

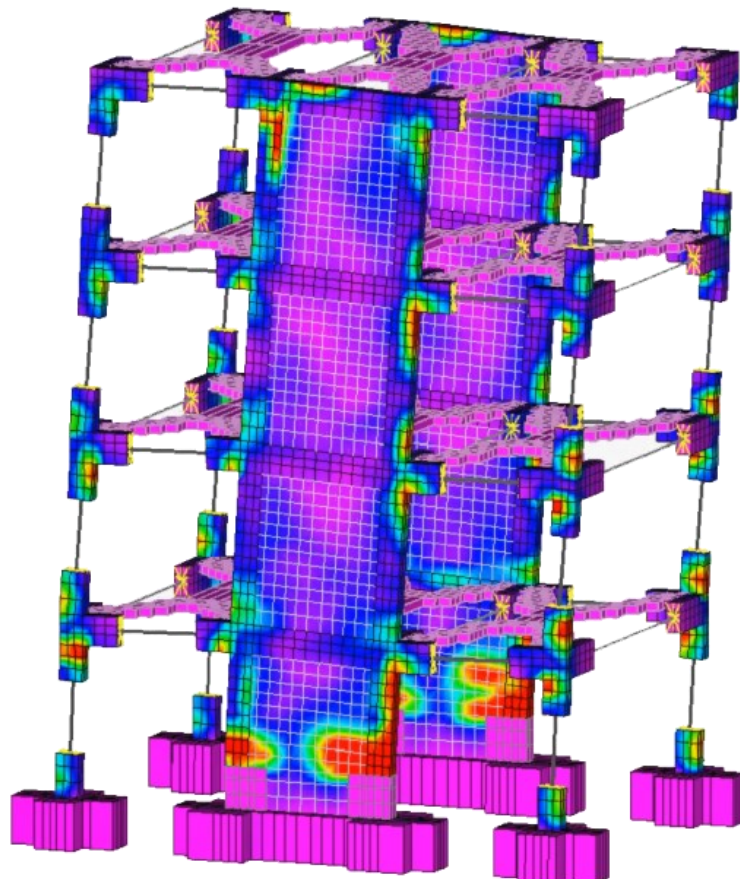
# COMPDYN 2021

*8<sup>th</sup> International Conference  
on Computational Methods in Structural Dynamics  
and Earthquake Engineering*

## PROCEEDINGS

### Volume II

M. Papadrakakis, M. Fragiadakis (Eds.)







## **COMPDYN 2021**

### **Computational Methods in Structural Dynamics and Earthquake Engineering**

Proceedings of the 8<sup>th</sup> International Conference on Computational  
Methods in Structural Dynamics and Earthquake Engineering  
Streamed from Athens, Greece  
28-30 June 2021

Edited by:

**M. Papadrakakis**

National Technical University of Athens, Greece

**M. Fragiadakis**

National Technical University of Athens, Greece

#### **A publication of:**

Institute of Structural Analysis and Antiseismic Research  
School of Civil Engineering  
National Technical University of Athens (NTUA)  
Greece

**COMPDYN 2021**

**Computational Methods in Structural Dynamics and Earthquake Engineering**

M. Papadrakakis, M. Fragiadakis (Eds.)

First Edition, September 2021

© The authors

ISBN (set): **978-618-85072-5-8**

ISBN (vol II): **978-618-85072-4-1**

## PREFACE

This volume contains the full-length papers presented in the 8<sup>th</sup> International Conference on Computational Methods in Structural Dynamics and Earthquake Engineering (COMPDYN 2021) that was streamed from Athens, Greece on June 28-30, 2021.

COMPDYN 2021 is one of the 32 Thematic Conferences of the European Community on Computational Methods in Applied Sciences (ECCOMAS) which were held in 2021 and is also a Special Interest Conference of the International Association for Computational Mechanics (IACM). The purpose of this Conference series is to bring together the scientific communities of Computational Mechanics, Structural Dynamics and Earthquake Engineering, to act as a forum for exchanging ideas in topics of mutual interests and to enhance the links between research groups with complementary activities. We believe that the communities of Structural Dynamics and Earthquake Engineering will benefit from their exposure to advanced computational methods and software tools which can highly assist in tackling complex problems in dynamic and seismic analysis and design of structures, while also giving the opportunity to the Computational Mechanics community to be exposed to very important engineering problems of great social interest.

The COMPDYN 2021 Conference is supported by the National Technical University of Athens (NTUA), the European Association for Structural Dynamics (EASD), the European Association for Earthquake Engineering (EAEE), the Greek Association for Computational Mechanics (GRACM).

The editors of this volume would like to thank all authors for their contributions. Special thanks go to the colleagues who contributed to the organization of the Minisymposia and to the reviewers who, with their work, contributed to the scientific quality of this e-book.

**M. Papadrakakis**

National Technical University of Athens, Greece

**M. Fragiadakis**

National Technical University of Athens, Greece



## ACKNOWLEDGEMENTS

The conference organizers acknowledge the support towards the organization of the “8<sup>th</sup> International Conference on Computational Methods in Structural Dynamics and Earthquake Engineering”, to the following organizations:

- European Community on Computational Methods in Applied Sciences (ECCOMAS)
- International Association for Computational Mechanics (IACM)
- European Association for Structural Dynamics (EASD)
- European Association for Earthquake Engineering (EAEE)
- Greek Association for Computational Mechanics (GRACM)
- Hellenic Society for Earthquake Engineering (HSEE)
- School of Civil Engineering, National University of Athens (NTUA)

### Plenary Speakers and Invited Session Organizers

We would also like to thank the Plenary and Semi-Plenary Speakers and the Minisymposia Organizers for their help in the setting up of a high standard Scientific Programme.

**Plenary Speakers:** Sondipon Adhikari, Peter Betsch, Hong Hao, Boris Jeremic, Geert Lombaert , Gabriele Milani , Shinobu Yoshimura

**Semi-Plenary Speakers:** Denis Duhamel, Fernando Fraternali, Muneo Hori, Alexander Idesman , Jean-Mathieu Mencik, Giuseppe Muscolino

**MS Organizers:** Christoph Adam, Hamid Ahmadi, Ada Amendola, Giulia Angelucci, António Arêde, Davide Arezzo, Nikolaos P. Bakas, Rui Carneiro Barros, Manuel Braz-César, Bruno Briseghella, Eleonora Bruschi, Bruno Calderoni, Guido Camata, Luca Caracoglia, Sandro Carbonari, Donatello Cardone, Claudia Casapulla, Serena Cattari, Nicola Cavallaghi, Liborio Cavaleri, Dimitrios Chronopoulos, Francesco Clementi, Marco Gaetani d’Aragona, Mario D’Aniello, Dario De Domenico, Maria Teresa De Risi, Matt DeJong, Carlo Del Gaudio, Ciro Del Vecchio, Pedro Delgado, Mariano Di Domenico, Raffaele Di Laora, Marco Di Ludovico, Luigi Di Sarno, Fabio Di Trapani, Beatrice Faggiano, Marco Filippo Ferrotto, Amedeo Flora, Antonio Formisano, Michalis Fragiadakis, Fernando Fraternali, Fabio Freddi, André Furtado, Stefano Galassi, Emanuele Gandelli, Linda Giresini, José A. González, Chiara Iacovino, Alper Ilki, Maria Iovino, Konstantinos Katakalo, Jin-Gyun Kim, Radek Kolman, Daniele Losanno, George C. Manos, Giuseppe Carlo Marano, George Markou, Angelo Masi, Konstantinos G. Megalooikonomou, Gabriele Milani, Lucia Minnucci, Fabrizio Mollaioli, Michele Morici, Lukas Moschen, Jiří Náprstek, Vanni Nicoletti, Ehsan Noroozinejad, Roger Ohayon, K. C. Park, Carlo Pettorruso, Vagelis Plevris, Maria Polese, Virginio Quaglini, Giuseppe Quaranta, Laura Ragni, Gian Andera Rassati, Paolo Ricci, Hugo Rodrigues, Emmanouil Rovithis, Juan Chiachío Ruano, Manuel Chiachío Ruano, Antonio Sandoli, Fabrizio Scozzese, Salvatore Sessa, Anastasios Sextos, P. Benson Shing, Castorina Silva Vieira, Aram Soroushian, Enrico Spacone, James Swanson, Francesca Taddei, Kumar Tamma, Marco Tanganelli, Roberto Tartaglia, Anton Tkachuk, Savvas Triantafyllou, Grigorios Tsinidis, Yiannis Tsompanakis, Enrico Tubaldi, Filippo Ubertini, Nicolò Vaiana, Humberto Varum, Michalis Vassiliou, Ilaria Venanzi, Gerardo M. Verderame, Stefania Viti, Marco Vona

## SUMMARY

<b>Preface</b> .....	iii
<b>Acknowledgements</b> .....	iv
<b>Contents</b> .....	ix

## VOLUME I

<b>PLENARY</b> .....	1
<b>SEMI-PLENARY</b> .....	28

### Minisymposia

<b>MS 1: INFLUENCE OF INFILL MASONRY WALLS IN THE RESPONSE AND SAFETY OF BUILDINGS</b> .....	63
<i>Organized by Humberto Varum, Hugo Rodrigues, Enrico Spacone</i>	
<b>MS 2: REPAIR AND RETROFIT OF STRUCTURES</b> .....	111
<i>Organized by Ciro Del Vecchio, Marco Di Ludovico, Alper Ilki</i>	
<b>MS 3: RECENT ADVANCES AND CHALLENGES IN GEOTECHNICAL EARTHQUAKE ENGINEERING</b> .....	202
<i>Organized by Castorina Silva Vieira, Yiannis Tsompanakis</i>	
<b>MS 4: ADVANCEMENTS IN NUMERICAL MODELLING AND SEISMIC INTERVENTION TECHNIQUES OF HISTORICAL MASONRY STRUCTURES</b> .....	231
<i>Organized by Francesco Clementi, Nicola Cavalagli, Antonio Formisano, Gabriele Milani, Vagelis Plevris</i>	
<b>MS 6: ADVANCES ON SEISMIC ASSESSMENT AND LOCAL COLLAPSE MECHANISMS OF RIGID BLOCKS IN STRUCTURES AND INFRASTRUCTURES</b> .....	637
<i>Organized by Claudia Casapulla, Linda Giresini, Francesca Taddei, Ehsan Noroozinejad</i>	
<b>MS 7: NEW ADVANCES IN COMPUTATIONAL MODELLING AND EXPERIMENTAL TESTING OF INFILLED FRAMES (2ND EDITION)</b> .....	779
<i>Organized by Fabio Di Trapani, Liborio Cavaleri, Guido Camata, P. Benson Shing</i>	
<b>MS 8: A MATTER OF SCALE: FROM REAL-TIME MONITORING TO AREA-WIDE SEISMIC RISK ASSESSMENT</b> .....	987
<i>Organized by Konstantinos G. Megalooikonomou</i>	
<b>MS 9: NONLINEAR MODELLING AND ASSESSMENT OF EXISTING REINFORCED CONCRETE ELEMENTS</b> .....	1016
<i>Organized by Mariano Di Domenico, Paolo Ricci, Gerardo M. Verderame</i>	

<b>MS 10: VULNERABILITY OF MUSEUM'S COLLECTIONS DYNAMIC RESPONSE, SAFETY ASSESSMENT AND DIGITAL INNOVATIONS .....</b>	<b>1125</b>
<i>Organized by Stefania Viti, Marco Tanganelli, Stefano Galassi</i>	
<b>MS 11: RECENT FINDINGS AND OPEN ISSUES IN SEISMIC PERFORMANCE ASSESSMENT OF AS-BUILT AND RETROFITTED EXISTING RC BUILDINGS .....</b>	<b>1188</b>
<i>Organized by Maria Teresa De Risi, Carlo Del Gaudio, André Furtado, Gerardo M. Verderame, Humberto Varum</i>	
<b>MS 12: ADVANCES IN COMPUTATIONAL MODELLING, EXPERIMENTAL TESTING AND OPTIMIZATION OF SEISMIC RETROFITTING.....</b>	<b>1322</b>
<i>Organized by Liborio Cavaleri, Marco Filippo Ferrotto, Fabio Di Trapani, Giuseppe Carlo Marano</i>	
<b>MS 13: MODELLING AND SOLUTION STRATEGIES FOR DYNAMIC PROBLEMS .....</b>	<b>1416</b>
<i>Organized by Aram Soroushian, Kumar Tamma</i>	
<b>MS 14: SEISMIC ASSESSMENT AND RETROFITTING OF EXISTING STEEL STRUCTURES .....</b>	<b>1492</b>
<i>Organized by Luigi Di Sarno, Fabio Freddi, Mario D'Aniello</i>	
<b>MS 16: DYNAMIC RESPONSE ASSESSMENT IN RAIL TRACK ENGINEERING .....</b>	<b>1550</b>
<i>Organized by Lukas Moschen, Grigorios Tsinidis, Christoph Adam, Anastasios Sextos</i>	
<b>MS 17: RECENT DEVELOPMENTS IN ROCKING STRUCTURES .....</b>	<b>1574</b>
<i>Organized by Matt DeJong, Michalis Vassiliou</i>	
<b>MS 19: ADVANCES IN THE OPTIMUM DESIGN AND CONTROL OF LARGE STRUCTURES UNDER DYNAMIC LOADS .....</b>	<b>1712</b>
<i>Organized by Fabrizio Mollaioli, Giulia Angelucci, Bruno Briseghella, Giuseppe Carlo Marano, Giuseppe Quaranta</i>	
<b>MS 20: COMPUTATIONAL DESIGN AND MODELING OF TENSEGRITY SYSTEMS FOR APPLICATIONS IN SCIENCE AND ENGINEERING .....</b>	<b>1825</b>
<i>Organized by Fernando Fraternali, Ada Amendola</i>	
<b>MS 22: CONDITION BASED MAINTENANCE AND POST-PROGNOSTICS OF COMPOSITE STRUCTURES: AN ENHANCED PLATFORM .....</b>	<b>1874</b>
<i>Organized by Dimitrios Chronopoulos, Savvas Triantafyllou, Juan Chiachío Ruano, Manuel Chiachío Ruano</i>	
<b>MS 23: ADVANCED MODELS AND NUMERICAL METHODS IN DYNAMICS, WAVE PROPAGATION AND COUPLED PROBLEMS .....</b>	<b>1892</b>
<i>Organized by José A. González, Radek Kolman, Anton Tkachuk, Jiří Náprstek, K. C. Park</i>	
<b>MS 24: LIFE-CYCLE RISK-BASED STRUCTURAL ASSESSMENT AND COST ANALYSIS .....</b>	<b>1941</b>
<i>Organized by Ilaria Venanzi, Filippo Ubertini, Luca Caracoglia</i>	
<b>MS 25: MONITORING, IDENTIFICATION AND VIBRATION CONTROL OF STRUCTURES .....</b>	<b>2014</b>
<i>Organized by Rui Carneiro Barros, Manuel Braz-César</i>	
<b>MS 26: SEISMIC SAFETY ASSESSMENT OF STRUCTURES .....</b>	<b>2157</b>
<i>Organized by Pedro Delgado, António Arêde</i>	

<b>MS 27: TIMBER-BASED ELEMENTS: RECENT ADVANCEMENTS FOR NEW AND EXISTING SEISMIC-RESISTANT STRUCTURES .....</b>	<b>2195</b>
<i>Organized by Antonio Sandoli, Bruno Calderoni, Beatrice Faggiano</i>	
<b>MS 29: SEISMIC PROTECTION OF NON-STRUCTURAL COMPONENTS: RECENT DEVELOPMENTS AND FUTURE CHALLENGES .....</b>	<b>2388</b>
<i>Organized by Luigi Di Sarno, Michalis Fragiadakis</i>	
<b>MS 30: DYNAMIC PROTECTION SYSTEMS AND DEVICES: EXPERIMENTAL TESTS, MATHEMATICAL MODELING AND DESIGN METHODS .....</b>	<b>2435</b>
<i>Organized by Nicolò Vaiana, Daniele Losanno, Salvatore Sessa</i>	
<b>MS 32: SIMPLIFIED METHODOLOGIES FOR PERFORMANCE AND LOSS ASSESSMENT AT BUILDING OR TERRITORIAL SCALE .....</b>	<b>2557</b>
<i>Organized by Maria Polese, Marco Gaetani d'Aragona</i>	

## VOLUME II

### Minisymposia

<b>MS 33: EXPERIMENTAL MEASUREMENTS AND NUMERICAL SIMULATION ON PROBLEMS IN THE FIELD OF EARTHQUAKE ENGINEERING AND STRUCTURAL DYNAMICS .....</b>	<b>2718</b>
<i>Organized by George C. Manos, Konstantinos Katakalos</i>	
<b>MS 34: FRAGILITY CURVES FOR EXISTING BUILDINGS: OPEN CHALLENGES IN THEIR DEFINITION AND USE FOR SEISMIC RISK ANALYSES .....</b>	<b>3059</b>
<i>Organized by Serena Cattari, Angelo Masi</i>	
<b>MS 35: RECENT ADVANCES IN SEISMIC ISOLATION AND SUPPLEMENTAL DAMPING SYSTEMS FOR VIBRATION CONTROL .....</b>	<b>3187</b>
<i>Organized by Virginio Quaglini, Eleonora Bruschi, Emanuele Gandelli, Carlo Pettoruso</i>	
<b>MS 36: METHODOLOGIES AND ADVANCED TOOLS FOR SEISMIC RISK ASSESSMENT, MANAGEMENT, AND MITIGATION: ADVANCES AND OPEN CHALLENGES .....</b>	<b>3305</b>
<i>Organized by Marco Vona, Donatello Cardone, Amedeo Flora, Chiara Iacovino</i>	
<b>MS 37: RISK ASSESSMENT OF BRIDGES AND ROAD NETWORKS SUBJECTED TO NATURAL HAZARDS .....</b>	<b>3377</b>
<i>Organized by Michele Morici, Fabrizio Scozzese, Lucia Minnucci</i>	
<b>MS 38: DYNAMIC SOIL-FOUNDATION-STRUCTURE INTERACTION: DEVELOPMENTS AND EMERGING ISSUES .....</b>	<b>3577</b>
<i>Organized by Emmanouil Rovithis, Raffaele Di Laora, Maria Iovino</i>	
<b>MS 39: THE CONTRIBUTION OF DYNAMIC TESTS AND STRUCTURAL MONITORING ON THE SEISMIC RISK ASSESSMENT AND MITIGATION .....</b>	<b>3697</b>
<i>Organized by Davide Arezzo, Sandro Carbonari, Vanni Nicoletti</i>	



<b>MS 40: ARTIFICIAL INTELLIGENCE &amp; MACHINE LEARNING IN DESIGN AND ASSESSMENT OF STRUCTURES .....</b>	<b>3795</b>
<i>Organized by George Markou, Nikolaos P. Bakas</i>	

<b>MS 41: SEISMIC PERFORMANCE OF STRUCTURES WITH ISOLATION AND/OR ENERGY DISSIPATION DEVICES .....</b>	<b>3912</b>
<i>Organized by Enrico Tubaldi, Laura Ragni, Dario De Domenico, Hamid Ahmadi</i>	

<b>MS 42: ADVANCES IN MODEL REDUCTION TECHNIQUES OF COMPUTATIONAL AND STRUCTURAL DYNAMICS .....</b>	<b>4111</b>
<i>Organized by Jin-Gyun Kim, K. C. Park, Roger Ohayon</i>	

<b>MS 43: ANALYSES AND DESIGN OF STEEL JOINTS UNDER CYCLIC ACTION .....</b>	<b>4134</b>
<i>Organized by Roberto Tartaglia, Mario D'Aniello, Gian Andera Rassati, James Swanson</i>	

## **Thematic Sessions**

<b>TS 5: DYNAMICS OF CONCRETE AND MASONRY STRUCTURES .....</b>	<b>4226</b>
<b>TS 14: NUMERICAL SIMULATION METHODS FOR DYNAMIC PROBLEMS .....</b>	<b>4331</b>
<b>TS 15: OPTIMUM DESIGN AND CONTROL IN STRUCTURAL DYNAMICS AND EARTHQUAKE ENGINEERING .....</b>	<b>4428</b>
<b>TS 17: PERFORMANCE-BASED EARTHQUAKE ENGINEERING .....</b>	<b>4558</b>
<b>TS 19: REPAIR AND RETROFIT OF STRUCTURES .....</b>	<b>4729</b>
<b>TS 20: SEISMIC ISOLATION .....</b>	<b>4816</b>
<b>TS 21: SEISMIC RISK AND RELIABILITY ANALYSIS .....</b>	<b>4853</b>
<b>TS 27: STEEL STRUCTURES.....</b>	<b>4906</b>
<b>TS 28: STOCHASTIC DYNAMICS.....</b>	<b>4926</b>
<b>TS 31: NUMERICAL SIMULATION OF GEOTECHNICAL PROBLEMS.....</b>	<b>4946</b>
<b>TS 32: DYNAMICS OF STEEL AND SLENDER STRUCTURES.....</b>	<b>5108</b>
<b>TS 33: AEROELASTICITY, SOUND AND VIBRATION AND BRIDGE DYNAMICS .....</b>	<b>5179</b>
<b>TS 34: NONLINEAR AND IMPACT DYNAMICS.....</b>	<b>5307</b>

# CONTENTS

## VOLUME I

### PLENARY

SEISMIC VULNERABILITY OF MASONRY HISTORICAL STRUCTURES: A SIMPLE ADAPTIVE NURBS FE APPROACH FOR THE LIMIT AND THE SUBSEQUENT NON-LINEAR STATIC ANALYSIS WITH FEW DOFS .....	1
<i>Nicola Grillanda, Gabriele Milani</i>	

### SEMI-PLENARY

SOME RECENT ADVANCES IN THE WAVE FINITE ELEMENT METHOD .....	28
<i>Denis Duhamel, B. Claudet, T. Hoang, G. Foret, Jean-Mathieu Mencik</i>	
DYNAMIC ANALYSIS OF PERIODIC STRUCTURES AND METAMATERIALS VIA WAVE APPROACHES AND FINITE ELEMENT PROCEDURES .....	42
<i>Jean-Mathieu Mencik, Denis Duhamel</i>	

### Minisymposia

#### MS 1: INFLUENCE OF INFILL MASONRY WALLS IN THE RESPONSE AND SAFETY OF BUILDINGS

IMPACT OF MASONRY INFILL VARIABILITY ON THE ESTIMATION OF FLOOR RESPONSE SPECTRA IN RC BUILDINGS .....	63
<i>Gianrocco Mucedero, Daniele Perrone, Emanuele Brunesi, Ricardo Monteiro</i>	
EFFECT OF IN-PLANE/OUT-OF-PLANE INTERACTION IN INFILL WALLS ON THE FLOOR SPECTRA OF REINFORCED CONCRETE BUILDINGS .....	84
<i>Mariano Di Domenico, Paolo Ricci, Gerardo M. Verderame</i>	
SEISMIC LOSS ANALYSIS OF A CODE-DESIGNED INFILLED RC BUILDING ACCOUNTING FOR INFILL MODEL CLASS UNCERTAINTY .....	102
<i>Fabio Romano, Mohammad S. Alam, Maria Zucconi, Marco Faggella, Andre R. Barbosa, Barbara Ferracuti</i>	

#### MS 2: REPAIR AND RETROFIT OF STRUCTURES

SEISMIC BEHAVIOR OF SUBSTANDARD EXTENDED RECTANGULAR RC COLUMNS JACKETED WITH SPRAYED GFRM .....	111
<i>Muhsin Can Lülecı, Bilal Sari, Ugur Demir, Muhammed Maraslı, Alper İlki</i>	
DAMAGE EVOLUTION FOR REPAIRABILITY OF SUBSTANDARD BEAM-COLUMN JOINTS .....	120
<i>Özgür Yurdakul, Ciro Del Vecchio, Marco Di Ludovico, Ladislav Řoutil, Özgür Avşar</i>	

EXPERIMENTAL RESPONSE AND NUMERICAL MODELLING OF TWO-STOREY INFILLED RC FRAME .....	131
<i>Ciro Del Vecchio, C. Moliterno, Marco Di Ludovico, Gerardo Mario Verderame, Andrea Prota, Gaetano Manfredi</i>	
DEFENCE OF ARCHITECTURAL HERITAGE: EXPERIMENTAL CAMPAIGN ON MASONRIES REINFORCED WITH NATURAL FRCM COMPOSITE MATERIALS .....	141
<i>Riccardo Liberotti, Nicola Cavalagli, Federico Cluni, Massimiliano Gioffrè, Chiara Pepi, Vittorio Gusella</i>	
NUMERICAL MODELLING AND ANALYSIS OF ECCENTRIC BRACING WITH VERTICAL SHEAR LINKS .....	151
<i>Gaetano Cantisani, Emilio Rodontini, Gaetano Della Corte</i>	
PERFORMANCE OF EXISTING REINFORCED CONCRETE ARCH BRIDGES UNDER CURRENT NON SEISMIC LOADS .....	164
<i>Giovanni Crisci, Francesca Ceroni, Gian Piero Lignola, Andrea Prota</i>	
A SUSTAINABLE SOLUTION FOR THE SEISMIC STRENGTHENING OF RC EXISTING BUILDINGS THROUGH THE HPDF SYSTEM (HPDF): A CASE STUDY .....	180
<i>Giuseppe Ventura, Vincenzo Manfredi, Angelo Masi, Giuseppe Santarsiero, Andrea Digrisolo</i>	
APPLICATION OF C-FRP SHEETS FOR STRUCTURAL REPAIRING OF RC BEAM-COLUMN CONNECTIONS DAMAGED UNDER CYCLIC LOADING – EXPERIMENTAL STUDY .....	191
<i>Emmanouil Golias, Stavroula Katsimante, Eirini Ziavra, Konstantinos Kirtsonis, Constantin E. Chaliotis, Chris C. Karayannis</i>	
 <b>MS 3: RECENT ADVANCES AND CHALLENGES IN GEOTECHNICAL EARTHQUAKE ENGINEERING</b>	
SEISMIC VULNERABILITY OF SHALLOW UNDERGROUND CAVITIES IN SOFT ROCK .....	202
<i>Stefania Fabozzi, Filomena De Silva, Marco Nocentini, Edoardo Peronace, Emilio Bilotta, Massimiliano Moscatelli</i>	
EFFICIENCY OF SEISMIC LIQUEFACTION MITIGATION METHODS FOR EXISTING STRUCTURES .....	212
<i>Alexandros Valsamis, Taxiarchoula Limnaiou, Achilleas Papadimitriou</i>	
PREDICTING RAILWAY TRACK DISPLACEMENTS WITH THE HARDENING SOIL SMALL STRAIN MODEL NEAR CRITICAL SPEED .....	222
<i>Jesús Fernández-Ruiz, Pedro Alves Costa</i>	
 <b>MS 4: ADVANCEMENTS IN NUMERICAL MODELLING AND SEISMIC INTERVENTION TECHNIQUES OF HISTORICAL MASONRY STRUCTURES</b>	
NON-DESTRUCTIVE AND DESTRUCTIVE TESTS ON OPUS INCERTUM MASONRY PANELS .....	231
<i>Francesca Autiero, Giuseppina De Martino, Marco Di Ludovico, Andrea Prota</i>	
PRELIMINARY NONLINEAR STATIC AND DYNAMIC ANALYSIS OF THE MAIN PYRAMID OF HUACA DE LA LUNA, PERU .....	244
<i>Selman Tezcan, Miguel a. Pando, Rafael Aguilar, Benjamin Castañeda, Carol Rojas, Renato Perucchio</i>	

MODELING STRATEGIES FOR NON-LINEAR SEISMIC ANALYSES: COMPARISON AMONG EFM AND FEM RESULTS ON AN EXISTING URM CASE STUDY .....	258
<i>Marco Pegoraro, Elisa Saler, Matteo Salvalaggio, Maria Rosa Valluzzi</i>	
ANALYSIS OF THE DAMAGE STATE OF A MONUMENTAL BUILDING BY CONSIDERING THE VARIATIONS IN SOIL CONDITIONS .....	268
<i>Erica Lenticchia, Gaetano Miraglia, Stefania Coccimiglio, Rosario Ceravolo</i>	
ADVANCED NUMERICAL PREDICTION OF UNREINFORCED U-SHAPED MASONRY WALLS LOADED OUT-OF-PLANE .....	278
<i>Jacopo Scacco, Luís C. Silva, Graça Vasconcelos, Gabriele Milani, Paulo B. Lourenço</i>	
LOW-COST BASE ISOLATION SYSTEMS FOR UNREINFORCED MASONRY BUILDINGS IN DEVELOPING COUNTRIES .....	286
<i>Nagavinothini Ravichandran, Daniele Losanno, Fulvio Parisi</i>	
NONLINEAR STATIC ANALYSIS OF MASONRY BUILDINGS THROUGH FIBRE-BASED CAPACITY MODELLING .....	298
<i>Elia Acconcia, Valentina Buonocunto, Fulvio Parisi</i>	
A DISCRETE-MACRO-ELEMENT-MODEL FOR THE IN-PLANE ANALYSIS OF MASONRY STRUCTURES STRENGTHENED BY FRCMS .....	309
<i>Paolo Zampieri, Riccardo Piazzon, Bartolomeo Pantò, Carlo Pellegrino</i>	
NUMERICAL MODELLING OF DIAGONAL COMPRESSION TESTS ON MASONRY PANELS STRENGTHENED BY FRCM .....	318
<i>Francesca Ferretti, Francesco Saverio Murgo, Claudio Mazzotti</i>	
EMPIRICAL AND MECHANICAL ANALYSIS METHODS FOR SEISMIC VULNERABILITY ASSESSMENT OF CLUSTERED BUILDINGS OF HISTORICAL CENTRES: A CASE STUDY .....	331
<i>Antonio Formisano, Giovanni Mochi, Nicola Chieffo</i>	
SETTLEMENT-INDUCED DAMAGE ASSESSMENT IN UNILATERAL MASONRY-LIKE STRUCTURES: A PIECEWISE RIGID DISPLACEMENT APPROACH .....	338
<i>Ida Mascolo, Antonio Fortunato</i>	
ON THE USE OF DIGITAL TWINS FOR SEISMIC STRUCTURAL HEALTH MONITORING OF A MONUMENTAL MASONRY TOWER .....	346
<i>Alban Kita, Nicola Cavalagli, Ilaria Venanzi, Filippo Ubertini</i>	
MICROMECHANICAL ANALYSIS OF UNREINFORCED AND REINFORCED MASONRY ARCHES .....	354
<i>Daniela Addressi, Cristina Gatta, Mariacarla Nocera, Domenico Liberatore</i>	
ANALYTICAL AND NUMERICAL ANALYSIS OF S. MARTINO'S DEI GUALDESI CHURCH DAMAGED DURING THE 2016 CENTRAL ITALY SEISMIC SEQUENCE .....	367
<i>Ivis Cescatti, Michol Rampado, Veronica Follador, Francesca da Porto, Claudio Modena</i>	
A NURBS-BASED NUMERICAL APPROACH FOR THE ASSESSMENT OF MASONRY VAULTS UNDERGOING DIFFERENTIAL SETTLEMENTS .....	380
<i>Andrea Chiozzi, Nicola Grillanda, Gabriele Milani, Antonio Tralli</i>	



NUMERICAL MODELLING OF BONDED BRICKWORK UNDER CYCLIC COMPRESSION LOADING .....	387
<i>Mohammad Asad, Tatheer Zahra, Julian Thamboo</i>	
FULL 3D CAD PROCEDURE FOR THE LIMIT ANALYSIS OF LONGHU PAGODA IN CHINA .....	398
<i>Peixuan Wang, Alessandro De lasio, Jacopo Scacco, Gabriele Milani, Shengcai Li</i>	
ROLE OF REPEATED SEISMIC EVENTS ON THE COLLAPSE OF TWO CALIDARIA IN ROME DATING BACK TO THE IMPERIAL AGE .....	406
<i>Francesca Faleri, Nicola Grillanda, Selman Tezcan, Renato Perucchio, Gabriele Milani</i>	
3D ADVANCED NUMERICAL MODELLING OF A CATALAN-LAYERED MASONRY VAULT UNREINFORCED AND REINFORCED WITH GLASS-TRM MATERIALS AND SUBJECTED TO VERTICAL SUPPORT MOVEMENTS .....	415
<i>Elisa Bertolesi, Gabriele Milani, José M. Adam, Pedro A. Calderón</i>	
DYNAMIC ANALYSIS OF MASONRY CHIMNEYS BY MEANS OF A SIMPLE RIGID BEAM MODEL .....	423
<i>Daniele Baraldi, Gabriele Milani, Vasilis Sarhosis</i>	
COMPARATIVE ANALYSIS AMONG DIFFERENT ANALYSIS PROGRAMS FOR SEISMIC VULNERABILITY EVALUATION OF A MASONRY BUILDING COMPOUND IN THE DISTRICT OF NAPLES .....	433
<i>Generoso Vaiano, Antonio Formisano</i>	
TERRITORIAL ANALYSIS OF SEISMIC PERFORMANCE OF ANCIENT CHURCHES: METHODS AND APPLICATION TO CASE STUDIES .....	447
<i>Michele D'Amato, R. Laguardia, Rosario Gigliotti, Antonio Formisano</i>	
FE MODELING OF A SEISMIC ISOLATOR MADE OF HDR AND REGENERATED EPDM .....	456
<i>Gaetano Pianese, Gabriele Milani, Antonio Formisano</i>	
INFLUENCE OF CROSSLINKING ON THE SEISMIC PERFORMANCE OF UNBONDED FIBER REINFORCED ELASTOMERIC ISOLATORS (UFREI) MADE OF REGENERATED RUBBER .....	463
<i>Gaetano Pianese, Davide Torrini, Gabriele Milani, Antonio Formisano</i>	
COMBINING OPERATIONAL MODAL ANALYSIS AND GENETIC ALGORITHMS TO UNDERSTAND THE ACTUAL STRUCTURAL BEHAVIOR OF HISTORICAL CONSTRUCTIONS .....	470
<i>Gianluca Standoli, Georgios Panagiotis Salachoris, Maria Giovanna Masciotta, Francesco Clementi</i>	
SEISMIC ASSESSMENT OF MASONRY CROSS VAULTS THROUGH NON-LINEAR STATIC ANALYSES .....	487
<i>Marco Alforno, Alessia Monaco, Fiammetta Venuti, Chiara Calderini</i>	
“SCAGLIA ROSSA” EXPERIMENTAL CAMPAIGN AND MODEL UPDATING FOR NUMERICAL DAMAGE EVALUATION .....	497
<i>Georgios Panagiotis Salachoris, Erica Magagnini, Francesco Clementi</i>	
BEHAVIOUR FACTOR ASSESSMENT OF ANCIENT MASONRY TOWERS THROUGH AN INNOVATIVE SIMPLIFIED PUSHOVER METHOD .....	508
<i>Alessandro De lasio, Peixuan Wang, Gabriele Milani, Bahman Ghiassi</i>	

FE PUSHOVER ANALYSES OF A 20TH-CENTURY MASONRY CHIMNEY IN SPAIN: COLLAPSE BEHAVIOR AND NUMERICAL UNCERTAINTIES .....	519
<i>Alessandro De Iasio, Gabriele Milani, Jose M. Adam</i>	
FINITE ELEMENT ANALYSIS OF JUMA MOSQUE IN UZBEKISTAN BASED ON LASER SCANNING AND AMBIENT STUDIES .....	530
<i>Shakhzod Takhirov, Bahodir Rakhmonov</i>	
CONTINUOUS AND DISCONTINUOUS DESCRIPTIONS OF BLOCKED STRUCTURES: THE CASE STUDY OF SANTISSIMO CROCIFISSO CHURCHES IN PRETARE (ITALY) .....	539
<i>Francesco Clementi, Angela Ferrante, Ersilia Giordano, Stefano Lenci</i>	
LATTICE DISCRETE MODELING OF OUT-OF-PLANE BEHAVIOR OF IRREGULAR MASONRY .....	546
<i>Micaela Mercuri, Madura Pathirage, Amedeo Gregori, Gianluca Cusatis</i>	
NUMERICAL STUDY ON SEISMIC RETROFIT OF URM WALLS USING TIMBER PANELS .....	563
<i>Davide Cassol, Ivan Giongo, Maurizio Piazza</i>	
OPTIMIZATION OF EMPIRICAL SEISMIC VULNERABILITY ASSESSMENT FOR MASONRY BUILDINGS FOLLOWING NONLINEAR ANALYSIS .....	581
<i>Eugen Onescu, Iasmina Onescu, Marius Mosoarca</i>	
NONLINEAR SIMULATION OF MASONRY VAULTS UNDER EARTHQUAKE LOADING .....	595
<i>Adam Plavsic, Bartolomeo Pantò, Corrado Chisari, Lorenzo Macorini, Bassam A. Izzuddin, Ingrid Boem, Natalino Gattesco</i>	
LOW-COST RUBBER COMPOUNDS FOR FIBER-REINFORCED ELASTOMERIC ISOLATORS: RECOVERED POWDERS AND WASTE OILS FROM RUBBER MANUFACTURING PROCESSES .....	607
<i>Gaetano Pianese, Gabriele Milani, Federico Milani, Ahmad Basshofi Habieb</i>	
HORIZONTAL FORCE CAPACITY OF A HEMI-SPHERICAL DOME .....	614
<i>Carlo Olivieri, Anna Castellano, Isabella Elia, Antonio Fortunato, Ida Mascolo</i>	
SEISMIC RETROFITTING TECHNIQUES FOR EXISTING MASONRY BUILDINGS .....	626
<i>Ida Mascolo, Antonio Fortunato, Carlo Olivieri, Antonio Gesualdo</i>	
 <b>MS 6: ADVANCES ON SEISMIC ASSESSMENT AND LOCAL COLLAPSE MECHANISMS OF RIGID BLOCKS IN STRUCTURES AND INFRASTRUCTURES</b>	
PRELIMINARY DESIGN METHOD FOR ROCKING AND NEGATIVE STIFFNESS SYSTEMS .....	637
<i>Natalia Reggiani Manzo, Michalis Vassiliou</i>	
PREFABRICATED REINFORCED CONCRETE CLADDING PANELS SUPPORTS: DESIGN AND NUMERICAL MODELLING .....	649
<i>Flavio Stochino, Fausto Mistretta, Mario Lucio Puppio, Mauro Sassu</i>	

INFLUENCE OF THE ELASTO-PLASTIC BEHAVIOR OF TIE-RODS IN THE RESPONSE OF ROCKING MASONRY WALLS THROUGH SEISMIC DEMAND HAZARD CURVES .....	664
<i>Fabio Solarino, Linda Giresini, Pietro Croce</i>	
GRAPHICAL METHODS, KINEMATIC AND FINITE ELEMENT ANALYSIS OF THE PREMILCUORE MASONRY BRIDGE ...	682
<i>Linda Giresini, Daniela De Paola, Mario Lucio Puppio, Giovanni Buratti</i>	
REDUCTION OF HOUSNER'S COEFFICIENT OF RESTITUTION FOR MASONRY WALLS UNDER ONE-SIDED ROCKING .....	702
<i>Linda Giresini, Pietro Croce</i>	
AN EQUIVALENT VISCOUS DAMPING PROPOSAL FOR BLOCK-BASED ROCKING MODELS .....	717
<i>Georgios Vlachakis, Carla Colombo, Anastasios Giouvanidis, Anjali Mehrotra, Nathanael Savalle, Paulo B. Lourenço</i>	
PROBABILISTIC SEISMIC FRAGILITY FOR ROCKING MASONRY FAÇADES USING CLOUD ANALYSIS .....	727
<i>Armando Benenato, Stefania Imperatore, Gian Piero Lignola, Barbara Ferracuti</i>	
MODELLING OF THE OUT-OF-PLANE BEHAVIOUR OF UNREINFORCED MASONRY PANELS USING THE DISCRETE MACRO-ELEMENT METHOD (DMEM) .....	738
<i>Valeria Cusmano, Bartolomeo Pantò, Ivo Calì, Paulo B. Lourenço</i>	
VISUAL PROGRAMMING FOR MACRO-BLOCK ANALYSIS OF MULTI-STOREY MASONRY BUILDINGS .....	752
<i>Elham Mousavian, Luca Umberto Argiento, Claudia Casapulla</i>	
OUT-OF-PLANE RESPONSE OF T-SHAPED MASONRY WALLS STRENGTHENED WITH CFRP INJECTED ANCHORS: MODELLING AND DESIGN PROVISIONS .....	764
<i>Alessandra Maione, Claudia Casapulla, Francesca Ceroni, Marco Di Ludovico, Andrea Prota</i>	
<b>MS 7: NEW ADVANCES IN COMPUTATIONAL MODELLING AND EXPERIMENTAL TESTING OF INFILLED FRAMES (2ND EDITION)</b>	
NUMERICAL MESO-MODEL FOR REINFORCED CONCRETE FRAMES WITH RETROFITTED MASONRY INFILL .....	779
<i>Gianni Blasi, Daniele Perrone, Maria Antonietta Aiello</i>	
ASSESSMENT OF OUT-OF-PLANE STRENGTH OF MASONRY INFILLS ACCORDING TO EC6 .....	795
<i>Laura Liberatore</i>	
INFLUENCE OF PRIOR IN-PLANE DAMAGE ON THE OUT-OF-PLANE RESPONSE OF NON-LOAD BEARING UNREINFORCED MASONRY WALLS UNDER SEISMIC LOAD .....	808
<i>Bogdan Šakić, Aleksa Milijaš, Marko Marinković, Christoph Butenweg, Sven Klinkel</i>	
EXPERIMENTAL INVESTIGATION OF BEHAVIOUR OF MASONRY INFILLED RC FRAMES UNDER OUT-OF-PLANE LOADING .....	829
<i>Aleksa Milijaš, Bogdan Šakić, Marko Marinković, Christoph Butenweg, Sven Klinkel</i>	
STRUCTURAL CONCEPTS IN THE DESIGN OF MASONRY-INFILLED STEEL FRAMES .....	847
<i>Dario Sokic, Damir Markulak, Tihomir Doksanovic, Ivan Radic</i>	

A SIMPLE METHODOLOGY FOR THE INFILL MASONRY WALL STIFFNESS ESTIMATION .....	860
<i>Vanni Nicoletti, Davide Arezzo, Sandro Carbonari, Fabrizio Gara</i>	
ASSESSMENT OF DAMAGE TO MODERN REINFORCED CONCRETE BUILDINGS – ENGINEERING ANALYSIS OF THE M6.4 ALBANIA EARTHQUAKE, 26TH OF NOV. 2019 .....	871
<i>Lars Abrahamczyk, Davorin Penava, Melad Haweyou, Filip Anić, Arturo E. Schultz, Jeff Rautenberg</i>	
INFLUENCE OF THE INFILL TYPOLOGY IN THE EVALUATION OF THE ANNUAL LOSSES OF RC STRUCTURES THROUGH THE APPLICATION OF A NEW METHOD .....	886
<i>Andrea Rossi, Paolo Morandi, Riccardo R Milanese, Guido Magenes</i>	
LOCAL EFFECTS DUE TO THE SEISMIC INTERACTION BETWEEN INNOVATIVE DUCTILE MASONRY INFILLS AND RC ELEMENTS .....	899
<i>Riccardo R. Milanese, Valentino Bolis, Simone Pelucco, Paolo Morandi, Guido Magenes, Marco Preti</i>	
A DEGRADING BOUC-WEN DATA-DRIVEN MODEL FOR THE CYCLIC BEHAVIOR OF MASONRY INFILLED RC FRAMES .....	913
<i>Matteo Pellicciari, Stefano Sirotti, Fabio Di Trapani, Bruno Briseghella, Giuseppe Carlo Marano, Camillo Nuti, Angelo Marcello Tarantino</i>	
SEISMIC PERFORMANCE OF PAKISTANI-TECHNIQUE INFILLED REINFORCED CONCRETE FRAMES .....	923
<i>Nisar Ali Khan, Alessandro Vittorio Bergami, Camillo Nuti, Giorgio Monti, Marco Vailati, Bruno Briseghella</i>	
GENERATION OF OUT-OF-PLANE FRAGILITY FUNCTIONS FOR IN-PLANE DAMAGED UNREINFORCED MASONRY INFILLS .....	935
<i>Bharat Pradhan, Liborio Cavaleri, Vasilis Sarhosis, Marco Filippo Ferrotto</i>	
EMPIRICAL FORMULATION OF THE OUT-OF-PLANE RESISTANCE OF INFILLED FRAMES .....	955
<i>Fabio Di Trapani, Alessandro Vizzino, Giovanni Tomaselli, P. Benson Shing</i>	
MECHANICAL VS EMPIRICAL MODELS FOR MODELS IN-PLANE RESPONSE OF INFILLED FRAMES: RELIABILITY 7 COMPARISON AND VALIDATION OF A NEW DATA-DRIVEN MODEL .....	970
<i>Fabio Di Trapani, Giovanni Tomaselli, Gabriele Bertagnoli</i>	
 <b>MS 8: A MATTER OF SCALE: FROM REAL-TIME MONITORING TO AREA-WIDE SEISMIC RISK ASSESSMENT</b>	
EARTHQUAKE EARLY WARNING AND RAPID RESPONSE SYSTEM BASED ON SMART SEISMIC AND MONITORING SENSORS EMBEDDED IN A COMMUNICATION PLATFORM AND COUPLED WITH BIM MODELS .....	987
<i>Georgios Balaskas, Benno Hoffmeister, Christoph Butenweg, Marco Pilz, Anna Bauer</i>	
MONITORING OF A PRESTRESSED BRIDGE MODEL BY ULTRASONIC MEASUREMENT AND VIBRATION RECORDINGS .....	999
<i>Chun-Man Liao, Falk Hille, Daniel Fontoura Barroso, Ernst Niederleithinger</i>	



COMPARATIVE NON-STRUCTURAL VULNERABILITY ASSESSMENT METHODS FOR HISTORICAL RESIDENTIAL MASONRY BUILDINGS .....	1008
<i>Filippos Alogdianakis, Konstantinos G. Megalooikonomou, Georgios S. Papavasileiou</i>	

## **MS 9: NONLINEAR MODELLING AND ASSESSMENT OF EXISTING REINFORCED CONCRETE ELEMENTS**

STUDY OF BIAxIAL SHEAR FAILURE ENVELOPE OF REINFORCED CONCRETE COLUMNS .....	1016
<i>Beatrice Belletti, Simone Ravasini, Andrea Alberici</i>	

EVALUATION OF THE SEISMIC VULNERABILITY OF EXISTING PRE-CODE RC CORE STRUCTURAL SYSTEMS THROUGH NON-LINEAR PUSHOVER ANALYSES .....	1027
<i>Beatrice Belletti, Enzo Martinelli, Elena Michelinì, Francesca Vecchi</i>	

CALIBRATION AND VALIDATION OF AN OVERDAMPED DISPLACEMENT ADAPTIVE PROCEDURE FOR SEISMIC ASSESSMENT OF INFILLED RC FRAMES .....	1039
<i>Francesca Barbagallo, Melina Bosco, Aurelio Gheris, Edoardo Michele Marino, Pier Paolo Rossi</i>	

CYCLIC TESTING OF 1:40 SCALE CANTILEVER RC ELEMENTS WITH DIGITALLY MANUFACTURED REINFORCEMENT .....	1053
<i>Lorenzo Del Giudice, Rafal Wrobel, Antonios Katsamakas, Christian Leinenbach, Michalis Vassiliou</i>	

R/C COLUMN MODELLING USING ANSYS AND LOADING RATE AND MESH METHOD INFLUENCE STUDIES .....	1063
<i>Theodora Mitkou, Theodoros Chrysanidis</i>	

CALIBRATION AND NUMERICAL MODELING OF RC BEAM-COLUMN JOINTS DESIGNED FOR GRAVITY LOADS .....	1085
<i>Marcello Sabene, Maria Zucconi, Stefano Pampanin, Barbara Ferracuti</i>	

ASSESSMENT OF THE RESPONSE ENVELOPE OF REINFORCED CONCRETE MEMBERS WITH DIFFERENT FAILURE MODES .....	1097
<i>Mariano Di Domenico, Paolo Ricci, Gerardo M. Verderame</i>	

SEISMIC ASSESSMENT OF AN EXISTING RC BUILDING AFFECTED BY SLOW-MOVING LANDSLIDES INDUCED DISPLACEMENTS MONITORED BY REMOTE SENSING TECHNIQUE .....	1112
<i>Annalisa Mele, Andrea Miano, Diego Di Martire, Donato Infante, Andrea Prota, Massimo Ramondini</i>	

## **MS 10: VULNERABILITY OF MUSEUM'S COLLECTIONS DYNAMIC RESPONSE, SAFETY ASSESSMENT AND DIGITAL INNOVATIONS**

VULNERABILITY OF ART WORKS TO BLAST HAZARD: THE FOUNTAIN OF NEPTUNE IN FLORENCE .....	1125
<i>Marco Domaneschi, Marco Tanganelli, Stefania Viti, Gian Paolo Cimellaro</i>	

SIMPLIFIED ANALYSES FOR THE MODEL SETTING OF SCULPTURES: THE "OCEANO" BY GIAMBOLOGNA .....	1135
<i>Marco Tanganelli, Stefano Galassi, Stefania Viti</i>	

VULNERABILITY ASSESSMENT OF MONUMENTAL ARTWORKS USING CONTACT TIME-HISTORY ANALYSIS .....	1145
<i>Raffaele Gagliardo, Michele Godio, Lucrezia Cascini, Francesco Portioli, Raffaele Landolfo</i>	

THE TARANTOLA ETRUSCAN PEDIMENT: NDT AND 3D MODEL CONTENT .....	1153
<i>Anna Livia Ciuffreda, Massimo Coli, Tessa Donigaglia, Paola Ilaria Mariotti, Teresa Salvatici, Gabriela Simoni</i>	
CORRELATION OF VULNERABILITY AND CONSERVATION BETWEEN ARTISTIC ASSETS AND STRUCTURAL ELEMENTS: CAMPAIGN OF THERMOGRAPHIC SURVEYS ON THE FRESCOS OF THE TEMPLAR CHURCH OF SAN BEVIGNATE .....	1170
<i>Riccardo Liberotti, Federico Cluni, F. Faralli, Vittorio Gusella</i>	
 <b>MS 11: RECENT FINDINGS AND OPEN ISSUES IN SEISMIC PERFORMANCE ASSESSMENT OF AS-BUILT AND RETROFITTED EXISTING RC BUILDINGS</b>	
EVALUATION OF A NUMERICAL MODELLING APPROACH FOR THE SIMULATION OF RETROFITTED RC ELEMENTS .....	1188
<i>Ines Sousa, Rita Couto, Rita Peres, José Miguel Castro, Rita Bento</i>	
EXPERIMENTAL INVESTIGATION ON ANCHORAGE PERFORMANCE OF EMBEDDED SMOOTH REBARS SUBJECTED TO CYCLICNG LOADING .....	1201
<i>Anthony Paderno, Simone Pelucco, Marco Preti</i>	
OUT-OF-PLANE TESTING OF MASONRY INFILL WALLS MADE WITH LIGHTWEIGHT CONCRETE BLOCKS .....	1212
<i>M. Agante, André Furtado, Hugo Rodrigues, António Arêde, P. Fernandes, Humberto Varum</i>	
SELECTION OF OPTIMAL SEISMIC RETROFITTING FOR EXISTING SCHOOL BUILDINGS THROUGH MULTI- CRITERIA DECISION MAKING .....	1223
<i>Wilson Carofilis, Nicholas Clemett, Giammaria Gabbianelli, Gerard O'Reilly, Ricardo Monteiro</i>	
NUMERICAL INVESTIGATIONS ON THE RESIDUAL CAPACITY AND ECONOMIC LOSSES OF EARTHQUAKE- DAMAGED REINFORCED CONCRETE WALL STRUCTURES .....	1242
<i>Cristiana Ceccarelli, Simona Bianchi, Livio Pedone, Stefano Pampanin</i>	
SIMPLIFIED LOSS ESTIMATION IN INFILLED RC BUILDINGS: MECHANICAL METHOD AND VALIDATION .....	1261
<i>Carlo Del Gaudio, Maria Teresa De Risi, Gerardo Mario Verderame</i>	
SEISMIC PERFORMANCE ASSESSMENT OF AS-BUILT AND RETROFITTED RC BUILDINGS CONSIDERING THE INFLUENCE OF INFILLS: PRE-'70 LOW-MIDE RISE CASE-STUDIES .....	1275
<i>Maria Teresa De Risi, Santa Anna Scala, Carlo Del Gaudio, Gerardo Mario Verderame</i>	
MAPPING PERFORMANCE-TARGETED RETROFITTING TO SEISMIC FRAGILITY REDUCTION .....	1301
<i>Karim Aljawhari, Roberto Gentile, Carmine Galasso</i>	

## **MS 12: ADVANCES IN COMPUTATIONAL MODELLING, EXPERIMENTAL TESTING AND OPTIMIZATION OF SEISMIC RETROFITTING**

EXPERIMENTAL STUDY ON THE IN-PLANE RESPONSE OF ADOBE MASONRY WALLS STRENGTHENED WITH TEXTILE REINFORCED MATRIX SYSTEMS .....	1322
<i>Paolino Cassese, Luigi Fenu, Domenico Asprone, Antonio Occhiuzzi, Fulvio Parisi</i>	
GENETIC OPTIMIZATION FOR THE DESIGN OF SEISMIC RETROFITTING OF PLANE RC FRAMES WITH BUCKLING RESTRAINED BRACES (BRBS) .....	1333
<i>Giovanni Minafò, Gaetano Camarda</i>	
INFLUENCE OF THE EFFECTIVENESS FACTORS IN ASSESSING THE SHEAR CAPACITY OF RC BEAMS STRENGTHENED WITH FRP .....	1345
<i>Piero Colajanni, Salvatore Pagnotta</i>	
OPTIMIZATION OF STEEL-JACKETING RETROFITTING OF SHEAR-CRITICAL AND DUCTILITY CRITICAL RC FRAME STRUCTURES BY A NOVEL GENETIC ALGORITHM FRAMEWORK .....	1368
<i>Antonio Pio Sberna, Fabio Di Trapani, Giuseppe Carlo Marano</i>	
EXPECTED ANNUAL LOSS ORIENTED SEISMIC RETROFITTING OPTIMIZATION OF RC FRAME STRUCTURES USING A NEW AI-BASED FRAMEWORK .....	1383
<i>Fabio Di Trapani, Antonio Pio Sberna, Giuseppe Carlo Marano</i>	
THE ROLE OF THE SUSTAINED LOADS ON THE BEARING CAPACITY OF REINFORCED CONCRETE COLUMNS RETROFITTED BY STEEL JACKETS .....	1401
<i>Marco Filippo Ferrotto, Bharat Pradhan, Liborio Cavaleri</i>	

## **MS 13: MODELLING AND SOLUTION STRATEGIES FOR DYNAMIC PROBLEMS**

CASE STUDY OF CONNECTIVITY OF DIGITAL TWINS AND EXPERIMENTAL SYSTEMS .....	1416
<i>Matthew Bonney, Paul Gardner, David Wagg, Robin Mills</i>	
AN ADAPTIVE FAST NONLINEAR ANALYSIS (AFNA) ALGORITHM FOR RAPID TIME HISTORY ANALYSIS .....	1426
<i>Bowei Li, Wei-Chu Chuang, Seymour M.J. Spence</i>	
A NOVEL METHOD FOR THE GENERATION OF FULLY NON-STATIONARY SPECTRUM COMPATIBLE ARTIFICIAL ACCELEROGRAMS .....	1437
<i>Federica Genovese, Giuseppe Muscolino, G. Biondi, E. Cascone</i>	
AN APPLICATION OF THE PROPER ORTHOGONAL DECOMPOSITION METHOD FOR NONLINEAR DYNAMIC ANALYSIS OF REINFORCED CONCRETE STRUCTURES SUBJECTED TO EARTHQUAKES .....	1445
<i>Naim Ayoub, Walid Labri, Joseph Pais, Lucie Rouleau, Jean-François Deu</i>	
MULTI-RESOLUTION FINITE WAVELET DOMAIN METHOD FOR FAST TRANSIENT DYNAMIC ANALYSIS IN HOMOGENEOUS AND HETEROGENEOUS RODS AND BEAMS .....	1458
<i>Dimitris K. Dimitriou, Christos V. Nastos, Dimitris A. Saravanos</i>	

A TECHNIQUE FOR TIME INTEGRATION WITH STEPS LARGER THAN THE EXCITATION STEPS: REVIEW OF THE PAST AND ADDRESSING THE EXISTING CHALLENGES AND A PERSPECTIVE OF THE FUTURE .....	1476
<i>Aram Soroushian</i>	

#### **MS 14: SEISMIC ASSESSMENT AND RETROFITTING OF EXISTING STEEL STRUCTURES**

A SIMPLIFIED APPROACH FOR THE ESTIMATION OF SEISMIC VULNERABILITY OF STEEL MOMENT RESISTING FRAMES .....	1492
<i>Rosario Montuori, Elide Nastri, Vincenzo Piluso, Paolo Todisco</i>	

PRELIMINARY NUMERICAL ANALYSIS OF THE SEISMIC RESPONSE OF STEEL FRAMES WITH MASONRY INFILLS RETROFITTED BY BUCKLING RESTRAINED BRACES .....	1506
<i>Fernando Gutiérrez-Urzúa, Fabio Freddi, Luigi Di Sarno, Jing-Ren Wu, Mario D'Aniello, Raffaele Landolfo, Stathis Bousias</i>	

NUMERICAL MODELLING OF MASONRY INFILL WALLS IN EXISTING STEEL FRAMES .....	1519
<i>Luigi Di Sarno, Jing-Ren Wu, Fabio Freddi, Mario D'Aniello, Stathis Bousias, Fernando Gutiérrez-Urzúa, Raffaele Landolfo, Nikolaos Stathas</i>	

HYBRID COLD-FORMED/TUBULAR MODULAR STRUCTURAL SYSTEM WITH INNOVATIVE JOINTS .....	1532
<i>Luís Carlos Silva, Hélder David Craviero, Trayana Tankova, Rui Simões, Ricardo Costa, Mario D'Aniello, Raffaele Landolfo, Luís Simões da Silva</i>	

SEISMIC ASSESSMENT OF BEAM-TO-COLUMN JOINTS FOR A NON-CONFORMING MRF EXISTING STRUCTURE ....	1542
<i>Roberto Tartaglia, Mario D'Aniello, Aldo Milone, Raffaele Landolfo</i>	

#### **MS 16: DYNAMIC RESPONSE ASSESSMENT IN RAIL TRACK ENGINEERING**

APPLICATION AND ASSESSMENT OF A DYNAMIC SOIL-BRIDGE-TRAIN INTERACTION MODEL .....	1550
<i>Benjamin Hirzinger, Christoph Adam</i>	

SEISMIC FRAGILITY ANALYSIS OF RAILWAY RC BRIDGES. ACCOUNTING FOR BRIDGE-TRAIN INTERACTION BASED ON A NOVEL FORMULATION FOR CONSTRAINED DYNAMICAL SYSTEMS AND A CO-SIMULATION TECHNIQUE .....	1562
<i>Sotiria Stefanidou, Elias Paraskevopoulos</i>	

#### **MS 17: RECENT DEVELOPMENTS IN ROCKING STRUCTURES**

REDUCTION OF LOCAL DAMAGES IN PRECAST POST-TENSIONED SEGMENTAL BRIDGE PIERS .....	1574
<i>Parya Ahmadi, Ehsan Ahmadi, Mohammad M. Kashani</i>	

BASE VERSUS TOP ACTIVE CONTROL TO IMPROVE DYNAMIC AND SEISMIC PERFORMANCES OF RIGID BLOCKS .	1583
<i>Angelo Di Egidio, Alessandro Contento, Stefano Pagliaro</i>	

UNIFORM RISK SPECTRA FOR NEGATIVE STIFFNESS SYSTEMS .....	1596
<i>Natalia Reggiani Manzo, Christos Lachanas, Michalis Vassiliou, Dimitrios Vamvatsikos</i>	
SEISMIC BEHAVIOR OF ARCHAEOLOGICAL MULTIDRUM COLUMNS AT THE POMPEII SITE .....	1607
<i>Francesca Autiero, Giuseppina De Martino, Marco Di Ludovico, Andrea Prota</i>	
THE INFLUENCE OF IMPACT MODELLING ASSUMPTIONS ON THE DYNAMIC BEHAVIOUR OF FLEXIBLE ROCKING OSCILLATORS .....	1618
<i>Huanian Zhu, Manolis Chatzis, Sinan Acikgoz</i>	
QUANTIFYING SEISMIC RESILIENCE OF SINGLE-COLUMN ROCKING BRIDGES – A COMPARATIVE STUDY .....	1626
<i>Anastasios Giouvanidis, You Dong</i>	
DYNAMIC RESPONSE OF MULTI-STOREY STRUCTURES SEISMICALLY ISOLATED USING KINEMATIC BEARINGS ....	1641
<i>Kosmas E. Bantilas, Ioannis E. Kavvadias, Lazaros Vasiliadis, Anaxagoras Elenas</i>	
THE EFFECT OF IMPACT MODELING ON THE SEISMIC RESPONSE OF MULTI-STOREY PODIUM STRUCTURES .....	1657
<i>Ioannis E. Kavvadias, Kosmas E. Bantilas, Lazaros Vasiliadis, Anaxagoras Elenas</i>	
3D ROCKING MOTION: BLIND PREDICTION CONTEST RESULTS AND INFLUENCE OF EVALUATION METRIC ON THE RANKINGS .....	1672
<i>Michalis F. Vassiliou, Marco Broccardo, Cihan Cengiz, Matt Dietz, Luiza Dihoru, Selim Gunay, Khalid M. Mosalam, George Mylonakis, Anastasios Sextos, Bozidar Stojadinovic</i>	
FINITE ELEMENT MODELLING OF A RC ROCKING WALL WITH ADDITIONAL STEEL REBARS .....	1688
<i>Michele Egidio Bressanelli, Andrea Belleri, Jose Ignacio Restrepo</i>	
CYCLIC TEST OF A PRECAST BRIDGE COLUMN FOR SUSTAINABLE BRIDGE DESIGN .....	1700
<i>Natalia Reggiani Manzo, Michalis Vassiliou</i>	
 <b>MS 19: ADVANCES IN THE OPTIMUM DESIGN AND CONTROL OF LARGE STRUCTURES UNDER DYNAMIC LOADS</b>	
STUDY OF THE INFLUENCE OF SEISMIC ACTION ON THE CONSTRUCTION COST OF THE LOAD-BEARING STRUCTURE OF A TEN-STOREY R/C BUILDING .....	1712
<i>Panagiotis Sioulas, Theodoros Chrysanidis, Nikolaos Alamanis, Grigorios Papageorgiou</i>	
ASSESSMENT AND RETROFITTING OF A RC BUILDING THROUGH A MULTI-HAZARD APPROACH: SEISMIC RESISTANCE AND ROBUSTNESS .....	1725
<i>Martina Scalvenzi, Fabio Freddi, Fulvio Parisi</i>	
OPTIMAL LATERAL RESISTING SYSTEMS FOR HIGH-RISE BUILDINGS UNDER SEISMIC EXCITATIONS .....	1737
<i>Giulia Angelucci, Giuseppe Quaranta, Fabrizio Mollaioli</i>	
NON-INVASIVE VIBRATING CONTROL OF THE ZOSER PYRAMID .....	1751
<i>Masoud Shadlou, Pierfrancesco Cacciola, Ashraf Ayoub, Youssef Rashed, Alessandro Tombari</i>	

OPTIMUM DESIGN OF A HYBRID ISOLATION DEVICE FOR SERVER RACKS USING CONSTRAINED DIFFERENTIAL EVOLUTION ALGORITHM .....	1767
<i>Luca Aceto, Giuseppe Quaranta, Guido Camata, Bruno Briseghella, Enrico Spacone</i>	
INNOVATIVE MASS-DAMPING-BASED APPROACHES FOR SEISMIC DESIGN OF TALL BUILDINGS .....	1778
<i>Elena Mele, Diana Faiella, Mario Argenziano</i>	
DIAGRID SYSTEM COUPLED WITH SHEAR WALLS: ANALYTICAL INVESTIGATION ON THE DYNAMICAL RESPONSE IN TALL BUILDINGS .....	1793
<i>Giuseppe Lacidogna, Giuseppe Nitti, Domenico Scaramozzino, Alberto Carpinteri</i>	
OPTIMUM DAMPING OF SLENDER MONOPOLE TOWERS BY GYROSCOPIC STABILIZER .....	1803
<i>Gian Felice Giaccu, Luigi Fenu, Bruno Briseghella, Camillo Nuti</i>	
VIBRATION CONTROL OF WIND TURBINE TOWERS WITH KDAMPER-BASED DESIGNS .....	1812
<i>Konstantinos Kapasakalis, Ioannis Antoniadis, Evangelos Sapountzakis</i>	
 <b>MS 20: COMPUTATIONAL DESIGN AND MODELING OF TENSEGRITY SYSTEMS FOR APPLICATIONS IN SCIENCE AND ENGINEERING</b>	
ADAPTIVE BENDING-ACTIVE MODULES FOR A TENSILE SOLAR SHADING SYSTEM .....	1825
<i>Alessandro D'Ambrosio, Maria Matheou, Rosario Montuori, Elide Nastri</i>	
A MESOSCALE TENSEGRITY MODEL OF SPIDER DRAGLINE SILK FIBER .....	1834
<i>Ada Amendola, Narinder Singh, Cornelia Rodenburg, Chris Holland, Fernando Fraternali</i>	
GEOMETRIC PATTERNS AND DYNAMICS OF FOLDABLE MODULI FOR ADAPTIVE FAÇADES .....	1840
<i>Veronica Abbate, Enrico Babilio, Filipe Amarante dos Santos, Narinder Singh, Fernando Fraternali</i>	
MODELING AND DESIGN OF PERIODIC LATTICES WITH TENSEGRITY ARCHITECTURE AND HIGHLY NONLINEAR RESPONSE .....	1848
<i>Andrea Micheletti, Claudio Intrigila, Nicola Nodargi, Edoardo Artioli, Fernando Fraternali, Paolo Bisegna</i>	
A DYNAMIC-STIFFNESS APPROACH FOR DAMPED LOCALLY-RESONANT TIMOSHENKO BEAMS .....	1856
<i>Andrea Francesco Russillo, Giuseppe Failla, Antonina Pirrotta, Fernando Fraternali</i>	
SEISMIC METAMATERIALS WITH TENSEGRITY ARCHITECTURE .....	1867
<i>Filipe Santos, Narinder Singh, Ada Amendola, Fernando Fraternali, Andrea Micheletti</i>	
 <b>MS 22: CONDITION BASED MAINTENANCE AND POST-PROGNOSTICS OF COMPOSITE STRUCTURES: AN ENHANCED PLATFORM</b>	
RECONSTRUCTION OF MATERIAL STIFFNESS PROPERTIES FROM DISPERSION RELATIONS USING GENETIC ALGORITHMS .....	1874
<i>Victor Thierry, Wen Wu, Dimitrios Chronopoulos, Sergio Cantero-Chinchilla</i>	

PARTICLE FILTER-BASED HYBRID DAMAGE PROGNOSIS CONSIDERING BIAS .....	1881
<i>Tianzhi Li, Francesco Cadini, Claudio Sbarufatti</i>	

### **MS 23: ADVANCED MODELS AND NUMERICAL METHODS IN DYNAMICS, WAVE PROPAGATION AND COUPLED PROBLEMS**

DISPERSION ANALYSIS OF BULK ACOUSTIC WAVES IN PIEZOELECTRIC MEDIA DISCRETIZED BY ENERGY-ORTHOGONAL FINITE ELEMENTS .....	1892
<i>Francisco J. Brito Castro</i>	

DISPERSION DESIGN OF 1D PERIODIC DISCRETE SYSTEMS USING LOG-DET HEURISTICS .....	1922
<i>Anton Tkachuk, Mykola Tkachuk</i>	

AN EFFICIENT PRECONDITIONER FOR MODAL FREQUENCY RESPONSE .....	1934
<i>Tobias Willerding</i>	

### **MS 24: LIFE-CYCLE RISK-BASED STRUCTURAL ASSESSMENT AND COST ANALYSIS**

FRAGILITY ASSESSMENT OF WIND-EXCITED VIDEO SCREEN ROOMS IN HIGH-RISE BUILDINGS .....	1941
<i>Fabio Rizzo, Laura Ierimonti, Stefano Sacconi, Ilaria Venanzi</i>	

FRAGILITY OF EXISTING ITALIAN BRIDGES TO TRAFFIC LOADS .....	1950
<i>Giacomo Miluccio, Daniele Losanno, Fulvio Parisi, Edoardo Cosenza</i>	

TOWARDS THE DEVELOPMENT OF A COMPREHENSIVE FRAMEWORK FOR LIFE CYCLE COST ANALYSIS OF BRIDGES SUBJECTED TO MULTIPLE HAZARDS .....	1961
<i>Stefano Sacconi, Laura Ierimonti, Ilaria Venanzi, Filippo Ubertini</i>	

LIFE-CYCLE COST ANALYSIS OF TALL BUILDINGS IN SYNOPTIC, MIXED WIND LOAD CLIMATES BY LAYERED STOCHASTIC APPROXIMATION MONTE-CARLO METHOD .....	1973
<i>Lei Zhang, Luca Caracoglia</i>	

APPLICATION OF BAYESIAN FE MODEL SELECTION FOR SHM OF A MONUMENTAL MASONRY PALACE THROUGH SEMI-SUPERVISED LEARNING .....	1988
<i>Laura Ierimonti, Nicola Cavalagli, Enrique García-Macías, Ilaria Venanzi, Filippo Ubertini</i>	

A NEURAL NETWORK-BASED APPROACH FOR SEISMIC-INDUCED DAMAGE ASSESSMENT OF STEEL LIQUID STORAGE TANKS .....	2003
<i>Laura Micheli, Mahmoud Faytarouni</i>	

### **MS 25: MONITORING, IDENTIFICATION AND VIBRATION CONTROL OF STRUCTURES**

APPLICATION OF WAVELET TRANSFORMS ON ACCELERATION RECORDS: PRACTICAL APPROACH .....	2014
<i>Vladimir Vukobratović, Trevor Yeow, Koichi Kusunoki</i>	

NUMERICAL INVESTIGATION ON THE PRINCIPAL STRESS ROTATION EFFECT UNDER EARTHQUAKE LOADINGS ..	2022
<i>Zhe Wang, Yunming Yang</i>	
ENRICHED BEAM FINITE ELEMENT MODELS WITH TORSION AND SHEAR WARPING FOR DYNAMIC ANALYSIS OF FRAME STRUCTURES .....	2033
<i>Daniela Addessi, Paolo Di Re, Cristina Gatta</i>	
EARTHQUAKE-INDUCED STRUCTURAL POUNDING BETWEEN TWO INELASTIC SDOF STRUCTURAL SYSTEMS .....	2058
<i>Pedro Folhento, Rui Barros, Manuel Braz-César</i>	
INFLUENCE OF STRUCTURAL INELASTIC BEHAVIOR IN THE STUDY OF COLLIDING SDOF STRUCTURES .....	2085
<i>Pedro Folhento, Rui Barros, Manuel Braz-César</i>	
VIRTUAL SENSING AND STRAIN ESTIMATION ON AN OFFSHORE WIND TURBINE USING SUPERVISED LEARNING .....	2112
<i>Marius Tarpø, Sandro Amador, Evangelos Katsanos, Mattias Skog, Johan Gjørdvad, Rune Brincker</i>	
SIMPLIFIED METHODS FOR FREQUENCY ESTIMATION OF SMALL WIND TURBINE TOWER .....	2121
<i>Anelise Dick, Rui Carneiro-Barros, Manuel Braz-César</i>	
FINITE ELEMENT MODEL CALIBRATION EFFECTS ON THE STATIC AND DYNAMIC RESPONSE OF A METALLIC HOLLOW TOWER .....	2132
<i>Anelise Dick, Rui Carneiro-Barros, Manuel Braz-César</i>	
PARAMETRIC STUDY OF LATTICE TOWERS ON THE INFLUENCE OF WIND ACTION FOR DIFFERENT TYPOLOGIES OF BRACING .....	2143
<i>Rui Carneiro-Barros, Luís Barros</i>	
 <b>MS 26: SEISMIC SAFETY ASSESSMENT OF STRUCTURES</b>	
EXPERIMENTAL IN-PLANE LATERAL RESPONSE OF A FULL-SCALE ADOBE MASONRY WALL WITH OPENING .....	2157
<i>Paolino Cassese, Luigi Fenu, Domenico Asprone, Antonio Occhiuzzi, Fulvio Parisi</i>	
INFLUENCE OF BEAM-TO-COLUMN CONNECTIONS IN SEISMIC VULNERABILITY ASSESSMENT OF STEEL STRUCTURES .....	2170
<i>Giammaria Gabbianelli, Daniele Perrone, Emanuele Brunesi</i>	
ASSESSMENT OF RC HOLLOW-PIERS FOR SEISMIC LIMIT STATE OF DAMAGE - DIRECT REPAIR COSTS .....	2185
<i>Pedro Delgado, Naiara Silva, Mário Marques, António Arêde</i>	
 <b>MS 27: TIMBER-BASED ELEMENTS: RECENT ADVANCEMENTS FOR NEW AND EXISTING SEISMIC-RESISTANT STRUCTURES</b>	
OPTIMIZATION OF THE SLIP FORCE IN A NOVEL FRICTION-BASED CONNECTION FOR THE E-CLT TECHNOLOGY ..	2195
<i>Angelo Aloisio, Francesco Boggian, Roberto Tomasi</i>	



EXPERIMENTAL AND NUMERICAL INVESTIGATION OF INNOVATIVE DUCTILE AND REPLACEABLE ANCHORING SYSTEMS FOR WOOD SHEAR WALLS UNDER SEISMIC LOADS .....	2211
<i>Georgios Balaskas, Vera Wilden, Benno Hoffmeister</i>	
ANALYTICAL AND NUMERICAL MODELLING OF THE IN-PLANE RESPONSE OF TIMBER DIAPHRAGMS RETROFITTED WITH PLYWOOD PANELS .....	2227
<i>Michele Mirra, Marianthi Sousamli, Michele Longo, Geert Ravenshorst</i>	
MOMENT-CURVATURE DIAGRAMS FOR CLT PANELS ACCOUNTING FOR ORTOGONAL TO GRAIN COMPRESSION TIMBER PROPERTIES .....	2254
<i>Antonio Sandoli, Claudio D'Ambra, Maria Lippiello, Carla Ceraldi, Bruno Calderoni, Andrea Prota</i>	
REINFORCING STOP-SPLAYED SCARF JOINTS WITH TIMBER PEG: ROLE OF SLENDERNESS .....	2272
<i>Carla Ceraldi, Claudio D'Ambra, Maria Lippiello, Antonio Sandoli, Andrea Prota</i>	
IMPACT OF RETROFIT OF RC FRAMES BY CLT PANELS AND FRICTION DAMPERS .....	2287
<i>Francesca Barbagallo, Giuseppe Margani, Edoardo M. Marino, A. Moretti, Carola Tardo</i>	
SEISMIC STRENGTHENING OF EXISTING URM STRUCTURES THROUGH CLT ELEMENTS: NUMERICAL ANALYSIS OF THE APPLICATION OF A NOVEL INTERVENTION TECHNIQUE .....	2300
<i>Matteo Salvalaggio, Marco Pegoraro, Elisa Saler, Umberto Turrini, Maria Rosa Valluzzi</i>	
POST-TENSIONED LOW DAMAGE TIMBER WALLS WITH DISSIPATIVE DEVICES BEHAVIOUR: NUMERICAL PREDICTION .....	2314
<i>Valentina Tomei, Maria Zucconi, Barbara Ferracuti</i>	
MANSORY-INFILLED RC FRAMES STRENGTHENED WITH CROSS-LAMINATED TIMBER PANELS .....	2323
<i>Zabih Mehdipour, Jorge Branco, Iztok Sustersic, Leonardo Filipe Rodrigues, Paulo Lourenço</i>	
INFLUENCE OF PERPENDICULAR WALLS ON THE LATERAL STIFFNESS OF CLT SHEAR WALLS .....	2336
<i>Elisabetta Maria Ruggeri, Giuseppe D'Arenzo, Marinella Fossetti, Werner Seim</i>	
POST-TENSIONED LOW DAMAGE CLT WALLS WITH REPLACEABLE HYSTERETIC DEVICES – CONCEPT, EXPERIMENTAL AND NUMERICAL CHARACTERIZATION .....	2352
<i>Luca Pozza, Luca Benedetti, Valentina Tomei, Barbara Ferracuti, Maria Zucconi, Claudio Mazzotti</i>	
TIMBER BEAM-TO-COLUMN JOINT WITH STEEL LINK: DESIGN AND MECHANICAL CHARACTERIZATION THROUGH NUMERICAL INVESTIGATION .....	2359
<i>Giacomo Iovane, Beatrice Faggiano</i>	
A NUMERICAL STUDY ON A TIMBER-BASED SEISMIC RETROFIT INTERVENTION FOR MASONRY INFILLED CONCRETE FRAMES .....	2366
<i>Francesco Smirolto, Davide Viel, Ivan Giongo, Maurizio Piazza</i>	

**MS 29: SEISMIC PROTECTION OF NON-STRUCTURAL COMPONENTS: RECENT DEVELOPMENTS AND FUTURE CHALLENGES**

COMPREHENSIVE NONLINEAR ANALYSIS OF FAILURES OF FIRE-SPRINKLER SYSTEM BASED ON FINITE ELEMENT MODELLING AND AMBIENT VIBRATION TESTS .....	2388
<i>Shakhzod Takhirov, Amir Gilani</i>	
IMPROVEMENT OF DYNAMIC AND SEISMIC BEHAVIOUR OF CABINETS THROUGH CONTROLLED DEFORMATION .....	2396
<i>Stefano Pagliaro, Angelo Di Egidio, Alessandro Contento</i>	
NUMERICAL MODELING OF ROCKING AND SLIDING CYLINDRICAL COLUMNS UNDER SEISMIC EXCITATION .....	2408
<i>Antonios Katsamakas, Michalis Vassiliou</i>	
SEISMIC RISK ASSESSMENT OF ROCKING BUILDING CONTENTS .....	2421
<i>Michalis Fragiadakis, Spyridon Diamantopoulos</i>	

**MS 30: DYNAMIC PROTECTION SYSTEMS AND DEVICES: EXPERIMENTAL TESTS, MATHEMATICAL MODELING AND DESIGN METHODS**

SOME RECENT ADVANCES ON THE MODELING OF THE HYSTERETIC BEHAVIOR OF RATE-INDEPENDENT PASSIVE ENERGY DISSIPATION DEVICES .....	2435
<i>Nicolò Vaiana, Ciro Napolitano, Luciano Rosati</i>	
SEISMIC PROTECTION OF CULTURAL HERITAGE ARTEFACTS BY MEANS OF ELASTOMERIC ISOLATORS: A CASE STUDY .....	2446
<i>Davide Pellecchia, Stefania Lo Feudo, Nicolo Vaiana, Jean-Luc Dion, Luciano Rosati</i>	
TUNING THE LATERAL RESPONSE OF UNBONDED FIBER REINFORCED ELASTOMERIC ISOLATORS (U-FREIS): EXPERIMENTAL-NUMERICAL FINDINGS .....	2456
<i>Simone Galano, Andrea Calabrese, Daniele Losanno</i>	
ON THE VERTICAL RESPONSE OF FIBER REINFORCED ELASTOMERIC ISOLATORS (FREIS) UNDER COMBINED VERTICAL AND LATERAL LOADING .....	2468
<i>Simone Galano</i>	
SEISMIC ISOLATION OF LIGHTWEIGHT STRUCTURES THROUGH WIRE ROPE DEVICES: PRELIMINARY EXPERIMENTAL RESULTS AND SIMULATION .....	2488
<i>Mariacristina Spizzuoco, Giorgio Serino</i>	
REAL-TIME HYBRID SIMULATION OF A STRUCTURE WITH CIRCULAR FIBER REINFORCED ISOLATORS .....	2498
<i>Carlos Riascos, Semion Klopov, Johannio Marulanda, Peter Thomson, Giorgio Serino</i>	
A COMPARATIVE STUDY ON THE ACCURACY AND EFFICIENCY OF TWO BIAXIAL HYSTERETIC MODELS SUITABLE FOR ELASTOMERIC BEARINGS .....	2511
<i>Nagavinothini Ravichandran</i>	

LABORATORY CHARACTERIZATION OF A RECLAIMED RUBBER COMPOUND FOR LOW-COST ELASTOMERIC ISOLATORS .....	2525
<i>Fabrizia Cilento, Daniele Losanno, Luigi Piga</i>	
EFFECT OF EXTREMELY LOW TEMPERATURE ON MECHANICAL PROPERTIES OF A LARGE SIZE LRB .....	2536
<i>Gokhan Ozdemir, Esengul Cavdar, Volkan Karuk</i>	
STIFF DYNAMIC ABSORBERS FOR THE VERTICAL SEISMIC PROTECTION OF STRUCTURES .....	2543
<i>Marina Kalogerakou, Konstantinos Kapasakalis, Ioannis Antoniadis, Evangelos Sapountzakis</i>	
 <b>MS 32: SIMPLIFIED METHODOLOGIES FOR PERFORMANCE AND LOSS ASSESSMENT AT BUILDING OR TERRITORIAL SCALE</b>	
ACCURATE COLLAPSE CAPACITY QUANTIFICATION FOR INFILLED RC FRAME BUILDINGS .....	2557
<i>Al Mouayed Bellah Nafeh, Gerard O'Reilly</i>	
DEVELOPMENT OF A PYTHON-BASED STOREY LOSS FUNCTION GENERATOR .....	2573
<i>Davit Shahnazaryan, Gerard O'Reilly, Ricardo Monteiro</i>	
ASSESSMENT OF POST-EARTHQUAKE DAMAGES ON ITALIAN SCHOOL BUILDINGS PORTFOLIO OVER THE LAST 50 YEARS .....	2591
<i>Sergio Ruggieri, Chiara Tosto, Daniele Perrone, Giuseppina Uva, Maria Antonietta Aiello</i>	
SEISMIC RISK ASSESSMENT FOR THE ITALIAN RESIDENTIAL MASONRY BUILT STOCK AND EFFECTIVENESS OF DIFFERENT MITIGATION STRATEGIES .....	2606
<i>Pietro Carpanese, Veronica Follador, Elisa Saler, Francesca da Porto</i>	
THE USE OF STICK-IT MODEL FOR EDP ASSESSMENT IN EXISTING RC INFILLED TYPOLOGIES .....	2619
<i>Marco Gaetani d'Aragona, Maria Polese, Marco Di Ludovico, Andrea Prota</i>	
APPLICATION OF THE EMPIRICAL PREDICTIVE DAMAGE MODEL OF HISTORICAL CHURCHES .....	2631
<i>Claudia Canuti, Michele Morici, Andrea Dall'Asta, Graziano Leoni</i>	
A SEISMIC RISK ASSESSMENT FRAMEWORK FOR LOSS ESTIMATION OF CRITICAL INFRASTRUCTURE – HOSPITALS CASE .....	2643
<i>Paolo Basso, Saimir Osmani, Matteo Scolari, Ruben Valsecchi</i>	
CAESAR II: AN ITALIAN DECISION SUPPORT TOOL FOR THE SEISMIC RISK. THE CASE STUDY OF TORRE PELLICE, VILLAR PELLICE AND PINEROLO MUNICIPALITIES .....	2659
<i>Giulio Zuccaro, Francesca Linda Perelli, Daniela De Gregorio, Daniele Masi</i>	
OPEN MODELS AND SOFTWARE FOR ASSESSING THE VULNERABILITY OF THE EUROPEAN BUILDING STOCK .....	2678
<i>Helen Crowley, Vitor Silva, Luis Martins, Xavier Romão, Nuno Pereira</i>	

PELL-SCHOOLS A STANDARDIZED AND INTEROPERABLE PLATFORM FOR THE SEISMIC VULNERABILITY AND ENERGY EFFICIENCY DATA MANAGEMENT OF ITALIAN SCHOOLS .....	2689
<i>Laura Blaso, Sonia Giovinazzi, Simona Bianchi, Livio Pedone, Chiara Ormando, Paolo Clemente, Stefano Pampanin, Nicoletta Gozo, Giuseppina Giuliani, Maurizio Pollino</i>	

EFFECT OF BUILDING SAMPLE SELECTION ON SEISMIC FRAGILITY CURVES FOR RC BUILDINGS AT TERRITORIAL SCALE .....	2707
<i>Maria Zucconi, Fabio Romano, Barbara Ferracuti</i>	

## VOLUME II

### Minisymposia

#### MS 33: EXPERIMENTAL MEASUREMENTS AND NUMERICAL SIMULATION ON PROBLEMS IN THE FIELD OF EARTHQUAKE ENGINEERING AND STRUCTURAL DYNAMICS

ANALYTICAL INVESTIGATION OF THE TENSILE EXPERIMENTS MODELING THE ELONGATION DEGREE OF R/C WALLS FOR STUDYING THE LATERAL BUCKLING PHENOMENON .....	2718
<i>Theodoros Chrysanidis, Vassilis Panoskaltsis</i>	

ANALYTICAL INVESTIGATION OF THE TENSILE EXPERIMENTS TO PRISMS WITH VARYING LONGITUDINAL RATIO FOR STUDYING THE LATERAL BUCKLING OF R/C WALLS .....	2730
<i>Theodoros Chrysanidis, Vassilis Panoskaltsis</i>	

PRELIMINARY CONSIDERATIONS ON THE LOSS OF SUPPORT FOR PRECAST BEAM ELEMENTS .....	2744
<i>Marius Eteme Minkada, Simone Labò, Alessandra Marini, Andrea Belleri</i>	

SEISMIC PERFORMANCE OF BELL TOWERS .....	2754
<i>George C. Manos</i>	

STUDYING THE PERFORMANCE OF STONE MASONRY ARCH BRIDGES EMPLOYING IN-SITU MEASUREMENTS AND NUMERICAL PREDICTIONS .....	2769
<i>George C. Manos, N. Simos</i>	

EXPERIMENTAL IDENTIFICATION OF MECHANICAL AND DYNAMIC CHARACTERISTICS OF 3D PRINTING SPECIMENS .....	2791
<i>Ioannis E. Kavvadias, Konstantinos Tsongas, Dimitrios Tzetzis, Kosmas E. Bantilas, Lazaros Vasiliadis, Anaxagoras Elenas</i>	

INVESTIGATION OF LOW COST SMAS UNDER ELEVATED TEMPERATURES .....	2800
<i>Sofia Piliafa, Lazaros Melidis, Lambros Kotoulas, Nikolaos Makris, Konstantinos Katakalos</i>	

EXPERIMENTAL AND NUMERICAL INVESTIGATION OF THE PLASTIC CYCLIC BEHAVIOUR OF SIMPLE STEEL COUPONS .....	2808
<i>Alexandra Nalmpantidou, George C. Manos</i>	

EXPERIMENTAL TESTS AND NUMERICAL STUDY OF THE PLASTIC CYCLIC BEHAVIOUR OF A STEEL BEAM-TO-COLUMN CONNECTION .....	2824
<i>George C. Manos, Alexandra Nalmpantidou</i>	
DYNAMIC AND VIBROACOUSTIC RESPONSE OF TIMBER FLOOR PANELS. MEASUREMENTS AND NON-LINEAR NUMERICAL SIMULATIONS .....	2843
<i>Magdalini Titirla, Sarah Benakli, Walid Larbi</i>	
THE USE OF INTELLIGENT FACADES FOR UPGRADING ENERGY AND SEISMIC DEMANDS OF EXISTING R/C STRUCTURE .....	2852
<i>Lazaros Melidis, Efthymios A. Kechagias, Konstantinos Katakalos, George C. Manos</i>	
EXPERIMENTAL AND NUMERICAL INVESTIGATION OF FRP STRENGTHENED R/C BEAM-TO-COLUMN JOINTS SUBJECTED TO CYCLIC SEISMIC-TYPE LOADING .....	2863
<i>Lazaros Melidis, George C. Manos, J. Maranos, Konstantinos Katakalos</i>	
THE BEHAVIOR OF PARTIALLY GROUTED MASONRY WALLS SUBJECTED TO OUT OF PLANE SEISMIC TYPE LOADS. LABORATORY MEASUREMENTS AND NUMERICAL SIMULATIONS .....	2875
<i>George C. Manos, Lazaros Melidis, Lampros Kotoulas, Konstantinos Katakalos</i>	
IN PLANE BEHAVIOR OF PARTIALLY GROUTED MASONRY WALLS USING A NEW CLAY UNIT. LABORATORY MEASUREMENTS AND NUMERICAL SIMULATIONS .....	2885
<i>George C. Manos, Lazaros Melidis, Lampros Kotoulas, Konstantinos Katakalos</i>	
EXPERIMENTAL AND NUMERICAL INVESTIGATION OF THE OUT OF PLANE BEHAVIOR OF THERMAL INSULATED MASONRY WALLS .....	2895
<i>George C. Manos, Lazaros Melidis, Konstantinos Katakalos, Anthimos Anastasiadis</i>	
EXPERIMENTAL & NUMERICAL INVESTIGATION OF LAP-SPLICED R/C COLUMNS UNDER THREE POINT BENDING & AXIAL COMPRESSION .....	2903
<i>Pelagia Kastiza, Lazaros Melidis, Konstantinos Katakalos</i>	
DEVELOPMENT OF AN EXPERIMENTAL SETUP FOR MEASURING THE EFFECTIVENESS OF STRENGTHENED PRESTRESSED CONCRETE CYLINDER PIPES (PCCP) .....	2913
<i>Sofia Gkaraklova, Lazaros Melidis, George C. Manos, Konstantinos Katakalos</i>	
MECHANICAL PROPERTIES CHARACTERISATION OF FRPS UNDER ELEVATED TEMPERATURES .....	2922
<i>Christina Papadimitriou, Lambros Kotoulas, Nikolaos Makris, Lazaros Melidis, Konstantinos Katakalos</i>	
EXPERIMENTAL TESTING CAMPAIGN AND NUMERICAL MODELLING OF AN INNOVATIVE BASE-PLATE CONNECTION FOR PALLET RACKING SYSTEMS .....	2934
<i>Bonaventura Tagliaferro, Rosario Montuori, Ioannis Vayas, Sofia Antonodimitraki, Magdalini D. Titirla, Marco Simoncelli, Xenophon Lignos</i>	
STUDY OF THE INFLUENCE OF UNDERLYING SOFT-SOIL LAYERS ON THE DYNAMIC AND EARTHQUAKE RESPONSE OF BELL TOWERS .....	2943
<i>George C. Manos</i>	

THE INFLUENCE OF WOODEN ROOF CONNECTION ON THE DYNAMIC AND EARTHQUAKE RESPONSE OF OLD INDUSTRIAL STONE MASONRY BUILDINGS .....	2965
<i>George C. Manos, Lampros Kotoulas</i>	
EXPERIMENTAL AND ANALYTICAL INVESTIGATION OF THE STRENGTHENING OF TRADITIONAL TIMBER FRAMES .....	2983
<i>Ioannis Stavrou, Panayiotis Demosthenous, Stelios Papastilianou, Milton Demosthenous</i>	
NUMERICAL SIMULATIONS OF THE EXPERIMENTAL RESULTS OF STEEL FRAME MODEL WITH ROOF ROLLER SYSTEM SUBJECTED TO DYNAMIC BASE EXCITATIONS .....	2997
<i>Nikodemos Kouroufexis, Milton Demosthenous</i>	
EXPERIMENTAL AND NUMERICAL INVESTIGATION OF A MASONRY MODEL BUILDING SUBJECTED TO DYNAMIC BASE EXCITATIONS .....	3007
<i>Stefania Demosthenous, Milton Demosthenous</i>	
PASSIVE CONTROL ISSUES ON THE LONGITUDINAL AND TRANSVERSE VIBRATIONS OF FLEXIBLE PYLONS .....	3021
<i>George Manolis, George Dadoulis</i>	
PSEUDO-DYNAMIC ANALYSES OF INFILLED REINFORCED CONCRETE FRAMED STRUCTURES WITH PRIOR DAMAGES AFTER ADVANCED RETROFIT .....	3036
<i>Theodoros Rousakis, Evgenia Anagnostou, Theodora Fanaradelli</i>	
EXPERIMENTAL AND NUMERICAL STUDY OF SELF-SUPPORTING DOUBLE SKIN METAL FACED MINERAL WOOL PANELS .....	3049
<i>Sofia Gkaraklova, Lazaros Melidis, George C. Manos, Konstantinos Katakalos</i>	
 <b>MS 34: FRAGILITY CURVES FOR EXISTING BUILDINGS: OPEN CHALLENGES IN THEIR DEFINITION AND USE FOR SEISMIC RISK ANALYSES</b>	
SEISMIC FRAGILITY ASSESSMENT FOR A CLASS OF RC SCHOOL BUILDINGS IN ITALY LEVERAGING DETAILED AND REDUCED-ORDER MODELS .....	3059
<i>Sergio Ruggieri, Giuseppina Uva</i>	
FRAGILITY CURVES FOR RC FRAMED BUILDINGS CONSIDERING CUMULATIVE DAMAGE DUE TO EARTHQUAKE GROUND MOTION AND SLOW-MOVING LANDSLIDES .....	3073
<i>Fulvio Parisi, Elia Acconcia</i>	
FRAGILITY CURVES FOR ITALIAN RESIDENTIAL MASONRY BUILDINGS WITH RETROFIT INTERVENTIONS .....	3083
<i>Veronica Follador, Marco Donà, Pietro Carpanese, Francesca da Porto</i>	
FRAGILITY MODELS FOR EXISTING MASONRY INFILLED RC FRAMES IN THE EMILIA AREA .....	3098
<i>Gianluca Salamida, Nicola Buratti</i>	
FRAGILITY ASSESSMENT OF THE ITALIAN MASONRY SCHOOL BUILDING ASSET FOR RISK EVALUATION AT NATIONAL SCALE .....	3113
<i>Elisa Saler, Veronica Follador, Pietro Carpanese, Francesca da Porto</i>	

DERIVATION OF SEISMIC FRAGILITY CURVES OF A GRAVITY-LOAD DESIGNED RC SCHOOL BUILDING THROUGH NLTHA .....	3127
<i>Elisa Saler, Pietro Carpanese, Veronica Follador, Francesca da Porto</i>	
TYPOLOGICAL ANALYSIS AND VULNERABILITY CURVES FOR MASONRY CHURCHES .....	3141
<i>Elvis Cescatti, Veronica Follador, Francesca da Porto</i>	
COMPARATIVE STUDY ON TWO ANALYTICAL MECHANICAL-BASED METHODS FOR DERIVING FRAGILITY CURVES TARGETED TO MASONRY SCHOOL BUILDINGS .....	3155
<i>Serena Cattari, Sara Alfano, Daria Ottonelli, Elisa Saler, Francesca da Porto</i>	
ROLE OF DESIGN LEVEL AND INFILL ARRANGEMENT ON THE SEISMIC FRAGILITY CURVES OF ITALIAN RC EXISTING BUILDINGS .....	3176
<i>Angelo Masi, Vincenzo Manfredi, Giuseppe Nicodemo, Andrea Digrisolo</i>	
 <b>MS 35: RECENT ADVANCES IN SEISMIC ISOLATION AND SUPPLEMENTAL DAMPING SYSTEMS FOR VIBRATION CONTROL</b>	
EXPERIMENTAL AND NUMERICAL ASSESSMENT OF ISOLATION SEISMIC DEVICE FOR RETROFIT OF INDUSTRIAL EXISTING SHED .....	3187
<i>Luca Mari, Virginio Quaglini, Carlo Pettoruso, Eleonora Bruschi</i>	
INVESTIGATION OF THE BREAKAWAY FRICTION INFLUENCE ON THE SEISMIC RESPONSE OF BUILDINGS ISOLATED WITH CURVED SURFACE SLIDERS .....	3204
<i>Eleonora Bruschi, Virginio Quaglini, Emanuele Gandelli</i>	
SUPPLEMENTAL ENERGY DISSIPATION WITH PRESTRESSED LEAD EXTRUSION DAMPERS (P-LED): EXPERIMENTS AND MODELING .....	3216
<i>Carlo Pettoruso, Eleonora Bruschi, Virginio Quaglini</i>	
AN INNOVATIVE STEEL DAMPER WITH ADAPTIVE HYSTERETIC BEHAVIOR .....	3230
<i>Emanuele Gandelli, Johan Distl, Peter Huber, Christian Braun</i>	
INVESTIGATIONS ON INTER-STOREY SEISMIC ISOLATION AS A TECHNIQUE FOR ADDING UPPER STOREYS .....	3248
<i>Enrico Bernardi, Marco Donà, Francesca da Porto, Ping Tan</i>	
FUNCTIONAL ACCEPTANCE TESTS FOR THE SEISMIC ISOLATION DEVICES OF THE NEW SAN GIORGIO BRIDGE IN GENOA .....	3267
<i>Marcello Cademartori, Andrea Miano, Antimo Fiorillo, Alessandro Aliotta, Marco Di Ludovico, Andrea Prota, Simone Dellacasagrande, Alaeddine Fatnassi, Daniele Pastorelli</i>	
MODELING STRATEGIES FOR THE LATERAL RESPONSE OF CURVED SURFACE SLIDER DEVICES UNDER EXTREME DISPLACEMENT DEMANDS .....	3281
<i>Marco Furinghetti, Alberto Pavese</i>	
ASSESSMENT OF THE SHEAR PROPERTIES OF HDRBS UNDER DIFFERENT COMPRESSION LEVELS .....	3294
<i>Eleonora Bruschi, Emanuele Gandelli, Carlo Pettoruso, Virginio Quaglini</i>	

## **MS 36: METHODOLOGIES AND ADVANCED TOOLS FOR SEISMIC RISK ASSESSMENT, MANAGEMENT, AND MITIGATION: ADVANCES AND OPEN CHALLENGES**

A FRAMEWORK FOR THE ASSESSMENT OF SEISMIC DAMAGE SCENARIOS IN THE EMILIA-ROMAGNA REGION, ITALY .....	3305
<i>Elena Simoni, Nicola Buratti, Claudio Mazzotti</i>	
THE USE OF AN INTEGRATED APPROACH FOR BUILDING INVENTORY AND EFFECTS ON RISK ESTIMATIONS AT THE TERRITORIAL SCALE .....	3323
<i>Maria Polese, Marco Di Ludovico, Gabriella Tocchi, Andrea Prota</i>	
SEISMIC ASSESSMENT OF MASONRY BUILDINGS AT TERRITORIAL SCALE .....	3338
<i>Chiara Iacovino, Amedeo Flora, Donatello Cardone, Marco Vona</i>	
INVESTIGATING GROUND-MOTION DURATION EFFECTS ON BUILDING PORTFOLIO LOSS ESTIMATES .....	3360
<i>Kenneth Otárola, Roberto Gentile, Luis Sousa, Carmine Galasso</i>	

## **MS 37: RISK ASSESSMENT OF BRIDGES AND ROAD NETWORKS SUBJECTED TO NATURAL HAZARDS**

RELIABILITY-BASED ASSESSMENT OF A MASONRY ARCH BRIDGE UNDER FLOOD EVENTS .....	3377
<i>Carlos Andres Mendoza Cabanzo, Monica Patricia Santamaria Ariza, Hélder S. Sousa, Jose Antonio Campos e Matos</i>	
SIMPLIFIED FRAGILITY ANALYSIS OF MULTI-SPAN ISOSTATIC RC-BRIDGES CONSIDERING AN INCOMPLETE KNOWLEDGE LEVEL .....	3389
<i>Andrea Nettis, Domenico Raffaele, Giuseppina Uva</i>	
SCOUR-INDUCED DYNAMIC PROPERTIES MODIFICATION OF MASONRY ARCH BRIDGES WITH DIFFERENT GEOMETRY .....	3407
<i>Fabrizio Scozzese, Laura Ragni, Enrico Tubaldi, Fabrizio Gara</i>	
INFLUENCE OF THE PIERS' HEIGHT ON THE FRAGILITY ASSESSMENT OF ITALIAN R.C. LINK SLAB BRIDGES .....	3418
<i>Lucia Minnucci, Fabrizio Scozzese, Andrea Dall'Asta, Sandro Carbonari, Fabrizio Gara</i>	
PERFORMANCE-BASED EARTHQUAKE ENGINEERING ANALYSIS OF SHORT-MEDIUM SPAN STEEL-CONCRETE COMPOSITE BRIDGES .....	3430
<i>Daniele Corritore, Fabrizio Paolacci</i>	
SEISMIC VULNERABILITY ANALYSIS OF THE HISTORICAL SS FILIPPO E GIACOMO MASONRY ARCH BRIDGE IN ASCOLI PICENO (ITALY) .....	3445
<i>Graziano Leoni, Fabrizio Gara, Michele Morici</i>	
ROC-BASED PERFORMANCE EVALUATION OF DATA CLEANSING TECHNIQUES FOR FALSE ALARM RISK REDUCTION IN CONTINUOUSLY MONITORED BRIDGES .....	3458
<i>Valentina Giglioni, Enrique García-Macías, Ilaria Venanzi, Laura Ierimonti, Filippo Ubertini</i>	
RC TIED-ARCH BRIDGES: TYPOLOGICAL ANALYSIS FOR THE DEFINITION OF RETROFIT INTERVENTIONS .....	3470
<i>Valentina Pernechele, Elisa Saler, Francesca da Porto, Claudio Modena</i>	



APPLICATION TO AN URBAN BRIDGE STOCK OF A PRIORITIZATION PROCEDURE BASED ON SEISMIC ASSESSMENT COMPARED WITH THE NOVEL ITALIAN GUIDELINES .....	3484
<i>Elisa Saler, Valentina Pernechele, Giovanni Tecchio, Francesca da Porto</i>	
ANALYTICAL PROBABILISTIC RESILIENCE ESTIMATION FOR BRIDGES UNDER NEAR-FAULT EARTHQUAKES .....	3499
<i>Yang Liu, Da-Gang Lu, Fabrizio Paolacci</i>	
SIMPLIFIED ANALYTICAL-MECHANICAL METHODOLOGY FOR STRUCTURAL-SEISMIC SAFETY ASSESSMENT OVER TIME OF RC BRIDGES AFFECTED BY CORROSION PHENOMENA .....	3520
<i>Matteo Gentile, Filippo Molaioni, Stefano Pampanin</i>	
REAL-TIME ASSESSMENT OF PERFORMANCE INDICATORS FOR BRIDGES TO SUPPORT ROAD NETWORK MANAGEMENT IN THE AFTERMATHS OF EARTHQUAKE EVENTS .....	3536
<i>Chiara Ormando, Ugo Ianniruberto, Paolo Clemente, Sonia Giovinnazzi, Maurizio Pollino, Vittorio Rosato</i>	
DIAGNOSTICS OF HISTORICAL STEEL BRIDGES: THE CASE OF THE VALENCIAN RAILROAD NETWORK .....	3551
<i>Valentino Sangiorgio, Andrea Nettis, Giuseppina Uva, Juan A. García-Cerezo, Pedro A. Calderón, Humberto Varum, Jose M. Adam</i>	
TOWARDS A UNIFIED SEISMIC- FLOOD HAZARD MODEL FOR RISK ASSESSMENT OF ROADWAY NETWORKS IN GREECE .....	3569
<i>Anna Karatzetzou, Sotiria Stefanidou, Stefanos Stefanidis, Grigorios Tsinidis, Dimitrios Pitilakis</i>	
<b>MS 38: DYNAMIC SOIL-FOUNDATION-STRUCTURE INTERACTION: DEVELOPMENTS AND EMERGING ISSUES</b>	
DYNAMIC CROSS-INTERACTION BETWEEN TWO CLOSELY-SPACED SHALLOW FOUNDATIONS .....	3577
<i>Enza Zeolla, Filomena de Silva, Stefania Sica</i>	
ON THE SITE-AMPLIFICATION AND SOIL-STRUCTURE INTERACTION IN URM STRUCTURES: USE OF FRAGILITY CURVES TO ASSESS THE SIMPLIFIED CODE-APPROACH .....	3589
<i>Andrea Brunelli, Filomena de Silva, Serena Cattari</i>	
ELASTODYNAMIC ANALYSIS OF LATERALLY LOADED PILES: MODIFICATIONS TO A SIMPLIFIED ENERGY APPROACH .....	3605
<i>Jamie J. Crispin, George Mylonakis</i>	
ON THE EFFECTIVENESS OF EXPERIMENTALLY-DERIVED FOUNDATION IMPEDANCE FUNCTIONS .....	3617
<i>Chiara Amendola, Filomena de Silva, Dimitrios Pitilakis, Francesco Silvestri</i>	
NUMERICAL ANALYSIS ON THE INFLUENCE OF DYNAMIC SOIL-STRUCTURE INTERACTION IN SORIA ARCH DAM: A CASE STUDY .....	3633
<i>J.C. Galván, L.A. Padrón, J.J. Aznárez, O. Maeso</i>	
SOIL-CAISSON-BRIDGE PIER-DECK DYNAMIC INTERACTION UNDER STRONG EARTHQUAKES: THE INFLUENCE OF PRIMARY AND SECONDARY SOIL NONLINEARITIES .....	3645
<i>Domenico Gaudio, Sebastiano Rampello</i>	

INFLUENCE OF SCOUR ON DYNAMIC IMPEDANCES OF BRIDGE SHALLOW FOUNDATIONS .....	3658
<i>Christos Antonopoulos, Enrico Tubaldi, Sandro Carbonari, Fabrizio Gara, Francesca Dezi</i>	

KINEMATIC PILE-HEAD BENDING UNDER LARGE EARTHQUAKE-INDUCED SHEAR STRAINS .....	3671
<i>Stefano Stacul, Emmanouil Rovithis, Raffaele Di Laora</i>	

ASPECTS OF SEISMIC SOIL-PILE-STRUCTURE INTERACTION IN SOFT CLAY BY CENTRIFUGE TESTING .....	3685
<i>Maria Iovino, Emmanouil Rovithis, Raffaele Di Laora, Cristiano D'Alterio, Luca de Sanctis, Thejesh K. Garala, Stuart Haigh, Gopal S. Madabhushi</i>	

### **MS 39: THE CONTRIBUTION OF DYNAMIC TESTS AND STRUCTURAL MONITORING ON THE SEISMIC RISK ASSESSMENT AND MITIGATION**

LONG TERM MONITORING OF THE SANTA MARIA DI COLLEMAGGIO BASILICA .....	3697
<i>Angelo Aloisio, Riccardo Cirella, Antonacci Elena, Rocco Alaggio</i>	

AMBIENT VIBRATION TEST ON AN EXISTING PRESTRESSED CONCRETE BRIDGE .....	3720
<i>Alessandra De Angelis, Giacomo Esposito, Giuseppe Maddaloni, Edoardo Cosenza, Maria Rosaria Pecce</i>	

MODAL ANALYSIS OF THE HISTORICAL SS FILIPPO E GIACOMO MASONRY ARCH BRIDGE IN ASCOLI PICENO (ITALY) .....	3731
<i>Fabrizio Gara, Graziano Leoni, Michele Morici</i>	

THE TRACKING OF MODAL PARAMETERS FOR A REINFORCED CONCRETE BUILDING DURING LOW-MEDIUM INTENSITY EARTHQUAKES .....	3743
<i>Davide Arezzo, Vanni Nicoletti, Sandro Carbonari, Fabrizio Gara</i>	

FIRST RESULTS OF LONG-TERM MONITORING OF PORTICO VARANO IN THE CAMERINO DUCAL PALACE (ITALY) .....	3752
<i>Leonardo Cipriani, Andrea Dall'Asta, Graziano Leoni, Michele Morici, Alessandro Zona</i>	

DEVELOPMENT OF LOW COST SENSORS FOR MONITORING OF STRUCTURES .....	3762
<i>Giuseppe Maddaloni, Alessandra De Angelis, Francesco Minicozzi, Claudio Martino, Maria Rosaria Pecce</i>	

CALIBRATION OF NUMERICAL MODELS TO SUPPORT SHM: THE CONSOLI PALACE OF GUBBIO, ITALY .....	3778
<i>Serena Cattari, Daniele Sivori, Sara Alfano, Laura Ierimonti, Nicola Cavalagli, Ilaria Venanzi, Filippo Ubertini</i>	

### **MS 40: ARTIFICIAL INTELLIGENCE & MACHINE LEARNING IN DESIGN AND ASSESSMENT OF STRUCTURES**

RAPID DESIGN OF R/C COLUMNS USING MACHINE LEARNING TECHNIQUES .....	3795
<i>Vassilis Papanikolaou, Aristotelis Charalampakis</i>	

DEVELOPMENT OF A NEW FUNDAMENTAL PERIOD FORMULA BY CONSIDERING SOIL-STRUCTURE INTERACTION WITH THE USE OF MACHINE LEARNING ALGORITHMS .....	3801
<i>Vicky-Lee Taljaard, Dewald Z. Gravett, Christos Mourtas, George Markou, Nikolaos Bakas, Manolis Papadrakakis</i>	
PREDICTING THE SHEAR CAPACITY OF REINFORCED CONCRETE SLENDER BEAMS WITHOUT STIRRUPS BY APPLYING ARTIFICIAL INTELLIGENCE ALGORITHMS .....	3810
<i>Zelda Spijckerman, Nikolaos Bakas, George Markou, Manolis Papadrakakis</i>	
STRUCTURAL DAMAGE PREDICTION UNDER SEISMIC SEQUENCE USING NEURAL NETWORKS .....	3820
<i>Petros C. Lazaridis, Ioannis E. Kavvadias, Konstantinos Demertzis, Lazaros Iliadis, Antonios Papaleonidas, Lazaros K. Vasiliadis, Anaxagoras Elenas</i>	
AUTOMATED ESTIMATION OF BUILDING HEIGHT THROUGH IMAGE PROCESSING .....	3837
<i>Pietro Carpanese, Marco Donà, Francesca da Porto</i>	
MACHINE LEARNING TECHNIQUES FOR THE ESTIMATION OF LIMIT STATE THRESHOLDS AND BRIDGE-SPECIFIC FRAGILITY ANALYSIS OF R/C BRIDGES .....	3848
<i>Sotiria Stefanidou, Vassilis Papanikolaou, Elias Paraskevopoulos, Andreas Kappos</i>	
LINKS OF AESTHETIC VALUE OF MULTI-CURVATURE ARTIFACTS, WITH THEIR STRUCTURAL BEHAVIOR, UTILIZING MACHINE LEARNING ALGORITHMS .....	3857
<i>Nikolaos Bakas, Neofytos Christofi, John Bellos, Dimitrios Antoniou, George Markou</i>	
PERFORMANCE AND SCALABILITY OF DEEP LEARNING MODELS TRAINED ON A HYBRID SUPERCOMPUTER: APPLICATION IN THE PREDICTION OF THE SHEAR STRENGTH OF SLENDER RC BEAMS .....	3878
<i>Nikolaos Bakas, George Markou, Dimos Charmpis, Kyriakos Hadjiyiannakou</i>	
PREDICTION OF THE EIGENPERIODS OF MDOF SHEAR BUILDINGS USING NEURAL NETWORKS .....	3894
<i>Vagelis Plevris, German Solorzano</i>	
 <b>MS 41: SEISMIC PERFORMANCE OF STRUCTURES WITH ISOLATION AND/OR ENERGY DISSIPATION DEVICES</b>	
SEISMIC PERFORMANCE OF STRUCTURES EQUIPPED WITH BRB .....	3912
<i>Paolo Castaldo, Enrico Tubaldi, Laura Gioiella</i>	
EFFECT OF LEAD RUBBER BEARING (LRB) MODELING TECHNIQUE ON THE SEISMIC RESPONSE OF BASE-ISOLATED BRIDGES .....	3930
<i>Vahid Aghaeidoost, Ahm Muntasir Billah</i>	
AN ADVANCED MODEL FOR THE FLUID VISCOUS DAMPER BRITTLE FAILURE .....	3942
<i>Laura Gioiella, Fabrizio Scozzese, Enrico Tubaldi, Laura Ragni, Andrea Dall'Asta</i>	
SEISMIC PERFORMANCE OF STEEL MRFS RETROFITTED WITH BRBS: INFLUENCE OF THE DESIGN DECISIONS FOR THE DEVICES .....	3957
<i>Fernando Gutiérrez-Urzuá, Fabio Freddi</i>	

EXPERIMENTAL INVESTIGATION OF SPHERICAL RUBBER SEISMIC ISOLATION BEARINGS .....	3970
<i>Antonios Katsamakas, Gabriel Belser, Michalis Vassiliou, M. Blondet, Božidar Stojadinovic</i>	
EXPERIMENTAL SEISMIC POST-TENSIONING PERFORMANCE AND LONG-TERM EFFECTS OF A POST-TENSIONED TIMBER FRAMED MODEL WITH DISSIPATIVE SYSTEMS .....	3982
<i>Antonio Di Cesare, Felice Carlo Ponzo, Nicla Lamarucciola, Domenico Nigro</i>	
EXPERIMENTAL COMPARISON BETWEEN FLAT AND CURVED SLIDING CONDITIONS FOR THE RESPONSE EVALUATION OF CURVED SURFACE SLIDER DEVICES .....	3992
<i>Alberto Pavese, Marco Furinghetti</i>	
THE NEW CAMERINO UNIVERSITY RESEARCH CENTER: DESIGN OF THE BASE-ISOLATED BUILDING AND DYNAMIC TESTING .....	4005
<i>Andrea Dall'Asta, Graziano Leoni, Fabio Micozzi, Laura Gioiella, N. Ceccolini, Laura Ragni</i>	
VARIATION IN RESPONSE OF A BRIDGE SEISMICALLY ISOLATED WITH LRBS UNDER THE EFFECT OF LOW AMBIENT TEMPERATURE .....	4015
<i>Esengul Cavdar, Volkan Karuk, Gokhan Ozdemir</i>	
SEISMIC PROTECTION OF MULTI-STORY STRUCTURES WITH NOVEL VIBRATION ABSORPTION DEVICES COMBINING NEGATIVE STIFFNESS AND INERTER .....	4026
<i>Konstantinos Kapasakalis, Georgios Florakis, Ioannis Antoniadis, Evangelos Sapountzakis</i>	
MULTI-LEVEL OPTIMISATION OF NONLINEAR VISCOUS DAMPERS FOR SEISMIC RETROFIT OF SUBSTANDARD STEEL FRAMES .....	4046
<i>Dario De Domenico, Iman Hajirasouliha</i>	
SEISMIC RETROFIT OF EXISTING PRECAST RC BUILDINGS WITH DISSIPATIVE DEVICES BASED ON CARBON WRAPPED STEEL TUBES .....	4058
<i>Lucia Praticò, Andrea Vittorio Pollini, Devis Sonda, Nicola Buratti</i>	
METAMODELING CHOICES FOR SEISMIC VULNERABILITY ASSESSMENT OF BRB-RETROFITTED LOW-DUCTILITY RC FRAMES .....	4078
<i>Jayadipta Ghosh, Fabio Freddi</i>	
NUMERICAL INVESTIGATION OF RUBBER BEARINGS WITH LOW SHAPE FACTOR UNDER SEISMIC EXCITATION .....	4091
<i>Alessandra Orfeo, Enrico Tubaldi, Alan Muhr, Daniele Losanno</i>	
INELASTIC RESPONSE MODES OF SEISMICALLY ISOLATED STRUCTURES: FAILURE OF THE ISOLATORS OR DAMAGE IN THE ISOLATED STRUCTURE? .....	4100
<i>Anastasios Tsiavos, Tomislav Markić, David Schlatter, Božidar Stojadinović</i>	
 <b>MS 42: ADVANCES IN MODEL REDUCTION TECHNIQUES OF COMPUTATIONAL AND STRUCTURAL DYNAMICS</b>	
A NEW PARALLEL ALGORITHM FOR THE OPTIMUM EMBEDDED REBAR MESH GENERATION FOR LARGE-SCALE REINFORCED CONCRETE STRUCTURES .....	4111
<i>Dewald Gravett, George Markou</i>	

ON THE APPLICATION OF GENERALISED SCHUR COMPLEMENTS TO SUBSYSTEM-LEVEL VARIABILITY QUANTIFICATION .....	4120
<i>Vladimir Yotov</i>	

#### **MS 43: ANALYSES AND DESIGN OF STEEL JOINTS UNDER CYCLIC ACTION**

BEHAVIOUR OF LAP SHEAR RIVETED CONNECTIONS WITH CONSTRUCTIONAL IMPERFECTIONS .....	4134
<i>Aldo Milone, A. De Martino</i>	

BEHAVIOR OF INNO3D JOINTS UNDER MONOTONIC AND CYCLIC LOADING .....	4142
<i>Arash Poursadrollah, A. De Martino</i>	

DESIGN AND ANALYSIS OF FREEDAM FRAMES: COMPARISON WITH TRADITIONAL CONNECTIONS .....	4149
<i>Maria Maglio, Camilla Naddei, Elide Nastri, Rosaria Russo, Paolo Todisco</i>	

COMPONENT MODELLING OF CONNECTIONS BETWEEN CIRCULAR-HOLLOW-SECTIONS AND THROUGH- ALL MEMBERS .....	4177
<i>A. Saldutti, Sabatino Di Benedetto, Massimo Latour, Gianvittorio Rizzano</i>	

SEISMIC RESPONSE OF INNOVATIVE CFS WALLS BRACED WITH UHS STEEL BARS: EXPERIMENTAL INVESTIGATION .....	4185
<i>Alessia Campiche</i>	

VALIDATION OF NOVEL SEISMIC DESIGN CRITERIA FOR LIGHTWEIGHT STEEL BUILDING IN EUROPE .....	4199
<i>Sarmad Shakeel, Marica Navarra, Alessia Campiche</i>	

BEHAVIOUR OF T-STUB UNDER MODE 2 AND 3 WITH HV AND HR BOLTS .....	4212
<i>Roberto Tartaglia, Mario D'Aniello</i>	

INFLUENCE OF THE JOINT BEHAVIOUR ON THE PERFORMANCE OF ORTHOGONAL EXOSKELETONS FOR SEISMIC RETROFIT .....	4219
<i>Roberto Tartaglia, Gianmaria Di Lorenzo, Antonio Formisano, Raffaele Landolfo</i>	

#### **Thematic Sessions**

##### **TS 5: DYNAMICS OF CONCRETE AND MASONRY STRUCTURES**

EVALUATION OF THE SEISMIC BEHAVIOR OF HISTORICAL CHURCHES REINFORCED BY CROSS-LAM ROOF- STRUCTURES .....	4226
<i>Nicola Longarini, Pietro Crespi, Marco Zucca</i>	

SEISMIC RESPONSE OF SEVEN EXISTING REINFORCED CONCRETE CHIMNEYS EQUIPPED WITH TUNED MASS DAMPERS UNDER FIVE STRONG SEISMIC EVENTS .....	4248
<i>Pietro Giuseppe Crespi, Nicola Longarini, Marco Valente, Marco Zucca</i>	

SHAKING TABLE TEST ON THE EFFECTS OF SHEAR WALLS FOR LONG-SPAN KOREAN TRADITIONAL TIMBER STRUCTURE .....	4262
<i>Yeong-Min Kim</i>	
INVESTIGATION OF THE IMPACT OF SEISMIC ZONE TO THE COST OF CONSTRUCTION OF A 5-STOREY R/C BUILDING .....	4272
<i>Theodoros Chrysanidis, Nikolaos Alamanis, Grigorios Papageorgiou, Georgia Kaouri</i>	
FLEXURAL PERFORMANCE OF CONCRETE BEAMS UNDER CYCLIC LOADING .....	4283
<i>Waseem Khan, Saleem Akhtar, Aruna Rawat, Anindya Basu</i>	
A MULTILAYER SHELL ELEMENT FOR NONLINEAR ANALYSIS OF R/C SHEAR WALLS .....	4294
<i>Vassilis Papanikolaou, Christos Karakostas, Konstantinos Morfidis, Emmanouil Baboukas</i>	
COMPARISON OF THE EFFICIENCY OF MINIMUM-THICKNESS CIRCULAR AND PARABOLIC ARCHES FOR VARIOUS GRAVITY CONDITIONS .....	4302
<i>Nicos Kalapodis, Georgios Kampas, Thomas McLean, Christian Malaga-Chuquitaype</i>	
LARGE-DISPLACEMENT RESPONSE OF UNREINFORCED MASONRY STRUCTURES: COMPARISON BETWEEN ANALYTICAL SOLUTIONS AND DEM MODELS INCLUDING OPEN-SOURCE SOFTWARE .....	4317
<i>Igor Bouckaert, Michele Godio, João Pacheco de Almeida</i>	
<b>TS 14: NUMERICAL SIMULATION METHODS FOR DYNAMIC PROBLEMS</b>	
NONLINEAR FINITE ELEMENT MODELS FOR EMBEDDED BASE CONNECTIONS .....	4331
<i>Nicolas Mora Bowen, Pablo Torres Rodas</i>	
LOCAL SCALE DAMPING MODEL FOR REINFORCED CONCRETE ELEMENTS .....	4341
<i>Clotilde Chambreuil, Cédric Giry, Frédéric Ragueneau, Pierre Léger</i>	
NUMERICAL STUDY ON THE DAMPING CHARACTERISTICS OF A SHOCK ABSORBER VALVE UTILIZING DIFFERENT VELOCITIES THROUGH CFD ANALYSIS .....	4353
<i>Yousif Badri, Thaer Syam, Sadok Sassi, Mohammed Hussein, Jamil Renno, Saud Ghani</i>	
ENERGY HARVESTING FROM RAILWAY VIBRATIONS – A NUMERICAL STUDY BASED ON BEAM-ON-ELASTIC-FOUNDATION UNDER QUASI-STATIC LOADING .....	4363
<i>Shahd Elshafei, Mohammed Hussein, Jamil Renno, Asan Mutalif</i>	
IMPACT FACTORS DERIVED FROM INTERNAL FORCES IN TIMOSHENKO BEAMS SUBJECTED TO CONCENTRATED MOVING LOADS .....	4373
<i>Benjamín Pinazo, Salvador Monleón, Carlos Lázaro, Pedro Museros</i>	
ON THE DEVELOPMENT OF A NOVEL APPROACH FOR SIMULATING ELASTIC BEAMS IN DUALSPHYSICS WITH THE USE OF THE PROJECT CHRONO LIBRARY .....	4385
<i>Salvatore Capasso, Bonaventura Tagliafierro, Iván Martínez-Estévez, José M. Domínguez, Joe El Rahi, Vasiliki Stratigaki, Alejandro J.C. Crespo, Rosario Montuori, Peter Troch, Moncho Gómez-Gesteira, Giacomo Viccione</i>	

DIGITAL SIMULATION OF WIND FIELD VELOCITY FOR EVALUATING PROPER STIFFNESS INDICATORS OF WINDOW MULLIONS .....	4400
<i>Gian Felice Giaccu, Antonio Cazzani</i>	
ANALYTICAL/NUMERICAL SOLUTIONS TO THE PROBLEM OF THE DYNAMIC RESPONSE OF AN ELASTIC PLATE ON A CONTINUOUSLY NON-HOMOGENEOUS CROSS-ANISOTROPIC VISCOELASTIC SOIL TO A MOVING LOAD .....	4407
<i>Niki D. Beskou, Edmond V. Muho</i>	
 <b>TS 15: OPTIMUM DESIGN AND CONTROL IN STRUCTURAL DYNAMICS AND EARTHQUAKE ENGINEERING</b>	
OPTIMAL DESIGN OF TID-BASED SYSTEM FOR THE CONTROL OF WIND-INDUCED VIBRATION IN TALL BUILDINGS THROUGH CULTURAL ALGORITHM .....	4428
<i>Luis Lara-Valencia, Mateo Ramírez-Acevedo, José Brito, Daniel Caicedo, Yosef Farbiarz</i>	
A PARAMETRIC ANALYSIS OF THE SEISMIC PERFORMANCE OF BRIDGES AS A FUNCTION OF THE DCFP DEVICE PROPERTIES .....	4439
<i>Paolo Castaldo, Guglielmo Amendola</i>	
SEISMIC PERFORMANCE OF BRIDGES ISOLATED WITH FPS .....	4452
<i>Paolo Castaldo, Guglielmo Amendola</i>	
CRITICAL ACCELERATION, SEISMIC SLIDING DISPLACEMENT AND SMART DESIGN OF CANTILEVER WALLS .....	4467
<i>Loukas C. Katsenlis, Constantine A. Stamatopoulos, Vassilis P. Panoskaltis</i>	
COMPARISON OF CONTROL ALGORITHMS APPLIED TO AN HYBRID MASS DAMPER ATTACHED TO AN WIND TURBINE TOWER .....	4481
<i>Pedro Rocha, Suzana Avila</i>	
PRELIMINARY STUDY OF AN ARDUINO CONTROLLED SHAKE TABLE TO LOW-FREQUENCY TEST .....	4494
<i>Ledymar F. Moreno, Marcus V. G. de Moraes, Suzana M. Avila</i>	
EFFICIENT DAMPER DESIGN METHOD FOR ELASTIC-PLASTIC MDOF STRUCTURES UNDER CONSECUTIVE-LEVEL EARTHQUAKES .....	4508
<i>Hiroki Akehashi, Izuru Takewaki</i>	
DIFFERENTIATION OF THE CONSTRUCTION COST OF A FIFTEEN STOREY R/C BUILDING DEPENDING ON THE SEISMIC HAZARD ZONE .....	4520
<i>Paulina Tselempi, Theodoros Chrysanidis</i>	
DOES THE SEISMICITY OF THE AREA HAVE AN IMPACT ON THE CONSTRUCTION COST OF THE LOAD-BEARING STRUCTURE OF R/C BUILDINGS? .....	4535
<i>Thomas-Erik Makris, Theodoros Chrysanidis</i>	

IMPROVING ENERGY DISSIPATION CAPACITY OF NATURALLY BUCKLING BRACES UNDER LOW-CYCLE FATIGUE LOADS .....	4547
<i>Shadiya Jamshiyas, Kazuhiro Hayashi, Xiaopo Yang, Konstantinos Skalomenos</i>	

## **TS 17: PERFORMANCE-BASED EARTHQUAKE ENGINEERING**

NUMERICAL MODELING OF SLIP RESPONSE OF Laterally SWAYING BRIDGE PIERS' TENSILE REINFORCEMENT .....	4558
<i>Konstantinos G. Megalooikonomou</i>	

SEISMIC RISK ASSESSMENT OF A PROCESS PLANT UNIT ACCOUNTING FOR DYNAMIC INTERACTION .....	4568
<i>George Karagiannakis, Luigi di Sarno</i>	

A COMPARATIVE STUDY ON SEISMIC RESPONSE OF A SUPER HIGH-RISE BUILDING USING CONVENTIONAL AND MODAL PUSHOVER ANALYSIS .....	4582
<i>Xianlong Zhang, Hao Wu, Qiao Yu, Yang Liu, Lingzhi Li, Wannan Xu, Junyan Zhou</i>	

NUMERICAL PARAMETRIC STUDY OF GRILLE-TYPE STEEL CONCRETE COMPOSITE SHEAR WALL FOR SEISMIC REGIONS .....	4593
<i>Tian Wang, Qiao Yu, Hao Wu, Yang Liu, Lingzhi Li, Xianlong Zhang</i>	

SEISMIC RELIABILITY OF BRIDGES ISOLATED WITH FPS .....	4607
<i>Paolo Castaldo, Guglielmo Amendola, Luca Giordano, Diego Gino, Elena Miceli</i>	

INTENSITY MEASURES PROPERTIES AND SELECTION FOR RISK ANALYSIS ON STRUCTURES SUBJECTED TO EARTHQUAKE INDUCED BUILDING POUNDING WITH A NON SMOOTH CONTACT DYNAMICS METHOD .....	4621
<i>Thomas Langlade, David Bertrand, Stéphane Grange, Gabriel Candia, Juan Carlos de la Llera</i>	

ESTIMATION OF DUCTILITY IN ASYMMETRIC-PLAN STRUCTURES .....	4633
<i>Kaan Kaatsiz, Halûk Sucuoğlu</i>	

A MULTI-OBJECTIVE DISPLACEMENT-BASED DESIGN PROCEDURE OF VISCOUS AND HYSTERETIC DAMPED BRACES FOR THE SEISMIC PROTECTION OF RC BUILDINGS .....	4646
<i>Fabio Mazza, Carlo Pasceri</i>	

EFFECT OF THE DAMPING RATIO OF THE NON-STRUCTURAL COMPONENTS ON FLOOR ACCELERATION DEMANDS IN TORSIONALLY IRREGULAR BUILDINGS .....	4660
<i>Ankur Jain, Mitesh Surana</i>	

EXPLORING THE EXPECTED INCREASE OF COSTS AND LOSS REDUCTION BY RAISING THE BAR IN SEISMIC DESIGN: COMPARISON OF ALTERNATIVE DESIGN METHODOLOGIES AND EARTHQUAKE-RESISTANT TECHNOLOGIES .....	4670
<i>Francesca Gentili, Jonathan Ciurlanti, Simona Bianchi, Stefano Pampanin</i>	

SEISMIC RESPONSE OF A TRANSPARENT PAVILION MADE OF STRUCTURAL GLASS .....	4688
<i>Dimitra V. Achillopoulou, Nikoleta K. Stamataki</i>	



ON THE USE OF INSTANTANEOUS POWER FOR NEAR-FAULT RECORD MODIFICATION .....	4697
<i>Esra Zengin, Norman Abrahamson</i>	
SEISMIC DESIGN OF STEEL FRAMES WITH INTENTIONALLY ECCENTRIC INDUCTION-HEAT TREATED STEEL BRACES .....	4706
<i>Thomas Whittall, Konstantinos A. Skalomenos</i>	
AN EFFICIENT RECORD-TRUNCATION SCHEME FOR PULSE-LIKE RECORDS USING A WAVELET-BASED APPROACH .....	4720
<i>Vicky Dimakopoulou, Michalis Fragiadakis, Ioannis Taflampas</i>	
 <b>TS 19: REPAIR AND RETROFIT OF STRUCTURES</b>	
NUMERICAL MODELLING OF SHEAR BOND TESTS ON EXTERNALLY STRENGTHENED MASONRY SPECIMENS ....	4729
<i>Ottavio Tamborrino, Daniele Perrone, Marianovella Leone</i>	
A DISPLACEMENT-BASED DESIGN PROCEDURE OF VISCOUS DAMPED STEEL EXOSKELETONS FOR THE SEISMIC RETROFITTING OF RC FRAMED BUILDINGS .....	4742
<i>Fabio Mazza, Egidio Mollo</i>	
DEBONDING ANALYSIS OF FRCM COMPOSITES FOR STRUCTURAL UPGRADING OF RC STRUCTURES .....	4758
<i>Maria Teresa Cristofaro, Angelo D'Ambrisi, Francesco Focacci, Raffaele Nudo, Gianfranco Stipo, Marco Tanganelli, Mario De Stefano</i>	
NODAL DISSIPATIVE DEVICES FOR SEISMIC PROTECTION OF PRECAST RC STRUCTURES .....	4772
<i>Fabrizio Comodini, Angelo D'Ambrisi, Marco Mezzi</i>	
INVESTIGATION OF THE RESPONSE OF INTERFACES OF CFRP SHEET STRENGTHENING SCHEMES ENHANCED WITH TOUGHENED EPOXY ADHESIVE LAYERS APPLIED IN CORRODED CONCRETE SUBSTRATES .....	4782
<i>Dimitra Achillopoulou</i>	
SEISMIC RETROFITTING OF SINGLE-STORY RC PRECAST BUILDINGS THROUGH A NOVEL METALLIC HYSTERETIC DEVICE .....	4789
<i>Chiara Di Salvatore, Gennaro Magliulo, Maria G. Castellano, Nicola Caterino</i>	
COMPRESSIVE STRENGTH EVALUATION OF BLUE MOSQUE MINARET STONES WITH ULTRASONIC TESTING ....	4800
<i>Gulen Uncu, Şahin Dede, Eser Çaktı</i>	
EXPERIMENTAL INVESTIGATION OF SHEAR STRENGTH OF SOLID BRICK URM WALLS RETROFITTED WITH TRM JACKET .....	4808
<i>Athanasia Thomoglou, Athanasios Karabinis</i>	

## **TS 20: SEISMIC ISOLATION**

METAFoundation AS A NEW APPROACH FOR SEISMIC ISOLATION OF BUILDINGS .....	4816
<i>Stefania Fiore, Domenico Magisano, Giovanni Finocchio, Massimo Chiappini</i>	

SEISMIC PERFORMANCE OF DOUBLE FRICTION PENDULUM BEARINGS UNDER HORIZONTAL AND VERTICAL EXCITATION .....	4824
<i>Ioannis E. Kavvadias</i>	

SEISMIC DEVICES FOR STEEL STORAGE STRUCTURES .....	4834
<i>Marco Simoncelli, Bonaventura Tagliaferro, Rosario Montuori</i>	

ANALYSIS OF THE PARTICLES DISTRIBUTION INFLUENCE ON THE RECYCLED RUBBER PROPERTIES TO BE USED AS A MATRIX OF LOW-COST SEISMIC ISOLATORS .....	4845
<i>Carolina Rojas Cabrera, Lizeth F. Ortega Escobar, Ingrid E. Madera Sierra, Daniele Lossano, Albert R. Ortíz Lasprilla</i>	

## **TS 21: SEISMIC RISK AND RELIABILITY ANALYSIS**

THE EFFECT OF SOIL-STRUCTURE INTERACTION AND LIQUEFACTION ON THE SEISMIC VULNERABILITY OF TYPICAL PORT STEEL LIGHT-FRAME WAREHOUSES .....	4853
<i>Stella Karafagka, Stavroula Fotopoulou, Anna Karatzetzou, Giorgos Malliotakis, Dimitrios Pitilakis</i>	

COMPARATIVE ASSESSMENT OF EMPIRICAL AND MECHANICAL APPROACHES FOR THE ESTIMATION OF THE SEISMIC FRAGILITY OF ORDINARY MASONRY BUILDINGS TYPE IN THE INNER CENTRAL ITALY .....	4869
<i>Ilaria Capanna, Franco Di Fabio, Massimo Fragiocomo</i>	

EVALUATION OF SEISMIC RESILIENCE OF RC-BUILDINGS SUBJECTED TO REPEATED EARTHQUAKE USING RESILIENT INDEX AND FRAGILITY SURFACE FUNCTIONS .....	4880
<i>Moustafa Moufid Kassem, Fadzli Mohamed Nazri, Ahmad Mohamad El-Maissi</i>	

A SIMPLIFIED APPROACH FOR THE VULNERABILITY ASSESSMENT OF REGULAR AND IRREGULAR REINFORCED CONCRETE BIULDINGS AT THE LARGE SCALE .....	4896
<i>Valentina Blasone, Alberto Basaglia, Raffaele De Risi, Flavia De Luca, Enrico Spacone</i>	

## **TS 27: STEEL STRUCTURES**

GENERELIZED MACROELEMENT FOR GEOMETRIC AND MATERIALLY NON-LINEAR ANALYSIS OF STEEL MEMBERS .....	4906
<i>Konstantinos Morfidis</i>	

## **TS 28: STOCHASTIC DYNAMICS**

GAUSSIAN AND NON-GAUSSIAN WIND TUNNEL PROCESSES .....	4926
<i>Marco Di Giovanni, Piero D'Asdia</i>	

RANDOM PROCESS PEAKS PREDICTION: A LITERATURE OVERVIEW .....	4934
<i>Marco Di Giovanni, Piero D'Asdia</i>	
 <b>TS 31: NUMERICAL SIMULATION OF GEOTECHNICAL PROBLEMS</b>	
EFFECT OF SOIL PROFILE CHARACTERISTICS ON THE SEISMIC SLIDING DISPLACEMENT OF SLOPES .....	4946
<i>Loukas C. Katsenis, Constantine A. Stamatopoulos, Vassilis P. Panoskaltsis</i>	
EFFECT OF 1D VERTICAL VARIABILITY OF SHEAR MODULUS ON THE SEISMIC RESPONSE OF SITES .....	4963
<i>Mounia Menoun Hadj Brahim, Hamid Afra</i>	
A PARAMETRIC STUDY OF “WEAK LAYER” EFFECTS ON THE SEISMIC RESPONSE OF LIQUEFIABLE SOIL PROFILES .....	4973
<i>Yannis Tsiapas, Maria Spanea, George Bouckovalas</i>	
COUPLED ANALYSIS OF SEISMIC PILE-TENDON-PLATFORM INTERACTION IN LIQUEFIABLE SEABED .....	4983
<i>Yannis Chaloulos, Yannis Tsiapas, George Bouckovalas, Konstantinos Bazaios</i>	
STATE-OF-THE-ART INVESTIGATION OF WIND TURBINE STRUCTURES BY CONSIDERING THE SOIL- STRUCTURE INTERACTION PHENOMENON .....	4993
<i>Dewald Gravett, George Markou</i>	
MODELLING THE IMPACT OF GAPPING BEHAVIOUR ON MONOPILE MOUNTED OFFSHORE WIND TURBINE DYNAMICS .....	5005
<i>Stephen Williams, Loizos Pelecanos, Antony Darby</i>	
SOIL-STRUCTURE INTERACTION IN THE SEISMIC VULNERABILITY ANALYSIS OF RC BUILDINGS. APPLICATION TO A CASE STUDY BUILDING LOCATED IN SOUTHWESTERN SPAIN .....	5015
<i>Maria-Victoria Requena-Garcia-Cruz, Antonio Morales-Esteban, Percy Durand-Neyra, Emilio Romero-Sanchez</i>	
FREE VIBRATION RESPONSE OF LONG MULTI-SPAN BRIDGES ACCOUNTING FOR SOIL-STRUCTURE INTERACTION .....	5028
<i>Pieter Reumers, Geert Lombaert, Geert Degrande</i>	
THREE DIMENSIONAL DYNAMIC INTERACTION OF ADJACENT FOUNDATIONS ON A HALFSpace WITH LOCAL INHOMOGENITY APPLYING A COUPLED ITM-FEM APPROACH .....	5039
<i>Julian Freisinger, Gerhard Müller</i>	
NUMERICAL ANALYSIS ON SHALLOW FOUNDATIONS LATERAL DISCONNECTION .....	5066
<i>Fausto Somma, Alessandro Flora, Emilio Bilotta, Giulia Viggiani</i>	
INFLUENCE OF THE DYNAMIC SOIL-STRUCTURE INTERACTION IN CONCRETE FRAMES WITH INCORPORATED VISCOUS DAMPERS .....	5078
<i>Andrés Mauricio Cortés Arias, Francisco Peña Ocampo, Orlando Cundumí Sánchez</i>	

COMPUTATIONAL MODELING AND PARAMETRIC STUDY OF PILE GROUPS .....	5093
<i>Mariana Lazarini, Miguel Paula, Manuel Braz-César</i>	

## **TS 32: DYNAMICS OF STEEL AND SLENDER STRUCTURES**

ADVANCES IN COMPUTATIONAL AND ANALYTICAL MODELS FOR COLUMN BASE CONNECTIONS .....	5108
<i>Pablo Torres-Rodas</i>	
INFLUENCE OF EARTHQUAKE MECHANISMS TO THE SEISMIC RESPONSE OF STEEL MOMENT FRAMES .....	5124
<i>Liseth Campos, Pablo Torres-Rodas, Pablo Quinde, Fabricio Yopez</i>	
SEISMIC ACTION COMBINATION RULES FOR THE DESIGN OF AZIMUTH-INDEPENDENT STRUCTURES .....	5134
<i>Nikolaos Karaferis, Dimitrios Vamvatsikos</i>	
INVESTIGATING THE OVERTURNING STABILITY OF UNANCHORED CONTAINERS WITH FINITE ELEMENT SIMULATIONS .....	5142
<i>Stefanos Gkatzogiannis, Peter Knoedel, Thomas Ummenhofer</i>	
GREEN BANK RADIO TELESCOPE: WIND INDUCED EFFECTS ON FEED-ARM .....	5159
<i>Gian Felice Giaccu, Luca Gallisai, Steven White, Richard Prestage, Luca Caracoglia</i>	
PARAMETRIC STUDY OF STEEL COLUMN-BASE CONNECTION SUBJECTED TO BIDIRECTIONAL BENDING AND AXIAL COMPRESSION .....	5165
<i>Md. Asif Bin Kabir, Ahm Muntasir Billah</i>	

## **TS 33: AEROELASTICITY, SOUND AND VIBRATION AND BRIDGE DYNAMICS**

GEOMETRICALLY NON-LINEAR FREE IN-PLANE VIBRATION OF FUNCTIONALLY GRADED CIRCULAR ARCH WITH UNIFORM CROSS SECTION .....	5179
<i>Omar Outassafte, Ahmed Adri, Yassine El Khouddar, Said Rifai, Rhali Benamar</i>	
ANALYSIS OF GEOMETRICALLY NON-LINEAR FREE VIBRATIONS OF FUNCTIONAL GRADED BEAMS IN A THERMAL ENVIRONMENT .....	5191
<i>Yassine El Khouddar, Ahmed Adri, Omar Outassafte, Issam El Hantati, Said Rifai, Rhali Benamar</i>	
PERSPECTIVES ON THE ACCELERATION OF THE NUMERICAL ASSESSMENT OF FLUTTER AND BUFFETING RESPONSE OF BRIDGE DECKS .....	5201
<i>Julien Heremans, Anass Mayou, Vincent Denoël</i>	
SIMULATING LOW FREQUENCY SOUND TRANSMISSION LOSS OF MOUNTED PANELS .....	5214
<i>Moris Kalderon, Andreas Paradeisiotis, Ioannis Antoniadis</i>	
INVESTIGATION OF A METHODOLOGY FOR DESCRIBING FAN BLADE FLUTTER LIMITATIONS INDUCED BY NON-LINEAR FRICTION AT BLADE ROOTS .....	5232
<i>Nicolas Ombret, Maxime De Pret, Alain Dugeai, Fabrice Thouverez, Laurent Blanc, Thomas Berthelon</i>	

GEOMETRICALLY NON-LINEAR FREE IN-PLANE VIBRATION OF STEPPED CIRCULAR ARCH .....	5255
<i>Omar Outassafte, Ahmed Adri, Yassine El Khouddar, Said Rifai, Rhali Benamar</i>	
SIMPLE AND COMPLEX MODELLING OF SEAT-TYPE ABUTMENT-BACKFILL SYSTEMS .....	5266
<i>Ioannis G. Mikes, Andreas J. Kappos</i>	
INFLUENCE OF THE CONTINUITY OF THE BALLASTED TRACK ON THE DYNAMIC RESPONSE OF A SIMPLY SUPPORTED HIGH SPEED RAILWAY BRIDGES .....	5283
<i>Said El Hankari, Rachid Dkiouak, Khalid Roky</i>	
A FRAMEWORK ON THE DYNAMIC RESPONSE OF TALL STRUCTURES TO NON-STATIONARY WIND USING DESIGN SPECTRUM .....	5299
<i>Jing Song, Pedro Martinez-Vazquez, Konstantinos A. Skalomenos</i>	
 <b>TS 34: NONLINEAR AND IMPACT DYNAMICS</b>	
GEOMETRICALLY NONLINEAR FORCED TRANSVER VIBRATIONS ANALYSIS OF TAPERED EULER-BERNOULLI BEAMS .....	5307
<i>Issam El Hantati, Ahmed Adri, Hatim Fakhreddine, Said Rifai, Rhali Benamar</i>	
POWDER SNOW IMPACT OF TALL VIBRATING STRUCTURES .....	5318
<i>Andrin Caviezel, Stefan Margreth, Kseniya Ivanova, Betty Sovilla, Perry Bartelt</i>	
GEOMETRICALLY NONLINEAR FREE VIBRATIONS OF FULLY CLAMPED MULTI-STEPPED BEAMS CARRYING MULTIPLE MASSES .....	5331
<i>Issam El Hantati, Ahmed Adri, Hatim Fakhreddine, Said Rifai, Rhali Benamar</i>	
COMPARISON BETWEEN DYNAMIC NONLINEAR ANALYSIS WITH ASCE 7-10 AND ASCE 7-16 IN CONCRETE FRAMES WITH VISCOUS DAMPERS INCORPORATED .....	5342
<i>Juan Sebastián Cundumí García, Orlando Cundumí Sánchez</i>	
FRAGILITY CURVES DEFINITION OF EXISTING REINFORCED CONCRETE BUILDINGS DESIGNED FOR GRAVITY LOADS .....	5357
<i>Alberto Basaglia, Marco Terrenzi, Enrico Spacone</i>	
STOCHASTIC NONLINEAR RESPONSE OF STRUCTURAL SYSTEMS ENDOWED WITH SINGULAR MATRICES SUBJECT TO COMBINED PERIODIC AND STOCHASTIC EXCITATIONS .....	5367
<i>Ioannis P. Mitseas, Peihua Ni, Vasileios C. Fragkoulis, Fan Kong, Michael Beer, Michalis Fragiadakis</i>	

## ANALYTICAL INVESTIGATION OF THE TENSILE EXPERIMENTS MODELING THE ELONGATION DEGREE OF R/C WALLS FOR STUDYING THE LATERAL BUCKLING PHENOMENON

Theodoros A. Chrysanidis<sup>1</sup>, Vassilis P. Panoskaltis<sup>1</sup>

<sup>1</sup> Demokritos University of Thrace  
University Campus Xanthi-Kimmeria, P.C. 67100, Xanthi, Greece  
theodoros\_gr@yahoo.com, vpanoska@civil.duth.gr

---

### Abstract

*In the context of the present work, the influence of the degree of tension on the phenomenon of transverse instability of reinforced concrete walls is examined. The present investigation is basically analytical but it contains experimental results of 4 test specimens published from the first author in the past. These specimens simulate the extreme boundary edges of structural walls. All columns simulate only the extreme reinforced areas of the walls, in order to study the basic mechanism of the phenomenon. The detailing of the specimens consists of 4 rebars with a diameter of 8 mm for each bar. The geometric dimensions are the same for all specimens. What differentiates the specimens from each other is the degree of tension they have sustained. More specifically, the tensile degrees used are 10%, 20%, 30%, 50%. The loading stages of each specimen for all specimens are as follows: (a) Uniaxial central tensile loading on each test specimen, (b) Uniaxial central compression loading on each specimen till its failure due to buckling or due to an excess of its cross-section compressive strength. The present study focuses on the tensile loading stage only. Extreme tensile strains are also used, e.g., 30% and 50%, to take into account the cases of extreme seismic excitations. First, the experimental results from a previous publication are presented and afterwards they are followed by the numerical investigation of these 4 specimens using appropriate finite element software. Useful conclusions are drawn regarding the precision of the experimental tests investigating the influence of the degree of elongation on the phenomenon of transverse buckling. These conclusions are substantiated both experimentally and analytically, as the results of the tensile experiments are compared with the corresponding results of the analytical investigation.*

**Keywords:** Degree of elongation, Lateral buckling, Structural walls, Tensile loading

---

## 1 INTRODUCTION

Structural behavior and soil-structure interaction has troubled engineers worldwide for various types of structures [1]–[10]. Structural walls play an important role in the structures' behavior and safety against horizontal loads and especially against earthquake cyclic loading [11], [12]. It is well-known that the vast part of seismic loading is resisted by seismic walls in reinforced concrete structures [13]–[26]. One critical mode of failure which can appear during earthquake cyclic loading is the out-of-plane buckling of R/C shear walls [27]–[36]. It has been observed that such type of failure is so critical that can lead to partial or total collapses of multi-storey reinforced concrete buildings [37]. This phenomenon can appear when the boundary edges of seismic walls have sustained a large size of tensile loading during the first semi-cycle of seismic loading and then are subjected to a compressive loading during the second semi-cycle of earthquake loading [38]–[41]. Transverse buckling appears when the cracks formed during the first stage of tensile loading have such a large width that makes it impossible to be closed during the second stage of compressive loading [42]–[51]. The fact that the cracks cannot close when compression loading is applied leads to the wall buckling transverse to its plane. This phenomenon is called in international bibliography lateral buckling or transverse buckling or out-of-plane buckling and sometimes instead of using the word “buckling”, the word “instability” is preferred.

The present study uses experimental tests performed in the past by the first author trying to investigate the mechanical parameters affecting the transverse instability [28]. These specimens were subjected to tensile strain equal to 10‰, 20‰, 30‰ and 50‰. In the framework of the present work, the four specimens subjected to tensile loading are modelled using finite element software and the results of this analytical investigation are compared to the existing experimental results concerning the tensile loading stage. It is noted that the experiments have taken place in the Laboratory of Strength of Materials of Aristotle University of Thessaloniki and the analysis of the results has taken place in Demokritos University of Thrace.

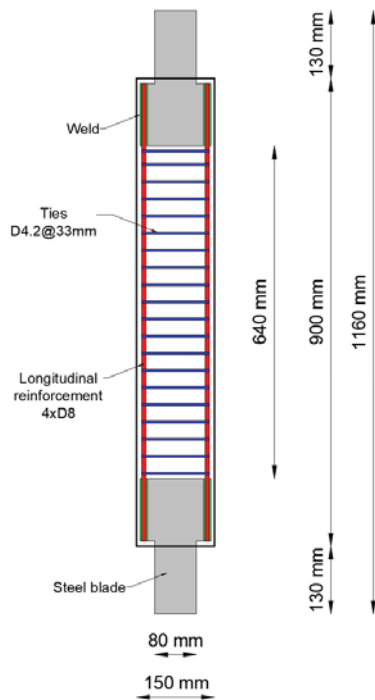
## 2 EXPERIMENTAL RESEARCH

### 2.1 Test specimen characteristics

The experimental investigation for the four test specimens has been described in detail by the first author in the past [28]. Figure 1a shows the geometrical characteristics of the four test specimens, while Figure 1b displays the load test setup used for the application of the tensile loading. It is noted the fact that the tensile loading is the first stage of the two loading stages. In the framework of the present study, only the experimental results of the tensile loading stage are compared to the analytical ones. Table 1 shows the test specimens' characteristics.

N/A	Specimen	Dimensions (cm)	Longitudinal reinforcement	Transverse reinforcement	Longitudinal reinforcement ratio (%)	Degree of elongation (‰)
1	L-10	15x7.5x76	4xD8	D4.2@33 mm	1.79	10.00
2	L-20	15x7.5x76	4xD8	D4.2@33 mm	1.79	20.00
3	L-30	15x7.5x76	4xD8	D4.2@33 mm	1.79	30.00
4	L-50	15x7.5x76	4xD8	D4.2@33 mm	1.79	50.00

Table 1: Dimensions of the test specimens.



(a)



(b)

Figure 1: (a) Vertical reinforcement layout, (b) Test setup for tensile loading.

## 2.2 Materials

For all test specimens, materials used for their construction and their characteristics were also described by the first author in the past [28]. Table 2 displays the concrete resistance for all test specimens at 28 days and at the day that the compression test has taken place while Table 3 shows the mechanical properties for the longitudinal steel and the transverse ties.

N/A	Specimen	Concrete cube resistance (28 days) (MPa)	Concrete cube resistance (Compression test day) (MPa)	Concrete cylinder resistance (Compression test day) (MPa)
1	L-10	24.89	28.00	23.00
2	L-20	24.89	28.00	23.00
3	L-30	23.33	25.56	20.56
4	L-50	24.89	28.00	23.00

Table 2: Concrete mechanical properties.

Reinforcement	Yield strength (MPa)	Ultimate strength (MPa)
D8 (Longitudinal reinforcement)	603.77	743.10
D4.2 (Transverse ties)	552.02	670.91

Table 3: Reinforcement mechanical properties.



## 2.3 Experimental results

Each one of the four test specimens has been subjected to a different degree of elongation according to Table 1 and the results published by the first author in the past [28]. Figure 2 displays the shape of test specimens after the uniaxial tensile test has taken place. It is obvious that several cracks of different width have formed after the tensile loading according to the degree of elongation applied to each specimen.

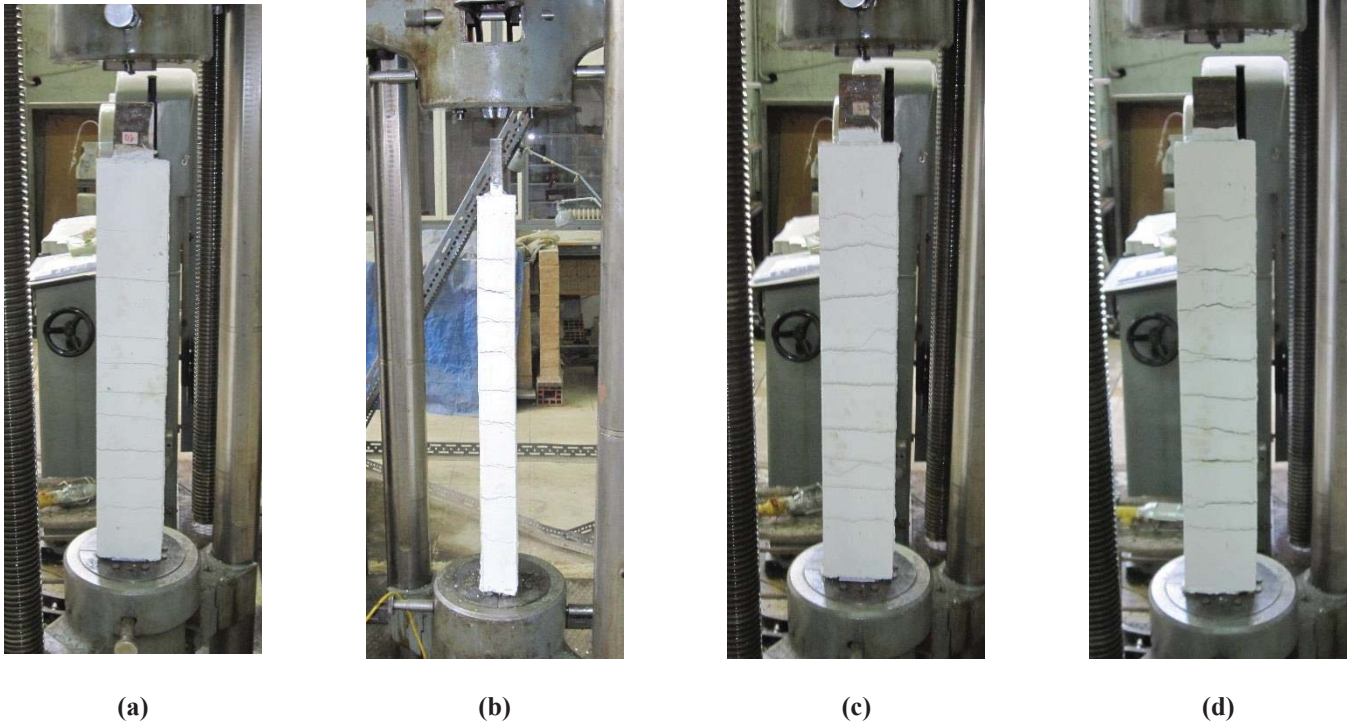


Figure 2: Specimens with low reinforcement ratio after the uniaxial tensile test: (a) L-10, (b) L-20, (c) L-30, (d) L-50

## 3 ANALYTICAL RESEARCH

### 3.1 Modeling of test specimens

The analytical research has taken place using a finite element software. 3D elements were used in this software to model all four test specimens subjected to tensile loading. It is noted, as it has been said before, that the present work focuses on modeling only the first stage of loading; meaning the tensile loading path till certain preselected and different degrees of elongation. For the concrete material, the inelastic concrete model found in the software library of isotropic plasticity has been chosen. For the reinforcement bar material, the properties derived from experiments are inserted in the software to model the inelastic behaviour of reinforcement steel. A bilinear isotropic model has been chosen for the behaviour of rebar steel. The same inelastic model has been selected to model the behaviour of the steel used for the transverse ties. This model is again the bilinear isotropic model. 3D finite elements having an edge of 2 cm are used for the modeling of the concrete column section. Both the longitudinal reinforcement and the transverse ties are modeled using 3D finite elements having a length equal to 1 cm. Figure 3 shows the 3D model of the column either for the whole column section or the reinforcement steel only. The column model is considered fixed at its base.

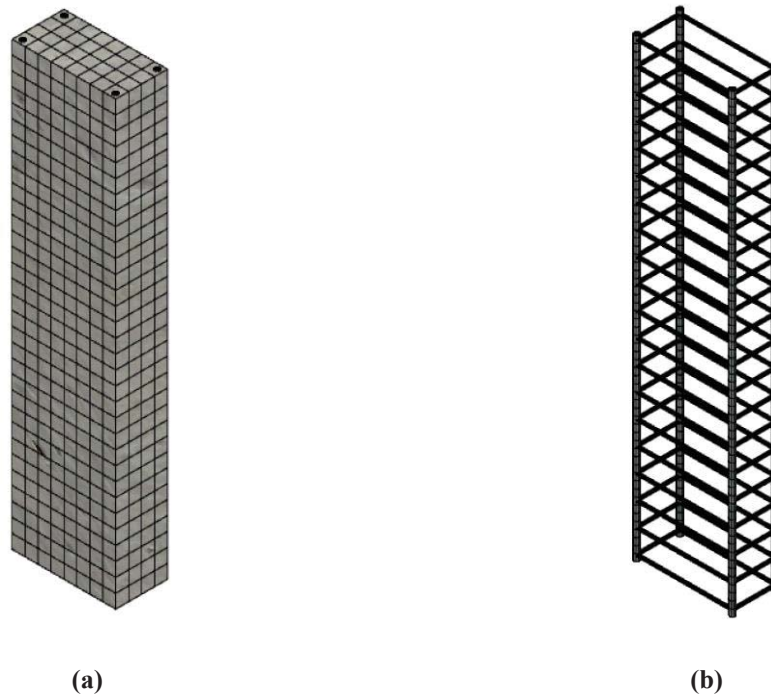


Figure 3: (a) 3D model for column, (b) 3D model for the column reinforcement.

### 3.2 Analytical results

Figure 4 displays the displacement along the column height after the end of the tensile loading test for all four test specimens. The displacement is zero at the fixed column base.

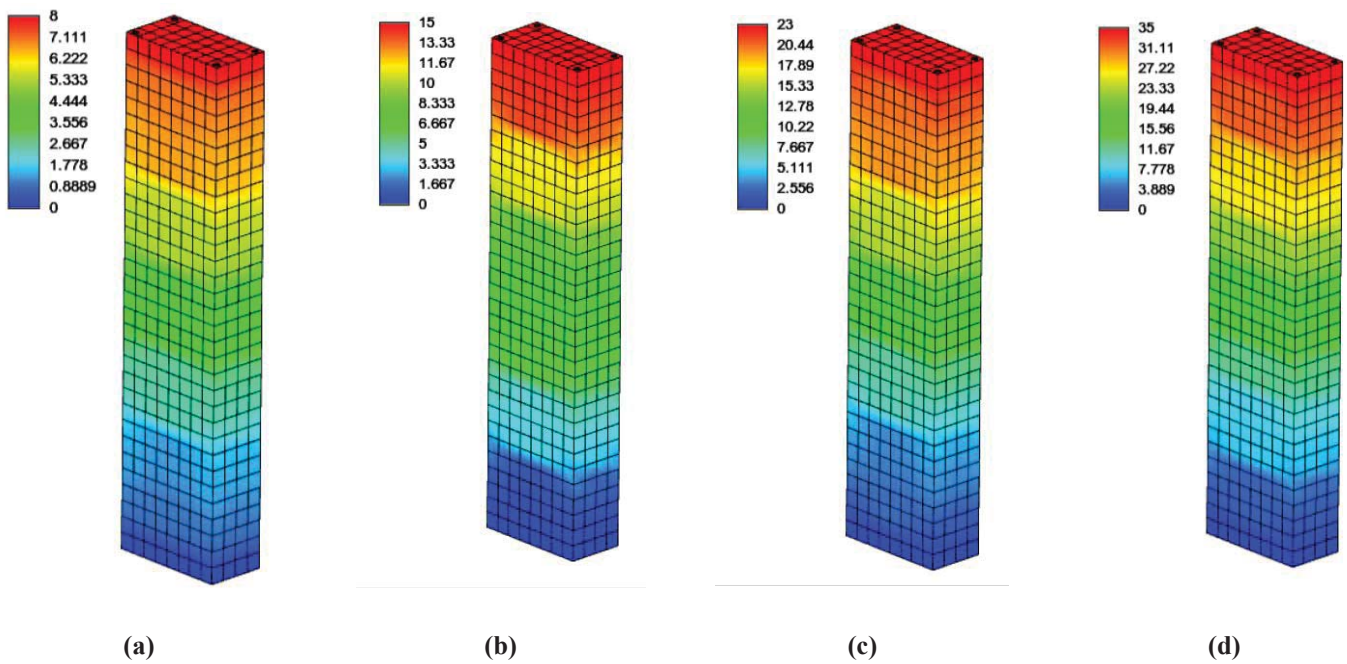


Figure 4: Displacement along the column axis at the end of the tensile test: (a) L-10, (b) L-20, (c) L-30, (d) L-50

## 4 ANALYSIS OF RESULTS

### 4.1 Analytical versus experimental results

A comparison takes place between the load versus elongation diagrams which have resulted from the experimental tensile tests and the tests applied to the analytical models of the four specimens modeling the boundary edges of seismic walls (Figures 5-8).

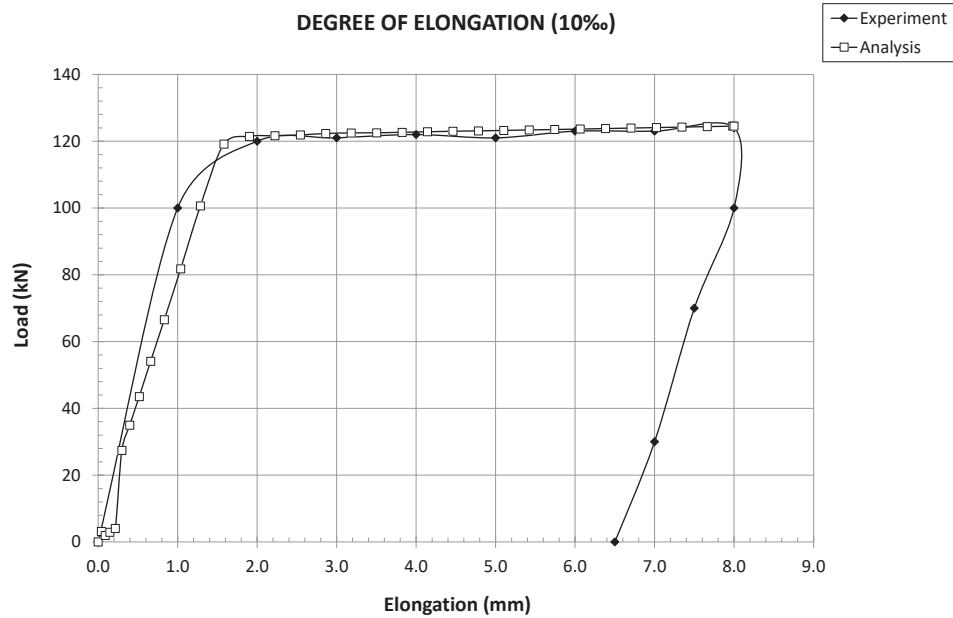


Figure 5: Load versus elongation diagram for specimen L-10.

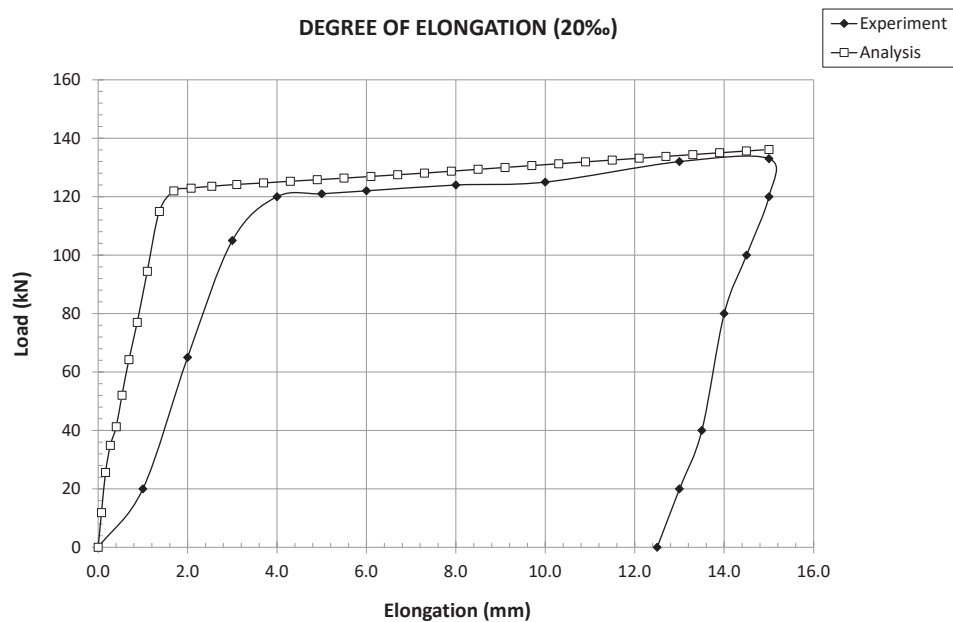


Figure 6: Load versus elongation diagram for specimen L-20.

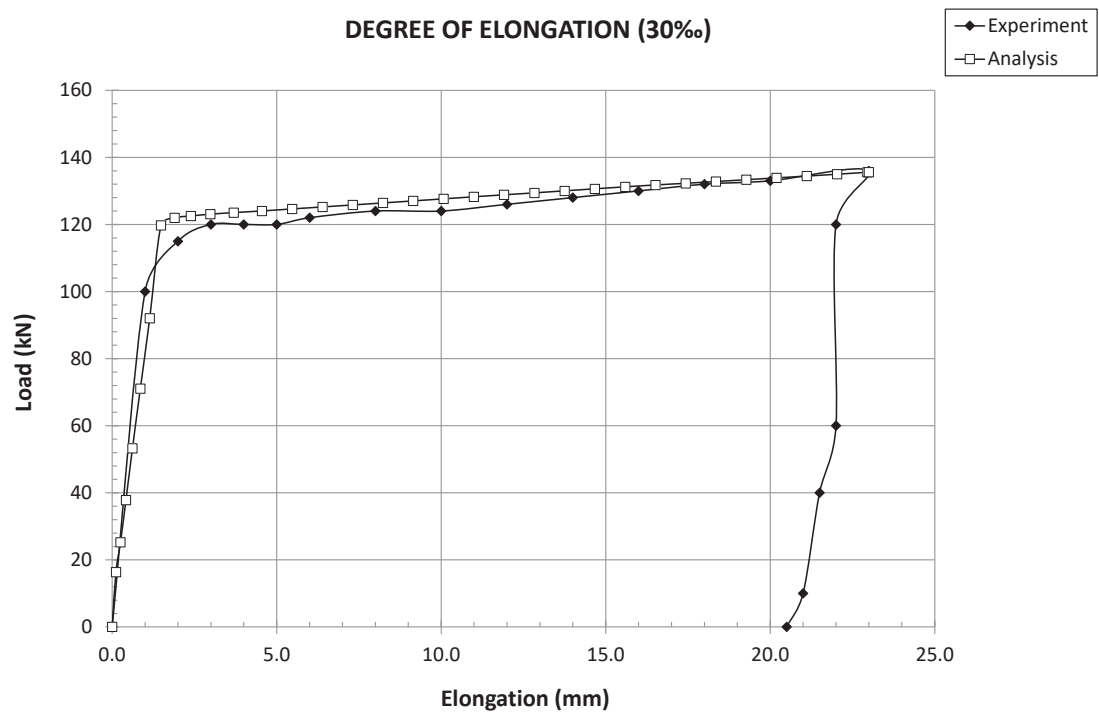


Figure 7: Load versus elongation diagram for specimen L-30.

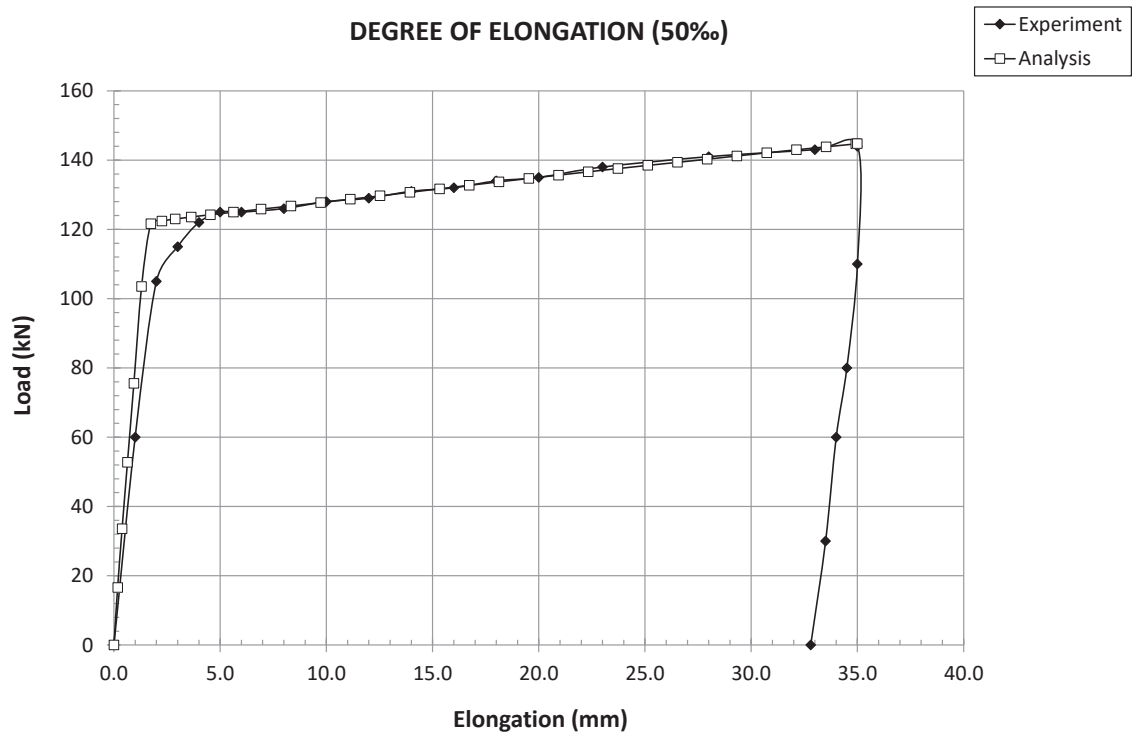


Figure 8: Load versus elongation diagram for specimen L-50.

## 4.2 Analysis of results

The analysis of the previous results leads to the following:

1. Figure 4 displays the displacement along the vertical axis which is the Z-axis and coincides with the height of the prism specimens modeling the boundary edges of structural walls. It can be seen that each specimen is strained till the preselected displacement according to the preselected degree of elongation.
2. The vertical displacement is zero at the base of the prisms since the base is rigid (Figure 4). The maximum vertical displacement is found towards the upper part of the specimens where the tensile load is applied. The same phenomenon takes place in the tensile experiments where the tensile load is applied at the upper part of the test specimens while at the bottom part the test specimens are held rigidly by the grapples of the tensile machine.
3. It is obvious that there is an almost perfect correlation between the experimental and the analytical results for all test specimens (Figures 5-8). The elastic branch is the same both in the experiments and the analysis. The same thing applies for the plastic branch after the yielding. The plastic branch of the analyses coincides with the plastic branch from the tensile tests.
4. Yielding takes place almost at the same load both for the tests and the analyses for all test specimens.
5. There is only one exception concerning test specimen L-20 (Figure 6). The plastic branch for this specimen is almost the same both for the experiment and the relevant analysis. There is a noticeable deviation for the elastic branch of the diagrams. This can be explained probably due to a slip that might have taken place during the onset of the application of the tensile load for this specimen. Probably, an initial slip and a relevant error to the measured elongation might have led to an experimental elastic branch with smaller inclination.
6. The effective length of the test specimens is the one which has been modelled only since this is the length in which the tensile elongation appears (Figure 1). The effective length is equal to 640 mm (Figure 1).

## 5 CONCLUSIONS

The results stemmed from the tensile experiments and the relevant analytical procedures concerning the behavior of the boundary edges of seismic walls under the tensile stage of load application has led to the following conclusions:

1. There is an almost excellent correlation between the experimental results and the analytical results concerning the tensile loading. The analysis has taken place using 3D finite elements.
2. The elastic branch, the yielding point and the plastic branch coincide almost perfectly for almost all specimens except one where the deviation noticed for the elastic branch only can be attributed probably to slip effects and thus, to deviations concerning the measuring of the elongation.
3. The degree of elongation is a very crucial mechanical parameter that affects tremendously the behavior of the boundary edges of structural walls and its investigation has to be applied in the proper and right way following a correct procedure. The convergence between the experimental and the numerical results proves that the procedure applied, probably, follows the right path.
4. A future research could and should model the whole test specimen and not only the effective length in order to simulate even more precisely the experimental behavior.



**REFERENCES**

- [1] N. Alamanis, "Influence of random soil strength properties on the earthquake vulnerability of slopes with embedded oil and natural gas pipelines," *Energy Systems*, 2020, doi: 10.1007/s12667-020-00394-9.
- [2] N. Alamanis and P. Dakoulas, "Investigation on the effect of spatial variability of soil properties on permanent seismic displacements of slopes in load," in *14th Baltic Sea Geotechnical Conference 2020*, 2020.
- [3] N. Alamanis and P. Dakoulas, "Effect of spatial variability of soil properties on the stability and permanent seismic displacements of highway slopes," in *The 17th European Conference on Soil Mechanics and Geotechnical Engineering*, 2019.
- [4] N. Alamanis and P. Dakoulas, "Effect of the spatial variability of soil properties on the seismic vulnerability of slopes with embedded oil and natural gas pipelines," in *6th International Conference on "Energy, Sustainability and Climate Change" (ESCC 2019)*, 2019.
- [5] N. Alamanis and P. Dakoulas, "Vulnerability of soil slopes against seismic damage based on the effect of spatial variability of soil properties on the development of permanent seismic displacements," in *International Conference on Research in Engineering, Technology and Science*, 2019.
- [6] A. Mouratidis, C. Daniilidou, and G. Papageorgiou, "Evaluation of pavement maintenance and strengthening techniques," in *Bituminous Mixtures and Pavements VII, Proceedings of the 7th International Conference on Bituminous Mixtures and Pavements (ICONFBMP 2019)*, 2019, pp. 516–523.
- [7] N. Alamanis, G. Papageorgiou, P. Chantzopoulou, and I. Chouliaras, "Investigation on the influence of permeability coefficient  $k$  of the soil mass on construction settlements. Cases of infrastructure settlements in Greece," *Wseas Transactions on Environment and Development*, vol. 15, pp. 95–105, 2019.
- [8] G. Papageorgiou, N. Alamanis, I. Chouliaras, and P. Kapsali, "Decision making for designing infrastructure projects: The case of the city of Larissa, Greece," *Journal of Engineering and Architecture*, vol. 7, no. 1, pp. 115–125, 2019, doi: 10.15640/jea.v7n1a13.
- [9] G. Papageorgiou and A. Mouratidis, "Defining threshold values for pavement surface characteristics," *Proceedings of the Institution of Civil Engineers (ICE) - Transport*, vol. 168, no. 3, pp. 223–230, 2015, doi: 10.1680/tran.12.00028.
- [10] G. Papageorgiou and A. Mouratidis, "A mathematical approach to define threshold values of pavement characteristics," *Structure and Infrastructure Engineering*, vol. 10, no. 5, pp. 568–576, 2014.
- [11] K. Christidis and K. Trezos, "Experimental investigation of existing non-conforming RC shear walls," *Engineering Structures*, vol. 140, no., pp. 26–38, 2017, doi: <https://doi.org/10.1016/j.engstruct.2017.02.063>.
- [12] T. Terzioglu, K. Orakcal, and L. M. Massone, "Cyclic lateral load behavior of squat reinforced concrete walls," *Engineering Structures*, vol. 160, 2018, doi: 10.1016/j.engstruct.2018.01.024.
- [13] J. W. Wallace, "Performance-Based Design of Tall Reinforced Concrete Core Wall

- Buildings,” *Geotechnical, Geological and Earthquake Engineering*, vol. 17, pp. 279–307, 2010, doi: 10.1007/978-90-481-9544-2\_12.
- [14] R. Serrette and D. P. Nolan, “Reversed Cyclic Performance of Shear Walls with Wood Panels Attached to Cold-Formed Steel with Pins,” *Journal of Structural Engineering*, vol. 135, no. 8, pp. 959–967, 2009, doi: 10.1061/(asce)st.1943-541x.0000037.
- [15] H. S. Lee and D. W. Ko, “Seismic response characteristics of high-rise RC wall buildings having different irregularities in lower stories,” *Engineering Structures*, vol. 29, no. 11, pp. 3149–3167, 2007, doi: 10.1016/j.engstruct.2007.02.014.
- [16] X. Lu and Y. Chen, “Modeling of Coupled Shear Walls and Its Experimental Verification,” *Journal of Structural Engineering*, vol. 131, no. 1, pp. 75–84, 2004, doi: 10.1061/(asce)0733-9445(2005)131:1(75).
- [17] M. Hassan and S. El-Tawil, “Inelastic dynamic behavior of hybrid coupled walls,” *ASCE Journal of Structural Engineering*, vol. 130, no. 2, pp. 285–296, 2004, doi: 10.1061/40616(281)83.
- [18] L. M. Massone and J. W. Wallace, “Load-Deformation Responses of Slender Reinforced Concrete Walls,” *ACI Structural Journal*, vol. 101, no. 1, pp. 103–113, 2004.
- [19] P. Riva, A. Meda, and E. Giuriani, “Cyclic behaviour of a full scale RC structural wall,” *Engineering Structures*, vol. 25, no. 6, pp. 835–845, 2003, doi: 10.1016/S0141-0296(03)00020-8.
- [20] A. Rutenberg, “The seismic shear of ductile cantilever wall systems in multistorey structures,” *Earthquake Engineering and Structural Dynamics*, vol. 33, no. 7, pp. 881–896, 2004, doi: 10.1002/eqe.384.
- [21] Y. Chiou, Y. Mo, F. Hsiao, Y. Liou, and M. Sheu, “Experimental and analytical studies on large-scale reinforced concrete framed shear walls,” *Symposium Paper*, vol. 211, no., pp. 201–222, 2003.
- [22] T. A. Duffey, C. R. Farrar, and A. Goldman, “Low-Rise Shear Wall Ultimate Drift Limits,” *Earthquake Spectra*, vol. 10, no. 4, pp. 655–674, 2003, doi: 10.1193/1.1585792.
- [23] Y. L. Mo, J. Zhong, and T. T. C. Hsu, “Seismic simulation of RC wall-type structures,” *Engineering Structures*, vol. 30, no. 11, pp. 3167–3175, 2008, doi: 10.1016/j.engstruct.2008.04.033.
- [24] I. Ghorbani-Renani, N. Velev, R. Tremblay, D. Palermo, B. Massicotte, and P. Léger, “Modeling and testing influence of scaling effects on inelastic response of shear walls,” *ACI Structural Journal*, vol. 106, no. 3, pp. 358–367, 2009.
- [25] J. D. Aristizabal-Ochoa, “Seismic Behavior of Slender Coupled Wall Systems,” *Journal of Structural Engineering*, vol. 113, no. 10, pp. 2221–2234, 2008, doi: 10.1061/(asce)0733-9445(1987)113:10(2221).
- [26] P. Bisch and A. Coin, “Seismic behaviour of slightly reinforced concrete walls: Experiments and theoretical conclusions,” *Bulletin of Earthquake Engineering*, vol. 5, no. 1, pp. 45–65, 2007, doi: 10.1007/s10518-006-9014-1.
- [27] T. Chrysanidis, “Evaluation of Out-of-Plane Response of R/C Structural Wall Boundary Edges Detailed with Maximum Code-Prescribed Longitudinal

- Reinforcement Ratio,” *International Journal of Concrete Structures and Materials*, vol. 14, no. 1, 2020, doi: 10.1186/s40069-019-0378-4.
- [28] T. Chrysanidis, “Influence of elongation degree on transverse buckling of confined boundary regions of R/C seismic walls,” *Construction and Building Materials*, vol. 211, pp. 703–720, Jun. 2019, doi: 10.1016/J.CONBUILDMAT.2019.03.271.
- [29] T. Chrysanidis and I. Tegos, “Does reinforcement ratio affect displacements due to lateral buckling behavior of concrete walls?,” *International Journal of Applied Engineering Research*, vol. 12, no. 3, pp. 382–388, 2017.
- [30] T. Chrysanidis and I. Tegos, “Influence of elongation degree on out-of-plane buckling of R/C structural walls with a medium high reinforcement ratio,” *International Journal of Civil Engineering and Technology*, vol. 7, no. 4, pp. 358–364, 2016.
- [31] T. Chrysanidis and I. Tegos, “Size of seismic tensile strain and its influence on the displacements due to transverse buckling of ultra-highly reinforced structural walls,” *ARPJ Journal of Engineering and Applied Sciences*, vol. 11, no. 23, pp. 13884–13890, 2016.
- [32] T. Chrysanidis and I. Tegos, “Displacements and mode of failure of medium high reinforced walls due to transverse buckling,” *International Journal of Engineering Development and Research*, vol. 4, no. 3, pp. 628–634, 2016.
- [33] T. Chrysanidis, “Low Reinforced Shear Walls: Displacements and Failure Modes Due to Lateral Buckling,” *International Journal of Science and Engineering Investigations*, vol. 5, no. 55, pp. 143–148, 2016.
- [34] T. Chrysanidis, “Degree of Elongation of Maximum Code-Prescribed Reinforced Walls: Modes of Failure and Displacements of Lateral Buckling Phenomenon,” *International Journal of Trend in Research and Development*, vol. 3, no. 4, pp. 435–440, 2016.
- [35] T. Chrysanidis, “Size of seismic tensile strain and its influence on the lateral buckling of highly reinforced concrete walls,” *IOSR Journal of Mechanical and Civil Engineering*, vol. 11, no. 1, pp. 18–22, 2014, doi: 10.9790/1684-11121822.
- [36] T. Chrysanidis and I. Tegos, “Out-of-plane buckling of highly reinforced seismic walls: Displacements and mode of failure,” *International Journal of Civil Engineering and Technology*, vol. 5, no. 6, pp. 101–107, 2014.
- [37] C. Alarcon, M. Hube, R. Jünemann, and J. de la Llera, “Characteristics and displacement capacity of reinforced concrete walls in damaged buildings during 2010 Chile earthquake,” *Bulletin of Earthquake Engineering*, vol. 13, pp. 1119–1139, 2015, doi: <https://doi.org/10.1007/s10518-015-9727-0>.
- [38] A. Haro, M. Kowalsky, Y. Chai, and G. Lucier, “Boundary elements of special reinforced concrete walls tested under different loading paths,” *Earthquake Spectra*, vol. 34, no. 3, pp. 1267–1288, 2018, doi: 10.1193/081617EQS160M.
- [39] K. Herrick and M. Kowalsky, “Out-of-plane buckling of ductile reinforced structural walls due to in-plane loads,” *Journal of Structural Engineering*, vol. 143, no. 3, pp. 1–15, 2016, doi: 10.1061/(asce)st.1943-541x.0001660.
- [40] Y. Chai and S. Kunnath, “Minimum thickness for ductile RC structural walls,” *Engineering Structures*, vol. 27, no. 7, pp. 1052–1063, Jun. 2005, doi:



- 10.1016/j.engstruct.2005.02.004.
- [41] T. Welt, L. Massone, J. LaFave, D. Lehman, S. McCabe, and P. Polanco, “Confinement behavior of rectangular RC prisms simulating wall boundary elements,” *Journal of Structural Engineering*, vol. 143, no. 4, pp. 1–12, 2017, doi: 10.1061/(asce)st.1943-541x.0001682.
  - [42] T. Chrysanidis and V. Panoskaltsis, “Does the degree of tensile strain have an impact on the cracking behavior of vertical structural elements?,” in *IOP Conference Series: Materials Science and Engineering, 2020 5th International Conference on Civil Engineering and Materials Science (ICCEMS 2020)*, 2020, vol. 897, doi: 10.1088/1757-899X/897/1/012004.
  - [43] T. Chrysanidis and V. Panoskaltsis, “Evaluation of cracking behavior of R/C vertical components reinforced with varying longitudinal reinforcement ratios,” in *Proceedings of the XI International Conference on Structural Dynamics (EURODYN 2020)*, 2020, pp. 3186–3197, doi: 10.47964/1120.9260.18887.
  - [44] T. Chrysanidis and V. Panoskaltsis, “Experimental investigation of the influence of tensile strain on the cracking of R/C vertical structural elements,” in *Proceedings of the XI International Conference on Structural Dynamics (EURODYN 2020)*, 2020, pp. 3174–3185, doi: 10.47964/1120.9259.18582.
  - [45] T. Chrysanidis and I. Tegos, “Influence of elongation degree on the behavior of R/C structural walls with maximum code-prescribed reinforcement ratio,” in *Proceedings of the 170th International Conference on Civil and Environmental Engineering (ICCEE 2017)*, 2017, pp. 8–12.
  - [46] T. Chrysanidis and I. Tegos, “How does degree of elongation affect lateral buckling behavior of seismic walls?,” *American Academic and Scholarly Research Journal*, vol. 7, no. 4, pp. 266–272, 2015.
  - [47] T. Chrysanidis and I. Tegos, “The influence of the degree of elongation to the displacements of structural walls with low-reinforced end-sections,” *American Academic and Scholarly Research Journal*, vol. 7, no. 4, pp. 259–265, 2015.
  - [48] T. Chrysanidis and I. Tegos, “The influence of the degree of elongation to the displacements of seismic walls with maximum code-prescribed reinforcement ratio,” *American Academic and Scholarly Research Journal*, vol. 7, no. 4, pp. 273–279, 2015.
  - [49] T. Chrysanidis, “The influence of the degree of tensile strain to the ultimate strength and mode of failure of seismic walls with low-reinforced end-sections,” *American Academic and Scholarly Research Journal*, vol. 6, no. 4, pp. 337–343, 2014.
  - [50] T. Chrysanidis, “The influence of tensile strain of the high-reinforced end sections of seismic walls to their displacements and mode of failure,” in *Proceedings of the International Conference on Recent Trends in Engineering and Technology – 2014 (IJBRMM’s ICRTET 2014)*, 2014.
  - [51] T. Chrysanidis and I. Tegos, “Does degree of elongation affect displacements of structural walls?,” *American Academic and Scholarly Research Journal*, vol. 6, no. 4, pp. 344–350, 2014.

## ANALYTICAL INVESTIGATION OF THE TENSILE EXPERIMENTS TO PRISMS WITH VARYING LONGITUDINAL RATIO FOR STUDYING THE LATERAL BUCKLING OF R/C WALLS

Theodoros A. Chrysanidis<sup>1</sup>, Vassilis P. Panoskaltzis<sup>1</sup>

<sup>1</sup> Demokritos University of Thrace  
University Campus Xanthi-Kimmeria, P.C. 67100, Xanthi, Greece  
theodoros\_gr@yahoo.com, vpanoska@civil.duth.gr

---

### Abstract

*In the context of the present work, the influence of the longitudinal reinforcement ratio on the phenomenon of lateral buckling of reinforced concrete walls is examined. The present investigation is basically analytical but it contains experimental results of 6 test specimens published from the first author already. These specimens simulate only the extreme boundary edges of structural walls to study the basic mechanism of the transverse instability phenomenon. The elongation degree used for all six specimens is equal to 30‰. The geometric dimensions are the same for all specimens. What differentiates the specimens from each other is the longitudinal reinforcement ratio. More specifically, the longitudinal reinforcement ratios used are 1.79%, 2.68%, 3.18%, 3.68%, 4.02% and 4.19%. The loading stages for all specimens are as follows: (a) Uniaxial central tensile loading on each test specimen, (b) Uniaxial central compression loading on each specimen till its failure due to buckling. The present study focuses on the tensile loading stage only. Extreme tensile strain of 30‰ is used to take into account the cases of extreme seismic excitations. First, the experimental results from an already accepted publication are presented and afterwards they are followed by the numerical investigation of these 6 specimens using appropriate finite element software. Useful conclusions are drawn regarding the precision of the experimental tests investigating the influence of the longitudinal reinforcement ratio on the phenomenon of transverse buckling. These conclusions are substantiated both experimentally and analytically, as the results of the tensile experiments are compared with the corresponding results of the analytical investigation.*

**Keywords:** Longitudinal reinforcement ratio, Lateral buckling, Seismic walls, Tensile load

---

## 1 INTRODUCTION

Engineers worldwide have been troubled for the structural behavior and soil-structure interaction for various types of structures [1]–[10]. Structural walls play an important role in the structures' behavior and safety against horizontal loads and especially against earthquake cyclic loading [11], [12]. It is well-known that the vast part of seismic loading is resisted by seismic walls in reinforced concrete structures [13]–[26]. One critical mode of failure which can appear during earthquake cyclic loading is the lateral buckling of R/C shear walls [27]–[36]. It has been observed that such type of failure is so critical that can lead to partial or total collapses of multi-storey reinforced concrete buildings [37]. This phenomenon can appear when the boundary edges of seismic walls have sustained a large size of tensile loading during the first semi-cycle of seismic loading and then are subjected to a compressive loading during the second semi-cycle of earthquake loading [38]–[41]. Transverse buckling appears when the cracks formed during the first stage of tensile loading have such a large width that makes it impossible to be closed during the second stage of compressive loading [42]–[50].

The present study uses experimental tests performed already by the first author trying to investigate the mechanical parameters affecting the transverse instability [51]. These specimens were all subjected to tensile strain equal to 30‰ but they had a different longitudinal reinforcement ratio. In the framework of the present work, the six specimens subjected to tensile loading are modelled using finite element software and the results of this analytical investigation are compared to the existing experimental results concerning the tensile loading stage. It is noted that the experiments have taken place in the Laboratory of Strength of Materials of Aristotle University of Thessaloniki and the analysis of the results has taken place in Demokritos University of Thrace.

## 2 EXPERIMENTAL RESEARCH

### 2.1 Test specimen characteristics

The experimental investigation for the six test specimens has been described in detail by the first author already [51]. Figure 1a shows the geometrical characteristics of one of the six test specimens and more specifically the test specimen detailed with longitudinal reinforcement of 4 bars of 8 mm diameter and 2 bars of 10 mm diameter. Figure 1b displays the load test setup used for the application of the tensile loading. It is noted the fact that the tensile loading is the first stage of the two loading stages. In the framework of the present study, only the experimental results of the tensile loading stage are compared to the analytical ones. Table 1 shows the test specimens' characteristics.

N/A	Specimen	Dimensions (cm)	Longitudinal reinforcement	Transverse reinforcement	Longitudinal reinforcement ratio (%)	Elongation degree (‰)
1	S-1.79-4Ø8	15x7.5x76	4xD8	D4.2@33 mm	1.79	30.00
2	S-2.68-6Ø8	15x7.5x76	6xD8	D4.2@33 mm	2.68	30.00
3	S-3.19-4Ø8+2Ø10	15x7.5x76	4xD8+2xD10	D4.2@33 mm	3.18	30.00
4	S-3.68-4Ø10+2Ø8	15x7.5x76	4xD10+2xD8	D4.2@33 mm	3.68	30.00
5	S-4.02-4Ø12	15x7.5x76	4xD12	D4.2@33 mm	4.02	30.00
6	S-4.19-6Ø10	15x7.5x76	6xD10	D4.2@33 mm	4.19	30.00

Table 1: Dimensions of the test specimens.

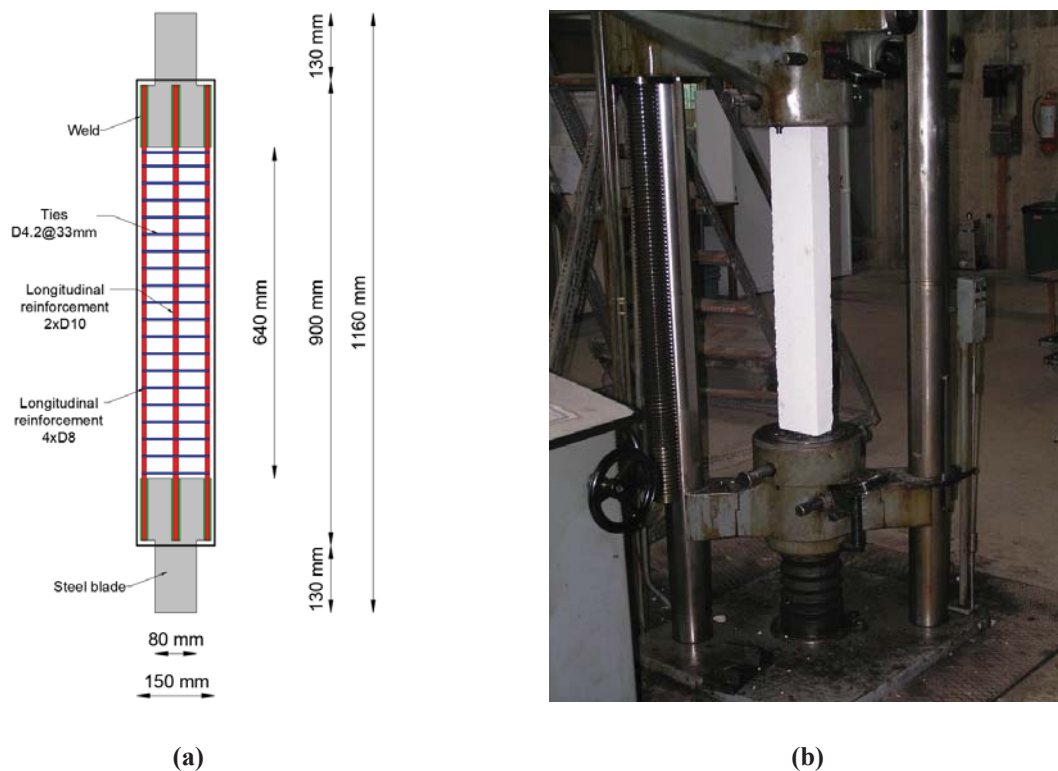


Figure 1: (a) Vertical reinforcement layout (Reinforcement differs for each specimen. Example shows a typical longitudinal reinforcement 4xD8+2xD10.), (b) Test setup for tensile loading.

## 2.2 Materials

Materials used and their characteristics were also described by the first author already [28]. Table 2 displays the concrete mechanical properties and Table 3 the steel characteristics.

N/A	Specimen	Concrete cube resistance (28 days) (MPa)	Concrete cube resistance (Compression test day) (MPa)	Concrete cylinder resistance (Compression test day) (MPa)
1	S-1.79-4Ø8	23.33	25.56	20.56
2	S-2.68-6Ø8	22.22	27.55	22.55
3	S-3.19-4Ø8+2Ø10	22.82	25.78	20.78
4	S-3.68-4Ø10+2Ø8	22.82	25.78	20.78
5	S-4.02-4Ø12	23.26	27.85	22.85
6	S-4.19-6Ø10	23.26	27.85	22.85

Table 2: Concrete mechanical properties.

Reinforcement	Yield strength (MPa)	Ultimate strength (MPa)
D8 (Longitudinal reinforcement)	603.77	743.10
D10 (Longitudinal reinforcement)	552.02	670.91
D12 (Longitudinal reinforcement)	560.27	666.43
D4.2 (Transverse ties)	552.02	670.91

Table 3: Reinforcement mechanical properties.

### 2.3 Experimental results

Each one of the six test specimens has been subjected to the same degree of elongation according to Table 1 and the results have been published by the first author already [51]. Figure 2 displays the shape of test specimens after the uniaxial tensile test has taken place. It is obvious that several cracks of different width have formed after the tensile loading according to the longitudinal reinforcement ratio that each specimen has.

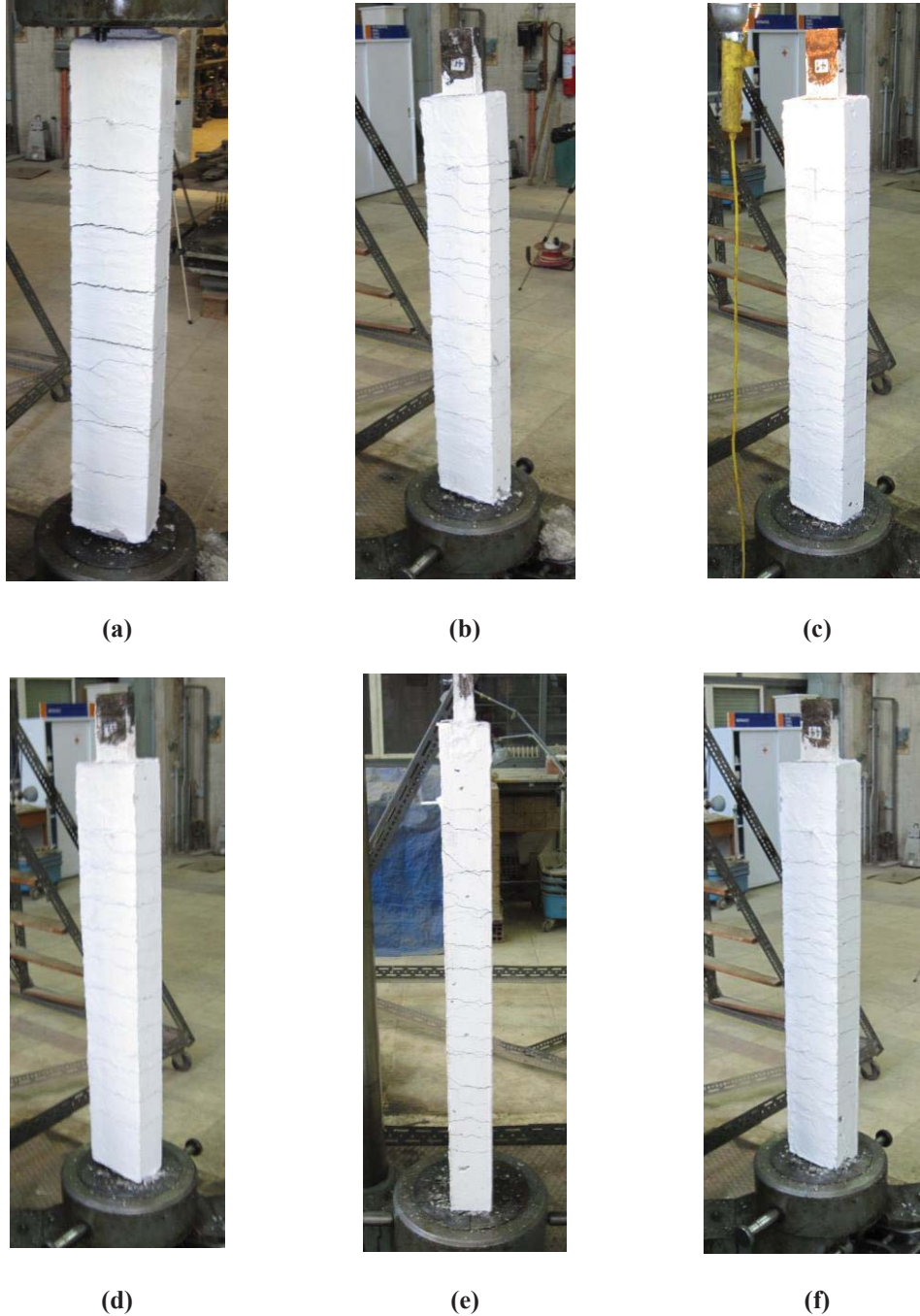


Figure 2: State of specimens after the end of the tensile experiment: (a) S-1.79-4Ø8, (b) S-2.68-6Ø8, (c) S-3.19-4Ø8+2Ø10, (d) S-3.68-4Ø10+2Ø8, (e) S-4.02-4Ø12, (f) S-4.19-6Ø10



### 3 ANALYTICAL RESEARCH

#### 3.1 Modeling of test specimens

The analytical research has taken place using 3D elements to model specimens subjected only to tensile loading. Inelastic models are used both for concrete and steel. Figure 3 shows the 3D model both for the whole column section and its corresponding reinforcement steel.

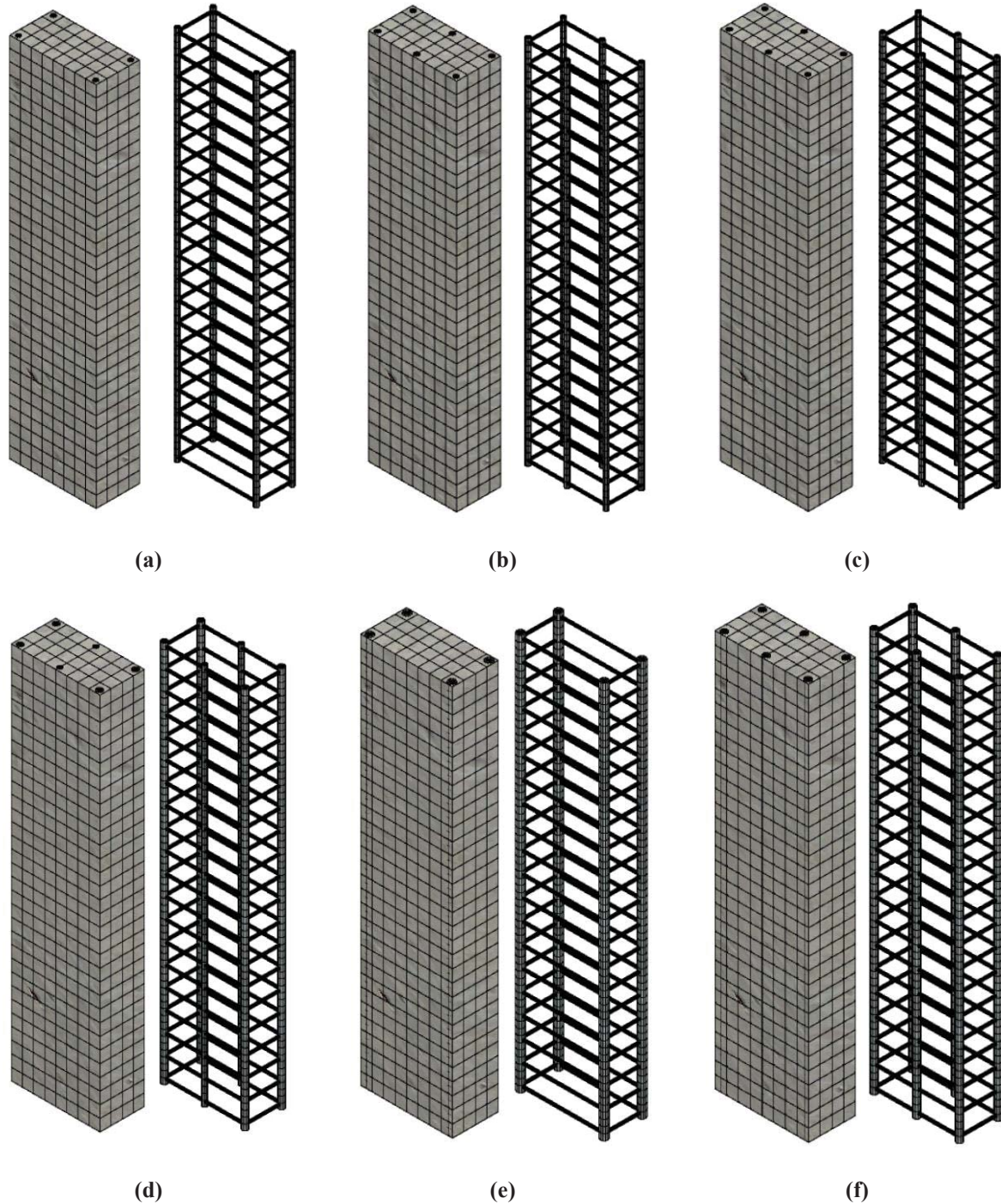


Figure 3: 3D model for column and reinforcement for: (a) S-1.79-4Ø8, (b) S-2.68-6Ø8, (c) S-3.19-4Ø8+2Ø10, (d) S-3.68-4Ø10+2Ø8, (e) S-4.02-4Ø12, (f) S-4.19-6Ø10

### 3.2 Analytical results

Figure 4 displays the displacement along the column height after the end of the tensile loading test for all six test specimens. The displacement is zero at the fixed column base.

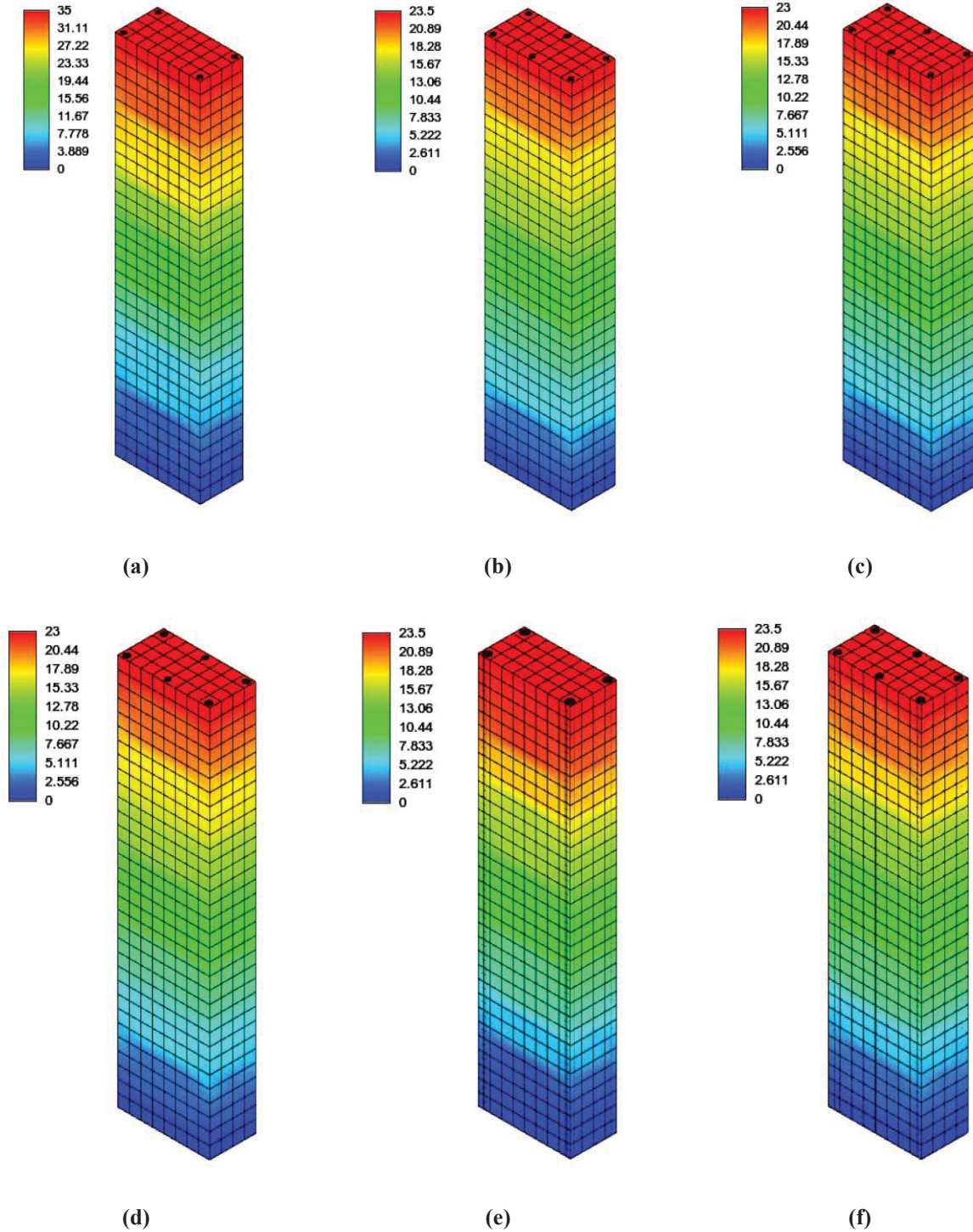


Figure 4: Displacement along the column axis at the end of the tensile test (mm): (a) S-1.79-4Ø8, (b) S-2.68-6Ø8, (c) S-3.19-4Ø8+2Ø10, (d) S-3.68-4Ø10+2Ø8, (e) S-4.02-4Ø12, (f) S-4.19-6Ø10

## 4 ANALYSIS OF RESULTS

### 4.1 Analytical versus experimental results

Figures 5-10 show the comparison between the experimental and the analytical diagrams of load versus elongation for specimens modeling the boundary edges of R/C walls.

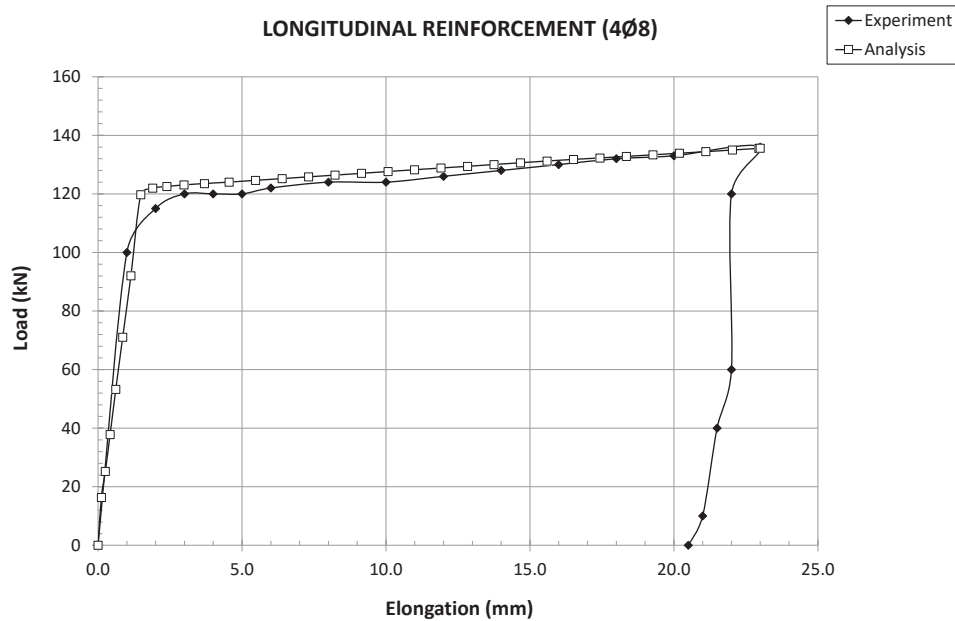


Figure 5: Load versus elongation diagram for specimen S-1.79-4Ø8.

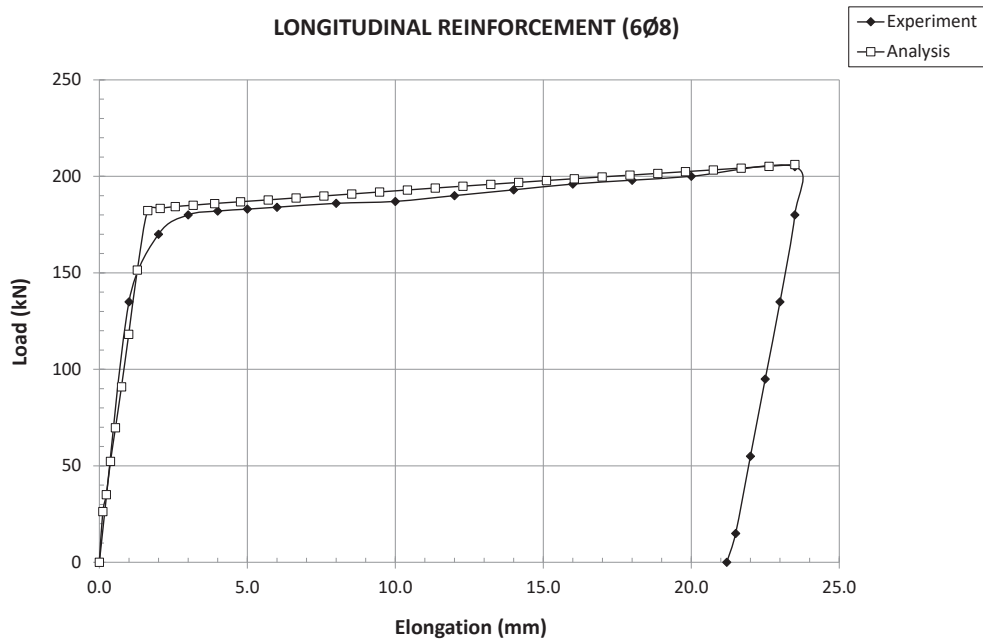


Figure 6: Load versus elongation diagram for specimen S-2.68-6Ø8.



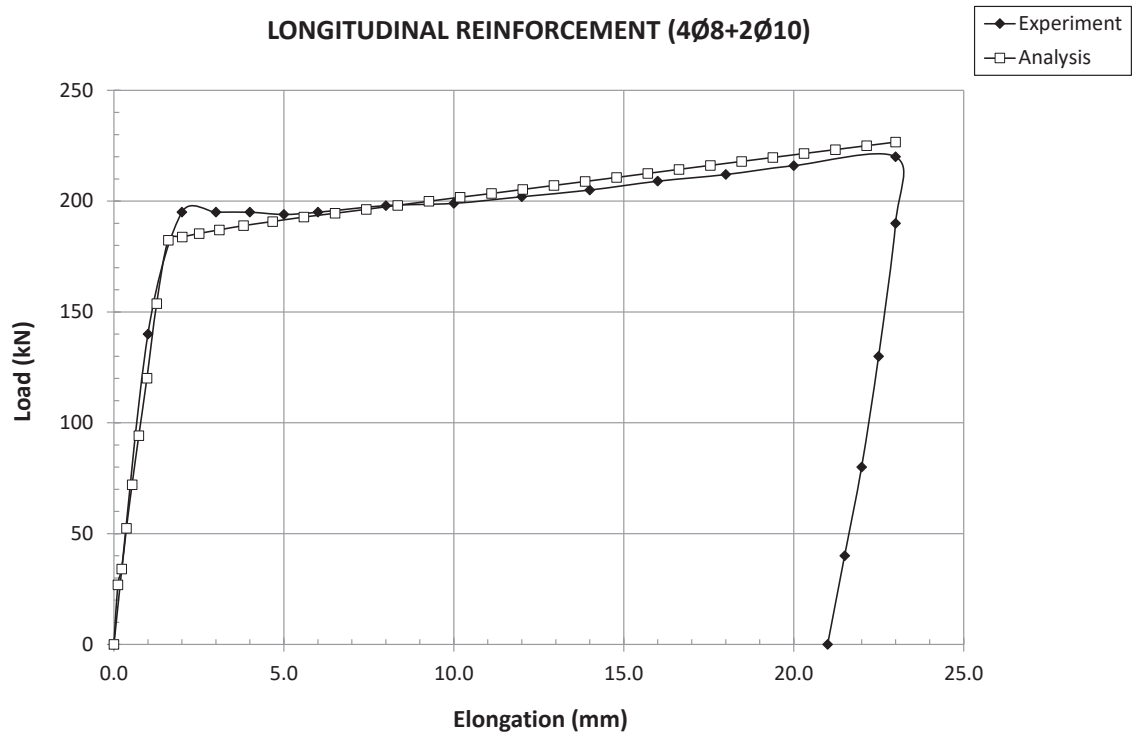


Figure 7: Load versus elongation diagram for specimen S-3.19-4Ø8+2Ø10.

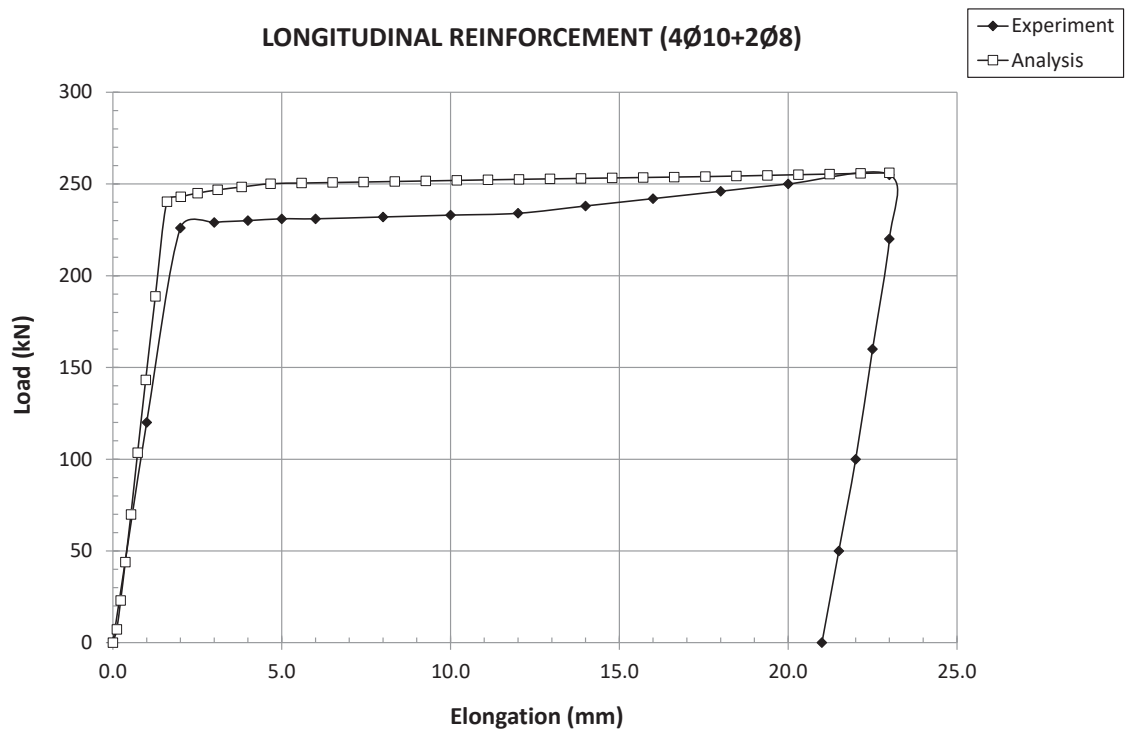
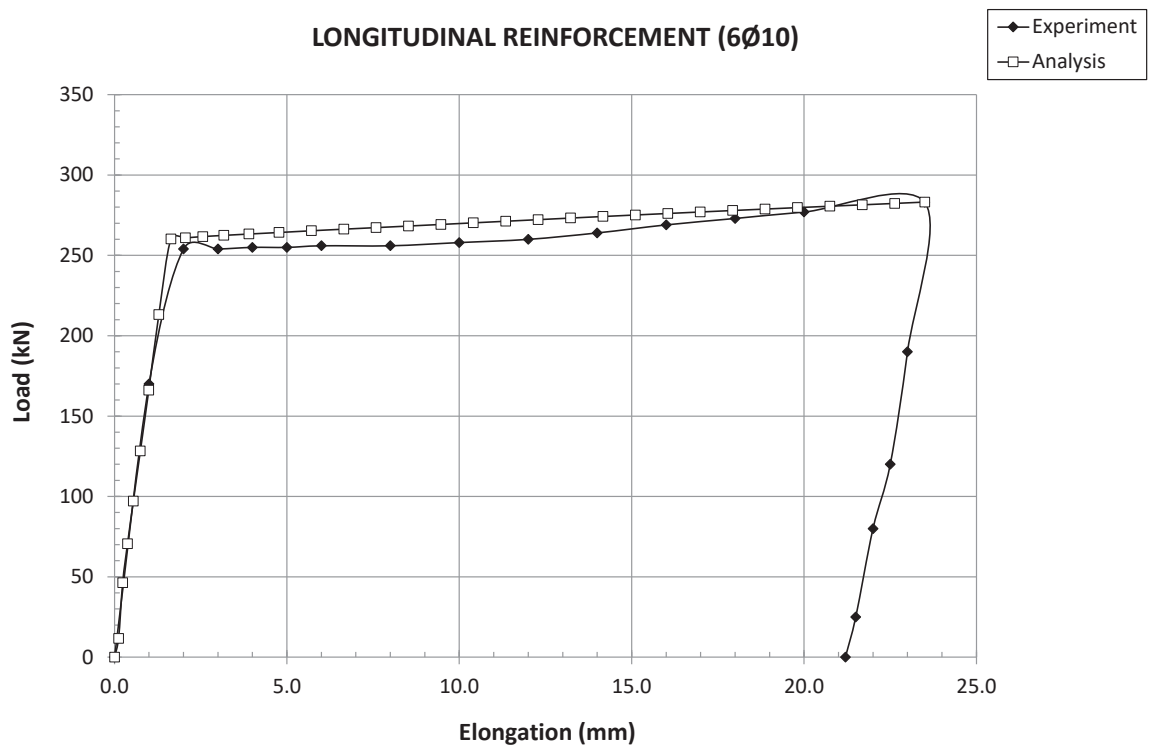
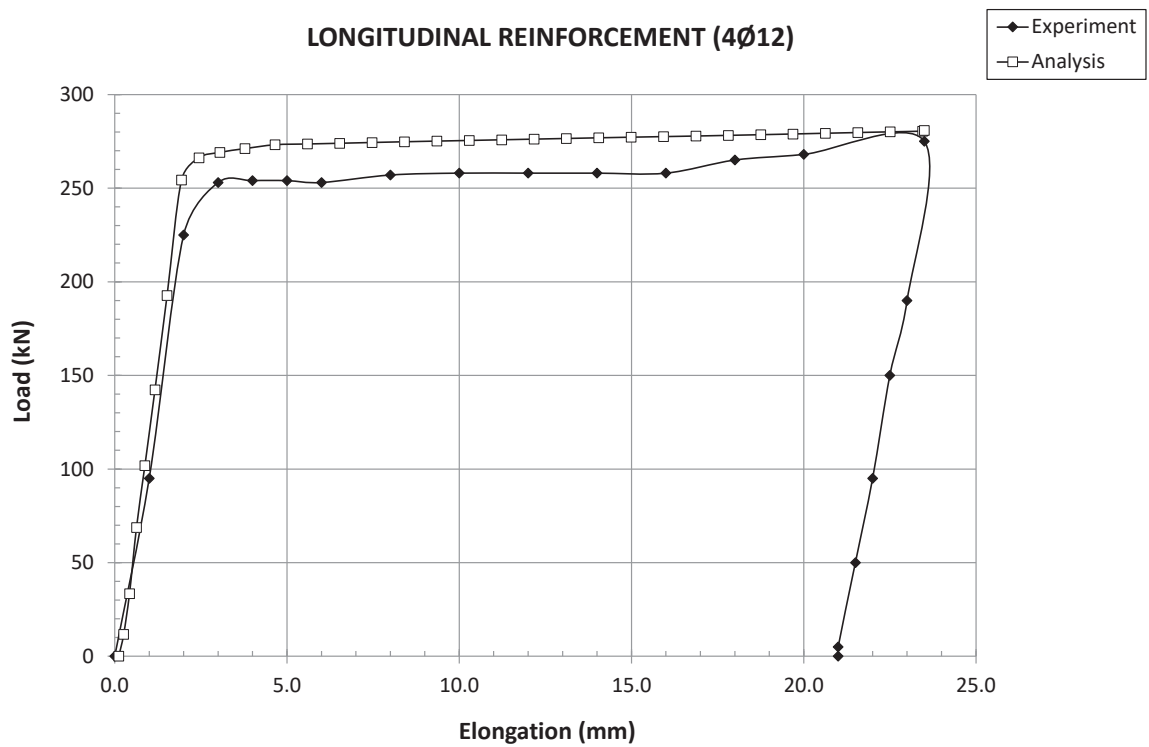


Figure 8: Load versus elongation diagram for specimen S-3.68-4Ø10+2Ø8.



## 4.2 Analysis of results

The analysis of the previous results leads to the following:

1. Figure 4 shows that the vertical displacement is zero at the base of the prisms since the base is rigid. The maximum vertical displacement is found towards the upper part of the specimens where the tensile load is applied. The same phenomenon at the tensile experiments, too.
2. It is obvious that there is a very good correlation between the experimental and the analytical results for all test specimens (Figures 5-10). This very good correlation can be noticed both for the elastic and the plastic branch, as well as for the point of yield.
3. The 640 mm effective length of the test specimens is the one which has been modelled only since this is the length in which the tensile elongation appears (Figure 1).

## 5 CONCLUSIONS

The conclusions resulted from the tensile experiments and the relevant analytical procedures concerning the behavior of the extreme edges of R/C walls are:

1. There is a very good correlation between the experimental results and the analytical results concerning the tensile loading. This very good correlation has to do with the elastic branch, the yielding point and the plastic branch for all six specimens.
2. The longitudinal reinforcement ratio is a significant mechanical parameter that affects the behavior of the extreme edges of seismic walls and its investigation has to be applied in the proper and right way following a correct procedure. The good convergence between the experimental and the numerical results proves that the procedure applied, probably, follows the correct methodology.
3. A future research could and should model the whole test specimen and not only the effective length in order to simulate even more precisely the experimental behavior.

## REFERENCES

- [1] N. Alamanis, "Influence of random soil strength properties on the earthquake vulnerability of slopes with embedded oil and natural gas pipelines," *Energy Systems*, 2020, doi: 10.1007/s12667-020-00394-9.
- [2] N. Alamanis and P. Dakoulas, "Investigation on the effect of spatial variability of soil properties on permanent seismic displacements of slopes in load," in *14th Baltic Sea Geotechnical Conference 2020*, 2020.
- [3] N. Alamanis and P. Dakoulas, "Effect of spatial variability of soil properties on the stability and permanent seismic displacements of highway slopes," in *The 17th European Conference on Soil Mechanics and Geotechnical Engineering*, 2019.
- [4] N. Alamanis and P. Dakoulas, "Effect of the spatial variability of soil properties on the seismic vulnerability of slopes with embedded oil and natural gas pipelines," in *6th International Conference on "Energy, Sustainability and Climate Change" (ESCC 2019)*, 2019.
- [5] N. Alamanis and P. Dakoulas, "Vulnerability of soil slopes against seismic damage based on the effect of spatial variability of soil properties on the development of permanent seismic displacements," in *International Conference on Research in Engineering, Technology and Science*, 2019.

- [6] A. Mouratidis, C. Daniilidou, and G. Papageorgiou, "Evaluation of pavement maintenance and strengthening techniques," in *Bituminous Mixtures and Pavements VII, Proceedings of the 7th International Conference on Bituminous Mixtures and Pavements (ICONFBMP 2019)*, 2019, pp. 516–523.
- [7] N. Alamanis, G. Papageorgiou, P. Chantzopoulou, and I. Chouliaras, "Investigation on the influence of permeability coefficient  $k$  of the soil mass on construction settlements. Cases of infrastructure settlements in Greece," *Wseas Transactions on Environment and Development*, vol. 15, pp. 95–105, 2019.
- [8] G. Papageorgiou, N. Alamanis, I. Chouliaras, and P. Kapsali, "Decision making for designing infrastructure projects: The case of the city of Larissa, Greece," *Journal of Engineering and Architecture*, vol. 7, no. 1, pp. 115–125, 2019, doi: 10.15640/jea.v7n1a13.
- [9] G. Papageorgiou and A. Mouratidis, "Defining threshold values for pavement surface characteristics," *Proceedings of the Institution of Civil Engineers (ICE) - Transport*, vol. 168, no. 3, pp. 223–230, 2015, doi: 10.1680/tran.12.00028.
- [10] G. Papageorgiou and A. Mouratidis, "A mathematical approach to define threshold values of pavement characteristics," *Structure and Infrastructure Engineering*, vol. 10, no. 5, pp. 568–576, 2014.
- [11] K. Christidis and K. Trezos, "Experimental investigation of existing non-conforming RC shear walls," *Engineering Structures*, vol. 140, no., pp. 26–38, 2017, doi: <https://doi.org/10.1016/j.engstruct.2017.02.063>.
- [12] T. Terzioglu, K. Orakcal, and L. M. Massone, "Cyclic lateral load behavior of squat reinforced concrete walls," *Engineering Structures*, vol. 160, 2018, doi: 10.1016/j.engstruct.2018.01.024.
- [13] J. W. Wallace, "Performance-Based Design of Tall Reinforced Concrete Core Wall Buildings," *Geotechnical, Geological and Earthquake Engineering*, vol. 17, pp. 279–307, 2010, doi: 10.1007/978-90-481-9544-2\_12.
- [14] R. Serrette and D. P. Nolan, "Reversed Cyclic Performance of Shear Walls with Wood Panels Attached to Cold-Formed Steel with Pins," *Journal of Structural Engineering*, vol. 135, no. 8, pp. 959–967, 2009, doi: 10.1061/(asce)st.1943-541x.0000037.
- [15] H. S. Lee and D. W. Ko, "Seismic response characteristics of high-rise RC wall buildings having different irregularities in lower stories," *Engineering Structures*, vol. 29, no. 11, pp. 3149–3167, 2007, doi: 10.1016/j.engstruct.2007.02.014.
- [16] X. Lu and Y. Chen, "Modeling of Coupled Shear Walls and Its Experimental Verification," *Journal of Structural Engineering*, vol. 131, no. 1, pp. 75–84, 2004, doi: 10.1061/(asce)0733-9445(2005)131:1(75).
- [17] M. Hassan and S. El-Tawil, "Inelastic dynamic behavior of hybrid coupled walls," *ASCE Journal of Structural Engineering*, vol. 130, no. 2, pp. 285–296, 2004, doi: 10.1061/40616(281)83.
- [18] L. M. Massone and J. W. Wallace, "Load-Deformation Responses of Slender Reinforced Concrete Walls," *ACI Structural Journal*, vol. 101, no. 1, pp. 103–113, 2004.
- [19] P. Riva, A. Meda, and E. Giuriani, "Cyclic behaviour of a full scale RC structural

- wall,” *Engineering Structures*, vol. 25, no. 6, pp. 835–845, 2003, doi: 10.1016/S0141-0296(03)00020-8.
- [20] A. Rutenberg, “The seismic shear of ductile cantilever wall systems in multistorey structures,” *Earthquake Engineering and Structural Dynamics*, vol. 33, no. 7, pp. 881–896, 2004, doi: 10.1002/eqe.384.
- [21] Y. Chiou, Y. Mo, F. Hsiao, Y. Liou, and M. Sheu, “Experimental and analytical studies on large-scale reinforced concrete framed shear walls,” *Symposium Paper*, vol. 211, no., pp. 201–222, 2003.
- [22] T. A. Duffey, C. R. Farrar, and A. Goldman, “Low-Rise Shear Wall Ultimate Drift Limits,” *Earthquake Spectra*, vol. 10, no. 4, pp. 655–674, 2003, doi: 10.1193/1.1585792.
- [23] Y. L. Mo, J. Zhong, and T. T. C. Hsu, “Seismic simulation of RC wall-type structures,” *Engineering Structures*, vol. 30, no. 11, pp. 3167–3175, 2008, doi: 10.1016/j.engstruct.2008.04.033.
- [24] I. Ghorbani-Renani, N. Velev, R. Tremblay, D. Palermo, B. Massicotte, and P. Léger, “Modeling and testing influence of scaling effects on inelastic response of shear walls,” *ACI Structural Journal*, vol. 106, no. 3, pp. 358–367, 2009.
- [25] J. D. Aristizabal-Ochoa, “Seismic Behavior of Slender Coupled Wall Systems,” *Journal of Structural Engineering*, vol. 113, no. 10, pp. 2221–2234, 2008, doi: 10.1061/(asce)0733-9445(1987)113:10(2221).
- [26] P. Bisch and A. Coin, “Seismic behaviour of slightly reinforced concrete walls: Experiments and theoretical conclusions,” *Bulletin of Earthquake Engineering*, vol. 5, no. 1, pp. 45–65, 2007, doi: 10.1007/s10518-006-9014-1.
- [27] T. Chrysanidis, “Evaluation of Out-of-Plane Response of R/C Structural Wall Boundary Edges Detailed with Maximum Code-Prescribed Longitudinal Reinforcement Ratio,” *International Journal of Concrete Structures and Materials*, vol. 14, no. 1, 2020, doi: 10.1186/s40069-019-0378-4.
- [28] T. Chrysanidis, “Influence of elongation degree on transverse buckling of confined boundary regions of R/C seismic walls,” *Construction and Building Materials*, vol. 211, pp. 703–720, Jun. 2019, doi: 10.1016/J.CONBUILDMAT.2019.03.271.
- [29] T. Chrysanidis and I. Tegos, “Does reinforcement ratio affect displacements due to lateral buckling behavior of concrete walls?,” *International Journal of Applied Engineering Research*, vol. 12, no. 3, pp. 382–388, 2017.
- [30] T. Chrysanidis and I. Tegos, “Influence of elongation degree on out-of-plane buckling of R/C structural walls with a medium high reinforcement ratio,” *International Journal of Civil Engineering and Technology*, vol. 7, no. 4, pp. 358–364, 2016.
- [31] T. Chrysanidis and I. Tegos, “Size of seismic tensile strain and its influence on the displacements due to transverse buckling of ultra-highly reinforced structural walls,” *ARP Journal of Engineering and Applied Sciences*, vol. 11, no. 23, pp. 13884–13890, 2016.
- [32] T. Chrysanidis and I. Tegos, “Displacements and mode of failure of medium high reinforced walls due to transverse buckling,” *International Journal of Engineering Development and Research*, vol. 4, no. 3, pp. 628–634, 2016.

- [33] T. Chrysanidis, "Low Reinforced Shear Walls: Displacements and Failure Modes Due to Lateral Buckling," *International Journal of Science and Engineering Investigations*, vol. 5, no. 55, pp. 143–148, 2016.
- [34] T. Chrysanidis, "Degree of Elongation of Maximum Code-Prescribed Reinforced Walls: Modes of Failure and Displacements of Lateral Buckling Phenomenon," *International Journal of Trend in Research and Development*, vol. 3, no. 4, pp. 435–440, 2016.
- [35] T. Chrysanidis, "Size of seismic tensile strain and its influence on the lateral buckling of highly reinforced concrete walls," *IOSR Journal of Mechanical and Civil Engineering*, vol. 11, no. 1, pp. 18–22, 2014, doi: 10.9790/1684-11121822.
- [36] T. Chrysanidis and I. Tegos, "Out-of-plane buckling of highly reinforced seismic walls: Displacements and mode of failure," *International Journal of Civil Engineering and Technology*, vol. 5, no. 6, pp. 101–107, 2014.
- [37] C. Alarcon, M. Hube, R. Jünemann, and J. de la Llera, "Characteristics and displacement capacity of reinforced concrete walls in damaged buildings during 2010 Chile earthquake," *Bulletin of Earthquake Engineering*, vol. 13, pp. 1119–1139, 2015, doi: <https://doi.org/10.1007/s10518-015-9727-0>.
- [38] A. Haro, M. Kowalsky, Y. Chai, and G. Lucier, "Boundary elements of special reinforced concrete walls tested under different loading paths," *Earthquake Spectra*, vol. 34, no. 3, pp. 1267–1288, 2018, doi: 10.1193/081617EQS160M.
- [39] K. Herrick and M. Kowalsky, "Out-of-plane buckling of ductile reinforced structural walls due to in-plane loads," *Journal of Structural Engineering*, vol. 143, no. 3, pp. 1–15, 2016, doi: 10.1061/(asce)st.1943-541x.0001660.
- [40] Y. Chai and S. Kunnath, "Minimum thickness for ductile RC structural walls," *Engineering Structures*, vol. 27, no. 7, pp. 1052–1063, Jun. 2005, doi: 10.1016/j.engstruct.2005.02.004.
- [41] T. Welt, L. Massone, J. LaFave, D. Lehman, S. McCabe, and P. Polanco, "Confinement behavior of rectangular RC prisms simulating wall boundary elements," *Journal of Structural Engineering*, vol. 143, no. 4, pp. 1–12, 2017, doi: 10.1061/(asce)st.1943-541x.0001682.
- [42] T. Chrysanidis and I. Tegos, "The influence of the degree of elongation to the ultimate strength and mode of failure of RC walls reinforced with the maximum code-prescribed longitudinal reinforcement ratio," in *Proceedings of the 2013 International Van Earthquake Symposium*, 2013.
- [43] T. Chrysanidis and I. Tegos, "The influence of the degree of elongation of the longitudinal reinforcement of the high-reinforced end sections of ductile structural walls to their ultimate strength and mode of failure," in *Proceedings of the Vienna Congress on Recent Advances in Earthquake Engineering and Structural Dynamics (VEESD 2013)*, 2013.
- [44] T. Chrysanidis and I. Tegos, "The influence of the longitudinal reinforcement ratio of R/C walls to their displacements due to failure of transverse instability under extreme seismic loads," in *Proceedings of the Vienna Congress on Recent Advances in Earthquake Engineering and Structural Dynamics (VEESD 2013)*, 2013.
- [45] T. Chrysanidis and I. Tegos, "The influence of the degree of elongation of the ultra

- high-reinforced end sections of R/C walls to their displacements and mode of failure,” in *Proceedings of the 2013 International Van Earthquake Symposium*, 2013.
- [46] T. Chrysanidis and I. Tegos, “The influence of the degree of elongation to the displacements and mode of failure of medium-reinforced ductile structural walls,” in *Proceedings of the Engineering a Concrete Future: Technology, Modeling and Construction (fib Symposium 2013)*, 2013.
- [47] T. Chrysanidis and I. Tegos, “The influence of ratio of the longitudinal reinforcement of the boundary edges of structural walls to the resistance against lateral instability of earthquake-resistant reinforced concrete structural walls,” in *Proceedings of the 15th World Conference on Earthquake Engineering (15th WCEE 2012)*, 2012.
- [48] T. Chrysanidis and I. Tegos, “The influence of tension strain of wall ends to their resistance against lateral instability for low-reinforced concrete walls,” in *Proceedings of the 15th World Conference on Earthquake Engineering (15th WCEE 2012)*, 2012.
- [49] T. Chrysanidis, “Evaluation of lateral buckling phenomenon using R/C prisms detailed with an ultra high reinforcement ratio,” in *Emerging Trends in Engineering Research and Technology Vol. 3*, L. Salisu, Ed. London, UK: Book Publisher International, 2020, pp. 55–64.
- [50] T. Chrysanidis and I. Tegos, “Can the diameter of longitudinal bars of extreme edges of R/C walls halt transverse buckling?,” in *Emerging Trends in Engineering Research and Technology Vol. 3*, L. Salisu, Ed. London, UK: Book Publisher International, 2020, pp. 65–72.
- [51] T. Chrysanidis, “The effect of longitudinal reinforcement ratio on the lateral buckling behavior of R/C walls modelled using prism elements,” *Journal of Building Engineering*, vol. 42, no. 102456, 2021, doi: 10.1016/j.jobee.2021.102456.



## PRELIMINARY CONSIDERATIONS ON THE LOSS OF SUPPORT FOR PRECAST BEAM ELEMENTS

Marius Eteme Minkada<sup>1</sup>, Simone Labò<sup>1</sup>, Alessandra Marini<sup>1</sup> and Andrea Belleri<sup>1</sup>

<sup>1</sup> University of Bergamo  
via Marconi 5, 24044, Dalmine, Bergamo, Italy  
{marius.etememinkada, simone.labo, alessandra.marini, andrea.belleri}@unibg.it

---

### Abstract

*One of the main objectives to be achieved for the safety of industrial precast buildings with simple friction beam-to-column connections is the reduction of their relative displacement. This goal is generally achieved through a global strengthening of the building or by locally introducing mechanical connecting devices between the elements. However, for low seismicity areas, these interventions may not be required, and it could be interesting to evaluate the level of safety achieved by simple friction; such an information would allow for instance the prioritization of the retrofit interventions.*

*This paper aims to establish criteria for evaluating the loss of support probability in existing precast buildings in the case of a seismic event. The behavior of the friction connection is evaluated through a simplified model that describes the behavior of a portal frame composed of two columns and one beam. The equations of motion are derived, and a parametric analysis is performed by investigating the influence of the geometry of the structural elements, the non-linear behavior of the columns, and the friction coefficient used in the column-beam connections for varying horizontal and vertical seismic acceleration. The objective of the sensitivity analysis is to provide some preliminary considerations about the influence of the main parameters that characterize the existing precast structure on the loss of the support probability.*

**Keywords:** Precast buildings; friction connection; beam-to-column connection; simplified models.

---



## 1 INTRODUCTION

The Italian building stock encompasses many precast concrete structures; the main advantage of this construction technology lies on high quality control materials and the short construction time. The typical structural layout of these buildings consists of a single story with a rectangular plan in which the bearing structure is made of prefabricated columns supporting double tapered prestressed beams. A great share of these buildings was designed before the enforcement of modern anti-seismic regulation codes and, therefore, they were not designed to withstand the horizontal loads.

The seismic events that occurred in 2012 in Emilia-Romagna, Veneto and Lombardy, highlighted the main vulnerabilities of existing precast industrial buildings [1, 2, 3, 4, 5, 6, 7, 8, 9]; the main vulnerabilities consist in the breaking of the fork, the overturning of the infill panels, the reaching of the ultimate rotation of the column, the loss of the beam-to-column support and/or the loss of the support of other roofing elements [10, 11, 12, 13, 14, 15, 16, 17]. The loss of the support is due to the absence of adequate structural detailing in the connection between beam and columns.

To date, in Italy, the implementation of mechanical devices between the structural elements of precast buildings (e.g. column and beam at the beam-to-column support) is required for new buildings and new technological solution have been studied in recent years [18]; such a detailing was not common practice in the past. However, for low seismicity areas, the seismic retrofit of these connections may not be necessary, and it could be interesting to evaluate the level of safety achieved by simple friction; such an information would allow for instance the prioritization of the retrofit interventions.

The problem of loss of support in friction beam-column connections has been previously addressed: Magliulo et al. [6] and Belleri et al. [1] evaluated the minimum value of the friction coefficient required to avoid the sliding of the beam under the hypothesis of perfect correlation between the maximum values of the horizontal and vertical components of the seismic inputs; Demartino et al. [19] approached the problem by defining simplified numerical finite element models of the friction beam-column connection, starting from the equations of motion of the friction connection considering a rigid block model having two degrees of freedom. Furthermore, the effect of the seismic-hazard disaggregation was considered. The results showed that the minimum friction coefficient required to prevent the sliding of the beam depends on the period of the structure and the damping coefficients used in the equations.

In this paper, a new analytical model is proposed for the evaluation of the seismic response of a simple portal frame with friction beam-column connections. The portal frame is described by means of a dynamic system with four degrees of freedom (DOF), 3 horizontal and 1 vertical. The main novelty introduced by the present work relies on the simplified model proposed and on the evaluation of the influence of various parameters. Section 2 describes the proposed numerical model. In section 3, parametric analyses are carried out to evaluate the influence of the main parameters on the global response of the simplified model. In section 4, the analytical model is compared with finite element nonlinear time history analyses, carried out on a selected reference structure. Finally, a concise discussion of the results obtained in sections 3 and 4 and some considerations on possible improvements of the proposed model are made.

## 2 SIMPLIFIED SYSTEM DEVELOPMENT

The simplified 4DOF system used to describe the transverse portal-like response of a typical precast industrial building is here introduced and described. Similar models were adopted in previous research work [20, 21, 22, 23, 19].

## 2.1 Simplified model

The lateral displacement of the 2 columns and the displacement of the beam is described through a system characterized by 3 horizontal DOFs plus 1 vertical DOF (Figure 1b); the simplified system consists of 3 masses connected by springs ( $k_1, k_{12}, k_{23}, k_3$ ) and viscous dampers ( $c_1, c_{12}, c_{23}, c_3$ ) and subjected to the ground horizontal and vertical accelerations ( $\ddot{X}_g, \ddot{Y}_g$ ). The chosen degrees of freedom to describe the behavior of the system are the horizontal displacements of the top of the two columns ( $u_1, u_3$ ), and the horizontal and vertical displacement of the beam ( $u_2, v_2$ ). The simplified system is drawn in Figure 1b.

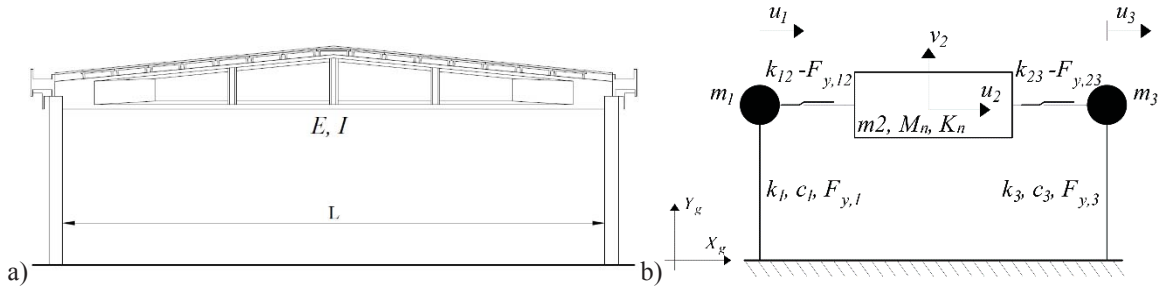


Figure 1: a) layout of a typical portal-like precast industrial building; b) simplified 3DOF system adopted.

The parameters used to describe the considered simplified systems are here presented; the subscripts refer to the element considered (i.e. 1 for the left-side column; 2 for the beam; 3 for the right-side column) or, in the case of connections, the elements that are connected by the link (e.g. subscript- $i$  refers to the DOF of the element- $i$ , while the subscript- $ij$  refers to the link describing the relative displacement between the element- $i$  and the element- $j$ ). The element-1 and the element-3 are described by the masses  $m_1$  and  $m_3$ , the elastic stiffnesses  $k_1$  and  $k_3$ , the damping coefficients  $c_1$  and  $c_3$ , and, to consider the nonlinear behavior of the columns, the yielding forces  $F_{y,1}$  and  $F_{y,3}$ , respectively. The element-2, represented by the mass  $m_2$ , is connected to the element-1 and element-3 by means of friction connections. The elastic stiffnesses  $k_{12}$  and  $k_{23}$  are associated for instance with the neoprene pads. The friction forces are  $F_{y,12}$  and  $F_{y,13}$ .

As for the vertical component of element-2, the generalized mass ( $M_n$ ) and the generalized stiffness ( $K_n$ ) are introduced to represent the participating mass and stiffness of the  $n$ -th vertical mode of the beam. In this work only the first vertical mode is considered; consequently, the subscript - $n$  is set to be equal to 1 ( $M_1, K_1$ ).

In the analyses described in the following section, the main parameter investigated is the relative displacements between the beam and the supporting columns ( $\delta_{12}, \delta_{13}$ ). For sake of clarity,  $\delta_{12}$  can be calculated as the difference between  $u_2$  and  $u_1$ ; similar considerations can be drawn for  $\delta_{13}$ .

## 2.2 Equations of motion and solving method

The free-body model of the 4DOF system is represented in Figure 2.

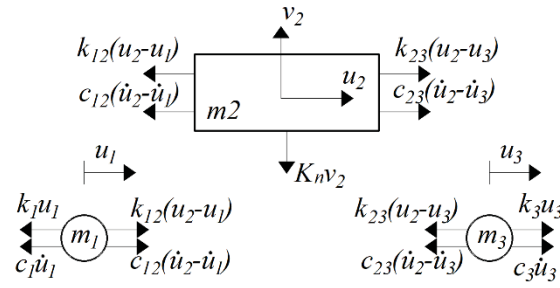


Figure 2: Free-body diagrams of the 3DOF system.

By enforcing balance to horizontal translation of element-1, element-3, it yields:

$$m_1 \ddot{u}_1 + k_1 u_1 + c_1 \dot{u}_1 - k_{12}(u_2 - u_1) - c_{12}(\dot{u}_2 - \dot{u}_1) = -m_1 \ddot{X}_g \quad (1)$$

$$m_3 \ddot{u}_3 + k_3 u_3 + c_3 \dot{u}_3 + k_{13}(u_3 - u_2) + c_{13}(\dot{u}_3 - \dot{u}_2) = -m_3 \ddot{X}_g \quad (2)$$

The horizontal equilibrium on element-2 is

$$m_2 \ddot{u}_2 + k_{12}(u_2 - u_1) + c_{12}(\dot{u}_2 - \dot{u}_1) - k_{13}(u_3 - u_2) - c_{13}(\dot{u}_3 - \dot{u}_2) = -m_2 \ddot{X}_g \quad (3)$$

The vertical component of element-2, expressed through its time-derivative in principal coordinates [24], is

$$\partial v / \partial t = [-K_1 v_2 - M_1 \ddot{v}_2] \cdot \frac{1}{M_1} \quad (4)^1$$

For a simply supported beam [24]

$$\begin{aligned} M_1 &= m_2 / 2 \\ K_1 &= \frac{\pi^4 EI}{2L^3} \end{aligned} \quad (5)$$

Where  $E$  and  $I$  are the elastic modulus and the moment of inertia of the horizontal beam, respectively, and  $L$  is the length of the beam.

From the vertical displacement expressed in principal coordinates, the shear at the beam ends ( $V(0, t)$  and  $V(L, t)$ ) can be derived as a function of the time ( $t$ ).

$$V(0, t) = \left[ -EI \cdot \left( \frac{\pi}{L} \right)^3 \right] \cdot v(t) \quad (6)^2$$

$$V(L, t) = -V(0, t) = \left[ EI \cdot \left( \frac{\pi}{L} \right)^3 \right] \cdot v(t)$$

It is worth noting that  $V(x, t)$  does not account for the mass  $m_2$ ; the total vertical force on the column  $-i$  ( $N_i$ ) can be calculated by the algebraic sum of  $V(x, t)$  and the generalized mass multiplied by the gravity constant ( $M_1 g$ ).

The inelastic behavior of element-1, element-3 and of the link simulating the simple beam-column friction support is modeled by the Bouc-Wen hysteresis law [25]. The nonlinear behavior of the columns is accounted for by substituting  $k_i u_i$  (Eq. 1 and Eq. 2) with  $P(t)$

$$P(t)_{column} = \alpha \cdot k_i \cdot u_i + (1 - \alpha) k_i \cdot \delta_{y,i} \cdot Z(t) \quad (7)$$

where  $-i$  is 1 for element-1 and 2 for the element-2,  $\alpha$  is the post yielding stiffness ratio, and  $Z$  is an internal variable whose behavior is described by its derivative:

<sup>1</sup>  $\ddot{v} = \partial^2 v / \partial t^2$

<sup>2</sup>  $\Phi'' = \partial^2 \Phi / \partial x^2$

$$\frac{dZ}{dt} = \left( \frac{1}{\delta_{y,i}} \right) \cdot (\dot{u}_i - \gamma \cdot |\dot{u}_i| \cdot Z(t) \cdot |z(t)|^{n-1} - \nu \cdot \dot{u}_i \cdot |z(t)|^n) \quad (8)$$

$n$ ,  $\nu$ , and  $\gamma$  are dimensionless quantities,  $n$  governs the smoothness of the curve in the proximity of the yielding point,  $\nu$  and  $\gamma$  control the size and the shape of the hysteretic loop ( $|\nu| + |\gamma| = 1$ ). In this case, the yielding force of the hysteresis model is derived as a function of the columns features and it is introduced through the parameter  $F_{y,i} = k_i \cdot \delta_{y,i}$  (Eq. 7).

A similar procedure can be followed for the friction beam-to-column support; in this case, the subscript  $-ij$  is set equal to 12 and 23 for the left and right connection, respectively, and the displacements  $u_{12}$  and  $u_{23}$  refer to the relative displacement between the 2DOFs ( $u_2 - u_1$  and  $u_2 - u_3$ ). Moreover, to simulate the simple friction support, the yielding forces of the links ( $F_{y,12}$  and  $F_{y,13}$ ) are derived according to the Coulomb's Law. Defining a friction coefficient  $\mu$  to characterize the contact between the column and the beam, the Coulomb's Law define the friction force ( $F_{y,ij}$ ) as the product between  $\mu$  and the total vertical force acting on the top of the column- $i$  ( $N_i$ ). Eq. 7 becomes

$$P(t)_{friction} = \alpha \cdot k_{ij} \cdot u_{ij} + (1 - \alpha) \cdot (\mu \cdot (\pm V(0, t) + M_1 g)) \cdot Z(t) \quad (9)$$

The equations of motion are solved with the function Ode45 [26], a versatile ordinary differential equation solver that adopts the Runge-Kutta method with a variable time step. The algorithm requires the conversion of the second-order differential equations into an equivalent system of first-order equations.

### 3 PARAMETRIC ANALYSIS

The input parameters varied in the parametric analyses are summarized in Table 1.

Parameter	Symbol	Value or range	
Behavior factor	$q$	1, 1.75, 2.5, 3.25, 4.0	[ - ]
Damping ratio	$\zeta_i$	1,3	[%]
Friction coefficient	$\mu$	0.1337, 0.5	[ - ]
Vertical component	$V_{mode}$	No, 1 <sup>st</sup> Mode	[ - ]
Ground Motion	GM	Mirandola, Amatrice	[ - ]

Table 1: Input parameters varied in the parametric analyses.

For the sensitivity analyses, the masses  $m_1$  and  $m_3$  are assumed equal to half of the self-weight of the single column, the elastic stiffnesses  $k_1$  and  $k_3$  are calculated from the geometry of the columns and account for a 50% reduction of the elastic modulus of the reinforced concrete due to cracking. All these parameters can be derived by the layout and the column cross-section of the reference case described in the next Section. A viscous damping model is considered; the damping coefficients  $c_1$  and  $c_3$  are considered equal and they are calculated in the parametric analyses by varying the damping ratio  $\zeta_i$  as indicated in Table 1 (with  $-i$  equal to 1 or 3), while the damping ratio of the vertical mode of the beam ( $\zeta_2$ ) is set equal to 0.01 [19]. As for the nonlinearity,  $n$ ,  $\nu$ , and  $\gamma$  are assumed, for the columns, equal to 1, 0.5, 0.5, respectively, while equal to 25, 0.5, 0.5, for the simple friction support, respectively. In both cases the post yielding ratio is set equal to 0.001. The friction coefficient  $\mu$  is varied among the values 0.1337 to simulate a neoprene-concrete interface [17] and 0.5 to consider a concrete-concrete interface [27]. The stiffness of the Bouc-Wen hysteresis of the friction support is set equal to  $k_{12} = k_{23} = 49000$  [N/m] [17] for  $\mu = 0.1337$ , while it is assumed equal to 1832461 [N/m] when the

friction coefficient is set equal to 0.5. The cases with and without the vertical DOF are both performed to evaluate the influence of the vertical component. The analyses are performed considering as seismic input the main shocks recorded in the L'Aquila station (Italy) during the 2008 seismic events, and in the Mirandola station (Italy) during the 2012 seismic events.

### 3.1 Parametric analyses and preliminary considerations

The results of the parametric analyses are reported in Figure 3 as a function of  $q$  in terms of ratio between the relative displacement ( $\delta_{12} = u_2 - u_1$ ) and  $\delta_R$ , corresponding to the value  $\delta_{12}$  obtained in the reference case with  $\zeta_I = \zeta_3 = 3\%$ ,  $\mu = 0.1337$ ,  $q = 1$ , and without the vertical component (indicated in the plot with a full black circle). Considering the geometric symmetry of the system, the same results would be obtained plotting  $\delta_{13}$ .

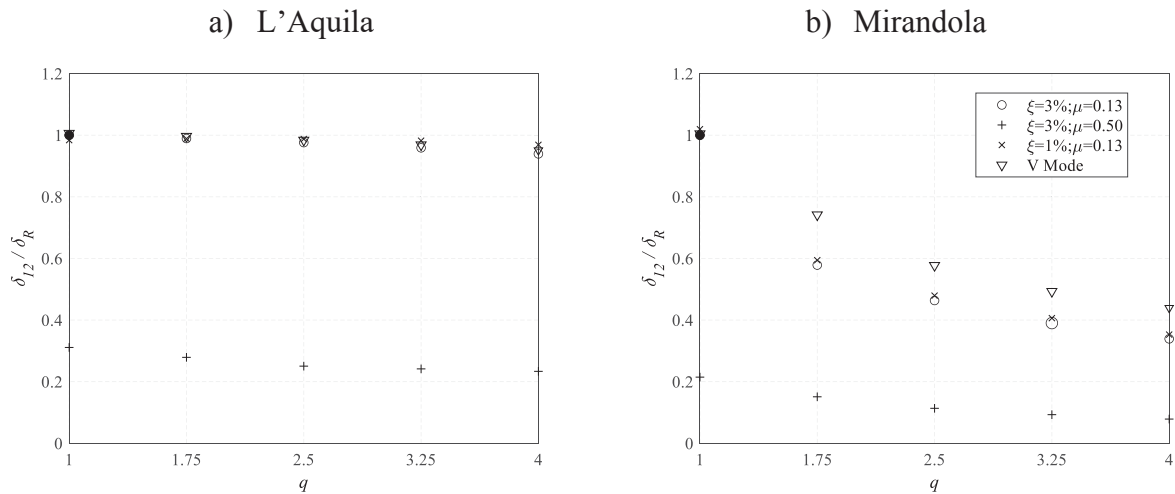


Figure 3: Parametric analyses results for the different ground motions considered. For both the GM the results are plotted as a function of  $q$  as the ratio between the relative displacement ( $\delta_{12}$ ) and  $\delta_R$  corresponding to  $\delta_{12}$  of the reference case ( $\zeta_I = \zeta_3 = 3\%$ ,  $\mu = 0.1337$ ,  $q = 1$ , No V Mode).

Increasing the behavior factor ( $q$ ) the relative displacement ( $\delta$ ) decreases following an almost linear trend;  $q$  affects more the case of Mirandola (with  $q = 4$ , almost 60% reduction) than the case of L'Aquila (with  $q = 4$  almost 10% reduction).

The friction parameter ( $\mu$ ) significantly affects the relative displacement between the beam and the columns; increasing  $\mu$  such relative displacement decreases.

The relative displacements increase by considering the vertical component; the maximum increasing value is shown in the case of Mirandola (+30%); this is considered a reasonable result observing that Mirandola is the site in which the maximum values of the vertical component were recorded. As for the case of L'Aquila, the increase is lower. Introducing  $\zeta = 0.01$  leads to variations that range between  $\pm 2\%$  with respect to the reference case.

## 4 REFERENCE CASE

To validate the simplified model presented, time history analyses have been carried out on a reference case study resembling a typical '70s precast industrial building. The building is supposed to be located in Mirandola (Emilia-Romagna, Italy). The building has a rectangular plan and story height (under the beam) equal to 5.35 (m). The bearing structure is made of precast frames designed according to the regulation codes at that time. The main frame of the building is composed of 2 columns and a double-tapered beam with a net span equal to 10.65 (m); accordingly, an I-section beam with a variable height between 0.40 (m) and 1.50 (m) is supposed.

The portal-to-portal distance is about 6.70 (m) and an overall roof weight of 2.40 (kN/m<sup>2</sup>) is assumed. The columns have a square cross-section 0.34x0.34 (m<sup>2</sup>) with a longitudinal reinforcement ratio equal to 0.8 (%). Furthermore, each column has a RC fork at the top, in which the beam is housed thus creating a simple-friction connection. A C28/35 concrete (28 MPa characteristic cylindrical strength), and Feb38k (380 MPa characteristic yield strength) steel are considered.

#### 4.1 Finite Element Model

The model and the analyses are carried out with the finite element software MidasGen 2020 [28]. Beams and columns are modeled as beam elements; the double-tapered beam is modeled as an elastic element with equivalent rectangular cross-section 0.12x0.85 (m<sup>2</sup>). Being simply lying on the columns, it should not be directly damaged by seismic loading. To account for the nonlinear behavior of the columns, Takeda lumped plastic hinges are introduced.

As for the constraints, the columns are fixed at the base while the beam-to-column connection is modeled using a “Friction Pendulum” general link with a very high radius of curvature. The link in the global vertical direction of the beam-column connection is set to behave as a rigid compression-only element.

Parametric analyses are carried out for four different cases by varying the parameters  $\zeta$ ,  $\mu$ , and  $V Mode$  reported in Table 1; the main shock recorded in the Mirandola station during the 2012 seismic events and a behavior factor ( $q$ ) equal to 2.5 are assumed. The considered cases are summarized in Table 2.

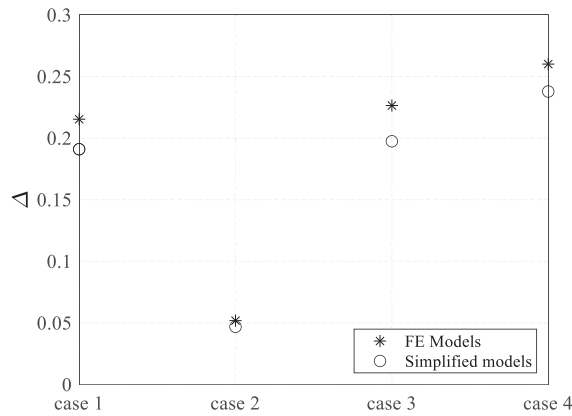
#### 4.2 Results and discussion

Figure 4 shows the results in terms of the ratio between the relative beam-column displacement and the beam support length indicated by the code ( $\Delta = \delta_{ij} / \delta_{REF}$ ). In this case,  $\delta_{REF} = 11.55\text{cm}$  is considered [29].

According with the preliminary consideration made in Section 3, the results show that the relative displacement decreases when the friction coefficient increases (-16%),  $\Delta$  increase when the vertical component (1<sup>st</sup>  $V Mode$ ) is considered; in particular, the relative displacement increases by 17% compared to the reference case. By varying the damping ratio (from  $\zeta_i=3\%$  to  $\zeta_i=1\%$ ) an increase of the relative displacement of approximately 5% compared to the reference case is showed.

Second, with the empty circle, the results obtained from the finite element model and the simplified model are compared. From the comparison, it can be observed that the simplified model can accurately predict the relative displacement between the beam and the column at the beam to column support. In this case, the maximum variation is about -10% with respect to the FEM model; the underestimation of the relative displacement could be due to the different models used for describing the beam-column connection in the two models and to the higher number of degrees of freedom in the FE model.





	$\zeta_i$	$\mu$	$V Mode$
case 1	3%	0.13	No
case 2	3%	0.50	No
case 3	1%	0.13	No
case 4	3%	0.13	Yes

Table 2: Considered cases in the parametric analyses.

Figure 4: Parametric analyses results for the different model considered and comparison between the FEM and the simplified model. The results are expressed in terms of ratio between the relative displacement ( $\delta_{ij}$ ) and the length of the support ( $\delta_{REF}$ ).

## 5 CONCLUSIONS

In this paper, a simplified model to evaluate the behavior of precast portal frames with beam-to-column simple friction connection is presented. The behavior of the portal frame has been investigated through a 4DOF model and parametric analyses have been carried out by varying the main parameters of the frame and of the simple friction connection ( $q$ ,  $\zeta$ ,  $\mu$ ,  $V Mode$ ).

The results of the parametric analyses showed that the friction coefficient ( $\mu$ ) is the parameter that most significantly affect the relative displacement between the columns and the beam. The vertical component of the ground motion is another parameter that should be accurately considered in the evaluation of the beam- loss of support is; if the vertical component of the ground motion is not considered, there is an underestimation of the relative displacements between the beam and the columns, thus resulting in an unconservative approach. Finally, the more the non-linear behavior of the structure, the less is the relative displacement between the beam and the column; the parameter  $\zeta$  (i.e. damping ratio) does not significantly affect the relative displacement. The results of the parametric analyses have been validated and assessed through a 2D finite element model.

## REFERENCES

- [1] A. Belleri, E. Brunesi, R. Nascimbene, M. Pagani and P. Riva, "Seismic performance of precast industrial facilities following major earthquakes in the Italian territory," *Journal of performance of constructed facilities*, vol. 29, no. 5, 2015.
- [2] A. Belleri, M. Torquati, P. Riva and R. Nascimbene, "Vulnerability assessment and retrofit solutions of precast industrial structures," *Earthquake and structures*, vol. 8, no. 3, pp. 801-820, 2015.
- [3] A. Belleri, "Displacement based design for precast concrete frames with not-emulative connections," *Engineering structures*, vol. 141, pp. 228-240, 2017.
- [4] M. Ercolino, G. Magliulo and G. Manfredi, "Failure of a precast RC building due to Emilia Romagna earthquakes," *Engineering structures*, vol. 118, pp. 262-273, 2016.
- [5] D. A. Bournas, P. Negro and F. F. Taucer, "Performance of industrial buildings during the Emilia earthquakes in Northern Italy and recommendations for strengthening," *Bulleting of earthquake engineering*, vol. 12, no. 5, pp. 2383-2404, 2014.
- [6] G. Magliulo, M. Ercolino, C. Petrone, O. Coppola and G. Manfredi, "The Emilia Earthquake: seismic performance of precast reinforced concrete buildings," *Earthquake Spectra*, pp. 891-912, May 2014.
- [7] F. Minghini, E. Ongaretto, V. Ligabue, M. Savoia and N. Tullini, "Observational failure analysis of precast buildings after the 2012 Emilia earthquakes," *Earthquakes and structures*, vol. 11, no. 2, pp. 327-346, 2016.
- [8] E. Nistri, M. Vergato and M. Latour, "Performance evaluation of seismic retrofitted RC precast industrial building," *Earthquakes and structures*, vol. 12, no. 1, 2017.
- [9] M. Palanci, S. M. Senel and A. Kalkan, "Assessment of one story existing precast industrial buildings in Turkey based on fragility curves," *Bulleting of earthquake engineering*, vol. 15, no. 1, pp. 271-289, 2017.
- [10] E. Brunesi, R. Nascimbene, D. Bolognini and D. Belotti, "Experimental investigation of the cyclic response of reinforced precast concrete framed structures," *PCI Journal*, vol. 60, no. 2, pp. 57-79, 2015.
- [11] A. Belleri, M. Torquati, A. Marini and P. Riva, "Horizontal cladding panels: in-plane seismic performance in precast concrete buildings," *Bulleting of earthquake engineering*, vol. 14, pp. 1103-1129, 2016.
- [12] A. Belleri, F. Cornali, C. Passoni, A. Marini and P. Riva, "Evaluation of out-of plane seismic performance of column-to-column precast concrete cladding panels in one-storey industrial buildings," *Earthquake engineering and structural dynamics*, vol. 47, pp. 397-417, 2017.
- [13] B. Dal Lago, P. Negro and A. Dal Lago, "Seismic design and performance of dry-assembled precast structures with adaptival joints," *Soil dynamics and earthquake engineering*, vol. 106, pp. 182-195, 2018.
- [14] M. Torquati, A. Belleri and P. Riva, "Displacement-based assessment for precast concrete frames with non-emulative connections," *Journal of earthquake engineering*, 2018.
- [15] I. Iervolino, A. Spillatura and P. Bazzurro, "RINTC e project: risk assessment of existing residential reinforced concrete buildings in Italy," in *7th ECCOMAS thematics*



- conference on computational methods in structural dynamics on earthquake engineering*, 2019.
- [16] M. Ercolino, D. Belotti, G. Magliulo and R. Nascimbene, "Vulnerability analysis of industrial RC precast buildings designed according to model seismic codes," *Engineering structures*, pp. 67-78, 2018.
  - [17] M. Bosio, A. Belleri, P. Riva and A. Marini, "Displacement-based simplified seismic loss assessment of Italian precast buildings," *Journal of earthquake engineering*, vol. 24, no. 1, pp. 60-81, 2020.
  - [18] M. E. Bressanelli, M. Bosio, A. Belleri, P. Riva and P. Biagiotti, "Crescent-moon beam-to-column connection for precast industrial buildings," *Frontiers*, 2021.
  - [19] C. Demartino, G. Monti and I. Vanzi, "Seismic loss-of-support conditions of frictional beam-to-column connections," *Structural Engineering and Mechanics*, vol. 61, pp. 527 - 538, 2017.
  - [20] A. Pompei, A. Scalia and M. A. Sumbatyan, "Dynamics of rigid block due to horizontal ground motion," *Journal of Mechanical Engineering*, vol. 124, no. 7, pp. 713-717, 1998.
  - [21] T. Taniguchi, "Non-linear response analyses of rectangular rigid bodies subjected to horizontal and vertical ground motion," *Earthquake engineering and structural dynamics*, vol. 31, no. 8, pp. 1481-1500, 2002.
  - [22] D. Lopez Garcia and T. T. Soong, "Sliding fragility of block-type non-structural components," *Earthquake engineering and structural dynamics*, vol. 32, no. 1, pp. 131-149, 2003.
  - [23] D. Lopez Garcia and T. T. Soong, "Sliding fragility of block-type non-structural components," *Earthquake engineering and structural dynamics*, vol. 32, no. 1, pp. 111-129, 2003.
  - [24] A. K. Chopra, *Dynamics of structures*, Earthquake engineering research institute, Berkeley CA, 1995.
  - [25] Y.-K. Wen, "Method for Random Vibration of Hysteretic System," *Journal of the Engineering Mechanics Division*, vol. 102, no. 2, pp. 249-263, 1976.
  - [26] I. The MathWorks, *Matlab*, 2017.
  - [27] R. Raths and J. Inc, *design handbook. Precast and Prestressed Concrete*, vol. 3rd, P. C. Institute, Ed., PCI, 1985.
  - [28] MidasGEN, "Analysis Manual for Midas GEN," 2020.
  - [29] M. Ercolino, *Seismic behavior of one-story precast buildings*, Ph.D. Thesis, University of Naples, 2014.

## SEISMIC PERFORMANCE OF BELL TOWERS

George C. Manos

<sup>1</sup> Laboratory of Strength of Materials and Structures, Aristotle University  
e-mail: gmanos@civil.auth.gr

---

### Abstract

*The dynamic and earthquake response of bell towers is examined here. The dynamic characteristics of two bell tower were measured in-situ through a series of free vibration tests that were performed following a strong earthquake sequence. Subsequently the dynamic and earthquake response of one of these bell towers was numerically simulated employing a 3-D elastic numerical simulation shell of the bell tower and its foundation. The earthquake response is examined for a variety of load combination conditions employing design spectra as well as the ground motion recorded at a small distance from this bell tower during a prototype earthquake motion. This study is further included to examine the influence of the soil-foundation interface. Towards this end, the non-linear uplift mechanism of the foundation block from the underlying soil is numerically simulated. The earthquake response is examined comparatively in terms of global response parameters, such as base shear, overturning moment, and top displacements as well as peak stress values at particular parts of the bell tower that stress concentration occurs. These response values are studied in a comparative way in order to validate these numerical simulations with the observed performance.*

**Keywords:** Bell towers, In-situ Dynamic Measurements, Numerical Simulation, Earthquake Response, Soil-structure Interaction.

---

## 1 INTRODUCTION

Bell towers are structures that are of particular interest regarding their dynamic and earthquake response, which has been the subject of research in the past ([3] to [10]). A large number of bell towers with dimensions much larger than the ones examined here are located in numerous cities in Italy and elsewhere. The largest percentage of these bell towers is built by stone or brick masonry. In many cases earthquake activity constitutes the major cause of serious damage for bell towers that many times leads to partial or total collapse ([1] and [2]). Consequently, there is a major international concern for the stability of numerous bell towers. This resulted to significant international research effort that includes in-situ monitoring of the response of bell towers on a temporary basis, like the one attempted here, or more sophisticated and on a permanent basis ([3] to [10]). Foundation problems for bell towers are evident in many case the most celebrated being Pisa's grand bell tower in Italy, that is quoted as a major medieval engineering error. Therefore, the soil flexibility is also an area of research interest for these structures especially when their dynamic and earthquake response is under investigation ([12] to [20]).

The purpose of this investigation is to study the seismic performance of relatively new bell towers compared to the old ones. Two of these relatively new bell towers, namely the bell tower of Agios Gerasimos at Lixouri [21] and the bell tower of Panayia Argiliotissa at Havriata, are selected for further in-depth study. Both structures are made of reinforced concrete and are distinct for the following reasons. A review of the seismic performance of bell towers and especially those located in Kefalonia, Greece is presented in [21] and [22].



Figure 1a. Stamp issued in 1953 by the Greek Post Organization



Figure 1b. Partial collapse of the bell tower at the village of Kourouklata during the recent 2014 earthquake sequence

## 2 IN-SITU MEASUREMENTS

In the present work a summary of in-situ measurements is presented again for two bell towers located in the island of Kefalonia. These bell towers are : a) The bell tower of Agios Gerasimos at Lixouri. b) The bell tower at the village of Havriata. Information on these two bell towers are also included in [21] and [22]. The basic geometrical features of these two bell towers are depicted in figure 2. Both bell towers were constructed after a catastrophic earthquake sequence in 1953 which destroyed numerous bell towers in this island. Both bell towers

are made of reinforced concrete and did not sustain any structural damage during the recent 2014 earthquake sequence despite the severity of the earthquake ground motion.

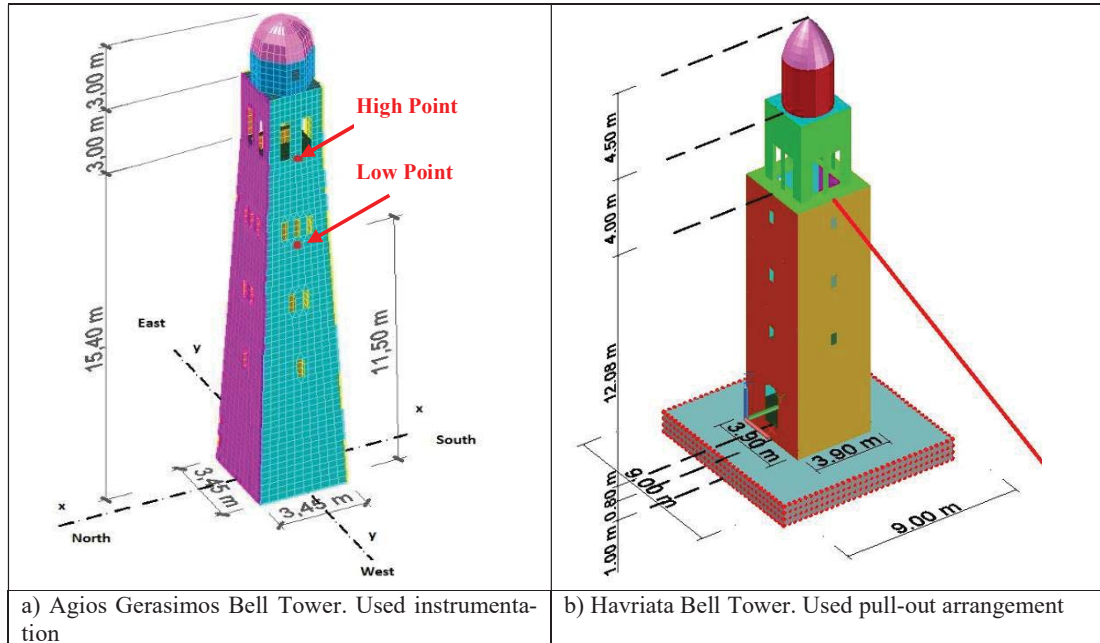


Figure 2. The Agios Gerasimos bell tower at Lixouri (left) and the Panagia Agriliotissa Bell tower at Havriata (right)

### 2.1. In-situ Measurements of Agios Gerasimos Bell Tower

The dynamic characteristics of this bell tower were measured in-situ through a series of free vibration tests that were performed following the damaging earthquake sequence 3<sup>rd</sup> of February 2014 seismic. The dynamic characteristics of this bell tower were measured in-situ through a series of free vibration tests that were performed following the damaging earthquake sequence 3<sup>rd</sup> of February 2014 seismic. A set of two tri-axial accelerometers were utilized together with a digital data acquisition system. These accelerometers were fixed at two locations along the height of the bell tower. The first accelerometer was fixed on a horizontal reinforced concrete (R/C) slabs which was built internally on this bell tower and was connected in a monolithic way with all four peripheral R/C walls. This R/C slab was immediately below the bells and could be reached through a R/C staircase which was also built internally and was also connected in a monolithic way with the peripheral R/C walls. This R/C slab was located at 15.4m from the ground level, which is named here “High Measuring Point (up)” and the accelerometer fixed at this level is depicted in figure 2a. The second tri-axial accelerometer was also fixed internally on the West R/C wall at a location 11.5m from ground level, which is named here “Low Measuring Point (down)”. It can be seen that both instruments were located at an axis of symmetry of this structure named y-y in figure 2a (East-West).

The bell tower was excited by a pull-out free vibration test sequence ([20], [21] and [22]). More details are included in [21]. Figure 3 depicts the measured bell tower response at the low and high measuring point during a pull-out in-situ test. The presence of a quite dominant frequency is quite clear in these free vibration dynamic acceleration responses. This dominant response frequency, which is equal to 2.343Hz (0.427 sec. period), was extracted from transforming the obtained measurements in the frequency domain through a Fast Fourier Transform (FFT) algorithm.

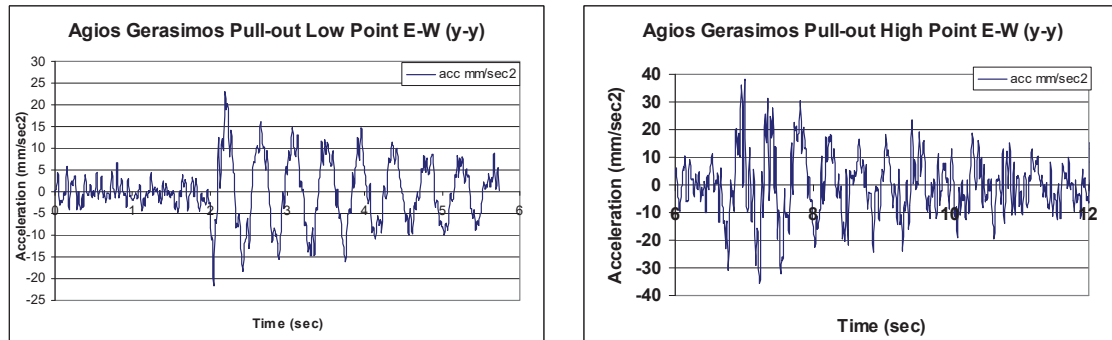


Figure 3. Free vibration horizontal acceleration response at the “Low and High measuring points” of the Agios Gerasimos bell tower at Lixouri

### 2.3. In-situ Measurements of the Bell Tower belonging to the Panayia Agriliotissa.

The church of Panayia Agriliotissa church at Havriata village, built in 1693, is partially supported by a backfill and a system of retaining walls depicted in figure 4. The dynamic characteristics of this bell tower were measured in-situ through a series of pull-out excitations tests (see Manos et al, [21]), which were performed on 10<sup>th</sup> October, 2015, approximately twenty (20) months after the damaging earthquake sequence of 3<sup>rd</sup> of February 2014. This type of excitation that was also employed for the bell tower of Agios Gerasimos at Lixouri [21], namely pull-out excitation. The level of this pull-out excitation was capable of producing horizontal vibrations by exciting mainly the horizontal translational eigen-modes of this bell tower. This dynamic response could be capture by the employed tri-axial velocity sensors with a sensitivity of 0.001mm/sec and a data acquisition system with a sampling frequency of 400Hz. The velocity response measurements were made by securing the velocity sensors at 5 levels along the height of the bell tower. This is depicted in figure 4 whereby for each level the vertical distance from level 0 is also indicated e.g. at 0.80m (level 1), 3.84m (level 2), 6.78m (level 3), 9.83m (level 4), 12.88m (level 5).

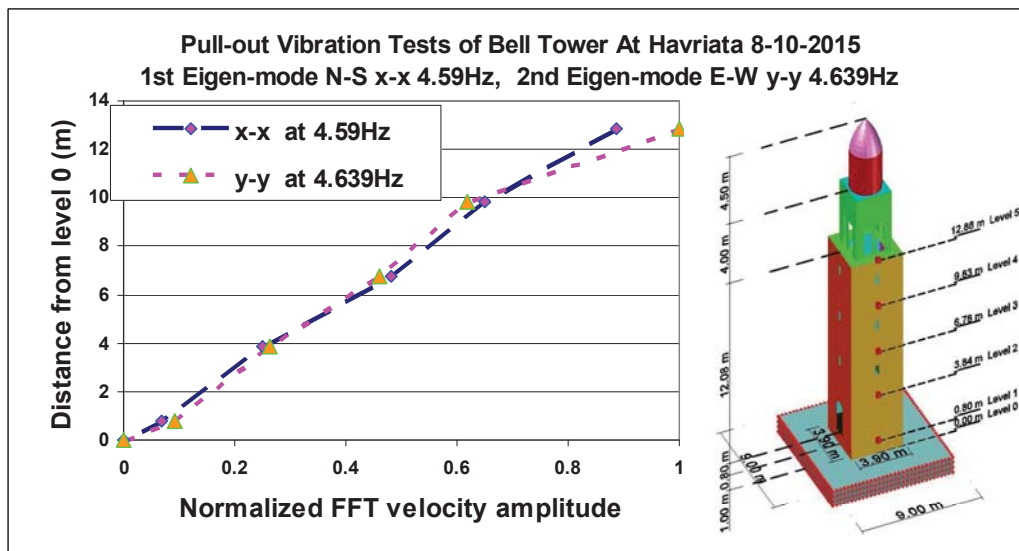


Figure 4. FFT velocity response amplitudes along the height of the Havriata bell tower for the main eigen-frequencies.

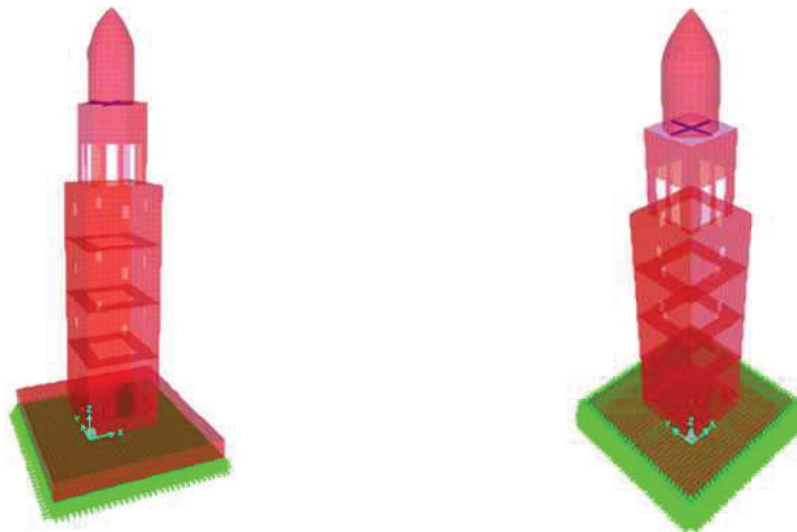
From the analysis of the measured velocity response in the frequency domain the main eigen-frequency values were obtained equal to 4.59Hz for the N-S (x-x) and 4.639Hz for the E-



W (y-y) directions, respectively. These frequency values, as will be explained, correspond to the 1<sup>st</sup> and 2<sup>nd</sup> horizontal translational modes. This is concluded from the same frequency analysis by selecting and plotting along the height in figure 4 (left) the FFT amplitudes that correspond to these frequency values, as obtained from the measured vibration response along the height of the bell tower at each one of the five (5) selected levels. The plotted in figure 4 FFT amplitude variation along the bell tower height for these specific eigen-frequency values are normalized, thus representing the mode shapes of the two N-S and E-W eigen-modes. As can be seen in this figure, the resulting mode shapes have an almost linear variation along the height from level 0 to level 5 thus representing the translational horizontal mode-shapes of the bell tower in the N-S (x-x) and E-W (y-y) directions.

### 3 NUMERICAL SIMULATION OF THE DYNAMIC AND EARTHQUAKE RESPONSE OF THE PANAYIA AGRILIOTISSA BELL TOWER AT HAVRIATA

The dynamic response of this bell tower was numerically simulated employing a linear elastic dynamic analysis utilizing shell elements assumed to be of reinforced concrete as an isotropic material with a Young's Modulus equal to  $E=10000\text{MPa}$  and typical to reinforced concrete. The bells were assumed to weight 500kgf. They were simulated with a steel beam that was placed at the right location and height where the actual steel beam supporting the bells is located. A mass and weight multiplier was used for this beam to account for the extra mass and weight of the bells. The geometry and thickness of the external walls, the slabs and the top vault of this bell tower were included in this numerical simulation.



a) Foundation block simply-supported      b) Foundation block supported with 3-D links  
Figure 5. 3-D numerical simulation of the Havriata bell tower

The foundation was assumed to be a mass-less concrete block of total thickness equal to 1m that was numerically formed by the following parts (figure 5):

- Two mass-less and stiff horizontal slabs with a thickness 0.45m were located one at zero (0) level and the other at a depth of 1.0m from zero (0) level. These slabs represent the upper and lower horizontal planes of the foundation concrete block. In addition, four mass-less and stiff vertical slabs having a thickness 1.0m were also added. Two of these slabs were placed at the x-z plane and the other two at the y-z plane of the numerical model. These ver-

tical slabs represent the peripheral vertical planes of the foundation block facing the East-West (x-z plane) and the North-South (y-z plane) directions. In this way the foundation block was formed that represents in itself a very rigid part of the whole structure. In order to approximate the possibility of a flexible interface between this foundation block and the surrounding soil volume two types of boundary conditions were introduced in this numerical model. In the first case all the points of the bottom slab of this foundation block were simply supported whereas in the second case all these points were connected to the supporting media with 3 directional linear springs with a stiffness equal to 5000000KN/m, a value that corresponds to a very stiff soil (see also Manos and Kozikopoulos [21]).

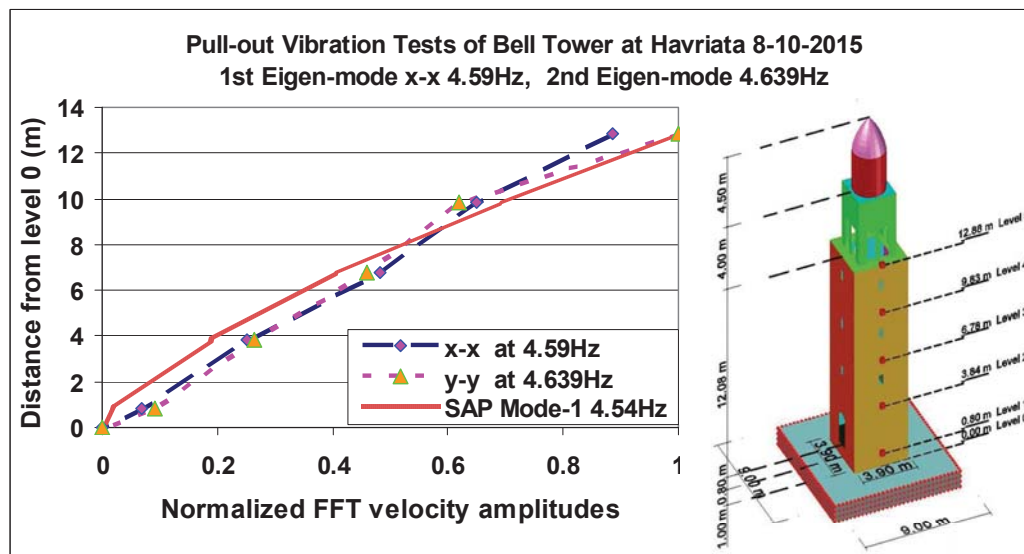


Figure 6. Comparison of measured and predicted dynamic characteristics of the Havriata bell tower.

In figure 6 the numerically predicted N-S / E-W eigen-frequencies values and eigen-mode shapes (SAP Mode-1) are compared with the corresponding measurements (N-S x-x and E-W y-y). Only the numerical results for the x-x 1<sup>st</sup> mode are plotted in this figure because the corresponding results for the second y-y mode are almost identical, due to the geometric symmetry of this bell tower. The plotted eigen-mode shape is limited to that part of the bell tower where measurements of its dynamic response were obtained from the in-situ campaign, as already described, from level 0 to level 5. As can be seen in this figure reasonably good agreement can be seen between both the measured and numerically predicted eigen-mode shape as well as the eigen frequency values. The numerical results obtained from the simply supported foundation block are almost identical to the corresponding results obtained from the numerical model whereby the foundation block is supported by 3-D stiff links (5000000KN/m), as already described. Thus, in the case of the Havriata bell tower it was not necessary to employ less stiff 3-D links at the soil foundation interface in order to reach a reasonably good agreement between measured and numerically predicted dynamic response characteristics for this structure. On this point it is important to underline that in the case of the bell tower of Agios Gerasimos at Lixouri [21], whereby the authors followed an identical methodology for in-situ measurements and numerical simulation, it was necessary in-order to reach such a reasonable degree of agreement between measured and predicted dynamic response to use 3-D links with a stiffness value equal to 21000KN/m. The obvious conclusion is that in the case of the Havriata bell tower the flex-

ibility of the surrounding soil volume exercised much less influence on its dynamic response than in the case of the Agios Gerasimos at Lixouri bell tower. This observation is in good agreement with the overall picture of the two locations as the Havriata bell tower is located at the top of a hill whereas the Agios Gerasimos bell tower is located at a close distance from the harbor almost at sea level. However, it must also be underlined that this conclusion is based on in-situ dynamic response measurements generated from relatively very low level excitations and it should not be extended to the very intense excitation that both structures were subjected to during the earthquake sequence of 3<sup>rd</sup> February, 2014. On the contrary, as will be described in the following, both structures were subjected to very intense earthquake excitations during the 3<sup>rd</sup> of February 2014 seismic event [1].



Figure 7a. The damaged longitudinal peripheral masonry South wall of the church after the seismic event of 3<sup>rd</sup> February 2014

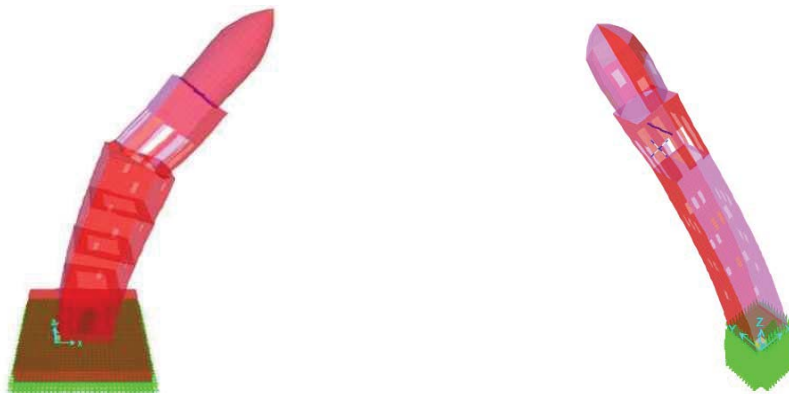


Figure 7b. The failure of the retaining wall and the backfill at the South side of The Theotokos church of Havriata

Figure 7b show the failure of the retaining wall and the backfill at the South side of the Theotokos church of Havriata, at a distance of less than 50m from the bell tower. Moreover, the church of Panayia Agriliotissa of Havriata developed also significant structural damage (figure 7a). These observations represent visual evidence of the severity of the ground motion of this seismic event. In addition, both in Lixouri as well as in Havriata the seismic excitation was recorded [1, 21, 22], by strong motion accelerographs located at close distance from either bell tower (approximately 300m).

It must be underlined that the Havriata bell tower was designed and constructed well after 1996, when the provisions of the new Greek seismic code became mandatory ([11], [23], [24]). The adopted in the case of Agios Gerasimos bell tower design acceleration/force levels for its seismic design could not be ascertained up to now. However, in this case from eye witness reports the foundation block in the case of Agios Gerasimos bell tower was much thicker and as such was included in the numerical simulation.





a) Theotokos bell tower at Havriata.

Translational mode N-S (x-x)

T=0.220sec, f=4.54Hz, (stiff soil)

b) Agios Gerasimos bell tower at Lixouri.

Translational mode N-S (x-x)

T=0.425sec, f=2.35Hz, (medium soil)

Figure 8. Comparison of translational eigen-modes and eigen-frequencies of the Theotokos bell tower at Havriata and the Agios Gerasimos bell tower at Lixouri.

In figure 8, the mode-shape of the 1<sup>st</sup> translational eigen-mode of the Havriata bell tower is shown, as predicted numerically for the full height of this bell tower (from level 0 to the top). In the same figure the measured 1<sup>st</sup> eigen-frequency and eigen-mode in either the North-West or the North-South direction is also indicated. A good agreement can be seen between the measured and the numerically predicted values. It must be underlined that in the case of the Havriata bell tower the foundation block was supported at its base to the soil with a series of link elements representing stiff-soil conditions. In figure 8a and 8b, the mode shapes of the 1<sup>st</sup> translational eigen-mode for the Havriata and the Agios Gerasimos bell towers are depicted, respectively. As can be seen in these figures, the flexible soil in the case of the Agios Gerasimos bell tower leads to an increase in the flexibility of the whole structure. On the contrary, the stiff soil in the case of the Havriata bell tower results to a relatively stiff structure and leads to a more pronounced response of its upper part which is relatively more flexible than its lower part.

#### 4.1. Results from the design spectral curves

In this section the performance of the Havriata bell tower will be studied adopting earthquake force levels according to the type-2 Euro-Code 8 design spectra for soil category D. Moreover, the design ground acceleration for the island of Kefalonia, as specified by the seismic zoning map of the new seismic code of Greece, equal to 0.36g (g the acceleration of gravity) is also adopted. The importance factor for the bell tower is set equal to 1. A critical point is the value of the behaviour factor (q).

$$q = q_0 k_w \geq 1.5$$

where:  $q_0$  is the basic value of the behaviour factor, dependent on the type of the structural system and on its regularity in elevation;

$k_w$  is the factor reflecting the prevailing failure mode in structural systems with walls

For reinforced concrete structures that are formed by uncoupled walls, as one can classify the Havriata bell tower, the minimum value for the behaviour factor is  $q_0 = 3$  [23]. This value can become even higher when the detailing ensures behaviour of high ductility. At the same time, because of the dimensions of the bell tower and the presence of the bells at its upper part, such a structure could be considered as partly resembling an inverted pendulum in which case the behaviour factor value ranges from  $q_0 = 1.5$  to 2.0. The value of  $q_0$  given for inverted pendulum systems may be increased, if it can be shown that a correspondingly higher energy dis-

sipation is ensured in the critical region of the structure. The value of  $k_w$  for the bell tower can range from 1 to 1.43. Part of the concept of high values for the behaviour factor is based on the fact that the strong seismic ground motion effect will be absorbed from ductile inelastic hysteretic response of its structural members and thus reduce the overall structural response in a way similar to that of an overdamped elastic response associated to reduced levels of seismic forces. For the purposes of this study a value of  $q=3$  could be adopted for the behaviour factor considering this bell tower as an RC wall system. In a complementary study the inelastic response spectral curves were derived for the two horizontal components of the ground motion recorded at Havriata at a small distance of the bell tower during the strongest event on the 3<sup>rd</sup> of February, 2014. These inelastic spectral curves were derived for an assumed ductility factor value  $m=3$ , to be in accordance with the adopted value of the behaviour factor adopted for the design spectra derived from the provisions of Euro-Code 8, as described above. These are depicted in the following figure 9 for the East-West and the North-South horizontal components of the named recording of the ground motion at Havriata.

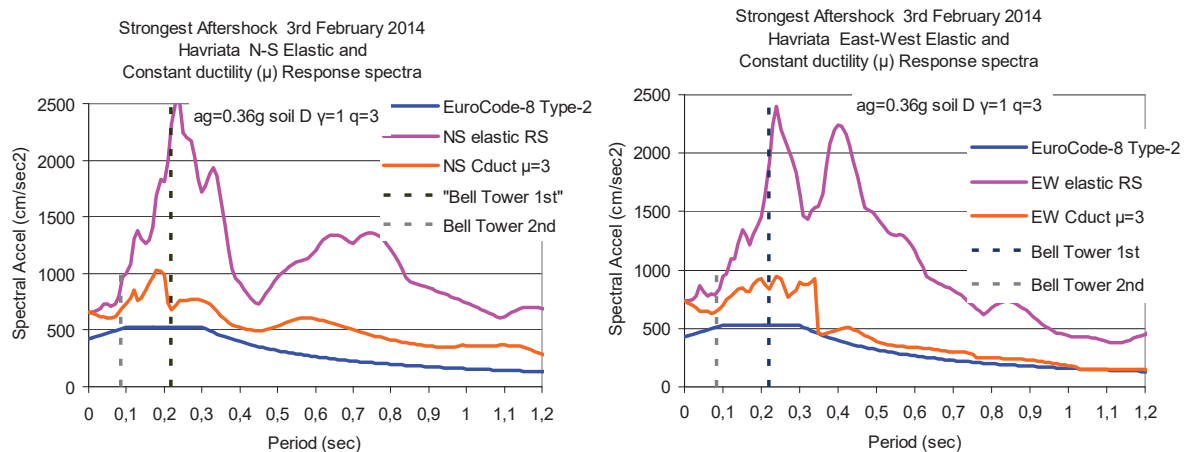


Figure 9. The response and the design spectra for the Havriata Bell tower

In figure 9, the eigen-period values of the 1<sup>st</sup> and 2<sup>nd</sup> eigen-modes in either the North-South or the East-West directions are also indicated. Apart from the Euro-Code-8 design spectral curves and the inelastic ( $m=3$ ) constant ductility spectral curves of the Havriata strong motion record in the two horizontal directions, the corresponding elastic spectra curves are also plotted. As can be seen from these plots, the inelastic constant ductility curve values are larger than the corresponding Euro-Code 8 design spectral values for both eigen-periods and for both directions. Similarly, the elastic response spectral curve values are much higher than the corresponding inelastic constant ductility ( $m=3$ ) spectral curves. Moreover, the following observations can be made.

- The 1<sup>st</sup> eigen-period value for the Havriata bell tower corresponds to the period range with the relatively large spectral values. This is also the case for the Agios Gerasimos bell tower.
- The presence of the relatively flexible soil in the case of the Agios Gerasimos results in a larger eigen-period value (0.425sec) than the corresponding eigen-period value for the Havriata bell tower (0.220sec). These numerically predicted eigen-period values were validated by the in-situ measurements.
- The presence of the flexible soil in the case of the Lixouri also influenced the seismic ground motion as can be seen when the response spectral curves of Lixouri ground motion

record [1] are compared with the corresponding response spectral curves of Havriata ground motion record. Thus, it can be seen that in the case of the Havriata ground motion the period range with the largest spectral values is from 0.15sec to 0.4sec whereas in the case of the Lixouri ground motion record this period range was sifted to 0.3sec to 0.6sec.

The modal analysis results of the numerical model of the Havriata bell tower resting on links representing stiff soil conditions are listed in the following table. In this numerical model the part that simulates the foundation block which is below the ground surface is represented by a rigid box formed by relatively rigid finite elements in a way that the weight of the actual foundation block is realistically approximated. At the same time these elements are assumed to be practically mass-less as not to interfere in an unrealistic way with the dynamic system of this structure. Moreover, in order to account for the influence of soil deformability the link elements supporting the foundation block to the soil were provided with a damping ratio equal to 10% of critical.

Table . Modal Participating Mass Ratios

Mode	Period	UX	UY	UZ	SumUX	SumUY	SumUZ
Number	Sec	Unitless	Unitless	Unitless	Unitless	Unitless	Unitless
1	<b>0,22</b>	<b>0,52381</b>			0,52381	0	0
2	<b>0,219</b>		<b>0,5114</b>		0,52381	0,5114	0
3	<b>0,086</b>	<b>0,21565</b>			0,73946	0,5114	0
4	<b>0,084</b>		<b>0,2085</b>		0,73946	0,7199	0
5	0,062				0,73952	0,7199	0
6	<b>0,05</b>			<b>0,51</b>	0,73952	0,7199	0,51
7	0,041	0,06824			0,80776	0,7199	0,51
8	0,04		0,0646		0,80776	0,7845	0,51
9	0,039	0,00473			0,81249	0,7845	0,51
10	0,032	0,05812			<b>0,87061</b>	<b>0,7845</b>	<b>0,51</b>

Table . Base Reactions

Load case	CaseType		GlobalFX (tnf)	GlobalFY (tnf)	GlobalFZ (tnf)
DEAD (with Foundation)	LinStatic	Max			534,6 / 225,6*
1. EuroCode 8 q=3	LinRespSpec	Max	<b>70,1 / 13%</b>	<b>70,1 / 13%</b>	
2. EW-res spectra Con. Duc. m=3	LinRespSpec	Max		<b>104,4 / 20%</b>	
3. NS-res spectra Con. Duc. m=3	LinRespSpec	Max	<b>90,9 / 17%</b>		
4. Dead + EC8x-x + 0.3EC8y-y	LinRespSpec	Max	<b>70,1 / 13%</b>	<b>20.4</b>	534,6 / 225,6*
5. Dead+0.3 EC8x-x + EC8y-y	LinRespSpec	Max	<b>21.0</b>	<b>67.8</b>	534,6 / 225,6*
6. Dead+(RSEW + 0.3RSNS) m=3	LinRespSpec	Max	<b>27.3</b>	<b>104.4</b>	534,6 / 225,6*
7. Dead+(RSEW + 0.3RSNS) m=3	LinRespSpec	Max	<b>90.9</b>	<b>31.3</b>	534,6 / 225,6*

- with and without the weight of the foundation block. The listed percentage values in this table were derived from comparing the base shear values in each case with the total weight of the bell tower including the foundation

As can be seen from the modal participating mass ratio values listed in the above table the 1<sup>st</sup> and second translational modes in the x-x (North-South) and the y-y (East-West) direction mobilize a considerable part (more than 72%) of the total mass of the superstructure. The rest of the higher order modes used in the subsequent dynamic spectral analyses (up to 10 modes) mobilize up to 87% and 78.5% of the total mass of the superstructure in the x-x and y-y horizontal directions, respectively. Therefore, no further amplification of the dynamic response was employed. The resulting base shear values are listed in Table . The listed percentage val-

ues in this table were derived from comparing the base shear values in each case with the total weight of the bell tower including the foundation. As can be seen, the seismic force levels when the constant ductility response spectra curves are employed are higher (20% of the total weight) than those employing the Euro-Code-8 design spectral curves (13% of the total weight). The same is obviously valid when the load combinations, described in load cases No. 6 and 7 (constant ductility response spectra) are compared with load cases No. 4 and 5 (Euro-Code-8 design spectra).

Load Cases	Top of Tower Hor. Displ. (mm)	Base Shear (tnf)	Over Moment (tnf-m)	Vertical link force* (tnf)
4. Dead + EC8x-x + 0.3EC8y-y	U <sub>x</sub> =14.75 / U <sub>y</sub> =4.48	Q <sub>x</sub> =70 Q <sub>y</sub> =20	M <sub>x</sub> =1301 M <sub>y</sub> =-1911	0.14 / -2.09
5. Dead + 0.3 EC8x-x + EC8y-y	U <sub>x</sub> =4.43 / U <sub>y</sub> =14.69	Q <sub>x</sub> =21 Q <sub>y</sub> =67	M <sub>x</sub> =1900 M <sub>y</sub> =-1305	0.06 / -2.06
6. Dead + (RSEW + 0.3RSNS) m=3	U <sub>x</sub> = 5.72 / U <sub>y</sub> =23.11	Q <sub>x</sub> =27 Q <sub>y</sub> =104	M <sub>x</sub> =2389 M <sub>y</sub> =-1381	0.60 / -2.06
7. Dead + (RSNS + 0.3RSEW) m=3	U <sub>x</sub> =19.06 / U <sub>y</sub> =7.01	Q <sub>x</sub> =91 Q <sub>y</sub> =31	M <sub>x</sub> =1449 M <sub>y</sub> =-2164	0.55 / -2.50

\* The vertical force that develops at the link connecting the foundation block with the soil located at the North-West corner of this foundation block

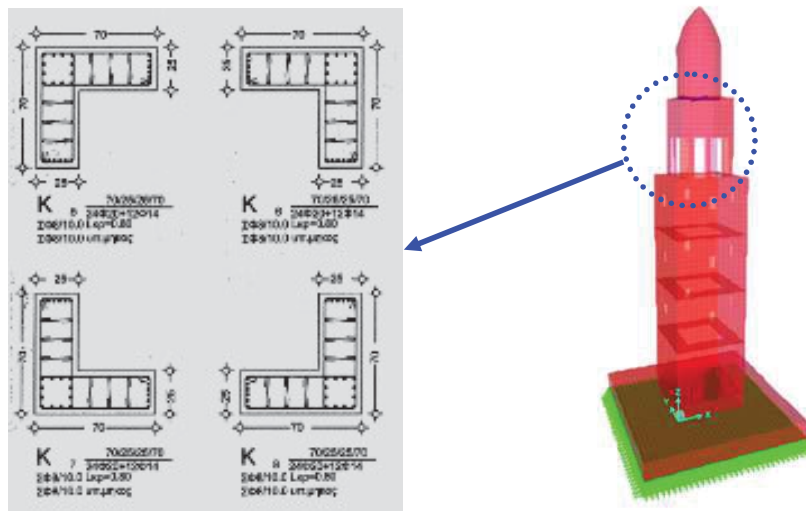


Figure 10. Structural detailing of the columns at the level supporting the bells

Figure 10 depicts the structural detailing of the part of the bell tower with the columns above the level 12.00m, which as depicted in figures 11, is highly stressed both in tension and shear from the load combinations that include either the EuroCode-8 design spectral curves or the constant ductility response spectral curves of the recorded ground motion during the strongest earthquake event of the 2014 sequence. This bell tower was designed according to the provisions of the Euro-code 8 by a designer civil engineer (see acknowledgements) assuming design ground acceleration 0.36g, behaviour factor  $q=3$ , importance factor  $\gamma=1$ , and soil category B according to the provisions of the new Greek seismic code. The quality of the concrete was C20/25 and the reinforcing steel S400s (assumed yield stress equal to 400MPa). As was shown in figure 10, the inelastic spectral acceleration curves derived from the recorded ground motion assuming ductility factor equal to  $m=3$  re-

sult in base shear values approximately 50% higher than the corresponding base shear values derived from the Euro-Code-8 design spectral values (see Table ). It was underlined that no structural damage could be seen at this bell tower after the event despite the fact that it was subjected to earthquake forces exceeding the level of the assumed earthquake forces in the design. The same can be seen when one compares the maximum displacement response values predicted to develop at the top of the bell tower employing the Euro-Code-8 design spectra with the corresponding constant ductility response spectra curves. The same can be seen when one compares the stress levels that develop at the columns of the part of the bell tower below the level where the bells are located. This part of the structure is selected because the columns located at this part of the whole structural system develop relatively high level of stresses. These stress levels can be met successfully by the reinforcing details of these columns.

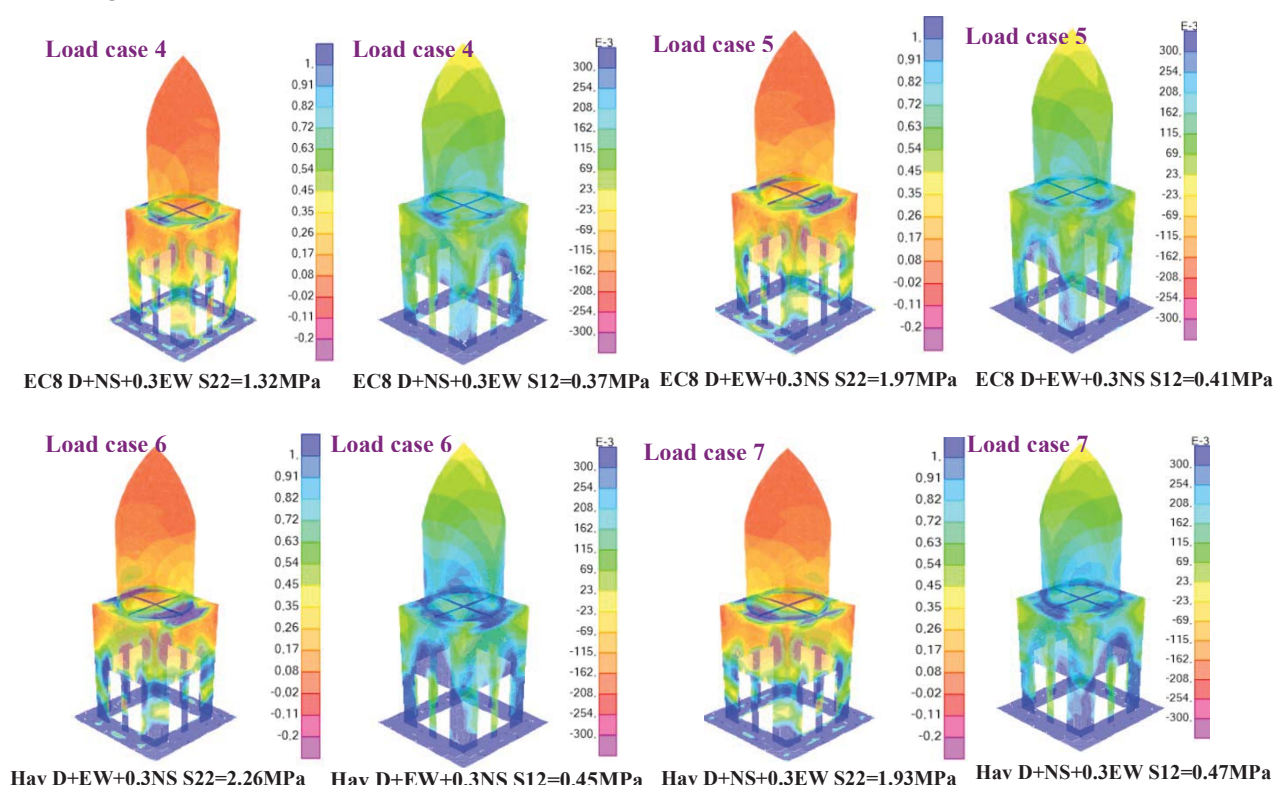


Figure 11. Stress levels that develop at the part of the bell tower supporting the bells for the various loading conditions

#### 4 CONCLUSIONS

- The measured 1<sup>st</sup> eigen-period values compare well with the numerically predicted values for both bell towers. The 1<sup>st</sup> eigen-period value for the Havriata bell tower corresponds to the period range with the relatively large spectral values. This is also the case for the Agios Gerasimos bell tower.
- The presence of the relatively flexible soil in the case of the Agios Gerasimos results in a larger eigen-period value (0.425sec) than the corresponding eigen-period value for



the Havriata bell tower (0.220sec). The employed numerical simulations recognized this fact by employing the appropriate support conditions of the foundation block.

- The seismic force levels when the constant ductility response spectra curves are employed are higher (20% of the total weight) than those employing the Euro-Code-8 design spectral curves (13% of the total weight).
- The bell tower columns above the level 12.00m, represent the part of the bell tower which is highly stressed both in tension and shear.
- No structural damage could be seen at this bell tower after the event despite the fact that it was subjected to earthquake forces exceeding the level of the assumed earthquake forces in the design.

## ACKNOWLEDGEMENTS

The authors would like to thank Civil Engineer L. Rouchotas for providing information relevant to the design of the Havriata bell tower. Moreover, the authors would like to thank the priest and the council of the Theotokos church during the in-situ measurements.

- To the memory of Nick Simos, Senior Researcher, Brookhaven National Laboratory, U.S.A.

## REFERENCES

- [1] GEER - EERI - ATC - Cephalonia GREECE *Earthquake Reconnaissance January 26th/ February 2nd 2014 Version 1: June 6 2014*
- [2] Papazachos, B. and Papazachou, K., 1989, 1997, 2003. The earthquakes of Greece, *Zitis Publ., Thessaloniki*, 356 pp., 304 pp., 286 pp. (in Greek).
- [3] L. de Stefani, R. Scotta, M. Lazzari, A. Saetta. Seismic improvement of Slender Bell Tower and Minarets. – *PROHITECH, Antalya, Turkey, 2014*
- [4] R. M. Azzara, L. Zaccarelli, A. Morelli, T. Trombetti. Seismic Monitoring of the Asinelli and Garisenda Medieval Towers in Bologna (Italy), an Instrumental Contribution to the Engineering Modeling Directed to their Protection. - *PROHITECH, Antalya, Turkey, 2014*
- [5] Casolo Siro, Uva Giuseppina. Non-Linear dynamic analysis of masonry towers under natural accelerograms accounting for soil-structure interaction. – *COMPDYN 2013 - Kos Island, Greece, June 12-14, 2013*
- [6] A. Saisi, C. Gentile, L. Cantini. Post – Earthquake assessment of a masonry tower by on – site inspection and operational modal testing. – *COMPDYN 2013 - Kos Island, Greece, June 12-14, 2013*
- [7] D. Colapieto, A. Fiore, A. Netti, F. Fatiguso, G. Marano, M. de Fino D. Cascella, A. Antocona. Dynamic identification and evaluation of the seismic safety of a masonry bell tower in the south Italy. – *COMPDYN 2013 - Kos Island, Greece, June 12-14, 2013*
- [8] R. Guidorzi, R. Diversi, L. Vincenzi, C. Mazzotti, V. Simioli. Structural monitoring of the Tower of the Faculty of Engineering in Bologna using MEMS –based sensing. – *EURODYN 2011 – Leuven, Belgium, 4-6 July 2011*

- [9] C. Blasi M. Carfagni, S. Carfagni. The use of impulsive actions for the structural identification of Slender monumental buildings- *STREMAH-1991 - Seville, Spain, 14-16 May 1991*
- [10] S. Dumorier, W.P. De Wilde. Finite element study of the Tower of Brussels City Hall – *STREMAH 1995 – Chania, Crete, Greece, 1995.*
- [11] G.C. Manos, Seismic Code of Greece, Chapter 17, International Handbook of Earthquake Engineering: "Codes, Programs and Examples", edited by Mario Paz, by Chapman and Hall, ISBN 0-412-98211-0, 1994.
- [12] G.C. Manos, et al. (1996) "Predictions of the dynamic characteristics of a 5-story R.C. building at the Volvi Euro-SeisTest Site, utilizing low-intensity vibrations", *3rd European Conference on Structural Dynamics, Eurodyn 1996, Florence, II, 877–884.*
- [13] G. C. Manos, (1998). "The Dynamic Response of a 5-story Structure at the European Test site at Volvi-Greece." *6th U.S. National Earthquake Engineering Conference, May 31 - June 4, Seattle, Washington, U.S.*
- [14] G. C., Manos, et al.. (2004). "Dynamic and Earthquake Response of Model Structures at the Volvi – Greece European Test Site." *13th World Conference on Earthquake Engineering, Vancouver, Canada.*
- [15] G. C., Manos, V. Kourtides, V.J. Soulis, A.G. Sextos, A. G., and P. Renault, (2006). "Study of the dynamic response of a bridge pier model structure at the Volvi - Greece European Test Site." *8th National Conference on Earthquake Engineering, April 18-22, San Fransisco, U.S.A.*
- [16] G.C. Manos, V. Kourtides, A. Sextos, P. Renault, S. Chiras "Study of the dynamic soil-structure interaction of a bridge pier model based on structure and soil measurements" *9<sup>th</sup> Canadian Conf. on Eartquake Engineering, Ottawa, Ontario, Canada, 26-29 June 2007.*
- [17] G.C. Manos, V. Kourtides, A. Sextos, S. Chiras "Soil-Foundation-Bridge Pier Interaction at the Euro-Seis Test Site", *4<sup>th</sup> Int. Conference on Geotechnical Engineering, Thessaloniki, 24-28 June, 2007.*
- [18] G.C. Manos, V. Kourtides, A. Sextos, "Model Bridge Pier Foundation- Soil Interaction implementing, in-situ / shear stack testing and numerical simulation", *14WCEE, Beijing, CHINA, 2008.*
- [19] Manos George, "Consequences on the urban environment in Greece related to the recent intense earthquake activity", *Int. Journal of Civil Engineering and Architecture, Dec. 2011, Volume 5, No. 12 (Serial No. 49), pp. 1065–1090.*
- [20] G. C. Manos , K.D. Pitilakis, A.G. Sextos, V. Kourtides, V. Soulis, J. Thauampth, "Field experiments for monitoring the dynamic soil-structure-foundation response of model structures at a Test Site" *Journal of Structural Engineering, American Society of Civil Engineers, Special Issue "Field Testing of Bridges and Buildings, D4014012, Vol. 141, Issue 1, January 2015.*
- [21] G.C. Manos and E. Kozikopoulos, "In-Situ Measured Dynamic Response of the Bell tower of Agios Gerasimos in Lixouri-Kefalonia, Greece and its Utilization in the Numerical Predictions of its Earthquake Response", *COMPDYN 2015, 5th ECCOMAS Thematic Conference on, Computational Methods in Structural Dynamics and Earthquake Engineering, Crete Island, Greece, 25–27 May 2015.*

- [22] G.C. Manos, D. Naxakis, V. Soulis, “The Dynamic and Earthquake Response of a Two-story Old R/C Building with Masonry Infills in Lixouri-Kefalonia, Greece, Including Soil-Foundation Deformability, *COMPDYN 2015, 5th ECCOMAS Thematic Conference on, Computational Methods in Structural Dynamics and Earthquake Engineering, Crete Island, Greece, 25–27 May 2015*.
- [23] Eurocode 8: Design of structures for earthquake resistance - Part 1: General rules, seismic actions and rules for buildings, *FINAL DRAFT prEN 1998-1, December 2003*.
- [24] EAK-2000 Greek seismic Code (in Greek).



## STUDYING THE PERFORMANCE OF STONE MASONRY ARCH BRIDGES EMPLOYING IN-SITU MEASUREMENTS AND NUMERICAL PREDICTIONS

G.C. Manos<sup>1</sup> and N. Simos<sup>+</sup>

<sup>1</sup> Laboratory of Strength of Materials and Structures, Aristotle University  
e-mail: gcmayos@civil.auth.gr

<sup>+</sup> Brookhaven National Laboratory, U.S.A.

---

### Abstract

*The present study presents a series of in-situ measurements conducted at selected old stone masonry bridges, using up-to-date system identification techniques, in an effort to identify their dynamic characteristics in terms of eigen-frequencies, eigen-modes and damping properties. All these information is part of a data base that can be used in the future as a reference for identifying noticeable changes in these dynamic characteristics as part of a structural health monitoring effort for these bridges. Moreover, this information provides a basis for building realistic numerical simulations towards studying the structural behaviour of such stone masonry bridges and assessing their expected structural behaviour in extreme future seismic events. Selected in-situ measurements are presented together with their use in building numerical models of various levels of complexity. These numerical models are finally utilized in assessing the expected performance of specific case studies of stone masonry bridge structures in Greece towards meeting the demands of extreme events that include design earth-quake loads. The described system identification technique can also be linked to specific actions, such as earthquake activity, and thus serve as warning for specific maintenance counter-measure.*

**Keywords:** Stone Masonry Bridges, In-situ Vibration Measurements, System Identification, Numerical Simulation, Foundation Deformability, Plaka Bridge Collapse.

---

## 1 INTRODUCTION

In what follows selective results are presented from an extensive study, which focused on old stone masonry bridges that are located mainly in the prefectures of Western Macedonia and Epirus and Thessaly in Greece (Gialeridis 1995, Grassos 2007, Milas 2016, Psimarni et al 2000). These bridges are examples of out-standing stone-masonry construction that was dominant for a long period in these parts of Greece (Figs. 1a and 1b).



Figure 1a. Konitsa Bridge, Ipiros, Greece.



Figure 1b. Plaka Bridge, Ipiros, Greece. (Before its collapse in 1<sup>st</sup> February 2015)

The use of the stone masonry arch that is utilized in forming stone masonry bridges was extensively used in the times of the Roman Empire as part of the transportation system that was established and linked the various provinces of the Roman Empire. Evidence of stone masonry arch bridges prior to Roman times is not known although stone masonry structures in the East Mediterranean area for other uses date to prehistoric times. A well known use of arch/vault stone masonry structural form is the one that can be seen at the royal tombs which have been excavated during the last 200 years in many places in Greece.

The royal tomb of Atræus at Mycenae-Greece utilized stone masonry to form an underground vaulted structure with a diameter at its base of 14.60m and a height of 13.30m constructed with 33 subsequent series of stone masonry along the height. The use of such vaulted stone masonry structures demonstrates the efficient utilization of this structural form in order to bear efficiently the dead loads as well as the weight of the overlying soil volume in a state of stress dominated by compression. The use of the stone masonry arch/vault type formation is also evident in the structural system of the royal tombs of the Macedonian kings at Vergina in Northern Greece, dated from 350 B.C. and excavated during the last 30 years. Despite the use of arch/vaulted stone masonry structural formations for these underground Macedonian royal tombs at Vergina in Northern Greece there is no evidence of such structural formations being used for bridges at that time. The remains of an ancient Roman bridge is located between Vergina and Thessaloniki. These remains correspond today to only one main arch with a span of 15m and height of 7.5m. This surviving part of a Roman stone masonry bridge is dated between 50 A.D. and 150 A.D. and it is located at a close distance (25km) from the Macedonian palaces of Vergina and Pella and 30km from the city of Thessaloniki.

The old stone masonry bridges that survive today have been built during the 18th and 19th century. They were used to connect villages located in rough mountainous terrain bridging currents that could be quite turbulent during part of the year. This type of transporting people, animals and goods was accomplished using a relatively narrow deck with width vary-ing from 2.0m to 3.0m. On the contrary, their size spans from 8m to 40m when a single arch is employed (Konitsa) or over 70m for multi-arch structures (Plaka). More information on the

geometry, construction characteristics and mechanical properties of the employed materials are given by Manos et al. (2016). Today, these structures have retain but only a small part of this primary function, as new roads and bridges have been built to facilitate the contemporary transportation needs. Despite this fact they have recently attracted considerable attention as cultural heritage structures together with an effort to become parts of a network of mountain trails. Because a number of people use these structures as visitors a conservation effort was also initiated for their maintenance. Our study has also partly such an objective. That is to obtain information through in-situ instrumentation and measurements on the vibration characteristics of these structures at a given time in a health monitoring framework, as described in section 2. In addition, these in-situ measurements are complemented with a numerical investigation that has as first target to form realistic numerical simulations of such old stone masonry structures. Moreover, to employ next such realistic numerical simulations in order to assess the behaviour of these old stone masonry bridges to a combination of loads that include accidental actions, such as forces generated from earthquakes or flooding.



Figure 2a. The studied old stone masonry bridge of Saint Vissariona 23rd August, 2017. Span of main arch 28.9m and height 16.3m



Figure 2b. The studied old stone masonry bridge of Aziz Aga 31st August, 2016. Span of main arch 28m and height 13.5m.

## 2 IN-SITU MEASUREMENTS OF THE DYNAMIC CHARACTERISTICS OF THE STUDIED STONE BRIDGES

In measuring the dynamic response of all the studied stone bridges two types of excitation were mobilized. The first, namely ambient excitation, mobilized the wind, despite the variation of the wind velocity in amplitude and orientation during the various tests. Due to the topography of the areas where these stone bridges are located, usually a relatively narrow gorge, the orientation of the wind resulted in a considerable component perpendicular to the longitudinal bridge axis. This fact combined with the resistance offered to this wind component by the façade of each bridge produced sufficient excitation source resulting in small amplitude vibrations that could be recorded by the employed instrumentation. The second type of excitation that was employed, namely vertical in-plane excitation, was produced from a sudden drop of a weight on the deck of each stone masonry bridge (Aoki 2007, Manos 2015a, 2015b, 2016, 2017, Ozden et al 2012, Ruocci et al. 2013).

The level of this second type of excitation was capable of producing mainly vertical vibrations; however, depending on the location of the stone-bridge that such an excitation was applied, horizontal vibratory response components could also be recorded. From the recorded three-component response the in-plane and out-of-plane eigen-frequencies and eigen-modes of each studied stone masonry bridge structure could be identified. The employed tri-axial velocity sensors had a sensitivity of 0.001mm/sec and a data acquisition system with a sam-

pling frequency of 800Hz. The wind orientation relative to the geometry of each bridge structure coupled with the bridge stiffness properties could excite mainly the 1st symmetric out-of-plane eigen-modes. The variability of the wind orientation could also excite, although to a lesser extend, some of the other in-plane and out-of-plane eigen-modes. The drop weight excitation in various locations combined with the placement of the sensors in selected locations was capable of capturing the in-plane as well as out-of-plane modes of response. A careful study of the numerous in-situ response measurements together with the assistance of numerical simulation tools and a back analysis process resulted for such stone bridges in their dynamic system identification. This process is presented in what follows for two old masonry bridges, namely the Saint Vissariona Bridge at Pile, in Trikala prefecture (figure 2a) and the bridge of Aziz-Aga, at Grevena prefecture (figure 2b).

Due to space limitations only selective measurements of the out-of-plane response, which was recorded utilizing either the wind or the drop weight excitation are included here. More information is reported by Manos et al. (2016).

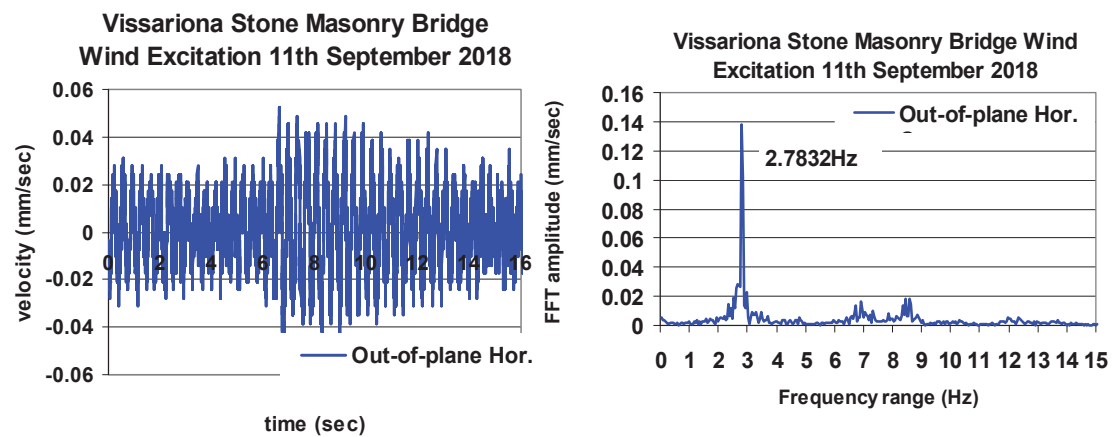


Figure 3. Wind excitation Saint Vissariona Bridge 9th September, 2018. Out-of-plane horizontal component.

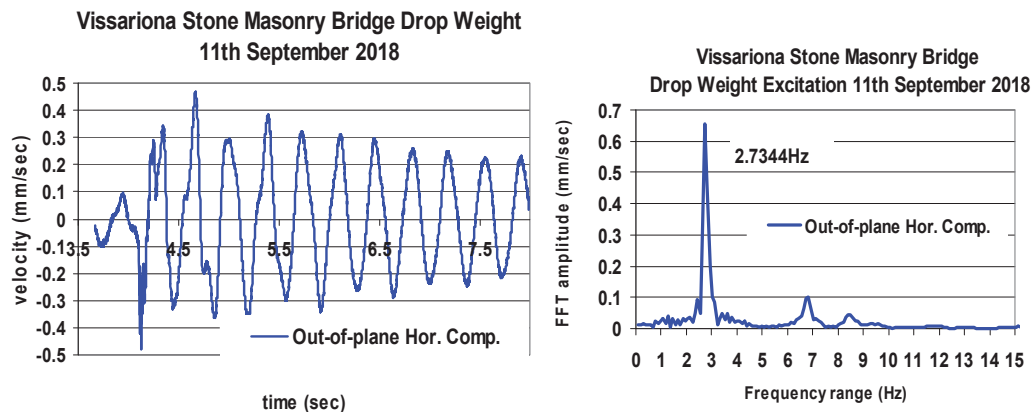


Figure 4. Drop weight excitation Saint Vissariona Bridge 9th September, 2018. Out-of-plane horizontal component.

In figure 3, the out-of-plane horizontal component response of the Saint Vissariona bridge is presented due to wind excitation. The time history plot is shown at the left hand side of this figure with the corresponding FFT plot shown at the right hand side. As dominant frequency



the value of 2.7832Hz can be identified. Figure 4 depicts the corresponding out-of-plane horizontal component response, in terms of time history and FFT plots, for the same bridge due this time to the drop weight excitation. The dominant frequency value is this time equal to 2.7344Hz. For the Aziz Aga stone bridge the out-of-plane horizontal component response, in terms of time history and FFT plots, due to the drop weight excitation is depicted in figure 5. As can be seen in this figure the dominant eigen-frequency is equal to 3.4668Hz. By studying further the FFT plots of figures 4 and 5 one can also identify through the other two distinct peaks the eigen-frequencies of two more high-order out-of-plane response eigen-modes.

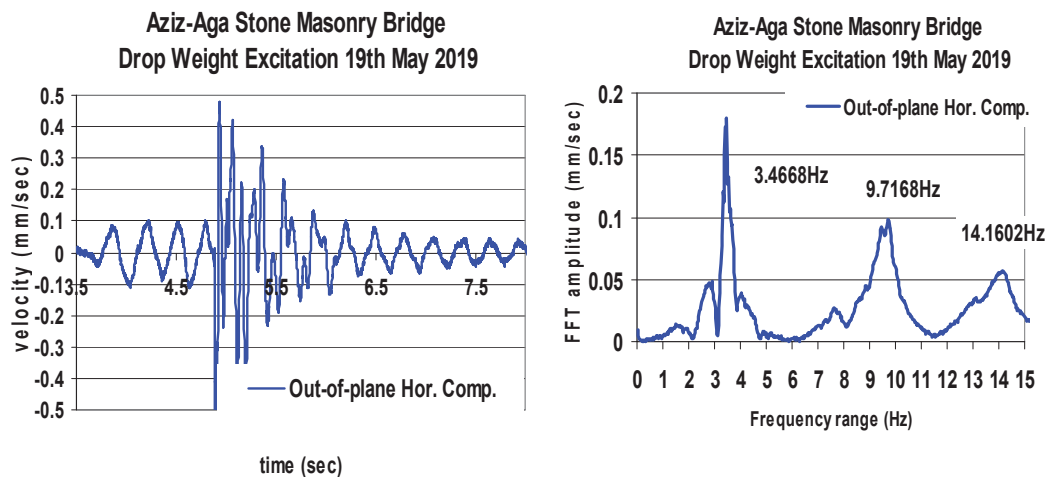


Figure 5. Drop weight excitation Aziz-Aga Bridge 19th May, 2019. Out-of-plane horizontal component

### 3 NUMERICAL SIMULATION OF THE DYNAMIC RESPONSE RECORDED IN-SITU UTILIZING LINEAR-ELASTIC RESPONSE ASSUMPTIONS.

Initially, in the following section an attempt is made to employ a variety of linear-elastic numerical simulations for a relatively simple arch bridge.



Figure 6. The single arch stone masonry bridge at Kryineri (Molista).

This structure bridges one of the streams that flows towards Sarantaporos river between the mountains of Grammos and Smolikas at the prefecture of Ipirous. This valley was and still is

one of the main links between the prefectures of Macedonia and Ipirous in Greece. Apart from this bridge there were other bridges in this valley that do not exist today. One of these bridges that survive today, which bridges the upper part of Sarantaporos river near its origin (Eptachori) is the two-arch bridge of Drosopigi, located near the village with the same name, the birth place of the second author of this work (figure 7). Both Drosopigi bridge and the Kryoneri bridge were initially studied numerically by Simos and Manos [24]. In section 3.1. the numerical simulation of the Kryoneri Bridge is again presented together with corresponding measurements performed in-situ.



Figure 7. The two-arch stone masonry bridge at Drosopigi.

### 3.1 The stone masonry bridge at Kryoneri

This is a relatively simple stone masonry bridge of a single arch, as shown in figure 6. The clear span of this bridge is 8.25m, the height from the river bed to the key of the arch (bottom fiber) 5m and the width of this bridge at the key of the arch 2.4m. Figures 8a and 8b depict the main out-of-plane and in-plane eigen-modes of this bridge, respectively.

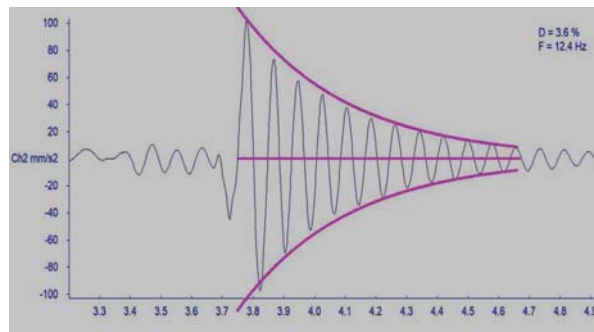


Figure 8a. Out-of-plane 12.744Hz Damping 3.7%

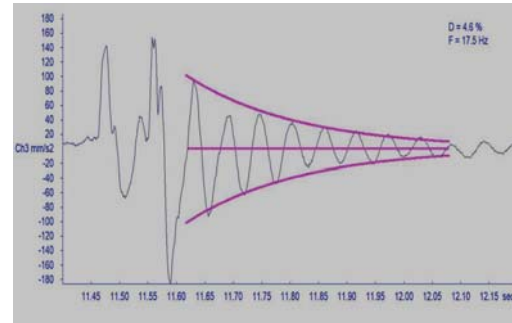


Figure 8b. 1st In-plane 17.578 Hz Damping 4.6%

As can be seen in figures 8a and 8b the first out-of-plane eigen frequency was measured in-situ to be equal to 12.744Hz, whereas the first in-plane eigen-frequency was measured to be equal to 17.578, which is considerably higher than the 1<sup>st</sup> out-of-plane. It must be underlined here that the drop weight excitation process was utilized in situ to obtain these eigen-frequency values. Moreover, from stone samples taken in-situ the following mechanical characteristics were obtained from laboratory tests.

Table 1. Molista stone cubes. Compression test results November 2018

Code No	Width (mm)	Thickness (mm)	Area (mm <sup>2</sup> )	Height (mm)	Slenderness ratio H/l	Ultimate Compression (KN)	Ultimate Compressive stress (MPa)
1	61	57	3477	61	1.000	363.0	104.4
2	57	60.5	3448.5	48	0.817	392.4	113.8
3	59	57	3363	70	1.207	412.0	122.5
4	50	60.5	3025	64	1.164	255.1	84.3
<b>Average compressive strength value (MPa)</b>							<b>106.25</b>
<b>Standard deviation (MPa)</b>							<b>16.4</b>
<b>Young's Modulus E=40GPa, Average Tensile Strength = 6.56MPa</b>							

The subsequent numerical analysis followed three different numerical simulations. All of them assumed linear-elastic behaviour and homogenization of the stone masonry. The first approach is the simplest of the three simulating the bridge through the middle longitudinal plane of symmetry utilizing thick shell finite elements, as shown in figure 9. The supports for all the nodes forming the horizontal abutment base contact was assigning zero translations ( $u_x=u_y=u_z=0$ ) and zero rotations ( $\phi_x, \phi_y, \phi_z$ ) along all three axes. The supports for all the nodes forming the inclined abutment base contact was assigning only zero translations along all three axes ( $u_x=u_y=u_z=0$ ). The second approach uses brick finite elements and in this way the full geometry of the bridge is portrayed, as shown in figure 10a. In the third approach the numerical simulation includes also the valley substrate as a continuation of the abutments of this bridge in a way shown in figure 10b. In all these analyses the homogenized masonry Young's modulus was assumed equal to 2000MPa and the homogenized masonry special density 25.5KN/m<sup>3</sup>

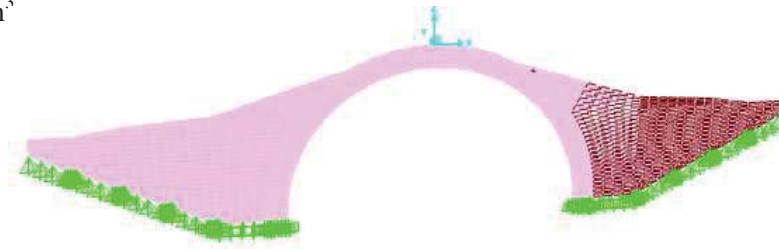


Figure 9. 3-D numerical simulation of the single-arch stone masonry bridge at Kryoneri (Molista) employing thick shell finite elements.

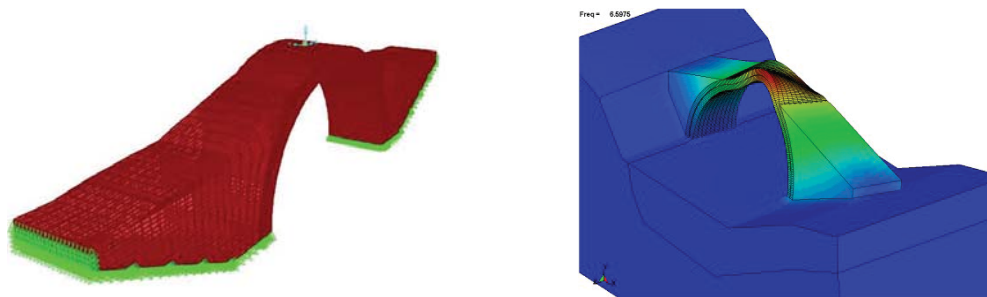


Figure 10. a) 3-D numerical simulation of the single-arch stone masonry bridge at Kryoneri (Molista) employing brick finite elements. b) 3-D numerical simulation of the single-arch stone masonry bridge at Kryoneri (Molista) together with part of the valley substrate employing brick finite elements.

From the eigen-frequency values listed in figure 11 good agreement is reached between the eigen-frequency values obtained by the 3-D numerical simulation of the single-arch stone masonry bridge at Kryoneri (Molista) employing either thick shell finite elements or the 3-D numerical simulation employing brick finite elements.



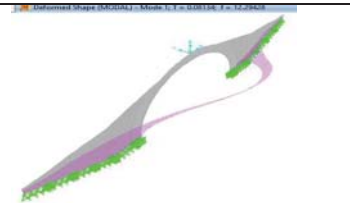

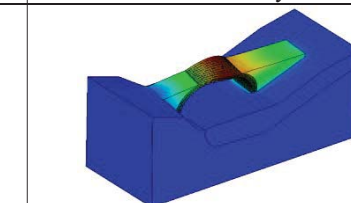
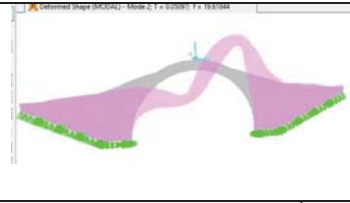
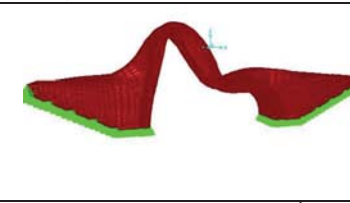
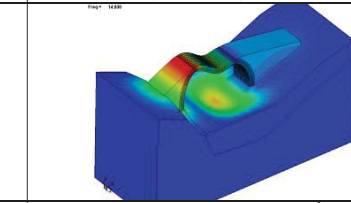
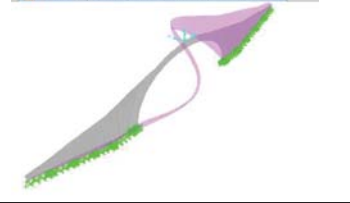

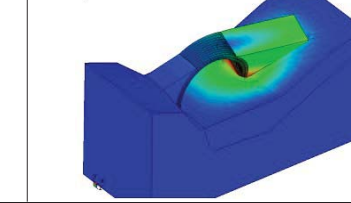
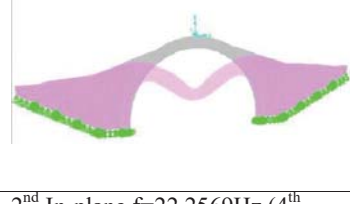
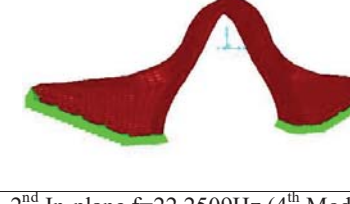
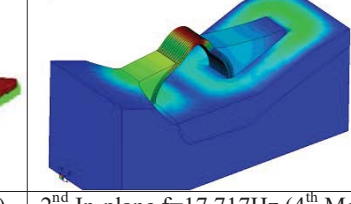
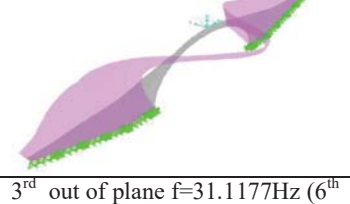
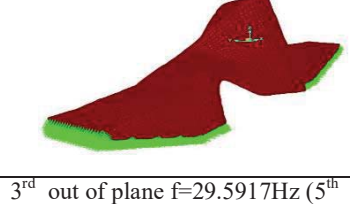
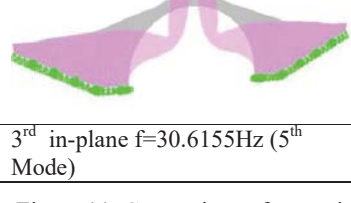
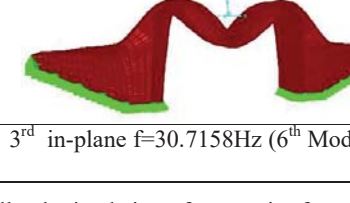
3-D Numerical simulation thick shell finite elements	3-D Numerical Simulation brick finite elements	3-D Numerical Simulation brick finite elements with valley substrate
		
1 <sup>st</sup> out of plane $f=12.2943\text{Hz}$ (1 <sup>st</sup> Mode). <b>Measured 12.744Hz</b>	1 <sup>st</sup> out of plane $f=11.4383\text{Hz}$ (1 <sup>st</sup> Mode). <b>Measured 12.744Hz</b>	1 <sup>st</sup> out of plane $f=6.3049\text{Hz}$ <b>right abutment</b> (1 <sup>st</sup> Mode).
		
1 <sup>st</sup> in- plane $f=19.6184\text{Hz}$ (2 <sup>nd</sup> Mode). <b>Measured 17.578 Hz</b>	1 <sup>st</sup> in- plane $f=19.6472\text{Hz}$ (2 <sup>nd</sup> Mode). <b>Measured 17.578 Hz</b>	1 <sup>st</sup> in- plane $f=14.938\text{Hz}$ (2 <sup>nd</sup> Mode). <b>Measured 17.578 Hz</b>
		
2 <sup>nd</sup> out of plane $f=21.3738\text{Hz}$ (3 <sup>rd</sup> Mode)	2 <sup>nd</sup> out of plane $f=22.0209\text{Hz}$ (3 <sup>rd</sup> Mode)	2 <sup>nd</sup> out of plane <b>right abutment</b> $f=12.422\text{Hz}$ (3 <sup>rd</sup> Mode)
		
2 <sup>nd</sup> In-plane $f=22.2569\text{Hz}$ (4 <sup>th</sup> Mode). <b>Measured 23.438 Hz</b>	2 <sup>nd</sup> In-plane $f=22.2509\text{Hz}$ (4 <sup>th</sup> Mode). <b>Measured 23.438 Hz</b>	2 <sup>nd</sup> In-plane $f=17.717\text{Hz}$ (4 <sup>th</sup> Mode). <b>Measured 23.438 Hz</b>
		
3 <sup>rd</sup> out of plane $f=31.1177\text{Hz}$ (6 <sup>th</sup> Mode)	3 <sup>rd</sup> out of plane $f=29.5917\text{Hz}$ (5 <sup>th</sup> Mode)	
		
3 <sup>rd</sup> in-plane $f=30.6155\text{Hz}$ (5 <sup>th</sup> Mode)	3 <sup>rd</sup> in-plane $f=30.7158\text{Hz}$ (6 <sup>th</sup> Mode)	

Figure 11. Comparison of numerically obtained eigen-frequencies from the three numerical approaches between themselves and with specific in-situ measured values.



When comparing the numerical results of the 3-D numerical simulation of the single-arch stone masonry bridge at Kryoneri (Molista) together with part of the valley substrate employing brick finite elements it can be observed that the inclusion of the soft alluvium substrate introduces a considerable flexibility in the structural system as a whole. Moreover, a number of the first in-plane and out-of-plane significant eigen-modes are influenced by the flexibility of the abutments as they are supported on the alluvium substrate. This is underline in both figures 11 and 12. It must be underlined that the used method of excitation is of such an intensity that is unable to mobilize such an interaction between the abutments of the Kryoneri bridge and the alluvium substrate that can be of significance. This is the reason that these numerical values are not compared in figure 11 with the corresponding measured in-situ values.

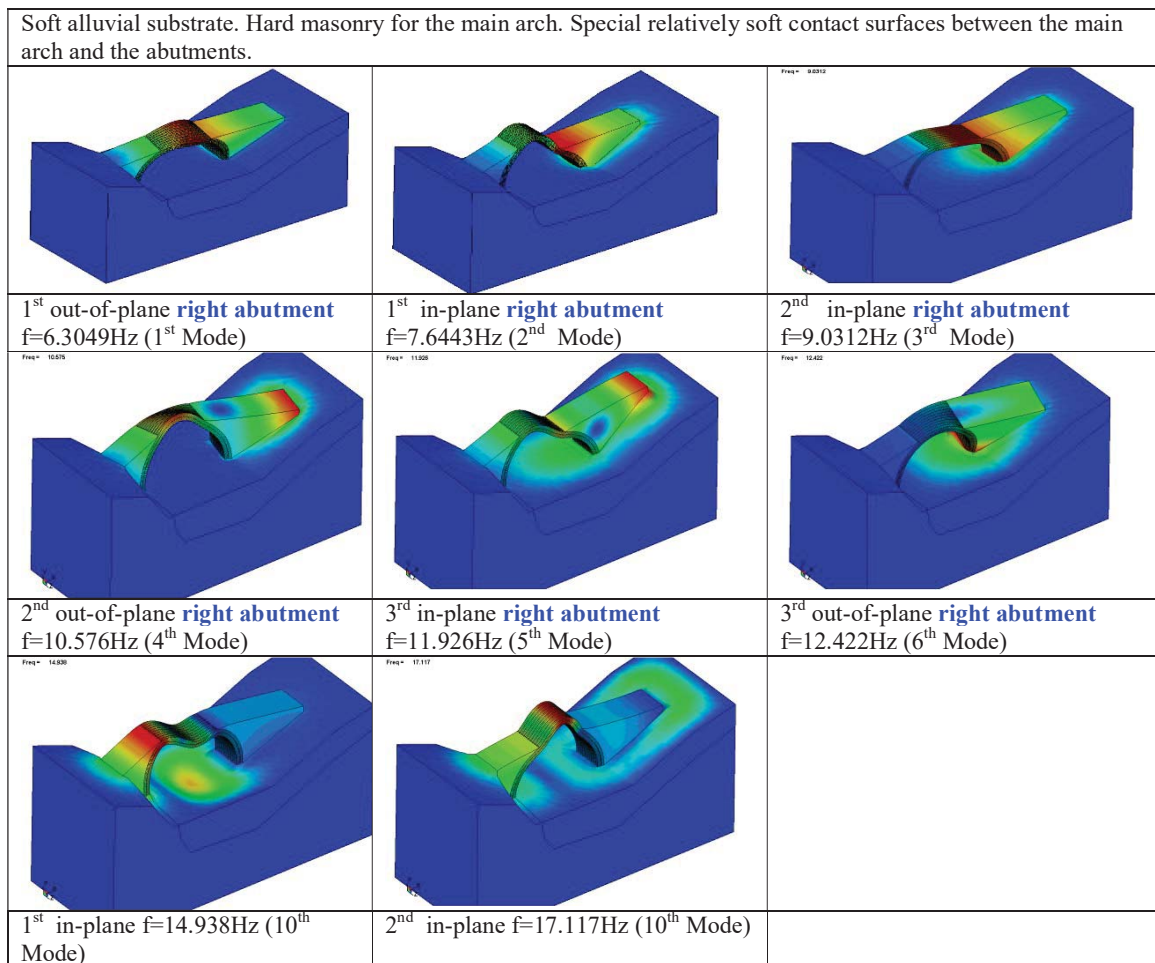



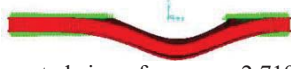










Figure 12. Eigen-modes and eigen-frequencies obtained from a 3-D numerical simulation of the single-arch stone masonry bridge at Kryoneri (Molista) together with part of the valley substrate employing brick finite elements.

### 3.2 The numerical simulation of relatively large stone masonry arch bridges

In this section numerically simulate the eigen-frequencies and eigen-modes of Saint Vissariona and Aziz Aga stone masonry bridges, as they resulted from the dynamic system identification process, based on the measured in-situ numerous dynamic response records. These

stone masonry arch bridges are much larger than the simple arch bridge examined in section 3.1. At this initial stage the basic assumption of the numerical simulation is the linear elastic response approximation. The overall geometry of the various parts as well as their overall thickness was reproduced as was measured in-situ. The numerical simulation tried to reproduce the primary arch and the secondary arch separately. Moreover, separately were reproduced the abutments and the foundation footings. Thin layers of more flexible material (mortar layers) were introduced in regions where such main parts were connected. Reported by Manos et al. (2016) is a limited study of the mechanical characteristics of stone and mortar samples taken from a prototype bridge which collapsed in 2015 and is currently rebuilt. More information of this bridge's performance is presented by Manos et al. (2019).

Initially, for simplicity purposes, these numerical simulations are made in the 3-D domain representing the bridge structure with its mid-surface employing thick shell finite elements (SAP2000).



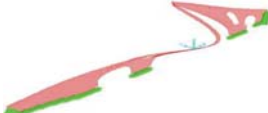







Table 2. Measured and predicted eigen-frequencies for Saint Vissariona stone masonry bridge		
Eigen-modes and measured eigen-frequencies	3-D numerical simulation with <b>shell elements</b> representing the longitudinal mid-section	3-D numerical simulation with <b>solid elements</b> representing the full geometry of the stone bridge
(1)	(2)	(2)
<b>1<sup>st</sup> Out-of-plane</b> Measured eigen-frequency 2.832Hz	 Pred. eigen-frequency 2.784Hz, $m_y=40.3\%$	 Computed eigen-frequency 2.719Hz
<b>2<sup>nd</sup> Out-of-plane</b> Measured eigen-frequency 5.029Hz	 Pred. eigen-frequency 5.270Hz, $m_y=0.0$	 Computed eigen-frequency 5.240Hz
<b>1<sup>st</sup> In-plane</b> Measured eigen-frequency 7.129Hz	 Pred. eigen-frequency 8.38Hz, $m_x=9.27\%$ $m_z=0.4\%$	 Computed eigen-frequency 8.392Hz
<b>3<sup>rd</sup> Out-of-plane</b> Measured eigen-frequency 8.839Hz	 Pred. eigen-frequency 9.184Hz, $m_y=20.5\%$	 Computed eigen-frequency 8.202Hz
<b>2<sup>nd</sup> In-plane</b> Measured eigen-frequency 9.570Hz	 Pred. eigen-frequency 9.45Hz, $m_x=0.002\%$ $m_z=9.7\%$	 Computed eigen-frequency 9.475Hz
<b>3<sup>rd</sup> In-plane</b> Measured eigen-frequency 13.037Hz	 Pred. eigen-frequency 12.69Hz, $m_x=0.01\%$ $m_z=14.1\%$	 Computed eigen-frequency 12.712Hz

The predicted eigen-frequency values obtained from this type of numerical simulation are listed in column 2 of tables 2 and 3 for the stone masonry bridges of Saint Vissariona and Aziz Aga, respectively. The corresponding modal mass participation ratio values are also listed in this table. The out-of-plane and the in-plane horizontal directions are denoted with the axes y-y and x-x, respectively, whereby z-z is the vertical axis. At a second stage an alternative 3-D numerical was carried out whereby all the various parts of each bridge were represented employing solid prismatic finite elements. The predicted eigen-frequency values

obtained from this type of numerical simulation are listed in column 3 of tables 2 and 3 for the stone masonry bridges of Saint Vissariona and Aziz Aga, respectively.

The corresponding eigen-mode shapes are also included in these tables. The various main parts of this stone masonry bridge, that is the primary and the secondary arches, the abutments, the deck, the mandrel walls and the parapets were simulated in such a way that narrow contact surfaces could be introduced between them, representing in this way a different “softer” medium. All available information, measured during the in-situ campaign, on the geometry of each one of these parts was used in building up these numerical simulations. The mechanical property values obtained from the stone and mortar sample tests were utilized (see Manos et al. (2016). Moreover, there is important information that is needed in order to form with some realism the boundary conditions at the river bed and banks. The lack of specific studies towards clarifying in a systematic way all these uncertainties represents a serious limitation in the numerical simulation process. The approximation adopted in this study is a process of back simulation (Manos et al. 2015a, 2015b, Simos et al. 2017, 2018). This is done by adopting values for these unknown mechanical stone masonry properties, respecting at the same time all the measured geometric details, which result in reasonably good agreement between the measured and predicted in this way eigen-frequency values.

Table 3. Measured and predicted eigen-frequencies for Aziz Aga stone masonry bridge

Eigen-modes and measured eigen-frequencies	3-D numerical simulation with <b>shell elements</b> representing the longitudinal mid-section	3-D numerical simulation with <b>solid elements</b> representing the full geometry of the stone bridge
(1)	(2)	(3)
<b>1<sup>st</sup> Out-of-plane</b>		
Measured eigen-frequency 3.4670Hz	 Computed eigen-frequency 3.360Hz	 Computed eigen-frequency 2.618Hz
<b>2<sup>nd</sup> Out-of-plane</b>		
Measured eigen-frequency 6.250Hz	 Computed eigen-frequency 5.857Hz	 Computed eigen-frequency 4.399Hz
<b>1<sup>st</sup> In-plane</b>		
Measured eigen-frequency 8.398Hz	 Computed eigen-frequency 7.920Hz	 Computed eigen-frequency 7.776Hz
<b>3<sup>rd</sup> Out-of-plane</b>		
Measured eigen-frequency 7.764Hz	 Computed eigen-frequency 8.024Hz	 Computed eigen-frequency 6.150Hz
<b>2<sup>nd</sup> In-plane</b>		
Measured eigen-frequency 9.375Hz	 Computed eigen-frequency 9.440Hz	 Computed eigen-frequency 9.332Hz

Following this approximate process the boundary conditions introduced in both numerical simulations at all the boundaries, either at the river bed or the river banks, were constraining to zero the translational displacement in the two horizontal and the vertical direction. It was observed from a sensitivity analysis that was performed by Manos et al. (2016) for a number of stone masonry bridges that introducing fixity boundary conditions for the first type of numerical simulation influences, as expected, the out-of-plane and not the in-plane stiffness of the studied stone masonry bridges. Moreover, for the Saint Vissariona and Aziz Aga Bridge whereby the main central arch is supported at the North end in adjacent arches rather than in a rocky river bank the influence of the variation of the boundary conditions, as expected, is again less pronounced.

The value of the corresponding measured eigen-frequency values is included in the first column of tables 2 and 3. These values, as already mentioned, were obtained from the system identification study for each bridge based on the numerous measurements of the vibratory response recorded in-situ utilizing either wind or drop weight excitations (see figures 3, 4 and 5). When the predicted eigen-frequencies obtained from the shell elements numerical simulation of Saint Vissariona bridge (Table 2 column 2) are compared with those obtained from the solid elements numerical simulation (Table 2 column 3) a good agreement is observed for all the listed numerically predicted eigen-modes apart for the third out-of-plane eigen-mode. When this comparison is made between the numerically predicted eigen-frequency values with the ones deduced from the in-situ measurements (Table 2 column 1), a good agreement can be observed for the 1st and 2nd out-of-plane and for the 2nd and 3rd in-plane eigen-modes, for both types of numerical simulations. For the 3rd out-of-plane eigen-mode the numerical simulation employing shell element is in better agreement with the measured value than the numerical simulation employing solid elements. Both types of numerical simulation predict an eigen-frequency value for the 1st in-plane eigen-mode that differs substantially for the measured value. This discrepancy is of need of further research. When the predicted eigen-frequencies obtained from the shell elements numerical simulation of Aziz Aga bridge (Table 3 column 2) are compared with those obtained from the solid elements numerical simulation (Table 3 column 3) a good agreement is observed for all three in-plane numerically predicted eigen-modes but not for the corresponding three out-of-plane eigen-modes. When this comparison is made between the numerically predicted eigen-frequency values with the ones deduced from the in-situ measurements (Table 3 column 1), a good agreement can be observed between the measured and predicted values for the 1st type of numerical simulation employing shell finite elements. The predicted values employing solid finite elements are in reasonable agreement with the measured values only for the in-plane eigen-modes but not for the out-of-plane eigen-modes. This must be attributed to the effect of the boundary conditions for the numerical simulation employing solid elements.

#### 4 SEISMIC BEHAVIOUR OF THE SAINT VISSARIONA BRIDGE

This section includes results from a series of simplified numerical simulations of the Saint Vissariona stone masonry bridge when it is subjected to a combination of actions that include the dead weight (D) combined with extreme actions generated from seismic ground motions (Sevim Baris, et al., 2011, Kiyono J., et al. 2012). The seismic forces were defined by making use of the current definition of the seismic forces by EURO-Code 8 (2004). Towards this horizontal design spectral curves were derived (figure 13) based on the horizontal design ground acceleration. This value, as it is defined by the zoning map of the current Seismic Code of Greece, is equal to 0.16g (g the acceleration of gravity) for the location of the Saint Vissariona bridge located at Pyle Trikala Prefecture of Greece (EAK 2000, ITSAK 2019). Further-

more, it is assumed that the soil conditions belong to category B because of the bridge is founded near the banks of the river bed and not directly at a rocky sub-terrain. The importance factor was assigned to a value equal to 1.2 whereas the foundation coefficients was assigned a value equal to one (1.0); the damping ratio is considered equal to 5% and the behaviour factor is equal to 1.5 (unreinforced masonry).

It must be pointed out that the flexibility of the foundation that was taken into account in the numerical simulation of stone masonry bridges in the past was not considered here. Two types of numerical analyses were performed. In the first type of numerical analysis, the dynamic spectral method was employed making use of the contribution of twelve modes, which include the dominant in-plane and out-of-plane eigen-modes. Moreover, an amplification factor was introduced in order to compensate for the fact that only a portion of the total mass is mobilized by these eigen-modes in the in-plane and out-of-plane directions. In the second type of numerical analysis equivalent horizontal seismic forces are applied either in the in-plane ( $E_x$ ) or in the out-of-plane ( $E_y$ ) directions. These forces are of an almost triangular distribution along the height of this bridge with the maximum value applied at the key of the central arch. Moreover, the base shear that results by applying these equivalent horizontal seismic forces is approximately equal to the base shear that results from the dynamic spectral analyses (Manos 2015c). This is done by adjusting the amplitude of the equivalent horizontal seismic forces. In what follows results from this second type of analyses are presented and discussed.

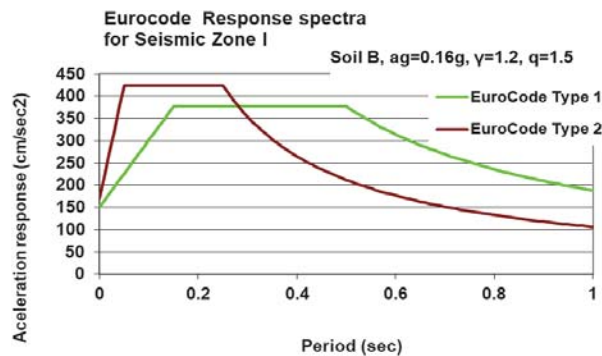


Figure 13. Design acceleration spectral curves.

Load combinations which included the simultaneous application of the dead load ( $D$ ) and the equivalent horizontal seismic forces either in the in-plane ( $D + E_x$ ) or in the out-of-plane ( $D + E_y$ ) directions have been considered. The obtained deformation and stress results for the Saint Vissariona stone masonry bridge as obtained from these load combinations are shown in the following figures 14 to 16. Figure 14 shows the deformation and in-plane stress distribution patterns of Saint Vissariona bridge due to its dead load. As can be seen in this figure, the deformation of the key of the central arch due to dead load is relatively small ( $u_z = -3.46\text{mm}$ ). In addition the maximum tensile stress value is also relatively small ( $\sigma_{\max} = 0.200\text{MPa}$ ) and develops at a confined region at the deck of the bridge above the left and right abutments. The minimum compressive stress value is of the order of  $\sigma_{\min} = -0.70\text{MPa}$  that can be easily sustained by such stone masonry construction. Figure 15 shows the deformation and in-plane stress distribution patterns of Saint Vissariona bridge due to the load combination including the dead load and the in-plane equivalent horizontal seismic forces. Again, the in-plane deformation of the key of the central arch due to this load combination is relatively small ( $u_x = 1.70\text{mm}$   $u_z = -4.51\text{mm}$ ). However, it can be seen that the region at the deck above the left abutment develops a considerable increase in the maximum tensile stress value



( $\sigma_{\max}=0.500\text{MPa}$ ). Such tensile stress values represent a relatively high tensile stress demand for stone masonry. The region that this high tensile stress value develops correlates with the deformation pattern of the bridge for this load combination. Again, the minimum compressive stress value is of the order of  $\sigma_{\min}=-0.70\text{MPa}$  that can be easily sustained by such stone masonry construction.

#### **Dead Load**

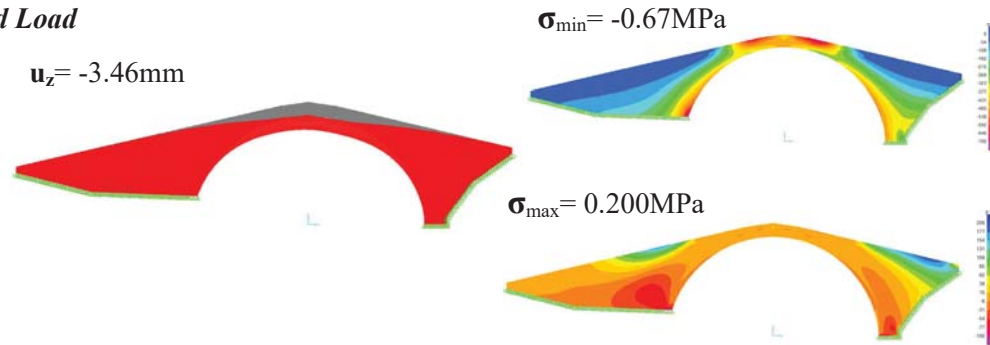


Figure 14. Deformation and in-plane stress distribution patterns of Saint Vissariona bridge due to the dead load

#### **Dead Load + Ex**

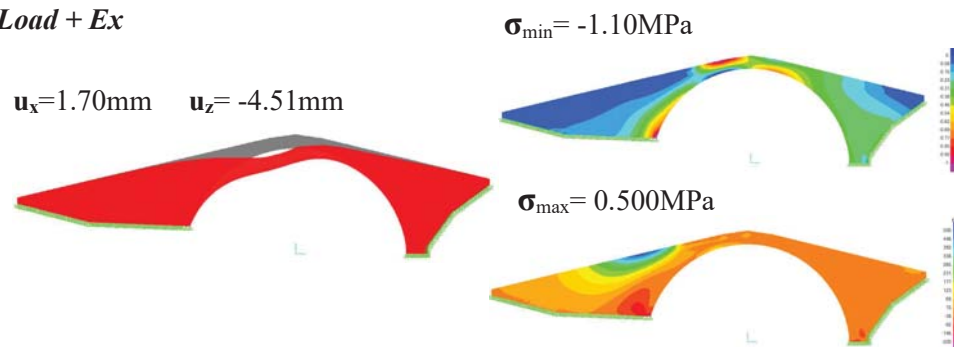


Figure 15. Deformation and in-plane stress distribution patterns of Saint Vissariona bridge due to dead load and equivalent in-plane seismic horizontal forces

#### **Dead Load + Ey**

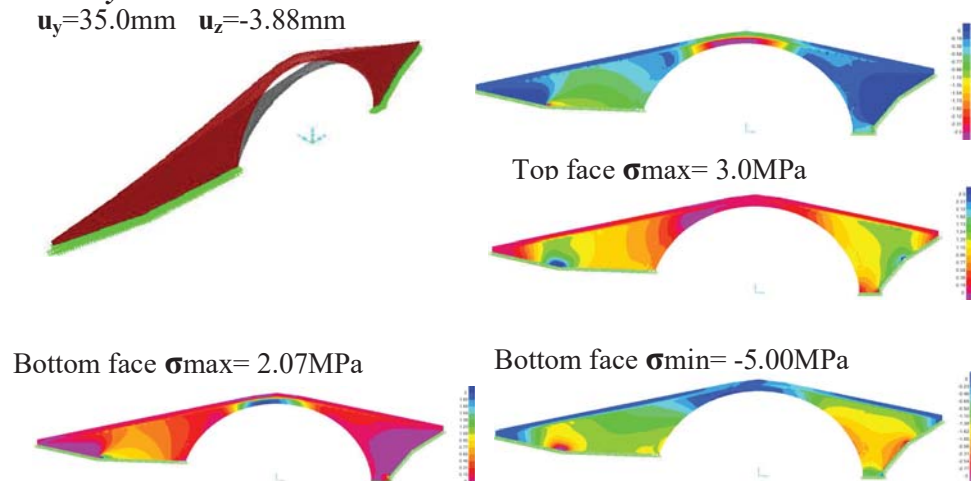


Figure 16. Deformation and out-of-plane stress distribution patterns at the facades (top and bottom) of Saint Vissariona bridge due to dead load and equivalent out-of-plane seismic horizontal forces

Figure 16 shows the deformation and out-of-plane stress distribution patterns at the two extreme faces (top and bottom) of Saint Vissariona stone masonry bridge due to the load combination of the dead load and the out-of-plane horizontal equivalent seismic forces. As can be seen in this figure, the out-of-plane horizontal deformation of the key of the central arch due to this load combination is relatively large ( $u_y=35.0\text{mm}$   $u_z=-3.88\text{mm}$ ). As a result, large maximum tensile stress values develop at the central region of the main arch (Bottom face  $\sigma_{\max}=2.07\text{MPa}$ ) as well as at the region where the left abutment joins the foundation. Such tensile stress values represent a relatively very high tensile stress demand for stone masonry. Again, the minimum compressive stress value is of the order of  $\sigma_{\min}=-5.00$  that, despite the relatively large amplitude, can be easily sustained by such stone masonry construction. As can be seen from the results of such a simplified numerical analysis the Saint Vissariona bridge can be quite vulnerable for earthquake ground motions that are dictated from the current seismic code. According to historical information this stone masonry bridge was built on 1514 A.D. In 1967 this stone masonry bridge was declared cultural monument by the Greek Ministry of Culture and in 2000 the surrounding area was also declared as a region in need of special protection by the same Ministry (Greek Government Gazette 1967). During the last century the most intense earthquake activity related to this bridge must be considered the Sofades in Karditsa earthquake sequence on 30th of April 1954 which is assigned by Papazachos et al. (1989) a magnitude of 7.0 at the Richter scale with an epicenter approximately 50km from the site of Saint Vissariona bridge. It was not possible up to now to find any record of structural damage relating this earthquake to Saint Vissariona bridge despite the fact that there are reports of substantial structure damage which was widespread in the Thessalia prefecture.

## 5 INFLUENCE OF THE FOUNDATION DEFORMABILITY.

In the preceding sections 3 and 4 the piers and the abutments of the examined stone masonry bridges were assumed to be supported in non-deformable soil-foundation interface. In what follows a preliminary study of the influence of deformable soil where a stone masonry is found is carried out. The Plaka stone masonry bridge collapsed on the 1st of February 2015 due to the flooding of the Arachthos river. Figure 17a depicts this bridge as it was standing before this collapse whereas figure 17b shows the remains of the abutments after the collapse of the bridge due to the flooded river which is also shown in the same figure. Figure 17c depicts the collapsed bridge ten months afterwards (12th December 2015) whereas figure 17d depicts the picture (19th October 2019) of the reconstruction of the old bridge in the same overall geometry and using materials and constructions techniques as close as possible to the original construction. Recently (7th December 2019), it was announced that the primary arch of the reconstructed new Plaka stone masonry bridge was completed by placing the top key stones at the top-middle of this primary arch. Manos et al. (2017) investigated, through a simplified linear analysis approach, the effect of the flooding forces acting on the Plaka bridge structure adopting the assumption that the foundation of its mid-pier footing was on a relatively flexible soil.

In addition, the damage suffered by the main arch during an explosion that occurred in 1944, was also included in this study. More information can be found in Manos et al 2017.

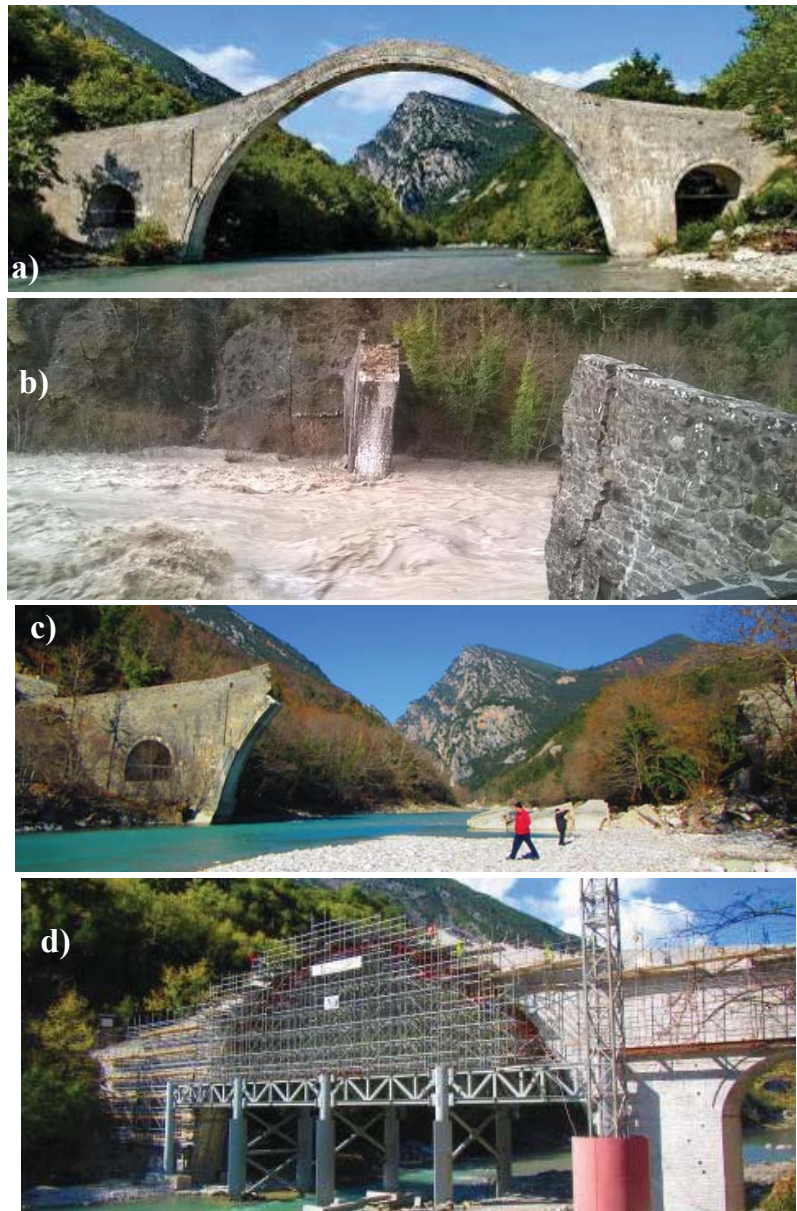


Figure 17. Collapse from flooding and reconstruction of the Plaka stone masonry bridge

Figures 18a,b,c depict the displacement and stress response of the Plaka bridge under the combined action of the gravity and flooding forces, taking into account the arch damage as well as the deformability of the soil under the footing of the mid-pier. The maximum vertical deflection response, shown in figure 18a, is equal to 21.95mm at the top middle of the central arch. At the same location, the horizontal in-plane displacement is equal to 4.5mm ( y-y direction), whereas the out-of-plane horizontal displacement (x-x direction, flow of river) is equal to 0.87mm. The maximum (tensile) stress response is depicted in figures 18b and 18c. As can be seen, at the central arch region (figure 18c) the maximum stress value is equal to 0.764MPa whereas at the left relief arch region the maximum stress value is equal to 2.579MPa (figure 18b).



Simos et al. (2017). Investigated the collapse of the Plaka Stone Bridge due to extreme flooding using high fidelity, three-dimensional non-linear numerical analysis and sensitivity studies. The potential of a number of postulated scenarios in initiating failure and leading to the eventual collapse of the bridge were explored aided by sensitivity analyses relying on non-linear finite element modeling, augmented by actual material properties of the structural elements deduced from laboratory tests following the collapse. More information can be found in Simos et al. 2017.

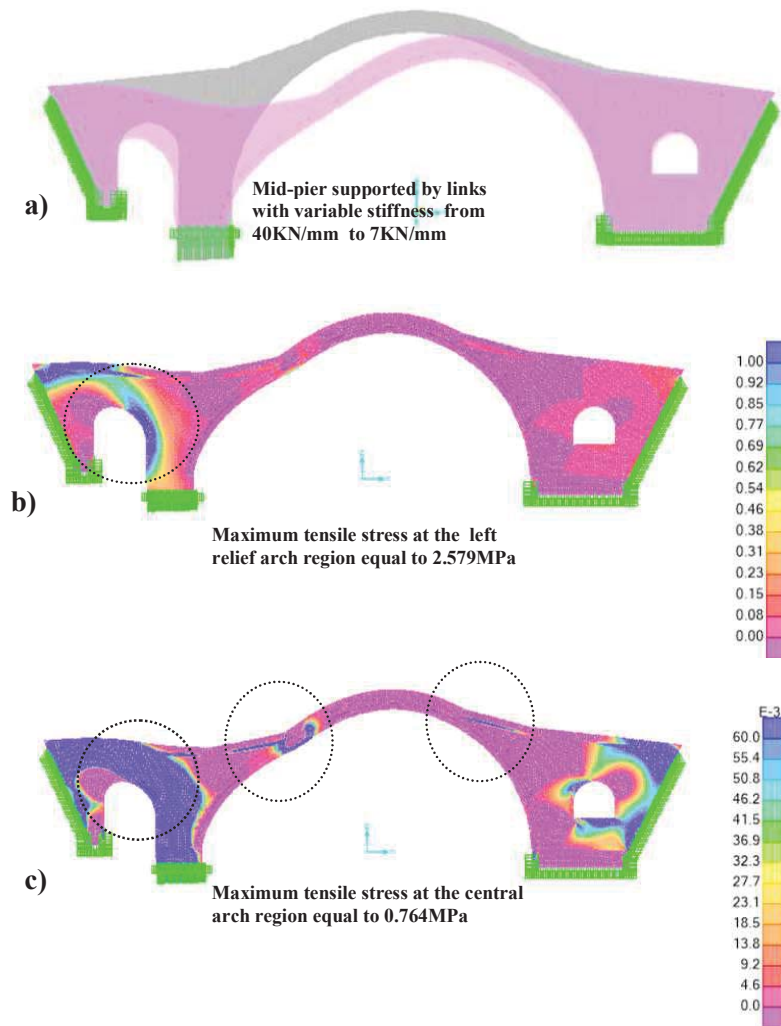


Figure 18. Displacement and stress response of the Plaka stone masonry bridge

The numerical analysis and the failure scenario postulated and presented in detail in this study tend to support that the triggering of the collapse and the most-likely cause was the undermining by the flood (scouring of the river bed and hydrodynamic loads) of the central pier. In what follows the Plaka Bridge is numerically simulated this time together with a volume of soil under its foundation of the piers and the abutments within the river bed, as is shown in figure 19. Elastic properties are assigned to this volume in an effort to approximate the flex-

ibility of the foundation under the footings of the piers located within the river bed and to further research on the collapse mechanisms.

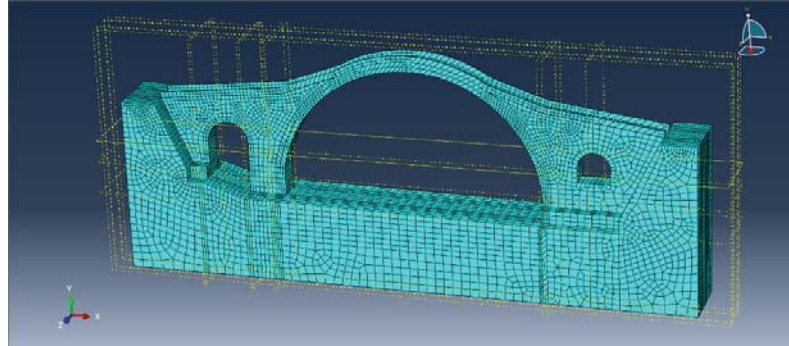


Figure 19. Numerical simulation of the Plaka bridge together with a volume of soil.

Apart from numerically simulating the flexibility of the foundation in these way seven critical cross sections, five at the central arch, one at the left relief arch and one at the right relief arch, were numerically simulated employing contact surfaces which could allow a non-linear plasticification response to develop, according to an assumed cohesive constitutive law. In order to check how this numerical model reproduces the effect of the foundation flexibility, simulated as described, the gravity forces were gradually applied till they reached a final level equal to the gravity forces amplified by a factor of 2. The obtained response, in terms of amplified displacement response is shown in figure 20a whereas figure 20b is indicating the plasticification of the mentioned contact surfaces.

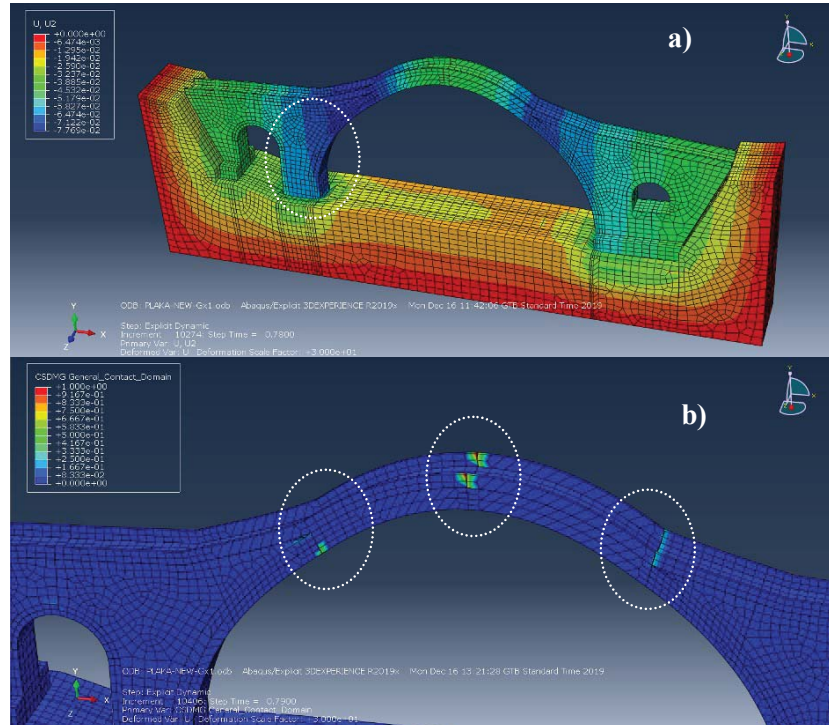


Figure 20. Vertical deflection of the mid-pier footing (a) together with the corresponding plastification (b) of critical cross-sections of the Plaka bridge for vertical forces 80% of gravity.

Figures 20a and 20b depict the numerical response when the applied forces reach the level of 80% of gravity. At this stage the vertical deflection of the footing of the mid-pier, due to the flexibility of the underlying soil, is approximately 30mm. This deflection of the footing is sufficient to cause the initiation of plastification in three contact surfaces at the encircled critical regions of the central arch, indicated in figure 20b. It is of interest to observe that two of the locations of the plastification of figure 20b coincide with the regions of tensile stress concentration in figure 18c.

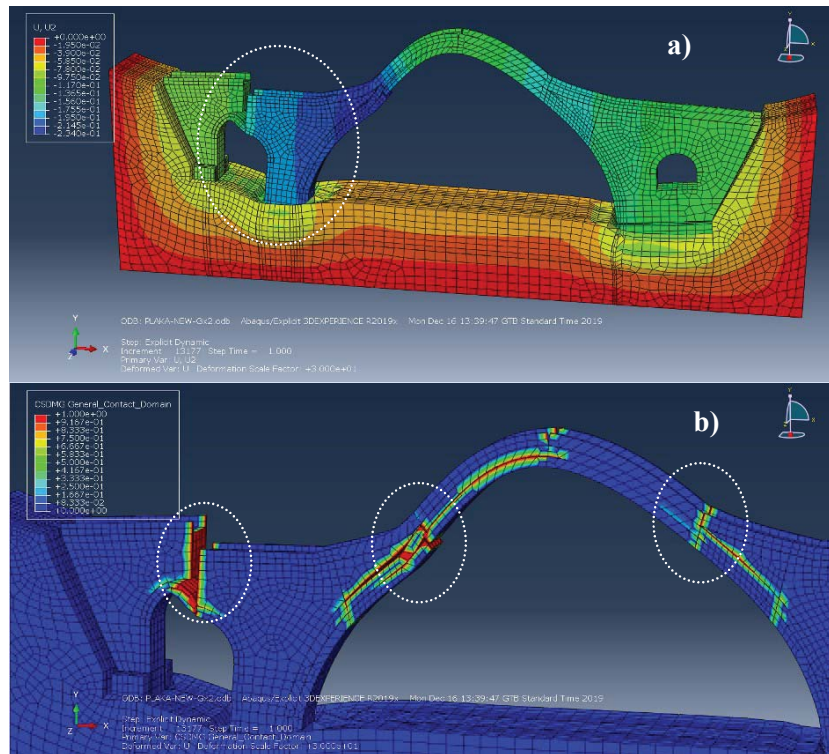


Figure 21. Vertical deflection of the mid-pier footing (a) together with the corresponding plastification (b) of critical cross-sections of the Plaka bridge for vertical forces 200% of gravity.

Figures 21a and 21b depict the numerical response when the applied forces reach gradually the level of 200% of gravity. At this stage the vertical deflections of the footing of the mid-pier, due to the flexibility of the underlying soil, reach the level of 200mm. Such level of deflections of the footing are detrimental to the structure as can be seen figure 21b. The plastification is widespread in all the contact surfaces being more pronounced at the left and right critical regions of the mid-pier. These plotted deformation pattern of the bridge bears resemblance to the collapse mechanism of the Plaka bridge depicted in figures 17b, 17c. Thus, the numerical response obtained at the end of the described gradual loading sequence shows signs of non-linear structural response which can be considered as realistic. This investigation is still under way. Stone bridge behaviour employing advanced non-linear analyses tools were also utilized by Drosopoulos et al (2006), Korompilias (2015), Simos et al. (2018).

## 6 CONCLUSIONS

- Stone masonry construction has a long tradition in many places worldwide. Stone masonry bridges built many centuries ago are one such example. Despite the rigidity and resilience of stone masonry bridges they are in need of maintenance in order to preserve them as part of

the built cultural heritage. Towards this end in-situ measurement campaigns were conducted on a number of stone masonry bridges in order to identify their dynamic characteristics in terms of eigen-frequencies, eigen-modes and damping properties. This information is believed to represent a valuable basis for building realistic numerical simulations of the structural behaviour of such bridges as well as for their structural health monitoring.

- The simplified numerical analyses yielded numerical predictions of bridge deformations and stresses that are useful in understanding the structural behaviour and the structural damage potential for such masonry structures.

- The peak tensile values predicted when design seismic forces were applied for the Saint Vissariona bridge are many times above the tensile strength of the stone masonry thus indicating the severe potential structural damage for this old stone masonry bridge from the design earthquake. The most vulnerable parts of the bridge, as obtained from the location of the peak tensile stress concentration, is a wide area at the crest of the main central arch of the bridge as well as at the abutment near the foundation.

- The integrity of the stone masonry in various parts of the bridge is an additional maintenance issue of considerable importance. Intervention recommendations for such stone masonry bridges should include clauses for applying preparatory actions of measurements and analyses like the ones included here together with established principles that govern a major retrofitting / maintenance effort for cultural heritage together with effective retrofitting / maintenance techniques that are proven to be durable.

- The described system identification technique can also be utilized in identifying changes of stiffness that may be linked to specific actions, such as earthquake activity, and thus serve as warning for certain maintenance counter-measures.

- As shown from the numerical predictions, the flexibility of the foundation, which may be partly attributed to long or short term erosion of the bridge footings, results in detrimental response for the Plaka bridge. These predicted peak tensile stress values are well beyond the stone masonry strength. Consequently, they could well have contributed towards the February 2015 collapse.

- The peak tensile values predicted when design seismic forces were applied for the Plaka bridge are many times above the tensile strength of the stone masonry thus indicating the severe potential structural damage for this old stone masonry bridge from the design earthquake. The most vulnerable parts of the bridge, as obtained from the location of the peak tensile stress concentration, is a wide area at the crest of the main central arch of the bridge as well as the mid-pier internal side footing. Thus, these earthquake vulnerability predictions for the Plaka bridge indicate that had the bridge not collapsed from flooding the design earthquake would have led to its structural damage and its partial collapse.

- Results from advanced non-linear numerical analyses show that such numerical simulations can reproduce in a realistic way the collapse failure scenario and support the hypothesis that the most-likely cause of the collapse of the Plaka bridge.

## REFERENCES

- [1] Aoki T., et al, (2007), "Theoretical and Experimental Dynamic Analysis of Rakanji Stone Arch Bridge, Honyabakei, Oita, Japan," 7th International Conference on Motion and Vibration Control, MOVIC 04.



- [2] Drosopoulos G.A., Stavroulakis G.E., Massalas C.V., (2006) “Limit analysis of a single span masonry bridge with unilateral frictional contact interfaces,” *Engineering Structures* 28 (2006) 1864–1873.
- [3] EAK (2000), Provisions of Greek Seismic Code 2000 , OASP, Athens, December 1999. Revisions of seismic zonation introduced in 2003.
- [4] Eurocode 8 (2004) - Design of structures for earthquake resistance – Part 1 and Part 2: Bridges, DRAFT No 3. European Committee for Standardization; 2004.
- [5] Galeridis A. (1995) “The Stone Masonry Bridges in Thessalia”, Technical Chamber of Greece, Eptalofos, Athens, Greece (In Greek).
- [6] Gazette of the Greek Government (1967), (ΦΕΚ 352/Β/31-5-1967) and (ΦΕΚ 194/Β/21-2-2000), (in Greek).Grassos G. (2007), “The stone masonry arch bridges of Greece”, Center of environmental education Makrinitas, Editor G. Grassos, ISBN: 978-960-98043-9-4, (in Greek). <http://kpe-makrin.mag.sch.gr>.
- [7] ITSAK (2019) Institute of Engineering Seismology and Earthquake Engineering (ITSAK), Data Base of Greek Earthquake Strong Motions.
- [8] Kiyono J., et al. (2012), “Seismic Assessment of Stone Arched Bridges,” 15 WCEE, Lisboa, Portugal, 2012.
- [9] Korompilias D., (2015), “Study of the inelastic behaviour of the Konitsa bridge using an inelastic model for masonry and applying strengthening methods,” PhD Thesis, Univ. Of Patras, Greece, (in Greek).
- [10] Manos G.C. (2011), “Consequences on the urban environment in Greece related to the recent intense earthquake activity”, *Int. Journal of Civil Eng. and Architecture*, Dec., Volume 5, No. 12 (Serial No. 49), pp. 1065–1090.
- [11] Manos G.C. et al. (2015a), “Field experiments for monitoring the dynamic soil-structure-foundation response of model structures at a Test Site” *Journal of Structural Engineering*, American Society of Civil Engineers, Special Issue “Field Testing of Bridges and Buildings, D4014012, Vol. 141, Issue 1, January 2015.
- [12] Manos G.C. and Kozikopoulos E., (2015b) “In-situ Measured Dynamic Response of the Bell Tower of Agios Gerasimos in Lixouri-Kefalonia, Greece and its Utilization of the Numerical Predictions of its Earthquake Response”, *COMPDYN* 2015, Greece.
- [13] Manos G.C., Kotoulas L., Soulis V., Felekidou O. (2015c), “Numerical Simulation of the Limit Non-Linear Behaviour of Unreinforced Masonry under In-plane State of Stress from Gravitational and Seismic Actions”, *COMPDYN* 2015, Greece.
- [14] Manos G.C., Nick Simos N. and Kozikopoulos E. (2016) “The Structural Performance of Stone-Masonry Bridges”, Chapter 4, *Structural Bridge Engineering*, ISBN 978-953-51-2689-8, Print ISBN 978-953-51-2688-1, <http://dx.doi.org/10.5772/64752>.
- [15] Manos G.C., Kozikopoulos E., Kotoulas L., Simos N. (2017), “In-situ Measurements Related to the Performance of Stone Masonry Bridges in Greece”, *COMPDYN* 2017, 6th ECCOMAS Thematic Conference on Computational Methods in Structural Dynamics and Earthquake Engineering, M. Papadrakakis, M. Fragiadakis (eds.), Rhodes Island, Greece.
- [16] Manos G., Simos N., Lambri-Gaitana N. (2019), “Dynamic and Seismic Behaviour of Stone Masonry Bridges in Greece Utilizing In-situ Measurements and Numerical Pre-

- dictions”, COMPDYN 2019, 7th ECCOMAS Thematic Conference on Computational Methods in Structural Dynamics and Earthquake Engineering, M. Papadrakakis, M. Fragiadakis (eds.), Crete, Greece.
- [17] Milas Iraklis, (2016), “Stone Bridges”, Ethnos Travel Book, Ethnos Publications, ISBN:978-960-577-122-5 (in Greek).
- [18] Ozden Caglayan B., Kadir Ozakgul and Ovunc Tezer, (2012), “Assessment of a concrete arch bridge using static and dynamic load tests” *Structural Engineering and Mechanics*, Vol. 41, No. 1 (2012) 83-94
- [19] Papazachos B.K. and Papazachou K. (1989) “Earthquakes in Greece”, Ziti publishers, Thessaloniki, Greece, (In Greek).
- [20] Psimarni K., Georgopoulos A., Balodimos D.D. (2000), “Development of a Geographic Information System for the Traditional Bridges of Central Zagori,”, Report to the Municipality of Zagori, in Greek.
- [21] Ruocci G., Quattrone A., Zanotti Fragonara L., Ceravolo R., De Stefano A., (2013) “Experimental Testing of a Masonry Arch Bridge Model Subject to Increasing Level of Damage”, IRIS, Chapter 6, Industrial Safety and Life Cycle Engineering, VCE Vienna Consulting Engineers, [www.vce.at](http://www.vce.at), ISBN 978-3-200-03179-1.
- [22] SAP2000, Integrated Software for Structural Analysis and Design, Computers and Structures Inc.
- [23] Sevim Baris, et al., (2011), “Finite element model calibration effects on the earthquake response of masonry arch bridges,” *Finite Elements in Analysis and Design*, 47 (2011), 621–634
- [24] Simos N. and. Manos G.C, (2013), “Numerical Analysis of Seismic Response of Natural Stone Arch Bridges-Field Observations and a Case Study,” COMPDYN 2013, <http://www.eccomasproceedings.org/cs2013/>
- [25] Simos N., Manos G.C., Kozikopoulos E., Kotoulas L. “On the Assessment of the Plaka Bridge Collapse using Non-linear Analysis Preventable or Doomed?”, COMPDYN 2017, 6th ECCOMAS Thematic Conference on Computational Methods in Structural Dynamics and Earthquake Engineering, M. Papadrakakis, M. Fragiadakis (eds.), Rhodes Island, Greece, 15–17 June 2017.
- [26] Simos N., Manos G.C., Kozikopoulos E. (2018), “Near- and far-field earthquake damage study of the Konitsa stone arch bridge”, *Engineering Structures* 177 (2018) 256–267, <https://doi.org/10.1016/j.engstruct.2018.09.072>.

## EXPERIMENTAL IDENTIFICATION OF MECHANICAL AND DYNAMIC CHARACTERISTICS OF 3D PRINTING SPECIMENS

Ioannis E. Kavvadias<sup>1</sup>, Konstantinos Tsongas<sup>2</sup>, Dimitrios Tzetzis<sup>2</sup>, Kosmas E. Bantilas<sup>1</sup>,  
Lazaros Vasiliadis<sup>1</sup>, Anaxagoras Elenas<sup>1</sup>

<sup>1</sup>Department of Civil Engineering, Democritus University of Thrace  
Campus of Kimmeria, Xanthi 67100, Greece  
e-mail: {ikavvadi, kbantila, lvasilia, elenas}@civil.duth.gr

<sup>2</sup>Digital Manufacturing and Materials Characterization Laboratory, School of Science and Technology  
International Hellenic University  
14km Thessaloniki - N. Moudania, Thermi GR57001, Greece  
{k.tsongas, d.tzetzis}@ihu.edu.gr

---

### Abstract

*Additive manufacturing is at the forefront of research activities worldwide, as the commercial exploitation of this technology is expected to displace some traditional manufacturing methods over the next few years. The aim of this research is the identification of the dynamic characteristics of three-dimensional printing specimens. The specific specimens, composed of 3D printed parts, correspond to elastic single and multiple degree of freedom oscillators. Moreover, parts that represent rigid rocking columns are constructed. Bending tests are performed in order to identify the stiffness of the elastic oscillators. Moreover, experimental results of free vibrations are presented in order to investigate the dynamic response of the rocking parts. The dynamic behavior verification through analytical solutions will highlight the adequacy of 3D printing specimens for conducting experimental research in structural dynamics.*

**Keywords:** Additive Manufacturing, Fused Deposition Modeling, Structural Dynamics, Earthquake Engineering, Rocking Structures, Experimental Investigation.

---

## 1 INTRODUCTION

Additive manufacturing technology is widely applied to optimize products in several industries and more specifically in the field of civil engineering [1] where the efforts have been intensified recently towards the implementation and testing of prototypes. Additive Manufacturing (AM), also known as 3D Printing, allows the fabrication of fully personalized designs with geometrical complexity, while it decreases the use of tools, the cost during prototyping steps and the fabrication time [2]. No requirement of molds, costly tools, milling, and sanding processes are the main reasons why it is a low-cost production method. Even though the basic methods of thermoplastics forming (extrusion, injection molding, thermoforming) are the mainstream in the polymers industry, 3D printing is more efficient, time saving, and minimizes the use of raw materials [3]. During the past few decades, different applications of 3D printing have been investigated in various industries, due to the interest of scientists, engineers, and the medical community [4]. The extensive use of 3D printing in recent years has increased the interest in Fused Deposition Modelling (FDM), which is a widely used method for 3D printing, due to good efficiency, easy material deposition and low costs [5]. Over the last years, bio-based polymers, such as poly (lactide acid) (PLA), have attracted much attention in 3D printing, replacing petroleum-based polymers, due to its availability from renewable and environmentally friendly resources as well its outstanding properties as high tensile strength and modulus [6, 7], demonstrating simultaneously high-stiffness and high-damping properties, worthy of further functional studies [8]. The application of PLA in FDM technology raises year by year [9]. The mechanical response of 3D printed PLA was found better than injection-molded PLA [10]. However, PLA has some disadvantages, such as poor thermal stability and surface, as well as brittleness which make it unsuitable for some large-scale end uses.

In the present research project, the exploitation of 3D printing in seismic testing was investigated. Especially, the seismic response of rocking podium strictures (RPSs) [11-13] was experimentally investigated. RPSs are comprised of an elastic superstructure placed on the top of a rocking story. Thus, 3D printed parts representing rocking columns and elastic oscillators were constructed. Evaluating the mechanical and the dynamic properties of the specimens by comparing the behavior with the analytical solution results, significant remarks arise regarding the capability of 3D printing in earthquake engineering experimental research. In the current study, preliminary results obtained by bending tests of the elastic members, as well as free rocking oscillation tests of rocking columns and frames are presented and discussed.

## 2 ROCKING PODIUM STRUCTURES

The first detailed study of the dynamic response of structures seismically isolated using a purely rocking floor at the base, considering that the superstructure behaves like a single degree of freedom elastic oscillator, was carried out by Bachmann et al. [11]. Based on the sdof model of the superstructure, Bantilas et al. [12] investigated the parameters that affect the elastic demands of RPSs. Later studies of Bantilas et al. [13] highlighted the critical effect of the higher vibration modes on the dynamic response of RPSs consisted of multiple degree of freedom (mdof) elastic superstructure. Experimental investigation of RPSs consisted of sdof superstructure has been also conducted [14]. The presence of curved extensions at the base of the rocking columns results in rolling and rocking rocking response [15]. The idealization of the model of mdof elastic oscillator fixed on the top of a rocking frame which is comprised of kinematic bearings is illustrated in Figure 1(a). Moreover, a typical configuration of the kinematic bearings is presented in Figure 1(b).



The rigid frame consists of a cap beam with mass  $m_b$  and  $N$  freestanding columns with mass  $m_c$ , semi-diagonal length  $R = \sqrt{H^2 + B^2}$ , rotational moment of inertia around its center of mass  $I_{cm}$ , and slenderness  $\alpha = \arctan(B/H)$ . In case of kinematic bearings with curved wedges and total slenderness  $\tan \alpha' = B'/H$ , the post uplift stiffness during rolling response depends on the radius of curvature  $r$  of the extensions, while the wedge's angle  $\beta$  sets the limit between rolling and rocking response. The superstructure is determined by the mass matrix  $\mathbf{M}$ , the stiffness matrix  $\mathbf{K}$  and the damping matrix  $\mathbf{C}$ . The equations of motion of the examined structural system are presented in the aforementioned literature.

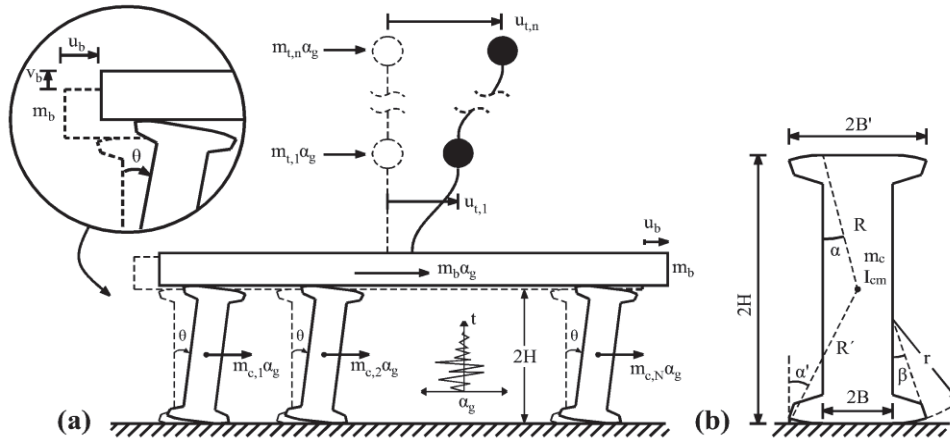


Figure 1: (a) Schematic representation of the analytical model, (b) geometric configuration of a typical kinematic bearing.

For the scope of the experimental investigation, rocking podium structures comprised by a couple of kinematic bearings, and superstructures which were formed by stiff plates and two flexible walls were designed. In total, three different sets of kinematic bearings were constructed. Moreover, a one storey superstructure, a three storey superstructure and a rigid superstructure were configured. In order to obtain comparable response results, the total mass of the superstructures is equal, while the flexible superstructures demonstrate the same fundamental vibration period.

Each rocking column has height  $2H = 150$  mm and slenderness  $\alpha = 0.15$  rad. Thus, the width was  $2B = 22.5$  mm. Regarding the kinematic bearings with the curved extensions, the total width was  $2B' = 45$  mm and the wedges' radius of curvature  $r = 50$  and  $75$  mm. The rocking parts were placed on the top of a stiff plate.

The dynamic properties of the elastic oscillators should be in accordance with the scale of the rocking parts. Thus, taking into account that the height of the rocking parts is scaled down by a factor of 20, the period of the elastic oscillators must be scaled down by in order to represent a full size podium structure. Assuming that a typical three storey structure demonstrate period  $T_t = 0.3$  s, the period of the specimens should be  $T_t = 0.07$  s. The elastic oscillators are comprised of stiff plates and flexural walls. The stiff plates have dimensions  $150 \times 150 \times 6$  mm.

The vertical parts have height and width equal to 150 mm. The most important dimension, which is defined by the targeted period, is the thickness of the walls. Considering that in typical structures the distribution of floor masses is constant, the translational stiffness distribution throughout the structure affects the lateral displacement profile and the effective mass of the fundamental vibration mode. Due to the assembly of the superstructure the plates should be considered as rigid, while the walls as flexible. As such, only translational Dofs were considered. The relative translational stiffness between the floors was determined by solving the eigenvalue problem [17]. Regarding the mdof superstructure, the eigenvalue problem was solved in reverse

assuming triangular lateral displacement profile [16]. As such, given that the Young's modulus of PLA is  $E = 3.2$  GPa, the thickness of the walls of the sdof superstructure was 4.85 mm, while for the mdof superstructure the thicknesses were 6.35 mm, 5.83 mm and 4.80 mm for the walls of the 1st, the 2nd and the 3rd storey respectively.

The individual structural members of the examined structural system were designed in SolidWorks CAD software (Dassault Systèmes, SolidWorks Corporation, Waltham, MA, USA). Except of the geometric characteristics referred above, of great importance was the detailed design of the regions where the assembly of the kinematic bearings with the base plate and the cup beam, and the plates with the flexible walls took place. In Figure 2 indicative structural members, as well as the details of the plates, as they are designed, are illustrated.

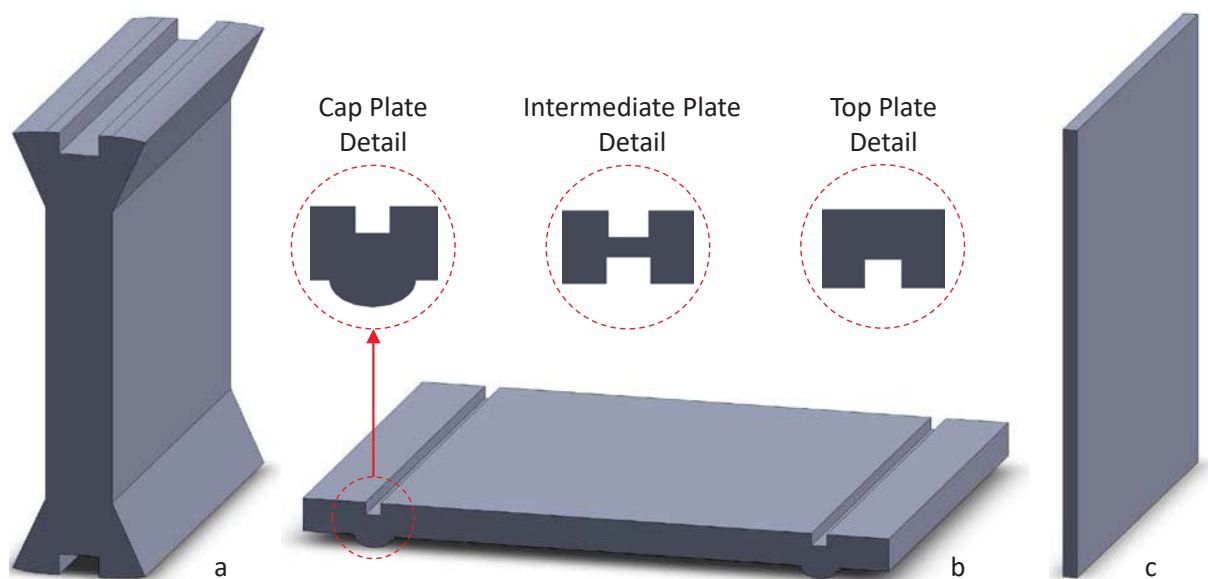


Figure 2: CAD models of (a) a kinematic bearing, (b) a plate and (c) an elastic wall.

### 3 EXPERIMENTAL METHODS

#### 3.1 Fabrication of 3D printed specimens

All specimens tested in this study were produced on a BCN3D Sigma R17 3D printer (BCN3D, Barcelona, Spain) with a 2.85 mm filament diameter. BCN3D Cura was used as slicing Software. Only system integrated (default) variations of production parameters were used in the comparative analysis. The printing parameters used were: nozzle extrusion temperature of 220° C, heat bed temperature of 60°C, deposition line (layer) height 0.3 mm, deposition line width 0.8 mm and printing speed of 60 mm/s. Deposition speed was therefore not considered a variable in this study and a constant extrusion velocity was selected for all specimens, based on device parameters (e.g., effective printing range). Also, 3D printing was performed in a standard laboratory without temperature or humidity control.

The kinematic bearing specimens have been 3D printed with an infill density of 20%, as illustrated in Figure 3a. For the plates, an infill density of 30% was considered optimal (Figure 3b). Figure 3c demonstrates the elastic wall specimens that were 3D printed as hollow sections. For all specimens two lines were printed on the perimeter to form the outer shell, which is typical in FDM prints. Figure 3d shows an assembly of a rocking podium structure consisted of a three storey superstructure. It has to be mentioned that in order to avoid sliding, a low friction tape has been applied over the contact region between the bearings and the plates.

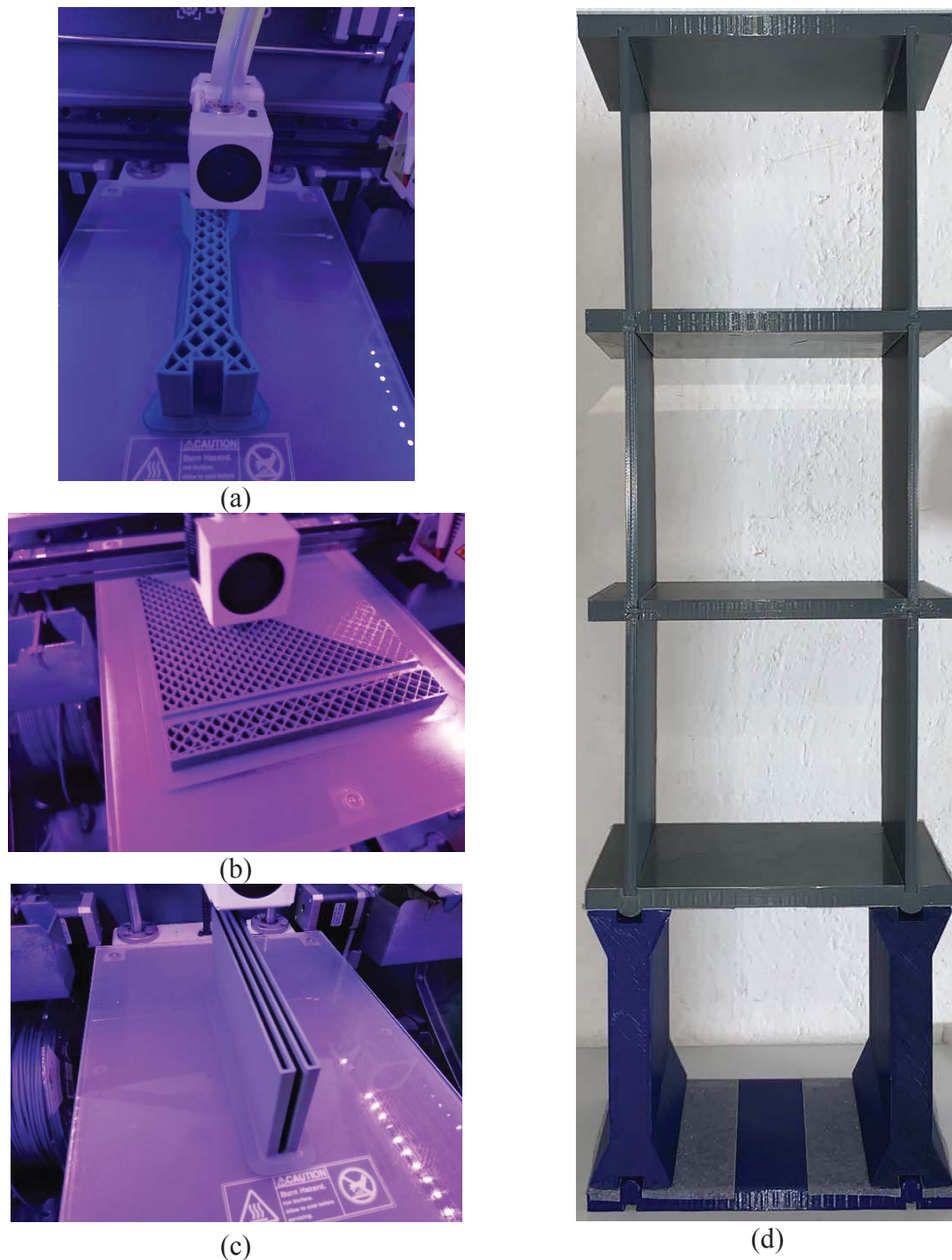


Figure 3: 3D printed (a) kinematic bearing, (b) plate, (c) elastic wall and (d) assembly of a rocking podium structure.

### 3.2 Bending tests

The 3D printed wall structures were subjected under 3-point bending tests using a universal Testometric M500-50AT testing machine equipped with 50 kN load cell, according ASTM D590. The support span was set to be 110 mm. At least three specimens were prepared and

tested. The loading and supports noses have a diameter of 10 mm. The crosshead speed was set to be 5 mm/min.

### 3.3 Free oscillation tests

The kinematic response of a kinematic bearing and a rocking frame, under free oscillation, was measured by motion tracking analysis of image sequences. For this scope the dynamic behavior is captured by a Canon EOS 5D MKIV camera with a Canon EF 24-70mm f/2.8 L USM II lens. The measurement of the displacements was performed using the Kinovea [18] software. Kinovea is a free and open source 2D motion tracking software that analyzes video files, even without markers. However, in order to improve the reliability of the measurements passive markers were assigned on the specimens.

## 4 MECHANICAL AND KINEMATIC BEHAVIOR OF 3D PRINTED SPECIMENS

Preliminary investigation of the identification of mechanical and kinematic properties of 3D printed specimens has been performed. These 3D printed parts will be used to construct the examined RPSs for the purpose of the current research program.

Orientation can also have a significant impact on print time. The 3D printing direction was purposely selected. For functional parts, it is important to consider the application and the direction of the loads. FDM parts are much more likely to delaminate and fracture when placed in tension in the Z direction compared to the XY directions.

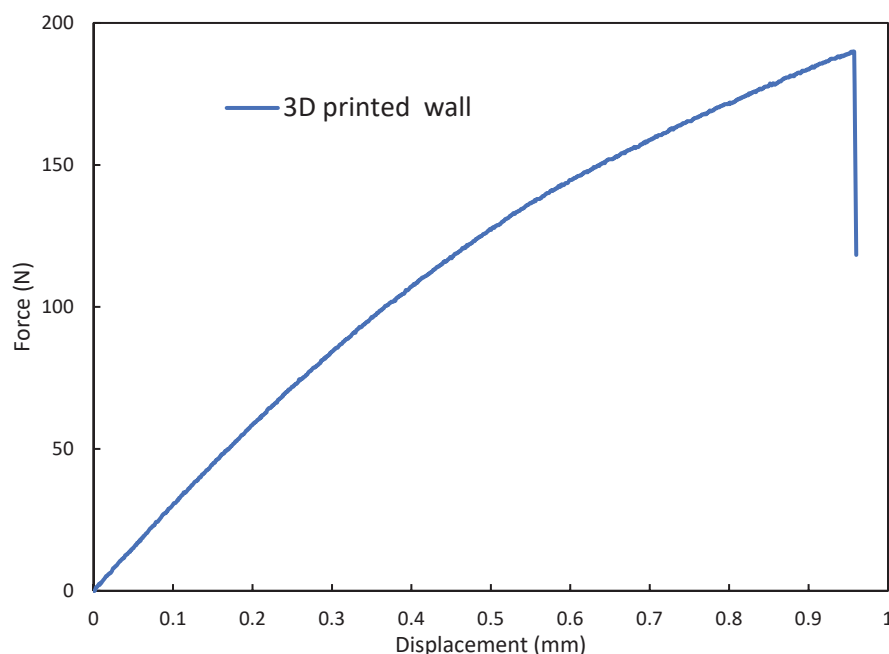


Figure 4: Typical force-displacement curve of a 3D printed elastic wall.

The force-displacement response of a 3D printed elastic wall has been determined with flexural tests. The typical force-displacement curve is illustrated in Figure 4. It can be observed that the maximum force that was applied on the 3D printed elastic wall was 205 N. The deflection at break was 0.95 mm. The flexural stiffness is a criterion of measuring deformability. The flexural stiffness of a structure is a function based upon two essential properties: the elastic modulus,  $E$  (stress per unit strain) of the material that composes it, and the moment of inertia,

$I$ , a function of the cross-sectional geometry. In terms of flexural stiffness  $EI$ , the mean measured value was  $8.5 \times 10^6 \text{ Nmm}^2$ , while the theoretical calculations during the design process were given at  $9 \times 10^6 \text{ Nmm}^2$ .

In Figure 5 the experimental time histories of an individual kinematic bearing and a rocking frame under free oscillation are presented comparatively with the analytical solution. Regarding the kinematic bearing with radius of curvature  $r = 50 \text{ mm}$ , the responses are demonstrated in terms of horizontal displacement of its center of mass (Figure 5a). The analytical response was calculated given the design properties of the bearing, while the coefficient of restitution that defines the energy dissipation during impact was assumed as provided by Bachmann et al. [15]. Given the geometry of the kinematic bearing and the printing properties, the non-dimensional moment of inertia  $\bar{I}_0 = 1.354$ . Where  $\bar{I}_0 = I_0 / (m_c R^2)$ , and  $I_0$  is the rotational inertia of the column with respect to the pivot point. In Figure 5b the response of a rocking frame consisted of the kinematic bearings with radius of curvature  $r = 50 \text{ mm}$  is displayed. The analytical solution was derived by Makris and Vassiliou [19]. The time history is given in terms of the cap beams' horizontal displacement. In general, the analytical solution predicts well enough the response time histories. Furthermore, the coefficient of restitution seems to provide with high precise the energy dissipation during impact. However, the differences between the responses, especially in case of the kinematic bearings, lead to significant remarks. It has to be mentioned the fact that although the amplitude of the negative values of the responses are in good agreement, the measured positive displacements are higher than those of the analytical solution. Moreover, the peak positive value after impact is almost equal to the negative extreme value before impact. These remarks imply a non-symmetric specimen. Although the initial design was totally symmetric, the eccentricity may occur due to imperfections of the external geometry or due to non-symmetric pattern of the infill. In order to capture the response of the specimens with higher accuracy, validation of the analytical solution is needed.

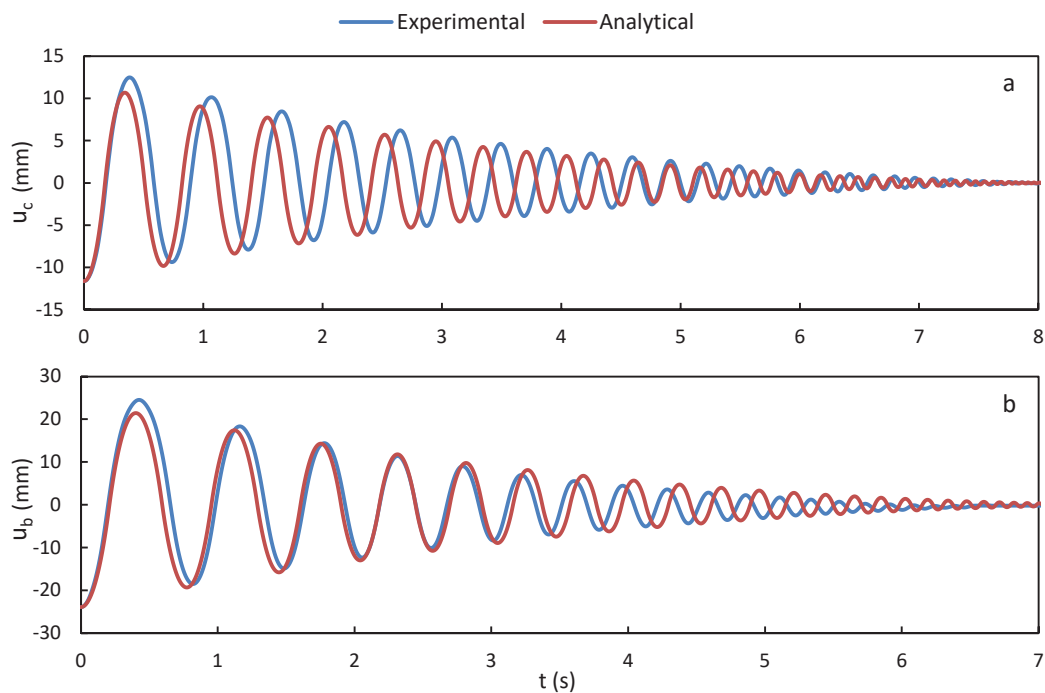


Figure 5: Response under free oscillation of (a) a kinematic bearing and (b) a rocking frame.



## 5 CONCLUSIONS

In the present research project, the exploitation of 3D printing in seismic testing is investigated. 3D printed parts representing rocking columns and elastic oscillators were manufactured with Fused Deposition Modeling technology. The mechanical and the dynamic properties were assessed. The measured mechanical response was very close to the designed. Considering the dynamic behavior, minor deviations to the designed geometry were observed. Therefore, the 3D printing procedure can be potentially utilized for seismic testing. In a future study, the construction of a redesigned and more complex structural system could be done, through the process of additive manufacturing, along with a thorough examination of the dynamic behavior via the utility of proper experiments.

## ACKNOWLEDGEMENTS

This research is co-financed by Greece and the European Union (European Social Fund-ESF) through the Operational Programme «Human Resources Development, Education and Lifelong Learning» in the context of the project "Reinforcement of Postdoctoral Researchers - 2nd Cycle" (MIS-5033021), implemented by the State Scholarships Foundation (IKY).

## REFERENCES

- [1] L. Del Giudice, M. F. Vassiliou, Mechanical properties of 3D printed material with binder jet technology and potential applications of additive manufacturing in seismic testing of structures. *Additive Manufacturing*, **36**, 101714, 2020.
- [2] C.M. González-Henríquez, M.A. Sarabia-Vallejos, J. Rodriguez-Hernandez, Polymers for additive manufacturing and 4D-printing: Materials, methodologies, and biomedical applications. *Progress in Polymer Science*, **94**, 57-116, 2019.
- [3] K. Gnanasekaran, T. Heijmans, S. Van Bennekom, H. Woldhuis, S. Wijnia, G. de With, H. Friedrich, 3D printing of CNT-and graphene-based conductive polymer nanocomposites by fused deposition modeling. *Applied materials today*, **9**, 21-28, 2017.
- [4] C. Wang, W. Huang, Y. Zhou, L. He, Z. He, Z. Chen, X. He, S. Tian, J. Liao, B. Lu, Y. Wei, M. Wang, 3D printing of bone tissue engineering scaffolds. *Bioactive materials*, **5**(1), 82-91, 2020.
- [5] P. Szymczyk-Ziółkowska, M.B. Łabowska, J. Detyna, I. Michalak, P. Gruber, A review of fabrication polymer scaffolds for biomedical applications using additive manufacturing techniques. *Biocybernetics and Biomedical Engineering*, **40**(2), 624-638, 2020.
- [6] D. Rasselet, A.S. Caro-Bretelle, A. Taguet, J.M. Lopez-Cuesta, Reactive compatibilization of PLA/PA11 blends and their application in additive manufacturing. *Materials*, **12**(3), 485, 2019.
- [7] W.J. Choi, K.S. Hwang, H.J. Kwon, C. Lee, C.H. Kim, T.H. Kim, S.W. Heo, J.H. Kim, J.Y. Lee, Rapid development of dual porous poly (lactic acid) foam using fused deposition modeling (FDM) 3D printing for medical scaffold application. *Materials Science and Engineering: C*, **110**, 110693, 2020.
- [8] M. Mansour, K. Tsongas, D. Tzetzis, Measurement of the mechanical and dynamic properties of 3D printed polylactic acid reinforced with graphene. *Polymer-Plastics Technology and Materials*, **58**(11), 1234-1244, 2019.

- [9] V. Mazzanti, L. Malagutti, F. Mollica, FDM 3D printing of polymers containing natural fillers: A review of their mechanical properties. *Polymers*, **11(7)**, 1094, 2019.
- [10] Y. Song, Y. Li, W. Song, K. Yee, K.Y. Lee, V.L. Tagarielli, Measurements of the mechanical response of unidirectional 3D-printed PLA. *Materials and Design*, **123**, 154-164, 2017.
- [11] J.A. Bachmann, M.F. Vassiliou, B. Stojadinović, Dynamics of rocking podium structures. *Earthquake Engineering and Structural Dynamics*, **46(14)**, 2499-2517, 2017.
- [12] K.E. Bantilas, I.E. Kavvadias, L.K. Vasiliadis, Analytical investigation of the seismic response of elastic oscillators placed on the top of rocking storey. *Bulletin of Earthquake Engineering*, **19**, 1249-1270, 2021.
- [13] K.E. Bantilas, I.E. Kavvadias, L.K. Vasiliadis, Seismic response of elastic multidegree of freedom oscillators placed on the top of rocking storey. *Earthquake Engineering and Structural Dynamics*, **50(5)**, 1315-1333, 2021.
- [14] Bachmann J.A., Jost C., Studemann Q., Vassiliou M.F., Stojadinović B., An analytical model for the dynamic response of an elastic SDOF system fixed on top of a rocking single-storey frame structure: experimental validation. *7th European Congress on Computational Methods in Applied Sciences and Engineering*, Crete Island, Greece, 2016.
- [15] J.A. Bachmann, M.F. Vassiliou, B. Stojadinović, Rolling and rocking of rigid uplifting structures. *Earthquake Engineering and Structural Dynamics*, **48(14)**, 1556-1574, 2019.
- [16] G.E. Thermou, S.J. Pantazopoulou, A.S. Elnashai, Global interventions for seismic upgrading of substandard RC buildings. *Journal of Structural Engineering*, **138(3)**, 387-401, 2012.
- [17] A.K. Chopra, *Dynamics of Structures: Theory and Applications to Earthquake Engineering*. Prentice Hall, 1995.
- [18] <https://www.kinovea.org/>
- [19] N. Makris, M.F. Vassiliou, Planar rocking response and stability analysis of an array of free-standing columns capped with a freely supported rigid beam. *Earthquake Engineering and Structural Dynamics*, **42(3)**, 431-449, 2013.



## INVESTIGATION OF LOW COST SMAs UNDER ELEVATED TEMPERATURES

Sofia Piliafa<sup>1\*</sup>, Lazaros Melidis<sup>1</sup>, Lambros Kotoulas<sup>1</sup>, Nikolaos Makris<sup>1</sup> and Konstantinos Katakalos<sup>1</sup>

<sup>1</sup> Aristotle University of Thessaloniki  
Laboratory of Experimental Strength of Materials and Structures, Thessaloniki, 54124  
e-mail: {spiliafa, kkatakalo}@civil.auth.gr, {lpkotoulas, nsvmakris}@gmail.com  
<https://strength.civil.auth.gr>

---

### Abstract

*Nowadays much emphasis has been placed on studying smart materials because of their ability to change their particular properties in a controlled manner by external stimuli. Shape memory alloys belong to the wider category of intelligent materials and exhibit two unique characteristic behaviors, superelasticity and shape memory effect, making them differ from conventional materials. These effects are due to diffusionless transformations between austenitic and martensitic phases. The SME occurs because a temperature-induced phase transformation reverses deformation and the pseudoelasticity achieves large, recoverable strains with little to no permanent deformation, as well, but it relies on more complex mechanisms. Innovative, low cost iron-based shape memory alloys (Fe-Mn-Si SMAs) with good workability, machinability, and weldability have been drawing much attention during the last two decades regarding to their potential application in engineering such as prestressing of concrete or coupling devices. In the present work we carried out experiments on monotonic mechanical loading, low-cycle fatigue and thermal loading in the laboratory of Experimental Strength of Materials and Structures of Aristotle University of Thessaloniki, so as to investigate in practice their behavior and all their special characteristics that already exist in the current literature.*

**Keywords:** low cost iron-based shape memory alloys, thermomechanical characterization, civil engineering applications.

---

## 1 INTRODUCTION

Shape memory alloys (SMAs) are metallic materials which belong to the wider category of smart materials. The last decades they have attracted the interest regarding to their potential application in engineering, due to their good mechanical properties including fatigue behavior, corrosion resistance and their ability to damp and absorb energy. [1-3] Shape memory alloys display two distinct crystal structures or phases (austenitic and martensitic phase), which depend on temperature and internal stress. Martensite exists at lower temperatures while austenite exists at higher temperatures. When an SMA is in martensite form at lower temperatures, the metal can easily be deformed into any shape. When the alloy is heated, it goes through transformation from martensite to austenite. In the austenite phase, the memory metal «remembers» its initial shape, before deformation [4]. Because of that, shape memory alloys exhibit two unique characteristic behaviors, superelasticity and shape memory effect. The loading–unloading cycle typically shows a pronounced hysteresis loop. In the shape memory effect, a large residual strain remains after unloading, which can be recovered by heating [5]. The two most prevalent shape-memory alloys are copper-aluminium-nickel and nickel-titanium (NiTi) which are preferable for most applications due to their stability and practicability [6]. However, low-cost, iron-based Shape Memory Alloys (Fe-Mn-Si SMAs) have been drawing much attention during the last three decades[7,8]. Fe-Mn-Si SMAs can be passive or active components in civil structures to reduce damage caused by environmental impacts or earthquakes [3]. Other possible applications of SMAs in civil engineering are passive vibration damping and energy dissipation, active vibration control, actuator applications, and the utilization of the SME (Shape memory effect) for prestressing or tensioning. Among those possible applications, the pre-stressing of structures using fixed shape memory alloys has attracted a considerable attention [8]. In contrast to conventional prestressing, neither anchoring systems nor hydraulic devices are necessary for applying the prestressing force, since prestressing is achieved by the shape memory effect produced by heating. This heating can be implemented by electrical resistance heating (Joule heating). However, to be suitable for prestressing, an SMA needs to have certain properties, such as a large and stable recovery stress [10,11]. The aim of this work is to broaden the knowledge of iron-based Shape memory alloys' mechanical behavior, which is now limited, through laboratory tests. The experimental work presented in this paper focuses on characterizing the thermo-mechanical response of the Fe-SMA through experiments on monotonic mechanical loading, low-cycle fatigue and thermal loading, carried out in the laboratory of Experimental Strength of Materials and Structures of Aristotle University of Thessaloniki. Stress and temperature were the investigation parameters.

## 2 MATERIALS AND METHODS

To characterize the thermo-mechanical response, four dog-bone shaped tensile specimens with a gauge length of 60 mm and cross-section of 1.5 x 9 mm<sup>2</sup> were prepared from the original (Fe-SMA) plate. (see table 1) Then, unidirectional mechanical tests were performed using the Instron tensile testing machine equipped with a climate chamber which can be operated in a temperature range between 20°C (RT-Room Temperature) and 250°C. Instron machine contains also an integrated static load cell of 50 kN capacity and the Bluehill software which gives us the results of an experiment in a diagram form of load – strain. (see figure 1) During the tests, the strain evolution was measured with a clip-on extensometer. The stress–strain behavior of the alloy was characterized by applying tensile mechanical loading and unloading, in the two first specimens, under displacement-controlled conditions with a loading rate of 1 mm/min. The

recovery stresses as a function of the temperature were also measured in strain-controlled tests in the two other specimens. Firstly, the samples were subjected to 4 and 1% tensile strain and then heated to 160 and 250°C, respectively, and subsequently cooled down to RT, keeping the gauge length constant during the whole experiment. In Table 1 we depict all details of the experimental sequence. The heating rate was set to 6°C/min. As far as cooling is concerned it was held in a physical way, so the coolest temperature reached was approximately 20°C and the cooling rate was slow. (see figure 2)

Table 1: Detailed information of experiments

Name	Dimensions (mm)		Loading	T (°C)	Target strain	Comments
	t	b				
<b>Specimen 1</b>	1.50	9.15	MUT <sup>*1</sup>	RT(=23)	Up to failure	
<b>Specimen 2</b>	1.56	9.68	LCF <sup>*2</sup>	RT	Strain 4‰	
	1.56	9.68	LCF	RT	Strain 9‰	
	1.56	9.68	LCF	RT	Strain 3.5%	
	1.56	9.68	LCF	RT	Strain 6.5%	
	1.56	9.68	MUT	RT	Up to failure	
<b>Specimen 3</b>	1.52	9.03	TL <sup>*3</sup>	160		Prestrain 4% & complete unloading
	1.52	9.03	MUT	RT	Up to failure	
<b>Specimen 4</b>	1.55	9.41	TL	250		Prestrain 1% & Complete unloading
	1.55	9.41	MUT	RT	Up to failure	

\*1Monotonic Uniaxial Tension, \*2Low Cycle Fatigue (n=3), \*3Thermal Loading (n=1)

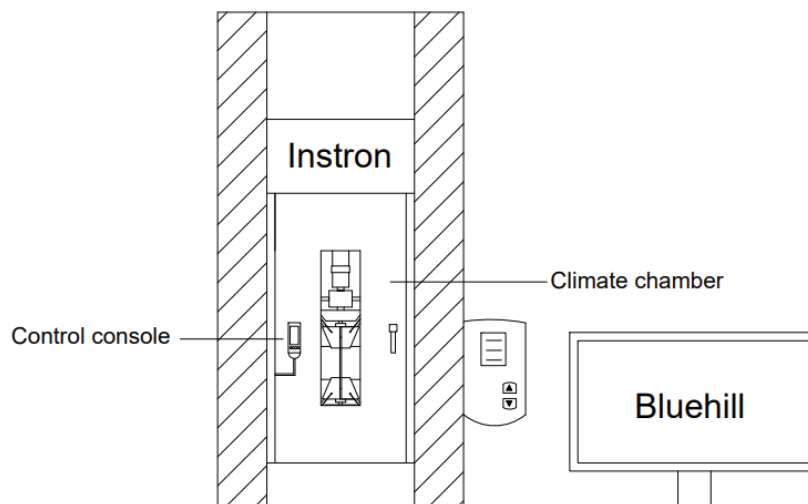


Figure1. Experimental setup with climate chamber

As mentioned before, the two first specimens (specimen 1 & 2) are tested under displacement-controlled conditions. Each one is placed carefully in suitable grips for its cross-

section, so as not to have slip losses and tension loads be applied right. Their dimensions are measured (1.5 x 9.15) mm and (1.56 x 9.68) mm, respectively, using a caliper. The first one is tested under monotonic, uniaxial tension loading up to failure. Specimen 2 is submitted to five low – cycle fatigue tests of three loading – unloading cycles with a different target strain each time. Target and residual strains of each cycle are given collectively in the table 2 below:

Table 2: Target and residual strains of each low-cycle fatigue test.

No of Cycle	Target strain	Residual strain
1st cycle	4‰	1.8‰
2nd cycle	9‰	5‰
3rd cycle	3.5%	2.8%
4th cycle	6.5%	5.8%

When four cycles are completed a gradual increase of loading is applied with the same rate of 1mm/min, as before.

Following the previous investigations, specimens 3 and 4 are tested in thermal loading. Each one is placed carefully in suitable grips for its cross-section, so as not to have slip losses and tension loads be applied right. Their dimensions are measured (1.52 x 9.03) mm and (1.55 x 9.41) mm, respectively, using a caliper. We have applied an initial pre-strain and total unloading to both specimens. When the protocol set is activated, the temperature starts increasing from 20°C (RT-Room Temperature) to the default values of 160 and 250°C with a rate of 6°C/min. When the heating is completed, the temperature is held for a few minutes, in order to achieve uniform temperature distribution in the specimen. When opening the climate chamber, cooling starts naturally and a Room Temperature of 20°C is reached. (details in table 3) After that, the extensometer is placed again, and monotonic uniaxial loading is forced to the specimen up to failure. Figure2 present the aforementioned thermal protocol.

Table 3: Required time for heating and cooling.

Target temp. (°C)		Heating time (min)	Constant time (min)	Cooling time (min)
Temp. (°C)	150	20	5	10
	260	60	5	40

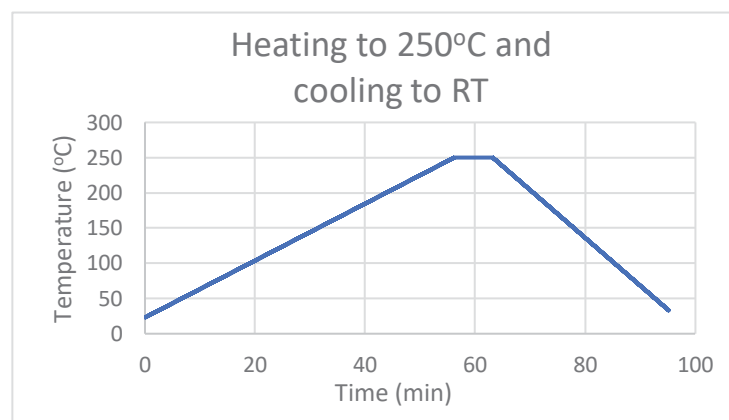


Figure 2: Time – Temperature diagram for heating to 250°C and cooling to RT

### 3 RESULTS

The following table 4 summarizes the results obtained from the experimental campaign occurred in the Laboratory for Strength of Materials and Structures.

Table 4. Summarized results

Name	Max. Load (kN)	Max. Stress (Mpa)	Max. Strain (%)	T (°C)	Residual strain (‰)
<b>Specimen 1</b>	13,734	1000	33	RT(=23)	Up to failure
<b>Specimen 2</b>	5,540	367	0,4	RT	1,8
	7,816	518	0,9	RT	5,0
	10,133	671	3,5	RT	29
	11,085	734	6,5	RT	58
	14,481	959	33	RT	Up to failure
<b>Specimen 3</b>	2,750	180	0,15	160	None
	9,230	672	35	RT	Up to failure
<b>Specimen 4</b>	3,870	250	0,19	250	None
	13,546	928	37	RT	Up to failure

Specimen 1 was monotonically loaded at room temperature up to failure. Figure 3 depicts the strain-strain graph of this coupon. An ultimate load of 13,734kN, which corresponds to 1000 MPa was recorded. The maximum measured strain was equal to 33%. It is obvious that at room temperature Fe-SMAs exhibit a high strength value together with high plasticity.

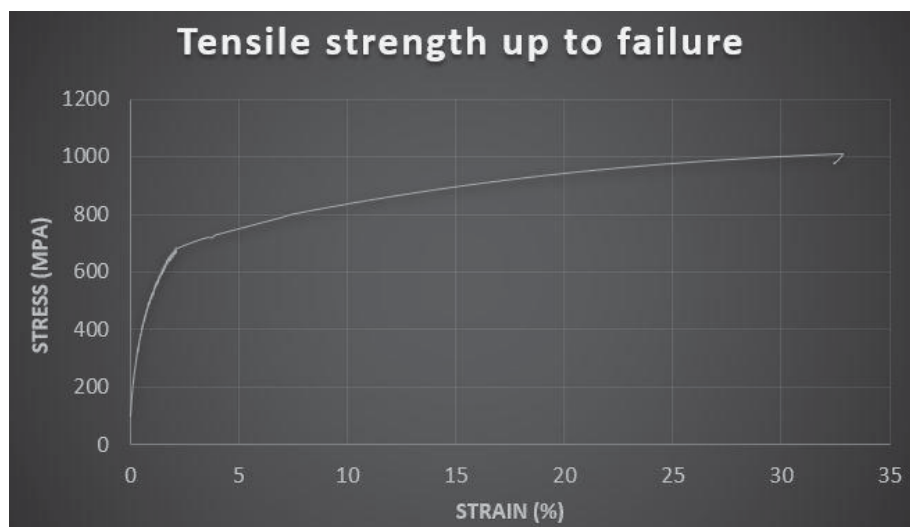
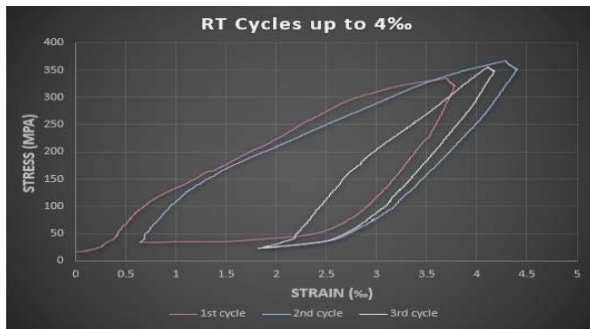
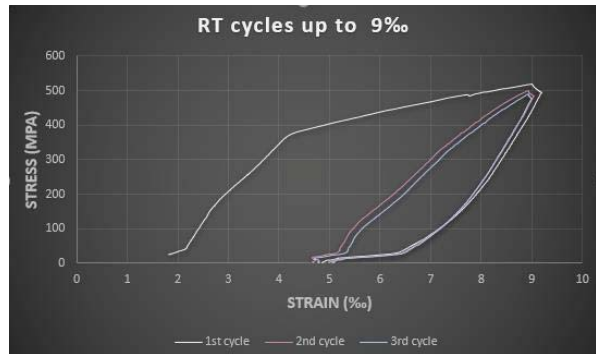
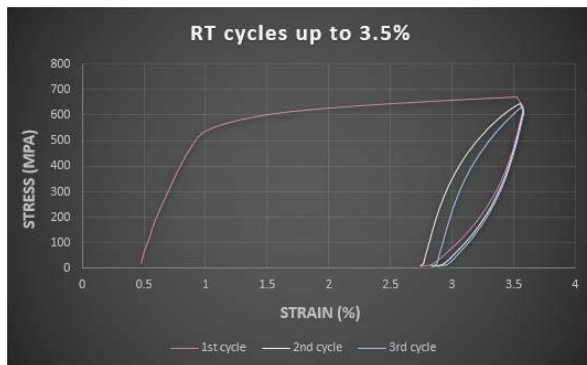
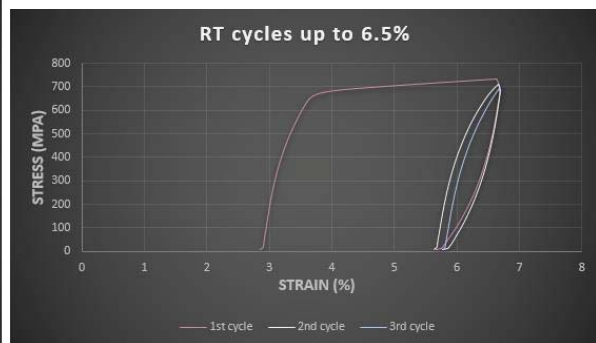


Figure 3.  $\sigma$ - $\epsilon$  graph for specimen 1

Specimen 2 was loaded for several cycles (see table 1), at room temperature but at different loading rates. The first 3 cycles were performed up to a strain limit of 4‰. The following at a strain limit of 9‰, value which was increased to 35‰ and 65‰. Finally, specimen 2 was loaded up to failure. Figures 4a to 4

Figure 4a.  $\sigma$ - $\epsilon$  graph for specimen 2 (4‰ target strain)Figure 4b.  $\sigma$ - $\epsilon$  graph for specimen 2 (9‰ target strain)Figure 4c.  $\sigma$ - $\epsilon$  graph for specimen 2 (35‰ target strain)Figure 4d.  $\sigma$ - $\epsilon$  graph for specimen 2 (65‰ target strain)

Concerning the pre-strain of 4‰ we noticed that the residual strain changed significantly when we slightly increased the target strain value, which means the investigated Fe-SMA is sensitive to the defined pre-strain value, leading to very different residual strains.

The further increase of the target strain from 4 to 9‰, leads to a gradient change of the  $\sigma$ - $\epsilon$  graphs' inclination (initial yield of the material), shortly after 4‰. The target strain remained stable to 9‰ at both three cycles, so loops follow a more regular behavior, having the same values of residual strains.

The following pre-strain levels are reaching 3.5% and 6.5% respectively. The mechanical behavior of alloy becomes clearly elastoplastic and the residual strains after unloading are becoming significant. (see figures 3c and 3d) Finally a loading-unloading sequence 12 cycles we applied monotonic uniaxial tension to the coupon specimen up to failure. When the sample reaches its fracture point stress of 959 MPa we measure an ultimate strain of 33%.

Comparing the overall behavior of specimen 1 and specimen 2 we could say that the loading-unloading of 12 cycles (low-cycle fatigue) did not affect the Fe-SMA's mechanical behavior.

Specimens 3 and 4 were used to investigate the thermomechanical behavior of the tested Fe-SMA's alloy. Specimen 3 was pre-strained to a level of 4% and was unloaded to RT conditions. A low stress of 25 MPa is kept constant to avoid grips' slip. Then the temperature was increased from RT to 160°C. When heating is activated a low increase of load is noticed which is soon decreased until we reached the target temperature of 160°C. From that temperature level until the cooling to room temperature (20°C) conditions, the load starts increasing. The increase of almost 180 MPa depicts the prestress effect of the coupon. The aforementioned behavior is demonstrated in figure 5b. Similarly, specimen 4 was heated to 250°C and left to cool to RT. For the target temperature of 250°C we measured an imposed



stress equal to 250MPa. (see figure 6b). Finally, both specimens after the thermal loading-unloading were imposed to uniaxial tension up to failure. Figures 5a and 6a show the overall  $\sigma$ - $\epsilon$  behavior of the tested specimens 3 and 4.

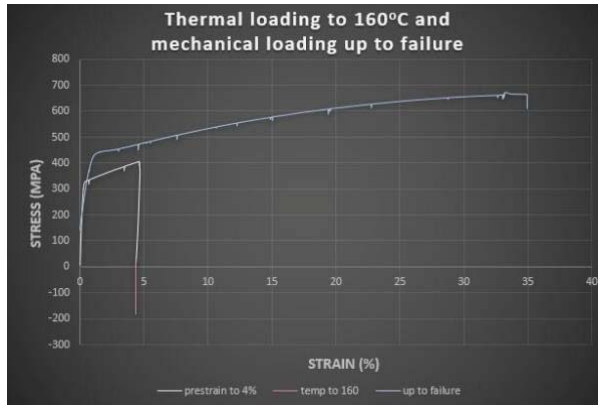


Figure 5a.  $\sigma$ - $\epsilon$  graph for specimen 3

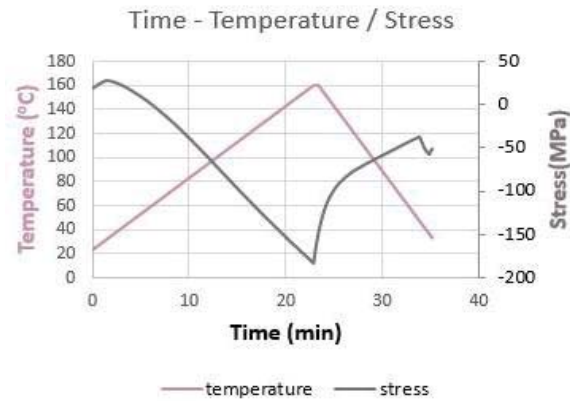


Figure 5b. Thermomechanical behavior of specimen 3

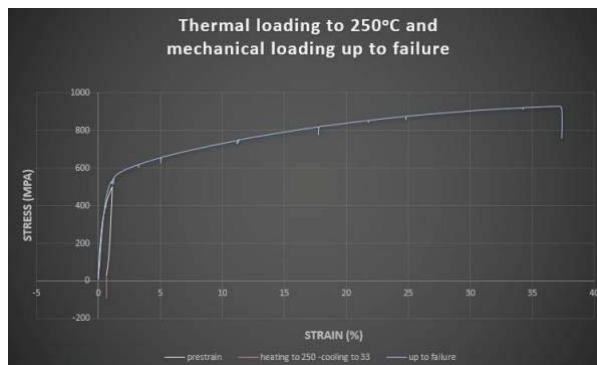


Figure 6a.  $\sigma$ - $\epsilon$  graph for specimen 4

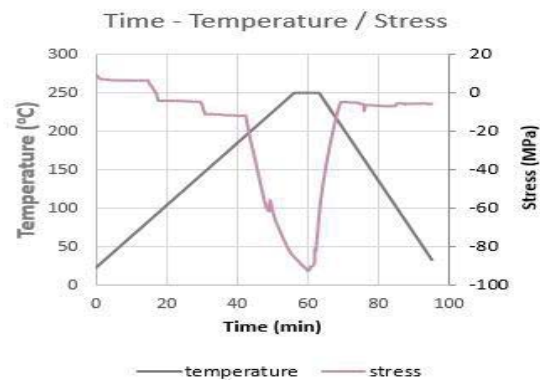


Figure 6b. Thermomechanical behavior of specimen 4

## 4 CONCLUSION

- At room temperature Fe-SMAs exhibit a high strength value together with high plasticity.
- The investigated Fe-SMAs are sensitive to the imposed pre-strain value, leading to different residual strains
- The loading-unloading of 12 cycles (low-cycle fatigue) did not affect the Fe-SMA's mechanical behavior.
- Different levels of target temperature lead to different prestress levels

## ACKNOWLEDGMENTS

Part of the aforementioned research “Investigation of the thermomechanical for smart materials to monotonic and low-cycle fatigue conditions” has been co-funded by Greece and



European Union through the Operational Program “EDBM-103: SUPPORT FOR RESEARCHERS EMPHASIZING YOUNG RESEARCHERS – 2<sup>nd</sup> CYCLE” (project code: 5047899) which are gratefully acknowledged.



## REFERENCES

- [1] L. Janke , C. Czaderski , M. Motavalli and J. Ruth ,Applications of shape memory alloys in civil engineering structures - Overview, limits and new ideas, Materials and Structures 2005
- [2] G. Songa, N. Maa, H.-N. Lib ,Applications of shape memory alloys in civil structures, Engineering Structures (2006)
- [3] A.R. Khaloo1 , P. Piran Aghl2 , I. Eshghi3, APPLICATION OF SMA IN CONCRETE STRUCTURES
- [4] [https://depts.washington.edu/matseed/mse\\_resources/Webpage/Memory%20metals/how\\_shape\\_memory\\_alloys\\_work.htm](https://depts.washington.edu/matseed/mse_resources/Webpage/Memory%20metals/how_shape_memory_alloys_work.htm)
- [5] W.J. Lee, B. Weber ↑ , C. Leinenbach, Recovery stress formation in a restrained Fe–Mn–Si-based shape memory alloy used for prestressing or mechanical joining, Construction and Building Materials (2015)
- [7] A. Arabi-Hashemi a , W.J. Lee b , C. Leinenbach, Recovery stress formation in FeMnSi based shape memory alloys: Impact of precipitates, texture and grain size, Materials and Design 2018
- [8] W. J. Lee, R. Partovi-Nia, T. Suter and C. Leinenbach\*, Electrochemical characterization and corrosion behavior of an Fe-Mn-Si shape memory alloy in simulated concrete pore solutions, Materials and Corrosion 2016
- [9] Zhizhong Dong, Ulrich E. Klotz, Christian Leinenbach\*, Andrea Bergamini, Christoph Czaderski, and Masoud Motavalli ,A Novel Fe-Mn-Si Shape Memory Alloy With Improved Shape Recovery Properties by VC Precipitation, Advanced Engineering Materials 2009
- [10] W J Lee, B Weber, G Feltrin, C Czaderski, M Motavalli and C Leinenbach , Stress recovery behaviour of an Fe–Mn–Si–Cr–Ni–VC shape memory alloy used for prestressing, Smart Materials and Structures 2013
- [11] W.J. Lee, B. Weber, G. Feltrin, C. Czaderski, M. Motavalli, C. Leinenbach, Phase transformation behavior under uniaxial deformation of an Fe–Mn–Si–Cr–Ni–VC shape memory alloy, Materials Science & Engineering 2013

## EXPERIMENTAL AND NUMERICAL INVESTIGATION OF THE PLASTIC CYCLIC BEHAVIOUR OF SIMPLE STEEL COUPONS

Alexandra Nalmpantidou, George C. Manos

Lab. of Strength of Materials and Structures  
Dpt. Civil Engineering, A.U.Th.  
Egnatia Odos, Panepistimioupoli  
[gcmayos@civil.auth.gr](mailto:gcmayos@civil.auth.gr), [a.nalmpantidou@posteo.de](mailto:a.nalmpantidou@posteo.de)

---

### Abstract

*Steel beam-to-column connections under a cyclic sinusoidal loading history were studied. The investigation of the cyclic response of the steel beam-to-column connections contained an experimental and numerical part. The experimental part included a number of full-scale specimens having a cross section of IPE240 or IPE300 and a height of 1.0m which were rigidly connected to a much stiffer steel beam thus representing a steel beam-to-column connection. These specimens were tested to failure being subjected to a cyclic sinusoidal point load of continuously increasing amplitude. Next, a numerical study is performed in an effort to simulate the observed behaviour of these steel beam-to-column connections and their response is presented and discussed. The material test data for the numerical simulation of the steel beam-to-column connection were provided from simple steel coupons which were taken from the T-Beam specimens after testing. The cross-section of these coupons was 6.2mm x 8.0mm and their height equal to 16.5mm. A number of such simple steel coupons were tested having as main variable the nature of the load (monotonic or cyclic) and the variation of the loading frequency. From the observed behaviour it can be concluded that an increase in the strain rate results in an increase of the stress values beyond the yield. Next, a numerical study is performed in an effort to simulate the observed behaviour of these simple steel coupons. Experimental and numerical results of the material steel coupons are presented in this paper. It can be concluded that the combined constitutive law can be quite successful in yielding realistic prediction of the cyclic response provided the appropriate values for the parameters defining this constitutive law from the experimental test data, in combination with the option of the dynamic increase factor (DIF) in order to take into account the strain rate effect.*

**Keywords:** Steel beam-to-column connection, Simple steel coupons, cyclic response, Numerical Simulation, Comparison of measured and predicted response, strain rate effects

---

## 1 INTRODUCTION

Moment resistant frames are commonly used in seismic areas because of their excellence on seismic resistance whereby the performance of beam-to-column connections are of particular importance especially when these structures are subjected to strong earthquake ground motions ([1], [2], [3]). Usually these connections undergo large moment reversals during the earthquake excitation, thus it is important to exhibit stable plastic flexural response in order to provide dissipative capability, without the development of undesired damage patterns, and in this way prevent any kind of local or global instability.

In a previous investigation by Manos, Nalmpantidou and Anastasiadis ([10]) the performance of steel beam-to-column joints was studied first by examining steel beam-to-column welded joint specimens at the laboratory subjecting them to cyclic seismic-type low-cycle fatigue loading and then by numerically simulating the observed performance of the same specimens. Similar studies have been performed in the past by other researchers. Despite the fact that many similar experiments have been performed in the past ([4], [5]), this investigation provided at first hand all the information required for the numerical analyses. That is, the exact geometric and material characteristics of the specimens as well as specific information on the type of loading conditions and on the measured response. The numerical simulation was performed utilizing a commercial software package that is thought to be suitable to simulate the observed response and the non-linearity that developed and included large plastic strains and local instabilities.

One parameter that was found to be of significance in this investigation was the definition of the material characteristic of the steel T-Beam specimens that were investigated ([6], [8], [10], [11]). In order to assess the performance of structural steel components it is important to know the material properties. Quasi-static material tests are usually performed to obtain these parameters, however they may no longer represent the dynamic behaviour of the material during an earthquake, because as expected the loading frequency during an earthquake exceeds the loading frequency during the quasi-static material tests. In order to predict the response of a structure during an earthquake a good knowledge of the material behavior for the numerical simulation is important.

The T-Beam specimens were tested under cyclic load with the frequency of this loading being one of the variables that was studied. For this reason, it was necessary to study the material properties in light of the fact that the imposed cyclic loading was not of the constant slow-rate monotonic type that usually characterizes the material properties of steel structural elements. For this purpose, the following experimental sequence was carried out. From each of the tested steel T-Beams a number of coupon samples were taken, as is described in section 2. These samples were tested in axial tension/compression under cyclic loading with the frequency of the loading being one of the main variables. In addition, apart from these samples being tested by cyclic load additional samples of the same T-Beam specimens were tested applying the tension in a monotonic way. From all these tests results were obtained that shed some light on the influence of the nature of loading (cyclic or monotonic) as well as on the frequency of this loading. The results have been used to develop cyclic hardening parameters and dynamic increase factors suitable for incorporation into numerical models in order to predict the material behavior of structural members subjected to cyclic loading under several different frequencies. Summary results of this experimental sequence are presented and discussed in section 3. The numerical analysis of the observed performance is presented in section 4. The ABAQUS commercial software package was utilized for this purpose.

## 2 MATERIALS AND EXPERIMENTAL SETUP

The coupon samples for the tests aiming for the material characterization were obtained by removing parts of the flanges from the previously tested T-Beam specimens that were located away from the locations of the plastic hinge locations which developed during the T-Beam tests ([10],[12]). The testing of these T-Beam specimens is described in the work by Manos et al. ([10]) and is not repeated here.



Figure 1a. Coupon 6R1-6 (6.7mm x 6.7mm,  $\ell = 16\text{mm}$ )    Figure 1b. Coupon 6R1-5 (7.95mm x 7.80,  $\ell = 16\text{mm}$ )

The coupons to be tested were formed by machining the parts removed from the flanges, as shown in figures 1a and 1b. These coupons had a narrow central part of relatively small cross section with a small length ( $\ell = 16\text{mm}$ ) and this part was designed to provide the necessary information for the material characterization. Through the two larger parts, which were provided with holes in order their attachment to the loading reaction frame to approximate pinned support conditions, the coupon was attached to the loading reaction frame. At the top and bottom of the coupon steel brackets are employed to attach the coupon sample using cylindrical pins. These brackets are in turn firmly attached to the reaction loading frame. At the top bracket a load cell is also attached that monitors the variation of the applied axial load.

The cross section of the narrow part remained constant all along its 16mm length. Its dimensions (x, y) were accurately measured (figures 2a, 2b and 2c). Moreover, strain gauges were attached at the middle of all the sides of this rectangular prismatic narrow part. These strain gauges were placed in the longitudinal direction of this steel prismatic part in order to measure the variation of the axial strain that developed during the variation of the axial load. The dimensions of the cross section of this narrow part combined with its length dictated almost uniform tension / compression conditions prohibiting the development of any distortions from local buckling, especially when large plastic strains developed in this narrow central part. Through the readings of the strain gauges the eccentricity of the axial load application could be checked and controlled.

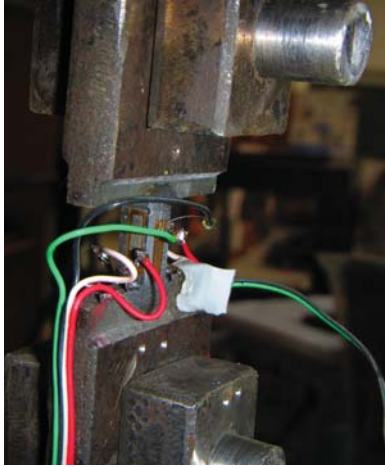


Figure 2a. Coupon 9R1-2 (6.2mm x 8.0mm,  $\ell = 16.5$ mm)

Section A-A

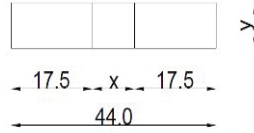


Figure 2b. Dimensions of the coupon

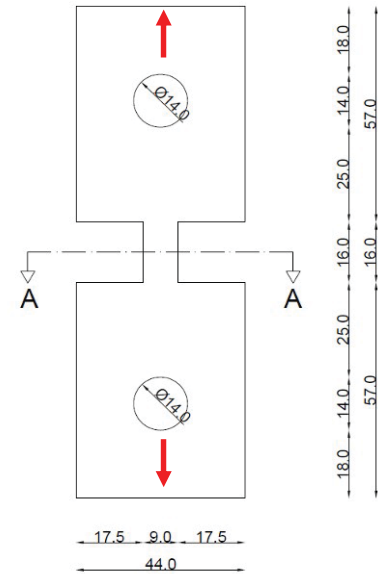


Figure 2c. Dimensions of the coupon

### 3 OBSERVED PERFORMANCE AND CORRESPONDING MEASUREMENTS.

As already mentioned, one of the main variables of this investigation was the nature of loading, being either cyclic or monotonic. The second variable was the frequency of the cyclic loading or the rate that the monotonic loading was applied, as will be indicated in what follows.

#### 3.1 Monotonic loading

A summary of the results obtained when the specimens were subjected to monotonic axial tensile loading is presented below. The characterization of the applied load in terms of loading rate (slow or fast) and the origin code name of the T-Beam are mentioned in the presentation of these test results. In figure 3a the axial stress versus axial strain response is shown from two coupons taken from T-Beam 9R1; one of them was tested with slow strain rate whereas the other one with fast strain rate. As can be seen from this figure, this variation of the strain rate during the monotonic application of the applied load resulted in a significant change in the yield stress value as well as in the plasticized part of the response beyond the yield point. Next, figure 3b shows the response of axial stress versus axial strain from two coupons tested both at slow strain rate; one of them was taken from T-Beam 9R1 while the other from T-Beam 10R1. As can be seen from this figure, the response obtained from these two coupons is rather similar. By studying the two figures, we are led to the conclusion that increasing the strain rate from slow to fast leads to an increase in the yield stress as well as in the stress values beyond the yield point.

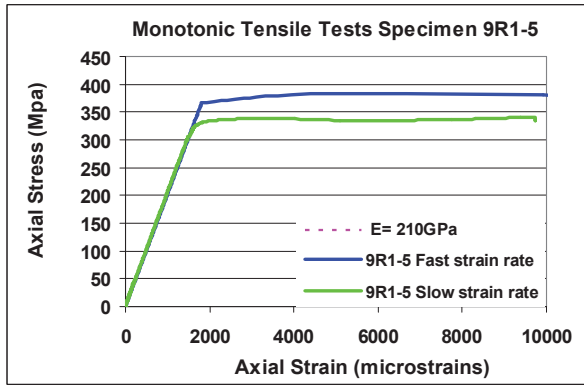


Figure 3a. Coupons taken from T-Beam 9R1 tested with slow and fast strain rate

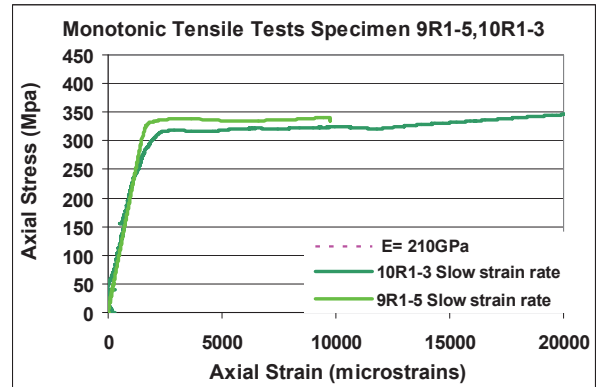


Figure 3b. Coupons taken from T-Beam 9R1 and T-Beam 10R1 both tested with slow strain rate

### 3.2 Cyclic loading

Following on from our previous work ([12]), this paper will present results from the material test coupons taken from the flanges of the T-Beam 8R1. In figure 4 and 5 the obtained axial stress versus axial strain responses are shown as they were measured and subjected to a number of cyclic loading tests. The strain rate during all these tests varied from fast to slow, as it resulted from the application of the axial tensile/compressive load from a sinusoidal variation with a frequency of 0.005Hz to 2.0Hz.

In figure 4a the cyclic response of a coupon taken from T-Beam 8R1 is shown. This response resulted by applying the axial load in a sinusoidal way with a frequency of 2.0Hz thus producing a rather fast strain rate. In figure 4b the cyclic response of a coupon also taken from T-Beam 8R1 is shown. This response resulted by applying the axial load in a sinusoidal way with a frequency of 0.005Hz thus producing a slow strain rate. Figure 5 shows the cyclic response of a coupon taken from T-Beam 8R1 obtained by applying the axial load in a sinusoidal way with a frequency ranging from 0.005Hz to 2.0Hz. The response obtained during the test whereby the cyclic load was varied with a frequency equal to 0.05Hz is considered as a rather slow strain rate test whereas the one with a frequency equal to 0.1Hz as a rather moderately fast strain rate test. Finally, the response obtained during the test whereby the cyclic load was varied with a frequency equal to 2.0Hz is considered as a rather fast strain rate test.



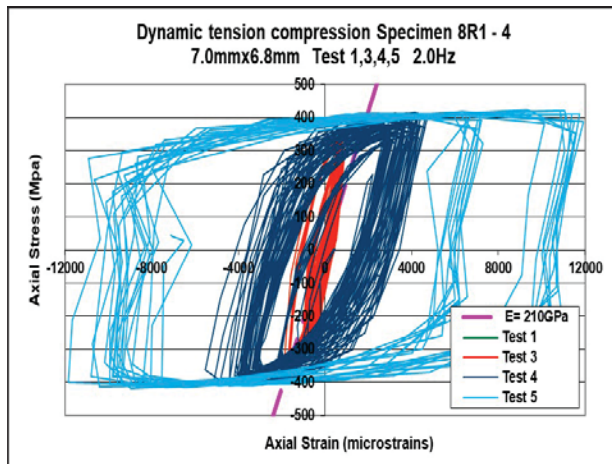


Figure 4a. Cyclic response with axial load varying in a sinusoidal way with a frequency of 2.0Hz. Coupon taken from T-Beam 8R1 tested with a rather fast strain rate

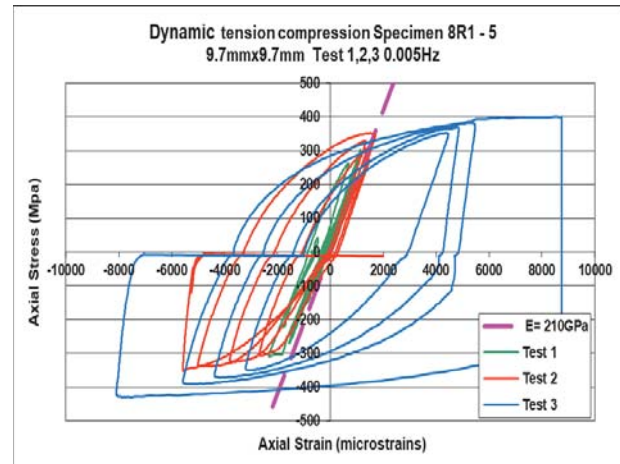


Figure 4b. Cyclic response with axial load varying in a sinusoidal way with a frequency of 0.005Hz. Coupon taken from T-Beam 8R1 tested with a slow strain rate

As can be seen from these figures (4a, 4b, and 5) the yield point can be hardly distinguished from the obtained axial stress versus axial strain response. However, as can be seen in figure 5, the variation of the strain rate during the cyclic application of the applied load resulted in a significant change in the plasticized part of the response beyond yield as it was also observed in figure 3a for the monotonic application of the load. It can be concluded from both figures 3a and 5 that the increase in the strain rate results in a noticeable increase both at the yield stress as well as at the stress values beyond the yield point for strain values larger than the yield strain.

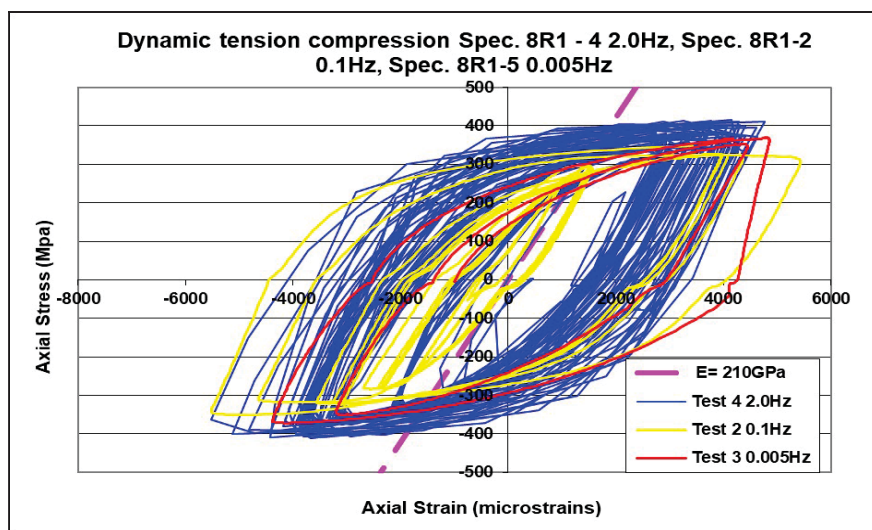


Figure 5. Cyclic response when axial load is varying in a sinusoidal way with frequency values in the range from 0.005Hz to 2.0Hz. Coupons taken from T-Beam 8R1 tested with slow as well as with fast strain rate

In figure 6, a comparison between the axial stress versus axial strain response from four coupons under cyclic and monotonic loading is shown; one of them is taken from T-Beam 8R1, one of them is taken from T-Beam 10R1 and two of them are taken from T-Beam 9R1. Coupon 8R1 was tested with a cyclic loading frequency equal to 2.0Hz (Tests 3, 4, 5) producing a rather fast strain rate. Two coupons from T-Beam 9R1 were tested by applying the tensile



load in a monotonic way; one of them with a slow strain rate (INSTRON static 9R1-5) and the other one with a fast strain rate (INSTRON quick 9R1-5). Finally, the fourth specimen was taken from T-Beam 10R1 and was tested by applying monotonic load with a slow strain rate (INSTRON static 10R1-3). The two main observations that were made before can also be seen in this figure.

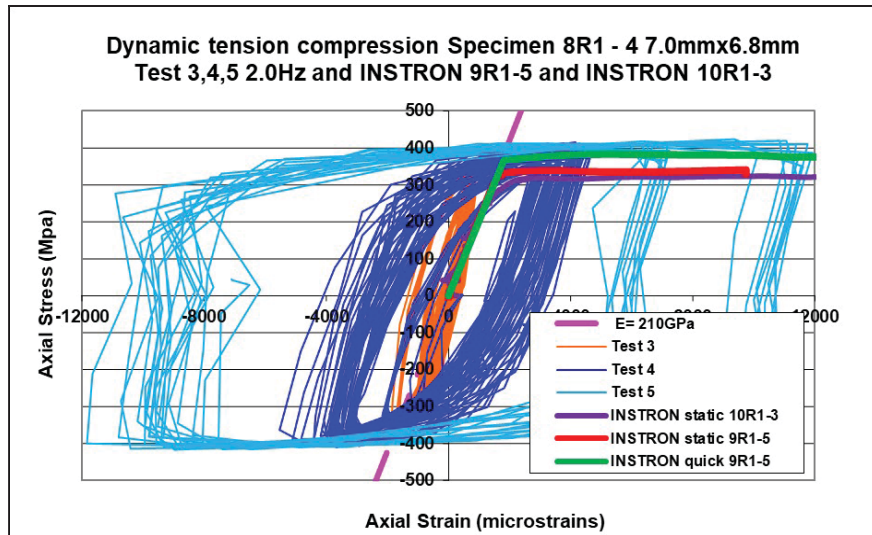


Figure 6. Monotonic / cyclic axial stress - strain response. The cyclic axial load is varying in a sinusoidal way with frequency value equal to 2.0Hz (T-Beam 8R1). Monotonic response from coupons taken from T-Beam 9R1 and 10R1 tested either with slow or with fast strain rate

From the above observed performance it can again be concluded that,

- a) During the monotonic application of the load an increase in the strain rate resulted in an increase in the yield stress value as well as in the stress values of the plasticized part of the response beyond the yield point. In addition to this the observed axial stress versus axial strain response from different coupons subjected to the same slow strain rate monotonic load is quite similar.
- b) The application of the cyclic load with slow, moderately fast or rather fast strain rate resulted in axial stress versus axial strain response whereby the yield point is hardly distinguishable but despite of this the strain rate effect can be clearly seen. Furthermore the application of the cyclic load with slow, moderately fast or rather fast strain rate resulted in axial stress versus axial strain response that has stress values beyond the yield point that exhibit a noticeable increase with the increase in the strain rate.
- c) From the limited results presented here the effect of the cyclic nature of the loading results in a more pronounced increase of the stress values with the increase in the strain rate than when the load is applied in a monotonic way.

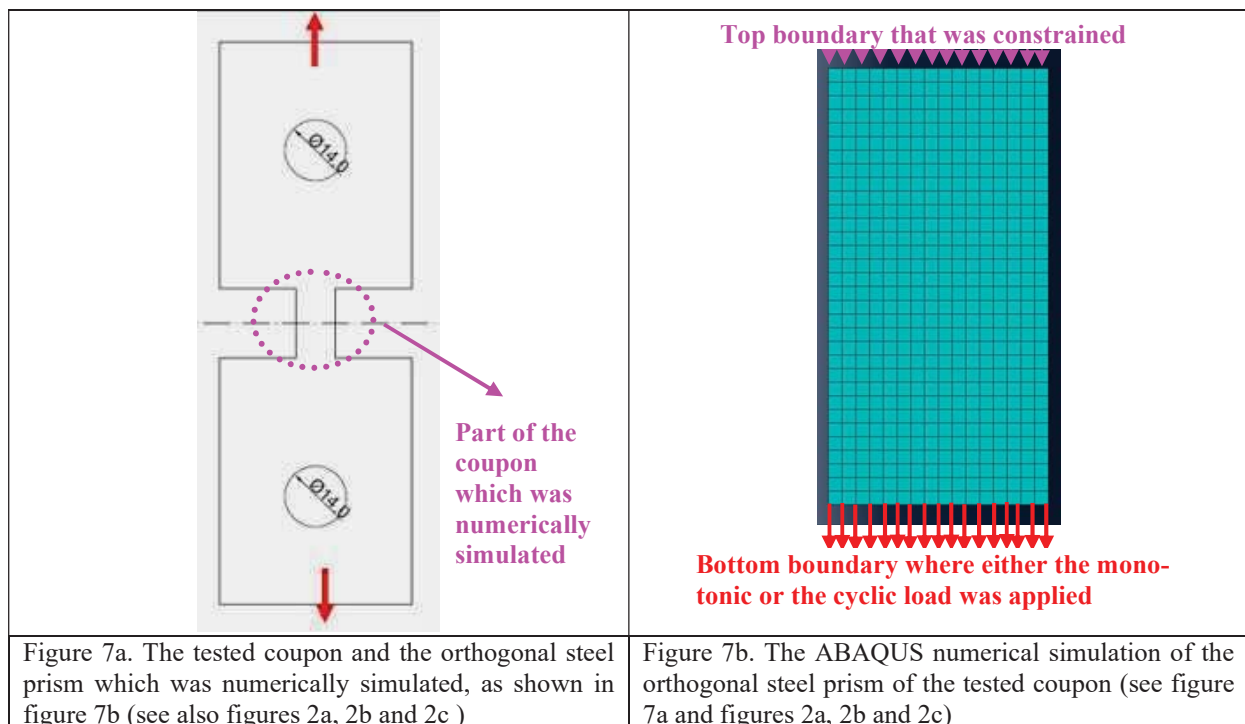
## 4 NUMERICAL SIMULATION OF THE TENSION AND CYCLIC TESTS

### 4.1 Numerical modeling.

As mentioned in section 2 simple specimens having the shape of an orthogonal prism were taken from the flanges and were applied to monotonic tension or / and to cyclic tensile / compressive load with a sinusoidal time variation having a given amplitude and frequency. A

number of such simple specimens were tested and their results are presented and discussed in section 3 having as main variable the variation of the loading frequency and the nature of the loading (monotonic or cyclic). In order to simulate numerically the behavior of these specimens a numerical study was performed utilizing the commercial software package ABAQUS [7].

The orthogonal prism of the experimental sequence (figure 7a), which was represented through the finite element 2-D mesh, is shown in figures 7b. The prism was considered to be represented with absolute fixity conditions in the numerical simulation on the top side whereas on the bottom side either the monotonic or the cyclic load was applied. The other two sides were left unconstrained. However, the rigid body in-plane as well as the out-of-plane horizontal displacement response was also constrained.



In order to simulate the variation of the load in time as either fast or slow monotonic load or as cyclic load with varying sinusoidal cyclic frequency, the displacement control option was utilized whereby an imposed displacement was defined as a function of time and displacement amplitude. Dynamic implicit analyses were in-order for this software to take into account the different load frequencies. Following the load variation that was applied during testing the numerical analyses were also performed with monotonic load (with either slow or fast strain rate) and with cyclic load (again with either slow, moderate or fast strain rate). The imposed displacement variation was introduced to the software in tabular form identical with the one that was applied to the corresponding specimen during the experimental sequence. The adopted discretization scheme (figure 7b) is believed to be considerably fine in an effort to capture numerically the observed behavior.

## 4.2 Material modeling

In the framework of the numerical investigation a parametric study was conducted that focused on the way the steel material properties were introduced in the numerical simulation. In our previous work two different approaches were tried ([12]). According to the first approach

the measured tensile steel properties were modified accordingly in order to be introduced in the numerical simulation through the ABAQUS combined hardening material constitutive law whereas in the second approach the measured properties were introduced in the numerical simulation through the ABAQUS isotropic hardening constitutive law. Furthermore in both cases different yield stress ratios for different strain rates were taken into account.

In this work the focus lies in the numerical simulation of the material tests through the ABAQUS combined hardening material constitutive law. There are several ways in this commercial software package [7] to define a combined hardening material constitutive law in order to capture the cyclic response of a specimen. The evolution law of this model consists of two components: a nonlinear kinematic hardening component, which describes the translation of the yield surface in stress space through the back-stress, and an isotropic hardening component, which describes the change of the equivalent stress defining the size of the yield surface, as a function of plastic deformation [7]. In the present study the combined hardening constitutive law is defined through the values that are given to certain relevant parameters. For the nonlinear kinematic hardening component these parameters are a)  $\sigma|_0$ , the yield stress at zero equivalent plastic strain, b)  $C_k$  and  $\gamma_k$  (material constants that can be calibrated from test data) and for the isotropic hardening model these parameters are c)  $\sigma|_0$ , equivalent yield stress, d)  $Q_\infty$  and  $b_{iso}$  (material constants that can be calibrated from test data). Values for these parameters were calculated from the test data that were obtained from the experimental process from the tests of steel samples and were utilized in the parametric study that was performed in the present work. The nonlinear kinematic hardening component of the model defines the change of back-stress  $\alpha$  and is given by Equation (1). All stress strain data are taken from a stabilized cycle from the test data as shown in figure 8.

$$\alpha_k = C_k / \gamma_k (1 - e^{-\gamma_k \epsilon^{pl}}) + \alpha_{k,1} e^{-\gamma_k \epsilon^{pl}} \quad (1)$$

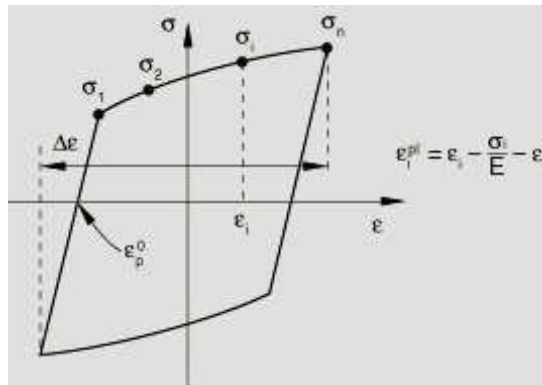


Figure 8. Stress strain data for a stabilized cycle

The isotropic component defines the change of the size of the yield surface  $\sigma^0$  as a function of equivalent plastic strain  $\epsilon^p$  as shown in figure 9 and is given by Equation (2).

$$\sigma^0 = \sigma|_0 + Q_\infty (1 - e^{-b_{iso} \epsilon^p}) \quad (2)$$

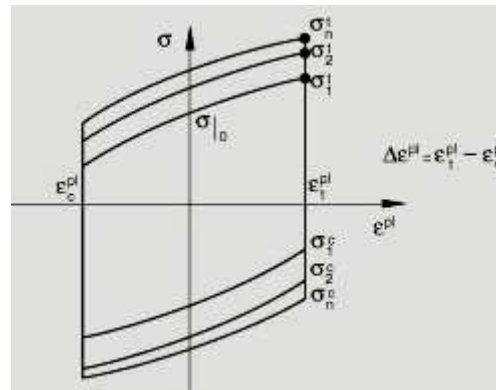


Figure 9. Symmetric strain cycle

Abaqus allows the specification of strain rates effects with the option of rate dependent data at combined and isotropic hardening constitutive law. In order to define the strain rate effect the use of a dynamic increase factor (DIF) was utilized based on the work of Malvar and Crawford [9]. The same values for DIF that were calculate and introduced as input in tabular form in terms of a ratio of the yield stress versus the equivalent plastic strain rate to be used in the particular case being analyzed, from our previous work [12] are also being used in this paper. The work of Malvar and Crawford [9] is based on numerous experimental data from a literature review on the effects of strain rates on the properties of steel reinforcing bars for reinforced concrete structural elements. The dynamic increase factor (DIF) is the amplification by DIF of the value a certain mechanical property (yield stress or maximum stress) has under low strain rate loading conditions (static) to another condition whereby because of the nature of loading (dynamic) the strain rate has a larger value than before. A relationship is proposed by Malvar and Crawford ([9]) that a DIF value can be derived for a given strain rate increase and thus evaluate through this DIF the corresponding for this increased strain rate amplified yield and ultimate stress values. This formulation is valid for bars with yield stresses between 290 and 710 MPa and for strain rates between  $10^{-4} \text{ sec}^{-1}$  and  $225 \text{ sec}^{-1}$ . Figure 10 depicts the variation of DIF with the variation of the strain rate. This approach was presently followed use as reference control properties the yield stress found for the slow rate monotonic axial tension test with coupon 9R1-5 (see figure 5).

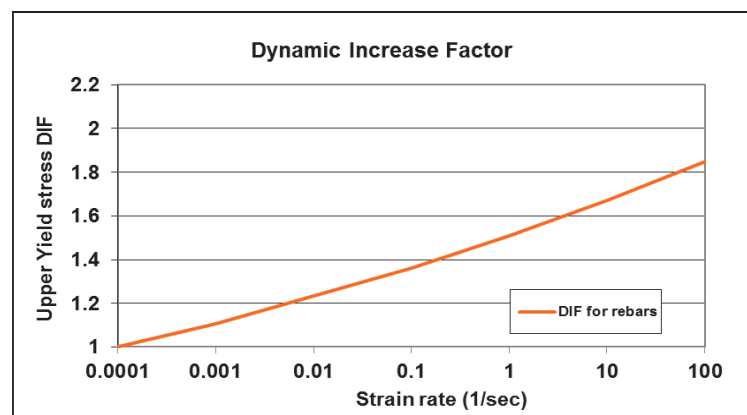


Figure 10. Dynamic increase factor which has been considered for the numerical investigation

### 4.3 Numerical results for monotonic axial tensile load cases

Figure 11 shows a comparison between the axial stress – axial strain monotonic tensile response obtained from the numerical analysis of coupon 9R1-5 and 10-3 loaded under slow strain rate conditions (duration of loading 700 seconds) and coupon 9R1-5 loaded under fast strain rate conditions (duration of loading 2.5 seconds) for both constitutive laws of isotropic hardening and combined hardening together with the option of the DIF.

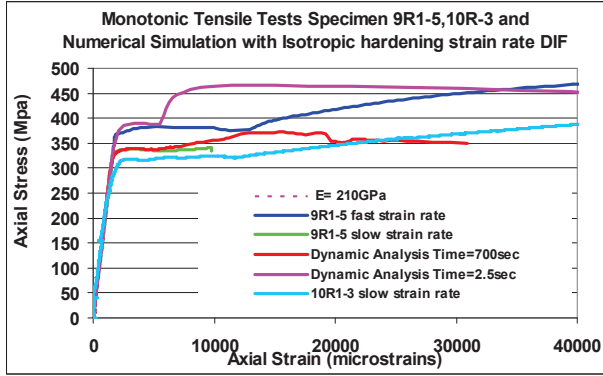


Figure 11a. Monotonic axial tension numerical simulation with isotropic hardening constitutive law for coupon 9R1-5 and 10R-3 for strain values up to 40000 microstrains.

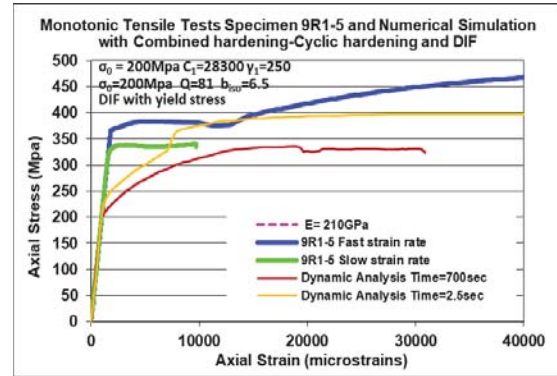


Figure 11b. Monotonic axial tension numerical simulation with combined hardening constitutive law for coupon 9R1-5 for strain values up to 40000 microstrains.

As can be seen in figure 11a, the numerical simulation including the isotropic hardening with the DIF option is quite sensitive to the effect of the strain rate variation. Moreover, the numerical response agrees quite well with the observed response for strain values smaller than 6000 micro-strains. In the case of the slow strain rate there is a certain discrepancy between predicted and observed stress values for strains larger than 10000 micro-strains and smaller than 20000 micro-strains. Similarly, in the case of the fast strain rate there is again a certain discrepancy between predicted and observed stress values for strains larger than 6000 micro-strains and smaller than 25000 micro-strains.

In figure 11b depicts the axial stress-strain numerical response employing combined hardening constitutive law together with the DIF options for coupons 9R1-5 submitted to monotonic tension load with slow strain rate conditions (duration of loading 700 seconds) and with fast strain rate conditions (duration of loading 2.5sec). The material parameters that were calculated from test data from test coupons that were taken from T-Beam 9R1 and were used to define the combined hardening constitutive law with cycling hardening are:

Combined hardening parameters:

Yield stress at plastic strain  $\sigma|_0=200\text{Mpa}$ ,  
Kinematic Hardening Parameter  $C_k=28300$

Gamma  $\gamma_k=250$

Cyclic hardening parameters:

Equivalent stress  $\sigma|_0=200\text{Mpa}$

Q-Infinity parameter  $Q_\infty=81$

Hardening parameter  $b_{iso}=6.5$

As indicated in figure 11b there is no good agreement between numerical simulation and measured response. The reason for that could be that the kinematic hardening model, which includes the combined hardening, is for simulating the cyclic loading of metals and not monotonic tensile behaviour (Abaqus). From the relevant graph it can be easily seen that a value for the yield point equal to 200Mpa is assigned for the slow strain rate tension test (duration of loading 700 sec) which is the same value of the yield stress at zero equivalent plastic strain from a stabilised cycle  $\sigma|_0=200\text{Mpa}$ . This value was obtained from the test data of the cycling loading. Furthermore, the numerical simulation is quite sensitive to the effect of the strain rate variation, as can be seen in the plotted response. An increase of the yield and ultimate stress can be seen from the case when the specimen is subjected to a relatively slow loading (which corresponds to a slow strain rate) to the case when the specimen is subjected to a relatively fast loading (which corresponds to a fast strain rate).

#### 4.4 Numerical results for cyclic axial tension / compression load cases

This section presents numerical results of the experimental investigation carried out with material test coupons obtained from T-Beam 8 under cyclic axial tension /compression load cases. The necessary material parameters for the numerical simulation were calculated from the experimental data based on Equations (1) and (2) mentioned in section 4.2. These values are as follows:

Combined hardening parameters:

Yield stress at plastic strain  $\sigma|_0=200\text{-}220\text{Mpa}$ ,

Kinematic Hardening Parameter  $C_k=34000$

Gamma  $\gamma_k=250$

Cyclic hardening parameters:

Equivalent stress  $\sigma|_0=200\text{-}220\text{Mpa}$

Q-Infinity parameter  $Q_\infty=85$

Hardening parameter  $b_{iso}=6.5$

Figures 12a and 12b depict the axial stress-strain numerical response employing combined hardening constitutive law with cyclic hardening together with the DIF options for coupons 8R1-5 and 8R1-3 submitted to cyclic tension / compression load resulting in a slow strain rate condition (variation in time of the sinusoidal cyclic load equal to 0.005Hz) and in a moderately slow strain rate condition (variation in time of the sinusoidal cyclic load equal to 0.01Hz). As indicated in these figures a reasonably good agreement between numerical predictions and measured response was achieved for values of the parameters  $\sigma|_0=220\text{Mpa}$ ,  $C_k=34000$ ,  $\gamma_k=250$ ,  $Q_\infty=85$ ,  $b_{iso}=6.5$  for a cyclic load equal to 0.005Hz and a cyclic load equal to 0.01Hz. This good agreement between measured and predicted values can be seen for the yield and ultimate stress values as well as for the shape of the hysteretic loops.



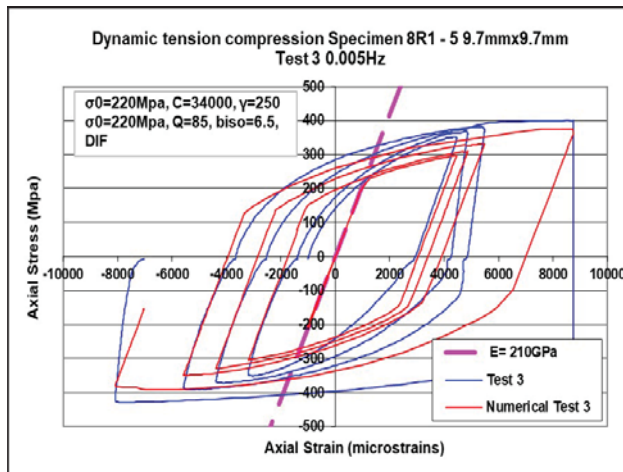


Figure 12a. Numerical axial stress strain response employing combined hardening constitutive law for coupons 8R1-5 submitted to cyclic tension/compression load resulting in a slow strain rate

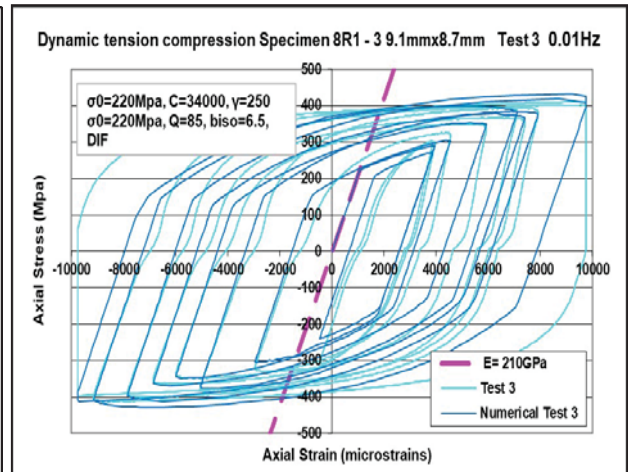


Figure 12b. Numerical axial stress strain response employing combined hardening constitutive law for coupons 8R1-3 submitted to cyclic tension/compression load resulting in a moderately slow strain rate

Figures 13a and 13b depict the axial stress-strain numerical response employing combined hardening constitutive law with cyclic hardening together with the DIF options for coupons 8R1-2 and 8R1-4 submitted to cyclic tension / compression load resulting in a moderately fast strain rate condition (variation in time of the sinusoidal cyclic load equal to 0.1Hz) and in a fast strain rate condition (variation in time of the sinusoidal cyclic load equal to 2.0Hz). As indicated in these figures, reasonably good agreement between numerical predictions and measured response was achieved adopting values of the parameters  $\sigma_0=200\text{Mpa}$ ,  $C_k=34000$ ,  $\gamma_k=250$ ,  $Q_\infty=85$ ,  $b_{iso}=6.5$  for cyclic loads applied with frequencies equal to either 0.1Hz or 2.0Hz. For numerically simulating these relatively high loading frequency tests the value of  $\sigma_0$  equal to 200Mpa was adopted the yield stress at plastic strain and the equivalent stress instead of 220Mpa, which was used in the numerical simulation for the relatively load loading frequencies of 0.005Hz and 0.01Hz. This value of 200Mpa led to a better agreement between the experimental results and the numerical simulation for the yield and ultimate stress values as well as for the shape of the hysteretic loops.



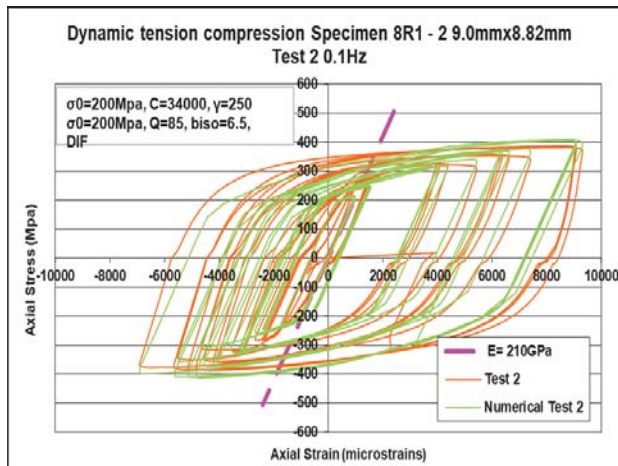


Figure 13a. Numerical axial stress strain response employing combined hardening constitutive law for coupons 8R1-5 submitted to cyclic tension/compression load resulting in a slow strain rate

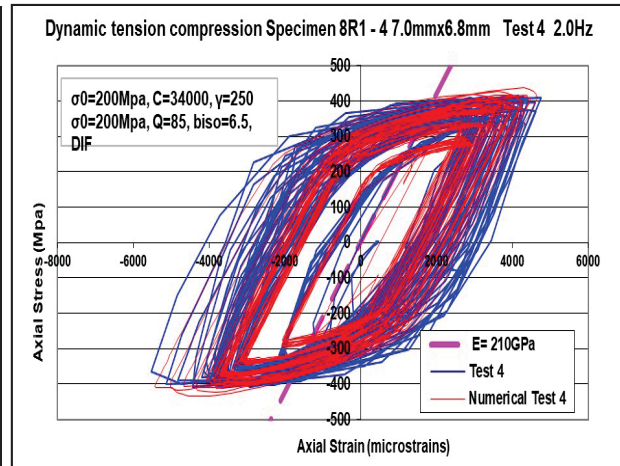


Figure 13b. Numerical axial stress strain response employing combined hardening constitutive law for coupons 8R1-3 submitted to cyclic tension/compression load resulting in a moderately slow strain rate

From this numerical study it can again be concluded that a numerical simulation based on the combined constitutive law employing values of the necessary parameters from test data (such as  $\sigma_0$ , the yield stress at zero equivalent plastic strain, and  $C_k$  and  $\gamma_k$  the material constants) is quite successful in yielding realistic predictions of the cyclic response. Moreover, utilising the an inclusion of the DIF option, such a numerical simulation can be also sensitive to the observed strain rate effect. Therefore, it is reasonable to believe that it would also be successful in simulating the behaviour of more complex structural elements under a variety of loading which can result in different strain rate conditions.

## 5 CONCLUSIONS

- An extensive experimental sequence was conducted testing relatively small dimension coupons to axial monotonic or cyclic loading with a variety of strain rate conditions. These coupons were formed from steel parts taken from the flanges of T-beam steel section that were previously tested to destruction by cyclic seismic-type loading. The current study is an extension of the previous research in an effort to first quantify the strain rate effect in a controlled way and next to be able to effectively simulated utilizing existing numerical tools. From the current investigation the following findings could be stated.
- An increase in the strain rate during the monotonic application of the load resulted in an increase in the yield stress value as well as in the stress values of the plasticized part of the response beyond the yield point.
- Additional experimental data from the analysis of more T-Beams under cyclic loading to be added to the existing ones led to the same conclusion as before that
  - a)The application of the cyclic load with slow, moderately fast or rather fast strain rate resulted in axial stress versus axial strain response whereby the yield point is hardly distinguishable. Thus the strain rate effect can be clearly seen.
  - b)The application of the cyclic load with slow, moderately fast or rather fast strain rate resulted in axial stress versus axial strain response that has stress values beyond the yield point that exhibit a noticeable increase with the increase in the strain rate.

- From the subsequent numerical study it can be concluded that the combined constitutive law is quite successful in yielding realistic prediction of the cyclic response but not of the monotonic tensile response; the appropriate values of the parameters defining this constitutive law (such as  $\sigma|_0$ , the yield stress at zero equivalent plastic strain,  $C_k$ ,  $\gamma_k$ ,  $Q_\infty$  and  $b_{iso}$  the material constants) must be calibrated from test data. In this case, the numerical simulation employing the same material constitutive law together with an DIF inclusion is reasonable to believe that it would also be successful in simulating the behaviour of more complex structural elements for loading introducing a variety of strain rate conditions.
- Both the experimental and the numerical part of this study are still under way; thus the above conclusions should be considered as preliminary.

## ACKNOWLEDGEMENTS

The authors would like to acknowledge the assistance of M. Theofanous, Dr. Civil Engineer, Lecturer at the Department of Civil Engineering of the University of Birmingham, for all his valuable advice related to the numerical simulation. The technical assistance of T. Koukouftopoulos in preparing the experimental arrangement is also gratefully acknowledged.

- To the memory of Hiroshi Akiyama, Professor of the University of Tokyo, Japan and of Heki Shibata, Professor of Industrial Science, University of Tokyo, Japan.

## REFERENCES

- [1] Akiyama H. Earthquake-Resistant Limit-State Design for Buildings. University of Tokyo Press: Tokyo, 1985.
- [2] Anastasiadis A., Mosoarca M., Gioncu V., Mazzolani F. M., “Some thoughts for the prediction of the local inelastic capacity of MRF subjected to seismic actions”, 8<sup>th</sup> STESSA Conf. on the Behavior of Steel Structures in Seismic Areas, Tongji Univ., Songhai China, July 2015.
- [3] Ballio Giulio &. Castiglioni, Carlo A, “Seismic Behaviour of Steel Sections”, J. Construct. Steel Research 29 (1994) 21-54
- [4] Castiglioni Carlo A., Mouzakis Harris P., Carydis Panayotis Gr. (2007): “Constant and Variable Amplitude Cyclic Behavior of Welded Steel Beam-to-Column Connections”, Journal of Earthquake Engineering, 11:876–902, 2007, 11:6, 876-902, doi.org/10.1080/13632460601188027.
- [5] El Hassouni A, Plumier A., Cherrabi A. “Experimental and numerical analysis of the strain-rate effect on fully welded connections”, Journal of Constructional Steel Research (2010), doi 10.1016/j.jcsr.2010.09.02
- [6] Gioncu V, Petcu D. “Available rotation capacity of wide-flange beam and beam-columns part 1, 2.”, Journal of Constructional Steel Research 1997; 43: 161-244.

- [7] Hibbitt, Karlsson, Sorensen. Inc. ABAQUS user's manual volumes I–V and ABAQUS CAE manual. Version 6.10.1. Pawtucket, USA; 2010.
- [8] Lee Kyungkoo and Stojadinovic Bozidar, “Low-cycle fatigue limit on seismic rotation capacity for US steel moment connections”, 13th World Conference on Earthquake Engineering, Vancouver, B.C., Canada, August 1-6, 2004, Paper No. 90.
- [9] Malvar, L. J. and John E. Crawford J. E. (1998), “Dynamic increase factor for steel reinforcing bars”, Twenty-Eighth DDESB Seminar, Orlando, FL.
- [10] Manos G.C., A. Nalmpantidou A., Kourtides A., Anastasiadis A., (2015), “Cyclic response of a steel beam to column connection – an experimental and numerical study”, CompDyn 2015, M. Papadrakakis, V. Papadopoulos, V. Plevris (eds.), Crete Island, Greece, 25–27 May 2015.
- [11] Vayas I. “Investigation of the cyclic behavior of steel beams by application of low-cycle fatigue criteria.” Behavior of Steel Structures in Seismic Areas STESSA 1997; 350-357.
- [12] Manos G.C., A. Nalmpantidou A., (2019), “Experimental and numerical study of the cyclic behaviour of a steel beam-to-column connection”, CompDyn 2019, M. Papadrakakis, M. Fragiadakis (eds.), Crete Island, Greece, 24–26 June 2019.

## EXPERIMENTAL TESTS AND NUMERICAL STUDY OF THE PLASTIC CYCLIC BEHAVIOUR OF A STEEL BEAM-TO-COLUMN CONNECTION

G.C. Manos, A. Nalmpantidou

Laboratory for Strength of materials and Structures  
Dpt. Civil Engineering, A.U.Th.pt. Civil Engineering, A.U.Th.  
Egnatia Odos, Panepistimioupoli  
[gcmayos@civil.auth.gr](mailto:gcmayos@civil.auth.gr), [a.nalmpantidou@posteo.de](mailto:a.nalmpantidou@posteo.de)

---

### Abstract

*Steel beam-to-column connections under a cyclic sinusoidal loading history were studied. The investigation of the cyclic response of the steel beam-to-column connections contained an experimental and numerical part. The experimental part included a number of full-scale specimens having a cross section of IPE240 or IPE300 and a height of 1.0m which were rigidly connected to a much stiffer steel beam thus representing a steel beam-to-column connection. These specimens were tested to failure being subjected to a cyclic sinusoidal point load of continuously increasing amplitude. Each specimen experienced yielding and plastic rotation till the final damage, which occurred either in the form of local instability of the flanges or fracture. Next, a numerical study is performed in an effort to simulate the observed behaviour of these steel beam-to-column connections and their response is presented and discussed. The material test data for the numerical simulation of the steel beam-to-column connection were provided from simple steel coupons which were taken from the T-beam specimens after testing. Experimental and numerical results of the beam-to-column connections are presented and discussed in this paper. It can be concluded that the employed numerical simulation can be quite successful in yielding realistic prediction of the cyclic response of the steel beam-to-column, provided that the material model in this numerical simulation was equipped with the appropriate values for the parameters defining the material constitutive law from the experimental test data.*

**Keywords:** Steel beam-to-column connection, Simple steel coupons, cyclic response, Numerical Simulation, Comparison of measured and predicted response, strain rate effects

---

## 1 INTRODUCTION

Steel frame structures are commonly used in seismic areas because of their excellence on seismic resistance. This type of structures are usually composed of moment resistant frames whereby the performance of beam-to-column connections are of particular importance especially when these structures are subjected to strong earthquake ground motions [1, 2, 5]. Usually these connections undergo large moment reversals during the earthquake excitation, thus it is important to exhibit stable plastic flexural response in order to provide dissipative capability, without the development of undesired damage patterns, and in this way prevent any kind of local or global instability. However, two recent earthquakes, in Northridge, California 1994 and Kobe Japan 1995, revealed the vulnerability of this type of construction. Premature cracks were observed at welded connections of steel beam-to-column joints leading to brittle failure without prior warning (obvious yielding) at the area around the weld. Such a failure mode or the development of local buckling when beam-to-column connections undergo low-cycle fatigue seismic-type of loading is of particular research interest [3, 4, 9, 14].

The fatigue life of steel beam-to-column joints depends on the amplitude of the imposed loading cycles and the hysteretic behavior of the constituent material that is linked with the amplitude and rate of the developing plastic strains. In order to investigate the fatigue life of steel beam-to-column joints several fatigue testing investigations have been proposed leading to tests that can be categorized in two groups. Testing regimes in which the elastic strain amplitude is higher than the plastic strain amplitude and testing regimes in which the plastic strain dominates. The first type of tests is generally referred as high cycle fatigue (HCF); these tests typically involve more than  $10^6$  cycles to cause failure. The second type of tests is named low cycle fatigue (LCF) test and the number of cycles to failure generally ranges from  $10^2$  to  $10^4$  cycles and this is usually employed for testing the seismic performance of steel beam-to-column joints [6, 8, 11, 12, 15].

The current work studies the performance of steel beam-to-column joints first by examining steel beam-to-column welded joint specimens at the laboratory subjecting them to cyclic seismic-type low-cycle fatigue loading as is explained in section 2. Next, the performance of the same specimens is simulated numerically. Similar studies have been performed in the past by other researchers. Despite the fact that many similar experiments have been performed in the past [6, 8], the current experimental investigation was considered as necessary in order to provide at first hand all the information required for the numerical analyses. That is, the exact geometric and material characteristics of the specimens as well as specific information on the type of loading conditions and on the measured response. The numerical simulation is performed utilizing a commercial software package that is thought to be suitable to simulate the observed response and the non-linearities that developed and included large plastic strains and local instabilities.

## 2 MATERIALS AND EXPERIMENTAL SETUP

### 2.1 Tested specimens

Two full-scale specimens, namely T-Beam 8 and T-Beam 8R1 INV have been constructed with prototype steel cross sections in order to form a beam-to-column joint. Both specimens were of the same geometry and used as the beam part a IPE 300 steel section and as the column part a HEA 300 steel section. These two parts were welded together, as shown in figures 1 and 2, to form the beam-to-column connection to be tested .

The IPE 300 beam was to a steel base plate having a thickness of 20mm welded and this steel plate in turn was bolted to the HEA 300 column (figure 1 and 2). Furthermore, in order



to avoid the brittle type of failure at the welds joining the IPE 300 beam part with the base steel plate two or six 20mm thick steel stiffeners of triangular shape (with a height of 150mm and width of 150mm) were welded at either side of the IPE 300 section connecting its flanges with the base plate as shown in figures 1 and 2. The T-Beam 8 specimen had in total two identical triangular steel stiffeners on each side of the flanges welded and the T-Beam 8R1 INV specimen had in total 6 steel stiffeners 3 evenly spaced on each side of the flanges. The height of the IPE 300 beam part was 1200mm and was connected on its upper part with the forcing fixtures that were provided by a double acting hydraulic actuator. This actuator was controlled by a servo-hydraulic digital electronic controller providing the desired imposed cyclic horizontal displacement amplitude at a distance of 1000mm from the base plate. The two IPE 300 beam-to-column connection specimens were tested as shown in figures 1 and 2. Both specimens were of the same overall geometry having webs with thickness equal to 7mm. The flange thickness varied from 10.2mm for the west flange and 10.5mm for the east flange.

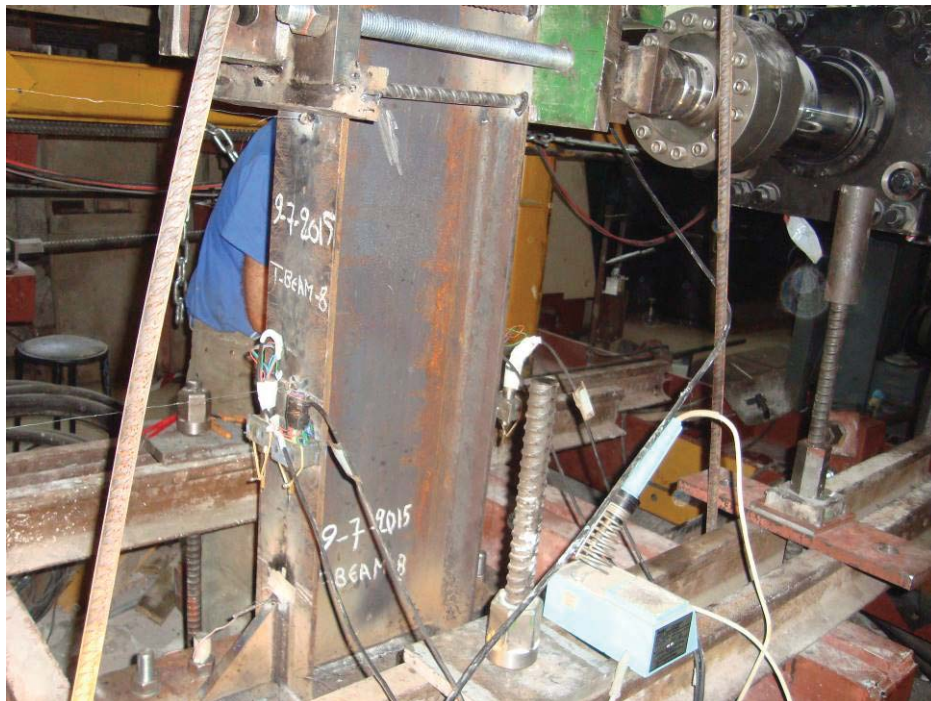


Figure 1. Details of the experimental setup with the tested IPE 300 T-Beam 8 beam-to-column joint specimen

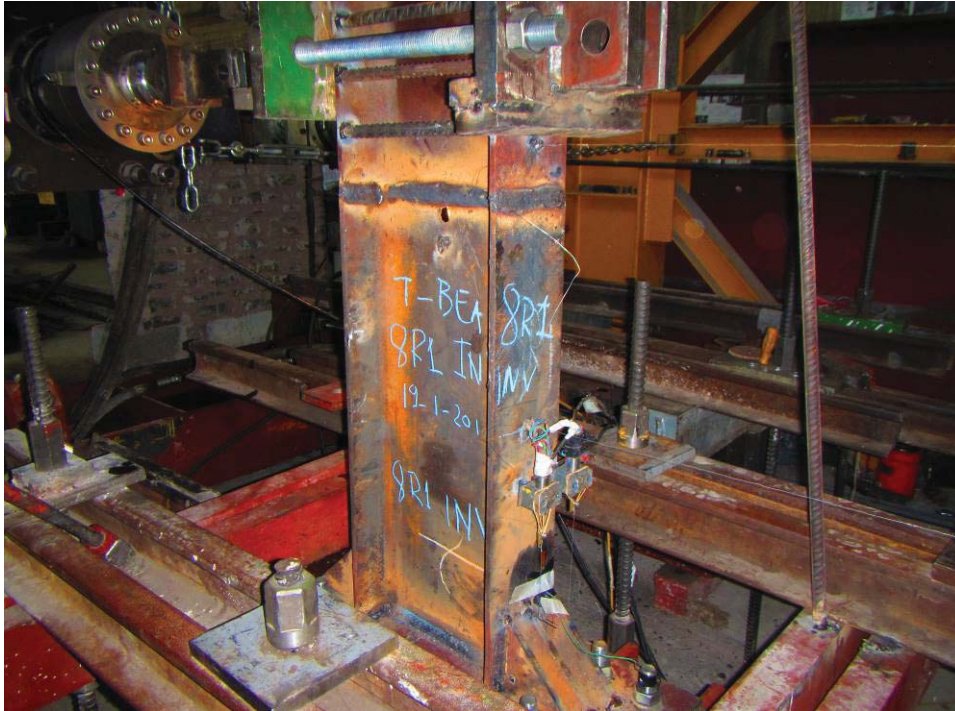


Figure 2. Details of the experimental setup with the tested IPE 300 T-Beam 8R1 INV beam-to-column joint specimen

## 2.2 Loading arrangement

The tested specimens were subjected to a cyclic seismic-type loading arrangement. An extensive discussion on the loading protocols was presented by Krawinkler [11]. This is a very important and difficult issue as on one hand it is believed that it influences the resulting performance and on the other hand it poses demands on the capabilities of the experimental facility [6, 7, 8, 11, 12, 15]. As this work at its present stage aims to produce results that will be utilized for validating the numerical capabilities of existing software rather than checking the validity of code provisions the used loading protocol does not comply exactly with ones suggested by Krawinkler and other researchers [6, 7, 11, 15]. Instead, a series of sinusoidal horizontal cyclic displacements were used and were imposed on the top of the IPE 300 beam part, as shown in figures 1,2 and 4. Both specimens were rigidly attached on the strong floor of the Laboratory of Strength of Materials and Structures of Aristotle University. The hydraulic actuator was attached on the strong metal frame which together with the strong floor forms this experimental facility. The imposed horizontal displacement and the resulting horizontal load leads to the development of a bending moment at the beam-to-column connection which, if of sufficient amplitude, is expected to bring this part of the beam-to-column connection to a certain limit state condition, as will be explained in section 3. The imposed horizontal displacement in amplitude and frequency content is controlled by the electronic servo-controller. A relatively simple imposed displacement protocol is depicted in figure 3. It consists of thirteen (13) groups of 3 full sinusoidal cycles. In each group the imposed maximum displacement amplitude remains constant and keeps gradually increasing from one group to the next in a prescribed manner, as a percentage of the maximum target displacement. The difficulty in imposing this protocol accurately lies on the fact that the target displacement is known at best through predictions that may differ considerably from the actual target displacement that,



when imposed, will produced the desired phenomena. The protocol depicted in this figure was adopted in the current study in a general sense. That is, the amplitude of the imposed horizontal displacement kept increasing from one group to the next till the plastification of the tested specimens led to some type of failure, as will be described in section 3. One distinct difference in the followed loading protocol for the specimen T-Beam 8 is the fact that the frequency content was relatively low (0.005Hz) as to allow this test to be characterized as a dynamic test accompanied with low level of strain rate. On the contrary, the loading protocol for T-Beam 8R1 INV specimen was relatively high (0.1Hz) that is characterized as cyclic test of relatively medium level strain rate.

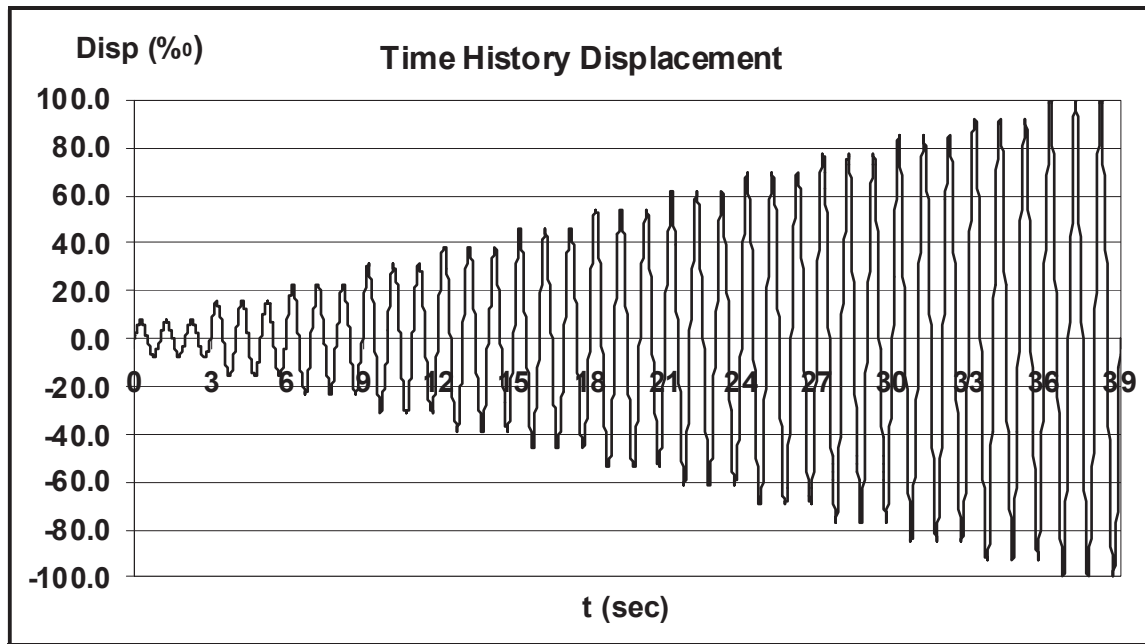


Figure 3. Typical cyclic seismic-type imposed displacement protocol for low fatigue loading

### 2.3 Instrumentation

Instrumentation was provided capable to record the dynamic response of the specimen at the top in terms of imposed horizontal displacement (LVDT 01, figure 4) and horizontal force. In addition, four displacement transducers (LVDT 02, LVDT 03, LVDT 04 and LVDT 05) were attached to the specimen in order to record the relative vertical displacement of two sets of horizontal cross sections of each specimen near the plastification zone (figures 1, 2 and 4). The first set of horizontal cross sections was that at the base, where the IPE 300 part was welded at the base steel plate) and the one 500mm higher. Utilizing LVDT 02 and LVDT 03 the relative elongation or shortening between these two cross sections of the specimen was measured at the flanges of both sides of the IPE 300 section. The second set of horizontal cross sections was that at 150mm from the base, where the triangular stiffeners ended, and the one 100mm higher. Utilizing LVDT 03 and LVDT 04 the relative elongation or shortening between these two cross sections of the specimen was measured at the flanges of both sides of the IPE 300 section. In this way, it became possible to deduce from the measured response the rotation between the first and the second set of these horizontal cross sections. The second set of horizontal cross sections is of particular importance as the highly plastified region (plastic hinge), which was expected to develop during the experimental sequence, lies between the

horizontal cross-sections of the second set. Indeed, the used instrumentation was able to capture the plastification of this region from the initial stages of yielding till the final stages of local instability. In addition, a set of strain gauges was also provided in order to control in a different way the initiation and development of plastification in this zone.

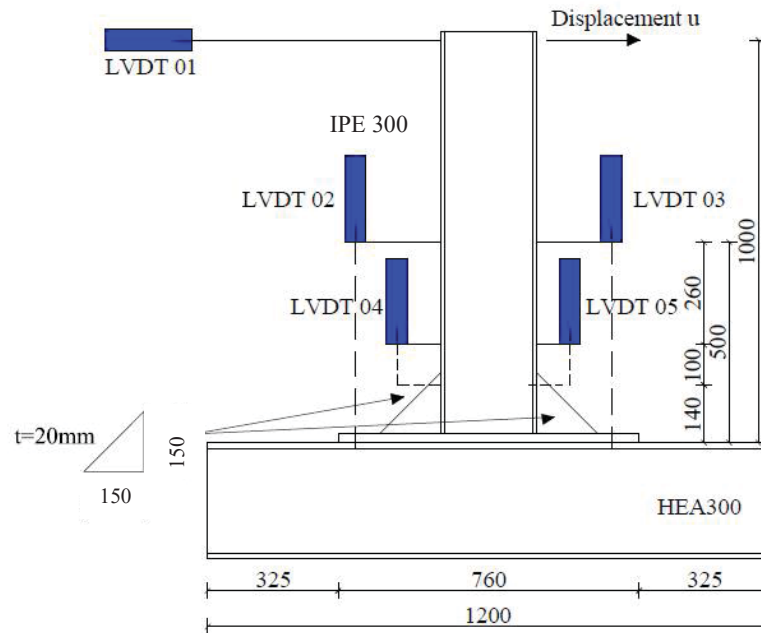


Figure 4. Experimental set-up with the geometry of the specimens, the instrumentation and loading

Figures 5 and 6 depict the instrumentation of this zone near the beam-to-column joint. The used hydraulic actuator can also be seen in figure 5 whereas in figure 6 the vertical displacement transducer utilized to measure the relative elongation or shortening between two horizontal cross sections above the stiffener having a distance between them equal to 100mm can also be seen (second set of horizontal cross sections).



Figure 5. Instruments located near the beam-to-column joint.



Figure 6. Measuring the relative elongation/shortening between two horizontal cross sections above the stiffener

## 2.4 Steel tensile properties

In order to input the proper information related to the steel characteristic in the finite element program monotonic tensile tests from similar T-Beam IPE300 beams and cyclic tests from T-Beam 8 with different loading frequencies were performed with coupons taken from the specimens. These coupons were taken from the flanges of the specimens after the completion of the relevant test sequence. In order to measure the material properties of the virgin steel prior to any plastification and permanent straining these coupons were taken from the upper part of the IPE 300 beam sections near the section where the imposed displacement was applied. More detailed information about the material steel coupons and the corresponding results are given in the work of Manos G.C. and Nalmpantidou A. [18].

## 3 OBSERVED PERFORMANCE AND CORRESPONDING MEASUREMENTS.

### 3.1 Observed over-all performance and actual damage

Each specimen experienced plastic rotation above the stiffeners that was captured by the employed instrumentation. Despite the fixity of the attachment of the specimens on the strong floor part of the imposed horizontal displacement was consumed by the rotation of the specimen at its fixed base as well as of the elastic response along the height apart from the plastic rotation that developed at the desired location above the stiffeners. Fortunately, despite the limitations of the capabilities of the experimental facility it was possible to attain the plastic limit state for both studied specimens and produce the expected form of damage. This is depicted in figures 7 for specimen T-Beam 8 and figure 8 for specimen T-beam 8R1 INV.

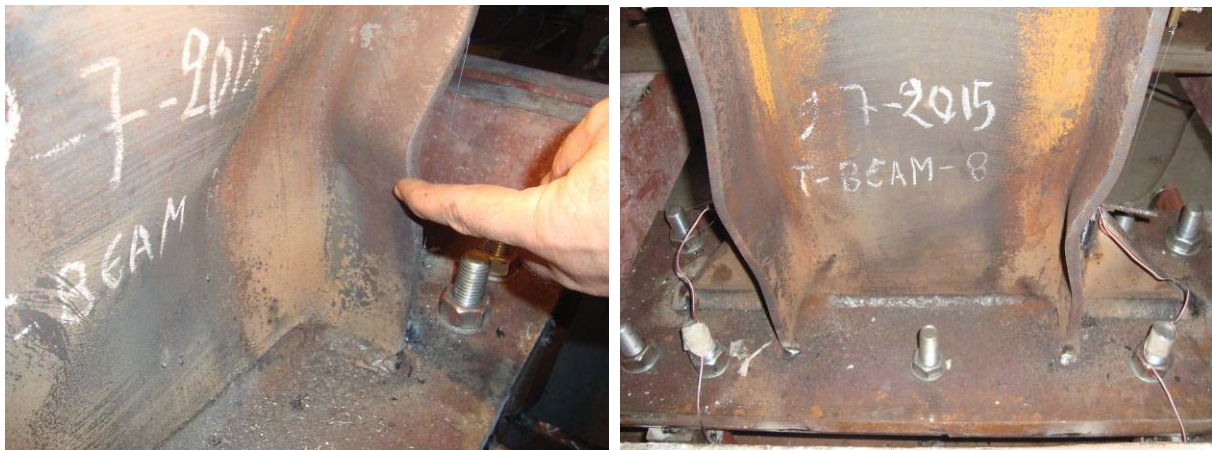


Figure 7. Plastification of specimen T-Beam 8 at the end of test - 11



Figure 8. Plastification of specimen T-Beam 8R1 INV at the end of test - 14

### 3.2 Measured response in terms of plastic rotations at the plastic hinge.

Figure 9, depicts the full loading sequence in terms of horizontal displacement at the top of the specimen T-Beam 8 that could be deduced from the employed instrumentation as directly linked with the elastic/plastic rotation at the zone of the specimen extending at a length of 100mm above the stiffeners of the IPE 300 beam (figures 4 and 6). The corresponding development of the plastic rotation with time in this plastic hinge region is shown in figure 10. The imposed loading history in terms of plastic hinge rotation and the corresponding horizontal displacement at the top of specimen T-Beam 8R1 INV is shown in figure 11 and 12.



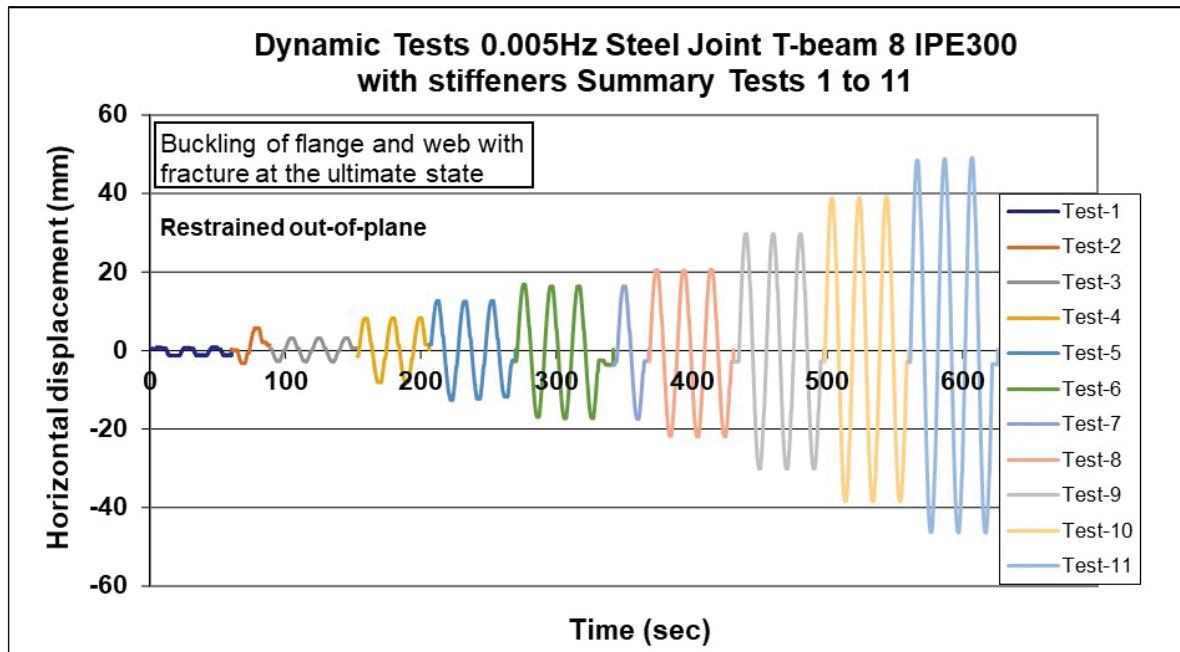


Figure 9: Horizontal displacement at the top of specimen T-Beam 8 due to the plastic rotation at the plastic hinge region.

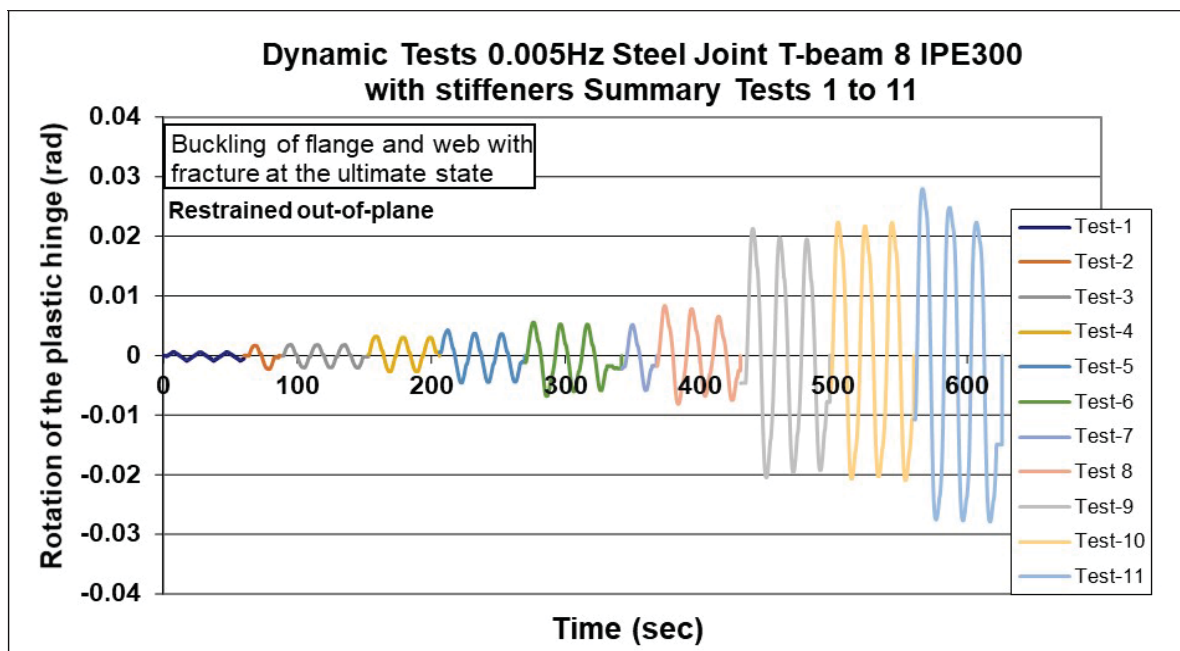


Figure 10: Plastic rotation at the plastic hinge region due to horizontal displacement at the top of specimen T-Beam 8.

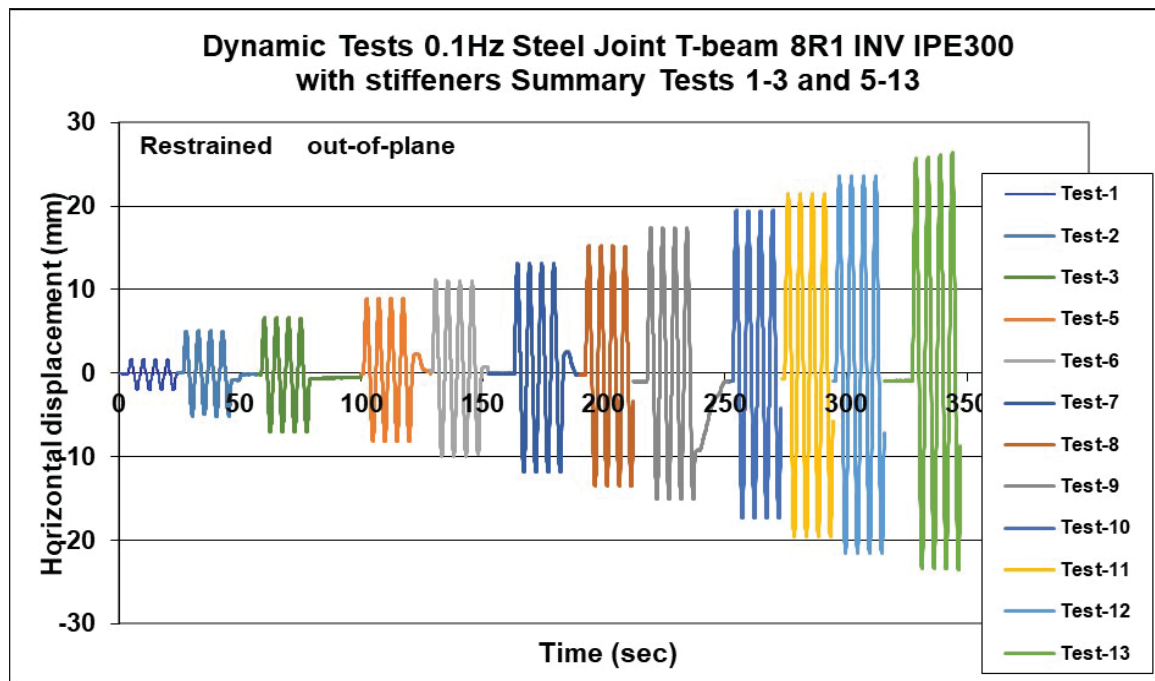


Figure 11: Horizontal displacement at the top of specimen T-Beam8R1 INV due to the plastic rotation at the plastic hinge region.

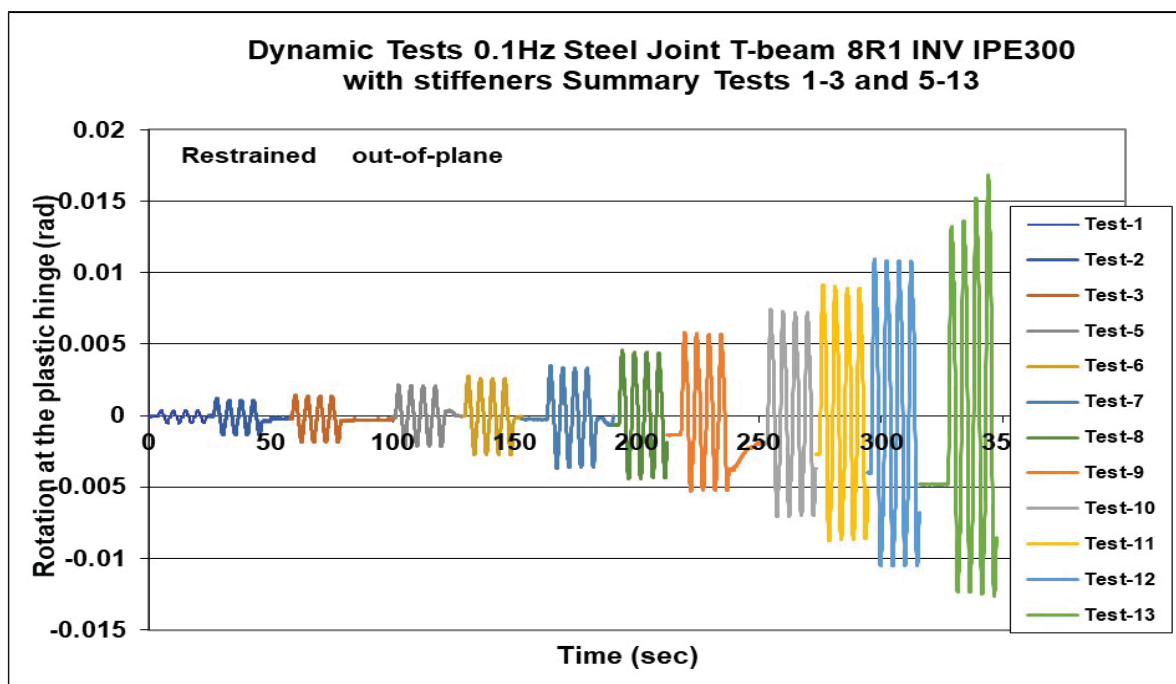


Figure 12: Plastic rotation at the plastic hinge region due to horizontal displacement at the top of specimen T-Beam 8R1 INV.

As can be seen in figures 10 and 12 specimen T-Beam 8 reaches the flexural plastic limit for plastic hinge rotations of the order of 0.027 radians and specimen T-Beam 8R1 INV of the order of 0.015 radian, having undergone a considerable number of low-fatigue cycles



[10, 13, 14]. Moreover, both specimens failed by developing local instability at the plastic region in the form of flange local buckling and eventually fracture. Figures 13 and 14 portray the observed cyclic response in terms of bending moment and plastic hinge rotation, for specimens T-Beam 8 and T-Beam 8R1 INV, respectively. The bending moment values were deduced at a section above the stiffeners from the measured horizontal load.

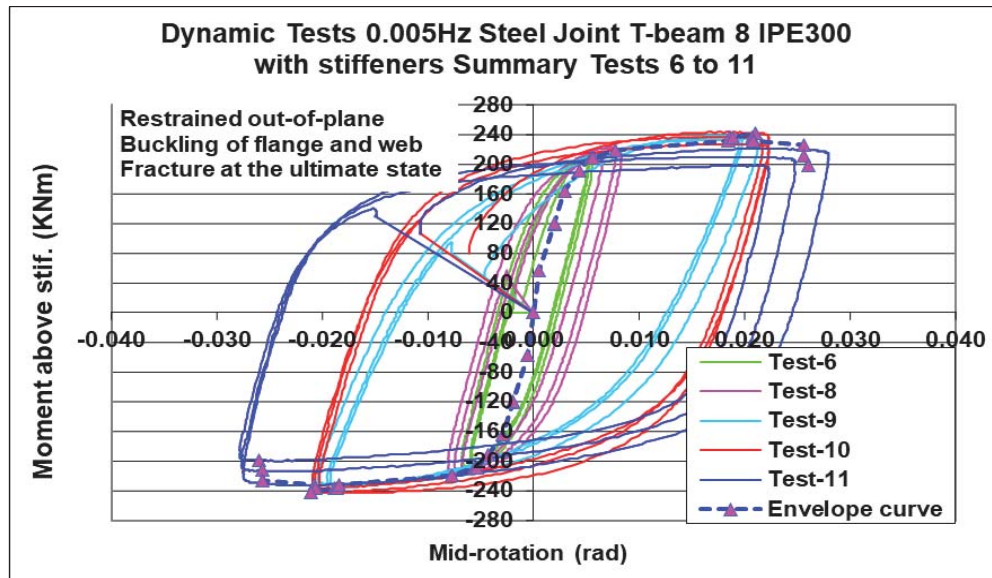


Figure 13: Measured cyclic response of the plastic hinge for specimen T-Beam 8.

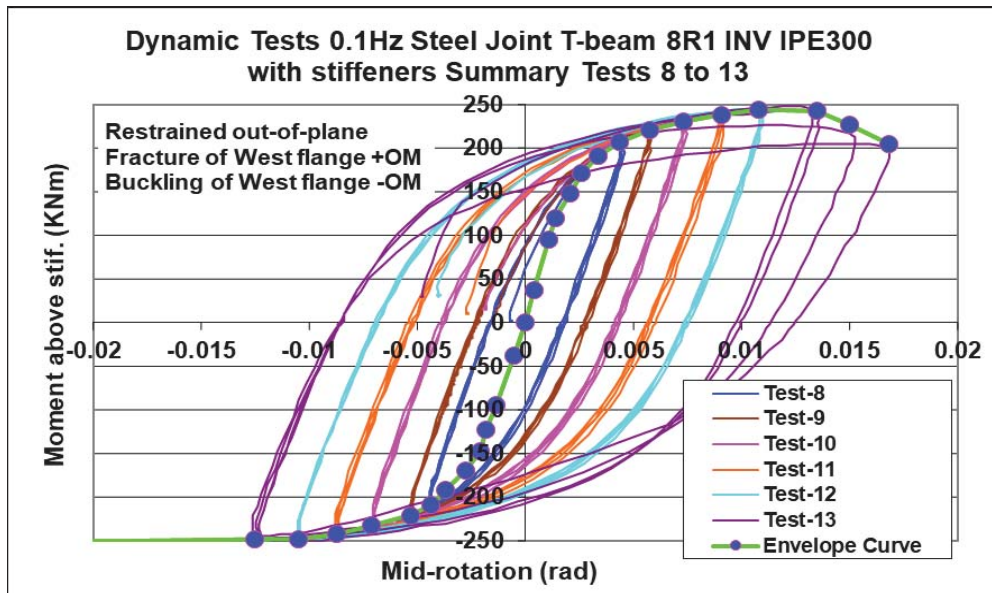


Figure 14: Measured cyclic response of the plastic hinge for specimen T-Beam 8R1 INV.

In both figures 13 and 14 a corresponding envelop curve is also plotted with a dashed blue line for T-Beam 8 specimen and a green line for T-Beam 8R1 INV specimen. As can be seen, both specimens developed large cycles of stable plastic response before reaching their failure mode thus dissipating considerable energy in terms of hysteretic damping. Figure 15

depicts this hysteretic cyclic response through the corresponding envelop curves. As can be seen from the comparison of these two envelope curves in figure 17 there is a slight difference in the specimens performance in terms of maximum flexural baring capacity and plastic hinge rotation corresponding to that flexural capacity. The measured flexural capacity is of the order of 244 KNm and 248 KNm for specimens T-Beam 8 and T-Beam 8R1 INV, respectively. The plastic hinge rotation values corresponding to these flexural capacity values are for the T-Beam 8 specimen approximately 0.018 rad and for the T-Beam 8R1 INV specimen approximately 0.012 rad. Consequently, it can be concluded that the variation in the loading frequency from 0.005Hz of the T-Beam 8 specimen to 0.1Hz of the T-Beam 8R1 INV specimen led to a decrease in the value of the plastic hinge rotation of the maximum flexural baring capacity with the increase of the loading frequency. Finally from the overall envelope curve a slight increase in the flexural capacity of T-Beam 8R1 INV specimen can be observed with increasing loading frequency and increasing strain rate.

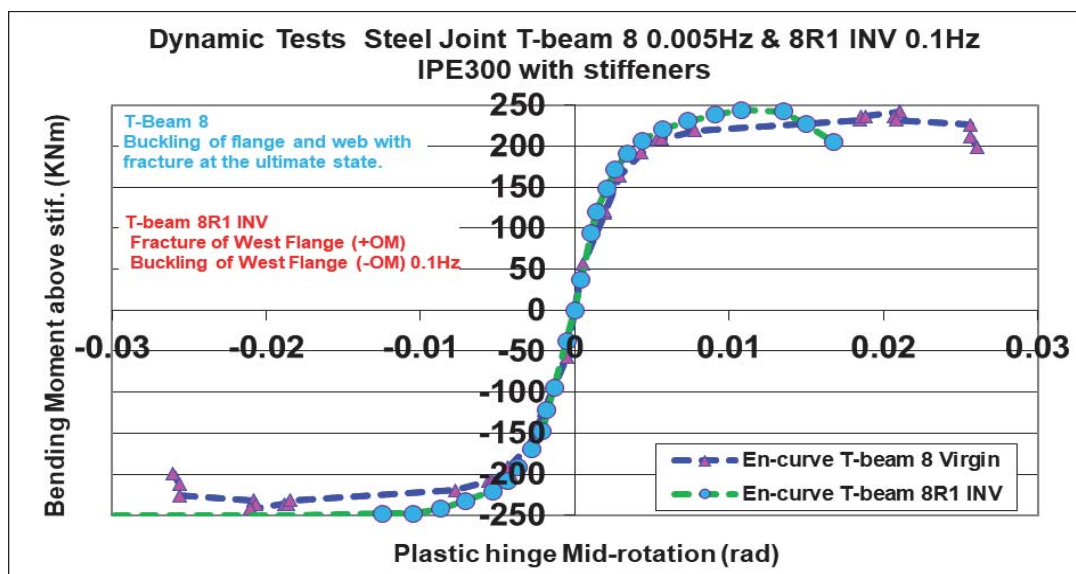


Figure 15: Measured cyclic response of the plastic hinge in terms of envelop curves for both specimens T-Beam 8 and T-Beam 8R1 INV.

## 4 NUMERICAL SIMULATION OF THE OBSERVED CYCLIC RESPONSE AND PERFORMANCE

### 4.1 Numerical modeling.

The commercial software ABAQUS [16] was utilized in this numerical simulation effort. In doing so, the IPE 300 beam part of the experimental sequence was reproduced through the finite element representation as accurately as possible. This is shown in figure 16 whereby it can be seen that the numerical simulation extended all the way from the top section where the horizontal load was imposed to the bottom horizontal section where the IPE 300 beam was welded to the base plate. Moreover, the triangular stiffeners with their actual thickness and geometry were also included in this numerical simulation. The whole surface of the IPE 300 and the stiffeners at the bottom level where the specimens were welded to the base plate was considered to be represented with absolute fixity conditions in the numerical simulation. In addition, the horizontal displacement of the specimen outside the loading plane was con-

strained. The discretization scheme that was adopted was considerably fine in an effort to be able to catch numerically the observed local modes of buckling of the flanges in the plastic hinge region.



Figure 16: Employed numerical model.

## 4.2 Material modeling

In the framework of the numerical investigation a parametric study was conducted that focused on the way the steel material properties were introduced in the numerical simulation. Two different approaches were tried. According to the first approach the measured tensile steel properties were introduced in the numerical simulation through the Abaqus isotropic hardening parameters whereas in the second approach the measured properties were modified accordingly in order to be introduced in the numerical simulation through the ABAQUS combined hardening material model [16]. More information on this approach can be obtained from the previous work by Manos G.C. et al [19].

In this work the focus relies in the numerical simulation of the material tests through the ABAQUS combined hardening material constitutive law. There are several ways in this commercial software package [16] to define a combined hardening material constitutive law in order to capture the cyclic response of a specimen. The evolution law of this model consists of two components: a nonlinear kinematic hardening component, which describes the translation of the yield surface in stress space through the back-stress, and an isotropic hardening component, which describes the change of the equivalent stress defining the size of the yield surface, as a function of plastic deformation [16]. In this study the combined hardening constitutive law is defined through the values that are given to certain relevant parameters. Values for these parameters were calculated from the test data that were obtained from the experimental process from the tests of steel samples that were taken from the T-Beam specimens and can be seen in the work by Manos G.C and Nalmpantidou A. [18].

This software (Abaqus) allows the specification of strain rates effects with the option of rate dependent data at combined and isotropic hardening constitutive law. In order to define the strain rate effect the use of a dynamic increase factor (DIF) was utilized based on the work of Malvar and Crawford [9]. The work of Malvar and Crawford [20] is based on numerous

experimental data from a literature review on the effects of strain rates on the properties of steel reinforcing bars for reinforced concrete structural elements. The dynamic increase factor (DIF) is the amplification by DIF of the value a certain mechanical property (yield stress or maximum stress) has under low strain rate loading conditions (static) to another condition whereby because of the nature of loading (dynamic) the strain rate has a larger value than before. A relationship is proposed by Malvar and Crawford [20] that a DIF value can be derived for a given strain rate increase and thus evaluate through this DIF the corresponding for this increased strain rate amplified yield and ultimate stress values. Figure 17 depicts the dynamic increase factor considered for the numerical simulation.

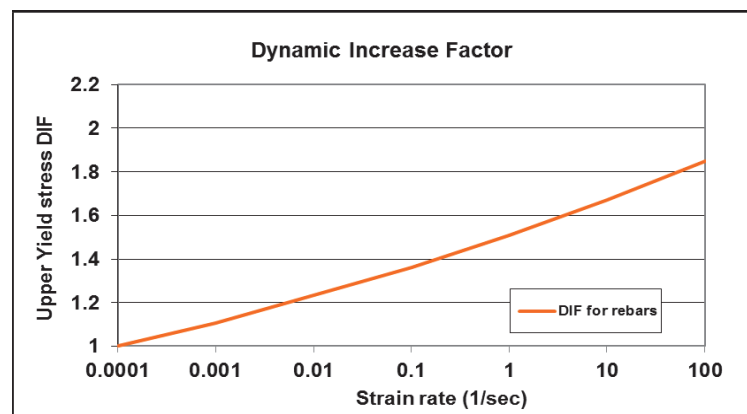


Figure 17. Dynamic increase factor which have been considered for the numerical investigation

#### 4.3 Numerical results from the parametric study

This section will present numerical results of the experimental investigation carried out with T-Beam 8 and T-Beam 8R1 INV under cyclic tests. The necessary material parameters for the numerical simulation were calculated from the experimental data of simple steel coupons taken from T-Beam 8 and are the following:

Combined hardening parameters:

Yield stress at plastic strain  $\sigma|_0=180\text{-}200\text{Mpa}$ ,

Kinematic Hardening Parameter  $C_k=34000$

Gamma  $\gamma_k=250$

Cyclic hardening parameters:

Equivalent stress  $\sigma|_0=180\text{-}200\text{Mpa}$

Q-Infinity parameter  $Q_\infty=85$

Hardening parameter  $b_{iso}=6.5$

Combined hardening parameters:

Yield stress at plastic strain  $\sigma|_0=100\text{-}140\text{Mpa}$ ,

Kinematic Hardening Parameter  $C_k=51800$

Gamma  $\gamma_k=250$

Cyclic hardening parameters:

Equivalent stress  $\sigma|_0=100\text{-}140\text{Mpa}$

Q-Infinity parameter  $Q_\infty=305$

Hardening parameter  $b_{iso}=6.5$   
 Combined hardening parameters:  
 Yield stress at plastic strain  $\sigma_0=140\text{Mpa}$ ,  
 Kinematic Hardening Parameter  $C_k=59520$   
 Gamma  $\gamma_k=250$   
 Cyclic hardening parameters:  
 Equivalent stress  $\sigma_0=140\text{Mpa}$   
 Q-Infinity parameter  $Q_\infty=30$   
 Hardening parameter  $b_{iso}=6.5$

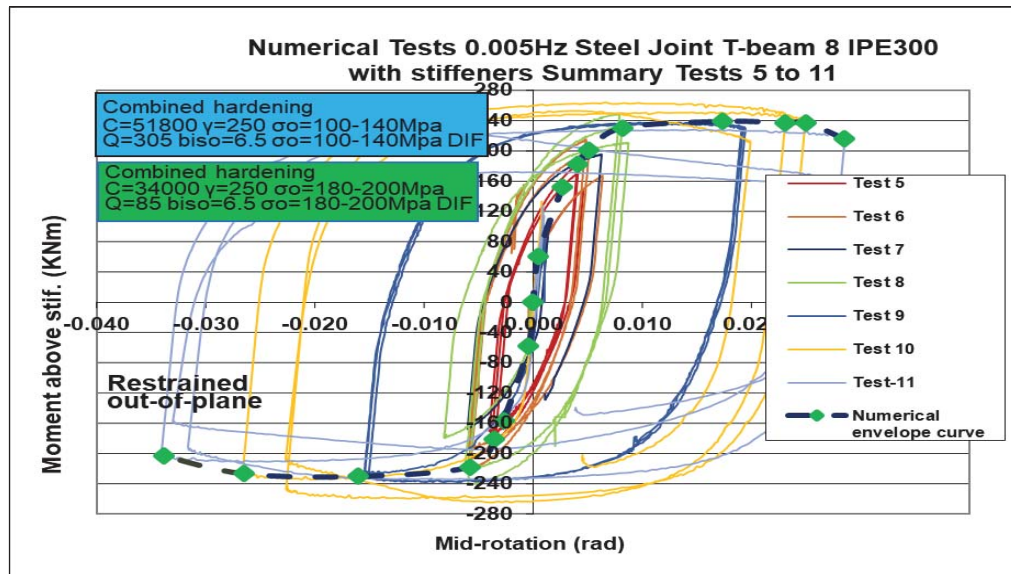


Figure 18. Numerical predictions of the cyclic response of the plastic hinge for specimen T-Beam 8

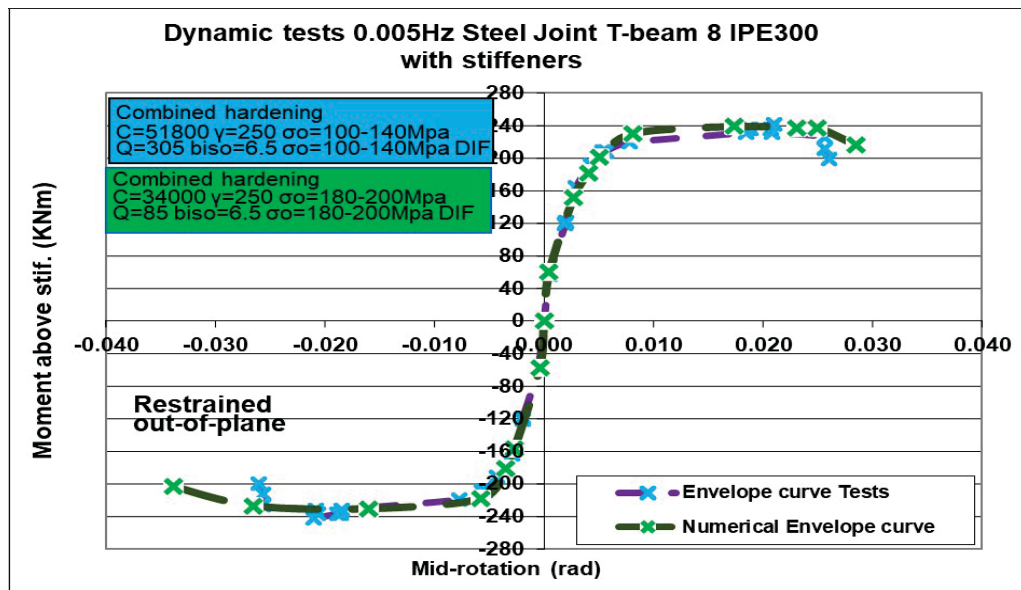


Figure 19. Predicted cyclic response of the plastic hinge in terms of envelope curves for specimen T-Beam 8 together with the measured response



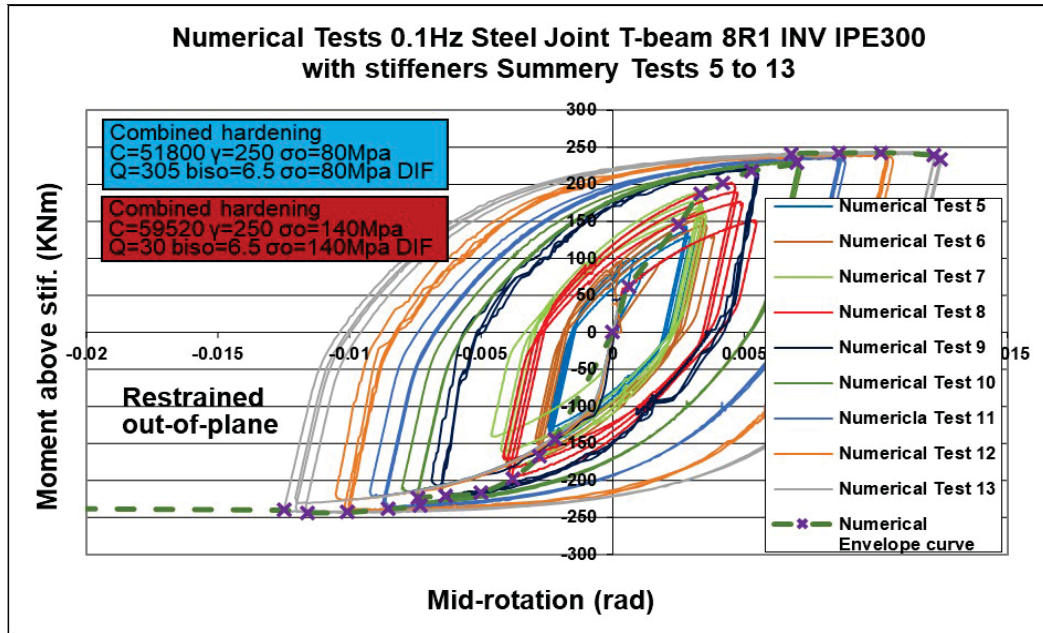


Figure 20. Numerical predictions of the cyclic response of the plastic hinge for specimen T-Beam 8R1 INV

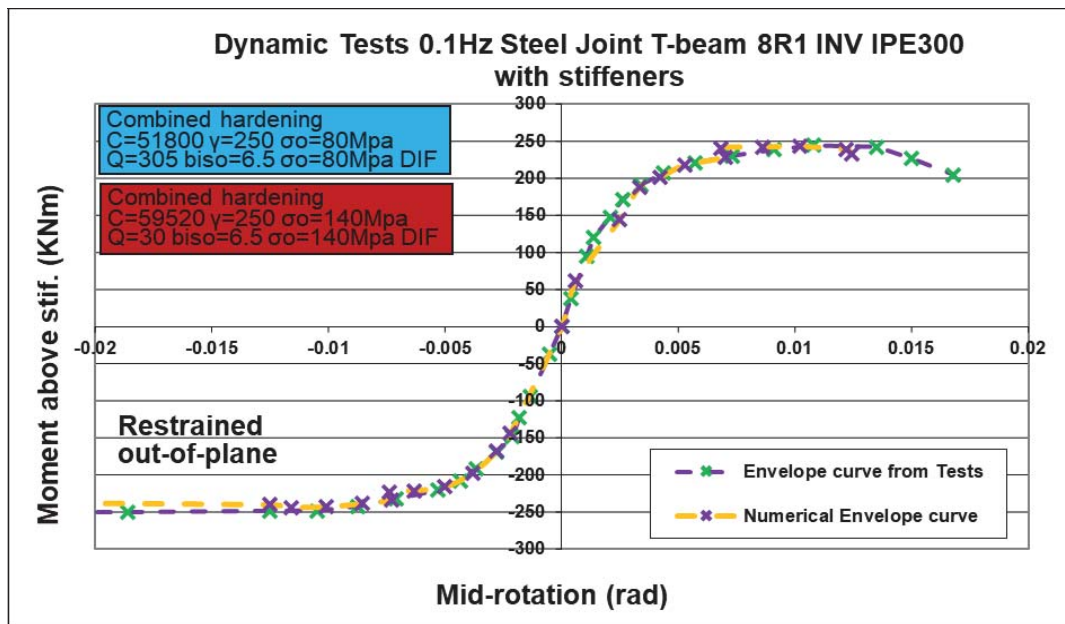


Figure 23. Predicted cyclic response of the plastic hinge in terms of envelope curves for specimen T-Beam 8R1 INV together with the measured response

In figure 18 and 20 are the results of the numerical simulation of T-Beam 8 and T-Beam 8R1 INV and the corresponding envelope curves shown. As can be seen specimen T-Beam 8 reaches the flexural plastic limit for plastic hinge rotations of the order of 0.027 radians and



specimen T-Beam 8R1 INV of the order of 0.015 radian, having undergone the same number of low-fatigue cycles [10, 13, 14] as the experimental setup.

Figure 19 and 21 compare the envelop curves predicted by the numerical simulation for specimens T-Beam 8 and T-Beam 8R1 INV, respectively, with the corresponding envelop curves of the measured cyclic response for the same specimens. The predicted response was obtained by using the combined hardening material model and as can be seen there is a small variation between the measured flexural capacity and rotation at the plastic hinge and the numerical simulation with higher values of the numerical simulation for T-Beam 8 specimen. Furthermore the predicted cyclic response of T-Beam 8R1 INV has a quite good agreement between the measured flexural capacity and rotation at the plastic hinge and the numerical simulation.

## 5 CONCLUSIONS

- The seismic performance of a steel beam-to-column connection was studied by subjecting two specimens of such steel beam-to-column connection specimens to imposed cyclic displacements with a variety of low to medium range strain rates. The tested specimens were constructed with prototype steel sections welded in a typical fashion.
- Both specimens developed local flange buckling modes of failure for plastic hinge rotation values approximately equal 0.027 radians for T-Beam 8 specimen and 0.015 radians for T-Beam 8R1 INV specimen. For values of plastic hinge rotation higher than 0.027 radians for T-Beam 8 specimen and 0.15 radians for T-Beam 8 R1 INV specimen the deterioration of the flexural capacity became substantial for both specimens as the local flange buckling mode of failure prevailed.
- The consequence of the previous observation is that the employed strain rate variation in the used loading sequence of specimen T-Beam 8 with 0.005Hz from that of the loading sequence of specimen T-Beam 8R1 INV with 0.1 Hz led to a decrease in the value of the plastic hinge rotation of the maximum flexural baring capacity with the increase of the loading frequency. From the overall envelope curve a slight increase in the flexural capacity of T-Beam 8R1 INV specimen can also be observed with increasing loading frequency and increasing strain rate. However, this is a partial conclusions based on rather limited data. Therefore more research is needed to further investigate the strain rate influence on the beam-to-column connections earthquake performance.
- The numerical simulation of the tested specimens utilizing the capabilities of a commercial software package yielded reasonable good agreement between both the measured and predicted cyclic response in terms of maximum flexural capacity, dissipation characteristics and deterioration of the flexural capacity. It is of utmost importance to have realistic estimates of the values of the parameters are  $\sigma_0$  (yield stress at zero equivalent plastic strain),  $C_k$  and  $\gamma_k$  (material constants) which define the steel combined hardening material behaviour.

## ACKNOWLEDGEMENTS

The authors would like to acknowledge the assistance of M. Theofanous, Dr. Civil Engineer, Lecturer at the Department of Civil Engineering of the University of Birmingham, for all his valuable advice related to the numerical simulation. The technical assistance of T.

Koukouftopoulos in preparing the experimental arrangement is also gratefully acknowledged.

- To the memory of Hiroshi Akiyama, Professor of the University of Tokyo, Japan and of Heki Shibata, Professor of Industrial Science, University of Tokyo, Japan.

## REFERENCES

- [1] Akiyama H. Earthquake-Resistant Limit-State Design for Buildings. University of Tokyo Press: Tokyo, 1985.
- [2] Anastasiadis A., Mosoarca M., Gioncu V., Mazzolani F. M., “Some thoughts for the prediction of the local inelastic capacity of MRF subjected to seismic actions”, 8<sup>th</sup> STESSA Conf. on the Behavior of Steel Structures in Seismic Areas, Tongji Univ., Songhai China, July 2015.
- [3] Anastasiadis A, Gioncu V, Mazzolani FM. “New trends in the evaluation of available ductility of steel members.” Behavior of Steel Structures in Seismic Areas STESSA 2000; 3-26.
- [4] Anderson, James C., Nastar Navid, Rojas Fabian, “Low-Cycle Fatigue Effects on Steel Moment Frames”, Safety, Reliability and Risk of Structures, Infrastructures and Engineering Systems – Furuta, Frangopol & Shinozuka (eds)© 2010 Taylor & Francis Group, London, ISBN 978-0-415-47557-0
- [5] Ballio Giulio &. Castiglioni, Carlo A, “Seismic Behaviour of Steel Sections”, J. Construct. Steel Research 29 (1994) 21-54
- [6] Castiglioni Carlo A., Mouzakis Harris P., Carydis Panayotis Gr. (2007): “Constant and Variable Amplitude Cyclic Behavior of Welded Steel Beam-to-Column Connections”, Journal of Earthquake Engineering, 11:876–902, 2007, 11:6, 876-902, doi.org/10.1080/13632460601188027.
- [7] Clark P, Frank K, Krawinkler H, Shaw R. Protocol for fabrication, inspection, testing, and documentation of beam-column connection tests and other experimental specimens. SAC Steel Project Background Document, Report No. SAC/BD-97/02, 1997.
- [8] El Hassouni A, Plumier A., Cherrabi A. “Experimental and numerical analysis of the strain-rate effect on fully welded connections”, Journal of Constructional Steel Research (2010), doi 10.1016/j.jcsr.2010.09.02
- [9] Federal Emergency Management Agency. Interim testing protocols for determining seismic performance characteristics of structural and nonstructural components. FEMA 461 Draft Document, Applied Technology Council, Redwood City, CA, 2007.
- [10] Gioncu V, Petcu D. “Available rotation capacity of wide-flange beam and beam-columns part 1, 2.”, Journal of Constructional Steel Research 1997; 43: 161-244.
- [11] Krawinkler H. Loading histories for cyclic tests in support of performance assessment of structural components. The 3rd International Conference on Advances in Experimental Structural Engineering, San Francisco, 2009.

- [12] Lamarche Charles-Philippe and Tremblay Robert, “Seismically induced cyclic buckling of steel columns including residual-stress and strain-rate effects”, *Journal of Constructional Steel Research* 67 (2011) 1401–1410, doi:10.1016/j.jcsr.2010.10.008
- [13] Lee Kyungkoo and Stojadinovic Bozidar, “Low-cycle fatigue limit on seismic rotation capacity for US steel moment connections”, 13th World Conference on Earthquake Engineering, Vancouver, B.C., Canada, August 1-6, 2004, Paper No. 90.
- [14] Vayas I. “Investigation of the cyclic behavior of steel beams by application of low-cycle fatigue criteria.” *Behavior of Steel Structures in Seismic Areas STESSA 1997*; 350-357.
- [15] Yu Jiao, Satoshi Yamada, Shoichi Kishiki and Yuko Shimada, “Evaluation of plastic energy dissipation capacity of steel beams suffering ductile fracture under various loading histories” *Earthquake Engng Struct. Dyn.* 2011; 40:1553–1570.
- [16] Hibbitt, Karlsson, Sorensen. Inc. ABAQUS user’s manual volumes I–V and ABAQUS CAE manual. Version 6.10.1. Pawtucket, USA; 2010.
- [17] Nip, K.H., Gardner L., Davies C.M., Elghazouli A.Y., “Extremely low cycle fatigue tests on structural carbon steel and stainless steel”, *Journal of Constructional Steel Research* 66 (2010) 96-110, doi:10.1016/j.jcsr.2009.08.004
- [18] Nalmpantidou A., Manos G.C., “Experimental and numerical investigation of the plastic cyclic behavior of simple steel coupons”, *COMPDYN 2021*, Streamed from Athens, Greece, June 2021
- [19] Manos G.C., A. Nalmpantidou, V.Kourtides, A. Anastasiadis “Cyclic response of a steel beam to column connections – an experimental and numerical study”, *COMPDYN 2015*, Crete Island, Greece, May 2015
- [20] Malvar, L. J. and John E. Crawford J. E., “Dynamic increase factor for steel reinforcing bars”, *Twenty-Eighth DDESB Seminar*, Orlando, FL., 1998

## DYNAMIC AND VIBROACOUSTIC RESPONSE OF TIMBER FLOOR PANELS. MEASUREMENTS AND NON-LINEAR NUMERICAL SIMULATIONS

Magdalini Titirla<sup>1</sup>, Sarah Benakli<sup>1</sup>, and Walid Larbi<sup>1</sup>

<sup>1</sup> Structural Mechanics and Coupled Systems Laboratory (LMSSC), Conservatoire National des Arts et Métiers (CNAM), Paris,  
292 rue Saint-Martin, 75141 Paris Cedex 03, France  
{magdalini.titirla, sarah.benakli, walid.larbi}@lecnam.net

---

### Abstract

*The present work concerns the dynamic and vibroacoustic response of timber floor panels as well as the study of the effect of material nonlinearities and damping. Each panel is composed of glued laminated beams and wood constituting the floor. The dimensions of the panels are defined to ensure appropriate implementation and transport conditions. For these reasons, the width of the panels is fixed at 2.40 m, and the length is 7.2 m. Two types of floor panels were investigated with and without struts. A numerical approach based on 3D finite element method is used to solve the problem. Our finite element model and the mechanical properties of the used materials are first validated from comparisons with experimental tests carried out in statics [1]. A dynamic non-linear analysis of the timber floor panels has been then conducted under a walking time history and the vibroacoustic response of the system is finally investigated.*

**Keywords:** Timber structures, dynamic analysis, vibroacoustic, numerical and experimental measurements, non-linear.

---

## 1 INTRODUCTION

The use of wood as construction material increased in Europe during the last decades. Compared to steel or reinforced concrete buildings, the timber buildings are more sensitive to dynamic loading, especially in terms of vibroacoustic comfort. Furthermore, due to the complexity of wood material and different structural details it is more difficult to predict the accurate response due to dynamic loading.

Floor vibrations and structure-borne sound in residential buildings can be induced by several sources such as people walking indoors, machines vibration. Excessively high sound and/or vibration levels cause annoyance and discomfort for residents. Low frequency prediction tools are needed to access the dynamic behavior of a timber floor in an early design phase to ultimately reduce the low frequency impact noise. This highlights the need to improve the design of multi-story timber buildings such that vibration levels and the need of further investigation on this field.

In the European countries, the vibration of timber floors is regulated by the serviceability limit states (SLS) requirements of Eurocode [2]. In addition, a lot of researchers have started to investigate this field. Initially, the vibration issues of different types of flooring systems (composite, concrete, steel with timber) was identified under the action of human activities by Bachmann & Ammann [3], Williams & Waldron [4], Da Silva et al. [5] and Ebrahimpour & Sack [6].

In the present work attention is focused on the dynamic and vibroacoustic response of timber floor panels as well as the study of the effect of material nonlinearities and the damping ration. The first part of this study focuses on the validation of the finite elements (FE) model with the appropriate selected experimental results, in order to be a reliable tool for the further part of this study. After the validation, dynamic analyses were conducted under a walking load time history of a person in the middle of each floor panel, and then the vibroacoustic of these panels are presented.

## 2 A SHORT DESCRIPTION OF THE INVESTIGATED TIMBER FLOOR PANELS

Two types of floor panels were investigated (with and without struts). The floor panels have been proposed by Fuentes et al [1] and analyzed only in static analysis. The dimensions of the panels were defined to ensure appropriate implementation and transport conditions. For these reasons, the width of the panels was fixed at 2.40 m, and the length was 7.2 m. Each floor panel was consisted of glued laminated beams, joists and floor of 25mm. The first one, referred to herein as PAN\_Fl, consisted of two (2) beams, thirteen (13) joists and the floor, while the second one, referred to herein as PAN\_Fl\_struts, was like the previous one but with struts (Figure 1). The design of these floor panels meted the requirement of Part 1-1 of Eurocode 5 [2]. The material of the main parts of the floor panels was categorized in the class GL32h.

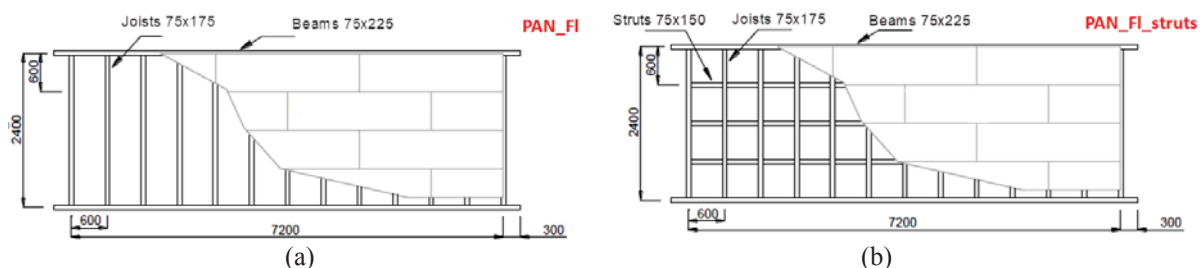


Figure 1: Geometric configuration of: (a) PAN\_Fl, (b) PAN\_Fl\_struts (values in mm).

### 3 VALIDATION OF FEM FOR FLOOR PANELS IN STATIC ANALYSIS

The FE method is a widely employed approach to develop numerical prediction models in construction industry and more and more researchers are used it [7-9]. By performing numerical simulations, experimental acoustical tests can be reduced, and parametric studies can also be carried out to investigate the influence of specific geometrical changes in construction as well as the influence of the variations/uncertainties in material properties, which always have a mark able influence on the results [10-12].

The FE analysis calibration study included analytical modelling of the two panels. Elastoplastic orthotropic material models were used with non-linear hardening associated with material densification. Table 1 summarises the details of the material properties.

Table 1: Main material parameters.

Quality	$E_1$ (MPa)	$E_2$ (MPa)	$E_3$ (MPa)	$f_{m,k}$ (MPa)	$\nu_{12}$	$\nu_{13}$	$\nu_{23}$	$\rho$ (kg/m <sup>3</sup> )
GL32h	13500	450	450	32.5	0.35	0.35	0.09	420

The 3D FEM model geometry reproduced the actual geometry of the experiments, as well as the simulation used the same boundary conditions and loading as in the experimental program (see Figure 1 and 2).

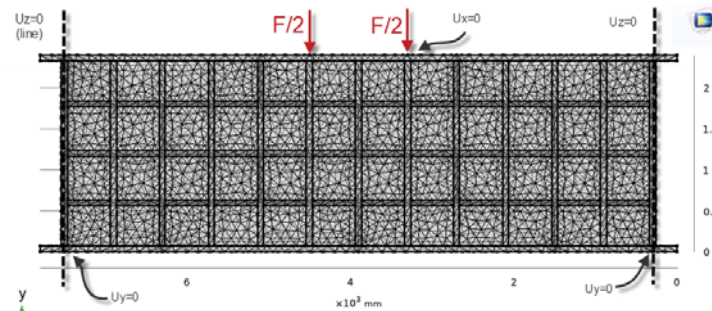


Figure 2: Configuration of floor panels PAN\_Fl\_struts.

Alternative finite element models were conducted to identify the best meshing. It is known that a finer mesh density provides higher accuracy but also increases the computational time without improving substantially the accuracy of the results, therefore, a tradeoff between time and accuracy becomes crucial. In our model tetrahedral solid elements were used with high level of optimization in order to avoid inverted curved elements, too large or too small elements. In total 16335 elements were used for the PAN\_Fl and 21954 for the PAN\_Fl\_struts.

In this section, static analyses have been performed with increasing load until the failure of the panels. The nonlinear solver uses an affine invariant form of the damped Newton method. The numerical results were compared with the experimental ones and the validation of the model was based on: (i) the force-displacement curves, and (ii) the deformation shape of the bottom beam during different loads, for the both floor panels.

Figures 3 and 4 compare the experimental and the numerical results of the panels PAN\_Fl and PAN\_Fl\_struts respectively. Part (a) presents the force – displacement curves at the middle of the panel, part (b) illustrates the shape of the deflection along the bottom beam of each panel, while part (c) shows the deformation shape of each panel for a selected force (45kN for the panel PAN\_Fl and 65kN for the panel PAN\_Fl\_struts). It is important to notice that in the Figures 3c and 4c the panels are illustrated without the floors in order to verify the shape of the beams and the joists. As it is shown, the numerical monotonic curve follows the envelope



of the experimental response. Therefore, the numerical loading curve can be reliably used to assess the stiffness and strength of the investigated panels and the proposed FE model in order to establish the individual and combined effects of various parameters on the response of the panels and, in so doing, to identify the significance of the numerical contribution to produce results that are harder to obtain experimentally.

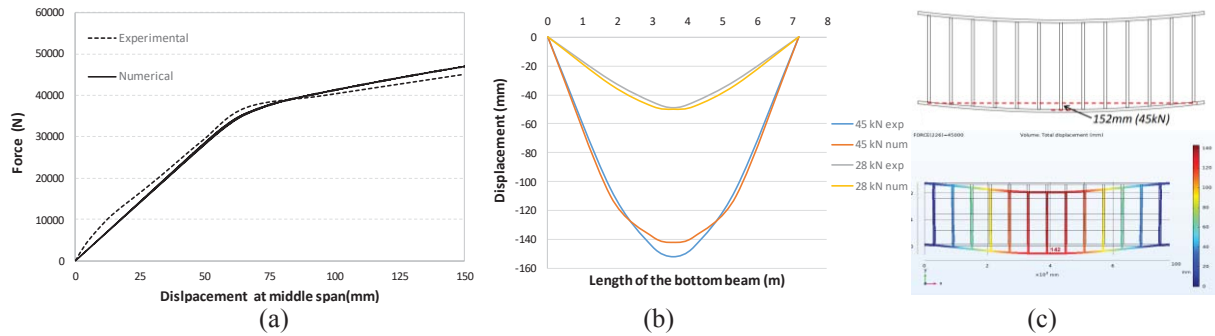


Figure 3: Comparison of experimental and numerical results for the panel PAN\_Fl.

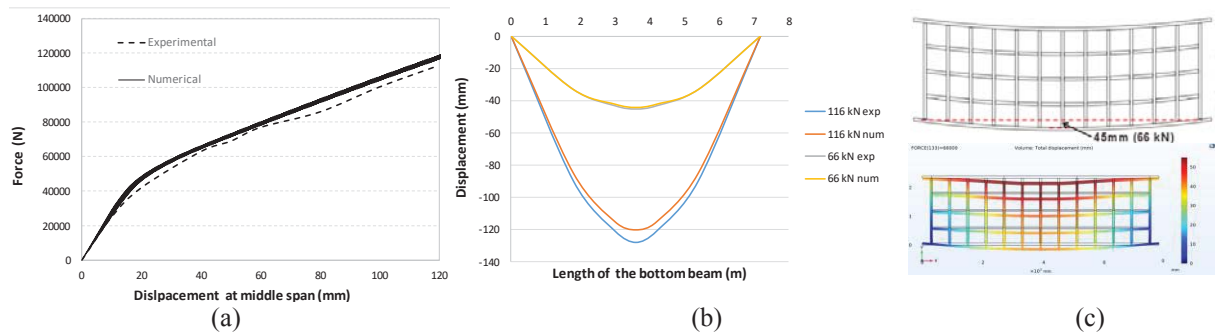


Figure 4: Comparison of experimental and numerical results for the panel PAN\_Fl\_struts.

#### 4 DYNAMIC ANALYSIS

The aim of this section is to use the proposed FE model in order to investigate the dynamic response of these panels in different vibration loading. A dynamic analysis of a structure differs from a corresponding static analysis mainly in two ways. While a static analysis assumes that a structure is in complete equilibrium with its surroundings a dynamic analysis takes into consideration the structure's true response when subjected to a force. Furthermore, a static analysis treats the loads as static, which means that they varies sufficiently slowly with time. On the other hand, there are a lot of loads that in fact are dynamic, that is, they varies rather quickly with time [13]. Vibrations may be described as oscillations around the statically equilibrium of a structure [14]. Vibrations arise when time-varying disturbances, either forces or displacements, interact with the inertia properties of an affected medium. The dynamic response of a structural system is affected by the material properties, the damping, the properties of the system as whole, and the presence of non-structural elements, such as floor coverings, ceilings etc [15].

Damping is the most important parameter which significantly influences the response of occupants to floor vibrations even though it hardly affects the fundamental frequency  $f_i$ . This is because damping is an intrinsic property of structural systems that influences oscillation amplitudes and the rate of decay under forced and free vibrations, respectively [16]. Previous research has shown that the timber floors constructed with engineered I-joists had a damping ratio  $\zeta = 2 - 4\%$  [17] while the floors with metal-webbed joists only had a very low damping

ratio  $\zeta = 0.86\%$  which is below  $1\%$  [18]. This indicates that the design damping ratio  $\zeta = 1\%$  proposed in EN 1995-1-1 [2] may not cover all timber floor types so an average damping ratio  $\zeta = 2\%$  is proposed in order to cover most practical cases [19].

#### 4.1 Case study

In this study the two panels of PAN\_Fl and PAN\_Fl\_struts were analysed under a walking loading time history of one person 75kg in the middle of each panel (on the spot) with a total duration of 2.6 sec. In this study only the effects of a damping ration were presented. Figure 5 describes the investigated panels with the details of boundary conditions, load time histories, while Table 2 summarizes the investigated cases. The beams of the panels are the part that is being connected with the columns of the structures. The stiffness of these connections can varies as it depends on the type of the connection as Titirla et al have been presented [20-23], but in this study only the case of a rigid connection was presented.

Each harmonic of the loading function can cause resonance with a natural frequency of the floor, and it is the walking pace frequency that gives the worst-case response that should be used for design. The pace frequency ( $f_p$ ) for walking has a mean value of 2.0 Hz. The standard walking load of a person can then be described as a series of consecutive steps, where each step is given by a polynomial function which is proposed by Harpel et al. [24].

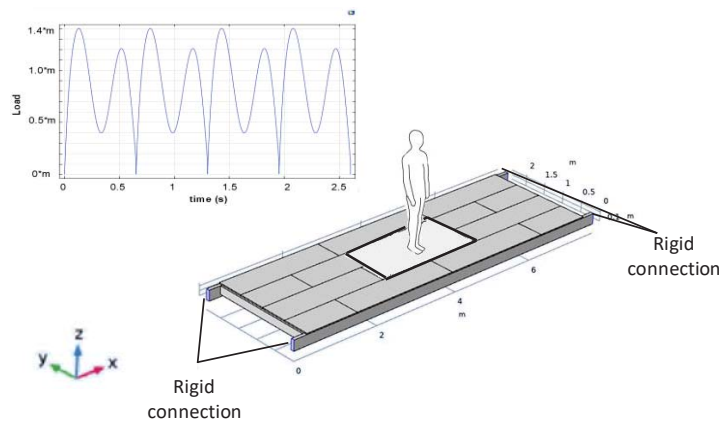


Figure5: Walking time history and boundary condition of the panels.

Table 2: Description of the case studies.

Panel	Boundary conditions	Damping	Name
PAN_Fl	Rigid	0%	PAN_Fl
PAN_Fl	Rigid	1%	PAN_Fl_d
PAN_Fl_struts	Rigid	0%	PAN_Fl_struts
PAN_Fl_struts	Rigid	1%	PAN_Fl_struts_d

#### 4.2 Comparison of the results

In the present numerical study a damping ratio equal to  $1\%$  was selected, according to EN 1995-1-1 [2]. The comparison of the results, given in Figure 5, shows that the maximum vertical displacement was reduced  $1.4\%$  for the PAN\_Fl and  $0.5\%$  for the PAN\_Fl\_struts according to damping, while the maximum acceleration in the middle of the span was reduced equal to  $10\%$  and  $2.5\%$  respectively. It can be observed that each transient vibration signal contains a high initial peak and decays. The peak values of a transient vibration are governed by system stiffness and mass, but not by damping. Damping is a measure of how quickly the

response of vibrating system decay after the loading period; as a result the effects of the damping during the walking loading of 2.6sec were not as much remarkable.

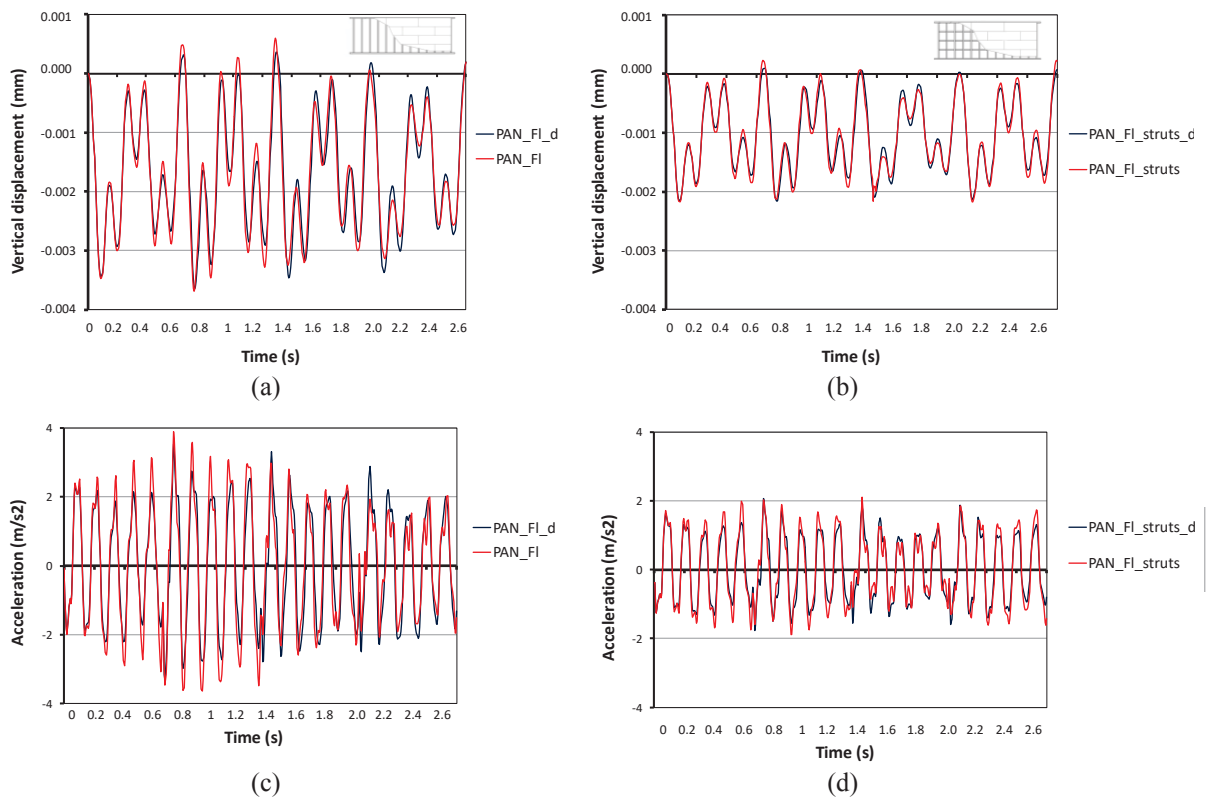


Figure 5: Time histories of (a) the vertical displ. at the middle of the panel PAN\_Fl, (b) the vertical displ. at the middle of the panel PAN\_Fl\_struts, (c) the acceleration at the middle of the panel PAN\_Fl, (d) the acceleration at the middle of the panel PAN\_Fl\_struts.

## 5 VIBROACOUSTIC

Structures when subjected to time varying loads will vibrate and generate acoustic waves. The characteristics of the acoustic waves generated by the structure may depend on the vibration behavior of the structure, which in turn depends on different factors such as the properties of structural materials, types of loads, location of load application, structural configuration, boundary conditions, etc. The determination of the true vibro-acoustic characteristics of a structure is essential for the correct prediction of the actual vibration and sound radiation behaviors of the structure. Therefore, because of its importance, the vibro-acoustic characterization of structures has drawn close attention and a lot of researchers are working in this field [25-27].

The aim of this session is to study the influence of the two configurations (PAN\_Fl and PAN\_Fl\_struts) on the impact sound transmission of a floor. For this reason the previous panels with the rigid connections were investigated; but this time the analyses were focused on the frequency domain. The Acoustics interface uses the Pressure Acoustics, Frequency Domain module to solve the governing wave equation that is complemented with sound sources as boundary condition. The speed of the sound in the air equal to 343 m/s and the density of 1.2 kg/m³ were taken into account in this study.

The radiated sound power level for the reference case is shown in Figure 7. The large amplitude peaks observed in the frequency response make it possible to identify the critical resonance frequencies to be avoided.

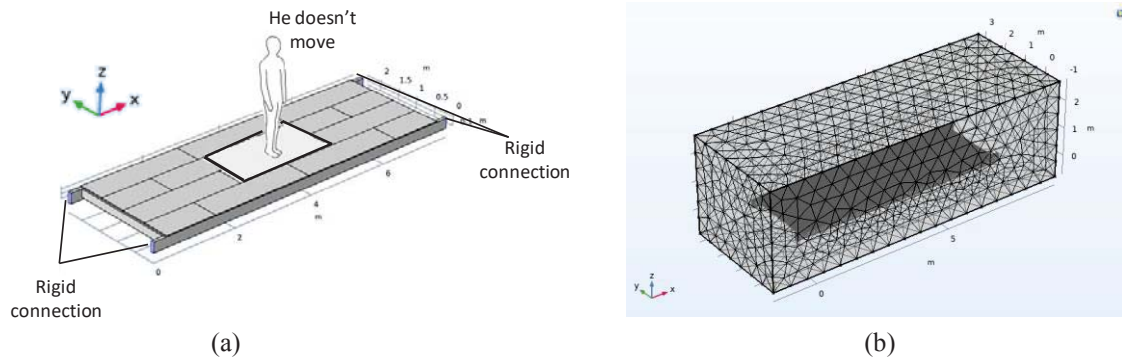


Figure6: (a) the model with the additional mass and the boundary conditions, (b) the mesh for the floor elements and the air.

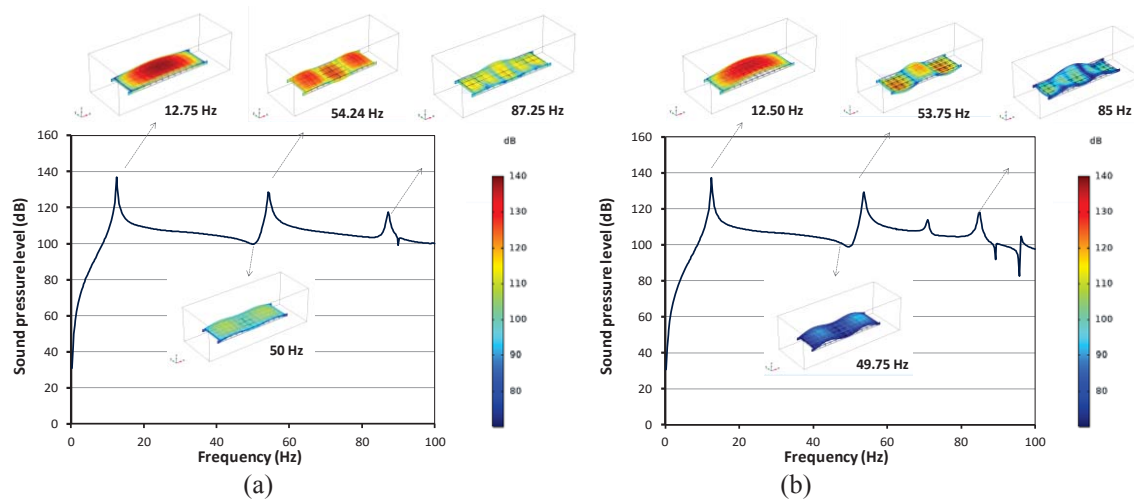


Figure 7: The radiated sound power level of the plate surface for the panel (a) PAN\_Fl and (b) PAN\_Fl\_struts.

## 6 CONCLUSIONS

In the present work attention is focused on the dynamic and vibroacoustic response of timber floor panels as well as the study of the effect of the damping ration. In this study the two panels of PAN\_Fl and PAN\_Fl\_struts were analysed in static and dynamic analyses. Based on the findings of this study new conclusions are drawn :

- The validation of the numerical simulation is based on the envelope experimental behavior of the two difference floor panel. The response of the panel PAN\_Fl was used to build the numerical model while the response of the panel PAN\_Fl\_struts was used to validate the previous model.
- The success of the deployed numerical simulation is fully demonstrated by comparing the shape of the load–displacement curves with the experimental ones. Therefore, it is a reliable tool for the simulation of the hysteretic behavior of these timber floor panels and can be used in further studies.
- The peak values of a transient vibration are governed by system stiffness and mass, but not by damping. Damping is a measure of how quickly the response of vibrating system decay after the loading period; as a result the effects of the damping during the walking

loading of 2.6 sec were not as much remarkable. The comparison of the results shows that the maximum vertical displacement was reduced 1.4 % for the PAN\_Fl and 0.5% for the PAN\_Fl\_struts according to damping, while the maximum acceleration in the middle of the span was reduced equal to 10 % and 2.5% respectively.

- iv. The analysis of the vibroacoustic response of the system made it possible to identify the most radiant resonance frequencies.

## REFERENCES

- [1] S. Fuentes, E. Fournely & A. Bouchaïr, Experimental study of the in-plan stiffness of timber floor diaphragms. *European Journal of Environmental and Civil Engineering*, **18**:10, 1106-1117, 2014.
- [2] CEN. 2004. EN 1995-1-1:2004, Eurocode 5: design of timber structures. Part 1–1: general common rules and rules for buildings. *European Committee for Standardization*, Brussel, Belgium.
- [3] H. Bachmann, and W. Ammann, Vibrations in structures induced by man and mechanics. IABSE – AIPC – IVBH, Switzerland, 1987.
- [4] M.S. Williams, and P. Waldron, Evaluation of methods for predicting occupant induced vibrations in concrete floors. *The Structural Engineer*, **72**(20), 334-340, 1994.
- [5] J.G.S. Da Silva, P.C.G. Da S. Vellasco, de Andrade, F.J.C.P. da Soeiro, and R.N Werneck, An evaluation of the dynamical performance of composite slab. *Computers and Structures*, **81**, (18-19), 1905-1913, 2003.
- [6] A. Ebrahimpour, and R.L. Sack, A review of vibration serviceability criteria for floor structures. *Computers and Structures*, **83**, 2488-2494, 2005.
- [7] W. Larbi, Numerical modeling of sound and vibration reduction using viscoelastic materials and shunted piezoelectric patches. *Computers & Structures*, **232**, 105822, 2020.
- [8] M. Titirla, P. Papadopoulos, I. Doudoumis, Finite Element modelling of an innovative passive energy dissipation device for seismic hazard mitigation. *Engineering Structures*, **168**, 218-228, 2018.
- [9] W. Larbi, L. Pereira da Silva, J.-F. Deü, An efficient FE approach for attenuation of acoustic radiation of thin structures by using passive shunted piezoelectric systems. *Applied Acoustics*, **128**, 3-13, 2017.
- [10] M. Titirla, K. Katakalo, Evaluation of an innovative passive mitigation device through experimental and numerical investigation. *COMPADYN 2017, 6th ECCOMAS Thematic Conference on Computational Methods in Structural Dynamics and Earthquake Engineering*, Rhodes Island, Greece; 06/2017.
- [11] W. Larbi, J.-F. Deü, R. Ohayon, Finite element formulation of smart piezoelectric composite plates coupled with acoustic fluid. *Composite Structures*, **94** (2), 501-509, 2012.
- [12] M.D, Titirla, P.Papadopoulos, Finite Element investigation of a new seismic energy absorption device. *COMPADYN 2015, 5th ECCOMAS Thematic Conference on Computational Methods in Structural Dynamics and Earthquake Engineering*, Crete Island, Greece; 05/2015.
- [13] R.R. Craig, A.J. Kurdila, Fundamentals of Structural Dynamics, 2nd Edition, Wiley, ISBN 978-0-471-43044-5, 2006.
- [14] A.K. Chopra, Dynamics of structures - Theory and Applications to Earthquake Engineering, Prentice Hall - Pearson Highered, 2012.



- [15] ISO 10137 Bases for design of structures - Serviceability of buildings and walkways against vibrations, Second edition, International Organization for Standardization, 2007.
- [16] L.J. Hu, Y.H. Chui, D.M. Onysko, Vibration serviceability of timber floors in residential construction. *Prog. Struct. Eng. Mater.* **3**, 228–237, 2001.
- [17] J. Weckendorf, B. Zhang, A. Kermani, D. Reid, Damping characteristics of timber flooring systems. *The 10th world conference on timber engineering (WCTE10)*, Miyazaki, Japan; June 2008.
- [18] B. Zhang, J. Weckendorf, A. Kermani, Vibrational performance of metal-webbed timber floors. *The 11th world conference on timber engineering (WCTE-11)*, Riva del Garda, Trentino, Italy; June 2010.
- [19] British Standards Institution. UK NA to BS EN 1995-1-1:2004+A1:2008 UK National Annex to Eurocode 5: Design of timber structures – Part 1-1: General – Common rules and rules for buildings; 2009.
- [20] M. Titirla, E. Ferrier, L. Michel, On the mechanical behaviour of innovative moment connections between composite floor panels and glulam columns, *International Journal of Architectural Heritage - Conservation, Analysis, and Restoration*, 2020 doi.org/10.1080/15583058.2020.1836529.
- [21] M. Titirla, L. Michel, E. Ferrier, Mechanical behaviour of glued-in rods (carbon and glass fibre-reinforced polymers) for timber structures — An analytical and experimental study, *Composite Structures*, **208**, 70-77, 2019.
- [22] M. Titirla, L. Michel, E. Ferrier, Mechanical behavior of hybrid floor panels to timber columns joints, *9th International Conference on Fibre-Reinforced Polymer (FRP) Composites in Civil Engineering (CICE 2018)*, Paris, France, 17-19 July 2018.
- [23] M. Titirla, L. Michel, E. Ferrier, Innovative connections between hybrid floor panels and timber columns able to reduce the deflection of the panels big span. *COMPDYN 2019, 7th ECCOMAS Thematic Conference on Computational Methods in Structural Dynamics and Earthquake Engineering*, Crete Island, Greece; 24-26 June 2019.
- [24] FC Harper, WJ Warlow, BL Clarke, The forces applied to the floor by the foot in walking. *Wear* **4**(6):495–497, 1961.
- [25] W. Larbi, J.-F. Deü, R. Ohayon, Vibroacoustic analysis of double-wall sandwich panels with viscoelastic core, *Computers & Structures*, **174**, 92-103, 2016.
- [26] W. Larbi, J.-F. Deü, M. Ciminello, R. Ohayon, Structural-acoustic vibration reduction using switched shunt piezoelectric patches: A finite element analysis, *Journal of Vibration and Acoustics*, **132** (5), 051006, 2010
- [27] N. Reboul, C Grazide, N. Roy, E. Ferrier, Acoustic emission monitoring of reinforced concrete wall-slab connections, *Construction and Building Materials*, **259**, 2020.



## THE USE OF INTELLIGENT FACADES FOR UPGRADING ENERGY AND SEISMIC DEMANDS OF EXISTING R/C STRUCTURE

Lazaros Melidis<sup>1</sup>, Efthymios A. Kechagias<sup>1</sup>, Konstantinos Katakalos<sup>1</sup>, George C. Manos<sup>1</sup>

<sup>1</sup> Aristotle University of Thessaloniki  
Laboratory of Experimental Strength of Materials and Structures, Thessaloniki, 54124  
e-mail: {lazmelidis; ekechagi; kkatakalo; gcmmanos}@civil.auth.gr <https://strength.civil.auth.gr>

---

### Abstract

*The installation of exterior facades made of metal elements in buildings is a dual function application: On one hand it alters the facade, through architectural modifications, and on the other it creates the conditions for the improvement of energy efficiency of the building, utilizing the gap that develops between old and new facade. In order to ensure that the suspension and anchoring system can safely receive both static and dynamic loads, which will strain the construction during its life cycle, it is necessary to carry out a set of controls that will ensure exactly this: the static and anti-seismic adequacy of the used suspension and anchoring system. For this reason, a building consisting of frames was chosen, on the perimeter of which masonry was placed and, then, the metal facades were hung on the masonry, through the use of appropriate joints. Through Dynamic Spectral Analysis and Time History Analysis, the adequacy or not of the suspension system was examined, but also the effects that the system had on the modal, strain and deformation sizes of the building. In the end, it was concluded that the attachment of elements to the facade of the building, although it is done for architectural or other purposes, brings about significant changes in its seismic response and, therefore, must be adequately studied.*

**Keywords:** Metal facades, Metal links, Structural Dynamics, Earthquake Engineering, Assessment of dynamic characteristics, Ventilated facade.

---

## 1 INTRODUCTION

### 1.1 Ventilated facades

In modern times, architectural design invests heavily in facade cladding, considering them often part of the original design of the building but also an appropriate solution in cases of reconstruction or renovation of exterior facades and siding. In addition, facade cladding panels are used as partial interventions in facades, in balcony cladding, fencing or the creation of awnings and blinds. There is a plethora of materials that can be used in facade cladding! Examples include titanium zinc, copper, aluminum, bakelites, HPL (High Pressure Laminates) panels, ceramic tiles and colored fiber reinforced cement boards. A ventilated facade is a construction method whereby a physical separation is created between the outside of the facade and the interior wall of the building. This separation creates an open cavity allowing the exchange of the air contained between the wall and the outer cladding.



Figure 1: Titanium zinc facade.



Figure 2: Copper facade.



Figure 3: Ceramic tiles facade.



Figure 4: Colored fiber reinforced cement boards facade.

### 1.2 Fixing brackets

To support the facade, a suspension system or fixing brackets system is required. In order for the system in use to be deemed as sufficient, it must first be examined whether the fixing bracket can safely receive the required loads (axial and shear) and then whether it can safely transfer them to the concrete frame and/or masonry infill. Thus, at first, the strength of the fixing bracket is examined, based on the requirements arising from the analysis model and depending on the specifications set by the bracket's manufacturer. It is then checked whether these requirements are covered by the capacities set by the regulations, in this case KAN.EPE.

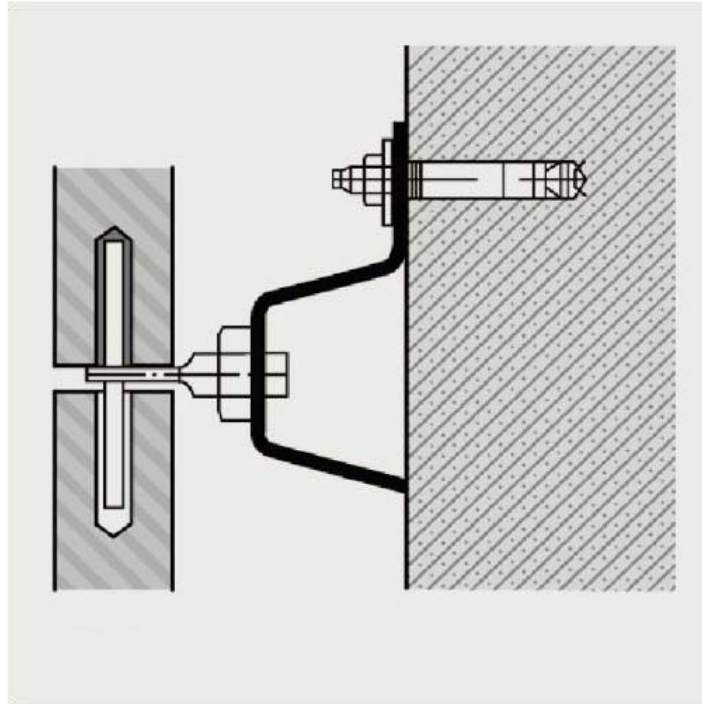


Figure 5: Fixing bracket.

## 2 BUILDING GEOMETRY AND CHARACTERISTICS

The external dimensions of the building are 22.20x22.20 m. In the direction of the X-axis there are 6 frames, with a net opening of 17.00 m and a distance of 3.50 m between them. The columns have dimensions 1.10x0.30 m, with the large dimension parallel to the X-axis. The class of the concrete used was evaluated, in current terms, in category C20 / 25 and the reinforcement steel in S135 / 150 [1]. The building has previously been deemed in need of seismic reinforcement [1].

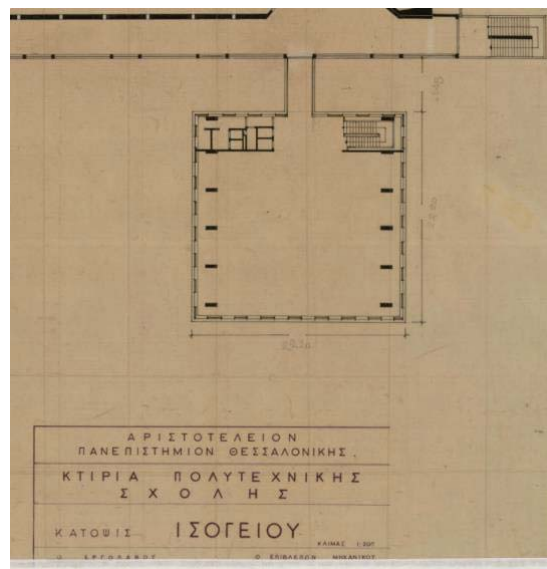


Figure 6: Ground floor plan.

### 3 ANALYSIS

#### 3.1 Analysis Methods

To assess the dynamic characteristics of the building, the Dynamic Spectral Analysis was applied in a fully elastic model, in order to evaluate the adequacy of the support joints and the anchoring system. Furthermore, a Dynamic Time History Analysis was performed on an elastic-partially plastic, non-linear model, in which the joints would yield if they exceeded a certain limit, in order to better analyze the response of the structure in an earthquake scenario.

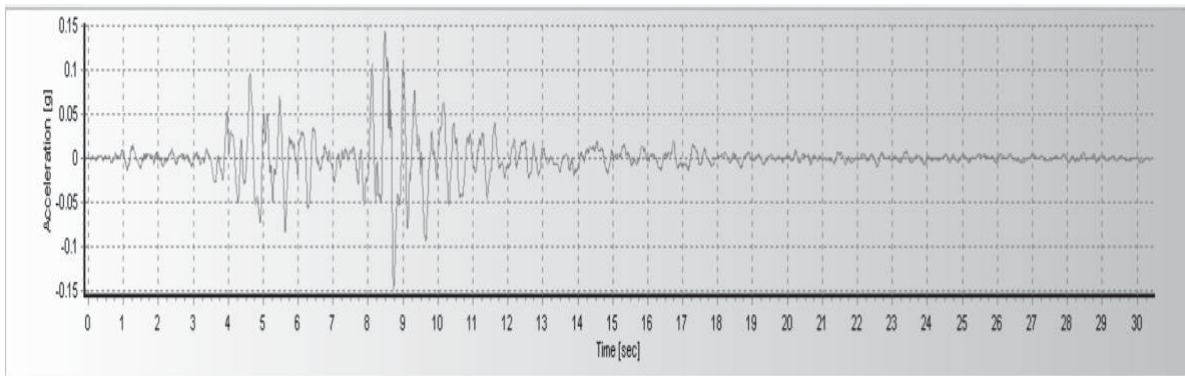


Figure 7: Accelerometer of the Thessaloniki earthquake of 1978.

The E.C. 8 [2] spectrum was used for the Dynamic Spectral Analysis as well as the spectrum obtained from the accelerometer of the 1978 Thessaloniki earthquake. The accelerometer of the Thessaloniki earthquake of 1978 was used for the Dynamic Time History Analysis. The area of Thessaloniki is categorized as ground type B, where  $a_g = 0.16g$ . The accelerometer was obtained from a ground type D area and therefore had to be properly adjusted to ground category B, in order to be compatible with the soil conditions present at the building site. Below, a graph showcasing the acceleration expressed in g in regard to the oscillation period is depicted, for the spectrum of E.C. 8 in ground category B, as well as the spectrum obtained from the accelerometer for ground category D and ground category B.

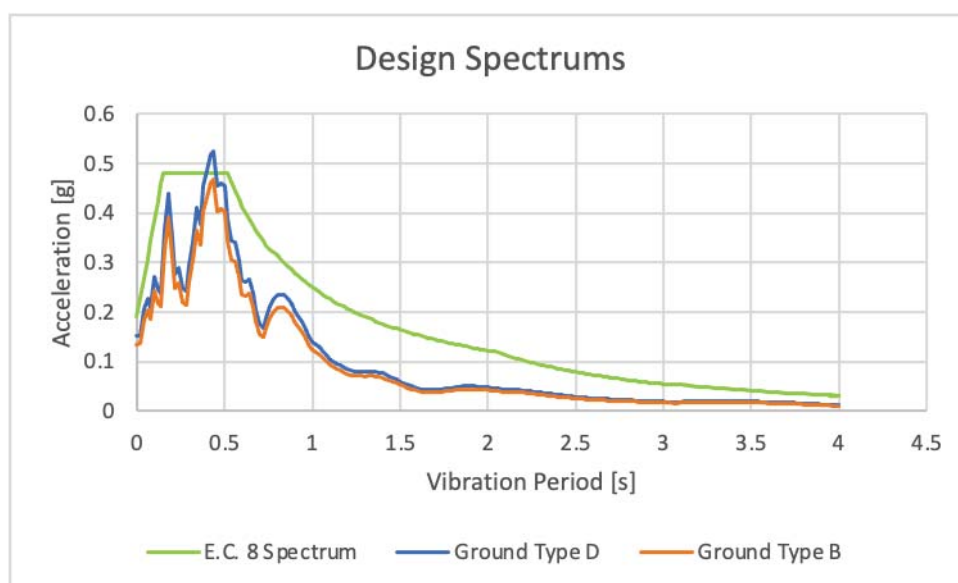


Figure 8: Design Spectrums used in analysis.



### 3.2 Analysis Models

Three analysis models were used:

- The first model consisted mainly of linear elements, beams and columns, which simulates the current state of the building.
- In the second model, a perimeter of filling masonry was added, in order for the metal facades to be added in a later state, which was also the reference model for the comparisons made.
- In the third model the metal facades were added and comparisons were made.

The analyzes were performed with the help of SAP2000.

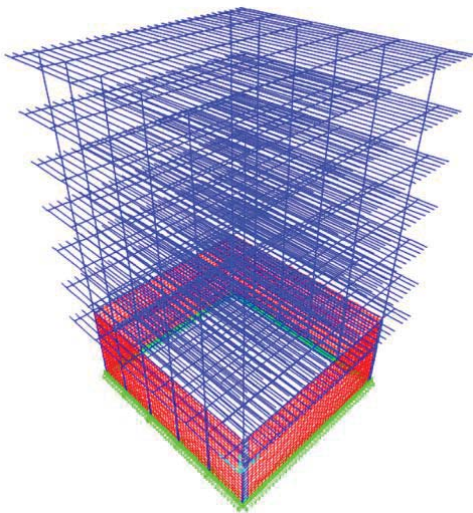


Figure 9: Basic linear model.

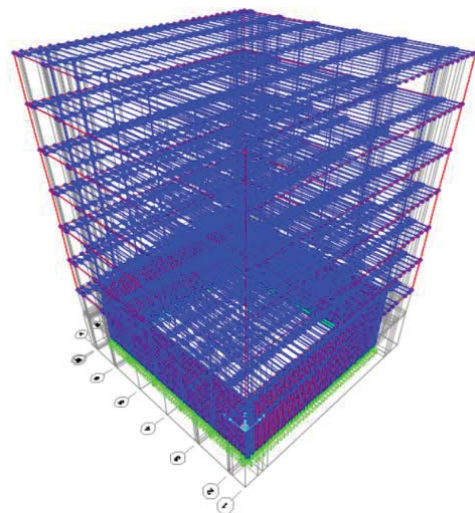


Figure 10: Masonry infilled model.

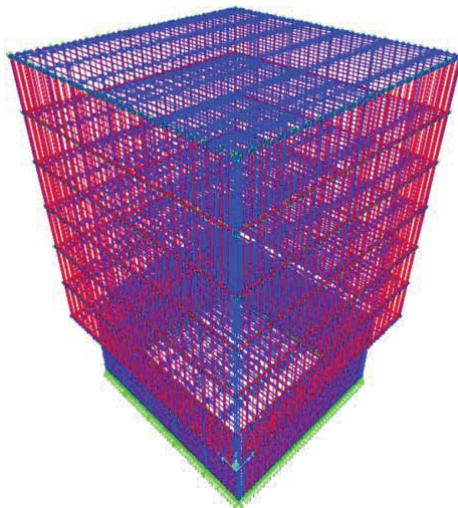


Figure 11: Metal facade model.

### 3.3 Vibration Periods

A sufficient number of eigenmodes was used for each scenario during the analysis. For the first case 6 eigenmodes were used, which activated 60 % of the oscillating mass. For the second case 9 eigenmodes were used, which activated 60% of the oscillating mass. For the third case, significantly more eigenmodes were needed, a total of 30, due to the excessive

number of elements added by the exterior facades. The activated mass in this case amounted to 55 % of the oscillating mass. Appropriate multiplying factors were used in the Dynamic Spectral Analysis, according to the specifications of E.C. 8 to accommodate the activated oscillating mass.

Eigenmode	Vibrating Period [s]		
	Without masonry	With masonry	With facades
<b>1</b>	2.179	0.717	0.453
<b>2</b>	2.136	0.687	0.423
<b>3</b>	1.634	0.285	0.391
<b>4</b>	0.689	0.177	0.390
<b>5</b>	0.591	0.168	0.383
<b>6</b>	0.494	0.161	0.376
<b>7</b>	-	0.112	0.376
<b>8</b>	-	0.111	0.374
<b>9</b>	-	0.097	0.370
<b>20</b>	-	-	0.244
<b>30</b>	-	-	0.171

Table 1: Vibrating Periods for analysis scenarios.

It is worth noting that the first model is very flexible, which leads to high vibrating periods and low spectral accelerations. The addition of masonry infill leads to a significant reduction of the vibrating period. Furthermore, the addition of metal facades makes the building even more rigid and leads to the development of maximum spectral accelerations, according to E.C. 8.

## 4 ANALYSIS RESULTS

### 4.1 Base shear

For each scenario, the base shear was calculated in both directions, as the base reaction from the analysis.

Case	Base Reaction [kN]		
	Without masonry	With masonry	With facades
<b>E.C.8-X</b>	5128	13969	24625
<b>E.C.8-Y</b>	5524	14740	21857
<b>Thess-X</b>	3117	8861	27597
<b>Thess-Y</b>	2744	9703	21221

Table 2: Base reactions for analysis scenarios.

With the addition of the masonry infill the base reaction almost triples. The addition of the metal facades further doubles the base reaction, in the case of E.C. 8, and triples it in the Thessaloniki 1978 scenario.

### 4.2 Reference column strain

In order to assess the influence that the metal facade has on the seismic response of the building, a corner column was used as a reference point. The axial, shear and moment that was calculated in each scenario was compared, at the level of each floor.



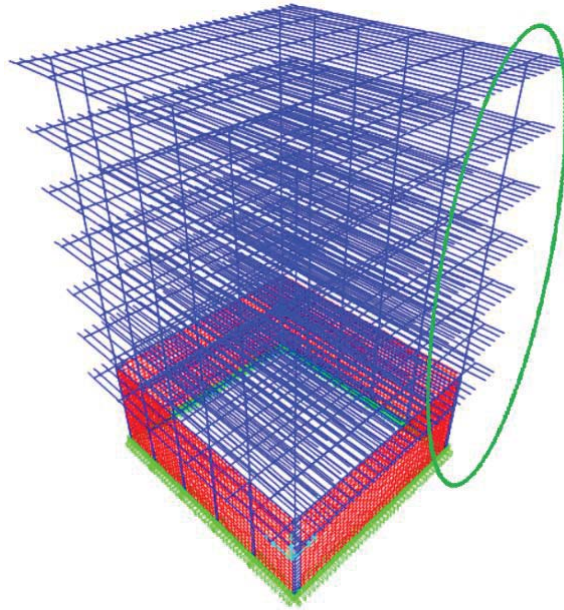


Figure 12: Metal facade model.

The addition of masonry infill multiplied the axial load by an average factor of 6, while the shear and moment loads dropped by 50 % in average. This was due to the redistribution of strain to the intermediate columns.

The addition of the metal facades had almost no effect to the axial load, but it increased the shear and moment loads by 35 % in average.

#### 4.3 Reference column top displacement

The top displacement for the first model was relatively high, mainly due to the low stiffness of the building. The second model, although with a higher base shear, developed a lesser top displacement, due to the increased stiffness offered by the masonry infill. The third model had slightly increased top displacement, due to the higher base shear and the fact that the facades did not contribute significantly to the stiffness of the model.

Case	Top displacement [cm]		
	Without masonry	With masonry	With facades
<b>E.C.8-X</b>	17.8	8.7	7.0
<b>E.C.8-Y</b>	15.6	8.4	7.0
<b>Thess-X</b>	14.5	5.1	7.8
<b>Thess-Y</b>	12.4	5.3	6.8

Table 3: Top displacements for analysis scenarios.

## 5 ASSESSMENT OF BEARING CAPACITY

### 5.1 Fixing brackets

The manufacturer's strengths were taken for the assessment of bearing capacity and were compared with the results of the analysis. For a 2 mm displacement, the bracket was considered to have failed.

Code	Type	Size(mm)	Support	Loading direction	Loadbearing capacity	
					At elastic behavior of material (without residual displacement)	At displacement 2 mm
ET710001.00 (07varioQ172)	double	62/40/160	fixed	vertical	6,40 kN	14,45 kN
ET710002.00 (07varioQ82)	double	62/75/160	fixed	horizontal	6,07 kN	10,86 kN
ET710002.00 (07varioQ82)	double	62/75/160	movable	horizontal	5,04 kN	10,95 kN
ET710002.00 (07varioQ82)	double	62/75/160	fixed	vertical	6,04 kN	10,33 kN
ET710003.00 (07varioQ102)	double	60/100/160	fixed	vertical	4,65 kN	7,03 kN
ET710003.00 (07varioQ102)	double	60/100/160	fixed	horizontal	1,45 kN	6,38 kN
ET710005.00 (07varioQ152)	double	60/150/160	fixed	vertical	3,67 kN	5,03 kN
ET710004.00 (07varioQ172)	double	60/125/160	fixed	vertical	3,42 kN	6,67 kN
ET710004.00 (07varioQ172)	double	60/125/160	fixed	horizontal	5,17 kN	10,93 kN
ET710004.00 (07varioQ172)	double	60/125/160	movable	horizontal	7,15 kN	10,15 kN
ET710014.00 (07varioQ18)	single	60/180/90	fixed	vertical	0,38 kN	0,46 kN
ET710006.00 (07varioQ182)	double	60/180/160	fixed	vertical	2,40 kN	3,32 kN
ET710015.00 (07varioQ21)	single	60/210/90	fixed	vertical	0,36 kN	0,41 kN

Figure 13: Fixing brackets' loadbearing capacities.

Case	Axial		Shear	
	Yields	Failures	Yields	Failures
E.C.8-X	30	0	88	0
E.C.8-Y	48	0	10	0
Thess-X	31	0	90	0
Thess-Y	50	0	5	0

Table 4: Number of brackets yield and failed.

In total, 644 elements were examined. In the worst scenario, 90 of them surpassed the yield limit and none failed.

## 5.2 Anchorage system

The ultimate force under tension the anchor can bear is calculated [3]:

$$N_{ud} = \pi \cdot d \cdot l_b \cdot f_{bd} \quad (1)$$

Where  $N_{ud}$  is the ultimate force under tension the anchor can bear,  $d$  the diameter of the anchorage,  $l_b$  the anchorage length and  $f_{bd}$  the tensile strength of the material anchorage takes place.

The ultimate force under shear the anchor can bear is calculated [3]:

$$F_{ud} = 0.65 \cdot d^2 \cdot \sqrt{f_{cd} \cdot f_{yd}} \quad (2)$$

Where  $F_{ud}$  is the ultimate force under shear the anchor can bear,  $d$  the diameter of the anchorage,  $f_{cd}$  is the compressive strength of the material anchorage takes place, in this case masonry, and  $f_{yd}$  is the steel tensile strength.

For the interaction of the two phenomena the formula used is [3]:

$$\left(\frac{N_{sd}}{N_{ud}}\right)^{3/2} + \left(\frac{F_{sd}}{F_{ud}}\right)^{3/2} = 1 \quad (3)$$

Where  $N_{sd}$  is the axial load from the analysis,  $N_{ud}$  is the ultimate force under tension the anchor can bear, as calculated above,  $F_{sd}$  is the shear force from the analysis and  $F_{ud}$  is the ultimate force under shear the anchor can bear, as calculated above.

All anchorages were deemed sufficient, with the maximum ratio of demand to capacity being  $\eta_{max}=77.4\%$ .

## 6 DYNAMIC TIME HISTORY ANALYSIS

For the Dynamic Time History Analysis, the accelerometer from the earthquake of Thessaloniki of 1978 was used as a ultimate limit scenario and 60% of it as a serviceability limit scenario, according to KAN.EPE. The links were assigned non-linear properties. Three scenarios were designed, earthquake by the X-axis, earthquake by Y-axis and their SRSS directional combination. Approximately 20 % of the elements surpassed their yield limit during the SRSS directional combination of the ultimate limit scenario. None failed. For the serviceability limit scenario 4 % of the elements surpassed their yield limit during the SRSS directional combination. None failed. In both cases, the brackets used were deemed sufficient.

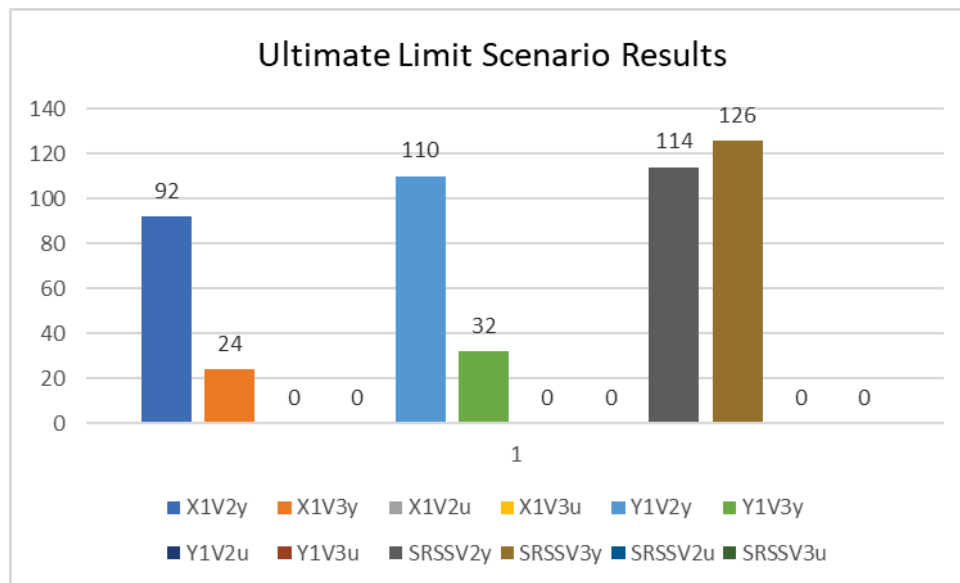


Figure 14: Ultimate Limit Scenario Results.

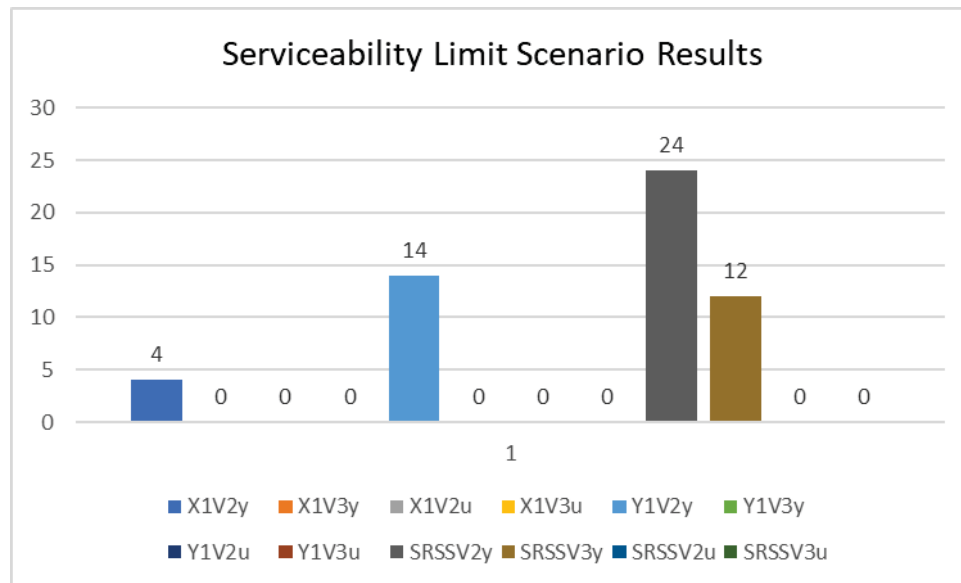


Figure 15: Serviceability Limit Scenario Results.

## 7 CONCLUSION

- The addition of masonry infilled increases the building's stiffness.
- Exterior facades further increase, to a lesser extent, the building's stiffness, the strain developed at the building's frames and its top displacement.
- Retrofitting may be needed in some cases.
- The links used were deemed sufficient.

## ACKNOWLEDGMENTS

Part of the aforementioned research "Intelligent Facades for Nearly Zero Energy Buildings (IF – ZEB)" has been co-funded by Greece and European Union through the Operational Program "Erevno - Dimiourgo - Kainotomo" (project code: T1EDK-02045) which are gratefully acknowledged.

## REFERENCES

- [1] I. Avramidis, *Αντισεισμική ενίσχυση του κτιρίου Αγρονόμων και Τοπογράφων Μηχανικών της Πολυτεχνικής Σχολής του Α.Π.Θ., 4<sup>th</sup> International Colloquium on Computation of Shell and Spatial Structures (IASS-IACM 2000)*, Chania, Crete, Greece, June 4-7, 2000.

- [2] Manos, G.C., Melidis, L., Katakalos, K., Kotoulas, L., Anastasiadis, A., Chatziastrou, C., “Masonry panels with external thermal insulation subjected to in-plane diagonal compression”, *Case Studies in Construction Materials*, Volume 14, June 2021, Article number e00538
- [3] G.C.Manos, K.Katakalos, L.Melidis, A.Anastasiadis, “The behaviour of masonry infills with thermal insulation facades under out of plane seismic type loads (in Greek), 4th Panhellenic Conference on Earthquake Engineering and Technical Seismology (2019).
- [4] C. Manos, L. Melidis, K. Katakalos, V. Soulis, A. Anastasiadis, Unreinforced masonry with thermal insulation facades in multi-story buildings subjected to seismic type loads, The 17th World Conference on Earthquake Engineering (2020).
- [5] P. Antoniadou, M. Symeonidou, E. Kyriaki, E. Giama, S.N. Boemi, S. Chadiarakou, A.M. Papadopoulos, High performance building Facades for Zero Energy Buildings in Greece: state of the art and perspectives, *IOP Conference Series: Earth Environ. Sci.* 410 (1) (2020), doi:<http://dx.doi.org/10.1088/1755-1315/410/1/012036>.
- [6] A.M. Papadopoulos, State of the art in thermal insulation materials and aims for future developments, *Energy Build.* 37(1)(2005) 77-86, doi:<http://dx.doi.org/10.1016/j.enbuild.2004.05.006>.
- [7] European Committee for Standardization (C.E.N.), *Eurocode 8, Design of structures for earthquake resistance – Part 1: General rules, seismic actions and rules for buildings. EN 1998-1: 2004E.*, Brussels, 2004.
- [8] Earthquake Planning and Protection Organization (Ο.Α.Σ.Π.), *KAN.EΠΕ.*, Athens, 2013.
- [9] E. Kechagias, *Αποτίμηση και ενίσχυση υφιστάμενου φορέα οπλισμένου σκυροδέματος με χρήση μεταλλικών προσόψεων.*, Thessaloniki, 2020.

## EXPERIMENTAL AND NUMERICAL INVESTIGATION OF FRP STRENGTHENED R/C BEAM-TO-COLUMN JOINTS SUBJECTED TO CYCLIC SEISMIC-TYPE LOADING

Lazaros Melidis<sup>1</sup>, George C. Manos<sup>2</sup>, J. Maranos<sup>3</sup>, K. Katakalo<sup>4</sup>

<sup>1,2,3,4</sup> Lab. Strength of Materials and Structures, Aristotle University  
[lazmelidis@gmail.com](mailto:lazmelidis@gmail.com), [gcmmanos@civil.auth.gr](mailto:gcmmanos@civil.auth.gr), [jmaranos@gmail.com](mailto:jmaranos@gmail.com), [kkatakalo@civil.auth.gr](mailto:kkatakalo@civil.auth.gr)

**Keywords:** R/C beam-to-column joints, Flexural behaviour, FRP strengthening, FRP jackets mechanical anchored

### Abstract

*The behaviour of R/C beam-to-columns joints is experimentally and numerically investigated here. A 1:3 scaled specimen is constructed and tested under cyclic seismic type loading at the Laboratory of Strength of Materials and Structures (Aristotle University of Thessaloniki). The reinforcing details prohibit the appearance of shear failure modes. Thus, this study focuses on the bending behavior of the structural members forming the R/C joint as built and strengthened with FRP jacketing. The main focus of this study is the effectiveness of the strengthening system adopted here. The FRP layers are mechanically anchored using steel sections in the joint region in order to prevent the premature delamination of the FRP layers and the proper distribution of stresses through the anchoring system to the structural members. The observed at the laboratory behaviour is portrayed in terms of horizontal load versus horizontal displacement cyclic response as well as bending moment cyclic response that develops at the beams and columns forming this R/C joint. Apart from the observations of this R/C joint behaviour based on the laboratory measurements this R/C subassembly was numerically simulated. The used numerical models include detailed modeling of all material used assigned with nonlinear constitutive laws derived by material testing. By comparing the numerical results with the corresponding experimental measurements, the validity of the employed numerical simulation is validated. Both experimental and numerical results demonstrate the satisfactorily behavior of the strengthening system used here.*



## 1 INTRODUCTION

The behavior of RC beam to column joints subjected to seismic type cyclic loading is studied here ([2], [7], [9]). For this purpose, a 1:3 scaled 3-D reinforced concrete (RC) joint specimen was constructed and tested at the laboratory of Strength of Materials and Structures of Aristotle University ([4], [5], [6], [10], [11]), shown in figure 1. The experimental campaign included testing of the joint specimen at 3 stages. Firstly, the virgin joint, following the same specimen with retrofitted beams applying FRP sheets and the retrofitted specimens with both beams and columns strengthened using FRP sheets. In order to achieve the desired flexural strengthening of the structural members an anchoring system, formed by steel angles and bars around the joint core, is used to mechanically anchor the FRPS sheets.

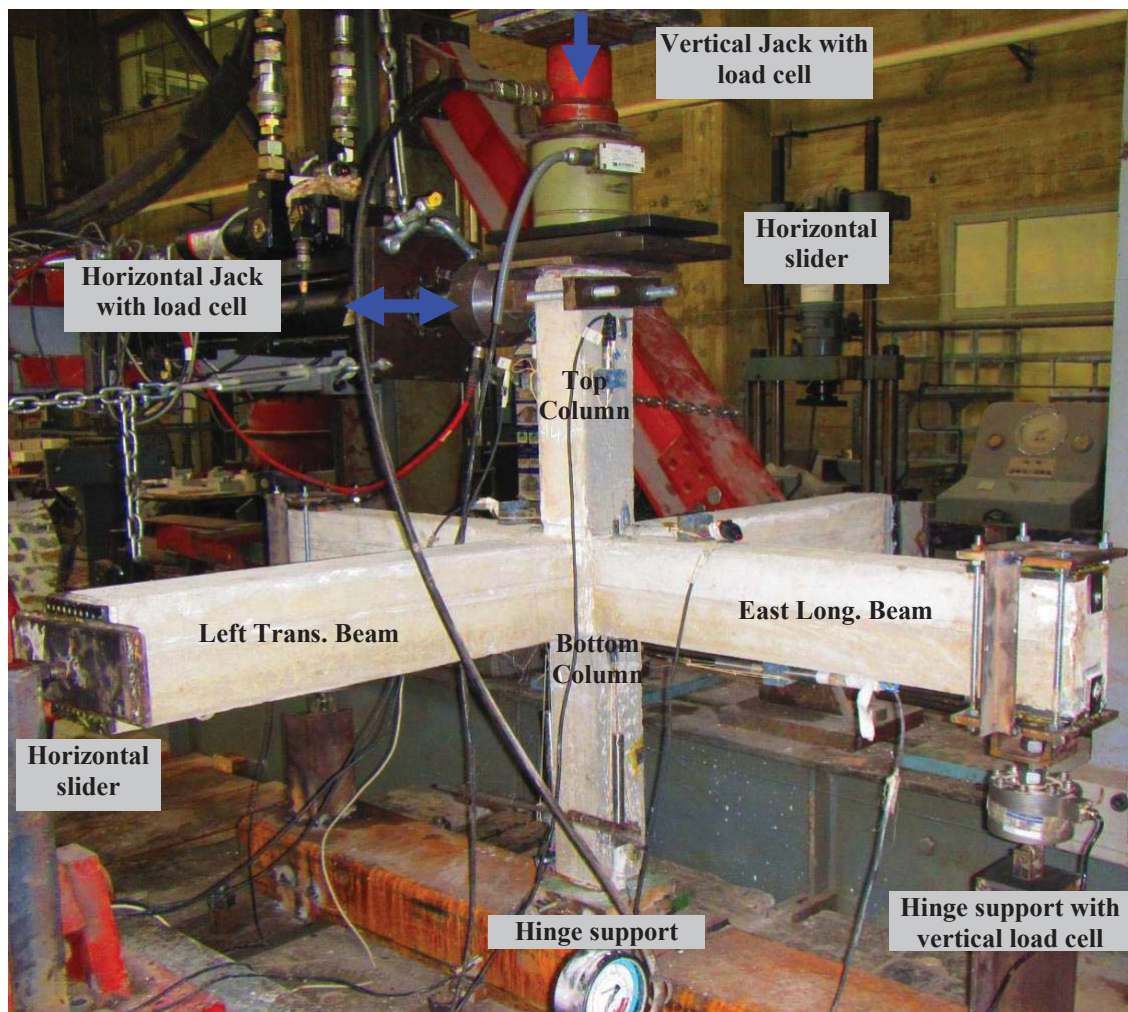


Figure 1. Interior RC joint model at Aristotle University – Experimental set-up.

In addition, 3-D numerical simulations of the tested specimens are also formed. These numerical models were subjected to monotonic loading instead of the cyclic loading sequence adopted at the experimental procedure resembling the envelope curve measured during testing. The reinforcing detailing of the tested specimen was such as to prohibit the development of any shear mode of failure. Therefore, this study focuses on numerically simulating the flexural response and mode of failures of the structural members that form this 3-D joint and

not on the failure of the joint core. The numerical models follow a micro-modeling approach. The concrete volume is represented together with the embedded longitudinal and transverse reinforcement in an explicit way. Both materials are governed by nonlinear material laws which have been derived by material testing. For the strengthened models the FRPs sheets are simulated by shell elements given an elastic constitutive law, as the predominant mode of failure of the FPP sheets is the debonding from the structural member's surface and not the FRP's rupture. Thus, the debonding failure is predicted by the non-linear interface assigned between the FRP sheets and the concrete's surfaces given a tensile and shear stress limit. Nonlinear Static analysis (pushover analysis) is next conducted to determine ultimate load, deflection capability and failure mechanisms. By comparing the measured behaviour with the corresponding numerical predictions an attempt is made to check the validity of the employed numerical simulations.

## 2 FEATURES OF THE EXPERIMENTA SEQUENCE

In what follows a brief description of a 1:3 scaled specimen of RC beam-to-column joint is presented. This scaled model was constructed and tested at the Laboratory of Strength of Materials of Aristotle University. The specimens tested at Aristotle University did not include an RC slab. Details of this specimen are shown in figures 1 and 2. Further details are included in the published works by Manos et al. ([4], [5], and [6]). The East (E) and West (W) longitudinal beams have at their ends a hinge support which is also provided with a load cell capable of recording the vertical (upwards or downwards) reaction at these supports. The transverse beam North (N) and South (S) ends are free to deflect vertically as well as to slide horizontally at the E-W direction of the cyclic horizontal load (as is shown in figure 1) being in contact with a sliding surface at these locations. The horizontal movement of these transverse beam ends at the N-S directions is restrained. The end of the bottom column is restrained in the two horizontal as well as at the vertical direction though a hinged support.

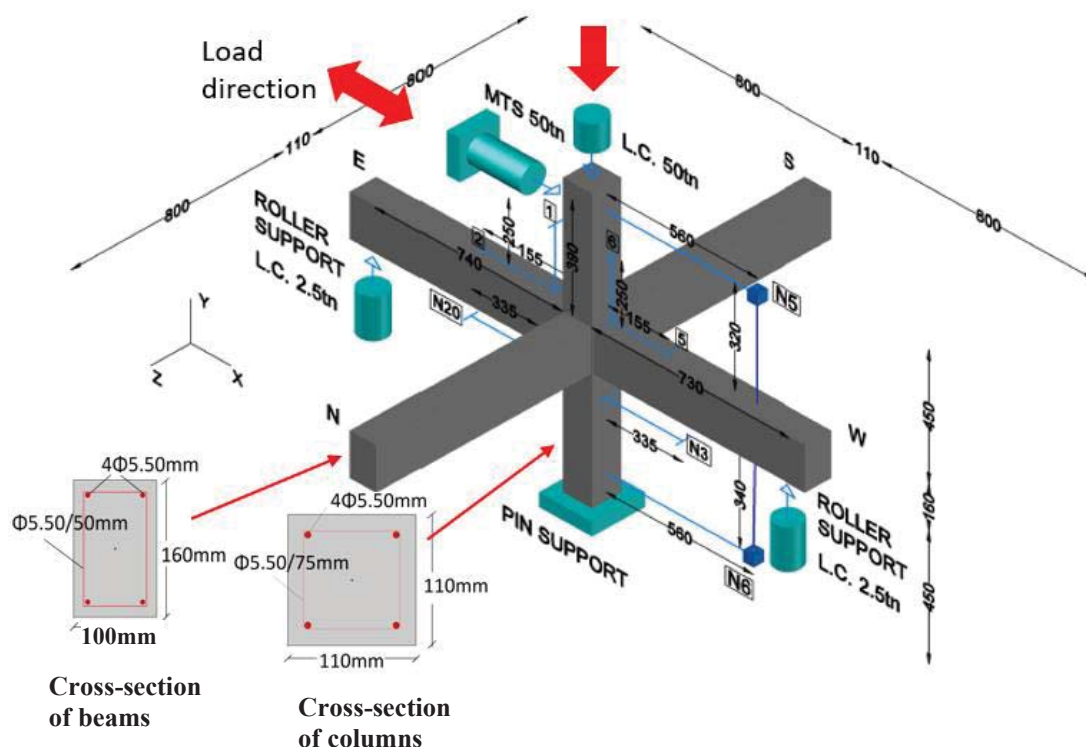


Figure 2. Interior RC joint model at Aristotle University – Experimental set-up and instrumentation scheme.

The top of the column is attached to the horizontal dynamic actuator capable of applying an imposed cyclic horizontal displacement in the E-W directions, as depicted in figures 1 and 2. The corresponding horizontal load is measured in this location by a horizontal load cell. Before any horizontal displacement is applied at the top of the column, a vertical load of 5.0tnf is applied through a jack and kept constant throughout each test. This load is monitored through a vertical load cell. These vertical load cell and jack were supported on top of the column through a set of sliders in such a way as not to restrict the horizontal movement of the top of the column (figure 1).

Apart from the load cells described before a number of displacement transducers were also provided in order to monitor the horizontal displacement of the top of the column at the point of horizontal cyclic load application as well as the horizontal displacement of the axis of the longitudinal beam. In addition, for both left and right longitudinal beams as well as top and bottom columns displacement transducers were provided capable of recording the relative extension or contraction of their top and bottom fiber near the joint in an effort to measure directly the rotation of each part of these structural elements during the flexural response of the whole RC joint. The geometry of the cross-sections of the beams and columns of this specimen are shown in figures 1 and 2 together with the details of the used reinforcing arrangement (see also table 1). The mechanical properties of the concrete and the steel used to build this specimen are listed in table 2 from axial compression and tensile tests with coupons taken during the construction. All RC beams and columns were provided with steel stirrups spaced in a way to prohibit the development of any form of shear failure. Both the longitudinal and transverse reinforcement was formed by smooth small diameter reinforcing bars according to similitude requirements ([4], [5], and [6]).

Columns		Longitudinal beams		Transverse beams	
width b (mm)	height h (mm)	width b (mm)	height h (mm)	width b (mm)	height h (mm)
110	110	100	160	100	160
Longitudinal Reinforcing bars Number / diameter (mm)					
4 / Ø5.5mm		2 / Ø5.5mm + 2 / Ø5.5mm			

Table 1. Details of RC joints (figure 1)

Steel reinforcing bars	Yield stress $f_y$ (MPa)	Yield strain $\epsilon_y$	Ultimate stress $f_u$ (MPa)	Ultimate strain $\epsilon_u$
Diameter Ø5.50mm longitudinal	311	0.08	425	0.22
Diameter Ø5.50mm (stirrups)	360	0.06	542	0.20

Table 2. Mechanical properties of used reinforcing bars (figure 1)

### 3 RESULTS AND OBSERVATION FROM THE MEASURED BEHAVIOUR

Figure 3a depicts the variation of the applied horizontal cyclic load versus the corresponding horizontal displacement of the tested RC beam-to-column joint that develops either at the top of the column or at the axis of the longitudinal beam (approximately at the mid-height of the specimen). The maximum load measured was equal to 8.69KN. The observed damage at the East beam cross-section is depicted in figure 3b.



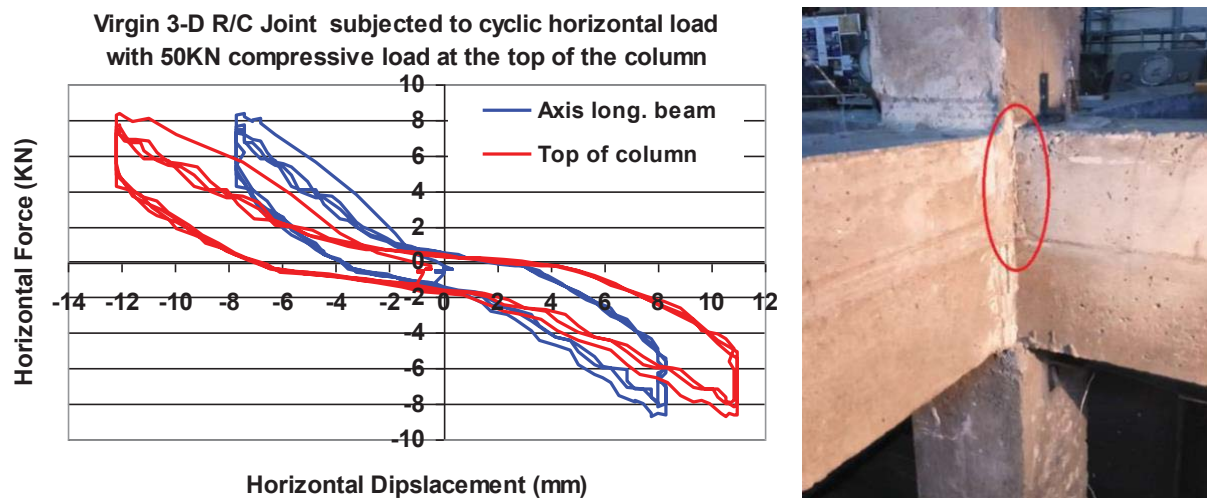


Figure 3. a) Cyclic load versus the corresponding horizontal displacement response of the RC beam-to-column interior joint model tested at Aristotle University. b) observed cracking at the East beam cross-section

Following, a strengthening technique was adopted only for the longitudinal beams. In these members two CFRP sheets were bonded in both faces. Near the joint core steel angles were placed together with circular bars in order to support mechanically the FRP layers and prohibit the premature delamination as depicted in figure 4. The response of the specimen with strengthened beams in terms of applied load versus the horizontal displacement at the top of the column is given in figure 5 together with the observed damage pattern. In this case, the cracking occurs at the bottom column's cross-section near the joint core. The maximum load measured was equal to 12.54KN.



Figure 4. The examined strengthening method: The anchoring system consisting of steel parts is placed around the joint area and the CFRP sheets are bonded to the longitudinal beam faces.

Next, the same strengthening technique was used for the column sections as well. Three CFRP sheets were bonded at each face of the column members. Again the specimen was subjected to cyclic horizontal loading. The variation of the applied horizontal cyclic load versus the corresponding horizontal displacement of the tested RC beam-to-column joint that

develops at the top of the column is shown in figure 6. The maximum load observed was equal to 16.63KN.

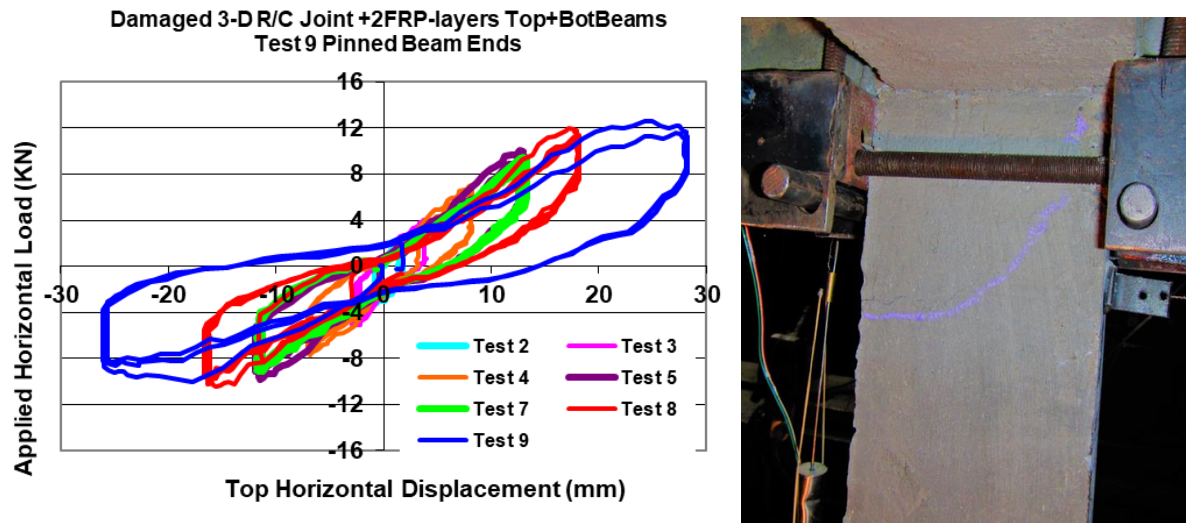


Figure 5. a) Cyclic load versus the corresponding horizontal displacement response of the RC beam-to-column joint with FRP strengthened beams. b) observed cracking at the East beam cross-section

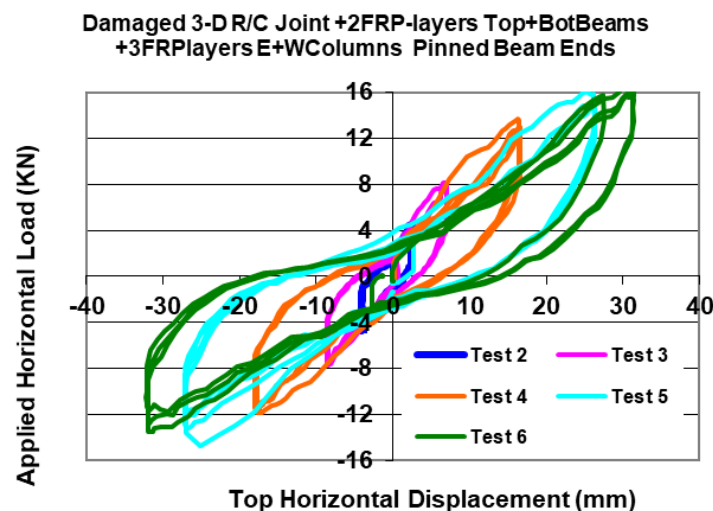


Figure 6. a) Cyclic load versus the corresponding horizontal displacement response of the RC beam-to-column joint with FRP strengthened beams and columns. b) observed cracking at the East beam cross-section

#### 4 NUMERICAL SIMULATIONS OF THE OBSERVED BEHAVIOUR

The numerical models discussed here utilize solid elements for the concrete volume as shown in figure 7a, together with wire elements for the numerical representation of the reinforcing bars as shown in figure 7b. Reinforcing bars were added within the concrete volume representing the actual reinforcing bars. The reinforcing bars were in full contact with the surrounding concrete through the relevant option (embedded region) provided in the software [1].

Non-linear constitutive laws were adopted in this numerical simulation for either the concrete or the steel elements. These stress-strain constitutive laws are based on the corresponding measured axial compression or tension tests performed with specimens taken during the

construction of the RC beam-to-column mock-up at the laboratory of Strength of Materials and Structures of Aristotle University. The vertical load of 5.0tnf was initially applied and kept constant, while the horizontal force at the top of the column was applied in a gradually increasing manner, following a step-by-step time history pushover analysis. The response of the virgin joint model is given in figure 8 in comparison with the corresponding experimental measurements in terms of applied load versus the horizontal displacement at the top of the column. Figure 9 depicts the formation of plastic hinges at beam cross sections. As can be seen in this figure, large principal plastic strains appear to develop at the edges of the beam ends near the joint faces corresponding to areas of the concrete volume that develops flexural cracks (figure 9a). In figure 9b the reinforcing bars, at the same locations where the concrete develops high principal plastic strains, develop high tensile stress that have values larger than the yield stress of the reinforcing steel ( $f_y=311\text{MPa}$ , Table 2). The yielded reinforcing longitudinal bars are marked with red color. Therefore, in this 3-D numerical simulation the plastic hinges in the beams are numerically represented explicitly in this detailed manner.

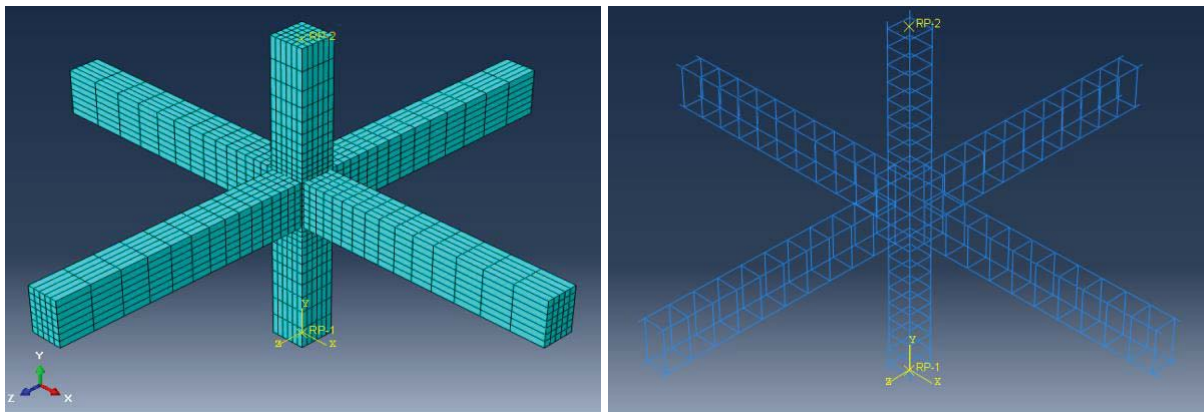


Figure 7. 3-D numerical simulation of the RC beam-to-column joint tested at the laboratory of Strength of Materials and Structures of Aristotle University. a) The numerical simulation of the concrete volume. b) The numerical simulation of the longitudinal and transverse reinforcement.

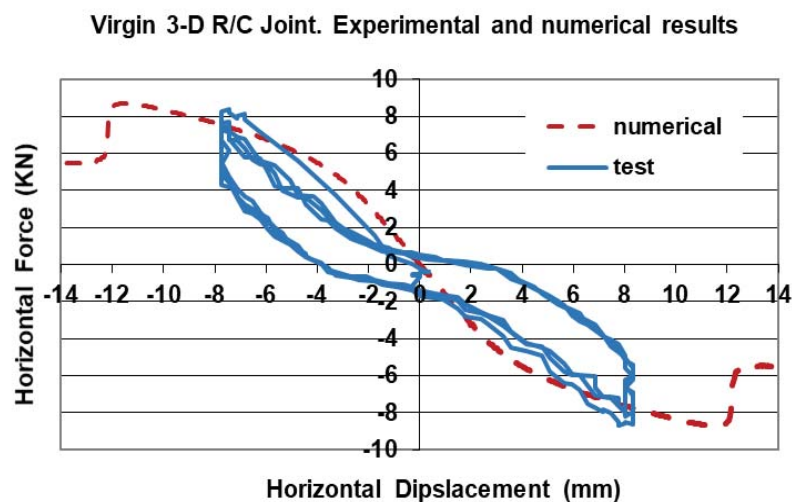


Figure 8. Comparison between the measured horizontal force versus horizontal displacement at the top for the virgin RC joint tested with the 3-D numerical predictions



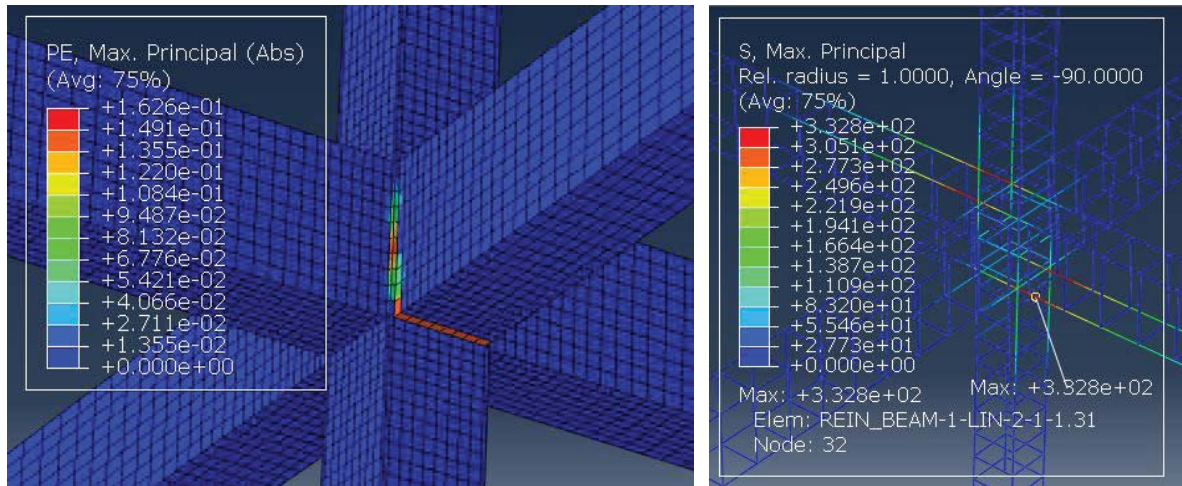


Figure 9. Virgin RC joint numerical response. a) The distribution of plastic strains at the beams near the region that they meet the RC joint. b) Distribution of axial stress at the longitudinal reinforcement of longitudinal beams. The yielded reinforcing longitudinal bars are marked with red color.

Following, the anchoring system was simulated with simple contact with the R/C joint and the FRP sheets were bonded to the beams and attached at the anchoring system (figure 10a). The response of this model in terms of applied load versus the horizontal displacement at the top column is depicted in figure 10b together with the corresponding experimental measurements. Figure 11 shows the plastic strains developed at concrete's volume. Large plastic strains develop at the column cross sections near the joint. At the same location the vertical reinforcing bars develop high tensile stresses, larger than the yield limit (table 2). Thus, plastic hinges are formed in column's cross section.

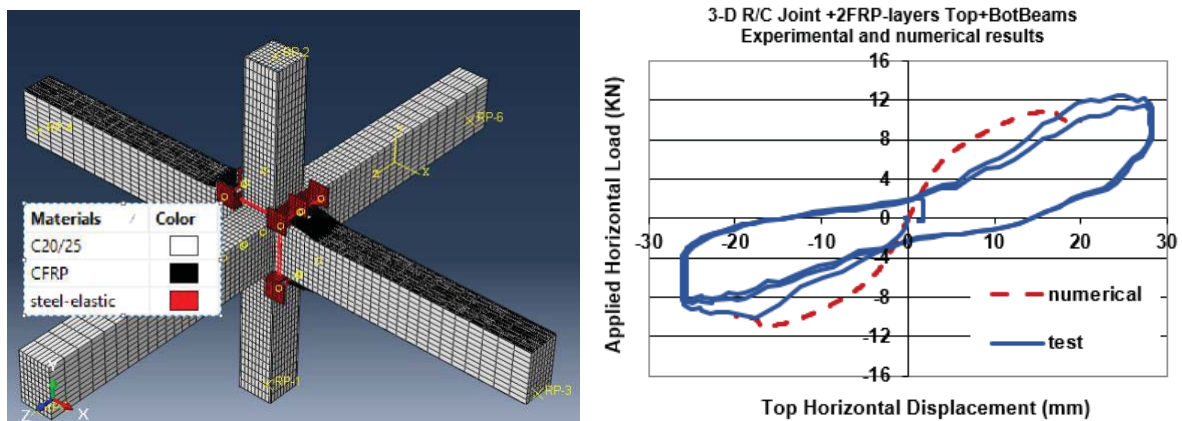


Figure 10. a) The numerical model of joint with FRP strengthened beams. b) Comparison between the measured horizontal force versus horizontal displacement at the top for the joint with FRP strengthened beams and the corresponding numerical prediction

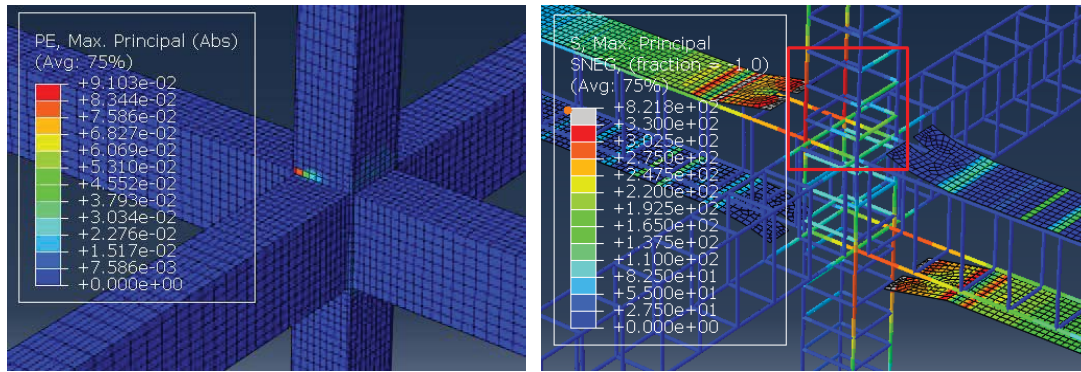


Figure 11. Joint with strengthened beams. a) The distribution of plastic strains at the column near the region that meet the RC joint. b) Distribution of axial stress at the longitudinal reinforcement and FRP sheets of longitudinal beams. The yielded reinforcing longitudinal bars are marked with red color.

Next, FRP sheets were attached at the two faces of the top and bottom column following the same methodology as previously described, 2 CFRP sheets to beams and 3 CFRP sheets to columns (figure 12a). The response of this model in terms of applied load versus the horizontal displacement at the top column is depicted in figure 12b together with the corresponding experimental measurements. Figure 13 shows the plastic strains developed at concrete's volume. Large plastic strains develop at the beam cross sections near the joint. At the same location the reinforcing bars develop high tensile stresses, larger than the yield limit (table 2). Thus, plastic hinges are formed in column's cross section.

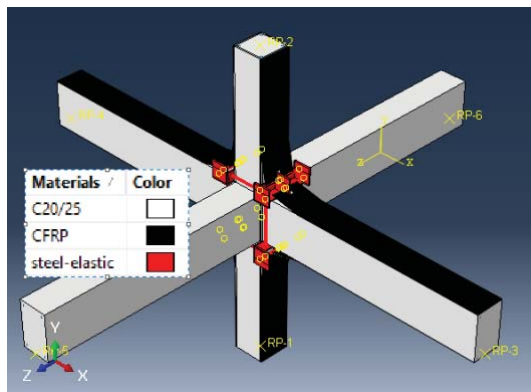


Figure 12. a) The numerical model of joint with FRP strengthened beams and columns. b) Comparison between the measured horizontal force versus horizontal displacement at the top for the joint with FRP strengthened beams and columns and the corresponding numerical prediction

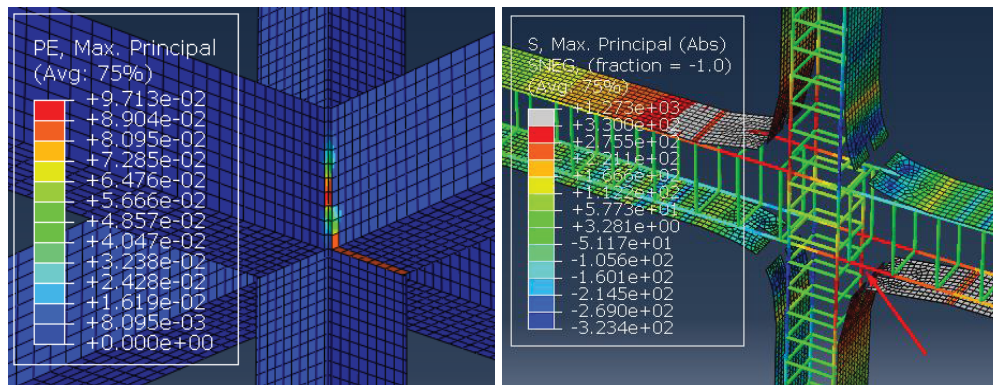


Figure 13. Joint with strengthened beams and columns. a) The distribution of plastic strains at the beam, near the region that meet the joint core. b) Distribution of axial stress at the longitudinal reinforcement and FRP sheets. The yielded reinforcing longitudinal bars are marked with red arrow.

## 5 DISCUSSION OF THE OBTAINED RESULTS.

In section 3 the experimental results of the tested R/C joints are given. The virgin 3D joint was tested under cyclic horizontal load with a constant vertical load equal to 50KN. Following, the damaged specimen was strengthened with 2 CFRP sheets bonded at the longitudinal beams. Subsequently, 3 FRP sheets were placed to the column as well. In all cases the FRP layers were attached to the examined anchoring system placed near the joint core region. The virgin joint exhibited a maximum load equal to 8.69KN, while cracking appeared at the beam cross sections near the joint. The beam strengthened joint exhibited greater maximum load, 12.54KN, while cracking was observed at the bottom column. Finally, the joint with both beams and columns strengthened exhibited a maximum load equal to 16.63KN.

Afterward, numerical models were developed using all the geometrical and the mechanical properties of the tested specimen. Three models are examined with correspondence with the above mentioned tests. The virgin model exhibited a maximum load equal to 8.70KN, while cracking appeared at the beam cross sections near the joint. The beam strengthened joint exhibited greater maximum load, 10.96 KN, while cracking was observed at the bottom column. Finally, the joint with both beams and columns strengthened exhibited a maximum load equal to 12.55 KN, while the beam cross section showed cracking.

Specimen	Experimental results		Numerical results	
	Maximum load (KN)	Observed mode of failure	Maximum load (KN)	Observed mode of failure
Virgin	8.69	Cracking of beam sections	8.70	Plastic strains at concrete and rebar of beams
Beams Strengthened (2 sheets)	12.54	Cracking of column sections	10.96	Plastic strains at concrete and rebar of column
Columns Strengthened (3 sheets)	16.63	Cracking of beam sections	12.55	Plastic strains at concrete and rebar of beams

Table 3 Summary experimental measurements and numerical predictions

## 6 CONCLUSIONS

The behavior of RC beam-to-column joints subjected to seismic type cyclic loading is studied here as built and subsequently strengthened using CFRP sheets. The strengthening methodology aims to upgrade the flexural capacity of the structural members and for this purpose an anchoring system near the joint area is used. The observed behaviour is portrayed in terms of horizontal load versus horizontal displacement cyclic response. Apart from the laboratory observations numerical simulations were conducted. The main conclusions are enlisted below:

- The anchoring system employed in the discussed experimental campaign successfully prohibited the delamination of FRP sheets near the joint core and ensured the stresses distribution. Thus, the structural subassembly bearing capacity is increased by 44% and 91% for the beam strengthened specimen and the both beams and columns FRP strengthened specimen.
- The used 3-D numerical simulations of the tested RC joint successfully represented the observed flexural non-linear response of this RC structural sub-assembly, as for each case satisfactorily captured the mode of failure.



- Regarding the bearing capacity predicted by these numerical models again the numerical simulation can be considered successful up to point. The strengthened models exhibited an increase of maximum load by 27% and 44% for the beam strengthened specimen and the both beams and columns FRP strengthened models, which are smaller than the corresponding laboratory measurements. This can be explained by the fact that during the analysis damage on the interface between FRP sheets and R/C members was observed, while the experimental procedure did not exhibit such a failure. Thus, the bearing capacity's increase is limited. Therefore, the properties of these interfaces should be further investigated.

## REFERENCES

- [1] Manos, G.C., Melidis, L., Katakalos, K., Kotoulas, L., Anastasiadis, A., Chatziastrou, C., "Masonry panels with external thermal insulation subjected to in-plane diagonal compression", *Case Studies in Construction Materials*, Volume 14, June 2021, Article number e00538
- [2] Joglekar M., Murry P., Jirsa J. and R. Klinger R. (1984) "Full Scale Tests of Beam-Column Joints",
- [3] Mahin S.A. and Bertero V.V. (1977), "RCCOLA: A computer program for Reinforced Concrete Column Analysis", Dept. Civil Engineering, University of California, Berkeley, U.S.A.
- [4] Manos G.C., Yasin B., J. Thaumpta J., D. Mpoufides D. (1998) "The Simulated Earthquake Response of two 7-story R.C. Planar Model Structures - A Shear Wall and a Frame with Masonry Infills", 6th U.S. National Earthquake Engineering Conference, 1998.
- [5] Manos G.C., Thaumpta J., Yasin B., Triamataki M., Demosthenous M. (1998), "The Dynamic Response of a 5-story Structure at the European Test site at Volvi-Greece", 11th European Earthquake Engineering Conference.
- [6] Manos G.C., Pitilakis K.D., Sextos A.G., Kourtides V., Soulis V., Thauampteh J., (2015), "Field experiments for monitoring the dynamic soil-structure-foundation response of model structures at a Test Site" *Journal of Structural Engineering*, American Society of Civil Engineers, Special Issue "Field Testing of Bridges and Buildings, D4014012, Vol. 141, Issue 1, January 2015.
- [7] Melidis L. (2017), "Study of the Behaviour of Reinforced Concrete Columns and Beams that form a 3-D Joint Before and After Retrofitting", Postgraduate Thesis, Dept. Civil Engineering, Aristotle University, (in Greek).
- [8] Manos G.C., Theofanous M. and Katakalos K. (2014), "Numerical simulation of the shear behaviour of reinforced concrete rectangular beam specimens with or without FRP-strip shear reinforcement", *Advances in Engineering Software*, Elsevier, Elsevier, Vol. 67, pp. 47-56, 31-1-2014.
- [9] Park R. and Paulay T. (1974), "Reinforced Concrete Structures".
- [10] Wallace B. and Krawinkler H. (1983), "Small-scale Model Experimentation on R/C Assemblies", U.S. – Japan Research Program, Dept. Civil Engineering, Stanford University, Report No. 74, June 1983.

- [11] Melidis, L., & Manos, G. C. (2019). Reinforced concrete 3-D beam-to-column joints subjected to cyclic seismic-type loading. Laboratory measurements and numerical simulations. *COMPdyn Proceedings*, 1, 225–239. doi.org/10.7712/120119.6915.19164

## THE BEHAVIOR OF PARTIALLY GROUTED MASONRY WALLS SUBJECTED TO OUT OF PLANE SEISMIC TYPE LOADS. LABORATORY MEASUREMENTS AND NUMERICAL SIMULATIONS

George C. Manos<sup>1</sup>, Lazaros Melidis<sup>2</sup>, Lampros Kotoulas<sup>3</sup>, Kostas Katakakos<sup>4</sup>

<sup>1,2,3,4</sup> Lab. Strength of Materials and Structures, Aristotle University

[gcmayos@civil.auth.gr](mailto:gcmayos@civil.auth.gr), [lazmelidis@gmail.com](mailto:lazmelidis@gmail.com), [kotoulaslambros@gmail.com](mailto:kotoulaslambros@gmail.com), [kkatakakos@civil.auth.gr](mailto:kkatakakos@civil.auth.gr)

---

### Abstract

*A number of ungrouted and grouted masonry walls were built at the laboratory of Strength of Materials and Structures of Aristotle University using an innovative clay unit vertically perforated. This vertically perforated clay unit was designed and produced with the proper holes in order to host the required horizontal and vertical reinforcing steel bars. At the same time the remaining holes are filled with expanded polystyrene parts capable to provide sufficient thermal insulation and drastically reduce the energy consumption. The specimens constructed with the thin mortar method using a high strength mortar and employing vertical reinforcing bars of different diameters. The measured behavior is depicted here in terms of horizontal applied load versus the horizontal displacement at mid height. Furthermore, numerical models were developed in order to simulate the observed behaviour of the tested specimens by modeling separately the masonry panels as homogenized material and linear beam elements representing the employed longitudinal (vertical) reinforcement. The numerically simulated behavior resembles the measured load-deformation response of the tested specimens and the observed actual damage at the end of the tests.*

**Keywords:** Partially grouted masonry, out of plane bending, Laboratory measurements, Numerical Simulations.

---



## 1 INTRODUCTION

The vulnerability of unreinforced masonry walls subjected to seismic loads was highlighted during past earthquake events [1, 2]. The employment of reinforcing bars to construct earthquake resistant partially grouted masonry structures with acceptable performance is one possible solution. The in-plane behavior of such structures has been widely investigated. Manos et al. [3, 4] tested partially reinforced piers with different reinforcing schemes under in plane cyclic loads. Recent studies investigate the in-plane behavior of reinforced masonry walls using new clay units with the appropriate thermal properties in an effort to improve the structures energy consumption [5, 6]. Over the literature there are both experimental and numerical investigations about the out of plane response of reinforced masonry walls focusing on the effect of the aspect ratio, boundary conditions, reinforcing ratio etc. [7, 8].

An ongoing research of Laboratory of Strength of Materials and Structures deals with partially grouted reinforced masonry walls constructed with a novel clay unit. A key issue in the construction of these walls is the masonry unit employed. The geometry of this new unit was defined using parametric numerical predictions taking into consideration not only the mechanical properties, but also parameters like thermal properties, production cost and ease of construction practice [9, 10]. In this paper the out of plane behavior of ungrouted and partially grouted masonry wallets is discussed. Results are presented from tests of unreinforced masonry wallets or reinforced with vertical rebars of different diameters, which are subjected to cyclic out of plane bending. The mechanical properties of all the employed materials are defined through testing. Following, numerical models were developed utilizing all the geometrical and mechanical properties in order to replicate the experimentally measured out of plane behaviour. All these results are presented and discussed focusing on the influence of the reinforcing arrangement in the overall in plane response.

## 2 SPECIMEN CONSTRUCTION AND MATERIAL PROPERTIES

The geometry of the employed clay unit is depicted in Figure 1. The basic mechanical properties of this unit were measured at the Laboratory. More specific, unit's compressive strength perpendicular to the bed joint and parallel to the bed joint are measured by compression test according to EN772-1 [11]. The proposed reinforced masonry system uses the construction technique of thin mortar joint. The mechanical properties of the mortar material used, were obtained by material testing according to EN1015-19 [12]. The same mortar is used as grout to fill the vertical holes when a rebar is placed. Additionally, tensile tests for the used reinforcing steel bars with diameter 10mm, 14mm and 16mm were conducted. The above mentioned properties are listed at table 1 and table 2.

The used vertically perforated units with nominal dimensions length=210mm, height=240mm and thickness=300mm form a vertical hole between the units with dimensions about 75x75mm aiming to be used for the placement of the concentrated vertical reinforcing bar (figure 1).

All specimens were built by builders following the relevant prototype work conditions. The constructed specimens (length 970mm, height 1700mm and a thickness of 300mm) were tested under cyclic out of plane bending. Before the out of plane loading, all specimens were subjected to uniform compressive load equal to  $4t_n$ , which was kept constant during the out of plane loading sequence and was measured by a load cell. The horizontal load was applied at the mid height of each wallet by an actuator and was measured by a load cell. Displacement transducers were also used to measure the out of plane deflection of each specimen. All measurements were used to obtain the performance of each specimen in terms of out of plane load applied at mid-height versus the out of plane deflection, as it is showed below (section 3).

<b>Brick unit</b>	
mean compressive strength perpendicular to bed joints ( $f_b$ )	8.12 MPa
mean compressive strength parallel to bed joints ( $f_{b,h}$ )	2.73 MPa
<b>Mortar</b>	
compressive strength ( $f_m$ )	13.47 MPa
flexural strength ( $f_{mt}$ )	2.80 MPa

Table 1: mechanical properties of masonry materials used.

steel bar's diameter	yield stress (MPa)	ultimate stress (MPa)	yield strain	ultimate strain
D10mm	580	680	2.9‰	10‰
D14mm	540	670	2.7‰	12‰
D16mm	530	640	2.6‰	11‰

Table 2: mechanical properties of steel reinforcing bars

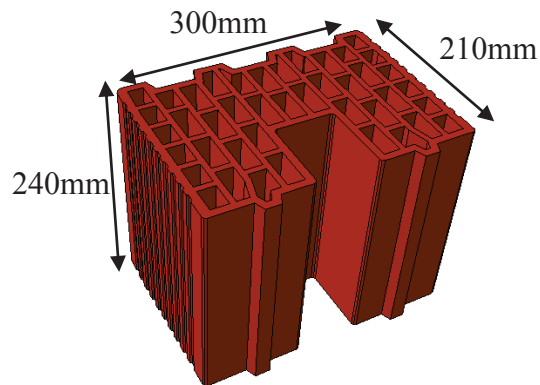


Figure 1: The geometry of the novel brick unit (left) and the employment of vertical bars (right)

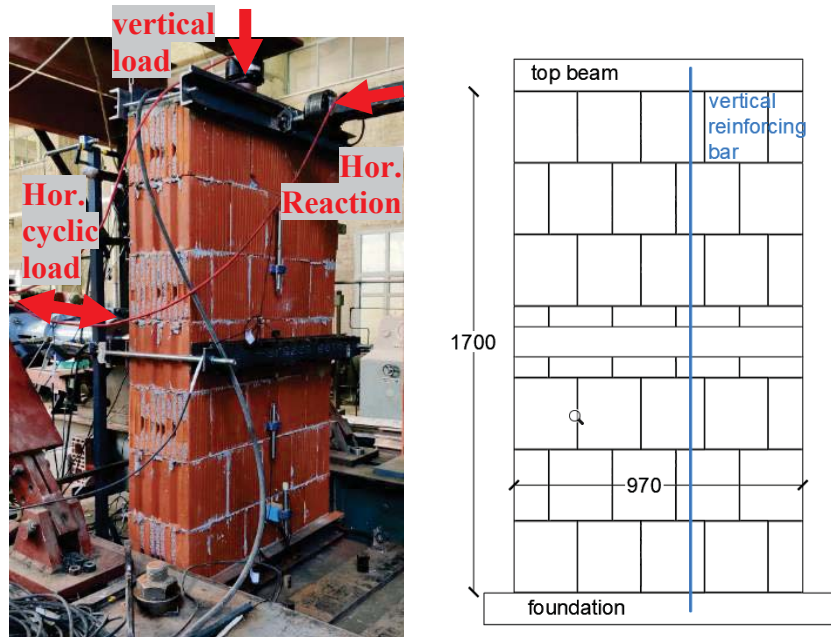


Figure 2: Experimental set-up (left) and the geometry of tested specimens (right)

### 3 EXPERIMENTALLY OBSERVED BEHAVIOR

The observed out of plane performance of the tested specimens with or without vertical reinforcing bars is presented and discussed in terms of the variation of the out of plane load applied at mid-height versus the out of plane deflection together with the observed damage. Firstly, the performance of the unreinforced wallet is given. Figure 3 (right) depicts the observed performance of the unreinforced masonry wallet without any reinforcement, which represents the control specimen. As can be seen a linear behavior is observed till the first cracking at the minimum load (-5.0KN). At this point the flexural failure of the bed joint develops and it is followed by a sudden decrease of bearing capacity. Following, for the next cycles the bearing capacity is almost constant (+2.3KN, -3.0KN). This performance can be characterized rather brittle. At the same figure (figure 4 left) the formation of horizontal cracking along the bed joint at mid height is depicted.

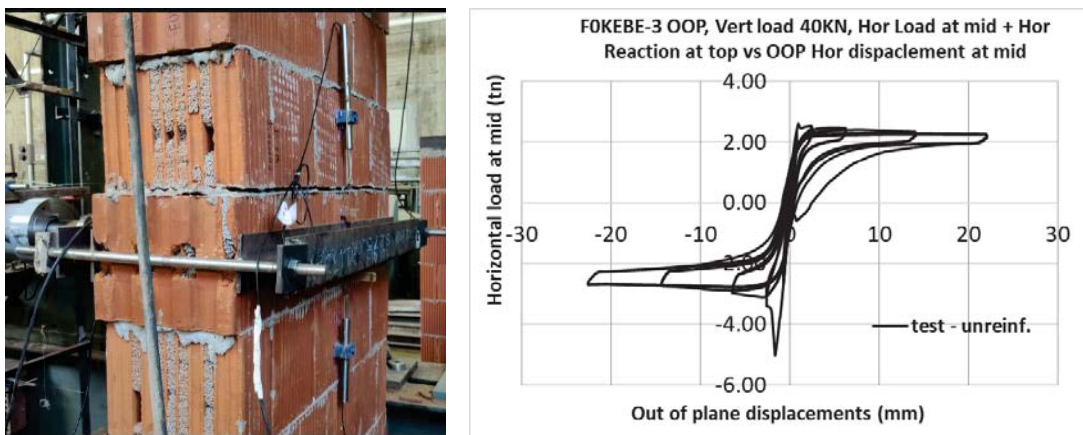


Figure 3: Damage pattern of bare wallet (left) and its response in terms load versus deflection (right)

Following, the response of the tested specimens with vertical reinforcing bars is presented. Figure 4 depicts the observed damage and the variation of the out of plane load applied at mid-height versus the out of plane deflection for a specimen with a vertical rebar of diameter 10mm placed at a vertical grouted hole. The bed joint failure develops again for a negative load about -5.0KN, but for the next cycles a ductile behavior is observed with maximum and minimum measured load +4.8KN and -6.0KN respectively. The formation of horizontal crack at the mid-height bed joint characterizes the observed mode of failure for this specimen.

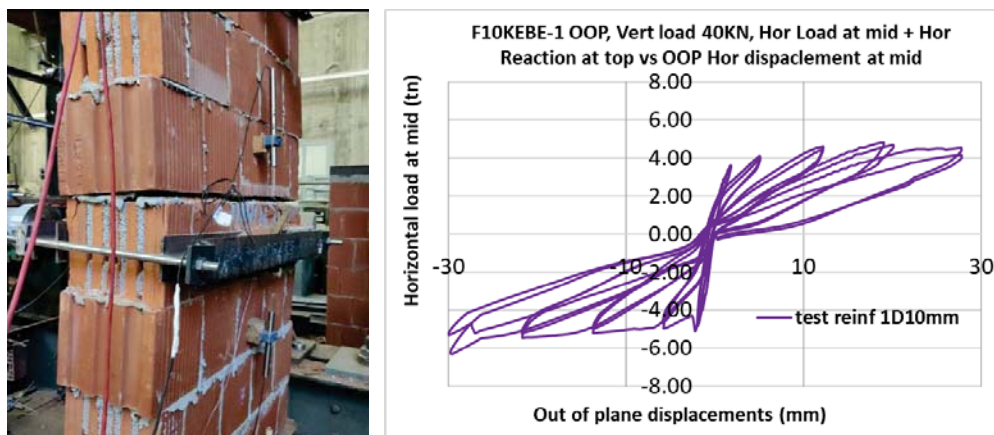


Figure 4: Damage pattern of reinforced wallet with D8mm reinforcing bars and its response in terms load versus deflection (right)



The response of the tested specimens with vertical reinforcing bars with diameter 14mm and 16mm is depicted in figures 5 and 6 in terms of variation of the out of plane load applied at mid-height versus the out of plane deflection and the observed damage pattern. In both cases, the bed joint failure develops again for a negative load about -5.0kN and for the next cycles a ductile behavior is observed with a maximum and minimum measured load +5.9kN/-6.1kN and +6.1kN/-6.2kN for the wallets with reinforcing bar with diameter 14mm and 16mm respectively. The formation of horizontal crack at the mid-height bed joint characterizes the observed mode of failure for these specimens. For the latter stages of the cyclic loading compressive failure of the outer face of bricks developed.

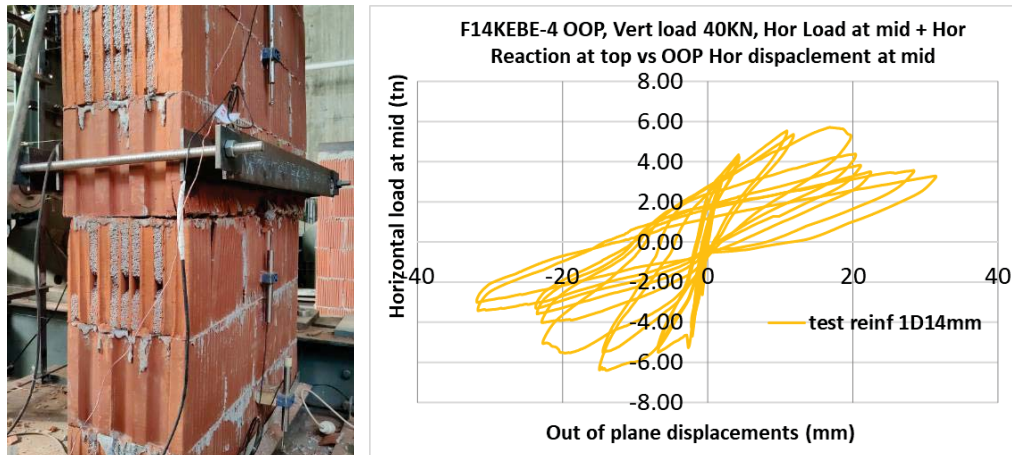


Figure 5: Damage pattern of reinforced wallet with D8mm reinforcing bars (left) and its response in terms of load versus deflection (right)

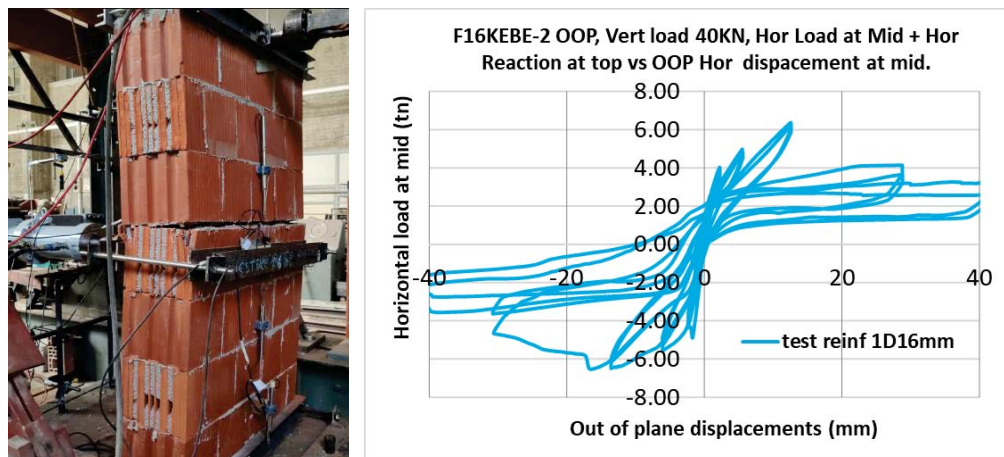


Figure 5: Damage pattern of reinforced wallet with D8mm reinforcing bars (left) and its response in terms of load versus deflection (right)

#### 4 NUMERICAL MODELING

Three-dimensional finite element numerical models were formed, adopting a macro modeling approach with a homogenized material obeying the Concrete Damaged Plasticity (CDP) constitutive law for the masonry, that can satisfactorily represent the behaviour of brittle materials, like concrete or masonry, with different stress – strain laws for compression and tension. Two different material laws were formed resembling the ungrouted and grouted masonry parts. These two laws differ in the Young's Modulus and the compressive strength. The material properties assigned to material laws are listed in table 3 and they were obtained by ma-

terial testing on prism masonry specimens according to corresponding EN Standrads [13,14]. The vertical reinforcing bars were simulated by wire elements given an elasto-plastic material law obtained by the laboratory measurements (see table 2). A perfect bond between masonry and reinforcing bars were assumed. The geometry and details of the numerical model are depicted in figure 6. The numerical predictions includes two monotonic pushover analysis for “negative” and “positive” deflection.

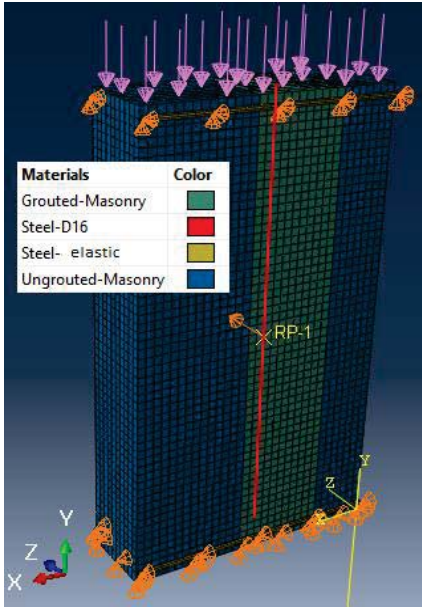


Figure 6: 3D view of the numerical model of the reinforced masonry wallet with a vertical D16mm reinforcing bar.

Concrete Damaged Plasticity – material model assigned to masonry panel		
	UngROUTED masonry	Grouted masonry
Young's Modulus (MPa)	4000 MPa	4700 MPa
Compressive strength (MPa)	3.6 MPa	4.30 MPa
Flexural strength (MPa)	0.2 MPa	0.2 MPa

Table 3: Parameters of CDP constitutive law for masonry material

The damaged pattern of the unreinforced wallet’s numerical model is depicted in figure 7 together with the comparison of the variation of horizontal applied load with out of plane deflection response with the corresponding tested specimen. A very good agreement both in load – displacement curve and in the observed mode of failure.

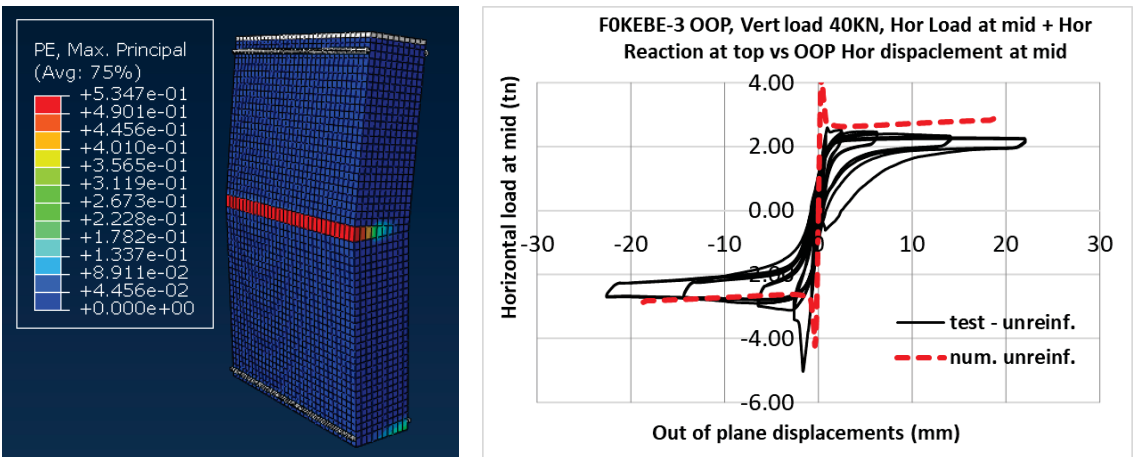


Figure 7: Plastic strains – damage pattern of unreinforced numerical model at the end of loading (left) and its response in terms horizontal applied load versus out of plane deflection (right)

Following, in the previous model a vertical reinforcing bar is added as shown in figure 6 with wire elements. The reinforcing bar is of diameter 10mm, 14mm or 16mm as in the tested

specimens. Figures 8, 9, 10 depict a comparison between experimental results and the corresponding numerical predictions for the 3 above mentioned reinforced wallets. In general, a good agreement is observed both in the load – deflection response and in the damage pattern. Additionally, rebar's and masonry's panel plastic strains at the end of the analysis, for an out of plane displacement about 30mm are depicted. The reinforced wall with 1D10mm has relatively large plastic strains developed in the vertical rebars at the bottom and at the mid-height. On the other side, reinforced walls with 1D14mm and 1D16mm developed greatly smaller and no plastic strains at the rebar elements respectively. In these two models significant plastic strains are developed at the compressive zone at the mid-height cross-section indicating compressive failure.

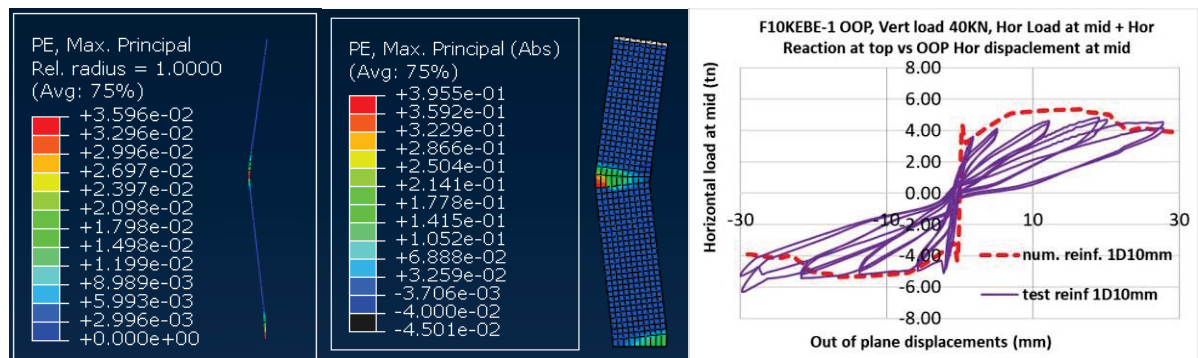


Figure 8: Plastic stains at rebar and masonry panel (left) and horizontal applied load versus out of plane deflection response of numerical model with 1D10mm vertical reinforcing bar, compared with the corresponding experimental measurements (right).

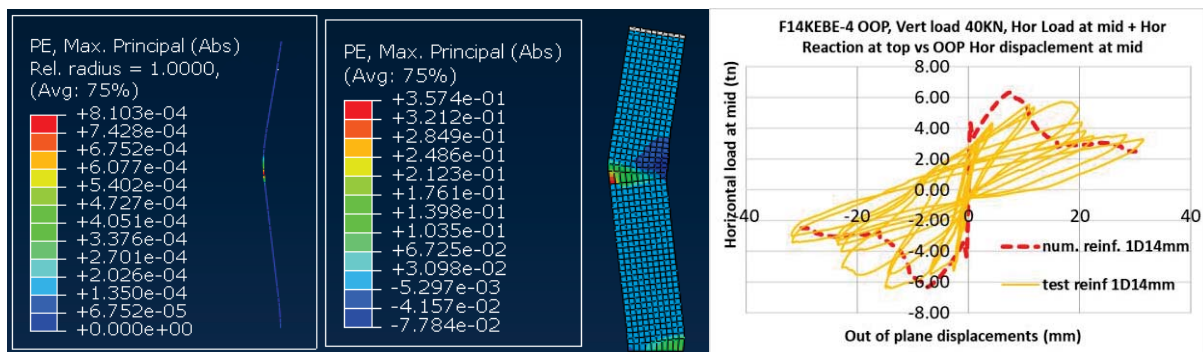


Figure 9: Plastic stains at rebar and masonry panel (left) and horizontal applied load versus out of plane deflection response of numerical model with 1D14mm vertical reinforcing bar, compared with the corresponding experimental measurements (right).

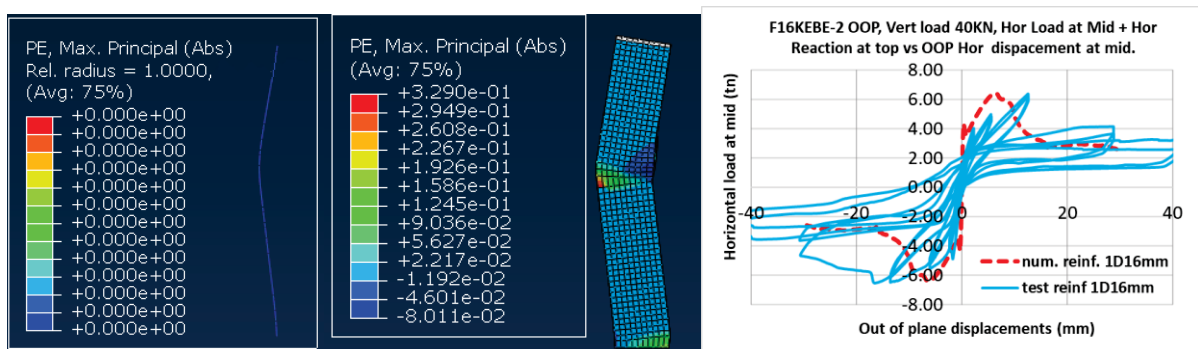


Figure 10: Plastic stains at rebar and masonry panel (left) and horizontal applied load versus out of plane deflection response of numerical model with 1D16mm vertical reinforcing bar, compared with the corresponding experimental measurements (right).



## 5 DISCUSSION

Figure 3 depicts the response of the unreinforced masonry wall. The applied load is increasing till the bed joints failure starts followed by a sudden drop of the applied load, which from this point and for greater out of plane displacements remains almost constant. As it is showed in figures 4, 5, 6 the existence of a vertical reinforcing bar leads to a further increase of the applied load after the bed joint's failure and as the out of plane deflection is increased. The table below includes the maximum / minimum load for each specimen and the corresponding deflections. For all specimens the mode of failure was the same and was characterized by the bed joints cracking at the mid-height section.

Apart from the bearing capacity increase, the existence of vertical reinforcing bars contributes to relatively fat hysteresis loops under the cyclic loading compared to the unreinforced specimen's performance. This fact indicates that the reinforcing rebars have exceeded their yield limit and developed plastic strains contributing in that way to a much more ductile response for the reinforced specimens. Vertical rebar's yield is also confirmed by the numerical predictions. Figures 8, 9, 10 depicts the developed plastic strains of reinforcing bars for an out of plane imposed deflection about 30mm.

Specimen detail	Experimental measurements		Numerical predictions	
	Minimum load (corresponding displacement)	Maximum load (corresponding displacement)	Minimum load (corresponding displacement)	Maximum load (corresponding displacement)
Unreinforced	-5.04 tn (-1.63mm)	2.59 tn (0.94mm)	-4.23tn (-0.38mm)	4.23tn (0.38mm)
Reinforced 1D10mm	-6.31 tn (-30.20mm)	4.85 tn (22.63mm)	-5.35 tn (-16.62mm)	5.35 tn (16.62mm)
Reinforced 1D14mm	-6.40 tn (-10.92mm)	5.72 tn (22.62mm)	-6.31 tn (-7.31mm)	6.31 tn (7.31mm)
Reinforced 1D16mm	-6.54 tn (-16.50mm)	6.37 tn (12.54mm)	-6.43 tn (-6.25mm)	6.43 tn (6.25mm)

Table 2: Summary results of all tested and numerically simulated wallets. Maximum/minimum load is given together with the corresponding displacement

## 6 CONCLUSIONS

The behavior of reinforced masonry wallets under out of plane bending is discussed here, mainly focusing on the contribution of the vertical reinforcing bars in the overall wallet's response. Apart from the experimental observations, numerical models were developed using all the available information about the mechanical properties of the materials used and the geometrical details in an effort to numerically reproduce the behavior observed at the laboratory. The main conclusions are listed below:

- The observed mode of failure of all specimens was the cracking along the bed joint at mid-height joint
- The existence of reinforcing bar, placed vertically at a grouted hole, contributed in an increase of maximum load measured, proportional to the rebar's cross section.
- The unreinforced masonry wallet exhibited a rather brittle performance, as after the bed joint's crack a sudden loss of the applied load occurred. On the contrary, reinforced masonry walls performed much more ductile exhibiting an "elastic – plastic" response.

- The vertical rebar of diameter 14mm and 16mm, while leading to a further increase of maximum load, exhibit a less ductile behavior compared to the reinforced wall with 1D10mm vertical rebar, due to the failure of the compressive zone at the mid height.
- The developed numerical models discussed here can satisfactorily capture the observed mode of failure, the maximum load measured and up to a point the force – deflection curves.

## ACKNOWLEDGEMENTS

All materials for the construction of the specimens were provided by “KEBE S.A. (Northern Greece Ceramics)”. Part of the aforementioned research “Innovative construction system of reinforced masonry with anti-seismic, thermal-insulating and environmental friendly characteristics (TheSeisMas)” has been co-funded by Greece and European Union through the Operational Program “Erevno - Dimiourgo - Kainotomo” (project code: T1EDK-03314) which are gratefully acknowledged.



Co-financed by Greece and the European Union

## REFERENCES

- [1] Manos G (2011), “Consequences on the urban environment in Greece related to the recent intense earth-quake activity”, Int. Journal of Civil Engineering and Architecture, Volume 5, No. 12 (Serial No. 49), pp. 1065–1090.
- [2] Manos G.C. (2020) “The 30th of October Samos-Greece Earthquake. Issues relevant to the protection of structural damaged caused by strong earthquake ground motions”, Journal Architecture and Engineering, Volume 5 Issue 4, <https://aej.spbgasu.ru/index.php/AE>, DOI: 10.23968/2500-0055-2020-5-4-03-17
- [3] G.C. Manos, L. Kotoulas, L. Melidis, K. K. (2019). Partially grouted reinforced brick masonry wall specimens made in Greece subjected to in-plane seismic loadingQ experimental observations and numerical prediction. 13th North American Masonry Conference.
- [4] Manos, G. C., Kotoulas, L., Melidis, L., & Katakalos, K. (2019). Partially grouted reinforced masonry piers under seismic-type in-plane loads. Experimental measurements and non-linear numerical simulations. COMPDYN Proceedings, 1, 252–268. <https://doi.org/10.7712/120119.6917.19257>
- [5] Mosele, F., & Da Porto, F. (2011). Innovative clay unit reinforced masonry system: Testing, design and applications in Europe. Procedia Engineering, 14, 2109–2116. <https://doi.org/10.1016/j.proeng.2011.07.265>
- [6] Loureço, P. B., Vasconcelos, G., Medeiros, P., & Gouveia, J. (2010). Vertically perforated clay brick masonry for loadbearing and non-loadbearing masonry walls. Construction and Building Materials, 24(11), 2317–2330. <https://doi.org/10.1016/j.conbuildmat.2010.04.010>

- [7] Da Porto, F., Mosele, F., & Modena, C. (2011). Cyclic out-of-plane behaviour of tall reinforced masonry walls under P- $\Delta$  effects. *Engineering Structures*, 33(2), 287–297. <https://doi.org/10.1016/j.engstruct.2010.10.004>
- [8] Noor-E-Khuda, S., & Dhanasekar, M. (2020). On the out-of-plane flexural design of reinforced masonry walls. *Journal of Building Engineering*, 27(December 2018), 100945. <https://doi.org/10.1016/j.jobbe.2019.100945>
- [9] Kotoulas, L., Manos, G. C., Melidis, L., Katakalos, K., & Manolis, G. (2019). Unreinforced masonry materials under axial compression or four-point flexure. Laboratory measurements and numerical simulations. *COMPdyn Proceedings*, 1, 345–358. <https://doi.org/10.7712/120119.6923.19346>
- [10] Manos, G. C., Melidis, L., & Katakalos, K. (2020). PARTIALLY REINFORCED MASONRY PIERS UNDER SEISMIC-TYPE LOADS. MEASUREMENTS AND NUMERICAL SIMULATIONS. 17th World Conference on Earthquake Engineering.
- [11] EN 772-1:2011 - Methods of test for masonry units Part 1: Determination of compressive strength.
- [12] EN 1015-11:2019 - Methods of Test for Mortar for Masonry - Part 11: Determination of flexural and compressive strength of hardened mortar.
- [13] EN 1052-1:1999 – Methods of test for Masonry – Part 1: Determination of compressive strength
- [14] EN 1052-2:1999 – Methods of test for Masonry – Part 2: Determination of flexural strength

## IN PLANE BEHAVIOR OF PARTIALLY GROUTED MASONRY WALLS USING A NEW CLAY UNIT. LABORATORY MEASUREMENTS AND NUMERICAL SIMULATIONS

George C. Manos<sup>1</sup>, Lazaros Melidis<sup>2</sup>, Lampros Kotoulas<sup>3</sup>, Kostas Katakalo<sup>4</sup>

<sup>1,2,3,4</sup> Lab. Strength of Materials and Structures, Aristotle University

[gcmayos@civil.auth.gr](mailto:gcmayos@civil.auth.gr), [lazmelidis@gmail.com](mailto:lazmelidis@gmail.com), [kotoulaslambros@gmail.com](mailto:kotoulaslambros@gmail.com), [kkatakalo@civil.auth.gr](mailto:kkatakalo@civil.auth.gr)

---

### Abstract

*A new innovative clay brick unit is used for the construction of partially grouted masonry walls. This new unit aims to provide both the required mechanical properties and thermal insulating properties. The behavior of masonry specimens constructed with this unit and thin mortar method under in plane loads is discussed here. The basic mechanical properties of the examined construction system are measured by a series of material tests, prism tests under combined shear and compression and wallets under compression tests. The laboratory measurements are compared with the defined by EC6 values. Following, diagonal compression tests were conducted at the Laboratory of Strength of Materials and Structures (Aristotle University of Thessaloniki) to ungrouted and grouted masonry wallets with different reinforcing details employing horizontal reinforcing steel bars placed at the prefabricated holes of the clay unit. The effect of the reinforcing steel bars in the bearing capacity and in the post peak behavior is investigated. Apart from the experimental investigation, numerical models simulating these tests were developed utilizing all the geometrical properties of the specimens and the mechanical properties of the materials used. The numerically simulated behavior resembles the measured load-deformation response of the tested specimens and the observed actual damage at the end of the tests.*

**Keywords:** Partially grouted masonry, In plane behavior, Laboratory measurements, Numerical Simulations.

---

## 1 INTRODUCTION

The vulnerability of unreinforced masonry walls subjected to seismic loads was highlighted during past earthquake events [1, 2]. The employment of reinforcing bars to construct earthquake resistant partially grouted masonry structures has been widely investigated. Manos et al. [3, 4] tested partially reinforced piers with different reinforcing schemes. For the tested piers with a height over length ratio equal to 1 and horizontal reinforcing ratio values larger than 0.085%, the flexural response together with the rather ductile plastic rotation response at the bottom of the wall, similar to a plastic-hinge mechanism. Additionally, some of the specimens exhibited extensive compressive failures on the compression zone. Other researchers [5, 6] investigated the influence of the horizontal shear reinforcement in partially grouted masonry piers subjected to combined horizontal and vertical loads. It was observed that shear reinforcement not only provided additional resistance, but also improved the post-cracking performance. Recent studies investigate the behavior of reinforced masonry walls using new clay units with the appropriate thermal properties in an effort to improve the structures energy consumption together with an acceptable structural performance [7, 8]. Again, the importance of bricks mechanical properties was noted as the deformation of walls appeared to be limited by the brittleness of the units, as toe crushing develops for some walls, leading also to a low dissipation of energy.

An ongoing research of Laboratory of Strength of Materials and Structures deals with partially grouted reinforced masonry walls constructed with a novel clay unit. A key issue in the construction of these walls is the masonry unit employed. The geometry of this new unit was defined using parametric numerical predictions taking into consideration not only the mechanical properties, but also parameters like thermal properties, production cost and ease of construction practice [9, 10]. In this paper the in-plane behavior of ungrouted and partially grouted masonry wallets is discussed. Results are presented from tests of unreinforced masonry wallets or reinforced with horizontal rebars of different diameters, which are subjected to in-plane diagonal compression. The mechanical properties of all the employed materials are defined through testing. Following, numerical predictions of this measured in-plane behaviour are also included. All these results are presented and discussed focusing on the influence of the reinforcing arrangement in the overall in plane response.

## 2 SPECIMEN CONSTRUCTION AND MATERIAL PROPERTIES

The geometry of the employed clay unit is depicted in Figure 1. The basic mechanical properties of this unit were measured at the Laboratory. More specific, unit's compressive strength perpendicular to the bed joint and parallel to the bed joint are measured by compression test according to EN772-1 [11]. The proposed reinforced masonry system uses the construction technique of thin mortar joint. The mechanical properties of the mortar material used, were obtained by material testing according to EN1015-19 [12]. Additionally, tensile tests for the used reinforcing steel bars with diameter 6mm and 8mm were conducted. The above mentioned properties are listed at table 1 and table 2.

The used vertically perforated units with nominal dimensions length=210mm, height=240mm and thickness=300mm had properly shaped to form two horizontal channels in order to embody the horizontal reinforcement (figure 1). Additionally, vertical holes are formed between the clay units used for the vertical reinforcing bars.

All specimens were built by builders following the relevant prototype work conditions. The constructed specimens (1340mm by 1340mm and a thickness of 300mm) were tested under diagonal compression. The used experimental set up are depicted in figure 2. This simple loading scheme to study the in-plane performance of masonry panels is specified by ASTM



E519-15 [13] and by RILEM Technical Recommendations for “Testing and Use of Construction Materials” [14].

<b>Brick unit</b>	
mean compressive strength perpendicular to bed joints ( $f_b$ )	8.12 MPa
mean compressive strength parallel to bed joints ( $f_{b,h}$ )	2.73 MPa
<b>Mortar</b>	
compressive strength ( $f_m$ )	13.47 MPa
flexural strength ( $f_{mt}$ )	2.80 MPa

Table 1: mechanical properties of masonry materials used.

steel bar's diameter	yield stress (MPa)	ultimate stress (MPa)	yield strain	ultimate strain
D6mm	605	650	3.00‰	4%
D8mm	550	657	2.75‰	15%

Table 2: mechanical properties of steel reinforcing bars

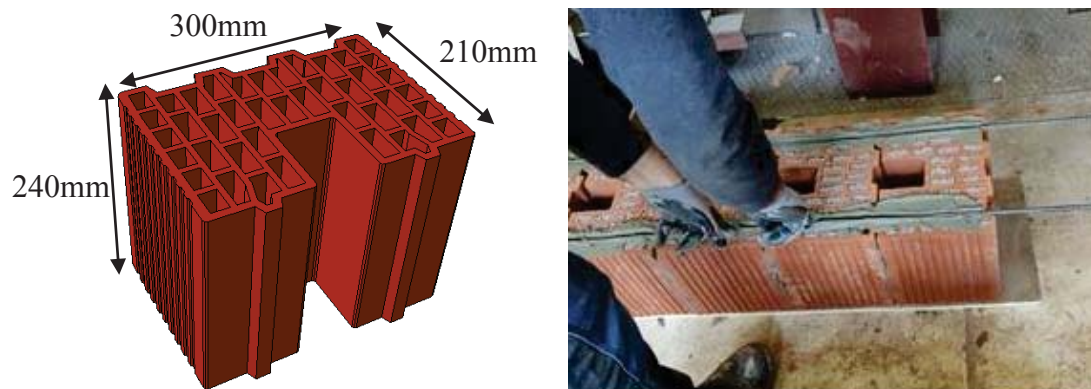


Figure 1: The geometry of the novel brick unit (left) and the employed of horizontal bars (right)

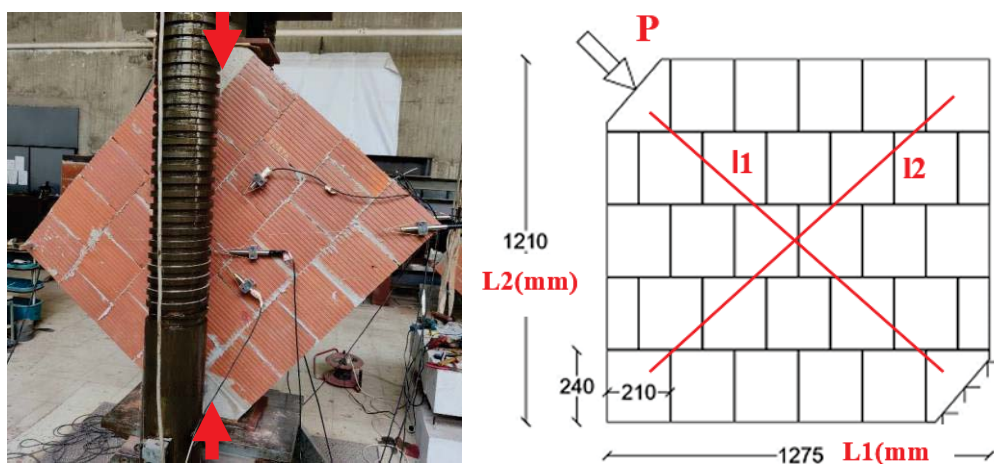


Figure 2: Experimental set-up (left) and the employed of horizontal bars (right)



The vertical compressive load was monotonic and was applied at a relative slow rate being measured by a load cell. Displacement transducers were also used to measure the vertical and horizontal variation of the length of the two main diagonals at both facades of the loaded specimen. By utilizing these displacement transducers, the variation of the diagonal lengths was monitored together with the variation of the applied vertical load throughout the whole of the loading sequence employing an automatic data recording acquisition system. The observed performance for each tested specimen is presented in section 3 in terms of the variation of the equivalent shear stress versus the corresponding shear strain, obtained as described before.

All measurements were used to obtain the performance of each specimen in terms of the variation of the equivalent shear stress ( $\tau_s$ ) versus shear strain ( $\gamma$ ) calculated through equations 1 and 2, as is described in ASTM E519-15 [13]. Each specimen was designed to be tested under diagonal compression along one of its main diagonals having a concrete block at the top and bottom corner of the vertical diagonal of each specimen in order to facilitate the application of the compressive diagonal load (fig. 3).

$$\tau_s = (0.707 * P) / [0.5 * (L1 + L2) * t] \quad (1)$$

$$\gamma = |\delta l1| / l1 + |\delta l2| / l2 \quad (2)$$

*P*: the applied vertical load.

*L1 and L2*: the length of the sides of the wallet as indicated in figure 2.

*l1 and l2*: the length of the vertical and horizontal diagonals the variation of which is monitored with displacement transducers attached on the brick façade of the wallet as indicated in figure 2.

$\delta l1$  and  $\delta l2$ : the variation of the relevant lengths *l1* and *l2* as they occur during the variation of the applied load (*P*).

*t*: the thickness of the masonry panel (neither the thickness of the thermo-insulating attachment nor the thickness of the adhesive mortar are included).

### 3 EXPERIMENTALLY OBSERVED BEHAVIOR

The observed diagonal compression performance of the tested specimens with or without horizontal reinforcing bars is presented and discussed in terms of the variation of the equivalent shear stress ( $\tau_s$ ) versus shear strain ( $\gamma$ ) (equations 1 and 2) together with the observed damage. Firstly, the performance of the unreinforced wallets is given. Figure 4 (right) depicts the observed performance of the unreinforced masonry wallet without any reinforcement, which represents the control specimens. As can be seen the shear strength value is of the order of 0.56MPa and the equivalent shear-stress versus shear strain variation characterizes this performance as being rather brittle. At the same figure (4a) the formation of a typical diagonal tension crack characterizes the observed mode of failure.

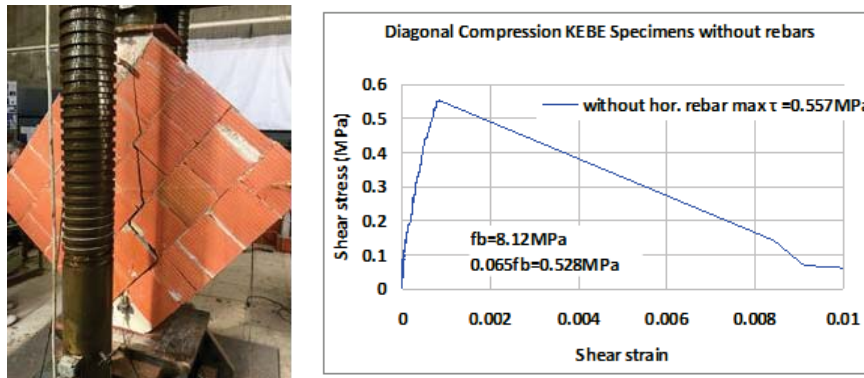


Figure 3: Damage pattern of bare wallet (left) and its response in terms of shear stress versus shear strain (right)

Following, the response of the tested specimens with horizontal reinforcing bars is presented. Figure 4 depicts the observed damage and the variation of the equivalent shear stress ( $\tau$ ) versus shear strain ( $\gamma$ ) (equations 1 and 2) for a specimen with 2 horizontal bars of diameter 6mm at each bed joint. Figure 5 depicts the observed damage and the variation of the equivalent shear stress versus shear strain for a specimen with 2 horizontal bars with diameter of 8mm at each bed joint. As can be seen the shear strength value for the reinforced specimens is slightly increased. The formation of a typical diagonal tension crack characterizes the observed mode of failure for these specimens.

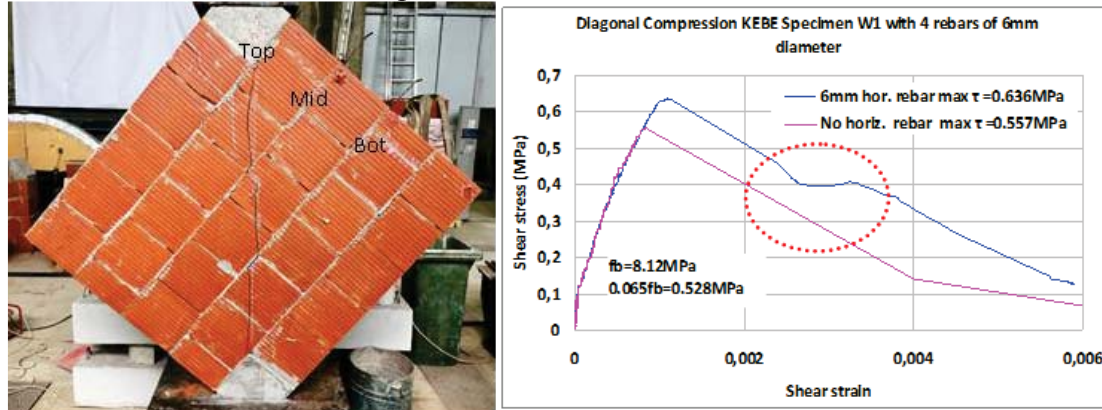


Figure 4: Damage pattern of reinforced wallet with D8mm reinforcing bars and its response in terms of shear stress versus shear strain (right)

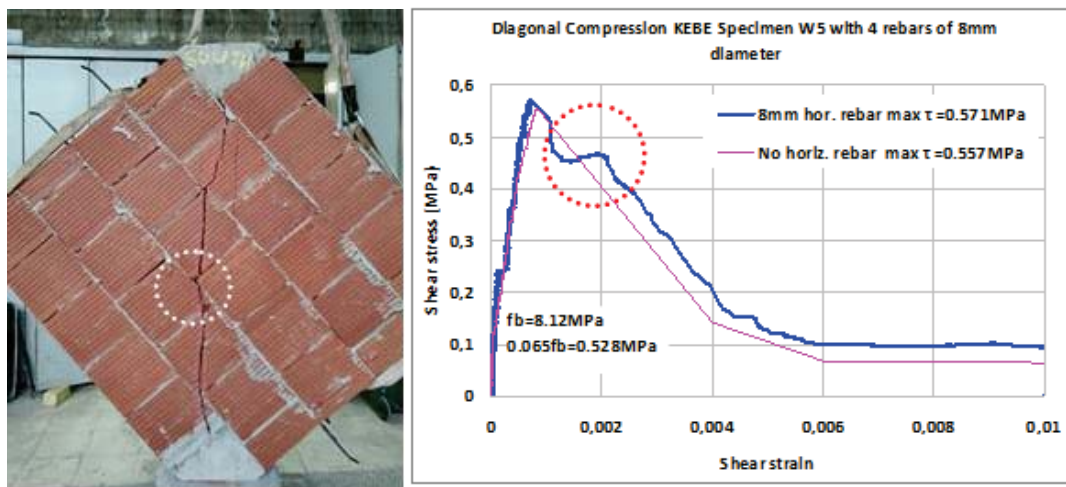


Figure 5: Damage pattern of reinforced wallet with D8mm reinforcing bars (left) and its response in terms of shear stress versus shear strain (right)

#### 4 NUMERICAL MODELING

Three-dimensional finite element numerical models were formed, adopting a macro modeling approach with a homogenized material obeying the Concrete Damaged Plasticity (CDP) constitutive law for the masonry, that can satisfactorily represent the behaviour of brittle materials, like concrete or masonry, with different stress – strain laws for compression and tension. The numerical model resembling the unreinforced wallet was calibrated in order to capable follow the behavior observed at the laboratory. All the parameters used for the constitutive law are listed at table 3. The geometry and details of the numerical model are depicted in figure 6.

Concrete Damaged Plasticity – material model assigned to masonry panel					
Elastic properties		Compressive behavior		Tensile behavior	
Young's Modulus (MPa)	4000	Yield stress MPa	Plastic stain	Yield stress MPa	Plastic stain
Poisson's ratio	0.15	3.60	0	0.48	0
		0	0.01	0	0.01

Table 3: Parameters of CDP constitutive law for masonry material

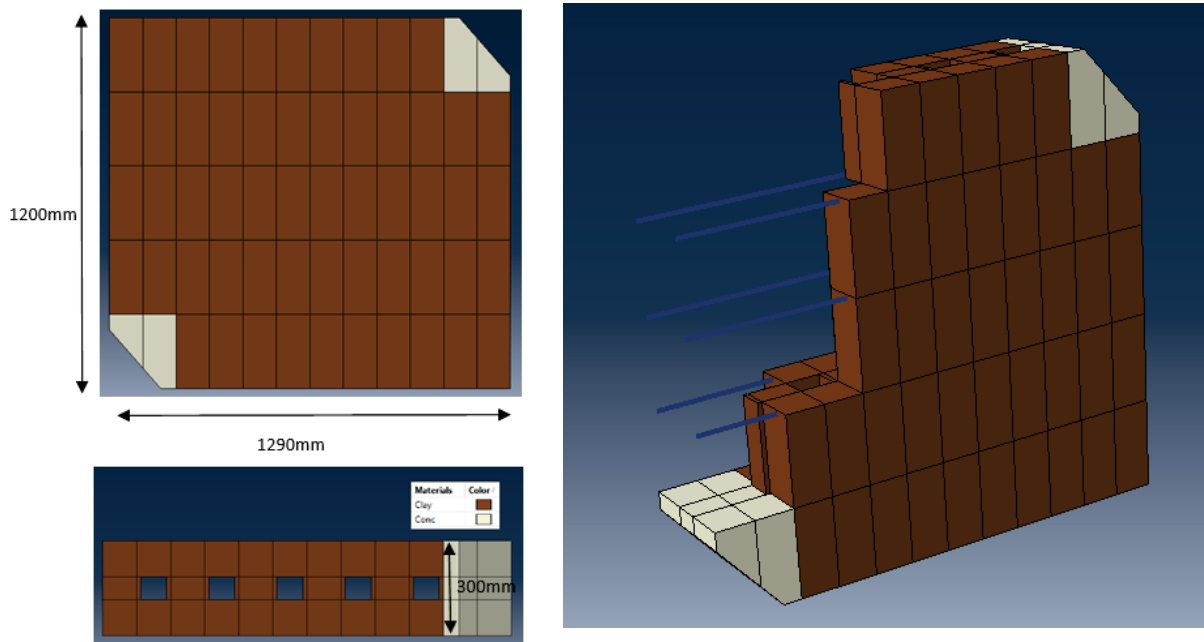


Figure 6: Numerical model. Front view and top view (left) and 3D view of the model with the embedded reinforcing steel bars (right)

The damaged pattern of the unreinforced wallet's numerical model is depicted in figure 7 together with the comparison of shear stress - shear strain response with the corresponding tested specimen. A very good agreement is observed both in the stress – strain response and in the damage pattern observed.

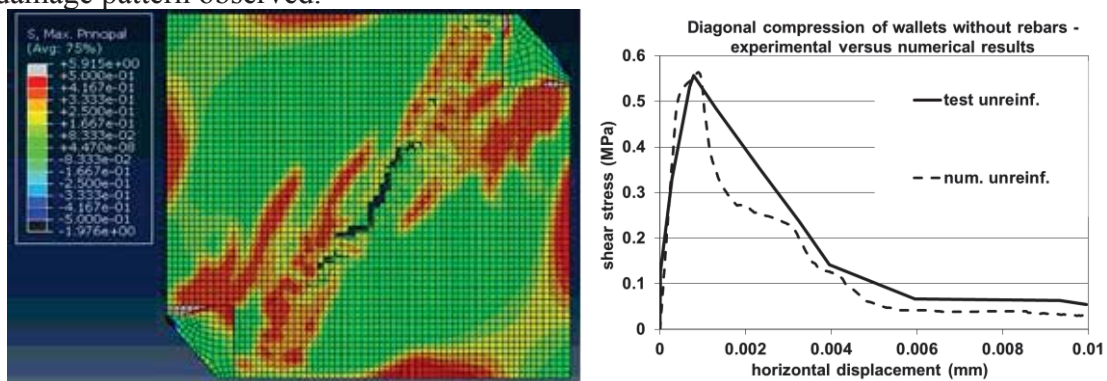


Figure 7: Maximum principal stress (MPa) and damage pattern of unreinforced numerical model at the step of maximum load (left) and its response in terms of shear stress versus shear strain (right)

Following, in the previous model horizontal reinforcing bars are added as shown in figure 6 with wire elements. The reinforcing bars are of diameter 6mm or 8mm as in the tested specimens. These bars are assigned with an elasto-plastic material law obtained by material testing



(section 2). A perfect bond between rebars and the masonry panel is assumed. The damaged pattern of the numerical model and a comparison of shear stress - shear strain response with the corresponding tested specimens is shown in figure 8 and 9 for the model with horizontal bars with diameter 6mm and 8mm respectively. In general, a good agreement is observed both in the stress – strain response and in the damage pattern. Additionally, the developed axial stresses of the horizontal rebars are depicted in figure 10 at the step of maximum load for both reinforced models, in an effort to explain the contribution of the horizontal reinforcing bars in the overall response.

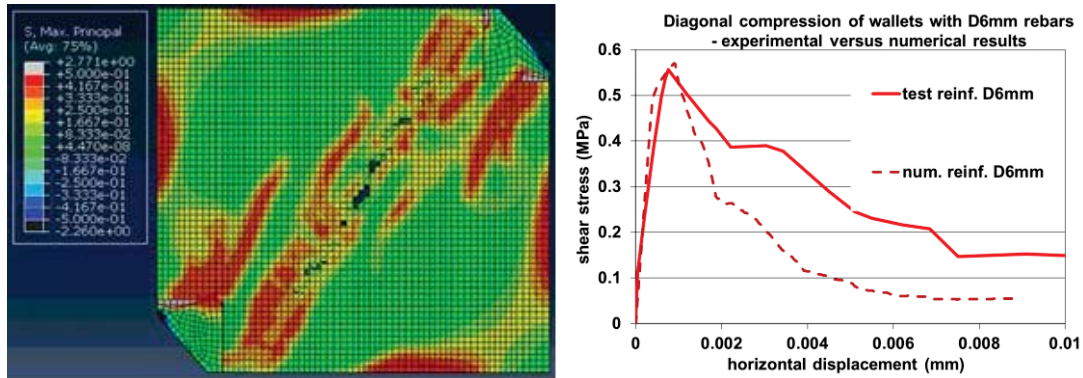


Figure 8: Maximum principal stresses (MPa) and damage pattern of reinforced with D6mm horizontal bars numerical model at the step of maximum load (left) and its response in terms of shear stress versus shear strain (right)

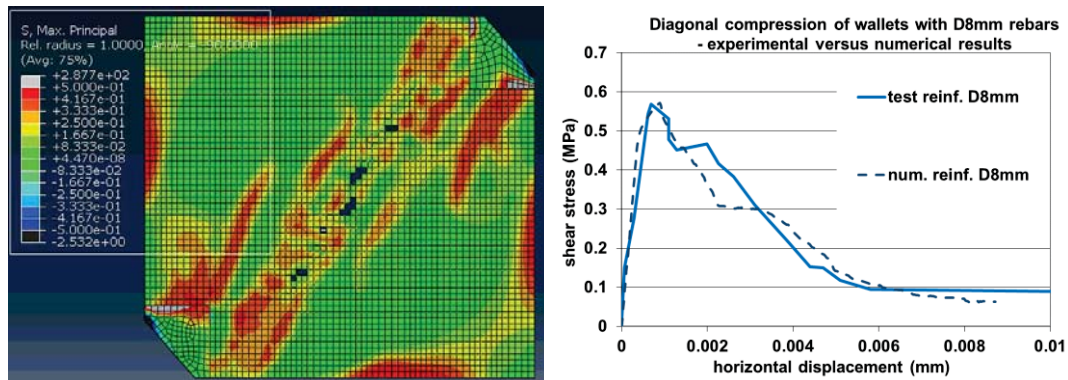


Figure 9: Maximum principal stresses (MPa) and damage pattern of reinforced with D8mm horizontal bars numerical model at the step of maximum load (left) and its response in terms of shear stress versus shear strain (right)

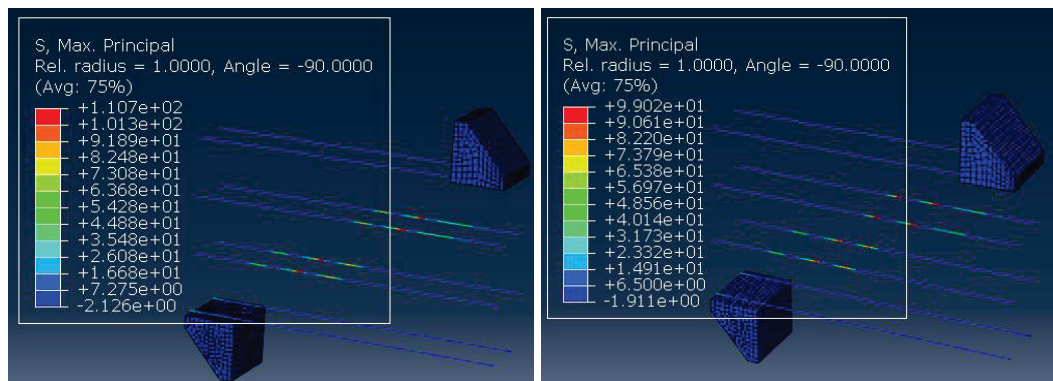


Figure 10: Developed axial stresses (MPa) of reinforcing bars at the step of maximum load for D6mm bars (left) and D8mm bars (right)

## 5 DISCUSSION

Figure 12 depicts the response in terms of equivalent shear stress versus shear strain for unreinforced and reinforced with horizontal reinforcing steel bars with diameter either 6mm or 8mm. The corresponding numerical predictions are also shown in the same figure. In all cases it is clear that there is no remarkable increase of shear strength due to the reinforcing steel bars. Over the literature there are studies reporting similar observations by diagonal compression test either on reinforced masonry wallets [15] or on strengthened wallets with steel bars mounted near masonry's surface [16]. This is explained by the fact that till the maximum load, reinforcement's stresses are not great. When the non-linear behavior occurs and masonry's cracks are widening the reinforcing bars develop greater stress. Thus, the existence of horizontal reinforcing bars seems to improve the post peak response leading to a less brittle declining brunch.

The shear strength is highly affected by the clay unit's compressive strength as the diagonal cracking propagates through the clay units. This mode of failure is predicted in Eurocode 6 [17] as the shear strength is prevailed by an upper limit of  $0.065 \cdot f_b$  (units' mean compressive strength). In the examined case this limit is calculated 0.528 MPa, pretty close to the shear strength values obtained by the diagonal compression tests.

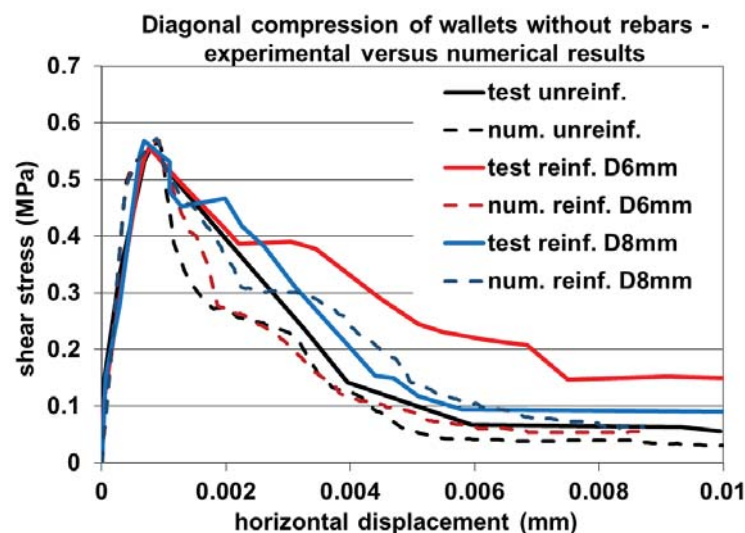


Figure 11: Response of both tested specimens and numerical models for unreinforced and reinforced configuration

## 6 CONCLUSIONS

The behavior of reinforced masonry wallets under diagonal compression is discussed here, mainly focusing on the contribution of the horizontal reinforcing bars in the overall wallet's response. Apart from the experimental observations, numerical models were developed using all the available information about the mechanical properties of the materials used in an effort to numerically reproduce the behavior observed at the laboratory. The main conclusions are enlisted below:

- The horizontal reinforcing bars are not clearly increase masonry's shear strength, but they contribute for the increase on the ductility.
- The observed damage pattern of the diagonal cracking does not change when horizontal reinforcing bars are added and it is directly linked with the compressive strength of clay units used.

- The developed numerical models, after calibrated with the unreinforced specimen's response, can satisfactorily capture the observed behavior of reinforced masonry wallets both in terms of shear stress – shear strain response, but also in the damage pattern.

## ACKNOWLEDGEMENTS

All materials for the construction of the specimens were provided by “KEBE S.A. (Northern Greece Ceramics)”. Part of the aforementioned research “Innovative construction system of reinforced masonry with anti-seismic, thermal-insulating and environmental friendly characteristics (TheSeisMas)” has been co-funded by Greece and European Union through the Operational Program “Erevno - Dimiourgo - Kainotomo” (project code: T1EDK-03314) which are gratefully acknowledged.



Co-financed by Greece and the European Union

## REFERENCES

- [1] Manos G (2011), “Consequences on the urban environment in Greece related to the recent intense earth-quake activity”, Int. Journal of Civil Engineering and Architecture, Volume 5, No. 12 (Serial No. 49), pp. 1065–1090.
- [2] Manos G.C. (2020) “The 30th of October Samos-Greece Earthquake. Issues relevant to the protection of structural damaged caused by strong earthquake ground motions”, Journal Architecture and Engineering, Volume 5 Issue 4, <https://aej.spbgasu.ru/index.php/AE>, DOI: 10.23968/2500-0055-2020-5-4-03-17
- [3] G.C. Manos, L. Kotoulas, L. Melidis, K. K. (2019). Partially grouted reinforced brick masonry wall specimens made in Greece subjected to in-plane seismic loadingQ experimental observations and numerical prediction. 13th North American Masonry Conference.
- [4] Manos, G. C., Kotoulas, L., Melidis, L., & Katakalos, K. (2019). Partially grouted reinforced masonry piers under seismic-type in-plane loads. Experimental measurements and non-linear numerical simulations. COMPDYN Proceedings, 1, 252–268. <https://doi.org/10.7712/120119.6917.19257>
- [5] Calderón, S., Sandoval, C., & Arnau, O. (2017). Shear response of partially-grouted reinforced masonry walls with a central opening: Testing and detailed micro-modelling. Materials and Design, 118(January), 122–137. <https://doi.org/10.1016/j.matdes.2017.01.019>
- [6] K. C. Voon, J. M. I. (2006). Experimental In-Plane Shear Strength Investigation of Reinforced Concrete Masonry Walls. Journal of Structural Engineering.
- [7] Mosele, F., & Da Porto, F. (2011). Innovative clay unit reinforced masonry system: Testing, design and applications in Europe. Procedia Engineering, 14, 2109–2116. <https://doi.org/10.1016/j.proeng.2011.07.265>



- [8] Loureço, P. B., Vasconcelos, G., Medeiros, P., & Gouveia, J. (2010). Vertically perforated clay brick masonry for loadbearing and non-loadbearing masonry walls. *Construction and Building Materials*, 24(11), 2317–2330. <https://doi.org/10.1016/j.conbuildmat.2010.04.010>
- [9] Kotoulas, L., Manos, G. C., Melidis, L., Katakalos, K., & Manolis, G. (2019). Unreinforced masonry materials under axial compression or four-point flexure. Laboratory measurements and numerical simulations. *COMPdyn Proceedings*, 1, 345–358. <https://doi.org/10.7712/120119.6923.19346>
- [10] Manos, G. C., Melidis, L., & Katakalos, K. (2020). PARTIALLY REINFORCED MASONRY PIERS UNDER SEISMIC-TYPE LOADS. MEASUREMENTS AND NUMERICAL SIMULATIONS. 17th World Conference on Earthquake Engineering.
- [11] EN 772-1:2011 - Methods of test for masonry units Part 1: Determination of compressive strength.
- [12] EN 1015-11:2019 - Methods of Test for Mortar for Masonry - Part 11: Determination of flexural and compressive strength of hardened mortar.
- [13] ASTM E519-15 (2015) Standard test method for diagonal tension (shear) in masonry assemblages. American Society for Testing Material
- [14] RILEM LUMB6 (1994) Diagonal tensile strength tests of small wall specimens (1991). Rilem recommendations for the testing and use of constructions materials. RILEM, pp 488–489.
- [15] Haach, V. G., Vasconcelos, G., & Lourenço, P. B. (2014). Study of the behaviour of reinforced masonry wallets subjected to diagonal compression through numerical modelling. 9th International Masonry Conference 2014, 1–11.
- [16] Ismail, N., Petersen, R. B., Masia, M. J., & Ingham, J. M. (2011). Diagonal shear behaviour of unreinforced masonry wallettes strengthened using twisted steel bars. *Construction and Building Materials*, 25(12), 4386–4393. <https://doi.org/10.1016/j.conbuildmat.2011.04.063>
- [17] EN1996-1-1:2005 Eurocode 6 - Design of masonry structures - Part 1-1: General rules for reinforced and unreinforced masonry structures

## EXPERIMENTAL AND NUMERICAL INVESTIGATION OF THE OUT OF PLANE BEHAVIOR OF THERMAL INSULATED MASONRY WALLETS

George C. Manos<sup>1</sup>, Lazaros Melidis<sup>2</sup>, Kostas Katakalos<sup>3</sup>, Anthimos Anastasiadis<sup>4</sup>

<sup>1,2,3</sup>, Lab. Strength of Materials and Structures, Aristotle University  
[gmanos@civil.auth.gr](mailto:gmanos@civil.auth.gr), [lazmelidis@gmail.com](mailto:lazmelidis@gmail.com), [kkatakal@civil.auth.gr](mailto:kkatakal@civil.auth.gr)

<sup>4</sup> Dr. Civil Engineer, Research Associate, Thessaloniki, Greece,  
[anastasiadis@asacon.eu](mailto:anastasiadis@asacon.eu)

### Abstract

*Multi-story buildings are composed of multi-bay steel or R/C frames having unreinforced masonry panels considered as non-structural elements not included in the structural design. Such structures are subjected to strong earthquake motions, leading to potentially damaging conditions for the masonry in the form of in-plane damage or/and its dislocation and partial collapse. This study focuses on the out of plane response of unreinforced masonry panels built with clay bricks units horizontally perforated representing a typical masonry infill subassembly. The examined masonry panels constructed and tested at the Laboratory of Strength of Materials and Structures (Aristotle University of Thessaloniki) are subjected to cyclic out of plane bending as built or attached with different thermal insulating facades. The response of these tests is presented in terms of horizontal load applied versus the corresponding horizontal displacement in an effort to record the influence of the thermal façade on masonry's response. Moreover, numerical models were developed in order to replicate the observed at the laboratory behavior. These models include non linear constitutive material laws together with non linear interfaces to represent the debonding of the thermal insulating facades. The measured response is presented and discussed together with the corresponding effort to numerically simulate the observed performance.*

**Keywords:** ETICS, Thermal insulation, Out of plane behavior of masonry wallets, numerical investigation

## 1 INTRODUCTION

Unreinforced masonry panels are used in multi-story buildings made of steel or reinforced concrete (R/C) to form the exterior facades or the interior partitions. Thermo-insulating panels are also attached on the exterior facades of these masonry panels in order to improve the energy efficiency of these building as well as to reduce noise and moisture penetration. This type of masonry façades is widely applied in many countries ([1, 2]). These masonry infills are considered as non-structural elements and they are not included in the structural design. However, they interact with the surrounding structural members, when such structures are subjected to strong earthquake motions. This is because masonry infills are forced to follow the displacement response of the supporting surrounding structural members (slabs, columns and beams) leading to potentially damaging conditions due to simultaneous in plane and out of plane loads. One of the most serious consequence of either of these forcing scenarios, when the seismic forces are considered as acting either separately (in-plane or out-of-plane) or combined, is the dislocation and partial collapse of such unreinforced masonry panels ([3, 4]). Figure 1a depicts a typical damage pattern observed in numerous multi-story buildings in Durres, Albania due to the recent strong earthquake sequence (26th November, 2019). Similar damage patterns have been observed in many past strong earthquake sequences in Greece (Athens 1999) and Italy (L' Aquila 2009).



Figure 1. Typical damage pattern observed in masonry infills. a) Albania, Durres 2019. b) Italy, L' Aquila 2009. c) Greece, Athens 1999.

EuroCode 6 ([5]), while accepting that vertical unreinforced masonry panels are subjected to both in-plane and out-of-plane seismic forces, includes design provisions based on the assumption of un-coupled in-plane and out-of-plane limit states. This simplification has been adopted in the large majority of relevant past research either for masonry walls or for infill masonry panels, similar to the ones studied here. The current research follows this simplification in the effort to study the influence of thermo-insulating attachments on the seismic performance of masonry panels [6, 7]. Only the out of plane behaviour for a thermo-insulated masonry panel is studied here. This is done by subjecting in the laboratory masonry wallets to simple loading conditions in order to generate stress fields within such specimens simulating similar stress fields in a masonry panel out-of-plane direction. The influence of a thermo-insulating attachment for the in-plane behaviour of masonry panels has been investigated and discussed before [3,4 8]. Results are presented from tests employing unreinforced masonry wallets, having relatively simple boundary conditions, which are subjected to out of plane bending. The mechanical properties of all the employed thermo-insulating materials are defined through testing. Following, numerical models were developed utilizing all the geometrical and mechanical properties in order to replicate the experimentally measured out of plane

behaviour. All these results are presented and discussed focusing on the influence of the external thermal insulation system (ETICS) in the overall out of plane response.

## 2 SPECIMEN CONSTRUCTION AND MATERIAL PROPERTIES

The specimens are masonry sub-assemblies which are constructed and tested at the Laboratory of Strength of Materials and Structures (Aristotle University of Thessaloniki, Greece). The thermo-insulating materials are produced by “FIBRAN Anastasiadis Dimitrios S.A.” and are applied on the specimens to be tested in the same way that are applied in prototype construction. A cross section of a masonry wallet attached with ETICS is depicted in figure 2. All specimens were built with the same 12-hole clay brick unit of nominal dimensions length=320mm, height=180mm and thickness=150mm. This brick unit is commonly used in prototype construction for this type of un-reinforced masonry panels in multi-story buildings in Greece. Similarly, a relative weak general-purpose mortar was used for all specimens. The thermo-insulating layer was added to one side of all specimens two months following their construction following the relevant construction practice. Three different thermo-insulating materials, with code names XPS, EPS and Petro, were investigated, having a panel thickness of 100mm. Specimens of all materials used for building these specimens were taken during construction and tested for determining the relevant mechanical characteristics. The mechanical properties of masonry materials are listed in table 1. Due to space limitations, the mechanical properties of ETICS materials are not reported here. However, their mechanical properties and the bond strength between ETICS and masonry substrate together with the in-plane behavior of thermal insulated masonry wallets are extensively discussed before [8].

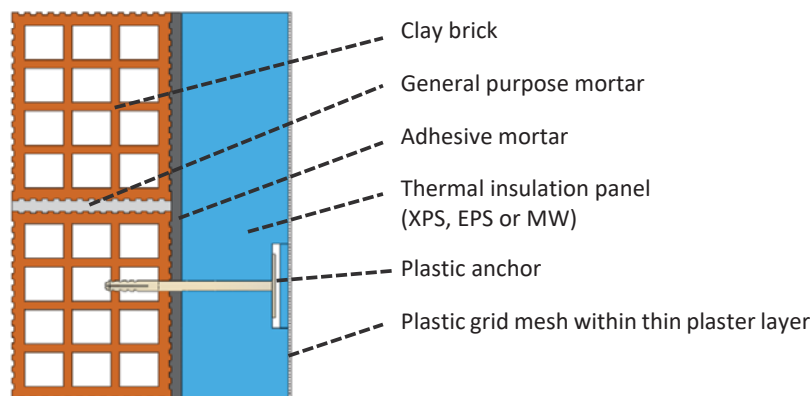


Figure 2 Typical cross-section of a thermal insulated infill wall.

<b>Brick unit</b>	
mean compressive strength perpendicular to bed joints ( $f_b$ )	2.97 MPa
<b>Mortar</b>	
compressive strength ( $f_m$ )	2.15 MPa
flexural strength ( $f_{mt}$ )	1.16 MPa

Table 1 mechanical properties of masonry materials used

The behavior of 4 wallets subjected to out of plane bending is discussed here. The first one is bare without any thermal insulation. The other three specimens are thermal insulated with MW, EPS and XPS panels with thickness 100mm respectively. The dimensions of these wallets are depicted in figures 3a and 3b. The out-of-plane load was applied at a horizontal cross-

section located at the mid-height of wallet as depicted in figure 3. The applied out-of-plane load and the corresponding out-of-plane displacement at the mid-height central point of the wallet was recording during the test with a data acquisition system.

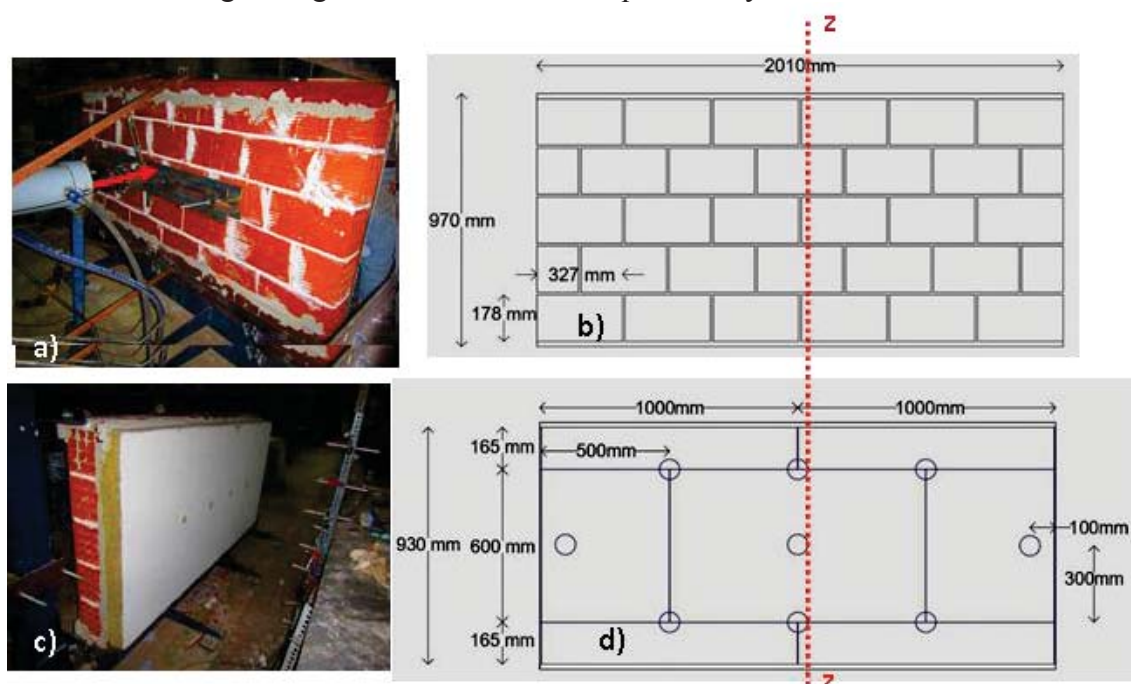


Figure 3. Out-of-plane flexure of a masonry wallets. a) and b) View from the brick façade. c) and d) View from the thermo-insulating (mineral wool) façade. The circles indicate the location of the anchors.

### 3 EXPERIMENTALLY OBSERVED BEHAVIOR

The observed out of plane performance of the tested specimens with or without thermal insulations is presented and discussed in terms of the out of plane load applied at mid-height versus the out of plane deflection together with the observed damage. Firstly, the observed performance of the bare masonry wallet without any insulation, which represents the control specimen. A linear behavior is observed till the first cracking at the minimum load (8.81kN) for an out of plane deflection about 2mm. At this point the flexural failure of the bed joint develops and it is followed by a sudden decrease of bearing capacity (figure 4).

Following, the response of the tested specimens with external thermal insulation panels are presented. The masonry specimen attached with MW panels with thickness of 100mm exhibited a maximum load 14.77kN for an out of plane deflection 5mm. The masonry wallets insulated with EPS and XPS with thickness 100mm reached a maximum load 35.62kN and 38.91kN respectively for out of plane deflection 5mm and 3mm respectively. The mode of failure of the thermal insulated panels included bed joint flexural cracking followed by a partial debonding of the thermal façade's panels.





Figure 4. Damage pattern of bare wallet

#### 4 NUMERICAL MODELING

Three-dimensional finite element numerical models were formed, adopting a macro modeling approach with a homogenized material obeying the Concrete Damaged Plasticity (CDP) constitutive law for the masonry, that can satisfactorily represent the behaviour of brittle materials, like concrete or masonry, with different stress – strain laws for compression and tension. The material law resembling the masonry part was calibrated to match the response of the corresponding wallet specimen. The attachment of the thermal insulation panels to the masonry is done with a layer of adhesive mortar which is numerically simulated with two layers of interfaces; the first interface is joining the mortar joint with the numerical simulation of the masonry and it is assigned with a perfect bond whereas the second interface is joining the mortar joint to the numerical simulation of the thermo-insulating panel and it is assigned with a cohesive-friction interface. The thermo-insulating panels were numerically simulated by 3-D finite elements. The ETICS properties and interface properties were defined from results obtained from material testing [8]. In this way, the measured flexural response was numerically simulated, utilizing the capabilities of commercial software [9]. The numerical predictions include one monotonic pushover analysis for deflection where the thermal panel are on the tensile face. All the numerical prediction for the bare and the insulated models are depicted in figure 5. The corresponding damage patterns are depicted in figure 6. In this figure, the plastic strains of the model are depicted resembling the horizontal cracking of the bare wallet of the mid bed joint (6a) and the detachment of the thermal panel following the bed joint failure (6a), as that was the predicted mode of failure for all insulated wallet models.



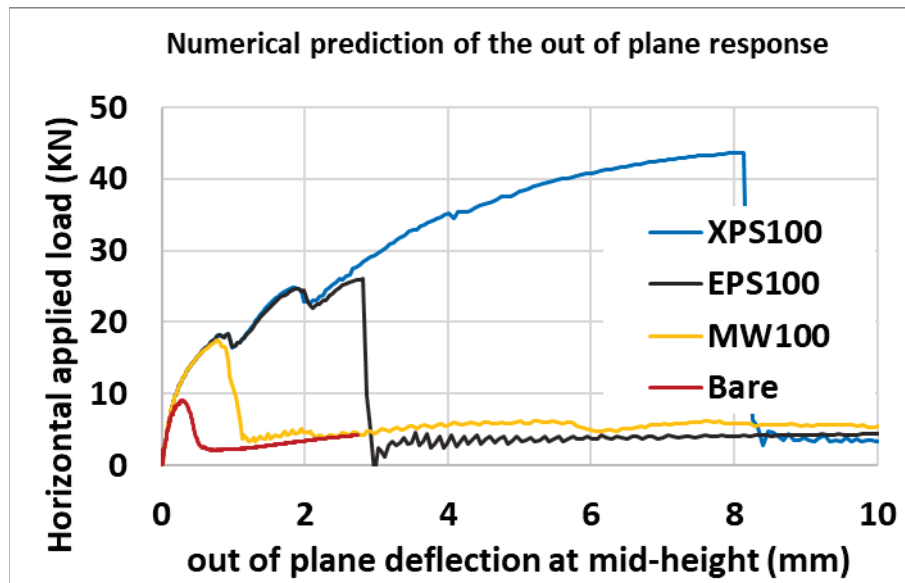


Figure 5. Numerical predictions of the tested specimens in terms of applied load versus the out of plane deflection at mid-height

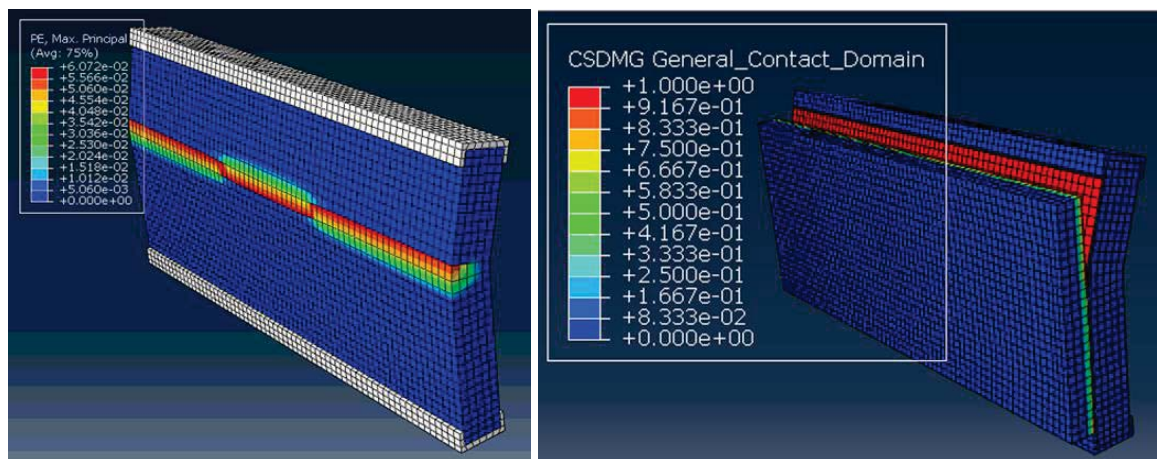


Figure 6. Plastic strains of the bare wallet model (a). The failure of the interface between adhesive mortar and insulation panel appeared for all insulated panels (b).

## 5 DISCUSSION

The behavior of 4 wallets, one bare and three attached with different insulating panels with thickness 100mm is discussed here. For these wallets both experimental results and numerical predictions are given. The table below (table 2) includes the absolute maximum load for each specimen and the corresponding deflections. For all specimens the mode of failure was the same and was characterized by the bed joints cracking at the mid-height section. Both the tested specimens and the numerical models exhibited partial detachment of the external thermal insulation following the bed joints crack.

Specimen detail	Experimental measurements		Numerical predictions	
	Absolute maximum load (KN)	Deflection at maximum load	Absolute maximum load (KN)	Deflection at maximum load
Bare	8.81	2mm	8.96	0.4mm
MW 100mm	14.77	5mm	17.55	0.8mm
EPS 100mm	35.62	5mm	26.09	2.8mm
XPS 100mm	38.91	3mm	43.59	8.1mm

Table 2. Summary results of all tested and numerically simulated wallets. Absolute maximum load is given together with the corresponding displacement

## 6 CONCLUSIONS

The behavior of thermal insulated wallets under out of plane bending is discussed here, mainly focusing on the response and the contribution of the ETICS employed in the overall wallet's response. Apart from the experimental observations, numerical models were developed using all the available information about the mechanical properties of the materials used and the geometrical details in an effort to numerically reproduce the behavior observed at the laboratory. The main conclusions are listed below:

- The observed mode of failure of all specimens was the cracking along the bed joint at mid-height joint. However, the existence of ETICS contributed in an increase of maximum load measured. The thermal insulated wallets exhibited larger bearing capacity. This increase differs depending on the panels used. The measured increment of load increase is 68%, 304% and 342% for MW, EPS and XPS insulating panels respectively.
- The developed numerical models discussed here can satisfactorily capture the observed mode of failure. All models exhibited plastic strains in a horizontal cross section resembling the failure of the tested specimens. Following the detachment of the thermal panels occurred, as it was observed during the experimental sequence. Additionally, the models discussed here can satisfactorily capture the maximum load increase and the force – deflection curves up to a point.

## ACKNOWLEDGMENTS

All materials for the construction of the specimens were provided by “FIBRAN Anastasiadis Dimitrios S.A.”. Part of the aforementioned research “Intelligent Facades for Nearly Zero Energy Buildings (IF – ZEB)” has been co-funded by Greece and European Union through the Operational Program “Erevno - Dimiourgo - Kainotomo” (project code: T1EDK-02045) which are gratefully acknowledged.



Co-financed by Greece and the European Union

**REFERENCES**

1. Antoniadou, P., Symeonidou, M., Kyriaki, E., Giama, E., Boemi, S. N., Chadiarakou, S., & Papadopoulos, A. M. (2020). High performance building façades for Zero Energy Buildings in Greece: State of the art and perspectives. *IOP Conference Series: Earth and Environmental Science*, 410(1). <https://doi.org/10.1088/1755-1315/410/1/012036>
2. Touloupaki, E., & Theodosiou, T. (2017). Optimization of external envelope insulation thickness: A parametric study. *Energies*, 10(3). <https://doi.org/10.3390/en10030270>
3. Manos, G. C., Melidis, L., Soulis, V., Katakalos, K., & Anastasiadis, A. (2020). The in-plane and out-of-plane behaviour of masonry panels with thermo-insulating attachment. *Brick and Block Masonry - From Historical to Sustainable Masonry*, 952–959. <https://doi.org/10.1201/9781003098508-135>
4. Masonry, U., Thermal, W., Facades, I., Buildings, I. N. M., To, S., & Type, S. (2020). UNREINFORCED MASONRY WITH THERMAL INSULATION FACADES IN MULTI-STORY BUILDINGS SUBJECTED TO SEISMIC TYPE LOADS.
5. EN1996-1-1:1998 Euro-code 6 - Design of masonry structures - Part 1-1: General rules for reinforced and unreinforced masonry structures
6. Sagar, S. L., Singhal, V., Rai, D. C., & Gudur, P. (2017). Diagonal shear and out-of-plane flexural strength of fabric-reinforced cementitious matrix-strengthened masonry wallets. *Journal of Composites for Construction*, 21(4), 1–13. [https://doi.org/10.1061/\(ASCE\)CC.1943-5614.0000796](https://doi.org/10.1061/(ASCE)CC.1943-5614.0000796)
7. Gkournelos, P. D., Triantafillou, T. C., & Bournas, D. A. (2020). Integrated Structural and Energy Retrofitting of Masonry Walls: Effect of In-Plane Damage on the Out-of-Plane Response. *Journal of Composites for Construction*, 24(5), 04020049. [https://doi.org/10.1061/\(ASCE\)CC.1943-5614.0001066](https://doi.org/10.1061/(ASCE)CC.1943-5614.0001066)
8. Manos, G. C., Melidis, L., Katakalos, K., Kotoulas, L., Anastasiadis, A., & Chatziastrou, C. (2021). Masonry panels with external thermal insulation subjected to in-plane diagonal compression. *Case Studies in Construction Materials*, 14, e00538. <https://doi.org/10.1016/j.cscm.2021.e00538>
9. Abaqus Unified FEA - SIMULIATM by Dassault Systèmes.

## EXPERIMENTAL & NUMERICAL INVESTIGATION OF LAP-SPLICED R/C COLUMNS UNDER THREE POINT BENDING & AXIAL COMPRESSION

Pelagia Kastiza<sup>1</sup>, Lazaros Melidis<sup>2</sup>, and Kostas Katakalos<sup>3</sup>

<sup>1,2,3</sup> Lab. Strength of Materials and Structures, Aristotle University

peggykast12@gmail.com, lnmelidis@civil.auth.gr, kkatakal@civil.auth.gr

---

### Abstract

*There is a valuable research work around the strength capacity of lap spliced rebars in columns specifically in accordance with bond-slip behavior or column's seismic response. Nonetheless, lap splicing of rebars with anchored ends under combined bending and compressive loads has not yet been fully explored with due consideration of its components. It is imperative to investigate a column's behavior under bending for different levels of axial load ratio and with different reinforcing configurations employing either plain or ribbed steel bars. This paper comparatively demonstrates the results of experimental and non-linear numerical simulations pertaining to the effect of splice strength and anchoring on the compression lap splicing of rebars in concrete column. The experimental specimens are composed by prototype-scale square columns with dense or sparse stirrups, measuring 250x250 mm and 2000 mm in length, while the steel reinforcement includes a lap splice length of 400mm. Some of the tested specimens were reinforced with plain spliced bars with anchored ends; while others included ribbed spliced bars with free ends. All the specimens were tested under simultaneous bending and constant concentric, axial loading of  $\nu=0.1$ . Finally, the investigation results outline the influence of lap splice to the structural integrity of the column as a part of a composite system and generally evaluate the resistance of the lap splices in a plastic joint area, under parametric analysis.*

**Keywords:** column, lap-splices, non-linear parametric analysis, plastic joint, three points bending, axial load ratio

---

## 1 INTRODUCTION

In multistorey buildings, the columns of every single storey bear different levels of axial loading because of the scaled weight of the overhead storeys and it would be ideal if each of the column's longitudinal rebars could be placed as one single piece throughout the structure's entire height. This however cannot be accomplished in many cases for practical reasons and indicates the necessity of lap splices. Straight lap splices are employed in reinforced concrete to transfer loads from one steel reinforcing bar to another through the bonding between the embedding concrete and the two bars along a lapped length. Moreover, it is convenient to lengthen the steel bar via lap splice in a variety of cases, but when lapping steel bars from successive stories, it is essential to ensure the correct transmission of forces from the rebars of the superjacent floor to the rebars of the subjacent floor. This can be achieved by welding; however, this method has a few technical difficulties and it is used only in special occasions. As a result, the practice usually followed is the rebar lap-splicing as for instance with the help of anchorage hooks in the lap splice ends. ([1], [2]) As long as the cooperation between concrete and lap-spliced rebars is ensured and during the column's loading combination of bending and axial loading, the spliced bars interact with each other, following a complex force transfer mechanism, unlike the behavior of the individual ones. As a result, three stages of stresses development arise as shown in fig.1. Experimental studies have shown, however, that the bond slip behavior (associated with either splitting or pullout) in a lap splice region is similar to that of individual embedded bars and it is generally accepted that there is a small deviation between the load-carrying capacity of lap-spliced rebars and an individual bar.([1],[3]) A critical issue is when lap splices are located at potential plastic hinge regions and it is essential to study the factors which influence the structural integrity of those columns. This paper focuses on different parameters affecting the bearing capacity of R/C columns. The rebars type, the presence of internal anchorages (hooks) and the stirrups density for a stable interface stiffness coefficient are investigated. The steel-concrete interface properties are formed under the scope of the CEB-FIB bond stress-slip behavior pattern while the models include longitudinal reinforcement with ribbed or smooth bars, dense or sparse stirrups. ([4], [5])

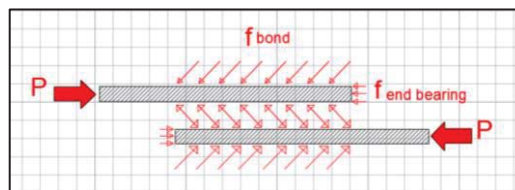


Figure 1: Components of compression lap spliced bars inside a column

## GEOMETRY OF SPECIMENS & MATERIAL PROPERTIES

The column specimens include longitudinal reinforcement of eight steel bars (plain and ribbed) of  $\Phi 12\text{mm}$  diameter, four for every side of the column due to the lap splice of the rebars, while there is also a transverse reinforcement of  $\Phi 8$  steel stirrups. The nominal yield stress value of steel occurred from the experimental process of tension of a steel rebar equal to  $f_y=549\text{MPa}$ . The Young's modulus of the steel is  $200000\text{ MPa}$  and the Poisson's ratio is  $0.3$ . The reinforcement includes straight lap splices, which are employed in reinforced concrete to transfer loads from one steel reinforcing bar to another by bond between the embedding concrete and the two bars along the overlap length of  $L_b, t=33D_b=400\text{ mm}$ . The compressive strength of concrete is given in terms of the characteristic compressive strength of  $150\text{ mm}$  size cubes tested at  $28\text{ days}$  ( $f_{ck}$ ) and is equal to  $20\text{ MPa}$ . The result has been derived from the



laboratory experimental process of the compression of three, cubic, concrete specimens. As far as the steel concrete interface operation is concerned, a bond-slip model is used to assess the anchorage capacity of a bar. The bond failure pattern follows the three stages of CEB-FIB proposed model and it is schematically represented in Fig.2. Its failure is characterized by the initiation and propagation of cracks in the concrete-steel interface. [2]

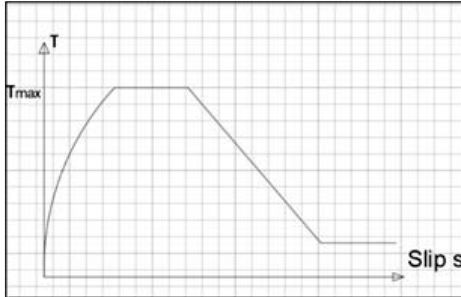


Figure 2: Bond-slip behavior relationship

Concrete	
Compressive strength $f_{ck}$	20 MPa
Reinforcing steel bars	
Yield stress $f_y$	549 MPa
Ultimate stress $f_u$	672 MPa
Ultimate strain $\epsilon_u$	0.10

Table 1: Column specimens' structural identity

The investigation refers to a column part of a square cross section of 25x25cm, which constitutes a member of a bigger and more complex columns-plate system. Specifically, the investigation area is a two meters region between two columns, interrupted by an integrated slab, including a lap splice length of 400mm, starting from the middle of the slab (50 cm away from the inferior and 125cm from the superior support, respectively). One half of the tested column specimens included longitudinal reinforcement of plain rebars with anchored ends sparse or dense stirrups, while the other half included ribbed rebars with free ends, with sparse or dense stirrups. The specimens were subjected to a loading combination of a three point bending, and a constant, axial loading equal to the first floor weight. The bending load was applied as horizontal displacement through a jack and was imposed in the inferior end of the lap spliced rebars, just in the middle of the bottom slab. What follows is the experimental and numerical investigation of the loading combination effects on the column specimens.

### 3 EXPERIMENTAL INVESTIGATION & RESULTS

The laboratory experimental process included the test of eight column specimens of a prototype-scale, by being placed in a laboratory experimental setup with maximum loading capacity of 600tn. The specimens were subjected to a three-point bending with a simultaneous axial, concentric loading which was kept constant during the test. Specifically, two actuators were installed on the top and bottom of a column specimen so as to impose the axial load and one hydraulic jack was placed vertically at the bottom end of the lap spliced rebars of the column specimen, to apply a constant displacement throughout the test, on an area of the column where a plastic hinge was going to form. That displacement represents the horizontal force that column accepts by the bottom slab. The tested column specimens developed similar failure modes. [6]

The vertical load – displacement experimental results show that the presence of plus stirrups in the specimens with plain rebars, did not significantly ameliorate the structural correspondence of the specimen, while the presence of the axial loading lead to the rise of the load capacity of the column up to 30kN and the displacement of the area of interest was increased by 2mm, while the widen of the cracking in the vulnerable areas of the lap splice was mitigated. [7]



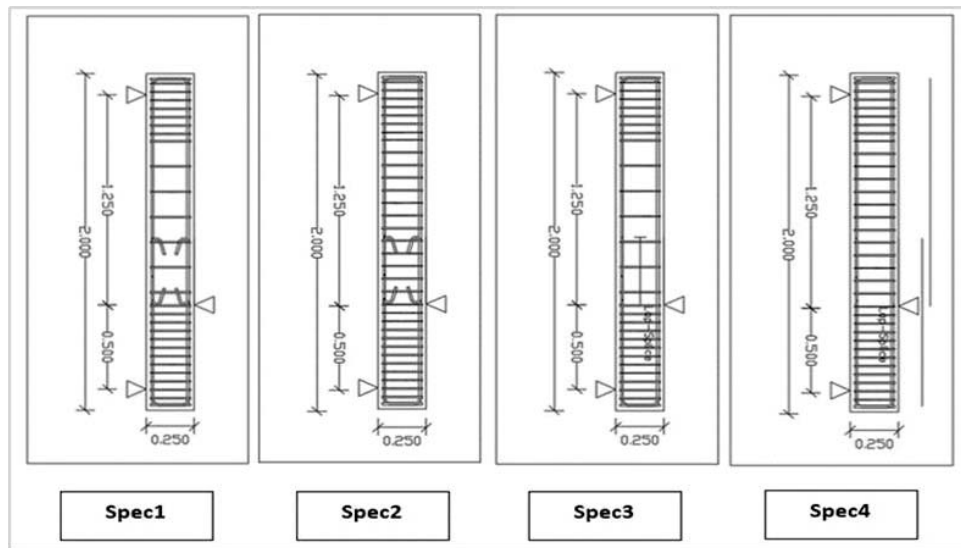


Figure 3: The geometry of the tested specimens

Spec ID	Altered parameters						
	Axial load ratio	Anchor age	Rebars type		Stirrups	Exp P (tn)	Exp D (mm)
			smooth	ribbed			
1-2	0	x	x	-	sparse	4	10
2-2	0	x	x	-	dense	3.3	8
3-2	0	-	-	x	sparse	4	3.3
4-2	0	-	-	x	dense	5	6.5
1-1	0.1	x	x	-	sparse	6	13.8
2-1	0.1	x	x	-	dense	6.2	10
3-1	0.1	-	-	x	sparse	6.9	6
4-1	0.1	-	-	x	dense	6.5	6

Table 2: Experimental results of the 8 specimens tested



Figures 4,5,6: (left) The column specimen placed on the experimental setup of 600tn, subjected to 3 points bending through an imposed displacement by the vertical piston and axial loading of 70kN. (right): Regions of column's specimen failure -small-scale cracks (optics No.1). (bottom): Regions of local cracking at the anchoring regions of lap splices ends (optics No.2)

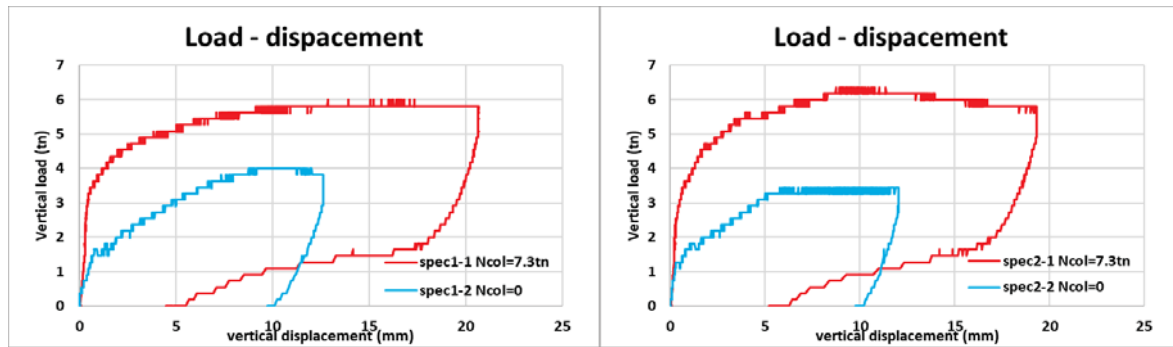


Figure 7: The comparison of the experimental results of column specimens with sparse (on the left) and dense stirrups (on the right) under axial loading case of  $N=0$  and  $N=70\text{kN}$

## 4 NUMERICAL SIMULATION & RESULTS

### 4.1 Simulation of the column model

The presented modeling approach utilizes all the geometrical and mechanical properties described above (section 2). A detailed modeling is used. Concrete and longitudinal rebars are represented with 3D finite elements assigned with a Concrete Damaged Plasticity constitutive law and an elasto-plastic constitutive law respectively. Stirrups are simulated using wire elements and elasto-plastic material law. Between concrete and longitudinal rebars a cohesive – friction behavior (see figure 2), while stirrups is assumed to be perfectly embodied into the concrete. Two different models are investigated. The first one represents column with plain bars and anchors at rebars edges and the second one with free edges simulating the column reinforced with ribbed rebars. Additionally, different bonding strength between concrete and steel bars is given. The relatively poor bond strength between concrete and smooth rebars is given  $1\text{MPa}$ , while the bond strength between concrete and ribbed rebars is given  $5\text{MPa}$ . Below all numerical predictions carried out are listed together with the reinforcing detail and the column's axial compressive load (table 3).

Specimen ID	Altered parameters					Load capacity (tn)		Displacement range (mm)	
	Axial load ratio	Anchorage presence	Rebars type		Stirrups presence	Exp P	Num P	Exp D	Num D
			smooth	ribbed					
1-2	0	x	x	-	sparse	4	4.1	10	14.6
2-2	0	x	x	-	dense	3.3	4.3	8	15.5
3-2	0	-	-	x	sparse	4	4.1	3.3	3.3
4-2	0	-	-	x	dense	5	3.8	6.5	3
1-1	0.1	x	x	-	sparse	6	5.6	13.8	14.14
2-1	0.1	x	x	-	dense	6.2	5.8	10	14.75
3-1	0.1	-	-	x	sparse	6.9	5.5	6	3.8
4-1	0.1	-	-	x	dense	6.5	5.1	6	3.9

Table 3: Specimens' description with the experimental & numerical results

## 4.2 Numerical results investigation

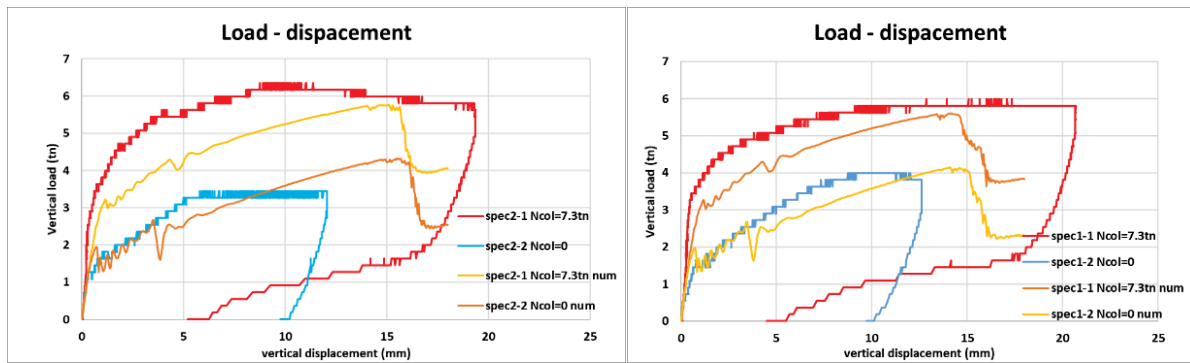


Figure 8: Plot of numerical results for  $v=0$  &  $v=0.1$ , of specs 2-1, 2-2 (left) and of specs 1-1, 1-2 (right)

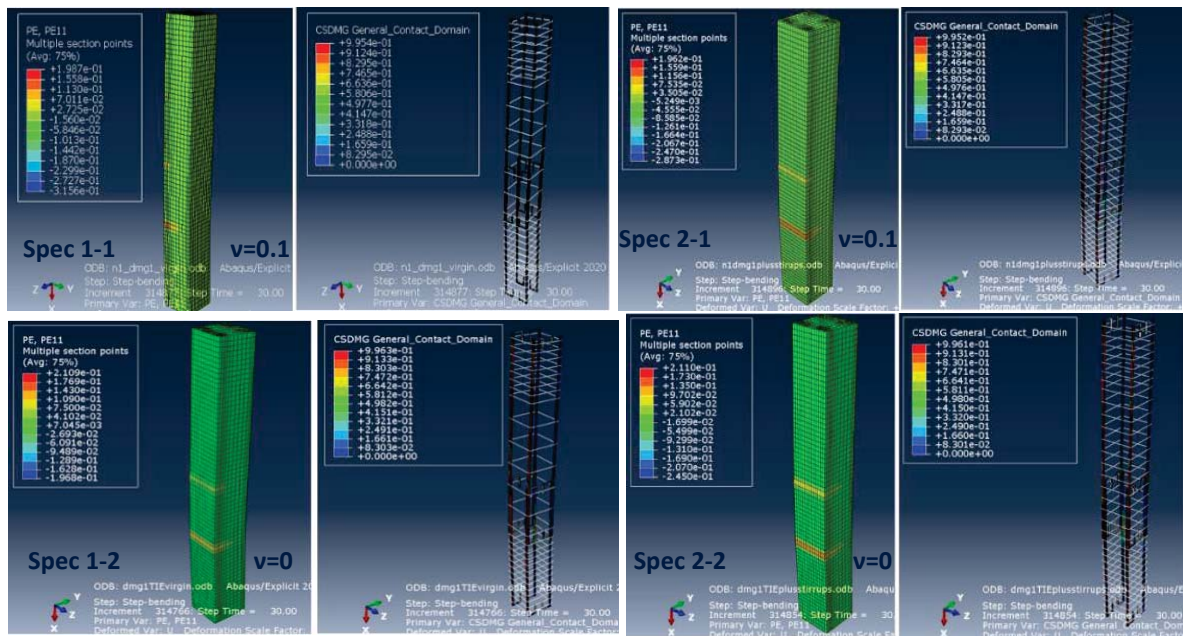


Figure 9: Failure modes: Plastic strains of concrete and CSDMG for specimens 1-1, 2-1 ( $v=0.1$ ) & 1-2, 2-2 ( $v=0$ ) with plain rebars and internal anchoring

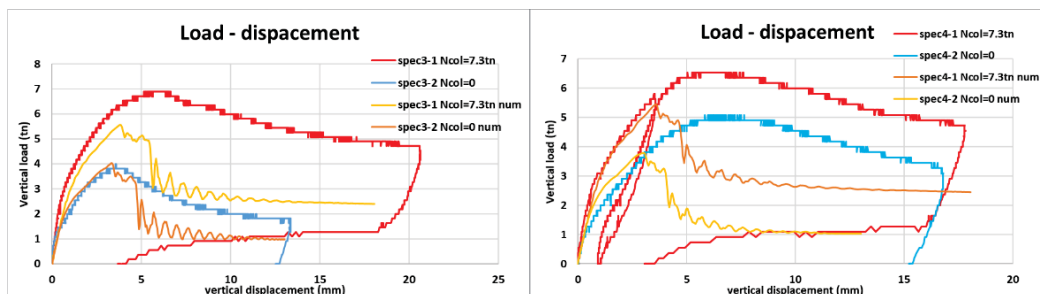


Figure 10: Plots of numerical results for  $v=0$  &  $v=0.1$ , of specs 3-1, 3-2 (left) and of specs 4-1, 4-2 (right)

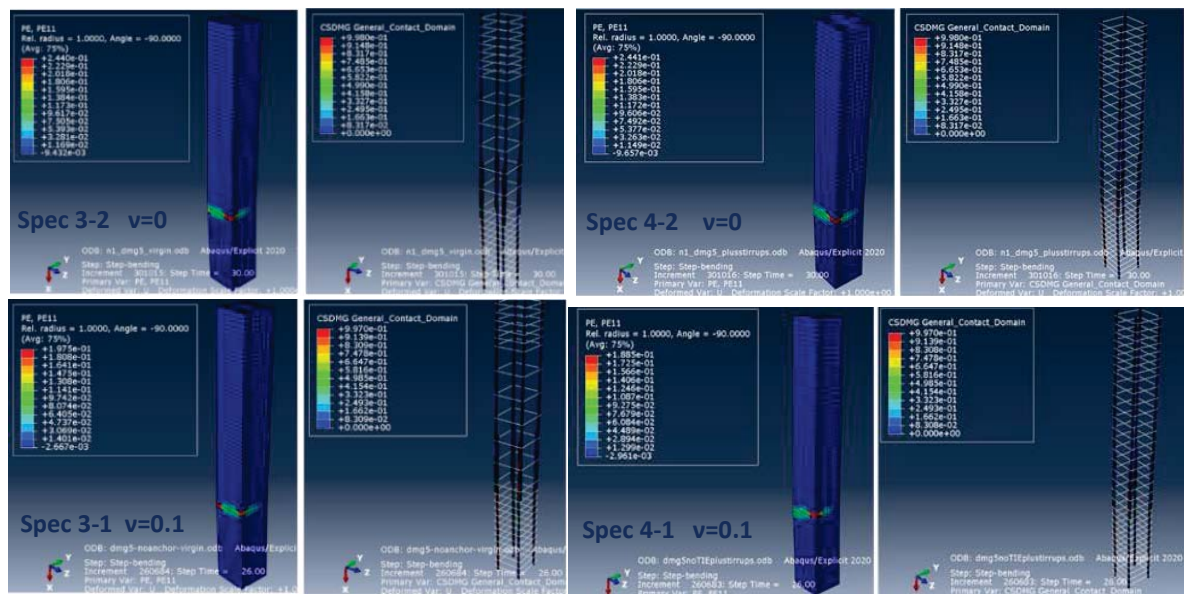


Figure 11: Failure modes: Plastic strains of concrete and CSDMG for specimens 3-2, 4-2 ( $v=0$ ) & 3-1, 4-1 ( $v=0.1$ ) with ribbed rebars

#### • Numerical results evaluation

Spec ID	experimental results		numerical results		exp-num deviation rate		
	P(tn)	d(mm)	P(tn)	d(mm)	P(tn)	P(%)	d(mm)
1-1	6	8-13	5.6	14	0.4	7.14	1-4
1-2	4	9-11	4.1	14.6	0.1	2.5	3.6-5.6
2-1	6.2	10	5.8	14.8	0.4	6.9	4.8
2-2	3.3	7-10	4.3	15.5	1	30.3	5.5-8.5
3-1	6.9	6	5.5	4	1.4	25.5	2
3-2	4.1	3.3	4.1	3.3	0	0	0
4-1	6.5	6	5.1	4	1.4	27.5	2
4-2	5	6.5	3.8	3	1.2	31.6	3.5

Table 4: Validation of the numerical results

The maximum undertaken loads and displacements for the numerical investigation for  $v=0$  and 0.1 lie between 3.8-5.8tn and 3-15.5mm respectively and are higher for the anchored specimens. There is also a satisfactory exploitation rate of the concrete's and steel's load-bearing capacity for the plain reinforced specimens as it is observed a strong anchorages' resistance which causes local damage to the concrete at the lap splice ends, the plot also shows delayed load drop and increased steel deformation and displacement. However, when the rebars are laid out freely without anchoring at the ends, the strength of the concrete steel interface is reinforced only by the interface bond between the surface of the rebar and the circumferential concrete. A premature load drop is observed for a smaller displacement due to the weak resistance of the steel ribs against anchors. It is concluded that the presence of anchors at the rebars' ends, contributes in a significant rate to the utilization of the bearing capacity of the individual materials, steel and concrete, prolonging increase in load intake and deformation for the specimen. The plastic deformation of the concrete and the steel stress at the anchors' areas



are intensified due to the exceeding of the concrete tensile strength by the stress intensity of the surrounding steel.

## 5 DISCUSSION ON THE INVESTIGATIONAL RESULTS

A general convergence is observed between the experimental and the numerical results, included the failure modes. The same loading combination with displacement control was used in both experimental tests and numerical simulation. As far as the failure patterns are concerned, Fig.12 compares the tensile damage nephogram obtained from the numerical simulation with the surface cracks obtained from the experimental test of the same specimen. The two failure modes are similar with extended cracks being concentrated on the bottom lap spliced end where the developed stress is higher for the ribbed reinforced specimens 3, 4. While, in the case of specimens 1 and 2, the cracking was developed on the concrete surface of both the anchored lap splice ends. According to the plots of the numerical and experimental results of undertaken load and displacement, a satisfactory convergence rate was achieved in the terms of the maximum load, the corresponding displacement, and the slope of the curves. (*Table 5*) In addition, the strength of the interface was simulated by realistic cohesion stresses and the expected forms of failure were induced. As a result, a reliable numerical tool has been developed and quantified so as to predict the response of critical RC members under the influence of various loading factors.

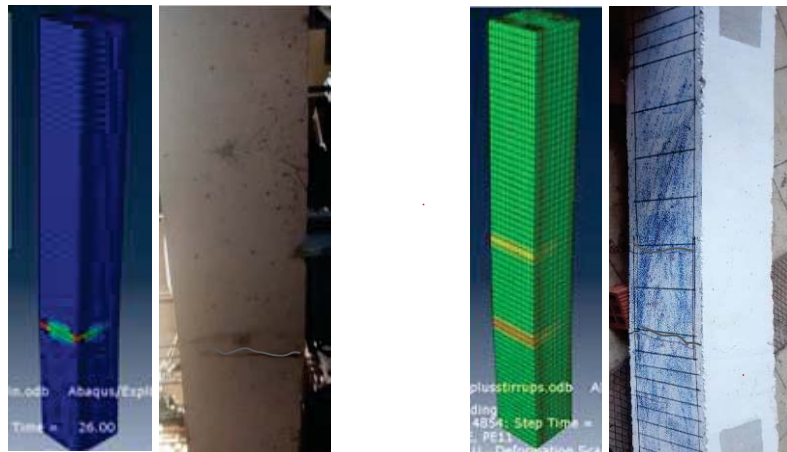


Figure 12: Comparison of the numerical and experimental failure modes of the ribbed (left) and plain with internal anchoring (right), reinforced specimens

Spec ID	Test results (tn)	Simulation results (tn)	Convergence rate (%)
1-2	4	4.1	97.6
2-2	3.3	4.3	76.7
3-2	4	4.1	97.6
4-2	5	3.8	76
1-1 v1	6	5.6	93.3
2-1 v1	6.2	5.8	93.6
3-1 v1	6.9	5.5	79.7
4-1 v1	6.5	5.1	78.5

Table 5: Comparison of the ultimate undertaken load of column specimens for  $v=0$  &  $v=0.1$

## 6 CONCLUSIONS

An experimental and a numerical study was performed on full scale RC column specimens to evaluate the behavior of lap splices as a part of a complex structural system under the load combo of three point bending and a constant compression on the edges. The type of longitudinal reinforcement, the presence of stirrups, the free and anchored ends of the lap spliced rebars and the magnitude of the load ratio, were the main parameters considered in this study. According to the tests results, including the global behavior of the splices and the failure modes that the column specimens develop, the major findings of this study are as follows:

- The absence of anchorage leads to the premature slip of the lap spliced rebars and to early load drop under the insufficient exploitation of the materials' properties.
- The presence of dense stirrups does not essentially contribute to the rise of the undertaken load but it reduces the deformation of the concrete, by restricting the opening of the surficial cracking.
- The proposed finite element model of Abaqus for RC column is in good agreement with the experimental results such as load carrying capacity, displacement, failure mode and CEB-FIB bond stress-slip behavior pattern.
- The maximum undertaken load and the respective displacement are getting greater for both the plain and ribbed reinforced specimens as the axial load ratio rises from 0 to 7tn.
- The main difference among the results for specimens with ribbed and plain rebars, is the fact that the absence of anchoring leads to early load drop and a low exploitation of material properties, as the slip of the ribbed rebars happens prematurely.
- The presence of the lap splice implies a failure mode connected with the slip of the reinforcing bars.
- The higher degree of failure in the column specimens, for both the numerical and experimental results, is located in the plastic joint area, on the bottom end of the lap splice length.



## REFERENCES

- [1] S.P. Tastani, S. J. Pantazopoulou, *Direct Tension Pullout Bond Test: Experimental Results*, M.ASCE, Journal of Structural Engineering Vol. 136, Issue 6, 2010.
- [2] Delso Juan Murcia, P. Benson Shing, *Bond-Slip Model for Detailed Finite-Element Analysis of Reinforced Concrete Structures*, M.ASCE, Journal of Structural Engineering Vol. 141, Issue 4, 2015.
- [3] Dionysis Biskinis, Michael N. Fardis, *Models for FRP-wrapped rectangular RC columns with continuous or lap-spliced bars under cyclic lateral loading*, Engineering Structures Volume 57, Pages 199-212, 2013
- [4] Luccioni, López, Danesi Bibiana María, Daniel Ernesto, Rodolfo Francisco, *Bond-Slip in Reinforced Concrete Elements*, Journal of Structural Engineering Vol. 131, Issue 11, 2005.
- [5] Zanuy Carlos, Iván M. Díaz, *Stress distribution and resistance of lap splices under fatigue loading*, Engineering Structures Volume 175, Pages 700-710, 2018.
- [6] M.A Najafgholipour, S.M Deghan, M.Khani, A. Heidari, *The performance of lap splices in RC beams under inelastic reversed cyclic loading*, Structures Volume 15, Pages 279-291, 2018.
- [7] H.Kupfer, H.K Hilsdorf, H. Rusch, *Biaxial strength of concrete*, Journal of the American Concrete Institute, Vol.66, No.8, pp.656-666, 1969.

## DEVELOPMENT OF AN EXPERIMENTAL SETUP FOR MEASURING THE EFFECTIVENESS OF STRENGTHENED PRESTRESSED CONCRETE CYLINDER PIPES (PCCP)

Sofia Gkaraklova<sup>1</sup>, Lazaros Melidis<sup>1</sup>, George C. Manos<sup>1</sup> and Konstantinos Katakalos<sup>1,\*</sup>

<sup>1</sup> Aristotle University of Thessaloniki  
Laboratory of Experimental Strength of Materials and Structures, Thessaloniki, 54124  
e-mail: {kkatakalo,gcmanos}@civil.auth.gr, {sofiagked,lazmelidis}@gmail.com  
<https://strength.civil.auth.gr>

---

### Abstract

*This paper presents the results of a numerical investigation on the behavior of Prestressed Concrete Cylinder Pipes (PCCP) under the Three Edge Bearing Test (TEBT) (diametrical compression test). The main goal is to develop an experimental setup in the lab in order to evaluate the efficiency of different strengthening schemes with Fiber Reinforced Polymer (FRP) repair methods. The PCCP specimens under evaluation are assumed to be prefabricated parts of an existing water infrastructure network. For practical reasons we chose to define a typical length of 1.0m for all investigated numerical specimens. On the whole, four (4) pipe models are considered: a non-prestressed initial specimen, a prestressed virgin specimen, a strengthened prestressed specimen with internally applied FRP sheet and a last strengthened prestressed specimen with externally applied FRP sheet. The numerical assessment of External Load Crushing Strength by the Three Edge Bearing Test Method is realized using 3D FEM software and in compliance with the terms of ASTM C-497 standard. The developed experimental setup will be fabricated in the Laboratory for Strength of Materials and Structures “LSMS” of Civil Engineering Faculty of Aristotle University of Thessaloniki (AUTH). For all four (4) numerically examined models we employed all the geometrical and mechanical properties of materials from existed PCCP pipes, that LSMS had the chance to measure in the past. The numerically simulated models were evaluated and discussed in terms of load-deformation response and observed limit states of damages.*

**Keywords:** Prestressed Concrete Cylinder Pipes (PCCP), External Load Crushing Strength, Three Edge Bearing Test, Numerical simulation.

---

## 1 INTRODUCTION

Prestressed Concrete Cylinder Pipes (PCCPs) were first manufactured in 1942 as lined cylinder pipe. The prestressing wire in lined cylinder pipe is wrapped directly around the steel cylinder. A second type of PCCP was developed in 1952 that has concrete encasement of the steel cylinder on both sides. Known as embedded cylinder pipe, it differs from lined cylinder pipe by the encapsulation of its steel cylinder in a concrete core. Therefore, the prestressing wire is wrapped around the concrete core rather than the steel cylinder as in lined cylinder pipe. The typical diameter ranges for lined and embedded cylinder pipe are between 0.40 to 1.50 meters and 0.75 to 6.50 meters, respectively. PCCPs are typically manufactured according to the American Water Works Association (AWWA) standard C304. [1,9]. With the onward maturity of the prestressed concrete technology of the latest years, PCCPs have been used in oil, water conservancy, hydropower engineering and other areas. Also, it has been demonstrated that in the sector of large diameter pipes, PCCPs are more competitive than any other type of pipes [2-4]. In recent years, research has been conducted in the field of experimental and numerical study of concrete pipes utilizing the Three Edge Bearing Test (TEBT) and Finite Element Method (FEM) simulation respectively [5-7]. Another interesting and growing segment of scientific study is the investigation of the strengthening repair methods of PCCPs implementing novel FRP and CFRP technology [8-10].

The “Laboratory of Strength of Materials and Structures” of Aristotle University of Thessaloniki has commenced a research project, which scope is to investigate both experimentally and numerically the mechanical behavior of PCCPs. This project aspires to address issues such as the response of PCCPs under the Three Edge Bearing Test (TEBT) and under internally applied fluid pressure, as well as the effectiveness of specific strengthening repair methods. In the current paper part of these results are presented. More specifically, the behavior of two (2) pipes specimens (one with and one without prestress) under TEBT is examined experimentally and numerically and the efficiency of two (2) strengthening methods (internal and external confinement of PCCPs with FRP double mantle) is assessed.

## 2 EXAMINED SPECIMENS AND EXPERIMENTAL SETUP

The geometry of the examined pipes is depicted in Figure 1 and the denomination of the four (4) specimens alongside with their main dimensions is presented in Table 1. All specimens have the same internal diameter, i.e., 1.80m, while the external diameter is 2.16m for Spec 2, Spec 3, Spec 4 and 1.98m for Spec 1.

The External Load Crushing Strength of the examined pipes specimens is calculated by utilizing the Three-Edge Bearing Test Method in accordance with ASTM C-497 standard. The experimental setup scheme is outlined in Figure 2, along with the real experimental configuration developed at the “Laboratory of Strength of Materials and Structures” of Aristotle University of Thessaloniki. In total, an instrument which measures the applied load (load cell) and four (4) Linear Variable Differential Transducers (LVDTs) were installed. Also, deformation strips were selectively placed at some points in order to have better control of the loading process and enhance the accuracy of the experimental device, especially in the area of the failure.

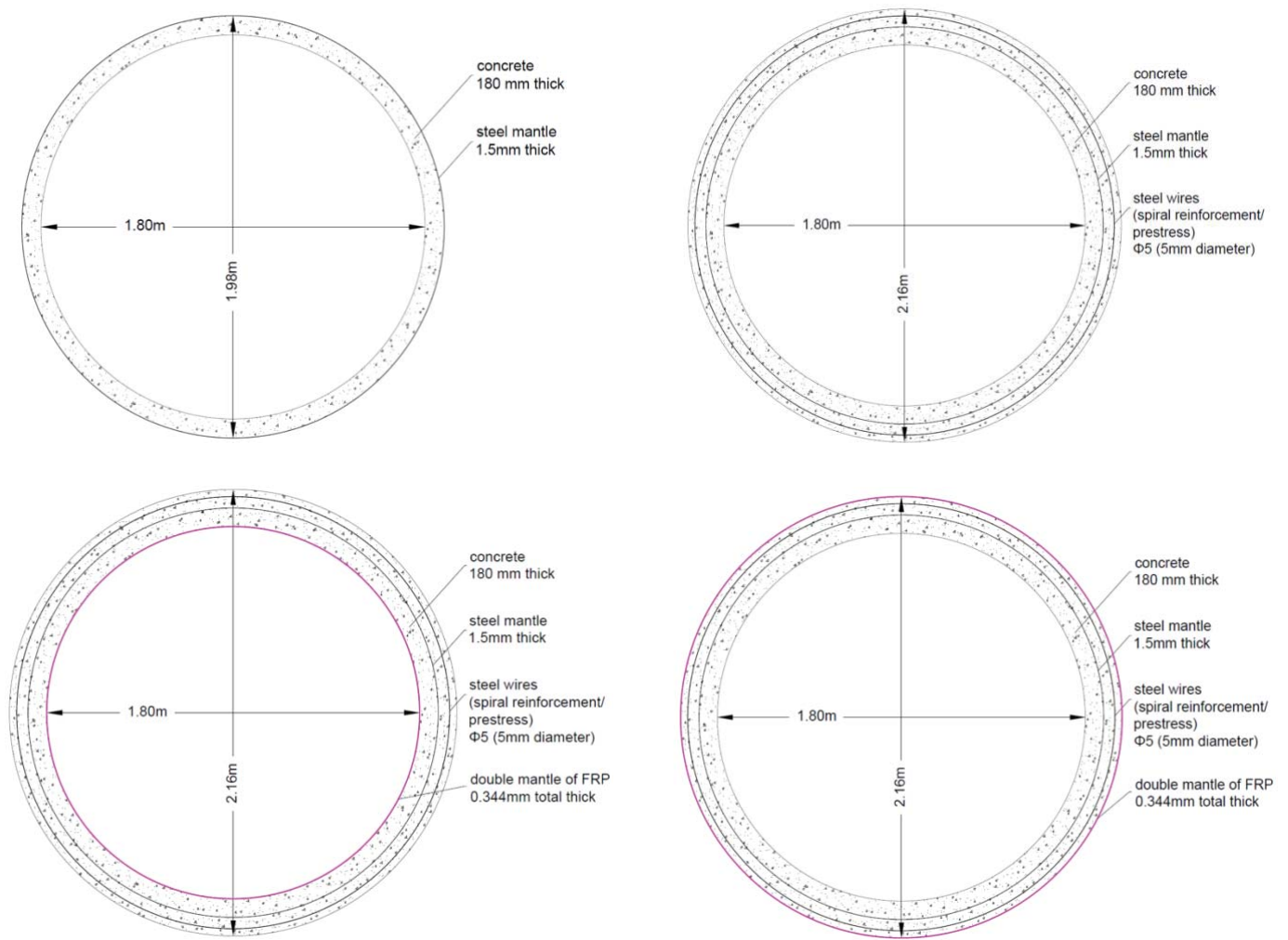


Figure 1: Geometry of the four (4) examined models: unprestressed maternal – Spec 1 (top-left), prestressed maternal – Spec 2 (top-right), FRP internally strengthened prestressed – Spec 3 (bottom-left) and FRP externally strengthened prestressed – Spec 4 (bottom-right)

Specimen Name	Description	External Diameter/ Internal Diameter
Spec 1	Maternal unprestressed specimen	1.98/1.80
Spec 2	Maternal prestressed specimen	2.16/1.80
Spec 3	FRP internally strengthened, prestressed specimen	2.16/1.80
Spec 4	FRP externally strengthened, prestressed specimen	2.16/1.80

Table 1: Geometric properties of the four (4) examined specimens

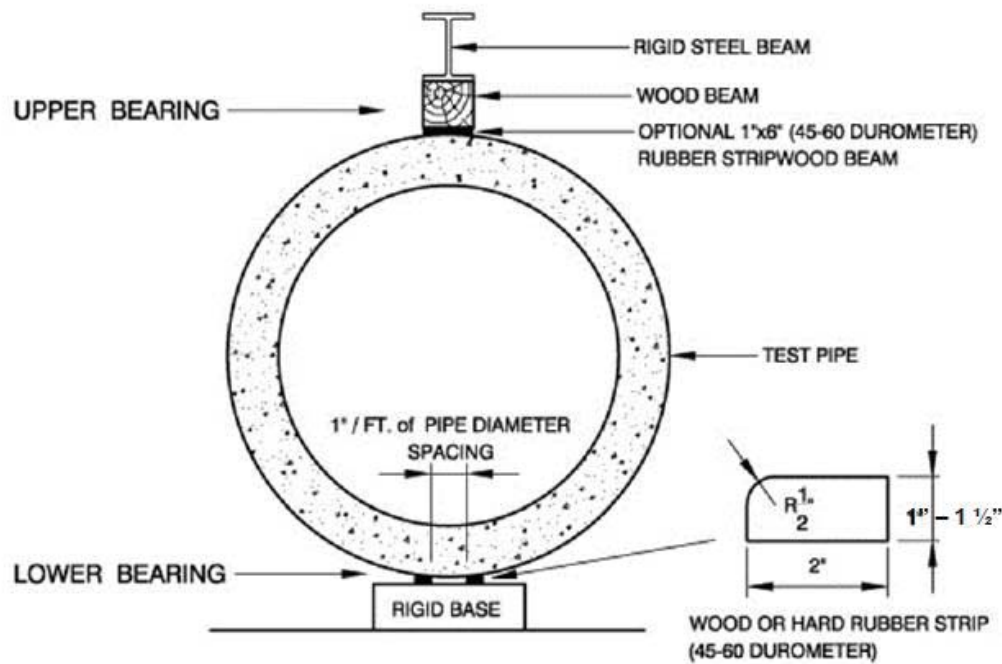


Figure 2: Scheme (top) of the experimental setup of the Three Edge Bearing Test as per ASTM C-497

### 3 NUMERICAL MODELING

Three-dimensional finite element numerical models have been built adopting a macro modeling approach with homogenized non-linear material laws. It should be underlined that all materials that compose the pipe specimens have been tested at the “Laboratory of Strength of Materials and Structures” of Aristotle University of Thessaloniki and have been adopted in the Finite Element Analysis (FEA) software in order to non-linear realistic numerical models. All the parameters used for the constitutive law are listed at table 2. The models of the four (4) specimens are presented in Figure 3.

Material law assigned to concrete – Concrete Damaged Plasticity					
ELASTIC PROPERTIES		COMPRESSIVE BEHAVIOR		TENSILE BEHAVIOR	
Mass Density (ton/mm <sup>3</sup> )	2.5E-09	Yield Stress (MPa)	Plastic Strain	Yield Stress (MPa)	Plastic Strain
Young's Modulus (MPa)	39000	11.88	0	1	0
Poisson's ratio	0.25	35.3	0.0012	0	0.005
		43	0.0021		
		48	0.0028		
		43.2	0.0043		

		9.6	0.02		
Material law assigned to steel mantle – Plastic					
ELASTIC PROPERTIES		TENSILE BEHAVIOR			
Mass Density (ton/mm³)	7.85E-09	Yield Stress (MPa)	Plastic Strain		
Young’s Modulus (MPa)	200000	300	0		
Poisson’s ratio	0.30	300	0.0085		
		390	0.0485		
		420	0.0985		
		450	0.4		
		360	0.42		
		40	0.45		
Material law assigned to steel wires – Plastic					
ELASTIC PROPERTIES		TENSILE BEHAVIOR			
Mass Density (ton/mm³)	7.85E-09	Yield Stress (MPa)	Plastic Strain		
Young’s Modulus (MPa)	210000	1400	0		
Poisson’s ratio	0.30	1500	0.0007		
		1600	0.0012		
		1700	0.0022		
		1800	0.0047		
		30	0.015		
Material law assigned to Fiber Reinforced Polymer (FRP) - Elastic					
ELASTIC PROPERTIES					
Mass Density (ton/mm³)	1E-09				
Young’s Modulus (MPa)	240000				
Poisson’s ratio	0.15				

Table 2: Parameters of constitutive laws for concrete, mantle steel, wires steel and FRP materials



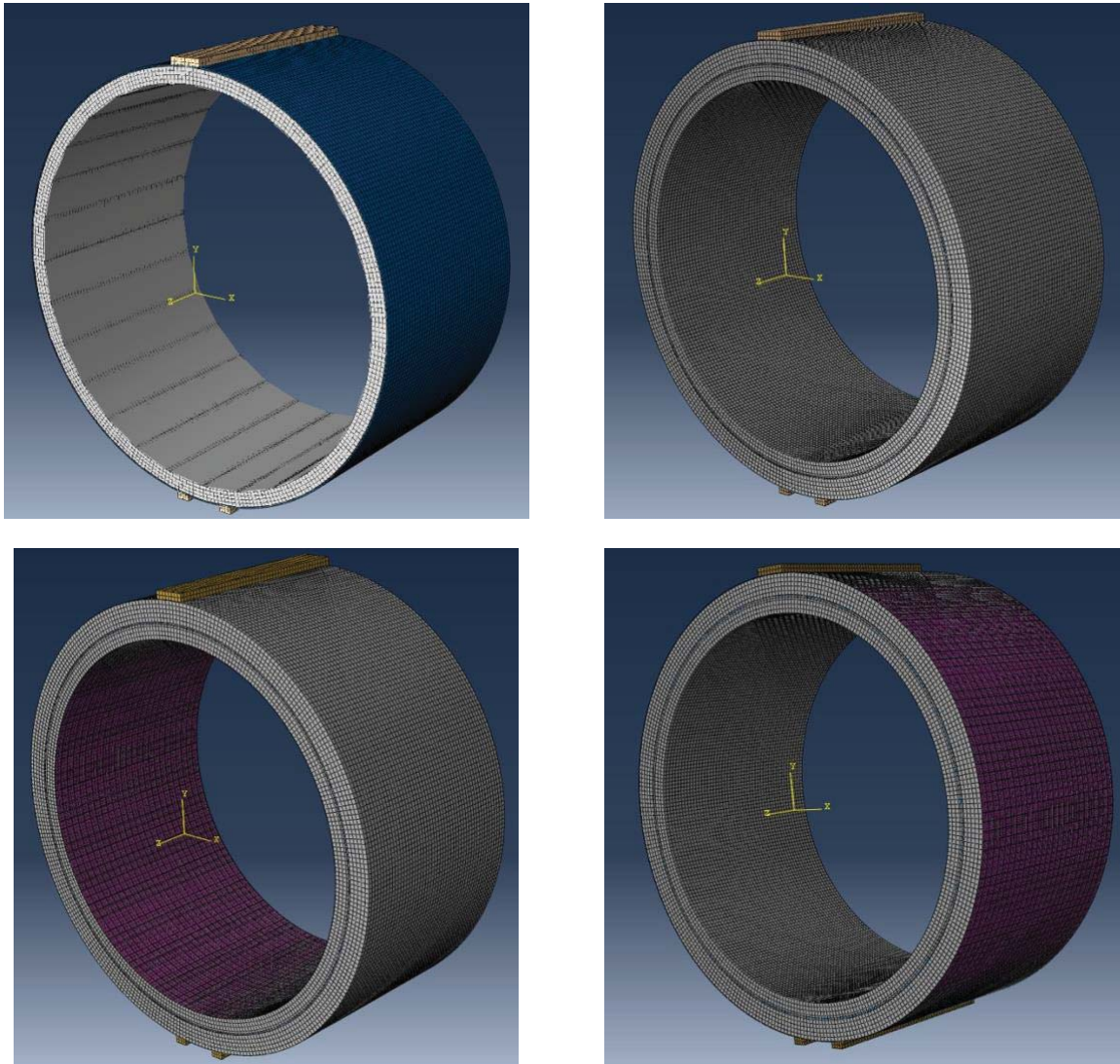


Figure 3: FEM Models of the four (4) examined specimens: maternal unprestressed – Spec 1 (top-left), maternal prestressed – Spec 2 (top-right), FRP internally strengthened & prestressed – Spec 3 (bottom-left) and FRP externally strengthened & prestressed – Spec 4 (bottom-right)

The numerically obtained results were initially evaluated in terms of applied load – developed deformations graphs, as presented in figures 4. It is depicted that for all 4 models we manage to get a non-linear behavior. In addition, the adopted numerical methodology, of applying loads and imposing restrains (experimental setup in the lab) resulted to very rational data since we were able to yield the utilized materials, obtain the bearing capacity of all models and get the post maximum decrease behavior.

Moreover, we see that the bearing capacity is increasing by adding, initially the prestress (Spec2) then by applying internally FRP sheets (Spec3) and finally by applying externally FRP sheets. It has to be mentioned that the depicted results are estimations of the real performance of the PCCP pipes and they aim to predict in a realistic way the performance of a PCCP pipe and evaluate the efficiency of strengthening schemes.

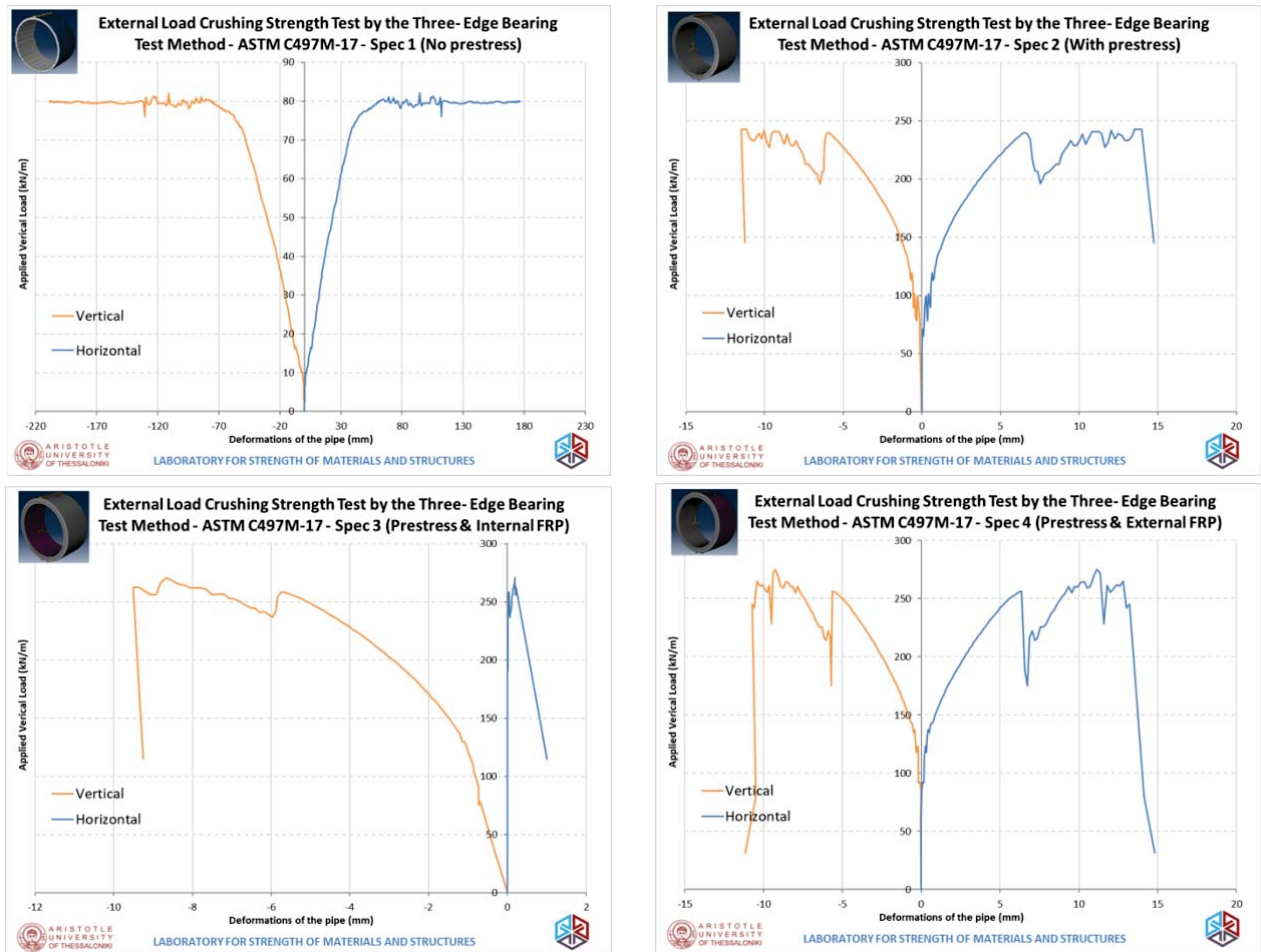


Figure 4: Numerical results - diagrams of applied force, vertical deflection and horizontal swelling of Spec 1 (top-left), Spec 2 (top-right), Spec 3 (bottom-left) and Spec 4 (bottom-right)

Figure 5 presents (plastic strain components) the damage pattern that is attained in the numerical simulations. It is depicted that plastic strains are developed on the faces of PCCP model that suffers from tension. These are the regions that we expect to get the developed cracks, under the present loading conditions. The developed damage pattern indicates the qualitatively realistic FE model.

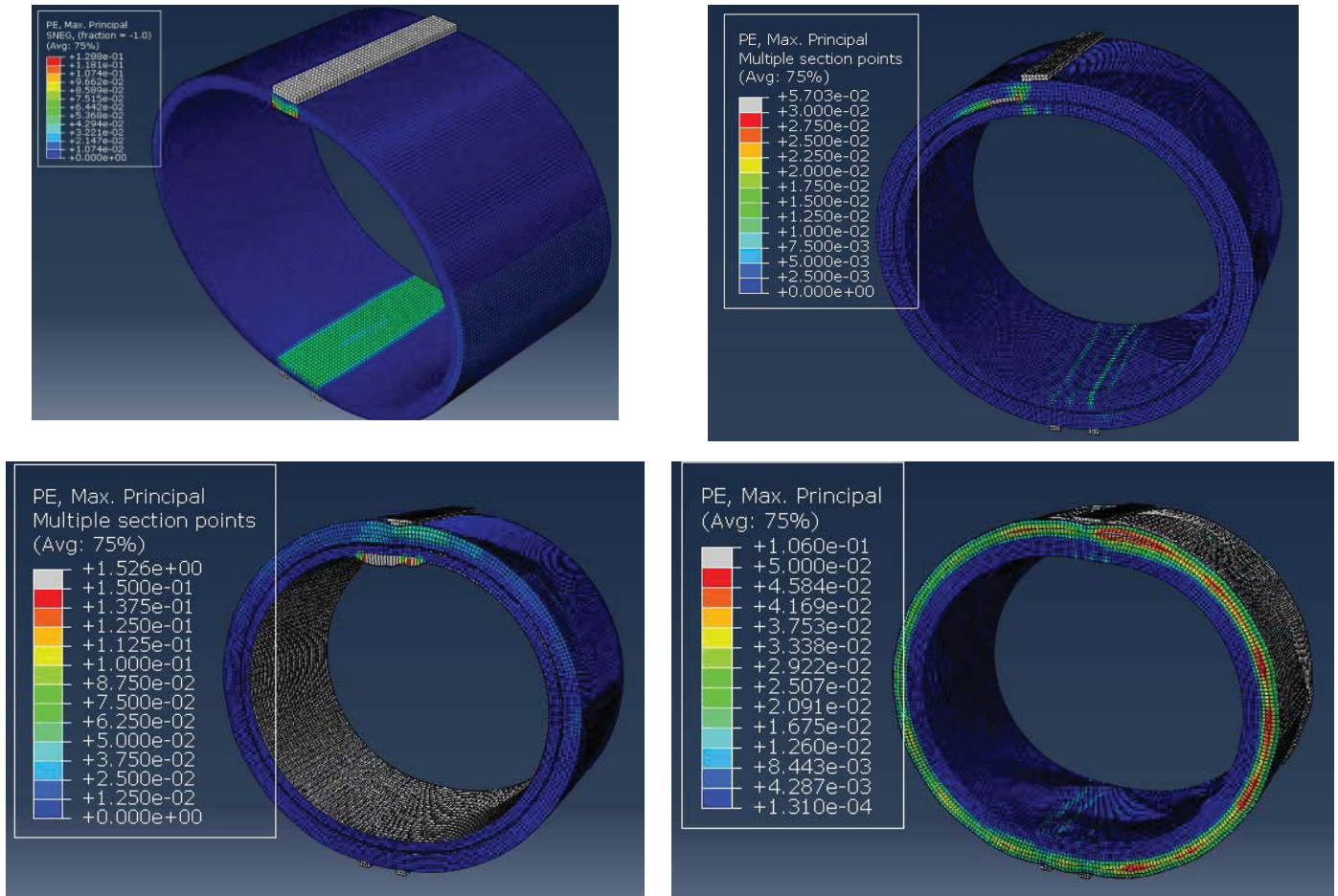


Figure 5: Numerical results - plastic strain components (PE) of Spec 1 (top-left), Spec 2 (top-right), Spec 3 (bottom-left) and Spec 4 (bottom-right)

Taking under consideration the aforementioned results, it is clear that the maternal prestressed specimen (Spec 2) develops 3 times larger strength than the maternal unstressed specimen (Spec 1). This is indicative of the highly significant contribution of the perimetric prestress and how important it is that it remains active and is not disabled by any damages or corrosion. Also, as expected, the strengthened specimens (Spec 3 and Spec 4) demonstrate greater bearing capacity than the maternal prestressed specimen (Spec 2). More specifically, the FRP internally strengthened specimen (Spec 3) indicated an increase of 12.4% in maximum bearing capacity compared to the maternal prestressed specimen (Spec 2), while the FRP externally strengthened specimen (Spec 4) demonstrated a similar behavior.

## 4 CONCLUSIONS

The behavior of Prestressed Concrete Cylinder Pipes (PCCPs) under the Three Edge Bearing Test (TEBT) is discussed here, mainly focusing on the contribution of the FRP strengthening method in the PCCPs response. Numerical models were developed using all the available information about the mechanical properties of the materials used in an effort to numerically reproduce the realistic behavior of the pipe. The goal is to estimate the bearing capacity of the



models, their damage patterns and finally quantify the experimental setup that has to be constructed in the Lab. The main conclusions are enlisted below:

- The perimetric spiral prestress is very significant as it increases the bearing capacity of the concrete pipe by 3 times.
- The strengthening of the PCCP with FRP is efficient and results in a 12,5% growth of the bearing capacity
- The developed 3-D FEM models, are considered realistic and can be utilized to built the experimental setup in the Lab

## REFERENCES

- [1] AWWA C304-14(R19) Design of Prestressed Concrete Cylinder Pipe
- [2] ShaopingSun, Yongfeng Guo, Application of PCCP, Special Structures. 2003,20(3):28-31
- [3] Zhijun Rong, Mancang Hao, et al. Comparison on PCCP Pipe, PCP Pipe and Steel Pipe, Shanxi hydrotechnics, 2000.11:48-50
- [4] Hu Liansheng, Mancang Hao, Prestressed Concrete Cylinder Pipe (PCCP) and Its Development, Shanxi hydrotechnics 6, 84-85
- [5] Facundo L. Ferradoa, Mario R. Escalantea and Viviana C. Rougiera, Simulation of the three-edge bearing test: 3d model for the study of the strength capacity of SFRC pipes, Mecánica Computacional, Vol XXXVI, págs. 195-204, San Miguel de Tucumán, 6-9 November 2018
- [6] Amin Darabnoush Tehrani, Finite element analysis for ASTM C-76 reinforced concrete pipes with reduced steel cage, MSc Thesis, University of Texas at Arlington, 2016
- [7] Yuliang Wang, Yongqing Bi, Xiaojie Zhou, Mechanical capacity analysis of large diameter prestressed concrete cylinder pipe (PCCP), Applied Mechanics and Materials Vols. 166-169 (2012) pp 3214-3219
- [8] Michael J. Karantzakis, Constantinos P. Antonopoulos, Dimitrios V. Skamagis, Strengthening of Large Diameter PCCP Pipe with External Application Of FRP, FRPRCS-University of Patras, Patras, Greece, July 16-18, 2007
- [9] M. Gabbitas; K. Eysaman; A. B. Pridmore; J. Kiladis; J. Halls , City of Baltimore SW Diversion 78-in. Diameter PCCP:2,140 LF Continuous Carbon Fiber Pipe Rehabilitation, ASCE Pipelines 2015 pp 1245-1256
- [10] Tarek Alkhrdaji, Ph.D., P.E.; Silvia Rocca, Ph.D., P.E.; and Nestore Galati, Ph.D., P.E., PCCP Rehabilitation using Advanced Hybrid FRP Composite Liner, ASCE Pipelines 2013 pp 672-681

## MECHANICAL PROPERTIES CHARACTERISATION OF FRPs UNDER ELEVATED TEMPERATURES

Christina Papadimitriou<sup>1\*</sup>, Lambros Kotoulas<sup>1</sup>, Nikolaos Makris<sup>1</sup>, Lazaros Melidis<sup>1</sup> and Konstantinos Katakalos<sup>1</sup>

<sup>1</sup> Aristotle University of Thessaloniki  
Laboratory of Experimental Strength of Materials and Structures, Thessaloniki, 54124  
e-mail: {chrdimpap,kkatakalo}@civil.auth.gr, {lpkotoulas,nsvmakris}@gmail.com  
<https://strength.civil.auth.gr>

---

### Abstract

*Fiber-reinforced polymers (FRP) are rapidly gaining acceptance from the construction sector due to their large effectiveness. They are mainly used as confining reinforcement for concrete columns and as tensile reinforcement for concrete beams and slabs. FRPs are already used to a large extent at applications such as bridges and parking lots, where elevated temperatures are not the main risk. Their increasing use as structural reinforcement is hampered by the concern related with their behavior at elevated temperatures as the relevant research is deficient. Thanks to the significant advantage of FRPs' mechanical properties, further investigation into the influence of heating on their mechanical behavior may solve many doubts. The present study examines the influence of temperatures of 50, 100 and 250°C on the tensile strength of FRP laminates with carbon fibers (CFRP). In addition, the resistance of CFRP specimens to low-cycle thermal loading at the temperatures of 50, 100 and 250°C under constant tensile load was investigated. The experiments carried out in the laboratory of Experimental Strength of Materials and Structures of Aristotle University of Thessaloniki.*

**Keywords:** fiber reinforced polymer, thermomechanical characterization, elevated temperatures, civil engineering applications.

---

## 1 INTRODUCTION

The FRPs are composite materials consisting of continuous high-strength fibers, which are embedded into a polymer matrix (usually organic) [1]. The fibers are the reinforcing elements, whereas the polymer matrix is the connecting material which protects them and transfers the loads to and between the fibers [1]. In the construction sector, the main types of fibers used are glass, carbon (inorganic) and aramid fibers (organic polymers). The use of these materials in civil engineering applications is constantly expanding, due to their important advantages. High resistance to corrosion, high strength-to-weight ratio, high stiffness, appropriate fatigue performance, electric insulation and easy installation are some of them [2],[3]. However, FRPs, according to surveys, show sensitivity to high temperatures. Elevated temperatures cause reduction in elastic modulus and strength [2]. These possibly result in large deflections, loss of reinforcement and eventually collapse [2].

Specifically, the glass transition temperature  $T_g$  is an important parameter to be considered, as above this the mechanical characteristics of the FRPs are reduced dramatically [4]. The polymer is converted from a hard, glassy material to a soft and rubbery one [2]. This leads to loss of adhesion and fibers' removal from the matrix. The resin is no longer able to transfer the loads evenly to the fibers [4]. As a result, some of the fibers are being further loaded, probably exceed their strength and fail [4]. It is also marked that a significant increase in temperature, except in the case of fire, can be caused by direct exposure to sunlight [4]. Especially, dark surfaces are able to reach temperatures of 70°C [4].

The effects of elevated temperatures on the mechanical properties of FRPs are of concern and research into this is limited. However, thanks to the significant advantages of FRPs it is worth further investigation. The present experimental work focuses on the thermo-mechanical behavior of the CFRPs laminates under monotonic mechanical loading, low-cycle fatigue and thermal loading. The experiments carried out in the laboratory of Experimental Strength of Materials and Structures of Aristotle University of Thessaloniki and the investigation parameters were the tensile stress and the temperature.

## 2 MATERIALS AND METHODS

The material of the specimens which were used in the current research was FRP laminate with unidirectional carbon fiber layers embedded in organic matrix with  $T_g=58$  °C. According to the manufacturer data sheet, layer's thickness was 0.129 mm, and the tensile strength and the elastic modulus of dry fibers were 4,000 MPa and 230,000 MPa, respectively. Twenty CFRP specimens of 250 mm length, 15 mm width and 1.8 mm thickness were prepared for the tests. (see figure 1) Their dimensions were measured using a digital caliper. Nine of them were tested at room temperature ( $RT=16$  °C) and they were used as controls while the rest of the specimens were exposed to elevated temperatures (50, 100, 250 °C).



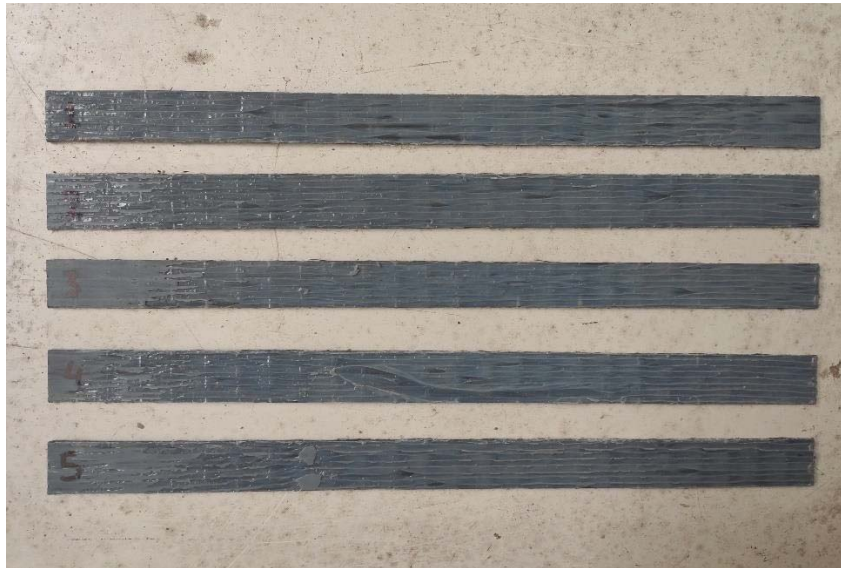


Figure 1: Investigated specimens.

The tensile tests were performed using a universal testing machine Instron of 50 kN maximum capacity. Concurrently, the Bluehill software was used for the data export. (see figure 2) A clip-on extensometer was installed in order to measure the strain values. The tensile testing was conducted using a standard head stroke rate of 2.0 mm/min until failure. The Instron machine was equipped with an electric furnace for the heating of the specimens. The maximum operating temperature of the furnace is 260 °C and the applied heating rate was 10 °C/min. The cooling up to the room temperature was held in a physical way, so the cooling rate was relatively slow. While the furnace was closed the deflection was measured by the Instron machine head stroke. The experimental setup for both room and elevated temperatures is shown in figure 3.

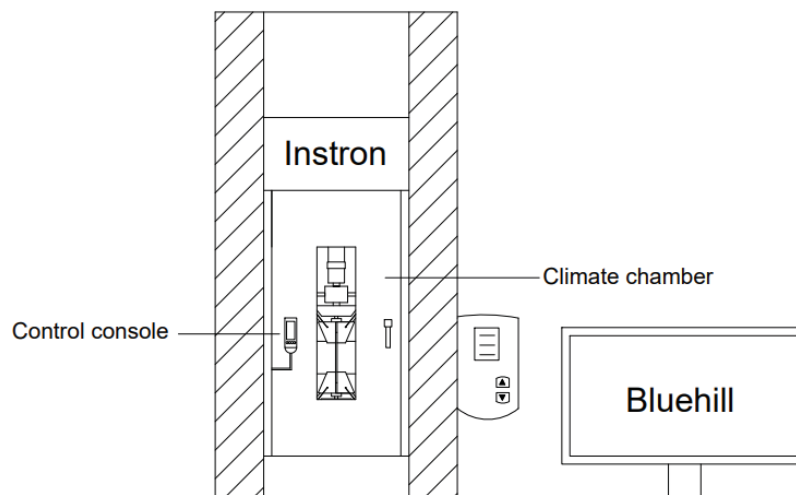


Figure 2: Experimental setup with climate chamber [5].

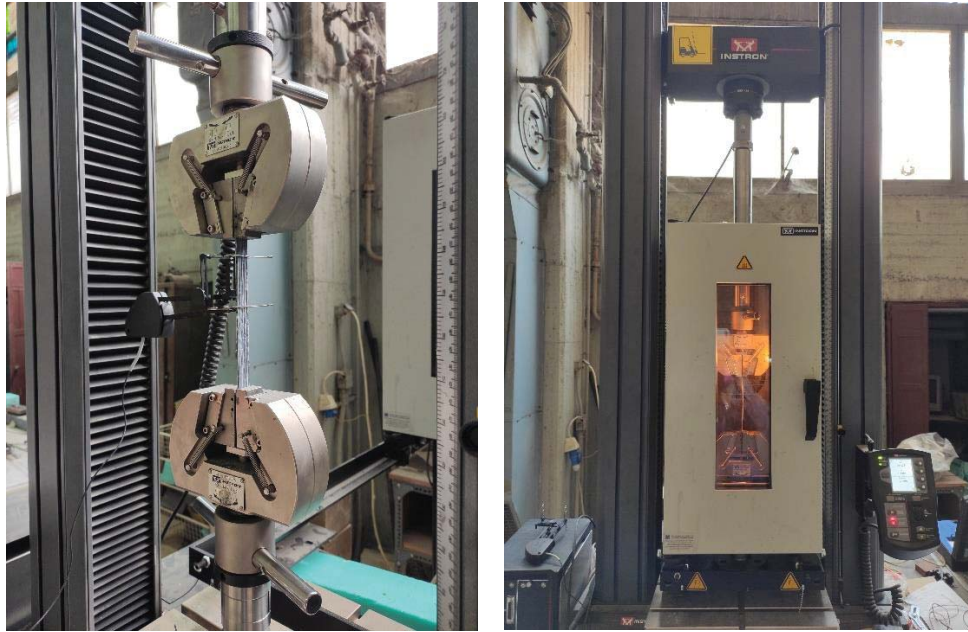


Figure 3: Experimental setup for room temperature and for elevated temperatures.

As mentioned, nine tests were occurred at room temperature (16 °C). The first five specimens (FRPspec1-5) were tested under monotonic, uniaxial tension until failure. From the average value of these specimens' strength, their maximum tensile strength was determined. Subsequently, four specimens were submitted to low-cycle fatigue tests of fifty loading-unloading cycles. The maximum load of the cycle was equal to the 50% of the average tensile strength for the two specimens (FRPspec6,14) and 75% for the other two specimens (FRPspec7,15). The rate of the tensile loading was 1000 N/min for the cyclic tests. After the fatigue loading the four specimens were tested under monotonic, uniaxial tension up to failure. The information of experiments under room temperature is shown in table 1.

Table 1: Detailed information of experiments under room temperature.

Name	Dimensions (mm)		Loading	T (°C)	Comments
	t	b			
FRPspec1	1.63	15.74	MUT* <sup>1</sup>	RT(=16)	MUT up to failure
FRPspec2	1.74	17.26	MUT	RT	MUT up to failure
FRPspec3	1.71	14.68	MUT	RT	MUT up to failure
FRPspec4	1.65	16.56	MUT	RT	MUT up to failure
FRPspec5	1.78	15.95	MUT	RT	MUT up to failure
FRPspec6	2.06	16.26	LCF* <sup>2</sup> , MUT	RT	LCF (50 cycles) with max load 50% of the tensile strength and MUT up to failure
FRPspec14	1.74	15.15	LCF, MUT	RT	LCF (50 cycles) with max load 50% of the tensile strength and MUT up to failure
FRPspec7	1.98	16.04	LCF, MUT	RT	LCF (50 cycles) with max load 75% of the tensile strength and MUT up to failure
FRPspec15	1.85	16.34	LCF, MUT	RT	LCF (50 cycles) with max load 75% of the tensile strength and MUT up to failure

\*1Monotonic Uniaxial Tension, \*2Low Cycle Fatigue (n=50)

The rest eleven specimens were exposed under elevated temperatures. The first six of them were submitted to thermal loading at temperatures of 50 °C (FRPspec8,11), 100 °C (FRPspec9,12) and 250 °C (FRPspec10,13). Once the furnace reached the target temperature, each specimen remained at this temperature for 30 min in order to obtain a uniform temperature distribution. When the specimen FRPspec8 was heated at 50 °C, the uniaxial tensile test was performed at that temperature level. However, the tensile tests for the FRPspec11, the FRPspec9,12 and the FRPspec10,13 at 50 °C, 100 °C and 250 °C, respectively, were performed after the specimens left to cool down to room temperature (16 °C). The cooling process was achieved by opening the door of the furnace. After the cooling, the specimens were tested under monotonic, uniaxial tension until failure, as described before.

In fact, CFRPs applied in concrete structures are usually under both imposed load and elevated temperatures from the environmental changes. Therefore, we decided to investigate the last five specimens under cyclic thermal loading while applying at the time uniform axial tensile loading. These specimens were subjected to monotonic, uniaxial tension constantly at 50% of their average tensile strength. A standard head stroke rate of 2.0 mm/min was used until the target load value. Then, the specimens remained under this constant axial load. After three minutes, cyclic thermal loading was imposed to the specimens. We reached the temperatures of 50 °C (FRPspec16), 100 °C (FRPspec17,18) and 250 °C (FRPspec19,20). The low-cycle thermal loading consisted of heating-cooling cycles up to failure. The maximum number of the cycles was three. Each cycle concluded the heating process with a rate of 10 °C/min, a holding time of 15 min at the target temperature and the cooling process to the room temperature (16 °C). Figure 4 presents the thermal protocol for each temperature. Specifically, the FRPspec16, which completed successfully the three thermal loading cycles, was additionally subjected to monotonic, uniaxial tension until failure at the temperature of 50 °C. The information of experiments under elevated temperature is shown in table 2.

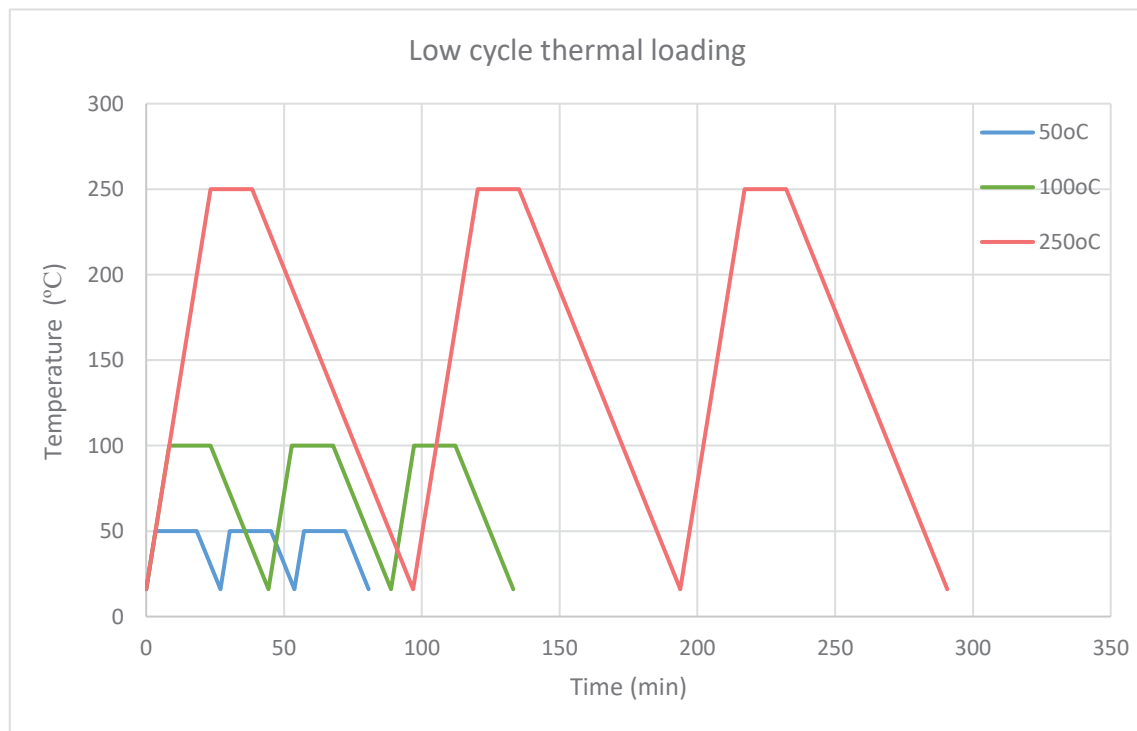


Figure 4: Time – Temperature diagram for cyclic thermal loading (heating to 50, 100 and 250°C and cooling to RT=16°C).

Table 2: Detailed information of experiments under elevated temperatures.

Name	Dimensions (mm)		Loading	T (°C)	Comments
	t	b			
FRPspec8	1.90	16.25	TL <sup>*3</sup> , MUT	50	TL (1 cycle) and MUT up to failure
FRPspec11	1.99	15.96	TL, MUT	50	TL (1 cycle) and MUT up to failure
FRPspec9	1.84	16.05	TL, MUT	100	TL (1 cycle) and MUT up to failure
FRPspec12	2.04	15.76	TL, MUT	100	TL (1 cycle) and MUT up to failure
FRPspec10	1.89	15.96	TL, MUT	250	TL (1 cycle) and MUT up to failure
FRPspec13	1.78	13.98	TL, MUT	250	TL (1 cycle) and MUT up to failure
FRPspec16	1.73	14.52	MUT and LCTL <sup>*4</sup>	50	MUT with constant load 50% of the tensile strength and concurrently LCTL up to failure (max 3 cycles)
FRPspec17	1.80	14.45	MUT and LCTL	100	MUT with constant load 50% of the tensile strength and concurrently LCTL up to failure (max 3 cycles)
FRPspec18	1.71	16.68	MUT and LCTL	100	MUT with constant load 50% of the tensile strength and concurrently LCTL up to failure (max 3 cycles)
FRPspec19	1.73	13.40	MUT and LCTL	250	MUT with constant load 50% of the tensile strength and concurrently LCTL up to failure (max 3 cycles)
FRPspec20	1.87	11.05	MUT and LCTL	250	MUT with constant load 50% of the tensile strength and concurrently LCTL up to failure (max 3 cycles)

\*3Thermal Loading, \*4Low Cycle Thermal Loading (n=3)

### 3 RESULTS

Table 4 presents the results of all the CFRP specimens. Concerning to the control specimens, the average tensile strength of dry fibers of the specimens FRPspec1-5, which were monotonically loaded at room temperature up to failure, was 4,410.82 MPa, their average ultimate strain was 17.47‰ and their average elastic modulus of dry fibers was 252.52 GPa. Their stress-strain curves are shown in figure 5.

Table 4: Summarized results

Name	Loading	T (°C)	Max Tensile Stress (MPa)	Max Tensile Stress of dry fi- bers (MPa)	Max Strain (‰)	Elastic Modu- lus of dry fibers (GPa)	Comments / Mode of failure
FRPspec1	MUT	RT(=16)	719.59	4,546.28	17.86	254.61	Fracture of fibers
FRPspec2	MUT	RT	664.65	4,482.52	16.75	267.61	Fracture of fibers
FRPspec3	MUT	RT	657.99	4,361.10	18.53	235.35	Fracture of fibers
FRPspec4	MUT	RT	711.28	4,548.91	18.39	247.36	Fracture of fibers
FRPspec5	MUT	RT	596.49	4,115.30	15.81	260.30	Fracture of fibers
FRPspec6	LCF, MUT	RT	565.99	4,519.17	20.45	220.98	Fracture of fibers
FRPspec14	LCF, MUT	RT	646.27	4,358.59	21.69	200.98	Fracture of fibers

<b>FRPspec7</b>	LCF, MUT	RT	531.52	4,079.09	16.12	253.08	Fracture of fibers
<b>FRPspec15</b>	LCF, MUT	RT	612.95	4,395.18	18.84	233.25	Fracture of fibers
<b>FRPspec8</b>	TL, MUT	50	490.90	3,615.14	13.67	264.52	Fracture of fibers
<b>FRPspec11</b>	TL, MUT	50	569.99	4,396.47	17.68	248.67	Fracture of fibers
<b>FRPspec9</b>	TL, MUT	100	393.61	2,807.13	10.14	276.95	Fracture of fibers
<b>FRPspec12</b>	TL, MUT	100	518.15	4,097.00	27.66	148.11	Fracture of fibers
<b>FRPspec10</b>	TL, MUT	250	577.98	4,234.06	15.51	272.99	Fracture of fibers
<b>FRPspec13</b>	TL, MUT	250	669.88	4,621.66	19.60	235.80	Fracture of fibers
<b>FRPspec16</b>	MUT and LCTL	50	356.98	2,393.71	15.21		It completed successfully the three thermal loading cycles. <i>The values of the first line refer to the LCTL under constant tension and the values of the second line refer to the MUT up to failure.</i>
			487.61	3,269.66	19.32	169.27	
<b>FRPspec17</b>	MUT and LCTL	100	348.07	2,428.37	12.95	187.46	Failure at the heating process of the first cycle at 64°C. <i>The values refer to the LCTL under constant tension.</i>
<b>FRPspec18</b>	MUT and LCTL	100	317.71	2,105.78	24.14	87.23	Failure at the cooling process of the first cycle at 31°C. <i>The values refer to the LCTL under constant tension.</i>
<b>FRPspec19</b>	MUT and LCTL	250	388.48	2,604.95	15.55	167.53	Failure at the heating process of the first cycle at 61°C. <i>The values refer to the LCTL under constant tension.</i>
<b>FRPspec20</b>	MUT and LCTL	250	327.22	2,371.75	23.63	100.36	Failure at the heating process of the first cycle at 151°C. <i>The values refer to the LCTL under constant tension.</i>



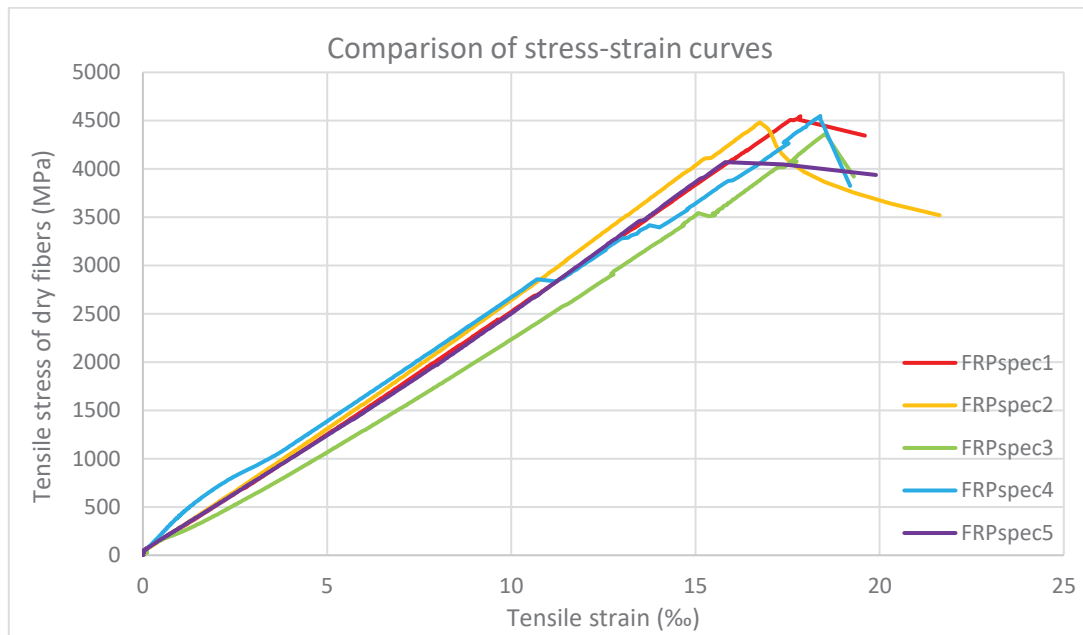
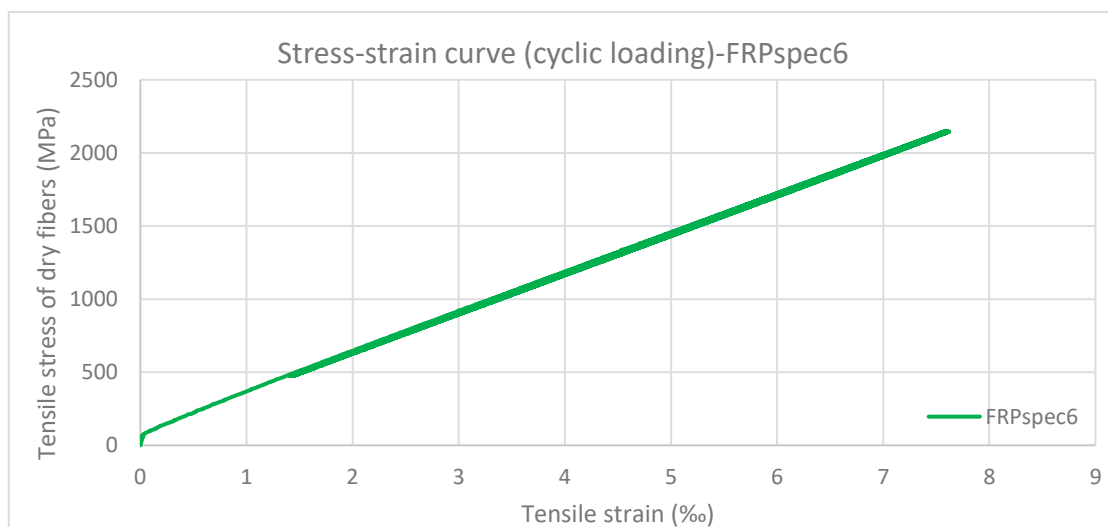


Figure 5: Stress-strain curves for monotonic uniaxial tension at room temperature.

The specimens FRPspec6,14 and FRPspec7,15 were submitted to fatigue tests of fifty loading-unloading cycles with maximum load of 50% and 75% of the average tensile strength, respectively. (see figure 6) Resulted from the monotonic, uniaxial tension that followed, the average tensile strength of dry fibers was 4,438.88 MPa and 4,237.14 MPa for the FRPspec6,14 and the FRPspec7,15, respectively. Consequently, the low-cycle fatigue did not affect the specimens FRPspec6,14, but it reduced the CFRPs tensile strength of dry fibers by 3.94% for FRPspec7,15. Besides, the average ultimate strain did not appear significant change as its value was 21.07‰ and 17.48‰ for the FRPspec6,14 and the FRPspec7,15, respectively. It should also be mentioned that low-cycle fatigue does not affect the stiffness of the CFRPs as their elastic modulus of dry fibers remain at the same level. The stress-strain curves of monotonic tensile loading of the specimens are shown in figure 7.





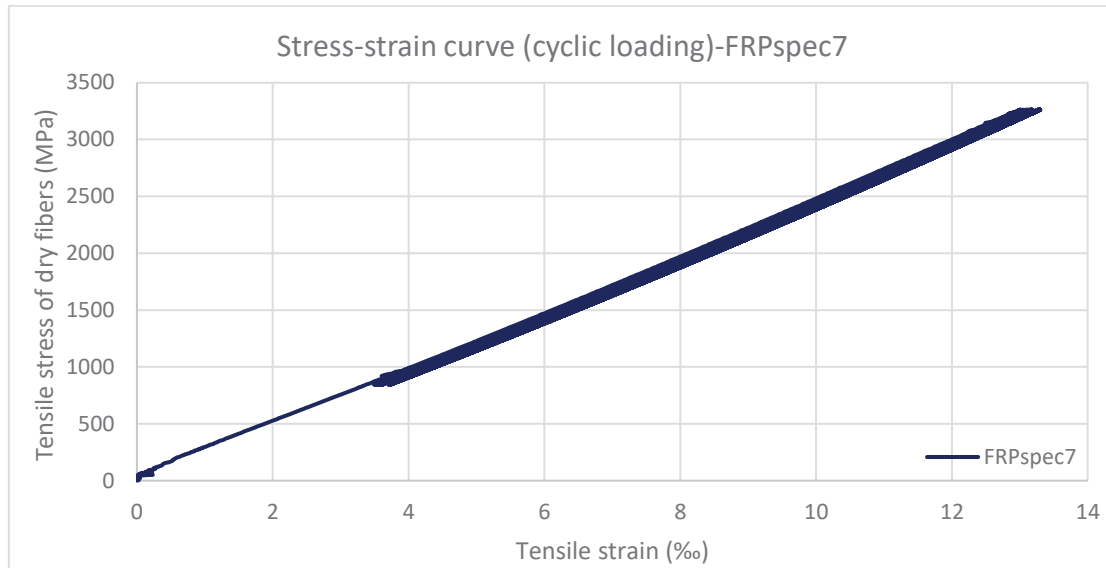


Figure 6: Stress-strain curves for low-cycle fatigue with max load 50% (FRPspec6) and 75% (FRPspec7) of the tensile strength.

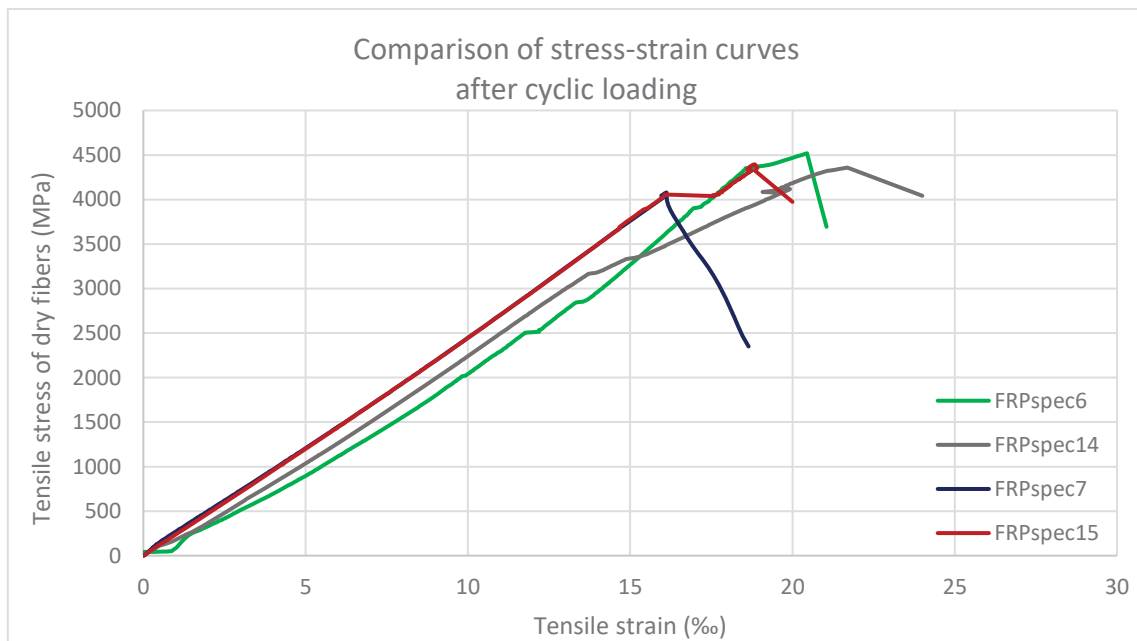


Figure 7: Stress-strain curves of monotonic, uniaxial tension at room temperature after low-cycle fatigue.

The specimens FRPspec8-13,16-20 were exposed to different temperatures during the experiments as it mentioned before. Figure 8 presents the stress-strain curves of monotonic, uniaxial tensile tests which were conducted after the specimens' heating and cooling (FRPspec8-13). FRPspec8 is an exception as the tensile test was possible to be held at the temperature of 50 °C without slip of the specimen. The specimen's tensile strength of dry fibers was 3,615.14 MPa and its ultimate strain was 13.67‰. Observing the samples after heating, those exposed to 100 and 250 °C softened a lot and the resin turned easily into powder with the application of pressure by the machine. In addition, the FRPspec10,13 acquired a dark black colour. However, it was observed that the samples regained their hardness after cooling and the resin was no longer frail. A worth noting conclusion is that the tensile strength of dry fibers of the specimens after exposure at the temperatures of 50, 100 and 250 °C for 30 min did not appear decrease.

The fact that the samples were left to cool significantly contributed to this result. The ultimate strain and the elastic modulus of dry fibers of these specimens did not appear any important change, too.

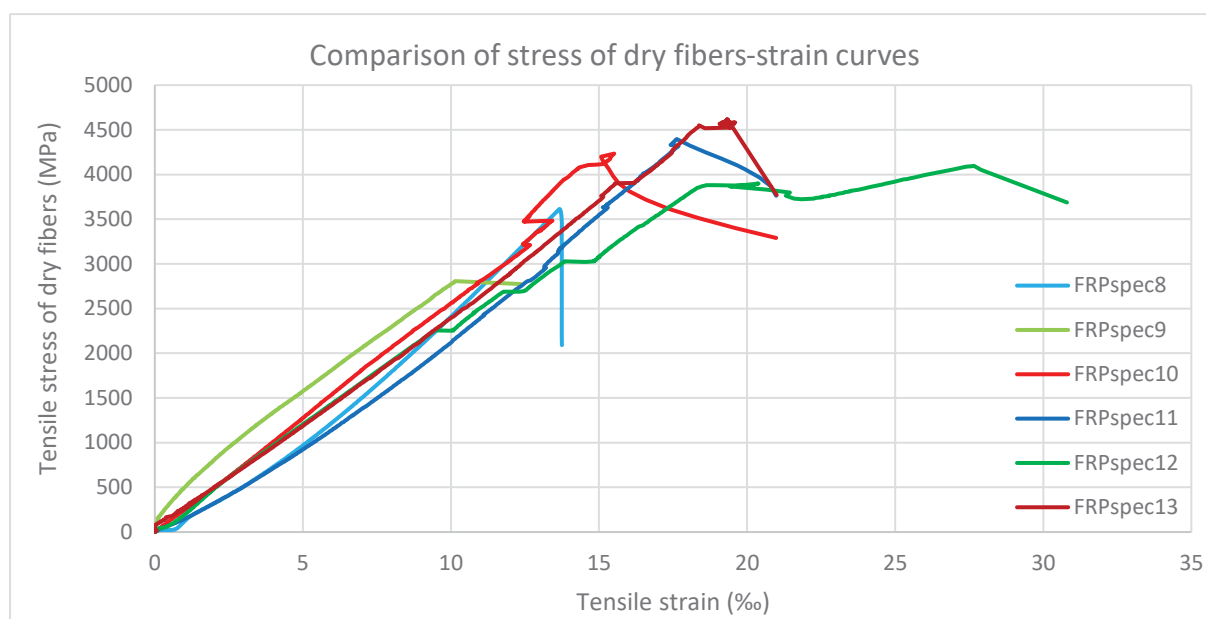


Figure 8: Stress-strain curves of monotonic, uniaxial tensile tests after exposure to the temperatures of 50 °C (FRPspec8,11), 100 °C (FRPspec9b,12) and 250 °C (FRPspec10,13) and then cooling.

The specimens FRPspec16-20 were under both constant tensile load and thermal loading of maximum three heating-cooling cycles. The stress-strain curves of these tests are shown in figure 9. The only sample which managed to complete three heating-cooling cycles without failure was FRPspec16. The maximum temperature of each cycle at this test was 50 °C. After the thermal cyclic loading, FRPspec16 was tested under monotonic tension. The specimen's tensile strength of dry fibers was 3,269.66 MPa, its ultimate strain was 19.32 % and its elastic modulus of dry fibers was 169.27 GPa. According to this, the tensile strength and the elastic modulus of dry fibers are decreased after the heating-cooling cycles.

At higher temperatures, heating combined with the continuous loading had an important impact on the CFRPs' strength as the four samples failed during the first cycle. FRPspec17 failed at the heating process at 64 °C, FRPspec18 failed at the cooling process at 31 °C, FRPspec19 failed at the heating process at 61 °C and FRPspec20 failed at the heating process at 151 °C. The first two of these samples were supposed to be exposed to maximum temperature of 100 °C and the last two to maximum temperature of 250 °C.

It is necessary to mention that the heating rate was 10 °C/min. Because of this slow rate, the specimens remained at high temperature for a long time. If the heating rate was faster, may the FRPs resisted for more thermal loading cycles. The deterioration of the CFRP, due to the long time remaining at high temperature, was also obvious from the mode of failure of the FRPspec20 and its fibers' dark colour. Some of the specimens which were exposed to elevated temperatures are shown after their failure in figure 10.

From the specimens which were supposed to be exposed to maximum temperature of 100 °C and 250 °C, the FRPspec18 and FRPspec20 remained at high temperatures for a longer time than the FRPspec17 and the FRPspec19, which failed earlier. It is also evident from the figure 9 that staying at high temperatures under constant load for longer time causes greater deflections and significant reduction in the modulus of elasticity. The ultimate strain and the elastic

modulus of dry fibers of the FRPspec18 were 24.14 % and 87.23 GPa, respectively, and of the FRPspec20 were 23.63 % and 100.36 GPa, respectively.

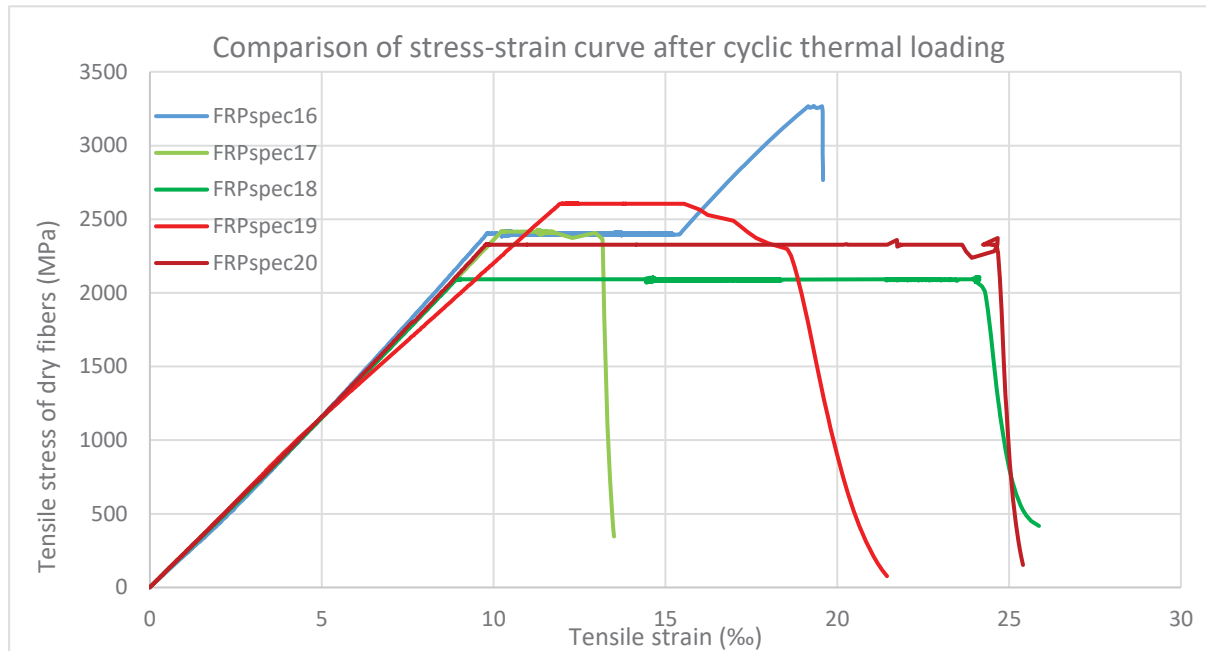


Figure 9: Stress-strain curves of low-cycle thermal loading under constant tensile load. The maximum temperatures of heating-cooling cycles were 50 °C (FRPspec16), 100 °C (FRPspec17,18) and 250 °C (FRPspec19,20).

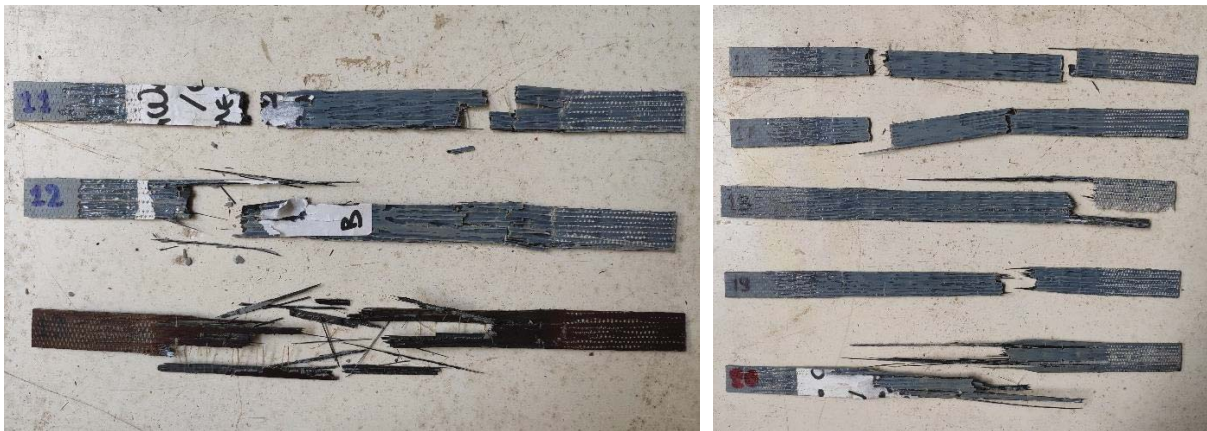


Figure 10: Specimens, exposed to elevated temperatures, after their failure.  
FRPspec11,12,13 were exposed to 50,100 and 250 °C, respectively (TL, MUT).  
FRPspec16, FRPspec17,18 and FRPspec19,20 were exposed to 50,100 and 250 °C, respectively (MUT and LCTL).

#### 4 CONCLUSION

- At room temperature CFRP laminates appear high tensile strength and elastic modulus.
- Low-cycle fatigue at room temperature reduces in a small percentage the CFRP laminates' tensile strength. This reduction is obvious when the maximum load of the cycle is high enough.
- Low-cycle fatigue at room temperature does not affect the stiffness of the CFRPs, as their elastic modulus remain at the same level.

- When CFRP laminates are exposed to elevated temperatures (100 °C, 250 °C) the resin softens and turns easily into powder if pressure is applied. In addition, the FRPs acquire a dark black colour at 250 °C.
- Because of the resin's deterioration under elevated temperatures, the CFRP specimens slip from the machine's grips during the tensile testing. Therefore, better gripping is needed.
- CFRPs cooled after exposure to elevated temperatures, regain their hardness and the resin is no longer frail. Their tensile strength does not show decrease.
- The cyclic thermal loading under constant tensile load causes degradation of CFRP laminates, as their tensile strength is reduced after the heating-cooling cycles.
- The cyclic thermal loading under constant tensile load reduces the elastic modulus of CFRP laminates. The higher temperatures the CFRPs are exposed to, the greater reduction of the elastic modulus is caused.
- The longer time the CFRP laminates remain at high temperatures under constant tensile load, the greater deflections and reduction in their elastic modulus are caused.

## ACKNOWLEDGEMENTS

Part of the research “MECHANICAL PROPERTIES CHARACTERISATION OF FRPS UNDER ELEVATED TEMPERATURES” has been co-funded by Greece and European Union through the Operational Program “EDBM-103: SUPPORT FOR RESEARCHERS EMPHASIZING YOUNG RESEARCHERS – 2<sup>nd</sup> CYCLE” (project code: 5047899) which are gratefully acknowledged.



## REFERENCES

- [1] M.Z. Naser, R.A. Hawileh, J.A. Abdalia, Fiber-reinforced polymer composites in strengthening reinforced concrete structures: A critical review. *Engineering Structures*, **198**, 2019.
- [2] S.B. Singh, A. Sethi, A Review of Performance of Fibre Reinforced Polymer Strengthened Structures Under Fire Exposure. *Civil Engineering Department, Birla Institute of Technology and Science, Pilani, India*, 2017.
- [3] H. Ashrafi, M. Bazli, E.P. Najifabadi, A.V. Oskouei, The effect of mechanical and thermal properties of FRP bars on their tensile performance under elevated temperatures, *Construction and Building Materials*, **157**, 1001-1010, Tehran, Iran, 2017
- [4] K. Spirakos, Reinforcement of structures for seismic loads, **288**, 176-177, Athens, 2004
- [5] S. Piliafa, Investigation of the thermomechanical for smart materials to monotonic and low-cycle fatigue conditions, 71, Aristotle University of Thessaloniki, Greece, 2020

## EXPERIMENTAL TESTING CAMPAIGN AND NUMERICAL MODELLING OF AN INNOVATIVE BASE-PLATE CONNECTION FOR PALLET RACKING SYSTEMS

**Bonaventura Tagliaferro<sup>1\*</sup>, Rosario Montuori<sup>1</sup>, Ioannis Vayas<sup>2</sup>, Sofia Antonodimitraki<sup>2</sup>,  
Magdalini D. Titirla<sup>3</sup>, Marco Simoncelli<sup>4</sup>, Xenophon Lignos<sup>2</sup>**

<sup>1</sup>University of Salerno  
Via Giovanni Paolo II, 132, 84084 Fisciano SA, Italy  
{btagliaferro,r.montuori}@unisa.it

<sup>2</sup>National Technical University of Athens, Institute of Steel Structures  
Iroon Politehneiou 9, 15780 Zografos, Athens, Greece  
e-mail: vastahl@central.ntua.gr; lignosx@central.ntua.gr

<sup>3</sup>Structural Mechanics and Coupled Systems Laboratory (LMSSC)  
Conservatoire National des Arts et Métiers (CNAM), Paris, 292 rue Saint-Martin, 75141 Paris Cedex  
03, France  
titirlamagdalini@gmail.com

<sup>4</sup>Politecnico di Milano  
Department of Architecture, Built Environment and Construction Engineering Milano, Italy  
marco.simoncelli@polimi.it

**Keywords:** Steel Structures, Adjustable Pallet Racks, Seismic Standards, Eurocode

**Abstract.** *The problem of the high fragility of upright frames of pallet racking systems against lateral forces raises an important question for researchers. This lack of seismic performance can be attributed to a small degree of internal overdetermination of the system, as is also acknowledged by the European Standard for adjustable pallet racking structures (EN16681), which only takes into account the low-dissipative behaviour for these structures. This paper presents an innovative base-plate connection that can provide the upright frames of pallet racking systems with a certain degree of global ductility, thus improving the seismic attitude of these structures when seismically stimulated along the cross-aisle direction. A design procedure for the specimens to be tested is proposed, which aims at guiding the system design toward localizing yielding strains in the plates of the base connections, as the principles of the capacity design posit. The proposed base-plate connection is tested under monotonic and cyclic loads to better understand its properties and, by inference, its dynamic characterization, which could be utilized in a lighter numerical model in order to study overall performance improvement. Additionally, a numerical model of the specimen, as tested in the Laboratory of Steel Structures at the National Technical University of Athens (Greece), which has been calibrated and validated in accordance with experimental tests results, is presented.*



## 1 INTRODUCTION

The structural frames of racking structures are often composed of open cold-formed thin-walled steel members, that typically do not guarantee plastic capacities of their cross section [1, 2]. This poses a new issue: it is well-known that the capacity of structure systems to resist seismic actions in the nonlinear range generally permits their design for forces smaller than those corresponding to a linear elastic response. Another issue is related to the behaviour of structures in the post-elastic range; it becomes vital to control the force distribution [3] in order to control the structure collapse, as well the lateral displacements [4, 5]. Such approach is what allows designing building with design spectra [see 6], which generally correspond to an onset of elastic spectra by introducing a conventional parameter that accounts for the capacity of the structure to dissipate energy. Nevertheless, storage racks can still provide a degree of energy dissipation if other non-conventional mechanisms are considered [7, 8, 9]. For example, if designed so, beam-to-column and base-plate connections can exhibit an inelastic behavior which could be used to keep using the same approach [10, 11]. Nonetheless, the European Framework for steel structures does not allow yet to concentrate any damage on beam-to-column connections [12].

Cross-aisle frames often have a truss-like structure system: two uprights are laced up by different diagonal patterns, the most common of which are *X*-shaped diagonal and *D*-shaped diagonal. The cross-aisle structural scheme tends to have fewer internal degrees of freedom, thus making fragile collapse modes most likely. Hence, as also shown by many works [13], the lateral resistance of the overall frame is greatly affected by the flexural behaviour of the base-plate connections, which may be as well the only place where plastic deformation can safely take place [14]. The high lateral stiffness of the upright frames is also cause of concern for the happenstance of excessive accelerations at decks level. It is safe to say that the sliding of pallets on the supporting beams can be the most serious threat to the shedding of goods, which can either endanger the health of workers/customers or even damage some structural parts thus leading to cascading effects. In the cross-aisle direction, the fundamental period is generally short, comprised between 0.7s and 1.0s [15].

The seismic responses of the two principal directions of pallet racking structures are rather different. In the down-aisle direction, the great flexibility provided by connections and the absence of spine bracings reflect in significantly high value of the fundamental period of vibrations

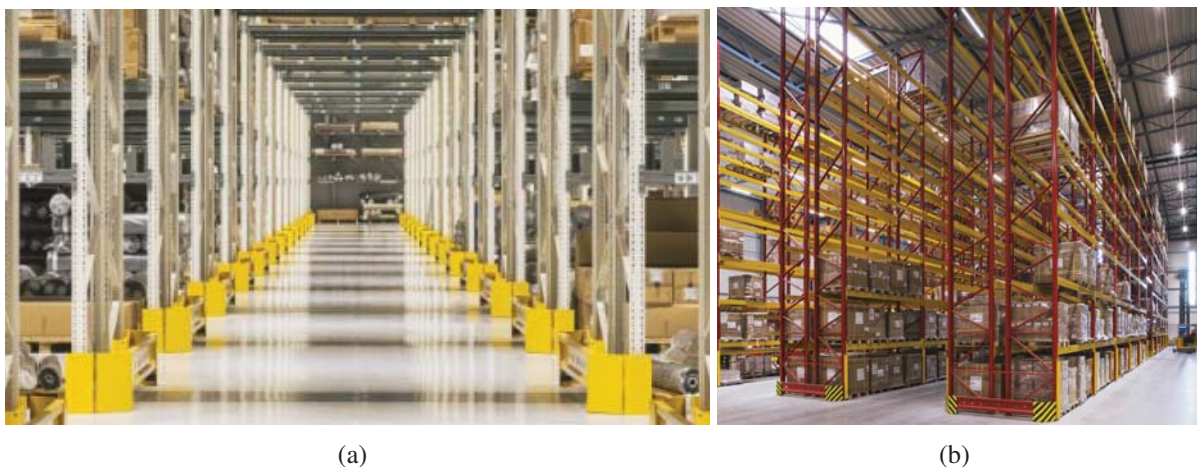


Figure 1: (a) and (b) Warehouse stores with pallet racks (courtesy of NEDCON B.V.).



( $T$ ), sometimes up to 3.50s, which are the typical values observed for high-rise and tall steel buildings. The adherence of this structural scheme with ordinary structures has made a great body of research focus on this subject and its performance is well understood although it needs to manage a great variety of numerical special features [16].

Under lateral dynamic loads, owing to the presence of open thin-walled cross-sections, rack bearing elements are often prone to local and/or distortional buckling phenomena, which largely precede the attainment of the cross section yielding capacity. Therefore, to enforce classical design procedure, it is important to rely exclusively on the post-yielding capacity of connections. Cross-aisle frames can hardly locate plastic deformations within their inner connections, though it might be possible to design such a connection with that in mind. On the other hand, the connections between upright and building slab are characterised by a very limited degree of flexural stiffness and bending resistance, mainly limited by the column cross-section ultimate resistance capacity. In most of the cases, when the cross-aisle direction is considered, the seismic action can pose a risk for the overturning, which becomes the most dangerous limit state. Nevertheless, as it happened for the beam-to-column connections, the nonlinear cyclic behaviour can provide a non-negligible ductility to the structure. For this reason, as suggested by [17], attention must be paid on the design of base-connections to be allowed to use a behaviour factor  $q$  greater than 1 (but however lower than 2) in the seismic structural analysis;

Upright frames can be designed as *low-dissipative structural behaviour* (DCL), as recognised by EN 16681. This circumstance is addressed by EC8, and a *behaviour factor* is as well allowed, used to allow designers to perform elastic analyses and, at the same time, account for nonlinear phenomena. EC8 clearly identifies the use of  $q \leq 1.50$  for this class. It is stated that such value accounts for overall structural *overstrengths*. With reason, for example, for DCL class, it is advised to avoid cross sectional class 4, for it does not guarantee enough overstrength. In contrast with this last clause, EN 16681 affirms that the behaviour factor accounts for the *energy dissipation capacity* of the structure.

This work presents the results of a experimental tests and numerical simulations to investigate the cyclic response of a base-plate connection designed for adjustable pallet racking systems. The experimental tests, which were carried out in the Laboratory of Steel Structures, NTUA (Athens, Greece), are described, and results for a monotonic and a cyclic load path are reported. Hence, the specimen was reproduced in a mesh-based numerical framework, giving further insight about the mechanical behaviour of the specimen under study.

## 2 EXPERIMENTAL CAMPAIGN

### 2.1 Specimen

A base-plate connection for adjustable pallet racking systems was conceived to provide structures with energy-dissipation capacity. The behavior of this type of connection is reminiscent of a T-stub mechanism mainly subjected to axial load, which is generally used to model the top and bottom tee of beam-to-column connections; in such situations, the working principles are well-understood and the performance under cyclic loads proved to be quite remarkable (Piluso and Rizzano 2008) [18]).

All specimens have been assembled by welding steel plates composing the base plate, 6mm thick, and the bracket, 5mm thick, made of S235 ( $f_y = 235 \text{ MPa}$  and  $f_u = 415 \text{ MPa}$ ) steel fastened through the flanges by means of two M20 bolts made of 8.8 class high strength steel [6]; the upright, supplied by NEDCON B.V. (The Netherlands), having an overall depth of 120 mm and an overall width of 94 mm, was made of steel S350D and is connected to the bracket

by means of 8 M8 bolts 8.8 class. The photographic image and the schematic view representing the test specimen are given in Fig. 2. In order to guarantee an optimal stress distribution in the profile, the upright was cut 425 mm long ( $\approx$  four times its depth). Its upper cross section is welded to an end-plate that is hence bolted to the actuator head, where the load cell is located.

The base-plate connection was tested under monotonic and cyclic loads in the Laboratory of Steel Structures, NTUA (Athens, Greece). In Fig. 2(a), the experimental setup is shown, where the testing machinery and the specimen are indicated. The static actuator has a stroke of  $\pm 150$  mm and can reach up to  $300 \text{ kN}$ ; the accuracy of measuring equipment belongs to the 1 class of accuracy, thus giving an expected error on the measurement of  $\pm 1.5 \text{ kN}$ . Aiming at assessing the axial performance solely, the degree of freedom activated by the actuator is along the axis of the column stub (vertical).

## 2.2 Results

The monotonic test was performed by applying a displacement time history from 0 – 28 mm, with a constant velocity equal to  $v = 0.15 \text{ mm/s}$ . The cyclic protocol was defined in accordance with the AISC Seismic Provisions (AISC 2002), which provides a test sequence given as a function of the peak deformation  $\delta_y$ , with a decreasing number of cycles as the load step increases (Fig. 3(a)). The specimens were instrumented with two LVDTs located on both sides of the base plate to measure the uplift displacement.

The results of the tests are reported in Fig. 3. The two tests show an overall good agreement in terms of overall behaviour, providing good performance accounting for the cyclic consistency of the loops. The post-elastic performance of the tested specimen arises from the exploitation of

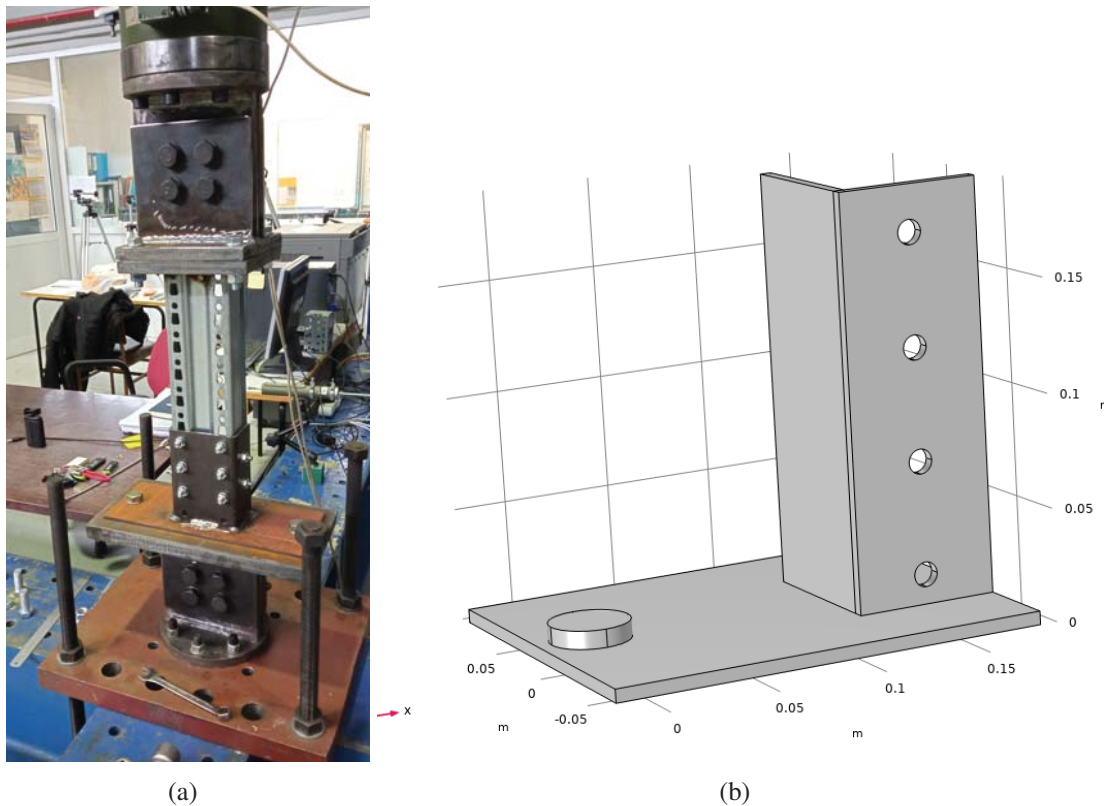
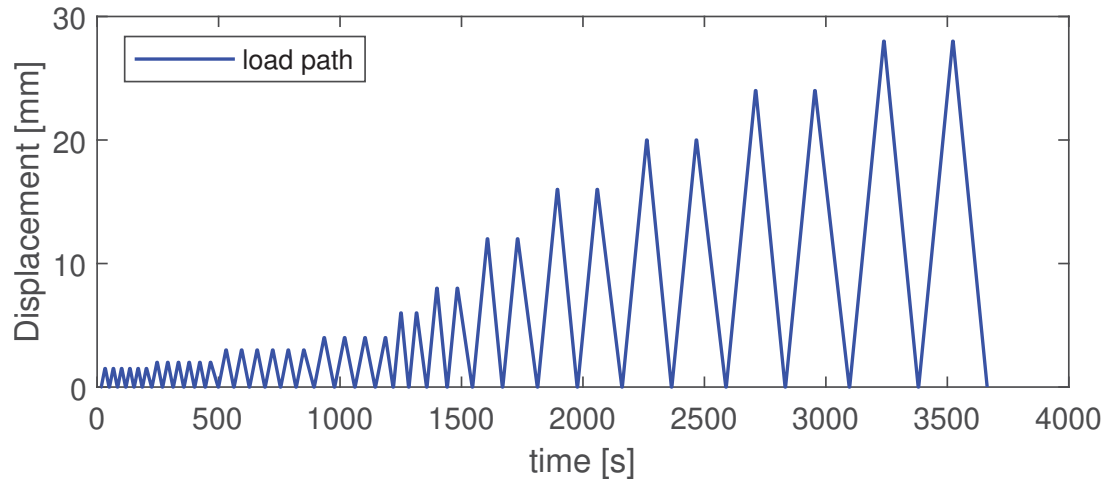


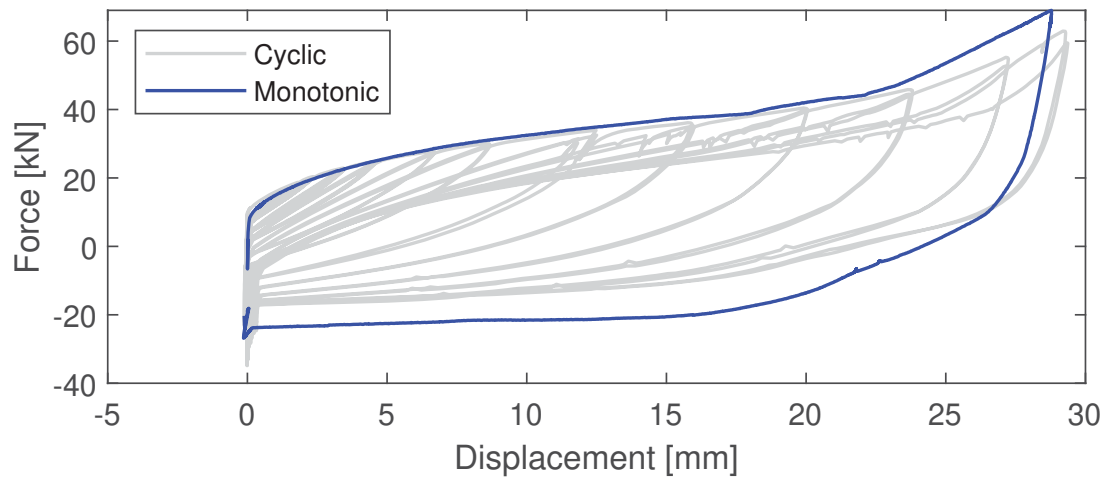
Figure 2: (a) Photographic image of the specimen as in the experimental setup. (b) 3D view of the base-plate assembly.

the dissipative failure mechanism (Type 1 mechanism [12]), which can be promoted by design guaranteeing strong-bolt weak-flange resistance relationship. It is characterized by the formation of a plastic hinge in the T-stub flanges, plus a circular pattern around the bolt's axis (ref. Fig. 4).

As it can be noticed, the shape of the cycles can be related to similar experimental results, in which the performance of T-stub connections was studied, accounting for energy dissipation capacity and stiffness degradation for the pinching of the hysteresis loops [18].



(a)



(b)

Figure 3: (a) Cyclic loading protocol and (b) experimental results of the tests.

### 3 NUMERICAL MODELLING

As the finite element (FE) method is widely employed as an approach to develop numerical prediction models, many researchers have been using it to support their investigation [19, 20, 21]. In this study, the COMSOL software has been used. The Johnson-Cook hardening law was used to model the strain rate dependency of the plastic hardening; the material properties are presented in Section 2.1 of this study. The 3D FE model geometry reproduced the half geometry of the experiments, using symmetric conditions in order to minimize the computation effort. As well as the simulation used similar boundary conditions and loading as in the experimental



Figure 4: Lateral view of the specimen at the end of the monotonic test

program. A sensitivity analysis was conducted to identify the best meshing and, in total, 79759 elements were used (4-nodes solid elements). Contact conditions between two surfaces are governed by kinematic constraints in the normal and tangential directions. The normal stress at contact is either zero when there is a gap between the two surfaces, or compressive when the surfaces are in contact. The contacts are defined in the augmented Lagrangian method with the penalty factor controls. In addition, material and geometric nonlinearities have been taken into account. The nonlinear solver uses an affine invariant form of the damped Newton method. In this section, static analyses have been performed with increasing displacement, in the same fashion of the experimental test. The numerical results were compared with the experimental ones and the validation of the model was based on: (i) the force-displacement curves, and (ii) the deformation shape of the specimen (Figure 5).

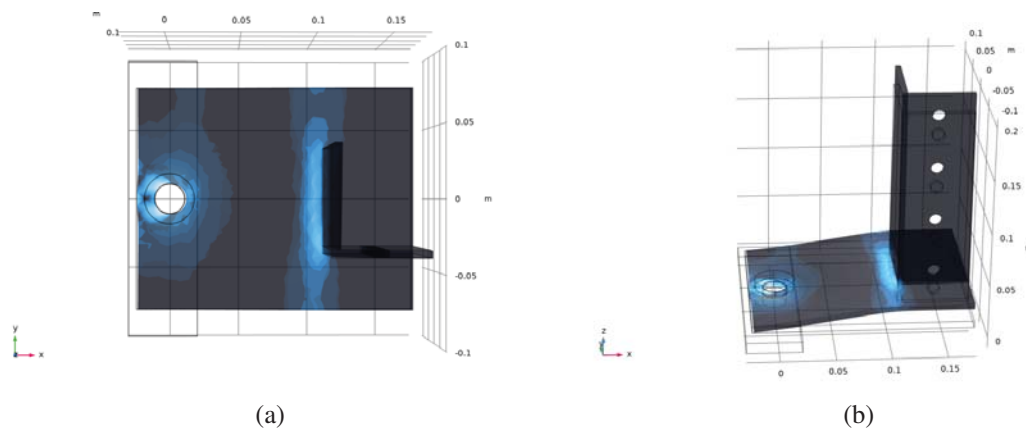


Figure 5: Top (a) and 3D (b) view of the specimen at the end of the monotonic test; the right hand side picture highlights the plastic hinge in correspondence of the T-stub web and a circular pattern around the bolt.

#### 4 CONCLUSIONS AND FUTURE RESEARCH NEEDS

This work explores the performance of a T-stub-like connection that can be used to improve the seismic performance of pallet racking systems, with the aim of increasing the energy dissipation capacity of the upright frames. The sample was shown to have similar performance to a standard T-stub, which is widely used to model the overall 3D behaviour of beam-to-column connections of steel structures. This type of connection can be used for the construction of new lateral resisting structures, as well as for the retrofitting of existing ones, where lateral loads are

a problem.

## 5 ACKNOWLEDGEMENTS

The first author's Ph.D. scholarship is granted by the Italian Ministry for Education, University and Research (MIUR) as part of the program "Dottorati Innovativi a caratterizzazione industriale", ID DOT 1328490–3, funded by the European Union (Structural Funding ERDF-ESF for "Research and Innovation" 2014-2020). The authors are grateful for the support.

Parts of the test set-up were delivered gratis by J Dimitriou Ltd Kataskevastiki. This support is acknowledged.

Part of the material used for the testing campaign was provided by NEDCON B.V. (The Netherlands). The authors would like to express their very great appreciation to Ir. Jan Hermanek.

## 6 CONFLICTS OF INTEREST

The authors declare no conflict of interest. The funders had no role in the design of the study; in the collection, analyses, or interpretation of data; in the writing of the manuscript, or in the decision to publish the results.

## REFERENCES

- [1] Rosario Montuori, Giammaria Gabbianelli, Elide Nastri, and Marco Simoncelli. Rigid plastic analysis for the seismic performance evaluation of steel storage racks. *Steel and Composite Structures*, 32(1):1–19, 07 2019.
- [2] Giammaria Gabbianelli, Francesco Cavalieri, and Roberto Nascimbene. Seismic vulnerability assessment of steel storage pallet racks. *Ingegneria Sismica*, 37:18–40, 06 2020.
- [3] Rosario Montuori, Elide Nastri, and Vincenzo Piluso. Advances in theory of plastic mechanism control: closed form solution for mr-frames. *Earthquake Engineering & Structural Dynamics*, 44(7):1035–1054, 2015. doi: <https://doi.org/10.1002/eqe.2498>. URL <https://onlinelibrary.wiley.com/doi/abs/10.1002/eqe.2498>.
- [4] R. Montuori, E. Nastri, and B Tagliafierro. An optimal seismic force pattern for uniform drift distribution. *Buildings*, 9(11):231, 2019. doi: <https://doi.org/10.3390/buildings9110231>.
- [5] R. Montuori, E. Nastri, and B. Tagliafierro. Residual displacements for non-degrading bilinear oscillators under seismic actions. *Mechanics Research Communications*, 111: 103651, 2021. ISSN 0093-6413. doi: <https://doi.org/10.1016/j.mechrescom.2020.103651>. URL <https://www.sciencedirect.com/science/article/pii/S0093641320301798>.
- [6] European Committee for Standardization CEN, EN1998-1. *Eurocode 8 - Design of Structures for Earthquake Resistance-Part 1: General Rules, Seismic Actions and Rules for Buildings*. CEN, 2005.
- [7] Magdalini D. Titirla and Panikos Papadopoulos. Finite element investigation of a new seismic energy absorption device through simultaneously yield and friction. Crete Island, Greece, 05 2015. COMPDYN 2015, 5th ECCOMAS Thematic Conference on Computational Methods in Structural Dynamics and Earthquake Engineering.



- [8] Magdalini D. Titirla, Panikos K. Papadopoulos, and Ioannis N. Doudoumis. Finite element modelling of an innovative passive energy dissipation device for seismic hazard mitigation. *Engineering Structures*, 168:218–228, 2018. ISSN 0141-0296. doi: <https://doi.org/10.1016/j.engstruct.2018.04.081>. URL <https://www.sciencedirect.com/science/article/pii/S0141029617330547>.
- [9] Marco Simoncelli, Bonaventura Tagliafierro, and Rosario Montuori. Recent development on the seismic devices for steel storage structures. *Thin-Walled Structures*, 155:106827, 2020. ISSN 0263-8231. doi: <https://doi.org/10.1016/j.tws.2020.106827>.
- [10] E. Jacobsen and R. Tremblay. Shake-table testing and numerical modelling of inelastic seismic response of semi-rigid cold-formed rack moment frames. *Thin-Walled Structures*, 119:190 – 210, 2017. ISSN 0263-8231. doi: <https://doi.org/10.1016/j.tws.2017.05.024>.
- [11] Stella Avgerinou, Xenophon Lignos, Dimitris Tsarpalis, and Ioannis Vayas. Full-scale tests on used steel storage racks. *Steel Construction*, 12(3):231–242, 2019. doi: 10.1002/stco.201900009.
- [12] Eurocode 3. *Design of Steel Structures*. European Committee for Standardization, Brussels, 2005.
- [13] Zhaoqi Huang, Yue Wang, Xianzhong Zhao, and Ken S. Sivakumaran. Determination of the flexural behavior of steel storage rack baseplate upright connections with eccentric anchor bolts. *Thin-Walled Structures*, 160:107375, 2021. ISSN 0263-8231. doi: <https://doi.org/10.1016/j.tws.2020.107375>.
- [14] Magdalini D. Titirla, Konstantinos Katakalo, Giulio Zuccaro, and F Fabbrocino. On the mechanical modeling of an innovative energy dissipation device. *Ingegneria Sismica*, 34, 06 2017.
- [15] Bonaventura Tagliafierro, Rosario Montuori, and Maria Gabriella Castellano. Shake table testing and numerical modelling of a steel pallet racking structure with a seismic isolation system. *Thin-Walled Structures*, Under review, 2021.
- [16] Claudio Bernuzzi and Marco Simoncelli. Steel storage pallet racks in seismic zones: Advanced vs. standard design strategies. *Thin-Walled Structures*, 116:291 – 306, 2017. ISSN 0263-8231. doi: <https://doi.org/10.1016/j.tws.2017.03.002>.
- [17] EN 16681. *Steel Static Storage Systems – Adjustable Pallet Racking Systems – Principles for Seismic Design*. European Committee for Standardization, Brussels, 2016.
- [18] Vincenzo Piluso and Gianvittorio Rizzano. Experimental analysis and modelling of bolted t-stubs under cyclic loads. *Journal of Constructional Steel Research*, 64(6):655–669, 2008. ISSN 0143-974X. doi: <https://doi.org/10.1016/j.jcsr.2007.12.009>.
- [19] Magdalini D. Titirla and Konstantinos Katakalo. Evaluation of an innovative passive mitigation device through experimental and numerical investigation. pages 353–361, 01 2017. doi: 10.7712/120117.5425.18065.
- [20] M. Titirla, A. Chalot, L. Michel, and E. Ferrier. 3d finite element modelling of novel strengthening solutions for RC wall/slab connections. *Ingegneria Sismica - International Journal of Earthquake Engineering*, 37(3):64–83, 2020.



- [21] Rosario Montuori, Elide Nastri, Vincenzo Piluso, and Alessandro Pisapia. Ultimate behaviour of high-yielding low-hardening aluminium alloy i-beams. *Thin-Walled Structures*, 146:106463, 2020. ISSN 0263-8231. doi: <https://doi.org/10.1016/j.tws.2019.106463>. URL <https://www.sciencedirect.com/science/article/pii/S0263823119310109>.

## **STUDY OF THE INFLUENCE OF UNDERLYING SOFT-SOIL LAYERS ON THE DYNAMIC AND EARTHQUAKE RESPONSE OF BELL TOWERS**

**G.C. Manos<sup>1</sup>**

<sup>1</sup> Emeritus Professor and Ex-Director of the Lab. of Strength of Materials and Structures, Aristotle  
University  
e-mail: gmanos@civil.auth.gr

---

### **Abstract**

The dynamic and earthquake response of a bell towers founded on soft soil layers is examined here. The dynamic and earthquake response of such a bell towers is numerically simulated together with a number of layers of the underlying soil. The earthquake response is examined for a variety of load combination conditions employing design spectra as well as the ground motion recorded at a small distance from this bell tower during a prototype earthquake motion. Towards this end, the variation of the recorded ground motion due to the flexibility of these underlying soil layers is also examined. The earthquake response is examined comparatively in terms of global response parameters, such as base shear, overturning moment, and top displacements as well as peak stress values at particular parts of the bell tower that stress concentration occurs. These response values are studied in a comparative way in order to validate these numerical simulations with the observed performance.

**Keywords:** Bell towers, In-situ Dynamic Measurements, Numerical Simulation, Earthquake Response, Soil-structure Interaction.

---

## 1 INTRODUCTION

Bell towers are structures that are of particular interest regarding their dynamic and earthquake response, which has been the subject of research in the past. A large number of bell towers with dimensions much larger than the ones examined here are located in numerous cities in Italy and elsewhere. The largest percentage of these bell towers is built by stone or brick masonry. In many cases earthquake activity constitutes the major cause of serious damage for bell towers that many times leads to partial or total collapse ([1] to [16]). Consequently, there is a major international concern for the stability of numerous bell towers. This resulted to significant international research effort that includes in-situ monitoring of the response of bell towers on a temporary basis, like the one attempted here, or more sophisticated and on a permanent basis. Foundation problems for bell towers are evident in many cases the most celebrated being Pisa's grand bell tower in Italy, that is quoted as a major medieval engineering error. Therefore, the soil flexibility is also an area of research interest for these structures especially when their dynamic and earthquake response is under investigation ([19] to [28]).

This investigation was initiated by the observed performance of two relatively new bell towers. Both these bell towers, built by reinforced concrete (RC) and founded on an RC foundation block did not sustain any structural damage. They were both founded on relatively flexible soil although they were not any visible signs of soil deformation at the aftermath of the strong seismic ground motion. For both towers in-situ measurements were performed aiming to investigate their main dynamic characteristics. From these measurements it became apparent that the flexibility of the underlying soil layers could have exerted an influence on the seismic performance of these bell towers that should not be ignored. This was initially attempted by altering the flexibility of the supports of the RC foundation block utilizing linearly flexible links between the foundation block and the underlying soil. This was successful, up to a point, as shown by comparing the numerically predicted in this way fundamental translational periods of these bell towers to the corresponding values found from the in-situ measuring campaign. However, in this way the adopted approach did not address the influence of the existing structures to the assumed earthquake ground motion, which was recorded at some distance from these structures which were of considerable height (23m) with a foundation block of considerable dimensions (4.5m x 4.5m in plan and more than 1m thick). Moreover, it was interesting to observe that in the case of one of these bell towers (Havriata) the nearby church was damaged as well as the South slope of the hill that both the bell tower and the church were located showed signs of distress (see figures 1). In what follows, an investigation is performed aimed to study the bell tower dynamic and earthquake response by numerically simulating the structure of the bell tower and its foundation together with a considerable volume of the underlying soil. This investigation, for simplicity purposes, is performed in the 2-D domain and assumes linear behaviour of both the soil and the superstructures. At a later stage, this study can be extended at a later stage to a more complex numerical simulation in the 3-D domain which could also include a more realistic behaviour of the soil volume than that which is assumed at present. In what follows initially the acceleration at the bedrock is approximated. Next, the response of the soil volume is studied in three different configurations; the first assumes only the given soil volume the second this soil volume with a simple superstructure numerically simulating the church and the third configuration includes the given soil volume together with simple numerical simulations of both the church and the bell tower. The obtained numerical predictions are presented and discussed.



Fig. 1. The Church and the bell tower of the Panagia Agriliotissa at Havriata, Kefalonia-Greece together with the interior and exterior damage of the church and the South slope.

## 2 ESTIMATING THE ROCK ACCELERATION.

In what follows a study is performed using the ground acceleration (figure 2) recorded during the 3rd of February 2014 earthquake sequence at Havriata village in Kefalonia island [3]. The two horizontal and the vertical components of this record are used as input together with a soil volume that is assumed to be 30m deep. For layers deeper than 30m it is assumed that these layers have mechanical properties close to those of a rocky formation. The soil volume above this rocky substrate is divided in three layers having a 10m depth each. Three dif-

ferent soil profiles are studied whereby the properties of the upper layer are only varied whereas the properties of the other two underlying layers remain constant. Two types of analyses are performed using a 2-D software for this purpose. The first type of analysis assumes linear behaviour of the soil volume that depends on the given elastic mechanical properties of the soil layers. The second type of analysis assumes a certain soil non-linear behaviour as it is simulated by given options in this software [17].

## 2.1 Linear behaviour of the underlying soil layers.

Initially, linear behaviour of the underlying soil layers are assumed with elastic properties listed in table 1. The following values of the soil properties are listed in this table. Young's Modulus  $E$  (Mpa), Shear Modulus  $G$  (Mpa), Mass density  $\rho$  (KNsec<sup>2</sup>/m<sup>4</sup>), and Shear wave velocity  $v$  (m/sec) given by equation 1.

$$v = (G / \rho)^{0.5} \quad (1)$$

Depth (m)	Soil Profiles	E (MPa)	G (MPa)	$\rho$ (KNsec <sup>2</sup> /m <sup>4</sup> )	$v$ (m/sec)
0 to -10	1 <sup>st</sup> Profile	465	194	1.835	325
0 to -10	2 <sup>nd</sup> Profile	300	125	1.835	261
0 to -10	3 <sup>rd</sup> Profile	100	41.67	1.835	150
-10 to -20	1 <sup>st</sup> , 2 <sup>nd</sup> and 3 <sup>rd</sup> Profiles	1000	417	1.835	477
-20 to -30	1 <sup>st</sup> , 2 <sup>nd</sup> and 3 <sup>rd</sup> Profiles	2000	833	1.835	674
Deeper than -30m	1 <sup>st</sup> , 2 <sup>nd</sup> and 3 <sup>rd</sup> Profiles	50000	20833	1.835	1066

Table 1. Elastic properties of the soil layers

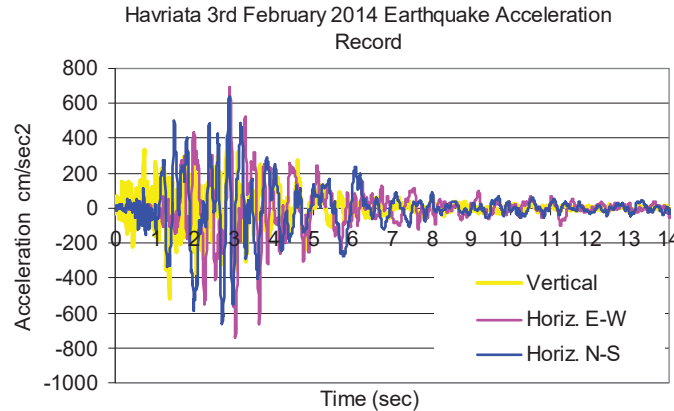


Figure 2. The recorded at Havriata earthquake ground motion in terms of two horizontal and the vertical acceleration components.

In what follows, the software STRATA [17] assuming linear behaviour of all the underlying soil layers with values of these elastic properties listed in table 1. Based on these values and using as input information the acceleration components of the recorded ground motion at the surface of the Havriata town the corresponding components are obtained at bedrock, assumed to be at layers deeper than 30m from the soil surface. The results are obtained in two forms, either as acceleration time history or as the relevant acceleration elastic response spectral curve (for 5% damping ratio). Along these lines a parametric study is performed whereby the 3 three soil profiles listed in table 1 were analyzed. The obtained results in terms of either acceleration time history components at bedrock or acceleration elastic response spectral curves (for 5% damping ratio) are depicted in



figure 2 (soil profile 1) for the two horizontal and the vertical component of the Havriata 3<sup>rd</sup> of February 2014 record of the earthquake ground motion. For soil profiles 2 and 3 the corresponding results are depicted in figures 3 and 4, respectively. As it is listed in figures 2, 3 and 4 as well as from the values listed in Table 1 soil profile 1 corresponds to a relatively stiff soil, soil profile 2 to a moderately stiff soil whereas soil profile 3 corresponds to a relatively flexible soil.

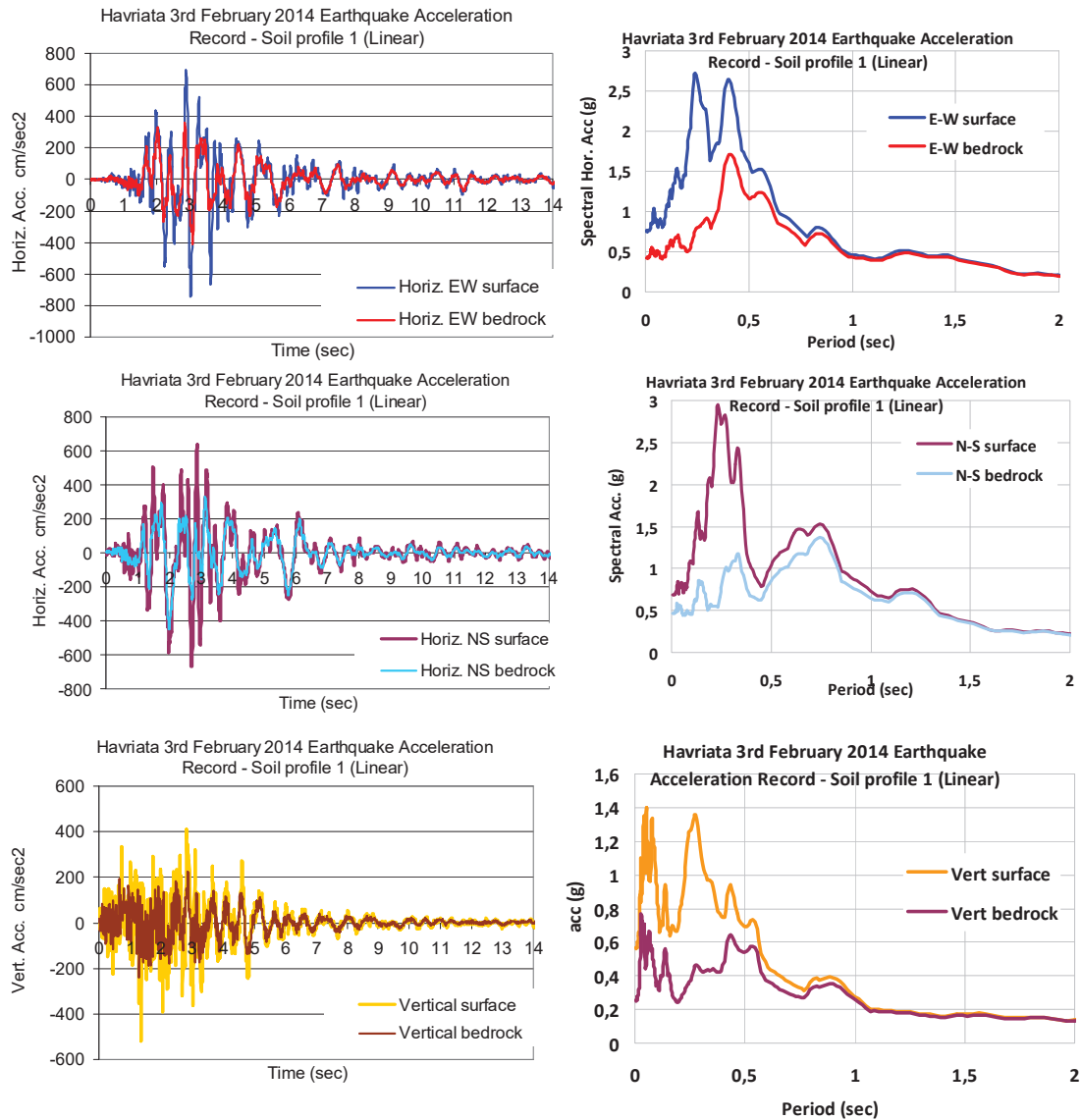


Figure 2. The obtained acceleration components at the bedrock for the Havriata earthquake ground motion in terms of two horizontal and the vertical acceleration components or the corresponding elastic response spectral curves (for 2% damping ratio). **Soil Profile 1 (Linear) Upper layer relatively stiff.**



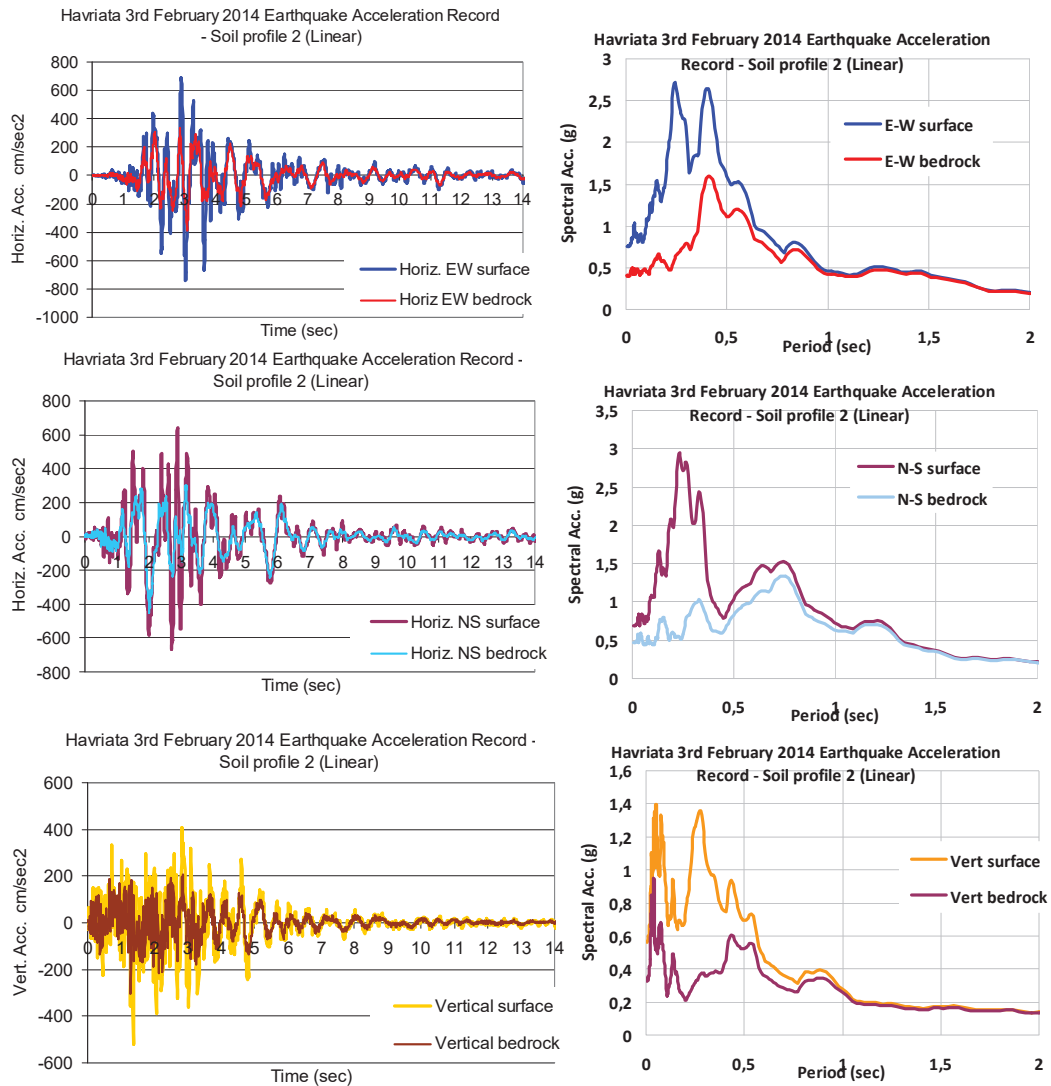
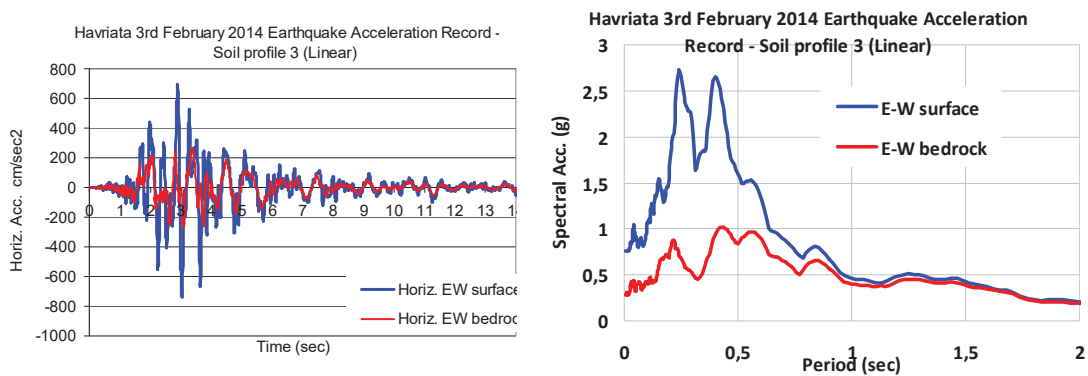


Figure 3. The obtained acceleration components at the bedrock for the Havriata earthquake ground motion in terms of two horizontal and the vertical acceleration components or the corresponding elastic response spectral curves (for 2% damping ratio). **Soil Profile 2 (Linear) Upper layer moderately flexible.**



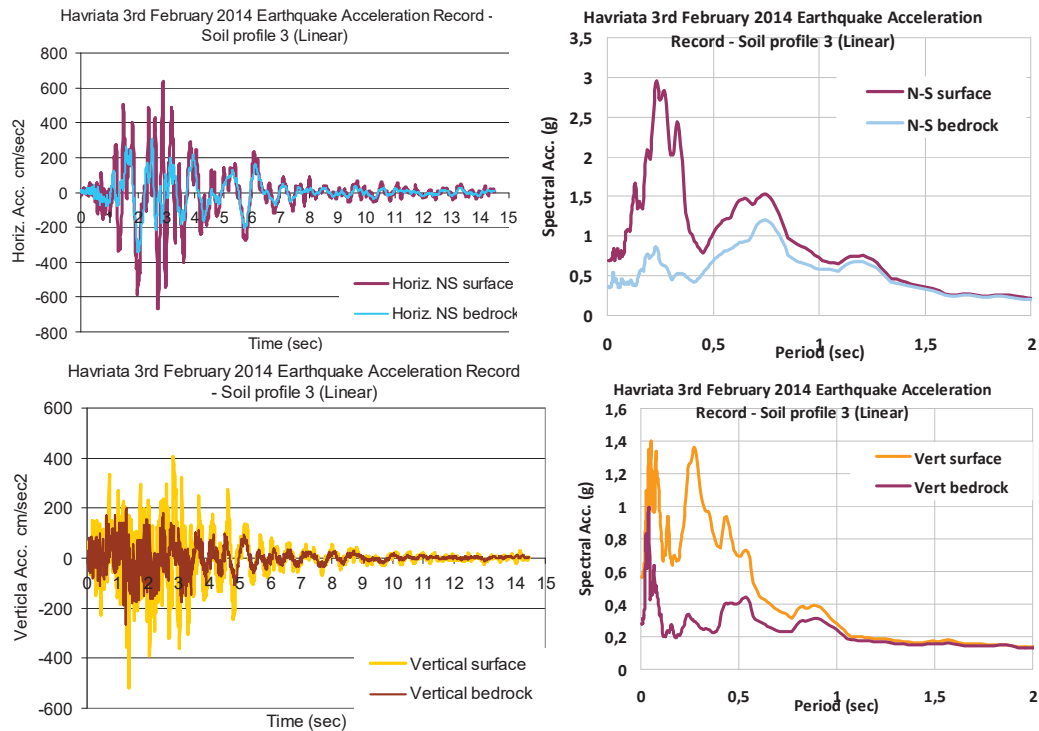


Figure 4. The obtained acceleration components at the bedrock for the Havriata earthquake ground motion in terms of two horizontal and the vertical acceleration components or the corresponding elastic response spectral curves (for 2% damping ratio). **Soil Profile 3 (Linear) Upper layer relatively flexible.**

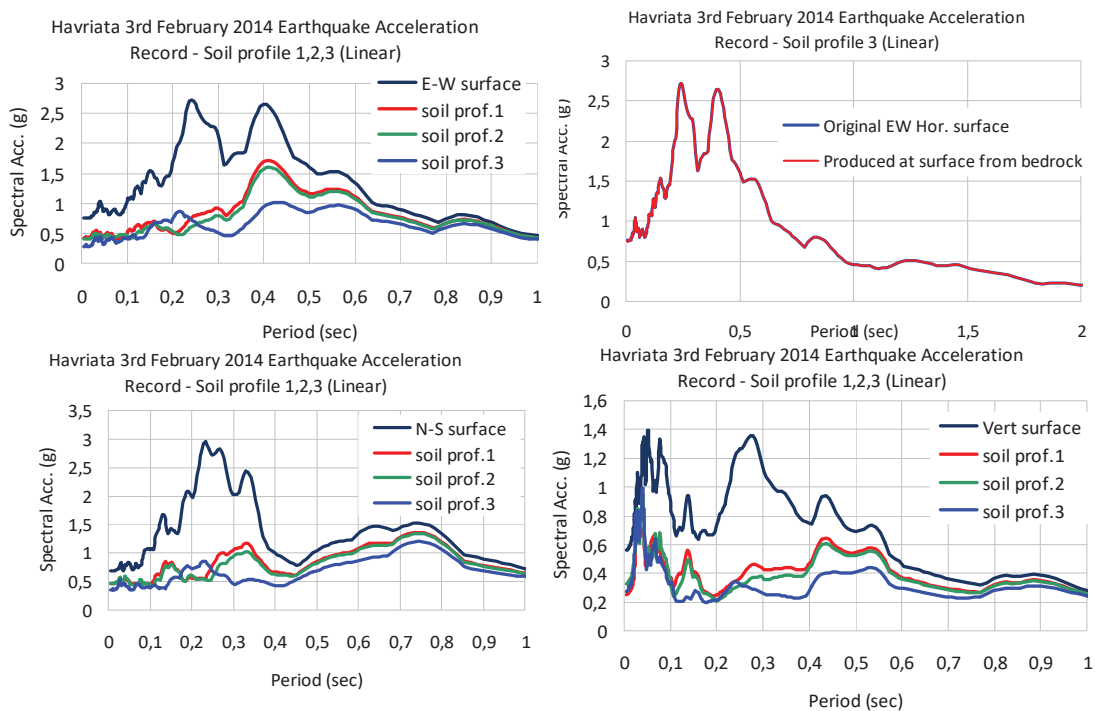


Figure 5. Comparison of the acceleration spectral curves obtained from the recorded components of the seismic ground motion at Havriata and the corresponding acceleration spectral curves from the acceleration components obtained from STRATA software at the bedrock for the three soil profiles.

Figure 5 summarizes the results of figures 2, 2 and 4 in terms of acceleration spectral curves derived from the acceleration components obtained at bedrock by utilizing STRATA software assuming soil properties for three soil profiles listed in table 1 and assuming linear behaviour. In the same figures the spectral curves at the surface of the soil volume derived from the three components of the recorded seismic ground motion at Havriata are also plotted. Moreover, at the top right of this figure the spectral curve of the East-West component of the recorded during the seismic event ground motion is compared with the corresponding spectral curve found by applying the STRATA software in the inverse way. That is, using as bedrock acceleration the one found for soil profile 3 is used as input to obtain through this software the acceleration at the surface of the soil-volume. Then, the spectral acceleration curve for 5% damping ratio is found and potted. As can be seen, these two spectral acceleration curves, the original one from the actual record and the one employing STRATA software, combining the direct and the inverse process, are identical. Moreover, from the results depicted in figures 2, 3, 4 and 5 it can be seen that that both the acceleration time histories and the corresponding acceleration spectral curves are deflated when they are compared with the corresponding values at the soil volume surface of the originally recorded ground acceleration. It can also be observed, that this deflation, is larger for soil profile 3 than for either soil profile 2 or soil profile 1. Inversely, the more flexible the soil profile the more intense the amplification of the ground acceleration at the surface either in terms of time history or acceleration spectral values.

## 2.2 Non-Linear behaviour of the underlying soil layers

The linear analyses with the STRAT software, previously described, were followed by additional analyses assuming non-linear properties for the underlying soil layers. Two additional soil profiles were used here, as a non-linear variation of the linear 3<sup>rd</sup> soil profile listed in table 1. First, the 4<sup>th</sup> soil profile is formed by assuming at the upper soil layer (0 to -10m depth) the soil properties representative of “Imperial Valley soil”, which is an option included in the software and represents relatively stiff soil. Next, the 5<sup>th</sup> soil profile is formed by assuming at the upper soil layer (0 to -10m depth) the soil properties representative of the “Idriss weak clay”, which is another option included in the software and represents relatively flexible soil. These two soil profiles are listed in table 2. Again, the properties of the layers deeper than -10m are the same for both the 4<sup>th</sup> and the 5<sup>th</sup> soil profile as listed in table 2. In reference [18] a study on the influence of the plasticity index (PI) on the cyclic stress-strain parameters of saturated soils needed for site-response evaluations and seismic microzonation is presented. Ready-to-use charts are included, showing the effect of PI on the location of the modulus reduction curve  $G/G_{max}$  versus cyclic shear strain  $\gamma_c$ , and on the material damping ratio  $\lambda$  versus  $\gamma_c$  curve. The charts are based on experimental data from 16 publications encompassing normally and overconsolidated clays ( $OCR=1-15$ ), as well as sands. It is shown that PI is the main factor controlling  $G/G_{max}$  and  $\lambda$  for a wide variety of soils; if for a given  $\gamma_c$  PI increases,  $G/G_{max}$  rises and  $\lambda$  is reduced. Similar evidence is presented showing the influence of PI on the rate of modulus degradation with the number of cycles in normally consolidated clays. It is concluded that soils with higher plasticity tend to have a more linear cyclic stress-strain response at small strains and to degrade less at larger  $\gamma_c$  than soils with a lower PI. Possible reasons for this behavior are discussed. A parametric study is presented showing the influence of the plasticity index on the seismic response of clay sites excited by the accelerations recorded on rock in Mexico City during the 1985 earthquake”. For the 4<sup>th</sup> and 5<sup>th</sup> soil profiles the non-linear variation of the assumed shear modulus and damping depending on the strain amplitude is depicted in figures 5 and 6.

Layer No. Depth (m)	4 <sup>th</sup> Non-linear Profile Relatively stiff soil	5 <sup>th</sup> Non-linear Profile Relatively flexible soil
Layer 1 (0 to 10m)	Imperial Valley (Soils 0-300ft)	Idriss, Weak-Clay
Layer 2 (-10m to -20m)	Vucetic & Dobry PI=100	Vucetic & Dobry PI=100
Layer 3 (-20m to -30m)	Vucetic & Dobry PI=200	Vucetic & Dobry PI=200

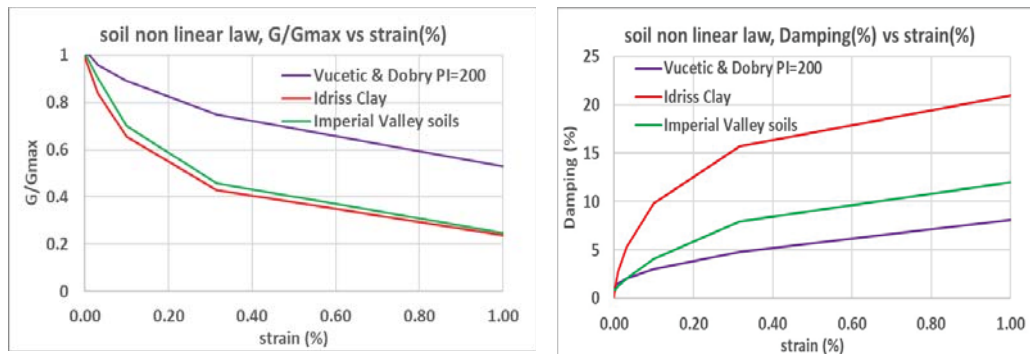
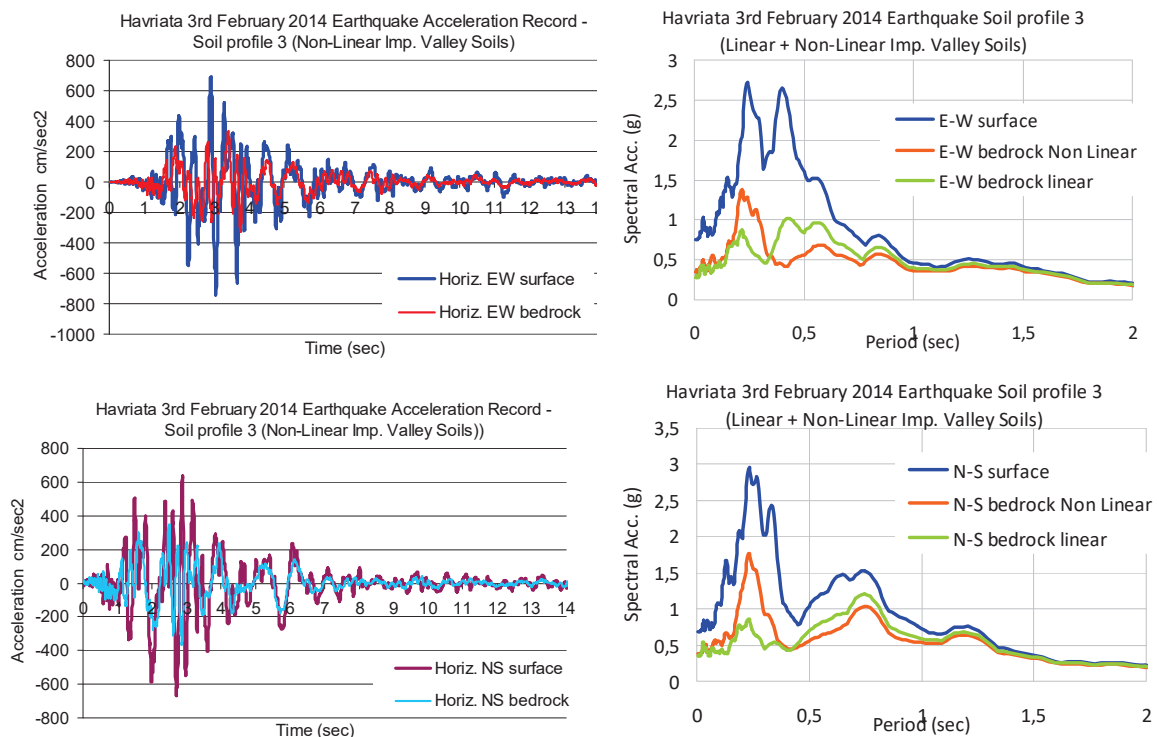
Table 2. Non-linear soil profiles 4<sup>th</sup> and 5<sup>th</sup>.

Figure 6. The assumed non-linear variation of the shear modulus with strain amplitude (left). The assumed non-linear variation of the damping ratio with strain amplitude (right).



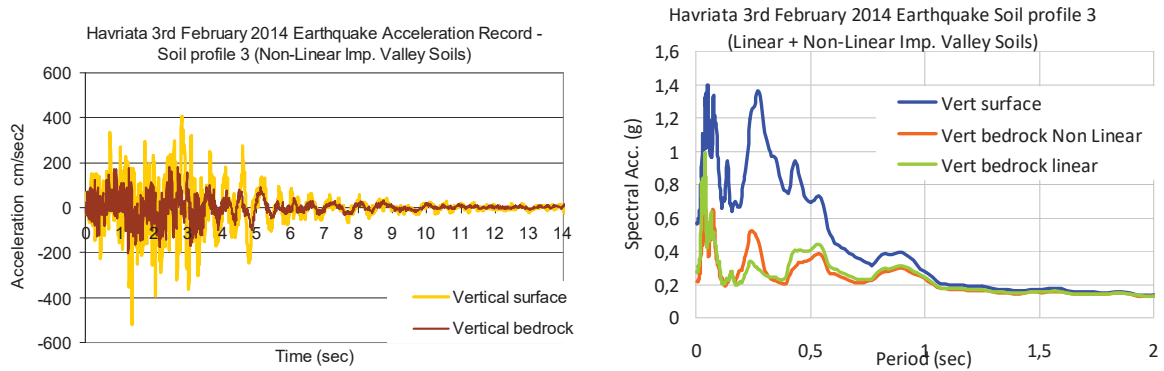


Figure 7. The obtained acceleration components at the bedrock for the Havriata earthquake ground motion in terms of two horizontal and the vertical acceleration components or the corresponding elastic response spectral curves (for 2% damping ratio). **Soil Profile 4<sup>th</sup> (Non-Linear) Upper layer relatively stiff.**

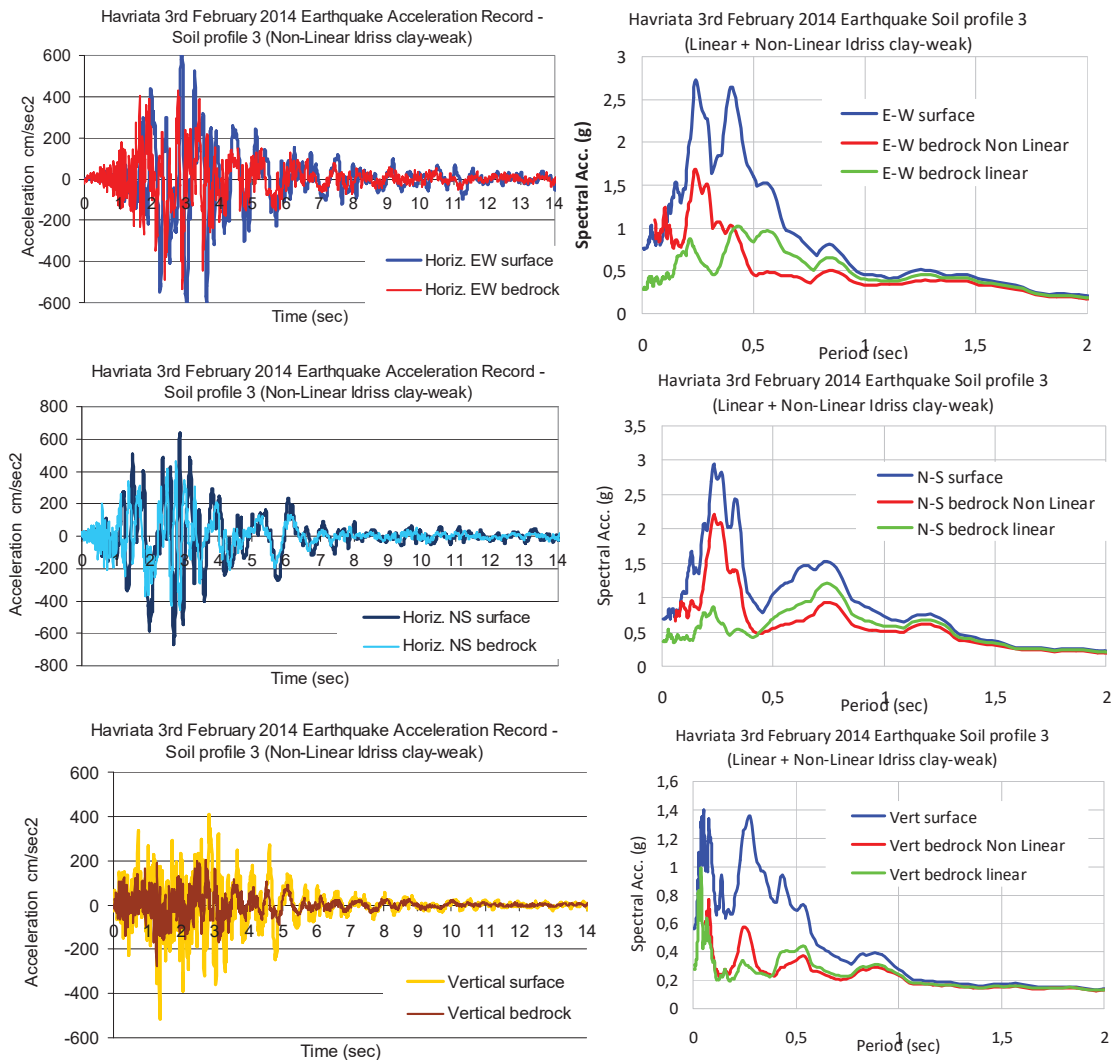
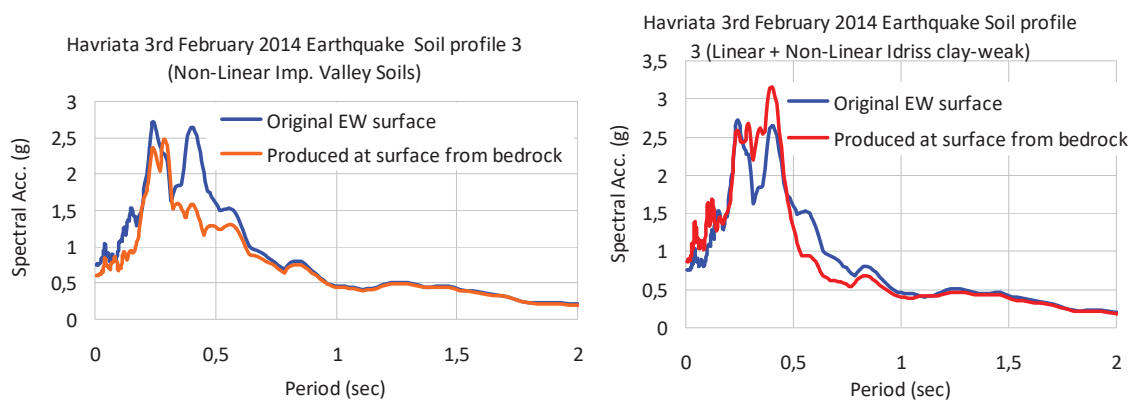


Figure 8. The obtained acceleration components at the bedrock for the Havriata earthquake ground motion in terms of two horizontal and the vertical acceleration components or the corresponding elastic response spectral curves (for 2% damping ratio). **Soil Profile 5<sup>th</sup> (Non-Linear) Upper layer relatively flexible.**

The obtained acceleration at bed rock, in terms of either acceleration time histories or response spectral curves are depicted in figures 7 and 8 for soil profiles 4<sup>th</sup> and 5<sup>th</sup>, respectively. In the spectral curves plots the corresponding spectral curves for soil profile 3 assuming linear behaviour are also plotted. In the same plots the corresponding seismic ground acceleration recorded during the February 2014 earthquake sequence, either in terms of time history or in terms of the corresponding acceleration spectral curves for 5% damping ratio are also shown. Moreover, in figure 9 the spectral curve of the East-West component of the recorded during the seismic event ground motion is compared with the corresponding spectral curve found by applying the STRATA software in the inverse way. That is, using as bedrock acceleration the one found for soil profile 4 (left of figure 9) or soil profile 5 (right of figure 9) is used as input to obtain through this software the acceleration at the surface of the soil-volume. Then, the spectral acceleration curve for 5% damping ratio is found and plotted in this figure. As can be seen, these two spectral acceleration curves, the original one from the actual record and the one employing STRATA software, combining the direct and the inverse process, are differing with the best agreement achieved for soil profile 5. As was observed from the results obtained assuming linear behaviour from the results depicted in figures 7 and 8 it can be seen that that assuming non-linear behaviour both the acceleration time histories and the corresponding acceleration spectral curves are deflated when they are compared with the corresponding values at the soil volume surface from the originally recorded ground motion. It can also be observed, that for small eigen-period values (0.1 to 0.4 sec) this deflation, is smaller when assuming non-linear (soil profiles 4 and 5) than when assuming linear behaviour (soil profile 3). Inversely, the non-linear soil behaviour the less intense the amplification of the ground acceleration at the surface either in terms of acceleration spectral values for small eigen-period values (0.1 to 0.4 sec). The opposite is true for relatively large period values (0.4 to 1.0 sec). Following the inverse approach for soil profile 4 and 5 and assuming non-linear behaviour it can be seen that for soil profile 5 (figure 9, right) the predicted spectral values in the period range from 0.3sec to 0.4 sec there are amplified when compared with the corresponding values of the original record. The opposite is true for soil profile 4 (figure 9, left).



ground motion at Havriata and the corresponding acceleration spectral curves from the acceleration components obtained from STRATA software at the bedrock for the three soil profiles.

### 3 TWO DIMENSIONAL (2-D) NUMERICAL SIMULATION OF THE SOIL LAYERS, THE CHURCH AND THE BELL TOWER.

In what follows an 2-D numerical simulation is presented of the soil layers studied in section 2 assuming linear behaviour. Again, three soil layers are numerically simulated with a depth of 10m each having mechanical properties the ones listed in Table 1 for soil profile 3.



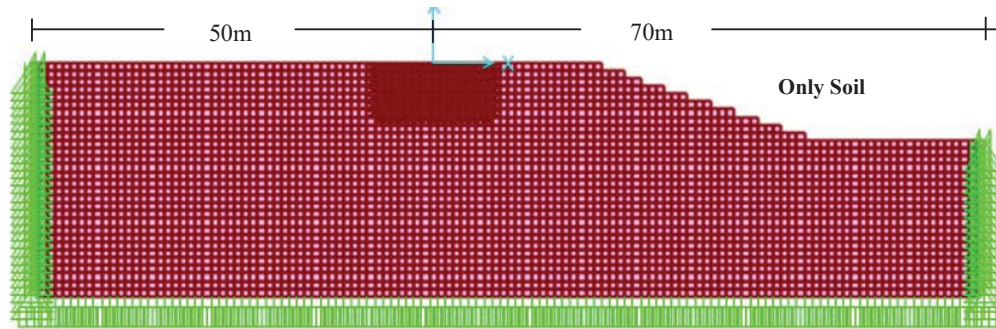


Fig. 10. 2-D Numerical simulation of the soil layers under the bell tower and the church (up to 30m depth and 120m long)

At the depth of 30mm from the surface the boundary is considered with fixed base conditions. At this boundary, the North-South acceleration time history was applied, obtained for the bedrock through STRATA software for soil profile 3, as described in section 3. The length of the soil formation is equal to 120m, with the vertical boundaries being confined with horizontal links having a finite stiffness of 1000KN/mm. An attempt is made to numerical simulate the slope of the hill present at the South side of the damaged church at Havriata (see fig 1). An attempt was also made to have a 2-D numerical representation of the bell tower and the church respecting their basic dimensions and the relative distance between them. Moreover, the eigen-period values for the fundamental North-South translational eigen-modes. The dynamic characteristics of these simple representations of either the bell tower or the church are in good agreement with corresponding values found from more detailed 3-D numerical representations of these structures being also partially validated with in-situ measurements.

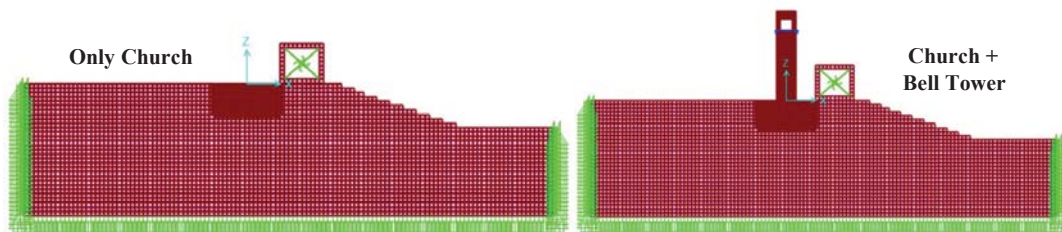


Fig. 11. 2-D Numerical simulation of the soil layers under the bell tower and the church (up to 30m depth) together with simple numerical models of the church, the bell tower and its foundation.

### 3.1. Study of eigen-modes and eigen-periods

In figures 10 and 11 the studied 2-D numerical simulations for the three configurations, namely “only Soil”, “only Church” and “Church+Bell Tower” are shown. In all these configurations the numerical simulation of the soil volume remains the same. Moreover, in all the analyses the employed excitation also remains the same, that is bedrock horizontal component that was derived by applying STRATA software for soil profile 3 (linear behaviour – Table 1) using as input the North-South horizontal component of the seismic ground motion recorded in the village of Havriata during the 3rd of February 2014 earthquake sequence (see figure 4).

In what follows first the numerically predicted eigen-modes and eigen-periods are shown for the previously described three configurations. These are presented in the form of a table (Tables 3, 4 and 5) listing the first seven (7) eigen-modes in terms of eigen-period values with the corresponding modal mass participation ratio values. These eigen-modes are with respect

to one horizontal (x-x) and one vertical (z-z) directions. Figures 13, 14 and 15 depict the corresponding mode-shapes.

Only Soil-3	Period (sec)	UX %	UZ %	SumUX %	SumUZ %
Mode 1	<b>0,289</b>	<b>32.0</b>	0	32.0	0
Mode 2	0,241	0.1	0	32.0	0
Mode 3	0,202	1.0	1.2	34.0	1.2
Mode 4	<b>0,196</b>	0.3	<b>26.0</b>	34.0	28.0
Mode 5	0,190	0.1	4.3	34.0	32.0
Mode 6	0,182	0	0.9	34.0	33.0
Mode 7	0,177	1.3	0.7	36.0	33.0

Table 3. Eigen-periods and modal mass participation ratio – Only Soil (Soil-3)

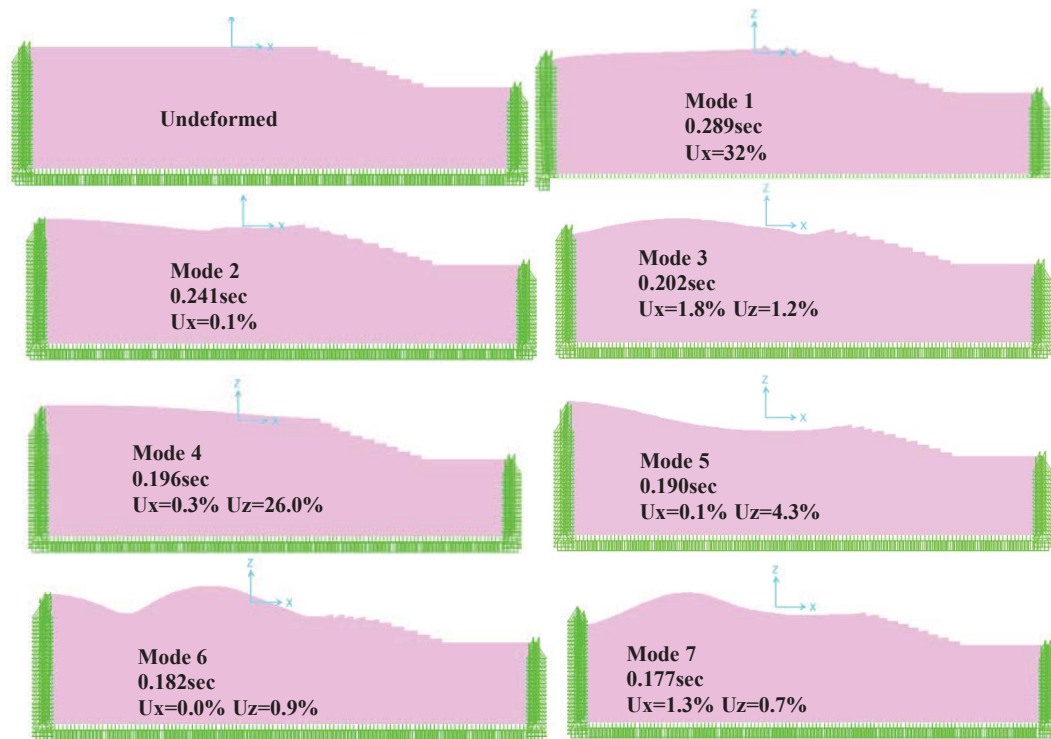


Figure 12. Eigen-modes, eigen-periods and modal mass participation ratio – Only Soil-3

Only Soil-1	Period (sec)	UX %	UZ %	SumUX %	SumUZ %
Mode 1	<b>0,200</b>	<b>55.2</b>	0.1	55.2	0.1
Mode 2	0,158	0.2	0	55.4	0.1
Mode 3	<b>0,141</b>	0.9	<b>45.8</b>	56.3	45.9
Mode 4	0,133	1.7	5.1	57.9	51.1
Mode 5	0,130	0.7	0	58.6	51.1
Mode 6	0,118	0.7	3.9	59.4	55.0
Mode 7	<b>0,112</b>	<b>10.5</b>	0.1	69.9	55.1

Table 4. Eigen-periods and modal mass participation ratio – Only Soil (Soil-1)

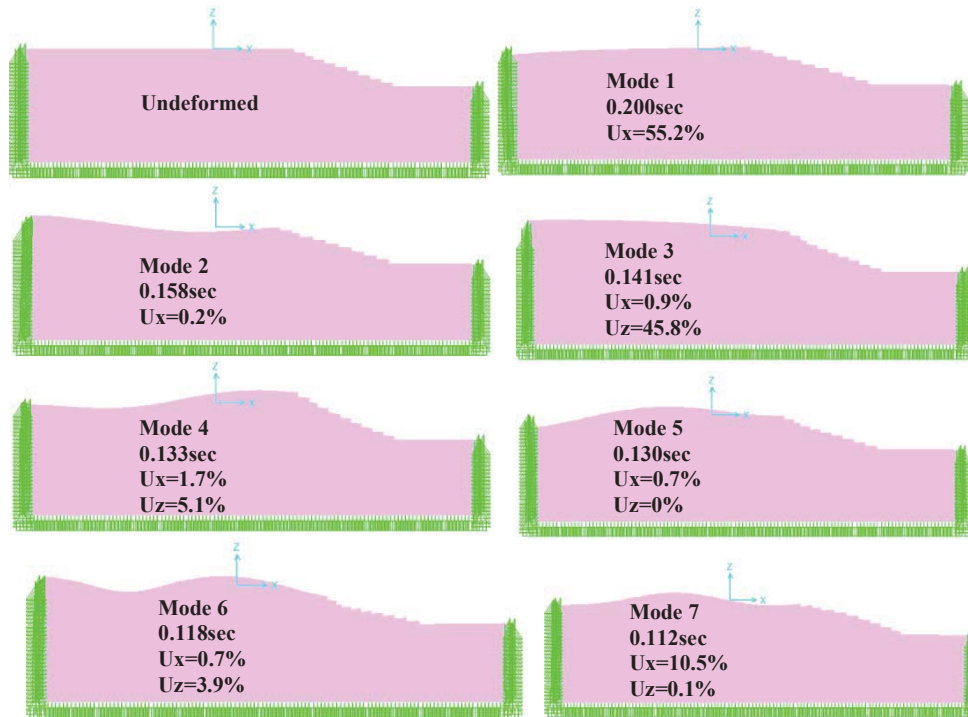


Figure 13. Eigen-modes, eigen-periods and modal mass participation ratio – Only Soil-1

Soil-3 + Church	Period (sec)	UX %	UZ %	SumUX %	SumUZ %
Mode 1	<b>0,301</b>	<b>23.8</b>	0	23.8	0
Mode 2	0,267	8.1	0	31.9	0
Mode 3	0,236	0.2	0	32.1	0
Mode 4	0,203	1.8	2.4	33.9	2.4
Mode 5	<b>0,197</b>	0.4	<b>29.9</b>	34.3	32.4
Mode 6	0,193	0	0.8	34.3	33.2
Mode 7	0,183	0.1	0.2	34.5	33.4

Table 5. Eigen-periods and modal mass participation ratio – Only Church (Soil-3)

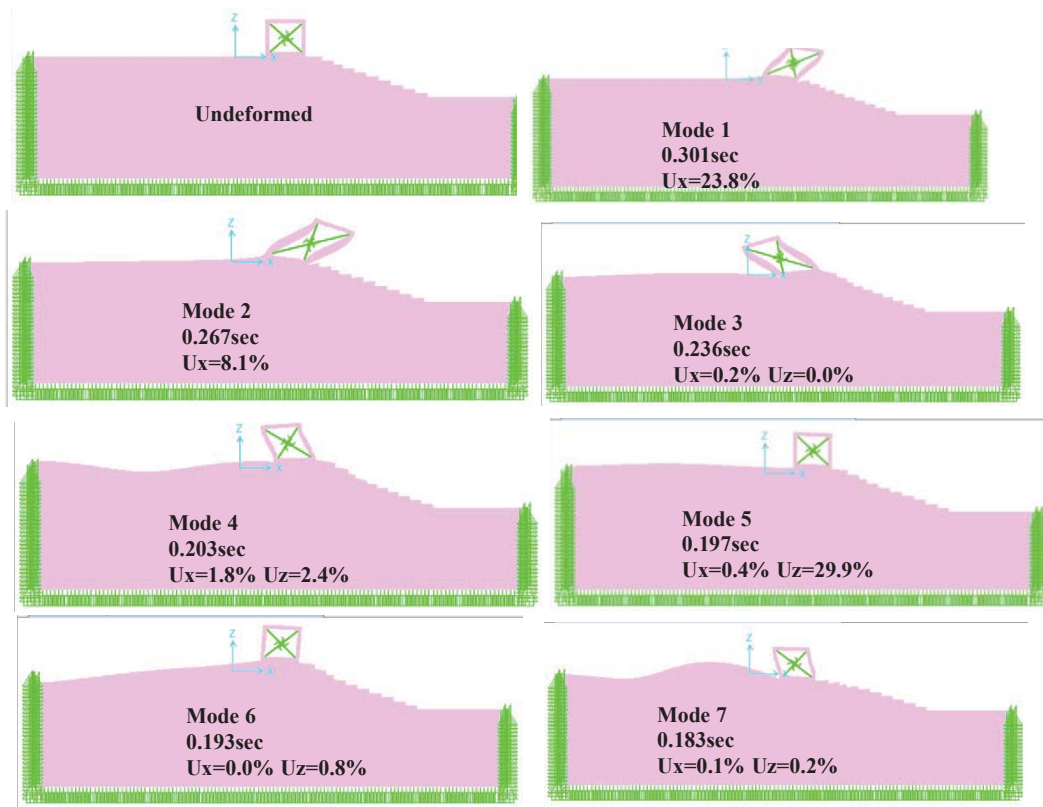


Figure 14. Eigen-modes, eigen-periods and modal mass participation ratio – Church Soil-3

Soil-1 + Church	Period (sec)	UX %	UZ %	SumUX %	SumUZ %
Mode 1	0,232	4.5	0	4.5	0
Mode 2	<b>0,198</b>	<b>50.8</b>	0.1	55.3	0.1
Mode 3	0,155	0.3	0	55.7	0.1
Mode 4	0,141	0.7	0	56.4	47.9
Mode 5	<b>0,134</b>	1.5	<b>47.8</b>	57.8	51.8
Mode 6	0,129	1.0	0.1	58.8	51.9
Mode 7	0,116	0.1	3.0	59.0	54.9

Table 6. Eigen-periods and modal mass participation ratio – Church (Soil-1)

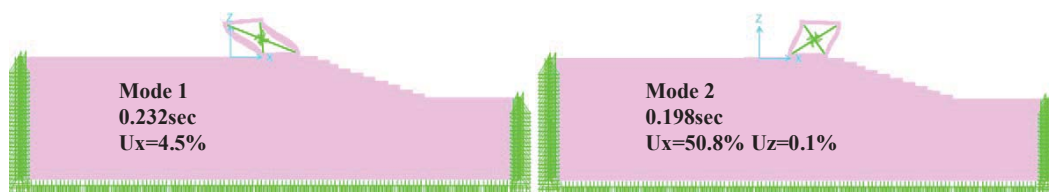


Figure 15. Eigen-modes, eigen-periods and modal mass participation ratio – Church Soil-1

Soil-3 + Church + Tower	Period (sec)	UX %	UZ %	SumUX %	SumUZ %
Mode 1	<b>0,326</b>	<b>9.8</b>	0	9.8	0
Mode 2	<b>0,294</b>	<b>13.2</b>	0	23.0	0
Mode 3	<b>0,261</b>	<b>9.2</b>	0	32.2	0
Mode 4	0,231	0.5	0	32.7	0
Mode 5	<b>0,201</b>	0.3	<b>23.1</b>	33.0	23.1
Mode 6	<b>0,196</b>	1.6	<b>8.9</b>	34.5	31.9
Mode 7	0,194	0	0.5	34.5	32.5

Table 7. Eigen-periods and modal mass participation ratio – Church + Bell Tower (Soil-3)

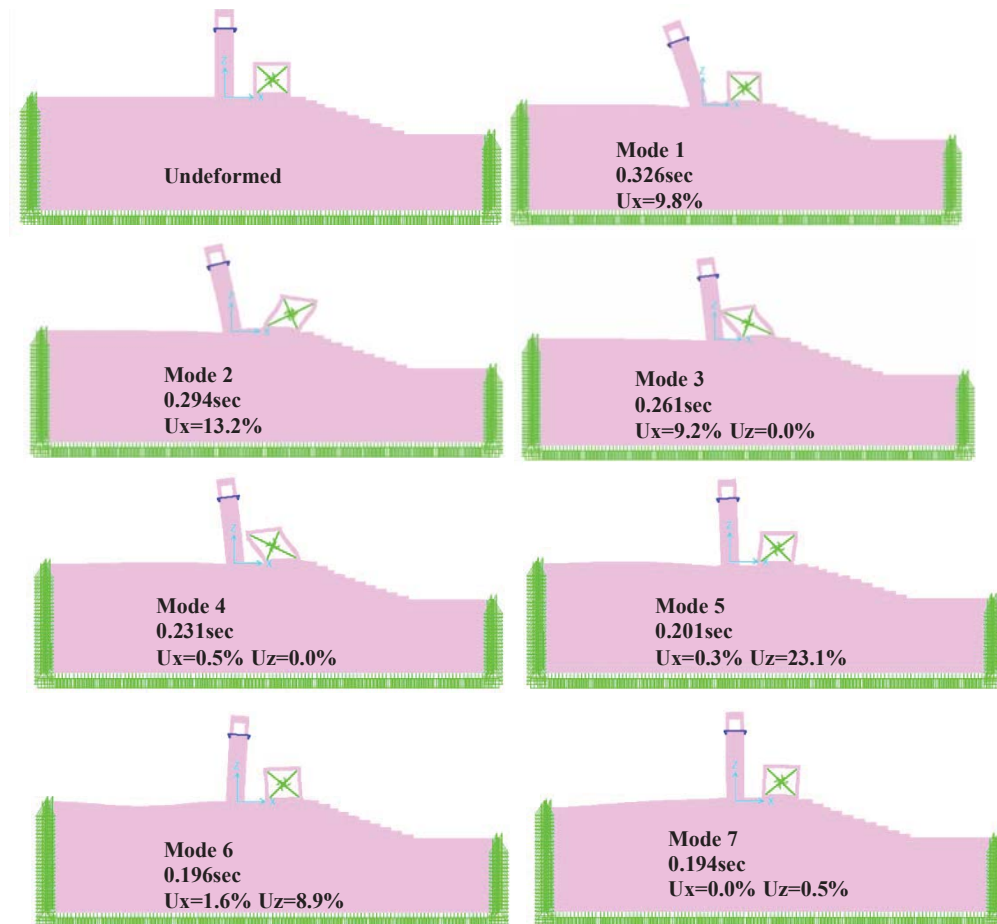


Figure 16. Eigen-modes, eigen-periods and modal mass participation ratio – Church + Bell Tower Soil-3

Soil 1+ Church+Tower	Period (sec)	UX %	UZ %	SumUX %	SumUZ %
Mode 1	<b>0,232</b>	5.4	0	5.4	0
Mode 2	<b>0,216</b>	<b>12.9</b>	0	18.3	0
Mode 3	<b>0,193</b>	<b>37.3</b>	0.1	55.6	0.1
Mode 4	<b>0,155</b>	0.4	0	56.0	0.1
Mode 5	<b>0,142</b>	0.5	<b>49.7</b>	56.5	49.8
Mode 6	<b>0,134</b>	1.1	0.9	57.6	50.7
Mode 7	<b>0,128</b>	1.4	0.4	59.0	51.2

Table 8. Eigen-periods and modal mass participation ratio – Church + Bell Tower (Soil-1)



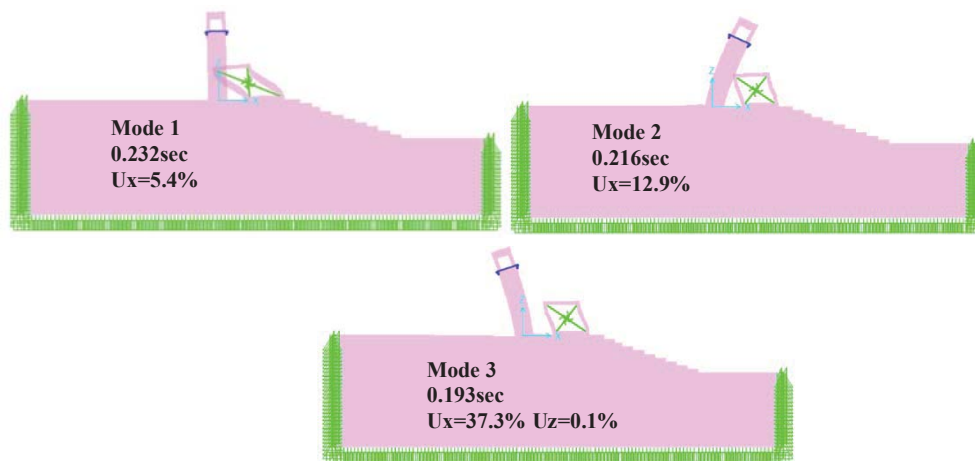


Fig. 17. Eigen-modes, eigen-periods and modal mass participation ratio–Church+Bell Tower (Soil-1)

For soil profile 3 it can be seen from tables 3,5 and 7 and from figures 12, 14 and 16 the main horizontal translational x-x eigen-modes are at 0.3sec period range whereas the corresponding main vertical z-z translational eigen-modes are at the period range of 0.2sec for all three studied configurations. Both these modes mobilize approximately 30% of the total mass. For soil profile 1 it can be seen from tables 4,6 and 8 and from figures 13, 15 and 17 the main horizontal translational x-x eigen-modes are at 0.22sec period range whereas the corresponding main vertical z-z translational eigen-modes are at the period range of 0.14sec for all three studied configurations. Both these modes mobilize approximately 50% of the total mass.

Only <b>Soil-3</b>	Period (sec)	UX %	UZ %
Mode 1	0,289	32.0	0
Mode 4	0,196	0.3	26.0
<b>Soil-3 + Church</b>	Period (sec)	UX %	UZ %
Mode 1	0,301	23.8	0
Mode 5	0,197	0.4	29.9
<b>Soil-3 + Church+Tower</b>	Period (sec)	UX %	UZ %
Mode 1	0,326	9.8	0
Mode 2	0,294	13.2	0
Mode 3	0,261	9.2	0
Mode 5	0,201	0.3	23.1
Mode 6	0,196	1.6	8.9
Only <b>Soil-1</b>	Period (sec)	UX %	UZ %
Mode 1	0,200	55.2	0.1
Mode 3	0,141	0.9	45.8
Mode 7	0,112	10.5	0.1
<b>Soil-1 + Church</b>	Period (sec)	UX %	UZ %
Mode 1	0,232	4.5	0
Mode 2	0,198	50.8	0.1
Mode 5	0,134	1.5	47.8
<b>Soil-1 + Church+Tower</b>	Period (sec)	UX %	UZ %
Mode 1	0,232	5.4	0
Mode 2	0,216	12.9	0
Mode 3	0,193	37.3	0.1
Mode 5	0,142	0.5	49.7

Table 9. Summary of the main eigen-periods and modal mass participation ratio values



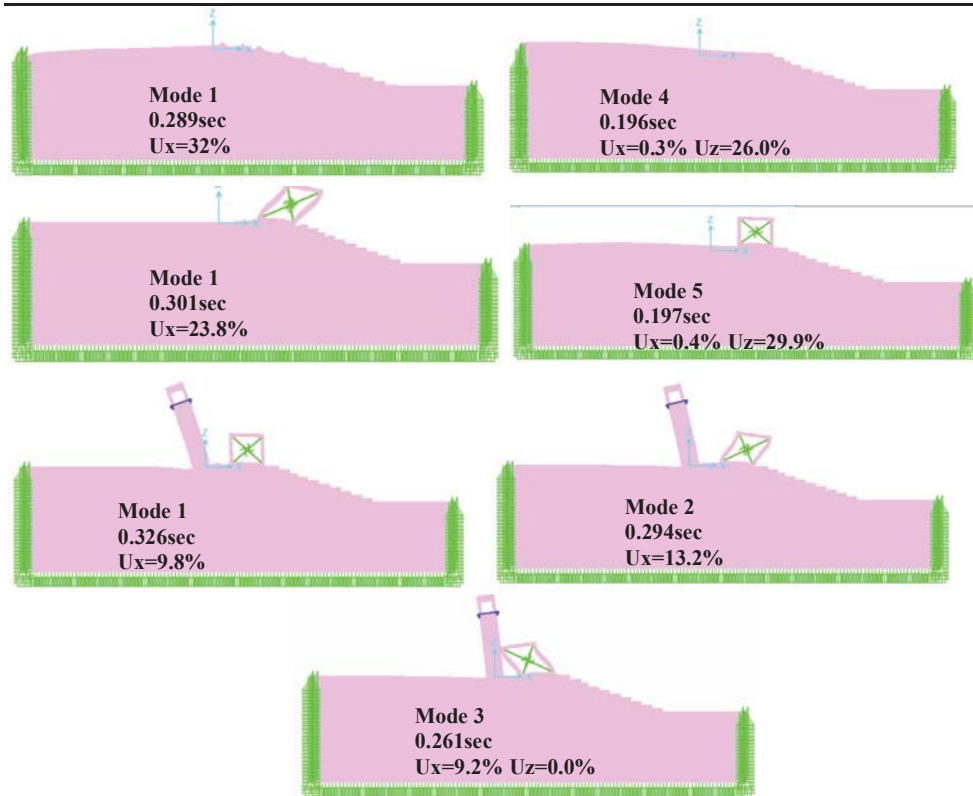


Figure 18. Summary of the main eigen-modes, eigen-periods and modal mass participation ratio – for all three configurations. (**Soil-3**)

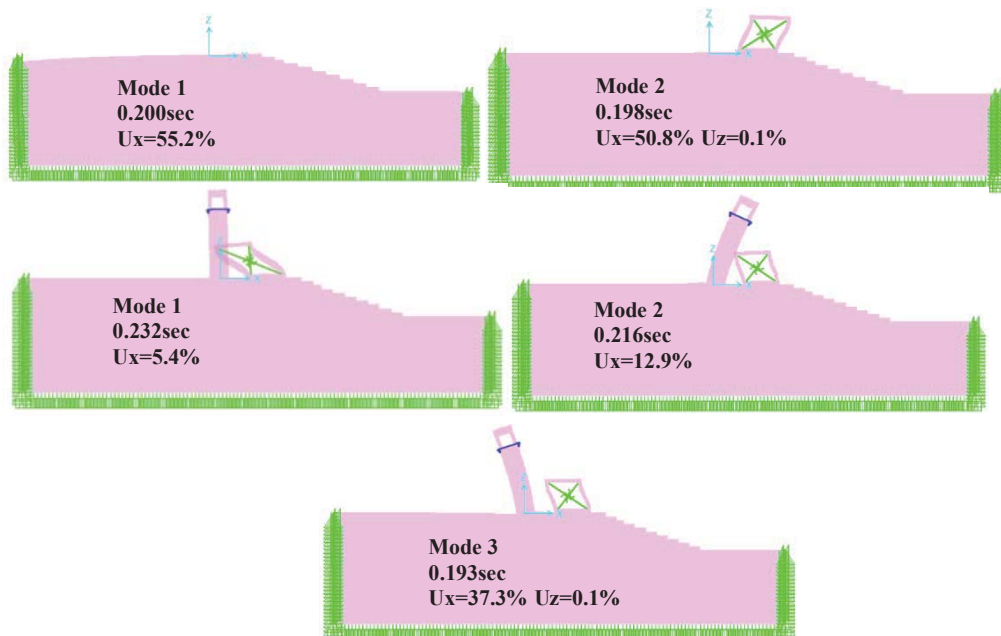


Figure 19. Summary of the main eigen-modes, eigen-periods and modal mass participation ratio – for all three configurations. (**Soil-1**)

These eigen-mode and eigen-period results are also summarized in table 9 and figure 18 (Soil profile 3) and figure 19 (Soil profile 1). As can be seen from table 9 and from figures 18 and 19 the presence of the bell tower together with the church introduces a larger number of eigen-modes that participate in a significant way either in the x-x or in the z-z translation. The values of the eigen-periods of these eigen-modes for the configuration of the “bell tower + church” are quite close to the corresponding period range of either the configuration of “only soil” or the “soil and church”. It is also interesting to note that for the configuration of the “bell tower + church” the first translational x-x eigen mode involves mainly the bell tower whereas the second and the third translational x-x eigen-modes involve both the bell tower and the church. As was expected, the eigen-periods of the main eigen-modes or the relatively stiff soil profile (soil-1) have smaller values (0.22sec) than the corresponding values (0.3sec) for the relatively flexible soil profile (soil-3). It is interesting to note that for both soil profiles the most significant horizontal translational eigen-modes involve the bell tower together with the church. Therefore, from the study of these eigen-modes it can be concluded that the flexibility of the soil results in vibratory modes coupling both the bell tower and the church. The detrimental effect of the foundation-soil flexibility has been demonstrated in many cases of Greek Orthodox stone masonry churches damaged from past earthquake activity ([19] to [30]).

#### 4 CONCLUSIONS

- The increased flexibility of the upper soil layers of the studied soil formation results in the coupling of the dynamic response of the bell tower and the church. This is evident from the study of the significant mode shapes.
- The increased flexibility of the upper soil layers of the studied soil formations and the coupling of the dynamic response of the bell tower and the church results in a vertical acceleration response at the locality between the bell tower and the church which of comparable amplitude to that of the vertical acceleration recorded at the soil surface directly from the seismic event.
- The above conclusions may partly explain the severity of structural damage that was observed at the church of the Panagia Agriliotissa at Havriata, Kefalonia-Greece, as depicted in figure 1.
- Attention should be given in erecting new bell towers of considerable height at location close to existing masonry churches. The amplification of the seismic response of the church, due to such dynamic coupling effects, could be critical especial for old masonry structures having relatively small resistance to considerable seismic forces, as was the case for the studied church at Havriata.

#### REFERENCES

- [1] Papazachos, B. and Papazachou, K., 1989, 1997, 2003. The earthquakes of Greece, *Zitis Publ., Thessaloniki*, 356 pp., 304 pp., 286 pp. (in Greek).
- [2] Manos George, “Consequences on the urban environment in Greece related to the recent intense earthquake activity”, *Int. Journal of Civil Engineering and Architecture*, Dec. 2011, Volume 5, No. 12 (Serial No. 49), pp. 1065–1090.
- [3] GEER - EERI - ATC - Cephalonia GREECE *Earthquake Reconnaissance January 26th/ February 2nd 2014 Version 1: June 6 2014*

- 
- [4] G.C. Manos “The 30th of October Samos-Greece earthquake. Issues relevant to the protection from structural damage caused by strong earthquake ground motions.”, *Journal of Architecture and Engineering*, Vol 5, Issue 4, December 2020, <https://aej.spbgasu.ru/index.php/AE>
  - [5] L. de Stefani, R. Scotta, M. Lazzari, A. Saetta. Seismic improvement of Slender Bell Tower and Minarets. – *PROHITECH, Antalya, Turkey, 2014*
  - [6] R. M. Azzara, L. Zaccarelli, A. Morelli, T. Trombetti. Seismic Monitoring of the Asinelli and Garisenda Medieval Towers in Bologna (Italy), an Instrumental Contribution to the Engineering Modeling Directed to their Protection. - *PROHITECH, Antalya, Turkey, 2014*
  - [7] Casolo Siro, Uva Giuseppina. Non-Linear dynamic analysis of masonry towers under natural accelerograms accounting for soil-structure interaction. – *COMPDYN 2013 - Kos Island, Greece, June 12-14, 2013*
  - [8] A. Saisi, C. Gentile, L. Cantini. Post – Earthquake assessment of a masonry tower by on –site inspection and operational modal testing. – *COMPDYN 2013 - Kos Island, Greece, June 12-14, 2013*
  - [9] D. Colapieto, A. Fiore, A. Netti, F. Fatiguso, G. Marano, M. de Fino D. Cascella, A. Antocona. Dynamic identification and evaluation of the seismic safety of a masonry bell tower in the south Italy. – *COMPDYN 2013 - Kos Island, Greece, June 12-14, 2013*
  - [10] R. Guidorzi, R. Diversi, L. Vincenzi, C. Mazzotti, V. Simioli. Structural monitoring of the Tower of the Faculty of Engineering in Bologna using MEMS –based sensing. – *EURODYN 2011 – Leuven, Belgium, 4-6 July 2011*
  - [11] C. Blasi M. Carfagni, S. Carfagni. The use of impulsive actions for the structural identification of Slender monumental buildings- *STREMAH-1991 - Seville, Spain, 14-16 May 1991*
  - [12] S. Dumorier, W.P. De Wilde. Finite element study of the Tower of Brussels City Hall – *STREMAH 1995 – Chania, Crete, Greece, 1995.*
  - [13] G.C. Manos and E. Kozikopoulos, “In-Situ Measured Dynamic Response of the Bell tower of Agios Gerasimos in Lixouri-Kefalonia, Greece and its Utilization in the Numerical Predictions of its Earthquake Response”, *COMPDYN 2015, 5th ECCOMAS Thematic Conference on, Computational Methods in Structural Dynamics and Earthquake Engineering, Crete Island, Greece, 25–27 May 2015.*
  - [14] G.C. Manos, D. Naxakis, V. Soulis, “The Dynamic and Earthquake Response of a Two-story Old R/C Building with Masonry Infills in Lixouri-Kefalonia, Greece, Including Soil-Foundation Deformability, *COMPDYN 2015, 5th ECCOMAS Thematic Conference on, Computational Methods in Structural Dynamics and Earthquake Engineering, Crete Island, Greece, 25–27 May 2015.*
  - [15] G.C. Manos and E. Kozikopoulos “Seismic performance of bell towers in Kefalonia-Greece during the 2014 earthquake sequence”, *6th ECCOMAS Thematic Conference on Computational Methods in Structural Dynamics and Earthquake Engineering M. Papadrakakis, M. Fragiadakis (eds.) Rhodes Island, Greece, 15–17 June 2017.*
  - [16] George C. Manos , Evaggelos Kozikopoulos , Lambros Kotoulas “In-situ Measurements and Numerical Simulations of the Dynamic and Seismic Response of Bell Towers”, *16th European Conf. Earthquake Engineering, Thessaloniki-Greece, 2018.*

- [17] Albert R. Kottke and Ellen M. Rathje “Technical Manual for Strata” *PEER Report 2008/Pacific Earthquake Engineering Research Center College of Engineering University of California, Berkeley October 2008.*
- [18] Vucetic & Dorby, “Effect of Soil Plasticity on Cyclic Response”, *ASCE, Journal of Geotechnical Engineering, Vol. 117, Issue 1 (January 1991)*
- [19] G.C. Manos, et al. (1996) "Predictions of the dynamic characteristics of a 5-story R.C. building at the Volvi Euro-SeisTest Site, utilizing low-intensity vibrations", *3rd European Conference on Structural Dynamics, Eurodyn 1996, Florence, II, 877–884.*
- [20] G. C. Manos, (1998). “The Dynamic Response of a 5-story Structure at the European Test site at Volvi-Greece.” *6th U.S. National Earthquake Engineering Conference, May 31 - June 4, Seattle, Washington, U.S.*
- [21] G. C., Manos, et al.. (2004). “Dynamic and Earthquake Response of Model Structures at the Volvi – Greece European Test Site.” *13th World Conference on Earthquake Engineering, Vancouver, Canada.*
- [22] G. C., Manos, V. Kourtides, V.J. Soulis, A.G. Sextos, A. G., and P. Renault, (2006). “Study of the dynamic response of a bridge pier model structure at the Volvi - Greece European Test Site.” *8th National Conference on Earthquake Engineering, April 18-22, San Fransisco, U.S.A.*
- [23] G.C. Manos, V. Kourtides, A. Sextos, P. Renault, S. Chiras “Study of the dynamic soil-structure interaction of a bridge pier model based on structure and soil measurements” *9th Canadian Conf. on Earthquake Engineering, Ottawa, Ontario, Canada, 26-29 June 2007.*
- [24] G.C. Manos, V. Kourtides, A. Sextos, S. Chiras “Soil-Foundation-Bridge Pier Interaction at the Euro-Seis Test Site”, *4th Int. Conference on Geotechnical Engineering, Thessaloniki, 24-28 June, 2007.*
- [25] G.C. Manos, V. Kourtides, A. Sextos, “Model Bridge Pier Foundation- Soil Interaction implementing, in-situ / shear stack testing and numerical simulation”, *14WCEE, Beijing, CHINA, 2008.*
- [26] G. C. Manos , K.D. Pitilakis, A.G. Sextos, V. Kourtides, V. Soulis, J. Thauampth, “Field experiments for monitoring the dynamic soil-structure-foundation response of model structures at a Test Site” *Journal of Structural Engineering, American Society of Civil Engineers, Special Issue “Field Testing of Bridges and Buildings, D4014012, Vol. 141, Issue 1, January 2015.*
- [27] George C. Manos , Evaggelos Kozikopoulos , Lambros Kotoulas , Vasilios Soulis “The Earthquake Performance of Stone Masonry Basilica Churches in Kefalonia, Greece Including Wall Detachment and Foundation Deformability”, *16th European Conf. Earthquake Engineering, Thessaloniki-Greece, 2018.*
- [28] George C. Manos, Lambros Kotoulas and Evangelos Kozikopoulos “Evaluation of the Performance of Unreinforced Stone Masonry Greek “Basilica” Churches When Subjected to Seismic Forces and Foundation Settlement”, *Journal, buildings, Published: 30 April 2019*
- [29] Eurocode 8: Design of structures for earthquake resistance - Part 1: General rules, seismic actions and rules for buildings, *FINAL DRAFT prEN 1998-1, December 2003.*

- [30] G.C. Manos, Seismic Code of Greece, Chapter 17, International Handbook of Earthquake Engineering: "Codes, Programs and Examples", *edited by Mario Paz, by Chapman and Hall, ISBN 0-412-98211-0, 1994.*

## THE INFLUENCE OF WOODEN ROOF CONNECTION ON THE DYNAMIC AND EARTHQUAKE RESPONSE OF OLD INDUSTRIAL STONE MASONRY BUILDINGS

G.C. Manos<sup>1</sup> and L. Kotoulas<sup>2</sup>

<sup>1</sup> Professor Emeritus, Lab. Strength of Materials and Structures, Aristotle University  
gcmanos@civil.auth.gr

<sup>2</sup> Post-graduate student, Lab. Strength of Materials and Structures, Aristotle University  
lpkotoulas@gmail.com

---

### Abstract

*Unreinforced masonry made of stone and low strength mortar has been used for centuries in forming the structural system of old type buildings. Wooden roofs were also used as part of such structural systems. The influence of the connections of such wooden roofs with the vertical masonry walls is the objective of this study. A number of old stone-masonry buildings used as leather factories in the island of Samos-Greece are employed in this investigation. The wooden roofs of these buildings collapsed either partly or totally during the recent earthquake of October 2020. Initially, the dynamic behaviour typical forms of such buildings with wooden roofs are studied. A variation of the connections of such a wooden roof with the vertical stone masonry walls is studied in a parametric way. Next, the earthquake response of the same structural formations are also studied using again the variation of these connections as the main parameter. Towards this end earthquake design spectra are used as well as the acceleration recordings of this earthquake ground motion by an instrument located in the Samos island. Numerical simulation results are presented and discussed. Through the comparison of the obtained numerical predictions with the observed behaviour the validity of the numerical approach is discussed.*

**Keywords:** Wooden roof, Stone masonry; weak mortar; Gravitational forces, Seismic actions,

---



## 1 INTRODUCTION

An earthquake occurred 16km North from the Greek island of Samos on the 30<sup>th</sup> of October 2020 (11:51GMT) with a magnitude of M6.7 (Fig. 1). This island is located at the East side of the Aegean Sea an area seismically active ([1], to [7]) The main event caused widespread structural damage mainly at numerous low-rise old unreinforced masonry buildings of this island. It all also caused heavy damage and collapse of multi-story reinforced concrete (R/C) buildings at the city of Izmir located at the coastline of mainland Turkey towards the North-East, approximately 60km from the epicenter of this earthquake. This study focuses on the effects of this seismic strong motion on the Greek island of Samos. The Institute of Engineering Seismology and Earthquake Engineering (ITSAK) operates a strong motion accelerometer at the city of Vathi, the capital of Samos. The ground accelerations at Vathi due to the main shock were recorded by this instrument (see preliminary report of ITSAK, [6] and ETAM [7]) having peak horizontal ground acceleration 227cm/sec<sup>2</sup> and peak vertical ground acceleration 134cm/sec<sup>2</sup>. The main event was followed by a considerable number of aftershocks, with the aftershock sequence being still active. (Fig. 2).



Figure 1. Map indicating the epicenter of the 30<sup>th</sup> of October 2020 seismic event

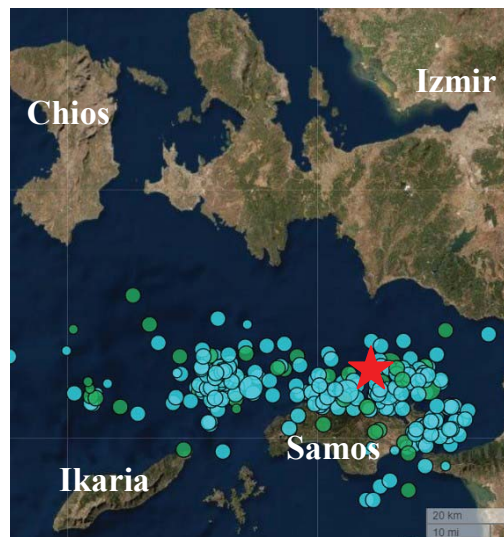


Figure 2. The epicenter of the 30<sup>th</sup> of October 2020 main event and the following aftershock sequence

The most spectacular structural damage could be observed at the two main cities in the island, its capital (Vathi) and Karlovaisi 25km to the West (Fig. 3). Due to the location of the epicen-

ter, having the same epicentral distance from both Vathi and Karlovasi, and due to the generating mechanism of this earthquake that followed an almost East-West fault line, as can be seen from the aftershock sequence, it can be reasonably assumed that the strong motion characteristics at Karlovasi would be quite similar to those of the recorded strong motion at Vathi. This assumption will be made use of in the section presenting selected numerical analyses predictions of the structural response of damaged buildings [8].

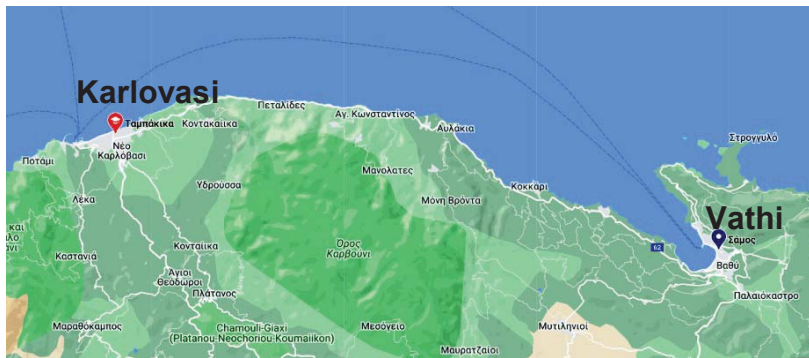


Figure 3. Map of the North coast-line of the island of Samos where the two main cities of Vathi and Karlovasi are located.

### 1.1 The recorded ground motion

In figure 3 the recordings of the earthquake ground motion, in terms of ground acceleration, velocity and displacement in the two horizontal directions are shown [6]. Due to the location of the epicenter, the same epicentral distance of both the city of Vathi and the city of Karlovasi from the epicenter (see figures 1, 2, 3) and due to the generating mechanism of this earthquake that followed the almost East-West fault line, as can be seen from the aftershock sequence it can be reasonably assumed that the strong motion characteristics at Karlovasi would be quite similar to those of the recorded strong motion at Vathi.

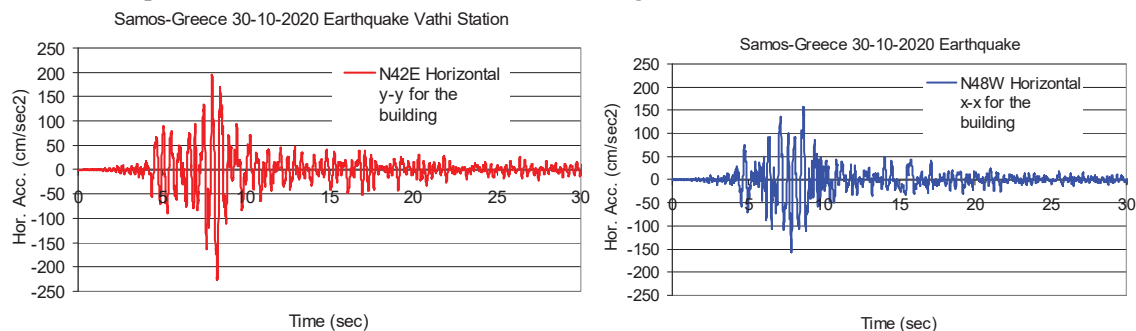


Figure 4. Horizontal ground acceleration recorded at 30<sup>th</sup> October 2020 at Vathi by an instrument managed by the Institute of Earthquake Engineering and Engineering Seismology (ITSAK, see reports [6] and [7]).

Figure 5 depicts the inelastic acceleration response spectral curves of the two horizontal components of the recorded ground motion at Vathi (Fig. 4) for 5% damping ratio and ductility factor  $m=1.5$ . In the same figure the design spectral curves as predicted by Euro-Code 8 are also shown. These design spectral curves were obtained for ground design acceleration equal to  $0.24g$  ( $g$ = the acceleration of gravity) and for two different soil categories either soil C (flexible soil) or soil D (very flexible soil). This peak design ground acceleration is in accor-

dance with the seismic zoning map of Greece [ ]. It is also assumed that the soil conditions near the coastline either at Vathi or at Karlovasi will belong to either one of these two soil conditions. Moreover, these design spectral curves are employing damping ratio equal to 5% and response modification factor  $q=1.5$  (the same as the ductility factor value for the inelastic spectral curves) and importance factor equal to 1 ( $\gamma=1$ ). Finally, the design spectral curves are obtained for either type 1 or type 2 earthquake design motion, as specified by Euro-Code 8 [ ]. Type 2 is suppose to represent an earthquake hazard from an event with a magnitude lesser than  $M=5.5$  on the Richter scale.

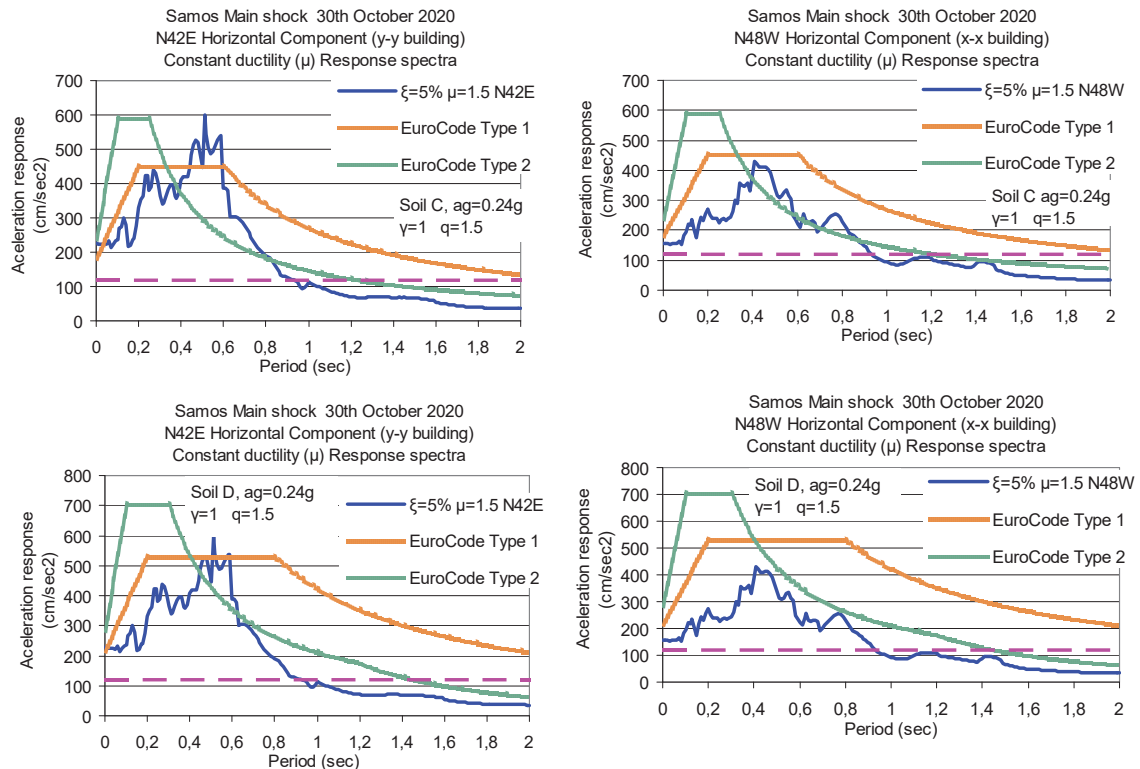


Figure 5. Comparison of inelastic response spectra (based on the horizontal ground acceleration recorded at 30<sup>th</sup> October 2020 at Vathi. [ ]) and Euro-code 8 design spectra.

From the comparison between these inelastic response spectra (based on the horizontal ground acceleration recorded at 30th October 2020 at Vathi and the corresponding Euro-code 8 design spectra (either Type 1 or 2 and either soil category C or D, [9] to [14]) the following observations can be made. **a)** Type 1 design spectra agree better with the inelastic response spectra (based on the recorded ground motion) than type 2 design spectra. **b)** The type 1 design spectra for soil category D have spectral acceleration amplitudes that are larger in almost all the plotted period range than the corresponding inelastic response spectra values (based on the recorded ground motion). **c)** The type 1 design spectra for soil category C have spectral acceleration amplitudes that are larger in almost all the plotted period range, apart from the period range between 0.45sec. and 0.61sec., than the corresponding inelastic response spectra values (based on the recorded ground motion).

## 2 ANALYSED STRUCTURES

In many Greek islands as well as at the old part of city-centers in many Greek cities a considerable number of old buildings still survives despite the destruction due to the military operations or the frequent earthquake activity. A considerable number of such buildings were demolished to give room to the extended urban development that took place after World War II and the tourism activity that followed, particularly in the islands. However, during the last four decades a conservation effort became quite strong endorsing a number of such building in a conservation register being under special legislative protection. In this category belong the buildings depicted in figures 6 and 7. These buildings were used as leather processing factories an activity that was prominent in Samos island from the end of the 9<sup>th</sup> century till World War II when started declining. A number of these buildings were left unoccupied and without any maintenance, which makes them vulnerable to strong earthquake excitations apart from the used construction system which unreinforced stone masonry walls covered by a wooden roof



Figure 6. Old industrial buildings under conservation status



Figure 7. Old industrial buildings (Tambakia) at the coastline of Karlovasi

The earthquake performance of this type of structures is dominated by certain response mechanisms that can be characterized as “global”. These mechanisms include a) the connection of the wooden roof to the masonry walls b) the interconnection of the masonry walls at the corners and c) the foundation deformability including the potential of partial uplifting at the foundation due to tensile forces arising from excessive overturning moment response and uneven foundation settlements (see [13], [17]). All these mechanisms are non-linear in nature and it is many times difficult to quantify them in order to include their influ-





the top of the roof is assumed equal to 10m. Eight (8) trusses are assumed to form the wooden roof equally spaced along the x-x direction, as shown in figure 9. This wooden roof is connected to both the longitudinal walls at certain location through the transverse beams forming the bottom part of these wooden trusses. Moreover, This wooden roof is also connected by a series of longitudinal wooden beams with the gables of the two transverse wall (parallel to the y-y direction). In the subsequent numerical analysis the x-x direction is presumed to coincide with the N48W component of the recorded ground motion whereas the y-y direction with the N42E component.

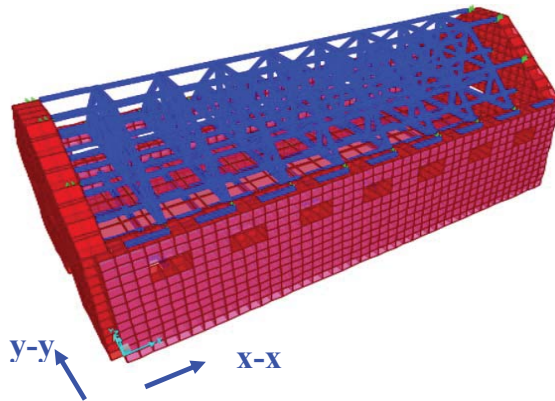
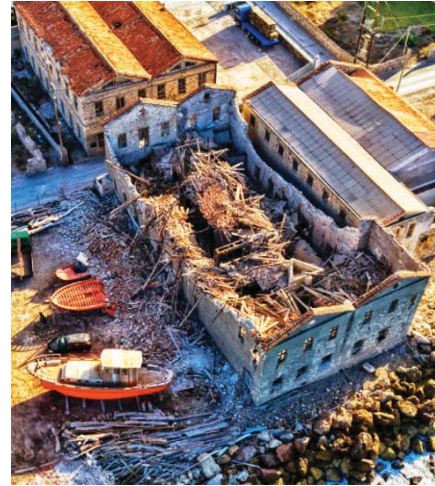


Figure 9. Simplified numerical model of a typical industrial building



10. A two-story twin industrial building of unreinforced masonry

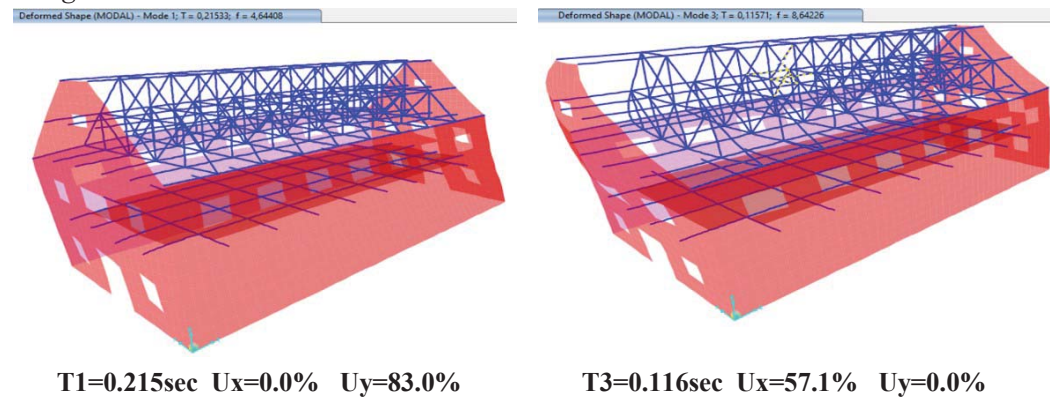
As already mentioned, the influence of the connections of the wooden roof with the peripheral masonry walls is the objective of this parametric simplified numerical simulation. This is done as follows. Initially, the wooden beams are considered as pinned to the masonry walls, capable of transferring axial and shear forces (not bending moments) in a way that the displacements of the wooden end is the same as the point of the masonry wall it is connected to (rigid connection). Next, this connection is done through flexible 3-D links with limited stiffness thus allowing a relative displacement between the end of the wooden beam at its connecting location of the masonry wall. By decreasing the stiffness of these 3-D links the level of force that can be transferred between these two media can be limited. Moreover, by decreasing the stiffness of these 3-D links the restraint that is enforced by the interaction between the wooden roof and the masonry walls is also decreased. These effects will be shown in the following discussion. It should be recognized that is a simplification of the actual interaction that is a more complex non-linear mechanism than what is described here. Despite this simplification, the influence of such a flexible connection is being presented and discussed here.

## 2.2 Modal analysis.

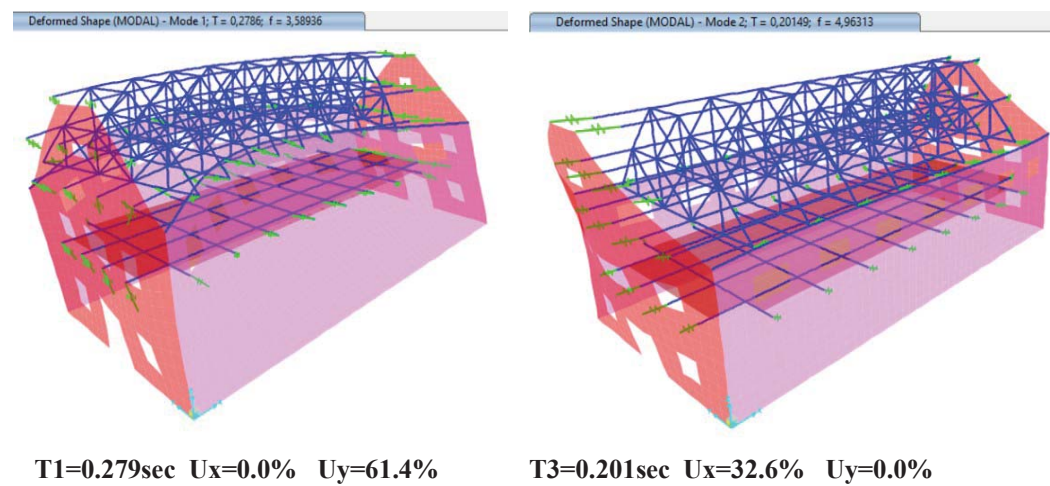
Initially, the most significant eigen-modes of the simplified numerical model depicted in figure 9 having three different wooden-beam to masonry-wall connections is studied. As mentioned, these connections are: 1-Rigid, 2-Moderately flexible and 3-Flexible. The obtained modal shapes, modal periods and modal mass participation ratio values are presented in what follows.



### 1-Rigid connections



### 2-Moderately flexible connections



### 3-Flexible connections

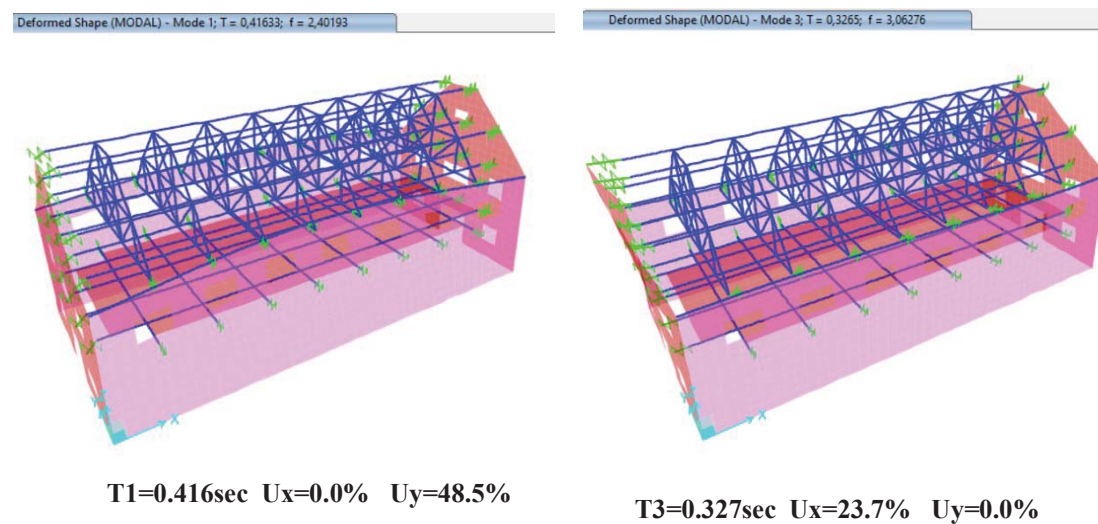


Figure 11. Eigen-modes for the simplified numerical model of the industrial building for Rigid, Moderately flexible and Flexible connections between the wooden roof beams and the masonry walls.

The following summarize the influence of the attempted simplified relaxation of the connections between the wooden roof beams and the masonry walls on the dynamic characteristics of the studied structural system.

- As expected, the increase in the flexibility of the connections between the wooden roof beams and the masonry walls results in an increase of the corresponding eigen-period values of the studied system from 0.215 sec. to 0.416 sec. for the mainly translational eigen-mode in the transverse y-y direction and from 0.116sec. to 0.327 sec. for the mainly translational eigen-mode in the longitudinal x-x direction.
- The increase in the flexibility of the connections between the wooden roof beams and the masonry walls results in a decrease in the corresponding modal mass participation ratio value. This is pronounced for the transverse y-y translational 1<sup>st</sup> eigen-mode (from 83% to 48.5%) but even more pronounced for the longitudinal x-x translational 3<sup>rd</sup> eigen-mode (from 57.1% to 23.7%).

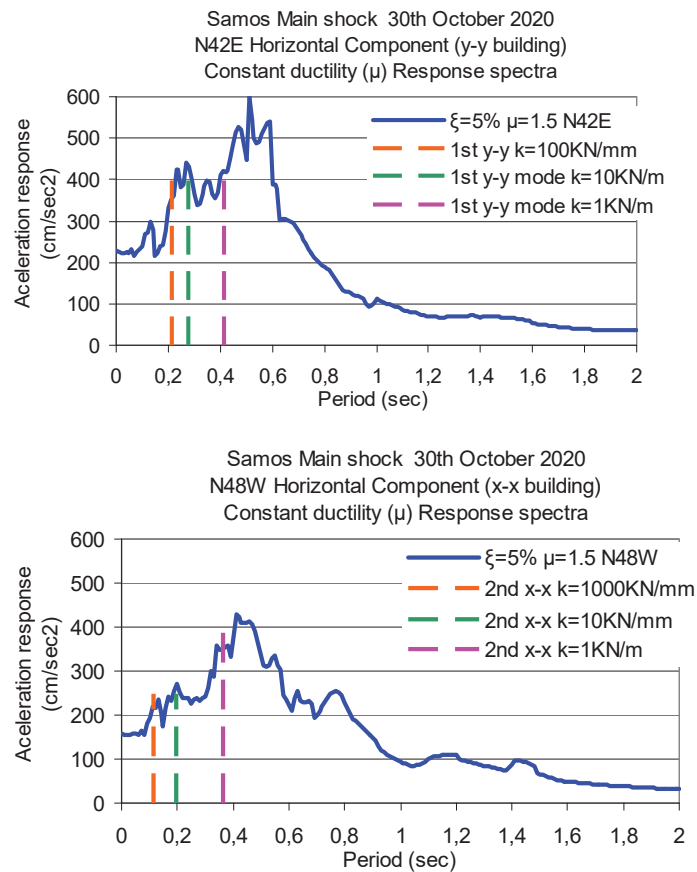


Figure 12. Inelastic acceleration response spectral curves ( $m=1.5$ ) based on the recorded ground acceleration together with the variation of the eigen-periods for the main y-y and x-x translational eigen-modes as they resulted from the simplified numerical model of the industrial building for Rigid, Moderately flexible and Flexible connections between the wooden roof beams and the masonry walls.

In figure 12 the variation of the eigen-periods for the main y-y and x-x translational eigen-modes, as they resulted from the simplified numerical model of the industrial building for Rigid, Moderately flexible and Flexible connections between the wooden roof beams and

the masonry walls, are plotted together with the corresponding inelastic acceleration response spectral curves ( $m=1.5$ ). These inelastic acceleration spectral curves are based on the recorded ground acceleration together for the Samos island earthquake (30<sup>th</sup> October 2020). As can be seen from these plots the increased flexibility of the connections between the wooden beam roofs and the masonry walls will also result in an increase of the corresponding spectral acceleration value thus leading to a relevant increase on the seismic force levels for the studied structure. At the same time these increased inelastic spectral acceleration values are more in agreement with the corresponding Euro-Code 8 design spectral values, as already discussed on the basis of figure 5, than those of the rigid connections.

### 3 NUMERICAL EARTHQUAKE PERFORMANCE

In this section the numerical earthquake performance of the studied structure is presented in terms of a) maximum displacement values at the top of the masonry walls b) maximum normal and shear stress values of the masonry walls c) maximum axial force values that developed at the connections between the wooden roof beams and the masonry walls. All these values were obtained through dynamic spectral elastic analysis using the inelastic spectral curves depicted in figure 12. The presented results are for two specific load combinations:

1<sup>st</sup> Load Combination: Dead + ResSp N42E + 0.3 ResSp N48W

2<sup>nd</sup> Load Combination: Dead + ResSp N42E + 0.3 ResSp N48W

Dead= The dead load of the masonry walls and the roof.

ResSp N42E = The earthquake forces resulting from the dynamic spectral analysis in the y-y (transverse direction).

ResSp N48W = The earthquake forces resulting from the dynamic spectral analysis in the x-x (longitudinal direction)

As was done for the modal analysis the earthquake performance is examined utilizing the simplified numerical model depicted in figure 9 having the described before three different wooden-beam to masonry-wall connections (e.g. 1-Rigid, 2-Moderately flexible and 3-Flexible). In figure 13 includes the results obtained from the simplified numerical simulation assuming rigid connections of the wooden roof beams with the masonry walls. In figure 13a and 13b the displaced masonry walls of the structure are depicted in figures 13a and 13b for load combinations with the seismic forces applied either mainly in the transverse N42E or mainly in the longitudinal N48W directions, respectively. Figures 13c depicts the normal stress (S22) distribution whereas figure 13d the shear stress (S12) distribution for a load combination with the seismic forces applied mainly along the transverse N42E direction. Figure 13e depicts the normal stress (S22) distribution for a load combination with the seismic forces applied mainly along the longitudinal N48W direction. Figure 13f depicts the distribution of the axial forces that develop at the roof wooden beams for a load combination with the seismic forces applied mainly along the transverse N42E direction whereas figure 13g depicts the axial forces that develop at the roof wooden beams for a load combination with the seismic forces applied mainly along the longitudinal N48W direction. The results for moderately flexible (figures 14) or for flexible connections (figure 15) are also shown.

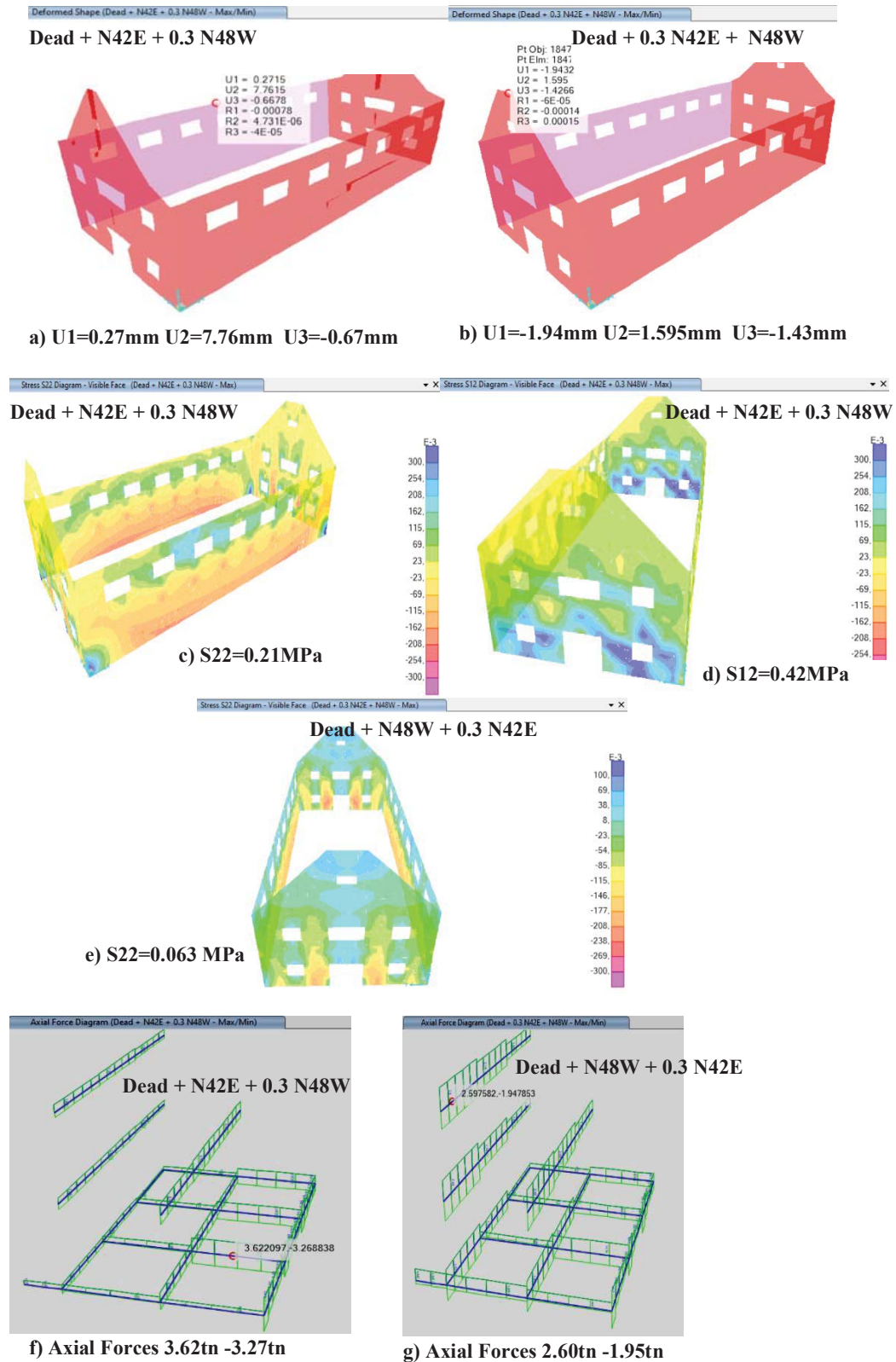


Figure 13. Structural response results. Rigid connections of the wooden roof beams with the masonry walls



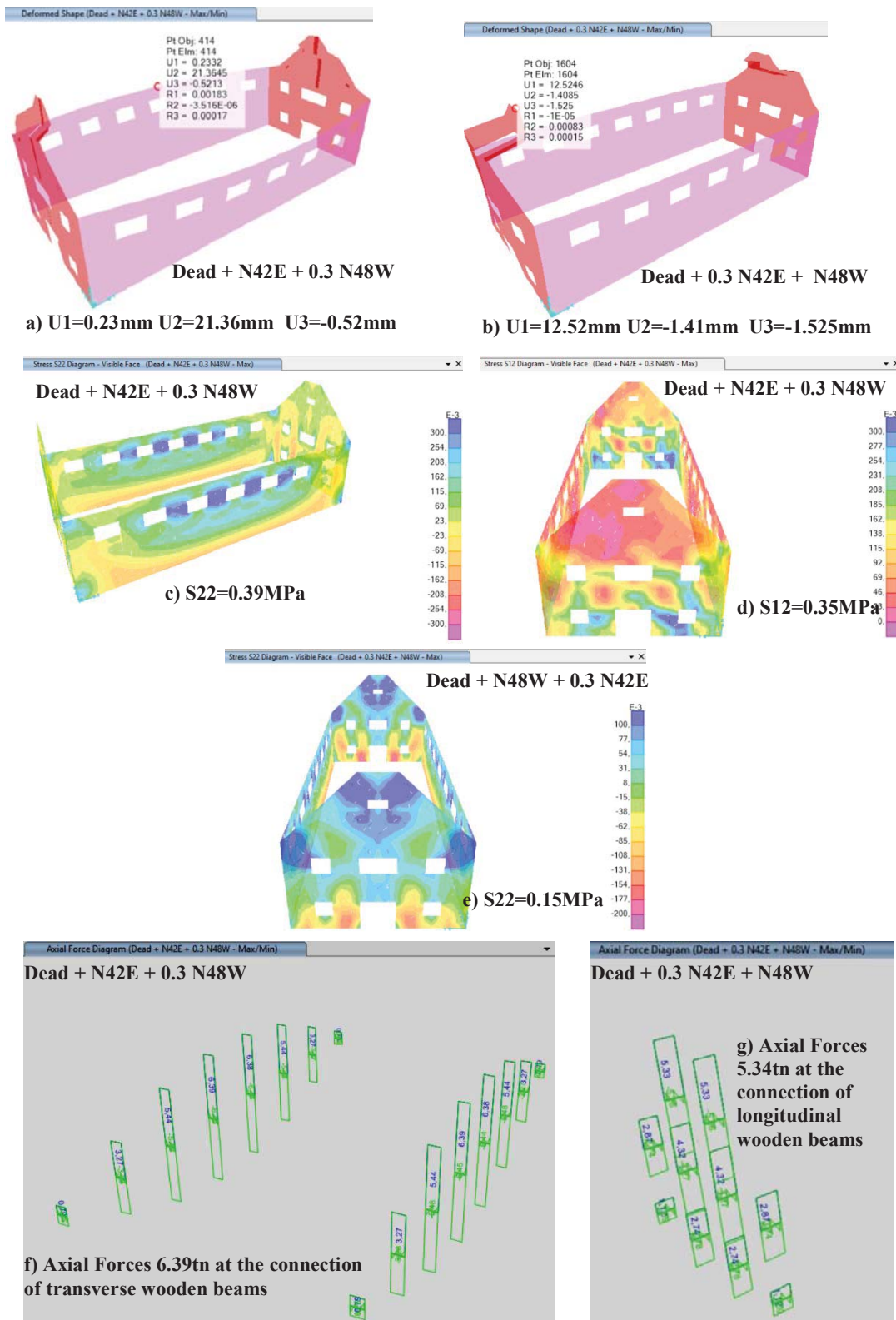


Figure 14. Structural response results. Moderately flexible connections of the wooden roof beams with the masonry walls

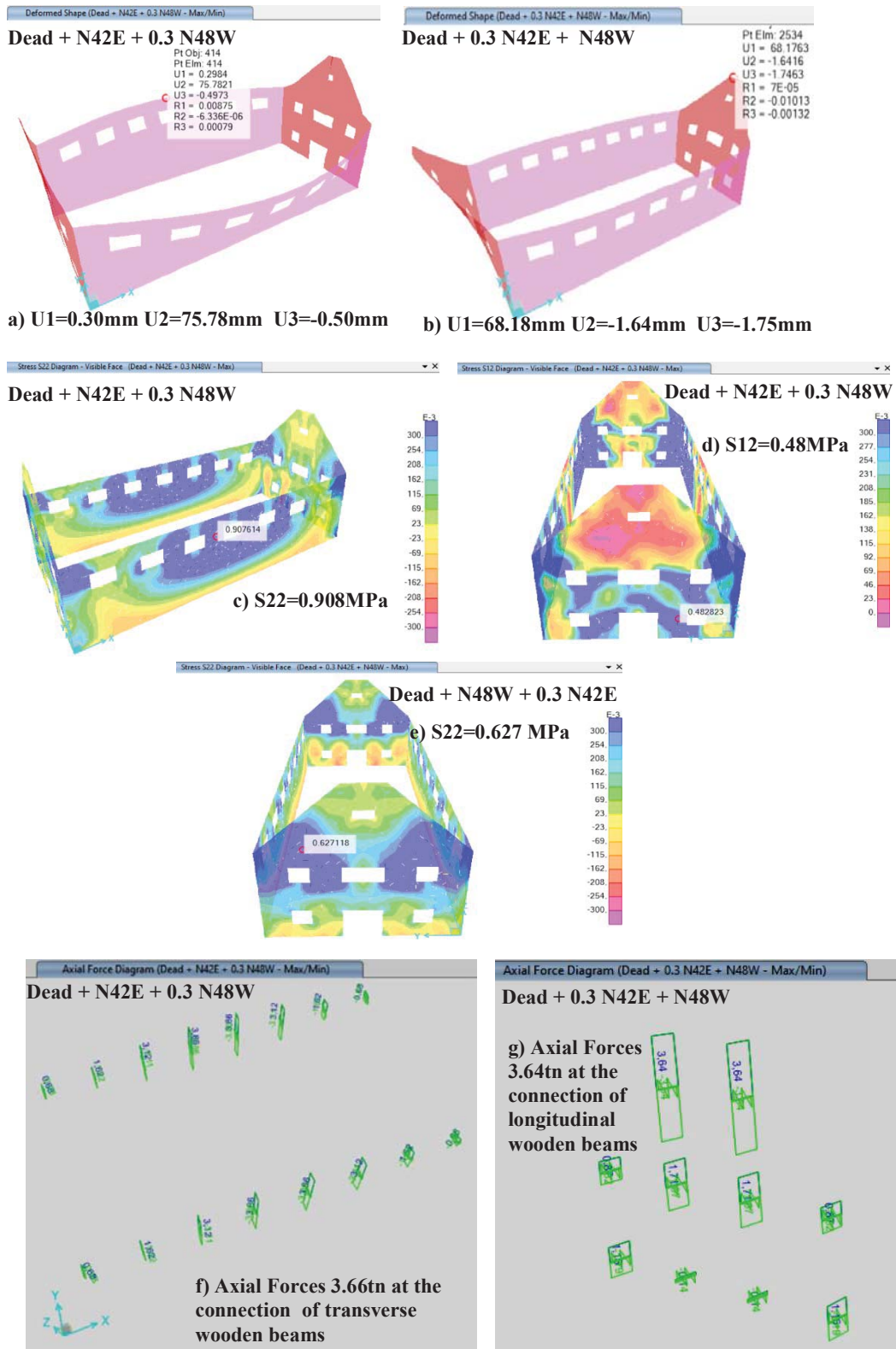


Figure 15. Structural response results. Flexible connections of the wooden roof beams with the masonry walls



Table 1. Peak values of the response parameters resulting from the simplified numerical analyses

Numerical Model-Roof Connection cases	Out of plane y-y displ. of longitudinal walls (mm)	Out of plane x-x displ. of Transverse walls (mm)	Normal stress Longit. Walls S22 (MPa)	Normal stress Transv. Walls S22 (MPa)	Shear stress Longit. Walls S12 (MPa)	Axial or connection forces Transv. Beams (tn)	Axial or connection forces Longit. Beams (tn)
(1)	(2)	(3)	(4)	(6)	(5)	(7)	(8)
<b>Rigid</b> Qy=352tn Qx=175tn	7.76	1.94	0.21	0.063	0.42	3.62	2.60
<b>Moderately Flexible</b> Qy=306tn Qx=195tn	21.36	12.52	0.39	0.15	0.35	6.39 / 6.39mm*	5.34 / 5.34mm*
<b>Flexible</b> Qy=372tn Qx=259tn	75.78	68.18	0.908	0.627	0.48	3.66 / 36.6mm*	3.64 / 36.4mm*

\* the relative axial displacement between the wooden roof beam and the masonry wall at the location of their connection

Table 1 summarizes all the peak response values from the results plotted in figures 13, 14 and 15. In the first column of this table each of the three analyzed cases of connection between the wooden roof beams and the masonry walls is denoted. At the same column the peak horizontal base shear values are also listed for each case, as they resulted from the dynamic spectral (see figure 12) analyses along the x-x (N48W perpendicular to the transverse walls) and y-y (N42E perpendicular to the longitudinal walls) directions (see figure 9). As already discussed, because of the variation of the amplitudes of the employed inelastic spectral curves with the eigen periods values (figure 12) the structural system with the flexible roof-to-masonry connections is subjected to the highest seismic force amplitudes in both x-x and y-y directions. Consequently, part of the significant amplification of the obtained displacement and stress response for this case as compared with the cases of either the rigid or the moderately flexible connections is partly due to this fact. However, another large part of this amplification must be attributed to the fact that the flexible connections exercise limited restraint in prohibiting the masonry walls to displace, especially in the out-of-plane direction. This is evident by comparing the out-of-plane peak displacement values of either at the top of the longitudinal walls (column 2 of table 1) or at the top of the transverse walls (column 3 of table 1). As can be seen, an increase flexibility in these wooden roof beam to masonry wall connections result in a large increase in the out-of-plane displacements at the top of either the longitudinal or the transverse masonry walls. This in turn results in a corresponding increase in the peak (tensile) axial stress values normal to the bed joints (S22) for either the longitudinal masonry walls (column 4 of table 1) or the transverse masonry walls (column 5 of table 1). In contrast, the moderate variation in the peak shear stress value of the transverse masonry walls is in line with the corresponding variation of the base shear value in the y-y direction (Qy, column 1 of table 1). Finally, the increase in the flexibility of the wooden roof beam to masonry wall connections result in a decrease, as expected, in the axial force value that is transmitted through these connections (columns 7 and 8 table 1). It is also interesting to note that the rigid connections between the wooden roof beams and the masonry walls, which is an unrea-

listic ideal case, results in relatively small out-of-plane displacement values, despite the fact that the resulting axial forces at the connection locations are also relatively small. On the contrary, the increase in the flexibility of these connections from moderately flexible to flexible results in a decrease at the level of axial force which is in agreement with the resulting increase of the out-of-plane displacement at the top of the masonry walls. In columns 7 and 8 of table 1 the relative axial displacement between the wooden roof beam and the masonry wall at the location of their connection is also listed. As can be seen, the increase flexibility of this connection means in a sense a large relative displacement between the wooden roof beam and the masonry wall. This practically means that there is a possibility of a loss of support of the wooden roof beam when this relative displacement becomes excessive, as is the case of the flexible connection assumed in this simplified numerical simulation. This is the case portrayed by the collapsed roof in figures 7 and 10. Obviously, this simplified analysis is only qualitative. In order to obtain realistic numerical predictions it is necessary to include in the numerical analysis a valid numerical description of the non-linear connection mechanism ([31] to [36]).

#### 4 CONCLUSIONS

- The recent earthquake sequence in the Greek island of Samos gave the opportunity of assessing the earthquake performance of various types of structure in Greece. It can be stated that the enforcement in 1995 of the “New Greek Seismic Code” together with the provisions of the Euro-Codes has substantially increased the safety level of structures against earthquakes. A significant expansion of the strong motion network of accelerographs that covers the whole of Greece provides very important information on the characteristics of the earthquake strong ground motion that is very useful in assessing the consequences of the intense earthquake activity to the built environment. The relevant data base is enriched with valuable information on the characteristics of the earthquake strong ground motion that is very useful to designers and contractors.
- A source of seismic risk that can result in human loss was highlighted by this earthquake event. It is generated by old and weak unreinforced masonry structures which are left unoccupied and not maintained by their owners due to various social-economic non-incentives and complications. This category includes numerous old buildings that belong to culture heritage being listed in conservation status. The group of old stone- masonry buildings with wooden roof that were used as leather processing factories at Karlovassi-Samos belong to this category.
- Numerical tools combined with realistic measurements of the seismic forces generated by a strong earthquake ground motions can be utilized to explain the observed structural damage. They can also be utilized in the subsequent retrofitting effort. Towards this objective, the present numerical study investigated the influence of the flexibility of the connections between the wooden roof beams and the masonry walls of such old stone masonry industrial buildings.
- The flexible connections exercise limited restraint in prohibiting the masonry walls to displace, especially in the out-of-plane direction. Consequently, such increased flexibility results in relatively large displacement and stress response demand for the masonry walls that could be detrimental leading to mainly flexural type failures. This is to be expected for masonry construction with low flexural capacities. At the same time, the increase in the flexibility of these connections results in a decrease of the level of axial force which

is in agreement with the resulting increase of the out-of-plane displacement at the top of the masonry walls.

- At the same time, the increased flexibility of wooden roof beams to masonry wall connections also results in large relative displacement between the wooden roof beam and the masonry walls. This practically means that there is a possibility of a loss of support of the wooden roof beam when this relative displacement becomes excessive, as is the case of the flexible connection assumed in this simplified numerical simulation.
- The present simplified analysis is only qualitative. In order to obtain realistic numerical predictions it is necessary to include in the numerical analysis a valid numerical description of the non-linear connection mechanisms. Moreover, there is also need to obtain measured capacities of such connections through laboratory measurement focusing to this problem.

## REFERENCES

- [1] Ambrazeys, N.N. et.al. "Prediction of Horizontal Response Spectra in Europe" Int. J. of Earth. Engin. and Struct. Dyn., pp. 371-400, Vol. 25, No. 4, April 1996.
- [2] Ambrazeys, N.N. et.al. "Prediction of Vertical Response Spectra in Europe" Int. J. of Earthquake Engineering and Structural Dynamics, pp. 401-414, Vol. 25, No. 4, April 1996.
- [3] Carydis, P.G., Tilford, N.R., Brandow, G.E. and Jirsa, J.O. "The Central Greece Earthquakes of February-March 1981, A Reconnaissance and Engineering Report", National Academy Press, Washington, D.C., Report No. CETS-CND-018, pp 162, 1982.
- [4] Papazachos, B.C. (1990) "Seismicity of the Aegean and the Surrounding Area", Tectonophysics, 178, 287-308.
- [5] Manos G.C., "Consequences on the urban environment in Greece related to the recent intense earthquake activity", Int. Journal of Civil Engineering and Architecture, Dec. 2011, Volume 5, No. 12 (Serial No. 49), pp. 1065–1090.
- [6] The Earthquake of Oct. 30, 2020, M6.7 (11:51GMT) North of Samos Island (Greece): Observed strong ground motion on Samos island. Institute of Earthquake Engineering and Engineering Seismology (ITSAK) , Preliminary report, October 2020.
- [7] Preliminary report on the Samos 30th October 2020 earthquake. Hellenic Society of Earthquake Engineering, ETAM,-report- Samos-2020 earthquake, November 2020.
- [8] Manos G.C. "The 30th of October Samos-Greece Earthquake. Issues Relevant to the Protection from Structural Damage Caused by Strong Earthquake Ground Motions", Journal of Architecture and Engineering, Volume 5 Issue 4 (2020), eISSN: 2500-0055, <http://aej.spbgasu.ru/>
- [9] Paz. M. International Handbook of Earthquake Engineering: "Codes, Programs and Examples", edited by Mario Paz, Chapter 17, Greece by G.C. Manos, Chapman and Hall, ISBN 0-412-98211-0, 1994.
- [10] Organization of Earthquake Planning and Protection of Greece (OASP),. (2001).Guidelines for Level- A earthquake performance checking of buildings of public occupancy», Athens.

- [11] Organization of Earthquake Planning and Protection of Greece (OASP), (2011). Guidelines for Retrofitting in Reinforced Concrete Buildings, Athens.
- [12] EAK-2000 Greek seismic Code.
- [13] Provisions of Greek Seismic Code with revisions of seismic zonation”, Government Gazette, Δ17α /115/9/ΦΝ275, No. 1154, Athens, 12 Aug. 2003.
- [14] ELOT EN 1998-1/2005-05-12, Eurocode 8: Design of structures for earthquake resistance - Part1: General rules, seismic actions and rules for buildings.
- [15] Croci G., “The Conservation and Structural Restoration of Architectural Heritage”, Computational Mechanics Publication, 1998, ISBN 1 85312 4826.
- [16] Limoge Schraen C., Giry C., Desprez C., Ragueneau F., “Tools for a large-scale seismic assessment method of masonry cultural heritage”, Structural Studies, Repair and Maintenance of Cultural Heritage, STREMAH XIV, WIT press (2015), ISBN 978-1-84564-968-5.
- [17] Lagomarsino Sergio “Damage assessment of churches after L’Aquila earthquake (2009)” Bulletin of Earthquake Eng. 2011, DOI 10.1007/s10518-011-9307-x.
- [18] Modena C. et.al., “ L’Aquila 6th April 2009 Earthquake: Emergency and Post-emergency Activities on Cultural Heritage Buildings” Claudio Modena C. et.al. , Chapter 20, Earthquake Engineering in Europe, Geotechnical, Geological, and Earthquake Engineering 17, DOI 10.1007/978-90-481-9544-2\_20, Springer Science+Business Media B.V. 2010.
- [19] Manos G.C. and Papanaooum E., “Earthquake Behaviour of a R/C Building Constructed in 1933 before and after its Repair” STREMAH 2009, Tallin, 22-24 June, 2009.
- [20] Manos G.C., Soulis V., Diagouma A. (2008) “Numerical Investigation of the behavior of the church of Agia Triada, Drakotrypa, Greece”, Journal in Advances in Engineering Software 39 (2008) 284-300.
- [21] Manos G.C., Soulis V. J & Karamitsios N., “The Performance of Post-Byzantine churches during the Kozani-1995 Earthquake – Numerical Investigation of their Dynamic and Earthquake Behaviour”, 15WCEE, 2012, Portugal.
- [22] Manos G.C. & Karamitsios N., “Numerical simulation of the dynamic and earthquake behavior of Greek post-Byzantine churches with and without base isolation”, Earthquake Engineering Retrofitting of Heritage Structures, Design and evaluation of strengthening techniques, pp. 171-186, Edited By: S. Syngellakis, Wessex Institute of Technology, UK, ISBN: 978-1-84564-754-4, eISBN: 978-1-84564-755-1, 2013.
- [23] Manos G.C., Kotoulas L., Felekidou O., Vaccaro S. and Kozikopoulos E. “Earthquake damage to Christian Basilica Churches – Application of an expert system for the preliminary in-plane design of stone masonry piers” , STREMAH-2015, A Coruna, Spain, 13-15 July, 2015.
- [24] Manos G.C., “The Seismic Behaviour of Stone Masonry Greek Orthodox Churches” Journal of Architecture and Engineering, Vol. 1, Issue 1, March 2016, pp. 44-53, <https://aej.spbgasu.ru/index.php/AE/index>
- [25] Manos G.C., Kotoulas L., Matsou V., Felekidou O. “Dynamic and Earthquake Behaviour of Greek Post-Byzantine Churches with Foundation Deformability – Experimental Investigation of Stone Masonry Materials Properties”, Springer Publishing, I. N. Psy-

- charis (seds.), I.N. Psycharis et al. (eds.), *Seismic Assessment, Behavior and Retrofit of Heritage Buildings and Monuments*, Computational Methods in Applied Sciences 37, DOI 10.1007/978-3-319-16130-3\_9.
- [26] Manos G., Kozikopoulos E., Kotoulas L., Soulis V. “The Earthquake performance of stone masonry Basilica churches in Kefalonia-Greece including wall detachment and soil foundation deformability”, 16th European Conf. Earthquake Engineering, Thessaloniki-Greece, 2018.
- [27] Kotoulas L., Manos G.C. “Unreinforced stone masonry churches in Greece under gravitational and earthquake actions”, 7th ECCOMAS Thematic Conference on Computational Methods in Structural Dynamics and Earthquake Engineering M. Papadrakakis, M. Fragiadakis (eds.), Crete, Greece, 24–26 June 2019.
- [28] Manos G.C., Kotoulas L., and Kozikopoulos E., (2019) “Evaluation of the Performance of Unreinforced Stone Masonry Greek “Basilica” Churches When Subjected to Seismic Forces and Foundation Settlement”, *Buildings* 2019, 9, 106; doi:10.3390/buildings9050106.
- [29] Manos GC & L Kotoulas. *Unreinforced Stone Masonry Churches under Gravitational and Earthquake Actions*, CompDyn 2019, Crete, Greece 2019.
- [30] Soulis V. J. and Manos G. C., Numerical Simulation and Failure Analysis of St. Konstantinos Church, after the Kozani Earthquake”, *International Journal of Civil Engineering* (2019) 17:949–967, <https://doi.org/10.1007/s40999-018-0345-5>
- [31] Manos, George C., Clough, Ray W., Mayes, Ronald L “Shaking table study of single-story masonry houses: dynamic performance under three component seismic input and recommendations”, Report UCB/EERC-83/11.
- [32] Gulkan P., Clough R.W., Manos G.C. and Mayes R.L. “Seismic Testing of Single-story Masonry Houses : Part 1”, *Journal of Str. Eng. ASCE*, Vol. 116, No 1, January 1990, pp. 235-256.
- [33] Gulkan P., Clough R.W., Manos G.C. and Mayes R.L. “Seismic Testing of Single-story Masonry Houses : Part 2”, *Journal of Str. Eng. ASCE*, Vol. 116, No 1, January 1990, pp. 257-274.
- [34] Manos G.C., Mpoufidis D., Zafiriou Th, “The seismic behaviour of a Pre-cast R/C industrial complex subjected to the 1999 Athens-Greece Earthquake”, 16th European Conf. Earthquake Engineering, Thessaloniki-Greece, 2018.
- [35] European Committee for Standardization, Eurocode 6; “Design of Masonry Structures, Part 1-1:General Rules for Building. Rules for Reinforced and Unreinforced Masonry”, EN 1996-1-1:2005.
- [36] Katakalos K.V., Arnaoutis I., and Manos G.C. “Identification of failure mechanism of the Ottoman bath (Hamam) at Apollonia (Pazarouda) – Exploitation of historical data”, *Joural Case Studies in Construction Materials*, 2020.

## EXPERIMENTAL AND ANALYTICAL INVESTIGATION OF THE STRENGTHENING OF TRADITIONAL TIMBER FRAMES

Ioannis Stavrou<sup>1</sup>, Panayiotis Demosthenous<sup>1</sup>, Stelios Papastylianou<sup>1</sup>  
and Milton Demosthenous<sup>2</sup>

<sup>1</sup>Civil Engineer, MSc Student, Frederick University, Nicosia, Cyprus

<sup>2</sup>Dr. Civil Engineer, Professor, Frederick University, Nicosia, Cyprus  
eng.dm@frederick.ac.cy

---

### Abstract

*This paper deals with the experimental investigation of the behavior of timber frames with or without infill panels. The examined infill panels are diagonal timber bracers, masonry infill and OSB. The main scope of this effort is the investigation of the influence of the infill panels to the strengthening and the global behavior of these frames. At the first stage the mechanical properties of the used materials, such as timber, brick, mortar and masonry were defined through experimental tests. An additional number of tests were completed in order to define the capacity of the joints between two timber members focused on the shear capacity and the extraction of nails which used for the connection of timber members. All these data will be used for the numerical simulations of the experimental studied timber frames. At the second stage, eight timber frames were designed, constructed and tested at the metallic reaction frame of Frederick University under lateral monotonic loadings until the ultimate limit state. The lateral loading as well the lateral displacement and the uplift of the column which was under tension were measured and recorded using a data acquisition system. At the same time the observed modes of failures were reported. At last, but not least, the evaluation of these measurements through various analytical methods was completed. Through this effort the relation between the lateral displacement and the uplift is examined, the absorbed energy from each timber frame is estimated and the contribution of each infill system to the global behavior of the timber frame systems is defined and discussed.*

**Keywords:** Timber frame, infill panels, experimental investigation, analytical evaluation

---



## 1 INTRODUCTION

The majority of the historic buildings, both in Eastern Mediterranean region and throughout Europe, were built with load-bearing masonry wall system. Of particular interest, is the timber frame with masonry infill. A masonry timber frame is consisted by many parts created by horizontal, vertical and diagonal timber elements (fig. 1). The ease of construction, on one hand and the availability of the natural material, on the other hand, played an important role, on the wide use of the system throughout the world. The long term existence of this system, proves its efficiency and its durability throughout the centuries. Even today, the timber frame system, in various forms and types, still plays a leading role in the Building industry. Many experimental and numerical investigations have dealt with the behavior and response of this system. Many of them are presenting a qualitative evaluation of this system, under static and seismic loading. While, this study evaluates, with the aid of experimental approach, the behaviour of various strengthening typologies of the system, in a way that this would be helpful to the maintenance and even strengthening procedures of existing structures [ 1, 2, 3, 4 ].

An experimental investigation approach, aiming to the strengthening techniques of historic timber frames is designed and is under develop at the Frederick University in Cyprus. The present study is focused on the basic part of a timber frame as explained above, as the first step of this effort in order to understand well the behavior of such systems under lateral seismic loadings, the mechanisms of failure as well the contribution of various techniques for the strengthening of masonry timber frames. Therefore, eight (8) different timber frame specimens with various techniques of strengthening were designed, constructed and tested under monotonic lateral static loading. At the first stage the mechanical properties of the used materials, such as timber, brick, mortar and masonry were defined through experimental tests. An additional number of tests were completed in order to define the capacity of the joints between two timber members focused on the shear capacity and the extraction of nails which used for the connection of timber members. All these data will be used for the numerical simulations of the experimental studied timber frames. During the experimental sequence of frame specimens, a monitoring and data acquisition system was used for the recording of the lateral loading and the horizontal displacement on the top of the frames. In addition to that, the uplift of column which is under tension was recorded during the loading procedure. All these results are evaluated, presented and discussed in what follow with emphasis on the contribution of various strengthening techniques on the behavior of these frames.

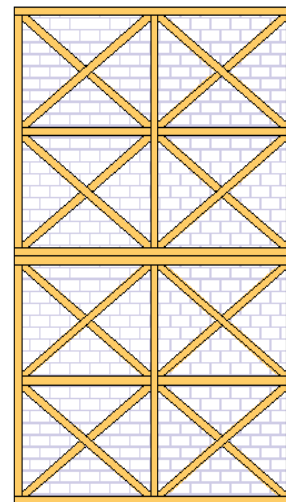


Figure 1. Masonry timber frames on the upper storey of building structure in Cyprus

## 2 DESIGN AND CONSTRUCTION OF THE EXPERIMENTAL TIMBER FRAMES

### 2.1 Mechanical properties of the materials

A number of tests were completed for the definition of the mechanical properties of the used materials such as timber, brick, mortar and masonry. The properties of these materials will be used for the numerical simulations and structural analysis of experimental frame specimens.

For the construction of masonry walls, lime mortar and bricks were used. Their mechanical properties were defined according to the provisions of European standards. The compressive strength of masonry was defined using triplet specimens (consisted by three bricks connected with mortar) and was founded out equal to 13.2 Mpa.

It is well known that timber is orthotropic material. Therefore, the used timber for the construction of timber frames was tested under compression loadings in two cases, parallel and perpendicular to the grain, again according to the provisions of European standards. For each case three specimens were tested. The results from these tests are presented in figure 2 in terms of stress - strain.

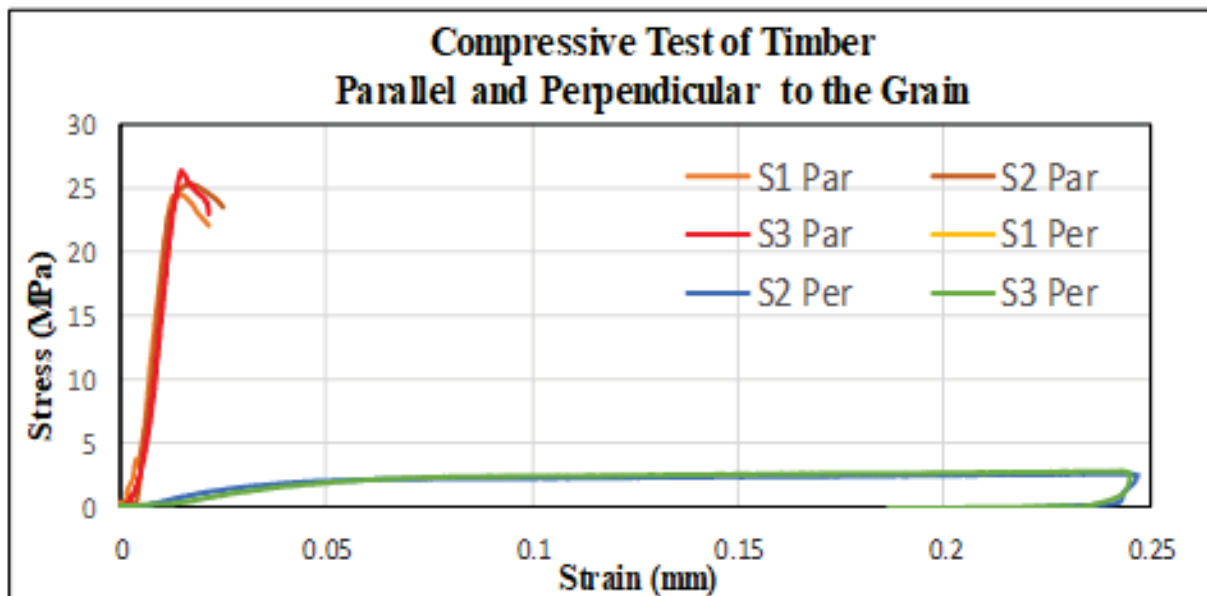


Figure 2. Stress - strain curves of timber under compression

### 2.2 Capacity of the joints of timber elements

All the timber elements were connected with nails. The capacity of these joints is characterized by the shear resistance and resistance to the extraction of the nails under axial tension. Therefore a number of experimental tests were completed to define the shear capacity and the capacity to the extraction of nails. In both cases (shear and extraction capacity) the tests includes various number of nails (one, two or three) for the connection of timber elements.

For the extraction of the nails six specimens were tested. In three of them the timber elements were connected with two nails and in the case of the other three specimens three nails were used. For the shear capacity five specimens were tested. Each specimen was consisted by three timber elements arranged in parallel configuration. The central one was connected

with the external timber elements using nails. For two specimens two nails were used (1+1) and for three specimens four nails (2+2).

During the tests, the applied loading (shear or tension) and the displacement between the connected timber elements were measured. In any case, after the completion of each test, the capacity corresponds to one nail was estimated. These results are noted in figures 3 & 4. In the same figures, the average value of the capacity of one nail is given with a solid line.

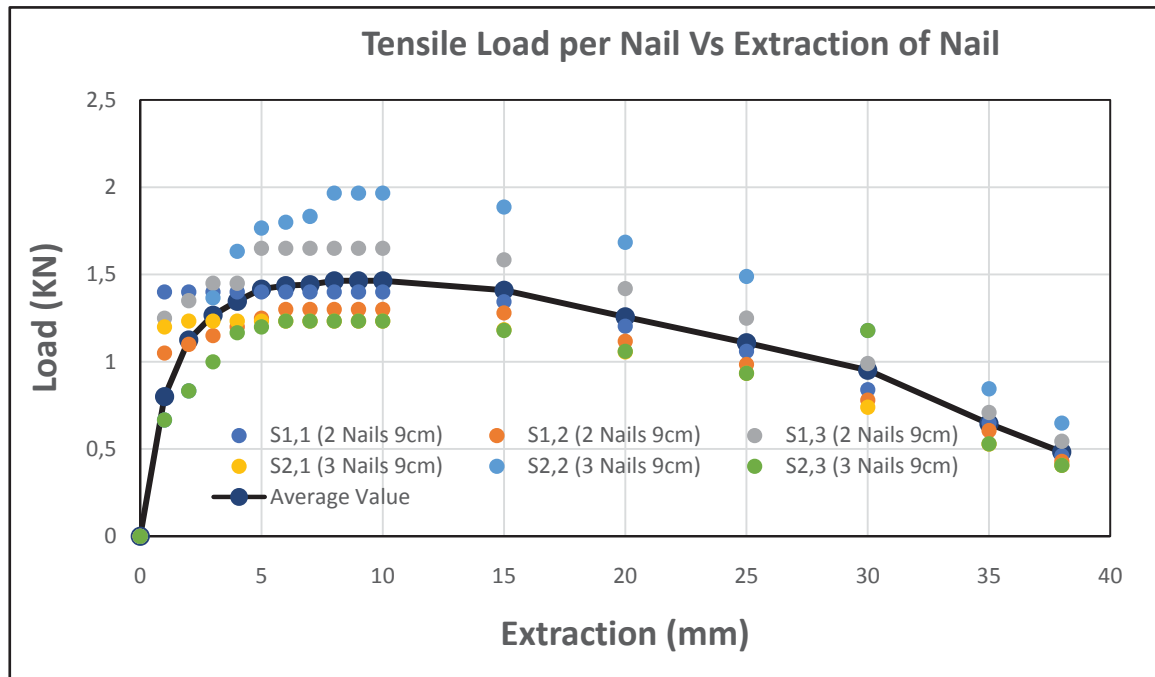


Figure 3. Experimental measurements from the extraction of nails tests

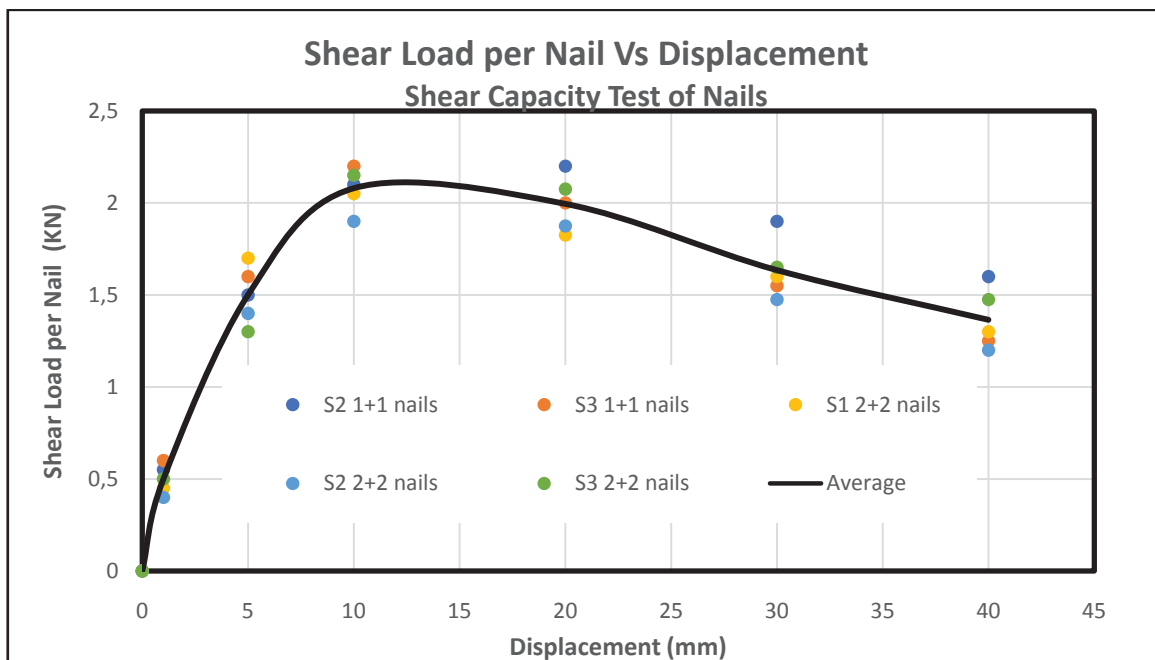


Figure 4. Experimental measurements for the shear capacity nails

### 2.3 Design and construction of experimental timber frames

As mentioned above, the experimental specimens examined in this paper represent a basic part of a real timber frame (see figure 1) in order to understand well the behavior and the failure mechanisms of such sub-system as basic background to understand and explain these topics of a whole frame system as well to understand and record the influence of various strengthening techniques to the behavior of timber frames such as diagonal timber bracers, masonry infill and the OSB as infill panel. Therefore, eight (8) timber frames in various forms were designed and constructed (figure 5). All experimental timber frames have rectangular shape with height 0.77m (77cm) and the same bay between the two vertical timber columns (77cm).

- The first frame, which will be referred as reference frame in what follow (2CTF), consisted by an horizontal timber beam as base level. Two vertical columns are connected at the base beam with nails. The top level of these columns are connected also with a timber beam using nails.
- The second one has the same configuration, however one more timber column is attached at the middle of the bay (3CTF).
- The third one has also the same configuration with the reference frame including diagonal timber bracers (2CXTF).
- The fourth one is the same with the reference one but with masonry infill (2CMTF).
- The fifth one, as timber frame, is the same with the third one including also masonry infill (2CXMTF).
- The sixth one has the same timber skeleton with the reference one however two OSB panels were used as infill panel attached in both sides of the frame (2CTF - 2- OSB).
- The seventh one has the same timber skeleton with the third one (with diagonal bracers) but only one OSB panel was attached at one side (2CXTF - 1- OSB).
- The eight one has the same timber skeleton with third one (with diagonal bracers) but in this case two OSB panels were used as infill panel attached in both sides of the frame (2CXTF - 2- OSAB).

The facade of all the above experimental timber frames are presented in figure 5.

## 3 EXPERIMENTAL TESTS OF TIMBER FRAMES

### 3.1 Experimental setup

All experimental timber frames were attached at the metallic reaction frame of Frederick University and were subjected to lateral monotonic loading (figure 6). The timber beam at the base of the frames was fixed at the horizontal steel beam of the reaction frame. The lateral loading was applied at the top of the timber frame using an hydraulic jack. In order to avoid local modes of failures due to the point load, an additional timber beam was fixed at the top beam of the frames with an expansion to the hydraulic jack. Therefore, the lateral load was applied in uniform distribution to the top beam of the timber frames.

Two displacement transducers (LVDT) were used to measure the displacements of the timber frames. The first one measured the horizontal displacement at the top of the timber frames. The second one was attached at the base of the frame in order to measure the uplift of the timber column which was under tension during the experimental loading. This uplift was happened due to the extraction of the nails which connected the timber column with the beam at the base level. The measurements of the LVDT' s as well the loadings applied from the hydraulic jack were restored in a data acquisition system in time domain.

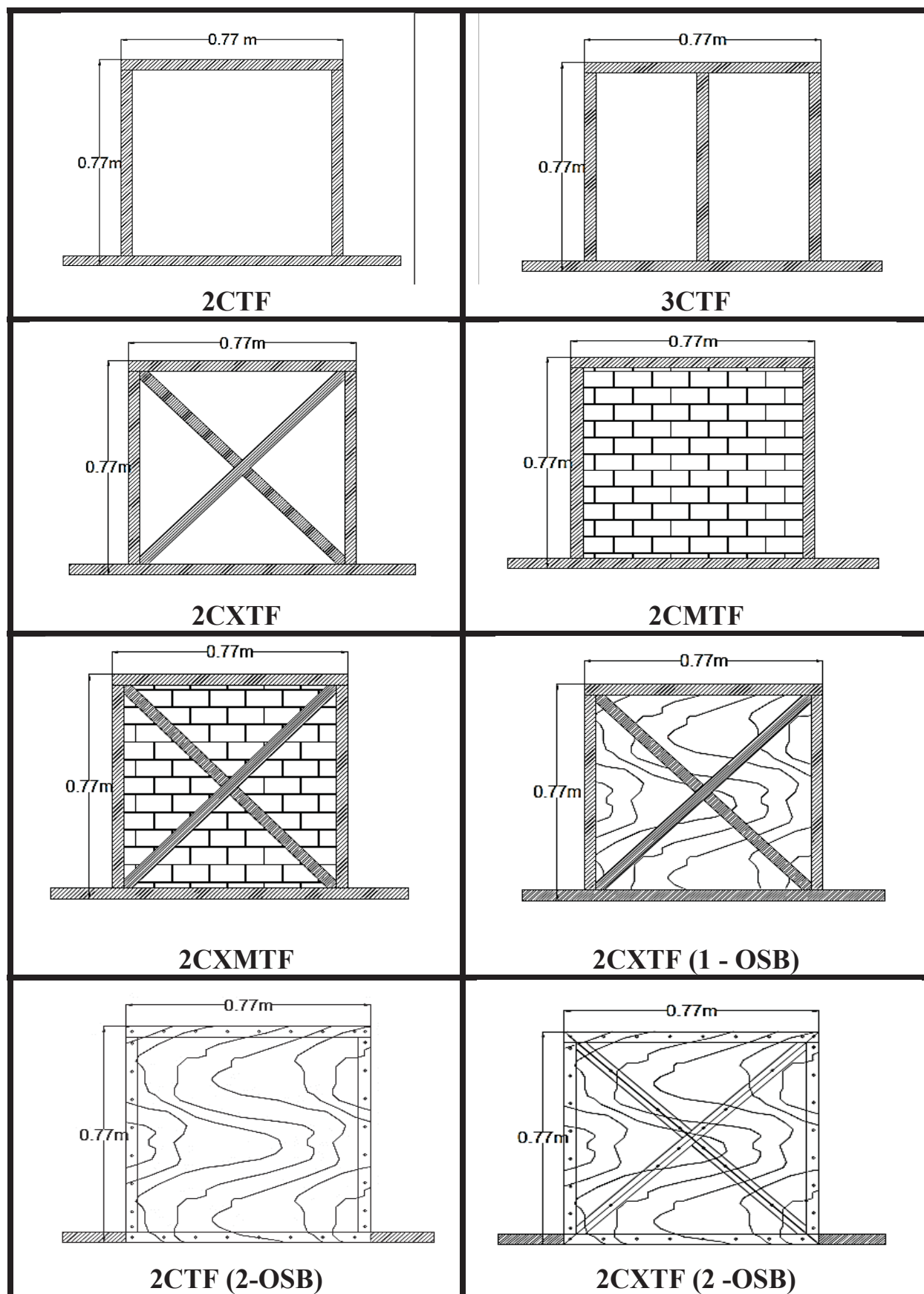


Figure 5. Configuration and dimensions of experimental timber frames



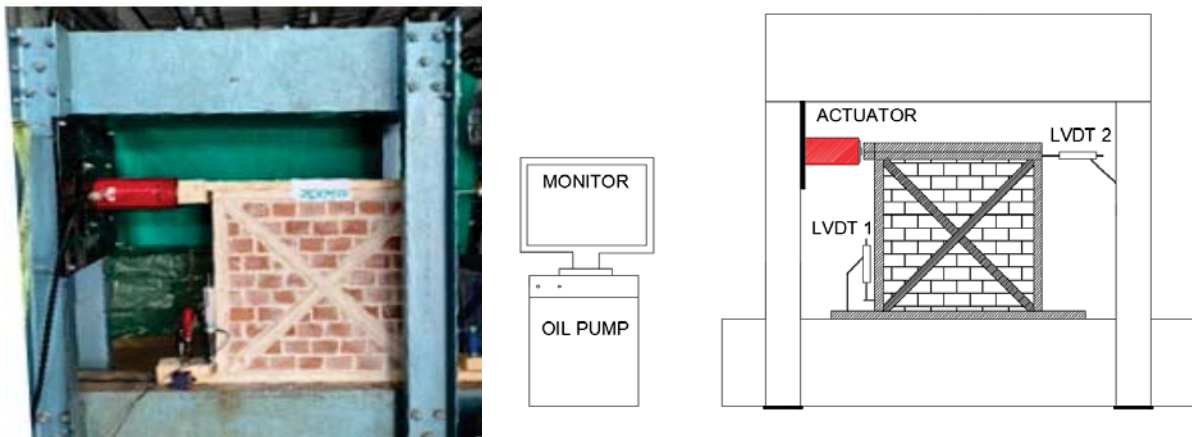


Figure 6. Experimental setup

### 3.2 Experimental measurements

The lateral horizontal load vs the horizontal displacements for all the timber frames are presented in figure 7. We can see that the timber frames 2CTF and 3CTF (pure frames) have almost the same behavior with the lower level of the lateral received load but with higher level of lateral displacements without uplift. The timber frames with OSB can receive the higher level of the external loading. The other timber frames (with masonry infill or/and diagonal bracers), simulating traditional timber frames, have a capacity between the two previous categories as mentioned above (pure timber frames and timber frames with OSB). Similar observations can be made and for the measurements of the uplift at the bottom of the left timber column with tensile stress (figure 8).

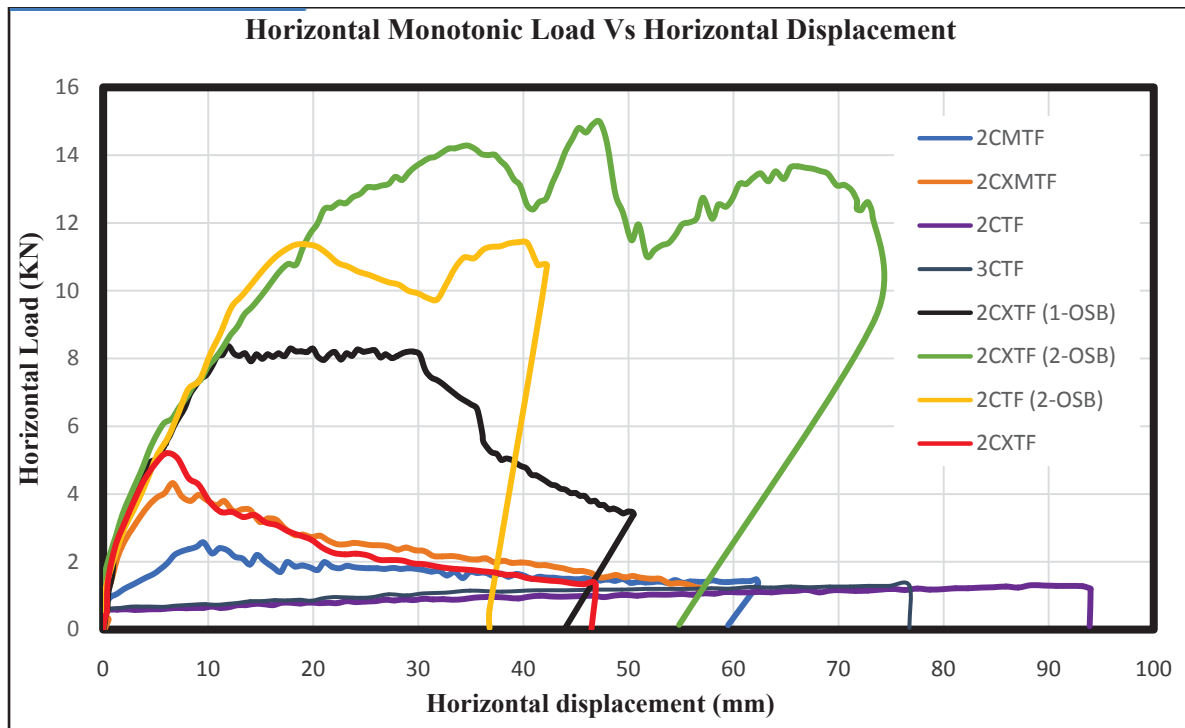


Figure 7. Horizontal monotonic load vs horizontal displacements



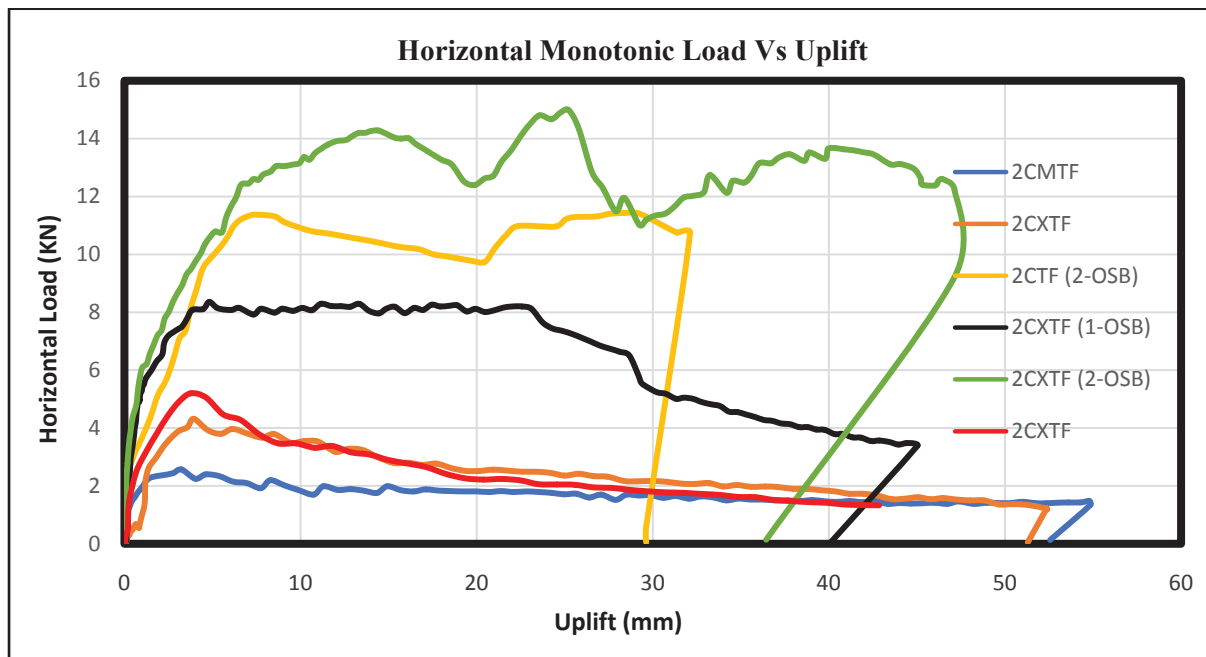


Figure 8. Horizontal monotonic load vs Uplift of the left timber column

### 3.3 Observed damages

The pure frames consisted only by columns and beams (2CTF & 3CTF) developed only horizontal displacements without any uplift at the left column. After the un-load of these frames a remain displacement was observed. The deformation shape of these frames it looks like pure shear deformation which is mean that the actual resistance during the test was the shear resistance of the nails which connected the timber structural elements (figure 9).

In the case of timber frames with diagonal bracers (2CXTF & 2CXTF (1-OSB)) the behavior is characterized by horizontal displacements and uplift of the left column at the base level as well the uplift of the diagonal timber element connected at this joint. After the un-load of these frames a remain displacement was observed as well uplift at the base level due to the extraction of the nails (figure 9).

The timber frames with masonry infill develop similar behavior with those with diagonal timber bracers including remain uplift and horizontal displacement after un-loading. However in this case it was founded out that there are significant damages on the masonry infill characterized by disconnection from the timber frame as well diagonal shear cracks were observed. These damages are more serious in the case of timber frame without diagonal timber bracers (2CMTF). In addition to that, a flexural deformation on the left column was observed due to the interaction between the masonry infill and the left timber column (figure 9).

The last two timber frames with OSB infill (2CTF - 2- OSB & 2 CXTF -2 -OSB) developed much difference behavior. Due to the OSB infill panel which was connected with the surrounding frame (columns and beams), the beam at the base level developed flexural deformation created by vertical loadings applied through the connections of the beam with the OSB. After the un-load of these frames the remain displacement and uplift was observed to be much smaller than the previous cases. However, a flexural deformation is remained at the beam at the base level (figure 9).



Figure 9. Modes of the observed failures of the timber frames

## 4 EVALUATION AND ANALYSIS OF THE EXPERIMENTAL MEASUREMENTS

### 4.1 Evaluation and analysis of the horizontal displacements of the timber frames

In this section the horizontal displacements of the timber frames are examined until the max. lateral load ( $F_{max}$ ) with the assumption of linear behavior. From this point of view, the total horizontal displacement ( $X$ ) of each frame is consisted by two parts ( $X_1 + X_2$ ). The first one ( $X_1$ ) is created due to the uplift. Assuming of a rigid body rotation of the frame system, the  $X_1$  is equal to the uplift ( $X_1 = \text{uplift}$ ). However, an additional horizontal displacement ( $X_2$ ) is created due to the shear and bending deformation of the timber frame. This approach is presented in figure 10. The values of the  $X$  (total displacement), the  $X_1$  and the  $X_2$  are presented in figure 11 for six timber frames which developed uplift during the tests.

At a second step, the values of the  $X_1$  and  $X_2$  are divided by the total displacement ( $X$ ) in order to find the contribution of each part to the total displacements in percentage (figure 12). As can be seen, in the case of masonry infill timber frame without diagonal bracers (2CMTF) the contribution from the uplift to the total displacement is more than 75%, however in the case of masonry timber frame with diagonal bracers (2CXMTF) this contribution is reduced approximately up to 55%. In the case of timber frame with diagonal bracers (2CXTF) the contribution from the uplift is approximately about 33%. The more significant observation from this analysis is that, all the frames with OSB infill panel the contribution from the uplift ( $X_1$ ) to the total displacement ( $X$ ) is almost the same in all the cases, approximately up to 42%. From this point of view it can be said that the behavior of timber frames with OSB infill panel is more predictable. However, this observation must be verified through a numerical investigation.

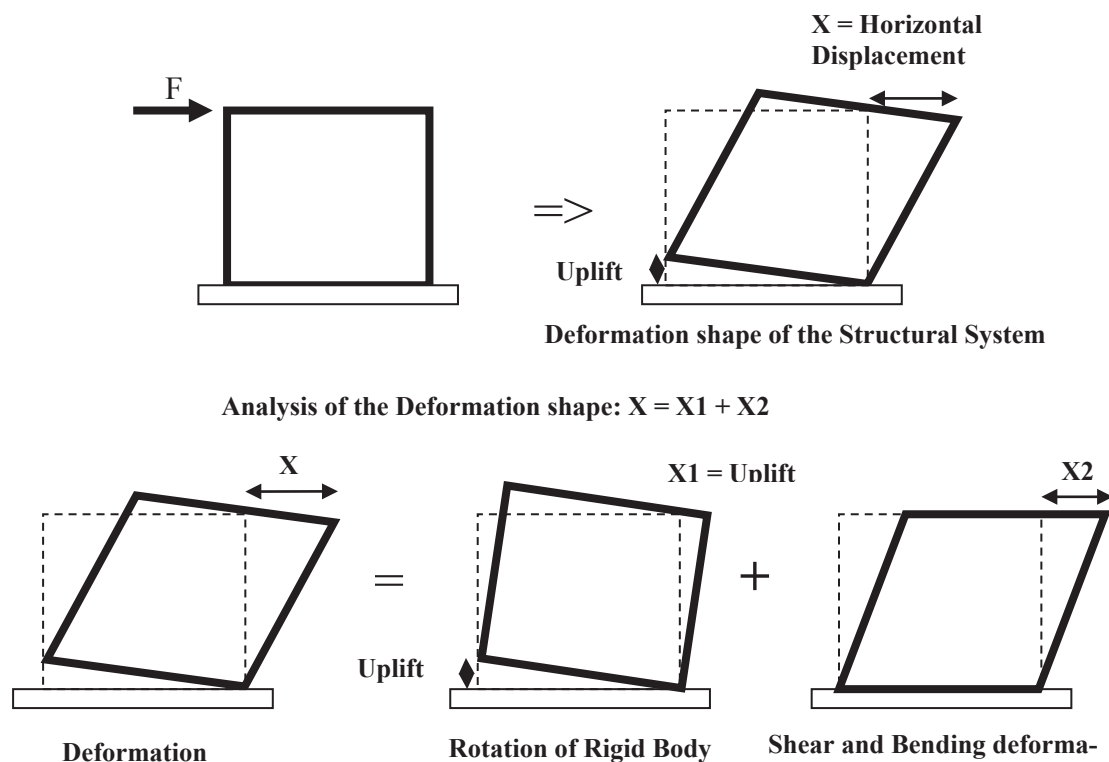


Figure 10. Analysis of the total displacement

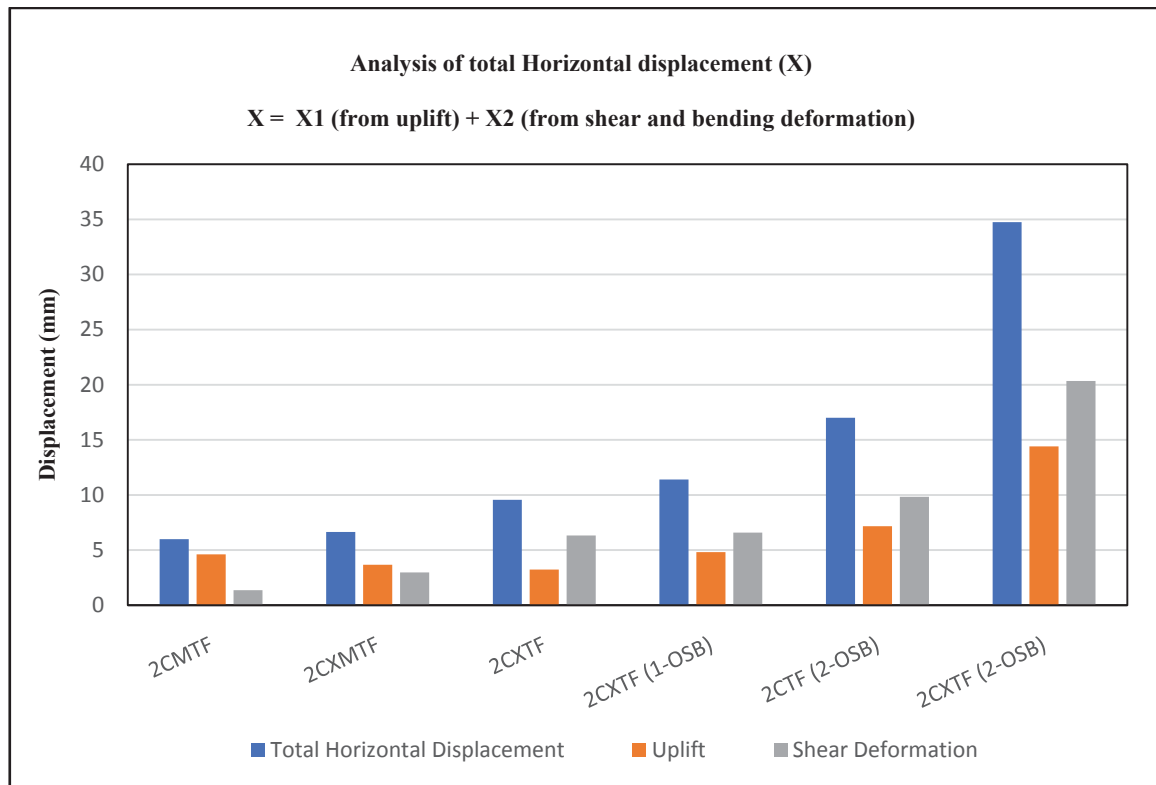


Figure 11. Analysis of the total displacement

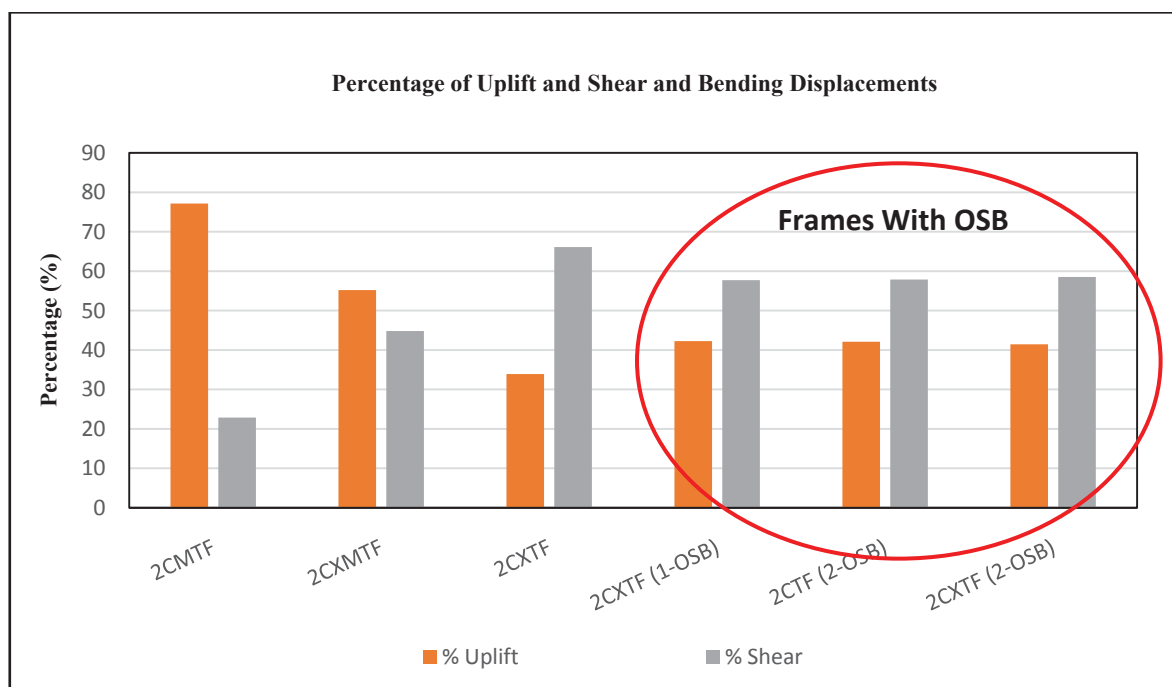


Figure 12. Percentage contribution of uplift and shear and bending deformation to the total horizontal displacement

#### 4.2 Evaluation and analysis of the global behavior of the timber frames and contribution of the strengthening techniques

The main scope of this effort is to investigate the influence of the strengthening techniques to the global behavior of the studied timber frames. For that, the quantity of energy absorbed by each frame and the correlation of this energy with that of the reference frame (2CTF) is presented. For each timber frame, the absorbed energy was estimated by the area below the curve of Lateral Force Vs Horizontal Displacement as defined by the experimental measurements. This absorbed energy was estimated until 40mm horizontal displacement for all the studied frames (figure 13). After that, the absorbed energy of each frame is correlated with absorbed energy of the reference frame (2CTF). The results from this effort are presented in table 1.

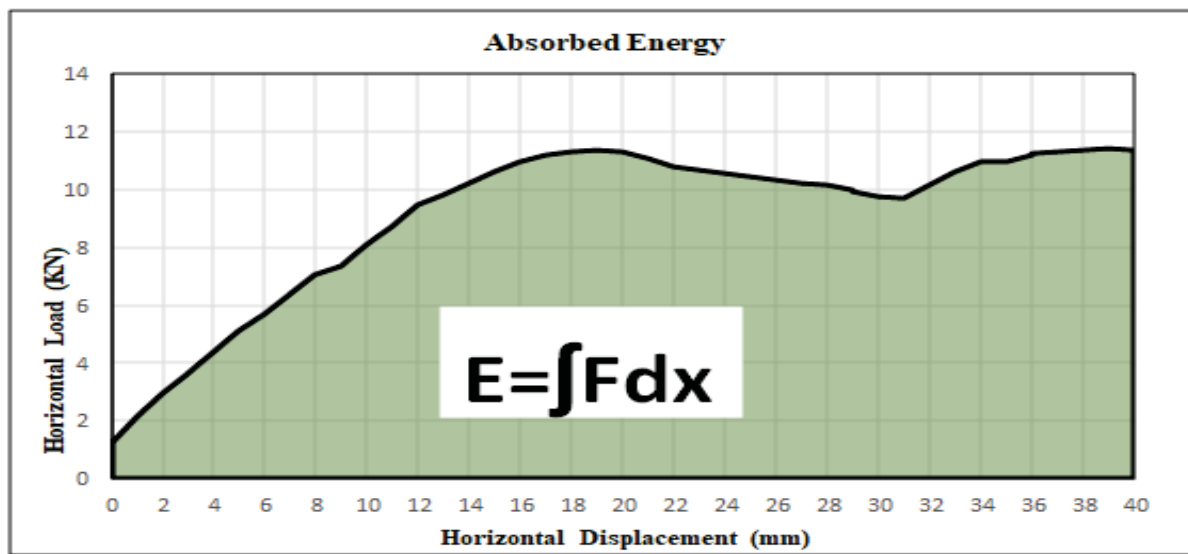


Figure 13. Procedure for the estimation of the absorbed energy for each timber frame

Timber Frame	Absorbed Energy (J)	Ratio of Absorbed Energy (frame i / 2CTF)	Increasing of Absorbed Energy
2CTF	32.5	1.00	0.0 %
3CTF	40.6	1.24	24 %
2CMTF	73.75	2.26	126 %
2CXTF	113.0	3.47	247 %
2CMXTF	114.0	3.50	257 %
2CXTF (1 - OSB)	277.35	8.53	753 %
2CTF (2 - OSB)	363.4	11.21	1021 %
2CXTF (2 - OSB)	429.7	13.22	1222 %

Table 1. Result from the estimation of the absorbed energy and correlation with the reference frame (2CTF)



At a second step, the contribution of each strengthening technique to the increasing of the absorbed energy is examined. For that, the contribution of an additional vertical timber column, the masonry infill, the diagonal timber bracers and the OSB as infill panel are examined. In the first stage the difference in absorbed energy between two timber frames with only difference the examined strengthening technique is estimated. If there were more cases with that, the average value of them was taken in the account. Finally the amplification factor for each intervention technique was estimated. This amplification factor describes how many times there is increasing of the absorbed energy of the reference frame (2CTF) if the strengthening technique would be applied on the reference frame. The results from this procedure are summarize in table 2. According to these results, it can be said that the panel of one OSB has much higher contribution to the absorbed energy than the other strengthening techniques. Actually the contribution of one panel of OSB is more than two times than that from the diagonal bracers and almost four times than that from the masonry infill. At last, but not least, it can be said that the additional vertical timber column has very low contribution to the absorbed energy, however this technique must be examined in various cases and structural configurations for more safety and realistic conclusions.

Strengthening Technique	Formula	Absorbed Energy (J)	Average value	Amplification factor (Str. tech./2CTF)
Additional one vertical column	$3CTF - 2CTF$	8.1	8.1	0.25
Masonry infill	$2CMTF - 2CTF$	41.25	41.25	1.3
Diagonal bracers	$2CXTF - 2CTF$	80.5	73.5	2.25
1 OSB panel infill	$2CXTF (2OSB) - 2CTF (2OSB)$	66.3		
	$2CXTF (1OSB) - 2CXTF$	164.35	162.7	5.0
	$[2CXTF (2OSB) - 2CXTF] / 2$	158.35		
	$[2CTF(2OSB) - 2CTF] / 2$	165.45		

Table 2. Contribution of each strengthening technique to the absorbed energy

## 5 CONCLUSIONS

The behavior of eight (8) timber frames was investigated under lateral monotonic loadings through an extended experimental investigation accompanied by the analysis and the evaluation of the experimental measurements. The reference timber frame was consisted by two vertical columns connected at the base level and at the top level with horizontal beams. The timber elements were connected with nails. All the other timber frames were strengthened using various strengthening techniques, such as additional vertical timber column, masonry infill, diagonal timber bracers and OSB as infill panel. According to the observed damages and the evaluation of the experimental results, the followed conclusions can be made:

- The predominant modes of the observed failures can be characterized by the uplift of the vertical timber column which was under tension, due to the extraction of the nails at the base level, as well by shear and bending deformation of the frame. After the unloading of the experimental frames, significant remained displacement of all the examined frames was observed.
- In the case of the timber frames with masonry infill, sliding and disconnection of the masonry infill from the surrounding frame accompanied also by cracks of the masonry infill were occurred.
- In the case of timber frames with OSB as infill panel, a flexural deformation at the bottom beam was observed due the connection of this beam with the OSB.
- It was founded out that the max. values of the received lateral load ( $F_{max}$ ) is strongly depended by the strengthening technique with those of the timber frames with OSB to received much higher max. horizontal load than the other cases.
- The total displacement is consisted by two parts. The first one is the contribution from the uplift and the second one is the contribution from the shear and bending deformation of the frames. This contributions are varied however in the case of timber frames with OSB were founded to be constant.
- Finally, the increasing of the absorbed energy by the OSB it was founded out that is much higher than the absorbed energy by the frames strengthened with other techniques. Also, the diagonal bracers has almost two times higher contribution in the absorbed energy than that by the masonry infill.

## REFERENCES

- [1] Dima DI, Dutu A. Traditional buildings with timber frame and various infills in Romania. Presented at the World Conference on Timber Engineering (WCTE), Wien, Austria; 2016.
- [2] Gólkan P, Langenbach R. The earthquake resistance of traditional timber and masonry dwellings in Turkey. Presented at the 13th World Conference on Earthquake Engineering (WCEE), Vancouver, B. C., Canada; 2004.
- [3] Dutu A, Niste M, Spatarelu I. In-plane static cyclic tests on traditional Romanian houses' walls. Presented at the 16th European Conference on Earthquake Engineering (ECEE), Thessaloniki, Greece; 2018.
- [4] Makarios, T., and M. Demosthenous. 2006. Seismic response of traditional buildings of Lefkas Island. *Greece, Engineering Structures* 28:364–295.

## NUMERICAL SIMULATIONS OF THE EXPERIMENTAL RESULTS OF STEEL FRAME MODEL WITH ROOF ROLLER SYSTEM SUBJECTED TO BASE EXCIATATIONS

Nikodemos Kouroufexis<sup>1</sup> and Milton Demosthenous<sup>2</sup>

<sup>1</sup>Civil Engineer, MSc, Frederick University, Nicosia, Cyprus  
nikodemoskouroufexis@gmail.com

<sup>2</sup>Dr. Civil Engineer, Professor, Frederick University, Nicosia, Cyprus  
eng.dm@frederick.ac.cy

---

### Abstract

This paper deals with the experimental and numerical investigation of the effectiveness of a Rolling Mass to the reducing of the resonance response of an experimental and a numerical model of one storey structural system utilizing the shaking table of Frederick University. At the first stage, a sweep test including a range of frequencies of excitations was completed in order to define the resonance response of a steel experimental model simulating one storey building. At the second stage the design and the manufacture of a simple Rolling Mass was completed and its dynamic properties were defined through a sequence of experimental tests with sinusoidal base excitations. At the third stage, the Rolling Mass was attached at the roof of the steel experimental model structure and the influence of that to the resonance response of the model structure was investigated in various cases. Through this investigation the stiffness and the mass ratio of the Rolling Mass system to those of the model structure were defined in order to have the higher level of the reduction of the resonance response. At last but not least, based on the results from the experimental investigation, a numerical model of one storey real structure was designed with or without Rolling Mass at the roof level. This numerical model was subjected also under sinusoidal base excitations in order to study the effectiveness of the Rolling Mass to the resonance response. The normalized results from the experimental investigation of the experimental model structure and those from the numerical investigations of the real model structure were founded out in enough good correlation. The results of this effort are presented and discussed.

**Keywords:** Shaking table, Rolling Mass, Resonance Response

---

## 1 INTRODUCTION

During dynamic loading of structures, such as winds, earthquakes or vibrations due to the operation of machines installed on the structures, a resonance response can be occurred, when the frequency of vibration is equal, or almost equal, with the predominant natural frequency of the structure. The level of forces (or accelerations and displacements) generated by resonance vibration are generally too large and usually they don't be acceptable, both for the operation and the safety of the structure. This response is related also with the damping of the structure so as the damping is increased the resonance response is decreased .

The more practical way to reduce the vibration of a structural system is to change its dynamic properties through the strengthening or changing the mass of the system. However, these interventions are very difficult to be applied in many structural systems. In this case, the most effective and economic way to reduce the vibration is to apply an additional dynamic system at a discrete location of the existing structure to change its dynamic properties in order to avoid the resonance. Tuned Mass Dampers (TMDs) belongs into this category of devices. The TMD system is designed taking in the account many parameters and especially the frequency of resonance. It is effective only over a narrow frequency band very close to the resonance frequency. This problem was under investigation in many research efforts [1, 2, 3, 4]. The design, manufacture and installation of TMD is a very complicated and expensive procedure. Therefore, for these reasons, today they can have applications only on very specific structures. The sliced mass (SM) and the Rolling Mass (RM) have similar behavior and effects with the TMD. Except of the effectiveness, these specific systems have many differences with the TMD such as the manufacture procedure, the installation on the structures, the cost as well the design and the control of their response. On the other hand, the sliced mass (SM) and the rolling mass (RM) can easily be manufactured and installed on a structure but very difficult to be controlled in the way for the reduction of the resonance response.

This paper deals with the experimental and numerical investigation of the effectiveness of a Rolling Mass (RM) to the reducing of the resonance response of un experimental [5] and a numerical model of one storey structural system. For the purposes of this effort the shaking table of Frederick University was used.

- At the first stage, a sweep test including a range of frequencies of excitations was completed in order to define the resonance response of a steel experimental model simulating one storey building.
- At the second stage the design and the manufacture of a simple Rolling Mass (RM) was completed and its dynamic properties were defined through a sequence of experimental tests with sinusoidal base excitations.
- At the third stage, the RM was attached at the roof of the steel experimental model structure and the influence of that to the resonance response of the model structure was investigated in various cases. Through this investigation the stiffness and the mass ratio of the RM to those of the model structure were defined in order to have the higher level of the reduction of the resonance response.
- At last but not least, based on the results from the experimental investigation, a numerical model of one storey real structure was designed with or without Rolling Mass (RM) at the roof level. This numerical model was subjected also under sinusoidal base excitations in order to study the effectiveness of the RM to the resonance response. The normalized results from the experimental investigation of the experimental model structure and those from the numerical investigations of the real model structure were founded out in enough good correlation.

## 2 EXPERIMENTAL INVESTIGATION

### 2.1 Experimental model structure and results from sweep test

For the purpose of this investigation, a flexible steel frame system in small scale was used consisted by two flexible vertical elements and a rigid slab. From this point of view we can assume that this model represent a Single Degree of Freedom (SDOF) system. Before any test, the mass and the stiffness of this model were measured. This model was fixed at the platform of the shaking table and was subjected on a range of frequencies of excitations (1.5 - 8.5Hz) with step 0.5Hz, including of course in this range of frequencies the predominant frequency of this steel frame. In all the cases the max. base acceleration was kept constant ( $2.0\text{m/sec}^2$ ). The base acceleration as well the acceleration response of the experimental model were measured in time domain and restored using a data acquisition system (figure 1). Through this sequence of tests (well known as sweep test) the resonance response of the SDOF system was defined as well the predominant frequency and the viscous damping of the experimental model. The results of the resonance response from this test are summarized in figure 2.

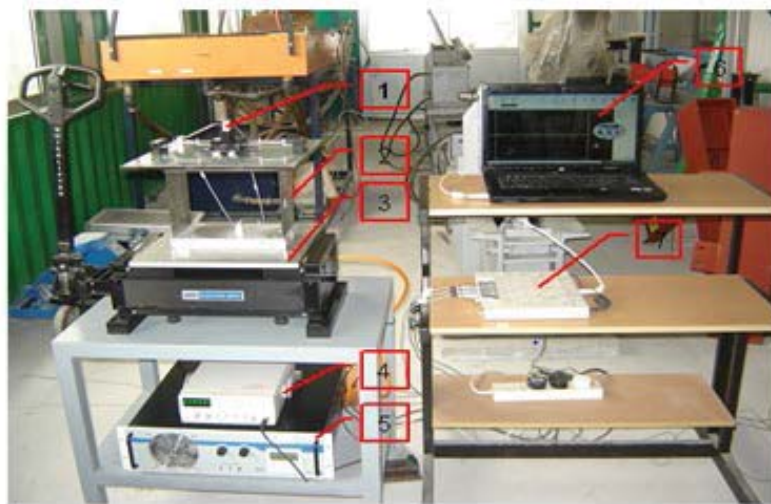


Figure 1: The experimental setup with the model structure

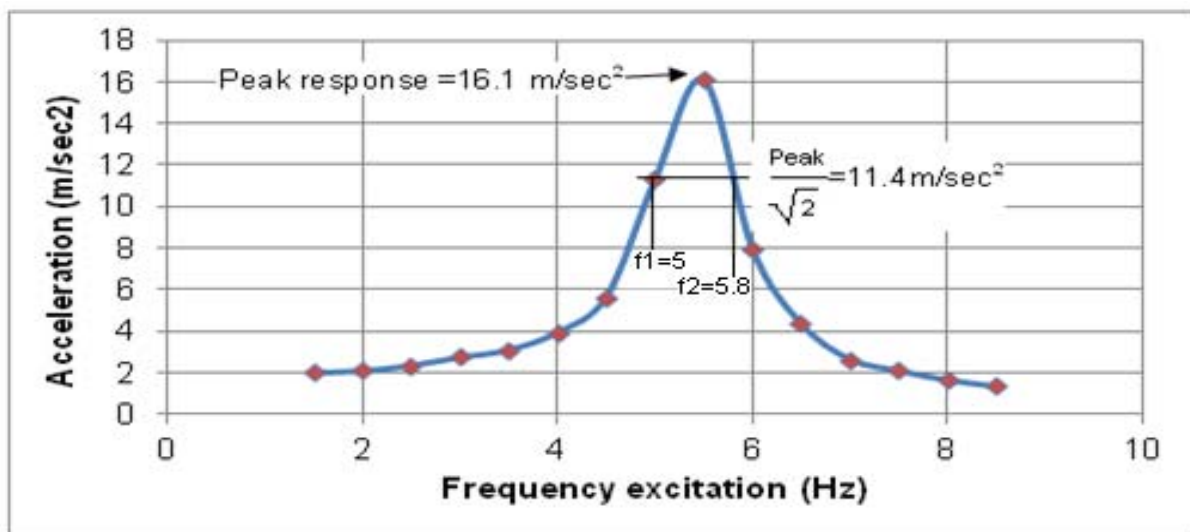


Figure 2: The resonance response of the experimental model



## 2.2 Experimental Rolling Mass (RM) and results from sweep test

At the second stage the design and the manufacture of a single Rolling Mass (RM) was completed. It is a symmetrical system with four rollers, free standing in a metallic plate and able to roll in horizontal direction. At the edge of this plate two rigid metallic systems were fixed. The rolling mass was connected with these rigid metallic systems with springs arranged in symmetrical configuration (figure 3). This system was attached at the platform of the shaking table and was subjected to a range of frequencies of excitations with constant max. base acceleration but with various values of mass of the RM and various values of stiffness of the springs. Before any test the stiffness of the used springs were measured. For each test, the base acceleration as well the response acceleration of the RM were measured and restored. Using these data, the resonance response of the RM, the predominant frequency and the viscous damping were estimated. The results from one case from this sequence of tests are presented in figure 4.

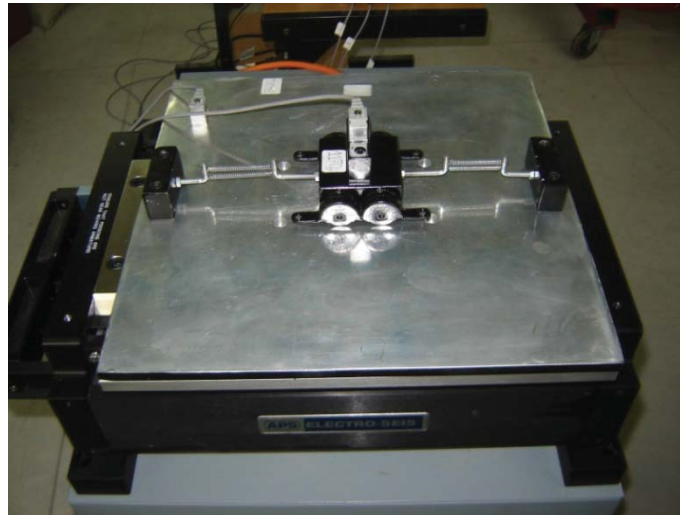


Figure 3: The rolling mass on the shaking table

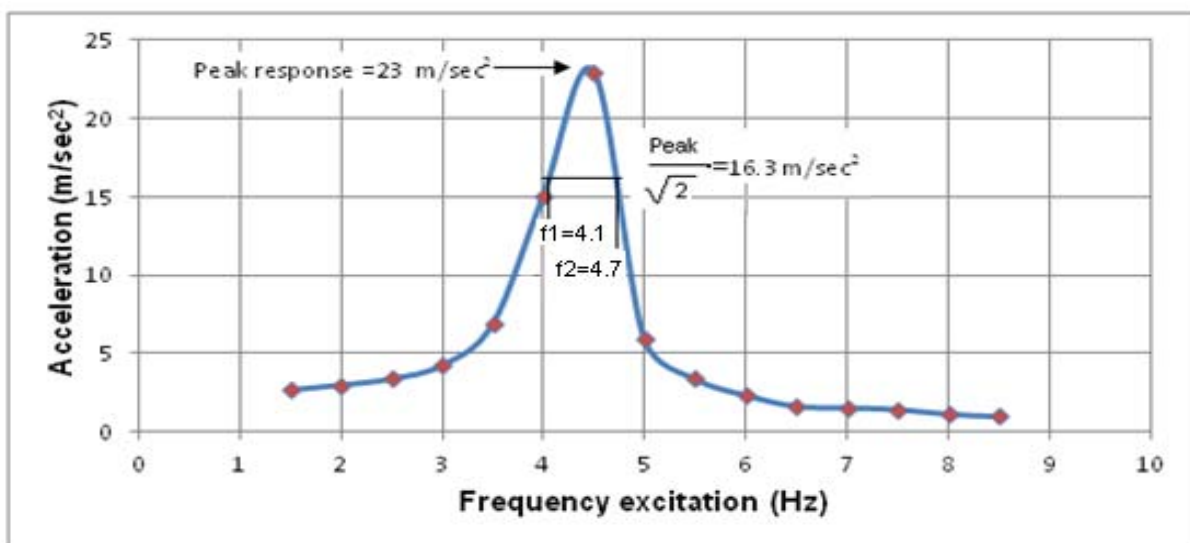


Figure 4: Resonance response of the Rolling Mass (RM)

### 2.3 Experimental model structure with RM and results from sweep test

At the third stage, the system with the RM was attached at the roof of the model structure and was subjected in a large number of sinusoidal base excitations using the same range of frequencies and max. base acceleration as in the previous tests (figure 5). The results from a test are presented in figure 6 and correlated with those from the resonance response of the experimental model without the RM. As can be seen the response of the experimental model with RM is reduced drastically in a narrow band of frequencies closed to the resonance frequency (figure 6). However, two other peaks of the response of this system with RM are occurred but with lower level of amplitudes, one at the left of the resonance frequency with frequency F1 and one at the right with frequency F2. The left one represent the case with in-phase response of the RM with that of the model structure and the right one the case of the out-of-phase response.

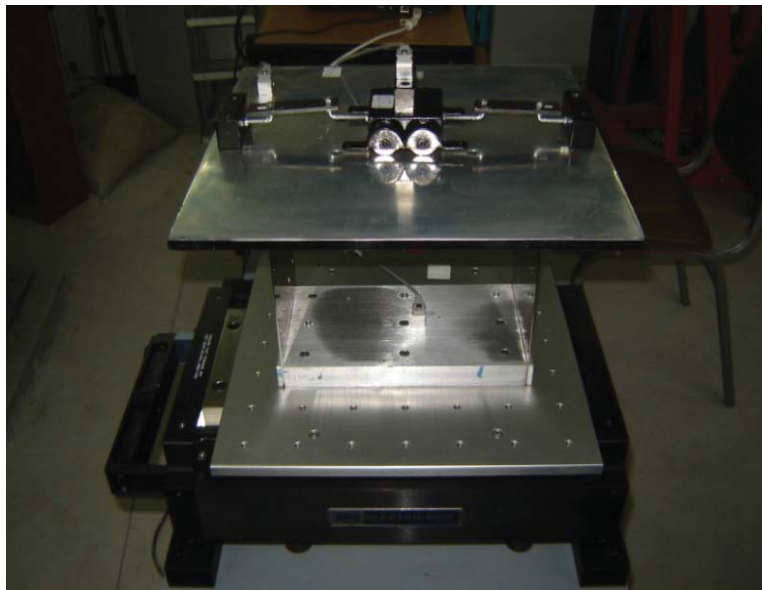


Figure 5: The experimental model with the RM on the shaking table

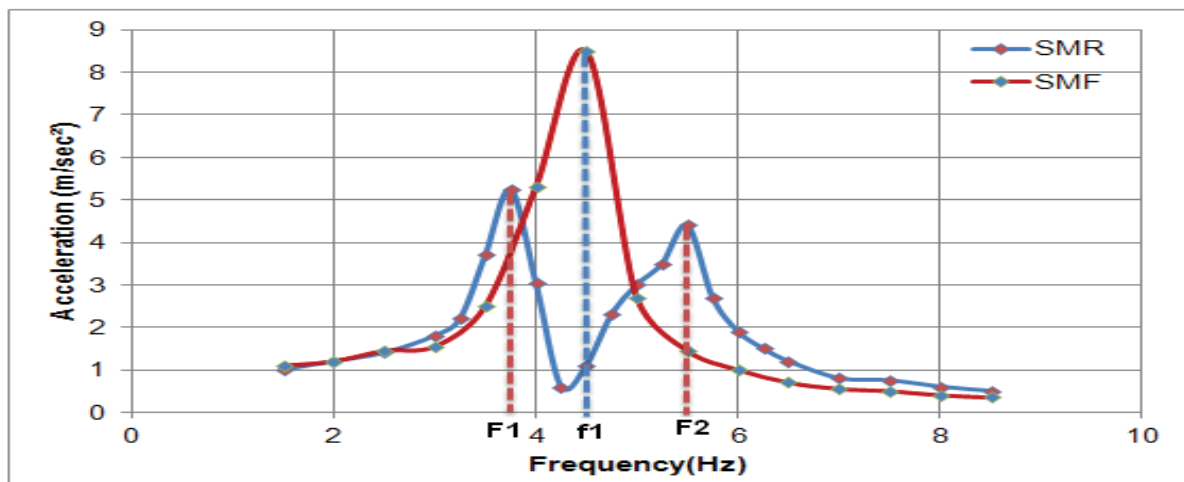


Figure 6: Correlation of the resonance response of the experimental model without the RM (SMF) with the response of the same model with the RM (SMR)

## 2.4 Results from experimental parametric investigations

An extended parametric investigation with 13 sweep tests were completed in order to examine the influence of the mass and the predominant frequency of the RM to the response of the model structure. In the first case, the mass ratio ( $k = \text{mass of RM} / \text{mass of model structure}$ ) was kept constant ( $k=16\%$ ) but the frequency of RM was changed from test to test ( $\delta = \text{natural frequency of RM} / \text{natural frequency of model structure}$ ) using different springs. Seven sweep tests were completed in the same range of frequencies and constant max. base acceleration as before. The results from this investigation are presented in figure 7. As can be seen, the response of the model structure with RM is changed drastically from test to test. In the second case, the ratio of frequencies was kept constant and equal to one ( $\delta=1$ ) and the ratio of mass ( $k$ ) was changed from test to test fixing additional masses on the RM. The results from six sweep tests are presented in figure 8. As can be seen, in this case the response of the model structure with RM is more constant. However, it was founded out that the lower amplitude of the response is occurred in the case when the ratio of the mass of the RM over the mass of the model structure is 10% ( $k=10\%$ ).

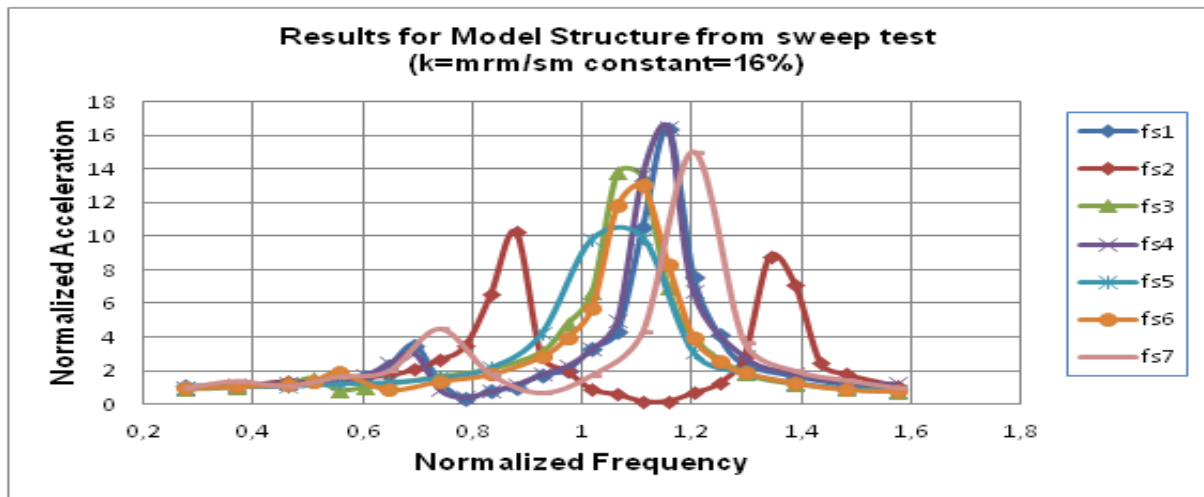


Figure 7: Experimental results of the experimental model with RM from seven sweep tests with constant ratio of masses ( $k=16\%$ )

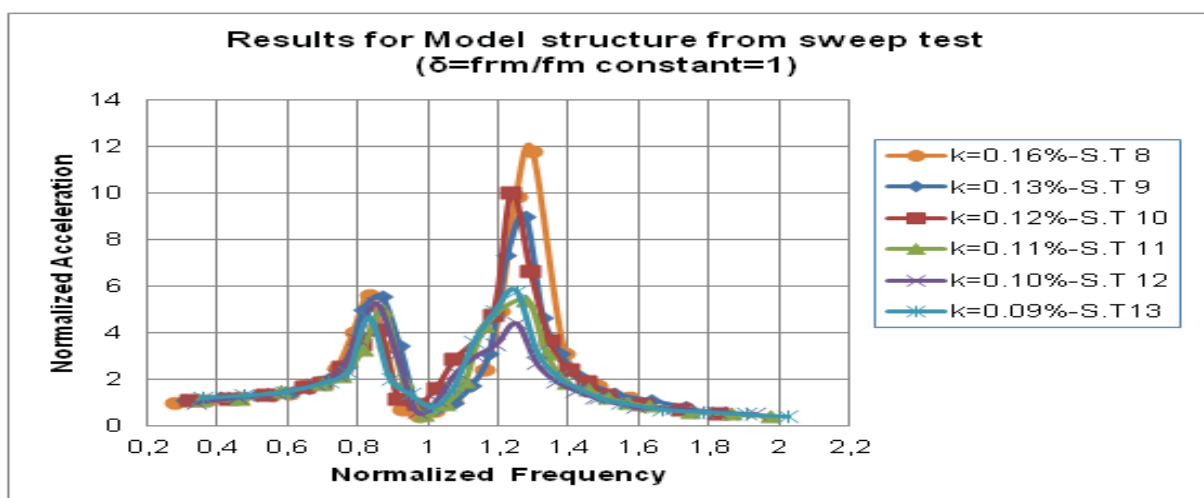


Figure 8: Experimental results of the experimental model with RM from six sweep tests with constant ratio of frequencies ( $\delta=1$ )

## 2.5 Prediction of the fundamental frequencies of experimental model with RM

At first, the assumption that the experimental model without the RM is a Single Degree of Freedom (SDOF) system is adopted. Therefore, the case of the experimental model with RM assumed that is a Two Degree of Freedom (2DOF) system. Using analytical methods from structural dynamic theories, the prediction of the fundamental frequencies of the experimental model with RM ( $F_1$ ,  $F_2$ ) and the difference between these two frequencies ( $F_2 - F_1$ ) are estimated. The  $F_1$  corresponds to the 1st mode with the in-phase response of the model structure and the RM and the  $F_2$  corresponds to 2nd mode with out-of-phase response. The predicted results from the analysis of 13 experimental sweep tests are presented in figures 9 and correlated with those which measured during the experimental tests. As can be seen from the diagrams of this figure, there are enough good correlation between experimental results and the predicted values. These observations allowed us to continue the investigation of this problem through numerical simulations as will be presented in the follow section.

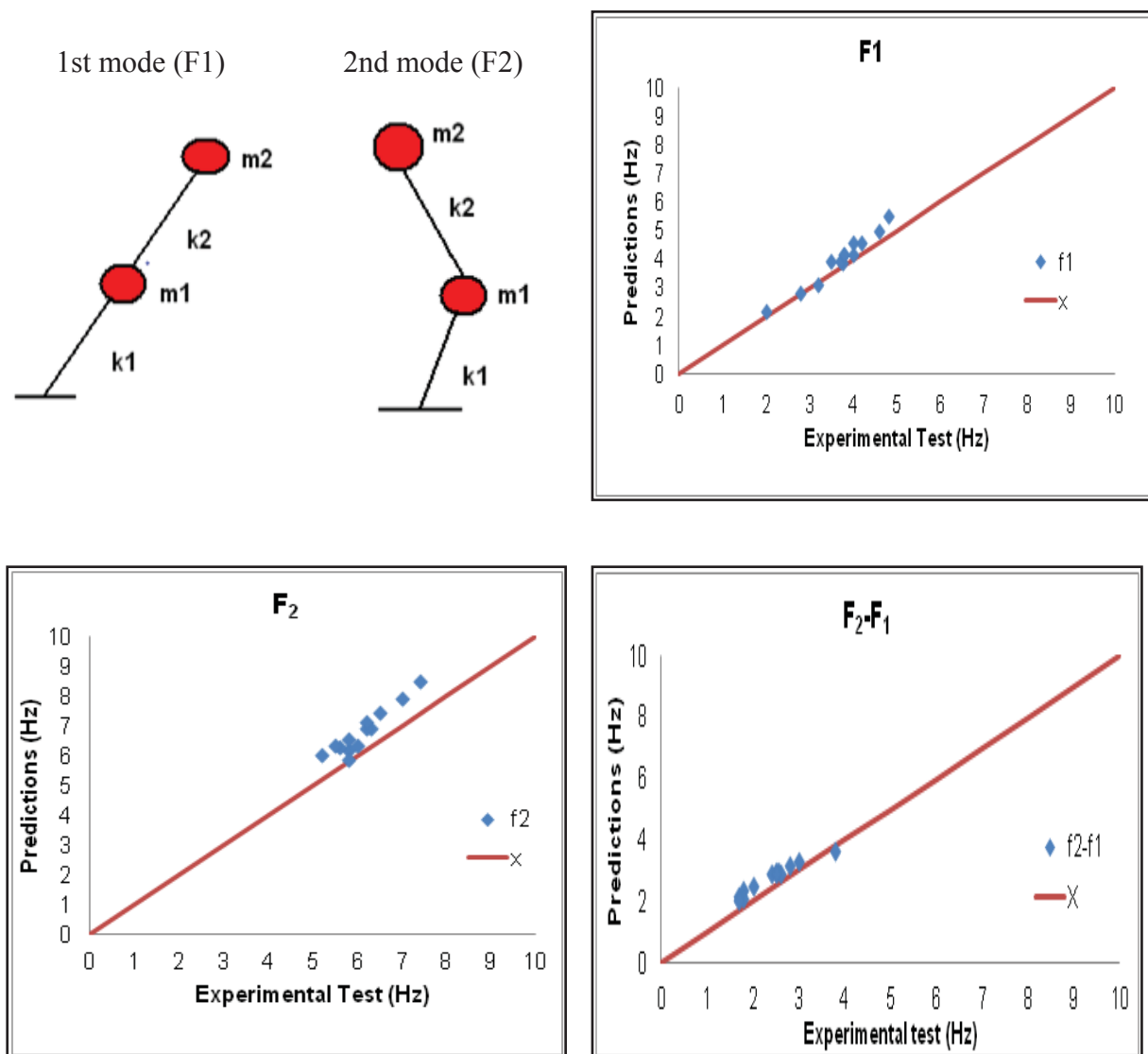


Figure 9: Prediction of fundamental frequencies of the experimental model with RM and correlation with the experimental result

### 3 NUMERICAL INVESTIGATION

#### 3.1 Description of the numerical model

Based on the results from the experimental investigation, a numerical model of one storey frame of a real structure with height 3.0m was designed with or without Rolling Mass (RM) at the roof level. This structural model is consisted by two columns and an horizontal rigid beam. At the first stage, through a modal analysis the predominant frequency of the structural system without the RM was founded out ( $f_0=2.85\text{Hz}$ ). The two columns are expanded over the beam as rigid elements. The mass of the RM was defined to be equal to 10% of the mass of the model of the real structure and to be very stiff using horizontal and diagonal braces. The attach of the RM at the middle of the beam was done through specific supports. The restrictions of these supports were defined in order to allow the horizontal displacement in two horizontal directions but without creation of bending moments, simulating the roller supports of the experimental model. Using horizontal springs, the RM was connected with the rigid elements over the columns in both directions (figure 10). Through an extended numerical investigation the characteristics of the horizontal springs as well those of the specific supports were defined with the main scope the predominant frequency of the RM to be equal to the predominant frequency of the numerical model of the frame structure (2.85Hz). This model structure with RM was subjected in a sweep test for various frequencies keeping constant the max. base acceleration. The shape of the used sinusoidal signal was similar to that developed by the shaking table as it is presented in figure 11.

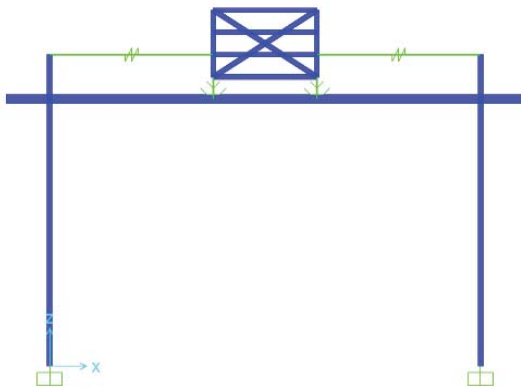


Figure 10: Numerical model of frame system with the RM at the roof

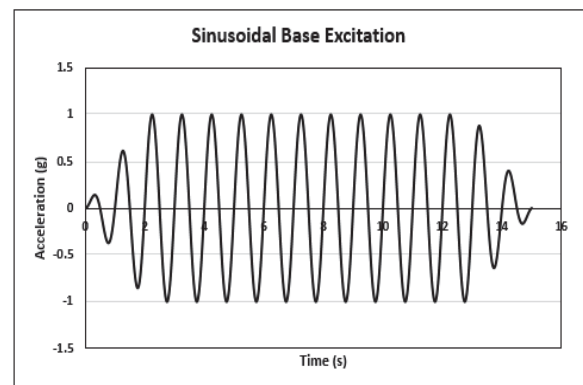


Figure 11: Shape of the sinusoidal base acceleration

#### 3.2 Modal and step by step time history analysis

An extended modal analysis of the numerical models was completed to define the predominant modes of them because the final design of the numerical model with RM is based on the modal characteristics, both the structural system and the RM. As has been mentioned above, at the first stage the predominant frequency of the frame structure without the RM was founded out. At the second stage the characteristics of the used springs and the those of the supports of the RM on the rigid beam were defined with the main scope the fundamental frequency of the RM to be equal to that of the frame system. Finally, the predominant modes of the frame system with the RM were estimated using SAP2000. The first two mode shapes of this model are presented in figure 12 giving also the corresponding values of frequencies. As can be seen, the 1st mode describes an in-phase response of the structural system with that of the RM with  $f_1=2.43\text{Hz}$  and the 2nd mode an out-of-phase response with  $f_2=3.45\text{Hz}$ .



After that, a step by step time history analysis of the structural system with RM was completed using as time history of the base acceleration the shape which was presented in figure 11 and for various values of frequencies and max. base accelerations. The results from two cases are presented in figures 13 & 14. In the first case (figure 13) the frequency excitation was equal to the fundamental frequency of the 1st mode,  $f_1=2.43\text{Hz}$ . The black line correspond to the base acceleration (excitation), the red one to the acceleration response of the frame system and the blue one to the acceleration response of the RM. As can be seen from this figure, there is in-phase response of the frame system with the RM however, the max. acceleration of the RM is much higher than that of the frame system. In the second case (figure 14) the frequency excitation was equal to the fundamental frequency of the 2nd mode,  $f_2=3.45\text{Hz}$ . In this case, out-of-phase response is occurred between the RM and the frame system but also in this case the max. acceleration of the RM is much higher than that of the frame system. All these observations are in a good agreement with those from the experimental investigation.

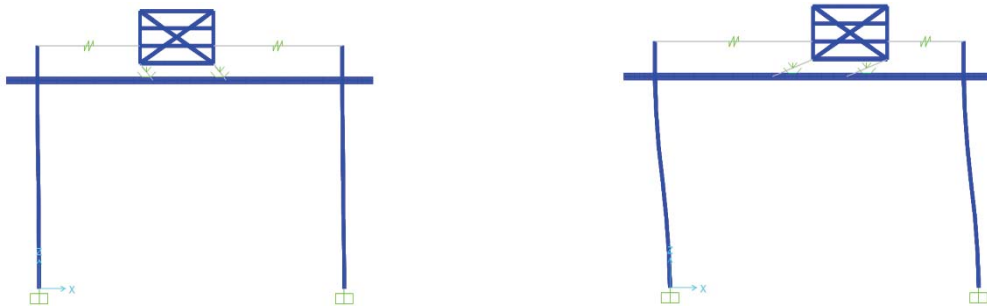


Figure 12: Mode shapes of 1st mode ( $f_1=2.43\text{Hz}$ ) and 2nd mode ( $f_2=3.45\text{Hz}$ ) of the structural model with RM

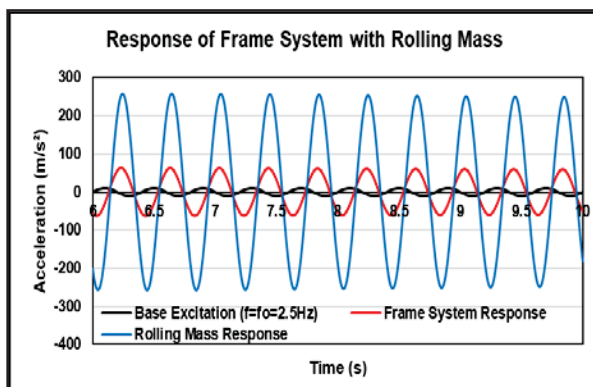


Figure 13: In-phase response - freq. ex.  $f_1=2.43\text{Hz}$

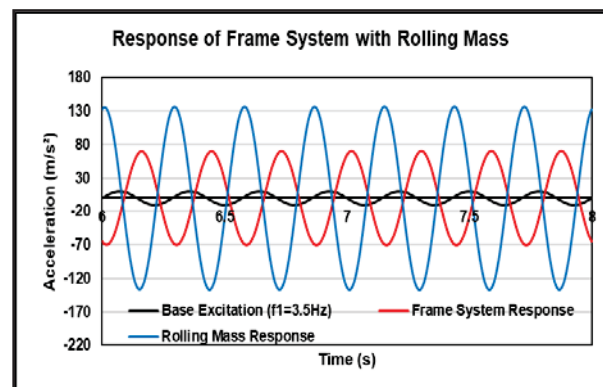


Figure 14: Out-of-phase response- freq. ex.  $f_1=3.45\text{Hz}$

### 3.3 Results for sweep analysis and correlation with experimental results

The numerical models of the frame structure with and without RM attached at the roof beam were subjected in a sweep analysis in a range of frequencies of excitation and constant max. base acceleration. The results from these analyses are summarized in figure 15 in normalized form (response acceleration / resonance max. acceleration response) together with the corresponding normalized results of the experimental model from the sweep tests. As can be seen from this figure there is a good agreement between numerical and experimental results. Some differences between the results of the two models are under investigation.

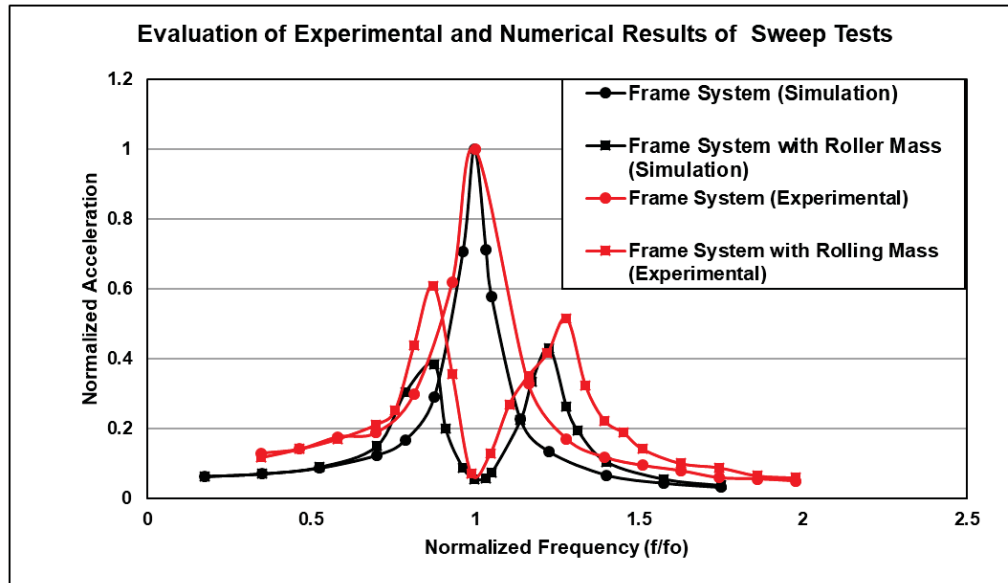


Figure 15: Correlation of numerical and experimental results

#### 4 CONCLUSIONS

Through the experimental and numerical investigation of this paper, the follow conclusions can be made:

- During the experimental investigation it was founded out that the Rolling Mass (RM) can be used in experimental models in order to reduce the resonance response.
- The reduction of the resonance response becomes higher when the mass ratio (mass of the RM / mass of the structure) is equal to 10% and the frequency of the rolling mass is equal to that of the structure.
- In phase and out-of-phase response of RM to that of the frame structure can develop but in both cases the response is much lower than that developed during resonant response of the structure without the RM.
- A good correlation was observed between numerical and experimental normalized results, therefore similar conclusions can be made also from the numerical investigation

#### REFERENCES

- [1] Haga.Y. ed al. (1992). Tuned mass Damper for long-period buildings. Tsukuba, p.p.2311-2317.
- [2] Winkel, B. Keith. L. (2008). Peak-Frequency Responses and Tuned Mass Dampers Exciting Applications of Systems of Differential Equations. UMAP. p30.
- [3] Chey, M-H. ed al. (2009). Energy-dissipative Semi-Active Tuned Mass Damper Building Systems for Structural Damage Reduction. p15.
- [4] Lides, T. (2009). Improving the performance of the semi-active tuned mass damper. Oulu Finland: University of Oulu. p159
- [5] Theodosiou, A. (2012). Experimental investigation of the dynamic response of model structures with active rolling mass, Final Year Project, Department of Civil Engineering, Frederick University, Supervisor, Prof. Milton Demosthenous

## EXPERIMENTAL AND NUMERICAL INVESTIGATION OF A MASONRY MODEL BUILDING SUBJECTED TO DYNAMIC BASE EXCITATIONS

Stefania Demosthenous<sup>1</sup> and Milton Demosthenous<sup>2</sup>

<sup>1</sup>Civil Engineer, MSc Student, Frederick University, Nicosia, Cyprus  
st006796@stud.fit.ac.cy

<sup>2</sup>Dr. Civil Engineer, Professor, Frederick University, Nicosia, Cyprus  
eng.dm@frederick.ac.cy

---

### Abstract

*Many research efforts are continued nowadays around the world to validate numerical tools for masonry structures using at the same time results from experimental works. The present paper belongs in these efforts. At the first stage, this paper deals with the design of a simple masonry building in prototype scale (1:1) including earthquake resistance design. After that, the same structure was also designed in scale 1:10 in order to have the same distribution of stresses under vertical and earthquake loadings, the same level of tensile stresses gravity loadings at the critical zones and the same modes of vibrations under dynamic loadings. From this point of view, it was assumed that this model building in scale 1:10 can develop the same structural behavior with the corresponding prototype. Therefore, this model building in scale 1:10 was constructed and tested using the shaking table of Frederick University. During these tests, the acceleration of the base excitation and the acceleration response of the structure were recorded. Using these measurements from the case of 0.3g response acceleration, the max. dynamic loading of the model was estimated by multiply the response acceleration with the mass of the model. This load was applied to the numerical model with surface finite elements and structural analysis was completed. By the evaluation of the numerical results using Mohr-Coulomb failure criterion, the locations and the type of damages were specified which founded out in a good correlation with the observed damages during the experimental tests. Finally, the same cases of loadings were used for the structural analysis of the prototype structure as well the same procedure for the evaluation of the numerical results. These results developed by the prototype model are correlated with those from the numerical model of the experimental model and discussed.*

**Keywords:** Masonry, finite elements, shaking table, numerical simulations, failure criterion

---

## 1 INTRODUCTION

The protection of the ancient monuments and historical structures is in the main interest for more than 100 years. In order to protect them from bad and catastrophic interventions, international chapters and relevant codes have been adopted and they are in practice in various countries. The documentation of these structures, as the first stage of the works for their protection, includes the structural analysis of them under vertical, seismic and other cases of loadings with the main scope the assessment and evaluation of their existing capacity. At the second stage, one more structural analysis must be completed to examine their capacity for the suggested intervention scheme. However, it is well known that the majority of monumental and historical structures are masonry structures, consisted by stones or bricks which are arranged in various formations and connected with mortars. Therefore, the masonry is a synthetic and inhomogeneous material. In addition to that, the masonry can be characterized as orthotropic and brittle material. On the other hand, the masonry structures are consisted by 2D and 3D structural elements such as walls, piers, arches, vaults, cross vaults and domes having a global behavior during earthquakes much deferent than that of contemporary structures.

For all these reasons, the simulation and the structural analysis of masonry structures is a very complicated procedure. In the past, many techniques were suggested based on many assumptions and with many questions about the accuracy of the results from these methods. The same problems are existing also for the design of new masonry structures, as described by the EC6 (EN1996). The last 40 years, the used methods for the simulation and structural analysis of masonry structures are based on the Finite Element Method (FEM) utilizing computer software. At the first period the 2D models of structures were used simulating the structural elements with linear elements. Approximately, after 1990 the surface finite elements are the most common used elements for the simulation of masonry structures and more recently the solid elements.

However, many research efforts are continued nowadays around the world to validate numerical tools for masonry structures using at the same time results from experimental works. These works use various experimental methods for the testing of materials, masonry walls and models of masonry building structures studied and tested with compressive machines, lateral static or cycling loadings on a reaction frame and using a shaking table to produce dynamic and earthquake base excitations of studied models. In parallel to the experimental tests, various numerical techniques are used, utilizing software of finite elements to simulate the experimental models and study them under the same loading conditions such as those used during experimental investigation. Through this procedure and by the correlation of experimental and numerical results the numerical tools are calibrated and after that they are used for extended numerical and parametric investigations [1, 2, 3, 4].

Following the previous examples and for the same scope, an extended research effort has been established at the Laboratory of Mechanics of Frederick University including testing of materials, experimental tests on models of masonry structures and numerical simulations. The present paper, at the first stage, deals with the design, the construction and testing on the shaking table of a masonry model structure in scale 1:10 [5]. At the second stage numerical simulations and structural analyses of the experimental model was completed using various levels of seismic actions as recorded during the test. The results from structural analyses were evaluated using Mohr-Coulomb failure criterion and the estimated locations of failures are correlated with those observed during the experimental tests. At last, but not least, the same procedure of structural analysis was developed for the corresponding prototype structure (scale 1:1) and the results are correlated with those from the numerical model of the experimental model in scale 1:10 and discussed.

## 2 DESIGN AND CONSTRUCTION OF THE EXPERIMENTAL MODEL

### 2.1 Mechanical properties of the materials

A usual limestone for the construction of monumental and historical structures in Cyprus was used for the construction of the model structure. This stone belong to the Pachna Geological Formation (located at the Tochni area) and was supplied by the Tochni Quarries in units with dimensions of 0.04mx0.03mx0.02m as required for the construction of the model structure in scale 1:10. A lime/sand ratio 1:4 was used for the lime-mortar mixture that was used for bonding the bricks using the thin sand produced from crashing of the Tochni's stone. The dimensions of the timber used for the roof beams were 0.009mx0.019x0.45m.

An extended experimental sequence of tests was performed on the stones, mortar, masonry units and timber, in order to define the mechanical properties of these materials. Three compressive tests of model stone/brick were performed in order to find its compressive strength ( $f_{bc}$ ) and its modulus of elasticity ( $E$ ). Table 1 summarizes these tests for each specimen. The compressive strength of mortar was founded out  $f_{cm}=0.303\text{Mpa}$ . In addition, three compressive tests of masonry triplets were performed in order to find the compressive strength of masonry wall ( $f_{wc}$ ) and the modulus of elasticity ( $E$ ) (table 2). Apart from compressive tests, shear stress tests were also performed in order to identify the shear strength without compression ( $f_{ws}$ ) of the masonry wall (table 3). The masonry tensile strength ( $f_{wt}$ ) was assume to be equal to the shear strength. These properties were used for the simulation, structural analysis and evaluation of numerical results for both, the prototype building structure (scale 1:1) and the experimental model (scale 1:10).

STONE 4cm X 3cm X 2cm	$f_{bc}$ (MPa)	$E_b$ (MPa)
SPECIMEN1 (S1)	49.46	874.67
SPECIMEN2 (S2)	48.24	867.77
SPECIMEN3 (S3)	43.7	769.73
Average	47.13	837.39

Table 1: Mechanical characteristics of model stones 4cm x 3cm x 2cm

WALL	$f_{wc}$ (MPa)	$E$ (MPa)
TRIPLER 1 (T1)	14.52	880.17
TRIPLER 2 (T2)	15.7	639.91
TRIPLER 3 (T3)	21.96	13.83
Average	17.393	511.303

Table 2: Mechanical characteristics of masonry wall

TRIPLER	$f_{ws}$ (MPa)
T1	0.08
T2	0.1
T3	0.08
Average	0.087

Table 3: Shear testing results of the masonry wall



## 2.2 Design of the prototype masonry building in scale 1:1 and the experimental model in scale 1:10

At first stage a single storey masonry building was designed with dimensions of those of typical traditional houses as build before and until very early of the 20<sup>th</sup> century in Cyprus [5]. The architectural design of such houses was usually consisted by an open plan type of space with dimensions 4.0m x 7.0m and a height of approximately 3.0m. Two door openings with a width of 1.4m are presented at the center of the larger dimension of the plan, while the thickness of the masonry wall is 0.4m. The two opposite large walls are connected at the roof level with timber beams supporting a traditional horizontal roof system covered by soil materials. The structural and earthquake resistance design of this building was completed according to the provisions of EN-1996 (EC6) and EN-1998 (EC8) and the corresponding National Annexes of Cyprus [5]. For that, the same materials properties (stone, mortar, masonry & timber) as used for the construction of the experimental model in scale 1:10 were used.

After that, the same structure was also designed in scale 1:10 and constructed (fig. 1). As can be seen, additional masses were attached at the roof level according to basic rules for the design of experimental models in small scaling. Through this effort the final design of model structure was defined in order to have similar distribution of stresses under vertical and earthquake loadings, similar level of stresses at the critical areas and the similar shapes of the predominant modes of vibrations under dynamic loadings. From this point of view, it is assumed that this model building in scale 1:10 can develop the same structural behavior with the corresponding prototype. The correlation of the first three modes of the prototype structure (scale 1:1) and the model one in scale 1:10 are presented in figure 2. As can be seen there is a good agreement between the two models.

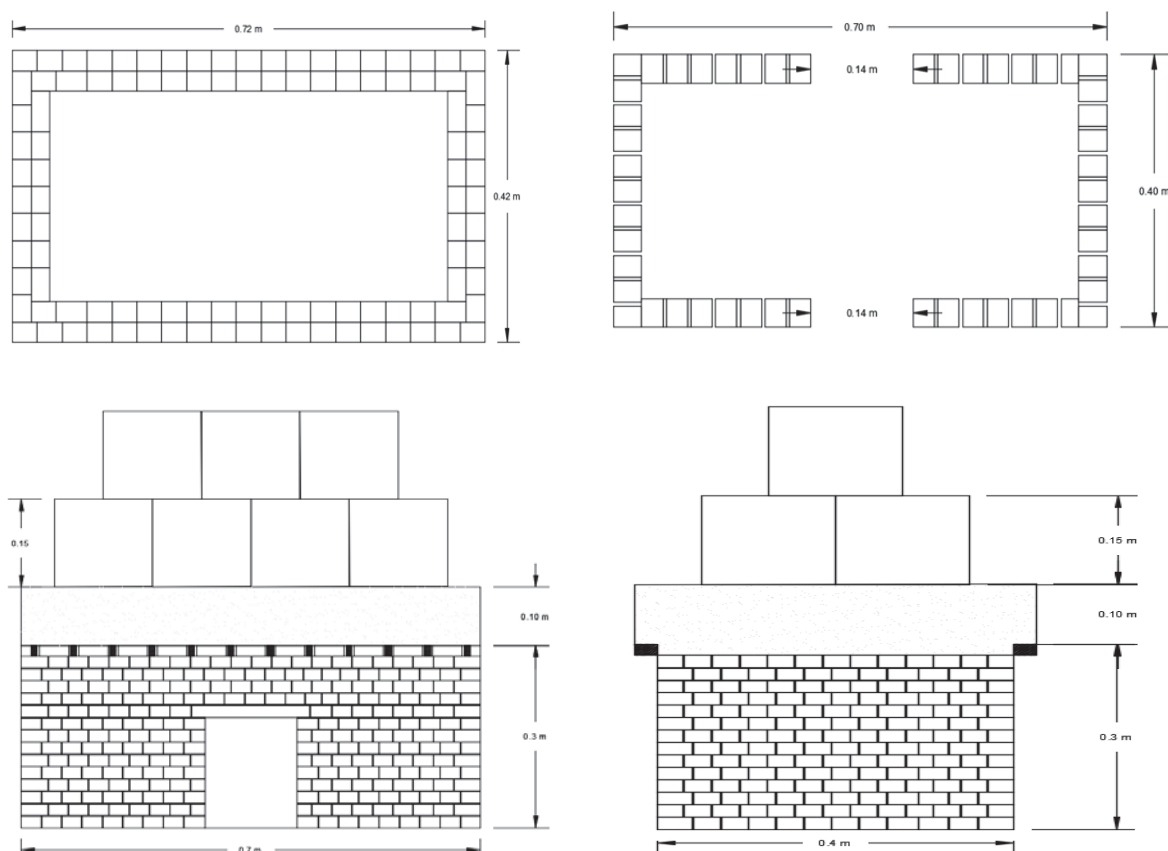


Figure 1: Drawings with the dimensions of the experimental model in scale 1:10

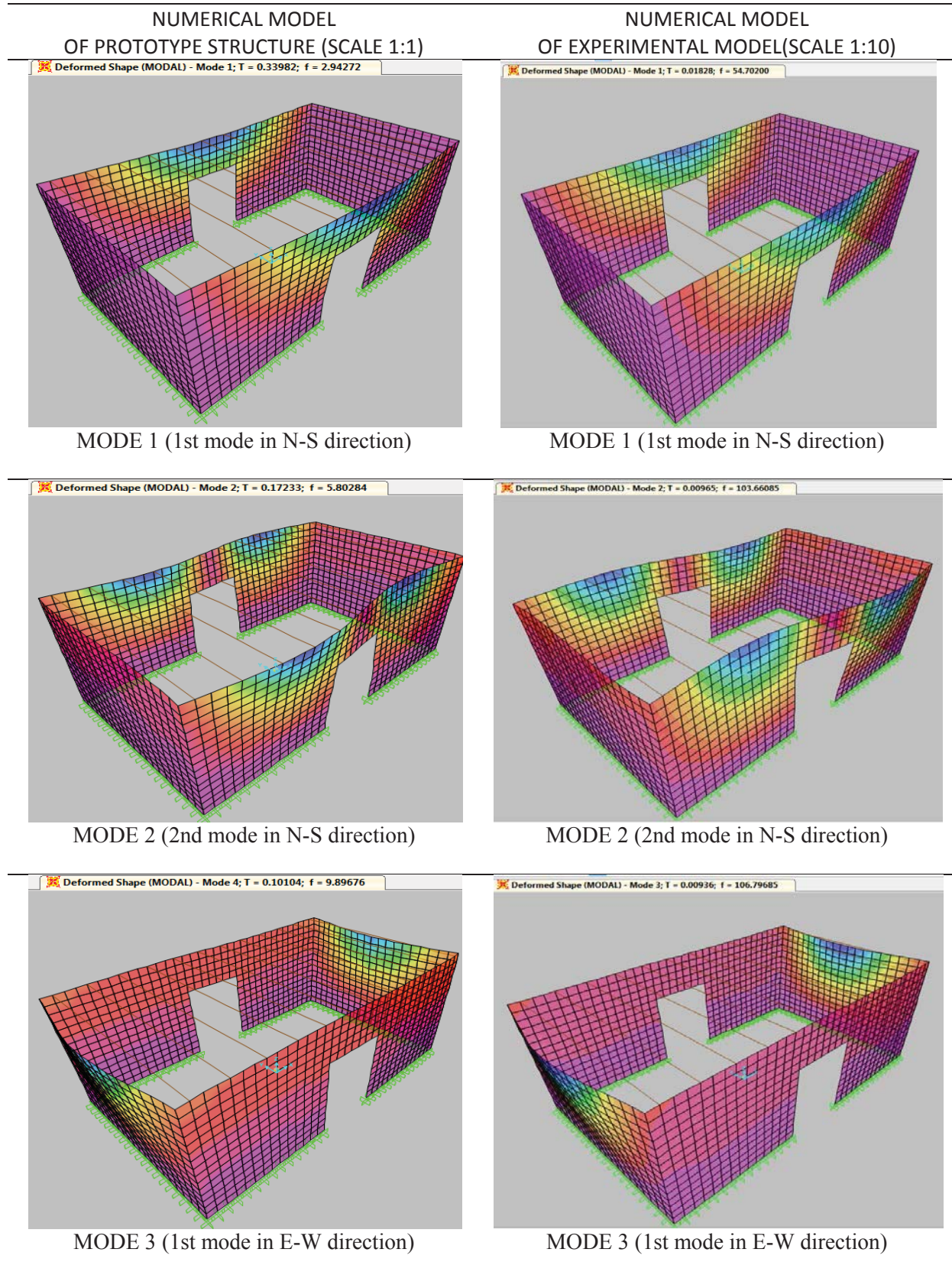


Figure 2: Correlation of the first three modes of the numerical models of the prototype structure (scale 1:1) and the experimental model (scale 1:10)

### 3 EXPERIMENTAL TESTS

#### 3.1 Experimental setup

The model structure was attached at the expanded platform of the shaking table of Frederick University which can move in one direction (E-W) (figure 3). Four accelerometers were used for the recording of the base excitation (CH. 1) and the response of the experimental model at the top of the masonry walls (CH.2, CH.3 and CH.4) (figure 4). One of them attached at the middle of the west wall (CH.2) and one at the middle of the north wall (CH.3). The last one (CH. 4) attached at the edge of the west wall. By the evaluation of the records from this accelerometer with the one from CH. 2, the possible torsional response or out of phase response of the model can be estimated. All these instruments were connected with the data acquisition system for the recording the signals from the excitation and the response of the model.

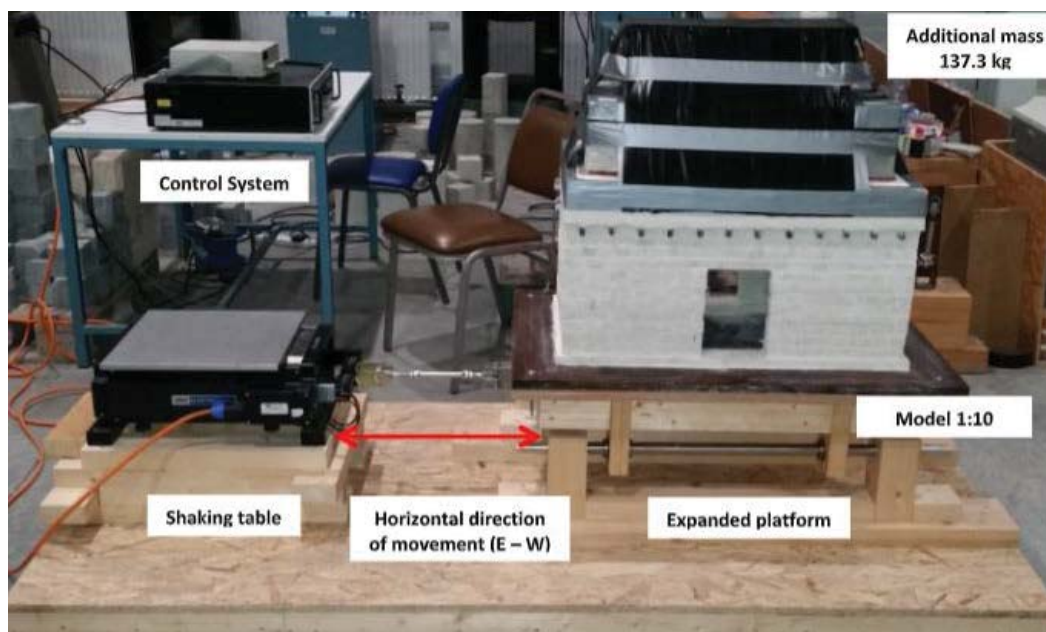
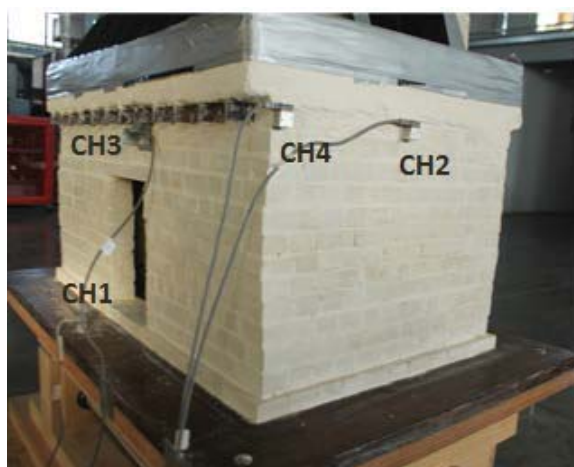


Figure 3: Experimental configuration



- CH1: Base Excitation
- CH2: Mid Top of West wall – (E-W)
- CH3: Mid Top of North wall – (N-S)
- CH4: Edge of West Wall – (E-W)

Figure 4: Instrumentation of the experimental model



### 3.2 Sequence of the experimental tests

The main scope of this effort is to examine the behavior of the model structure under earthquake base excitations. However, at the present investigation, the model structure was tested in various other cases with the main scope to understand its behavior under dynamic loadings. Therefore, the experimental sequence includes:

- Impulse tests for the estimation of the dynamic properties (period and viscous damping) (figure 5). However after the evaluation of these results it was founded out much differences with those from numerical simulations due to the interaction of the system with the shaking table platform. Therefore, an extended sequence of tests are under progress.
- Sinusoidal base excitations in a various range of frequencies and amplitude of the excitations but in low level to avoid the occurrence of damages
- Random white noise base excitations in various levels in order to moderate the occurrence of damages (figure 6). During these tests, damages were occurred when the max. acceleration response in E-W direction was 0.3g.

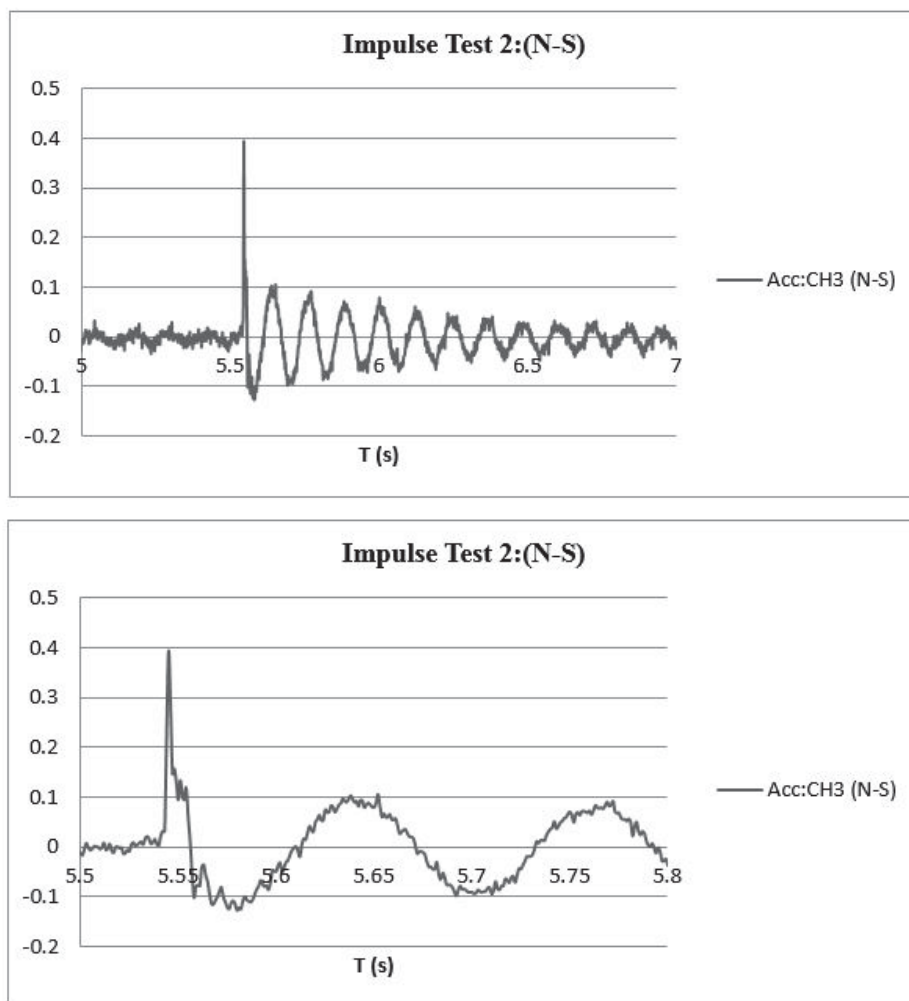


Figure 5: Acceleration records from impulse test in N-S direction

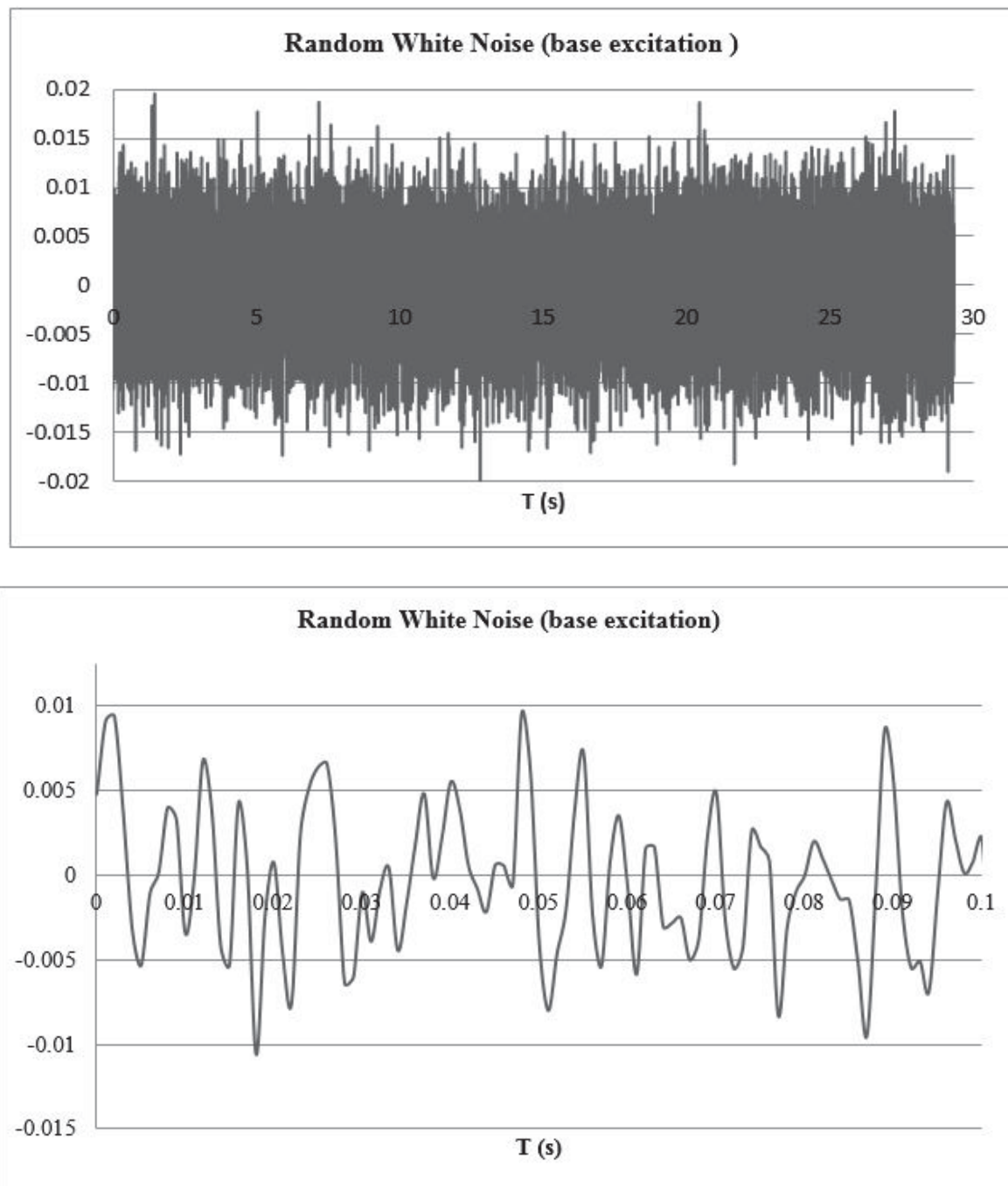


Figure 6. Base acceleration during random white noise

### 3.3 Observed damages

As has been mentioned, during random white base excitations tests, the first damages were observed in masonry walls located in direction E-W. These damages can be divided in two groups. The first group includes cracks at the mortar joints close to the upper corners of the openings which are expanded in diagonal direction up to the roof level. The second group includes also cracks at the mortar joints at the bottom of the corners of the masonry walls (figures 7 & 8). As has been also mentioned in the previous paragraph, these cracks were observed when the max. acceleration response was 0.3g in E-W direction. However, maybe these cracks were created as micro cracks during previous lower level of acceleration response.



Figure 7: Observed diagonal cracks at the corner of the opening and at the bottom corner of the walls

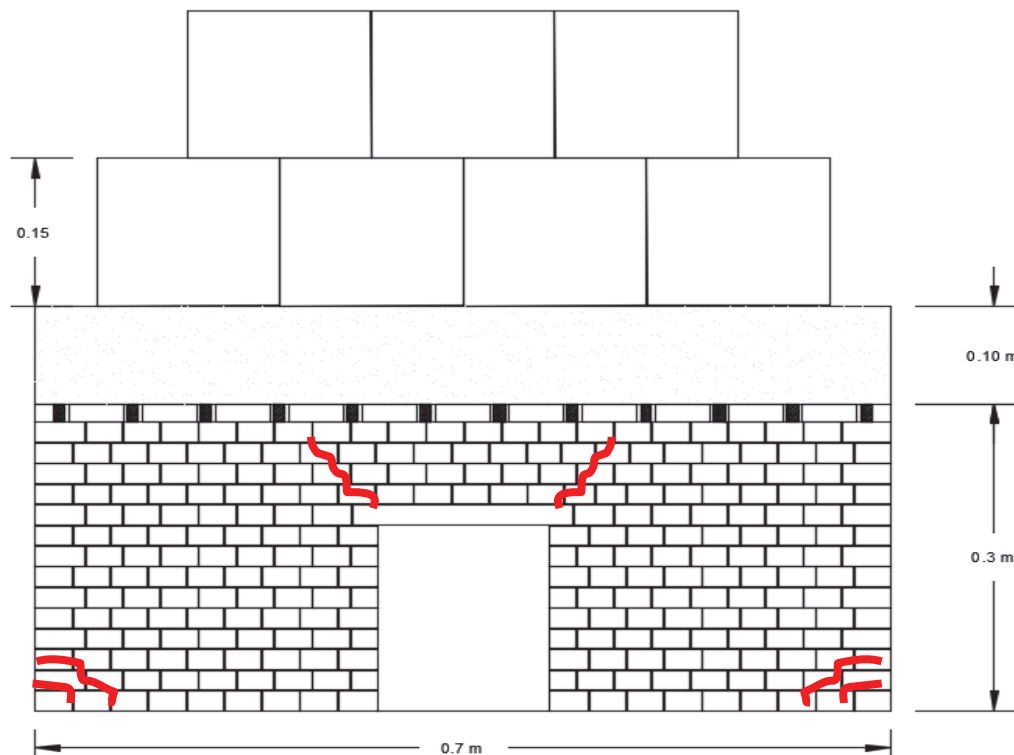


Figure 8: Location of cracks on the facade of the experimental model



## 4 NUMERICAL SIMULATIONS AND STRUCTURAL ANALYSIS

### 4.1 Simulations of loadings and structural system

During the experimental tests it was founded out that the damages were observed when the max. response acceleration was 0.3g. The created loadings on the structural model were estimated through a simple method as explain in what follow (fig. 9). The horizontal seismic force ( $F$ ) at the top of the masonry walls was estimated by multiply the additional masses with the max. value of the recorded acceleration. This force is distributed as horizontal load at the timber beams ( $f_i$ ). The horizontal force from the additional masses creates also a bending moment at the top of the masonry walls ( $M$ ). The vertical loading from the additional masses ( $N$ ) is also distributed at the timber beams ( $N_i$ ) in combination with those created by the bending moment ( $N_{mi}$ ). In addition to that, horizontal loadings are created also on the masonry walls ( $f_{wi}$ ). All these loadings with the gravity load of the masonry wall were used for the study of a masonry wall in E-W direction under vertical loads and horizontal static loadings. A mesh with 2cmX2cm finite elements was used for the simulation of the masonry wall with the assumption of isotropic material using the software SAP200 (fig. 10).

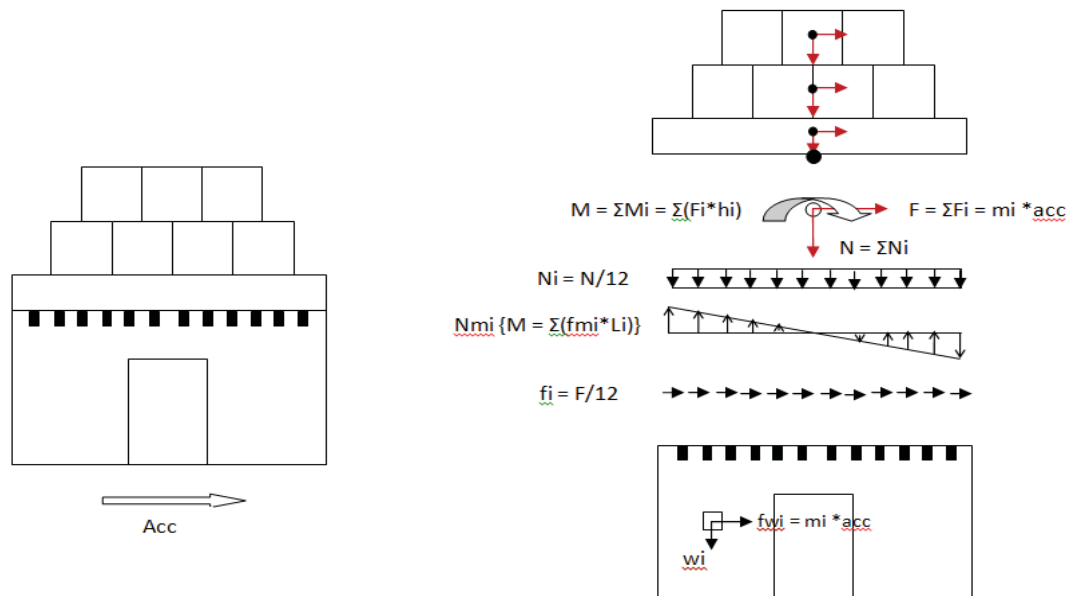


Figure 9. Estimation of the seismic loads

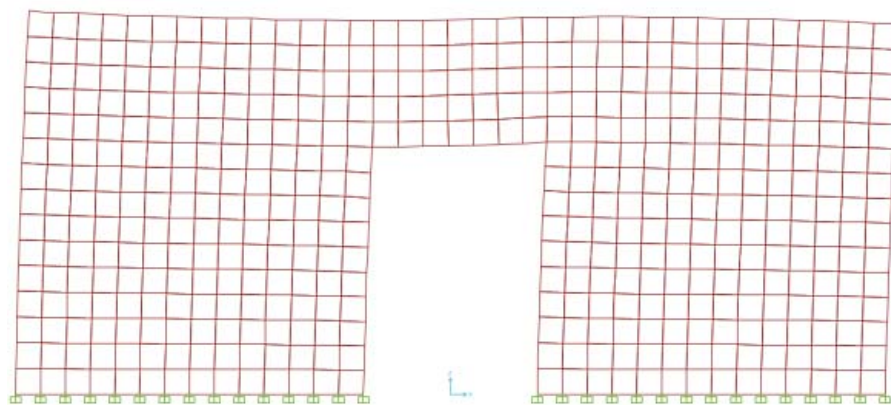


Figure 10. Numerical model under lateral seismic loadings

#### 4.2 Structural analysis and evaluation of the results of the experimental model

The vertical stresses (S22) (compression or tension) of the numerical model are shown in figure 11 as well the shear stresses (S12) in figure 12. From these figures, it can be seen that at the left bottom of the wall significant tensile stress is created however the compressive strength is in lower level in the opposite site. Exactly the opposite will be occurred if the lateral load is applied to the opposite direction. The results of the stresses (S22 & S1) from this analysis were evaluated using Mohr - Coulomb failure criterion ( $\tau$ -  $\sigma$ ). For the design of the envelope of the failure criterion the tensile, the shear and the compressive strength of masonry wall were used as defined from the experimental tests. This evaluation is presented in figure 13. Each point presents the corresponding results of the of shear (S12) and normal (S22) stresses of a joint of a finite element. The points which are in outside area of the failure criterion is mean that the corresponding joint of the finite element is failed. These finite elements are colored in the mesh (figure 13). By the correlation of this mesh with the figure 8 it can be said that the numerical results are in a good agreement with the locations and the type of the observed damages during the experimental test showing only tensile mode of failures.

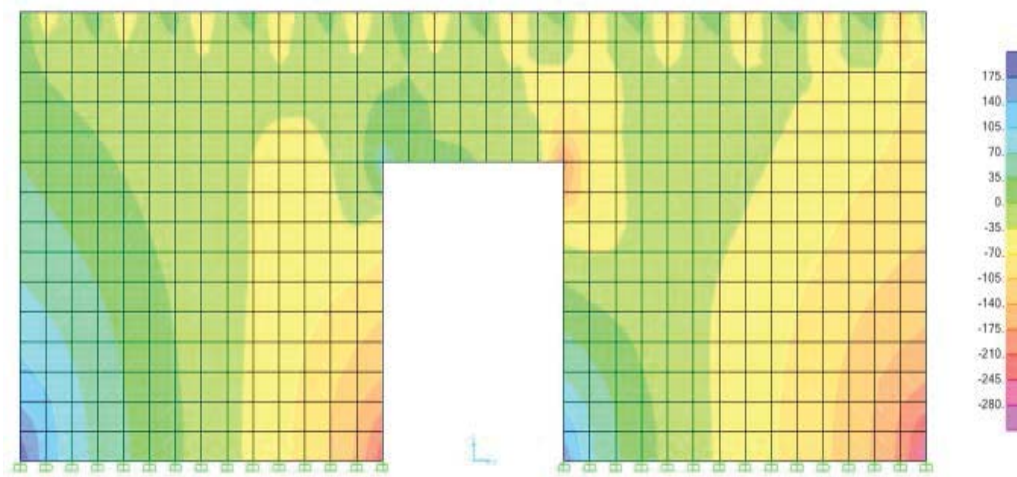


Figure 11. Vertical normal stress (S22) due to vertical and horizontal seismic loadings

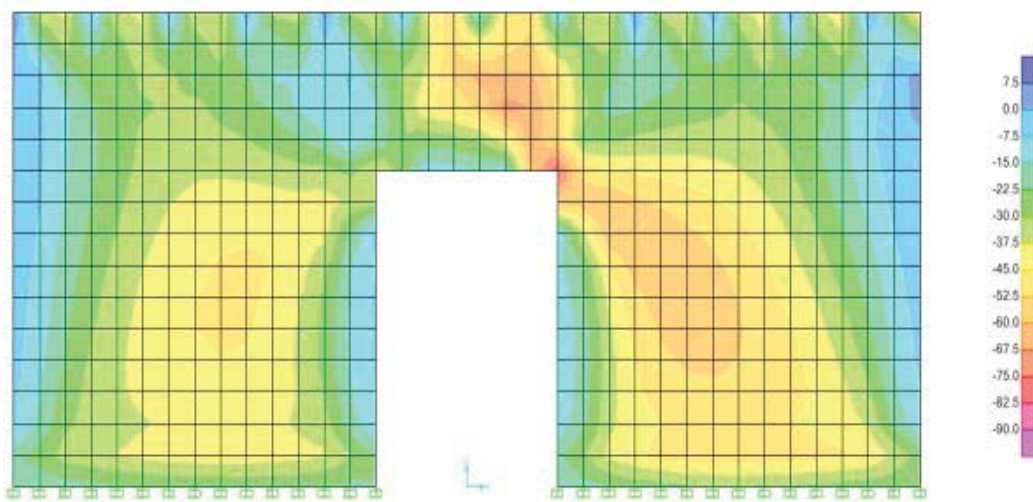


Figure 12. Shear stress (S12) due to vertical and horizontal seismic loadings

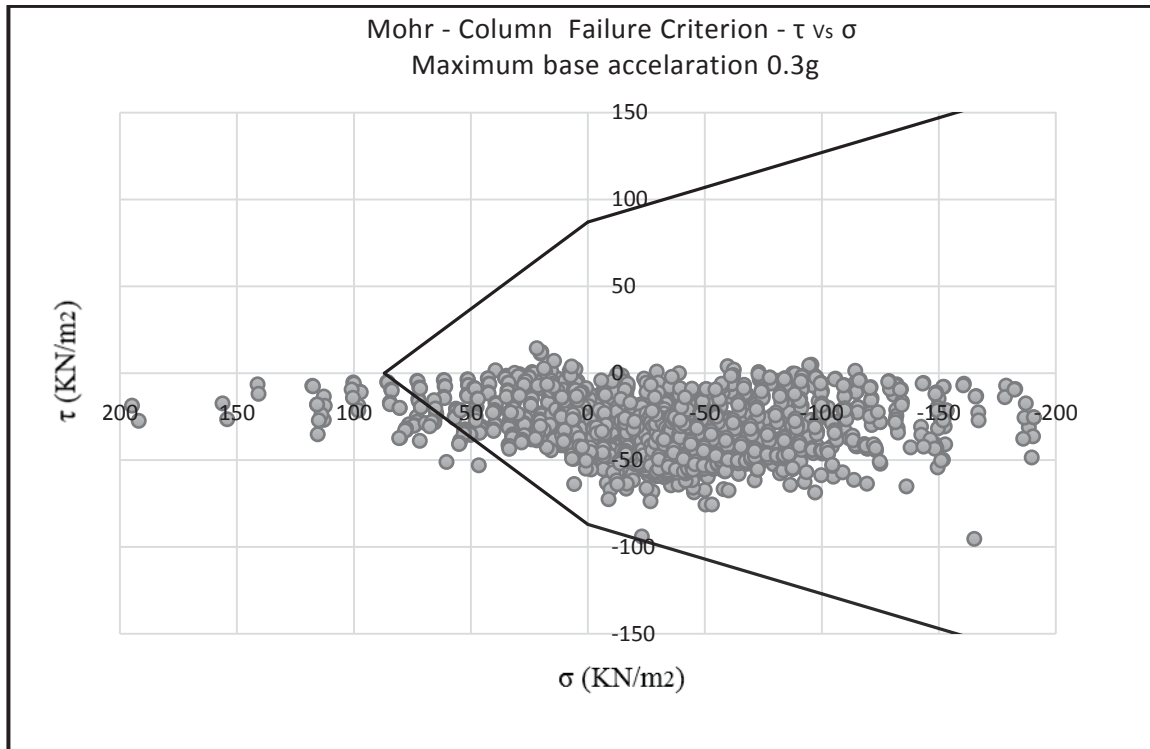


Figure 13. Mohr Column Criterion - Maximum base acceleration 0.3g

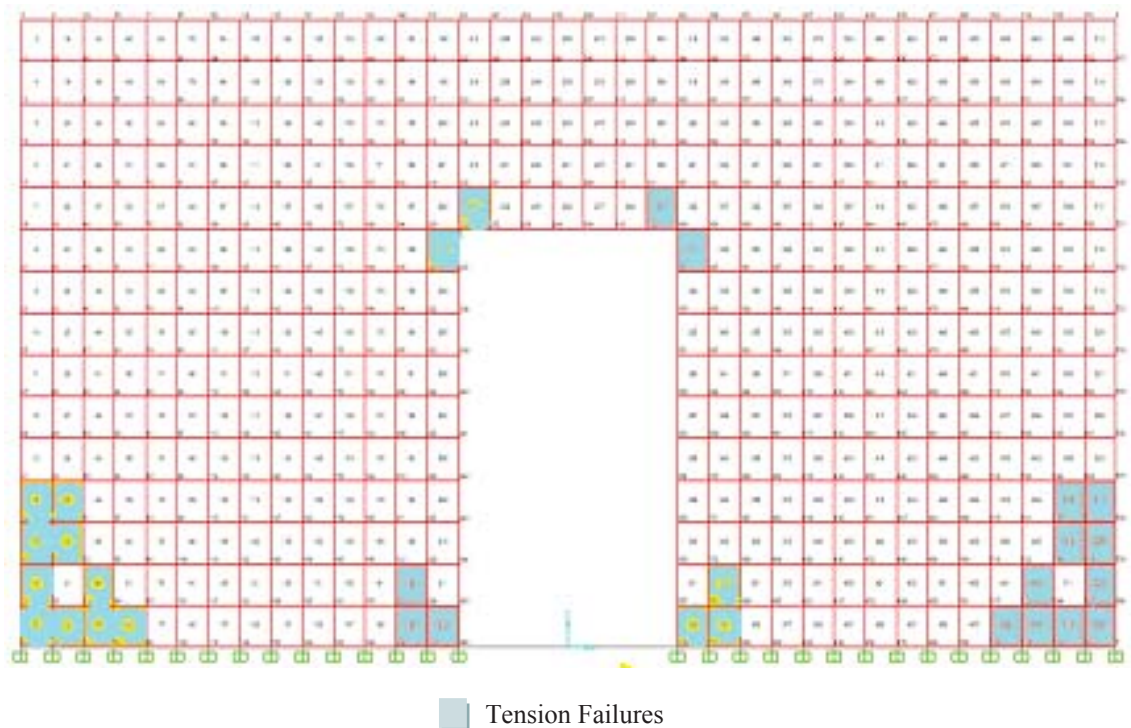


Figure 14. Evaluation of the numerical results with Mohr - Coulomb failure criterion and colored of the finite elements with failure of the experimental model (scale 1:10)

### 4.3 Structural analysis and evaluation of the results of the prototype structure

The same procedure for the simulation of the loadings and the structural system was applied also for the prototype structure defining the max. response acceleration 0.3g. However this system is without additional masses therefore the loadings due to the response acceleration are created only on the roof system and the masonry walls. Although the we have the same distribution of vertical normal stresses (S22) and shear stresses (S12), the max. values of these stress were founded much higher than those developed in the case of the experimental model. Also, for the evaluation of the numerical results the Mohr - Coulomb failure criterion was used with the main scope to find the location and the type of failures.

As can be seen in figure 14, the combination of vertical normal stresses (S22) with the shear stresses (S12) of more joints of the finite elements were founded to exceed the failure criterion. On the other hand, we can see that except of the exceed of the tensile stresses there is also a significant exceeding of the shear strength at the area with lower level of normal stresses which define cracks of the joint mortars. The joints of finite elements and the corresponding finite elements with exciding of the level of stresses defined by the envelope of the failure criterion are colored in the mesh (figure 14). By this figure we can see that the tensile failures on the numerical model of prototype structure are in a good agreement with those occurred on the numerical model of the experimental model. However, and in addition to that as have been mentioned above, shear failures are founded out especially in an horizontal line at the bottom of the wall which can be characterized as sliding mode failures, as well the initiation of diagonal cracks can be mentioned.

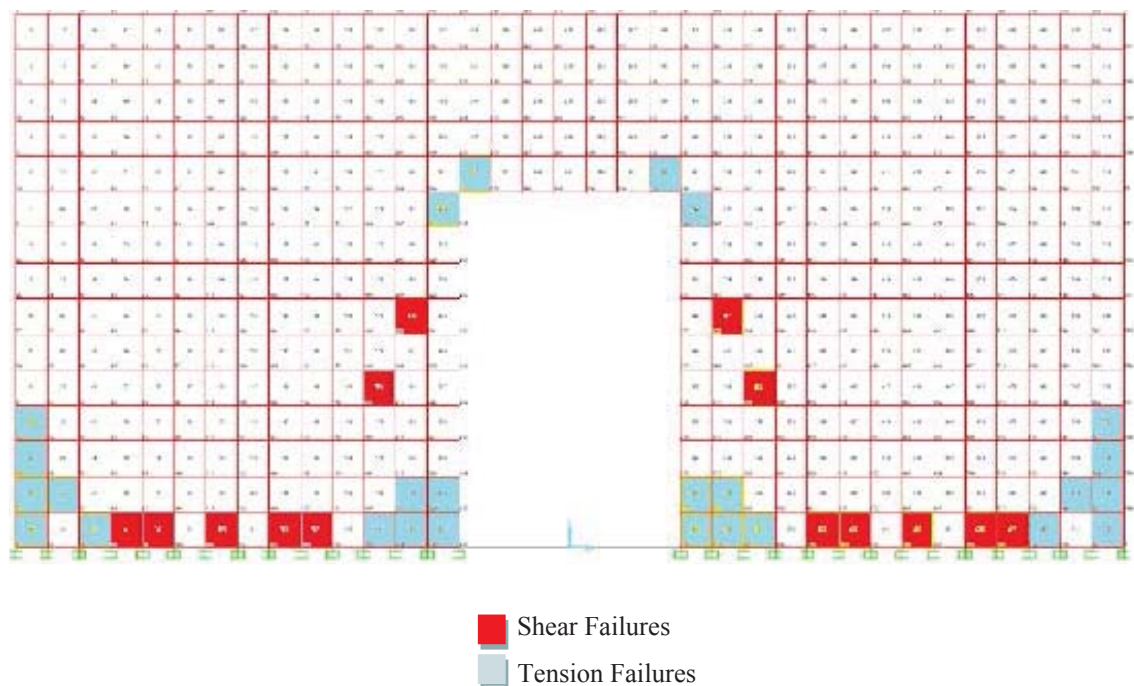


Figure 15. Evaluation of the numerical results with Mohr - Coulomb failure criterion and colored of the finite elements with failure of prototype structure (scale 1:1)



## 5 CONCLUSIONS

Through this effort, a simple masonry building (prototype building in scale 1:10) was designed and at the same time an experimental model building was designed and constructed in scale 1:10 of the prototype building. Specific rules were adopted for that focused on the modal analysis results, the distribution of stresses under vertical loadings and the level of the tensile stresses. The experimental model was subjected in various base excitations using the shaking table of Frederick University. However, before the design and the construction of the experimental model, the mechanical properties of the used materials (stone, mortar, masonry and timber) were defined through experimental tests. The scopes of this effort was:

Firsts, to validate the numerical results from the structural analysis of the experimental model with those from the experimental tests, focus on the correlation of the type and the location of the observed damages, using the Mohr - Coulomb failure criterion for the evaluation of the numerical results. which designed according to the mechanical properties of the used materials. From this point of view it was found out enough good correlation between the experimental and numerical results which both of them developed only bending modes of failures by the exceeding of the tensile strength.

Second, the numerical results of the experimental model (in scale 1:10) to be able to reproduce similar behavior of the prototype one (in scale 1:10), again focus on the observed location and type of damages. From this point of view it can be said that it was founded out differences between two numerical models. Although, in both of them were founded out tensile mode of failures at the same locations of the numerical models, the model of prototype structure developed also shear failures. Due to that, the quantity and the effectiveness of the additional masses applied to the experimental must be checked and resigned.

## REFERENCES

- [1] G.C. Manos, V. Soulis, J. Thawabteh, 2003, "Numerical Investigation of Mortar – Joint Modes of in-plane failure Utilizing Unreinforced Masonry Assemblages", 9th North American Masonry Conference, Clemson Univ., North Carolina, USA
- [2] G.C. Manos, V.J. Soulis, J. Thawabteh, 2003 "Non-linear Numerical Simulation of the Mortar Joints' Failure Mechanism Utilizing Unreinforced Masonry Assemblages", 6th Intern. Symp. on Computer methods in Str.l Masonry, Italy.
- [3] Paulo Candeias, A. Campos Costa, Ema Coelho, 2004, "Shaking table tests of 1:3 reduced scale models of four story unreinforced masonry buildings", 13th World Conference on Earthquake Engineering Vancouver, B.C., Canada
- [4] Lakshmi Keshav, and V. G. Srisanthi, 2012, Masonry CSEB Building Models under Shake table Testing-An Experimental Study, World Academy of Science, Engineering and Technology, International Journal of Civil and Environmental Engineering Vol:6, No:12
- [5] S. Demosthenous, 2016, Experimental and Numerical Investigation of a Masonry Model Building Structure in scale 1:10, Final Year Project, Dept. of Civil Engineering, Frederick University, Supervisor, M. Demosthenous



## PASSIVE CONTROL ISSUES ON THE LONGITUDINAL AND TRANSVERSE VIBRATIONS OF FLEXIBLE PYLONS

George D. Manolis<sup>1</sup>, and George I. Dadoulis<sup>2</sup>

<sup>1</sup> Department of Civil Engineering  
Aristotle University, Thessaloniki 54124, Greece  
e-mail: gdm@civil.auth.gr

<sup>2</sup> Department of Civil Engineering  
Aristotle University, Thessaloniki 54124, Greece  
gdadoulis@civil.auth.gr

---

### Abstract

*The influence of passive mass dampers and base isolators on the vibratory motion of flexible beams with uniform cross-section, viewed as a special case of the non-uniform one, is examined herein for both axial and flexural vibrations. Use of such beams is widespread, both in a mechanical engineering setup (e.g., wind turbines, aircraft blades) as well as in a civil engineering setup (e.g. pylons, antennas). We start with an analytical solution to the governing equations of motion to recover the eigenproperties of a cantilevered pylon in the presence of a top mass and base springs. This is followed by the complete solution for the case of harmonic ground motion using modal analysis. Results are finally presented in term of transmissibility functions, defined as the ratio of the top pylon displacement amplitude to that of the base motion, so as to identify the frequency range where the presence of these external control devices is beneficial.*

**Keywords:** Pylons, Flexible Structures, Vibrations, Passive Control, Elastic Waveguides, Lumped Mass, Soil Springs

---

## 1 INTRODUCTION

The kinematic and stress fields that develop in elastic beams are dependent on the material properties, the geometry and on the external loads. For dynamic loads, retaining a continuous distribution of the mass of the beam along its length yields an elastic waveguide [1,2] that can exhibit flexural, axial and torsional vibrations. Beams in flexure with a non-uniform cross-section are governed by a fourth order, linear partial differential equation (PDE) with variable coefficients, while for the other two modes of vibration the equations of motion are PDE of second order. It is also possible to have coupling between the axial and flexural vibrations, which requires solution of two coupled PDE. Furthermore, if a lumped mass is placed at the top of the beam, or if its foundation is elastic, then the boundary conditions change and are no longer homogeneous. These two additions modify the structural response of the beam and their presence can be viewed as a means of passive structural control. A discussion of the circumstances under which the effects of rotatory inertia and shear deformation must be considered, and whether or not coupling of flexural and axial vibrations is important, have been found elsewhere [3,4]. In general, for flexible pylons serving as part of power transmission lines and as telecommunication antennas, and for the frequency range of ambient vibrations generated by traffic, the aforementioned effects seem to be of minor importance. We note that this frequency range is roughly *20-200 Hz*, with flexural vibrations occurring in the lower part and axial vibrations in the higher part of the spectrum. On the other hand, the Bernoulli-Euler beam theory fails and has to be upgraded to Rayleigh's model with the rotatory inertia of the cross-section included in the equations of motion, for high vibration frequencies in excess of *500 Hz*.

The literature is rich in the solution of continuous beams under dynamic loads [5], but research interest remains strong, because these elements play a pivotal role in structural engineering (e.g., column elements) and in mechanical engineering (e.g., blades). In the interest of brevity, we simply mention here a recent paper [6] on an exhaustive analysis of wind turbines in an offshore environment under all three response modes (bending, compression, torsion) to a variety of environmentally-induced loads. From our perspective, the field of application of this work, which is continuation of a previous publication [4], is structural health monitoring (SHM). More specifically, modern advances in hardware have rendered possible the use of wireless sensors that send signals to a central processing unit, which in turn evaluates them to decide if the integrity of the structure in question has been compromised [7,8]. To stem the flow of large data over time, it is essential that these sensors be equipped with software based on reliable and efficient numerical models representing the structure in question. This way, computations can be carried out locally to produce results against which the recorded signals may be compared. This allows for a first evaluation of the recorded data, which can be discarded if it just shows a routine response of the structure to ambient vibrations. Furthermore, an SHM system can be placed within an artificial intelligence (AI) environment [9], which would serve to monitor the structural response in the absence of an overseer and give alert signals when it becomes evident that the structure in question is experiencing duress due to environmentally induced loads and needs to be inspected.

In here, we examine simple methods for passive vibration protection of a cantilevered pylon used as part of an electric transmission line for railways by formulating the equations of motion for flexural and axial vibrations. The pylon is then augmented with either of two elementary passive structural control devices, namely a lumped mass at the top and a base isolator in the form of springs at the base. The magnitude of the lumped mass has to be relatively small compared to the total mass of the pylon so as to serve as a secondary system [10] whose fixed-base natural frequency can be tuned with respect to the eigenfrequencies of the pylon.

## 2. MATHEMATICAL MODELS FOR NON-UNIFORM BEAMS

We will formulate the mathematical models for the tapered cantilevered pylon shown in Fig. 1, where placement of a lumped mass at the top and of springs at the base serve as rudimentary passive damping devices. Then, the uniform cross-section cantilevered pylon can be recovered as a special case. By considering in Fig. 1 the force and moment equilibrium of a differential segment  $dx$  under distributed longitudinal  $p(x, t)$  and transverse  $f(x, t)$  loads, we obtain the coupled governing equations of motion as

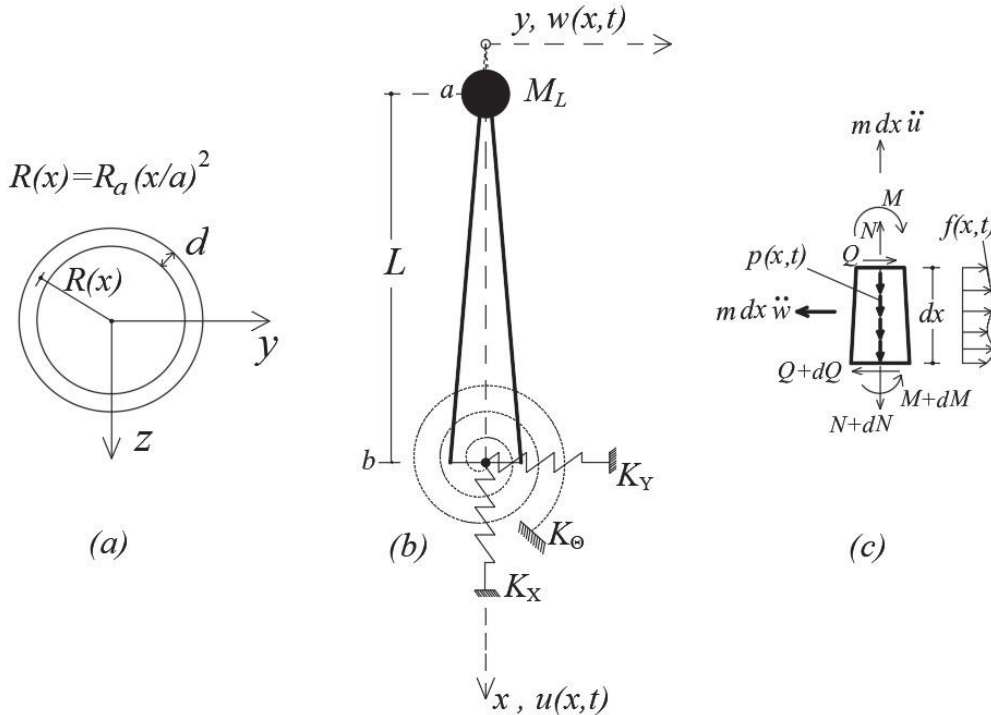


Figure 1. Cantilevered pylon with (a) ring cross-section of variable radius  $R$ ; (b) length  $L$  with added mass and springs at the ends and (c) the free body diagram.

$$\frac{\partial}{\partial x} \left( EA(x) \frac{\partial u(x, t)}{\partial x} \right) - \frac{\partial}{\partial x} \left[ Q(x, t) \frac{\partial w(x, t)}{\partial x} \right] - m(x) \frac{\partial^2 u(x, t)}{\partial t^2} = p(x, t) \quad (1a)$$

$$\frac{\partial^2}{\partial x^2} \left( EI(x) \frac{\partial^2 w(x, t)}{\partial x^2} \right) - \frac{\partial}{\partial x} \left[ N(x, t) \frac{\partial w(x, t)}{\partial x} \right] + m(x) \frac{\partial^2 w(x, t)}{\partial t^2} = f(x, t) \quad (1b)$$

In the above,  $u(x, t)$  and  $w(x, t)$  are the axial and transverse displacements, respectively and  $m(x)$  is the distributed mass. Next, the axial force, bending moment and shear force are defined as  $N = EA(x)(\partial u / \partial x)$ ,  $M = -EI(x)(\partial^2 w / \partial x^2)$  and  $Q = -E \frac{\partial}{\partial x} (I(x) \partial w^2 / \partial x^2)$ .

Initial conditions are assumed to be zero, and three sets of boundary conditions are considered, which respectively address the fixed base case, the fixed base case with a lumped mass at the top, and the base isolated case:

$$M(a, t) = Q(a, t) = N(a, t) = 0 \text{ and } w(b, t) = \partial w(b, t) / \partial x = u(b, t) = 0 \quad (2a)$$

$$M(a, t) = 0, Q(a, t) = M_L \ddot{w}(a, t), N(a, t) = M_L \ddot{u}(a, t) \text{ and } w(b, t) = \partial w(b, t) / \partial x = u(b, t) = 0 \quad (2b)$$

$$M(a, t) = Q(a, t) = N(a, t) = 0 \text{ and } M(b, t) = -K_\theta \partial w(b, t) / \partial x, Q(b, t) = -K_Y w(b, t), N(b, t) = -K_X u(b, t) \quad (2c)$$

In the above,  $x = a$  is the top and  $x = b$  is the base of the cantilevered pylon with length  $L = b - a$ . The lumped mass  $M_L$  placed at the top influences both axial and flexural vibrations, whereas the base springs  $K_X, K_Y, K_\theta$  respectively influence the longitudinal motion, the transverse motion and the base rotation.

## 2.1 Harmonic vibrations

By ignoring the coupling terms  $\frac{\partial}{\partial x} \left[ Q \frac{\partial w}{\partial x} \right]$  and  $\frac{\partial}{\partial x} \left[ N \frac{\partial w}{\partial x} \right]$  for the range of frequencies considered in here, and by differentiating the variable stiffness terms, we recover the following equations:

$$EA(x)u'' + \left[ \frac{\partial EA(x)}{\partial x} \right] u' - m(x)\ddot{u} = -p(x, t) \quad (3a)$$

$$EI(x)w'''' + 2 \left[ \frac{\partial EI(x)}{\partial x} \right] w''' + \left[ \frac{\partial^2 EI(x)}{\partial x^2} \right] w'' + m(x)\ddot{w} = f(x, t) \quad (3b)$$

In the above,  $EA(x)$  and  $EI(x)$  are the aggregate axial and flexural stiffness that varies along the pylon length  $a \leq x \leq b$ . The notation introduced now involves primes (') and dots (·) to denote differentiation with respect to the spatial coordinate  $x$  and time  $t$ .

We now consider a slender, circular cylindrical pylon with a cross-section in the form of an annulus of constant thickness  $d$  and variable radius  $R(x)$ , which is a rather common design for pylons. The reference radius is the mean radius of the cross-section defined as  $R = R_{ext} - d/2$ , where  $R_{ext}$  is the external radius, see Fig. 1. For small thickness  $d$ , the cross-section area, moment of inertia and polar moment of inertia are closely approximated as  $A = 2\pi dR$ ,  $I = \pi R^3 d$ ,  $J = 2I$ , while the mass per unit length is  $m = \rho A$ . We adopt a general representation of a radius that changes quadratically with height, i.e.  $R(x) = R_a \cdot (x/a)^2$ , with  $R_a$  the mean radius at the top. Then, the following expressions for the pylon stiffness and mass are recovered:

$$EA(x) = (EA)_0 \left( \frac{x}{a} \right)^2, \quad EI(x) = (EI)_0 \left( \frac{x}{a} \right)^6, \quad m(x) = m_0 \left( \frac{x}{a} \right)^2 \quad (4)$$

where  $(EA)_0, (EI)_0, m_0$  are reference values computed at the top, i.e. for  $R(x = a) = R_a$ . Note that it is possible to handle material properties that are also position dependent, so long as the aggregate stiffness and mass values obey Eq. (4). We finally note in passing that torsional vibrations are of minor importance as ambient ground vibrations are unlikely to elicit torsion at the base of the shaft.

Assuming a time harmonic environment, the input and the response can be written in terms of position dependent amplitudes times the exponential term  $\exp(i\omega t)$ ,  $i = \sqrt{-1}$ , where  $\omega$  (rad/s) is the frequency of vibration. Therefore, the dependent variables are now the amplitudes of the axial and flexural vibration  $W(x), U(x)$  and we also define the corresponding amplitude of the external distributed forces as  $F(x), P(x)$ . The governing equations for harmonic motion are now

$$[x^2 U'' + 2x U'] + \omega^2 m_0 \left( \frac{x}{a} \right)^2 \frac{a^2}{(EA)_0} U = - \frac{a^2}{(EA)_0} \cdot P(x) \quad (5a)$$

$$[x^6 W'''' + 12x^5 W''' + 30x^4 W''] - \omega^2 m_0 \left( \frac{x}{a} \right)^2 \frac{a^6}{(EI)_0} W = \frac{a^6}{(EI)_0} \cdot F(x) \quad (5b)$$

which respectively are a Bessel equation of fractional order for the axial motion and Euler's equation for the flexural motion.

### 3. SOLUTIONS FOR LONGITUDINAL AND TRANSVERSE VIBRATIONS

To recover analytical solutions to the above equations, we first derive the homogeneous solution and then solve for the eigenvalue problem to recover the eigenproperties of the pylon, first for axial and then for flexural vibrations. The general form of the homogeneous solutions to Eq. (5) in the frequency domain are

$$U(x) = x^{-\frac{1}{2}} \cdot \{A_1 J_{(-\frac{1}{2})}(\alpha x) + A_2 J_{(+\frac{1}{2})}(\alpha x)\}, \quad x > 0 \quad (6a)$$

$$W(x) = B_1 |x|^{r_1} + B_2 |x|^{r_2} + B_3 |x|^{r_3} + B_4 |x|^{r_4} \quad (6b)$$

In the above,  $J_{(q)}$  are the Bessel functions of first kind and fractional order  $q$ , while exponents  $r_i$ ,  $i = 1, 4$  are non-repeated complex numbers. Also,  $A_i, B_i$  are constants of integration to be determined from the boundary conditions.

For flexural vibrations, Euler's equation (5b) requires a preliminary transformation of variables as  $x = e^y$ ,  $y = \ln(x)$  to convert it into a differential equation with constant coefficients. The characteristic polynomial for this differential equation that must be solved for determining the exponents  $r_i$  is  $r^4 + 6r^3 + 5r^2 - 12r - \beta^4 = 0$ . Solution to the aforementioned quartic polynomial yields complex roots in the form  $B_j x^{r_j} = B_j x^{a_j + i b_j} = B_j x^{a_j} \{\cos(b_j x) + i \sin(b_j x)\}$ ,  $i = \sqrt{-1}$ . In our case,

$$\begin{aligned} r_1 &= -\frac{3}{2} + \frac{\sqrt{(17 + 4\sqrt{(4 + \beta^4)})}}{2}, r_2 = -\frac{3}{2} - \frac{\sqrt{(17 + 4\sqrt{(4 + \beta^4)})}}{2} \\ r_3 &= -\frac{3}{2} + i \frac{\sqrt{(4\sqrt{(4 + \beta^4)} - 17)}}{2}, r_4 = -\frac{3}{2} - i \frac{\sqrt{(4\sqrt{(4 + \beta^4)} - 17)}}{2} \end{aligned}$$

with  $W(\xi) =$

$$= \xi^{-\frac{3}{2}} \left( B_1 \xi^{\frac{\sqrt{(k+17)}}{2}} + B_2 \xi^{-\frac{\sqrt{(k+17)}}{2}} + B_3 \sin\left(\frac{\sqrt{(k-17)}}{2} \ln \xi\right) + B_4 \cos\left(\frac{\sqrt{(k-17)}}{2} \ln \xi\right) \right) \quad (7)$$

where  $k = 4\sqrt{(\beta^4 + 4)}$  and for a dimensionless spatial parameter  $\xi \in [1, b/a]$ .

We adopt the Kelvin solid model with a complex elasticity modulus in the form  $E^* = E(1 + i\delta)$ ,  $\delta = \eta\omega/2E$ , where  $E$  is the original real-valued elasticity modulus and  $\eta$  is a constant in the viscoelastic stress-strain law. For concrete, the dimensionless damping coefficient  $\delta$  values have been experimentally determined to range as 1% – 5%, values which respectively correspond to pre-stressed and to weathered concrete. This complex number representation of the elastic modulus filters into the pressure and shear wave speeds  $c_p, c_s$ , and into the wave numbers for axial and flexural vibrations.

If tapering is ignored and the pylon cross-section is uniform with radius  $R_a$ , then the above homogeneous solutions reduce to

$$U(x) = A_1 \cos(\alpha x) + A_2 \sin(\alpha x), \alpha^2 = \omega^2/c_p^2 \quad (8a)$$

$$W(x) = B_1 \cos(\beta x) + B_2 \sin(\beta x) + B_3 \cosh(\beta x) + B_4 \sinh(\beta x), \beta^4 = \omega^2 \frac{\rho A_0}{EI_0} \quad (8b)$$



### 3.1 The eigenvalue problem

The eigenvalue problem derives from imposing homogeneous boundary conditions, see Eq. (2a). The boundary conditions corresponding to the lumped mass and the elastic springs can be rendered homogeneous as well, leading to a more complicated solution for the eigenfunctions  $\Phi_n(x), n = 1, 2, \dots, \infty$ . The corresponding eigenvalues  $f_n$  (Hz) are recovered during this process by solving for the roots of a transcendental equation. More specifically, the solutions given in Eq. (6a) for axial vibrations and in Eq. (7) for flexural vibrations can be respectively recast in matrix form as

$$[G(\omega)][A] = \{0\}, [H(\omega)][B] = \{0\} \quad (9)$$

respectively, with the former matrix size being  $2 \times 2$  and the latter being  $4 \times 4$ . These matrices respectively contain Bessel functions and trigonometric functions evaluated at the two ends  $x = a, b$  of the pylon. By setting the matrix determinants equal to zero and solving for the roots of resulting transcendental equations using the Newton-Raphson method, the eigenvalues of the pylon are recovered. Finally, the eigenfunctions are evaluated starting with a back-substitution of the eigenvalues in Eq. (9) and usually setting one of the coefficients of the vectors  $\{A\}, \{B\}$  equal to one.

### 3.2 External loads

When external loads are present, one can opt to either employ modal analysis or to find a particular solution for the right-hand sides (RHS) of Eq. (5) corresponding to time harmonic forces, in which case the complete solution is the addition of the homogeneous and particular parts. For ambient vibrations in the form of ground motion, a complication arises due to the fact that one must distinguish between the displacement of the cantilever relative to its base, and its total displacement which is the addition of both. The generic form of ground motion, be it in the vertical or horizontal directions, is  $x_g(t) = x_{go} \exp(i\Omega t)$ , where  $X_{go}(m)$  is a mean value for the ground displacements and  $\Omega$  (rad/s) is the frequency of vibration. Assuming  $U, W$  are relative to the base, then the RHS of Eq. (1) are  $f(x, t) = p(x, t) = m(x) \cdot \Omega^2 \cdot x_{go} \cdot \exp(i\Omega t)$ . Two frequency ranges are relevant to the pylons considered here due to the passage of high speed trains: (i) High frequency base accelerations in the vertical direction in the range  $f = \Omega/2\pi = 100 - 200$  Hz that result from the train's wheels running across rails that have minor imperfections and (ii) low frequency base accelerations in the horizontal direction in the range  $f = 20 - 40$  Hz as the train moves rapidly and generates forward travelling elastic waves in the soil.

### 3.3 Mass dampers and base springs

If the pylon has a lumped mass  $M_L$  at the top, one boundary condition for each of the axial and flexural vibrations involves the acceleration at  $x = a$ . In a steady-state environment, these acceleration amplitudes are  $-\omega^2 U(x), -\omega^2 W(x)$ , to which the amplitude of the base acceleration  $\Omega^2 \cdot x_{go}$  must be added. This still allows for a reformulation of the boundary conditions of Eq. (2b) in the homogeneous form specified by Eq. (9). The boundary conditions of Eq. (2c) involving the base isolation springs  $K_X, K_Y, K_\theta$  are simpler to implement because they involve relative displacements. For the flexural vibration case, each of the translational and rotational springs are examined separately. Since the eigenvalue formulation matrix equations resulting from the imposition of the boundary conditions are complex, there is some economy in computation to be gained if their inversion is carried out in closed form. This is trivial for the  $2 \times 2$  matrix  $G(\omega)$  that yields constants  $A_1, A_2$ . It becomes more involved

for the  $4 \times 4$  matrix  $H(\omega)$  that yields constants  $B_1, B_2, B_3, B_4$ , and we give as example in the Appendix the transcendental equation that yields the flexural eigenfrequencies for a lumped mass  $M_T$  at the top of the pylon.

#### 4. EIGENPROPERTIES OF PYLONS WITH PASSIVE CONTROL DEVICES

Following the modal analysis approach previously discussed, we will focus on pylons with a uniform cross-section, as being the more general reference case.

##### 4.1 Longitudinal vibrations

The transient axial displacement for the damped catilevered pylon is as follows:

$$u(x, t) = \{\sum_{n=1}^{\infty} b_n^* \Phi_n(x)\} \cdot (e^{i\omega t}) \quad (10a)$$

$$b_n^* = x_{g0} z^{*2} \cdot \int_0^L \Phi_n(x) dx / \{(k_n^2 - z^{*2}) \int_0^L \Phi_n^2(x) dx\} \quad (10b)$$

In the above, summation is over all  $n = 1, 2, \dots \infty$  eigenmodes, while complex coefficient  $z^*$  has real and imaginary parts given by

$$Re(z^*) = \omega \sqrt{\frac{\rho}{E}} \frac{1}{D} \sqrt{\frac{D+1}{2}}, \quad Im(z^*) = -\omega \sqrt{\frac{\rho}{E}} \frac{1}{D} \sqrt{\frac{D-1}{2}} \quad (11)$$

with  $D = (1 + \delta^2)$ . The eigenfunction is defined in the interval  $0 \leq x \leq L$  as  $\Phi_n(x) = \cos(k_n x)$ .

If a lumped mass  $M_L = R_M M_T$  is placed at the top of the pylon, the axial displacement is

$$u(x, t) = \{\sum_{n=1}^{\infty} b_n^* \Phi_n(x) + ax\} \cdot (e^{i\omega t}) \quad (12a)$$

$$b_n^* = x_{g0} z^{*2} \cdot \{\int_0^L \Phi_n(x) dx + a \int_0^L x \Phi_n(x) dx\} / \{(k_n^2 - z^{*2}) \int_0^L \Phi_n^2(x) dx\} \quad (12b)$$

with coefficient  $a = \frac{x_{g0}/L}{\{(\Gamma^2/\omega^2) - 1\}}$ ,  $\Gamma^2 = \frac{E^*}{\rho R_M L^2}$  and complex coefficient  $z^*$  given by Eq. (11).

##### 4.2 Transverse vibrations

As in the above, reconstitution of the transverse displacement using modal analysis for the damped, flexible pylon with uniform cross-section is given as

$$w(x, t) = \{\sum_{n=1}^{\infty} b_n^* \Phi_n(x)\} e^{i\omega t}, \quad b_n^* = \frac{x_{g0} z^{*4} \int_0^L \Phi_n(x) dx}{(k_n^4 - z^{*4}) \int_0^L \Phi_n^2(x) dx} \quad (13)$$

with the real and imaginary parts of the complex coefficient  $z^*$  given as

$$Re(z^*) = \sqrt{\frac{\omega}{r}} \sqrt[4]{\frac{\rho}{E}} \sqrt{\frac{1}{2\sqrt{D}} + \frac{\sqrt{D+1}}{2\sqrt{2}D}}, \quad Im(z^*) = -\sqrt{\frac{\omega}{r}} \sqrt[4]{\frac{\rho}{E}} \sqrt{\frac{1}{2\sqrt{D}} - \frac{\sqrt{D+1}}{2\sqrt{2}D}} \quad (14)$$

and where  $r = \sqrt{I/A}$  is the radius of gyration of the cross-section. The general form of the eigenfunctions is

$$\Phi_n(x) = \sin(k_n x) + \sinh(k_n x) + C_n \cdot (\cos(k_n x) + \cosh(k_n x)) \quad (15)$$

When a horizontal base spring  $K_Y$  is placed at the pylon's base, then constants  $C_n$  appearing in the eigenfunctions are given below as

$$C_n = \frac{\sin(k_n L) + \sinh(k_n L) - (EI/K_Y) \cdot k_n^3 \cdot (-\cos(k_n L) + \cosh(k_n L))}{-(\cos(k_n L) + \cosh(k_n L)) + (EI/K_Y) \cdot k_n^3 \cdot (\sin(k_n L) + \sinh(k_n L))} \quad (16)$$

Next, when a rotational spring  $K_\theta$  is placed at the base, the new constants  $C_n$  are now

$$C_n = \frac{\cos(k_n L) + \cosh(k_n L) + (EI/K_\theta) \cdot k_n \cdot (-\sin(k_n L) + \sinh(k_n L))}{-(-\sin(k_n L) + \sinh(k_n L)) - (EI/K_\theta) \cdot k_n \cdot (-\cos(k_n L) + \cosh(k_n L))} \quad (17)$$

## 5. NUMERICAL STUDIES FOR A FLEXIBLE PYLON

The aim here is to derive transmissibility ( $TR$ ) functions for both axial and flexural vibrations of a cantilevered pylon serving as part of the network for electrified railway lines. The pylon material is pre-stressed concrete, and the relevant geometric and mechanical properties are given in Table 1 below, including  $M_T$ , the total mass of the pylon. All subsequent computations were carried out in a Python programming environment [11], where computation times did not exceed **8 sec** for the  $TR$  functions that follow, which are parametric in the mass ratio  $R_M = M_L/M_T$  and in the spring  $K_X, K_Y, K_\theta$  constants.

$a$ (m)	$b$ (m)	$d$ (m)	$R(a)$ (m)	$R(b)$ (m)
39.5	49.5	0.0875	0.215	0.3375

$E$ (kPa)	$\rho$ (tn/m <sup>3</sup> )	$m_0$ (tn/m)	$M_T$ (tn)	$\delta$ (%)
$44.4 \cdot 10^6$	2.55	0.301	3.84	5.0

Table 1: Properties of the pre-stressed R/C cantilevered pylon

### 5.1 Preliminary calculations

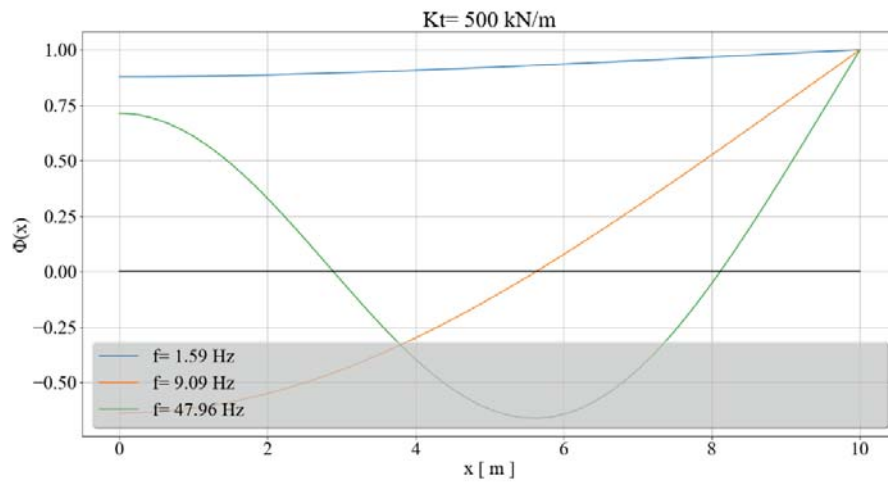
We define an equivalent, uniform cantilevered pylon that has a constant cross-section defined by the base radius  $R(b)$  through-out its height. This is simply done for comparison purposes with the tapered one, and Table 2 lists the first three axial and flexural eigenfrequencies for both types of pylons. We observe that the difference in the first fundamental frequency of the pylon is in the neighborhood of **5%** between the tapered and the uniform cross-section variants. Further such comparison studies can be found in Ref. [4].

Pylon type	$f_1$ (Hz) axial	$f_2$ (Hz) axial	$f_3$ (Hz) axial	$f_1$ (Hz) flexural	$f_2$ (Hz) flexural	$f_3$ (Hz) flexural
Uniform	104.3	312.9	521.6	5.57	34.92	97.78
Tapered	114.0	316.5	523.7	5.84	30.47	80.85

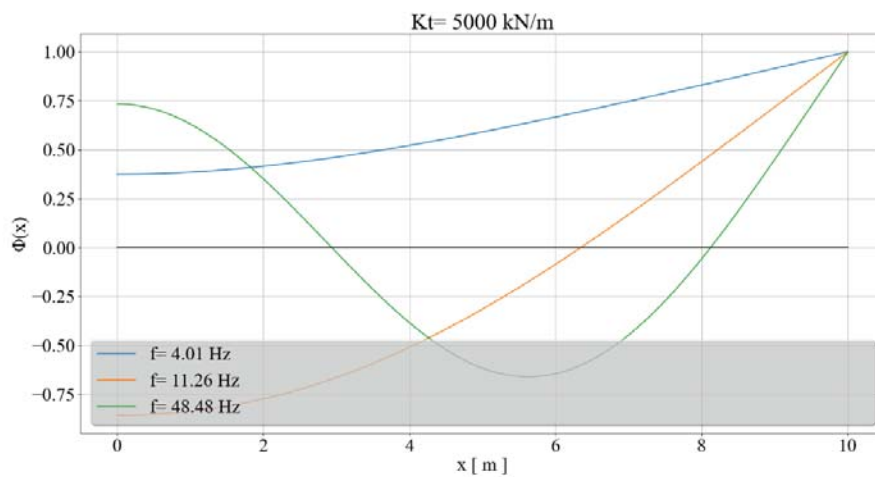
Table 2: Comparison of the eigenvalues between R/C pylon uniform and tapered cross section.

### 5.2 The eigenvalue problem for a base-isolated pylon with a uniform cross-section

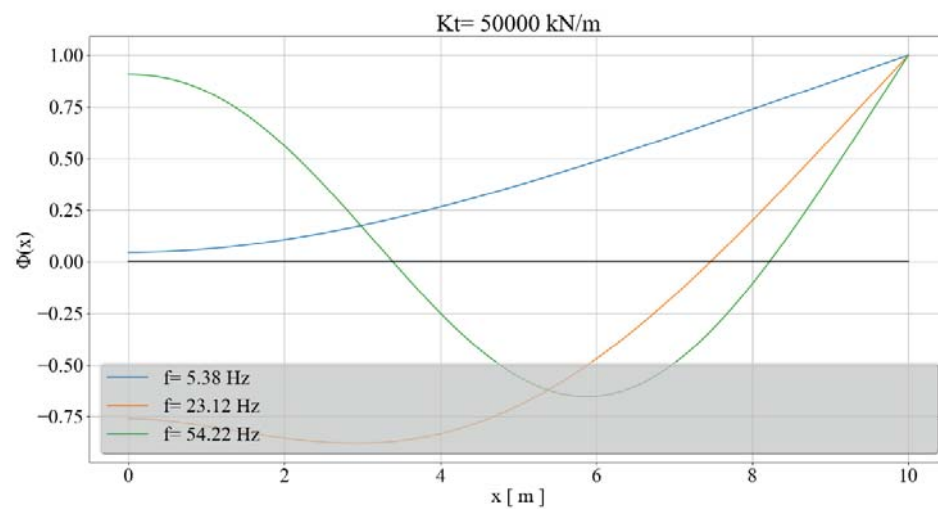
For illustrative purposes, Fig. 2 below shows the pylon's first three flexural eigenmodes for the case of a translational spring  $K_Y$  whose value increases so that in Fig. 2(c) the fixed-base pylon case is recovered.



(a)



(b)



(c)

Figure 2: First three eigenfrequencies and eigenfuntions of a flexible pylon under transverse vibrations as a function of the translational base spring magnitude: (a) Soft spring,  $K_Y=500$  kN/m, (b) intermediate spring,  $K_Y=5,000$  kN/m and (c) stiff spring  $K_Y=50,000$  kN/m.

Also, Fig. 3 is a convergence study on how the first three flexural eigenfrequencies of the base isolated pylon converge to the values for the fixed-base case as the magnitude of the translational and rotational base springs increases

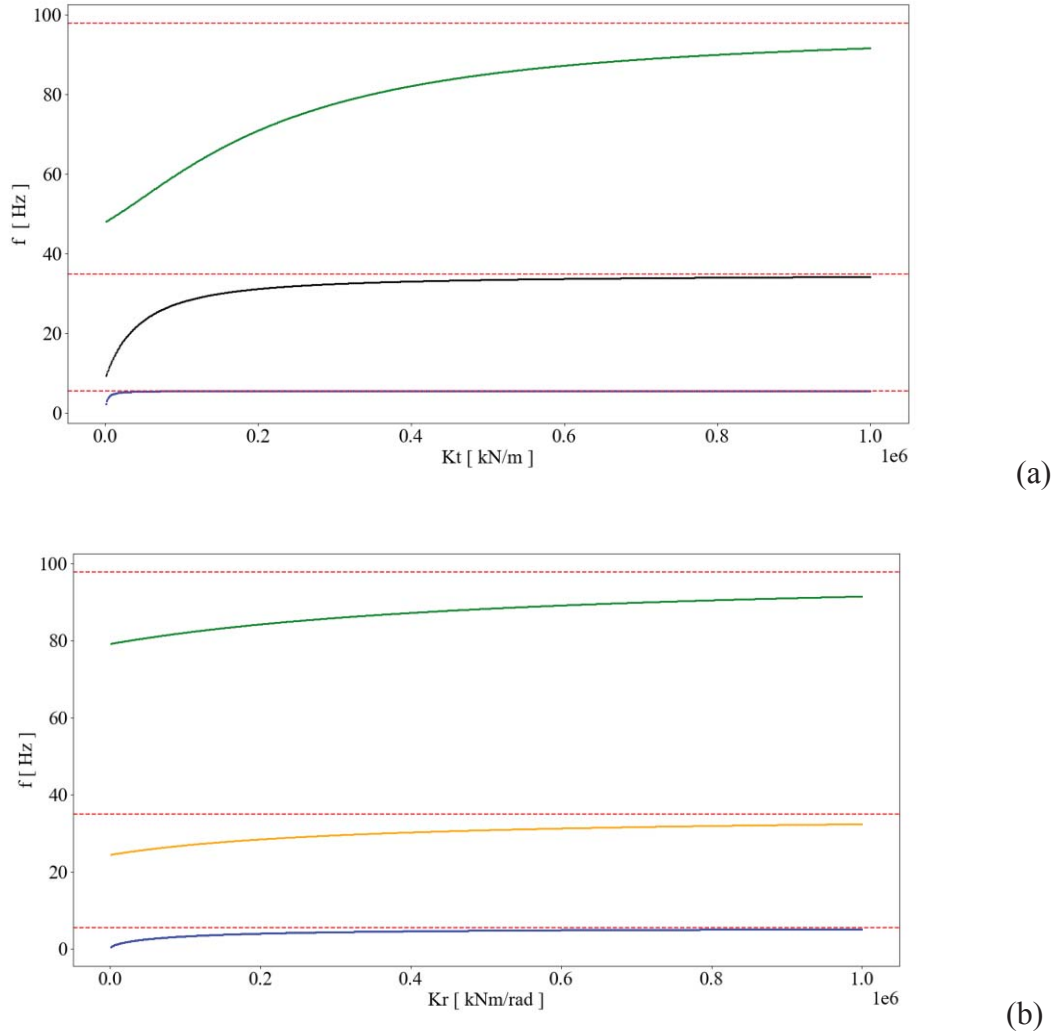


Figure 3: Convergence study on the first three flexural eigenfrequencies of the base-isolated pylon as a function of spring stiffness: (a) translational spring  $K_Y$  and (b) rotational spring  $K_\Theta$ . Note: The dotted red line is for the fixed-base pylon.

### 5.3 Transmissibility functions for longitudinal vibrations

We next proceed to recover  $TR$  functions for the reference case of the equivalent uniform pylon, keeping in mind that tapering basically acts as a perturbation of the first eigenfrequencies of an equivalent pylon with a uniform cross-section. Since the eigenfrequencies of pylons are widely spaced, we resort to  $\log\text{-}\log$  plots. Starting with Fig. 4, we observe that until the first axial eigenfrequency is reached, the presence of the lumped mass at the top is of minor



consequence, but still somewhat detrimental. However, as the frequency continues to go up, the lumped mass starts actively reducing the motion by as much as an order of magnitude, and even a small mass of 10% of  $M_T$  is effective. Note here the emergence of a new eigenfrequency, otherwise absent when there is no top mass. The situation with the vertical base spring is quite different, because at low frequencies, below the first eigenfrequency, we have substantial decrease in the  $TR$  values as compared to the fixed base, which roughly corresponds to the spring with the largest values, namely  $K_X=5 \cdot 10^6 \text{ kN/m}$ . As the frequency goes up, the  $TR$  exhibit minor fluctuations but the motion de-amplification is still substantial.

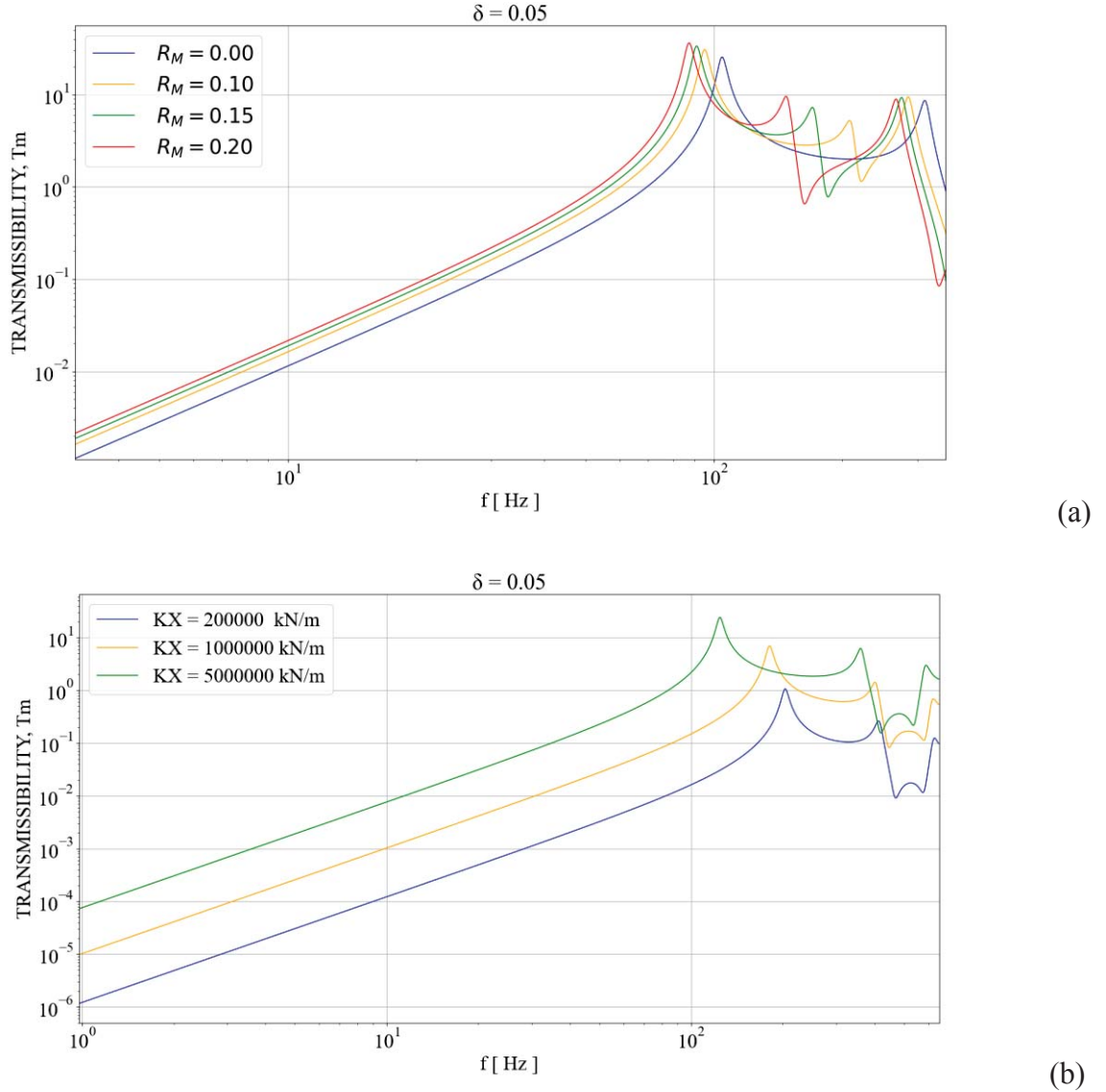


Figure 4: Transmissibility functions  $TR$  between top and ground displacement amplitudes versus frequency  $f$  for longitudinal pylon vibrations under a normalized sinusoidal ground acceleration input and for a damping  $\delta$  value of 5% as a function of: (a) mass ratio  $R_M=M_L/M_T$ ; (b) vertical base spring  $K_X$  values.

#### 5.4 Transmissibility functions for transverse vibrations

We continue with Fig. 5 for flexural vibrations, where the  $TR$  functions for the base isolation springs present a rather complicated situation. Assuming that the highest spring values

approach the fixed-base case, then base isolation springs are ineffective at low frequencies, i.e. those below the first flexural eigenfrequency. As we move past that value, only the horizontal spring is effective in producing de-amplification of motion. Finally, the rotational spring remains ineffective at both the low and high ends of the frequency spectrum, where it shifts the fixed-base dominant eigenfrequency to lower values. It is effective only when the external frequency of vibration approaches a narrow frequency range around the fixed-base pylon eigenfrequencies.

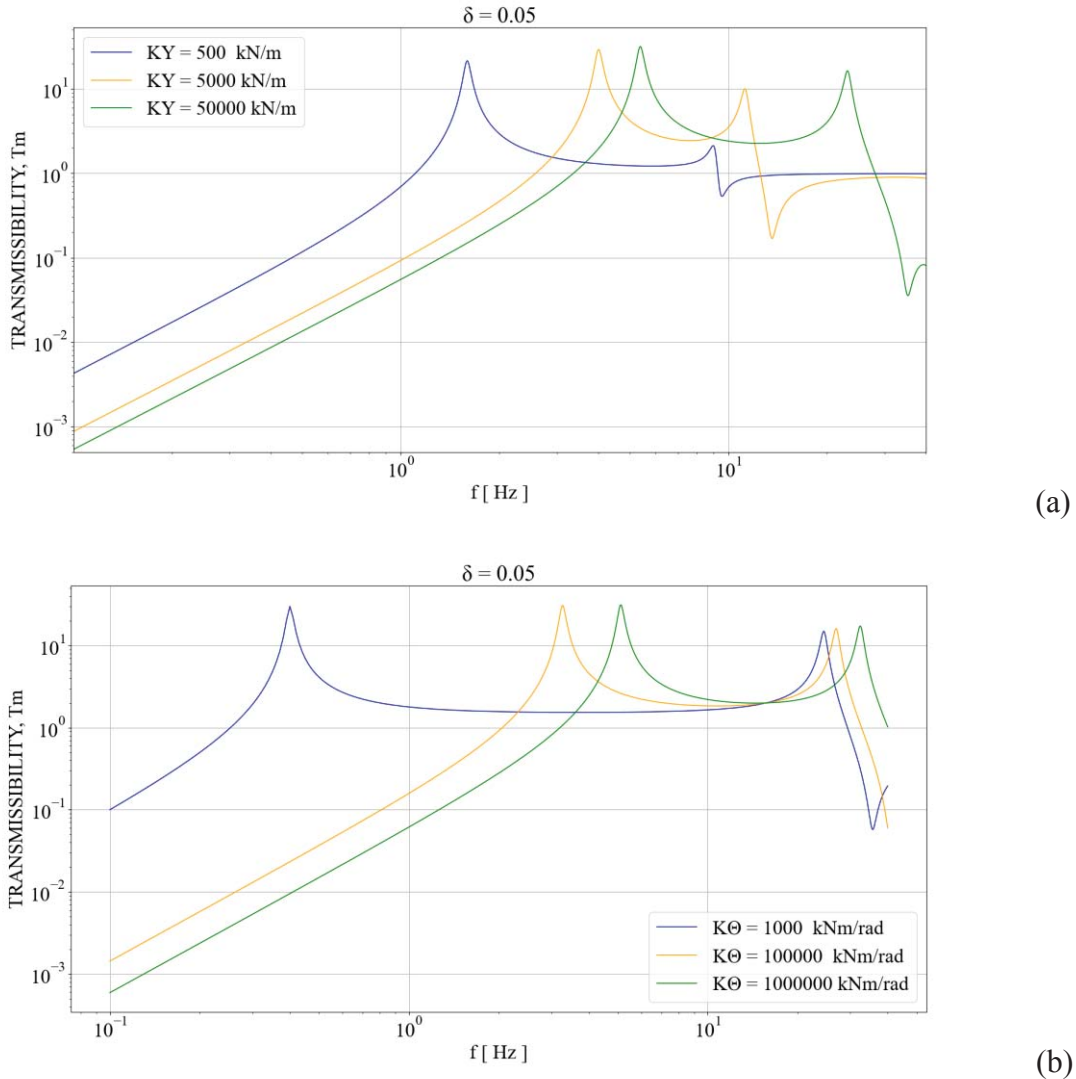


Figure 5: Figure 4: Transmissibility functions  $TR$  between top and ground displacement amplitudes versus frequency  $f$  for transverse pylon vibrations under a normalized sinusoidal ground acceleration input and for a damping  $\delta$  value of 5% as a function of: (a) horizontal base spring  $K_Y$  values and (b) rotational base spring  $K_\Theta$  values.

## 6. CONCLUSIONS

In this work, we have derived solutions for the transmission of motion between the top and base of a cantilevered pylon, to which either a lumped mass is attached at the top or springs are inserted at the base for the purpose of acting as passive control devices. Of course, it may be that a lumped mass is already attached to the pylon, as would for lighting devices, cable

supports, signal transmission apparatus, etc., which implies that the results generated here are still applicable. The same holds true if the pylon is founded on soft soil, in which case we have soil-structure-interaction phenomena and the ground is replaced by an equivalent set of springs.

For a typical R/C pylon used in electric rail lines, with vibrations induced by passing trains in both the vertical direction and on the horizontal plane, the presence of the lumped mass at the top of the pylon is beneficial in the high frequency range, where we see an amplitude reduction in the pylon displacements. Conversely, in the low frequency range as compared to the pylon fundamental eigenfrequency, the presence of a lumped mass ranges is of minor significance and may even be detrimental. Similar conclusions can be drawn in reference to the presence of base isolation springs that become effective in the higher frequency range. In the low frequency range, however, their presence is detrimental, as they result in an increase in amplitude at the top for transverse vibrations, but beneficial for longitudinal vibrations.

The presence of a lumped mass and of base isolation springs becomes important when viewed in terms of SHM, because these passive damping mechanisms can be upgraded to a semi-active status [9]. For instance, it may be possible to allow for the lumped mass to fluctuate as the pylon structural vibrations unfold with time, provided a suitable mechanism can be added for this purpose. In addition, there would have to be a control algorithm, as for instance a predictor-corrector method that computes the imminent displacement at the top of the pylon and energizes the mechanism if this displacement exceeds a prescribed limit. A similar situation can be envisaged for the case of a base isolation mechanism. In both cases, the use of control algorithms pre-supposes the existence of robust and efficient structural analysis capabilities, as would be the case for the analytical solutions presented herein.

**Acknowledgement:** The authors acknowledge support from the German Research Foundation (DFG) projects SM 281/14-1 entitled “Data-driven analysis models for slender structures using explainable artificial intelligence” and SM 281/20-1 entitled "Resilient infrastructure based on cognitive buildings", Prof. K. Smarsly, University of Hamburg-Harburg, coordinator.

## REFERENCES

- [1] K.F. Graff, *Wave motion in elastic solids*, Ohio State University Press, 1975.
- [2] E. Kausel, *Advanced structural dynamics*, Cambridge University Press, 2017.
- [3] I. Elishakoff, J. Kaplunov, E. Nolde, Celebrating the centenary of Timoshenko’s study of effects of shear deformation and rotatory inertia, *Applied Mechanics Reviews of ASME*, **67**, 060802-1, 2015.
- [4] G.D. Manolis, G. I. Dadoulis, S.I. Pardalopoulos, K. Dragos, Analytical models for the monitoring of flexible antennas under environmentally induced dynamic loads, *Acta Mechanica*, **231**, 3621-3624, 2020.
- [5] J.C. Snowdon, *Vibration and shock in damped mechanical systems*, J. Wiley, 1968.
- [6] C.C. Chaves-Júnior, R.F. de Alencar Araujo, C.M.C. de Souza, A.C.A. Ferreira, P.M.V. Ribeiro, A collocation method for bending, torsional and axial vibrations of offshore wind turbines on monopile foundations, *Ocean Engineering*, **217**, 107735, 2020.

- [7] S. Nagarajaiah, S. Dyke, J.P. Lynch, A. Smyth, A. Agrawal, M. Symans and E. Johnson, Current directions of structural health monitoring and control in USA. *Advances in Science and Technology*, **56**, 277-286, 2008.
- [8] C.R. Farrar and K. Worden. *Structural health monitoring: A machine learning perspective*. J. Wiley, 2012.
- [9] K. Smarsly and K.H. Law, A migration-based approach towards resource-efficient wireless structural health monitoring. *Advanced Engineering Informatics*, **27:4**, 625-635, 2013.
- [10] S. I. Pardalopoulos, G. D. Manolis, An engineering approach for evaluating the dynamic response of acceleration-sensitive secondary systems in flexible structures, *Earthquake Engineering and Structural Dynamics*, 2021. <https://doi.org/10.1002/eqe.3438>
- [11] *Python Software Foundation*, Beaverton, Oregon, USA, 2001. [www.python.org](http://www.python.org)

## APPENDIX

We derive here the transcendental equation for flexural vibrations of a tapered pylon with a lumped mass  $M_L$  at the top, whose numerical solution by the Newton-Raphson method yields the eigenfrequencies. This derivation assumes that this mass is activated by the relative transverse motion  $w(x, t)$  of the pylon, which is the case that appears often in the literature. We should note, however, that the mass is influenced by the total motion that includes the base motion  $x_g(t)$ . Finally, recovery of the first three eigenmodes is usually deemed sufficient for any subsequent dynamic analysis. More specifically, we start with the shear force boundary condition

$$Q(a, t) = M_L \ddot{w}(a, t) \Rightarrow -EI'(a)w''(a, t) - EI(a)w'''(a, t) = M_L \ddot{w}(a, t)$$

We follow with a substitution for  $w(x, t)$  in terms of the generalized coordinates  $q(t)$  and the eigenfunctions  $\Phi(x)$ :

$$-EI'(a)W'''(a)q(t) - EI(a)W''''(a)q(t) = M_L W(a)\ddot{q}(t)$$

However, the generalized coordinates obey the single degree-of-freedom equation as

$$\ddot{q}(t) + \omega^2 q(t) = 0 \Rightarrow \ddot{q}(t) = -\omega^2 q(t)$$

Since the bending moment at the pylon's top is zero, we have that  $M(a) = 0 \Rightarrow \Phi''(a) = 0$ . Manipulation of the boundary condition equation yields

$$-EI(a)W''''(a)q(t) = M_L W(a)\ddot{q}(t) = M_L W(a)(-\omega^2)q(t) \Rightarrow EI(a)W''''(a) = M_L W(a)\omega^2$$

Next, we use the dimensionless length  $\xi = \frac{x}{a}$ ,  $\xi \in [1, b/a]$  and of moment of inertia of the tapered pylon  $I = I_0(x/a)^6 = I_0 \xi^6$  to recover the following equation:

$$EI_0 \Phi''''(1)/a^3 = M_L W(1)\omega^2 \quad (\text{A.1})$$

The total mass of the pylon  $M_T$  is then computed as

$$M_T = \int_{x=a}^{x=b} \rho \, 2\pi d R_O \left(\frac{x}{a}\right)^2 dx = \int_{\xi=b/a}^{\xi=1} \rho \, 2\pi d R_O \xi^2 a d\xi = (2\pi R_O d) \frac{a}{3} \rho \left(\frac{b^3}{a^3} - 1\right) = A_O \frac{a}{3} \rho \left(\frac{b^3}{a^3} - 1\right) = \rho A_O \Lambda, \text{ where } \Lambda = \frac{a}{3} \left(\frac{b^3}{a^3} - 1\right), R = \frac{M_L}{M_T}, \text{ and } \beta^4 = \frac{\rho A_O a^4}{EI_O} \omega^2.$$

By inserting the above expressions in Eq. (A.1) we recover that

$$-\left(\frac{M_L}{\rho A_O \Lambda}\right) \left(\frac{\omega^2 \rho A_O a^4}{EI_O}\right) \frac{\Lambda}{a} W(1) + W''''(1) = -R \cdot \beta^4 \cdot \left(\frac{\Lambda}{a}\right) \cdot W(1) + W''''(1) = 0$$

We now introduce the homogeneous solution for flexural vibrations as

$$W(\xi) = \xi^{-\frac{3}{2}} \left\{ B_1 \xi^{\frac{\sqrt{(k+17)}}{2}} + B_2 \xi^{-\frac{\sqrt{(k+17)}}{2}} + B_3 \sin\left(\frac{\sqrt{(k-17)}}{2} \ln \xi\right) + B_4 \cos\left(\frac{\sqrt{(k-17)}}{2} \ln \xi\right) \right\}$$

where  $k = 4\sqrt{(\beta^4 + 4)}$ . Now we can define the following quantities:

$$A_1(\xi) = \xi^{-\frac{3}{2}} \xi^{\frac{\sqrt{(k+17)}}{2}}, A_2(\xi) = \xi^{-\frac{3}{2}} \xi^{-\frac{\sqrt{(k+17)}}{2}}, \\ A_3(\xi) = \xi^{-\frac{3}{2}} \sin\left\{\frac{\sqrt{(k-17)}}{2} \ln(\xi)\right\}, A_4(\xi) = \xi^{-\frac{3}{2}} \cos\left\{\frac{\sqrt{(k-17)}}{2} \ln(\xi)\right\}$$

The full set of boundary conditions for the lumped mass at the top is

$$W(b/a) = 0, W'(b/a) = 0, W''(1) = 0, -R \cdot \beta^4 \cdot \Lambda \cdot a^{-1} \cdot W(1) + W''''(1) = 0$$

Finally, to recover the wave numbers, the determinant of the  $4 \times 4$  matrix is set equal to zero:

$$\det = \begin{bmatrix} \alpha_1 & \alpha_2 & \alpha_3 & \alpha_4 \\ \beta_1 & \beta_2 & \beta_3 & \beta_4 \\ \gamma_1 & \gamma_2 & \gamma_3 & \gamma_4 \\ \delta_1 & \delta_2 & \delta_3 & \delta_4 \end{bmatrix} = 0 \quad (\text{A.2})$$

The matrix terms appearing in Eq. (A.2) are as follows:

$$\alpha_1 = A_1(b/a), \alpha_2 = A_2(b/a), \alpha_3 = A_3(b/a), \alpha_4 = A_4(b/a) \\ \beta_1 = A_1'(b/a), \beta_2 = A_2'(b/a), \beta_3 = A_3'(b/a), \beta_4 = A_4'(b/a) \\ \gamma_1 = A_1''(1), \gamma_2 = A_2''(1), \gamma_3 = A_3''(1), \gamma_4 = A_4''(1) \\ \delta_1 = -R \left(\frac{k^2}{16} - 4\right) \cdot \left(\frac{\Lambda}{a}\right) A_1(1) + A_1''''(1), \delta_2 = -R \left(\frac{k^2}{16} - 4\right) \cdot \left(\frac{\Lambda}{a}\right) A_2(1) + A_2''''(1) \\ \delta_3 = -R \left(\frac{k^2}{16} - 4\right) \cdot \left(\frac{\Lambda}{a}\right) A_3(1) + A_3''''(1), \delta_4 = -R \left(\frac{k^2}{16} - 4\right) \cdot \left(\frac{\Lambda}{a}\right) A_4(1) + A_4''''(1)$$



## PSEUDO-DYNAMIC ANALYSES OF INFILLED REINFORCED CONCRETE FRAMED STRUCTURES WITH PRIOR DAMAGES AFTER ADVANCED RETROFIT

Theodoros Rousakis<sup>1</sup>, Evgenia Anagnostou<sup>1</sup>, and Theodora Fanaradelli<sup>1</sup>

<sup>1</sup> Democritus University of Thrace, Department of Civil Engineering,  
Xanthi, Greece  
e-mail: {trousak,eanagno,tfanarad}@civil.duth.gr

---

### Abstract

*This study investigates suitable models for the analysis of innovative retrofits in infilled (and bare) reinforced concrete frames. It focuses on the detrimental effects of prior damages and deficiencies in frames such as corroded steel reinforcements or inadequate lap-splices in columns that may lead to premature failures and structural collapses. It investigates numerically the beneficial effects of innovative interventions on deficient RC frames, through pseudo-dynamic 3-dimensional finite element analyses. The intervention involves infill wall with special thermal insulating clay brick orthoblocks, having at the boundary interface with the RC frame, an advanced seismic joint made of highly deformable polyurethane. The technique has been already validated experimentally in frames without corroded or lap-spliced bars [1] (as well as for a four-column structure in project named “INfills and MASONry structures protected by deformable POLyurethanes in seismic areas” – INMASPOL [2,3]). The analyses suggest that the 3dimensional FE models may reproduce with satisfactory accuracy the mechanical behavior of FRP retrofitted deficient columns. Further, they suggest that the deficient RC frames after the innovative composite retrofit achieve higher base shear load than the original bare RC frame without corroded or lap-spliced bars, at comparable top displacement ductility.*

**Keywords:** Finite Element, retrofit, reinforced concrete frame, brick infill, polyurethane seismic joint

---

## 1 INTRODUCTION

Reinforced concrete (RC) structures in seismic and coastal regions often present accumulated damage due to corrosion of steel reinforcement [4] among others. Further, the columns may include several deficiencies such as inadequate lap-splices of bottom steel bars [5, 16] among others. Available innovative materials and intervention techniques such as steel fiber systems or fiber reinforced polymers (FRPs) in the form of sheets, strips and ropes are widely used. Suitable diagnosis and retrofit of deficient members can improve their strength, delay further corrosion of the reinforcement as well as reduce deformations at the serviceability limit stage [5-11, 17].

Furthermore, the behavior of RC frames with masonry infills is significantly affected by the stiffness and the difference in yield-failure deformation between the RC frames and the masonry infills. The majority of buildings are constructed by brittle materials (clay bricks or concrete). Flexible frames cannot support high loads at low excitations and this can cause damage to the infills in normal (frequent) earthquakes. In the case of aftershocks, damaged infills may fail in and/or out of plane and collapse, causing human injuries. On the other hand, if the infill is too strong compared to the columns, it may cause their detrimental shear failure. Seismic isolation of the infills through structural Polyurethane Flexible Joints (PUFJ) may result in desirable RC frame – infill interaction enhancing the elastic stiffness and base shear while maintaining significant displacement ductility of the composite frames [1-3]. PUFJs can be used to fill cracks or joints or to bond composite materials (for masonry see [12]). In cases the fiber retrofit is applied with standard epoxy resins or inorganic matrices, the sequence of failures of the infilled RC frames remains unchanged, revealing a significant accumulation of damage for relative displacement of the frame between 0.5% - 1.5% [13]. Recent analytical studies have shown that strengthening with PUFJs may delay infill damage and thus enables the engagement of multiple different infills in a building frame. This aspect increases their shear capacity significantly [3].

However, during an experimental campaign involving large scale frames, only a few parameters can be investigated due to the high demand of resources and time. 3D finite element modelling and analyses may help address the effects of critical design parameters or deficiencies or damages in frames, by further developing already validated models in RC columns and in half RC column-foundation specimens retrofitted or not (see [14,15]).

This study investigates analytically the performance of bare RC frames with corroded reinforcements or inadequate bar lap-splices. Further, their corresponding RC frame counterparts with an innovative infill and PUFJ seismic joint are included in the parametric investigation. The infill wall is made of special thermal insulating clay bricks (orthoblocks with vertical direction of holes), having at the boundary interface with the RC frame an advanced seismic joint made of highly deformable polymer (PUFJ). The technique has been already validated experimentally in frames without corroded or lap-spliced bars in [1] (as well as for a four-column structure in INMASPOL [2,3]). The parametric analyses reveal the effects of damages and deficiencies on the performance of seismic resistant frames and the potential of innovative retrofits with seismic polymer joints.

## 2 FINITE ELEMENT MODELLING

This study develops suitable models for the analytical investigation of innovative retrofits in infilled (and bare) framed structures with prior structural deficiencies, based on the prior numerical validation of 3D FE models of isolated columns with deficiencies.

## 2.1 Concrete

The behavior of concrete is captured with the Riedel–Hiermaier–Thoma (RHT) model [18–20] (ANSYS, Autodyn [21]), suitable for similar geological materials under dynamic loading situations. The RHT is a constitutive model for brittle materials and is a combined plasticity and shear damage model in which the deviatoric stress in the material is limited by a generalized failure surface of the form (Eq. 1)

$$f(P, \sigma_{eq}, \theta, \dot{\varepsilon}) = \sigma_{eq} - Y_{TxC(P)} * F_{CAP(P)} * R_{3(\theta)} * (F)_{RATE(\dot{\varepsilon})} \quad (1)$$

where  $\sigma_{eq}$  is the uniaxial compressive strength,  $Y_{TxC(p)}$  is the fracture surface,  $F_{CAP(P)}$  is a dimensionless cap function which activates the elastic strength surface within the RHT material model at high pressures,  $R_{3(\theta)}$  is the third invariant dependence term and  $(F)_{RATE(\dot{\varepsilon})}$  is the strain rate effect represented through fracture strength with plastic strain rate.

## 2.2 Longitudinal and Transverse Steel Bars

In Explicit Dynamics analyses, plastic deformation is computed by reference to the Von Mises yield criterion (also known as Prandtl–Reuss yield criterion). This states that the local yield condition is (Eq. 2)

$$(\sigma_1 - \sigma_2)^2 + (\sigma_2 - \sigma_3)^2 + (\sigma_3 - \sigma_1)^2 = 2Y^2 \quad (2)$$

where  $\sigma_1, \sigma_2, \sigma_3$  are the first, second and third principal stresses and  $Y$  is the yield stress of steel reinforcement under tension.

For the elastic part of the response of the longitudinal and transverse steel was chosen the “Isotropic Elasticity” model. The “Bilinear Isotropic Hardening” model was used to define the yield stress ( $Y$ ) as a linear function of plastic strain,  $\varepsilon_p$  (Eq. 3)

$$Y = Y_0 + A * \varepsilon_p \quad (3)$$

where  $Y_0$  is the yield strength and  $A$  is the tangent modulus.

## 2.3 Brick

Brick is modeled with Young’s modulus equal to 3800 MPa and Poisson’s Ratio equal to 0.25. The orthotropic elasticity material properties with tensile strength in X, Y and Z directions are 1.49 MPa, 3.89 MPa and 1.49 MPa, respectively.

## 2.4 Fiber Reinforced Polymers (FRP)

The retrofitted isolated specimens were externally confined with 2 layers of carbon FRP [5]. The FRP jacket was applied over a height of 600 mm at the base of the column. The thickness of one layer of CFRP was  $t_f=0.13$  mm, the elastic modulus was  $E_f=230$  GPa and the failure strain was  $\varepsilon_{uf}=0.015$ , while the corners of the section were rounded with radius of  $r=30$  mm. FRP jacket was modelled as an orthotropic elastic material. For the analyses, the material properties were reduced to 59,160 MPa for the elastic modulus along the direction of carbon fibers in order to take into account both the fibers and impregnation polymer. In addition, the thickness of the jacket was suitably increased so that the elastic modulus multiplied by the thickness of the jacket, in both cases, provides the same axial rigidity value.

## 2.5 Polyurethane

The frame specimen is the brick infilled RC frame with polymer joints of 2cm thick at 3 sides, simulating application to existing buildings. The 3-sided gap was filled in with PUFJ polymer through by injection. Polymer for PUFJ was of type Sika PM. The elastic modulus, strength and ultimate elongation of the polymer were 4 MPa, 1.4 MPa and 110%, respectively in a tensile test and the Poisson ratio 0.47. Polyurethane is modeled as an isotropic elasticity material.

## 2.6 Element Type

Concrete and bricks were eight-node elements "Hexahedral Solid Elements". The internal steel reinforcement was 2-node element "Beam (Line) Elements" with the ability to develop large axial deformations. More details on the FE modelling and analysis procedure can be found also in [14, 15].

## 3 VALIDATION OF FE MODELS

The analytical study presented herein includes two phases. At the first phase the accuracy of the prediction performance of the constructed 3D FE models are validated against the experimental results of 2 selected real scale RC frames from the study by [1]. Specimen A1F is the bare RC frame of the series and it is designed according to current Eurocodes. This real scale frame has plane dimensions of 270 cm long beam with extensions of 30 cm in both sides and height of 245 cm (245 cm to the level of the diaphragm). The columns are of cross section dimensions of 25 cm×25 cm and have 8Φ16 longitudinal continuous rebars (without lap-splices) and Φ10/100 mm closed stirrups (peripheral and rhombic). The columns have two top extensions of 30 cm as well as a common foundation beam with dimensions 30 cm×40 cm×355 cm. The top beam has cross section dimensions of 25 cm×25 cm and is reinforced with 8Φ14 longitudinal rebars and Φ10/100 mm closed stirrups (peripheral). The dimensions of the RC frame and the detailing of the internal steel reinforcement are depicted in Figure 1a.

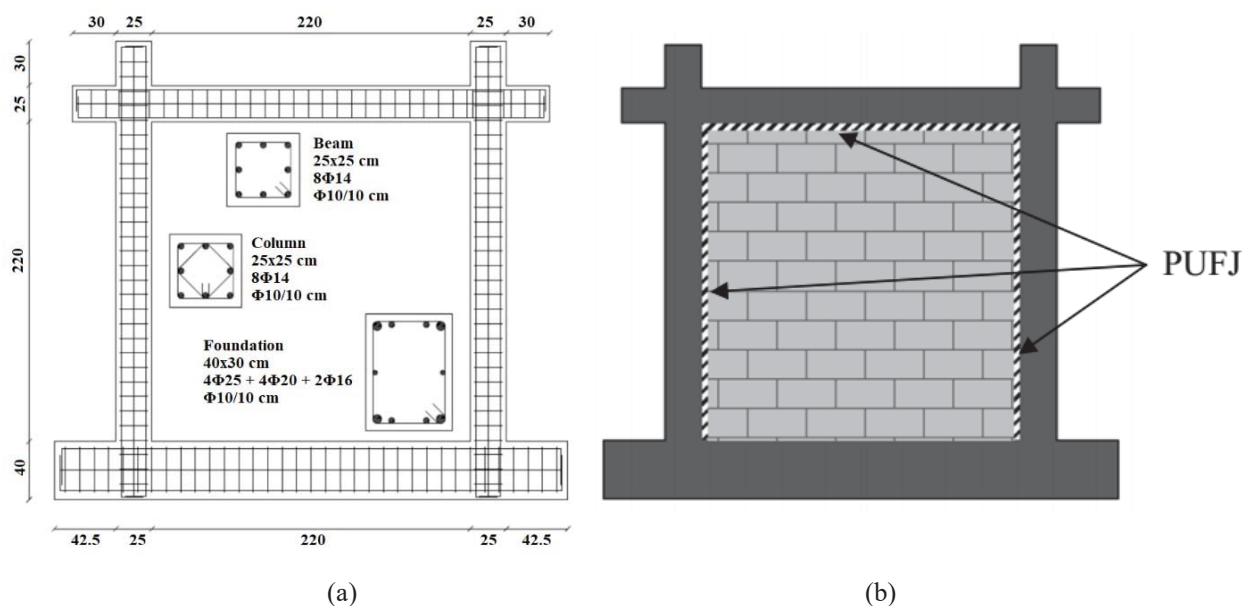


Figure 1: (a) Dimensions of the RC frame and detailing of internal steel reinforcement and (b) Specimen B2 with 3-sided polymer joint applied on existing infill (adapted by [1]).

Specimen B2 is identical to the A1F frame with addition of infill wall with special thermal insulating clay bricks (orthoblocks with vertical direction of holes), having at the boundary interface with the RC frame, advanced seismic joint made of highly deformable polymer. The polyurethane joint is 2 cm thick, placed at 3 sides (at 2 vertical interfaces and at top interface) which is depicted in Figure 1b. The two columns of the frame have been subjected to 375 kN concentric load each. Then, the horizontal actuator imposed cycles of gradually increased displacements at the top beam. More details on the experimental setup and test results of the 2 selected frames can be found in [1].

Figures 2a and 2b show in black and black-grey curves the experimental envelope base shear – top displacement curves of the two frames for (+) and (-) push respectively. It should be mentioned that the innovative orthoblock infill with the PUFJ seismic joint increased the elastic stiffness of the frame as well as the maximum base shear of the frame from 164 kN (A1F frame push +) and 134 kN (A1F frame push -) to 192.8 kN (B2 frame push +) and 167 kN (B2 frame push -) when the orthoblock-PUFJ is used. Further, the top displacement ductility of the infilled frame B2 was remarkable, with negligible base shear reduction up to 3.5% drift for push (+).

The analytical predictions of the FE analyses are in red color and compare well with the experimental ones in terms of maximum and ultimate base shear as well as in terms of top displacement at maximum bearing load and at ultimate (see figure 2).

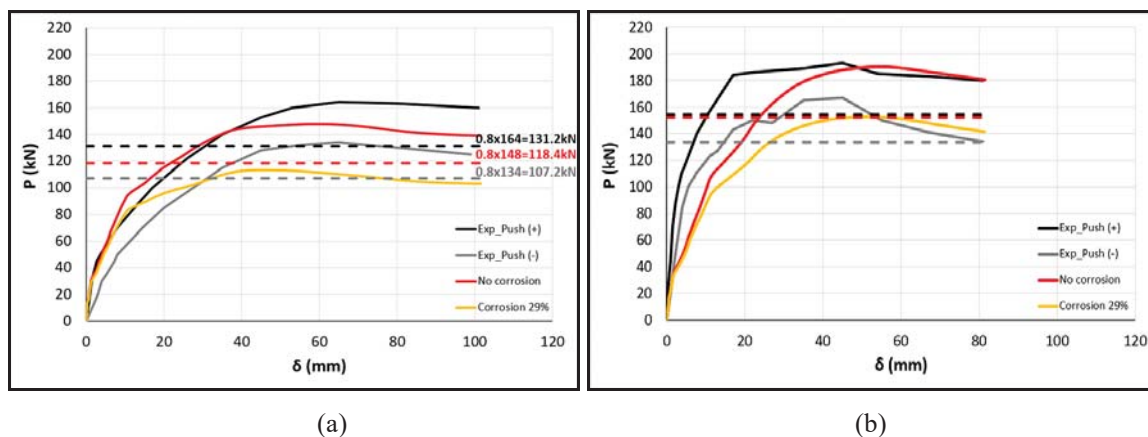


Figure 2: Analytical base shear force -displacement curve for (a) A1F and (b) B2 with no and 29% corrosion, compared against the experimental ones.

## 4 PARAMETRIC FE ANALYTICAL INVESTIGATION

At the second phase, the study utilizes the modelling approach presented in [15] for RC columns with lap-spliced steel bars or with corroded reinforcements. The corresponding developments are introduced in the frames A1F and B2 to investigate the effects of the implementation of orthoblock infill with seismic PUFJ on the P-d performance of deficient frames in need of retrofit.

### 4.1 Corrosion of steel reinforcement

Anagnostou and Rousakis [15] validated the simplified FE approach on the analysis of RC columns with corroded steel bars of varying degree of corrosion utilizing the experiments by [5]. The half column specimens had section dimensions 20 cm x 30 cm and height 120 cm. The concrete strength and steel yield stress was  $f_c=25.5$  MPa and  $f_{yL}=460$  MPa and the normalized axial load  $\nu=0.18$ . Four different degrees of corrosion were investigated experimen-



tally. The FE analytical results in [15] suggest there is reduction of the force received by the longitudinal bars under tension compared to the uncorroded column, as the degree of corrosion increases (in accordance with the mass loss of the steel). The strength and the ductility of RC column decrease and the reduction of strain in corroded steel bars is significant. Finally, for a high degree of corrosion, fracture of steel longitudinal bars is expected.

A corrosion of about 10% results in negligible reduction of the ultimate chord rotation [5] while a higher than 20% leads to a dramatic reduction of the yielding and ultimate strength. The column NS-X16 presented a reduction in experimental ultimate displacement of about 28% and in strength about 10% with respect to uncorroded one. This corrosion level is considered in this study the limit one for a column satisfying the seismic code requirements.

Herein, the analytical and experimental results (for both directions, push + and push -) of specimens NS-X0 and NS-X16 (0 and 16% corrosion, respectively) for the maximum and ultimate lateral force ( $P_{\max}$ ,  $P_u$ ) and the corresponding displacements ( $\delta_{P_{\max}}$ ,  $\delta_{P_u}$ ) are presented and compared in Table 1. The parameter used for the comparisons in all tables is the Absolute Divergence (AD), also known as Absolute Error (AE). It is defined as follows:

$$AD = \frac{|a_{anal.} - a_{exp.}|}{a_{exp.}} \quad (4)$$

AD requires the absolute experimental values ( $a_{exp.}$ ) to be subtracted by the analytical ones ( $a_{anal.}$ ) and then divided by the experimental ones ( $a_{exp.}$ ). The divergence between the experimental and analytical values at characteristic states for the columns is low (Table 1). All comparisons with loads and displacements at characteristic states suggest the analytical predictions are satisfactory. More details can be found in [15].

	NS-X0			NS-X16		
	Exp.	Anal.	AD (%)	Exp.	Anal.	AD (%)
$P_{\max}$ (+) (kN)	60.70	54.56	10.11	50.90	49.56	2.64
$\delta_{P_{\max}}$ (+) (mm)	20.00	20.87	4.35	18.00	42.12	134.00
$P_{\max}$ (-) (kN)	52.00	54.56	4.92	50.00	49.56	0.88
$\delta_{P_{\max}}$ (-) (mm)	15.00	20.87	39.13	30.00	42.12	40.40
$P_u$ (+) (kN)	51.60	46.38	10.12	43.27	42.13	2.63
$\delta_{P_u}$ (+) (mm)	81.10	73.75	9.06	55.10	52.86	4.07
$P_u$ (-) (kN)	44.20	46.38	4.92	42.50	42.13	0.88
$\delta_{P_u}$ (-) (mm)	70.00	73.75	5.36	55.00	52.86	3.89

Table 1: Comparative results for specimens NS-X0 and NS-X16 with different corrosion levels.

The same approach was adopted for the frames A1F and B2. The scenario concerns 29% mass loss due to corrosion for all the steel bars and stirrups, including the two columns along with the beam. All analyses are stopped at the same displacement, as the experimental one. Figure 2a presents the analytical base shear force – displacement curve of frame A1F with 29% corrosion while figure 2b the curve of B2 with 29% of corrosion, both in yellow color.

The dashed lines mark the 20% drop of the maximum values of the analytical and experimental base shears (for both directions, push + and -), considered as the lowest acceptable threshold of base shear at failure according to several seismic codes. In particular (see Table 2), for frame A1F without corrosion these experimental limit values for push (+) and (-) are  $0.8 \times 164 = 131.2$  kN and  $0.8 \times 134 = 107.2$  kN respectively. The analytical prediction is  $0.8 \times 148 = 118.4$  kN, being around the average of experimental ones. Analysis for A1F with

29% corrosion reveals maximum base shear of 113.35 kN which is around the analytical 80% value at failure for uncorroded frame. Further, the ultimate base shear is 103.26 kN, lower than the experimental limits and far lower than the analytical failure limit of 118.4kN. It seems that the base shear degradation at ultimate because of 29% corrosion in bare frame A1F is 30.2% (i.e. from 148 kN to 103.26 kN), concluding corroded A1F as insufficient. This load drop is far higher than in isolated columns (15.6%) as all steel reinforcements of the frame are considered corroded.

	A1F (No corrosion, No lap)			A1F (29% corrosion)		A1F (11d <sub>bL</sub> lap length)	
	Exp.	Anal.	AD (%)	Anal.	AD (%)	Anal.	AD (%)
P <sub>max</sub> (+) (kN)	164.00	148.00	9.76	113.35	23.41	139.67	5.63
δP <sub>max</sub> (+) (mm)	65.00	59.93	7.80	46.25	22.83	53.34	11.00
P <sub>max</sub> (-) (kN)	133.40	148.00	10.94	113.35	23.41	139.67	5.63
δP <sub>max</sub> (-) (mm)	65.00	59.93	7.80	46.25	22.83	53.34	11.00
P <sub>u</sub> (+) (kN)	159.90	139.14	12.98	103.26	25.79	131	5.9
δP <sub>u</sub> (+) (mm)	101.50	101.50	-	101.50	-	101.5	-
P <sub>u</sub> (-) (kN)	124.70	139.14	11.58	103.26	25.79	131	5.9
δP <sub>u</sub> (-) (mm)	99.00	101.50	-	101.50	-	101.5	-

Table 2: Comparative results for specimens A1F with different corrosion levels and lap lengths.

For frame B2 without corrosion, the corresponding experimental limit values for push + and - are  $0.8 \times 192.8 = 154.2$  kN and  $0.8 \times 167 = 133.6$  kN respectively (Table 3). The corresponding analytical prediction is  $0.8 \times 190.25 = 152.2$  kN, being around the experimental push + value. Analysis for B2 with 29% corrosion reveals maximum base shear of 152.66 kN which is around the analytical value at failure for uncorroded frame. Further, the ultimate base shear is 141.48 kN, which is higher than the limit experimental value for push – direction. However, this base shear degradation at ultimate because of 29% corrosion, is 25.6% (i.e. from 190.25 kN to 141.48 kN), concluding corroded A1F marginally as insufficient. Interestingly, if B2 frame is considered the retrofitting scenario for A1F corroded bare frame, then the analytical behavior of corroded A1F retrofitted with orthoblock infills and PUFJ (corroded B2) is somewhat better than the analytical behavior of uncorroded A1F. Indeed, the maximum base shear of B2 corroded is 152.66 kN (higher than 148kN in A1F uncorroded). Further, the ultimate base shear is also higher. Given the unique characteristics of PUFJ for emergency retrofits providing a short curing period of some hours [1-3], this innovative retrofit could enable the corroded frame to sustain P-d demands equivalent to the uncorroded one.

	B2 (No corrosion, No lap)			B2 (29% corrosion)		B2 (11d <sub>bL</sub> lap length)	
	Exp.	Anal.	AD (%)	Anal.	AD (%)	Anal.	AD (%)
P <sub>max</sub> (+) (kN)	192.80	190.25	1.32	152.66	19.76	165.04	13.25
δP <sub>max</sub> (+) (mm)	44.80	54.70	22.10	51.70	5.48	53.72	1.79
P <sub>max</sub> (-) (kN)	166.60	190.25	14.20	152.66	19.76	165.04	13.25
δP <sub>max</sub> (-) (mm)	44.80	54.70	22.10	51.70	5.48	53.72	1.79
P <sub>u</sub> (+) (kN)	179.00	180.42	0.79	141.48	21.58	147.76	18.10
δP <sub>u</sub> (+) (mm)	81.40	81.40	-	81.40	-	81.4	-
P <sub>u</sub> (-) (kN)	134.50	180.42	34.14	141.48	21.58	147.76	18.10
δP <sub>u</sub> (-) (mm)	81.40	81.40	-	81.40	-	81.4	-

Table 3: Comparative results for specimens B2 with different corrosion levels and lap lengths.

Figures 3 and 4 present the concrete damage of the specimens A1F and B2. Frames A1F with 29% corrosion and uncorroded present similar damage accumulation. Damage occurs mostly at the bottom and the top of the columns (critical regions) and inside the joints. Specimen B2 with 29% corrosion presents damage at similar regions but of lower severity as the damage is also distributed inside the orthoblock infill.

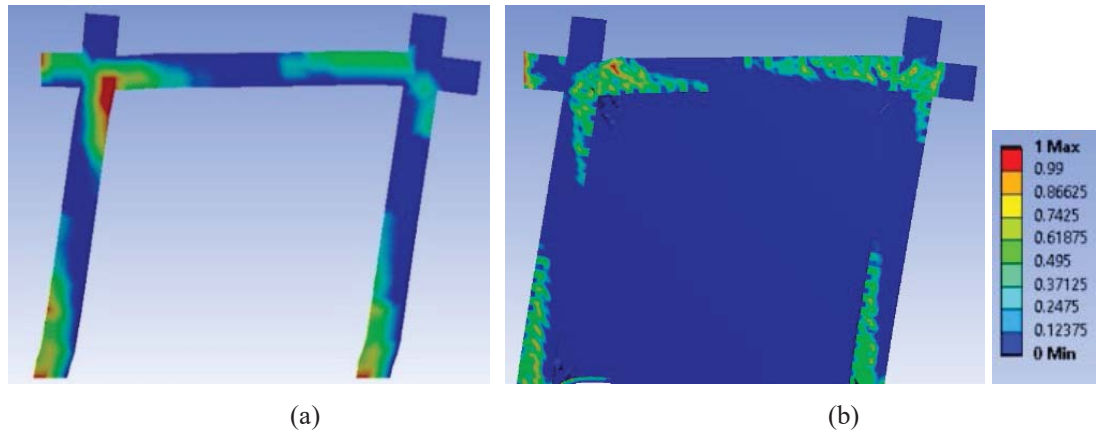


Figure 3. Concrete damage of specimen A1F with (a) no corrosion/no lap splices, and specimen B2 with (b) no corrosion/no lap splices (magnification factor 2).

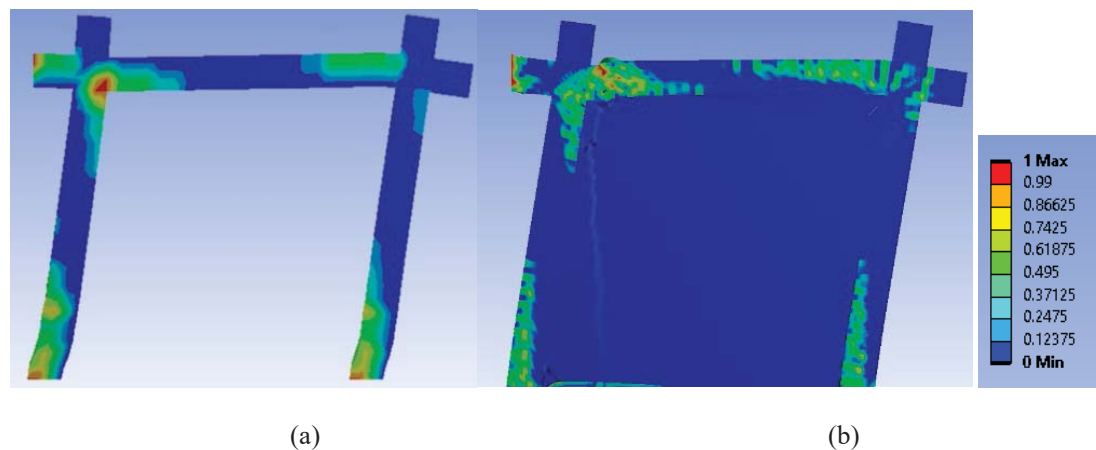


Figure 4. Concrete damage of specimen A1F with (a) 29% corrosion at total displacement 101.50 mm and specimen B2 with (b) 29% corrosion at total displacement 81.40 mm (magnification factor 2).

#### 4.2 Lap-spliced longitudinal bars

Anagnostou and Rousakis [15] have verified the 3D FE models of columns with lap-spliced longitudinal bars utilizing the experiments by [22]. The half columns had section dimensions 25 cm×50 cm and height 160 cm. The concrete strength varied among columns  $f_c=26.9\text{--}32.9$  MPa, and steel yield stress  $f_{yL}=514$  MPa. The normalized axial load was  $\nu=0.26\text{--}0.30$ , while three different lap-splice lengths of 15 times the diameter of the longitudinal bar ( $15d_{bL}$ ),  $30d_{bL}$  and  $45d_{bL}$  were examined. Table 4 cites the analytical and experimental results of columns with no bar laps or with bar lap lengths of  $15d_{bL}$  and  $30d_{bL}$  confined with 2 layers of FRP. All comparisons with loads and displacements at characteristic states suggest the analytical predictions are satisfactory. Column with  $15d_{bL}$  lap-splices (R-P2L1) shows a significantly reduced base shear (a mean reduction of about 20%) and reduced deformation capacity

compared with the column without laps (R-P2L0). Column with 30d<sub>bL</sub> (R-P2L3), achieves ultimate displacement similar to that of R-P2L0 but at marginally lower base shear (around 4%). Similarly, the analytical maximum axial force developed on the bars under tension at the lap region at the base of column R-P2L3 is 134.63 kN. This force is 9% lower than the axial force of 147.89kN in R-P2L0. For the column R-P2L1 the corresponding axial force is 85.49 kN, being 57% of the one in column R-P2L0. Therefore, the steel bars in the lap do not yield (analytical yield tensile force on the bar is 130.8 kN).

	R-P2L0			R-P2L1			R-P2L3		
	Exp	Anal	AD (%)	Exp	Anal	AD (%)	Exp	Anal	AD (%)
P <sub>max</sub> (+) (kN)	240.00	217.73	9.28	175.00	176.86	1.06	215.00	209.11	2.74
δP <sub>max</sub> (+) (mm)	48.50	34.84	28.16	19.50	27.77	42.41	48.50	38.13	21.38
P <sub>max</sub> (-) (kN)	194.00	217.73	12.23	168.00	176.86	5.27	208.00	209.11	0.53
δP <sub>max</sub> (-) (mm)	38.50	34.84	9.51	19.00	27.77	46.16	34.50	38.13	10.52
P <sub>u</sub> (+) (kN)	192.00	174.18	9.28	140.00	141.49	1.06	172.00	167.29	2.74
δP <sub>u</sub> (+) (mm)	70.40	75.37	7.06	54.40	58.46	7.47	75.20	66.85	11.10
P <sub>u</sub> (-) (kN)	155.20	174.18	12.23	134.40	141.49	5.27	166.40	167.29	0.53
δP <sub>u</sub> (-) (mm)	64.00	75.37	17.77	50.00	58.46	16.92	65.00	66.85	2.85

Table 4: Comparative results for specimens R-P2L0, R-P2L1 and R-P2L3 with different lap lengths.

The same approach was adopted for the frames A1F and B2. The scenario concerns the insufficient lap-splice case of 15d<sub>bL</sub>. However, this lap length is further reduced to 11d<sub>bL</sub> accordingly, based on the different concrete strength of the frames (C30 quality) that corresponds to higher bond strength of the bars inside concrete than the one in the columns by [22] (C20 quality). All analyses are stopped at the same displacement, as the experimental one. Figure 5a presents the analytical base shear force – displacement curve of frame A1F with 11d<sub>bL</sub> lap length while figure 5b the curve of B2 with 11d<sub>bL</sub> lap length, both in green color.

Analysis for A1F with 11d<sub>bL</sub> lap length reveals maximum base shear of 139.67 kN (see Table 2) which is only 5.63% lower than the analytical value at maximum for the frame without laps (148 kN). The corresponding ultimate base shear is 131 kN (only 11.4% lower than 148 kN, correspondingly). The ultimate base shear in A1F with laps is higher than all limit values of 20% drop (experimental or analytical), being sufficient globally, despite insufficient laps. It seems that the base shear degradation at ultimate because of insufficient lap-splices is higher in isolated half column specimens revealing a shear force of 141.49 kN. The corresponding maximum base shear in column without lap-splices is 217.13 kN, denoting a drop of 34.8% (3 times higher). The reason for this, may be attributed to the engagement of the sections on the top of the columns of the frame at higher extend, to compensate for the insufficiency of the bottom sections (redistribution effects).

Analysis for B2 with 11d<sub>bL</sub> lap length reveals maximum base shear of 165.04 kN which is 14.4% lower than the analytical value at maximum for the frame B2 without laps (Table 3). The ultimate base shear in B2 with laps is 147.76 kN (22.3% lower, correspondingly). This value is around the analytical limit value of 20% drop for frame B2 without laps (152.2kN), being only marginally insufficient globally, despite heavily insufficient laps. Further, if B2 frame is considered the retrofitting scenario for A1F bare frame with laps, then the analytical behavior of corroded A1F retrofitted with orthoblock infills and PUFJ (corroded B2) is far better than the analytical behavior of A1F without laps. Indeed, the maximum base shear of B2 with laps is 165.04 kN (higher than 148kN in A1F without laps). Further, the ultimate base shear is 147.76 kN (Table 3), compared with 139.14 kN in A1F without laps (Table 2).

In this case, orthoblock-PUFJ emergency retrofit [1-4], could enable the lap-spliced frame to sustain P-d demands higher than the A1F frame without laps.

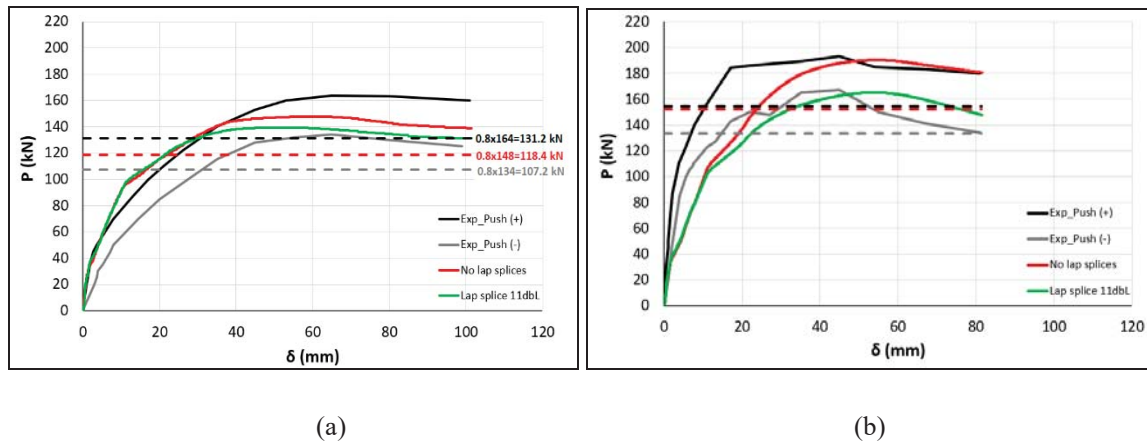


Figure 5. Analytical base shear force -displacement curve for (a) A1F and (b) B2 with no and 11dbL lap length, compared against the experimental ones.

Figure 6a presents the undeformed lap length region of 11dbL while figures 6b and 6c the slippage of the bars of frames A1F and B2 at ultimate. In both cases the analyses suggest that the lap-spliced bars reach their yielding force under tension (96.5 kN) despite the slip.

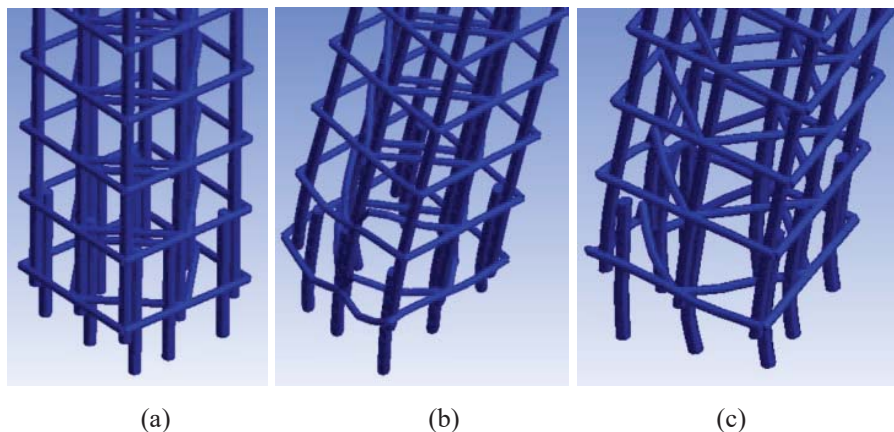


Figure 6. (a) Undeformed 11dbL lap length, (b) Slippage of longitudinal steel bars of specimen A1F at ultimate displacement of 101.5 mm and (c) B2 at ultimate displacement of 81.4 mm (magnification factor 10).

Figures 7a and 7b suggest that both frames present similar damage accumulation. Damage occurs mostly at the bottom and the top of the columns (critical regions) and inside the joints. Specimen B2 with 11dbL lap-splices presents damage of higher severity than in A1F, at the upper left beam-column joint region and at the bottom of the right column. However, the maximum shear force does not drop below 80% of the maximum experimental and analytical values.



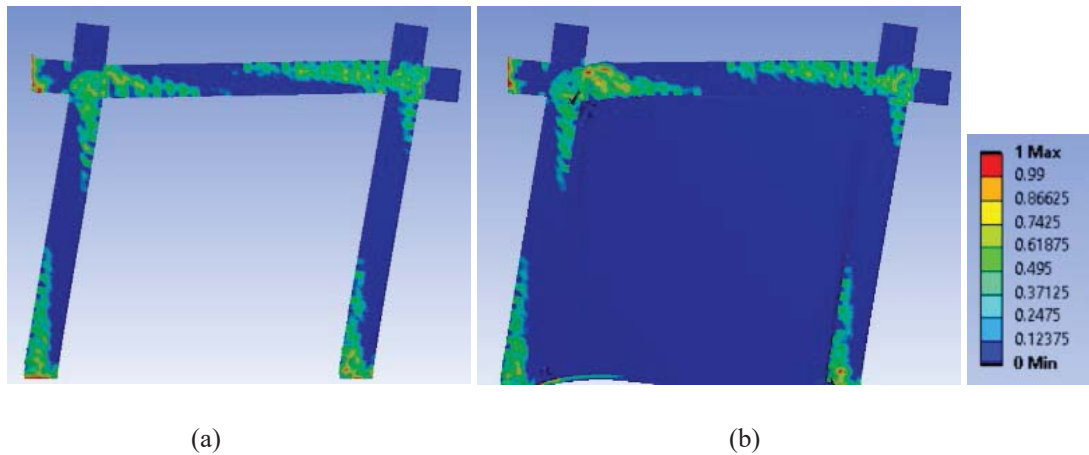


Figure 7. Concrete damage of specimens with  $11d_{bL}$  lap length of (a) A1F and (b) B2.

## 5 CONCLUSIONS

The analytical results of the developed FE models for frames A1F and B2 compare well with the experimental results. Further, the frames are suitably integrated to assess analytically their performance when they suffer 29% mass loss of their steel reinforcements due to corrosion or when the bottom column reinforcements have insufficient lap-splices of  $11d_{bL}$  length. Reference experiments of the international literature in half column specimens are utilized to validate the produced models.

The analytical results are mainly assessed based on the lowest acceptable threshold of 20% drop for the base shear at failure when compared with the maximum base shear of the frame (according to several seismic codes) without damages or deficiencies. Further, the investigated deficiencies cause no significant degradation of the elastic stiffness of the frames.

The corrosion of 29% steel mass loss to all reinforcements in bare frame A1F, results in ultimate base shear that is 30.2% lower than the maximum base shear in uncorroded A1F. Therefore, the frame is in need of retrofit as insufficient. In corroded B2 the corresponding drop is lower, 25.6%, considering it marginally as insufficient. However, if corroded B2 is considered the retrofit scenario for corroded A1F with orthoblocks and PUFJ, then the base shear at maximum and at ultimate are both higher than the corresponding values in A1F uncorroded, at comparable top displacement ductility. Therefore, it can be considered an efficient retrofit (especially as emergency one). However, such high levels of corrosion should be treated with caution.

The insufficient lap-splice of  $11d_{bL}$  to the bottom bars of the columns in bare frame A1F results in ultimate base shear that is only 11.4% lower than the maximum base shear in A1F without laps. The ultimate base shear in A1F with laps is higher than all limit values of 20% drop (experimental or analytical), being sufficient globally, despite insufficient laps (in isolated half column specimens the drop was 3 times higher). In B2 with lap-splices, the corresponding drop is 22.3%, considering it as marginally insufficient, despite insufficient laps. Further, if B2 frame is considered the retrofitting scenario for A1F bare frame with laps, then the analytical behavior of A1F with insufficient laps and retrofitted with orthoblock infills and PUFJ (B2 with lap-splices) is far better than the analytical behavior of A1F without laps. Orthoblock-PUFJ could enable the frame with lap-splices to sustain P-d demands higher than the A1F frame without laps, at comparable top displacement ductility.

## 6 ACKNOWLEDGMENTS

This research is co-financed by Greece and the European Union (European Social Fund-ESF) through the Operational Programme «Human Resources Development, Education and Lifelong Learning 2014- 2020» in the context of the project “Advanced Material Retrofits of Infilled Framed Reinforced Concrete Structures With Predamages Against Collapse” (MIS 5050146)

## REFERENCES

- [1] A.T. Akyildiz, A. Kwiecień, B. Zając, P. Triller, U. Bohinc, T. Rousakis, A. Viskovic, Preliminary in-plane shear test of infills protected by PUFJ interfaces. *17<sup>th</sup> International Brick and Block Masonry Conference from Historical to Sustainable Masonry (IB2MaC 2020)*, Krakow, Poland, July 5-7, 2020.
- [2] T. Rousakis, A. Ilki, A. Kwiecień, A. Viskovic, M. Gams, P. Triller, B. Ghiassi, A. Benedetti, Z. Rakicevic, C. Colla, O.F. Halici, B. Zając, L. Hojdys, P. Krajewski, F. Rizzo, V. Vanian, A. Sapalidis, E. Papadouli, A. Bogdanovic, Deformable Polyurethane Joints and Fibre Grids for Resilient Seismic Performance of Reinforced Concrete Frames with Orthoblock Brick Infills. *Polymers*, **12**, 2869, 2020.
- [3] T. Rousakis, Brick walls Interventions with FRPU or PUFJ and of RC columns with FR in Brick-Infilled RC Structures with the use of Pushover Beam-Column Element Analysis and Pseudo-Dynamic 3D Finite Element Analysis. *17<sup>th</sup> International Brick and Block Masonry Conference from Historical to Sustainable Masonry (IB2MaC 2020)*, Krakow, Poland, July 5-7, 2020.
- [4] C. Goksu, A. Ilki, Seismic Behavior of Reinforced Concrete Columns with Corroded Deformed Reinforcing Bars. *ACI Structural Journal*, **113(5)**, 1053-1064, 2016.
- [5] S.N. Bousias, M.N. Fardis, A.I. Spathis, D. Biskinis, Concrete or FRP jacketing of concrete columns for seismic retrofitting. S.T. Wasti, G. Ozcebe eds. *Advances in Earthquake Engineering for Urban Risk Reduction*. Nato Science Series: IV: Earth and Environmental Sciences, vol 66. Springer, 2006.
- [6] C.G. Papakonstantinou, K. Katakalos, Flexural behavior of reinforced concrete beams strengthened with a hybrid inorganic matrix - Steel fiber retrofit system. *Structural Engineering and Mechanics*, 31(5), 567-585, 2009.
- [7] G.G. Triantafyllou, T.C. Rousakis, A.I. Karabinis, Corroded RC beams patch repaired and strengthened in flexure with fiber-reinforced polymer laminates. *Elsevier Journal of Composites Part B: Engineering*, **112**, 125-136, 2017a.
- [8] G.G. Triantafyllou, T.C. Rousakis, A.I. Karabinis, Analytical assessment of the bearing capacity of RC beams with corroded steel bars beyond concrete cover cracking. *Elsevier Journal of Composites Part B: Engineering*, **119**, 1325-140, 2017b.
- [9] G.G. Triantafyllou, T.C. Rousakis, A.I. Karabinis, Effect of patch repair and strengthening with EBR and NSM CFRP laminates for RC beams with low, medium and heavy corrosion. *Elsevier Journal of Composites Part B: Engineering*, **133**, 101-111, 2018.

- [10] C.E. Chalioris, V.K. Kytinou, M.E. Voutetaki, C.G. Karayannis, Flexural Damage Diagnosis in Reinforced Concrete Beams Using a Wireless Admittance Monitoring System—Tests and Finite Element Analysis. *Sensors*, **21(3)**, 679, 2021.
- [11] C.G. Karayannis, E. Golias, Full scale tests of RC joints with minor to moderate seismic damage repaired using C-FRP sheets. *Earthquake and Structures*, **15(6)**, 617–627, 2018.
- [12] B. Zając, A. Kwiecień, Thermal stress generated in masonries by stiff and flexible bonding materials. *9<sup>th</sup> International Masonry Conference*, Guimarães, Portugal, 2014.
- [13] L. Koutas, T.C. Triantafillou, S.N. Bousias, Analytical modeling of masonry-infilled RC frames retrofitted with textile-reinforced mortar. *Journal of Composites for Construction*, **19(5)**, 2014.
- [14] T.D. Fanaradelli, T.C. Rousakis, 3D Finite Element Pseudodynamic Analysis of Deficient RC Rectangular Columns Confined with Fiber Reinforced Polymers under Axial Compression. *Polymers*, **12(11)**, 2546, 2020.
- [15] E. Anagnostou, T.C. Rousakis, 3D Finite Element Analysis of FRP Retrofitted Seismic Resistant Reinforced Concrete Columns with Lap Splices or Prior Damages. *Submitted for publication*, 2021.
- [16] G. Kalogeropoulos, A.D. Tsonos, Cyclic performance of RC columns with inadequate lap splices strengthened with CFRP jackets. *Fibers*, **8(6)**, 39, 2020.
- [17] K. Katakalos, G. Manos, C. Papakonstantinou, Seismic retrofit of R/C T-beams with steel fiber polymers under cyclic loading conditions. *Buildings*, **9(4)**, 101, 2019.
- [18] W. Riedel, Beton unter dynamischen Lasten: Meso- und makromechanische Modelle und ihre Parameter. *Fraunhofer Verlag*, 2004.
- [19] W. Riedel, N. Kawai, K. Kondo, Numerical Assessment for Impact Strength Measurements in Concrete Materials. *International Journal of Impact Engineering*, **36**, 283–293, 2006.
- [20] W. Riedel, K. Thoma, S. Hiermaier, E. Schmolinske, Penetration of Reinforced Concrete by BETA-B-500, Numerical Analysis using a New Macroscopic Concrete Model for Hydrocodes. *9<sup>th</sup> Internationales Symposium Interaction of the Effects of Munitions with Structures*, Berlin Strausberg, Germany, May 3–7, 1999.
- [21] ANSYS®, Academic Research Release 15.0. *SAS IP Inc*, Canonsburg, PA, USA, 2003.
- [22] S.N. Bousias, T.C. Triantafillou, M.N. Fardis, L. Spathis, B.A. O'Regan BA, Fiber-reinforced polymer retrofitting of rectangular reinforced concrete columns with or without corrosion. *Structural Journal*, **101(4)**, 512–520, 2004.

## EXPERIMENTAL AND NUMERICAL STUDY OF SELF-SUPPORTING DOUBLE SKIN METAL FACED MINERAL WOOL PANELS

Sofia Gkaraklova<sup>1</sup>, Lazaros Melidis<sup>1</sup>, George C. Manos<sup>1</sup> and Konstantinos Katakalos<sup>1,\*</sup>

<sup>1</sup> Aristotle University of Thessaloniki  
Laboratory of Experimental Strength of Materials and Structures, Thessaloniki, 54124  
e-mail: {kkatakakal,gcmanos}@civil.auth.gr, {sofiagked,lazmelidis}@gmail.com  
<https://strength.civil.auth.gr>

---

### Abstract

*The present study presents the results of experimental and numerical investigation on the behavior of self-supporting, double skin metal faced insulating sandwich panels under compression, tension and shear. More specifically, appropriate number of specimens is subjected to compression, tension and shear loads at the “Laboratory for Strength of Materials and Structures” (LSMS) Department of Civil Engineering of Aristotle University of Thessaloniki (AUTH) in compliance with the terms of BS EN 14509:2013 standard. In addition, numerical models simulating the compression and tension tests are developed and the mechanical properties of the materials composing the insulating panels are calibrated. As a result, stress – strain laws for both compression and tension behaviours of the product are determined. Moreover, numerical model simulating the shear test is built by implementing the previously formed material laws with analytical stress-strain relations for compression and tension. Finally, the response of the numerical model under shear test is compared to the experimental one and consequently the accuracy of determined material laws is assessed.*

**Keywords:** Composite, Self-supporting double skin metal faced MW panels, Experimental tests, Numerical simulation, Material law, Validation

---

## 1 INTRODUCTION

Sandwich panels are modern pre-fabricated construction components used as cladding elements for different types of buildings. Sandwich panels consist of an insulating core material covered by two faces which are typically made of thin metal sheets. The materials can be configured in many possible combinations. For instance, for the cover layers thin metal faces, timber-based plates or glass fiber reinforced plastics can be used. The insulating core layer in most cases is made of structured foams like polyurethane (PUR), polystyrene (PS) or of mineral wool (MW). Sandwich panels are used as light-weight roofs and wall claddings in industrial and commercial buildings. Usually, the structures are loaded by permanent loads, like self-weight, snow and wind loads. However, additional loads like temperature differences between external and internal metal faces or creep of the core must be taken into account for statical calculations of sandwich panels structures. The high load bearing capacity of sandwich panels is the result of a rigid connection between the core material and the cover layers. The bending moment is distributed to the two faces (e.g., for panels with flat faces in the form of axial forces) and the shear loads are borne by the core layer. In standard applications, the panels are mounted and fixed on a load-bearing substructure of beams or purlins. Sandwich panels can reduce the problem of lateral torsional buckling of this substructure of beams or purlins by providing stabilization either by shear stiffness or by torsional restraint. [1,2].

For the structural behavior of sandwich panels, it is necessary to consider all of the potential failure modes: tensile failure of the faces (due to tensile stress), local buckling (wrinkling) of the faces (due to compressive stress), and shear failure of the core or the adhesion between the core and face. In sandwich panels with thin strongly profiled faces, two additional failure modes are introduced: shear strength of the webs in a profiled face and the support reaction capacity of a profiled face [3,4].

The European standard BS EN 14509:2013 [5], or European Recommendations published by the European Convention for Constructional Steelwork (ECCS) and the International Building Council (CIB) do not provide detailed design methods for sandwiches with strongly profiled faces. Determination of the load bearing capacity required for the design of sandwich panels is to a large degree based on test results [6].

Pokharel and Mahendran [7,8] implemented Finite Element Analysis Method (FEM) in order to investigate the structural behavior of flat and lightly profiled sandwich panels. The investigation of structural behavior and failure analysis of composite structures through the use of finite element analyses have also been presented in [9] and [10].

The objective of this paper is to investigate experimentally and numerically lightly profiled insulating panels but most importantly develop a methodology for calibrating and determining materials' law that would enable an accurate simulation and estimation of the structural behavior of these composite panels.

## 2 EXAMINED SPECIMENS AND EXPERIMENTAL PROCEDURE

All the experimental tests are executed at the "Laboratory of Strength of Materials and Structures" of Aristotle University of Thessaloniki (AUTH) in compliance with EN 14509:2013 standard. The insulating panel under examination is in fact a sandwich section that consists of two metal faces of thickness 0.45mm, called "lamellas" and a core material between them which is Mineral Wool (MW). This panel is denominated as SP. The profile of the studied section is depicted in Figure 1. Three (3) panel thickness values,  $d_c$ , are considered in the present research: 50mm, 80mm and 100mm.



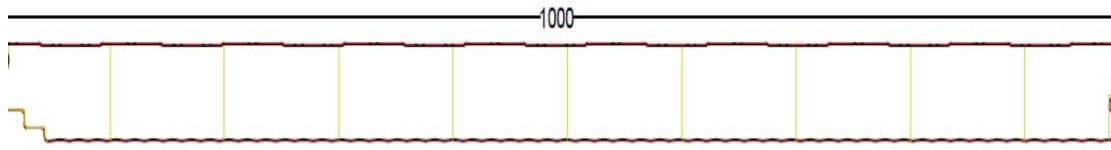


Figure 1: Profile of the examined self-supporting, double skin metal faced insulating SP

The compressive strength ( $f_{cc}$ ) and elasticity modulus ( $E_{cc}$ ) of the examined panel is measured by testing six (6) specimens of each thickness in compliance with the procedure described in paragraph A.2 of EN 14509: 2013 standard. The specimens, as recommended in EN 826 standard (compressive behavior of thermal insulation products) should have a square cross-section of dimensions between 50 and 300mm. In the present study prisms of 100x100mm are used. Also, six (6) specimens of the same dimensions are tested for evaluating the tensile behaviour of the panels and measuring their tensile strength ( $f_{ct}$ ) and elasticity modulus ( $E_{ct}$ ) in accordance with the paragraph A.1 of EN 14509: 2013. Finally, the terms of paragraph A.3 of the aforementioned paragraph are implemented for testing three (3) SP specimens of length of 1000mm and width of 100mm under “shear test with two-point loads” and estimating the ultimate shear strength ( $f_{cv}$ ) and shear modulus ( $G_c$ ). The properties of the specimens and details of the procedures are listed below in Table 1.

Examined Characteristics	Test Method/Procedure	Specimens' dimensions			min number of tested specimens
		thickness $d_c$ (mm)	length (mm)	width (mm)	
Compressive strength and modulus	EN 14509:2013 A.2	50, 80, 100	100	100	6
Tensile strength and modulus	EN 14509:2013 A.1	50, 80, 100	100	100	6
Shear strength and modulus	EN 14509:2013 A.3	50, 80, 100	1000	100	3

Table 1: Properties of tested specimens and experimental procedures

### 3 EXPERIMENTAL RESULTS

In this section the results of the experimental tests are presented. Figures 2, 4 and 6 illustrate the damage pattern of compression, tension and shear, respectively. In Figure 3 the compression stress – strain curve is depicted and the average values of strength and elasticity modulus are presented. The same applies to Figure 5, which refers to tensile behavior, while Figure 7 illustrates the maximum applied load – deflection curve of the examined specimens and shear strength and modulus average rates are displayed.

Observing Figure 3, one can see that the thickness of insulating panels has little effect on their performance under compression test as the characteristic values of compressive strength and elasticity modulus have little difference for the three examined width rates. Also, it is not clear if this little impact is negative or positive since the compressive strength of SP 80mm thick is smaller than that of 50mm, but greater than that of 100mm.

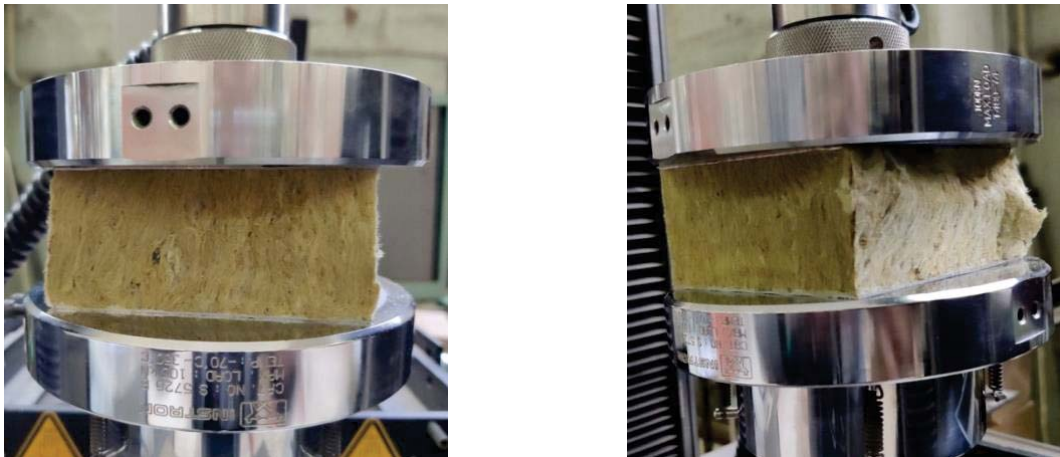


Figure 2: Indicative photographs of SP specimen before (left) and after (right) compression test

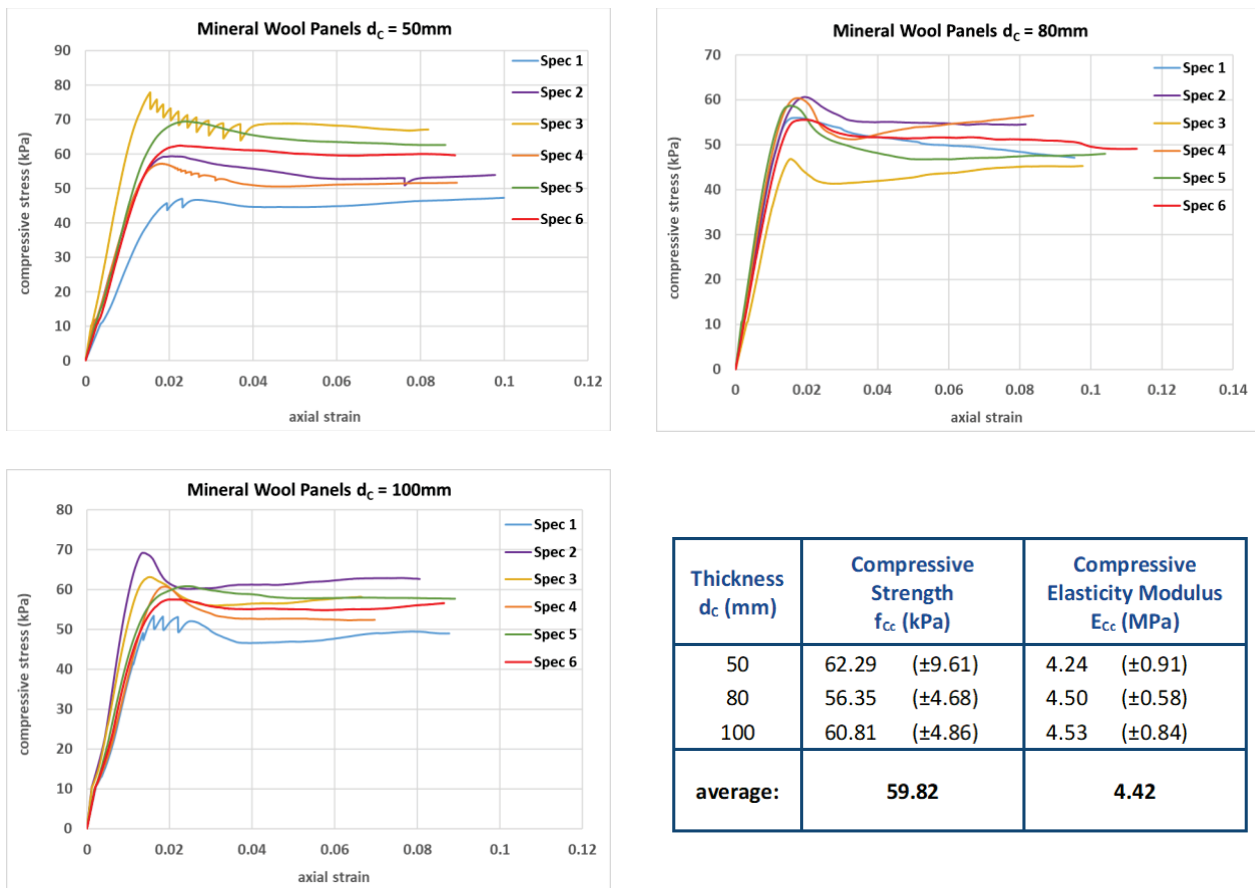


Figure 3: Compressive strength-strain diagrams of six (6) specimens of thickness  $d_c=50\text{mm}$  (top-left),  $d_c=80\text{mm}$  (top-right),  $d_c=100\text{mm}$  (bottom-left) and table of average compressive strength and elasticity modulus values (bottom-right)

The experimental results revealed that the performance of SP under tension test (Figure 5) is deteriorate to that under compression (Figure 3) as the average tensile strength amounts approximately to 10kPa while the average compressive strength is about 60kPa, i.e., 6 times greater. Another interesting finding is that the tensile elasticity modulus of the examined

insulating panels is roughly 1/8 of the compressive modulus, fact that is depicted in the corresponding curves' slope angle.

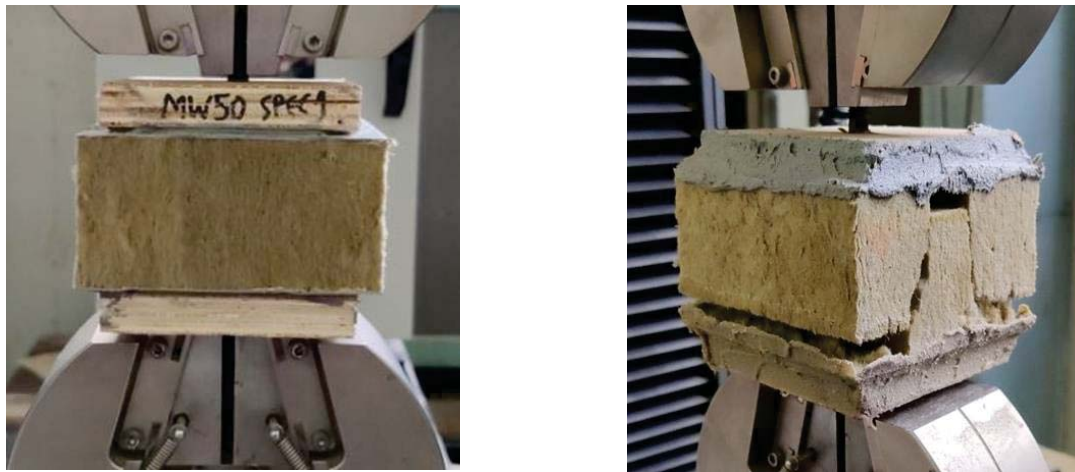


Figure 4: Indicative photographs of SP specimen before (left) and after (right) tension test

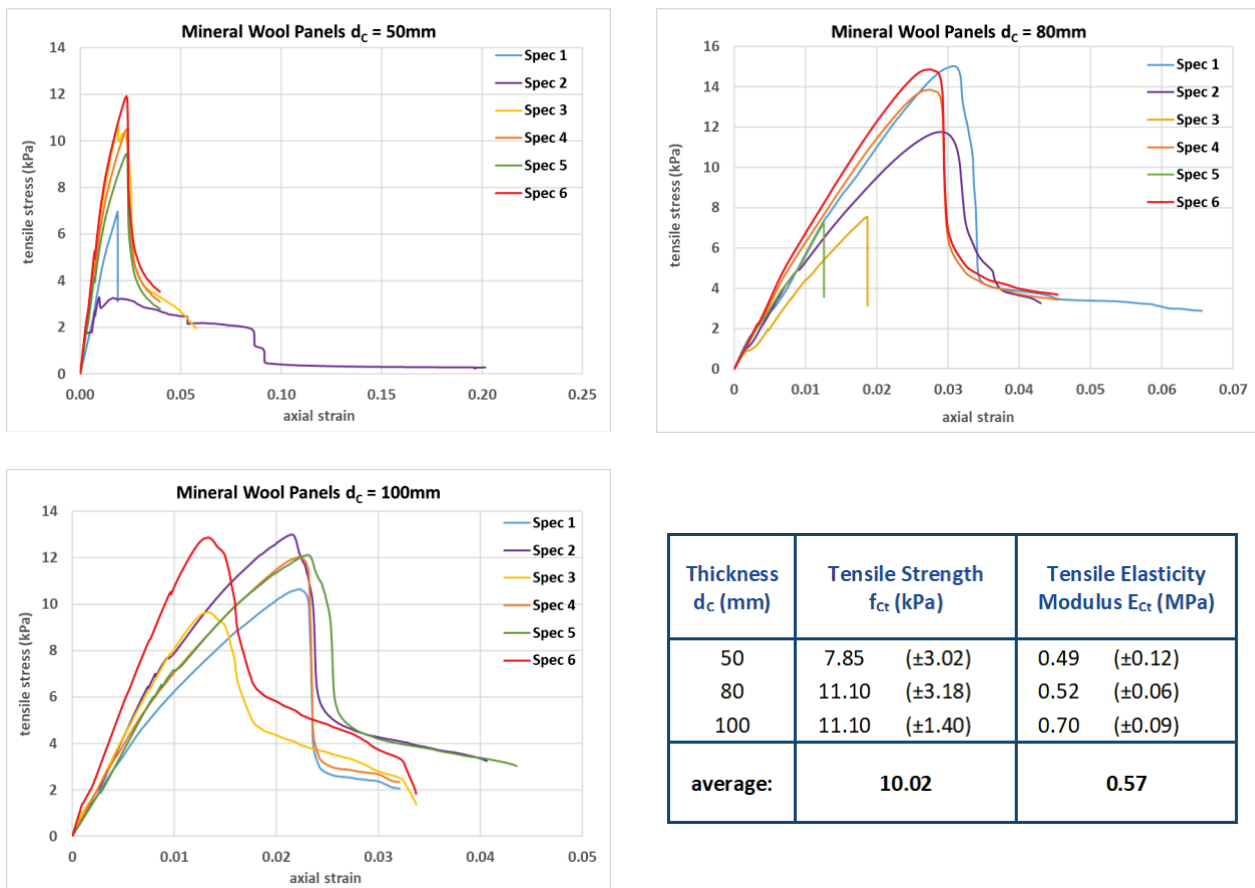


Figure 5: Tensile strength-strain diagrams of six (6) specimens of thickness  $d_c=50\text{mm}$  (top-left),  $d_c=80\text{mm}$  (top-right),  $d_c=100\text{mm}$  (bottom-left) and table of average tensile strength and elasticity modulus values (bottom-right)

The performance of SP under shear test is very sound as shown in Figure 7. The shear strength average value amounts to 3255kPa, 54 times greater than the compressive strength and

325 than the tensile strength. This happens because of the high contribution of lamellas (steel panels) to the tensile behavior of SP product (lamella material's properties listed in section 4).

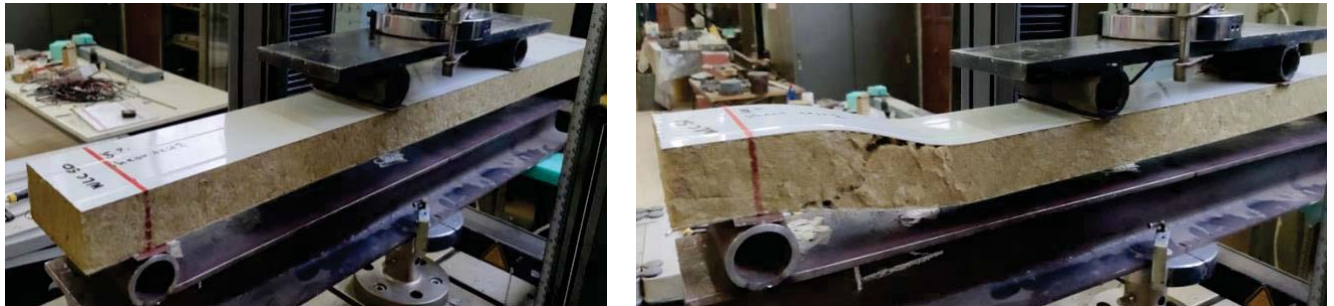


Figure 6: Indicative photographs of SP specimen before (left) and after (right) shear test

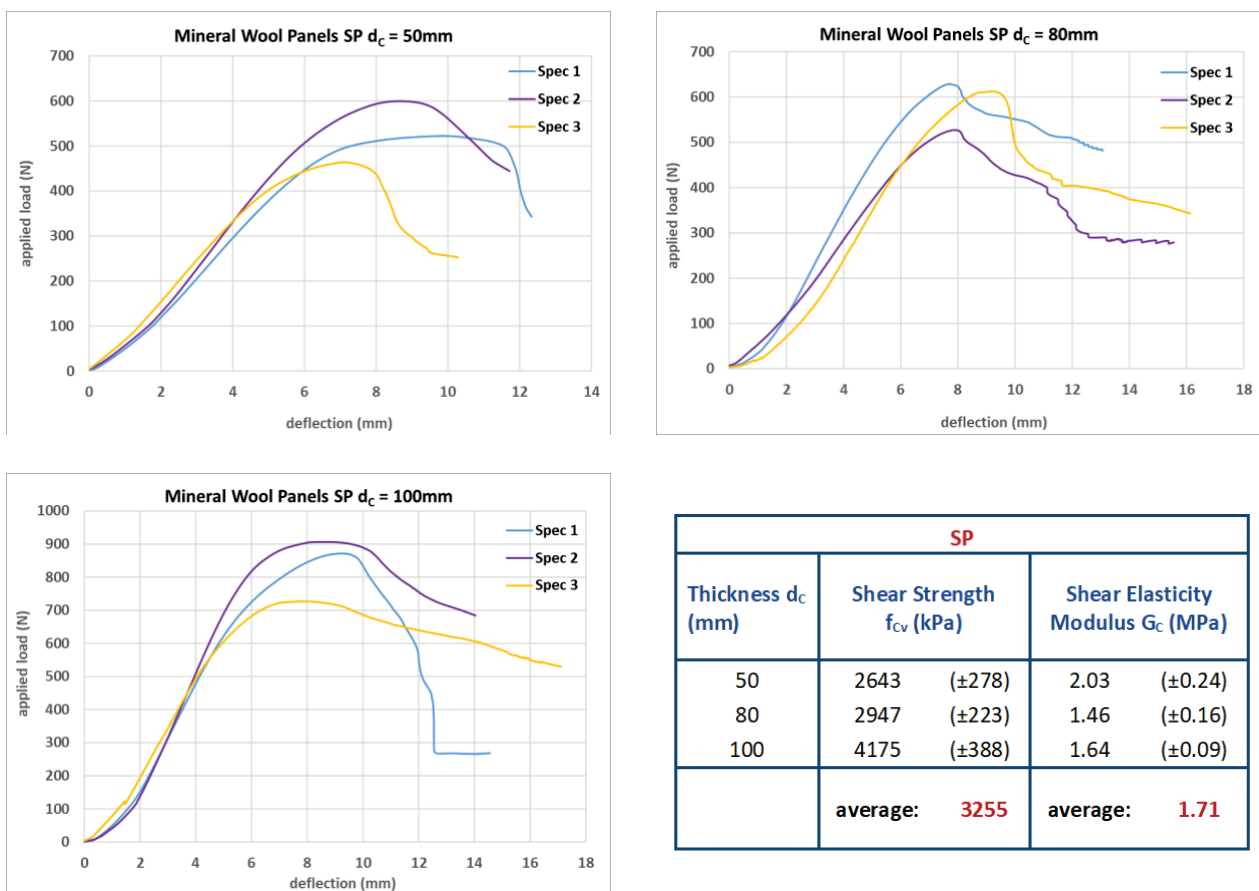
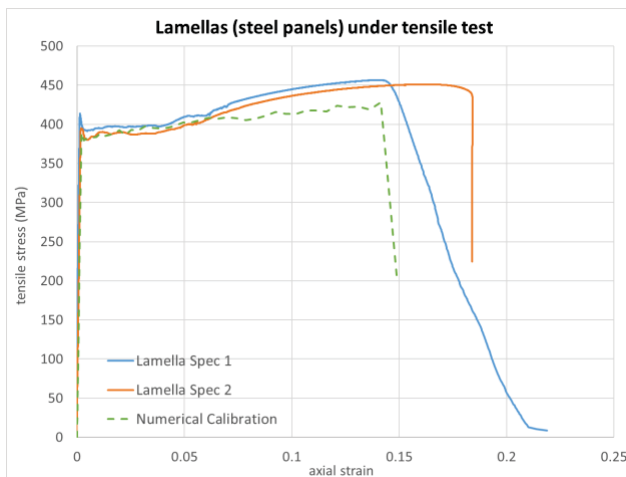


Figure 7: Applied load-deflection diagrams of three (3) specimens of thickness  $d_c=50\text{mm}$  (top-left),  $d_c=80\text{mm}$  (top-right),  $d_c=100\text{mm}$  (bottom-left) and table of average shear strength and elasticity modulus values (bottom-right)

#### 4 NUMERICAL MODELING

Three-dimensional finite element numerical models have been developed adopting a macro modeling approach with homogenized non-linear material laws. It should be underlined that the steel face (lamella) of the insulating panel has been at first tested separately at the “Laboratory of Strength of Materials and Structures” of Aristotle University of Thessaloniki and the

material's mechanical properties have been calibrated in a Finite Element Analysis (FEA) software. The results of this calibration are presented in Figure 9 and the material's properties are listed in Table 2. After that, the compression and tension tests have been simulated and both the compressive and tensile characteristics of the core material (MW) have been calibrated in order to achieve the actual behaviour of the panels, observed at the laboratory. For indicative reasons and in order to avoid a lengthy paper, only the calibration of panels of width  $d_c=50\text{mm}$  under compression is demonstrated below. The same procedure is followed for each thickness value for both compression and tension tests. Finally, a material law that satisfies all cases is determined and its parameters are presented in Table 3 and these parameters become the input for FEM simulation of shear tests.



tension	
stress (MPa)	plastic strain
380	0
500	0.1581
50	0.1881

Table 2: The calibrated material law for lamellas of SP

Figure 9: Calibration of tensile behavior of lamellas (steel panels of thickness of 0.45mm)

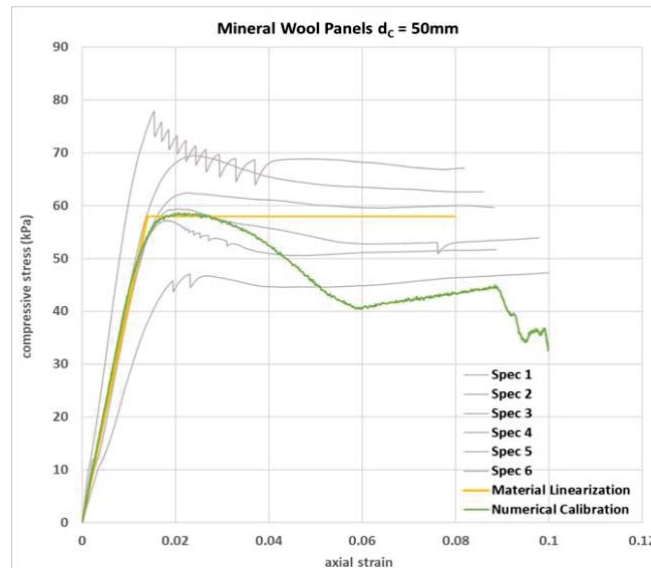


Figure 10: Calibration of compression behavior of the insulating panels of thickness  $d_c=50\text{mm}$



compression		tension	
stress (MPa)	plastic strain	stress (MPa)	plastic strain
0.035	0	0.0075	0
0.0175	0.05176	0.0020	0.03324

Table 3: The calibrated material law for Secret Fix Panels (SP)

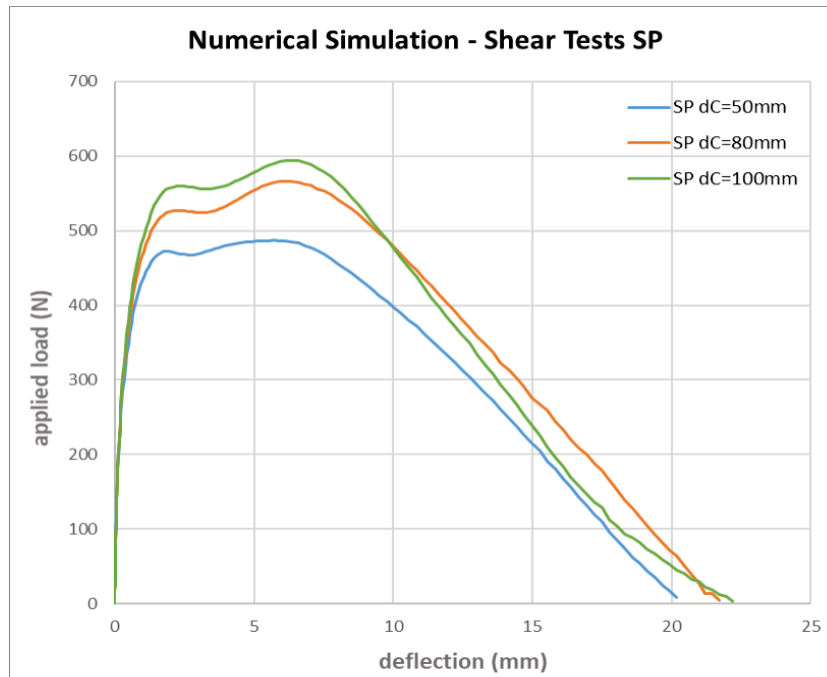


Figure 11: Applied load-deflection curves for numerical FEM simulation of SP

Comparing Figures 7 and 11, one can observe a very good correlation as the results of numerical simulation approach adequately the experimental ones. More specifically, the maximum load values achieved in FEA simulation for SP of thickness of 50mm and 80mm are very close to the real ones (Figure 7), while the maximum load of 100mm thick SP is a little lower than the experimental (600N against 750N – Figure 7). Moreover, the load-deflection curves achieved in numerical simulation have greater slopes angle, which possibly can be attributed to elasticity modulus scarce assess. This could be investigated further. Finally, the damage pattern under shear test in FEA software is illustrated below (Figure 12), which is very realistic, comparing to the one observed in laboratory (Figure 6)

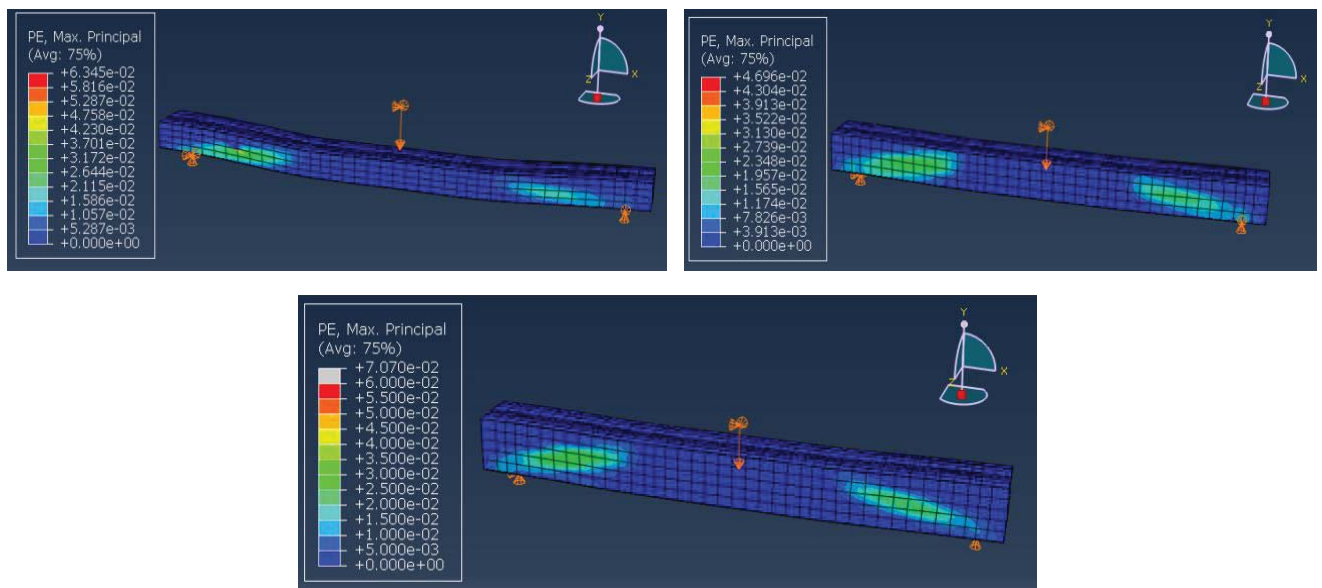


Figure 12: Illustrated damage pattern in FEM simulation models for SP of width  $d_c=50\text{mm}$  (top-left),  $d_c=80\text{mm}$  (top-right) and  $d_c=100\text{mm}$  (bottom)

## 5 CONCLUSIONS

The performance of insulating MW Panels SP behavior under compression, tension and shear loadings is discussed here, mainly focusing on the FEM simulation capacity to accurately approach the experimental results. The main conclusions are enlisted below:

- The compressive strength of SP is about 6 times greater than the tensile strength. The shear strength of SP is about 54 times greater than the compressive strength and 325 than the tensile, which is mainly attributed to the high contribution of lamellas (steel panels) to shear behavior.
- The thickness of SP has little impact on its performance under compression and tension tests.
- The developed 3-D FEM models, after experimental tests and numerical validation of the materials, can satisfactorily capture the observed shear behavior of the insulating panels, especially in terms of the maximum load bearing capacity, but also in the damage pattern.

## REFERENCES

- [1] Barrett, P. et al., edited (2010) W056 – Special Track, 18<sup>th</sup> CIB World Building Congress, May 2010 Salford, United Kingdom. CIB Publication 342. 84 p.
- [2] Zenkert, D. (1997), The Handbook of Sandwich Construction, Chameleon Press, London
- [3] Metod Čuk – Franc Kosel – Nenad Zrnić – Boris Jerman, An Analysis of Continuous Sandwich Panels with Profiled Faces, Journal of Mechanical Engineering 63(2017)12, 746-753
- [4] Davies, J.M. (2001), Lightweight Sandwich Construction, Blackwell Science, Oxford, DOI:10.1002/9780470690253

- [5] EN 14509:2013 Self-Supporting Double Skin Metal Faced Insulating Panels - Factory Made Products - Specifications. European Committee for Standardization, Brussels
  - [6] Misiek, T., Hassinen, P. (2010), Unified Approach for the Local Buckling Of Sandwich Panels and Trapezoidal Sheeting, Proceedings: W056 – Special Track 18<sup>th</sup> CIB World Building Congress, Salford, p. 14-26
  - [7] Pokharel, N., Mahendran M. (2004), Finite element analysis and design of sandwich panels subject to local buckling effects, Thin-Walled Structures, vol. 42, no. 4., p. 589-611, DOI:10.1016/j.tws.2003.08.002
  - [8] Pokharel, N., Mahendran M. (2005), An investigation of lightly profiled sandwich panels subject to local buckling and flexural wrinkling effects, Journal of Constructional Steel Research, vol. 61, no. 7, p. 984-1006, DOI:10.1016/j.jcsr.2004.12.008
  - [9] Rädcl, F., Lange, J. (2011), Tragfähigkeit von Sandwichelementen mit profilierten Deckschichten und Öffnungen. Stahlbau, vol. 80, no. 9, p. 656-661, DOI:10.1002/stab.201101469
- Ilić, I., Petrovic, Z., Maksimović, M., Stupar, S., Stamenković, D. (2012), Computation method in failure analysis of mechanically fastened joints at layered composites, Strojniški vestnik – Journal of Mechanical Engineering, vol. 58, no. 9, p. 553-559, DOI:10.5545/sv-jme.2011.157

## SEISMIC FRAGILITY ASSESSMENT FOR A CLASS OF RC SCHOOL BUILDINGS IN ITALY LEVERAGING DETAILED AND REDUCED-ORDER MODELS

Sergio Ruggieri<sup>1</sup>, Giuseppina Uva<sup>1</sup>

<sup>1</sup> Polytechnic University of Bari  
Via Amendola, 70126 Bari, Italy  
{sergio.ruggieri, giuseppina.uva}@poliba.it

---

### Abstract

*A study is presented on the seismic fragility analysis of a class of existing RC school buildings in Puglia, Southern Italy. Firstly, we defined a taxonomy for identifying a homogenous building class, through the collection of typological data, such as construction age, number of storeys and construction materials. After, by means of the available Census data on Italian school buildings, we selected 735 units in the focused area to assembly a proper database to involve in the phase of numerical modelling and analysis. To assess fragility, we employed two modelling options: (a) a single-degree-of-freedom approach, by evaluating the backbone of the simplified models; (b) a multi-degree-of-freedom approach, by means of some index buildings of the class for which a full knowledge of geometrical and mechanical properties is available, as well as their spatial nonlinear numerical models. Nonlinear time history analyses were performed on all simplified models to define specific class fragility, accounting for any source of variability (record-to-record and building-to-building). The results of the investigation are compared in terms of class fragility curves, in order to highlight the differences between the two modelling approaches.*

**Keywords:** Class Fragility Curves, Typological Data, SDOF Models, MDOF Models.

---

## 1. INTRODUCTION

The studies about seismic fragility at class-level of buildings have recently become increasingly numerous among researchers, which try to individuate the main sources of vulnerability and to reduce the related risk of several typologies of building portfolios. Of growing interest are the investigations focused on the existing building stock, which is often characterized by an high probability of damage, especially if subjected to earthquakes. Several examples of the catastrophic effects given by earthquakes are available, with regard to different building typologies having different social importance, such as residential [1-2], strategic (e.g., schools [3-4] or hospital), precast and ecclesiastical buildings [5]. A myriads of approaches can be employed for defining fragility functions for class-level assessment purposes, in which four macro-categories can be identified: (i) empirical [6-7], (ii) mechanical [8-11], (iii) judgemental [12] and (iv) hybrids methods. Among these, in this study we are going to argue about mechanical ones, focusing on the results achievable by different modelling approaches.

Generally, the mechanical methods allow to perform fragility/vulnerability assessment through a direct derivation of the relationship between seismic intensity and damage states/losses. This is possible by means of the analysis results (usually nonlinear dynamic or static) carried out on numerical models, which simulate a single or a class of buildings. The results of a fragility function, elaborated for large-scale purpose, is strictly related to the quantity and the quality of the numerical models at disposal, which in turn depends from the available data. With this regard, Silva et al. [13] defined the two extreme options: (a) few detailed multi-degree-of-freedom (MDOF) models; (b) many single-degree-of-freedom (SDOF) models. The first option consists in the selection of few real (or idealized) archetypes representative of a certain building class, characterized by a detailed knowledge of all structural components and all geometrical and mechanical properties. This is the case of the so-called index-buildings, which are usually selected through the expert opinions of the analyst, as made in [10,14]. Obviously, an incorrect selection of the index-building properties can lead to a misleading fragility evaluation, frustrating the related analysis efforts. The second option consists in an extensive analysis process on a large number of reduced-order models, generated on the base of few data and outlined through simple computations. The easy management and the evident discount in terms of analysis efforts makes the SDOF models the most attractive option, as shown in several literature works [15-16], although the loss of accuracy in each single model (e.g. local responses, structural irregularities) assumes a key role in the fragility estimate. In the middle, other methods are available from the scientific literature, balancing accuracy vs. complexity and quantity vs. quality of numerical models [17-19].

In all cases, by referring to class-level fragility, the starting point is the definition of a building taxonomy, which can vary on the basis of the sample size. As a matter of fact, to represent the overall fragility of a specific class via simple SDOF models, few data are necessary, such as the construction material, the year of construction or the number of storeys. On the other hand, the adoption of complex MDOF models requires the knowledge of detailed information, which implies a not always sustainable economic and computational burden in the investigation and analysis phases.

Anyway, the goodness of the fragility function is strongly influenced by two not negligible aspects: (a) the analysis method (b) the uncertainty treatment. On the analysis side, static pushover (SPO) analysis [20] and nonlinear response history analysis (NRHA) contend for the title of best, where the first approach wins in simplicity and intuitiveness, while the second approach dominates the first one in the prediction of seismic response of buildings, accounting for the real nature of earthquakes (use of ground motions) and for the features variability of any kind of buildings (e.g., structural irregularities, influence of higher modes). On the uncertainty side, NRHA approach can be preferred in class-fragility analysis, where record-to-record variability can be taken into account by



evaluating its contribute on the basis of the number of records employed, the selected intensity measure (IM) and the investigated engineering demand parameter (EDP). In addition to this kind of uncertainty, the intra-building and the inter-building uncertainties are to consider, where the first one refers to the uncertainty in the knowledge of each investigated building and the second one aims to define the variability of each building in the selected ensemble to represent the class.

In this wide range of options, a study on the fragility function of a class of real school buildings in Puglia (Southern Italy) is provided, by exploring the two abovementioned modelling extremes: many simple SDOF models vs. few complex MDOF models. Given a building taxonomy, the comparison among fragility curves at safety limit-states is provided, by using the results of 10 complex MDOF models selected from the work by Ruggieri et al. [21] and the response of 735 SDOF models elaborated from the information contained in some freely available exposure databases (ISTAT Census data [22], ARISTOTELES Project [23], Open Data about Italian schools provided by Italian Ministry of University and Research (MIUR) [24]). Fragility functions will be developed by opting for a NRHA approach, as well as by running cloud analyses on MDOF models and incremental dynamic analyses (IDAs) on SDOF models [25]. For the case at hand, we can anticipate that the seismic behaviour of SDOF models (e.g., backbone curve), which could be evaluated through any number of methods proposed by the scientific literature, has been evaluated looking at the MDOF models, their modelling assumptions and their seismic response.

## 2. MODELLING METHODOLOGIES FOR SDOF SYSTEMS FOR CLASS-LEVEL ASSESSMENT PURPOSES

The use of SDOF models for developing class fragility/vulnerability functions has been often adopted by researchers to limit the computational burden for larger sets of buildings [15-16]. The parametrization of the inelastic behaviour of SDOF, as well as the backbone shape, can be elaborated through different fairly popular procedures. For example, Ruiz-García and Miranda [26] elaborated a probabilistic approach to estimate the maximum inelastic displacement demands of SDOF systems, by providing a new version of the  $R$ - $\mu$ - $T$  (strength ratio-ductility-period) relationship [27], through the definition of the constant-strength inelastic displacement ratios. Vamvatsikos and Cornell [28] proposed a pushover-based approach to investigate the dynamic behaviour of SDOF models, simulated through a quadri-linear backbone and contextually, authors developed the SPO2IDA tool. The same approach was involved in the analytical studies developed in FEMA P440A [29], which presents the force-displacement capacity of some spring typologies to employ in SDOF systems for simulating different building behaviours, expressed in terms of maximum inter-story drift ratio ( $\theta_{max}$ ) vs. the normalized base shear on the yield value ( $V_b/V_{b,y}$  or  $F/F_y$ ). Lagomarsino and Giovinazzi [30], proposed the relationships to relate macro-seismic and mechanical-based approaches, in which authors provided criteria to trace the SDOF backbone curves for several class of European buildings. Vamvatsikos and Aschheim [31] adopted the paradigm of Performance-Based Design, by means of Yielding Frequency Spectra approach, to define an equivalent SDOF model from a MDOF one, as well as after applied by Kohrangi et al. [32] in the vulnerability model for buildings in the municipality of Isfahan, Iran.

Herein, we are adopting the procedure suggested in [32], by assuming a backbone curve of SDOF models (and the boundary control points for the spring to employ, in terms of  $\theta_{max}$  vs.  $F/F_y$ ) according to the seismic behaviour of full MDOF models, given a building taxonomy. With regard to the building taxonomy, it is necessary that both SDOF and MDOF models are belonging to same class, which is defined by the parametrization of at least five parameters, usually available in freely online databases: construction typology ( $CT$ ), year of construction ( $CY$ ), number of storeys ( $NS$ ) and

two values among in-plan area ( $A$ ), total volume ( $V$ ), interstorey height ( $H_i$ ) and total height ( $H_{TOT}$ ). Within the online databases containing the required information, the parameters  $A$  and  $V$  are often available and they can be employed by means of simple equations and assumptions, to estimate all the key features of the building taxonomy. In particular, knowing  $CT$ ,  $CY$  and  $NS$ , the other parameters can be found with the following equations (or with the inverse formulations):

$$H_{TOT} = \frac{V}{A} \quad (1)$$

$$H_i = \frac{H_{TOT}}{NS} \quad (2)$$

In addition, assuming the typical values of gravity loads ( $L$ ) for the selected building class, it is possible to compute the total mass ( $M$ ) and the total weight ( $W$ ) of the buildings:

$$L = G + \psi_{k2} \cdot Q_k \quad (3)$$

$$W = A \cdot L \cdot NS \quad (4)$$

$$M = \frac{W}{g}; m_i = \frac{M}{NS} \quad (5)$$

where  $G$  and  $Q$  are, respectively, the dead and the accident loads,  $\psi_{k2}$  is the combination coefficient for the quasi-permanent  $k^{th}$  load,  $g$  is the gravity acceleration and  $m_i$  is the mass of the  $i^{th}$  storey. While  $Q$  can be defined on the basis of the prescriptions provided by the current building code,  $G$  is an unknown parameter, which can be established on the basis of the typical features of the building typology investigated. To support the definition of  $G$ , the knowledge of the technologies and the loads detected on some MDOF buildings is fundamental, in order to identify the most employed typologies of slabs, external and internal masonry infills, floor tiles and other finishes.

To define the SDOF behaviour, the formulation defined in [31] and developed in [32] can be employed, where the parameters of an equivalent SDOF are provided. In particular, given the building taxonomy, the approach consists in the definition of eight parameters and a SDOF backbone shape. Among the eight parameters,  $NS$  and  $H_i$  are directly identified from the input building database. Three of the eight parameters can be fixed a-priori, as well as the participation factor ( $\Gamma$ ) and the mass participation factor ( $a_1$ ) for the first vibration mode and the conventional damping ratio ( $\zeta$ ). For the case at hand, both  $\Gamma$  and  $a_1$  can be fixed equal to 1, as suggested in [32]. The remaining three parameters are:

- The base shear coefficient,  $C_y$ , identified as the ratio between the yield base shear and the total weight of the structure ( $V_{b,y}/W$ );
- The yield storey drift,  $\theta_y$ , evaluated on the real elastic behaviour of MDOF building;
- The coefficient of distortion,  $\alpha_{COD}$ , which represents the ratio between the peak interstorey drift and the related roof drift, as following defined:

$$\alpha_{COD} = \frac{\theta_{max}}{\theta_R} \quad (6)$$

Operationally,  $C_y$  can be defined on the yield code spectrum given the yield displacement ( $\delta_y$ ), because it is equivalent to yield spectral acceleration (expressed in unit of  $g$ ). To define  $\delta_y$  as suggested in [31], the following equation can be adopted:

$$\delta_y = \frac{\theta_y \cdot (NS \cdot H_i)}{\Gamma \cdot \alpha_{COD}} \quad (7)$$

Eq. 7 depends from the parameters  $\theta_y$  and  $\alpha_{COD}$ , where the first one can be defined by observing the behaviour of the available MDOF structures, while  $\alpha_{COD}$  can be defined according to [33, 34]. This parameter is the simpler way to define the deformation behaviour of buildings and, for a generic MDOF system,  $\alpha_{COD}$  ranges between 1.1 and 1.4 as long as the building behaves as elastic. After the

yielding and for higher values of  $\theta_{max}$ ,  $\alpha_{COD}$  tends to increase, as shown in [31]. For a one-storey building  $\alpha_{COD}$  is equal to 1. Once that all the eight parameters are defined, the period of each SDOF system ( $T^*$ ) can be evaluated as:

$$T^* = 2\pi \cdot \sqrt{\frac{\delta_y}{c_y \cdot g}} \quad (8)$$

Finally, to define the backbone shape of SDOF system, it is possible to pursue different options, basing on the expected behaviour of the simulated buildings. The simpler option is the elastic-plastic shape, while to better simulate the post-elastic behaviour it is possible to refer to the parametric capacity curve shapes provided by FEMA-P440A [29]. The presented SDOF models can be employed in the fragility function, by means of the results provided by the analysis phase. Some additional remarks can be added for the development of the procedure. Firstly, for a class-level purpose, different seismic actions can be considered within the focused area and the definition of the yield spectral acceleration can be differentiated on the basis of the buildings localization. After, some of the eight parameters, such as  $\theta_y$ , can be established a-priori on the basis of the *CY* of the buildings and the reference building code [32]. Nevertheless, the detailed knowledge of the structural behavior of some MDOF structures, representative of the building class, can be used for having a reliable indication about the effective values to employ in the procedure. In the end, also the adoption of the FEMA-P440A backbone curves [29] could represent a simplification. Also for this aspect, the seismic response of few MDOF structures belonging to the identified class can be employed for a calibration of a specific-class backbone curve shape, to involve in the fragility function through the simplified modelling approach.

### 3. DEFINITION OF AN HOMOGENEOUS CLASS OF SCHOOL BUILDINGS IN PUGLIA, SOUTHERN ITALY

The starting point of this study is represented by 15 real RC school buildings in the province of Foggia, Puglia, Southern Italy. In particular, for these buildings, which present a generalized in plan irregularity, a near-full information of the geometrical and mechanical features is available and, according to the work by Ruggieri et al. [21], the 3D numerical models of buildings and the related pushover analyses in both directions are at disposal. Following the procedure in Section 2, within this sample of buildings, it is possible to define an homogenous subset aimed to identify a building taxonomy, according to some key parameters and additional historical information.

Firstly, all buildings present a *NS* ranging from 2 to 3, which suggest that the entire sample is constituted by low-rise buildings, also according to the classification provided by HAZUS [35]. After, concerning to the *CT*, all buildings are RC moment-frame buildings, which do not present RC walls and all buildings present infill panels (in some cases, the eternal frames are totally infilled, while in others they are partially infilled and presenting ribbon windows). The discriminant parameter is the *CY*. Despite all buildings were designed between 60' and 80', three main historical aspects have to be considered to define the building taxonomy [23]:

- After some modifications occurred in 1935 and in 1969, the Apulian seismic map was upgraded in 1981, and some municipalities of the Province of Foggia (North of the Region) were redefined from non-seismic to low-seismic areas, as shown in Figure 1.
- Between 1972 and 1979, Italian governments released a new version of the Italian building code, in which new design rules were introduced accounting for the first anti-seismic requirements.
- In the subsequent years to the Second World War (from 1945 to 1950), new buildings difficultly presented RC moment-frame structural systems, because it was very likely the

presence of masonry structural parts. This evidence was caused by the aftermaths of the Fascism that previously forbade the use of the steel in Italy.

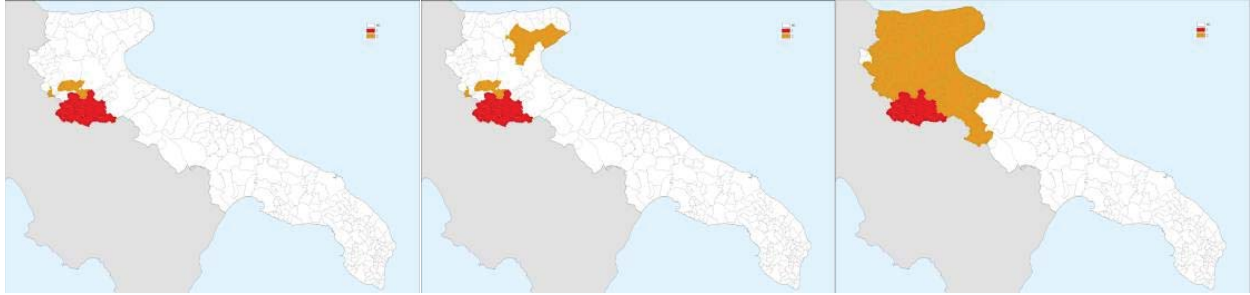


Figure 1 – Evolution of the seismic classification in Apulian Region with reference to, respectively, 1935/03/25, 1962/11/25 and 1981/3/7 [23]. The white part indicates non-seismic areas, the orange part indicates a low-seismic areas (zone 2) and the red part indicates a medium-high seismic areas (zone 1)

Then, with regard to *CY*, the buildings belonging to homogenous class are the ones built between the 1950 and 1979 and located in the municipalities classified as non-seismic areas (according to the seismic classification provided by Italian governments and shown in Figure 1), within the indicated time period. According to the identified building taxonomy, 10 of 15 school buildings fall under the homogenous class. Figure 2 reports the pushover curves in both main directions (X and Y, according to the reference system adopted in [21]) for the new subset of buildings, labelled as B1-B10 (From the total sample, B3, B4, B5, B6 and B10, as defined in [21], have been excluded and the remaining 10 buildings have been renumbered).

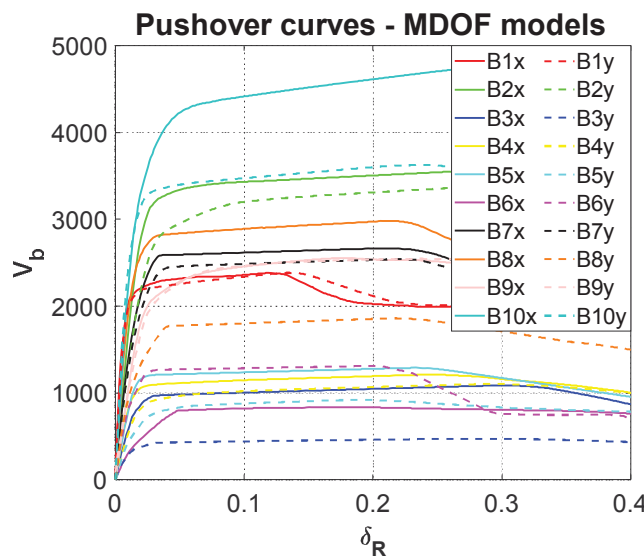


Figure 2 – Pushover curves in both directions (X,Y) of the 10 RC school buildings, belonging to the identified building class

For a purpose of class-level assessment, given the building taxonomy, several buildings can be identified from freely available databases, for which few data are at disposal. For the case at hand, two open databases have been consulted and elaborated: (a) database developed in ARISTOTELES Project [23] and (b) Open Data about Italian schools provided by Italian Ministry of University and Research (MIUR) [24]. From the first database, which was based on the ISTAT Census data [22], information about all the existing schools in Puglia have been gathered with reference to 2001. In particular, data on *CY*, *CT*, *NS*, *V*, *A*, municipalities where buildings are located and the related seismic evolution in the time were extracted. From the second database, information about all the existing



schools in Italy have been collected with reference to 2019. In detail, it presents only the exact location of each school building (municipality, address, postal code) and information on  $CY$ ,  $A$  and  $V$ . In both databases, each unit presents an univocal code to identify the school. By matching the two databases through the comparison of the common data (univocal code, municipality,  $CY$ ,  $A$  and  $V$ , evaluated with a certain tolerance) and with regard to the given building taxonomy, 735 existing RC school buildings have been selected. All data have been elaborated according to the Eqs. 1-5. More in detail, after the evaluation of  $H_i$  and  $H_{TOT}$  for all buildings, a value of  $L$  equal to  $6 \text{ kN/m}^2$  has been supposed, given by the assumption of a value of  $G$  equal to  $5 \text{ kN/m}^2$ , a unique value of  $Q_k$  equal to  $3 \text{ kN/m}^2$  and a value of  $\psi_{k2}$  equal to 0.3 in accordance with the Italian Building code (NTC18) [36]. Figure 3 reports the geographical distribution of all identified buildings, where the greater part of the units are located in the South and in the Central of the Region, while only few buildings have been considered in the North, accounting for the existing seismic zoning in the assumed time interval.

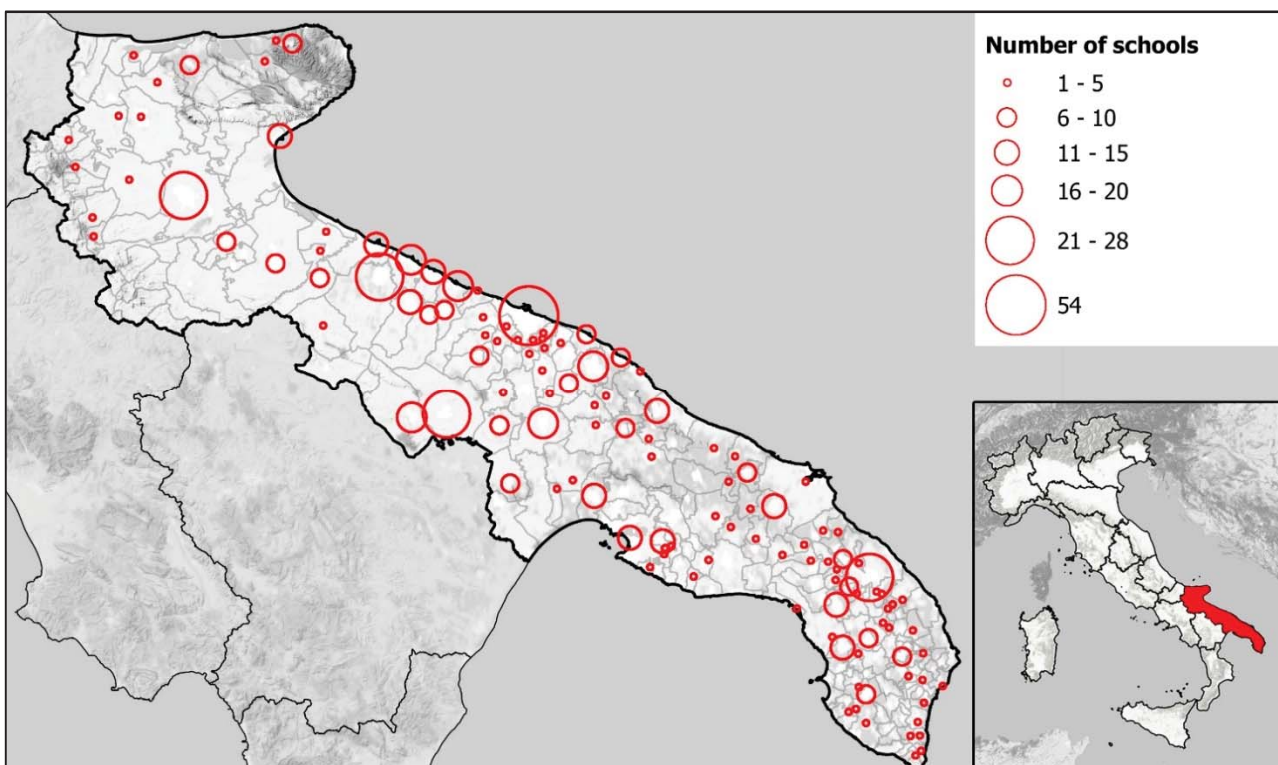


Figure 3 – Distribution of the selected 735 school buildings along the Region, according to the given taxonomy

#### 4. SEISMIC FRAGILITY ASSESSMENT AT CLASS-LEVEL

##### 4.1 Numerical models

For both samples made by 10 MDOF and 735 SDOF systems, different modelling strategies have been employed. Concerning to the modelling of the 10 full models of the known school buildings, the reference is the work made in Ruggieri et al. [21], where the nonlinear MDOF models were carried out through a lumped plasticity approach and by implementing all the geometrical and mechanical features at disposal. As just shown in Figure 2, a ductile behaviour is assumed, by neglecting for simplicity the influence of shear mechanisms and infill panels. Nevertheless, as declared in [21], shear failures given by low transversal reinforcement of structural elements can be evaluated a posteriori, by checking the brittle mechanisms of beams and columns. After, all the 735 buildings belonging to the homogenous class have been elaborated for a SDOF approach. More in detail, looking at the SPO curves of the 10 MDOF structures, a value of  $\theta_y$ , equal to 0.25% has been



fixed while, according to [32], the values of  $\alpha_{COD}$  are assumed equal to 1, 1.25 and 1.35, respectively for 1-storey, 2-storeys and 3-storeys buildings. Using Eq. 7, the values of  $\delta_y$  have been defined for all buildings. Later, assuming an elastic code spectrum, the values of  $C_y$  have been defined, which are the same values of the spectral accelerations. Finally, by means of Eq. 8, the values of  $T^*$  have been determined. With regard to the assumed elastic code spectrum, the seismic actions in the regional capital (Bari, which is in the Central of the Bari) has been considered, as good compromise between the higher seismicity in the North and the lower seismicity in the South. Still, in the elastic code spectrum has been computed by using an unitary behavior factor and by considering an usage class adequate to school buildings, with a coefficient equal to 1.5. Lastly, no any amplification factors due to e.g., soil and topography categories have been considered. For few cases of the buildings investigated, high values of  $V_{by}$  are obtained, considering high values of  $A$ , as typical for school buildings in the focused geographic zone. In addition, a large set of  $T^*$  is identifiable, which ranges about from 0.3 s to 0.8 s and given by the different  $NS$  that characterize buildings in the considered sample.

Therefore, all 735 buildings have been modelled through nonlinear SDOFs oscillators. In particular, the springs of the SDOF systems have been simulated by using OpenSees software [37], opting for a Pinching4 material to define the quadri-linear force-displacement capacity boundaries. Regarding to the backbone capacity of the springs employed in the SDOF models, “spring 3b” provided by FEMA-P440A [29] has been considered. As a matter of fact, according to the modelling strategy adopted for the MDOF structures, a ductile behaviour has been accounted for, as visible in the backbone curve shape reported in Figure 4 (right), which also reports the boundary control points of the backbone curve. All coordinates of the normalized hinge (each point is indicated with a letter, labelled from  $A$  to  $G$ ) are specified in Table 1 and they are reported in terms of  $\theta_{max}$  vs.  $F/F_y$ . In conclusion, the results about SDOF models are displayed in Figure 4 (left), where capacity curves of 735 models are displayed in terms of  $C_y$  and  $\delta_R^*$  (light grey lines) as well as the mean and the standard deviation of all realizations (black lines).

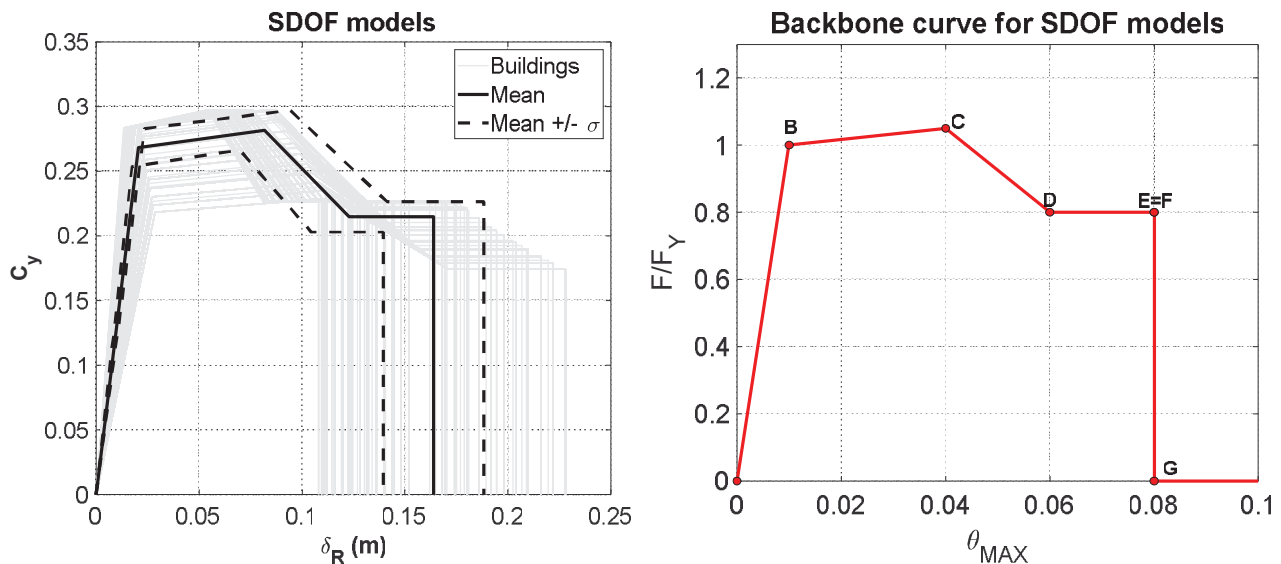


Figure 4 – Capacity curves of the 735 SDOF models generated, displaying mean and standard deviation (left); Backbone curve of SDOF models, according to the prescriptions provided by FEMA-P440A [29] (right)

Table 1. Coordinates of the boundary control points of the Spring “3b” by FEMA-P440A [29], expressed in terms of  $F/F_y$  vs.  $\theta_{max}$ 

Structural system	Quantity	B	C	D	E	F	G
Spring 3b - FEMA-P440A [29]	$F/F_y$	1.00	1.05	0.80	0.80	0.80	0.00
	$\theta_{max}$	0.01	0.04	0.06	0.08	0.08	0.08

#### 4.2 Seismic analysis and class fragility function

The structural response of the 735 SDOF models have been investigated through NRHAs, according to the IDA methodology, while the MDOF models were investigated through SPOs analyses and NRHAs [21]. These latter analyses were performed according to a practice-oriented principle (computational cost reduction) and, for this reason, only few NRHAs have been carried out. With regard to the number of records employed, MDOF models were subjected to a set of 11 ground motion records characterized by two horizontal components, to investigate 3D models in both main directions. For sake of comparison, the same set of 11 ground motion records has been employed herein, by running IDAs with all the 22 horizontal components to each SDOF model. Figure 5 shows an example of the analyses performed on the numerical models, both for SDOF and MDOF systems, by assuming as IM the average spectral acceleration ( $AvgSa$ ) evaluated in a range period from 0.2 s to 2 s and as EDP, the values of  $\theta_{max}$ . In particular, IDAs on the SDOF model n. 10 are shown in the left graph while cloud analyses on B1 are shown in the right graph, where black and red dots indicate, respectively, non-collapsed and collapsed points (Both models are characterized by a  $NS$  equal to 2). Regarding to the cloud analyses on 3D models, the results have been recorded in both main directions and, for sake of comparison they are expressed in a unique IM-EDP plane, by considering as response the square-root-of-sum-of-squares rule of the  $\theta_{max}$  in both main directions. Having the structural responses for both sets of models, fragility analysis have been performed. In particular, the fragility functions are differently developed for the two modelling extremes. For identifying the EDP distribution conditioned by the IM value, a power law approximation has been developed on the structural responses of MDOF systems [38], while an IM-basis approach has been employed to IDA results of SDOF systems.

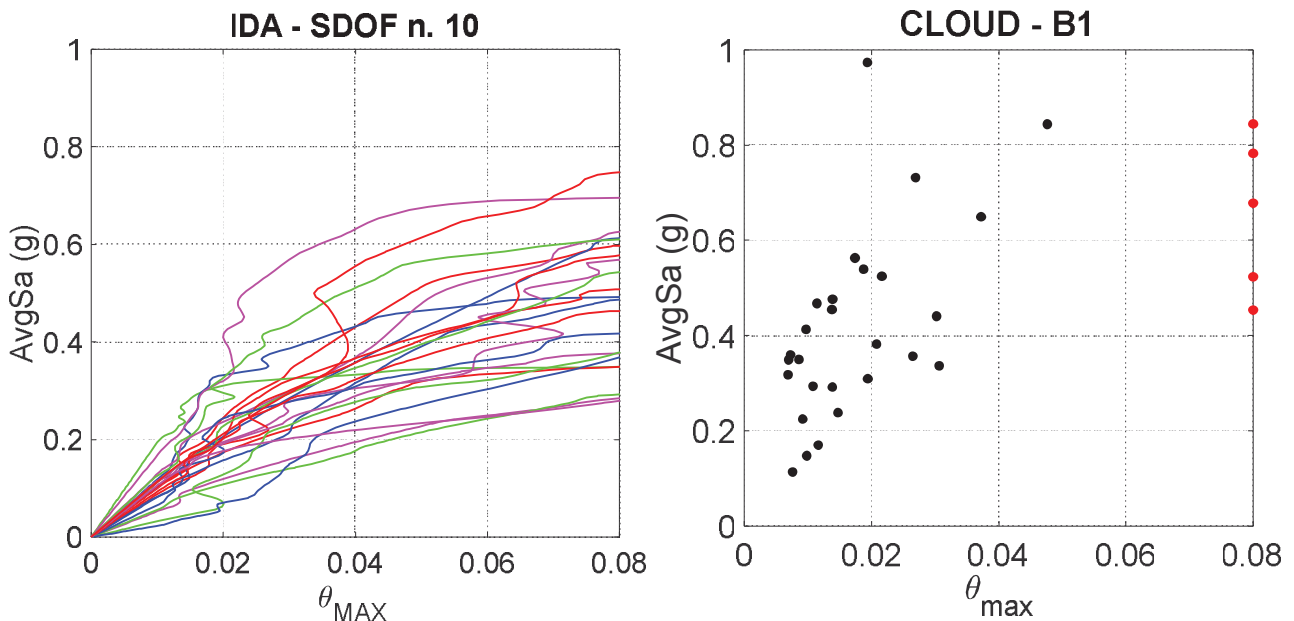


Figure 5 – IDAs on SDOF models (plot for SDOF model n. 50) vs. cloud analysis on MDOF model (plot for building B1, where black and red dots indicate, respectively, non-collapsed and collapsed points)

With regard to the limit-states to investigate, in this study all evaluations have been referred to the safety limit-states, considering that the collapse mechanisms can be given by brittle and ductile failures. In a practice-oriented view, three limit-states have been defined, as well as near-collapse (NC) for brittle and ductile mechanisms and life-safety (LS) for ductile mechanisms. While the achievement of the limit-states can be evaluated independently on each MDOF system by observing the effective structural behaviour of the simulated buildings, a different approach needs to be employed for SDOF models. As a matter of fact, despite a large sample of SDOF models allows to provide a good coverage of all buildings falling into the entire class, this modelling approach does not guarantee an accurate structural failures prediction, especially in the cases of structural irregularities and of higher modes relevance. To establish a valid approach that combines the effective local and global behaviours provided by MDOF models and the simplified estimates provided by SDOF models, fixed values of  $\theta_{max}$  have been assumed for both the involved modelling approaches. In particular, a  $\theta_{max}$  equal to 0.5% has been assumed for NC-brittle limit-state, while thresholds equal to 3.2% and 4.3% have been assumed, respectively, for LS- and NC-ductile limit-states.

These limits are selected by extending the mean values of the thresholds obtained for the buildings selected from the work by Ruggieri et al. [21] to the overall behaviour of the backbone curves for SDOF models. Looking at the boundary control points in the backbone capacity curve (Figure 4, right), NC ductile limit-state is fixed on the branch *C-D*, which identifies the softening part that leads to the residual lateral strength, while LS is fixed in the branch *B-C*, precisely at the end of the hardening phase.

Once that fragility curves have been evaluated for all units of the identified class, accounting for all limit-states of interest (NC - brittle, LS and NC - ductile) and for the two modelling and analysis approaches (cloud on 10 MDOF vs. IDAs on 735 SDOF), class fragilities are estimated by virtue of the laws of total expectation and total variance. In particular, the ensemble lognormal mean ( $\mu_C$ ) is given by the mean of all individual lognormal means, while the related dispersions ( $\beta_C$ ) are evaluated through the sum of the squares of the intra-building and inter-building dispersions. The class fragility curves are displayed in Figure 6, in terms of probability of exceedance of the building capacity conditioned by the IM value assumed for the limit-state considered ( $P[IM > IM_C | IM]$ , where  $IM_C$  is the capacity IM), both for the 735 SDOF models (left, with all fragility curves for all individual units, displayed in light grey) and the 10 MDOF models (right). Table 2 reports the values of the fragility curves parameters, in terms of  $\mu_C$  and  $\beta_C$ .

The comparison among the two modelling options shows that for the NC-brittle limit-state, the values of  $\mu_C$  and  $\beta_C$  are similar while for the LS-ductile and NC-ductile limit-states, the values of  $\mu_C$  and  $\beta_C$  obtained by SDOF models are lower than the ones provided by MDOF models. Nevertheless, considering the percentage difference obtained in terms of  $\mu_C$  for NC-brittle limit state, which is in the order of 50%, it is evident how the two modelling approaches do not return comparable results. This is mainly due to the structural irregularity presented by MDOF structures (and by school buildings in general), which cannot be predicted by a simple SDOF modelling approach. As a matter of fact, as shown in Figure 5, the results obtained by SDOF models are conservative, also for lower values of  $\theta_{max}$  and for an elastic behaviour, which should return similar values of  $\mu_C$  for a fixed EDP value. These disparities in results lead to improve the simplified modelling approaches for fragility analysis at class-level, especially for irregular buildings. Other reasons can justify the obtained differences, considering that the higher dispersions of the fragility curves obtained by the MDOF models can be addressed to the combination of some aspects: (i) few models are available for representing the class; (ii) few NRHAs have been performed on MDOF structures; (iii) the continuous IM-EDP representation through power law is characterized by a certain approximation degree. Obviously, the choice of running few NRHAs on MDOF models allow to reduce the computational cost related to the analysis, which represents a limit in a large-scale analysis. On the SDOF approach

side, the main advantage of the approach is the possibility to consider the differences in median responses of the sample (inter-building dispersion) and the structural responses given by the set of records employed (intra-building dispersion). On the other hand, the knowledge of the structural behaviour of some MDOF structures could play a key role in the SDOF system definition, because it could allow to better fix some parameters, e.g. backbone curve shape, limit-state thresholds, besides to account for the structural irregularities. In the end, the proposed comparison shows advantages and disadvantages of the two modelling and analysis extremes in the seismic fragility prediction at class-level, with different results that require further investigations, especially for the SDOF modelling.

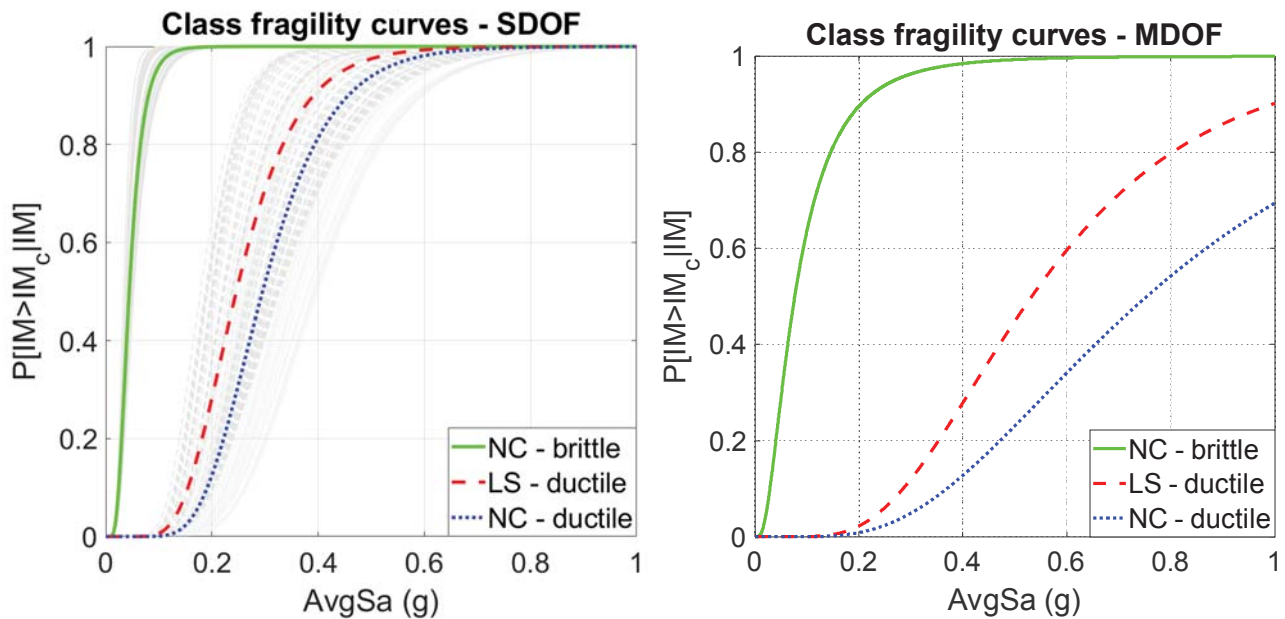


Figure 6 – Fragility curves for the specific-class investigated, accounting for safety limit-states (NC - brittle, LS and NC - ductile) and for the two modelling approaches (SDOF and MDOF)

Table 2.  $\mu_c$  and  $\beta_c$  values for fragility curves of the specific-class investigated, accounting for safety limit-states (NC - brittle, LS and NC - ductile) and for the two modelling approaches (SDOF and MDOF)

Model	NC (Brittle)		LS (Ductile)		NC (Ductile)	
	$\mu_c$	$\beta_c$	$\mu_c$	$\beta_c$	$\mu_c$	$\beta_c$
SDOFs	0.045	0.466	0.246	0.340	0.296	0.362
MDOFs	0.077	0.763	0.533	0.488	0.753	0.557

## 5. CONCLUSION

A study on the seismic fragility of existing RC school buildings in Southern Italy is presented, by leveraging on few detailed MDOF models and a large sample of simplified SDOF models. In the first step, a building taxonomy for the specific-class has been investigated, by defining the ranges of some typological parameters, such as the construction typology, the year of construction and the building height. After, by using the available data from some freely databases containing information about Italian school buildings and based on the Census data, 735 buildings have been selected and a SDOF modelling approach has been employed. The lateral behaviour of the 735 models has been defined on the basis of methodology developed in [31, 32], and they have been compared with 10 buildings belonging to the class, for which a full modelling and the nonlinear analyses results are available [21]. The entire sample of 735 reduced-order models have been generated and investigated through IDAs. The comparison among the safety fragility curves obtained by the two modelling

approaches, the two analysis methods and the two samples of buildings having a different size, provides different results for safety limit-states, as well as brittle and ductile ones. The differences confirm the evidence that the SDOF modelling herein adopted is low accurate to predict the behaviour of irregular buildings, also for low EDP values, which imply an elastic behaviour of buildings. Generally, conservative estimates are provided by SDOF models, with higher values of medians and dispersions for MDOF models. From the MDOF side, the choice of index buildings that effectively represents the class is the main hurdle, as well as the complexity and the effort for an extensive analysis phase. On the other hand, MDOF system represents the best way to reproduce the seismic response of the class, accounting for global and local behaviour. From the SDOF side, the methodology allows to consider a more accurate estimate of the structural responses for the given building class, accounting for any source of variability (record-to-record and building-to-building). In the end, the characterization of the simple models could require the knowledge of the overall behaviour of more complex structures belonging to the class, which drives to find future calibration processes, especially for irregular structures as school buildings. The employment of the two modelling extremes in class fragility studies and subjected to different nonlinear analyses suggests advantages and disadvantages of both methodologies, as well as the necessity to further investigations to improve the approaches at class-level.

## ACKNOWLEDGMENTS

Authors thank Prof. Dr. Dimitrios Vamvatsikos for his kind help and insightful suggestions in the development of the work. The research presented in this article was funded by the Italian Department of Civil Protection in the framework of the national project DPC-ReLUIs 2019-2021.

## REFERENCES

- [1] Zuccaro, G., Perelli, F. L., De Gregorio, D., & Cacace, F. (2020). Empirical vulnerability curves for Italian masonry buildings: evolution of vulnerability model from the DPM to curves as a function of acceleration. *Bulletin of Earthquake Engineering*, 1-21.
- [2] Del Gaudio, C., Di Ludovico, M., Polese, M., Manfredi, G., Prota, A., Ricci, P., & Verderame, G. M. (2020). Seismic fragility for Italian RC buildings based on damage data of the last 50 years. *Bulletin of Earthquake Engineering*, 18(5), 2023-2059.
- [3] Di Ludovico, M., Digrisolo, A., Moroni, C. et al. (2018) Remarks on damage and response of school buildings after the Central Italy earthquake sequence. *Bull Earthquake Eng.* <https://doi.org/10.1007/s10518-018-0332-x>
- [4] Ruggieri S., Tosto C., Perrone D., Uva G., Aiello M. A. (2021) Assessment of post-earthquake damages on Italian school building portfolios over the last 50 years. In *COMPDYN 2021, 8th ECCOMAS Thematic Conference on Computational Methods in Structural Dynamics and Earthquake Engineering*.
- [5] Ruggieri, S., Tosto, C., Rosati, G., Uva, G., & Ferro, G. A. (2020). Seismic Vulnerability Analysis of Masonry Churches in Piemonte after 2003 Valle Scrivia Earthquake: Post-event Screening and Situation 17 Years Later. *International Journal of Architectural Heritage*, 1-29.
- [6] Rossetto, T. and Elnashai, A. (2003) Derivation of Vulnerability Functions for European-Type RC Structures Based on Observational Data. *Journal of Engineering Structures*, 25, 1241-1263.
- [7] Rota, M., Penna, A. and Strobbia, C. L. (2008) Processing Italian damage data to derive typological fragility curves. *Soil Dynamics and Earthquake Engineering*, 28(10-11), 933-947.



- [8] Aiello, M. A., Ciampoli, P. L., Fiore, A., Perrone, D., Uva, G. (2017) Influence of infilled frames on seismic vulnerability assessment of recurrent building typologies. *Ingegneria Sismica*, 34(4), 58-80.
- [9] Ruggieri, S., Porco, F. & Uva, G. (2020) A practical approach for estimating the floor deformability in existing RC buildings: evaluation of the effects in the structural response and seismic fragility. *Bull Earthquake Eng* 18, 2083–2113. <https://doi.org/10.1007/s10518-019-00774-2>
- [10] Vamvatsikos, D., Bakalis, K., Kohrangi, M., Pyrza, S., Castiglioni, C. A., Kanyilmaz, A.... & Proença, J. M. (2020). A risk-consistent approach to determine EN1998 behaviour factors for lateral load resisting systems. *Soil Dynamics and Earthquake Engineering*, 131, 106008.
- [11] Uva, G., Ciampoli, P., Leggieri, V., Nettis, A., Ruggieri, S. (2019) A Mechanical Approach for Estimating Regional Fragility Curves Of Existing Rc Buildings Stock In Puglia. In *COMPDYN 2019 7th ECCOMAS Thematic Conference on Computational Methods in Structural Dynamics and Earthquake Engineering*.
- [12] Ruggieri S., Perrone D., Leone M., Uva G., Aiello M.A. (2020) A prioritization RVS methodology for the seismic risk assessment of RC school buildings. *International Journal of Disaster Risk Reduction*. Vol. 51, 101807. <https://doi.org/10.1016/j.ijdr.2020.101807>
- [13] Silva V., Akkar S., Baker J.W., Bazzurro P., Castro J.M., Crowley H., Dolsek M., Galasso C., Lagomarsino S., Monteiro R., Perrone D., Pitilakis K., Vamvatsikos D. (2019) Current challenges and future trends in analytical fragility and vulnerability modelling. *Earthquake Spectra*, DOI: 10.1193/042418EQS1010.
- [14] Porter, K., Farokhnia, K., Vamvatsikos, D., and Cho, I., (2015). Guidelines for Component-Based Analytical Vulnerability Assessment of Buildings and Nonstructural Elements, Tech. Rep. 2014-10, Global Earthquake Model, Pavia, Italy.
- [15] Silva. V.. Crowley. H.. Varum. H.. Pinho. R.. and Sousa. L.. (2014). Investigation of the characteristics of Portuguese regular moment-frame RC buildings and development of a vulnerability model. *Bulletin of Earthquake Engineering* 13. 1–36.
- [16] Villar-Vega M, Silva V, Crowley H, Yepes C, Tarque N, Acevedo AB, Hube MA, Gustavo CD, Santa María H. (2017) Development of a Fragility Model for the Residential Building Stock in South America. *Earthquake Spectra*; 33(2): 581–604.
- [17] Borzi B., Pinho R., Crowley H. (2008) Simplified Pushover-Based vulnerability analysis for large scale assessment of RC buildings. *Engineering Structures*, 30(3): 804-820.
- [18] Jamšek. A.. & Dolšek. M. (2020). Seismic analysis of older and contemporary reinforced concrete frames with the improved fish-bone model. *Engineering Structures*. 212. 110514.
- [19] Ruggieri S., Chatzidaki A., Vamvatsikos D., Uva G. (2021) Reduced-order models for the seismic assessment of plan-irregular low-rise moment-frame buildings. *Earthquake Engineering and Structural Dynamics* (submitted - under review)
- [20] Ruggieri, S., & Uva, G. (2020). Accounting for the spatial variability of seismic motion in the pushover analysis of regular and irregular rc buildings in the new Italian building code. *Buildings*, 10(10), 177.
- [21] Ruggieri S., Porco F., Uva G., Vamvatsikos D. (2021) Two frugal options to assess class fragility and seismic safety for low-rise reinforced concrete school buildings in Southern Italy. *Bulletin of Earthquake Engineering*. DOI: 10.1007/s10518-020-01033-5.
- [22] Italian National Institute of Statistics (ISTAT), 15° Censimento generale della popolazione e delle abitazioni (2011). Website: <https://www.istat.it/it>. in Italian.
- [23] Greco R., Marano G., Mezzina M., Milella S., Raffaele D., Palmisano F., Porco F., Trulli I., Uva G., Il Progetto ARISTOTELES. Un’analisi Tecnico-Economica Sulle Strutture Scolastiche in Puglia (In Italian).

- [24] Italian Ministry of University and Research (MIUR), Portale unico della scuola (2019) Website: <https://dati.istruzione.it/> (In Italian).
- [25] Vamvatsikos, D., and Cornell, C. A. (2002) Incremental dynamic analysis. *Earthquake Engineering & Structural Dynamics*, 2002, 31(3), 491–514.
- [26] Ruiz-García, J., and Miranda, E. (2007) Probabilistic estimation of maximum inelastic displacement demands for performance-based design, *Earthquake Engineering and Structural Dynamics* 36, 1235–1254.
- [27] Miranda E., Ruiz-Garcia J. (2002) Evaluation of approximate methods to estimate maximum inelastic displacement demands. *Earthquake Engineering and Structural Dynamics*. Vol. 31, No. 3, pp. 539-560.
- [28] Vamvatsikos D., Cornell C.A. (2006) Direct estimation of the seismic demand and capacity of oscillators with multi-linear static pushovers through IDA. *Earthq Eng Struct Dyn*, 35:1097–1117.
- [29] FEMA-P440A (2009) Effects of Strength and Stiffness Degradation on Seismic Response. Applied Technology Council: 201 Redwood Shores Parkway, Suite 240, Redwood City, California 94065.
- [30] Lagomarsino S, Giovinazzi S. (2006) Macroseismic and mechanical models for the vulnerability and damage assessment of current buildings. *Bulletin of Earthquake Engineering*; 4(4): 415–443.
- [31] Vamvatsikos D, Aschheim MA. (2016) Performance-based seismic design via yield frequency spectra. *Earthquake Engineering and Structural Dynamics*; 45(11): 1759–1778.
- [32] Kohrangi, M., Bazzurro, P. & Vamvatsikos, D. Seismic risk and loss estimation for the building stock in Isfahan. Part I: exposure and vulnerability. *Bull Earthquake Eng* (2021). <https://doi.org/10.1007/s10518-020-01036-2>
- [33] Moehle JP. (1992) Displacement-Based Design of RC Structures Subjected to Earthquakes. *Earthquake Spectra* 1992; 8(3): 403–428.
- [34] Katsanos EI, Vamvatsikos D. (2017) Yield frequency spectra and seismic design of code-compatible RC structures: an illustrative example. *Earthquake Engineering and Structural Dynamics*; 46(11): 1727–1745.
- [35] FEMA, HAZUS99 Technical Manual. Service Release 2, Federal Emergency Management Agency, Washington, D.C., USA, 2001.
- [36] DM 17/01/2018, Aggiornamento delle Norme Tecniche per le Costruzioni. *Gazzetta Ufficiale* n. 42. del 20/02/2018. Rome. 2008. (In Italian)
- [37] McKenna F. (2011) OpenSees: a framework for earthquake engineering simulation. *Comput Sci Eng*;13:58–66.
- [38] Cornell. C. A., Jalayer. F., Hamburger. R. O., and Foutch. D. (2002) Probabilistic Basis for 2000 SAC Federal Emergency Management Agency Steel Moment Frame Guidelines. *Journal of Structural Engineering*.

## FRAGILITY CURVES FOR RC FRAMED BUILDINGS CONSIDERING CUMULATIVE DAMAGE DUE TO EARTHQUAKE GROUND MOTION AND SLOW-MOVING LANDSLIDES

Fulvio Parisi<sup>1</sup>, Elia Acconcia<sup>1</sup>

<sup>1</sup> Department of Structures for Engineering and Architecture, University of Naples Federico II  
via Claudio 21, 80125 Naples, Italy  
e-mail: fulvio.parisi@unina.it, elia.acconcia@unina.it

---

**Abstract.** *Differential settlements during earthquake ground shaking at the base of framed buildings located on the crest of slopes can produce heavy damage. This reflects the importance of considering ground shaking and co-seismic vertical displacements as interacting hazards in seismic fragility assessment. Slow-moving landslides are indeed secondary hazards of earthquakes that can induce significant damage accumulation, increasing the seismic vulnerability of structures. This paper presents the main findings of a seismic fragility analysis that was carried out on RC framed structures representative of low-rise, pre-code, residential Italian buildings. The methodology behind this study made use of fibre-based structural models and sequential nonlinear static analysis, which allowed the simulation of structural response to both earthquake ground motion and differential settlements with acceptable computational cost. Based on multivariate regression models available in the literature and random sampling of structures, seismically-induced settlements at the base of each structure were simulated considering multiple intensity measures (IMs) of seismic ground shaking. The correlation between the selected IMs was derived through a recent database of 250 accelerograms, which allow a wide representation of seismic hazard in the whole Italian territory for seismic risk assessment. The buildings were analysed with OpenSees software, assuming four performance limit states for characterization of seismic fragility at multiple levels of structural damage. The comparison between fragility curves associated with earthquake ground shaking only and those derived considering differential settlements allows the impact of cumulative damage to be evaluated.*

**Keywords:** Seismic fragility, Reinforced concrete buildings, Fibre-based plasticity modelling, Earthquake-induced landslides, Cumulative damage.

---

## 1 INTRODUCTION

Post-earthquake reconnaissance missions have shown that earthquakes often produce slope instability, resulting in landslides that can exacerbate seismic damage to buildings and infrastructure and hence both life and economic losses. Buildings located on the crest of slopes can experience co-seismic displacements associated with slow-moving earthquake-induced landslides. This suggests considering the interaction between earthquake ground shaking and such landslides in seismic risk assessment of buildings. In this context, the development of probabilistic methodologies allows engineers, decision makers and stakeholders to carry out a multi-hazard risk analysis accounting for different sources of uncertainty in shaking and landslide hazards, vulnerability, and exposure.

In recent years, research developments in this field have been made, particularly in the case of reinforced concrete (RC) buildings but usually neglecting the uncertainties on their geometry and material properties that play a role in performance-based seismic assessment of existing structures. Foutopoulou and Pitilakis [1–3] studied the vulnerability of buildings to earthquake-induced landslides, making use of three-dimensional finite element (FE) modeling and nonlinear time history analysis of both the slope and building. Nonetheless, that computational strategy can be too computationally demanding for seismic vulnerability assessment of building classes that are spatially distributed within a region.

In this study, a computationally efficient method for probabilistic vulnerability assessment of RC buildings subjected to earthquake-induced landslide hazard is presented. The proposed methodology builds upon a recent selection of strong ground motions oriented towards large-scale risk assessment of buildings, which allows incorporating correlation between different intensity measures (IMs) used for earthquake ground shaking and slow-moving landslides.

## 2 METHODOLOGY

The vulnerability assessment described in this paper is based on a probabilistic procedure that allows modelling and propagation of uncertainties through fragility analysis, which is a well-established method in earthquake engineering [4]. After that a class of buildings with RC frame structure was selected, the correlation between two IMs used to describe the intensity of earthquake ground shaking and slow-moving landslide was investigated. In this respect, the selected IMs were the peak ground acceleration (PGA) and peak ground velocity (PGV), the correlation of which was investigated via 250 accelerograms that were recently selected in the ReLUIIS-DPC 2019-2021 research project. The accelerograms were characterized by a wide amplitude range reflecting design spectra for L'Aquila, Italy (with return period ranging from 50 to 10,000 years), which was found to give a good representation of seismic hazard over the entire Italian territory [5]. Each accelerogram was characterized by a (PGA, PGV) pair, so the correlation between those IMs was studied over a set of 250 data points. More specifically, PGA and PGV were selected to measure the intensity of shaking and landslide, respectively.

After that seismic input was defined, the authors modelled the uncertainties in structural properties of the selected buildings, creating the basis for random generation of structural models. Random sampling was based on Monte Carlo simulation, which was fully implemented in MATLAB [6]. The structural capacity of RC buildings was defined through a fibre-based FE modelling approach using OpenSees software [7]. The seismic performance assessment of each random model of the RC structure was carried out by means of a sequence of nonlinear static analyses, in which the structural system was first subjected to incremental vertical differential settlement associated with the landslide, and subsequently to incremental horizontal displacement associated with earthquake ground shaking. Hence, the sequential nonlinear static analysis consisted of a nonlinear static analysis under incremental vertical settlement and a pushover

analysis of the structure. The range of settlements impressed to the structure was based on the study by Foutopolou and Pitilakis [8], who proposed a predictive model that allows the prediction of peak co-seismic displacement based on the slope's characteristics and seismic input IMs. This allowed seismic displacement demand associated with slow-moving landslide to be predicted. Seismic displacement demand associated with ground shaking was evaluated according to the N2 method [9]. Seismic fragility of the selected buildings was evaluated with respect to four performance limit states corresponding to increasing damage levels. Each fragility point was derived under increasing PGA, allowing subsequent fitting of lognormal probability distribution to fragility data for development of fragility curves.

In the following sections, the methodology used in this study is described in detail.

## 2.1 Selection of buildings

The building class under study is that of low-rise residential buildings with RC frame structure built in Italy. The uncertainty modelling of those buildings involved consideration of both geometric and material properties. The case-study buildings had two storeys and rectangular plan, with frame systems consisting of 2 spans parallel to the slope crest and 3, 5, or 7 spans in the perpendicular direction. Beams were assumed to have the same span length in each longitudinal and transverse frame of the structure.

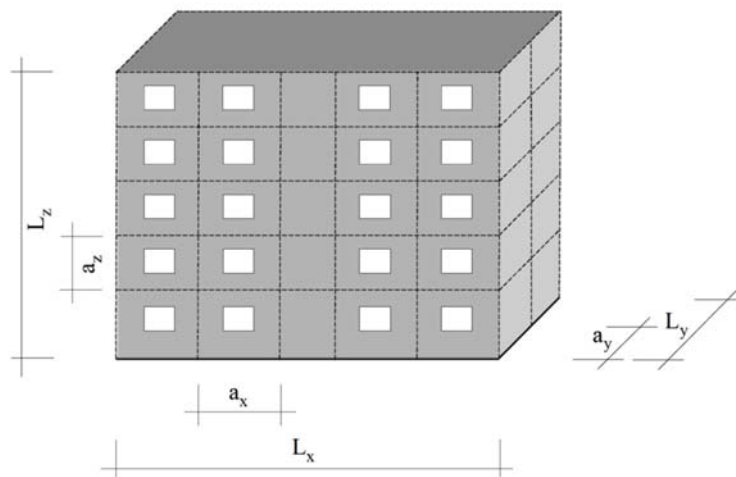


Figure 1: Case-study building with geometric random properties.

The mechanical properties of materials were identified by grouping the buildings by construction time according to the evolution of Italian codes. Both buildings built before 1971 (i.e., the year that marked the transition from design to gravity loads only to design for earthquake resistance) and those built between 1971 and 2008 in non-seismic areas according to past seismic zoning of Italy, were considered as pre-code. Low-code buildings were assumed to be those built in seismic areas between 1915 and 2008 according to old seismic design criteria (first-generation earthquake-resistant buildings). Medium-code and high-code buildings are those built after 2008, the former designed in low ductility class (second-generation earthquake-resistant buildings) and the latter in a high ductility class (third-generation earthquake-resistant buildings).

This study investigated the fragility of pre-code RC buildings built before 1971, assuming the following material properties: concrete with compressive strength having a mean value



$f_{cm} = 16.0$  MPa and coefficient of variation  $CoV = 31\%$  [10]; and reinforcing steel with yield strength having a mean value  $f_{ym} = 369$  MPa and  $CoV = 20\%$  [11].

## 2.2 Simulated design of structures

The design of the structural elements was carried out using the design methods used at the time of construction [12,13] and the Italian code in force in the same period [14] (Table 1).

Item	Variable	Value
Columns	$b$ [m]	Derived by simulated design
	$h$ [m]	
	$h_i$ [m]	3.00
	$c$ [mm]	30
Beams	$b$ [m]	Derived by simulated design
	$h$ [m]	
	$l$ [m]	[4, 6]
	$c$ [mm]	30

Table 1: Geometric properties.

The selected buildings were designed against gravity loads only according to the permissible stress method, which was based on the assumption of permissible stresses, linear elastic behaviour of materials, and effects superposition. Table 2 outlines the properties adopted for sizing of beams and columns.

Item	Property	Value
Concrete	$R_{ck}$	160 kg/cm <sup>2</sup>
	$\sigma_{c,adm,c}$	45 kg/cm <sup>2</sup>
	$\sigma_{c,adm,b}$	50 kg/cm <sup>2</sup>
Steel	$\sigma_{f,adm}$	1400 kg/cm <sup>2</sup>
Beams	$A_{c,min}$	300×300 mm <sup>2</sup>
	$A_f$	0.8% $A_{min}$
	$B$	300 mm
	$H$	$r\sqrt{M/b}$
	$A_f$	$t\sqrt{Mb}$
	$r$	0.446
	$t$	0.00174
	$A_{f,min}$	4 Ø12
	Stirrups	Ø6 @ min( $L_{min}/2$ ; $10\phi_{min}$ )

Table 2: Parameters for simulated design of beams and columns.

## 2.3 Definition of performance limit states

The displacement approach used for vulnerability assessment suggests defining the performance limit states (LS) in relation to the strain capacity of the elements considered. According

to the literature [3,12], the strain thresholds listed in Table 3 were assumed in terms of maximum strains of steel ( $\varepsilon_s$ ) and concrete ( $\varepsilon_c$ ) as a function of the construction period. This definition of limit states is in line with the fibre-based FE modelling of the structure, which allows axial strain in materials to be monitored during structural analysis.

Limit State	Analytical definition
LS1	$\varepsilon_{ct,max} = \varepsilon_{ctp}$
LS2	$\varepsilon_{s,max} = 0.0125$ ; $\varepsilon_{cc,max} = 0.0045$
LS3	$\varepsilon_{s,max} = 0.025$ ; $\varepsilon_{cc,max} = 0.006$
LS4	$\varepsilon_{s,max} = 0.045$

Table 3: Definition of limit states.

LS1 was associated with slight damage and was assumed to be attained when the maximum tensile strain in concrete  $\varepsilon_{ct,max}$  reached the cracking strain  $\varepsilon_{ctp}$ . LS2 was associated with moderate damage and was assumed to be attained when either the maximum tensile strain in steel  $\varepsilon_{s,max}$  reached 0.0125 or the maximum compressive strain in concrete  $\varepsilon_{cc,max}$  reached 0.0045. Similar criteria were adopted for LS3 and LS4, which were respectively associated with severe damage and near collapse. In detail, LS3 was assumed to be attained when either  $\varepsilon_{s,max}$  reached 0.025 or  $\varepsilon_{cc,max}$  reached 0.006. The collapse limit state, i.e. LS4, was assumed to be attained when  $\varepsilon_{s,max}$  reached 0.045.

### 3 DISPLACEMENT DEMAND DUE TO EARTHQUAKE-INDUCED LANDSLIDE

As briefly discussed in Sect. 2, 250 accelerograms compatible with design spectra for L'Aquila, Italy (with return period ranging from 50 to 10,000 years), were selected to cover a very wide range of shaking intensities and to allow risk assessment at any site of Italy. Figure 3 shows a bi-logarithmic scatter plot of PGA and PGV for selected ground motions.

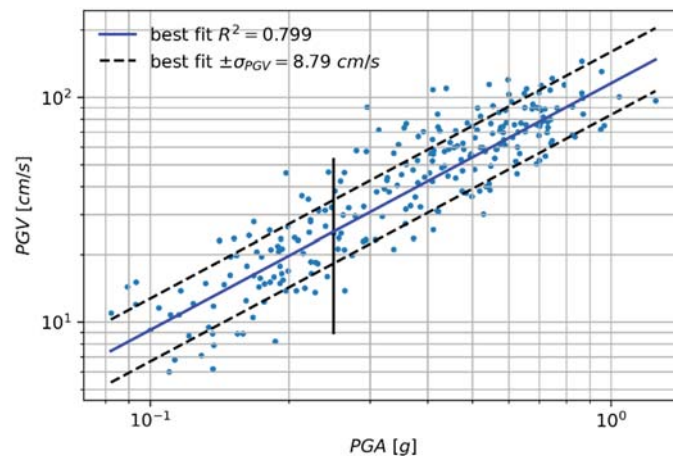


Figure 2: Correlation between PGV and PGA of selected accelerograms.

A regression analysis was performed using the power function as model, which on the bi-logarithmic plane is represented by a straight line. Based on the ( $PGA$ ,  $PGV$ ) pairs of the selected accelerograms, the following equation was obtained:

$$PGV = 121.3PGA^{1.097} \quad (1)$$

with a coefficient of determination  $R^2 = 0.799$  and standard deviation  $\sigma_{PGV} = 8.79$  cm/s. Such a regression model allows the random generation of PGV conditioned upon PGA as expected conditional value of PGA plus a sample of the model error, the latter being assumed as lognormal random variable with zero mean and standard deviation equal to  $\sigma_{PGV}$ . Figure 4 shows the distribution of PGV given  $PGA = 0.25g$ .

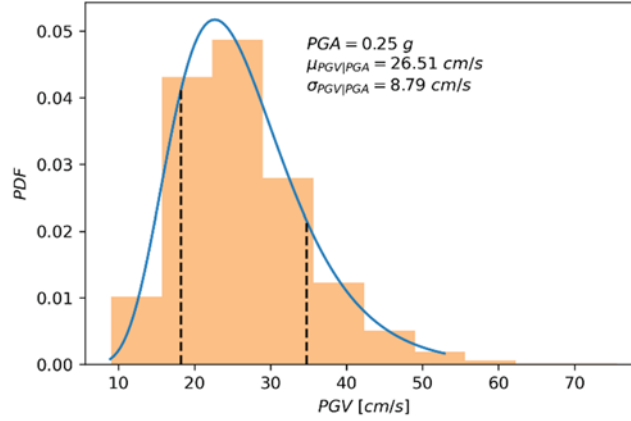


Figure 3: Probability distribution of conditional PGV given  $PGA = 0.25g$ .

In order to evaluate the permanent displacement  $D$  induced by the earthquake, the study conducted by Fotopoulou and Pitilakis [5] was taken into account. Those researchers developed 5 different predictive models based on single or multiple IMs. In this study, the following predictive model was used:

$$\ln(D) = -8.360 + 1.873 \ln(PGV) - 0.347 \ln(k_y/PGA) - 5.964 k_y \pm 0.64 \epsilon \quad (2)$$

which allows the prediction of  $D$  given  $PGA$ ,  $PGV$  and  $k_y$ , assuming  $k_y$  as yield acceleration coefficient of the slope,  $\epsilon$  is the standard normally distributed variable with zero mean and unit standard deviation and 0.64 is the logarithmic standard deviation.

To take into account the different configurations of the slope, reference was made to the yield acceleration coefficient  $k_y$  that summarizes the effects of both geometric and mechanical characteristics of the slope, the relative location of the building with respect to the slope, and the effects of gravity loads transmitted from the building to the slope.

To cover the majority of cases, 5 values of the parameter  $k_y$  were considered, namely, 0.05g, 0.10g, 0.15g, 0.20g, and 0.25g. For each  $k_y$ -value, 10 levels of PGA between 0 and 1.0g were considered, resulting in 50 combinations. For each value of  $k_y$  and  $PGA$ ,  $10^3$  samples of the building class were randomly generated through Monte Carlo method in order to obtain a sample that is representative of the existing buildings.

#### 4 SEQUENTIAL STRUCTURAL ANALYSIS

The analysis was conducted using the OpenSees opensource software [7]. OpenSees allows users to simulate the response of structural and geotechnical systems subjected to seismic input and/or other types of actions. The construction of a finite element model and subsequent analysis must be implemented in OpenSees through a code in TCL or with more recent versions in Python. For this reason, OpenSees is well suited for applications in the research field, especially when using parametric models for the evaluation of building classes.

Once the geometric, mechanical and load models were defined, the analysis procedure consisted in the application of gravity loads through a first analysis step with force control.

Afterwards, a modal analysis was carried out to identify the first-mode shape to define the corresponding profile of horizontal seismic actions.

The second analysis stage consisted in the application of the settlement at the base of the columns subjected to the landslide. That analysis was carried out with displacement control, assuming a gradually increasing displacement with step equal to 1 mm. In each analysis step, the reaction force at the base of the columns affected by the settlement was computed to check whether columns were compressed. Otherwise, the support at the base nodes was removed in the subsequent analysis phases.

At this point, a nonlinear incremental static (pushover) analysis was performed with displacement control to assess the structural performance under horizontal seismic actions. The roof centroid was assumed as a control point and the first-mode shape of the structure was used to generate the lateral load profile proportional to the product of modal displacements by inertia masses. Pushover analysis was carried out by increasing the roof displacement by 10 mm until a peak base shear degradation of 75% was attained.

Structural performance was assessed during each analysis stage, checking whether axial strains in frame members reached their limit states thresholds outlined in Table 3. In that way, the capacity in terms of displacement associated with each limit state was evaluated.

Whilst seismic demand in terms of vertical displacement was predicted through the model into Eq. (2), the seismic demand associated with horizontal ground shaking was estimated according to the N2 method [9]. Accordingly, the base shear versus roof displacement curve derived through pushover analysis was transformed into the corresponding capacity curve of an equivalent single-degree-of-freedom (SDOF) system, allowing the seismic demand assessment by means of inelastic displacement spectra. The displacement demand was computed for each considered PGA level and compared to the capacity associated with each limit state, allowing the authors to assess whether each limit state was exceeded.

## 5 DEVELOPMENT OF FRAGILITY CURVES

Given a prescribed value of  $k_y$ , for each PGA level the conditional probability of exceeding a prescribed limit state was estimated as the ratio of the number of failure cases  $N_f$  to the total number of simulations (i.e.,  $N_{sim} = 10^3$ ). This allowed the computation of counted fragility under varying PGA. A lognormal probability distribution was then fitted to fragility points to develop a fragility curve for each limit state. Figure 6 shows the fragility curves corresponding to  $k_y = 0.15g$  for all limit states, considering either ground shaking only (dashed lines identified as EQ in the figure legend) or both the combined effect of seismic ground shaking and co-seismic settlement due to slow-moving landslide (solid lines identified as EQ + L in the figure legend). Table 4 outlines the median value of PGA, denoted by  $PGA_{50}$ , and dispersion  $\beta$  corresponding to each limit state.

LS	Ground shaking		Ground shaking + landslide	
	$PGA_{50}$ [g]	$\beta$	$PGA_{50}$ [g]	$\beta$
LS1	0.0055	0.7535	0.0055	0.7535
LS2	0.1312	0.4327	0.1054	0.4125
LS3	0.1752	0.4292	0.1403	0.4120
LS4	0.7233	0.4051	0.3034	0.4204

Table 4: Median and dispersion of fragility curves.

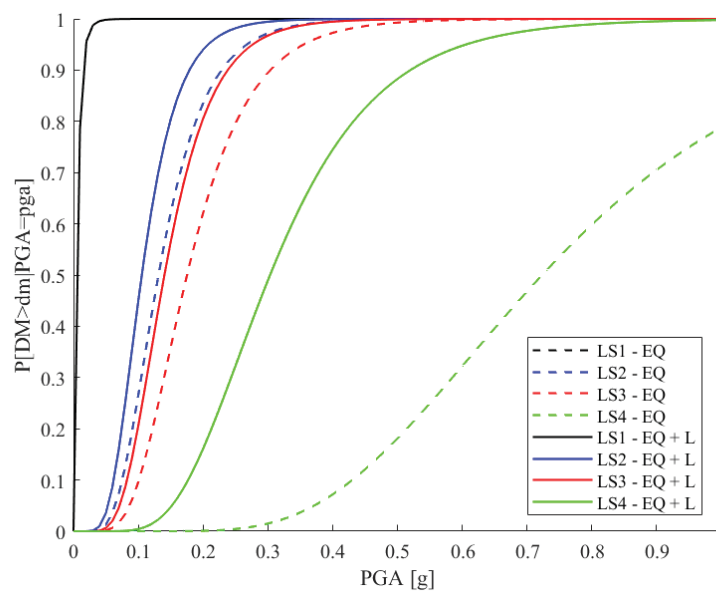


Figure 4: Fragility curves.

The fragility curves show a high vulnerability of the case-study building class even without considering the effect of co-seismic settlement. As expected, slight damage (LS1) consisting of concrete cracking takes place at very low levels of  $PGA$ . For the limit state of collapse (LS4), the co-seismic settlement has a major impact on seismic vulnerability, reducing  $PGA_{50}$  from 0.72g to 0.30g. A lower increase in median  $PGA$  with decreasing dispersion is found for the limit states of moderate damage (LS2) and severe damage (LS3).

The horizontal distance between median values of the fragility curves is a measure of the ductility available in the structure of the case-study buildings. In this respect, the relatively small distance between the fragility curves corresponding to LS2 and LS3 indicates a rather limited ductility of pre-code RC buildings.

## 6 CONCLUSIONS

In the present study, the seismic vulnerability of existing RC buildings subjected to earthquake-induced landslides has been assessed. Buildings placed upstream of the slope and therefore exposed to the effects of co-seismic settlements were considered. Lumping the geometric and geotechnical characteristics of the slopes as well as the presence and relative distance of buildings through the yield acceleration coefficient, 1000 building samples were randomly generated, based on Monte Carlo method. For each sample, a simulated design was carried out to determine the dimensions of the member cross-sections and their reinforcement. Each building model was modelled and analysed in OpenSees by first imposing co-seismic vertical displacements associated with slow-moving landslide and then horizontal displacements associated with seismic ground shaking. Seismic performance under both earthquake-induced landslide and horizontal ground shaking was evaluated through nonlinear static analysis with displacement control. For each sample, the displacement capacity corresponding to four limit states was evaluated and compared to demand, allowing fragility estimation under varying  $PGA$ . The lognormal distribution was fitted to fragility points to develop fragility curves.

The proposed methodology makes it possible to assess the vulnerability of RC frame buildings to seismically-induced landslides through a fully mechanics-based approach. This allows drawbacks of empirical vulnerability assessment methods to be overcome, particularly when observed damage data on buildings struck by earthquake-induced landslides are lacking. It is



also emphasised that the proposed methodology based on fibre-based FE modelling and sequential nonlinear static analysis has a very low computational cost with respect to nonlinear time history, allowing a very large number of simulations on 3D building structures. For each case study (i.e., yield acceleration coefficient), 10,000 analyses on 1000 structural models subjected to 10 levels of seismic intensity were carried out on a personal computer equipped with 8 cores, a 3.6 GHz processor and 32 GB RAM. This allowed 1 analysis per minute, leading to a total duration of 7 days for the entire fragility analysis to be completed.

## ACKNOWLEDGMENTS

This study was developed in the framework of POR GRISIS project (Gestione dei rischi e sicurezza delle infrastrutture a scala regionale), which was funded by Campania Region through POR FESR 2014-2020 programme.

## REFERENCES

- [1] S.D. Fotopoulou, K.D. Pitilakis, Fragility curves for reinforced concrete buildings to seismically triggered slow-moving slides. *Soil Dynamics and Earthquake Engineering*, **48**, 143-161, 2013.
- [2] S.D. Fotopoulou, K.D. Pitilakis, Probabilistic assessment of the vulnerability of reinforced concrete buildings subjected to earthquake induced landslides, *Bulletin of Earthquake Engineering*, **15**, 5191–5215, 2017.
- [3] S.D. Fotopoulou, K.D. Pitilakis, Vulnerability assessment of reinforced concrete buildings at precarious slopes subjected to combined ground shaking and earthquake induced landslide. *Soil Dynamics and Earthquake Engineering*, **93**, 84-98, 2017.
- [4] K.A. Porter, R.P. Kennedy, R.E. Bachman, Creating fragility functions for performance-based earthquake engineering. *Earthquake Spectra*. **23** (2), 471-489, 2007.
- [5] V. Manfredi, A. Masi, R. Paolucci, A.G. Ozcebe, C. Smerzini, Selection and frequency-scaling of seismic input for deriving analytical fragility curves of RC existing buildings, *Bulletin of Earthquake Engineering* (to be submitted).
- [6] MATLAB (R2019b). Natick, Massachusetts: *The MathWorks Inc.*, 2018.
- [7] F. McKenna, OpenSees: A framework for earthquake engineering simulation. *Computing in Science & Engineering*, **13**(4), 58-66, 2011.
- [8] S.D. Fotopoulou, K.D. Pitilakis, Predictive relationships for seismically induced slope displacements using numerical analysis results. *Bulletin of Earthquake Engineering*, **13**, 3207–3238, 2015.
- [9] P. Fajfar, Capacity spectrum method based on inelastic demand spectra, *Earthquake Engineering and Structural Dynamics*, **28**, 979-993, 1999.
- [10] A. Masi, M. Vona, Vulnerability assessment of gravity-load designed RC buildings: Evaluation of seismic capacity through non-linear dynamic analyses. *Engineering Structures*, **45**, 257–269, 2012.

- [11] G.M. Verderame, A. Stella, E. Cosenza, Le proprietà meccaniche degli acciai impiegati nelle strutture in ca realizzate negli anni '60. *Proceedings of X Congresso Nazionale "L'Ingegneria Sismica in Italia"*, Potenza-Matera, 2001.
- [12] H. Crowley, R. Pinho, J. J. Bommer, A Probabilistic Displacement-based Vulnerability Assessment Procedure for Earthquake Loss Estimation. *Bulletin of Earthquake Engineering*, **2**, 173–219, 2004.
- [13] L. Santarella, *Il cemento armato – La tecnica e la statica, vol. I*, Hoepli, 1956.
- [14] Regio Decreto del 16/11/1939 n. 2229, *Norme per la esecuzione delle opere in conglomerato cementizio semplice ed armato*, Rome.

## FRAGILITY CURVES FOR ITALIAN RESIDENTIAL MASONRY BUILDINGS WITH RETROFIT INTERVENTIONS

Veronica Follador<sup>1,3</sup>, Marco Donà<sup>2,3</sup>, Pietro Carpanese<sup>3</sup>, and Francesca da Porto<sup>3</sup>

<sup>1</sup> Depart. of ICATAM - University of Brescia  
Via Branze, 43, 25123, Brescia (IT)  
v.follador@unibs.it

<sup>2</sup> Earthquake Engineering Research & Test Center – Guangzhou University  
Guang Yuan Zhong Rd. 248, 510405 Guangzhou, China  
dona\_marco@gzhu.edu.cn

<sup>3</sup> Depart. of Geosciences - University of Padova  
Via G. Gradenigo, 6, 35131 Padova, Italy  
veronica.follador@unipd.it, marco.dona.1@unipd.it, pietro.carpanese@phd.unipd.it,  
francesca.daporto@unipd.it

---

### Abstract

*The earthquakes of the last decades have shown that the Italian residential masonry built heritage has high seismic vulnerability, in particular when considering structures built before 1919. For this reason, it is necessary to develop effective large-scale risk mitigation strategies in order to reduce the huge losses that could occur in the aftermath of an earthquake. In this paper some retrofit interventions applicable mainly to old buildings are presented, explaining their advantages and potential. These interventions are then implemented, through Vulnus 4.0 software, on a database of 205 buildings built before 1919, previously analyzed in their as-built state.*

*Fragility curves are then developed for each building, and are processed in order to create a vulnerability model for different construction periods that takes into account the possible retrofit intervention strategies. Therefore, this procedure allows a comparison between pre and post retrofit intervention fragility, and the results in terms of curves can be used for large scale damage and risk simulations.*

**Keywords:** Residential Masonry Buildings, Territorial-Scale Seismic Vulnerability, Fragility Model, Retrofit intervention.

---

## 1 INTRODUCTION

Over the last decades, Italy has been affected by very impactful seismic events, which caused thousands of casualties and around 180 billion euros of economic losses, in terms of recovery and reconstruction costs [1]. It is clear that those high economic and human costs are no longer sustainable, and large-scale mitigation policies need to be pursued.

In this context, Italian institutions (in particular the Department of Civil Protection - DPC) are working in synergy with the scientific community to find effective seismic risk mitigation strategies [1-3]. In particular, the work presented in this paper is part of a project carried out by ReLUIS (Network of University Laboratories for Earthquake Engineering) and EUCENTRE (European Centre for Training and Research in Earthquake Engineering), and coordinated by DPC. The aim of the project is to develop large scale vulnerability models for consolidated buildings, and then to perform cost-benefit analyses that can give an estimate of the payback time of seismic retrofit interventions. The final purpose is to elaborate mitigated risk maps that simulate different preventive strategies, thus making it possible to identify prioritization and convenience ranking for the different interventions.

In order to do so, one must assess the variation of seismic vulnerability between the as-built configuration and the case where particular seismic retrofit interventions were performed. The estimation of seismic vulnerability, i.e. the propensity of structures to suffer damage after a seismic event of a given intensity, is usually defined by fragility curves. A fragility curve is a probabilistic distribution that expresses the probability of occurrence of a certain damage state in relation to seismic intensity. Usually, lognormal cumulative fragility curves are used [4].

In literature there are several methods to define fragility curves: a) empirical methods, in which fragility curves are calibrated from damage data survey in areas affected by seismic events [5-8]; b) analytical (mechanical) methods, based on structural models and analyses that simulate the seismic behavior of buildings [9-13]; and c) hybrid methods, which have characteristics from both a) and b) methods [14].

In this study, a mechanical simplified procedure was used to obtain fragility curves for Italian residential masonry buildings with eight different types of intervention. This study focuses on residential historical buildings: these are usually stone (mainly random) and solid brick masonry buildings, with timber floors and roofs and in most cases without any retaining elements, such as tie-rods or beams. In particular, buildings dating from before 1919 were analyzed, as they represent the 29.4% of the Italian masonry heritage and the 18.1% of the entire Italian residential building stock [15], but made for the most of damage observed in recent events.

The paper firstly presents the most common seismic retrofit interventions in Italy for the analyzed building type, and defines the main modifications that these interventions produce in structural and mechanical parameters. Then, the selected interventions were simulated in a database composed of 205 Pre-1919 masonry buildings. The program used for the analysis and the elaboration of the fragility curves is the *Vulnus vb 4.0* software [16, 17].

Then, the curves obtained by *Vulnus* are post-processed according to the Donà et al. [18] methodology, in order to obtain a single fragility model.

## 2 INTERVENTIONS FOR SEISMIC RETROFIT OVERVIEW

Interventions for seismic improvement can be grouped in the following categories [19, 20] according to their aim: a) interventions targeting strength and compactness of walls; b) interventions that improve connections, and c) interventions aimed at strengthening and stiffening horizontal diaphragms.

## 2.1 Masonry strengthening and compacting

In case of historical ordinary buildings, the materials that compose the load-bearing stone masonry structure are often not very performing in terms of mechanical characteristics. Several techniques can be applied to improve masonry performance, provided a careful evaluation of the most suitable intervention with respect to the typology and the quality of the masonry is previously carried out [19-21].

When the stone masonry is inconsistent and characterized by the presence of voids (two or three leaves masonry), the most used and effective interventions are grout or mortar injections [22-24]. This type of intervention consists in the grouting of the wall's core through a regular pattern of drilled holes, previously cleaned by water or compressed air. Injections are performed from the bottom to the top of the walls with controlled pressure.

In case of damaged or inconsistent masonry, it is also possible to realize reinforced concrete jackets [25] made of cement or lime-based mortars and a steel mesh or fabrics reinforcement. To the ends of a successful intervention, the reinforcements on both sides need to be well anchored to the wall by the means of transversal connections (Figure 1a).

With stone ashlar or brick masonry, but either with poorly performing resistant elements or poor quality mortars, the most suitable interventions are bed-joint repointing (also reinforced with metal bars) or the application of FRCM-TRM (Fibre/Fabric Reinforced Cementitious Matrix/Mortar – Textile Reinforced Mortars) plasters [26, 27]. The latter consists of reinforced plasters made with glass, carbon, aramid or polypropylene fiber meshes, coated in inorganic matrices based on lime or cement mortar. These reinforcements can be widespread to the entire surface of the walls or applied locally (Figure 1b) [28, 29].

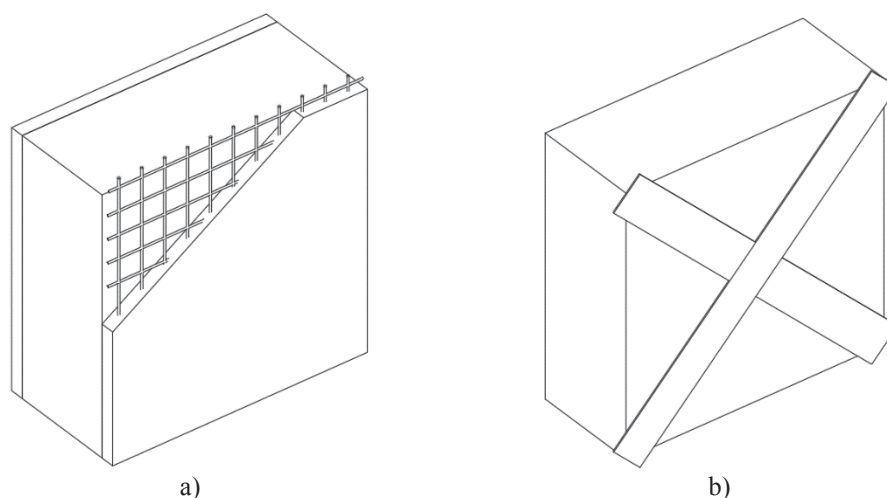


Figure 1: Reinforced concrete jackets (a) and example of application of FRCM-TRM (b).

The condition of multiple leaves that are not adequately connected to each other can occur in both brick and stone masonry. In order to guarantee the overall functioning of the wall, it is possible to insert artificial transverse elements in its thickness (made of reinforced concrete or metal profiles), or metal tie-rods (made of smooth or threaded bars) with an anti-expulsion function [22, 22]. This type of intervention is feasible only if the masonry is consistent enough to ensure the solidarization between the faces.

## 2.2 Improvement of connections and box-like behavior

The seismic behavior of existing masonry buildings also depends on the connections between structural elements (wall-to-wall and wall-to-floor). These connections are necessary to



enable the global behavior of the building and to prevent the activation of out-of-plane mechanisms, however they are generally inadequate in more ancient buildings.

The connections among the walls can be obtained through local interventions, although the application of connecting elements between parallel opposite walls (such as steel tie-rods and cables or external confining rings) has proved to be one of the most effective [19, 25]; moreover, tie-rods are a traditional technique which is also highly compatible. Usually, steel threaded bars are placed at floor levels, in the two main directions of the building, along the load-bearing walls, although in more recent times they may also have been combined with diagonally crossed systems. Tie-rods must be positioned at floor level in conjunction with the nodes (along external and inside walls, Figure 2a).

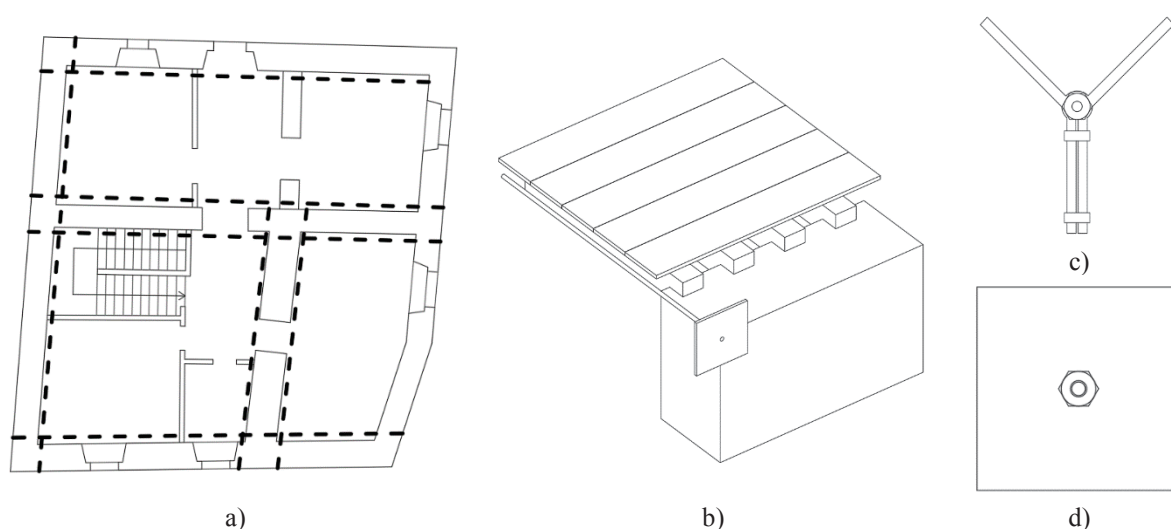


Figure 2: Ties positioning (a, b) and examples of external anchors (c, d).

In general, the tie-rods placed on the upper levels of the building have a crucial role for the local equilibrium of the walls. For an effective intervention, the contrasting masonry must be sufficiently consistent and resistant to sustain the local force applied by a tie's anchor; for this reason, localized interventions are recommended, such as hydraulic mortar injections, reinforcement or replacement of individual degraded elements, assuming that the general state of the masonry is sufficiently good.

Another possible intervention is the insertion of tie-beams just at the top or at all levels of a building. According to past Italian seismic codes [30, 31] they must have been made of reinforced concrete, but this was recently proved to be more detrimental than beneficial to seismic behavior as a consequence of high weight and poor compatibility with random masonry [19, 20, 32]. Therefore, a new generation of tie beams was proposed, adopting reinforced masonry or steel structural shapes [33].

### 2.3 Strengthening and stiffening of horizontal diaphragms

Horizontal diaphragms in seismic conditions should redistribute horizontal loads from load-bearing walls orthogonal to the earthquake direction to those parallel to it, in order to oppose the highest strength.

Timber floors are based on the assembly of overlapping elements, which are able to withstand and distribute vertical stresses, but not horizontal ones. This is due to the lack of adequate connections between the elements of the horizontal structure (inadequate in-plane stiffness) and between the horizontal structure and the vertical one (inadequate wall to floor connection).

Considering the fundamental partitioning action of floors, interventions aim at not only decreasing plan deformability, but also strengthening the connections between floors and walls have to be performed. However, an excessive strengthening, like that obtained by floor replacement with reinforced concrete slabs, would be ineffective, or even pejorative from a seismic retrofit point of view [20, 34].

For what concerns historical buildings, several techniques have been developed respecting traditional construction practice and avoiding at the same time the negative increase of weight at the floor level [26].

Some examples of interventions that improve the diaphragm action are wooden planking and application of diagonal metallic belts or composite material strips. These interventions can be executed on the intrados or on the extrados of the floor. With regard to residential buildings without valuable floors, interventions on the extrados are preferable.

In order to increase the in-plane stiffness, the addition of single or double wooden planks over the existing one can be considered (in orthogonal direction or at  $45^\circ$ , using tongue-and-groove joints with nails or screws as connectors) [35, 36] (Figure 3).

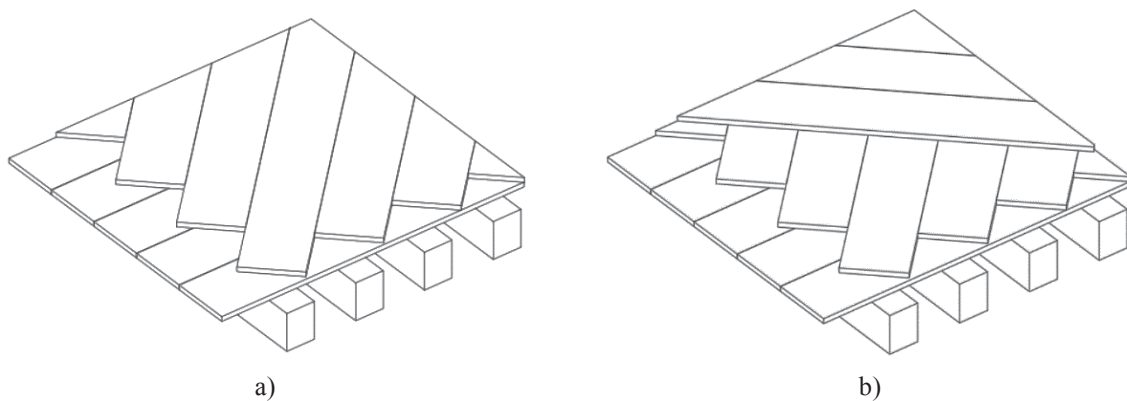


Figure 3: Reinforced timber floor with single planking inclined at  $45^\circ$  (a); reinforced timber floor with double planking crossed at  $+45^\circ$  and  $-45^\circ$  (b).

Interventions that do not modify floor stiffness but assure an adequate connection with walls are perimeter steel plates anchored with dowels to the walls [37] and distributed anchors at the ends of floor joists. These have to be injected with mortars or resins on the wall, or anchored externally; on the inner side, they have to be nailed to joists or upper boards, thus binding the floor to the wall (Figure 4) [38, 39].

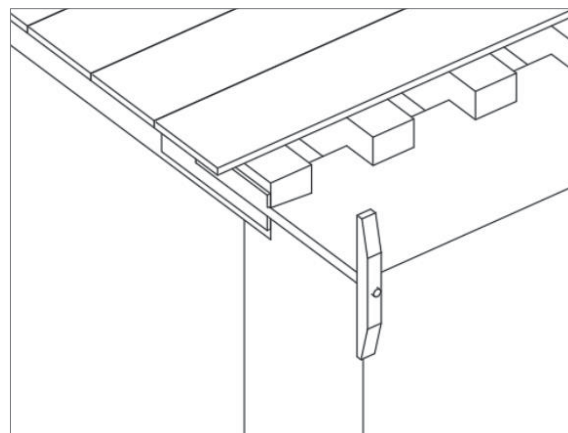


Figure 4: Example of connection floor-to-wall.

### 3 ANALYSIS TOOL AND IMPLEMENTATION OF INTERVENTIONS

Once the best performing retrofit interventions were analyzed, it was possible to select the most suitable method and tools to start the implementation phase.

#### 3.1 Analysis method

The software used for the analysis is Vulnus vb 4.0 [16, 17], originally developed by A. Bernardini, R. Gori and C. Modena (University of Padova). Vulnus can analyze load-bearing masonry structures through limited information (geometry, material properties, construction details, qualitative information) by means of limit analysis.

The Vulnus methodology is based on the calculation of the critical horizontal accelerations that cause the activation of the main out-of-plane collapse mechanisms for each wall, and in-plane shear failure of the two main parallel wall systems. These critical accelerations are then normalized to gravity acceleration  $g$  and returned in terms of indices  $I1$  and  $I2$  for the in-plane and out-of-plane response, respectively.

More specifically, the index  $I1$  represents the shear resistance calculated on the weakest direction of the building, eventually corrected in case of irregularities that may cause non-uniform distributions of normal and tangential stresses. On the other hand, the index  $I2$  depends on the possible out-of-plane kinematic mechanisms and it corresponds to the minimum value of the sum of two sub-indices,  $I2'$  and  $I2''$ . In particular,  $I2'$  evaluates a building's resistance to mechanisms which involve a vertical strip of its walls (overall overturning of the wall, overturning and flexural failure of the top storey).  $I2''$  instead evaluates the resistance to mechanisms developing across the breadth of a walls (horizontal masonry strips): a) bending and arching mechanism failure, b) overturning and flexural collapse of the arch shoulders, and c) detachment of the transverse walls, always at the last storey.

In addition, a third index  $I3$  represents qualitative features of the building (not included in the other two indices).  $I3$  is calculated as the weighted normalized sum (between 0 and 1) of the scores derived by the "Second Level" form of GNDT [40]. Specifically, the form consists of 11 parameters, to which a quality class from A to D (where A is the best condition) is assigned; each qualitative class is then associated to a numerical score.

Once the three indices  $I1$ ,  $I2$  and  $I3$  have been calculated, Vulnus performs a vulnerability analysis using the fuzzy sets theory. The fuzzy approach allows to consider uncertainties associated to those parameters which are not directly measured and to the variability of the mechanical characteristics of the materials.

Using this approach, Vulnus calculates three fragility curves, which represent the mean (White curve) and the extreme probabilities (Lower-Bounds and Upper-Bounds curves) of reaching or exceeding the triggering acceleration of in-plane or out-of-plane mechanisms. For this reason, the damage state (DS) associated to the resulting fragility curves is a DS2-3, with reference to the scale proposed by the European Macroseismic Scale (EMS-98) [41].

#### 3.2 Implementation of retrofit interventions

On the basis of the considerations presented in section 2 and of direct field observations [32, 42], some interventions were considered as the most effective for Pre-1919 buildings. These interventions are presented in Table 1.

Vulnus allows to carry out simplified vulnerability analyses of masonry buildings. This implies that interventions must also be implemented in a simplified way. In fact, some intervention could be directly implemented by the options already present in the software, whereas others had to be implemented indirectly, reproducing the effect of the intervention on the building's overall behavior.

The implementation methodology of the selected interventions is presented below. Some interventions were also implemented in combination (as shown in Table 1).

*individual interventions*

MSN1	1 <sup>st</sup> stage	of masonry strengthening (stone: injection – brick: reinforced plaster)
MSN2	2 <sup>nd</sup> stage	
TR	addition of tie-rods	
FLR	stiffening of floors (light interventions)	

*combined interventions*

MSN1+TR	first stage of masonry strengthening + addition of tie-rods	
MSN1+FLR	first stage of masonry strengthening + stiffening of floors	
MSN2+TR	second stage of masonry strengthening + addition of tie-rods	
MSN2+FLR	second stage of masonry strengthening + stiffening of floors	

Table 1: Implemented retrofit interventions.

Two stages of retrofit interventions of strengthening of masonry are proposed. The first stage (MSN1) considers the application of light or single interventions, whereas the second one (MSN2) implies the concurrent application of more types of intervention or the implementation of a single intervention with all possible expedients to ensure the best results. The masonry interventions proposed in this study, according to the type of masonry, are: on random multi-leaf stone mainly injections are suggested, whereas the application of FRCM-TRM reinforced plaster is preferred in the case of stone ashlar or brick masonry. To simulate these interventions through Vulnus, the corrective coefficients shown in Table 2 were applied. The coefficients refer to table C8.5.II available in [43], and represent a medium increase of the mechanical characteristics of the materials composing the building owing to different type of intervention. It can be observed that the first step brings a similar improvement among different masonry types. Instead, the implementation of more invasive and heavy interventions on stone masonry, characterized by values of the mechanical parameters lower than the ones associated to brick masonry, gives greater improvements, although not exceeding the values of the mechanical characteristics of brick masonry. Lastly, the interventions considered require the addition of material, which is estimated to determine an average increase of masonry specific weight by 5%.

	MSN1	MSN2
Stone masonry	1.7	2.4
Solid brick masonry	1.5	1.8
Tuff masonry	1.6	1.9

Table 2: Multiplicative coefficients used.

The insertion of tie-rods (TR) was directly implemented in Vulnus. In fact, the software provides the possibility to enter the number of ties present in both main directions of the building. TR intervention was implemented by placing, for each main direction of the building, an adequate number of rods (two rods, one per side, placed parallel to the internal partitions, and one rod to the perimeter walls).

As regards to floor interventions (FLR), the most effective solutions for historical buildings are the insertion of bracing systems or the installation of double wooden planks, in order to increase the stiffness without overloading. Since in Vulnus floor types determine just the dead loads on walls, diffuse chains have been placed to simulate the improved box-like behavior when floors are stiffened. In addition, to further increase the diaphragms' reaction of the model, the floor-to-wall friction coefficient was increased to account for the improved connection achieved by the intervention.

In order to update the class of the Second Level GNDT form parameters, used by Vulnus to elaborate the final curves, the modifications that each intervention brings to the as-built configuration were studied. Of the 11 parameters of the form, those linked to the interventions analyzed are: quality of the resistant system, floor type, roof type and state of maintenance. The value assigned to other parameters in as-built conditions was maintained in strengthened ones. In Table 3 the adopted changes, made with reference to the manual of the form [40], are reported.

GNDT parameter	MSN1 MSN2	TR	FLR	MSN1+TR MSN2+TR	MSN1+FLR MSN2+FLR
Resistant system	<b>A</b>			<b>A</b>	<b>A</b>
Floors			<b>A</b>		<b>A</b>
Roof		+ 1 class	+ 1 class	+ 1 class	+ 1 class
State of maintenance	<b>A</b>			<b>A</b>	<b>A</b>

Table 3: Modified classes for the GNDT parameters considered.

## 4 FRAGILITY MODEL WITH RETROFIT INTERVENTIONS

The present study is in continuity with past analyses [44, 45] in which a database of more than 500 buildings was analyzed using Vulnus 4.0 and fragility sets were obtained for ten macro-types (five age and two height classes) of as-built residential masonry buildings. Specifically, the eight interventions identified in the previous chapters have been implemented on those 205 buildings which belonged to the Pre-1919 macro-typology of the original database. Then, the elaboration of the specific fragility sets for each intervention was carried out following the procedure proposed by Donà et al. [18].

### 4.1 Methodological approach

As already mentioned, the Vulnus software produces three fragility curves associated with an average probability (White) and two extreme probabilities (Upper- and Lower-Bounds), corresponding to a damage state DS2-3.

In order to define a single fragility model for the two macro-typologies considered in this study (Pre-1919 Low-Rise buildings, i.e. 1 and 2 floors, and Pre-1919 Mid-Rise buildings, i.e. 3, 4 and 5 floors), in the first place the White, Upper- and Lower-Bounds curves were processed separately. The curves of each building were averaged firstly by municipality, in order to maintain a geographical representativeness, and then by number of floors and age of construction, considering for each sub-typology the actual real distribution obtained from 2001 ISTAT census data [15].

Subsequently, the fragility model of Lagomarsino and Cattari [10] was calibrated on the mechanical fragility model obtained for DS2-3, in order to represent seismic fragility over the five damage states (from DS1 to DS5). In this way, a new mechanically based heuristic fragility model was derived.



Lastly, the different sets obtained for White, Upper- and Lower-Bounds were combined, with the aim of developing a single fragility set (LUW). This operation allows to maintain the average fragility defined by the White curves (assumed as the most likely fragility), but at the same time to increase the dispersion parameter, thus resulting more suitable to represent the vulnerability of the built stock on a large scale.

In Figure 5, the main steps of this procedure [18] are presented.

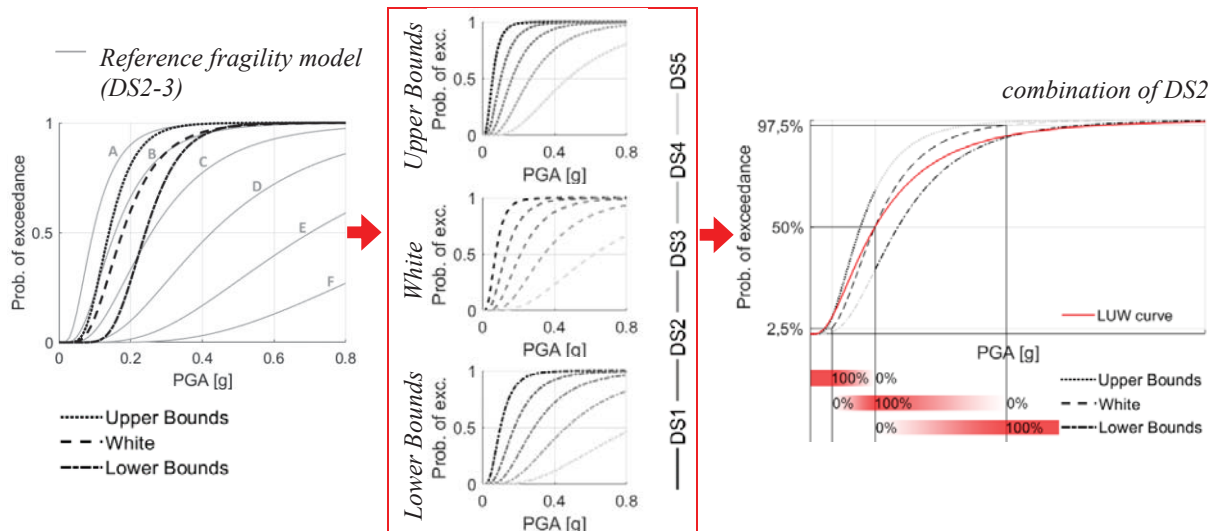


Figure 5: Procedure used to define the mechanical-heuristic fragility model from the mechanical one obtained through Vulnus [18].

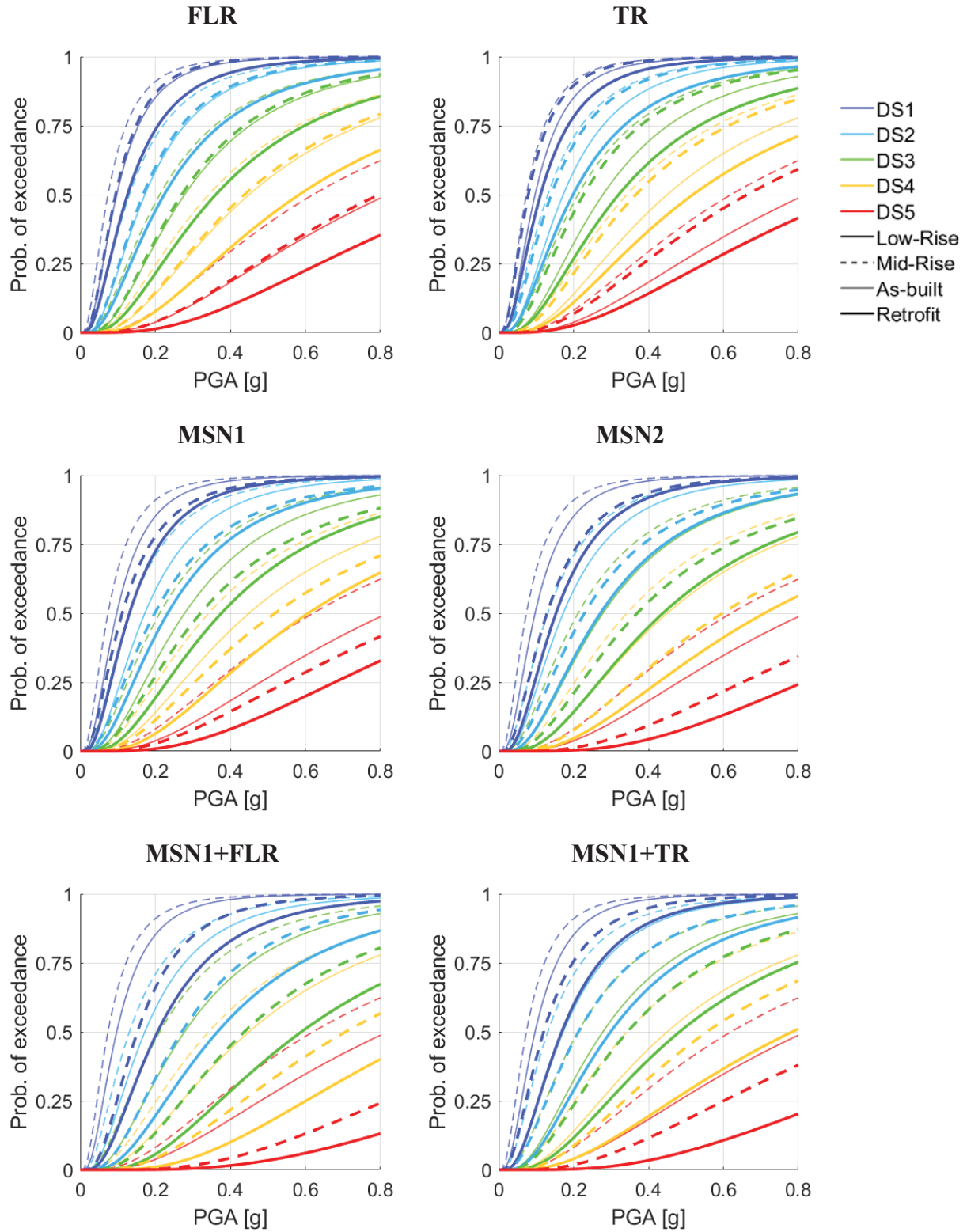
## 4.2 Fragility sets and results

The procedure presented in §4.1 was recursively carried out for each intervention considered. In this way, the fragility sets related to the Pre-1919 buildings for the two height classes Low-Rise (1 and 2 storeys) and Mid-Rise (3, 4 and 5 storeys) were obtained, and it was possible to compare the fragility curves of the as-built configuration with the curves obtained after the simulation of the interventions.

It should be noticed that, despite the validity of the method [18], the models presented below (Figure 6) do not allow to evaluate the effects that the interventions may produce limited to some DSs (e.g. reduction of severe damage but not of slighter one), but provide just an overall indication of their effectiveness.

As expected, the graphs in Figure 6 show that the greatest variation in vulnerability occurs with the application of combined interventions. Considering individual interventions, the insertion of tie-rods (TR) produces underperforming results, while the intervention on floors (FLR) gives slightly better outcomes. The greatest effectiveness derives from two-steps interventions applied to increase masonry strength and compactness (MSN1, MSN2). When the floors or ties interventions are combined with masonry strengthening (MSN1+FLR, MSN1+TR, MSN2+FLR, MSN2+TR), the floors interventions appears to be more effective than the tie-rods ones.

Furthermore, the different effectiveness of interventions in Low-Rise and Mid-Rise buildings can be examined. The interventions on the floors and those related to the insertion of tie-rods are more effective if applied to Low-Rise buildings, whereas for Mid-Rise buildings the vulnerability reduction is smaller. This leads to the conclusion that the height of the building plays a fundamental role in the variation of vulnerability.



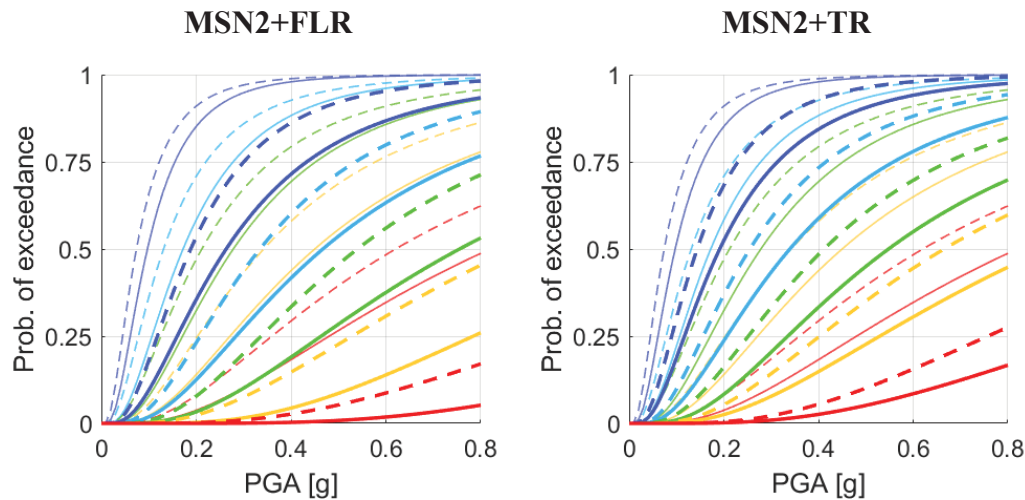


Figure 6: Comparison of fragility sets developed for Pre-1919 buildings in as-built condition and with retrofit for the interventions analyzed.

## 5 CONCLUSIONS

- The paper presents a study that provides mechanical-heuristic seismic fragility curves of Pre-1919 Italian residential masonry buildings, subject to seismic retrofit interventions. In particular, eight type of intervention were analyzed: two steps of intervention concerning the strengthening of the walls (MSN1, MSN2), insertion of tie-rods (TR), stiffening and improvement of diaphragm behavior of the floors (FLR), as well as the combination of these interventions (MSN1+TR, MS1+FLR, MS2+TR, MS2+FLR).
- The software Vulnus 4.0 was used, and the fragility curves (White, Upper-Bound and Lower-Bound) were obtained for eight retrofit solutions, on a dataset of 205 buildings. Then, the procedure by Donà et al. [18] was applied and fragility sets for the retrofit interventions have been derived, so that they could be compared with the as-built fragility curves.
- In general, the results show that masonry strengthening is overall more effective than any other intervention. Moreover, combined interventions are more effective than single ones. It should be noticed that the reduction of vulnerability deriving from a combination of two interventions is not the simple sum of that obtained from individual ones.
- Possible future developments are the extension of this study to residential masonry buildings belonging to construction periods starting from 1919, which have different characteristics and may require different retrofit interventions.

## ACKNOWLEDGEMENTS

Special thanks are due to the Italian Department of Civil Protection (DPC), which funded this study in the framework of the *ReLUIS-DPC Project 2019-2021 – Work Package 4: MARS (Maps of Risk and Scenarios of seismic damage) – Task 6: Preventive strategies: comparative analysis in terms of risk on a national scale (Strategie preventive: analisi comparata in termini di rischio a scala nazionale)*.

## REFERENCES

- [1] Italian Civil Protection Department of the Presidency of the Council of Ministers – DPC, National risk assessment - Overview of the potential major disasters in Italy: seismic, volcanic, tsunami, hydro-geological/hydraulic and extreme weather, droughts and forest fire risks. 2018.
- [2] M. Dolce, A. Prota, B. Borzi, F. da Porto, S. Lagomarsino, G. Magenes, C. Moroni, A. Penna, M. Polese, E. Sperenza, Seismic risk assessment of residential buildings in Italy: Methodology overview and main results. *Bulletin of Earthquake Engineering*, 2020.
- [3] F. da Porto, M. Donà, A. Rosti, M. Rota, S. Lagomarsino, S. Cattari, B. Borzi, M. Onida, D. De Gregorio, F.L. Perelli, C. Del Gaudio, P. Ricci, E. Speranza, Comparative analysis of the fragility curves for Italian residential masonry and RC buildings *Bulletin of Earthquake Engineering*, 2021.
- [4] G.M. Calvi, R. Pinho, G. Magenes, J.J. Bommer, L.F. Restrepo-Veléz, H. Crowley, The development of seismic vulnerability assessment methodologies for variable geographical scales over the past 30 years. *ISET J Earthq Technol*, **43**, 75–104, 2006.
- [5] M. Rota, A. Penna, C. Strobbia, Processing Italian damage data to derive typological fragility curves. *Soil Dyn Earthq Eng*, **28**(10), 933–947, 2008.
- [6] T. Rossetto, I. Ioannou, D.N. Grant, Existing empirical fragility and vulnerability functions: Compendium and guide for selection. *GEM Technical Report 2013-X*, GEM Foundation, Pavia, Italy, 2013.
- [7] A. Rosti, M. Rota, A. Penna, Empirical fragility curves for Italian URM buildings. *Bulletin of Earthquake Engineering*, 2020.
- [8] G. Zuccaro, F.L. Perelli, D. De Gregorio, F. Cacace, Empirical vulnerability curves for Italian masonry buildings: evolution of vulnerability model from the DPM to curves as a function of acceleration. *Bulletin of Earthquake Engineering*, 2020.
- [9] S. Lagomarsino, S. Cattari, Fragility functions of masonry buildings, (Chapter 5), K. Pitilakis, H. Crowley, A.M. Kaynia eds. *SYNER-G: Typology Definition and Fragility Functions for Physical Elements at Seismic Risk*, Vol. 27, 111- 156, Springer 2014.
- [10] D. D’Ayala, A. Meslem, D. Vamvatsikos, K. Porter, T. Rossetto, V. Silva, Guidelines for analytical vulnerability assessment of low/mid-rise buildings. *Vulnerability Global Component Project*, 2015.
- [11] C. Del Gaudio, P. Ricci, G.M. Verderame, A class-oriented mechanical approach for seismic damage assessment of RC buildings subjected to the 2009 L’Aquila earthquake. *Bulletin of Earthquake Engineering*, **16**(10), 4581-4605, 2018.
- [12] B. Borzi, M. Faravelli, A. Di Meo, Application of the SP-BELA methodology to RC residential buildings in Italy to produce seismic risk maps for the national risk assessment. *Bulletin of Earthquake Engineering*, 2020.
- [13] M. Vettore, M. Donà, P. Carpanese, V. Follador, F. da Porto, M.R. Valluzzi, A Multilevel Procedure at Urban Scale to Assess the Vulnerability and the Exposure of Residential Masonry Buildings: The Case Study of Pordenone, Northeast Italy, *Heritage*, **3**, 1433–1468, 2020.

- [14] A.J. Kappos, G. Panagopoulos, C. Panagiotopoulos, G. Penelis, A hybrid method for the vulnerability assessment of RC and URM buildings. *Bulletin of Earthquake Engineering*, **4**, 391-413, 2006.
- [15] Italian National Institute of Statistics (ISTAT 2001) Website and data warehouse, 2001. <https://www.istat.it/it/censimenti-permanenti/censimenti-precedenti/popolazione-e-abitazioni/popolazione-2001>
- [16] A. Bernardini, M. Gori, C. Modena, Application of coupled analytical models and experimental knowledge to seismic vulnerability analyses of masonry buildings, A. Koridze ed. *Earthquake damage evaluation and vulnerability analysis of Building structures*, INEEC, Omega Scientific, Ozon, 161-180, 1990.
- [17] M.R. Valluzzi, Manuale d'uso del programma Vulnus 4.0, programma originario di A. Bernardini, R. Gori, C. Modena, versione Vb a cura di M.R. Valluzzi, contributi di G. Benincà, E. Barbetta, M. Munari, 2009. (In Italian)
- [18] M. Donà, P. Carpanese, V. Follador, L. Sbrogio, F. da Porto, Mechanics-based fragility curves for Italian residential URM buildings. *Bulletin of Earthquake Engineering*, 2020.
- [19] C. Modena, M.R. Valluzzi, F. da Porto, F. Casarin, Structural Aspects of The Conservation of Historic Masonry Constructions in Seismic Areas: Remedial Measures and Emergency Actions. *International Journal of Architectural Heritage*, **5**, 539-558, 2011.
- [20] Y. Saretta, L. Sbrogio, M.R. Valluzzi, Seismic response of masonry buildings in historic centres struck by the 2016 Central Italy earthquake. Calibration of a vulnerability model for strengthened conditions, *Constr. Build. Mater.* (in press).
- [21] C. Modena, F. Pineschi, M.R. Valluzzi, Valutazione Della Vulnerabilità Sismica Di Alcune Classi Di Strutture Esistenti: Sviluppo E Valutazione Di Metodi Di Rinforzo. Roma: Cnr-Gruppo Nazionale Per La Difesa Dai Terremoti, 2000. (In Italian)
- [22] M.R. Valluzzi, F. da Porto, C. Modena, Behavior and modeling of strengthened three-leaf stone masonry walls. *Materials and Structures*, **37**, 184–192, 2004.
- [23] N. Mazzon, M.R. Valluzzi, T. Aoki, E. Garbin, G. De Canio, N. Ranieri, C. Modena, Shaking table tests on two multi-leaf stone masonry buildings. *11<sup>th</sup> Canadian Masonry Symposium*, Toronto, Canada, May 31–June 3, 2009.
- [24] B. Silva, M. Dalla Benetta, F. da Porto, M.R. Valluzzi, Compression and Sonic Tests to Assess Effectiveness of Grout Injection on Three-Leaf Stone Masonry Walls. *International Journal of Architectural Heritage*, **8**, 408-435, 2014.
- [25] C. Modena, F. Casarin, F. da Porto, E. Garbin, N. Mazzon, M. Munari, M. Panizza, M.R. Valluzzi, Structural interventions on historical masonry buildings: review of Eurocode 8 provisions in the light of the Italian experience. E. Cosenza ed. *Eurocode 8 Perspectives from the Italian Standpoint*, 225 – 236, Napoli, Doppiavoce, 2009.
- [26] F. da Porto, M.R. Valluzzi, M. Munari, C. Modena, A. Arêde, A.A. Costa, Strengthening of Stone and Brick Masonry Buildings. A.A. Costa, A. Arêde, H. Varum (eds) *Strengthening and Retrofitting of Existing Structures. Building Pathology and Rehabilitation*, vol 9. Springer, Singapore, 2018.
- [27] M. Giaretton, D. Dizhur, E. Garbin, J. Ingham, F. da Porto, In-plane strengthening of clay brick and block masonry walls using textile-reinforced mortar. *J. Compos. Constr.*, **22**(5), 2018.



- [28] CNR-DT 215/2018, Istruzioni per la progettazione, l'esecuzione ed il controllo di interventi di consolidamento statico mediante l'utilizzo di compositi fibrorinforzati a matrice inorganica. National Research Council, Roma, Italy, 2019. (In Italian)
- [29] A. Borri, M. Corradi, G. Castori, A. Molinari, Stainless steel strip – A proposed shear reinforcement for masonry wall panels. *Construction and Building Materials*, **211**, 594-604, 2019.
- [30] MLP 1986, Ministry of Public Works, ministerial decree 24/01/1986, norme tecniche relative alle costruzioni antisismiche. (in Italian)
- [31] MLP 1981, Ministry Of Public Works, Ministerial Decree No. 198, 02/07/1981, Normativa Per Le Riparazioni E Il Rafforzamento Degli Edifici Danneggiati Dal Sisma Nelle Regioni Basilicata, Campania E Puglia. (In Italian)
- [32] M. Vettore, Y. Saretta, L. Sbrogiò, M.R. Valluzzi, A New Methodology for the Survey and Evaluation of Seismic Damage and Vulnerability Entailed by Structural Interventions on Masonry Buildings: Validation on the Town of Castelsantangelo sul Nera (MC), Italy. *Int. J. Archit. Herit.*, 1–26, 2020.
- [33] A. Borri, R. Sisti, M. Corradi, A. Giannantoni. Experimental Analysis of Masonry Ring Beams Reinforced with Composite Materials. *16th international brick and block masonry conference*, Padua, Italy, 26–30 June, 2016.
- [34] G. Magenes, A. Penna, I.E. Senaldi, M. Rota, A. Galasco, Shaking Table Test of a Strengthened Full-Scale Stone Masonry Building with Flexible Diaphragms, *International Journal of Architectural Heritage*, **8**, 349–375, 2014.
- [35] M.R. Valluzzi, E. Garbin, M. Dalla Benedetta, C. Modena, In-plane strengthening of timber floors for the seismic improvement of masonry buildings. *World Conf. on Timber Engineering (WCTE)*, Curran Associates, Red Hook, NY, 2010.
- [36] M.R. Valluzzi, E. Garbin, M. Dalla Benedetta, C. Modena, Experimental assessment and modelling of in-plane behaviour of timber floors. *VI Int. Conf. on Structural Analysis of Historical Constructions (SAHC08)*, Bath, United Kingdom, July 2nd-4<sup>th</sup>, 2008.
- [37] E. Giuriani, A. Marini, G. Plizzari, Experimental behavior of stud connected wooden floors undergoing seismic action. *International Journal for Restoration of Buildings and Monuments/Internationale Zeitschrift für Bauinstandsetzen und Bau-denkmalspflege*, **11**(1), 3-24, 2005.
- [38] D. Dizhur, M. Giaretton, J. Ingham, URM wall-to-diaphragm and timber joist connection testing. *Proc. Int. Mason. Soc. Conf*, 2018.
- [39] M. Giaretton, I. Giongo, D. Dizhur, Field testing of unreinforced masonry wall-to-diaphragm connection via through-bolt plate anchors and timber blocking. *Mason. Int.*, **32**, 63–71, 2019.
- [40] M. Ferrini, A. Melozzi, A. Pagliazzi, S. Scarparolo, Rilevamento della vulnerabilità sismica degli edifici in muratura. Manuale per la compilazione della Scheda GNDT/CNR di II livello. Regione Toscana, 2003. (In Italian)
- [41] G. Grünthal, European Macroseismic Scale. *Chaiers du Centre Européen de Géodynamique et de Séismologie*, vol. 15. Luxembourg, 1998.

- [42] M.R. Valluzzi, L. Sbrogiò, Y. Saretta, H. Wenliuhan, Seismic response of masonry buildings in historical centres struck by the 2016 Central Italy earthquake. Impact of building features on damage evaluation. *Int. J. Archit. Herit.*
- [43] Circolare Esplicativa 21 gennaio 2019, n. 7 C.S.LL.PP. Istruzioni per l'applicazione dell'«Aggiornamento delle “Norme tecniche per le costruzioni”» di cui al decreto ministeriale 17 gennaio 2018, Roma, 2019. (In Italian)
- [44] M. Donà, P. Carpanese, V. Follador, F. da Porto, Derivation of mechanical fragility curves for macro-typologies of Italian masonry buildings. M. Papadrakakis, M. Fragiadakis eds. *7th ECCOMAS Thematic Conference on Computational Methods in Structural Dynamics and Earthquake Engineering (COMPDYN 2019)*, Crete, Greece, June 24-26, 2019.
- [45] M. Donà, P. Carpanese, V. Follador, F. da Porto, L. Xu, L. Sbrogiò, Seismic fragility and risk of Italian residential masonry heritage. *17th International Brick and Block Masonry Conference (IB2MaC 2020)*, Kraków, Poland, July 5-8, 2020.

## FRAGILITY MODELS FOR EXISTING MASONRY INFILLED RC FRAMES IN THE EMILIA AREA

G. Salamida<sup>1</sup>, N. Buratti<sup>2</sup>

<sup>1</sup> CIRI - Edilizia e Costruzioni (University of Bologna)  
Via del Lazzaretto 15/5, Bologna  
e-mail: gianluca.salamida2@unibo.it

<sup>2</sup> DICAM (University of Bologna)  
Viale Risorgimento 2, Bologna  
nicola.buratti@unibo.it

---

### Abstract

*Fragility models are important tools for seismic risk assessment and seismic damage scenarios estimation. Some models are already available in the literature, however, in the case of infilled RC frames, further investigations are necessary, given the high uncertainty about their behaviour. In fact, damage observations following seismic events, suggest that the presence of masonry infills can strongly influence the response of reinforced concrete (RC) frames and affect their collapse mechanisms. The main goal of this work is to contribute to the seismic vulnerability assessment of the existing building stock in the Emilia-Romagna region in northern Italy, developing fragility models for infilled RC frame buildings. On the basis of an analysis of both census data on the existing building stock and on damage survey forms after the 2012 Earthquake, a set of representative structures was defined and modelled with finite elements, adopting a concentrated plasticity approach. Different modelling approaches of the infill walls were considered, using single and multi-strut models, in order to simulate shear failure in columns. Non-linear static (push-over) analyses were then carried out on these models to obtain their capacity curves. Displacement demands were computed using simplified procedures (IN2 method). The definition of damage levels in the models was based on the achievement of local deformation capacity limits of structural and non-structural elements, according to the classification provided by the EMS-98 Macro-seismic scale. Fragility curves were finally obtained by considering uncertainties in material properties, by means of the Response Surface method, as well as ground-motion record-to-record variability.*

**Keywords:** RC frames, masonry infills, fragility curves, pushover analysis, seismic fragility.

---

## 1 INTRODUCTION

Many of the buildings currently present in the European area date back to several decades ago and were built without seismic design criteria, due to changes in the seismic classification of the territory and to the considerable evolution of structural design codes in the most recent years; hence the interest and the need for studies on existing buildings. Within a probabilistic framework, an important tool for assessing the seismic vulnerability of existing buildings are fragility curves, which associate the probability of exceeding a certain damage level to different levels of a certain measure of ground-motion intensity.

After the Emilia earthquake (northern Italy) in May 2012, many of the studies on existing buildings focused on masonry buildings [1] and prefabricated structures [2, 3], i.e. the types on which the most severe damage was observed. Studies have also been carried out on reinforced concrete frames with masonry infills [4]; in particular, fragility curves have been developed in [5], for some models of representative buildings, based on capacity limits associated with the damage levels defined by the EMS-98 macro-seismic scale. Furthermore, this study provided a damage scenario for the area hit by the Emilia earthquake, also making predictions on the cumulative damage caused by multiple seismic events. The typical damage observed following seismic events raises the need to use models capable of describing the local interaction phenomena between frames and infill panels [6, 7]. Preventive considerations are necessary on the choice of materials characteristics, with particular attention to the masonry infill properties, which can strongly influence the structural behaviour of the building and, consequently, the assessment of its vulnerability [8].

The present work presents the fragility curves for existing residential Reinforced Concrete (RC) frame structures with masonry infills, and is part of a larger study aimed at assessing the seismic vulnerability of the existing building heritage in the Emilia area. These fragility curves are obtained analysing, by means of nonlinear static analyses and Response Surface metamodells [9], a series of case study structures, which in terms of geometry, dimensions and mechanical characteristics, can be considered representative of the fraction of the existing building stock under study.

## 2 REFERENCE BUILDINGS

### 2.1 Characteristics of the building stock

In order to define the case study buildings, preliminary investigations were made to acquire information about the main characteristics of the existing building stock: in particular, reference was made to the data of the AEDES forms (i.e. post-earthquake damage evaluation forms used in Italy), compiled following the Emilia earthquakes, occurred in May 2012, and census data provided by ISTAT (National Institute of Statistics), from the 15th general population and housing census, for the areas of Bologna, Ferrara and Modena. Analysing the available data on existing buildings, once the construction type and intended use of interest have been identified, all data was filtered by construction period, number of storeys, average floor surface and regularity.

The data from the AEDES forms and census, restricted to RC frame structures for residential use, involve sample consisting of 1573 and 58980 buildings, respectively: it is clear that the census data offer a broader and more general vision than the AEDES data, which instead concern a small part of the building stock, as they are compiled only for a subset of the buildings affected by the earthquake, i.e., in general, for buildings that have shown some damage. On the other hand, AEDES data can provide important information of the structural features of the

buildings that were most susceptible to damage. Figure 1 shows the distribution of the number of floors in the dataset.

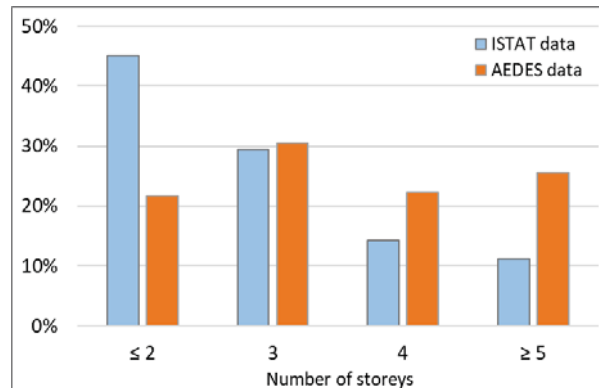


Figure 1: Number of storeys of existing building stock.

There is a clear prevalence of low-rise buildings, with less than 2 floors, for the ISTAT data, in contrast to the AEDES forms data, which show an opposite trend for buildings with a greater number of floors (in detail 4 or greater than or equal to 5): this can suggest that, in general, buildings with a higher number of floors, although they constitute a smaller percentage of the building stock, also constitute the most fragile part. According to ISTAT data, almost 58% of the RC frame structures were built between the 50s and 70s, a time period characterized by the complete lack of seismic design criteria in the area affected by the 2012 earthquake.

For the definition of the geometry in plan and elevation of the models to be studied, the data on the average floor surface was analysed and correlated with the number of floors (as shown in Figure 2). It should be noticed that only the AEDES forms provide this data. The range of floor areas between 100 m<sup>2</sup> and 170 m<sup>2</sup> is common for buildings with a low number of floors, while it is not very frequent in buildings with 5 or more floors. The range of surfaces between 170 and 300 m<sup>2</sup> characterizes a large part of the sample of buildings, being present in a relatively high percentage in all categories based on the number of floors (between 23.7% and 39.2%), in particular for structures with a number of floors equal to or greater than 4. Floor areas from 300 to 500 m<sup>2</sup> mainly characterize buildings with a number of floors greater than or equal to 4.

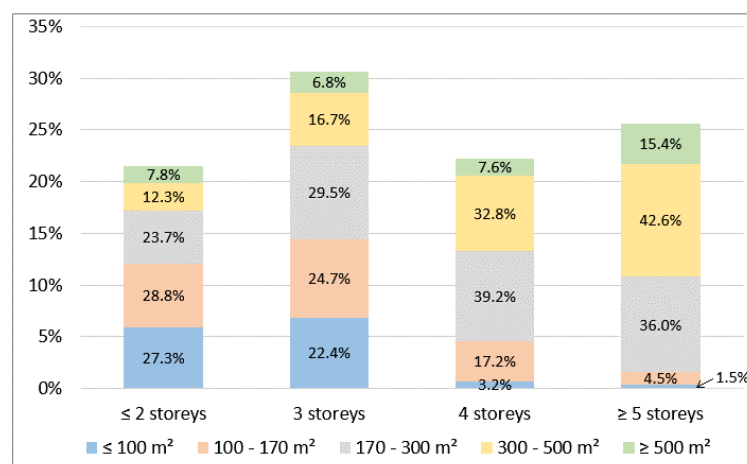


Figure 2: Average floor area and number of storeys (AEDES data).

It should be specified that the relationship between the average floor area and the number of floors may not fully represent the actual building stock, but only a subset of it, as only the



AEDES forms makes this information available. However, as specified above, it can be thought that these data provide more direct information on the most fragile part of the building stock and is therefore of greatest interest in the context of assessing the seismic vulnerability of existing buildings.

## 2.2 Definition of case study structures

On the basis of the characteristics observed, two types of building were defined: in particular a 2-storey and a 4-storey building. The plan surface area of each building (see Table 1) was chosen in such a way as to obtain structures that are as representative as possible of the existing stock.

In order to conduct non-linear static analyses, two-dimensional models were created. However, since the existing buildings in the area under consideration often feature frames with different features in different horizontal directions, two models were considered for each structure. The direction indicated with X corresponds to the one of main frames, while Y corresponds to the one of slabs, which are assumed as one-way.

MODEL	<i>X direction</i>			<i>Y direction</i>			Plan surface [m <sup>2</sup> ]
	n° bays	span length [m]	Lx [m]	n° bays	span length [m]	Ly [m]	
2 storey	3	4.5	13.5	3	4	12	162
4 storey	4	4.5	18	3	4	12	216

Table 1: Main geometric features of benchmark buildings.

## 2.3 Simulated design

A simulated design was carried out on the reference buildings, to define the size of the cross-sections of the structural elements and the relative reinforcements. To this purpose, it is of primary importance to place the buildings in an appropriate regulatory context. Based on the ISTAT census data on the construction period for the sample of buildings analysed, it is believed that the period of greatest interest, spans from the 50s to the 70s.

In the simulated design of the structures, the method of admissible stresses was used, respecting the requirements set out in the Italian structural design code issued in 1976 [10], thus considering it the reference standard. All the structures have been designed for vertical loads only; unlike the perimeter beams, shallow wide beams were considered for the internal frames, a typical solution of residential buildings, in which, due to architectural requirements, the thickness of beams is maintained within the thickness of slabs. Permanent loads were assumed equal to 5 kN/m<sup>2</sup> while live loads to 2 kN/m<sup>2</sup>. A concrete with a characteristic compressive strength  $R_{ck}$  equal to 25 MPa was considered for the simulated design. For the characterization of the reinforcing bars, reference was made to a series of studies on the mechanical characteristics of the steels used in RC structures in the 1960s [11]: in particular, smooth bars were used, with a median yield stress equal to 369.9 MPa, which lead to an allowable stress of 155 MPa. The stirrup spacing in columns is assumed equal to 25 cm. The size of columns depends on their axial stress, evaluated on the basis of tributary areas, while the beams were designed only for the bending moment due to the vertical loads. In particular, the perimeter beams have a section with dimensions 30x50 cm, while the cross-section of roof beams are 30x45 cm. The internal main beams have a section of 75x24 cm. Secondary beams, i.e. in the Y direction, are also considered, but of reduced dimensions.

### 3 MODELLING

The case study buildings must be schematized in a finite element model that is able to simulate the nonlinear structural response under to horizontal loads, both for structural elements (beams and columns) and non-structural elements, such as masonry infills. An approach based on lumped plasticity was adopted in the modelling. Finite element modelling was carried out through the OpenSees software [12]. The model of each structure was not limited only to one infilled frame (external frame), but involved the modelling of two frames side by side (Figure 3): one infilled and one bare frame, bound to undergo the same floor displacements, under a rigid diaphragm assumption.

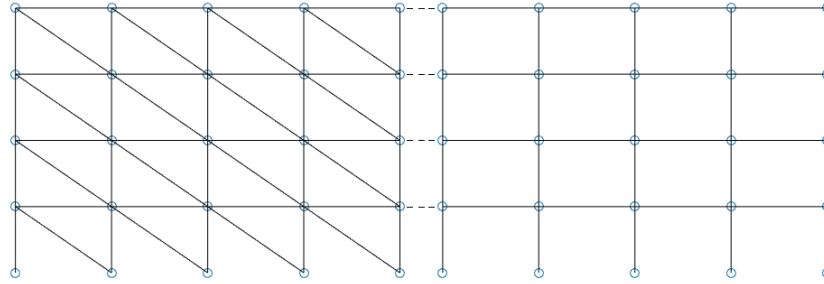


Figure 3: Example of the adopted modelling scheme.

#### 3.1 Frame elements

The frame elements (beams and columns) have been modelled using linear elastic elements, with rotational springs at their ends (*ZeroLength* elements). A moment-rotation relationship characterized by a three-linear envelope was adopted, defined by three characteristic points, which represent the yield condition, the ultimate condition, and the complete loss of strength. the latter is defined by the slope of the degrading branch, until zero moment, based on the Ibarra, Medina and Krawinkler model [13]. For each hinge the rotation capacity, corresponding to the yield ( $\theta_{y,s}$ ) and ultimate ( $\theta_{u,s}$ ) conditions was evaluated based on the approach suggested by Eurocode 1998-part 3 [14] for estimating the yield ( $\theta_y$ ) and ultimate ( $\theta_u$ ) chord rotations of RC members:

$$\theta_y = \phi_y \frac{L_v + a_v z}{3} + 0.0014 \left( 1 + 1.5 \frac{h}{L_v} \right) + \frac{\varepsilon_y}{d - d'} \frac{d_{bl} f_y}{6 \sqrt{f_c}} \quad (1)$$

$$\theta_u = \frac{1}{\gamma_{el}} 0.016 (0.3^v) \left[ \frac{\max(0.01; \omega')}{\max(0.01; \omega)} f_c \right]^{0.225} \left( \min \left( 9; \frac{L_v}{h} \right) \right)^{0.35} 25^{\alpha \rho_{sx} \frac{f_{yw}}{f_c}} (1.25^{100 \rho_d}) \quad (2)$$

where  $\phi_y$  is the yield curvature of the element cross-section,  $L_v$  is the shear span length,  $h$  is the cross-section depth;  $\omega$  and  $\omega'$  are, respectively, the mechanical reinforcement ratio of the tension and compression longitudinal bars;  $f_c$ ,  $f_y$  and  $f_{yw}$  are the concrete compressive strength, the longitudinal reinforcement yield tension and the stirrup yield tension, respectively, (MPa);  $\varepsilon_y$  is the steel elastic modulus;  $d_{bl}$  is the mean diameter of longitudinal tension reinforcement;  $d$  and  $d'$  are the depths to the tension and compression reinforcement, respectively;  $z$  is the internal lever arm length and  $a_v$  is equal to 1.0 if shear cracking is expect to precede the end section flexural yielding and it is equal to 0 otherwise;  $\rho_{sx}$  is the ratio of transverse reinforcement in loading direction (x);  $\rho_d$  is the diagonal reinforcement ratio;  $\alpha$  is the confinement effectiveness ratio;  $\gamma_{el}$  is equal to 1.5 for primary seismic elements and it is equal to 1.0 otherwise;  $v$  is the normalized axial force.

Some of the parameters in Eqns. 1 and 2 are not constant during a pushover analysis, however, given the limited number of storeys of the case study buildings, the axial force in the columns was assumed as constant, and due to non-seismic gravitational loads only. The shear span length  $L_v$  was defined on the basis of some preliminary analyses that led to the choice of the following values: half the length of the element for beams and columns, with the exception of the first storey columns, for which a point of contraflexure placed at 2/3 of the length, starting from the base, was assumed. Values of  $\theta_y$  and  $\theta_{um}$  were corrected, according to Eurocode 1998-part 3 rules, in order to consider lapping of reinforcing bars, the presence of smooth bars and the lack of seismic details.

In modelling the beam-spring assembly, the flexural behaviour of each element of the frame has been traced back to that of two equivalent cantilever beams. The effective moment-rotation relationship for the rotational springs was defined by subtracting from the total chord rotation (beam-spring system) the chord rotation due to the elastic deformation of the element, as reported below:

$$\theta_{y,s} = \theta_y - \frac{M_y L_v}{3EJ} \quad (3)$$

$$\theta_{u,s} = \theta_{um} - \frac{M_u L_v}{3EJ} \quad (4)$$

$$\theta_{uc,s} = \theta_{u,s} + \frac{M_u \theta_y}{\alpha_c M_y} \quad (5)$$

where  $\theta_{y,s}$  is the spring rotation at yielding,  $\theta_{u,s}$  is the spring rotation at ultimate condition and  $\theta_{uc,s}$  is the spring rotation corresponding to the complete loss of strength;  $\alpha_c$  is a percentage of the elastic branch stiffness of the backbone curve and it defines the slope of the degrading branch.

### 3.2 Masonry infills

Masonry infills were modelled adopting equivalent struts, using *Truss* elements, which follows the constitutive law proposed by Panagiotakos and Fardis [15] (as shown in Figure 4), implemented in the form of a three-linear force-displacement curve through the *Hysteretic* material of the OpenSees library.

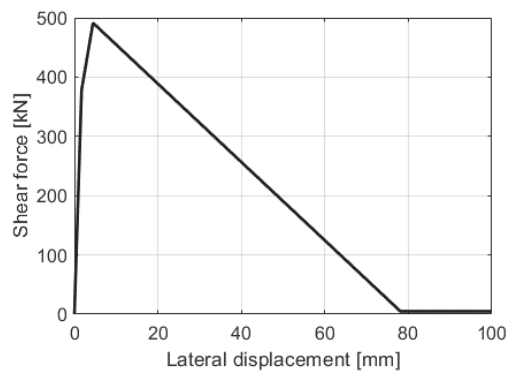


Figure 4: Example of the adopted force-displacement relationship for masonry infills.

The initial behaviour of the infill depends on the initial shear stiffness of the panel, defined as:

$$K_I = \frac{G_w L_w t_w}{h_w} \quad (6)$$

in which  $G_w$  is the masonry shear elastic modulus,  $L_w$  and  $h_w$  are the effective length and height of the panel, respectively and  $t_w$  is its thickness. The horizontal force corresponding to the first shear cracking depends on the shear cracking strength  $\tau_{cr}$ :

$$F_{cr} = \tau_{cr} A_w = \tau_{cr} L_w t_w \quad (7)$$

The stiffness of the second branch of the backbone curve corresponds to the axial stiffness of the equivalent masonry strut, as follows:

$$K_2 = \frac{E_w b_w t_w}{d_w} \quad (8)$$

where  $E_w$  is the masonry elastic modulus,  $d_w$  is the diagonal length of the infill panel and  $b_w$  represents the width of the equivalent strut, which was calculated with the formulation proposed in [16]:

$$b_w = d_w \cdot 0.175 (\lambda h_w)^{-0.4} \quad (9)$$

$$\lambda = \sqrt[4]{\frac{E_w t_w \sin(2\theta)}{4E_c J_p h_w}} \quad (10)$$

The parameter  $\lambda$  defines the relative stiffness of the RC frame and the infill panel, according to the formulation developed in [17], in which  $E_c$  is the concrete elastic modulus,  $J_p$  is the moment of inertia of the columns of the surrounding frame and  $\theta$  is the inclination angle of the panel with respect to the horizontal. The overstrength ratio, i.e. the ratio between the maximum strength of the masonry strut and the shear cracking strength, is equal to 1.3, while the stiffness of the degrading branch is 3% of the initial elastic stiffness, until a residual strength assumed as 1% of the peak force.

Different equivalent truss geometries were considered; in particular, single- and three-strut models (Figure 5). The first is able to adequately describe the global behaviour of an infilled frame, characterized by an increase in stiffness and resistance compared to a bare frame, but it is not able to simulate the local shear-failure mechanisms in columns due to the interaction with masonry infills. The second one, on the other hand, is capable of taking into account the local interaction phenomena between the frame and the infill panel.

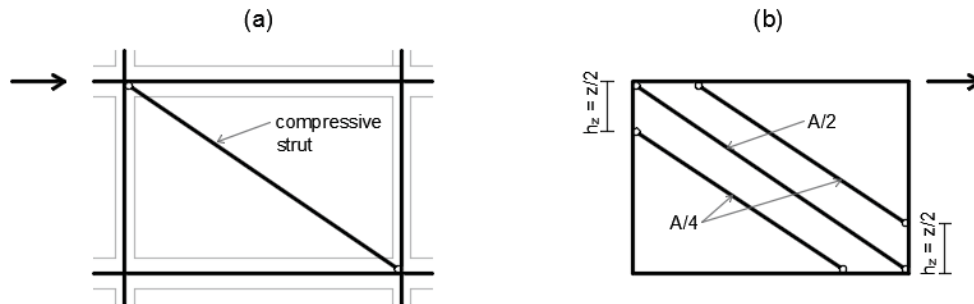


Figure 5: (a) single-strut model; (b) three-strut model.

In the three-strut models the total strut area is distributed among the three truss elements, considering 50% for the centre element and 25% for the others. The end node distance of side

truss elements from a frame node  $h_z = z / 2$  (see Figure 5) is based on an estimate of the size of the contact area between the infill and the frame, where  $z$  is calculated as follows:

$$z = \frac{\pi}{2\lambda} \quad (11)$$

The mechanical characteristics of masonry, such as the elastic modulus, the shear elastic modulus and the shear cracking tension, were defined after [6]. In particular,  $E_w$  and  $G_w$  were set to 1495 MPa and 598 MPa, respectively, while  $\tau_{cr}$  was set to 0.36 MPa.

The presence of openings in masonry infills was considered, assuming a percentage of openings  $\alpha_w = 14\%$ , evenly distributed. Therefore, simple relationships based on the definition of reduction coefficients directly applicable to the strut areas were used; in particular, reference was made to the following formulation [18]:

$$\lambda_{op} = 1 - 2\alpha_w^{0.54} + \alpha_w^{1.14} \quad (12)$$

## 4 ANALYSIS METHODOLOGY

Non-linear static analyses were carried out using OpenSees software. For each case study structure, pushover analyses were performed both in X and Y directions, assuming two different distributions for the horizontal forces: one proportional to the storey masses (uniform distribution), and one dependent on the shape of the first mode of vibration (linear distribution). The outputs of the pushover analyses were then processed using the MATLAB<sup>®</sup> software, with which a procedure for calculating the displacement demand was also implemented (see Section 4.2).

### 4.1 Damage levels for numeric models

Five levels of damage were defined, deriving them from the EMS-98 macro-seismic scale [19]. Each of these damage states (from DS1 to DS5) was associated to with the achievement of a certain local capacity in terms of displacement. On the basis of the modelling choices made, it was convenient to define the damage to the structural elements as a function of the deformation of the rotational springs that represent the plastic hinges. Damage on the infill panels was defined based on the deformation in the corresponding truss elements. The criteria adopted are as follows:

- DS1 – slight damage: is reached when the first cracks appear in the masonry infills, i.e. when the cracking force of the struts is reached.
- DS2 – moderate damage: this state occurs when either one RC member yields or one truss element reaches its peak strength.
- DS3 – heavy damage: this state occurs when either one of the truss elements reaches its ultimate displacement or one plastic hinge reaches a rotation corresponding to 3/4 of the ultimate rotation capacity.
- DS4 – very heavy: this state occurs when in one of the columns there is a resisting moment degradation of 20% after the peak resisting moment.
- DS5 – collapse: this state occurs when the total resisting base shear of the structure becomes equal to 20% of the residual capacity of the bare frames.

In addition to the five damage states described above, a further level of damage (DS5<sub>shear</sub>) was considered based on to the achievement of the shear strength in the structural elements (typically in the columns). Shear failure is a fragile failure mechanism which, although not specifically mentioned on the EMS-98 scale, represents very heavy damage. The shear strength



has been defined according to the current Italian structural design code [20]. Each level of damage was associated to a specific displacement of the control point.

## 4.2 Capacity curves

Sample results for the buildings studied are reported in Figure 6. These plots contrast the different behaviour of bare frames and the infilled frames, the latter being characterized by higher initial stiffness and maximum strength as well as by a relevant loss of strength, after the masonry struts failure. The capacity curve of the entire building was obtained combining infilled and bare frames, as discussed in Section 3.

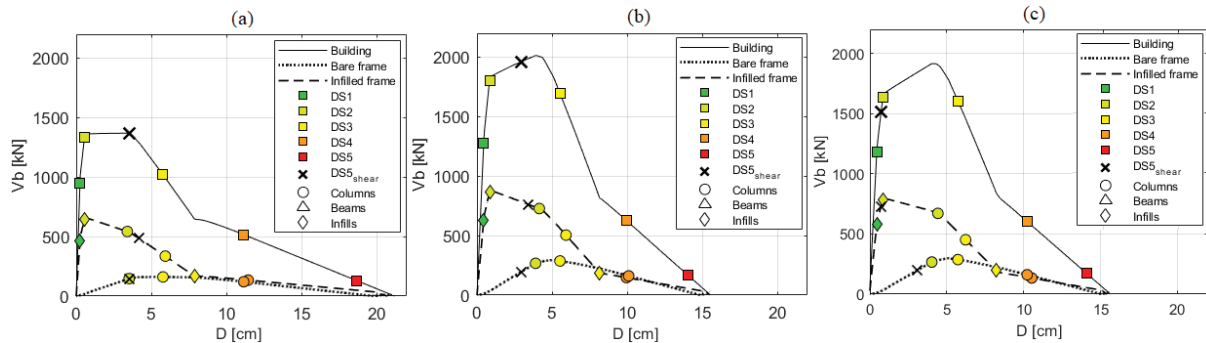


Figure 6: Capacity curves for in the X direction with mass proportional force distribution for the 2-storey single-strut model (a); 4-storey with single-strut model (b); 4-storey building, three strut model (c). For further details about geometrical characteristics see Table 1.

The observed collapse mode is predominantly characterized by soft floor mechanisms at the base of buildings. This behaviour is favoured by several factors: the low quality of detailing; the lack of capacity design criteria in design; furthermore, the failure of the infill panels in one floor tends to create a soft storey condition. These factors favour the formation of plastic hinges in columns rather than in beams. The plots in Figure 6 also show the capacity limits associated to the five damage levels under consideration. In the curves shown in Figure 6, it can be observed that the damage level DS2 is characterized by the rupture of the infills rather than by the yielding of the frame elements; conversely DS3 occurs first in the frame. In the 3-strut model (Figure 6-c) it can be observed that the columns shear failure occurs approximately when the peak resistance of the infills is reached, i.e. when the pressure of the panel on the contact area with the frame is maximum. It should be noted that also in the single-strut models shear failures can occur, but these models are not able to simulate the local interaction between the frames and the masonry infills occurring at the ends of columns and beams.

## 4.3 Evaluation of the displacement demand

In pushover analyses the displacement demand on a structure, associated with a certain IM value, such as PGA or spectral acceleration, is computed based on the definition of an equivalent SDOF system and specific  $R-\mu-T$  relationships. The present study was based on the IN2 method [21], which is applicable to systems characterized by a significant strength degradation as infilled frame structures. The method requires a preliminary multi-linearization of the pushover curve, respecting the underlying areas equality criteria, as shown in Figure 7.

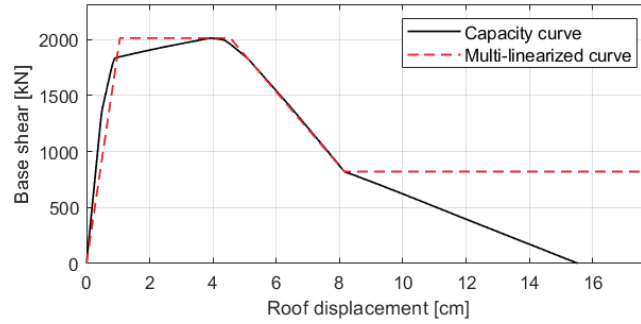


Figure 7: Example of multi-linearization of the 4-storey building capacity curve.

Given an elastic spectrum in terms of acceleration the calculation of the displacement demand first passes through the study of an equivalent SDOF system, and the evaluation of an appropriate inelastic demand spectrum. For the calculation of this latter and of the required ductility, reference was made to the relation  $R-\mu-T$  proposed in [22]. This procedure requires an elastic spectrum with a standard Newmark-Hall shape. The elastic spectrum adopted in the present study was defined according to the current Italian structural design code [20], considering a return time of 475 years and assuming a position of the site close to the epicentres of the main shocks that stroke the Emilia area. The IN2 curves in terms of PGA are shown in Figure 8, for 2 and 4 storey buildings, considering a single strut model for masonry infills.

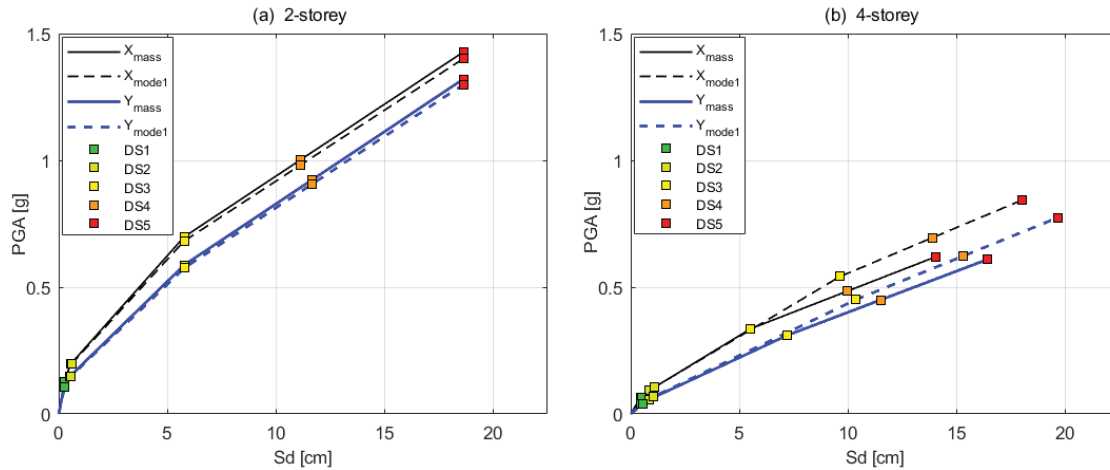


Figure 8: IN2 curves for the 2-storey (a) and 4-storey building (b) single-strut models.

## 5 FRAGILITY ANALYSIS

This section is dedicated to the seismic fragility assessment of the case study buildings. Considering the numerical models presented, a fragility analysis was conducted, with the aim of obtaining fragility curves that relate the probability of reaching the damage levels discussed in Section 4.1 to the values of Peak Ground Acceleration (PGA). To this aim it is necessary to consider the uncertainties that affect the problem under consideration. These are mainly related to: material properties, modelling uncertainties, record-to-record variability and prediction capacity of the analysis method adopted. Random Variables (RV) were used in order to describe these uncertainties. The RVs chosen are (see Table 2): concrete compressive strength  $f_c$ ; steel yielding stress  $f_y$ ; chord rotation at yielding  $\theta_y$ ; chord rotation at ultimate condition  $\theta_{um}$ ; coefficient  $\alpha_c$ , which determines the slope of the post capping stiffness of RC members; lateral force  $F_{inf}$  and lateral drift  $D_{inf}$  of the infills force-displacement relationship. In particular, different variabilities have been assumed for  $F_{inf}$  and  $D_{inf}$  relatively to the cracking point and

the peak point of the infills behaviour curve. The variables described above influence the behaviour of the building, in particular, affecting the capacity curve. However, the  $R-\mu-T$  relation used to determine the inelastic spectra in the calculation of the displacement demand, provides an average value of the required ductility. Therefore, a certain variability was assumed also for the ductility demand [22], this represents both the uncertainty on the prediction provided by the adopted analysis method and record-to-record variability. A log-normal distribution has been assumed for all RVs and the corresponding coefficients of variation are shown in Table 2. The coefficient of variation for concrete compressive strength was evaluated in order to fall within the limit values set for the concrete acceptance criteria, while that relating to the coefficient  $\alpha_c$  was defined in order to obtain a median value comparable with the formulation reported in [23], and extreme values contained within the range tested in [24].

For each building model, given a set of random values of the RVs, defined a loading direction and a distribution of forces it is possible to compute a capacity curve, which can then be used to find scaling factor for the elastic response spectrum that leads to a displacement demand equal to the capacity associated to a certain DS. The PGA of the so obtained scaled spectrum represents a measure of the structural capacity for the DS under consideration. By repeating this procedure for more samples of the RVs is possible to obtain a sample of the PGA capacity values associated to a certain DS, the cumulative probability distribution of these values represents, the fragility curve relative to the considered damage level. However, such a procedure is computationally inefficient because it requires a large number of samples. Therefore, Response Surface (RS) models were introduced in order to find empirical relationships between the structural capacities for each of the DSs under consideration and the values of the RV. A RS is a statistical regression model that interpolates, within a certain domain, the values of a response variable – PGA capacity for a certain DS in this case – as a function of a set of independent variables.

RV	Distribution	CoV	Reference
$f_c$	Log-normal	0.20	
$f_y$	Log-normal	0.08	[11]
$\theta_y$	Log-normal	0.331	[5]
$\theta_{um}$	Log-normal	0.54	[23]
$\alpha_c$	Log-normal	0.55	
$F_{inf} = [F_{cr}; F_{max}]$	Log-normal	[0.3; 0.3]	[5]
$D_{inf} = [D_{cr}; D_{max}]$	Log-normal	[0.3; 0.7]	[5]
$\mu$ (ductility)	Log-normal	0.70	[22]

Table 2: Random Variables and uncertainty parameters.

In order to obtain data for fitting the RS models, the Central Composite Design (CCD) criterion was used in order to define a set of values of the RVs to be used for the pushover analyses. Since, as discussed later, the ductility demand was not considered in the RS models, the number of RVs is 7, which according to CCD correspond to  $2^7 + 2 \cdot 7 + 1 = 143$  combinations of the RV values to be used for pushover analyses. These are carried out for each model, for each direction and for each distribution of forces. The form of RS model adopted for each structure, for the  $i$ -th DS associated to a loading direction and a force distribution is:

$$\ln(PGA_{DS \geq DS_i}) = b_0 + b_1 \ln(f_c) + b_2 \ln(f_y) + b_3 \ln(\theta_y) + b_4 \ln(\theta_{um}) + b_5 \ln(\alpha_c) + b_6 \ln(F_{inf}) + b_7 \ln(D_{inf}) + \varepsilon \quad (13)$$

where  $b_0$  to  $b_7$  are unknown regression coefficients, and  $\varepsilon$  is a normal error term. Their values were estimated by means of linear regression. The standard deviation of the error term was the

augmented considering the uncertainty on the ductility demand [22]. Since a log-normal distribution for the RVs was assumed,  $\ln(PGA_{DS} \geq DS_i)$  is a linear combination of normally distributed variables and therefore assumes a normal distribution which is fully defined by its mean value and standard deviation. The cumulative distribution function for  $\ln(PGA_{DS} \geq DS_i)$  represents the fragility curve for the  $i$ -th DS. As mentioned above, fragility curves are obtained for the different main directions of the building and for the different horizontal force profiles (Figure 9).

Fragility curves for the X and Y directions of each building (Figure 9-a) were obtained by considering the highest probability value (worst case) between the curves associated to the two different lateral load distributions. In order to provide a global assessment of the building's seismic vulnerability, direction-independent fragility curves were also evaluated; these curves were obtained as the average exceedance probability for generic DS for the two different directions (Figure 10). Considering the worst case between the X and Y directions would in fact lead to a systematic overestimation of the building's vulnerability. The fragility curves obtained for 2 and 4-storey buildings show that the latter is more vulnerable than the former, with differences in the probability of damage higher than 30%, in particular for the DS3, DS4, DS5 and DS5<sub>shear</sub> in the PGA range between 0.2 g and 0.6 g.

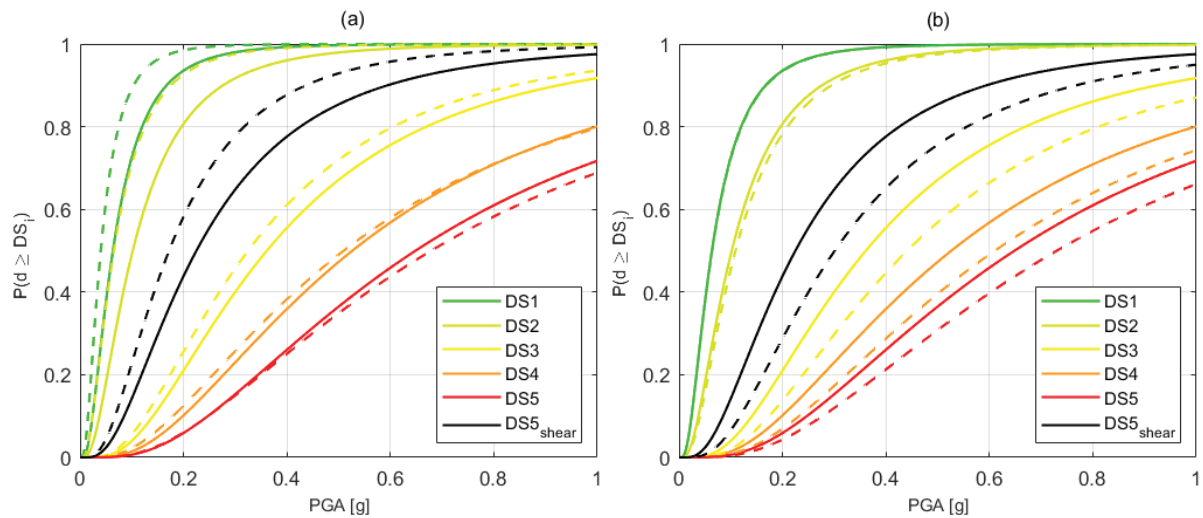


Figure 9: Fragility curves for the 4-storey building: (a) X (solid line) and Y direction (dashed line); (b) force distribution proportional to storey masses (solid line) and to the first mode (dashed line).

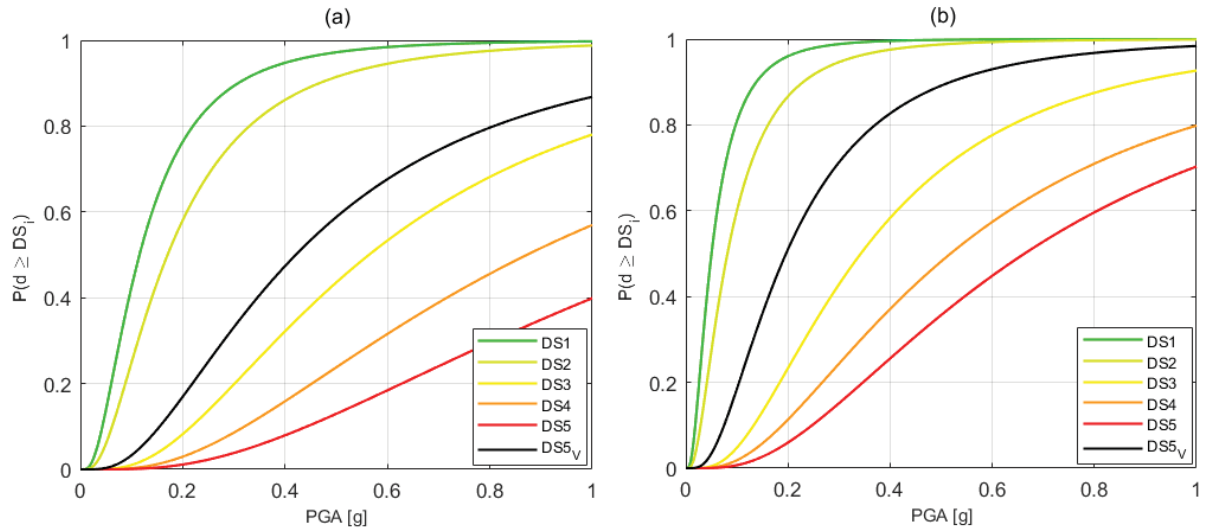


Figure 10: Global capacity curves (single strut model): 2-storey (a) and 4-storey building (b).

The fragility curves for the 4-storey building modelled with 3 equivalent struts are shown in Figure 11. For the frame members a flexural behaviour similar to the case of the single strut model was observed, however, with this model, an anticipated shear failure at the ends of the columns can be triggered, due to the local interaction between the infill panel and the surrounding frame. The fragility curve associated with shear failure is very close to the curve associated with DS2, corresponding to the first condition to occur between the infill peak strength and yielding of the frame elements. In the three-strut model the shear failure of the columns tends, therefore, to occur at the maximum strength in the masonry struts and to anticipate the columns yielding.

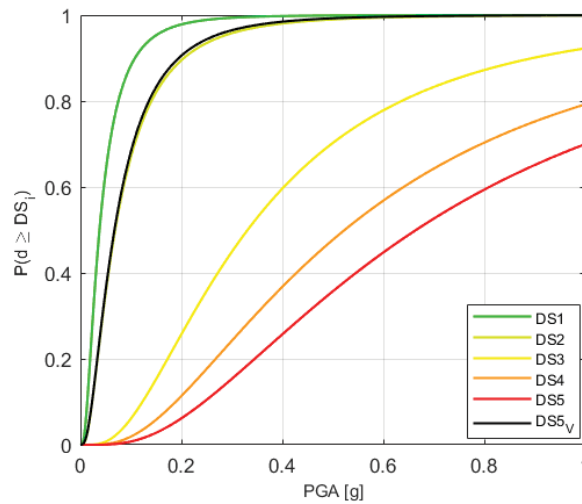


Figure 11: Global capacity curves for the 4-storey building (three strut model).

## 6 CONCLUSIONS

With this work we have contributed to the seismic vulnerability assessment of RC frames with masonry infills. Starting from a study on the characteristics of the existing building stock in the Emilia area, case study buildings were defined, then modelled with finite elements considering the contribution of masonry infills. Non-linear static analyses were carried out on



the obtained models and the capacity in terms of PGA associated with different DSs was evaluated. Fragility curves were finally developed for the examined buildings using RS models. Different infills models were considered, in order to simulate the fragile shear failure in the columns. However, the three-strut modelling used here, while capturing the local interaction described, are not able to adequately describe the behaviour of the structure after the shear failure has been detected. Fragility curves have also been presented for shear failure, but in these terms, more work is needed.

## ACKNOWLEDGEMENTS

The financial support of the Italian Civil Protection Department, DPC-RELUIS 19-21 research project, Workpackage WP17, is gratefully acknowledged.

## REFERENCES

- [1] Penna, A., Morandi, P., Rota, M. et al. Performance of masonry buildings during the Emilia 2012 earthquake. *Bull Earthquake Eng* 12, 2255–2273 (2014).
- [2] Buratti, N., Minghini, F., Ongaretto, E., Savoia, M., Tullini, N., Empirical seismic fragility for the precast RC industrial buildings damaged by the 2012 Emilia (Italy) earthquakes. *Earthquake Engineering and Structural Dynamics*, 2017, 46(14), pp. 2317–2335.
- [3] Savoia, M., Buratti, N., Vincenzi, L., Damage and collapses in industrial precast buildings after the 2012 Emilia earthquake. *Engineering Structures*, 2017, 137, pp. 162–180.
- [4] Ricci P., De Risi M.T., Verderame G.M., Manfredi G., (2013). Influence of infill distribution and design typology on seismic performance of low- and mid-rise RC buildings. *Bulletin of Earthquake Engineering*, DOI 10.1007/s10518-013-9453-4.
- [5] Verderame, G., Ricci, P., De Luca, F., Del Gaudio, C., & De Risi, M. T. (2014). Damage scenarios for RC buildings during the 2012 Emilia (Italy) earthquake. *Soil Dynamics and Earthquake Engineering*, 66, 385–400.
- [6] G. Uva, D. Raffaele, F. Porco, A. Fiore, On the role of equivalent strut models in the seismic assessment of infilled RC buildings. *Engineering Structures* 42 (2012) 83–94.
- [7] A.F. Mohammad, M. Faggella, R. Gigliotti, E. Spacone, Seismic performance of older R/C frame structures accounting for infills-induced shear failure of columns. *Engineering Structures* 122 (2016) 1–13.
- [8] Daniele Perrone, Marianovella Leone, Maria Antonietta Aiello, Non-linear behaviour of masonry infilled RC frames: Influence of masonry mechanical properties. *Engineering Structures* 150 (2017) 875–891.
- [9] Buratti, N., Ferracuti, B., Savoia, M., Response Surface with random factors for seismic fragility of reinforced concrete frames. *Structural Safety*, 2010, 32(1), pp. 42–51.
- [10] Decreto Ministeriale 16 giugno 1976 – *Norme tecniche per la esecuzione delle opere in cemento armato normale e precompresso e per le strutture metalliche*.

- 
- [11] Verderame GM, Stella A., Cosenza E. (2001). Le proprietà meccaniche degli acciai impiegati nelle strutture in c.a. realizzate negli anni 60'. *X Convegno nazionale "L'Ingegneria Sismica in Italia"*, Potenza-Matera, 9-13 settembre.
- [12] McKenna, F., Fenves, G.L., Scott, M.H. (2004). OpenSees: Open System for Earthquake Engineering Simulation. Pacific Earthquake Engineering Research Center. University of California, Berkeley, CA, USA. <http://opensees.berkeley.edu>.
- [13] Ibarra, L. F., Medina, R. A., and Krawinkler, H. (2005). Hysteretic models that incorporate strength and stiffness deterioration, *Earthquake Engineering and Structural Dynamics*, Vol. 34, 12, pp. 1489-1511.
- [14] EN 1998-3:2005, *Eurocode 8 – Design of structures for earthquake resistance – Part 3: Assessment and retrofitting of buildings*.
- [15] Panagiotakos, T. B., & Fardis, M. N., (1996): "Seismic Response of Infilled R/C Frames Structures", Proc. of the 11th World Conference on Earthquake Engineering, Mexico, paper 225.
- [16] Klingner, R. E., & Bertero, V. V., (1976): "Infilled frames in earthquake-resistant construction", Report EERC 76-32, Earthquake Engineering Research Center.
- [17] Stafford Smith, B., (1966): "Behavior of Square Infilled Frames", Journal of the Structural Division, Vol. 92, n. ST1, pp. 381-403.
- [18] P.G. Asteris, I.P. Giannopoulos, C.Z. Chrysostomou, Modeling of Infilled Frames With Openings. The Open Construction and Building Technology Journal, 2012, 6, (Suppl 1-M6) 81-91.
- [19] Grünthal, G. ed. 1998. 'European Macroseismic Scale 1998 (EMS-98)', Cahiers du Centre Européen de Géodynamique et de Séismologie 15, Helfent-Betrangle (Luxembourg).
- [20] Decreto Ministeriale 17-01-2018: Norme tecniche per le costruzioni (GU Serie Generale n.42 del 20-02-2018 - Suppl. Ordinario n. 8).
- [21] Dolšek, M., Fajfar, P. (2005). Simplified non-linear seismic analysis of infilled reinforced concrete frames. *Earthquake Engineering and Structural Dynamics*, 34(1), 49-66.
- [22] Dolšek, M., Fajfar, P. (2004). Inelastic spectra for infilled reinforced concrete frames. *Earthquake Engineering and Structural Dynamics*, 33(15), 1395-1416.
- [23] Haselton, C.B., A.B. Liel, S. Taylor Lange, and G.G. Deierlein (2008). Beam-Column Element Model Calibrated for Predicting Flexural Response Leading to Global Collapse of RC Frame Buildings, PEER Report 2007/03, *Pacific Engineering Research Center, University of California, Berkeley, California*.
- [24] Ibarra, L. F., and Krawinkler, H. (2005). Global collapse of frame structures under seismic excitations, *Technical Report 152, The John A. Blume Earthquake Engineering Research Center, Department of Civil Engineering, Stanford University, Stanford, CA*.

## FRAGILITY ASSESSMENT OF THE ITALIAN MASONRY SCHOOL BUILDING ASSET FOR RISK EVALUATION AT NATIONAL SCALE

E. Saler<sup>1,2</sup>, V. Follador<sup>2</sup>, P. Carpanese<sup>2</sup>, and F. da Porto<sup>2</sup>

<sup>1</sup> Dept. of Civil, Environmental and Mechanical Engineering, University of Trento  
Via Mesiano 77, 38123 Trento, Italy  
e-mail: elisa.saler@unitn.it

<sup>2</sup> Dept. of Geosciences, University of Padova  
Via Gradenigo 6, 35131 Padova, Italy  
{veronica.follador, francesca.daporto}@unipd.it; pietro.carpanese@phd.unipd.it

---

### Abstract

*Seismic risk and scenario assessments at large-scale provide important science-based tools to support governments and civil protection departments in investment policies and emergency planning. In this framework, school buildings are particularly significant due to the consequences of their damage or collapse and their relevance, as public buildings, in emergency planning. The evaluation of risk requires the definition of its components, i.e., hazard, exposure and vulnerability. To assess the seismic vulnerability of masonry school building assets, this paper presents the fragility curves derived for 265 building types, based on the Italian school building census. Parametric analyses were carried out on 14 representative prototype schools, using a mechanics-based model which considers both in-plane and out-of-plane mechanisms. More than 7500 sample fragilities were calculated and linearly combined to obtain fragility curves representing the Italian taxonomy of masonry school buildings. A macro-seismic heuristic model from the literature was then calibrated to derive a fragility set for each school type, for five damage states, from slight damage to complete collapse. Finally, the paper compares the outcome fragility curves and fragility sets from the literature for residential buildings, highlighting the specificities of school seismic vulnerability. Indeed, masonry school buildings are frequently characterized by intrinsic geometric deficiencies due to significant inter-story height and great distance between transverse walls, both affecting the out-of-plane response and, therefore, the overall seismic fragility.*

**Keywords:** Fragility curves, School buildings, Masonry buildings, Seismic risk, Large-scale assessment.

---

## 1 INTRODUCTION

School buildings are crucial elements of structural and infrastructure assets for communities. The social impact of their collapse associated to seismic events is huge, in terms of both casualties and social dispersion. After the collapse of a primary school in San Giuliano di Puglia (Italy) in 2002 [1], the Italian government issued a national plan to evaluate the seismic vulnerability of the entire stock of relevant and strategic structures, including school buildings [2].

Detailed modeling and analyses are very time consuming, and therefore not suitable to manage large stocks of buildings, while tools based on fragility curves of building types better respond to this need. Fragility curves provide a correlation between a seismic intensity measure, such as the Peak Ground Acceleration (PGA), and the probability that a structure exceeds a damage state (DS). Fragility curves for school buildings were obtained for Nepalese schools, after processing data on observed damage caused by the 2015 Nepal earthquake [3], while Gentile et al. [4] derived fragility curves for Indonesian schools by means of non-linear dynamic analyses.

Different approaches are available to define fragility curves: empirical, based on observed damage after a seismic event [5–8]; mechanical, based on structural modeling, either detailed [9] or simplified [10–13]; and hybrid, based on both empirical data and models [14, 15]. These methods have been largely applied to ordinary and residential buildings. Moreover, vulnerability assessment at urban scale of the built asset specific for a regional area [16] has aroused a large interest, as it allows a more precise estimation of risk.

The taxonomy of buildings exposed to risk is fundamental to define building types and their distribution at large scale, requiring typological analyses of the building census of the analyzed area. In particular for Italy, regional taxonomies have been provided in the literature, while the evaluation of national macro-classes representative of the entire national school asset has yet to be defined. A typological study of masonry school buildings in the crater of the Central Italy seismic sequence (2016) was provided by Ottonelli et al. [17], while masonry school types were classified for the Friuli-Venezia Giulia region by Gattesco and Boem [18].

Especially for the Italian framework, the fragility analysis of specific classes of structures, such as school buildings, based on an extensive taxonomy describing the national stock, is required to assess risk at large scale and to optimize the allocation of funds for mitigation strategies. This aim is carried out by a cooperative national project (*ReLUIS-DPC Project 2019-2021*) by will of the Italian Department of Civil Protection, in which this contribution is included.

This paper presents the derivation of seismic fragility curves for unreinforced masonry (URM) school buildings by means of extensive parametric analyses carried out by applying a mechanics-based model [19, 20] which considers both the in-plane (IP) and the out-of-plane (OOP) mechanisms, as well as an index of the structural quality [21]. The approach has been already effectively applied to residential URM buildings and validated by simulating the damage scenario caused by the 2009 L'Aquila earthquake [22, 23]. In the present paper, a set of 14 representative prototype school buildings were analyzed, varying different parameters, i.e., number of stories, quality of construction details, floor weight, type of masonry and related panel thickness. The contribution aims to provide fragility curves which cover all the macro-classes based on the Italian school census, defined by a limited number of parameters, i.e., construction age, number of stories, plan area, and type of masonry.

## 2 ITALIAN SCHOOL BUILDING ASSET

A general taxonomy of Italian school buildings was derived according to the School Building Registry (SBR) of the Italian Ministry of Education [24], which classifies a large amount of the Italian school asset, based on a limited number of parameters, i.e., construction material and age, number of stories, plan area, and types of floors and roof. In this framework, data from the Italian SBR (2005) for masonry schools, amounting to more than ten thousand buildings, were used to define the macro-classes for which the fragility model, presented hereinafter, was derived.

Figure 1 illustrates the distribution of typological characteristics of masonry school buildings comprised in the national census. In particular, Figure 1a shows the distribution of construction ages, which appears to be covered quite evenly. Then Figure 1b provides the distribution of the number of stories, with a peak corresponding to the case of two-story buildings, and Figure 1c shows the prevalence of small to medium schools, according to their plan area. Lastly, the combinations of couples of these parameters are shown in Figure 1d with the number of stories given the construction age, Figure 1e with the distribution of plan area given the construction age, and Figure 1f with the number of stories associated to the plan area.

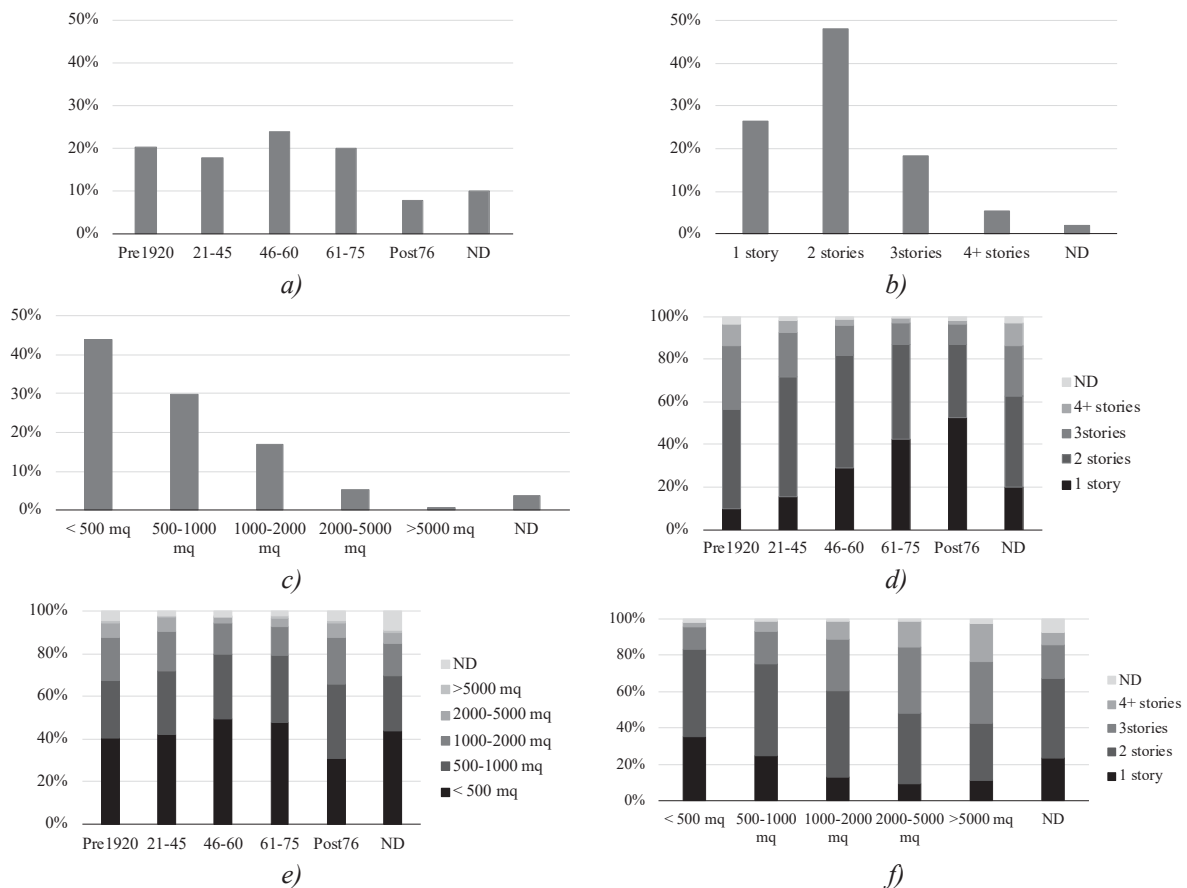


Figure 1: Distribution of typological characteristics of masonry buildings in Italian School Building Registry.

The analysis of the distribution of the typological characteristics of the masonry school buildings in the SBR allowed the definition of a finite number of prototype buildings to be used in the derivation of fragility curves, as described in the following sections. Considering significant combinations of the typological parameters, 14 masonry school buildings were selected from the databases collected by research groups from the Universities of Genova, Pa-



dova, and Trieste, so as to ensure a good representativeness of the national school building taxonomy; their typological characteristics are reported in Table 1. The typical shapes of school building plans, included in the analysis by choosing representative prototype buildings, are shown in Figure 2.

School ID	Age	N. stories	Plan area [m <sup>2</sup> ]	Plan shape
S1	Before 1920	3	<500	Rectangular
S2	Before 1920	2	>2000	U-shape
S3	Before 1920	2	1000-2000	Cloister
S4	Before 1920	3	1000-2000	U-shape
S5	1921-1945	2	500-1000	Rectangular
S6	1921-1945	2	<500	Rectangular
S7	1921-1945	2	<500	T-shape
S8	1921-1945	2	1000-2000	U-shape
S9	1921-1945	2	500-1000	T-shape
S10	1946-1960	2	1000-2000	L-shape
S11	1946-1960	2	<500	Rectangular
S12	1946-1960	2	<500	Rectangular
S13	1961-1975	1	<500	Square
S14	After 1976	1	<500	Square

Table 1: Typological characteristics of prototype school buildings.

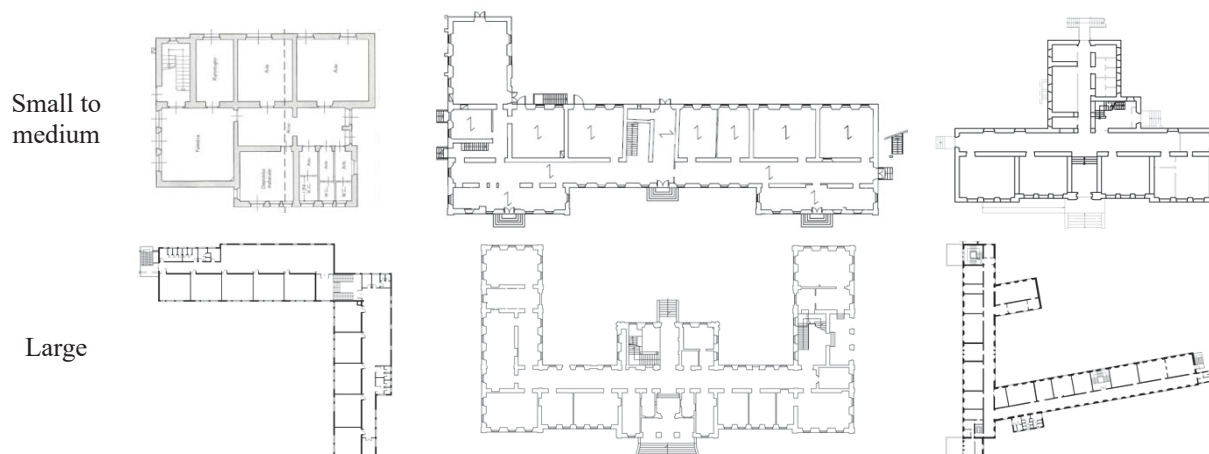


Figure 2: Typical shapes of school building plans.

N. stories	Construction details	Floor weight	Type of masonry	Thickness of masonry [cm]
1	No ring-beam, no tie-rod (LQD)	Light	Random rubble	30-70
2	Tie-rods (MQD)	Heavy	Stone ashlar	30-70
3	Ineffective ring-beam (HQD ineff)		Clay bricks w/ lime mortar	25-50
4	Effective ring-beam (HQD)		Clay blocks w/ cement mortar	30-45

Table 2: Parameters and ranges of variation considered in parametric analyses.

Preserving the geometric properties of each building, a parametric analysis was carried out, increasing the size of the school dataset, which lead to more than 7500 realizations imple-

mented through the simplified mechanical model. Table 2 reports parameters and their range of variation included in the analyses.

The mechanical properties of masonry were assumed according to Italian Code [25], considering two values for the masonry strength: the minimum value reported in the regulation, and a maximum value obtained by applying code-compliant improving coefficients, to take into account possible interventions carried out during the lifetime of the structure.

### 3 MECHANICS-BASED APPROACH FOR FRAGILITY ASSESSMENT

The simplified mechanics-based approach *Vulnus 4.0* [19, 20], which allows the implementation of a significant amount of analyses with a limited computational effort, was applied for the fragility assessment of the above described prototype schools. The modeling procedure allows seismic analyses to be implemented accounting for both the In-Plane (IP) shear resistance of the building and the trigger of potential Out-Of-Plane (OOP) mechanisms, together with a vulnerability rate deriving from the II level GNDT form [21]. *Vulnus 4.0* provides three outcome indexes: i) the first index ( $i_1$ ) expresses the ratio, for the weakest plan direction, between the IP shear resistance and the weight of the building; ii) the second index ( $i_2$ ) describes the susceptibility to OOP mechanisms (i.e., overturning, flexural failure, and arch compression failure), calculated by means of kinematic analyses; and iii) the third index ( $i_3$ ) considers qualitative factors, included in II level GNDT form, which can affect the seismic vulnerability of a building, such as the masonry quality as well as the type of floors, also considering those configurations which strongly worsen the seismic response (i.e., heavy and rigid floor on weak random masonry).

Then, the combination of the indexes is carried out through fuzzy set theory, allowing the probabilistic evaluation of the influence of both not quantifiable parameters, summarized in the  $i_3$  index, and uncertainties of quantifiable parameters (e.g., mechanical properties of masonry), which are considered in the calculation of indexes  $i_1$  and  $i_2$ . The outcome of vulnerability analysis with *Vulnus 4.0* consists in three fragility curves: an average curve, called *white*, which describes the most probable distribution; and two extreme conditions, defined as *lower* and *upper*, representing the lower and the upper bounds, respectively.

Fragility curves, which expresses the probability of exceedance of a damage state, are derived as log-normal cumulative probability functions, which are described by two parameters: the mean value ( $IM_{mean}$ ) and the standard deviation ( $\beta$ ).

The resulting set represents the cumulative probability of exceeding a medium-severe damage state (DS), according to the definition provided by the European macro-seismic scale (EMS98) [26], which is an intermediate DS between 2 (i.e., trigger of OOP mechanisms) and 3 (i.e., IP global shear failure). The DS identified by the *Vulnus 4.0* fragility set is therefore conventionally referred to as DS2-3, hereinafter.

As mentioned before, the parametric analysis generated more than 7500 realizations and thus, the same amount of DS2-3 fragility sets, which were then combined to finally derive 265 fragility sets, to be associated with school macro-classes, according to the typological parameters included in the Italian school building census. An exposure matrix was assumed, based on expert judgement, to linearly combine curves obtained from each case of the parametric analysis, keeping the *white*, *lower* and *upper* curves separate. Table 3 reports the percentage of the exposure matrix used for the recombination in macro-classes starting from subtypes of masonry, while Table 4 shows the percentage of recombination for different level of quality details, whose definition has been given in Table 2.

The fragility sets for macro-classes describing the damage state 2-3 were then extended to a complete set of five fragility curves, capable of describing the probability of exceedance of

the five damage states given by the EMS98 [26], from DS1 (slight damage) to DS5 (complete collapse).

The final complete sets took into account both the average *white* curve and the extreme bounds, by means of a geometric combination, detailed as follows. The above described procedure was developed for residential buildings [27] and afterwards, in the present work, applied to school buildings.

	Before 1920	1921-45	1946-60	1961-75	After 1976
Random rubble	30%	30%	10%	10%	-
Stone ashlar	35%	35%	27%	27%	10%
Clay bricks	35%	35%	54%	44%	27%
Clay blocks	-	-	9%	19%	63%

Table 3: Assumed exposure matrix of type of masonry during construction ages.

	Before 1920	1921-45	1946-60	1961-75	After 1976
LQD	20%	15%	10%	-	-
MQD	50%	35%	50%	30%	15%
HQD ineff	30%	30%	-	-	-
HQD	-	20%	40%	70%	85%

Table 4: Assumed exposure matrix of quality of construction details during construction ages.

To obtain fragility sets representing five DSs, each DS2-3 fragility set was referred to the fragility model proposed by Lagomarsino and Cattari, in 2014 [13], which was derived from a previously presented macro-seismic model [15]. For the present application, the correlation law between the Peak Ground Acceleration (PGA) and the macro-seismic intensity was set according to Margottini et al. [28]. The reference model represents fragility distributed on five DSs for the six vulnerability classes (from A to F) defined by EMS98 [26], on the basis of the intrinsic correlation between macro-seismic intensity and damage state. The macro-seismic reference model was thus calibrated on the macro-class fragility sets obtained with the mechanical procedure *Vulnus 4.0*, through the steps described as follows:

1. An average curve DS2-3 was derived for the six vulnerability classes, through the linear combination of the available DS2 and DS3 fragility curves. Figure 3a shows fragility curves from macro-seismic model for all vulnerability classes, with DS2 and DS3 curves highlighted in solid blue lines, and DS2-3 highlighted in solid black lines.
2. Each fragility set from the mechanical model was then represented through a combination of compatible DS2-3 curves of two vulnerability classes, calculated at the previous step. A genetic algorithm (NSGA-II [29]) was implemented to evaluate the optimal linear combination, by minimizing both the absolute and the relative errors between the curves, calculated through the least squares and the difference between the areas, respectively.
3. A set of five fragility curves (i.e., representing five DSs) was derived for each macro-class of school buildings through the optimal coefficient that was previously calculated, for the linear combination of vulnerability classes. Figure 3b reports, as an example, the fragility curve DS2-3 from the mechanical model for two-story masonry schools built before 1920 (solid red line), which resulted to be an optimal combination of DS2-3 curves for vulnerability classes B and C, which are represented in blue and black solid lines, respectively. Fragility curves for DSs from 1 to 5, for the school macro-class, was then derived as a combination of each DS curves from the macro-seismic model, in this case considering the curves associated with vulnerability classes B and C.

This procedure was applied to each macro-class of school buildings for all the curves previously derived through *Vulnus 4.0*, namely the *white*, *lower* and *upper* curves.

Finally, a procedure for geometric combination (named LUW [22, 23]) was implemented in order to include, in the proposed fragility model, the uncertainties considered in *Vulnus 4.0* analysis by means of fuzzy theory. Thus, the procedure allowed *white*, *upper* and *lower* curves to be combined for each macro-typology and for each DS.

The LUW procedure preserves the mean value of the *white* curve; it uses *upper* and *lower* distributions in 2.5% and 97.5% fractals of the *white* probability, respectively. Between 2.5% and 50% of the *white* probability, it linearly combines *white* and *upper* curves, while a linear combination of *white* and *lower* curves is calculated between 50% and 97.5%.

For example, Figure 4 illustrates how LUW procedure was applied to two-story masonry schools built before 1920 and, thereby, the final fragility set was derived.

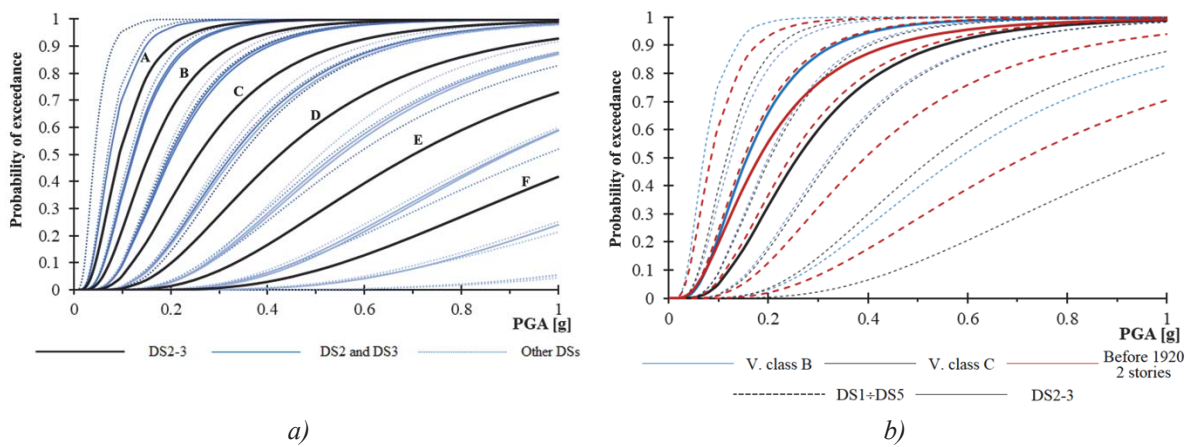


Figure 3: a) Average curves DS2-3 for macro-seismic reference model, b) calibration of macro-seismic model for one school macro-class.

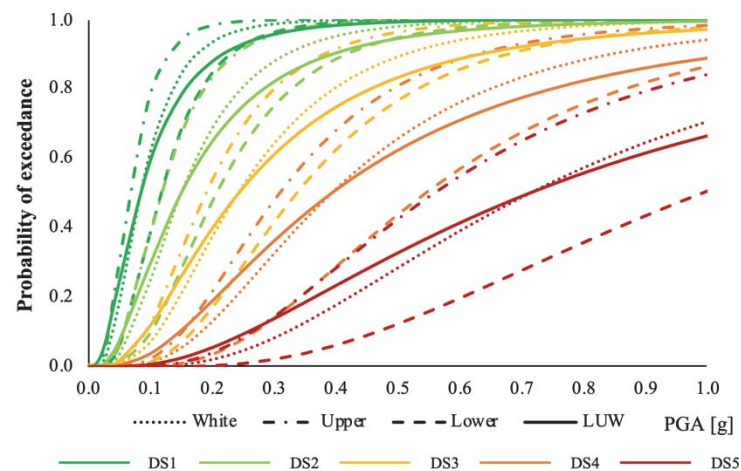


Figure 4: Application of LUW procedure on a set of fragility curves.

#### 4 RESULTS AND PROPOSED FRAGILITY MODEL

This section presents the outcomes of this study, starting from the fragility sets associated to a Damage State 2-3, which were obtained through the mechanical approach *Vulnus 4.0*. Figure 5 illustrates the mechanical fragility curves obtained from the combination, according to the above-described exposure matrix, of the fragility curves resulting from the above-

described extensive parametric analysis. The figure reports a summary of the results considering two parameters (i.e., number of stories and construction age).

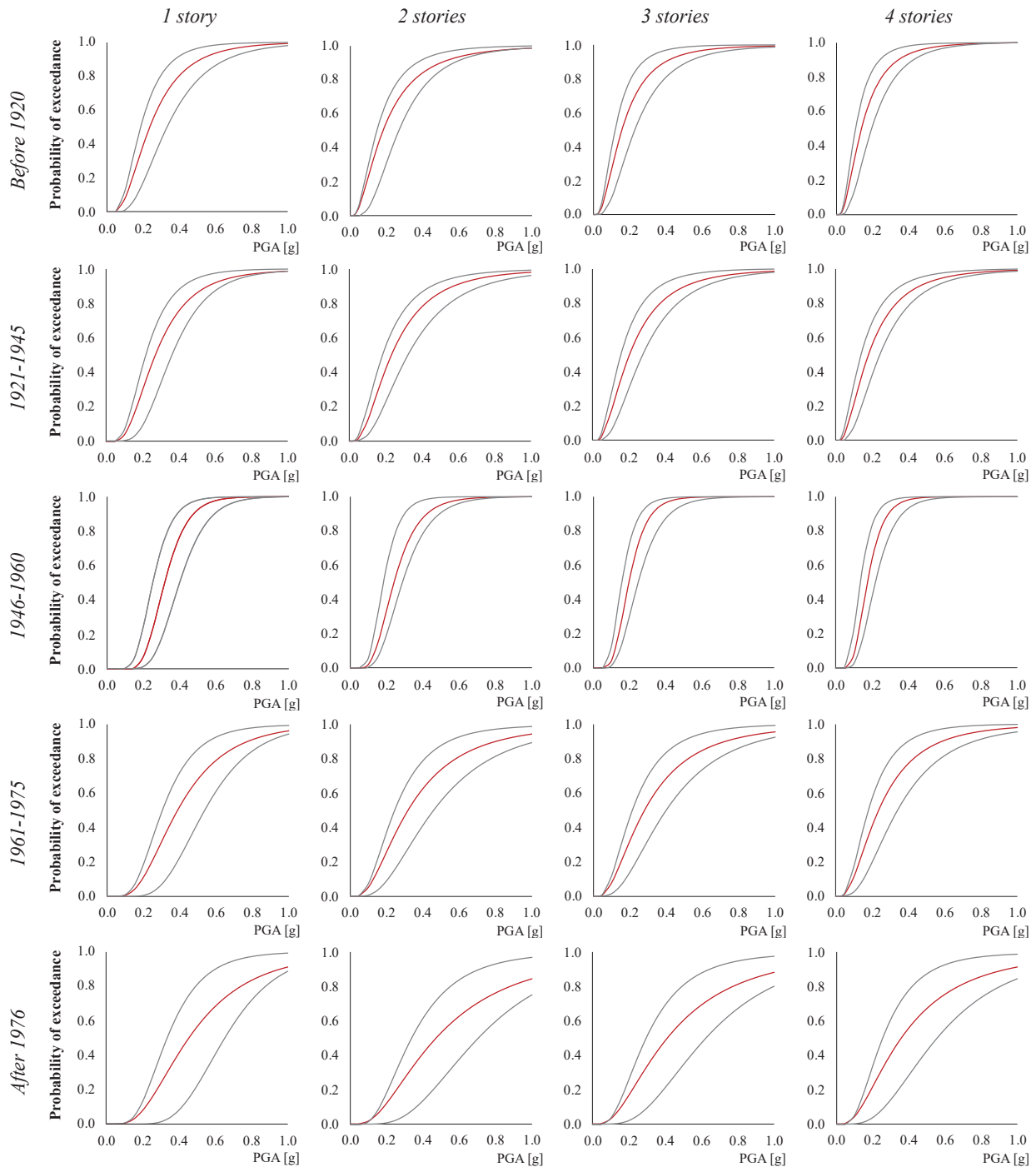


Figure 5: Mechanical fragility curves for DS2-3; white curves in red between upper and lower bounds.

Macro-class fragility tends to slightly increase as the number of stories increases, while it appears to be more evidently influenced by the construction age. Furthermore, an increase in the dispersion was observed as the overall fragility decreases (e.g., for more recent construction ages).

A novel fragility model was derived for Italian masonry school buildings for macro-classes based on a limited number of parameters included in the SBR (i.e., number of stories, con-



struction age, plan area, and type of masonry). In addition, more general classes were derived from the aggregation of specific school types, for instance all single-story masonry schools built before 1919 (in this case, curves for specific plan area and type of masonry were combined together).

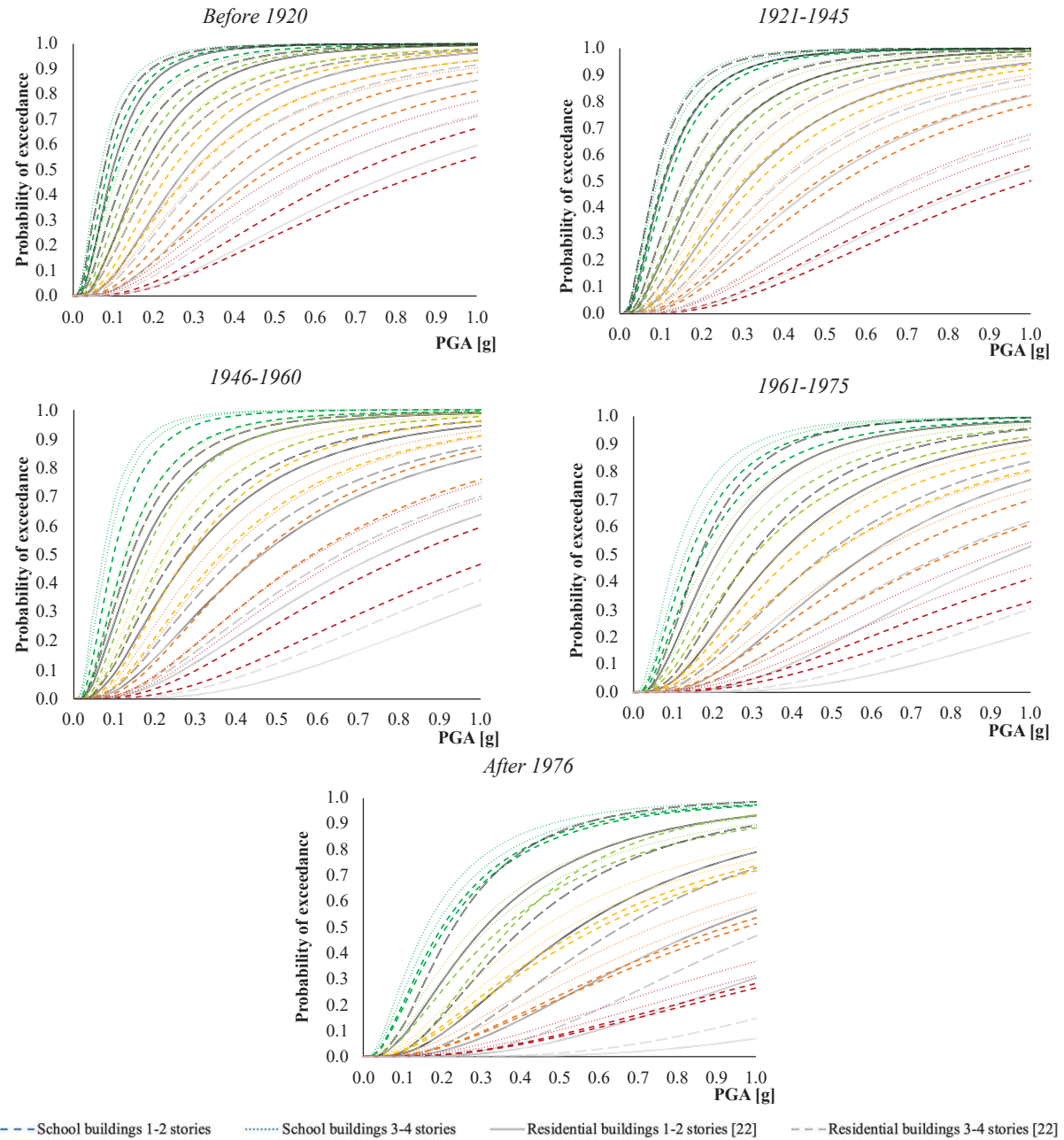


Figure 6: Comparison between fragility models for masonry schools and for masonry residential buildings [22].

The reduction in the number of parameters allowed the proposed fragility model to be compared to fragility curves from the literature, previously derived for residential buildings by Donà et al. [22]. Since the development methodology was the same, the differences in the fragility models are due to the variation of building types. Figure 6 reports the proposed fragility model for the Italian masonry school buildings classified, according to the number of stories and the construction age, and their comparison to fragility curves for residential buildings of comparable macro-classes.

It can be observed that, before 1945, the fragilities of schools and residential buildings are similar. On one hand, in fact, better material quality and more frequent applications of retrofit and restoration interventions can be expected for public relevant buildings such as schools; on the other hand, school buildings present an intrinsic geometric vulnerability (i.e., higher inter-story and great distance between transverse walls, orthogonal to façades) which increase their susceptibility towards OOP mechanisms. After 1945, also the residential construction industry improved, as described in the reference study by Donà et al. [22]. Thus, the geometric vulnerability factors of schools prevailed in the fragility model and, therefore, school structures appear to be more fragile than residential buildings. A note of caution is due regarding the interpretation of results as they are strongly influenced by the assumed exposure matrix for the combination of school macro-classes.

The trends of the mean value of the proposed fragility curves are reported in Figure 7 to highlight how they can be affected by the different parameters taken into account. The factors increasing vulnerability were confirmed to be the age, the great number of stories, the plan area, which is often related to plan complexity, and the poor quality of the material.

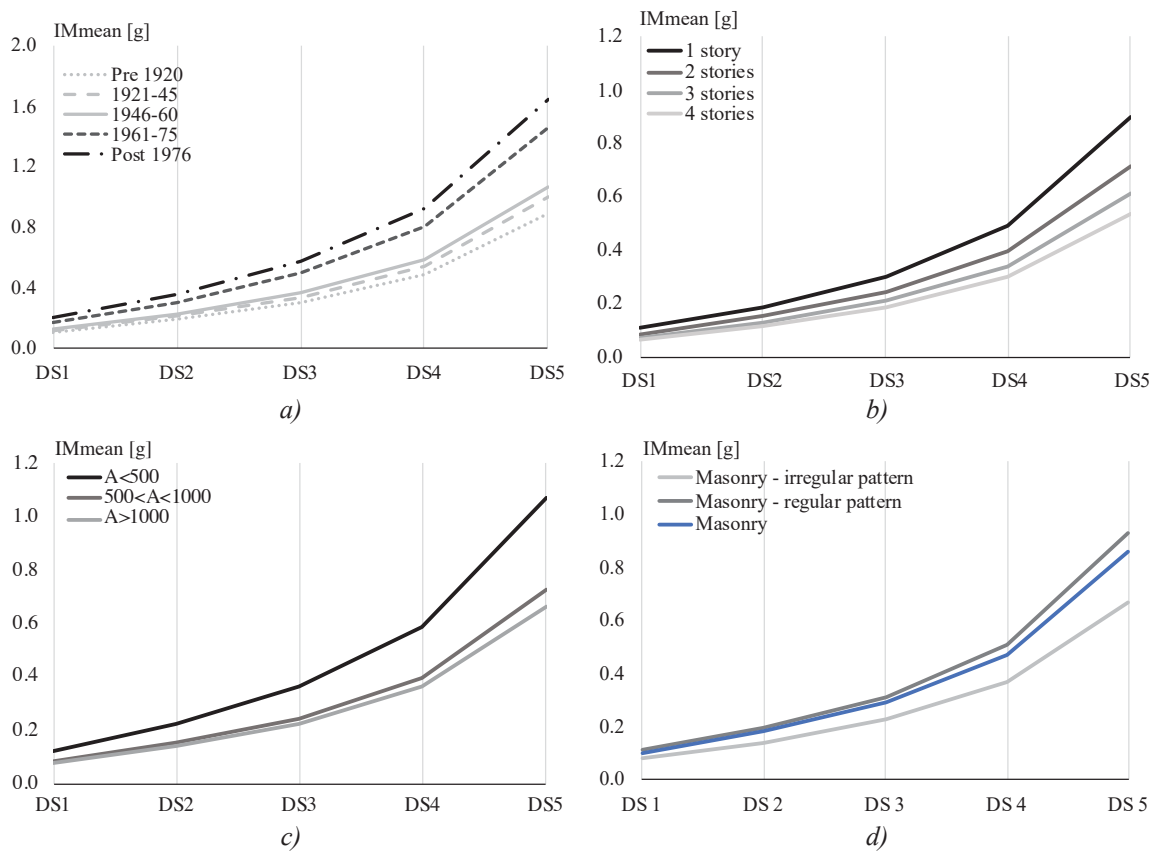


Figure 7: Trend of mean value as following parameters vary: a) construction age, b) number of stories, c) plan area in square meters, and d) type of masonry.

Focusing on construction age, two groups can be identified due to a perceptible gap in the trends of mean values: before 1960 and after 1960, when modern clay blocks and high-quality construction details began to spread in the construction use, years before code provisions (which started, in Italy, in the 1980s) [30]. Plan area appeared to affect the vulnerability and two groups can be identified based on their response: small buildings and, on the other hand, medium-large structures. Thus, for plan area greater than 500 m<sup>2</sup>, an increased vulnerability due to plan complexity shall be expected.

## 5 CONCLUSIONS

- The present paper has illustrated the derivation on fragility curves for the Italian masonry school building asset, on the basis of a limited number of parameters included in the Italian school building registry: the construction age, the number of stories, the plan area, and the type of masonry.
- The simplified mechanical modeling procedure *Vulnus 4.0* was used, as it allows a large amount of analyses to be performed in a suitably short time. The mechanical model considers both IP and OOP mechanisms, together with an index which summarizes qualitative vulnerability factors, according to the II level GNDT form [21].
- A parametric analysis was implemented through *Vulnus 4.0*, resulting in a fragility set, comprised of three fragility curves (i.e., average *white* curve, a lower-bound and an upper-bound), for each macro-class of school structures. Fragility sets were associated to an intermediate DS between 2 and 3, and therefore called DS2-3. Then, a macro-seismic model from the literature [13, 15] was calibrated to extend the mechanical fragility sets to five damage states, according to EMS98 [26]. Lastly, average *white* curves were combined to upper and lower bounds increasing dispersion, thereby leading to a better treatment of uncertainties.
- A novel fragility model was proposed and compared to a likewise developed fragility model from the literature for masonry residential buildings [22]. Interestingly, for the construction period before 1919 and between the two World Wars, school buildings and residential structures present similar fragilities, suggesting that the intrinsic geometric vulnerability of schools was balanced by the better quality of public construction industry. Otherwise, after 1945, also the residential construction industry had improved and, therefore, school buildings appear to be more seismically fragile than ordinary buildings.
- This research contributes to current knowledge of seismic risk assessment and mitigation by providing a broad fragility assessment of a particular type of relevant structures (i.e., school buildings), at national scale. This study was focused on the Italian building asset and construction use, to which both the database analysis and the exposure matrix are referred. A limitation of this study was the lack of information regarding the distribution of masonry quality and construction details during the ages at national scale; this additional information would have allowed the exposure matrices, here based on expert judgement, to be calibrated. Further investigations are requested to retrieve data, consistent at national scale, for specific types of structures.
- This contribution will be used to develop maps of seismic risk and damage scenario for Italy. The proposed fragility sets will represent the vulnerability component in the convolution with hazard and exposure to evaluate seismic risk. This evaluation will be possible thanks to the IRMA platform [31], specifically developed by Eucentre, within the framework of a cooperative national project. The final aim will be a deep knowledge of seismic risk, to mitigate the impact of earthquakes which have caused casualties, huge economic losses on the residential asset [32,33] and on the production sector [34, 35] and, above all for schools, an unquantifiable social impact.

## ACKNOWLEDGEMENTS

Special thanks are due to the Italian Department of Civil Protection (DPC), which funded this study in the framework of the *ReLUIIS-DPC Project 2019-2021 – Work Package 4: MARS (Maps of Risk and Scenarios of seismic damage) – Task 7: Fragility models and curves for schools and other strategic or relevant buildings*. A special thanks to the Work Group for the effective cooperation, especially to the research units of the Universities of Genova, coordinated by Prof. Serena Cattari, and Trieste, coordinated by Prof. Natalino Gattesco, for sharing data of prototype schools included in the study.

## REFERENCES

- [1] N. Augenti, E. Cosenza, M. Dolce, G. Manfredi, A. Masi, L. Samela, Performance of school buildings during the 2002 Molise, Italy, earthquake, *Earthq. Spectra*. **20**, 2004. <https://doi.org/10.1193/1.1769374>.
- [2] OPCM 3431/2005, All 2 - Norme Tecniche per il Progetto, la Valutazione e L'Adeguamento Sismico degli Edifici (in Italian), Ordinary Suppl. Off. Gazzette Ital. Repub. N°107 10th May 2005. 1–139.
- [3] N. Giordano, F. De Luca, A. Sextos, F. Ramirez Cortes, C. Fonseca Ferreira, J. Wu, Empirical seismic fragility models for Nepalese school buildings, *Nat. Hazards* **105**, 339–362 (2020). <https://doi.org/10.1007/s11069-020-04312-1>.
- [4] R. Gentile, C. Galasso, Y. Idris, I. Rusydy, E. Meilianda, From rapid visual survey to multi-hazard risk prioritisation and numerical fragility of school buildings, *Nat. Hazards Earth Syst. Sci.* **19**, 2019, 1365–1386. <https://doi.org/10.5194/nhess-19-1365-2019>.
- [5] M. Rota, A. Penna, C.L. Strobbia, Processing Italian damage data to derive typological fragility curves, *Soil Dyn. Earthq. Eng.* **28**, 2008 933–947. <https://doi.org/10.1016/j.soildyn.2007.10.010>.
- [6] A. Rosti, M. Rota, A. Penna, Empirical fragility curves for Italian URM buildings, *Bull. Earthq. Eng.*, 2020. <https://doi.org/10.1007/s10518-020-00845-9>.
- [7] G. Zuccaro, F.L. Perelli, D. De Gregorio, F. Cacace, Empirical vulnerability curves for Italian masonry buildings: evolution of vulnerability model from the DPM to curves as a function of acceleration, *Bull. Earthq. Eng.*, 2020. <https://doi.org/10.1007/s10518-020-00954-5>.
- [8] C. Del Gaudio, G. De Martino, M. Di Ludovico, G. Manfredi, A. Prota, P. Ricci, G.M. Verderame, Empirical fragility curves for masonry buildings after the 2009 L'Aquila, Italy, earthquake, *Bull. Earthq. Eng.* **17**, 2019, 6301–6330. <https://doi.org/10.1007/s10518-019-00683-4>.
- [9] A. Masi, A. Digrisolo, V. Manfredi, Fragility curves of gravity-load designed RC buildings with regularity in plan, *Earthq. Struct.* **9**, 2015, 1–27. <https://doi.org/10.12989/eas.2015.9.1.001>.
- [10] B. Borzi, H. Crowley, R. Pinho, Simplified pushover-based earthquake loss assessment (SP-BELA) method for masonry buildings, *Int. J. Archit. Herit.* **2**, 2008, 353–376. <https://doi.org/10.1080/15583050701828178>.
- [11] A.B. Acevedo, J.D. Jaramillo, C. Yepes, V. Silva, F.A. Osorio, M. Villar, Evaluation of

- the seismic risk of the unreinforced masonry building stock in Antioquia, Colombia, *Nat. Hazards*. **86**, 2017, 31–54. <https://doi.org/10.1007/s11069-016-2647-8>.
- [12] D. D’Ayala, A. Meslem, D. Vamvatsikos, K. Porter, T. Rossetto, V. Silva, Guidelines for Analytical Vulnerability Assessment of Low/Mid-Rise Buildings, Vulnerability Global Component Project., GEM Tech. Rep. 2015-08 v1.0.0. 08, 2015, 162.
- [13] S. Lagomarsino, S. Cattari, Fragility Function of Masonry Buildings, in: K. Pitilakis, H. Crowley, A.M. Kaynia (Eds.), SYNER-G Typology Defin. Fragility Funct. Phys. Elem. Seism. Risk Build. Lifelines, Transp. Networks Crit. Facil., 2014. <https://doi.org/10.1007/978-94-007-7872-6>.
- [14] A.J. Kappos, G. Panagopoulos, C. Panagiotopoulos, G. Penelis, A hybrid method for the vulnerability assessment of R/C and URM buildings, *Bull. Earthq. Eng.* **4**, 2006, 391–413. <https://doi.org/10.1007/s10518-006-9023-0>.
- [15] S. Lagomarsino, S. Giovinazzi, Macroseismic and mechanical models for the vulnerability and damage assessment of current buildings, *Bull. Earthq. Eng.* **4**, 2006, 415–443. <https://doi.org/10.1007/s10518-006-9024-z>.
- [16] M. Vettore, M. Donà, P. Carpanese, V. Follador, F. da Porto, M.R. Valluzzi, A Multi-level Procedure at Urban Scale to Assess the Vulnerability and the Exposure of Residential Masonry Buildings: The Case Study of Pordenone, Northeast Italy, *Heritage* **3**, 2020 1433–1468. <https://doi.org/10.3390/heritage3040080>.
- [17] D. Ottonelli, S. Alfano, S. Cattari, M. Di Ludovico, A. Prota, Structural and damage data analysis of a stock of URM schools struck by the 2016/2017 Central Italy earthquake, in: XVIII CONVEGNO ANIDIS - L’ingegneria Sismica Ital., Pisa University Press, Ascoli Piceno, 15-19 September 2019, 2019: pp. 43–53.
- [18] N. Gattesco, I. Boem, Classification of Friuli-Venezia Giulia masonry school buildings for seismic risk models purposes, in: XVIII CONVEGNO ANIDIS - L’ingegneria Sismica Ital., Ascoli Piceno, 15-19 September 2019, 2019: pp. 79–86.
- [19] A. Bernardini, R. Gori, C. Modena, M.R. Valluzzi, Vulnus 4.0 - Automatic procedure for the seismic vulnerability analysis of masonry buildings (in Italian), 2009.
- [20] M.R. Valluzzi, User Manual of Vulnus\_4.0, original program by Bernardini Gori A, Modena R C, Vb version edited by Valluzzi MR, with contributions by Benincà G, Barbetta E, Munari M (in Italian), 2009.
- [21] GNDT-SSN, Scheda di esposizione e vulnerabilità e di rilevamento danni di primo livello e secondo livello (muratura e cemento armato) (in Italian), 1994.
- [22] M. Donà, P. Carpanese, V. Follador, L. Sbrogio, F. da Porto, Mechanics-based fragility curves for Italian residential URM buildings, *Bull. Earthq. Eng.*, 2020 1–34. <https://doi.org/10.1007/s10518-020-00928-7>.
- [23] M. Donà, L. Xu, P. Carpanese, V. Follador, F. da Porto, L. Sbrogio, Seismic fragility and risk of Italian residential masonry heritage, in: Brick Block Mason. - From Hist. to Sustain. Mason., 2020. <https://doi.org/10.1201/9781003098508-16>.
- [24] L. 23/1996: Regulation for School Buildings (in Italian), Off. Gazzette Ital. Repub. N°15 19th January 1996. Rome, Italy, 1996
- [25] Circ 21/01/2019 N.7, Istruzioni per l’applicazione dell’«Aggiornamento delle “Norme tecniche per le costruzioni”» di cui al decreto ministeriale 17 gennaio 2018. (Italian



- Guideline), Suppl. Ordin. Alla “Gazzetta Uff. n. 35 Del 11 Febbraio 2019 - Ser. Gen. (n.d.) 337. <https://www.gazzettaufficiale.it/eli/gu/2019/02/11/35/so/5/sg/pdf>.
- [26] G. Grunthal, EMS98 - *European Macroseismic Scale 1998*, Conseil de l’Europe - Cahiers du Centre Européen de Géodynamique et de Séismologie, Luxembourg, 1998.
  - [27] M. Donà, P. Carpanese, V. Follador, F. Porto, Derivation of mechanical fragility curves for macro-typologies of Italian masonry buildings, in: M. Papadrakakis, M. Fragiadakis (Eds.), Proc. 7th ECCOMAS Them. Conf. Comput. Methods Struct. Dyn. Earthq. Eng., Crete, Greece, 2019: pp. 24–26.
  - [28] C. Margottini, D. Molin, L. Serva, Intensity versus ground motion: A new approach using Italian data, *Eng. Geol.* **33**, 1992. [https://doi.org/10.1016/0013-7952\(92\)90034-V](https://doi.org/10.1016/0013-7952(92)90034-V).
  - [29] K. Deb, A. Pratap, S. Agarwal, T. Meyarivan, A fast and elitist multiobjective genetic algorithm: NSGA-II, *IEEE Trans. Evol. Comput.* **6**, 2002. <https://doi.org/10.1109/4235.996017>.
  - [30] D.M.LL.PP. 20/11/1987, Norme tecniche per la progettazione, esecuzione e collaudo degli edifici in muratura e per il loro consolidamento (in Italian), Off. Gazzette Ital. Repub. N°285 5th December 1987. (1987).
  - [31] B. Borzi, M. Onida, M. Faravelli, D. Polli, M. Pagano, D. Quaroni, A. Cantoni, E. Speranza, C. Moroni, IRMA platform for the calculation of damages and risks of Italian residential buildings, *Bull. Earthq. Eng.*, 2020. <https://doi.org/10.1007/s10518-020-00924-x>.
  - [32] M. Dolce, A. Prota, B. Borzi, F. da Porto, S. Lagomarsino, G. Magenes, C. Moroni, A. Penna, M. Polese, E. Speranza, G.M. Verderame, G. Zuccaro, Seismic risk assessment of residential buildings in Italy, *Bull. Earthq. Eng.*, 2020. <https://doi.org/10.1007/s10518-020-01009-5>.
  - [33] F. da Porto, M. Donà, A. Rosti, M. Rota, S. Lagomarsino, S. Cattari, B. Borzi, M. Onida, D. De Gregorio, F. L. Perelli, C. Del Gaudio, P. Ricci, E. Speranza (2021) Comparative analysis of the fragility curves for Italian residential masonry and RC buildings. *Bull. Earthq. Eng.*, 2021. <https://doi.org/10.1007/s10518-021-01120-1>.
  - [34] Donà, M., Bizzaro, L., Carturan, F., & da Porto, F. Effects of business recovery strategies on seismic risk and cost-effectiveness of structural retrofitting for business enterprises. *Earthquake Spectra*, **35**(4), 2019, 1795-1819.
  - [35] Braga, F., Gigliotti, R., Monti, G. et al. Speedup of post earthquake community recovery: the case of precast industrial buildings after the Emilia 2012 earthquake. *Bull Earthquake Eng* **12**, 2405–2418, 2014. <https://doi.org/10.1007/s10518-014-9583-3>

## DERIVATION OF SEISMIC FRAGILITY CURVES OF A GRAVITY- LOAD DESIGNED RC SCHOOL BUILDING THROUGH NLTHA

E. Saler<sup>1,2</sup>, P. Carpanese<sup>2</sup>, V. Follador<sup>2</sup>, and F. da Porto<sup>2</sup>

<sup>1</sup> Dept. of Civil, Environmental and Mechanical Engineering, University of Trento  
Via Mesiano 77, 38123 Trento, Italy  
e-mail: elisa.saler@unitn.it

<sup>2</sup> Dept. of Geosciences, University of Padova  
Via Gradenigo 6, 35131 Padova, Italy  
pietro.carpanese@phd.unipd.it; {veronica.follador, francesca.daporto}@unipd.it

---

### Abstract

*School buildings are considered relevant structures and their safety towards seismic actions shall be verified in consideration of the significant consequences of their collapse. With reference to Italy, most reinforced concrete (r.c.) schools were built after the second world war and in the later years of the economic boom, before a widely applied seismic regulation. In fact, seismic classification of Italy was a long process developing throughout the XX century, with significant areas which were not considered seismic until the early 2000s.*

*The paper presents the evaluation of the seismic behavior of a representative 2-story Italian r.c. school building designed for gravitational loads only, and the derivation of a fragility curve set describing the seismic behavior of the macro-class of buildings. A series of Non-Linear Time History Analyses (NLTHA), with sets of natural ground motion records of increasing intensity, were implemented on two fiber models, developed in Midas GEN, representing the bare frame (BF) and the infilled frame (IF) configurations, respectively. Inter-story drift ratio (IDR) was chosen as demand parameter to identify the Damage State (DS) exceeded by each analysis and explicitly calculated for the analyzed structure. Fragility curve sets, describing five increasing DSs, were derived, for both the BF and the IF configurations, through the statistical processing of NLTHA results. A comparison of the calculated fragilities, between BF and IF models, is finally provided.*

**Keywords:** Fragility curves, school buildings, RC frame, gravitational load design, Non-linear time history analysis.

---

## 1 INTRODUCTION

Italy is one of the most seismic prone countries of Europe, where earthquakes have caused casualties, unusable buildings, huge economic losses for both the residential [1,2] and the industrial [3,4] assets, and damage to the cultural heritage with heavy repercussions on the tourism sector [5]. Furthermore, the global impact of strong seismic events on communities is hardly quantifiable. In this framework, schools play a crucial role due to the high social impact of their collapse, threatening children and youth, and their unusability in the aftermath of a seismic event [6,7]. Thus, an estimation of seismic risk and damage scenario related to school buildings is required to deepen knowledge of disaster risk (Priority 1 of the *Sendai Framework for Disaster Risk Reduction 2015–2030* [8]).

With this aim, a national project has been established by the Italian Department of Civil Protection (DPC) and the Laboratories University Network of seismic engineering (ReLUIS consortium), to develop maps of seismic risk and damage scenarios for different classes of buildings (e.g., ordinary buildings, schools, and churches) at a national scale [1,9].

Risk estimation requires the definition of hazard, exposure and vulnerability of the built asset. Various methodologies have been developed to assess vulnerability at large scale, and they are mainly based on the derivation of fragility curves (i.e., cumulative density function expressing the probability of exceeding a damage state). Empirical approaches provide the description of damage probability (through damage probability matrices – DPM) based on the post-event observed damage [10–13]. These methods provide realistic fragility estimates, which however strongly depend on collected data, and thus on the building taxonomy of the region interested by the seismic event. Lack of damage data (e.g., for certain levels of seismic intensity or for specific building types) can be overcome using hybrid methods [14,15], based on both empirical data and mechanical models, of which some examples are presented as follows. Numerous studies have focused on developing fragility curves by means of mechanics models. Among the others, mechanics-based vulnerability assessment of structures can be based on simplified procedures [16–19], including Displacement-Based approaches [20–22], as well as on non-linear time history analyses (NLTHA) [23,24].

This contribution provides a proposal of vulnerability assessment of a specific class of school buildings (i.e., two-story r.c. frame designed for gravitational loads only), by deriving fragility curves through NLTHA performed on a finite element (F.E.) model of a prototype school. To investigate the influence of infills on the seismic response, two different models were implemented to simulate the dynamic behavior of both bare frame (BF) and infilled frame (IF).

Seven ground motion suites, each consisting of 10 accelerograms, were selected based on spectrum-similarity criteria, with reference to the elastic spectrum of L'Aquila, Italy, for seven increasing return periods. The investigated demand parameter was the interstory drift ratio, which was associated to damage states (DSs) through threshold values from the literature [9,25]. Then, the statistical processing of NLTHA outcomes was carried out to estimate the parameters (i.e., median value and standard deviation) of the log-normal cumulative density function (CDF), allowing fragility curves to be derived, and then compared.

The IF model shows a regular distance among DS fragility curves, while the slightly higher ductility of the BF configuration is found in the distribution of fragility curves, resulting more spaced.

## 2 ITALIAN SCHOOL BUILDING ASSET

The reference dataset for the risk assessment at national scale is the Italian school building registry (SBR) of the Ministry of Education [26] which gathers almost 50,000 school build-

ings, of which 16,522 are r.c. structures. School buildings are registered on the basis of a limited number of parameters: construction material and age, number of stories, plan area, and types of floors and roof. The distributions of typological characteristics of the r.c. schools are reported in Figure 1. Reinforced concrete schools result to be built mainly after 1961, with a prevalence of low-rise structures, with one or two stories. Similarly, the distribution of plan area shows a prevalence of small to medium buildings, up to 2,000 m<sup>2</sup>. However, the amount of larger buildings is not negligible, and moreover they present a significant exposure.

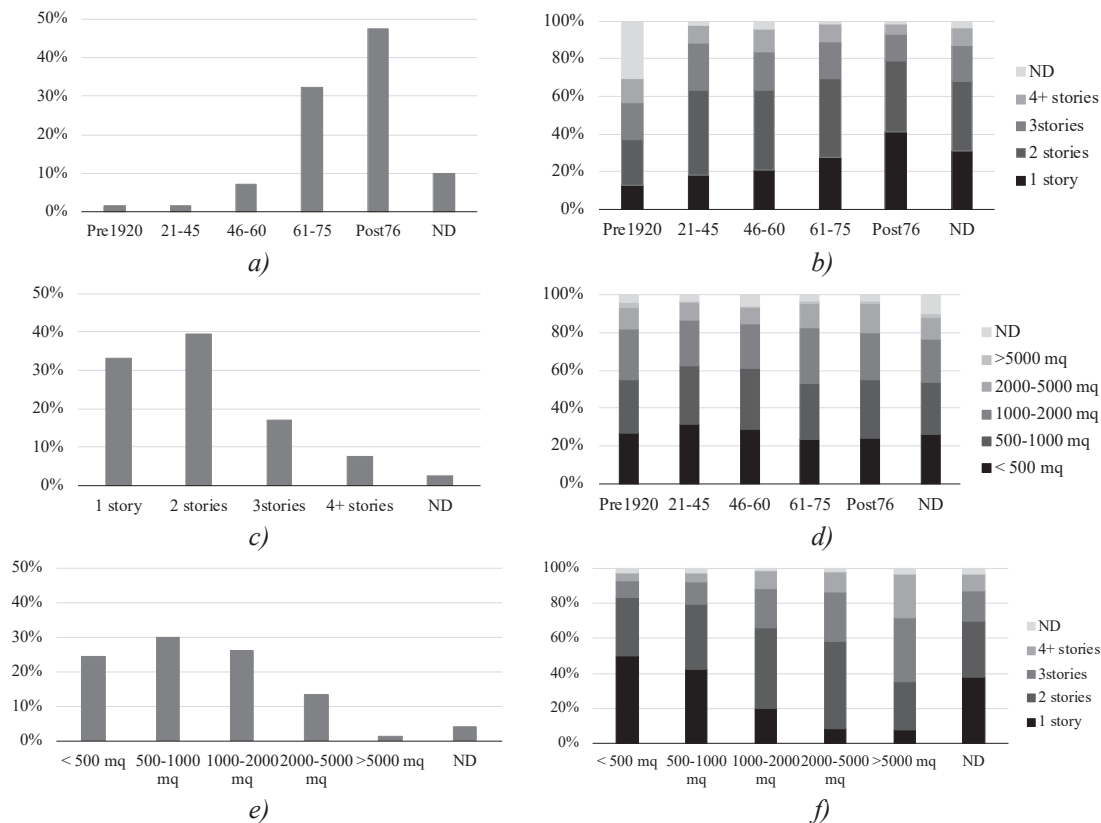


Figure 1: Typological characteristics of r.c. buildings in Italian SBR: a) construction age; b) number of stories given age; c) number of stories; d) plan area given age; e) plan area; f) number of stories given plan area

The processing of the dataset allowed the identification of a series of macro-classes adequate for risk analyses at a national scale, i.e., based on a limited number of parameters which distribution is available on the country (construction material, number of stories, and age). Each macro-class is assumed to be homogeneous from a seismic vulnerability point of view; thus, a single set of fragility curves, describing the probability of exceeding various damage states, can be assigned to each macro-class. Fragility models of macro-classes can be developed through the analysis of prototype structures, selected on the basis of representativeness criteria, so that results can be extended on a national scale.

This paper presents, as case study, the fragility assessment for a prototype r.c. school, representative of the macro-class of two-story school buildings built between 1961 and 1975.

## 2.1 Selected prototype r.c. school building

The selected school building consists in a two-story r.c. bi-directional frame (weak columns/strong beams), designed in 1966 for gravitational loads only. The retrieved original project documentation reported both the detail of reinforcement for each structural element and

the class of smooth rebars (i.e., AQ50), while no data was found regarding the concrete class. Thus, a mean cylinder compressive strength ( $f_{cm}$ ) equal to 20 MPa was assigned according to Masi et al. [27].

The school, which plan is shown in Figure 2, presents significant openings on the façades of classrooms, with five bays of the frame entirely infilled with hollow clay bricks with modest void area, approximately equal to 35% (Figure 3). Infills panels are 13 cm thick (one header).

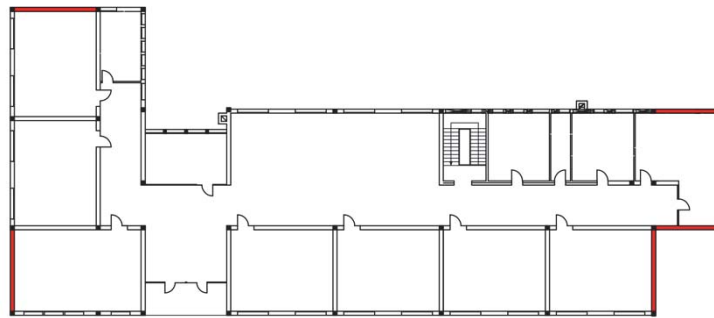


Figure 2: School plan with indication of infilled bays (in red).

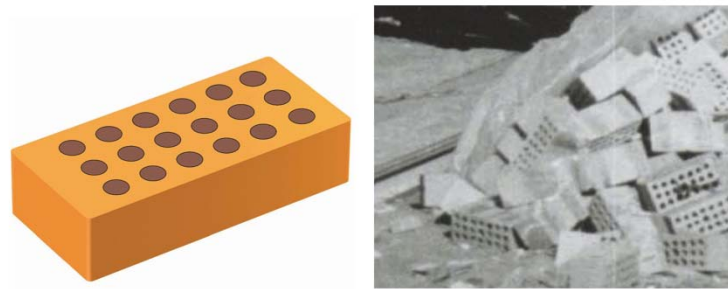


Figure 3: Hollow clay brick used for infill panels and photo of coeval school construction site.

### 3 FRAGILITY ASSESSMENT THROUGH NLTHA

#### 3.1 Modelling of bare frame and of masonry infills

Two numerical models of the prototype building were implemented through the software Midas GEN [28]. For r.c. structural elements a fiber model [29] was developed, on the basis of the original project documentation. The constitutive laws of materials were assumed according to Mander [30] for concrete, accounting for confinement, and Menegotto and Pinto [31] for steel, considering an hardening behavior.

To investigate the influence of infills on the global behavior of the structure, two different models were implemented: a first one simulating the bare frame, and a second one representing the infilled frame (as shown in Figure 4a).

Prior studies have experimentally defined the seismic response of both thin masonry infills [32–34] and thick panels [35,36], with reference to hollow blocks with high void area. Thus far, no experimental data were available on masonry infill walls with low void area. The seismic behavior of masonry infills is affected by the interaction of in-plane (IP) and out-of-plane (OOP) responses. Some detailed models have been developed to catch this combined effect through numerical simulations [37,38], however, up to now, hardly applicable to fragility assessment.



For the purposes of this study, a single-strut macro-model was implemented for infill panels, as it allows an efficient simulation of the infill influence on the global structural behavior, with limited numerical effort [39]. The equivalent thickness of the infill strut was estimated according to Stafford Smith (1967) [40] and Mainstone (1974) [41], through the following equations.

$$\frac{w}{d} = 0.175\lambda_h^{-0.4} \quad ; \quad \lambda_h = \left[ \frac{E_{inf}t_{inf}\sin(2\theta)}{4E_cI_cH_{inf}} \right]^{\frac{1}{4}} \quad (1)$$

The ratio between the equivalent thickness ( $w$ ) and the length ( $d$ ) of the strut is expressed as a function of the relative stiffness  $\lambda_h$ , which depends on Young's Modulus of both infill ( $E_{inf}$ ) and columns ( $E_c$ ), thickness ( $t_{inf}$ ) and height ( $H_{inf}$ ) of the infill panel, moment of inertia of r.c. columns ( $I_c$ ), and infill diagonal inclination ( $\theta$ ).

Due to the lack of experimental tests to calibrate the constitutive law of masonry infill struts, the model proposed by Panagiotakos and Fardis was assumed [42]. The infill strut constitutive law is shown in Figure 4b.

Results of the eigenvalue analysis are reported in Table 1 for the first three vibration modes. The infilled frame model has lower vibration periods and presents lower torsional deformation. Hence, the presence of infills, besides increasing the stiffness of the model, regularizes it.

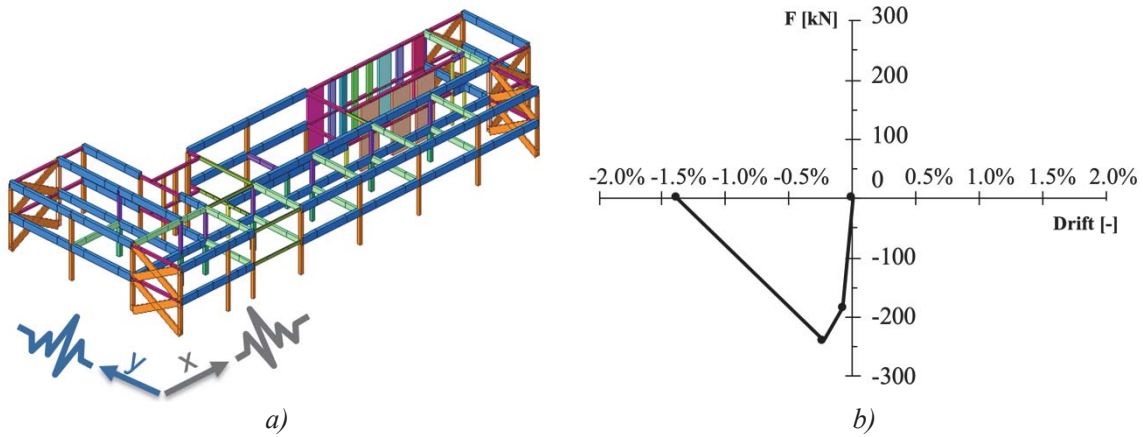


Figure 4: a) F.E. model with infills and b) infill strut constitutive law.

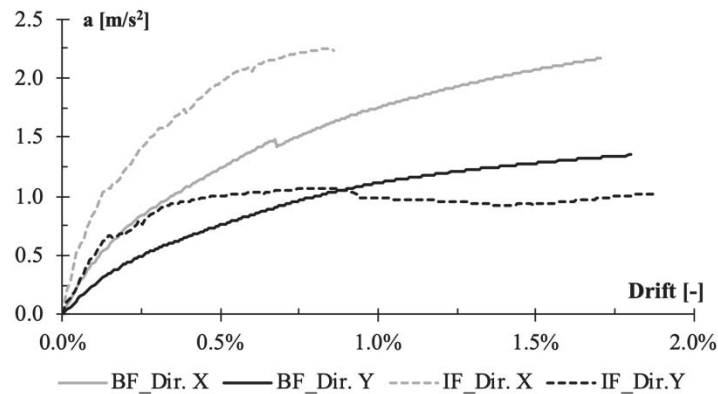


Figure 5: Results of non-linear static analyses for BF and IF models.

Mode	$T [s]$	<i>Bare frame model</i>			$T [s]$	<i>Infilled frame model</i>		
		$m_{Tx} [\%]$	$m_{Ty} [\%]$	$m_{Rz} [\%]$		$m_{Tx} [\%]$	$m_{Ty} [\%]$	$m_{Rz} [\%]$
1	1.111	-	81.93	-	0.844	-	87.58	-
2	1.037	-	-	81.40	0.708	26.32	-	62.62
3	0.758	82.32	-	-	0.592	60.92	-	27.56

Table 1: Dynamic properties for first three vibration modes.

A preliminary non-linear static analysis (NLSA) was performed on the model to evaluate the response of both bare and infilled frame in the two main directions. Capacity curves resulting from NLSA are reported in Figure 5 in terms of acceleration (i.e., base shear normalized with respect to building mass) and global drift (i.e., top displacement normalized with respect to building height). As it can be expected, X-direction has a higher stiffness than Y-direction, which instead appears to be more ductile even in the IF configuration. The effect of infills is more evident for X-direction (which presents three infilled bays) than for Y-direction (two infilled bays).

### 3.2 Definition of ground motion records

The selection of ground motion suites was carried out through the procedure *Select&Match*, proposed by Paolucci et al. [43], with the aim of providing a large set of input ground motion records for a wide range of intensity levels to be used for the derivation of site-independent fragility curves. For this purpose, a target spectrum referring to the site of L'Aquila, Italy, for increasing return periods (i.e., 50, 100, 200, 475, 975, 2475, and 5000 years) was defined to select ground motions of increasing intensity. A suite of ten spectrum-similar ground motion records was defined for each reference return period, with a similarity criteria less strict than the code-compliant spectrum compatibility [44,45], in order to define site-independent ground motion sets.

The values of peak ground acceleration (PGA) of the selected ground motions are reported in Figure 6, compared to PGAs of the reference spectrum, for increasing return periods. A higher dispersion can be observed for greater return periods.

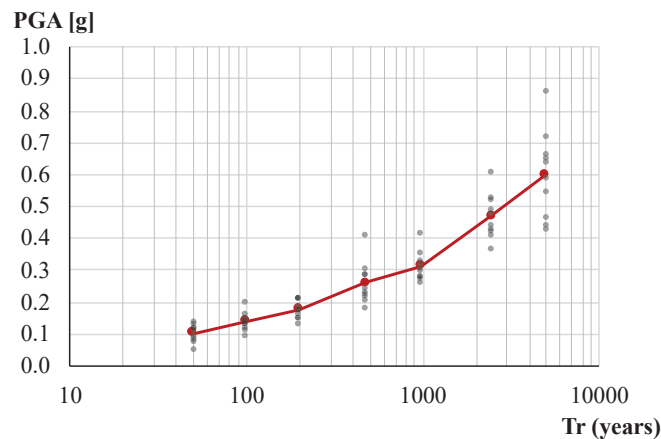


Figure 6: PGAs of selected accelerograms (grey) compared to PGAs of reference spectrum (red).

Seventy accelerograms were selected and applied to models (both BF and IF) separately in the two main directions, in order to more clearly associate each level of PGA to the investigated engineering demand parameter (EDP). Thus, for each model, 140 NLTHA were carried out.

### 3.3 Definition of the EDP

Fragility assessment by means of numerical analyses requires the definition of reference demand parameters, which should have a good correlation with damage. In this case, the maximum interstory drift ratio (IDR) was selected to describe both structural and non-structural damage, as reported in the macro-seismic scale EMS98 [46] for five increasing damage states (DSs).

Research in the field of fragility curves for existing reinforced concrete buildings has proposed IDR thresholds to distinguish between DSs which can be reached and exceeded by a structure: slight damage, moderate damage, severe damage, partial collapse and complete collapse. Masi et al. [9] proposed five IDR thresholds in r.c. frames designed for gravitational loads only, considering both structural and non-structural elements. The correlation between IDR thresholds and DSs was evaluated by means of parametric non-linear dynamic analyses, where the global damage was quantified in terms of ductility demand and capacity of structural elements.

More recently, the observation of RC buildings damaged by seismic events led to the definition of IDR thresholds which take into account the seismic response of infills for the first three DSs. An extended review and processing of the available experimental data from the literature, in terms of drift capacity of infill panels, was presented in Del Gaudio et al. [25], providing novel median IDR capacities, which were then validated based on the assessment of losses caused by the L'Aquila earthquake [47].

Table 2 compares IDR thresholds from the aforementioned studies. It can be observed that the first set is more conservative for the second, third, and fourth limits, thus including the exceeding of DSs by infill panels of the second proposed set. Thus, in the present study, the IDR thresholds were assumed according to Masi et al. [9], except for the first threshold which resulted to be more conservative according to Del Gaudio et al. [25]

A shortcoming of this selected set is that the same IDR thresholds were assumed for both BF and IF models, even though different modelling strategies affect the development of story displacements. The difference mainly regards lower DSs, while it tends to decrease for higher DSs, where the contribution of infills is strongly reduced. Further investigations are needed to evaluate the most suitable set of thresholds, distinguishing between BF and IF model. In this framework, BF model is here presented only for comparison purposes.

	DS <sub>0</sub>	DS <sub>1</sub>	DS <sub>2</sub>	DS <sub>3</sub>	DS <sub>4</sub>	DS <sub>5</sub>
Masi et al. [9],	0.1%	0.25%	0.5%	1.0%	2.5%	
Del Gaudio et al. [25]	0.08%	0.32%	0.94%	1.78%	-	
Selected IDR	0.08%	0.25%	0.5%	1.0%	2.5%	

Table 2: IDR thresholds for five damage states for RC frames designed for gravitational loads only.

### 3.4 Derivation of fragility curves

The outcomes of NLTHA are presented in Figure 7 using cloud plots, reporting each resulting maximum interstory drift ratio associated with the PGA that generated it, with the indication of IDR thresholds.

The BF model shows higher IDR values associated to ground motions of moderate intensity compared to IF model, thus more realizations overcome IDR thresholds for DS<sub>3</sub> and DS<sub>4</sub>. As a consequence, the DS<sub>3</sub> threshold in particular is exceeded in advance in the BF model, as it will become evident from the comparison of the derived fragility curves. The most populated damage state for BF configuration results to be DS<sub>4</sub> (partial collapse). On the contrary, infilled model appears to have a lower general dispersion, and more homogeneously populated

DSs. For the selected seismic input, no NLTHA provides a maximum IDR smaller than the first threshold ( $DS_0$ ).

NLTHA results falling between two IDR thresholds represent the cases in which the building reached or exceeded the DS enclosed by the thresholds. PGA values for each IDR range were processed in order to estimate parameters of fragility curves (i.e., log-normal CDF), expressed as follows:

$$P(D \geq DS_i | PGA) = \Phi \left[ \frac{\ln(PGA/\mu_{DS_i})}{\beta_{DS_i}} \right] \quad (2)$$

where  $P(D \geq DS_i | PGA)$  indicates the conditional probability of exceeding a damage state  $DS_i$  given a PGA value,  $\Phi$  is the standardized normal CDF, and  $\mu_{DS_i}$  and  $\beta_{DS_i}$  are the parameters of the CDF (i.e., the median value and the logarithmic standard deviation, respectively).

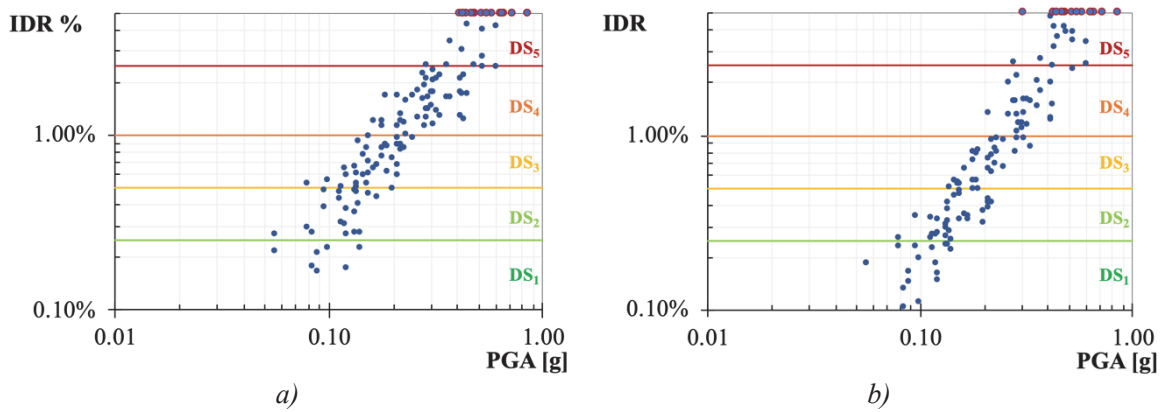


Figure 7: Cloud plots of resulting maximum IDR associated with generating PGA for a) BF and b) IF.

The standard deviation of the proposed fragility curves was computed through the SRSS (i.e., Square Root of Sum of Squares) combination of three different component: i)  $\beta_D$  expressing dispersion due to record-to-record variability; ii)  $\beta_C$  related to uncertainties associated to structural capacity, assumed equal to 0.3 according to HAZUS-FEMA [48] for Pre-Code buildings; and iii)  $\beta_{M(DS)}$  related to uncertainties in the estimation of median value of EDP thresholds for each DS, assumed equal to 0.4 according to HAZUS-FEMA [48].

$$\beta_{DS_i} = \sqrt{\beta_D^2 + \beta_C^2 + \beta_{M(DS)}^2} \quad (3)$$

The estimation of the probability of exceedance towards global collapse by means of mechanical models might be affected by convergence problems which can be expected in strongly non-linear field [49]. According to the proposal by Jalayer et al. [50], it was assumed that  $DS_5$  is reached through two separate conditions: i) IDR greater than the last threshold (i.e., 2.5%), identified hereinafter as *NoC* cases, since the model did not numerically “collapse”; or ii) dynamic instability (due to large displacements as well as failed convergence of the software) [51], identified hereinafter as *Col* cases. Both conditions contributed to derive the  $DS_5$  fragility curve, estimated by implementing the following equation based on total probability theorem:

$$P(D \geq DS_5 | PGA) = P(D \geq DS_5 | PGA, NoC)(1 - P(Col | PGA)) + P(Col | PGA) \quad (4)$$

NLTHA results for which dynamic instability occurred are shown in Figure 7 with a red border, and their probability of occurrence was computed through a logistic regression model. Please refer to Jalayer et al. [50] for further details.

The derived fragility curves are shown in Figure 8, which compares, for both BF and IF models, probability functions with logarithmic standard deviation for either record-to-record variability or all the dispersion components. The values of the estimated parameters are reported in Table 3. Figure 9 provides a comparison between BF and IF models in terms of plotted fragility curves and trend of median value  $\mu_{DSi}$ .

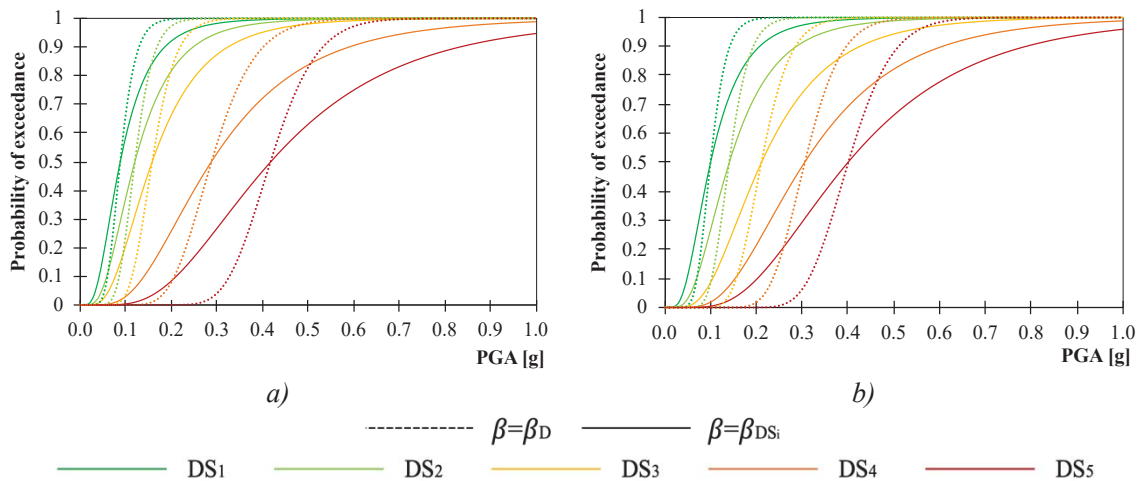


Figure 8: Fragility curves derived from a) BF and b) IF models.

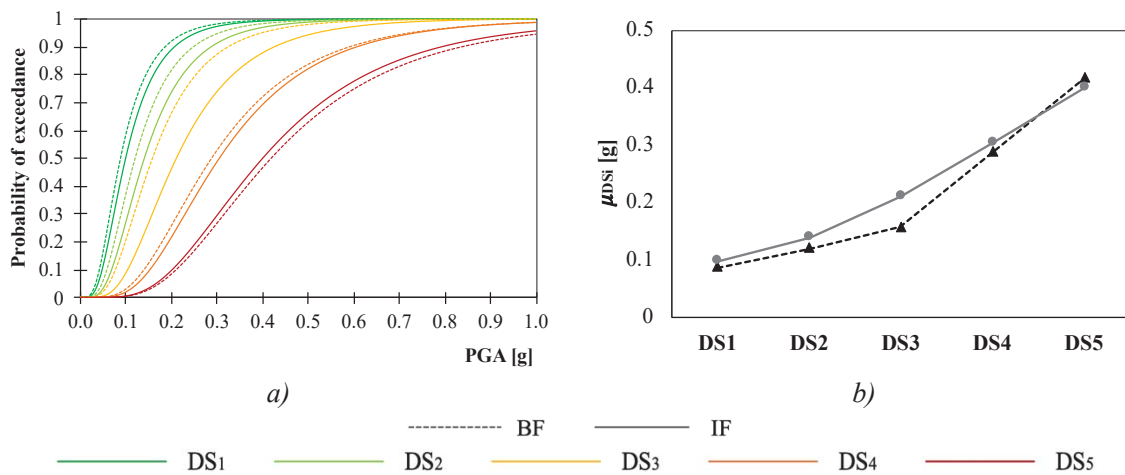


Figure 9: Comparison between BF and IF models in terms of a) fragility curves and b) median value  $\mu_{DSi}$ .

	<i>Bare frame model</i>			<i>Infilled frame model</i>		
	$\mu_{DSi}$	$\beta_D$	$\beta_{DSi}$	$\mu_{DSi}$	$\beta_D$	$\beta_{DSi}$
DS <sub>1</sub>	0.088	0.300	0.583	0.099	0.278	0.572
DS <sub>2</sub>	0.120	0.265	0.566	0.140	0.250	0.559
DS <sub>3</sub>	0.158	0.256	0.562	0.211	0.236	0.553
DS <sub>4</sub>	0.288	0.259	0.563	0.305	0.203	0.540
DS <sub>5</sub>	0.417	0.190	0.535	0.400	0.189	0.535

Table 3: Estimated median values and logarithmic standard deviations.



Infilled frame model showed a more homogeneously distributed behavior, with regular distance between different DSs. On the contrary, outcome from bare frame model provided the anticipation of the first three DSs, which can be related to threshold values not adapted to the BF configuration.

Results suggest a slightly more ductile behavior of the BF configuration, with a greater distance among DS curves, in accordance with both results of aforementioned NLSA and previous studies [52,53].

#### 4 CONCLUSIONS

- The present paper has discussed the derivation of fragility curves for a macro-class of school buildings starting from a representative prototype building. The case study is a two-story r.c. frame school, built in the 1960s and designed for gravitational loads only.
- The fiber model of both the bare frame and infilled frame configurations were developed through Midas Gen software [28] to implement a series of non-linear time history analyses. For the IF configuration a single-strut macro-model of the infills was implemented. Due to the significant presence of openings, only five bays on each story were modelled as infilled.
- A suite of 70 ground motion records was selected based on the procedure proposed by Paolucci et al. [43], based on spectrum-similarity, instead of spectrum-compatibility, in order to obtain a site-independent set.
- The selected ground motions were applied to both BF and IF models in the two main directions and the maximum interstory drift ratio was recorded and chosen as demand parameter, related to the damage state of the structure. IDR thresholds to distinguish among different damage states were assumed according to previous studies from the literature [9,25].
- Results from NLTHA were plotted in terms of maximum IDR and the peak ground acceleration of the ground motion that generated it. The statistical post-processing of resulting cloud plot provides the derivation of fragility curves (i.e., log-normal CDF of the probability of exceedance) for five damage states from EMS 98 [46].
- This research contributes to the current knowledge of seismic risk of a relevant class of structures (i.e., school buildings). This contribution will be part of a study that aims to develop maps of seismic risk and damage scenario for Italian school asset, thanks to the IRMA platform [54], specifically developed by Eucentre for this purpose.

#### ACKNOWLEDGEMENTS

Special thanks are due to the Italian Department of Civil Protection (DPC), which funded this study in the framework of the *ReLUIIS-DPC Project 2019-2021 – Work Package 4: MARS (Maps of Risk and Scenarios of seismic damage) – Task 7: Fragility models and curves for schools and other strategic or relevant buildings*. A special thanks to the Work Group for the effective cooperation, especially to the task coordinators, Prof. Serena Cattari and Prof. Angelo Masi.

## REFERENCES

- [1] M. Dolce, A. Prota, B. Borzi, F. da Porto, S. Lagomarsino, G. Magenes, C. Moroni, A. Penna, M. Polese, E. Speranza, G.M. Verderame, G. Zuccaro, Seismic risk assessment of residential buildings in Italy, *Bull. Earthq. Eng.*, 2020. <https://doi.org/10.1007/s10518-020-01009-5>.
- [2] F. da Porto, M. Donà, A. Rosti, M. Rota, S. Lagomarsino, S. Cattari, B. Borzi, M. Onida, D. De Gregorio, F. L. Perelli, C. Del Gaudio, P. Ricci, E. Speranza. Comparative analysis of the fragility curves for Italian residential masonry and RC buildings, *Bull. Earthq. Eng.*, 2021. <https://doi.org/10.1007/s10518-021-01120-1>.
- [3] M. Donà, L. Bizzaro, F. Carturan, F. da Porto, Effects of business recovery strategies on seismic risk and cost-effectiveness of structural retrofitting for business enterprises, *Earthq. Spectra*. **35**, 2019 1795–1819. <https://doi.org/10.1193/041918EQS098M>.
- [4] F. Braga, R. Gigliotti, G. Monti, F. Morelli, C. Nuti, W. Salvatore, I. Vanzi, Speedup of post earthquake community recovery: the case of precast industrial buildings after the Emilia 2012 earthquake, *Bull. Earthq. Eng.* **12**, 2014 2405–2418. <https://doi.org/10.1007/s10518-014-9583-3>.
- [5] M. Mazzocchi, A. Montini, Earthquake effects on tourism in Central Italy, *Ann. Tour. Res.* **28**, 2001, 1031–1046. [https://doi.org/10.1016/S0160-7383\(01\)00008-1](https://doi.org/10.1016/S0160-7383(01)00008-1).
- [6] D. Perrone, G.J. O'Reilly, R. Monteiro, A. Filiatrault, Assessing seismic risk in typical Italian school buildings: From in-situ survey to loss estimation, *Int. J. Disaster Risk Reduct.* **44**, 2020, 101448. <https://doi.org/10.1016/j.ijdr.2019.101448>.
- [7] M. Di Ludovico, A. Digrisolo, C. Moroni, F. Graziotti, V. Manfredi, A. Prota, M. Dolce, G. Manfredi, Remarks on damage and response of school buildings after the Central Italy earthquake sequence, *Bull. Earthq. Eng.* **17**, 2019, 5679–5700. <https://doi.org/10.1007/s10518-018-0332-x>.
- [8] United Nations, Sendai Framework for Disaster Risk Reduction 2015-2030, Geneva, Switzerland, 2015. [https://www.unisdr.org/files/43291\\_sendaiframeworkfordrren.pdf](https://www.unisdr.org/files/43291_sendaiframeworkfordrren.pdf)
- [9] A. Masi, S. Lagomarsino, M. Dolce, V. Manfredi, D. Ottonelli, Towards the updated Italian seismic risk assessment: exposure and vulnerability modelling, *Bull. Earthq. Eng.* 2021. <https://doi.org/10.1007/s10518-021-01065-5>.
- [10] F. Braga, M. Dolce, D. Liberatore, A statistical study on damaged buildings and an ensuing review of the MSK-76 scale., in: *Proc. Seventh Eur. Conf. Earthq. Eng.*, Athens, Greece, 1982.
- [11] M. Rota, A. Penna, C.L. Strobbia, Processing Italian damage data to derive typological fragility curves, *Soil Dyn. Earthq. Eng.* **28**, 2008 933–947. <https://doi.org/10.1016/j.soildyn.2007.10.010>.
- [12] C. Del Gaudio, M. Di Ludovico, M. Polese, G. Manfredi, A. Prota, P. Ricci, G.M. Verderame, Seismic fragility for Italian RC buildings based on damage data of the last 50 years, *Bull. Earthq. Eng.*, 2020. <https://doi.org/10.1007/s10518-019-00762-6>.
- [13] M. Vettore, Y. Saretta, L. Sbrogio, M.R. Valluzzi, A New Methodology for the Survey and Evaluation of Seismic Damage and Vulnerability Entailed by Structural Interventions on Masonry Buildings: Validation on the Town of Castelsantangelo sul Nera (MC), Italy, *Int. J. Archit. Herit.*, 2020 1–26.

- <https://doi.org/10.1080/15583058.2020.1766159>.
- [14] A.J. Kappos, G. Panagopoulos, C. Panagiotopoulos, G. Penelis, A hybrid method for the vulnerability assessment of R/C and URM buildings, *Bull. Earthq. Eng.* **4**, 2006, 391–413. <https://doi.org/10.1007/s10518-006-9023-0>.
  - [15] S. Lagomarsino, S. Giovinazzi, Macro seismic and mechanical models for the vulnerability and damage assessment of current buildings, *Bull. Earthq. Eng.* **4**, 2006, 415–443. <https://doi.org/10.1007/s10518-006-9024-z>.
  - [16] S. Lagomarsino, S. Cattari, Fragility Function of Masonry Buildings, in: K. Pitilakis, H. Crowley, A.M. Kaynia (Eds.), SYNER-G Typology Defin. Fragility Funct. Phys. Elem. Seism. Risk Build. Lifelines, Transp. Networks Crit. Facil., 2014. <https://doi.org/10.1007/978-94-007-7872-6>.
  - [17] M. Donà, P. Carpanese, V. Follador, L. Sbrogiò, F. da Porto, Mechanics-based fragility curves for Italian residential URM buildings, *Bull. Earthq. Eng.*, 2020, 1–34. <https://doi.org/10.1007/s10518-020-00928-7>.
  - [18] M. Vettore, M. Donà, P. Carpanese, V. Follador, F. da Porto, M.R. Valluzzi, A Multi-level Procedure at Urban Scale to Assess the Vulnerability and the Exposure of Residential Masonry Buildings: The Case Study of Pordenone, Northeast Italy, *Heritage* **3**, 2020, 1433–1468. <https://doi.org/10.3390/heritage3040080>.
  - [19] C. Del Gaudio, M.T. De Risi, G.M. Verderame, Seismic Loss Prediction for Infilled RC Buildings via Simplified Analytical Method, *J. Earthq. Eng.*, 2021. <https://doi.org/10.1080/13632469.2021.1875940>.
  - [20] B. Borzi, H. Crowley, R. Pinho, Simplified pushover-based earthquake loss assessment (SP-BELA) method for masonry buildings, *Int. J. Archit. Herit.* **2**, 2008, 353–376. <https://doi.org/10.1080/15583050701828178>.
  - [21] B. Borzi, R. Pinho, H. Crowley, Simplified pushover-based vulnerability analysis for large-scale assessment of RC buildings, *Eng. Struct.* **30**, 2008, 804–820. <https://doi.org/10.1016/j.engstruct.2007.05.021>.
  - [22] G. Tecchio, M. Donà, C. Modena, Direct displacement-based design accuracy prediction for single-column RC bridge bents, *Earthq. Struct.* **9**, 2015, 455–480. <https://doi.org/10.12989/eas.2015.9.3.455>.
  - [23] A. Masi, Seismic vulnerability assessment of gravity load designed R/C frames, *Bull. Earthq. Eng.* **1**, 2003, 371–395. <https://doi.org/10.1023/B:BEEE.0000021426.31223.60>.
  - [24] A. Masi, A. Digrisolo, V. Manfredi, Fragility curves of gravity-load designed RC buildings with regularity in plan, *Earthq. Struct.* **9**, 2015, 1–27. <https://doi.org/10.12989/eas.2015.9.1.001>.
  - [25] C. Del Gaudio, M.T. De Risi, P. Ricci, G.M. Verderame, Empirical drift-fragility functions and loss estimation for infills in reinforced concrete frames under seismic loading, *Bull. Earthq. Eng.*, 2019. <https://doi.org/10.1007/s10518-018-0501-y>.
  - [26] L. 23/1996: Regulation for School Buildings, Off. Gazzette Ital. Repub. N°15 19th January 1996. Rome, Italy. (1996) (in Italian).
  - [27] A. Masi, A. Digrisolo, G. Santarsiero, Analysis of a large database of concrete core tests with emphasis on within-structure variability, *Materials (Basel)*. **12**, 2019. <https://doi.org/10.3390/ma12121985>.

- [28] MIDAS Information Technology Co., Midas Gen, (n.d.). [www.cspfea.net](http://www.cspfea.net).
- [29] E. Spacone, F.C. Filippidou, F.F. Taucer, Fibre beam-column model for non-linear analysis of rc frames: Part I. Formulation, *Earthq. Eng. Struct. Dyn.* **25**, 1996, 711–725.
- [30] J.B. Mander, M.J.N. Priestley, R. Park, Theoretical Stress-Strain Model for Confined Concrete, *J. Struct. Eng.* **114**, 1988, 1804–1826.
- [31] M. Menegotto, P.E. Pinto, Method of analysis for cyclically loaded RC plane frames including changes in geometry and non-elastic behaviour of elements under combined normal force and bending, in: *Symp. Resist. Ultim. Deform. Struct. Acted by Well Defin. Loads, International Association for Bridge and Structural Engineering*, Zurich, Switzerland, 1973.
- [32] G.M. Calvi, D. Bolognini, Seismic response of reinforced concrete frames infilled with weakly reinforced masonry panels, *J. Earthq. Eng.* **5**, 2001, 153–185. <https://doi.org/10.1080/13632460109350390>.
- [33] S. Hak, P. Morandi, G. Magenes, T.J. Sullivan, Damage control for clay masonry infills in the design of RC frame structures, *J. Earthq. Eng.* **16**, 2012, 1–35. <https://doi.org/10.1080/13632469.2012.670575>.
- [34] M. Minotto, N. Verlato, M. Donà, F. da Porto, Strengthening of In-Plane and Out-of-Plane Capacity of Thin Clay Masonry Infills Using Textile- and Fiber-Reinforced Mortar, *J. Compos. Constr.* **24**, 2020. [https://doi.org/10.1061/\(asce\)cc.1943-5614.0001067](https://doi.org/10.1061/(asce)cc.1943-5614.0001067).
- [35] P. Morandi, S. Hak, G. Magenes, Performance-based interpretation of in-plane cyclic tests on RC frames with strong masonry infills, *Eng. Struct.* **156**, 2018, 503–521. <https://doi.org/10.1016/j.engstruct.2017.11.058>.
- [36] F. da Porto, M. Donà, N. Verlato, G. Guidi, Experimental Testing and Numerical Modeling of Robust Unreinforced and Reinforced Clay Masonry Infill Walls, With and Without Openings, *Front. Built Environ.* **6**, 2020. <https://doi.org/10.3389/fbuil.2020.591985>.
- [37] M. Donà, M. Minotto, E. Saler, G. Tecchio, F. da Porto. Combined in-plane and out-of-plane seismic effects on masonry infills in RC frames, in: *Ing. Sismica*, 2017: pp. 157–173.
- [38] F. Mazza, A. Donnici, In-plane and out-of-plane seismic damage of masonry infills in existing r.c. structures: the case study of De Gasperi-Battaglia school in Norcia, *Bull. Earthq. Eng.*, 2021. <https://doi.org/10.1007/s10518-020-00981-2>.
- [39] F.J. Crisafulli, A.J. Carr, Proposed macro-model for the analysis of infilled frame structures, *Bull. New Zeal. Soc. Earthq. Eng.* **40**, 2007, 69–77. <https://doi.org/10.5459/bnzsee.40.2.69-77>.
- [40] B. Stafford Smith, Methods for predicting the lateral stiffness and strength of multi-storey infilled frames, *Build. Sci.* **2**, 1967. [https://doi.org/10.1016/0007-3628\(67\)90027-8](https://doi.org/10.1016/0007-3628(67)90027-8).
- [41] R.J. Mainstone, Supplementary note on the stiffnesses and strengths of infilled frames., *Build. Res. Establ. Build. Res. Stn.* (1974).
- [42] T.B. Panagiotakos, M.N. Fardis, Seismic response of infilled RC frame structures, in: *Proc. 11th World Conf. Earthq. Eng.*, 1996: pp. 1–8.

- [43] R. Paolucci, A.G. Ozcebe, C. Smerzini, A. Masi, V. Manfredi, Selection and spectral matching of recorded ground motions for earthquake engineering analysis. Overview of the S & M Matlab code and illustrative example for construction of fragility curves., 2020 (to be published).
- [44] Circ 21/01/2019 N.7, Istruzioni per l'applicazione dell'«Aggiornamento delle “Norme tecniche per le costruzioni” di cui al decreto ministeriale 17 gennaio 2018. (Italian Guideline), Suppl. Ordin. Alla “Gazzetta Uff. n. 35 Del 11 Febbraio 2019 - Ser. Gen. 337. (in Italian)
- [45] European Committee for Standardization, EN1998 Eurocode 8-1: Design of structures for earthquake resistance. Part 1: General rules, seismic actions and rules for buildings, 144 (2001) 55–60. <https://doi.org/10.1680/cien.144.6.55.40618>.
- [46] G. Grunthal, EMS98 - European Macroseismic Scale 1998, Conseil de l'Europe - Cahiers du Centre Européen de Géodynamique et de Séismologie, Luxemburg, 1998.
- [47] C. Del Gaudio, M.T. De Risi, G.M. Verderame, A simplified methodology for seismic repair costs assessment in RC buildings: an application to L'Aquila 2009 event, in: *Atti Del XVIII Convegno ANIDIS L'ingegneria Sismica Ital.* Ascoli Piceno, 15-19 September 2019.
- [48] FEMA - Federal Emergency Management Agency, HAZUS Earthquake Model Technical Manual 4.2 SP3, Washingt. DC. (2020). <https://www.fema.gov/>.
- [49] R. Villaverde, Methods to Assess the Seismic Collapse Capacity of Building Structures: State of the Art, *J. Struct. Eng.* **133**, 2007, 57–66. [https://doi.org/10.1061/\(asce\)0733-9445\(2007\)133:1\(57\)](https://doi.org/10.1061/(asce)0733-9445(2007)133:1(57)).
- [50] F. Jalayer, H. Ebrahimian, A. Miano, G. Manfredi, H. Sezen, Analytical fragility assessment using unscaled ground motion records, *Earthq. Eng. Struct. Dyn.* **46**, 2017, 2639–2663. <https://doi.org/10.1002/eqe.2922>.
- [51] D. Vamvatsikos, C. Allin Cornell, Incremental dynamic analysis, *Earthq. Eng. Struct. Dyn.* **31**, 2002, 491–514. <https://doi.org/10.1002/eqe.141>.
- [52] M. Dolšek, P. Fajfar, The effect of masonry infills on the seismic response of a four-storey reinforced concrete frame - a deterministic assessment, *Eng. Struct.* **30**, 2008, 1991–2001. <https://doi.org/10.1016/j.engstruct.2008.01.001>.
- [53] B. Pantò, I. Calì, P.B. Lourenço, Seismic safety evaluation of reinforced concrete masonry infilled frames using macro modelling approach, *Bull. Earthq. Eng.* **15**, 2017, 3871–3895. <https://doi.org/10.1007/s10518-017-0120-z>.
- [54] B. Borzi, M. Onida, M. Faravelli, D. Polli, M. Pagano, D. Quaroni, A. Cantoni, E. Speranza, C. Moroni, IRMA platform for the calculation of damages and risks of Italian residential buildings, *Bull. Earthq. Eng.*, 2020. <https://doi.org/10.1007/s10518-020-00924-x>.



## TYPOLOGICAL ANALYSIS AND VULNERABILITY CURVES FOR MASONRY CHURCHES

Elvis Cescatti<sup>1</sup>, Veronica Follador<sup>2</sup>, and Francesca da Porto<sup>1</sup>

<sup>1</sup> Depart. of Geosciences - University of Padova  
Via G. Gradenigo, 6, 35131 Padova (IT)  
elvis.cescatti@dicea.unipd.it; francesca.daporto@unipd.it

<sup>2</sup> DICATAM - University of Brescia  
Via Branze, 43, 25123, Brescia (IT)  
v.follador@unibs.it

---

### Abstract

*Masonry churches have a high intrinsic seismic vulnerability, demonstrated by the effects of the last earthquakes in Italy. In the present study a database of 1391 II level post-earthquake survey form (A-DC) has been analyzed. The forms were filled by the University of Padua, the University of Naples Federico II and the University of Naples Parthenope, under the coordination of the Department of Civil Protection, the Cultural Heritage Ministry (MiBACT) and the Italian Laboratories University Network of Seismic Engineering (Re-LUIS). The form were filled after the 2016/2017 Central Italy seismic sequence (889 forms), the 2012 Emilia earthquake (264 forms) and after the 2009 L'Aquila earthquake (238 forms). A typological investigation has been done as preliminary phase, and some vulnerability modifiers have been determined, with the aim of developing vulnerability and fragility curves dependent of poor but effective typological characteristics of the buildings.*

**Keywords:** Masonry Churches, Definition of Typologies, Vulnerability Curves, L'Aquila 2009, Emilia 2012, Central Italy 2016.

---

## 1 INTRODUCTION

In the last decades, great losses have occurred to the artistic and cultural heritage as a result of seismic events. In particular, serious damage has been suffered by churches [1-6], object of the present study. With the purpose of assess the safety conditions and collect the data of the damage suffered by ecclesiastical buildings, a specific form for the survey of damage churches [7, 8] was developed. The current version (A-DC form [9, 10]) consists of several sections, in which identification data, context description, damage data, safety evaluations and basic geometric information of the building are reported. As concern the damage survey, the form is based on the identification of the damage level (from 0 to 5) of 28 possible collapse mechanisms of macro-elements. Then, it is possible to obtain an overall damage index  $i_d$  (from 0 to 1) as a normalized average of the damage level of each mechanism.

The seismic events considered in this study are those in which the form for the damage survey of churches has been used in its actual version: the 2009 L'Aquila earthquake, the 2012 Emilia earthquake and the 2016/17 Central Italy seismic sequence. The surveys have been carried out under the coordination of the Department of Civil Protection (DPC) and the Ministry of Cultural Heritage and Tourism (MiBACT) by group of technicians (structural engineers, officials of the superintendence, fireman if the safety level was low). In particular, the authors have used A-DC forms filled mainly by the University of Padua, and in part by the University of Naples Federico II and the University of Naples Parthenope.

Churches are a peculiar type of building which has intrinsic seismic vulnerability due to its constructive and typological features (i.e. great lights, absence of intermediate diaphragms, large height to width ratio of walls, thrusting horizontal structures) [11]. Thus, in order to elaborate large-scale analysis, churches must be approached differently than ordinary buildings [2, 13, 14]. Usually, the evaluation of seismic risk at territorial scale requires the identification of different classes of buildings which have similar behavior [12]. For ordinary buildings, those classes are generally defined by the type of load-bearing structure (e.g. masonry, reinforced concrete, etc.) and by the constructive techniques and building regulations (mainly identifying with age of construction ranges). On the other hand, churches are usually load-bearing masonry buildings, distinguished by typological features more than constructive ones (e.g. presence of macro-elements, type of plan and façade, etc.). Therefore, the aim of this work is to identify typological characteristics that affect the vulnerability of the churches, in order to allow the elaboration of typological vulnerability and fragility curves that could account for different churches vulnerabilities and therefore be applied on large-scale seismic risk assessment according to the churches features.

## 2 TYPOLOGICAL DESCRIPTION OF THE SAMPLE

The database considered in the present study includes a total of 1391 post-earthquake survey A-DC forms [9, 10], filled mainly by the University of Padua, and in part by the University of Naples Federico II and the University of Naples Parthenope. Of these, 889 were collected following the 2016/2017 Central Italy earthquake sequence [6], 264 following the 2012 Emilia earthquake [4], and finally 238 following the 2009 L'Aquila earthquake [3]. Table 1 shows the geographical distribution of the surveys.

As already mentioned, in order to carry out the vulnerability analysis of churches it is necessary to consider the great geometrical and typological differences that they may present, which could lead to a very different seismic response. In particular, using the information collected from the A-DC forms and the photos of the post-earthquake surveys, the typological distributions of the churches affected by the three 2009, 2012 and 2016/17 earthquakes have been analyzed.

<i>Earthquake</i>	Regions (number of churches): province
<i>Central Italy 2016/17</i>	Marche (602): Ancona (AN), Ascoli Piceno (AP), Fermo (FM), Macerata (MC), Pesaro e Urbino (PU) Abruzzo (111): L'Aquila (AQ), Chieti (CH), Pescara (PE), Teramo (TE) Umbria (110): Perugia (PG), Terni (TR) Lazio (66): Frosinone (FR), Rieti (RI), Viterbo (VT)
<i>Emilia 2012</i>	Emilia Romagna (138): Bologna (BO), Ferrara (FE), Modena (MO), Reggio Emilia (RE) Lombardia (82): Cremona (CR), Mantova (MN) Veneto (44): Rovigo (RO)
<i>L'Aquila 2009</i>	Abruzzo (238): L'Aquila (AQ), Teramo (TE)

Table 1: Geographical distribution of the sample.

Specifically, the distribution of the following database parameters was studied [6]: a) type of plan (Figure 1); b) type of façade; c) masonry type; d) type of bell structure; and e) dimensions (volume).

The results in terms of the distribution of the analyzed features are collected in Table 2 and the typologies associated with each church belonging to the database, geographically located, are presented in Figure 2.

As regards to the type of plan, seven types were identified based on the number of naves, the presence of apse, transept and side chapels (Figure 1). Specifically: type 1 represents one nave churches with, simple rectangular plan, without apse or aggregated elements; type 2 is similar to type 1, with the addition of the apse; type 3 represents the most complex possibility for one nave churches (apse, transept and/or side chapels); type 4 is three or more naves church, with very complex plan (transept, chapels, apses at the end of naves and transept); type 5 is also a three or more naves church, with medium complex plan; type 6 represents the less complex typology of three naves churches (includes also the 2 naves churches); type 7 is circular or central plan (polygonal) church.

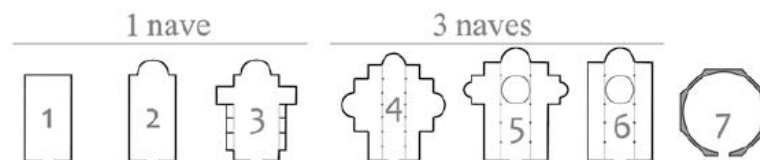


Figure 1: Schematic representation of the seven type of plan considered in this study.

The analysis of the sample showed that in Central Italy simpler churches are predominant. The most common types are 1 and 2, whereas with very small percentages are found types 3, 5 and 6; types 4 and 7 are just over 1%. Table 2 and Figure 2 show that the churches affected by the 2009 L'Aquila earthquake have many similarities with the ones of the 2016/17 Central Italy seismic sequence (both affect the central Apennine belt). In fact, the most widespread are type 1 and 2 churches (82.8 % CI and 66.9% AQ), but also, type 6 and type 3 are common. The trend identified in the Central Italy region changes considerably for the churches located in the Po Valley: the percentage of type 1 is very small (mostly oratories and minor private chapels). Instead, the more complex typologies (type 3, 6 and 5) are more widespread with a cumulative percentage of 61.4%. The numbers of types 4 and 7 remain marginal. Analyzing the geographical distribution, it can be observed that in the Apennine region there is a predominance of single nave churches (mainly typologies 1 and 2); the cases of churches with more naves are located in the less mountainous areas and in Abruzzo, and they belong to typology 6, so they

have a not excessively complex geometry. In the Po Valley the typologies present are distributed in the territory, and are not visibly dependent on geographical location.

The second feature analyzed is the type of façade. Four main types of façade have been identified: gabled, salient façade, quadrangular and polygonal. The cases that was not possible to trace back to one of these four types (e.g. churches with side entrances connected to adjacent buildings on several sides or churches with a large prothyrum or narthex) were excluded from the present analysis, because of the different seismic behavior of the façade macroelement.

With regard to the sample of Central Italy, there is a clear majority of gabled type, whereas the church façades of the L'Aquila earthquake belong in large part to the gabled and the quadrangular type. Instead, most of the churches in the Po Valley have salient and gabled façades.

The type of façade seems to have no correlation with geographical location (Figure 2) probably due to similar geographical conditions of the inspected area all enclosed in the plain.

Another important typological characteristic is the masonry type. Since the masonry texture is often covered by plaster, it is not always possible to determine the constituent material of the walls, unless more in-depth investigations are carried out. As for the façade, also for the masonry typology, the not identified cases have been excluded from the typological analysis.

Four masonry types have been distinguished: random stone, stone ashlar, brick masonry and mixed stone and brick masonry. The masonry parameter distribution is the most clearly readable: in Central Italy and L'Aquila samples, stone is the most common material (mainly random rubble), whereas in Emilia no cases of stone masonry but an almost totality of brick masonry have been identified. Figure 2 shows that the type of masonry depends almost exclusively on the geographical/topographical location. In the lowland areas and in the coastal strip only brick masonry (or mixed masonry at most) is present, whereas rising to a higher altitude and moving away from the coast, bricks begin to be flanked by the stone until it is completely replaced by it (this is particularly evident in the Central Italy earthquake).

Regarding the type of bell tower, four types have been identified: isolated bell tower, bell tower integrated or partially integrated with the church structure, bell gable and absence of bell tower. The samples of Central Italy and L'Aquila have similar distributions: the most common types are integrated bell tower and bell gable, whereas isolated bell tower is very uncommon. L'Aquila sample has also a 10% of cases in which the bell tower is absent. Also, for this parameter, the Emilia database is visibly different from the others, presenting for the most part integrated and isolated bell tower, and only few cases of bell gable. Figure 2 shows that, in this case, the differences between the distributions of the samples depend more on the territorial/regional area, rather than on altimetric or topographical factors.

The last of the typological features analyzed is the volume of the church. Since many forms were incomplete in the section related to the geometric survey, also this parameter is not identified for the all database. Six ranges of volume have been chosen: two ranges of very small and small churches (from 0 to 250 and from 250 to 500 m<sup>3</sup>), two of medium size churches (from 500 to 1000 and from 1000 to 2500 m<sup>3</sup>) and two ranges of large churches (from 2500 to 5000 and from 5000 m<sup>3</sup> upwards). Table 2 shows that in Central Italy and L'Aquila the most widespread churches are those of medium size, followed by small churches and lastly those of large size. Instead, in Emilia, the most of the churches have a large or medium volume. From a territorial distribution point of view, large churches are typically located in lowland areas or in correspondence of cities or important centers (Figure 2).

	Central Italy 2016/17		L'Aquila 2009		Emilia 2012	
	n	%	n	%	n	%
<i>Churches</i>	889		238		264	
<b><i>Plan shape</i></b>						
1	322	42.0%	103	43.6%	25	9.5%
2	313	40.8%	55	23.3%	71	26.9%
3	43	5.6%	29	12.3%	81	30.7%
4	13	1.7%	0	0.0%	5	1.9%
5	26	3.4%	8	3.4%	30	11.4%
6	38	5.0%	40	16.9%	51	19.3%
7	12	1.6%	1	0.4%	1	0.4%
<i>sum</i>	767	86.3%	236	99.2%	264	100.0%
<b><i>Façade typology</i></b>						
Gabled	572	74.4%	100	47.2%	104	41.8%
Salient	65	8.5%	16	7.5%	122	49.0%
Quadrangular	74	9.6%	71	33.5%	2	0.8%
Polygonal	58	7.5%	25	11.8%	21	8.4%
<i>sum</i>	769	86.5%	212	89.1%	249	94.3%
<b><i>Masonry typology</i></b>						
Random stone	318	43.6%	95	60.1%	0	0.0%
Stone ashlar	52	7.1%	30	19.0%	0	0.0%
Stone/Brick	141	19.3%	27	17.1%	2	0.9%
Brick	219	30.0%	6	3.8%	229	99.1%
<i>sum</i>	730	82.1%	158	66.4%	231	87.5%
<b><i>Bell tower typology</i></b>						
Bell tower isolated	17	2.5%	5	2.2%	63	24.0%
Bell tower integrated	351	52.5%	73	31.9%	146	55.5%
Bell gable	283	42.3%	127	55.5%	11	4.2%
No bell tower	18	2.7%	24	10.5%	43	16.3%
<i>sum</i>	669	75.3%	229	96.2%	263	99.6%
<b><i>Volume [m<sup>3</sup>]</i></b>						
0 - 250	100	12.7%	22	18.6%	14	6.1%
250 - 500	131	16.6%	17	14.4%	17	7.5%
500 - 1000	183	23.3%	28	23.7%	11	4.8%
1000 - 2500	185	23.5%	32	27.1%	47	20.6%
2500 - 5000	94	11.9%	12	10.2%	61	26.8%
> 5000	94	11.9%	7	5.9%	78	34.2%
<i>sum</i>	787	88.5%	118	49.6%	228	86.4%

Table 2: Statistical distribution of plan shape, façade type, masonry type, bell tower typologies and volume for the earthquake of Central Italy 2016/17, L'Aquila 2009 and Emilia 2012.

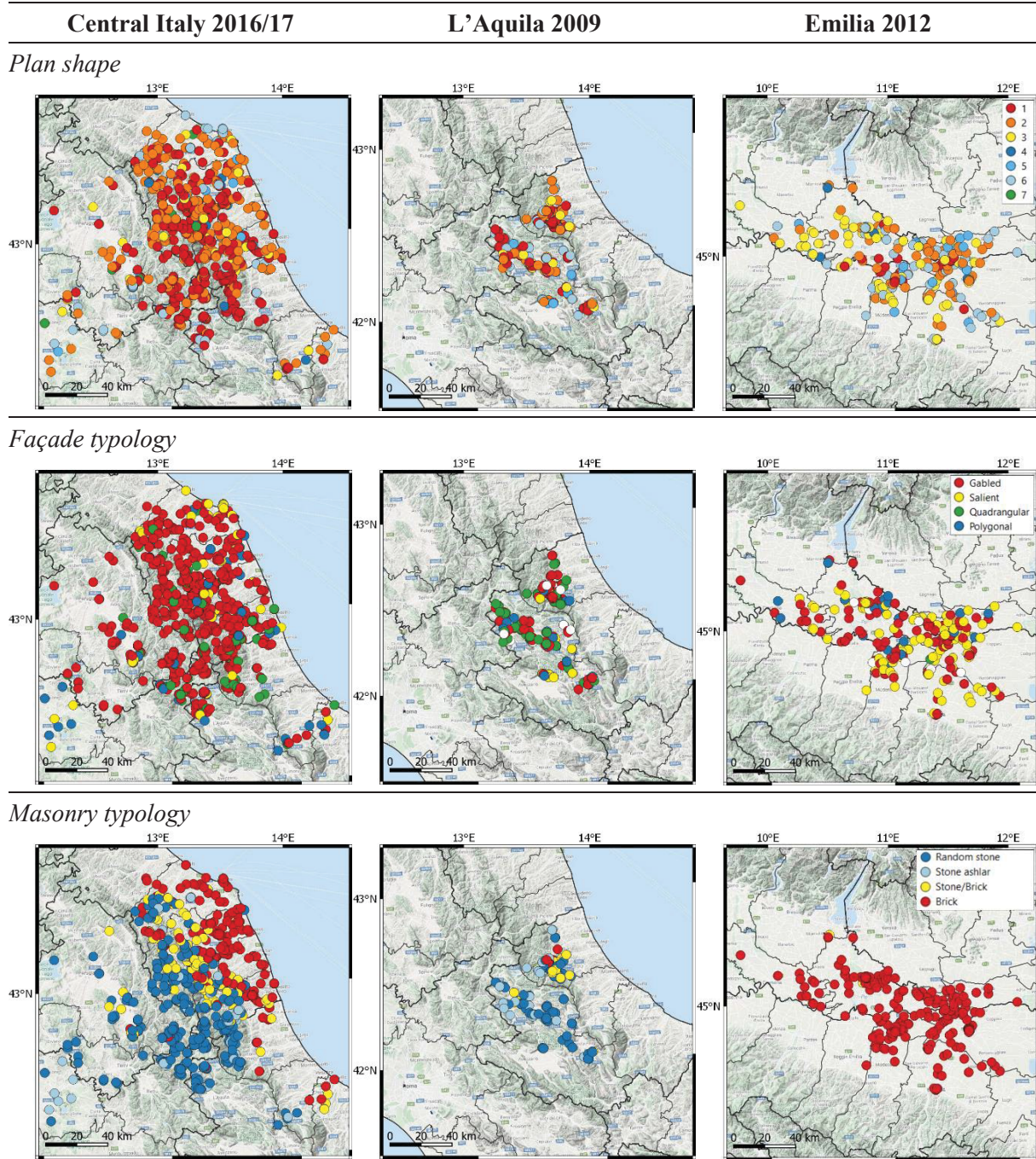
It can be concluded that Emilia churches are typologically very different from Central Italy and L'Aquila ones. The latter, belonging to the same geographical area, have more homogeneous characteristics, with some differences due to the proximity to the coast and to altimetric/topographical factors. In particular, the feature that the most depends on altitude is the masonry type, as a direct consequence of the availability of the different materials on site. The other parameters analyzed are not directly dependent on the altimetry, but are more related to the territorial/regional building traditions, especially evident in the type of façade and bell tower.

In summary, it emerges that the churches of Central Italy are mainly simple, medium size and single nave, with a gabled façade and a bell gable or a bell tower integrated into the structure of the church, built in stone (mostly random) in the Apennine area and brick in the coastal strip. Very similar are the churches affected by the L'Aquila earthquake, with the only difference that prefer a quadrangular façade and the cases with more than one nave are more widespread, although maintaining a very simple plan. Very different are the churches of Emilia and the Po



Valley regions, which have large complex plans with gabled or salient façades, with the presence of isolated or integrated bell tower and built almost exclusively in brick.

To compare several features, the maps in Figure 2 show that in Emilia there is a good correspondence between volume and complexity (typology of plan shape), whereas in Central Italy even when the churches are large the complexity is never high (particularly evident on the coastal strip).





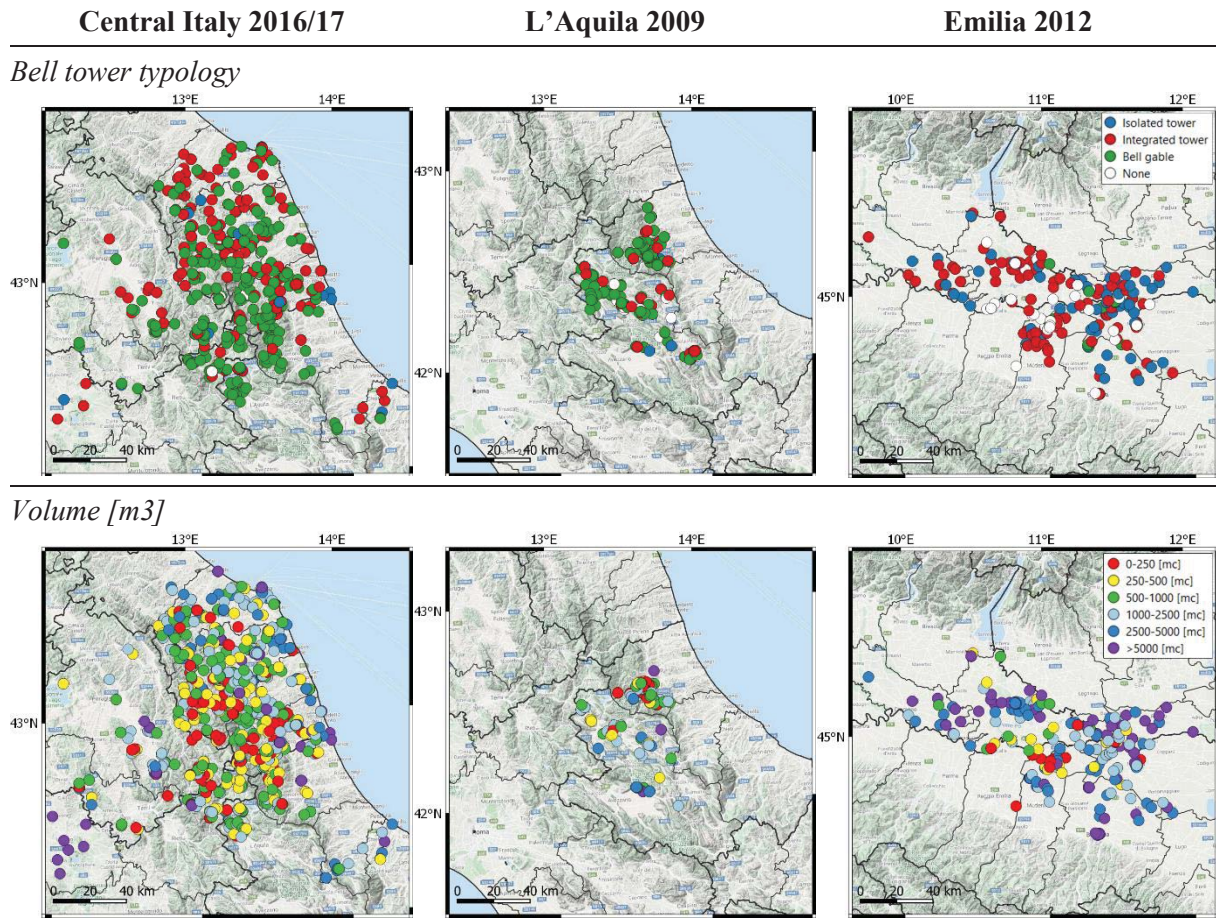


Figure 2: Map of the geographical distribution of different typological features for the earthquake of Central Italy 2016/17, L'Aquila 2009 and Emilia 2012.

### 3 VULNERABILITY CURVES

The seismic vulnerability of a building is defined as the propensity of the structure to suffer damage after a seismic event of a given intensity. It could be represented by a continuous function called vulnerability curve that relates the expected mean value of damage of a class of buildings to the seismic intensity. The latter is usually presented in terms of macroseismic intensity, but it can also be provided as peak ground acceleration-PGA values.

The formulation originally provided by [15] for residential buildings and further adapted to churches by Lagomarsino and Podestà [13] (1) was taken as reference to develop typological vulnerability curves.

$$\mu_d = 2,5 \left[ 1 + \tanh \left( \frac{I + 3.4375 \cdot \bar{i}_v - 8.9125}{q} \right) \right] \quad (1)$$

where  $\mu_d$  represents the mean damage grade ( $0 \leq \mu_d \leq 5$ ) as function of: the macroseismic intensity  $I$  expressed in accordance with the MCS scale [16], the mean vulnerability score  $i_v$  derived from the second level survey form for churches [17], and the ductility index  $q = 3$ .

In particular, a fitting procedure of the observational damage data collected was carried out using (2):

$$\mu_D = 2,5 \cdot [1 + \tanh(\alpha \cdot I_{MCS} + \beta)] \quad (2)$$

$$\text{with } \alpha = 1/q \quad (3)$$

$$\text{and } \beta = a \cdot i_v + b \quad (4)$$

and optimizing the value of  $\alpha$  and  $\beta$ .

The formulation (2) is equivalent to (1), but expressed in terms of the two parameters  $\alpha$  (3) and  $\beta$  (4). In this way, from the fitting procedure on mean damage values, the resulting vulnerability curve inherently includes the average value of  $i_v$  on the whole dataset. Indeed, as suggested below, the evaluation of different vulnerabilities classes or typologies could be related to a selected subset of homogenous churches.

### 3.1 Consideration on the damage index $i_d$

As mentioned before, the A-DC survey form allows to calculate an overall damage score (damage index)  $i_d$  for each church. In particular:

$$i_d = \frac{1}{5} \frac{\sum_{k=1}^n d_k}{n} \quad (5)$$

where  $n$  is the number of mechanisms that can be potentially activated in the church and  $d_k$  is the damage recorded in the  $k$ -th mechanism (from 0 to 5).

In order to be used for vulnerability and fragility analysis, the damage index  $i_d$  has to be converted to a damage level from 0 to 5, according to the EMS scale [18]. One of the most used correlation [13] is reported in Table 3.

Damage index $i_d$	0-0.05	0.05-0.25	0.25-0.4	0.4-0.6	0.6-0.8	0.8-1
Damage level (EMS98)	DS0	DS1	DS2	DS3	DS4	DS5
Description of the damage	<i>no damage</i>	<i>slight damage</i>	<i>moderate damage</i>	<i>heavy damage</i>	<i>very heavy damage</i>	<i>collapse</i>

Table 3: Correlation between the damage index  $i_d$  of the A-DC form and the damage level according to the EMS98 scale [13].

Using the correlation in Table 3, a process of discretization of a continuous quantity is carried out. This process is required to relate the result of the A-DC form to a damage level and to build damage probability matrices (DPM), but inevitably, it implies a great loss of detail. Moreover, this discretization slightly varies the overall mean description of the damage. For instance, considering a dataset of 101 churches equally distributed in the damage index  $i_d$  from 0 to 1, due to the different dimensions of each damage state, that discretization leads to an average  $\mu_D$  damage of 2.87 instead of the mathematical mean of 2.50. Figure 3 reports the real case of the 2016/17 Central Italy database with  $i_d$  multiplied by 5 to have a comparison. The graph shows how different the damage results can be: as expected, in general the mean damage obtained through the correlation proposed by Lagomarsino and Podestà [13] is higher then that obtained directly by the damage index  $i_d$ , but not in a consistent way. Indeed, in correspondence of some intensities (e.g  $I_{MCS}=8$  and  $I_{MCS}=9.5$ ) the difference is very low (about 0.15), while for others (e.g  $I_{MCS}=7.5$ ,  $I_{MCS}=8.5$  and  $I_{MCS}=10$ ) the difference is very impacting (0.5). This is a consequence of the specific distribution of the sample, and therefore it can generate unreliable results in terms of comparison analysis.

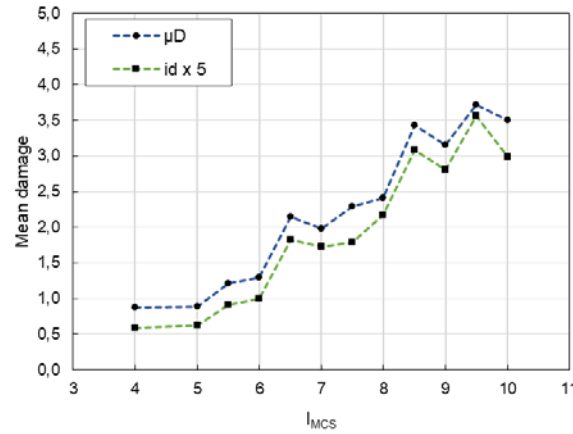


Figure 3: Comparison between the mean value of the damage expressed in terms of  $\mu_D$  and  $i_d$  for the Central Italy churches.

Therefore, since this study works directly on the average damage to figured out the vulnerability curve, and does not use the DPMs, it was decided to build the vulnerability curve in terms of damage index, using in place of the usual mean value  $\mu_d$  (2) the average  $i_d$  values (6):

$$i_d = 0,5 [1 + \tanh(\alpha \cdot I_{MCS} + \beta)] \quad (6)$$

The value of 2.5 is assumed as 0.5 accordingly to the domain of  $i_d$ . This choice has been made both to have more possibilities to adapt the curve to the observational values, and to use in a direct way the information obtained from the damage surveys, avoiding the loss of information deriving from the discretization of the value of  $i_d$ .

### 3.2 Fitting procedure

Once defined the formulation (6), some specification about the adopted fitting procedure are herein reported.

The two coefficients  $\alpha$  and  $\beta$  have been calibrated with the minimization of the total error. The ductility related coefficient  $\alpha$  was not keep fixed to  $q = 3$  since the observation of three different earthquakes and an extended sample shows a variability of this factor as reported in Table 4. As concern the  $\beta$  parameter, it was derived by the mean value of the observational damage indices of the A-DC forms, with a fitting procedure based on the minimization of the total error resulting from the sum of the square residual.

Table 4 reports values obtained from the fitting of eq. (6) and Figure 4 plot each vulnerability curve on the experimental data observed. As is possible to notice there is a good agreement between the observed data and the continuous curves with very limited errors.

	Central Italy 2016/17	L'Aquila 2009	Emilia 2012
$\alpha$	0.263	0.316	0.360
$\beta$	-2.205	-2.678	-2.471
<i>error</i>	$9.86 \times 10^{-04}$	$4.83 \times 10^{-04}$	$1.82 \times 10^{-03}$
$q$	3.807	3.161	2.778

Table 4: Value defined for the three analyzed earthquakes according to eq. (6)

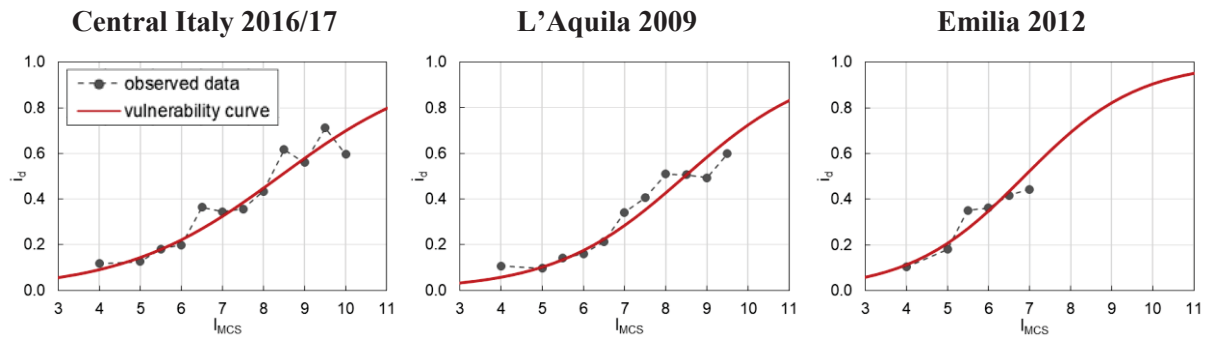


Figure 4: Vulnerability curves obtained from the three analyzed earthquakes

## 4 INFLUENCE OF TYPOLOGIES

Since the previously observed curves are defined on the whole dataset, hence accounting for the average vulnerability, the selection of homogenous dataset of churches with the same vulnerability may improve the overall evaluation.

Once defined the vulnerability model and the fitting method, it was possible to analyze the influence on seismic vulnerability of different typology characteristics that may lead to the homogenous subset above seek. Specifically, in this paper, the influence of masonry type and the number of naves are presented.

On the basis of the results reached in section 2 about the typological distribution of the churches belonging to the database, the following analyses have been carried out limited to the churches of Central Italy and L'Aquila, in order to guarantee the uniformity of the sample. Future more accurate analysis will allow to study the entire database, and come to overall results not affected by possible errors due to not considered features.

### 4.1 Influence of masonry type

The first typological parameter to be analyzed is the type of masonry. The categories already identified in the context of typological characterization have been further simplified and reduced to three: stone masonry (both ashlar and random rubble masonry), brick masonry and mixed stone and brick masonry.

Figure 5a shows that the two extreme categories (i.e. stone masonry and brick masonry) have a marked difference in terms of damage, whereas the behavior of the intermediate one (i.e. mixed masonry) seems to be less linear and tends to overlap with the former in correspondence of some  $I_{MCS}$ . This can be attributed to the great variability that mixed masonry can presents, sometimes with a predominance of stone, sometimes of brick. Moreover, it is possible that in some cases the particular disposition of the different materials composing the masonry leads to both particularly unfavorable and favorable consequences.

Therefore, this parameter proves to be relevant for the definition of seismic vulnerability. In Figure 5b the results of the fitting procedure are shown. In this elaboration, the behavior of mixed masonry churches emerges to be very similar to stone masonry ones, although those constructed in brick masonry proves to have a much better response to seismic actions.



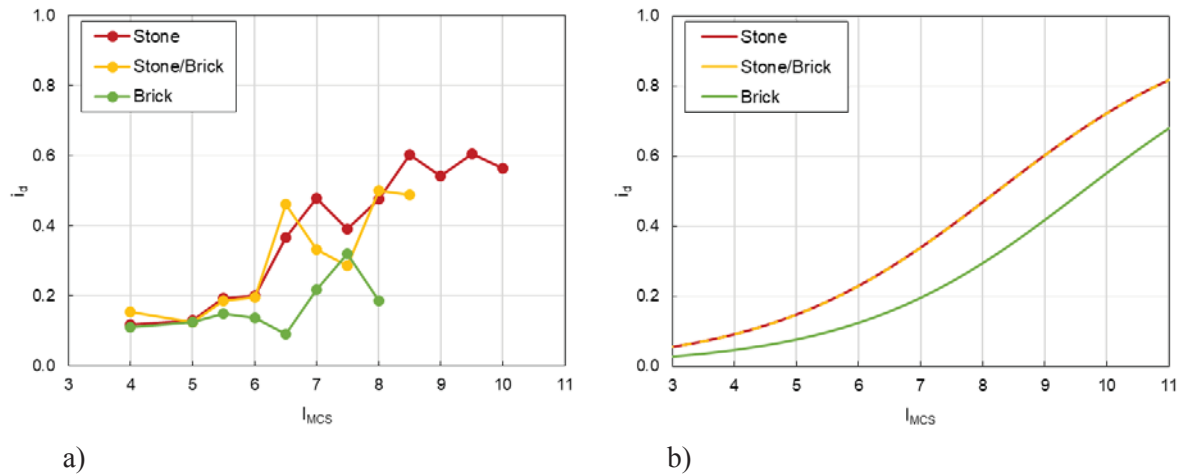


Figure 5: Mean  $i_d$  values for stone, mixed (stone/brick) and brick masonry churches (a) and resulting vulnerability curves (b).

#### 4.2 Influence of number of naves

The number of naves is the second typological feature analyzed. In particular, two classes were defined [19, 20]: one nave churches and more than one nave.

Figure 6a shows that for low value of  $I_{MCS}$  the damage observed for the two classes is similar. Then, with the increase of the intensity, the different behavior of the different types clearly emerges: churches with more than one nave tend to be less vulnerable compared to those with one nave. The different vulnerability is justified by the greater possibility of churches with several naves to absorb horizontal forces, thanks to the presence of colonnades and more widespread connections. On the other hand, the presence of such elements also makes less likely that all of them are damaged in a marked way; in fact, as the complexity increases, the weight of each macro-element decreases on the overall evaluation of the damage, leading on lower damage indices.

In Figure 6b, the vulnerability curves calibrated on the observed damage of both one and more than one nave churches.

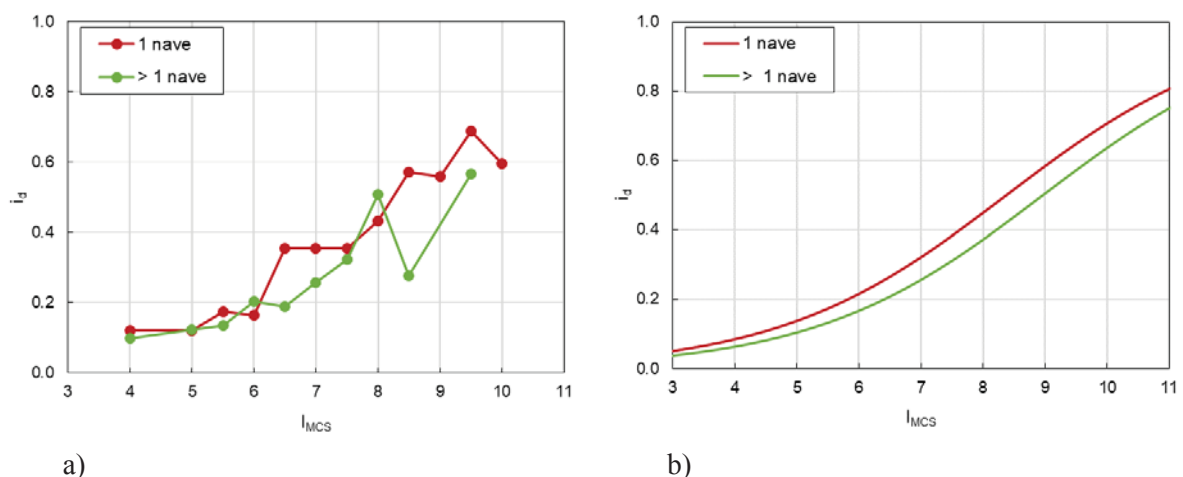


Figure 6: Mean  $i_d$  values for one nave and more than one nave churches (a) and resulting vulnerability curves (b).

## 5 CONCLUSIONS

- The present paper has presented a detailed typological distribution analysis of 1391 churches, affected by the 2009 L'Aquila earthquake, the 2012 Emilia earthquake and the 2016/17 seismic sequence of central Italy. The considered features have been plan shape, type of façade, masonry type, typology of bell tower, and volume of the church. It was figured out that the greater differences are due to the geographical and the altimetric/morphological location. In particular, churches of Central Italy regions are mainly simple, medium size and single nave, with a gabled or quadrangular façade and a bell gable or a bell tower integrated into the structure of the church, built in stone (mostly random) in the Apennine area and brick in the coastal strip. On the contrary, the churches located in the Po Valley regions generally have large complex plans with gabled or salient façades, with the presence of isolated or integrated bell tower and built almost exclusively in brick.
- Then, a methodology to derive vulnerability curves from damage data collected by the A-DC survey forms were defined starting from [13] and adapting the formulation to large scale and typological evaluation needs. Specifically, a reflection on the relation between the damage index  $i_d$  and the discrete damage value  $\mu_d$  was made and the vulnerability curves for the three analyzed earthquakes were provided.
- Lastly, the impact on seismic vulnerability related to the type of masonry and the number of naves of the churches was analyzed. Three different masonry typologies were defined (i.e. stone masonry, brick masonry and mixed stone and brick masonry), with the result that stone masonry and mixed masonry churches have a similar vulnerability, significantly higher than the one of brick masonry churches. Regarding the number of naves, one nave churches result more vulnerable of more than one nave ones, probably thanks to the presence of colonnades and widespread connections.
- Possible future developments are, first of all, the analysis of the influence of more typological parameters on the seismic vulnerability of churches. Then, an important further study is the extension of the procedure to the overall database, inclusive of Emilian churches.

## ACKNOWLEDGEMENTS

Special thanks are due to the Italian Department of Civil Protection (DPC), which funded this study in the framework of the *ReLUIS-DPC Project 2019-2021 – Work Package 4: MARS (MAPs of Risk and Scenarios of seismic damage) – Task 8: Models and fragility curves of churches (Modelli e curve di fragilità delle chiese)*.

## REFERENCES

- [1] F. Doglioni, A. Moretti, V. Petrini, P. Angeletti, *Le chiese e il terremoto. Dalla vulnerabilità constatata nel terremoto del Friuli al miglioramento antisismico nel restauro, verso la politica di prevenzione*. Trieste, Italy, Lint Editoriale Associati, 1994. (in Italian)
- [2] S. Lagomarsino, S. Podestà, Seismic Vulnerability of ancient churches: I. Damage assessment and emergency planning. *Earthquake Spectra*, **20**(2), 377–394, 2004 (a).

- [3] F. da Porto, F. Silva, C. Costa, C. Modena, Macro-scale analysis of damage to churches after earthquake in Abruzzo (Italy) on April 6, 2009. *Journal of Earthquake Engineering*, 16(6), 739-758, 2012.
- [4] S. Taffarel, M. Giaretton, F. da Porto, C. Modena, Damage and vulnerability assessment of URM buildings after the 2012 Northern Italy earthquakes. *16th International Brick and Block Masonry Conference (IBMAC 2016)*, Padua, Italy, June 26-30, 2016.
- [5] E. Cescatti, S. Taffarel, A. Leggio, F. da Porto, C. Modena, Macroscale damage assessment of URM churches after the 2016 sequence in Centre of Italy. XVII National Conference on L'Ingegneria sismica in Italia (ANIDIS 2017), Pistoia, Italy, September 17-21, 2017. (in Italian)
- [6] E. Cescatti, P. Salzano, C. Casapulla, D. Ceroni, F. da Porto, A. Prota, Damages to masonry churches after 2016–2017 Central Italy seismic sequence and definition of fragility curves. *Bull Earthquake Eng*, **18**, 297–329, 2020.
- [7] DPC, Survey form for the cultural heritage - damage to churches. G.U. no. 116, 21/05/2001, 2001. (in Italian)
- [8] S. Lagomarsino, L. Maggiolo, S. Podestà, Vulnerabilità sismica delle chiese: proposta di una metodologia integrata per il rilievo, la prevenzione ed il rilievo del danno in emergenza. X National Conference on L'Ingegneria sismica in Italia (ANIDIS 2001), Potenza-Matera, Italy, September 9-13, 2001. (in Italian)
- [9] DPCM 23/02/2006, Approval of forms for the seismic damage assessment of cultural heritage buildings. G.U. no. 55, 7/03/2006, 2006. (in Italian)
- [10] MiBACT, Direttiva 23 aprile 2015, Aggiornamento della direttiva 12 dicembre 2013, relativa alle “Procedure per la gestione delle attività di messa in sicurezza e salvaguardia del patrimonio culturale in caso di emergenze derivanti da calamità naturali. GU Serie Generale n.169 del 23-7-2015, 2015. (in Italian)
- [11] S. Lagomarsino, S. Podestà, Damage and vulnerability assessment of churches after the 2002 Molise, Italy, earthquake. *Earthquake Spectra*, **20**(S1), S271–S283, 2004c.
- [12] M. Dolce, A. Prota, B. Borzi, F. da Porto, S. Lagomarsino, G. Magenes, C. Moroni, A. Penna, M. Polese, E. Sperenza, Seismic risk assessment of residential buildings in Italy: Methodology overview and main results. *Bulletin of Earthquake Engineering*, 2020. <https://doi.org/10.1007/s10518-020-01009-5>
- [13] S. Lagomarsino, S. Podestà, Seismic Vulnerability of ancient churches: II. Statistical analysis of surveyed data and methods for risk analysis. *Earthquake Spectra*, **20**(2), 395–412, 2004b.
- [14] A. Penna, C. Calderini, L. Sorrentino, C.F. Carocci, E. Cescatti, R. Sisti, A. Borri, C. Modena, A. Prota, Damage to churches in the 2016 central Italy earthquakes. *Bull Earthquake Eng*, **17**, 5763–5790, 2019.
- [15] H. Sandi, I. Floricel, Analysis of seismic risk affecting the existing building stock. *10th European Conference on Earthquake Engineering*, Vienna, Austria, 28 August - 2 September, 1994.
- [16] A. Sieberg, Scala MCS (Mercalli-Cancani-Sieberg). *Geologie der Erdbeben, Handbuch der Geophysik*, **2**(4), 552–555, 1930.

- [17] Italian Ministry of Public Building and Works, G.U. no. 47. 2011, February 26. (suppl. ord. no. 54). Directive of the Prime Minister dated on 9/02/2011, Assessment and mitigation of seismic risk of cultural heritage with reference to the Technical Code for the design of constructions, issued by D.M. 14/1/2008, 2011. (in Italian)
- [18] G. Grunthal (ed.), *European Macroseismic Scale 1998*. Cahiers du Centre Européen de Géodynamique et de Séismologie, Luxembourg, 15, 1998.
- [19] G. De Matteis, E. Ciber, G. Brando, Damage probability matrices for three-nave masonry churches in Abruzzi after the 2009 L'Aquila earthquake. *International Journal of Architectural Heritage*, **10**(2-3), 120-145, 2016.
- [20] G. De Matteis, M. Zizi, Preliminary analysis on the effects of 2016 Central Italy earthquake on one-nave churches. R. Aguilar, D. Torrealva, S. Moreira, M.A. Pando, L.F. Ramos eds. *Structural analysis of historical constructions*, **18**, 1268-1279, RILEM Bookseries. Springer, Cham, 2019.

## COMPARATIVE STUDY ON TWO ANALYTICAL MECHANICAL-BASED METHODS FOR DERIVING FRAGILITY CURVES TARGETED TO MASONRY SCHOOL BUILDINGS

Cattari S.<sup>1</sup>, Alfano S.<sup>1</sup>, Ottonelli D.<sup>1</sup>, Saler E.<sup>2,3</sup> and da Porto F.<sup>2</sup>

<sup>1</sup> Dept. of Civil, Chemical and Environmental Engineering, University of Genoa  
Via Montallegro 1, 16145 Genoa  
e-mail: {serena.cattari,sara.alfano,daria.ottonelli}@unige.it

<sup>2</sup> Dept. of Geosciences, University of Padova  
Via Gradenigo 6, 3513 Padova  
{elisa.saler, francesca.daporto}@unipd.it

<sup>3</sup> Dept. of Civil, Environmental and Mechanical Engineering, University of Trento  
Via Mesiano 77, 38123 Trento

### Abstract

*Seismic events across several countries in the world have highlighted that strategic buildings, such as schools, may exhibit vulnerability levels that are in some cases higher than those of ordinary buildings. It follows the urgent need of reliable risk analyses to support the decision-making for large-scale mitigation policies. To this aim, the derivation of fragility curves, able to capture typological and constructive characteristics, constitutes an essential requisite. Within this context, the paper presents a comparative study on the use of two analytical-mechanical based methods for assessing fragility curves of Italian masonry school buildings. These are very often characterized by a number of stories rarely higher than three, presence of rigid floors, significant inter-story height, and great distance between transverse walls. Among the others, analytical approaches, either based on numerical or mechanical models, are more suitable to capture the effects of such features on the seismic vulnerability. The two methods discussed in the paper are “Vulnus Vb 4.0-2009”, developed at the University of Padova and based on the integrated use of mechanical and macroseismic approaches, and “DBV-Masonry (Displacement Based Vulnerability)”, a pure mechanical-based model developed at the University of Genoa. Both methods are applied to a stock of 14 masonry schools, selected as prototypes of Italian school masonry buildings. The critical review and comparative application of the two methods allow highlighting their similarities and differences in assessing the fragility associated to in-plane and out-of-plane failure mechanisms. Moreover, as some of the selected schools had been hit by the 2016-17 Central Italy earthquake sequence, the evidence of the real response allows assessing the actual reliability of the methods.*

**Keywords:** Masonry school building Fragility curves Analytical-mechanical models Seismic vulnerability.

---



## 1 INTRODUCTION

Schools constitute a key stone for the social and cultural life of people, beside to represent an essential place for supporting the growing of new generations. Despite the role they play, reconnaissance surveys of damage after many seismic events (*e.g.* as documented in Italy [1], [2]) have highlighted how strategic buildings or high-exposure buildings, such as schools, can present high levels of vulnerability and inadequate performance, in some cases comparable to those of ordinary ones. This has been confirmed also by vulnerability studies carried out in various countries across the world (*e.g.*, for Nepal [3], and for Iran [4]). The attention to the topic is also testified by various recent studies addressed to reduce risk and enhance resilience of schools (*e.g.*, [5],[6]), as well as some worldwide programs aimed to promote “safer schools” (*e.g.*, [7],[8]).

As known, derivation of fragility curves, able to capture the typological and constructive characteristics of the examined building stock, is a key point for reliable risk analyses, in order to support decision-making for large-scale mitigation policies. To date, few studies available in the literature have focused on fragility of unreinforced masonry (URM) schools. Fragility curves based on empirical approaches constitute a valuable resource, being based on the direct observation of damage (*e.g.*, derived for Peruvian [9] and Nepalese [10] schools). However, being usually based on a limited stock, their derivation faces the critical issues of less robust data, from a statistical point of view, than ordinary buildings. As a consequence, analytical approaches, either based on numerical or mechanical models [*e.g.*, [6], [11], [12], [13], [14]], are more suitable to capture the effects of specific features that affect the seismic vulnerability of such buildings.

Focusing on URM schools in Italy, the inventory of the Italian Ministry of Education, dated to 2005, indicates about 50,000 schools on the Italian territory, of which about 21% are masonry buildings. With respect the total URM stock, the distribution across the age is: 20% Pre1920, 18% 1921-45, 24% 1946-60, 20% 1961-75, 8% Post76; moreover, for the 10% the age is not available (indicated as NA in Figure 1). These schools are very often characterized:

- by low-rise, *i.e.*, the number of stories is rarely higher than three (see Figure 1);
- irregular plan: plans characterized by “T”, “L”, “C” shapes or with internal court. The latter is more frequently found for buildings that date back before 1920, in case their use changed along time;
- significant inter-story height;
- great distance between transverse walls;
- presence of rigid floors.

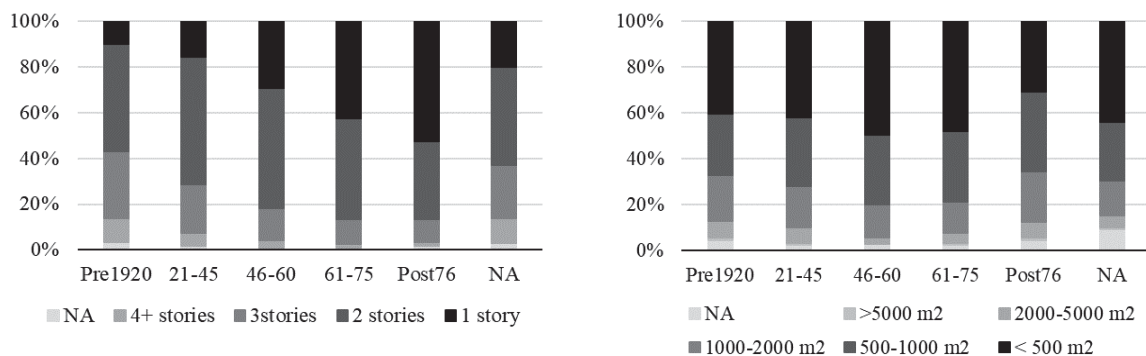


Figure 1. Distributions of Italian schools present in the Italian Ministry of Education inventory dated to 2005.

Within this context and being aware of the aforementioned high relevance of risk and resilience assessments of the national school asset, the Italian Civil Protection Department (DPC) conveyed the effort of several Italian Universities to update the National Risk Assessment already released in 2018 ([15], [16]), in order to include not only residential buildings but also other strategic classes, such as schools and churches. Thus, within the 2019–2021 research agreement between the Civil Protection Department (DPC) and the Network of University Laboratories for Earthquake Engineering (ReLUIS), the work package WP4 “Seismic Risk Maps -MARS” has been specifically conceived to address this scope [17]. One of the aims of the project is the derivation of seismic fragility models, able to describe the vulnerability of classes of schools characterized by seismic homogenous behavior.

Within this framework, the paper presents a comparative study on the use of two analytical-mechanical based methods for assessing fragility curves of schools; both of them have been adopted in the MARS project.

The two methods discussed in the paper are “Vulnus Vb 4.0-2009”, a hybrid model developed at the University of Padova, based on the integrated use of mechanical and macroseismic approaches [18], and the “DBV-*Masonry* (Displacement Based Vulnerability)”, a pure mechanical-based model originally developed at the University of Genoa [19] and further developed within the MARS project. Both methods assume a lognormal cumulative distribution to define fragility curves, that is thus defined by two parameters: the median value (i.e., the intensity measure, in this case the Peak Ground Acceleration, associated to the 50% probability of attaining the damage level under examination, indicated as  $IM_{DLi}$ ); and the log-normal standard deviation ( $\beta_{DLi}$ ). The fragility curves are associated to five damage levels ( $DL_i$ ,  $i = 1 \dots 5$ ), aimed to be consistent with those proposed in the EMS98 scale [20].

In this study, both methods were applied to a stock of 14 masonry schools, selected as prototypes of Italian school masonry buildings and described in §2. The assumptions on which the two methods are based are briefly recalled in §3, while the main aim of this contribution, which is the critical review and comparative application of the two methods, is presented in §4 by adopting – when possible – analogous hypotheses to estimate the seismic fragility of the schools under examination. Moreover, as some of the selected schools had been hit by the 2016-17 Central Italy earthquake sequence, the evidence of the real response allows some considerations on the reliability of the methods to be provided (§5).

## 2 DESCRIPTION OF THE ANALYZED PROTOTYPE SCHOOLS

The stock analyzed in the following is composed of 14 school buildings selected from three regional databases provided by the University of Naples and Genoa (database A) [21], the University of Padua (database B) [22] and the University of Trieste (C) [23]. Database A [21] includes school buildings from various areas of Central Italy; it groups data collected during support activity made by the ReLUIS consortium and DPC [24], requested by the Reconstruction Commissioner, nominated after the 2016/2017 Central Italy earthquake. Instead, database B and C refer to the data collected in the municipal area of Padua (B) and in the regional area of Friuli-Venezia Giulia (C). Database A, B and C contain 54, 25 and 92 masonry schools, respectively.

The 14 school buildings extracted from these databases were identified to be representative of Italian masonry schools. They were used within the MARS project – Task 4.7 [17] to derive fragility curves representative of sub-types with homogeneous seismic behavior, adopting them as “prototype buildings”.

The taxonomy for identifying these sub-types is based on the data available in the inventory set by the Italian Ministry of Education dated to 2005, namely: structural material (e.g.,

reinforced concrete, masonry, steel) and seismic resistant system (e.g., frame, shear walls); number of stories (i.e., 1,2,3, >4); plan area (i.e., <500 m<sup>2</sup>, 500-1000 m<sup>2</sup>, 1000-2000 m<sup>2</sup>, 2000-5000 m<sup>2</sup>, and >5000m<sup>2</sup>); diaphragm type (e.g., concrete slab with clay units, wooden floor); and roof type (i.e., flat, inclined, or mixed). Starting from this inventory, specific sub-types were defined to cover most of the Italian school building asset. In fact, as shown in Figure 1, the Italian URM school stock is mostly represented by low structures (mainly 2-story), with limited floor area (in most cases < 1000 m<sup>2</sup>), and mainly built before 1975.

These criteria addressed the choice of the 14 prototype schools. Table 1 gives an overview of the analyzed set in terms of construction age, plan shape, plan gross area, and inter-story height; nine schools date back to 1945, while the 65% of the stock is characterized by two floors, to better represent the national asset. Each school is identified by an alphanumeric ID, while the database from which the school was extracted is indicated in brackets.

While other literature works are dedicated to derive fragility curves representative the overall URM school taxonomy [25], as already specified in §1, this paper focuses on their derivation by explicitly referring to the original features of each prototype school (referred as the “as it is state” in the following): this is to facilitate a more accurate comparison between the two methods adopted in the paper and briefly recalled in §3.

ID School	Age	N. floors	Inter-story height [m]	Plan configuration	Plan gross area [m <sup>2</sup> ]
S1 (A)	Before 1919	3	NA	Elongated rectangular	< 500
S2 (B)	Before 1919	2	5.8 – 5.4	U-shape	> 2000
S3 (A)	Before 1919	2	NA	Cloister	1000-2000
S4 (A)	Before 1919	3	NA	C-shape	1000-2000
S5 (A)	1921-1945	2	4.4	Elongated rectangular	500-1000
S6 (A)	1921-1945	2	4.5 – 3.5	Rectangular	< 500
S7 (C)	1921-1945	2	4.6	Rectangular	< 500
S8 (C)	1921-1945	2/3	4.1 – 4.1 – 7.3/6.5	C-shape	1000-2000
S9 (A)	1921-1945	2	4.3 – 4.5	T-shape	500-1000
S10 (B)	1946-1960	2	3.15	L-shape	1000-2000
S11 (A)	1946-1960	2	3.0 – 2.9	Rectangular	< 500
S12 (C)	1946-1960	2	3.8	Rectangular	< 500
S13 (A)	1961-1975	1	3.5	Squared	< 500
S14 (A)	After 1976	1	3.0	Squared	< 500

Table 1. General data of examined prototype school buildings (NA stands for Not Available).

Figure 2 shows, for some prototype schools, a view of the plan, together with photos aimed to provide a general overview of the building. The variety of plans confirms what already introduced in §1 about the recurrence of irregular shapes.

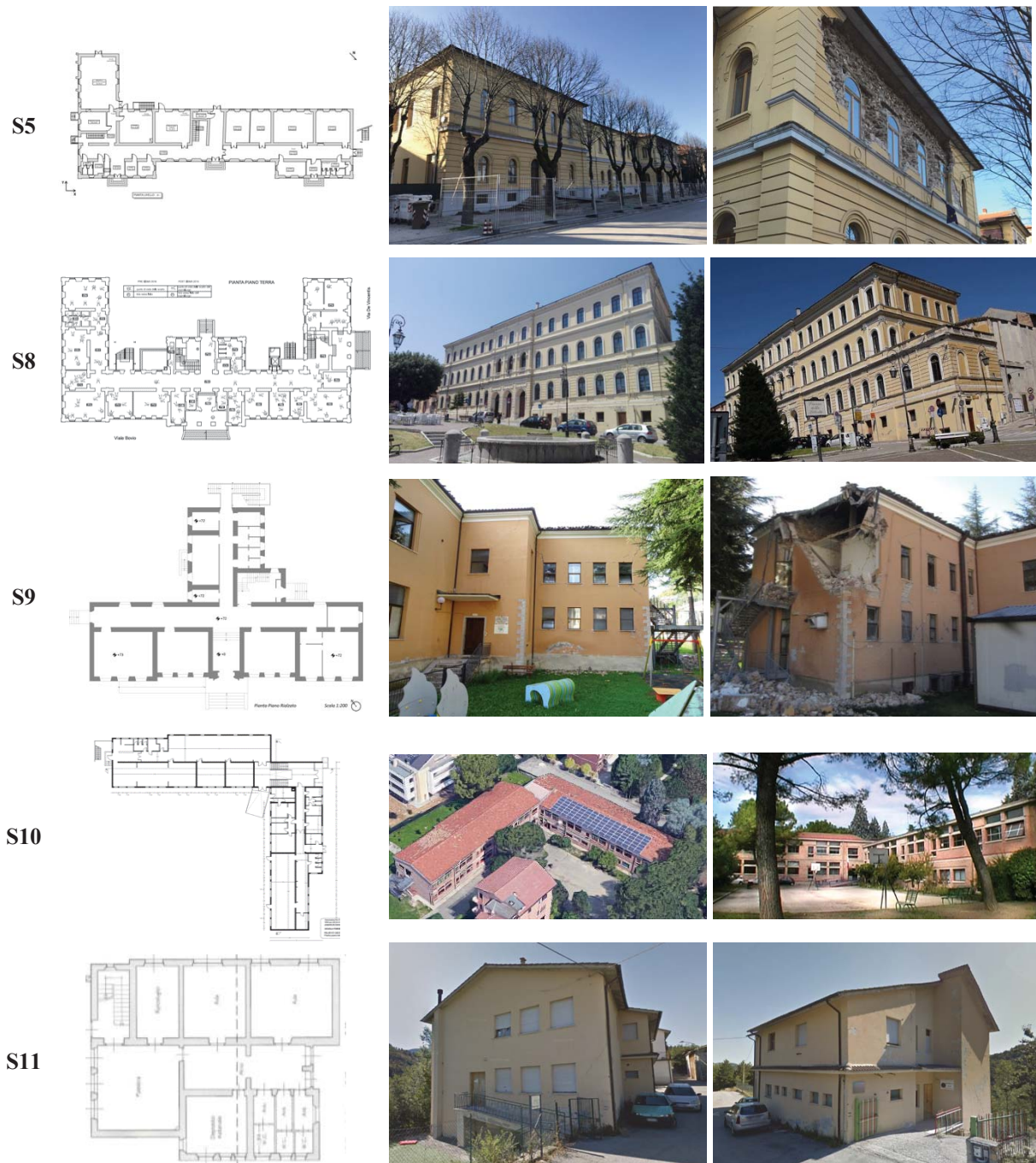


Figure 2. Plan shape and photos of some analyzed prototype schools.

For each prototype school, the basic data required for their typological and constructive characterization, as well as for the application of the two examined methods were collected, such as: the masonry type; the type of intermediate floors and roof; the resistant area for each story (in both directions); and the systemic presence of structural details, such as the presence of reinforced concrete (r.c.) ring beams or steel tie rods. Masonry type resulted quite heterogeneous. Conversely, intermediate floors was mainly ascribable to concrete slab with hollow clay blocks.



ID School	Resistant area [%]		Masonry type	Floor diaphragms	Roof	Structural Details
	X	Y				
S1	2.9	9.7	Solid bricks and lime mortar	Wooden floor	Wooden roof	Neither ring beams nor tie-rods systematic
S2	5.7 5.1	4.3 4.1	Solid bricks and lime mortar	r.c. slab	Wooden roof	r.c. ring beams
S3	9.7	8.0	Rubble stone	Vaults / Vaults with steel beams / r.c. slab with hollow clay blocks	Wooden roof	Partial presence of tie rods
S4	8.9 8.8 8.3	6.6 5.5 5.5	Solid bricks and lime mortar	Vaults	Wooden roof	Neither ring beams nor tie-rods systematic
S5	12.0 7.4	11.0 5.9	Rubble stone	Vaults with steel beams / r.c. slab with hollow clay blocks	Concrete slab with hollow clay blocks	r.c. ring beams along the perimeter of the roof
S6	6.9 7.6	4.2 4.3	Solid bricks and lime mortar	Concrete slab with hollow clay blocks	Concrete slab with hollow clay blocks	Neither ring beams nor tie-rods systematic
S7	5.9 5.9	4.8 4.6	Rubble stone with courses made by solid bricks	Concrete slab with hollow clay blocks / wooden floor / r.c. slab	Concrete slab with hollow clay blocks	r.c. ring beams
S8	5.4 5.0 6.8	6.9 5.6 8.7	Stone ashlar well-arranged	Concrete slab with hollow clay blocks / wooden floor	Wooden roof	r.c. ring beams on the first floor
S9	10.2 9.1	7.7 6.6	Stone ashlar well-arranged	Concrete slab with hollow clay blocks	Concrete slab with hollow clay blocks	r.c. ring beams along the perimeter of the roof
S10	2.7	1.9	Solid bricks and lime mortar	Concrete slab with hollow clay blocks	Concrete slab with hollow clay blocks	r.c. ring beams
S11	9.4 9.8	8.8 9.4	Simple stone with courses made by solid bricks	Concrete slab with hollow clay blocks	Concrete slab with hollow clay blocks	r.c. ring beams
S12	7.0	4.1	Solid bricks and lime mortar	Concrete slab with hollow clay blocks	Concrete slab with hollow clay blocks	r.c. ring beams
S13	3.7	3.7	Hollow blocks with cement mortar	Concrete slab with hollow clay blocks	Concrete slab with hollow clay blocks	r.c. ring beams
S14	Na	Na	Regular masonry	Rigid floor	Rigid floor	Neither ring beams nor tie-rods systematic

Table 2. Typological and constructive features of analyzed prototype schools.

## 2.1 Mechanical parameters adopted for prototype schools

For the application of the methods referred to in §3, the range of variation of the mechanical parameters of the masonry must be defined, in particular: the shear strength ( $\tau_0$ ), the masonry compressive strength ( $f_c$ ), and the tangential modulus of elasticity ( $G$ ). Since for most cases, direct mechanical characterization data were not available, reference values (plausible for the masonry types under examination) were assumed according to literature data ([26], [27], [28],



[29], [30], [31]). More specifically, the intervals recommended in the Italian Technical Code [32] were taken as reference. In particular, this Code provides firstly a basic range of values representative for a masonry that doesn't strictly follow the rules of thumbs (Table C8.5.I in [32]). Then corrective coefficients, which in most cases lead to an increase to the basic values, are proposed too (Table C8.5.II in [32]) with the aim of accounting for specific features which may influence the response of the masonry ([27], [33]), such as good quality mortar; good transversal connection between leaves; the presence of courses aimed to improve the horizontality of layers. The list of such corrective coefficients is summarized in Table 3 for sake of completeness.

Correction coefficient for the state of the art	Masonry Types							
	A	B	C	D	E	F	G	H
<b>Good quality mortar</b>	1.5	1.4	1.3	1.5	1.6	1.2	( <sup>b</sup> )	1.2
<b>Courses or borders <sup>a</sup></b>	1.3	1.2	1.1	1.2	-	-	-	-
<b>Transverse connections <sup>a</sup></b>	1.5	1.5	1.3	1.3	1.2	1.2	1.3 ( <sup>b</sup> )	-

<sup>a</sup> Correction coefficient relate solely to strength parameters

<sup>b</sup> "Good mortar" corresponds to a mortar with an average compressive strength ( $f_{mj}$ ) greater than 2 MPa. In this case the corrective coefficient can be set equal to  $f_{mj}^{0.35}$  ( $f_{mj}$  in Mpa).

Legend of masonry types: A – Random rubble stone masonry (pebbles, erratic, irregular stone); B – Uncut stone masonry with facing walls of irregular thickness; C – Ashlar masonry with good bonding; D – Irregular soft stone masonry (tuff, limestone, etc.); E – Regular soft stone masonry (tuff, limestone, etc.); F – Dressed rectangular stone masonry with no-soft stone; G – Solid bricks with lime mortar; H – Hollow blocks with cement mortar

Table 3. Correction coefficient for different types of masonry as proposed in [32].

Following this approach, for each school, the most plausible ranges of mechanical parameters were adopted. Smaller intervals of variation correspond to higher level of knowledge (see for example S9 and S5 in Figure 3). Conversely, in case of scarce data, the lack of knowledge lead to a higher residual uncertainty (i.e., a larger range of variation of the parameters). In particular, the highest range of variation was defined as follows (see for example S6 in Figure 3): the minimum value corresponds to the minimum proposed in Italian Technical Code [32]; the maximum value corresponds to the maximum proposed in the code, to which all the possible corrective coefficients were applied. The mechanical parameters of each school building used for the application of the analytical-mechanical models are reported in Table 4.

ID School	Specific feature of the masonry types of the school	fc [MPa]	$\tau_0$ [MPa] (min- max)		G [MPa] (min-max)	
		MEAN	MIN	MAX	MIN	MAX
<b>S1</b>	Low quality of mortar joints and stone texture	2.4	0.035	0.091	320	480
<b>S2</b>	NA	2.6	0.05	0.253	400	900
<b>S3</b>	NA	2.0	0.032	0.126	344	858
<b>S4</b>	Good mortar	2.6	0.075	0.253	600	900
<b>S5</b>	Low quality of mortar joints and stone texture	2.0	0.0245	0.0357	272	384
<b>S6</b>	NA	2.4	0.05	0.253	400	900
<b>S7</b>	Brick courses	2.4	0.043	0.072	346	492
<b>S8</b>	NA	2.7	0.056	0.074	500	660
<b>S9</b>	Good mortar and good transversal connection	3.4	0.0945	0.125	650	858
<b>S10</b>	NA	2.7	0.05	0.253	400	900
<b>S11</b>	Brick courses	2.9	0.062	0.106	500	858
<b>S12</b>	Good mortar	4.8	0.075	0.195	600	900
<b>S13</b>	NA	6.0	0.08	0.204	875	1680
<b>S14</b>	NA	2.6	0.05	0.253	400	900

Table 4. Mechanical parameters adopted for each school building (NA stands for Not Available).

Young's modulus was conventionally assumed to be three times the shear modulus ( $G$ ). Due to the limited influence of the masonry compressive strength in case of low-moderate axial load acting on walls (as usually the case of existing buildings), it was assumed deterministic and equal to the mean value of the range proposed in Italian Code [32] .

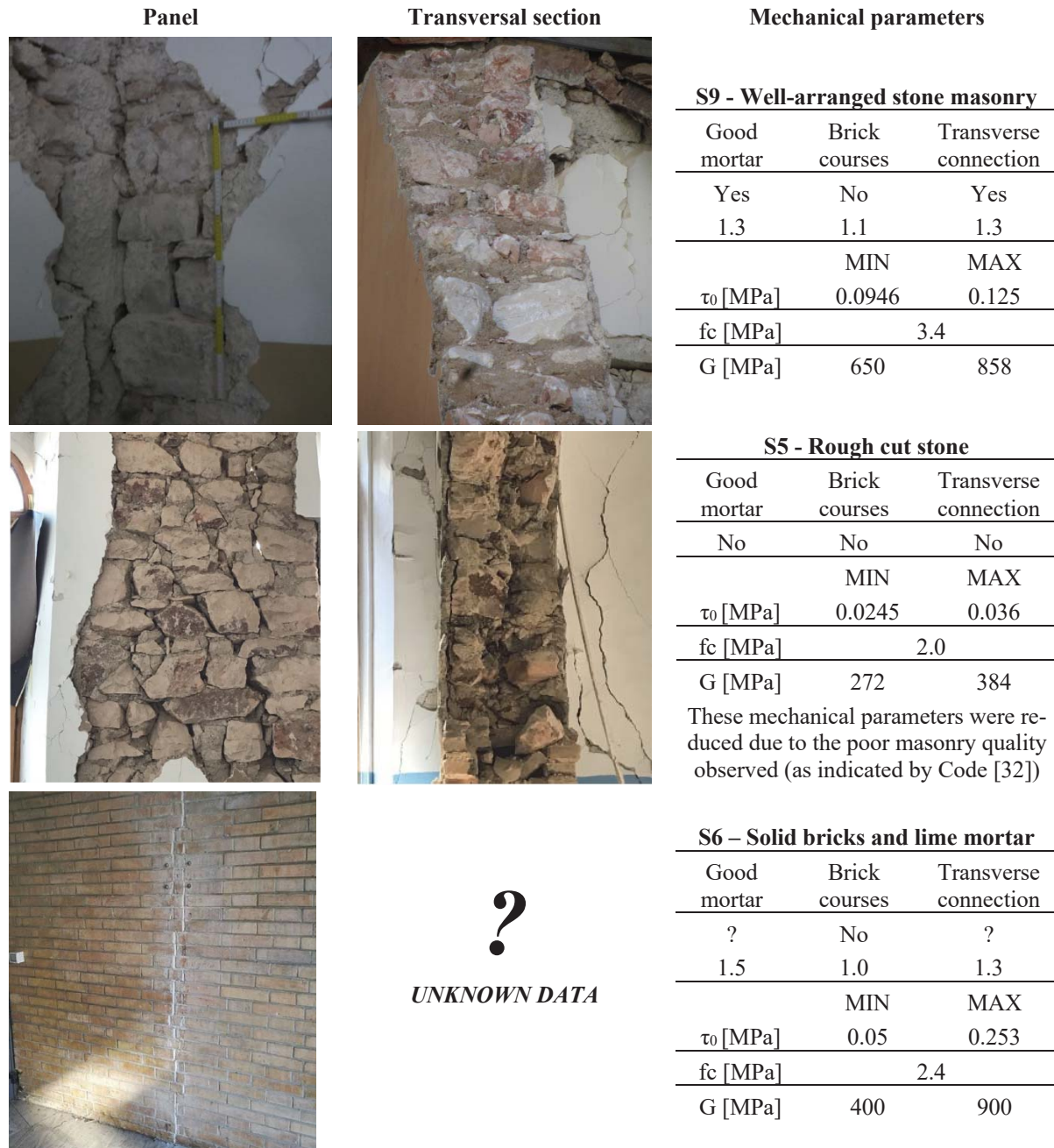


Figure 3. Frontal view and transversal section of masonry types of some prototype schools and final range of variation adopted for mechanical parameters.

### 3 BRIEF MENTION OF ANALYTICAL-MECHANICAL METHODS USED

#### 3.1 Mechanics-based modelling procedure *Vulnus*

The first simplified modelling procedure applied to the selected prototype schools was the mechanics-based approach developed at the University of Padova, which has been already

effectively applied to different territorial areas (i.e., from an urban area [34] to a national scale [18]). The approach is based on the simplified mechanical modelling procedure *Vulnus 4.0* [35] [36], which allows fragility assessment of unreinforced masonry buildings (URM) to be carried out considering both in-plane (IP) and out-of-plane (OOP) mechanisms, together with an index of the structural quality from 2<sup>nd</sup> level GNDT form [37]. The analysis of a URM building provides three indexes:

- $i_1$ , expressing the ratio between the IP shear resistance and the weight of the building for the weakest plan direction;
- $i_2$ , expressing the susceptibility to OOP mechanisms (both overturning and flexural failures), through the implementation of linear kinematic analyses;
- $i_3$ , quantifying vulnerability factors which affect the structural behavior (e.g., irregularity in elevation).

Then, the indexes are combined through fuzzy set theory, obtaining three fragility curves (derived as log-normal cumulative probability functions): one expressing the most probable distribution, called *white*, a lower- and an upper-bound. The fragility analysis of prototype schools was carried out referring to *white* curves. The resulting fragility refers to a medium-severe damage level (DL2-3), intermediate DS between 2 (given by trigger of OOP mechanisms) and 3 (given by IP global shear failure), according to the European macro-seismic scale (EMS98) [20].

Each DL2-3 curve was then extended to five fragility curves, from DL1 (slight damage) to DL5 (complete collapse), through the calibration of a fragility model proposed in [19], based on a previously presented macro-seismic model from the literature [38].

Figure 4 synthetically summarizes the basics of the procedure. For further details on the procedure, please refer to [1].

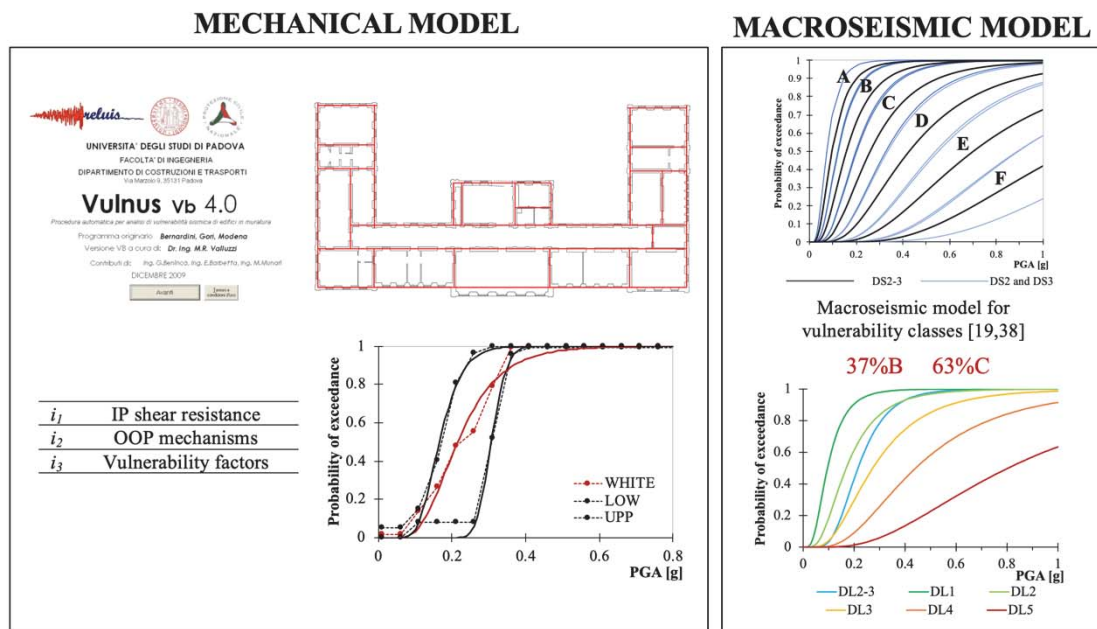


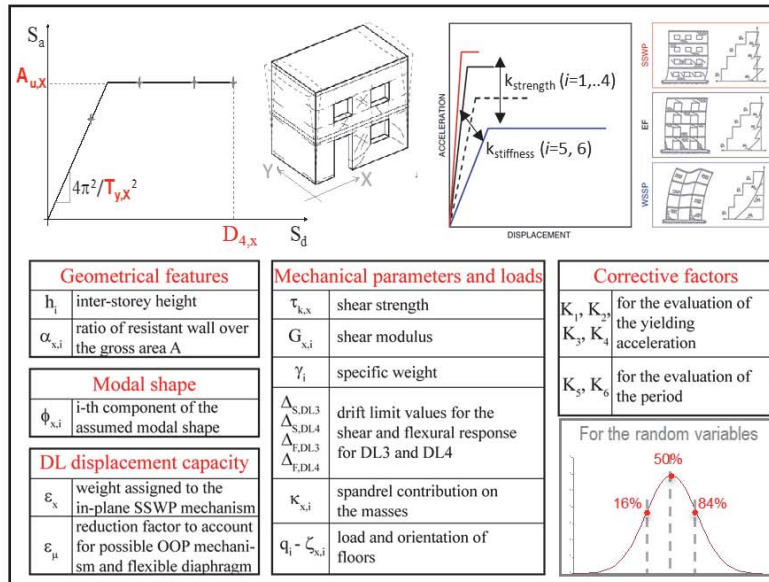
Figure 4. Basics of the *Vulnus* procedure.

### 3.2 DBV– *Masonry* model

The second simplified modelling procedure applied to the selected prototype schools was the mechanics-based approach developed at the University of Genoa [19].

The original approach was developed to derive fragility functions exclusively referring the global behavior of URM buildings associated to the in-plane walls response. The model firstly defines the capacity curve representative of the structural seismic response based on three variables (as in Figure 5): 1) the pseudo-elastic period of the structure  $T_y$ ; 2) the spectral acceleration at yielding  $A_y$  (equal to the ultimate one  $A_u$ , as no hardening is assumed); 3) the displacement capacity (associated to DL3 and DL4). The evaluation of these variables requires the definition of a limited number of mechanical and geometrical parameters, together with the assumption of a fundamental modal shape and the attribution of specific corrective factors ( $K_i$ ), aimed to account for the effects induced by the large set of constructive and morphological details that usually characterize existing buildings. The analytical formulation basically makes reference to the Strong-Spandrels Weak-Piers (SSWP) behavior, thus under the simplified assumption, for the evaluation of the overall base shear, that all masonry piers fail at the same time. Then, some of the aforementioned factors ( $K_i$ ) aims to correct this estimate in order to account for other possible behavior (like the Weak-Spandrels Strong-Piers – WSSP – or intermediate) induced by the lack of tie-rods and r.c. ring beams, or by the poor quality of spandrel elements (see [19] for further details). Once computed the capacity curve, the nonlinear static procedure based on the use of over-damped spectra [39] is adopted to compute the value of the IM that produces the attainment of DLs ( $IM_{DL}$ ). To this aim, proper rules are introduced to define the intermediate DLs on the capacity curve (i.e., DL1 and DL2) and the corresponding equivalent damping values ( $\xi_{DL}$ ) are evaluated. Finally, for the uncertainty propagation, various contributions are considered [19] and in particular the uncertainty associated to the structural capacity is computed by using the response surface method [40]. Figure 5 illustrates the basics of the method.

### CAPACITY CURVE



### FRAGILITY CURVE

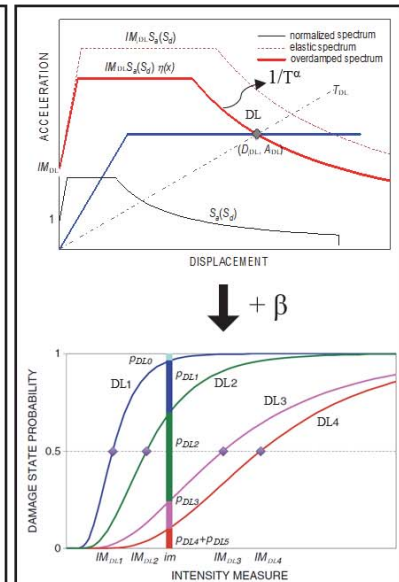


Figure 5. Basics of DBV-masonry model.

Starting from the original proposal of the model [19], within the MARS project as briefly summarized in the following, the authors from the University of Genoa made further refinements of the method that mainly concern, on the one hand, the estimate of the DLs displacement capacity, and, on the other hand, the evaluation of  $IM_{DL}$ .



As for the first issue, specific coefficients ( $\varepsilon_{\mu}$ ) aimed to limit the displacement capacity to introduce, even if in a simplified way, the possible activation of out-of-plane (OOP) mechanisms. At the current state of research, these coefficients only affect the DL3 and DL4 displacement capacity; their values vary from 0.4 to 0.9 and were defined on expert judgement, benefitting from the evidence of empirical fragility curves. They are applied when structural details, such as tie rods or r.c. ring beams, are absent, with values that as a function of both the masonry quality (more punitive in case of irregular masonry) and the floor types (more punitive in case of vaults or very flexible floors). Moreover, drift thresholds for defining DL3 and DL4 were updated and differentiated according to the masonry type to be consistent with the up-to-date experimental evidence ([28], [29], [31]) and the EMS98 damage levels (see Table 5).

As for the evaluation of  $IM_{DL}$ , a corrective factor was introduced to  $IM_{DL}$  in order to account for the approximation that nonlinear static procedures imply with respect to more refined methods, as nonlinear dynamic analyses. In particular, on basis of the work done by Marino et al. [41] a corrective factor equal to 1.45 was applied. The values of  $\xi_{DL}$  were computed according to Cattari and Lagomarsino [42] varying the structural details of the schools. Moreover, the ADSR spectral shape was refined including, in the branch usually adopted at constant velocity, the dependence on an  $\alpha$  coefficient (ranging from 1.1 to 1.4) to make it more consistent with evidence from actual recordings (see also [43]).

	Drift limit values for the shear (S) and flexural (F) response panels			
	S – DL3	S – DL4	F – DL3	F – DL4
<b>Min</b>	0.0025	0.0045	0.0035	0.007
<b>Max</b>	0.006	0.011	0.009	0.018

Table 5. Range of variation of drift thresholds adopted in *DBV-masonry* model.

#### 4 COMPARISON OF RESULTS

The results obtained from the two analytical-mechanical methods are compared as follows, in terms of both intermediate calculation ratios and parameters describing the fragility curves ( $IM_{DLi}$  and  $\beta_{DLi}$ ).

As for the first type of comparison, Figure 6 compares the parameter  $i_1$  from the *Vulnus* approach, to for the value of the base shear capacity normalized to the total mass from the *DBV-Masonry* model.

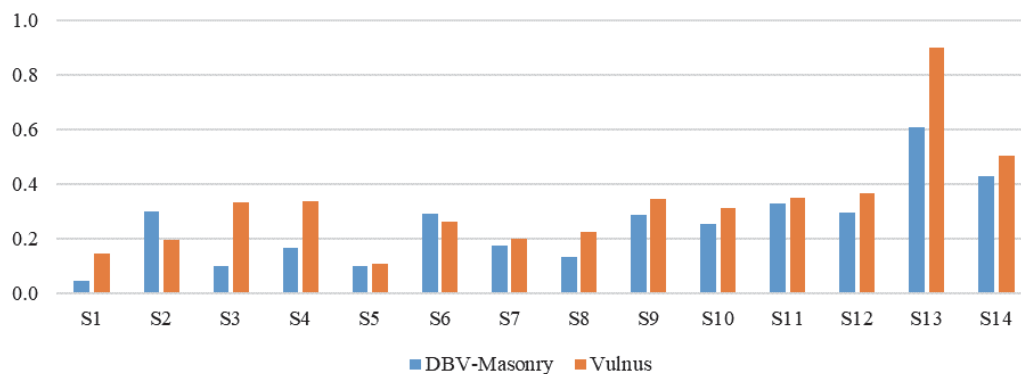


Figure 6. Comparison in terms of base shear normalized to total mass.

In general, a good correspondence is observed for most of schools. The highest difference, depicted in the cases S1, S3 and S4, is due to the strong penalization in the overall base shear capacity in the *DBV-Masonry* model given by the coefficients  $K_1$ ,  $K_2$ ,  $K_3$  and  $K_4$ , accounting



for poor structural details (e.g., the absence of tie rods and r.c. ring beams) and geometric irregularities. The complete set of corrective coefficients assigned to each school and applied to the overall base shear capacity are shown in Table 6. In the *Vulnus* procedure, in case of irregular buildings, the resistance area of walls is divided by a corrective factor (equal to 1.1) to consider the effects of the uneven distribution of stresses on the shear strength.

Ki factors of DBV- Masonry model	ID School													
	S1	S2	S3	S4	S5	S6	S7	S8	S9	S10	S11	S12	S13	S14
<b>K<sub>1</sub></b>	0.9	1.2	0.8	0.9	1.1	1.2	1.1	0.9	1	1.2	1.2	1.2	1.2	0.9
<b>K<sub>2</sub></b>	0.85	0.9	0.85	0.9	0.83	0.85	0.9	0.9	0.81	0.85	0.85	0.85	0.85	0.85
<b>K<sub>3</sub></b>	0.75	0.75	0.75	0.75	0.8	0.85	0.9	0.75	0.99	0.75	0.9	0.85	0.75	0.75
<b>K<sub>4</sub></b>	0.65	1	0.55	0.65	1	1	1	0.8	0.95	1	1	1	1	0.65

Table 6. Corrective factors used by DBV-Masonry model and applied to base shear capacity.

Figure 7 shows instead the comparison in terms of  $IM_{DLi}$  values. As recalled in §3.1, in the case of *Vulnus* approach, the value reported corresponds to a medium-severe damage level (DL2-3), whereas, in the case of the *DBV-Masonry* model, both values corresponding to DL2 and DL3 are reported separately. The comparison shows that in most cases the two models provide a good correspondence (such as for schools S1, S3, S4, S5, S9, S11 and S12), while in other cases the *DBV-Masonry* model provides greater median (less vulnerable structures) with respect to the *Vulnus* approach. This difference stems from the more significant role of the out-of-plane mechanisms, which are differently treated by the compared methods.

The values of the three indexes defined by the *Vulnus* approach are reported in Table 7; for schools with lower indexes  $i_2$ , also with respect to their  $i_1$  index, (i.e., structures more susceptible to OOP mechanisms) greater differences in the resulting  $IM_{DLi}$  values are found.

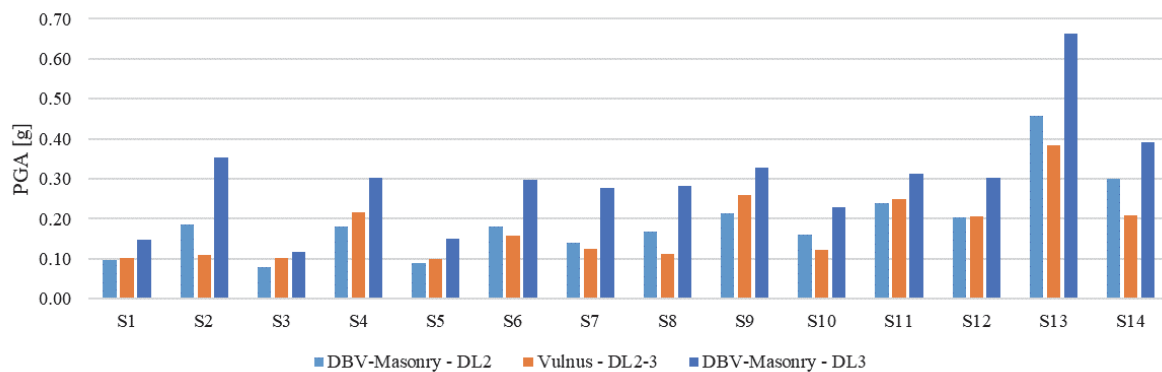


Figure 7. Comparison for the prototype schools in terms of median  $IM_{DLi}$  value (i.e., PGA in [g]).

Indexes Vulnus	Schools													
	S1	S2	S3	S4	S5	S6	S7	S8	S9	S10	S11	S12	S13	S14
<b>i1 [a/g]</b>	0.15	0.31	0.33	0.34	0.11	0.26	0.20	0.23	0.35	0.20	0.35	0.37	0.90	0.50
<b>i2 [a/g]</b>	0.16	0.10	0.09	0.27	0.14	0.18	0.15	0.12	0.31	0.11	0.30	0.20	0.36	0.19
<b>i3</b>	0.67	0.03	0.69	0.24	0.58	0.41	0.31	0.68	0.18	0.32	0.27	0.16	0.40	0.58

Table 7. Indexes obtained from *Vulnus* approach.

Indeed, in the *Vulnus* approach, the vulnerability of these schools is dominated by the activation of local mechanisms. Conversely, as described in §3.2, the *DBV-Masonry* model

includes the vulnerability associated to out-of-plane mechanisms only in a conventional way, by limiting the available global ductility.

Lastly, Figure 8 compares resulting fragility curves for some schools. As expected from the results illustrated in Figure 6 and Figure 7, for schools S9 and S11 the match of fragility curves is very good, while for schools S6 and S10 fragility curves derived from *Vulnus* approach are backward (describing a more vulnerable structure). This result is again mainly due to the different ways through which the two approaches treat the OOP mechanisms.

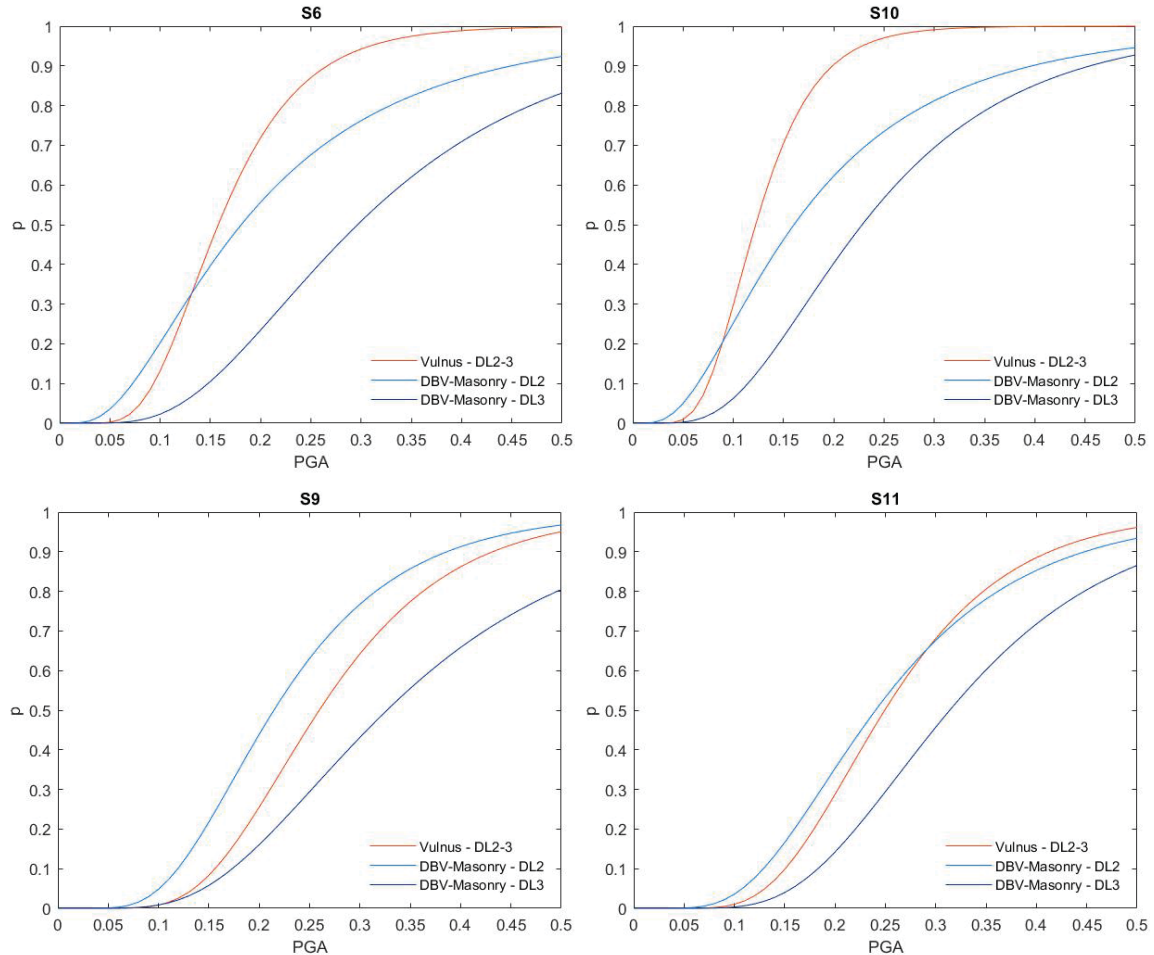


Figure 8. Comparison of fragility curves defined by DBV-Masonry (DL2 and DL3) and *Vulnus* approaches (DL2-3).

## 5 COMPARISON BETWEEN OBSERVED DAMAGE AND DPM ESTIMATED FROM FRAGILITY CURVES

As introduced in §2, some prototype schools were selected from those damaged and declared unusable after the seismic sequence that hit Central Italy in 2016/2017 [21]. Information on the actual damage of these schools was thereby available. These data are really valuable to preliminarily assess the reliability of the damage level estimated by fragility curves. Of course, a number of approximations were made to provide this comparison, since the aim of this study is far from an accurate simulation of the seismic response of these schools (e.g., made in other studies through refined 3D models and by performing nonlinear dynamic analyses [44]). Nevertheless, the comparison is useful in order to verify whether the damage predicted by fragility curves has the same order of magnitude of the observed damage; in addition, possible discrepancies might

emerge in the estimation of the consequences/losses when the fragility curves are then used for risk analyses scopes (e.g., [45]).



Figure 9. View of damaged schools S5, S9, and S11.

In order to make such a comparison, for each school an estimate is provided (Table 8) of the level of global damage observed and of the Peak Ground Acceleration that affected the structure ( $PGA_{2016/2017}$ ). The damage level was derived as part of the survey activities described in Di Ludovico et al. [24], based on a homogeneous approach which is consistent with the damage levels defined by the EMS98 scale [20]. The estimate of  $PGA_{2016/2017}$  is affected by more significant uncertainties. Only in one case (S9), the school, now demolished, was permanently monitored by the Italian Seismic Observatory of the Department of Civil Protection [46]. Thus, recorded data of the events that hit the school are available; in particular, the  $PGA_{2016/2017}$  associated to the most intense recorded seismic event (October 26<sup>th</sup>, 2016) is equal to 0.47g.

Conversely, in other cases, the maximum  $PGA_{2016/2017}$  value was derived from shake maps provided by INGV (Istituto Nazionale di Geofisica e Vulcanologia, INGV, <http://shake-map.rm.ingv.it/shake/index.html>). Attenuation laws and possible phenomena of amplification due to topography and stratigraphy, were considered, as well as third level seismic micro-zonation studies (MZ3), where available.

Specifically, for school S11, the PGA of the most significant event (August 24<sup>th</sup>, 2016) was defined equal to 0.30g, according to the shake maps provided by INGV. It was then multiplied by a coefficient equal to 1.2, in order to consider topographic amplification, consistently with Italian Code [47].

Concerning school S5, the PGA of the most severe event (October 26<sup>th</sup>, 2016) was derived from shake maps, equal to 0.15g. This school was subjected to strong phenomena of site effects, as confirmed by. Thus, a  $PGA_{2016/2017}$  equal to 0.23g was estimated. Further detailed numerical studies confirmed that the combination of structural vulnerability and amplification phenomena played a fundamental role in the response of this school [48].

ID School	Observed DL	Stratigraphic amplification	Topographic amplification	Estimated $PGA_{2016/2017}$ for computing the DPM from fragility curves [g]		
				Event	PGA from shake maps	Adopted PGA
S5	4	FA=1.45-1.63   Soil B	Plain	26/10/2016	0.15	0.23
S9	4	FA=1.37   Soil B	Slight slope	26/10/2016	0.47 (recorded)	0.47 (recorded)
S11	3	Soil B	Ridge	24/08/2016	0.30	0.36

Table 8. Estimated damage level and PGA for damaged prototype schools

The estimated  $PGA_{2016/2017}$  values were used to enter the fragility curves developed in §4 and then calculate the relative Damage Probability Matrix (DPM), and then the average damage level ( $\mu_d$ ) through the following expression:

$$\mu_D = \sum_{k=0}^5 p_k \cdot k \quad (1)$$

where  $p_k$  is the probability of reaching each damage grade  $k$  (from 1 to 5). As introduced in §3.2, the analytic-mechanical *DBV-Masonry* model allows fragility curves to be directly derived only for the first four damage levels. For the sake of comparisons, DL5 fragility curve was defined adopting a distance from DL4 curve consistent with the macroseismic model proposed by Lagomarsino and Giovinazzi [38] and adopted as reference also in the *Vulnus* model.

Figure 10 illustrates, for each school examined in this section, the fragility curves and the relative DPM; the vertical line in the graphs corresponds to the value of the  $PGA_{2016/2017}$  reported in Table 8.

In order to compare the average damage level ( $\mu_d$ ) with the observed damage, the continuous variable  $\mu_d$  shall be converted in a discrete number. To this aim, the binomial distribution was adopted [38], assuming that the upper bounds of each interval correspond to a probability of 0.5 in the associated cumulative distribution function. That leads to the conversion rule summarized in Table 9. The final values of the comparison are summarized in Table 10.

DLi	Conversion rule
1	$0.7 < \mu_d \leq 1.6$
2	$1.6 < \mu_d \leq 2.5$
3	$2.5 < \mu_d \leq 3.4$
4	$3.4 < \mu_d \leq 4.3$
5	$4.3 < \mu_d \leq 5$

Table 9. Criterion to convert the mean damage level into DLi discrete values.

Schools	Level of observed damage from real damage	Average damage level derived from fragility curves			
		Vulnus		DBV-Masonry	
		$\mu_D$	DL	$\mu_D$	DL
S5	4	3.67	4	3.21	3
S9	4	3.30	3	3.13	3
S11	3	2.87	3	2.78	3

Table 10. Comparison between observed and estimated damage levels from derived fragility curves.

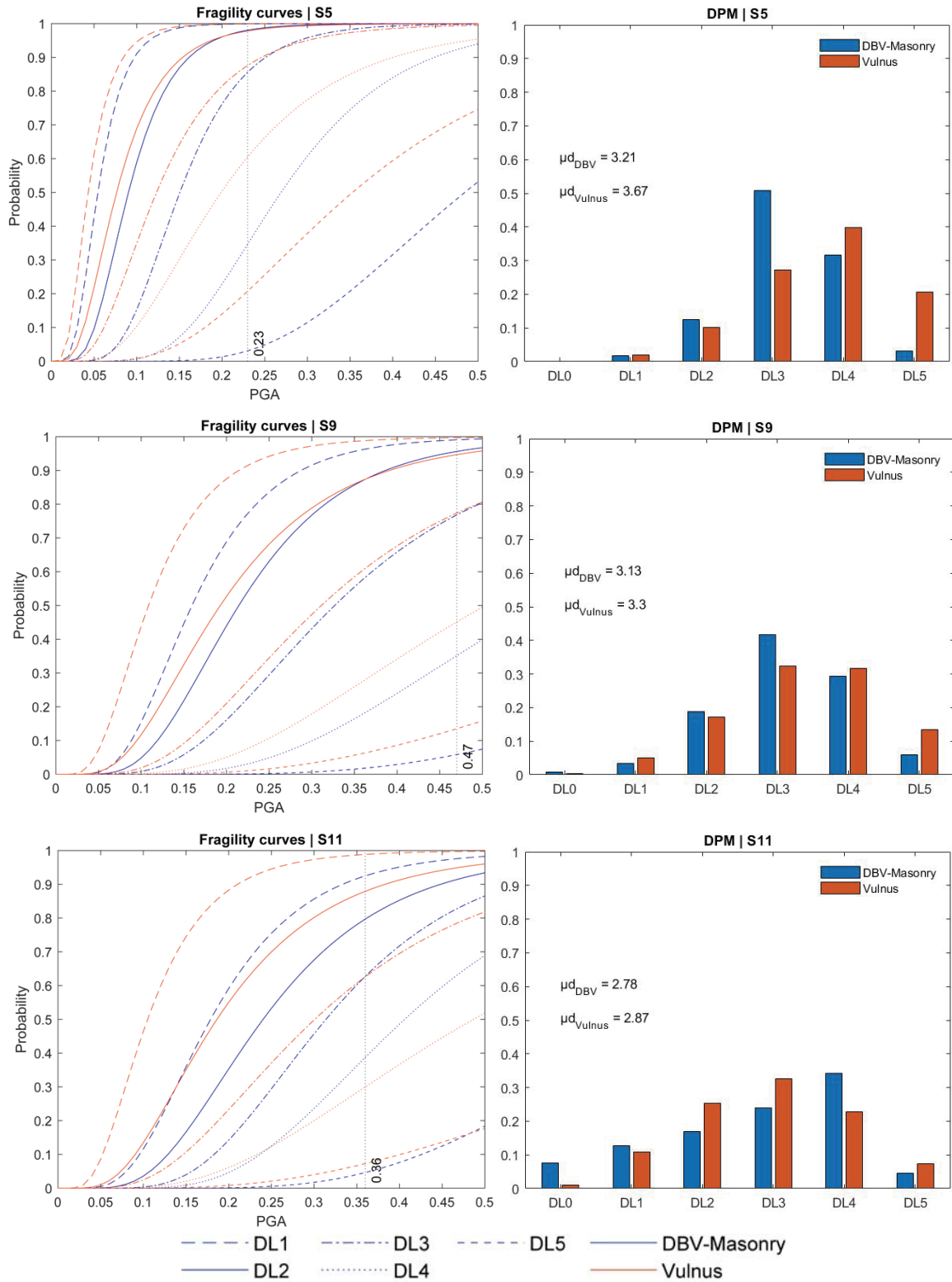


Figure 10. Comparison of fragility curves and DPM of damage prototype school buildings.

The comparison of results is satisfactory, in line with the general good correspondence discussed in §4.

In the case of school S5, the *DBV-Masonry* model slightly underestimates the damage level. In that case, the actual damage testified a clear dominance of the in-plane response of walls



(with very severe diagonal cracks in most piers of the first level, as shown in Figure 9) but also the activation of the out-of-plane response of part of the main façade. Thus, the aforementioned slight underestimation could be associated to the conventional way through which the *DBV-Masonry* model includes OOP mechanisms.

Concerning school S9, the results of both analytical-mechanical approaches slightly underestimate the actual damage level (i.e., the value of  $\mu_D$  is close to the lower threshold value for DL4); however, it is worth highlighting that the school suffered from damage accumulation phenomena [44], neglected by the derived fragility curves. In fact, although the  $PGA_{2016/2017}$  was associated to the most severe event, indeed some moderate damage already occurred due to the first shock (August 24<sup>th</sup>, 2016).

## 6 CONCLUSIONS

This paper has reported the comparison of results obtained from the application of two mechanical-analytical vulnerability models to a sample of 14 prototype schools, representative of the Italian school asset. In particular, the hybrid model based on the integrated use of mechanical and heuristic approach *Vulnus Vb 4.0-2009*, developed by the University of Padova, and the mechanical model *DBV-Masonry* developed by the University of Genoa were used. These vulnerability models aim at providing seismic vulnerability assessments of masonry buildings at territorial scale, to support seismic risk evaluations.

In this contribution, these approaches were applied to the selected prototype schools in their "as it is" configuration, to facilitate the comparison and without introducing the assumptions made necessary by the propagation of prototype buildings for the scopes of large scale assessment (as those addressed in MARS project illustrated in [17]).

The examined methods were compared in terms of derived fragility curves, as well as by analyzing intermediate parameters, such as the value of the base shear normalized to the total mass.

Results highlighted a good match between the two methods. The most relevant differences were found for buildings of which seismic vulnerability is potentially dominated by the trigger of local mechanisms; in these cases, the *DBV-Masonry* model, which takes into account the activation of out-of-plane mechanisms only conventionally, estimated a lower damage of the structure.

Lastly, the comparison between DPM estimated from fragility curves and observed damage has been provided for three schools of the sample, hit by the Central Italy earthquake. Results are promising and show a good capability of methods in forecasting the expected damage.

## ACKNOWLEDGEMENTS

The results presented in the paper were achieved in the national research project ReLUIS-DPC 2019 -2021 ([www.reluis.it](http://www.reluis.it)), supported by the Italian Civil Protection Department and, in particular, in the Work Package 4 (WP4 – “Seismic Risk Maps -MARS”, Coord. Proff. S. Lagomarsino and A.Masi). Moreover, the Authors thank the members of research units of UniNA (University of Naples Federico II - Coord. Prof. M.Di Ludovico) and UniTS (University of Trieste, Coord. Prof. N.Gattesco) for the data provided regarding prototype schools examined in the paper.

## REFERENCES

- [1] M. Di Ludovico, A. Digrisolo, C. Moroni, F. Graziotti, V. Manfredi, A. Prota, M. Dolce & G. Manfredi, Remarks on damage and response of school buildings after the Central Italy earthquake sequence. *Bull Earthquake Eng* **17**, 5679–5700, 2019. <https://doi.org/10.1007/s10518-018-0332-x>
- [2] M. Di Ludovico, A. Santoro, G. De Martino, C. Moroni, A. Prota, M. Dolce and G. Manfredi, Cumulative damage to school buildings following the 2016 central Italy earthquake sequence. *Bollettino di Geofisica Teorica ed Applicata* Vol. 60, n. 2, pp. 165-182, June 2019. DOI 10.4430/bgta0240
- [3] D. Gautam, R. Adhikari, R. Rupakhety and P. Koirala, An empirical method for seismic vulnerability assessment of Nepali school buildings. *Bull Earthquake Eng* **18**, 5965–5982, 2020. <https://doi.org/10.1007/s10518-020-00922-z>
- [4] H. Azizi-Bondarabadi, N. Mendes, P.B. Lourenço & N.H. Sadeghi, Empirical seismic vulnerability analysis for masonry buildings based on school buildings survey in Iran. *Bull Earthquake Eng* **14**, 3195–3229, 2016. <https://doi.org/10.1007/s10518-016-9944-1>
- [5] C. González, M. Niño & M.A. Jaimes, Event-based assessment of seismic resilience in Mexican school buildings. *Bull Earthquake Eng* **18**, 6313–6336, 2020. <https://doi.org/10.1007/s10518-020-00938-5>
- [6] D. D'Ayala, C. Galasso, A. Nassirpour, R.K. Adhikari, L. Yamin, R. Fernandez, D. Lo, L. Garciano and A. Oreta, Resilient communities through safer schools. *International Journal of Disaster Risk Reduction* Vol. 45, 2020. <https://doi.org/10.1016/j.ijdr.2019.101446>
- [7] UNISDR, Comprehensive School Safety, United Nations Office for Disaster Risk Reduction (UNDRR), 2014
- [8] WISS, Worldwide Initiative for Safe Schools - Vision: by 2030, Every School Will Be Safe, United Nations Office for Disaster Risk Reduction (UNDRR), 2013
- [9] A. Muñoz, M. Blondet, R. Aguilar, M. A. Astorga. Empirical fragility curves for Peruvian school buildings. *ERES 2007*. DOI 10.2495/ERES070261
- [10] N. Giordano, F. De Luca, A. Sextos, F. Ramirez Cortes, C. Fonseca Ferreira & J. Wu, Empirical seismic fragility models for Nepalese school buildings. *Natural Hazards*, 2020. <https://doi.org/10.1007/s11069-020-04312-1>
- [11] M. Yekrangnia, A. Bakhshi, M.A. Ghannad & M. Panahi, Risk assessment of confined unreinforced masonry buildings based on FEMA P-58 methodology: a case study—school buildings in Tehran. *Bull Earthquake Eng* **19**, 1079–1120, 2021. <https://doi.org/10.1007/s10518-020-00990-1>
- [12] N. Giordano, F. De Luca & A. Sextos, Analytical fragility curves for masonry school building portfolios in Nepal. *Bull Earthquake Eng* **19**, 1121–1150, 2021. <https://doi.org/10.1007/s10518-020-00989-8>
- [13] C. Michel, P. Hannewald, P. Lestuzzi, D. Fäh & S. Husen, Probabilistic mechanics-based loss scenarios for school buildings in Basel (Switzerland). *Bull Earthquake Eng* **15**, 1471–1496, 2017. <https://doi.org/10.1007/s10518-016-0025-2>

- [14] P. Hannewald, C. Michel, P. Lestuzzi, H. Crowley, J. Pinguet & D. Fäh, Development and validation of simplified mechanics-based capacity curves for scenario-based risk assessment of school buildings in Basel. *Engineering Structures* Vol 209, 2020. <https://doi.org/10.1016/j.engstruct.2020.110290>
- [15] Italian Civil Protection Department (2018) National Risk Assessment 2018. Overview of the potential major disasters in Italy. Updated December 2018
- [16] M. Dolce, A. Prota, B. Borzi, F. da Porto, S. Lagomarsino, G. Magenes, C. Moroni, A. Penna, M. Polese, E. Speranza, G.M. Verderame, G. Zuccaro, Seismic risk assessment of residential buildings in Italy. *Bull Earthquake Eng* , 2020. <https://doi.org/10.1007/s10518-020-01009-5>
- [17] A. Masi, S. Lagomarsino, M. Dolce, V. Manfredi & D. Ottonelli, Towards the updated Italian seismic risk assessment: exposure and vulnerability modelling. *Bull Earthquake Eng*, 2021. <https://doi.org/10.1007/s10518-021-01065-5>
- [18] M. Donà, P. Carpanese, V. Follador, L. Sbrogio, F. da Porto, Mechanics-based fragility curves for Italian residential URM buildings, *Bull Earthquake Eng* ,1–34, 2020. <https://doi.org/10.1007/s10518-020-00928-7>
- [19] S. Lagomarsino, S. Cattari, Fragility Functions of Masonry Buildings, in K. Pitilakis et al. (eds.), SYNER-G: Typology Definition and Fragility Functions for Physical Elements at Seismic Risk, Geotechnical, Geological and Earthquake Engineering 27, 2014. DOI 10.1007/978-94-007-7872-6\_5.
- [20] G. Grunthal, EMS98 - European Macroseismic Scale 1998, Conseil de l'Europe - Cahiers du Centre Européen de Géodynamique et de Séismologie, Luxemburg, 1998.
- [21] D. Ottonelli, S. Alfano, S. Cattari, M. Di Ludovico and A. Prota, Analisi statistiche dei dati tipologici e di danno delle scuole in muratura danneggiate dal terremoto del Centro Italia 2016/2017. *XVIII Convegno ANIDIS, L'ingegneria Sismica in Italia*. Settembre 15-19, Ascoli Piceno, Italia, 2019. (in Italian)
- [22] E. Saler, P. Carpanese, V. Pernechele and F. da Porto, Priority-ranking procedure to assess seismic vulnerability of school buildings at territorial scale. *XVIII Convegno ANIDIS, L'ingegneria Sismica in Italia*. Settembre 15-19, Ascoli Piceno, Italia, 2019.
- [23] N. Gattesco, I. Boem, Classificazione degli edifici scolastici in muratura in Friuli-Venezia Giulia, finalizzata alla costruzione di modelli di rischio. *XVIII Convegno ANIDIS, L'ingegneria Sismica in Italia*. Settembre 15-19, Ascoli Piceno, Italia, 2019. (in Italian)
- [24] M. Di Ludovico, C. Moroni, D. Abruzzese, A. Borri, B. Calderoni, S. Caprili, A. Dall'Asta, F. da Porto, G. De Martino, G. de Matteis, B. Ferracuti, S. Lagomarsino, G. Magenes, A. Mannella, A. Marini, A. Masi, C. Mazzotti, C. Nuti, A. Santoro, L. Sorrentino, E. Spacone, G.M. Verderame, A. Prota, M. Dolce, G. Manfredi, Il contributo di ReLUIIS nelle attività di supporto all'emergenza sismica del Centro Italia 2016. *XVIII Convegno ANIDIS, L'ingegneria Sismica in Italia*. Settembre 18-21, Pistoia, Italia, 2017. (in Italian)
- [25] E. Saler, V. Follador, P. Carpanese, F. da Porto, Fragility assessment of the Italian masonry school building asset for risk evaluation at national scale. *COMPDYN*, 28–30 June 2021, Streamed from Athens, Greece, 2021.

- [26] N. Augenti, F. Parisi, E. Acconcia, MADA: online experimental database for mechanical modelling of existing masonry assemblages *Proc. of the 15th World Conference on Earthquake Engineering*, Lisbon, 2012.
- [27] M. Krzan, S. Gostic, S. Cattari and V. Bosiljkov, Acquiring reference parameters of masonry for the structural performance analysis of historical building, *Bull. Earth. Eng.*, 13(1), 203-236, 2015.
- [28] F. Vanin, D. Zaganelli, A. Penna and K. Beyer, Estimates for the stiffness, strength and drift capacity of stone masonry walls based on 123 quasi-static cyclic tests reported in the literature. *Bull. Earth. Eng.*, 15(12), 2017, 5435-5479
- [29] P. Morandi, L. Albanesi, F. Graziotti, T. Li Piani, A. Penna and G. Magenes, Development of a dataset on the in-plane experimental response of URM piers with brick and blocks, *Construction and Building Materials*, 190, 593-611, 2018.
- [30] S. Boschi, L. Galano and A. Vignoli, Mechanical characterization of Tuscany masonry typologies by in situ tests, *Bull Earthquake Eng.*, 17(1), 413-438, 2019.
- [31] A. Rezaie, M. Godio and K. Beyer, Experimental investigation of strength, stiffness and drift capacity of rubble stone masonry walls, *Construction and Building Materials*, 251, 118972, 2020.
- [32] MIT 2019, Ministry of Infrastructures and Transportation, Circ. C.S.LI.PP. No. 7 of 21/1/2019. Istruzioni per l'applicazione dell'aggiornamento delle norme tecniche per le costruzioni di cui al Decreto Ministeriale 17 Gennaio 2018. G.U. S.O. n.35 of 11/2/2019. (In Italian)
- [33] A. Borri, M. Corradi, G. Castori, A. De Maria, A method for the analysis and classification of historic masonry, *Bull Earthquake Eng.*, 13(9), 2647-2665, 2015.
- [34] M. Vettore, M. Donà, P. Carpanese, V. Follador, F. da Porto and M.R. Valluzzi, A Multilevel Procedure at Urban Scale to Assess the Vulnerability and the Exposure of Residential Masonry Buildings: The Case Study of Pordenone, Northeast Italy, *Heritage*. 3 1433–1468, 2020. <https://doi.org/10.3390/heritage3040080>.
- [35] A. Bernardini, R. Gori, C. Modena, M.R. Valluzzi, *Vulnus 4.0 - Automatic procedure for the seismic vulnerability analysis of masonry buildings*, 2009. (in Italian)
- [36] M.R. Valluzzi, *User Manual of Vulnus 4.0*, original program by Bernardini Gori A, Modena R C, Vb version edited by Valluzzi MR, with contributions by Benincà G, Barbetta E, Munari M, 2009. (in Italian)
- [37] GNDDT-SSN, *Scheda di esposizione e vulnerabilità e di rilevamento danni di primo livello e secondo livello (muratura e cemento armato)*, (1994). (in Italian)
- [38] S. Lagomarsino, S. Giovinazzi, Macro seismic and mechanical models for the vulnerability and damage assessment of current buildings, *Bull Earthquake Eng.* 4 415–443, 2006. <https://doi.org/10.1007/s10518-006-9024-z>.
- [39] S.A. Freeman, The capacity spectrum method as a tool for seismic design. In: *Proceedings of 11th European conference of earthquake engineering*, Paris, France, 1998.
- [40] L.C. Pagnini, R.S. Vicente, S. Lagomarsino, H. Varum H, A mechanical model for the seismic vulnerability assessment of old masonry buildings. *Earthquake and Structures* 2(1):25–42, 2011.

- [41] S. Marino, S. Cattari, S. Lagomarsino, Are the nonlinear static procedures feasible for the seismic assessment of irregular masonry buildings? *Engineering Structures*, 200, 109700, 2019.
- [42] S. Cattari and S. Lagomarsino, “Masonry structures,” 151–200. in T. Sullivan and G. M. Calvi (ed.) *Developments in the Field of Displacement Based Seismic Assessment*. IUSS Press and EUCENTRE, Pavia, Italy, p 524, ISBN, 978-88-6198-090-7, 2013.
- [43] C. Smerzini, C. Galasso, I. Iervolino, R. Paolucci, Ground motion record selection based on broadband spectral compatibility, *Earthquake Spectra*, 30(4):1427-1448, 2014.
- [44] A. Brunelli, F. de Silva, A. Piro, F. Parisi, S. Sica, F. Silvestri and S. Cattari, Numerical simulation of the seismic response and soil–structure interaction for a monitored masonry school building damaged by the 2016 Central Italy earthquake. *Bull Earthquake Eng* . 19, 1181–1211, 2021. <https://doi.org/10.1007/s10518-020-00980-3>
- [45] A.W. Coburn, R.J.S. Spence, *Earthquake protection*, 2nd edn. Wiley, 2002.
- [46] S. Cattari, S. Degli Abbati, D. Ottonelli, C. Marano, G. Camata et al, Discussion on data recorded by the Italian structural seismic monitoring network on three masonry structures hit by the 2016–2017 Central Italy earthquake. *COMPDYN*, 24–26 June 2019, Crete, Greece, DOI 10.7712/120119.7044.20004.
- [47] NTC (2018) *Norme Tecniche per le Costruzioni*. DM 17/1/2018, Italian Ministry of Infrastructure and Transportation, G.U. n. 42, 20 February 2018, Rome, Italy (in Italian)
- [48] S. Cattari, S. Alfano, A. Brunelli, M. Angiolilli & F. De Silva, Investigating the combined role of the structural vulnerability and site effects on the seismic response of a URM school hit by the central Italy 2016 earthquake, 2021. *Submitted to Structures*.



## ROLE OF DESIGN LEVEL AND INFILL ARRANGEMENT ON THE SEISMIC FRAGILITY CURVES OF ITALIAN RC EXISTING BUILDINGS

A. Masi<sup>1</sup>, V. Manfredi<sup>1</sup>, G. Nicodemo<sup>1</sup>, A. Digrisolo<sup>1</sup>

<sup>1</sup> University of Basilicata – School of Engineering – Viale dell'Ateneo Lucano, 10 – 85100 Potenza – Italy

{angelo.masi, vincenzo.manfredi, giuseppe.nicodemo, andrea.digrisolo}@unibas.it

---

### Abstract

*Assessing the seismic vulnerability of existing buildings is a fundamental step in order to define mitigation programs in prone earthquake areas. In Italy, in 2019 the National Department of Civil Protection supported an ongoing research project involving its “Center of Competence” on seismic risk, ReLUIIS (Network of University Laboratories for Earthquake Engineering), with the cooperation of Eucentre (European Centre for Training and Research in Earthquake Engineering) to update the 2018 version of the National Risk Assessment. In this context, new fragility curves are being derived by using different approaches, whose results will be properly combined. In the paper, the purposely set up methodology for deriving analytical fragility curves through Non-Linear Dynamic Analyses (NLDAs) has been described. Further, results relevant to some Italian Reinforced Concrete (RC) building types have been shortly presented and analyzed, emphasizing the role of some key parameters affecting seismic vulnerability such as design level and infill arrangement.*

**Keywords:** RC existing buildings, seismic vulnerability assessment, non-linear dynamic analyses, fragility curves

---

## 1 INTRODUCTION

Past earthquakes have clearly pointed out the high level of seismic risk in Italy. According to the 2018 National Risk Assessment (NRA) [1, 2] released by the Department of Civil Protection (DPC), seismic risk mainly depends on the high vulnerability of the existing building stock, which was mostly built before the seismic classification of large part of the Italian territory and, consequently, without seismic rules. Seismic risk analyses in the 2018 NRA were carried out through the “Italian Risk Maps” (IRMA) platform [3], by combining the results obtained by different research units (RUs) belonging to two “Centers of Competence” of DPC, such as ReLUIIS (Network of University Laboratories for Earthquake Engineering) and Eucentre (European Centre for Training and Research in Earthquake Engineering). These results are mostly based on the empirical information reported in the Da.D.O. (Database of Observed Damage) database [4] collecting damage data relevant to the most damaging Italian earthquakes occurred in the last fifty years. Within the ongoing 2019-2021 DPC-ReLUIIS research project, the Work Package WP4 “Seismic Risk Maps - MARS” aims at preparing an updated version of the 2018 NRA by considering additional vulnerability models [5]. Specifically, in order to overcome the limited amount of observational damage data, in particular for Reinforced Concrete (RC) buildings, new sets of fragility curves (FCs) are being derived by using different approaches whose results will be properly combined [5]. In the present paper, the methodology for deriving analytical FCs especially for RC buildings through Non-Linear Dynamic Analyses (NLDAs) has been briefly described. Subsequently, the results for some RC building types have been analyzed in order to highlight the role of some key parameters affecting seismic vulnerability such as design level (i.e., gravity load design and earthquake resistant design) and infill arrangement (i.e., infills regularly arranged along the height and pilotis configuration).

## 2 METHODOLOGY

In the MARS research activity, a cloud-like approach has been adopted for deriving analytical Fragility Curves (FCs) through Non-Linear Dynamic Analyses (NLDAs). The methodology is based on ten main steps, as follows:

1. Identification of building classes
2. Selection of building types
3. Simulated design of building types
4. Modelling
5. Selection of Intensity Measure
6. Selection of representative ground-motion records
7. Non-linear dynamic analyses
8. Definition of relationship “structural response - damage level”
9. Treatment of fragility curves dispersion
10. Generation of analytical fragility curves

In order to identify building classes and typologies (steps 1-2), the knowledge of the attributes mainly affecting seismic vulnerability and its distribution over a building stock are crucial aspects in large-scale vulnerability studies [6, 7]. In this context, several sources of information are available in Italy (e.g., ISTAT census data [8], post-earthquake inspections [9], interview-based surveys [10]), each one characterized by different quality and accuracy of data. According to the 2011 ISTAT census of population and houses [8], the Italian building stock amounts to about 12 million buildings, most of them are masonry structures (more than 7 million) while about 4 million are RC ones. Due to the large number of masonry structures, almost half of the

Italian buildings have 2 storeys (i.e., low-rise type) while, for taller buildings, RC resisting frame structures were generally adopted. In terms of construction period, masonry buildings were mostly built up to the end of the 1970s while RC buildings became the structural type mainly adopted in Italy after the 1970s. Due to the low percentage of the Italian territory classified as seismic until 1980 (about 25%), most of the existing residential buildings were designed only for gravity loads. In case of seismic design, moderate lateral forces (i.e., equal to either 7% or 10% of the “seismic weight”) without anti-seismic criteria were used. Generally, both materials’ quality and design practice have growth over time. Similarly, as a result of the increasing attention to thermal and sound insulation requirements, different types of infills can be found, as reported in [11].

Summarizing the previous remarks, analytical FCs for Italian RC buildings have been derived by considering the following parameters (Figure 1):

- **period of construction**, three periods: ‘50s, ‘70s and ‘90s (consistent with the ranges 1946-70, 1971-90 and >1991 defined by ISTAT 2011);
- **design level**, two types: GLD buildings (i.e., designed only for gravity loads) and ERD buildings (i.e., earthquake resistant design);
- **number of storeys**, three types: Low-rise (i.e., 1-2 storeys, Figure 2a,d), Mid-rise (i.e., 3-5 storeys, Figure 2b,e) and High-rise ( $\geq 6$  storeys, Figure 2c,e);
- **infill arrangement**, three types: Regularly Infilled-frame (IF); Pilotis-frame (PF) and Bare frame (BF).

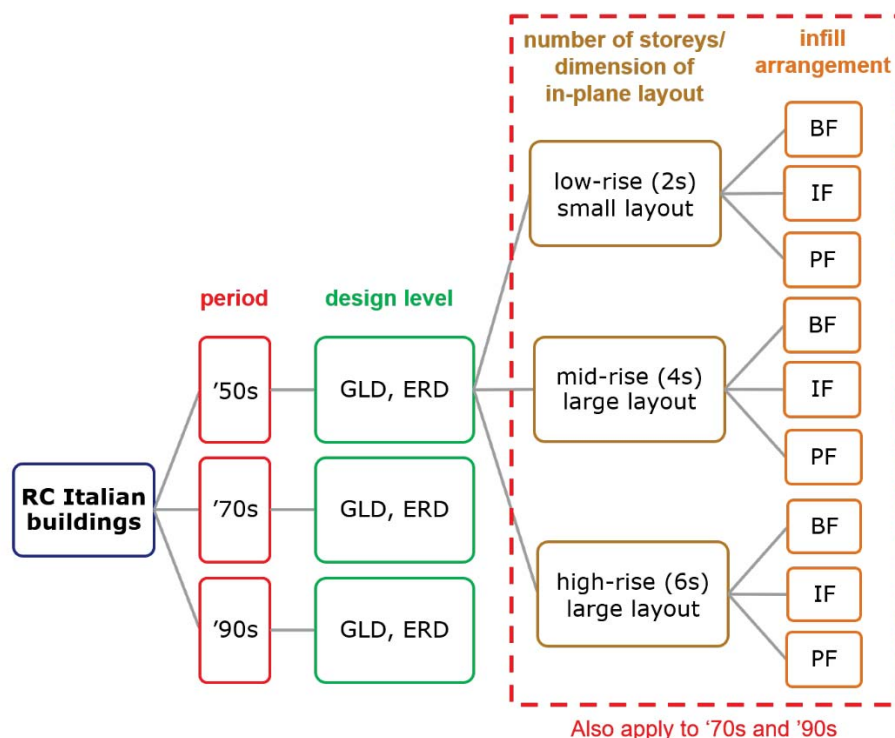
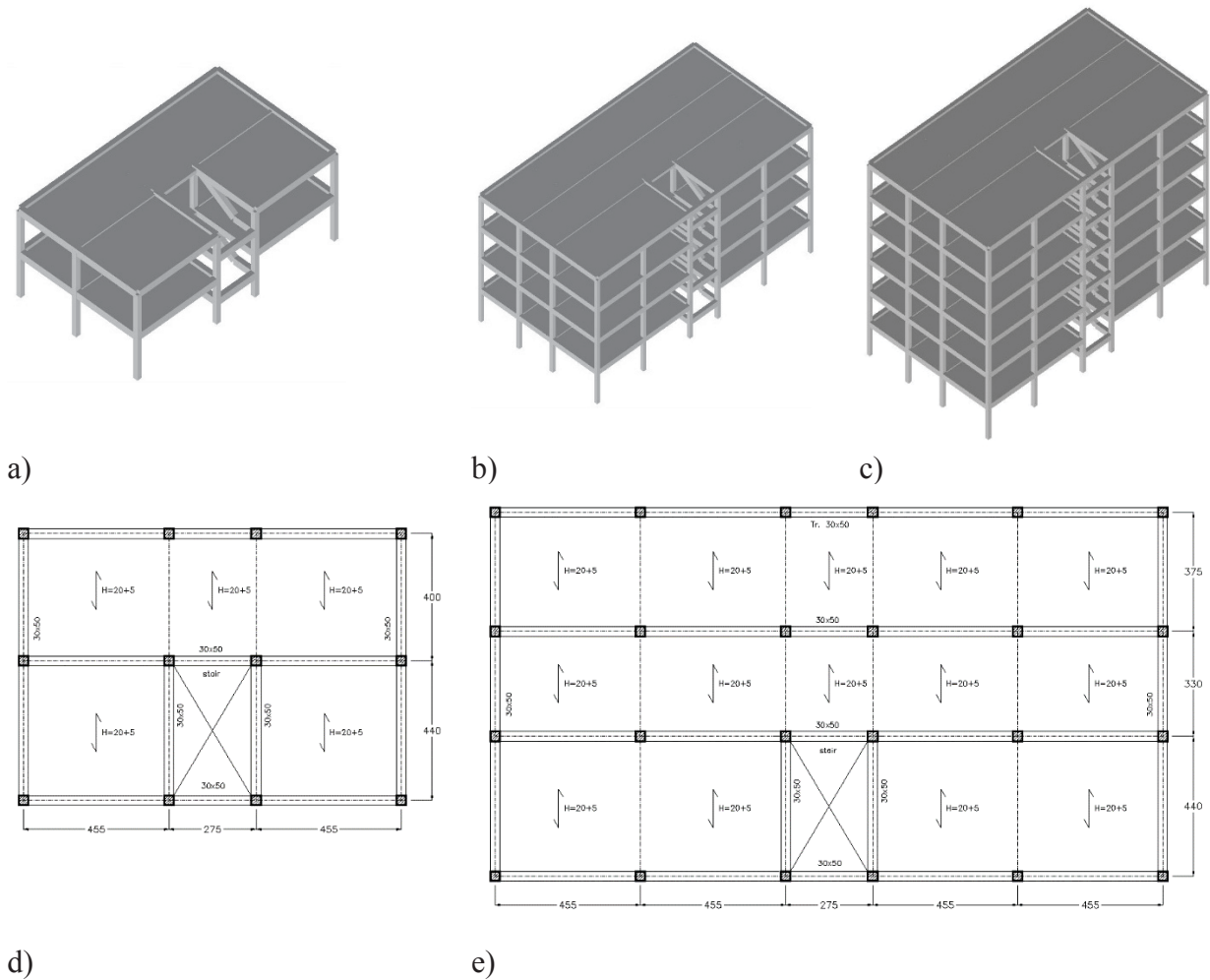


Figure 1: RC building types (from Masi et al. [5])

According to the above reported parameters, some building prototypes have been selected and detailed by means of the simulated design [12] carried out by taking into account the code in force, the quality of the typical materials and the design practice of the period. The selected structural layout is regular in-plan with different dimensions for low rise (Figure 2a,d) and mid/high rise (Figure 2b,c,e) types. For the ‘50s and ‘70s building types (both GLD and ERD

types), lateral load resisting frames (i.e., having rigid beams) are present only along the X direction and on the exterior frames. On the contrary, the '90s types show two frames (with flexible internal beams) along the two orthogonal in-plan directions. For all the considered building types, infills are double layers with empty cavity having different effective thickness (from 20 to 28 cm, ranging from '50s to '90s types) values and consistency (i.e., solid and hollow clay bricks).

Structural analyses have been performed by using the finite element code OpenSees [13]. A macro-modelling based on lumped plasticity has been adopted according to Ricci et al. [14]. Specifically, at both ends of each structural member, a bending moment–rotation ( $M-\theta$ ) relationship has been defined by adopting the Ibarra, Medina and Krawinkler model [15]. When a brittle failure is predicted (e.g., this typically occurs in the short columns of the staircase structure), the above-mentioned  $M-\theta$  relationship has been appropriately modified considering a bending moment value calculated as a function of the ultimate shear capacity according to the Sezen model [16]. On the basis of the mechanical properties of the constituent materials typically found in real buildings of the period under consideration [17, 18], mean strength values have been assumed in evaluating the structural capacity. Infill panels have been modelled by using an equivalent diagonal whose mechanical properties has been assumed according to [11, 19].



**Figure 2:** 3D view of 2 storey (a), 4 storey (b) and 6 storey (c), and in-plane layout of 2 storey (d), 4 storey and 6 storey (f) types (from Masi et al. [5])







A special attention has been paid to the selection of representative ground motion records for Non-Linear Dynamic Analyses (NLDAs). Specifically, a large set of real signals consistent with the Italian seismic hazard for soil condition consistent with A/B categories according to DM 17/01/2018 [20] has been selected and considered in terms of Peak Ground Acceleration (PGA). Although more effective Intensity Measures (IMs) could have been chosen (e.g., [21]), PGA represents the best compromise between a good correlation with the non-linear seismic response and practical constraints (i.e., data available from the Italian hazard map and standards of the IRMA platform). The considered signals with increasing intensity levels allow to reach all the EMS-98 damage levels [22] with an adequate number of data. Note that, for higher intensity levels (i.e., PGA values higher than 0.5-0.6g), a spectral matching procedure of real recorded motions has been adopted [23].

According to the lognormal cumulative distribution functions employed to define FCs, the standard deviation of the natural logarithm of the considered IM has been used to describe the total variability associated with a given damage level. In this framework, the overall uncertainty ( $\beta_{TOT}$ ) has been computed by considering three main sources of uncertainty, i.e., seismic demand ( $\beta_D$ ), inter/intra building capacity ( $\beta_C$ ) and damage thresholds' definition ( $\beta_{DS}$ ), and combined through a square root sum-of-the-squares (SRSS) rule, as follows:

$$\beta_{TOT} = \sqrt{\beta_D^2 + \beta_C^2 + \beta_{DS}^2} \quad (1)$$

Since  $\beta_D$  is directly evaluated from NLDAs as a function of the selected ground motion records, for the other sources of uncertainty (i.e.,  $\beta_C$  and  $\beta_{DS}$ ), suitable (deterministic) values from literature (e.g., [24]) and consistent with the Italian context have been considered.

In order to derive analytical FCs, the maximum interstorey drift (IDR) value along the height has been considered as earthquake demand parameter (EDP). From each NLDA, IDR value along the two in-plan directions has been evaluated and referred to the corresponding PGA value. For IDR value falling into a given damage level as defined according to a suitable relationship between damage levels and interstorey drift values, the median and the logarithmic standard deviation of the PGA value have been evaluated. An example of the relationship adopted for GLD building types is shown in Table 1 [21].

	D0	D1	D2	D3	D4	D5
<b>EMS-98 definition</b>	 SD = null NSD = null	 SD = null NSD = slight	 SD = slight NSD = moderate	 SD = moderate NSD = heavy	 SD = heavy NSD = very heavy	 Destruction
<b>Interstorey drift (%)</b>	< 0.1	0.1 – 0.25	0.25 – 0.5	0.5 – 1.0	1.0 2.5	>2.5

**Table 1:** Relationship between damage levels and interstorey drift values adopted for mid- and high-rise GLD buildings (from Masi et al. [21])

Finally, the FC related to a given damage level has been obtained by applying the well-known expression [24]:

$$P(D_k|PGA) = \Phi \left[ \frac{1}{\beta_{D,Dk}} \cdot \ln \left( \frac{PGA}{\overline{PGA}_{Dk}} \right) \right] \quad k=1,\dots,5 \quad (2)$$

where  $P(D_k|PGA)$  is the probability of exceedance of the  $k$ -th damage level  $D_k$  given a PGA value,  $\Phi$  is the standard normal (Gaussian) cumulative distribution function,  $\beta_{D,Dk}$  and  $\overline{PGA}_{Dk}$  denote the logarithmic standard deviation and median values, respectively. Note that  $\beta_{D,Dk}$



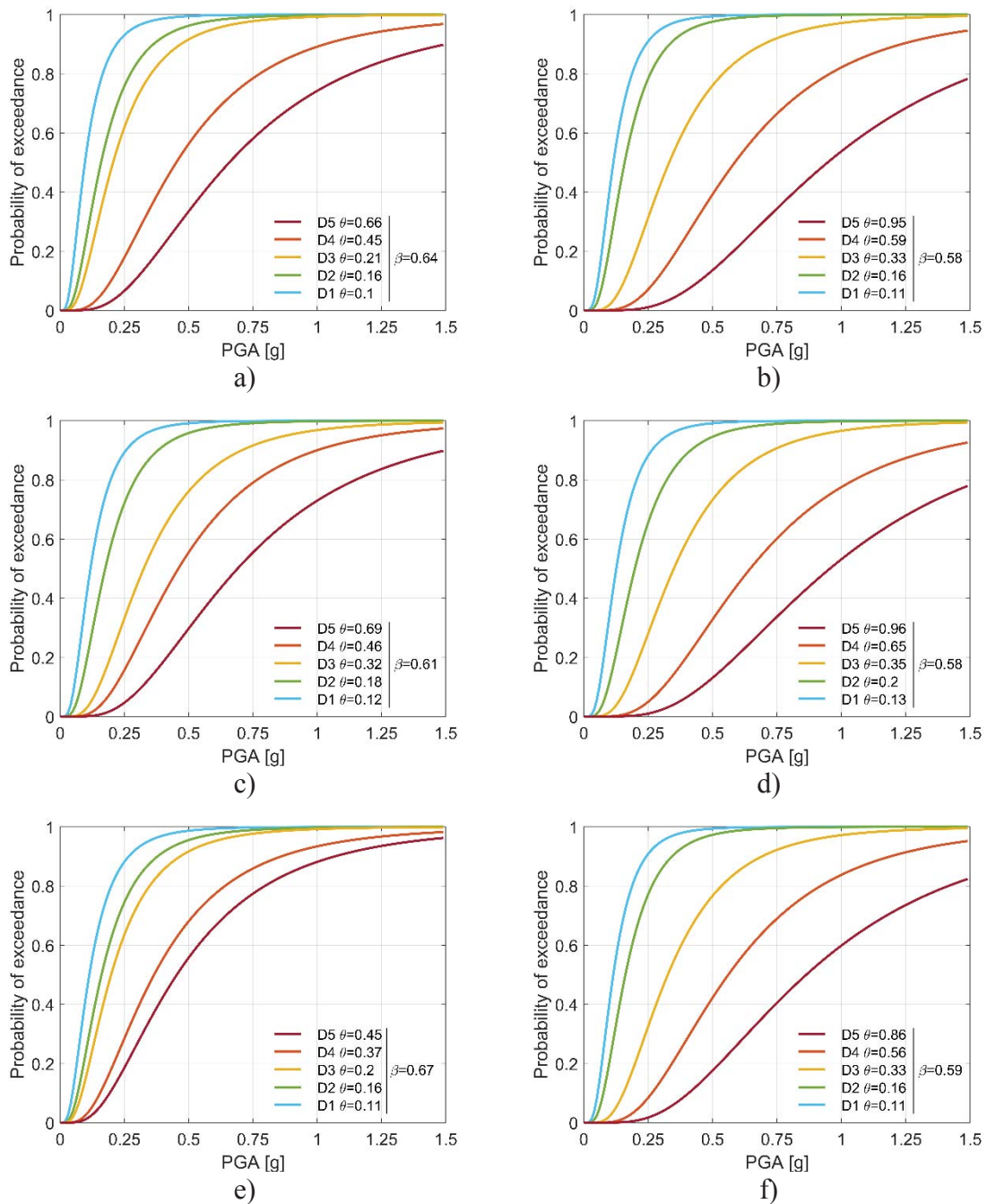
accounts for only the record-to-record variability as obtained from the NLDAs. In order to consider all sources of uncertainty, the values related to  $\beta_C$  and  $\beta_{DS}$  have to be added according to expression (1). Finally, in order to avoid unrealistic shapes of FCs (e.g., the intersection of the curves relevant to different damage levels), for each building type,  $\beta_{TOT}$  value has been evaluated as the mean of the results from each damage level.

### 3 ANALYSIS OF RESULTS

On the basis of the proposed methodology, fragility curves (FCs) for all the typological classes described previously have been derived. For sake of brevity, in the present paper only the FCs for the four-storey (4s) building type designed according to the 1970's standards have been shown. Results have been analyzed in order to highlight the role of some parameters such as infill arrangement and design level on seismic fragility. FCs related to the considered parameters (i.e., GLD and ERD design levels, presence/arrangement of infills according to BF, IF and PF configurations) are shown in Figure 3, as follows:

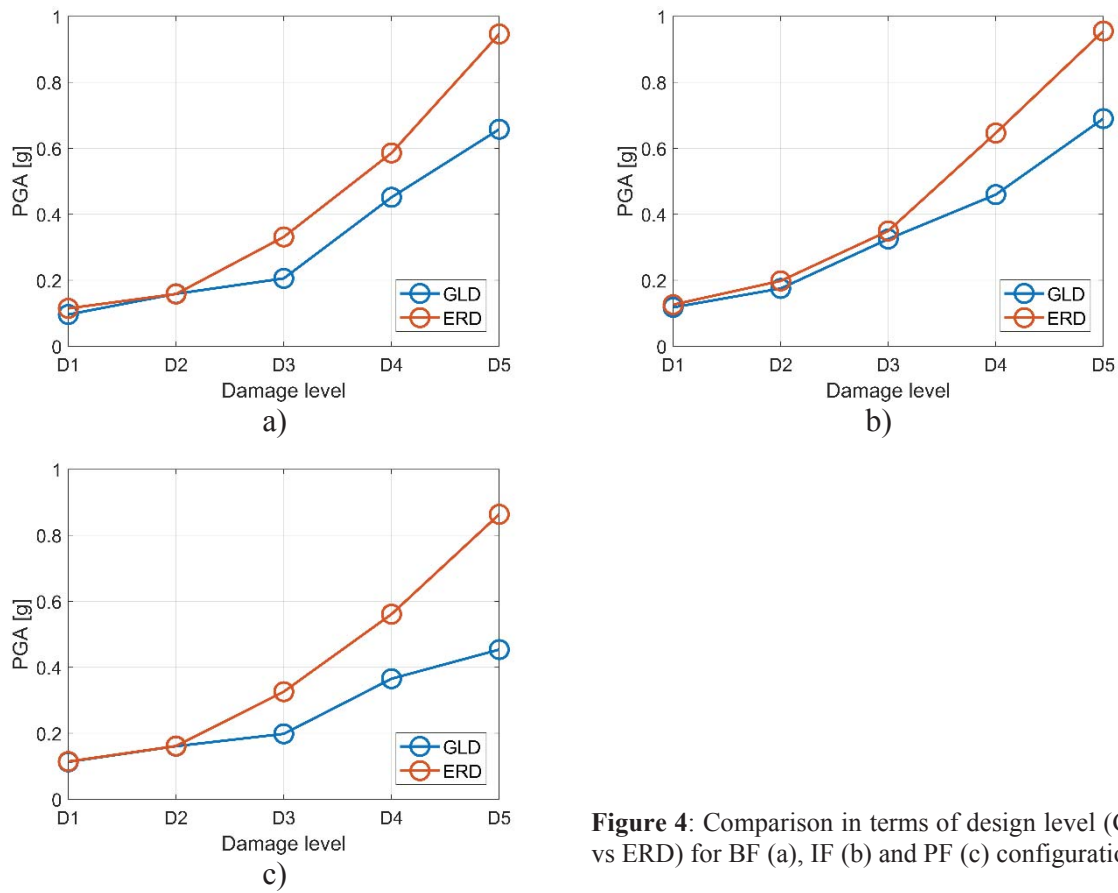
- GLD-BF in Figure 3a;
- ERD-BF in Figure 3b;
- GLD-IF in Figure 3c;
- ERD-IF in Figure 3d;
- GLD-PF in Figure 3e;
- ERD-PF in Figure 3f.

In the same figure, results in terms of median value of PGA (denoted as  $\theta$  and corresponding to the previously described  $\overline{PGA}_{DK}$ ) and dispersion ( $\beta$ , corresponding to the overall uncertainty  $\beta_{TOT}$  described above) for each damage level are reported. First of all,  $\beta$  values are in the range 0.58-0.67, with higher values for GLD types and lower ones for ERD. Further, for these latter types, similar values equal to about 0.58 are found. As for  $\theta$  values, the first damage level (D1) is reached at about 0.1g, irrespective of both design level and infill configuration, while greater differences are found for higher damage levels. In order to emphasize the role of the design level, Figure 4 shows a comparison in terms  $\theta$  values evaluated for each damage level. As expected, ERD types show better performance than GLD ones, especially for higher damage levels. Specifically, for IF configuration (Figure 4b),  $\theta$  value related to D5 (global collapse) is 0.96g for ERD and 0.69g (about -30%) for GLD. It is worth noting that, for lower damage levels (i.e., up to D3), similar  $\theta$  values are obtained for both ERD and GLD. This result mainly depends on two factors, that are i) no infill damage prevention design was required by the code considered for ERD types, thus providing a similar lateral stiffness value between ERD and GLD, ii) the same type of infills was adopted for both ERD and GLD types. These aspects are also confirmed from the results obtained for BF type, for which similar  $\theta$  values are found up to D2. The better performance of ERD with respect to GLD is even more emphasized in case of PF configuration. Indeed, the PGA median value at D5 evaluated for ERD type is approximately two times higher than for GLD type (0.86g and 0.45g, respectively for ERD and GLD).



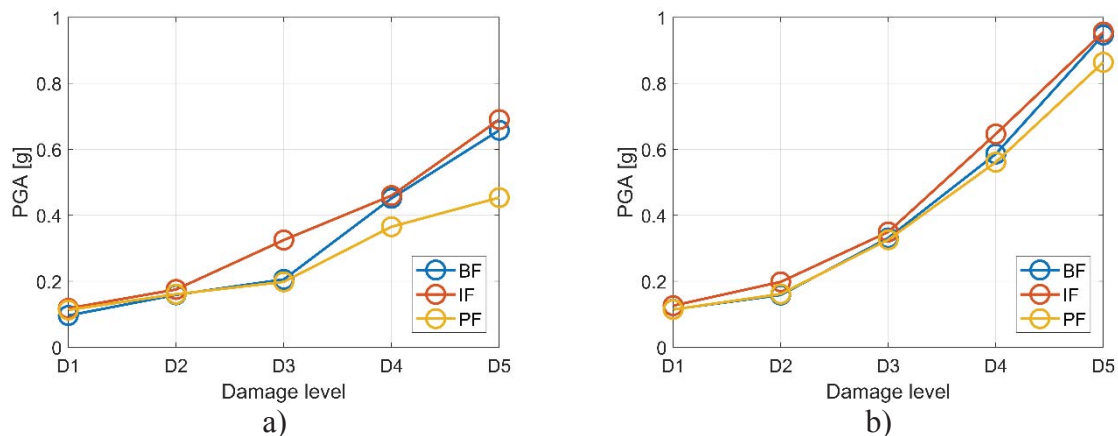
**Figure 3:** Fragility curves for the considered building types: GLD-BF (a); ERD-BF (b); GLD-IF (c), ERD-IF (d), GLD-PF (e), ERD-PF (f)

In order to highlight the role of infills on seismic performance, a comparison in terms of PGA median value by varying presence/arrangement of infills is shown in Figure 5a, for GLD type, and Figure 5b for ERD one. In general, IF types have better performance than PF ones, while intermediate results are found for BF. For GLD types, infills regularly arranged remarkably increase  $\theta$  values, especially for higher damage levels. On the contrary, for all damage levels, lower differences between IF and PF are found in case of ERD types. For example, for D5 evaluated for GLD,  $\theta$  value is equal to 0.69g for IF and 0.45g (about -35%) for PF. In case of ERD,  $\theta$  value related to IF is 0.96g while it is equal to 0.86g (about -10%) for PF.



**Figure 4:** Comparison in terms of design level (GLD vs ERD) for BF (a), IF (b) and PF (c) configurations

It is also noteworthy that, for higher damage levels, IF and BF types show similar seismic performance. Specifically,  $\theta$  values evaluated at collapse (D5) are equal to 0.69g and 0.66g for GLD-IF and GLD-BF, respectively, and 0.96g and 0.95g for ERD-IF and ERD-BF. To this purpose, it should be recalled that infills are very brittle components whose contribution to the lateral capacity of buildings decreases at higher IDR values associated with D4 and D5 damage levels.



**Figure 5:** Comparison in terms of presence/arrangement of infills for GLD (a) and ERD (b) building types

#### 4 FINAL REMARKS

Within the Work Package WP4-MARS of the 2019-2021 DPC-ReLUIIS research project, one of the main goals is to enrich the vulnerability models adopted in the 2018 National Risk Assessment by deriving additional fragility curves (FCs) from different approaches. In this context, a large set of analytical FCs through non-linear dynamic analyses has been obtained by considering some prototypes representative of the Italian building stock. Four main parameters have been considered to identify building classes, that are: (i) period of construction (three periods: '50s, '70s and '90s), (ii) design level (two levels: gravity load design, GLD, and earthquake resistant design, ERD), (iii) number of storeys (three heights: Low-rise, Mid-rise and High-rise), and (iv) infill arrangement (three configurations: Regularly Infilled-frame, IF, Pilotis-frame, PF, and Bare frame, BF).

In the paper, after a short description of the methodology, analytical FCs for the 4-storey RC building types designed according to 1970's standards have been analyzed in order to highlight the role of some parameters affecting seismic vulnerability, and specifically design level and infill arrangement.

As expected, although the '70s ERD types were poorly designed for lateral loads, significant differences (about 30%) in terms of PGA median values at collapse (D5) have been found between ERD and GLD types. On the contrary, similar performance has been found for the lower damage levels according to the EMS-98 classification (i.e., D1 and D2). This latter result mainly depends on two factors, that are: (i) no infill damage prevention design was required by the code considered for the '70s ERD types, thus providing a similar lateral stiffness value between ERD and GLD, (ii) the same type of infills was adopted for both ERD and GLD types in the '70s.

The presence of infills regularly arranged improves seismic performance, especially for buildings designed only for gravity loads (GLD type). As an example, for D5 damage level, PGA median value is equal to 0.69g for IF types, and 0.45g for PF ones, with a reduction around 35%. On the contrary, lower differences (about 10%) have been found in case of ERD types. The comparison between IF and BF types shows that the infill contribution to the lateral capacity of buildings is more appreciable for lower damage levels while, due to the brittle behaviour of infills, it becomes negligible at collapse.

#### ACKNOWLEDGEMENTS

The work reported in this article has been developed under the financial support of the Italian Department of Civil Protection, within the ReLUIIS-DPC 2019-21 Research Project, WP4 – Seismic Risk Maps (MARS), which is gratefully acknowledged.

## REFERENCES

- [1] Italian Civil Protection Department (DPC), *National Risk Assessment 2018. Overview of the potential major disasters in Italy*. Updated December 2018
- [2] M. Dolce, A. Prota, B. Borzi, F. da Porto, S. Lagomarsino, G. Magenes, C. Moroni, A. Penna, M. Polese, E. Speranza, G.M. Verderame, G. Zuccaro, Seismic Risk Assessment of residential buildings in Italy, *Bulletin of Earthquake Engineering*, <https://doi.org/10.1007/s10518-020-01009-5>, 2020
- [3] B. Borzi, M. Onida, M. Faravelli, D. Polli, M. Pagano, D. Quaroni D, A. Cantoni, E. Speranza, C. Moroni, IRMA platform for the calculation of damages and risks of residential buildings, *Bulletin of Earthquake Engineering*, <https://doi.org/10.1007/s10518-020-00924-x>, 2020
- [4] M. Dolce, E. Speranza, F. Giordano, B. Borzi, F. Bocchi, C. Conte, A. Di Meo, M. Faravelli, V. Pascale, Observed damage database of past Italian earthquakes: the Da.D.O. webgis. *Bollettino di Geofisica Teorica e Applicata*, 60(2): 141-164, 2019
- [5] Masi, S. Lagomarsino, M. Dolce, V. Manfredi, D. Ottonelli, Towards the updated Italian seismic risk assessment: exposure and vulnerability modelling. *Bulletin of Earthquake Engineering*, <https://doi.org/10.1007/s10518-021-01065-5>, 2021
- [6] M. Polese, M. Gaetani d'Aragona, A. Prota, Simplified approach for building inventory and seismic damage assessment at the territorial scale: an application for a town in southern Italy, *Soil dynamics and earthquake engineering*, 121 (2019) 405-420, 2019
- [7] G. Nicodemo, *Exposure modelling and loss estimation for seismic risk assessment of residential buildings: innovative methods and applications*, PhD thesis, University of Basilicata, Italy, <http://hdl.handle.net/11563/146804>, 2021
- [8] ISTAT, Italian National Institute of Statistics (2011) *15° Censimento della popolazione e delle abitazioni*, available at <http://www.istat.it>
- [9] G. Nicodemo, M. Pittore, A. Masi, V. Manfredi, Modelling exposure and vulnerability from post-earthquake survey data with risk-oriented taxonomies: AeDES form, GEM taxonomy and EMS-98 typologies. *International Journal of Disaster Risk Reduction*, 50, 101894. doi.org/10.1016/j.ijdr.2020.101894, 2020
- [10] G. Zuccaro, M. Dolce, D. De Gregorio, E. Speranza, C. Moroni, La scheda CARTIS per la Caratterizzazione Tipologico-Strutturale dei Comparti Urbani costituiti da edifici ordinari: valutazione dell'esposizione in analisi di rischio sismico. *Proceedings of the 34<sup>th</sup> GNGTS, Trieste, 2015*, 2015 (in Italian).
- [11] V. Manfredi, A. Masi, Seismic Strengthening and Energy Efficiency: Towards an Integrated Approach for the Rehabilitation of Existing RC Buildings. *Buildings* 8.3, 36, 2018.
- [12] A. Masi, Seismic vulnerability assessment of gravity load designed R/C frames. *Bulletin of Earthquake Engineering*, 1(3), 371-395, 2003.
- [13] F. McKenna, OpenSees: a framework for earthquake engineering simulation. *Computing in Science & Engineering*, Vol. 13, Issue 4, pp 58-66, 2011.
- [14] P. Ricci, V. Manfredi, F. Noto, M. Terrenzi, M.T. De Risi, M. Di Domenico, G. Camata, P. Franchin, A. Masi, F. Mollaioli, E. Spacone, G.M. Verderame, RINTC-e: Towards seismic risk assessment of existing residential reinforced concrete buildings in Italy,



- COMPDYN 2019, *7th ECCOMAS Thematic Conference on Computational Methods in Structural Dynamics and Earthquake Engineering*, M. Papadrakakis, M. Fragiadakis (eds.) Crete, Greece, 24–26 June, 2019
- [15] L.F. Ibarra, R.A., Medina, H., Krawinkler, Hysteretic models that incorporate strength and stiffness deterioration. *Earthquake engineering & structural dynamics*, 34(12), 1489–1511, 2005
  - [16] H. Sezen, *Seismic Response and Modeling of Reinforced Concrete Building Columns*. Ph.D. Thesis, Department of Civil and Environmental Engineering, University of California, Berkeley, CA, USA, 2002.
  - [17] G.M. Verderame, P. Ricci, M. Esposito, G. Manfredi, *STIL v1.0 – Software per la caratterizzazione delle proprietà meccaniche degli acciai da c.a. tra il 1950 e il 2000*. ReLUIS, Naples, Italy, 2012. Available at <http://www.reluis.it/>
  - [18] A. Masi, A. Digrisolo, G. Santarsiero, Concrete strength variability in Italian buildings: analysis of a large database of core tests. *Applied mechanics and materials*, 597, 283–290, 2014.
  - [19] A. Masi, V. Manfredi, G. Cetraro, In-plane performance of RC infilled frames under seismic actions: Experimental versus code provision values. In *Brick and Block Masonry—Trends, Innovations and Challenges*; Modena, C., da Porto, F., Valluzzi, M.R., Eds.; Taylor & Francis Group: London, UK, 2016; ISBN 978-1-138-02999-6.
  - [20] Ministerial Decree 17 January 2018, NTC 2018. *Aggiornamento delle “Norme Tecniche per le Costruzioni”*. GU n. 42, 20 February 2018
  - [21] A. Masi, A. Digrisolo, V. Manfredi, Fragility curves of gravity-load designed RC buildings with regularity in plan. *Earthquake and Structures* 9(1):1–27, 2015
  - [22] G. Grunthal, *European Macroseismic Scale*. Chaiers du Centre Européen de Géodynamique et de Séismologie, Vol. 15, Luxembourg, 1998
  - [23] R. Paolucci, A.G. Ozcebe, C. Smerzini, A. Masi, V. Manfredi, *Selection and spectral matching of recorded ground motions for earthquake engineering analysis*, available at <http://143.225.144.186:5000/>, 2020
  - [24] Federal Emergency Management Agency (FEMA), *Hazus-MH 2.1 Technical Manual: Earthquake Model*, developed by Federal Emergency Management Agency, Mitigation Division, Washington, D.C., 2012

## EXPERIMENTAL AND NUMERICAL ASSESSMENT OF ISOLATION SEISMIC DEVICE FOR RETROFIT OF INDUSTRIAL SHED

L. Mari<sup>1</sup>, V. Quaglini<sup>2</sup>, C. Pettorruso<sup>2</sup>, E. Bruschi<sup>2</sup>

<sup>1</sup> Moretti S.p.A., Director R&D  
via Gandhi 9, 25030 Erbusco (BS), Italy  
mari@morettispa.it

<sup>2</sup> Politecnico di Milano, Department of Architecture, Built Environment and Construction Engineering  
Piazza Leonardo da Vinci 32, 20133 Milan, Italy  
virginio.quaglini@polimi.it  
carlo.pettorruso@polimi.it  
eleonora.bruschi@polimi.it

---

### Abstract

*Prefabricated industrial sheds featured a high seismic vulnerability during the 2012 Emilia earthquake (Italy). The buildings typically exhibited a rigid collapse mechanism that was a consequence of the lack of connection between columns, beams and roof elements.*

*The study presents an experimental and numerical assessment of a novel isolation device which has been designed to improve the seismic performance of industrial sheds. The device, which is placed on the top of the column, exploits the movement of a rigid body on a sloped surface to provide horizontal stiffness and control the lateral displacement of the beam.*

*Biaxial tests are performed to investigate the effect of the vertical load, the velocity of sliding and the number of cycles on the force – displacement response of the device. To cope with the capacity of the testing equipment, the experimental campaign is carried out on a scaled model of the device, and the protocol is designed accounting for similarity requirements. The backbone curve of the tested prototype is eventually derived from the experimental data.*

*In the second part of the study, a 3D finite element model of the prototype is formulated in Abaqus and used to switch the backbone curve from the scaled model to the full-scale device. A parametric study is conducted to evaluate the influence of the inclination of the sloped surface and the coefficient of friction on the output force of the system.*

**Keywords:** Prefabricated sheds; seismic isolation; retrofit; experiments; reinforced concrete.

---

## 1 INTRODUCTION

In Italy, the seismic events of L'Aquila 2009, Emilia 2012 and Central Italy 2016 highlighted the vulnerability of the Italian stock on structures and infrastructures that were not designed according to modern seismic regulations.

The Emilia earthquake of May 2012 hit an area with a high density of productive activities, affecting mainly industrial buildings in precast reinforced concrete (RC) [1, 2] rather than in steel [3]. This seismic event caused a global economic damage of 13.27 billion of euros and estimates show that the loss of direct and indirect income was between 3 and 3.8 billion [4].

After Emilia earthquakes, the Italian Civil Protection Department prepared a summary (WG 2012) [5] of the main deficiencies of the precast industrial building structural performance. In this regard, it is worth also mentioning the study by Rossi et al. [6] about long-span-beam structure, which proposed a damage characterization to construct empirical fragility functions, cost and loss ratio curves referring to precast RC industrial buildings.

The existing industrial buildings in Italy are mainly characterized by a simple structural layout with columns pin-connected to beams that support the roof, which is an extremely vulnerable configuration under a seismic event. Indeed, the most severe damage, observed also during the event of Emilia 2012, is the loss of support and the consequent collapse of structural and non-structural elements [1, 2]. This kind of connections usually rely solely on friction and are inadequate to properly transfer the horizontal loads [7, 8, 9] and accommodate compatible rotations and displacements [10, 11, 12, 13, 14, 15].

In order to improve the seismic performance of poorly designed or deficient structures, a retrofit intervention needs to be planned and implemented at either local level or global one [3]. Local interventions usually consist of structural strengthening, applying rigid and resistant reinforcement that increase the capacity of deficient elements; such a reinforcement can be made of either steel, or high-strength fibers embedded into a cementitious or a polymeric matrix [16]. Conversely, global interventions are implemented by inserting in the structure particular devices, which either reduce the seismic input, by separating the motion of the superstructure from the motion of the ground (namely seismic isolation systems) or increase the total energy dissipation capacity (namely energy dissipation devices) [17,18] by concentrating on special elements out of the main load bearing structure the dissipation of most of the energy transmitted by the earthquake.

The study presents an experimental and numerical assessment of a novel isolation device which has been designed to improve the seismic performance of industrial sheds. The device, which is placed on the top of the column, exploits the movement of a rigid body on a sloped surface to provide horizontal stiffness, control the lateral displacement of the beam and dissipate with a friction mechanism part of seismic energy.

## 2 DEVICE DESCRIPTION

The isolation device is composed by two steel elements one concave and the other convex, truncated-pyramidal in shape. The two elements are coupled through the contact, total or partial, of their respective flat surfaces.

This isolation device is designed to be inserted at the junction between the columns and beam of a building and is intended to transmit the vertical load in the node. The horizontal displacement of the beam with respect to the column produced by an earthquake causes the sliding of the convex surface of the first element on the concave surface of the second element. This relative movement generates dissipation of a portion of the seismic energy introduced into the system through the friction generated in correspondence of the sliding contact.

The device is designed to transmit an axial load  $N_{\text{design}} = 360 \text{ kN}$  and perform a maximum displacement  $d_{\text{design}} = 60 \text{ mm}$ .

To make the loads developed by the device compatible with the capacity of the test equipment, the characterization was conducted on a prototype scaled by a geometric factor  $SL = 0.4$  and fabricated in steel (unit scale factor for modulus of elasticity  $SE = 1$ ). Applying the principle of similarity, the scaling factors for all mechanical quantities are determined (Table 1).

Size	Dimension	Scale factor
Length	[L]	$S_L = 0,4$
Elastic Modulus	[F] [L] <sup>-2</sup>	$S_E = 1,0$
Force	[F]	$S_F = (S_L)^2 = 0,16$
Pressure	[F] [L] <sup>-2</sup>	$S_p = 1,0$
Displacement	[L]	$S_d = 0,4$
Time	[T]	$S_T = (S_L)^{1/2} = 0,6324$
Velocity	[L] [T] <sup>-1</sup>	$S_V = (S_L)^{1/2} = 0,6324$
Frequency	[T] <sup>-1</sup>	$S_f = (S_L)^{-1/2} = 1,5811$

Table 21 Scale factor

This results in the following relationships between the design values of device force and displacement and the values that should be applied in tests to the scaled prototype (Table 2).

Size	Real scale	Prototype
Axial load	$N_{\text{design}} = 360 \text{ kN}$	$N_{\text{test}} = 57,6 \text{ kN}$
Displacement	$d_{\text{design}} = 60 \text{ mm}$	$d_{\text{test}} = 24 \text{ mm}$

Table 2 Relation between design and test parameters

The scale-down have the dimension shown in Figures 1 and 2.

SECTION A-A

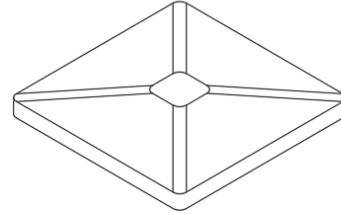
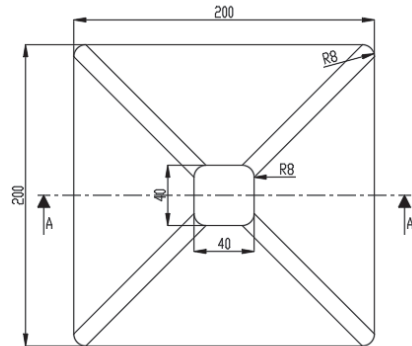
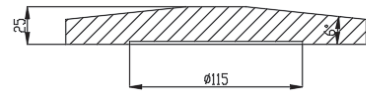


Figure 1 Geometrical characteristics of convex element

SECTION B-B

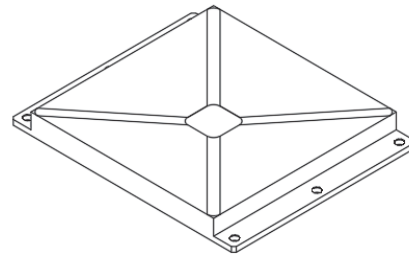
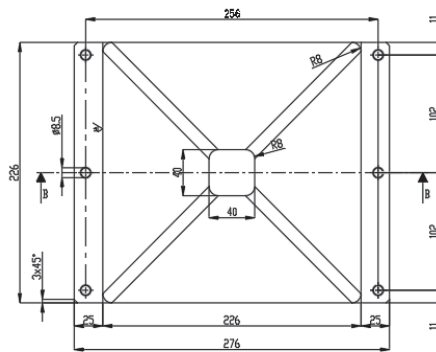
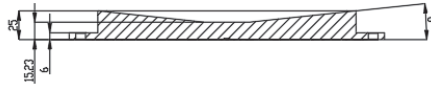


Figure 2 Geometrical characteristics of concave element



### 3 EXPERIMENTAL PROGRAM

#### 3.1 Tests setup and instrumentations

The test is performed on a pair of prototypes of equal size, mounted in an upside-down configuration to minimize the moment arising on the test machine due to the eccentricity of the load applied on the specimen while it is in a translated position.

The concave component is mounted on the moving slide, while the convex component is clamped to a fixed part of the testing machine, to the vertical actuator and the base respectively. The test configuration is shown in Figure 3.

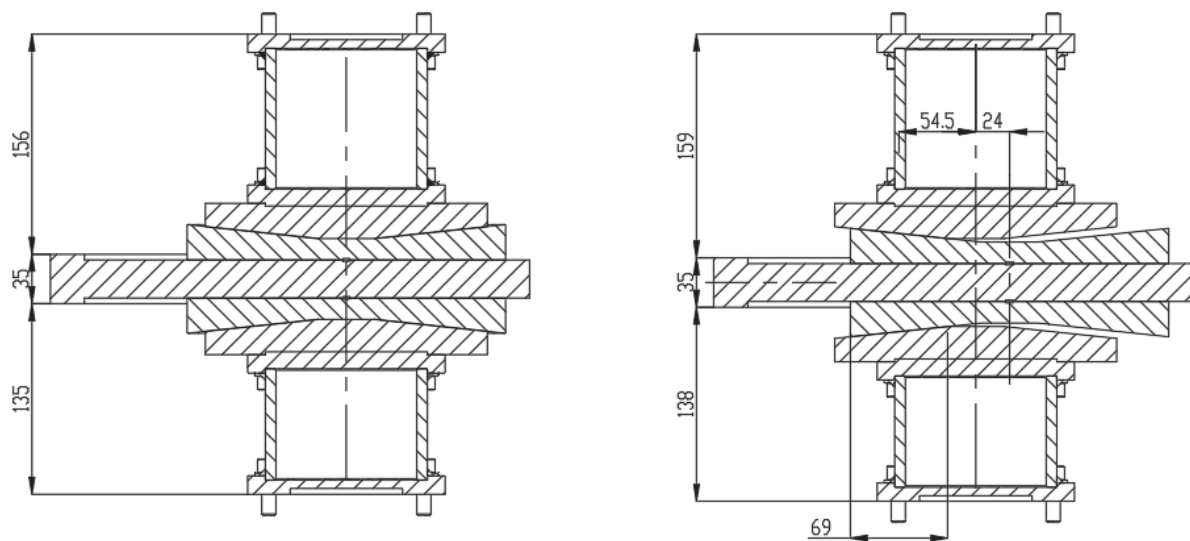


Figure 3 Setup configuration: on the left in centered configuration, on the right in translated position

The tests were conducted on a pair of prototypes with lubrication. Applying the axial load  $N_{test}$ , kept constant during the test, and simultaneously imposing a horizontal displacement through cycles of amplitude  $d_{test}$  at constant speed  $V_{test}$ . The test protocol, articulated in the execution of static and dynamic tests, reproduced for each combination of prototypes and type of lubrication is specified in Table 3a for the static and Table 3b for dynamic tests.

ID	Axial load	Displacement	Velocity	n. cycles
[-]	$N_{test}$ [kN]	$d_{test}$ [mm]	$V_{test}$ [mm/s]	[-]
S1	14,4	24	0,672	3
S2	28,8	24	0,672	3
S3	57,6	24	0,672	3

Table 3a Static test

ID	Axial load	Displacement	Velocity	n. cycles
[-]	$N_{test}$ [kN]	$d_{test}$ [mm]	$V_{test}$ [mm/s]	[-]
D2a	28,8	24	3,36	5
D2b	28,8	24	6,72	5
D2c	28,8	24	16,8	5
D2d	28,8	24	33,6	5
D3a	57,6	24	3,36	20

Table 3b Dynamic test

Tests were conducted using a biaxial testing system installed at the “Laboratorio Prove Materiali e Strutture per le Costruzioni del Politecnico di Milano”. The testing machine consists of a rigid frame with 4 columns and two fixed crossbeams, one lower and one upper, which form a closed ring in which the forces are confined [19].

The main characteristics of the test equipment are:

- Vertical load capacity: 500 kN
- Horizontal load capacity: 75 kN
- Horizontal displacement capacity: 100 mm

### 3.2 Results

The typical shape of the hysteretic horizontal force (F) - displacement (d) diagram of the prototype seismic device obtained in the cyclic tests is shown in Figure 4. In the force-displacement diagrams, the total force acting in the horizontal direction on the pair of prototypes is shown on the y-axis; the reaction force of the individual prototype corresponds to half of the force shown on the diagram.

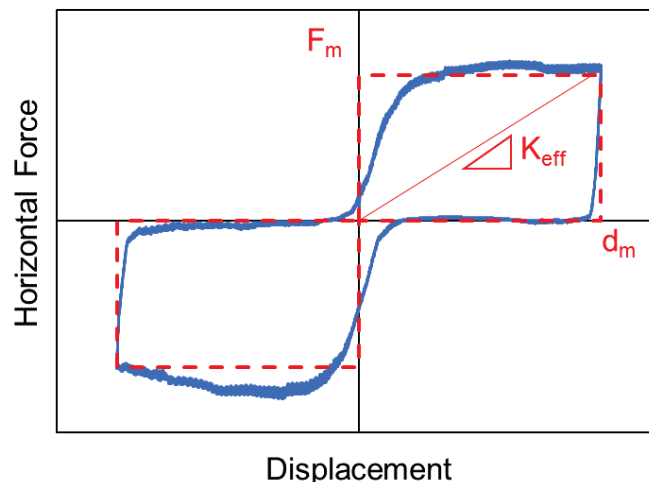


Figure 4 Hysteretic loop

The prototype device has a rigid-plastic constitutive law, characterized by an approximately constant reaction force up to the design displacement. The reaction force is provided by the sum of two contributions, each of which is ideally independent of the magnitude of the displacement: the first is the reaction force to the sliding of the convex element on the inclined plane formed by the surfaces of the concave element, and the second is the friction force generated during sliding.

In order to identify the characteristic parameters of the prototype, the hysteretic cycle is approximated by two cycles of rectangular shape placed in the first and third quadrant of the plane  $F - d$ , and such that the sum of their areas equals the area ( $A$ ) of the hysteretic cycle itself. Based on energy equivalence considerations, the following parameters are defined:

Energy dissipated in a cycle:

$$E_{diss} = \frac{A}{k_0} \quad (1)$$

Equivalent stiffness:

$$K_{eff} = \frac{E_{diss}}{2 (d_{test})^2} \quad (2)$$

Equivalent dynamic friction coefficient:

$$\mu_{eff} = \frac{E_{diss}}{4 d_{test} N_{test}} \quad (3)$$

where  $A$  [Nm] is the area of the hysteretic cycle, and the factor  $k_0 = 2$  takes into account the fact that the test is conducted simultaneously on two identical prototype devices (Figure 4).

### Static test

ID	Axial load	Velocity	n. cycles	Energy dissipated	Stiffness	Friction coefficient
[-]	$N_{test}$ [kN]	$V_{test}$ [mm/s]	[-]	$E_{diss}$ [Nm]	$K_{eff}$ [N/m]	$\mu$ (-)
S1	14,4	0,672	1	197	0,171	0,142
			2	202	0,175	0,146
			3	207	0,18	0,150
S2	28,8	0,672	1	314	0,272	0,114
			2	322	0,279	0,116
			3	331	0,287	0,120
S3	57,6	0,672	1	525	0,455	0,095
			2	539	0,468	0,097
			3	550	0,477	0,099

Table 4 Static test results

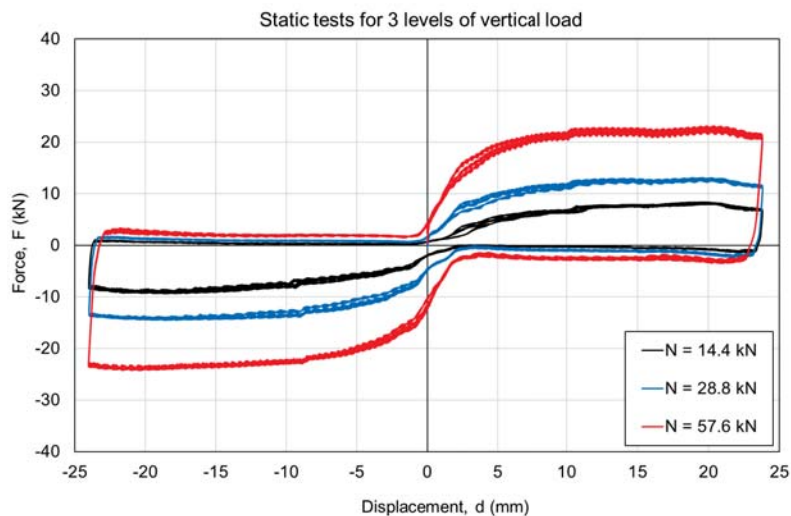


Figure 5 Static test curves

**Dynamic test**

ID	Axial load	Velocity	n. cycles	Energy dissipated	Stiffness	Friction coefficient
[-]	$N_{test}$ [kN]	$V_{test}$ [mm/s]	[-]	$E_{diss}$ [Nm]	$K_{eff}$ [N/m]	$\mu$ (-)
D2a	28,8	3,36	1	326	0,282	0,118
			2	335	0,29	0,121
			3	338	0,293	0,122
			4	339	0,293	0,123
			5	340	0,295	0,123
D2b	28,8	6,72	1	324	0,28	0,117
			2	327	0,283	0,119
			3	330	0,285	0,119
			4	330	0,285	0,12
			5	332	0,287	0,12
D2c	28,8	16,8	1	335	0,289	0,121
			2	330	0,285	0,119
			3	332	0,286	0,12
			4	333	0,287	0,12
			5	334	0,288	0,121
D2d	28,8	33,6	1	375	0,324	0,134
			2	353	0,304	0,126
			3	352	0,304	0,126
			4	353	0,304	0,126
			5	354	0,305	0,126

Table 5 Dynamic test D2 results

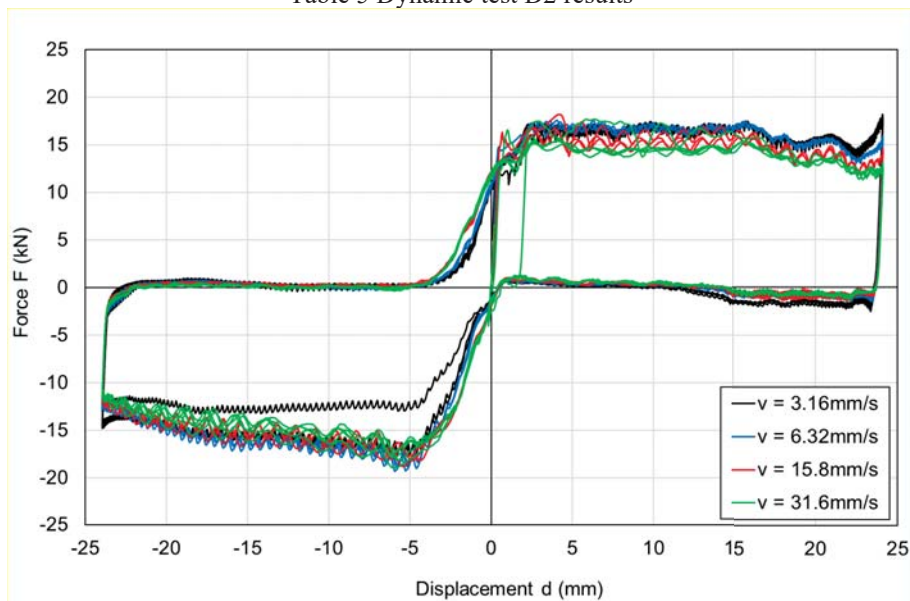


Figure 6 Dynamic test D2 diagram

ID	Axial load	Velocity	n. cycles	Energy dissipated	Stiffness	Friction coefficient
[-]	$N_{test}$ [kN]	$V_{test}$ [mm/s]	[-]	$E_{diss}$ [Nm]	$K_{eff}$ [N/m]	$\mu$ (-)
D3a	57,6	3,6	1	530	0,459	0,096
			2	537	0,465	0,097
			3	539	0,467	0,097
			4	545	0,471	0,098
			5	547	0,473	0,099
			6	551	0,477	0,1
			7	551	0,477	0,1
			8	558	0,483	0,101
			9	559	0,484	0,101
			10	560	0,485	0,101
			11	560	0,485	0,101
			12	562	0,487	0,102
			13	564	0,489	0,102
			14	568	0,492	0,103
			15	568	0,492	0,103
			16	570	0,493	0,103
			17	571	0,494	0,103
			18	571	0,494	0,103
			19	573	0,496	0,104
			20	573	0,496	0,104

Table 6 Dynamic test D3 result

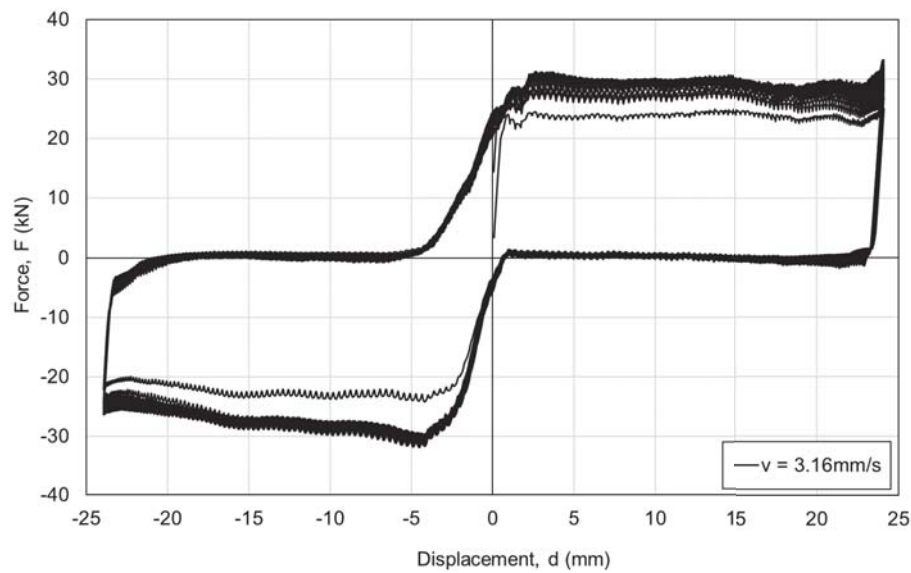


Figure 7 Dynamic test D3 diagram



## 4 NUMERICAL MODEL

### 4.1 Numerical description

Numerical model of the seismic isolation device described above was developed using the Abaqus CAE finite element calculation program [20].

The geometry of the numerical model of the prototype represents the one described previously that was subjected to experimental characterization tests at the Politecnico di Milano.

The numerical model takes into account only one device, and so there is only two elements, one convex and one concave. To simulate the behavior of the prototype it is developed an implicit dynamic analysis with full Newton solution technique.

The FEM model, like the prototype, is subject to a biaxial load. The boundary conditions that characterize the convex element are the distributed pressure of 11 MPa, whose resultant is 57,6 kN, applied on the external face, and the harmonic displacement with amplitude 24 mm. The concave element is fixed.

The numerical model was meshed with elements C3D8 (three-dimensional hexahedral element with 8 nodes) with maximum dimension equal to 8 mm. A total of #1016 elements were used for the convex element and #2034 elements for the concave element (Figure 8). The contact between the surfaces in creeping contact was modeled through the surface-to-surface contact command, defining the convex element as the master element, and formulating a hard contact constitutive behavior in the direction perpendicular to the contact surface, and a penalty constitutive behavior tangentially the contact surface [21]. The elements have elastic properties, Young modulus equal to  $E = 210'000$  MPa and Poisson's coefficient  $\nu = 0.30$ , corresponding to the characteristics of steel. The friction coefficient between the surfaces of the concave and convex element, based on experimental tests conducted on a device with lubricated surfaces, is assumed to be  $\mu = 0.10$ .

In the numerical modeling, in the absence of precise indications, it was assumed that in the initial configuration with perfectly centered concave and convex elements the two elements are in contact through the two flat faces.

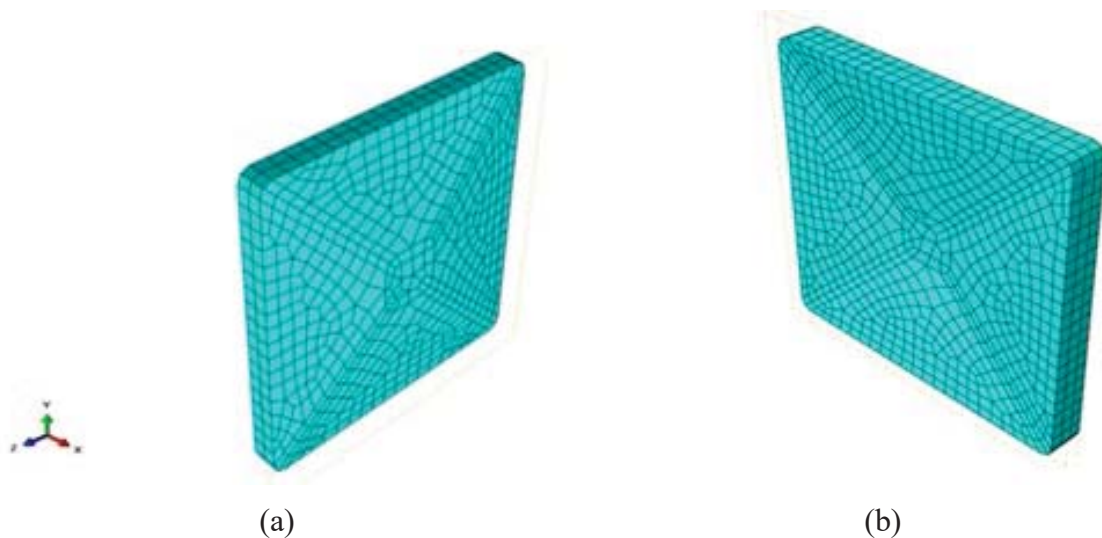


Figure 8 FEM model of the seismic energy dissipation device:(a) convex element; (b) concave element

## 4.2 Numerical result

The results of the numerical analyses are shown below for different motion trajectories of the convex component with respect to the concave component defined by angle  $\theta$  (Figure 9). The seismic dissipation device has four axes of symmetry, defined by the angles  $\theta = 0^\circ$ ,  $\theta = +90^\circ$ ,  $\theta = +45^\circ$ , and  $\theta = -45^\circ$ , the motions along two unidirectional trajectories were analyzed, directed according to the directions corresponding to the angles  $\theta = 0^\circ$  and  $\theta = 45^\circ$ , since the other two have the same characteristics as the two considered.

The results are expressed in the form of:

- force-displacement curves:
- reaction force vs. displacement
- reaction moment vs. displacement
- contact pressure distribution

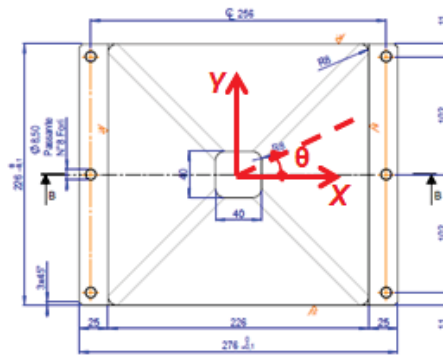


Figure 9 Definition of the reference system for the displacements

Figures 10 and 11 illustrate the force-displacement diagrams related to the analyses conducted imposing a unidirectional movement along the symmetry directions  $\theta = 0^\circ$  and  $\theta = +45^\circ$ .

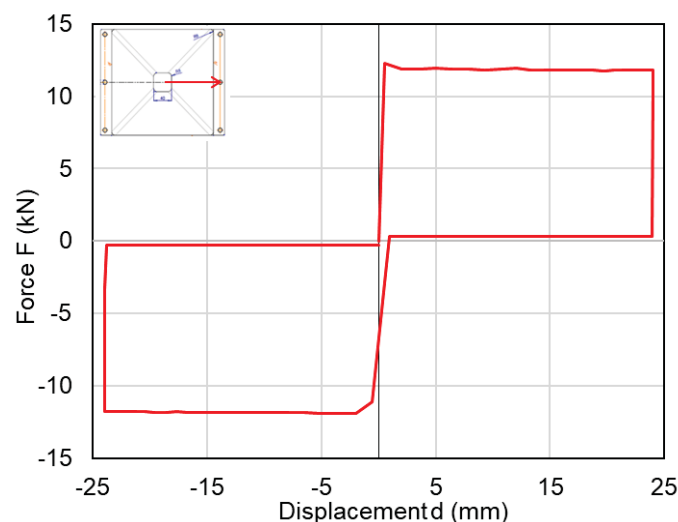


Figure 10 Force-displacement curve for unidirectional trajectory in direction  $\theta = 0^\circ$

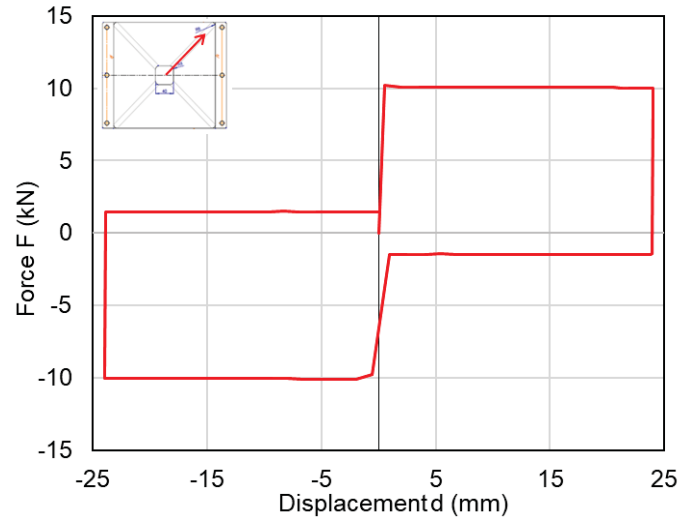


Figure 11 Force-displacement curve for unidirectional trajectory in direction  $\theta = 45^\circ$

The characteristic curve of the device moving according to a direction of symmetry presents the classical flag-shaped that characterizes a constant reaction force independent of the imposed displacement, but dependent on the direction of displacement. This behavior is consistent with the theoretical behavior corresponding to the movement of a solid on an inclined plane with friction, which provides a reaction force of the type

$$F = N [\sin \alpha \cdot \text{sign}(d) + \mu \cos \alpha \cdot \text{sign}(V)] \quad (4)$$

where  $F$  is the horizontal reaction,  $d$  is the imposed displacement,  $N$  is the vertical compressive load,  $\alpha$  is the tilt angle of the sliding surface,  $\mu$  is the coefficient of friction,  $V$  is the sliding velocity, and  $\text{sign}(\cdot)$  is the sign function. The first term on the right in Eq. (4) represents just the reaction force produced by motion on an inclined surface and the second term on the right the friction force:

- the effective angle of inclination  $\alpha$  of the device surface along the direction in which the trajectory develops is not constant but varies as the direction of motion defined by the angle  $\theta$  varies according to the relation

$$\alpha(\theta) = \max\{\arctan(h/L_0 \cdot \cos\theta); \arctan(h/L_0 \cdot \sin\theta)\} \quad (5)$$

where  $h$  and  $L_0$  are defined in figure 12.

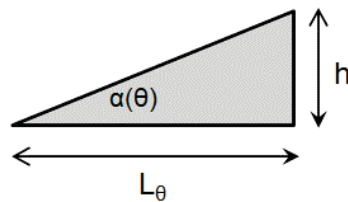


Figure 12 Descriptive geometric parameters of surface inclination along a generic direction  $\theta$

The equation (4) expresses the reaction force developed by the seismic dissipation device in the direction of motion, parallel to the trajectory of the convex component with respect to the concave component. On the other hand, the reaction force developed in the direction perpendicular to the trajectory is zero (Figure 13), and this is justified by the symmetry of the contact surfaces with respect to the direction of motion.

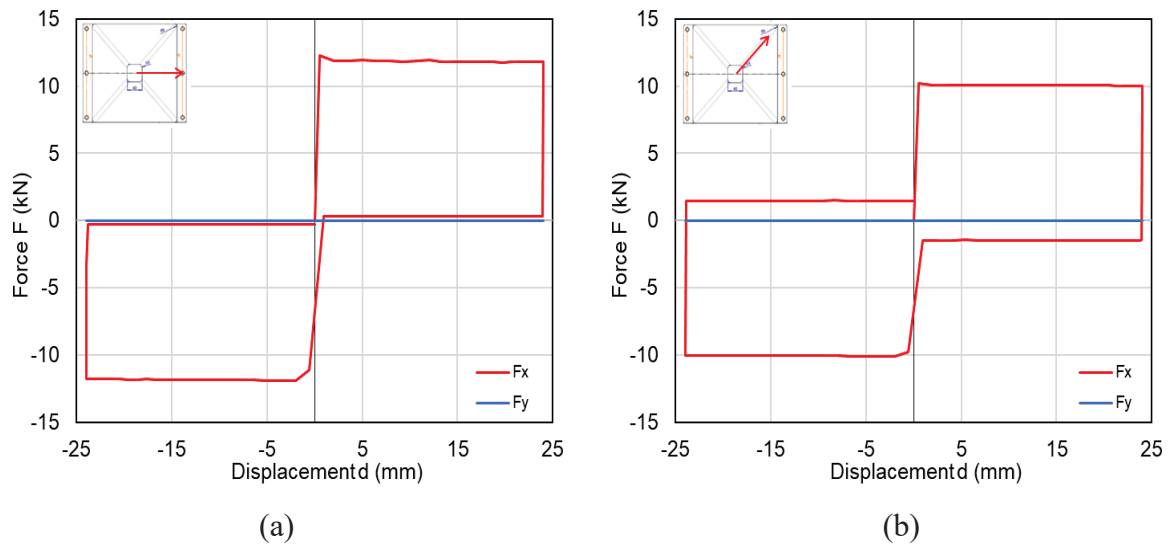


Figure 13 Reaction force parallel and perpendicular to the direction of motion: (a)  $\theta = 0^\circ$ ; (b)  $\theta = 45^\circ$

The reaction bending moment evaluated at the top of the column is shown in Figures 14. In agreement with the results presented in Figure 13, the moment acts only in the plane parallel to the direction of displacement, while the moment  $M_y$  acting in the perpendicular plane is zero. The moment has two contributions, one due to the horizontal reaction force  $F$  produced by the movement along the inclined plane, and the other due to the eccentricity of the vertical force  $N$  due to the displacement of the convex element.

The moment presents non-negligible values (equal to about 50% of the moment at maximum displacement) already for very small movements starting from the initial centered configuration, given by the product of the force  $F$  for the distance of its center of application from the base of the concave element (equal to the thickness of the plate), and grows further with the horizontal displacement  $d$  due to the vertical displacement of the center of application and especially by the eccentricity of the vertical force  $N$  that grows linearly with the displacement  $d$ .

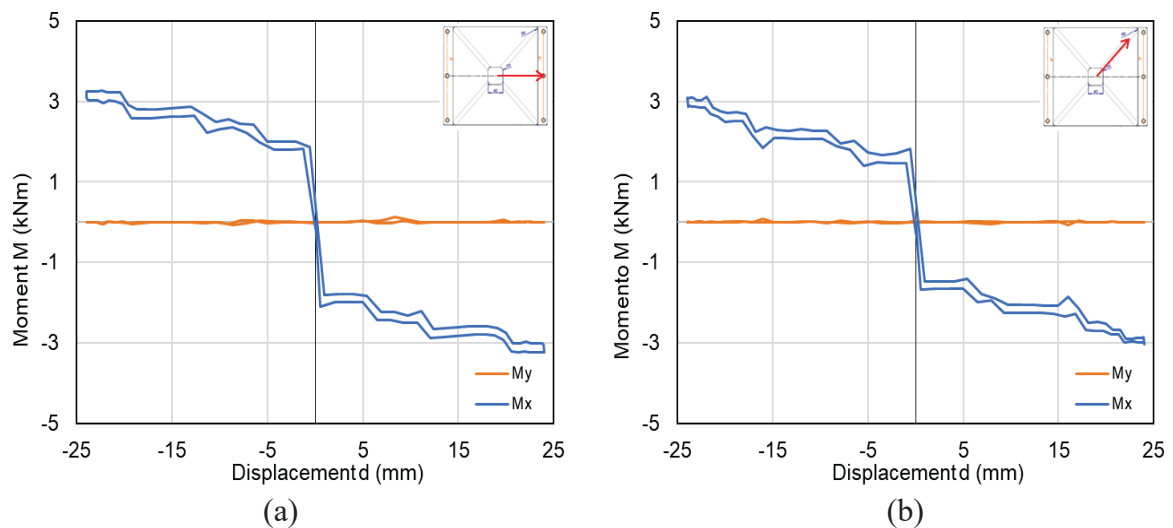


Figure 14 Bending moment at the top of the column: (a)  $\theta = 0^\circ$ ; (b)  $\theta = 45^\circ$

Figure 15 shows the distribution of contact pressures on the surface of the concave element for different values of displacement  $d$ , relative to the analysis with trajectory in the direction  $\theta = 0^\circ$ . As can be seen, the contact initially occurs at the horizontal plane at the bottom of the concave surface, but as the convex component begins to move, the contact is transferred to the inclined surface along which the motion develops. However, the contact remains localized over a limited area of the surface, corresponding to the area over which the tapered end of the convex member crawls, resulting in high contact pressures that, although below the yield strength of the steel, can potentially accelerate surface wear.

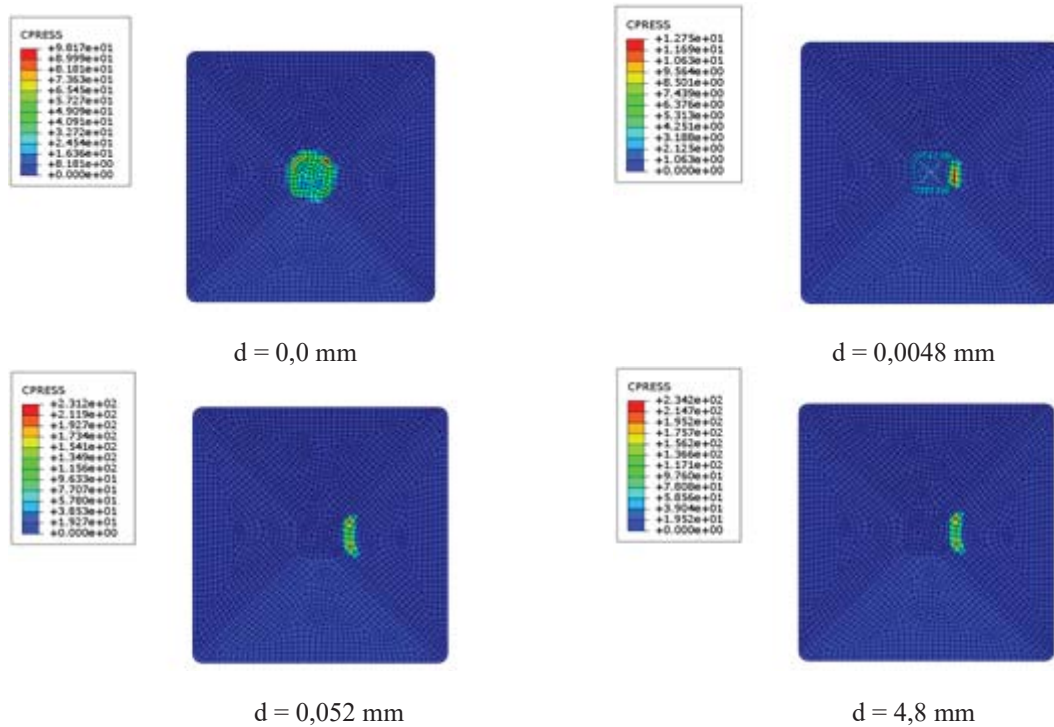


Figure 15 Contact pressures on the surface of the concave element for different values of displacement  $d$



## 5 DISCUSSION AND CONCLUSIONS

The force-displacement curves obtained from the numerical analyses carried out on the prototype and the corresponding experimental curves obtained in the experimental tests are compared in Figure 16.

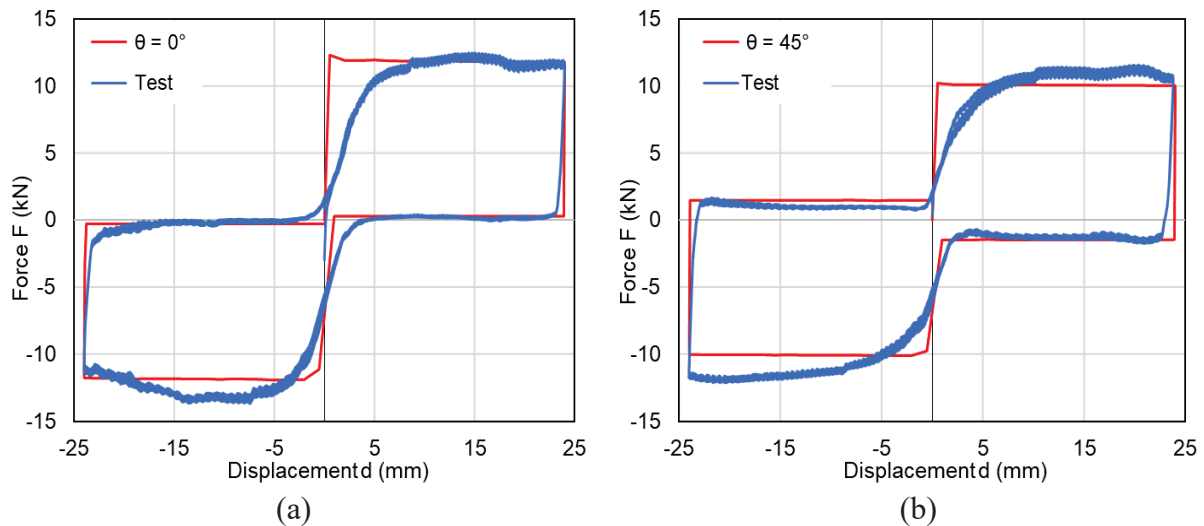


Figure 16 Experimental and numerical force-displacement curve: (a)  $\theta = 0^\circ$ ; (b)  $\theta = 45^\circ$

An acceptable correspondence between the experimental curves and the results of the numerical analyses is apparent. The biggest deviations are near the origin of the displacements and are attributed to the effective geometry of contact between the surfaces in the centered configuration of the device. Since the construction drawings provided by the customer and used for the formulation of the numerical model do not give indications on the construction tolerances, it was not possible to define a priori the characteristics of the initial contact to be reproduced in the analysis.

The horizontal reaction force is kept constant for displacements increasing in modulus and is only weakly influenced by the direction of the trajectory ( $\theta = 0^\circ$  vs.  $\theta = 45^\circ$ ), moreover this response is perfectly consistent with that predicted by a simplified analytical model that takes into account the reaction generated by the movement on an inclined plane and the reaction due to friction between surfaces.

Starting from the compared curves, the numerical model results validated. This allows to proceed to the development of the same starting first from a numerical study, to highlight possible criticalities of this device.

Among the developments will be interesting the study of one-dimensional trajectories along non-symmetrical axes and possible two-dimensional trajectories. In addition, as shown in the results of numerical analysis, a problem to be solved is the presence of the moment at the top of the column; it is possible through the development of this model to evaluate the possibility of introducing a hinge under the concave element in order to avoid eccentricity of the load.

Finally, it will be possible to model an industrial shed with the seismic dissipation device in order to evaluate the actual benefits induced by the presence of the devices.

## REFERENCES

- [1] A. Belleri, M. Torquati, P. Riva, R. Nascimbene, *Vulnerability assessment and retrofit solutions of precast industrial structures*, Earthquakes and Structures, Vol. 8 No. 3 (2015) 801-820.
- [2] M. Bosio, A. Belleri, P. Riva, A. Marini, *Displacement-Based Simplified Seismic Loss Assessment of Italian Precast Buildings*, Journal of Earthquake Engineering 2020, Vol. 24 , No. S1, 60-81.
- [3] A. Formisano, G. Di Lorenzo, R. Landolfo, *Seismic retrofitting of industrial steel buildings hit by the 2012 Emilia-Romagna earthquake: a case study*, Conference Proceedings – October 2018.
- [4] E. Artioli, R. Battaglia, A. Tralli, *Effects of 2012 Emilia earthquake on industrial buildings of early '900 on the Po river line*, Engineering Structures, 56 (2013) 1220-1233.
- [5] “Linee di indirizzo per interventi locali e globali su edifici industriali mono piano non progettati con criteri anti-sismici”, Avallabile from: [http://www.reluis.it/Linee\\_di\\_indirizzo\\_GDL\\_Capannoni.pdf](http://www.reluis.it/Linee_di_indirizzo_GDL_Capannoni.pdf)
- [6] L. Rossi, M. Stuppazzini, D. Parisi, B. Holtschoppen, G. Ruggieri, C. Butenweg, *Empirical Fragility Functions and loss curves for Italian business facilities based on the 2012 Emilia-Romagna earthquake official database*, Bulletin of Earthquake Engineering 2020, 18:1693-1721.
- [7] G. Magliulo, G. Fabbrocino, G. Manfredi, “*Seismic assessment of existing precast industrial buildings using static and dynamic nonlinear analyses*”, Earthquakes Structures 2008, 30(9), 2580-2588
- [8] L. Liberatore, L. Sorrentino, D. Liberatore, LD. Decanini, “*Failure of industrial structures induced by the Emilia (Italy) 2012 earthquakes*”, Engineering Failure Analysis 2013, 34, 629-647.
- [9] A. Belleri, B. Moaveni, J.I. Restrepo, (2014), “*Damage assessment through structural identification of a three-story large-scale precast concrete structure*”, Earthquake Engineering Structure Dynamic., 43(1), 61-76.
- [10] A. Belleri, E. Brunesi, R. Nascimbene, M. Pagani, and P. Riva, *Seismic performance of precast industrial facilities following major earthquakes in the Italian territory*. Journal of Performance of Constructed Facilitiesdoi 2014 :10.1061
- [11] A. Belleri, M. Torquati, P. Riva, and R. Nascimbene. *Vulnerability assessment and retrofit solutions of precast industrial structures*. Earthquake and Structures 2015, 8 (3): 801–20.
- [12] E. Brunesi, R. Nascimbene, D. Bolognini, D. Bellotti. *Experimental investigation of the cyclic response of reinforced precast concrete framed structures*. PCI Journal 2015 (2): 57–79.
- [13] C. Casotto, V. Silva, H. Crowley, R. Nascimbene, R. Pinho. *Seismic fragility of Italian RC precast industrial structures*. Engineering Structures 2015 94: 122–36.
- [14] Colombo, A., P. Negro, G. Toniolo, and M. Lamperti.2016. *Design guidelines for precast structures with cladding panels*. JRC Technical report

- [15] C. Demartino, I. Vanzi, G. Monti, C. Sulpizio, *Precast industrial buildings in Southern Europe: Loss of support at frictional beam-to-column connections under seismic actions*, Bulletin of Earthquake Engineering 2016 (1): 259–94.
- [16] F. Mazza, M. Mazza, *Seismic retrofitting of gravity- loads designed r.c. framed buildings combining CFRP and hysteretic damped braces*, Bulletin of Earthquake Engineering 2019, 17:3423-3445.
- [17] D. A. Bournas, P. Negro, F. Taucer, *Performance of industrial buildings during the Emilia earthquakes in Northern Italy and recommendations for their strengthening*, Bulletin of Earthquake Engineering 2014, vol. 12, 2383–2404.
- [18] P. Martinelli, M. G. Mulas, *An innovative passive control technique for industrial precast frames*, Earthquake Structures 2010: 32 1123-1132.
- [19] V. Quaglini, P. Dubini, C. Poggi, *Experimental assessment of sliding material for seismic isolation system*, Bulletin of Earthquake Engineering, 2012 10:717-740
- [20] Abaqus/CAE 2017 Documentation. Analysis User's Manual, Simulia; 2017.
- [21] V. Quaglini, E. Gandelli, P. Dubini, *Numerical investigation of curved surfaced sliders under bidirectional orbits*, Ingegneria Sismica - International Journal of Earthquake Engineering 2019, Vol. 2.

## INVESTIGATION OF THE BREAKAWAY FRICTION INFLUENCE ON THE SEISMIC RESPONSE OF BUILDINGS ISOLATED WITH CURVED SURFACE SLIDERS

E. Bruschi<sup>1</sup>, V. Quaglini<sup>1</sup>, and E. Gandelli<sup>1</sup>

<sup>1</sup> Politecnico di Milano, Department of Architecture, Built Environment and Construction Engineering,  
Piazza Leonardo da Vinci 32, 20133 Milan, Italy  
e-mail: {eleonora.bruschi, virginio.quaglini, emanuele.gandelli}@polimi.it

---

### Abstract

*Under a seismic excitation the response of a building isolated with curved surface sliders (CSSs) is highly influenced by the breakaway friction coefficient, which is a parameter that governs the transition between the sticking and the sliding behaviour of the isolators. Its effect is detrimental especially in case of low-to-moderate earthquakes; in fact, the inertia forces are not able to overcome the breakaway frictional resistance of the CSS isolators and the structure behaves as a fixed-base building, thus experiencing higher acceleration, inter-storey drifts and internal forces than the isolated building. Usually this parameter is disregarded because the majority of structural analysis programs implement the dynamic friction coefficient only throughout the response history analysis; this leads to a possible overestimation of the displacement demand for the isolation system but a likely unsafe design for the superstructure.*

*In this contribution, the frictional resistance to sliding before the breakaway is simulated through a bidirectional plasticity domain, coded in a finite element of the isolator formulated in OpenSees. Based on this formulation, an exhaustive parametric analysis comprising a range of friction coefficients and superstructure properties is implemented considering a number of natural spectrum-compatible bidirectional ground motions of different intensity levels and frequency contents.*

*Through the review and discussion of the results, the study provides insight into the implications of including the breakaway coefficient in non-linear time history analyses, and recommendations useful to predict the trigger acceleration at which sliding motion starts.*

**Keywords:** Base isolation, Curved surface slider, Friction coefficient, Breakaway effect, Nonlinear time history analyses.

---

## 1 INTRODUCTION

The Curved Surface Slider (CSS) is one of the most popular isolation hardware, whose behaviour depends on two fundamental parameters, namely the coefficient of friction ( $\mu_{dyn}$ ) and the effective radius of curvature ( $R_{eff}$ ) of the sliding surfaces.

During the motion of the CSS, the dynamic friction coefficient at sliding surface  $\mu_{dyn}$  usually increases from a minimum value  $\mu_{LV}$ , in the low-velocity regime, to a steady value  $\mu_{HV}$ , in the high-velocity range, as described by the Eq. (1) of Constantinou et al. [1]:

$$\mu_{dyn} = \mu_{HV} - (\mu_{HV} - \mu_{LV})e^{(-\alpha v)} \quad (1)$$

where  $\alpha$  is the transition rate parameter and  $v$  is the velocity. Nowadays, available commercial FE codes, such as SAP2000 [2] and MIDAS GEN [3], are still based on the friction model of Eq. (1).

However, this formulation is not able to predict the actual response of CSS isolators in the sticking phase preceding the triggering of the sliding motion. In fact, experimental findings reveal that at the beginning of the motion and at any momentary sticking of the sliding surfaces, e.g. at motion reversal, the friction coefficient attains a higher value than  $\mu_{dyn}$ , which is known as the static friction coefficient  $\mu_{ST}$ . This parameter is governed by chemical bonds arising at the interface between the contact surfaces during the sticking phase and the number and strength of these bonds increases with the duration of sticking; indeed, the static coefficient of friction that contrasts the start of the motion (usually denoted as the breakaway friction coefficient  $\mu_B$ ) is reasonably larger than the value observed at motion reversal  $\mu_{rev}$ . Therefore, to properly simulate the actual response of CSSs during both the breakaway and the sliding phase, the numerical formulation should include the breakaway friction coefficient besides the dynamic friction coefficient [4]. Disregarding  $\mu_B$  from the friction model leads to an underestimation of the peak floor accelerations and maximum inter-storey drifts transferred to the superstructure, which are likely to be experienced in the sticking phase before the breakaway.

Some authors ([5] and [6]) developed friction models suitable to account for both forms of static coefficient of friction, at breakaway and at motion reversal. However, both formulations have some drawbacks: in [5] the study was limited to unidirectional trajectories (underestimating the decrease in damping capability induced by frictional heating [7]) and there was no distinction among the different contributions of friction coefficients at the breakaway and at motion reversal, as it implicitly assumed  $\mu_B = \mu_{rev} = \mu_{ST}$ . Also in [6], the work consisted in unidirectional non-linear time history analyses (NLTHAs) and the low-velocity friction coefficient  $\mu_{LV}$  was replaced by the static coefficient of friction  $\mu_{ST}$ , leading to a possible underestimation of the maximum displacement of CSS  $d_{max}$ , as well as an overestimation of the residual displacement  $d_{res}$  [4].

Gandelli et al. [8] studied the effect of different breakaway levels and friction materials on the response of a mid-rise building protected by means of CSS isolators, confirming that the breakaway friction has a major effect on the peak floor acceleration and on the shear at the isolation level, whereas the influence on the maximum displacement of CSS  $d_{max}$  is usually modest. However, the study was conducted only on one building prototype under unidirectional ground-motion, therefore the authors could not claim a general validity for its conclusion.

The present work consists in a more extensive parametric study comprising a significant number of NLTHAs in which different properties of both superstructure and CSS isolation system are taken into account, in order to draw more general conclusions on the effect of the breakaway friction on the seismic response in terms of peak floor acceleration, inter-storey drift, base shear and CSSs displacement demand.



## 2 PARAMETRIC STUDY

A broad parametric study is carried out, performing 9072 bidirectional NLTHAs with the structural analysis program OpenSees [9]. The analyses include different properties of the superstructure, namely number of storeys and base mass to floor mass ratio ( $m_b/m_f$ ), as well as different properties of the CSS isolation systems, considering three friction classes representative of low friction (LF), moderate friction (MF) and high friction (HF) sliding materials. The analyses are performed considering a large group of natural ground motion records having different intensity levels and frequency contents.

### 2.1 Structural models

The case-study structures consist of three RC buildings, conceived as moment-resisting frames of two-storey, four-storey, and six-storey. The structures are designed in compliance with the Italian Building Code NTC2018 [10] and are characterized by a double-symmetric, square plan with three bays of 6 m in both horizontal directions and a constant inter-storey height of 3 m, **Figure 1**.

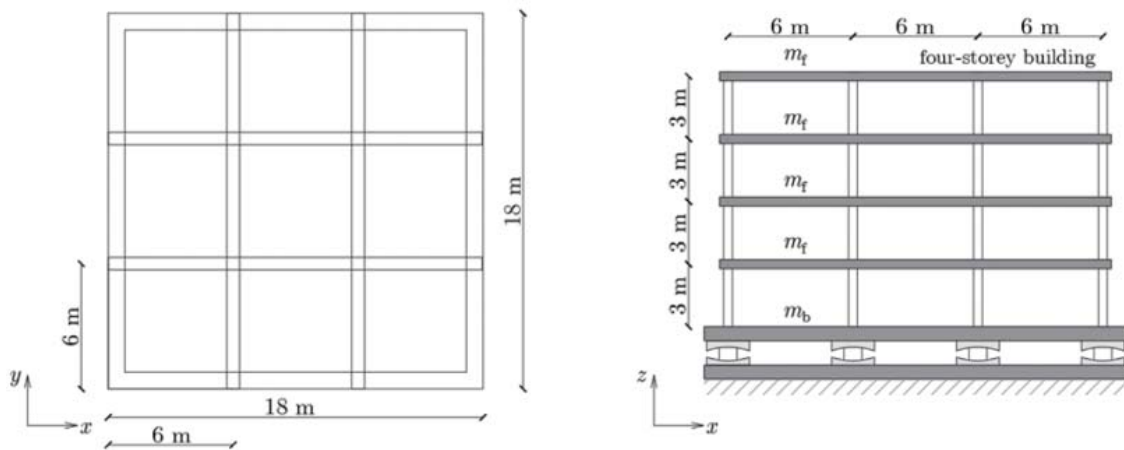


Figure 1: Plan view and front view of representative four-storey building

The concrete compressive strength  $f_c$  is equal to 25 MPa and the steel yield strength  $f_y$  is equal to 450 MPa. Additional information regarding geometry of the structural elements, design loads and fundamental periods are reported in [4].

The structures are modelled in OpenSees [9] as linear elastic systems with *ElasticBeamColumn elements* [11] for beams and columns with appropriate cross-sectional characteristics. The floor slabs are modelled as rigid diaphragms, by using the *RigidFloorDiaphragm* [11] multi-points constraint, imposing the nodes belonging to the same floor to have the same displacement. Therefore, the floor mass ( $m_f$ ) can be lumped at a master node located at the centroid of each floor, along with a mass moment of inertia about vertical axis.

The buildings are isolated with sixteen CSS isolators located underneath each column and connected to each other via a base slab of mass  $m_b$  acting as a rigid diaphragm, which prevents differential displacements. Two base mass to floor mass ratios ( $m_b/m_f = 1.0$  and  $= 2.0$ ) are considered for each building, thus including six different building configurations in the parametric study, in order to verify if this parameter has an influence on the seismic response of the case-study structures.

The damping of the base-isolated system is modelled with a substructure approach, by separating the superstructure component alone from the base isolation system [12] and the superstructure is characterized by a stiffness proportional damping.

The CSSs have an effective radius of curvature  $R_{eff} = 3000mm$ , which corresponds to an undamped period  $T_{iso} = 2\pi(R_{eff}/g)^{0.5} = 3.48s$ , and are modelled with a reduced version of the *BVNC* element developed by Gandelli et al. [13]. The reduced version of this element (hereinafter referred as *BV* element, **Figure 2**) accounts for the breakaway and the velocity effects only. The transition between static and dynamic friction is accomplished by two distinct plastic material models, one for the static friction ruling the breakaway phenomenon, and the other for the dynamic friction after the initiation of the sliding motion. In particular, the *VelDependent* friction model of the *SingleFPSSimple3d* element [11] is used to describe the dynamic friction coefficient, according to the exponential formulation of Eq. (1), excluding the influence of the normal force and of the heating phenomena on the variation of the friction coefficient.

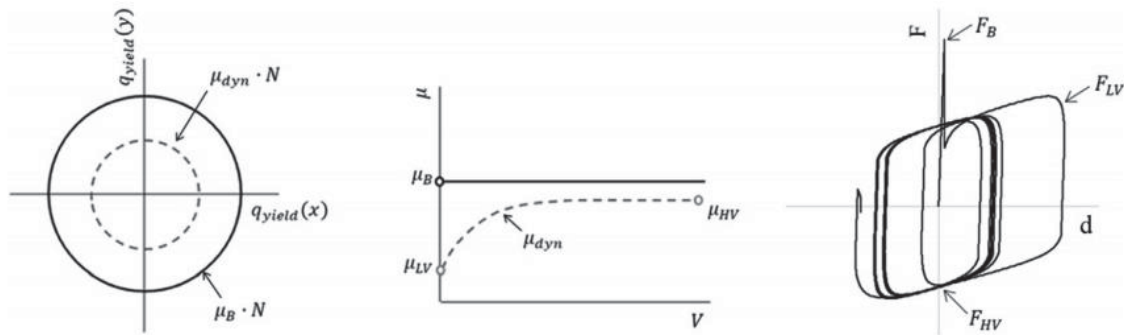


Figure 2: The *BV* element adopted in the present study: relevant bidirectional plasticity domain (left), associated friction model (centre) and response of the element to a sinusoidal excitation (adapted from Gandelli et al. [13])

The study includes three friction classes representative of low friction (LF), moderate friction (MF) and high friction (HF) sliding materials; each friction class has different low-velocity  $\mu_{LV}$  and high-velocity  $\mu_{HV}$  friction coefficients (**Table 1**) with a ratio  $\mu_{HV}/\mu_{LV} = 2.5$ , as indicated in previous literature studies ([14] and [15]). The case  $\mu_B/\mu_{LV} = 1$  corresponds to no-breakaway and is used as baseline reference for comparison, corresponding to the friction models usually implemented in structural analysis programs. The second case  $\mu_B/\mu_{LV} = 2$  corresponds to intermediate breakaway that typically occurs with lubricated sliding material; while, the third case  $\mu_B/\mu_{LV} = 4$  is the high breakaway, that may be caused by unfavourable effects induced by low temperature, poor maintenance conditions of the sliding surfaces, mounting defects [16], as well as possible permanent setting of the surfaces. The value  $\mu_B/\mu_{LV} = 4$  is selected according to the work of Constantinou et al. [1].

For all friction classes, the transition rate parameter  $\alpha$  from the low-velocity to the high-velocity friction is set to 0.0055s/mm.

Friction class	Friction coefficient ( $\mu_{LV}, \mu_{HV}$ )	Breakaway class	Breakaway friction ( $\mu_B$ )	Friction ID
LF	(0.01, 0.025)	$\mu_B/\mu_{LV}=1$	0.01	LF_1
		$\mu_B/\mu_{LV}=2$	0.02	LF_2
		$\mu_B/\mu_{LV}=4$	0.04	LF_4
MF	(0.03, 0.075)	$\mu_B/\mu_{LV}=1$	0.03	MF_1
		$\mu_B/\mu_{LV}=2$	0.06	MF_2
		$\mu_B/\mu_{LV}=4$	0.12	MF_4
HF	(0.05, 0.125)	$\mu_B/\mu_{LV}=1$	0.05	HF_1
		$\mu_B/\mu_{LV}=2$	0.10	HF_2
		$\mu_B/\mu_{LV}=4$	0.20	HF_4

Table 1: Parameters of the dynamic friction and of the breakaway considered in the parametric study

## 2.2 Seismic input

Non-linear dynamic analyses have been performed considering natural ground motions characterized by two horizontal components, whereas the vertical component of the seismic input is ignored. The accelerograms are selected from the European strong-motion database [17] by means of the software REXEL v. 3.5 [18].

The parametric study is performed considering two installation sites: Lamezia Terme (latitude  $38.58^\circ$ , longitude  $16.18^\circ$ ) and Naples (latitude  $40.86^\circ$ , longitude  $14.28^\circ$ ), which respectively belong to the seismic zone 1 (high probability of occurrence of strong earthquakes) and the seismic zone 2 (moderate probability of occurrence of strong earthquakes) of the old national classification [19]. The accelerograms are consistent with the elastic spectrum associated to an ordinary structure with nominal life  $V_n = 50$  years and functional class II corresponding to  $c_u = 1.0$ . Both serviceability limit state (SLD) and life-safety limit state (SLV) are used for the selection of the accelerograms; a topography condition  $T_1$  and two different soil conditions, designated as soil class A and soil class C, are considered. For each installation site, soil class and limit state, a suite of 21 independent bidirectional natural ground motion records are selected with a magnitude range  $M_w$  between 5 and 8. In order to include different fault distances, these 21 records include 7 events recorded at epicentral distance  $R_{ep}$  between 0 and 10 km, 7 events with  $R_{ep}$  between 10 and 20 km and the remaining 7 events with  $R_{ep}$  between 20 and 50 km. Additional details pertaining to the input ground motions are provided in [4] and **Figure 3**.

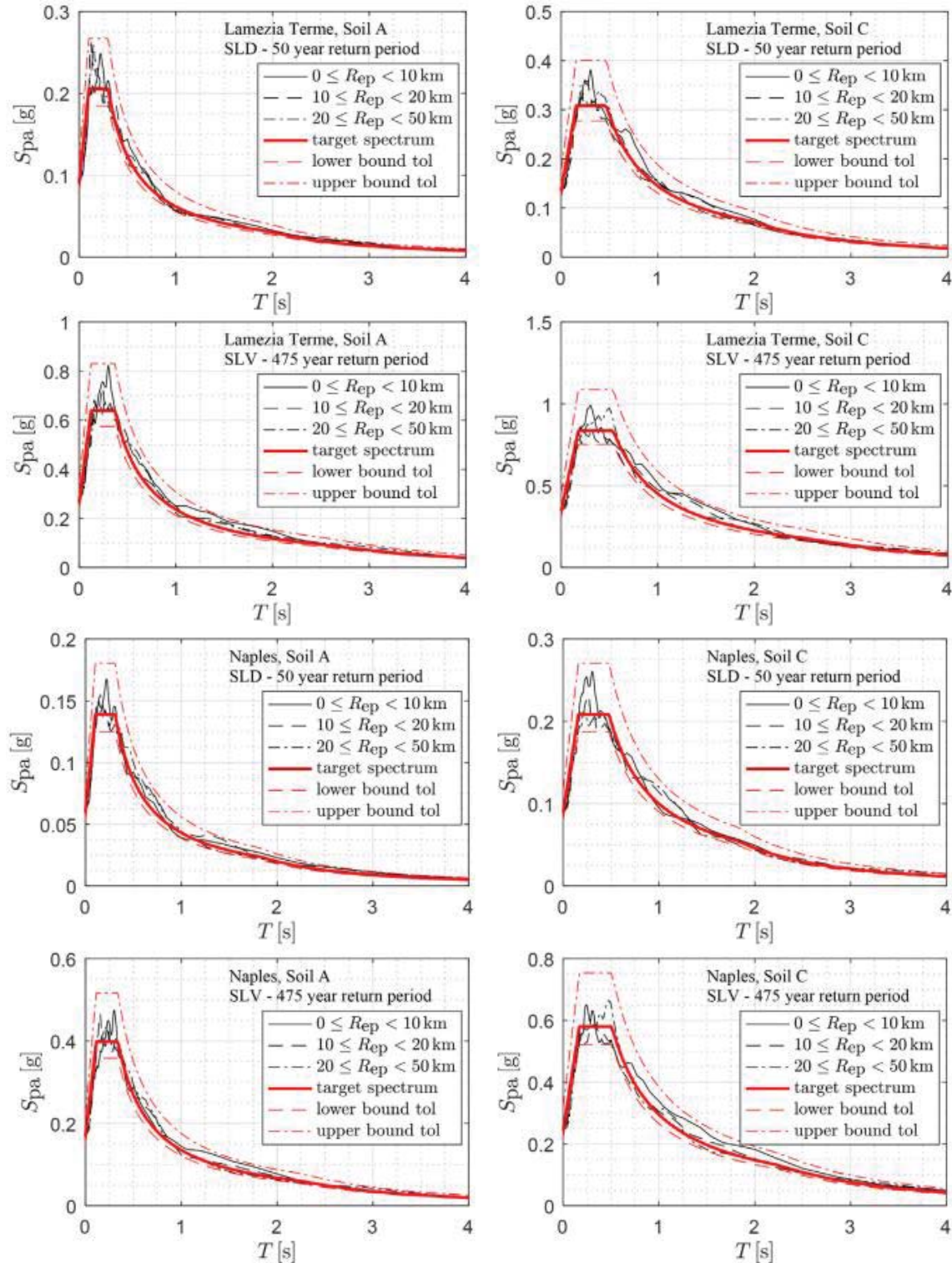


Figure 3: Target response spectra and median response spectra for the two installation sites, two soil classes and three epicentral distances

### 3 RESULTS AND DISCUSSION

The output of the NLTHAs on the base-isolated structure is analysed in terms of four response parameters representative of both the superstructure response and the base isolation system response, namely (i) Peak Floor Acceleration (*PFA*), (ii) Inter-storey Drift Ratio (*IDR*),

(iii) displacement of the base isolation system ( $d_{iso}$ ), and (iv) shear force carried by the isolation system normalized to the total seismic weight  $V_{iso}/W_{tot}$ , where  $W_{tot}$  is given by the sum of  $W_{ss}$  (equal to the sum of the seismic weight of each floor) and  $W_{bs}$  (equal to the seismic weight of the base). The maximum values of each parameter are extracted from the 9072 NLTHAs and then statistically processed to obtain average maximum response quantities.

**Figure 4** and **Figure 5** show the average response parameters of the base-isolated buildings in terms of *PFA*, maximum *IDR*, isolators' displacement  $d_{iso}$ , and normalized shear force carried by the isolation unit  $V_{iso}/W_{tot}$ , for serviceability earthquakes at SLD and life-safety earthquakes at SLV respectively. The results are organized distinguishing between the three friction classes (LF, MF and HF) and the three breakaway classes  $\mu_B/\mu_{LV} = 1.0, 2.0, 4.0$ , where  $\mu_B/\mu_{LV} = 1.0$  represents the baseline reference model.

Referring to SLD case (**Figure 4**), the breakaway friction tends to increase the *PFA*, maximum *IDR* and maximum normalized  $V_{iso}$ , in comparison to the baseline reference model  $\mu_B/\mu_{LV} = 1.0$ . MF and HF friction class isolators show a similar trend for all the three parameters with a more relevant increase than that LF friction class isolators, especially for  $\mu_B/\mu_{LV} = 4.0$ . On the other hand, the isolators' peak displacement  $d_{iso}$  does not seem to be affected by the breakaway friction, indeed, the three curves do not show substantial differences compared to the baseline reference model  $\mu_B/\mu_{LV} = 1.0$ .

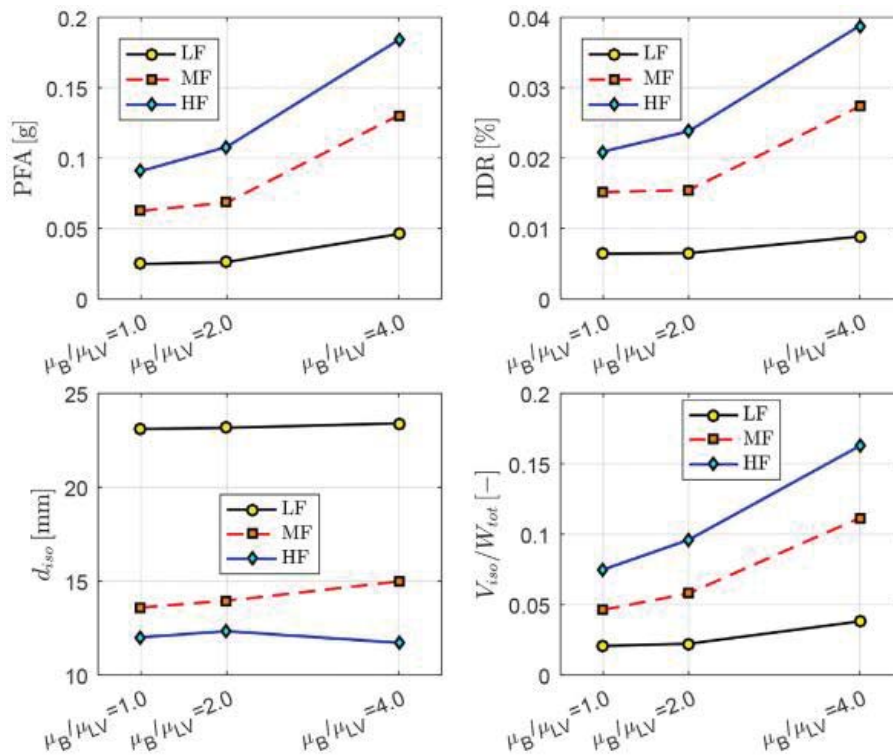
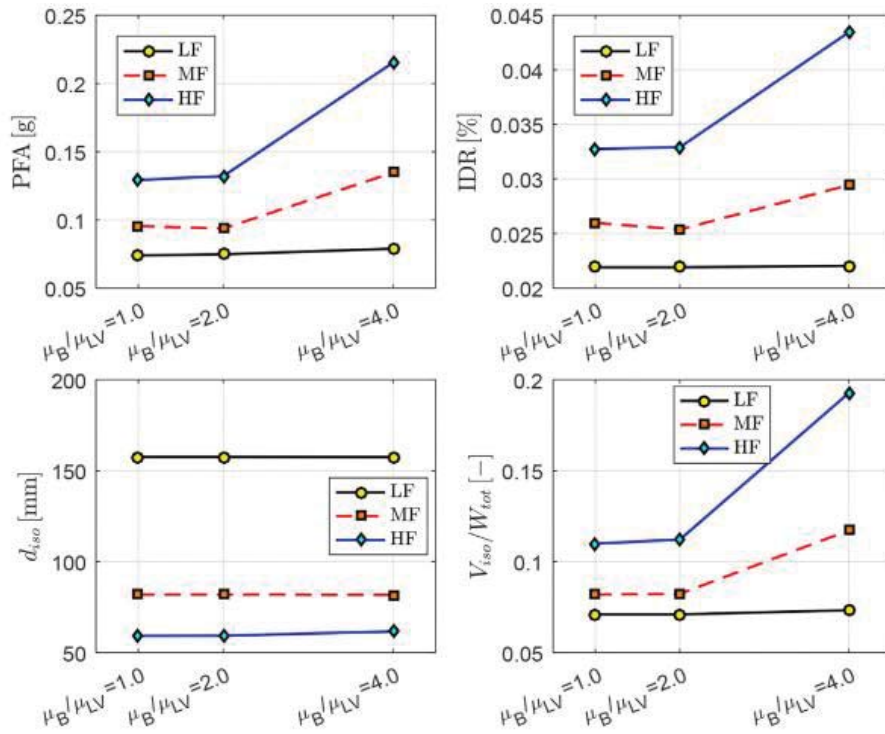


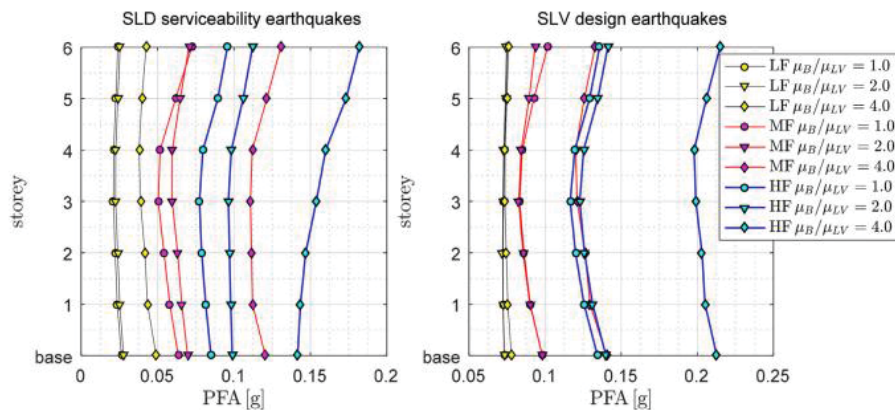
Figure 4: Average response parameters (*PFA*, *IDR*,  $d_{iso}$ ,  $V_{iso}/W_{tot}$ ) at SLD

With regard to SLV case (**Figure 5**), LF friction class isolators seem not influenced by the breakaway friction, while both MF and HF friction class CSSs increase significantly the *PFA*, maximum *IDR* and maximum normalized  $V_{iso}$ , especially for  $\mu_B/\mu_{LV} = 4.0$ . Also for SLV, as in SLD, the maximum displacement of the isolators  $d_{iso}$  is not influenced by the breakaway friction coefficient.



Figure 5: Average response parameters (PFA, IDR,  $d_{iso}$ ,  $V_{iso}/W_{tot}$ ) at SLV

The results of **Figure 4** and **Figure 5** are confirmed by looking at the overall behaviour of the superstructure in terms of *PFA*s, **Figure 6**. The superstructure model analysed in NLTHAs experiences higher *PFA*s due to the delayed engagement of the isolators at both SLD and SLV. **Figure 6** shows that under low-to-moderate intensity earthquake, typical of SLD, the breakaway friction has a major influence especially in case of MF and HF friction class; in fact, CSSs with higher coefficient of friction may remain in the sticking phase over the entire duration of the ground motion, consequently the structure behaves as a fixed-based building and the *PFA*s are much higher than the isolation building scenario.

Figure 6: Average PFA profiles at SLD (left) and SLV (right) along the height of the 6-storey building for different friction classes and  $\mu_B/\mu_{LV}$  ratios

Based on the previous considerations, a fundamental design parameter is the trigger acceleration  $a_{trigger}$ , meant as the minimum value of the ground acceleration capable of activating the sliding motion; indeed, for earthquakes characterized by a peak ground acceleration lower than  $a_{trigger}$ , the isolation system would not be activated, with potential detrimental conse-

quences on the internal forces in the superstructure. The most simple way to analytically determine  $a_{trigger}$  is referring to the simple two-degree-of-freedom (2DOF) system, consisting of two masses, namely superstructure mass  $m_s$  and base mass  $m_b$ , connected to the ground by a CSS bearing with coefficient of friction at breakaway  $\mu_B$  [8]. The sliding motion is triggered when the shear force through the CSS exceeds the resisting breakaway frictional force  $F_B$  evaluated as  $\mu_B(m_s+m_b)g$ , where  $g$  is the acceleration of gravity [4] and this condition is achieved when the ground motion acceleration  $a_g$  is larger than the trigger value  $a_{trigger}$ .

In 439 out of 9072 NLTHAs the CSSs were not engaged at all over the duration of the ground motion, meaning that the inertia force induced by the ground motion acceleration was not able to overcome  $F_B$ . As expected, all these cases belong to the low-intensity serviceability earthquakes, SLD.

**Figure 7** shows the relationship among the no-activation cases with the breakaway friction coefficients  $\mu_B$ , the soil class and the epicentral distance. The number of no-activation cases increases with increasing of  $\mu_B$ , and all the cases are concentrated in the range 0.10 – 0.20. No-activation cases seem marginally influenced by the epicentral distance of the earthquake, as the trend is almost equally distributed among the three values  $R_1$  ( $0 \text{ km} \leq R_{ep} \leq 10 \text{ km}$ ),  $R_2$  ( $10 \text{ km} \leq R_{ep} \leq 20 \text{ km}$ ) and  $R_3$  ( $20 \text{ km} \leq R_{ep} \leq 50 \text{ km}$ ). Whereas the soil class show a significant influence on the occurrence of no-activation condition, since 374 out of the 439 cases are obtained for rigid soil condition (soil A), and only the remaining 65 cases are observed for medium soil conditions (soil C), typically characterized by higher values of  $PGA$  (Peak Ground Acceleration) and of spectral acceleration corresponding to the fundamental period of the superstructure.

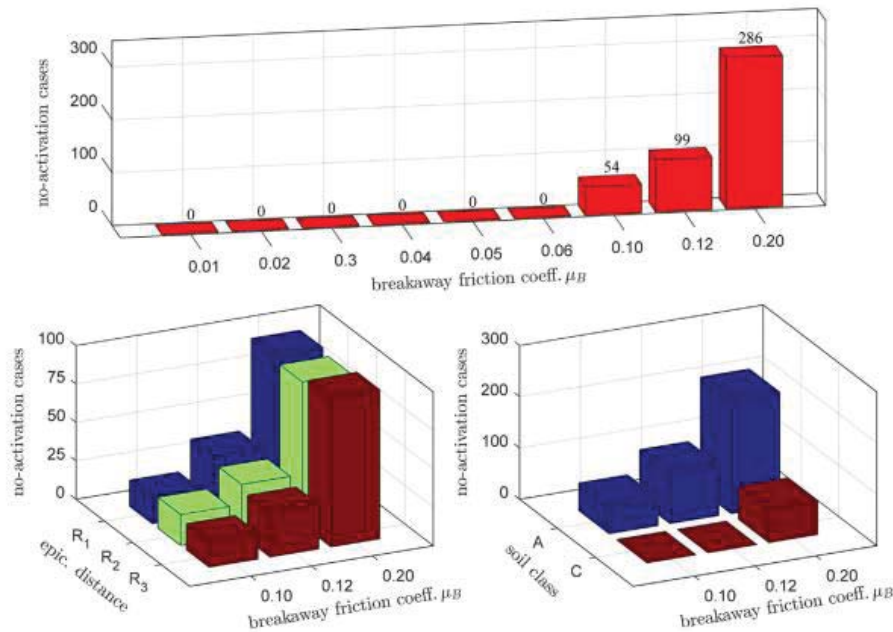


Figure 7: No-activation cases in relationship to the breakaway friction coefficient (top) and sub-analysis depending on the epicentral distance (bottom left) and soil class (bottom right)

The parametric study has also included two values of the mass ratio  $m_b/m_f$ , however the influence of this parameter on the results in terms of  $a_{trigger}$  as well as in terms of the considered seismic response parameters did not show a clear trend, and seems to be marginal at least for the building configurations and seismic excitations considered in this study.

## 4 CONCLUSIONS

The study investigated the influence of the breakaway friction coefficient  $\mu_B$  on the seismic response of base-isolated buildings, by implementing in OpenSees [9] a friction model capable to reproduce the transition between the breakaway friction  $\mu_B$  in the sticking phase and the velocity-dependent friction model in the subsequent sliding phase.

In order to draw the most general conclusions, an extensive parametric study comprising more than 9000 bidirectional NLTHAs has been performed, including three case-study buildings with increasing number of stories (2, 4 and 6), two different mass distributions ( $m_b/m_f = 1.0$  and  $= 2.0$ ), three friction classes (LF, MF and HF) and three breakaway friction classes ( $\mu_B/\mu_{LV} = 1.0, 2.0$  and  $4.0$ ), **Table 1**. For the characterization of the seismic input, two intensity levels of the earthquake excitations, associated to either serviceability SLD or life-safety SLV limit states, two soil characteristics (class A and class C), three epicentral distances ( $R_{ep} = 0\div 10\text{km}$ ,  $10\div 20\text{km}$  and  $20\div 50\text{km}$ ) and two installation sites (Lamezia Terme and Naples) have been considered, thus including 168 spectrum-compatible bidirectional components of ground motion acceleration.

The results showed that in both SLD and SLV conditions, the sliding motion may be delayed by a high breakaway frictional resistance, and the CSSs may persist in the sticking phase for a relatively long part of the ground motion, affecting significantly the seismic response of the superstructure and of the isolation system. In fact, the buildings experienced higher inter-storey drifts *IDRs* and peak floor accelerations *PFA*s, as well as the isolation system engaged significantly higher normalized shear force  $V_{iso}$ , whereas was marginally affected in terms of displacement  $d_{iso}$ .

Especially when the breakaway coefficient is relatively high and the base-isolated structures are subjected to low-to-moderate intensity earthquakes (typical of SLD), the CSSs may persist in the sticking phase over the entire duration of the ground motion. This phenomenon was observed in 439 out of the 9072 NLTHAs included in the parametric study, and the majority (85%) occurred for ground motions relevant to soil class A. It is likely that this occurs because both the *PGA* (Peak Ground Acceleration) and the spectral acceleration corresponding to the fundamental period of the superstructure are higher in the soil class C than in the soil class A.

Although these conclusions are confined to the examined cases, the present work provides some insight into the effects of breakaway friction coefficient on the seismic response of base-isolated buildings, highlighting the necessity to include this parameter in the NLTHAs.

## REFERENCES

- [1] M.C. Constantinou, A. Mokha, A. Reinhorn. Teflon bearings in base isolation II: modeling. *Journal of Structural Engineering ASCE*, **116**(2), 455–474, 1990. [https://doi.org/10.1061/\(ASCE\)0733-9445\(1990\)116:2\(455\)](https://doi.org/10.1061/(ASCE)0733-9445(1990)116:2(455)).
- [2] Computer and Structures. SAP2000 Analysis Reference, Vol. 1., 1997, Berkeley.
- [3] Midas, Midas Gen V7.6.1, 2008, On-line Manual, <http://www.MidasUser.com>.
- [4] E. Gandelli, D. De Domenico, P. Dubini, M. Besio, E. Bruschi, V. Quaglini. Influence of the breakaway friction on the seismic response of buildings isolated with curved surface sliders: Parametric study and design recommendations, *Structures*, **27**, 788–812, 2020, <https://doi.org/10.1016/j.istruc.2020.06.035>.
- [5] V. Quaglini, M. Bocciarelli, E. Gandelli, P. Dubini. Numerical assessment of frictional heating in sliding bearings for seismic isolation. *Journal of Earthquake Engineering*, **18**(8), 1198–1216, 2014. <https://doi.org/10.1080/13632469.2014.924890>.
- [6] E. Fagà, P. Ceresa, R. Nascimbene, M. Moratti, A. Pavese. Modelling curved surface sliding bearings with bilinear constitutive law: effects on the response of seismically isolated buildings. *Material and Structures*, **49**(6), 2179–2196, 2015. <https://doi.org/10.1617/s11527-015-0642-2>.
- [7] V. Quaglini, E. Gandelli, P. Dubini. Numerical investigation of curved surface sliders under bidirectional orbits, *Ingegneria Sismica - International Journal of Earthquake Engineering*, **2**, 2019, Pàtron editore
- [8] E. Gandelli, V. Quaglini. Effect of the static coefficient of friction of curved surface sliders on the response of an isolated building. *Journal of Earthquake Engineering*, 2018. <https://doi.org/10.1080/13632469.2018.1467353>.
- [9] F. McKenna, G. Fenves, M. Scott. Computer program OpenSees: open system for earthquake engineering simulation, 2006, <https://opensees.berkeley.edu>.
- [10] NTC2018. CSLLPP - Consiglio Superiore dei Lavori Pubblici. Norme Tecniche per le Costruzioni. Gazzetta Ufficiale 495 della Repubblica Italiana, No. 42 of 20 February 2018. Rome, Italy, (in Italian).
- [11] OpenSeesWiki, online manual, available at: [http://opensees.berkeley.edu/wiki/index.php/Main\\_Page](http://opensees.berkeley.edu/wiki/index.php/Main_Page).
- [12] D. De Domenico, G. Falsone, G. Ricciardi. Improved response-spectrum analysis of base-isolated buildings: a substructure-based response spectrum method. *Engineering Structures*, **162**, 198–212, 2018. <https://doi.org/10.1016/j.engstruct.2018.02.037>.
- [13] E. Gandelli, M. Penati, V. Quaglini, G. Lomiento, E. Miglio, G. Benzoni. A novel OpenSees element for single curved surface sliding isolators. *Journal of Soil Dynamics and Earthquake Engineering*, **119**, 433–454, 2019, <https://doi.org/10.1016/j.soildyn.2018.01.044>.
- [14] M.C. Constantinou, P. Tsopelas, A. Kasalanati, E.D. Wolff. Property modification factors for seismic isolation bearings. Report No. MCEER-99-0012, 1999, National Center for Earthquake Engineering Research, Buffalo.

- [15] V. Quaglini, E. Gandelli, P. Dubini, MP Limongelli. Total displacement of curved surface sliders under nonseismic and seismic actions: a parametric study. *Structural Control and Health Monitoring*, **24**(12):e2031, <https://doi.org/10.1002/stc.2031>.
- [16] A. Pavese, M. Furinghetti, C. Casarotti. Investigation of the consequences of mounting-laying defects for curved surface slider devices under general seismic input. *Journal of Earthquake Engineering*, **23**(3), 377–403, 2019. <https://doi.org/10.1080/13632469.2017.1323046>.
- [17] N. Ambraseys, P. Smit, R. Sigbjornsson, P. Suhadolc, B. Margaris. Internet-Site for European Strong-Motion Data, European Commission, Research-Directorate General, Environment and Climate Programme 2002.
- [18] I. Iervolino, C. Galasso, E. Cosenza. REXEL: computer aided record selection for code-based seismic structural analysis. *Bulletin of Earthquake Engineering*, **8**, 339–362, 2010. <https://doi.org/10.1007/s10518-009-9146-1>.
- [19] OPCM 3274. Ordinanza del Presidente del Consiglio dei Ministri n. 3274. Primi elementi in materia di criteri generali per la classificazione sismica del territorio nazionale e di normative tecniche per le costruzioni in zona sismica [in Italian], 2003.



## SUPPLEMENTAL ENERGY DISSIPATION WITH PRESTRESSED LEAD EXTRUSION DAMPERS (P-LED): EXPERIMENTS AND MODELING

C. Pettoruso<sup>1\*</sup>, E. Bruschi<sup>1</sup>, V. Quaglini<sup>1</sup>

<sup>1</sup> Politecnico di Milano, Department of Architecture, Built Environment and Construction Engineering,  
Piazza Leonardo da Vinci 32, 20133 Milan, Italy  
e-mail: { carlo.pettoruso, eleonora.bruschi, virginio.quaglini }@polimi.it

---

### Abstract

*Supplemental energy dissipation devices are employed both in new and retrofitted constructions in order to prevent structural damage, increase life-safety and achieve a desired level of performance. Among these devices, hysteretic dampers have been proven to be an appropriate and economically affordable solution to reduce the vulnerability of ordinary structures, such as residential, school and industrial buildings. The study presents an experimental and numerical investigation of a Prestressed Lead Extrusion Damper (P-LED), an emerging energy dissipation device which provides energy dissipation by means of the plastic extrusion of lead through an orifice created between a containing tube and a moving shaft and achieves high specific output force by preloading of the working material.*

*The experimental investigation is performed following the provisions set in the European standard EN 15129 for Displacement Dependent Devices. A damper prototype is tested in cyclic tests at different displacement amplitudes and in a monotonic ramp up to the amplified design deformation. The damper shows a rigid-plastic behavior, without strength degradation regardless of the imposed deflection; the shape of the hysteresis loops is essentially rectangular, resulting in an effective damping of 0.55, very close to the maximum theoretical level; the device is able to sustain multiple cycles of motion at the basic design earthquake displacement, anticipating a maintenance-free operation even in presence of repeated ground shakes. A 3D finite element model of the P-LED is formulated in Abaqus and validated upon the results of the experimental tests. The model enlightens that the output force of the damper accounts for two contributions, namely the extrusion force of the lead and the friction force between the lead and the moving shaft. The model is then used in a parametric study to investigate the influence of the device dimensions, namely the diameters of the shaft, of the containing tube and of the bulge, and the length of the shaft, on the output force. The numerical data points are fitted by a simple model which can be used for design of the damper to a specific quasi-static force.*

**Keywords:** Lead Extrusion Damper, EN 15129, energy dissipation, experimental assessment, finite element model.

---

## 1 INTRODUCTION

Supplemental energy dissipation is employed both in new and retrofitted constructions in order to prevent structural damage, increase life-safety and achieve a desired level of performance ([1],[2]), appearing an appropriate and economically affordable solution to reduce the vulnerability of ordinary structures, such as residential, school and industrial buildings [3]-[6].

Current energy dissipation devices can be classified in two main categories [7]: (i) the so-called fluid viscous dampers, where the dissipation is achieved through the lamination of a viscous fluid forced by a piston to pass through an orifice or a valving system, and whose behavior strictly depends on the fluid velocity; (ii) the hysteretic dampers, which are further classified in hysteretic steel dampers, friction dampers and metal extrusion dampers, depending on the mechanism actually used to dissipate the seismic energy.

Most of the dampers used in residential, school and industrial buildings belong to the hysteretic damper's category ([2],[4],[6],[8] and [9]), whose constitutive law mainly depends on the displacement.

Supplemental energy dissipation is typically implemented by providing the structure with dissipative bracing systems, made of steel braces incorporating dissipation devices [10]. This approach is aimed at achieving two effects, namely increase the structural stiffness, which reduces the structural displacement, and dissipate much of the seismic energy, which reduces the structural acceleration [11].

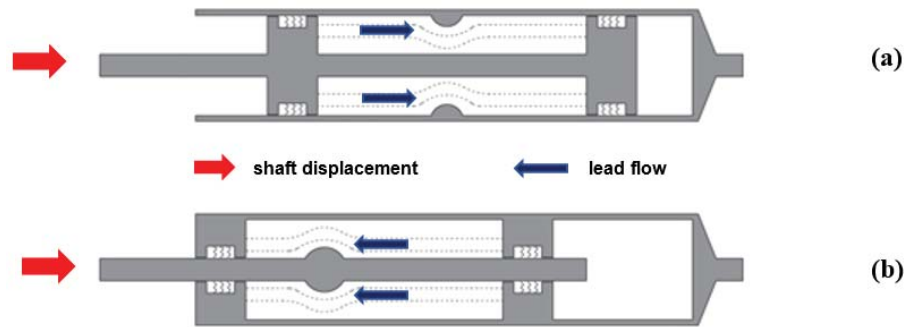
However, though in principle dissipative braces represent a viable solution to protect any kind of building, they show some drawbacks such as increased internal forces in beams and columns, modification of the building layout, and in case of retrofit, the need of a significant amount of construction work, resulting in heavy disturbance to the occupants [12]. For these reasons, their application is more feasible in new constructions, where the provision of the dissipative braces can be planned since the beginning, rather than for retrofit, because of architectural issues posed by the braces, like interference with the design of the façade and position of the openings [12]. Another issue concerns the fact that the design of dissipative bracing systems is performed respecting the "structural safety requirement" at the Ultimate Limit State only ([2],[10],[13]-[15]); indeed, the devices are designed not to be engaged under normal service loads and weak seismic excitations [12]. Consequently, under small earthquakes, a structure equipped with dissipative braces is subjected to greater accelerations than the bare configuration [5]. Moreover, tests carried out at the University of Basilicata (Italy) [16] have shown that the significant reduction of the frame lateral deformation, brought by the introduction of the hysteretic braces, is counteracted by a huge increase of Peak Floor Accelerations [5]. Similar results were obtained also from the numerical analyses performed by Gandelli et al. [17] on a hospital building equipped with dissipative bracing systems. This phenomenon has detrimental consequences especially to acceleration-sensitive non-structural components [5],[17]. In recent years, some researchers suggested using new kind of systems to control multi-levels of earthquake energy [6], to achieve stable deformation, increase structural ductility, and increase energy dissipation capacity with different stiffnesses [5], [18], [19] and [20].

Moreover, because of low-cycle fatigue and residual stresses of steel dampers, or large permanent deformations of friction and extrusion dampers, after a severe earthquake hysteretic dampers need to be replaced or restated, with consequent costs but also with a potential threat to the safety of the structure, which is left exposed to aftershocks which may occur in the aftermath of the main event.

In conclusion, a more robust form of energy dissipation is needed that satisfies several objectives [21]: (i) more compact and architecturally less invasive design in order to be ideally

located within the beam-column joint region; (ii) should not require maintenance after a major earthquake, in order to guarantee a high safety level and maintain an economical appeal, especially for the retrofitting of conventional buildings; (iii) should not be at risk of low-cycle fatigue bar fracture; (iv) should ensure the re-centering of the structure; and (v) the cost of devices should be economical compared with conventional design solutions.

An emerging energy dissipation device likely to satisfy these conditions is the lead extrusion damper [22], [23], which dissipates energy through the plastic extrusion of lead, forced to flow through an annular restriction (Figure 1) provided either from a constriction of the tube (a), or a bulged shaft (b).



**Figure 1: Longitudinal sections of lead extrusion damper: (a) constricted tube type; (b) bulged shaft type. Adapted from [24]**

Two forces contribute to the overall output force of the device, namely the frictional resistance of the working material against the moving shaft, and the extrusion resistance of the lead that is forced to flow through the annular orifice [25], [26], making the device weakly dependent upon the velocity [27]. A part of the energy is immediately dissipated as heat, which induces softening of the working material and reduces its strength. However, the effect is temporary, because when the device is allowed to cool down, the original value of resistive force is recovered [26]. The other part of the energy is stored in the deformed lead which quickly recrystallizes and regains its original properties, resulting in consistent force across multiple cycles of response without any strain hardening or loss of strength or stiffness [23].

The main drawback of this device is the formation of voids within the working material during extrusion, which is attributed to compression of the lead: as the shaft moves, the material is compressed into a smaller volume leading to the formation of a trailing void [28], causing a decrease of the energy dissipation. For this reason, the lead extrusion dampers used in the first structural applications were quite large, in order to provide sufficient reaction force [22], [23]. Only in the first decade of the 21st century, Rodgers ([28], [29]) proposed an improved version called HF2V (High Force to Volume) where a substantial increase in the specific force was achieved by preloading the working material during the assembly. Increasing the internal pressure of the system reduced the formation of trailing voids and increased the reaction force and the force-to-volume ratio, allowing a more compact design. This device presents an essentially rectangular hysteretic curve, which maximizes the amount of energy dissipation for a given applied force and displacement with a stable and repeatable behavior, an insignificant sensitivity to aging and environment, compact dimensions, and low cost [29]-[31].

The present study deals with the Prestressed Lead Extrusion Damper (P-LED), which achieves high specific output force by preloading of the working material [28]. The performance of the damper is assessed experimentally to verify the compliance to the requirements of the European standard [32]. Then, a finite element model is formulated and used to investigate the influence of the device dimensions on the output force. The numerical data points are

fitted by a simple model which can be used for design of the damper to a specific quasi-static force.

## 2 EXPERIMENTAL INVESTIGATION

### 2.1 Description of the prototype

A bulged-shaft type Prestressed Lead Extrusion Damper has been experimentally investigated in the study. The prototype has four main components, namely the bulged shaft, the tube, the cap and the working material (Figure 2). Tube, shaft and cap are made of structural steel, while the working material is 99.99% pure lead. The shaft is plated with hard chromium (70  $\mu\text{m}$  thickness) in order to minimize friction and wear when sliding through the bushing provided in the cap. The cap is fixed to the tube wall by means of eight screws.

The characteristic dimensions of the device are: shaft diameter  $D_s = 32$  mm; bulge diameter  $D_{blg} = 42$  mm; inner diameter of the tube  $D_{cyl} = 60$  mm; length of shaft in contact with the working material  $D_s = 95$  mm. The design deflection is  $d_{bd} = 20$  mm in either direction (i.e., 40 mm total stroke). To maintain the reaction aligned along the major axis of the device and avoid bending of the shaft, self-lubricating spherical hinges with a minimum rotation capacity of  $\pm 2^\circ$  are provided at both ends of the damper, namely at one end of the shaft and on the bottom of the tube.

During the assembling process, the working material was prestressed to a nominal force of 280 kN (corresponding to an average pressure of 138 MPa on lead) by tightening the screws connecting the cap to the tube wall. Pre-stressing the working material was aimed at increasing the friction between the tube and the shaft and preventing coring out of the lead as the bulge is forced through.

Three thermocouples were inserted into  $\varnothing 5$  mm blind holes drilled in the lateral wall of the containing tube, about 5 mm away from the chamber filled with the working material, in order to measure the temperature rise during the extrusion process.

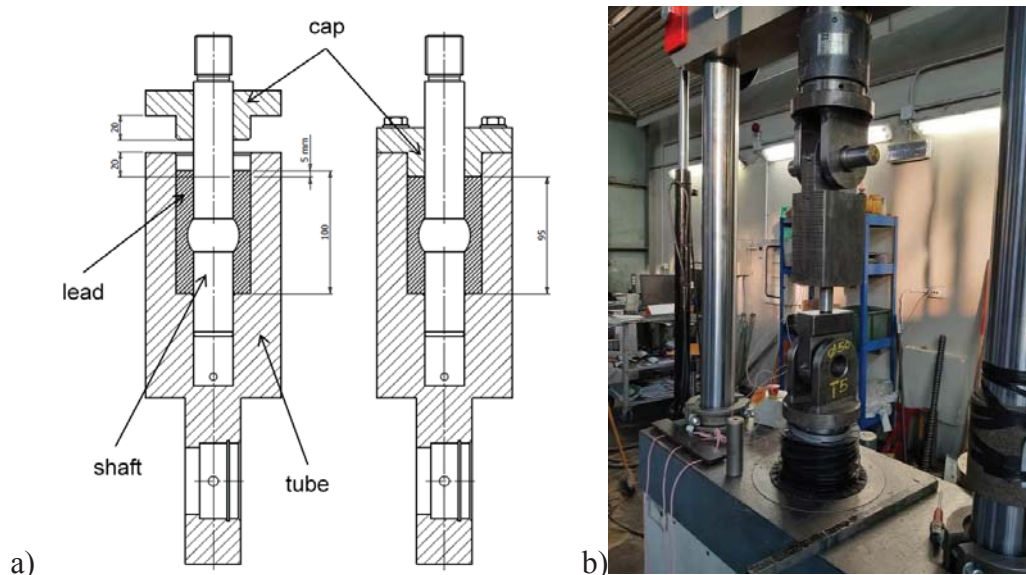


Figure 2: (a) Cross-section of the bulged-shaft P-LED; (b) prototype on the testing machine

### 2.2 Experimental procedure

The experiments were performed at the Materials Testing Laboratory of Politecnico di Milano, using a 500 kN servohydraulic testing machine (MTS Systems, Eden Prairie, MN).



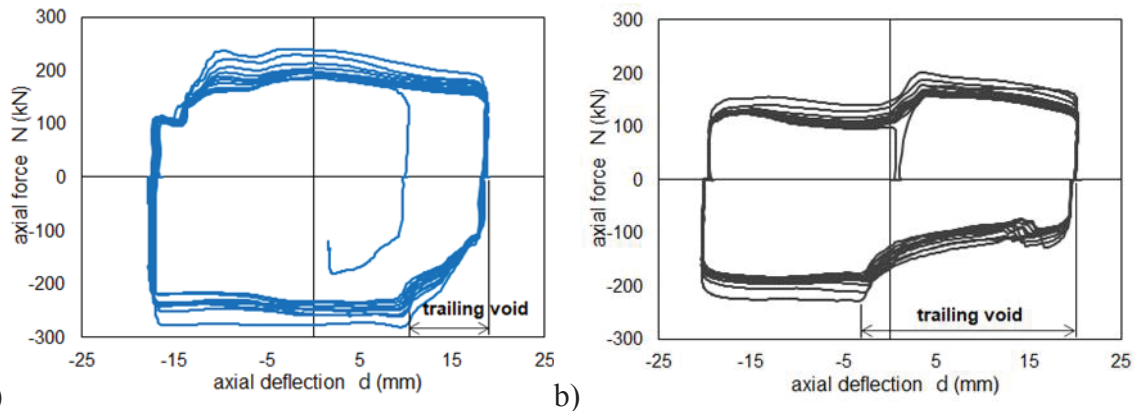
The specimen was subjected to the type testing protocol prescribed in the European standard EN 15129 [32] for assessment of Displacement Dependent Devices, i.e. damping systems whose reaction force depends essentially on the displacement. The hysteretic force-deflection response was evaluated by imposing harmonic cycles of increasing amplitude at 25%, 50% and 100 % of the design deflection  $d_{bd} = 20$  mm, at a loading frequency of 0.5 Hz. Five cycles for each intermediate amplitude and ten cycles for the maximum amplitude were applied. Eventually, a ramp test at 0.1 mm/s rate was performed to the amplified design displacement  $\gamma_b \gamma_x d_{bd} = 26.4$  mm (where  $\gamma_b = 1.1$  and  $\gamma_x = 1.2$  are the amplification factor and the reliability factor given in the standard, respectively), to assess the failure condition under quasi-static condition.

It is here noted that according to the standard the type tests performed on one specimen of a device can be deemed valid also for new models of the device with same geometry, working materials and constraints, provided that the geometrical linear differences between the new and the tested model are less than 20% and the results can be suitably extrapolated to the new device.

In order to assess the recovery of the original output force after cooling of the working material, at the end of the experimental protocol requested by the standard the prototype was left at rest for 45 minutes and then subjected to a second series of 10 cycles to  $d_{bd}$ .

### 3 RESULTS AND DISCUSSION

The force–displacement behavior of the P-LED prototype at the design deflection  $d_{bd} = 20$  mm is shown in Figure 3: in Figure 3(a) the prototype is subjected to the preload of 280 kN to prestress the lead, while in Figure 3(b), the prototype was tested without application of the preload. The hysteresis loops in Figure 3(a) have an almost rectangular shape, but for some “cut-outs” at motion reversals which are attributed to a small trailing void, that occurred in the lead in spite of the initial prestress. However, after the cut-out, the force achieves an essentially constant level, thus maximizing the amount of energy dissipation. From the shape of the hysteresis loop the length of the trailing void created behind the bulge is estimated to be approximately 9 mm over a total stroke of 40 mm. In Figure 3(b), the size of the trailing void increases to about 23 mm, significantly reducing the dissipated energy; also the output force is substantially smaller than in the previous case (e.g., 187 kN vs. 228 kN at the third cycle) due to the lower confinement of lead and the decrease in the extrusion resistance.

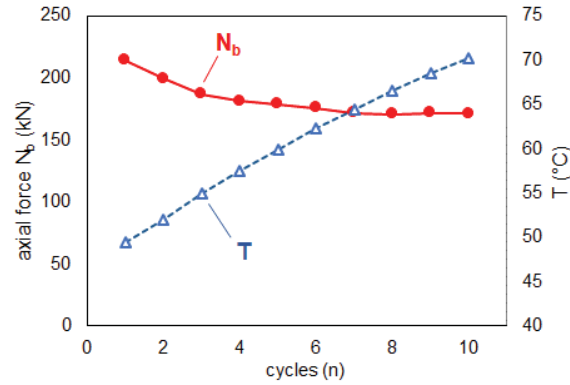


**Figure 3: (a) Hysteresis loops of the P-LED prototype preloaded at 280 kN and tested to the design deflection  $d_{bd} = 20$  mm; (b) hysteresis loops of the prototype without prestressing**

The strength of the device declines as the number of cycles proceeds due to heating of lead (Figure 4); the output force  $N_b$  (evaluated as the average force on each branch, after the cut-out) shrinks from 205 kN at the first cycle to 170 kN at the tenth cycle in extension, and from 243 kN to 193 kN in compression. The largest decrease occurs between the first and the third



cycle (-13%), and then the force tends to approach a steady value. It must be here recalled that the temperature reported in the panel in Figure 4 was measured in the steel wall of the tube, about 5 mm away from the lead, and therefore underestimates the actual temperature of the working material.



**Figure 4: Progress of output force (mean value between extension and compression) and temperature within the tube wall vs. number of cycles**

Two quantities are calculated at each cycle and used to characterize the response of the P-LED, namely the effective stiffness  $K_{\text{eff}} = N_b/d_b$  and the effective damping  $\xi_{\text{eff}} = 2A_{\text{cycle}}/(\pi 4 K_{\text{eff}} d_b)$ , where  $N_b$  is the output force of the prototype,  $d_b$  is the maximum cycle deflection and  $A_{\text{cycle}}$  is the area of the hysteresis loop.

The European standard [32] requires that both  $K_{\text{eff}}$  and  $\xi_{\text{eff}}$  remain essentially constant as the cycles proceed <sup>(a)</sup> subscript 3 is relevant to quantities assessed at the third load cycle, and subscript  $i$  is relevant to quantities at the  $i$ -th cycle, excluding the first cycle ( $i \geq 2$ )

Table 1); in particular, except for the first cycle, the difference among the cycles must remain within the 10%.

Requirement <sup>(a)</sup>	Test results		
	$d_b = 5\text{mm}$	$d_b = 10\text{mm}$	$d_b = 20\text{mm}$
$ K_{\text{eff},i} - K_{\text{eff},3}  / K_{\text{eff},3} < 0.10$	0.024	0.035	0.098
$ \xi_{\text{eff},i} - \xi_{\text{eff},3}  / \xi_{\text{eff},3} < 0.10$	0.012	0.046	0.024

<sup>(a)</sup> subscript 3 is relevant to quantities assessed at the third load cycle, and subscript  $i$  is relevant to quantities at the  $i$ -th cycle, excluding the first cycle ( $i \geq 2$ )

**Table 1: Stability requirements for Non Linear devices [32] and results of the tests on the P-LED prototype**

The average value of  $\xi_{\text{eff}}$  evaluated over 10 cycles performed at the design deflection is 0.55, i.e. 86% of the effective damping of an ideally rectangular loop, confirming the good dissipation capacity of the P-LED. After cooling lead recrystallizes and recovers its original properties, thereby providing a reliable and consistent response even in case of multiple loading sequences occurring within short time: after the execution of the experimental program prescribed by the standard, the prototype was left at ambient temperature for 45 minutes and then subjected to a second sequence of cycles at  $d_{b,i}$ ; the stiffness and damping were practically unchanged from the previous sequence, with a -4% difference on  $K_{\text{eff}}$  and 0% on  $\xi_{\text{eff}}$  at the third cycle (curves labelled as “ $d_b = 20\text{ mm}$  (2)” in Figure 5).

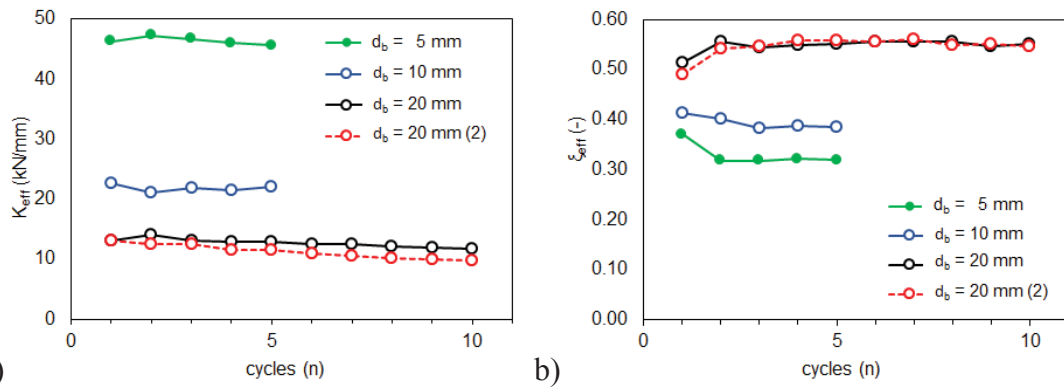


Figure 5: Plots of (a) effective stiffness  $K_{eff}$ , and (b) effective damping  $\xi_{eff}$  of the P-LED vs. number of cycles at different deflection amplitudes  $d_b$

Eventually, in the monotonic ramp test (Figure 6) the prototype was able to sustain the amplified design deflection  $\gamma_x \gamma_{bd} d_{bd}$  without leakage of working material. The force–deflection curves presents an initial peak which is ascribed to the transition from the static to the kinetic friction between lead and shaft [26] and then stabilizes at a constant level, demonstrating the ability to accommodate the prescribed displacement without any damage or deterioration of stiffness.

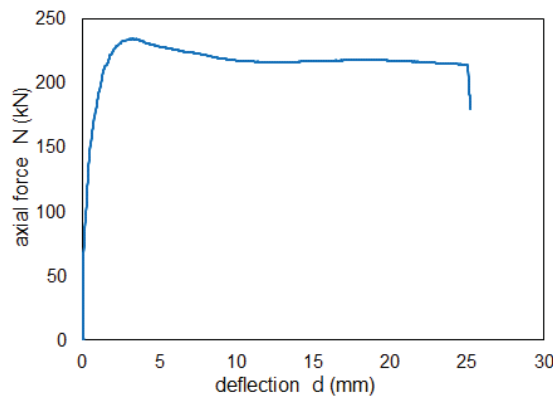


Figure 6: Force–deflection relationship of P-LED under quasi-static condition

## 4 NUMERICA INVESTIGATION

### 4.1 FE model

A 3D finite element model of the prototype presented in Section 2 was formulated in the general-purpose software Abaqus/CAE 6.14-2 [33], using 4-node bilinear axisymmetric elements type C4X4. By exploiting the symmetry of the system about its longitudinal axis, only half of the prototype is modelled.

The model includes four parts: the shaft, the tube, the plug and the working material (Figure 7). The region of the working material is meshed with fine mesh (maximum size 3.3 mm) along the shaft region where large deformation is expected, in order to allow realistic simulation of lead flow around the shaft (Figure 7(b)), without severe distortion of the elements, which may cause abortion of analysis.

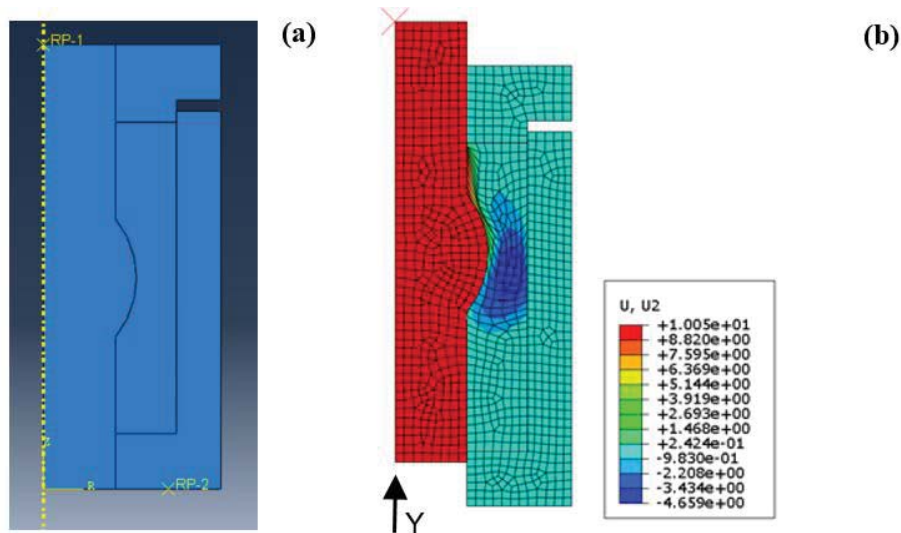


Figure 7: (a) Physical model of P-LED; (b) lead flow through the orifice between bulge and containing tube during motion of the shaft (U2: displacement in Y direction, unit: mm)

Lead is modelled as an elastic-almost perfectly plastic material (a small hardening is introduced in order to avoid convergence issues), and S450 steel is assumed for shaft, tube and cap regions. The modelling parameters of the FE model are as tabulated in Table 2 [34]. Hard contact is introduced at the interface between shaft and tube and between shaft and cap, while hard contact in normal direction, and frictional behavior in shear direction is assumed at the interfaces between lead and shaft and between lead and containing tube, where the coefficient of friction counts  $\mu = 0.15$  and  $\mu = 0.30$  respectively. The analyses are performed in two steps. In the first step, prestressing of the working material is simulated by applying a constant force of 280 kN uniformly distributed on the upper surface of the cap, pressing the cap on the lead. In the second step, dynamic implicit analysis is performed by imposing a cyclic displacement history to the shaft. Three analyses are conducted, with displacement amplitude of 5 mm, 10 mm and 20 mm, respectively.

Properties	Steel		Lead	
E [GPa]	210		16.4	
$\nu$ [-]	0.33		0.44	
$\rho$ [kg/mm <sup>3</sup> ]	$7.85 \times 10^{-6}$		$8 \times 10^{-6}$	
Plastic behavior	Plastic Strain		Stress [MPa]	
	0		450	
	0.2		500	
	0.001		20.5	
	0.002		21.5	
	0.1		22.0	
	0.3		22.5	
			23.0	

$E$ =Young's Modulus [GPa],  $\nu$  = Poisson's Ratio [-],  $\rho$  = density [kg/mm<sup>3</sup>]

Table 2: Material properties used in the FE model

The quasi-static output force vs. deflection curves calculated from the model are compared to the experimental curves evaluated at the third cycle of each test. The agreement between model and experimental data is good in the first and in the third quadrant of the diagram, but some deviation is observed at motion reversals (Figure 8). This is due to the fact that the numerical model does not account for trailing void, i.e. no gap can occur between working material and shaft as the bulge passes through the lead.

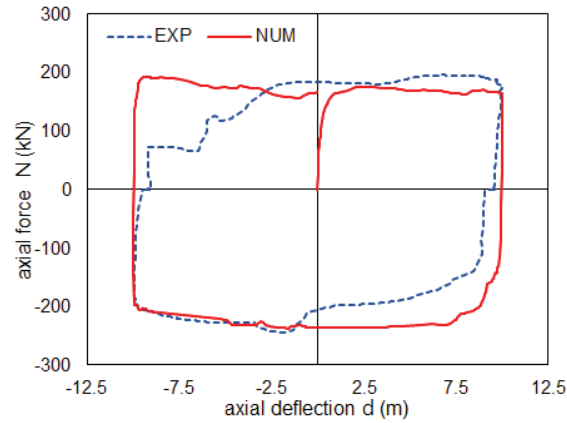


Figure 8: Comparison between calculated (NUM) and experimental (EXP) hysteresis loop

#### 4.2 Effect of device dimensions

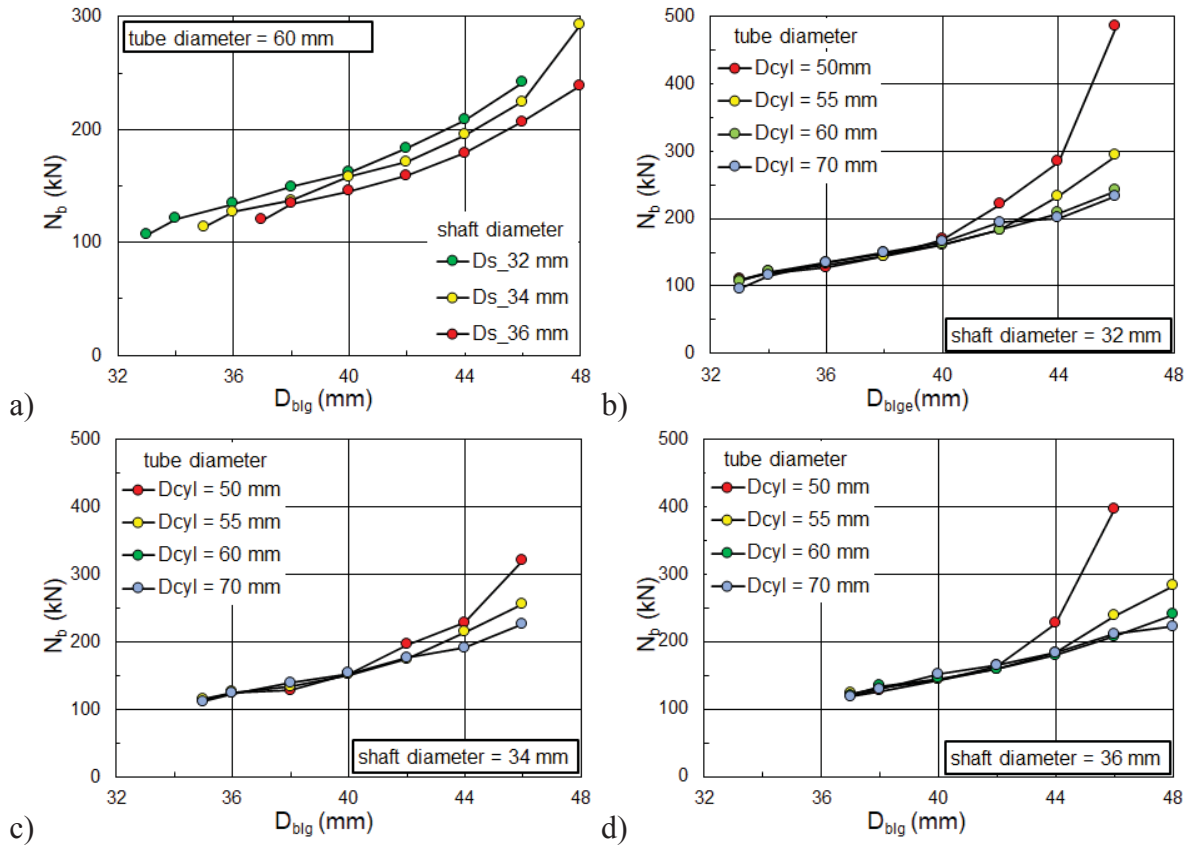
The numerical model is then applied to investigate combinations of a wide range of device dimensions (Table 3), to enable device optimization and further delineate the contributions of friction and extrusion forces to the overall reaction force produced by the device. In each analysis the compressive force on the lead is adjusted to the actual cross-section of the working material in order to provide an average pressure of 138 MPa.

Dimensions [mm]		Values
$D_s$		32 – 34 – 36
$D_{blg}$	33 – 34 – 35 – 37 – 38 – 40 – 42 – 44 – 46	
$D_{cyl}$		50 – 55 – 60 – 70
$L_s$		75 – 95 – 115

$D_s$  = Shaft diameter,  $D_{blg}$  = Bulge diameter,  $D_{cyl}$  = tube diameter,  $L_s$  = shaft length

Table 3: Device dimensions investigated in the study

The importance of either force contribution can be appreciated in Figure 9(a), where the first data point of each plot represents the situation where the extrusion force is negligible ( $D_{blg} \approx D_s$ ), and the output force is essentially provided by the frictional resistance of the prestressed lead on the lateral surface of the moving shaft (the relative velocity on the tube surface is almost null); a larger shaft diameter corresponds to a larger contact area and hence a larger frictional force. In contrast, increasing the bulge diameter  $D_{blg}$  reduces the area of the annular orifice through which lead flows, and thereby increases the extrusion resistance; this contribution is independent of  $D_s$  and becomes more important as  $D_{blg}$  approaches  $D_{cyl}$ . It is worth noting that only for large values of  $D_{blg}$ , i.e.  $D_{blg} > 44$  mm, the contribution from extrusion becomes equal to, or larger than, the frictional resistance. A similar conclusion (i.e. the friction force is a large part of the overall response) was reported in previous studies which compared the response of bulged, constrained and straight (i.e. without bulge) shafts [25], [27]. Figure 9(b), 9(c) and 9(d) show the effect of the tube diameter. When  $D_{blg}$  is small in comparison to  $D_{cyl}$  ( $D_{blg}/D_{cyl} \leq 0.8$ ), the output force is not influenced by the diameter of the tube; in contrast when the gap is small (less than 4 mm in the examined cases) the extrusion resistance has a steep increase, inducing large forces that can eventually lead to structural failure of the rod or the cap screws.



**Figure 9: Influence of device dimensions of P-LED on the quasi-static output force  $N_b$ : (a) influence of shaft diameter  $D_s$  and bulge diameter  $D_{blg}$  for assigned tube diameter  $D_{cyl} = 60$  mm and shaft length  $L_s = 95$  mm; (b) (c) (d) influence of tube diameter  $D_{cyl}$  and bulge diameter  $D_{blg}$  for assigned shaft diameter  $D_s = 32$  mm,  $D_s = 34$  mm, and  $D_s = 36$  mm, respectively**

## 5 CONCLUSIONS

The study investigated the behavior of an emerging energy dissipation device, namely Pre-stressed Lead Extrusion Damper (P-LED). The device provides energy dissipation through the plastic extrusion of lead through an orifice created between a containing tube and a bulged shaft, and achieves high specific output force though preloading of the working material during the assembly.

A prototype of the P-LED was experimentally assessed according to the provisions of the European standard EN 15129 [32] for displacement dependent devices. The damper exhibits a consistent rigid-plastic behavior without strength degradation regardless of the imposed displacement up to the amplified deflection prescribed by the standard. The influence of the rate of deflection is weak over the tested range and can be ignored from a practical point. Cyclic tests were used to evaluate the response of the damper at different displacement amplitudes. Neglecting the effects of trailing voids at motion reversals, the hysteresis loops have an essentially rectangular shape with an equivalent damping ratio of 0.55, close to the maximum theoretical value of 0.63.

The tested specimen is able to sustain multiple sequences of motion at the basic design earthquake displacement, demonstrating its ability to provide maintenance-free operation even in presence of repeated ground shakes. Though a certain softening of the working material is observed due to heating, the changes in stiffness and damping capacity over 10 cycles at the design deflection lie within the  $\pm 10\%$  bound. Besides, the effect of heating is only tem-



porary, and when the damper is cooled down to ambient temperature, the stiffness and damping characteristics return to their original value.

A 3D finite element model of the P-LED device was formulated and validated against the experimental data. The numerical formulation was then used, in a parametric study, to investigate the effect of the device dimensions on the output force. The main parameters determining the response of the P-LED are found to be the annular area of lead around shaft and the projected area of the bulge, which are related to the extrusion force of the working material, and the area of the lateral surface of the shaft, which is proportional to the friction force arising from the relative motion between shaft and lead.

## REFERENCES

- [1] A. Di Cesare, F. C. Ponzo, D. Nigro. Assessment of the performance of hysteretic energy dissipation bracing systems. *Bulletin of Earthquake Engineering*, 12(6), 2777–2796, 2014; DOI: 10.1007/s10518-014-9623-z.
- [2] A. Di Cesare, F. C. Ponzo. Seismic retrofit of reinforced concrete frame buildings with hysteretic bracing systems: design procedure and behaviour factor. *Hindawi, Shock and Vibration*, Volume 2017, Article ID 2639361, DOI: 10.1155/2017/2639361.
- [3] F. Aliakbari, S. Garivani, A.A. Aghakouchak. An energy based method for seismic design of frame structures equipped with metallic yielding dampers considering uniform inter-story drift concept, *Engineering Structures* 2020, 205, 110114, <https://doi.org/10.1016/j.engstruct.2019.110114>.
- [4] S. Garivani, S.S. Askariani, A.A. Aghakouchak. A.A. Seismic design of structures with yielding dampers based on drift demands, *Structures* 2020, 28, 1885–1899, <https://doi.org/10.1016/j.istruc.2020.10.019>.
- [5] E. Gandelli, S. Chernyshov, J. Distl, P. Dubini, F. Weberd, A. Taras. Novel adaptive hysteretic damper for enhanced seismic protection of braced buildings, *Soil Dynamics and Earthquake Engineering* 2021, 141, 106522, <https://doi.org/10.1016/j.soildyn.2020.106522>.
- [6] M.Z. Golmoghany, S.M. Zahrai. Improving seismic behavior using a hybrid control system of friction damper and vertical shear panel in series, *Structures* 2021, 31, 369–379, <https://doi.org/10.1016/j.istruc.2021.02.007>.
- [7] C. Christopoulos, A. Filiatrault. Principles of passive supplemental damping and seismic isolation. IUSS Press 2006, Pavia.
- [8] C. Durucan, M. Dicleil. Analytical study on seismic retrofitting of reinforced concrete buildings using steel braces with shear link, *Engineering Structures* 2010, 32, 2995–3010, doi:10.1016/j.engstruct.2010.05.019.
- [9] F. Mazza, A. Vulcano. Equivalent viscous damping for displacement-based seismic design of hysteretic damped braces for retrofitting framed buildings, *Bulletin of Earthquake Engineering* 2014, 12, pages2797–2819, DOI 10.1007/s10518-014-9601-5.
- [10] F. Mazza, A. Vulcano. Displacement-based design procedure of damped braces for the seismic retrofitting of r.c. framed buildings, *Bulletin of Earthquake Engineering* 2015, 12:2121–2143, DOI 10.1007/s10518-014-9709-7.
- [11] F. Yang, G. Wang, M. Li. Evaluation of the Seismic Retrofitting of Mainshock-Damaged Reinforced Concrete Frame Structure Using Steel Braces with Soft Steel Dampers. *Applied Science* 2021, 11, 841. <https://doi.org/10.3390/app11020841>.
- [12] J.E. Martínez-Rueda. On the evolution of energy dissipation devices for seismic design, *Earthquake Spectra* 2002, Volume 18, Issue 2, Pages 309–346.
- [13] CSLLPP (Consiglio Superiore dei Lavori Pubblici). Circolare 21 gennaio 2019, n. 7 C.S.LL.PP. Istruzioni per l'applicazione dell'«Aggiornamento delle “Norme tecniche per le costruzioni”» di cui al decreto ministeriale 17 gennaio 2018, Roma; 2019, in Italian.

- [14] F. Braga, F. Buttarazzi, A. Dell'Asta, W. Salvatore. Protezione sismica di edifici in c.a. con controventi dissipativi in acciaio. Dario Flaccovio Editore 2015; (in Italian).
- [15] G. Lomiento, N. Bonessio, F. Braga. Design criteria for added dampers and supporting braces. *Seismic Isolation and Protection Systems* 2010, 1(1):55–73.
- [16] F.C. Ponzo, A. Di Cesare, N. Lamarucciola, D. Nigro. Seismic design and testing of post-tensioned timber buildings with dissipative bracing systems. *Frontiers in Built Environment* 2019, 5(104). <https://doi.org/10.3389/fbuil.2019.00104>.
- [17] E. Gandelli, A. Taras, J. Disti, V. Quaglini. Seismic retrofit of hospitals by means of hysteretic braces: influence on acceleration-sensitive non-structural components. *Frontiers in Built Environment* 2019, 5(100), DOI: [doi.org/10.3389/fbuil.2019.00100](https://doi.org/10.3389/fbuil.2019.00100).
- [18] Z. Li, H. Dong, X. Wang, M. He. Experimental and numerical investigations into seismic performance of timber-steel hybrid structure with supplemental dampers, *Engineering Structures* 2017, 151, pp. 33-43, [10.1016/j.engstruct.2017.08.011](https://doi.org/10.1016/j.engstruct.2017.08.011).
- [19] A. Naeem, J. Kim J. Seismic performance evaluation of a multi-slit damper, *Engineering Structures* 2019, 189, pp. 332-346, [10.1016/j.engstruct.2019.03.107](https://doi.org/10.1016/j.engstruct.2019.03.107).
- [20] T. Balendra, C.H. Yu, F.L. Lee. An economical structural system for wind and earthquake loads. *Engineering Structures* 2001, 23:491–501. [https://doi.org/10.1016/S0141-0296\(00\)00061-4](https://doi.org/10.1016/S0141-0296(00)00061-4).
- [21] G.W. Rodgers, K.M. Solberg, J.G. Chase, J.B. Mander, B.A. Bradley, R.P. Dhakal, L. Li. Performance of a damage-protected beam-column subassembly utilizing external HF2V energy dissipation devices. *Earthquake Engineering and Structural Dynamics* 2008b, 37(13): 1549-1564, DOI: [10.1002/eqe.830](https://doi.org/10.1002/eqe.830).
- [22] W.H. Robinson, L.R. Greenbank. Properties of an extrusion energy absorber. *Bulletin of the New Zealand National Society for Earthquake Engineering* 1975, 8(3), 187-191.
- [23] W.H. Robinson, L.R. Greenbank. An extrusion energy absorber suitable for the protection of structures during an earthquake. *Earthquake Engineering & Structural Dynamics* 1976, 4(3), 251-259, DOI: [10.1002/eqe.4290040306](https://doi.org/10.1002/eqe.4290040306).
- [24] W.J. Cousins, T.E. Porrit. Improvements to lead-extrusion damper technology. *Bulletin of the New Zealand National Society for Earthquake Engineering* 1993, 26, 342-348.
- [25] V. Vishnupriya, G.W. Rodgers, J.B. Mander, J.G. Chase. Precision design modelling of HF2V devices. *Structures* 2018, 14, 243-250, DOI: [10.1016/j.istruc.2018.03.007](https://doi.org/10.1016/j.istruc.2018.03.007).
- [26] G.W. Rodgers, J.G. Chase, J.B. Mander, J.B. Repeatability and high-speed validation of supplemental lead-extrusion energy dissipation devices. *Advances in Civil Engineering* 2019, Article ID 7935026, DOI: [10.1155/2019/7935026](https://doi.org/10.1155/2019/7935026).
- [27] J.C. Golodrino, J.G. Chase, G.W. Rodgers, G.A. MacRae, C.G. Clifton. Velocity dependence of HF2V devices using different shaft configurations. *Annual Conference of the New Zealand Society for Earthquake Engineering* 2012, Christchurch, New Zealand, paper 99.
- [28] G.W. Rodgers, J.G. Chase, J.B. Mander, N.C. Leach, C.S. Denmead. Experimental development, tradeoff analysis and design implementation of high force-to-volume damping technology. *Bulletin of the New Zealand National Society for Earthquake Engineering* 2007a, 40(2), 35-48.

- [29] G.W. Rodgers, J.B. Mander, J.G. Chase, R.P. Dhakal, N.C. Leach, C.S. Denmead. Spectral analysis and design approach for high force-to-volume extrusion damper-based structural energy dissipation. *Earthquake Engineering and Structural Dynamics* 2008a, 37(2), 207-223, DOI: 10.1002/eqe.752.
- [30] G.W. Rodgers, J.G. Chase. Testing of Lead Extrusion Damping devices undergoing representative earthquake velocities. *Annual Conference of the New Zealand Society for Earthquake Engineering* 2013, Wellington, New Zealand.
- [31] D.A. Latham, A.M. Reay, S. Pampanin. Kilmore Street Medical Centre: application of an advanced flag-shape steel rocking system. *Annual Conference of the New Zealand Society for Earthquake Engineering* 2013, Wellington, New Zealand.
- [32] CEN, European Committee for Standardization (2009). EN 15129. Anti-seismic devices. Brussels.
- [33] Dassault Systemes Simulia Corp. (2017). Abaqus/CAE user's guide, Providence.
- [34] V. Vishnupriya, G.W. Rodgers, J.G. Chase. Finite Element Modelling of HF2V lead extrusion dampers for specific force capacities. *Procedure of the Pacific Conference on Earthquake Engineering and Annual Conference of the New Zealand Society for Earthquake Engineering* 2019, Auckland, New Zealand, paper 133.

## AN INNOVATIVE STEEL DAMPER WITH ADAPTIVE HYSTERETIC BEHAVIOR

Emanuele Gandelli<sup>1</sup>, Johan Distl<sup>1</sup>, Peter Huber<sup>1</sup>, Christian Braun<sup>1</sup>

<sup>1</sup> Maurer Engineering GmbH, R&D department  
Frankfurter Ring 193, 80807, München, Germany  
{e.gandelli, j.distl, p.huber, c.braun}@maurer.eu

---

### Abstract

*An ideal antiseismic technology should perform at high efficiency independently from the intensity of the ground shaking. However, traditional bilinear hysteretic dampers (BHDs) are commonly designed for severe ultimate limit state earthquakes resulting in a poor efficiency during weak but frequent events since they are engaged in their elastic region offering negligible damping. This can cause high peak floor accelerations (PFAs) that are detrimental for sensitive non-structural components, like elevators, and electric networks, whose integrity is essential for a prompt operation of the building after the quake. This shortcoming can be improved through a second generation of hysteretic dampers capable to produce different yielding levels based on the intensity of the occurring earthquake. Within this framework, the innovative Adaptive Hysteretic Damper (AHD) is presented in this paper. The results of force-displacement tests carried out on a 2.0MN prototype are argued and prove its robustness and reliability under several repeated cyclic motions. A simple design approach for braced frames implementing the AHDs is eventually proposed and applied to a real case-study building to quantify, through NLTH analyses, the enhanced seismic performances offered by this technology compared to traditional BHDs.*

**Keywords:** Steel Dampers, Adaptive Hysteretic Behavior, Serviceability Limit State, Ultimate Limit State, Non-structural Component.

---



## 1 INTRODUCTION

Among most advanced antiseismic design guidelines, the Eurocode 8 [1], embracing Performance Based Design (PBD) procedures [2], establishes two different seismic scenarios and relevant performance requirements:

- the most severe “Ultimate Limit State” (ULS) scenario features 10% of exceedance probability over the reference period  $V_R=50$  years (i.e. return period  $T_R=475$  years). Under ULS seismic events, the structure shall be capable to withstand the seismic loads without any global or local collapse preserving as well a residual lateral strength after the quake (“structural safety requirement” or “no-collapse requirement”);
- the less intense (but more frequent) “Serviceability Limit State” (SLS) scenario provides 10% of exceedance probability over the reference period  $V_R=10$  years (i.e. return period  $T_R=95$  years). Under SLS seismic events, the structure, besides not suffering any structural damage, shall remain fully operational (“damage limitation requirement”).

In order to meet the second requirement, “acceleration sensitive”, “drift-sensitive”, and “displacement sensitive” non-structural components (NSCs) should be protected against detrimental high peak floor accelerations (PFAs), interstorey-drifts ( $\Delta$ ), and absolute displacements (D) [3-5]. A list of most common NSCs grouped into these categories is given in Table 1. It is worth noting that the integrity of “drift-sensitive” NSCs should not represent a challenging target for structural engineers since usually enveloped, in average terms, by narrower or comparable SLS lateral deflection limits for structural elements. For instance, among weakest NSCs [3-6], curtain and infill walls, are characterized by a higher strength ( $\Delta_{lim}$ ) compared to more critical reinforced concrete columns ( $\Delta_{lim} = 0.75\%$  vs.  $\Delta_{lim} = 0.66\%$ ) [7]. Since characterized by several different layouts, the definition of the damage thresholds for “displacement-sensitive” NSCs often needs the “expert judgment”. However, the fulfillment of these checks can be easily ensured through conventional design approaches that usually aim to control the storeys’ lateral displacements [5]. On the contrary, the assessment of the integrity of “acceleration-sensitive” NSCs is more questionable since based on more complex “floor response spectrum” analyses that require the (rarely available) knowledge of the natural frequency and inherent damping of each NSC [8, 9]. Antiseismic technologies capable to minimize the spectral accelerations over a wide range of NSCs’ oscillation periods represent therefore the best option.

nonstructural components’ categories		
acc. sensitive	drift sensitive	disp. sensitive
false ceilings	infill walls	parapets
elevators	glass windows and doors	storage racks
UPS battery cabinets	pipelines	chimneys
UPS switchboard panels		thermal/seismic joints
UPS distribution panels		

Table 1: Most common “acceleration-sensitive”, “drift-sensitive”, and “displacement-sensitive” NSCs [3-5].

Among modern antiseismic technologies, Hysteretic Dampers (HDs), firstly introduced in the ‘70s of the last century [10], are typically installed in braced frames in order to dissipate the seismic energy through the plastic deformation of sacrificial mild steel components. Their force-displacement (F-d) response is not (or only scarcely) affected by velocity and is conventionally modelled by means of bilinear hysteretic models. Over the last thirty years, HDs ex-

exploiting axial loads, shear loads, bending, and torsion have been developed [11] and world-wide applied for the seismic protection of schools and hospitals [12, 13].

Despite the lower costs compared to other technologies (e.g. fluid viscous dampers), the use of HDs not always represents the best option for the protection of high-technological or strategic buildings [5]. Indeed, a recent experimental study [14] has shown that, on one hand, the introduction of the hysteretic braces allows a significant reduction of the frame lateral deformation, on the other hand, can trigger a huge increase (up to 300%) of PFAs. Enhancements in antiseismic technologies and new approaches based on low-damage methodologies are hence needed [15, 16]. Nevertheless, common methods for the design of new structures, as well as for the retrofit of existing ones, account the “structural safety requirement” at the ULS only [17-19]. In order to improve this unacceptable situation, the innovative Adaptive Hysteretic Damper (AHD), a device capable to modulate its effective damping and stiffness based on the intensity of the occurring earthquake, is presented in this paper. The reliability and robustness of the AHD under multiple excitations, is proven through experimental tests carried out on a full-scale 2.0MN prototype. Linear equivalent mechanical parameters to be exploited in simple response spectrum analyses for the design of braced frames implementing the AHDs are argued hereafter and exemplified through a case-study building. The comparison with the response calculated for the same building protected by conventional bilinear hysteretic dampers allows to claim the following achievements: (a) not impaired structural performance under severe ULS earthquakes; (b) enhanced protection of “acceleration-sensitive” NSCs under weak but frequent SLS events.

## 2 WORKING PRINCIPLE OF THE NEW DAMPER

Among common steel dampers, the Shear Hysteretic Panel (SHP) was the starting point for the development of the novel Adaptive Hysteretic Damper (AHD). The SHP consists of a steel plate with equally spaced openings delimiting a set of dissipative laminae (Fig. 1-left) [20]. The relative motion between the bottom and the upper edge of the SHP induces the shear deformation of the laminae first in the elastic and later in the plastic range (Fig.1-center) resulting in a typical bilinear hysteretic response (Fig.1-right). Despite SHPs exhibit a considerable energy absorption capacity and lateral stiffness even under small drift angles ( $\gamma_L = d/L$ ), that makes them very suitable for braced frames, their widespread application has been so far constrained by their unsatisfactory strength against out of plane loads (buckling).

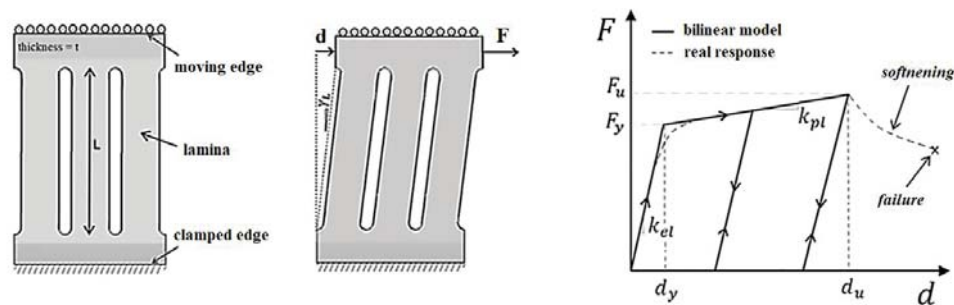


Figure 1: SHP damper: undeformed configuration (left), deformed configuration (centre), and typical bilinear F-d response (right).

The main novelties introduced by the AHD are shown in Fig. 2:

- the three-dimensional “hollow-section” arrangement of multiple laminae with an optimized “hourglass-shape” to form a dissipative core (the orange color element in Fig. 2-

left) capable to withstand high drift angles (hence displacement amplitudes) and overcome buckling problems. The clockwise alternated transmission of tension and compression loads at the corners of the core engages the shear deformation of the laminae;

- the “in series connection” between a minor (D1, green element) and a major (D2, orange element) dissipative core (Fig. 2-left) allows the development of an innovative “two-stages” hysteretic behavior (Fig. 2-right). The different yielding strengths of the minor ( $F_{y,D1}$ ) and major ( $F_{y,D2} > F_{y,D1}$ ) hysteretic cores are obtained by varying the number and/or the geometry of the hysteretic laminae. Two connection plates (CP) are used to link the dissipative cores to the main structural frame while a plate featuring a slotted hole, hereafter referred as “GAP-element”, is introduced to mutually link the two dissipative cores. This connector acts as a very stiff end-stroke stopper that: (a) during minor SLS earthquakes, allows the exclusive plastic engagement of the minor core; (b) during severe ULS events, enforces the activation of the major dissipative core to achieve higher levels of effective stiffness and equivalent damping.

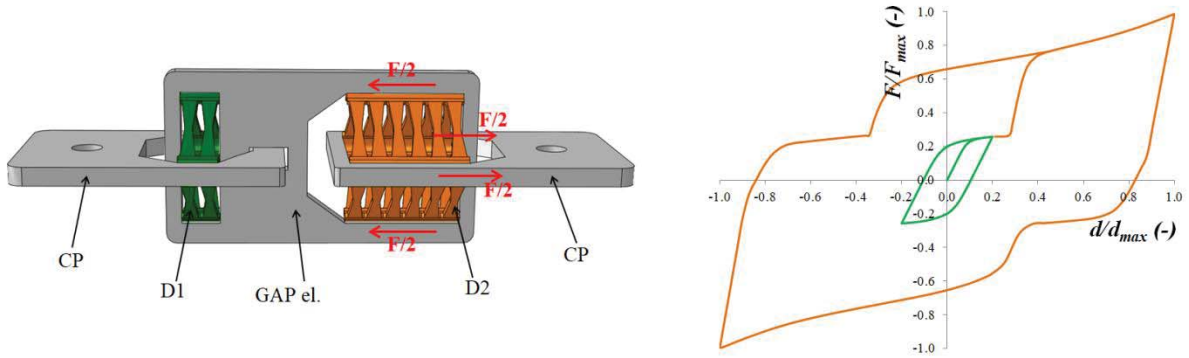


Figure 2: Adaptive Hysteretic Damper: device assembly (left) and innovative “two-stages” hysteretic loop (right).

Assuming that both the CP and the GAP elements offer very stiff elastic reactions ( $k_{el} \rightarrow +\infty$ ) even during the most severe design loads, the F-d backbone curve of the AHD (Fig. 3-left) can be described through an analytical model that depend on the following parameters only: (a) yielding force of the minor ( $F_{y,D1}$ ) and major ( $F_{y,D2}$ ) core; (b) elastic stiffness of the minor ( $k_{el,D1}$ ) and major ( $k_{el,D2} > k_{el,D1}$ ) core; (c) plastic stiffness of the minor ( $k_{pl,D1}$ ) and major ( $k_{pl,D2} > k_{pl,D1}$ ) core; (d) width of the slotted hole of the gap-connector ( $d_G$ ). Four different displacement fields can be distinguished:

- field A ( $d_{max} \leq d_{y,1}$ ): both D1 and D2 operate in their elastic regime ( $d_{y,1}$  denotes the yielding displacement of the minor core). The device reacts as a soft spring to SLS static and dynamic loads;
- field B ( $d_{y,1} < d_{max} \leq d_{ES}$ ): D1 is deformed in its plastic field while D2 still reacts in the elastic region ( $d_{ES} > d_G$  represents the displacement amplitude at the attainment of the contact in the gap-connector element). The device offers a minor effective stiffness and a certain damping level in order to minimize the effects of frequent SLS earthquakes;
- field C ( $d_{ES} < d_{max} \leq d_{y,2}$ ): the attained “contact condition” in the gap-element prevents any further deformation of D1 while, on the contrary, entrusts the incremental loads to D2 that is still reacting in its elastic regime ( $d_{y,2}$  denotes the yielding displacement of the minor core);

- field D ( $d_{y,2} < d_{max} \leq d_u$ ): the gap-element is still effective and D2 is eventually deformed in its plastic field maximizing the energy dissipation capacity of the damper and providing a higher effective stiffness in order to minimize the structural damages under strong ULS earthquakes.

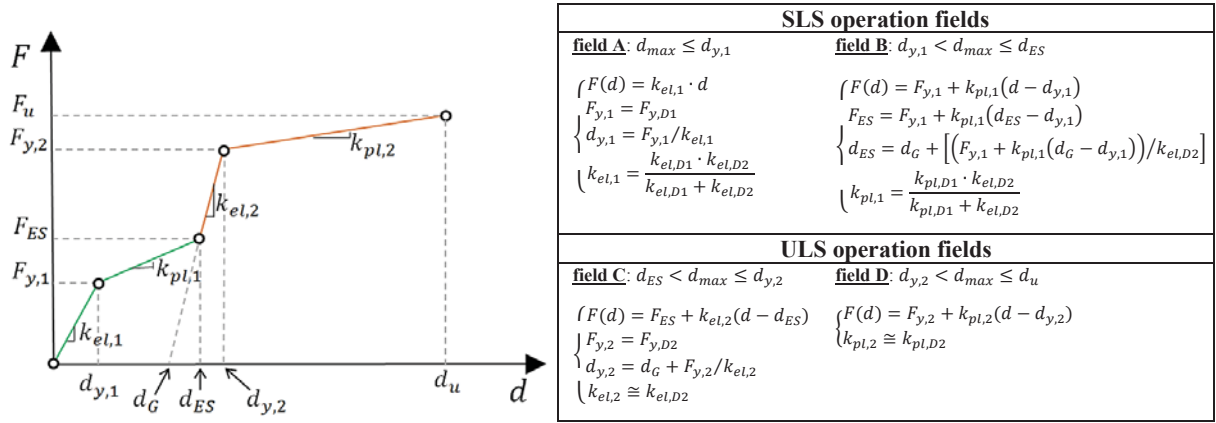


Figure 3: Force-displacement response of the AHD: backbone trend (left) and relevant analytical model (right).

### 3 EXPERIMENTAL TESTS

The force-displacement response of the AHD was assessed in displacement-controlled tests carried out at the Eucentre Lab. (Pavia, Italy) [21] on a full-scale prototype made of structural steel S355 and characterized by: (1) minor hysteretic core featuring  $F_{y,D1} = 450\text{kN}$ ,  $k_{el,D1} = 80\text{kN/mm}$ ,  $k_{pl,D1} = 6.0\text{kN/mm}$  (2) width of the hole in the gap-connector  $d_G = \pm 15\text{mm}$ ; (3) major hysteretic core featuring  $F_{y,D2} = 1350\text{kN}$ ,  $k_{el,D2} = 240\text{kN/mm}$ ,  $k_{pl,D2} = 18.0\text{kN/mm}$ .

According to the European Standard EN15129 (§ 6.2) [22], the testing protocol (Table 2) provided four runs with increasing displacement amplitudes equal to 25%, 50%, 100%, and 132% of the ULS design displacement ( $d_{bd}$ ), respectively. In particular, the first two runs provides “only” 5 cycles and are conceived to assess the response the device for low and medium intensity earthquakes, while the third run (10 cycles at 100% of  $d_{bd}$ ) is exploited to assess the degradation of the offered effective stiffness and damping due to low-cycle fatigue under severe ULS earthquakes. Eventually, in the last run, usually known as “displacement-capacity” test, the robustness of the damper is verified at the overload displacement  $d_{cd}$  obtained amplifying  $d_{bd}$  by a reliability ( $\gamma_x = 1.1$ ) and a safety ( $\gamma_b = 1.2$ ) factor [1].

run	ampl. (mm)	vel. (mm/s)	shape	cycles	notes
1	$\pm 16.3$	10	triangular	5	$= 0.25 \cdot d_{bd}$
2	$\pm 32.5$	10	triangular	5	$= 0.50 \cdot d_{bd}$
3	$\pm 65.0$	10	triangular	10	$= 1.00 \cdot d_{bd}$
4	$\pm 86.0$	10	triangular	1	$= 1.32 \cdot d_{bd}$

Table 2: Testing protocol.

During the tests, the deformations of the AHD were recorded through an electronic displacement transducer (LVDT) while instantaneous values of axial load by means of the load

cell of the testing machine. In this regard, Fig. 4 depicts the device in its maximum compression and elongation configurations (achieved during the “displacement-capacity” test) and Fig. 5 shows the recorded experimental loops (overlapped with the analytical backbone curve). The following results can be appreciated:

- a stable response of the AHD during runs No. 1-3. In particular, since the recorded loops of each run are practically overlapped, in agreement with the requirement of the EN 15129, both the energy dissipated per cycle ( $EDC$ ) and the effective stiffness ( $k_{eff}$ ) of the device did not degrade more than 10% due to the low-cycle fatigue;
- the absence of sudden stiffness-drops at max/min displacement amplitudes of run no. 4 witnessing the capability of the device to withstand even higher loads/deformations;
- a fair agreement between the analytical F-d backbone plot (red-dashed lines obtained through the Equations in the panel of Fig. 3) and the experimental data.

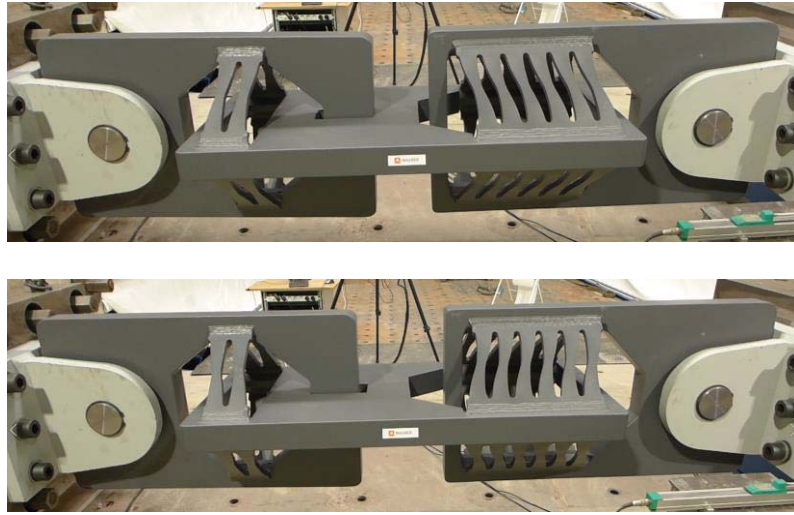


Figure 4: Maximum compression (top) and elongation (bottom) configurations reached by the AHD during run4.

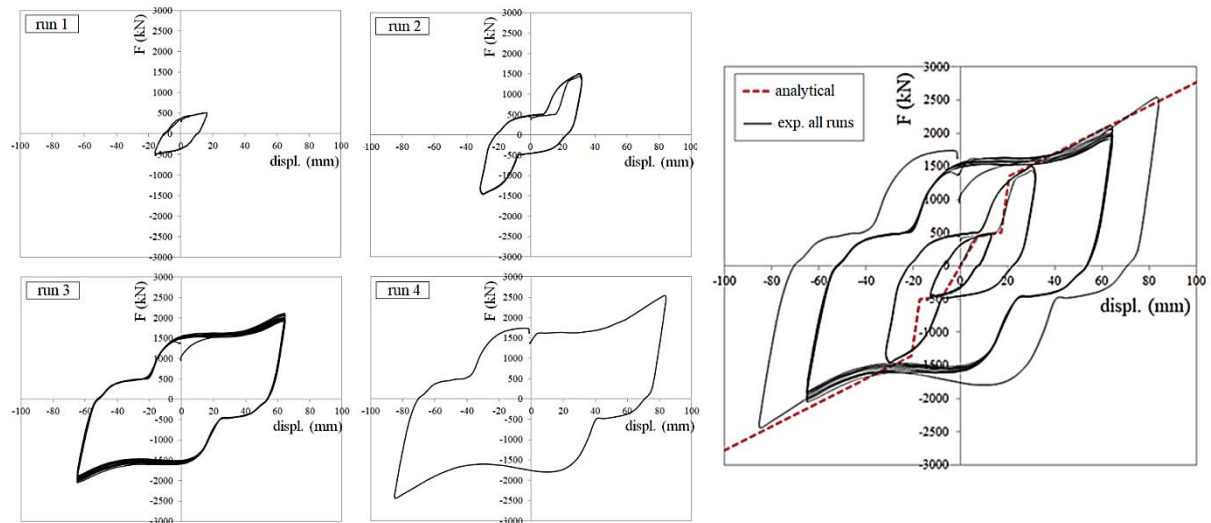


Figure 5: Recorded experimental loops.



#### 4 DESIGN OF BRACED FRAMES THROUGH SPECTRAL ANALYSIS

A recent study [23] has proven that the dynamic response, both in terms of maximum displacement and peak acceleration at roof level, of a multi-storey frame implementing the novel AHDs, can be predicted by means of simple iterative response spectrum analyses, where both the bare frame and the dissipative braces are schematized by means of linear equivalent SDOF systems. The basic assumption of this calculation method is the “a-priori knowledge” of the structural properties of the bare frame. This is always typical of retrofit-projects while for new buildings can be achieved through a preliminary design of the bare frame (e.g. accounting for the gravitational loads only). A modal analysis is hence performed to assess the participation factor  $\Gamma = m^*/\sum m_i\phi_i^2$  and the participating mass  $m^* = \sum m_i\phi_i$  of the fundamental mode shape. The lateral capacity of the bare frame is also appraised through nonlinear static (pushover) analyses under constant gravity loads and monotonically increasing horizontal loads (Fig. 6-left). Two distributions of lateral loads are considered, namely a “modal” pattern (resembling a triangular height-wise profile) and an “uniform” pattern as per EC8 provisions [1]. Among the two obtained capacity curves (base-shear  $F$  versus control-point displacement  $d$ ), the one associated to lowest strength is then processed (Fig. 6-right) in accordance with Annex B of EC8 [1]. The pushover curve ( $F; d$ ) of the MDOF system is then scaled by the modal participation factor  $\Gamma$  to obtain the capacity curve  $F^*-d^*$  of the equivalent single-degree-of-freedom (SDOF) system ( $F^* = \frac{F}{\Gamma}; d^* = \frac{d}{\Gamma}$ ). For clarity, hereinafter the quantities with superscript “\*” will refer to equivalent SDOF systems, and quantities devoid of suffix will refer to real MDOF systems. The yield force  $F_{y,F}^*$ , yield  $d_{y,F}^*$ , and ultimate displacement  $d_{u,F}^*$  (where subscript “F” stands for “frame”) are determined under the equal energy criterion assuming an ideal elastic-perfectly plastic force-displacement relationship.

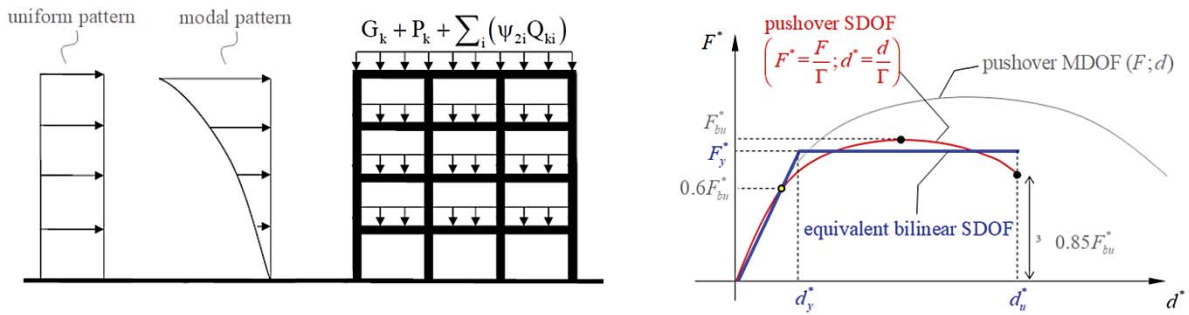


Figure 6: Qualitative representation of a pushover analysis (left) and definition of equivalent elastic-perfectly plastic SDOF system of the bare-frame (right).

Given a certain displacement demand ( $d_{max}^*$ ) of the seismic motion, the effective stiffness ( $k_{eff,F}^*$ ), and ductility demand ( $\mu_F^*$ ) of the bare frame are calculated as:

$$k_{eff,F}^* = \begin{cases} k_{el,F}^* = F_{y,F}^*/d_{y,F}^* & d_{max}^* \leq d_{y,F}^* \\ F_{y,F}^*/d_{max}^* & d_{y,F}^* < d_{max}^* \leq d_{u,F}^* \end{cases} \quad (1-a,b)$$

$$\mu_F^* = \begin{cases} 1 & d_{max}^* \leq d_{y,F}^* \\ d_{max}^*/d_{y,F}^* & d_{y,F}^* < d_{max}^* \leq d_{u,F}^* \end{cases} \quad (2-a,b)$$

In particular, it has been recently proven [23] that the design parameters of the AHD can be iteratively adjusted in order to achieve a desired displacement target at ULS ( $d_{targ,ULS}^*$ ) selected between two possible ranges: (1)  $d_{targ,ULS}^* \leq d_{y,F}^*$  when the goal is to maintain the frame in the elastic range; (2)  $d_{y,F}^* < d_{targ,ULS}^* < d_{u,F}^*$  when a certain level of plasticization of frame can be accepted.

The spectral analysis is then carried out approximating the response of the braced frame through two linear equivalent SDOF systems working in parallel (Fig. 7-left) and accounting for the frame ( $F^*$ ) and the damper ( $D^*$ ) responses. The effective vibration period of the braced frame ( $T_{eff,F+D}^*$ ) is conventionally calculated as:

$$T_{eff,F+D}^* = 2\pi \sqrt{\frac{m^*}{(k_{eff,F}^* + k_{eff,D}^*)}} \quad (3)$$

where  $k_{eff,D}^*$  is the effective lateral stiffness of the AHD (whose definition is given in next Section).

Adapting the original formulations for “in parallel damping mechanisms” [24], the equivalent viscous damping of the braced frame ( $\xi_{eq,F+D}^*$ ) can be calculated through the following weighted average [25]:

$$\xi_{eq,F+D}^* = \xi_{el,F}^* + \frac{\xi_{eq,F}^* E_{cum,F}^* + \xi_{eq,D}^* E_{cum,D}^*}{E_{cum,F}^* + E_{cum,D}^*} \quad (4)$$

being: (a)  $\xi_{el,F}^*$  the viscous damping offered by the frame in the elastic range (typically 5% and 2% for r.c. or steel structures, respectively); (b)  $E_{cum,F}^*$  and  $E_{cum,D}^*$  the energy dissipated by the frame and the AHD, respectively.

The estimation of the equivalent viscous damping ( $\xi_{eq,D}^*$ ) developed by the AHD is argued in the next Section while the one offered by frame ( $\xi_{eq,F}^*$ ) is calculated as [26]:

$$\xi_{eq,F}^* = \frac{a}{\pi} \cdot \left(1 - \frac{1}{\mu_F^b}\right) \cdot \left(1 + \frac{1}{(T_{eff,F+D}^* + c)^d}\right) \cdot \frac{1}{N} \quad (5)$$

being: (a)  $N = 1 + [1/(0.5 + c)^d]$ ; (b)  $a = 140$ ,  $b = 0.5$ ,  $c = 0.85$ ,  $d = 2$ .

For a generic set of AHD design parameters, i.e.  $i^{th}$  couple of parameters ( $T_{eff,F+D}^*, \xi_{eq,F+D}^*$ )<sup>(i)</sup>, the peak displacement of the braced frame is obtained by reducing the elastic (viscous damping 5%) spectral displacement ( $S_{d,ULS}(T_{eff,F+D}^*, 5\%)$ ) through the spectral reduction factor ( $\eta$ ) proposed in [24]:

$$\begin{cases} S_{d,ULS}(T_{eff,F+D}^*, \xi_{eq,F+D}^*)^{(i)} = \frac{1}{\eta^{(i)}} \cdot S_{d,ULS}(T_{eff,F+D}^*, 5\%) \\ \eta^{(i)} = \sqrt{7/(2 + \xi_{eq,F+D}^*)^{(i)}} \end{cases} \quad (6-a,b)$$

The mechanical parameters of the AHD ( $F_{y,D1}^*, F_{y,D2}^*, k_{el,D1}^*, k_{pl,D1}^*, k_{el,D2}^*, k_{pl,D2}^*, d_G^*$ ) are hence iteratively varied (Fig. 7, right) until the spectral displacement of the braced frame converges to the design target ( $|S_{d,ULS}(T_{eff,F+D}^*, \xi_{eq,F+D}^*)^{(i)} - d_{targ,ULS}^*| \leq tol$ , being  $tol$  a small enough tolerance parameter (e.g.  $tol = 0.01 \cdot d_{targ,ULS}^*$ ).

Since the iterative design process could seem not trivial (seven variable parameters), some “good practice” criteria that guide designers and practitioners to a fast identification of the optimal layout of the AHD are provided in Section 4.2. Moreover, in Section 5, specific rules for the spatial distribution of the AHD units at the different storey levels of the MDOF frame are also provided and applied to a real case-study building.

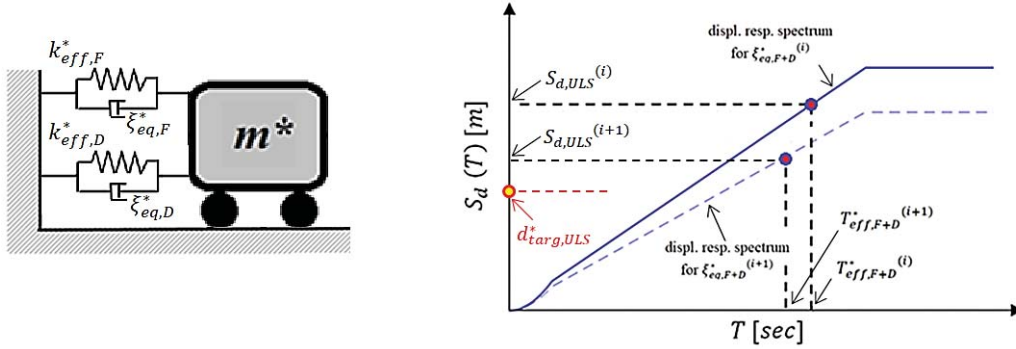


Figure 7: Proposed calculation method: rheological model (left) and iterative response spectrum analyses (right).

#### 4.1. Linear equivalent properties of the AHD

According to a good design practice, it is assumed hereafter that beam elements used to link the AHDs to the bare frame are very stiff and hence, even under severe earthquakes, undergo negligible elastic deformations without affecting the effective stiffness offered by the dampers [23]. Otherwise, a simple approach to account for the flexibility of link elements can be found in [19].

The effective stiffness provided by the AHD ( $k_{eff,D}^*$ ) reflects the “two-steps” hysteretic behaviour of the device (see Fig. 8) and, depending on the displacement demand ( $d_{max}^*$ ) and strength demand ( $F_{max}^*$ ) of the occurring earthquake (i.e. SLS or ULS), can be calculated as:

$$k_{eff,D}^* = \begin{cases} \frac{F_{y,1}^* + k_{pl,1}^* (d_{max}^* - d_{y,1}^*)}{d_{max}^*} & d_{max}^* \leq d_{ES}^* \text{ (at SLS)} \\ \frac{F_{ES}^* d_{ES}^* + F_{max}^* (d_{max}^* - d_{ES}^*)}{d_{max}^{*2}} & d_{max}^* \geq d_{y2}^* \text{ (at ULS)} \end{cases} \quad (7-a,b)$$

It is worth noting that, embracing the approach proposed in a recent study in [25], Eq. 7-b can be obtained equalizing the total elastic energy stored in the minor and major dissipative cores to the elastic energy stored in a virtually equivalent linear spring ( $E_{e,D}^* = E_{e,D1}^* + E_{e,D2}^*$ ):

$$\frac{1}{2} k_{eff,D}^* d_{max}^{*2} = \frac{1}{2} F_{ES}^* d_{ES}^* + \frac{1}{2} F_{max}^* (d_{max}^* - d_{ES}^*) \quad (8)$$

One can note that Eq. 8 alternatively means that the sum of the two blue shaded areas shown in Fig. 8-right is equal to the grey shaded one.

Despite an apparently simple “in series” arrangement of the two hysteretic cores, the effective damping offered by the AHD obeys to slightly more complex rules. Indeed, during minor SLS earthquakes ( $d_{max}^* \leq d_{ES}^*$ ), only the minor core (D1) is plastically engaged providing a certain energy dissipation (ductility level  $\mu_{D1}^* > 1$ ) while the major (D2) acts as a non-dissipative link ( $\mu_{D2}^* = 1$ ). On the contrary, under more demanding ULS displacements ( $d_{max}^* > d_{y2}^*$ ), the major core is activated experiencing a certain ductility demand ( $\mu_{D2}^* > 1$ )

while the deformation of the minor core is freezed at the maximum level allowed by the gap-connector ( $\mu_{D1}^* = d_{ES}^*/d_{y,1}^*$ ):

$$\mu_{D1}^* = \begin{cases} 1 & d_{max}^* \leq d_{y,1}^* \\ d_{max}^*/d_{y,1}^* & d_{y,1}^* < d_{max}^* \leq d_{ES}^* \\ d_{ES}^*/d_{y,1}^* & d_{max}^* > d_{ES}^* \end{cases} \quad (9-a \div c)$$

$$\mu_{D2}^* = \begin{cases} 1 & d_{max}^* \leq d_{y,2}^* \\ \frac{(d_{max}^* - d_G^*)}{(d_{y,2}^* - d_G^*)} & d_{max}^* > d_{y,2}^* \end{cases} \quad (10-a, b)$$

The equivalent viscous damping offered by the minor ( $\xi_{eq,D1}^*$ ) and major ( $\xi_{eq,D2}^*$ ) dissipative cores are calculated by means of the formulation proposed in [26] for bilinear hysteretic systems:

$$\xi_{eq,D(i)}^* = \frac{a}{\pi} \cdot \left( 1 - \frac{1}{\mu_{D(i)}^*{}^b} - 0.1 \cdot r_{(i)} \cdot \mu_{D(i)}^* \right) \cdot \left( 1 + \frac{1}{(T_{eff,F+D}^* + c)^d} \right) \cdot \frac{1}{N} \quad (11)$$

where: (a) the subscript "(i)" refers to the minor ( $i = 1$ ) or major ( $i = 2$ ) core, alternatively; (b)  $N = 1 + [1/(0.5 + c)^d]$ ; (c)  $a = 140$ ,  $b = 0.5$ ,  $c = 0.85$ ,  $d = 2$ ; (d)  $\mu_{Di}^*$  and  $r_i = k_{pl,Di}^*/k_{el,Di}^*$  are the ductility demand and hardening ratio, respectively.

Eventually, the overall equivalent viscous damping offered by the damper ( $\xi_{eq,D}^*$ ) is calculated through this weighted average [25]:

$$\xi_{eq,D}^* = \frac{\xi_{eq,D1}^* \cdot E_{cum,D1}^* + \xi_{eq,D2}^* \cdot E_{cum,D2}^*}{E_{cum,D1}^* + E_{cum,D2}^*} \quad (12)$$

being  $E_{cum,D1}^*$  and  $E_{cum,D2}^*$  the energy dissipated by the minor and major hysteretic core (Fig. 9), respectively.

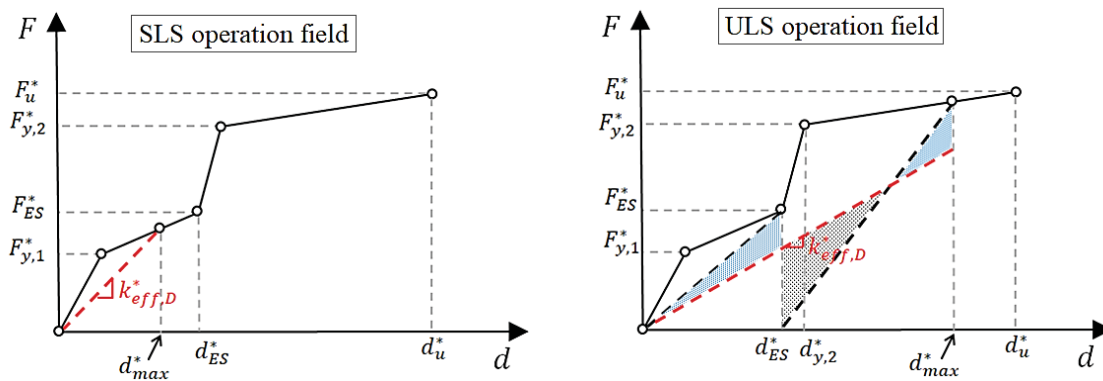


Figure 8: Definition of the damper effective stiffness for minor SLS displacements (left,  $d_{max}^* \leq d_{ES}^*$ ), and severe ULS displacements (right,  $d_{max}^* \geq d_{y,2}^*$ ).

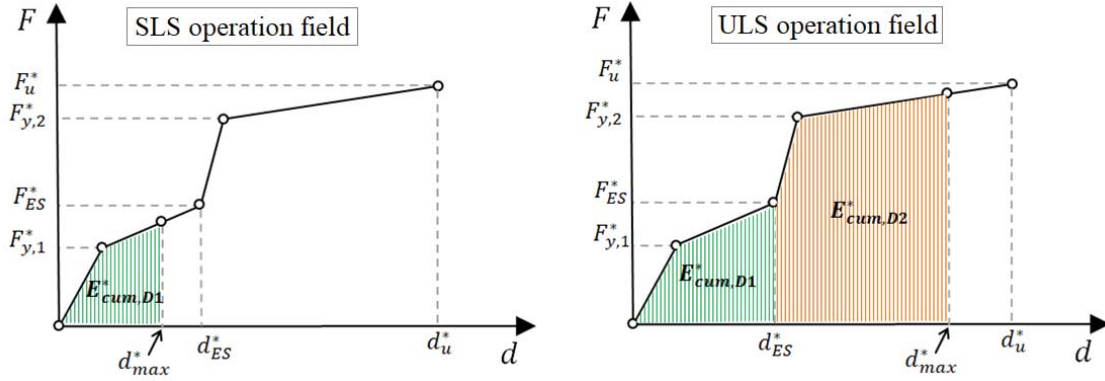


Figure 9: Definition of the energy dissipated by the two hysteretic cores for minor SLS displacements (left,  $d_{max}^* \leq d_{ES}^*$ ), and severe ULS displacements (right,  $d_{max}^* \geq d_{y,2}^*$ ).

#### 4.2. Simplified set of AHD design parameters

Due to the large number (seven) of the AHD design parameters ( $F_{y,D1}^*$ ,  $F_{y,D2}^*$ ,  $k_{el,D1}^*$ ,  $k_{el,D2}^*$ ,  $k_{pl,D1}^*$ ,  $k_{pl,D2}^*$ , and  $d_G^*$ ), the definition of the optimal damper layout could seem not easy. To overcome this issue, some criteria to simplify/reduce the variable parameters are provided hereafter. Within this framework, the ratios  $\alpha_F$ ,  $\alpha_k$ , and  $r$  are introduced to link the design parameters of the two hysteretic cores and those of the bare frame [23]:

$$\begin{cases} \alpha_F = F_{y,D1}^*/F_{y,D2}^* \\ \alpha_k = k_{el,D1}^*/k_{el,F}^* \\ r = k_{pl,D1}^*/k_{el,D1}^* = k_{pl,D2}^*/k_{el,D2}^* \end{cases} \quad (13-a \div c)$$

In particular, at designer's discretion,  $\alpha_k$  and  $r$  can be selected within the ranges ( $\alpha_F = 0.3 - 0.6$ ,  $\alpha_k = 2 - 15$ , and  $r = 0.01 - 0.10$ ) suggested in [23] leading to:

$$\begin{cases} F_{y,D1}^* = \alpha_F \cdot F_{y,D2}^* \\ k_{el,D1}^* = \alpha_k \cdot k_{el,F}^* \\ k_{el,D2}^* = (\alpha_k/\alpha_F) \cdot k_{el,F}^* \\ k_{pl,D1}^* = r \cdot \alpha_k \cdot k_{el,F}^* \\ k_{pl,D2}^* = r \cdot (\alpha_k/\alpha_F) \cdot k_{el,F}^* \end{cases} \quad (14-a \div e)$$

Moreover, accomplishing to the “adaptive working principle” of the AHD providing the exclusive engagement of the minor (D1) core during weak SLS events, a suitable criterion for the selection of the width ( $d_G^*$ ) of the gap-connector is [23]:

$$d_G^* = \gamma_x \cdot \gamma_b \cdot S_{d,SLS}(T_{eff,F+D}^*, \xi_{eq,F+D}^*) \quad (15)$$

being: (a)  $S_{d,SLS}(T_{eff,F+D}^*, \xi_{eq,F+D}^*)$  the spectral displacement calculated at SLS; (b)  $\gamma_x = 1.1$ , and  $\gamma_b = 1.2$  a reliability and a safety factor, respectively [1].

The “good practice” design assumptions described in this Section allow to reduce the number of variable parameters to the couple ( $F_{y,D2}^*$ ;  $\alpha_F$ ) leading to a fast identification of most suitable AHD layout.



## 5 A CASE-STUDY

In this Section, a seismic retrofit intervention of the “Piastra building” of the hospital complex of Lamezia Terme, a small city located in southern Italy, is designed through the previously proposed iterative spectral analysis. The beneficial effects offered by the AHDs, compared to traditional bilinear hysteretic dampers (BHDs), are discussed and quantified. For sake of simplicity, only the longitudinal frame of the “block C” is considered hereafter (Fig. 10-a). This building, erected in the early 70's, features a quite flexible r.c. frame (fundamental period equal to 1.06s) and would not be capable to survive the ULS design earthquake [4].

The reference retrofitting solution through conventional BHDs has been already proposed elsewhere [5]. In the same study, the characteristic parameters of both the real MDOF and the equivalent SDOF system of the bare frame are provided (Table 3).

The new retrofitting solution provides the replacement of the traditional BHDs with the innovative AHDs designed to ensure an unaltered degree of structural protection under severe ULS events, and offer an enhanced seismic response to minor SLS earthquakes. In this regard, according to the provisions of the Italian Building code [27], a severe “SLV” (ULS level) and a weak “SLO” (SLS level) design spectrum, featuring respectively  $PGA=0.45g$  and  $PGA=0.17g$ , were defined considering a topographic category T1, a nominal life of the building  $V_N = 100years$  (corresponding to a reference period  $V_R = c_u \cdot V_N = 200years$ ), and foundation-soil type B.

By analogy with the design-assumption of traditional BHDs [5], the ULS displacement target of the new retrofit-project is set to  $d_{targ,ULS} = 50mm$  ( $d_{targ,ULS}^* = d_{targ,ULS}/\Gamma = 36.8mm$ ) in order to maintain the frame in the elastic field and avoid the hammering with the adjacent “block B”. Besides this target, thanks to the iterative spectral procedure and the design criteria provided in the previous Section, the following set of AHD design parameters is detected to ensure minimal spectral accelerations under weak but frequent SLS earthquakes [23]:  $F_{y,D2}^* = 7300kN$ ,  $\alpha_F = 0.38$ ,  $\alpha_k = 15$ ,  $r = 0.075$ , and  $d_G^* = 14mm$ . The relevant effective period and equivalent viscous damping of the braced frame are: (i) at ULS design level,  $T_{eff,F+D}^* = 0.53s$ , and  $\xi_{eq,F+D}^* = 29.2\%$ ; (ii) at SLS design level,  $T_{eff,F+D}^* = 0.46s$ , and  $\xi_{eq,F+D}^* = 23.7\%$ . The (equivalent SDOF) design parameters of the selected AHD layout and those of the original BHD [5] are compared in Table 4.

real MDOF frame				
storey	$m_i$ (ton)	$\phi_i$ (-)	$F_{y,F,i}$ (kN)	$k_{el,F,i}$ (kN/mm)
1	1333	0.28	4703	344
2	1302	0.63	3886	187
3	954	1.00	2090	75
equivalent SDOF system				
$\Gamma$ (-)	$m^*$ (ton)	$F_{y,F}^*$ (kN)	$d_{y,F}^*$ (mm)	$k_{el,F}^*$ (kN/mm)
1.36	2148	4704	62.3	75.5

Table 3: Characteristic parameters of the bare frame: real MDOF system (F) and equivalent SDOF one (F\*).

novel AHD							traditional BHD		
$F_{y,D1}^*$ (kN)	$F_{y,D2}^*$ (kN)	$k_{el,D1}^*$ (kN/mm)	$k_{el,D2}^*$ (kN/mm)	$k_{pl,D1}^*$ (kN/mm)	$k_{pl,D2}^*$ (kN/mm)	$d_G^*$ (mm)	$F_{y,D}^*$ (kN)	$k_{el,D}^*$ (kN/mm)	$k_{pl,D}^*$ (kN/mm)
2760	7300	1133	2998	85.0	224.9	14.0	7000	1124	28.1

Table 4: Design parameters of the selected AHD compared to those of the traditional BHD (eq. SDOF systems).

Once defined the design parameters of the equivalent SDOF of the AHD, the the yielding force of the minor ( $F_{y,D1,i}$ ) and major ( $F_{y,D2,i}$ ) cores of the physical AHD devices installed at the  $i^{\text{th}}$  storey of the real MDOF frame are sized through this rule [23]:

$$\begin{cases} F_{y,D1,i} = \left( \frac{F_{y,F,i}}{F_{y,F}^*} \right) \left( \frac{F_{y,D1}^*}{n_{AHD,i} \cdot \cos \vartheta_i} \right) \\ F_{y,D2,i} = \left( \frac{F_{y,F,i}}{F_{y,F}^*} \right) \left( \frac{F_{y,D2}^*}{n_{AHD,i} \cdot \cos \vartheta_i} \right) \end{cases} \quad (16\text{-a,b})$$

and similarly for the elastic stiffness of the two cores:

$$\begin{cases} k_{el,D1,i} = \left( \frac{k_{el,F,i}}{k_{el,F}^*} \right) \left( \frac{k_{el,D1}^*}{n_{AHD,i} \cdot \cos^2 \vartheta_i} \right) \\ k_{el,D2,i} = \left( \frac{k_{el,F,i}}{k_{el,F}^*} \right) \left( \frac{k_{el,D2}^*}{n_{AHD,i} \cdot \cos^2 \vartheta_i} \right) \end{cases} \quad (17\text{-a,b})$$

resulting in the following plastic stiffnesses:

$$\begin{cases} k_{pl,D1,i} = r \cdot k_{el,D1,i} \\ k_{pl,D2,i} = r \cdot k_{el,D2,i} \end{cases} \quad (18\text{-a,b})$$

being: (a)  $F_{y,F,i}$  and  $k_{el,F,i}$  the overall lateral yielding-strength and elastic stiffness of the columns at the  $i^{\text{th}}$  storey level [19], respectively; (b)  $n_{AHD,i}$  the number of AHD units installed at the same level; (c)  $\vartheta_i$  the inclination angle of the dissipative braces (Fig. 10,b).

The “storey-distribution” of  $d_{GAP}^*$  among the AHD units installed at the different storey levels is assumed to reflect the fundamental mode shape [23]:

$$d_{G,i} = \Gamma_{\phi_1} \cdot (\phi_{1,i} - \phi_{1,i-1}) \cdot d_{GAP}^* \cdot \cos \vartheta_i \quad (19)$$

The complete set of design parameters of the real AHD units installed along the diagonal braces of each storey level are listed in Table 5.

The effectiveness of the new retrofitting solution is proven through NLTH analyses carried out in OpenSees FEM code [28] developing a specific modelling strategy for the AHD units [23]. Two sets of seven ground motion records (Fig. 11), one for the SLS and one for the ULS design spectrum, were identified by means of the software REXEL [29] enforcing the “spectrum compatibility” criterion in the range [0.15-2.0s]. According to the reference Standard [27], the structural integrity of the frame is checked at ULS and the serviceability of the hospital at SLS considering the average response over the seven independent history analyses.

level	$n_{\text{AHD},i}$ (-)	$\theta_i$ (°)	$F_{y,D1,i}$ (kN)	$F_{y,D2,i}$ (kN)	$k_{el,D1,i}$ (kN/mm)	$k_{el,D2,i}$ (kN/mm)	$r$ (%)	$d_{G,i}$ (mm)
1	12	54.8	399	1055	1293	3423	7.5	3.1
2	12	44.2	265	701	455	1205	7.5	4.8
3	12	51.3	163	432	240	635	7.5	4.4

Table 5: Design parameters of the different AHD units installed at each storey level.

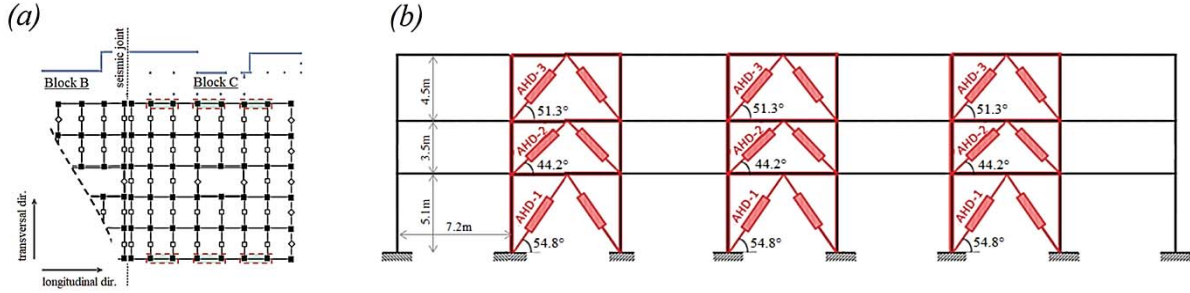


Figure 10: Spatial arrangement of the AHD units: (a) in-plan location; (b) vertical layout.

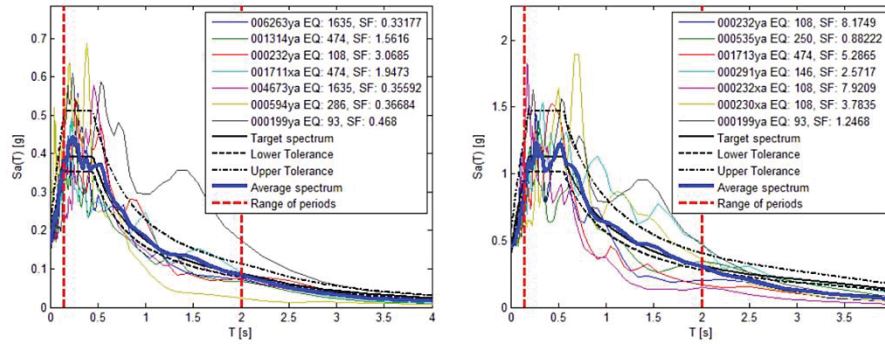


Figure 11: Selected ground motion records for NLTH analyses at SLS (left) and ULS (right).

According to the design assumption (i.e.  $d_{\text{target,ULS}}^* < d_{y,F}^*$ ), r.c. elements of the braced frame react to the seismic shaking remaining always in their elastic range. This is witnessed by Fig. 12 that shows the calculated displacement envelopes over the storey levels: the average peak displacement at roof level is equal to 16mm for SLS events and to 52mm ( $\cong d_{\text{target,ULS}}^*$ ) for ULS earthquakes. In particular at SLS, despite the “AHD solution” is a bit more flexible than the “BHD solution” (16mm vs. 13mm of peak displacement, respectively), thanks to the significant damping offered by the minor hysteretic core ( $\xi_{eq,F+D}^* = 23.7\%$ ), the displacement increase does not represent a hazard neither for “displacement-sensitive” nor for “drift-sensitive” NSCs. Indeed, as shown in Fig. 13-right, the largest inter-storey drift affects the 2<sup>nd</sup> columns level with a peak of 0.17% (practically identical to 0.16% calculated for the “BHD solution”) that is widely below the “immediate occupancy” average limits for both the weakest “drift-sensitive” NSC (0.75% for infill walls) [3] and r.c. column elements (0.66%) [7].

The enhanced protection level offered by the innovative AHDs is evident comparing the envelopes of PFAs at SLS (Fig. 13-left). The PFAs calculated at 3<sup>rd</sup> storey level are 0.20g and 0.42g for the retrofitting solution implementing the AHDs and the BHDs, respectively. This

achievement can be easily explained considering the lower effective period ( $T_{eff,F+D}^* = 0.33s$ ) and minor equivalent viscous damping ( $\xi_{eq,F+D}^* = 8.9\%$ ) offered by common BHDs (i.e. stiffer structure with lower energy dissipation capacity). As shown in Fig. 14, the huge reduction (-52%) of the PFAs leads also to markedly less demanding floor response spectra (calculated assuming a conventional viscous damping equal to 5%). These plots allow to compare the actual acceleration experienced by all NSCs (characterized different fundamental periods) installed at the different storey levels. For all oscillation periods in the range  $[0 - 4.0s]$ , the floor response spectrum of the new “AHD solution” lies practically always below that of the original “BHD solution” ensuring reduced peak values: -20%, -55%, and -53% for NSCs installed at first, second, and third storey level, respectively. Compared to the response offered by traditional BHDs, one can therefore conclude that the innovative AHDs, besides an unaltered protection level for both structural and non-structural drift-sensitive elements, can guaranty a considerably enhanced safeguard of “acceleration-sensitive” elements leading to a more prompt operation of the building after the quake and to likely reduced repairing costs.

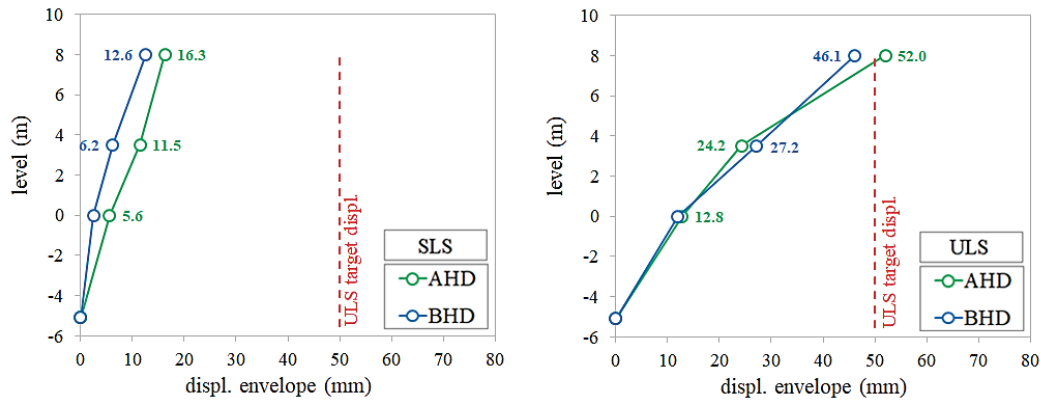


Figure 12: Average displacement envelopes calculated for the braced frame under SLS (left), and ULS (right) earthquakes.

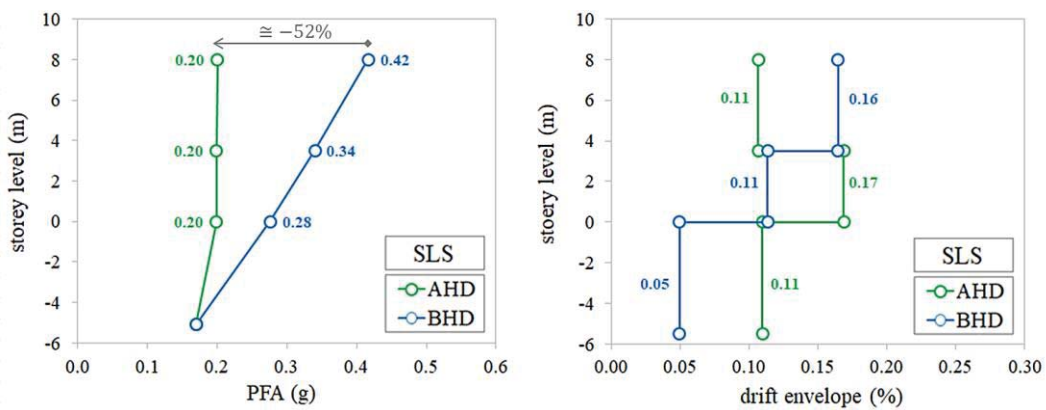


Figure 13: Average PFA (left) and inter-storey drift (right) envelopes calculated for SLS earthquakes.

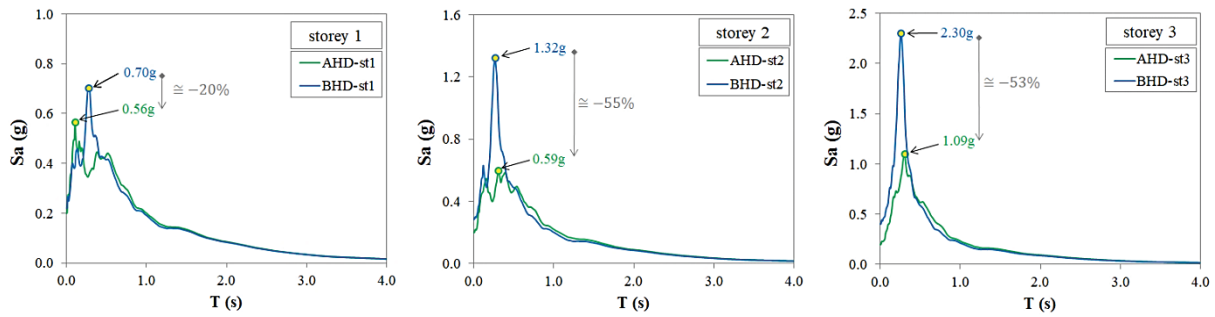


Figure 14: Average floor response spectra ( $\xi = 5\%$ ) calculated from acceleration time-histories obtained for SLS earthquakes: storey 1 (left), storey 2 (center), and storey 3 (right).

## 6 CONCLUSIONS

Traditional bilinear hysteretic dampers (BHDs) dampers are usually designed to guaranty the structural integrity of braced buildings under severe ULS seismic events. As a drawback, under weak but frequent SLS earthquakes, they practically behave as stiff springs causing high PFAs that are detrimental for “acceleration-sensitive” nonstructural components (NSCs).

To overcome this drawback, the innovative Adaptive Hysteretic Damper (AHD), capable to develop a two-steps hysteretic loop and to modulate its effective stiffness and damping based on the intensity of the occurring earthquake, has been presented claiming the following:

- results of experimental force-displacement tests have proven the reliability and robustness (i.e. stable response) of the device under repeated cyclic motions with increasing amplitudes;
- simple response spectrum analyses can be exploited for the design of braced buildings implementing the AHDs whose linear equivalent mechanical properties can be calculated through the analytical formulas provided in this paper;
- the main benefits arising from to the implementation of novel AHDs, rather than common BHDs, in braced frames have been quantified through NLTH analyses carried out on a case-study building. Very similar lateral displacements and inter-storey drifts envelopes have been calculated for the two structural systems, at both ULS and SLS design levels, resulting in the same protection level for structural and nonstructural sensitive elements. On the contrary, at SLS, the adoption of the new AHDs leads to markedly reduced peak floor (up to -52%) and spectral accelerations (up to -55%) ensuring: (a) an enhanced protection of “acceleration-sensitive” NSCs; (b) a more prompt response of the building after the quake; (c) likely reduced repairing costs.



## REFERENCES

- [1] CEN - Comité Européen de Normalisation, *EN 1998-1 - Eurocode 8: Design of structures for earthquake resistance – Part 1: General rules, seismic actions and rules for buildings*. Brussels, Belgium, 2004.
- [2] M.J.N. Priestley, Performance based seismic design. *12th World Conference on Earthquake Engineering (WCEE)*. Auckland, New Zealand, 2000.
- [3] G. Lupoi, P. Franchin, A. Lupoi, P.E. Pinto, G.M. Calvi, *Probabilistic Seismic Assessment for Hospitals and Complex-Social Systems*. ROSE Research Report No. 2008/02. IUSS Press, 2008.
- [4] E. Gandelli, V. Quaglini, P. Dubini, M.P. Limongelli, S. Capolongo, Seismic isolation retrofit of hospital buildings with focus on non-structural components. *Ingegneria Sismica - International Journal of Earthquake Engineering*, **36(2)**, 118-136, 2018.
- [5] E. Gandelli, A. Taras, J. Distl, V. Quaglini, Seismic retrofit of hospitals by means of hysteretic braces: influence on acceleration-sensitive non-structural components. *Frontiers in Built Environment – Earthquake Engineering section*, **5**, 2019.
- [6] FEMA, Federal Emergency Management Agency, *Earthquake Loss Estimation Methodology: HAZUS® Technical Manual*. National Institute of Building Sciences, Washington, DC, 1999.
- [7] A. Yakut, T. Solmaz, Performance based Displacement Limits for Reinforced Columns under Flexure. *15<sup>th</sup> World Conference on Earthquake Engineering*, Lisbon, Portugal, 2012.
- [8] P.M. Calvi, Relative Displacement Floor Spectra for Seismic Design of Nonstructural Elements, *Journal of Earthquake Engineering*, **28(9)**, 979-993, 2014.
- [9] C. Lima, E. Martinelli, Seismic Response of Acceleration-Sensitive Non-Structural Components in Buildings. *Buildings*, **9(1)**, 2018.
- [10] R.I. Skinner, R.G. Tyler, A.J. Heine, W.H. Robinson. Hysteretic dampers for protection of structures from earthquakes. *Bulletin of the New Zealand Society for Earthquake Engineering (NZSEE Bulletin)*, **13(1)**, 22-36, 1980.
- [11] A. Javanmardi, Z. Ibrahim, K. Ghaedi, H. Benisi, G. Muhammad, U. Hanif, State-of-the-Art Review of Metallic Dampers: Testing, Development and Implementation. *Archives of Computational Methods in Engineering*, 2019.
- [12] D. De Domenico, N. Impollonia, G. Ricciardi, Seismic retrofitting of confined masonry-RC buildings: The case study of the university hall of residence in Messina, Italy. *Ingegneria Sismica - International Journal of Earthquake Engineering*, **36(1)**, 54-85, 2019.
- [13] A. Wada, Y.H. Huang, M. Iwata, Passive Damping Technology for Buildings in Japan. *Progress in Structural Engineering and Materials*, **2**, 335-350, 2000.
- [14] F.C. Ponzo, A Di Cesare, N. Lamarucciola, D. Nigro, Seismic design and testing of post-tensioned timber buildings with dissipative bracing systems. *Frontiers in Built Environment*, **5(104)**, 2019.

- [15] T. Polocoser, J. Leimcke, B. Kasal, Report on the seismic performance of three-dimensional moment-resisting timber frames with frictional damping in beam-to-column connections. *Adv. Struct. Eng.*, **21**, 1652–1663, 2018.
- [16] W. Pu, C. Liu, F. Dai, Optimum hysteretic damper design for multistory timber structures represented by an improved pinching model. *Bull. Earthquake Eng.* **16**, 6221–6241, 2018.
- [17] F. Mazza, A. Vulcano, Displacement-based design procedure of damped braces for the seismic retrofitting of r.c. framed buildings. *Bulletin of Earthquake Engineering*, **13**(7), 2121-2143, 2015.
- [18] F. Braga, F. Buttarazzi, A. Dell'Asta, W. Salvatore, *Protezione sismica di edifici in c.a. con controventi dissipativi in acciaio*. Dario Flaccovio Editore, 2015.
- [19] A. Di Cesare, F.C. Ponzo, Seismic Retrofit of Reinforced Concrete Frame Buildings with Hysteretic Bracing Systems: Design Procedure and Behaviour Factor. *Shock and Vibration*, 2017.
- [20] R.W.K. Chan, F. Albermani, Experimental study of steel slit damper for passive energy dissipation. *Engineering Structures*, **30**(4), 1058-1066, 2008.
- [21] Eucentre Lab, Pavia (Italy), website at: <https://www.eucentre.it/laboratory-tests/?lang=en>
- [22] CEN - Comité Européen de Normalisation, *EN15129 - Antiseismic Devices*. Brussels, Belgium, 2009.
- [23] E. Gandelli, S. Chernyshov, J. Distl, P. Dubini, F. Weber, A. Taras, Novel adaptive hysteretic damper for enhanced seismic protection of braced buildings, *Soil Dynamics and Earthquake Engineering*, **141**, 2021.
- [24] M.J.N. Priestley, G.M. Calvi, M.J. Kowalsky, *Displacement-Based Seismic Design of Structures*, 2nd edition, Eucentre, 2007.
- [25] D. De Domenico, E. Gandelli, V. Quaglini, Adaptive isolation system combining low-friction sliding pendulum bearing and SMA-based gap dampers. *Engineering Structures*, **212**, 2020.
- [26] C.A. Blandon, M.J.N. Priestley, Equivalent viscous damping equations for direct displacement based design. *Journal of Earthquake Engineering*, **9** (no. spec02), 2005.
- [27] CSLLPP - Consiglio Superiore dei Lavori Pubblici. *Norme Tecniche per le Costruzioni - NTC2018*. Gazzetta Ufficiale della Repubblica Italiana, 2018.
- [28] F. McKenna, G.L. Fenves, M.H. Scott, B. Jeremic, *Open System for Earthquake Engineering Simulation (OpenSees)*. Pacific Earthquake Engineering Research Center (PEER), Berkeley, USA, 2000.
- [29] I. Iervolino, C. Galasso, E. Cosenza, REXEL: computer aided record selection for code-based seismic structural analysis. *Bulletin of Earthquake Engineering*, **8**, 339-362, 2010.

## INVESTIGATIONS ON INTER-STOREY SEISMIC ISOLATION AS A TECHNIQUE FOR ADDING UPPER STOREYS

Enrico Bernardi<sup>1,2</sup>, Marco Donà<sup>2</sup>, Francesca da Porto<sup>1</sup> and Ping Tan<sup>2</sup>

<sup>1</sup> Department of Geosciences, University of Padova, Via Gradenigo 6, 35131 Padova, Italy  
enrico.bernardi@dicea.unipd.it, francesca.daporto@unipd.it

<sup>2</sup> Earthquake Engineering Research & Test Center (EERTC), Guangzhou University, Guang Yuan  
Zhong Rd. 248, 510405 Guangzhou, China  
marco.dona.1@unipd.it, ptan@gzhu.edu.cn

---

### Abstract

*The inter-storey seismic isolation technique is becoming increasingly attractive for the seismic risk mitigation of buildings, also as alternative strategy to base isolation. The reasons for applying this technique can be various and of different nature, such as: architectural concerns, feasibility of construction, and performance benefits. An interesting application of this technique concerns its use for adding upper storeys to existing buildings, avoiding the increase of seismic forces on the substructure, or even reducing them. Therefore, this technique could also be effective for seismic retrofit applications, using the mass of the superstructure as a nonconventional TMD for controlling the dynamic response of the substructure.*

*Among the main issues concerning this application, there is the need to control the relative displacement between the two structural parts and the acceleration of the superstructure, while improving the seismic performance of the substructure.*

*In this paper, a multi-objective optimization method for the dynamic characteristics of the additional superstructure is presented, which uses a TMD approach and considers the performances of the substructure, isolation system and superstructure. A 3-storey (3 DOF) case study structure was taken as a reference, analysing a wide range of isolated masses, isolation periods and damping ratios. Time-history analyses are finally performed, based on the optimization results, in order to assess the effectiveness of both the optimization method and the isolation technique, also considering the structural non-linearity.*

**Keywords:** Inter-Storey Isolation System (IIS), Tuned Mass Damper (TMD), Multi-Objective Optimization, Frequency Response Functions, Time-History Analyses.

---

## 1 INTRODUCTION

The inter-storey isolation system (IIS) is becoming increasingly attractive, as it allows greater freedom in the structural conception of skyscrapers and multi-purpose buildings by defining two independent structures, i.e. substructure and superstructure, which may have different forms, materials and uses (e.g. [1, 2]). This represents both an advantage for architectural design and a sustainable solution for densely populated areas, as it allows significant savings on land use. Furthermore, in some cases, the base isolation technique encounters economic and technical issues that can prevent its application; for example, its application is often difficult and expensive in existing buildings, and generally more than applying isolation between storeys.

Moreover, the IIS technique can be applied to add extra storeys on the top of existing buildings, with appropriate vertical capacity, without increasing the base shear forces (e.g. [3, 4, 5]). In particular, the isolated superstructure, when properly designed, can be used as a Tuned Mass Damper (TMD) to improve the seismic behaviour of the substructure, thus making this technique very advantageous when retrofitting and elevation of the existing building are both required.

From a functional point of view, the IIS technique combines the functions of seismic isolation and mass damping; indeed, the isolation system is a filter for the inertial forces transmitted to the superstructure and, at the same time, induces the isolated superstructure to exert a mass damping action on the substructure, improving the seismic behaviour of the latter. In the literature, two main conceptual approaches can be identified, each of which focuses on one of the two main aspects of the IIS, i.e. seismic isolation or mass damping (TMD).

Studies that address the problem from the point of view of seismic isolation evaluate the interaction between the superstructure and the substructure, the effects of the higher vibration modes and their possible coupling, using frequency and mass ratios as design parameters (e.g. [6, 7, 8, 9, 10, 11, 12]), but also the optimal parameters of additional Fluid Viscous Dampers (FVDs) installed in the IIS (e.g. [2, 13, 14]). 3 degree-of-freedom (DOF) models (e.g. [8, 9]) or multi DOF models (e.g. [2, 10, 12]) are generally adopted, depending on the purpose of the study.

Other researchers, on the other hand, approach the study of the IIS following the strategy of mass damping, which is based on the principle of TMD, and considering the peculiarities of the IIS, namely the fact that the isolated mass also performs structural and housing functions in addition to that of dynamic control. The design parameters are the mass and frequency ratios between the TMD and the primary structure, and the damping ratio provided by the TMD. Generally, frequency and damping ratios are optimized for set values of mass ratio, using simplified 2 DOF models.

The concept of TMD for structural application was first introduced by [15], who applied a secondary mass to a single degree-of-freedom (SDOF) system harmonically excited. [16] first established a TMD design approach to suppress the peak displacement of an undamped SDOF system (primary structure) sinusoidally excited. This approach is based on the observation that all frequency response functions (FRFs) of the combined 2 DOF system (SDOF primary structure with TMD), obtained for various damping ratios of TMD, pass through two specific points (“fixed point theory”). Following the same design approach of [16], [17] derived the TMD design formula to optimize the performance of the undamped SDOF primary structure in the case of harmonic excitation at the base (more useful for earthquake engineering applications). Later, [18] proposed the equations for the optimal tuning parameters of the TMD in the case of damped SDOF primary structures. Then, [19] first conceived the idea of using a heavily damped vibration absorber (or TMD) to reduce the seismic response of the structure.

In particular, he suggested to tune the TMD in resonance with the primary structure and showed that its best performance is obtained when the two complex vibration modes of the resulting 2-DOF system have similar damping ratios, and approximately equal to the mean damping ratio between those of the TMD and the structure.

For several years, studies have focused on TMDs with low mass ratios, which are also often susceptible to tuning problems (e.g. [20]). Only more recently, various investigations have been directed towards TMDs with large mass ratios, also called nonconventional TMDs, given the growing interest in innovative applications such as mega-sub-control-structures (MSCS), inter-storey isolation systems and sliding roof systems (e.g. [21]). These TMDs have shown greater robustness than those with low mass ratios, due to their lower sensitivity to tuning (e.g. [22]). In particular, [23] showed that the design formulas proposed by [19] do not guarantee the equality of the modal damping ratios of the two complex modes in the case of TMD with mass ratios greater than 0.005; therefore, through a numerical procedure, [23] provided new design equations that result in equal damping ratios and equal frequencies for the two vibration modes. [24] validated the TMD tuning equations obtained by [23], proposing an analytical formulation that matches the same results. [25] proposed an alternative approach for tuning TMDs with large mass ratios, still equalizing the damping ratios but, at the same time, minimizing the maximum FRF amplitude associated with the displacement of the primary structure. The TMD damping ratio according to this last approach is significantly lower than that deriving from the model of [23], despite ensuring a similar efficiency of the TMD. [26] proposed an energy-based design methodology for non-conventional TMDs, which maximizes the ratio between the energy dissipated by the isolation system (located between the masses of a 2DOF system) and that of the input earthquake. [27] compared different optimization approaches, minimizing the variance of the responses (i) in displacement or (ii) in acceleration of the primary structure, or (iii) maximizing the energy dissipated by the TMD system (like [26]). [28] provided the equations for optimal TMD tuning, using a 2 DOF reduced-order model without damping in the main structure, minimizing (i) the maximum amplitudes of the base shear force under harmonic excitations, or (ii) the variance of the base shear force under a band-limited random excitation of white noise. [21], similarly to [25], proposed a TMD optimization approach that approximately equals the damping ratios of the 2 DOF system and, at the same time, minimizes its overall response; in particular, in addition to minimizing the FRF of the displacement of the primary structure, as done by [25], [21] simultaneously minimized the FRF of the acceleration of the nonconventional TMD, holding the latter also structural functions.

This paper investigates the inter-storey isolation system (IIS) as a technique for adding upper storeys to an existing building, improving at the same time its seismic behaviour. A 3-storey case study structure (without considering the IIS) is taken as a reference, analysing a wide range of isolated masses, isolation periods and damping ratios. First, some assessments are carried out on the effects that the IIS parameters (normalized to the substructure characteristics) have on the dynamic response of the substructure, using the complex modal analysis and evaluating the FRFs of the equivalent 2 DOF system. An alternative approach for tuning the IIS (or TMD) parameters is then proposed, carrying out two multi-objective optimizations that consider the performance of the substructure along with that of the isolation system (to limit the P- $\Delta$  effects on the substructure, *OPT1*) or along with that of the superstructure (to limit the TMD accelerations, *OPT2*). It is worth noting that high damping values in the IIS are effective in limiting the relative displacement of the isolators (and therefore the P- $\Delta$  effects) but could have negative effects on the overall structural behaviour, especially on the superstructure and its content (e.g. [2, 13, 14, 29]). Parametric time-history analyses are finally performed, based on the optimal solutions obtained for the IIS parameters, in order to assess the



effectiveness of the optimization method and therefore of the isolation technique, also considering the structural non-linearity.

## 2 CASE STUDY STRUCTURE AND PARAMETER DEFINITION

For reasons of clarity, even if the study presented here is of general applicability, reference was made to a generic three-storey structure, representative of regular RC frame buildings with a fundamental period of about 0.3 s. The building is shown in Figure 1 and is characterized by the following floor masses,  $m_1=m_2=350$  t and  $m_3=300$  t, and by the following storey stiffnesses,  $k_1=k_2=k_3=780$  kN/mm. Assuming that the structure can support additional floors (by its own capacity or through appropriate interventions), it is intended to add an isolated superstructure above it (which can therefore be defined as substructure), whose total mass is given by the masses of the isolation layer and the additional floors.

Conceptually, the IIS subdivides the structure into three main parts, i.e. the substructure, the isolation system and the superstructure. As said before, some relevant studies focusing on the aspect of seismic isolation analyse the structure using 3 DOF or multi DOF models, while other studies adopting TMD approaches evaluate the structural response using 2 DOF reduced-order models. However, as demonstrated in various studies (e.g. [7, 12]), when the mass ratio ( $\mu$ ) between the isolated mass and the mass of the substructure is less than 1, there is a “mass damping” behaviour, and therefore it is possible to neglect the higher vibration modes of the superstructure, simplifying the system with an equivalent 2 DOF model.

Thus, considering values of  $\mu$  in this study up to 1, both substructure and isolated superstructure were modelled with an equivalent SDOF model. In particular, the substructure is characterized by an angular frequency ( $\omega_{SDOF}$ ) of 21 rad/s (i.e., vibration period of about 0.3 s) and a damping ratio ( $\xi_{SDOF}$ ) of 5%; its equivalent mass ( $m_{SDOF}$ ) is 606 t and corresponds to the modal mass of the first vibration mode of the 3 DOF structure, calculated as in Equation 1, where  $\phi_1$  is the first eigenvector normalized to 1 and  $\mathbf{M}_{st}$  the mass matrix of the structure. On the other hand, the isolated superstructure is characterized by the parameters  $m_{IS}$  (sum of the masses of isolation and superstructure),  $\omega_{IS}$  and  $\xi_{IS}$  (angular frequency and damping ratio of the isolation system), as shown in Figure 1; the relation between  $m_{IS}$  and  $\omega_{IS}$  is given in Equation 2, where  $k_{IS}$  is the IIS stiffness. Considering the parameters of the isolated superstructure normalized to those of the substructure, as generally done in TMD approaches, the mass ( $\mu$ ) and frequency ( $\nu$ ) ratios in Equation 3 can be defined, which together with  $\xi_{IS}$  represent the dimensionless parameters of the nonconventional TMD to be optimized. Lastly, Equation 4 shows the matrices of mass ( $\mathbf{M}$ ), damping ( $\mathbf{C}$ ) and stiffness ( $\mathbf{K}$ ) of the 2 DOF reduced-order model (Figure 1b), as a function of the aforementioned parameters.

In this study, the optimization is performed for the parameters  $\nu$  and  $\xi_{IS}$ , considering the range from 0.05 to 1 for  $\nu$  and the range from 0.01 to 2 for  $\xi_{IS}$ , for set values of  $\mu$  (0.25, 0.5, 0.75 and 1).

$$m_{SDOF} = \phi_1^T \mathbf{M}_{st} \phi_1 \quad (1)$$

$$\omega_{IS} = \sqrt{\frac{k_{IS}}{m_{IS}}} \quad (2)$$

$$\mu = \frac{m_{IS}}{m_{SDOF}} \quad ; \quad \nu = \frac{\omega_{IS}}{\omega_{SDOF}} \quad (3)$$

$$\mathbf{M} = \begin{bmatrix} 1 & 0 \\ 0 & \mu \end{bmatrix} ; \quad \mathbf{C} = \begin{bmatrix} 2\xi_{SDOF}\omega_{SDOF} + 2\mu\xi_{IS}\nu\omega_{SDOF} & -2\mu\xi_{IS}\nu\omega_{SDOF} \\ -2\mu\xi_{IS}\nu\omega_{SDOF} & 2\mu\xi_{IS}\nu\omega_{SDOF} \end{bmatrix} ; \quad \mathbf{K} = \begin{bmatrix} \omega_{SDOF}^2 + \mu\nu^2\omega_{SDOF}^2 & -\mu\nu^2\omega_{SDOF}^2 \\ -\mu\nu^2\omega_{SDOF}^2 & \mu\nu^2\omega_{SDOF}^2 \end{bmatrix} \quad (4)$$

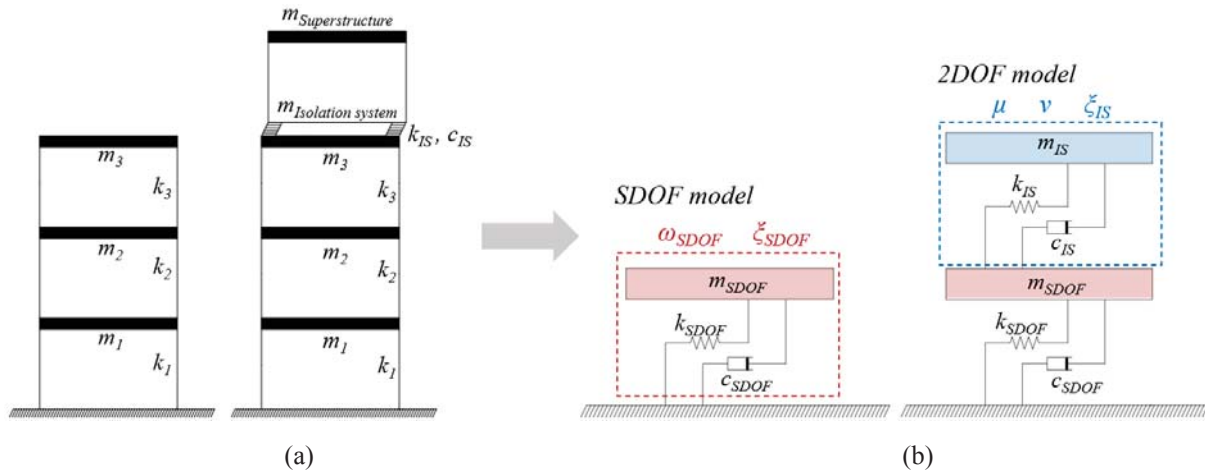


Figure 1: (a) MDOF models of the structure without and with IIS. (b) Related reduced-order models.

### 3 ASSESSMENT OF STRUCTURAL BEHAVIOUR IN FREQUENCY-DOMAIN

#### 3.1 Complex modal analysis

In traditional structural design, damping is assumed proportional to mass and stiffness and the results from classical modal analysis are not affected by it (as the  $\mathbf{C}$  matrix is not included in the problem formulation). When using non-proportional damping (e.g., in the case of IIS, where the damping is concentrated in some parts of the structure), the actual modal characteristics are different from the classical ones, and require a non-classical or complex modal analysis for their evaluation (e.g. [30]).

In this study the state-space formulation is adopted, which allows to decouple the equations of motion transforming the system with  $n$  second-order differential equations into a system with  $2n$  first-order differential equations, where  $n$  is the DOF number, namely:

$$\dot{\mathbf{v}}(t) = \mathbf{A}\mathbf{v}(t) + \mathbf{I}_g \ddot{u}_g(t) \quad (5)$$

where  $\mathbf{v}(t)$  is the state space vector at time  $t$ ,  $\mathbf{A}$  is the state space matrix,  $\mathbf{I}_g$  is the input vector and  $\ddot{u}_g(t)$  is the applied input process.  $\mathbf{v}(t)$ ,  $\mathbf{A}$  and  $\mathbf{I}_g$  are defined below:

$$\mathbf{v}(t) = \begin{bmatrix} \mathbf{x} \\ \dot{\mathbf{x}} \end{bmatrix}; \quad \mathbf{A} = \begin{bmatrix} \mathbf{0} & \mathbf{I} \\ -\mathbf{M}^{-1}\mathbf{K} & -\mathbf{M}^{-1}\mathbf{C} \end{bmatrix}; \quad \mathbf{I}_g = \begin{bmatrix} \mathbf{0} \\ -\boldsymbol{\tau} \end{bmatrix} \quad (6)$$

where  $\mathbf{x}$  and  $\dot{\mathbf{x}}$  are the relative displacement and relative velocity vectors, respectively;  $\mathbf{I}$  is the unitary matrix of dimensions  $2 \times 2$ ;  $\mathbf{M}$ ,  $\mathbf{K}$  and  $\mathbf{C}$  are the system matrices defined in Equation 4;  $\boldsymbol{\tau}$  is the unitary vector of dimensions  $2 \times 1$ . Therefore, the eigenvalue problem can be defined as:

$$\mathbf{A}\boldsymbol{\psi}_i = \lambda_i \boldsymbol{\psi}_i \quad (7)$$

where  $\lambda_i$  represents the eigenvalues and  $\boldsymbol{\psi}_i$  the eigenvectors.

Since the main objective of this study is the control of the seismic response of the substructure through the IIS, Figure 2 shows the results relating to the second vibration mode of the 2 DOF model (i.e., the mode associated with the deformation of the substructure), for  $\mu=0.5$ , values of  $v$  equal to 0.2, 0.4 and 0.6, and values of  $\zeta_{\text{IS}}$  in the range 0 - 2.

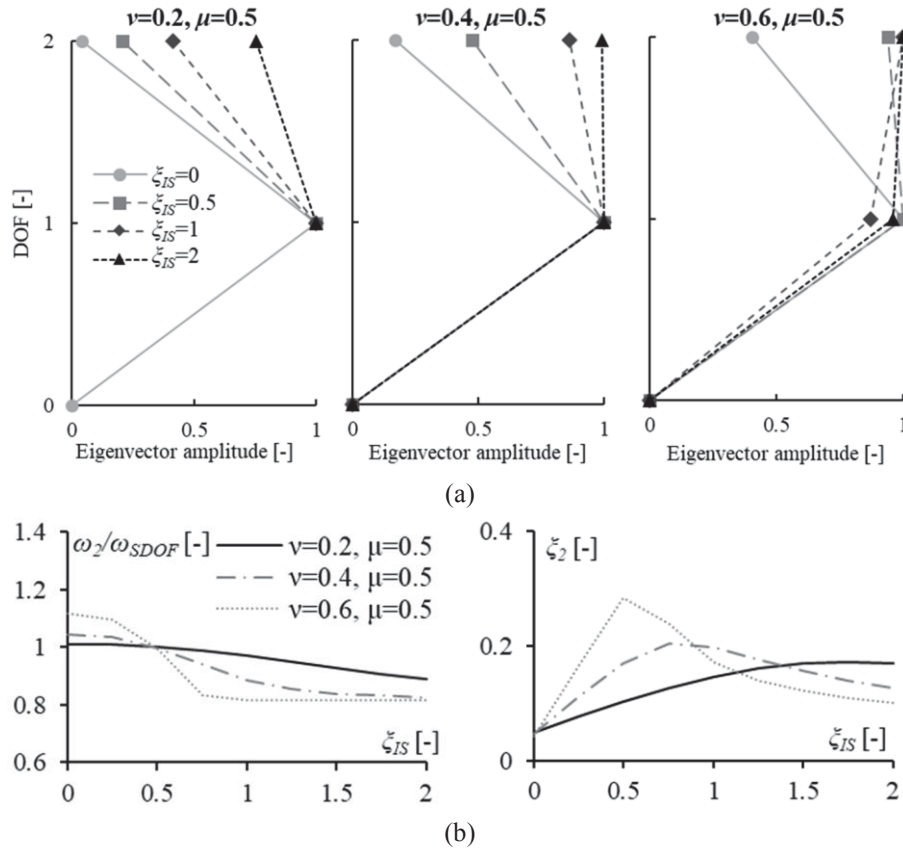


Figure 2: Complex modal analysis results of 2 DOF system, for  $\mu=0.5$ ,  $\nu=0.2, 0.4, 0.6$ ,  $\xi_{IS}=0 - 2$ : (a) eigenvectors of the second mode; (b) normalized frequency  $\omega_2$  and damping ratio  $\xi_2$  of the second mode, as a function of  $\xi_{IS}$ .

Figure 2a shows that, for low to medium values of the frequency ( $\nu$ ) and damping ( $\xi_{IS}$ ) ratios, the masses move in a decoupled way (characteristic behaviour of the isolated structures, due to the filter action exerted by the IIS), while increasing the value of the previous parameters the two masses reduce their relative displacement until, beyond certain values of  $\nu$  and  $\xi_{IS}$ , they move together. Instead, Figure 2b shows that, as  $\xi_{IS}$  increases, the frequency of the second mode ( $\omega_2$ ) is reduced, while the damping ratio of the second mode ( $\xi_2$ ) first increases and subsequently, for high  $\xi_{IS}$  values, it decreases. In particular, the peak of  $\xi_2$  seems to be corresponding to the change in concavity of the  $\omega_2/\omega_{SDOF}$  curve. These variations are greater for higher  $\nu$  values (i.e., for more rigid IIS), as the resulting 2 DOF system is more coupled in terms of mass displacement. In fact, a “perfect coupling” (for sufficiently high  $\nu$  and  $\xi_{IS}$  values) will lead to a single vibration mode having a modal mass equal to  $(m_{IS}+m_{SDOF})$  and a modal damping ratio equal to that of the substructure,  $\xi_{SDOF}$  (which justifies the reduction of  $\xi_2$  for high  $\xi_{IS}$  values).

### 3.2 Frequency Response Functions

To analyse the influence of the parameters  $\mu$ ,  $\nu$  and  $\xi_{IS}$  on the actual structural response, the frequency response functions (FRFs) of the equivalent 2 DOF systems (obtained parametrically by varying the values of  $\mu$ ,  $\nu$  and  $\xi_{IS}$  indicated in Section 2) were evaluated. FRFs express how a sinusoidal signal with a given input frequency is transferred within the system. In particular, the FRFs associated with the displacements ( $\mathbf{H}(\omega)$ ) and accelerations ( $\mathbf{H}_a(\omega)$ ) of the various DOF of the system can be defined as follow, where  $\omega$  is the excitation vibration frequency:

$$\begin{aligned}\mathbf{H}(\omega) &= -(-\omega^2 \mathbf{M} + i\omega \mathbf{C} + \mathbf{K})^{-1} \mathbf{M} \tau \\ \mathbf{H}_a(\omega) &= -\omega^2 \mathbf{H}(\omega) + \tau\end{aligned}\quad (8)$$

Specifically, the investigated FRFs concern the drift of the substructure (i.e., of the lower mass)  $|\mathbf{H}_1(\omega)|$ , the drift of isolation (i.e., between the two masses)  $|\mathbf{H}_2(\omega) - \mathbf{H}_1(\omega)|$ , and the acceleration of the superstructure (i.e., of the upper mass)  $|\mathbf{H}_{a2}(\omega)|$ . Figure 3 shows the trend of the selected FRFs with respect to the variation of  $\omega$  and one of the main parameters ( $\mu$ ,  $\nu$ ,  $\xi_{IS}$ ) at a time – therefore as 3D surfaces – assuming  $\mu=0.5$ ,  $\nu=0.4$  and  $\xi_{IS}=0.5$  as reference values for the other parameters. The following observations can be drawn:

- Increasing the values of  $\mu$  results in a reduction of  $|\mathbf{H}_1(\omega)|$  and  $|\mathbf{H}_{a2}(\omega)|$ , and therefore in a better structural performance in terms of drift of the substructure and acceleration of the superstructure; instead, the influence of  $\mu$  on  $|\mathbf{H}_2(\omega) - \mathbf{H}_1(\omega)|$  (i.e., on the isolation drift) is not very significant.
- Low values of  $\nu$  allow to limit the acceleration of the superstructure; intermediate values of  $\nu$  (e.g., between 0.4 and 0.6) seem the most effective solution to reduce the drift of the substructure; on the other hand, high values of  $\nu$  are optimal for reducing the isolation drift, even if they induce significant amplifications both on the substructure drift and on the superstructure acceleration.
- The increase in the  $\xi_{IS}$  values provides an effective initial reduction of the substructure drift and of the superstructure acceleration, at least up to medium-high values of  $\xi_{IS}$  (about 0.5), beyond which a further increase leads to a significant amplification of both  $|\mathbf{H}_1(\omega)|$  and  $|\mathbf{H}_{a2}(\omega)|$ . Instead,  $\xi_{IS}$  is always effective in reducing the isolation drift, as also confirmed by other studies (e.g., [2, 13, 14]).

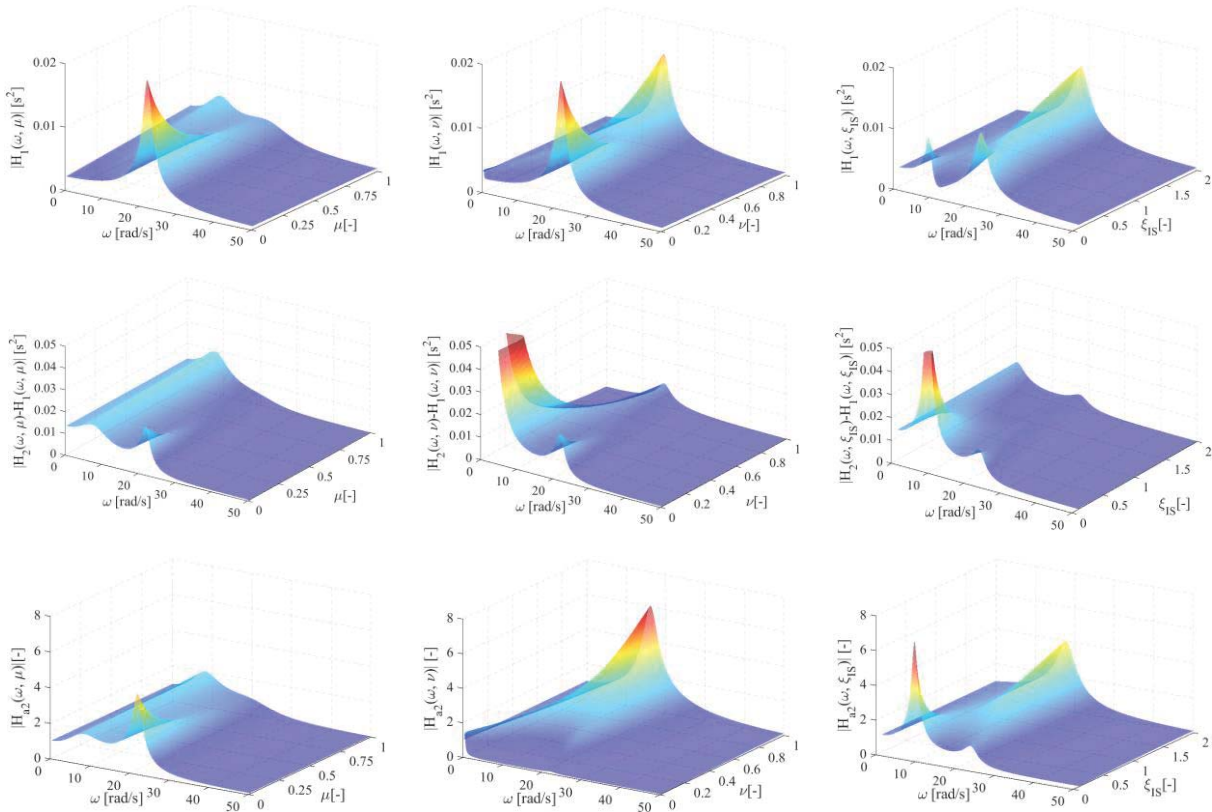


Figure 3: Trends of the FRFs as a function of  $\mu$ ,  $\nu$  and  $\xi_{IS}$ ; reference parameters:  $\mu=0.5$ ,  $\nu=0.4$  and  $\xi_{IS}=0.5$ .

## 4 MULTI-OBJECTIVE OPTIMISATION

### 4.1 Proposed approach

As seen in the Introduction, many of the literature studies on the optimization of TMD parameters (at least up to the most recent ones) seek the maximum effect of “mass damping” focusing on the minimization of the response of the primary system, thus neglecting the performance of the tuned mass (i.e., IIS drift and acceleration) in the optimization procedure. However, controlling the deflection of the isolators (and thus also the P-Δ effects on the substructure) and the acceleration of the superstructure can be of significant interest considering that the mass to be tuned is in fact a habitable building.

In order to model the stochastic nature of the seismic input, the Power Spectral Density (PSD) function of a zero-mean Gaussian stochastic process,  $\mathbf{S}(\omega)$ , is generally assumed; considering this type of process, the random vibration theory produces the following covariance matrices:

$$\begin{aligned} \text{Cov}[\mathbf{xx}^T] &= \int_{-\infty}^{\infty} \mathbf{H}(\omega) \mathbf{S}(\omega) \mathbf{H}(\omega)^{*T} d\omega \\ \text{Cov}[\ddot{\mathbf{x}}\ddot{\mathbf{x}}^T] &= \int_{-\infty}^{\infty} \mathbf{H}_a(\omega) \mathbf{S}(\omega) \mathbf{H}_a(\omega)^{*T} d\omega \end{aligned} \quad (9)$$

Furthermore, assuming the seismic excitation also as a white noise process, its PSD function is no longer dependent on  $\omega$  ( $\mathbf{S}(\omega)=S_0$ ); therefore, in order to obtain the optimal TMD parameters (i.e.,  $\mu$ ,  $\nu$ ,  $\xi_{IS}$ , variables of  $|\mathbf{H}(\omega)|$  and  $|\mathbf{H}_a(\omega)|$ ), the minimization of the integrals in Equation 9 is equivalent to the minimization of the integrals in Equation 10, where  $\sigma^2$  and  $\sigma_a^2$  are the displacement and acceleration variance, respectively.

$$\begin{aligned} \sigma^2/S_0 &= \int_{-\infty}^{\infty} |\mathbf{H}(\omega)|^2 d\omega \\ \sigma_a^2/S_0 &= \int_{-\infty}^{\infty} |\mathbf{H}_a(\omega)|^2 d\omega \end{aligned} \quad (10)$$

By defining the FRFs of the reference SDOF system, in terms of displacement ( $H_{SDOF}(\omega)$ ) and acceleration ( $H_{a,SDOF}(\omega)$ ) as:

$$\begin{aligned} H_{SDOF}(\omega) &= -(-\omega^2 + i\omega 2\xi_{SDOF}\omega_{SDOF} + \omega_{SDOF}^2)^{-1} \\ H_{a,SDOF}(\omega) &= -\omega^2 H_{SDOF}(\omega) + 1 \end{aligned} \quad (11)$$

the following Performance Indices ( $PI$ s) can be defined:

$$\begin{aligned} PI_1 &= \frac{\int_{-\infty}^{\infty} |\mathbf{H}_1(\omega)|^2 d\omega}{\int_{-\infty}^{\infty} |H_{SDOF}(\omega)|^2 d\omega} & PI_2 &= \frac{\int_{-\infty}^{\infty} |\mathbf{H}_2(\omega)|^2 d\omega - \int_{-\infty}^{\infty} |\mathbf{H}_1(\omega)|^2 d\omega}{\int_{-\infty}^{\infty} |H_{SDOF}(\omega)|^2 d\omega} & PI_3 &= \frac{\int_{-\infty}^{\infty} |\mathbf{H}_{a,2}(\omega)|^2 d\omega}{\int_{-\infty}^{\infty} |H_{a,SDOF}(\omega)|^2 d\omega} \end{aligned} \quad (12)$$

where,  $PI_1$  and  $PI_2$  are respectively the substructure drift variance and the isolation drift variance both normalized to the drift variance of the equivalent SDOF system, whereas  $PI_3$  is the



superstructure acceleration variance normalized to the acceleration variance of the SDOF system. Therefore, based on these  $PIs$ , the objective functions (OFs) are defined as follow:

$$OF_1 = \min(PI_1(\xi_{IS}, \nu)) \quad OF_2 = \min(PI_2(\xi_{IS}, \nu)) \quad OF_3 = \min(PI_3(\xi_{IS}, \nu)) \quad (13)$$

In particular, two multi-objective optimizations ( $OPT1$  and  $OPT2$ ) are performed, simultaneously minimizing  $OF_1$  and  $OF_2$  ( $OPT1$ ), or  $OF_1$  and  $OF_3$  ( $OPT2$ ), with the aim of controlling the substructure performance but, at the same time, also the deflection of the isolators or the acceleration of the superstructure.

In order to solve these multi-objective optimization problems, the well-known Non-dominated Sorting Genetic Algorithm NSGA-II (e.g. [31, 32]) was used. This algorithm, widely used in practical optimization problems, first creates an initial parent population  $P_0$ , of size  $N$ , with a random process; then, sorts this population according to the non-domination criterion (i.e., assigning to each solution a rank based on its non-domination level – e.g. 1 for the best level, 2 for the next one and so on – and minimising it); subsequently, it generates an offspring population  $Q_0$ , of size  $N$ , through binary tournament selection, recombination and mutation operations. Once the initial parent ( $P_0$ ) and offspring ( $Q_0$ ) populations are defined, an iterative procedure is carried out for a set number of generations (to be defined according to the stability and convergence of solution). This procedure allows to determine the parent and offspring populations at generation  $(k+1)$  starting from those at generation  $(k)$ . In particular, the solution  $P_{k+1}$ , of size  $N$ , is generated starting from the combined population  $R_k = P_k + Q_k$ , of size  $2N$ , based on two cascading criteria: the solutions preferred are (i) those of lesser (non-domain) rank and, among solutions of equal rank, (ii) those located in a less crowded region (selected by a crowding comparison operator). Using the new parent population ( $P_{k+1}$ ), through a binary tournament selection, crossover and mutation operations, the new offspring population ( $Q_{k+1}$ ) is then created. This procedure continues until the last generation required. The main parameters of this algorithm are therefore the number of generations, the size of the population sought and the mutation and crossover probabilities; the values set in this study for these parameters are shown in Table 1.

<i>Parameter</i>	<i>Value</i>
Generations	120
Population	80
Mutation probability	0.1
Crossover probability	0.9

Table 1: Parameters set for the NSGA-II algorithm.

## 4.2 Optimization results

The results obtained by the NSGA-II algorithm, i.e. the Pareto fronts, are shown in Figure 4 for both optimizations ( $OPT1$  and  $OPT2$ ). The main considerations are reported below.

- Overall, for the various cases analysed, the minimum values of  $OF_1$  ( $OF_{1min}$ ) are approximately equal to 0.4 (both for  $OPT1$  and  $OPT2$ ), indicating a clear reduction of the substructure drift due to the application of the IIS (i.e., of the isolated superstructure).
- Then, while the minimization of  $OF_2$  (in  $OPT1$ ) causes values of  $OF_1$  greater than 1, the minimization of  $OF_3$  (in  $OPT2$ ) allows values of  $OF_1$  always less than 1; this means that the solutions aimed at minimizing the superstructure acceleration do not cause an increase in the substructure drift compared to the case without IIS (i.e., the SDOF system), as instead occurs when the minimization of the isolation drift is sought.

- The values of  $OF_3$  show that the superstructure accelerations, when optimized, are significantly reduced compared to those of the existing substructure (i.e., the SDOF system).
- It is also worth noting that, as  $\mu$  increases, the minimum values of  $OF_1$  and  $OF_2$  increase – for *OPT1* (Figure 4a), whereas the minimum values of  $OF_1$  and  $OF_3$  decrease – for *OPT2* (Figure 4b).

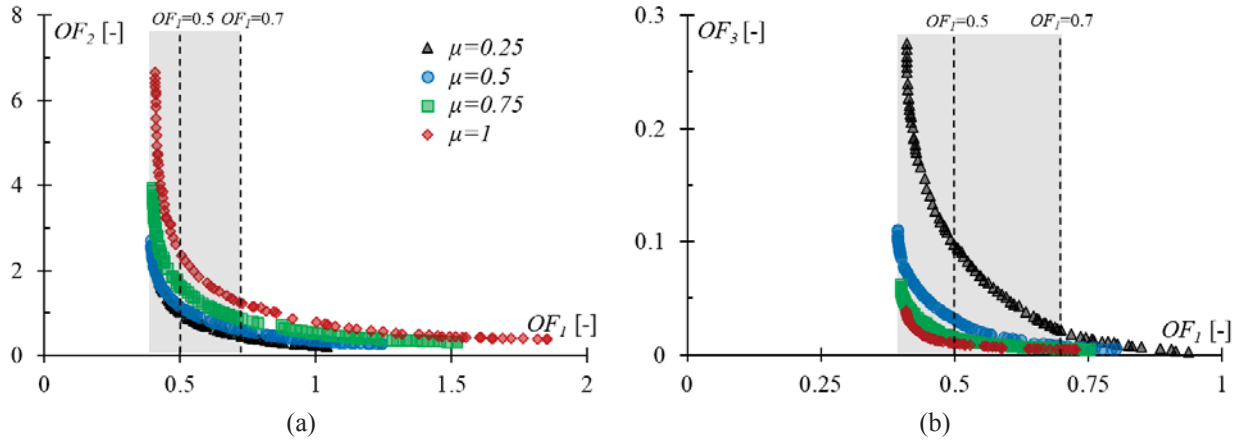


Figure 4: Pareto fronts (minimum values of OFs) for set values of  $\mu$ : (a) *OPT1*; (b) *OPT2*.

Since  $OF_1$  indicates the reduction of the variance of the substructure drift, a range from  $OF_{1min}$  to  $OF_1=0.7$  (i.e., 30% reduction) – as shown in Figure 4 – is considered effective for the purposes of this study; in particular, three values of  $OF_1$  were selected for subsequent evaluations (for both optimizations), namely  $OF_{1min}$ ,  $OF_1=0.5$  and  $OF_1=0.7$ .

Figure 5 shows the optimal values of the IIS (or TMD) parameters, for both *OPT1* (Figure 5a) and *OPT2* (Figure 5b), associated with the selected  $OF_1$  values. In particular, the optimal values of  $\zeta_{IS}$  and  $\nu$  are shown as a function of  $\mu$ , as well as the values of  $OF_2$  for *OPT1* and the values of  $OF_3$  for *OPT2*. The following observations can be derived:

- The  $OF_{1min}$  solutions (which minimize the variance of the substructure drift) are the same for both *OPT1* and *OPT2* optimizations, as expected. For these solutions, as  $\mu$  increases, the values of  $\zeta_{IS}$  increase and those of  $\nu$  decrease; therefore, these optimal solutions range from the “mass damping” behaviour towards that of “intermediate seismic isolation”, as already observed in previous studies.
- As regards the *OPT1* optimization, the reduction of  $OF_2$  (i.e., of the variance of the isolation drift) is associated with the increase of the values of  $\zeta_{IS}$  and  $\nu$ , that is, with solutions that induce a greater coupling between the two structural parts.
- On the other hand, regarding the *OPT2* optimization, reductions of  $OF_3$  (i.e., of the variance of the superstructure acceleration) are possible by increasing the values of  $\zeta_{IS}$  and reducing those of  $\nu$ , even significantly (especially for  $OF_1=0.7$  and low  $\mu$  values).
- Looking at the values of OFs as a function of  $\mu$ , it can be seen that  $OF_2$  is more sensitive for high values of  $\mu$ , whereas  $OF_3$  for low values of  $\mu$ . In these respective  $\mu$  ranges, multi-objective optimization is more effective and beneficial than single substructure performance optimization.
- The minimization of  $OF_3$  (see the case  $OF_1=0.7$ ), in the case of low values of  $\mu$ , is obtained by considerably reducing  $\nu$  (i.e., increasing the filter action offered by the IIS) and significantly increasing  $\zeta_{IS}$  (beyond the critical damping value for the presented study).

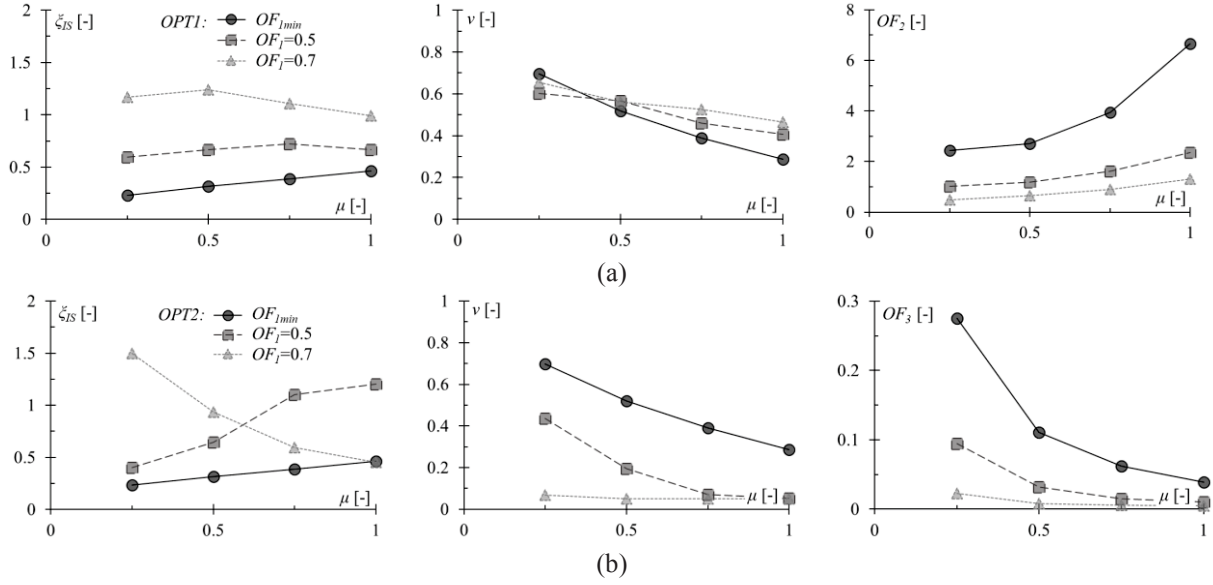


Figure 5: *OPT1* (a) and *OPT2* (b): optimal values of  $\zeta_{IS}$ ,  $\nu$ ,  $OF_2$  and  $OF_3$  as a function of  $\mu$  ( $OF_I=OF_{Imin}$ , 0.5, 0.7).

### 4.3 Comparison with other literature solutions

The optimal values of the IIS parameters ( $\zeta_{IS}$ ,  $\nu$ ) obtained for the  $OF_{Imin}$  solution (equal for *OPT1* and *OPT2*), which minimize the displacement variance of the primary system, are compared in Figure 6 with other relevant literature solutions, as the mass ratio  $\mu$  varies. These solutions are taken from: [17], who provided a closed-form solution for the TMD parameters in the case of an undamped primary SDOF system with base harmonic excitation; [25], who optimized the parameters of TMDs with large mass ratios by matching the damping ratios of the 2 DOF system while minimizing the maximum FRF amplitude associated with the displacement of the primary structure; [27], who proposed different approaches, including the minimization of the displacement variance of the primary structure (displacement approach) and the maximization of the energy dissipated by the TMD system (energy approach).

It is worth considering that the various solutions compared in Figure 6 refer to different values of the damping ratio of the primary structure ( $\zeta_{SDOF}$ ), i.e.: 0% for [17], 5% for [25] and this study, and 2% for [27]. However, as discussed in previous study (e.g. [25, 27, 21]), reasonable variations of  $\zeta_{SDOF}$  do not significantly affect the optimal TMD parameters.

As can be seen from these comparisons, the results obtained for  $OF_{Imin}$  are very similar to those obtained by the other literature approaches, and in particular by [27] (displacement approach).

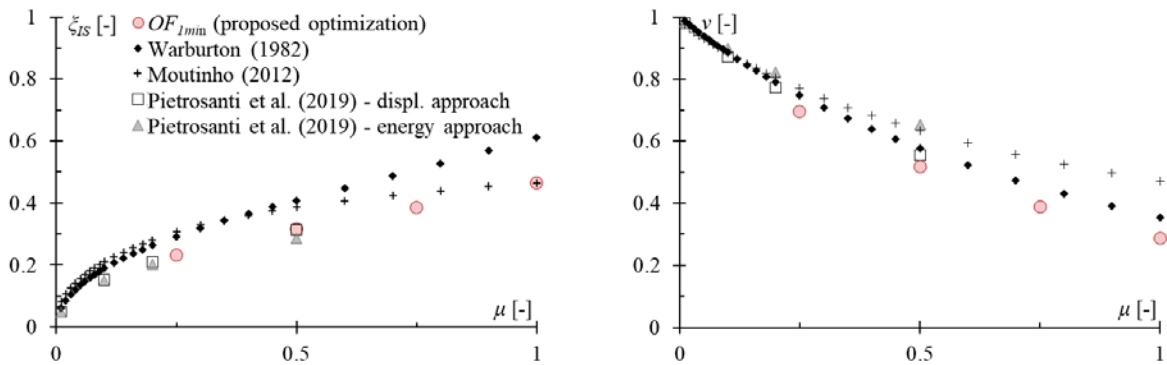


Figure 6: Optimal IIS parameters obtained in this study compared to other TMD solutions from the literature.

## 5 ASSESSMENTS THROUGH TH ANALYSES

### 5.1 Structure modelling and seismic input

This section shows the results of a Time History (TH) analysis, carried out on the 3 DOF case study structure (see Section 2) without and with IIS, in order to evaluate the optimization solutions previously obtained and therefore the effectiveness of the IIS technique.

The structure (see Figure 7) was modelled as a lumped mass system with a non-linear structural behaviour, assuming the bi-linear hysteretic law of Takeda for the substructure, which is often used to describe the behaviour of ductile RC frames. This hysteretic model was calibrated on the elastic stiffness of each storey, assuming a ratio  $r$  between the post-yield stiffness and the elastic stiffness equal to 0.2, and an inter-storey drift  $\delta_y$  at yield equal to 0.5%. The superstructure was modelled as a linear SDOF system, adopting for the IIS parameters ( $\nu$  and  $\xi_{IS}$ ) the optimal values obtained, associated with the mass ratio  $\mu=0.5$  and the solutions of  $OF_I = OF_{Imin}$ , 0.5 and 0.7, of both the optimizations performed (*OPT1* and *OPT2*).

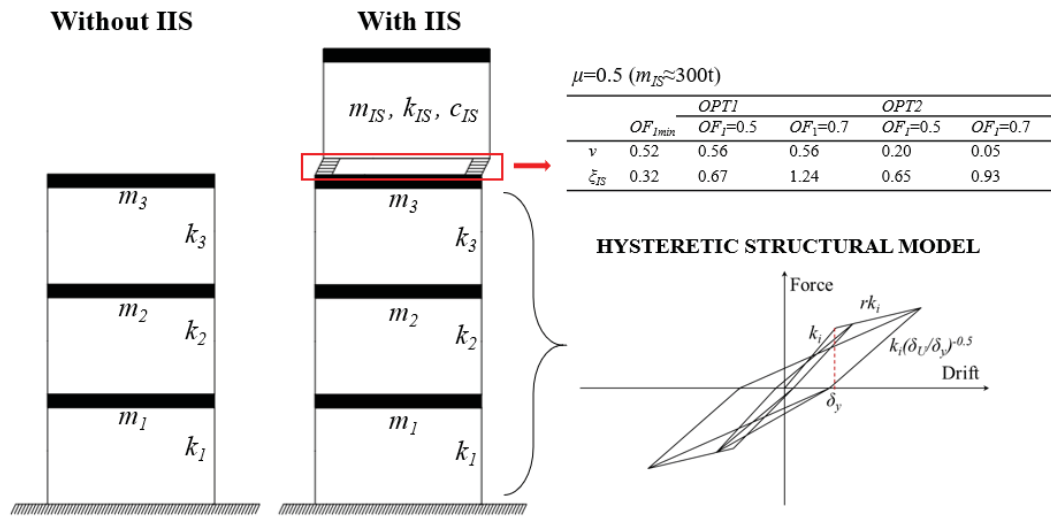


Figure 7: Hysteretic model of the substructure and optimal parameters of the IIS used for the TH analyses.

Time History analyses were performed for eight natural accelerograms, chosen among those of the European Strong-Motion Database (ESD, [33]). They were scaled to be compatible, on average, with the following elastic response spectrum of EC8: Type 1,  $a_g=0.25g$  (bed-rock acceleration) and soil B (i.e., soil factor  $S=1.2$ ); the peak ground acceleration PGA ( $=a_g \cdot S$ ) is  $0.3g$ . The main details of the natural records chosen are reported in Table 2, and the acceleration spectra are shown in Figure 8, together with that of EC8.

Ref.	Earthquake	Location	Date	$M_w$	Distance from epicentre [km]	Fault mechanism	Scale factor
Acc.1	Montenegro (aftershock)	Montenegro	1979/05/24	6.2	20	thrust	5.42
Acc.2	Campano Lucano	Italy	1980/11/23	6.9	33	normal (y)	3.02
Acc.3	Erzincan	Turkey	1992/03/13	6.6	13	strike slip	0.59
Acc.4	Ano Liosia	Greece	1999/09/07	6.0	18	normal	3.51
Acc.5	Campano Lucano	Italy	1980/11/23	6.9	33	normal (x)	3.04
Acc.6	Tabas	Iran	1978/09/16	7.3	57	oblique	1.71
Acc.7	Ano Liosia	Greece	1999/09/07	6.0	20	normal	0.32
Acc.8	Montenegro	Montenegro	1979/04/15	6.9	25	thrust	0.66

Table 2: Information on the assumed accelerograms.

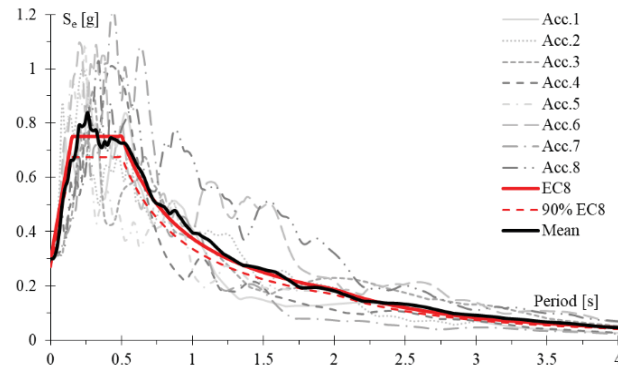


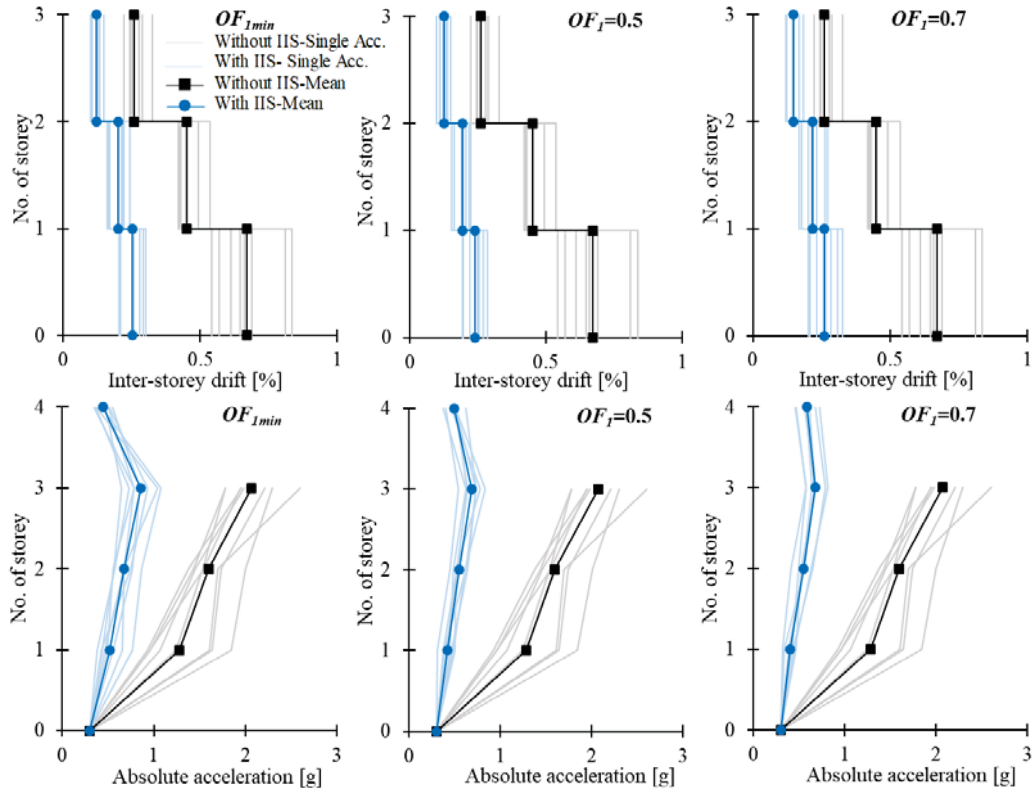
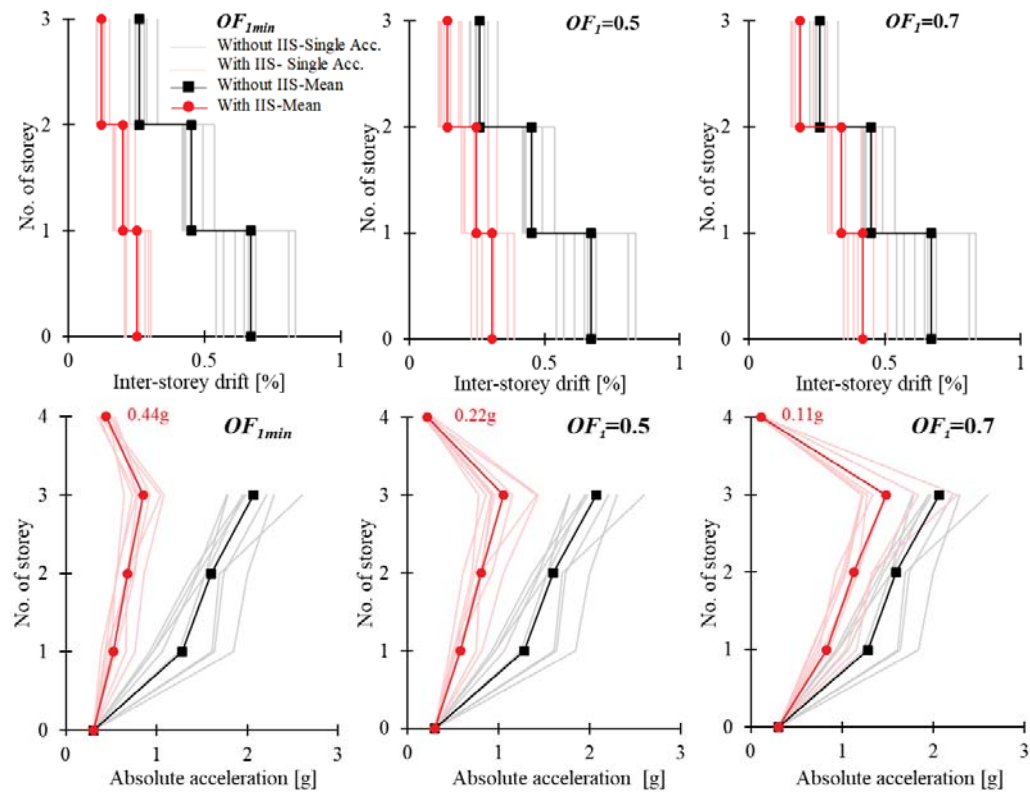
Figure 8: Acceleration response spectra compatible with the EC8 (Type 1) spectrum.

## 5.2 Analysis results

The main results obtained are shown in Figures 9 to 11. Figure 9 (for *OPT1*) and Figure 10 (for *OPT2*) shows the profiles of inter-storey drift and floor acceleration; in particular, they show the maximum values obtained from the analysis of the single accelerograms and the related average values. On the other hand, Figure 11 shows (for both *OPT1* and *OPT2*) the results obtained for the isolation drift ( $D_{IS}$ ). The following considerations can be drawn:

- All the optimal solutions adopted made it possible to significantly reduce both the maximum inter-storey drifts and the maximum floor accelerations in the substructure, compared to the case without IIS. In particular, in the case without IIS, the maximum drift values exceeded the yield limit drift ( $\delta_y=0.5\%$ ), causing inelastic structural deformations; instead, the optimal solutions of the IIS always allowed to remain in the elastic range.
- The  $OF_{Imin}$  solution, common to *OPT1* and *OPT2*, is associated with the better performance of the substructure in terms of inter-storey drift, as expected.
- For *OPT1* optimization, as the accepted value of  $OF_I$  increases (i.e., solutions  $OF_I=0.5$  and then  $OF_I=0.7$ ), the drift profiles of the substructure remain similar to those in the case of  $OF_{Imin}$ , i.e. there is no clear reduction in the substructure performance in terms of drifts, while it improves in terms of floor accelerations; then, as expected, the accelerations of the superstructure increase (albeit slightly), to the advantage of a greater reduction of the isolation drift (see Figure 11), due to the minimization of  $OF_2$  along with  $OF_I$ .
- For *OPT2* optimization, as the accepted value of  $OF_I$  increases (i.e.,  $OF_I=0.5$  and then  $OF_I=0.7$ ), the response of the substructure worsens compared to the case of  $OF_{Imin}$ , both in terms of maximum inter-storey drifts and floor accelerations; then, as expected, the accelerations of the superstructure are considerably reduced, due to the minimization of  $OF_3$  along with  $OF_I$ , at the expense of an increase in the deflection of the isolation system (with however acceptable values, as shown in Figure 11).
- It can be noted that moving away from the  $OF_{Imin}$  solution (e.g.,  $OF_I=0.7$ ), the *OPT1* results tend to give a more uniform response of the substructure along the building height, also reducing its variability with respect to the earthquake, whereas the *OPT2* results provide a greater decoupling between the two structural parts (typical of seismic isolation), reducing the control function on the substructure.




 Figure 9: Profiles of inter-storey drift and floor acceleration, for *OPT1* solutions.

 Figure 10: Profiles of inter-storey drift and floor acceleration, for *OPT2* solutions.

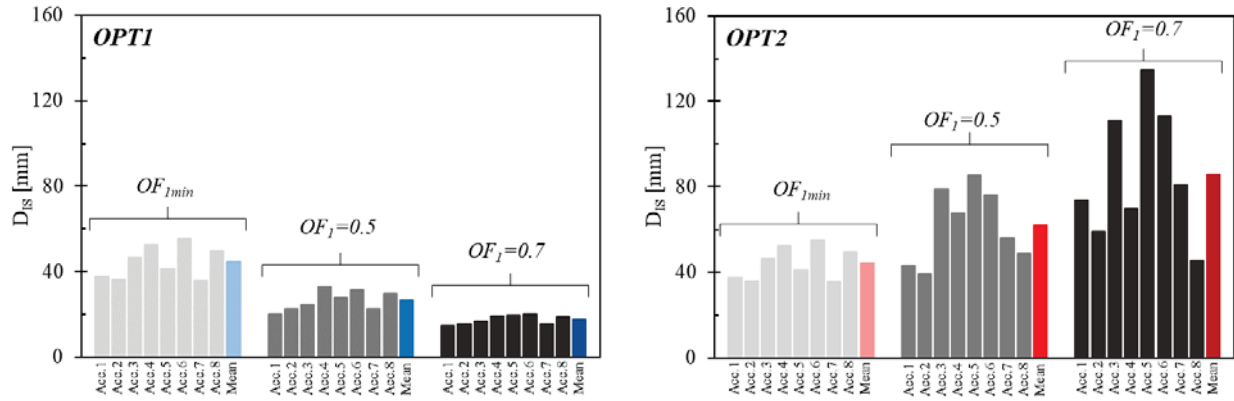
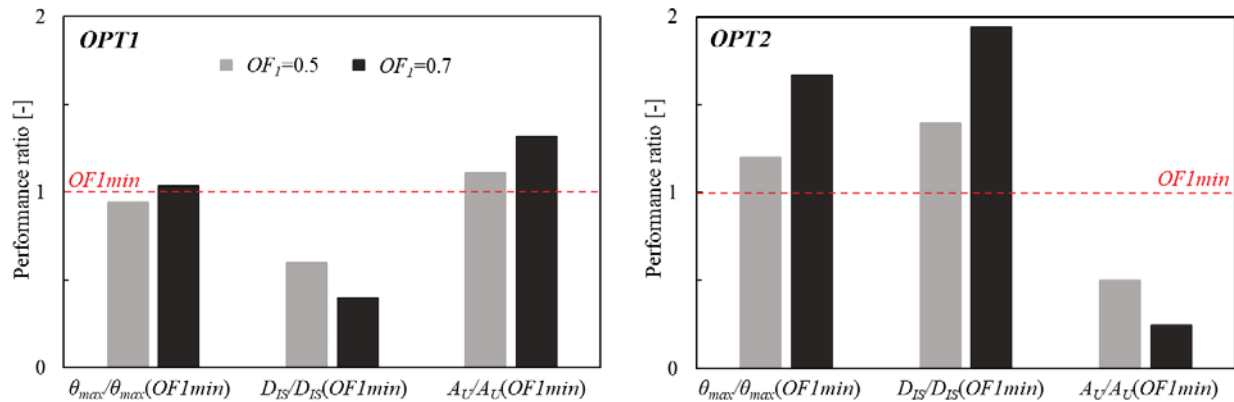

 Figure 11: Isolation drift ( $D_{IS}$ ) values resulting from both optimizations (*OPT1* and *OPT2*).

Figure 12 summarizes the main results obtained from the two optimizations. In particular, it shows the ratio between the average structural responses obtained for  $OF_I=0.5$  and  $OF_I=0.7$  and the respective ones obtained for  $OF_{Imin}$ , considering the following performance parameters: substructure drift ( $\theta_{max}$ , associated with  $OF_I$ ), isolation drift ( $D_{IS}$ , associated with  $OF_2$ ) and superstructure acceleration ( $A_U$ , associated with  $OF_3$ ).

Consistently with what was previously observed, and with respect to the  $OF_{Imin}$  solution (which minimizes the substructure drift), the *OPT1* optimization allows to strongly reduce  $D_{IS}$  (even more than 50%) while maintaining good performances in terms of  $\theta_{max}$  and  $A_U$ , which are only slightly amplified. On the other hand, the *OPT2* optimization allows strong reductions in  $A_U$  (greater than 50%) at the expense of appreciable amplifications of  $\theta_{max}$  and  $D_{IS}$ .


 Figure 12: Average structural responses (for the cases  $OF_I=0.5$  and  $0.7$ ) normalized to the case of  $OF_{Imin}$ .

## 6 CONCLUSIONS

A study investigating the inter-storey isolation system (IIS) as a technique for adding upper storeys to an existing building, while improving its seismic behaviour, is presented. A 3-storey case study structure (without considering the IIS) was taken as a reference.

The first part of the study evaluated the effects of the main parameters of the IIS (or non-conventional TMD) on the dynamic response of the substructure; these parameters are the ratios of damping ( $\xi_{IS}$ ), frequency ( $\nu$ ) and mass ( $\mu$ ), with  $\nu$  and  $\mu$  referring to the substructure characteristics. Given the prevailing “mass damping” behaviour for  $\mu$  values  $\leq 1$ , the structure was modelled with a reduced-order 2 DOF model. The evaluation was performed in the frequency domain, using the complex modal analysis and the frequency response functions

(FRFs) of the substructure drift, the isolation drift and the superstructure acceleration. The variations of the characteristics of the second vibration mode and of the FRFs were evaluated over the entire range assumed for the various parameters of the IIS (i.e.,  $\xi_{IS}$  from 0 to 2,  $\nu$  and  $\mu$  from 0 to 1). These preliminary assessments led to the subsequent definition of the methodology to optimize the IIS parameters.

In particular, two alternative multi-objective optimizations were proposed, named *OPT1* and *OPT2*, minimizing different objective functions (OFs). *OPT1* minimizes the variance of the substructure drift ( $OF_1$ ) along with that of the isolation drift ( $OF_2$ ); *OPT2* still minimizes the variance of the substructure drift ( $OF_1$ ), but together with the minimization of the acceleration variance of the superstructure ( $OF_3$ ).

The NSGA-II algorithm was used to solve the multi-objective problem, searching for the best solutions of  $\nu$  and  $\xi_{IS}$  for set  $\mu$  values. The solutions obtained from *OPT1* and *OPT2* were compared with each other, as well as with other relevant solutions from the literature. To this end, representative optimal solutions were selected from the Pareto fronts on the basis of the value of  $OF_1$ , i.e.  $OF_1 = OF_{1min}$  ( $\approx 0.4$ ), 0.5 and 0.7.

Finally, based on these optimal solutions, time-history analyses were performed, in order to verify the effectiveness of the optimization approach and therefore the beneficial effects of the IIS technique. For this purpose, a set of natural accelerograms was assumed, which is compatible with the EC8-Type1 spectrum, with soil B and PGA=0.3 g, and the substructure was modelled as a lumped mass 3 DOF system with a non-linear structural behaviour. Overall, the following conclusions can be drawn:

- The IIS technique, when its stiffness ( $\nu$ ) and damping ( $\xi_{IS}$ ) parameters are suitably optimized in relation to the isolated mass ratio ( $\mu$ ), seems effective in improving the seismic behaviour of the substructure (or existing structure).
- Considering the optimal solution that minimizes the variance of the substructure drift, i.e.  $OF_{1min}$ , the increase in the mass ratio (if allowed by the substructure in terms of vertical capacity) leads to a reduction of the optimal values of  $\nu$  and to an increase of those of  $\xi_{IS}$ , i.e. solutions that are more similar to those of seismic isolation. Consequently, increasing  $\mu$  reduces the accelerations of the superstructure but increases the drift of the isolation system.
- The *OPT1* optimization provides effective solutions to reduce the isolation drift while containing the maximum values of the substructure drift similar to those of the  $OF_{1min}$  solution. With the solutions of *OPT1*, a more uniform behaviour of the substructure is also obtained, minimizing floor accelerations.
- The *OPT2* optimization provides effective solutions to reduce the superstructure acceleration while containing the maximum values of the substructure drift similar to those of the  $OF_{1min}$  solution. With the solutions of *OPT2*, a more decouple behaviour between the two structural parts is also obtained, and therefore a lower reduction in the substructure accelerations.
- *OPT1* is particularly advantageous for the higher  $\mu$  values (for which the isolation drift is more sensitive –  $OF_2$ ), whereas *OPT2* for the lower  $\mu$  values (for which the superstructure acceleration is more sensitive –  $OF_3$ ). Finally, the solutions for  $OF_1=0.5$  seem a good compromise for both optimizations.

## REFERENCES

- [1] R. Zhang, B.M. Phillips, S. Taniguchi, M. Ikenaga, K. Ikago, Shake table real-time hybrid simulation techniques for the performance evaluation of buildings with inter-story isolation. *Structural Control Health Monitoring* 24. 1013 <https://doi.org/10.1002/stc.1971>, 2017
- [2] Y. Liu, J. Wu, M. Donà, Effectiveness of fluid-viscous dampers for improved seismic performance of inter-storey isolated buildings. *Engineering Structures* 169:276-292. <https://doi.org/10.1016/j.engstruct.2018.05.031>, 2018
- [3] F. L. Zhou, Seismic isolation of civil buildings in the People's Republic of China. *Progress in Structural Engineering and Materials* 1015 3(3):268-276. <https://doi.org/10.1002/pse.85>, 2001
- [4] M. Chey, J. Geoffrey Chase, J. Mander, A. Carr, Innovative seismic retrofitting strategy of added stories isolation system. *Frontiers of Structural and Civil Engineering*, 7, 13-23. <https://doi.org/10.1007/s11709-013-0195-9>, 2013
- [5] D. Faiella, B. Calderoni, E. Mele, Seismic Retrofit of Existing Masonry Buildings through Inter-story Isolation System: A Case Study and General Design Criteria. *Journal of Earthquake Engineering*, DOI: 10.1080/13632469.2020.1752854, 2020
- [6] M. Ziyaeifar, T. Noguchi, Partial mass isolation in tall buildings. *Earthquake Engineering and Structural Dynamics*, [https://doi.org/10.1002/\(SICI\)1096-9845\(199801\)27:1%3C49::AID-EQE718%3E3.0.CO;2-J](https://doi.org/10.1002/(SICI)1096-9845(199801)27:1%3C49::AID-EQE718%3E3.0.CO;2-J), 1998
- [7] P. Tan, Y. Zhang, F. Zhou, Optimal design and control mechanism study on story isolation system. *The 14<sup>th</sup> World Conference on Earthquake Engineering*, Beijing, China, October 12-17, 2008
- [8] S. J. Wang, K. C. Chang, J. S. Hwang, B. H. Lee, Simplified analysis of mid-story seismically isolated buildings. *Earthquake Engineering and Structural Dynamics*, <https://doi.org/10.1002/eqe.1004>, 2011
- [9] S. J. Wang, J. S. Hwang, K. C. Chang, M. H. Lin, B. H. Lee, Analytical and experimental studies on midstory isolated buildings with modal coupling effect. *Earthquake Engineering and Structural Dynamics*, <https://doi.org/10.1002/eqe.2203>, 2013
- [10] D.C. Charmpis, P. Komodromos, M.C. Phocas, Optimized earthquake response of multi-storey buildings with seismic isolation at various elevations. *Earthquake Engineering and Structural Dynamics*, <https://doi.org/10.1002/eqe.218>, 2012
- [11] D.C. Charmpis, M.C. Phocas, P. Komodromos, Optimized retrofit of multi-storey buildings using seismic isolation at various elevations: assessment for several earthquake excitations. *Bulletin of Earthquake Engineering*, <https://doi.org/10.1007/s10518-015-9737-y>, 2015
- [12] D. Faiella, E. Mele, Vibration characteristics and higher mode coupling in intermediate isolation systems (IIS): a parametric analysis. *Bulletin of Earthquake Engineering* DOI:10.1007/s10518-019-00637-w, 2019
- [13] M. Donà, E. Bernardi, A. Zonta, M. Minotto, F. da Porto, P. Tan, Effectiveness and optimal design of fluid-viscous dampers for inter-storey isolated buildings. *In Proc., XVIII ANIDIS Conf.*, Ascoli Piceno, Italy, 2019

- [14] M. Donà, E. Bernardi, A. Zonta, P. Tan, F. Zhou, Evaluation of optimal FVDs for inter-storey isolation systems based on surrogate performance models. *Bulletin of Earthquake Engineering*, 2021
- [15] H. Frahm, Devices for Damped Vibrations of Bodies, U.S. Patent No. 989958, Oct 30, 1909
- [16] J.P. Den Hartog, Mechanical Vibrations. *McGraw-Hill*, 3rd edition, 1947
- [17] G.B. Warburton, Optimum absorber parameters for various combinations of response and excitation parameters. *Earthquake Engineering and Structural Dynamics*, 10(3):381-401, 1982
- [18] H. Tsai, G. Lin, Optimum tuned-mass dampers for minimizing steady-state response of support-excited and damped systems. *Earthquake Engineering and Structural Dynamics*, 22(11):957-973, 1993
- [19] R. Villaverde, Reduction in seismic response with heavily-damped vibration absorbers. *Earthquake Engineering and Structural Dynamics*, <https://doi.org/10.1002/eqe.4290130105>, 1985
- [20] R. Rana, T.T. Soong, Parametric study and simplified design of tuned mass dampers. *Engineering Structures*, [https://doi.org/10.1016/S0141-0296\(97\)00078-3](https://doi.org/10.1016/S0141-0296(97)00078-3), 1998
- [21] M. Yahyai, L. Zebarjad, M. Head, M. Shokouhian, Optimum Parameters for Large Mass Ratio TMDs Using Frequency Response Function, *Journal of Earthquake Engineering*, <https://doi.org/10.1080/13632469.2019.1624228>, 2019
- [22] G. Bekdaş, S. M. Nigdeli, Metaheuristic based optimization of tuned mass dampers under earthquake excitation by considering soil-structure interaction. *Soil Dynamics and Earthquake Engineering* 92, 443–461. doi:10.1016/j.soildyn.2016.10.019, 2017
- [23] F. Sadek, B. Mohraz, A.W. Taylor, R.M. Chung, A method of estimating the parameters of tuned mass dampers for seismic applications. *Earthquake Engineering and Structural Dynamics*, 26(6):617-635, 1997
- [24] J. Miranda, On tuned mass dampers for reducing the seismic response of structures. *Earthquake Engineering and Structural Dynamics*, 34:847–865. DOI: 10.1002/eqe.461, 2005
- [25] C. Moutinho, An alternative methodology for designing tuned mass dampers to reduce seismic vibrations in building structures. *Earthquake Engineering and Structural Dynamics*, <https://doi.org/10.1002/eqe.2174>, 2012
- [26] A. Reggio, M. De Angelis, Optimal energy-based seismic design of non-conventional Tuned Mass Damper (TMD) implemented via inter-story isolation. *Earthquake Engineering and Structural Dynamics*, <https://doi.org/10.1002/eqe.2548>, 2015
- [27] D. Pietrosanti, M. De Angelis, M. Basili, Optimal design and performance evaluation of systems with Tuned Mass Damper Inerter (TMDI). *Earthquake Engineering and Structural Dynamics*, <https://doi.org/10.1002/eqe.2861>, 2017
- [28] Q. Zhou, M.P. Singh, X.Y. Huang, Model reduction and optimal parameters of mid-story isolation systems. *Engineering Structures*, <https://doi.org/10.1016/j.engstruct.2016.06.011>, 2016



- [29] M. Donà, A.H. Muhr, G. Tecchio, F. da Porto, Experimental characterization, design and modelling of the RBRL seismic-isolation system for lightweight structures. *Earthquake Engineering and Structural Dynamics* 46:831-853. 942 <https://doi.org/10.1002/eqe.2833>, 2017
- [30] A. S. Veletsos, C. E. Ventura, Modal analysis of non-classically damped linear systems. *Earthquake Engineering and Structural Dynamics*, doi: 10.1002/eqe.4290140205, 1986
- [31] K. Deb, A. Pratap, S. Agarwal, T. Meyarivan, A fast and elitist multiobjective genetic algorithm: NSGA-II. *IEEE Transactions on Evolutionary Computation*, <https://doi.org/10.1109/4235.996017>, 2002
- [32] C. Coello Coello, G.B. Lamont, D. Van Veldhuizen, Evolutionary Algorithms for Solving Multi-Objective Problems. *Genetic and Evolutionary Computation Series*, 2007
- [33] N. Ambraseys, P. Smit, R. Sigbjornsson, P. Suhadolc, B. Margaris, Internet-Site for European Strong-Motion Data. *European Commission, Research-Directorate General, Environment and Climate Programme*, 2002

## FUNCTIONAL ACCEPTANCE TESTS FOR THE SEISMIC ISOLATION DEVICES OF THE NEW SAN GIORGIO BRIDGE IN GENOA

**Marcello Cademartori<sup>1</sup>, Andrea Miano<sup>2</sup>, Antimo Fiorillo<sup>2</sup>, Alessandro Aliotta<sup>1</sup>, Marco Di Ludovico<sup>2</sup>, Andrea Prota<sup>2</sup>, Simone Dellacasagrande<sup>1</sup>, Alaeddine Fatnassi<sup>1</sup>, Daniele Pastorelli<sup>1</sup>**

<sup>1</sup> RINA Consulting  
Via Cecchi 6, Genoa, Italy  
{marcello.cademartori,alessandro.aliotta,s.dellacasagrande,alaeddine.fatnassi,daniele.pastorelli}@rina.org

<sup>2</sup> Department of Structures for Engineering and Architecture, University of Naples Federico II  
Via Claudio 21, Naples, Italy  
{andrea.miano,a.fiorillo,diludovi,a.prota}@unina.it

---

### Abstract

*The New San Giorgio Bridge has been built in a very short time between April 2019 and August 2020 in order to reconnect the highway system of the western part of Italy after the tragedy of the collapse of the Morandi Bridge, built in 1967 by prof. Riccardo Morandi. The new viaduct has a steel concrete composite closed section for the deck, a structural scheme of continuous beam with a total of 19 spans supported by elliptical concrete box piers with a maximum height of 40 m. The bridge is seismically isolated by means of friction pendulum devices and multidirectional bearings. In the transverse direction the seismic devices, except for two piers, are a combination of friction pendulum and shear fuses. The paper describes the construction supervision process for the functional acceptance tests of the bearing devices with respect to the Italian National Law, NTC2018, European norms EN15129 and EN1337, and in fulfilment with the Technical Specifications issued by the Italian Railway system (RFI) and Italian State Road Association (ANAS). The paper highlights the main issues encountered during the application of the several specifications for the certification and acceptance processes. A description of the different functional tests required during the construction supervision process is presented as well as an overview of the different acceptance criteria of the tests results. The aim is to provide useful recommendations for technicians involved in the definition of the seismic acceptance tests for bearing devices for highway bridges in the Italian and European contest.*

**Keywords:** New San Giorgio Bridge, Seismic isolation, Curved surface sliders, Certification, Acceptance Tests, Benchmark test.

---

## 1 INTRODUCTION

On the 14<sup>th</sup> August 2018 the highway Viaduct of the A10, one of the strategic roads of the northern part of Italy, collapsed. This tragedy caused the death of 43 people that were crossing the bridge in that moment.

The viaduct was designed between the 1964 and 1967 by the famous Italian Engineer prof. Riccardo Morandi and it was a cable stayed bridge structure with reinforced concrete post tensioned cables.

On December 2018, RINA Consulting was charged to develop the Project and Management, the Construction Supervision, the Health and Safety Management for the demolition of the Morandi Bridge and for the reconstruction of the Polcevera Viaduct, the Genoa new San Giorgio Bridge (called for brevity San Giorgio Bridge in the following) designed by the Arch. Renzo Piano. In this process, RINA took the role of technical and administrative support of the Commissioner all along the design process and it has been present during all the activities of demolition and reconstruction from the beginning to the end.

The San Giorgio Bridge has been designed by Italferr, starting from the concept of Arch. Renzo Piano, and has been built by a consortium called PerGenova and composed by WeBuild and Fincantieri. Because of the emergency, the reconstruction of the bridge was a very challenging task as it involved in parallel the project development and the construction phase.

As part of the Construction Supervision role, an important activity is the quality assurance that requires the control of the construction products on site as well as in the factories.

One of the most important task related to the quality control for the San Giorgio Bridge was related to the qualification and acceptance tests of the seismic devices and bearings installed in the viaduct to isolate the steel-concrete deck from the piers. This requires the development of a detailed “Testing Protocol” as part of the quality control activity and this document has been deployed taking into account: i) design specifications according to the design developed by Italferr; ii) drawings developed by the manufacturer Maurer SE and FIP-MEC; iii) European norms and Italian specifications; iv) technical capabilities of the testing devices present worldwide.

Figure 1 shows the San Giorgio Bridge after the construction phase. The testing program according to the construction and project plan aiming at match the main milestones in terms of deck launching and the time required to perform the tests. To this aim, the required functional tests have been organized in compliance with the construction plan requirement with the support and contribution of all the laboratories charged to execute the tests. Differently from other general design projects, in this case the acceptance process corresponds with the certification process, generating many issues normally not present. Indeed, in this case, the devices are not commercially produced elements, but have been realized “ad hoc” for the bridge, due to the requirements from the design specifications (e.g., the presence of the 100 meter spans and the condition of only 2 devices on each pier led to significant dimensions and acting forces for the devices).

This paper presents a detailed description of the whole testing program with a particular focus on the acceptance tests protocol, as well as a summary of the performance of the devices during the specified static and dynamic tests. Despite the demanding testing requirements in the new European norm, the results proved that the proposed design of the isolators successfully fulfilled the performance required for the acceptance of the devices.



Figure 1: Pictures of the San Giorgio Bridge.

## 2 THE SEISMIC ISOLATION SYSTEM OF THE SAN GIORGIO BRIDGE

The San Giorgio Bridge has a length of 1067 m and the road level is at a height of 40 m. The bridge has a steel-concrete composite deck with an overall width of 29.8 m and with a distance between the supports of 7 m. From the structural point of view, the bridge is a continuous beam with all spans' length of 50 m except for the three spans in the center (with a length of 100 m and for the spans near the abutments that are shorter).

The deck is seismically isolated from the piers. The supporting scheme has been designed to withstand the seismic actions, wind actions and thermal actions, particularly relevant in a bridge with a length of 1067 m without intermediate movement joints. Figure 2 shows a plan view of the bridge.

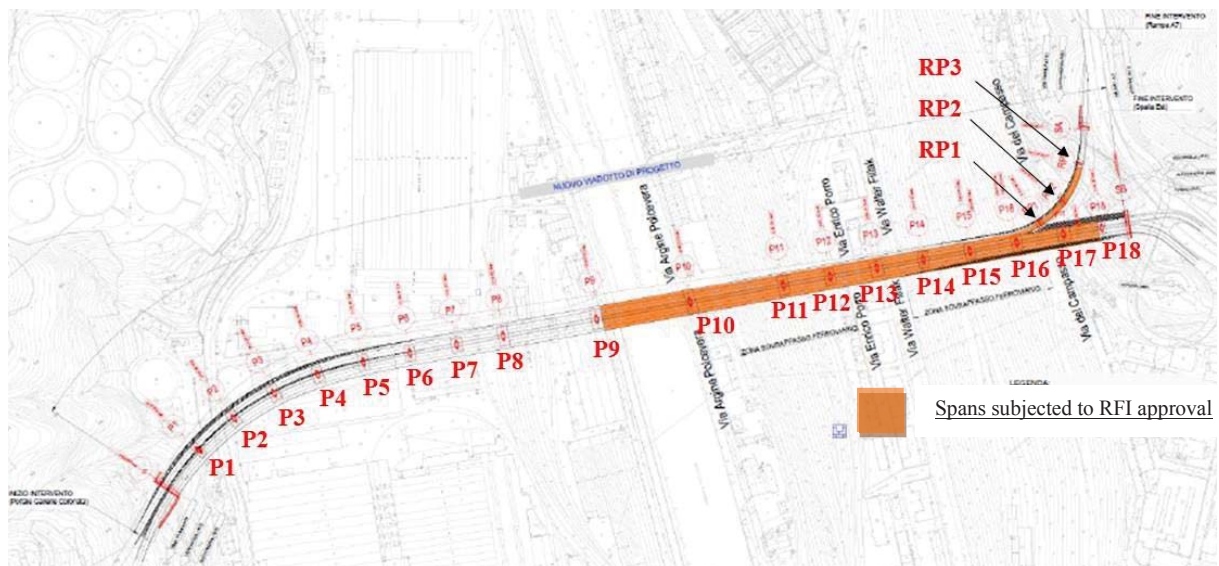


Figure 2: Plane view of the San Giorgio Bridge.

The bridge is equipped with the following devices (between the parenthesis, the nomenclature as per the UNI EN15129 [1] is reported), according to the plan view of Figure 2: i) two curved surface sliders (*friction pendulum*) on each pier from P2 to P17 with shear fuses for the device on the north side (*combined devices: curved surface sliders + fuses*) and without shear fuses for the device on the south side; ii) two multidirectional bearings on pier P1 and P18; iii) two multidirectional bearings on the abutments A, west side, and abutments B, east side; iv) a guided bearing in the center of the abutments; v) two curved surface sliders on the



piers RP1-RP2-RP3 of the ramp; vi) an elastomeric device in the center of the abutment A of the ramp; vii) two multidirectional bearings on the abutment A of the ramp.

The supporting system of the bridge has been designed to guarantee horizontal flexibility of the bridge during the seismic actions; this to increase the structural period of vibration and to reduce the seismic acceleration, while at the same time to limit the movement due to the wind actions. For this reason, the shear fuses are placed on the isolators in the south side of the piers from P2 to P17: these fuses aims at ensuring a fixed behaviour in the transversal direction for the serviceability limit states while they will break off in case of seismic event.

To avoid the direct contact between steel deck and concrete piers in case of extreme seismic events, the deck is also equipped with seismic restraints in the transversal direction in each pier and in the transversal and longitudinal direction in the abutments. Movement joints are provided only at the three abutments.

This paper focuses on the seismic certification and acceptance protocol followed for the curved surface sliders, friction pendulum and, then, for the categories i) and v) previously described. Moreover, a detailed discussion is provided with reference to the acceptance tests for the devices under investigation.

## 2.1 Seismic behavior of the curved surface sliders and combined devices

Curved surface sliders are seismic isolators that provide the four main functions of the base isolation (see UNI EN 15129, 3.1.26) through an appropriate arrangement of curved sliding surfaces; they use the characteristics of a pendulum to increase the natural period of the isolated structure. Several experimental and analytic studies on single and double concave surface sliders are present in literature, concerning different critical issues and the uniaxial and/or the biaxial response (e.g., [2-5]).

The curved main sliding surface of Curved Surfaces Sliders provides a restoring force at displacement  $d$ .

Energy is dissipated by friction due to movement in the main sliding surface. Rotations of the structure are accommodated by the secondary sliding surface.

Figure 3 shows the functional principle and main elements of curved surface sliders for the type A (see Table 1) curved surface sliders of the San Giorgio Bridge.

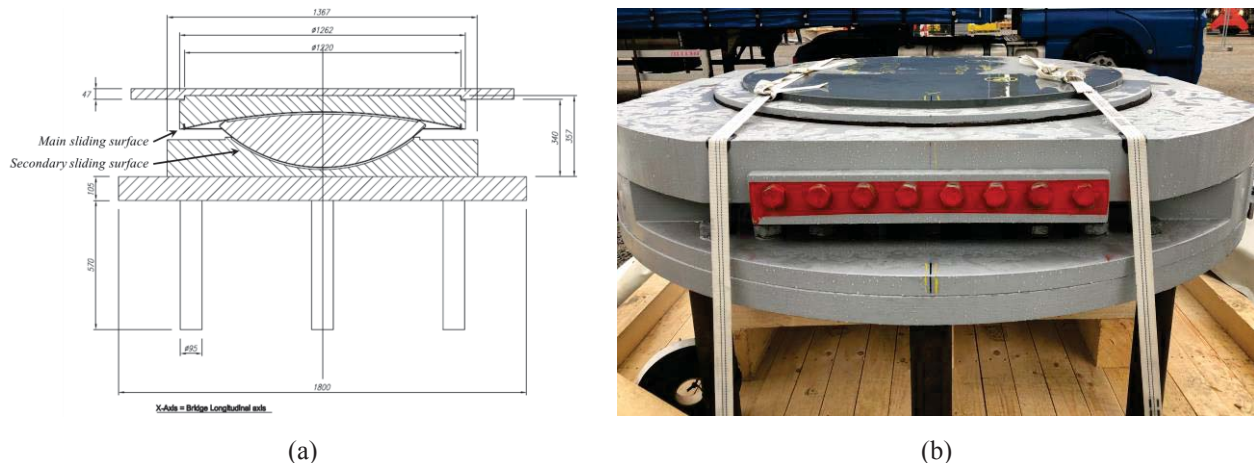


Figure 3: (a) Functional principle and main elements of Curved Surface Sliders for the type A (see Table 1) curved surface sliders of the San Giorgio Bridge; (b) picture of the device.

The constitutive law of this typology of devices in the horizontal plane, under constant axial load, is usually described with the following relationship [6]:



$$F = Mg \cdot \mu_{dyn} + \frac{Mg}{R} \cdot d \quad (1)$$

where:

F= horizontal force

Mg= N is the vertical force

R=radius of curvature of the device

d= horizontal displacement

$\mu_{dyn}$ =dynamic friction coefficient

The resultant hysteresis loop is reported in Figure 4.

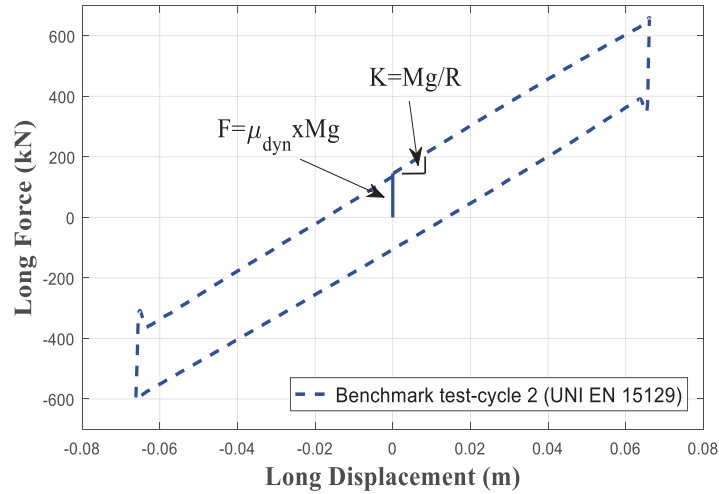


Figure 4: Force-Displacement relationship of the curved surface slider referred to the benchmark-cycle 2 test for one of the bridge devices.

Figure 5 shows the break-away friction, also called stick-slip effect, that is the forces recorded when the motion of the device starts [7], as well as the increase of force that is recorded with the inversion of the velocity.

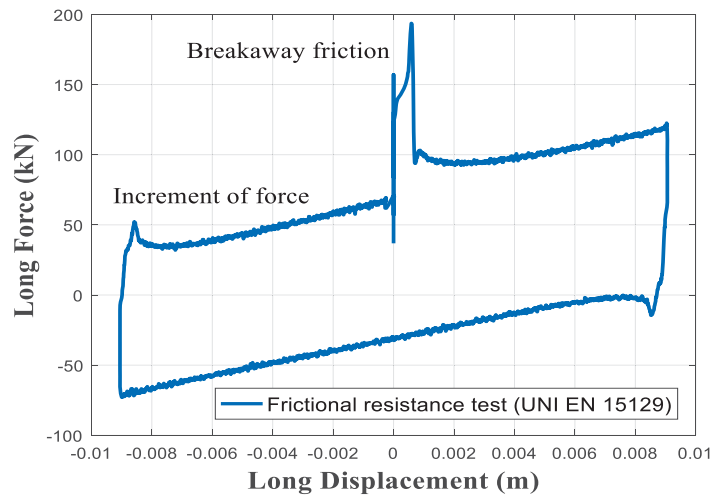


Figure 5: Experimental behavior of curved surface slider referred to the frictional resistance test for one of the bridge devices.

For the San Giorgio Bridge, the curved surface sliders are combined, in the transversal direction, with shear fuses. In this case, the device acts as a friction pendulum in the longitudi-

nal direction while for the transverse direction is fixed until a specific value of force is reached. Once the break-away force is reached the device has the same behavior in both the horizontal directions. The main objective of the combination of the shear fuses for the viaduct is to guarantee the benefits of the base isolation and to limit horizontal displacement under transversal wind loads.

### 3 THE CERTIFICATION AND ACCEPTANCE PROCESS FOR THE CURVED SURFACE SLIDERS IN THE EUROPEAN REGULATIONS FRAMEWORK

This chapter describes the certification and acceptance process for the curved surface sliders. Clearly, the design is directly linked to the recommendations of the country of realization of the construction. In the case of the San Giorgio Bridge, the Italian national code (NTC 2018, [8]) is inserted inside the context of European codes and specifically the UNI EN 15129 [1] and the UNI EN 1337 [9]. NTC 2018 [8] clearly separate the tests related to the certification process from the tests related to the acceptance process. This separation between certification and acceptance processes and the relative definition of the tests plan for the curved surface sliders is in perfect agreement with the suggestions of the UNI EN15129 [1] and UNI EN1337 [9]. Moreover, according to NTC 2018 [8] specific tests should be added based on the different type of isolators. For the case study of the San Giorgio Bridge, the curved surface sliders, described in Section 2, did not exist at the moment of the bridge design. They have been designed from the company *ad hoc* for the San Giorgio Bridge. Thus, in this case the certification and acceptance processes develop in parallel.

For the certification procedure, NTC 2018 (11.9.2) [8] requires that the anti-seismic devices must comply with the European standard harmonized UNI EN 15129 [1] and have the CE marking. The system of evaluation and verification of the constancy of performance, provided for in the aforementioned UNI EN 15129 [1], is applied. The certification procedures are intended to demonstrate that the device is capable of maintaining its functionality under the conditions of use envisaged throughout the life of the project.

For the acceptance procedure, NTC 2018 (11.9.3) [8] requires mandatory on-site acceptance checks for all the types of devices; furthermore, the Works Supervisor, before in-situ implementation, verifies the required certification documentation, and refuses the non-conforming devices. The Works Supervisor should also carry out the geometric verification and dimensional tolerances. The acceptance tests can be performed and certified by a laboratory that is able to guarantee adequate competence, equipment and organization. For the curved surface sliders, the methodology for the tests acceptance plan definition and for the relative evaluation criteria are those reported in the UNI EN 15129 [1] with reference to the Factory Production Control tests. Then, it is possible to use, for the purposes of acceptance tests, also the Factory Production Control tests carried out within the certification process of the devices in accordance with UNI EN 15129 [1] if (conditions respected for the case study San Giorgio Bridge): i) the sampling of the devices was carried out, on the lots destined for the specific site, by the Works Supervisor of construction site; ii) the tests are performed and certified by a laboratory with adequate expertise, equipment and organization; iii) the aforementioned certificates explicitly indicate the construction site (s) where the supply is used.

Finally, the devices subjected to certification or acceptance tests may be used in construction only if: i) the elements stressed in the non-linear field are replaced or if their resistance to low-cycle fatigue is at least one order of magnitude higher than the number of test cycles; ii) and in any case only after that they are subject to verification of their perfect integrity and full functionality.

The number of devices subjected to acceptance tests for the curved surface sliders is provided in Section NTC 2018 11.9.8.1 [8]. The acceptance tests must involve at least 20% of the

devices, in any case not less than 4 and no more than the number of devices to be implemented.

### 3.1 UNI EN 15129

The UNI EN 15129 [1] standard is the European standard for the description of the process of certification and acceptance for the curved surface sliders. The UNI EN 15129 [1] requirements have been integrated with additional tests required by national recommendations. However, a brief summary of the entire process of certification and acceptance processes is summarized herein. Chapter 10 of UNI EN 15129 [1] concerns the Assessment and Verification of the Constancy of the Performance (AVCP). It specifies that the conformity of the anti-seismic devices to the requirements of UNI EN 15129 [1] and to the performance declared from the producer have to be demonstrated through: i) type-product identification; ii) check of production in factory from the fabricator, including the assessment of the product.

Type-product identification is represented by the type tests that form the certification process together with the acquisition of the CE marking. According to UNI EN 15129 (10.2) [1], all the mechanical features of the sliders needed for the design to guarantee the service life, should be determined through type tests on full scale sliders, also including cyclic tests. The tests results should confirm the representative values of the mechanical features of the sliders.

Check of production in factory is represented by the factory production control (FPC) tests that form the acceptance process. According to UNI EN 15129 (10.3) [1], the fabricator should keep a FPC system to ensure that the sliders are in compliance with the performance declared in their essential features. The FPC includes also some specific tests for the devices and the check on the raw materials. These general rules are valid for all type of sliders, while the curved surface sliders are specifically analysed in Section 8.3.4 of UNI EN 15129 [1], defining the type tests (8.3.4.1) and the FPC tests (8.3.4.2).

Then, coherently with the purpose of this work, a focus is herein dedicated to the FPC tests to complete the acceptance of the devices. Section 8.3.4.2 of UNI EN 15129 [1] presents the tests to be implemented for the curved surface sliders (see Figure 6). In order to complete the FPC checks, the following tests are required:

- a) Vertical load bearing capacity (see Sect. 8.3.1.2.2.2 and 8.3.4.1.2 of UNI EN 15129 [1]);
- b) Frictional resistance force under service conditions (see Sect. 8.3.1.2.2.5 and 8.3.4.1.3 of UNI EN 15129 [1]);
- c) Test run P1, also called benchmark test (see Sect. 8.3.1.2.2.6 and 8.3.4.1.5 of UNI EN 15129 [1]).

The testing of raw materials and constituents shall be carried out in accordance with Tab. 16 of UNI EN 1337- 2:2004 [9] or, in case of other sliding materials, according regulations provided in the respective European Technical Approval (ETA).

In conclusion, Figure 6 summarizes the acceptance protocol of curved surface sliders in an European framework, based on recommendations described in this chapter. Note that in addition to the required tests from the UNI EN 15129 [1], additional tests recommended from the national codes and from other authorities involved in the project can be added to the tests protocol. Indeed, this was one of the main challenge of the acceptance test procedure: to ensure the compliance to all the European and Italian codes and at the same time to guarantee the fulfilment of the technical specifications issued by the Italian Railway system (RFI) and by the Italian State Road Association (ANAS).

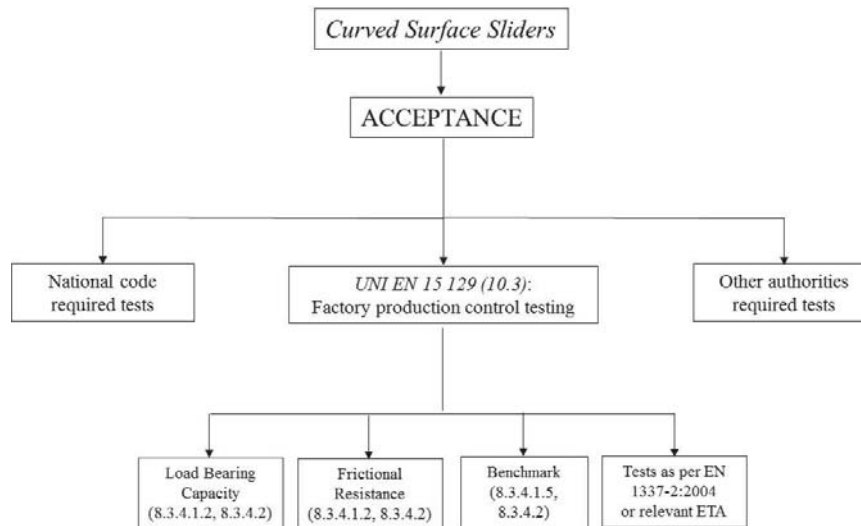


Figure 6: Flow-chart of acceptance protocol for the curved surface sliders.

In the case study of the San Giorgio Bridge, the Italian national code (NTC 2018, 11.9.8, [8]) suggests adding to the protocol another test, called Quasi Static test. Moreover, it is to note that in the case study of the San Giorgio Bridge, also the Technical Specifications issued by the Italian Railway system (RFI) and Italian State Road Association (ANAS) have been considered in the acceptance process. In particular, additional tests have been added to the acceptance protocol tests based on the recommendations of RFI, that in some cases proposed tests conceptually similar to the ones from UNI EN 1529 [1], but using different load conditions/setup conditions/acceptance parameters. In this paper, the acceptance tests required by the RFI specifications are not treated.

#### 4 ACCEPTANCE PROTOCOL TESTS: THE SAN GIORGIO BRIDGE CASE STUDY

The main objectives of the testing program carried out for the San Giorgio Bridge were: i) to guarantee the fulfilment of the applicable technical norms; ii) to guarantee the respect of the design planned performances; iii) to investigate the behaviour of the devices with respect to the comments and prescriptions issued by the different authorities during the approval process of the project (e.g. Technical Authority of the Italian Minister of Transportation and comments by the Commissioning Authority); iv) to investigate the durability and long-term behaviour of the devices applying all the tests available as per the most updated state of the art in this field.

All the above objectives have been addressed aiming at the same time at the respect of the project and construction plan.

Pursuing that the codes and specifications cannot regulate every aspects of complex phenomena, a pro-active role of the Construction Supervision team, in strong cooperation with the designer with the manufacturer and with the laboratories, has been deployed with the common purpose to verify the performance of the seismic devices while at the same time respecting the construction program.

The seismic acceptance tests have been performed in different testing facilities depending on their loading and displacement capacity and at the same time to make feasible the execution of different tests in parallel. Each testing facility was used for a similar group of devices to obtain more comparable results for similar bearings. The following laboratories have been involved in the experimental program:

- SismaLab under the supervision of the Polytechnic of Milan for the device of the ramp and for the shear fuses;
- Polytechnic of Milan using the external premises of FIP-MEC in Padua for the break-away tests of the combined device friction pendulum + fuses;
- Eucentre Lab in Pavia for friction pendulum and multidirectional bearings.

This section presents the acceptance protocol (UNI EN 15129 [1] FPC tests plus national code required tests) for the case study of the San Giorgio Bridge. Note that additional tests on the conformity of the characteristics of the materials in accordance with Tab. 16 of UNI EN 1337- 2:2004 [9] have been implemented. Moreover, under the supervision of the RFI specialists, other tests have been carried out based on their protocol. Table 1 reports the under investigation, the type of tests performed and the standard to which each test refers (tests done in accordance with the RFI specifications are not included here).

CURVED SURFACE SLIDERS TYPE	PIER	TEST			
<b>TYPE A:</b> 3 SLIDERS ON THE 100 METERS BAYS	P9/3, P10/3 and P11/2	Load Bearing Capacity UNI EN 15129	Frictional Resistance UNI EN 15129	Benchmark UNI EN 15129	Quasi-Static NTC 2018
<b>TYPE B:</b> 4 SLIDERS ON THE 50 METERS BAYS	P2/3, P13/3, P2/2 and P12/2				
<b>TYPE C:</b> 4 SLIDERS ON THE BRIDGE RAMP	RP3/R2, RP3/R3, RP2/R2 and RP1/R2				

Table 1: Summary of devices under investigation and relevant tests (see Figure 2 for labels).

The following nomenclature is used: the number after “P” refers to the pier number as reported in Figure 2, while the number after the “/” refers to the location of the devices on the pier (“3” for the northern support and “2” for the southern supports). The supports located on the southern side are combined devices (curved surface sliders + shear fuses).

The sliders types have been in depth discussed in Section 2 while the present section focuses on a critical discussion on the main issues occurred during the test program:

- Because the devices were not commercially produced elements, but have been realized “*ad hoc*” for the bridge, due to the requirements from the design specifications, the acceptance tests were carried out in parallel with those related to certification process. The UNI EN15129 [1] does not require full test for the combined devices in the acceptance tests protocol while it suggests only one test in the certification process. This may lead to significant issues in the cases in which the certification and acceptance processes correspond; indeed, high priority should be given to the combined device test, because it is crucial to verify that unexpected interferences between the components of the devices, that can affect the behavior of the whole device, are avoided. For the case study of the San Giorgio Bridge, the Construction Supervision team required the implementation of specific tests for the combined devices (tests in the transversal direction, break away tests on two sacrificial devices among others); however, they are not discussed in detail in this paper. During the combined tests, small modifications/upgrading can be necessary, such as in the case study, and this clearly point out that such a test should occur before the single components tests;
- The vertical loads are sometimes very high in particular for modern bridges (i.e. 1.3  $N_{ULS}$ =axial load from gravity load combination for ultimate limit states is required for the load bearing capacity test). This could imply that testing facilities may have not adequate capacity. These constraints should be taken into account in the design of structures/infrastructures to easily allow to tests the components (potentially in



the same geographical region of the construction), based on the current instrumentations availability of the laboratories; otherwise a significant increase of time and cost for testing not conventional devices should be considered. The norms should also provide specific procedures in such cases in order to simplify the whole procedure, by keeping the same safety level. The same problems may occur in terms of displacement requirements;

- the design of small friction values may imply that the calibration forces of the laboratory equipment can be comparable to forces to be measured; this can strongly affect the tests results.

Furthermore, as discussed in the following sections, the interpretation of some tests of UNI EN 15129 [1] may in some case not univocal or not always quantitative (e.g., see Faverage definition in the next Section).

From here, a specific focus is dedicated to the benchmark test, that is the more important dynamic test inside the requirements of UNI EN 15129 [1] in the acceptance phase.

#### 4.1 Benchmark test

In the context of the curved surface sliders acceptance tests, the benchmark test is required from UNI EN 15129 [1] with two purposes:

- 1) Verification of cycle stability in terms of fluctuation of the test force with respect to the average force;
- 2) Verification of the dynamic friction coefficient.

The load application method (UNI EN 15129 8.3.4.1.5 [1]) is reported as follows in Table 2, where  $d_{bd}$  is defined as the maximum design displacement of the device. During the test, a permanent vertical load  $N_{sd}$  (seismic combination) was applied to the device.

Type of test	Test run	Compression load $N_s$ [kN]	Displacement $d_0$ [mm]	Peak velocity $v_0$ [mm/s]	Number of complete cycles
Benchmark	P1	$N_{sd}$	$1 \times d_{bd}$	50	3

Table 2: Load application method for the benchmark test (UNI EN 15129 8.3.4.1.5 [1]).

About the test acceptance criteria, according to UNI EN 15129 8.3.1.6 [1], the movement in the sliding surfaces shall be regular and uniform and without producing any type of vibrations such as those induced by the stick-slip phenomenon. The force oscillation needs to be contained inside a variation range of  $\pm 5\%$  of the average restoring force, at any level of bearing displacement up to 85% of the maximum displacement required from the test protocol. The average restoring force shall be obtained from the best-fit straight line determined by the least square interpolation of the response between  $\pm 85\%$  of the maximum displacement.

Then the requirement for the satisfaction of the test can be summarized as:

$$\text{for } (-0.85) d_{bd} < d < (+0.85) d_{bd} : F_{\text{regression}} - (0.05 F_{\text{average}}) < F_{\text{test}} < F_{\text{regression}} + (0.05 F_{\text{average}}) \quad (2)$$

Moreover, the dynamic friction coefficient needs to fall within the limits specified by the Structural Engineer under the testing conditions specified in UNI EN 15129 8.3.4.1.5 [1]. Then, it is considered necessary to verify that the dynamic friction coefficient deriving from the test falls within the lower and upper bounds used in the design phase. The following check can be performed by calculating the average dynamic friction using the following formulation:

$$\mu = \frac{H}{2 \cdot (d^+ + |d^-|) \cdot V_{\text{load}}} \quad (3)$$

where:  $H$  = area subtended by the curve,  $d^+$  = maximum displacement,  $d^-$  = minimum displacement,  $V_{load}$  = vertical load. This value should vary inside the lower/upper bound range.

Then, the final requirement is that:

$$\mu_{lower\ bound} < \mu < \mu_{upper\ bound} \quad (4)$$

As for example, the results of the benchmark test on P10/3 slider (label producer MAU112E19-10) is discussed herein. Figure 7 shows the three force-displacement cycles of the test. Moreover, the displacements-time and forces-time plots for the 3 cycles are presented in Figure 8.

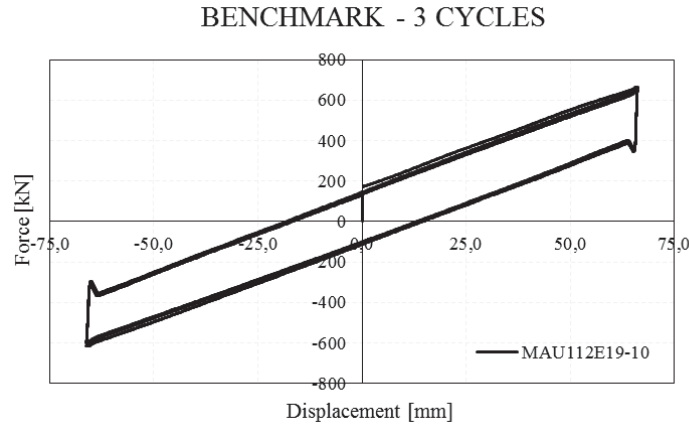


Figure 7: Displacement-force plot for the 3 cycles of the benchmark test.

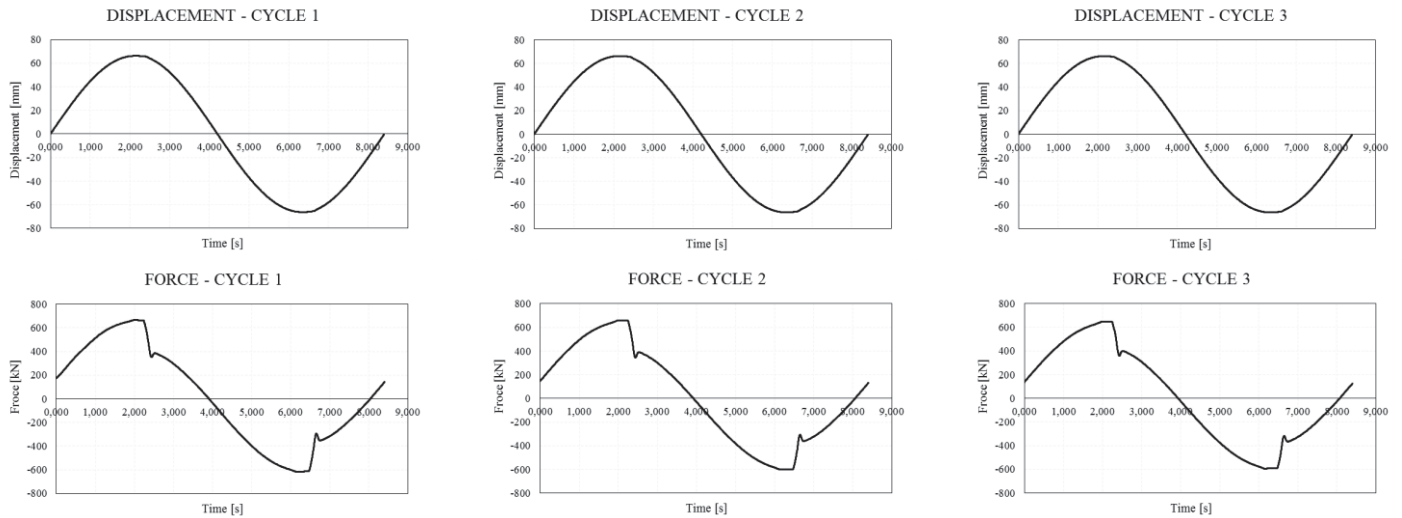


Figure 8: Displacements-time and forces-time plots for the 3 cycles.

Then, the graphical verification of the cycle stability in terms of fluctuation of the test force at each step with respect to the average force is presented in Figures 9-11 for the three cycles. It can be noted a continuous stability of the response has been registered through the 3 cycles investigated.

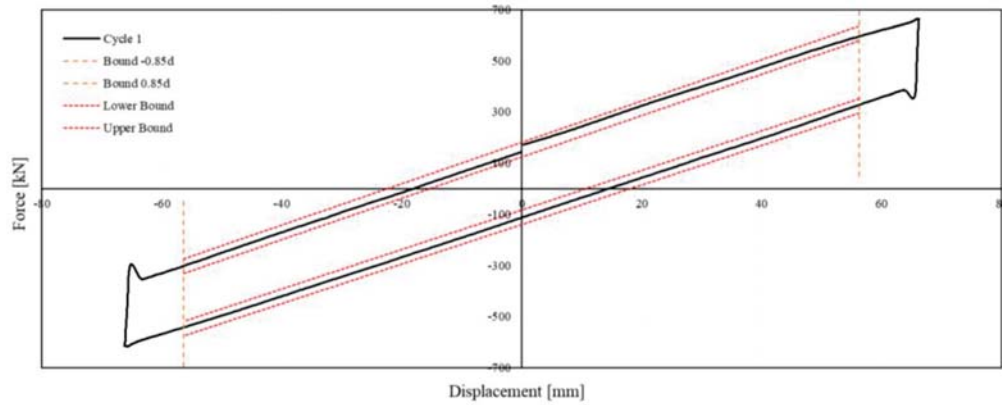


Figure 9: Stability verification for the cycle 1.

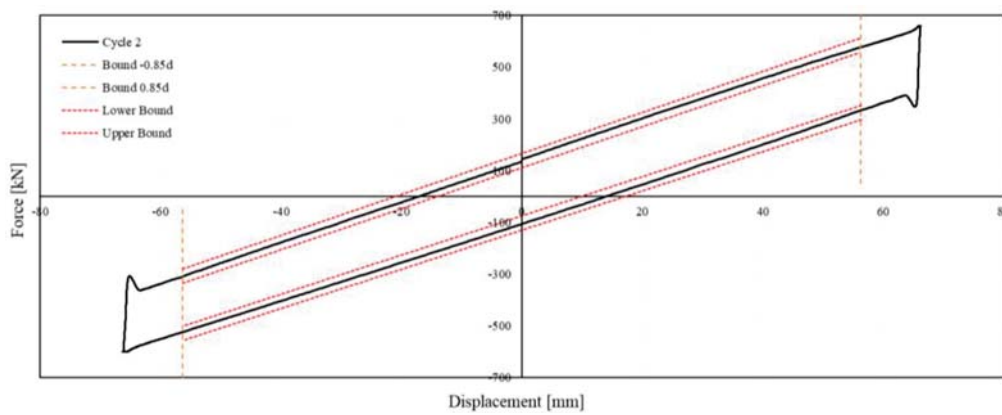


Figure 10: Stability verification for the cycle 2.

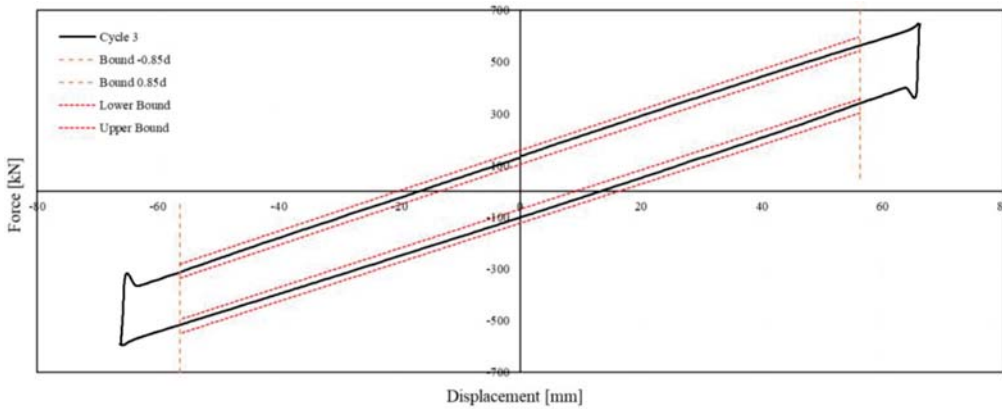


Figure 11: Stability verification for the cycle 3.

In accordance with Equation 3, the value of the dynamic frictional coefficient in the three cycles has been calculated and reported in Table 3.

Herein a summary of the dynamic frictional coefficient in the three cycles is reported (Table 3).

Cycle 1	Cycle 2	Cycle 3
0.5%	0.5%	0.5%

Table 3: Summary of the dynamic frictional coefficient in the three cycles.

The UNI EN 15129 [1] states that the average restoring force shall be obtained from the best-fit straight line determined by the least square interpolation of the response  $\pm 85\%$  of the test displacement peak. Fluctuations in horizontal force must be less than  $\pm 5\%$  of the average restoring force, at any level of displacement of the sliding isolator up to  $85\%$  of the test displacement peak. Thus, the procedure to identify for which value of this average restoring force the  $5\%$  interval should be calculated may lead to different interpretations (i.e. with respect to the interval in which the test outcome should be contained in order to satisfy the test). It is clear that this mentioned value should depend on an average of the maximum forces reached during the test in correspondence of the  $\pm 85\%$  of the test displacement peak, but a more straightforward explanation could help the users.

## 5 CONCLUSIONS

The San Giorgio Bridge has been built in a very short time between April 2019 and August 2020 in order to reconnect the highway system of the western part of Italy after the tragedy of the collapse of the Morandi Bridge. The new viaduct has a steel concrete composite closes section for the deck, a structural scheme of continuous beam with a total of 19 spans supported by elliptical concrete box piers with a maximum height of 40 m. The bridge is seismically isolated by means of a composition of friction pendulum devices and multidirectional bearings. One of the most important tasks related to the quality control for the San Giorgio Bridge is related to the qualification and acceptance tests of the seismic devices and bearings planed in the viaduct to isolate the steel-concrete deck from the piers. The testing program for the curved surface sliders was planned also considering the construction and project plan aiming at match the main milestones in terms of deck launching and the time required to perform the test. To do so, the required functional tests have been organized in compliance with the construction plan requirement with the important support and contribution of all the laboratories charged to execute the tests.

A detailed description of the whole testing program with a particular focus on the acceptance tests protocol, as well as a summary of the performance of the devices during the specified static and dynamic tests, has been discussed herein. Despite the demanding testing requirements in the new European norm, the results proved that the proposed design of the isolators successfully fulfilled the performance required for the acceptance of the devices. Differently from other general design projects, in this case the acceptance process corresponds with the certification process, generating many uncommon issues. In fact, in this case, the devices are not commercially produced elements, but have been realized “*ad hoc*” for the bridge, due to the requirements from the design specifications (e.g., the presence of the 100 meter spans and the presence of only two bearing per each pier have conducted to big dimensions and big forces for the devices). During the implementation of the tests program, many issues came out and have been deeply described through the paper.

Different important suggestions arisen from the experience of the preparation of the seismic acceptance tests.

First of all, it is important that the designer considers, since the design stage, to define devices with testable parameters. The vertical loads are sometimes very high in particular for modern bridges and the testing facilities may have not adequate capacity. The designers should design the structures/infrastructures in way that all the components are testable (potentially in the same geographical region of the construction), based on the current instrumentations availability of the laboratories to avoid significant time and cost increase in the certification/acceptance process. Specific standards may be introduced by technical norms and guidelines in such cases in order to simplify the whole procedure, by keeping the same safety level. A strong cooperation between the testing facilities, the designers, the manufacturers and

the Construction Supervision team is required in order to define the adequate tests able to assess the performances of the devices and hence guarantee a high level of quality control while at the same time respecting the construction and manufacturing schedule.

## ACKNOWLEDGMENTS

The authors would like to acknowledge the manufacturers Maurer SE and FIP-MEC for their professional cooperation during the whole project. A special thanks also goes to the laboratories (Eucentre, SismaLab and the Polytechnic of Milan) for their strong support in the definition of the seismic acceptance tests and for the assistance during the testing campaign. Finally, the authors wish to acknowledge the consortium PerGenova, the designer Italferr, the technical department of RFI and the Commissioning Authorities part of ANAS group for their technical support in the definition and interpretation of the tests.

## REFERENCES

- [1] UNI EN 15129 (CEN – Comité Européen de Normalisation, European Code): *Anti-seismic devices*, Brussels; 2018.
- [2] D.M. Fenz, M.C. Constantinou, Behaviour of the double concave friction pendulum bearing. *Earthquake Engineering and Structural Dynamics*, **35(11)**, 1403-1424, 2006.
- [3] V. Quaglini, M. Bocciarelli, E. Gandelli, P. Dubini, Numerical assessment of frictional heating in sliding bearings for seismic isolation. *Journal of Earthquake Engineering*, **18(8)**, 1198-1216, 2014.
- [4] A. Pavese, M. Furinghetti, C. Casarotti, Experimental assessment of the cyclic response of friction-based isolators under bidirectional motions. *Soil Dynamics and Earthquake Engineering*, **114**, 1-11, 2018.
- [5] A. Pavese, M. Furinghetti, C. Casarotti, Investigation of the consequences of mounting laying defects for curved surface slider devices under general seismic input. *Journal of Earthquake Engineering*, **23(3)**, 377-403, 2019.
- [6] G.M. Calvi, D. Pietra, M. Moratti, Criteri per la progettazione di dispositivi di isolamento a pendolo scorrevole. *Progettazione Sismica*, **3**, 2010.
- [7] P.M. Calvi, G.M. Calvi, Historical development of friction-based seismic isolation systems. *Soil Dynamics and Earthquake Engineering*, **106**, 14–30, 2018.
- [8] NTC 2018: Supplemento ordinario alla Gazzetta Ufficiale, n. 42 del 20 Febbraio 2018. Ministero delle Infrastrutture e dei Trasporti, Ministerial Decree DM 17 Gennaio 2018 “Aggiornamento delle Norme tecniche per le costruzioni” (in italian).
- [9] UNI EN 1337 part 2 (CEN – Comité Européen de Normalisation, European Code): *Structural bearings - Part 2: Sliding elements*, Brussels; 2004.



## MODELING STRATEGIES FOR THE LATERAL RESPONSE OF CURVED SURFACE SLIDER DEVICES UNDER EXTREME DISPLACEMENT DEMANDS

Marco Furinghetti<sup>1,2</sup> and Alberto Pavese<sup>1</sup>

<sup>1</sup> University of Pavia  
Via Ferrata 3, 27100 Pavia (Italy)  
marco.furinghetti@unipv.it  
a.pavese@unipv.it

<sup>2</sup> EUCENTRE  
Via Ferrata 1, 27100 Pavia (Italy)  
marco.furinghetti@eucentre.it

---

### Abstract

*Base isolation represents one of the most efficient strategy for the reduction of the structural vulnerability of buildings and bridges. Design procedures generally aim to provide the proper period shift, in order to reduce spectral acceleration values and, consequently, the base shear and internal forces. On the other hand, high displacement demands can be achieved, which can be partially limited by providing dissipative capacity through hysteretic behaviors. Although design procedures allow to fairly estimate the design displacement of the adopted devices, extreme seismic event can occur, and displacement higher than the design value can be experienced. Especially for Curved Surface Slider devices, if the displacement demand exceeds a certain geometrical limit, non-negligible damage can occur at the sliding pad, and variations in the force response are consequently noticed.*

*In this work modeling strategies for the computation of the seismic response of base-isolated buildings are presented, by considering extreme earthquake loading conditions. Analytical models are reported for Curved Surface Slider devices, calibrated through the experimental outcomes of tests performed at the Laboratory of EUCENTRE Foundation in Pavia (Italy). In addition, simplified dynamic systems are defined, which allow fast assessments of the global response of a base-isolated structure, even though extreme seismic events are applied. Results have been compared to the response returned by an experimental hybrid simulation, in order to evaluate the accuracy of the presented dynamic systems.*

**Keywords:** Base isolation, Curved Surface Slider, extreme earthquake loading, dynamic system, experimental hybrid simulation.

---

## 1 INTRODUCTION

Recent research works about seismic isolation have led to the definition of several modeling strategies for isolators, models which can be adopted in time history analyses for the assessment to building and bridge structural systems, by reducing significantly the uncertainty of the structural behavior prediction ([1], [7], [16]). The design of the proper period elongation, internal forces in the superstructure elements can be significantly reduced; on the other hand a large displacement demand may occur at the isolation level, even though lower values can be achieved, by means of the hysteretic characteristics of the implemented devices. Curved Surface Slider devices, among the others, represent one of the most suitable solutions for base-isolation ([2], [3], [10], [12], [13], [14]). Such isolators can actually accommodate large displacement demands, with potentially high dissipative capacities, which are provided by the frictional response of the induced sliding motion. In addition, residual displacements are effectively limited by the recentering behavior, due to the spherical shape of the sliding surfaces. However, recent risk assessment studies have shown that the base isolation technique in some cases can lead to higher seismic risk, with respect to their a correspondent fixed-base configuration. This is an unexpected outcome, since the isolation system is supposed to protect the superstructure against the effects of earthquake excitations. The main reason behind such results is related to the definition of the collapse condition that has is commonly assumed for isolation devices, which consists of the achievement of the design displacement. More specifically, a sliding base isolator is assumed to collapse once the internal reaches the edge of the implemented sliding surfaces, which corresponds to the maximum stroke of the device. This condition is generally considered as the maximum limit of the displacement capacity for sliding devices, because it is associated to the loss of functionality of the isolator. However, recent experimental research has led to evidence of extra-displacement capacity for such devices, with a controlled and limited force response ([6][8]); furthermore, the outcomes have been used for both model calibration and vulnerability assessments, in order to account for the effective ultimate conditions of the implemented isolators.

In this work the extra-stroke behavior of Double Curved Surface Slider devices has been modeled, in order to evaluate the response of a base isolated case study structure, subjected to a severe seismic event. An easy to implement analytical model of the extra-design response has been adopted, among the strategies available in the very recent literature, and results have been compared to a hybrid simulation, which has been performed at the Laboratory of EUCENTRE Foundation in Pavia (Italy). The outcomes of both the experimental hybrid and numerical simulations have been analyzed, in terms of isolation displacement and hysteretic responses, cumulative damage at the sliding pads equipped in the physical device and building base shear time series.

## 2 CASE STUDY STRUCTURE

The case study structure adopted in this research work consists of a reinforced concrete frame structure, which has been modeled by means of linear-elastic frame elements, by considering a reinforced concrete slab as an interface between the superstructure and the isolation layer, implemented through a mesh of shell elements (Figure 1).

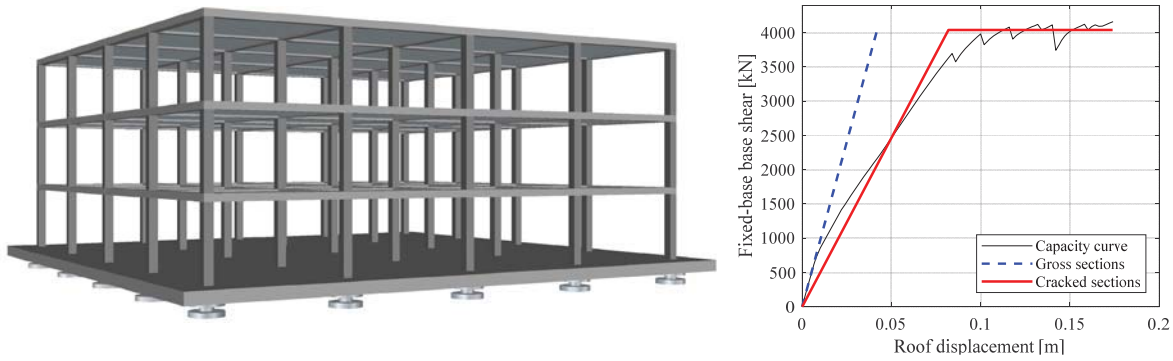


Figure 1: Case study structure.

The frame structure has four spans along both  $x$  and  $y$  directions with equal span length (6m each), and all floors have an interstorey height of 3m. Concerning the concrete slab, which represents the interface between the implemented isolation devices and the building, a thickness of 500mm has been adopted, and plan dimensions have been designed, by increasing the plan development of the superstructure of 1.5m along all directions (27m x 27m). For all the frame elements the flexural stiffness has been reduced, in order to better fit the linear-elastic branch of the bi-linear approximation of the capacity curve, as shown in Figure 1. The full capacity curve, in terms of base-shear vs. top displacement of the fixed-base configuration of the building has been obtained through a pushover analysis carried out through the software SeismoStruct ([15]), which allows to model force-based frame elements, with distributed plasticity and non-linear constitutive laws for materials (Mander's model for Concrete and Menegotto-Pinto's model for reinforcement steel); in addition, for concrete columns the proper confinement effects within the concrete core has been accounted for, in order to obtain realistic evaluation of both ductility and strength for all the implemented sections. Isolation devices are represented by Concave Surface Slider devices.

### 3 CHARACTERISTICS OF THE PHYSICAL DEVICE

The physical isolator consists of a Double Curved Surface Slider ([5]), which is actually the most typical configuration of sliding devices designed in real practice applications (Figure 2). Two spherical sliding surfaces with the same curvature radius have been implemented, both polished to mirror finish in order to achieve a roughness index  $R_a$  of 0,2 ([10]). Within the equal sliding surfaces, a non-articulated slider is installed, which is made up of a unique steel block (material S355JR): such an element houses two circular sliding pads, having same diameter (360mm) and same material composition, aiming at considering the same contact pressure and the same frictional properties at both the sliding interfaces. Both the radii of curvature of the spherical surfaces are 1600mm each, with internal slider height of 120mm: consequently, the equivalent radius of curvature of the device is approximately equal to 3080mm.

The device has been equipped with an innovative sliding material, which consists of a graded PTFE material, filled with bronze fibers. In addition, the sliding surface of the pad has been realized with dimpled recesses, with a light lubrication, in order to achieve the proper design friction coefficient, equal to 3% ([4]); the corresponding value of applied vertical load is equal to 1500kN. The maximum displacement, given the assumed plan geometric characteristics of sliding surfaces and internal slider, is equal to 172mm.

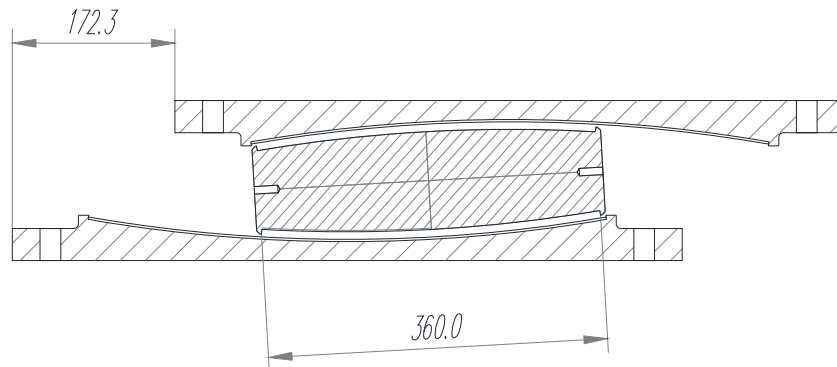
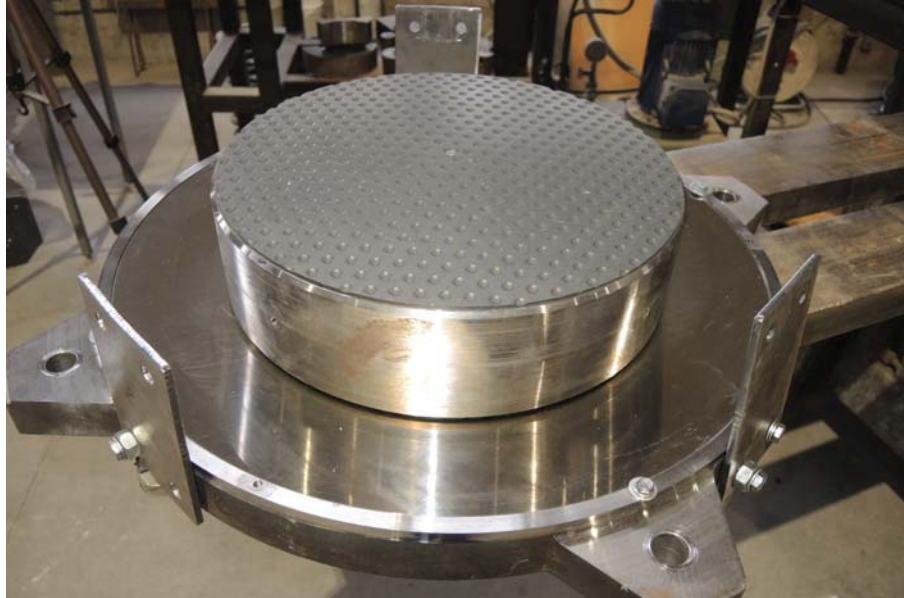


Figure 2: Tested physical device: definition of maximum displacement.

In order to consider a significant extra-stroke displacement demand, the maximum displacement to be considered for the simulation, which will define the proper scaling of the input signal, is defined according to the design value, increased by 50% of the sliding pad diameter, so that 25% of the pad is uncovered by each sliding surface ([6]). Thus, a maximum displacement of 350mm has been considered.

#### 4 NUMERICAL SUBSTRUCTURE AND DYNAMIC SYSTEM

The case study structure has been numerically modeled as an equivalent Multi Degree of Freedom oscillator, thanks to a special static condensation procedure, which has been applied to the full 3D FEM model of the structure ([9]). In Table 1 the resulting mass and stiffness matrices are reported.

941.3	0.0	0.0	0.0
0.0	589.7	0.0	0.0
0.0	0.0	589.7	0.0
0.0	0.0	0.0	397.1

236656	-329731	111851.3	-18776.6
-329731	617351.8	-377915	90295.5
111851.3	-377915	479479.9	-213416
-18776.6	90295.5	-213416	141894.8

Table 1: Mass (left [tons]) and stiffness (right [kN/m]) condensed matrices for the case study structure.

Such matrices allow to obtain dynamic properties almost overlapped of the ones related to the full FEM model; this result is a direct consequence of the adopted static condensation procedure, which allows to account for the actual flexural behavior in the out-of-plane direction for beams, together with torsional behavior of each floor. It is important to highlight that the response of the isolation system is not modeled by the stiffness matrix, since that contribution needs to be accounted for separately, especially for the hybrid simulation.

For both the hybrid test and the numerical simulation, the superstructure has been modeled through the definition of the aforementioned equivalent multi degree of freedom (MDOF) oscillator, with statically condensed mass and stiffness matrices. By adopting such matrices the actual dynamic properties of the overall structural systems are effectively reproduced, and approximately the same response of the full 3D FEM model can be obtained. Consequently, the dynamic system can be expressed as follows:

$$\overline{\overline{M}} \cdot \begin{pmatrix} \ddot{u}_0 \\ \ddot{u}_1 \\ \ddot{u}_2 \\ \ddot{u}_3 \end{pmatrix} + \overline{\overline{K}} \cdot \begin{pmatrix} u_0 \\ u_1 \\ u_2 \\ u_3 \end{pmatrix} + \langle F_{is} \rangle \cdot \begin{pmatrix} 1 \\ 0 \\ 0 \\ 0 \end{pmatrix} = -\overline{\overline{M}} \cdot \begin{pmatrix} 1 \\ 1 \\ 1 \\ 1 \end{pmatrix} \cdot \ddot{x}_g \quad (1)$$

Given:

- $\overline{\overline{M}}$  the condensed mass matrix of the system;
- $\overline{\overline{K}}$  the condensed stiffness matrix of the system;
- $u_i$  the translational degrees of freedom at the centre of mass location of the i-th floor;
- $\ddot{x}_g$  the considered ground acceleration time series;
- $\langle F_{is} \rangle$  the isolation force response.

A very low additional viscous damping has been considered for both simulations, namely 2%, modeled by means of the Rayleigh formulation, in order not to underestimate the overall response. The isolation system is considered separately in the dynamic system, and it is modeled as a single device, representative of the whole set of isolators. For the hybrid simulation, the isolation force is computed as a function of the force feedback of the Bearing Tester System, which is then scaled by the ratio between the total structural weight of the system and the applied vertical load to the device. On the other hand, in the numerical simulations, the following analytical expression can be adopted:

$$\langle F_{is} \rangle = W_{tot} \cdot \left( \frac{u_0}{R_{eq}} + k_\mu \cdot \mu \cdot f_{NF} \right) \quad (2)$$

Being:

- $W_{tot}$  the total structural weight of the system;
- $R_{eq}$  the equivalent radius of curvature of the device;
- $u_0$  the translational degree of freedom at the centre of mass location of the concrete slab (isolation level);
- $\mu$  the design friction coefficient;
- $f_{NF}$  a normalized frictional hysteretic parameter;
- $k_\mu = \mu / \mu_o$  a variation scale factor of the friction coefficient.



In order to model the frictional hysteretic response, a hysteretic parameter  $f_{NF}$  has been adopted, by assuming an elasto-plastic rule (Figure 3).

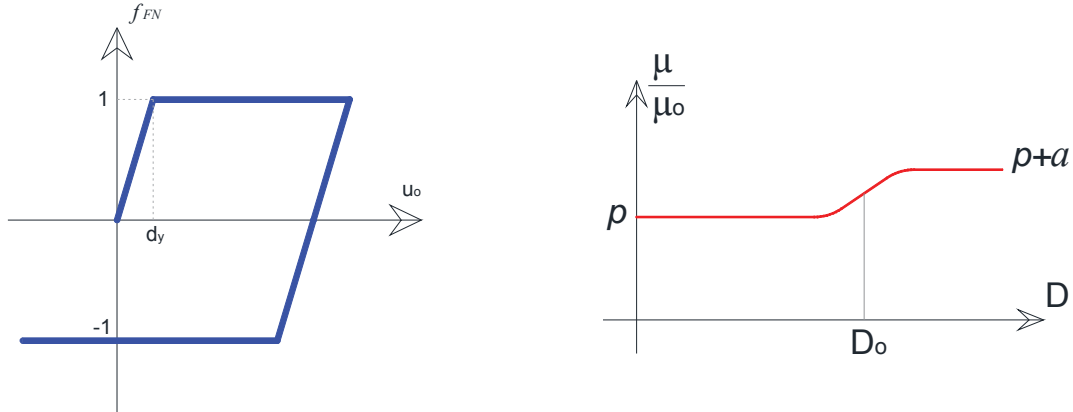


Figure 3: Analytical model of the frictional hysteretic (left) and extra-stroke (right) responses.

Since the overall system is supposed to be subjected to a severe seismic input, and consequently the design displacement of the isolation system is expected to be overcome, the extra-stroke behavior needs to be numerically modeled. Recent research works ([6], [8]) have shown good agreement between some experimental outcomes pseudo-dynamic tests in extra-stroke range for DCSS devices and possible numerical modeling strategies, namely:

- Analytical expression of the friction coefficient increase, for easy and fast structural assessments;
- An opensee link element for the extra-stroke response;
- An opensee link element, modeled for variable friction sliding isolators.

In this work the first strategy has been considered, by applying an analytical function, which increases the friction coefficient value, as the design displacement is exceeded. The increment of the friction coefficient in the extra-stroke range has been assumed equal to 50%.

## 5 SEISMIC INPUT

The input signal for both numerical and experimental hybrid simulations has been selected within the REXEL database ([11]), by checking the peak displacement of an equivalent Single Degree of Freedom (SDOF) system, with the non-linear hysteretic constitutive law of the implemented isolation system. The scale factor of the seismic event has been computed, aiming at obtaining a maximum displacement less than 350mm, which corresponds to the maximum displacement in the extra-stroke range considered in this study. A seismic event with a limited scale factor has been adopted, so that a realistic balance between amplitude and frequency content of the signal is ensured. Below the main characteristics of the selected earthquake are listed:

- Earthquake Name: *Gazli*
- Station ID: *KAR*
- Component: *x*

- Mw: 6.7
- Fault Mechanism: *reverse*
- Epicentral Distance [km]: 12.78
- Original PGA [g]: 0.717
- Scaled PGA [g]: 0.789
- Scale Factor [#]: 1.1

In Figure 4 graphical properties of the seismic event used for all the simulations are provided, in terms of time series of ground displacement and acceleration, together with the acceleration response spectrum at 5% damping.

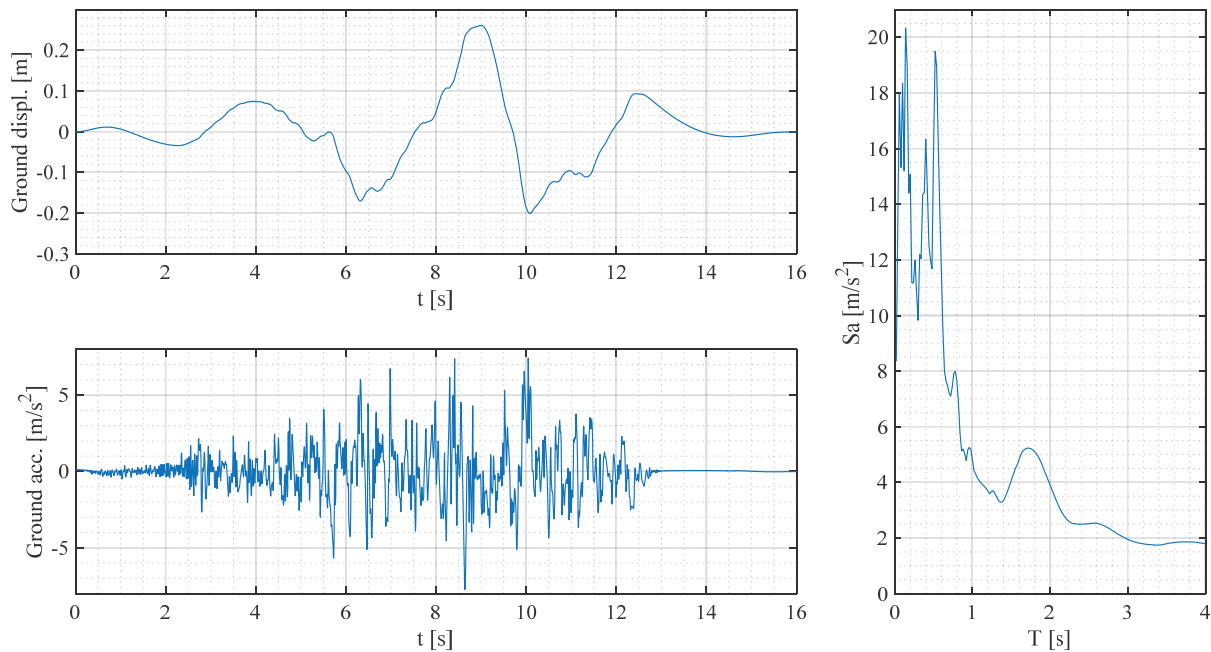


Figure 4: Characteristics of the adopted seismic event.

The resulting response spectrum show significantly high spectral coordinates at low periods, whereas more limited values can be noticed for high period values, much more related to the designed isolated system.

The hybrid simulation has been carried out by considering the superstructure as the aforementioned MDOF oscillator as a numerical substructure, whereas the full-scale device tested within the Bearing Tester System has been considered as the physical substructure, to carry out an earthquake simulation. To do so, within the hybrid simulation algorithm a time scale factor equal to 32 has been adopted.

## 6 RESULTS

Results of both numerical and experimental hybrid simulations are compared in this section, by focusing the attention on the isolation response, in terms of displacement demand and hysteretic behavior, and damage evidence at the implemented sliding pads has been checked after the test. In addition, the response of the superstructure has been analyzed, in order to assess if

the building has been subjected to excitations within the linear-elastic range. In Figure 5 the displacement time series of the isolation layer are compared, with respect to the design value.

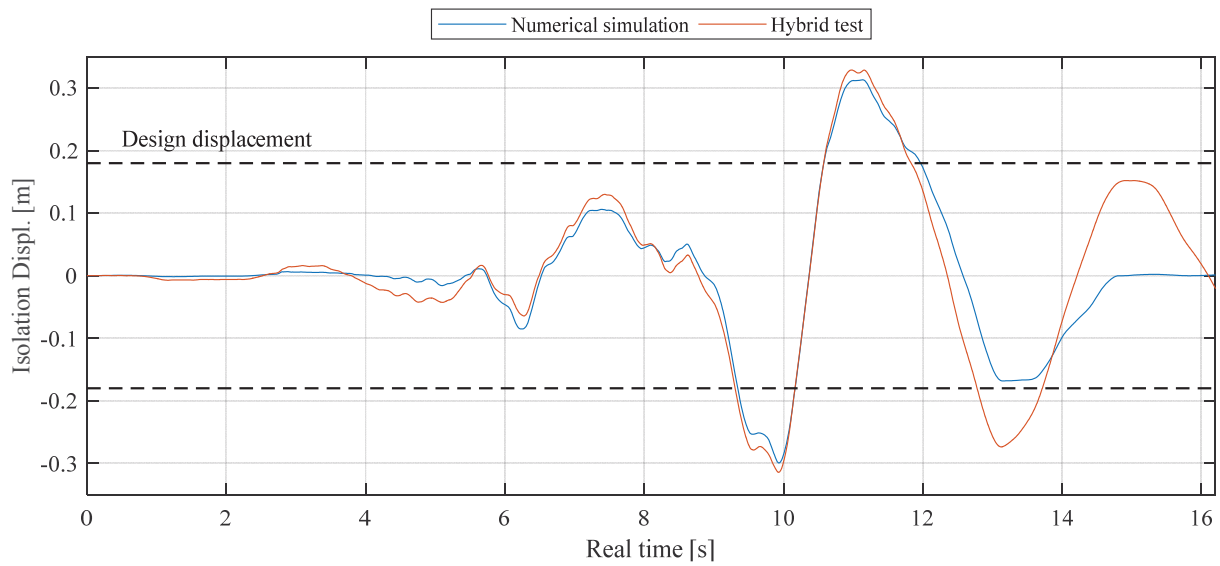


Figure 5: Isolation displacement response.

In Figure 6 the hysteretic response of the isolation system is provided, in terms of isolation force, normalized with respect to the total weight of the whole structural system.

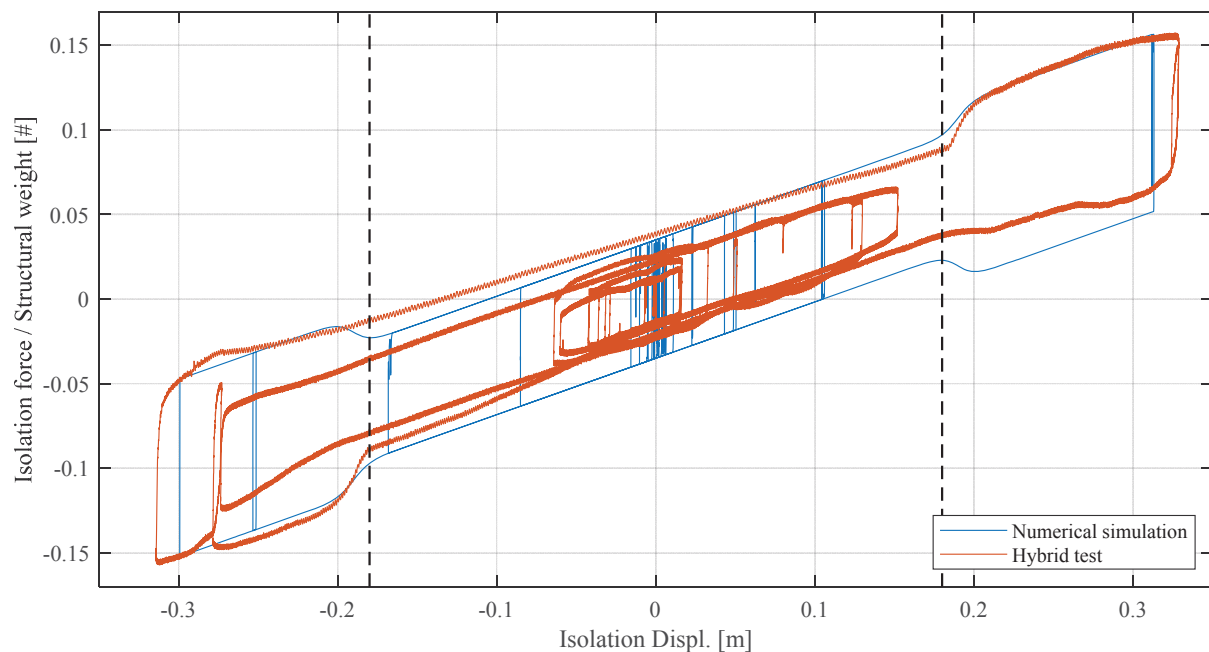


Figure 6: Isolation hysteretic behavior.

In Figure 7 the damage evidence at the sliding pad at the end of the experimental hybrid test are shown.



Figure 7: Damage evidence at the sliding pads.

In the hybrid simulation the full scale device has been subjected to displacement demands higher than the design value three times, at three consecutive peak displacement, under an approximately harmonic motion. The numerical simulation shown approximately an overlapped signal, exception made for the very last portion of the seismic event, where the design displacement is experimentally exceeded for the third time: at those time instants the numerical simulation returns lower displacement values, within the ordinary response of the isolator. The main reason of this final mismatching could be addressed to the degradation of the friction coefficient, which can be graphically noticed in the hysteretic response. Due to the subsequent extra-stroke displacement demands, significant damage occurs at the sliding interfaces, and this results into an increased pressure (caused by detachments of sliding material) and to a continuously decreasing friction coefficient. The degradation of the frictional properties finally leads to higher displacement demands, in comparison to the purely numerical model, which accounts for a constant friction coefficient. Nonetheless, for almost the whole duration of the simulation, the numerical model provides approximately overlapped signals, from both displacement and hysteretic responses, with a good estimate of the peak parameters. The increase of the friction coefficient modeled in the numerical simulation (+50%) due to the extra-stroke behavior fairly capture the experimental response of the full device in the hybrid test. Thus, results for the isolation system seems to suggest that the frictional properties may be influenced by the extra-stroke behavior, depending on the number of subsequent displacement demands exceeding the design value and, consequently, on the entity of the cumulative damage at the sliding pad.

Finally, in Figure 8 the building response is shown.

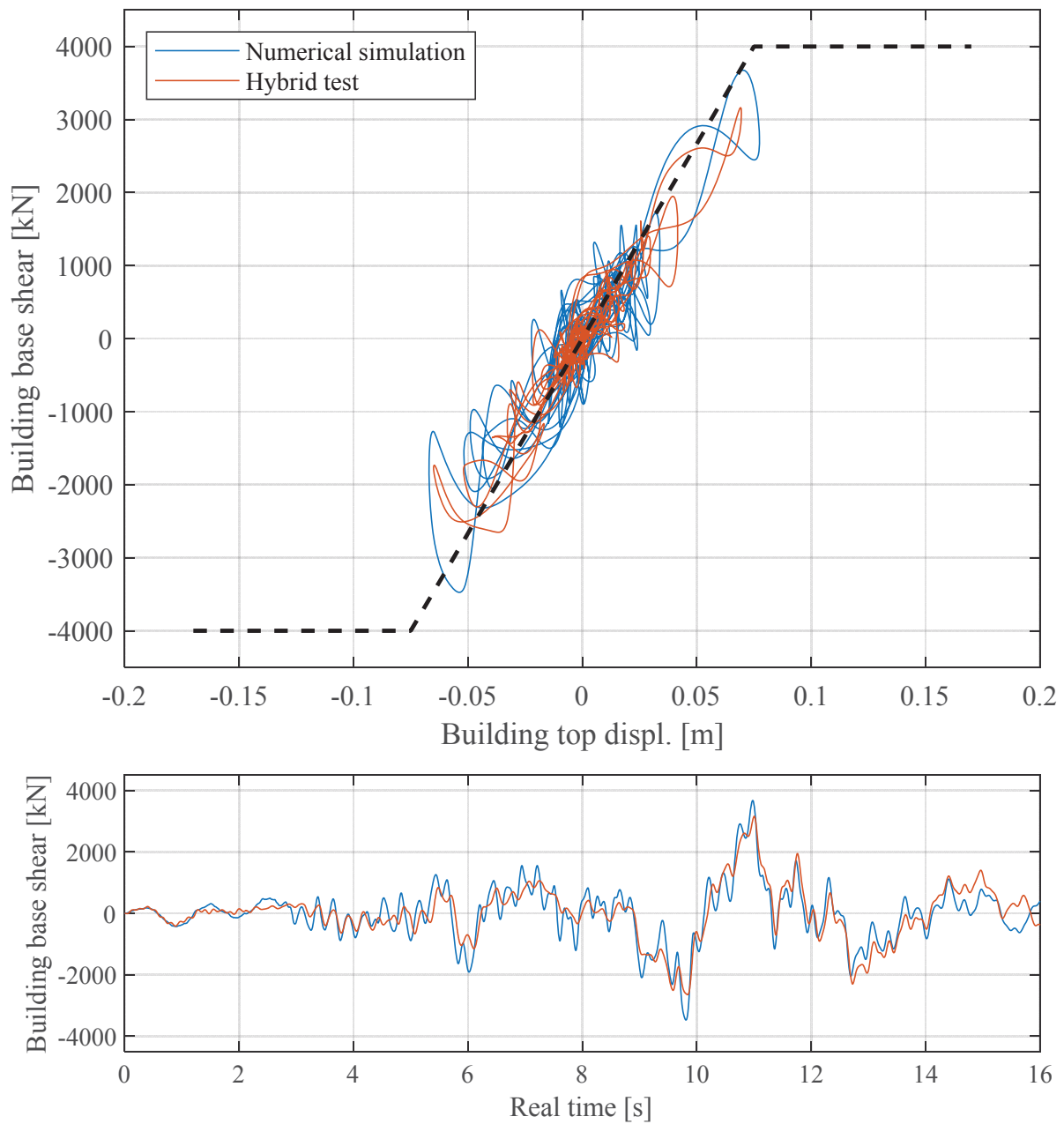


Figure 8: Building base shear response.

The building base shear response seems not to be significantly influenced by extra-stroke displacement demands at the isolation system, mainly because of the smooth increase of the friction coefficient which occurs, when the design displacement is overcome, according to the technology of devices under investigation. In addition, for the whole duration of the simulations, the building response is within the linear-elastic range, and confirm that the modeling assumptions of the MDOF system of the superstructure is fairly good for the considered system. The numerical simulation returns a slightly higher response in comparison to the experimental hybrid test, even though signals are very close one to each other.



## 7 CONCLUSIONS

In this work the response of a base isolated case study structure has been assessed, through a numerical simulation, by assuming an extreme seismic event. Specifically, the system has been subjected to an ad hoc selected earthquake, in order to overcome the design displacement at the isolation layer. The obtained results have been compared to the outcomes of a corresponding experimental hybrid test, in which the superstructure model represents the numerical substructure, whereas as a physical substructure a full-scale device has been tested within the Bearing Tester System of the Laboratory of EUCENTRE Foundation in Pavia (Italy). In the numerical simulation the extra-stroke behavior has been modeled by means of a specific function, which increases the friction coefficient, as the design displacement is overcome.

By analyzing both the experimental and numerical results, the following findings can be found:

- The numerical model can fairly represent the effective experimental hysteretic behavior of the physical device, when subjected to extra-design displacement demands;
- The displacement time series at the isolation level returned by the numerical simulation is approximately overlapped, in comparison to the outcomes of the hybrid test, exception made for the last phase of the event;
- Toward the end of the earthquake simulation, the numerical model underestimates the displacement response, with displacements within the ordinary stroke of the device, in comparison to the hybrid test, which show an additional extra-design displacement at the same time instants;
- The main reason for possible mismatching at the end of the seismic event could be addressed to the cumulative damage which develops at the implemented sliding pads: due to an increase of the contact pressure the friction coefficient value decreases, and consequently larger displacement demands can be found, in comparison to the numerical simulation which accounts for a constant friction coefficient in the ordinary response;
- Thus, subsequent extra-design displacement demands could lead to excessive cumulative damage, which may imply degradations of the frictional properties;
- The extra-stroke behavior seems to have negligible effects on the building response, in terms of base shear and top displacement signals.

Further experimental investigations are needed on the topic, in order to highlight eventual dependencies of the extra-stroke behavior on the common response parameters considered to characterize sliding isolators, such as sliding velocity and vertical load.

## ACKNOWLEDGMENTS

Part of the current work has been carried out under the financial support Italian Civil Protection, within the framework of the Executive Project DPC-EUCENTRE 2018 (Project 3 – Assessment of the seismic isolation of buildings through hybrid experimental/numerical simulations) and ReLUIS project 2019-2021 (WP15, Task 15.1).

## REFERENCES

- [1] Castaldo, P., Palazzo, B., Ferrentino, T. (2017) Seismic reliability-based ductility demand evaluation for inelastic base-isolated structures with friction pendulum devices, *Earthquake Engineering and Structural Dynamics*, **46**(8), 1245-1266
- [2] Castaldo, P., Palazzo, B., Alfano, G., Palumbo, M.F. (2018) Seismic reliability-based ductility demand for hardening and softening structures isolated by friction pendulum bearings, *Structural Control and Health Monitoring*, **25**(11), e2256
- [3] De Domenico D., Ricciardi G., Benzoni G. (2018) Analytical and finite element investigation on the thermo-mechanical coupled response of friction isolators under bidirectional excitation, *Soil Dynamics and Earthquake Engineering*, **106**, 131-147.
- [4] Dolce M, Cardone D, Croatto F (2005) Frictional behavior of steel-PTFE interfaces for seismic isolation. *Bulletin of Earthquake Engineering*, **3**, 75–99.
- [5] Fenz D, Constantinou MC, Behaviour of the double concave friction pendulum bearing. *Earthquake Engineering And Structural Dynamics*, **35**,1403–1424, 2006.
- [6] Furinghetti M., Yang T., Calvi P.M., Pavese A. (2021) Experimental evaluation of extra-stroke displacement capacity for curved surface slider devices. *Soil Dynamics and Earthquake Engineering*, <https://doi.org/10.1016/j.soildyn.2021.106752>.
- [7] Peng Y., Ma Y., Huang T., De Domenico D (2021) Reliability-based design optimization of adaptive sliding base isolation system for improving seismic performance of structures, *Reliability Engineering & System Safety*, DOI: <https://doi.org/10.1016/j.res.2020.107167>.
- [8] Ponzo F.C., Di Cesare A., Telesca A., Pavese A., Furinghetti M. (2021) Advanced Modelling and Risk Analysis of RC Buildings with Sliding Isolation Systems Designed by the Italian Seismic Code. *Applied Sciences*, <https://doi.org/10.3390/app11041938>.
- [9] Furinghetti M., Lanese I., Pavese A. (2020) Experimental assessment of the seismic response of a base isolated building through hybrid simulation technique, *Frontiers in Built Environment*, DOI: 10.3389/fbuil.2020.00033.
- [10] Furinghetti M, Pavese A, Quaglini V, Dubini P (2019) Experimental Investigation Of The Cyclic Response Of Double Curved Surface Sliders Subjected To Radial And Bidirectional Sliding Motions. *Soil Dynamics and Earthquake Engineering*, DOI: <https://doi.org/10.1016/j.soildyn.2018.11.020>.
- [11] Iervolino I, Galasso C, Cosenza E (2009), REXEL: computer aided record selection for code-based seismic structural analysis. *Bulletin of Earthquake Engineering*, DOI: 10.1007/s10518-009-9146-1.
- [12] Kumar M, Whittaker AS, Constantinou MC (2015) Characterizing friction in sliding isolation bearings. *Earthquake Engineering and Structural Dynamics*, **44**,1409–1425.
- [13] Lomiento G, Bonessio N, Benzoni G, Concave sliding isolator's performance under multi-directional excitation. *Ingegneria Sismica*, **30**:3,17-32, 2013.
- [14] Mazza F, Mazza M (2017) Sensitivity to modelling and design of curved surface sliding bearings in the nonlinear seismic analysis of base-isolated r.c. framed buildings. *Soil Dynamics and Earthquake Engineering*, **79**, 951-970.

- [15] Seismosoft. SeismoStruct 2016 – A computer program for static and dynamic nonlinear analysis of framed structures. 2016, available from <http://www.seismosoft.com>.
- [16] Tsiavos A, Sextos A, Stavridis A, Dietz M, Dihoru L, Nicholas A. (2020) Large-scale experimental investigation of a low-cost PVC ‘sand-wich’ (PVC-s) seismic isolation for developing countries. *Earthquake Spectra* **36**(4),1886-911.

## ASSESSMENT OF THE SHEAR PROPERTIES OF HDRBS UNDER DIFFERENT COMPRESSION LEVELS

E. Bruschi<sup>1</sup>, E. Gandelli<sup>1</sup>, C. Pettorosso<sup>1</sup>, and V. Quaglini<sup>1</sup>

<sup>1</sup>Department Architecture, Built Environment and Construction Engineering, Politecnico di Milano,  
Piazza Leonardo da Vinci 32, 20133 Milan, Italy  
{eleonora.bruschi, emanuele.gandelli, carlo.pettorosso, virginio.quaglini}@polimi.it

---

### Abstract

*Despite it is well known that the shear properties of High Damping Rubber Bearings (HDRBs) are affected by the instantaneous compression load developed during the seismic ground motion, only permissible variations of their design properties with frequency, temperature and ageing are prescribed in the standards while the influence of the compression level is usually disregarded.*

*Within this framework, this research addresses this drawback through both experimental and numerical investigations. In the first part of the study, small scale laminated isolators are tested on a custom biaxial machine in order to assess the secant modulus, and damping factor of the elastomeric compound under different compression levels. In the second part, the same phenomenon is investigated through cyclic shear tests on full scale HDRBs under three different levels of axial load. In the last part, a 3D finite element model of the isolator is eventually formulated in Abaqus FEM software. The mechanical response of the elastomer is simulated by means of a hyperelastic strain energy function combined with a relaxation function.*

*The experimental results highlight the substantial influence of the axial load on the damping capacity of the elastomer, while the shear modulus is less affected. The numerical analyses demonstrate that the vertical – horizontal coupled response of HDRBs can be accurately predicted, within the proposed formulation, with constitutive parameters estimated from simple uniaxial tests.*

**Keywords:** High Damping Rubber Bearings, shear modulus, equivalent viscous damping, axial load, experiments, numerical model.

---

## 1 INTRODUCTION

Base isolation is today a viable solution to mitigate the effects of earthquakes on constructions. The design of the base isolation hardware necessary to implement such strategy, such as elastomeric isolators and sliding bearings, has been developed in the past decades by many researchers and is today regulated by standards.

Rubber bearings have been used as seismic isolators since the mid of the '70s [1]. Today the most popular types of rubber isolators are the High Damping Rubber Bearings (HDRBs) and the Lead Rubber Bearings (LRBs). The mechanical characteristics of HDRBs affecting their performance as seismic isolators, namely stiffness and damping, depend only on the mechanical properties of the rubber compound. On the contrary, in LRBs the elastomer is required to provide the horizontal stiffness to the isolation system as well as a certain restoring capability, while the damping capacity relies on the hysteretic deformation of the lead core. A large variety of elastomeric compounds based on either natural or synthetic rubber is nowadays available for HDRBs and LRBs, with different damping, shear modulus, and vulcanization profile, according to proprietary techniques developed by the manufacturers.

An accurate characterization of the mechanical properties of the elastomer is fundamental for the design of HDRBs and LRBs. Nevertheless, despite of the large diffusion of these devices, some shaded areas still exist that need further investigation. One issue is the dependency of the mechanical properties on the environment [2]. To date, a large part of the studies on the behaviour of rubber for bridge bearings focused on their ageing deterioration [3]. However, the mechanical properties of elastomers can change due to a number of factors other than ageing, such as the strain amplitude, the frequency of loading, the number of cycles, and air temperature variations, and the response of a structure seismically isolated with rubber bearings can be strongly influenced by each of the above parameters [4].

According to the European Standard on anti-seismic devices [5], two sets of design properties must be determined for elastomeric isolators, the Upper Bound Design Properties (UBDP) leading to the maximum forces in the superstructure, and the Lower Bound Design Properties (LBDP) leading to the maximum displacements of the isolation system. Both UBDP and LBDP should be derived from tests performed on full scale devices, but for HDRBs the Standard allows to determine the effects of temperature, frequency and ageing by testing rubber specimens under pure shear, instead of full isolators, as it is acknowledged that the cyclic behaviour of steel reinforced rubber bearings is primarily governed by the mechanical properties of rubber [6]. An important factor that is generally ignored when testing rubber specimens is the influence of the compression stress on the shear properties of the elastomer, which was instead demonstrated to have a fundamental importance and needs to be taken into account for a correct understanding of the behaviour of HDRBs under service conditions [7].

One of the first studies addressing this topic was published by Aiken [8], who tested HDRBs with shape factors (ratio of load area to stress-free area of a single rubber layer) of 8.75 and 20 and design axial stresses of 3.2 and 5.1 MPa, respectively. The bearings were tested at several levels of compression stress, from 0 to 10 MPa for the first geometry and from 0 to 15 MPa for the second geometry, and the results showed an increase of both shear stiffness and damping with the compression load. Kelly [9] evaluated the performance of a rubber isolator characterized by nominal shear modulus of 0.86 MPa, damping of 15% and shape factor of 30. The compression stress was increased from 0 to 10.34 MPa, and the tests showed a negligible influence on the shear stiffness, while the damping increased from 13% to 17% (relative change of 30%).

Mori [10] tested five isolators differing for geometry and rubber mixture. When the axial load was small in comparison with the design value (say 34%), then the shear hysteresis loop



was a different shape from that one under the high applied axial load. Also, the area of the hysteresis loops became larger (i.e. damping increased) as the axial load was increased. On the contrary the influence of the axial load within the range between 0.68 and 1.25 times the design value on the shear stiffness was negligible. Iizuka [11] tested laminated elastomeric bearings with shape factor 20 under four different levels of compression (0; 4.90; 9.81; 19.60 MPa) up to 500% shear strain. The study confirmed the influence of the axial load on the nonlinear large-deformation shear behaviour of rubber, resulting in strain-hardening in the shear direction under small axial forces, but decrease in horizontal stiffness under large axial forces probably due to buckling of the rubber layers. Ryan [12] studied the behaviour of HDRBs with design axial stress of 3.2 MPa and shape factor of 8.27 and 20 respectively, subjected to the combined action of compression and shear force, concluding that in the range 0 to 10 MPa the shear stiffness of HDRBs decreases with increasing of the axial load.

From the review of the above literature it is clear that, though the influence of the axial load on the shear properties of HDRBs is a fact, the sensitivity of the individual bearing can vary significantly depending on the type and amount of fillers and by the amount of cross-linking of the mixture [13].

The paper presents some approaches for investigating the influence of the axial load on the shear properties of HDRBs from both an experimental and a numerical perspective. All the studies are performed on the same natural rubber compound. In the first part of the study, small scale prototypes of HDRBs are tested under varying axial load in the range of 0.5 to about 21 MPa, whereas in the second part the tests are performed on real scale isolators, and some experimental issues are put in evidence. Eventually, a numerical analysis is performed by using as case study the elastomeric isolator tested at full scale.

## 2 SMALL SCALE PROTOTYPES

### 2.1 Test pieces

Small circular test pieces (Fig. 1), with diameter  $D = 80$  mm, are used. Every piece includes 10 rubber layers, 4 mm in thickness each, alternated to 2 mm thick steel plates. The upper and the lower rubber layers are vulcanized to two thick (10 mm) steel plates that fit recessing holes in the plates of the testing machine. The test pieces are made of commercial rubber compound, categorized as “Normal” (hardness between 55 and 65 International Rubber Hardness Degree (IRHD)), with shear modulus  $G = 0.75$  MPa and equivalent viscous damping factor  $\xi = 12\%$ . The total thickness of rubber, which is the parameter that governs the maximum shear displacement, is 40 mm, while the primary and the secondary shape factors are  $S_1 = 5$  and  $S_2 = 2$ , respectively.  $S_1$  is defined as the ratio of the compressed area of the rubber layer divided by the area of lateral surface free to bulge, while  $S_2$  is the aspect ratio, i.e. the bearing diameter divided by the total rubber thickness [14].



Figure 1: Small scale HDRB test piece: picture of a specimen (left), and cross-section (right).

## 2.2 Test set-up

The biaxial testing system is illustrated in Fig. 2-left. The system consists of a stiff four columns steel frame equipped with two servo-hydraulic jacks. The vertical jack, rated 500 kN, applies the compressive load to the test piece, while the horizontal jack, rated 100 kN and with a 100 mm stroke, drives a shear plate that moves horizontally. The system permits to test simultaneously a pair of test pieces, placed symmetrically with respect to the shear plate in a double shear configuration (Fig. 2-right).

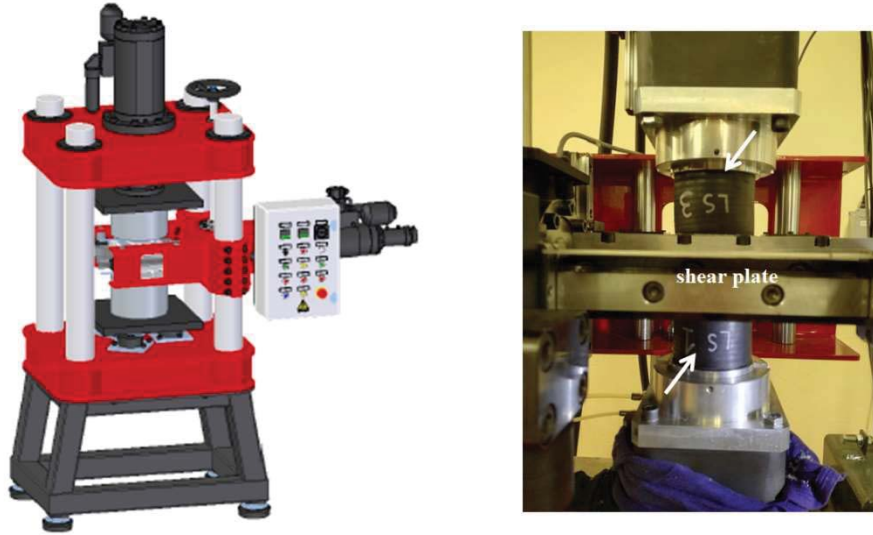


Figure 2: Schematic view of the biaxial test set-up (left), and test pieces in double shear configuration (right).

## 2.3 Test procedure

The sequence of tests performed on the pair of HDRB test pieces is outlined in Table 1. By adjusting the vertical load, the compression stress  $p$  is varied from a minimum value of 0.1 MPa to a maximum value of 24 MPa, with 3 MPa increments up to 12 MPa, and 6 MPa increments above 12 MPa. At each stress level, five full cycles of horizontal displacement are imposed with sinusoidal waveform, frequency  $f = 0.5$  Hz and amplitude 40 mm, resulting in a shear strain amplitude  $\gamma_a = 100\%$ . The sequence of tests is carried out in order of increasing vertical loads, with a dwell time of 30 minutes between any pair of tests in order to allow the viscoelastic recovery of the rubber. The tests are performed at a room temperature of  $19 \pm 2^\circ\text{C}$ .

$p$ (MPa)	$\gamma_a$ (%)	$f$ (Hz)	cycles
0.1 – 3 – 6 – 9	100	0.5	5
– 12 – 18 – 24			

Table 1: Test protocol for small scale HDRB test pieces.

## 2.4 Results

Fig. 3 illustrates the hysteretic shear force–displacement curves obtained at different levels of pressure ; in the diagrams, only the curve relevant at the third cycle is reported for each stress level. It is evident the large difference in shape between the curve at 0.1 MPa (i.e. virtually

without axial load), and the curves relevant to tests at  $p \geq 3$  MPa, with a substantial increase of the dissipated energy (i.e., the area enclosed in the loop).

From the horizontal force  $F$  and the horizontal deflection  $d$  of the single specimen, the shear stress  $\tau$  and shear strain  $\gamma$  of rubber are calculated as follows:

$$\tau = \frac{F}{A} \quad (1)$$

$$\gamma = \frac{d}{t_e} \quad (2)$$

where  $A$  is the area of the plan section of a rubber layer parallel to the direction of shear, and  $t_e$  is the total thickness of rubber subjected to shear. From the hysteretic shear stress–strain diagram, the secant shear modulus  $G$  and the equivalent viscous damping factor  $\xi$  are then calculated at each cycle:

$$G = \frac{\tau_2 - \tau_1}{2 \cdot \gamma_a} \quad (3)$$

$$\xi = \frac{EDC}{2\pi \cdot G \gamma_a^2} \quad (4)$$

where  $\tau_1$  and  $\tau_2$  are the stresses at the maximum shear deflections in either direction,  $EDC$  is the energy dissipated per cycle and  $\gamma_a = 1$  is the shear strain amplitude.

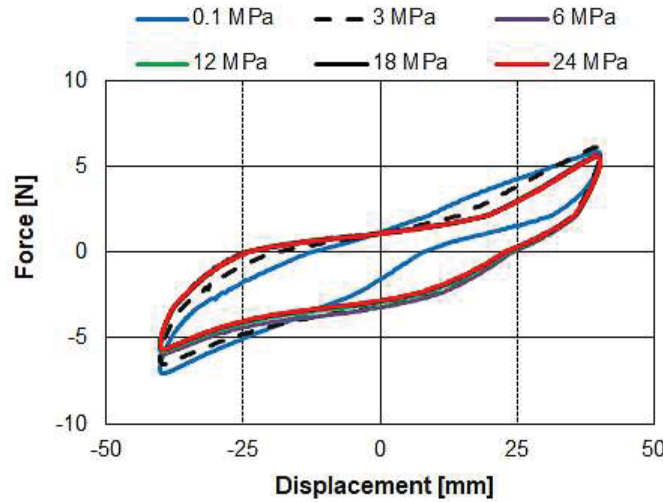


Figure 3: Shear force – displacement loops at different pressure levels.

Fig. 4 plots the change of  $G$  and  $\xi$  as a function of the compression stress  $p$ . The secant modulus has a 10% decrease when  $p$  rises from 3 MPa to 6 MPa, and holds constant for higher pressure levels. The equivalent viscous damping factor has a 38% increase when  $p$  is increased from 0.1 MPa to 3 MPa, and a further 10% increase at  $p = 6$  MPa, and then it holds substantially stable up to  $p = 24$  MPa.

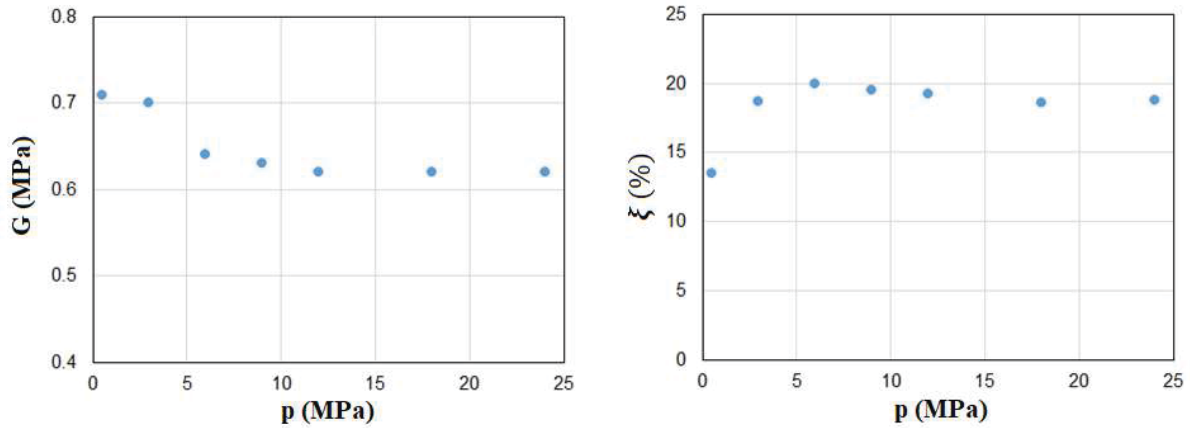


Figure 4: Influence of the compression stress on secant shear modulus (left) and equivalent viscous damping factor (right); values are determined at the third cycle.

### 3 FULL SCALE ISOLATORS

#### 3.1 Test pieces

The tests pieces are two HDRBs designed for an axial load  $N_{sd} = 1150$  kN and a seismic displacement  $d_{bd} = 250$  mm. The devices are circular in shape, with a diameter of 500 mm and a total thickness of 218 mm. Each HDRB consists of 14 rubber layers, 9 mm thick each, alternated with 13 steel plates, 4 mm thick, and 2 end plates of 20 mm thickness. The primary and the secondary shape factors are  $S_1 = 18.9$  and  $S_2 = 2$ , respectively. A sketch of the cross section of the isolator is shown in Fig. 5. The raw material is the same rubber compound used to manufacture the small scale test pieces.

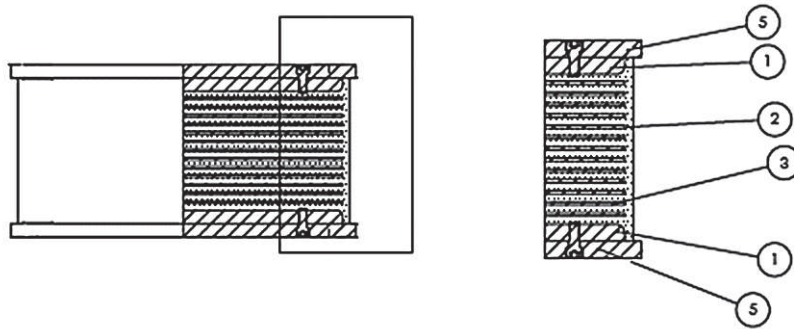


Figure 5: Sketch of the HDRD specimen, and cross-section details.

#### 3.2 Test set-up

The tests were performed at the Laboratory for Testing of Materials and Structures (SisLaB) at the University of Basilicata, using a custom bearing tester system (Fig. 6). The facility has load capacity of 8000 kN in the vertical direction and 1000 kN in the horizontal direction, and a displacement capacity of 1000 mm. The system incorporates a plate supported by low-friction bearings which moves in the horizontal direction, and allows to apply a shear force to the isolator. A single device can be tested each time.



Figure 6: The bearing tester system at University of Basilicata.

### 3.3 Test procedure

The sequence of tests performed on the HDRB isolators is illustrated in Table 2. The devices are tested at 0.45, 1.0 and 2.0 times the design axial load  $N_{sd}$ , which correspond to a compressive stress on rubber of 2.63, 5.85 and 11.70 MPa respectively. At each load level, three sinusoidal cycles are performed to a maximum displacement  $d_{bd} = 250$  mm, corresponding to a shear strain amplitude  $\gamma_a = 198\%$ , at a frequency  $f = 0.5$  Hz. The dwell time between two tests is of about 20 minutes. All tests are performed at room temperature.

$N$ (kN)	$d_{bd}$ (mm)	$f$ (Hz)	cycles
1150	250	0.5	3
530	250	0.5	3
2300	250	0.5	3

Table 2: Test protocol for HDRB isolators ( $N$ : axial load;  $d_{bd}$ : displacement amplitude).

### 3.4 Results

Fig. 7 illustrates the variation of the effective stiffness  $k_{eff}$ , evaluated at the maximum shear deflection, and the equivalent viscous damping factor  $\xi$  with the axial load. The shear stiffness at  $N_{sd}$  is found to decrease by 9% when the axial load is halved, and to decrease by 14% when the axial load is increased by a factor of 2. This behaviour, which is inconsistent with the findings of the small scale test, may be ascribed to the insufficient duration of the dwell time between the first and the second tests, at 1150 kN and 530 kN respectively, which could be too short to permit complete cooling of the isolator. Since the modulus of rubber decreases with increasing of temperature, this can explain the unexpected decay of stiffness at 0.45  $N_{sd}$ . The equivalent viscous damping factor has a more regular behaviour, with a negligible change when the design load is halved, and a 25% increase on average when the design load is increased by a factor of 2.

The secant modulus of the rubber can be calculated from the effective stiffness of the isolator. For a compressive stress of 5.85 MPa, corresponding to  $N_{sd}$ , the value of the secant



modulus derived from the tests on isolators counts  $G = 0.87$  MPa, which is 25% higher than the value ( $G = 0.7$  MPa) determined in the small scale tests; similarly, the equivalent viscous factor of the isolator is about 50% less than the relevant figure assessed on the small scale pieces (10.4% against 20%).

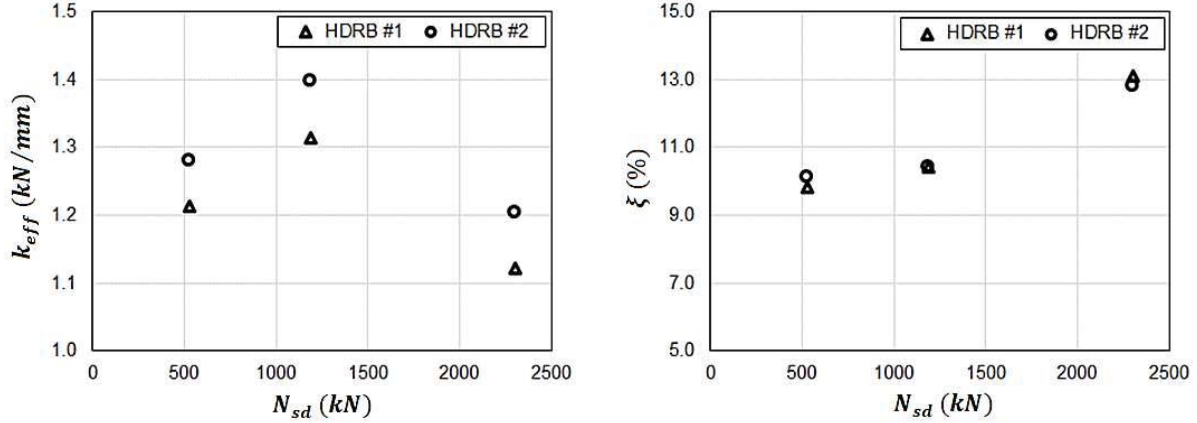


Figure 7: Influence of axial load on effective stiffness (left), and equivalent viscous damping factor (right) of full scale HDRBs; values determined at the third cycle.

## 4 FINITE ELEMENT INVESTIGATION

### 4.1 Numerical formulation

A 3D finite element model of the HDRB isolator shown in Fig. 5 has been formulated in the software program Abaqus. Taking advantage from the symmetry of the device, only half of the isolator has been modelled (Fig. 8). The size of the mesh of finite elements for the rubber layers is  $10 \times 4.5$  mm. The mechanical behaviour of the elastomer has been described by using a hyperelastic constitutive law [15] to represent the force-displacement relationship, and an exponential Prony series to represent the viscous behaviour. Model parameters have been calibrated based on experimental data obtained from uniaxial tensile tests and stress relaxation tests on rubber specimens (Fig. 9), according to the procedure described by [16]. Numerical analyses have been performed by simulating the application of an axial load on the isolator, and a concurrent displacement in the horizontal direction. The horizontal displacement is applied according to a sinusoidal waveform, with amplitude  $d_{bd} = 250$  mm and frequency  $f = 0.5$  Hz. Simulations have been performed for three values of axial load, namely  $N = 530$  kN,  $N = 1150$  kN, and  $N = 2300$  kN, with 3 cycles per load level.

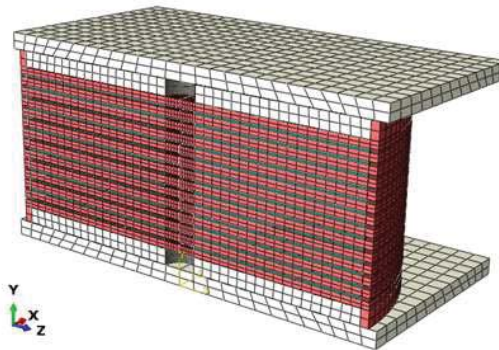


Figure 8: 3D finite element model of the HDRB isolator.

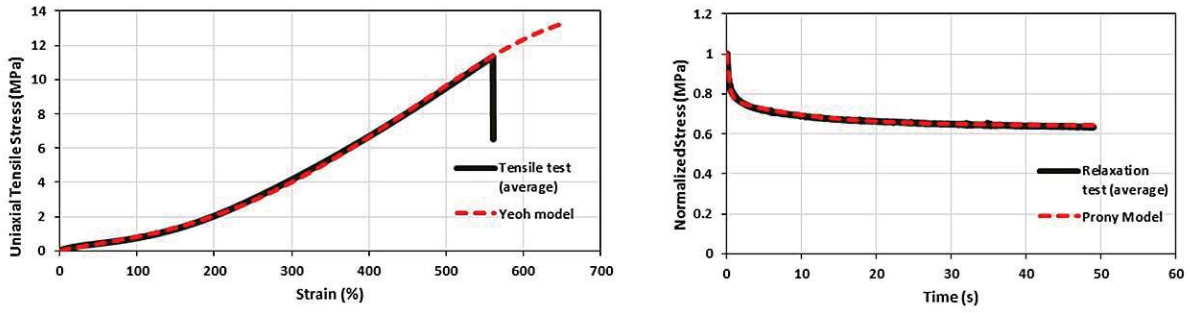


Figure 9: Calibration of elastomer constitutive parameters implemented in the finite element model of HDRB: hyperelastic Yeoh model (left), and Prony series (right).

## 4.2 Results

Fig. 10 compares the horizontal force – displacement curves predicted by the numerical code to the experimental curves obtained in the tests on full scale HDRBs. By considering the third cycle of loading, the agreement is fair for both the tests at  $N = 1150$  kN and  $N = 530$  kN, while at  $N = 2230$  kN the numerical model is capable to correctly reproduce the loading branch of the curve, but underestimates the actual damping and the dissipation capability of the isolator.

The effective stiffness and equivalent viscous damping factor calculated in the numerical analyses are eventually compared to the experimental values in Table 3. The numerical model calculates a decrease in stiffness when the axial load is increased from  $N_{sd}$  to  $2 N_{sd}$ , but  $k_{eff}$  does not change substantially when the axial load is reduced to  $0.5 N_{sd}$ . The accuracy of the numerical prediction is good as concern the stiffness (8% deviation at  $2 N_{sd}$ ), but the model underestimates the actual damping capacity of the isolators and is not able to capture the increase in viscous damping when  $N$  passes from  $N_{sd}$  to  $2 N_{sd}$  (30% deviation).

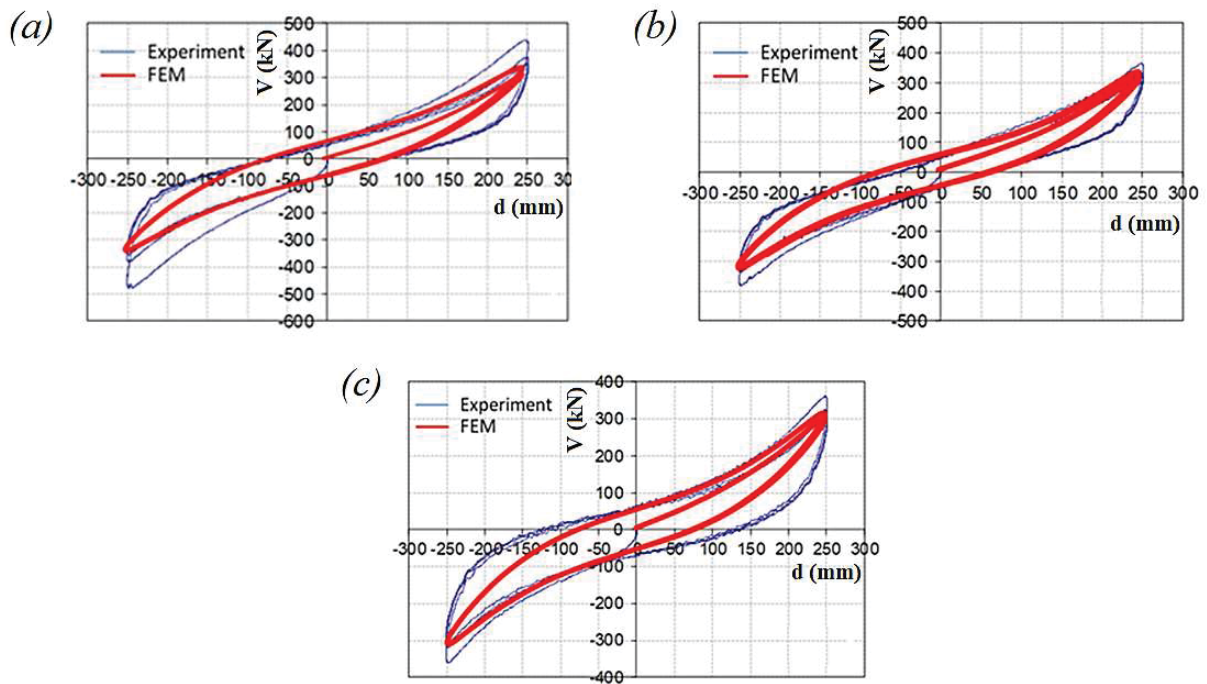


Figure 10: Comparison between experimental and numerical (FEM) force – displacement curves of the HDRB isolator at different levels of axial load: (a)  $N = 1150$  kN; (b)  $N = 530$  kN; (c)  $N = 2300$  kN.

$N$ (kN)	$k_{eff}$ (kN/mm)		$\xi$ (%)	
	EXP	FEM	EXP	FEM
1150	1.36	1.36	10.40	9.17
530	1.25	1.32	9.95	8.33
2300	1.16	1.26	12.95	9.03

Table 3: Experimental (EXP) and numerical (FEM) values of effective stiffness and equivalent viscous damping factor at different levels of axial load.

## 5 DISCUSSION

The study presents three different approaches to investigate the influence of the axial load on the properties in shear of HDRBs.

Experiments on small scale test pieces are rather cheap; indeed, the specimens are small and easy to manufacture, and a wide range of combinations of axial load and horizontal displacement can be tested at an affordable cost. Owing to the small size of the specimens, heating of the elastomer is expected to be small. Consistent results were obtained in the test campaign illustrated in this paper. However scaling effect may limit the accuracy of the extrapolation of the results to the real scale.

Tests on full scale isolators are expensive because require dedicated facilities and because the specimens are large and bulky. Moreover, heating of the isolator and its effect on the shear response may be not negligible in tests involving large energy inputs. Therefore in designing the experimental protocol an appropriate dwell time after each test must be envisaged in order to allow cooling of the specimens. However, since the tests are performed at the real scale, the results can be directly transferred to the application.

Numerical analyses allow to investigate many loading scenarios at a very limited cost, but the numerical model needs to be validated against experimental data to provide reliable results. Whereas accurate hyperelastic models are available to capture the actual stress – strain relationship of standard rubber, the viscous behavior of elastomeric compounds has not yet been effectively implemented into numerical codes.

## 6 CONCLUSIONS

The characterization of the effects of the axial load on the properties in shear of HDRBs is fundamental for developing accurate analyses and design of base isolation systems.

Examples of experimental and numerical approaches to investigate this subject have been presented in the paper. Whereas testing of small scale pieces is convenient at the stage of development and characterization of new rubber compounds, numerical analyses and testing of full scale isolators are most indicated at the final stage of design and validation of isolators for the real application.

Both small scale and large scale tests evidence that the axial load has a more substantial influence on the equivalent viscous damping than on the shear modulus of the elastomer. The numerical analyses demonstrate that the vertical – horizontal coupling of HDRBs can be deducted with a sufficient reliability from the characteristics of the elastomer measured in simple uniaxial tests, though more consistent models for viscous damping need to be formulated.

## REFERENCES

- [1] F. Naeim, J.M. Kelly, *Design of Seismic Isolated Structures*, Wiley, 1999.
- [2] M.C. Constantinou, A.S. Whittaker, Y. Kalpakidis, D.M. Fenz, G.P. Warn, Performance of Seismic Isolation Hardware under Service and Seismic Loading. *Technical Report MCEER-07-0012*, 2007.
- [3] Y. Itoh, H. Gu, K. Satoh, Y. Yamamoto, Experimental investigation on ageing behaviors of rubbers used for bridge bearings. *Structural Engineering / Earthquake Engineering*, JSCE, 23(1), 17s-31s, 2006.
- [4] A.C.T. Thompson, A.S. Whittaker, G.L. Fenves, S.A. Mahin, Property modification factors for elastomeric seismic isolation bearings. *The 14<sup>th</sup> World Conference on Earthquake Engineering (WCEE)*, October 12-17, Beijing, China, 2000.
- [5] CEN (European Committee for Standardisation), *EN15129 - Anti-seismic Devices*, 2009.
- [6] D. Cardone, G. Gesualdi, D. Nigro, Effects of air temperature on the cyclic behavior of elastomeric seismic isolators. *Bulletin of Earthquake Engineering*, 9(4), 1227-1255, 2011.
- [7] V. Quaglini, P. Dubini, G. Vazzana, Experimental assessment of High Damping Rubber under combined compression and shear. *ASME Journal of Engineering Materials and Technology*, 138, 0110021-9, 2016.
- [8] I.D. Aiken, J.M. Kelly, P.W. Clark, K. Tamura, M. Kikuchi, T. Itoh, Experimental studies of the mechanical characteristics of three types of seismic isolation bearings. *10<sup>th</sup> World Conference on Earthquake Engineering (WCEE)*. July 19-24, Madrid, Spain, 1992.
- [9] J.M. Kelly, *Earthquake-resistant design with rubber*, Springer-Verlag, London, UK, 1993.
- [10] T. Mori, P.J. Moss, N. Cooke, A.J. Carr, The Behavior Of Bearings Used For Seismic Isolators Under Shear And Axial Load. *Earthquake Spectra*, 15(2), 199-224, 1999.
- [11] M. Iizuka, A Macroscopic Model For Predicting Large-Deformation Behaviors Of Laminated Rubber Bearings. *Engineering Structures*, 22(4), 323-334, 2000.
- [12] K.L. Ryan, J.M. Kelly, A.K. Chopra, Experimental observation of axial load effects in isolation bearings. *ASME Journal of Engineering Mechanics*, 131(12), 1270-1278, 2005.
- [13] S.L. Burtcher, L.A. Dorfmann, Compression and shear tests of anisotropic high damping rubber bearings. *Engineering Structures*, 26(13):1979-1991, 2004.
- [14] G.M. Montuori, E. Mele, G. Marrazzo, G. Brandonisio, A. De Luca, Stability issues and pressure-shear interaction in elastomeric bearings: the primary role of the secondary shape factor. *Bulletin of Earthquake Engineering*, 14:569-597, 2016.
- [15] O.H. Yeoh, Some forms of the strain energy function for rubber. *Rubber Chemistry and Technology*, 66(5), 754-771, 1993.
- [16] A.B. Habieb, G. Milani, V. Quaglini, F. Milani, Experimentation and numerical modelling of recycled rubber pads for seismic isolation under accelerated ageing. *The 7<sup>th</sup> International Conference on Computational Methods in Structural Dynamics and Earthquake Engineering (COMPDYN)*, June 24-26, Crete, Greece, 2019.

## A FRAMEWORK FOR THE ASSESSMENT OF SEISMIC DAMAGE SCENARIOS IN THE EMILIA ROMAGNA REGION, ITALY

Elena Simoni<sup>1</sup>, Nicola Buratti<sup>2</sup>, and Claudio Mazzotti<sup>2</sup>

<sup>1</sup> DICAM - University of Bologna  
Via Risorgimento 2, Bologna  
e-mail: elena.simoni8@unibo.it

<sup>2</sup> DICAM – University of Bologna  
Via Risorgimento 2, Bologna  
{nicola.buratti, claudio.mazzotti}@unibo.it

---

### Abstract

*In the immediate aftermath of an earthquake, it is essential that emergency plans and damage scenarios are available so that civil protection agencies and risk-management organizations can detect and contain critical situations. These tools rely on the knowledge of the specific features of the potentially affected area, both in terms of intrinsic characteristics (e.g. morphology, near surface geology, etc.) and of elements at risk (e.g. building typologies, population distribution, etc.). All these pieces of information are combined in seismic-risk or damage scenario assessment procedures. This paper presents a framework developed for estimating seismic damage scenarios for the Emilia Romagna region in Northern Italy. Models for estimating ground-motion shake maps, based on regional attenuation relationships, spatial correlation models and soil data are first presented. These maps, which are computed considering different ground-motion intensity measures, are then combined with data on the spatial distribution of buildings, and fragility models. In order to consider the different sources of uncertainty, i.e. ground-motion intensity, definition of the fragility models, etc., a Monte Carlo simulation approach is used for estimating the distribution of buildings with different damage levels in each municipality. Finally, the paper presents comparisons with damage data observed after the 2012 Emilia earthquake.*

**Keywords:** Damage scenarios, Fragility assessment, Shake maps, Spatial correlation, Emilia earthquakes.

---



## 1 INTRODUCTION

Seismic risk assessment has the objective of identifying and highlighting the most vulnerable areas in a territory, and thus providing data to limit as much as possible earthquake-induced losses (e.g. economical, human lives, building stock, etc.). To this aim, damage scenarios can be estimated, both at national and regional scales. They are defined by studying past earthquake data in order to estimate the probability of exceeding different damage states in buildings and to quantify the expected losses. Up to date, there are many examples on how to derive damage scenarios, either based on site-specific analyses [1–5] or on larger-scales assessments [6]. After the 2012 earthquake studies have been focused on the Emilia-Romagna region [3,7]. Verderame et al. derived damage scenarios for reinforced concrete buildings and fragility curves were derived combining the Response Surface Method with nonlinear static analyses. Meroni et al. instead adopted the EMS-98 vulnerability classes definition to characterize the regional building stock and expressed its fragility in terms of macroseismic intensity.

The most commonly adopted procedures for the assessment of damage scenarios first require the identification of building types and the characterization of the building stock at the considered scale (i.e. urban, regional, national). In Italy the only complete catalog of the built heritage is the national Census, updated every ten years by the National Institute of Statistics (ISTAT). This survey, however, has the objective of mapping demographics and thus is very poor in terms of structural details of the investigated buildings. Nevertheless, some data are available concerning structural materials, number of stories and age of construction. Afterwards, estimates of the ground-motion intensity are needed. These are often given in the form of *shake-maps*, i.e. maps providing the spatial distribution of the values of a ground-motion Intensity Measure (IM). Finally, the effects of an earthquake on buildings are predicted combining data from shake maps and fragility models. These latter define the probability of exceeding a certain damage level as a function of the ground-motion intensity. Depending on the methodology employed for their derivation, fragility models can either be (i) *empirical* when obtained by fitting statistical models to observational data; (ii) *analytical* when calibrated upon numerical analyses on structural models; (iii) *experts' judgement-based* when estimated through experts' opinions.

Existing works [3,8] rely on already computed maps to derive vulnerability and exposure models. This study, however, wants to present a comprehensive approach in the definition of damage scenarios for the portion of the Emilia region affected by the 2012 Earthquakes. The adopted computational procedure for the derivation of shake maps is derived by literature studies but relies on specific attenuation relationships calibrated on the available ground motion recordings from the Emilia 2012 earthquakes. Fragility models, which are also specific for the context under consideration, are combined with the ground motion intensity and building distributions through a Monte Carlo simulation approach. This methodology allows to evaluate the damage distribution for each municipality in the area of interest. Outputs obtained with this procedure are then compared with the actual damage distribution observed after the 2012 Emilia earthquakes.

## 2 SHAKE MAPS FOR THE 2012 EMILIA EARTHQUAKES

Shake maps provide a graphical representation of the ground shaking intensity, described by means of an IM, and describe its distribution in an area affected by a seismic event. In the approach adopted here, the ground-motion intensity is first estimated for a regularly spaced grid by means of an attenuation relationship. These values are then combined with data for ground-motion recording stations using a spatial correlation model. The main steps of the procedure, as well as the models adopted, are described in the following.

## 2.1 The 2012 Emilia earthquakes

In May 2012, the provinces of Modena, Bologna and Ferrara, in northern Italy, were affected by a sequence of moderate seismic events which culminated in two main shocks on the 20<sup>th</sup> and 29<sup>th</sup> May, with moment magnitude equal to 6.1 and 6.0 [9], respectively. Ground-motion's data recorded during this seismic sequence was used to fit ground-motion attenuation models. Only the events with  $M_w \geq 5$  were considered to this purpose. Furthermore, since, as discussed in the following Section, the attenuation relationship's form adopted requires the definition of the geometry of the fault rupture plane, shocks for which this information was not available were excluded. Based on these criteria the four events listed in Table 1 were selected.

Event	Date	Municipality	Latitude [°]	Longitude [°]	Depth [Km]	$M_w$	GM records
20 <sup>th</sup> May main shock	2012-05-20 02:03:50	Finale Emilia	44.8955 0	11.26350	9.5	6.1	260
29 <sup>th</sup> May main shock	2012-05-29 07:00:02	Medolla	44.8417 0	11.06570	8.07	6	284
29 <sup>th</sup> May aftershock	2012-05-29 10:55:56	Cavezzo	44.8652 0	10.97950	4.35	5.5	182
29 <sup>th</sup> May aftershock	2012-05-29 11:00:22	San Possidonio	44.8660 0	10.97630	7.2	5.5	149

Table 1: Main information about the select events from the 20<sup>th</sup> and 29<sup>th</sup> May Emilia 2012 sequence [9].

## 2.2 Ground-motion attenuation relationships

Attenuation relationships are empirical statistical models that define the dependency of the values of an IM on seismological parameters as magnitude and source-to-site distance and other parameters such as type of soil at the site, style of faulting, bedrock depth, etc. The functional form employed in this study is

$$\ln(IM) = c_1 + c_2 \cdot M + c_3 \cdot \ln\left(\sqrt{R^2 + c_4^2}\right) + c_5 \cdot \ln(R + 25) + sf + \sigma_w \varepsilon_w + \sigma_b \varepsilon_b \quad (1)$$

where  $\ln(IM)$  is the natural logarithm of PGARotD50, defined according to Boore et al. [10] as the 50<sup>th</sup> percentile of the PGA values obtained rotating the acceleration horizontal components from 0 to 180°,  $M$  is the moment magnitude,  $R$  is the Joyne-Boore distance in km,  $sf$  is a term describing site amplification effects,  $\varepsilon_w$  and  $\varepsilon_b$  are intra- and inter-event standard normal error terms, respectively,  $c_1, \dots, c_5$  are unknown regression coefficients,  $\sigma_w$  and  $\sigma_b$  are unknown standard deviations associated to the intra- and inter-event variability, respectively. The term  $sf$  is defined as:

$$sf = c_6 \cdot S_B + c_7 \cdot S_C + c_8 \cdot S_D \quad (2)$$

where  $c_6, \dots, c_8$  are unknown regression coefficients and  $S_B, S_C$  and  $S_D$  are dummy variables representing different soil classes. In particular,  $S_B$  is 1 for soil class B and 0 otherwise,  $S_C$  is 1 for soil class C and zero otherwise and  $S_D$  is 1 for soil class D and 0 otherwise. The definition of soil classes is based on the Italian Building Code [11]. The values of the unknown coefficients in Equations (1) and (2) are estimated by means of nonlinear mixed effects regression

models, using recorded acceleration data from all the ground-motion recording stations at a distance shorter than 200 km from the epicenters of the earthquakes listed in Table 1. This table also reports the number of ground-motion records associated with each event. The model in Eq. (1) incorporates fixed and random effects. The former are parameters assumed as constant over the different groups of observations (each earthquake is a group), while random effects are random variables that assume a different value for each earthquake. The obtained attenuation relationship is plotted in Fig. 1 together with PGARotD50 data for the four events considered. Random effects do not vary significantly for each separate event which means that the between-event standard deviation is quite limited.

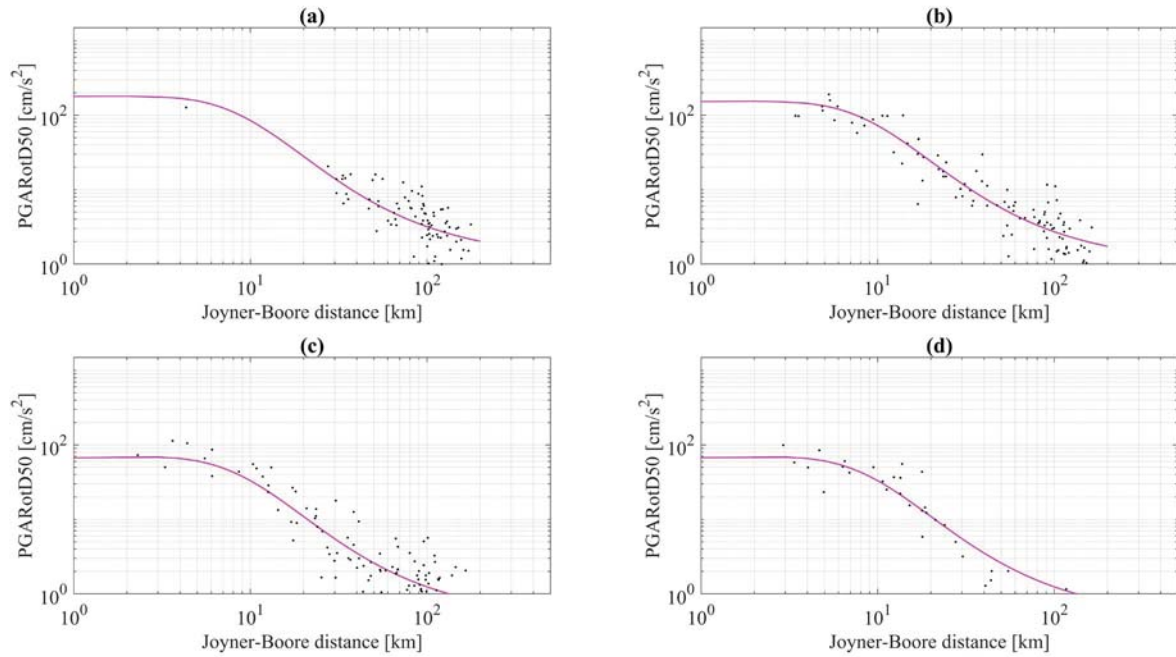


Fig. 1 – Attenuation relationship in logarithmic scale referred to an ideal rigid soil (class A). Blue dots are PGARot50 recordings for each event in terms of Joyner-Boore distance that have been referred to an equivalent soil type A. Event a) and b) are the main shocks of the 20<sup>th</sup> and 29<sup>th</sup> May respectively, while c) and d) are the 29<sup>th</sup> May aftershocks.

### 2.3 Spatial correlation models

Spatial correlation models must be defined for the computation of shake maps. In fact it has been observed that ground motion IM values are spatially correlated [12–14]. Clearly this correlation is not accounted for in the IM prediction given by attenuation relationships, which is for this reason called *unconditioned*. Shake maps instead combine the unconditioned distribution and recorded values, thus providing a *conditioned* distribution. Spatial correlation models were defined based on empirical semivariograms for the residuals obtained from the regression analysis carried out to fit the attenuation model. By visual comparison of different models, the spherical model was selected to fit the sample semivariograms. This model is defined as:

$$\gamma(h) = \begin{cases} \frac{3h}{2a} - \frac{1}{2} \left( \frac{h}{a} \right)^3 & \text{for } 0 \leq h \leq a \\ 1 & \text{for } h > a \end{cases} \quad (3)$$

being  $a$  the range and  $h$  the separation distance, whereas  $\gamma(h)$  is the semivariance. Spatial correlation is then obtained by subtracting the semivariance from unity.

## 2.4 Shake maps computation

As already mentioned in the previous sections, shake maps provide estimates of the spatial distribution of a ground motion IM over a certain area. Since a large number of ground-motion recordings is required in order to have reliable estimates, only the main events from the 20<sup>th</sup> and 29<sup>th</sup> May are considered from now on. Furthermore, it is also assumed that these events are those that contributed the most to building damage. Shake maps combine predictions from attenuation relationships, spatial correlation models and recorded IM values to derive estimates on a regular grid. The computational procedure adopted is derived from Bradley [13] and Worden et al. [15] and relies on the MVN theory. It is based on the hypothesis that the distribution of the natural logarithm of the IM produced by the earthquake  $e$  at site  $s$ , conditioned upon a set of  $N_{SMS}$  ground motion recordings,  $\ln(IM_{es}) | \ln(IM_{eSMS})$ , follows a multivariate normal distribution with mean value  $\mu_{\ln(IM_{es}) | \ln(IM_{eSMS})}$  and standard deviation  $\sigma_{\ln(IM_{es}) | \ln(IM_{eSMS})}$ :

$$\ln(IM_{es}) | \ln(IM_{eSMS}) \sim N(\mu_{\ln(IM_{es}) | \ln(IM_{eSMS})}, \sigma_{\ln(IM_{es}) | \ln(IM_{eSMS})}^2) \quad (4)$$

The mean value of this distribution can be estimated as:

$$\mu_{\ln(IM_{es}) | \ln(IM_{eSMS})} = \mu_{\ln(IM_{es})} + \Sigma_{\ln(IM_{es}), \ln(IM_{eSMS})} \Sigma_{\ln(IM_{eSMS}), \ln(IM_{eSMS})}^{-1} \delta_{W_{es}} + \delta_{B_e} \quad (5)$$

where  $\mu_{\ln(IM_{es})}$  is the unconditioned estimate of the mean value of the logarithm of the IM obtained by means of an attenuation relationship,  $\delta_{B_e}$  is the inter-event residual,  $\delta_{W_{es}}$  is a vector of intra-event residuals with  $N_{SMS}$  components,  $\Sigma_{\ln(IM_{eSMS}), \ln(IM_{eSMS})}$  is a variance-covariance matrix whose general term is defined as:

$$(\Sigma_{\ln(IM_{eSMS}), \ln(IM_{eSMS})})_{i,j} = \rho_{i,j} \sigma_W^2; \quad i = 1, \dots, N_{SMS}; \quad j = 1, \dots, N_{SMS} \quad (6)$$

being  $\rho_{i,j}$  the spatial correlation between the IM values at the  $i$ -th and  $j$ -th ground motion recording stations and  $\Sigma_{\ln(IM_{es}), \ln(IM_{eSMS})}$  is a variance-covariance matrix defined as:

$$(\Sigma_{\ln(IM_{es}), \ln(IM_{eSMS})})_{1,i} = \rho_{s,j} \sigma_W^2; \quad j = 1, \dots, N_{SMS} \quad (7)$$

Intra- and inter-event residuals are here determined by means of the attenuation relationship and are assumed to be normally distributed with null mean. The variance in Eq. (4) is computed as:

$$\sigma_{\ln(IM_{es}) | \ln(IM_{eSMS})}^2 = \sigma_W^2 - \Sigma_{\ln(IM_{es}), \ln(IM_{eSMS})} \Sigma_{\ln(IM_{eSMS}), \ln(IM_{eSMS})}^{-1} \Sigma_{\ln(IM_{eSMS}), \ln(IM_{es})} \quad (8)$$

Maps are computed for one event at time. In Figure 2 and the spatial distribution of PGARotD50 derived with the methodology just described is presented for the main shock of the 29<sup>th</sup> of May 2012, while Figure 3 shows the spatial distribution of the variance associated.

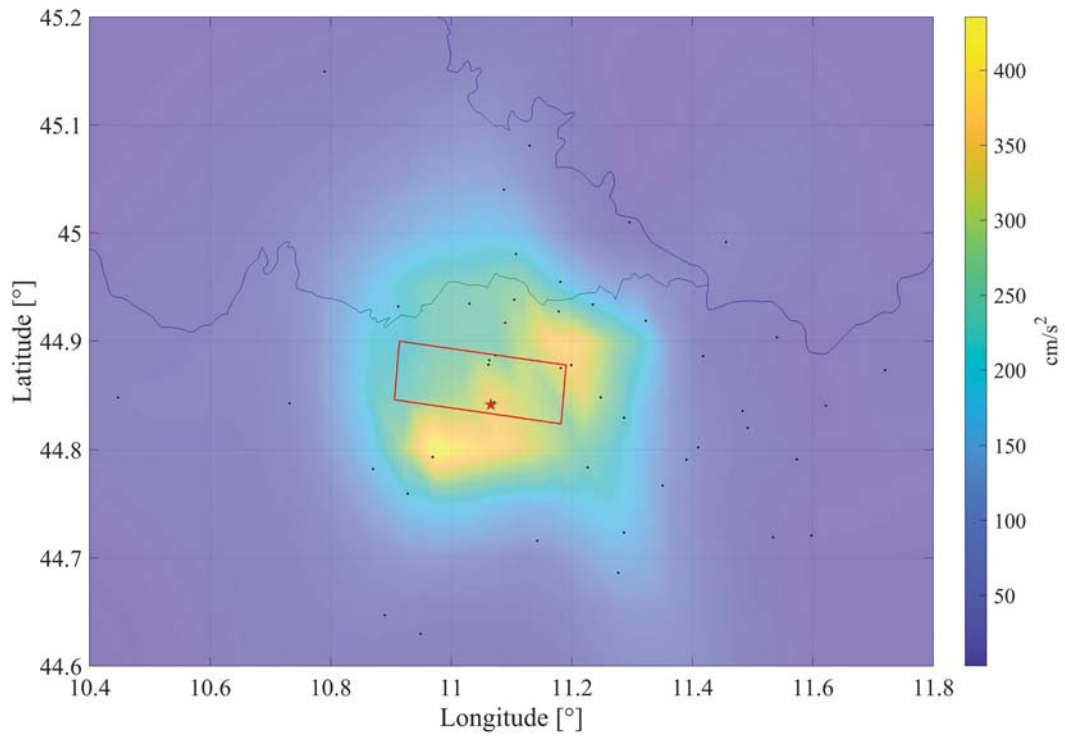


Fig. 2 - Shake map for the 29<sup>th</sup> of May 2012 event in terms of median PGARotD50 assuming uniform soil type C. Black dots are ground motion recording stations. The red polygon indicates the surface projection of the fault plane while the star symbol represents the position of the epicenter.

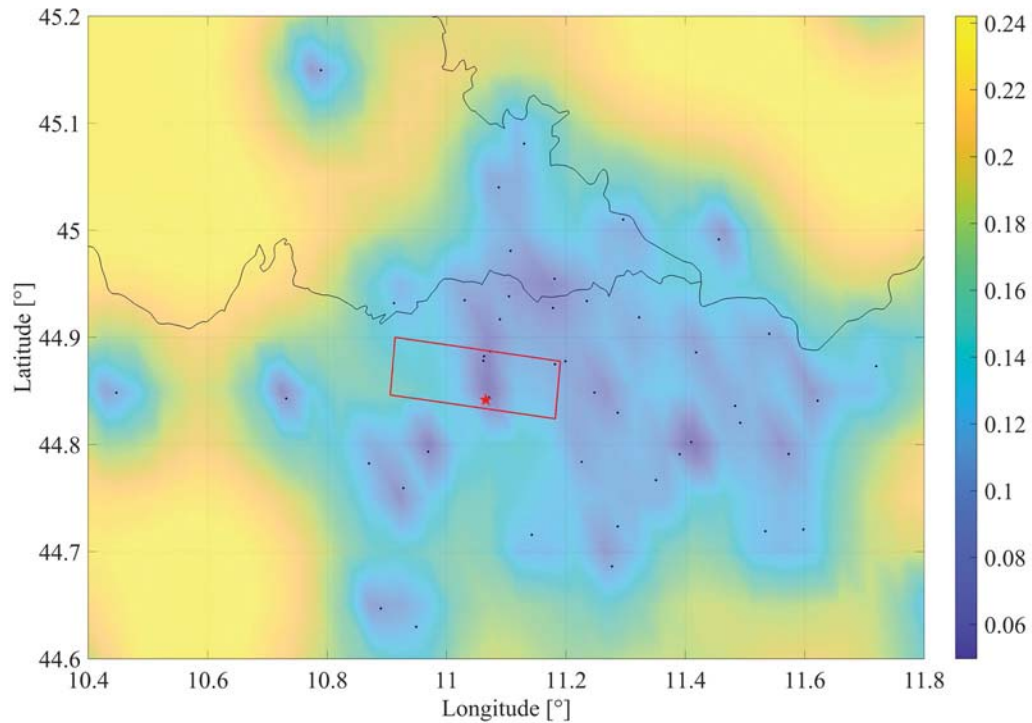


Fig. 3 - Spatial distribution of the variance associated with the  $\log_{10}(\text{PGARotD50})$  estimate. Variance is null in correspondence of ground motion recordings stations (black dots). The red polygon indicates the surface projection of the fault plane while the star symbol represents the position of the epicenter.



### 3 FRAGILITY MODELS

Fragility is generally referred to as the probability of exceeding a specific damage state conditioned to a certain ground motion IM value. Damage probability matrices (DPMs) describe fragility as a discrete quantity, relating the number of buildings with damage levels to some defined intervals of values of the IM [16,17]. To express fragility as a continuous function, parametric curves are often adopted. They represent the cumulative distribution function of the exceeding probability for the considered damage states. For the Emilia 2012 earthquakes a few specific models are available, both for masonry and reinforced concrete residential buildings. To carry out a damage scenario simulation, fragility models have to be consistent not only in terms of the building typology they refer to, but also in terms of adopted damage scale and ground motion IM considered. The following Sections describe the fragility models adopted in the present work; three different models for Reinforced Concrete (RC) and two models for unreinforced masonry structures.

#### 3.1 Fragility curves for unreinforced masonry structures

The characteristics of existing unreinforced masonry buildings are highly dependent on the quality and type of materials that can be found in a specific geographical area. For this reason, only models that have been derived from the Emilia-Romagna region residential masonry buildings were employed in this study. The first model used has been recently proposed by Ioannou et al. [18], and it is based on the analysis of damage data from the 2012 Emilia earthquake obtained from post-earthquake surveys. This dataset, however, is biased towards damaged buildings and the census [19] was used to complete the building stock with the undamaged buildings. Data was aggregated at the level of municipalities. It has often been highlighted [18,20,21] that this practice, common for empirical fragility assessment, reduces the level of detail in the building typology definition. The ground motion intensity was estimated using the attenuation model proposed by Bindi et al. [22]. Ioannou et al. then define several statistical models that relate 5 damage levels derived from EMS-98 to PGA, to the construction material (masonry, RC and other), to ground failure, and to the construction age. In the present study the model for masonry buildings was used.

The second set of curves was specifically derived by the authors in the present paper, based on statistical analysis of observational damage data. In a similar manner to the approach adopted in Ioannou et al., a complete database for masonry buildings, accounting for both the damaged and undamaged population, was obtained by combining information from post-earthquake surveys and census. The two sources were joined using the nearest neighbor criterion, i.e. for each post-earthquake survey form the nearest census building was deleted so that single entities are not double counted. Ground motion PGA values were estimated using maps derived according to the procedure described in Section 2. The fragility models obtained are based on logistic ordinal models, to avoid overlapping of fragility curves. The proportional odds assumption was introduced, thus considering that the slope of the curves is constant over the different damage levels. Specifically, a link logit function was used, and the covariate of the models was assumed to be constituted by the natural logarithm and squared natural logarithm of PGA, as shown in Eq. (9).

$$\Phi^{-1}(p_{i,j}) = \beta_{0,j} + \ln(IM_i) \beta_1 + \ln(IM_i)^2 \beta_2 \quad (9)$$

being  $\beta_{0,j}$  the intercept for each damage level, while  $\beta_1$  and  $\beta_2$  represent the slopes, constant among the different damage states. The two considered fragility models are shown in Fig. 4.

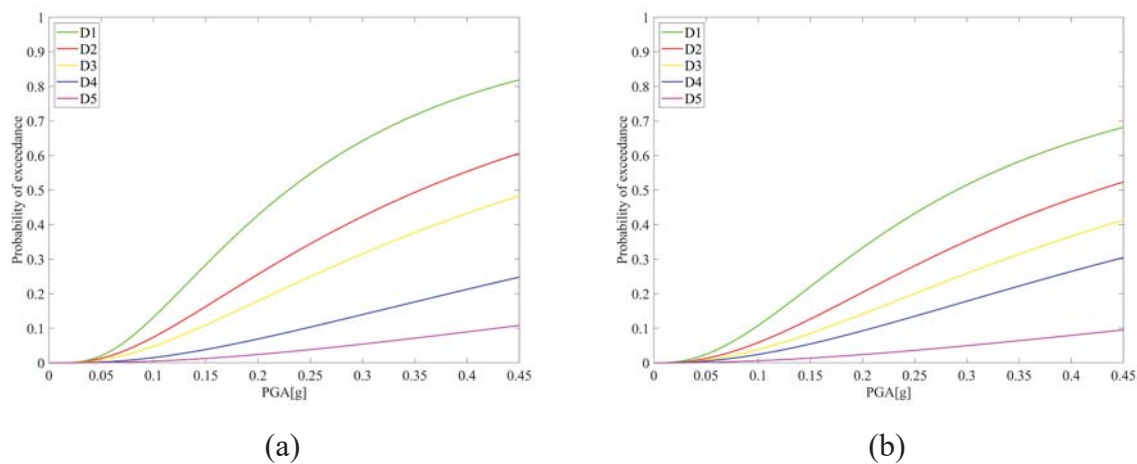


Fig. 4 – (a) Ioannou et al. [18] fragility curves and curves from the present work (b). Fragility is expressed in terms of PGA [g] for five different damage states.

### 3.2 Fragility curves for RC buildings

The first fragility model used in the present study was proposed by Verderame et al. [3]. These fragility curves were obtained by modeling infilled RC frames with 2 and 4 stories. Their geometry was defined after a detailed analysis of the damage distribution and of the residential building stock in some municipalities of the Emilia region while their structural detailing was derived referring to the post-1945 Italian regulations for RC buildings [23]. The capacity of these models was evaluated by means pushover analysis, while the IN2 method was used to estimate the displacement demand [24]. To derive fragility curves, damage thresholds expressed in terms of displacement capacity were first defined, while the variability of material characteristics or capacity parameters was accounted for by means of Response Surface meta-models. Lognormal fragility curves were obtained in terms of PGA for five different damage states, defined according to a mechanical interpretation of the EMS-98 scale [25].

The second fragility model adopted was developed by Salamida and Buratti [26] by applying nonlinear static analysis to study the structural response of 2- and 4-stories infilled RC frames, found to be the most common reinforced concrete residential building type in the Emilia region. Material properties and construction details were defined by means of simulated design, considering the Italian design adopted between 1950 and 1970. Damage states were defined from the EMS-98 scale as in Verderame et al., and fragility curves were calibrated separately for the different directions of application of the seismic action and for distributions of lateral loads. Overall fragility curves, were then computed as the mean probability of exceedance for the separate curves.

The third model used was proposed by Secci [27] and was developed through statistical analysis of data on the observed damage on RC buildings from the 2009 L'Aquila earthquake in Italy. For RC buildings it can be assumed that material properties are not strictly related to geography and local construction technologies. Furthermore, while analytical fragility models are generally biased though a very specific building typology, empirical models are able to account for the greater variability found in real buildings in terms of structural performance. Secci employed Bayesian regression to estimate the exceedance probability for five different damage states, based on the EMS-98, as a function of PGA. Damage levels were derived from post-earthquake surveys using the procedure proposed by Rota et al. [28]. The three considered fragility models are shown in Fig.5.

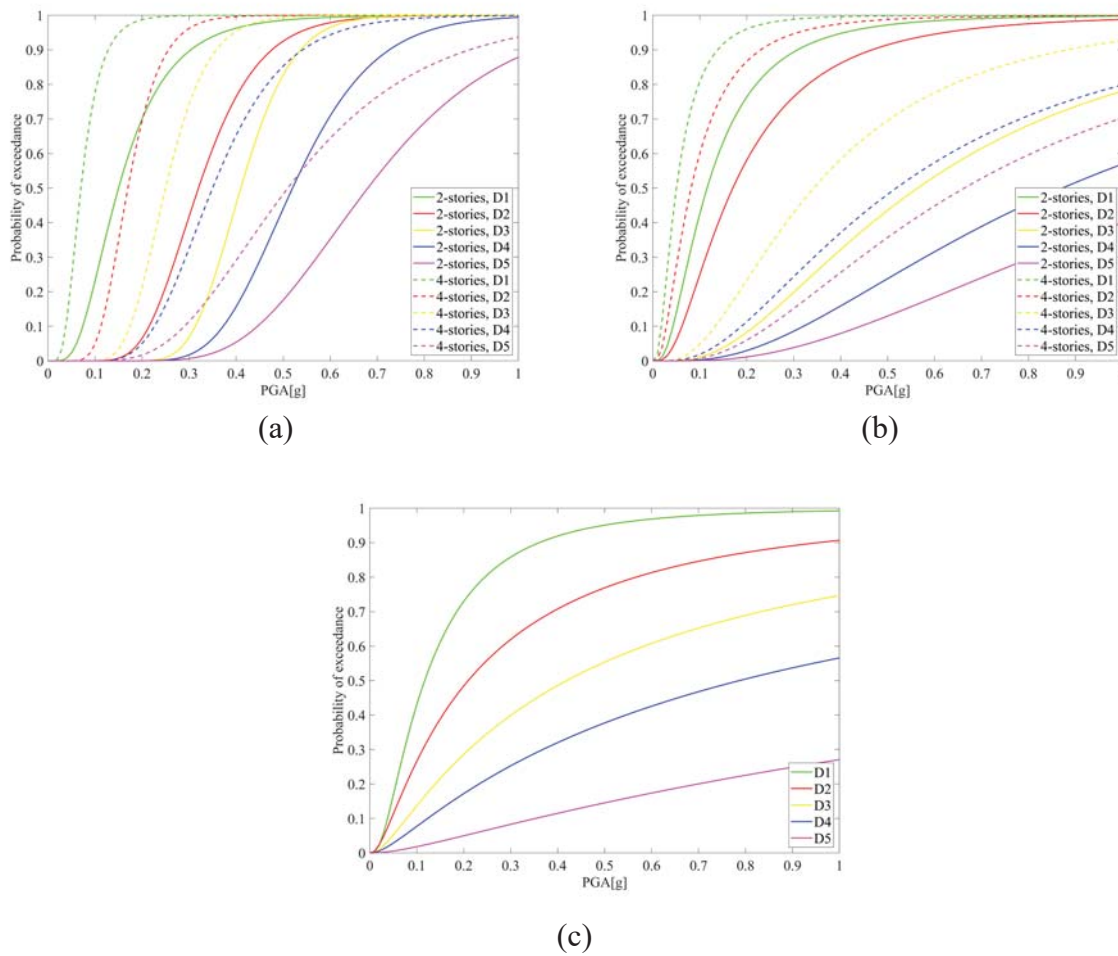


Fig. 5 – Fragility curves for RC buildings used in the present paper a) Verderame et al. [3], b) Salamida and Buratti [26], c) Secci [27]

#### 4 SIMULATION OF DAMAGE SCENARIOS

Damage scenarios are here derived only for municipalities within the epicentral area of the 2012 Emilia earthquake. Information regarding the building stock for each municipality is derived from the 2011 census [19]. The data used concerns geographical coordinates, construction material, age of construction and number of stories.

A Monte Carlo approach is then employed to evaluate a damage scenario in each municipality, for a given earthquake. First, the joint distribution of the ground motion intensity in terms of PGA at the locations of all the  $N_{b,k}$  buildings in the  $k$ -th municipality is estimated using the procedure described in Section 2. In particular, this distribution can be written as

$$\ln(\mathbf{IM})_k \sim N \left( \mathbf{M}_k, \left( \boldsymbol{\Sigma}_{\ln(IM_i), \ln(IM_j)} \right)_k \right) \quad (10)$$

where  $\mathbf{IM}_k$  is a random vector containing the  $N_{b,k}$  ground motion intensities associated to the buildings of the  $k$ -th municipality,  $\mathbf{M}_k$  is a vector containing the mean values of  $\ln(\mathbf{IM}_k)$ , and  $\left( \boldsymbol{\Sigma}_{\ln(IM_i), \ln(IM_j)} \right)_k$  is a variance-covariance matrix. The general element of this matrix is computed as per Eq. (6), though the spatial correlation and the standard deviation are referred to the ground-motion intensities at the locations of the  $i$ -th and  $j$ -th building.

The general iteration of the Monte Carlo simulations is then carried out as follows:

- i. A random sample of ground motion intensities is drawn from the distribution defined by Eq. (10).
- ii. A fragility model is randomly chosen among those defined in Section 3.1 and Section 3.2 for unreinforced masonry and RC buildings, respectively.
- iii. The probability of achieving the different damage levels (as well as no damage) is computed for each building combining data from i. and ii. When either the Verderame et al [3] or the Salomida and Buratti [21] fragility model is selected for RC buildings, the probabilities are computed considering the number of stories of each building (census data).
- iv. For each building a damage state is defined by comparing a random number drawn from a uniform PDF in the interval  $[0, 1]$  to the probabilities computed at step iii.

A number of 10000 simulations is carried out for each municipality. In the following, results are presented separately for masonry and RC residential buildings.

#### 4.1 Analysis of results for unreinforced masonry structures

To represent the simulation outcomes in a compact notation, histograms are used to visualize the mean number of buildings with the different damage levels, in contrast to damage data observed after the 2012 Emilia earthquakes.

Fig. 6, compares the distribution of damage in masonry buildings with reference to municipalities located within 10 km from the epicenter. It can be noted that buildings with low damage levels, such as D<sub>0</sub> or D<sub>1</sub> are overestimated by the simulation. To further investigate the simulated damage scenarios, municipalities outside the immediate epicentral area are considered, located at a distance larger than 10 km but still not further than 30 km. These areas are expected to be subjected to strong ground-motions, according to the computed shake map, but were not highly damaged, according to post-earthquake surveys. As shown in Fig. 7, in these municipalities, simulations predict higher damage levels than those observed. Damage scenarios, in fact, rely on fragility models that are calibrated on the whole observed damage database, thus, representing a mean trend in the damage observations among municipalities. This implies that this type of approach is better employed when evaluating the expected damage on a regional scale, while if used to derive damage scenarios at the municipality level, this could lead to underestimation or overestimation of the expected damage distribution.

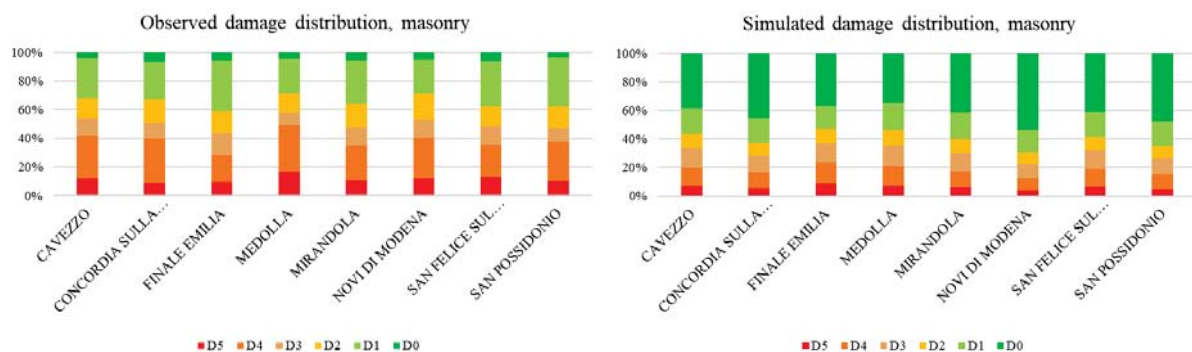


Fig. 6 - Comparison between observed (right) and mean values of the simulated (left) damage distribution for masonry buildings for municipalities in the immediate epicentral area (distance from epicenter < 10 km).



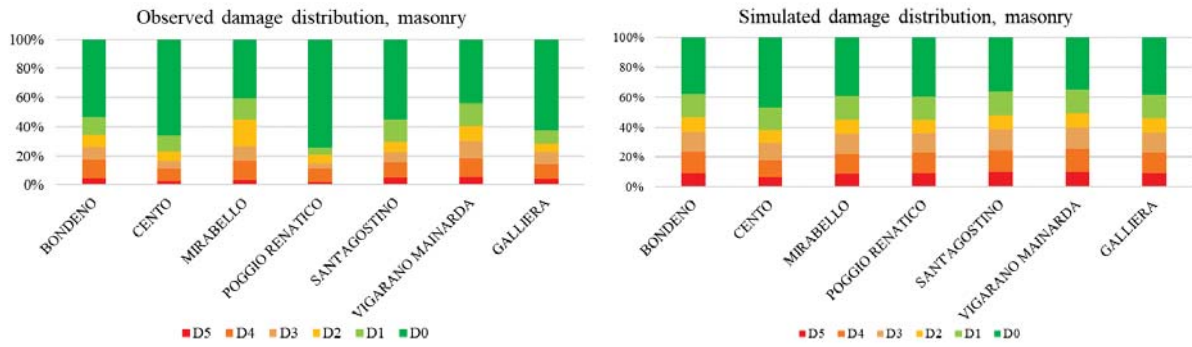


Fig. 7 - Comparison between observed (right) and mean values of the simulated (left) damage distribution for masonry buildings for municipalities in the slightly further epicentral area ( $10 \text{ km} < \text{distance from epicenter} < 30 \text{ km}$ ).

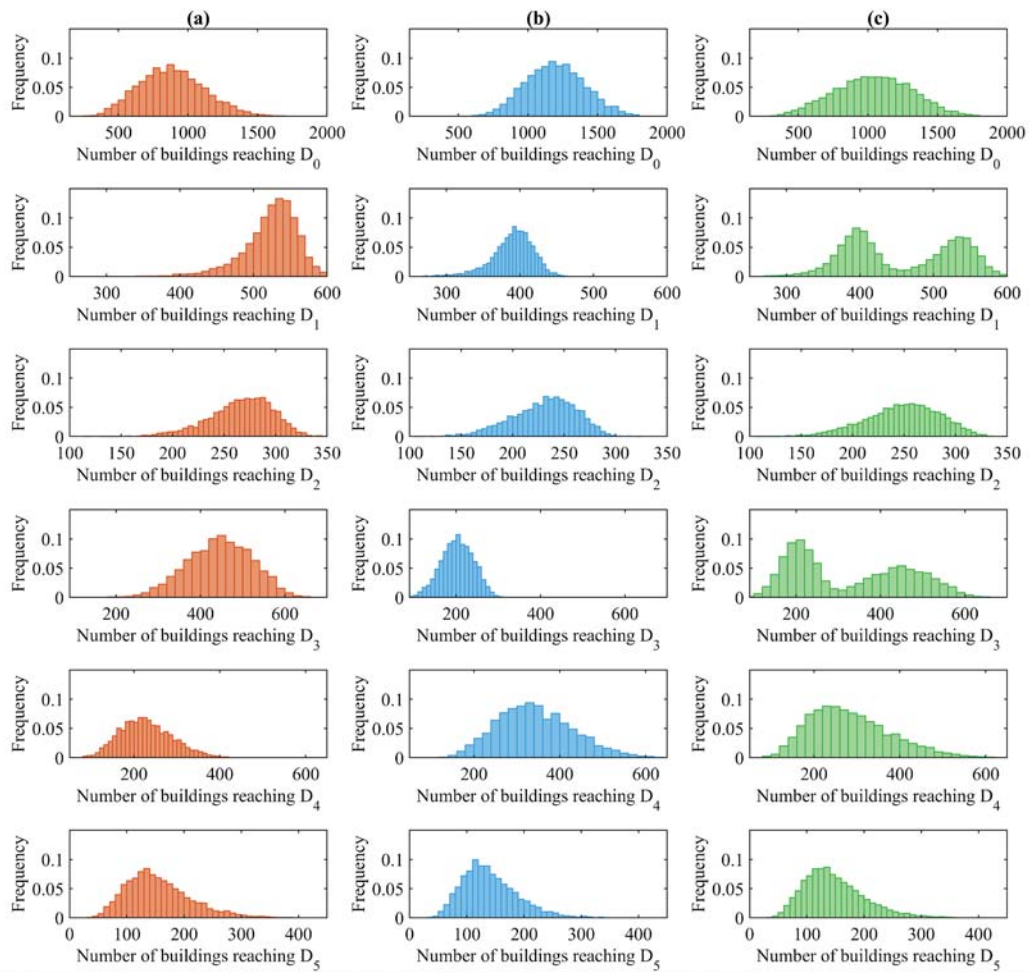


Fig. 8 – Histograms representing the distribution of the different damage levels among the 10000 simulations for the municipality of Mirandola. The a) column figures represent the contribution given by Ioannou et al. [18] fragility model, the b) column is the one given by the fragility model presented in the current paper, while c) represents the totality of the simulations.



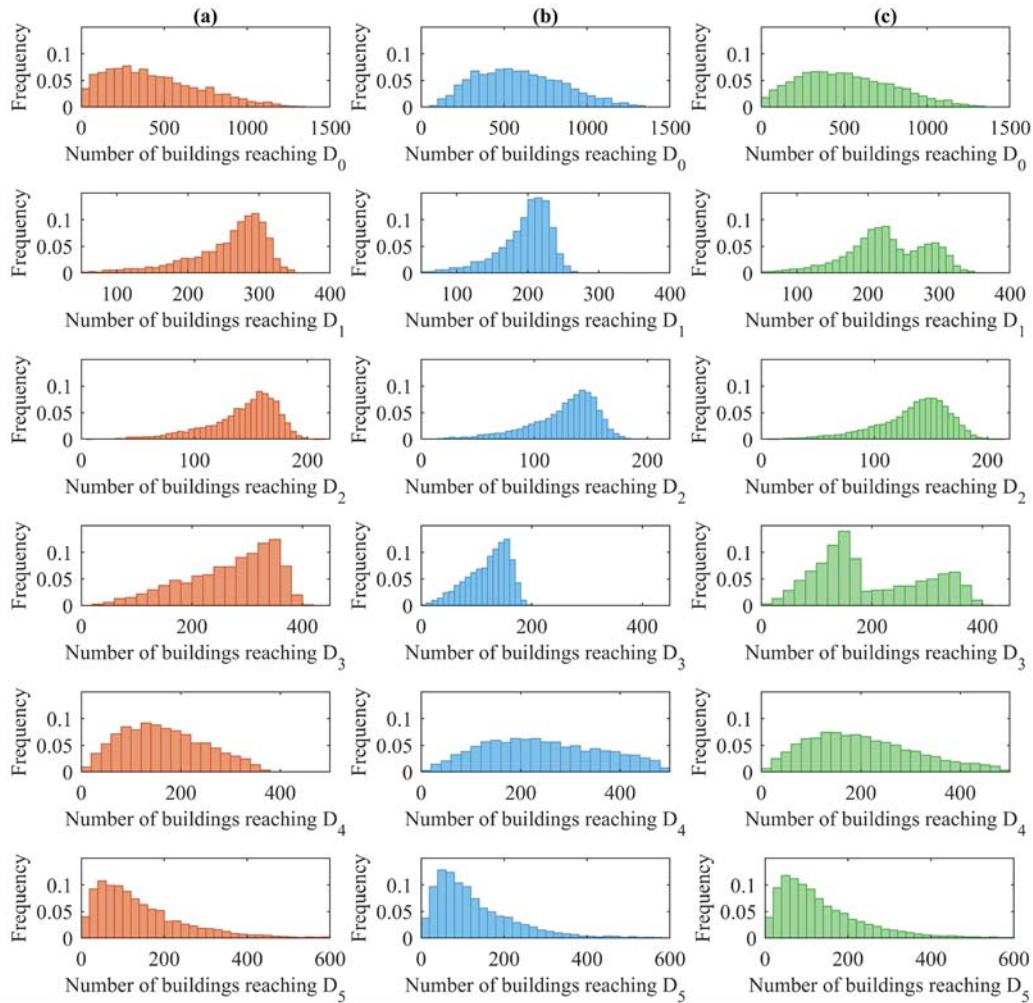


Fig. 9 - Histograms representing the distribution of the different damage levels among the 10000 simulations for the municipality of Sant'Agostino. The a) column figures represent the contribution given by Ioannou et al. [18] fragility model, b) is the one given by the fragility model presented in the current paper, while c) represents the totality of the damage levels distribution accounting for both models.

The variability of the simulation results is analyzed in Fig. 8 and Fig. 9 for the municipalities of Mirandola (MO) and Sant'Agostino (FE). It is evident, from both figures that buildings reaching D<sub>0</sub> have a high variability compared to other damage states. From the figures above, for levels D<sub>1</sub> and D<sub>3</sub> the two fragility models produce different results, while other damage states are quite coherent with each other.

#### 4.2 Analysis of the results for RC buildings

Results for reinforced concrete buildings, differently than those obtained for masonry structures, rely on both empirical and analytical fragility models. Analytical models are highly dependent on the assumptions introduced in the definition of structural models and can be very accurate in describing the behavior of that specific typology, while failing to account for the variability that characterizes the actual building stock. Comparison between observed and simulated damage distributions is presented in Fig. 10 for municipalities within 10 km from the epicenter that sustained significant damage, according to post-earthquake surveys. To further investigate the contribution given by each separate model, simulations are also run considering each fragility model one at a time and the so obtained damage distributions are presented for the same municipalities in Fig. 11.

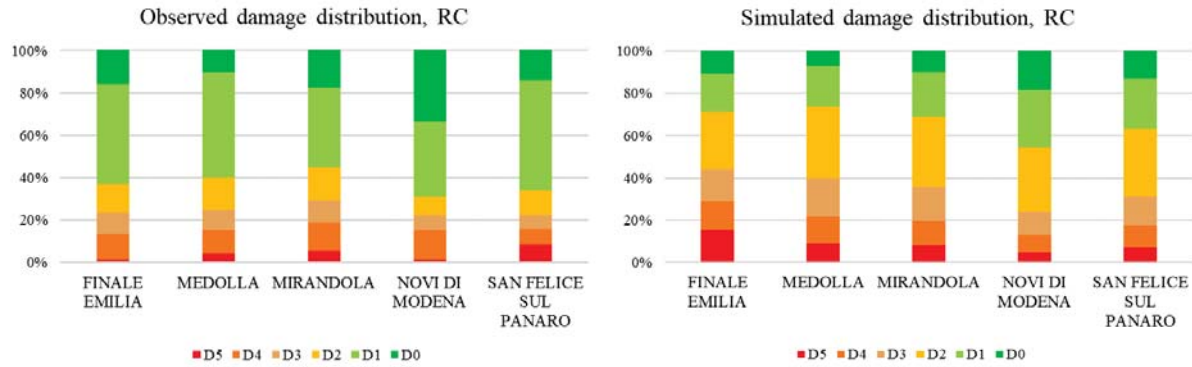


Fig. 10 - Comparison between observed (right) and mean values of the simulated (left) damage distribution for RC buildings for municipalities in the epicentral area (distance from epicenter < 10 km).

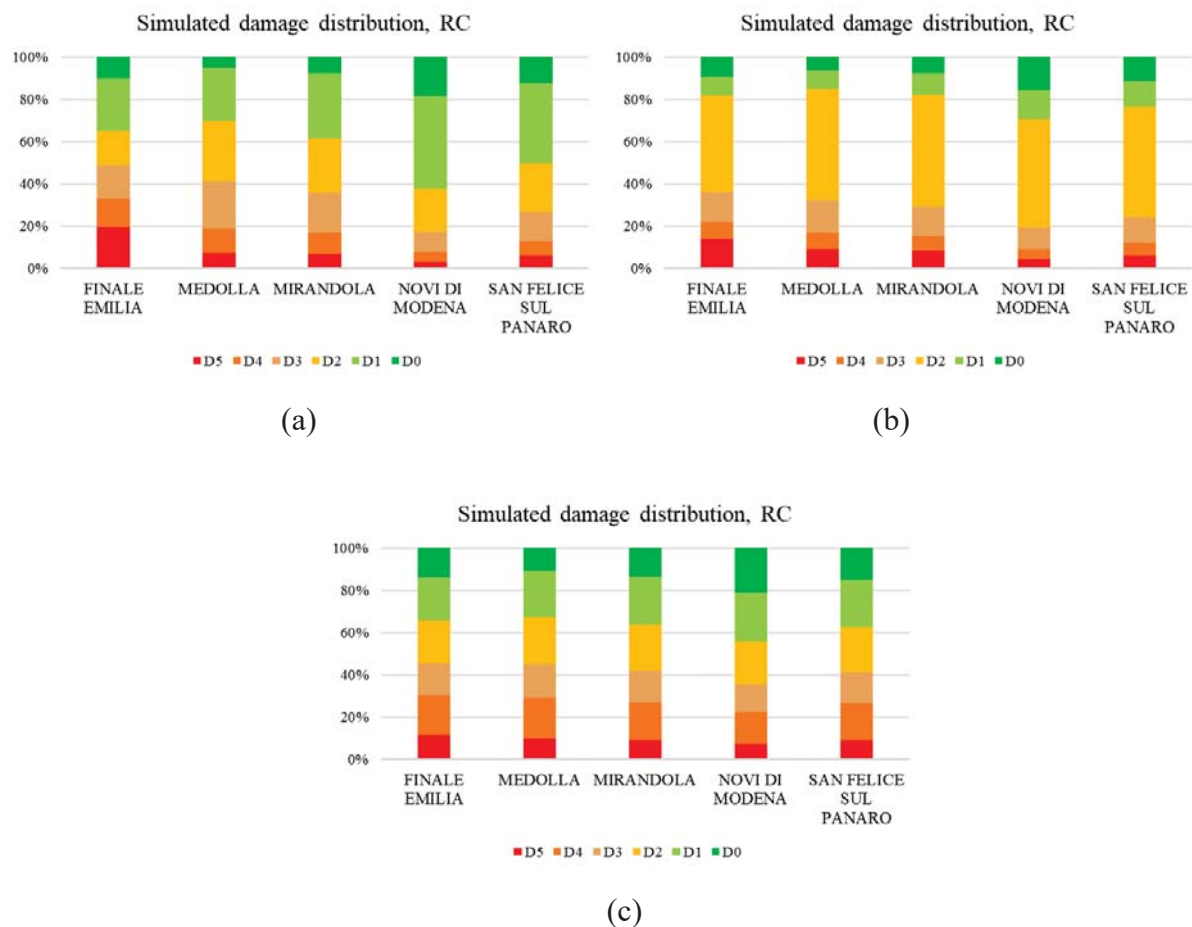


Fig. 11 – Mean value of the simulated damage distribution adopting either (a) Verderame et al. [3], (b) Salamida and Buratti [21] or Secci [27] fragility models.

Substantial differences can be observed comparing the observed and the simulated damage, both considering all fragility models together and separately. As already mentioned, Verderame et al. [3] and Salamida and Buratti [26] models adopt different sets of fragility curves depending on the height of buildings. To study the reliability of the adopted procedure, the number of stories distribution is analyzed in the subset considered and in the overall building database. First the census (Dat1) and the post-earthquake surveys (Dat2) databases are considered with

reference to the provinces of Bologna, Modena and Ferrara. Then the combined database (Dat3) is studied. Results are shown in Table 2.

Database	N. of stories					
	1	2	3	4	5	>5
<b>Dat1</b>	3.45 %	40.06 %	26.04 %	14.95 %	6.70 %	8.81 %
<b>Dat2</b>	29.10 %	18.14 %	17.87 %	14.69 %	7.96 %	11.31 %
<b>Dat3</b>	5.67 %	38.06 %	25.22 %	14.89 %	6.89 %	9.19 %

Table 2: Percentages with respect to the total of buildings separated for number of stories and database. Dat1 is the census dataset, Dat2 is the post-earthquake surveys one and Dat3 is the joint database

<b>Dat1</b>							
Municipality	N. of stories						Total #
	1	2	3	4	5	>5	
Finale Emilia	0.00 %	8.97 %	16.67 %	50.00 %	21.79 %	2.56 %	78
Medolla	0.00 %	4.65 %	16.28 %	51.16 %	27.91 %	0.00 %	43
Mirandola	3.85 %	5.68 %	16.63 %	31.03 %	41.38 %	1.42 %	493
Novi di Modena	1.69 %	2.82 %	9.60 %	21.47 %	60.45 %	3.95 %	177
San Felice sul Panaro	0.00 %	2.86 %	1.43 %	14.29 %	71.43 %	10.00 %	70
<b>Dat2</b>							
Municipality	N. of stories						Total #
	1	2	3	4	5	>5	
Finale Emilia	40.63 %	21.25 %	16.88 %	11.88 %	5.63 %	0.63 %	160
Medolla	40.00 %	22.22 %	22.22 %	14.44 %	0.00 %	0.00 %	90
Mirandola	30.38 %	16.46 %	14.77 %	16.46 %	11.18 %	0.00 %	474
Novi di Modena	26.06 %	28.87 %	23.94 %	9.15 %	4.93 %	0.00 %	142
San Felice sul Panaro	22.22 %	20.37 %	39.81 %	11.11 %	5.56 %	0.00 %	108
<b>Dat3</b>							
Municipality	N. of stories						Total #
	1	2	3	4	5	>5	
Finale Emilia	40.12 %	20.99 %	17.90 %	11.73 %	5.56 %	1.85 %	162
Medolla	40.00 %	22.22 %	22.22 %	14.44 %	0.00 %	0.00 %	90
Mirandola	29.45 %	18.00 %	14.93 %	16.36 %	10.84 %	9.00 %	489
Novi di Modena	19.59 %	38.66 %	24.23 %	8.25 %	4.12 %	4.64 %	194
San Felice sul Panaro	22.22 %	20.37 %	39.81 %	11.11 %	5.56 %	0.93 %	108

Table 3: Total number of buildings and percentages with respect to the number of stories for each municipality and database.

Remembering that Dat2 consists mainly of damaged buildings, and thus percentages can be intended as referring to the most fragile building typology, Dat1 and Dat3 coherently identify 2- and 3-stories structures as the most predominant typology. If the same analysis is conducted with respect to the single municipalities shown in Fig. 10 and Fig. 11, some changes can be observed. Table 3 highlights significant differences for the considered municipalities in the distribution of the number of stories. Specifically, Dat1 consists mainly of 4- and 5-stories structures and the total count is also lower than the corresponding quantity that has been surveyed in the same municipality. Thus, when combining Dat1 and Dat2 in Dat3, this final database

mostly consist of post-earthquake entries and the number of stories distribution reflects this, as well. However, damage scenarios are carried out relying on census data alone, which means that for some municipalities the dimension of the building stock may be underestimated. At the same time, errors may be introduced in the simulation due to misclassification of the number of stories, or of the type of construction material itself. Nonetheless, it has been shown in Table 2 that overall ratios are coherent among the different databases. It can be then said that damage scenarios produce reliable results when considering a regional scale but can lead to large misinterpretations if applied to a single municipality or limited scale. If damage scenarios aim to assess the expected fragility of single municipalities they have to be implemented starting from highly reliable and detailed data, especially with respect to those parameters that influence the chosen fragility models, such as the number of stories or construction age.

Finally, in an analogous way to what was done for masonry structures scenarios, the variability of the outcomes of the simulations is visualized in Fig. 12, disaggregated for the different fragility models considered. Damage level  $D_0$  histograms are similar for all considered models, while for other damage states results vary from model to model.

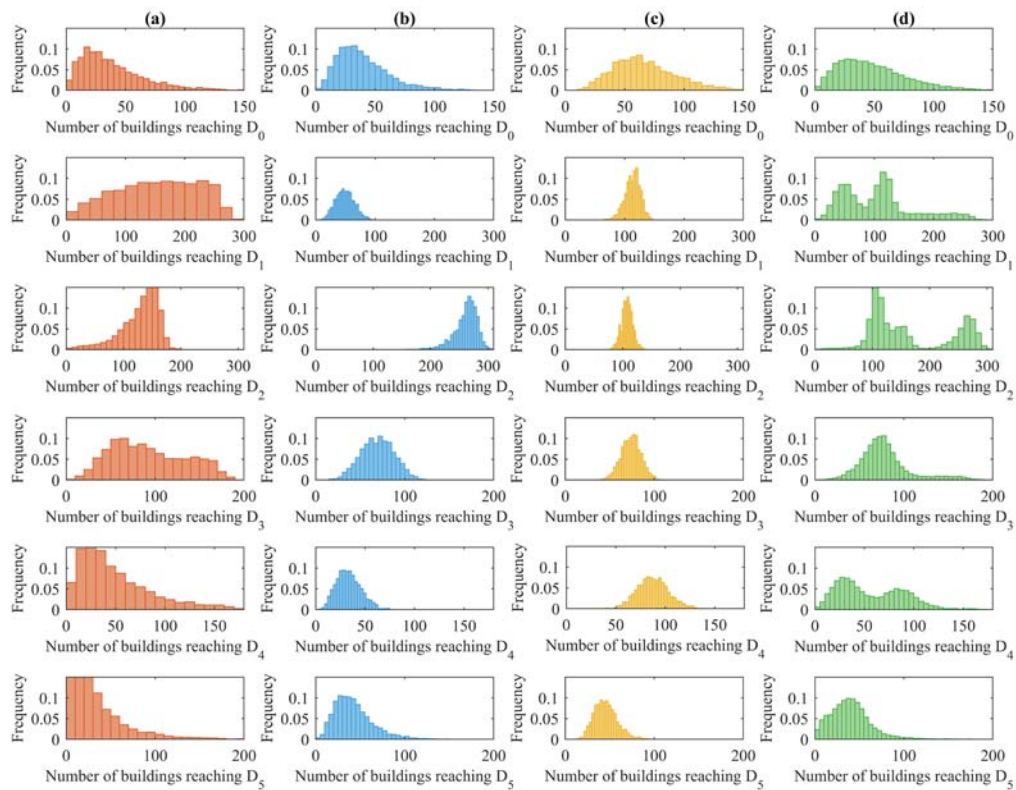


Fig. 12 – Histograms representing the distribution of the different damage levels among the 10000 simulations for the municipality of Mirandola. The a) column figures represent the contribution given by Verderame et al. fragility model [3], b) is the contribution from Salamida and Buratti’s fragility model [26], while c) represent the contribution given by the model proposed by Secci [27]. Finally, the totality of the damage levels distribution accounting for all models is represented in column c) plots.

## 5 CONCLUSIONS

The present paper illustrates a framework for the simulation of seismic damage scenarios in the Emilia Romagna region, in northern Italy. First attenuation relationships are defined as well as spatial correlation models in order to estimate shake maps for the Emilia 2012 earthquakes. These tools are then employed to carry out a Monte Carlo simulation to compute damage



scenarios for masonry and reinforced concrete residential buildings. Building stock information is obtained from the census, while fragility is estimated through models obtained from the available literature for both structural typologies. The simulated damage distribution is then compared to the observed one and results are discussed. It is derived that damage scenarios may be a powerful tool to obtain damage estimates on regional scale but may lead to overestimation or underestimation when applied to a reduced scale, such as at a single municipality level. These results are highly influenced by the quality of the building stock database (i.e. census) that introduces high uncertainties with respect to number of stories and construction material.

## ACKNOWLEDGEMENTS

The financial support of the Emilia-Romagna regional agency for Civil Protection and Territorial Safety is gratefully acknowledged.

## REFERENCES

- [1] L. Moya, E. Mas, S. Koshimura, F. Yamazaki, Synthetic building damage scenarios using empirical fragility functions: A case study of the 2016 Kumamoto earthquake. *International Journal of Disaster Risk Reduction*. **31** (March), 76–84, 2018.
- [2] A. Roca, X. Goula, T. Susagna, J. Chávez, M. González, E. Reinoso, A simplified method for vulnerability assessment of dwelling buildings and estimation of damage scenarios in Catalonia, Spain. *Bulletin of Earthquake Engineering*. **4** (2), 141–158, 2006.
- [3] G.M. Verderame, P. Ricci, F. De Luca, C. Del Gaudio, M.T. De Risi, Damage scenarios for RC buildings during the 2012 Emilia (Italy) earthquake. *Soil Dynamics and Earthquake Engineering*. **66** (November), 385–400, 2014.
- [4] M. Dolce, M. Marino, A. Masi, M. Vona, Uno scenario di danno sismico per la città di Potenza. in: X Congr. Naz. "L'ingegneria Sismica Ital., Potenza-Matera, 2001.
- [5] M. Dolce, A. Kappos, A. Masi, G. Penelis, M. Vona, Vulnerability assessment and earthquake damage scenarios of the building stock of Potenza (Southern Italy) using Italian and Greek methodologies. *Engineering Structures*. **28** (3), 357–371, 2006.
- [6] R. Spence, Earthquake Disaster Scenario Predictions & Loss Modelling for Urban Areas. , 2007.
- [7] F. Meroni, T. Squarcina, V. Pessina, M. Locati, M. Modica, R. Zoboli, A Damage Scenario for the 2012 Northern Italy Earthquakes and Estimation of the Economic Losses to Residential Buildings. *International Journal of Disaster Risk Science*. **8** (3), 326–341, 2017.
- [8] M. Dolce, B. Borzi, F. Da Porto, M. Faravelli, S. Lagomarsino, G. Magenes, et al., Mappe di rischio per il territorio Italiano. *Proceedings of the 18th Italian Conf on Earthq Eng ANIDIS*. (September), SS02-21 SS02-34, 2019.
- [9] L. Luzi, F. Pacor, R. Puglia, Italian Accelerometric Archive v3.0. Istituto Nazionale di Geofisica e Vulcanologia, Dipartimento della Protezione Civile Nazionale., 2019.
- [10] D.M. Boore, J. Watson-Lamprey, N.A. Abrahamson, Orientation-independent measures



- of ground motion. *Bulletin of the Seismological Society of America*. **96** (4 A), 1502–1511, 2006.
- [11] Ministero delle Infrastrutture e dei Trasporti, Aggiornamento delle «Norme tecniche per le costruzioni». *Gazzetta Ufficiale Della Repubblica Italiana*. (in Italian) , 1–198, 2018.
  - [12] K. Goda, H.P. Hong, Spatial correlation of peak ground motions and response spectra. *Bulletin of the Seismological Society of America*. **98** (1), 354–365, 2008.
  - [13] B.A. Bradley, Site-specific and spatially-distributed ground-motion intensity estimation in the 2010-2011 Canterbury earthquakes. *Soil Dynamics and Earthquake Engineering*. **61–62** (2014), 83–91, 2014.
  - [14] N. Jayaram, J.W. Baker, Correlation model for spatially distributed ground-motion intensities. *Earthquake Engineering & Structural Dynamics*. **38** , 1678–1708, 2009.
  - [15] C. Bruce Worden, E.M. Thompson, J.W. Baker, B.A. Bradley, N. Luco, D.J. Wald, Spatial and spectral interpolation of ground-motion intensity measure observations. *Bulletin of the Seismological Society of America*. **108** (2), 866–875, 2018.
  - [16] F. Braga, M. Dolce, D. Liberatore, A statistical study on damaged buildings and an ensuing review of the MSK-76 scale. *7th European Conference on Earthquake Engineering*. , 1982.
  - [17] R. Whitman, Damage probability matrices for prototype buildings. , 1973.
  - [18] I. Ioannou, S. Bertelli, E. Verrucci, V. Arcidiacono, T. Rossetto, Empirical fragility assessment of residential buildings using data from the Emilia 2012 sequence of earthquakes. Springer Netherlands, , 2021.
  - [19] Italian National Statistical Institute (ISTAT). 15th Italian Population and Housing Census, 2011
  - [20] M. Colombi, B. Borzi, H. Crowley, M. Onida, F. Meroni, R. Pinho, Deriving vulnerability curves using Italian earthquake damage data. *Bulletin of Earthquake Engineering*. **6** (3), 485–504, 2008.
  - [21] F. Meroni, V. Petrini, G. Zonno, Distribuzione Nazionale Della Vulnerabilità Comunale. *La Vulnerabilità Degli Edifici*. , 105–131, 2000.
  - [22] D. Bindi, F. Pacor, L. Luzi, R. Puglia, M. Massa, G. Ameri, et al., Ground motion prediction equations derived from the Italian strong motion database. *Bulletin of Earthquake Engineering*. **9** (6), 1899–1920, 2011.
  - [23] Regio Decreto Legge n. 2229 del 16/11/1939. Norme per la esecuzione delle opere in conglomerate cementizio semplice od armato. G.U. n. 92 del 18/04/1940 (in Italian).
  - [24] M. Dolšek, P. Fajfar, Simplified non-linear seismic analysis of infilled reinforced concrete frames. *Earthquake Engineering and Structural Dynamics*. **34** (1), 49–66, 2005.
  - [25] G. Grünthal, European Macroseismic Scale 1998. in: Cah. Du Cent. Eur. Géodynamique

Séismologie, Luxembourg, 1998.

- [26] G. Salamida, N. Buratti, Fragility models for existing masonry infilled RC frames in the Emilia area. in: 8th ECCOMAS Themat. Conf. Comput. Methods, , 2021.
- [27] E. Secci, Definizione di modelli di fragilità per edifici sulla base di dati sul danneggiamento relativi al terremoto dell'Aquila 2009, 2020.
- [28] M. Rota, A. Penna, C.L. Strobbia, Processing Italian damage data to derive typological fragility curves. *Soil Dynamics and Earthquake Engineering*. **28** , 933–947, 2008.

## THE USE OF AN INTEGRATED APPROACH FOR BUILDING INVENTORY AND EFFECTS ON RISK ESTIMATIONS AT THE TERRITORIAL SCALE

M. Polese<sup>1</sup>, M. Di Ludovico<sup>1</sup>, G. Tocchi and A. Prota<sup>1</sup>

<sup>1</sup> Department of Structures for Engineering and Architecture, University of Naples Federico II  
Via Claudio 21, 80125, Naples, Italy

e-mail: [mapolese@unina.it](mailto:mapolese@unina.it); [diludovi@unina.it](mailto:diludovi@unina.it); [gabriella.tocchi@unina.it](mailto:gabriella.tocchi@unina.it);  
[andrea.prota@unina.it](mailto:andrea.prota@unina.it)

---

### Abstract

*Large-scale seismic risk assessment is probably the most appropriate tool for investigating the consequences of earthquakes in a region of interest. Most of the existing risk-oriented studies focus on the seismic hazard evaluation and vulnerability assessment, while fewer efforts were performed in evaluating the influence of exposure modelling. The large-scale building inventory is generally conducted by relying on readily available sources of information, such as databases based on census data. However, the information contained in census databases are often limited to poor level data, such as building construction material, construction age and (not always available) the storey number. The use of inventory data for large scale application requires suitable rules to assign buildings typologies to vulnerability classes, that is an exposure model. Most of the existing exposure models are calibrated on building typological data available from post-earthquake survey data and therefore are based on data from specific geographic areas, namely the ones hit by damaging earthquakes. It is known that the distribution of building typologies can vary greatly for different areas of a country and the availability of construction material in the area. Furthermore, the evolution of construction techniques and the codes in force at the time of construction may affect the presence of a particular building's typology rather than another one. This study aims to evaluate the influence of a better knowledge level of the building environment on seismic risk at regional scale, investigating the variability of masonry building typologies distribution. The application is presented for two different Italian regions, showing that an improved characterization of regional vulnerability may strongly influence the impacts in terms of risk estimations.*

**Keywords:** exposure, vulnerability, inventory, local building typologies, Cartis

---

## 1 INTRODUCTION

In large scale seismic risk assessment, the buildings are clustered in relevant vulnerability classes based on the behavior that is expected during a seismic event, for which different vulnerability functions are defined. A common vulnerability classification is given by the European Macroseismic Scale EMS'98 [1], that categorizes buildings in 6 vulnerability classes (from A to F), based on the type of vertical structures, i.e. the construction material and code design level. Other vulnerability models identify vulnerability classes based on the construction material (masonry, reinforced concrete, steel, wood) taking into account as well other structural and non-structural elements features (e.g. [2]-[4]).

The distribution of buildings within the vulnerability classes in each territorial unit of analysis is given by building inventory. Different sources of information on people and residential buildings are available with global coverage at national and sub-national level (e.g. [5]-[7]); however, in order to compile building inventory Census database is often the primary employed source, thanks to their availability and diffusion on whole national territory. In Italy, census data on population and buildings, allowing to count building numerosness in terms of construction material, number of storeys and construction age, are produced by ISTAT, the national statistical institute. The data for each census tracts are available in aggregated form for privacy reasons, but the disaggregated census data on buildings are also available at provincial or municipality level, as shown in [8]-[9] and [10].

In general, to compile a building inventory at territorial scale starting from census data, a suitable exposure model is required to associate the building typology to vulnerability classes defined according to a vulnerability model. In the methodology adopted within last National Risk Assessment (NRA) for Italy [11], the exposure modelling defines the rules to assign building typology identified by ISTAT to EMS'98 vulnerability classes. Moreover, the methodology allowed to evaluate the risk by combination of the results obtained adopting different vulnerability/exposure models (VEM). Generally, exposure models may be calibrated based on building typological data available from post-earthquake surveys in Italy (e.g. [13] and [14]) or other available building-by-building survey databases (as in [15]) and eventually integrating them with expert judgment (e.g. [16]).

However, due to the high costs and time required, building-by-building survey campaign are generally carried out for limited areas in a country, such as urban districts or small municipalities, and the ones conducted after a noteworthy seismic event usually completely inspect only the municipalities with higher macroseismic intensity [17].

Thus, the exposure model used in national or sub-national risk assessment may be calibrated on data referred to a specific geographic area. However, the buildings' characteristics may be not the same for different areas of a country, likely due to variability in construction material diffusion and in construction techniques use for different regions.

Mostly for unreinforced masonry buildings, the type of vertical structure (e.g. regular, irregular, round stone, regular stone etc.), that has a clear influence on seismic vulnerability, may vary significantly: the type of stones can be influenced by the geography of the territory (e.g. the presence of quarries, waterways and volcanic areas) and in turn construction techniques are influenced by the type of stones, because some types of stones are better suited to be cut into square blocks. In Italy, in inland areas near to Apennine limestone is widespread while bricks are typical of the Adriatic coast and tuff of volcanic areas. This could explain the reason of large presence of irregular layout structures in the internal areas of the country and the presence of regular layout masonry structures in the areas characterized by the presence of bricks, tuff or travertine, as shown in [18]-[20].

A recent approach for the compiling of large-scale inventories is provided by Cartis [21], an interview-based form developed within “Territorial Themes” ReLUIS project financed by the Italian Civil Protection Department. The Cartis approach allows to rapidly survey ordinary building typologies in urban area, collecting information on buildings features useful for the building vulnerability classification. In this paper, we propose the use of Cartis database to improve the exposure modelling at regional scale. Adopting the methodology proposed in [22] and briefly recalled in the next paragraphs, the effects of the improved vulnerability characterization on risk assessment are evaluated for two Italian regions. Two exposure/vulnerability model recently proposed in Italy for unreinforced masonry buildings are adopted and the damage and risk assessment obtained from the original vulnerability/exposure models and from the ones updated through the Cartis-based inventory area compared. It will be shown that not negligible changes of the impacts may be observed, also depending on the analyzed region.

## **2 THE ADOPTED VULNERABILITY/EXPOSURE MODELS**

With the aim to investigate the effect of different typological distribution on the vulnerability assessment at the regional scale, two empirical vulnerability/exposure models that were recently proposed for masonry type buildings are adopted. The model proposed by Del Gaudio et al. [3], referred to as DG2019, is based on the statistical treatment of typological and damage data of masonry buildings damaged after the 2009 L’Aquila earthquake. The authors propose empirical based lognormal fragility curves for 14 masonry buildings classes, defined based on the combination of vertical structures (regular layout or good quality, irregular layout or poor quality structure with or without tie rods/beams) and horizontal structures (vaults with or without tie rods, beams with flexible, semi-rigid or rigid slabs), as shown in Table 1. Moreover, a set of fragility curves directly referred to construction age intervals, usable with a building classification based on census data, are also proposed. These age-dependent fragility curves are derived by a linear combination of the 14 sets of typological fragility curves, using the percentage of occurrence of each class within the 8 times intervals defined by ISTAT (< 1919, 1919-1945, 1946-1961, 1962-1971, 1972-1981, 1982-1991, 1991-2001, > 2001) reported in Table 1 as linear combination coefficients. To find out the distribution of buildings belonging to different age ranges, the data derived from the sample of 22,618 residential masonry buildings surveyed after L’Aquila earthquake are used. From this database analysis, it can be noted that most of the buildings built before 1945 are characterized by irregular layout (class 4B and 5B in Table 1), whit high percentage of vaults in oldest buildings (class 23BC), while modern buildings are characterized by regular layout and rigid floors.



Table 1 - Occurrence percentages of vulnerability classes into 8 time intervals, defined by [3].

	Vaults with or w/o tie rods		Beams with Flexible slab				Beams with Semi-rigid slab				Beams with Rigid slab			
	Irregular layout or poor quality	Regular layout or good quality	Irregular layout or poor quality		Regular layout or good quality		Irregular layout or poor quality		Regular layout or good quality		Irregular layout or poor quality		Regular layout or good quality	
			W/o tie rods or tie beams	With tie rods or tie beams	W/o tie rods or tie beams	With tie rods or tie beams	W/o tie rods or tie beams	With tie rods or tie beams	W/o tie rods or tie beams	With tie rods or tie beams	W/o tie rods or tie beams	With tie rods or tie beams	W/o tie rods or tie beams	With tie rods or tie beams
	23BC	23DE	4B	4C	4D	4E	5B	5C	5D	5E	6B	6C	6D	6E
<19	22%	3%	25%	5%	2%	1%	21%	6%	4%	2%	3%	2%	1%	2%
19-45	8%	2%	23%	3%	4%	1%	23%	6%	9%	4%	4%	3%	3%	7%
46-61	2%	1%	9%	1%	4%	1%	17%	6%	13%	8%	5%	7%	7%	20%
62-71	1%	0%	3%	1%	6%	1%	4%	3%	9%	9%	3%	5%	12%	43%
72-81	0%	0%	2%	0%	4%	1%	2%	1%	6%	8%	1%	2%	11%	62%
82-91	0%	0%	2%	0%	6%	2%	2%	1%	5%	6%	2%	2%	11%	62%
92-2001	2%	1%	4%	1%	7%	4%	3%	2%	5%	5%	2%	2%	10%	53%
>2001	3%	0%	3%	1%	5%	5%	4%	3%	3%	9%	3%	2%	6%	52%

The second model, proposed by Rosti et al. [23] referred to as RO2020, was derived considering the L'Aquila 2009 and Irpinia 1980 post earthquakes data. Eight building typologies were identified, based on quality of the masonry fabric (i.e. irregular layout or poor-quality masonry, regular layout and good-quality masonry), in-plane flexibility of diaphragms (i.e. flexible, rigid), presence (or absence) of connecting devices. These typologies were fused into three vulnerability classes (A: high vulnerability, B: medium vulnerability, C1: low vulnerability) based on classification rules proposed by Rota et al. [4], reported in Table 2. As one of the purposes of this study was to implement the model using IRMA platform [12] for its possible application for national risk assessment in Italy [11], the authors proposed an exposure model that defines the rules to assign the percentage of each census-based typologies for masonry buildings (defined based on construction age - < 1919, 1919-45, 1946-61, 1962-71, 1972-81, > 1981- and height level - L and MH) into the three vulnerability classes A, B and C1.

Table 2 - Definition of vulnerability classes based on type of vertical and horizontal structures and presence of connection devices, as reported in [4]

Horizontal structure	Irregular texture or poor quality masonry		Regular texture and good quality masonry	
	w/o connecting device	with connecting device	w/o connecting device	with connecting device
Flexible	A	A	B	C1
Semi-rigid	A	A	B	C1
Rigid	A	B	C1	C1
Vaults	A	B	C1	C1

This exposure model was calibrated through an optimization problem finalized to minimize the difference among a set of empirical fragility curves, derived by the sole dataset of masonry buildings damaged after 2009 L'Aquila earthquake, and the fragility curves previously derived for A, B and C1 vulnerability classes. The resulting exposure matrix is reported in Table 3.

Table 3 - Composition of the masonry building stock in terms of percentages of macro-categories belonging to the different vulnerability classes, according to [23]

Class of height	Low			Medium-High		
Vulnerability class	A-L	B-L	C1-L	A-MH	B-MH	C1-MH
<19	86%	0%	14%	97%	0%	3%
19-45	45%	44%	11%	22%	78%	0%
46-61	9%	59%	32%	0%	75%	25%
62-71	5%	4%	91%	0%	18%	82%
72-81	0%	0%	100%	0%	0%	100%
82-91	0%	0%	100%	0%	0%	100%

### 3 EXPOSURE MODELLING: A CARTIS-BASED APPROACH

The proposed methodology relies on Cartis form's information to re-calibrate the exposure models in different Italian regions. The 1<sup>st</sup> level "Cartis" form is an interview-based form finalized to the survey of ordinary building typologies in sub-areas of the town denominated Town Compartments TC, characterized by prevailing homogeneity of the built environment in terms of initial period of construction and/or constructive structural characteristics. Using Cartis approach is possible to detect buildings features having strong influence on seismic behavior, allowing a more refined classification for buildings. In addition to age of construction and number of storeys, for masonry building the type of masonry (e.g. irregular layout masonry or regular layout with square stones or bricks), the horizontal slab type (e.g. flexible, rigid or semi-rigid slabs), the type of vaults (if present) and the presence of tie rods or tie beams are some of the vulnerability factors considered in the form. For each TC the form allows to detect up to four different typologies for masonry buildings (MUR1, MUR2, MUR3, MUR4) and four for RC buildings (CAR1, CAR2, CAR3, CAR4).

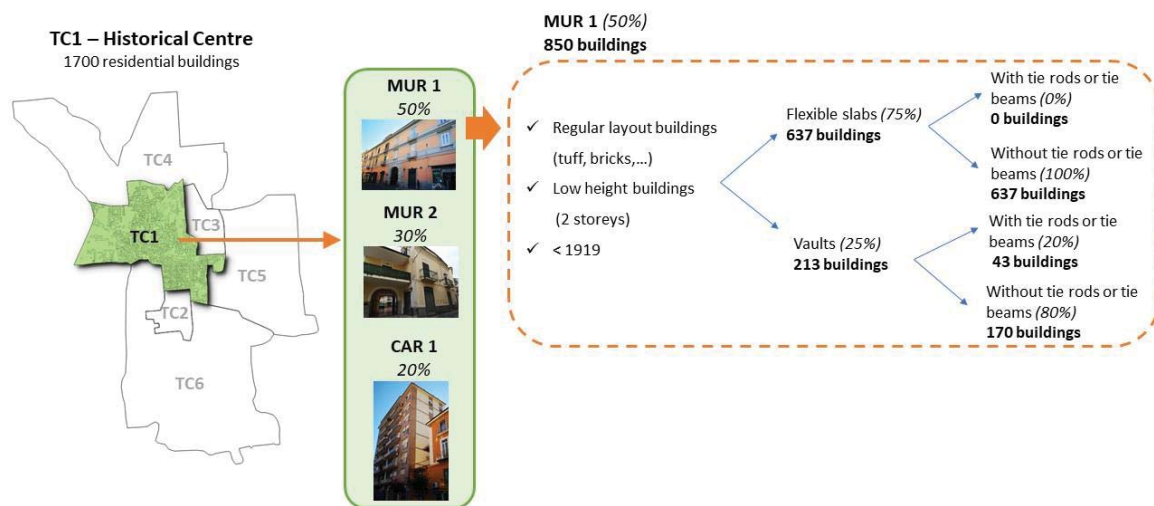


Figure 1 - Town Compartments for a town in the south of Italy and an example of buildings distribution for TC1, based on the related percentages reported in Cartis.

For each typology, the incidence percentages of the typology on the buildings in the TC are given. Therefore, given the total numbers of buildings in each TC, it is possible to derive the number of building belonging to different building typologies, and, consequently, considering all TCs in a town, the inventory at municipal level can be obtained. An example of the proce-

ture to derive the number of building for a masonry typology in a town compartment is reported in Figure 1.

Starting from the inventory compiled in towns where Cartis form is available, the occurrence percentage of building typologies at regional scale can be derived. Once the number of buildings belonging to defined structural types is obtained, it is possible to group them into vulnerability classes, according to the adopted vulnerability model.

In [22], based on the availability of Cartis-based inventory, a methodology for exposure modelling was proposed, that can be reassumed in the following steps:

- a) Compiling of Cartis-based inventory at urban scale, for all the towns where Cartis information is available.
- b) Deriving statistical distribution of building typologies at regional scale considering all the towns in the region for which Cartis-based inventory was compiled.
- c) Recalibration of exposure matrix with the percental distribution obtained by Cartis-based inventories, according to the vulnerability classes considered by the adopted vulnerability model.

Note that the reliability of the procedure is affected by the percentage of investigated towns as well as by their representativeness in terms of building and population number in a region.

As explained in [22], two slightly different approaches for the recalibration of the DG2019 and RO2020 models are applied. In DG2019 the age-dependent fragility curves to use with available ISTAT data was obtained by a linear combination of the fragility curves relative to the 14 building classes; therefore, after the recalibration of the exposure matrix a new set of age-dependent fragility curve has to be derived to evaluate the risk starting by census data. Differently, according to RO2020 model, only the exposure matrix was recalibrated, without modification of the fragility curves used for risk calculation. It is worth noting that the exposure matrices in DG2019 and RO2020 were obtained by statistical analysis of typological data relative to the sole buildings that were inspected after the 2009 L'Aquila earthquake. Thus, these matrices represent the typological distribution of a specific region (i.e. Abruzzo region). Therefore, a more accurate calibration procedure may improve the vulnerability characterization at regional level and consequently may affect the estimation of expected damage and impacts.

#### 4 APPLICATION FOR TWO ITALIAN REGIONS

The proposed procedure is applied for two Italian regions: Toscana and Veneto. In Toscana region 59 towns were surveyed through Cartis form, that represent about 22% of Toscana municipalities and 10% of regional inhabitants. In Veneto 35 towns were surveyed, representing the 6% of the municipalities and covering approximately the 11% of regional population.

According to the procedure previously described, the Cartis-based inventory is compiled for all the towns surveyed by Cartis form. Assuming the surveyed municipalities representative of the entire region, the percentage distribution of building typologies at regional level is obtained. It is worth noting that the Cartis database partially cover the whole regional territory, so this simplifying hypothesis could affect the reliability of estimations at regional scale. However, the present study represents a preliminary application to investigate the variability of vulnerability characterization at regional level and the results are expected to be updated when Cartis form on other municipalities will be compiled.

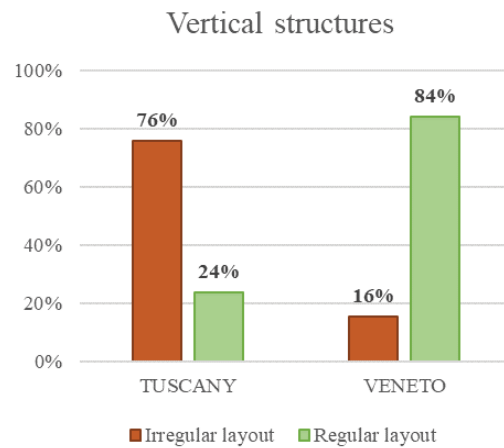


Figure 2 – Diffusion of the vertical (irregular or regular layout) types on masonry building stock at regional scale, derived by Cartis - based inventory.

The analysis of the regional inventories shows very different distribution of masonry building typologies. In Toscana irregular layout vertical structures are widespread, representing about 76% of masonry buildings, while in Veneto this typology characterizes just the 16% of the total, see Figure 2. Regarding horizontal structures type, the major difference between regional inventories is about the diffusion of semi-rigid slab type in irregular layout structures, about 36% in Toscana and almost absent in Veneto (2%), see Figure 3.

Once obtained the number of buildings with specific structural features (e.g. the number of masonry buildings with regular layout and vaults without tie rods), it's possible to group them into vulnerability classes according to DG2019 and RO2020 models and recalibrate the relative exposure matrices.

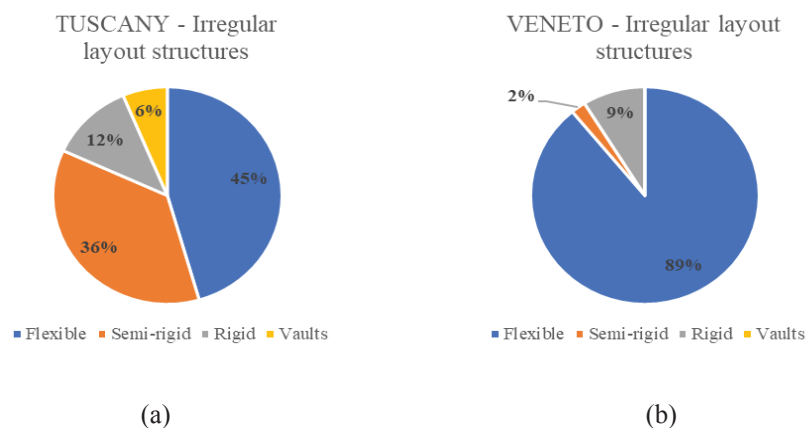


Figure 3- Diffusion of horizontal structure types for irregular layout buildings according to Cartis-based inventory, for Tuscany (a) and Veneto region (b).

The comparison with the DG2019 exposure model shows a considerable increase of irregular layout masonry structures in Tuscany for first and second time intervals (<1919, 1919-1945) (see Table 4). In particular, poor quality masonry structures without tie rods or tie beams and with flexible slabs (4B) and semi-rigid slabs (5B) are more widespread in Tuscany than in Abruzzo, according to the DG2019 matrix. Moreover, this type of structures represents a not negligible percentage of more recent built buildings.

Table 4 -DG2019 exposure matrix derived by Cartis-based inventory, for Tuscany region.

	Vaults with or w/o tie rods		Beams with Flexible slab				Beams with Semi-rigid slab				Beams with Rigid slab			
	Irregular layout or poor quality	Regular layout or good quality	Irregular layout or poor quality		Regular layout or good quality		Irregular layout or poor quality		Regular layout or good quality		Irregular layout or poor quality		Regular layout or good quality	
			W/o tie rods or tie beams	With tie rods or tie beams	W/o tie rods or tie beams	With tie rods or tie beams	W/o tie rods or tie beams	With tie rods or tie beams	W/o tie rods or tie beams	With tie rods or tie beams	W/o tie rods or tie beams	With tie rods or tie beams	W/o tie rods or tie beams	With tie rods or tie beams
	23BC	23DE	4B	4C	4D	4E	5B	5C	5D	5E	6B	6C	6D	6E
<19	8%	1%	43%	11%	5%	0%	23%	6%	0%	0%	1%	0%	1%	0%
19-45	3%	1%	21%	5%	7%	1%	41%	9%	1%	0%	7%	2%	3%	0%
46-61	0%	1%	12%	5%	8%	3%	31%	13%	7%	3%	7%	3%	5%	2%
62-71	0%	0%	1%	1%	1%	1%	1%	2%	1%	2%	12%	16%	22%	40%
72-81	0%	0%	1%	1%	1%	2%	1%	1%	1%	3%	10%	18%	16%	46%
82-91	0%	0%	0%	0%	1%	3%	0%	0%	1%	2%	12%	6%	14%	61%
92-2001	0%	0%	0%	0%	68%	1%	0%	0%	1%	0%	23%	0%	7%	0%
>2001	0%	0%	0%	0%	0%	0%	0%	0%	0%	0%	9%	0%	77%	15%

Table 5 - DG2019 exposure matrix derived by Cartis-based inventory, for Veneto region.

Vaults with or w/o tie rods		Beams with Flexible slab				Beams with Semi-rigid slab				Beams with Rigid slab				
	Irregular layout or poor quality	Regular layout or good quality	Irregular layout or poor quality		Regular layout or good quality		Irregular layout or poor quality		Regular layout or good quality		Irregular layout or poor quality		Regular layout or good quality	
			W/o tie rods or tie beams	With tie rods or tie beams	W/o tie rods or tie beams	With tie rods or tie beams	W/o tie rods or tie beams	With tie rods or tie beams	W/o tie rods or tie beams	With tie rods or tie beams	W/o tie rods or tie beams	With tie rods or tie beams		
	23BC	23DE	4B	4C	4D	4E	5B	5C	5D	5E	6B	6C	6D	6E
<19	0%	2%	35%	12%	24%	16%	1%	0%	0%	0%	4%	1%	3%	2%
19-45	1%	1%	15%	7%	24%	17%	0%	0%	0%	0%	9%	5%	12%	8%
46-61	0%	0%	0%	0%	3%	5%	0%	0%	0%	0%	4%	11%	32%	45%
62-71	0%	0%	0%	1%	2%	1%	0%	1%	0%	0%	4%	12%	45%	33%
72-81	0%	0%	0%	0%	0%	0%	0%	0%	0%	0%	1%	27%	48%	23%
82-91	0%	0%	0%	0%	0%	0%	0%	0%	0%	0%	2%	5%	58%	35%
92-2001	0%	0%	0%	0%	0%	0%	0%	0%	0%	0%	2%	15%	65%	18%
>2001	0%	0%	0%	0%	0%	0%	0%	0%	0%	0%	0%	0%	100%	0%

For Veneto region, irregular structures represent a significant percentage for older masonry buildings (<1919), but after 1950 almost the whole masonry buildings structures are regular layout structures with rigid floors (see Table 5). According to RO2020 model, it can be noted that for Tuscany region the differences between the original matrix and the recalibrated ones mostly concern masonry structures built between 1919 and 1945 and between 1946 and 1961, with many low-rise buildings classified in more vulnerable classes (Table 6). For Veneto a different distribution of older masonry buildings can be observed, with lower number of them classified as A (Table 7).



Table 6 - RO2020 Exposure matrix derived from Cartis-based inventory for Tuscany region.

Class of height	Low			Medium-High		
Vulnerability class	A-L	B-L	C1-L	A-MH	B-MH	C1-MH
<19	92%	6%	2%	90%	8%	2%
19-45	85%	11%	4%	85%	9%	5%
46-61	68%	19%	14%	70%	15%	15%
62-71	19%	15%	66%	14%	20%	65%
72-81	17%	17%	66%	10%	22%	67%
82-91	8%	11%	81%	17%	3%	80%

Table 7 - RO2020 Exposure matrix derived from Cartis-based inventory for Veneto region.

Class of height	Low			Medium-High		
Vulnerability class	A-L	B-L	C1-L	A-MH	B-MH	C1-MH
<19	51%	29%	21%	52%	24%	24%
19-45	24%	38%	38%	38%	24%	38%
46-61	0%	19%	81%	9%	8%	83%
62-71	4%	6%	90%	9%	19%	72%
72-81	0%	2%	98%	1%	46%	53%
82-91	2%	8%	91%	1%	3%	95%

#### 4.1 Damage and Risk assessment

The effects of a different vulnerability characterization at regional scale is evaluated with the aid of IRMA platform [12]. In the platform, different exposure/vulnerability models (VEM) and different sets of fragility curves can be employed. Deriving the exposure data from ISTAT 2011 database, the VEM is defined by an exposure matrix that identifies rules to classify the building typologies, derived by census data, into vulnerability classes adopted by the model. Using DG2019 approach the VEM is simply defined by building classes for age of construction, that are combined with the age-dependent fragility curves. In RO2020 approach, the VEM is defined by exposure matrix that provides the occurrence percentage of building classes (for age of construction and class of height) in the vulnerability classes identified in the model (A, B, C1), combined with the relative fragility curves. The improvement provided by the proposed procedure is evaluated comparing the outcomes of damage and risk assessment obtained by the adoption of the original set of age-dependent fragility curves and the exposure matrix, respectively for DG2019 and RO2020 model, with results obtained after the recalibration procedure.

Unconditional damage and risk assessment for 50 years timeframe is performed, that is an assessment obtained considering the probability of ground shaking severity in a selected time observation window according to PSHA based methodology. As both adopted VEM are for masonry buildings, the analyses are performed considering only this typology (masonry). Tables 8, 9, 10, 11 report the number of buildings for each damage state employing the original model (columns DG or RO) and the updated exposure modelling (columns DG+CA or RO+CA). The difference between the Cartis-based model and the original one is indicated as  $\Delta$  and the Regionalization factor RF, that can be considered as a parameter to represent variation in terms of expected damage due to a different exposure modelling, is calculated as the ratio of  $\Delta$  versus DG or RO, respectively for DG2019 and RO2020 model.

Table 8 - Number of buildings for each damage state, adopting the original exposure matrix DG2019 (DG) and the re-calibrated one based on CARTIS data (CARTIS) for Tuscany region.

	DG	DG+CA	$\Delta$	RF
<b>DS0</b>	138784	126798	-11986	-9%
<b>DS1</b>	133272	123662	-9610	-7%
<b>DS2</b>	59770	58576	-1194	-2%
<b>DS3</b>	81715	86155	4440	5%
<b>DS4</b>	88598	95497	6899	8%
<b>DS5</b>	46010	57462	11452	25%

Table 9 - Number of buildings for each damage state, adopting the original exposure matrix RO2020 (RO) and the re-calibrated one based on CARTIS data (CARTIS) for Tuscany region.

	RO	RO+CA	$\Delta$	RF
<b>DS0</b>	374663	340104	-34560	-9%
<b>DS1</b>	101790	111078	9288	9%
<b>DS2</b>	30561	41503	10942	36%
<b>DS3</b>	20040	26479	6439	32%
<b>DS4</b>	15714	21567	5853	37%
<b>DS5</b>	5381	7419	2038	38%

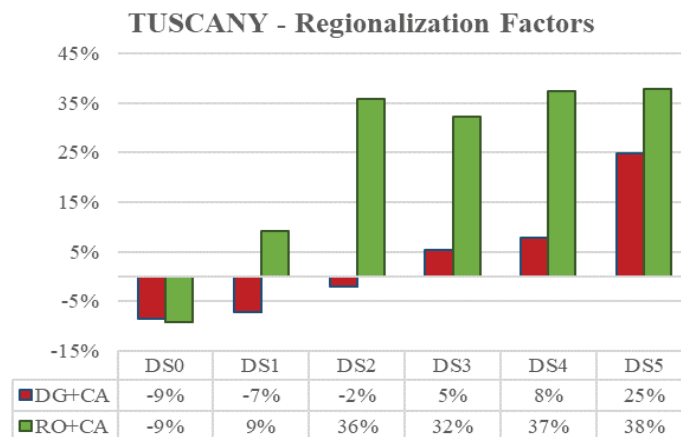


Figure 4 – The variation of number of buildings in each damage state with respect to the original model (i.e. the RF) obtained adopting the Cartis-based procedure (DG+CA for DG2019 and RO+CA for RO2020 model) for Tuscany region.

For Tuscany region, an increased number of building having medium-high damage states (DS3, DS4, DS5) can be observed according to Cartis-based model. Using DG2019 approach, the number of buildings that reach the heaviest damage grade (DS5) increases by +25%, while for the lower damage levels lower variations can be observed (see Figure 4). In reverse, adopting RO2020 model, with Cartis-based approach the numbers of buildings significantly increase for most of damage levels, with a value of RF grader than +30% from DS2 to DS5. This significant difference from DG2019 and RO2020 model is probably due to the different classification criteria. Indeed, according to RO2020 all the masonry buildings with irregular texture are classified as class A, the most vulnerable class, while in DG2019 different classes are identified for irregular layout buildings based on the horizontal structures type, to which different vulnerability level as well as fragility functions are associated. Therefore, for example, if for the second model irregular layout structures with rigid slab are less vulnerable than irregular layout structure without tie roads or tie beams with vaults, according to first one

these building are clustered in an unique class, the most vulnerable class A, greatly influencing the damage distribution.

For Veneto, a decrement of damaged buildings can be observed. Assuming the RF value for DS2 as reference, as it is representative of moderate damage, it can be observed a value of -30% according to DG2019 and -26% for RO2020. Differently to Tuscany region, for Veneto the presence of a small number of irregular layout structures, widespread only among oldest masonry building, leads to similar value of RF for both models (see Figure 5).

Table 10 - Number of buildings for each damage state, adopting the original exposure matrix DG2019 (DG) and the re-calibrated one based on CARTIS data (CARTIS) for Veneto region.

	DG	DG+CA	$\Delta$	RF
<b>DS0</b>	411779	504687	92907	23%
<b>DS1</b>	175772	145021	-30751	-17%
<b>DS2</b>	55532	39056	-16477	-30%
<b>DS3</b>	60906	39197	-21709	-36%
<b>DS4</b>	55843	34638	-21205	-38%
<b>DS5</b>	26863	24098	-2765	-10%

Table 11 - Number of buildings for each damage state, adopting the original exposure matrix RO2020 (RO) and the re-calibrated one based on CARTIS data (CARTIS) for Veneto region.

	RO	RO+CA	$\Delta$	RF
<b>DS0</b>	652750	673175	20425	3%
<b>DS1</b>	85160	78056	-7104	-8%
<b>DS2</b>	19676	14530	-5146	-26%
<b>DS3</b>	13587	10010	-3576	-26%
<b>DS4</b>	11031	7792	-3239	-29%
<b>DS5</b>	4493	3132	-1361	-30%

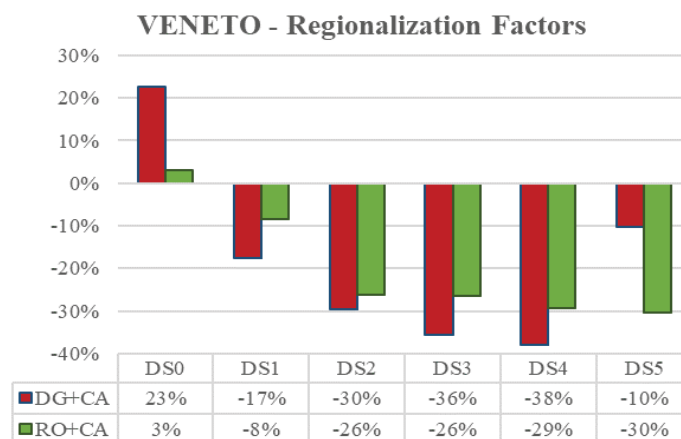


Figure 5 - The variation of number of buildings in each damage state with respect to the original model (i.e. the RF) obtained adopting the Cartis-based procedure (DG+CA for DG2019 and RO+CA for RO2020 model) for Veneto region.

The seismic risk in terms of economic losses is calculated, as well. In IRMA, the impact quantities are provided as a function of expected number of buildings affected by different damage level, according to the consequences model adopted in the recent national risk assessment for Italy (Dolce et al. 2020). The mean value of losses/m<sup>2</sup> among all the municipalities in each region is calculated and chosen as regional loss indicator. Likewise to what done previously, the regionalization factor due to losses RF<sub>L</sub> is evaluated.

Table 12 - Values of economic losses for each region analyzed, according to the different models adopted (DG2019 and the one recalibrated by Cartis-based approach).

	<b>L_DG/mq</b> <b>[€/mq]</b>	<b>L_CARTIS/mq</b> <b>[€/mq]</b>	<b>Δ [€/mq]</b>	<b>RF_L</b>
<b>TOSCANA</b>	566.9	621.1	54.2	<b>0.10</b>
<b>VENETO</b>	267.8	186.0	-81.8	<b>-0.31</b>

Table 13 - Values of economic losses for each region analyzed, according to the different models adopted (RO2020 and the one recalibrated by Cartis-based approach).

	<b>L_RO/mq</b> <b>[€/mq]</b>	<b>L_CARTIS/mq</b> <b>[€/mq]</b>	<b>Δ [€/mq]</b>	<b>RF_L</b>
<b>TOSCANA</b>	135.5	182.7	47.2	<b>0.35</b>
<b>VENETO</b>	65.1	50.3	-14.8	<b>-0.23</b>

## 5 CONCLUSIONS

The methodology proposed in [22] is adopted in this study to evaluate the effects of adopting improved exposure modelling on risk analysis. Cartis database is used to re-calibrate models relative to two existing empirical vulnerability models (DG2019 [3] and RO2020 [23]) for two Italian regions, Tuscany and Veneto. It is worth noting that this is a preliminary study about regional vulnerability characterization as the proposed exposure models are calibrated on the available Cartis' data on a limited number of municipalities in each region. However, the re-calibration procedure here proposed allows to detect the potential change in vulnerability region by region.

The main outcomes of the adopted approach can be summarized as follows:

- The use of Cartis-based approach leads to different distributions of building typologies at regional scale with respect to exposure models commonly calibrated on the base of empirical data derived on areas recently struck by an earthquake.
- The use of different exposure models at regional level has a significant influence on the damage assessment, also depending on the adopted vulnerability model. To assess such influence a parameter, the regionalization factor RF, may be defined to account for differences in damage assessment due to the use of improved exposure models with respect to original one. The RF referred to an intermediate damage state DS3 for Tuscany region is quite low adopting DG2019 model (5%), while assumes a value of +32% using RO2020 model. The reason of this discrepancy is probably due to the different vulnerability classification proposed by the models, that influence the damage distribution mostly for the regions where irregular layout structures are largely widespread.
- The influence of different exposure modelling at regional scale on economic losses can be effectively represented by regionalization factor associated to economic losses RF\_L. RF\_L may be used for a synthetic representation of the variation of risk estimation that can be obtained with improved exposure characterization.

As this study represents a first application toward the regional exposure assessment, the results obtained provide just a trend about vulnerability and risk at regional level and they can be improved when more data become available.

## ACKNOWLEDGMENTS

This study was performed within the framework of the PE2019–2021 joint program DPC-ReLUIS, WP2: “Inventory of existing building typologies” and WP4 “Risk maps and seismic damage scenarios”.

## REFERENCES

- [1] G. Grünthal European Macroseismic Scale, *Chaiers du Centre Européen de Géodynamique et de Séismologie*, Luxembourg, vol. 15, 1998.
- [2] F. Braga, M. Dolce, D. Liberatore, A statistical study on damaged buildings and an ensuing review of the MSK-76 scale, 1982, *In Proceedings of the seventh European conference on earthquake engineering*, Athens, Greece , 431-450, 1982.
- [3] C. Del Gaudio, G. De Martino, M. Di Ludovico, G. Manfredi, A. Prota, P. Ricci, GM Verderame, Empirical fragility curves for masonry buildings after the 2009 L’Aquila, Italy, earthquake. *Bull Earthq Eng* 17(11):6301–6330, 2019.
- [4] M. Rota, A. Penna, C.L. Strobbia, Processing Italian damage data to derive typological fragility curves. *Soil Dyn Earthq Eng* 28(10):933–947, 2008.
- [5] M. Pagani, J. Garcia-Pelaez, R. Gee, K. Johnson, V. Poggi, R. Styron, G. Weatherill, M. Simionato, D. Viganò, L. Danciu, D. Monelli, Global Earthquake Model (GEM) Seismic Hazard Map (version 2018.1 - December 2018), DOI: 10.13117/GEM-GLOBAL-SEISMIC-HAZARDMAP- 2018.1, 2018.
- [6] R. Spence, R. Foulser-Piggott, A. Pomonis, H. Crowley, P. Gue’guen, A. Masi, L. Chiauuzzi, G. Zuccaro, F. Cacace, C. Zulfikar, M. Markus, D. Schaefer, M.L. Sousa, A. Kappos, The European building stock inventory: creating and validating a uniform database for earthquake risk modeling and validating a uniform database for earthquake risk modeling risk modeling. In: *The 15th world conference on earthquake engineering*, Lisbon, Portugal, Sept 2012.
- [7] H. Crowley, V. Despotaki, D. Rodrigues, V. Silva, D. Toma-Danila, E. Riga, A. Karatzetzou, S. Fotopoulou, Z. Zugic, L. Sousa, S. Ozcebe, P. Gamba, Exposure model for European seismic risk assessment. *Earthquake Spectra*; DOI: 10.1177/8755293020919429, 2020.
- [8] M. Polese, M. Gaetani d’Aragona, A. Prota, Simplified approach for building inventory and seismic damage assessment at the territorial scale: an application for a town in southern Italy. *Soil dynamics and earthquake engineering*, 121:405-420, 2019.
- [9] M. Polese, M. Di Ludovico, M. Gaetani d’Aragona, A. Prota, G. Manfredi, Regional vulnerability and risk assessment accounting for local building typologies, *International Journal of Disaster Risk Reduction*, 43: 141400, 2020.
- [10] M. Polese, M. Di Ludovico, A. Prota, G. Tocchi, M. Gaetani d’Aragona, The use of Cartis form for inventory updating and effects on the vulnerability estimations at the territorial scale, *XVIII 25 Convegno Nazionale "L'Ingegneria Sismica in Italia"*, Paper ID 3508, Ascoli Piceno, September 2019 (in Italian).



- [11] M. Dolce, A. Prota, B. Borzi, F. da Porto, S. Lagomarsino, G. Magenes, C. Moroni, A. Penna, M. Polese, E. Speranza, G.M. Verderame, G. Zuccaro, Seismic risk assessment of residential buildings in Italy. *Bull Earthquake Eng.* <https://doi.org/10.1007/s10518-020-01009-5>, 2020.
- [12] B. Borzi, M. Onida, M. Faravelli, D. Polli, M. Pagano, D. Quaroni, A. Cantoni, E. Speranza, C. Moroni, IRMA platform for the calculation of damages and risks of residential buildings. *Bulletin of Earthquake Engineering*, DOI: 10.1007/s10518-020-00924-x, 2020.
- [13] A. Lucantoni, V. Bosi, F. Bramerini, R. De Marco, T. Lo Presti, G. Naso, F. Sabetta, Il rischio sismico in Italia. *Ingegneria Sismica*, 1, 5-35, 2001.
- [14] G. Di Pasquale, G. Orsini, R.W. Romeo, New developments in seismic risk assessment in Italy. *Bull Earthq Eng* 3:101–128, 2005.
- [15] F. Cacace, G. Zuccaro, D. De Gregorio, F.L. Perelli, Building Inventory at National scale by evaluation of seismic vulnerability classes distribution based on Census data analysis: BINC procedure. *International Journal of Disaster Risk Reduction*, 28, pp. 384-393, 2018.
- [16] A. Bernardini, S. Lagomarsino, A. Mannella, A. Martinelli, L. Milano, S. Parodi, Forecasting seismic damage scenarios of residential buildings from rough inventories: a case-study in the Abruzzi Region (Italy). *Proc. IMech E Part O: J. Risk and Reliability*, 224: 279-296, 2010.
- [17] M. Dolce, A. Goretti, Building damage assessment after the 2009 Abruzzi earthquake. *Bull Earthq Eng* 13(8):2241–2264, 2015.
- [18] F. Salmoiraghi F, Materiali naturali da costruzione, Milano, 1892.
- [19] F. Rodolico, Le pietre delle città d'Italia, Le Monnier, Firenze, 1965.
- [20] G. Zuccaro, M. Della Bella, F. Papa, Caratterizzazione tipologico strutturale a scala nazionale. *Atti 9° Convegno Nazionale ANIDIS, L'ingegneria Sismica in Italia*, Torino, 1999 (in Italian).
- [21] G. Zuccaro, M. Dolce, D. De Gregorio, E. Speranza, C. Moroni, La scheda CARTIS per la caratterizzazione tipologico- strutturale dei comparti urbani costituiti da edifici ordinari. Valutazione dell'esposizione in analisi di rischio sismico; In: *Proceedings of GNGTS*, 2015.
- [22] G. Tocchi, M. Polese, M. Di Ludovico, A. Prota, Regional based exposure models to account for local building typologies. *Bull Earthq Eng* (submitted).
- [23] A. Rosti, M. Rota, A. Penna, Empirical fragility curves for Italian URM buildings. *Bulletin of Earthquake Engineering*, DOI: 10.1007/s10518-020-00845-9, 2020.
- [24] M. Pagani, D. Monelli, G. Weatherill, L. Danciu, H. Crowley, V. Silva, M. Simionato, OpenQuake engine: an open hazard (and risk) software for the global earthquake model. *Seismol Res Lett* 85(3):692–702, 2014.
- [25] M. Stucchi, A. Akinci, E. Faccioli, P. Gasperini, L. Malagnini, C. Meletti, V. Montaldo, G. Valensise, Mappa di Pericolosità sismica del territorio Nazionale [http://zonesismiche.mi.ingv.it/documenti/rappor to\\_conclusivo.pdf](http://zonesismiche.mi.ingv.it/documenti/rappor to_conclusivo.pdf), 2004 (in Italian)

- [26] M. Stucchi, C. Meletti, V. Montaldo, H. Crowley, G.M. Calvi, E. Boschi, Seismic hazard assessment (2003-2009) for the Italian building code. *Bull Seism Soc of Am* 101:1885–1911, 2011.

## SEISMIC ASSESSMENT OF MASONRY BUILDINGS AT TERRITORIAL SCALE

C. Iacovino<sup>1</sup>, A. Flora<sup>1</sup>, D. Cardone<sup>1</sup> and M. Vona<sup>1</sup>

<sup>1</sup> School of Engineering, University of Basilicata, Italy

Viale dell'Ateneo Lucano, 10

{chiara.iacovino, amedeo.flora, donatello.cardone, marco.vona}@unibas.it

---

### Abstract

*In the last decades, a number of methodologies for the performance based-loss assessment of buildings have been proposed and developed. Among those, the PEER Performance-Based Earthquake Engineering (PBEE) methodology represents the most comprehensive approach providing probabilistic estimates of seismic losses. However, those procedures are suitable for building-specific evaluations, appearing extremely time-consuming if applied at the urban scale. Recently, many authors proposed simplified approaches relating the economic losses to the structural response (i.e. Engineering Demand Parameters, EDP) derived from analysis methods within the reach of the most practicing engineers. Many of these procedures have been also implemented in current seismic codes. In this paper a seismic loss assessment of the residential masonry building stock of the city center of Potenza is performed based on the simplified approach currently adopted within the Italian Seismic Risk Classification. After a preliminary typological characterization of the investigated structures, the mentioned methodology has been applied to derive the expected annual loss of masonry buildings, deriving information on the seismic resilience of the examined built heritage at urban scale. Preliminary socio-economic considerations of seismic scenarios at urban scale are discussed. The results presented herein are part of a comprehensive research activity performed within PON-AIM 2014-2020 project aimed at the definition of the seismic resilience of the examined area.*

**Keywords:** Masonry buildings, Seismic Risk Assessment, Vulnerability, Built Heritage.

---

## 1 INTRODUCTION

Observations from worldwide earthquakes illustrated the severe economic consequences in highly developed regions of society. In general, these economic consequences can be primarily attributed to: (i) direct economic losses associated with repairing damage within a structure [1], (ii) direct losses associated with injuries and casualties and (iii) indirect losses associated with the loss of income due to business disruption [2].

More in details, the economic losses from physical damage strongly influence the community's recovery capability, especially when a relevant portion of the building stock is represented by unreinforced masonry (URM) constructions. As a matter of fact, damage on masonry buildings usually involves expensive and time-consuming repairing activities that can be carried out only by expert builders, thus further enhancing the cost of the interventions. Moreover, the larger is the period of time requested to restore the operativity of the structure, the larger is the downtime, namely, the indirect losses associated with loss of productivity, business interruption and cost of occupants reallocation. All that considered, an appropriate loss estimation of buildings is crucial for the development of resilient communities in seismic prone areas [3], [4], providing risk-based information, which may help Governments, stakeholders and owners to define the priority of interventions or policies for disaster prevention.

In the last decade, several loss estimation methodologies have been proposed, although accurate quantification of loss is still a difficult task subject due to several uncertainties [5]-[8]. In recent years the accurate Performance Based Earthquake Engineering (PBEE) approach proposed by the US FEMA P-58 has been increasingly adopted for the seismic assessment of structures [9]. The method consists of a number steps implemented to provide information regarding the building's performances in terms of probability of exceedance (PoE) of specific Decision Variables (DV), such as monetary losses, casualties, downtime [10]. In the first step, a given site location and local characteristics are related to the seismic hazard expected from the surrounding region. In the second step, a probabilistic description of the seismic demand to the building at increasing levels of ground motion intensity is obtained from the results of a series of Nonlinear Response History Analyses (NRHAs). Subsequently, damage to individual structural and nonstructural components is estimated, through a suite of fragility curves, as a function of selected Engineering Demand Parameters (EDPs) (e.g., peak inter-story drifts, floor accelerations etc.) computed in the second step of analysis. Finally, expected losses are estimated through a set of suitable consequence functions, based on the level of damage sustained by each component.

The main output parameter of the PBEE approach is represented by the expected annual loss (EAL) [11], defined as the average economic loss expected to accrue every year in the structure, considering both the direct repair costs related to damage and the social costs associated to downtime. The synthetic information expressed by these parameters represents a powerful tool for the stakeholders. In particular, the EAL estimations in both the as-built and retrofitted configurations can be assumed as input parameters for a cost-benefit analysis, aimed at the rational choice of the optimal retrofit intervention among different options.

However the PBEE approach is still infrequently employed for the assessment of existing URM constructions. Difficulties in the application of the methodology arise in the calculation of the EAL involving the building's performance assessment at increasing intensity earthquakes. This requires significant computational efforts and is generally unaffordable for applications in the common practice.

Recently, simplified approaches, relating the economic losses to the structural response (engineering demand parameters, EDP) derived from analysis methods within the reach of the most practicing engineers, have been proposed [12], [13]. In particular, the main simplifica-

tion lies in relating a given performance level (PL) to an expected economic loss calculated based on specific story-based loss function [14] or pre-defined based on the actual structural typology [15]. The latter approach has been recently implemented within the Italian Seismic Risk Classification [16] to evaluate the “seismic quality” of existing buildings, providing a specific score system articulated in eight seismic risk classes. Generally speaking, the mentioned procedure appears useful when the amount information regarding the building geometry and structural details is limited and a reliable characterization of the seismic performances is uncertain. The Italian Seismic Risk Classification defines eight seismic performance-based risk classes in terms of EAL and structural collapse capacity. Those classes are employed to give an overall rating on a letter-based scale from A+ to G, similar to the appliances energy consumption scale used in Europe [17].

In this paper, the seismic loss assessment of the residential masonry building stock of the city center of Potenza (southern Italy) is presented. First of all, a complete identification and typological characterization of the residential masonry structures has been performed. Subsequently, different archetype buildings, one for each typology, have been implemented in the 3Muri environment [18] in order to derive their structural response through non-linear static analyses. Finally, based on the main Engineering Demand Parameters obtained in the previous step, the estimation of the EAL is performed according with the Italian guidelines seismic risk classification. The results in terms of monetary losses are then discussed to derive preliminary considerations on the economic and social impacts of probable seismic scenarios. A complementary study regarding the Reinforced Concrete (RC) residential buildings located in the examined area has been recently carried out [19].

## 2 OVERVIEW OF THE CONVENTIONAL APPROACH FOR THE ESTIMATION OF EXPECTED ANNUAL LOSS

The guidelines approved by the High Council of Public Works [16] define the methods addressing the seismic risk classification of constructions and the effectiveness of strengthening interventions. In particular, a conventional method is proposed based on the identification of the seismic performances towards four predefined limit states, namely Operational (SLO), Damage Limitation (SLD), Life Safety (SLV) and Collapse (SLC) [16]. The main novelty of the conventional method is represented by the introduction of two further conventional limit states: the Initial Damage (ID), resulting in a slight initial damage to the structural components and occurring for seismic events featuring a 10 years return period ( $T_r$ ) and the Reconstruction limit state (RLS), referring to seismic events causing a monetary loss corresponding to the total value of the construction [20].

The seismic risk class of the building is defined as the minimum between two classes: the IS-V class, associated to the Safety Index of the structure at the Life Safety Limit State, and the EAL class. The Safety Index is calculated as the ratio between  $PGA_{C,SLV}$  (PGA related to the capacity of the building at the Life Safety Limit State) and  $PGA_{D,SLV}$  (demand PGA prescribed by the code at Life Safety Limit State). The EAL-based score is related to the performances of the structure in terms of seismic losses (namely percentage of Expected Losses towards the total cost of the building, %RC) at different return periods  $T_r$  (namely Mean Annual Frequency of Exceedance, MAFE). More in details, the MAFE ( $\lambda$ ) is calculated according to Equation (1):

$$\lambda = \frac{1}{T_{rc}} = \frac{1}{T_{rd} (PGA_D / PGA_C)^{1/0.41}} \quad (1)$$

where  $T_{rc}$  and  $T_{rd}$  are the return periods related to capacity and demand respectively.



The guidelines [16] also provide conventional %RC, properly calibrated to include all the repair actions associated to a specific damage level.

Figure 1 shows the entire procedure for the EAL index calculation. First of all, a pushover analysis is required to assess the building performances at the four pre-defined limit states (SLO, SLD, SLV and SLC, Figure 1b). At this point, the Multiple Degrees of Freedom (MDOF) System is converted to an equivalent single degree-of-freedom (SDOF) system (Figure 1c). Then, for each limit state, the PGA associated to the building capacity ( $PGA_C$ ) can be calculated in the Acceleration Displacement Response Spectrum (ADRS) plane following the N2 method [21] (Figure 1d). In particular, the  $PGA_C$  is evaluated by scaling the response spectrum until the displacement demand matches the capacity at the reference limit state. Subsequently, based on the seismic hazard model adopted within the reference building code [22], the MAFE values corresponding to the mentioned limit states are determined (Figure 1e) and associated to the Expected Loss Ratios (%RC) prescribed in the guidelines [16]. For what concerns the ID limit state, an Expected Loss Ratio equal to 0% has been conventionally associated to a MAFE value equal to 0.1. Similarly, for the RLS an Expected Loss Ratio equal to 100% has been conventionally associated to a MAFE value equal to that calculated for the SLC limit state. A loss curve (multi-linear function) in the MAFE vs Expected Loss Ratio domain is thus obtained (Figure 1f). Finally, the EAL is computed by integrating the mentioned loss curve. More details about the described procedure are reported in [20]. Table 1 shows the risk classes for safety and economic assessment according to the mentioned guidelines [16].

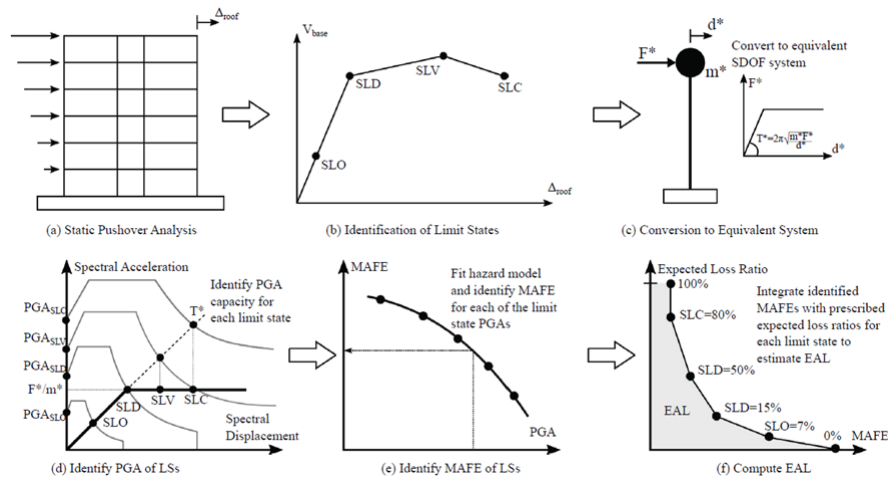


Figure 1: Steps of the Italian seismic risk classification scheme described in [23].

Safety assessment	Economic assessment	Risk class
IS-V (%)	EAL (%)	
$IS-V \geq 100$	$EAL \leq 0.5$	A+
$80 \leq IS-V < 100$	$0.5 \leq EAL < 1.0$	A
$60 \leq IS-V < 80$	$1.0 \leq EAL < 1.5$	B
$45 \leq IS-V < 60$	$1.5 \leq EAL < 2.5$	C
$30 \leq IS-V < 45$	$2.5 \leq EAL < 3.5$	D
$15 \leq IS-V < 30$	$3.5 \leq EAL < 4.5$	E
$IS-V < 15$	$4.5 \leq EAL < 7.0$	F
	$EAL \geq 7.5$	G

Table 1: Definition of risk classes as a function of both EAL and IS-V according to [16].

### 3 BUILDING TYPOLOGIES IDENTIFICATION FOR THE CITY CENTRE OF POTENZA

This work is carried out on the city of Potenza, located in Basilicata on a hill in the axial-active seismic belt (30 to 50 km wide) of southern Apennines. The city was hit by several strong earthquakes (intensity higher than or equal to VIII MCS). In particular, the 1826 and 1857 events caused severe damage in the entire town imposing a massive demolition and reconstruction activity in the historical city center [24]. In the aftermath of the Irpinia and Basilicata earthquake (November 1980), a massive reconstruction plan, funded by the Italian Government (law 219/81), involved several existing buildings in the Potenza municipality.

In this paper, the seismic assessment is referred to two main areas, namely the “old town center” and the “residential public housing neighborhood”, that can be considered as homogeneous zones (compartments) featuring specific historical, urbanistic and constructive peculiarities. Moreover, such compartments include most of the historical built heritage of the city, developed in two main periods: 1850-1950 and 1945-1990, respectively.

The specific building typologies inventory have been defined by combining the official national census database provided by the Italian Institute of Statistics (ISTAT) as the primary source for the classification of the building stock [25], integrated through secondary sources of information represented by extensive documental and virtual analysis and specific building surveys [26], [27]. More in details, a comprehensive documental analysis has been carried out based on the large database provided by the local organization of Social Housing (Azienda Territoriale per l'Edilizia Residenziale, ATER), directly involved in the residential compartment construction and in the post-seismic reconstruction after the Irpinia Earthquake (1980). Moreover, a number of building-by-building surveys, providing detailed data for both dimensional and structural peculiarities for a single building in an investigated area, have been performed. Finally, further information has been gathered interviewing local technicians with deep knowledge of the construction characteristics.

All that considered, the following main variables emerged as significant classification parameters: (i) masonry texture configuration (regular or irregular), (ii) horizontal structure typology (deformable, semi-rigid or rigid slab), (iii) presence of mixed structures (i.e. mixed masonry-RC structures), (iv) roof types, (v) presence of vaults, (vi) presence of seismic structural intervention. Based on the mentioned parameters, a preliminary macro-typologies inventory for the examined compartments has been defined, retrieving six macro-classes of masonry constructions (MUR).

The MUR1 and MUR2 typologies concern the first urban village built outside the historical center of the city in the 1920s. The MUR1 buildings feature squared local stone or solid brick masonries. Floors are mainly realized with hollow bricks and steel beams. The roof is pitched with wood structure and planking. This typology is characterized by the absence of vaults and mixed structures. Similar features have been retrieved for the MUR2 typology except for the vertical and horizontal structures, which are characterized by barely cut stone and vault floor with bricks and steel beams. The roof is pitched with brick-concrete slab. Over the years, some of the buildings included in the MUR2 typology have been subjected to strengthening interventions, consisting mainly of widespread connections (insertion of metal bars or RC beams). The MUR3 and MUR4 typologies, built in 1940-1960, group masonry constructions featuring solid brick masonry and lime mortar with rigid slab (reinforced brick-concrete) and connections between vertical walls and horizontal elements. In particular, the MUR4 typology is characterized by external masonry walls and internal RC beam-column systems. Both typologies show reinforced concrete pitched roof slab. The MUR5 and MUR6 typologies, built before 1920, are made of disorganized irregular stone masonry with friable mortar.

Such buildings have been retrofitted through different types of interventions (application of diffused tie-roads, filling the voids and/or cracks inside the wall by injecting of new mortar, substitution of damaged elements along cracking lines with new ones, etc.) performed after the Irpinia-Basilicata earthquake. The deformable slabs have been generally replaced by a rigid floor with reinforced brick-concrete slabs.

This preliminary inventory has been further refined considering other significant attributes emerged from the described documental and in situ investigations. Among those, irregularities in plan and the presence of connections between slabs and walls cannot be ignored for a comprehensive evaluation of the building typologies. In particular, based on the gathered data, masonry constructions in the investigated area can be grouped into three main classes: low-rise buildings “Lr” (1-2 stories), medium-rise buildings “Mr” (3-4 stories) and high-rise buildings “Hr” (5-6 stories). The mentioned number of stories ranges (1–2, 3–4, and 5–6) have been defined according with the considerations drawn in [28]. Indeed, all other variables being equal, masonry buildings featuring one to two stories exhibit a similar seismic behavior [28]. A similar criterion can be adopted for medium- and high-rise buildings.

In this optic, seventy-two typologies have been finally identified from the classification approach discussed above, as shown in Table 2.

MACRO-CLASS	Number of stories			Shape in plan		Slab-wall connections		ID
	Lr	Mr	Hr	Reg.	Irreg.	C	Nc	
MUR1	x			x		x		MUR1, Lr, Reg, C
	x			x			x	MUR1, Lr, Reg, Nc
	x				x	x		MUR1, Lr, Irreg, C
	x				x		x	MUR1, Lr, Irreg, Nc
		x		x		x		MUR1, Mr, Reg, C
		x		x			x	MUR1, Mr, Reg, Nc
		x			x	x		MUR1, Mr, Irreg, C
		x			x		x	MUR1, Mr, Irreg, Nc
			x	x		x		MUR1, Hr, Reg, C
			x	x			x	MUR1, Hr, Reg, Nc
			x		x	x		MUR1, Hr, Irreg, C
			x		x		x	MUR1, Hr, Irreg, Nc
MUR2	x			x		x		MUR2, Lr, Reg, C
	x			x			x	MUR2, Lr, Reg, Nc
	x				x	x		MUR2, Lr, Irreg, C
	x				x		x	MUR2, Lr, Irreg, Nc
		x		x		x		MUR2, Mr, Reg, C
		x		x			x	MUR2, Mr, Reg, Nc
		x			x	x		MUR2, Mr, Irreg, C
		x			x		x	MUR2, Mr, Irreg, Nc
			x	x		x		MUR2, Hr, Reg, C
			x	x			x	MUR2, Hr, Reg, Nc
			x		x	x		MUR2, Hr, Irreg, C
			x		x		x	MUR2, Hr, Irreg, Nc
MUR3	x			x		x		MUR3, Lr, Reg, C
	x			x			x	MUR3, Lr, Reg, Nc
	x				x	x		MUR3, Lr, Irreg, C
	x				x		x	MUR3, Lr, Irreg, Nc

		X		X		X		MUR3, Mr, Reg, C
		X		X			X	MUR3, Mr, Reg, Nc
		X			X	X		MUR3, Mr, Irreg, C
		X			X		X	MUR3, Mr, Irreg, Nc
			X	X		X		MUR3, Hr, Reg, C
			X	X			X	MUR3, Hr, Reg, Nc
			X		X	X		MUR3, Hr, Irreg, C
			X		X		X	MUR3, Hr, Irreg, Nc
MUR4	X			X		X		MUR4, Lr, Reg, C
	X			X			X	MUR4, Lr, Reg, Nc
	X				X	X		MUR4, Lr, Irreg, C
	X				X		X	MUR4, Lr, Irreg, Nc
		X		X		X		MUR4, Mr, Reg, C
		X		X			X	MUR4, Mr, Reg, Nc
		X			X	X		MUR4, Mr, Irreg, C
		X			X		X	MUR4, Mr, Irreg, Nc
			X	X		X		MUR4, Hr, Reg, C
			X	X			X	MUR4, Hr, Reg, Nc
			X		X	X		MUR4, Hr, Irreg, C
			X		X		X	MUR4, Hr, Irreg, Nc
MUR5	X			X		X		MUR5, Lr, Reg, C
	X			X			X	MUR5, Lr, Reg, Nc
	X				X	X		MUR5, Lr, Irreg, C
	X				X		X	MUR5, Lr, Irreg, Nc
		X		X		X		MUR5, Mr, Reg, C
		X		X			X	MUR5, Mr, Reg, Nc
		X			X	X		MUR5, Mr, Irreg, C
		X			X		X	MUR5, Mr, Irreg, Nc
			X	X		X		MUR5, Hr, Reg, C
			X	X			X	MUR5, Hr, Reg, Nc
			X		X	X		MUR5, Hr, Irreg, C
			X		X		X	MUR5, Hr, Irreg, Nc
MUR6	X			X		X		MUR6, Lr, Reg, C
	X			X			X	MUR6, Lr, Reg, Nc
	X				X	X		MUR6, Lr, Irreg, C
	X				X		X	MUR6, Lr, Irreg, Nc
		X		X		X		MUR6, Mr, Reg, C
		X		X			X	MUR6, Mr, Reg, Nc
		X			X	X		MUR6, Mr, Irreg, C
		X			X		X	MUR6, Mr, Irreg, Nc
			X	X		X		MUR6, Hr, Reg, C
			X	X			X	MUR6, Hr, Reg, Nc
			X		X	X		MUR6, Hr, Irreg, C
			X		X		X	MUR6, Hr, Irreg, Nc

Lr: low-rise buildings, Mr: medium-rise buildings, Hr: high-rise buildings, Reg: regular shape in plan, Irreg: irregular shape in plan, C: presence of slab-wall connections, Nc: absence of slab-wall connections.

Table 2: Building typologies inventory.

However, the number of masonry buildings actually included in some of the mentioned typologies classes is extremely limited. As a consequence, in order to reduce the computational efforts and also considering the slight incidence of a limited number of cases on the entire seismic assessment of the area, the typologies including a number of elements lower than three have been neglected. Seven typologies have been finally considered in what follows counting 213 buildings in total, distributed as reported in Table 3. For the sake of clarity, it is worth noting that, in this work, only isolated residential buildings have been taken into account. As a matter of fact, considering their inherent peculiarities, specific studies are needed for the seismic assessment of the historical-monumental and masonry aggregates located in the examined area. For the same reason, the MUR5 typology, composed by masonry aggregates, has not been included in Table 3.

Building typology	Number of buildings
MUR1,Hr,Reg,Nc	28
MUR3,Lr,Reg,C	20
MUR3,Mr,Reg,C	59
MUR3,Hr,Reg,C	31
MUR4,Mr,Reg,C	35
MUR4,Mr,Irreg,C	16
MUR6,Hr,Reg,C	24
Total	213

Table 3: Prevalent building typologies distribution.

## 4 CASE STUDIES

### 4.1 Archetype buildings

A series of archetype buildings, one for each typology, has been defined. The archetype referred to the first building typology (MUR1,Hr,Reg,Nc) is a five-story masonry building featuring a floor area equal to 317 m<sup>2</sup> (20.7 x 15.3 m) and a total height equal to 18 m (Figure 2). The vertical structure is composed by solid bricks, except for the first floor featuring an irregular stone masonry. The horizontal structure configuration consists in steel beams and hollow clay bricks. Three archetypes have been defined for the MUR3 building typology (Figures 3 to 5). The same dimensions in plan (23.4 x 12.4 m) have been adopted for all the mentioned archetypes, while different total height values have been considered: 7.1 m, 13.7 m and 20.3 m for “Lr”, “Mr”, and “Hr” building typologies, respectively. The vertical structure of the MUR 3 archetypes is composed by a solid brick masonry and lime mortar. On the other hand, RC floors with tie beams (connecting floors and masonry walls) have been adopted as horizontal structure. The building archetypes shown in Figure 6 and 7 are referred to MUR4. In both cases such archetypes feature a four-story mixed masonry-RC vertical structure. More in details, external masonry walls mixed with an internal RC beam-column system have been adopted. The MUR4 archetype buildings feature the same horizontal structure (reinforced brick-concrete floors) while differ in terms of plan configuration.

The last building prototype (Figure 8) refers to buildings located in the historical city center and involved in the reconstruction plan pursued in the aftermath of the Irpinia-Basilicata earthquake. The performances of the “ancient” masonry, characterized by disordered rubble stone with friable mortar and irregular sub-horizontal courses, were improved through widespread retrofit interventions (e.g., application of diffused tie-roads, injection grouting, damaged elements substitution, etc.). For what concerns the horizontal structure, the deformable



timber floors without steel chains and RC tie-beams were replaced by rigid floors with reinforced brick-concrete slab. The latter configuration has been implemented in the numerical model describing the MUR6 archetype (see Section 4.2).

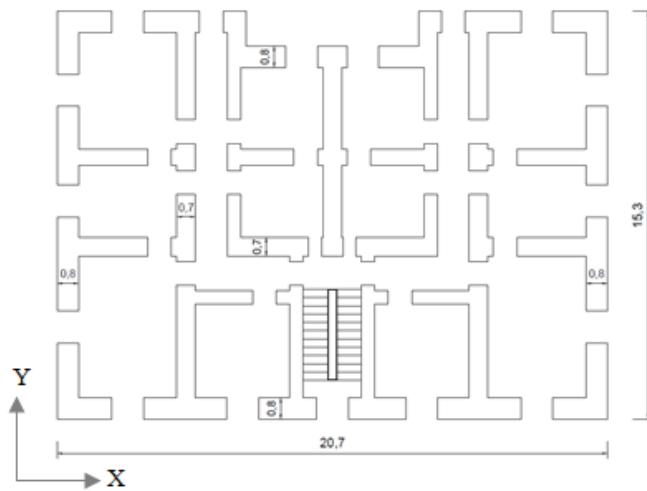


Figure 2: MUR1,Hr,Reg,Nc building typology: plan geometry of the first story (left) and a picture (right).

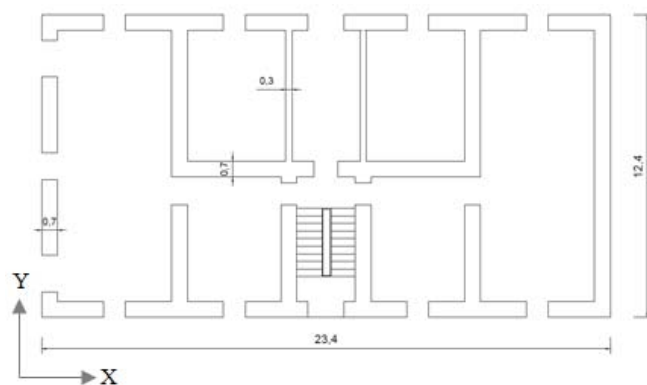


Figure 3: MUR3,Lr,Reg,C building typology: plan geometry of the first story (left) and a picture (right).

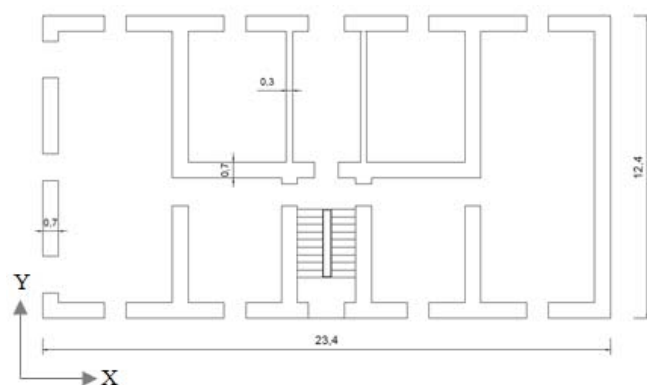


Figure 4: MUR3,Mr,Reg,C building typology: plan geometry of the first story (left) and a picture (right).

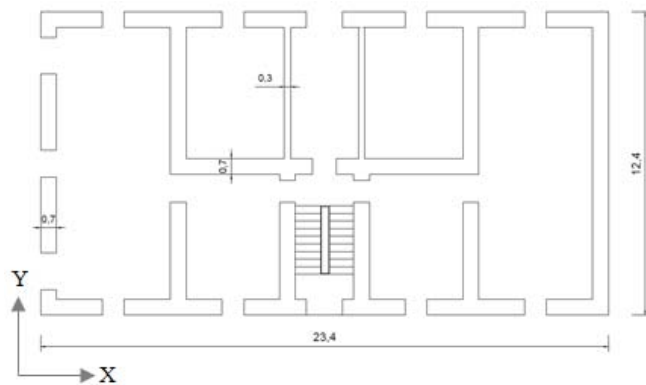


Figure 5: MUR3,Hr,Reg,C building typology: plan geometry of the first story (left) and a picture (right).

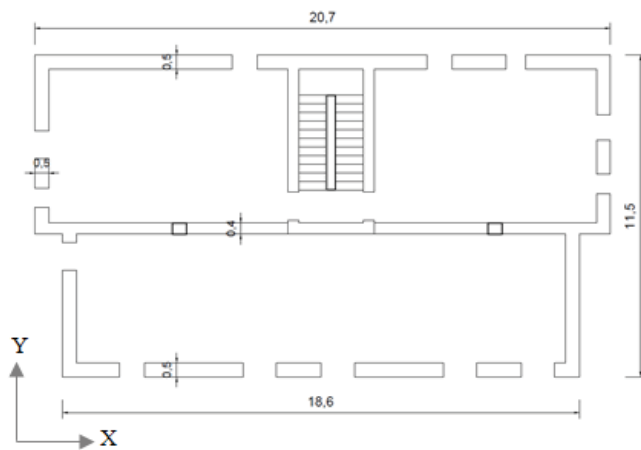


Figure 6: MUR4,Mr,Reg,C building typology: plan geometry of the first story (left) and a picture (right).

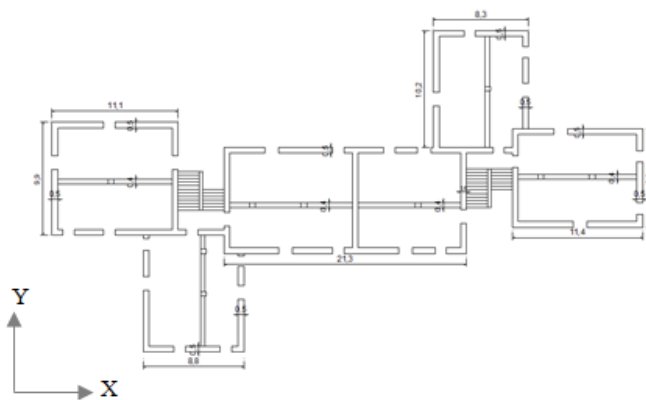


Figure 7: MUR4,Mr,Irreg,C building typology: plan geometry of the first story (left) and a picture (right).

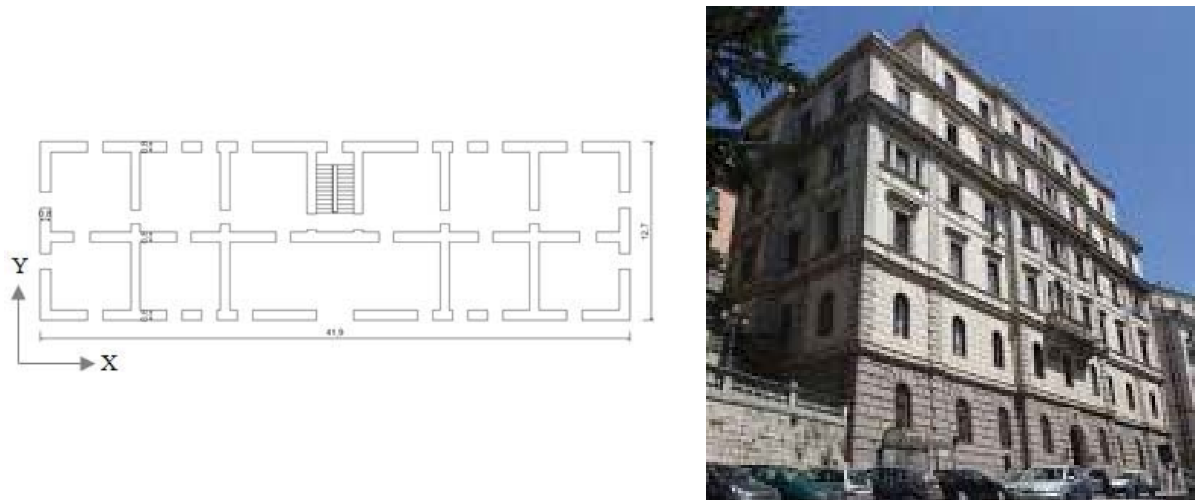


Figure 8: MUR6,Hr,Reg,C building typology: plan geometry of the first story (left) and a picture (right).

Generally speaking, the number of experimental campaigns aimed at the characterization of the mechanical properties of masonry is very limited if compared to the amount of data referred to concrete and reinforcements. As a matter of fact, the execution of exhaustive tests is frequently difficult due to both built heritage conservation issues and economic aspects [29]. Given the poor amount of data regarding the mechanical properties of the materials constituting the existing masonry buildings located in the examined area, reference to the typical values provided by the current Italian seismic code (Table C8.5.I [30]) have been taken into account. These values refer to historic masonry in poor conditions and have to be modified by corrective coefficients in the evidence of qualified characteristics, such as good mortar, presence of stringcourses etc.. Table 4 summarizes the values of the elastic and mechanical characteristics derived from the mentioned seismic code and adopted in the numerical models for irregular stone, barely cut stone and solid brick masonry panels.

Mechanical properties	Irregular stones	Barely cut stone	Brick and lime mortar
Comp. strength $f_{m,av}$ (MPa)	1.5	2	3.45
Shear strength $\tau_{0,av}$ (MPa)	0.025	0.043	0.09
Young modulus $E_{av}$ (MPa)	870	1230	1500
Shear modulus $G_{av}$ (MPa)	290	410	500

Table 4: Mechanical parameters adopted in the numerical models.

Finally, it is worth noting that all the archetype buildings are assumed to be located on a medium soil classified as soil type B, according with the current Italian seismic code [22]. For each archetype, the site hazard curve, defined based on the data provided by the INGV (Italian Institute of Geophysics and Volcanology), is expressed in terms of Mean Annual Frequency of Exceedance (MAFE<sub>i</sub>) as a function of the considered IM, namely, the Peak Ground Acceleration (PGA).

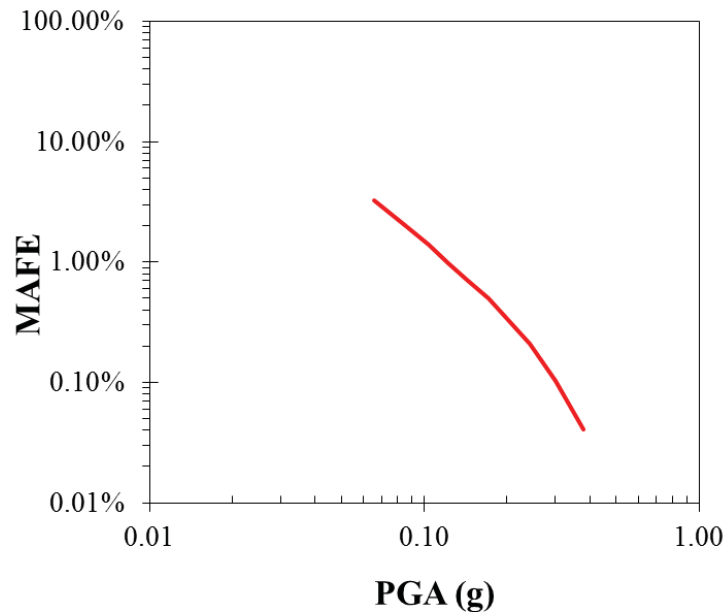


Figure 9: Hazard curve of the examined site, Potenza Soil Type B.

## 4.2 Numerical modeling

In order to assess the global behavior of the selected archetype buildings, 3d non-linear numerical models have been implemented in the 3Muri environment [18]. The mentioned software has been specifically developed for the evaluation of both local and global seismic response of URM buildings. 3Muri is based on the “Equivalent Frame Model” (EFM) approach. Generally speaking, a generic masonry wall with openings is idealized by identifying two main structural components, namely the piers and the spandrels, in which the non-linear response is concentrated, connected by a rigid area (nodes). The piers are the main vertically resisting elements while the spandrels couple the response of two adjacent piers. The identification of the geometrical properties of piers and spandrels is automatically performed by the software according to conventional criteria. The non-linear macro-element model implemented in 3Muri allows the two main failure modes, governing the response of masonry walls to be reproduced with a limited number of degrees of freedom. In terms of flexural behavior, rocking and crushing mechanisms are considered, whereas diagonal cracking and shear sliding are taken into account for shear failure. In order to define the ultimate shear and bending strength, simplified criteria are implemented in the software. The elastic behavior is defined considering the mechanical and geometrical properties of the masonry and a stiffness reduction factor is introduced to account for cracked conditions. It is worth noting that, in the numerical models of the archetypes included in the MUR4 building typology, the RC structural members have been modeled using non-linear lumped plasticity elements [18].

It is worth noting that the main assumption adopted in the numerical modeling is that the global behavior of the mentioned archetypes is fundamentally governed by the in-plane behavior of walls. In other words, the local mechanisms (mainly out-of-plane mechanisms) are not taken into account. This assumption is considered acceptable for most of the examined archetypes (namely all the archetypes except MUR1), since the systematic presence of RC ring beams is expected to reduce the vulnerability to local mechanisms [31]-[33]. The numerical models of the selected building prototypes are represented in Figure 10. As can be observed, the presence of staircase has been neglected at this step of the study.

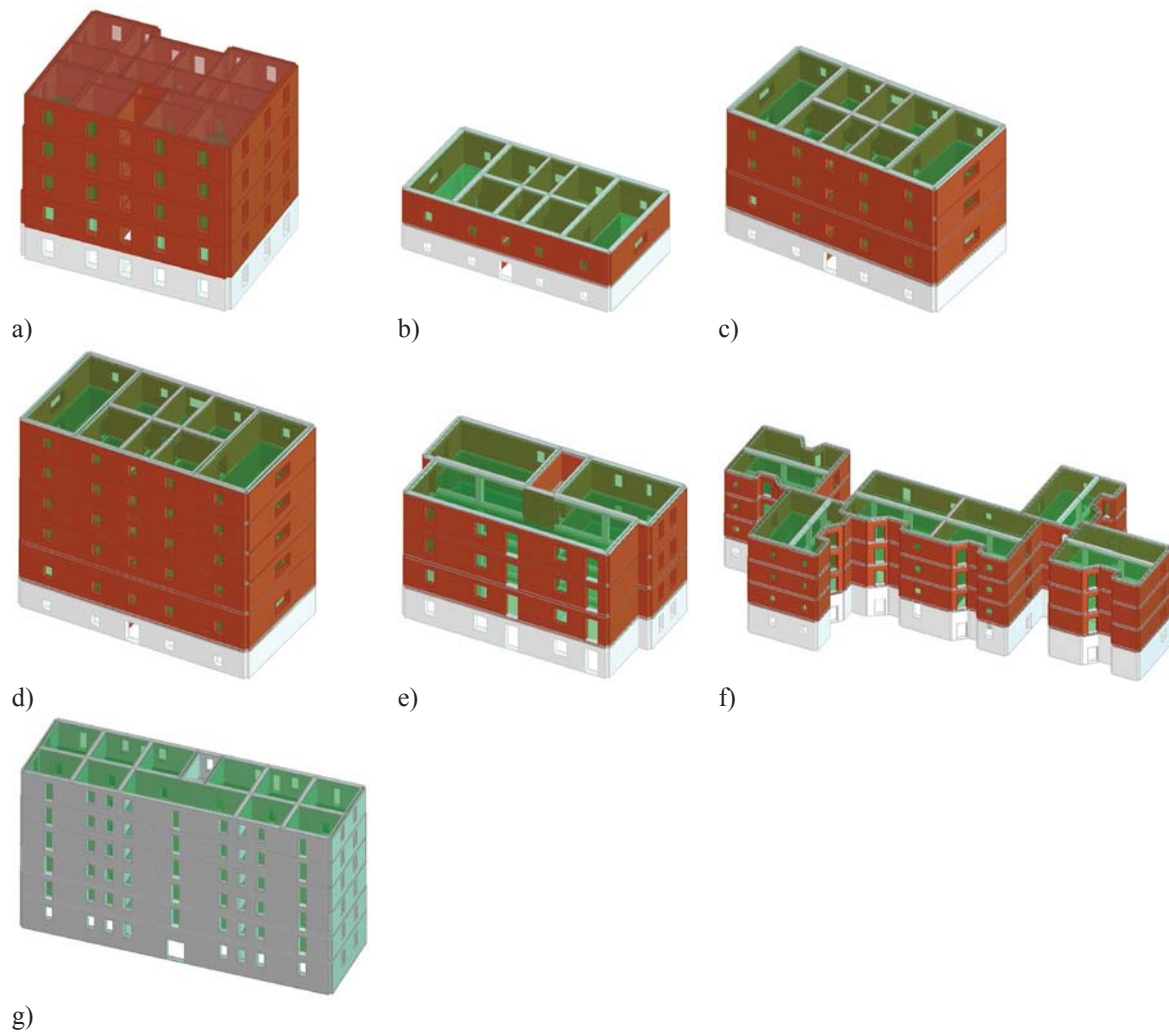


Figure 10: 3D view of the building typologies: a) MUR1,Hr,Reg,Nc; b) MUR3,Lr,Reg,C; c) MUR3,Mr,Reg,C; d) MUR3,Hr,Reg,C; e) MUR4,Mr,Reg,C; f) MUR4,Mr,Irreg,C; g) MUR6,Hr,Reg,C.

### 4.3 Analysis Results

Modal analyses have been performed in order to derive the dynamic characteristics of the selected buildings. Table 5 resumes the fundamental periods ( $T$ ) and participation masses ( $M$ ) of the examined numerical models. Each building prototype features similar fundamental periods along the principal directions. The lower period obtained with the MUR4 typology is probably associated to the contribution provided by the internal RC beam-column systems.

Building typology	$T_x$ (s)	$M_x$ (%)	$T_y$ (s)	$M_y$ (%)
MUR1,Hr,Reg,Nc	0.50	66	0.49	81
MUR3,Lr,Reg,C	0.17	77	0.18	72
MUR3,Mr,Reg,C	0.30	80	0.35	78
MUR3,Hr,Reg,C	0.49	78	0.56	78
MUR4,Mr,Reg,C	0.31	63	0.48	80
MUR4,Mr,Irreg,C	0.45	30	0.44	58
MUR6,Hr,Reg,C	0.53	69	0.63	78

Table 5: Modal parameters.



Non-linear seismic analyses have been performed along the main (X- and Y-) directions of the archetype buildings considering two different force distributions: (i) uniform (“Unif”) distribution, proportional to the mass, and (ii) linear (“Triang”) distribution, proportional to the shape of the fundamental mode of vibration.

Figure 11 to Figure 14 show the pushover curves in the two principal directions of each archetype. It is worth noting that the capacity curves in terms of base shear vs. top displacement have been cut off at a peak strength reduction of about 20% on the negative slope.

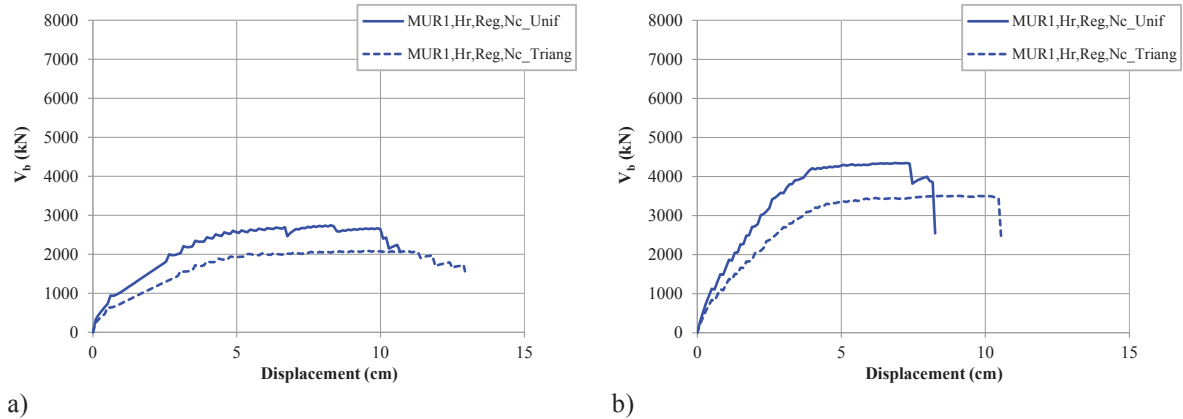


Figure 11: Pushover curves of the selected MUR1 building typology: a) X direction; b) Y direction.

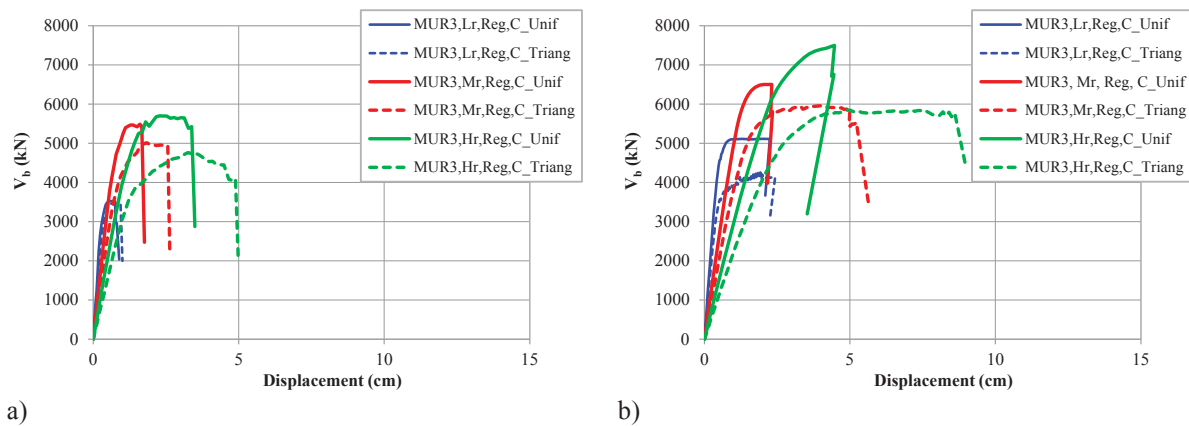


Figure 12: Pushover curves of the selected MUR3 building typologies: a) X direction; b) Y direction.

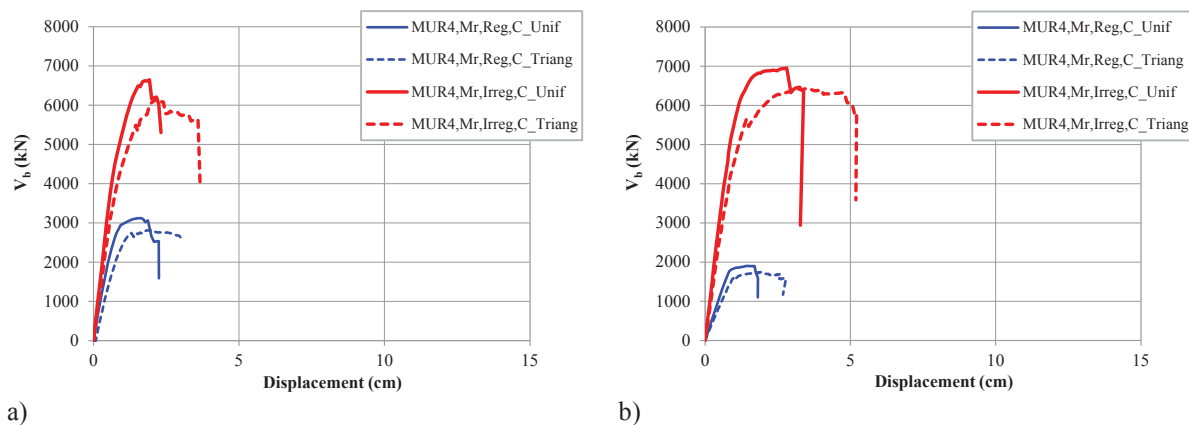


Figure 13: Pushover curves of the selected MUR4 building typologies: a) X direction; b) Y direction.

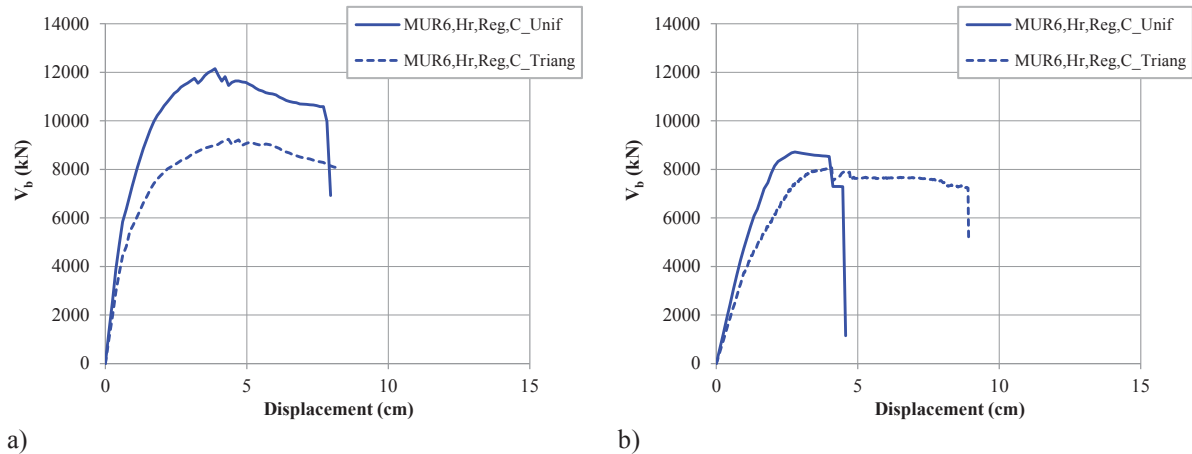


Figure 14: Pushover curves of the selected MUR6 building typologies: a) X direction; b) Y direction.

A different structural response has been obtained by using the two mentioned distributions. Obviously, the top displacement being equal, the maximum strength registered using the uniform distribution is larger than that obtained using the triangular distribution (the resultant of horizontal forces applied at each step of the analysis in the “Unif” distribution is double with respect to that associated to the “Triang” distribution). Moreover, while the uniform pattern produces a force concentration at first floor, a redistribution of loads is obtained with the triangular pattern, thus leading to a larger ductility capacity (of about 50%) of the examined structures. For the archetype buildings associated to MUR1 and MUR3, the lower value of the peak strength is registered in the X-direction (Figures 11 and 12). This is probably due to a lower number of resistant elements coupled with large openings along such direction. For what concerns the MUR4 archetypes, the more uniform distribution of openings and the presence of interior resistant elements (RC frames) counterbalance the structural response (in terms of peak strength) along the two main directions (Figure 13). For the MUR6 archetype, the larger value of the peak strength observed in the X-direction seems to be associated to the presence of a continuous internal masonry wall (with limited openings) along this direction (Figure 14). Finally, it is worth noting that the weakest structural response in terms of strength capacity has been observed for MUR1 and MUR4 archetype buildings. In the first case, such result seems to be related to the poor mechanical properties of the structural materials, compared to those of the remaining archetypes. On the other hand, for what concerns the MUR4 typology, the limited number of vertical resisting elements (in particular along the Y-direction) significantly affects the peak strength values.

Figure 15 to Figure 21 plot the damage patterns of the examined archetypes associated to the final step of the analysis. Different colors have been adopted to represent the failure modes of the involved structural elements.

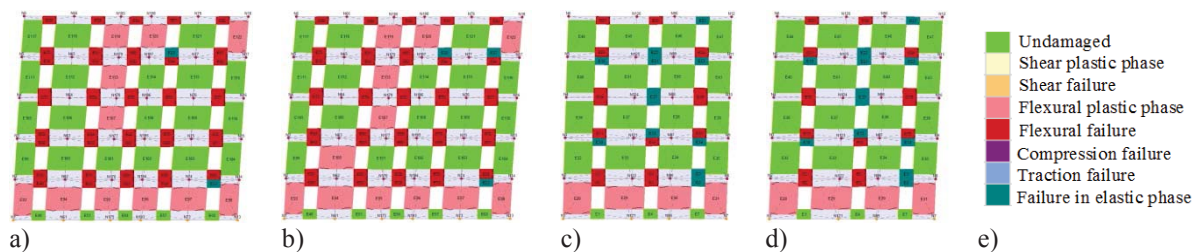


Figure 15: Damage pattern on the MUR1,Hr,Reg,Nc building: a) and b) front facade wall, respectively, for uniform and triangular load pattern; c) and d) side wall, respectively, for uniform and triangular load pattern; e) legend of the damage states associated to each masonry element.

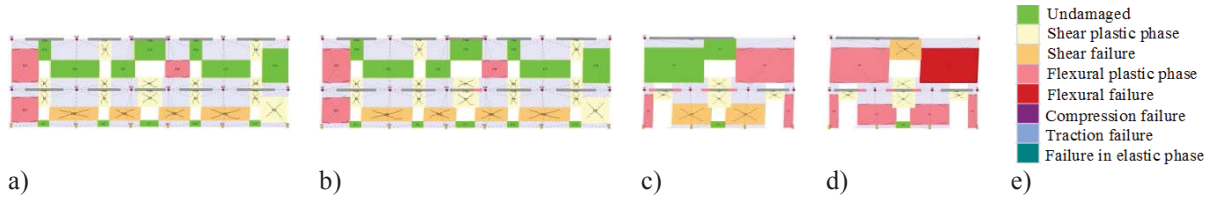


Figure 16: Damage pattern on the MUR3,Lr,Reg,C building: a) and b) front facade wall, respectively, for uniform and triangular load pattern; c) and d) side wall, respectively, for uniform and triangular load pattern; e) legend of the damage states associated to each masonry element.

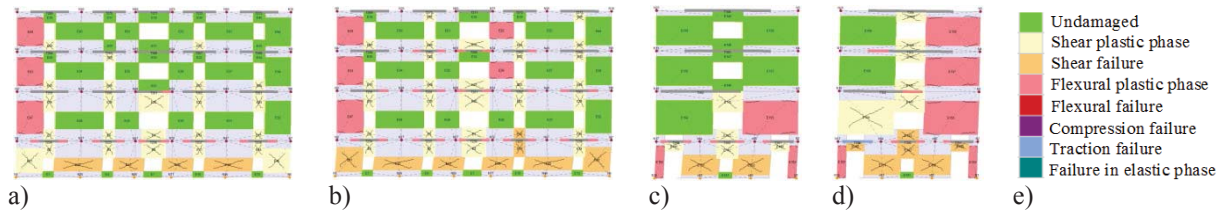


Figure 17: Damage pattern on the MUR3,Mr,Reg,C building: a) and b) front facade wall, respectively, for uniform and triangular load pattern; c) and d) side wall, respectively, for uniform and triangular load pattern; e) legend of the damage states associated to each masonry element.

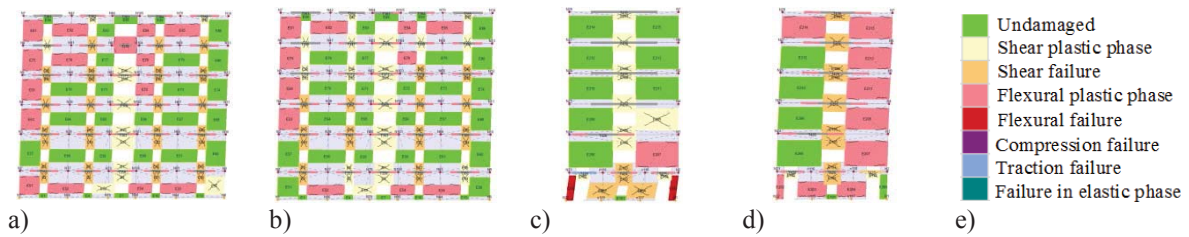


Figure 18: Damage pattern on the MUR3,Hr,Reg,C building: a) and b) front facade wall, respectively, for uniform and triangular load pattern; c) and d) side wall, respectively, for uniform and triangular load pattern; e) legend of the damage states associated to each masonry element.

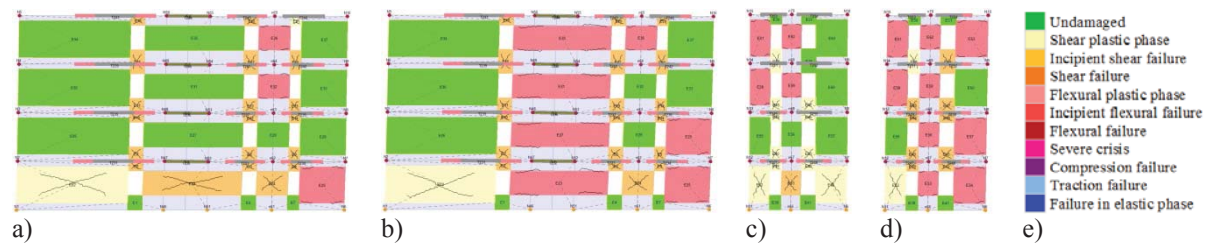


Figure 19: Damage pattern on the MUR4,Mr,Reg,C building: a) and b) front facade wall, respectively, for uniform and triangular load pattern; c) and d) side wall, respectively, for uniform and triangular load pattern; e) legend of the damage states associated to each masonry element.

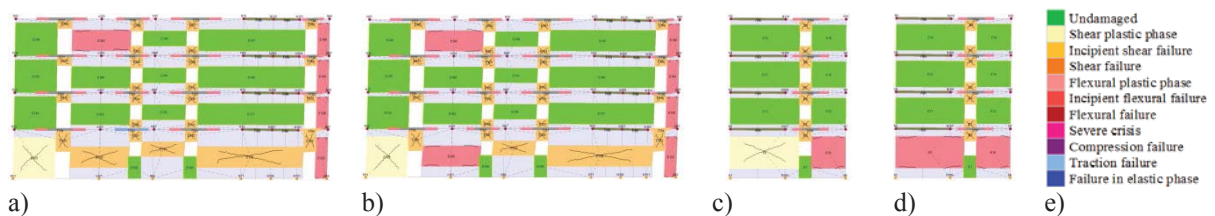


Figure 20: Damage pattern on the MUR4,Mr,Irreg,C building: a) and b) front facade wall, respectively, for uniform and triangular load pattern; c) and d) side wall, respectively, for uniform and triangular load pattern; e) legend of the damage states associated to each masonry element.

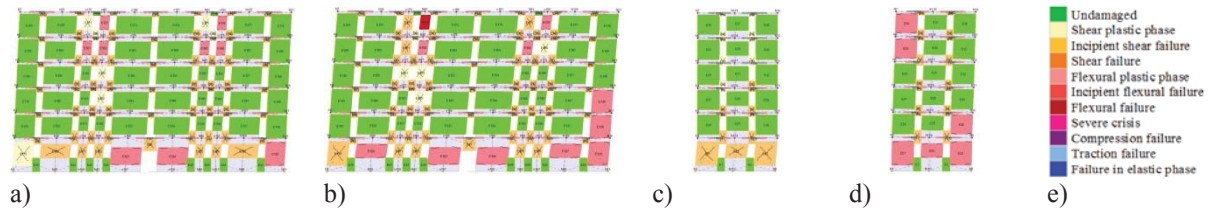


Figure 21: Damage pattern on the MUR6,Hr,Reg,C building: a) and b) front facade wall, respectively, for uniform and triangular load pattern; c) and d) side wall, respectively, for uniform and triangular load pattern; e) legend of the damage states associated to each masonry element.

The damage of the MUR1,Hr,Reg,Nc archetype building (Figure 15) is characterized by the flexural failure of spandrels triggering a strong piers-weak spandrel mechanism and, as a consequence, a rocking failure mode of piers [34]. In particular, the poor mechanical properties of the ground floor masonry produce a concentration of the flexural damage at the first story. Conversely, for what concerns the MUR3 and MUR4 archetypes, the RC floors with tie beams located at each level of the structure directly affect behavior of spandrels leading to a shear failure mode of such elements (Figures 16 to 20). Moreover, the rigid translation of the RC floors activates story mechanisms associated with shear collapse of the piers. Once again, the first story elements appear as the most vulnerable elements. A similar behavior has been observed for the MUR6 archetype building. However, the enhanced mechanical properties of such building typology lead to a reduced damage in the structural elements with respect to those observed for MUR3 and MUR4 archetypes. Finally, as mentioned above, the redistribution of loads associated to the triangular distribution corresponds to a redistribution of damage along the height of the examined buildings.

## 5 EXPECTED ANNUAL LOSS ESTIMATION

The conventional approach proposed within the Italian Seismic Risk Classification [16] and described in Section 2, has been applied to evaluate the “seismic quality” of the examined archetypes. For each archetype, the procedure has been performed four times (one for each non-linear analysis, i.e. two different load patterns coupled with two different main directions). The main outputs of the mentioned procedure are summarized in Table 6 and Table 7. It is worth noting that only the results corresponding to the non-linear analysis leading to the maximum value of EAL are reported. In particular, the return periods ( $T_r$ ) and MAFE ( $\lambda$ ) values for each target limit state are shown. The EAL values in the as-built configuration are provided in the third column of Table 7 and are expressed as a percentage of the Replacement Cost (RepC) of the building. The latter parameter has been estimated as the average cost of demolition and construction per square meter of similar new buildings, assumed equal to 954 €/m<sup>2</sup> according with [1].

Building typology	$T_{r, SLO}$ (years)	$\lambda_{SLO}$ (%)	$T_{r, SLD}$ (years)	$\lambda_{SLD}$ (%)	$T_{r, SLV}$ (years)	$\lambda_{SLV}$ (%)	$T_{r, SLC}$ (years)	$\lambda_{SLC}$ (%)
MUR1,Hr,Reg,Nc	65	1.54	30	3.33	211	0.47	393	0.25
MUR3,Lr,Reg,C	30	3.33	30	3.33	297	0.34	419	0.24
MUR3,Mr,Reg,C	75	1.33	30	3.33	139	0.72	233	0.43
MUR3,Hr,Reg,C	30	3.33	30	3.33	170	0.59	338	0.30
MUR4,Mr,Reg,C	36	2.78	30	3.33	87	1.15	147	0.68
MUR4,Mr,Irreg,C	46	2.17	30	3.33	119	0.84	207	0.48
MUR6,Hr,Reg,C	65	1.54	30	3.33	211	0.47	393	0.25

Table 6: Return periods ( $T_r$ ) and MAFE ( $\lambda$ ) values for each target limit state.



Building typology	RepC	EAL <sub>As-built</sub> (%RepC)	EAL <sub>Retrofitted</sub> (%RepC)
MUR1,Hr,Reg,Nc	1,812,848	1.60	1.0
MUR3,Lr,Reg,C	553,625	1.41	0.5
MUR3,Mr,Reg,C	1,107,251	1.45	0.5
MUR3,Hr,Reg,C	1,660,876	1.47	0.5
MUR4,Mr,Reg,C	908,399	1.89	1.0
MUR4,Mr,Irreg,C	2,207,556	1.67	1.0
MUR6,Hr,Reg,C	3,045,912	1.32	0.5

Table 7: EAL<sub>As-built</sub> and EAL<sub>Retrofitted</sub> values.

The results in terms of EAL<sub>As-built</sub> are in line with the considerations regarding the structural response of the examined buildings made in Section 4.3. As a matter of fact, the weak structural response observed for MUR1 and MUR4 archetypes produced larger values of EAL. On the contrary, lower values of EAL have been observed for the remaining archetypes, in particular for the MUR6 typology.

A general understanding of the potential socio-economic effects of the seismic scenarios at territorial scale has been obtained by monetizing the EAL<sub>As-built</sub> values, obtained for the each typology, with respect to the effective corresponding Replacement Cost (RepC). The monetary expected annual loss of the two compartments has been calculated by multiplying, for each building typology, the monetized EAL<sub>As-built</sub> value for the total number of elements of this category. As reported in Table 8, the total expected annual loss of the entire compartments (i.e., area's expected annual loss, AEAL) is equal to approximately 483 million Euros. To give some reference for the mentioned value, the latter can be compared to the area's total income (ATI) obtained multiplying the per capita income (PCI) measured in the examined area in the last year (equal to €16,522 [25]), by the total number of occupants (equal to 5730). In this optic, the ratio between AEAL and ATI is equal to approximately 5 (483 million divided by 94.7 million Euros).

Recently, the Italian 2019 Financial Law [35], introduced the so-called “Sisma Bonus” providing incentives, in terms of tax deductions, for seismic strengthening interventions on private buildings. These tax deductions range from 50% to 85% of the retrofit intervention's total cost. The incentives system is directly related to the risk classes of the Italian seismic risk classification guidelines and is associated to specific ranges of EAL (see Table 1 in Section 2). In particular, a 50% tax deduction can be obtained by implementing retrofit interventions without class improvement with respect to the as-built configuration. It can be raised up to 75% and 85% in case of improvement of one or two seismic risk classes, respectively. In any case, the maximum retrofitting expenditure amounts to €96,000 per property unit (single family house, apartment, etc.). Moreover, following the recent COVID19 pandemic, a special “Super Bonus” [36] up to 110% has been issued, with maximum retrofitting expenditure per property unit raised up to €136,000 also allowing the assignment of credit solution. In other words, the accrued credit can be transferred to third parties (financial institutions, banks, lenders), limiting or avoiding the economic burden for the stakeholders.

In this optic, for each building typology, the monetary EAL values obtained considering potential retrofit interventions, aimed at the improvement of two seismic classes with respect to the as-built condition, has been calculated (see the third column of Table 8). The reduction of EAL for each building typology ( $\Delta EAL = EAL_{As-built} - EAL_{Retrofit}$ ) is also reported (last column of Table 8). The total variation of the EAL ( $\Delta AEAL$ ) is thus equal to €264,440,931.



Assuming that all the buildings' owners exploit the maximum retrofit expenditure amount (i.e., 136,000 per property unit), the total cost of the potential interventions is equal to € 311,712,000. Therefore, less than two years would be sufficient to pay back the entire amount of the financial resources involved in the seismic protection improvement of the examined area's built heritage.

Building typology	EAL <sub>As-built</sub> (€)	EAL <sub>Retrofitted</sub> (€)	ΔEAL (€)
MUR1,Hr,Reg,Nc	81,215,592	50,759,745	30,455,847
MUR3,Lr,Reg,C	15,612,233	5,536,253	10,075,980
MUR3,Mr,Reg,C	94,725,285	32,663,892	62,061,394
MUR3,Hr,Reg,C	75,686,112	25,743,576	49,942,537
MUR4,Mr,Reg,C	60,090,581	31,793,958	28,296,623
MUR4,Mr,Irreg,C	58,985,896	35,320,896	23,665,000
MUR6,Hr,Reg,C	96,494,496	36,550,945	59,943,551
AEAL	482,810,195	218,369,264	264,440,931

Table 8: Monetized EAL values estimated for the examined building typologies.

## 6 CONCLUSIONS

The seismic loss assessment of masonry building stock located in the historical city center of Potenza has been performed based on the conventional approach currently used within the Italian Seismic Risk Classification [16]. First of all, the masonry buildings detected on the examined territory have been grouped in 7 typologies. Subsequently, 7 archetype buildings, each one featuring the structural, material and geometrical peculiarities of the corresponding building typology, have been modeled in the 3Muri environment. At this point, the mentioned simplified approach has been performed to derive the EAL of each archetype (i.e. building typology). The socio-economic effects of the seismic scenarios at territorial scale have been assessed, in first approximation, by comparing the EAL of the entire examined area with the current Area's Total Income (ATI) of the actual population. The ratio between EAL and ATI is equal to approximately 5.

Finally, considering the recent economic strategy adopted by the Italian Government to gradually reduce the seismic vulnerability of the existing building stock, a potential global retrofit intervention, aimed at the improvement of two seismic risk classes for all the masonry buildings located in the examined area, has been considered. The potential global intervention could significantly reduce the direct EAL of about 50%, from 483 to 218 million Euros. Moreover, considering that the maximum total amount of the intervention is equal to approximately 310 million of Euros, the pay-back period (namely the time needed to recover the cost of the investment) is about 1.2 years. Obviously, further studies, implementing specific retrofit interventions for each archetype, should be performed in order to precisely evaluate the actual economic effects and the structural performances in the retrofitted configuration. Moreover, further building typologies (historical-monumental and masonry aggregates) should be included to obtain a general understanding and a complete definition of the socio-economic impact at the territorial scale.

## AKNOWLEDGMENTS

This research has been developed within the PON-AIM 2014-2020 project, “Attraction and International Mobility”, Line 1, supported by the Italian Ministry of University and Public Instruction.

## REFERENCES

- [1] D. Cardone, A. Flora, B. Manganelli, Cost-benefit analysis of different retrofit strategies following a displacement based loss assessment approach: a case study. *Tenth U.S. National Conference on Earthquake Engineering Frontiers of Earthquake Engineering*, Anchorage, Alaska, USA, July 21-25, 2014. DOI: 10.4231/D3CF9J706.
- [2] D. Cardone, A. Flora, M. De Luca Picione, A. Martoccia, Estimating direct and indirect losses due to earthquake damage in residential RC buildings. *Soil Dyn. and Earth. Eng.*, **126**, 2019. DOI: 10.1016/j.soildyn.2019.105801.
- [3] M. Vona, A. Flora, E. Carlucci, E. Foscolo, Seismic Retrofitting Resilience-Based for Strategic RC Buildings. *Buildings*, **11**, 111, 2021. DOI: 10.3390/buildings11030111.
- [4] M. Vona, Proactive Actions Based on a Resilient Approach to Urban Seismic Risk Mitigation. *Open Constr. Build. Technol. J.*, **14**, 321–335, 2020. DOI: 10.2174/1874836802014010321.
- [5] D. Ottonelli, S. Cattari, S. Lagomarsino, Displacement-Based Simplified Seismic Loss Assessment of Masonry Buildings. *Journal of Earthquake Engineering*, **24**:sup1, 23-59, 2020. DOI: 10.1080/13632469.2020.1755747.
- [6] J. Snoj, M. Dolšek, Pushover-based seismic risk assessment and loss estimation of masonry buildings. *Earthquake Engng Struct Dyn.*, **49**, 567–588, 2020. DOI: 10.1002/eqe.3254.
- [7] B. Borzi, H. Crowley, R. Pinho, Simplified pushover-based earthquake loss assessment (SP-BELA) Method for masonry buildings. *Int J Architect Heritage: Conserv, Anal Restor.*, **2**(2–4), 353-376, 2008. DOI: 10.1080/15583050701828178.
- [8] J.K. Bothara, J.B. Mander, R.P. Dhakal, R.K. Khare, M.M. Maniyar, Seismic performance and financial risk of masonry houses. *ISET J Earthq Technol.*, **44**(3–4), 421-444, 2007.
- [9] K.A. Porter, An Overview of PEER’s Performance-Based Earthquake Engineering Methodology. *9th International Conference on Applications of Statistics and Probability in Civil Engineering*, 273(1995), 973–980, San Francisco, California, 2003.
- [10] S. Günay, K. M. Mosalam, PEER Performance-Based Earthquake Engineering Methodology, Revisited. *Journal of Earthquake Engineering*, **17**(6), 829–858, 2013.
- [11] K. A. Porter, J.L. Beck, Shaikhutdinov, R.V. Simplified estimation of economic seismic risk for buildings. *Earthquake Spectra*, **20**(4), 1239–63, 2004. DOI: 10.1193/1.1809129.
- [12] D. Cardone, G. Perrone, A. Flora, Displacement-Based Simplified Seismic Loss Assessment of Pre-70S RC Buildings. *Jour. of Earth. Eng.*, **24**:sup1, 82-113, 2020. DOI: 10.1080/13632469.2020.1716890

- [13] G. Perrone, D. Cardone, G.J. O'Reilly, T.J. Sullivan, Developing a direct approach for estimating expected annual losses of Italian buildings. *Jour. of Earth. Eng.*, 1–32, 2019. DOI: 10.1080/13632469.2019.1657988.
- [14] C.M. Ramirez, E. Miranda, Building specific loss estimation methods & tools for simplified performance based earthquake engineering. Technical Report No. 171, John A. Blume Earthquake Engineering Center, 2011, Stanford University.
- [15] T.J. Sullivan, G.M. Calvi, Considerations for the seismic assessment of buildings using the direct displacement-based assessment approach. Proc. of the ANIDIS Conference, 2011, Bari, Italy.
- [16] Ministry Decree n.58 28/02/2017 Allegato A: linee guida per la classificazione del rischio sismico delle costruzioni (in Italian). Italian Ministry of Infrastructures and Transport, Italy. <http://www.mit.gov.it/normativa/decreto-ministeriale-numero-58-del-28022017>.
- [17] EU Council. Council Directive 92/75/EEC of 22 September 1992 on the indication by labelling and standard product information of the consumption of energy and other resources by household appliances. Brussels, Belgium; 1992.
- [18] S. Lagomarsino, A. Penna, A. Galasco, S. Cattari, TREMURI program: an equivalent frame model for the nonlinear seismic analysis of masonry buildings. *Engineering Structures*, **56**, 1787–99, 2013. DOI: 10.1016/j.engstruct.2013.08.002.
- [19] A. Flora, D. Cardone, M. Vona, G. Perrone, A Simplified Approach for the Seismic Loss Assessment of RC Buildings at Urban Scale: The Case Study of Potenza (Italy). *Buildings*, **11**, 142, 2021. DOI: 10.3390/buildings11040142.
- [20] E. Cosenza, C. Del Vecchio, M. Di Ludovico, M. Dolce, C. Moroni, A. Prota, E. Renzi, The Italian guidelines for seismic risk classification of constructions: technical principles and validation. *Bulletin of Earthquake Engineering*, **16**, 5905–5935, 2018. DOI: 10.1007/s10518-018-0431-8.
- [21] P. Fajfar, A nonlinear analysis method for performance based seismic design. *Earthq Spectra*, **16**, 573–592, 2000.
- [22] D.M. 17 Gennaio 2018 (D.M. 2018). Technical code for constructions (in Italian). G.U. n. 42 del 20/2/2018. Rome, Italy.
- [23] G.J. O'Reilly, D. Perrone, M. Fox, R. Monteiro, A. Filiatrault, Seismic assessment and loss estimation of existing school buildings in Italy. *Engineering Structures*, **168**, 142–162, 2018. DOI: 10.1016/j.engstruct.2018.04.056.
- [24] F.T. Gizzi, N. Masini, Historical earthquakes and damage patterns in Potenza (Basilicata, Southern Italy). *Annals of geophysics*, **50**(5), 2007.
- [25] Italian National Statistics Institute (ISTAT). 15th National Census on Buildings and Population. 2014, Rome, Italy (in Italian).
- [26] C. Iacovino, A. Flora, D. Cardone, M. Vona, Defining a masonry building inventory for the city of Potenza. *20th International Conference on Computational Science and Applications (ICCSA 2020)*, LNCS 12250, 914–927, 2020. DOI: 10.1007/978-3-030-58802-1\_65.
- [27] A. Flora, C. Iacovino, D. Cardone, M. Vona, Typological inventory of residential Reinforced Concrete buildings for the city of Potenza. *20th International Conference on*

- Computational Science and Applications (ICCSA 2020)*, LNCS 12250, 899–913, 2020. DOI: 10.1007/978-3-030-58802-1\_64.
- [28] M. Polese, M. Di Ludovico, A. Prota, G. Tocchi, M. Gaetani d’Aragona, Utilizzo della scheda Cartis per aggiornamento dell’inventario ed effetto sulle stime di vulnerabilità a scala territoriale, *XVIII Convegno Anidis*, Ascoli Piceno, 15-19 settembre 2019. (In Italian).
  - [29] G. Milani, M. Valente, Failure analysis of seven masonry churches severely damaged during the 2012 Emilia-Romagna (Italy) earthquake: non-linear dynamic analyses vs conventional static approaches. *Eng Fail Anal*, **54**, 13–56, 2015. DOI: 10.1016/j.engfailana.2015.03.016.
  - [30] MIT 2019, Circolare n. 7 del 21 gennaio 2019. Istruzioni per l’applicazione dell’Aggiornamento delle “Norme tecniche per le costruzioni” di cui al decreto ministeriale 17 gennaio 2018.
  - [31] J. Milosevic, S. Cattari, R. Bento, Definition of fragility curves through nonlinear static analyses: procedure and application to a mixed masonry-RC building stock. *Bulletin of Earthquake Engineering*, **18**, 513–545, 2020. DOI: 10.1007/s10518-019-00694-1.
  - [32] G. Magenes, A. Penna, I. Senaldi, M. Rota, A. Galasco, Shaking table test of a strengthened fullscale stone masonry building with flexible diaphragms. *J Archit Herit Conserv Anal Restor*, **8**(3), 349–375, 2014. DOI: 10.1080/15583058.2013.826299
  - [33] D. D’Ayala, E. Speranza, An integrated procedure for the assessment of seismic vulnerability of historic buildings. In: *Proceedings of the 12th European conference on earthquake engineering*, London, 2002.
  - [34] P. Foraboschi, Coupling effect between masonry spandrels and piers. *Materials and Structures*, **42**, 279–300, 2009. DOI: 10.1617/s11527-008-9405-7.
  - [35] Law 145/2018. In Bilancio di Previsione dello Stato per l’Anno Finanziario 2019 e Bilancio Pluriennale per il Triennio 2019-2021 (Legge di Bilancio 2019); n.302 del 31/12/2018; Gazzetta Ufficiale della Repubblica Italiana: Roma, Italy, 2018. (In Italian).
  - [36] Law 77/2020. In Conversione in Legge, con Modificazioni, del Decreto-Legge 19 Maggio 2020, n. 34, Recante Misure Urgenti in Materia di Salute, Sostegno al Lavoro e all’Economia, Nonche’ di Politiche Sociali Connesse all’Emergenza Epidemiologica da COVID-19; n.180 del 18/07/2020; Gazzetta Ufficiale della Repubblica Italiana: Roma, Italy, 2020. (In Italian).

## INVESTIGATING GROUND-MOTION DURATION EFFECTS ON BUILDING PORTFOLIO LOSS ESTIMATES

Kenneth Otárola-Madriral<sup>1</sup>, Roberto Gentile<sup>2</sup>, Luis Sousa<sup>3</sup>, and Carmine Galasso<sup>1,2</sup>

<sup>1</sup> Scuola Universitaria Superiore (IUSS) Pavia, Pavia, Italy  
e-mail: kenneth.otarola@iusspavia.it

<sup>2</sup> University College London, London, United Kingdom  
e-mail: {r.gentile, c.galasso}@ucl.ac.uk

<sup>3</sup> AIR worldwide London Ltd., London, United Kingdom  
e-mail: LSousa@air-worldwide.com

---

### Abstract

*Earthquake-induced ground-motion duration can be an important factor to consider when assessing ground-motion damage potential, as evidenced by recent earthquake events worldwide. In current practice, duration is commonly relegated to implicit, qualitative considerations. This study introduces a framework to explicitly quantify the influence of duration on building portfolio direct economic losses. To this end, a simulation-based probabilistic risk modelling framework is developed for different synthetic building portfolios impacted by a case-study seismic source. Two building typologies, representative of distinct vulnerability classes in southern Europe, are considered. A simulation-based probabilistic seismic hazard analysis is performed, explicitly simulating duration jointly with spectral-shape-related intensity measures. Sets of long and one-to-one spectrally-equivalent short duration ground-motion records are selected and then used jointly to perform nonlinear dynamic analysis and derive fragility models for each considered building typology. Fragility relationships are derived by using average spectral acceleration as the primary intensity measure and: 1) maximum inter-storey drift ratio as a demand parameter, indirectly accounting for ground-motion duration (through the adopted nonlinear modelling strategy); 2) maximum inter-storey drift ratio as demand parameter, explicitly considering duration as an intensity measure together with spectral shape, in a vector-valued format. For each case, vulnerability models are developed by combining the fragility relationships with a building-level damage-to-loss model. The portfolio expected annual losses estimated using the described vulnerability models are critically compared and discussed. Depending on the location/portfolio, the impact of ground-motion duration can be significant, and the proposed approaches allow an analyst to account for it in a practical way.*

**Keywords:** Ground-motion duration; nonlinear dynamic analysis; maximum inter-storey drift ratio; building portfolio loss.

---



## 1 INTRODUCTION

Earthquake events have been responsible for devastating human, environmental and economic losses in modern societies over the years. Portfolio risk assessment represents the first step towards developing risk reduction and resilience-enhancing strategies for earthquake-prone regions. Earthquake risk assessment generally requires three main modelling components: a probabilistic seismic hazard model (simulating representative earthquake scenarios in time and space and assessing the resulting ground-shaking intensity across a geographical area at risk); a comprehensive exposure dataset (containing details on the location and characteristics of the assets at risk in the geographic area of concern); and a set of (physical) vulnerability models for those exposed assets/asset types (e.g., [1]), quantifying the susceptibility to damage, or other forms of loss (e.g., downtime and casualties), of structures and their contents because of the hazard impact. This latter component plays a significant role in earthquake risk modelling/risk reduction since reducing physical vulnerability leads to a direct decrease in the associated seismic risk. Therefore, understanding and quantifying the various earthquake-induced ground-motion characteristics driving seismic vulnerability becomes crucial.

Current seismic design and risk assessment procedures commonly characterise ground motions in terms of amplitude and frequency-related parameters (e.g., spectral ordinates) without explicitly considering ground-motion duration. Large-magnitude events worldwide, often resulting in long-duration ground motions [2] (e.g., the 2010 Maule Chile earthquake, moment magnitude,  $M_w$  8.8; the 2011 Tohoku Japan,  $M_w$  9.0) caused billions of dollars in losses, emphasising the need to account for ground-motion duration in practical earthquake risk assessment exercises. The importance (and influence) of amplitude and frequency-related parameters on ground-motion-induced damage and losses have been comprehensively investigated and quantified. However, a consensus has not been reached yet concerning the impact of ground-motion duration on structural response, building performance, and resulting damage/losses.

The main difficulty in quantifying the effect of duration on seismic response of structures is related to the challenging task of decoupling this specific effect from the impact of other ground-motion characteristics. Duration is considered an essential factor in assessing a ground-motion damage potential, but its significance remains unclear, partly because of the somehow contradictory and inconclusive results of some past studies (e.g., [3]). Such conflicting findings from prior studies mainly result from the adopted definition of strong-motion duration, the structural demand parameters utilised to quantify damage, and the inadequacy of the numerical models in capturing the stiffness and strength cyclic and in-cycle deterioration of different structural systems.

Some studies (e.g., [4]) have demonstrated that while duration has no significant effect on peak-based demand parameters (e.g., maximum inter-story drift ratio, MIDR), it can have a significant effect on cumulative demand parameters (e.g., dissipated hysteretic energy, EH). On the other hand, studies that utilised analytical models accounting for stiffness and strength cyclic and in-cycle deterioration (e.g., [5]) demonstrated that long-duration ground motions impact cumulative damage and collapse capacities. However, the degree of importance of duration effects may vary depending on the structural system under consideration.

Significant advances on the topic have been recently made due to the increasing availability of reliable long-duration ground-motion records and improved deteriorating nonlinear structural models incorporating the destabilising P- $\Delta$  effects (e.g., [2], [6]). These studies focused primarily on the influence of ground-motion duration on structural collapse capacity and structural collapse risk, using novel ground-motion selection procedures to isolate the effects of duration from the response spectral shape by using “spectrally equivalent” long- and short-duration ground-motion records. This approach assumes a weak correlation between spectral

shape (i.e., spectral acceleration ordinates) and duration (i.e., significant duration), which may not be a realistic assumption in some cases.

Literature describing how duration affects structural fragility for different damage states and their evaluation is not widely available. In [7], this modelling challenge was tackled using two different approaches. In the first approach, the effect of duration was decoupled from the effects of amplitude and spectral shape by assembling sets of spectrally equivalent long- and short-duration ground motions. Those sets of records were employed in comparative incremental dynamic analyses to derive fragility and vulnerability models using realistic SDoF deteriorating nonlinear models. Formal hypothesis testing was also employed to assess the analyses results' statistical significance quantitatively. The second approach employed the generalised conditional intensity measure (GCIM) method to select hazard-consistent ground motions. Those ground motions were used as an input to multiple stripe analyses using realistic MDoF deteriorating nonlinear models. The impact of duration was investigated by variance analysis and in terms of vector-valued fragility and vulnerability models.

Most of the existing studies, as noticed, focus on structural response/building performance assessment, and very few on building-specific loss assessment (e.g., [8]). To the best of the authors' knowledge, no past studies investigated the effect of ground-motion duration on building-portfolio direct economic losses. Accurately quantifying the potential impact of ground-motion duration on portfolios of buildings located in seismically prone regions, as proposed in this study, can be of interest to different stakeholders (e.g., property owners, (re)-insurers).

The study begins with an overview of the simulation-based risk assessment framework employed in the study. The proposed methodology relies on probabilistic seismic hazard analysis (PSHA), incremental dynamic analysis-based [9] fragility derivation (scalar and vector-valued models are considered [10]), and simulation-based loss estimation. The approach is applied to two synthetic portfolios of the same size, located in the fault-parallel orientation with respect to a case-study strike-slip fault. Different structural types are considered for each portfolio, including gravity-designed and seismically-designed reinforced concrete (RC) frames. The results are discussed considering the effects of ground-motion duration on the median loss and expected annual loss (EAL) of the considered location/portfolios at different distances from the case-study fault.

## 2 SIMULATION-BASED SEISMIC LOSS ASSESSMENT

The implemented simulation-based risk assessment framework [11] is schematically illustrated in Figure 1. Sections 2.1 to 2.4 describe the relevant hazard, exposure and vulnerability framework components and the associated direct loss estimations within this framework.

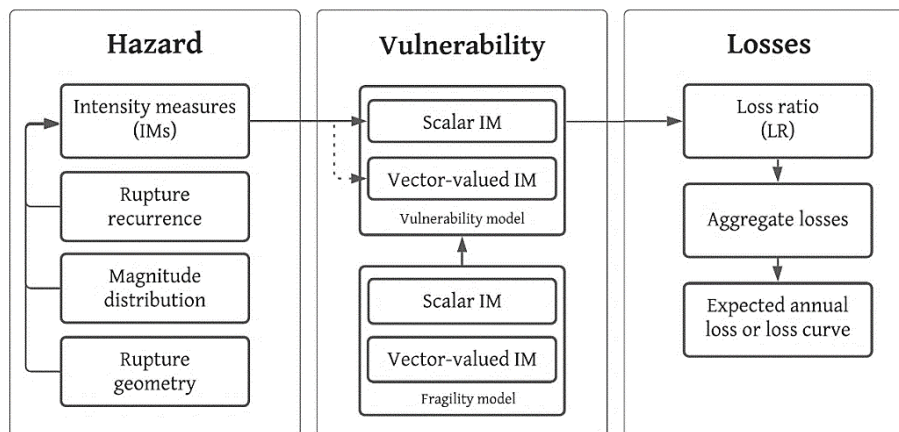


Figure 1: Simulation-based risk assessment framework.

Event-based PSHA [12] is used to simulate 1) seismicity in the considered region as described by a source model; and 2) the resulting ground shaking at the considered set of locations by using a ground-motion model (GMM). Specifically, a stochastic event set (i.e., a stochastic catalogue) is generated for a given time span, chosen based on the minimum rate of exceedance of interest. The number of earthquake occurrences within this period is simulated by sampling the probability distribution for the considered source model's rupture occurrence. The geometry (constraining the earthquake rupture location) and the magnitude-frequency distribution (defining the average annual occurrence rate over a magnitude range) describe the considered source models. For each event in the catalogue, the corresponding magnitude is first simulated from the magnitude-frequency distribution. Next, following the Joyner-Boore source-to-site distance definition, the distance to the rupture for each location of interest is assigned (shallow rupture with a dip angle of  $90^\circ$  and strike of  $0^\circ$ ). Then, ground-motion intensity measures (IMs) of interest are sampled from the probability distributions defined by the GMM, accounting for cross-IM correlation. The set of simulated ground-shaking IMs at the various locations forms a ground-motion field; various ground-motion fields are generated to capture the aleatory variability (both inter- and intra-event) in the GMM.

Given a suite of site-independent ground-motion records with similar spectral shape but different durations, fragility, and vulnerability models (scalar and vector-valued) are derived for each considered building type within the considered portfolios. For each location, building type and simulated IMs, the loss ratio is calculated using the appropriate vulnerability model accounting indirectly or directly for ground-motion duration. The total portfolio loss is calculated by summation over all the building locations in each simulation.

Loss exceedance curves (mean annual frequency, MAF, of exceedance vs loss ratio/loss value) for specific buildings/locations and the entire portfolio can be estimated using the obtained ground-motion fields, leading to lists of events and corresponding loss ratios/loss values. The lists are sorted from the highest loss ratio/loss value to the lowest. The rate of exceedance of each loss ratio/loss value is computed by dividing the number of exceedances of that loss ratio by the length of the event set (eventually multiplied by the number of stochastic event sets, if more than one set are generated). By assuming a Poisson distribution of the occurrence model, the probability of exceedance of each loss ratio/loss value can also be estimated. The portfolio EAL can be calculated by averaging over all the simulations and events.

## 2.1 Hazard

A Poisson model is used to simulate the events' earthquake occurrence on the considered fault. The characteristic earthquake-recurrence model by [13] is adopted to simulate each event associated  $M_w$ . It consists of a log-linear recurrence relationship (i.e., frequency of occurrence vs  $M_w$ ) for moderate (non-characteristic) events and a constant probability branch of occurrence for large (characteristic) events. This model is based on observations that during repeated ruptures occurring on the same fault (or fault system), some characteristics, such as fault geometry, source mechanism, and seismic moment, remain approximately constant over a significant time. The magnitude-dependent length of the rupture is obtained from the equations proposed by [13]. The Joyner-Boore distance is used to define the source-to-site distances for the set of locations of interest.

The amplitude- and duration-based ground-motion IMs (i.e., average spectral acceleration, AvgSa and significant duration,  $D_{S5-95}$ ) are simulated for each seismic event in the stochastic catalogue using the approach presented in [14] for correlated random realisations from a multivariate lognormal distribution (including cross-IM correlation). The AvgSa and  $D_{S5-95}$  realisations are obtained using appropriate GMMs (i.e., [15]; [16]) and empirical correlation models (i.e., [17]; [18]) for spectral acceleration (Sa) ordinates (to estimate AvgSa) and  $D_{S5-95}$ . It is

worth noting that different models should be considered and combined in a logic tree to consider the epistemic uncertainties included in the framework. Nevertheless, one set of models is utilised since the study focuses on introducing the proposed simulation-based loss estimation framework and relative loss results.

It is also worth mentioning that only the combined (intra- and inter-event) GMM uncertainty is considered in this study for simplicity (and computational efficiency), with no consideration of ground-motion spatial correlation (among the locations of the portfolio). Yet, a full correlation for the buildings pertaining to one single site is implicitly assumed since ground shaking is herein simulated for each location (rather than for each building). Many studies (e.g., [19]) have shown that the spatial correlation in ground-motion IMs has important implications on probabilistic seismic hazard and loss estimates of spatially distributed systems (e.g., building portfolios). Inclusion of spatial correlation of IMs into the seismic risk analysis may often result in the likelihood of observing more significant (and in some instances smaller) losses for a portfolio distributed over a typical city-scale when compared against simulations in which this correlation is neglected. Therefore, in practice, the spatial correlation must be included. This is a future development of the current study.

## 2.2 Exposure

Various building portfolios located nearby a causative fault are considered. Each portfolio consists of several equally spaced locations (i.e., sites). In each location, a group of buildings of different typologies (or taxonomy) is collocated (i.e., the exposure is “lumped” at the considered sites). Each portfolio is also moved (utilising 3 km intervals) horizontally through the entire region (perpendicularly to the fault) to assess the ground-motion duration influence on the loss curves/EAL with respect to the distance from the fault.

## 2.3 Vulnerability

Fragility relationships are derived by using incremental dynamic analysis (IDA) with AvgSa as the primary IM and: 1) MIDR as a demand parameter, indirectly accounting for duration, through an advanced nonlinear structural model; 2) MIDR as demand parameter, explicitly considering duration as an IM together with spectral shape, in a vector-valued format. For each case, vulnerability models are developed by combining the fragility relationships with a building-level damage-to-loss model. It is worth noting that MIDR can account indirectly for the duration since the hysteretic models utilised here ([20]; [21]) accounts for the cyclic and in-cycle strength and stiffness deterioration of the structural components based on the EH of the components, following the deterioration rule developed by [22].

When using a scalar IM (i.e., AvgSa), the probability of reaching or exceeding a damage state (DS) at a given IM level can be estimated as the fraction of records for which this DS occurs at a level lower than the defined IM. This probability can be calculated as shown in equation 1, assuming a lognormal distribution.

$$P(DS \geq ds_i | IM) = \Phi \left[ \frac{\ln(IM/\mu)}{\beta} \right] \quad (1)$$

The fragility relationship mean,  $\ln(\mu)$ , and standard deviation,  $\beta$  (i.e., dispersion), are computed with equations 2 and 3 (i.e., by using the method of moments estimator as described in [23]). In these equations,  $n$  is the number of considered ground-motions;  $IM_i$  is the intensity measure value associated with the onset of a DS for the  $i^{\text{th}}$  ground motion.  $\Phi$  is the CDF of the standard Gaussian distribution.

$$\ln(\mu) = \frac{1}{n} \sum_{i=1}^n \ln(IM_i) \quad (2)$$

$$\beta = \sqrt{\frac{1}{n-1} \sum_{i=1}^n \left[ \ln\left(\frac{IM_i}{\mu}\right) \right]^2} \quad (3)$$

When using a vector-valued IM (i.e., [AvgSa, Ds<sub>5-95</sub>] in this study), although only a single IM parameter is scaled during IDA, it is still possible to determine the effects of other IMs. In such context, IM<sub>2</sub> (i.e., Ds<sub>5-95</sub>) can explain part of the variation of the associated IM<sub>1</sub> (i.e., AvgSa). Therefore, the probability of exceeding the IM<sub>1</sub> associated with the target EDP (i.e., MIDR) level can be expressed in terms of a conditional distribution of IM<sub>1</sub> given IM<sub>2</sub>. Linear regression is used to find the conditional mean of  $\ln IM_1$  given  $\ln IM_2$  as shown in equation 4.  $\beta_0$  and  $\beta_1$  are coefficients estimated from linear regression using the data points. The conditional standard deviation ( $\sigma_{\ln IM_1 | \ln IM_2 = \ln im_2}$ ) of  $\ln IM_1$  given  $\ln IM_2$  is estimated computing the standard deviation of the regression residuals (root mean squared error).

$$\mu_{\ln IM_1 | \ln IM_2 = \ln im_2} = \beta_0 + \beta_1 \ln IM_2 \quad (4)$$

If the conditional distribution of  $\ln IM_1$  given  $\ln IM_2$  is assumed to be Gaussian, the conditional mean and standard deviation calculated completely define the conditional distribution of  $\ln IM_1$  associated with reaching an EDP level. Thus, the CDF of this conditional distribution can be estimated as in equation 5, where  $\Phi$  is the CDF of the standard Gaussian distribution.

$$P(IM_1 < im_1 | DS = ds_i, IM_2 = im_2) = \Phi\left(\frac{\ln im_1 - \mu_{\ln IM_1 | \ln IM_2 = \ln im_2}}{\sigma_{\ln IM_1 | \ln IM_2 = \ln im_2}}\right) \quad (5)$$

Damage loss ratios (DLRs) are usually estimated empirically through post-earthquake reconnaissance data or employing expert judgment. These ratios are site-specific and building-type-specific and must be carefully selected while developing vulnerability models (e.g., [24]). For this study, the DLRs suggested by [25] are considered. The definition of the damage loss ratios is shown in Table 1 (from no damage, DS0 to collapse, DS5).

DSs	DS0	DS1	DS2	DS3	DS4	DS5
DLRs	0.00	0.01	0.10	0.35	0.75	1.00

Table 1: Definition of damage-to-loss ratios.

Vulnerability models are expressed here in terms of loss ratio (LR), i.e., the repair-to-replacement cost ratio of the building conditional on the level of ground-shaking IM. Such functions are derived according to equation 6, using the law of total expectation.  $DLR_i$  is the damage-to-loss ratio for the  $i^{\text{th}}$  damage level DS, whilst  $P(DS = ds_i | IM)$  is the probability that the DS is equal to  $ds_i$  (probability of being in each damage state). It is worth noting that IM here could be a single IM composed only by AvgSa, or a vector-valued IM including AvgSa and Ds<sub>5-95</sub> as derived above, resulting in vector-valued vulnerability relationships.

$$LR(IM) = \sum_i DLR_i P(DS = ds_i | IM) \quad (6)$$



## 2.4 Loss assessment

For each event and IM simulation (i.e., ground-motion field), the mean LR is computed using the pertinent vulnerability models. This process is replicated for each location within the portfolio, and each considered building typology,  $t$ . According to [11], for each computed LR, the ground-up loss at each of the  $n_{loc}$  locations is calculated through equation 7, assuming  $N_{b,t}$  buildings of typology  $t$  for which the replacement cost is equal to  $CR_{b,t}$ . Such cost (cost of structural/non-structural component and contents inclusive) is often provided in the exposure model. The loss ratio for every location for a given IM is calculated with equation 8.

$$L_{loc}(IM) = \sum_t LR_{b,t}(IM) N_{b,t} CR_{b,t} \quad (7)$$

$$LR_{loc}(IM) = \frac{L_{loc}(IM)}{CR_{loc}} = \frac{\sum_t LR_{b,t}(IM) N_{b,t} CR_{b,t}}{\sum_t N_{b,t} CR_{b,t}} \quad (8)$$

Assuming that  $CR_{b,t} = CR$  for each  $b$ , the equation 8 is simplified into equation 9, in which  $n_{b,t} = N_{b,t} / \sum_t N_{b,t}$  is the proportion of building typologies,  $t$ . Considering that the distribution of buildings  $n_b$  is uniform through the portfolio, the portfolio LR is calculated as the mean of loss ratios per location (equation 10). Given such assumptions, there is no need to assume any  $CR$  nor the number of buildings at the given location for each building typology without jeopardising the result generality. The outcome is expressed in terms of loss exceedance curves and EAL, representing the expected loss per year (statistical mean loss) and is used as an estimate of the annual insurance premiums to cover the peril [26]. The EAL is calculated, averaging the portfolio LR for each event and simulation in the stochastic catalogue.

$$LR_{loc}(IM) = \frac{\sum_t LR_{b,t}(IM) N_{b,t}}{\sum_t N_{b,t}} = \sum_t LR_{b,t}(IM) n_{b,t} \quad (9)$$

$$L_{loc}(IM) = \frac{\sum_{loc} L_{loc}}{CR_{port}} = \frac{\sum_{loc} LR_{loc} CR_{loc}}{\sum_{loc} CR_{loc}} = \frac{\sum_{loc} LR_{loc}}{n_{loc}} \quad (10)$$

## 3 ILLUSTRATIVE APPLICATION

### 3.1 Considered ground-motion records

The ground-motion dataset employed in this study is a subset of the Pacific Earthquake Engineering Research Center NGA-West2 database [27]. Sets of long and one-to-one spectrally-equivalent short duration ground-motion records are used herein as described by [2]. Firstly, a set of long duration records is selected considering all the records within the NGA-West2 database complying with the following criteria: a)  $10 \text{ km} \leq R_{rup} \leq 250 \text{ km}$ ; b)  $30 \text{ s} \leq D_{s5-95} \leq 60 \text{ s}$ ; c) a minimum  $M_w = 5$ ; d) a minimum  $PGA = 0.1 \text{ g}$ ; and e) a minimum  $PGV = 10 \text{ cm/s}$ .  $R_{rup}$  is the minimum distance to the rupture surface;  $M_w$  is the moment magnitude of an earthquake; and  $PGA$  and  $PGV$  are the peak ground acceleration and peak ground velocity of the ground motions, respectively. Secondly, the companion set of short-duration records is assembled, selecting a corresponding record with  $D_{s5-95}$  smaller than 25 s for each long record, and closely matching the response spectrum of the long-duration record. The ones with the lowest sum of squared errors (SSE vary from 0.19 up to 0.95) are chosen from all the candidate short duration records. Finally, 200 ground-motion records are utilised (see Figure 2). The selected sets of

short- and long-duration records are finally combined together to cover a wide range of relevant IM values in performing nonlinear dynamic analysis of the considered archetype frames.

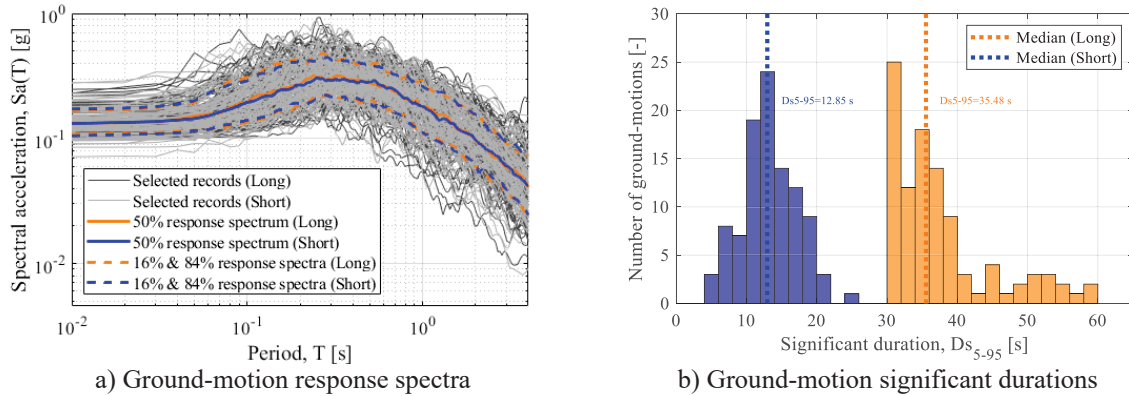


Figure 2: Selected ground-motion records.

### 3.2 Considered building typologies

The considered mid-rise reinforced concrete (RC) building models represent distinct vulnerability classes in southern Europe. The total building height is equal to 13.5 m, with a first storey of 4.5 m, upper storeys of 3 m and a bay width of 4.5 m in both directions [28]. Two moment-resisting frames are considered using the same geometry. The first case-study frame, termed as special-code frame, is designed and detailed according to the seismic provisions of the EC8 for high ductility class [29]. These provisions include capacity design, various requirements in terms of cross-sectional dimensions and seismic detailing to ensure a ductile global performance and preventing the formation of localized brittle failure modes. The other frame, termed as pre-code frame, is designed for gravity loads only as per the Royal Decree n. 2239 of 1939 [30] that regulated the structural design in Italy until 1974. Therefore, this frame does not conform to modern seismic requirements. A non-ductile behaviour characterizes it due to the lack of strength hierarchy rules, sufficient longitudinal reinforcement, poor confinement, and susceptibility to develop brittle failure mechanisms (see [31] for more details). According to this distinction, the two case-study frames include a pre-code bare (PB) frame and a special-code bare (SB) frame. Figure 3a depicts the elevation layout of these frames.

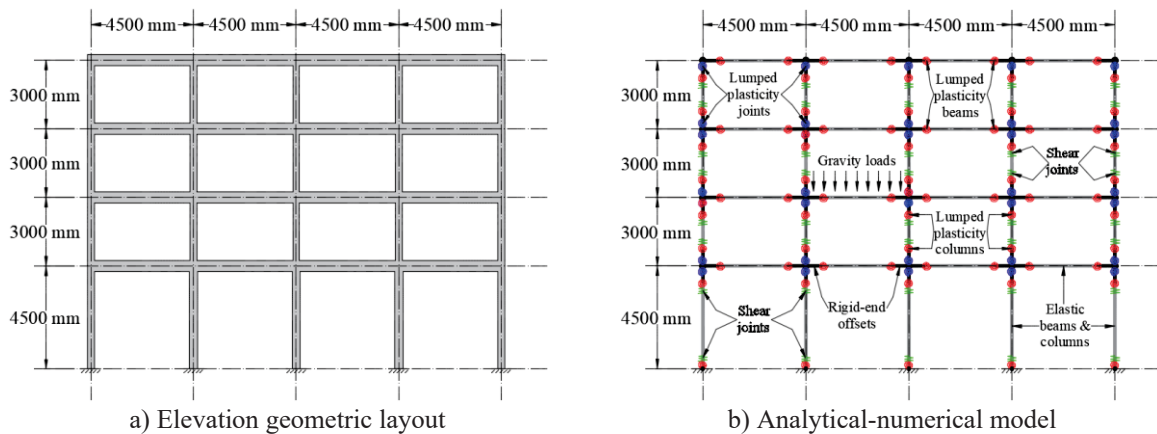


Figure 3: Geometric elevation definition and modelling strategy of the buildings.

Regarding the materials used for each building, their mean mechanical properties, such as the concrete compressive strength and the rebar steel yield strength, represent those typically adopted in southern Europe. For the pre-code frame, mean concrete mechanical properties are

obtained from [32] and [33], while for the special-code frame are obtained from [34] and based on the current practice. The described material properties are summarised in Table 2.

Parameter	Symbol	Units	Pre-code	Special-code
Compressive strength of concrete	$f_{cm}$	MPa	19	37
Modulus of elasticity of concrete	$E_c$	MPa	26670	32600
Yield strength of rebar steel	$f_{ym}$	MPa	360	490
Modulus of elasticity of rebar steel	$E_s$	MPa	200000	200000

Table 2: Properties of the reinforced concrete.

The case-study structure response is simulated by two-dimensional numerical models adopting the finite element software OpenSees [35], as shown in Figure 3b. For all the case studies, gravity loads are uniformly distributed on the beams and masses concentrated at master joints on different floors. Besides, elastic damping is modelled through the Rayleigh model [36], using a 5% viscous damping ratio on the first two vibration modes. Moreover, geometric nonlinearities are included to account for P- $\Delta$  effects.

A lumped plasticity approach is utilised to model both beams' and columns' nonlinear behaviour using zero-length rotational springs. Beam-column end-offsets and floor diaphragms are modelled as rigid. The moment-rotation constitutive relationship for beam and columns is consistent with the models developed by [37]. The peak-oriented hysteretic model (as defined by [20] and further refined by [21]) describes the strength and stiffness deterioration (cyclic and in-cycle). For pre-code frames only, nonlinear shear springs are added in series to the rotational ones to account for brittle mechanisms consistent with the model developed by [38].

Structure-specific MIDR thresholds for five DSs are calibrated via pushover analyses by reviewing multiple measurable criteria according to [31], which are based on [39] and [29]. The pushover load patterns are defined according to the first mode shape, as indicated in [29]. The selected DSs thresholds are shown in Table 3. Some relevant information on the case-study buildings' dynamic behaviour, such as the first- and second-mode vibration periods and the corresponding mass participation ratios, is summarised in Table 4.

Case-study frames	Damage states				
	DS1	DS2	DS3	DS4	DS5
PB	0.15%	0.25%	1.40%	2.00%	3.50%
SB	0.17%	0.40%	2.70%	3.85%	8.00%

Table 3: Definition of damage state thresholds for MIDR.

Parameter	PB frame	SB frame
Fundamental structural period	$T_1=0.83$ s; $T_2=0.25$ s	$T_1=0.50$ s; $T_2=0.15$ s
Mass participation ratio	94.50%	91.96%

Table 4: Fundamental structural periods and mass participation ratios.

### 3.3 Considered building portfolios

Two synthetic building portfolios are considered in this study. As shown in Figure 4, a fault-parallel “zone” is first defined as located next to a case-study strike-slip fault. The zone is defined so that the closest sites are located at 5 km minimum from the fault; each portfolio is moved perpendicularly from the fault to assess the effects of distance on ground-motion duration (and, consequently, losses). Within the considered zone, the centroid of each location in the portfolio is distributed on a uniform lattice approximately 3 km-spaced. Thus, a 9 km<sup>2</sup> area

pertains to each location. Such choice allows attaining a balance between computational burden and accuracy in the outcomes [11].

A 36 km x 36 km base portfolio is used as a standard size and is considered representative of a small region. Two different exposure configurations are also considered, considering that each location has the same building composition. These configurations involve a single building typology (i.e., PB or SB) only.

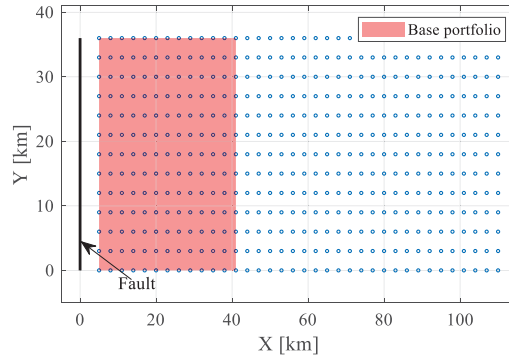


Figure 4: Geometric definition of building portfolios.

### 3.4 Considerations for the stochastic catalogue

The considered case-study strike-slip fault is defined by the characteristic earthquake-recurrence model shown in [40]. The necessary parameters for this model are assumed as follows:  $m_c=6.4$  (characteristic earthquake magnitude);  $b=1$  ( $b$ -value of the Gutenberg–Richter law);  $M_{\min}=5$ ;  $M_{\max}=6.9$ ; and  $\Delta m_1=1$  (interval below the magnitude level  $m_c$ , required in the considered probabilistic model). A rock soil type is assumed for each portfolio's location with shear wave velocity in the first 30 m of soil  $V_{s30}=800$  m/s.

A 10000-year stochastic catalogue is considered; for each event, 500 realisations of the IMs are generated. This maximum time and the number of simulations is selected based on the current catastrophe risk modelling practice and correspond to a good balance in terms of statistical validity of the loss estimates and computational burden. As discussed, AvgSa is selected as the primary IM, and it is calculated in the period range  $[T_2:2T_1]$  for both case-study frames (consistently with [41]).

## 4 RESULTS

### 4.1 Effects of ground-motion duration on hazard

Ground-motion duration increases with the distance from the source due to the scattering and dispersion of seismic waves and the difference in the arrival times of waves propagating at different velocities and traversing different paths (e.g., [42]; [43]; [44]). However, duration also depends on local site conditions, with longer duration ground-motions typically observed at sites with softer soils due to repeated seismic wave reflections within the soft-soil layer and the respective dynamic amplification [45].

Figure 5a and Figure 5c show the obtained AvgSa and  $Ds_{5-95}$  hazard curves (individual simulations and median); while Figure 5b and Figure 5d show the AvgSa and  $Ds_{5-95}$  ground-motion fields (median), considering 2500-year mean return period (MRP) for one of the two index buildings (i.e., PB). As expected, the AvgSa values decrease, and the  $Ds_{5-95}$  values increase with distance. It is worth noting that the AvgSa ground-motion field varies for each of the index buildings (not shown here for brevity) since AvgSa is structure-dependent. At the same time,

the  $DS_{5-95}$  ground-motion field is the same for every index building. In the PB case, AvgSa ranges from around 0.05 g to 1.10 g; the  $DS_{5-95}$  ranges from approximately 20 s to 70 s.

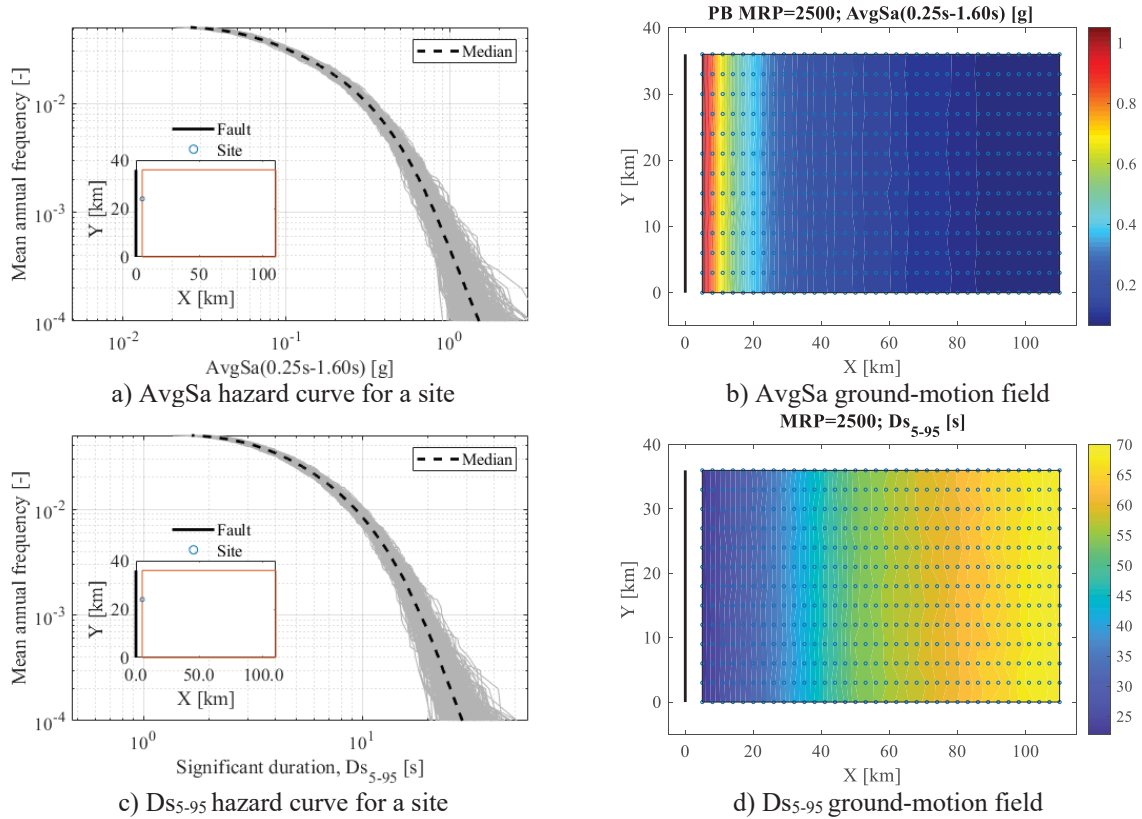


Figure 5: Simulation-based PSHA results for the region.

#### 4.2 Effects of ground-motion duration on vulnerability

Figure 6a-b show the fragility and vulnerability models obtained using AvgSa as an IM after performing the IDA for the PB frame. These relationships implicitly account for the significant duration since the structure hysteretic models can well capture the cyclic and in-cycle strength and stiffness deterioration (using the EH dissipated in each component) and the ratcheting of MIDR accentuated by the  $P$ - $\Delta$  effects. Similar behaviour is presented in different empirical damage models such as the Park and Ang damage index [46].

Figure 6c-d show the fragility and vulnerability models obtained using AvgSa and  $DS_{5-95}$  in a vector-valued format after performing the IDA. The fragility and vulnerability surfaces explicitly account for the ground-motion duration since  $DS_{5-95}$  can describe part of the variability of AvgSa, even if the latter is scaled during the nonlinear procedure. It could be noticed from the results that ground-motion duration mainly affects the higher DSs (i.e., DS3, DS4 and DS5), whilst the lower damage states (i.e., DS1 and DS2) remain approximately unaffected. This explained why the vulnerability surface exhibits a slight but steady increase in the loss ratio due to duration. On the other hand, the fragility relationship surface for DS5 exhibits a more significant (i.e., steeper) increase from short to long durations (i.e., from 1 s up to 60 s as depicted in the figure). In every case, the duration effects are consistently more apparent at lower durations and increase as AvgSa increases.

It is worth mentioning that the previous results are consistent among all the index buildings considered in this study. The fragility and vulnerability models are structure-dependent; therefore, these models vary accordingly per each case study (not shown here for brevity).



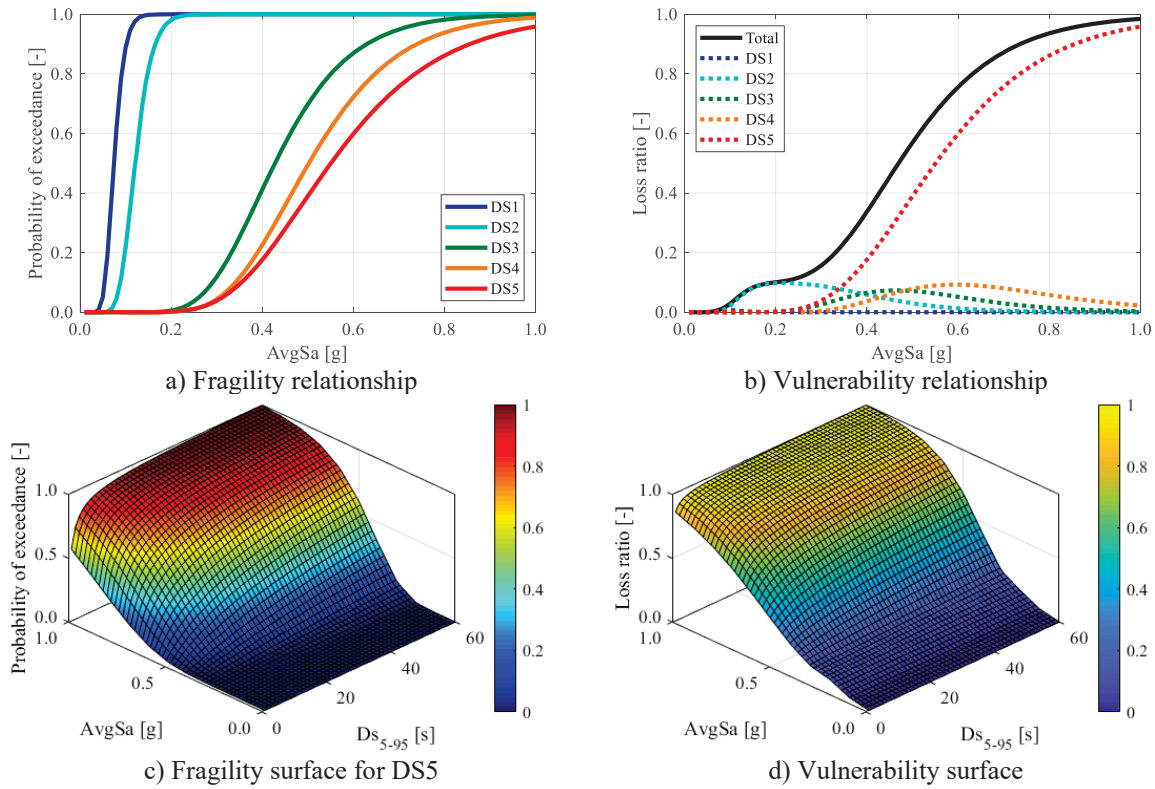


Figure 6: Fragility and vulnerability models for PB frame.

#### 4.3 Effects of ground-motion duration on losses

Figure 7a-b presents the median normalised loss ratio (NLR) corresponding to 2500 years MRP at each location within the region (i.e., normalised loss maps), computed as shown in equation 11. As expected, the NLR increases with distance when the IM explicitly accounts for duration (i.e., utilising the previously described vector-valued IM). The latter result is more apparent for the SB frame case, where the NLR can reach values around 60%. It is important to note that losses decrease dramatically with distance, and low LR values are obtained for sites located far away from the source (e.g., at 100 km from the source). Therefore, small fluctuations in LR estimates at these locations can result in obtaining high NLR values. Thus, these high NLRs may not necessarily represent significant differences in the loss estimates from a practical point of view.

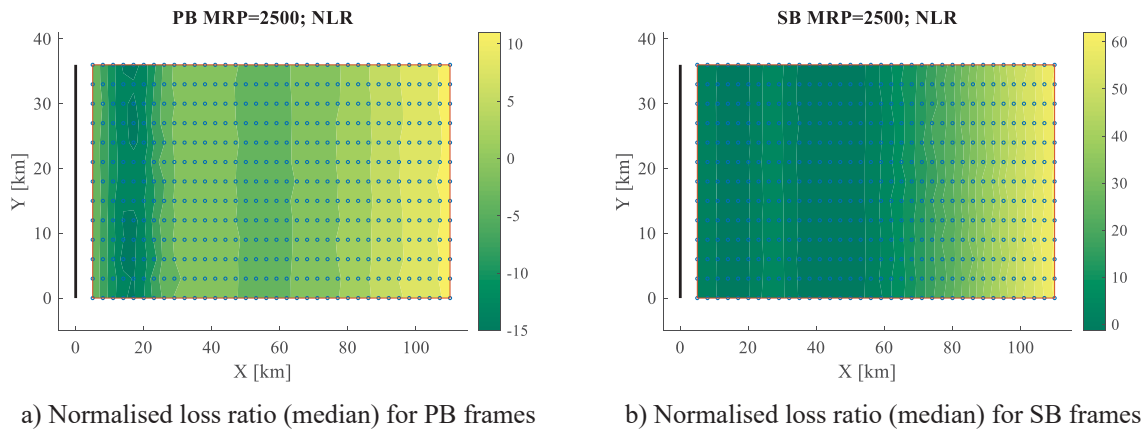


Figure 7: Normalised loss ratio (median) for PB and SB frames (MRP = 2500 years) [%].

It is worth noting that the results obtained for the SB frame are not consistent with the ones obtained when using the PB frame since, for locations relatively near the source (from 5 km to 25 km from the source), the NLR is higher when AvgSa is used as a scalar IM. This indicates that using duration in the vector-valued IM can increase or decrease the NLR value with respect to the scalar IM, given the region seismic hazard, exposure, and vulnerability models under consideration.

$$\frac{[\text{LR}(\text{IM}_{\text{vector}})_{\text{MRP}=2500 \text{ years}} - \text{LR}(\text{IM}_{\text{scalar}})_{\text{MRP}=2500 \text{ years}}]}{\text{LR}(\text{IM}_{\text{vector}})_{\text{MRP}=2500 \text{ years}}} \quad (11)$$

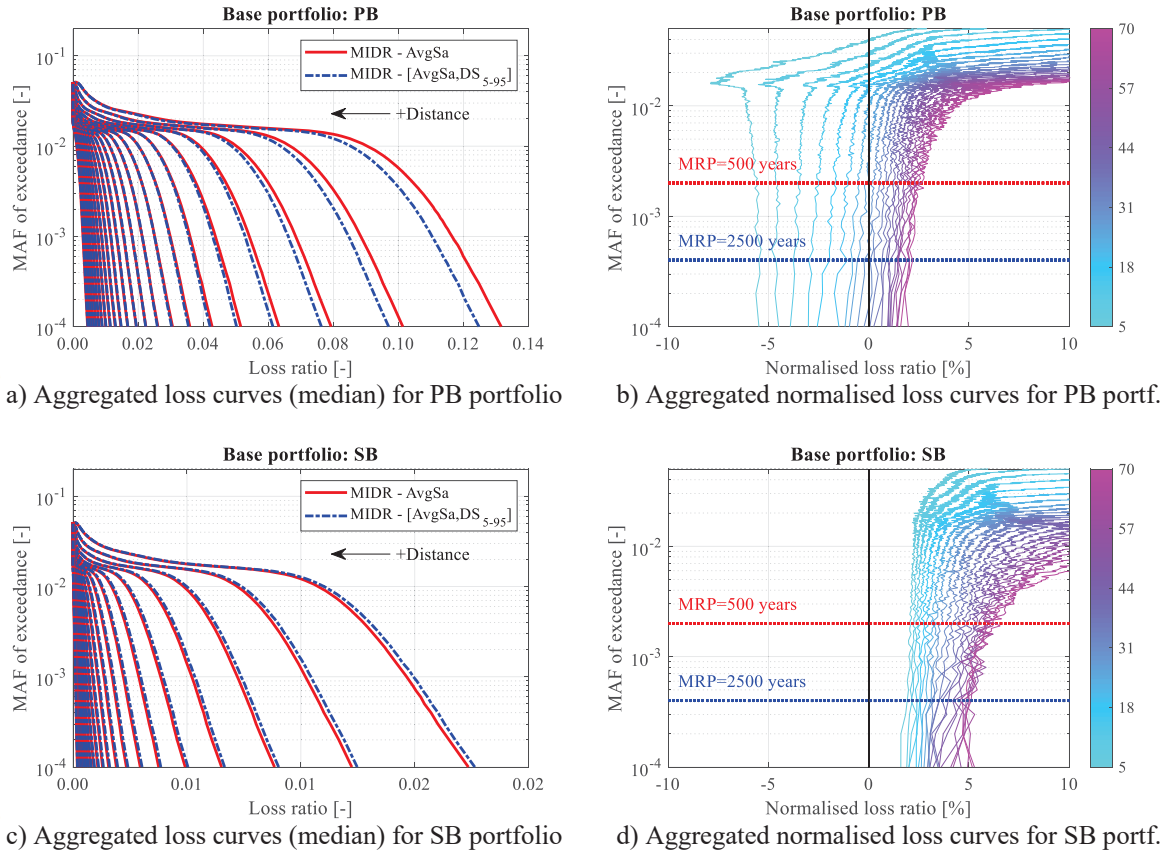


Figure 8: Aggregated loss curves (median) pairs and aggregated normalised loss curves (median) varying with distance for PB and SB portfolios. The colour bar represents the distance from the source [km].

Figure 8a-d offers a better picture of how losses (i.e., LR or NLR as appropriate) and their mean annual frequency of exceedance (for different MRP) vary with distance. The left panels in these figures show the aggregated loss curves (median) for portfolios located at different distances from the source and using AvgSa or [AvgSa, Ds<sub>5-95</sub>] respectively (the distance increase from right to left as indicated). The right panel in these figures show the corresponding aggregated normalise loss curves (median) for selected portfolios (the aggregated normalise loss curves are estimated using equation 11 for every MRP associated with each mean annual frequency of exceedance, MAFE). The results are shown for two portfolios composed of PB (see Figure 8a-b) and SB (see Figure 8c-d) frames for the considered base portfolio size.

Regarding the portfolio made exclusively of PB buildings, when using AvgSa as an IM, the obtained LR are higher in the vicinity of the source than those computed when using [AvgSa, Ds<sub>5-95</sub>] as an IM. Thereby, accounting explicitly (i.e., using the vector-valued IM) for duration near the source provides lower LR estimates. The previous behaviour varies with

distance up to 25 km from the source approximately; in this case, the losses computed using [AvgSa, Ds<sub>5-95</sub>] as an IM are higher than those estimated using AvgSa as IM. The previous results are valid for MAFEs below roughly 1/100 years, as noticed in the figures. For relatively large MAFE value (above 1/100 years), the NLR are higher than 10%, indicating that the vector-valued IM can better capture duration effects for moderate seismic events.

Interestingly for the portfolio made of SB buildings, when using AvgSa as an IM, the resulting LR results are lower than those obtained when [AvgSa, Ds<sub>5-95</sub>] is used as an IM. This may be due to the fact that a special-code frame (i.e., SB frame) with higher levels of strength and ductility can dissipate higher EH levels. Since significant duration is better correlated to structures behaving in such a way, its effect could be more apparent when duration is considering explicitly for intensity levels that are not causing structural collapse. In contrast, a pre-code building (i.e., PB frame) may collapse given the same intensity level without dissipating significant amounts of EH (as it occurs next to the source). These results reinforced the idea that the vector-valued-based vulnerability model can better capture duration effects given the considered seismic hazard, exposure, and vulnerability models.

The EAL is a suitable parameter to represent portfolio losses; therefore, the EAL is computed for all the possible distances within the region for the same portfolios analysed above. The outcome depends strongly on the portfolio composition when using both vulnerability models (i.e., scalar- and vector-valued-based vulnerability models). For the portfolio including only PB buildings, differences between the EAL values are at most 6% (next to the source). In contrast, for the portfolio composed of SB buildings, EAL differences can reach up to 9% (far from the source). The noticeable trend among all distances is that, when EAL is used as a loss metric, there is a non-significant difference between using a scalar IM and a vector-valued IM accounting implicitly and explicitly for ground-motion duration, respectively.

## 5 CONCLUSIONS

This study investigated the influence of earthquake-induced ground-motion duration on estimating seismic losses for building portfolios using a simulation-based risk assessment framework. The aim was to examine how this ground-motion feature influences different loss estimates, investigating whether duration matters (depending on the location/portfolio) and should be included in the seismic risk assessment practice. The main conclusions of this work are summarised as follows:

- As expected, given the utilised GMMs, AvgSa intensity decrease and Ds<sub>5-95</sub> increase with distance from the source;
- Duration can be implicitly or explicitly considered when fragility and vulnerability models are constructed. In general, the outcomes (i.e., loss estimates) do not match;
- Vector-valued fragility and vulnerability models may perform better in capturing the impact of ground-motion duration;
- The loss curves and EAL decrease rapidly with distance from the source; after 25 km-30 km, the differences when using a scalar and a vector-valued IM may be neglected;
- Building portfolio loss assessment is influenced by ground-motion duration, and its effect depends on the portfolio location and composition;

This study provided a first look at how to account for earthquake-induced ground-motion duration in building-portfolio loss estimation, and its results may not be generalised. Essential aspects such as the size of the portfolio, a realistic composition of the portfolio (e.g., mixed building typologies in the considered exposure), the use of more building typologies, complex source models, among others, were not considered in the paper but will be investigated in future developments of the study.

## REFERENCES

- [1] V. Silva, H. Crowley, H. Varum, and R. Pinho, "Seismic risk assessment for mainland Portugal," *Bull. Earthq. Eng.*, vol. 13, no. 2, 2015, doi: 10.1007/s10518-014-9630-0.
- [2] R. Chandramohan, J. W. Baker, and G. G. Deierlein, "Quantifying the influence of ground motion duration on structural collapse capacity using spectrally equivalent records," *Earthq. Spectra*, vol. 32, no. 2, 2016, doi: 10.1193/122813EQS298MR2.
- [3] J. Hancock and J. J. Bommer, "A state-of-knowledge review of the influence of strong-motion duration on structural damage," *Earthquake Spectra*, vol. 22, no. 3. 2006, doi: 10.1193/1.2220576.
- [4] C. A. Cornell, "Does Duration Really Matter?," 1997.
- [5] M. Raghunandan and A. B. Liel, "Effect of ground motion duration on earthquake-induced structural collapse," *Struct. Saf.*, vol. 41, 2013, doi: 10.1016/j.strusafe.2012.12.002.
- [6] M. A. Bravo-Haro and A. Y. Elghazouli, "Influence of earthquake duration on the response of steel moment frames," *Soil Dyn. Earthq. Eng.*, vol. 115, 2018, doi: 10.1016/j.soildyn.2018.08.027.
- [7] K. Otárola-Madrigal, L. Sousa, R. Gentile, and C. Galasso, "Impact of earthquake-induced ground-motion duration on nonlinear structural performance," MSc thesis, University of Pavia and University School of Advanced Studies (IUSS) Pavia, 2020.
- [8] S. H. Hwang, S. Mangalathu, and J. S. Jeon, "Quantifying the effects of long-duration earthquake ground motions on the financial losses of steel moment resisting frame buildings of varying design risk category," *Earthq. Eng. Struct. Dyn.*, 2020, doi: 10.1002/eqe.3403.
- [9] D. Vamvatsikos and C. A. Cornell, "Applied incremental dynamic analysis," *Earthq. Spectra*, vol. 20, no. 2, 2004, doi: 10.1193/1.1737737.
- [10] J. W. Baker, "Probabilistic structural response assessment using vector-valued intensity measures," *Earthquake Engineering and Structural Dynamics*, vol. 36, no. 13. 2007, doi: 10.1002/eqe.700.
- [11] R. Gentile and C. Galasso, "Accounting for directivity-induced pulse-like ground motions in building portfolio loss assessment," *Bull. Earthq. Eng.*, 2020, doi: 10.1007/s10518-020-00950-9.
- [12] M. Pagani, D. Monelli, G. A. Weatherill, and J. Garcia, "The OpenQuake-engine Book: Hazard," *GEM Found.*, 2014.
- [13] D. L. Wells and K. J. Coppersmith, "New empirical relationships among magnitude, rupture length, rupture width, rupture area, and surface displacement," *Bull. - Seismol. Soc. Am.*, vol. 84, no. 4, 1994.
- [14] B. A. Bradley, "A ground motion selection algorithm based on the generalized conditional intensity measure approach," *Soil Dyn. Earthq. Eng.*, vol. 40, 2012, doi: 10.1016/j.soildyn.2012.04.007.
- [15] K. W. Campbell and Y. Bozorgnia, "NGA-West2 ground motion model for the average horizontal components of PGA, PGV, and 5% damped linear acceleration response spectra," *Earthq. Spectra*, vol. 30, no. 3, 2014, doi: 10.1193/062913EQS175M.
- [16] K. Afshari and J. P. Stewart, "Physically parameterized prediction equations for significant duration in active crustal regions," *Earthq. Spectra*, vol. 32, no. 4, 2016, doi: 10.1193/063015EQS106M.
- [17] J. W. Baker and N. Jayaram, "Correlation of spectral acceleration values from NGA ground motion models," *Earthq. Spectra*, vol. 24, no. 1, 2008, doi: 10.1193/1.2857544.
- [18] B. A. Bradley, "Correlation of significant duration with amplitude and cumulative



- intensity measures and its use in ground motion selection,” *J. Earthq. Eng.*, vol. 15, no. 6, 2011, doi: 10.1080/13632469.2011.557140.
- [19] G. A. Weatherill, V. Silva, H. Crowley, and P. Bazzurro, “Exploring the impact of spatial correlations and uncertainties for portfolio analysis in probabilistic seismic loss estimation,” *Bull. Earthq. Eng.*, vol. 13, no. 4, 2015, doi: 10.1007/s10518-015-9730-5.
  - [20] L. F. Ibarra, R. A. Medina, and H. Krawinkler, “Hysteretic models that incorporate strength and stiffness deterioration,” *Earthq. Eng. Struct. Dyn.*, vol. 34, no. 12, 2005, doi: 10.1002/eqe.495.
  - [21] D. G. Lignos and H. Krawinkler, “Deterioration Modeling of Steel Components in Support of Collapse Prediction of Steel Moment Frames under Earthquake Loading,” *J. Struct. Eng.*, vol. 137, no. 11, 2011, doi: 10.1061/(asce)st.1943-541x.0000376.
  - [22] M. Rahnema and H. Krawinkler, “Effects of Soft Soil and Hysteresis Model on Seismic Demands,” *John A. Blume Earthq. Eng. Cent. Tech. Rep. Ser.*, vol. TR108, no. 108, 1993.
  - [23] K. Porter, R. Kennedy, and R. Bachman, “Creating fragility functions for performance-based earthquake engineering,” *Earthq. Spectra*, vol. 23, no. 2, 2007, doi: 10.1193/1.2720892.
  - [24] T. Rossetto and A. Elnashai, “Derivation of vulnerability functions for European-type RC structures based on observational data,” *Eng. Struct.*, vol. 25, no. 10, 2003, doi: 10.1016/S0141-0296(03)00060-9.
  - [25] G. Di Pasquale, G. Orsini, and R. W. Romeo, “New developments in seismic risk assessment in Italy,” *Bull. Earthq. Eng.*, vol. 3, no. 1, 2005, doi: 10.1007/s10518-005-0202-1.
  - [26] K. Mitchell-Wallace, M. Jones, J. Hillier, and M. Foote, *Natural catastrophe risk management and modelling: A Practitioner’s Guide*. 2017.
  - [27] T. D. Ancheta *et al.*, “PEER NGA-West2 Database,” *PEER Rep.*, no. May 2013, 2013.
  - [28] S. Minas and C. Galasso, “Accounting for spectral shape in simplified fragility analysis of case-study reinforced concrete frames,” *Soil Dyn. Earthq. Eng.*, vol. 119, 2019, doi: 10.1016/j.soildyn.2018.12.025.
  - [29] Eurocode 8, “European Standard EN 1998-3:2005: Design of structures for earthquake resistance - Part 3: Assessment and retrofitting of buildings,” *Com. Eur. Norm. Brussels*, vol. 3, no. 2005, 2005.
  - [30] Consiglio dei ministri, “Regio Decreto Legge n. 2229 del 16/11/1939.” G.U. n.92 del 18/04/1940, 1939.
  - [31] K. Aljawhari, R. Gentile, F. Freddi, and C. Galasso, “Effects of ground-motion sequences on fragility and vulnerability of case-study reinforced concrete frames,” *Bull. Earthq. Eng.*, 2020, doi: 10.1007/s10518-020-01006-8.
  - [32] G. M. Verderame, G. Manfredi, and G. Frunzio, “Le proprietà meccaniche dei calcestruzzi impiegati nelle strutture in cemento armato realizzate negli anni ‘60,” *X Congr. Naz. "L'Ingegneria Sismica Ital. - ANIDIS*, 2001.
  - [33] G. M. Verderame, P. Ricci, M. Esposito, and F. C. Sansiviero, “Le Caratteristiche Meccaniche degli Acciai Impiegati nelle Strutture in C.A. Realizzate dal 1950 al 1980,” *Aicap- Reluis*, 2011.
  - [34] N. Mohammad Noh, L. Liberatore, F. Mollaioli, and S. Tesfamariam, “Modelling of masonry infilled RC frames subjected to cyclic loads: State of the art review and modelling with OpenSees,” *Eng. Struct.*, vol. 150, 2017, doi: 10.1016/j.engstruct.2017.07.002.
  - [35] S. Mazzoni, F. McKenna, and M. Scott, “Open system for earthquake engineering simulation (OpenSees),” *Berkeley, Calif.*, 2006.
  - [36] F. Zareian and R. A. Medina, “A practical method for proper modeling of structural



- damping in inelastic plane structural systems,” *Comput. Struct.*, vol. 88, no. 1–2, pp. 45–53, Jan. 2010, doi: 10.1016/j.compstruc.2009.08.001.
- [37] T. B. Panagiotakos and M. N. Fardis, “Deformations of reinforced concrete members at yielding and ultimate,” *ACI Struct. J.*, vol. 98, no. 2, 2001, doi: 10.14359/10181.
- [38] E. J. Setzler and H. Sezena, “Model for the lateral behavior of reinforced concrete columns including shear deformations,” *Earthq. Spectra*, vol. 24, no. 2, 2008, doi: 10.1193/1.2932078.
- [39] T. Rossetto *et al.*, “FRACAS: A capacity spectrum approach for seismic fragility assessment including record-to-record variability,” *Eng. Struct.*, vol. 125, 2016, doi: 10.1016/j.engstruct.2016.06.043.
- [40] V. Convertito, A. Emolo, and A. Zollo, “Seismic-hazard assessment for a characteristic earthquake scenario: An integrated probabilistic-deterministic method,” *Bull. Seismol. Soc. Am.*, vol. 96, no. 2, 2006, doi: 10.1785/0120050024.
- [41] A. K. Kazantzi and D. Vamvatsikos, “Intensity measure selection for vulnerability studies of building classes,” *Earthq. Eng. Struct. Dyn.*, vol. 44, no. 15, 2015, doi: 10.1002/eqe.2603.
- [42] M. D. Trifunac and A. G. Brady, “A study on the duration of strong earthquake ground motion,” *Bull. Seismol. Soc. Am.*, vol. 65, no. 3, 1978.
- [43] S. Stein and M. Wyssession, *An Introduction to Seismology, Earthquakes, and Earth Structure*. Oxford, UK: Blackwell Publishing Ltd., 2003.
- [44] D. M. Boore and E. M. Thompson, “Path durations for use in the stochastic-method simulation of ground motions,” *Bull. Seismol. Soc. Am.*, vol. 104, no. 5, 2014, doi: 10.1785/0120140058.
- [45] R. Dobry, I. M. Idriss, and E. Ng, “Duration characteristics of horizontal components of strong-motion earthquake records,” *Bull. Seismol. Soc. Am.*, vol. 68, no. 5, 1978.
- [46] Y. Park and A. H. -S. Ang, “Mechanistic Seismic Damage Model for Reinforced Concrete,” *J. Struct. Eng.*, vol. 111, no. 4, 1985, doi: 10.1061/(asce)0733-9445(1985)111:4(722).

## RELIABILITY-BASED ASSESSMENT OF A MASONRY ARCH BRIDGE UNDER FLOOD EVENTS

Carlos Mendoza<sup>1</sup>, Mónica Santamaria<sup>2</sup>, Hélder S. Sousa<sup>3</sup> and José C. Matos<sup>4</sup>

<sup>1</sup> MSc student, University of Minho, ISISE, Department of Civil Engineering  
Guimarães, Portugal

e-mail: carlos\_amc1@hotmail.com

<sup>2</sup> Ph.D. candidate, University of Minho, ISISE, Department of Civil Engineering  
Guimarães, Portugal

email: id8021@alunos.uminho.pt

<sup>3</sup> Postdoc researcher, University of Minho, ISISE, Department of Civil Engineering  
Guimarães, Portugal

e-mail: sousa.hms@gmail.com

<sup>4</sup> Assistant Professor, University of Minho, ISISE, Department of Civil Engineering  
Guimarães, Portugal

e-mail: jmatos@civil.uminho.pt

---

### Abstract

*Natural disasters are unavoidable and can cause serious damage to bridges, which may lead to catastrophic losses both human and economic. In the US more than 45% of bridge collapses are caused by flood events in which more than one-third are caused by scouring effects. In 2015, part of the Tadcaster bridge, a masonry arch bridge in North Yorkshire UK, collapsed during a flooding event. This tragedy was followed by another one in 2019 when a masonry bridge collapsed in the same county. Therefore, the assessment of bridges susceptible to these events is of paramount importance as to identify possible mitigation needs. The objective of the present paper is to present a consistent framework to obtain the reliability index of a masonry arch bridge (MAB), under flood hazard that is subject to local scour, using surrogate models to reduce the computational effort of the probabilistic analysis. The proposed framework is tested on a MAB located in Portugal. A two-dimensional numerical model is constructed where the random variables that affect the structural capacity and the scour geometry were considered. The results show the failure mechanism of the MAB when subjected to scour-induced settlements, therefore allowing to identify the vulnerable zones along the arch's length. The presented methodology can be used to assess the bridge performance under a flood event, thus providing useful information for bridge management and monitoring. Moreover, it can be further developed to include fragility analysis and vulnerability assessment.*

**Keywords:** • Masonry bridges, Local Scour, Reliability, Surrogate Models.

---

## 1 INTRODUCTION

Bridges have a higher design life than most common structures. During this period, bridge management is fundamental to maintain a satisfactory performance of the structure. To achieve this goal, information regarding the state of the bridges is essential when making decisions that involve the maintenance of the structure [1]. Masonry arch bridges (MAB) represent a large part of the European network (railway and roadway), hence by identifying the safety level of the bridge, suitable maintenance strategies can be applied [2].

Bridges are structures that face harsh environmental condition; therefore, should be able to withstand potential hazards such as flooding, earthquakes, among others [3]. Natural disasters are often unavoidable and can cause serious damage to bridges, which may cause catastrophic losses both human and economic. Floods account for a large percentage of all bridge failures [4]. Nowadays, the effects of climate change may produce larger and more frequent peak river discharges, which could induce the mobilization of sediment from riverbeds, and around piers and abutments (i.e., increased risk of scouring). Bridge collapses have been experienced worldwide. In 2015, part of the Tadcaster bridge, a masonry arch bridge in North Yorkshire, collapsed during a flood event [5]. Therefore, the assessment of bridges susceptible to these phenomena (namely flood, scour, trapped debris, among others) is of utmost importance as to identify possible mitigation needs.

When assessing bridges under loading conditions resulting from environmental conditions, the lack of available information causes high uncertainties when representing the environmental actions and the parameters of the materials [2]. Explicitly considering the uncertainties can mitigate this lack of information. Moreover, limit analysis-based structural assessment in combination with probabilistic-based approaches has been used to predict ultimate loading carrying capacity and safety verification of Portuguese MAB [6]. Thus, a full probabilistic analysis for the reliability-based assessment of MAB under floods for ultimate limit states should be implemented.

Due to the complexity of the probabilistic analysis, the objective of the present work is to propose a consistent framework to reduce the computational costs to obtain the reliability index associated with a failure mode of masonry arch bridges (MAB) under flood hazard. This will allow to assess the performance of bridges that may affect the efficiency of important sections of the roadway network if damaged by a flood event. The proposed framework is tested on a MAB “Ponte da Vala do Carregado” located in Portugal. A numerical model is constructed in LimitState:GEO software (<http://www.limitstate.com>) [7]. The model implemented the random variables that affect the structure capacity [2] and the scour geometry, such as shape and depth derived from flood conditions [8].

## 2 METHODOLOGY

The methodology considered in this work is shown in Figure 1. First, a numerical model is developed using a software based on limit state analysis. Then, a surrogate model is defined to perform a sensitivity analysis which allows to identify the most influent variables on the ultimate capacity of the bridge [2]. Later, a new surrogate model based on the most relevant variables is introduced which uses a low number of evaluations, thus reducing the computational costs of the full probabilistic analysis [6], [9]. Finally, the reliability index is computed based on the subset simulation technique [10].

For this study, the procedure was implemented for different scour profiles. This approach allows assessing the bridge reliability under local scouring from a case study.

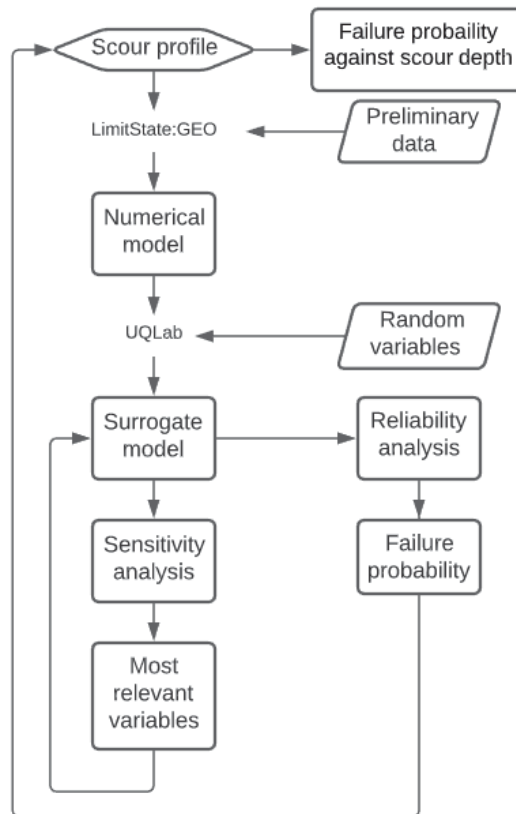


Figure 1: Framework for reliability assessment of MAB under local scouring.

### 3 NUMERICAL MODEL

The case study “Vala do Carregado” is a railway masonry arch bridge located in Vila Franca de Xira, Portugal (see Figure 2). The three-span bridge has a total span of around 30m, and it is supported by direct foundations. Earliest reports of the bridge date from 1881 when the bridge was built. After that, there is information regarding reinforcement of the arch barrel, until subsequent studies were conducted, and it was concluded that the bridge should be replaced [11].

According to the performed studies, it was found that the bridge foundations presented poor soil conditions, which were incompatible with the foundation system, and hydraulic capacity was below the requirements of the design flood (corresponding to a 100-year return period) [11]. For these reasons, the Vala do Carregado bridge before being replaced is considered as representative of the typical Portuguese railway masonry arch bridges which require particular attention.

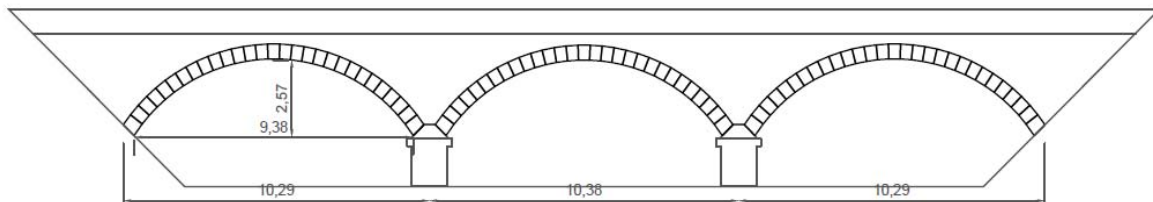


Figure 2: Case study (dimensions in meters).

A two-dimensional limit state model was developed using LimitState:GEO which is designed to rapidly analyze the ultimate limit state for a wide variety of 2D geotechnical problems by using the computational limit analysis technique named Discontinuity Layout

Optimization (DLO) [12]. The software was selected due to the reliability of its results when assessing the collapse mechanisms of MABs, while allowing to model the soil parts of the bridge and its interaction with other materials (*e.g.*, concrete, masonry) [13]. Moreover, the software allows fast and computational efficiency which is key when performing probabilistic analysis.

Only the parameters defining the yield surface are required for the material models used by LimitState:GEO. The following models were used to define the different components of the case study: (i) a Mohr-Coulomb model was employed to represent the soil parts of the bridge, namely riverbed and backfill; (ii) fully rigid blocks, where no slip-line can pass through it at any load, were utilized for modelling masonry blocks and foundations; and (iii) cutoff materials were used to model joints, which allows modelling tension cracks or crushing by limiting the tensile or compressive stress, respectively [12].

Load models are used to represent the real loading that a bridge is subjected to. Some studies have been made regarding the reliability of Portuguese MABs, which are based on the documentation provided by the Portuguese railway authorities (Infraestruturas de Portugal) [2]. The load model is composed of four-point loads spaced by 1.6 m. Two distributed loads are also defined within the load mode, but studies have shown that even by not considering them the most unfavorable case scenario is still achieved [14].

By assuming that there is no failure (nor excessive deformation) in the spandrel walls, then the bridge capacity will depend mainly on the arch barrel and the backfill. Therefore, 2D limit state analyses are best suited for in-plane assessment of bridge reliability. Nevertheless, it is worth mentioning that bridges with increased backfill height are more vulnerable to out-of-plane failure of the spandrel (*i.e.*, less load carrying capacity) [15].

The water table was assumed to be acting on top of the structure due to the inadequacy of the masonry arch bridge to withstand the design flood (100-year return period) as concluded by the hydraulic modelling [11]. Moreover, studies have been made showing the effects of the water level in MAB, in which for a fully submerged bridge (with backfill fully saturated) a reduction in its load-bearing capacity near 40% was found [7]. Thus, to have the most unfavorable scenario, all soil materials are considered fully saturated and a water table near the surface level is assumed.

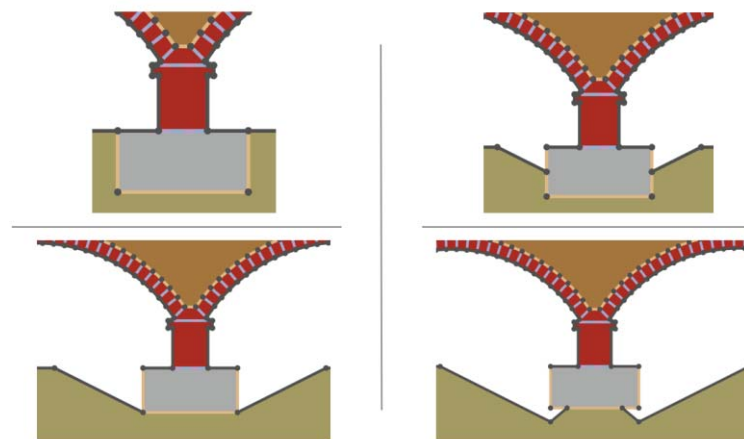


Figure 3: Scour profiles (No scour, minor, moderate, and extensive).

The scour cavity is affected by several factors including soil type, flow velocity and turbulence, and foundation geometry [16]. Studies have been made in which several shapes for local scouring were defined and studied [8].

There are three main forms of scour around foundations, upstream, downstream and at the sides. When analyzing in-plane behavior, only the effects of the local scour due to the separa-



tion of the flow (*i.e.*, at the sides) will be considered. The profile geometry was defined by considering not only different damage states but scour depths and shape of the foundation. Figure 3 depicts the proposed scour cavities which represent different damage levels (minor, moderate, extensive) which are related to the ratio between scour depth and foundation height ( $d_s/D$  equal to 0.50, 1.00, 1.36) [8], [16], [17].

By analyzing the ultimate capacity of the bridge in terms of an adequacy factor (see Figure 4), which is based on how many loads increments the structure can withstand before collapsing, it is possible to evaluate the safety level of the bridge. In the following chapter, a stochastic approach is conducted to evaluate the reliability of the structure under the effects of local scouring.

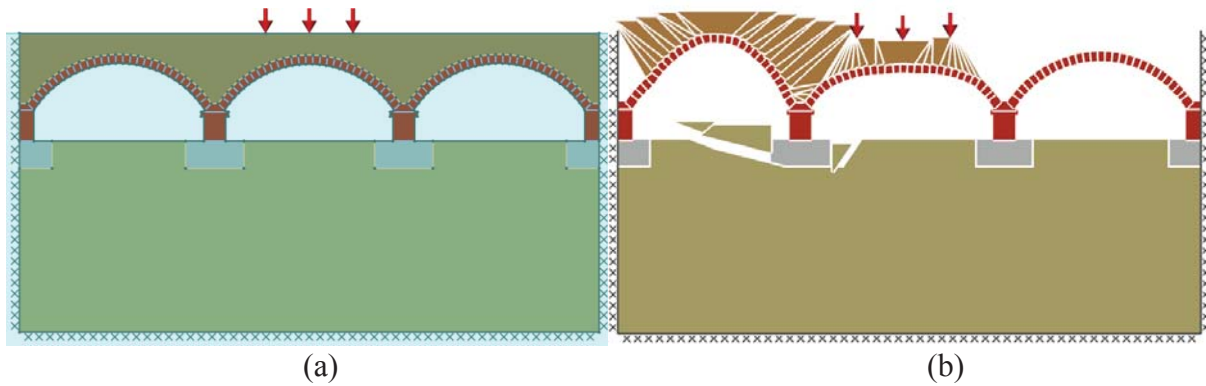


Figure 4: 2D Limit-state model without local scouring (a) geometry (b) failure for an adequacy factor of 4.235

## 4 PROBABILISTIC ANALYSIS

In structural design, there are many uncertainties related to loading and load-carrying capacities. Fundamentally, structures do not have a zero probability of failure due to the random variables involved in the design, construction, and operation processes [18].

To compute the reliability index of the case study, first some random variables that are involved in the load-carrying capacities of the structure must be defined and assessed. Resistance parameters and density of each material comprising the structure are considered. In Table 1, each variable with its distribution type and parameters are presented.

ID	Description	Element	Nominal Values	Units	CV (%)	Type	Reference
FA <sub>S</sub>	Friction angle	Soil	34,61	tan( $\phi$ )	10,0	Lognormal	[19]
SD <sub>S</sub>	Saturated density	Soil	20,50	kN/m <sup>3</sup>	5,0	Lognormal	[19]
D <sub>C</sub>	Density	Concrete	25,00	kN/m <sup>3</sup>	10,0	Gaussian	[20]
SD <sub>B</sub>	Saturated density	Backfill	20,00	kN/m <sup>3</sup>	12,5	Gaussian	[21]
C <sub>B</sub>	Cohesion	Backfill	30,00	kPa	15,0	Gaussian	[6]
FA <sub>B</sub>	Friction angle	Backfill	30,00	°	10,0	Gaussian	[6]
D <sub>M</sub>	Density	Masonry	16,00	kN/m <sup>3</sup>	10,0	Gaussian	[22]

Table 1: Random variables used in the probabilistic analysis.

### 4.1 Surrogate model

The use of reliability methods is limited due to the vast computational cost they often require. Therefore, metamodeling techniques (*e.g.*, polynomial chaos, kriging, among others) have been widely used. Comparisons between different surrogate models have been conducted, and Kriging based metamodels using subset simulations (AK-SS [10]) have been proven

to be efficient to describe non-linear limit state functions, allowing a great representation of the behavior of the function using 19 evaluations [9]. To optimize the probabilistic assessment of the structure by reducing the number of evaluations (*i.e.*, numerical models), a surrogate model was built using UQLab, a general-purpose Uncertainty Quantification framework [23].

The assessment of the load-carrying capacity of a masonry arch bridge can be approximately represented by a non-linear limit state function, as shown traditionally by the Military Engineering Experimental Establishment (MEXE) method. This method has its roots in idealized elastic structural modelling, which mainly depends on geometrical parameters and densities of materials (*e.g.*, masonry and backfill) [24].

Therefore, an experimental design of 20 runs generated by using the Latin Hypercube Sampling Method (LHS) was used [9]. Then, a Kriging metamodel using UQLab was created and validated based on the random variables previously defined. The surrogate model uses a universal trend type, an anisotropic ellipsoidal Matérn 5/2 correlation function, used to define the Gaussian process and cross-validation estimation method. For the validation of the metamodel, two different sources of error estimation were implemented. First, the leave one out method, and second a validation experimental design of 10 runs using LHS; the errors found were  $4.11\text{e-}03$  and  $8.28\text{e-}03$ , respectively.

## 4.2 Sensitivity analysis

To reduce the number of relevant variables in the response of the structure, a sensitivity analysis was performed using UQLab. Analysis of covariance (ANCOVA) was used to produce helpful sensitivity indices for both correlated and uncorrelated input variables using a covariance decomposition method [25].

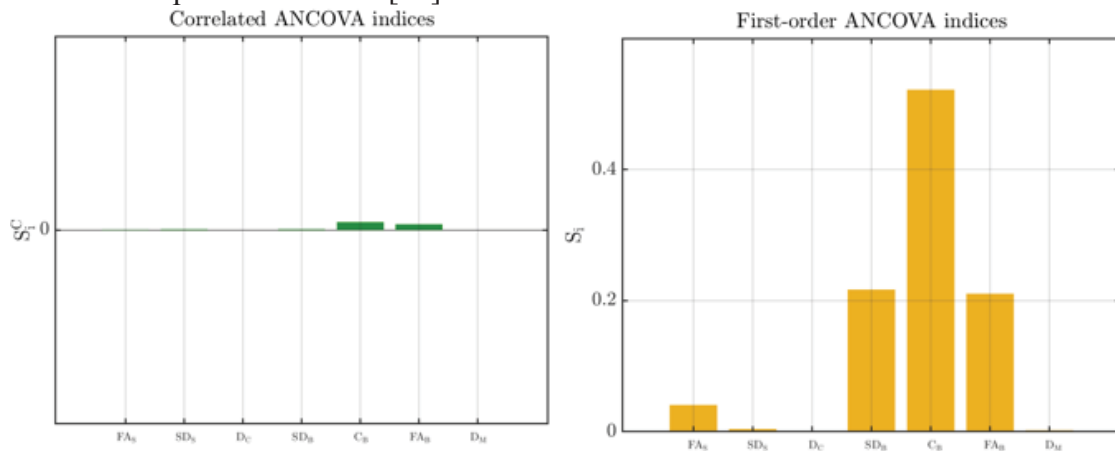


Figure 5: ANCOVA indices

As it can be observed from Figure 5, the parameters with the most influence over the load-carrying capacity are the ones used to describe the backfill soil. This was expected given that most of the capacity of the bridge for in-plane behavior (and excluding the spandrel) comes from the backfill [15]. Furthermore, the soil underneath the foundation has an impact on the capacity, which is expected as a portion of the soil is being mobilized by the foundation. As the correlated ANCOVA indices are small in magnitude, the correlation among input variables has only a weak effect on the response sensitivity.

Then, the same process used to define the surrogate model is used, but instead of the seven variables, only the main four are used. This gives a more efficient metamodel without compromising its reliability.

### 4.3 Reliability analysis

By using the surrogate model based on the relevant variables, an experimental design of 10000 simulations using Monte-Carlo (MC) sampling method was generated (Figure 6). Then, a Gumbel distribution was fitted based on the generated histogram of adequacy factors (*i.e.*, collapsing loads), which allowed to define the resistance curve  $R$ . Additionally, model uncertainties for limit state models (defined by a Gaussian distribution of mean 1 and COV 1%), was also considered [6]. The loading curve  $S$  was defined using existing data fitted to a Gumbel distribution, which is described by a mean equal to 184.41 kN and a COV of 9.06% [2].

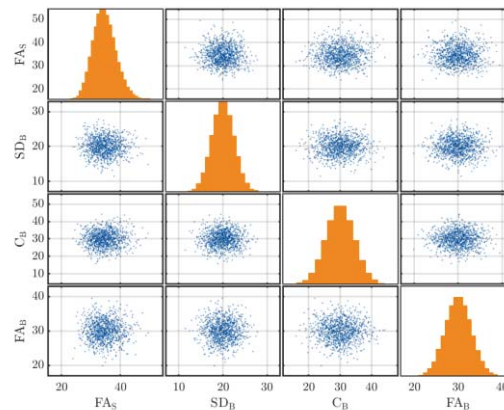


Figure 6: MC experimental design.

To obtain the reliability index of the structure for a given profile of local scour, traditional methods like MC may require numerous simulations to converge with a satisfactory level of accuracy. Therefore, subset simulation techniques are employed herein to overcome this limitation by solving simpler reliability problems with intermediate thresholds (Figure 7) [26].

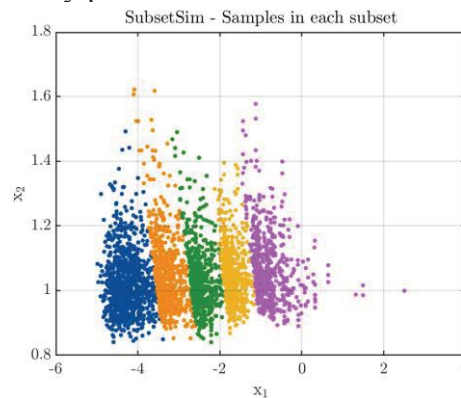


Figure 7: Subset simulation samples discretization.

Once the reliability analysis is completed, the failure probability and reliability index are obtained. In the following chapter, the different results obtained for each scour profile will be presented and discussed.

## 5 INFLUENCE OF SCOUR DEPTH IN THE RELIABILITY OF THE STRUCTURE

Each scour profile produces a different impact on the reliability of the structure, and it is important to understand how changes in the scour depth ( $d_s$ ) in relation to the foundation

height ( $D$ ) may affect the load-bearing capacities of the bridge. Next, the results for the different scour scenarios are presented.

First, the sensitivity analysis shows some differences among the scour profiles (see Figure 8). It can be seen that the variables related to the backfill are the ones with the most influence on the load-bearing capacity of the bridge (in-plane analysis) [15]. Moreover, due to the removal of soil at the base of the foundation (*i.e.*, changes  $ds/D$ ), the parameters related to the soil beneath the river have less influence when the scour hole increases, as can be observed in Figure 9 by the differences between the failure modes for each scour profile.

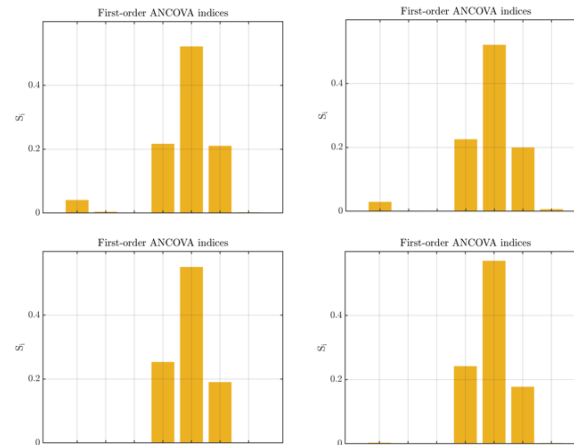


Figure 8: Results of the sensitivity analysis for each scour profile (no scour, minor, moderate, and extensive).

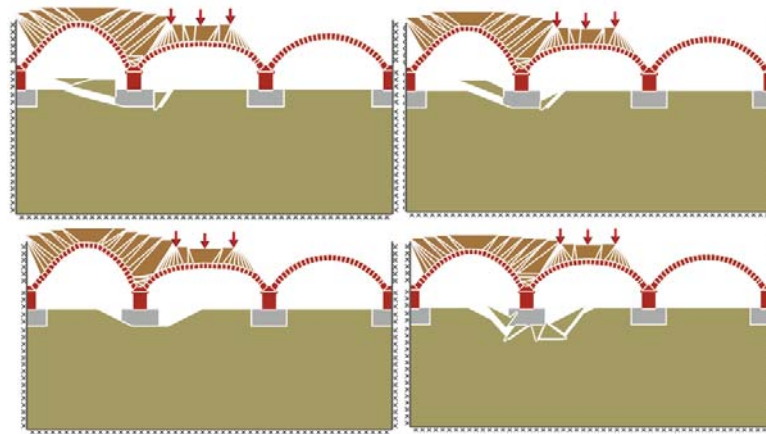


Figure 9: Failure modes of each scour profile (no scour, minor, moderate, and extensive).

Among the different scour scenarios, the failure mode remains largely the same, *i.e.*, in each case, failure of the backfill is achieved by incrementing the railroad load applied at surface level. Moreover, failure at the riverbed is reached due to the mobilization of the foundation. Meanwhile, both arch failures show the characteristic shape of the hinging mechanism [27].

Then, the respective surrogate models are defined, and the capacity curve of the structure for each of the scour profiles are built (see Figure 10). It can be observed that the capacity of the bridge decreases with each increment of the scour depth. As expected, the loss of bearing capacity for scour depth values lower than the foundation height is slight, *i.e.*, the capacity curve largely maintains its properties which indicates a slight decrease in the bridge reliability index [8].

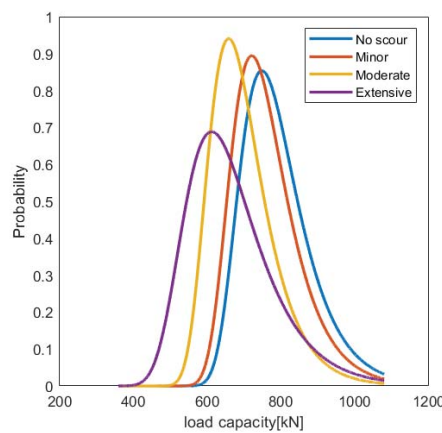


Figure 10: Resistance curve R of each scour profile.

However, when analyzing the extensive scour profile, the capacity curve changes drastically which may be occasioned by failure of the soil under the foundation. Finally, the values of reliability and failure probability are plotted against the scour depth ( $ds/D$ ) in Figure 11.

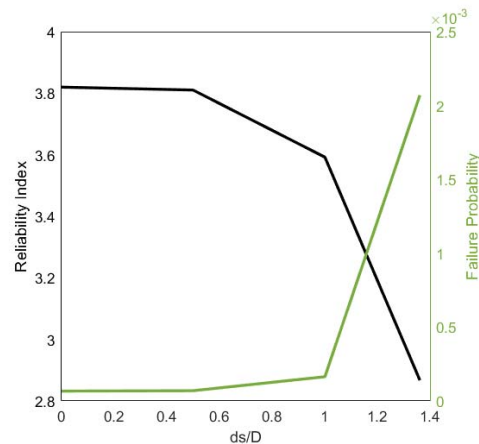


Figure 11: Reliability index and probability failure against scour depth

From Figure 11 it can be seen that the reliability index decreases greatly when the local scour starts to extend below the foundation. This situation may cause problems with extensive settlements of the bridge which may induce instability on the arch barrel and consequently bridge collapse [8]. For none of the scour profiles the structure fulfills the target reliability for safety, i.e.  $\beta_{\text{target}}=4.3$  for structures with consequences involving high human and economic losses, according to the NP 1990 [28].

## 6 CONCLUSIONS

The present work established an efficient framework for reliability assessment of MAB subject to flood-induced scour. The methodology was validated through a case study bridge located in Portugal. Based on the obtained results, the following conclusions can be made:

- By using surrogate model techniques, it is possible to perform several numbers of experiments, that otherwise would be time-consuming and would demand high computational cost, with a satisfactory level of reliability. Thus, optimizing and improving probabilistic analyses. Regarding the study of the reliability of MAB, it was possible to examine different scenarios of local scouring by analyzing different random variables at an efficient computational cost.



- By performing a sensitivity analysis, the most relevant variables when assessing the bridge capacity were obtained and validated by literature. As discussed before, the soil parameters used to describe the behavior of the backfill are the ones that have the most impact when computing the load-bearing capacity of the in-plane performance of a MAB [15].
- To understand the behavior of the bridge under local scouring, the ultimate limit state function was defined by considering the randomness of the bridge loading capacity and different scour profiles, which allowed assessing the bridge performance under floods. In each of the proposed scenarios, failure of the backfill was achieved by incrementing the railroad load applied at the surface level. Moreover, the arches under the mobilized portion of the backfill presented shapes that resemble failure by hinging mechanism [27].
- As expected, the loss of bearing capacity becomes considerable when the scour depth surpasses the foundation depth. Failure of the soil under the foundation may explain the differences of the capacity curve, as found for the extensive scour scenario. It should be noted that the variation of the lateral erosion (*i.e.*, dimension below the foundation) for the same scour depth, even though was not considered, influences the bridge capacity [8].
- The case study presented an initial reliability of 3.82 which indicates a probability of failure of  $6.68e-05$ . When increasing the scour depth up to 1.36 times the foundation height (extensive level), the reliability index decreased up to 2.87 with a failure probability of  $2.07e-03$ . Consequently, none of the scour scenarios fulfill the target reliability in the codes [28], which indicates that the bridge presents a poor performance under flooding events.

This study represents the first approach to assess the reliability of MAB subject to the effects of scour and floods. It is recommended to expand upon this work by analyzing out of plane behavior and investigate the effects of the bridge geometry and other flood-related effects that may influence the bridge performance. Finally, vulnerability analysis considering direct and indirect consequences may provide useful information for bridge management and decision making.

## ACKNOWLEDGMENTS

This work was partly financed by FCT / MCTES through national funds (PIDDAC) under the R&D Unit Institute for Sustainability and Innovation in Engineering Structures (ISISE), under reference UIDB / 04029/2020.

The second author would like to thank FCT – Portuguese Scientific Foundation for the research grant SFRH/BD/144749/2019.

This project has received funding from the European Union’s Horizon 2020 research and innovation programmed under grant agreement No 769255. This document reflects only the views of the author(s). Neither the Innovation and Networks Executive Agency (INEA) nor the European Commission is in any way responsible for any use that may be made of the information it contains.



## REFERENCES

- [1] L. Quirk, J. Matos, J. Murphy, and V. Pakrashi, “Visual inspection and bridge management,” *Struct. Infrastruct. Eng.*, vol. 2479, no. July, pp. 1–13, 2017, doi: 10.1080/15732479.2017.1352000.

- [2] V. N. Moreira, J. Fernandes, J. C. Matos, and D. V. Oliveira, "Reliability-based assessment of existing masonry arch railway bridges," *Constr. Build. Mater.*, vol. 115, pp. 544–554, 2016, doi: 10.1016/j.conbuildmat.2016.04.030.
- [3] A. Decò and D. M. Frangopol, "Risk assessment of highway bridges under multiple hazards," *J. Risk Res.*, vol. 14, no. 9, pp. 1057–1089, 2011, doi: 10.1080/13669877.2011.571789.
- [4] L. Deng, W. Wang, and Y. Yu, "State-of-the-Art Review on the Causes and Mechanisms of Bridge Collapse," *J. Perform. Constr. Facil.*, vol. 30, no. 2, p. 04015005, 2015, doi: 10.1061/(asce)cf.1943-5509.0000731.
- [5] F. T. Ekuje, "Bridge Scour – Climate Change Effect," 2018.
- [6] B. Conde, J. C. Matos, D. V. Oliveira, and B. Riveiro, "Probabilistic-based structural assessment of a historic stone arch bridge," *Struct. Infrastruct. Eng.*, vol. 0, no. 0, pp. 1–13, 2020, doi: 10.1080/15732479.2020.1752261.
- [7] K. M. Hulet, C. C. Smith, and M. Gibert, "Load-carrying capacity of flooded masonry arch bridges," *Proc. Inst. Civ. Eng. Bridg. Eng.*, vol. 159, no. 3, pp. 97–103, 2006, doi: 10.1680/bren.2006.159.3.97.
- [8] P. Zampieri, M. A. Zanini, F. Faleschini, L. Hofer, and C. Pellegrino, "Failure analysis of masonry arch bridges subject to local pier scour," *Eng. Fail. Anal.*, vol. 79, no. May, pp. 371–384, 2017, doi: 10.1016/j.engfailanal.2017.05.028.
- [9] H. Guimarães, J. C. Matos, and A. A. Henriques, "An innovative adaptive sparse response surface method for structural reliability analysis," *Struct. Saf.*, vol. 73, pp. 12–28, 2018, doi: 10.1016/j.strusafe.2018.02.001.
- [10] X. Huang, J. Chen, and H. Zhu, "Assessing small failure probabilities by AK-SS: An active learning method combining Kriging and Subset Simulation," *Struct. Saf.*, vol. 59, pp. 86–95, 2016, doi: 10.1016/j.strusafe.2015.12.003.
- [11] Infraestruturas de Portugal, "Modernização da Linha do Norte- Trecho Vila Franca de Xira (Norte) - Azambuja," 2001.
- [12] LimitState: GEO Manual, "LimitState: GEO Manual," vol. 44, no. 0, 2010.
- [13] M. Gilbert, C. C. Smith, and T. J. Pritchard, "Masonry arch analysis using discontinuity layout optimisation," *Proc. Inst. Civ. Eng. Eng. Comput. Mech.*, vol. 163, no. 3, pp. 155–166, 2010, doi: 10.1680/eacm.2010.163.3.155.
- [14] S. De Santis, "Load-carrying capability and seismic assessment of masonry bridges," *Engineering*, no. February, 2011.
- [15] B. Pulatsu, E. Erdogmus, and P. B. Lourenço, "Influence of soil-backfill depth on the strength and behavior of masonry arch bridges in the transverse direction," *13th North Am. Mason. Conf.*, no. June, pp. 15–25, 2019.
- [16] B. A. Vijayasree, T. I. Eldho, B. S. Mazumder, and N. Ahmad, "Influence of bridge pier shape on flow field and scour geometry," *Int. J. River Basin Manag.*, vol. 17, no. 1, pp. 109–129, 2019, doi: 10.1080/15715124.2017.1394315.
- [17] S. Mitoulis and S. Argyroudis, "Survey for bridge restoration after floods," no. January, 2021.
- [18] A. S. Nowak and K. R. Collins, *Reliability of structures*. Mc Graw Hill, 2000.

- [19] JCSS PROBABILISTIC MODEL CODE, “Section 3.7: Soil properties,” *JCSS Probabilistic Model Code*, no. August, 2006.
- [20] T. Choudhury and H. B. Kaushik, “Treatment of uncertainties in seismic fragility assessment of RC frames with masonry infill walls,” *Soil Dyn. Earthq. Eng.*, vol. 126, no. July, p. 105771, 2019, doi: 10.1016/j.soildyn.2019.105771.
- [21] P. Zampieri, M. A. Zanini, and F. Faleschini, “Derivation of analytical seismic fragility functions for common masonry bridge types: methodology and application to real cases,” *Eng. Fail. Anal.*, vol. 68, pp. 275–291, 2016, doi: 10.1016/j.engfailanal.2016.05.031.
- [22] L. Su, X. long Li, and Y. pang Jiang, “Comparison of methodologies for seismic fragility analysis of unreinforced masonry buildings considering epistemic uncertainty,” *Eng. Struct.*, vol. 205, no. October 2019, p. 110059, 2020, doi: 10.1016/j.engstruct.2019.110059.
- [23] S. Marelli and B. Sudret, “UQLab: a Framework for Uncertainty Quantification in MATLAB,” in *The 2nd International Conference on Vulnerability and Risk Analysis and Management (ICVRAM 2014)*, 2014, pp. 2554–2563, doi: 10.1061/9780784413609.257.
- [24] J. Wang and C. Melbourne, “Mechanics of MEXE method for masonry arch bridge assessment,” *Proc. Inst. Civ. Eng. Eng. Comput. Mech.*, vol. 163, no. 3, pp. 187–202, 2010, doi: 10.1680/eacm.2010.163.3.187.
- [25] C. Xu and G. Z. Gertner, “Uncertainty and sensitivity analysis for models with correlated parameters,” *Reliab. Eng. Syst. Saf.*, vol. 93, no. 10, pp. 1563–1573, 2008, doi: 10.1016/j.res.2007.06.003.
- [26] S. K. Au and J. L. Beck, “Estimation of small failure probabilities in high dimensions by subset simulation,” *Probabilistic Eng. Mech.*, vol. 16, no. 4, pp. 263–277, 2001, doi: 10.1016/S0266-8920(01)00019-4.
- [27] B. Pulatsu, E. Erdogmus, and P. B. Lourenço, “Comparison of in-plane and out-of-plane failure modes of masonry arch bridges using discontinuum analysis,” *Eng. Struct.*, vol. 178, no. August 2018, pp. 24–36, 2019, doi: 10.1016/j.engstruct.2018.10.016.
- [28] NP EN 1990: 2009, “Norma Portuguesa - Eurocódigo 0 - Bases para o projeto de estruturas,” *Inst. Port. da Qual.*, vol. 1999, p. 88, 2009.

## SIMPLIFIED FRAGILITY ANALYSIS OF MULTI-SPAN ISOSTATIC RC-BRIDGES CONSIDERING AN INCOMPLETE KNOWLEDGE LEVEL

Andrea Nettis<sup>1</sup>, Domenico Raffaele<sup>1</sup>, Giuseppina Uva<sup>1</sup>

<sup>1</sup>Department of Civil, Environmental, Land, Building Engineering and Chemistry  
Polytechnic University of Bari, Bari, Italy  
e-mail: {a.nettis, d.raffaele, g.uva}@poliba.it

---

### Abstract

*The prediction of the seismic vulnerability of bridges is a challenging task for road managers which need to include structural risk prioritisation in their Bridge Management Systems. The large number of bridges designed without anti-seismic requirements and the uncertainties resulting from the lack of knowledge data (e.g. design documents and blueprints), strongly affect the feasibility of this process. A simplified approach for performing fragility analysis considering the epistemic uncertainty associated with an incomplete knowledge level is described. Uncertainties are considered through the statistical generation of a population of index-bridges, which are analysed utilizing a simplified modelling approach and the capacity method spectrum method applied with real ground-motion spectra. The proposed approach is applied on a case-study simply supported-girder RC bridge of the Basilicata provincial road network. The modelling and the influence of the epistemic uncertainty on the fragility are discussed for two knowledge levels corresponding to different data collection strategies. Finally, a validation of the proposed approach is carried out through a comparison with a refined modelling approach and non-linear dynamic analyses.*

**Keywords:** fragility analysis, RC bridges, capacity spectrum method, nonlinear static procedures, seismic risk, cloud analysis.

---

## 1 INTRODUCTION

Improving the safety of road networks is a challenging task for transportation infrastructure managers in natural-hazard-prone countries. In the aftermath of strong earthquakes, an inadequate seismic response of bridges may provoke direct and indirect losses, e.g. structural damages, economic losses or issues in managing post-event emergency. In most of the developed countries, the majority of the roadway/railway bridges were designed according to old regulatory codes lacking adequate anti-seismic design recommendations. For instance, in Italy, a high amount of bridges was built during the '60s and '70s decades [1] when most of the Italian territory was not considered an earthquake-prone zone. Therefore, road managers have to deal with risk prioritization of large bridges portfolios, to identify structures that could exhibit poor performance in the aftermath of a seismic event. Low cost- and time-demanding analytical approaches for calculating fragility relationships and quantifying the risk of bridges are required.

In this context, many literature studies investigated the adoption of typological fragility assessment approaches for bridges (e.g. [2–5]). The HAZUS model [6] is a well-known reference on this topic. These simplified methodologies, based on a typological classification [7,8] assume that the performance of bridges belonging to the same class is similar. One or more archetype structures, representative of each typological class, are identified and analysed to achieve class fragility curves, possibly considering the variability of geometrical/constructive characteristics within the class. The accuracy of these approaches is strictly linked to the classification scheme adopted, usually defined on a judgemental-empirical basis, that could not be directly related to the expected seismic performance [9]. Furthermore, typological approaches neglect structure-specific components and geometrical features that could be crucial in the vulnerability of bridges belonging to the same class (e.g. specific geometry, deck-pier connection type) [10].

On the other hand, recent studies focus on structure-specific approaches. Among them, simplified displacement-based assessment (DBA) algorithms are proposed and tested. Sadan et al. [11] proposed a simplified DBA approach for multi-span continuous girder RC bridges, which is recently refined by Gentile et al. [12,13] and Perdomo et al. [14]. Cardone [15] proposed displacement-based damage state thresholds for bridge components to be used within the DBA algorithm. These DBA approaches were also extended for simplified fragility function calculations by Cademartori et al. [16]. Stefanidou and Kappos [17] presented a hybrid methodology for bridge-specific fragility analysis suitable for bridge portfolio applications, using simplified elastic analysis. A different approach is adopted by Borzi et al. [18], that, by using a comprehensive database to store bridge data, developed an automated tool to build refined finite element models and to perform nonlinear time history analysis (NLTHA)-based fragility analysis for probabilistic seismic assessment within bridge portfolio applications.

Generally, within both a typological or structure-specific probabilistic seismic assessment framework, aleatory and epistemic uncertainties should be considered. These are respectively associated with the random nature of the seismic action or to the knowledge limit about mechanical properties (geometry, material etc.), modelling assumptions or capacity models. Epistemic uncertainties are modelled as random variables and appropriate statistical distribution. These are generally considered by statistical sampling techniques for generating a population of structures representative of the main one. This process burdens considerably the whole assessment procedure since multiplies the number of required analyses. A preliminary adequate knowledge level of the structure(s) being analysed could beneficially limit the number of uncertainties. However, a refined data collection phase may be unaffordable: on-site diagnostic inspections are time- and cost-consuming and bridge databases are lacking design data and blueprints which mostly were lost by management authority operators or stored into



inaccessible archives. In the case of wide epistemic uncertainty, refined numerical models and analysis techniques are not a feasible solution and simplified fragility analysis methodologies should be applied.

In this study, a bridge-specific fragility analysis approach accounting appropriately for aleatory and epistemic uncertainties is proposed. The method adopts simplified mechanical models and capacity spectrum method (CSM) algorithms to perform cloud-based fragility analysis. The methodology aims to consider the uncertainty connected to the initial knowledge that particularly affects the seismic assessment of RC bridges when the input data are limited. Other types of epistemic uncertainties are neglected.

A refined description of the procedure, which currently is developed for multi-span isostatic (simply-supported) reinforced concrete (RC) bridges, is reported in Section 2. In Section 3, the procedure is applied to a case-study RC bridge for illustrative purpose. Preliminary validation of the simplified seismic performance assessment algorithm for fragility analysis is also provided using NLTHA as a benchmark.

## 2 DESCRIPTION OF THE METHODOLOGY

The simplified methodology to perform fragility analysis of bridges considering aleatory and incomplete-knowledge-based (hereinafter simply knowledge-based) uncertainties is described in this section. It resorts to simplified mechanical models, which are commonly used for the seismic analysis of isostatic multi-span bridges. A population of index-models is generated to consider the knowledge-based uncertainties, while the aleatory ones are represented by an appropriate suite of ground motions. The fragility analysis is performed by using a cloud approach for each index-model. A population of fragility curves representing the fragility of the main bridge can be thus generated and be used for simplified indicators of seismic risk. A synthetic flowchart is reported in Figure 1.

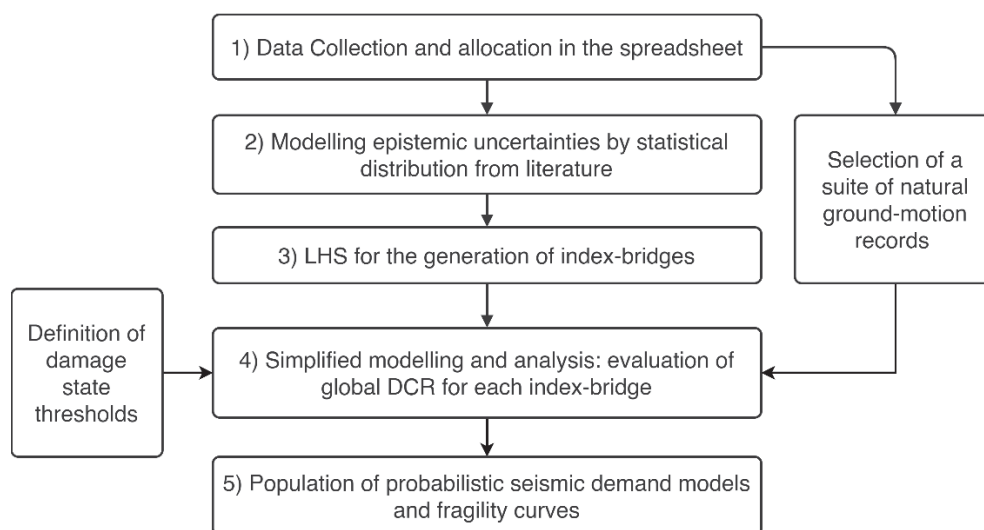


Figure 1: Flowchart of the proposed methodology

### 2.1 Uncertainty modelling

The first step of the methodology involves a data-collection process (Figure 1, step 1) that can be performed through fast in-situ inspections supported by innovative remote-sensing technologies such as drones equipped with optical sensors and photogrammetry algorithms. An example of how these new tools can be applied to effectively and quickly retrieve geometric

and constructive data on bridges is reported in [19]. The completeness of the data collection can be affected by environmental constraints around the investigated bridge or by the proper constructive characteristics (e.g. inaccessible areas for natural obstacles or inability to collect images underneath the deck).

After this process, the knowledge-based uncertainties to be considered in the probabilistic seismic assessment can be identified (Figure 1, step 2). Geometry parameters, mechanical properties of the materials or the structural members, structural details, which are not assumed “deterministic”, can be modelled as uncertainties and represented by random variables with appropriate statistical distributions. The latter can be identified based on literature studies. Zelaschi et al. [20] and Nielson et al. [21] proposed sets of statistical distributions to model appropriately the geometric parameters and the material properties of subclasses of highway bridges in Italy or the US, respectively. If literature references are not available, lacking data should be assumed based on engineering judgement. Furthermore, if more than one bridge is analysed within the same road network, lacking data on one bridge can be assumed for similarity with respect to the other bridges of the same typology within the same road network. Note that only engineering-relevant epistemic uncertainties should be modelled to avoid undesired burdening of the process. As anticipated, other types of epistemic uncertainty (e.g. the capacity models or for the definition of damage state thresholds), which are not considered in this study, can be similarly represented.

Epistemic uncertainties are usually modelled by introducing the random generation of a population of models (herein named index-bridges) “deterministically” characterised by variables selected from the corresponding statistical distributions by using statistical sampling techniques (Figure 1, step 3). To this aim, the standard or Latin Hypercube Sampling (LHS) Monte Carlo methodologies are generally used. The LHS [22] is widely used in literature for the probabilistic seismic analysis of both single or portfolios of bridges (e.g. [23,24]) and is usually preferred over the standard Monte Carlo technique since it requires less computational effort. In the LHS framework, the cumulative distributions of the random variables  $X_j$  are divided into  $N$  equal probability intervals (stratification of the input), where  $N$  is the target number of realizations, and a single value is randomly extracted from each interval. The output samples are  $N$  vectors of size  $j$ , in turn, composed by values randomly paired under the assumption that these belong to different intervals. At the end of the sampling process, convergence in statistics should be checked to reach a number of models being representative of the real distribution and convenient in terms of computational effort. At the end of the simulation process, a set composed of  $N$  bridge realizations is obtained. Each realisation is “deterministically” characterised and can be directly analysed.

In addition to the knowledge-based uncertainty, the (aleatory) uncertainty linked to the random nature of the seismic action (i.e. record-to-record variability) should be modelled (Figure 1, step 4). In the proposed procedure, a cloud-based approach [25] is adopted to perform fragility analysis. To this aim, a wide suite of earthquake-induced ground motions representative of the seismic hazard condition of the site is needed. The selection of ground motions should be addressed reflecting the soil classification of the site and mean values of magnitude and distance of likely seismic events provided by an appropriate hazard de-aggregation for the site of interest. Additional recommendations for the record selection are reported by Jalayer et al. [25].

## **2.2 Simplified approach for seismic performance assessment**

In the following sub-section, the process for calculating the performance of the index-bridges under specific earthquake-induced ground motions, is described. Based on the fundamentals of

nonlinear static procedures, equivalent single-degree-of-freedom (SDoF) capacity curves are attained analytically (in both longitudinal and transverse direction) and subjected to a capacity spectrum-based approach performed with real (un-smoothed) response spectra. Some assumptions of the proposed methodology are reported hereafter. Only the nonlinear response of the substructure members and the deck-substructure connection systems is considered, while the deck is supposed to respond elastically during the earthquake excitation. At this stage of the development, the foundations are modelled as fully-fixed constraints at the pier base according to [18,26]. However, the proposed procedure can be extended to account for soil-structure interactions following the methodology by Ni et al. [27]. The bi-directional effects of the seismic shaking are also neglected and each index-bridge is analysed separately in the transverse and longitudinal directions.

To reduce the necessary computational effort in analysing the index-bridges, a simplified seismic performance assessment strategy should be used within the procedure. The strategy proposed in this study is based on a simplified mechanical modelling approach suitable for multi-span isostatic bridges: the Individual Pier Model (IPM). However, it is worth mentioning that the general scheme of the proposed methodology (Figure 1) can be applied to other bridge typologies if suitable simplified modelling approaches are available (e.g. [28] for continuous-deck bridges). The IPM is a simplified strategy to analyse the seismic response of isostatic bridges with adjacent independent simply supported deck analysed in the transverse direction [1,15,16]. This approach is valid if relative rotations between the deck and the piers along the vertical axis are allowed. The seismic behaviour of each deck-pier/abutment subassembly can be analysed separately and can be represented by an equivalent SDoF multi-linear force-displacement law. This latter is obtained by combining the force-displacement relationships of the connection system (e.g. bearing devices, shear keys) and of the piers, assuming that these components act as a series system.

The force-displacement behaviour of single-column piers can be calculated according to [29,30]. To this aim, bilinear moment-curvature analyses are used, calculated by means of simplified surrogate meta-models [31,32] or programming routines [33]. The force-displacement law of framed piers can be achieved via simplified analytical methods based on mechanism analysis [34] or by simply aggregating the force-displacement laws of the columns acting in parallel in double-bending condition. If the flexibility of the bearings is negligible (i.e. fixed bearings) these can be assumed rigid and only the nonlinear behaviour of the pier is considered in the IPM. However, in most of the existing simply-supported bridges, the behaviour of the bearing devices should be considered. As an example, old fixed bearings (e.g. steel hinges or pin bearings) could experience brittle shear failures, followed by a pure friction (concrete-concrete) behaviour until deck-unseating phenomenon. Moreover, neoprene bearings were widely used in Italy between 1960 and 1990 [35] and can considerably affect the displacement profile of the IPM given their high deformability. Their shear strength is governed only by friction between rubber and concrete surfaces. The slipping of this type of bearings implies a nonlinear behaviour of the subassembly with large relative displacements between the deck and the pier. If present, the contribution of shear keys should be considered. Multilinear force-displacement laws for the mechanical characterisation of bearing devices and shear keys are reported in Cardone [15]. The cumulative force-displacement law of the deck-pier connection system can be attained by the sum of contribution of the bearing devices acting in parallel (i.e. the total base shear is the sum of the shear absorbed by the different devices subjected to the same top displacement).

The capacity curve of the equivalent SDoF representative of each subassembly can be calculated in a simplified way, assuming that its effective mass ( $m_{sub}$ ) is entirely lumped in the centre of mass of the deck. Under the assumption of a series system, for a given value of the

base shear ( $V_b$ ), the effective displacement of the equivalent SDoF system ( $\Delta_{sub}$ ) is given by the sum of the displacements of the pier ( $\Delta_{pier}$ ) and bearing system ( $\Delta_{bear}$ ), obtained by interpolating the respective constitutive laws at  $V_b$ .

To identify the performance of each subassembly under a specific ground-motion record the CSM [36] is applied. Particularly, the algorithm proposed by the authors [37] to apply the CSM with real spectra for fragility analysis is adopted. To this aim, the equivalent SDoF force-displacement law is converted in a capacity spectrum. The equivalent viscous damping of the subassembly ( $\xi_{sub}$ ) associated with each value of  $\Delta_{sub}$  can be computed by Equation (1) aggregating the equivalent viscous damping of the pier ( $\xi_{pier}$ ) and the deck-pier connection system ( $\xi_{bear}$ ). For each  $\xi_{sub}$ , the spectral reduction factor  $\eta_{sub}$  can be calculated to compute overdamped spectra and to identify the performance point (PP). To calculate  $\xi_{pier}$  and  $\xi_{bear}$  the ductility-based formulations by Priestley et al. [29] can be applied. At the end of this process, the seismic performance of each subassembly under a given seismic action can be calculated.

$$\xi_{sub} = \frac{\Delta_{pier}\xi_{pier} + \Delta_{bear}\xi_{bear}}{\Delta_{sub}} \quad (1)$$

The IPM can be used to analyse the response of the bridge in the longitudinal direction if the width of the expansion joints between adjacent decks allows for relative displacement between the subassemblies. This approach is usually suitable for bridges where the expansion joints between the independent decks are seismically designed: each subassembly responds independently until the closure of the joints is reached. In this case, the tributary seismic mass of each subassembly is strictly influenced by the type of bearing devices (fixed or free) and their capacity to transfer shear forces.

Conversely, if a premature closure of the joints is expected (e.g. non-seismically designed joints, designed for thermal dilatations only) or in presence of shock-transmitters, the bridge subassemblies act as a parallel system. In this case, the subassemblies resist a portion of the global seismic action depending on the proper (secant-to-top-displacement) stiffness. If the closure of the deck-abutment joint is expected, the abutment-backfill interaction should be appropriately considered in the simplified model [5]. The force-displacement relationships related to an equivalent SDoF of the entire bridge is calculated: the force-displacement laws of each deck-pier subassembly are aggregated, assuming that all the subassemblies are subjected to the same deck displacement (only one degree of freedom) which is axially rigid. Given a pre-determined target displacement of the deck, the shear force in each subassembly can be achieved by interpolating the corresponding force-displacement laws. These are summed up to calculate the total base shear. Repeating this process for incremental control node displacement, the equivalent SDoF capacity curve is obtained. For each step, the equivalent viscous damping ( $\xi_{eff}$ ) is calculated via Equation (2) where  $N$  is the total number of  $i$  subassemblies. The capacity curve is thus subjected to the CSM [37] to calculate the PP.

$$\xi_{eff} = \frac{\sum_{i=1}^N \xi_{sub,i} V_{sub,i}}{\sum_{i=1}^N V_{sub,i}} \quad (2)$$

### 2.3 Methodology for fragility analysis

After the calculation of the performance demand for each index-bridge subjected to each of the selected ground-motion records, the fragility analysis is performed. Fragility curves express the probability to reach or exceed a damage state (DS) conditioned to a given value of seismic

intensity. Note that fragility analysis of complex systems, like bridges, composed of multiple components, is not a straightforward task, since, the DS of the bridge is related to the DS of the different members (e.g. piers, bearings, abutments). The proposed procedure requires the analyst to define DS thresholds for each bridge member depending on the number of limit states of interest. Recommendations for defining DS thresholds for RC components, bearing devices, shear keys, etc are reported by Cardone [15]. Deterministic DS thresholds are defined in this procedure. However, the uncertainty on the DS thresholds should be easily accounted for according to e.g. [3,23].

The system fragility is defined based on the DS of the different components. In this study, the bridge is simply considered a series system and the weakest member determines the DS of the bridge [25]. The performance of each  $i$ -th bridge component (e.g. pier, bearing system, abutment) under the  $j$ -th ground motion with respect to a given DS, is expressed by a Demand Capacity Ratio ( $DCR$ ) calculated with Equation (3). The global bridge  $DCR_j$  related to the  $j$ -th ground-motion record is the maximum of the  $DCR_{i,j}$  of the different  $i$ -th components. As an example, if only the piers, the bearings and the abutments are considered as critical components, the global  $DCR_j$  is given by Equation (4) where the  $p$ ,  $b$  and  $ab$  subscripts indicate piers, bearings and abutments, respectively.

$$DCR_{ij}^{DS} = \frac{\Delta_{ij}}{\Delta_i^{DS}} \quad (3)$$

$$DCR_j^{DS} = \max (DCR_{p1,j}^{DS}, \dots, DCR_{pN,j}^{DS}, DCR_{b1,j}^{DS}, \dots, DCR_{bN,j}^{DS}, DCR_{ab1,j}^{DS}, DCR_{ab2,j}^{DS}) \quad (4)$$

Various literature studies focus on the definition of optimal intensity measures (IM) for probabilistic seismic analysis of bridges. The appropriate type of IM should be chosen

depending on the scope of the application with reference to its efficiency, sufficiency, practicality and hazard computability. An in-depth study about this is reported in e.g. [21,38].

In this study, fragility functions represent the probability that (the “weakest” member of) the index-bridge reaches a unitary DCR given a determined value of IM and are calculated via a cloud analysis approach [28]. Firstly, the results of the previous analyses are organized in couples of  $IM_j - DCR_j$  (i.e. the “cloud data”). It is assumed that a power-law model ( $DCR = aIM^b$ ) best expresses the relationship between the structural demands and IM [39]. The parameter  $[a, b]$  are estimated fitting a linear model to the cloud data transformed in the natural logarithmic scale using the least square method. This is expressed by Equation (5) where  $\alpha_{DCR|IM}$  represents the median DCR (50% to be exceeded) conditioned to the IM value for a given DS. The dispersion of the demand around the median estimated with the regression model is assumed constant varying the IM and is given Equation (6) where  $M$  is the number of ground motion records. Once,  $\alpha_{DCR|IM}$  and  $\beta_{DCR|IM}$  are calculated (simply  $\alpha$  and  $\beta$  hereinafter), the fragility function,  $P(DCR > 1|IM)$ , and can be expressed by Equation (7) where  $\Phi(\cdot)$  is the standard cumulative distribution functions (CDF).

$$\ln(DCR) = \ln \alpha_{DCR|IM} = \ln(a) + b \ln(IM) \quad (5)$$

$$\beta_{DCR|IM} = \sqrt{\frac{\sum_{j=1}^M (\ln DCR_j - \ln a(IM_j)^b)^2}{M - 2}} \quad (6)$$



$$P(DCR > 1|IM) = \Phi\left(\frac{\ln \alpha_{DCR|IM}}{\beta_{DCR|IM}}\right) = \Phi\left(\frac{\ln a(IM)^b}{\beta_{DCR|IM}}\right) \quad (7)$$

Following this approach, the obtained fragility function is calculated for each index-bridge accounting for demand uncertainty only (i.e. record-to-record variability). The influence of the knowledge-based uncertainty is represented by the variability within the entire dataset of fragility curves related to the index-bridges. This population of fragility curves can be synthesized using specific percentiles of the dataset of the medians and the dispersions [40].

A synthetic fragility curve comprehensive of both aleatory and epistemic uncertainty can be defined by calculating the median  $\alpha_{bridge}$  for a given DS as the median of the population of  $\alpha_k$  related to the  $k$ -th index-bridges with Equation (7). The overall dispersion ( $\beta_{bridge}$ ) should account for both the dispersion of the fragility curves of the single index-models ( $\beta_k$ ) and the dispersion around the medians. These contributions are combined with the SRSS rule.

For risk-based prioritisation purposes, the seismic risk and its variability linked to epistemic uncertainty can be calculated. As an example, the simplified strategies by [41] can be used to calculate the mean annual frequency of exceeding a determined DS ( $\lambda_{DS}$ ).

$$\ln \alpha_{bridge} = \left(\sum_{k=1}^N \ln \alpha_k\right)/N \quad (8)$$

$$\beta_{bridge} = \sqrt{\left(\frac{1}{N} \sum_{k=1}^N \beta_k\right)^2 + \left(\frac{1}{N} \sum_{k=1}^N \ln \alpha_k - \ln \alpha_{bridge}\right)^2} \quad (9)$$

### 3 APPLICATION OF THE PROPOSED METHODOLOGY TO A CASE-STUDY BRIDGE

The proposed framework is applied on a case-study bridge, part of the Basilicata provincial road-network. Two time- and cost-saving approaches are used to perform the data collection, leading to two different levels of knowledge about the geometrical and constructive features of the bridge. The following sections describe the data collection approach, the modelling of uncertainties and the results of the fragility analysis. This section aims to practically describe how to apply the proposed algorithm dealing with real bridges and provide a preliminary validation of the adopted simplified mechanical modelling strategy in fragility analysis.

#### 3.1 Description of the bridge, data collection approaches and uncertainties

The main features of the case-study bridge are reported in Figure 2. The bridge exhibits an isostatic structural scheme with five 30 m-long spans. The superstructure is composed of simply supported independent adjacent decks consisting of precast RC girders having a I-shaped cross section. The height of the single-column piers, having circular cross section (diameter equal to 2.60 m) ranges between 6.6 and 13.6 m. Although the exact year of design is unknown, it is assumed that the bridge was built between the 1980-1984 and designed according to the *D.M. 3 marzo 1975* and *D.M. 2 agosto 1980* [42,43] for seismic and bridge traffic loads, respectively. Note that this information can be easily retrieved from road managers' databases or, if necessary, modelled as knowledge-based uncertainty as follows.

The data collection is performed according to two data collection methodologies. The first exploits open-source Google Earth Street View data and a dataset of images collected on-site and is indicated hereinafter as low-knowledge level (KL1). The geometry was characterized by

means of image processing and measurements by GE data and images. The second data collection approach uses imagery collected by a drone-based survey and photogrammetric elaborations and is identified as high-knowledge level. Further information about this drone-based data collection methodology is reported in [19]. A (Excel-based) data-form is used to store the information in a suitable format to be directly used by a sequence of programming routines developed in MATLAB [44]. These routines perform the statistical sampling for modelling uncertainty and the simulated design of columns (sub-section 2.1) and the fragility analysis according to the simplified mechanics-based approach (sub-sections 2.2 and 2.3).

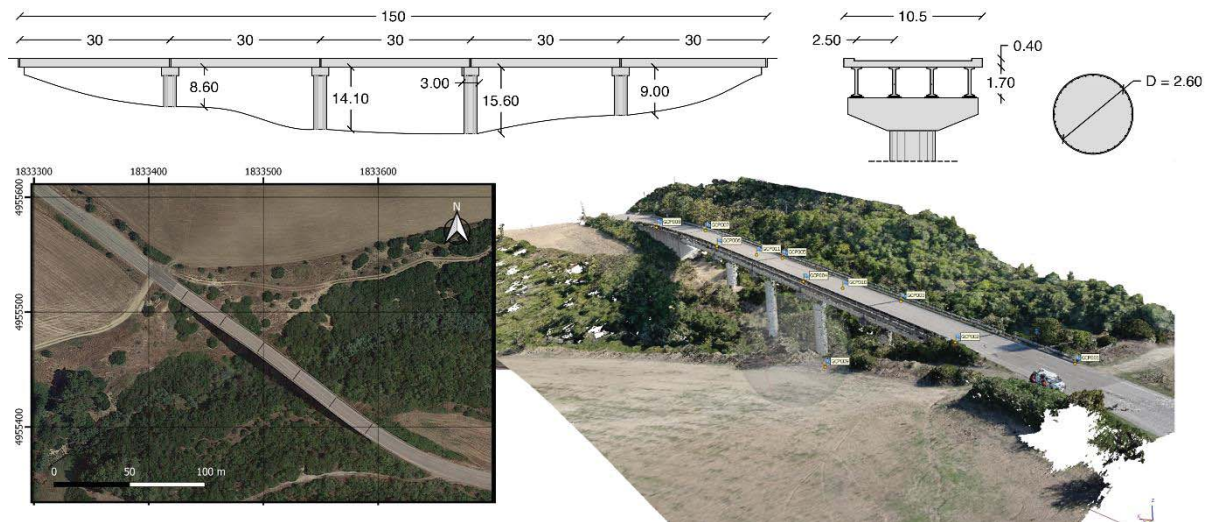


Figure 2: Geometric and constructive characterization of the case-study bridge [19].

Table 1 lists the uncertainties defined via some statistical distributions derived from literature studies [3,20,23,24,45] and engineering judgement. For parameters whose statistical distributions are not available, the maximum uncertainty is assumed using a uniform distribution (continuous or discrete) [40]. Although statistical distributions from different contexts (e.g. United States) are used, it is expected that more data about Italian highway bridges will be available in future, improving the reliability of such an approach. Table 1 differentiates the uncertainties associated with low- and high- knowledge levels (KL1 and KL2). With reference to KL1, no information on the typology of the bearing devices placed between the superstructure and the pier caps is detected. Therefore, in addition to the parameters listed in the table, the variability of two configurations of bearing typology are assumed: fixed/free bearings and neoprene bearings. In the first configuration, the bearings are assumed to be fixed in the transverse direction, while a fixed and a movable bearing line is placed on the top of each pier in longitudinal direction. Also, a variability between three and four devices per bearing line (two lines in total) is assumed. The width of the expansion gaps is low and not measurable at this knowledge level. It is assumed varying according to [3,23] and confirmed by [16] for not seismically designed Italian bridges. Conversely, the KL2 allows for identifying that the deck cross-section is composed of four precast girders (thus four devices per bearing line) and neoprene bearings of 4 cm-thickness; the gap size between the deck and abutments is fixed at 2.5 cm.

The variability in the design class of the materials ( $f_{ck}$  and  $f_{yk}$ ) is modelled. Mean and dispersion of the mean strength values of concrete and steel ( $f_{ck}$  and  $f_{yk}$ ) are calculated depending on the characteristic values assuming a coefficient of variation of 0.09 and 0.18 [24].

The LHS is performed to generate the population of models. For each model, the longitudinal reinforcement layout is calculated by means of a simulated design procedure. An appropriate MATLAB routine was developed to perform this task according to Italian old regulatory codes for bridges. The procedure automatically neglects the couples of design concrete and steel classes which lead to an incompatible design with respect to the old reference code. Since in the '70-'90 decades, the design of transverse reinforcements of bridge columns was dictated by constructive needs rather than mechanical because of the low seismic design actions the volumetric ratio of the transverse reinforcement ( $\rho_t$ ) is modelled with a uniform distribution (Table 1).

The uncertainty about the seismic action is considered via an appropriate ground-motion suite. A dataset of 100 natural ground-motion records is selected from the SIMBAD database [46] consistently with the characteristic of soil type [47], magnitude and distance of expected earthquakes in the site. The magnitude and distance de-aggregation is achieved using the software Rexel [48]. The ground motions compatible with these requirements are firstly collected (176 ground motions). Then, the 100 records with the highest PGA (geometric mean of the two directions) were selected to perform the fragility analysis. The PGA of the selected record varies between 1.77 and 0.16 g.

Parameter	Knowledge Level	Distribution	Distr. Param.	
Characteristic compressive concrete strength ( $f_{ck}$ )	KL1-KL2	Uniform (Discrete)	25-30-35	MPa
Characteristic tensile steel strength ( $f_{yk}$ )	KL1-KL2	Uniform (Discrete)	375-440	MPa
Mean concrete compressive strength ( $f_{cm}$ )	KL1-KL2	Normal	$\mu = 1, \sigma = 0.18$	Factor
Mean steel Tensile Strength ( $f_{ym}$ )	KL1-KL2	Normal	$\mu = 1, \sigma = 0.09$	Factor
Transverse reinforcement volumetric ratio ( $\rho_t$ )	KL1-KL2	Uniform	0.05-0.1*	%
Abutment gap size	KL1	Normal	$\mu = 24.5, \sigma = 5$	mm
Shear modulus of neoprene bearings (G)	KL1-KL2	Uniform	$l = 0.8, u = 1.2$	MPa
Thickness of neoprene bearings ( $t_b$ )	KL1	Uniform	$l = 40, u = 70$	mm
Abutment passive stiffness	KL1-KL2	Uniform	$l = 0.5, u = 1.5$	Factor
Mass variability (G1+G2)	KL1	Uniform	$l = 0.9, u = 1.1$	Factor

Table 1: Variability in geometrical/constructive bridge characteristics depending on the knowledge level (KL)

### 3.2 Modelling assumptions and damage states

Once the models are completely characterised, the seismic assessment is performed according to the CSM-based procedure (sub-section 2.2). To this aim, the moment-curvature relationships of the piers are calculated using CUMBIA [33]. This analysis shows that the flexure governs the seismic behaviour and damage state of the piers. An elastic perfectly-plastic behaviour is assigned to the neoprene bearings, assuming that the maximum strength is reached for slipping between the neoprene and the concrete surfaces, as suggested by Cardone [15] for low-thickness neoprene bearings. The stiffness of each neoprene bearing device is equal to  $k_b = GA/t_b$  (G is the shear modulus, A is the area of the pad) and the slipping strength is calculated assuming a friction coefficient ( $\mu$ ) equal to 0.4. The flexibility of the fixed bearings is neglected together with their shear failure (i.e. it is implicitly assumed that the maximum shear of the subassembly is reached before the shear failure of the fixed bearings). Finally, the

longitudinal response of the abutment-backfill systems for seat type abutments is calculated as proposed in [49,50], while its transverse deformability is neglected.

To provide validation for the simplified performance assessment approach, the bridge is also analysed by means of NLTHA performed in Opensees [51]. A refined numerical modelling strategy is adopted in this case. The RC-piers are modelled via *BeamWithHinges* elements composed of an internal elastic part and a nonlinear hinge at the base. The *Hysteretic* material is used to model the nonlinear cyclic behaviour of the plastic hinges, expressed by means of a sectional moment-curvature law. The deck and the pier caps are represented by elastic beam elements. *TwoNodesLink* elements are utilised to capture the nonlinearity of the bearing devices (*elastic-perfectly-plastic* material) and the abutment-backfill interactions (*impact* material). A tangent stiffness proportional damping is defined for NLTHA [29]. Moreover, a 5% Rayleigh damping model is assigned.

An overview of the local damage state thresholds used to compute the DCR for each component is reported in Table 2. The most damaged component determines the global damage state. The thresholds correspond to slight damage (DS1), severe damage (DS2) and collapse prevention (DS3).

Element	DS1	DS2	DS3	Note
Piers (flexural)	$\Delta_y$	$\Delta_y + 2/3(\Delta_u - \Delta_y)$	$\Delta_u$	$\Delta_y$ and $\Delta_u$ are the yielding and ultimate displacement of the pier.
Neoprene bearings (slipping)	$\Delta_{fr}$	$\Delta_{pad}$	$\Delta_{uns}$	$\Delta_{fr} = (\mu P / k_b)$ is the displacement corresponding to the friction strength attainment, $P$ is the compressive load of the bearing device. $\Delta_{pad}$ is the dimension of the bearing device in the considered direction. $\Delta_{uns}$ corresponds to deck unseating
Sliding bearings	—	—	$\Delta_{uns}$	$\Delta_{sl}$ is the displacement capacity of the bearing device
Abutment-backfill system	$\Delta_{gap}$	$\Delta_{pbw}$	$1.1 \Delta_{pbw}$	$\Delta_{pbw}$ is the displacement at the reaching of passive backfill pressure calculated starting from $k_{bw} = k_i w (h/1.7)$ and $P_{bw} = h_w w p_i (h/1.7)$ , where $h$ and $w$ are the height and width of the abutment backwall, $k_i$ is equal to 11.5 (kN/mm)m and $p_i$ is 239 kPa.

Table 2: Damage state thresholds for each considered components

### 3.3 Convergence in the statistics

Reaching convergence in random sampling is essential for the accuracy of the final fragility estimations. This section aims at identifying the number of index-bridges in the population necessary to achieve robustness in the results, to ensure that the addition of other samples does not involve strong modifications of the final results. This is necessary to identify a sample size which reflects a compromise between computational effort (more index-models, more calculations) and representativeness of the generated population (more index-models, higher accuracy). For this task, the KL1 is considered, where an higher influence of uncertainties is expected with respect to the KL2 case.

First, a first sampling is performed, producing a population of 500 index-bridges. This dataset is analysed, calculating the corresponding set of 500 fragility curves. For this task, PGA is used as IM and DS3 is only considered. A dataset of medians of the fragility curves are collected and their 50<sup>th</sup> percentile ( $\alpha_{opt}$ ) is extracted and assumed as an optimal estimation of the median IM associated with the fragility of the whole population. The 10<sup>th</sup> and 90<sup>th</sup>



percentiles are calculated also, providing optimal estimates of the variability in the median IM of the population leading DS3.

This process is repeated several times reducing the sampling size ( $N_s = [200, 100, 50, 25, 15]$ ). The stability of the counterparts ( $\alpha_{N_s}$ ) with respect to the optimal values is evaluated calculating the relative errors. Figure 3 reports that errors within a range of 10% are achieved when a sample size of 50 realisations is selected. Clearly, this result is strongly related to the adopted uncertainties for this selected bridge, and further studies should investigate the sample size varying the expected influence of the uncertainty.

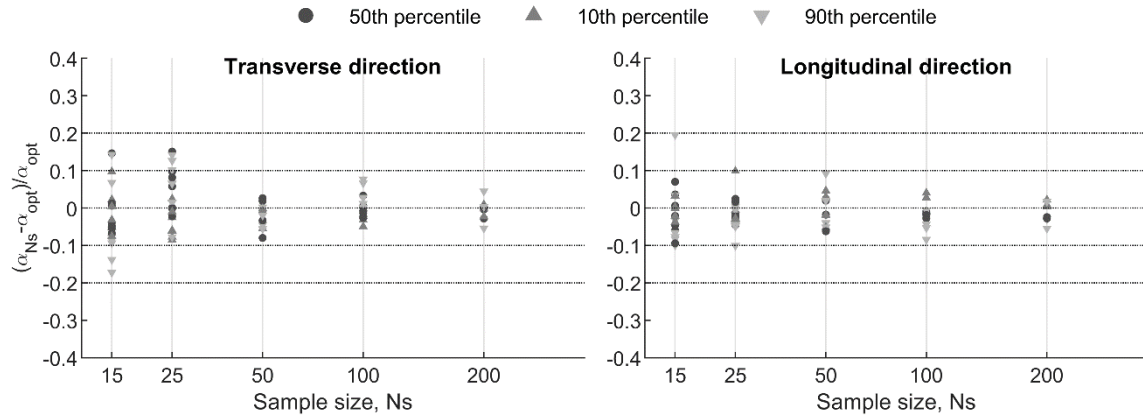


Figure 3: Relative errors on 50<sup>th</sup>, 10<sup>th</sup> and 90<sup>th</sup> of the median IM with respect to the sample size

### 3.4 Discussion on results

In this subsection, the results of the fragility analysis are discussed to evaluate the influence of the incomplete knowledge level and the reduction of this effect due to a reduction of the general uncertainty. Also, the errors induced by the simplified analysis approach with respect to refined NLTHA are evaluated. The results are numerically listed in Table 3 and graphically shown in Figure 4. Particularly, Table 3 reports the values of the median IM (i.e. PGA) associated with the 50<sup>th</sup> percentile of the fragility population (Eq. (8)) and the per cent relative difference ( $err_{DS}^{10/90th} = (\alpha_{DS}^{10/90th} - \alpha_{DS}^{50th}) / \alpha_{DS}^{50th} * 100$ ) of the 10<sup>th</sup> and 90<sup>th</sup> percentile with respect to the 50<sup>th</sup> one to numerically evaluate the influence of uncertainties. These per cent differences are represented by the amplitude of the “bundle” in Figure 4 representing synthetically the fragility curve population. As expected, the influence of a low-knowledge level, quantified by the 10<sup>th</sup> and 90<sup>th</sup> percentiles, is strongly reduced with a more accurate data collection. This effect is noticeable for the transverse direction, while it is slighter for the longitudinal where the damage is governed by the abutment-backfill interaction that is less affected by the uncertainties. In the transverse direction, the 10<sup>th</sup> and 90<sup>th</sup> percentiles of the median IM of the population change in a range which reaches [-50; +50]% of the 50<sup>th</sup> percentiles regardless of the DS.

Figure 5 better explains this outcome, showing the population of fragility curves for the KL1 case at DS2 (chosen for illustrative purposes). Red curves correspond to index-bridges having fixed/free bearings, while blue ones indicated index-bridges where neoprene bearings are present. Moreover, the pattern of the curve is related to the critical member which reaches DS, i.e. pier (flexure), bearing device or abutment-backfill system. Figure 5a shows that in the transverse direction, the variability in critical member induces wide variability in fragility curve parameters. The group of index-bridges with neoprene bearings (red) are generally associated with lower fragility (lower probability of reaching DS) than the index-bridges where fixed bearings are present and piers are damaged for flexure. The neoprene bearings produce a beneficial effect in the vulnerability in the transverse direction, since their slipping prevents



further increase of shear force in the piers, enhancing the ductility of the bearing-pier subassemblies. This outcome is consistent with [18]. This explains the general increase in  $\alpha_{DS}^{50th}$  for KL2, where only neoprene bearings are modelled, with respect to KL1 (Table 3). In this case, the maximum variability of  $\alpha_{DS}$  is registered at DS3 and corresponds to the range [-30.48; +13.81] %.

Case	$\alpha_{DS1}^{50th}$	$err_{DS1}^{10th}$	$err_{DS1}^{90th}$	$\alpha_{DS2}^{50th}$	$err_{DS2}^{10th}$	$err_{DS2}^{90th}$	$\alpha_{DS3}^{50th}$	$err_{DS3}^{10th}$	$err_{DS3}^{90th}$
Transverse direction									
KL1-CSM	0.64	-41.62	49.77	1.34	-40.59	49.01	2.05	-39.98	49.15
KL2-CSM	0.82	-24.09	12.77	1.66	-28.70	12.91	2.33	-30.48	13.81
KL2-NLTHA	0.80	-19.07	11.67	1.58	-24.11	11.64	2.38	-28.46	19.99
Longitudinal direction									
KL1-CSM	0.26	-34.95	31.05	0.71	-20.44	28.47	0.78	-23.65	35.99
KL2-CSM	0.24	-7.57	5.24	0.64	-13.74	34.59	0.68	-14.29	36.81
KL2-NLTHA	0.25	-5.86	3.66	0.67	-12.90	36.23	0.71	-13.61	37.91

Table 3: Median PGA (50<sup>th</sup>) and per cent shift associated with 10<sup>th</sup> and 90<sup>th</sup> percentiles

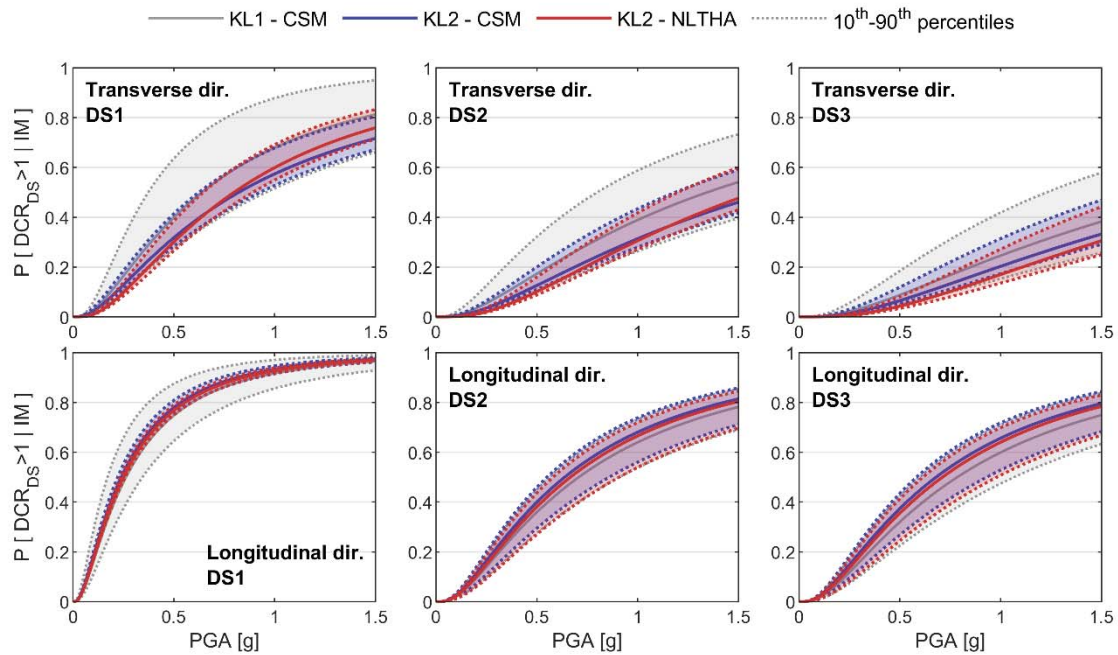


Figure 4: Fragility curves and associated variability for the case-study bridge considering the KL1 (analysed via CSM) and KL2 (analysed via CSM and NLTHA).

As shown in Figure 5b, in the longitudinal direction, it is very common among the analysed index-bridges that the abutment-backfill system induces the DS2. This is confirmed by [5] for non-seismically designed bridges. The presence of neoprene bearings is unfavourable for the fragility of the case-study bridge in this case. Indeed, the index-bridges where fixed bearings are present exhibit a lower probability to be damaged since the piers collaborate with the abutment-backfill system in resisting the total amount of seismic action. Conversely, neoprene bearings decrease the stiffness of the deck-pier subassemblies inducing a higher amount of seismic action directly transferred to the abutment and anticipating the reaching of DS2. It is

observed that in the longitudinal direction, the  $\alpha_{DS}$  ranges in a narrower interval with respect to the transverse direction.

Figure 4 evidences the general accuracy provided by the simplified CSM for fragility analysis with respect to NLTHA. In this case, the relative error between the two approaches on the median IM of the fragility curves (50<sup>th</sup> percentile) is lower than 5% regardless of the DS and the analysis direction. This evidences that, for this case study, the assumptions of the simplified IPM, that neglects the interactions between the subassemblies, and the equivalent viscous damping strategy is appropriate. However, this should be considered as a first outcome and other tests are needed for other case-study bridges or using more efficient IM in the calculation of fragility curves,

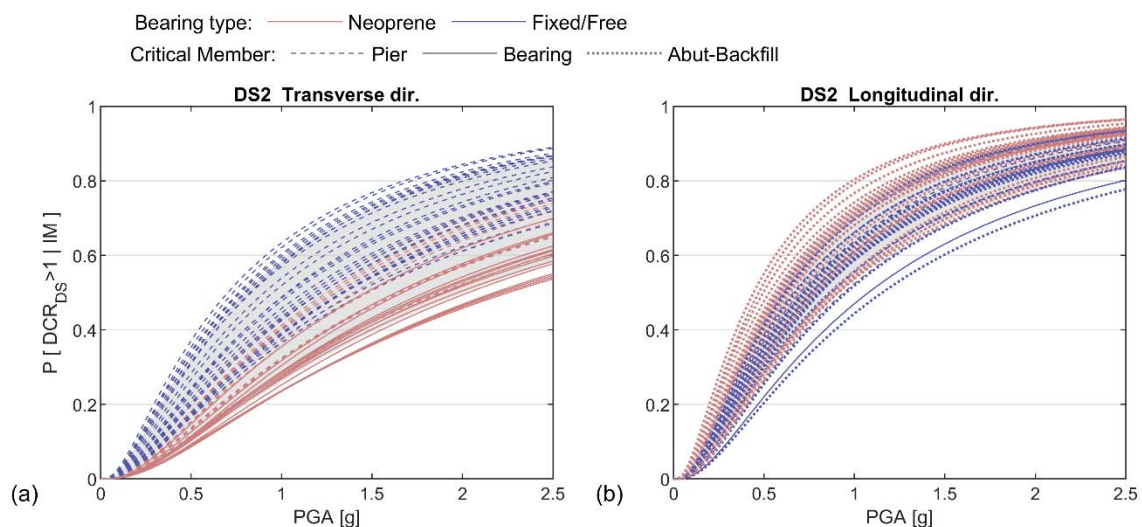


Figure 5: Population of fragility curves for the KL1 case at DS2. Different colours aim to distinguish the bearing type of the index-bridge, different patterns indicate different critical members. The grey area indicated the area between the 10<sup>th</sup> and the 90<sup>th</sup> percentiles.

## 4 CONCLUSIONS

In this study, a simplified methodology to perform fragility analysis of bridges directly accounting for uncertainties linked to an incomplete knowledge level is described. These knowledge-based uncertainties are considered by means of the statistical generation of a population of index bridges. The analysis of index-bridges is based on a simplified modelling approach, suitable for isostatic typical Italian bridges, and the capacity spectrum method used to evaluate the performance of index-bridges under a specific earthquake record. The performance of the single index-bridge is synthesized by a set of Demand-Capacity Ratios which is used to fit regression-based probabilistic seismic demand models and compute fragility curves. The fragility of the main bridge is represented by a population of fragility curves and the influence of knowledge-based uncertainties can be quantified by extracting significant percentile values of the population.

The proposed approach is applied on a case-study bridge of the Basilicata (Italy) provincial road network. The case-study section is aimed at illustrating the different steps of the procedure. Two data collection approaches are performed using different data sources involving two knowledge levels characterised by different degree of completeness. The case-study section tests the appropriate sample size to generate a representative population of index-bridges and provide a validation of the simplified analysis approach by means of the comparison with non-linear time history analysis on a refined numerical model. The fragility analysis shows that the response of the abutment-backfill system in the longitudinal direction is decisive for the

fragility of this case study whose deck-abutment gap size is not seismically designed. In the transverse direction, the fragility of the bridge is affected by the bearing typology and the lack of this information strongly increases the influence of the uncertainties. It can be stated that an adequate preliminary data collection should address the width of the abutment-deck gap and the typology of the deck abutment connections. The employment of typological approaches that neglect these components could involve severe inaccuracies in fragility estimations of bridge portfolios.

Finally, it is worth mentioning that further validations are needed to investigate the accuracy of the simplified fragility analysis methodology for different bridge types as continuous deck bridges.

## 5 ACKNOWLEDGEMENTS

The research presented in this paper was partially funded by the Italian Department of Civil Protection in the framework of the national project DPC-ReLUIIS 2019-2021.

## REFERENCES

- [1] Pinto PE, Franchin P. Issues in the upgrade of Italian highway structures. *J Earthq Eng* 2010;14:1221–52. <https://doi.org/10.1080/13632461003649970>.
- [2] Choi E, DesRoches R, Nielson B. Seismic fragility of typical bridges in moderate seismic zones. *Eng Struct* 2004. <https://doi.org/10.1016/j.engstruct.2003.09.006>.
- [3] Nielson BG, DesRoches R. Seismic fragility methodology for highway bridges using a component level approach. *Earthq Eng Struct Dyn* 2007. <https://doi.org/10.1002/eqe.655>.
- [4] Avşar Ö, Yakut A, Caner A. Analytical fragility curves for ordinary highway bridges in Turkey. *Earthq Spectra* 2011. <https://doi.org/10.1193/1.3651349>.
- [5] Moschonas IF, Kappos AJ, Panetsos P, Papadopoulos V, Makarios T, Thanopoulos P. Seismic fragility curves for greek bridges: Methodology and case studies. *Bull Earthq Eng* 2009. <https://doi.org/10.1007/s10518-008-9077-2>.
- [6] FEMA. Multi-Hazard Loss Estimation Methodology, Earthquake Model, Hazus®-MH, Technical Manual. 2003.
- [7] Zelaschi C, Monteiro R. Towards a Taxonomy for Portuguese Rc Bridges 2017:652–62. <https://doi.org/10.7712/120117.5447.17003>.
- [8] Hancilar U, Taucer F. Guidelines for typology definition of European physical assets for earthquake risk assessment - SYNER-G Reference Report 2. 2013. <https://doi.org/10.2788/68751>.
- [9] Mangalathu S, Jeon J-S, Padgett JE, DesRoches R. Performance-based grouping methods of bridge classes for regional seismic risk assessment: Application of ANOVA, ANCOVA, and non-parametric approaches. *Earthq Eng Struct Dyn* 2017. <https://doi.org/10.1002/eqe.2919>.
- [10] Stefanidou SP, Kappos AJ. Bridge-specific fragility analysis: when is it really necessary? vol. 17. Springer Netherlands; 2019. <https://doi.org/10.1007/s10518-018-00525-9>.

- [11] Şadan OB, Petrini L, Calvi GM. Direct displacement-based seismic assessment procedure for multi-span reinforced concrete bridges with single-column piers. *Earthq Eng Struct Dyn* 2013. <https://doi.org/10.1002/eqe.2257>.
- [12] Gentile R, Nettis A, Raffaele D. Effectiveness of the Displacement-Based seismic performance Assessment for continuous RC bridges and proposed extensions. *Eng Struct* 2020;in press:110910. <https://doi.org/10.1016/j.engstruct.2020.110910>.
- [13] Nettis A, Gentile R, Uva G, Raffaele D. Validation of an analytical displacement-based pushover for multi-span continuous deck bridges. *COMPdyn Proc.*, 2019.
- [14] Perdomo C, Monteiro R. Extension of displacement-based simplified procedures to the seismic loss assessment of multi-span RC bridges. *Earthq Eng Struct Dyn* 2020. <https://doi.org/10.1002/eqe.3389>.
- [15] Cardone D. Displacement limits and performance displacement profiles in support of direct displacement-based seismic assessment of bridges. *Earthq Eng Struct Dyn* 2014. <https://doi.org/10.1002/eqe.2396>.
- [16] Cademartori M, Sullivan TJ, Osmani S. Displacement - based assessment of typical Italian RC bridges. *Bull Earthq Eng* 2020. <https://doi.org/10.1007/s10518-020-00861-9>.
- [17] Stefanidou SP, Kappos AJ. Methodology for the development of bridge-specific fragility curves. *Earthq Eng Struct Dyn* 2017;46:73–93. <https://doi.org/10.1002/eqe.2774>.
- [18] Borzi B, Ceresa P, Franchin P, Noto F, Calvi GM, Pinto PE. Seismic Vulnerability of the Italian Roadway Bridge Stock. *Earthq Spectra* 2014.
- [19] Nettis A, Saponaro M, Nanna M. RPAS-based framework for simplified seismic risk assessment of Italian RC-bridges. *Buildings* 2020. <https://doi.org/10.3390/BUILDINGS10090150>.
- [20] Zelaschi C, Monteiro R, Pinho R. Parametric Characterization of RC Bridges for Seismic Assessment Purposes. *Structures* 2016;7. <https://doi.org/10.1016/j.istruc.2016.04.003>.
- [21] Padgett JE, Nielson BG, DesRoches R. Selection of optimal intensity measures in probabilistic seismic demand models of highway bridge portfolios. *Earthq Eng Struct Dyn* 2008. <https://doi.org/10.1002/eqe.782>.
- [22] Olsson A, Sandberg G, Dahlblom O. On Latin hypercube sampling for structural reliability analysis. *Struct Saf* 2003. [https://doi.org/10.1016/S0167-4730\(02\)00039-5](https://doi.org/10.1016/S0167-4730(02)00039-5).
- [23] Tavares DH, Padgett JE, Paultre P. Fragility curves of typical as-built highway bridges in eastern Canada. *Eng Struct* 2012;40:107–18. <https://doi.org/10.1016/j.engstruct.2012.02.019>.
- [24] Monteiro R. Sampling based numerical seismic assessment of continuous span RC bridges. *Eng Struct* 2016;118:407–20. <https://doi.org/10.1016/j.engstruct.2016.03.068>.
- [25] Jalayer F, Ebrahimian H, Miano A, Manfredi G, Sezen H. Analytical fragility assessment using unscaled ground motion records. *Earthq Eng Struct Dyn* 2017;46:2639–63. <https://doi.org/10.1002/eqe.2922>.
- [26] Calvi GM, Pinto PE, Franchin P. Seismic design practice in Italy. In: Chen W-F, Duan

- L, editors. *Bridg. Eng. Handb. 2nd Ed. Seism. Des.*, CRC-Press; 2013.
- [27] Ni P, Petrini L, Paolucci R. Direct displacement-based assessment with nonlinear soil-structure interaction for multi-span reinforced concrete bridges. *Struct Infrastruct Eng* 2014;10:1211–27. <https://doi.org/10.1080/15732479.2013.802813>.
  - [28] Nettis A, Gentile R, Uva G, Raffaele D. SOME APPLICATIONS OF A DISPLACEMENT-BASED PROCEDURE FOR THE SEISMIC RESPONSE OF CONTINUOUS GIRDER RC-BRIDGES. 3rd Int. Conf. Int. Conf. Recent Adv. Nonlinear Des. Resil. Rehabil. Struct. (CoRASS 2019), 2019.
  - [29] Priestley MJN, Calvi GM, Kowalsky MJ. *Displacement-based seismic design of structures*. IUSS Press, Pavia, Italy; 2007.
  - [30] Raffaele D, Porco F, Fiore A, Uva G. Simplified vulnerability assessment of reinforced concrete circular piers in multi-span simply supported bridges. *Struct Infrastruct Eng* 2014;10:950–62. <https://doi.org/10.1080/15732479.2013.772642>.
  - [31] Gentile R, Porco F, Raffaele D, Uva G. Simplified moment-curvature relationship in analytical form for circular RC sections. *Bull New Zeal Soc Earthq Eng* 2018;51:145–58.
  - [32] Gentile R, Raffaele D. Simplified analytical Moment-Curvature relationship for hollow circular RC cross-sections. *Earthq Struct* 2018;15:419–29. <https://doi.org/10.12989/eas.2018.15.4.419>.
  - [33] Montejo LA, Kowalsky MJ. Set of codes for the analysis of reinforced concrete members. *Environ Eng* 2007.
  - [34] Gentile R, del Vecchio C, Pampanin S, Raffaele D, Uva G. Refinement and Validation of the Simple Lateral Mechanism Analysis (SLaMA) Procedure for RC Frames. *J Earthq Eng* 2019:1–29. <https://doi.org/10.1080/13632469.2018.1560377>.
  - [35] Tortolini P, Petrangeli M, Lupoi A. Criteri per la verifica e la sostituzione degli appoggi in neoprene di viadotti esistenti in zona sismica. 14th Ital. Conf. Seism. Eng., Bari: 2011.
  - [36] Freeman SA. Development and use of capacity spectrum method. *Proc. 6th U.S. Natl. Conf. Earthq. Engng.*, Seattle: CD-ROM, EERI, Oakland; 1998.
  - [37] Nettis A, Gentile R, Raffaele D, Uva G, Galasso C. Cloud Capacity Spectrum Method: accounting for record-to-record variability in fragility analysis using nonlinear static procedures. (Under Rev *Soil Dyn Earthq Eng* n.d.
  - [38] Zelaschi C, Monteiro R, Pinho R. Critical Assessment of Intensity Measures for Seismic Response of Italian RC Bridge Portfolios. *J Earthq Eng* 2017. <https://doi.org/10.1080/13632469.2017.1342293>.
  - [39] Cornell CA, Jalayer F, Hamburger RO, Foutch DA. Probabilistic basis for 2000 SAC federal emergency management agency steel moment frame guidelines. *J Struct Eng* 2002. [https://doi.org/10.1061/\(ASCE\)0733-9445\(2002\)128:4\(526\)](https://doi.org/10.1061/(ASCE)0733-9445(2002)128:4(526)).
  - [40] Celik OC, Ellingwood BR. Seismic fragilities for non-ductile reinforced concrete frames - Role of aleatoric and epistemic uncertainties. *Struct Saf* 2010;32:1–12. <https://doi.org/10.1016/j.strusafe.2009.04.003>.
  - [41] Dolšek M. Simplified method for seismic risk assessment of buildings with



- consideration of aleatory and epistemic uncertainty. *Struct Infrastruct Eng* 2012;8:939–53. <https://doi.org/10.1080/15732479.2011.574813>.
- [42] Decreto Ministro dei Lavori Pubblici (DM) 3 marzo 1975 -Approvazione delle norme tecniche per le costruzioni in zone sismiche. G.U. 8-4-1975, n.93; 1975.
- [43] Decreto Ministeriale (DM) 2 agosto 1980 - Criteri Generali e prescrizioni tecniche per la progettazione, esecuzione e collaudo dei ponti 1980.
- [44] The MathWorks Inc. MATLAB . version 9.5.0.944444 (R2018b) 2018.
- [45] Cardone D, Perrone G, Sofia S. A performance-based adaptive methodology for the seismic evaluation of multi-span simply supported deck bridges. *Bull Earthq Eng* 2011. <https://doi.org/10.1007/s10518-011-9260-8>.
- [46] Smerzini C, Galasso C, Iervolino I, Paolucci R. Ground motion record selection based on broadband spectral compatibility. *Earthq Spectra* 2014;30:1427–48. <https://doi.org/10.1193/052312EQS197M>.
- [47] Forte G, Chioccarelli E, De Falco M, Cito P, Santo A, Iervolino I. Seismic soil classification of Italy based on surface geology and shear-wave velocity measurements. *Soil Dyn Earthq Eng* 2019;122. <https://doi.org/10.1016/j.soildyn.2019.04.002>.
- [48] Iervolino I, Galasso C, Cosenza E. REXEL: Computer aided record selection for code-based seismic structural analysis. *Bull Earthq Eng* 2010. <https://doi.org/10.1007/s10518-009-9146-1>.
- [49] Caltrans. Seismic Design Criteria Version 1.7. Calif Dep Transp Sacramento, CA, US 2013.
- [50] Sextos A, Mackie K, Stojadinovic B, Taskari O. Simplified P-y relationships for modeling embankment-abutment systems of typical California bridges. 14th World Conf. Earthq. Eng. Beijing, China, 2008.
- [51] McKenna F. OpenSees: A framework for earthquake engineering simulation. *Comput Sci Eng* 2011. <https://doi.org/10.1109/MCSE.2011.66>.

## SCOUR-INDUCED DYNAMIC PROPERTIES MODIFICATION OF MASONRY ARCH BRIDGES WITH DIFFERENT GEOMETRY

F. Scozzese<sup>1</sup>, L. Ragni<sup>2</sup>, E. Tubaldi<sup>3</sup>, F. Gara<sup>2</sup>

<sup>1</sup> University of Camerino  
Viale della Rimembranza 63100 Ascoli Piceno, Italy  
e-mail: fabrizio.scozzese@unicam.it

<sup>2</sup> Università Politecnica delle Marche  
Via Breccie Bianche, Ancona (AN), Italy  
{laura.ragni, f.gara}@univpm.it

<sup>3</sup> University of Strathclyde  
75 Montrose Street, G1 1XQ Glasgow, UK  
enrico.tubaldi@strath.ac.uk

---

### Abstract

*This paper, focused on the effect of local scour actions on masonry bridges, represents a follow-up of a previous study conducted by the authors aimed at analysing the effect of a localised scour-induced settlement of the pier on the modal properties of the bridge (i.e., frequencies and mode shapes). Results from the previous study showed as the scour phenomenon, even at its early stages could induced a non-negligible variability of the transverse modal shape of a masonry arch bridge selected as case study. In this paper, the work is continued by analysing how the bridge geometry can affect the aforesaid results. To this aim, bridges with three different geometry (130 m length, 100 m length, 50 m length) are analysed by simulating the scour evolution under the piers and by monitoring the modal response at different stages of the excavation. Accurate finite element models are developed in Abaqus, accounting for both mechanical and geometrical nonlinearities.*

**Keywords:** masonry, bridges, scour, Abaqus FEM, arch bridges, modal shapes, OMA.

---

## 1 INTRODUCTION

Scour is a natural phenomenon caused by the erosion or removal of streambed or bank material from bridge foundations due to flowing water [1-3].

This action is among the most common causes of bridge failure worldwide [2-4], leading to notable direct and indirect losses, as witnessed by the numerous cases of scour-induced collapses occurred worldwide [5-8].

Masonry arch bridges are particularly vulnerable to this phenomenon, due to their high stiffness and the usually shallow footings. The relevance of the problem is also witnessed by the increasing number of works dealing with this issue, e.g., numerical studies employing soil-foundation-structure interaction models with different level of complexity [4, 9], works proposing advanced models for describing the cracking mechanism evolution in the masonry components [10-13], and studies oriented towards dynamic identification and scour monitoring [14-17]. Moreover, besides the studies fully dedicated to the seismic response [18, 19], the literature offers an always growing number of papers focused on vulnerability and resilience assessment of masonry bridges under multiple hazard (mainly earthquakes and floods) [20, 21].

In the recent years, studies have been also carried out to investigate the possibility of detecting scour by tracking the changes of the dynamic properties of the bridge-foundation-soil system (see e.g., the studies of [22, 23] in the context of masonry arch bridges, or the ones of [24, 25] for steel and reinforced concrete bridges).

In particular, the study conducted in 2020 by [5] has shown as the scour phenomenon, even at its early stages could induced a non-negligible variability of the transverse modal shape of a masonry arch bridge selected as case study, thus opening the way to mode-shape based scour monitoring techniques. Very recently (in 2021) the work of [26] presented an approach to detect stiffness loss arising due to scour based on relative changes of vertical-pier mode shape amplitudes, by testing the method through a scaled experimental model of a bridge traversed by a vehicle.

Within this framework and as follow-up of [5], the present paper focuses on the effects of a localized scour-induced settlement of the pier on the modal properties (i.e., frequencies and mode shapes) of multi-span masonry arch bridges. In particular, the investigation initiated in [5] is herein extended to bridges with three different geometries: 7-spans 130 m length, 5-spans 100 m length, 3-spans 50 m length. For each of the three bridges an accurate 3D finite element model is first developed in Abaqus [27], accounting for both mechanical and geometrical nonlinearities; then numerical simulations are performed to assess the modal response sensitivity at different stages of the scour process evolution (a single pier is assumed to experience scour).

## 2 CASE STUDIES

A masonry arch bridge typology very common in the existing Italian infrastructural stock (but also diffused in Europe and worldwide) is considered in this study, and three different geometric schemes are analysed: a 7-spans bridge (131.20 m long), a 5-spans bridge (98.80 m long) and a 3-spans bridge (54.40 m long).

All the bridges have the following features [5, 28] in common: the spans are 16.00 m long; the piers are all identical with a plan size of 9.5 m x 3.2 m, excluding the extreme circular parts with a radius of 2.0 m along the transverse direction (Y direction); the arches have thickness of 0.95 m and a radius of 11.58 m; spandrel walls have thickness of 0.65 m; the pier foundations have a rectangular plan shape of 11.00 m x 3.90 m and their height is 4.15 m. More details about the bridge geometry are given in Figure 1, The longitudinal views of the bridges are provided in Figure 1; two sections (one transversal and one longitudinal) are shown in Figure 2.

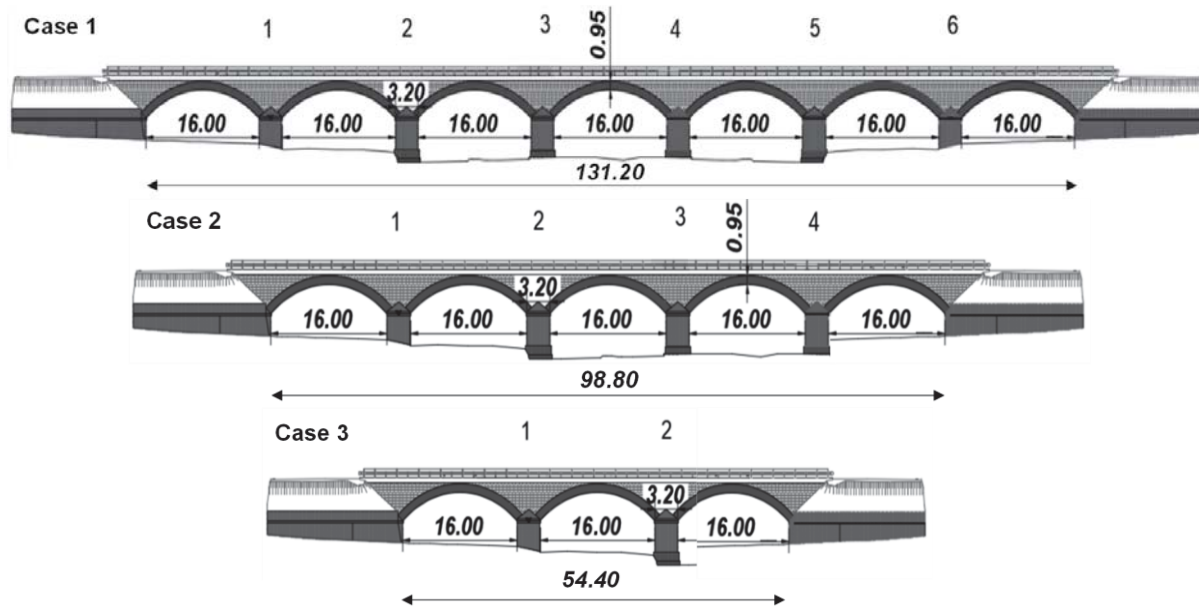


Figure 1. Longitudinal view and geometries of the three case studies.

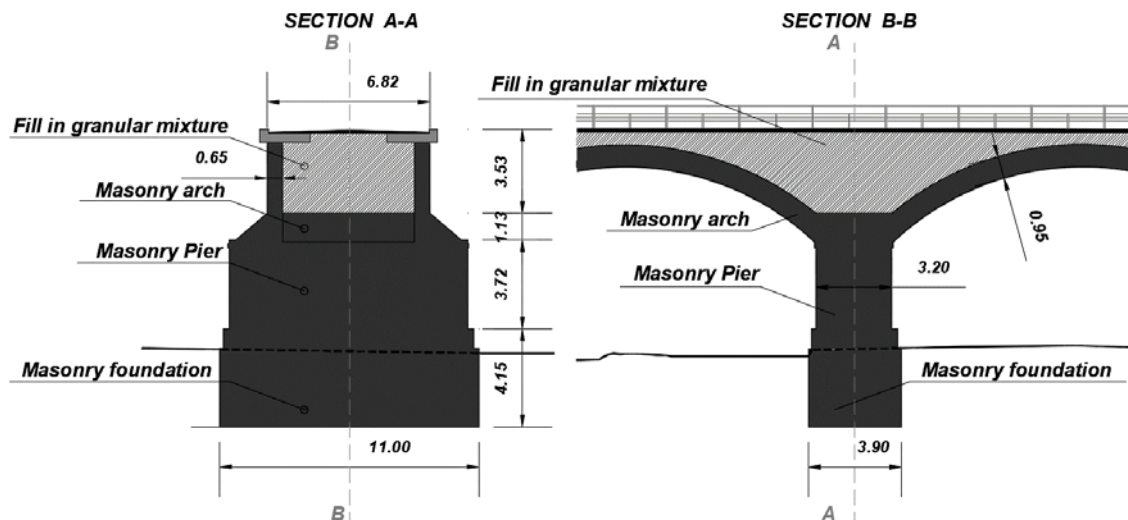


Figure 2. Sections and details common for all the masonry arch bridges.

The materials mechanical properties are taken from [5] and are based on both in-situ and laboratory characterization tests. Table 1 provides a summary of the main mechanical properties of the bridge materials, in terms of density  $\rho$ , Young's modulus  $E$ , yield stress in compression  $f_{y,c}$  (or cohesion  $c$  for what concerns the backfill) and peak tensile stress  $f_{y,t}$ .

Table 1. Material properties.

Material [-]	$\rho$ [t/m <sup>3</sup> ]	$E$ [kN/m <sup>2</sup> ]	$c - f_{y,c}$ [kN/m <sup>2</sup> ]	$f_{y,t}$ [kN/m <sup>2</sup> ]
Masonry (Arches & Spandrels)	1.80	3100000	2000	150
Masonry (Piers)	1.75	2900000	2000	150
Backfill	1.70	250000	10	0
Abutment	1.90	300000	-	-

Riverbed features are assumed according to the case study analysed in [5], where both geophysical and mechanical soil characterizations were achieved through a set of in-situ tests and laboratory tests. The riverbed properties, made of with highly dense gravel and sands (alluvial deposit extending 27 m below the surface), are collected in Table 2 (friction angle  $\phi$ , Young's modulus  $E$ , Poisson's ratio  $\nu$ , shear modulus  $G$ , soil density  $\rho$ , and average shear waves velocity  $v_s$ ).

Table 2. Soil parameters.

$\phi$ [°]	$E$ [kN/m <sup>2</sup> ]	$\nu$ [–]	$G$ [kN/m <sup>2</sup> ]	$\rho$ [t/m <sup>3</sup> ]	$v_s$ [m/s]
38	1065000	0.45	370000	2.0	430

### 3 MODELLING STRATEGY

#### 3.1 General details of the finite element model and material constitutive laws

A 3D model of each case study (Figure 3) is developed in ABAQUS 2017 [27] by following the strategy adopted in [5] and briefly recalled below.

The bridge model is built by using continuum solid linear hexahedral 8-nodes elements of type C3D8R, with 6 degrees of freedom per node.

A coarser mesh is attributed to master parts in defining contact pairs interaction, in order to avoid penetration at the interface. Moreover, the mesh discretisation is set in order to attain of a good trade-off between results' accuracy and computational effort, with element dimensions varying between 0.35 m and 0.75 m.

The model accounts for both geometrical and mechanical nonlinearities.

The behaviour of the masonry components in the linear elastic field is described by assigning the properties summarised in Table 1. The non-linear behaviour is described through the Concrete Damage Plasticity (CDP) model with the parameters reported in [5].

For the fill material, a linear elastic model is employed, together with a Mohr-Coulomb failure criterion, characterized by a friction angle of 55° and a cohesion of 10 kN/m<sup>2</sup>.

As schematically shown in Figure 4, the interaction between the different bridge components is simulated by means of the following nonlinear frictional/cohesive interfaces [4, 5, 10] (see [5] for a detailed discussion of the topic): a frictional interface is used to describe the interaction between the fill and the other bridge components along the tangential direction (the tangential behaviour is characterised by a friction coefficient of 0.60); a “hard-contact” behaviour is assumed along the normal direction, allowing separation but preventing penetration between the parts in contact; cohesive interactions are used for the other interfaces (i.e., spandrel-to-arch, spandrel-to-pier and arch-to-pier), simulating the behaviour of mortar joints between the parts. Moreover, a damage criterion is introduced, whose initiation is governed by the attainment of the maximum nominal stress values along the normal and tangential directions, equal to  $f_{n,max} = 150$  kN/m<sup>2</sup> (Table 1) and  $f_{t,max} = 1.4 \cdot f_{n,max} = 220$  kN/m<sup>2</sup>, respectively. The damage evolution is described by the Benzeggagh-Kenane mixed mode fracture criterion, with a power-law exponent of 2.2, and the values of normal and shear fracture energies are assumed equal to  $G_{f,n} = 0.05$  kN/m and  $G_{f,s} = 0.10$  kN/m, respectively. To improve convergence, a damage stabilization criterion is also used, by defining a viscous coefficient of  $10^{-5}$  kNs/m.



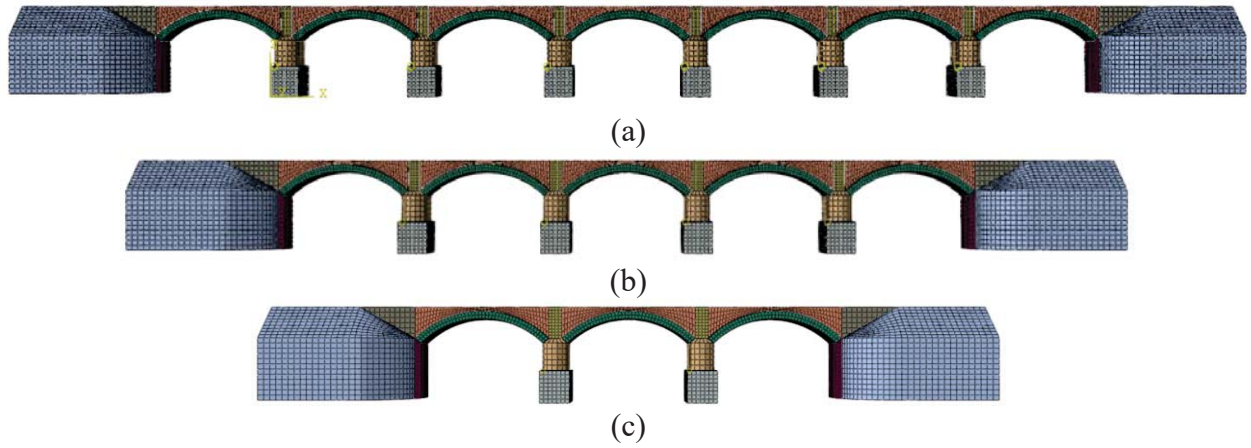


Figure 3. Finite element models: (a) 7-spans, (b) 5-spans and (c) 3-spans bridge.

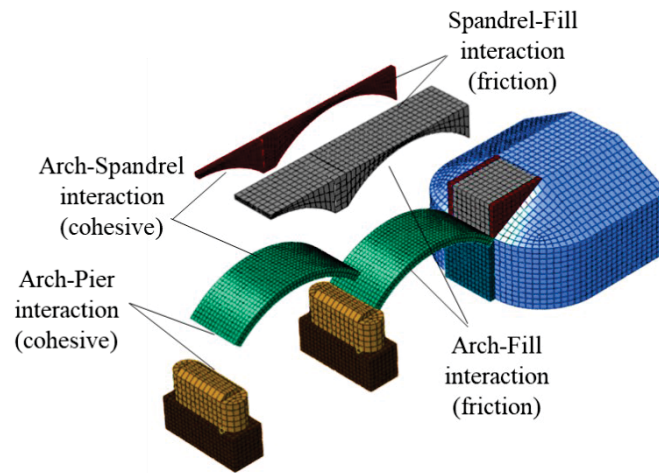


Figure 4. FE model with highlighted materials interface types.

### 3.2 Scour numerical simulation

A Winkler modelling approach is employed to describe the soil-foundation interaction (Figure 5). The relationship between the soil pressure and the corresponding settlement is described through the following set of equivalent soil stiffness constants (Table 3)  $k'_x = \frac{k_x}{A_x}$ ,  $k'_y = \frac{k_y}{A_y}$ ,  $k'_z = \frac{k_z}{A_z}$ , with  $k_x, k_y, k_z$  (kN/m) provided by Gazetas [29] and  $A_x, A_y, A_z$  foundation areas. However, different impedances formulations [30] might also be used.

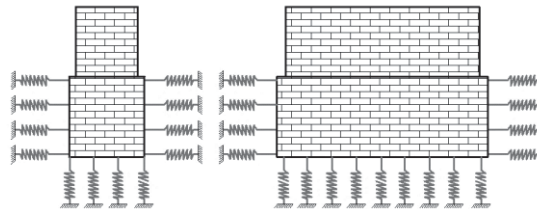


Figure 5. Impedances along the  $x, y, z$  directions

Table 3. Soil stiffness constants.

$k'_x$ [kN/m <sup>3</sup> ]	$k'_y$ [kN/m <sup>3</sup> ]	$k'_z$ [kN/m <sup>3</sup> ]
220000	420000	940000

The scour process evolution is numerically modelled according to the simplified procedure proposed in [5], which can be synthetised as follows (Figure 6):

- The hole shape is described by a constant inverted pyramidal form [4].
- The vertex of the pyramid is assumed along a vertical line passing through the centre of the upstream face of the pier, the upstream slope of the hole is taken equal to friction angle at rest of the soil,  $\phi$ , whereas the downstream slope is approximately half that value, consistently with [2].
- The scour hole slope along the direction perpendicular to the flow is equal to  $5/6 \cdot \phi$ .
- Being the shape of the scour hole fixed, the hole geometry is completely defined by the maximum scour depth  $y_s$ , identifying the scour hole vertex, and by the value of the friction angle of the soil.
- A time-history analysis is performed in Abaqus in which, at each time step, the level of the maximum scour depth is increased and the depth of the centroid of each cohesive element representing the foundation-soil interaction is compared with the depth of scour at the same location: if the element centroid is within the scour hole, then the element is deactivated.
- In this study, the simulation of the deepening of the scour hole is described by considering 8 discrete steps.

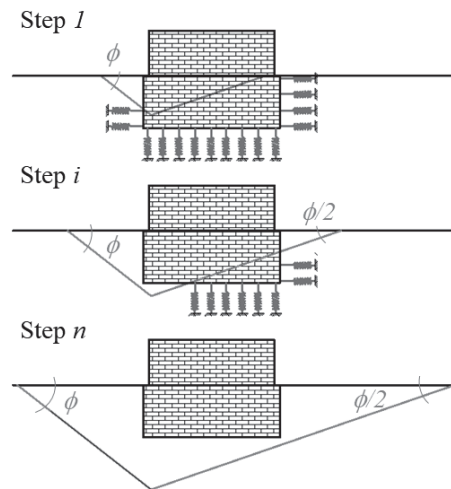


Figure 6. Scheme of scour progression modelling.

Step 0 corresponds to the starting condition, with gravity loads acting on the bridge (self-weight loads plus a uniform pressure of  $6.6 \text{ kN/m}^2$  simulating the road pavement loads) and no scour. From Step 1 to Step 7, the scour development is simulated by considering increments of  $y_s$  equal to  $1.0 \text{ m}$  per step, for a total maximum scour depth of  $7.0 \text{ m}$  attained at Step 7, corresponding to an excavation of  $3.0 \text{ m}$  under the base of the pier's foundation (whose height is  $4.15 \text{ m}$ ).

At the end of step of analysis, a eigenvalues analysis is performed in order to evaluate the modal shapes and the frequencies of the bridges at the current state (i.e., at the current level of scour). Further details about the simulation and the solver setting are given in [5]. In this study,

the scour is assumed to occur on one single pier only, corresponding to the most extreme one (i.e., near the right abutment).

#### 4 SCOUR INFLUENCE ON BRIDGES DYNAMIC PROPERTIES

In this section the influence of the scour progression on the modal properties of the three bridges is assessed. In particular, for each bridge configuration, the modification of the transversal modal shapes is graphically displayed (Figure 7, Figure 8, Figure 9); it is worth noting that the sequence of mode shapes shown in the figures should be read from the top (no scour taking place) to the bottom (maximum scour excavation).

The variation of the corresponding natural frequencies is reported as well (Table 4 and Table 5): Table 4 illustrates the evolution of the frequency with the scour depth progression, while Table 5 collects the percent variation with respect to the reference value at Step 0.

Despite the different values of the reference frequencies observed by three bridges, a common pattern can be found in the results of this investigation. Indeed, the changes of the modal frequency are very low for increasing scour depths between 0.0 m and 4.0 m, with a percentage decrease of 1.5% - 2.44% at Step 4 (i.e., with  $y_s = 4.0$  m). From this point on, the effects of the scour on the modal frequency become more and more significant, with percentage reductions higher than 20% at Step 5 (i.e., 1.0 m of excavation under the pier), while very high reductions (>46%) are observed for  $y_s = 6.0$  m (i.e., 2.0 m of excavation under the pier).

Table 4. Modal frequency evolution (Hz) at different scour levels.

Bridge	Step 0	Step 1	Step 2	Step 3	Step 4	Step 5	Step 6
	0.0 m	1.0 m	2.0 m	3.0 m	4.0 m	5.0 m	6.0 m
7-spans	6.455	6.453	6.445	6.428	6.357	5.077	3.431
5-spans	6.048	6.045	6.031	6.016	5.952	4.750	3.199
3-spans	6.110	6.101	6.067	6.041	5.961	4.750	3.200

Table 5. Modal frequency percent variation (%) at different scour levels.

Bridge	Step 0	Step 1	Step 2	Step 3	Step 4	Step 5	Step 6
	0.0 m	1.0 m	2.0 m	3.0 m	4.0 m	5.0 m	6.0 m
7-spans	0.00	-0.03	-0.15	-0.42	-1.52	-21.35	-46.85
5-spans	0.00	-0.05	-0.28	-0.53	-1.59	-21.46	-47.11
3-spans	0.00	-0.15	-0.70	-1.13	-2.44	-22.26	-47.63

If from one side the frequency changes remain negligible for a “long time” of scour process evolution, the mode shapes (Figure 7, Figure 8, Figure 9) are found to be more sensitive to the effect of scour. Indeed, a non-negligible variability of the transverse mode shapes is observed on all the three bridges starting from the early stages of the scour phenomenon, i.e., for  $y_s$  between 1.5 and 2.0 m, before the stages of excavation under the pier’s foundation. As the scour proceeds, the mode shape becomes always more local and interesting the subsiding pier.

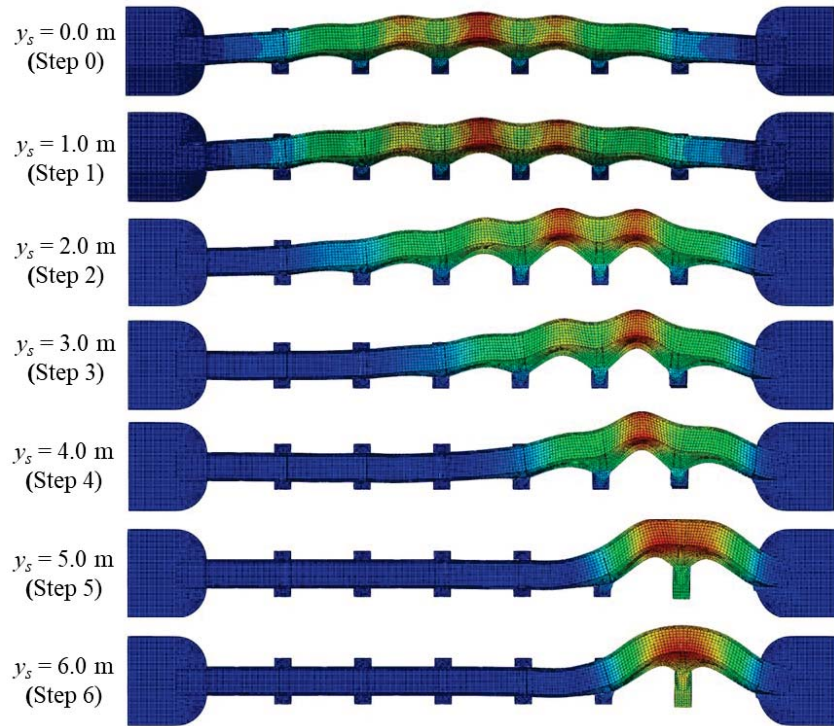


Figure 7. Transverse mode shapes variation for different scour depths.

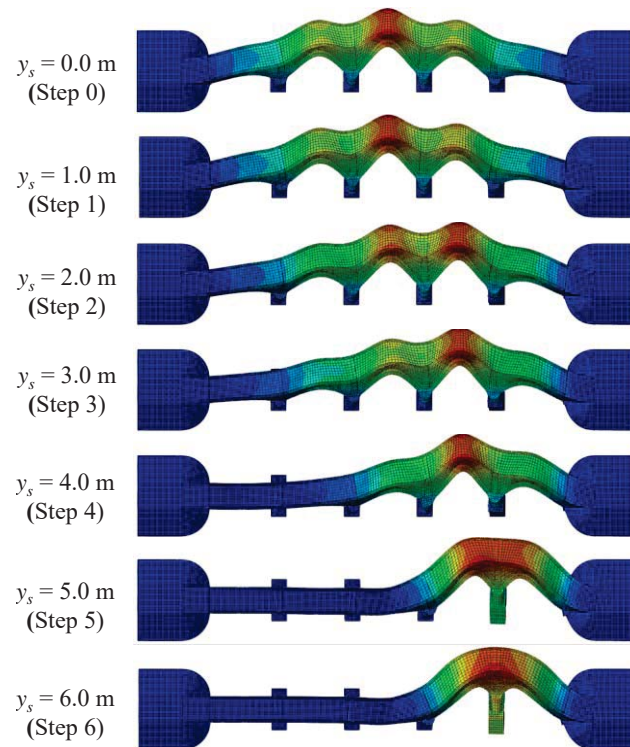


Figure 8. Transverse mode shapes variation for different scour depths.



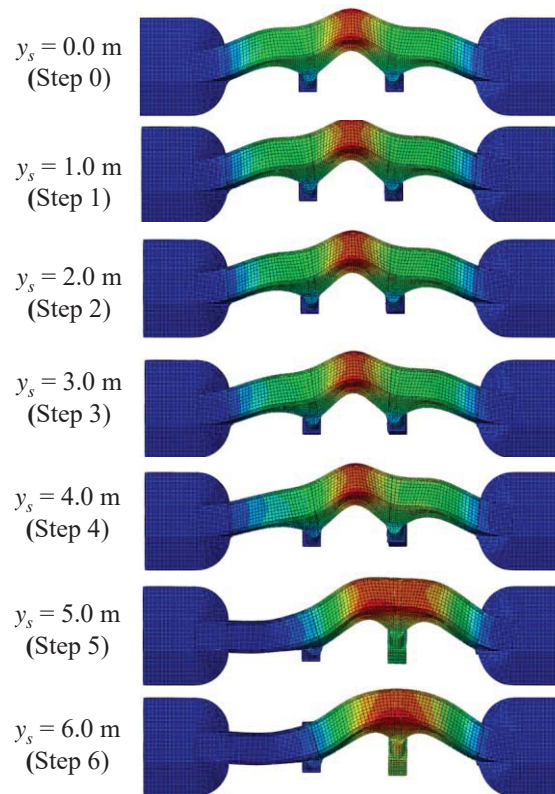


Figure 9. Transverse mode shapes variation for different scour depths.

## 5 CONCLUSIONS

The effects of a localized scour-induced settlement of the pier on the modal properties (i.e., frequencies and mode shapes) of masonry arch bridges are analysed. As extension of the study of [5], bridges with three different geometries (130 m length, 100 m length, 50 m length) are analysed by simulating the scour evolution under the piers and by monitoring the modal response at different stages of the excavation. Accurate finite element models are developed in Abaqus, accounting for both mechanical and geometrical nonlinearities.

No significative differences are observed among the analysed case studies, characterised by different geometries but equal static scheme, materials and boundary conditions. The results of [5] and the relevant main conclusions thus still hold and can be summarised as follows:

- are negligible if the scour depth involves only the lateral sides of the foundation.
- The modal frequency changes become noticeable (higher than 20%) only when the soil underneath the pier is eroded; for this reason, the suitability of a *frequency-oriented* identification system based on ambient vibrations might be compromised.
- Conversely, the transverse mode shapes exhibit a very high sensitivity to scour, even at the early stages of the phenomenon; in light of this, a *mode shape-oriented* identification system might be appropriate for monitoring the scour evolution over the time and thus intervene timely in order to avoid failure or damage development on masonry bridges.

However, the study shall be extended to a wider set of case studies in order to verify the effectiveness of the proposed OMA-based identification technique as a scour monitoring and early warning strategy in those cases in which scour affects a larger number of piers (scour on a single pier is analysed in this work).



Moreover, an ongoing study is aimed at developing a probabilistic hazard discharge model accounting for the scour refill process due to live-bed flood conditions, based on the recent work [31]. This hazard model will be exploited within a time-dependent risk assessment probabilistic framework for bridges, which may also integrate other source of hazards (e.g., earthquakes [32]).

## REFERENCES

- [1] Pizarro, A., Manfreda, S., & Tubaldi, E. (2020). The science behind scour at bridge foundations: A review. *Water*, 12(2), 374.
- [2] Hoffmans GJCM, Verheij HJ. Scour Manual. Routledge; 2017. doi:10.1201/9780203740132.
- [3] Melville BW, Coleman SE. Bridge scour. Water Resources Publications, LLC; 2000.
- [4] Tubaldi E, Macorini L, Izzuddin BA. Three-dimensional mesoscale modelling of multi-span masonry arch bridges subjected to scour. *Engineering Structures* 2018;165:486–500. doi:10.1016/J.ENGSTRUCT.2018.03.031.
- [5] Scozzese, F., Ragni, L., Tubaldi, E., & Gara, F. (2019). Modal properties variation and collapse assessment of masonry arch bridges under scour action. *Engineering Structures*, 199, 109665.
- [6] Sousa JJ, Bastos L. Multi-temporal SAR interferometry reveals acceleration of bridge sinking before collapse. *Natural Hazards and Earth System Sciences* 2013;13:659–67. doi:10.5194/nhess-13-659-2013.
- [7] Gavin K, O'Brien EJ. Sustainable Maintenance and Analysis of Rail Transport Infrastructure (SMART rail) Railway bridge safety and condition assessment View project Smart Rail View project. 2012.
- [8] Maddison B. Scour failure of bridges. *Proceedings of the Institution of Civil Engineers - Forensic Engineering* 2012;165:39–52. doi:10.1680/feng.2012.165.1.39.
- [9] Zampieri P, Zanini MA, Faleschini F, Hofer L, Pellegrino C. Failure analysis of masonry arch bridges subject to local pier scour. *Engineering Failure Analysis* 2017;79:371–84. doi:10.1016/J.ENGFAILANAL.2017.05.028.
- [10] Zhang Y, Tubaldi E, Macorini L, Izzuddin BA. Mesoscale partitioned modelling of masonry bridges allowing for arch-backfill interaction. *Construction and Building Materials* 2018;173:820–42. doi:10.1016/J.CONBUILDMAT.2018.03.272.
- [11] Milani G, Lourenço PB. 3D non-linear behavior of masonry arch bridges. *Computers & Structures* 2012;110–111:133–50. doi:10.1016/J.COMPSTRUC.2012.07.008.
- [12] Tubaldi, E., Minga, E., Macorini, L., & Izzuddin, B. A. (2020). Mesoscale analysis of multi-span masonry arch bridges. *Engineering Structures*, 225, 111137.
- [13] Rainieri, C., Notarangelo, M. A., & Fabbrocino, G. (2020). Experiences of dynamic identification and monitoring of bridges in serviceability conditions and after hazardous events. *Infrastructures*, 5(10), 86.
- [14] Maroni, A., Tubaldi, E., Ferguson, N., Tarantino, A., McDonald, H., & Zonta, D. (2020). Electromagnetic sensors for underwater scour monitoring. *Sensors*, 20(15), 4096.
- [15] Civera, M., Calamai, G., & Fragonara, L. Z. (2021, April). System identification via Fast Relaxed Vector Fitting for the Structural Health Monitoring of masonry bridges. In *Structures* (Vol. 30, pp. 277-293). Elsevier.
- [16] Wan Mohtar, W. H. M., Muad, A. M., Porhemmat, M., Ab. Hamid, H., & Whayab, S. S. (2021). Measuring scour level based on spatial and temporal image analyses. *Structural Control and Health Monitoring*, 28(1), e2645.

- [17] Lee, M., Yoo, M., Jung, H. S., Kim, K. H., & Lee, I. W. (2020). Study on Dynamic Behavior of Bridge Pier by Impact Load Test Considering Scour. *Applied Sciences*, 10(19), 6741.
- [18] Zampieri, P., Perboni, S., Tetougueni, C. D., & Pellegrino, C. (2020). Different Approaches to Assess the Seismic Capacity of Masonry Bridges by Non-linear Static Analysis. *Front. Built Environ*, 6, 47.
- [19] Gönen, S., & Soyöz, S. (2021). Seismic analysis of a masonry arch bridge using multiple methodologies. *Engineering Structures*, 226, 111354.
- [20] Argyroudis, S. A., Mitoulis, S. A., Hofer, L., Zanini, M. A., Tubaldi, E., & Frangopol, D. M. (2020). Resilience assessment framework for critical infrastructure in a multi-hazard environment: Case study on transport assets. *Science of The Total Environment*, 714, 136854.
- [21] Argyroudis, S. A., & Mitoulis, S. A. (2021). Vulnerability of bridges to individual and multiple hazards-floods and earthquakes. *Reliability Engineering & System Safety*, 107564.
- [22] Ruocci G. Application of the SHM methodologies to the protection of masonry arch bridges from scour. PhD Thesis, Polytechnic University of Torino, 2010.
- [23] Foti S, Sabia D. Influence of Foundation Scour on the Dynamic Response of an Existing Bridge. *Journal of Bridge Engineering* 2011;16:295–304. doi:10.1061/(ASCE)BE.1943-5592.0000146.
- [24] Ju SH. Determination of scoured bridge natural frequencies with soil–structure interaction. *Soil Dynamics and Earthquake Engineering* 2013;55:247–54. doi:10.1016/J.SOILDYN.2013.09.015.
- [25] Prendergast LJ, Hester D, Gavin K, O’Sullivan JJ. An investigation of the changes in the natural frequency of a pile affected by scour. *Journal of Sound and Vibration* 2013;332:6685–702. doi:10.1016/J.JSV.2013.08.020.
- [26] Malekjafarian, A., Kim, C. W., OBrien, E. J., Prendergast, L. J., Fitzgerald, P. C., & Nakajima, S. (2020). Experimental Demonstration of a Mode Shape-Based Scour-Monitoring Method for Multispan Bridges with Shallow Foundations. *Journal of Bridge Engineering*, 25(8), 04020050.
- [27] Abaqus, V. (2014). 6.14 Documentation. Dassault Systemes Simulia Corporation, 651. 2014.
- [28] Ragni L, Scozzese F, Gara F et al. Dynamic identification and collapse assessment of Rubbianello Bridge. In *IABSE Symposium, Guimaraes 2019: Towards a Resilient Built Environment Risk and Asset Management - Report*. pp. 619–626.
- [29] Gazetas G. Formulas and Charts for Impedances of Surface and Embedded Foundations. *Journal of Geotechnical Engineering* 1991;117:1363–81. doi:10.1061/(ASCE)0733-9410(1991)117:9(1363).
- [30] Carbonari S, Morici M, Dezi F, Leoni G. A lumped parameter model for time-domain inertial soil-structure interaction analysis of structures on pile foundations. *Earthquake Engineering & Structural Dynamics* 2018;47:2147–71. doi:10.1002/eqe.3060.
- [31] Link O, García M, Pizarro A, Alcayaga H, Palma S. (2020). Local Scour and Sediment Deposition at Bridge Piers during Floods. *J Hydraul Eng*, 146(3), 04020003.
- [32] Scozzese, F., Tubaldi, E., & Dall’Asta, A. (2020). Assessment of the effectiveness of Multiple-Stripe Analysis by using a stochastic earthquake input model. *Bulletin of Earthquake Engineering*, 1-37.

## INFLUENCE OF THE PIERS' HEIGHT ON THE FRAGILITY ASSESSMENT OF ITALIAN R.C. LINK SLAB BRIDGES

L. Minnucci<sup>1</sup>, F. Scozzese<sup>2</sup>, A. Dall'Asta<sup>2</sup>, S. Carbonari<sup>1</sup> and F. Gara<sup>1</sup>

<sup>1</sup> DICEA – Università Politecnica delle Marche  
Via Breccie Bianche, Ancona (AN), Italy  
l.minnucci@pm.univpm.it, {s.carbonari, f.gara}@univpm.it

<sup>2</sup> SAAD – University of Camerino  
Viale della Rimembranza, Ascoli Piceno (AP), Italy  
{fabrizio.scozzese, andrea.dallasta}@unicam.it

### Abstract

*Recent seismic events occurred in Central Italy drew the attention towards the resilience of the Italian road network, which is characterized by a significant number of old reinforced concrete bridges and viaducts. In this context, the fragility assessment of existing bridges is crucial, since their collapse or loss in functionality after earthquakes may lead to significant economic and social consequences.*

*This work focuses on the fragility assessment of reinforced concrete multi-span continuous bridges, which is a widespread structural typology in Italy. The study aims to individuate fragilities relevant to both local and global mechanisms, considering bridge components such as piers, bearings and deck members, in order to highlight the most vulnerable ones compromising the whole structural response under the seismic action. A probabilistic framework is developed considering both the site-dependent seismic hazard and the most important Engineering Demand Parameters (EDPs) characterizing the structural response. The first one accounts for the record-to-record variability as well as the parameters governing the seismic scenario in which the structure is located, while the latter ones are individuated depending on the structural typology and the identified vulnerabilities. Multiple Stripe Analyses are performed with the aim of providing insights about the seismic response of the bridge class at hand and of furnishing the fragility curves for all the response parameters relevant for the structural system. Starting from a real case study located in Centre Italy, a couple of reinforced concrete bridge models is developed in order to consider the influence of different heights for the piers and to provide a forecast for the structural behaviour of the selected bridge class. The models are able to capture the failure mechanisms most likely to occur. Performance thresholds are chosen for each bridge component considering the relevant limit state demands according to the current codes and literature. As a result, fragility curves provide useful insights about the main structural deficiencies of the system at hand.*

**Keywords:** *Italian bridge fragility, bridge heritage, earthquake damage, reinforced concrete infrastructures.*

---

## 1 INTRODUCTION

Fragility assessment is fundamental for a proper probabilistic characterization of the consequences of natural hazards such as earthquakes or flood-related ones [1]-[2] on existing infrastructures. Concerning the seismic vulnerability of bridges, a common practice is that of defining homogeneous fragility classes for cataloguing bridges based on their geometric and mechanical characteristics, deck cross section, static scheme and typology of vertical supporting elements [3]-[5]. Among the several bridge classes, this paper focuses on the particular but widespread typology of Reinforced Concrete (RC) Link Slab (LS) jointless bridges, which are highly representative of the Italian existing infrastructural network and, at the same time, can be commonly found in the infrastructural stock of many other countries [6]-[10]. The interest in such bridge class, and in general in bridges and viaducts, has grown due to earthquakes occurred in Italy in the recent years as well as due to the catastrophic events involving strategical structures in the regional road network (e.g. the collapse of the Morandi's bridge in Genova in 2018).

To the authors' knowledge, no detailed probabilistic studies have been performed yet to investigate LS RC bridges properly. Thus, the wide use of this engineering solution deserves a deeper investigation, considering that in most cases existing LS bridges were designed according to old standards, which lack attention and detailing with respect to seismic actions. For this purpose, two RC simply supported multi-span LS bridges are considered as representative case studies for the bridge class at hand. The geometries are derived from an existing LS bridge in Central Italy [11] and differ for the height of the piers to compare the response of tall and short piers on the overall behaviour of the structural system. A simulated project is preliminary developed following typical design rules of Italian codes of the 70's [12] and nonlinear finite element models are developed to perform numerical nonlinear Time Histories (TH) analyses. A conditional probabilistic approach is adopted, based on Multiple Stripe Analysis (MSA) [13] and on a stochastic ground motion model for the seismic scenario characterization. Different demand parameters are monitored to properly assess the seismic response of the system, and fragility curves are estimated for the damage mechanisms most likely to occur in LS bridges.

## 2 LS BRIDGES: VULNERABILITIES

LS bridges are characterized by simply supported beams constituted by reinforced or prestressed concrete girders, linked at the slab level by means of steel bars to make the slab continuous. This technical solution, also used as a retrofit technique in existing bridges with separated spans, belongs to the wider category of jointless bridges, where the adoption of links instead of expansion joints is an economical and efficient alternative to reduce the vulnerability of the entire structural system. In fact, water leaking through the joints is the major cause for the deterioration of bearings and supporting structures, while debris accumulation in the joints may causes damage to the deck for the prevented thermal expansion. Consequently, LSs require a lower maintenance effort and costs; an example of link connection is illustrated in Figure 1.

Kinematic links are usually designed considering longitudinal loads acting at the slab level. The effectiveness of link slabs as retrofit intervention in presence of live and thermal loads has been investigated in the literature [6]-[8] but no probabilistic approach useful to the fragility and risk evaluation of this structural component has been employed yet. It is also worth to mention that no evaluation of the performance of links under transverse loads was required by past codes, so that their behaviour is unknown in occurrence of a seismic event. It is well known that structural problems can arise not only in vertical and supporting elements, but also



3420



with  $\Phi(\cdot)$  denoting the standard normal cumulative distribution function,  $\theta$  the median fragility value (i.e., the *IM* level with 50% probability of exceedance),  $\beta$  the *IM* standard deviation. In this paper, the fragility function parameters  $(\hat{\theta}, \hat{\beta})$  are obtained by maximizing the logarithm of the likelihood function, since the maximum likelihood represents an appropriate fragility fitting strategy [28].

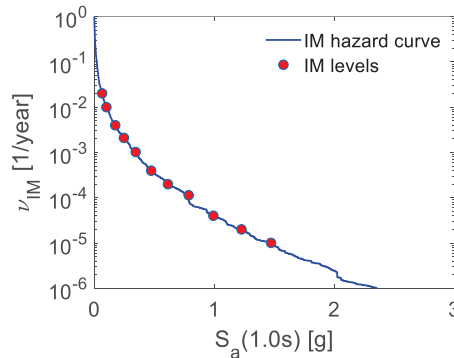


Figure 2: IM hazard curve for  $S_a(T)$  at  $T=1.0$  s and discretization in 11 IM levels.

## 4 APPLICATIONS

### 4.1 Geometry and structural details of the case studies

Two multi-span simply supported pre-stressed concrete bridges are considered as case studies. To better represent the existing Italian bridge stock, it is assumed that the bridges were constructed in the 70's, before the emanation of seismic design codes at national and European level [23], [29].

The LS bridges are 131 m long, with 5 simply supported 25 m long spans. The case studies present the same superstructure. The bridge deck is composed of a cast-on-site 12.50 m wide slab on three V-shaped pre-stressed concrete girders. This geometry is a typical choice for pre-stressed concrete girder cross-sections and derives from an existing LS bridge in Central Italy. Figure 3 shows the cross-section shape (original design document).

Spans present connections at the slab level realized through the kinematic links, made by DYWIDAG bar groups with diameter  $\varnothing 40$  mm. The bar arrangement is made according to the static scheme in the longitudinal direction presented in Figure 4, where a fixed constraint is located at the abutment on the right side, and according to the relevant distribution of axial forces (due to seismic actions in the longitudinal direction of the bridge).

RC girders, at both piers and abutments, are supported by a set of 3 neoprene semi-rigid bearings. The bearings mechanical behaviour is the same along the two horizontal directions.

Vertical supporting elements are single piers with a full reinforced concrete circular cross section with a parallelepiped cap on top. The two case studies differ for the height of the piers, that is calculated according to a nondimensional ratio  $H/D$  equal to 3 and 7 respectively, where  $H$  is the height and  $D$  the cross-section diameter. The latter is the same for both the case studies and constant along the bridge. The choice of a different height allows to investigate effects of the seismic action in case of short and tall piers.

A simulated design has been performed according to the Italian DM 03.03.1975 [12], considering both gravity and seismic loads. The first derives directly from the deck self-weight, while the latter are modelled as equivalent seismic forces applied separately along the transverse and longitudinal direction of the bridge in order to design piers and link bars. Following the code requirements, the minimum longitudinal reinforcement ratio of 1% is assumed for the piers that have a diameter of 2.0 m. Concerning materials, a  $f_c = 30$  MPa concrete is as-

sumed and effects of the confinement on piers are considered according to [30]. Link bars are made of harmonic steel (DYWIDAG bars) while neoprene bearings are characterized by a shear modulus  $G = 1$  MPa.

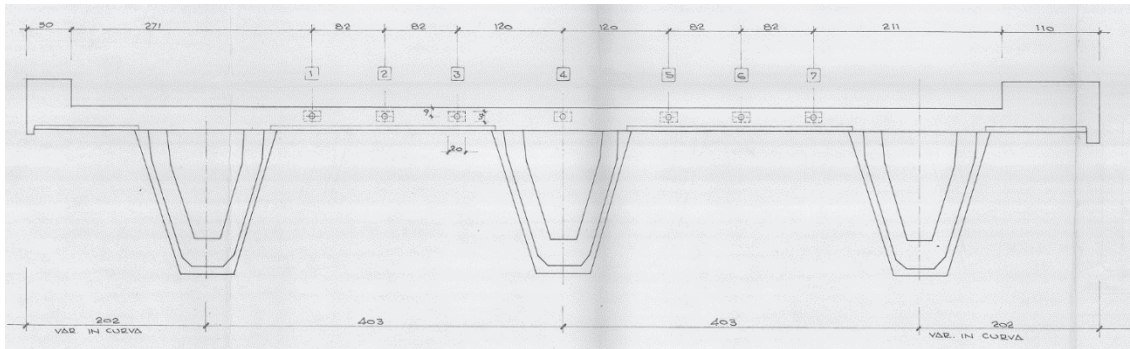


Figure 3: Pre-stressed concrete deck cross-section. Source: design project of the road links among SS76 road, A14 highway, Falconara airport and SS16 road, ANAS, 18.02.1986.

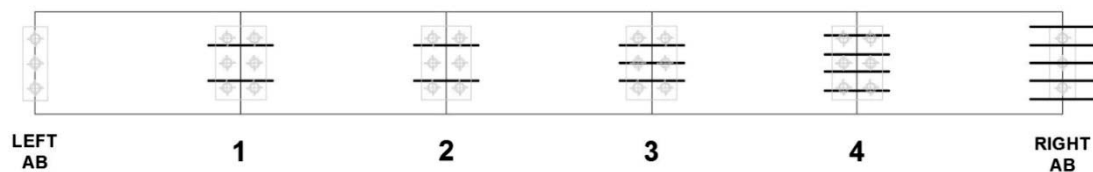


Figure 4: Scheme of link bar arrangement at the slab level.

## 4.2 Numerical models

Three-dimensional nonlinear models are developed in OpenSees [31] to perform TH nonlinear dynamic analyses.

Since no plastic deformation is expected on the deck girders, the latter are modelled as *elastic beam-column* elements and the hypothesis correctness is verified a-posteriori.

Link slabs are modelled as displacement-based beam-column elements (*dispBeamColumn element*) with fibre section to catch the bar stress state under the transverse seismic load. Link bars are modelled through fibre elements with *Steel02* elastic-plastic law, while the concrete slabs adopt a fibre cross section with *Concrete01* uniaxial material.

Pier caps are assumed as rigid elements and are modelled by *rigidLink beam* elements connecting the deck beam ends to the bearings. Bearings are modelled through *zero-length* elements with *Steel01* uniaxial material having elastic-plastic law to simulate the deformability of the bearing and the sliding between concrete surface and neoprene once the static friction is exceeded. The constitutive law of neoprene bearings and the value assumed for the friction coefficient ( $\mu_1 = 0.25$ ) are derived from the available literature.

Columns are modelled using displacement-based fibre elements (*dispBeamColumn element*), which are able to take into account the evolution of the plastic hinge at the base of the pier. The pier cross section, a circular reinforced concrete discretised fiber section, is built so that effects of the confinement on the concrete, modelled as *Concrete01*, are considered according to [30]. For the sake of simplicity, piers and abutments are assumed to be fixed at their base although the authors recognise the significance of soil-structure interaction effects in the response of bridges, especially in the case of soft soils [32].

### 4.3 Fragility analysis

In order to examine the most significant damaging mechanisms occurring with seismic action, three Engineering Demand Parameters (EDPs) are selected: 1) the pier top maximum displacement, which controls  $\chi$  ductile mechanisms of the piers; 2) the bearing maximum displacement; 3) the maximum strain on the link-slab steel bars. The performance of these components is assessed referring to two main limit states, corresponding to the occurrence of plastic mechanisms (piers or bars yielding or the onset of sliding phenomena at the bearings) and to the reaching of the ultimate condition at collapse (pier collapse or bars fracture or maximum displacement of the bearings). In the following, the first is indicated as  $d_y$  while the second as  $d_u$ . The performance thresholds associated to the considered limit states are shown in Table 1. Concerning piers, a cross-sectional analysis is performed to evaluate yielding and ultimate curvatures from which the relevant displacement thresholds are computed according to the static scheme of the piers.

Limit State	Link bars $\epsilon_{\text{bar}} [-]$	Piers $u_p [m]$		Bearings $u_b [m]$
		H/D = 3	H/D = 7	
Yielding/Damage ( $d_y$ )	0.0046	0.027	0.152	0.045
Collapse ( $d_u$ )	0.0400	0.111	0.405	0.200

Table 1: Performance levels and related demand threshold values for the bridge components.

## 5 RESULTS

Results are shown in terms of fragility curves. For each investigated component, charts on the left illustrate the structural response for the case with short piers, while charts on the right pertain to the bridge with tall piers. Black curves refer to the damage limit state  $d_y$ , while red curves to the collapse  $d_u$ . Moreover, the label “Bridge Joint” is used in this case to indicate the pier position (Figure 4). Figure 5 compares fragility curves for pier displacements. It is evident that the vulnerability of vertical elements changes between the two structural models and diminishes with the pier height. Piers never reach the collapse limit state; however, short piers present a sensibly higher vulnerability at damaging than tall ones. For H/D = 3, piers 1 and 3 present a similar vulnerability while in the central pier damage occurs at lower *IMs*, that is related to the 1<sup>st</sup> natural vibration mode in the transverse direction, which significantly involves the middle pier. This phenomenon is less evident in the case of long piers. Differences between pier n. 2 and 3 can be attributed to the different capacity of the kinematic links, offered by the link bars on the slab: indeed, the number of link bars on the superstructure changes and influence the pier response. Overall, as the link bars increase in number, the pier demand in terms of displacement decreases (i.e. a higher *IM* is needed to induce damage). In both structural models, pier n. 4 never experiences damage: the phenomenon can be reasonably attributed to the presence of the fixed abutment on the right.

Concerning the link bars, it is possible to notice from Figure 6 that effects of the change of the pier height are slight on the strain at limit state  $d_y$  while much more evident at collapse  $d_u$ . This is particularly evident for joints n. 1 and 2, where the number of bars is minimum, and joint 4. In both configurations, joint n. 2 presents the highest vulnerability, due to the low number of bars and the central position. Due to the fixed abutment on the right, the vulnerability of joint n. 4 is higher than that of joint n. 3. Above results can be explained since the demand in the links due to longitudinal actions (for which they are designed) is sensibly different from the demand due to transverse excitation. For link bars, both damage and collapse

limit states can be reached, denoting the fundamental role of the superstructure response on the definition of an overall behaviour for the bridge. Moreover, it is evident that links are the weakest components of the structural system at both damage and (excepting for bearing n. 1) collapse limit states.

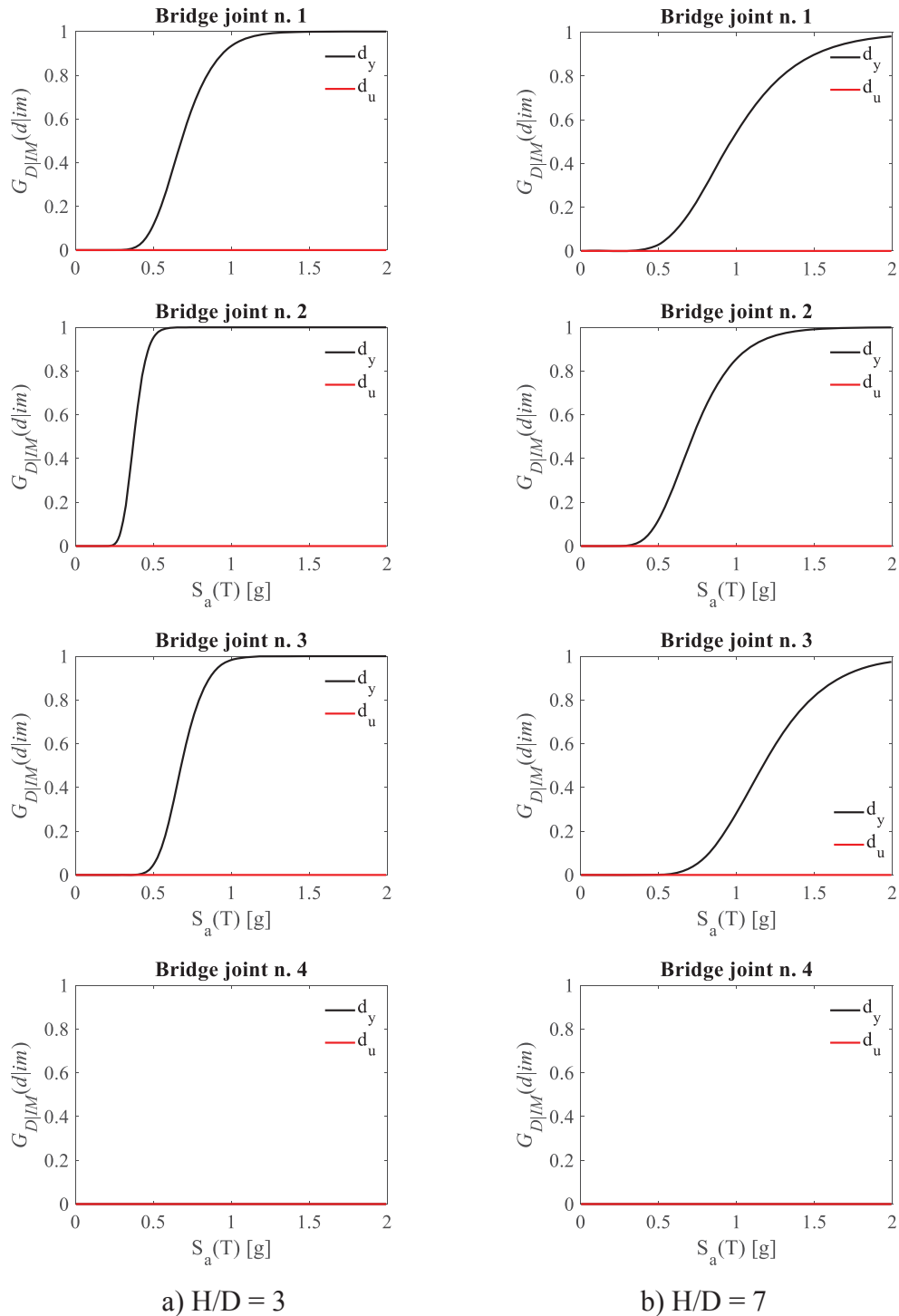


Figure 5: Fragility curves for pier displacements: (a) short piers and (b) tall piers.

Finally, Figure 7 shows fragility curves for bearing displacements. This EDP reveals as the most influenced by the  $H/D$  ratio. For short piers, a higher vulnerability of bearings is obtained. It is worth noticing that, similarly to the behaviour of piers, bearings of joint n. 4 never

collapse since the restraint provided by the fixed abutment influences prevent excessive displacements. The influence of the link disposition can be found on the different response of bearings on joints n. 2 and 3; in detail, bearings at joint n. 2, where the number of bars is the lowest, are more vulnerable than bearings at joint n. 3.

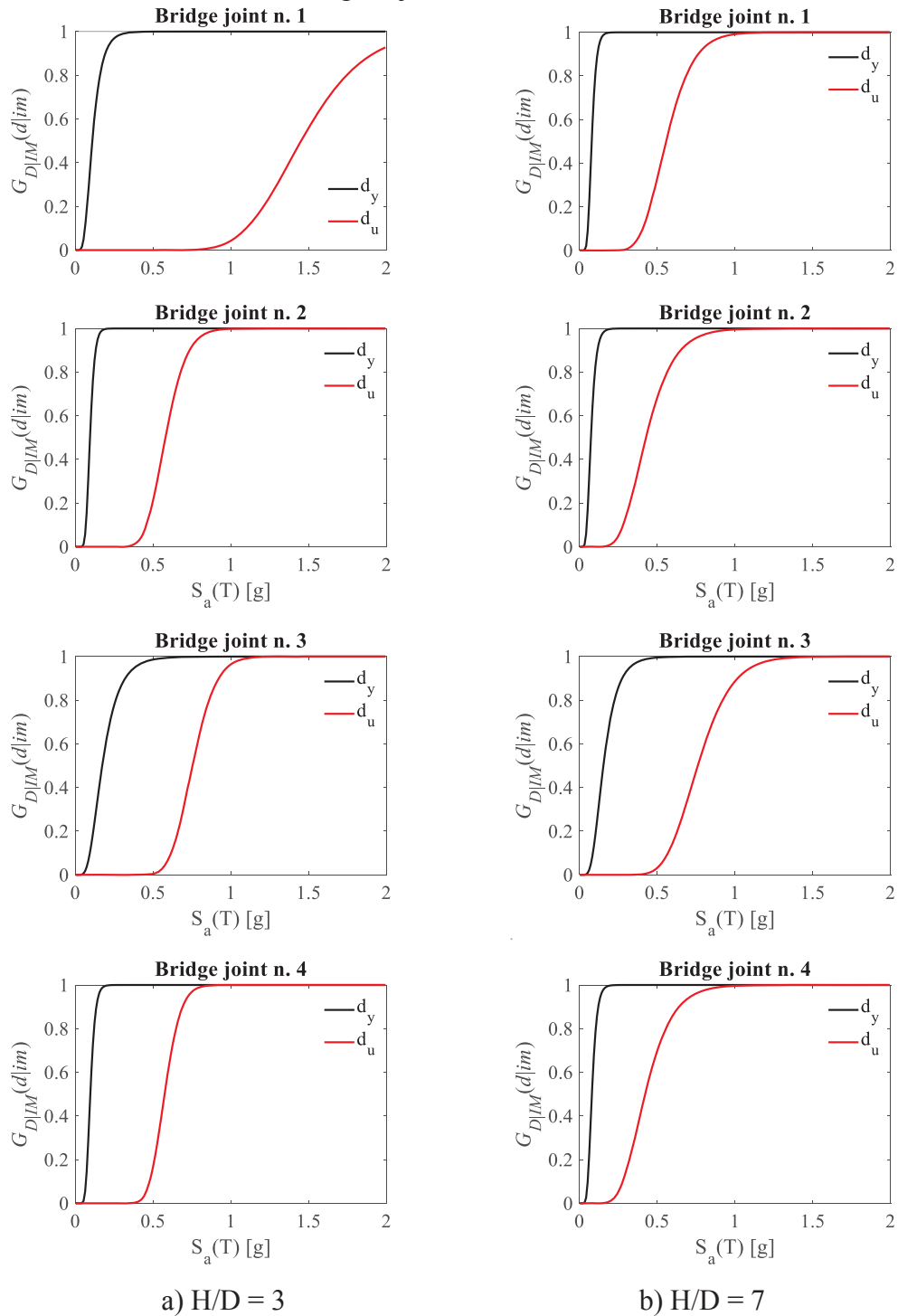


Figure 6: Fragility curves for link bar strain: (a) short piers and (b) tall piers.



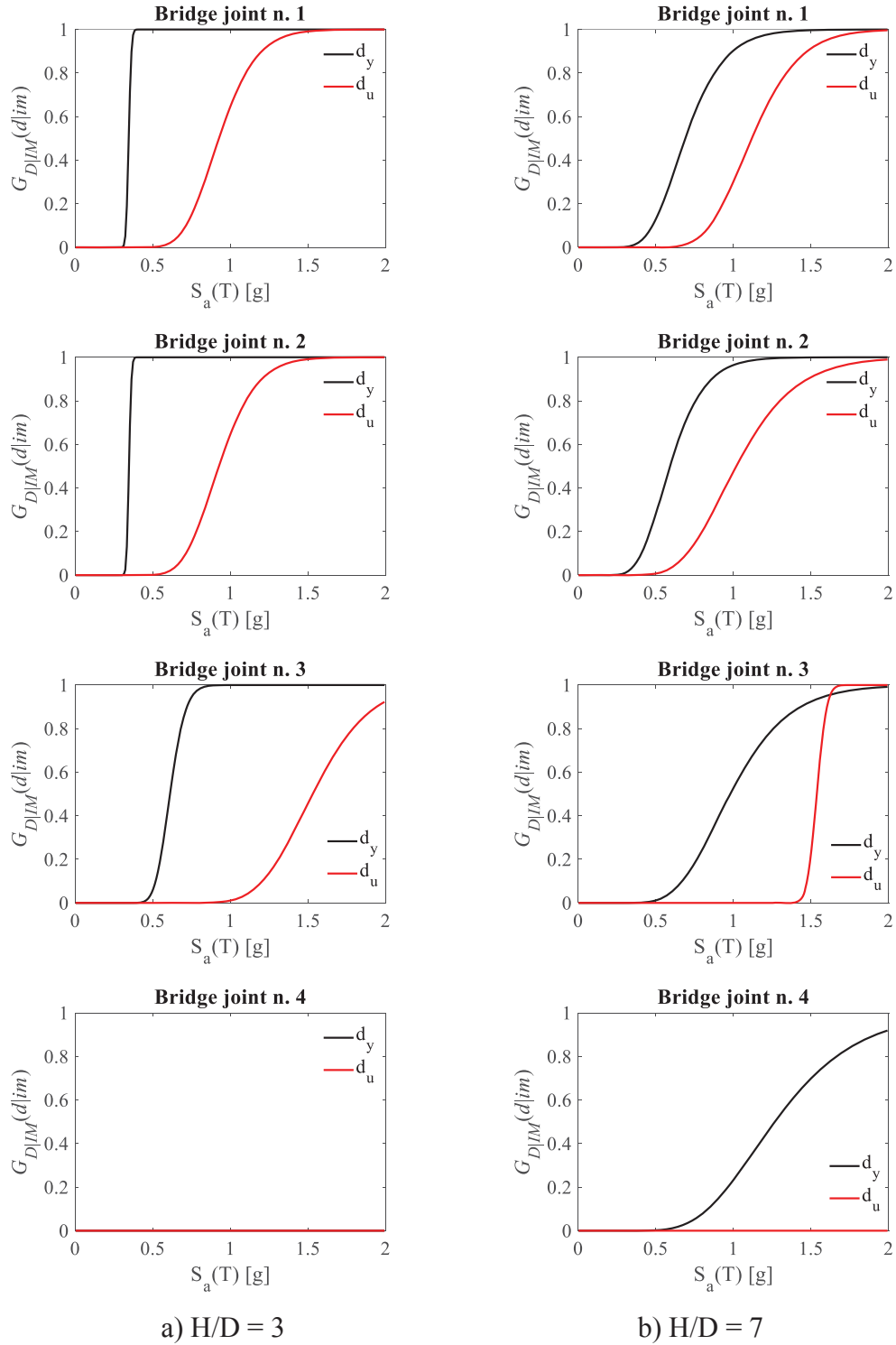


Figure 7: Fragility curves for bearing displacements: (a) short piers and (b) tall piers.

Overall, it should be remarked that a detailed comparison of results between the two different case studies is tough due to their intrinsic different dynamic response to the seismic excitation promoted by the different fundamental periods of the two structural systems. However, results highlight that the seismic vulnerability of links and bearings of LS RC bridges deserves attention. Further data analysis will be carried out to provide a more effec-

tive insight into the effects of the piers' height on the overall bridge typology response through a wider range of the H/D ratio.

## 6 CONCLUSIONS

A first insight into the fragility assessment of LS RC bridges, which is a widespread typology on the Italian national territory, has been investigated in this paper, starting from two representative case studies of the bridge typology. A robust and versatile probabilistic framework based on the use of the multiple stripe analysis tool is adopted to perform seismic analyses. The typical vulnerabilities of the considered structural typology are investigated through three fundamental engineering demand parameters, involving both the superstructure and the supporting structures, such as piers and bearings. Case studies, representative of the typology at hand, are selected to investigate the significance of the damage mechanisms in case of both short and long piers. Detailed numerical models are developed to capture the main vulnerability mechanisms potentially taking place at earthquake occurrence. Results are shown as fragility curves considering two main limit states associated to damage and collapse condition of piers, kinematic links and bearings.

It is possible to conclude that the investigated existing bridge typology may suffer different types of local failures and these affects in a complex way the global structural response and the consequent damage scenario expected for a strong earthquake. Results highlight that the vulnerability of links and bearings of LS RC bridges deserve attention in seismic analysis. In particular, the distribution of damage in the links is quite difficult to predict since they are usually design with only reference to longitudinal actions, which provides a demand distribution sensibly different of that induced by transverse excitations. Further studies on the fragility assessment of LS bridges will be necessary to provide an overall view on the vulnerability of the bridge class at hand and to address the role of the geometric parameters, such as the here investigated H/D ratio, on the overall behaviour of the bridge, as well as on the significance of each damage mechanism.

The approach adopted in this paper for the fragility estimation allows to separately analyse the vulnerability of the different bridge components at the limit states of interest, as a classical strategy in the scientific literature. However, current studies by the authors aim to develop a more detailed procedure for the fragility assessment, concerning the quantification of the damage extension and the evolution of the failure mechanisms within the bridge structure, as fundamental information for a proper and detailed quantification of consequences and costs associated to the seismic risk. The novel procedure can be applied to different bridges configurations or typologies, and also reveals sufficiently general for the analysis of various bridge components and the associated possible failure mechanisms.

## REFERENCES

- [1] Scozzese F, Ragni L, Tubaldi E, Gara F. (2019). Modal properties variation and collapse assessment of masonry arch bridges under scour action. *Engineering Structures*, 199, 109665.
- [2] Ragni L, Scozzese F, Gara F et al. (2019): Dynamic identification and collapse assessment of Rubbianello Bridge. In *IABSE Symposium, Guimaraes 2019: Towards a Resilient Built Environment Risk and Asset Management – Report*, 619–626.
- [3] Nielson BG, DesRoches R (2007): Seismic fragility curves for typical highway bridge classes in the Central and South-eastern United States. *Earthquake Spectra*, 23, 615–633.

- [4] Ramanathan K, DesRoches R, Padgett JE (2010): Analytical fragility curves for multispan continuous steel girder bridges in moderate seismic zones. *Transportation Research Record*, 2202(1), 173-182.
- [5] Mangalathu S, Jeon JS, Padgett JE, DesRoches R (2016): ANCOVA-based grouping of bridge classes for seismic fragility assessment. *Engineering Structures*, 123, 379-394.
- [6] Briseghella B, Siviero E, Zordan T (2004): A composite integral bridge in Trento, Italy: Design and Analysis. In *IABSE Symposium Report*, 88(6), 297-302.
- [7] Caner A, Zia P (1998): Behavior and design of link slabs for jointless bridge decks. *PCI journal*, 43, 68-81.
- [8] Caner A, Dogan E, Zia P (2002): Seismic performance of multi simple-span bridges retrofitted with link slabs. *Journal of Bridge Engineering*, 7(2), 85-93.
- [9] Sevgili G, Caner A (2009): Improved seismic response of multisimple-span skewed bridges retrofitted with link slabs. *Journal of Bridge Engineering*, 14(6), 452-459.
- [10] Wang C, Shen Y, Zou Y, Zhuang Y, Li T (2019): Analysis of Mechanical Characteristics of Steel-Concrete Composite Flat Link Slab on Simply-Supported Beam Bridge. *KSCE Journal of Civil Engineering*, 1-10.
- [11] Gara F, Regni M, Roia D, Carbonari S, Dezi F (2019) Evidence of coupled soil-structure interaction and site response in continuous viaducts from ambient vibration tests. *Soil Dynamics and Earthquake Engineering*, 120, 408,422.
- [12] Ministero delle Infrastrutture e dei Trasporti (1975): D.M.03.03.1975, *Approvazione delle norme tecniche per le costruzioni in zone sismiche*, G.U. n.93, 08.04.1975.
- [13] Jalayer, F, Cornell CA (2009): Alternative non-linear demand estimation methods for probability-based seismic assessments. *Earthquake Engineering & Structural Dynamics*, 38(8), 951-972.
- [14] Carbonari S, Gara F, Dall'Asta A, Dezi L (2016): Shear Connection Local Problems in the Seismic Design of Steel-Concrete Composite Decks. *Conference on Italian Concrete Days*, 341-354.
- [15] Dezi L, Carbonari S, Dall'Asta A, Gara F, Minnucci L (2018): Seismic behaviour of steel-concrete composite bridge decks. *Steel and Steel-concrete composite structures in seismic areas: advances in research and design*. Research Project RP3, ReLUIS-DPC 2014-2018. Napoli: Doppia Voce. ISBN 978-88-89972-74-8, 451-478.
- [16] Tubaldi E, Barbato M, Dall'Asta A (2010): Transverse seismic response of continuous steel-concrete composite bridges exhibiting dual load path. *Earthquakes and Structures*, 1(1), 21-41.
- [17] Tubaldi E, Barbato M, Dall'Asta A (2011): Influence of model parameter uncertainty on seismic transverse response and vulnerability of steel–concrete composite bridges with dual load path. *Journal of Structural Engineering*, 138(3), 363-374.
- [18] Tubaldi E, Dall'Asta A (2012): Transverse free vibrations of continuous bridges with abutment restraint. *Earthquake engineering & structural dynamics*, 41(9), 1319-1340.
- [19] Scozzese F, Dall'Asta A, Tubaldi E (2019): Seismic risk sensitivity of structures equipped with anti-seismic devices with uncertain properties. *Structural Safety*, 77, 30-47.

- [20] Au SK, Beck JL (2003): Subset simulation and its application to seismic risk based on dynamic analysis. *Journal of engineering mechanics*, 129(8), 901-917.
- [21] Ramanathan KN (2012): *Next generation seismic fragility curves for California bridges incorporating the evolution in seismic design philosophy*. Georgia Institute of Technology.
- [22] Xie Y, Zhang J, DesRoches R, Padgett JE (2019): Seismic fragilities of single-column highway bridges with rocking column-footing. *Earthquake Engineering & Structural Dynamics*, 48(7), 843-864.
- [23] European Committee for Standardization (CEN). (2005): Eurocode 8: Design of structures for earthquake resistance – Part 2: Bridges. *EN 1998-2*.
- [24] Atkinson GM, Silva W (2000): Stochastic modeling of California ground motions. *Bulletin of the Seismological Society of America*, 90(2), 255-274.
- [25] Boore DM (2003): Simulation of ground motion using the stochastic method. *Pure and applied geophysics*, 160(3-4), 635-676.
- [26] Jalayer F, Beck JL (2008): Effects of two alternative representations of ground-motion uncertainty on probabilistic seismic demand assessment of structures. *Earthquake Engineering & Structural Dynamics*, 37(1), 61-79.
- [27] Porter K, Kennedy R, Bachman R (2007): Creating fragility functions for performance-based earthquake engineering. *Earthquake Spectra*, 23(2), 471-489.
- [28] Baker JW (2015): Efficient analytical fragility function fitting using dynamic structural analysis. *Earthquake Spectra*, 31(1), 579-599.
- [29] Ministero delle Infrastrutture e dei Trasporti (2018): D.M.17.01.2018, *Aggiornamento delle Norme Tecniche per le Costruzioni*, G.U. n.42, 20.02.2018.
- [30] Mander JB, Priestley MJ, Park R (1988): Theoretical stress-strain model for confined concrete. *Journal of structural engineering*, 114(8), 1804-1826.
- [31] McKeena F, Fenves G, Scott M (2015): Open System for Earthquake Engineering Simulation (OpenSees). *Pacific Earthquake Engineering Research Center (PEER)*, University of California: Berkeley, CA.
- [32] González F, Padrón LA, Carbonari S, Morici M, Aznárez JJ, Dezi F, Leoni G (2019) Seismic response of bridge piers on pile groups for different soil damping models and lumped parameter representations of the foundation. *Earthquake Engineering and Structural Dynamics*, 48(3), 306-327.

## PERFORMANCE-BASED EARTHQUAKE ENGINEERING ANALYSIS OF SHORT-MEDIUM SPAN STEEL-CONCRETE COMPOSITE BRIDGES

Daniele Corritore<sup>1</sup>, Fabrizio Paolacci<sup>1</sup>

<sup>1</sup> Department of Engineering, Roma Tre University  
e-mail: [fabrizio.paolacci@uniroma3.it](mailto:fabrizio.paolacci@uniroma3.it), [daniele.corritore@uniroma3.it](mailto:daniele.corritore@uniroma3.it)

---

### Abstract

*In this paper, the results of the performance-based earthquake engineering (PBEE) analysis, carried out to assess the seismic behaviour of short-medium span steel-concrete composite I-girder bridges, are presented and discussed. The selected case study is part of a group of bridges analysed within the SEQBRI project, funded in 2012 by the European Union, which deals with a systematic development of the PBEE analysis for short-medium span steel-concrete composite I-girder bridges. In this respect, fragility and damage analysis of the selected bridge are performed using a proper component-based numerical model along with wide experimental campaign. These outcomes are then integrated in the decision-making analysis, where the selected decision variable is the repair cost ratio of the bridge. The results show the good performances of short medium span steel-concrete composite bridges, both for minor and major damage scenarios.*

**Keywords:** Performance based earthquake engineering, steel-concrete composite bridges, loss analysis, concrete cross beam.

---



## 1 INTRODUCTION

Nowadays, short-medium span steel-concrete composite I-girder bridges (SCC) made of hot rolled steel beams are very popular, owing to their short construction time and reduced costs. Moreover, they are very adequate for seismic areas for their limited weight. These bridges can be easily designed for static loading, according to Eurocode 4, [1]; however, the effects of seismic loading has not been yet adequately investigated, and thus, they may exhibit damages even in low-seismicity zones.

In general, steel-concrete composite bridges with hot rolled sections for small and medium spans, (range between 25-40 m), exhibit several advantages in terms of: small total depth of composite section, no pre-stressing in concrete slab, low dead weight and limited foundations and settlements of supports, simple erection methods. The SEQBRI project, funded in 2012 by the European Union and conceived on these premises, deals with a systematic development of the Performance-Based Earthquake Engineering, [2], for short-medium span steel-concrete composite I-girder bridges that includes seismic input randomness, demand and damage analysis as well as economic cost-benefit estimations, [3]. In particular, a new type of connection between steel girder and piers that use a transverse concrete cross beam (CCB) is taken into account. The steelwork parts of the composite beams are prepared in factory and equipped with steel elements for connections (plates, holes, welded studs...). The steel girders are placed on the head of the piers without any propping; subsequently, the slab is concreted and the continuity of the composite beam is completed by concreting the beam joints and the transverse beams over the pier. This kind of joint has been studied in the past but only for static load conditions, [4-5]. In this paper, the results of the performance-based earthquake engineering (PBEE) analysis, carried out to assess the seismic performance of short-medium span steel-concrete composite I-girder bridges, are presented and discussed. The selected case study is part of a group of bridges analysed within the SEQBRI project, [3]. In this respect, fragility and damage analysis of the selected bridge are performed based on a proper component-based numerical model and a wide experimental campaign, [6-7]. These outcomes are then integrated in the decision making analysis, where the selected decision variable is the repair cost ratio of the bridge.

## 2 DESCRIPTION OF THE CASE STUDY

The analyzed case study is a straight 2-span deck consisting of 4 main girders HE600B of S460 steel grade with 2.65m in-between distance (Figure1). The bridge is 40.00 m long and consists of 2 spans; the total width of the road cross-section is 10.60 m, with carriageway 6.50 m wide and 2 sidewalks 2.05 m wide. The thickness of the concrete slab is equal to 25 cm. At the abutments, the steel girders are fixed to an end reinforced concrete crossbeam 0.60 m wide. The deck is simply supported on normal damping rubber bearings.

At the intermediate pier, the steel girders are fixed to an intermediate reinforced concrete crossbeam 0.90 m wide (Figure2). A wall type pier 0.60 m thick and 7.00 m wide is used. It is assumed that the foundation soil is categorized as type B according to EN1998. In this example, the SSI effect is neglected.

Different types of CCB configurations have been applied in several occasions, [8]. Many of them are variants of the configurations included in the standard DIN-FB-104, [9]. These configurations are proposed in order to manage mainly vertical dead and live loads, which produce negative moments at supports. For bridges subjected to seismic actions, significant tensile forces might be exhibited also at the bottom flange of the steel girder, especially when monolithic connection between CCB and pier is formed. Because of the CCB configuration is the most crucial detail, in order to identify the better solution for applicability in seismic prone areas, within the SEQBRI project the DIN FB variant C of the CCB has been chosen to be

analytically and experimentally investigated. Moreover, two new variants, based on the DIN FB variant B, have been designed and investigated.

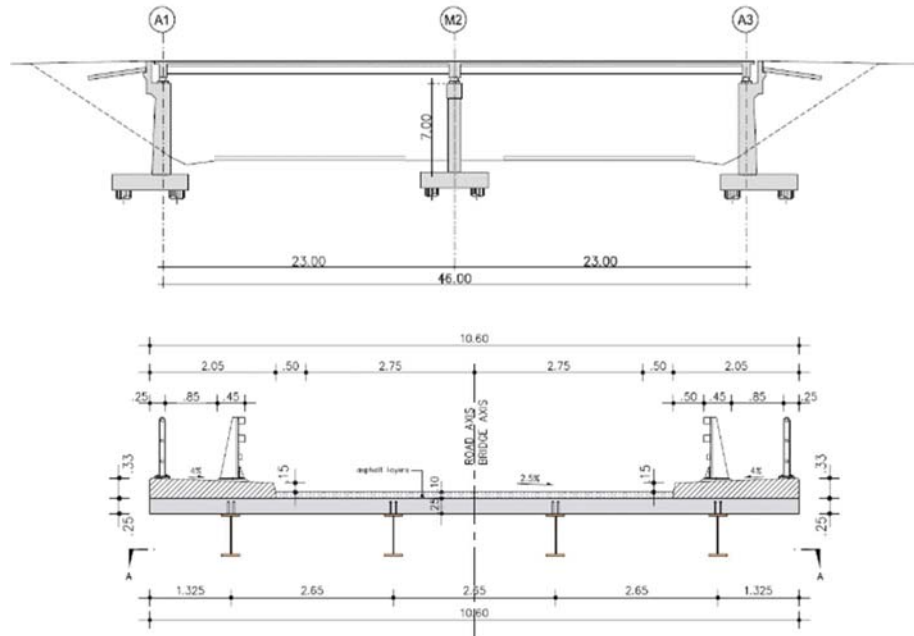


Figure 1. Longitudinal section and cross section at span for selected case study

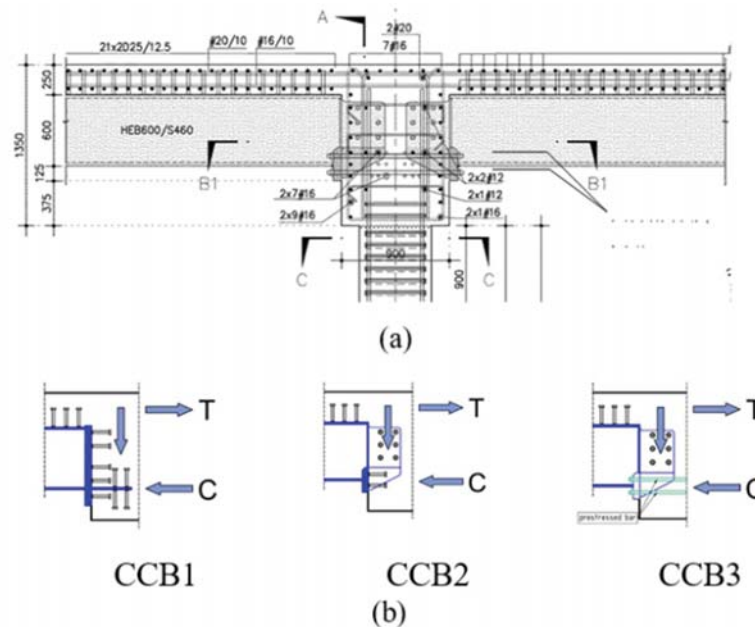


Figure 2. (a) Pier-Deck joint with Concrete Cross Beam, (b) Static behavior of Pier-to-deck Joints

The idea is to transfer the forces from the composite girder to the CCB through contact and dedicated groups of shear studs. For this reason, in the new configurations, the steel flanges are not inserted into the CCB and the height of the head plate is limited (Figure 2). A broad

description of these typologies and of the experimental tests can be found in Abbiati et al., [6] and Paolacci et al., [7]. In what follows the vulnerability of the selected bridge with CCB3 (see Figure 2b) is analyzed in the framework of PBEE. In this kind of CCB, the tensile force at the top flange is transferred gradually to the longitudinal reinforcement (or reversely a potential compression force to the concrete slab) through a group of vertical studs, which are placed on the top flange of the girder before the CCB. The shear force is transferred to the CCB through a group of horizontal studs, transversally placed at the sides of the girder's web, which is inserted into the CCB. These studs are subjected only to pure shear, action that is compatible to their actual function. The tensile stress at the bottom flange of the steel girder is transferred through anchor bars inserted throughout holes present in the web. The bars are tensioned after hardening of concrete and imposition of dead loads and are not bounded. The duct of each anchor should be filled with grease, in order to offer the opportunity for inspection, re-tension or even replacement in case of extreme seismic events.

### 3 NUMERICAL MODELING OF CONCRETE CROSS BEAM –STEEL GIRDER CONNECTION

A component based mechanical model of the CCB3 connection was developed in the code OpeSEES, [10]. This model (Figure 3) was used to analytically reproduce the experimental tests executed on I-girder subassemblies of the bridge. In [7] the results of the test campaign are presented and discussed. The aim was the definition of a refined model that faithfully approximates the real behavior of the sample and that allows the extension of the model to several cases.

Nonlinearities have been explicitly considered in the steel girders, concrete slab, pier, shear headed studs of the CCB, shear headed studs between girder and slab. Steel girder and concrete slab have been modeled using nonlinear beam elements with fiber sections. The steel girder and the slab have been connected by elastic beam elements with high stiffness; whereas, the shear and axial behavior of the vertical connecting studs has been modeled using nonlinear links with elasto-plastic behaviour.

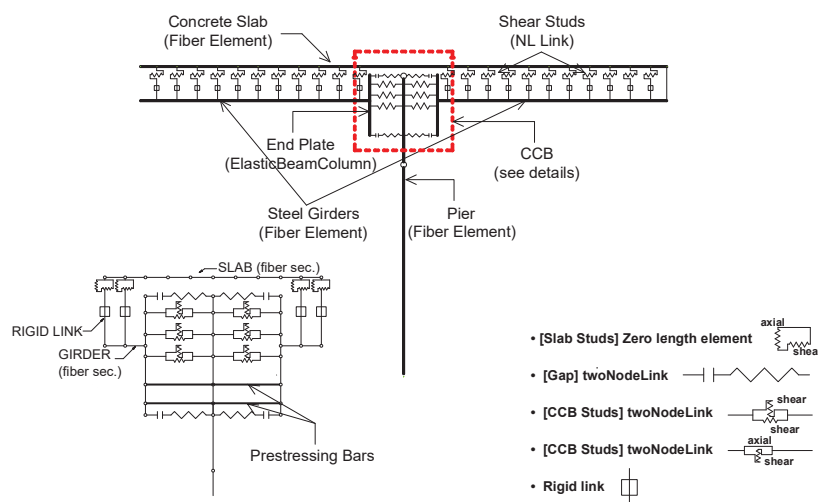


Figure 3. Numerical model of the pier-deck joint with Concrete Cross Beam



Fig. 4 – Experimental setup

Strength of the single shear stud  $Q_u$  has been calculated according to CEN 1994, [1], while the related stiffness has been evaluated by mean of the shear load-slip curves (Q-s) defined in [11]:

$$\frac{Q}{Q_u} = \alpha \sqrt{1 - e^{-\beta s}} + \gamma s \quad (1)$$

with  $\alpha = 0.97$ ,  $\beta = 1.3$ ,  $\gamma = 0.0045 \text{ mm}^{-1}$ .

The vertical head plates welded on the steel girders and directly in contact with the transverse concrete beam have been modeled by rigid links. The CCB have been modeled by elastic beam elements with vertical axis. Nonlinearities in the CCB were considered by modeling shear studs and prestressing bars separately. Moreover, in order to reproduce the constraint in compression due to the presence of the concrete crossbeam, four compression gap elements have been used both at left and right sides of the CCB joints at two different levels, as shown in Figure 3, [12]. A simplified evaluation of the stiffness of the gap has been performed, assuming that the compressive force coming from the girder would act uniformly on a surface equal to the area of the vertical head-plate.

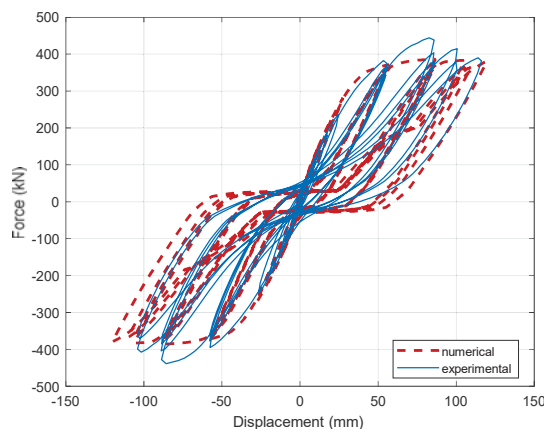


Figure 5. Numerical and experimental hysteretic response

Studs welded in the transverse direction on the web plate entering the CCB are simulated with nonlinear links in the vertical and horizontal direction. Each link simulates the effect of  $\phi 25$  mm shear studs. Their strength and stiffness has been calculated as for the studs in the slab. The two levels of pretension bars (Dywidag type) in the bottom area of the CCB, have been modeled by two elastic truss elements.

The 2-D FE model for concrete cross beam is shown in the following figure. This model has been validated through a wide experimental campaign. The setup of a test and a numerical/experimental comparison of the hysteretic force-displacement cycle are illustrated, respectively, in Figure 4 and in Figure 5.

#### 4 SEISMIC INPUT SELECTION

A group of 14 accelerograms has been selected from the PEER ground motion database in order to best approximate the Eurocode8 type 1 Response Spectrum, [13]. A set of records have been picked out from the database according to the following hazard parameters: magnitude range  $M_w = 5.8-7.0$ , distance from the fault rupture comprised in a range 15-40 km and local soil type B. Successive-ly, 14 records have been selected among these so that their mean spectrum best approximate the target spectrum. A scaling factor has been applied to each input signal in order to minimize the dispersion of the mean spectra compared to the Eurocode spectrum. The scaling factor modifies the original record only in amplitude.

#### 5 PROBABILISTIC SEISMIC DEMAND ANALYSIS OF CASE STUDIES

The author's name should include first name, middle initial and surname. It should be written centered, in 12pt boldface Roman, 12pt below the title.

In the perspective of a Cost-Effective Risk Analysis, as the final goal of the application of the PBEE procedure, the elements (structural or finishing) whose damage and repairing item could be significant must be identified. Accordingly, the damage mechanisms and the Engineering Demand Parameters (EDP) through which they can be quantified by a numerical structural analysis must be defined. The selected EDPs for the chosen representative case study are listed hereafter, according to the classification of Mackie and Stojadinovic [14], and Tubaldi et al. [15]:

1. Global EDPs:
  - Pier drift top displacement of the pier normalized with respect to the total height.
2. Intermediate EDPs
  - Bending moment-curvature ( $M_{max}, \chi_{max}$ ) of the pier at the bottom section.
  - Bending moment-rotation of the CCB connection.
3. Local EDPs
  - Maximum force and relative displacement of shear studs in the CCB in the horizontal direction.

The bending moment and the curvature of the CCB connection have been obtained for both the left and right sides of the joint. The bending moment of the composite section just before the side of interest, has been defined as follows:

$$M_{max} = M_{slab} + M_{girder} + \Delta N \cdot z \quad (2)$$



where  $M_{slab}$  is the bending moment of the slab,  $M_{girder}$  the bending moment of the girder,  $\Delta N$  the axial force in the slab and  $z$  the level arm (distance between girder and slab). The rotation of one side of the joint is given by the rotation of the vertical end plate with respect to the undeformed configuration.

Incremental dynamic analyses have been performed, [16], and multi-record IDA curves of the structural response quantities mentioned above have been built. Since the properties of the seismic response depend on the intensity of the ground shaking, a comprehensive assessment requires numerous nonlinear dynamic analyses at various levels of intensity in order to represent different possible earthquake scenarios. The selected scan of PGA is in the range (0.1g - 2.0g). The multi-record IDA response of the pier drift, obtained as mean value of the multi-record IDA, is shown in Figure 7. The mean value of the drift ratio for a PGA of 2.0g is about 7%. The typical collapse ratio of 4%, [17], is reached around 1.2g of PGA. For a PGA of 0.3g, which corresponds to the PGA of response spectrum type 1 (soil B) chosen for the design of the bridge, the drift ratio is about 1.0%. Analyzing the moment-curvature relationship, not shown here for brevity, it can be noticed the nonlinear behaviour of the section at the base of the pier.

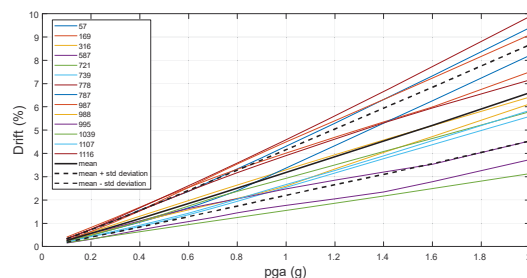


Figure 7. IDA-Drift ratio of the pier

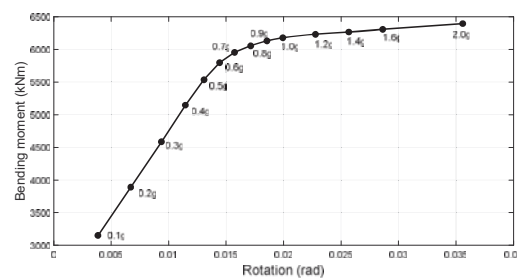


Figure 8. Bending moment-Rotation (mean values) of CCB left side

Pier yields at its base for earthquakes characterized by PGA of 0.4g while plastic hinge develops for stronger seismic actions. Ultimate value is obtained between 1.2 g and 1.4 g.

In Figure 8 the bending moment-rotation relationship (mean value) of CCB at left side, that is the maximum absolute bending moment versus the corresponding rotation of left side of the joint, is shown. It can be noticed that the onset of nonlinear behaviour takes place "after" the yielding of the pier, or rather for higher values of PGA (0.8-0.9 g). Representative force-slip curves of the CCB shear studs, not shown here for brevity, showed that, when the lower group begins to yield, around 0.5g, the upper levels of connectors are subject to smaller levels of stress. In particular, 1st group is still in the elastic range. The bigger deformations of the last line of studs are in agreement with the fact that during the seismic action the neutral axis in the CCB is closer to the first rows of connectors. In conclusion, for events with a PGA of 0.3g or under, the critical part is the pier only with the formation of a plastic hinge at its base while the concrete crossbeam does not seem to be affected by any relevant damage. First level of damage within the intermediate CCB starts to arise from 0.5-0.6g, value of PGA for which the lower group of studs within the CCB yield.

## 6 DAMAGE ANALYSIS AND FRAGILITY CURVES

In order to implement performance-based earthquake engineering method for the representative case of small-medium span composite bridge and investigate its vulnerability, it has been necessary to accurately assess the probability of reaching particular levels of damage. For this purpose, a correlation process between the most representative engineering demand parameters and damage measures has been made. Piers are often the most vulnerable elements in a bridge

and column failure can have catastrophic consequences. Excessive deformations can result in spalling of cover concrete, buckling of longitudinal reinforcement or bar fracture. Concrete cover spalling represents the first flexural damage state, in which there are marginal safety implications, there may be a possible short-term loss of function, and the cost to repair concrete spalling could be significant. Buckling and fracture of the longitudinal bars represent damage states in which safety implications are significant, partial replacement may be required, and a longer term loss of function may occur. In order to quantitatively implement PBEE for the considered reinforced wall-type pier, in this work the three damage conditions above mentioned have been considered as damage measures. The equations proposed by Berry and Eberhard, [18], for damage estimation have been used to relate the pier EDP and DS. Assuming that the DS occur in sequence (with DS1 preceding DS2 which, in turn, precedes DS3 and so on), the corresponding EDP can be ordered ( $EDP_1 \leq EDP_2 \leq EDP_3 \leq \dots$ ). Assuming, as an example, three DS, the joint probability density function of the variables  $EDP_1 \leq EDP_2 \leq EDP_3$  can be assumed as follows:

$$p_{EDP_1, EDP_2, EDP_3}(EDP_1, EDP_2, EDP_3) = \begin{cases} \frac{1}{k} p_L(EDP_1, EDP_2, EDP_3) & \text{if } EDP_1, EDP_2, EDP_3 \\ 0 & \text{otherwise} \end{cases} \quad (3)$$

where  $p_{EDP_1, EDP_2, EDP_3}(\cdot)$  is a joint lognormal distribution function of three random variables. The constant  $k$  in the previous equation is a normalization constant. A more detailed explanation of the previous equation can be found in Alessandri et al., [19]. Figure 9 shows the four probabilities of the DS conditioned to the EDP evaluated for the pier. The correlation between the DS has been considered and the Damage States were assumed to occur in sequence (with concrete spalling preceding bar buckling, which, in turn, precedes bar fracture). For the shear headed studs of the beam-to-beam concrete connection, two levels of damage have been considered. In particular, first level of damage is the yielding of the studs, assumed as the last point of their elastic behaviour in the elasto-plastic constitutive law chosen in the model. The second level of damage corresponds to the complete rupture of the stud, taken from the research work of Gattesco and Giuriani, [11]. The rupture of a shear headed stud, monotonically loaded, takes place for a horizontal slip of 9.7 mm. By assuming that the EDP is log-normally distributed, the probability of damage conditioned to the IM,  $P(DS|IM)$ , known as fragility function, is evaluated by the convolution of the  $P(DS|EDP)$  and  $P(EDP|IM)$ :

$$Pr(DS|im) = \int_{EDP} Pr(DS|EDP) dG(EDP|IM) dEDP \quad (4)$$

The DS0 in the figure corresponds to a negligible damage for which no repair items is considered. As shown in Figure 10, the probability of having cover spalling is over 15% for 0.3g of PGA. It grows then very fast, reaching 80% at 0.75g, then reduces because of bar buckling and bar fracture become more probable. The probability of having bar buckling is under 10% until 0.8g and reaches 30% at 2g. The risk of bar fracture seems to arise only for strongest seismic inputs. The probability of fracture of the reinforcement is under 10% until 0.8g, it is almost 30% for 1.6g and reaches 35% for 2.0g. Figure 10 show the fragility function evaluated for the pier base.

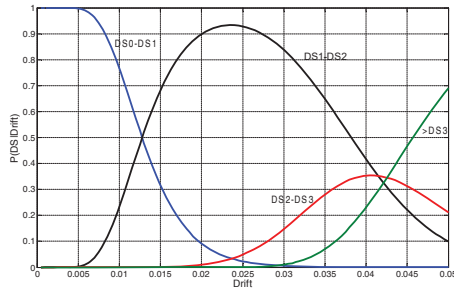


Figure 9. Conditional probability functions of the DS for the pier

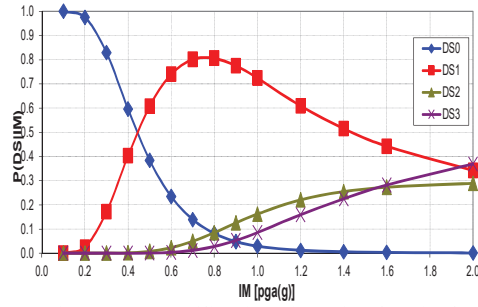


Figure 10. Fragility functions for the pier base

## 7 COST-EFFECTIVE RISK ANALYSIS

Cost-effective risk evaluation is the very last step of the global integrated probabilistic performance-based evaluation procedure used for SEQBRI project. The result of this phase is a decision model, which is based on Decision Variables (DV) pertaining to the use of a structure given a level of sustained damage. Decision models are mathematical relations between damage measures (DMs) and decision variables (DVs). Commonly used decision variables describe losses in terms of repair cost, interruption in service (downtime or repair time), or loss of life: thus, decision models are also called loss models. The decision model may have several parts those that relate DMs to repair quantities (Q) and those that relate Q back to repair cost or repair time. A completely different set of decision variables focuses on the remaining capacity of the structure to function as intended. For example, the return of a highway bridge to differing degrees of functionality in a highway network is also an important loss criterion. Functionality may be measured in terms of lateral load resistance in aftershocks, traffic volume, lane and speed reductions, or access for emergency vehicles. The main DV here adopted is the repair/construction cost ratio (Direct cost). This choice comes from the goal to provide an immediate economic measure of earthquake performance of the assessed structure. Indirect costs like downtimes are not explicitly considered in the analysis. Global earthquake demand is defined in terms of peak ground acceleration (PGA), which represents the most commonly used intensity measure for structural seismic analysis and design issues. Local engineering demand parameters (EDP) consist in variables related to structural elements deformation or load, such as pier drift or bending moments. Damage states are expressed in terms of EDP limit values and associated damage or repair amounts expressed in terms of percentage of structural quantities (concrete cracking surface and/or volume, percentage of broken or yielded reinforcement rebars, percentage of broken studs or rotation angle for example for what concerns CCB). At the end, the ultimate goal is to evaluate the cumulative probability distribution function of the decision variables DV (cost and/or repair duration), as expressed by the PBEE framework Integral defined by Equation (4):

$$\lambda(DV < dv) = \int_{IM} \int_{DM} \int_{EDP} G(DV|DM) dG(DM|EDP) dG(EDP|IM) |d\lambda(IM)| \quad (5)$$

where  $G(\cdot)$  represents the complementary cumulative distribution function of the considered variables.

Most of those different successive analysis parameters and intermediate outcomes, result from the previous tasks, including numerical non-linear analysis and experimental evaluations. At each steps, results are addressed in terms of probabilistic quantities such as mean values,

deviation or probability of exceedance (see previous paragraphs). Repair costs and duration databases are collected from different former projects, US and French repair data, [3]. Additional (but rather sparse) data are also collected from road/bridges maintenance services concerning European recent « real field » seismic events such as Aquila earthquake. Analysis preferentially focuses on direct costs related to structural damages, since indirect costs appears to be very depending on the context (country, location, proximity of big cities, economical/industrial activities, toll-roads) and are not directly related to SEQBRI project bridge typology and specificity (SCC bridges with CCB).

### 7.1 Direct losses evaluation

Direct cost evaluation is essentially based on repair quantities evaluated for different parts or elements of the structure for a given intensity measure or damage scenario and on associated unit repair costs. Repair cost estimation (and loss modeling in general) is almost always a structural system problem, not simply determined at the component level. Therefore, it is often necessary to combine (sum) numerous scalar values in order to obtain, for example, a total cost. For this matter, the bridge system is disaggregated into individual components or ensembles, such as the columns or CCB, denoted as performance groups (PGs) that are damaged, assessed, and repaired together using a specific combination of different repair methods. Each of those performance groups is also sub-divided into individual elements or sub-PGs.

### 7.2 Performance Groups

Different damage-states (DS) are defined for each performance group. The tested case-study is thus broken down into performance groups (PGs) for each major bridge component. Each performance group represents a collection of structural components that act as a global-level indicator of structural performance and that contribute significantly to repair-level decisions. Performance groups are not necessarily the same as load resisting structural components. For example, non-structural components may also be a performance group, since they also suffer damage and contribute to repair costs. The PGs generally correspond to things that are observable as a unit. Grouping bridge components into performance groups allows for more meaningful damage assessment than grouping by component. The definition of the PGs used for the SCC bridges with CCB corresponds to the following structure disaggregation. Four performance groups have been defined for this study (foundations are excluded):

- PG1: Pier (bottom)
- PG2: Pier (top)
- PG3: Concrete Cross beams
- PG4: Deck: including concrete slab, steel girders and superstructures/equipment.

### 7.3 Damage States and associated repair methods and quantities

Each damage state corresponds to only one repair method. Selection of repair methods is a crucial step in computing the repair-related decision variable, repair cost ratios and repair time. A selection of repair methods specific for the damage states has been made based on Caltrans database, [13], of typical repair techniques, since it has been defined to be generalizable and usable for performance-based evaluation of other structures. Each performance group contains a number of discrete damage states (DS) corresponding to repair quantities needed for restoring the bridge. The damage states are numbered from DS0 to DS3 with higher numbers indicating more severe damage. The DS0 damage state corresponds to the onset of damage when repair costs begin to accumulate. For analysis, the repair cost of the bridge is treated as 0 € below the

DS0 level of damage. Damage beyond DS0 are needed to be repaired and costs begin to accumulate. Slight damage less than DS0 is assumed to be insignificant and not needing repair. Damage computation requires the definition of maximum possible repair quantities to define an upper limit to the quantities and costs. The upper limit is called DS3, since it corresponds to the most severe possible damage state for the elements in a performance group. DS3 usually corresponds to complete failure and replacement of all elements in the entire performance group. Details on repair methods here adopted can be found in [3].

#### 7.4 Damage Scenario and loss analysis

To evaluate the expected repair cost of a structure as consequence of a seismic event in a given reference time period, one or more damage scenario must be defined. Its definition, which considers repairing items more or less large, reflects a level of the intensity measure (IM) of the ground motion at the site. Two damage scenarios have been defined; they are described in Table 1 and Table 2.

Table 1. Damage States (DS) for Minor scenario.

Performance Group	DS	Description
PG1 (Pier at base)	DS1	Seal cracks and minor removal and patching of concrete
PG2 (Pier at top)	DS0	----
PG3	DS1	Seal cracks and minor removal and patching of concrete
PG4	DS2	Seal cracks, clean deck and apply methacrylate

Table 2. Damage States (DS) for Minor scenario

Performance Group	DS	Description
PG1 (Pier at base)	DS2	Seal cracks, major patching
PG2 (Pier at top)	DS1	Seal cracks and minor removal and patching of concrete
PG3	DS2	Replacement of CCB
PG4	DS2	Seal cracks, clean deck and apply methacrylate

According to the methodology developed in ([3] and [13], once the scenario has been defined its average cost can be calculated by summing the costs of the repairing items associated to each PG. Figure 11 shows the repair-to-rebuild ratio for both minor and major scenarios. Figure 12 shows the cost disaggregated for PGs. From the results it clearly appears that PG1 (base of piers) contributes most to minor damage scenario expected cost at high value of the PGA, while peak contribution is from PG3 (cross beams) at lower values of PGA for the minor scenario and over the whole range of PGA for the major damage scenario.



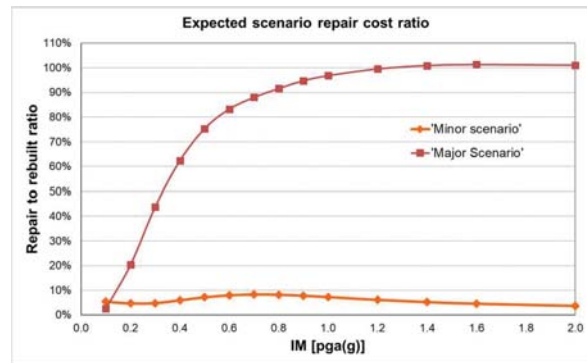


Figure 11. Expected repair cost conditioned to IM for the selected scenarios.

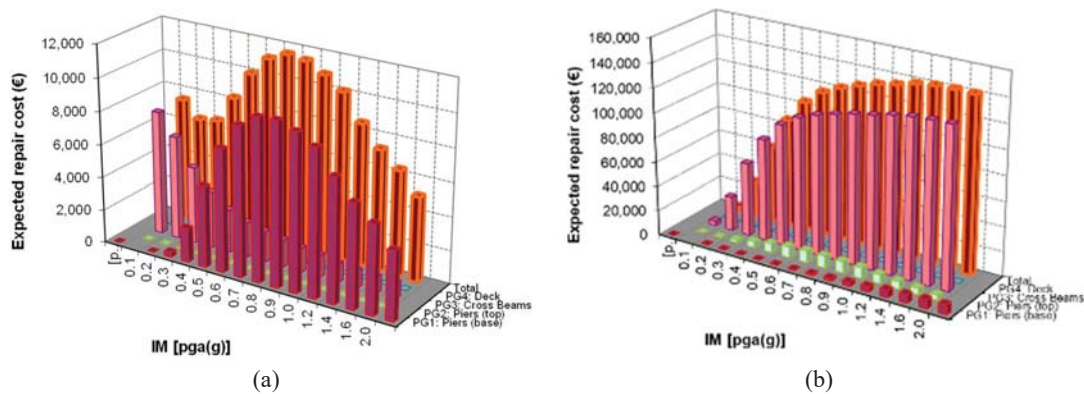


Figure 12. Disaggregation of the expected (a) minor and (b) major scenario repair cost by PG

From these curves it appears that the contribution for the minor damage scenario is mainly from epoxy inject cracks and repairing minor spalls, independently of earthquake intensity. For major damage scenario temporary support of the deck begins to rise rapidly as a contributing cost for higher intensities. It also can be noted that one repair quantity can dominate because several performance groups require that item. Figure 13 shows the probability of occurrence of the selected scenarios.

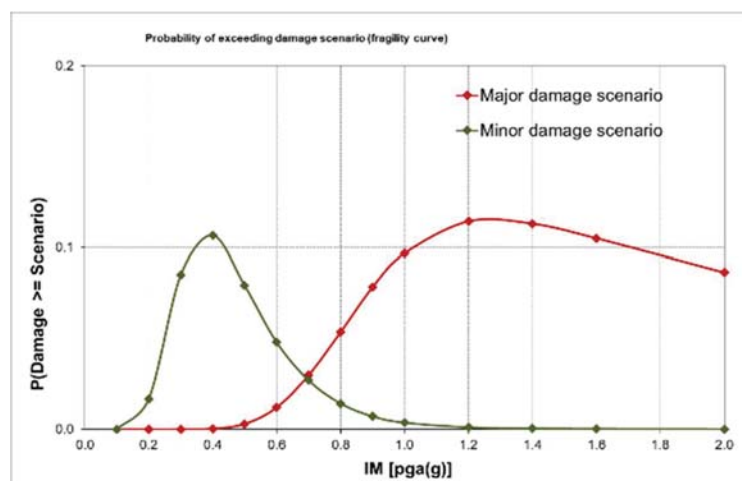


Figure 13. Probability of occurrence of the expected (a) minor and (b) major scenario

From the application of the methodology to the case study the following observations can be drawn:

- Significant probability of occurrence of the minor damage scenario are due to  $0.3g < \text{PGA} < 0.6g$ ;
- Significant probability of occurrence of the major damage scenario are due to  $\text{PGA} > 0.7g$ ;
- An overall expected repair ratio between 5-8% is obtained for the minor damage scenario and  $>20\%$  for  $\text{PGA} > 0.2g$  for major damage scenario;
- PG1, PG2 (pier) and PG3 (CCB) mainly govern the decision-making analysis given that their associated costs results particularly important. Therefore, any optimization action should act on these elements.

## 8 CONCLUSIONS

The SEQBRI project dealt with the full application of the next-generation Performance-Based Earth-quake Engineering methodology (PBEE) employed for the assessment of a new type of steel concrete composite (SSC) bridges endowed with a special pier-to-deck connection (Concrete Cross Beam).

The development of the PBEE framework for SCC bridges can be considered a novel contribution to the foundation of a new generation of earthquake engineering seismic codes for bridges in Europe. The results are novel. In particular, they entail:

- A better understanding of the seismic behaviour of SCC bridges with CCB;
- A reliable definition of limit states for this new type of bridges
- A proposal of a decision-making tool based on next-generation PBEE methodology for SCC bridges with CCB in moderate/strong seismic prone areas.
- A significant improvement of seismic design state-of-the-art of SCC bridges with CCB, through the development of design guidelines for improving Eurocodes for the assessment of bridges in seismic prone areas.

It is evident that the application of this complex framework can be totally justified only when important damage conditions are expected and for which the adoption of non-linear models and probabilistic analyses appear justifiable. Given the fact that small-medium SCC bridges with CCB exhibit in mean important damage conditions only for  $\text{PGA} > 0.25g$ , it appears reasonable to employ the PBEE methodology only for PGA values of  $0.35g$  or greater. These PGA values characterize the most active prone-areas in Europe. For lower PGA values the design approaches to be adopted can rely on current design approaches prescribed by Eurocodes, where partial safety factors cover aleatory uncertainties. In summary, no specific rules are provided by Euro-codes to design CCBs, so, the design procedure pro-posed in the SEQBRI project can be profitable used for this purpose.

## ACKNOWLEDGMENTS

The Present work is supported by the funds of the Euro-pean Project SEQBRI: “Performance-Based Earthquake Engineering Analysis of Short-Medium Span Steel-Concrete Composite Bridges”, Grant N° RFSR-CT-2012-00032. This project has partially received funding from the Italian Ministry of Education, University and Research (MIUR) in the frame of the Departments of Excellence (Grant L. 232/2016).

## REFERENCES

- [1] CEN 1994 2006. “Eurocode 4: Design of composite steel and concrete structures”, Brussels, 2006.
- [2] Porter, K. A. 2000. An Overview of PEER’s Performance-Based Earthquake Engineering Methodology. Ninth International Conference on Applications of Statistics and Probability in Civil Engineering (ICASP9) July 6-9, 2003, San Francisco.
- [3] Paolacci, F., et al., 2017. “Performance-based earthquake engineering analysis of short medium span steel-concrete composite bridges”, Final Report, SEQBRI Project, Contr. No: RFSR-CT-2012-00032, Research Fund for Coal and Steel. ISBN 978-92-79-65612-5, ISSN 1831-9424, DOI:10.2777/48012.
- [4] Lachal, A, Aribert, J.M. 2002. National program MIKTI, Conception de tabliers performants dans le domaine des petites portées. Sujet 1-B: Techniques innovantes de raboutage, Cahier.
- [5] Somja, H., Kaing, S., Lachal, A. 2012. New beam-to-beam joint with concrete embedding for composite bridges Experimental study and finite element modelling *Journal of Constructional Steel Research*, Vol 77, 210–222
- [6] Abbiati G., Cazzador E., Alessandri S., Bursi O.S., Paolacci F., De Santis S. 2018. Experimental characterization and component-based modeling of deck-to-pier connections for composite bridges, *Journal of Constructional Steel Research*, 150, pag. 31-50, DOI: 10.1016/j.jcsr.2018.08.005.
- [7] Paolacci F., Giannini R., Alessandri S., Corritore D., (2018), An experimental investigation on the seismic response of a new pier-to-deck connection for composite short-medium span bridges, submitted to *Journal of Traffic and Transportation Engineering*, Volume 5, Issue 6, December 2018, Pages 439-453, DOI: 10.1016/j.jtte.2018.10.002
- [8] Hanswille, G. 2007. “Composite bridges in Germany – State of the Art“, *Proceedings of 7th German Japanese Bridge Symposium*, Osaka.
- [9] DIN FB 104 2009, DIN-Fachbericht 104 - Verbundbrücken (Composite steel and concrete bridges). Berlin, 2009
- [10] Mazzoni, S., McKenna, F., Scott, M.H., Fenves, G.L. 2009. Open System for Earthquake Engineering Simulation User Command-Language Manual, Pacific Earthquake Engineering Research Center, University of California, Berkeley, May, 2009.
- [11] Gattesco, N., Giuriani E. 1996. “Experimental Study on Stud Shear Connectors Subjected to Cyclic Loading,” vol. 38, no. 1, pp. 1–21, 1996.
- [12] Paolacci, F., Giannini, R., Alessandri, S., Corritore, D. 2018. On the cyclic behaviour of new pier-to-deck connections for short-medium span composite I-girder bridges. *Journal of traffic and transportation engineering*. 2018; 5(6): 439-453.
- [13] CEN 1998-1:2005. Design of Structures for Earthquake Resistance Part 1: General Rules, Seismic Actions and Rules for Buildings. *Comité e Européen de Normalisation: Brussels*, 2005.
- [14] Mackie, K.R., Wong, J.M., Stojadinovic, B. 2008. “Integrated Probabilistic Performance-Based Evaluation of Benchmark Reinforced Concrete Bridges”. *Pacific Earthquake Engineering Research Center*.

- [15] Tubaldi, E., Barbato, M., and Dall'Asta, A. 2010. "Transverse seismic response of continuous steel-concrete composite bridges exhibiting dual load path". *Earthquake and Structures* 1:1, 21-41.
- [16] Vamvatsikos, D., Cornell, C.A. 2002. Incremental dynamic analysis. *Earthquake Engineering and Structural Dynamics* 2002; 31:491–514.
- [17] FEMA 356 2000: Prestandard and Commentary for the Seismic Rehabilitation of Buildings, Prepared by American Society of Civil Engineers, Washington, D.C. (U.S.A.), November.
- [18] Berry, M.P., Eberhard, M. 2003. "Performance models for flexural damage in reinforced concrete columns". *PEER Report*, 2003/18.
- [19] Alessandri, S., Giannini, R. and Paolacci, F. 2013. Aftershock risk assessment and the decision to open traffic on bridges, *Earthquake Engng. Struct. Dyn.*, 42: 2255–2275.

## SEISMIC VULNERABILITY ANALYSIS OF THE HISTORICAL SS FILIPPO E GIACOMO MASONRY ARCH BRIDGE IN ASCOLI PICENO (ITALY)

G. Leoni<sup>1</sup>, F. Gara<sup>2</sup>, and M. Morici<sup>1</sup>

<sup>1</sup> University of Camerino, School of Architecture and Design  
63100 Ascoli Piceno, Italy  
e-mail: {graziano.leoni, michele.morici} @unicam.it

<sup>2</sup> Università Politecnica delle Marche, Department of Construction, Civil Engineering and Architecture  
60131 Ancona, Italy  
f.gara@univpm.it

---

### Abstract

*The bridge was built in 14th century and had undergone very complex vicissitudes related mainly to exceptional floods; it was partially rebuilt twice and other strengthening works were carried out over the time. The bridge, which is almost completely built with travertine blocks, has a total length of 146 m and follows a slightly curved path. Six arches, the main of which is semi-circular with span of 25 m and the others are lancet arches with span of about 8 m, support the carriageway that is about 8 m wide. The piers and abutments are founded on the bedrock and consequently some piers are deeply embedded in the sandy gravel deposit. A 3D numerical Finite Element Model has been developed integrating data available from the geometric survey and calibrating the mechanical parameters starting from experimental tests. The global seismic vulnerability of the bridge has been evaluated comparing the capacity curves of the bridge obtained by means a static nonlinear pushover analysis with the Italian Standard seismic demand. In addition, local vulnerability verifications of spandrel walls have been carried out by means a linear kinematic analysis.*

**Keywords:** Stone Masonry Bridges, Finite Element Models, Vulnerability Analysis, Experimental In-Situ Tests.

---



## 1 INTRODUCTION

The presence of unreinforced masonry arch bridges in the Italian roads networks is very widespread and given that high seismic risk of some areas, it is very important for the public network authorities to evaluate their capacity.

Evaluation of the capacity of a historical masonry structure is a difficult task because of many uncertainties associated with the knowledge of the structure in its current conditions (original structure and structural changes due to repair enlargement and retrofit works, different construction systems and different materials, structural and material degradation and damages, soil and foundation modifications) and also due to modelling techniques complexity as well as to analysis methods. In this sense, after a deep historical analysis and a complete geometrical and structural survey, sophisticated measurement techniques are necessary to catch the real behaviour of the structure, especially the mechanical properties of the structural materials and the global dynamic behaviour.

Regarding the material survey, both traditional techniques and innovative methods are available but non destructive techniques are generally preferred when dealing with historic and valuable structures. Numerous procedures for the evaluation of the mechanical properties of structural materials have been proposed and the mapping of the building evolution or construction details that can be adopted even in cases where retrofitting interventions have been carried out. The dynamic tests, the subsequent structural identification and the updating of a numerical model of the structure to match the experimental results [1-3] is the most widely diffused approach. The experimental modal parameters evaluated starting from the dynamic tests, can then be used to update refined finite element models able to describe the real behaviour of structures, which can be required for structural verifications and for designing repair and retrofit works [4-6].

Regarding the modelling techniques, in the last decades several procedure was developed aimed to predict the behaviour to arch masonry bridges. The difficulty to describe the interaction between the filling material and the resistant masonry arch requires the use of a complex and effective structural model [7]. Generally methodologies, based on Limit Analysis [8-11] and non linear incremental techniques [12-15], are usually refer to bidimensional arches. Improved bidimensional models, which take into account the arch-fill interaction, were also developed [17-18]. In addition, three-dimensional FEM models [18-20] allow both a complete description of the bridge geometry and detailed constitutive models. Regarding the seismic assessment of masonry arch bridges, only a few studies are available today concern the procedure to evaluation of the safety of the bridge [21].

This paper presents the global seismic vulnerability of the SS. Filippo and Giacomo Bridge over the Tronto river at Ascoli Piceno, in the centre of Italy. The bridge was built in the XIV century and was then subjected to many changes for repair, strengthening, retrofit, and enlargement works. This results in a large complexity of the structural organism, due to interaction between parts of different age which are made of materials with different mechanical properties. Due to these uncertainties and considering the importance of the bridge an accurate analysis of its current conditions was deemed essential to obtain a reliable predictive finite element model to be used for the design of seismic retrofit. First of all a historic study and geometric survey of the bridge were developed. For the material properties in-situ tests, both destructive and non-destructive, were carried out, to evaluate the quality of the travertine block masonry. These information were used to develop a refined 3D finite element model that was tuned based on the experimental modal parameters; in particular, the Young's modulus of some materials initially defined according to standard values suggested by codes, was calibrated to fit the dynamic behaviour obtained experimentally. Starting from the calibrated

modal, the capacity curves of the bridge obtained by means a static nonlinear pushover analysis are evaluated considering the elastoplastic materials for the bridge and adopting the yield criterion of Mohr–Coulomb. The capacity is compared with the Italian Standard seismic demand, following the well known “N2 method” included in the European codes [22]. In addition, local vulnerability verifications of spandrel walls have been carried out by means a linear kinematic analysis.

## 2 “SS. FILIPPO AND GIACOMO” BRIDGE

“SS. Filippo and Giacomo” Bridge rises in the outskirts of Ascoli Piceno town crosses the Tronto River, and is built between two rock escarpments one of which is characterized by an important slope (Figure 1).

It has a total length of 146 m and maximum height over 20 m, and it is constituted by six arches. The main arch crosses the river during its regular flow and has a semicircular shape with span of about 25 m. The arch barrel has the minimum thickness of 0.90 m at the crown and increases up to 1.40 m at the imposts. The other five arches are lancet shaped with span of about 8 m. The depth of the fill at the crowns of arches is variable from about 6.0 to 7.5 m. The aspect of the present “SS. Filippo and Giacomo” Bridge derives from a complex sequence of events occurred over almost six hundred years life (Figure 2).



Figure 1: Aerial photogrammetric bridge view.

The former bridge, dating back to the second half of XIV century, was probably constituted by four semicircular arches. It was seriously damaged by a flood occurred in 1453 that produced the collapse of three arches at the right side, the bridge rebuilding started around 1464, rebuilding the collapsed section with lancet arches reducing spans with respect to the original arches.

A second exceptional flood, occurred in 1528, produced the collapse of the main arch survived to the previous event. This was rebuilt starting from 1545 by means of two parallel barrel-vaults: the vault placed downstream, about 3 m wide, has remained almost unchanged; the vault placed up-stream, with variable width, underwent an important vertical settlement (of about 0.4 m) and was finally rebuilt in 1667 by placing wooden and iron ties aimed at tightening together the two parts. In 1721, a new flood produced the collapse of a not well specified wall (probably a wing wall or a part of the abutment at the left riverbank).

A cutwater was realized to protect the main pier in 1794. The two arches sustained by the main pier were restored between 1835 and 1836. At the end of these works, two barrel-vaults

were built instead of reinstating the earth fill at the extrados of the main arch in order to facilitate the maintenance of the structure. The two vaults are sustained by the bridge spandrel walls.

Works to reduce the slope of the upper road were carried out between 1849 and 1850: the spandrel walls were raised placing an earth fill in between after having stabilized the system by means of transverse ties placed at two meters from the old top level. At the same time, the ending bend was modified placing side travertine corbels with variable span up to 1 m in order to widen the carriageway. Such corbels were then connected by brick arches having thickness of 0.30 m. A new order of internal lightening rooms was built over the main arch during this phase; the rooms are spaced as the external pensile arches so that the stone corbels are placed in the walls separating the rooms. Each room is vaulted orthogonally to the lower level previously realized.

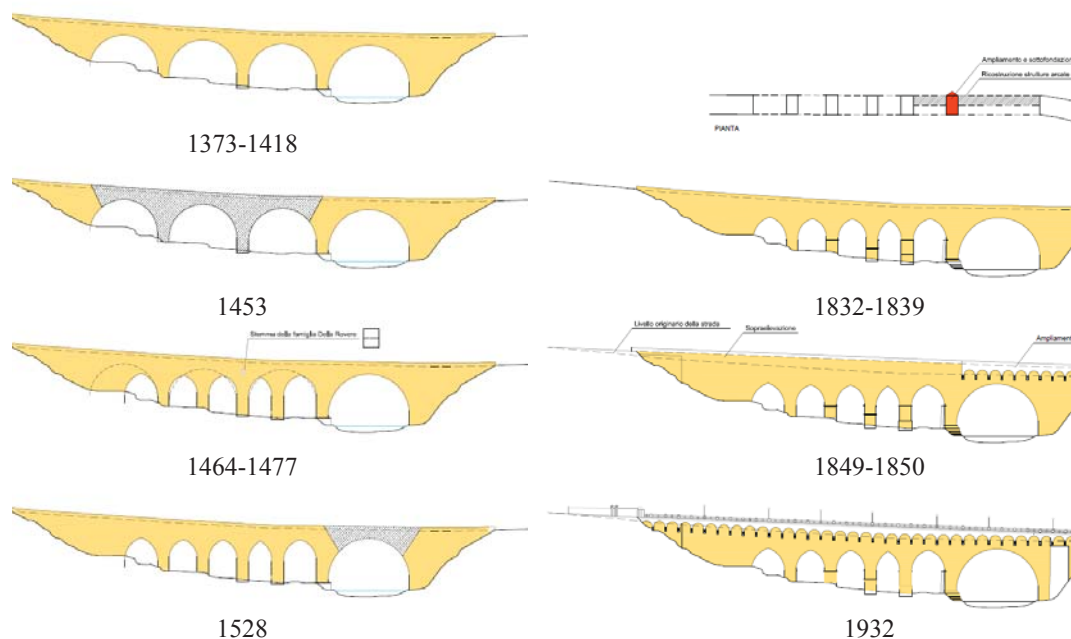


Figure 2: Synopsys of historical vicissitudes.

## 2.1 Current geometrical configuration and crack pattern

The bridge rises between two rock escarpments produced by erosion of Tronto River (Figure 3). The left escarpment has a rather high slope ( $52^\circ$ ) whereas the right one is less sloping ( $31^\circ$ ). The gorge is characterized by a sandy gravel deposit on the right riverbank, with variable thickness up to 10 m, whereas the sandstone bedrock is outcropping at the left riverbank. Investigations carried out in correspondence of piers P1, P2 and P3 demonstrated that foundations are placed at the sandstone bedrock which is horizontal; despite other specific analyses were not carried out for the other piers (P4 and P5) there is no evidence (vertical settlements) that these are founded over the deposit; the sandy gravel deposit is thus placed around the pier but not under the foundation layer.

The bridge exhibits a crack pattern characterized by cracks with vertical orientation located at the mortar joints. Such cracks are located at the base section of piers P1, P2 and P3 (Figure 4) and may be attributed to stress states due to vertical loads associated to the settling of masonry that is widely characterized by deteriorated mortar joints.



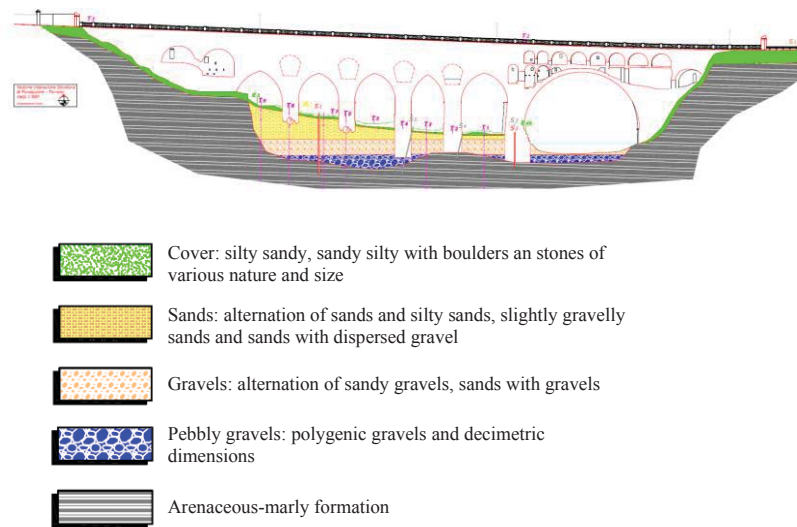


Figure 3: Geological configuration and foundation level.



Figure 4. (a) crack pattern at the bottom of pier P1; (b) cracks of pier P3.

## 2.2 Geometrical and material survey

The range-based survey used to acquire geometrical/metric data was made by means of a 3D-TOF laser scanner technique. Both the external geometry and the geometry of the various internal vaulted rooms over the main arch, at the pier top and at the abutments, were surveyed. Wooden and steel ties, placed to avoid the spandrel wall overturning toward outside were also surveyed in the accessible zones. The acquired data-set was then processed to obtain a refined 3D geometrical model that was later used to generate a structural model with very precise geometry and rigorous mass distributions. Such a kind of survey revealed to be extremely useful in the case under consideration characterized by a very complex geometry.

## 3 TESTS ON MATERIALS

Materials were characterized by onsite tests namely two tests with single flat jacks and one test with double flat jacks. Three compression tests on travertine speci-mens sampled by means of masonry coring were also executed. Sampling and test locations are reported in Figure 5.

Masonry coring permitted to observe that the pier structure is characterized by an external curtain, having variable thickness and realized with Ascoli Piceno travertine squared blocks, and an important inter-nal, rather irregular, rubble stone infill characterized by the presence of water in the lower parts.

Compressive tests carried out on the three specimens gave scattered results with minimum strength  $16.9 \text{ N/mm}^2$ . The double flat jack test carried out at the base of pier P2 provided a linear behavior in the stress range investigated (up to about  $4 \text{ N/mm}^2$ ), characterized by Young's modulus of about  $6600 \text{ N/mm}^2$ . Single flat jack tests carried out at the base of piers P1 and P2 permitted the estimation of the stress state in the external masonry curtains. For pier P1 the stress state obtained is higher than for pier P2, as expected; in particular the normal vertical stress in P1 is about  $1.3 \text{ N/mm}^2$  while for pier P2 it is about  $0.5 \text{ N/mm}^2$ .

For what concerns the masonry of the interior vaulted rooms, tests were not carried out because from the inspection and the laser scanner survey it was evident that it is a good brick masonry. Never-theless, it is worth noticing that such components are not expected to give a significant contribution to the overall behavior of the structure excepting for the mass.

The two kinds of masonry constituting the bridge structure can be classified according to catalogs re-reported in design guidelines and standards. Italian Standards [23-24] provide the mechanical characteristic reported in Table 1.

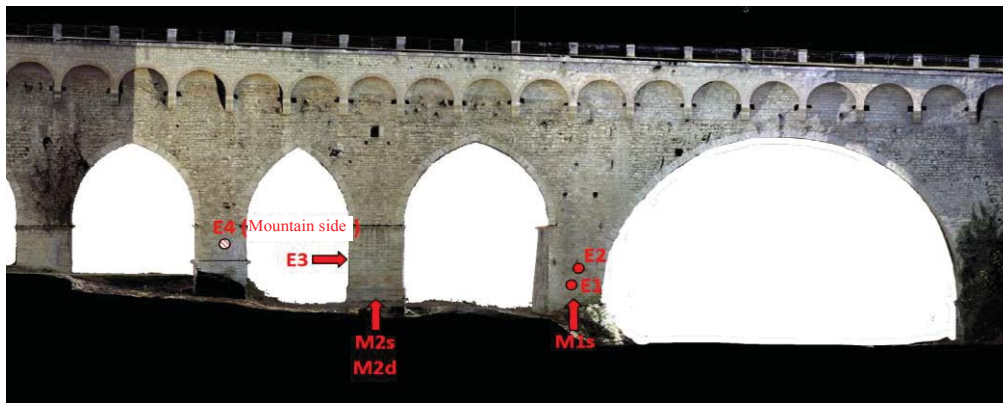


Figure 5. Location of sampling and onsite tests

Masonry	E ( $\text{N/mm}^2$ )	G ( $\text{N/mm}^2$ )	w ( $\text{kN/m}^3$ )
Curtains of stone squared blocks with poor core	1680 2240	546 658	22
Bricks with lime mortar	1200 1800	400 600	18

Table 1. Mechanical characteristics deriving from on-site tests

In addition the modal parameters of the bridge, i.e. natural frequencies, damping ratios and mode shapes, are experimentally estimated by means of operational modal analysis starting from the accelerations of the deck recorded during ambient vibration measurements which are mainly due to traffic, wind and microtremors. Results obtained from this test was adopted to calibrate the elastic value of the materials used in the model.



#### 4 STRUCTURAL MODEL OF THE BRIDGE

The 3D Finite Element Model (FEM) intended for the structural analyses is developed in Straus7 [25] starting from the data available from the laser scanner survey. In order to avoid excessive refinement of the mesh due to details that do not actually affect the overall behavior of the bridge, the geometry was simplified. Part of the soil portion in the riverbed at the base of internal piers was included in the model, to take into account the particular geological formation and capture the soil-pier interaction phenomena. In addition, all internal rooms and the earth fill was considered in the model to capture the real stiffness and mass distribution in the structure (Figure 6a).

The finite element model is obtained with a mesh of 4-node tetrahedral elements with linear interpolation shape functions (Tetra4). The mesh is generated by importing a closed poly-surface constructed by approximating the geometry obtained with the laser scanner survey. Based on previous consideration, the geometry was simplified imposing the maximum length of the element edge of 1.0 m for the bridge structure, whereas it was increased up to 4.5 m for the elements belonging to the soil deposit (Figure 6b). Fixity restraints are placed at the deposit base and at the structure sections interacting with the sand stone formation. All the materials, including earth fills and the soil deposit, are considered to be linear elastic and isotropic.

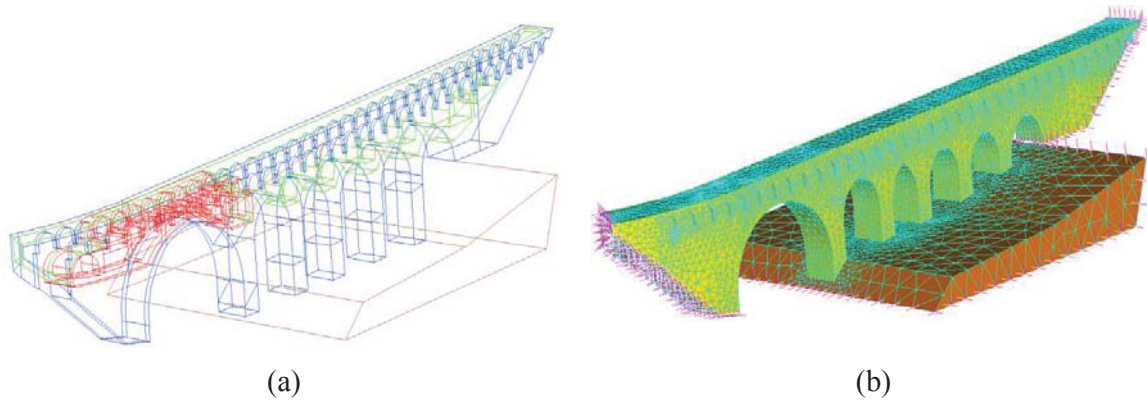


Figure 6. (a) Geometrical model; (b) Finite element model.

The mechanical parameters of the finite element model were assumed elastic-plastic, considering the yield criterion of Mohr–Coulomb. Regarding the initial condition, elastic parameters are calibrated by fitting the experimental modal parameters with numerical ones relevant to the finite element model previously discussed. Regarding the soil parameters, they are derived from geotechnical in situ tests, while the infill materials are hypothesized based on construction techniques.

Materials	E (N/mm <sup>2</sup> )	G (N/mm <sup>2</sup> )	w (kN/m <sup>3</sup> )	c (N/mm <sup>2</sup> )	φ [°]
Travertine masonry	7000	2414	22	0.256	76.0
Brick masonry	1282	427	18	0.214	72.0
Earth infill material	666	238	18	0.010	42.5
Base soil deposit	666	243	19	0.010	32.0

Table 4. Mechanical parameters considered in the analyses

## 5 SEISMIC DEMAND

The area where the bridge is located falls within an area of medium seismic hazard. According to the seismic Italian Standard Code [23-24], in Figure 7a is reported the seismic hazard curve at the arch bridge site in terms of Peak Ground Acceleration (PGA)  $a_g$ , varying the return period  $T_R$ . Considering the  $T_R$  equal to 475 years, the PGA assume the value of  $a_g = 0.178g$ . For the site effect, a subsoil category B been assumed for the subsoil condition and category  $T_2$  regarding the topographic condition. In Figure 7b is reported the corresponding elastic response spectrum considering for the site considered in the following analyses.

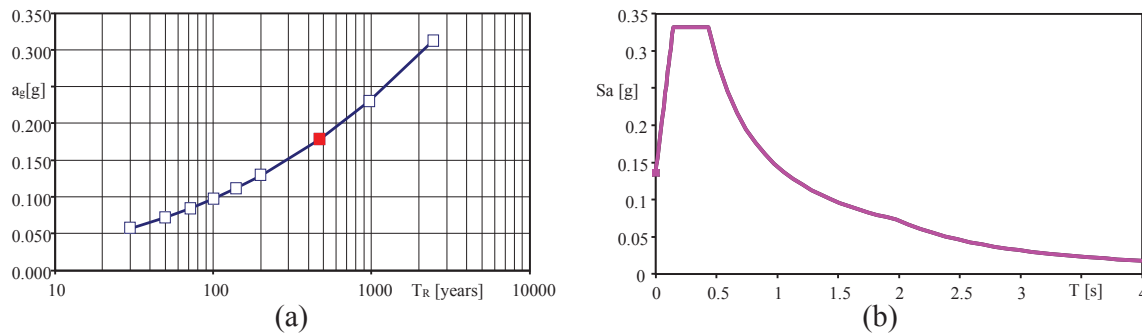


Figure 7. (a) Seismic hazard curve at the arch bridge site; (b) Elastic response spectrum

## 6 EVALUATIO OF THE SEISMIC CAPACITY

### 6.1 Non linear static analysis

The assessment of the capacity of the masonry arch bridge is evaluated following the methods included in the European codes, based on the N2 method [26], that combines the non-linear static analysis of the multi-degree of freedom model with the response spectrum analysis of an equivalent single degree of freedom system.

Capacity analyses is performed by applying two different distributions of the lateral loads: a “modal” pattern (which will be hereafter referred to as “mode 1”) corresponding to a distribution of the acceleration proportional to the 1<sup>st</sup> modal shape; a “uniform” pattern, based on lateral forces proportional to mass regardless of elevation (uniform response acceleration).

During the loading process, the transversal displacement of the control point located in the position of maximum modal deformation is monitored, in order to trace the pushover curve in terms of the equivalent lateral load. Afterwards, the pushover curve is transformed into a simplified bilinear force-displacement relationship for an equivalent inelastic SDOF system, based on the equivalence of energy between two systems. Results relevant to SDOF system is reported in the plane Acceleration-Displacement Response Spectra (ADRS) and evaluating the inelastic spectrum for the return period  $T_R^*$  consistent with the capacity of the equivalent SDOF (condition of equal displacement).

Figures 10a-b and Figures 11a-b reports the stresses of the component ZZ and XX respectively considering the distribution of lateral loads proportional to 1<sup>st</sup> modal shape at the end of analysis in positive/negative Y direction.

Figures 12a-b and Figures 13a-b reports the stresses of the component ZZ and XX respectively considering the distribution of lateral loads proportional to mass regardless of elevation at the end of analysis in positive/negative Y direction.

Figures 10c-Figures 13c shows the equivalent SDOF evaluated starting from the non-linear pushover analyses, and Figures 10d-Figures 13d shows the verifications in verification in ADRS plane.

Finally, Table 5 summarise the Index Risk ( $I_R$ ) evaluated by the expression [27]:

$$I_R = \frac{T_R}{T_R^*} \quad (1)$$

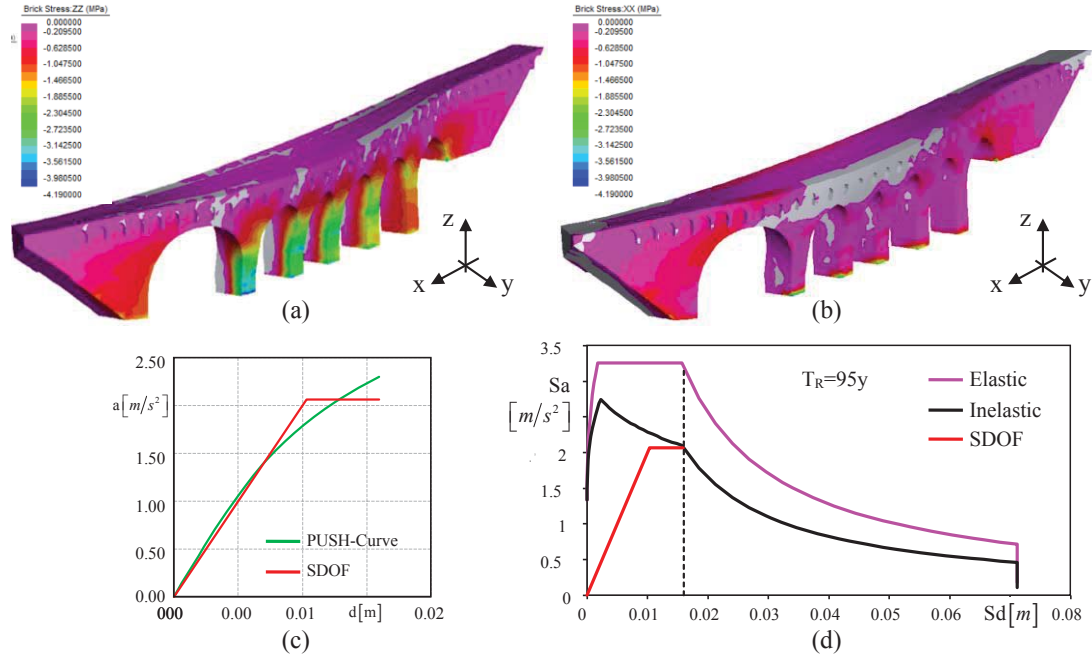


Figure 8. Pushover analysis considering lateral load proportional to 1<sup>st</sup> modal shape (Y+ direction): (a) ZZ stresses components at the maximum displacements; (b) XX stresses components at the maximum displacements; (c) bilinear equivalent SDOF; (d) verification in ADRS plane.

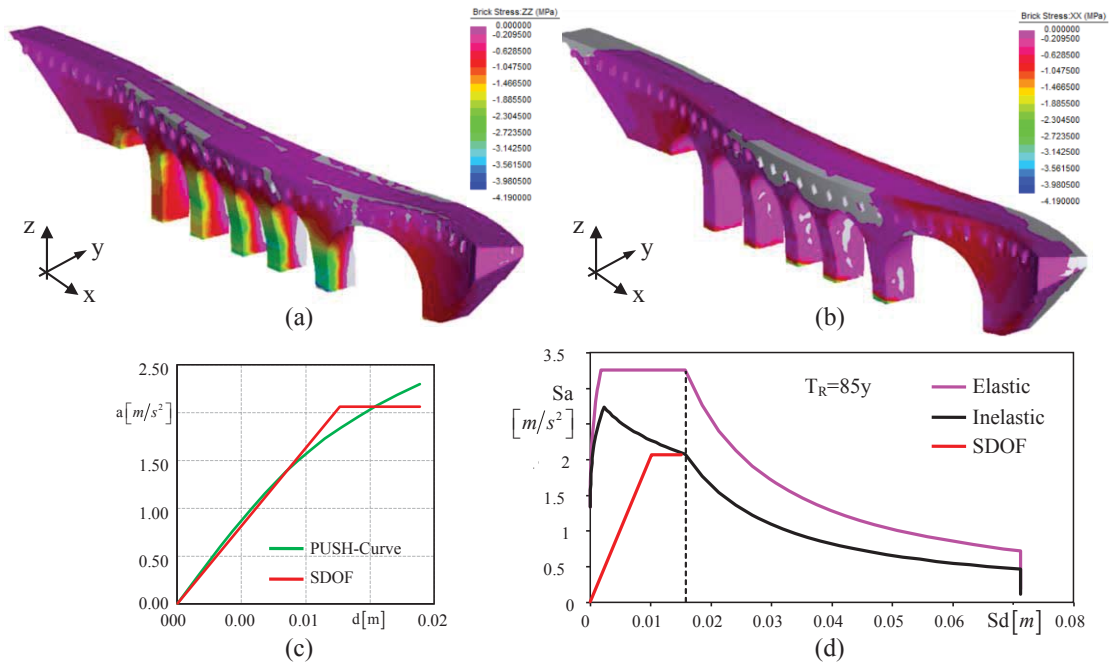


Figure 9. Pushover analysis considering lateral load proportional to 1<sup>st</sup> modal shape (Y- direction): (a) ZZ stress-components at the maximum displacements; (b) XX stresses components at the maximum displacements; (c) bilinear equivalent SDOF; (d) verification in ADRS plane.

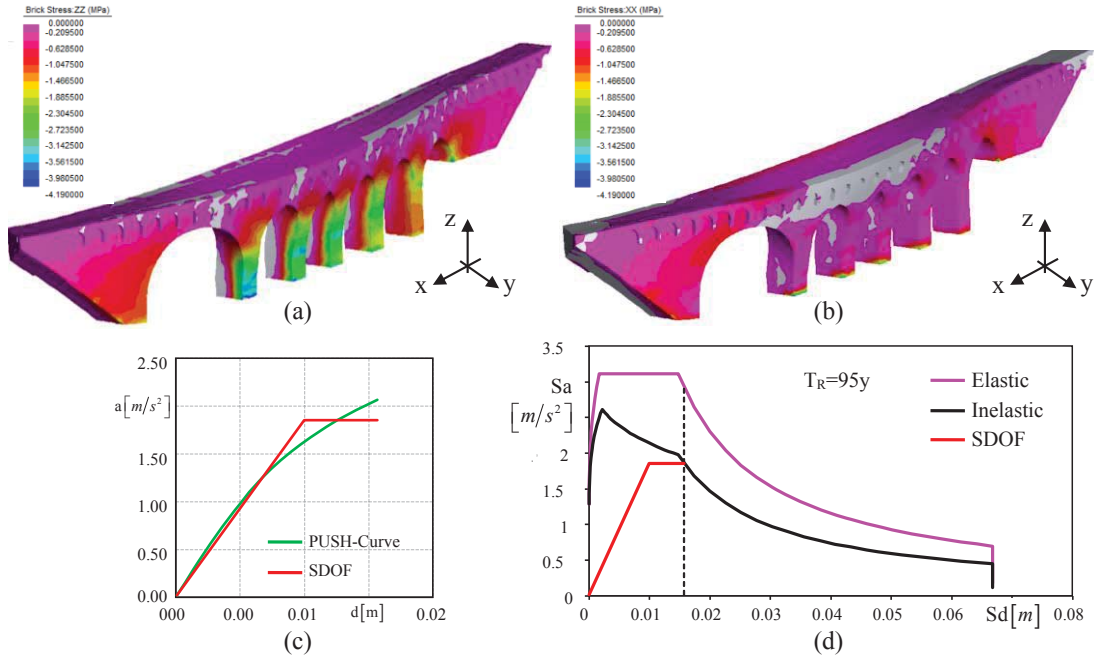


Figure 10. Pushover analysis considering lateral load proportional to masses distribution (Y+ direction): (a) ZZ stresses components at the maximum displacements; (b) XX stresses components at the maximum displacements; (c) bilinear equivalent SDOF; (d) verification in ADRS plane.

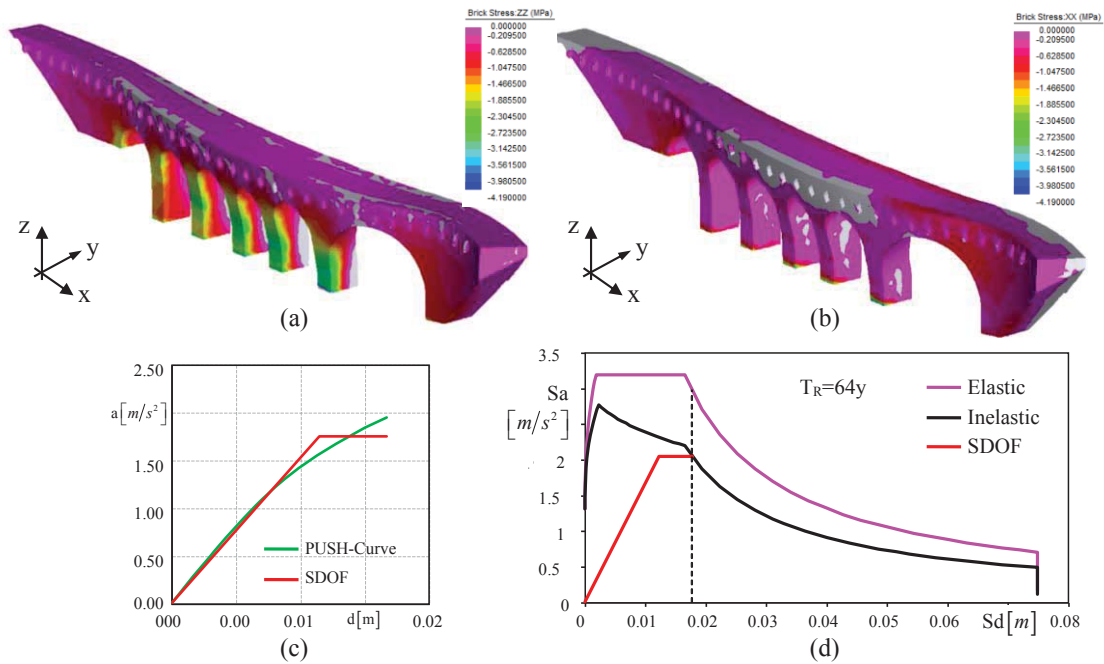


Figure 11. Pushover analysis considering lateral load proportional to masses distribution (Y- direction): (a) ZZ stresses components at the maximum displacements; (b) XX stresses components at the maximum displacements; (c) bilinear equivalent SDOF; (d) verification in ADRS plane.

Analysis	$I_R$
MODE Y+	0.20
MODE Y-	0.20
MASS Y+	0.18
MASS Y-	0.13

Table 3. Index Risk

## 6.2 Local analysis

The main local vulnerabilities consist in the overturning of the bridge tympanum characterized by the presence of earth filling, in the portion of the bridge above the secondary arches. Assuming the inefficiency of a head connection of the bridge tympanum, the possibility of overturning of the single wall or single hanging arch is expected; it is assumed that the tie added on the occasion of the raising of the bridge are efficient and that therefore the overturning takes place at the tax rate of the arches.

The assessment of local vulnerability is conducted by means of a linear kinematic analysis with reference to the bridge segment between the axes of two consecutive arches placed in correspondence with the third arch (Figure 14a).

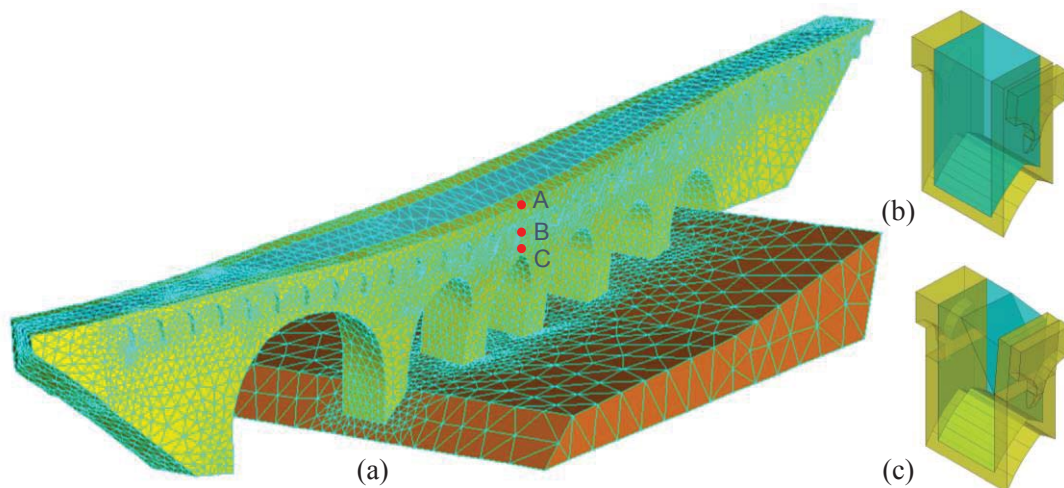


Figure 12. Comparison between experimental and theoretical vibration modes

Figure 14b reported the mechanism single hanging arch, while Figure 14c reported the mechanism relevant to the formation of an active thrust wedge of the infilling material. Regarding the first mechanism the risk index assumed the value  $I_R = 0.08$ , while for the second mechanism  $I_R = 0.09$ . In both evaluations, the seismic demand is evaluated considering the seismic action corresponding the first period of vibration and behaviour factor equal 2.

## 7 CONCLUSIONS

The assessment of the seismic vulnerability of a historical masonry bridge, characterized by an unusual geometry deriving by very complex historical vicissitudes, has been presented. The capacity is compared with the with the Italian Standard seismic demand, following the well-known “N2 method”; furthermore, local vulnerability verifications of spandrel walls have been carried out by means a linear kinematic analysis.



The bridge rises in a gorge and is founded on a sand-stone deposit that is outcropping at the abutments. The bridge is constituted by six different arches whose piers are founded on the sand-stone formation and are embedded for significant sections (up to 10 m) into the fluvial deposit constituted by sandy-gravel soil.

A laser scanner survey was crucial to obtain a model encompassing all main features of the real structure such as the inner lightening rooms, with very irregular geometry, as well as the pensile arches constructed to enlarge the carriageway.

The onsite tests permitted to evaluate the main mechanical characteristics of the materials and to estimate the stress state in critical sections of the piers.

The operational modal analysis, used to detect the dynamic behavior of the bridge, was decisive for tuning a finite element model capable of predicting the overall behavior of the bridge, and adopted to evaluate the seismic capacity of the arch bridge.

## REFERENCES

- [1] C. Gentile, A. Saisi. Operational modal testing of historic structures at different levels of excitation. *Constr Build Mater* 48:1273–1285, 2013.
- [2] C. Costa, D. Ribeiro, P. Jorge, R. Silva, A. Arêde, R. Calçada. Calibration of the numerical model of a stone masonry railway bridge based on experimentally identified modal parameters. *Engineering Structures* 123, 354–371, 2016.
- [3] S. Gonen, S. Soyoz. Dynamic Identification of Masonry Arch Bridges Using Multiple Methodologies. In: Epp D.S. (eds) *Special Topics in Structural Dynamics & Experimental Techniques*, Volume 5. Conference Proceedings of the Society for Experimental Mechanics Series. Springer, Cham., 2021.
- [4] A. De Sortis, E. Antonacci, F. Vestroni. Dynamic identification of a masonry building using forced vibration tests. *Eng Struct*, 27(2): 155-165, 2005.
- [5] H. Ahmadian, G.M. Gladwell, F. Ismail. Finite element model identification using modal data. *J Sound Vib*, 172(5): 657-669, 1994.
- [6] J.E. Mottershead, M.I. Friswell. Model updating in structural dynamics: a survey. *J Sound Vib*, 167(2): 347-375, 1993.
- [7] B. Conde, L. Díaz-Vilariño, S. Lagüela, P. Arias. Structural analysis of Monforte de Lemos masonry arch bridge considering the influence of the geometry of the arches and fill material on the collapse load estimation. *Construction and Building Materials* 120, 630–642, 2016.
- [8] J. Heyman. *The masonry arch*. Chichester: Ellis Horwood; 1982.
- [9] M. Gilbert, C. Melbourne. Rigid-block analysis to masonry arches. *Structural Engineering*; 72: 356–361, 1994.
- [10] TG. Hughes, MJ. Blackler. A review of the UK masonry assessment methods. *Proceedings of the Institution of Civil Engineers*, 110: 373–382, 1995.
- [11] Boothby T. Collapse modes of masonry arch bridges. *Journal of the British Masonry Society*. 9 (2): 62–69, 1995.

- [12] C. Molins, P. Roca. Capacity of masonry arches and spatial frames. *J Struct Eng*, 124: 653–663, 1988.
- [13] A. Brencich, U. De Francesco. Assessment of multi-span masonry Arch bridges. Part I: a simplified approach, Part II: examples and applications. *J Bridge Eng ASCE*, 9 (November): 582–598, 2004.
- [14] A. Audenaert, P. Fanning, L. Sobczak, H. Peremans. 2-D analysis of arch bridges using an elasto-plastic material model. *Engineering Structure*; 30: 845–855, 2008.
- [15] A. Thavalingam, N. Bicanic, J.I. Robinson, D.A. Ponniah. Computational framework for discontinuous modelling of masonry arch bridges. *Computers and structures*, 79: 1821–1830, 2001.
- [16] A. Cavicchi, L. Gambarotta. Collapse analysis of masonry bridges taking into account arch–fill interaction. *Engineering Structures*, 27: 605–615, 2005.
- [17] A. Cavicchi, L. Gambarotta. Lower bound limit analysis of masonry bridges including arch–fill interaction. *Engineering Structures*, 29: 3002–3014, 2007.
- [18] M.E. Stavroulaki, B. Riveiro, G.A. Drosopoulos, M. Solla, P. Koutsianitis, G.E. Stavroulakis. Modelling and strength evaluation of masonry bridges using terrestrial photogrammetry and finite elements. *Advances in Engineering Software* 101, 136–148, 2016. <https://doi.org/10.1016/j.advengsoft.2015.12.007>
- [19] P.J., Fanning, T.E. Boothby. Three-dimensional modelling and full-scale testing of stone arch bridges. *Journal of Computers and Structures* 2001; 79 (29–30):2645–2662.
- [20] F. Scozzese, L. Ragni, E. Tubaldi, F. Gara. Modal properties variation and collapse assessment of masonry arch bridges under scour action. *Engineering Structures* 199, 15 November 2019, 109665, 2019.
- [21] S. Gönen, S. Soyöz. Seismic analysis of a masonry arch bridge using multiple methodologies. *Engineering Structures* 226, 1 January 2021, 111354, 2021.
- [22] Eurocode 8: Design of structures for earthquake resistance- part 1: General rules, seismic actions and rules for buildings.
- [23] *Norme tecniche per le costruzioni*. D.M. Ministero Infrastrutture e Trasporti 2018, Supplemento ordinario alla “Gazzetta Ufficiale n. 42 del 20 febbraio 2018 - Serie generale (In italian), 2018
- [24] *Istruzioni per l'applicazione delle Nuove norme tecniche per le costruzioni di cui al decreto ministeriale 14 gennaio 2018*. Ministero delle Infrastrutture e dei Trasporti e Consiglio Superiore dei Lavori Pubblici, Circolare 21 gennaio 2019, n. 7. *Gazzetta Ufficiale* n. 35 del 11 febbraio 2019 - supplemento ordinario n. 5 (in Italian), 2019.
- [25] Straus7, G+D Computing Pty Limited, <http://www.straus7.com>
- [26] P. Fajfar, A nonlinear analysis method for performance-based seismic design, *Earthquake Spectra* 16 (3) 573–592), 2000.
- [27] *Valutazione e riduzione del rischio sismico del patrimonio culturale con riferimento alle NTC 14 gennaio 2008*. DPCM 9 febbraio 2011, G.U.R.I., Roma, Italy (in Italian), 2011.

## ROC-BASED PERFORMANCE EVALUATION OF DATA CLEANSING TECHNIQUES FOR FALSE ALARM RISK REDUCTION IN CONTINUOUSLY MONITORED BRIDGES

Valentina Giglioni<sup>1</sup>, Enrique García-Macías<sup>2</sup>, Ilaria Venanzi<sup>2</sup>, Laura Ierimonti<sup>2</sup> and Filippo Ubertini<sup>2</sup>

<sup>1</sup>Department of Civil and Environmental Engineering, University of Perugia. Via G. Duranti 93, Perugia - 06125, Italy.  
e-mail: valentina.giglioni1@studenti.unipg.it

<sup>2</sup> Department of Civil and Environmental Engineering, University of Perugia. Via G. Duranti 93, Perugia - 06125, Italy.  
e-mail: {enrique.garciamacias, ilaria.venanzi, laura.ierimonti, filippo.ubertini}@unipg.it

**Keywords:** Bridge monitoring, ROC curves, Structural Health Monitoring, Data cleansing, False alarm.

**Abstract.** *Maintenance and prevention of roadway bridges is an important societal and economic challenge where structural health monitoring systems can play a major role. The main reason lies in the significant number of ageing infrastructures requiring a strategy to evaluate their structural integrity and durability as well as to enable structural prognosis. In the context of unsupervised learning processes, damage detection can be accomplished by tracking deviations of dynamic parameters from their normal conditions using specific tools, named control charts. However, the main drawback of dealing with changes in modal properties is represented by their high sensitivity to environmental and operational factors. It follows that these effects must be necessarily removed to obtain suitable damage sensitive features. In this regard, the selection of a particular statistical model for data cleansing inevitably influences the distribution of the residuals, the control chart and therefore the damage detection. To overcome this issue, in the present paper an original methodology is developed, based on Receiving Operating Characteristic (ROC) curves, which provides a new decision-support tool for the definition of the best environmental effects' removal technique. Residuals stemming from the application of different data cleansing methods, plotted in control charts are conceivably distinguished in False Positives, True Positives, False Negatives and True Negatives. Consequently, ROC curves are computed and compared, each one referred to a particular data cleansing procedure, among which Principal Component Analysis, Multiple Linear Regression and more and to a specific damage class. The proposed approach is applied in the illustrative case study of the Z24 Bridge, located in the canton Bern near Solothurn, Switzerland. The results of the application of the procedure demonstrated that ROC curves are a suitable tool for defining the optimal damage threshold and the most effective environmental effects' removal technique, in order to minimize the occurrence of false alarms.*

## 1 INTRODUCTION

Structural Health Monitoring (SHM) has become increasingly popular in the field of Civil Engineering. The main reason lies in the necessity to better manage the significant number of ageing structures and infrastructures. In particular, bridges represent critical elements in modern transport networks, hence the importance to develop strategies ensuring their safety as well as correct prevention [1]. Within this context, long-term vibration-based SHM systems represent a suitable solution [2]. Such methods provide modal parameters' estimate by exploiting OMA analysis and allow to identify damage-induced anomalies through statistical pattern recognition techniques.

However, a major challenge in application of SHM systems to civil structures and infrastructures is represented by the high sensitivity of dynamic properties to environmental and operational conditions [3]. For this reason, in order to minimize the significant risk of masking early stage damages, several techniques to remove environmental effects from monitoring data are continuously being developed in the SHM community. The basic idea is to create a proper statistical model able to reproduce the part of variance in frequency estimates that is associated with changes in environmental conditions. To this aim, common statistical tools such as Multiple Linear Regression (MLR) [3, 4] and Principal Component Analysis (PCA) [5] are broadly investigated in the literature.

Once a proper statistical model is selected, it is possible to compute quantities, called residuals, that are only minimally affected by environmental effects and therefore suitable to be used as damage-sensitive features [6]. In this framework, Novelty Analysis through control charts [7] represents a common statistical process control tool useful to identify the beginning of a damage mechanism. In particular, proper statistical distances between newly acquired data and a baseline population allow to detect any outlier consistently overpassing a fixed threshold. As a consequence, it is clear that the definition of the threshold in the classification (damage or non-damaged) represents one of the major issues, inevitably producing erroneous predictions as False Positives and False Negatives.

Therefore, with the aim to minimize the rate of damage detection errors in view of an effective monitoring, a strategy to select, for the specific case study, the most appropriate technique to remove environmental effects is highly required. Such purpose is accomplished in this paper by proposing a new decision-support tool to optimally solve the statistical model selection problem, which heavily affects the distribution of the residuals and hence, damage detection. The new methodology described in the present work is based on the use of ROC [8] curves as performance metrics, aiming at providing a quantification of damage classification errors. Despite the popularity of ROC in several application fields [9], their use for optimal statistical pattern recognition within the context of damage detection, is still lacking.

In order to bridge this research gap, the basic idea of this paper is to supply objective criteria allowing to define (i) which data cleansing technique would ensure the best damage identification and (ii) which cut-off value minimizes the number of false positives and false negatives.

Preliminarily, residuals are calculated and plotted in different control charts. Then, several ROC curves, each one referred to a particular statistical model and to a specific damage scenario, are computed and afterwards assessed by measuring the entire two-dimensional area underneath the curve (AUC). Hence, this strategy can be formulated as an optimization problem, aiming at selecting the curve with the higher AUC, which corresponds to the most suitable model for data cleansing purposes.

## 2 BACKGROUND

In order to discern damage-induced changes in the natural frequencies time-histories, several tools have been recently used to remove environmental and operational effects. This section briefly presents an overview on MLR, PCA and the Gaussian Mixture Model (GMM) and provides a description of the basic theory of Novelty Analysis, commonly utilized to detect the occurrence of damage by means of proper statistical distances.

### 2.1 Statistical models handling environmental and operational effects

Multiple Linear Regression (MLR) exploits linear correlations between one or more dependent variables, called estimators and a group of independent variables, defined as predictors. In this case, dependent variables are natural frequencies, while independent variables are typically environmental and operational factors. The linear statistical model should be able to study the influence of each predictor on the dependent variables and then, to predict future values of the natural frequencies when only the predictors are known [4].

Another well-established methodology, the Principal Component Analysis, has the primary purpose to reduce the dimensionality of a data set without producing significant losses of data variance. It consists in transforming a set of observations of possibly correlated variables into a group of uncorrelated variables, called principal components (PCs). Firstly, the original data are projected into the vectorial space generated by the PCs. Then, according to this approach, a subset of those PCs providing the largest contributions to the variance of the original data can be retained and assumed representative of the environmental and operational factors. As a result, it is possible to estimate natural frequencies by moving back the reduced subset of PCs onto the original space [5, 6].

In order to handle non-linear environmental/operational effects, Gaussian Mixture Model (GMM) represents an efficient tool, which is based on grouping damage sensitive features (e.g. natural frequencies) in the training period into different clusters. Considering that the data set in the training period is non-normally distributed, this approach consists in introducing  $K$  clusters, described by Gaussian distributions, and assuming a linear superposition of them equal to the probability density function of the data set in the training period [10, 11]. Once the  $K$  clusters have been defined, new acquired data can be assigned to the cluster with minimal Mahalanobis distance.

### 2.2 Novelty analysis

The selection of the proper statistical model, successful in reproducing environmental effects on dynamic signatures, allows to compute the residual error matrix  $\mathbf{E}$  as:

$$\mathbf{E} = \mathbf{Y} - \hat{\mathbf{Y}} \quad (1)$$

which contains quantities that are minimally affected by environmental factors and therefore assumed as damage sensitive features. It follows that any damage pattern can be inferred by observing anomalies in the distribution of  $\mathbf{E}$ .

To this aim, Novelty Analysis through the use of control charts represents a statistical tool able to associate significant deviations of natural frequencies from normal conditions, in terms of statistical outliers, with the occurrence of damage. Firstly, it is necessary to define a reference condition, containing data sets collected in a training period, in which the structure is assumed to remain healthy. Consequently, any new data point is compared with such baseline population by means of properly defined statistical distances. In this framework, the  $T^2$ -statistic is adopted,



defined as:

$$T^2 = r \cdot (\bar{\mathbf{E}} - \bar{\bar{\mathbf{E}}})^T \cdot \Sigma^{-1} \cdot (\bar{\mathbf{E}} - \bar{\bar{\mathbf{E}}}) \quad (2)$$

where  $r$  is an integer parameter referred to as subgroup size,  $\bar{\mathbf{E}}$  is the mean of the residuals computed in the subgroup of the last  $r$  observations, while  $\bar{\bar{\mathbf{E}}}$  and  $\Sigma$  are the mean value and the covariance matrix of the residuals statistically estimated in the training period, respectively. Once several values of the statistical distance steadily overcome the Upper Control Limit (UCL), a change in the distribution of the residuals may have been occurred. Therefore, damage-induced anomalies not encountered in the training period are conceivably identified. In this context, the limit threshold (UCL) is computed as a certain percentage of the standard deviation of the control chart in the training period.

### 3 METHODOLOGY

#### 3.1 ROC curves

A Receiver Operating Characteristic (ROC) curve represents a graphical tool which allows to quantify the performance of a process, varying the threshold position, and to statistically evaluate the erroneous predictions related to false detection.

Firstly, it is necessary to illustrate all the possible outcomes provided by the control chart (Fig. 1 a)):

- True Negative (TN): the data set point before damage lying under the UCL;
- False Positive (FP): the data set point before damage lying above the UCL;
- False Negative (FN): the data set point after damage lying under the UCL;
- True Positive (TP): the data set point after damage lying above the UCL;

The confusion matrix  $C$  can be constructed starting from the knowledge of TP, FP, TN and FN:

$$C = \begin{bmatrix} \text{TP} & \text{FP} \\ \text{FN} & \text{TN} \end{bmatrix}; \quad (3)$$

In order to characterize a ROC curve, some statistical measures, evaluating the performance of a binary classification test, are introduced hereafter.

The true positive rate TPr defines how many correct positive results occur among all positive samples. It is also known as *sensitivity* (SE) or *probability of detection*:

$$\text{TPr} = \frac{\text{TP}}{\text{TP} + \text{FN}} = \frac{\text{True Positives}}{\text{All positive cases}} \quad (4)$$

The false positive rate FPr, or *probability of false alarms*, counts how many incorrect positive results occur among all negative samples:

$$\text{FPr} = \frac{\text{FP}}{\text{FP} + \text{TN}} = 1 - \text{SP} = \frac{\text{False Positives}}{\text{All negative cases}} \quad (5)$$

where SP, called as *specificity* or true negative rate, describes how many correct negative results occur among all negatives samples.

A ROC curve plots the true positive rate (TPr) against false positive rate (FPr) at various classification thresholds. The basic theory is that a very low threshold produces 100% of false and true positives, classifying all the items as positive. On the contrary, a very high threshold could never indicate damage, resulting in 0% of false and true positives. It is important to highlight that the model's accuracy increases when the curve comes closer to the upper-left-hand corner of the ROC space and decreases, vice versa, when the curve comes closer to the 45° diagonal (Fig. 1 b).

The performance of a ROC curve is commonly evaluated by computing the Area Under the Curve (AUC), indicated in Fig. 1 c). Considering normalized units, AUC values go from 0 to 1. It is worth pointing out that this parameter is equivalent to the probability that a classifier will rank a randomly chosen positive instance higher than a randomly chosen negative one [8]. It can be defined as follows:

$$AUC = \int_0^1 ROC(f)df \quad (6)$$

where  $f$  and  $ROC(f)$  indicate, respectively, the false positive rate (FPr) and the corresponding true positive rate (TPr).

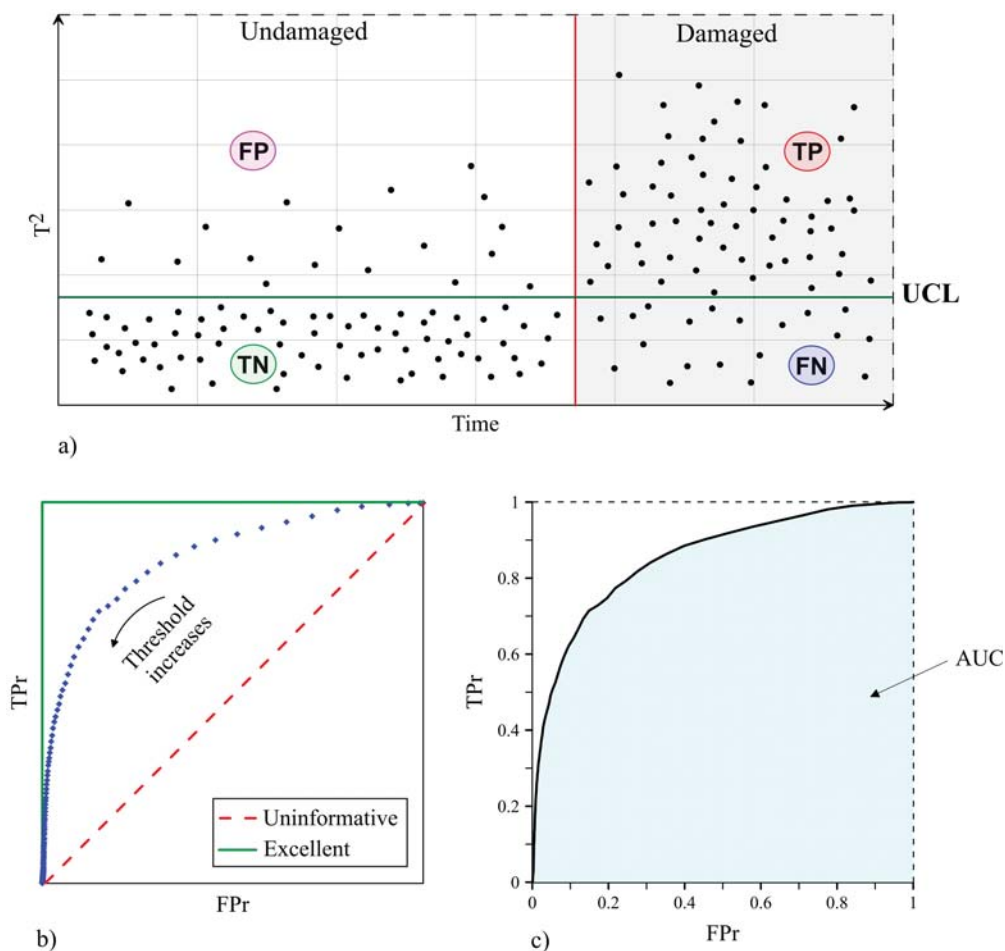


Figure 1: a) control chart items' classification: True Positive (TP), False Positive (FP), True Negative (TN) and False Negative (FN); b) different typologies of ROC curves; c) definition of AUC.

### 3.2 Selection of the best data cleansing technique

The methodology for selecting the best data cleansing technique is provided in Fig. 2 a). Preliminarily,  $m$  statistical models and  $d$  damage scenarios (real or simulated) are taken into account, with the purpose to evaluate and compare models' performance, varying the type of damage.

It is interesting to point out that damage data are rarely available in the field of civil engineering. Therefore, the use of suitable virtual models to simulate different damage scenarios becomes necessary. In these cases, damage-induced variations of modal properties predicted by the structural model can be artificially introduced into the monitoring data through constant shifts in the time series of identified modal frequencies.

By applying Eq. (1), residuals can be computed and then plotted in  $(m \times d)$  control charts. As a result, by counting the data set points belonging to each class, labelled as FP, TP, FN and TN,  $(m \times d)$  ROC curves are obtained, varying the classification threshold. Each curve is referred to a particular statistical model (or data cleansing technique), and to a specific damage scenario. In order to conceivably evaluate the behavior of different curves in a quantitative point of view, AUC is computed to provide a measure of performance across all possible classification thresholds. The basic theory of the proposed approach is to select the curve with the higher AUC, corresponding to the most performing model with an excellent capability in discerning between the positive and negative classes. This translates into an optimization problem:

$$i_{opt} = \arg \max_i (J_i) \quad (7)$$

$$J_i = \sum_{j=1}^d \text{AUC}_{ij} \quad (8)$$

where  $\text{AUC}_{ij}$  represents the area under the ROC curve for the  $i^{th}$  statistical model and the  $j^{th}$  damage scenario, with  $i = 1, 2, \dots, m$  and  $j = 1, 2, \dots, d$ .

### 3.3 Optimal threshold selection

In order to minimize false alarms and missing alarms, the selection of the optimal classification threshold has an extremely important role. To this aim, the proposed methodology, schematically presented in Fig. 2 b), involves the use of *Youden index* ( $Y$ ), which is a useful parameter allowing to provide a summary measure about model's performance. It is calculated in ROC space and conceptually represents the vertical distance between a point on the ROC curve and the  $45^\circ$  line. Typically, a high value of the *Youden index* corresponds to a well performing ROC curve (close to the upper-left-hand corner) leading to a high percentage of true positive rate over false positive rate. The index is calculated as follows:

$$Y = \text{SE} + \text{SP} - 1 \quad (9)$$

Once the most performing model is defined, the idea is to compute *Youden index* for each  $j^{th}$  damage scenario, varying classification thresholds. The maximum values,  $Y_{max}(j)$ , correspond to a specific damage threshold, which is denoted as  $T(j)$ .

However, it is important to underline that such procedure implies the inspection of several thresholds, each one related to a specific damage scenario. As a solution, the strategy proposed in this paper aims at fixing the optimal threshold as the minimum among the  $T(j)$ , so that the SHM system is able to detect even the smallest damage:

$$T_{opt} = \min \{T(j)\} \quad (10)$$

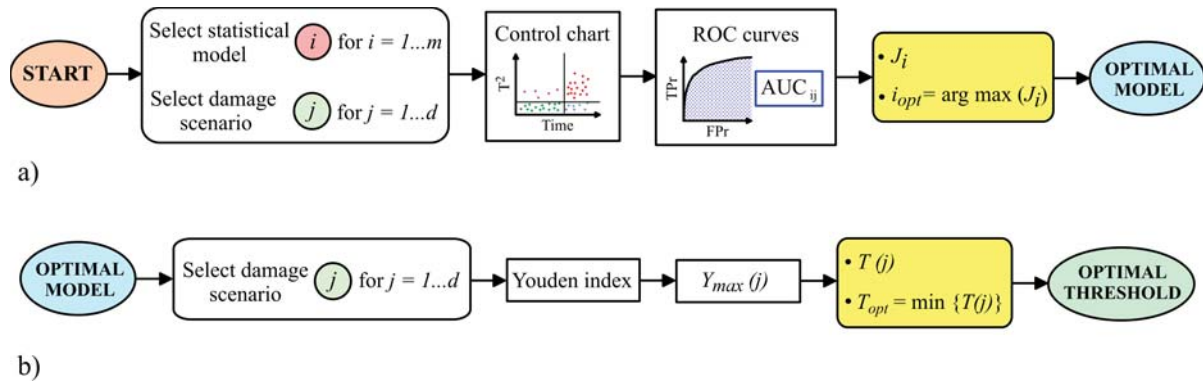


Figure 2: a) flow chart of the proposed methodology to select the most performing statistical model; b) flow chart of the proposed procedure for the optimal threshold selection.

## 4 APPLICATION CASE STUDY: Z24 BRIDGE

This section presents a general overview about the geometry and the monitoring system of the Z24 bridge and discuss, additionally, the results obtained by application of the proposed methodology on the investigated case study. To this aim, the available monitoring data are collected, processed and analysed through a specific MATLAB code, called MOSS, implemented by García-Macías et al. [12].

### 4.1 General description

The Z24 Bridge (Fig. 3) was located in the canton Bern, Switzerland, overpassing the national highway between Bern and Zurich. It was a post-tensioned concrete box girder bridge with a main span of 30 m and two side spans of 14 m. The two triplets of concrete columns at both ends were connected via concrete hinges to the girder, while two concrete piers, representing the intermediate supports of the bridge, were clamped into the girders and situated at the end points of the main span (Fig. 3 b)).

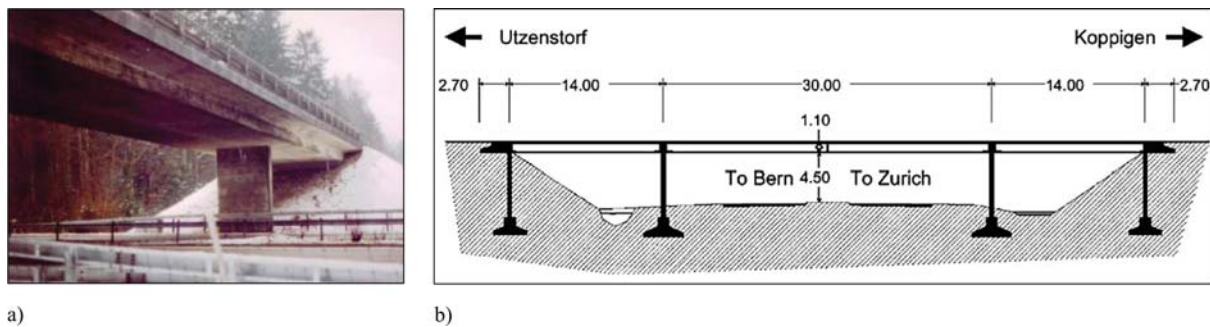


Figure 3: Z24 bridge: a) general view [13], b) longitudinal section [14].

The bridge was demolished at the end of 1998 to build a larger side span bridge. However, before demolition, it was continuously monitored from November 1997 till September 1998, with the aim to provide both environmental and vibration data for dynamic behavior's assessment. In particular, progressive damage tests were carried out during the summer of 1998 (shortly before the complete demolition of the bridge) in order to study the influence of different realistic damage scenarios on the modal properties.

Sensors to measure accelerations as well as environmental parameters were spread across the bridge. More specifically, among 16 accelerometers, only 8 were properly working. Data from all sensors were captured every hour with a sampling frequency of 100 Hz, resulting in 24 measurements per day.

#### 4.1.1 Definition of the damage scenarios

With the aim to evaluate modal parameters' variations in view of a prompt damage detection, frequency tracking has been performed over time, as depicted in Fig. 4.

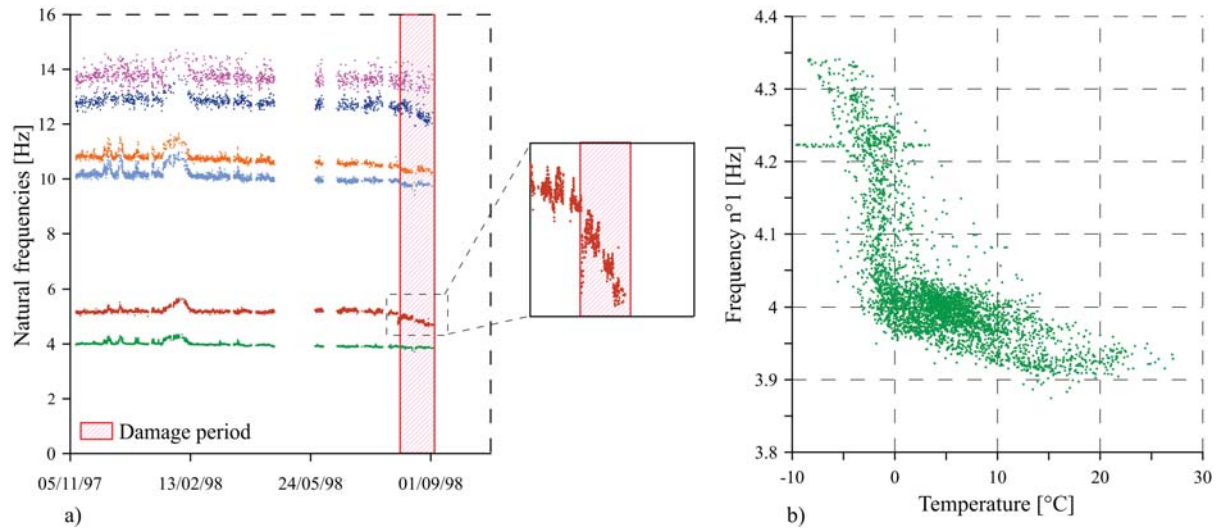


Figure 4: a) frequency tracking of the Z24 Bridge; b) relation between the first natural frequency and the temperature.

Between August 10<sup>th</sup> and September 4<sup>th</sup> 1998, the bridge was subjected to progressive damage tests. In particular, four damage scenarios ( $d = 4$ ) are taken into account in the present work:  $d_1$ ,  $d_2$ ,  $d_3$  and  $d_4$  indicate, respectively, the whole damage period (10<sup>th</sup> August - 4<sup>th</sup> September), the first portion of damage period (10<sup>th</sup> August - 18<sup>th</sup> August), the second portion (19<sup>th</sup> August - 26<sup>th</sup> August) and finally, the third one (27<sup>th</sup> August - 4<sup>th</sup> September).

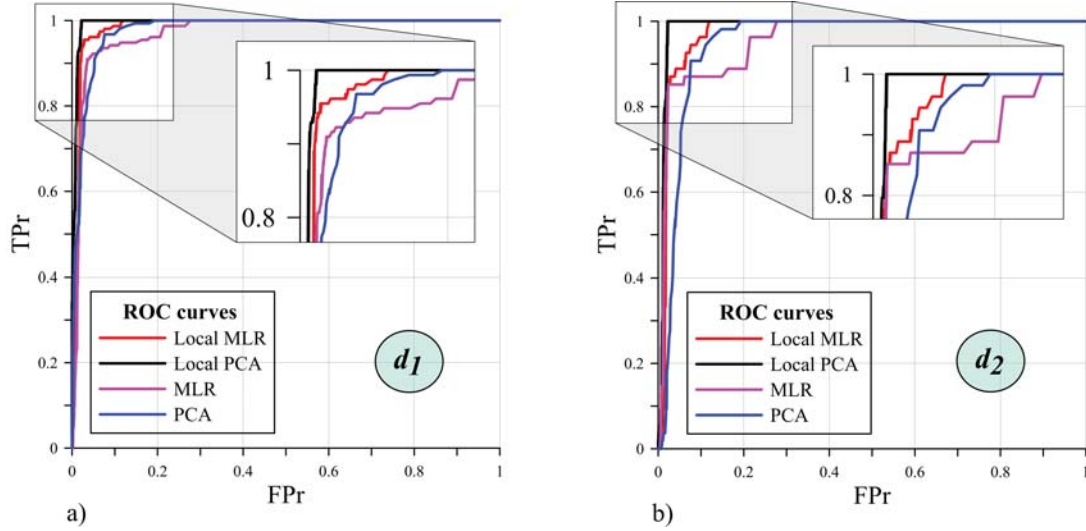
#### 4.1.2 Comparison between different statistical models

In order to get residuals, four data cleansing techniques ( $m = 4$ ) are considered, namely Multiple Linear Regression (MLR), Principal Component Analysis (PCA), Local MLR and Local PCA. The application of every statistical model, varying damage scenarios, leads to different control charts, each one referred to the  $i^{th}$  model and the  $j^{th}$  damage condition. By counting false positives, true positives, false negatives and true negatives, outgoing from every control chart, ROC curves are computed empirically by varying the classification threshold. Following the proposed methodology, AUC values are calculated and afterwards collected in Table 1.

It can be noticed that ROC curves exhibit a good behavior if the whole damage period ( $d_1$ ) is considered (Fig. 5 a)), even though slightly more performing results are visible when dealing with larger damage severity (e.g.  $d_4$ ), since the probability to discern true positive items highly increases. Conversely, when damage to be identified is not so marked (e.g.  $d_2$ ), AUC values get inevitably worse allowing, though, to clearly distinguish various performance levels associated to the  $m$  models, as shown in Fig. 5 b).



d	AUC			
	PCA	Local PCA	MLR	Local MLR
$d_1$	0.979	0.994	0.973	0.984
$d_2$	0.953	0.988	0.959	0.975
$d_3$	0.988	0.996	0.971	0.984
$d_4$	0.997	0.999	0.989	0.993

Table 1: *AUC* values for  $m$  statistical models and  $d$  damage scenarios.Figure 5: Comparison between the different statistical models in terms of ROC curves. a, b) ROC curves computed for the whole damage period ( $d_1$ ) and for the first portion of damage period ( $d_2$ ), respectively.

Since the damage inferred to the bridge was significant, it is necessary to point out that every model managed to yield extremely performing ROC curves, regardless of the selected damage scenario. However, in order to find out which is the best technique to remove environmental effects, the proposed optimization problem is applied. Following Eq. (7), the argument of the maximum of the objective function,  $i_{opt}$ , corresponds to the Local PCA model, the one providing the best performance in terms of AUC.

Due to the fact that the damage inferred to the structure progressively increases during the monitoring time, it could be interesting to identify which technique stands out in detecting damage first. To this aim, each control chart associated to the  $i^{th}$  model is taken into account and the portion corresponding to damage is afterwards divided into a certain number of steps. By computing and plotting AUC values at every step, as shown in Fig. 6, it comes to the light that Local PCA results to be the best model in a global view, while MLR turned out to be the fastest technique to detect damage.

#### 4.1.3 Selection of the optimal threshold

Once Local PCA is identified as the most performing model, it is crucial to minimize damage errors such as false positives and false negatives. This translates into the selection of the optimal threshold, leading to the higher TPr over the FPr within the ROC space. To this aim, *Youden index* is computed for every  $j^{th}$  damage scenario, varying the classification threshold. Table 2

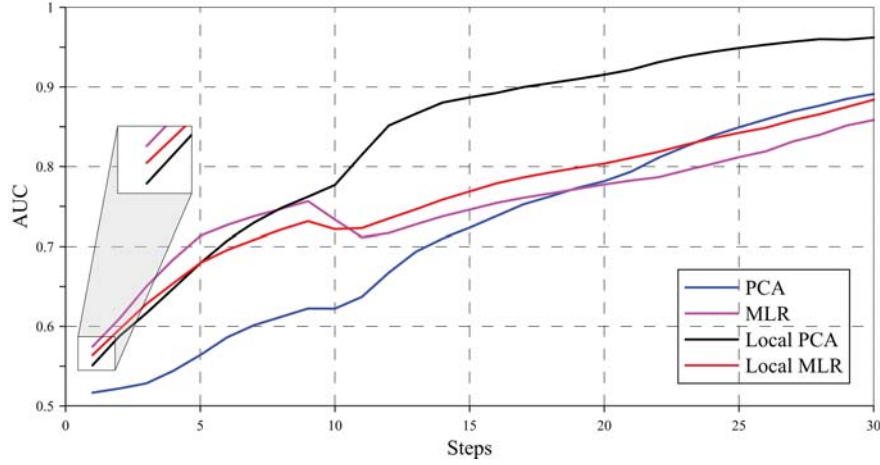


Figure 6: Comparison between  $m$  models in terms of AUC, computed at every step throughout the damage period.

summarizes the maximum values  $Y_{max}(j)$  with the corresponding thresholds  $T(j)$ .

d	Local PCA	
	$Y_{max}$	$T$
$d_1$	0.978	0.196
$d_2$	0.978	0.196
$d_3$	0.990	0.424
$d_4$	0.993	0.493

Table 2: Maximum values of *Youden index* ( $Y_{max}$ ) for every damage scenario and the corresponding thresholds ( $T$ ).

With the growing of damage severity, it is possible to highlight (i) an increase of the optimal threshold and (ii) an enlargement of the interval containing the maximum values of *Youden index*, as clearly visible in Fig. 7 a).

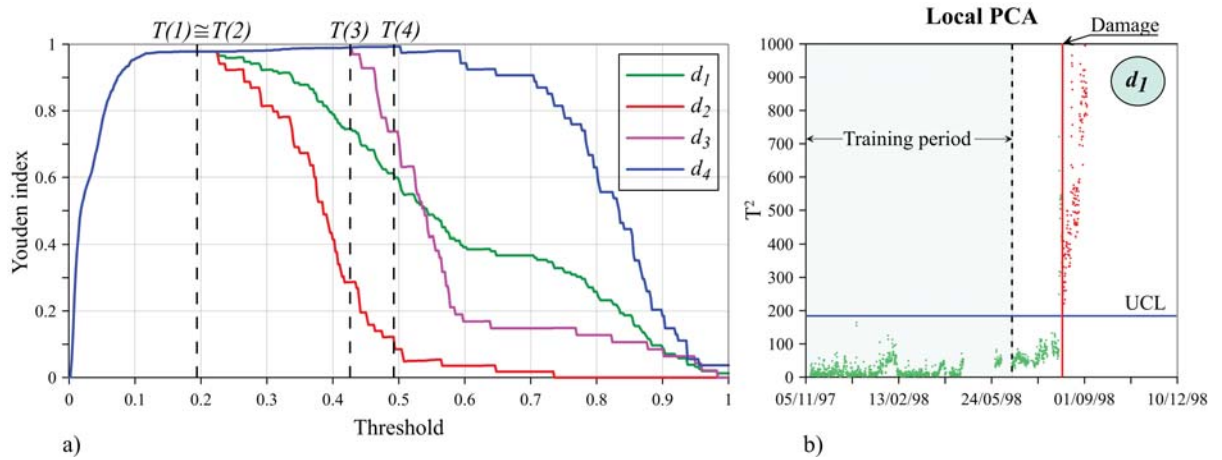


Figure 7: a) *Youden index* for  $d$  damage scenarios, varying the classification thresholds; b) control chart of the Z24 bridge obtained for a specific damage scenario ( $d_1$ ) by setting Local PCA as statistical model and  $T_{opt}$  as UCL.

However, as shown in Table 2, the methodology has provided several thresholds, each one related to a specific damage scenario. To overcome this issue, the optimal value  $T_{opt}$ , required to set the UCL of the control chart, is selected as the minimum:  $T_{opt} = \min \{T\} = 0.196$ . The control chart obtained by considering Local PCA as statistical model and  $d_1$  as damage scenario is depicted in Fig. 7 b), where the UCL is set equal to the optimal threshold computed using Eq. (10). It is easy to point out the excellent capability of this data cleansing technique (i.e. Local PCA) in correctly classifying the outcomes throughout the possible thresholds, notably avoiding the false negatives detection.

## 4.2 Discussion of the results

The relation between the identified natural frequencies and temperature may significantly affect the selection of the best environmental effects removal technique. Regarding the Z24 bridge, such relation is non-linear, as shown in Fig. 4 b). This could be the key for the interpretation of the results, as local approaches are typically useful to handle non-linear environmental/operational effects. In this particular case study, Local PCA (Principal Component Analysis applied to single clusters), in comparison with linear regression analysis (MLR), turned out to be the statistical model with the highest capability in minimizing erroneous predictions in view of a reliable damage detection.

## 5 CONCLUSIONS

The present paper provides a new decision-support tool for the definition of the best technique to remove environmental effects, as well as for the selection of the optimal classification threshold, minimizing false alarms and missing alarms. The proposed methodology is based on the use of ROC curves as performance metrics, which are computed and compared, in terms of AUC, for a variety of statistical models and different damage scenarios. Therefore, the selection of the best statistical model is carried out in the form of an optimization problem. Moreover, keeping fixed the most performing technique, the parameter *Youden index* is introduced to find out the optimal threshold for every damage scenario. Finally, in order to let the SHM system detect even the smallest damage, the strategy is to select the lowest value as optimal UCL.

The developed procedure has been exemplified by application in the Z24 bridge case study. The results illustrate that all the models managed to clearly detect the huge damage progressively inferred to the bridge. Local PCA, though, has showed a higher capability to correctly classify the outcomes of the control chart, proving to be the optimal model to remove environmental effects for an effective damage detection.

In conclusion, the provided methodology represents a valid tool to statistically evaluate the performance of different data cleansing techniques, by supplying reliable performance metrics within unsupervised damage detection under changing environment. The procedure is general and can be implemented in manifold SHM applications, considering different statistical models and different damage scenarios.

## Acknowledgements

The supports of the Italian Ministry of University and Research (MIUR) and the University of Perugia are acknowledged, within the Program “Dipartimenti di eccellenza 2018-2022”.

## REFERENCES

- [1] B.J.A. Costa, F. Magalhães, T. Cunha, J. Figueiras, Rehabilitation assessment of a century steel bridge based on modal analysis. *Engineering Structures*, **56**, 260–272, 2013.
- [2] O. Avci, O. Abdeljaber, S. Kiranyaz, M. Hussein, M. Gabbouj, D.J. Inman, A review of vibration-based damage detection in civil structures: From traditional methods to Machine Learning and Deep Learning applications. *Mechanical Systems and Signal Processing*, **147**, 2021.
- [3] A. Kita, N. Cavalagli, F. Ubertini, Temperature effects on static and dynamic behavior of Consoli Palace in Gubbio, Italy. *Mechanical Systems and Signal Processing*, **120**, 180–202, 2019.
- [4] F. Magalhães, A. Cunha, E. Caetano, Vibration based structural health monitoring of an arch bridge: From automated OMA to damage detection. *Mechanical Systems and Signal Processing*, **28**, 212–228, 2012.
- [5] A.-M. Yan, G. Kerschen, P. De Boe, J.-C. Golinval, Structural damage diagnosis under varying environmental conditions - Part I: A linear analysis. *Mechanical Systems and Signal Processing*, **19**, (4), 847–864, 2005.
- [6] E. García-Macías, I. Venanzi, F. Ubertini, Metamodel-based pattern recognition approach for real-time identification of earthquake-induced damage in historic masonry structures. *Automation in Construction*, **120**, 2020.
- [7] K. Worden, H. Sohn, C.R. Farrar, Novelty detection in a changing environment: Regression and interpolation approaches. *Journal of Sound and Vibration*, **258** (4), 741–761, 2002.
- [8] T. Fawcett, An introduction to ROC analysis. *Pattern Recognition Letters*, **27**, (8), 861–874, 2006.
- [9] L. Ierimonti, I. Venanzi, F. Ubertini, ROC analysis-based optimal design of a spatio-temporal online seismic monitoring system for precast industrial buildings. *Bulletin of Earthquake Engineering*, **19**, (3), 1441–1466, 2021.
- [10] J. Kullaa, Structural health monitoring under nonlinear environmental or operational influences. *Shock and Vibration*, **2014**, 2014.
- [11] C.M. Bishop, Pattern Recognition and Machine Learning. *Springer*, 2006.
- [12] E. García-Macías, F. Ubertini, MOVA/MOSS: Two integrated software solutions for comprehensive Structural Health Monitoring of structures. *Mechanical Systems and Signal Processing*, **143**, 2020.
- [13] G. Steenackers, P. Guillaume, Structural health monitoring of the Z-24 bridge in presence of environmental changes using modal analysis. *Conference Proceedings of the Society for Experimental Mechanics Series*, **18**, 2005.
- [14] KU Leuven, Z24 bridge benchmark, <https://bwk.kuleuven.be/bwm/z24>, accessed on 19th March 2021.

## RC TIED-ARCH BRIDGES: TYPOLOGICAL ANALYSIS FOR THE DEFINITION OF RETROFIT INTERVENTIONS

Valentina Pernechele<sup>1</sup>, Elisa Saler<sup>2,3</sup>, Francesca da Porto<sup>3</sup> and Claudio Modena<sup>1</sup>

<sup>1</sup> Institute for Construction Technologies – National Research Council (ITC-CNR)  
Corso Stati Uniti 4, 35127 Padova, Italy  
e-mail: pernechele@itc.cnr.it; claudio.modena@unipd.it

<sup>2</sup> Dept. of Civil, Environmental and Mechanical Engineering, University of Trento  
Via Mesiano 77, 38123 Trento, Italy  
e-mail: elisa.saler@unitn.it

<sup>3</sup> Dept. of Geosciences, University of Padova  
via Gradenigo 6, 35131 Padova, Italy  
e-mail: {elisa.saler, francesca.daporto}@unipd.it

---

### Abstract

*The Italian bridge asset is characterized by aged structures, most of which made of reinforced concrete, needing retrofit interventions to improve both their seismic performance and load-bearing capacity towards the increased traffic volume. In order to provide a series of guidelines for retrofit, a research project, carried out by the ReLUIS consortium supported by the Italian Department of Civil Protection, aims to identifying typological deficiencies and vulnerability of the main type of bridges widespread on the Italian territory, defining typological interventions. This paper presents the outcomes of the ongoing research focusing on RC tied-arch bridges, frequently built in the period between the two world wars. A typological study was carried out to define the main design deficiencies and construction details, and how degradation acts on this type of bridge, besides the main structural vulnerability to both gravitational and seismic loads. Numerical and parametrical analyses were carried out on a representative prototype tied-arch bridge with RC hangers, dating back to 1930s. The structural behavior was assessed by means of numerical analysis on FEM models, allowing the evaluation of the static and seismic capacity, the definition of the most vulnerable elements, and thus, the identification of the most suitable type of retrofit interventions.*

**Keywords:** Bridge stock, bridge degradation, condition state assessment, bridge seismic vulnerability, prioritization.

---



## 1 INTRODUCTION

Bridges are the most critical structures in transportation networks and [1], in many developed countries, such as Italy, most of them were built more than 40 years ago [2]. According to the CNR, the National Council for Research of Italy, many of those structures are at risk nowadays for their age [3]; in addition, structural typologies, technologies, and materials used for bridges were very different from those used today [4].

An out-of-service bridge might cause significant economic losses (i.e., costs for users, owners, and operators); maintaining them in service conditions is therefore desirable [2]. Proper inspections and timely maintenance are too often unfulfilled due to limited economic budgets and a widespread approach based on emergency, which is leading to a progressive deterioration of structures [5].

In the last ten years, a series of tragic collapse of bridges occurred in Italy [6, 7], pointing out the need for a regulatory direction to the problem. Then, in 2019, novel Guidelines for existing bridges [8] were issued, defining a methodology for inspection, prioritization, and verification of existing bridges.

Research has provided scientific-based tools to manage bridge stocks [9, 10, 11, 12] and to prioritize retrofit actions [13, 14, 15, 16], while the investigation of the most suitable types of retrofit has yet to be deepened in a framework of multi-criteria typological analyses.

Hence, a national project, funded by the Italian Department of Civil Protection (DPC), has been carried out by the *ReLUIS* consortium, with the purpose of identifying typological deficiencies of the main type of bridges and thereby defining the more suitable types of retrofit interventions. The present contribution, in particular, focuses on reinforced concrete (r.c.) tied-arch bridges.

R.c. tied-arch bridges are comprised by one or more arches, a tying chord, also called bow-string girder or tie-girder, which often corresponds to the deck system (i.e., girders and slab), and a series of hangers connecting the arches to the bow-string girders. These ones, located below the arches, absorb their horizontal thrust [17], allowing, on a theoretical level, the transmission of only vertical forces to the substructures. Bridges of this type often date back to the period between the two world wars and, due to their age, their safety is jeopardized by both degradation and increasing in the traffic volume [18].

The dynamic behavior and finite element (F.E.) model calibration of this type of bridges were previously studied by Turker et al. [19] and Brisighella et al. [20], which focused their analyses on specific case studies. Similarly, an extensive study including experimental non-destructive tests was carried out on a r.c. bowstring bridge in the Sicily region (Italy) [21, 22]. The influence of the hanger arrangement was investigated by Vlad et al. [23], through numerical simulations on 3D F.E. model.

The present paper proposes a critical examination of the available literature and of retrieved original projects. In order to operate in a typological framework, the most common characteristics of r.c. tied-arch bridges in Italy are illustrated, based on data collection carried out at national scale. Moreover, numerical analyses on a FEM model of a representative case study are presented, considering both gravitational and seismic actions. The identification of typological deficiencies, confirmed by results from the analysis of the case study, allowed classes of intervention to be suggested.

## 2 TYPOLOGICAL STUDY

R.c. arch bridges were widely built starting from the early 20<sup>th</sup> century, especially to overcome rivers where either a significant freeboard was required (e.g., for navigable canals) [24]

or the clearance space between the road level and substructures was limited [21]. These bridges were frequently built in-situ by constructing a temporary centering [24].

Various sub-types of r.c. tied-arch bridges can be identified based on the following geometric and structural characteristics: i) the hanger material (i.e., r.c., prestressed r.c. or steel); ii) the hanger arrangement (i.e., vertical, radial or inclined), iii) type of crossbeams. Hence, these parameters were included in a preliminary data collection carried out at national scale which results are reported in the following section.

## 2.1 Dataset of r.c. tied-arch bridges in Italy

A dataset was collected, comprised of almost 90 r.c. tied-arch bridges, evenly distributed on the Italian area. The distribution of the main geometric and structural characteristics for bridges part of this stock are reported as follows.

Figure 1 reports the distribution of general characteristics of the identified bridges, i.e., the year of construction, the number of spans, and the span length. It was observed that the vast majority of the identified bridges were built in the period 1919-1946, between the two world wars; unfortunately, this datum was not available (NA) for a significant part of the stock. R.c. tied-arch bridges appeared to be mainly single-span, while span lengths were quite heterogeneous. Then, the hanger typology was observed, and Figure 2 reports the distribution of their arrangement, material, and spacing. Finally, the types of crossbeams were investigated (Figure 3). On the basis of the data collected, it was assumed that the most common type of r.c. tied-arch bridge in Italy has r.c. vertical hangers and orthogonal crossbeams.

Some examples of tied-arch bridges in Italy are reported in Figure 4.

## 2.2 Construction details

By consulting original project documentations retrieved for several r.c. tied arch bridges in Italy, it was possible to detect the common construction details and to deduce the design method of the time.

Concrete compressive strength ranges from high resistance (i.e., mean value of cube compressive strength  $R_{cm}$  around 40 MPa) to very low mechanical properties, found in one case [21]; these cases cannot be considered negligible due to the ancient construction age. Reinforcement bars were smooth, consistently with construction age, and small diameters ( $\phi 6-8$  mm) were used for stirrups. Arches are segmental, with different values of the ratio between rise and span. They were designed to resist mainly to compression, based on the design criteria for masonry arches, and therefore they were relatively poorly reinforced.

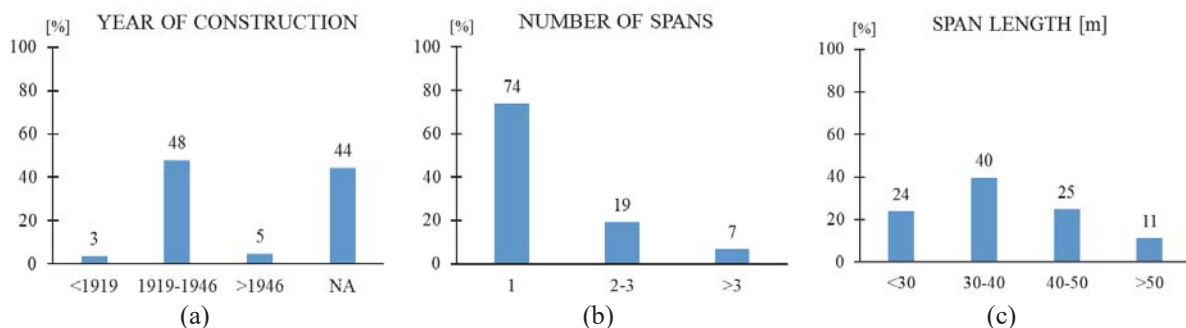


Figure 1: General characteristics of bridges in dataset: a) years of construction, b) number of spans, and c) span length.

Hanger spacing varies in the range 2 - 4 meters, depending on the span of the bridge, and therefore on the generated stresses. The hanger joints, both to the arch and to the tie-girder, were designed as hinges, with insufficient reinforcement details to transfer flexural actions.

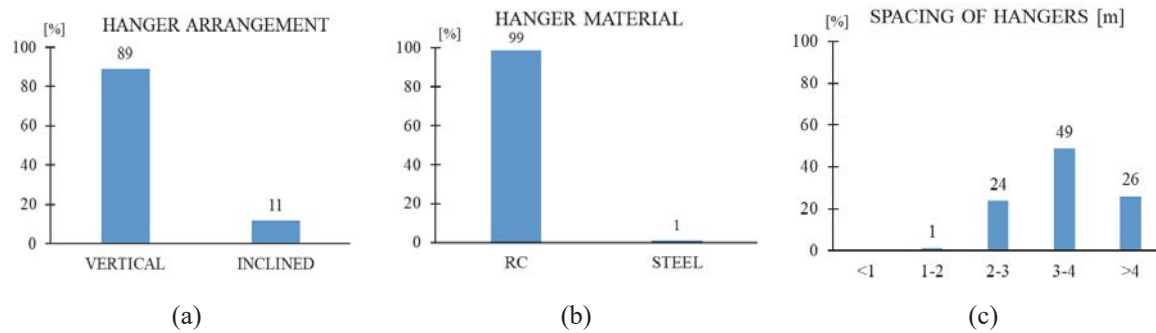


Figure 2: Hanger characteristics for bridges in dataset a) arrangement, b) material, and c) spacing.

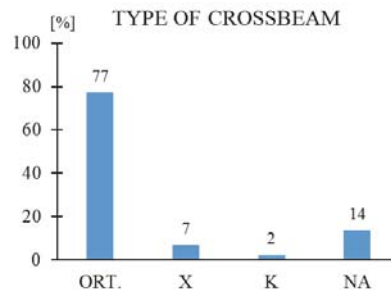


Figure 3: Distribution of type of crossbeams for bridges in dataset.

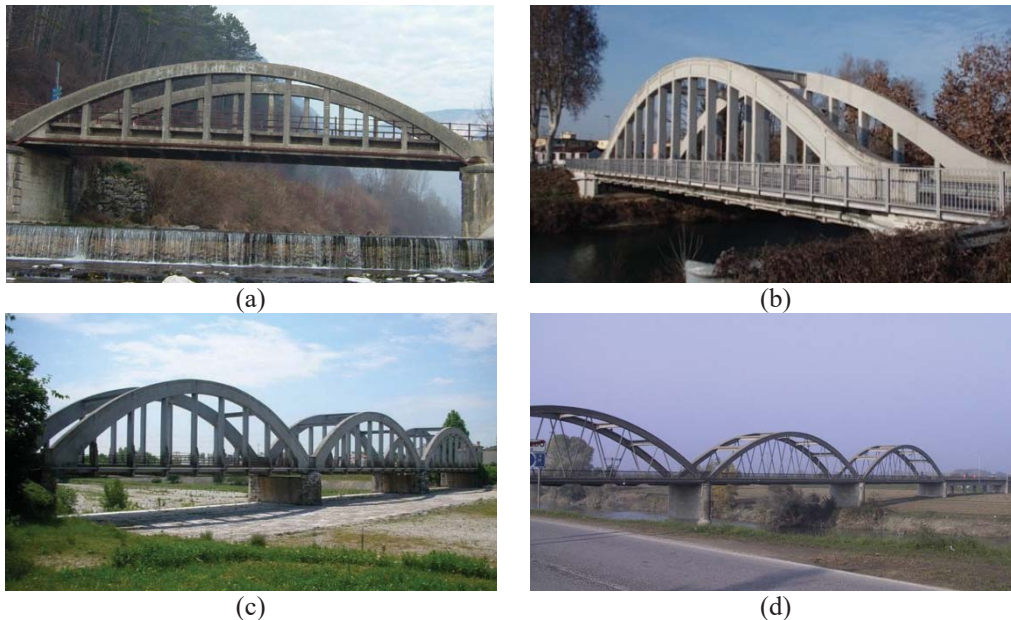


Figure 4: Bridges characterized by a) vertical r.c. hangers [25], b) vertical r.c. hangers and orthogonal crossbeams, c) vertical r.c. hangers and orthogonal crossbeams (multi-span) [25], and d) inclined r.c. hangers and orthogonal crossbeams (multi-span) [25].

### 2.3 Degradation and structural deficiencies

The macro-class of bridges here investigated resulted to be subjected to degradation effects and structural deficiencies, both affected the structural safety. The present section describes the main typical issues that can be found in r.c. tied-arch bridges.

The effects of degradation are caused by environmental actions (i.e., physical, chemical, and biological), and aggravated by many factors, such as incorrect construction details, low quality of materials, and lack or insufficient maintenance. The main and most common effect of degradation on r.c. bridges is the spalling of concrete, with consequent corrosion of the exposed reinforcement bars. Besides the susceptibility to degradation of all the elements of a r.c. tied-arch bridge, the observation of this phenomenon [26] suggests that hangers and deck structure are the most affected elements (Figure 5). To preserve both deck system and substructures, an effective system to drain rainwater is needed. In the case of steel hangers, the degradation of the material can cause the relaxation of hangers, with consequent redistribution of stresses, and the damage of anchors, which might lead to the detachment of the relative hangers.



Figure 5: Spalling of concrete and corrosion of exposed rebars on: a) r.c. hanger and b) deck [25].

Not only is structural safety threatened by degradation, it might be also reduced by structural deficiencies influencing the response to both static and seismic loads.

Considering gravitational loads, substructures can be statically inadequate, as a result of original design deficiency and/or an increase in traffic loads (e.g., an increase in the arch thrust, no longer absorbed by the tie-girder, transferred to the abutments). The low quality of materials, poorly reinforced sections, and inadequate supports are the main static design deficiencies for the superstructure. As commonly found in existing bridges, the supporting system, connecting the substructure to the superstructure, is often inadequate to current traffic loads.

Most of r.c. tied-arch bridges in Italy were built long before the emanation of seismic codes, they were therefore not designed for seismic actions, making these structures intrinsically vulnerable to earthquakes. The most significant inadequacy is found for supports and substructures, due to both high levels of stress born by devices and the risk of support loss that can occurred in simply supported bridges. Poorly reinforced piers are vulnerable to horizontal stresses, towards either flexural or shear mechanisms. Focusing on the arches, the phenomenon of out-of-plane instability due to seismic actions is not negligible, mainly in case of missing or insufficient bracing system.

### 3 CASE STUDY

The case study presented and analyzed hereinafter is an existing r.c. tied-arch bridge, dating back to 1931 and located in the Veneto region, in north-east Italy. The case study was selected



based on representativeness criteria, as it has a series of widespread characteristics, previously illustrated in the national dataset presentation. In detail, it is a single-span bridge, with a span length of almost 40 meters; it has r.c. vertical hangers (spacing 2.5 meters) and three orthogonal r.c. crossbeams (Figure 6 and 7). The deck consists of longitudinal and transverse beams, and a slab. The r.c. abutments founded on piles.

Furthermore, prior to implement analyses, original project documentation was retrieved, including representation of the construction details, which are reported in Table 1. No data was available on concrete, which were then assumed according to a similar bridge built in the region [27]. Two different set of data were available deriving from experimental tests carried out on two r.c. tied-arch bridges in the Veneto region. The one providing lower material strength was chosen based on both conservative criteria and geographic similarity of sites, leading to assume a concrete resistance class C20/25.



Figure 6: Case study – r.c. tied-arch bridge.

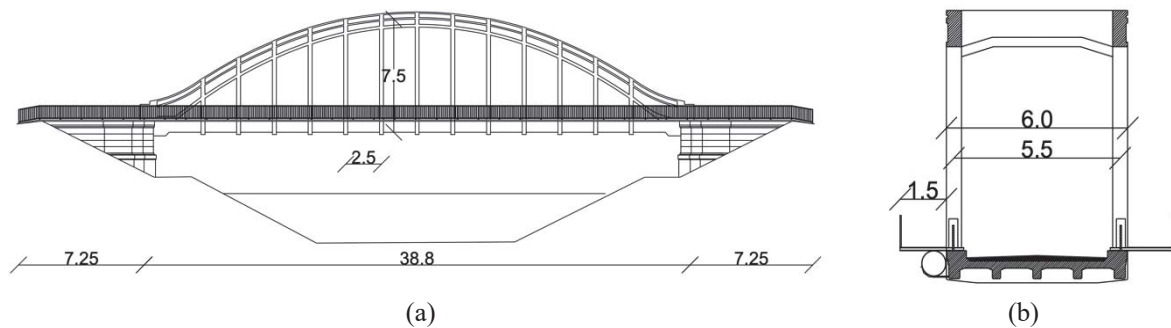


Figure 7: a) Longitudinal and b) transverse view of case study.

Element	Section	Reinf.	Element	Section	Reinf.
		4+4Φ20 2Φ14 2Φ14 4+4Φ20			4Φ30 4Φ30 4Φ30 4Φ30 4Φ30
		B=0.20 H=0.50 2Φ16 4Φ20 4Φ16			B=0.30 H=0.40 2Φ22 4Φ28 4Φ28



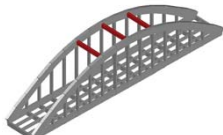
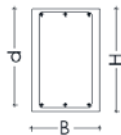

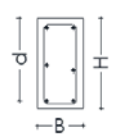
		$B=0.40$ $H=0.60$	$3\Phi 18$ $3\Phi 18$			$B=0.25$ $H=0.50$	$2\Phi 22$ $2\Phi 22$ $2\Phi 22$
-----------------------------------------------------------------------------------	-----------------------------------------------------------------------------------	----------------------	--------------------------	------------------------------------------------------------------------------------	-------------------------------------------------------------------------------------	----------------------	----------------------------------------

Table 1: Section and reinforcements of bridge elements.

In 1994, a restoration intervention was carried out, by rebuilding the deck slab and restoring all the concrete elements, which showed diffused spalling. During this intervention two metal footways were added on the outer sides. Prior to the restoration intervention, experimental tests were performed on the smooth reinforcement bars, which showed a yield strength greater than 450 MPa, and an ultimate strength greater than 600 MPa.

Traffic loads have been limited to 7.5 tons, as a result of the static verification performed in 1994; the limitation persists nowadays, thus it was considered in the definition of loads for the analysis.

### 3.1 FE model

A 3D F.E. models was implemented using the software Midas Civil [28], according to the current configuration, with the external metal footways (Figure 9). All of the bridge members were modelled through *beam* elements.

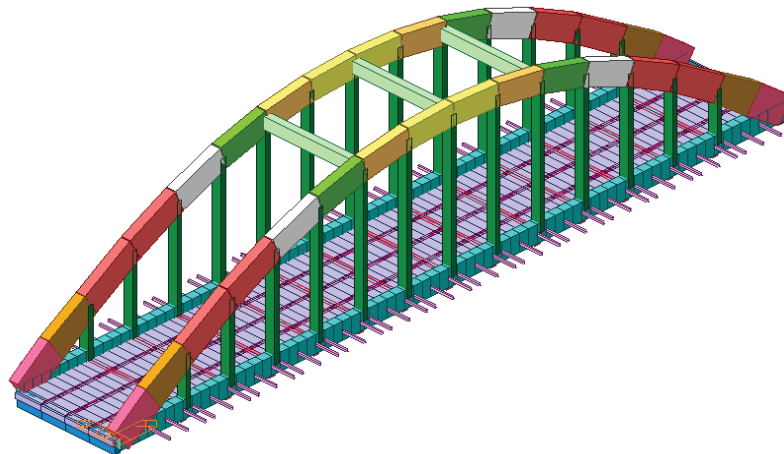


Figure 9: F.E. model based on current configuration.

Specific attention was paid to the study on the joints between hangers and the tie-girder or the arch, respectively. To study the behavior of these connections, a parametric analysis was carried out, modelling the hangers through either *beam* or *truss* elements.

The assumption of beam elements to model the behavior of hangers undergo the condition that the flexural stresses at the joints does not overcome the resistant bending moment. This condition resulted to be not verified. Moreover, reinforcements of the hangers consist in steel bars hooked at the ends, with insufficient degree of connection to transfer flexural stresses. Thus, it can be stated that hangers mainly have an axial behavior, which is better modelled through *truss* elements.

A comparison was also made of the stresses deriving from the two above-mentioned models, in order to verify that modelling with truss was conservative.

In general, the model with *truss* elements showed increased stresses for both the arch and the tie-girder, and a relative increase in vertical displacements. An exception is given by bending moments acting on both the arch and the tie-girders for self-weight, which were reduced in the model with *truss* elements.

Nevertheless, using *truss* elements to model hangers resulted to be more suitable for this type of bridges, and thus, safety verifications were carried out on this model configuration. Results of the comparison between modelling strategies are shown in Table 2.

		Arch			Tie-girder		
		M	N	Dz	M	N	Dz
		[kNm]	[kN]	[mm]	[kNm]	[kN]	[mm]
Self-weight	<i>Beam</i>	125	-1593	6,8	53	1263	6,9
	<i>Truss</i>	109	-1603	6,9	45	1277	7,1
	$\Delta$ [%]	-13%	+1%	+2%	-15%	+1%	+3%
Permanent and accidental loads	<i>Beam</i>	1229	-4541	24,5	650	3619	27,1
	<i>Truss</i>	1387	-4579	27,9	734	3677	30,6
	$\Delta$ [%]	+12%	+1%	+14%	+13%	+2%	+13%

Table 2: Stress comparison between modelling strategies for hangers: using *truss* or *beam* elements.

### 3.2 Static and seismic assessment

Due to the lack of in situ investigations on materials, the level of knowledge for the structure was defined as limited (KL1) and thus a confidence factor  $CF=1.35$  was assumed [29]. Safety verifications towards both static and seismic load combinations were performed according to Italian regulations, included the novel guidelines for existing bridges [8].

Four traffic load combinations were considered for static verifications, the first was defined according to Italian code [30, 31] and thus referred to as “NTC18” hereinafter. Three load combinations were assumed according to Italian Guidelines for existing bridges [8] to evaluate the level of safety ensured by the structure: operativity, transitivity 1, and transitivity 2. In fact, each of these combinations corresponds to traffic load layouts with decreasing return periods, thus providing an effective tool for the evaluation of measures to be adopted. The load combination transitivity 2 was defined considering a traffic limitation that allows the transit of vehicles up to 7.5 tons.

The values of stresses resulted from the analyses are reported in Table 3. A general relief of the elements can be observed, due to the decrease in traffic loads with respect to NTC18 configuration.

Results of ULS strength verifications are reported in Figure 10, which represents the minimum demand/capacity ratio ( $D_d/C_d$ ) for each element. The tie-girders and the longitudinal beams results to be the most critical elements, which satisfy the verifications only for the less demanding load combination (i.e., transitivity 2). The deck deficiencies stem from the poor distribution capacity of the slab, besides the increased in traffic loads with respect to the period of construction.

Figure 11 compares outcomes from the analyses in terms of axial load and bending moment with the limit domain of tie-girders.

Safety verification towards seismic action were carried out with reference to three decreasing return period  $T_R$  (i.e., 75 years, 30 years, and 5 years); the first one referred to a design working life of 50 years increased of a factor 1.5 for relevant structures, according to Italian Code [30], while lower return period were assumed according to Italian Guidelines for existing bridges [8].

The elastic response spectrum was conventionally referred to L'Aquila, Italy, a site with moderate-high seismicity.

A linear dynamic analysis was carried out. The obtained first three modes of vibration are shown in Figure 12: the first one results to be transverse, which corresponds to the out-of-plane direction of the arches; the second mode is vertical; and the third one have a predominantly torsional component.

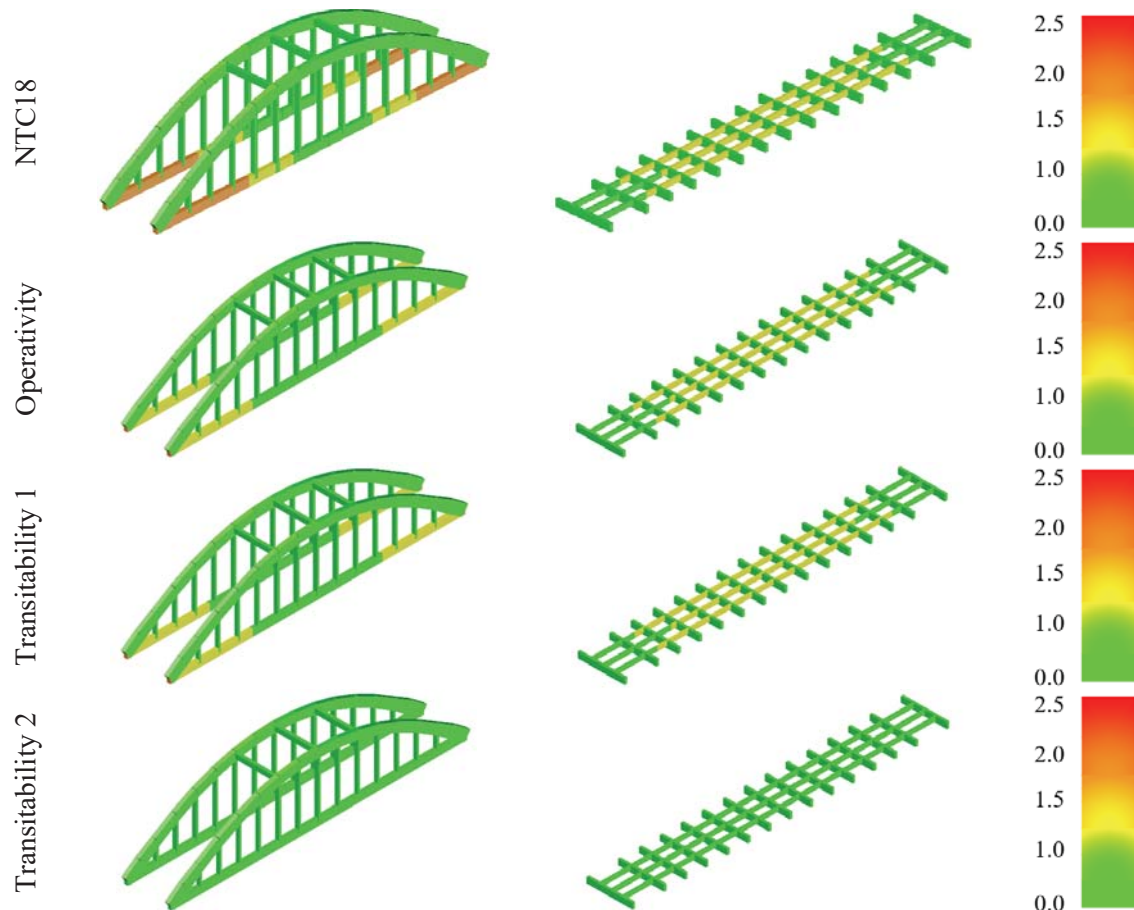


Figure 10: Safety verifications for static load combinations in terms of demand/capacity ratio.

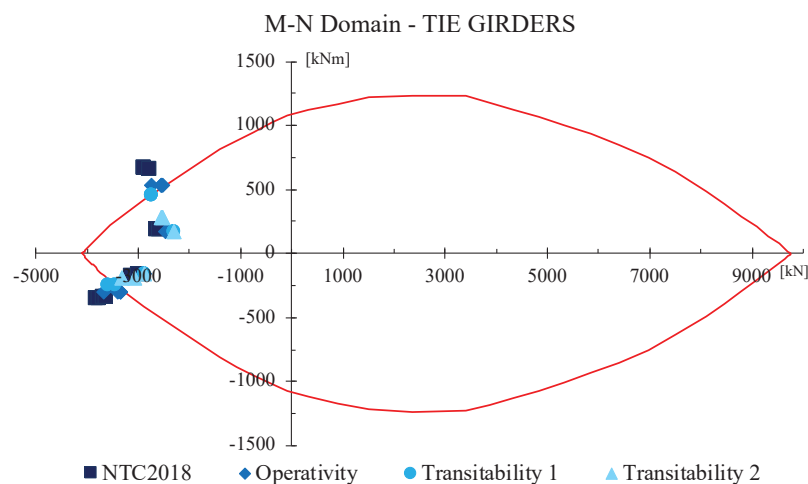


Figure 11: M-N limit domain of tie-girders with plotted outcomes of static analyses.

<b>ARCH</b>								
	$N_{max}$		$M_{ymax}$		$M_{ymin}$		$V_{max}$	
	[kN]	[%]	[kNm]	[%]	[kNm]	[%]	[kN]	[%]
<i>NTC18</i>	-3664		1250		263		273	
<i>Operativity</i>	-3293	10%	1021	18%	225	15%	225	17%
<i>Transitability 1</i>	-3402	7%	895	28%	258	2%	200	27%
<i>Transitability 2</i>	-3190	13%	608	51%	177	33%	140	49%
<b>TIE-GIRDER</b>								
	$N_{max}$		$M_{ymax}$		$M_{ymin}$		$V_{max}$	
	[kN]	[%]	[kNm]	[%]	[kNm]	[%]	[kN]	[%]
<i>NTC18</i>	3821		657		-360		497	
<i>Operativity</i>	3402	11%	527	20%	-305	15%	417	16%
<i>Transitability 1</i>	3468	9%	455	31%	-250	31%	329	34%
<i>Transitability 2</i>	3231	15%	275	58%	-192	47%	244	51%
<b>HANGER</b>								
	$N_{max}$							
	[kN]	[%]						
<i>NTC18</i>	531							
<i>Operativity</i>	454	15%						
<i>Transitability 1</i>	415	22%						
<i>Transitability 2</i>	330	38%						

Table 3: Comparison of stresses acting on bridge for the analyzed traffic load combinations.

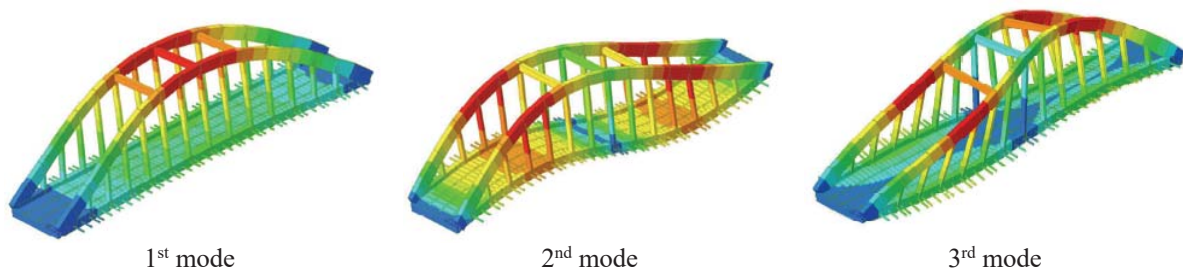


Figure 12: First three modes of vibration of analyzed bridge.

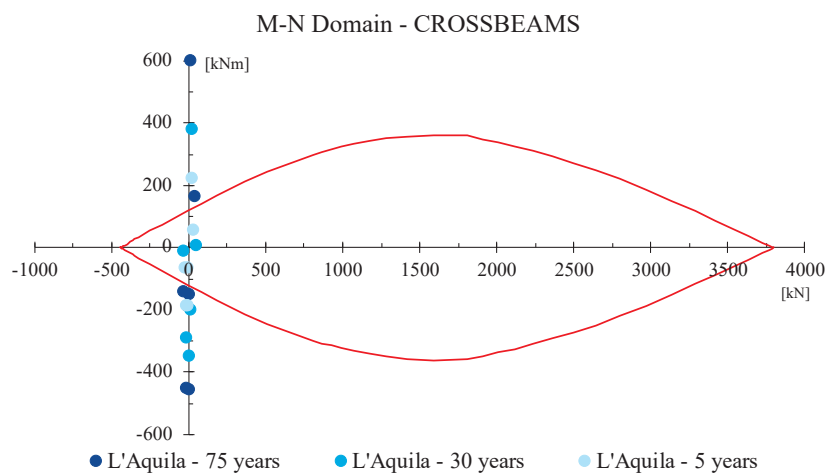


Figure 13: M-N limit domain of crossbeams with plotted outcomes of seismic analyses.

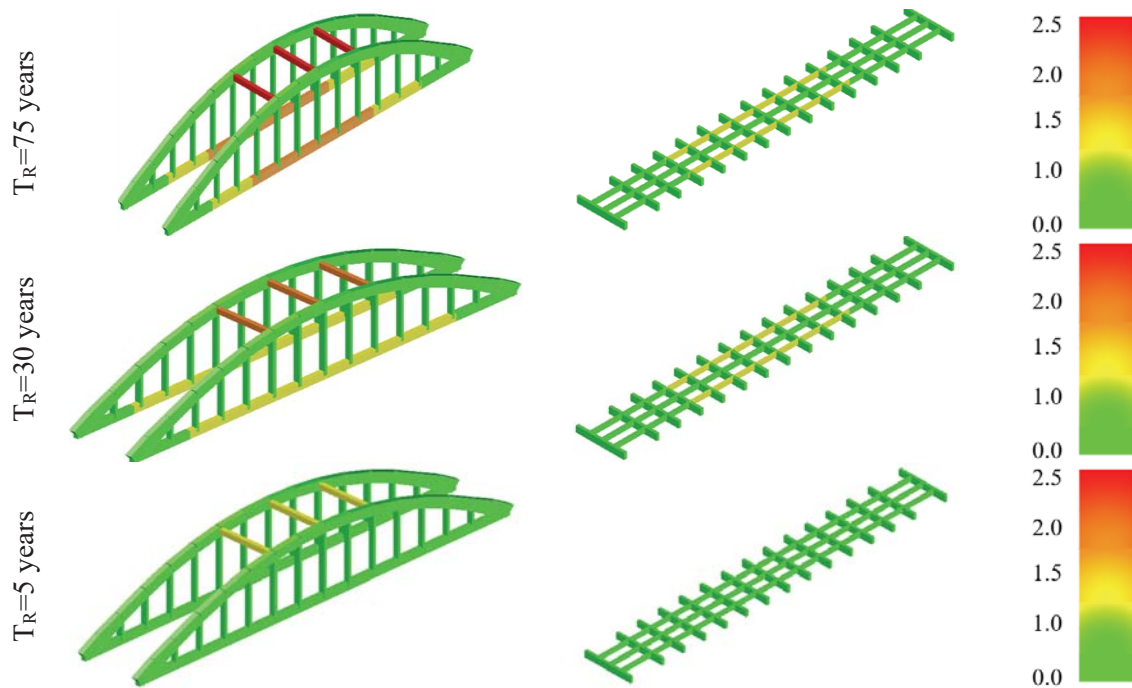


Figure 14: Safety verifications for seismic load combinations in terms of demand/capacity ratio.

According to the results of seismic verifications, the most stressed elements are the crossbeams, which have the function of preventing the out-of-plane instability of the arches. Crossbeams appear to have a significant seismic vulnerability, showing inadequate safety indices also for low seismic actions (Figure 13). In addition, tie-girders shows a deficiency for seismic actions as well. Figure 14 reports the results of seismic verifications in terms of minimum demand/capacity ratio for each structural member.

Results suggest the most suitable classes of intervention to be applied to r.c. tied-arch bridges. Being aware of specific features of each unique existing structures is fundamental to design the proper retrofit intervention; however, useful direction can stem from typological studies. In the present study the following typological classes of intervention were identified:

- post-stressing the tie-girders, in order to improve the capacity of absorbing the arch thrust;
- replacing supports with a novel isolation system, able to reduce actions on both substructures and superstructures.

In addition, since the r.c. deck slab is commonly inadequate in existing r.c. bridges [26], a strengthening intervention on this element shall be considered.

#### 4 CONCLUSIONS

- A typological study of RC tied-arch bridges in Italy was carried out in order to identify structural characteristics and main deficiencies. Various sub-types of r.c. tied-arch bridges have been identified based on the hanger material and arrangement, and the arch bracing system. On the basis of data collected at national scale, it was assumed that the most common type of r.c. tied-arch bridge has r.c. vertical hangers and orthogonal crossbeams.
- Increasing traffic loads, poorly reinforced sections and degradation (mainly acting on hangers and deck structure) are the main causes of reduced structural safety. In addition, due to their age of construction, most r.c. tied-arch bridges in Italy were not designed for seismic actions, making them intrinsically vulnerable to earthquakes.



- Based on representativeness criteria, a case study was selected and analyzed through numerical modeling. It is a single-span bridge built in 1931; it has r.c. vertical hangers and orthogonal r.c. crossbeams. The tie-girders and the longitudinal beams results to be the most critical elements towards static combinations, while crossbeams have a significant seismic vulnerability, showing inadequate safety indices also for low seismic actions.
- Future developments will focus on improving the knowledge of the case study and on identifying the most suitable type of retrofit interventions. The former will be pursued through a dynamic identification and experimental tests on materials. The presented study suggests that the most suitable types of intervention are the following: i) the application of a post-stress system to the tie-girders, in order to improve the capacity of absorbing the arch thrust, and ii) the replacement of supports with a novel isolation system.

## ACKNOWLEDGEMENTS

Special thanks are due to the Italian Department of Civil Protection (DPC), which funded this study in the framework of the *ReLUIS-DPC Project 2019-2021 – Work Package 5: Retrofit interventions for existing bridges*. In addition, thanks to the municipality of Padova for providing the original project of the case study and thanks to Andrea Gennaro for the support in numerical analysis.

## REFERENCES

- [1] E. Uzgider, M. Aydogan, O. Caglayan, et al, Performance of a Tied-Arch Reinforced Concrete Railway Bridge: Rating, Safty Assessment, and Bond Length Evaluation. *J Perform Constr Facil* 23:366-371. 2009. [https://doi.org/10.1061/\(asce\)cf.1943-5509.0000016](https://doi.org/10.1061/(asce)cf.1943-5509.0000016)
- [2] A. Del Grosso, D. Inaudi, L. Pardi, Overview of european activities in the health monitoring of bridges. *First International Conference of Bridge Maintenance, Safety and Management, IABMAS*, 2002.
- [3] A. Occhiuzzi, *Direttore CNR-ITC sul viadotto Morandi di Genova* – Press Note, [www.cnr.it](http://www.cnr.it). 2018.
- [4] P.G. Malerba, Inspecting and repairing old bridges: experiences and lessons. *Structure and Infrastructure Engineering*, 10:4, 443-470, 2014.
- [5] F. Braga, G. Buratti, A. Cosentino, A. Dall'Asta, G. De Matteis, R. Gigliotti, M. Mezzina, F. Morelli, C. Ristori, W. Salvatore, Multi-level approach for the assessment bridge and viaducts within road networks. *XVIII Convegno ANIDIS*, 2019.
- [6] M. di Prisco, M. Colombo, P. Martinelli, D. Coronelli, The technical causes of the collapse of Annone overpass on SS. 36. *In Italian Concrete Days*, 2018.
- [7] G.M. Calvi, M. Moratti, G.J. O'Reilly, N. Scattareggia, R. Monterio, D. Malomo, P. M. Calvi, R. Pinho, Once upon a Time in Italy: The Tale of the Morandi Bridge. *Structural Engineering International*, 29:2, 198-217, 2019. <https://doi.org/10.1080/10168664.2018.1558033>

- [8] CSLP n.88/2019. Linee guida per la classificazione e gestione del rischio, la valutazione della sicurezza ed il monitoraggio dei ponti esistenti. (in Italian) Assemblea Generale 11.04.2020.
- [9] P.D. Thompson, E.P. Small, M. Johnson, A.R. Marshall, The Pontis Bridge Management System. *Structural Engineering International, J Int Assoc Bridg Struct Eng*, 1998. <https://doi.org/10.2749/101686698780488758>
- [10] H. Hawk, E.P. Small, *The BRIDGIT Bridge Management System. Structural Engineering International, J Int Assoc Bridg Struct Eng* **8**, 1998. <https://doi.org/10.2749/101686698780488712>
- [11] R.J. Woodward, D.W. Cullington, A.F. Daly, et al, *BRIME - Bridge Management in Europe*. Final Rep 227, 2001.
- [12] D. Zonta, R. Zandonini, F. Bortot, A reliability-based bridge management concept. *Structural Infrastructural Engineering*, **3**:215–235, 2007. <https://doi.org/10.1080/15732470500315740>
- [13] A. Montepara, F. Merusi, F. Giuliani, Sviluppo di una nuova metodologia per la valutazione delle priorità di intervento di manutenzione di ponti e viadotti. *17° Convegno Naz della Soc Ital Infrastrutture Viarie*, 2008. (in Italian)
- [14] S. Sathananthan, T. Onoufriou, M.I. Rafiq, A risk ranking strategy for network level bridge management. *Structural Infrastructural Engineering* **6**:767–776, 2010. <https://doi.org/10.1080/15732470802383677>
- [15] S. Valenzuela, H. De Solminihac, T. Echaveguren, Proposal of an integrated index for prioritization of bridge maintenance. *Journal of Bridge Engineering* **15**:337–343, 2010. [https://doi.org/10.1061/\(ASCE\)BE.1943-5592.0000068](https://doi.org/10.1061/(ASCE)BE.1943-5592.0000068)
- [16] E. Saler, V. Pernechele, M. Anastasio, M. Minotto, G. Tecchio, Macroscale vulnerability and condition state assessment of bridges at municipality level. *XVIII ANIDIS*. 2019.
- [17] D. Ribeiro, A. Pedro, R. Calçada, R. Delgado, Experimental analysis and model updating of a bowstring arch railway bridge. *7<sup>th</sup> European Conference on Structural Dynamics, Eurodyn*, 2008.
- [18] P. Lonetti, A. Pascuzzo, A. Davanzo. Dynamic Behavior of Tied-Arch Bridges under the Action of Moving loads. *Math Probl Eng* 2016. <https://doi.org/10.1155/2016/2749720>
- [19] T. Türker, A. Bayraktar, Structural safety assessment of bowstring type RC arch bridges using ambient vibration testing and finite element model calibration. *Meaus J Int Meas Confed* **58**:33-45. 2014. <https://doi.org/10.1016/j.measurement.2014.08.002>
- [20] B. Briseghella, N. Gallino, C. Gentile, T. Zordan, Finite element modelling of a tied arch bridge form operational modal analysis. In: *ARCH'07 – 5<sup>th</sup> International Conference on Arch Bridges*, 2007.
- [21] E. Lo Giudice, G.L. Di Marco, M. Gallo, R. Mantione. The bridge over the river Cassibile: a structure in r/c Bowstring scheme dating 1930. **8**. 2016. (in Italian)
- [22] E. Lo Giudice, G.L. Di Marco, M. Gallo, R. Mantione, V. Carlisi. Indagini non distruttive sul ponte ad arco in c.a. sul fiume Cassibile. IuPnD, Milano, 2017.
- [23] M. Vlad, G. Kollo, V. Marusceac. A modern approach to tied-arch bridge analysis and design. *Acta Technica Corviniensis – Bulletin of Engineering*. 2015.

- [24] P. Margiotta. *I ponti ad arco in calcestruzzo sostenuti da cavi nelle fasi di costruzione ed esercizio*. PhD Thesis in Structural Engineering – XXII Cycle, ICAR09, University of Palermo, 2011. (in Italian)
- [25] C. Modena, SM Ingegneria s.r.l., <https://www.smingegneria.it>. It visited on April 2020.
- [26] C. Modena, *Adeguamento statico, sismico e funzionale di ponti esistenti: alcuni casi studio*. INGENIO, 2016. (in Italian)
- [27] S. Zuccotto, *Manutenzione di ponti ad arco a via inferiore: il caso del ponte di Pedescala*. Master Thesis in Strctural Engineering, University of Padova, 2007. (in Italian)
- [28] Midas Civil, *On-line Manual – Civil structure design system*. 2018. [http://manual.midasuser.com/EN\\_Common/Civil/865/On-line\\_Manual.htm](http://manual.midasuser.com/EN_Common/Civil/865/On-line_Manual.htm)
- [29] EC 1998-3 (2005) Eurocode 8, Design of structures for earthquake resistance-Part 3: Assessment and retrofitting of buildings. European Committee for Standardization.
- [30] NTC2018, D.M. 17/01/2018. Aggiornamento delle “Norme tecniche per le costruzioni” (in Italian), Off. Gazzette Ital. Repub. N°42 20h Febr. 2018. (2018).
- [31] Circ 21/01/2019 N.7. Istruzioni per l’applicazione dell’«Aggiornamento delle “Norme tecniche per le costruzioni”» di cui al decreto ministeriale 17 gennaio 2018. (Italian Guidelines), Suppl. Ordin. Alla “Gazzetta Uff. n. 35 Del 11 Febbraio 2019. <https://www.gazzettaufficiale.it/eli/gu/2019/02/11/35/so/5/sg/pdf>.

## APPLICATION TO AN URBAN BRIDGE STOCK OF A PRIORITIZATION PROCEDURE BASED ON SEISMIC ASSESSMENT COMPARED WITH THE NOVEL ITALIAN GUIDELINES

E. Saler<sup>1,3</sup>, V. Pernechele<sup>2</sup>, G. Tecchio<sup>3</sup> and F. da Porto<sup>3</sup>

<sup>1</sup> Dept. of Civil, Environmental and Mechanical Engineering, University of Trento  
Via Mesiano 77, Trento, Italy  
e-mail: elisa.saler@unitn.it

<sup>2</sup> Institute for Construction Technologies - National Research Council (ITC-CNR)  
Corso Stati Uniti 4, 35127 Padova, Italy  
e-mail: pernechele@itc.cnr.it

<sup>3</sup> Dept. of Geosciences, University of Padova  
Via Gradenigo 6, 35131 Padova, Italy  
e-mail: {giovanni.tecchio, francesca.daporto}@unipd.it

---

### Abstract

*The challenge of large-stock maintenance with limited budget is faced by administrations in charge which need tools for management and intervention prioritization. This need is especially perceived for bridges which are strategic structures and represent crucial elements in roadway networks. Since 2016, a combined prioritization procedure has been applied to the bridge stock of the Municipality of Padova (Italy) to assess both the condition state, accounting for degradation, and the seismic vulnerability. The proposed methodology evaluates the level of degradation through visual inspections and type-specific forms for the defect survey, while the seismic vulnerability is assessed by means of fragility curves previously obtained by the authors for typical Italian bridges. This contribution focuses on the application of the seismic-based prioritization. The identification of the bridge typologies which appeared to be more seismically fragile is presented, comparing this aspect with results from the recently issued novel Italian Guidelines for the management of existing bridges.*

**Keywords:** Bridge stock, bridge degradation, condition state assessment, bridge seismic vulnerability, prioritization.

---

## 1 INTRODUCTION

Roadway networks represent strategic infrastructures for the civil protection system, since they are fundamental for post-event emergency management. Thus, disaster risk mitigation requires also to improve the reliability of infrastructure networks, especially their most vulnerable elements, such as bridges.

Most of Italian bridges were built before 1980 [1], with no seismic provisions, since the seismic classification of large part of the country was completed only by the early 2000s.

Focusing on seismic vulnerability of bridge assets, fragility curves represent an effective tool to describe the susceptibility of a structure to seismic damage. They express the probability of exceedance of a certain performance level (or damage state [2]) for a given value of intensity measure, for instance the peak ground acceleration (PGA).

An extensive review of the fragility assessment approach in the literature was provided by Muntasir Billah and Shahria Alam [3]. Analytical models are widely used to derive fragility functions, as they can be applied to general taxonomies of structure. One of the most acknowledged analytical approaches is the derivation of fragility curves through non-linear time history analysis (NLTHA) applied to mechanical models (e.g., [4–6]), also considering the effect of degradation on structural performance [7]. Mechanics-based vulnerability assessment of bridges can be also carried out through simplified procedures, such as Displacement-Based approaches [8,9] or limit analysis applied to arch bridges [10,11].

A number of authors have focused on seismic vulnerability assessment of typical bridges of a particular region or country, so as to better catch the local bridge taxonomy [12–14].

Moreover, bridges are particularly subjected to degradation, due to their exposure to environmental agents, as well as other natural hazards (e.g., flood, scour, and landslide) [15]. In addition, some structures, such as orthotropic steel deck bridges, might be subjected to fatigue phenomena, even if recently built [16].

In this framework, structural health monitoring (SHM) systems can be applied to the most critical or strategic structures, to efficiently collect information on structural integrity and durability [17].

Nevertheless, the maintenance and retrofit of large bridge stock is a challenging theme for administrations in charge, that need to allocate limited funds.

A series of scientific-based bridge management systems (BMS) have been proposed since the early 90s [18–21]. In addition, prioritization procedures are commonly required when infrastructure maintenance has been neglected for a long time, leading to the need of an extensive restoration and retrofit campaign which must be first addressed to the most critical structures [20]. Various prioritization approaches have been proposed by researchers, such as, among the others [22–24].

More recently, research has started to focus on combined prioritization approaches, which include seismic vulnerability and degradation. In this framework, in 2020, novel guidelines for existing bridges were issued in Italy [25]. They proposed a novel simplified and multi-level procedure to prioritize further verifications and interventions on bridges part of a stock, based on a multi-risk approach, which considers structural safety accounting for degradation, as well as seismic, hydraulic, and hydrogeological risks. The main limitation of the proposed procedure is that it groups bridges in attention classes, but it has not the purpose of a detailed ranking by rating each structure.

This paper discusses a priority ranking procedure which evaluates both degradation effects and seismic vulnerability (the former through visual inspections and defect survey, and the latter by using fragility curves from the literature), as described by the authors in Saler et al. [26]. The estimate of degradation effects was carried out according to a simplified procedure



available in the literature [27], whereas the proposed seismic assessment approach was devised so as to be consistent with it.

Since 2016, the prioritization approach has been applied to an urban bridge stock consisting of more than 160 bridges. The analyzed urban area, whose specific features are described in the paper, is the Municipality of Padova, in North-East Italy.

This contribution is focused on seismic evaluation, for which a comparison with the procedure proposed by Italian Guidelines is provided [25].

## 2 THE BRIDGE INVENTORY OF PADOVA, ITALY

The current section presents the bridge stock managed by the Municipality of Padova (i.e., comprised of structures for which the local administration is directly in charge, as well as bridges which overcoming roads of the municipality network). Since 2016, an extensive campaign of visual inspection and survey has been carried out, allowing a detailed taxonomy of the stock to be devised.

The bridge inventory of Padova consists of 162 bridges of various types, whose characteristics reflect the topography and urbanization of the area. The city of Padova is very ancient, the first urban settlement was founded in the XII century BC, and surrounded by rivers and artificial canals, useful in the past for both transportation and defense purposes. A certain number of bridges from the Roman and Medieval ages are still operational. Railway network passes across the historical center (HC), where the railway station is located. Thus, a series of bridges were built to overcome railways tracks.

Figure 1 shows some examples of type of bridges of the Padova inventory.

Aggregated distributions of structural and typological characteristics of the bridge inventory are reported in Figure 2, unbundling data related to the HC, so as to highlight its particular features. The related meaning of symbols is reported in Table 1.

Most bridges in the inventory are road bridges, followed by pedestrian bridges, most of which were built in the last 20 years, to enhance pedestrian safety against the increasing traffic volume. The construction age of the asset is quite heterogeneous, with a peak of structures built before 1920, including most of the masonry arched bridges in the historical center. Then, a second peak period of construction is found between 1960 and 1980, due to the expansion outside the historical center of both urbanized and productive areas. Finally, the last period of enlargement of the urban network have occurred in the last 20 years, corresponding to the construction of the most recent part of the suburban beltway, carried out in the early 2000, as well as to the realization of most pedestrian bridges, as aforementioned.

Most bridges in the HC are masonry or r.c. structures. Several cases were surveyed in which an r.c. deck was built next to a masonry arch to allow the carriageway to be widened. Out of the HC, the majority of bridges (almost 60%) has r.c. or prestressed r.c. deck, and the prevalence increases to 70% if only road bridges are considered.

While representing a minority part of the stock, other types of bridges (i.e., with masonry or steel deck) represents a not negligible portion of an urban asset like the Padova inventory. On the contrary, datasets referring to highway networks [13,14] reported bridge types other than r.c. structures to be rarer than in the analyzed case.

Focusing on static scheme, in the HC most bridges are arched (all of masonry structures as well as a number of r.c. arch) or girders, either simply supported or continuous.

Outside the HC the distribution of static schemes appears more heterogeneous, with a peak corresponding to simply supported girders.

In the Padova inventory there are mainly single-span bridges, with also a significant set of structures with two or three spans. A greater number of spans is rare, and mainly located out of the historical center.

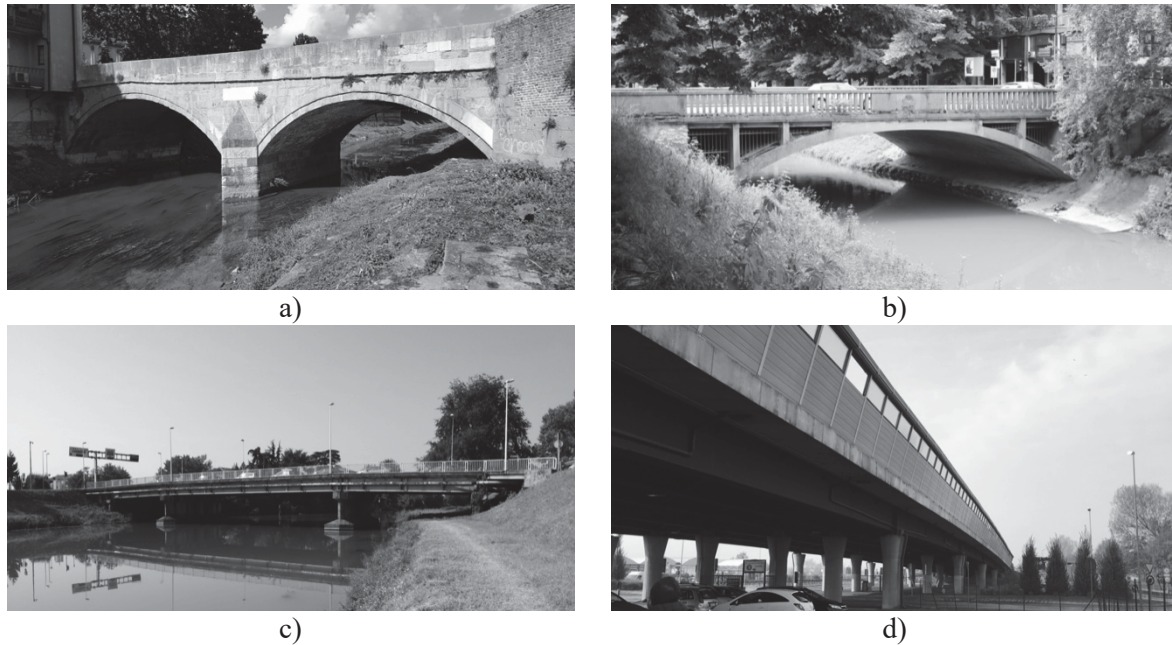


Figure 1: Examples of types of bridges of Padova inventory: a) masonry arch; b) r.c. arch; c) r.c. girder deck; and d) mixed steel-r.c. girder deck.

Small (<20m) to medium (20-40 m) bridges are mainly found in the urban area, also due to its flat topography and high population density. Spans tend to be on average shorter in the HC, with a mode in the range 10-20 meters, while outside the HC the span length mode is in the range 20-30 m (steel and precast r.c. technologies allowed longer spans to be realized). An exception inside the HC is due to the presence of the railway station and tracks, which require greater span length, up to 50 m, to be properly overcome.

Generally, reinforced concrete appears to be the most used material for substructures, although masonry was used for ancient structures. In the historical center is therefore more common to find masonry abutments. Lastly the distribution of height and type of piers is provided (obviously referring to only multi span bridges – 24 in the HC, 50 out of HC). Pier height is mainly shorter than 8 meters, due to the flat topography of the area. Thus, squat configuration is more common for wall piers, which represent the most common type in the HC. Outside the HC also frame piers are fairly common, since this type is more suitable for structures with greater transverse width (i.e., with larger carriageways).

Nevertheless, the following sections are focused only on bridge types which are more susceptible to seismic damage (see the following Table 2), excluding light and flexible structures which are negligibly affected by seismic actions (i.e., steel arch bridges and cabled structures).

<i>DC</i>	Reinforced concrete (r.c.) deck	<i>RET-SIM</i>	Reticular – simply supported
<i>DPC</i>	Prestressed r.c. deck	<i>CBL</i>	Stayed cable or suspended bridge
<i>DM</i>	Masonry deck	<i>AM</i>	Masonry abutment
<i>DS</i>	Steel deck	<i>AC</i>	R.c. abutment
<i>DCS</i>	Mixed steel-r.c. deck	<i>PSC</i>	Circular single pier
<i>ARCH</i>	Arch	<i>PW</i>	Wall pier
<i>SIM</i>	Simply supported	<i>PF2</i>	Two-column frame pier
<i>GER</i>	Gerber scheme	<i>PFM</i>	Multi-column frame pier
<i>CONT</i>	Continuous spans		

Table 1: List of symbols.

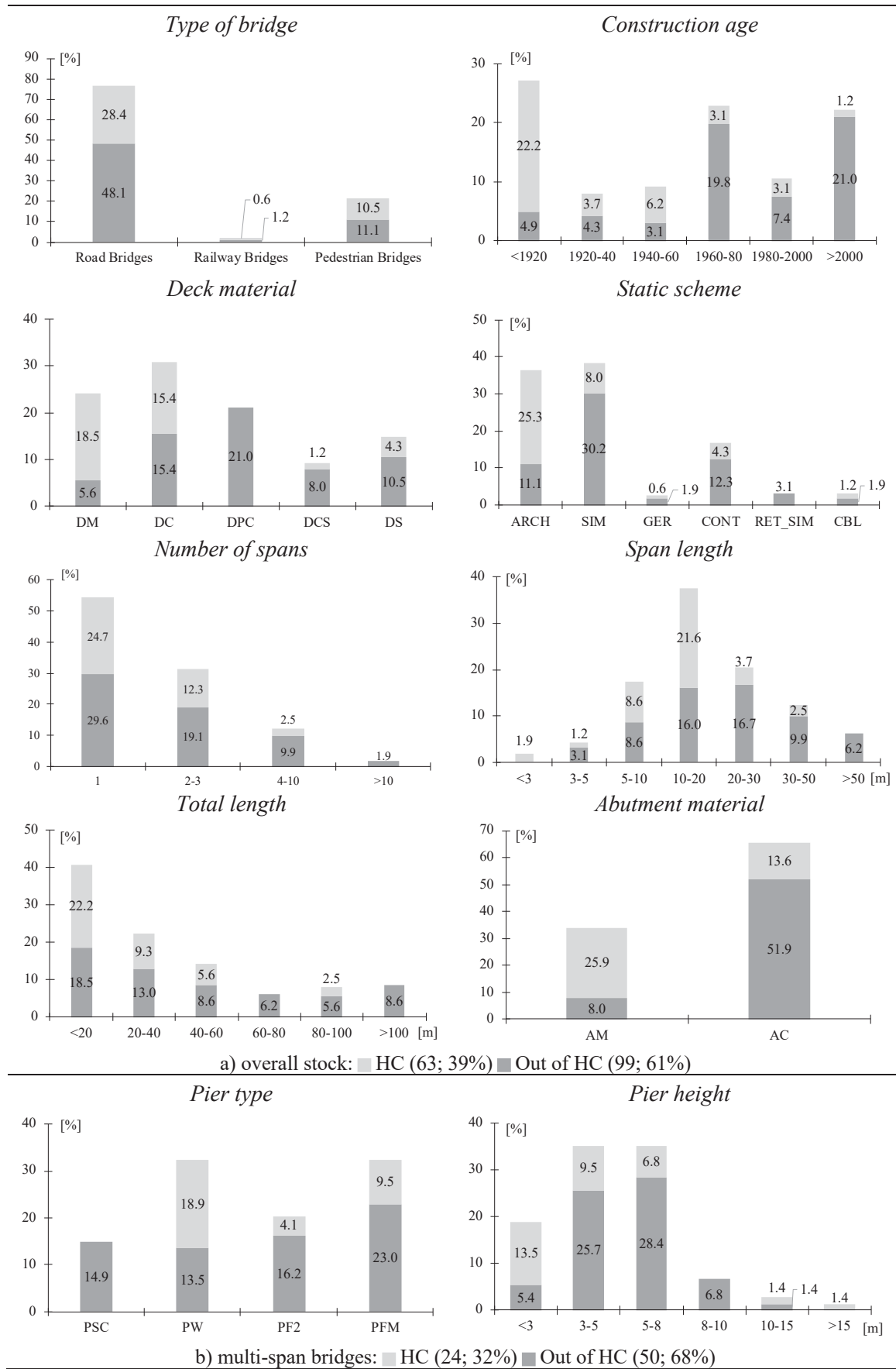


Figure 2: Typological characteristics of bridges of Padova inventory: a) overall stock; b) multi-span bridges.

### 3 SEISMIC-BASED RANKING PROCEDURE

The effects on a structure of both degradation and earthquake depends on its type and on structural members which determine how the structure responses. For instance, some components are more affected by degradation (e.g., Gerber saddles). The identification of bridge macro-classes, based on construction material and static scheme, is reported in Table 2, while Table 3 lists the structural components mainly involved in the structural response and the related mechanisms which were considered in the vulnerability assessment.

The evaluation of seismic vulnerability was carried out through fragility curves previously derived by the authors [8,11], defined for ranges of geometric and structural parameters, for example different fragility curves are assigned for segmental and circular arches. Both Life Safety and Damage limit states (LSLS and DLS, respectively) were considered.

Structural Material	Static Scheme
<i>Masonry</i>	Arch
<i>Reinforced concrete</i>	Arch
	Girder
<i>Steel</i>	Girder
	Reticular

Table 2: Macro-classes of bridges based on construction material and static scheme.

Element	Collapse mechanisms
<b><i>Single span masonry arch</i></b>	
Arch	<i>Longitudinal mechanism</i>
Spandrel wall	<i>Spandrel wall overturning</i>
<b><i>Multi span masonry arch</i></b>	
Arch - Pier	<i>Longitudinal mechanism</i>
Arch - Pier	<i>Transverse mechanism</i>
Spander wall	<i>Spandrel wall overturning</i>
<b><i>Single span reinforced concrete/steel bridge</i></b>	
Support	<i>Support failure</i>
Support	<i>Loss of support of deck</i>
Abutment	<i>Shear/Sliding</i>
Abutment	<i>Flexural mechanism</i>
<b><i>Multi span reinforced concrete/steel bridge</i></b>	
Support	<i>Support failure</i>
Support	<i>Loss of support of deck</i>
Abutment	<i>Shear/Sliding</i>
Abutment	<i>Flexural mechanism</i>
Pier	<i>Shear</i>
Pier	<i>Flexural mechanism</i>
<b><i>Reinforced concrete arch</i></b>	
Support	<i>Support failure</i>
Support	<i>Loss of support of deck</i>
Abutment	<i>Shear/Sliding</i>
Abutment	<i>Flexural mechanism</i>
Arch	<i>Longitudinal mechanism</i>

Table 3: Structural components and relative seismic mechanism for bridge macro-classes.

The probability of exceeding each limit state was processed as described in detail in Saler et al. [26], obtaining a rating value (Total Sufficiency Rating – TSR [26,27]) for each bridge, ranging from 1 (highest vulnerability) to 100 (lowest vulnerability). Seismic classes were defined on the basis of seismic rating, as reported in Table 4, which as well provides an interpretation of seismic classes according to the urgency of intervention. This was defined according to a recommendation [28] of the Italian Department of Civil Protection on how to use results of seismic verifications of relevant and strategic structures, made mandatory by Italian Code OPCM 3274/2003 [29].

	Seismic classes	TSR <sub>seismic</sub>	Urgency of intervention
Priority ↓	As	76-100	Long-term intervention – no need for planning
	Bs	51-75	Mid-term planning of intervention
	Cs	26-50	Short-term planning of intervention
	Ds	1-25	Immediate planning of intervention

Table 4: Seismic classes and relative urgency of intervention.

As an example, the calculation of the seismic rating value for one representative bridge is reported as follows. The case study is a precast r.c. girder bridge; it has three spans, each one simply supported (on simple neoprene bearing pads). It has r.c. abutments and squat r.c. wall piers.

The failure mechanisms which were included in the evaluation were both shear and flexural failure of piers and abutments, as well as the failure of supports. For each mechanism the probability of exceeding either LSLs or DLS was calculated by means of fragility curves, based on the expected peak ground acceleration (PGA) for the site of the structure. Then, for each structural element, the probability of exceeding each LS was assumed to be the maximum probability among the potential mechanisms for the specific bridge component.

Then, the exceedance probability associated to the global response of the bridge was computed by combining the probability of its components, through the upper-bound approach proposed by Choi et al. [4]. The upper-bound, which is more conservative and therefore used to calculate the global exceedance probability, is based on the assumption of statistically independent structural components. The values of exceedance probability for the presented case study are reported in Table 5.

For each limit state, the exceedance probability was associated to a Condition Factor (CF) [26,27], assigned as illustrated in Figure 3, which was then used to calculate the above-mentioned seismic Total Sufficiency Rating (TSR<sub>seismic</sub>), including corrective coefficients to take into account the importance of the bridge in the network [27]. The final rating of the structure is obtained as the minimum TSR between the rates calculated for LSLs and DLS; the seismic class of the structure is then assigned accordingly (Table 6).

A seismic class Ds was therefore assigned to the presented case study, which resulted to have a very low seismic rating, and thus a high priority for intervention planning.

Element	DLS	LSLS
Supports	3.523E-04	2.775E-02
Abutments	0.000E+00	1.898E-05
Piers	9.948E-01	1.832E-01
Global	9.948E-01	2.059E-01

Table 5: Exceedance probability of structural components and of entire bridge and for case study.



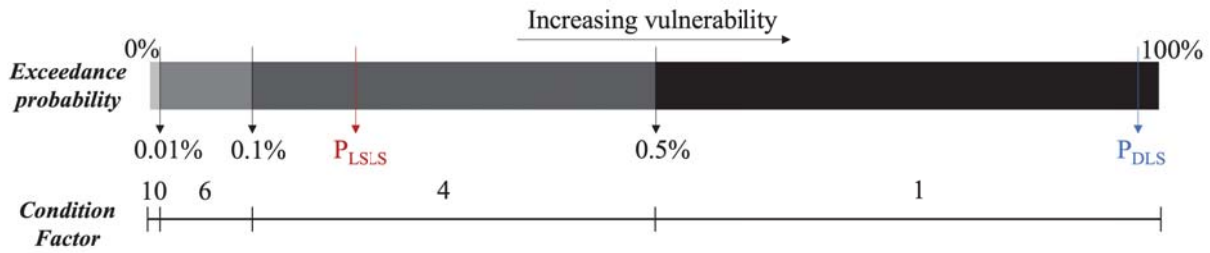


Figure 3: Condition factors associated to exceedance probability with values for case study for LSL and DLS.

	DLS	LSLS	Final
TSR <sub>seismic</sub>	9	36	9
Seismic Class	Ds	Cs	Ds

Table 6: Evaluated seismic rating and class for case study.

### 3.1 Application to the Padova bridge inventory

The seismic-based ranking procedure was applied to 145 bridges of the Padova inventory belonging to macro-classes identified as prone to seismic damage.

The proposed procedure takes into account the local hazard through the demand PGA which value allows the probability of exceeding a LS to be obtained by using fragility curves. Since, in the current paper, the procedure was applied to an urban area with homogeneous seismic hazard classification (i.e., ground acceleration on soil A  $a_g \simeq 0.1g$  for relevant and strategic structures), no variability in the results is due to different hazard input, while it can be assumed to be linked to structural and typological characteristics.

Results are provided as follows in terms of seismic classes. Figure 4 reports the obtained seismic classes, for both bridges in the historical center and outside of it. The majority of structures in the HC are classified Cs (i.e., needing short-term retrofit interventions), while outside the HC, most bridges (64%) fall in the best two classes (As and Bs).

To better understand these distributions, Figure 5 provided the obtained seismic classes, disaggregated on the basis of construction age, deck material, and static scheme, for the entire stock (graphs) and for either HC or the areas outside it (tables).

Comparing the frequency of seismic classes for bridges inside and outside the HC (observing the distributions based on construction age, deck material, and static scheme) a generalized greater seismic vulnerability of the historical center network is confirmed. Higher frequencies are reported for class Cs in the HC, and for the first two classes (As and Bs) outside the HC.

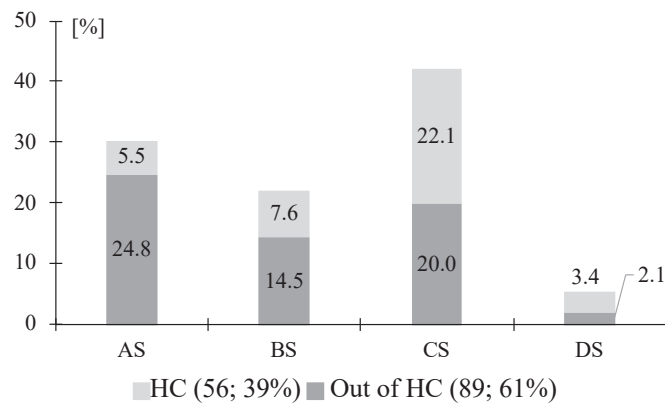


Figure 4: Distribution of seismic classes obtained for earthquake prone bridges of Padova inventory.

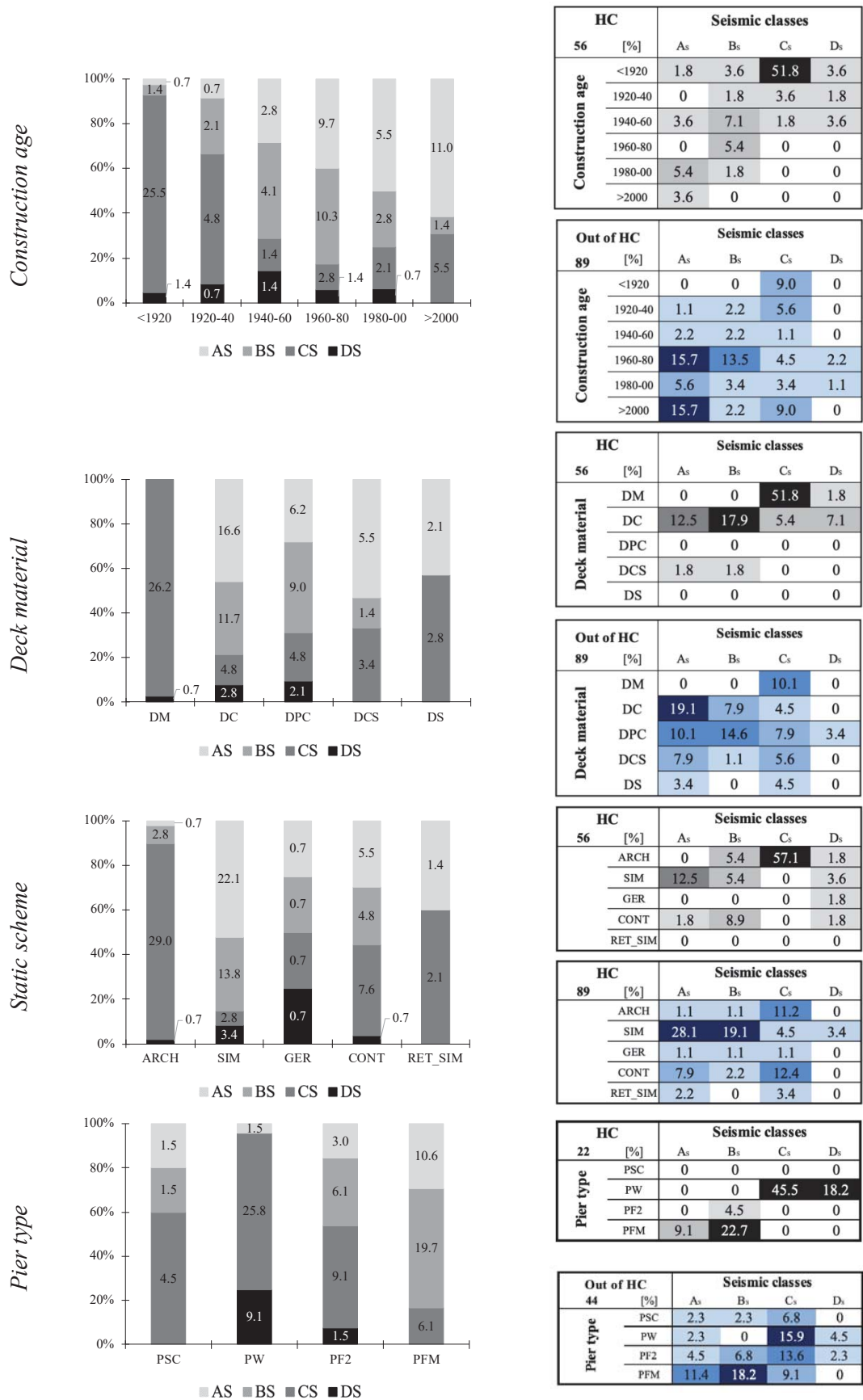


Figure 5: Obtained seismic classes for earthquake prone bridges of Padova inventory disaggregated on the basis of construction age, deck material, and static scheme.

Focusing on the distribution of seismic classes during construction periods, as expected, a larger amount of As-classified structures is found as the age of bridges decreases. The vast majority of bridges built before 1920 falls in seismic class Cs, while various distributions are found in the intermediate ages. Bridges built in the decades 1940s-1960s present the larger portion of structures classified Ds (i.e., needing immediate planning for seismic retrofit interventions).

An interesting correlation emerges analyzing the distribution of seismic classes for different deck materials; most of masonry bridges are classified Cs (leading to the high percentage of structures classified Cs among bridges built before 1920 and with arch static scheme). The critical mechanism for the majority of these bridges was indeed the overturning of spandrel walls, leading to the same seismic class.

R.c. bridges (both ordinary and precast) report the highest percentage of Ds classified structures. The most vulnerable structures, in this case, presents squat wall piers, with high probability of exceeding the trigger of shear mechanism at Damage LS.

A limited number (22) of steel bridges was analyzed in this contribution, since various steel structures were excluded due to their lightness and flexibility. None of this type of structures is classified Ds. Although caution must be applied to the interpretation of results due to the small sample size, a possible explanation for this might be that steel bridges are, on average, of recent construction.

The application of seismic-based prioritization allows typological intervention to be identified, based on specific deficiencies which characterized some types of bridges. Retrofitting all the masonry arched bridges classified Cs by means of tie-rods, to prevent spandrel wall overturning, is a fast intervention, with low impact and cost and great efficiency. Indeed, it allows bridges to change seismic class from Cs to As, with great impact on the global vulnerability of the stock, requiring limited effort.

A common deficiency for girder bridges is given by inadequate support devices. To replace supports with more efficient isolation systems would allow seismic vulnerability of structures to be reduced, with also a decreasing in the forces transferred to substructures.

#### 4 COMPARISON WITH ITALIAN GUIDELINES

Very recently, novel Italian Guidelines for the assessment of bridge stocks were issued [25]. The proposed multi-level approach includes a procedure to classify bridges in five “warning levels” (i.e., high, medium-high, medium, medium-low, low) [30]. The estimation of warning levels, indeed, represent “Level 2” of the guideline procedure, preceded by inventory of the analyzed asset and visual inspection, and followed by detailed evaluations and verifications.

The approach allows the combination, through logical operators, of warning levels referring to various natural hazards (i.e., seismic, hydraulic, and hydrogeological), as well as to degradation effects.

The evaluation of warning levels associated to seismic risk was carried out for the above-described bridge inventory of Padova. In this section results from Italian Guidelines are presented and compared to the outcomes of the proposed seismic-based ranking procedure.

The main difference between the outcomes of these approaches is that the Guidelines group structures in warning levels, in which homogeneous risk is assumed, while the proposed ranking procedure provides a quantitative rating, allowing bridges to be sorted according to the estimated vulnerability.

The approach provided by the Guidelines combines, through logic paths, factors of hazard, exposure and vulnerability, which in turn depend on the following parameters: i) hazard parameters are the peak ground acceleration, topography, and type of soil; ii) exposure parameters are traffic volume, average span length and importance of the bridge; iii) vulnerability parameters

are construction material, static scheme and span length, as well as degradation level and design criteria (whether seismic design was considered or not).

Figure 6 compares the distribution of seismic classes, obtained with the above-described seismic based ranking procedure, and the warning level toward seismic risk obtained from the application of Italian Guidelines [25]. First, the classification of all the seismic prone bridges of the Padova inventory are reported (Figure 6a). The guideline approach provides more conservative results, with most bridges which presents a high or medium-high warning level, and no structure with low warning level. For a local administration in charge with a relatively large stock of structure, it could be challenging to manage the outcomes of guideline prioritization, as the number of bridges requiring urgent verifications remains high. Moreover, when an extensive retrofit campaign must be planned, allocating limited funds, the identification of a manageable number of most critical structures is necessary.

Results of the different approaches are compared also on the basis of deck material (Figure 6b), construction age (Figure 6c), and static scheme (Figure 6d).

Generally, results from the guideline approach are confirmed to be more conservative; an exception is given by masonry arch bridges, which classification according to Guidelines is quite heterogeneous, while they were classified mainly Cs by the proposed seismic-based prioritization. This result may be explained by the fact that the evaluation of warning level according to Italian Guidelines is focused on the Life-Safety LS of the structure, thus some damage mechanisms involving secondary elements (e.g., spandrel walls in masonry arch bridges) may be not directly included. On the contrary, the proposed seismic-based approach includes this kind of mechanisms, which, in case of masonry arch bridges, results to be the most critical, affecting the seismic classification. R.c. bridges report the highest percentage of the worst classified structures, for both the approaches.

The distribution of the most vulnerable structure, according to the analyzed procedure, across the age of construction is slightly different, with a concentration of high warning level [25] in the period 1960-1980, while, as mentioned before, bridges built in the preceding decades (1940-1960) present the peak of Ds-classified structures.

The guideline procedure results to be punitive in particular for bridges with simply supported deck (both simply supported girder and Gerber scheme deck), which however present a peak of worst classified structures also by applying the proposed seismic based ranking procedure.

## 5 CONCLUSIONS

- This paper discusses a priority ranking procedure presented by the authors in Saler et al. [26]. Since 2016, the prioritization approach has been applied to an urban bridge stock managed by the Municipality of Padova, in North-East Italy.
- An extensive campaign of visual inspection was carried out, allowing a detailed taxonomy of the urban stock to be devised and presented in the current contribution by means of aggregated distributions of structural and typological characteristics. Data related to the historical center have been unbundled, so as to highlight its particular features.
- The evaluation of the seismic vulnerability of the stock through fragility curves for various mechanisms allows some indications about typological interventions to be deduced: i) masonry arched bridges are mainly subjected to spandrel wall overturning, thus the application of tie-rods (with low cost and impact) is suitable to improve the seismic response of this type of bridges; ii) girder bridges often have inadequate support systems which replacement with isolation devices can reduce the seismic vulnerability of both substructures and superstructures.

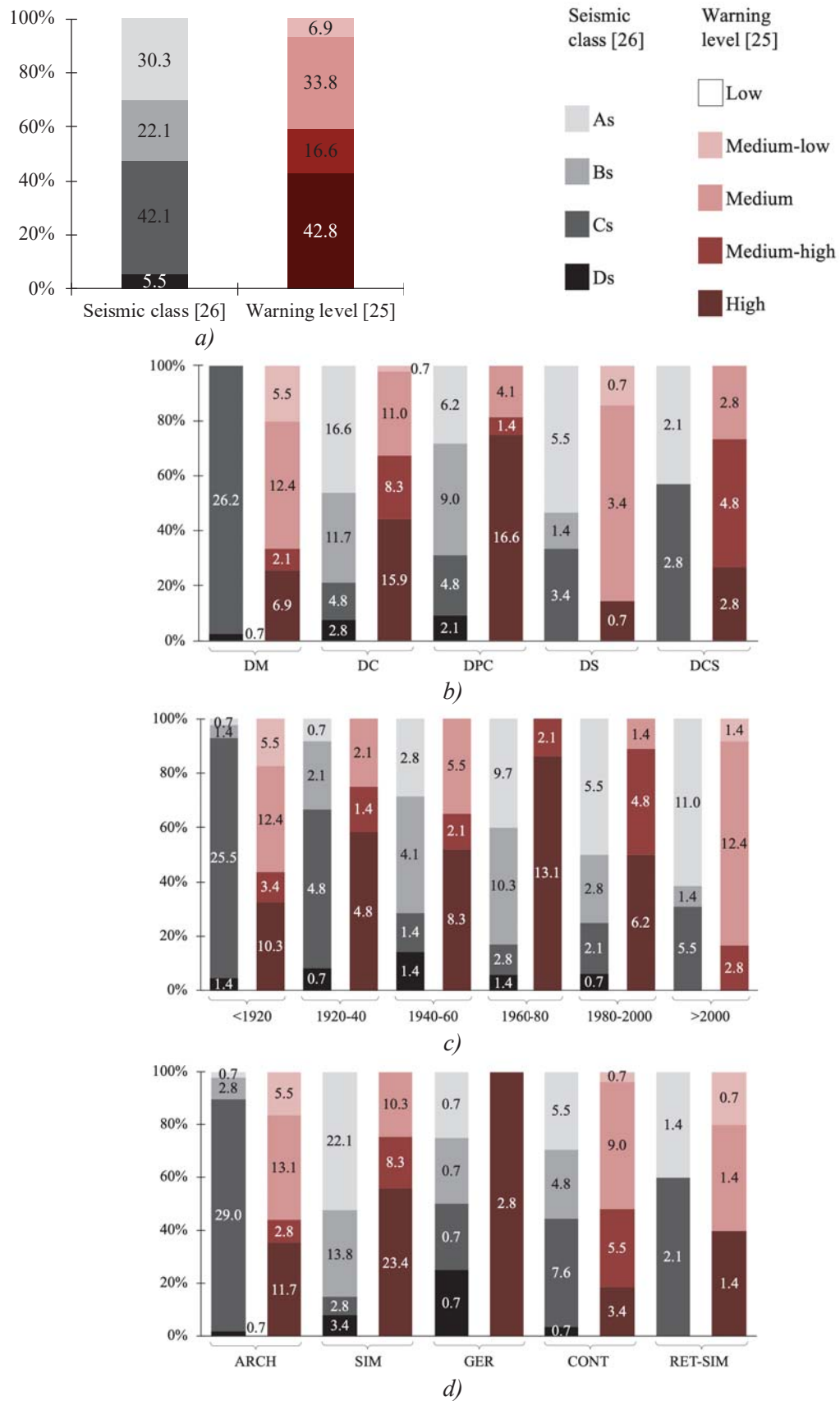


Figure 6: Comparison of seismic class [26] and warning level [25] distributions: a) general; b) based on deck material; c) based on construction age; and d) based on static scheme.



- The evaluation of seismic warning levels according to novel Italian Guidelines on existing bridges [25] was carried out for the bridge inventory of Padova. Italian Guidelines group structures in warning levels (homogeneous risk), while the proposed approach rates each structure, allowing bridges to be sorted according to their vulnerability.
- Results from the applied procedures have been compared. Guidelines resulted to be more conservative, with most bridges presenting a high or medium-high warning level, and no structure with low warning level. However, similar results might be difficult to be managed by local administrations in charge, for the high number of bridges requiring urgent verifications to be urgently planned.

## ACKNOWLEDGEMENTS

Special thanks are due to the Municipality of Padova which partly funded this work.

## REFERENCES

- [1] A. Del Grosso, D. Inaudi, L. Pardi, Overview of European activities in the health monitoring of bridges, *First Int. Conf. Bridg. Maintenance, Saf. Manag.*, 2002 1–8.
- [2] G. Grunthal, EMS98 - European Macroseismic Scale 1998, Conseil de l'Europe - Cahiers du Centre Européen de Géodynamique et de Séismologie, Luxembourg, 1998.
- [3] A.H.M. Muntasir Billah, M. Shahria Alam, Seismic fragility assessment of highway bridges: a state-of-the-art review, *Struct. Infrastruct. Eng.* **11**, 2015, 804–832. <https://doi.org/10.1080/15732479.2014.912243>.
- [4] E. Choi, R. DesRoches, B. Nielson, Seismic fragility of typical bridges in moderate seismic zones, *Eng. Struct.* **26**, 2004, 187–199. <https://doi.org/10.1016/j.engstruct.2003.09.006>.
- [5] Y. Pan, A.K. Agrawal, M. Ghosn, S. Alampalli, Seismic fragility of multispan simply supported steel highway bridges in New York State. II: Fragility analysis, fragility curves, and fragility surfaces, *J. Bridg. Eng.* **15**, 2010, 462–472. [https://doi.org/10.1061/\(ASCE\)BE.1943-5592.0000055](https://doi.org/10.1061/(ASCE)BE.1943-5592.0000055).
- [6] D.H. Tavares, J.E. Padgett, P. Paultre, Fragility curves of typical as-built highway bridges in eastern Canada, *Eng. Struct.* **40**, 2012, 107–118. <https://doi.org/10.1016/j.engstruct.2012.02.019>.
- [7] J. Ghosh, J.E. Padgett, Aging considerations in the development of time-dependent seismic fragility curves, *J. Struct. Eng.* **136**, 2010, 1497–1511. [https://doi.org/10.1061/\(ASCE\)ST.1943-541X.0000260](https://doi.org/10.1061/(ASCE)ST.1943-541X.0000260).
- [8] G. Tecchio, Simplified displacement-based approaches for seismic design and vulnerability assessment of multi-span rc bridges, PhD Thesis, University of Padova, 2013.
- [9] G. Tecchio, M. Donà, C. Modena, Direct displacement-based design accuracy prediction for single-column RC bridge bents, *Earthq. Struct.* **9**, 2015, 455–480. <https://doi.org/10.12989/eas.2015.9.3.455>.
- [10] F. da Porto, G. Tecchio, P. Zampieri, C. Modena, A. Prota, Simplified seismic

- assessment of railway masonry arch bridges by limit analysis, *Struct. Infrastruct. Eng.* **12**, 2015, 567–591. <https://doi.org/10.1080/15732479.2015.1031141>.
- [11] G. Tecchio, M. Donà, F. da Porto, Seismic fragility curves of as-built single-span masonry arch bridges, *Bull. Earthq. Eng.* **14**, 2016, 3099–3124. <https://doi.org/10.1007/s10518-016-9931-6>.
- [12] D. Cardone, G. Perrone, M. Dolce, a Numerical Procedure for the Assessment of Highway Bridges in Seismic Area, in: *Proc. ECCOMAS Themat. Conf. Comput. Methods Struct. Dyn. Earthq. Eng. (COMPDYN, 2007)* Rethymno, Crete, Greece, 2007: pp. 13–16.
- [13] P.E. Pinto, P. Franchin, Issues in the upgrade of Italian highway structures, *J. Earthq. Eng.*, 14:8, 1221–1252, 2010. <https://doi.org/10.1080/13632461003649970>.
- [14] B. Borzi, P. Ceresa, P. Franchin, F. Noto, G.M. Calvi, P.E. Pinto, Seismic vulnerability of the Italian roadway bridge stock, *Earthq. Spectra.* **31**, 2015, 2137–2161. <https://doi.org/10.1193/070413EQS190M>.
- [15] L. Deng, W. Wang, Y. Yu, State-of-The-Art Review on the Causes and Mechanisms of Bridge Collapse, *J. Perform. Constr. Facil.* **30**, 2016, 1–13. [https://doi.org/10.1061/\(ASCE\)CF.1943-5509.0000731](https://doi.org/10.1061/(ASCE)CF.1943-5509.0000731).
- [16] G. Tecchio, F. Lorenzoni, M. Caldon, M. Donà, F. da Porto, C. Modena, Monitoring of orthotropic steel decks for experimental evaluation of residual fatigue life, *J. Civ. Struct. Heal. Monit.* **7**, 2017, 517–539. <https://doi.org/10.1007/s13349-017-0240-9>.
- [17] F. Lorenzoni, N. De Conto, F. da Porto, C. Modena, Ambient and free-vibration tests to improve the quantification and estimation of modal parameters in existing bridges, *J. Civ. Struct. Heal. Monit.* **9**, 2019, 617–637. <https://doi.org/10.1007/s13349-019-00357-4>.
- [18] P.D. Thompson, E.P. Small, M. Johnson, A.R. Marshall, The Pontis Bridge Management System, *Struct. Eng. Int. J. Int. Assoc. Bridg. Struct. Eng.*, 1998,. <https://doi.org/10.2749/101686698780488758>.
- [19] H. Hawk, E.P. Small, The BRIDGIT Bridge Management System, *Struct. Eng. Int. J. Int. Assoc. Bridg. Struct. Eng.* **8**, 1998. <https://doi.org/10.2749/101686698780488712>.
- [20] R.J. Woodward, C. D.W., A.F. Daly, P.R. Vassie, P. Haardt, R. Kashner, R. Astudillo, C. Velando, B. Godart, C. Cremona, B. Mahut, A. Raharinaivo, Lau, I. Markey, L. Bevc, I. Peruš, BRIME - Bridge Management in Europe, Final Rep. (2001) 227.
- [21] V. Gattulli, L. Chiaramonte, Condition assesment by visual inspection for a bridge management system, *Comput. Civ. Infrastruct. Eng.* **20**, 2005, 95–107. <https://doi.org/10.1111/j.1467-8667.2005.00379.x>.
- [22] A. Montepara, F. Merusi, F. Giuliani, Sviluppo di una nuova metodologia per la valutazione delle priorità di intervento di manutenzione di ponti e viadotti, 17° Convegno Naz. Della Soc. Ital. Infrastrutture Viarie. (2008).
- [23] S. Valenzuela, H. De Solminihac, T. Echaveguren, Proposal of an integrated index for prioritization of bridge maintenance, *J. Bridg. Eng.* **15**, 2010, 337–343. [https://doi.org/10.1061/\(ASCE\)BE.1943-5592.0000068](https://doi.org/10.1061/(ASCE)BE.1943-5592.0000068).
- [24] D.Y. Yang, D.M. Frangopol, Risk-informed bridge ranking at project and network levels, *J. Infrastruct. Syst.* **24**, 2018. [https://doi.org/10.1061/\(ASCE\)IS.1943-555X.0000430](https://doi.org/10.1061/(ASCE)IS.1943-555X.0000430).

- [25] C.S.LL.PP, Linee Guida per la classificazione e gestione del rischio, la valutazione della sicurezza ed il monitoraggio di ponti esistenti (in Italian), 2020.
- [26] E. Saler, V. Pernechele, M. Anastasio, M. Minotto, G. Tecchio, Macroscale vulnerability assessment of bridges at municipality level, in: Atti Del XVIII Convegno ANIDIS L'ingegneria Sismica Ital. Ascoli Piceno, 15-19 Settembre 2019, 2019.
- [27] C. Pellegrino, A. Pipinato, C. Modena, A simplified management procedure for bridge network maintenance, *Struct. Infrastruct. Eng.* **7**, 2011, 341–351. <https://doi.org/10.1080/15732470802659084>.
- [28] Italian Department of Civil Protection, Clarifications on the management of the results of seismic verifications carried out in compliance with OPCM 3274/2003 (in Italian), (2010). <http://www.protezionecivile.gov.it/documents/20182/0/Gestioneverifiche.pdf/c6870ced-e049-494c-84de-2689d83b993c>.
- [29] OPCM 3274/2003, All. II - Technical standards for the project, the assessment and the seismic retrofit of buildings (in Italian), (2003).
- [30] F. Braga, G. Buratti, A. Cosentino, A. Dall, G. De Matteis, Multi-level approach for the assessment of bridge and viaducts within road networks, in: Atti Del XVIII Convegno ANIDIS L'ingegneria Sismica Ital. Ascoli Piceno, 15-19 Settembre 2019, 2019.

## ANALYTICAL PROBABILISTIC RESILIENCE ESTIMATION FOR BRIDGES UNDER NEAR-FAULT EARTHQUAKES

Yang Liu<sup>1</sup>, Da-Gang Lu<sup>2</sup>, Fabrizio Paolacci<sup>3</sup>

<sup>1</sup> College of Architecture and Environment, Sichuan University  
e-mail: liuyang6886@163.com

<sup>2</sup> School of Civil Engineering, Harbin Institute of Technology  
e-mail: ludagang@hit.edu.cn

<sup>3</sup> Department of Engineering, Roma Tre University  
e-mail: [fabrizio.paolacci@uniroma3.it](mailto:fabrizio.paolacci@uniroma3.it)

---

### Abstract

*The seismic resilience is becoming an important indicator for the performance assessment of structures and infrastructure systems. This paper proposes a probabilistic approach based on seismic fragility analysis to assess the seismic resilience of steel-concrete composite bridges. By considering the structural and seismic uncertainties in different analysis steps of this approach, the sample generation process for probabilistic demand models is simplified, which largely reduced the computational burden. To deeper understand the seismic resilience and better describe the uncertainties, the estimation interval of the expected resilience is given, while the uncertainties are considered in fragility and propagated to the resilience. This approach is applied to a new typology of steel-concrete composite bridge endowed with concrete cross beams, which has been analyzed within the European Research Project SEQBRI. The results show that this probabilistic approach can largely speed up the process of seismic resilience assessment, while both the aleatory and epistemic uncertainties are considered. Meanwhile, the resilience of the bridge is assessed under both the near-fault and the far-field ground motions which aim to study the influence of near-fault earthquakes on the seismic resilience.*

**Keywords:** Seismic resilience; seismic fragility; steel-concrete composite bridges; near-fault earthquakes.

---

## 1 INTRODUCTION

The concept of seismic resilience has been fast developing in recent years, which plays an important role in performance assessment especially for infrastructure systems. The structural condition of bridges is one of the key aspects of the functionality of transportation networks, which must correspond to an acceptable resilience level to guarantee the efficient flow of people and services (Deco et al. 2013). However, the approach on seismic resilience assessment for bridges has not been yet adequately investigated, being in general difficult to be performed especially for near-fault earthquakes.

Deterministic approaches for seismic resilience evaluation have been developed in the past by many researches. Bruneau et al. (2003) proposed the preliminary framework of seismic resilience assessment. Xu et al. (2007), Frangopol and Bocchini (2011) were interested in the recovery scheduling optimization, while Cimellaro et al. (2010) developed the recovery functions based on empirical formulas. Further developments proposed a probabilistic treatment of the seismic resilience. For example, Deco et al. (2013) suggested a probabilistic approach for resilience prediction based on fragility analysis, while Karamlou and Bocchini (2015) assessed the accuracy of traditional fragility methods for resilience prediction.

The performance-based earthquake engineering (PBEE) approach has been broadly proposed to assess the seismic performance of structures and supporting decision-makers in disaster management. The probabilistic approach adopted by PBEE allows considering the intrinsic randomness related to earthquakes and structures. In this respect, a seminal work concerning the probabilistic seismic demand analysis (PSDA) was performed by Shome (1999), in which the uncertainty of the seismic demand was accounted for. Cornell et al. (2002) derived the demand fragility functions to combine the inherent uncertainties of seismic hazard and structural response. Deco and Frangopol (2013) proposed a method for resilience calculation of bridges in seismic prone-areas including structural uncertainties and variability in the restoration process and rehabilitation costs.

It is worth mentioning that the epistemic uncertainties, which derive mainly from the inadequacy of FE models, cannot be totally neglected (Ellingwood et al. 2009). However, in the previous analyzed works, the epistemic uncertainty for resilience analysis has not been correctly accounted for, which should instead be quantitatively calculated for improving the accuracy of probability models. Therefore, an advancement towards this direction appears necessary.

According to the above-depicted framework, this paper presents a probabilistic approach to estimate the seismic resilience for bridges. For this purpose, analytical seismic fragility functions are used, accounting for both aleatory and epistemic uncertainty associated with earthquake event, structural response and expected damage (Lu et al. 2014). The point and interval estimation methods are firstly used for the expected recovery curves, which allow to easily estimate the seismic resilience and help decision-makers in predicting the seismic performance of bridges. The procedure is then applied to a short-span steel-concrete composite (SCC) bridge which has been analyzed within the Project SEQBRI. In order to estimate the seismic performance of bridges under an extreme event, the effect of near-fault earthquakes is considered. Finally, simplified seismic fragility analysis and seismic resilience estimation of the case study are performed.

## 2 ASSESSMENT METHODOLOGY

In this section, a simplified method to assess the seismic resilience of bridges is presented, which consists of four steps as illustrated in Fig. 1:



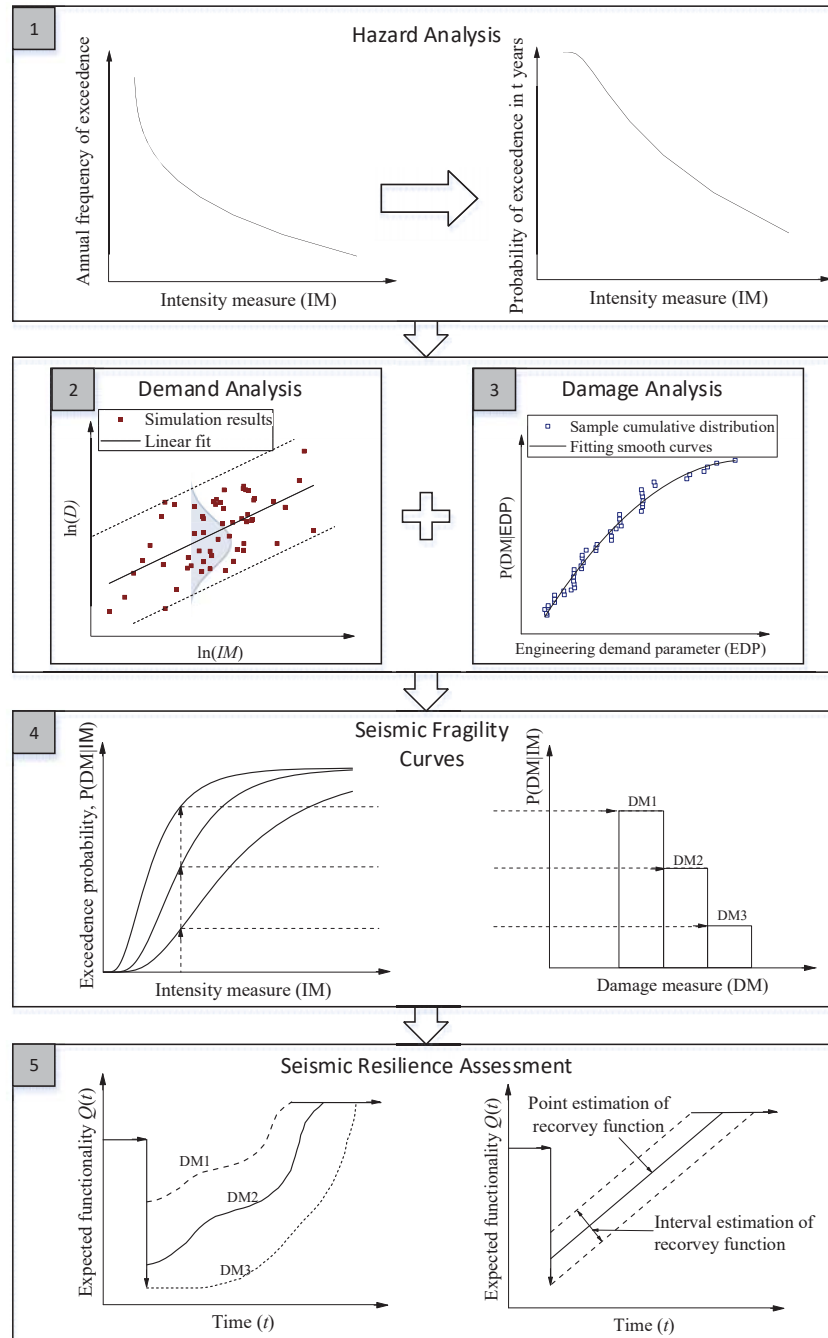


Fig. 1 Analysis stages of assessment methodology

1. **Seismic hazard analysis.** The classical Probabilistic Seismic Hazard Analysis (PSHA) is here in adopted, which provides the mean annual frequency (MAF) of exceedance of a selected intensity measure (IM) for all possible sources generating an earthquake (Cornell 1968);
2. **Seismic demand analysis.** Among different nonlinear demand estimation methods for the PSDA, the Cloud Analysis (CA) certainly is the commonly used. This method consists in

generating cloud of Engineering Demand Parameter (EDP) values for a set of earthquake ground motion records characterized by a hazard-consistent IM. Basic and improved versions of CA have been proposed to account for the inherent randomness of the seismic action in the form of record-to-record variability only or also the epistemic uncertainty, related to the modelling (Bazzurro 1998; Cornell et al. 2002; Ellingwood et al. 2009). In this work only the basic version has been implemented to evaluate the probability of exceedance (POE) of a given demand level.

3. **Damage Analysis.** The damage analysis aims at predicting the structural damage at component level as function of demand parameters. Any damage level, usually expressed in terms of Damage Measures (DM), presents variability with EDP due to the uncertainty of material properties and structural response history (Gardoni et al 2002).
4. **Fragility Analysis.** In this step, the POE of a given DM conditioned to a selected IM is determined by adopting an analytical approach. By assuming a lognormal distribution, a closed-form formulation of demand and capacity fragility curves is proposed, which accounts for epistemic uncertainty as well.
5. **Resilience estimation.** This is the last step that consists in the seismic resilience assessment for different structural damage level caused by the earthquake event, considering the uncertainty associated with the restoration process.

This paper focuses on the previous steps and proposes a methodology based on numerical simulation, which is described in the following sub-sections.

## 2.1 Probabilistic seismic demand models (PSDA)

The purpose of PSDA is to establish a probabilistic relationship between the selected EDP and IM (Tondini and Stojadinovic 2012).

It is assumed that the seismic demand  $D$  follows a lognormal distribution (Cornell et al. 2002). The probability of exceeding the demand level  $d$  conditioned on  $IM = x$  can be expressed as:

$$P[D \geq d | IM = x] = 1 - \Phi \left[ \frac{\ln(d) - \ln(m_D)}{\beta_{D|IM}} \right] = 1 - \Phi \left[ \frac{\ln\left(\frac{d}{m_D}\right)}{\beta_{D|IM}} \right] \quad (1)$$

where,  $m_D$  is the median of the demand parameter EDP,  $\beta_{D|IM}$  is the dispersion of the demand about its median value conditioned to  $IM$ , and  $\Phi(\cdot)$  is the standard normal cumulative distribution function. Additionally,  $m_D$  can be assumed linear in the log-log space (Cornell et al. 2002). Consequently, the probabilistic seismic demand model (PSDM) can be expressed as

$$\ln(m_D) = a + b \ln(IM) \quad (2)$$

in which,  $a$  and  $b$  are regression parameters, which could be assessed by a linear regression analysis on the logarithmic maximum response versus  $\ln IM$ . Accordingly, the logarithmic standard deviation could be estimated by the following formula:

$$\beta_{D|IM} = \sqrt{\frac{\sum_{i=1}^N [\ln(d_i) - \ln(m_D)]^2}{N-2}} \quad (3)$$

Previous studies on bridges clearly demonstrated that the uncertainty from earthquakes events is much bigger than that of structures (Wen et al. 2003; Padgett and Des-Roches 2007). For this reason, in the following only the randomness due to the earthquake is considered by selecting suites of ground motions and generating samples of EDPs. For this approach simplified, the computational burden is reduced several times in time-history analysis.

## 2.2 Seismic fragility functions

The seismic fragility represents the probability of occurrence or exceeding specified levels of damage in the considered range of IMs. This can also be expressed in terms of probability of the seismic demand (D) exceeding the seismic capacity (C) at the component or system level, conditioned on  $IM=x$ :

$$F_R(x) = P(DM|IM = x) = P(D > C|IM = x) \quad (4)$$

Assuming that the capacity (C) obeys lognormal distribution, using Equations (1) and (2), the fragility function can be further derived as:

$$F_R(x) = \Phi \left[ \frac{\ln(m_{D|IM}) - \ln(m_C)}{\sqrt{\beta_{D|IM=x}^2 + \beta_C^2}} \right] = \Phi \left[ \frac{\ln(aIM^b) - \ln(m_C)}{\sqrt{\beta_{D|IM=x}^2 + \beta_C^2}} \right] \quad (5)$$

where,  $\mu_C$  and  $\beta_C$  are, respectively, the median and the dispersion of the capacity. These parameters can be evaluated performing the probabilistic damage analysis adopting either experimental or numerical approaches (Melchers 1999). The fragility function can be further derived as:

$$F_R(x) = \Phi \left[ \frac{\ln(aIM^b) - \ln(m_C)}{\sqrt{\beta_{D|IM=x}^2 + \beta_C^2}} \right] = \Phi \left[ \frac{\ln(m_{D|IM}) - \ln(m_C)}{\sqrt{\beta_{D|IM=x}^2 + \beta_C^2}} \right] = \Phi \left[ \frac{\ln(x/m_R)}{\beta_R} \right] \quad (6)$$

where,  $\mu_R$  and  $\beta_R$  are, respectively, the median and the dispersion of the fragility, obviously, the parameters of the fragility can be re-formulated as (Lu et al. 2014):

$$m_R = \left( \frac{m_C}{a} \right)^{\frac{1}{b}} \quad (7)$$

$$\beta_R = \left( \frac{1}{b} \right) \sqrt{\beta_{D|IM=x}^2 + \beta_C^2} \quad (8)$$

## 2.3 Probabilistic seismic resilience assessment

In the field of civil engineering, the seismic resilience is defined as the ability of structures to contain the effects of a seismic event adopting effective measures to recover functionality after disasters and mitigate the effects of the future seismic risk (Bruneau et al. 2003). However, resilience is a multi-faceted concept, which covers too broadly social and technical aspects to be defined with a single analytical function. In the present paper the following definition of resilience index R is adopted (Deco et al. 2013):

$$R = \frac{\int_{t_0}^{t_0+t_h} Q(t) dt}{t_h} \quad (9)$$

where  $Q(t)$  is the functionality of the structure, which depends on time  $t$ ,  $t_0$  is the occurrence time of the earthquake, and  $t_h$  is the investigated time horizon. Based on the total probability theorem, the estimation of structural functionality at any specific time  $t$  after an earthquake can be calculated. Assuming a limited range of earthquake intensity, the expected functionality (" $Q$ ") (" $t$ ") can be computed as following (Karamlou et al. 2015),

$$\bar{Q}(t) = \sum_i^{n_{IM}} P(IM = i) \sum_j^{n_{DS}} P(DS = j|IM = i) Q_j(t) \quad (10)$$

where, " $P(IM = i)$ " is the probability of occurrence of the earthquake while the intensity  $IM=i$ , computed by using PSHA for the bridge location site (FEMA445). The second item of the right hand of the equation, " $P(DS = j | IM = i)$ ," is the vulnerability expressed as the probability of being in the damage state  $j$  conditioned on " $IM = i$ ".  $Q_j(t)$  is the time-variant functionality of the structure in the case of initial damage state  $j$ . Being different from buildings, the functionality of highway facilities (e.g., bridges) is usually defined as the carrying capacity of traffic under normal situations (ATC13).

## 2.4 Quantification of uncertainties, point estimation and interval estimation

In the field of civil engineering, the seismic resilience is defined as the ability of structures to con

In order to develop reliable probabilistic models the various sources of uncertainties need to be quantified. Two broad types of uncertainties in probability models have to be dealt with: aleatory uncertainties and epistemic uncertainties. The formers are involved in the modeling and evaluation of low-probability, high-consequence events in nature, which are caused by the inherent variability and randomness in nature, and cannot be influenced by the observation. The epistemic uncertainties arise from our limited knowledge, imperfect modeling and simplifications (Ellingwood and Kinali 2009).

As shown in Equation (6), the two probabilistic models of demand and capacity can be integrated into a unitary probabilistic model of the fragility. Alternatively, the fragility model can be separated into a probabilistic demand and a capacity model.

Following the first approach, the uncertainty of the demand and the capacity are considered separately. Referring to the probabilistic seismic demand analysis (PSDA), the dispersion  $\square D|IM$  represents the aleatory uncertainty raised from the randomness of the earthquake records input. That can be directly calculated in the PSDA. The epistemic uncertainty of the demand is instead not included in this model. This approach has been justified by Karamlou and Bocchini (2015) that have evaluated the epistemic uncertainty arising from the different assumptions used to build the probabilistic seismic demand models (PSDM). The effect of this uncertainty on the fragility is limited, whose influence range is smaller than 10%. For this reason, in the following only the aleatory uncertainty  $\square D|IM$  will be accounted for.

In the probabilistic capacity analysis, the capacity dispersion  $\square C$  generally contains two components of uncertainty (Wen et al. 2003), which is defined as:

$$\beta_C = \sqrt{\beta_{CR}^2 + \beta_{CU}^2} \quad (11)$$

where the dispersion  $\square CR$  is the aleatory uncertainty arising from the randomness of the structural capacity, which can be assessed based on some experimental studies. The dispersion  $\square CU$  presents the epistemic uncertainty of capacity, which depends on the effects of the different sample sizes selection in probabilistic capacity seismic analysis (Ellingwood 2001; Ellingwood and Kinali 2009). The substitution of Equation (11) into Equation (8) leads to the point estimation of the fragility function considering the epistemic uncertainty:

$$F_R(x) = \phi \left[ \frac{\ln(x/m_R)}{\beta_R} \right] = \phi \left[ \frac{\ln(ax^b) - \ln(m_C)}{\sqrt{\beta_{D|IM=x}^2 + \beta_{CU}^2 + \beta_{CR}^2}} \right] \quad (12)$$

where the epistemic uncertainty of the fragility is presented by the dispersion  $\square CU$  of the capacity.

In the second approach, the epistemic uncertainty in the fragility model is assumed unitary, which can be directly considered as the epistemic uncertainty of the median  $m_R$  of the fragility curve (Eq. (6)). Therefore, the median of the fragility can be expressed as

$$M_R = \varepsilon m_R \quad (13)$$

in which the  $\varepsilon$  is the random error of the median value.

It is assumed that the median of the fragility follows the lognormal distribution, whose median and dispersion are  $m_R$  and  $\square RU$  (Ellingwood and Kinali 2009; Lu et al. 2014). According to the definition of the confidence level  $C$ , we have:

$$\Phi \left[ \frac{\ln(m_{R,\alpha}/m_R)}{\beta_{RU}} \right] = 1 - \alpha \quad (14)$$

where,  $m_{R,\alpha}$  is the fractile of the median given the confidence level  $\alpha$ , which can be further derived as:

$$m_{R,\alpha} = m_R \exp[-\beta_{RU} \Phi^{-1}(\alpha)] = \left(\frac{m_C}{a}\right)^{\frac{1}{b}} \exp[-\beta_{RU} \Phi^{-1}(\alpha)] \quad (15)$$

Then, the interval estimation of the fragility function becomes:

$$F_R(x) = \Phi \left[ \frac{\ln(x/m_R)}{\beta_R} \right] = \Phi \left\{ \frac{\ln x / (m_C/a)^{\frac{1}{b}} \exp[-\beta_{RU} \Phi^{-1}(\alpha)]}{\sqrt{\beta_{D|IM=x}^2 + \beta_{CR}^2}} \right\} \quad (16)$$

where the dispersion of the fragility  $\square R$  just represents the aleatory uncertainty of the fragility, which can be calculated by the first method mentioned above. The belief interval is assumed to have lower and higher bounds equal respectively to 16% and 84%:

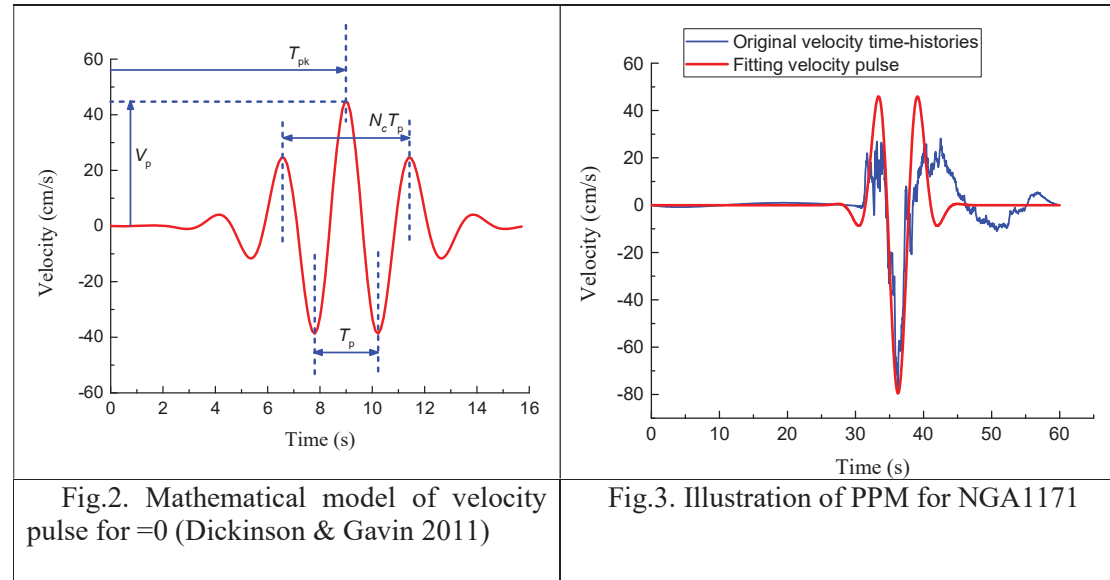
$$m_{R,16\%}(x) = m_{RR} \exp(-\beta_U), m_{R,84\%}(x) = m_{RR} \exp(\beta_U) \quad (17)$$

Equation 10 shows clearly the process of the uncertainty propagation from the hazard, the fragility and the recovery functionality to the expected recovery functionality. The uncertainty in  $Q$  consists of corresponding to the uncertainty in  $P(IM=i)$ ,  $P(DM=j|IM=i)$  and  $Q_j$ . The functionality restoration of bridges is affected by a large amount of uncertainties associated with the condition of the disaster area, the decisions of disaster relief, the support from surrounding areas, etc. (Frangopol et al. 2011). Given that the related research regarding to this uncertainty is limited in the literature, additional research is needed to address this shortcoming. For the sake of brevity, the uncertainty associated to the  $Q_j$  is here neglected in this content. It is assumed that all the uncertainty for the expected recovery functionality is derived from the occurrence of the earthquake and the damage. Then, the epistemic uncertainty in  $Q$  derived from decision making could be considered in the fragility analysis.

### 3 DETERMINATION OF PULSE-LIKE GROUND MOTIONS

It is well known that the near-fault (NF) earthquakes can induce significant seismic damages to the structures. The single or multiple pulses observed in their velocity time histories is the key characteristic for this type of ground motions. With respect to this feature, those ground motions can obviously induce higher seismic demands (Bertero et al. 1978; Hall et al. 1995; Chopra and Chintanapakdee 2001; Alavi and Krawinkler 2001, 2004). Consequently, it is strongly suggested to use this type of ground motions for the seismic assessment of bridges.

In the following, a method to quantify the strong velocity pulse that characterizes NF pulse-like ground motions is introduced (Zhai et al. 2013). The least-square fitting (LSF) technique is firstly used to find best matching with the main velocity pulse of the real ground motion of a simplified numerical model of the time history. Then, the parameters of the velocity pulse (e.g., period of pulse, peak velocity) are identified by using the peak-point method (PPM). Finally, the energy index ( $E_p$ ) is defined and calculated to determine, for the selected natural earthquake records, the pulse-like ground motions (Baker 2007; Zhai et al. 2013).



As shown in Fig.2, the pulse model is defined as (Dickinson & Gavin 2011):

$$v_p(t; V_p, T_p, N_c, T_{pk}, \varphi) = V_p \exp \left[ -\frac{\pi^2}{4} \left( \frac{t - T_{pk}}{N_c T_p} \right)^2 \right] \times \cos \left( 2\pi \frac{t - T_{pk}}{T_p} - \varphi \right) \quad (18)$$

in which  $v_p$  is the velocity pulse,  $V_p$  and  $T_p$  are respectively the amplitude and the period of the pulse,  $N_c$  and  $T_{pk}$  represent the number of cycles and the location in the pulse time-history,



and  $\phi$  is the phase of the pulse. The LSF algorithm is used to match the original velocity pulse and the simplified mathematical model, which is used to remove the high-frequency content of the real ground motions. Based on the PPM (Osaki 2008; Baker 2007), the peak velocity is extracted from the original velocity time histories to locate the velocity valley, and then the time interval of velocity valley is defined as the pulse period. Fig.3 illustrates the extracted velocity pulse for the NGA1171 ground motion.

With the aim to identify, among the selected natural records, the pulse-like ground motion, an energy-based method is used (Baker 2007). In this study, the determination indicator is defined as (Zhai et al. 2013):

$$\begin{cases} E_p = \int_{t_s}^{t_e} dE(t) = E(t_e) - E(t_s) \\ E(t) = \frac{\int_0^t v^2(\tau) d\tau}{\int_0^\infty v^2(\tau) d\tau} \end{cases} \quad (19)$$

in which  $E_p$  is the energy index,  $E(t)$  is the cumulative energy of the ground motion at time  $t$ ,  $t_s$  and  $t_e$  represent respectively the starting and ending time of the velocity pulse and  $v(\tau)$  is the velocity time-history.

According to the recent studies (Zhai et al. 2013), the ground motions are determined as the pulse-like ground motions when the value of  $E_p$  is greater than 0.3. While the peak ground velocity is greater than 30cm/s, the failure probability of this method is about 1.5%. That means some non-pulse-like ground motions may be determined as the pulse-like ground motions. Since the number of the pulse-like ground motions is limited, this standard with value 0.3 is used.

## 4 PROBABILISTIC RESILIENCE CALCULATION OF A SHORT-SPAN STEEL-CONCRETE COMPOSITE BRIDGE

### 4.1 Description of the bridge and its finite element model

The case study is a typical short span overpass with two lanes, currently under investigation within the European Project SEQBRI (Paolacci et al. 2016). The bridge is 40.00m long and consists of 2 spans of 20.00m each.

The bridge presents two spans of 20.0 m each for a total length of 40.0 m (Fig. 4). The roadway width of bridge is 10.6 m, including 6.5 m wide carriageway and two sidewalks of 2.05m wide each. Four HE600B steel girders of S460 steel grade are used, with 2.65 m in-between distance. The thickness of the concrete slab is 25cm. The steel girders are monolithically connected to the pier by a reinforced concrete crossbeam (CCB) 0.9 m wide, whereas they are simply supported on normal (low) damping bearings at the abutment through an additional CCB.

Details of the CCB configuration are shown in Fig. 5. The pier of wall type is 7.0 m height, 0.6 m thick and 7.0 m wide. The foundation soil is assumed to be categorized as type B according to EN1998 (BIBLIO) and the soil structure interaction effect is neglected.

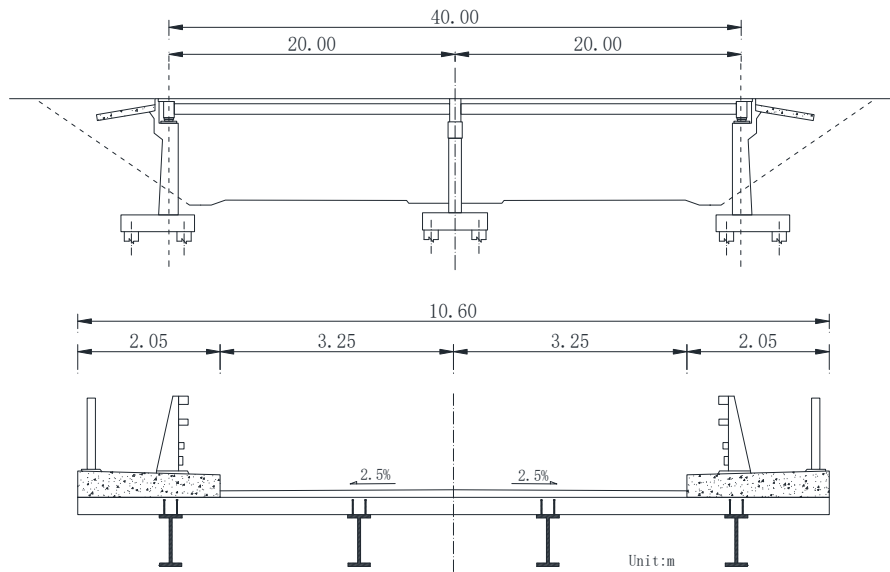


Fig. 4. Longitudinal section and cross section at span

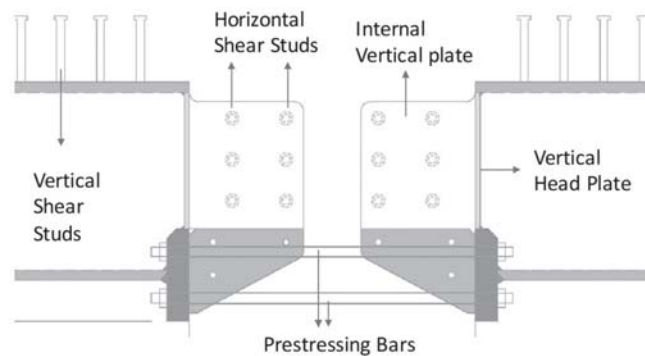


Fig. 5. CCB configuration

The 3D finite element (FE) model illustrated in Fig. 6 has been developed by using the OpenSees software (McKenna et al. 2007). In this model, the nonlinearities of materials are explicitly considered. In particular, the nonlinear beam elements with fiber cross-sections are used to model the single steel girder and the tributary concrete slab (Fig. 6 and 7). The Menegotto-Pinto model is adopted to simulate the mechanical behavior of steel girders and slab reinforcement, whereas the Kent and Park model is used to reproduce the mechanical behavior of concrete.

Nonlinear links with elasto-plastic behavior are used to model the vertical shear studs connecting the steel girders to the slab as well as the shear studs within the CCB. The strength of the shear studs has been evaluated in accordance with CEN (2006), while the stiffness has been evaluated by means of the load-slip curves experimentally defined by Gattesco and Giuriani (1996), even though different other recent proposal has been formulated (Shim et al. 2004; Lee et al. 2005).

Horizontal elasto-plastic links are also used to simulate the shear studs along the deck whereas the vertical direction and the rotation are constrained by rigid links between girders and slab.

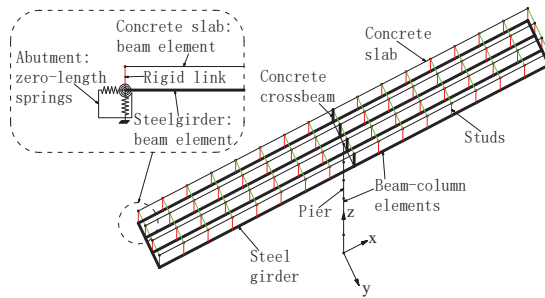


Fig. 6. 3-D finite element model

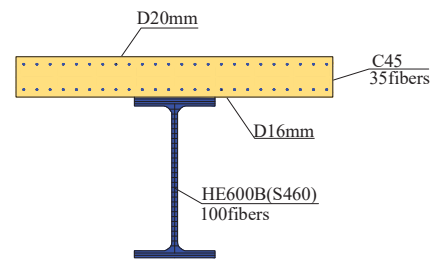


Fig. 7. Fiber sections of the single composite beam

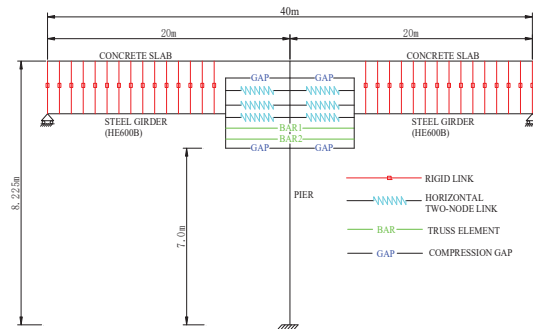


Fig. 8. 2D view of the model and details of the CCB modeling of the single composite beam

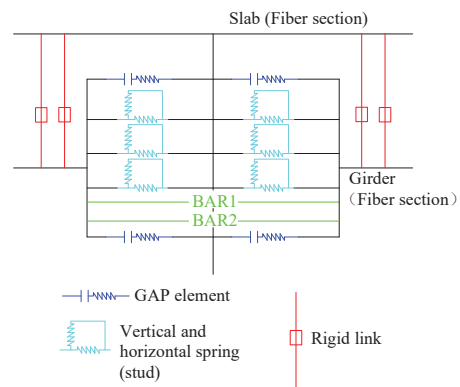


Fig. 9. 2D Component-based model of CCB joint

The behavior of the CCB joint is difficult to reproduce. For this reason, a component-based model has been recently proposed (Paolacci et al. 2014), which is currently under experimental investigation.

Rigid links are used to model the vertical head plates welded on the steel girders and directly in contact with the transverse concrete beam. Different non-linear links reproducing the behavior of the horizontal shear headed studs within the joint are connected to these rigid links according to the CCB configuration (Fig. 5). In order to reproduce the constraint in compression due to the presence of the CCB, gap elements are adopted at both left and right sides of the CCB joint at two different heights, as shown in Fig. 8. A simplified evaluation of the stiffness of the gap elements is performed, assuming that the compressive force transmitted by the girder would act uniformly on the contact area of the vertical head plate. The two groups of prestressing bars at the bottom area of the CCB, are modeled by two elastic truss elements. The 2-D FE model for concrete cross beam is shown in detail in Fig. 9.

#### 4.2 Selection of input ground motions

The case study is a typical short span overpass with two lanes, currently under investigation within the European Project SEQBRI (Paolacci et al. 2016). The bridge is 40.00m long and consists of 2 spans of 20.00m each.

Based on PEER strong ground motion database, a suite of ground motion records has been selected, which includes 60 near-fault (NF) pulse-like ground motions and 60 far-field (FF) ground motions. Two hazard conditions are adopted to select NF ground motions: moment magnitudes (MW) greater than 6.0 and site-to-source distances (R) less than 20 km (Stewart et

al. 2002; Bary and Rodriguez-Marek 2004). Additionally, the dimensionalized peak ground velocity (PGV) and peak ground acceleration (PGA) were imposed to be greater than 0.2 (Kwon and Elnashai 2006; Padgett 2008; Zhai et al. 2012). The FF ground motion records were selected to match the PGA and MW of the NF records, but with  $R > 20$  km. The selected NF ground motions were recorded during the following 5 strong earthquake events: Imperial Valley Earthquake (America, 1979), Palm Springs Earthquake (America, 1986), Northridge Earthquake (America, 1994), ChiChi Earthquake (Taiwan, 1999) and Kocaeli Earthquake (Turkey, 1999); the 80 FF ground motions records belongs to the previous strong seismic events, with the addition of Whittier Narrows Earthquake (America, 1987) and Kobe Earthquake (Japan, 1995). Table 1 reports the selected NF ground motions.

Based on the identification approach described in section 3, all the NF ground motions have been identified as pulse-like ground motions. Due to the limited space, only their energy index  $E_p$  is shown in Fig. 10.

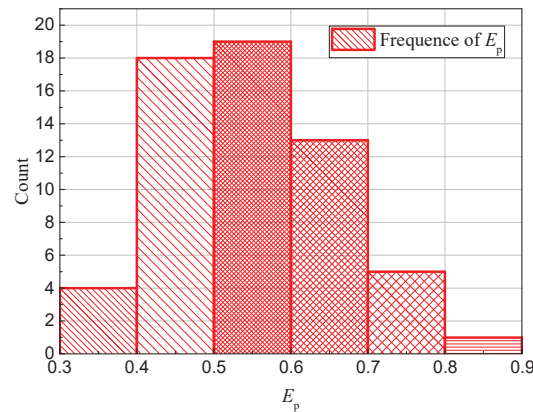


Fig. 10. Energy index  $E_p$  for NF ground motions selected

### 4.3 Fragility analysis

As stated before, the main damage is expected to be in the pier, which is the most vulnerable element of the bridge with potential catastrophic consequences. Usually piers experience different degrees of damaging, from the cover spalling of concrete to the buckling of longitudinal reinforcement or bar fracture. In what follows these three damage levels have been assumed as Damage Measures. Berry and Eberhard (2003), developed empirical equations to estimate deformations at the above damage levels calibrated with a series of existing experimental tests from the UW-PEER reinforced concrete column performance database, which include the performance of over 400 columns. Concrete cover spalling represents the initial damage state that may cause a possible short-term loss of functionality along with a significant repair cost. Bar buckling and fracture represent instead damage states in which safety implications are particularly important, which may imply partial replacement and a longer term loss of functionality. Concrete cover spalling, bar buckling and bar fracture can be defined as a moderate, extensive and complete damage condition. A closed-form of the median value of the drift (mC) was proposed by Berry and Eberhard for damage estimation, which read:

$$\begin{aligned}
 \frac{\Delta_{sp}^{calc}}{L} (\%) &= 1.6 \left( 1 - \frac{P}{A_g f'_c} \right) \left( 1 + \frac{L}{10D_e} \right) && \text{Concrete cover spalling} \\
 \frac{\Delta_{bb}^{calc}}{L} (\%) &= 3.25 \left( 1 + k_e \rho_{eff} \frac{d_b}{D_e} \right) \left( 1 - \frac{P}{A_g f'_c} \right) \left( 1 + \frac{L}{10D_e} \right) && \text{Bar buckling} \\
 \frac{\Delta_{bf}^{calc}}{L} (\%) &= 3.25 \left( 1 + k_e \rho_{eff} \frac{d_b}{D_e} \right) \left( 1 - \frac{P}{A_g f'_c} \right) \left( 1 + \frac{L}{10D_e} \right) && \text{Bar fracture}
 \end{aligned} \tag{20}$$

where  $k_e = 40$ ,  $\rho_{eff} = 0.307$  volumetric transverse reinforcement ratio,  $f'_c$  concrete compressive strength,  $d_b$  diameter of the longitudinal reinforcement,  $D_e$  column depth,  $P$  axial load at the column base,  $A_g$  gross area of the cross-section and  $L$  distance from the column base to the point of contra flexure. An alternative representation of the damage condition in the pier is the plastic deformation at bottom section. The corresponding levels of damage, obtained in the pier, are for concrete cover spalling 1.37%, for buckling 4.25% and for fracture 8.96 %.

According to the HAZUS99 (1999), the damage indices represented the damage of bridge piers are defined as the ductility ratio. Using the case data, the damage indices are calculated and converted to the drift ratio. The results are 0.63% for slight damage, 1.31% for moderate damage, 4.31% for extensive damage and 12.3% for complete damage. Compared to the results of Berry and Eberhard method, the values of damage indices for moderate damage and extensive damage are close. The usefulness of this method is manifested. For the experimental results which are generally considered being more reliable, the results of Berry and Eberhard method for moderate, extensive and complete damage are defined as the main damage indices while the slight damage index of the HAZUS results is the supplement. The comprehensive damage index of the pier is listed in Table 3.

Table 3. Damage index for pier drift ratio

	Slight damage	Moderate damage	Extensive damage	Complete damage
Damage index (Drift ratio)	0.63%	1.37%	4.25%	8.96%

Concerning the aleatory uncertainties considered in fragility analysis, the dispersion of capacity fragility  $\square C$  is assumed equal to 0.3 based on the experimental data elaborated by Berry and Eberhard (2003). In Fig. 11 the seismic fragility curves with intensity measures  $S_a$  are shown; it is evident that the POE of any level of damage in the pier is larger for the NF pulse-like ground motions. In fact, in the considered range of the IMs, the maximum probability of exceeding bars buckling in the NF region is about 90%, while in FF region is about 60%; the probability of bars fracture is about 30% under NF pulse-like ground motions and only 5% in the FF region.



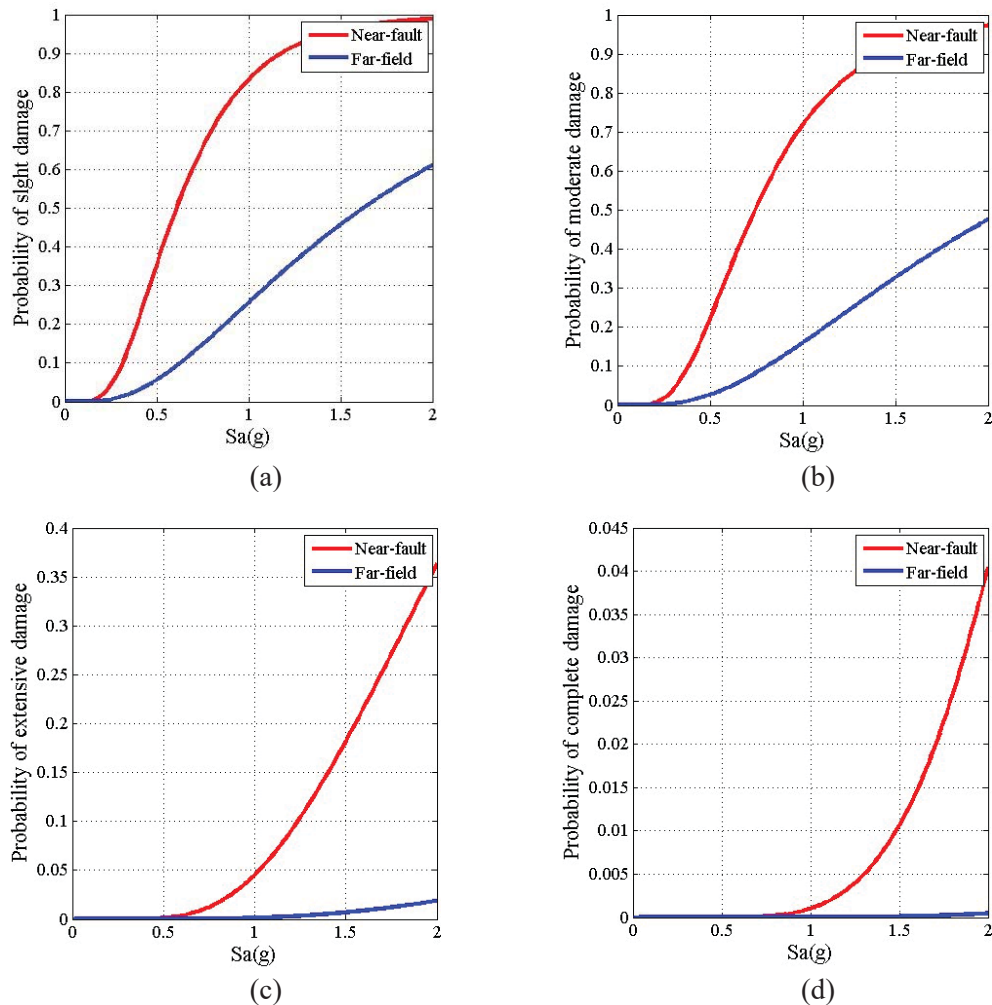


Fig. 11. Comparison of fragility curves of piers with the given IMs on longitude: (a) slight damage, (b) moderate damage, (c) extensive damage, and (d) complete damage

In contrast to aleatory uncertainties, which are essentially irreducible, the epistemic uncertainties generally can be reduced through additional knowledge provided at the expense of more comprehensive (and costly) data acquisition and analysis. Existing studies indicated that the dispersion of fragility in terms of epistemic uncertainties can be assumed as 0.2 (Ellingwood et al. 2009; Haleem et al. 2010).

With the point estimation and interval estimation method mentioned in section 2.4, the fragility curves for near-fault earthquakes considering both aleatory and epistemic have been developed. They are illustrated in Fig. 12. The epistemic uncertainties are labelled as EU. The bounds of the belief interval is assumed to 16% and 84%.

Considering the epistemic uncertainty discussed in Section 2.4, seismic fragility curves with point estimation and interval estimation have been developed. Fig. 12 depicts fragility curves for each limit state. For slight damage and moderate damage, the probability considering epistemic uncertainties is similar to the probability with only aleatory uncertainties, and the epistemic uncertainty can be neglected. But the probability with EU is always bigger than the probability without EU in the considered range of IM. So it is meaningful to consider the

epistemic uncertainty for fragility estimation when the bridges face to extreme events, which can in-duce the extensive damage and complete damage.

It is easy to see that the interval of probability estimation is increasing with the damage. A possible reason is that the epistemic uncertainties reduce the accuracy of probabilistic models for the heavy damage states.

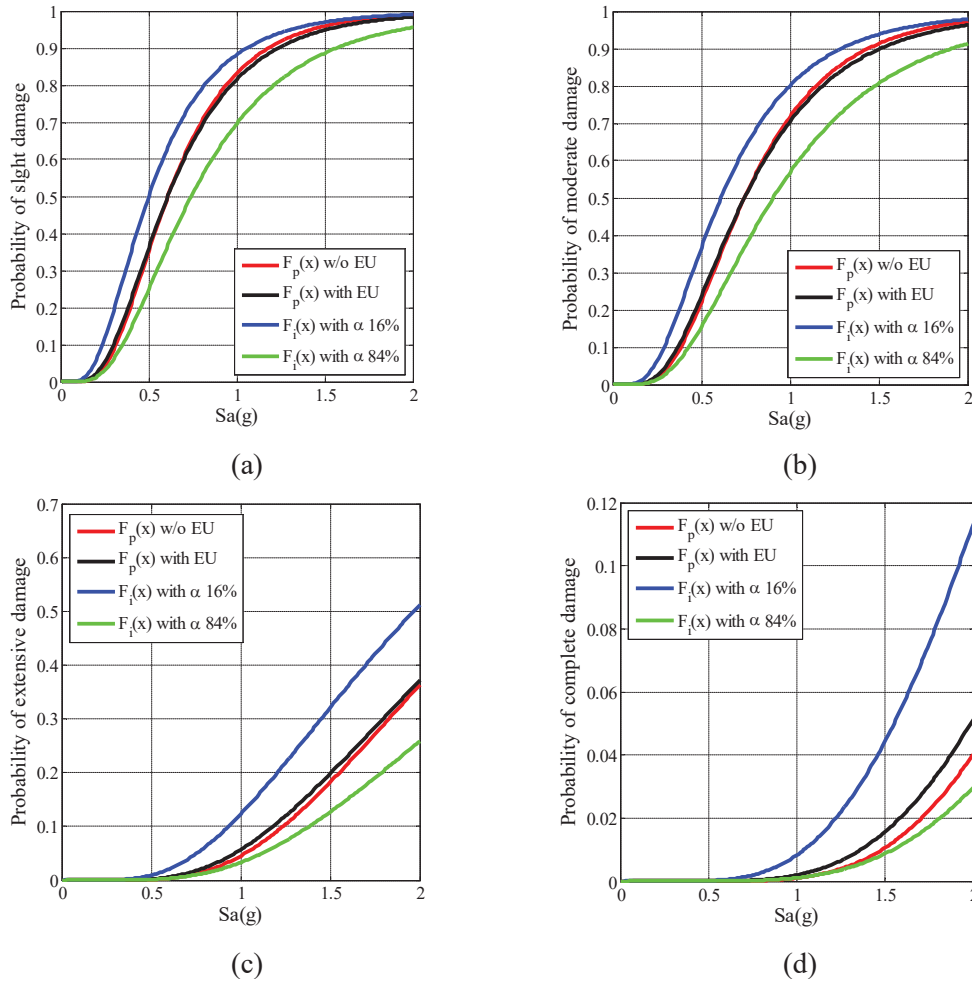


Fig. 12. Point and interval estimate for near-fault earthquake fragility curves considering epistemic uncertainty: (a) slight damage, (b) moderate damage, (c) extensive damage, and (d) complete damage

#### 4.4 Probabilistic Resilience estimation

System and component level fragility curves have been shown in the previous section. Based on these data, the seismic resilience analysis of the selected case study has been performed following the method presented in Section 2.3. The bridge is assumed to be located in Los Angeles, California, USA, whose hazard curves, for a reference life of 100 years, has been provided by the the United States Geological Survey (USGS).

Considering the scarcity of statistical data concerning loss and post-earthquake recovery for bridges, in this work the loss estimation for highway bridges in California (ATC-13, 1985) has been used. In particular, the functionality recovery functions proposed by expertise-based surveys have been adapted for seismic resilience estimation. The selected recovery function is

specific for steel-concrete composite highway bridges, whose functionality is defined as the traffic capacity and the category is 25c.

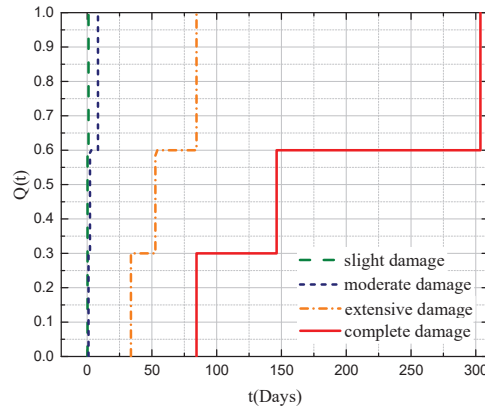


Fig. 13. Functionality recovery profiles from ATC-13

The recovery profiles of the function are listed in tabular form and present the mean time required to recover specific percentage (30%, 60%, 100%) of normal functionality. For the present study, referring to the damage definition provided by ATC-13, the damage states 2 through 5 are assumed to be the corresponding damage states from slight to complete damage. The selected recovery function is presented in Fig.13.

According to ATC-13, the time horizon investigated for the functionality recovery function from is 303.6 days. Consequently, the time horizon of the expected functionality restoration is limited to maximum of 303.6 days by using Equation (7).

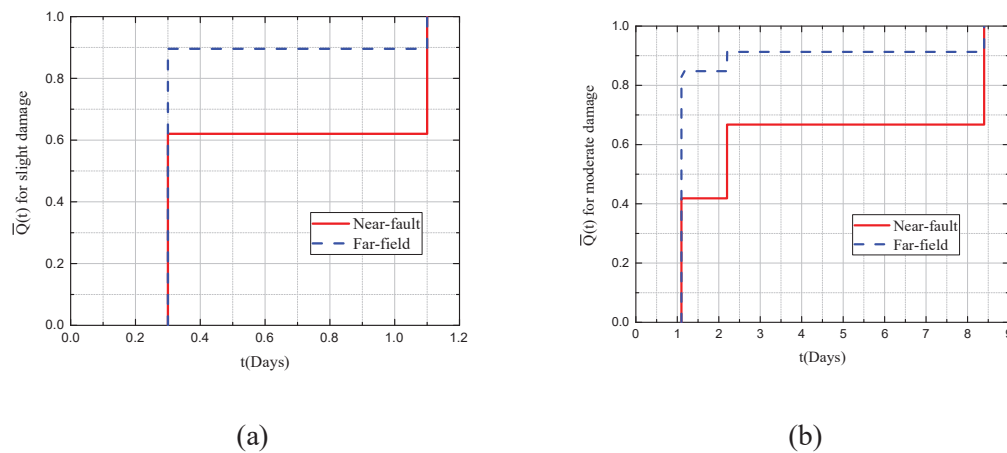


Fig. 14. Expected functionality recovery of bridge at different damage levels: (a) slight damage, (b)moderate damage, (c)extensive damage, and (d)complete damage

Fig. 14 illustrates the expected functionality recovery processes of the bridge for each damage state. Two recovery profiles are presented in the figures both for near-fault and far-field earthquakes. The expected functionality recovery of the whole bridge is instead shown in Fig. 15. Assuming that the total recovery time is constant and the initial damage is null, the obtained functionality paths appears rather different. It can be easily seen that the damage caused by

near-fault earthquakes is more hard to be recovered. In other words, the seismic resilience demand of the bridge struck by near-fault earthquakes is larger than resilience demands coming from far-field earthquakes.

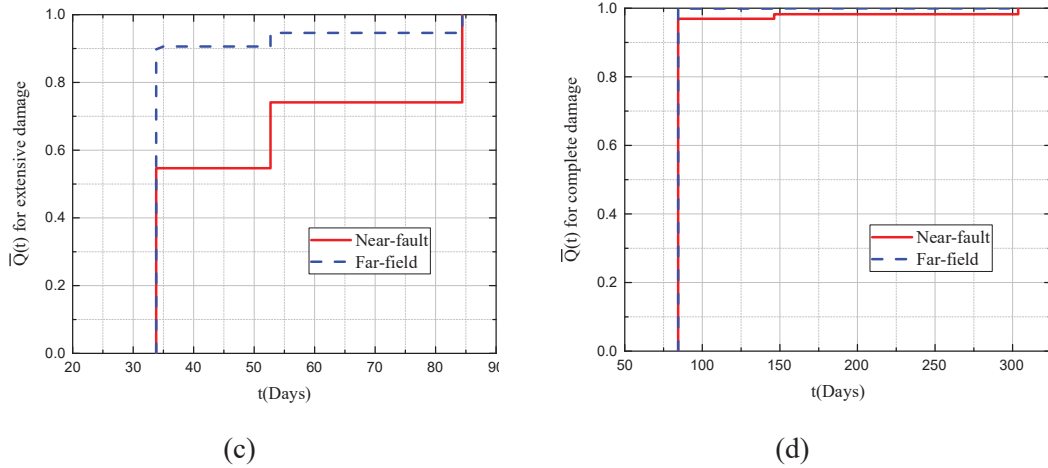


Fig. 14. Expected functionality recovery of bridge at different damage levels: (a) slight damage, (b) moderate damage, (c) extensive damage, and (d) complete damage

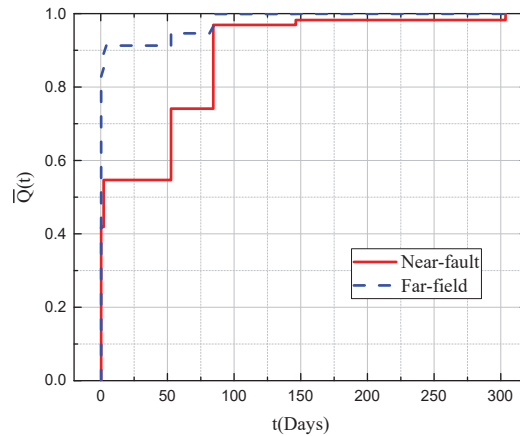


Fig. 15. Expected functionality recovery of whole bridge

Using the fragility curves with epistemic uncertainties (Fig. 16 and 17), the expected functionality recovery estimation can be developed also by using Equation (10). The interval estimation of recovery curves presents a variation tendency similar to fragility curves, which is more uncertain for higher damage. As shown in Fig. 15, it is easy to find that the interval estimation width is broaden for increasing recovery time. This is caused by the increasing of epistemic uncertainty with damage states and the variation of recovery service.

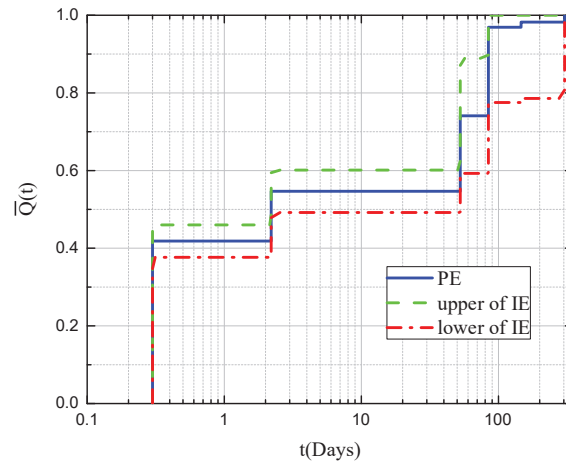


Fig.17. Interval estimation and point estimation of expected functionality recovery for whole bridge

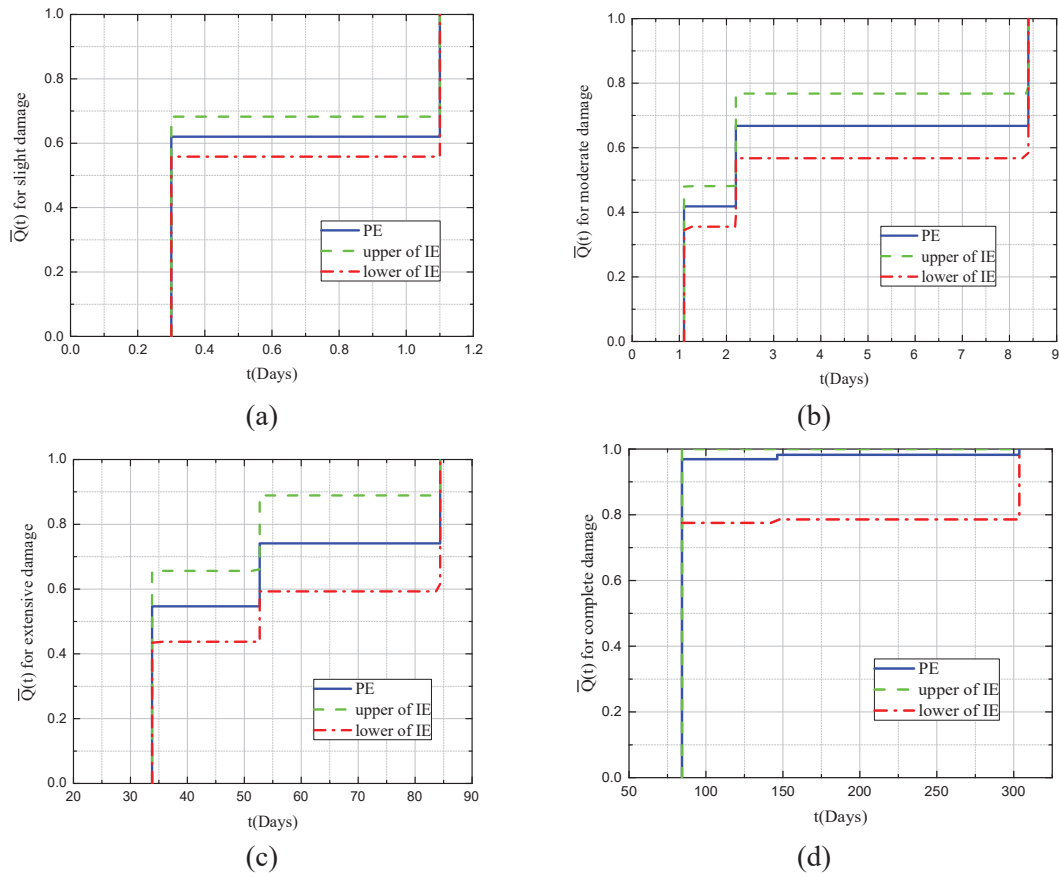


Fig. 16. Point estimation and interval estimation of expected functionality recovery at different damage levels: (a)slight damage, (b)moderate damage, (c)extensive damage, and (d)complete damage

The resilience of the bridge can be determined using Equation (9). The resilience index is shown in Table 4. It can be found that the resilience of the bridge struck by far-field earthquakes



(0.98) is larger than that under near-fault earthquakes (0.89). The horizon of resilience interval estimation for this type of bridges under the near-fault earthquakes ranges from 0.91 to 0.86.

Table 4. The expected resilience index of bridge

	Near-fault	Far-field
Expected resilience index	0.89	0.98
Upper of interval estimation	0.91	-
Lower of interval estimation	0.86	-

## 5 CONCLUSIONS

The probabilistic seismic resilience of steel concrete composite bridges with concrete cross beams is estimated by a simulation approach and the resilience demand after the near-fault earthquake events is quantified. The following conclusions are obtained:

1. The assessment process of seismic resilience is performed in a probabilistic way by using the seismic fragility analysis and considering both aleatory and epistemic uncertainties derived respectively from earthquakes and the structure.
2. It has been found that the uncertainties of the restoration path increase along the time and when more severe damage occurs.
3. The near-fault pulse-like earthquakes have significant effects on the seismic performance of the bridge. The result have shown that the estimation resilience of the bridge under NF earthquakes is about 10% less than FF earthquakes; the function restoration indicates that the bridge under NF earthquakes is more difficult to recover than that under FF earthquakes.
4. It has been demonstrated that the simplified approach proposed in this paper can be profitably used to approximately and easily estimate the seismic resilience of a steel concrete composite bridge. This suggests further developments devoted to the extension of the method for the calculation of the resilience of bridge network systems.

It has been found that the main barrier for the seismic resilience assessment is limited by the scarce number of studies investigating the functionality recovery functions. In this respect, current on-going research activities concerning this aspect will lead to better restoration process models, which it will increase the assessment accuracy..

## ACKNOWLEDGMENTS

The authors would like to thank the Editor and the anonymous reviewers for their constructive comments and valuable suggestions to improve the quality of the article. The financial supports received from the National Science Foundation of China (Grant Nos. 51378162, 51908384), and the China Postdoctoral Science Foundation (2020M673223) is gratefully appreciated. The present work is also supported by the funds of the European Project SEQBRI: “Performance-Based Earthquake Engineering Analysis of Short-Medium Span Steel-Concrete Composite Bridges”, Grant N° RFSR-CT-2012-00032.

## REFERENCES

- [1] Alavi B, Krawinkler H (2001) Effects of near-fault ground motions on frame structures. Technical Report, Blume Center Report 138, Stanford, California
- [2] Alavi B, Krawinkler H (2004) Behavior of moment-resisting frame structures subjected to near-fault ground motions. *Earthquake engineering & structural dynamics* 33, 687–706
- [3] ATC (1985) Earthquake damage evaluation data for California. Technical Report ATC-13, Applied Technology Council (ATC), Redwood City, CA
- [4] Baker JW (2007) Quantitative classification of near-fault ground motions with wavelet analysis. *Bulletin of the Seismological Society of America* 97(5): 1486-1501
- [5] Bazzurro P (1998) Probabilistic Seismic Demand Analysis. PhD Dissertation. Stanford University: UMI
- [6] Berry MP, Eberhard M (2003) Performance Models for Flexural Damage in Reinforced Concrete Columns. PEER Report, 2003/18
- [7] Bertero VV, Mahin SA, Herrera RA (1978) Aseismic design implications of near - fault San Fernando earthquake records. *Earthquake engineering & structural dynamics* 6(1): 31-42
- [8] Bray JD, Rodriguez-Marek A (2004) Characterization of forward-directivity ground motions in the near-fault region. *Soil dynamics and earthquake engineering* 24(11): 815-828
- [9] Bruneau M, Chang SE, Eguchi RT, Lee GC, O'Rourke TD, Reinhorn AM, Shinozuka M, Tierney K, Wallace AW, von Winterfeldt D (2003) A framework to quantitatively assess and enhance the seismic resilience of communities. *Earthquake Spectra* 19(4):733–752
- [10] CEN (European Committee for Standardization) (2004) Design of composite Steel and Concrete Structures. Eurocode 4, Brussels
- [11] Chopra AK, Chintanapakdee C (2001) Comparing response of SDF systems to near-fault and far-fault earthquake motions in the context of spectral regions. *Earthquake Engineering & Structural Dynamics* 30(12): 1769-1789
- [12] Cimellaro GP, Reinhorn AM, Bruneau M. (2010) Seismic resilience of a hospital system. *Structure and Infrastructure Engineering* 6(1–2):127–144
- [13] Cornell CA (1968) Engineering seismic risk analysis. *Bulletin of the Seismological Society of America* 58(5): 1583-1606
- [14] Cornell CA, Jalayer F, Hamburger RO, Foutch DA (2002) Probabilistic basis for 2000 SAC federal emergency management agency steel moment frame guidelines. *Journal of Structural Engineering* 128(4): 526–533
- [15] Decò A, Bocchini P, Frangopol DM (2013) A probabilistic approach for the prediction of seismic resilience of bridges. *Earthquake Engineering & Structural Dynamics* 42(10): 1469-1487
- [16] Dickinson BW, Gavin HP (2011) Parametric statistical generalization of uniform hazard earthquake ground motions. *Journal of Structural Engineering(ASCE)* 137(3): 410-422
- [17] Ellingwood BR (2001) Earthquake risk assessment of building structures. *Reliability Engineering & System Safety* 74(3): 251-262

- [18] Ellingwood BR, Kinali K. (2009). Quantifying and communicating uncertainty in seismic risk assessment. *Structural Safety* 31(2): 179-187
- [19] Federal Emergency Management Agency (FEMA) (2006) Next-generation performance-based seismic design guidelines. Technical Report FEMA-445, Washington, D.C.
- [20] Frangopol DM, Bocchini P (2011) Resilience as optimization criterion for the rehabilitation of bridges belonging to a transportation network subject to earthquake. *Proceedings of the ASCE 2011 Structures Congress SEI 2011*, Ames D, Droessler TL, Hoit M (eds). Las Vegas, NV; 2044–2055.
- [21] Gardoni P, Der-Kiureghian A, Mosalam KM (2002) Probabilistic capacity models and fragility estimates for reinforced concrete columns based on experimental observations. *Journal of Engineering Mechanics* 128(10): 1024-1038
- [22] Gattesco N, Giuriani E (1996) Experimental study on stud shear connectors subjected to cyclic loading. *Journal of Constructional Steel Research* 38(1): 1-21
- [23] Haleem K, Abdel-Aty M, Mackie K (2010) Using a reliability process to reduce uncertainty in predicting crashes at unsignalized intersections. *Accident Analysis & Prevention* 42(2): 654-666
- [24] Hall JF, Heaton TH, Halling MW, et al (1995) Near-source ground motion and its effects on flexible buildings. *Earthquake spectra* 11(4): 569-605
- [25] Federal Emergency Management Agency (FEMA) (1999) Earthquake loss estimation methodology: User's Manual. HAZUS99, Washington D.C.
- [26] Karamlou A, Bocchini P (2015) Computation of bridge seismic fragility by large-scale simulation for probabilistic resilience analysis. *Earthquake Engineering & Structural Dynamics* 44(12): 1959-1978
- [27] Kwon OS, Elnashai A (2006) The effect of material and ground motion uncertainty on the seismic vulnerability curves of RC structure. *Engineering structures* 28(2): 289-303
- [28] Lee PG, Shim CS, Chang SP (2005) Static and fatigue behavior of large stud shear connectors for steel-concrete composite bridges. *Journal of Constructional Steel Research* 61(9):12, 70-85
- [29] Liu Y, Lu DG, Paolacci F (2015) Multivariate probabilistic seismic demand analysis of steel-concrete composite Bridges under Near-fault Pulse-like Ground Motions. *Multispan large bridges*, Portugal
- [30] Lu DG, Yu XH, Jia MM, et al (2014) Seismic risk assessment for a reinforced concrete frame designed according to Chinese codes. *Structure and Infrastructure Engineering* 10(10): 1295-1310
- [31] McKenna F, Mazzoni S, Scott MH, Fenves GL (2007) OpenSees command language manual. Pacific Earthquake Engineering Research Center, University of California, Berkeley, July
- [32] Melchers RE (1999) *Structural reliability: Analysis and prediction* (2nd Ed.). Wiley, New York
- [33] Osaki Y (2008) *Spectral analysis in earthquake engineering*. Seismological Press, Beijing
- [34] Padgett JE, Des-Roches R (2007) Sensitivity of seismic response and fragility to parameter uncertainty. *Journal of Structural Engineering* 133(12): 1710-1718

- [35] Padgett JE (2008) Selection of optimal intensity measures in probabilistic seismic demand models of highway bridge portfolios. *Earthquake Engineering and Structural Dynamics* 37:711-725
- [36] Paolacci F, Giannini R (2014) Toward a performance-based earthquake engineering analysis of short-medium span steel-concrete composite bridges. Second European Conference on Earthquake Engineering and Seismology. Istanbul
- [37] Paolacci F, et al (2016) Performance-based earthquake engineering analysis of short-medium span steel-concrete composite bridges (SEQBRI), European research fund for coal and steel (RFCS). Grant N°RFSR-CT-2012-00032, 2012-2015, Final Report, March 2016
- [38] Shim CS, Lee PG, Yoon TY (2004) Static behavior of large stud shear connectors. *Engineering Structures* 26:18, 53-60
- [39] Shome N (1999) Probabilistic Seismic Demand Analysis of Non-linear Structures. PhD Dissertation, Stanford University
- [40] Stewart JP, Chiou SJ, Bray JD, et al (2002) Ground motion evaluation procedures for performance-based design. *Soil dynamics and earthquake engineering* 22(9): 765-772
- [41] Tondini N, Stojadinovic B (2012) Probabilistic seismic demand model for curved reinforced concrete bridges. *Bulletin of Earthquake Engineering* 10: 1455-1479
- [42] U.S. geological hazard science center (2012) <http://geohazards.usgs.gov/hazardtool/application.php>. Accessed 15 September 013
- [43] Wen YK, Ellingwood BR, Veneziano D, et al (2003) Uncertainty modeling in earthquake engineering. MAE center project FD-2 report
- [44] Xu N, Guikema SD, Davidson RA, Nozick LK, Çağnan Z, Vaziri K (2007) Optimizing scheduling of post-earthquake electric power restoration tasks. *Earthquake Engineering and Structural Dynamics* 36(2): 265–284
- [45] Zhai C, Chang Z, Li S, Chen ZQ, Xie L (2013) Quantitative identification of near-fault pulse-like ground motions based on energy. *Bulletin of the Seismological Society of America* 103(5): 2591-2603.

## **SIMPLIFIED ANALYTICAL-MECHANICAL METHODOLOGY FOR STRUCTURAL-SEISMIC SAFETY ASSESSMENT OVER TIME OF RC BRIDGES AFFECTED BY CORROSION PHENOMENA**

**M. Gentile<sup>1</sup>, F. Molaioni<sup>2</sup>, S. Pampanin<sup>1</sup>**

<sup>1</sup> Sapienza University of Rome, Department of Structural and Geotechnical Engineering  
Via Eudossiana 18, 00184, Rome, Italy  
matteo.gentile8@gmail.com, stefano.pampanin@uniroma1.it

<sup>2</sup> University of Rome Tor Vergata, Dept. of Civil Engin. and Computer Science Engin. (DICII),  
Via del Politecnico 1, Rome, 00133, Italy  
filippo.molaioni@uniroma2.it

---

### **Abstract**

*Existing R.C. bridge structures are generally subject to intense environmental attacks. Over time, environmental actions can trigger structural deterioration effects, the most common of which is the rebars corrosion. As steel reinforcement corrosion could reduce the capacity of R.C. members, the seismic safety of R.C. bridges could be compromised by these phenomena. In accordance with international guidelines, the initial assessment of bridges is carried out by identifying and grading defect-indices after a visual inspection of the structure. This study arises from the need to find a quantitative correlation between the grading scale adopted in the evaluation of defect-indices and the impact of corrosion effects on RC members capacity and safety, also evaluating the evolution over time of degradation. A practical simplified, whilst mechanical-based, analytical methodology for assessing the seismic safety starting from defect-index visual assessment of RC bridges subject to degradation corrosive attacks, is presented and applied to a case study RC bridge representative of the main characteristics of the viaducts of Italy. Different chloride damage scenarios related to defect-indices are considered for the piers of the case study bridge and the seismic safety of the structure is analytically evaluated. Two corrosion rate limit conditions are then considered to evaluate (upper and lower bound) effects on seismic safety over time. Finally, an estimate of the epistemic uncertainty due to the visual assessment of the damage is performed to obtain the structure collapse probability. The analytical results underline that the seismic safety is strongly influenced both by the location and the evolution of corrosion phenomena over time. By identifying the safety and collapse probability of the structures, the proposed methodology can be used as a decision-making support tool regarding the need for intervention with maintenance/restoration/retrofit solutions.*

**Keywords:** Reinforced Concrete, Bridges, Seismic Safety, Seismic Assessment, Corrosion, Collapse Probability.

---



## 1 INTRODUCTION

The structural-seismic safety assessment of existing reinforced concrete bridges is a long-standing key topic in civil engineer [1]. The Italian territory, characterized by medium-high seismicity, has a large stock of old RC bridge structures, typically prior to the introduction of seismic-resistant and durability principles and code provisions [2-4]. Deterioration phenomena may be triggered by aggressive environmental conditions for RC structures lacking adequate construction details. In these cases, corrosion of reinforcing rebars represents the most frequent and dangerous deterioration phenomenon. Once activated, corrosion can occur in a uniform or localized manner; uniform corrosion is caused by humid and carbon dioxide-rich environmental conditions; pitting corrosion instead activates due to the penetration of chloride ions in concrete, a frequent case for bridges due to the application of de-icing salts.

Corrosion of the steel reinforcement affects the mechanical properties of the materials, leading to reduction of the resistant section of the steel bars and of the reinforcement deformation capacity, cracking of cover concrete, and deterioration of the bond strength. In recent decades, considerable efforts have been devoted to understanding the mechanical behavior of corroded R.C. members. In Rodriguez et al. 1997 [5], Castel et al. 2000 [6], Meda et al. 2014 [7] experimental tests were carried out to evaluate flexural, shear and cyclic behavior. The effects on material properties such as stress-strain and/or bond strength laws were identified in Alonso et al. 1996 [8], Almusallam et al. 2001 [9], Apostolopoulos et al. 2008 [10], Imperatore et al. 2017 [11], FIB Model Code 2020 [12]. The reinforcing bars corrosion phenomenon is characterized by two phases [13]: the initiation phase, when atmospheric agents penetrate the concrete until the reinforcement depassivation, and the propagation phase when the impact on materials further evolve over time. Since the seismic performance of bridge structures is highly dependent on the mechanical behavior of its elements, thus on the state of decay, the assessment of seismic structural safety of existing structures and infrastructures should take into account the quantitative evaluation of capacity reduction and its impact on performance/safety due to rebars corrosion.

Given the key strategic role of bridge structures within a country's road network, and the potentially substantial socio-economic costs associated with demolition-reconstruction interventions, several national and international guidelines on the evaluation of existing reinforced concrete bridges have been issued in recent years [14,15]. The common goal is to develop practical and reliable bridge-state assessment procedure and define appropriate maintenance-retrofit solutions for degraded and unsafe structures. Some of these guidelines (e.g., [14]), provide for a multilevel (tiers) approach based on the identification of defect indices following a

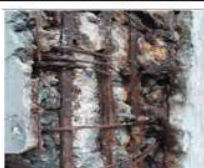
Visual Inspection	Defect	Severity (G)	Extention (k1)	Intensity (k2)	Total Score
	Umidity	x	x	x	G * k1 * k2
	Concrete Deterioration	x	x	x	
	Cracking	x	x	x	
	Cover Spalling	x	x	x	
	Stirrups Corrosion	x	x	x	
	Rebars Corrosion	x	x	x	
Relative Defect Coefficient				$\sum_i G_i * k1_i * k2_i$	

Figure 1: Example of Defect Indices Datasheet

visual inspection of the structure: for each area of the bridge the defects are identified, and through "qualitative scores" the severity and extent of the defects are graded. Figure 1 shows an example on how these approaches work. The Relative Defect Coefficient (DS) is calculated from the weighted sum of the individual defects (G) multiplied by the intensity ( $k_1$ ) and extension ( $k_2$ ) coefficients. Depending on the overall scoring (DS), the codes provide procedures that may highlight the need for more in-depth investigations, aimed at verifying the effective structural capacity, or the possibility of carrying out only maintenance interventions or proceeding with the downgrading of the bridge.

In the authors' opinion, such approach, based on visual inspections, could and should be further developed using mechanical-based methodologies in order to quantitatively evaluate the potential capacity-reduction of RC structural members and, therefore, of the structures static and seismic safety.

The aim of this work is to develop and integrate a quantitative mechanical-based assessment of RC members to the visual inspection and defect indices qualitative "scoring" approach in order to suggest a methodology for structural and seismic safety assessment of deteriorated RC bridges. To achieve this goal, a practical analytical methodology [16,17,18,19,20], whilst mechanical-based, referred to as SLaMA (Simple Lateral Mechanism Analysis) is further extended to for the evaluation of the seismic performance/safety evaluation of existing bridges, specifically including considerations on the capacity assessment of corroded RC structural members. In this work, the seismic safety of a case study reinforced concrete bridge, representing an archetype of widespread bridge typologies in Italy, affected by corrosion phenomena, is evaluated. Three different degradation scenarios are considered: corrosion intensity in terms of percentage mass loss is chosen consistently with three different defect indices, defined according to [14], thus integrating a quantitative measure to the visual inspection approach. Corrosion effects on members capacity reduction are analytically calculated as reported in [11,21,22]. The global seismic capacity of the bridge is determined and therefore the safety index defined in [14] is calculated. Considering different corrosion propagation models [23,24,25,26], upper and lower bounds for corrosion rates are adopted, and the seismic safety reduction over time is assessed. The uncertainty related to the location and extent of degradation is evaluated, and finally, using a simplified probabilistic approach [27] the fragility curves associated to the bridge collapse probability are calculated as a function of the peak ground acceleration for each degradation scenario.

## 2 SLAMA-BRIDGE METHODOLOGY INCLUDING DETERIORATION EFFECTS

The proposed procedure, schematically shown in the flow-chart of Figure 2, consists of the simplified seismic assessment of existing RC bridges based on the SLaMA approach for bridges [16,17,18,19], integrated with the evaluation of element capacity reduction evaluation due to corrosion of the reinforcement bars. As a first step, the seismic capacity of the pier is calculated determining the force-displacement curve. In this phase, it is crucial to correctly identify the 'critical section' where the plastic hinge and potential associated energy dissipation is expected to occur and develop. Generally, for bridges piers the plastic hinge region is expected to be located as the base, given their cantilever scheme; however, in case of localized environmental corrosive attack, the structural deterioration can modify the structural nonlinear behavior, and consequently, the critical sections can be relocated [28].

Therefore, it is important to support such estimation on the specifically planned visual inspections of the degradation. As part of the members capacity evaluation, the interaction between flexure and shear mechanisms is taken into account by comparing the force-displacement curve and the degrading-shear capacity curve calculated according to [29].

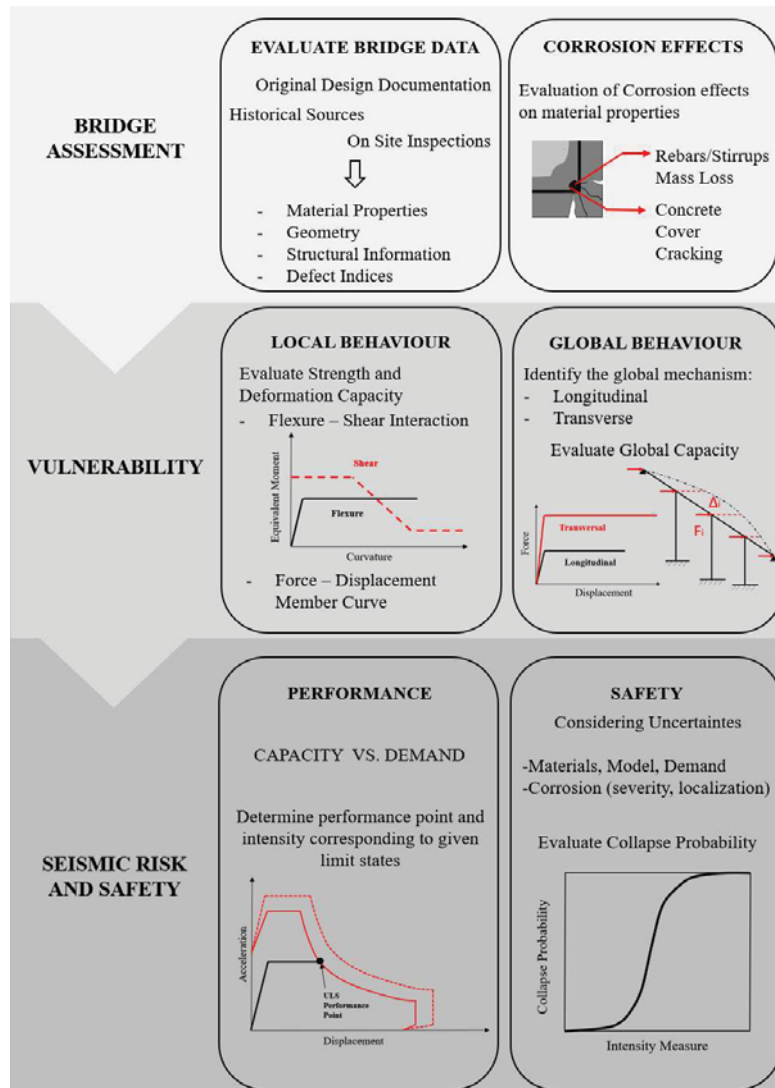


Figure 2: Methodology Flow Chart

In this paper, the evaluation of the plastic hinge length is calculated as the average value of the results related to different formulations available in the literature [30,31,32]. In a section analysis (or fiber numerical model) approach, the corrosion effect is taken into account by reducing the mechanical properties of the reinforcements as reported in [11] and by reducing the concrete cover compressive strength to consider the cracking induced by oxides expansion [33,34]. The overall seismic capacity of the bridge is evaluated separately for the longitudinal and transverse directions. The relationship between the local and global capacity is closely related to the static scheme of the bridge. The most common schemes for existing reinforced concrete bridges are continuous beam and supported beam ones. As reported in [35], in case of supported beams, and in the absence of seismic restraints, each pier behaves independently therefore, in a simplified way, the performance of the bridge is governed by the performance of the weakest (performance-wise) pier, both in longitudinal and transverse direction. On the other hand, in the case of continuous beam scheme: in the longitudinal direction, same top displacement can be assumed for all piers and the overall capacity is obtained by adding in parallel the individual

capacities of each pier; in the transverse direction, following a displacement approach presented in [36], the global capacity curve is obtained by adding the singles piers capacity in proportion to the piers effective displacement identified for the principal vibration mode of the structure. The global displacement instead is determined by referring to an equivalent SDOF. The seismic safety is measured through the safety index  $\zeta_E$  (also referred to as IS-V and %NBS in the ITA2017 and NZSEE2017 guidelines, respectively) [14, 16, 29], or Capacity/Demand ratio, obtained by comparing the bridge capacity curve with the ADRS seismic demand spectrum SLV limit state [29].

One of the objectives of this paper is the further extension of the analytical assessment methodology to account for the potential reduction of safety over time. To achieve this scope, an extensive literature review on research on the corrosion rate models available in the literature has been carried out, both for the carbonation and for the chlorides attack phenomenon. Since pitting corrosion due to chloride attack is characterized by a higher rate (Figure 3), in this work this typology is considered for the deterioration scenarios applied to the structure.

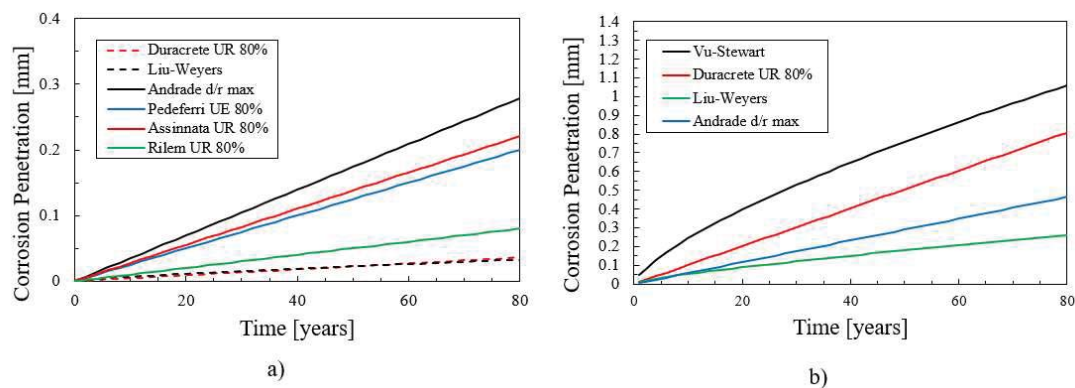


Figure 3: Corrosion rate models. a) Carbonation. b) Chlorides attack.

In the Defect Indices Approach through visual inspections, no explicit empirical or theoretical relationships are associated to the determination of the so called “extension” and “intensity” coefficients, and, at this stage, there are no quantitative correlation between the grading scale and the actual mechanical material properties reduction, making a structural mechanical assessment that takes into account deterioration phenomena not applicable.

To overcome these issues, a probabilistic approach is adopted in this work: the probability of the structure to overcome a certain damage level is determined as a function of the seismic intensity. The fragility curves can be calculated through analytical or empirical methods. In [27] most of the analytical methods adopted for buildings are presented. In [37] empirical methods are proposed for the calculation of the fragility curves according to the considered structure.

For the sake of simplicity and in the absence of more detailed data, in the simplified collapse probability assessment procedure herein proposed for a corroded reinforced concrete bridge structure, variations in the main factors affecting the corroded member capacity are considered, in particular: the location of the critical section, the amount of lost mass and the number of bars involved. Extensive analyses have been carried out varying both parameters.

In this way both corrosion location and intensity uncertainty related to the assumed deterioration scenarios are accounted and then combined, as recommended in [28], through SRSS rule with the epistemic (model and material characteristics) and aleatoric (seismic demand) uncertainties  $\beta$  value of 0.6 suggested in [37].

### 3 CASE STUDY BRIDGE

#### 3.1 Geometric and mechanical characteristics

The case study Bridge is an archetype representative of typical characteristics of a large number of R.C. bridges in the Italian territory (Figure 4). The geometry, material properties and static scheme of the bridge were selected through the analysis of a database of the Italian bridges in central Italy [20]. The database shows a strong prevalence of supported beam scheme, therefore herein selected for the case study. The bridge consists of four 30 m spans. Deck beams consist of I-shape prestressed reinforced concrete with prestressed 7-wire strands with straight longitudinal profile. The Piers have hollow polygonal section. Table 1 reports the key geometric characteristics of piers. The material mechanical properties (Table 2) have been selected as average values of the concrete cubic compressive strength and of the reinforcement yield strength values available in the database. In this regard, it is worth noting that material properties design values are obtained by reducing the mean values by partial safety factors and knowledge factor according to the Italian Code Provisions NTC2018 and associated Commentary 2019 for existing Structures and Infrastructures [14,29].

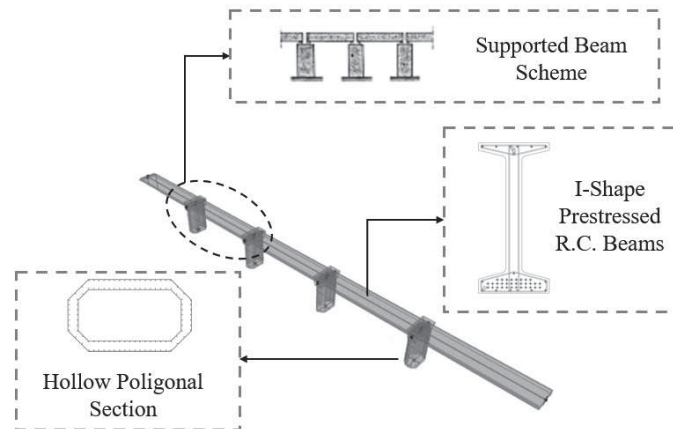


Figure 4: Archetype example for Italian Territory bridges

Pier Section	Lenght	$A_{conc}$	$\Phi_{long}$	$\rho_{long}$	$\Phi_t$	s
	[m]	[m <sup>2</sup> ]	[mm]	[%]	[mm]	[mm]
	10	7	20	0.45	10	250

Table 1: Case study piers geometry



Concrete				Steel			
$f_{cd}$	$E_{cm}$	$\epsilon_{c0}$	$\epsilon_{cu}$	$f_{yd}$	$E_s$	$\epsilon_{sy}$	$\epsilon_{su}$
[MPa]	[GPa]	[-]	[-]	[MPa]	[GPa]	[-]	[-]
26.80	29.57	0.2	0.35	375.00	210.00	0.18	6.75

Table 2: Case study piers material properties

As regards the seismic demand, conditions of high seismicity were considered. Reference is made to the L'Aquila site, representative of the seismology of central Apennine Italy. A nominal life  $V_N = 100$  years and an Importance Level IV (Important strategic functions structures) [29] are considered in order to account for the strategic function of the bridge structure. In Table 3 the main parameter of the elastic acceleration response spectrum are presented for the limit states of (Fully) Operational (SLO), Damage Control (SLD), Life Safety (SLV) and Collapse Prevention (SLC).

$P_{VR}$	$T_R$	LIMIT STATE	$a_g$	$F_0$	$T^*_C$
[-]	[years]	[-]	[g]	[-]	[s]
81%	120	SLO	0.15	2.3	0.30
63%	201	SLD	0.19	2.31	0.32
10%	1898	SLV	0.41	2.44	0.38
5%	2475	SLC	0.45	2.46	0.38

Table 3: Response spectrum parameters

Three different degradation scenarios are applied to the case study bridge in order to evaluate the potential losses in terms of seismic safety due to the corrosion effects. Each scenario, representative of a specific degradation level, is associated to the “Relative Defect Coefficient” evaluated according to the qualitative defect sheets of the Italian guidelines for the evaluation of existing bridges. In Figure 5 visual examples for assumed degradation scenarios are given.

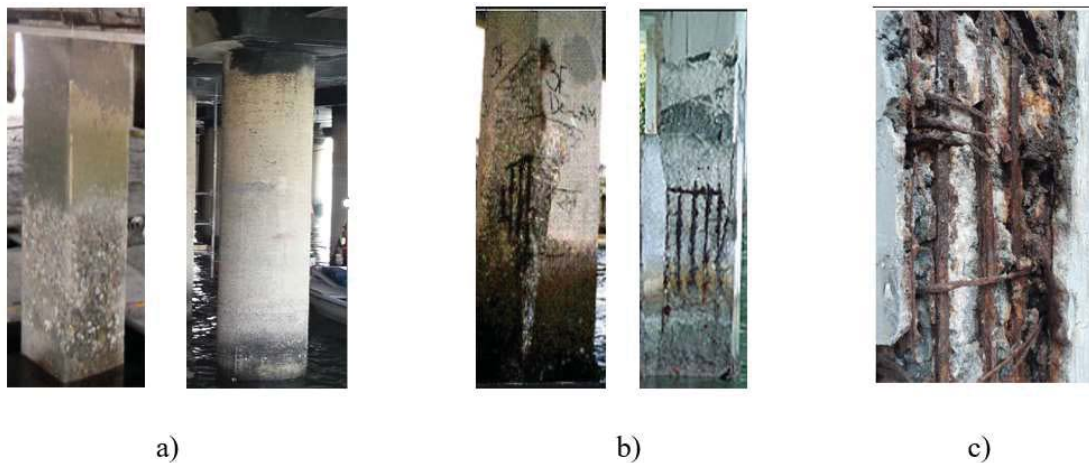


Figure 5: Examples of degradation scenarios: a) Low degradation – Scenario 1. b) Medium degradation – Scenario 2. c) High degradation – Scenario 3.

<b>Scenario 1 - Low Degradation</b>				
Defect	Severity	Extention	Intensity	Total Score
Umidity	4.00	0.50	1.00	2.00
Concrete Deterioration	2.00	0.50	1.00	1.00
Cracking	2.00	1.00	0.20	0.40
Rebars Corrosion	5.00	0.20	0.20	0.20
Relative Defect Coefficient				3.60
<b>Scenario 2 - Medium Degradation</b>				
Defect	Severity	Extention	Intensity	Total Score
Umidity	4.00	0.50	1.00	2.00
Concrete Deterioration	2.00	0.50	1.00	1.00
Cracking	2.00	1.00	1.00	2.00
Cover Spalling	2.00	0.20	1.00	0.40
Stirrups Corrosion	3.00	0.50	0.50	0.75
Rebars Corrosion	5.00	0.20	0.50	1.25
Relative Defect Coefficient				7.40
<b>Scenario 3 - High Degradation</b>				
Defect	Severity	Extention	Intensity	Total Score
Umidity	4.00	0.50	1.00	2.00
Concrete Deterioration	2.00	0.50	1.00	2.00
Cracking	2.00	1.00	1.00	2.00
Cover Spalling	2.00	0.20	1.00	2.00
Stirrups Corrosion	3.00	0.50	0.50	1.50
Rebars Corrosion	5.00	0.20	0.50	1.25
Relative Defect Coefficient				10.75

Table 4: Degradation scenarios parameters considered for the case study

In Table 4 the degradation parameters assumed for each scenario are presented. For the Scenario 1, low degradation conditions are considered: it is assumed that corrosive agents have broken the protective film of the bars but the corrosion of the latter has just begun ( $M_{\text{loss}} = 5\%$ ), the most obvious defect being the extensive deterioration of the concrete with capillary cracking. In Scenario 1, the extent of the degradation is considered localized. The position of deterioration is parametrically shifted to assess the influence of the location of the damage on the capacity of the structure. For the Scenario 2, medium degradation conditions are considered with rebars corrosion ( $M_{\text{loss}} = 15\%$ ) and partial detachment of the concrete cover. Also for Scenario 2 the extent of the deterioration is assumed localized. For the Scenario 3, severe and limit conditions are considered: rebars corrosion is high ( $M_{\text{loss}} = 25\%$ ) and the stirrups are no longer considered resistant, the concrete cover has spalled and the extent of the damage affects a large part of the pier. In Table 5 the corrosion consequences on material properties are presented for each scenario, the reinforcement mass loss values ( $M_{\text{loss}}$ ) were chosen consistently with values found in the literature for chlorides corrosion [11, 35].

	Steel					Concrete	
	$M_{loss}$	$\varepsilon_{sy}$	$\varepsilon_{su}$	$f_{ym}$	$f_{um}$	$w$	$f_{c,rid}$
	[-]	[-]	[-]	[Mpa]	[Mpa]	[mm]	[Mpa]
Scenario 1	5%	0.20%	5.13%	337.57	489.67	0.12	26.37
Scenario 2	15%	0.12%	2.97%	260.27	389.00	0.82	24.21
Scenario 3	25%	0.09%	1.72%	186.11	288.33	4.09	21.12

Table 5: Corrosion consequences on material properties

Given the high uncertainty of the corrosion rate, an upper and a lower bound were identified through the study of predictive models available in the literature and adopted to evaluate the reinforcement mass losses,  $M_{loss}$  for the case study bridge over a period of 15 years. The limit values of the corrosion rates together with the consequent  $M_{loss}$  values assumed over time are shown in Figure 6.

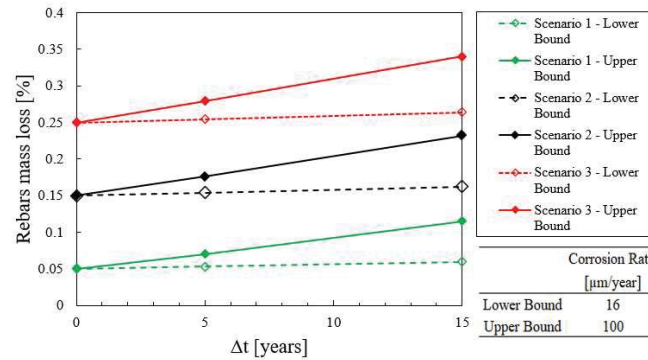


Figure 6: Corrosion intensity evolution for each scenario: a) Lower bound corrosion rate. b) Upper bound corrosion rate

### 3.2 Safety reduction and risk assessment results

The models described above for the strength and ductility losses for structural members subject to corrosion were applied to the structure for the three deterioration scenarios. Figure 7 shows the moment-curvature curve for the weakest bridge pier for the non-corroded case and each corrosion scenario considered. It can be noted that as the degradation increases, a marked loss of element ductility is observed. This effect is mainly due to the reduction in terms of steel ultimate deformation capacity.

Then the bridge seismic capacity for each scenario was calculated. In Figure 8 the global capacity curves and expected performance within a ADRS (Acceleration Displacement Response Spectrum) domain are presented for the longitudinal direction. Worth noting that, as the seismic safety in the transverse direction did not present significant problems for any scenario, albeit with a reduction in vulnerability, the results have been herein omitted. As it can be observed, in the longitudinal direction the seismic safety check is no longer satisfied for all scenarios. The safety index reduces from  $\zeta_e=1.15$  for the non-corroded case to a  $\zeta_e=0.98$ , 0.71 and 0.61, for scenario 1, 2 and 3.

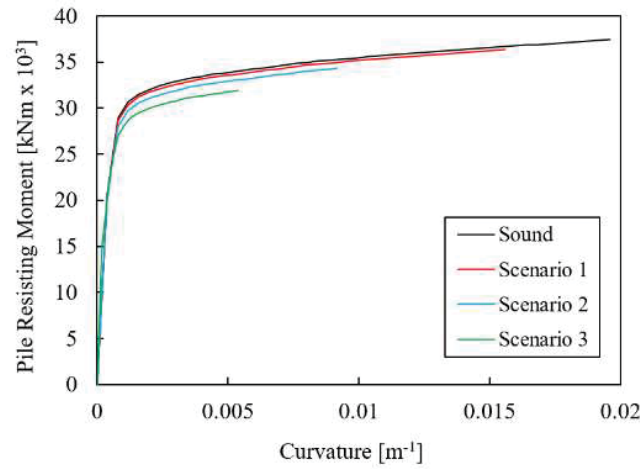


Figure 7: Moment-curvature relationship for the base section of bridge piers

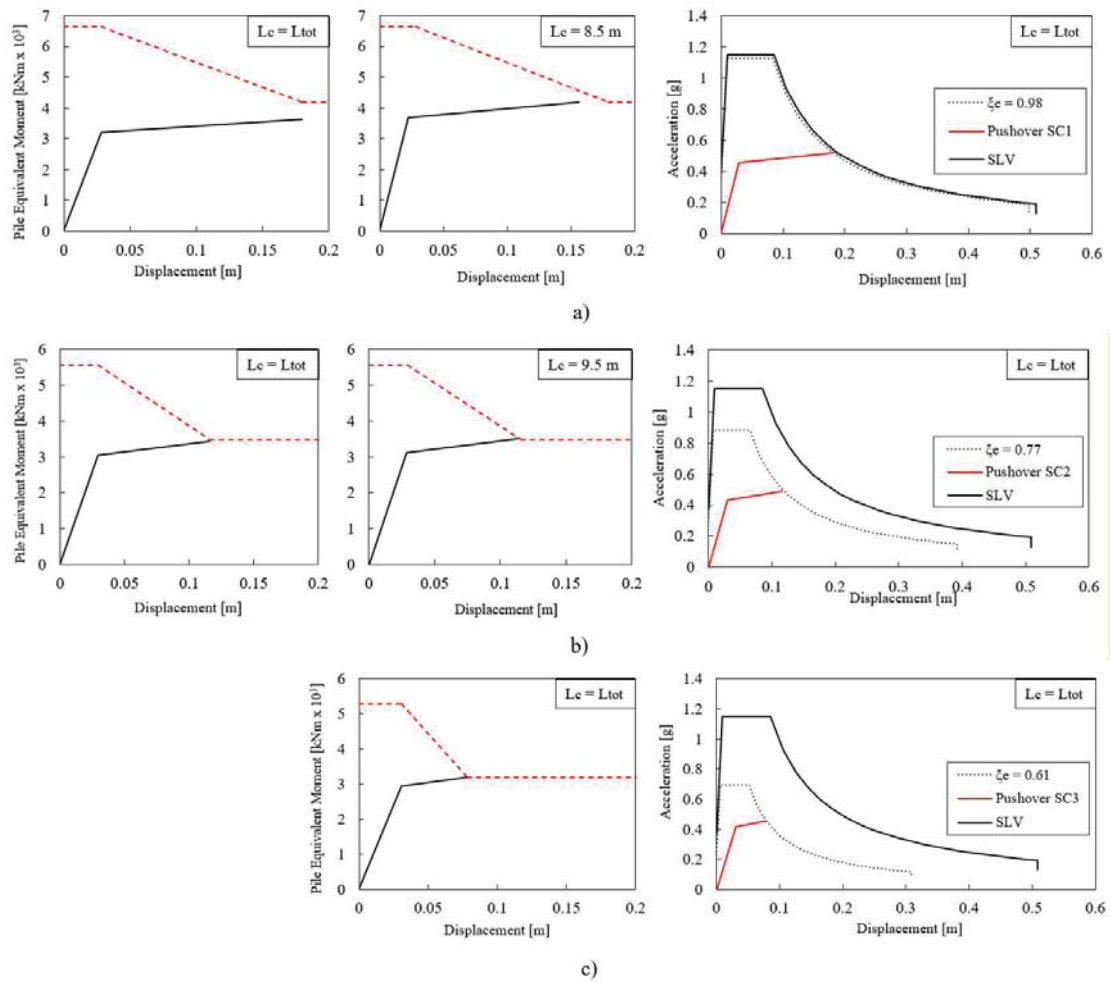


Figure 8: Capacity curves and safety index evaluation for the case study bridge. a) scenario 1. b) scenario 2. c) scenario 3.

Considering the upper and lower bound corrosion rate values previously described, the decay of the Safety Risk index over time is evaluated and shown in Figure 9. For the case study, a maximum percentage loss of seismic safety in 15 years of about 47% for scenario 3 is assessed. Reduction due to the upper bound corrosion rate in 15 years is about 15%, while for the lower bound is about 2.5% highlighting the extreme importance of this parameter characterized by high uncertainty.

In order to calculate the collapse probability of piers, variations in the intensity (3-30%  $M_{loss}$ ), in the number of corroded bars, in the critical damaged section location (base section, 0.25L, 0.5L) are considered. Altogether a sample of 186 performance data of the structure referred to the achievement of the ultimate displacement of the pile is obtained. The reference parameter is the PGA, peak ground acceleration, associated with a given damage state. The damage states considered are the displacement limits reported in the study in [39]. For the Collapse Prevention limit state the displacement limit considered is the ultimate one. The values obtained for the corrosion localization and damage uncertainties and the combination of the two with the epistemic and aleatoric uncertainties are reported in Table 6.

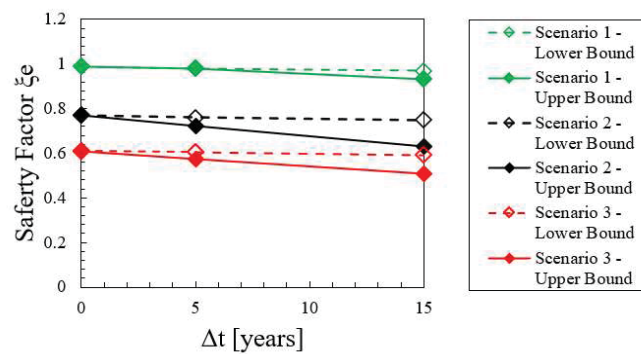


Figure 9: Safety factor decay over time due to corrosion development

	PGA	$\beta_{\text{model+materials+demand}}$	$\beta_{\text{localization}}$	$\beta_{\text{damage}}$	$\beta_{\text{localization+damage}}$	$\beta_{\text{total}}$
	[g]	[-]	[-]	[-]	[-]	[-]
Sound	0.43	0.6	-	-	-	0.6
Scenario 1	0.4	0.6	0.17	0.16	0.24	0.65
Scenario 2	0.35	0.6	0.17	0.16	0.24	0.65
Scenario 3	0.31	0.6	0.17	0.16	0.24	0.65

Table 6: Main parameters for fragility curves calculation

The collapse probability curves were then calculated for the non-corroded bridge and each scenario considered. The results are reported in Figure 10. As the severity of the deterioration increases, the fragility curve shifts to the left. This indicates that, as expected, as the damage from deterioration increases, there is a greater probability of collapse for a given PGA (seismic intensity).



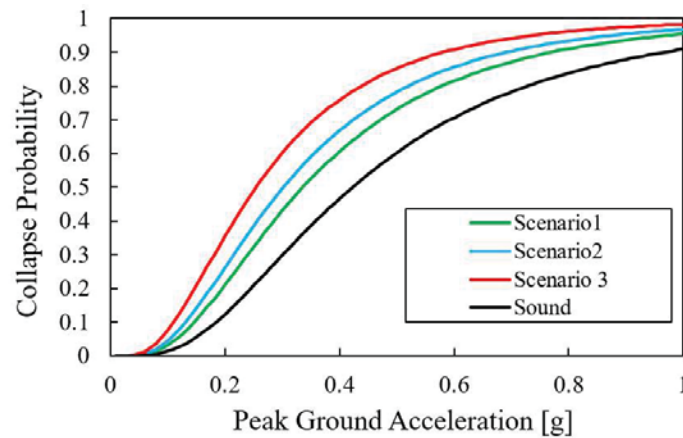


Figure 10: Collapse probability - Pier

#### 4 CONCLUSIONS

In this work, a practical methodology for the seismic safety assessment of reinforced concrete bridges subject to corrosion phenomena was presented. Furthermore, considering different corrosion propagation models, seismic safety losses were also evaluated over time. The methodology was applied to a case study bridge (archetype), representative of the most typical technology and structural scheme adopted in the Central Italy territory. Finally, considering the epistemic and aleatoric uncertainties related to the materials, to the model, to the seismic demand, and to the corrosion intensity and localization starting from a defect index, the methodology allows to calculate the collapse probability curves, considering the ultimate displacement of the piers as Engineer Demand Parameter and the PGA taken as Intensity Measure.

The assessment results of the case study show that for bridges with supported beam static scheme the sensitivity to corrosion phenomena may significantly undermine the structure seismic safety. For the most severe deterioration scenario, results in terms of safety factor and fragility curve show the need for retrofit intervention to recover the initial safety level. Results obtained for the mild and medium intensity scenarios, on the other hand, do not seem to cause immediate and significant reductions in safety. Yet the study of the evolution of corrosive phenomena over time shows that, in the case of high corrosion rates, safety may be compromised within a few years. For these cases it should also be considered that time can cause the deterioration to evolve not only in intensity but also in extension, thus potentially moving in a short time into a more severe deterioration scenario. In these cases, therefore, although structural restoration interventions might not be urgent, continuous monitoring and appropriate maintenance plans including preventive “light” restoration interventions might be critical to preserve the integrity and safety of the bridge in the long-term.

The analyses carried out show a significant loss of capacity in the case of localization of a weak section along the height of the pier rather than at the base.

The methodology presented, both for its simplicity and its effectiveness can represent a useful support tool integrating the visual inspection approach for assessing the corrosion effects on the R.C. bridge piers and therefore evaluating the overall structure seismic capacity. It can, therefore, represents a valuable decision support tool in terms of retrofit/restoration/maintenance

priorities related to the seismic performance of the structure. Further improvement and refinement of the methodology are needed and are under developments, to include further sources of material deterioration as well as local and global failure mechanisms.

Yet, in the authors' opinion, the high uncertainty associated with the corrosion phenomena, both in terms of mechanical consequences and in evolution over time, remains the main issue in the evaluation of seismic capacity. In this regard, the fragility curves evaluated through the proposed methodology can somehow account for this lack of current knowledge in the form of aleatoric and epistemic uncertainties. In any case, an adequate integration of the various approaches, e.g. visual inspection, theoretical quantitative evaluation and mechanical on-site testing, within a unified framework and assessment procedure can lead to a robust hybrid procedure for a more reliable estimation and control of the static (and seismic) performance and safety of bridge structures.

## REFERENCES

- [1] Kawashima, K. (2000). Seismic design and retrofit of bridges. *Bulletin of the New Zealand Society for Earthquake Engineering*. <https://doi.org/10.5459/bnzsee.33.3.265-285>
- [2] Kumar, R., & Gardoni, P. (2014). Effect of seismic degradation on the fragility of reinforced concrete bridges. *Engineering Structures*. <https://doi.org/10.1016/j.engstruct.2014.08.019>
- [3] Mele, M., & Siviero, E. (1991). On the durability of reinforced and prestressed concrete structures. In *Courses and Lectures - International Centre for Mechanical Sciences*. [https://doi.org/10.1007/978-3-7091-2614-1\\_7](https://doi.org/10.1007/978-3-7091-2614-1_7)
- [4] Siemes, T., & Vries, H. De. (2002). *Overview Of The Development Of Service Life Design For Concrete Structures*. 1–10.
- [5] Rodriguez, J., Ortega, L. M., & Casal, J. (1997). Load carrying capacity of concrete structures with corroded reinforcement. *Construction and Building Materials*, 11(4), 239–248. [https://doi.org/10.1016/S0950-0618\(97\)00043-3](https://doi.org/10.1016/S0950-0618(97)00043-3)
- [6] Castel, A., François, R., & Arliguie, G. (2000). Mechanical behaviour of corroded reinforced concrete beams - Part 1: experimental study of corroded beams. *Materials and Structures/Materiaux et Constructions*, 33(233), 539–544.
- [7] Meda, A., Mostosi, S., Rinaldi, Z., & Riva, P. (2014). Experimental evaluation of the corrosion influence on the cyclic behaviour of RC columns. *Engineering Structures*, 76, 112–123. <https://doi.org/10.1016/j.engstruct.2014.06.043>
- [8] Alonso, C., Andrade, C., Rodriguez, J., & Diez, J. M. (1996). Factors controlling cracking of concrete affected by reinforcement corrosion. *Materials and Structures/Materiaux et Constructions*.
- [9] Almusallam, A. A. (2001). Effect of degree of corrosion on the properties of reinforcing steel bars. *Construction and Building Materials*, 15(8), 361–368. [https://doi.org/10.1016/S0950-0618\(01\)00009-5](https://doi.org/10.1016/S0950-0618(01)00009-5)
- [10] Apostolopoulos, C. A., & Papadakis, V. G. (2008). Consequences of steel corrosion on the ductility properties of reinforcement bar. *Construction and Building Materials*, 22(12), 2316–2324. <https://doi.org/10.1016/j.conbuildmat.2007.10.006>
- [11] Imperatore, S., Rinaldi, Z., & Drago, C. (2017). Degradation relationships for the mechanical properties of corroded steel rebars. *Construction and Building Materials*, 148, 219–230. <https://doi.org/10.1016/j.conbuildmat.2017.04.209>
- [12] fib Model Code 2020 . (2019). *Structural Concrete*. <https://doi.org/10.1002/suco.201970021>
- [13] Tuutti, K. (1977). CORROSION OF STEEL IN CONCRETE. *EUROCOR '77, Eur Congr on Met Corros, 92nd Event of the Eur Fed of Corros*, 655–661.
- [14] Ministero delle Infrastrutture e dei Trasporti. (2019). Linee Guida per la Classificazione e Gestione del Rischio, la Valutazione della Sicurezza ed il Monitoraggio dei ponti esistenti, allegate al parere del CSLPP n.88/2019.
- [15] FHWA. (1971). National Bridge Inspection Standards. *Federal Register*.

- [16] NZSEE (2017). New Zealand Society for Earthquake Engineering. The seismic assessment of existing buildings – technical guidelines for engineering assessments. Wellington, New Zealand;.
- [17] Pampanin, S., (2017) Towards the practical implementation of performance-based assessment and retrofit strategies for RC buildings: challenges and solutions, SMAR2017-Fourth conference on Smart Monitoring, Assessment and Rehabilitation of Structures, *Keynote Lecture*, 13-15 Sept, Zurich, Switzerland
- [18] Del Vecchio, C., Gentile, R. & Pampanin, S. (2017) The Simple Lateral Mechanism Analysis (SLaMA) for the seismic performance assessment of a case study building damaged in the 2011 Christchurch earthquake, *Research Report* N. 2016-02, University of Canterbury, Christchurch, New Zealand
- [19] Rotatori, R.M., (2019) “Valutazione della Vulnerabilità Sismica e Strategie di Miglioramento dei Viadotti a Travata in Calcestruzzo Precompresso attraverso la procedura SLaMa”, Laurea Magistrale (ME) Thesis (Supervisors: Prof. Ing. Stefano Pampanin and Prof. Ing. Fabio Brancaleoni), Department of Structural and Geotechnical Engineering, Sapienza University of Rome
- [20] Gentile, R., Nettis, A., & Raffaele, D. (2020). Effectiveness of the displacement-based seismic performance assessment for continuous RC bridges and proposed extensions. *Engineering Structures*. <https://doi.org/10.1016/j.engstruct.2020.110910>
- [21] Jeon, C. H., Lee, J. Bin, Lon, S., & Shim, C. S. (2019). Equivalent material model of corroded prestressing steel strand. *Journal of Materials Research and Technology*. <https://doi.org/10.1016/j.jmrt.2019.02.010>
- [22] Coronelli, D., & Gambarova, P. (2004). Structural Assessment of Corroded Reinforced Concrete Beams: Modeling Guidelines. *Journal of Structural Engineering*. [https://doi.org/10.1061/\(asce\)0733-9445\(2004\)130:8\(1214\)](https://doi.org/10.1061/(asce)0733-9445(2004)130:8(1214))
- [23] DuraCrete. (1998). *Modelling of degradation*, The European Union – Brite EuRam III.
- [24] Andrade, C., Alonso, C., & Sarfa, J. (2002). Corrosion rate evolution in concrete structures exposed to the atmosphere. *Cement and Concrete Composites*. [https://doi.org/10.1016/S0958-9465\(01\)00026-9](https://doi.org/10.1016/S0958-9465(01)00026-9)
- [25] Liu, T., & Weyers, R. W. (1998). Modeling the dynamic corrosion process in chloride contaminated concrete structures. *Cement and Concrete Research*. [https://doi.org/10.1016/S0008-8846\(98\)00259-2](https://doi.org/10.1016/S0008-8846(98)00259-2)
- [26] Vu, K. A. T., & Stewart, M. G. (2000). Structural reliability of concrete bridges including improved chloride-induced corrosion models. *Structural Safety*. [https://doi.org/10.1016/S0167-4730\(00\)00018-7](https://doi.org/10.1016/S0167-4730(00)00018-7)
- [27] FEMA. (2018). FEMA P-58-1: Seismic Performance Assessment of Buildings. Volume 1 – Methodology. *Fema P-58*.
- [28] Yuan, W., Guo, A., & Li, H. (2017). Seismic failure mode of coastal bridge piers considering the effects of corrosion-induced damage. *Soil Dynamics and Earthquake Engineering*. <https://doi.org/10.1016/j.soildyn.2016.12.002>
- [29] NTC, I. M. of I. and. (2018). Norme Tecniche per le Costruzioni. DM 17/1/2018. *Gazzetta Ufficiale Della Repubblica Italiana*.

- [30] Berry, M. P., Lehman, D. E., & Lowes, L. N. (2008). Lumped-plasticity models for performance simulation of bridge columns. *ACI Structural Journal*. <https://doi.org/10.14359/19786>
- [31] Panagiotakos, T. B., & Fardis, M. N. (2001). Deformations of reinforced concrete members at yielding and ultimate. *ACI Structural Journal*. <https://doi.org/10.14359/10181>
- [32] Priestley, M. J. N., & Park, R. (1987). STRENGTH OF DUCTILITY OF CONCRETE BRIDGE COLUMNS UNDER SEISMIC LOADING. *ACI Structural Journal*. <https://doi.org/10.14359/2800>
- [33] Coronelli, D., & Gambarova, P. (2004). Structural Assessment of Corroded Reinforced Concrete Beams: Modeling Guidelines. *Journal of Structural Engineering*. [https://doi.org/10.1061/\(asce\)0733-9445\(2004\)130:8\(1214\)](https://doi.org/10.1061/(asce)0733-9445(2004)130:8(1214))
- [34] Vecchio, F. J., & Collins, M. P. (1986). MODIFIED COMPRESSION-FIELD THEORY FOR REINFORCED CONCRETE ELEMENTS SUBJECTED TO SHEAR. *Journal of the American Concrete Institute*.
- [35] Progetto DPC-Reluis. (2009). *Linee guida e manuale applicativo per la valutazione della sicurezza sismica e il consolidamento dei ponti in c.a.*
- [36] Dwairi, H., & Kowalsky, M. (2006). Implementation of inelastic displacement patterns in direct displacement-based design of continuous bridge structures. *Earthquake Spectra*. <https://doi.org/10.1193/1.2220577>
- [37] FEMA, F. E. M. A. (2015). Hazus–MH 2.1: Technical Manual. *National Institute of Building Sciences and Federal Emergency Management Agency (NIBS and FEMA)*.
- [38] Dai, L., Wang, L., Bian, H., Zhang, J., Zhang, X., & Ma, Y. (2019). Flexural Capacity Prediction of Corroded Prestressed Concrete Beams Incorporating Bond Degradation. *Journal of Aerospace Engineering*. [https://doi.org/10.1061/\(asce\)as.1943-5525.0001022](https://doi.org/10.1061/(asce)as.1943-5525.0001022)
- [39] Cardone, D. (2014). Displacement limits and performance displacement profiles in support of direct displacement-based seismic assessment of bridges. *Earthquake Engineering and Structural Dynamics*. <https://doi.org/10.1002/eqe.2396>



## REAL-TIME ASSESSMENT OF PERFORMANCE INDICATORS FOR BRIDGES TO SUPPORT ROAD NETWORK MANAGEMENT IN THE AFTERMATHS OF EARTHQUAKE EVENTS

Chiara Ormando<sup>1</sup>, Ugo Ianniruberto<sup>1</sup>, Paolo Clemente<sup>2</sup>, Sonia Giovinazzi<sup>2</sup>, Maurizio Pollino<sup>2</sup> and Vittorio Rosato<sup>2</sup>

<sup>1</sup> Tor Vergata University  
Via Politecnico 1, 00133 Rome, Italy  
e-mail: [chiara.ormando@uniroma2.it](mailto:chiara.ormando@uniroma2.it), [ianniruberto@uniroma2.it](mailto:ianniruberto@uniroma2.it)

<sup>2</sup> ENEA (National Agency for New Technologies, Energy and Sustainable Economic Development)  
Lungotevere Thaon di Revel, 76 00196 Rome, Italy  
e-mail: ([sonia.giovinazzi@enea.it](mailto:sonia.giovinazzi@enea.it), [paolo.clemente@enea.it](mailto:paolo.clemente@enea.it), [maurizio.pollino@enea.it](mailto:maurizio.pollino@enea.it), [vittorio.rosato@enea.it](mailto:vittorio.rosato@enea.it))@enea.it

---

### Abstract

*CIPCast DSS, is a complex yet user-friendly and interoperable Decision Support System platform supporting the risk assessment and the real-time 24/7 operational monitoring of interdependent distributed critical infrastructures. CIPCast DSS is the reference platform for EISAC.it, the Italian node of the European Infrastructure Simulation and Analysis Centre. This paper presents the customization of CIPCast DSS to support the management of road networks in the aftermaths of an earthquake event, providing information on the damage and residual functionality of viaducts and bridges and the estimations of the earthquake-induced impacts in the surrounding natural and built environments. CIPCast DSS allows to support the identification of the areas and sections of the road networks that have been exposed to the ground shaking, and to estimate, in a simplified way, earthquake-induced damages for the road network components. Towards that fragility curves, numerical model analysis and data from Structural Health Monitoring (SHM) systems and sensors are used. The paper proposes physical damage indicators for bridges to be included in CIPCast DSS and the possible layout of SHM sensors to support their detection.*

**Keywords:** Highways, Bridges, Decision Support System, Emergency management, Earthquake-induced damage and impact, Structural Health Monitoring System.

---

## 1 INTRODUCTION

In Italy the road network is still the main transportation means for both people and goods; every year, about 8 millions vehicle and nearly 2 billion tons of goods (87% of the total Italian traded goods) travel along the Italian highway network [1]. Some sections of the Italian highway network (such as A24 and A25) are crucial for emergency operation in the event of crises and disasters. The business-as-usual maintenance and post-event effective management of highway networks are therefore fundamental to guarantee the well-being of the served communities, to support the logistic and the functionality of the economic systems and to guarantee a rapid and effective reconstruction and recovery after critical events.

Italy has more than 50 thousand kilometres of road and counts more than 2 thousand kilometres of artworks, more than half built before 1980 [1] when seismic prescriptions were almost inexistent. A meticulous assessment of the structural integrity of these structures is therefore imperative together with an evaluation of the resilience of the road network.

Particular attention should be paid to the vulnerability assessment of bridges and viaducts, considering the traffic load demand which they are subjected to (that might be higher than the one they were designed for), and the possible presence of pre-existing damage induced by environmental degradation and/or by critical event, such as earthquakes and floods.

Towards that the “*Linee Guida ponti*” [2] i.e. “*Guidelines for Risk Classification, Risk Management, Safety Evaluation and Monitoring of Existing Bridges*” released by MIT, Italian Ministry for Infrastructure and Transports, have defined a detailed operative framework for the classification and the structural safety assessment of the Italian bridges.

The idea presented in this paper is to embed the aforementioned institutional framework for the risk assessment of bridges in *CIPCast (Critical Infrastructure Protection risk analysis and foreCAST) Decision Support Systems (DSS)*, referred hereafter as *CIPCast DSS*, where scenario analysis can be performed considering also interdependencies and cascading effects, to support risk assessment and resilience enhancement of the whole road network. After a brief overview on worldwide initiatives to promote the resilience of highways and road networks and a non-exhaustive literature review on related DSS, the Italian platform *CIPCast DSS* is introduced and described as a potential tool for the risk analysis, the real-time monitoring, the business as usual as well as emergency management of Italian highway networks. In particular, the possible use of *CIPCast DSS* to support the post-earthquake management of highway networks is showcased in this paper, to provide to the control rooms and to the highway managers information on the earthquake-induced damage and residual functionality of bridges of the highway network as a whole, and on the possible impacts on the surrounding natural and built environments. In particular, the actual state and residual functionality of bridges is estimated in *CIPCast DSS* through Key Performance Indicators KPIs by combining the results obtained from empirical methods, numerical models, and, when available, performance indicators assessed from the data collected by SHM systems [3, 4].

## 2 OVERVIEW ON INITIATIVES AND TOOLS TO SUPPORT THE RESILIENCE OF HIGHWAY NETWORKS

The resilience and risk management of Critical Infrastructures (CIs), including highway networks, has been the subject of several ventures at national government level worldwide in the last decades.

In 2006, the U.S. Department of Homeland Security published the National Infrastructure Protection Plan (NIPP), subsequently revised in 2009 and in 2013, to outline how private sector parties and government departments should operate and interact to evaluate the

security, to ensure the resilience and to manage the risk of CIs. The main purposes of the NIPP are the identification of threats and hazards that might affect CIs, the reduction of CIs vulnerabilities and the development of strategies for mitigating the potential consequences induced by critical events. Industrial Control Systems (ICS), new Operational Technology (OT), as well as Intelligent Transport Systems (ITS) and Road Network Operations (RNO) have been introduced in order to reach these goals.

In 2011, following Fukushima natural and nuclear disaster (March 11<sup>th</sup>, 2011), Japan developed a program to promote the resilience of CIs (including energy, water and transportation infrastructures) to critical events, investing on the program approximately 210 billion dollars [5]. In 2018, Japan approved the *Fundamental Plan for National Resilience* defining the principles that governs the resilience of CI aiming to prevent loss of human life, to avoid the dysfunctionality of administrative and economic systems, to reduce physical damages on structures, infrastructures and goods and to ensure a rapid and effective recovery after critical events.

In 2015, the Australian government released the *Critical Infrastructure Resilience Strategy* to ensure the continued operation of CI in the face of different possible hazards; the aim being to support CI owners and operators to be efficient in the management of both foreseeable and unforeseeable risks.

In Europe, in 2018, the white paper “*Resilience Management Guidelines for Critical Infrastructures*”<sup>1</sup> was outlined by combining the outcomes of 5 Horizon 2020 projects<sup>2</sup> the white paper promotes the implementation of an *European Resilience Management Guideline for Infrastructures*.

As far as DSS tools are concerned, among several existing valid prototypes and operational tools, two have been selected for a brief presentation in this section as they have a good fit for purpose as far as the aforementioned CI resilience initiatives and policy frameworks are concerned, namely: REDARS<sup>TM</sup> and CIPCast DSS.

REDARS<sup>TM</sup> 2, Risks from Earthquake Damage to Roadway Systems [6] is a public-domain software promoted and financially supported in the U.S.A. by the Federal Highway Administration (FHWA) that, since 1993, has been sponsoring a Seismic Research Program.

REDARS<sup>TM</sup> 2 can support the assessment of seismic-induced hazards including ground motion, liquefaction, and surface fault rupture and, by considering the vulnerability of the highway assets, can support the estimation of earthquake-induced damages for different components of the highway network, for both simulated and real events.

After the assessment of earthquake-induced physical damage on the road network, REDARS<sup>TM</sup> 2 can be used for assessing the post-disaster traffic states and to evaluate their influence on traffic flows aiming to estimate the increased travel-time along key life-line routes and the resulting economic losses and impacts on the served community.

Simulated events can be run in REDARS<sup>TM</sup> 2 for planning purposes to estimate the effectiveness of various seismic retrofitting options and strategies towards the mitigation of the seismic risk for the highway network.

In case of real event REDARS<sup>TM</sup> 2 can support network managers to conduct an informed and aware decision-making process towards an effective emergency management [6] and to identify the needed remedial actions, their cost and benefits.

---

<sup>1</sup> [https://smr-project.eu/fileadmin/user\\_upload/Documents/Resources/WP\\_7/DRS\\_7\\_WHITE\\_PAPER\\_final\\_April2018.pdf](https://smr-project.eu/fileadmin/user_upload/Documents/Resources/WP_7/DRS_7_WHITE_PAPER_final_April2018.pdf)

<sup>2</sup> H2020 DRS-07-2014 Projects i.e.: DARWIN (<https://h2020darwin.eu/>), IMPROVER (<http://improverproject.eu/>), RESILIENS (<http://resiliens.eu/>), RESOLUTE (<http://resolute-eu.org/>) and SMR (<http://smr-project.eu/home/>);

CIPCast DSS is a WEBGIS-based software developed as part of the EU-funded FP7 project Critical Infrastructures Preparedness and Resilience Research Network, CIPRNet [7] for the real-time and operational (24/7) monitoring and risk analysis of built and natural environments, with special focus on the analysis of interdependent critical infrastructures such as electric power, water, telecommunication, road networks and strategic buildings.

CIPCast DSS is the main tool used by EISAC, the European Infrastructure Simulation and Analysis Centre, a European-wide network of national centres aiming to support the protection and resilience enhancement of Critical Infrastructures; the Italian EISAC center, namely<sup>3</sup> EISAC.it, already actively collaborating with providers of essential services, asset managers and operators of Cis, aims to collaborate with the Italian Department of Civil Protection (DPC), to support scenario and risk analysis for the protection and resilience enhancement of CIs.

In the following paragraphs, the functionalities of CIPCast DSS are briefly presented and discussed in relation to its possible use for supporting the emergency management of highway networks in the aftermaths of earthquake events and for risk mitigation purposes.

### 3 CIPCAST DSS FOR THE EFFECTIVE POST-EARTHQUAKE MANAGEMENT OF ROAD NETWORKS

CIPCast DSS could be applied in the management of highway networks, particularly in the decision-making process after an earthquake event [8]. The idea is to provide to operators and managers of the highway networks a tool, connected and interfaced with other tools, and deployed sensors (Figure 1), to be used both for the effective management of road networks in the aftermath of emergencies induced by natural events, including earthquakes. The focus of this paper is on the parameters used by CIPCast DSS to provide information to the asset managers on the safety and residual functionality of viaducts, and bridges in the aftermath of an earthquake event. A brief overview of how CIPcast DSS works, and which relevant databases are included in CIPCast geodatabases is provided here; a more exhaustive overview on the functions included in the platform can be found in [7], [8].

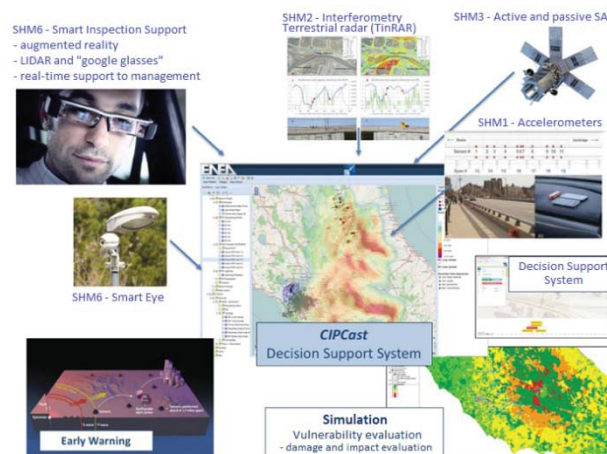


Figure 1: CIPCast DSS and possible connected tools and applications.

<sup>3</sup> EISAC.it (<http://www.eisac.it/>) was established in 2018 thanks to a collaboration agreement between ENEA, the Italian Agency for New Technologies, Energy and Sustainable Economic Development (<https://www.enea.it/en>) and INGV, the National Institute of Geophysics and Volcanology (<http://www.ingv.it/en/>).



CIPCast GeoDatabases, referred hereafter as CIPCast DBs allow the storing and management of large quantities of geospatial data obtained through GIS processing or from external sources including, among others, Open Data, field sensor data, third party or distributed repositories. The data can be stored locally or in different remote servers, accessible through services compliant with the Open Geospatial Consortium (OGC) standards. As far as the seismic assessment and management of the road networks is concerned CIPCast DBs include data for the assessment of both the seismic ground motion and seismic induced-hazard and for the characterisation of the seismic vulnerability of critical components such as bridges, viaducts tunnels and embankments. CIPCast DBs for the seismic hazard characterisation include among others: microzonation, faults location, surface faulting, liquefaction potential, earthquakes historical parametric catalogue; landslide and rock-fall hazard maps from past event and from satellite data SAR (Synthetic Aperture Radar) can be used (Figure 2).

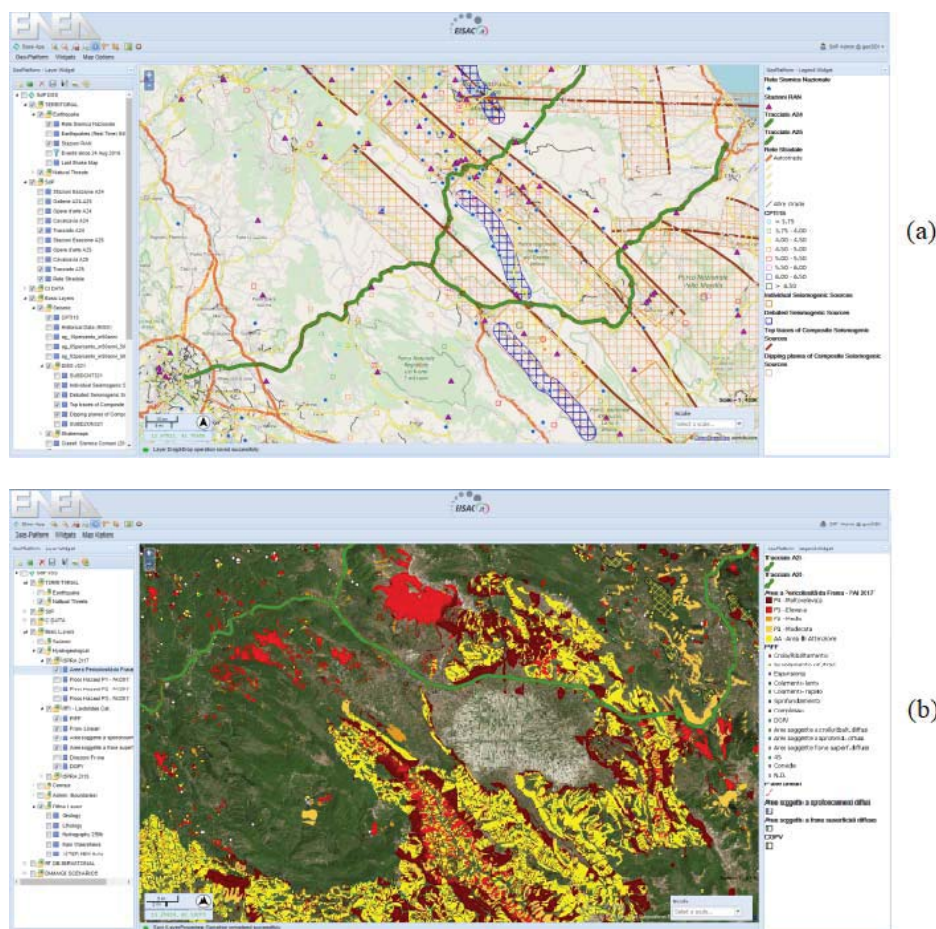


Figure 2: Example of geodata included in CIPCast DBs: (a) known faults location from INGV; and (b) landslide risk maps from P.A.I. (Piano Assetto Idrogeologico).

As far as the characterisation of viaducts or other artefacts are concerned, CIPCast can interface with external databases, via webservices, to collect and collate any already existing information thus avoiding duplication of data and waste of time. The idea is actually to promote the creation of a standardised interoperable platform, connected to CIPCast that will collate any relevant databases for viaducts or other road artefacts and that will allow to record new data [9]. As a matter of fact, since several years, ENEA, as part of the PELL (Public Energy Living Lab) project supported by the Italian Ministry of Economic Development,



MISE, has been promoted and boosted the digitization of data<sup>4</sup> and information related to the public administration, with special focus on energy-intensive and strategic infrastructures. The PELL standardised platform is already operative in several Italian municipalities for Public Lighting (PELL-IP, i.e. “Illuminazione Pubblica” in Italian) and is under development as far as schools [10, 11] and hospitals (PELL-Edifici, i.e. PELL-buildings) are concerned. For a possible PELL-viadotti [9] (i.e. Pell-viaducts), the idea would be: to collate, among others, data already included in national catalogues such as the “National Informatic Catalogue of Public Structure”, AINOP<sup>5</sup>, launched and managed by the Italian Ministry of Infrastructures and Transportation, MIT; to digitalise data that might have been collected in paper form by the PdCM (schede livello 1-2 ponti); to store, in a digital format, the data that need to be newly collected according to the forms expressly set by Linee Guida of the Italian MIT [2].

CIPCast-DSS for road networks (Figure 3) allows road network operators and emergency managers to gain, via a user-friendly WebGIS interface, real-time information on the position and extent of the ground motion and induced seismic hazard, in the aftermath of an earthquake event, as well as an estimate of the possible damage and impacts suffered by their network, that is continuously updated and made more reliable thanks to the flow of key performance indicators, KPIs, calculated from data collated through sensors deployed on some monitored components of the network.

In the first instance CIPCast DSS allow to visualise the position (coordinates of epicentre and hypocentre depth) and wave magnitude,  $M_w$ , of any occurring seismic event (overcoming the  $M_w=3$  threshold), in real time as soon as the information are made available by INGV (generally few minutes after the event).

Based on that, ground shaking maps are immediately computed by automatically implementing Ground Motion Prediction Equations (GMPEs) that can account also for possible site amplification. At the time, the GMPE provided by Bindi et al. [12] is implemented, but any other GMPE can be considered. The availability of this first estimate of the extent and severity of the seismic ground shaking along the road network allows identifying the segments and critical components, such as viaducts and embankment, that have presumably sustained higher accelerations and displacements and that might be worth inspecting as soon as possible. Possible warning about any reached threshold for the possible occurrence of earthquake-induced hazards (e.g. rockfall, landslides, permanent land deformation, liquefaction, fires following earthquake, etc.) or of any concurrent hazardous situation (e.g. severe/extreme weather, forest fires, flooding, etc.) are on the same time released by CIPCast. The official INGV shakemaps<sup>6</sup> are substituted to the simulated ones, as soon as they are made available (generally within an hour after the event).

Based on the simulated shake maps first, and on official shake maps then, a first estimate of the possible earthquake-induced physical damage to the main viaducts is performed by CIPCast implementing simplified approaches (Tier 1 and 2 approaches as explained in Section 4), based on the shaking sustained and accounting for any further possible concurrent hazards if necessary. Simultaneously, if a monitoring system is installed on viaducts, CIPCast can tune complement the estimation with the KPIs resulting from the data collected by the sensors (Tier 3 approach) thus allowing to obtain a more reliable assessment of the actual condition of the structure.

<sup>4</sup> According to the standards set by AgID, Agency for Digital Italy (<https://www.agid.gov.it/en>)

<sup>5</sup> <https://ainop.mit.gov.it/portale/#/>

<sup>6</sup> <http://shakemap.rm.ingv.it/shake4/>

Thanks to all the aforementioned real-time assessment, the most affected segments of the road are identified (Figure 3), and useful information on the residual functionality of the highway networks and on possible safe paths to evacuate the traffic can be evaluated. Through all the information displayable on the WebGIS interface of CIPCast, the asset managers can perform a more aware and participated decision-making process towards a safer and more effective emergency management.

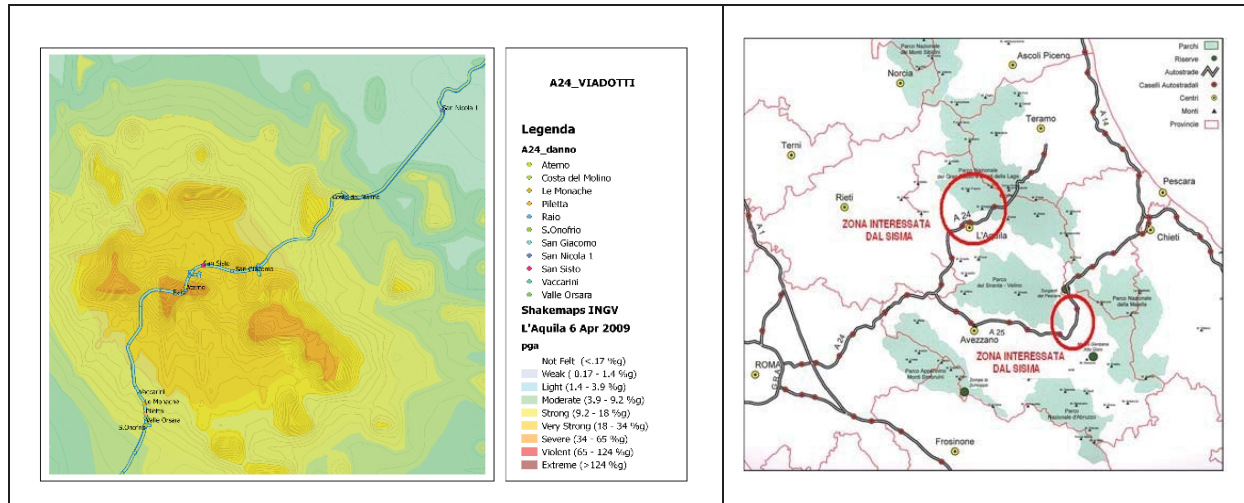


Figure 3: Ground shaking map of the April 6, 2009 L'Aquila Earthquake, overlaid with the highway route; the more severe damage to viaducts were actually identified in the viaducts located in the areas that experienced higher ground shaking.

#### 4 RISK INDICATOR AND SHM IN THE ACTIVE MANAGEMENT OF SEISMIC EVENT

During seismic emergency, as said before, CIPCast can evaluate the damage and the safety of viaducts through different methods based on the available information.

In CIPCast, three different tier of damage estimation would be implemented. Each tier corresponds to a different reliability which depends on the number of information required by the method of damage assessment. In Table 1, the three adopted tiers, in order of reliability, and their features are summarized.

For each tier, a Key Performance Indicator for the functionality level  $KPI_{SLO}$  and the damage level  $KPI_{SLV}$  can be defined to quickly evaluate the state of a bridge (Table 2) and actuate the most appropriate emergency plan.

##### 4.1 Tier 1 approach: empirical fragility curves

The first tier assesses the damage using fragility curves, which represent the probability of exceeding a predefined damage state (DS) as function of engineering demand such as peak ground acceleration (PGA), spectral acceleration (Sa) or spectral displacement (Sd).

A fragility curve can be defined through analytic or empirical methods. Analytic methods required a number of information too high to be used as a first level of damage assessment. So, CIPCast DSS implements the empirical method defined in the framework of RISK-UE project, based on empirical data collected after different seismic event.

The method divides viaducts into 15 categories, based on the parameters summarized in Table 2 and Table 3, and defines 4 different Damage State:

- D1: Minor damage,
- D2: Moderate damage,

- D3: Extensive Damage,
- D4: Complete Damage.

	Required information	Demand Parameter	Approach	Risk or damage KPI
Tier 1	Material, Column Bent Type, Span, Continuity Design (conventional or seismic) and Skew angle	Spectral acceleration $S_a(1s)$	Fragility curves	KPI <sub>1</sub>
Tier 2	Geometry, Material, Construction details and all the information to create a numerical model of the bridge	Time-history acceleration of the seismic event at the base of the structure	Numerical Model	KPI <sub>2</sub>
Tier 3	Geometry, material, construction detail	Quantity registered by SHM system	SHM	KPI <sub>3</sub>

Table 1: Tiered Approach.

Functionality level	KPI <sub>SLO</sub>	Damage level	KPI <sub>SLV</sub>
Operative bridge	<1	Low	<1
Bridge to verify	=1	Medium	=1
Inoperative bridge	>1	High	>1

Table 2: Value of KPI to evaluate the state of a bridge.

Material	Column Bent Type	Span Continuity	Design	Category
Concrete	Single	-	Conventional	1
			Seismic	2
		Simple Support	Conventional	3
			Seismic	4
	Multiple	Continuous	Conventional	5
			Seismic	6
		Simple Support	Conventional	7
			Seismic	8
		Continuous	Conventional	9
			Seismic	10
Steel	Multiple	Simple Support	Conventional	11
			Seismic	12
	All	Continuous	Conventional	13
			Seismic	14
	Other	-	-	15

Table 3: Risk-UE classification of bridges.

For each category, the method allows to define the probability of exceedance of the predefined damage states, knowing:

- The skew angle, i.e. the angle between the principal axis of minimum inertia of the pier and a line normal to roadway centreline
- The spectral acceleration at  $T=1s$  ( $S_a(1s)$ ) obtained from the response spectrum of the considered earthquake
- The number of spans.

Fixing the probability of the Damage State for which the viaduct is considered inoperable (SLO), and extremely damage (SLV), the value of the  $S_a(1s)$  inducing such states is defined respectively as  $S_{a\_SLO}$  and  $S_{a\_SLV}$ . For example, D2 and D3 levels of damage can be considered respectively to assess the spectral acceleration of the functionality level and the damage level. These values can be compared to the  $S_a(1s)$  of the response spectrum of the considered earthquake. Therefore, two KPIs can be defined by equations (1) and (2), respectively for the functionality level and the damage level.

$$KPI_{1(SLO)} = \frac{S_a}{S_{a(SLO)}} \quad (1)$$

$$KPI_{1(SLV)} = \frac{S_a}{S_{a(SLV)}} \quad (2)$$

## 4.2 Tier 2 approach: numerical models

The second tier assess the damage through a numerical model of the bridge. The required information on the viaduct increases with respect to tier 1. In order to create the numerical model, at least the following information are required:

- Structural type
- Materials and their properties
- Detailed geometry
- Construction details

If more information, such as presence of degradation phenomena, are known, the reliability of the method increases.

After the seismic event, based on the available information on both the earthquake and the structure, a linear or nonlinear analysis of the viaduct can be performed, and the dynamic response of the structure can be assessed. Some relevant parameters can be obtained to define the state of the viaduct. For example, for bridge with simple supported beams, considering an elastic numerical model, the following parameters should be determined:

- The horizontal displacements  $\Delta_t$  and  $\Delta_b$ , at the top and at the base of the piers, respectively, in order to calculate the drift of the pier  $\delta_p$
- The rotations  $\theta_t$  around the horizontal axis, at the top of the piers
- The horizontal relative displacement  $\delta_t$  between the deck and the top of the piers, if any
- The rotation  $\theta_b$  of beam section at the bearings
- The vertical displacement  $\delta_0$  of the beam at the half span

If a non-linear analysis is carried out, also the rotations  $\theta_b$  around the horizontal axis, at the base of the piers, should be evaluated. These parameters are simply represented in Figure 4.

In CIPCast DSS, the value of these parameters is compared to different threshold value, determined in order to detect the the functionality level and the damage level. Naming  $X_i$  the i-th parameter assessed from the model and  $X_{i(SLO)}$  and  $X_{i(SLV)}$  the threshold value,

respectively for the functionality and the damage level, the key performance parameters are defined by equations (3) and (4), respectively.

$$KPI_{2(SLO)} = \min \left( \frac{X_i}{X_{i(SLO)}} \right) \quad (3)$$

$$KPI_{2(SLV)} = \min \left( \frac{X_i}{X_{i(SLV)}} \right) \quad (4)$$

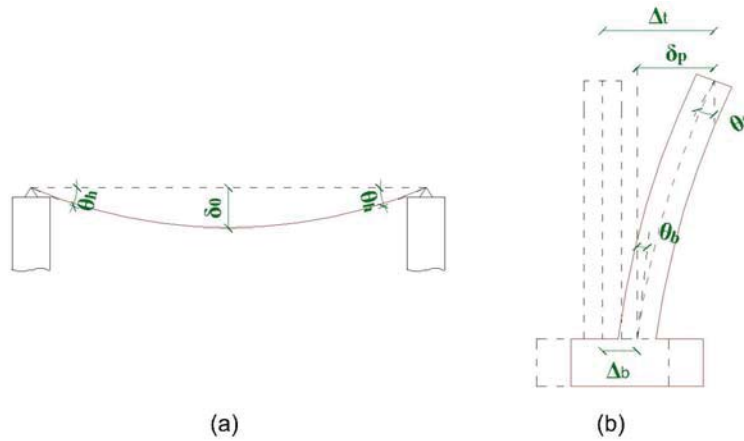


Figure 4: Relevant parameter to assess structural damage (tier 2).

#### 4.3 Tier 3 approach: SHM data processing and integration in the assessment

The third tier considers the use of a Structural Health Monitoring SHM system. In the following, the procedure to design a SHM system is reported:

- 1) Achievement of an accurate knowledge of the structure
- 2) Definition of the purpose of the monitoring system
- 3) Design of the monitoring system
- 4) Definition of the modality of data acquisition
- 5) Definition of the algorithm to elaborate the data
- 6) Choose of the interpretative model
- 7) Definition of the management process

Knowing the structure and the purpose of the monitoring, the SHM system must be design considering a great number of issues [13]. The monitoring time window (temporary or permanent system), the kind of sensors (inclinometers, strain gauges, displacement sensors, accelerometer...), the technologies (MEMS sensors, optical fiber sensors...), and instruments layout are chosen based on the scope of the monitoring [14].

In order to assess the actual health condition of a bridge during an earthquake, a permanent SHM system is required. The sensors work 24/7 but, to reduce the memory dimension of the data storage, the data recording starts only after a fixed number of sensors exceed a threshold value. So, CIPCast DSS receives, almost immediately, only the recordings of meaningful seismic events. For this purpose, different kind of instrument layout can be considered.

To immediately obtain time-histories of the same quantities evaluated by a numerical model and compare them to the threshold fixed value to eventually activate a state of alert or



emergency, with reference to a viaduct with simple supported beams, the following instruments layout can be used:

- displacement sensors (LVDT) at the top and base of the piers to measure their horizontal displacements,
- inclinometers at the top and base of the piers to measure their rotation around the horizontal axis,
- relative displacement sensors, for example radar sensor, between the header and the deck beams to monitor their relative horizontal displacement, if any,
- inclinometers on the deck beams to measure their rotation around the transversal axis,
- vertical displacement sensors of the beam at the half span.

This layout represents the minimum number of sensors required to assess the displacement of the structure only through a SHM system. Actually, for very different reasons, a smaller number of sensors could be used. In this way, there are not enough recording data to assess the state of the structure and the information must be updated with some parameters obtained performing a time-history analysis on the numerical model. The time history analysis is always possible if, at the base of the structure, 3 accelerometers are installed in three different perpendicular directions.

Another instruments layout, involving accelerometers, can be implemented. In this case, the following layout can be used:

- at the ground: 3 accelerometers to measure its acceleration along the longitudinal, transversal, and vertical directions,
- at the pile caps: almost one accelerometer along longitudinal, transversal, and vertical directions. If a more accurate evaluation is required, almost three unaligned sensors for each direction must be settled,
- on top of the piers: almost two accelerometers along the longitudinal direction and one along the transversal direction,
- on the beam: more sensors are required to properly assess its behaviour. The essential sensors are three unaligned vertical accelerometers: one (two) sensor at one-third of the span and two (one) sensors at three-third of the span. In addition, two unaligned accelerometers along transversal direction can be settled, one at one-third and the other at two-third of the span. Furthermore, one or two sensors in longitudinal direction can be disposed.

The values of the recorded acceleration provide some indication about the stress of the structure and, integrating the signal, information on velocity and displacement can be obtained.

However, this kind of pattern is commonly used to assess the dynamic properties of the bridge during an earthquake. Through a frequency domain analysis, the firsts modal shapes and their frequencies can be obtained. These values, evaluated for different earthquakes, can be compared, as shown in Figure 5, for the case of Cesi viaduct. The frequencies vary between the different seismic events and they decrease when the Arias Intensity of the Earthquake, calculated at the base of the bridge, increases. The strongest seismic event occurs on October 30, 2016. After this event, the frequencies returned to their initial values. The structure showed an elastic behaviour and, probably, the decrease of the frequencies is caused only by a non-linear behaviour [15].

To achieve a full representation of the health condition of the bridge both the first and second proposed layout can be implemented. Figure 6 shows an example of layout implemented in the monitoring of the jetty of Manfredonia. Figure 6(a) shows the accelerometer layout, which is repeated every six spans. Figure 6(b) shows the displacement sensor layout of a span.

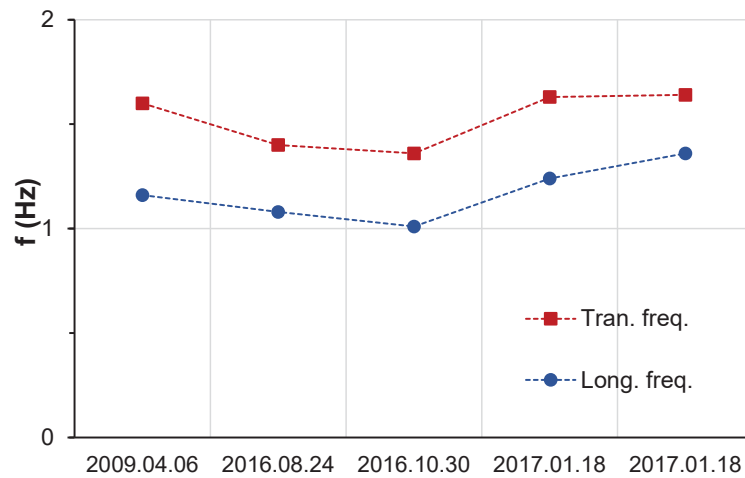


Figure 5: First natural frequency of Cesi viaduct during some consequent earthquakes.

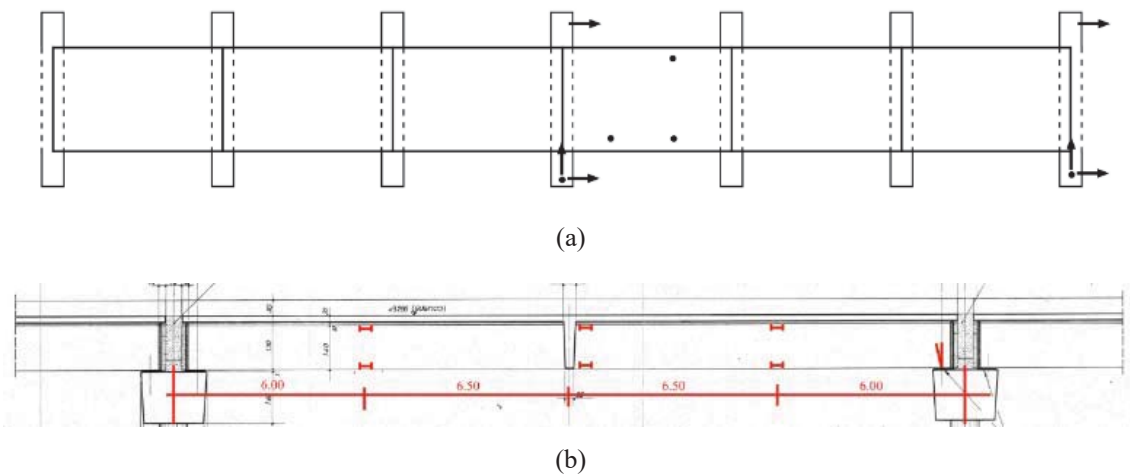


Figure 6: Layout of the (a) accelerometer and (b) displacement sensors for the jetty of Manfredonia.

This kind of monitoring system is useful also to assess the behavior of the structure in serviceable condition, considering ambient and traffic-induced vibrations [16]. Decreasing the threshold values which activate the data recording, CIPCast DSS can receive data of potential dangerous situation caused by travelling loads. The SHM efficiency increases if Weight In Motion (WIM) systems are included. These systems allow to obtain the weight and the speed of the vehicle crossing the bridge. Knowing this information, if, for equal weight and speed of vehicles, the deformations increase, the structure can be damaged. Detected the damage, the maintenance works can be scheduled.

In order to obtain complete information on the bridge status, also temperature sensors and weather control units, which measure humidity, air pressure, intensity of rain, and intensity and direction of wind, must be installed.

The analysis of all these sensor data allow to accurately define the actions on the bridge both in seismic and serviceable condition and, so, to better understand the structural response

of the viaduct and promptly detect dangerous situations. An example of such integrated and complete SHM systems is represented by the new San Giorgio bridge [17].

Depends on the features of the SHM system implemented on a bridge, the KPIs could be defined differently. The purpose of the authors is to define suitable KPIs for the most common situations.

## 5 CONCLUSIONS

After a briefly overview on the worldwide initiatives to promote the resilience of Critical Infrastructures and on develop Decision Support System for the management of the road networks, the features, and potentialities of the CIPCast DSS in use at EISAC.it have been described.

CIPCast DSS is a complex, yet user-friendly technological platform including different interoperable tools that enable the monitoring, the analysis, and the risk assessment of Critical Infrastructure. CIPCast DSS gathers and connects different vertical tools and through a powerful WebGIS interface, allows end-users to query databases DBs and to run simulation for supporting what-if analysis and decision-making processes. In the aftermaths of an earthquake, CIPCast DSS can effectively support the assessment of the residual functionality of the highway network. The paper has outlined the approached implemented within CIPcast and has originally introduced Key Performance Indicators, assessed from SHM system data, that CIPCast can use to tune and make a reliable estimation of possible damage. Therefore, CIPCast can assess the impact on the highway network functionality through simplified approaches, allowing an informed and aware decision-making process in the aftermath of seismic emergencies. The integration between CIPCast and SHM systems installed on viaducts, can effectively contribute to create “Smart Highway”, where different tools, analysis method and technologies work together 24/7 to ensure the resilience of the highway system.

## ACKNOWLEDGMENTS

The activities presented in the paper have been conducted in the framework of the following projects that are acknowledged: ARCH e RAFAEL.

## REFERENCES

- [1] F. Bontempi, *The control and the assessment of the safety of existing bridges – part 1 and part 2*. “Strade e autostrade” n°142 July/August 2020.
- [2] Ministero delle Infrastrutture e dei Trasporti. *Linee Guida per la Classificazione e Gestione del Rischio, la Valutazione della Sicurezza ed il Monitoraggio dei Ponti Esistenti*. MIT, D.M. 578 del 17/12/2020.
- [3] P. Clemente, A. De Stefano. *Novel methods in SHM and monitoring of bridges. Foreword*. Foreword to Special Issue of J. of Civil Structural Health Monitoring, Vol. 6, No. 3, Springer, 2016. <https://doi.org/10.1007/s13349-016-0185-4>.
- [4] P. Clemente. *Monitoring and evaluation of bridges. Lessons from the Polcevera Viaduct collapse in Italy*. Foreword to the Special Issue “Monitoring and evaluation of bridges following the Polcevera collapse” of the J. Civil Structural Health Monitoring, Springer, Vol. 10, No. 2, 177-182, 2020. <https://doi.org/10.1007/s13349-020-00384-6>.

- [5] A. DeWit. *Japan's "National Resilience" and the Legacy of 3-11*. The Asia-Pacific Journal, Vol.14, Issue 6, No. 1, March 15, 2016.
- [6] S. D. Werner, C. E. Taylor, S. Cho, JP. Lavoie, C. Huyck, C. Eitzel, H. Chung, R.T. Eguchi. *REDARS 2 Methodology and Software for Seismic Risk Analysis of Highway Systems*. Federal Highway Administration. Special Report MCEER-06-SP08. August 31, 2006.
- [7] A. Di Pietro, L. Lavallo, L. La Porta, M. Pollino, A. Tofani, V. Rosato. *Design of DSS for Supporting Preparedness to and Management of Anomalous Situation in Complex Scenario*. In: R. Setola, V. Rosato, E. Kyriakides and E. Rome (eds). *Managing the Complexity of Critical Infrastructures*. Studies in Systems, Decision and Control, vol.90. Springer International Publishing, 195-232. 2016. [https://doi.org/10.1007/978-3-319-51043-9\\_9](https://doi.org/10.1007/978-3-319-51043-9_9).
- [8] S. Giovinazzi, M. Pollino, V. Rosato, P. Clemente, G. Buffarini, L. La Porta, A. Di Pietro, F. Ciarallo, M. Lombardi. *A decision support system for the emergency management of highways in the event of earthquakes*. Atti del XVIII Congresso Nazionale "L'ingegneria Sismica in Italia" (Ascoli Piceno, 15-19 set 2019). SS05-101, No.3762, ANIDIS, Roma.
- [9] P. Clemente, S. Giovanizzi, M. Pollino, V. Rosato, L. Blaso, G. Giuliani, N. Gozo, C. Ormando. *Towards Standardized and Interoperable Platforms for Supporting the Seismic Vulnerability Assessment and Seismic Monitoring of Italian Bridges and Viaducts*. Eurostruct 2021 - 1<sup>st</sup> Conference of the European Association on Quality Control of Bridges and Structures. University of Padova, Italy, August 29 – September 1, 2021
- [10] L. Blaso, G. Buffarini, P. Clemente, S. Giovinazzi, S. Giuliani, G. Nicoletta, C. Ormando, M. Pollino, S. Bianchi, S. Pampanin, L. Pedone. *PELL-Schools a Standardized and Interoperable Platform for the Seismic Vulnerability and Energy Efficiency Data Management of Italian Schools*. COMPDYN 2021-8<sup>th</sup> ECCOMAS Thematic Conference on Computational Methods in Structural Dynamics and Earthquake Engineering. M. Papadrakakis, M. Fragiadakis (eds.). Streamed from Athens, Greece, 27–30 June 2021.
- [11] M. Annunziato, L. Blaso, G. Buffarini, P. Clemente, S. Giovinazzi, C. Meloni, S. Pampanin, S. Pizzuti, M. Pollino, V. Rosato. *PELL-Seismic School: piattaforma integrata, standardizzata ed interoperabile per supportare la valutazione della vulnerabilità sismica delle scuole italiane*. Atti del XVIII Congresso Nazionale "L'ingegneria Sismica in Italia" (Ascoli Piceno, 15-19 set 2019). SS13-110. No. 3735, ANIDIS, Roma. 2019.
- [12] D. Bindi, F. Pacor, L. Luzi, R. Puglia, M. Massa, G. Ameri. R. Paolucci. *Ground motion prediction equations derived from Italian strong motion database* Bulletin of Earthquake Engineering, 9(6), 1899-1920, 2011.
- [13] A. Gastineau, T. Jhonson, A. Schultz. *Bridge health monitoring and inspections systems – a survey of methods*. Department of Civil Engineering, University of Minnesota. 2009.
- [14] M. Furinghetti, A. Pavese. *Cloud Computing Strategies for Health Monitoring of Bridge Structural Systems*. Atti del XVIII Congresso Nazionale "L'ingegneria Sismica in Italia" (Ascoli Piceno, 15-19 set 2019). SS05-94. ANIDIS, Roma. 2019.

- [15] G. Bongiovanni, A. Cellilli, P. Clemente, S. Giovinazzi, C. Ormando. *Seismic response of a r.c. viaduct during different earthquakes*. SHMII-10 – 10<sup>th</sup> International Conference on Structural Health Monitoring of Intelligent Infrastructure, Porto, Portugal, 30 June-2 July, 2021.
- [16] P. Clemente, G. Bongiovanni, G. Buffarini, F. Saitta. *Structural health status assessment of a cable-stayed bridge by means of experimental vibration analysis*. J. of Civil Structural Health Monitoring, Springer, Vol. 9, No. 5, 655-669, 2019. <https://doi.org/10.1007/s13349-019-00359-2>.
- [17] P. Clemente, C. Ormando. *Monitoring system of the San Giorgio Bridge at Genoa, Italy*. The Monitor, Winter 2021, ISHMII. 2021.



## DIAGNOSTICS OF HISTORICAL STEEL BRIDGES: THE CASE OF THE VALENCIAN RAILROAD NETWORK

Valentino Sangiorgio<sup>1, 2, 3\*</sup>, Andrea Nettis<sup>2</sup>, Giuseppina Uva<sup>2</sup>, Juan A. García-Cerezo<sup>4</sup>,  
Pedro A. Calderón<sup>1</sup>, Humberto Varum<sup>3</sup>, Jose M. Adam<sup>1</sup>

<sup>1</sup> ICITECH - Instituto de Ciencia y Tecnología del Hormigón Universitat Politècnica de València  
Camino de Vera s/n, 46022, Valencia, Spain  
vsangio@upvnet.upv.es, joadmar@upv.es, pcaldero@upv.es

<sup>2</sup> Department of Civil, Environmental, Territorial, Building Engineering and Chemistry  
Polytechnic University of Bari  
via E. Orabona 4, 70125, Bari, Italy  
valentino.sangiorgio@poliba.it, andrea.nettis@poliba.it, [giuseppina.uva@poliba.it](mailto:giuseppina.uva@poliba.it)

<sup>3</sup>FEUP - Faculdade de Engenharia da Universidade do Porto  
R. Dr. Roberto Frias, 4200-465 Porto, Portugal  
[hvarum@fe.up.pt](mailto:hvarum@fe.up.pt)

<sup>4</sup>FGV – Ferrocarrils de la Generalitat Valenciana  
Avda. Villajoyosa, 2. 03016 Alicante  
[garcia\\_juacere@gva.es](mailto:garcia_juacere@gva.es)

### Abstract

*Exposure to aggressive environmental agents, aging and extreme weather events can seriously affect the performance of historical steel bridges. In the last decades, the need for diagnostic and monitoring of existing steel bridges became a huge widespread issue, as some recent catastrophic events pointed out (Mississippi River bridge, Minneapolis, Minnesota 2017; Kinzua Bridge State Park, Pennsylvania 2003). In this context, the need for monitoring and risk analysis of existing structures became an important concern for holders and administrators that are responsible for the construction operability and user safety. In particular, the issue of bridge inspections recently arose in the Valencian region (Spain) since a large number of railway riveted steel bridges were built between the end of the 19th and the beginning of the 20th Century. Today, after more than 100 years of existence, many bridges need repairing or strengthening interventions due to changes in service requirements or pathologies. This paper proposes a methodology for the identification of an analytical failure tree related to the structural response of the historical steel bridges located in the Valencian railroad network considering different critical phenomena and extreme events. Firstly, a suitable investigation plan has been developed to identify the typological, geometric, material and conservation characteristics of a case study. Subsequently, specific diagnostics (i.e. identification of the critical elements under traffic loads) is performed through a numerical model of the bridge calibrated by using the results of on-site static and dynamic tests. Once the critical elements are identified, some failure scenarios considering corrosion, fatigue and extreme events (e.g. earthquakes) are hypothesized in order to forecast consequence scenarios and achieve a failure tree of the bridge.*

**Keywords:** Historical Steel Bridges, Diagnostics, Failure Tree, On-Site Test, Calibration.

---

## 1 INTRODUCTION

Exposure to extreme natural events, aggressive environment and aging can compromise the structural performances of existing historical steel bridges jeopardizing the safety of users and of the bridge itself [1,2]. The dissemination and knowledge gained from recent failures have contributed to show the need for safe constructions, especially for critical infrastructure systems, with a high patrimonial value. Indeed, in the last decades, some recent catastrophic events pointed out the necessity of diagnosing and preventing serious damages and consequent collapse. Some of the recent catastrophic collapses of bridges occurred in Minnesota 2017 (Mississippi River bridge) and Pennsylvania 2003 (Kinzua Bridge State Park). Consequently, the perception of the society about historical steel bridges safety has changed radically, leading to the need of defining reliable tools for investigation, diagnostics mapping particular natural disasters [3,4].

The problem is highly widespread also in Europe, where *steel railway bridges* characterize the constructive heritage of the past century and are spread throughout the Countries even in small towns [5]. Indeed at European level, one of the main priorities of Horizon Europe (regarding secure societies) is to face the challenge of “*enhance the resilience of our society against natural and man-made disasters, ranging from the development of new crisis management tools to communication interoperability, and to develop novel solutions for the protection of critical infrastructure*”. Beyond this, *bridges collapse* is also dealt at a global level. United Nations’s Agenda 2030 identifies in the section “*sustainable cities and communities*” the following important topics: a) “*provide access to safe, affordable, accessible and sustainable transport systems*”, and b) “*reduce the number of deaths and the number of people affected and substantially decrease the direct economic losses relative to global gross domestic product caused by disasters*.”

In the related literature, there are numerous studies concerning the investigation and diagnostics of existing old structures [6,7,8]. These studies confirm that the design and construction criteria of the past do not consider a number of key principles to ensure the structures durability. In addition, the current service loads on the bridges are usually greater than those expected in the design phase of the past, due to the modern increase of people and freight transportation. As a result, there are many inadequacies and weaknesses in the existing steel bridges, particularly in their conceptual designs and structural details to resist cyclic loads.

A study of the ASCE Committee on Fatigue and Fracture Reliability [9] showed that eighty to ninety percent of failures in steel structures were related to *fatigue* and fractures. Vibrations, transverse horizontal forces (e.g. wind), distortions of member cross-sections, localized and diffused defects (such as corrosion damages) represent concurring causes of fatigue damage [10]. In addition, old bridges are usually characterized by their riveted connections and this is actually one of the weakest points of this type of steel structures. In this field, some research studies developed extensive tests concerning fatigue strength of rivets under shear loads demonstrating the insufficient performance level of this type of connection [11].

In this context, it is fundamental to investigate the contemporary presence of different typologies of damages in the *steel railway bridges* in order to understand the possible arising of concatenated failures. Some authors investigated how to include different typologies of damages in Finite Element Method (FEM) models [12]. In addition, fault trees are useful tools to get a complete overview of the possible arising of concatenated failures of different typologies (*fatigue*, *corrosion* damages, *seismic* damages) [13]. On the other hand, there are few attempts to connect a fault tree with a numerical FEM model. Typically the fault trees are heuristic approaches that only provide a decision support linked to the monitoring of the bridge. Research

and approaches to achieve the fault tree from the results of a structural model are missing in related literature.

This paper proposes a methodology to derive a fault tree from a FEM model (in this case calibrated by static and dynamic tests performed on-site). Hereafter, this novel graphical tool is named Analytical Failure Tree (AFT). Compared with the classical fault tree, the proposed AFT is not based on a heuristic approach, whereas it is achieved by numerical analysis and forecasting scenarios. In addition, this novel tool offers the advantage not only to numerically identify the component level failures (basic event) that cause the system level failure (top event) but also provides the possibility of displaying the failure events on a timeline. This is a useful tool also for stakeholders which can easily predict the remaining service life of the considered structure.

The proposed procedure is applied to a riveted steel bridges located in the Valencian railroad networks (Valencia region, Spain).

Particularly, the approach is articulated in three phases:

Firstly, a suitable investigation plan provides useful information (typological, geometric, material and conservation data) to characterize the bridge and its elements. The first step of the investigation plan is devoted to acquire geometrical information of the bridge. The second step provides useful historical data clarifying the history of the past structural interventions. The third and last steps of the investigation plan regard static and dynamic load tests performed directly on the bridge where a tailored monitoring system is installed to collect displacements in critical locations and stress/strains in significant structural components.

Secondly, starting from the information retrieved from the investigation plan, a FEM structural model of the bridge can be realized. The FEM model is calibrated exploiting the results in terms of strains on the monitored members by static and dynamic tests performed on the bridge and modal properties achieved by on-site measured vibrations.

Thirdly, phenomena such as corrosion, fatigue and other possible extreme events can be included and simulated with the FEM analysis. In this third phase, the procedure to derive the analytical failure tree of the bridge is explained. Moreover, by means of the FEM structural model simulating a different typology of damages and initial condition, it is possible to hypothesize different scenarios and consequently different analytical failure trees can be obtained.

## 2 THE HISTORICAL BRIDGES OF VALENCIAN RAILWAY NETWORK

In *Valencian region* a large number of *riveted steel bridges* were built to create the railroad network from the middle of the 19th century to the first decades of the 20th century when the use of steel in bridge construction was widespread. After more than 100 years of existence of this railroad network, many bridges need repairing or strengthening interventions due to changes in service requirements or pathologies. In addition, since the steel bridges have been subjected over the years to an increasing number of train passages (which means a large number of load cycles from the beginning to nowadays), the *fatigue* phenomena could affect their remaining life. In particular, fatigue often leads to a brittle fracture that, joined with a typical low level of redundancy of these types of structures, produces a high risk of collapse. Figure 1 shows two examples of old steel bridges in the Valencian railroad network.

In the last decades, the need for diagnostic and intervention of existing structures became a huge widespread issue for holders and administrators that are responsible for the construction

operability and user safety [14, 15]. In this context, an analytical failure tree of the bridge can be of great help in evaluating the diagnostic and monitoring of the structure.



**Figure 1.** Two examples of old steel bridges in the Valencian railroad network: “Quisi” (left) and “Ferrandet” (right) bridges.

## 2.1 The case-study bridge

The proposed methodology to derive an analytical failure tree from a FEM model is applied to the “Quisi” riveted steel bridge located in the Valencian railroad networks (Valencia region, Spain). The “Quisi” bridge is a multi-span truss deck bridge connecting the towns of Alicante and Denia, built between 1913 and 1915, which currently is still in-service within the Spanish railway network.

## 3 THE INVESTIGATION PLAN TO THE CHARACTERIZATION OF THE BRIDGE AND ITS ELEMENTS

The investigation plan procedure is devoted to identifying the geometrical, typological, dimensional and material information to characterize the bridge and its elements. In addition, this investigation plan provides useful information to realize and calibrate an effective FEM structural model able to simulate the performance of the bridge under a given load condition.

A preliminary historical analysis of the bridge is performed in order to retrieve the historical documentation useful to correctly identify the construction technique and be aware of possible modifications after construction. After achieving the documentation, the geometrical and visual survey can complete the information to obtain the geometric inspection of the complete system. Finally, static and dynamic load tests are performed directly on the bridges. Consequently, the FEM structural model can be realized, specific modelling assumption can be carried out thanks to the investigation and a calibration can be achieved exploiting the result of the static and dynamic load tests.

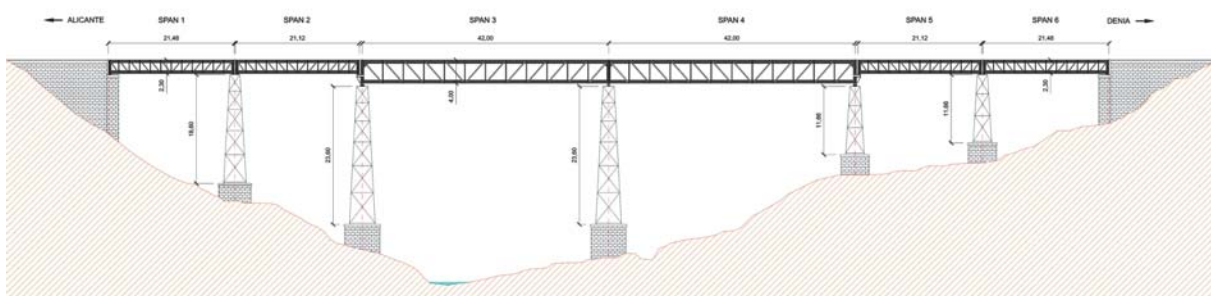
### 3.1 The investigation plan step 1: geometrical information of the bridge

The first step of the investigation plan is fundamental to identify the exact geometrical dimension of all the elements of the bridge. Useful geometrical and technical design documents of the bridge are retrieved and combined with no site investigations. In addition, in this step, photogrammetric processes of images acquired by drones or LiDAR techniques [16,17], can be used to acquire geometrical data which can be directly used to generate FEM models. A brief description of the resulting geometric and constructive features of the bridge is reported as follows. The bridge exhibits six spans for a total length of approximately 170 m. The first two, and the last two spans exhibit an isostatic structural scheme with simply supported deck trusses (approximate length 21.00 m). Conversely, the central spans (the third and the fourth) are characterised by a continuous truss deck (hyperstatic) having a total length of 84 m. The truss deck



is composed of two main truss beams, connected by transverse (i.e. floor) beams (which, in turn, sustain the stringers) and secondary lateral bracing systems at the level of the upper and lower chords. The two central spans present a continuous structural scheme, while the four lateral ones the scheme is isostatic.

The *sub-structure* system is constituted by 5 steel braced towers. The bracing system is arranged in panels, composed of X-bracing systems, considering the longitudinal and transverse direction of the bridge, respectively. At the top of the steel towers, 0.75 m-high beams are placed to absorb the gravity loads from the bearings. The legs are battened steel members: two built-up C-shaped parallel steel profiles are connected by steel plates, one per 0.85 m, creating an open-box cross-section. Rivets are used to connect the different steel elements together in each member. At the bottom of the steel towers, steel anchor bolts attach the legs to the masonry foundations. Figure 2 shows the geometrical drawing of the investigated bridge.

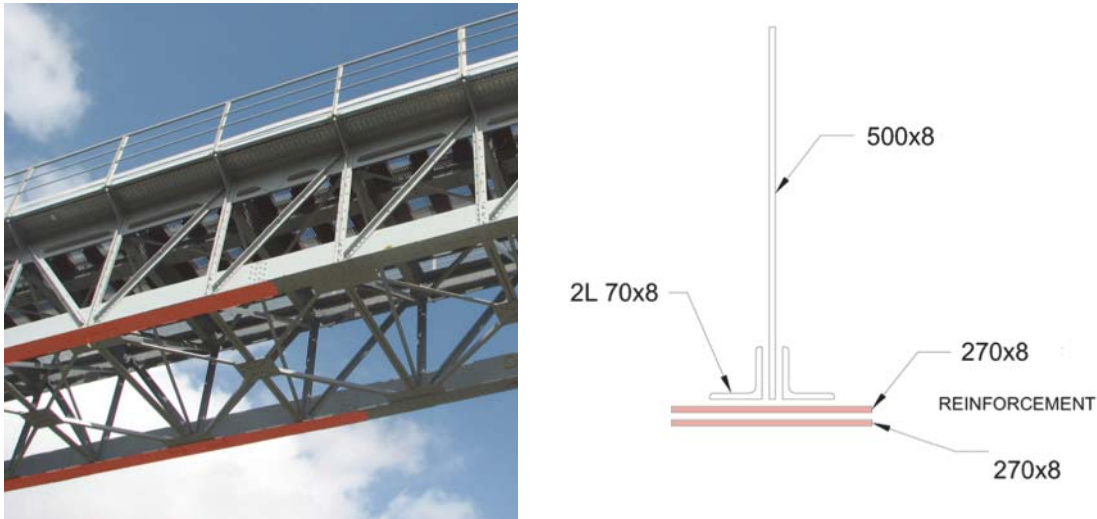


**Figure 2:** The geometrical drawing of the investigated bridge.

### 3.2 The investigation plan step 2: the historical analysis

After 100 years of useful life, the investigated bridge presents some structural criticalities related to corrosion and fatigue damages due to the operation time. In addition, the structure was designed and built according to the type of trains and railway traffic of the 20th century. In order to improve the structural safety of the bridge under the current conditions of use, in 2018 it underwent a substantial retrofit intervention. In this intervention, some reinforcing-plates were applied between the upper chords of the deck and the longitudinal members, to allow these elements to work together against the horizontal braking forces, in order to reduce the stresses in the cross beams. In addition, the dimensions of the upper and lower chord of the side members have been increased through the application of two additional bolted plate (8 mm-thick). Figure 3 emphasizes the intervention in the lower chord showed red in the photo (left part of the figure) and in a section of the structural detail (in the right).





**Figure 3:** Example of the intervention in the lower chord.

The last important retrofit intervention regards the replacement of bearing devices. Pot bearings (i.e. confined elastomeric bearings) are placed on the top of the steel towers and on the masonry abutments, preventing relative displacement between the deck and the substructure members in the transverse direction, while allowing longitudinal thermal deformations. Shock transmitters are also present to ensure the transmission of longitudinal seismic forces from the truss deck to the supporting steel towers.

### 3.3 The investigation plan step 3: static and dynamic load test

Beyond the geometrical dimension, the second important result of the investigation plan regards the mechanical and structural characteristics of the bridge.

Some mechanical tests (according to EN ISO 6892-1) [18] are performed in order to identify the characteristics of the materials. All the tested samples showed consistent results in terms of both yielding and ultimate strengths (Table 1.)

Sample	Yielding strength [MPa]	Ultimate strength [MPa]	Elongation [%]
Quisi	271	399	32

Table 1: Quisi tensile test results.

A *static load* test is performed: a train composed of two wagons, representative of the real service loads, is placed at the middle of each span and the stabilized *maximum deflection* of the truss is measured. Furthermore, the deformations in some significant truss components are registered thanks to the numerous strain and displacement sensors (Figure 4). In addition, a dynamic test is performed, in which a moving train travels on the bridge (speed of 30 km/h) and the strains and stresses of significant members are evaluated. This latter test allows for measuring bridge dynamic parameters such as the *modes of vibration* and *natural frequencies* by using a set of accelerometers during the same test.



**Figure 4:** Static and load test on the bridge.

#### 4 THE CALIBRATION OF THE STRUCTURAL MODEL

The FEM model is realized with the software SAP2000 (Computer and Structures INC (CSI). SAP2000 - Structural Analysis Program 2018) by exploiting the results of the described investigation plan. Figure 5 shows the structural model of the investigated Bridge. All the built-up members are modelled by single frame elements. The bearing devices connecting the trusses to the top beams of the towers are represented by linear *two-nodes links*. The elastic modulus of the steel is fixed at 210000 MPa and fully fixed foundations are considered. Rigid end zones are placed to model connection zones between the frame elements.



**Figure 5:** Structural Model of the investigated Bridge realised with SAP2000.

Some geometrical modelling assumption are necessary in order to reflect correctly the acquired information in the numerical model. In particular, the riveted connection beam-diagonal is modelled by using a fixed connection with rigid end offsets. Moreover, the isostatic span is assumed with the following external restraints: i) the fixed bearing modeled through pinned (i.e. fixed displacement) connection, ii) the movable bearing allowing a free longitudinal translation.

Figure 6 shows the connection between the isostatic span 2 (left), the hyperstatic span 3 (right) and the steel tower.



**Figure 6:** Connection between the isostatic span 2 (left), the hyperstatic span 3 (right) and the steel tower.

The structural model is calibrated in three steps: 1) identification of the fixity degree of connection between the diagonals and the chords, 2) calibration of the value of the gravity loads, 3) calibration of the model to simulate dynamic loads (the passage of the train).

#### 4.1 Calibration with static and dynamic loads

The calibration is performed via sensitivity analyses considering the variability in some modelling parameters. *Firstly*, the isostatic spans and hyperstatic spans are isolated from the model and are subjected to a load pattern representing the axle loads used for the static tests. A first calibration and sensitivity analysis concern the fixity degree of connection between the diagonals and the chords (rigid end offsets) provided by riveted connections; the frame mesh of the elements (element discretization) and Young modulus of the steel. This sensitivity analysis is carried out by hand, updating step-by-step the model and identifying the value of each parameter (or their combination) that best reflects the outcomes of the on-site tests. In this case, both the maximum deflection of the truss and the strain values are used for benchmarking the outcomes of the model.

*Secondly*, another sensitivity analysis is performed to calibrate the value of the gravity loads (considering also non-structural loads such as sleepers or rail profiles). For this aim, the results of a modal analysis performed using several mass values consistently with some assumptions about the non-structural loads are compared to the period of vibrations registered on-site. This process is repeated for one of the isostatic truss decks and the hyperstatic one.



Thirdly, a Moving Load Analysis is carried out in the SAP2000 environment simulating the dynamic load test performed on-site. This analysis leads to further refining of the previously-fixed parameters to best reflect the local strains value of some selected elements.

#### 4.2 Calibration results

The real on-site load test and the simulation performed via SAP2000 provides very similar results in terms of max deflection and first mode frequency. To provide an example Figure 7 shows that in the isostatic span the max deflection measured on-site is 5.5 mm and in the sensitivity analysis of the model, it ranges from 5.39- 6.06mm. Moreover, the first mode frequency is 8.79 Hz in the real test and ranges from 8.84 – 8.78 Hz in the sensitivity analysis of the model. These results of the sensitivity analysis demonstrate that the calibration is robust.

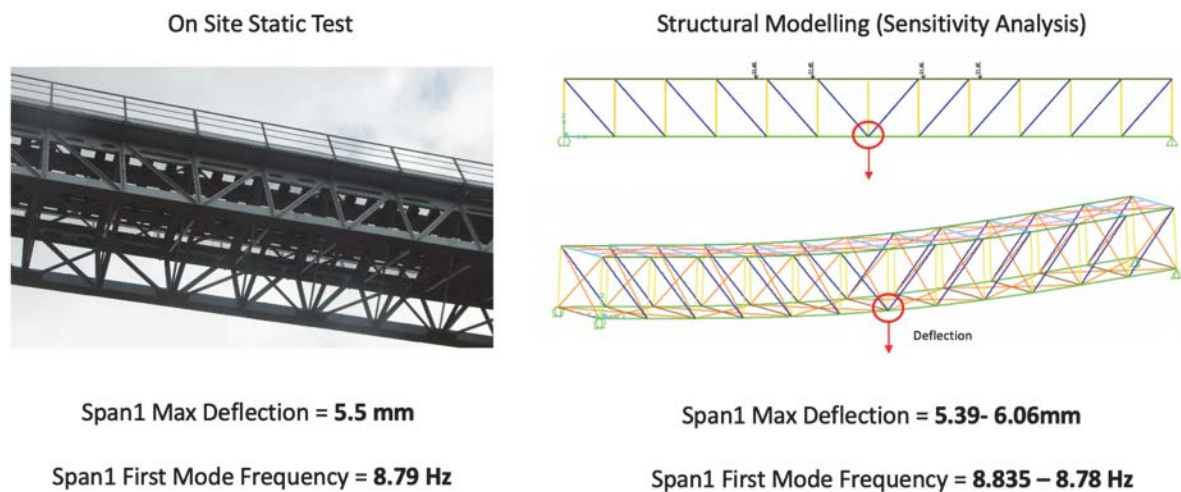
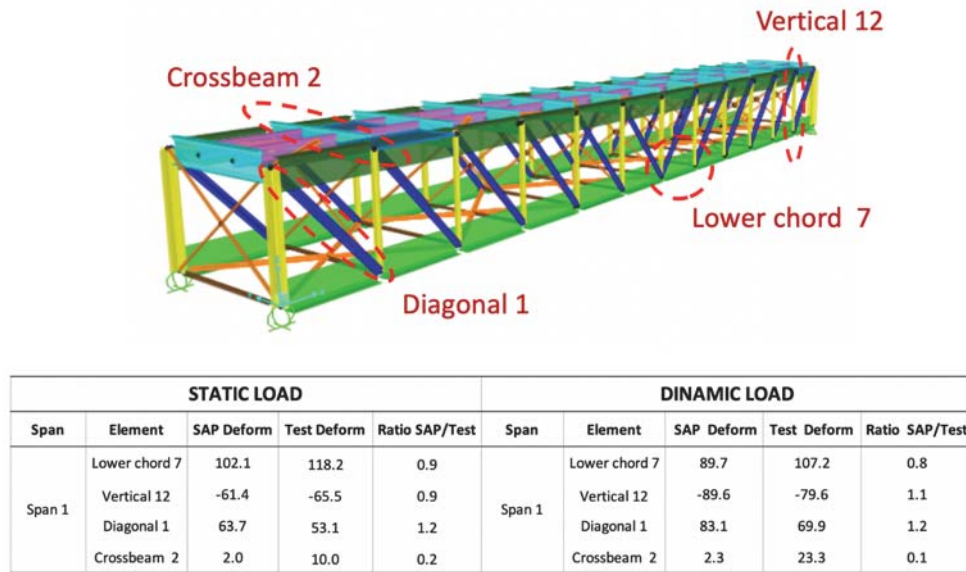


Figure 7: Static and modal test-based calibration of the isostatic Span 1

Beyond the max deflection and first mode frequency, all the strains sensors applied on the structural elements of the bridge are exploited for validating the calibration.

In particular, it is verified that the calibrated structural model (simulating the load tests) provides a deformation of the elements of the bridge compatible with that actually measured during the load tests (on which strain sensors are applied). In total, more than two hundred strain sensors are applied to the bridge, and consequently, numerous elements are available for validation. The comparison confirms the effectiveness of both the static and dynamic load simulation obtained with the calibrated structural model. Indeed, the ratio between the deformation obtained with the structural model and the deformation measured during the tests is on average equal to 0.923 (where 1 represents the perfect coherence among the two deformations). Figure 8 shows the comparison between the deformation of the elements of the Span 1 during the static and dynamic load tests, and the theoretical deformation achieved by using the SAP 2000 software.

In both in the static and load test, the only values that deviate from consistent behavior regards the cross beams. This situation occurs because cross beams take the load directly from the train. Consequently, the small differences of the model compared with the real bridge can cause overestimation or underestimation depending on the position of the train (load) on the bridge.



**Figure 8:** Comparison between the simulation (SAP 2000 software) and the real load test.

## 5 HOW TO GET AN ANALYTICAL FAILURE TREE OF THE BRIDGE

The calibrated model is the starting point to include different types of damages (e.g. corrosion, fatigue, natural hazards) in the analyses and achieve an analytical failure tree of the bridge. In this section, firstly it is explained how to include different damages in the structural model and secondly the procedure to achieve an analytical failure tree of the bridge is described. In order to have a complete overview of the possible damages of the bridge, different scenarios considering different combinations of corrosion, fatigue, earthquakes damages and different traffic volumes can be evaluated.

### 5.1 Evaluation of Corrosion Damage

The evaluation of the atmospheric corrosion is assumed on all the elements of the bridge according to the ISO 9224-2012 [19]. In particular, this approach assumes a uniform section reduction on the bridge elements. The speed of the steel corrosion depends on the type of steel and the aggressive environmental condition to which the element is exposed. In particular, the thickness reduction  $d$  is evaluated in function of the time of exposure according to the following equations:

$$\begin{cases} d_1(t) = r_{av} * t & \text{for } t < 10 \text{ Years} \\ d(t) = 10 * r_{av} + (t - 10) * r_{lin} & \text{for } t > 10 \text{ Years} \end{cases} \quad (1)$$

Where  $d_1(t)$  is the average depth of corrosion in the first 10 years of exposure,  $d(t)$  is the average depth of corrosion when the exposure time is more than 10 years;  $r_{av}$  is the average corrosion speed (during the first 10 years of exposure),  $r_{lin}$  is the average speed of stabilized corrosion (after an exposure time of 10 years), and  $t$  is the Exposure time. Moreover, the  $r_{av}$  and  $r_{lin}$  are tabulated values indicated in the ISO 9224-2012.



The reduction of the cross-section area of the elements calculated with the Equation (1) can be easily implemented in the structural model by property modifiers to the cross-section elements defined in SAP2000.

## 5.2 Evaluation of Fatigue Damage

The evaluation of the fatigue phenomenon can be evaluated according to the Miner's Rule [20]. The linear Miner's damage equation is widely used in engineering for its effectiveness and ease of application. This mathematical formulation allows for achieving the damage  $D$  of a specific element subjected to cyclic loads as follows:

$$D = \sum_{i=1}^k \frac{n_i}{N_i} \quad (2)$$

where  $N_i$  is the fatigue life of the element under some stress levels typically determined by laboratory tests and  $n_i$  is the number of load cycles of a given amplitude applied on the element. Moreover, when  $D$  is equal to 1, the component fails.

The value  $N$  can be achieved by using the curve Stress – Number of cycle (S-N) proposed by proposed in Kühn et al. [21] also applied in the Eurocode 3. In particular, some laboratory tests are performed to identify the S-N curve of the investigated bridge elements.

A previous investigation to achieve the curve S-N was performed in the laboratory of the ICITECH [22]. In particular, an upper cross beam and a full-scale bridge span of the Ferrandet Bridge was tested. The span and the cross beam have the same geometry and similar characteristics of spans 2 and 5 of the Quisi Bridge. To this aim, the results are valid for both the bridges as discussed in [22]. During the tests, Linear Variable Displacement Transducers (LVDTs) and Strain Gauge (SG) sensors were used to capture the possible nucleation and propagation of fatigue cracks.

Figure 9 shows the curve S-N of the investigated components of the bridge. In addition, an example of the application of the curve is showed in the following.

Let us assume that the structural model shows that the diagonal 12 of the Span1 suffer a load cycle of an amplitude of  $\Delta\sigma_c = 41 \text{ N/mm}^2$ . Consequently, thanks to the curve S-N it is possible to identify the amount of residual cycles before the component fails due to fatigue stress (that are approximately  $10^7$ ). It is worth noting that knowing the traffic on the bridge (number and typology of trains per day) it is possible to understand the remaining life of a component. The instant in time at which the failure occurs (considering a predetermined traffic condition) can be precisely identified.

The effects of fatigue phenomena can be accounted for in the numerical model, by appropriate reductions of the mechanical properties of the elements or by neglecting their contribution in case of fatigue failure. This operation should be performed by updating by-hand the model (e.g. no automatic procedure is available).

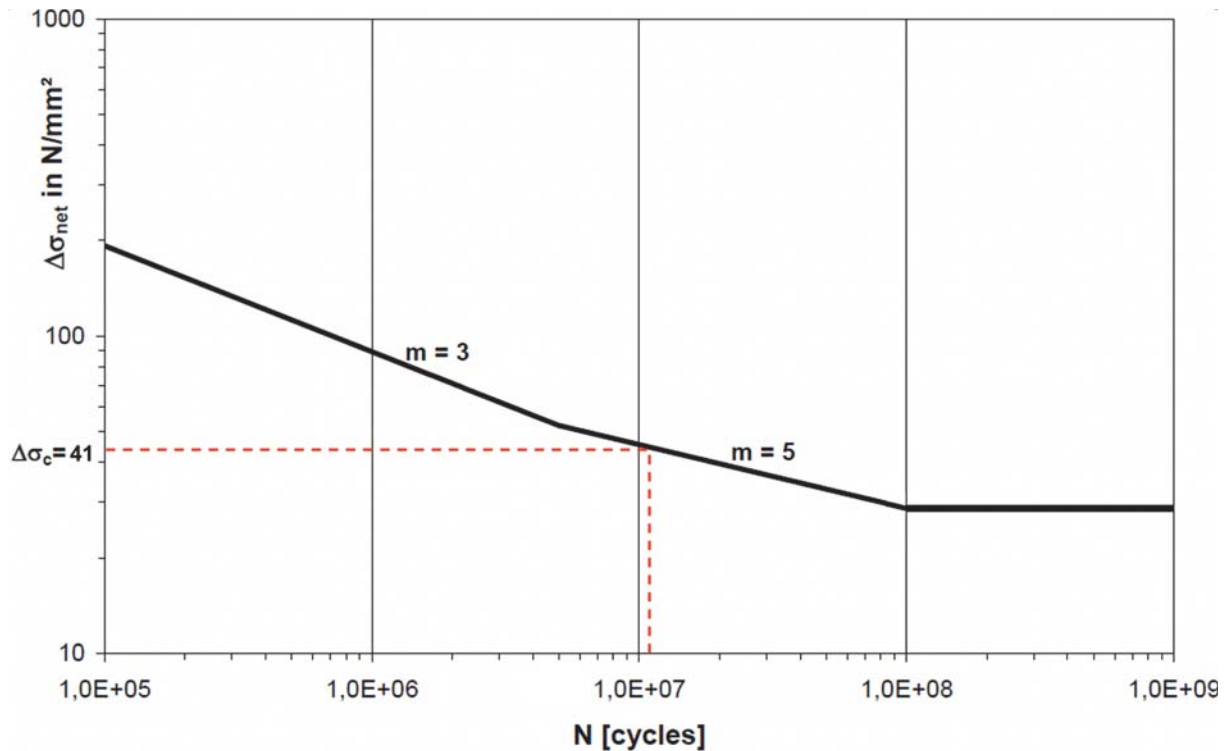


Figure 9: Curve Stress – Number of cycle for the components of the investigated Bridge: example of the application for the diagonal 12 of the Span1.

### 5.3 The evaluation of earthquake damage

Also the structural performance of the model under actions induced by natural hazards can be included in the analytical failure tree framework. As an example, in the case of seismic actions, state-of-the-art numerical analysis approaches (i.e. nonlinear static or nonlinear dynamic) can be performed to analyse the performance of the case-study structure under a given seismic action (i.e. code-based design action) or for a given earthquake scenario.

To this aim, a nonlinear numerical model should be adopted to predict the inelastic demand for each member during the seismic excitation. An appropriate modelling strategy should particularly consider the inelastic response of the substructure members which exhibit the highest probability to reach selected damage states, as proved in the large literature about the seismic response of multi-span bridges types [23,24]. To this aim, distributed- or lumped-plasticity strategies can be adopted. In the latter, plastic hinges should be used to predict the nonlinear axial response of bracing members (subjected to buckling or tensile yielding) and nonlinear axial-flexure response in the legs of the steel towers (Figure 10). Also, failures of the riveted connections or for shear should be considered. Appropriate recommendations about modelling and seismic analysis of truss bridges are reported in [25].

Nonlinear dynamic analyses are widely recognised as the most accurate strategies to predict the response of the case-study bridge under a given ground-motion shaking. However, such analysis approaches are very demanding in terms of computational efforts, particularly for complex structures such as steel truss bridges. Moreover, these analyses require models about the cyclic response of built-up steel members which are rarely available in the literature [26,27]. Conversely, nonlinear static procedures are less demanding with respect to nonlinear dynamic approaches. The accuracy of these simplified methods strongly depends on various assumptions (e.g. regular dynamic response) which can be not valid for typical steel truss bridges. However, according to [25], this simplified methodologies are effective for local analysis of substructure

members, such as steel towers, to identify the corresponding ductility capacity and failure mechanisms.

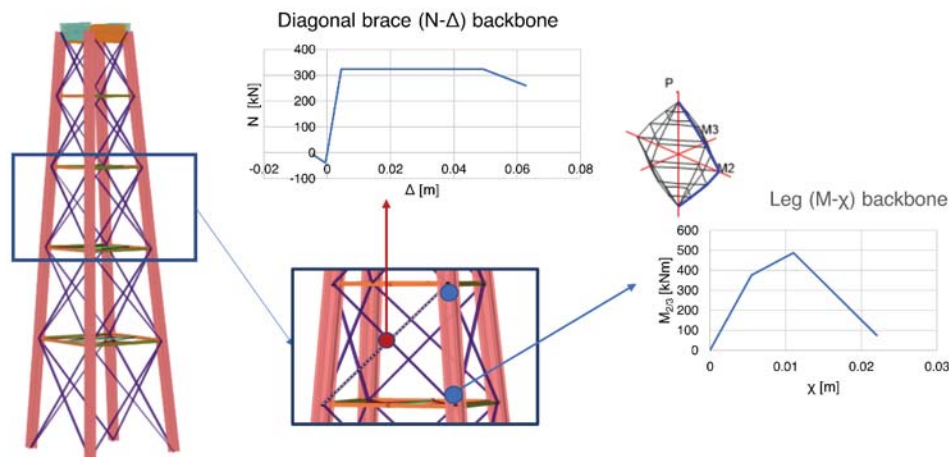


Figure 10: Modelling strategy (lumped-plasticity) for seismic response of supporting steel towers.

#### 5.4 The proposal of the analytical failure tree

In this subsection, the methodological process to achieve an analytical failure tree of a bridge is discussed. More precisely, the analytical failure tree is intended as a graphical representation developed on a timeline to show when faults can occur according to the structural model. In addition, the analytical failure tree also shows the connections among failures. A failure can be isolated without causing other consequences. In other cases, the failure can create a cascade effect. The analytical failure tree is also useful to understand the possible occurrence of serious cascade effects causing rapidly a global bridge collapse.

The analytical failure tree is obtained with an iterative process that concerns the evaluation of the amplitude of the load cycles from every element of the bridge (from the FEM model) and the related evaluation of the fatigue damages (and concurring causes) over time. In particular, the process is explained in the following bulleted list:

- 1) Initially there are no damages and the dynamic analysis is performed. Consequently, the stresses of all the elements (or components) are obtained from the FEM model;
- 2) The elements that undergo significant load cycles (named critical elements) according to the curve “Stress – Number of cycles” are considered. Fatigue and other concurring causes (e.g. corrosion) are evaluated over time by using procedures described in subsections 5.1 and 5.2;
- 3) The first element that fails in the instant  $t_I$  is identified;
- 4) The failure is shown in the analytical failure tree in the instant  $t_I$  (indicating component and cause);
- 5) The contribution of the damaged element is implemented, updating the FEM model (updated in the instant  $t_I$ ),
- 6) The new stresses of all the components (after  $t_I$ ) are obtained from the FEM model subjected to a new analysis,

- 7) If no other elements have reached a limit state it is possible to continue with the next step. If other elements have reached a limit state, the analytical failure tree and the structural model are updated by considering all the elements failed in the instant  $t_1$  and new stresses are evaluated (this step is repeated until the updating of the structural model does not cause other element reaching a limit state or a global failure is reached);
- 8) This phase is analogous to point 2. New fatigue damages and other concurring causes are evaluated over time;
- 9) The second element (or group of elements) fails in the instant  $t_2$ . If this second failure is related to the first one (instant  $t_1$ ), then it is placed on the same branch of the fault tree. On the contrary, if the second element fails is not related to the first one a new independent branch is drawn.
- 10) The process is repeated until the instant  $t_n$  is greater than a preset year or a global failure is achieved.

More in details, the rules to understand if two consecutive failures belong to the same branch are specified in the following. Let us assume the presence of two failures (a first failure in the instant  $a$ , and a second failure in successive instant  $b$ ). The conditions so that these two consecutive failures are positioned on the same branch of the failure tree are the following:

- 1) the two failures belong to the same span, or to two adjacent hyperstatic spans;
- 2) the element that undergoes the second failure (instant  $b$ ) suffers an increase in load due to the first failure (this condition can be identified when the numerical model is updated).

If these two conditions do not both occur, it means that the two damages are independent, and it is right to represent them differently on two different branches in the fault tree.

It is worth noting that in the proposed application, the failure can occur for the *fatigue* and all the other phenomena can only speed up the damage. Indeed, the *corrosion damage* causes a section reduction, that consequently can produce a premature fatigue failure. The *seismic damage* creates small structural damages (due to the low seismicity of the region in question) which in some cases can aggravate the effects to the fatigue damage. Other possible damages can occur as a consequence of the redistribution of loads after a fatigue failure. Consequently, the proposed approach is in line with the assumption demonstrated in the study of the ASCE Committee on Fatigue and Fracture Reliability [9] assessing that the failures in steel structures were related principally to *fatigue* and all the other phenomena are concurring causes that can involve the reaching of a limit state.

## 5.5 The analytical failure tree and different scenarios of the investigated bridge

The proposed analytical failure tree can consider different aggressive phenomena including corrosion, fatigue and it can also be used to understand the consequences of earthquake damages. In addition, different scenarios can be defined on the basis of the presence (with different intensity level) or absence of every aggressive phenomenon.

In particular, the *atmospheric corrosion* can produce a section reduction of the elements of the bridge. In an alternative scenario, corrosion can be avoided thanks to an effective maintenance and the use of adequate corrosion inhibitors.

The intensity of the *fatigue phenomenon* is strictly correlated to the traffic volume present on the bridge. The current traffic is about 32 trains per day, but it could be increased due to specific

needs of the region. Both the current and possible “traffic increased” scenario must be considered in order to have an exhaustive overview of the possible damage of the bridge.

The probability of occurrence of a *seismic event* of a given intensity is extremely connected to the hazard characteristics of the site. Even if the Valencian region has low seismicity, it is important to understand how the eventual presence of seismic damage would interact with other aggressive phenomena.

Consequently, it is possible to hypothesize eight damage scenarios corresponding with all the possible combination of *atmospheric corrosion*, *fatigue phenomenon* and presence or not of a *seismic event* (Table 2).

SCENARIOS	CORROSION	FATIGUE	SEISMIC EVENT
Scenario 1	No corrosion (Constant maintenance)	Current traffic volume	No seismic damage
Scenario 2	No corrosion (Constant maintenance)	Current traffic volume	Seismic event
Scenario 3	No corrosion (Constant maintenance)	Increased traffic volume	No seismic damage
Scenario 4	No corrosion (Constant maintenance)	Increased traffic volume	Seismic event
Scenario 5	Atmospheric corrosion	Current traffic volume	No seismic damage
Scenario 6	Atmospheric corrosion	Current traffic volume	Seismic event
Scenario 7	Atmospheric corrosion	Increased traffic volume	No seismic damage
Scenario 8	Atmospheric corrosion	Increased traffic volume	Seismic event

Table 2: Different damage scenarios.

For every different damage scenario, an analytical failure tree can be achieved in order to understand what types of damage could occur.

To provide an example, Figure 11 show an analytical failure tree for the Scenario 1 regarding the presence of an effective maintenance (to avoid corrosion), current traffic volume and no presence of seismic damage.

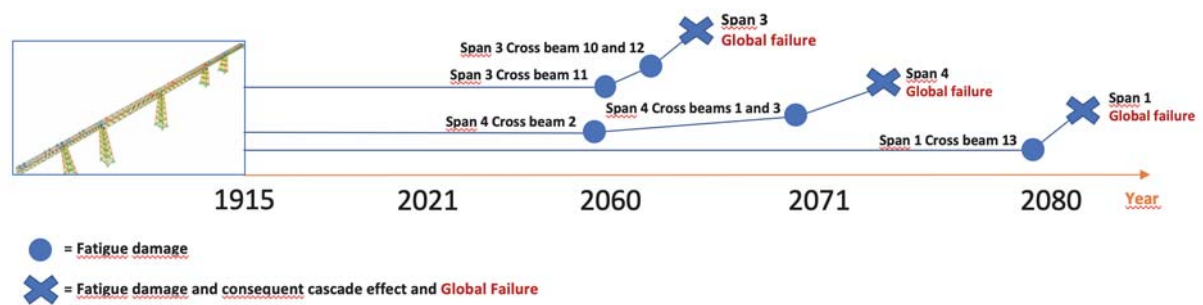


Figure 11: Analytical failure tree for the Scenario 1.



## 6 CONCLUSION

The work proposes a methodological approach to develop an analytical failure tree of historical steel bridges based on the calibration of a numerical FEM model able to include different damage scenarios in the analysis:

- i) The atmospheric corrosion phenomenon is evaluated in accordance with the ISO 9224-2012 assuming a uniform section reduction of the steel elements of the bridge.
- ii) The evaluation of the fatigue phenomenon exploits the Miner's Rule and the curve "Stress – Number of cycles" to identify the number of load cycles of a given amplitude that the element can experience before the failure.
- iii) The seismic damages can be included with state-of-the-art analysis approaches based on a nonlinear numerical model of the bridge representing its current condition.

Compared with the classical fault tree, the proposed analytical failure tree is achieved by exploiting a FEM model and numerical analysis. On the contrary, the classical fault tree is drawn based on the technician's expertise and by following a heuristic approach. In addition, the proposed failure tree has the advantage to displaying the failure events on a timeline.

The approach is applied to the real case study of a riveted steel bridge located in the Valencian railroad network (Spain) and the example of the analytical failure tree achieved for the scenario involving fatigue damaged related to 32 trains per day, absence of atmospheric corrosion and seismic damage is shown. The analytical failure tree obtained with the proposed approach can be useful for diagnostics, monitoring and forecast intervention by simulating different consequence scenarios.

Future research will perform an exhaustive investigation to achieve the analytical failure trees of several different scenarios in order to have a complete overview of the possible failures and any cascade effects on the investigated bridge.

## ACKNOWLEDGMENTS

The research presented in this paper was partially funded by the Italian Department of Civil Protection in the framework of the national project DPC-ReLUIs 2019-2021.

## REFERENCES

- [1] F.N. Catbas, A. E. Aktan, Condition and damage assessment: issues and some promising indices. *Journal of Structural Engineering*, **128**(8), 1026-1036, 2002.
- [2] J. Gocál, J.Odrobiňák, On the Influence of Corrosion on the Load-Carrying Capacity of Old Riveted Bridges. *Materials*, **13**(3), 717, 2020.
- [3] A. Iacobellis, M. Martellotta, A. Gioia, D. Prato, V. Totaro, R. Bonelli, G. Balacco, and A. A. M. G. Esposito, Investigation of a Flood Event Occurred on Lama Balice, in the Context of Hazard Map Evaluation in Karstic-Ephemeral Streams. in *International Conference on Computational Science and Its Applications*, Cham, Springer, vol 10964, pp. 317-333, 2018, [https://doi.org/10.1007/978-3-319-95174-4\\_26](https://doi.org/10.1007/978-3-319-95174-4_26)
- [4] G. Balacco, V. Totaro, A. Gioia, and A. F. Piccinni, Evaluation of Geomorphic Descriptors Thresholds for Flood Prone Areas Detection on Ephemeral Streams in the

- Metropolitan Area of Bari (Italy). in *International Conference on Computational Science and Its Applications*, Cham, Springer, vol. 11622, pp. 239-254, 2019, [https://doi.org/10.1007/978-3-030-24305-0\\_19](https://doi.org/10.1007/978-3-030-24305-0_19)
- [5] V. Sangiorgio, A.M. Mangini, I. Precchiazzi, A new index to evaluate the safety performance level of railway transportation systems. *Safety science*, **131**, 104921, 2020.
  - [6] V. Sangiorgio, G. Uva, M. A. Aiello, A multi-criteria-based procedure for the robust definition of algorithms aimed at fast seismic risk assessment of existing RC buildings. In *Structures*, **24**, 766-782 2020.
  - [7] V. Sangiorgio, G. Uva, J.M. Adam, Integrated seismic vulnerability assessment of historical masonry churches including architectural and artistic assets based on macro-element approach. *International Journal of Architectural Heritage*, 1-14, 2020.
  - [8] V. Sangiorgio, G. Uva, F. Fatiguso, A procedure to assess the criticalities of structures built in absence of earthquake resistant criteria. *REHABEND*, 2016, 631-639, 2016.
  - [9] ASCE, Committee on fatigue and fracture reliability of the committee on structural safety and reliability of the structural division. Fatigue reliability. *Journal of Structural Division. Proceedings of ASCE*, **108** 3–88, 1982.
  - [10] A. Brencich, L. Gambarotta, Assessment procedure and rehabilitation of riveted railway girders: The Campasso Bridge. *Engineering Structures*, **31**(1), 224-239, 2009.
  - [11] A. Pipinato, C. Pellegrino, O. S. Bursi, C. Modena, High-cycle fatigue behavior of riveted connections for railway metal bridges. *Journal of constructional steel research*, **65**(12), 2167-2175, 2009.
  - [12] R. Landolfo, L. Cascini, M. D’Aniello, F. Portioli, Gli effetti del degrado da fatica e corrosione sui ponti ferroviari in carpenteria metallica: Un approccio integrato per la valutazione della vita residua. *Riv Ital della Saldatura*, **63**(3), 367-77, 2011.
  - [13] C. Davis-McDaniel, M. Chowdhury, W. Pang, K. Dey. Fault-tree model for risk assessment of bridge failure: Case study for segmental box girder bridges. *Journal of infrastructure systems*, **19**(3), 326-334, 2013.
  - [14] M. Dağdeviren, İ. Yüksel, Developing a fuzzy analytic hierarchy process (AHP) model for behavior-based safety management. *Information Sciences*, **178**(6), 1717-1733, 2008.
  - [15] V. Sangiorgio, G. Uva, J.M. Adam, L. Scarcelli, Failure analysis of reinforced concrete elevated storage tanks. *Engineering failure analysis*, **115**, 104637, 2020.
  - [16] A. Nettis, M. Saponaro, M. Nanna, RPAS-based framework for simplified seismic risk assessment of Italian RC-bridges. *Buildings* 2020. <https://doi.org/10.3390/BUILDINGS10090150>.
  - [17] A. Khaloo, D. Lattanzi, K. Cunningham, R. Dell’Andrea, M. Riley Unmanned aerial vehicle inspection of the Placer River Trail Bridge through image-based 3D modelling. *Struct Infrastruct Eng* 2018. <https://doi.org/10.1080/15732479.2017.1330891>
  - [18] UNE EN ISO 6892-1:2017: Metallic materials - Tensile testing - Part 1: Method of test at room temperature, ISO 6892-1:2016.
  - [19] BS EN ISO 9224: 2012. Corrosion of metals and alloys—Corrosivity of atmospheres—Classification, determination and estimation, 2012.

- [20] Q. Sun, H.N. Dui, X.L. Fan, A statistically consistent fatigue damage model based on Miner's rule. *International Journal of Fatigue*, **69**, 16-21, 2014.
- [21] B. Kühn, M. Lukić, A. Nussbaumer, H.-P. Günther, R. Helmerich, S. Herion, M.H. Kolstein, S. Walbridge, B. Androic, O. Dijkstra, Ö. Bucak, Assessment of existing steel structures: recommendations for estimation of remaining fatigue life. *Joint Research Center*, 2008.
- [22] E. Bertolesi, M. Buitrago, J.M. Adam, P.A. Calderón, Fatigue Assessment of Steel Riveted Railway Bridges: Full-Scale Tests and Analytical Approach. 2021.
- [23] R. Gentile, A. Nettis, D. Raffaele, Effectiveness of the displacement-based seismic performance assessment for continuous RC bridges and proposed extensions. *Engineering Structures* **221**, 110910, 2020. <https://doi.org/10.1016/j.engstruct.2020.110910>.
- [24] M.F. Yilmaz, B. Çalayan, Seismic assessment of a multi-span steel railway bridge in Turkey based on nonlinear time history. *Nat Hazards Earth Syst Sci*, **18**, 231–40, 2018. <https://doi.org/10.5194/nhess-18-231-2018>.
- [25] T. Ho, R. Donikian, T. Hingham, C. Seim, A. Pan, Seismic retrofitting guidelines for complex steel truss highway bridges. Multidisciplinary Center for Earthquake Engineering Research State University of New York at Buffalo, Federal Highway Administration; 2006.
- [26] G. Della Corte, R. Landolfo, Lateral loading tests of built-up battened columns with semi-continuous base-plate connections. *Journal of Constructional Steel Research*, **138**, 783-798, 2017. <https://doi.org/10.1016/j.jcsr.2017.08.018>.
- [27] B.H. Hashemi, A. Poursamad Bonab, Experimental investigation of the behavior of laced columns under constant axial load and cyclic lateral load. *Engineering structures*, **57**, 536-543, 2013. <https://doi.org/10.1016/j.engstruct.2013.09.033>.

## TOWARDS A UNIFIED SEISMIC- FLOOD- HAZARD MODEL FOR RISK ASSESSMENT OF ROADWAY NETWORKS IN GREECE

Anna C. Karatzetizou<sup>1</sup>, Sotiria P. Stefanidou<sup>2</sup>, Stefanos P. Stefanidis<sup>3</sup>, Grigorios K.  
Tsinidis<sup>4</sup>, Dimitrios K. Pitilakis<sup>5</sup>

<sup>1, 2, 4, 5</sup> School of Civil Engineering, Aristotle University of Thessaloniki, 54124, Greece  
e-mail: {akaratze, ssotiria, gtsinidi, [dpitilak](mailto:dpitilak@civil.auth.gr)}@civil.auth.gr

<sup>3</sup> Faculty of Forestry and Natural Environment, Aristotle University of Thessaloniki, 54124, Greece  
e-mail: [ststefanid@gmail.com](mailto:ststefanid@gmail.com)

---

### Abstract

Roadway networks, playing a vital role in the economic prosperity of modern societies. Recent hazardous events in Greece, for instance, the 2021 Thessaly earthquake and floods and the heavy 2019 rainfall in Crete, have demonstrated the vulnerability of roadway networks to natural hazards, resulting in severe physical damage and important economic and societal losses. Severe damage on bridges and tunnels of roadway networks is commonly related to the effects of multiple hazards that may act independently during their life. However, the literature on risk assessment of the above elements is commonly focused on the effects of one hazard, disregarding the potential interaction effects of diverse hazards in a multi-hazard environment. In this context, there is an increasing need for reasonable and effective evaluation of the multi-hazard risk of transportation infrastructure. Research project INFRARES aspires to bridge this gap by gaining further insight into the risk assessment of bridges and tunnels of transportation networks in Greece, when subjected to separated and subsequent hazards, with particular emphasis being placed on seismic and flood hazards. The present paper briefly presents a unified methodology to homogenize the single seismic and flood hazard scenarios and develop appropriate single- and multi-hazard maps for Greece to be used in risk assessment of roadway networks. Seismic hazard data, referring to rock site conditions, developed within the SHARE research project ([www.share-eu.org](http://www.share-eu.org)), is initially selected and is properly amplified to account for site effects, by employing a simplified  $V_{s,30}$  model originating from morphology and topography data of each region in Greece. The seismic hazard is estimated for a return period of 475 years. Flood hazard zones are derived for whole Greece using newly developed data from the Joint Research Center of the European Commission (<https://data.jrc.ec.europa.eu/dataset>) for the 100-years return period scenario. Using the above input, both single hazard and multiple hazard models are developed and provided in terms of maps in GIS format. The model developed within this study is expected to be a valuable contribution towards the generation of a uniform multiple hazard model for the risk assessment of critical elements of transportation infrastructure in a multi-hazard environment.

**Keywords:** Natural hazards, earthquakes, floods, multi-hazard risk assessment.

---

## 1 INTRODUCTION

The reliability of roadway networks and their components, exposed to multiple natural hazards, is on the frontline of engineering research during the last three decades since potential damage on their critical components (e.g., bridges and tunnels) is strongly related to important direct and indirect economic losses. In this context, enhancing the resilience of roadway networks is key for a safety and an economic viewpoint. Disaster resilience is defined by the National Academies as “*the ability to prepare and plan for, absorb, recover from, and more successfully adapt to adverse events,*” while “*enhanced resilience allows better anticipation of disasters and better planning to reduce disaster losses – rather than waiting for an event to occur and paying for it afterward*” [1]. To achieve such enhanced resilience, civil infrastructure systems must not only survive natural disasters, but also recover to functional levels within acceptable time and cost limits.

The spatial extent of most civil infrastructure systems, including roadway networks, and the disparity of their elements make them susceptible to a wide range of natural hazards. Bridges and tunnels are considered to be the most critical components of urban and interurban transportation systems, and as such should ensure mobility and intercity connection after extreme hazard events. Bridge damage may cause significant disruption to a transportation system, resulting in severe substantial direct and indirect losses; for instance, the Loma Prieta 1989 earthquake resulted in more than 40 deaths due to bridge damage and \$1.8 billion monetary direct losses due to damage to the transportation infrastructure [2]. Flood due to heavy rainfall may result in substantial losses, as well; for example, in 2007, heavy rainfall in the UK affected the road network with estimated cost £60 million (The Parliamentary Office of Science and Technology, Post Note Number 362, October 2010). Extreme weather conditions, associated with recorded climate changes, e.g., floods and extreme temperatures, are expected to worsen the performance of many bridges in the near future [3]. Damage on bridges due to extreme weather conditions in Greece (e.g., reported damage due to heavy rainfall in Trikala in 2016 and in Crete in 2019) is more frequently recorded during the last years. Bridge damage related to flood, scouring and ground failures may result in collapse and traffic disruption. Although to a lesser extent, natural hazards may result in damage on tunnels as well. For instance, a large number of mountain tunnels suffered significant damage during the 1999 Chi-Chi earthquake in Taiwan, as well as during the 2008 Wenchuan earthquake in China [4].

During the last 30 years, several methods have been developed for the assessment of performance and vulnerability of bridges [5] and tunnels [4, 6] against seismic and flood hazard [7]. Recognizing the significant effects of multiple hazards, as well as of climate change, on the vulnerability of civil infrastructure, the research interest has been recently shifted upon the derivation of multi-hazard fragility curves [8]. However, the lack of knowledge in this field remains significant, when referring to transportation infrastructure, including roadway networks.

Regardless of the examined system or element at risk, one of the most critical steps of any multi-risk assessment methodology is the appropriate definition of multiple hazard scenarios under which the examined system or element may be subjected throughout its life.

Based on the above considerations, the main objective of the present paper is to present briefly a framework for the development of combined seismic- flood-hazard scenarios to be used for the risk assessment of critical elements of roadway networks, i.e., bridges and tunnels, referring to whole Greece. The proposed framework helps towards a unified seismic- flood hazard model, which will be used in within the research project INFRARES (<https://www.infrares.gr/>) that aims at assessing the risk and resilience of bridges and tunnels of roadway networks in Greece against the aforementioned hazards.



## 2 INFRARES PROJECT

A comprehensive methodology for the risk and resilience assessment of roadway networks in a multi-hazard environment, will be developed in the framework of INFRARES, focusing on bridges and tunnels. To meet the objectives of the project, various methodological frameworks will be used, associated with the following steps enclosed in the definition and assessment of risk: (i) exposure: an inventory of crucial elements of transportation systems, i.e., bridges and tunnels, which may be affected by diverse natural hazards, will be developed accounting for typologies found commonly in Greece. (ii) Multi-Hazard assessment: various scenarios of distinct and multiple natural hazards will be defined, focusing on earthquakes and floods since these hazards are considered more relevant for the risk assessment of the transportation infrastructure in Greece. This step will include also the definition of appropriate measures to describe the intensity of examined hazards. (iii) Vulnerability assessment: the degree of loss on the given element or set of elements at risk, when subjected to a specific natural hazard or to a combination of diverse hazards will be calculated, by employing comprehensive numerical analyses of the selected elements, while accounting thoroughly for the effects of ageing-related degradation phenomena of the elements, as well as of Soil-Structure Interaction (SSI) effects.

A fully parametrized software will accompany the methodology, allowing for its easier application by providing the provided time-dependent, multi-hazard fragility curves for roadway bridges and tunnels. Figure 1 presents a first draft of the general flowchart of the methodology that is being developed in the framework of the INFRARES project.

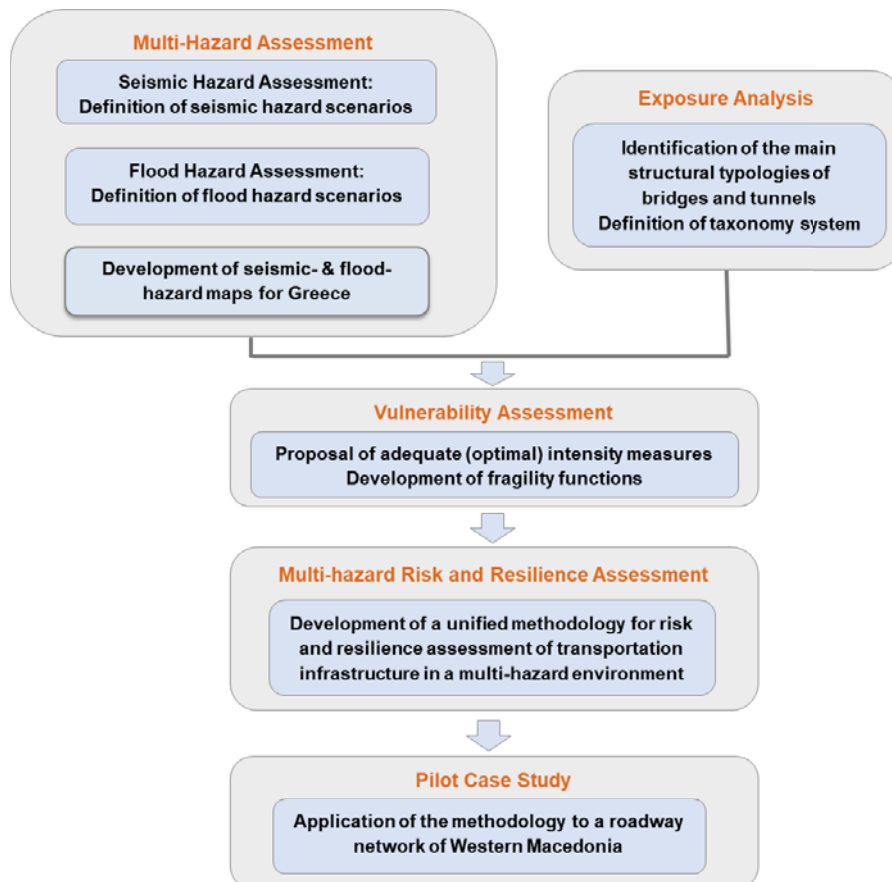


Figure 1: Flowchart of INFRARES project

In particular, INFRARES is expected to contribute on the State of the Art by providing an innovative methodology for the generation of multi-hazard maps, to be used for the definition of relevant scenarios in the framework of multi-hazard risk assessment of transportation or other civil infrastructure. In addition, new, analytical fragility curves and functions will be developed for various typologies of bridges and tunnels, and for distinct and/or combined hazards, considering in the latter case combinations of hazards that are relevant for Greece. Moreover, the damage state definitions within fragility analysis of bridges and tunnels will be case- and hazard-specific, considering different failure modes and damage mechanisms, to fill relevant knowledge gap. Finally, a resilience index will be proposed for bridges and tunnels typologies, as well as for roadway networks, referring to distinct hazards and various hazard combinations. In this context, the index will be appropriately modified so that to be applicable for multi-hazard assessment purposes. The methodology and the software could be used for rapid and rigorous pre- or post-event assessment of infrastructure or for post-event risk management, constituting very useful tools for stakeholders, operators, consultancies and public authorities.

In the following sections, we focus on one of the main steps of the methodology, namely the multi-hazard assessment. More specifically, we present an innovative methodology for the generation of multiple seismic- flood- hazard models in GIS format.

### **3 MULTIPLE HAZARD SCENARIOS FOR TRANSPORTATION INFRASTRUCTURE IN GREECE**

In the framework of the multi-hazard assessment approach adopted herein, diverse natural hazards and combined hazards scenarios are carefully selected, prioritized on the basis of the potential to cause damage on transportation infrastructure and further examined. After a thorough literature review and lessons learned from past hazards events, earthquakes and floods are selected as the most critical natural hazards for the assessment of the transportation infrastructure in Greece. Initially, each natural hazard is studied separately, while in a second phase we examine the combination of the two hazards, proposing a unified framework for multi-hazard scenarios. Both single or multiple hazards scenarios are visualized in the form of maps in GIS format, referring to whole Greece.

The main steps of the herein proposed framework are:

Step 1: Establish a ranking of the different types of natural hazards, considering potential interactions between them.

Step 2: Identify single-hazard models.

Step 3: Identify multi-hazard models, covering all potential intensities and relevant hazard interactions.

Step 4: Generate single- and multiple- hazard scenarios and relevant maps in GIS format for the assessment of transportation infrastructure in Greece.

For the sake of presentation of the framework, in the present paper, we consider for the seismic hazard the standard design/assessment seismic scenario with a return period equal to  $T_{m_s}=475$  years. For the flood hazard, we examine a design/assessment flood hazard scenario with a return period equal to  $T_{m_f}=100$  years.

### 3.1 Single hazard maps

In the present work, a unified methodology is employed to homogenize the single seismic and flood hazard scenarios. These single-hazard scenarios are displayed in the form of GIS maps and can be used for the risk assessment of any examined element. Moreover, they may be used to and develop appropriate maps for multi-hazard scenarios as discussed in section 3.2.

Seismic hazard data for rock site conditions, developed within the EU-funded research project SHARE (<https://www.share-eu.org>), is initially selected. This data is subsequently properly amplified to account for site effects, by employing a simplified  $V_{s,30}$  model, originating from morphology and topography data of the examined region. In the present study, the seismic hazard is estimated for a return period of 475 years.

More specifically, the seismic hazard estimates were extracted from the global seismic hazard map produced by Pagani et al. [89]. The hazard is expressed in terms of the Peak Ground Acceleration (PGA, as a fraction of  $g$ ) for a probability of exceedance of 10% in 50 years (equivalent to a 475-year return period) on rock (average shear-wave velocity down to 30 m -  $V_{s,30} = 760$  m/s). A detailed description of how the global seismic hazard model was developed may be found in Pagani et al. [9]. The seismic hazard analysis is performed using the OpenQuake engine [10], an open-source seismic hazard and risk calculation software developed, maintained and distributed by the Global Earthquake Model (GEM) Foundation. Recent studies on the use of the European Seismic Hazard ESHM13 [11] may be found in Riga et al. [12] and Karatzetzou et al. [13].

With reference to the flood hazard, flood hazard zones were derived for one scenario based on 100 years return period. In particular, a newly developed dataset for Europe referring to river flood hazard, was derived from the Join Research Center of the European Commission [14]. The flood hazard zones were based on the combination of river flow data, estimated through the hydrological model LISFLOOD, while the inundation simulations were performed with the 2D hydrodynamic modelling LISFLOOD-FP. Subsequently, the hazard was expressed in terms flood extent zones in different flood frequencies (e.g.,  $T=100$  means frequency 1-in-100-years).

Figure 2 portray the resulted single hazard maps for Greece for the examined seismic and flood hazards scenarios, respectively.

### 3.2 Multi-hazard maps

For the homogenization of the single hazard maps of Greece (i.e., seismic hazard map and flood hazard map, presented in section 3.1), we used a bivariate scaling system. This qualitative approach is often used to depict pairs of variables, whose mathematical combination might not be straightforward or possible, for instance, social vulnerability and natural hazards [15] or seismic and biological hazards [16]. In the herein proposed framework, we define four thresholds to classify each variable into *low*, *moderate*, *high* and *very high* hazard. These thresholds are created automatically in Arc-Gis using the quantile method. Then, we create a color matrix comprising all the combinations between the two variables. In this study, we combine the seismic hazard in terms of the PGA for the selected return period (475 years) with the river flood hazard in the terms of the percentage distribution of flood hazard zones, respectively for return period equal to 100 years. Figure 3, presents the resulted multiple-hazard map for Greece, for the examined scenarios.

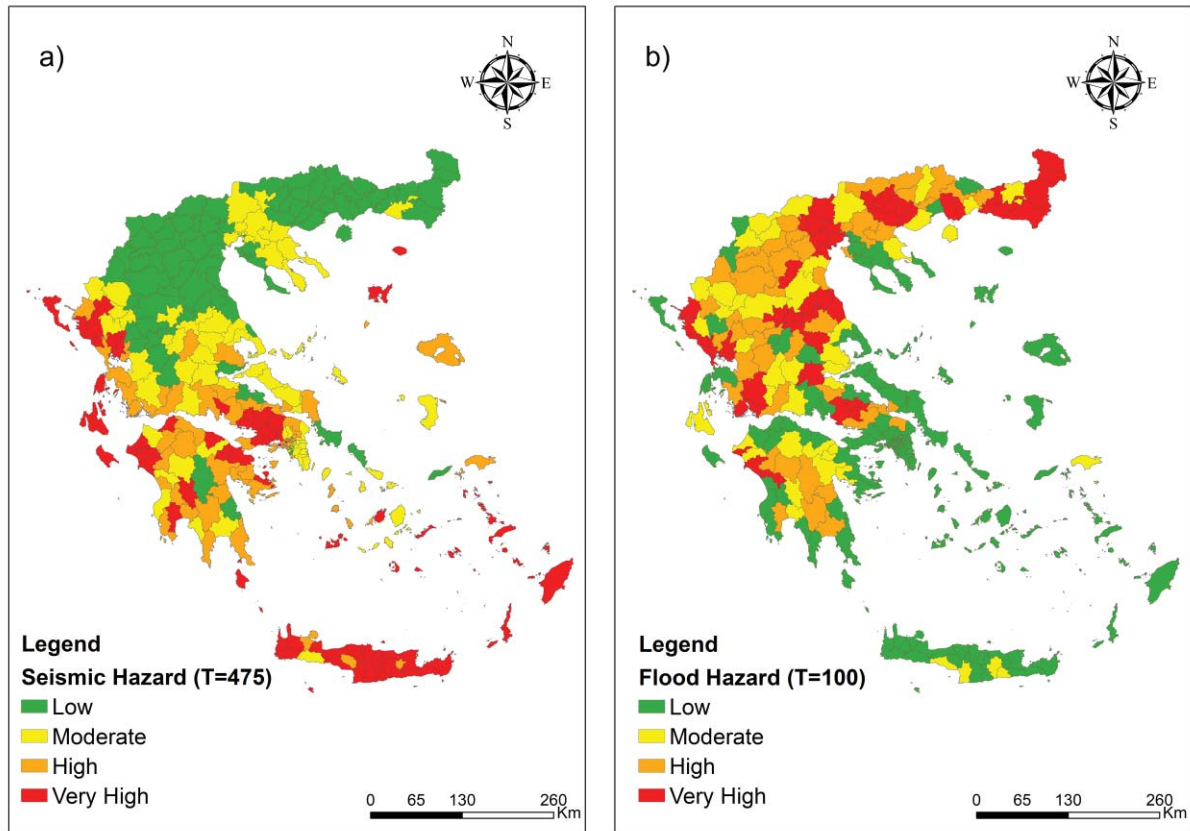


Figure 2: (a) Seismic hazard map for a return period equal to  $T_{m_s}=475$  years and (b) flood hazard map for a return period equal to  $T_{m_f}=100$  years for Greece

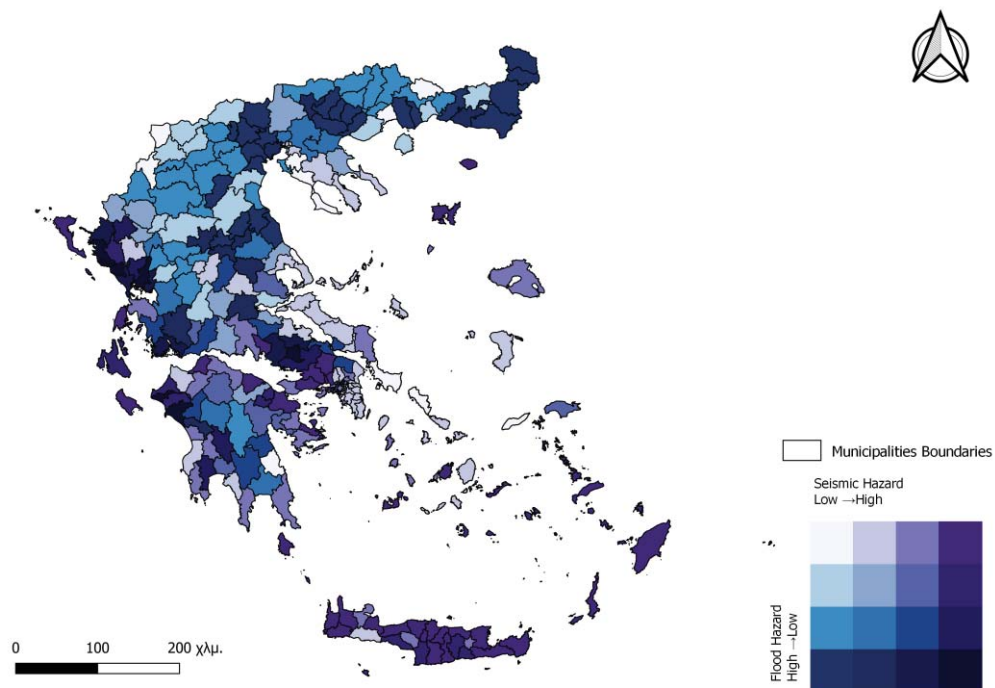


Figure 3: Bivariate map depicting the combination of seismic ( $T_{m_s}=475$  years) and flood ( $T_{m_f}=100$  years) hazard for Greece.

## 4 CONCLUSIONS

The present paper presented a unified framework to homogenize the single seismic and flood hazard scenarios and develop appropriate single- and multi-hazard maps for Greece to be used in an under-development methodology for the risk assessment of critical elements of transportation infrastructure in a multi-hazard environment. The work was developed within the INFRARES research project, which is also briefly presented.

With reference to seismic hazard; seismic hazard data for rock site conditions, developed within the SHARE research project ([www.share-eu.org](http://www.share-eu.org)), was initially selected and is properly amplified to account for site effects of various regions in Greece, by employing a simplified  $V_{s,30}$  model originating from morphology and topography data. The seismic hazard was estimated for whole Greece and for a 475-years return period scenario and plotted in a relevant map in GIS format.

Regarding flood hazard; flood hazard zones were derived for Greece from a newly developed database of the Joint Research Center of the European Commission [14] for one scenario based on 100 years return period. The resulted flood hazard was estimated for whole Greece and plotted in a relevant map in GIS format.

A bivariate scaling system was used for the homogenization of single-hazard maps referring to the above hazards. For the development of the multi-hazard map, four thresholds were automatically created in Arc-Gis to classify each hazard into *low*, *moderate*, *high* and *very high* level. A color matrix was then created comprising all the combinations between the two variables-hazards, leading to the creation of the multi-hazard map for whole Greece.

The framework presented within this study is expected to be a valuable contribution towards the generation of a uniform multiple hazard model for the risk and resilience assessment of roadway networks.

## ACKNOWLEDGEMENTS

The work reported in this paper was carried out in the framework of the research project INFRARES “Towards resilient transportation infrastructure in a multi-hazard environment” (<https://www.infrares.gr/>), funded by the Hellenic Foundation for Research and Innovation (HFRI) and General Secretariat for Research and Innovation (GSRI) under the “2<sup>nd</sup> Call for H.F.R.I. Research Projects to support Post-Doctoral Researchers”. (Project Number: 927).



**H.F.R.I.**  
Hellenic Foundation for  
Research & Innovation



## REFERENCES

- [1] S. L. Cutter & S. Carolina, Vulnerability to environmental hazards, *Progress in Human Geography*, **20(4)**, 529-539, 1999.
- [2] Y. Zhang, W. F. Cofer, D. I. Mclean, Analytical Evaluation of Retrofit Strategies for Multicolumn Bridges. *Journal of Bridge Engineering*, ASCE, **4(2)**, 143-150, 1999.
- [3] F. Nemry & H. Demirel, Impacts of Climate Change on Transport: A focus on road and rail transport infrastructures Impacts of Climate Change: A focus on road and rail transport infrastructure. *JRC Report*, Luxembourg, European Union, 2012.



- [4] G. Tsinidis, F. De Silva, I. Anastasopoulos, E. Bilotta, A. Bobet, Y.M.A. Hashash, C. He, G. Kampas, J. Knappett, G. Madabhushi, N. Nikitas, K. Pitilakis, F. Silvestri, G. Viggiani, R. Fuentes. Seismic behavior of tunnels: From experiments to analysis. *Tunnelling and Underground Space Technology*, **99**, 103334, 2020.
- [5] S. P. Stefanidou & A. J. Kappos, A., Methodology for the development of bridge-specific fragility curves. *Earthquake Engineering & Structural Dynamics*, **46**, 73-93, 2017.
- [6] S. Argyroudis, G. Tsinidis, F. Gatti, & K. Pitilakis, Effects of SSI and lining corrosion on the seismic vulnerability of shallow circular tunnels. *Soil Dynamics and Earthquake Engineering*, **98**, 244-256, 2017.
- [7] Lee, Jaebeom, Lee, Young-Joo, Kim, Hyunjun, Sim, Sung-Han, and Kim, Jin-Man. “A New Methodology Development for Flood Fragility Curve Derivation Considering Structural Deterioration for Bridges.” *Smart Structures and Systems* 17, no. 1 (January 25, 2016): 149–65. doi:10.12989/SSS.2016.17.1.149.
- [8] P. Gehl, & D. D’Ayala, System loss assessment of bridge networks accounting for multi-hazard interactions. *Structure and Infrastructure Engineering*, **2479**, 1–17, 2018.
- [9] M. Pagani, J. Garcia-Peláez, R. Gee, KL Johnson, V. Poggi, V. Silva, M. Simionato, RH Styron, D. Viganò, L. Danciu, D. Monelli, G. Weatherill G, The 2018 version of the global earthquake model: hazard component. *Earthquake Spectra*, doi: 10.1177/8755293020931866., 2020.
- [10] M. Pagani, D. Monelli, G. Weatherill, L. Danciu, H. Crowley, V. Silva, P. Henshaw, L. Butler, M. Nastasi, L. Panzeri, M. Simionato, D. Vigano, OpenQuake-engine: an open hazard (and risk) software for the global earthquake model. *Seismological Research Letters*, **85**, 692-702, 2014.
- [11] J. Woessner, L. Danciu, D. Giardini, H. Crowley, F. Cotton, G. Grünthal, G. Valensise, R. Arvidsson, R. Basili, M.B. Demircioglu, S. Hiemer, C. Meletti, RMW Musson, AN Rovida, K. Sesetyan, M. Stucchi, The SHARE Consortium (2015). The 2013 European Seismic Hazard Model: Key Components and Results, *Bulletin of Earthquake Engineering*, **13(12)**, 3553-3596, 2015.
- [12] E. Riga, A. Karatzetzou, S. Apostolaki, H. Crowley, K. Pitilakis. Verification of seismic risk models using observed damages from past earthquake events. *Bulletin of Earthquake Engineering*, doi: 10.1007/s10518-020-01017-5, 2021.
- [13] A. Karatzetzou, E. Riga, S. Apostolaki, S. Karafagka, K. Pitilakis, E. Lekkas. A Prioritization Scheme for Seismic Intervention in School Buildings. The case of Thessaloniki, Greece. *Proceedings of the 7th International Conference on Civil Protection & New Technologies (SAFE GREECE 2020)*, 14-16 October, on-line, 2020.
- [14] F. Dottori, L. Alfieri, A. Bianchi, J. Skoien, & P. Salamon, A new dataset of river flood hazard maps for Europe and the Mediterranean Basin region. *Earth System Science Data Discussions*, 1-35, 2021.
- [15] C. Emrich and S. Cutter, Social vulnerability to climate-sensitive hazards in the southern United States. *Weather, Climate, and Society*, **3(3)**,193-208, 2011.
- [16] V. Silva and N. Paul, Potential impact of earthquakes during the 2020 COVID-19 pandemic. *Earthquake Spectra*, **37(1)** 73-94, doi: 10.1177/8755293020950328, 2020

## DYNAMIC CROSS-INTERACTION BETWEEN TWO CLOSELY-SPACED SHALLOW FOUNDATIONS

Zeolla<sup>1</sup> E., de Silva<sup>2</sup> F., Sica<sup>1</sup> S.

<sup>1</sup> University of Sannio – Benevento (IT)

ezeolla@unisannio.it

stefsica@unisannio.it

<sup>2</sup> University of Naples Federico II, Naples (IT)

filomena.desilva@unina.it

---

### Abstract

*The cross interaction between two closely-spaced shallow foundations has been numerically investigated under static conditions and low-amplitude dynamic loading through a finite difference procedure implemented in the FLAC3D code. The motivation towards this research topic may be found in the increasingly growth of urbanization in modern metropolitan areas worldwide and in the urgent need for seismic requalification of vulnerable historical centres in ancient towns, where buildings are placed very close each other. Even though a disconnection between the superstructures exists, the response of their foundations (and that of the buildings themselves) may be coupled due to the continuity of the soil underneath. Consequently, the overall system response may be different from that predicted with reference to the simple scheme of an isolated footing or building. In the performed numerical study, the soil-foundation impedance functions of a single foundation were firstly compared to well-known literature closed-form solutions to validate the procedure from a numerical viewpoint. The analyses were then repeated with adding another footing identical to the first one and placed at a varying distance from it. The comparison between the response of the master foundation when modelled as isolated and as part of a group shows that the dynamic impedances of the footing in-group may remarkably change with respect to those of the isolated foundation. In particular, the stiffness (real part) increases at a frequency depending on footing-footing distance and the damping ratio increases or decreases depending to the type of imposed oscillation.*

**Keywords:** Soil-structure interaction, Dynamic Cross Interaction (DCI), Impedance functions, Shallow foundation, 3D numerical modelling

## 1 INTRODUCTION

With the rapid progress of urbanization, very closely-spaced buildings are increasingly being built in both large cities and smaller towns. The proximity among buildings could produce an interaction between them and, consequently, may cause a different response under both static and dynamic loading. As the former aspect concerns, the cross interaction between closely spaced footings could have effects on both settlement and bearing capacity evaluation. The first author that investigated the bearing capacity problem for a group of shallow footings was Stuart (1962) [22], who proposed to insert a sort of “efficiency factors” in the bearing capacity trinomial formula proposed by Terzaghi (1943) [23]. Depending on the width  $B$  of the footing, these corrective factors may be greater than one if the two footings are placed at a short distance  $S$  from each other ( $S < 3\div 4 B$ ), equal to one in the case of higher distance ( $S > 4\div 5 B$ ), so that each foundation behaves as isolated from the other, and equal to two in the case of  $S=0$ , i.e. when there is perfect contact between the two footings.

Under dynamic loading, the typical dynamic soil structure interaction evolves into a problem of cross interaction between multiple structures, better known in literature as Structure Soil Structure Interaction (SSSI) or Dynamic Cross Interaction (DCI). The study of SSSI may be handled with the same methods used for standard SSI problems in which a single footing (or structure) is involved. The available methods may, hence, be classified into analytical, semi-analytical or numerical approaches, experimental methods with observations on prototypes. Thanks to the rapid progress of computing procedures and hardware devices, nowadays the numerical methods are the most used approach for evaluating SSSI. Menglin et al. (2011) [11] produced an extensive literature review on structure-soil-structure interaction, in which it was highlighted that the SSSI terminology was firstly introduced into the scientific literature by Luco and Contesse (1973) [9], who investigated the interaction phenomenon between two or more buildings (modelled as shear walls) placed on rigid circular foundations and subjected to obliquely or vertically incident harmonic SH-waves. Through parametric studies, Luco and Contesse (1973) [9] found that a group of closely spaced buildings could be affected by cross interaction at frequencies close to the fundamental ones of the buildings and particularly in low frequency ranges. Any vibrating foundation was found to spread a wave field that could be seen as a disturbance affecting the adjacent foundations. In [9] the dynamic excitation was represented as an external load or a seismic wave field. In the first case, the response of the foundation was assessed through the frequency-dependent soil-foundation dynamic impedance, representing the soil-foundation response to the inertial action transmitted by the superstructure and linking the force (or moment) acting on the foundation to its displacement (or rotation). In the second case, the motion at the base of the structure was determined.

Based on the substructure method, Betti (1997) [19] proposed a methodology for the analysis of the 3D cross-interaction between two massless, rigid and embedded foundations. In the low-frequency range, the translational, rocking and torsional components of the impedance matrix show clear effects of cross-interaction, which tend to disappear as the frequency and distance between the adjacent foundations increase. Regarding the foundation input motion associated with incoming SH-, P-, and SV-waves, the case of vertically propagating waves is very indicative of the cross-interaction effects. With respect to each other, the two foundations present displacement and rotational components that are either in phase or  $180^\circ$  out-of-phase while, with respect to the free-field soil, they move with a phase shift that varies with frequency. By increasing the distance between the two foundations, each component of the foundation input motion approaches the corresponding one for the case of an isolated foundation. In the horizontal direction, the displacements of the second foundations are 10% lower than the value of the

first footing and the two foundations move completely out of phase with respect to each other and to the free field soil. For waves propagating with angles of inclination in both planes, vertical and horizontal, the motion of the two foundations becomes more complicated, showing differences in both amplitude and phase [19].

## 2 DEFINITION OF THE SOIL-FOUNDATION IMPEDANCE

Impedance functions represent the frequency-dependent stiffness and damping characteristics of the foundation-soil system, which link the forces acting on the foundation to its displacements. The typical expression of an impedance function is:

$$S_{ij}(\omega) = \bar{K}_{ij}(\omega) + i\omega\bar{C}_{tot,ij}(\omega) \quad (1)$$

with  $i = j = x, y, z$  for the translational motion along the three principal axes;  $i=t$  and without the  $j$ -term for the rotation around  $z$  (torsional mode) and  $i=r$  and  $j=x$  or  $y$  for the rotation around the  $x$  or  $y$  axes. The dynamic stiffness  $\bar{K}_{ij}$  is the product of the static stiffness  $K_{ij}$  and the dynamic stiffness coefficient  $k(\omega)_{ij}$ , while the total damping  $\bar{C}_{tot,ij}$  is the sum of a contribution related to the soil hysteretic damping ratio  $\beta$  and to the radiation damping. This latter is due to the waves scattering from the foundation and is the product of a static value  $C_{rad,ij}$  and a dynamic coefficient  $c_{rad,ij}(\omega)$ .

$$\bar{K}_{ij} = K_{ij} \cdot k(\omega)_{ij} \quad (2)$$

$$\bar{C}_{tot,ij} = C_{rad,ij} \cdot c(\omega)_{rad,ij} + \frac{2\bar{K}_{ij}\beta}{\omega} \quad (3)$$

The value of each term depends on the angular frequency,  $\omega$ , as well as on the foundation shape and embedment. Classical solutions are provided by Gazetas (1991) [5], Pais and Kausel (1988) [1] and Mylonakis et al. (2006) [14] assuming a rigid arbitrary-shaped foundation placed on the surface of an ideal halfspace or embedded in it. Additional formulations are available in literature to account for the variation of the shear stiffness variation with depth (Gazetas, 1991[5]; Vrettos, 1999 [24]), foundation embedment (e.g., Apsel and Luco, 1987 [2]), and flexibility (e.g., Iguchi and Luco, 1982 [6]).

In the following, the second subscript  $x, y, z$  referred to the translational components of the impedances will be omitted for the sake of brevity.

### 2. Numerical analysis

This section illustrates the procedure used in the performed study for the evaluation of the impedance functions. Through a finite difference commercial code, a single footing was firstly modelled and the obtained impedances were compared to the closed-form solutions published in literature (Gazetas, 1991[5]). Later, another foundation with the same geometric and load characteristics of the master one was added. The impedances for the double footing system

were compared to the corresponding values of the single foundation case to appreciate the cross-interaction effects.

## 2.1 Details on the numerical model and load application procedure

The 3D analysis domain (Figure 1) is a soil volume with a square plan (80m on each side), and a height of 50 m. Both the single (a) and the double foundations (b) were considered rectangular with a base  $B$  equal to 2m and a length  $L$  of 10m. Three different values of spacing between the two footings were considered ( $S=2, 1$  and  $0.5$  m) so that the ratio  $S/B$  was varied between 0.25 and 1. In the static conditions, fixed boundaries were placed at the bottom and lateral surfaces delimitating the soil volume, while quiet boundaries were activated during the dynamic analyses to delete the reflection of the outward propagating waves and allow the necessary energy radiation towards infinity. As soil behaviour concerns, a linear visco-elastic isotropic law was assigned to all soil elements. Viscous damping was introduced in the model through the Rayleigh formulation. Soil damping was set to a very low value so that the overall damping encompassed in the numerical simulations can be assumed to be totally radiative. The presence of the groundwater was not considered, so the analyses were conducted in total stress. Table 1 shows the physical and mechanical properties assigned to the soil in the parametric analysis.

Material properties	Unit	Value
Soil unit weight $\gamma$	[kN/m <sup>3</sup> ]	19.0
Bulk modulus $K$	[Mpa]	12.2
Shear modulus $G$	[MPa]	5.6
Shear wave velocity $V_s$	[m/s]	54.0

**Table 1: Parameters assigned to the soil in the numerical study.**



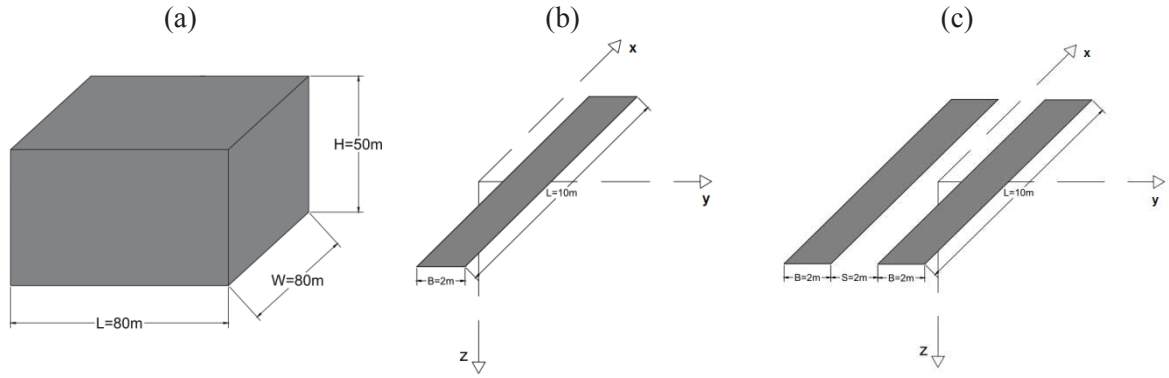


Figure 1: Analysis domain (a), single foundation (b) and double foundation system (c).

The structural element of the footing was not included within the numerical model, but its effect was accounted by applying a velocity field at all nodes placed on the foundation footprint. Since a uniform displacement field was applied to these nodes, the case of a rigid foundation ( $EI \rightarrow \infty$ ) was hence reproduced. In the static case, a constant velocity along x-, y- or z-directions was applied to all grid points of the contact area in order to calculate the corresponding translational stiffness components. To obtain the rotational stiffness, nodal velocities varying with a linear distribution with respect to the x and y axes of the footing and null in correspondence of the centre of the foundation were imposed. In this way, the moment acting around each horizontal axis was simulated. In the dynamic case, a harmonic function of velocity [ $v(t) = \omega A \cos(\omega t)$ ] has been applied, so that the imposed displacement  $s(t)$  is harmonic too and given by:

$$s(t) = A \sin(\omega t) \quad (4)$$

where  $A$  is the oscillation amplitude and the circular frequency  $\omega$  is linked to frequency  $f$  by the well-known relation,  $\omega = 2\pi f$ . Different values of the input frequency  $f$  were considered that is 1, 3, 5, 7, 9, 11 and 13 Hz. By imposing the harmonic velocity time-history at all nodes of the loaded area, the induced stress state is also harmonic, with an amplitude depending on the soil stiffness and out of phase with respect to the displacement due to all damping sources present in the model.

## 2.2 Interpretation method

By calculating the resultant of the contact stresses, the static stiffness in the vertical direction was obtained as:

$$K_z = \frac{F}{\delta} = \frac{\sum_{i=1}^N \sigma_{zzi} A_i}{\delta} \quad (5)$$

where  $A_i$  represented the area of the mesh elements below the loaded footprint,  $\sigma_{zzi}$  the contact pressure at the  $i$ -th node of the loaded area and  $\delta$  the displacement at the footing centre. The values obtained numerically were compared to those provided by the available literature solutions (Gazetas, 1991). For the other translational degrees of freedom (d.o.f.) of the footing, the static stiffnesses were calculated with the same procedure described above for the vertical direction.

The rotational stiffness was calculated as the ratio between the moment,  $M$ , and the applied rotation,  $\theta$ :

$$K_{ry} = \frac{M}{\vartheta} = \frac{\sum_{i=1}^N \sigma_{zzi} y_i A_i}{\vartheta} \quad (6)$$

and

$$K_{rx} = \frac{M}{\vartheta} = \frac{\sum_{i=1}^N \sigma_{zzi} x_i A_i}{\vartheta} \quad (7)$$

The moment has been obtained through integration of the vertical stresses computed below the foundation footprint, multiplied by the distance from the rotation axis, i.e.  $y_i$  or  $x_i$ . The rotation has been obtained as ratio between the vertical displacement obtained at the edge of the foundation footprint and the half-length (in x and y direction) of the foundation itself.

To obtain the impedance functions in the frequency domain, the Fourier transforms of the displacement and of the force were required. Having imposed a given velocity (therefore, a displacement) and not a load, it was better to calculate firstly the soil-foundation flexibility (inverse of stiffness) and then the impedance matrix as the inverse of the flexibility. As it is well known, the dynamic stiffness and damping correspond to the real and the imaginary parts of the impedance.

### 3 RESULTS

#### 3.1 Static case

In Table 2, the static stiffnesses computed through the procedure described above have been compared to those provided by Gazetas (1991) [5] closed-form equations. In the last column of Table 2, the percentage of variation between numerical and analytical values for each d.o.f. are listed. The analytical values were obtained by considering a single strip footing placed on a homogeneous half space with the same parameters reported in Table 1. From Table 2, it can be observed that the obtained numerical predictions are in good agreement with the values provided by the literature formulations, especially for the vertical and rotational degrees of freedom. The higher mismatch may be observed on the translational mode along x and y directions.

	Numeric value calculated	Gazetas (1991)	Variation (%)
$K_z$ [N/m]	9.62E+07	9.85E+07	-2.33
$K_y$ [N/m]	6.47E+07	8.75E+07	-26.06
$K_x$ [N/m]	6.07E+07	7.69E+07	-21.07
$K_{ry}$ Nm/m]	1.38E+09	1.46E+09	-5.48
$K_{rx}$ Nm/m]	1.25E+08	1.28E+08	- 2.30

**Table 2: Comparison between the static stiffness obtained through the developed numerical procedure and solutions proposed by Gazetas (1991)**

Figure 2 shows the results obtained for the system of two identical footings placed at different distance  $S$  between them. On the vertical axis of both figures, there is the percentage of variation of the translational (a) and rotational (b) static stiffness of the master footing when considered as part of a group and when considered alone. Since this percentage for all swaying motions and rotational  $K_{ry}$  are negative, the static stiffness of the footing in a group, as expected, is always smaller than that of the same foundation considered isolated ( $K_{\text{double}} < K_{\text{single}}$ ). In addition, for all modes the static stiffness of the master footing in a group decreases with decreasing the ratio  $S/B$  due to cross interaction effects. Singular is the case of the rotational

stiffness  $K_{rx}$  (long side of the footing), which is always positive ( $K_{rx\_double} > K_{rx\_static}$ ) and seems poorly affected by cross interaction when  $S/B$  is equal to 0.25.

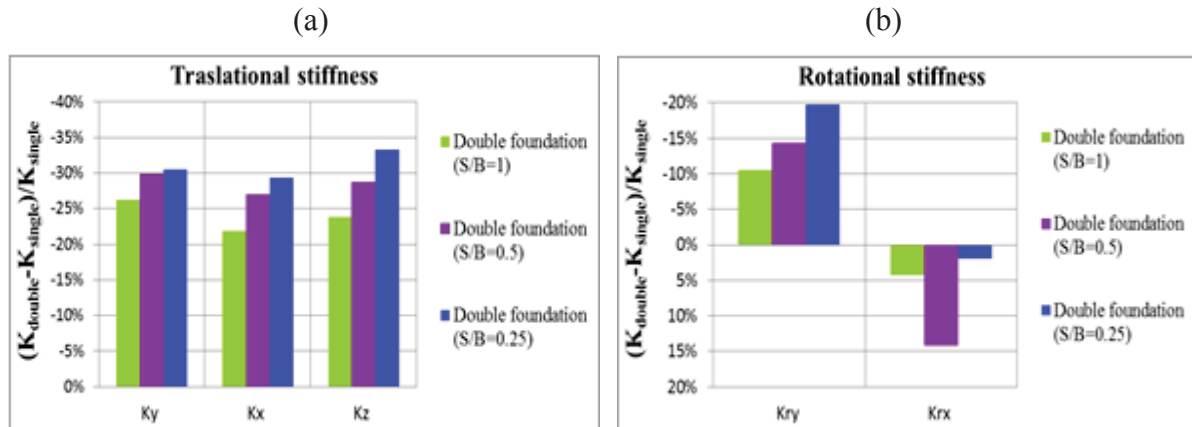


Figure 2: Static stiffness of the master foundation in group (double) or isolated (single) for the translational (a) and rotational (b) component of motion.

#### 4.2 Dynamic case

The variation of the dynamic coefficients against the dimensionless frequency  $a_0 = \omega B/V_s$  are plotted in the Figures 3-7 for different distance ratios,  $S/B$ . In addition, the impedances obtained numerically and analytically for the isolated footing have been superimposed for comparison.

For a single foundation, the obtained results (red line) are in excellent agreement with the analytical values (black line) provided by Gazetas (1991) equations up to a dimensionless frequency  $a_0$  equal to 1. For  $a_0 > 1$ , a slight mismatch is observed for the horizontal translational modes (Figures 4 and 5). Similar observations may be drawn for the radiation damping coefficients. The damping coefficients  $c_{rx}$  and  $c_{ry}$  (Figures 6 and 7), instead, are slightly higher than those obtained analytically in the whole range of dimensionless frequency  $a_0$ . In short, for the single footing the differences between the numerical and analytical predictions are quite small, so that the overall developed numerical procedure may be considered reliable.

With reference to the twin footing system, it can be observed that the impedances of the master foundation in the group are close to those of the single footing for low values of the frequency  $a_0$ . Conversely, there is a systematic increase of the stiffness coefficient for the footing in the group at higher frequencies, except for the rotational d.o.f. around the x-axis (long side in Figure 6). The dimensionless frequency at which the presence of an additional footing influences the results decreases with increasing  $S/B$ . Actually, the interference occurs when the wave originated from the clone foundation forces the master one to move out of phase with respect to its original motion. Such effect depends on the forcing frequency and on the  $S/B$  ratio. In fact, longer wavelengths, associated to lower frequencies, make closely-spaced foundations with smaller  $S/B$  (e.g.,  $S/B=0.25$ ) to move together without altering the response with respect to the isolated case. This means that closer are the foundations, higher is the frequency at which they interfere. No relevant differences may be recognized with changing the degree of freedom of the foundation.

The damping coefficients of the twin footing tend to increase with respect to that of the single foundation for the vertical motion (Figure 3) and this increase is proportional to  $S/B$ . Only for  $S/B=1$  there is a decrease starting from  $a_0=1$ , i. e. for a  $f=9$  Hz. The same trend is observed for the rotational d.o.f. around the y axis (Figure 7) and the opposite trend results for

the other translational components of motion (Figure 4 and 5). Such differences are associated to the fact that the wavefront originated by the twin footings interfere in a constructive or destructive way depending on the type of waves generated by the foundation motion.

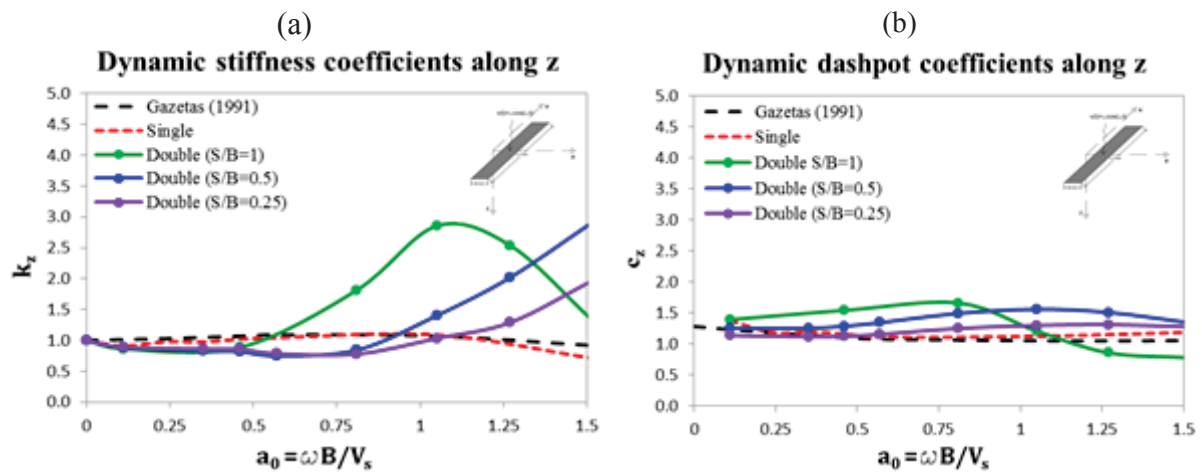


Figure 3: Vertical dynamic stiffness coefficients (a) and damping coefficients (b).

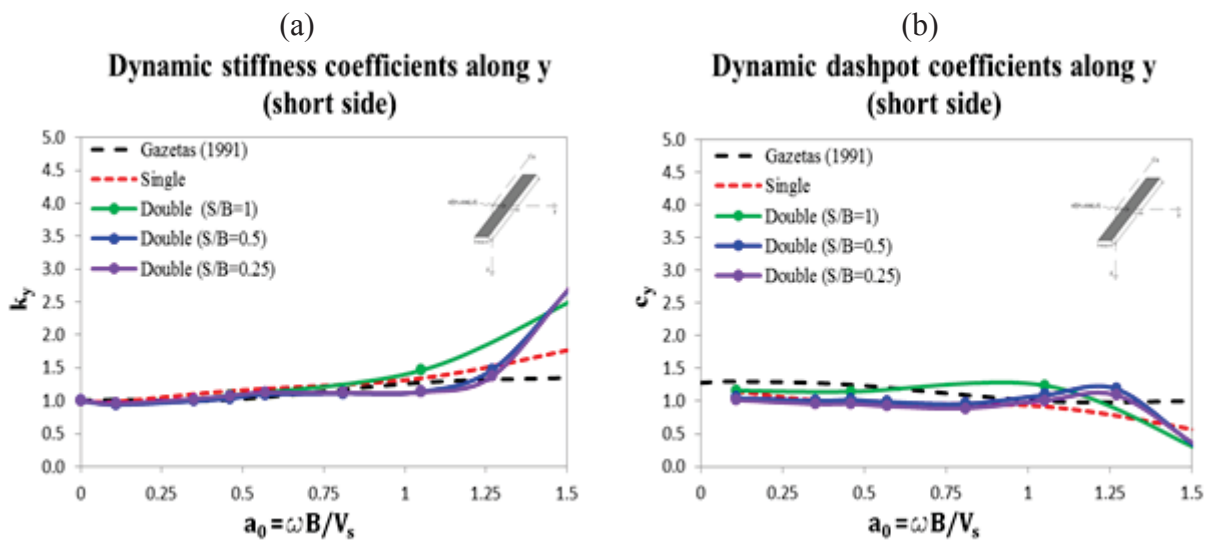


Figure 4: Horizontal dynamic stiffness coefficients (a) and damping coefficients (b) along short side.

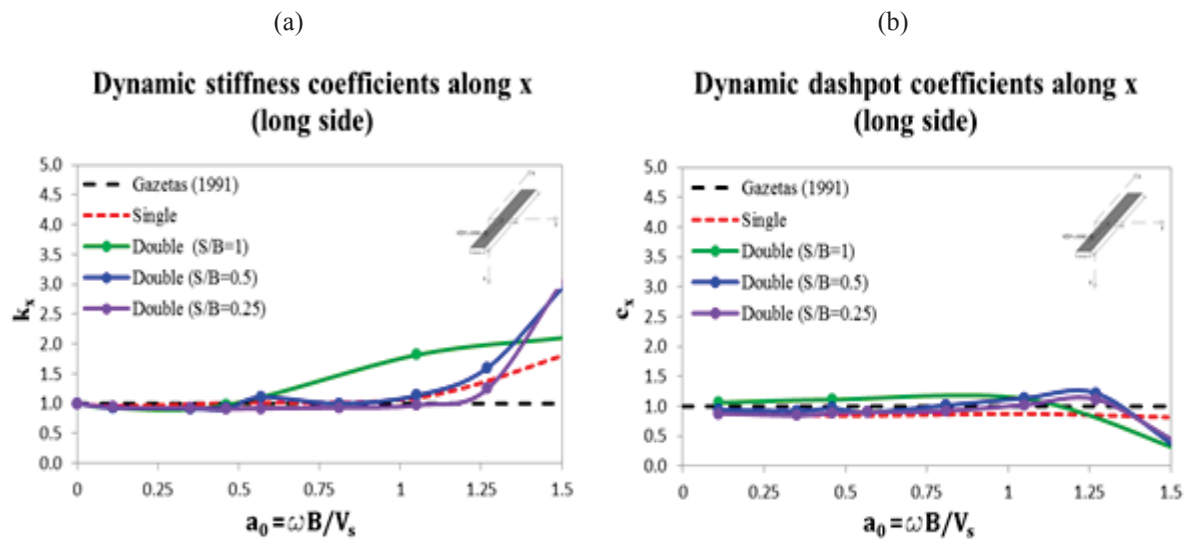


Figure 5: Horizontal dynamic stiffness coefficients (a) and damping coefficients (b) along long side.

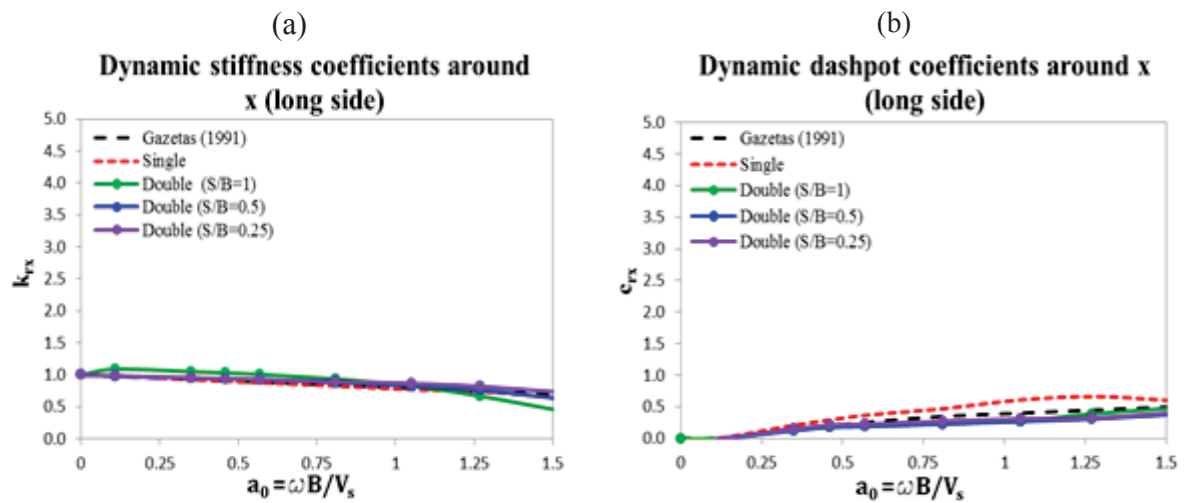


Figure 6: Rotational dynamic stiffness coefficients (a) and damping coefficient (b) around long side.



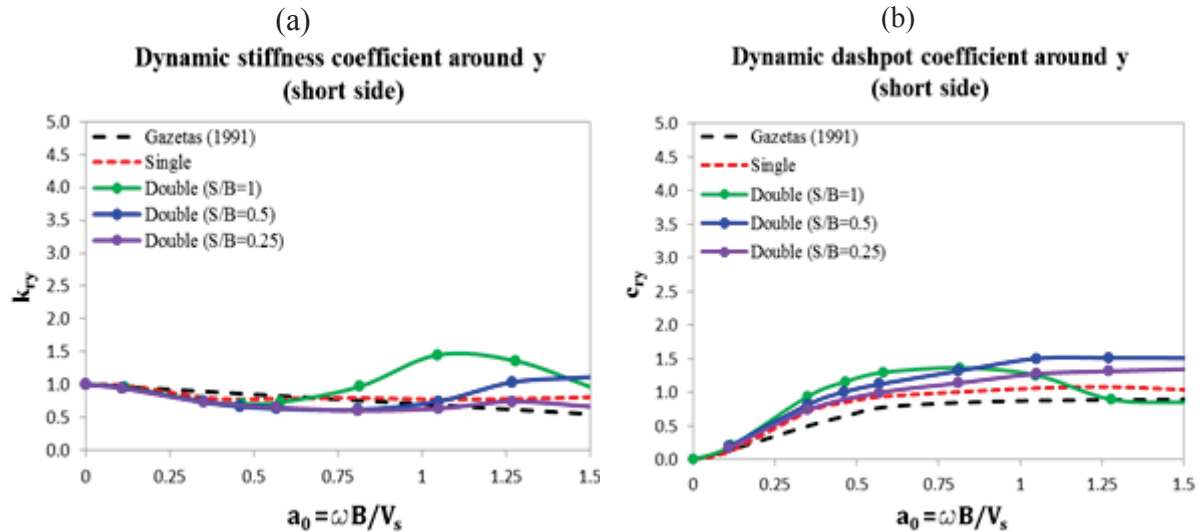


Figure 7: Rotational dynamic stiffness coefficients (a) and damping coefficients (b) around short side.

#### 4 CONCLUSIONS

The static and dynamic cross interaction between two closely-spaced shallow foundations was numerically investigated through a numerical procedure based on the finite difference technique. The cases of a single foundation and of two identical footings placed on the surface of a viscoelastic half-space were solved numerically.

For the single foundation case, the impedance functions thus obtained successfully reproduced those provided by Gazetas (1991) solutions.

For the twin foundation case, lower values of the static stiffness were found for almost all degrees of freedom due to cross-interaction effects. The dynamic stiffness coefficients were found coincident with those of the single foundation at low oscillation frequencies. Higher values were, instead, obtained for a typical dimensionless input frequency that markedly depends on footing-footing distance ratio  $S/B$ . The dynamic damping coefficients increase or decrease with respect to that of the single footing depending on the type of oscillation mode of the foundation. As a future perspective of the study, the current parametric study could be enriched with considering different configurations of the footing group, different values of soil damping, stiffness, foundation embedment and type of loading.

#### REFERENCES

- [1] Pais A., Kausel E., "Approximate formulas for dynamic stiffnesses of rigid foundations", Soil Dynamics and Earthquake Engineering 7 (4), 213-227
- [2] Apsel R. J. and Luco J., "Impedance functions for foundations embedded in a layered medium: An integral equation approach." Earthquake Engineering & Structural Dynamics 15 (1987): 213-231.
- [3] Braja M. Das and Larbi-Cherif Said, *Bearing capacity of two closely-spaced shallow foundations on sand*, Soils and Foundations, Vol.23, No. 1, (1983)
- [4] Vicencio F., Alexander N. A., *Dynamic structure-soil-structure interaction in unsymmetrical plan buildings due to seismic excitation*, Soil dynamics and earthquake engineering 127, 105817, (2019)

- [5] Gazetas, G. 1991, *Formulas and charts for impedances of surface and embedded foundations*, Journal of Geotechnical Engineering, 117(9), pp.1363-138.
- [6] Iguchi M. and Luco J., *Dynamic response of flexible rectangular foundations on an elastic half-space*, Earthquake Engineering & Structural Dynamics 9 (1981): 239-249.
- [7] Knappett J. A., Madden P., Caucis K., *Seismic structure-soil-structure interaction between pairs of adjacent building structures*, Géotechnique 65, No 5, 429 – 441, (2015)
- [8] Lee J., Eun J., *Estimation of bearing capacity for multiple footings in sand*, Computers and Geotechnics, 36, 1000-1008, (2009)
- [9] Luco JE, Contesse L., *Dynamic structure–soil–structure interaction*, Bulletin of the Seismological Society of America 1973;63(4):1289–303.
- [10] Wang J., Zhou D., *A simple model for vertical dynamic interaction among a group of strip footing rested on homogeneous half-space*, Shock and vibration Article ID 7382392, 12 pages, (2018)
- [11] Menglin L., Huaifeng W., Xi C., Yongmei Z., *Structure-soil-structure interaction: literature review*, Soil Dynamics and Earthquake Engineering Vol. 31, 1724 – 1731, (2011)
- [12] Alwalan M. F., *Interaction of closely spaced shallow foundations on sands and clays: a review*, International journal of advanced engineering research an science, vol.-5, issue 9, sept. (2018)
- [13] Pecce M.R., Sica S., Ceroni F., Principe B., *Soil-Structure interaction: the case study of a masonry tower*, NUMGE 2, pp. 1163-1168, (2014)
- [14] Mylonakis G., Nikolaou S., Gazetas G. (2006), *Footings under Seismic Loading: Analysis and Design Issues with Emphasis on Bridge Foundations*, Soil Dynamics and Earthquake Engineering, 26(9): 824-853
- [15] Gosh P., Sharma A., *Interference effect of two nearby strip footings on layered soil: theory of elasticity approach*, Acta Geotechnica, 5:189-198, (2010)
- [16] Gosh P., Rajesh S., Sai Chand J., *Linear and nonlinear elastic analysis of closely spaced strip foundations using Pasternak model*, Frontiers of Structural and Civil Engineering, 11(2): 228-243, (2017)
- [17] Prandtl L. (1921), *Über die Eindringungsfestigkeit (Härte) plastischer Baustoffe und die Festigkeit von Schneiden*, Zeit Angew Math Mech, (1):15–20.
- [18] Ge Q., Xiong F., Xie L., Chen J., Yu M., “*Dynamic interaction of soil-structure cluster*”, Soil dynamics and earthquake engineering 123, 16 – 30, (2019)
- [19] Betti R., *Effects of the dynamic cross-interaction in the seismic analysis of multiple embedded foundations*, Earthquake engineering and structural dynamics Vol. 26, 1005 – 1019 (1997)
- [20] Sica S., *Interaction between closely spaced strip footing*, wp16-sub task-16.3.3.-ur7 (Sannio-Sica), (2019).
- [21] Tileulioglu S., Stewart J. P., Nigbor R. L., *Dynamic stiffness and damping of a shallow foundation from forced vibration of a field test structure*, Journal of geotechnical and geoenvironmental engineering, April (2011)

- [22] Stuart JG., *Interference between foundations, with special reference to surface footings in sand*, Geotechnique 1964;12(1):15–20.
- [23] Terzaghi, K. (1943), *Theoretical Soil Mechanics*, Wiley, New York.
- [24] Vrettos C., *Vertical and rocking impedance for rigid rectangular foundations on soils with bounded non-homogeneity*, Earthquake Engineering & Structural Dynamics 28(12):1525 – 1540 (1999)

## ON THE SITE-AMPLIFICATION AND SOIL-STRUCTURE INTERACTION IN URM STRUCTURES: USE OF FRAGILITY CURVES TO ASSESS THE SIMPLIFIED CODE-APPROACH

A. Brunelli<sup>1</sup>, F. de Silva<sup>2</sup>, and S. Cattari<sup>1</sup>

<sup>1</sup> University of Genoa  
Genoa, Italy  
andrea.brunelli@edu.unige.it, serena.cattari@unige.it

<sup>2</sup> University of Naples Federico II  
Naples, Italy  
filomena.desilva@unina.it

---

### Abstract

*The paper investigates the effects of site-amplification and soil-foundation-structure interaction (SFS) on the fragility curves of a real unreinforced masonry (URM) structure. The building is inspired to a school with an irregular T-shape plan and is modelled according to the equivalent frame approach. The structure was ideally placed on a stiff rock outcrop (case FB A) or settled on four different soft soil profiles, including its real foundation subsoil. In the latter cases the base of the structural model was assumed as fixed (FB C) or endowed with springs (CB C) simulating the soil-foundation dynamic impedance. To evaluate the fragility curves, the corresponding structural models were analysed through non-linear dynamic analyses under 136 input motions, propagated in 1D soil models reproducing the selected profiles for FB C and CB C. The results were compared in the paper in terms of:*

- fragility curves calculated for five damage levels (defined to be conceptually consistent with those of the EMS98 scale) and expressed as a function of different intensity measures of the input motion;*
- average damage derived as a weighted average of the probability of failure associated to all the damage levels.*

*The comparison among the results of the different models highlights the expected increase of damage due to site effects and a beneficial effect of soil-structure interaction, mainly due to the increment of damping associated to the additional energy dissipated by the soil-foundation system. Finally, the average damage of FB C and CB C models were compared with those obtained from the fragility curves of a fixed base system in which site effects are considered through the conventional coefficients proposed in Codes (e.g. by the Eurocode 8), that neglect SFS. This latter approach is that followed in the current practice. The comparison demonstrates that the Code-based approach underestimates the fragility especially at high damage levels.*

**Keywords:** seismic site amplification, soil-structure interaction, fragility curves, unreinforced masonry structures, nonlinear dynamic analyses, code prevision.

## 1 INTRODUCTION

Various reconnaissance studies after seismic events [1, 2, 3] as well as more specific studies at scale of whole historical centres [4, 5, 6] testified as the site-amplification effects (either associated to topographic and soil stratigraphic effects) may play a relevant role, together with their vulnerability, in determining the resulting damage levels on existing unreinforced (URM) masonry. The microzonation studies, developed in various area in Italy after the recent seismic events [7, 8] that hit the country, confirmed this potential risk factor.

Together with this evidence at large scale or on huge building stocks, studies based on detailed models of prototype buildings and more refined analyses methods turn out very useful to understand the phenomenon and also deepen the potential effect of the soil-foundation-structure interaction (SFS). In [9] the topic is treated in a parametric way to attempt in providing a general overview of such effects on various structural typologies (classifiable according to their dynamic behaviour as “stiff” or “flexible”) concluding how the SFS may produce either beneficial or detrimental effects. The literature works specifically addressed to URM buildings are still very few, and usually focused to slender structures, like as towers or minarets [10, 11, 12], or massive monumental assets, like as fortresses [13, 14]. A recent very interesting case, that testified the possible role of SFS also on ordinary URM buildings, is constituted by the “P. Capuzi” school in Visso (MC, Italy). Being monitored as a strategic building by the Italian Seismic Observatory of Structures [15], the school response under the three mainshocks of the 2016-2017 Central Italy earthquake was recorded through numerous accelerometers installed in the building as well as the damage after each event was detected through on-site inspections. Although nowadays the school has been demolished due to the very severe damage occurred, all the precious data collected were very useful to validate numerical models and assess the role played by SFS phenomena in the seismic response of the school, like by [16, 17].

In particular, in [16] a compliant-base model has been successfully validated thanks to these data. This model, that works according to the equivalent frame modelling approach, is the one adopted also for the further developments presented in this paper, which focuses to both the site-amplification due to soil stratigraphic effects and the role played by SFS.

More specifically, the numerical strategy validated in [16] thanks to the actual recordings from the 2016-2017 Central Italy earthquake has been replicated by executing a huge set of nonlinear dynamic analyses (NLDA) with the final aim of developing fragility curves, similarly to what done for example by [5, 18, 19]. The model (briefly recalled at §2.3) has been analysed both as fixed at the base (FB) and endowed with springs (CB) simulating the soil-foundation dynamic impedance. NLDA have been performed according to the Cloud Method (see e.g. [20]) with a selection of records extracted from the SIMBAD database in [21, 22] to be representative of real events recorded on stiff rock outcrop. Then, they have been propagated by considering four different soft soil profiles (§2.1) representative of a class soil C (according to classification adopted in [23, 24]), including the real foundation subsoil of the school (§2.2). Fragility curves are defined assuming a log-normal distribution. The structural response from NLDA is interpreted according to a multiscale approach briefly described at §2, that allows to attribute to each records a damage level, defined to be conceptually consistent with those of the EMS98 scale [25]. Moreover, different intensity measures of the input motion have been considered in order to assess the sensitivity to the dispersion in the definition of the fragility curves (§3.1), namely the Peak Ground Acceleration (PGA) and the Spectral Acceleration corresponding to the fundamental period of the structure ( $S_a(T_1)$ ).

Finally, the average damage of FB C and CB C models were compared with those obtained from the fragility curves of a fixed base system in which site effects are considered in a simplified way through the conventional coefficients proposed in Codes (e.g. by the Eurocode 8 [24]),



that neglect SFS (§3.2). This latter approach is that followed in the current practice. The comparison aims to assess if the current Code-based approach is on the safe side or not, also varying the expected damage level (i.e. the nonlinear phase attained by the structure).

## 2 METHOD OF ANALYSIS

As introduced at §1, in this study fragility curves of a URM building endowed with shallow foundations were calculated accounting for both the amplification of the ground motion due to site effects and the dynamic soil-foundation-structure (SFS) interaction. Due to the low foundation embedment, the foundation input motion is expected to be equal to the free field motion, hence the latter was calculated through linear-equivalent one-dimensional site response analyses performed on four soil profiles. The resulting ground motion (illustrated at §2.3) was then used as input motion to perform non-linear dynamic analyses on:

- a fixed base structural model (indicated as FB C in the following);
- a compliant base structural model in which the base of each main wall is equipped with springs (indicated as CB C in the following).

The rich and huge amount of data from each nonlinear dynamic analysis carried out are interpreted according to a multiscale approach with the final aim of interpreting the simulated structural response through a synthetic parameter consisting in the global damage level. The latter has been defined to be conceptually consistent with the five ones defined in the EMS98 scale [25], that is (DL<sub>i</sub>,  $i=0\dots5$ ): DL0 - none; DL1 - negligible; DL2 - moderate; DL3 - severe; DL4 - very severe to near collapse; DL5 - collapse. In particular, the adopted multiscale approach, similarly to what originally proposed in [26], combines two heuristic criteria:

- a first one that directly refers to the global response scale, by defining proper thresholds of the displacement capacity of the building on pushover curves estimated from nonlinear static analyses. These thresholds are defined in terms of proper fractions of the overall base shear ( $V_b$ ): before the attainment of the maximum value ( $V_{b,max}$ ) to define the DL1 (equal to  $0.4 V_{b,max}$ ) and DL2 (equal to  $0.8 V_{b,max}$ ); after the attainment of the maximum value, i.e. on the softening phase of the curve, to define the DL3 (corresponding to a residual capacity equal to  $0.8 V_{b,max}$ ), DL4 (corresponding to a residual capacity equal to  $0.4 V_{b,max}$ ) and DL5 (corresponding to a residual capacity equal to  $0.2 V_{b,max}$ ).
- a second, based on the evaluation of damage severity and diffusion on vertical walls, that aims to monitor the spread of damage on the building. To this aim, the cumulative rate of walls that reached a given DL (graduated on five level) is computed. The attainment of the DL on a wall is checked in terms of the  $DL_{min}$  variable firstly introduced in [27]. This variable replaces the adoption of interstorey drift thresholds at the wall scale and the proposal assigns a damage level to the wall based on the minimum damage level attained by all the elements of a certain floor. This allows overcoming the definition of conventional interstorey drift thresholds, which are not suited to take into account the different damage mechanism exhibited by structural elements of different slenderness. A similar damage-assignment criterion has been recently pursued in Italian Structural Code [28]. The thresholds assumed for the cumulative rate have been defined to be consistent with the linguistic description of the damage grades of buildings proposed by the European Macroseismic Scale [25]; they are described in more detail in [29, 30].

According to this procedure, results of records can be properly grouped as those associated to the same resulting global DL.

Then, fragility curves were computed by estimating the probability of exceeding,  $p_{DLi}$ , the different damage levels, DL<sub>i</sub>, given a level of ground shaking quantified through the intensity

measure,  $IM$ . The  $p_{DLi}$  was computed from the lognormal distribution of  $IM$  causing the  $i^{th}$  DL and characterized by the median value  $IM_{mi}$  and the lognormal standard deviation  $\sigma$ .

$$p_{DLi}(DL > DLi|IM) = \Phi\left(\frac{\log IM|IM_{mi}}{\sigma}\right) \quad (1)$$

Where  $\Phi$  is the standard cumulative probability function.

Among possible intensity measures [31], in this study, the peak ground acceleration, PGA, and the spectral acceleration,  $Sa(T_1)$  referred to the bedrock input motion were used as  $IM$ . This choice is consistent with various studies on URM buildings [32, 33, 34]. In particular, the geometrical mean of the PGA and the  $Sa(T_1)$  associated to the predominant period along the X and Y directions of the numerical model was used. Since an elongation of the periods is expected for the compliant base models, the  $Sa(T_1)$  of the CB C case differs from those of the FB C case, while the PGA is obviously the same for the two models.

On basis of this procedure, the fragility curves resulting from the FB C model account only for site effects, while those of the CB C model consider both the site and SFS effects. Both cases have been then compared with the fragility curves of the same structure ideally placed on a stiff rock outcrop. The latter were obtained by analyzing the behavior of the fixed-base model subjected to the input motions representative of the bedrock condition (namely the FB A case in the following).

## 2.1 Analysed soil profiles

To study the influence of the soil stiffness on the results of FB C and CB C cases, four soil profiles were selected. The criterion adopted for the selection is that based on an equivalent shear wave velocity up to the bedrock depth,  $V_{seq}$ , falling in the range of class C (as defined by [23, 24]). The first profile (S1) is the actual soil below the “P. Capuzi” School of Visso, i.e. a sandy gravel layer (SG), covered and locally interbedded by clayey silt (CS) and silty clay (SC) lenses. The stiffness profile was measured through a MASW test [35] and several down-hole tests [36]. The on-site measured free field frequency obtained from HVSr tests allowed the back-calculation of the bedrock depth equal to 40 m. The shear wave velocity,  $V_s$ , is variable with depth with an equivalent value up to the bedrock equal to 281 m/s. Additional details on the geotechnical characterization of this soil profiles are reported in [16].

The second profile (S2) is the actual soil in the historic centre of Visso, investigated through two boreholes and a HVSr test [36]. The profile is made of clayey silt (CS) for the first 4 m, overlaying a 11 m thick sandy gravel layer (SG). The geological section of the Visso valley reported by [36] individuates the bedrock at a depth of 18 m. In lack of a direct measure of  $V_s$ , its value was obtained through a correlations law between  $V_s$  and the number of blows of SPT tests performed at a depth of 1.9 m in CS and 4.4 and 8.9 m in SG, respectively. Before the application, numerous correlation law available in the literature were checked against the results of down hole tests in the same valley. Such validation is not reported here for sake of brevity. The most successful correlations in the validation were used to characterize S2. In particular, the correlations by [37, 38] were used for CS, leading to the same  $V_s=162$  m/s, and by [39] for SG, leading to  $V_s=337$  m/s. The consequent equivalent  $V_s$  up to the bedrock depth is  $V_{seq}=272$  m/s. Finally, two other ideal clay (S3) and gravel (S4) profiles were considered with the bedrock placed at a depth of 40 m. In both cases  $V_s$  increases with depth. Its profile was calculated through the empirical laws by [40] for S3 and by [41] for S4, respectively. The resulting  $V_{seq}$  are 200 and 279 m/s, which are similar to those of S1 and S2.

Figure 1a summarizes the four soil and  $V_s$  profiles while Figure 1b reports their amplification functions. The latter have been calculated through a linear site response analysis performed by

using the STRATA software [42]. As highlighted by the resulting natural frequencies, there is a significant variety among the responses of the different soil profiles.

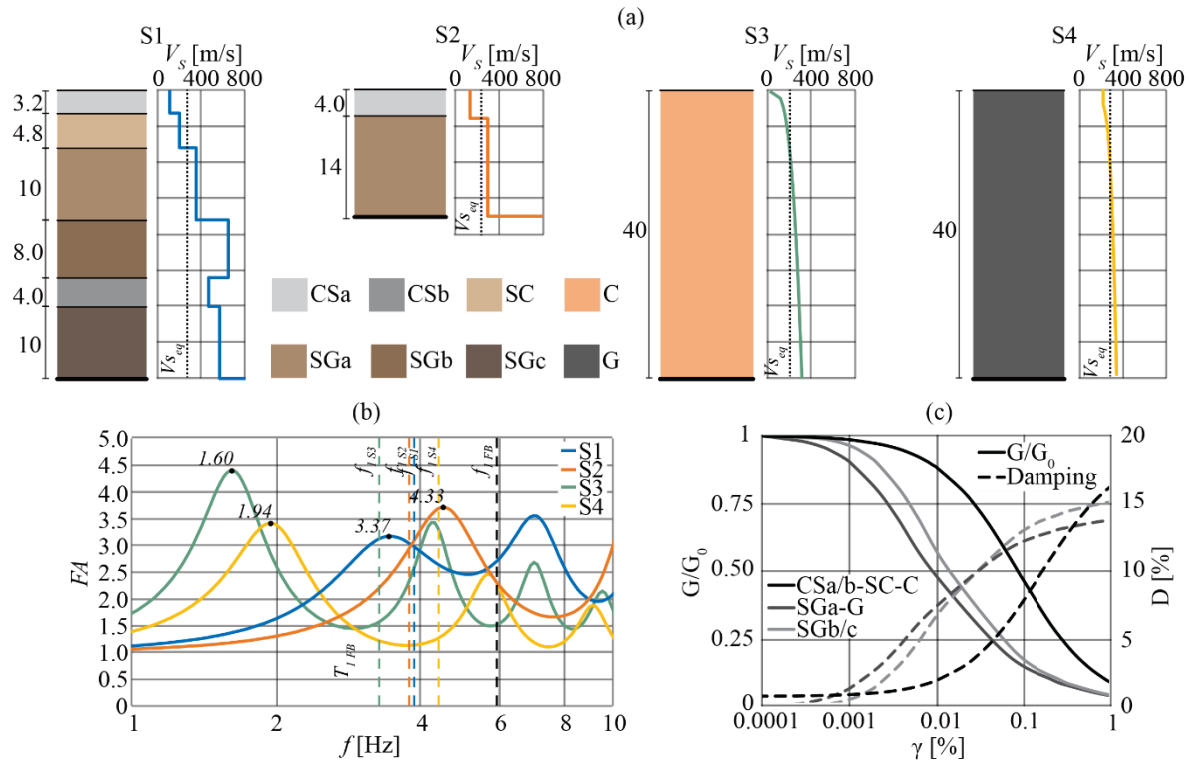


Figure 1: (a) layer with profile  $V_s$ ; (b) FA of the four stratigraphies and (c) decay curves of the soils considered.

Finally, Figure 1c shows the variation of the normalized shear modulus ( $G/G_0$ ) and the damping ratio ( $D$ ) with the shear strain ( $\gamma$ ) adopted in the linear equivalent site response analyses executed with the records of real earthquakes and performed again in the STRATA software. The curves adopted for the fine-grained soils in S1, S2 and S3 were obtained based on a comprehensive model calibrated by [43, 44] on the results of laboratory tests on comparable materials. The  $G/G_0$ - $\gamma$  curves obtained by [45], through laboratory tests on silty sandy gravel samples different confining stress were associated to the sandy gravel soil in S1, S2 and S4. The corresponding  $D$ - $\gamma$  curves were calculated by applying the model by [46] and the Masing criteria [47] to the  $G/G_0$ - $\gamma$  curves.

## 2.2 Results of site response analyses under records of real earthquakes

Figure 2 shows the acceleration time histories of the input motions employed to analyse the site effects in the four soil profiles described in §2.1. They were chosen from the Selected Input Motions for Displacement-Based Assessment and Design (SIMBAD) database [21, 22].

The selection includes the EW (Channel 1 (C1)) and NS (Channel 2 (C2)) components of accelerations recorded during 49 natural events at stations located on stiff rock outcrop, *i.e.*  $V_{s30}$  greater than 700 m/s. Some selected signals were slightly scaled to achieve the desired variability of the intensity measures to be used in the construction of the fragility curves of the FB A.

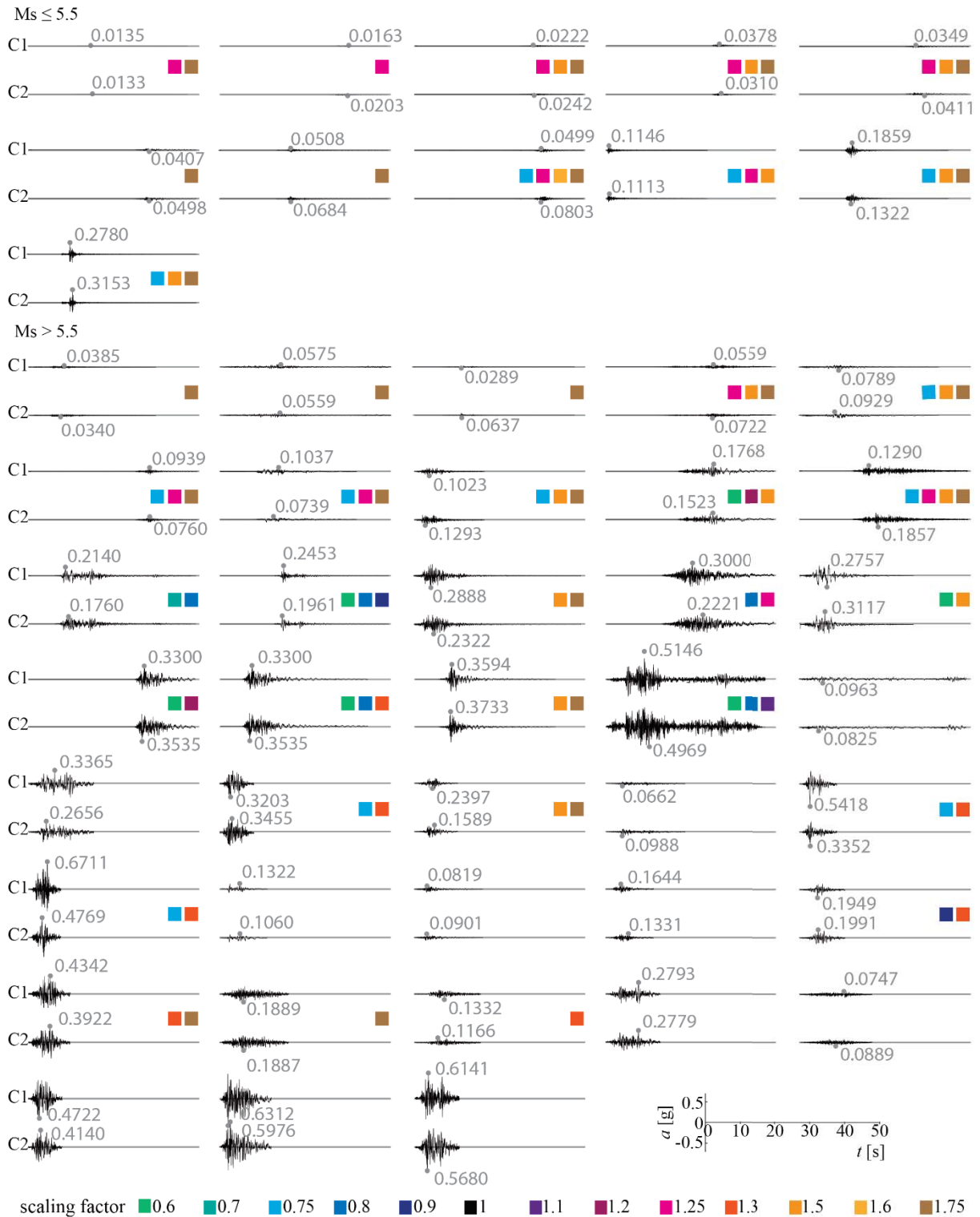


Figure 2: Time histories of the acceleration of the selected input motions.

Colours in Figure 2 indicate the scaling factors, when multiple colours are present, the same input motion was scaled more than once.

Figure 3 shows the mobilized  $G/G_0$  (a) and hysteretic damping ratio (b) calculated in the four considered soil profiles through site response analyses under each event. The mean values

mobilized in the soil volume, expected to be affected by the foundation motion (i.e. 1 m under foundation level) are reported. As expected, the highest effects of nonlinearity are recognized: for the profile S3, characterized by the lowest initial stiffness; and the gravel soil profile S4, characterized by the earliest development of stiffness reduction (see Figure 1c). Conversely the lowest nonlinearity corresponds to the shallowest bedrock producing the highest natural frequency, *i.e.* the stiffest response (see Figure 1b). The actual soil profile below the school, S1, shows an intermediate behaviour.

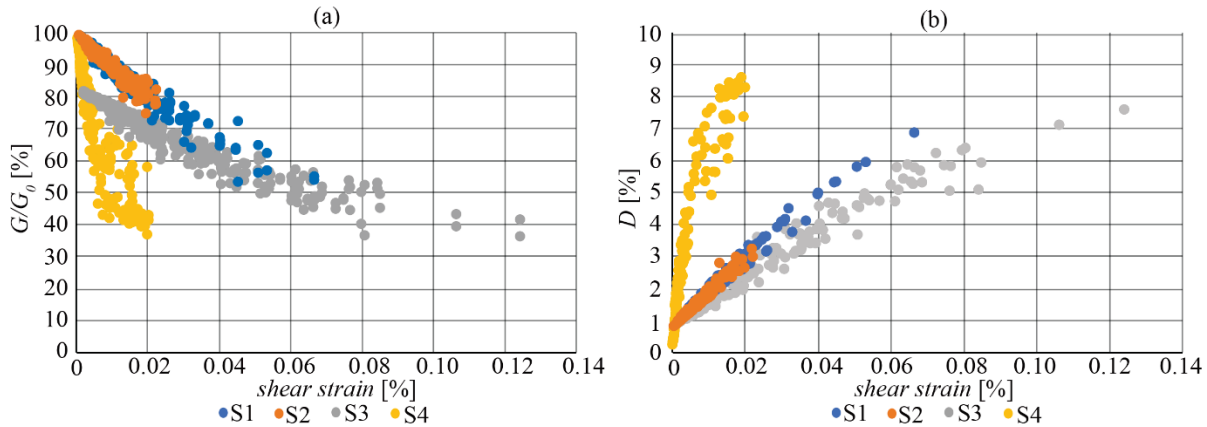


Figure 3: (a)  $G/G_0$  and (b) hysteretic damping ratio mobilized in the four soil profiles in significant volume during each site response analysis.

Figure 4 groups the analyses according to different ranges of  $Sa(T_1)$  of the free field motion resulting from the site response analyses and corresponding to the fixed-base period. The latter are reported in Table 1 together with the period of the CB models on the different soil profile, revealing that the different initial shear stiffness of the soil profiles significantly affects the CB C period.

Model	FB	CB -S1	CB -S2	CB -S3	CB -S4
$T_1$ [s]	0.1740	0.2580	0.2640	0.3050	0.2298

Table 1: first period of each model.

The comparison among the number of signals belonging to each group, reported in red on the top of Figure 4, shows that  $Sa(T_1)$  values on surface of profile S4 are lower than 1.5 g and mainly concentrated in the lowest amplitude ranges. The ranges associated with the highest  $Sa(T_1)$  are populated mainly by signals propagated in S1 and S3, highlighting that such profiles are more hazardous for the structural safety.

In the same Figure 4 the number of times in which  $Sa(T_1)$  of the CB models exceeds that of the FB ones is reported in percentage on the Y-axis. Except for S2 showing a more irregular trend, such percentage increases with increasing  $Sa(T_1)$  and is predominant (*i.e.* >50%) from  $Sa(T_1) > 0.75$  g. Hence, a detrimental effect of SFSI is shown on the seismic actions affecting the structure especially under the most severe input motions.



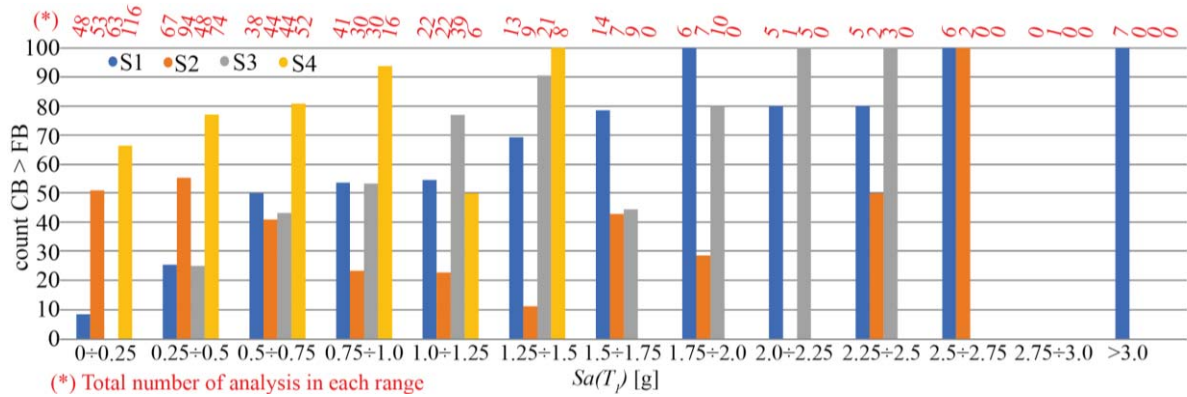


Figure 4: number of times in which  $Sa(T_1)$  of the CB model exceeds that of the FB.

### 2.3 Numerical model of the selected URM building

The 3D model of Visso school (Figure 5a) adopted for the execution of NLDA works according to the equivalent frame (EF) approach. It has been realized with the Tremuri software package [48] and has been calibrated in [16] thanks to the available data on the structure from the permanent monitoring and previous studies [35]. The choice of adopting the EF model is justified by the regular pattern of openings in walls and by the evidence from the actual seismic response [49], that clearly highlighted the concentration of cracks in specific portions of the walls (namely, the piers and spandrels, respectively identified in orange and green in Figure 5a). The constitutive law used allows for describing the nonlinear response until very severe damage levels at element scale (i.e.  $DL_E$  from 1 to 5) through progressive strength degradation corresponding to assigned drift values; with the aim of executing NLDA [34], the constitutive law includes also a hysteretic response (Figure 5b). The latter is based on a phenomenological approach that allows also to differentiate the hysteresis loops in spandrels and piers and also varying the prevailing failure mode (e.g. if dominated by the flexural response or diagonal shear cracking). For further details on mechanical panel properties and modelling assumptions the interested reader may refer to [16].

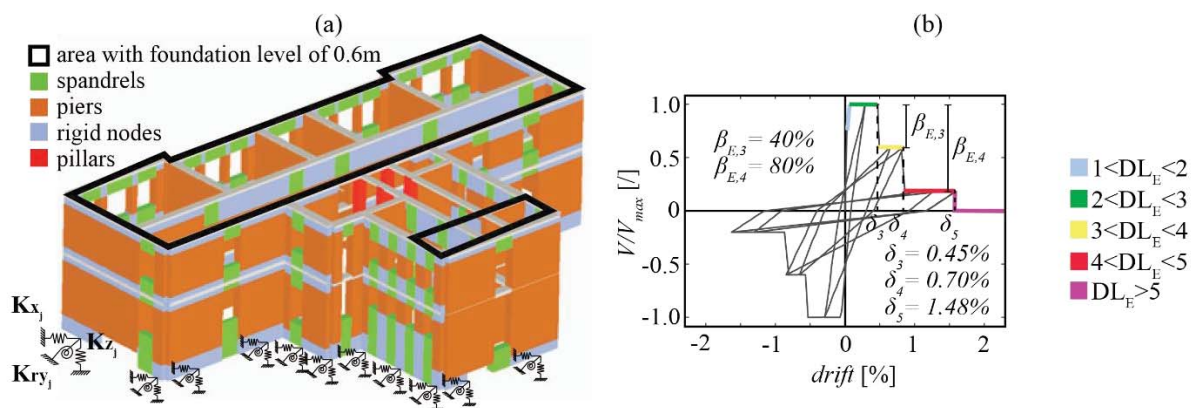


Figure 5: (a) 3D equivalent frame model with springs implemented in the CB model, (b) backbone and hysteretic response of masonry elements: piers under shear.

To simulate the base compliance, each foundation pier was equipped with springs (see Figure 5a), which stiffness was calibrated through the real part of the soil-foundation impedances by [50]. The foundation width was set equal to 0.90 m, while its length was defined by adding the

half-length of the spandrel panel to the size of the load-bearing wall. The value of the embedment was set to 0.6 m, except for the area indicated in Figure 5a, where the embedment increases up to 2.95 m due to the presence of an underground level. The soil was modelled as an equivalent linear half-space with a shear modulus equal to that mobilized at the foundation depth under each input motion. A full soil-foundation contact was assumed.

Firstly, the periods along the X and Y directions ( $T_x^*$  and  $T_y^*$ ) and the damping ratio ( $\beta_x$  and  $\beta_y$ ) of the SFS system were estimated through the replacement oscillator by [51]. To this aim, the building was approximated through a SDOF system with a viscous damping ratio equal to 3% and a lateral stiffness derived from the fundamental periods along the X and Y directions of the fixed base configuration (see [16]). To apply the formula by [51], the real and the imaginary parts of the monolithic foundation equivalent to the actual foundation systems were calculated from the sum of the real or imaginary parts of the impedances of the X-oriented (or Y-oriented) load-bearing walls. The contribution of the soil hysteretic damping mobilized at the foundation level (see Figure 3b) was added to the energy loss coefficients simulating the radiation damping ratio.

Then the frequency-dependent dynamic coefficients of the impedances were computed as a function of the resulting  $T_x^*$  and  $T_y^*$ , through an iterative procedure. To simulate the additional energy dissipation due to SFS interaction, the mean value of  $\beta_x$  and  $\beta_y$  was introduced as a Rayleigh damping ratio into the EF model. The calculation was repeated for each input motion: consequently, the impedances and the resulting  $T_x^*$  and  $T_y^*$  as well as the mean value of  $\beta_x$  and  $\beta_y$ , were updated according to the mobilized soil shear stiffness and damping ratio during each seismic response analysis (see Figure 3).

### 3 DESCRIPTION OF RESULTS

#### 3.1 Influence of site effects and SSI on the fragility curves

Table 2 reports the number of analyses (N), the median value  $IM_{50}$  (in acceleration unit g) and the standard deviation ( $\sigma$ ) used to generate the fragility curves of the fixed-base model analysed under the selected input motion (FB A).

Only few analyses, reported in brackets in Table 2, mobilize DL3, DL4 and DL5 for the FB A case; so the initial set of input motions described in Section 1.2 was integrated with the natural signals recorded on stiff soil and collected by [52]. However, the  $IM_{50}$  and  $\sigma$  resulting from the updated set of input motions are comparable with those obtained from the original selection (in brackets). There is only an increase, less than 10%, of the  $IM_{50}$  associated with DL5 in the case of PGA which results in a reduction of structural fragility.

	FB A				
	PGA		Sa( $T_1$ )		N
	$IM_{50}$	$\sigma$	$IM_{50}$	$\sigma$	
DL1	0.095	0.495	0.178	0.473	127
DL2	0.274	0.314	0.656	0.391	92
DL3	0.450 (0.413)	0.219 (0.255)	1.013 (0.969)	0.376 (0.423)	18 (10)
DL4	0.530 (0.488)	0.191 (0.147)	1.182 (1.156)	0.308 (0.299)	17 (7)
DL5	0.619 (0.562)	0.219 (0.178)	1.500 (1.428)	0.261 (0.314)	44 (12)

Table 2: Median value ( $IM_{50}$ ) and standard deviation ( $\sigma$ ) associated with to the various damage levels for the FB A model.

It is worth to remember that the IMs calculated for FB C and CB C refer to the bedrock. This implies that the  $IM_{50}$  values reduce moving from the FB A to FB C, independently of the soil profile. That highlights the expected increase of fragility for a fixed-base structure settled on soil type C with respect to that placed on soil type A, as shown in Figure 6 by way of example in the case of DL3.

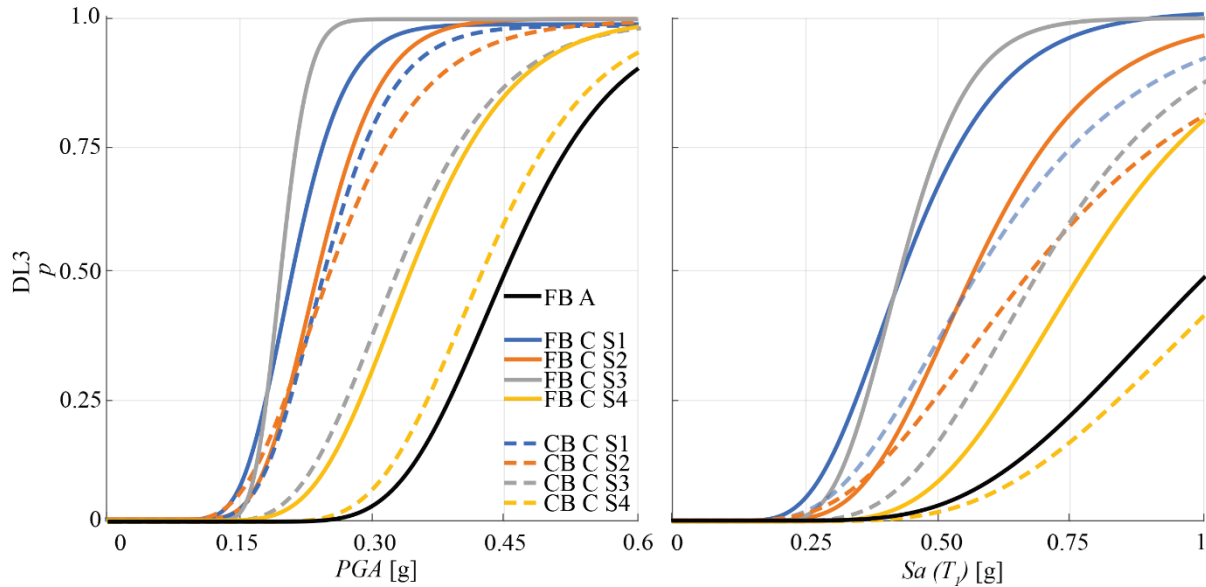


Figure 6: Comparisons between the curves obtained from the FB A, FB C and CB C assuming PGA and  $Sa(T_1)$  as IM in case of DL3.

The comparison with the CB C models reveals an increase of  $IM_{50}$  with respect to the FB C case. Such modification reduces the probability of failure on the building. Since the elongation of the CB C period produces an increment of the seismic actions with respect to the FB C case (see Figure 4 and Section 2.2), such beneficial effect is mainly due to the increase of damping ratio produced by the SFS interaction, as shown in Figure 6 by way of example for DL3. This general conclusion is however extendable to all DLs.

The same beneficial effect is evident by comparing the number of analyses that fall into the various  $DL_i$  for the FB C and CB C. There is in fact a reduction of the analyses in the more severe DLs for the CB C model, in particular for the profile S4 where the analyses in DL5 are only 3. Such reduced number of analyses reduces the reliability of the DL5 fragility curve for S4, hence this case will not be considered in the following interpretations. Obviously, the reliability of DL5 would have been improved by scaling through higher factors the signals originally selected, but such procedure would have led to unrealistically strong free field motions. Conversely, the low occurrence of DL5 for S4 (resulting from the numerical analyses) appeared much more realistic, because buildings settled on gravel are less prone to high damage since they are affected by lower seismic actions (see Figure 4) and benefit of higher soil damping.

The estimation of  $p_{DLi}$  through Equation 2 allows the computation of the mean damage  $\mu_d$  expected to affect the structure, as follows:

$$\mu_d = \sum_{i=0}^5 (p_{DLi} i) \quad (2)$$

where  $p_{DLi}$  is weighted by  $i=0,1,2,3,4$  or 5 passing from DL0 to DL5.

The calculation was performed by entering the curves of the case FB C and CB C with the values of PGA and  $Sa(T_1)$ , at the bedrock of each selected input motion. The  $\mu_d$  value may be conveniently converted into an equivalent discrete damage level by assuming a binominal

distribution, leading to the following conversion intervals: 0-0.7 for DL0; 0.7-1.6 for DL1; 1.6-2.5 for DL2; 2.5-3.4 for DL3; 3.4-4.3 for DL4; 4.3-5 for DL5. The latter ones have been used to define the “square metric” in Figure 7. These comparisons are reported considering as IM: the PGA in (a); and the  $Sa(T_1)$  in (b). The grey fillings indicate a difference of 1, 2 or 3 DLs between the mean damage of FB C and CB C. In the case of the PGA, SFS interaction always leads to a reduction of the expected damage, independently of the soil profile and the greatest beneficial effects at DL3-4, specially for S3. Considering the  $Sa(T_1)$ , the results are more dispersed. In any case there is a greater damage associated with the FB C model, but there are also some cases in which the CB C model leads to greater damage, specially at lowest DL in S1 and S2. In this case, it is worth to remind that also the IM changes among the models, because the fundamental period changes as shown in Table 1.

Despite these slight differences, the general conclusion on the SFS effects observed from the use of PGA and  $Sa(T_1)$  is the same.

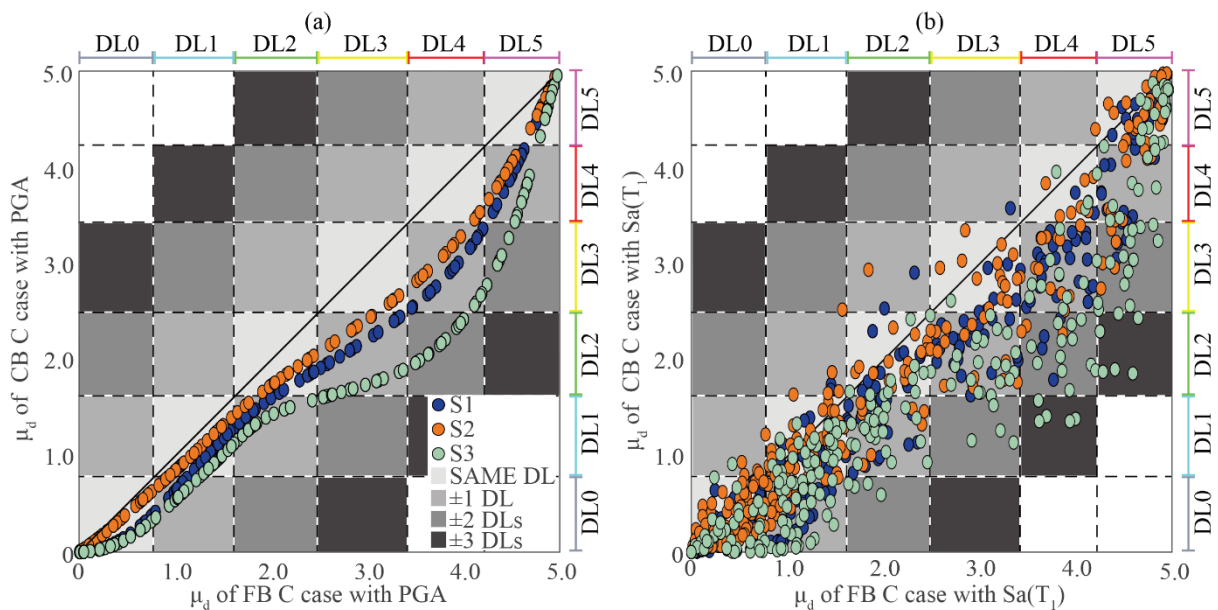


Figure 7:  $\mu_d$  between FB C and CB C for S1, S2 and S3 in case of (a) PGA and (b)  $Sa(T_1)$ .

### 3.2 Comparisons with the Eurocode previsions

In the most widespread cases of fragility curves generated for fixed base structures and stiff soil conditions (case FB A), site effects can be considered in the estimation of  $p_{DLi}$  in a simplified way, *i.e.* by entering in the curve with the IM amplified by the stratigraphic coefficient provided by Code. As an example, on the abscissa, Figure 8 shows the  $\mu_d$  resulting from the fragility curve of FB A in which the terms  $p_{DLi}$  in Equation 2 alternatively corresponds to peak ground (PGA\*) or the spectral ( $Sa(T_1)$ \*) accelerations, amplified according to the coefficient proposed by the [24]. This is equal to 1.5 for events with a surface wave magnitude lower than 5.5; otherwise it is equal to 1.15 (see Figure 2). When only site effects are considered (FB C) (see Figure 8a and b), EC8 underestimates the damage in any case and up to three damage levels. Soil-structure interaction reduces the gap between the  $\mu_d$  estimated through the Code conforming approaches and that estimated by explicitly accounting for the site effects joint to the soil structure interaction (CB C) (see Figure 8c and d). However, a difference of one DL (very rarely of two DLs) still results also for CB C. Such underestimation arguably would increase if the increment of damping ratio induced by SFS interaction was considered in the computation of the IM\*.



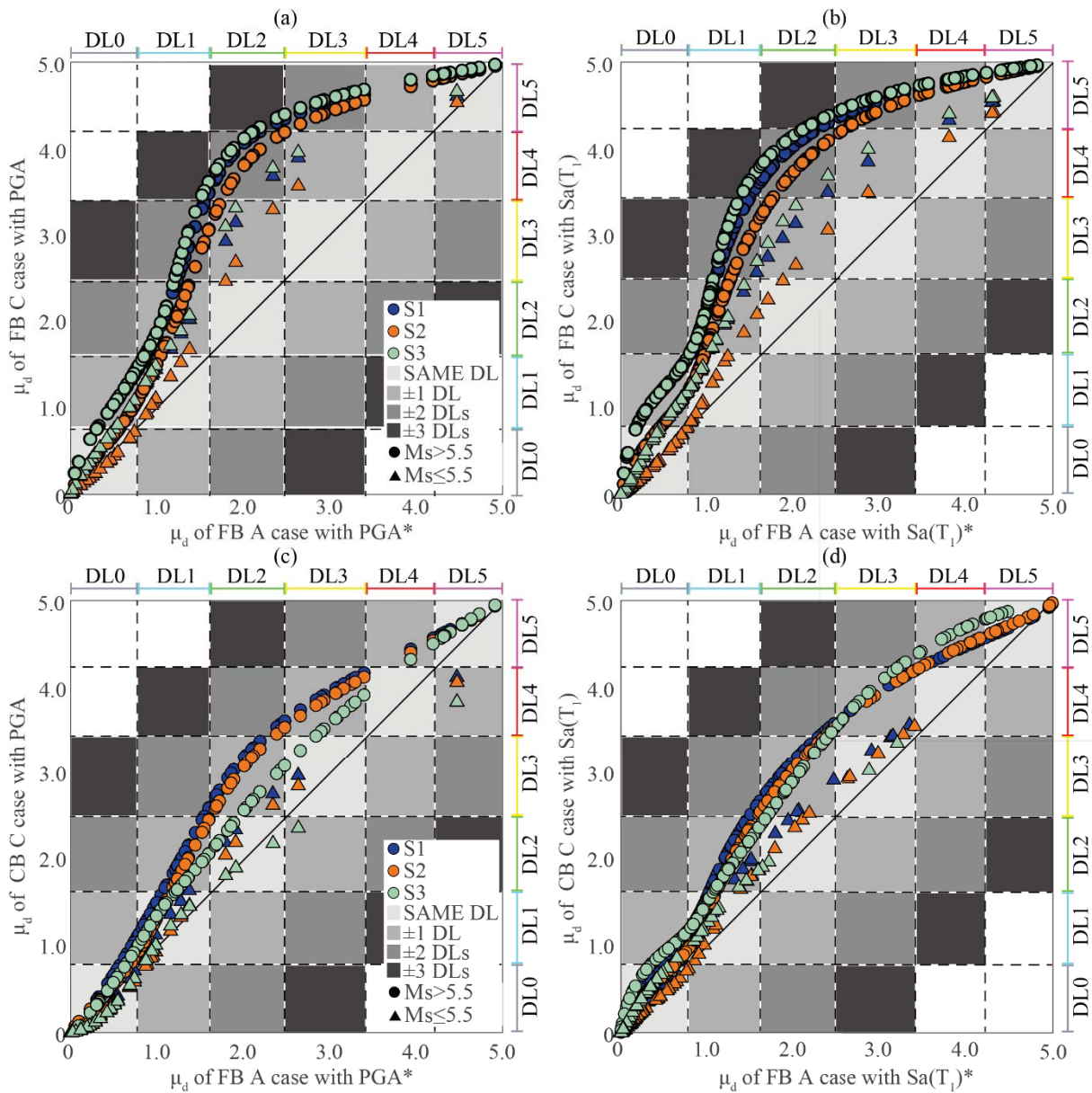


Figure 8: Comparison among the  $\mu_d$  resulting for the different analyzed cases from the curves expressed as a function of (a) PGA and (b)  $Sa(T_1)$  for FB C model, (c) and (d) for CB C model. In the FB A case, the  $PGA^*$  and  $Sa(T_1)^*$  values - amplified according to the coefficients proposed in the Eurocode 8 ([24]) - were used.

#### 4 CONCLUSIONS

The paper compares the fragility curves and the derived mean damages of a real URM structure ideally placed on stiff rock (FB A) or settled on four different soil profiles. The latter ones include its real foundation subsoil as well as other three with an equivalent shear wave velocity falling in the range of soil type C. The base of the structural model is alternatively assumed as fixed (FB C) or endowed with springs (CB C), simulating in that way the soil-foundation dynamic impedance.

The comparison among the results of the FB A and FB C cases shows the expected increase of the probability of failure when site amplifications are considered.



The comparison among FB C and CB C highlights: i) a general increase in the spectral accelerations affecting the model on springs; ii) a reduction of the probability of failure. As expected, the first effect (i) is due to the period elongation induced by the soil-foundation-structure interaction while the second (ii) is mainly ascribable to the increment of damping associated to the additional energy dissipated by the soil-foundation system.

The comparison among the results of models on the different soil profiles reveals that the highest damage levels are rarely achieved by structures placed on gravel. This is because they are affected by lower seismic actions and benefit of higher soil damping mobilized by the early development of nonlinearity in such soil types. Significant beneficial effects are also recognized for structures settled on soft clay again due to the significant damping mobilized by the considerable strain levels achieved in such profile.

Finally, the mean damages of FB C and CB C were compared with the values resulting from the probability of failures estimated by amplifying the intensity measure through the conventional coefficients proposed by Eurocode [24] to account for the site effects. The comparison shows that such simplified approach underestimates the damage up to two damage levels. Nevertheless, it is currently the most widespread procedure because fragility curves are mostly generated for fixed base structures and without considering site effects through site response analyses. Results achieved could be further developed in future works to improve also practice-oriented procedures.

## REFERENCES

- [1] A. Sextos, R. De Risi, A. Pagliaroli, S. Pagliaroli, S. Foti, et al., Local site effects and incremental damage of buildings during the 2016 Central Italy Earthquake sequence. *Earthq Spectra*, **34**(4), 1639-1669, 2018.
- [2] L. Sorrentino, S. Cattari, F. da Porto, G. Magenes, A. Penna, Seismic behaviour of ordinary masonry buildings during the 2016 central Italy earthquakes. *Bull Earthq Eng.*, **17**(10), 5583-5607, 2019.
- [3] J.P. Stewart, P. Zimmaro, G. Lanzo, S. Mazzoni, E. Ausilio, et al, Reconnaissance of 2016 central Italy earthquake sequence. *Earthq Spectra*, **34**(4), 1547-1555, 2018.
- [4] V. D'Amico, M. Mucciarelli, Validation through HVSR measurements of a method for the quick detection of site amplification effects from intensity data: an application to a seismic area in Northern Italy. *Soil Dyn Earthq Eng*, **22**(6), 475-483, 2002.
- [5] N. Chieffo, A. Formisano, Induced seismic-site effects on the vulnerability assessment of a historical centre in the Molise region of Italy: analysis method and real behaviour calibration based on 2002. *Earthq Geosci* **10** (1), 21,2020.
- [6] G. Brando, A. Pagliaroli, G. Cocco, F. Di Buccio, Site effects and damage scenarios: The case study of two historic centers following the 2016 Central Italy earthquake. *Engineering Geology*, **272**, 105674, 2020.
- [7] A. Pagliaroli, F. Pergalani, A. Ciancimino, A. Chiaradonna, M. Compagnoni, F. de Silva, S. Foti, S. Giallini, G. Lanzo, L. Luzi, L. Macerola, M. Nocentini, A. Pizzi, M. Tallini, C. Teramo, Site response analyses for complex geological and morphological conditions: relevant case-histories from 3<sup>rd</sup> level seismic microzonation in Central Italy, *Bull. Earthq. Eng.*, Special Issue: "Seismic Microzonation of Central Italy", 2019 <https://doi.org/10.1007/s10518-019-00610-7>.

- [8] G. Lanzo, F. Silvestri, A. Costanzo, A. d’Onofrio, L. Martelli, A. Pagliaroli, S. Sica, A. Simonelli, Site response studies and seismic microzoning in the Middle Aterno valley (L’aquila, Central Italy). *Bull. Earthq. Eng.* **9**, 1417, 2011.
- [9] F. Khosravikia, M. Mojtaba M. A. Ghannad, The effect of soil–structure interaction on the seismic risk to buildings. *Bull. Earthq. Eng.*, **16**, 3653-3673, 2018.
- [10] S. Casolo, V. Diana, G. Uva, Influence of soil deformability on the seismic response of a masonry tower. *Bull. Earthq. Eng.*, **15**, 1991-2014, 2017.
- [11] F. de Silva, Influence of soil-structure interaction on the site-specific seismic demand of masonry towers. *Soil Dyn Earthq Eng*, **131**, 106023, 2020.
- [12] A. Bayraktar, E. Hokelekli, Influences of earthquake input models on nonlinear seismic performances of minaret-foundation-soil interaction systems. *Soil Dyn. Earthq. Eng.* **139**, 2020.
- [13] A. Karatzetzou, D. Pitilakis, M. Kržan, V. Bosiljkov, Soil-foundation-structure interaction and vulnerability assessment of the Neoclassical School in Rhodes, Greece. *Bull Earthq Eng*, **13**, 411-428, 2015.
- [14] A. Fathi, A. Sadeghi, M.R. Emami Azadi, N. Hoveidae, Assessing the soil-structure interaction effects by direct method on the out-of-plane behavior of masonry structures (case study: Arge-Tabriz). *Bull. Earthq. Eng.*, 2020 <https://doi.org/10.1007/s10518-020-00933-w>.
- [15] M. Dolce, M. Nicoletti, A. De Sortis, S. Marchesini, D. Spina, F. Talanas, Osservatorio sismico delle strutture: the Italian structural seismic monitoring network. *Bull Earthq Eng* **15**(2), 621-641, 2017.
- [16] A. Brunelli, F. de Silva, A. Piro, S. Sica, F. Parisi, F. Silvestri, S. Cattari, Numerical simulation of the seismic response and soil-structure interaction for a monitored masonry school building damaged by the 2016 Central Italy earthquake. *Bull Earthq Eng.*, **19**(2), 1181-1211, 2021.
- [17] C. Ferrero, P.B. Lourenco, C. Calderini, Nonlinear modeling of unreinforced masonry structures under seismic actions: validation using a building hit by the 2016 Central Italy earthquake. *Frattura ed Integrità Strutturale*, **14**(51), 92-114, 2020.
- [18] F. Cavalieri, A.A. Correia, H. Crowley, R. Pinho, Seismic fragility analysis of URM buildings founded on piles: influence of dynamic soil–structure interaction models. *Bull. Earthq. Eng.* **18**, 4127-56, 2020.
- [19] D. Peduto, M. Korff, G. Nicodemo, A. Marchese, Empirical fragility curves for settlement-affected buildings: Analysis of different intensity parameters for seven hundred masonry buildings in The Netherlands. *Soils and Foundations*, **59**(2), 380-397, 2019.
- [20] F. Jalayer, H. Ebrahimian, A. Miano, G. Manfredi, H. Sezen, Analytical fragility assessment using unscaled ground motion. *Earthquake Engng Struct Dyn.*, 1-25 2017.
- [21] C. Smerzini, R. Paolucci, *SIMBAD: a database with Selected Input Motions for displacement Based Assessment and Design* – 3<sup>rd</sup> release by Department of Structural Engineering, Politecnico di Milano, Italy. Research Project DPC RELUIS, 2013.
- [22] I. Iervolino, C. Galasso, R. Paolucci, C. Smerzini, Ground Motion Record Selection Based on Broadband Spectral Compatibility. *Earthq. Spectra*, **30**(4), 1427-1448, 2014.

- [23] NTC, *Norme Tecniche per le Costruzioni*. DM 17/1/2018, Italian Ministry of Infrastructure and Transportation, G.U. n. 42, 20 February 2018, Rome, Italy, 2018 (in Italian).
- [24] CEN, EN 1998-1, Eurocode 8: *Design of structures for earthquake resistance - Part 1: General rules, seismic actions and rules for buildings*. Brussels: CEN, 2004.
- [25] G. Grünthal, *European macroseismic scale EMS-98*. European Seismological Commission, Sub-commission on Engineering Seismology, Working Group Macroseismic Scales, Luxembourg, 1998.
- [26] S. Lagomarsino, S. Cattari, PERPETUATE guidelines for seismic performance-based assessment of cultural heritage masonry structures, *Bull Earthq Eng*, **13**(1), 13-47, 2015.
- [27] S. Marino, S. Cattari, S. Lagomarsino, Are the nonlinear static procedures feasible for the seismic assessment of irregular existing masonry buildings? *Eng. Struct.*, **200**, 109700, 2019.
- [28] MIT, Istruzioni per l'applicazione dell'aggiornamento delle Norme tecniche per le costruzioni di cui al Decreto Ministeriale 17 gennaio 2018, Ministry of Infrastructures and Transportations, Rome, Italy, 2019 (in Italian).
- [29] D. Sivori, Ambient vibration tools supporting the model-based seismic assessment of existing buildings. PhD dissertation, University of Genoa, Italy, 2021.
- [30] S. Cattari, M. Angiolilli, Procedure for the attribution of EMS98-damage levels in masonry buildings from observed seismic damage or nonlinear analyses, *Bull Earthq Eng*, submitted.
- [31] J.J. Bommer, G. Magenes, J Hancock, P. Penazzo, The Influence of Strong-Motion Duration on the Seismic Response of Masonry Structures, *Bull. Earthq. Eng*, **2**, 1-26, 2004.
- [32] M. Zucconi, R. Ferlito, L. Sorrentino, Validation and extension of a statistical usability model for unreinforced masonry buildings with different ground motion intensity measures. *Bull. Earthq. Eng*, **18**, 767-795, 2020.
- [33] A. Mouyiannou, M. Rota, Selecting appropriate intensity measures for analytical state dependent fragility functions of URM buildings. *16<sup>th</sup> World Conference on Earthquake*, (16WCEE), Santiago, Chile, January 9-13, 2017.
- [34] S. Cattari, D. Camilletti, S. Lagomarsino, S. Bracchi, M. Rota, A. Penna, Masonry Italian Code-Conforming Buildings. Part 2: Nonlinear Modelling and Time-History Analysis. *J. Earthq. Eng.* **22**(2), 2010-2040, 2018.
- [35] ReLUIS-Task 4.1 Workgroup report, edited by S. Cattari, S. Degli Abbatì, D. Ottonelli, D. Sivori et al. *Report di sintesi sulle attività svolte sugli edifici in muratura monitorati dall'Osservatorio Sismico delle Strutture, Linea Strutture in Muratura*, ReLUIS report, Rete dei Laboratori Universitari di Ingegneria Sismica, 2018 (in Italian).
- [36] MZS3, *Report of the 3<sup>rd</sup> level Seismic Microzonation of Visso village*. Approved by the Working Group, May 29, 2018. <https://www.comune.visso.mc.it/avvisi-cms/microzonazione-sismica-iii-livello/>.
- [37] T. Imai, Y. Yoshimura, Elastic wave velocity and soil properties in soft soil. *Tsuchito-Kiso* **18** (1), 17-22, 1970 (in Japanese).
- [38] S.H.H. Lee, Analysis of the multicollinearity of regression equations of shear wave velocities. *Soils and Foundations*, **32**(1), 205-214, 1992.

- [39] Y. Ohta, N. Goto, Empirical shear wave velocity equations in terms of characteristic soil indexes. *Earthq. Eng. Struct. Dyn.*, **6**, 167-187, 1978.
- [40] A. d'Onofrio, F. Silvestri, Influence of Micro-Structure on Small-Strain Stiffness and Damping of Fine Grained Soil and Effects on Local Site Response. *International Conferences on Recent Advances in Geotechnical Earthquake Engineering and Soil Dynamics*, **15**, 2001.
- [41] B. O. Hardin, M. Kalinski, Estimating the Shear Modulus of Gravelly Soils. *J. Geotech. Geoenviron. Eng.*, **131**(7), 2005.
- [42] A. Kottke, E.M. R Rathje, *Technical manual for Strata*. Report No. 2008/10. Pacific Earthquake Engineering Research Center, University of California, Berkeley, 2008.
- [43] ReLUIS-WorkPackage 1, Deliverable UniNa, *Modellazione delle curve di decadimento del modulo di taglio e del fattore di smorzamento di alcuni terreni dell'Italia Centrale*, ReLUIS report, Rete dei Laboratori Universitari di Ingegneria Sismica (in Italian), 2018.
- [44] A. Ciancimino, G. Lanzo, G.A. Alleanza et al, Dynamic characterization of fine-grained soils in central Italy by laboratory testing. *Bull Earthq Eng*, **18**, 5503-5531, 2019.
- [45] T. Liao, N. Massoudi, M. Mchood, K.H. Stokoe, M.J. Jung, F.Y. Menq, Normalized shear modulus of compacted gravel. *18<sup>th</sup> international conference on soil mech Geotech eng. (ICSMGE)*, Paris, France, September 2-6, 2013.
- [46] W. Ramberg, W.R. Osgood, *Description of stress-strain curves by three parameters*. Natl Advis Comm Aeronaut, Washington DC, 1943.
- [47] G. Masing, Eigenspannungen und Verfestigung beim messing. *2<sup>nd</sup> Int congress of App Mech*, Zurich, Swiss, September 12-17, 1926.
- [48] S. Lagomarsino, A. Penna, A. Galasco, S. Cattari, TREMURI program: An equivalent frame model for the nonlinear seismic analysis of masonry buildings. *Eng Struct*, **56**, 1787-1799, 2013.
- [49] S. Cattari, G. Magenes, Benchmarking the software packages to model and assess the seismic response of unreinforced masonry existing buildings through nonlinear static analyses. *Bull Earthq Eng*, 2021. <https://doi.org/10.1007/s10518-021-01078-0>.
- [50] G. Gazetas, Formulas and charts for impedances of surface and embedded foundations. *J Geotech Eng*, **117**(9), 1363-1381, 1991.
- [51] A. Maravas, G. Mylonakis, D.L. Karabalis, Simplified discrete systems for dynamic analysis of structures on footings and piles. *Soil Dyn Earthq Eng*, **61-62**, 29-39, 2014.
- [52] R. Paolucci, A.G. Ozcebe, C. Smerzini, A. Masi, V. Manfredi, Selection and spectral matching of recorded ground motions for earthquake engineering analysis. *Internal report of RELUIS 2019 - WP4*, Mappe di rischio e scenari di danno sismico (MARS), 2020.

## ELASTODYNAMIC ANALYSIS OF Laterally LOADED PILES: MODIFICATIONS TO A SIMPLIFIED ENERGY APPROACH

Jamie J. Crispin<sup>1</sup>, and George E. Mylonakis<sup>123</sup>

<sup>1</sup> Department of Civil Engineering  
University of Bristol, Bristol, UK  
j.crispin@bristol.ac.uk, g.mylonakis@bristol.ac.uk

<sup>2</sup> Department of Civil Engineering  
University of California at Los Angeles, Los Angeles, CA, USA

<sup>3</sup> Department of Civil and Infrastructure Engineering  
Khalifa University, Abu Dhabi, UAE

---

### Abstract

*A simple, yet powerful analytical model for determining the dynamic response of laterally loaded piles has recently been proposed in a series of papers by Karatzia and Mylonakis. The method is essentially a finite-element formulation, based on the evaluation of a set of energy integrals to establish the dynamic stiffness and damping matrices at the pile head. The key ideas/assumptions behind the method are: (1) the soil around the pile is replaced by a bed of dynamic Winkler springs and dashpots accounting for soil stiffness and energy dissipation; (2) a shape function for pile deflection is employed along the whole pile length in each vibration mode; (3) the associated integrals can be solved in closed form. Solutions have been obtained for different soil profiles which provided realistic predictions of pile response to flexural loads. An implicit assumption of the method lies in the use of real-valued shape functions. While such functions greatly simplify the analysis by separating real and imaginary parts (thus leading exclusively to real-valued integrals), they have the disadvantage of ignoring the phase differences between pile movements at different depths.*

*This paper recognises that this simplification can lead to inaccurate results for inhomogeneous soil profiles, especially at high frequencies where phase differences among different points along the pile are significant. To overcome the problem, the possibility of using complex-valued shape functions, analogous to those employed in spectral finite-element methods is explored. It is shown, through comparison with rigorous numerical solutions (including FEM and BEM), that use of complex-valued shape functions improves the predictive power of the method.*

**Keywords:** Pile, Winkler, Finite Elements, Spectral Elements, Shape Function, Virtual Work.

---



## 1 INTRODUCTION

Winkler based models are well established for use in elastodynamic analysis of laterally loaded piles. Early work provided analytical expressions for the spring and dashpot coefficients based on a horizontal soil “slice” model [1, 2, 3]. Several subsequent studies provided solutions for pile stiffness and damping in homogeneous and inhomogeneous media, as well as kinematic response coefficients to seismic excitation [4, 5, 6, 8, 9, 10, 11, 12, 15, 16, 25, 26, 27]. A difficulty in employing such solutions in design lies in the inability to derive exact solutions for inhomogeneous media in the dynamic regime. An alternative approach is explored in this paper, by means of an energy formulation analogous to those used in finite-element methods, based on single shape function for the whole pile length. The method was introduced in pile dynamics by Dobry and Roesset [6] and later extended in a series of papers by Mylonakis and co-workers [8, 9, 10, 11, 16, 26]. The main assumptions of the method are: (1) the soil around and under the pile can be replaced by a bed of dynamic springs and dashpots accounting for soil stiffness and pile-soil energy dissipation (Winkler approximation); (2) a single shape function can be employed for the deflection of the whole pile for each vibration mode (Rayleigh approximation); (3) a virtual work formulation can be employed in which the associated one-dimensional integrals can be evaluated in closed form. In this way, the three-dimensional elastodynamic problem reduces to a handful of one-dimensional integrals which can be evaluated in closed form for different inhomogeneous soil media. The solutions have been shown to provide realistic predictions of pile response to flexural loads.

A simplification associated with the above method lies in the use of real-valued shape functions for pile deflection. While such functions greatly simplify the complex arithmetic by separating real and imaginary parts leading to exclusively real-valued integrals, they have the disadvantage of ignoring the phase differences between pile displacements at different depths. This paper recognises that this simplification can lead to inaccurate results for inhomogeneous soil profiles, especially at high frequencies where the phase differences between displacements at different elevations along the pile are significant. To overcome the problem, the possibility of using complex-valued shape functions, analogous to those employed in spectral finite element methods, is explored in this paper.

## 2 PROBLEM DEFINITION

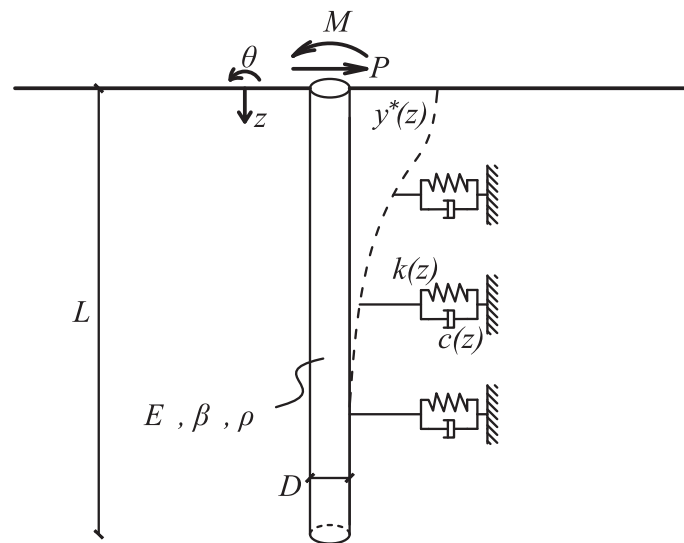


Figure 1: The dynamic Winkler model for a laterally loaded pile.

The dynamic Winkler model under consideration is shown in Figure 1. The pile is modelled as elastic Euler-Bernoulli beam with length,  $L$ , diameter,  $D$ , cross sectional area,  $A$ , second moment of area,  $I$ , mass density,  $\rho_p$ , elastic stiffness,  $E_p$  and hysteretic material damping coefficient,  $\beta_p$ . The last two terms can be expressed as a complex viscoelastic stiffness,  $E_p^* = E_p(1 + 2i\beta_p)$ .

A harmonic head load,  $P$ , and/or (anticlockwise positive) moment,  $M$ , are applied at an angular frequency,  $\omega$ , to the pile head. This is resisted by distributed Winkler springs and dashpots with coefficients  $k(z)$  and  $c(z)$ , respectively, which are often expressed as a complex-valued stiffness,  $k^* = k + i\omega c$ . The resulting pile displacement,  $y^*(z)$ , is also complex-valued, indicating a depth-varying phase difference from the applied load.

The governing equation describing the problem is obtained from the well-known expression for a beam under a distributed load [4]:

$$E_p^* I y^{*''''}(z) + [k(z) + i\omega c(z) - \rho_p A \omega^2] y^*(z) = 0 \quad (1)$$

where  $y^{*''''}(z)$  indicates the fourth derivative of  $y^*(z)$  with respect to depth,  $z$ .

Of most interest is the response at the pile head, which can be described using a complex-valued stiffness matrix,  $\mathbf{K}^*$ , defined as:

$$\mathbf{P} = \begin{bmatrix} P \\ M \end{bmatrix} = \mathbf{K}^* \mathbf{u}^* = \begin{bmatrix} K_{11}^* & K_{12}^* \\ K_{21}^* & K_{22}^* \end{bmatrix} \begin{bmatrix} y_0^* \\ \theta_0^* \end{bmatrix} \quad (2)$$

where  $\mathbf{P}$  and  $\mathbf{u}^*$  are the load and displacement vectors at the pile head, respectively, in which  $y_0^*$  is the pile head displacement and  $\theta_0^*$  is the pile head rotation (anti-clockwise positive). The components of the stiffness matrix  $K_{11}^*$ ,  $K_{22}^*$  and  $K_{12}^* (= K_{21}^*)$  are the swaying, rocking and cross swaying-rocking complex stiffnesses, respectively. Due to the linear-elastic nature of the problem, the matrix is symmetric ( $K_{12}^* = K_{21}^*$ ). In addition, with the sign convention chosen, all the stiffness terms are positive at low frequency.

For convenience, it is common to separate the complex stiffness components into real-valued spring and dashpot coefficients,  $K_{ij}$  and  $C_{ij}$ :

$$\begin{aligned} K_{ij} &= \mathcal{R}[K_{ij}^*] \\ C_{ij} &= \frac{1}{\omega} \mathcal{I}[K_{ij}^*] \end{aligned} \quad (3)$$

where  $\mathcal{R}[\ ]$  and  $\mathcal{I}[\ ]$  indicate the real and imaginary components, respectively.

### 3 CLOSED FORM SOLUTION

For the homogeneous case, where  $k(z) = k$  and  $c(z) = c$ , a complex wavenumber,  $\lambda^*$  can be introduced such that equation 1 reduces to:

$$\begin{aligned} y^{*''''}(z) + 4\lambda^{*4} y^*(z) &= 0 \\ \lambda^{*4} &= (k + i\omega c - \rho_p A \omega^2) / (4E_p^* I) \end{aligned} \quad (4)$$

This expression matches the well-known governing equation for the static Winkler model, with some terms substituted for complex-valued dynamic terms. Therefore, the static solution can be employed with the corresponding substitutions. For a long pile (longer than the active length, discussed later), the head stiffness matrix is given by [4]:

$$\mathbf{K}^* = \begin{bmatrix} 4E_p^* I \lambda^{*3} & 2E_p^* I \lambda^{*2} \\ 2E_p^* I \lambda^{*2} & 2E_p^* I \lambda^* \end{bmatrix} \quad (5)$$

This expression is simple and easy to implement. However, no closed-form solutions to equation 1 are known to the authors for any inhomogeneous stiffness profiles encountered in practice. In addition, although a closed-form solution is available for piles in layered soil (in the form of successive substitution into a formula for each layer), this results in an unwieldy expression. Instead, an approximate energy solution can be employed.

#### 4 ENERGY SOLUTION

Consider a pile in equilibrium subjected to an actual deflection  $y^*(z)$  under the influence of a set of external loads at the pile head and tip; the work done by a small virtual displacement,  $y_v(z)$ , on the system can be obtained by integrating equation 1:

$$E_p^* I \int_0^L y^{*''''}(z) y_v(z) dz + \int_0^L [k^*(z) - \rho_p A \omega^2] y^*(z) y_v(z) dz = 0 \quad (6)$$

This is known as the strong form of the equation; the desired weak form can then be obtained using integration by parts and the Euler-Bernoulli beam relationships at the pile head. Note that for long piles, the base response (and therefore upper integration limit) has negligible effect on the results. Therefore, these can be expressed as improper integrals:

$$P y_v(0) + M y_v'(0) = E_p^* I \int_0^\infty y^{*''}(z) y_v''(z) dz + \int_0^\infty [k^*(z) - \rho_p A \omega^2] y^*(z) y_v(z) dz = 0 \quad (7)$$

The stiffness matrix coefficients can then be obtained by dividing equation 7 by the displacement and virtual displacement at the pile head:

$$K_{ij}^* = E_p^* I \int_0^\infty \chi_i''(z) \chi_j''(z) dz + \int_0^\infty [k^*(z) - \rho_p A_p \omega^2] \chi_i(z) \chi_j(z) dz \quad (8)$$

where  $\chi_i(z)$  and  $\chi_j(z)$  are dimensionless, unitary shape functions describing the displacement and virtual displacement variation with depth, respectively.

A similar approach has previously been employed by [5, 6, 7] to obtain pile head dashpot coefficients for the swaying mode ( $C_{11}$ ). In the form shown here (for complex pile head stiffness), the method was first employed by [8]. Analytical expressions for layered soil were first included in [4, 8], a linear Winkler stiffness profile in [9], a parabolic Winkler stiffness profiles in [10] and a power-law and an exponential Winkler stiffness profiles in [11].

These solutions have used the following shape functions from the solution for homogeneous Winkler stiffness profiles [8]:

$$\begin{aligned} \chi_1(z) &= e^{-\mu z} [\sin(\mu z) + \cos(\mu z)] \\ \chi_2(z) &= \frac{e^{-\mu z}}{\mu} \sin(\mu z) \end{aligned} \quad (9)$$

where  $\mu$  is a real-valued average wavenumber analogous to  $\lambda^*$  for the static case ( $\omega = 0$ ), the inverse of which can be used as a characteristic pile wavelength [12]. For homogeneous profiles,  $\mu$  is set equal to  $\lambda^*$  in equation 4 with  $\omega = 0$  (the static case), calculating  $\mu$  for other Winkler stiffness profiles is discussed later. Note that the component  $\mathbf{K}^*$  ( $K_{ij}^*$ ) obtained in equation 8 corresponds to the subscripts of the shape function chosen for  $\chi_i$  and  $\chi_j$  [e.g.  $K_{ij}^*$  is obtained using  $\chi_i = \chi_1$  and  $\chi_j = \chi_2$ ].

These real-valued shape functions neglect the difference in phase of the response down the pile. However, they have the significant advantage that equation 8 can easily be separated into real-valued pile head stiffness and dashpot coefficients using equation 3. The pile head stiffness terms are given by [10, 11]:

$$K_{ij} = E_p I \int_0^\infty \chi_i''(z) \chi_j''(z) dz + \int_0^\infty k(z) \chi_i(z) \chi_j(z) dz - \rho_p A_p \omega^2 \int_0^\infty \chi_i(z) \chi_j(z) dz \quad (10)$$

The first two terms (the contribution of the pile flexural stiffness and soil stiffness, respectively) make up the static pile head stiffness and are independent of  $\omega$ . The last term is the contribution of the pile inertia and is often neglected in the analysis as it is typically a minor component [11].

The pile head damping terms are given by [10, 11]:

$$C_{ij} = \frac{2\beta_p E_p I}{\omega} \int_0^\infty \chi_i''(z) \chi_j''(z) dz + \frac{2\beta_s}{\omega} \int_0^\infty k(z) \chi_i(z) \chi_j(z) dz + \int_0^\infty c_r(z) \chi_i(z) \chi_j(z) dz \quad (11)$$

where the Winkler dashpot coefficient,  $c(z)$ , is split into the (hysteretic) material and radiation components,  $c_h$  and  $c_r$ , respectively, and  $\beta_s$  is the soil hysteretic material damping coefficient. The three terms of equation 11 correspond to the contributions of the pile material damping, soil material damping and radiation damping, respectively.

The simplification in equations 10 and 11 allows the pile head response to be evaluated from a few simple, real-valued, integrals. If the inertial term in equation 10 is neglected (note that in this paper it is not), only three unique integrals need to be evaluated. The first two are common to both equations, the first of which is also independent of the Winkler stiffness profile encountered. Analytical solutions for these integrals in closed-form are collated by [11] for all of the aforementioned Winkler stiffness profiles and a simple solution is included in [13] based on the result for homogeneous profiles.

## 5 APPLYING THESE SOLUTIONS: HOMOGENEOUS SOIL

In order to apply these solutions for homogeneous soil, only the Winkler spring and dashpot coefficients must be determined.

### 5.1 Selection of $k^*$

Various solutions are available for the selection of  $k^*$ , including analytical approximations and empirical functions fitted against numerical continuum solutions. The Winkler spring stiffness,  $k$ , is often assumed to be proportional to the elastic and/or shear moduli,  $E_s$  and  $G_s$ , respectively while the radiation dashpot coefficient,  $c_r$ , is often assumed to be proportional to the soil shear wave velocity,  $V_s = \sqrt{G_s/\rho_s}$ , where  $\rho_s$  is the soil mass density. A number of available expressions are tabulated in [14, 15, 16]. In this paper, three different approaches are considered.

The first approach is the horizontal slice model employed by [1, 2, 3]. The soil is modelled as discrete, infinite, horizontal slices under zero vertical normal strain. The equivalent spring and dashpot at the pile-soil interface is then solved in rigorously in closed-form. In [3] the hysteretic material damping is incorporated using complex-valued moduli from the correspondence principle of viscoelasticity [17]:

$$\begin{aligned} G_s &\rightarrow G_s^* = G_s(1 + 2i\beta_s) \\ E_s &\rightarrow E_s^* = E_s(1 + 2i\beta_s) \\ V_s &\rightarrow V_s^* = V_s \sqrt{1 + 2i\beta_s} \end{aligned} \quad (12)$$

This results in the following expression for the complex-valued stiffness,  $k^*$ :

$$\begin{aligned} k^* &= \pi G_s^* S^2 \frac{4K_1(q)K_1(s) + sK_1(q)K_0(s) + qK_0(q)K_1(s)}{sK_1(q)K_0(s) + qK_0(q)K_1(s) + qsK_0(q)K_0(s)} \\ S &= \frac{i\omega D}{2V_s \sqrt{1 + 2i\beta_s}} \\ q &= S \sqrt{\frac{1 - 2\nu_s}{2(1 - \nu_s)}} \end{aligned} \quad (13)$$

where  $K_\nu()$  is the modified Bessel function of the second kind of order  $\nu$ . While the analytic nature of this expression is appealing, it does yield zero static stiffness at low frequencies. In addition, due to the Bessel functions, this expression cannot be conveniently separated into real and imaginary parts in closed form.

As an alternative, [18] provided the simple expression in equation 14, which was fitted against numerical finite element results for a pile embedded in a homogeneous half space. The hysteretic damping term is treated approximately by only considering the effect on the real part of the stiffness.

$$\begin{aligned} k &= 1.2E_s \\ c_r &= 5\rho_s V_s D \\ c_h &= 2\beta_s \frac{k}{\omega} \end{aligned} \quad (14)$$

Finally, the model employed by [11] is considered. This model uses the [19] approach previously applied to this problem by [20, 21], which yields an improved version of the horizontal slice model that gives finite stiffness at low frequency. However, unlike in the previous models, this is only used employed for the real-valued coefficient, for which a simplified approximate expression is developed using the asymptotic behaviour of the Bessel functions. For the radiation damping coefficient, this model employs an improved version of the cone model introduced by [7]. Each horizontal slice is split into infinitesimal independent sectors through which both shear and compression waves propagate, resulting in a frequency dependant expression in terms of Bessel functions to which [11] fit the simple expression in equation 15. The hysteretic damping term is treated using the same approximation as in equation 14.

$$\begin{aligned} k &= \frac{4\pi G_s \eta_u^2}{(1+\eta_u^2)[\ln(4/\alpha_c) - \gamma] + \ln(\eta_u)} \\ c_r &= \pi \rho_s V_s D \left[ \frac{1}{4} + \frac{4}{5} \sqrt{\frac{2}{1-\nu_s}} \right] \left( \frac{\omega D}{V_s} \right)^{-0.4} \\ c_h &= 2\beta_s \frac{k}{\omega} \end{aligned} \quad (15)$$

where  $\gamma$  ( $\approx 0.577$ ) is the Euler-Mascheroni constant,  $\eta_u = \sqrt{(2 - \nu_s)/(1 - \nu_s)}$  is a compressibility coefficient and  $\alpha_c$  is a stiffness parameter (sometimes interpreted as a dimensionless cut-off frequency). Reference [11] provides simple power-law relationships between  $\alpha_c$  and the pile-soil stiffness ratio,  $E_p/E_s$ , for different soil profiles and pile head fixity conditions. For fixed head piles in homogeneous soil  $\alpha_c$  is given by:

$$\alpha_c = 1.227 \left( \frac{E_p}{E_s} \right)^{-1/4} \quad (16)$$

## 5.2 Comparison of methods

The performance of the closed-form and energy methods for each  $k^*$  is shown in Figure 2, in comparison with numerical continuum results from [22, 23]. The former used a boundary element method developed in [24] and the latter a finite element approach. The results are normalised by the well-known dimensionless frequency,  $a_0 = \omega D/V_s$ .

In general, the analytical closed-form solution matches the continuum results reasonable well. The energy solution also performs very well at low frequencies, with a low discrepancy from the closed-form solution. However, as frequency increases, it tends to underestimate the pile head stiffness and overestimate the pile head damping coefficient.



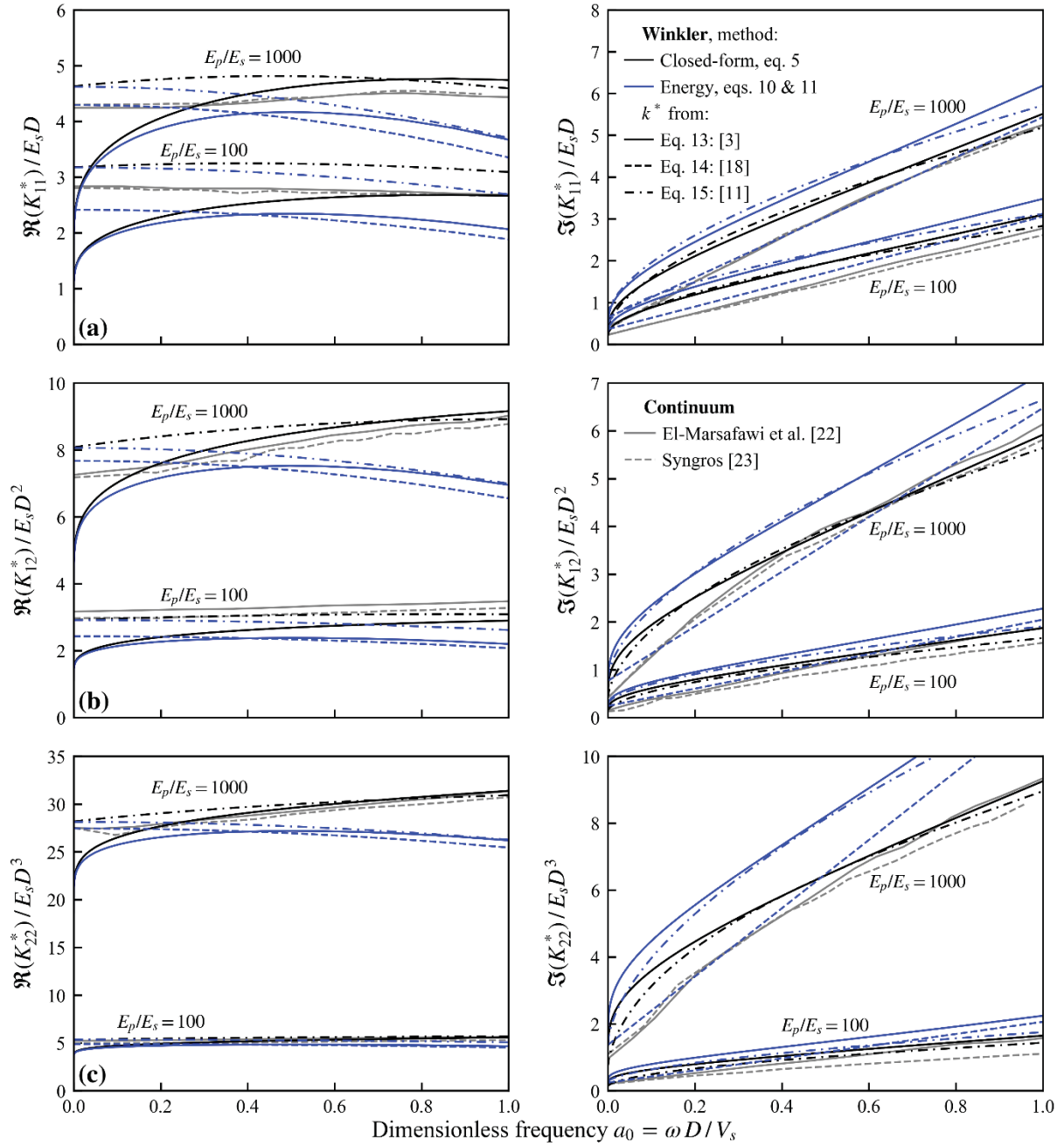


Figure 2: Normalised dynamic lateral head stiffness of piles embedded in a homogeneous half space; (a)  $K_{11}^*$  (b)  $K_{21}^*$  (c)  $K_{22}^*$  ( $\nu_s = 0.4$ ,  $\beta_s = 0.05$ ,  $\nu_p = 0.25$ ,  $\beta_p = 0.01$ ,  $\rho_p/\rho_s = 1.25$ ) (numerical data from Syngros 2004).

## 6 COMPLEX-VALUED SHAPE FUNCTIONS

In order to get better predictions at higher-frequencies, [16] suggest using complex valued shape functions,  $\chi_i^*$  and  $\chi_j^*$  based on the dynamic (rather than static) response for the homogeneous case. Therefore, equation 8 can be rewritten in the form:

$$K_{ij}^* = E_p I \int_0^\infty \chi_i^{*''}(z) \chi_j^{*''}(z) dz + \int_0^\infty [k^*(z) - \rho_p A_p \omega^2] \chi_i^*(z) \chi_j^*(z) dz \quad (17)$$

where  $\chi_1^*$  and/or  $\chi_2^*$ , given below, are substituted for  $\chi_i^*$  and  $\chi_j^*$  to get each of the complex stiffness terms as before.

$$\begin{aligned}\chi_1^*(z) &= e^{-\mu^* z} [\sin(\mu^* z) + \cos(\mu^* z)] \\ \chi_2^*(z) &= \frac{e^{-\mu^* z}}{\mu^*} \sin(\mu^* z)\end{aligned}\quad (18)$$

$\mu^*$  is now directly analogous to  $\lambda^*$ ; for homogeneous soil, if  $\mu^*$  is set equal to  $\lambda^*$ , equation 17 reproduces the complex stiffness terms from the closed-form solution exactly, as the phase difference between the responses at different depths is accounted for correctly. However, for inhomogeneous soil, the integrals in equation 17 are now also complex-valued, and harder to compute than the solution with real-valued shape functions.

## 7 APPLYING THESE SOLUTIONS: INHOMOGENEOUS SOIL

In order to compare the performance of the two different assumptions (real-valued and complex-valued shape functions), an example problem involving a pile embedded in an inhomogeneous half-space is considered. In this example, soil stiffness varies according to a linear function of depth with zero surface stiffness. As with the homogeneous case, a method to calculate  $k^*$  must be chosen. However, for inhomogeneous soil an appropriate method for selecting  $\mu$  or  $\mu^*$  must also be selected.

### 7.1 Selection of $k^*$

Only two of the  $k^*$  calculation approaches employed for homogeneous soil have been employed for this case, as the function fitted by [18] is specific to homogeneous soil. Equations 13 and 15 can be used as before, with  $G_s$  and  $V_s$  simply referring to the values at each depth, resulting in an inhomogeneous Winkler stiffness profile. In addition, the modified expression for  $\alpha_c$  for this case provided by [11] should be employed in place of equation 16:

$$\alpha_c = 1.667 \left( \frac{E_p}{E_{sD}} \right)^{-1/5} \quad (19)$$

where  $E_{sD}$  is the soil stiffness at a depth of one pile diameter.

However, the resulting functions describing the inhomogeneity in Winkler spring coefficients are not directly proportional to those describing the soil stiffness or shear wave velocity. Instead, for the solution described in equations 10 and 11, [11] suggests calculating  $k^*$  only at a depth of one diameter.  $k$  is then assumed proportional to the soil stiffness and  $c_r$  to the soil shear wave velocity (the square root of soil stiffness).

### 7.2 Selection of $\mu$

For inhomogeneous soils,  $\mu$  can be approximated as the average (static)  $\lambda$  value over a certain depth. An appropriate depth, suggested by [8], is the pile active length,  $L_a$ , which can intuitively be interpreted as the depth over which the soil stiffness has an effect on the pile head response, resulting in the following expression for  $\mu$ :

$$\mu = \frac{1}{L_a} \int_0^{L_a} \left( \frac{k(z)}{4E_p I} \right)^{1/4} dz \quad (20)$$

A number of expressions are available in the literature for  $L_a$ , based on various different definitions. Particularly useful to application is the value of  $\mu L_a = 2.5$  suggested by [25], this allows equation 20 to be used iteratively to obtain  $L_a$  and  $\mu$  for any arbitrary Winkler stiffness profile. For the specific case of power-law Winkler stiffness profiles, this was solved analytically by [26]. For the linear profile considered here this results in the expression:

$$L_a/D = \left[ \left( \frac{5}{4} \right)^8 \frac{\pi E_p}{k_D} \right]^{1/5} \quad (21)$$

where  $k_D$  is the Winkler spring stiffness at one diameter depth.

### 7.3 Selection of $\mu^*$

$\mu^*$  can be calculated using a similar approach as  $\mu$ , taking the average (complex)  $\lambda^*$  value over the active pile length:

$$\mu = \frac{1}{L_a} \int_0^{L_a} \lambda^*(z) dz$$

$$\lambda^*(z) = \left( \frac{k^*(z) - \rho_p A_p \omega^2}{4E_p^* I} \right)^{1/4} \quad (22)$$

As  $\mu^* L_a$  is complex valued, the expression suggested by [25] cannot be employed. Instead, the simple expression fitted by [23] to finite element results in the same soil profile is used here:

$$L_a/D = 2.5 \left( \frac{E_p}{E_{sD}} \right)^{1/5} \quad (23)$$

### 7.4 Comparison of methods

The performance of the two different shape function assumptions is shown in Figure 3, in comparison with numerical continuum results from [22, 23]. The results are normalised as before, using the shear wave velocity 20 diameters depth,  $V_{s,20D}$ , which was the pile length employed in the continuum solutions. An alternative normalisation,  $a_{0\mu}$ , (shown in equation 24) was suggested in [12, 27] using  $\mu$  directly. However, this was not suitable in this case due to the different  $\mu$  definition for each solution.

$$a_{0\mu} = \frac{\omega}{\mu V_s(1/\mu)} \quad (24)$$

As for the homogeneous case, the energy method with real-valued shape functions matches the continuum results for low frequencies, but significantly underestimates the pile head stiffness and overestimates the pile head damping coefficient at higher frequencies. However, the complex-valued shape functions result in a solution much closer to the continuum results. Note that a rigid boundary was employed in both continuum solutions as perfect absorbing boundaries are not available for the inhomogeneous soil profile. This is not a limitation for the Winkler model, therefore the undulations of the impedance functions and cut-off frequency evident in the continuum results are not present.

## 8 CONCLUSIONS

An energy method for predicting the head response of laterally-loaded piles according the dynamic Winkler model has been investigated and extended. The performance of the approach with the commonly employed, real-valued shape functions has been compared with numerical continuum results, as well as the closed-form (Winkler) analytical solution for homogeneous soil and an alternative solution employing complex-valued shape functions in inhomogeneous soil. Three different methods for selecting the Winkler stiffness coefficients have been employed. The following conclusions can be drawn:

- The simplifying assumption of real-valued shape functions allows analytical expressions for the (real-valued) pile head stiffness and damping terms to be obtained, such as those provided in [11].

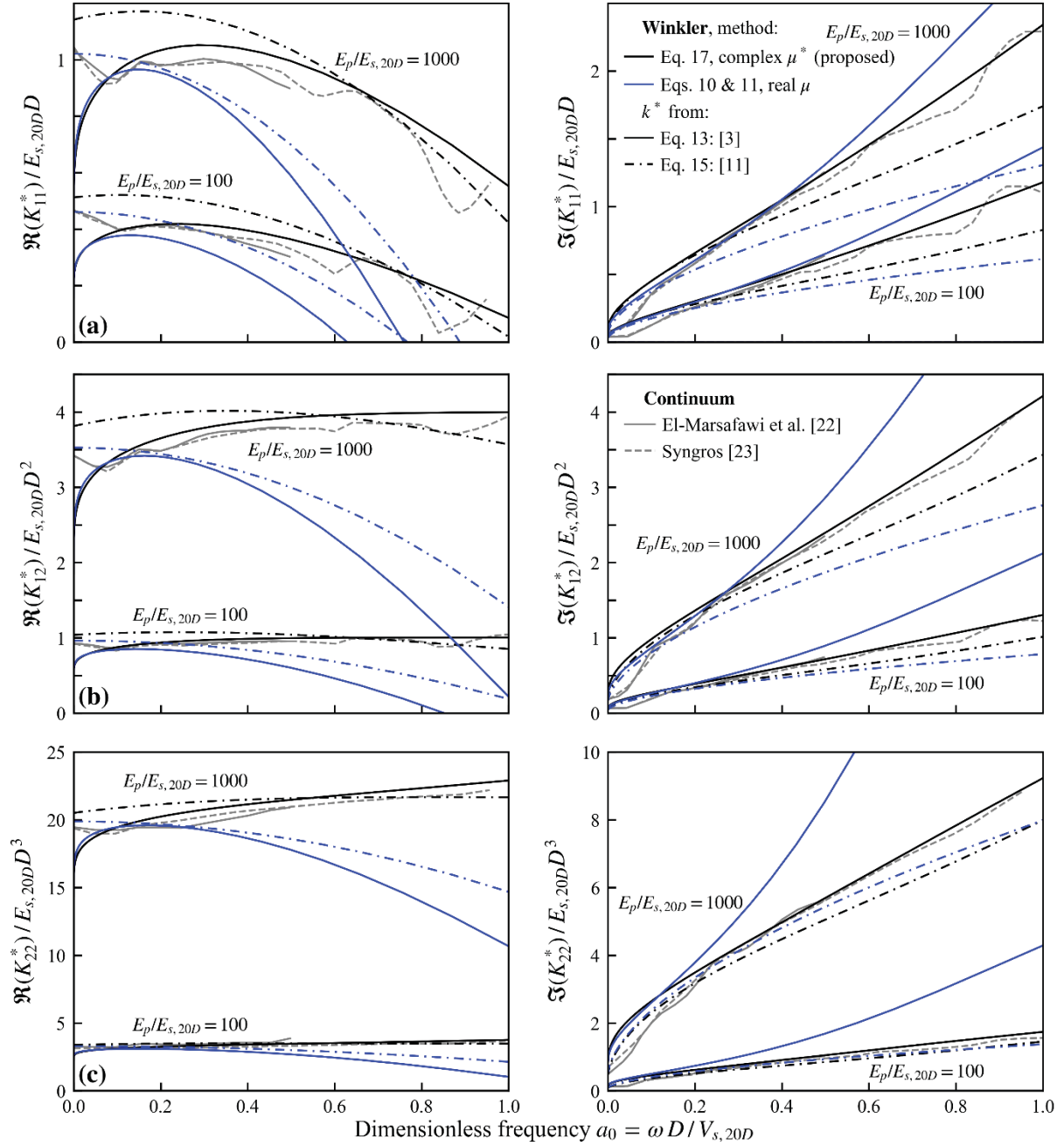


Figure 3: Normalised dynamic lateral head stiffness of piles embedded in an inhomogeneous soil with stiffness varying linearly with depth from a value of zero at the surface; (a)  $K_{11}^*$  (b)  $K_{21}^*$  (c)  $K_{22}^*$  ( $\nu_s = 0.4$ ,  $\beta_s = 0.05$ ,  $\nu_p = 0.25$ ,  $\beta_p = 0.01$ ,  $\rho_p/\rho_s = 1.25$ ) ( $L_a$  and numerical data from Syngros 2004).

- At low frequencies, the energy method with real-valued shape functions gives similar results to the analytical, closed-form Winkler solution for homogeneous soil. However, as the frequency increases it underestimates pile head stiffness and overestimates pile head damping.
- The solution employing complex-valued shape functions reproduces the homogeneous analytical solution in closed-form.
- For the inhomogeneous soil considered, both real-valued and complex-valued shape functions provide similar results at low frequencies. However, at higher frequencies the real-

valued shape functions result in underestimating pile head stiffness and overestimating pile head damping. This effect is more pronounced than for homogeneous soil.

- With the more rigorous complex-valued shape functions, the Winkler model performs well compared to the numerical continuum results in both the homogeneous and inhomogeneous soil profiles considered.

## REFERENCES

- [1] V.A. Baranov, On the calculation of excited vibrations of an embedded foundation (in Russian). *Voprosy Dynamiki i Prochnosti*, (14), Polytechnic Institute, Riga, Latvia, 195-209, 1967.
- [2] M. Novak, Dynamic stiffness and damping of piles. *Canadian Geotechnical Journal*, **11**(4), 574-578, 1974.
- [3] M. Novak, T. Nogami, F. Aboul-Ella, Dynamic soil reactions for plane strain case. *Journal of Engineering Mechanics, ASCE*, **104**(4), 953-959, 1978.
- [4] G. Mylonakis, G. Gazetas, Lateral vibration and internal forces of grouped piles in layered soil. *Journal of Geotechnical and Geoenvironmental Engineering, ASCE*, **125**(1), 16-25, 1999.
- [5] M.J. O'Rourke, R. Dobry, *Spring and dash pot coefficients for machine foundation on piles*. American Concrete Institute, Detroit, MI, USA. Report number SP-10, 177-198, 1978.
- [6] R. Dobry, E. Vicente, M.J. O'Rourke, J.M. Roesset, Horizontal stiffness and damping of single piles. *Journal of Geotechnical Engineering, ASCE*, **108**(3), 439-459, 1982.
- [7] G. Gazetas, R. Dobry, Simple radiation damping model for piles and footings. *Journal of Geotechnical Engineering, ASCE*, **110**(6), 937-956, 1984.
- [8] G. Mylonakis, *Contributions to static and seismic analysis of piles and pile-supported bridge piers*. Ph.D. thesis, State University of New York at Buffalo, 1995.
- [9] G. Mylonakis, D. Roumbas, Lateral impedance of single piles in inhomogeneous soil. *Proceedings of the 4th International Conference on Recent Advances in Geotechnical Earthquake Engineering and Soil Dynamics*, paper 6.27, San Diego, CA, USA, March 26-31, 2001.
- [10] X. Karatzia, G. Mylonakis, Horizontal response of piles in inhomogeneous soil: simple analysis. C. Soccodato, M. Maugeri eds. *Proceedings of the 2nd International Conference on Performance-based Design in Earthquake Geotechnical Engineering*, No 1117, Taormina, Italy, May 28-30 2012.
- [11] X. Karatzia, G. Mylonakis, Horizontal stiffness and damping of piles in inhomogeneous soil. *Journal of Geotechnical and Geoenvironmental Engineering, ASCE*, **143**(4), 04016113, 2017.
- [12] E. Rovithis, G. Mylonakis, K. Pitilakis, Dynamic stiffness and kinematic response of single piles in inhomogeneous soil. *Bulletin of Earthquake Engineering*, **11**(6), 1949-1972, 2013.



- [13] NEHRP, *Soil-structure interaction for building structures*. National Institute of Standards and Technology (NIST). Report number: GCR 12-917-21, 2012.
- [14] M. Shadlou, S. Bhattacharya, Dynamic stiffness of pile in a layered elastic continuum. *Géotechnique*, **64**(4), 303-319, 2014.
- [15] G. Anoyatis, A. Lemnitzer, Dynamic pile impedances for laterally-loaded piles using improved Tajimi and Winkler formulations. *Soil Dynamics and Earthquake Engineering*, **92**, 279-297, 2017.
- [16] G.E. Mylonakis, J.J. Crispin, Simplified models for lateral static and dynamic analysis of pile foundations. A.M. Kaynia eds. *Analysis of Pile Foundations Subject to Static and Dynamic Loading*, CRC Press, *in press*, 2021.
- [17] A.C. Pipkin, *Lectures on viscoelastic theory*. Springer, 1972.
- [18] J.M. Roesset, Stiffness and damping coefficients of foundations. M. O’Neil, R. Dobry eds. *Dynamic Response of Pile Foundations*, ASCE, 1-29, 1980.
- [19] V.Z. Vlasov, N.N. Leontiev, *Beams, Plates and Shells on Elastic Foundations*. Translated from Russian, Israel program for scientific translations, Washington, DC, USA. NIST No. N67-14238, 1966.
- [20] G. Mylonakis, Elastodynamic model for large-diameter end-bearing shafts. *Soils and Foundations*, **41**(3), 31-44, 2001.
- [21] G. Anoyatis, G. Mylonakis, A. Lemnitzer, Soil reaction to lateral harmonic pile motion. *Soil Dynamics and Earthquake Engineering*, **87**, 164-170, 2016.
- [22] H. El-Marsafawi, A.M. Kaynia, M. Novak, *Interaction factors and the superposition method for pile group dynamic analysis*. Geotechnical Research Center, Department of Civil Engineering, University of Western Ontario, Canada, Report number GEOT-1-92, 1992.
- [23] K. Syngros, *Seismic response of piles and pile-supported bridge piers evaluated through case histories*. Ph.D. thesis, The City College of the City University of New York, 2004.
- [24] A.M. Kaynia, E. Kausel, *Dynamic stiffness and seismic response of pile groups*. Department of Civil Engineering, Massachusetts Institute of Technology, Cambridge, MA, USA, Research report no. R82-03, 1982.
- [25] R. Di Laora, E. Rovithis, Kinematic bending of fixed-head piles in nonhomogeneous soil. *Journal of Geotechnical and Geoenvironmental Engineering, ASCE*, **141**(4), 04014126, 2015.
- [26] X. Karatzia, G. Mylonakis, Discussion of “Kinematic bending of fixed-head piles in non-homogeneous soil” by Raffaele Di Laora and Emmanouil Rovithis. *Journal of Geotechnical and Geoenvironmental Engineering, ASCE*, **142**(2), 07015042, 2016.
- [27] G. Anoyatis, R. Di Laora, A. Mandolini, G. Mylonakis, Kinematic response of single piles for different boundary conditions: analytical solutions and normalization schemes, *Soil Dynamics & Earthquake Engineering*, **44**, 183-195, 2013.

## ON THE EFFECTIVENESS OF EXPERIMENTALLY-DERIVED FOUNDATION IMPEDANCE FUNCTIONS

C. Amendola<sup>1</sup>, F. de Silva<sup>2</sup>, D. Ptilakis<sup>1</sup> and F. Silvestri<sup>2</sup>

<sup>1</sup> Dept. of Civil Engineering, Aristotle University of Thessaloniki, Greece  
e-mail: {chiaamen,dpitilakis}@civil.auth.gr

<sup>2</sup> University of Naples Federico II, Italy  
e-mail: {filomena.desilva,francesco.silvestri}@unina.it

---

### Abstract

*In the past decades, several experimental and analytical investigations showed that the dynamic behavior of buildings can be significantly affected by the interaction with a soft foundation soil. In such cases, the actual response of structures founded on shallow foundations can be successfully simulated if the structural model is equipped with springs and dashpots calibrated through frequency-dependent impedance functions. This paper discusses the results of a research project aimed at back-calculating the impedance functions of a shallow square foundation from records of the dynamic behavior of the EuroProteas soil-foundation-structure (SFS) facility, deployed at Euroseistest (Greece). To this aim, forced-vibration tests were executed under different frequencies and increasing loading amplitudes. The experimental impedances were compared with several analytical solutions available in the literature, accounting for different hypotheses on the subsoil model. This comparison improved when the shear wave velocity  $V_s$  used to define the analytical functions was reduced accounting for the strain level mobilized by the increasing amplitude of the applied force. A numerical model was realized in the SAP2000 software. The compliance of foundation soil has been introduced using elastic springs, the stiffness of which was calibrated considering either the analytical or the experimental impedances. The fundamental frequency obtained from a modal analysis of the SAP2000 model equipped with the springs calibrated on the experimental impedances turned out to reproduce the fundamental frequency of EuroProteas effectively measured on-site. Such results showed the effectiveness of using experimental impedance functions in the numerical simulations, especially when equivalent soil parameters are hard to define.*

**Keywords:** seismic soil-structure interaction; shallow foundations; forced-vibration tests; dynamic impedance functions

---

## 1. INTRODUCTION

It is customary in design practice to consider the structure fixed at its base, i.e. neglecting the interaction between the soil, foundation and structure (SFSI). Such hypothesis turns out to be realistic only for structures founded on very stiff soil. The up-to-date literature proves that neglecting SFSI effects may lead to an inaccurate evaluation of the actual seismic response of structures founded on soft soil [1]-[4]. The latter, instead, can be realistically simulated considering the deformability of the foundation soil through models endowed at their base through springs and dashpots [5],[6], whose stiffness and damping coefficients are calibrated through the frequency-dependent complex impedance functions.

Several analytical solutions [7]-[9] are available in the literature mostly considering simplified assumptions such as homogeneous soil with elastic behavior. Nevertheless, the equivalent stiffness in a layered soil volume involved in the foundation motion may be hard to define, if the wave velocity profile is not properly measured and accounted for. Moreover, the overburden pressure due to the structural weight can significantly influence the stress-dependent stiffness of the shallowest soil layers and, last but not the least, an increase in the loading force can lead to a non-negligible mobilization of non-linear soil behavior [1],[10]-[12].

In light of these uncertainties, full-scale experimental tests constitute an alternative strategy to evaluated frequency-dependent impedance functions. The earliest on-site studies available in the literature provided impedances for a limited range of frequency [13]-[15] or restricted to specific structures, such as an accelerograph station [16], and a nuclear reactor [17]. More recently, foundation impedance functions were identified from forced-vibration tests executed on a steel frame prototype in California [18] in the frequency range 5-15Hz.

This paper discusses the comparison between theoretical functions accounting for different hypotheses on the soil profile and the frequency-dependent experimental swaying and rocking impedances calculated from full-scale field tests on the single degree of freedom prototype EuroProteas in the EuroSeistest in Greece [19]. The objective of the study is to provide an evaluation on the reliability of field measurements of the impedance functions, in order to overcome the usual simplified assumptions on soil and foundation adopted by the analytical formulations.

## 2. IMPEDANCE FUNCTIONS

### 2.1. Definition

Impedances are complex expressions adopted to quantify the soil-foundation reaction when the structure is excited by a harmonic load,  $Fs$ , producing a shear force,  $V$ , and an overturning moment,  $M$ , on the foundation (see Figure 1a). The real part represents the stiffness and the imaginary part the radiation and material damping, which account for the energy scattered and dissipated through hysteresis in the subsoil [8]. When considering the degrees of freedom associated with the foundation swaying and rocking motion, the impedance function is a matrix that links  $V$  and  $M$  to the foundation displacement,  $u_f$ , and rotation,  $\theta_f$ . Moreover, for surface foundations, the out-of-diagonal terms can be neglected [9],[18], hence impedance matrix contains only the two diagonal terms, as follows:

$$\begin{bmatrix} \bar{V} \\ \bar{M} \end{bmatrix} = \begin{bmatrix} \bar{K}_x & 0 \\ 0 & \bar{K}_{\vartheta x} \end{bmatrix} \begin{bmatrix} u_f \\ \vartheta_f \end{bmatrix} \quad (1)$$

The terms of the impedance matrix are generally presented in the literature in the following explicit form:

$$\bar{K}_j = k_j(a_0)K_j + i\omega c_j(a_0)C_j \quad (2)$$

where  $j=x$  for the horizontal vibration and  $j=\vartheta x$  for rocking motion. The static stiffness  $K_j$ , and the dashpot coefficient,  $C_j$ , depend on the soil shear modulus,  $G$ , and Poisson's ratio,  $\nu$ , as well as on a characteristic dimension of the foundation (radius  $r$  or foundation half-width  $B$ ). The dynamic coefficients,  $k_j(a_0)$  and  $c_j(a_0)$ , depend on the vibration frequency,  $\omega$ , the characteristic dimension of the foundation,  $r$ , and the soil shear wave velocity,  $V_s$ , through the frequency factor,  $a_0 = \omega r / V_s$ .

Eqs. (1) can be solved in the frequency domain from the dynamic equilibrium of the structure-foundation system depicted in Figure 1b, as described by [19].

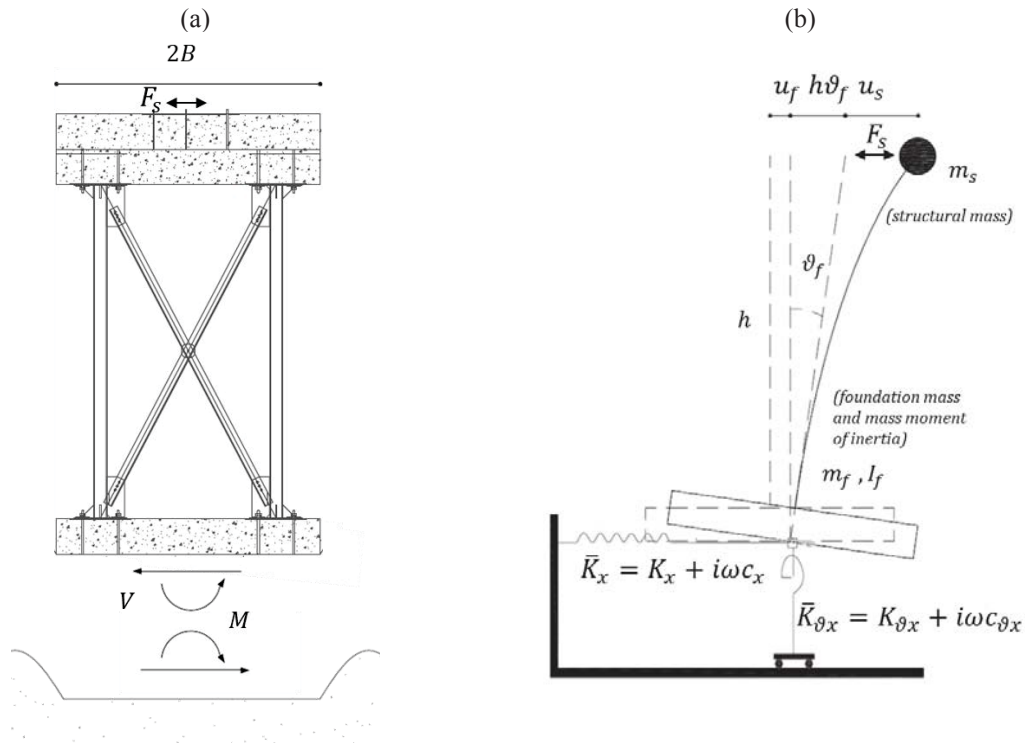


Figure 1: (a) Schematic view of the EuroProteas facility during forced vibration tests and associated reaction in the soil; (b) in-plane motion model of the single-degree-of-freedom system placed on translational and rotational springs adopted for the interpretation of experimental data. Modified after [19].

## 2.2. Analytical impedances

Different analytical functions are available in the literature for the real and complex impedance components, mostly referring to simplified conditions such as rigid massless foundation, more or less embedded in a subsoil which is typically assumed as an elastic homogeneous half-space [9],[10]. Nevertheless, [11],[20] suggest that the effect of soil inhomogeneity can be approximated with an equivalent halfspace with representative values of  $V_s$  and damping ratio averaged over depths equal to  $0.75r_{\vartheta x}$  and  $0.75r_x$ , where  $r_{\vartheta x}$  and  $r_x$  are the

rocking and swaying equivalent radii. Other widespread solutions (e.g. [21]) assume non-uniform soil profiles, including the case of a shallow layer stiffer or softer than the underlying halfspace [22]. Finally, non-linear soil behavior can play a crucial role under moderate to strong motions leading to a variation in the impedance functions. More recently, [23] introduced the effects of non-linear behavior, through a series of iterative linear analyses by updating the shear modulus and damping ratio consistently with the strain level induced by different excitation amplitudes. Reduction coefficients are then provided to reduce the real and imaginary parts of the analytical impedances by [9] when the excitation levels range from 0.01g to 1g.

Table 1 lists the analytical solutions and the associated hypotheses on the subsoil model adopted in this study to characterize the analytical impedance functions used for comparison with the experimental impedances back-calculated by [19]. The classic solution by Pais and Kausel [9] for a homogenous elastic halfspace was firstly selected for comparison; these equations are very similar to the widespread expressions given by [8] which therefore were not considered. Then, among all the different combinations of shear moduli of the layer and halfspace by Liou [22], a 50% reduction was considered between the shear moduli of the halfspace medium and that of the foundation deposit layer (i.e.  $G_2/G_1=0.5$ ). Finally, the solution by [23], accounting for soil nonlinearity, was checked. The dynamic coefficients corresponding to 0.01g and 0.2g were multiplied for the static stiffness expressions provided by [9].

Authors	Year	Soil
Pais and Kausel [9]	1988	Homogeneous elastic halfspace
Liou [22]	1993	Viscoelastic layer ( $G_1$ ) on a homogeneous halfspace ( $G_2$ ), $G_2/G_1=0.5$
Pitilakis et al. [23]	2013	Homogeneous equivalent linear (0.01g and 0.2g) halfspace

Table 1 Analytical impedance functions and associated subsoil models used for comparison with experimental data.

### 3. EXPERIMENTAL TESTS ON THE SISIFO PROJECT

#### 3.1. Experimental facility: EuroProteas in the Euroseistest

The above theoretical impedance functions were compared with the experimental results of the research project "Seismic Impedance for Soil-structure Interaction From On-site tests, SISIFO", funded by the HORIZON2020-supported program SERA the Seismology and Earthquake Engineering Research Infrastructure Alliance for Europe (<http://www.sera-eu.org/en/home/>). The SISIFO project aimed to investigate the effectiveness of different procedures of experimental identification of the impedance functions at prototype scale. For this reason, on-site tests were performed on the full-scale experimental facility of EuroProteas (Figure 2a) in the Euroseistest TST site located in the middle of Mygdonian valley in Northern Greece (Figure 2b).

EuroProteas consists of a simple steel frame supported by a 3m x 3m x 0.4m foundation raft, overtopped by two interconnected slabs each one of them identical to it (Figure 2a). The steel frame consists of four squared hollow steel columns (QHS 150mm x 150mm x 10mm) clamped on the foundation through steel bolts. L-shaped cross-braces (100mm x 100mm x 10mm) rigidly connect the steel columns all around the structure. The raft can be considered as an ideal 'shallow foundation' since the surrounding soil was intentionally removed before the execution of the tests discussed in the following. More details on the structural features are discussed by [19] and [24].



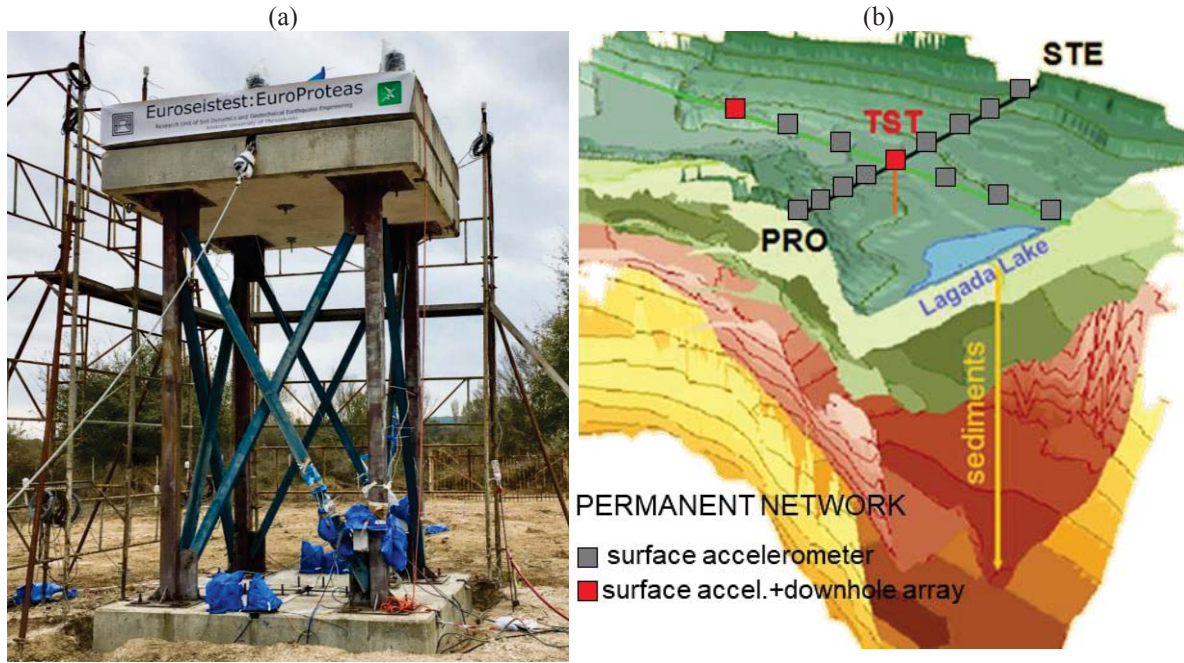


Figure 2 (a) Full-scale experimental facility of EuroProteas located (b) in the TST site, in the middle of the EuroSeistest.

The foundation subsoil was investigated and its dynamic properties were defined on the basis of extended geophysical and geotechnical in-situ and laboratory surveys reported in earlier studies [24]-[27]. The soil profile is composed of a first layer of silty-clayey sand about 7m thick, a layer of clayey-silty sand with local contents of gravel between 7m and 22m, and the last layer of marly silt and silty sand down to a depth of 30m. The shear wave velocity of the uppermost 6m was found to vary between 150m/s, as resulting from a DH test, and 100m/s, from the interpretation of further geophysical tests (see Figure 3a).

All the  $V_S$  profiles shown in Figure 3a refer to free-field investigations performed before the construction of the prototype. However, it must be observed that the increment of the mean effective stress due to the structural weight may have caused an increase in the initial shear stiffness at the shallowest depths [28]. Therefore, as suggested by [11],[18], the free-field velocity ought to be corrected to account for such a stiffening, by multiplying  $V_S$  for an overburden correction factor (hereafter  $OCF$ ) which can be computed as follows:

$$OCF = \left( \frac{\sigma'_v(z) + \Delta\sigma'_v(z)}{\sigma'_v(z)} \right)^{n/2} \quad (3)$$

where  $\sigma'_v(z)$  and  $\Delta\sigma'_v(z)$  are the effective vertical lithostatic stress and its increment due to the structural weight,  $n$  is an exponent increasing with soil plasticity index [29],[30]. Figure 3b reports the variation of  $OCF$  with depth between  $z=0.1$ m and  $z=6$ m (black solid line), calculated assuming  $n=0.5$  and adopting the Steinbrenner's solution for the vertical stress increment [31]. As expected,  $OCF$  is maximum at the foundation level and sharply decreases with depth. Previous studies in the literature [20] suggest to correct  $V_S$  profiles for  $OCF$  values averaged through appropriate depth intervals, in order to obtain a mean equivalent velocity profile. Following such a suggestion, Figure 3b also reports the values of  $OCF$  averaged over 50% (red solid line) and 100% (blue solid line) of the foundation width, i.e.  $2B$ .

The average increase of the free-field  $V_S$  is estimated to be equal to 35% ( $\overline{OCF}_B=1.35$ ) up to the foundation half-width,  $B$ , and 22% ( $\overline{OCF}_{2B}=1.22$ ) up to the total foundation dimension,  $2B$ . It follows that the actual velocity profile may present an inversion, with a greater value of  $V_S$  in the shallowest range of depths (i.e., that most interested by the foundation rocking motion) with respect to the soil volume mobilized by the foundation swaying.

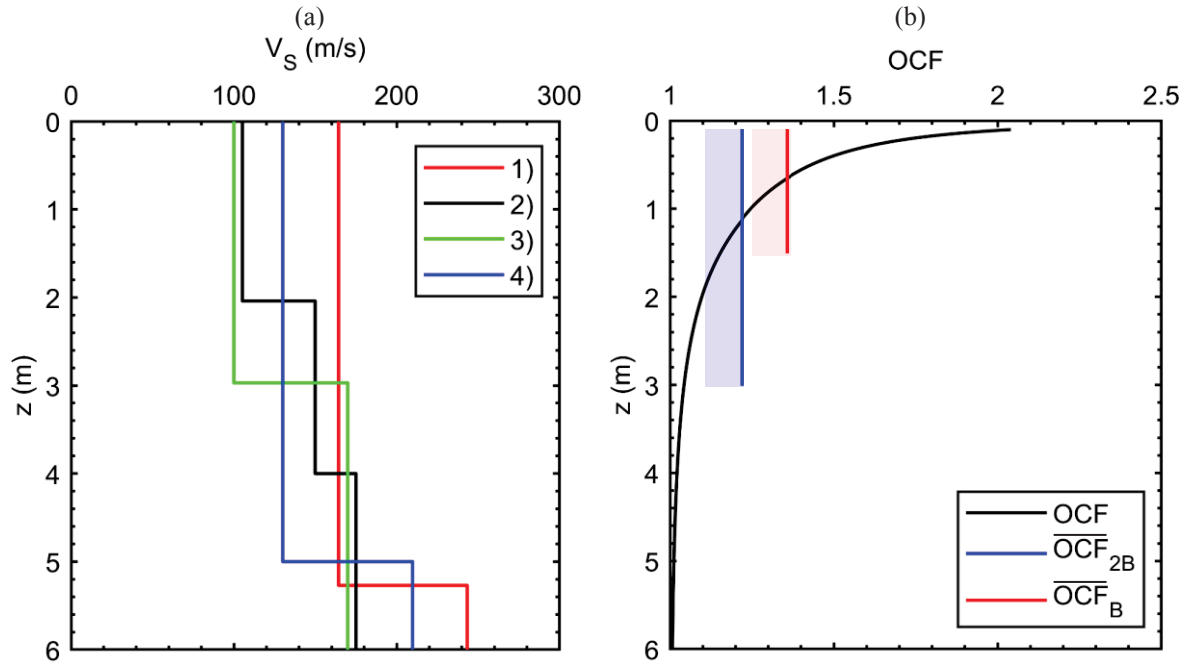


Figure 3 (a) Shear wave velocity profiles from 1) down-hole test before EuroProteas construction, 2) at a site approximately 50m away from the facility [25], 3) reference model of the valley cross-section from updated geophysical, geotechnical and numerical modeling [26], 4) profile from detailed geotechnical and geophysical surveys [27], as adapted from [24]; (b) overburden correction factor,  $OCF$ , for the EuroProteas foundation soil and its average along the foundation half-width,  $B$ , and width,  $2B$ .

### 3.2. Instrumentation layout and performed tests

The facility was instrumented with triaxial accelerometers (CMG-5TD and CMG-5TCDE, Guralp Systems Ltd) to record both the structural and the foundation response (Figure 4). In particular, the instrumentation layout consists of 5 accelerometers mounted on the roof, three along the axis parallel to the direction of shaking (in-plane) and two at the opposite corners of the slab, to capture possible out-of-plane motion. Additionally, four triaxial accelerometers were mounted in pairs at the opposite edges of the foundation slab along the direction of shaking, in order to ensure and validate the proper recording of the foundation's translational and rotational response. All the instruments were connected to external global positioning system (GPS) antennas and their sampling frequency was set to 200Hz. They were oriented along the positive  $x$ -direction of loading, which forms an angle of 30 degrees with the magnetic North. However, for sake of simplicity, the  $x$  and the  $y$  component of each record were tagged as North and East, respectively, as shown in Figure 4.

The dynamic response of the instrumented facility was firstly identified under random ambient noise test, in which the structural response was recorded with no external excitation. Free-vibration tests were also carried out by a ‘snap-back’ procedure, in which the roof was initially slightly displaced and thereafter released to induce the free vibration of the prototype structure (see [19]). The structure was then subjected to sinusoidal forced vibration tests, by

changing the frequency in a range of interest of earthquake engineering, i.e. from 1Hz to 10Hz, through a shaker mounted on the roof slab. The MK-500U (ANCO Engineers Inc) eccentric mass vibrator system was adopted as a source of harmonic excitation. The following equation controls the generated harmonic load:

$$F_s = E(2\pi f)^2 \sin(2\pi ft) \quad (4)$$

The frequency of the shaker force was held constant until the system reached the steady state. Four different forced vibration test series were executed, by changing the frequency of the excitation and adjusting the rotating mass through the vibrator's eccentricity of the shaker. Each applied frequency was locked for 60s and then incremented by 1Hz steps in the range 1Hz – 10Hz. The frequency step was reduced to 0.5Hz when approaching the first vibration mode, in order to more accurately record the resonance response.

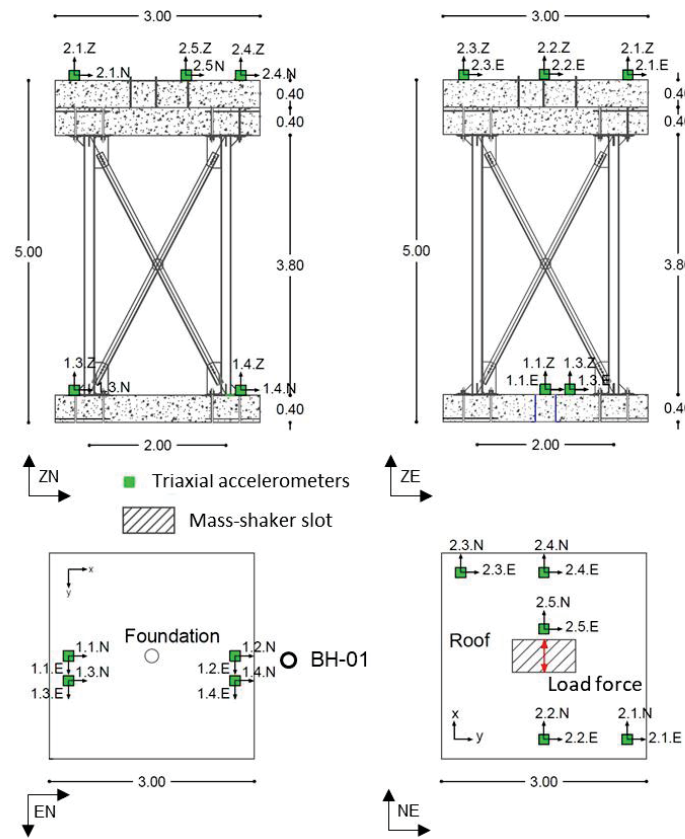


Figure 4 Instrumentation layout of the facility during the forced vibration tests.

Table 2 reports the details of the lowest and highest force amplitude tests, i.e. Forced-A and Forced-D, yielding the experimental impedance functions which were taken for comparison with the analytical solutions listed in Table 1.

Experiment	Frequency range $f = \omega/2\pi$	Force range (min-max) $E\omega^2$
(-)	(Hz)	(kN)
Forced-A	1-2-3-3.5-4-4.5-5-6-7-8-9-10	0.07-7.30
Forced-D	1-2-2.5-3-3.5-4-5-6-7-8	0.45-28.58

Table 2 Force and frequency range applied during Forced-A and Forced-D tests.

### 3.3. Experimental impedance functions

As detailed in [19], experimental impedance functions were back-calculated through Eqs. (1) from the data recorded during the forced vibration tests. The left side of the system of Eqs. (1) are the shear force,  $V$ , and the overturning moment,  $M$ , acting on the foundation. In the time domain, they result from the difference between the applied loads ( $F_s$  and  $F_s h$ ) and the inertia forces generated by the structural mass,  $m_s$ , the foundation mass,  $m_f$ , and its mass moment of inertia,  $I_f$ . The computational details are reported in [19] and here omitted for sake of brevity. The right side of Eqs. (1), i.e. the displacement array, defines the motion of the rigid foundation slab by two independent swaying,  $u_f$ , and rocking,  $\vartheta_f$ , kinematic components.

The foundation rocking,  $\vartheta_f$ , was computed as the difference between the double integration of vertical records 1.3Z and 1.4Z, divided by their distance. The foundation swaying,  $u_f$ , was calculated from the displacement obtained by integrating the acceleration recorded by sensor 1.4N minus the displacement induced by the foundation rocking, i.e.  $\vartheta_f h_f$ . The applied force defining the load vector was calculated according to Eq. (4), where the phase angle,  $\varphi$ , between the applied force itself and the response was assumed to equal to that characterizing the force-displacement time shift of a simple SDOF oscillator [32] with the overall damping  $\xi=5\%$  and the natural frequency  $f_n = 3.4\text{Hz}$  for Forced-A and  $3.0\text{Hz}$  for Forced-D which were inferred from the interpretation of noise and snap-back tests [19].

Figure 5 shows the real part of impedance functions calculated in [19] from Forced-A (full circles) and Forced-D (hollow circles) tests, for both swaying and rocking motions. As it can be observed from the plots, both swaying and rocking dynamic stiffness decrease with the increment of the excitation force, i.e. from Forced-A to -D, apparently due to the mobilization of non-linear soil behavior.

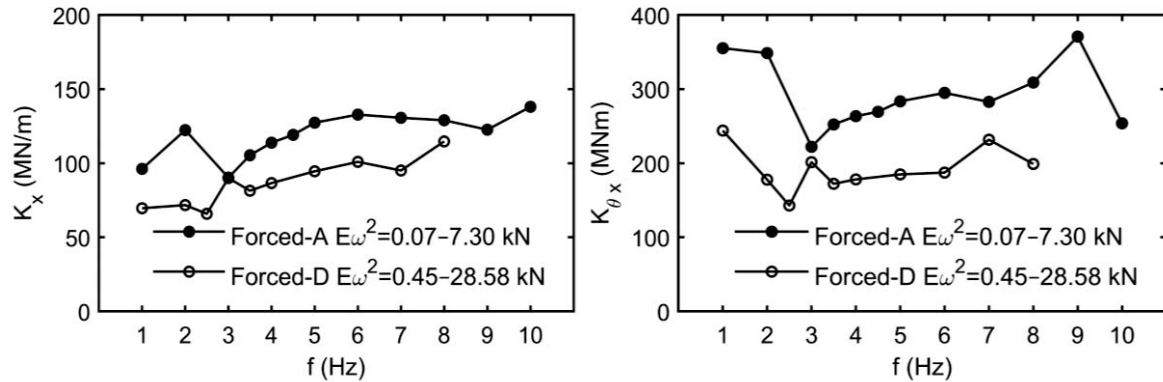


Figure 5 Comparison between the real part of impedance functions back-calculated from Forced-A (full circles) and Forced-D (hollow circles) vibration tests for swaying and rocking motion

### 3.4. Evidence of non-linear soil behavior from the experimental data

Mobilization of nonlinearity in the soil leads to a decrease of soil stiffness and to an increase of hysteretic damping, consequently modifying the foundation motion. For such a reason, soil properties defining impedance functions must be selected to properly account for the mobilized shear strain levels. An estimate of the peak shear strain amplitude,  $\gamma_{eff\max}$ , can be obtained from the ratio between the peak horizontal velocity recorded on the foundation,  $\dot{u}_f$ , and the shear wave velocity,  $V_s$  [33],[34].



The resulting mobilized shear strains during the Forced-A and -D tests are reported in Figure 6a. As expected, the strain amplitude increases with the level of the applied force, i.e. from Forced-A to -D. The system reaches the highest peak shear strain close to the resonance of the facility, i.e. around 3.0 and 2.5Hz, respectively under the Forced-A and -D tests [19],[35]. In correspondence of these values,  $\dot{u}_f$  resulted equal to 0.25cm/s and 0.9cm/s, which combined to a  $V_s$  equal to 100 m/s (see Figure 3a), yields to  $\gamma_{eff\ max}$  of the order of 0.0025% for Forced-A (blue hexagon in Figure 6a) and 0.009% for Forced-D (red hexagon in Figure 6) respectively. Figure 6b shows the variation of normalized shear modulus with the shear strain resulting from a resonant column test (reported in [24]) on a sample taken at a depth between 2.7m and 3.0m, from the borehole BH-01 close to the foundation. The plot revealed that the peak shear strain  $\gamma_{eff\ max}$  estimated for the Forced-A test is associated with a negligible reduction of the shear modulus, while  $\gamma_{eff\ max}$  for the Forced-D test produces a reduction of the shear modulus of the order of 25% of its initial value. Hence, soil nonlinearity is expected to affect rather significantly the experimental impedances derived from the Forced-D test.

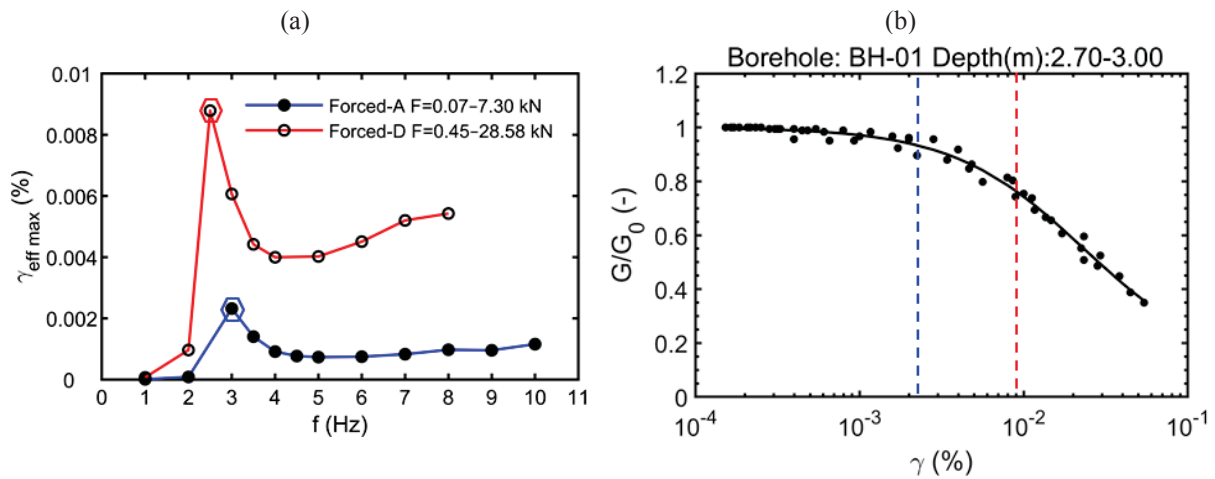


Figure 6 (a) Effective peak shear strain mobilized during Forced-A (full circles connected with a blue solid line) and Forced-D (hollow circles connected with a red solid line) tests, with resonance peaks highlighted by a blue and red marker, respectively; (b) peak strain amplitudes drawn with the same colors across the shear modulus reduction curve  $G/G_0$  (as adapted from [24]).

#### 4. CALIBRATION OF ANALYTICAL SOLUTIONS AGAINST ON-SITE IMPEDANCE FUNCTIONS

The best-fitting between the analytical and experimental impedances was investigated by changing the  $V_s$  value in the computation of the analytical value until the difference with the experimental impedance was minimized. Being both the impedances variable with frequency (see for instance Figure 5) the  $V_s$  was computed by minimizing the sum of the squares of the residuals (or offsets), defined as the difference between the analytical ( $K_{anal}$ ) and experimental ( $K_{exp}$ ) real part of impedances as follows:

$$RSS = \sum_{i=1}^n \left( K_{exp\ i} - K_{anal\ i}(V_s) \right)^2 \quad (5)$$

where  $i$  indexes the frequencies listed in Table 2.



The resulting  $RSS$  normalized with respect to the maximum value, i.e. that associated with  $K_{\theta x}$  under the test Forced-A, are reported in Table 3 along with the best-fitting  $V_s$  values.

	Forced-A					Forced-D			
	swaying		rocking			swaying		rocking	
	$(K_x)$		$(K_{\theta x})$			$(K_x)$		$(K_{\theta x})$	
	$V_S$	$RSS$	$V_S$	$RSS$		$V_S$	$RSS$	$V_S$	$RSS$
	m/s	%	m/s	%		m/s	%	m/s	%
Pais and Kausel	89	6	99	100	Pais and Kausel	77	5	81	34
Liou ( $G_2/G_I=0.5$ )	96	3	98	57	Liou ( $G_2/G_I=0.5$ )	83	2	79	20
Pitilakis et al. (0.01g)	92	6	96	68	Pitilakis et al. (0.2g)	95	3	96	34

Table 3 Minimum dimensionless values of Residual Sum of Squares ( $RSS$ ) associated with the shear wave velocity ( $V_s$ ) used to define the best-fitting analytical function for the swaying and rocking dynamic stiffness back-calculated after Forced-A and Forced-D tests.

The best-fit analytical stiffness is compared in Figure 7a for the swaying and in Figure 7b for the rocking motion to the experimental data of Forced-A (left) and Forced-D (right) tests.

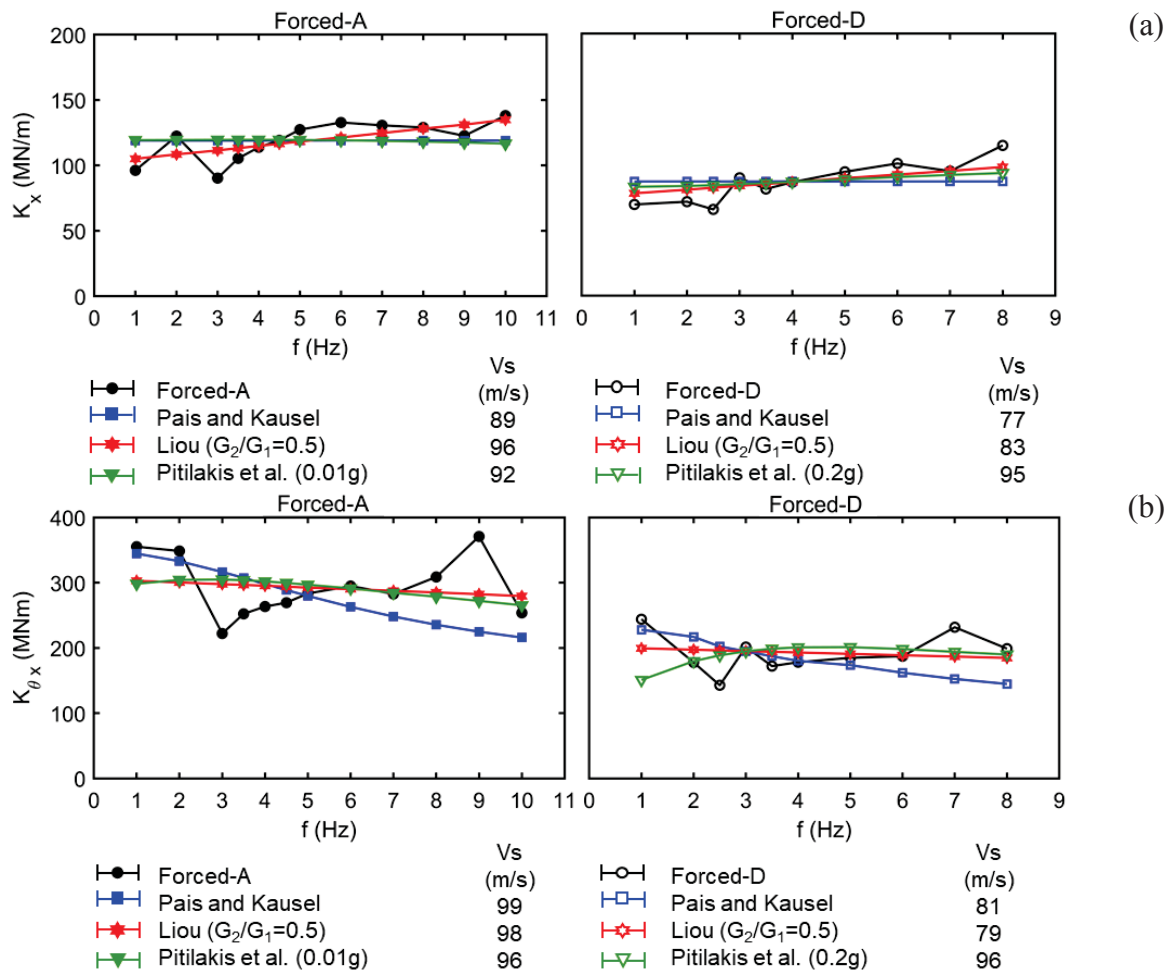


Figure 7 Comparison between the real part of experimental and analytical functions accounting for different values of shear wave profile for the foundation (a) swaying and (b) rocking for (left) Forced-A and (right) Forced-D tests.

For a given analytical solution, the best-fitting  $V_S$  depends on the considered foundation motion. With reference to the results of the Forced-A test, the highest discrepancy is observed for the solution by Pais and Kausel [9], which requires a  $V_S=89$  m/s to match the experimentally derived swaying impedance and a  $V_S=99$  m/s (i.e. with an increase of 11% with respect to the swaying) to match the rocking component. As it is well known [20],[36], the soil depth involved by foundation rocking is almost equal to the foundation half-width and that associated with the swaying motion to the foundation width. Hence the stiffness increase due to the EuroProteas overburden is expected to affect the rocking more than the swaying motion. As shown in Section 3.1 and Figure 3b, the relative difference between the OCF averaged up to the foundation halfwidth and width,  $\overline{OCF}_B$  and  $\overline{OCF}_{2B}$ , is exactly equal to 11%, i.e. that between the  $V_S$  values required to fit the rocking and swaying motions.

From a visual analysis of Figure 7 it appears that the best overall agreement between analytical solutions and experimental data (black symbols) is reached when considering the heterogeneous subsoil profile proposed by Liou [22] (red symbols). As reported in Table 3, such analytical impedances are associated with the lowest RSS for both swaying and rocking modes. Conversely, when considering analytical functions under simplified assumptions such as homogenous soil model (i.e. Pais and Kausel [9]), the match with experimental functions worsens (blue symbols) and the greatest RSS values are reached.

Both Table 3 and Figure 7 show that the "best fitting" shear wave velocity reduces when considering the Forced-D tests. Table 4 lists the ratio between the  $V_S$  used to define the analytical expressions for the best-fitting of Forced-D test results and the corresponding value for the Forced-A, for the two considered foundation motions.

	$V_{S \text{ Forced-D}}/V_{S \text{ Forced-A}}$	
	swaying	rocking
Pais and Kausel[9]	0.86	0.82
Liou ( $G_2/G_1=0.5$ )[22]	0.86	0.81
Pitilakis et al. [23]	1.03	1.00

Table 4 Shear wave velocity reduction from Forced-A to Forced-D, for both swaying and rocking motions.

The normalized shear wave velocity reduction ranges between 14% and 19% when adopting Pais and Kausel [9] and Liou [22] solutions. Such values are coherent with the experimental data reported in Figure 6b, revealing a reduction of the normalized shear modulus up to 25%, hence a  $V_S$  reduction up to 13%. When soil nonlinearity is directly considered in the analytical solution, as suggested by Pitilakis et al. [23], the best-fitting  $V_S$  is the same for the Forced-A and Forced-D tests, since soil properties consistent with the level of shear strain induced by shaking (i.e. 0.01g and 0.2g) are considered by the approach itself.

Finally, it is worth highlighting that the value of  $V_S$  matching the Forced-D test is less affected by the foundation motion than those matching the Forced-A. This is due to the fact that rocking motion mobilizes higher strain levels concentrated in the very shallow foundation soil, reducing its stiffness. Hence the initial inversion induced by the structural weight (see Section 3.1) is reduced, making the stiffness in the soil volume affected by the rocking and swaying motions more homogeneous.

## 5. NUMERICAL SIMULATION

A numerical simulation (Figure 8) with the finite element software SAP2000 allowed to determine the fixed-base (FB) and compliant-base (CB) dynamic response of the prototype.

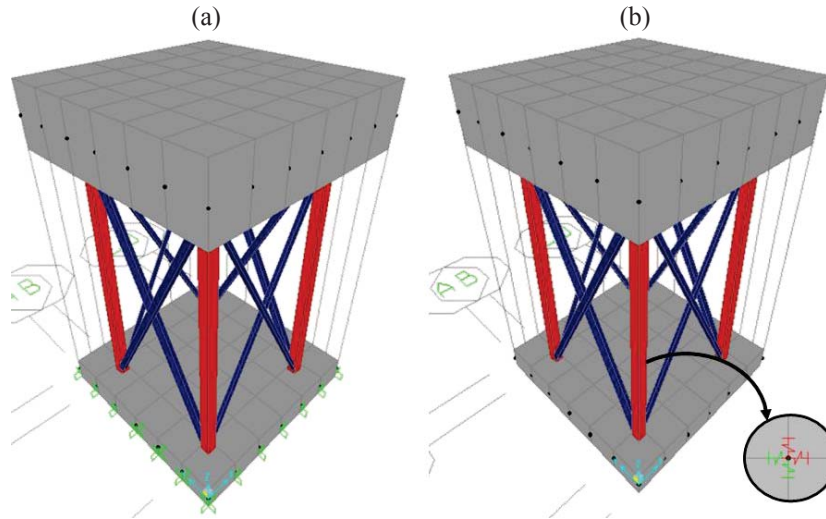


Figure 8 Numerical model for (a) the fixed-base, FB, and (b) compliant-base, CB, prototype.

Following the substructure approach, the numerical simulation of the compliant-base model, CB, was performed by restraining the base of the structural model with a system of springs. Their translational and rotational stiffness values were firstly characterized from the real part of the ‘linear’ experimental impedances, as resulting from Forced-A test for both swaying and rocking modes, with reference to the fundamental frequency of the system, i.e. 3Hz (see [19]), as in the usual procedure. To highlight the effectiveness of using experimental functions, the analysis was repeated by considering each analytical function listed in Table 1. In such a case, the calibration procedure followed in Section 4 was ignored and the shear wave velocity was assumed from the free-field measurements in Figure 4, as commonly done in lack of experimental impedance values. The minimum value of the range 100m/s - 150m/s of  $V_s$  measured in the uppermost 3 m of the layered soil profile was assumed, i.e. 100 m/s (Figure 3).

Results of modal analyses performed on the fixed-base and compliant-base models are reported in Table 5. They confirmed the expected strong influence of the soil-structure interaction on the dynamic response of the facility. In all cases, the fundamental frequency is significantly lower than the value of 9.13Hz resulting from the fixed-base model. Only when characterizing the springs with the experimental impedances, the results of the modal analysis were consistent with the on-site measurements, identifying a fundamental frequency around 3.0Hz under the Forced-A test. Such evidence highlights that the calibration of the compliant-base model through experimental impedances is possible and is even more accurate than the traditional analytical impedance functions because it implicitly accounts for soil inhomogeneity and nonlinearity, which are either neglected or hard to be quantified in the definition of analytical formula.

Foundation restraining system	frequency (Hz)	period (s)
FB (Fixed-base)	9.13	0.11
CB (Forced-A)	3.05	0.33
CB (Pais and Kausel [9])	3.11	0.32
CB (Liou ( $G_2/G_1=0.5$ ) [22])	3.38	0.30
CB (Pitilakis et al. (0.01g) [23])	3.44	0.29

Table 5 Fundamental frequency and period associated with the dominant response of the structure for the fixed-base and compliant-base conditions, considering experimental and analytical impedance functions.

## 6. CONCLUSIONS

The response of a structure resting on soft soil conditions may be different compared to the fixed-base assumption. In the up-to-date literature, SFSI is incorporated in the analysis of shallow foundations using the uncoupled 'substructure method'. The foundation compliance is taken into account through frequency-dependent impedance functions.

Several analytical functions are available in the literature depending on soil and foundation properties, varying with depth and strain level. In this study, theoretical functions accounting for different hypotheses on the subsoil model were calibrated against the impedance functions of a shallow square foundation back-figured from records of the dynamic behavior of the EuroProteas soil-foundation-structure (SFSI) facility, in the framework of the SISIFO project.

The experimental impedances evaluated under different values of forces applied by the shaker match reasonably well with the analytical frequency-dependent impedance functions calculated for varying shaking levels when changing the foundation soil properties according to the mobilized shear strain.

In this study, the agreement was found to increase considerably when considering an inversion in the soil velocity profile, as for the theoretical impedances proposed by Liou [22]. Such an effect is probably due to the increase of shear stiffness induced by the overburden pressure. To overcome the above limitation, future experimental campaigns addressed to evaluate impedance functions should include shear wave measurements after the installation of the prototype, for instance by means of a hole across the foundation slab, allowing for the execution of down-hole or cross-hole tests.

Moreover, when increasing the frequency-dependent amplitude of the force applied through the shaker, significant non-linear effects are induced; for such a reason, laboratory tests on specimens representative of the soil beneath the foundation are needed to investigate the role of inelastic soil behavior even at the lowest strain levels.

A numerical simulation in the SAP2000 software confirmed the effectiveness of using experimental impedance functions, especially when the soil parameters are hard to be defined. The comparison among the obtained predominant frequencies of the model equipped with springs calibrated on the experimental and analytical functions highlighted that the fundamental frequency of EuroProteas measured on-site is well-reproduced only if the experimental impedances are adopted in the analysis.

In conclusion, measurement of the foundation impedance can be a sound alternative strategy with respect to the predictive formulae. It does not require over-simplified assumptions on the geometrical and mechanical properties of both foundation and subsoil.

## 7. ACKNOWLEDGMENT

The Authors acknowledge support by the project "Seismology and Earthquake Engineering Research Infrastructure Alliance for Europe (SERA)". This project has received funding from the European Union's Horizon 2020 research and innovation programme under grant agreement No. 730900. The first Author has received fundings from the European Union's H2020 research and innovation programme under the Marie Skłodowska-Curie grant agreement N° 813137, project URBASIS. OASP-ITSACK is also acknowledged for providing part of the instrumentation and manpower for the execution of the tests.

## 8. REFERENCES

- [1] G. Mylonakis, G. Gazetas, Seismic soil-structure interaction: Beneficial or detrimental?, *Journal of Earthquake Engineering*, 4(3), 277–301, 2000.

- [2] R. Paolucci, Soil-structure interaction effects on an instrumented building in Mexico City. *European Earthquake Engineering*, 3, 33-44, 1993.
- [3] A. Piro, F. de Silva, F. Parisi, A. Scotto di Santolo, F. Silvestri, Effects of soil-foundation-structure interaction on fundamental frequency and radiation damping ratio of historical masonry building sub-structures. *Bulletin of Earthquake Engineering*, 18, 1187–1212, 2019.
- [4] F. de Silva, Influence of soil-structure interaction on the site-specific seismic demand of masonry towers. *Soil Dynamics and Earthquake Engineering*, 131, 2020.
- [5] A.S. Veletsos, J.W. Meek, Dynamic behavior of building-foundation systems. *Earthquake Engineering & Structural Dynamics*, 3(2), 121–138, 1974.
- [6] A.S. Veletsos, V.V. Nair, Seismic interaction of structures on hysteretic foundations. *Journal of Structural Engineering*, 101, 109-129, 1975.
- [7] A.S. Veletsos, B. Verbic, Vibration of viscoelastic foundations. *Earthquake Engineering & Structural Dynamics*, 2, 87–102. 1973.
- [8] G. Gazetas, Formulas and charts for impedances of surface and embedded foundations. *Journal of Earthquake Engineering*, 117(9), 1363–81, 1991.
- [9] A. Pais, E. Kausel, Approximate formulas for dynamic stiffnesses of rigid foundations. *Soil Dynamics and Earthquake Engineering*, 7(4), 213–27, 1988.
- [10] G. Gazetas, Analysis of machine foundation vibrations: state of the art. *Soil Dynamics and Earthquake Engineering*, 2(1), 2–42, 1983.
- [11] NIST, Soil-structure interaction for building structures. *Technical report*, US Department of Commerce, Washington, DC, 2012.
- [12] A. Di Tommaso, R. Lancellotta, D. Sabia, D. Costanzo, F. Focacci, F. Romaro, Dynamic identification and seismic behaviour of the Ghirlandina tower in Modena (Italy). *Proceedings of the AGI International Conference: Geotechnical Engineering for the Preservation of Monuments and Historic Sites*. Bilotta E., Lirer S., Viggiani C. (eds), Napoli, May 30-31 2013. 343-351, Taylor & Francis Group, London. ISBN 978-1-138-00055-1.
- [13] J.E. Luco, M.D. Trifunac, H.L. Wong, Isolation of soil-structure interaction effects by full-scale forced vibration tests. *Earthquake Engineering & Structural Dynamics*, 16, 1-21, 1988.
- [14] A.N. Lin, P.C. Jennings, Effect of embedment on foundation-soil impedance. *Journal of Engineering Mechanics*, 110(7), 1060-1075, 1984.
- [15] H.L. Wong, M.D. Trifunac, J. A. Luco, Comparison of soil-structure interaction calculations with results of full-scale forced vibration tests. *Soil Dynamics and Earthquake Engineering*, 7(1), 22-31, 1988.
- [16] C.B. Crouse, G.C. Liang, G.R. Martin, Experimental study of soil-structure interaction at an accelerograph station. *Bulletin of the Seismological Society of America*, 74(5), 1995-2013, 1984.
- [17] F.C.P. de Barros, J.E. Luco, Identification of foundation impedance functions and soil properties from vibration tests of the Hualien containment model. *Soil Dynamics and Earthquake Engineering*, 14, 229–48, 1995.
- [18] S. Tileylioglu, J.P. Stewart, R.L. Nigbor, Dynamic stiffness and damping of a shallow foundation from forced vibration of a field test structure. *Journal of Geotechnical and Geoenvironmental Engineering*, 137(4), 344–53, 2011.
- [19] C. Amendola, F. de Silva, A. Vratsikidis, D. Pitilakis, A. Anastasiadis, F. Silvestri, Foundation impedance functions from full-scale soil-structure interaction tests. *Soil Dynamics and Earthquake Engineering*, 141, 106523, 2021.



- [20] J. Stewart, S. Kim, J. Bielak, R. Dobry, M. Power, Revisions to soil structure interaction procedures in NEHRP design provisions. *Earthquake Spectra*, 19(3), 677-696, 2003.
- [21] H.L. Wong, J.E. Luco, Tables of impedance functions for square foundations on layered media. *International Journal of Soil Dynamics and Earthquake Engineering*, 4(2), 64–81, 1985.
- [22] G.S. Liou Impedance for rigid square foundation on layered medium. *Structural Engineering/Earthquake Engineering*, 10(2), 83-93, 1993.
- [23] D. Pitilakis, A. Modaressi-Farahmand-Razavi, D. Clouteau, Equivalent-linear dynamic impedance functions of surface foundations. *Journal of Geotechnical and Geoenvironmental Engineering*, 139(7), 1130-1139, 2013.
- [24] D. Pitilakis, E. Rovithis, A. Anastasiadis, A. Vratsikidis, M. Manakou, Field evidence of SFSI from full-scale structure testing. *Soil Dynamics and Earthquake Engineering*, 112, 89–106, 2018.
- [25] D. Raptakis, N. Theodulidis, K. Pitilakis, Data analysis of the euroseistest strong motion array in Volvi (Greece): standard and horizontal-to-vertical spectral ratio techniques. *Earthquake Spectra*, 14(1), 203–24, 1998.
- [26] K. Pitilakis, D. Raptakis, K. Lontzetidis, Th. Tika-Vassilikou, D. Jongmans. Geotechnical & geophysical description of EURO-SEISTEST, using field, laboratory tests and moderate strong-motion recordings. *Journal of Earthquake Engineering*, 3(3), 381–409, 1999.
- [27] D.G. Raptakis, F.J. Chavez-Garcia, K. Makra, K. Pitilakis. Site effects at Euroseistest-I. Determination of the valley structure and confrontation of observations with 1D analysis. *Soil Dynamics and Earthquake Engineering*, 19(1), 1–22, 2000.
- [28] B.O. Hardin, The nature of stress-strain behavior for soils. *Geotechnical Engineering Division Specialty Conference on Earthquake Engineering and Soil Dynamics*, ASCE, Pasadena (California), 1978.
- [29] C. Mancuso, F. Silvestri, F. Vinale, Soil properties relevant to seismic microzonation. *Proc. I Japanese-Turkish Conference on Earthquake Engineering*, Istanbul. Istanbul Technical University and Chamber of Civil Engineers, 1997.
- [30] A. d’Onofrio, F. Silvestri, Influence of micro-structure on small-strain stiffness and damping of fine grained soils and effects on local site response. *Proc. IV International Conference on 'Recent Advances in Geotechnical Earthquake Engineering and Soil Dynamics'*, S. Diego, 2001.
- [31] W. Steinbrenner, A rational method for determination of the vertical normal stresses under foundations, *Proceedings of the International Conference on Soil Mechanics and Foundation Engineering*, Cambridge, Massachusetts, 142-143, 1936.
- [32] A.K. Chopra, *Dynamics of Structures: Theory and applications to earthquake engineering*. 3th Edition New Jersey, USA: Prentice Hall Inc, 2003.
- [33] L.M. Star, S. Tileylioglu, M.J. Givens, G. Mylonakis, J.P. Stewart, Evaluation of soil-structure interaction effects from system identification of structures subject to forced vibration tests. *Soil Dynamics and Earthquake Engineering*, 116, 747-760, 2019.
- [34] F. de Silva, C. Amendola, D. Pitilakis, F. Silvestri, Comparisons among different techniques to derive the swaying and rocking stiffness and damping from field tests on a surface footing. (Submitted to *Journal of Geotechnical and Geoenvironmental Engineering*), 2021.
- [35] A. Vratsikidis, D. Pitilakis, Soil mass participation in soil-structure interaction by field experiments in EuroProteas. Silvestri F., Moraci N. (Eds.). *Earthquake Geotechnical Engineering for Protection and Development of Environment and Constructions*. London: CRC Press, 2019. <https://doi.org/10.1201/9780429031274>.

- [36] Gazetas G. Analysis of machine foundation vibrations: state of the art. *Soil Dynamics and Earthquake Engineering*, 2(1), 2-42, 1983.

## NUMERICAL ANALYSIS ON THE INFLUENCE OF DYNAMIC SOIL-STRUCTURE INTERACTION IN SORIA ARCH DAM: A CASE STUDY

J.C. Galván, L.A. Padrón, J.J. Aznárez, O. Maeso<sup>1</sup>

<sup>1</sup>Instituto Universitario de Sistemas Inteligentes y Aplicaciones Numéricas en Ingeniería  
(SIANI) Universidad de Las Palmas de Gran Canaria  
Edificio Central del Parque Científico y Tecnológico  
Campus Universitario de Tafira, 35017, Las Palmas de Gran Canaria, Spain  
{juancarlos.galvan, luis.padron, juanjose.aznarez, orlando.maeso}@ulpgc.es

---

### Abstract

Soria arch dam and reservoir is the largest infrastructure of this type that exists in the Canary Islands both in capacity and height which is located in the Island of Gran Canaria. The goal of this paper is the development of a numerical model for the analysis of the dynamic and seismic behavior of this arch dam. To do so the effects of the ground motion and of the canyon geometry on the dynamic response of the arch dam are studied in this paper. The seismic response of the arch dam subject to time harmonic shear waves impinging the dam site with a horizontal upstream and cross-stream free-field ground surface motion is analyzed. The numerical model includes both the concrete arch dam and the surrounding area, so that soil-structure interaction phenomena can be taken into account as accurately as possible. The model is used to evaluate the magnitude of soil-structure interaction and also the influence of the accuracy of the geometrical representation of the surrounding topography on such soil-structure interaction effects. To this end, two different numerical models are built. On the one hand, a Finite Element Model of the actual geometry of the concrete dam wall is developed and used to perform a modal analysis of the fixed-base model. On the other hand, several three-dimensional frequency-domain Boundary Element models of both the concrete dam and the surrounding topography are built; all of these models include the actual geometry of the dam wall and different approximations of the surrounding soil, ranging from a very simplified straight prismatic canyon to an elaborate model of the actual topography. These BEM models are used not only to estimate compliant-base natural frequencies and mode shapes, but also to study the seismic response of the system when subjected to incident planar seismic waves. The results show that the influence of the soil—structure interaction effects on the dynamic response of the system is quite significant. It is also shown that the asymmetry of the canyon might significantly affect the seismic response of the dam wall.

**Keywords:** Arch dam, Boundary Element Method, dynamic soil—structure interaction.

---

## 1 INTRODUCTION

Located in the south of the Island of Gran Canaria, between the municipalities of Mogán and San Bartolomé de Tirajana, the Soria dam is a concrete double-curvature arch dam. Soria arch dam and reservoir is the largest infrastructure of this type that exists in the Canary Islands both in capacity ( $32 \text{ hm}^3$ ) and height (120 m). The structure was constructed from 1962 to 1972. It is 120 meters in height (above foundation) and with a thickness of the crown cantilever decreasing from 17.30 m at the base to 3 m at the crest. It is provided with 5 galleries inside its body [1]. Some pictures of Soria dam are shown in Figure 1.



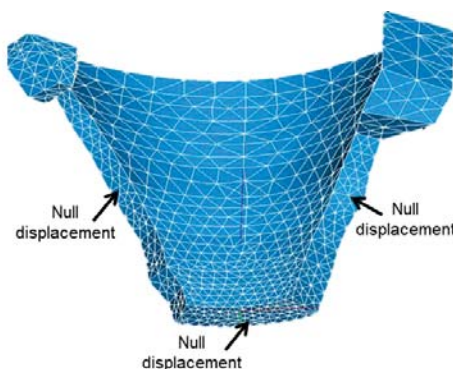
**Figure 1** : Soria arch dam (Gran Canaria).

The present study aims at building a three-dimensional numerical model for the analysis of the dynamic and seismic behavior of the Soria arch dam in order to analyze the influence of the soil-structure interaction effects, and of the accuracy of the geometrical representation of the surrounding topography.

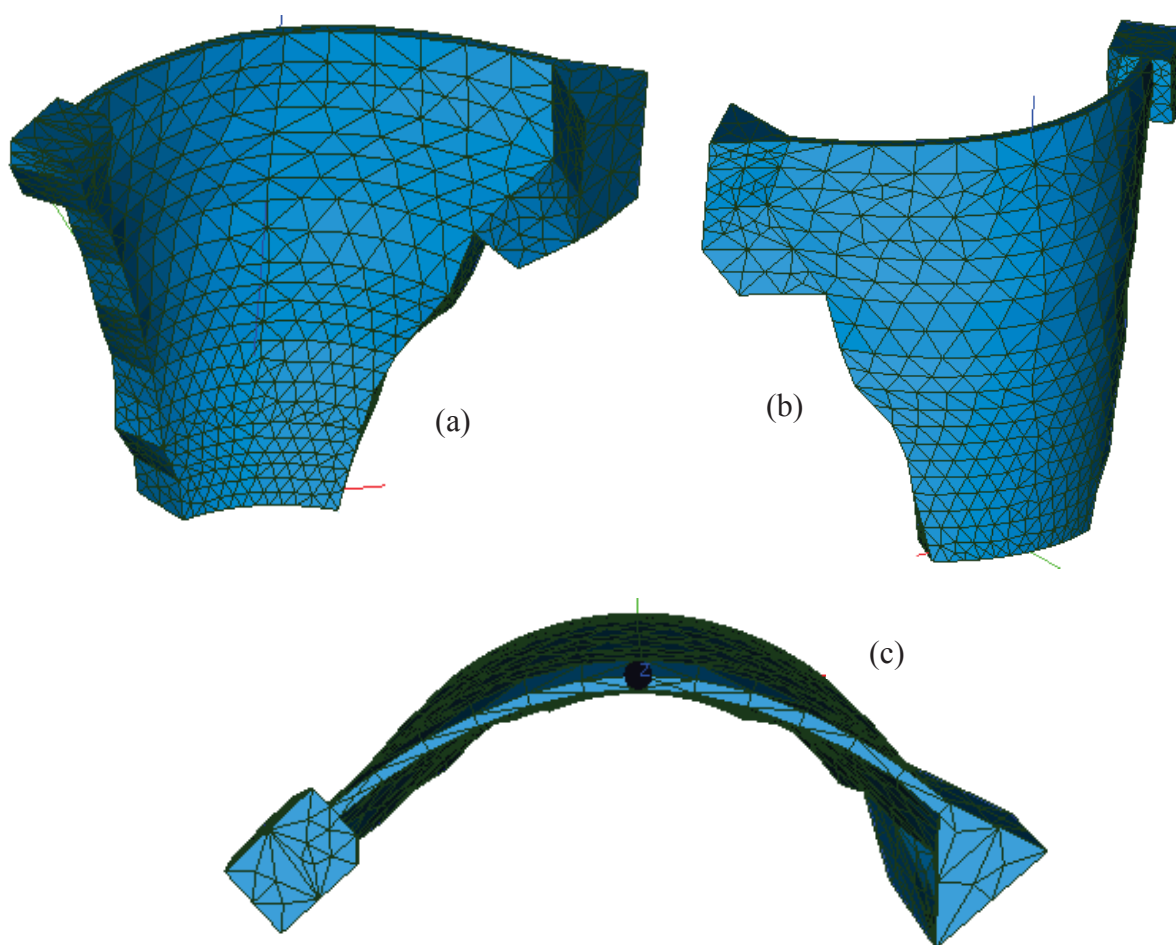
## 2 METHODOLOGY

Firstly, a geometrical model was developed consisting of two parts: the dam wall and the canyon. The geometry of the dam wall was constructed according to the information gathered from a specific study made in 1991 [2]; on the other hand, a geometrical representation of the actual canyon and surroundings was obtained from topographic information available in the databases of Gobierno de Canarias [3].

Secondly, a modal analysis was carried out. For that, a 3D finite element model of the dam wall was developed to obtain the mode shapes of vibration of the fixed-base model. Displacements along the abutments and base of the dam wall are assumed to be zero in this case (Figure 2). The finite element mesh corresponding to the geometry of the dam wall was constructed by means of 4250 tetrahedral 3D elements and 7805 nodes (Figure 3). For the Finite Element Analysis, Code\_Aster was used, which is a Finite Element Analysis software engine [4].



**Figure 2**: Boundary conditions in modal analysis.

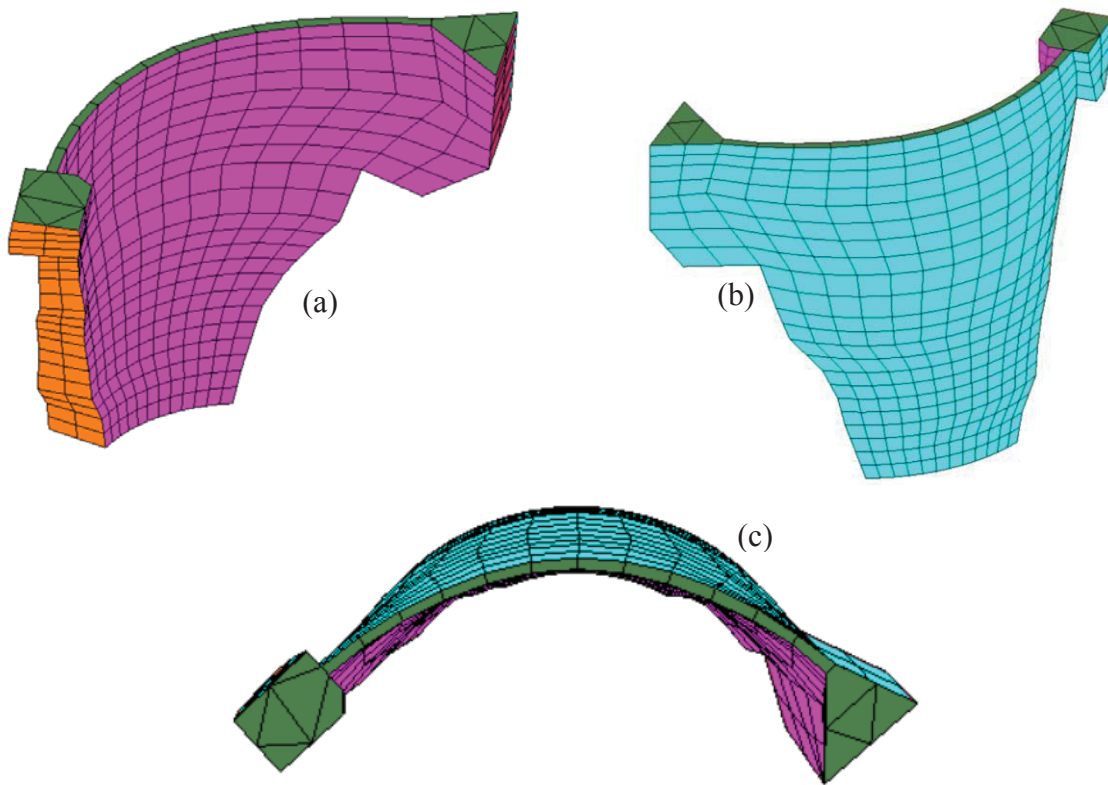


**Figure 3:** 3D mesh used for the FEM analysis. (a) downstream side view, (b) upstream side view and (c) top view.

Thirdly, to illustrate the differences in the dynamic response of the soil-structure system, harmonic analyses of the system, considering both fixed- and compliant-base configurations, were carried out using the multidomain Boundary Element Method (BEM) code in the frequency domain described in Maeso et al. [5, 6]. Wall and surrounding ground are modelled by means of boundary integral equations discretized into boundary elements, taking into account their specific characteristics and the interaction between them by using existing compatibility and equilibrium relationships on the variables defined for structure and soil in the nodes of the contact surfaces. Nine node quadratic quadrilateral elements and six node quadratic triangular elements with a parabolic approximation are used for the boundary elements discretization. The size of the wall elements is determined by the wavelength in the dam wall while in the soil free surface it is gradually increased as the distance from the area of interest increased. The Boundary Element Method allows to take intrinsically into account the unbounded character of the soil medium, without the need of absorbing boundaries or any other mathematical artifact. On the contrary, the free-field mesh is truncated at a distance such that only the scattered wave fields are sufficiently damped. Both structure and soil are considered as solid viscoelastic materials applying in these regions Navier's equation.



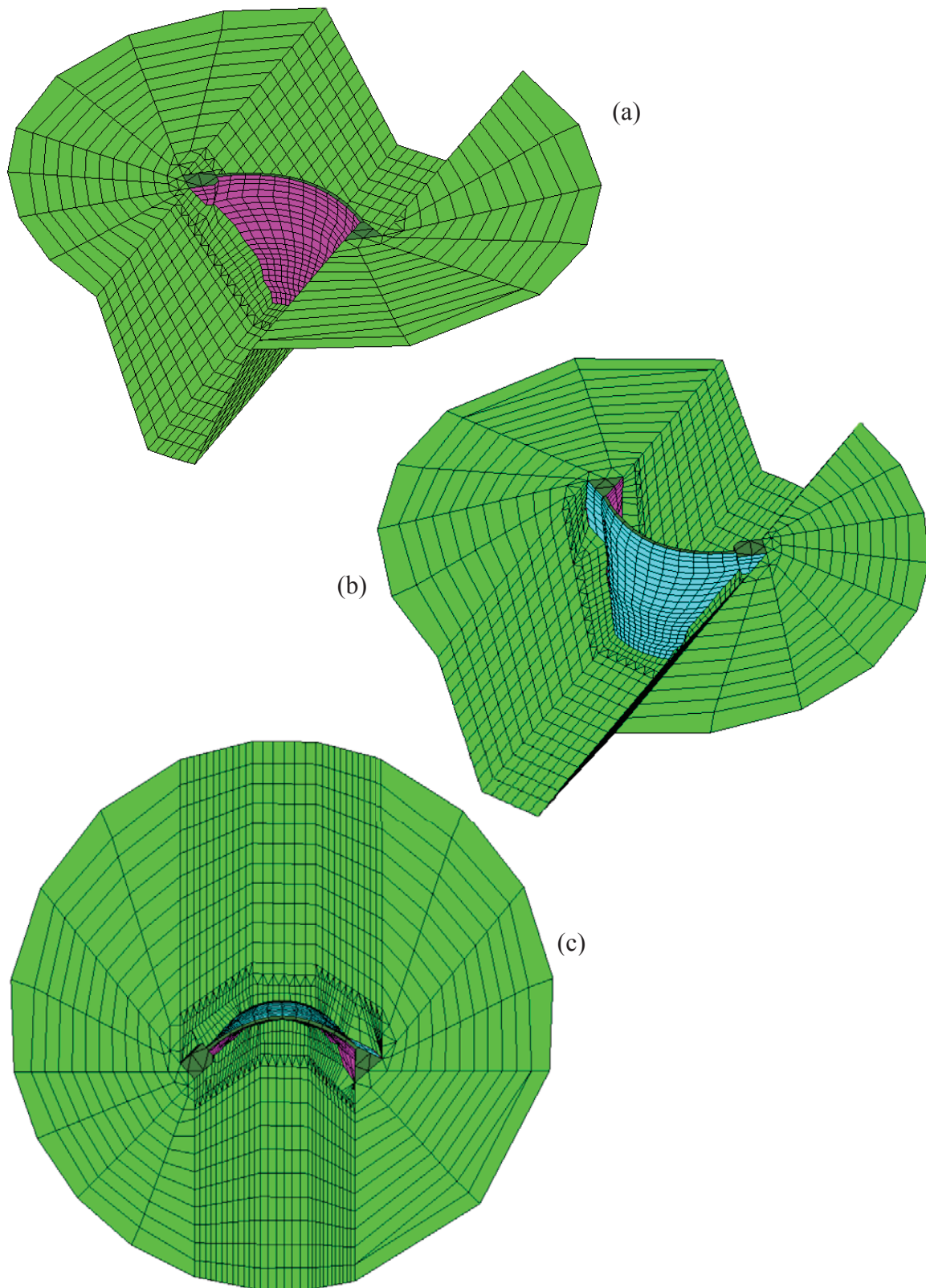
Figure 4 shows the boundary element mesh used for the fixed-base model. The influence of soil-structure interaction and of the accuracy of the geometrical representation of the surrounding topography on such soil-structure interaction effects needs to be evaluated. In order to do so, three of the BE discretizations are used. Figures 5, 6 and 7 show the actual geometry of the dam wall with different approximations of the surrounding soil, from a straight prismatic canyon with two different amounts of free-surface (Figures 5 and 6, free-surface extensions equal to two and three times the height of the dam wall, respectively) to a model of the actual topography (Figure 7, free-surface extensions equal to two times the height of the dam wall). As mentioned before, these four BEM models have been constructed by means of nine-node quadratic quadrilateral elements and six-node quadratic triangular elements where the number of nodes and elements are shown in table 1.



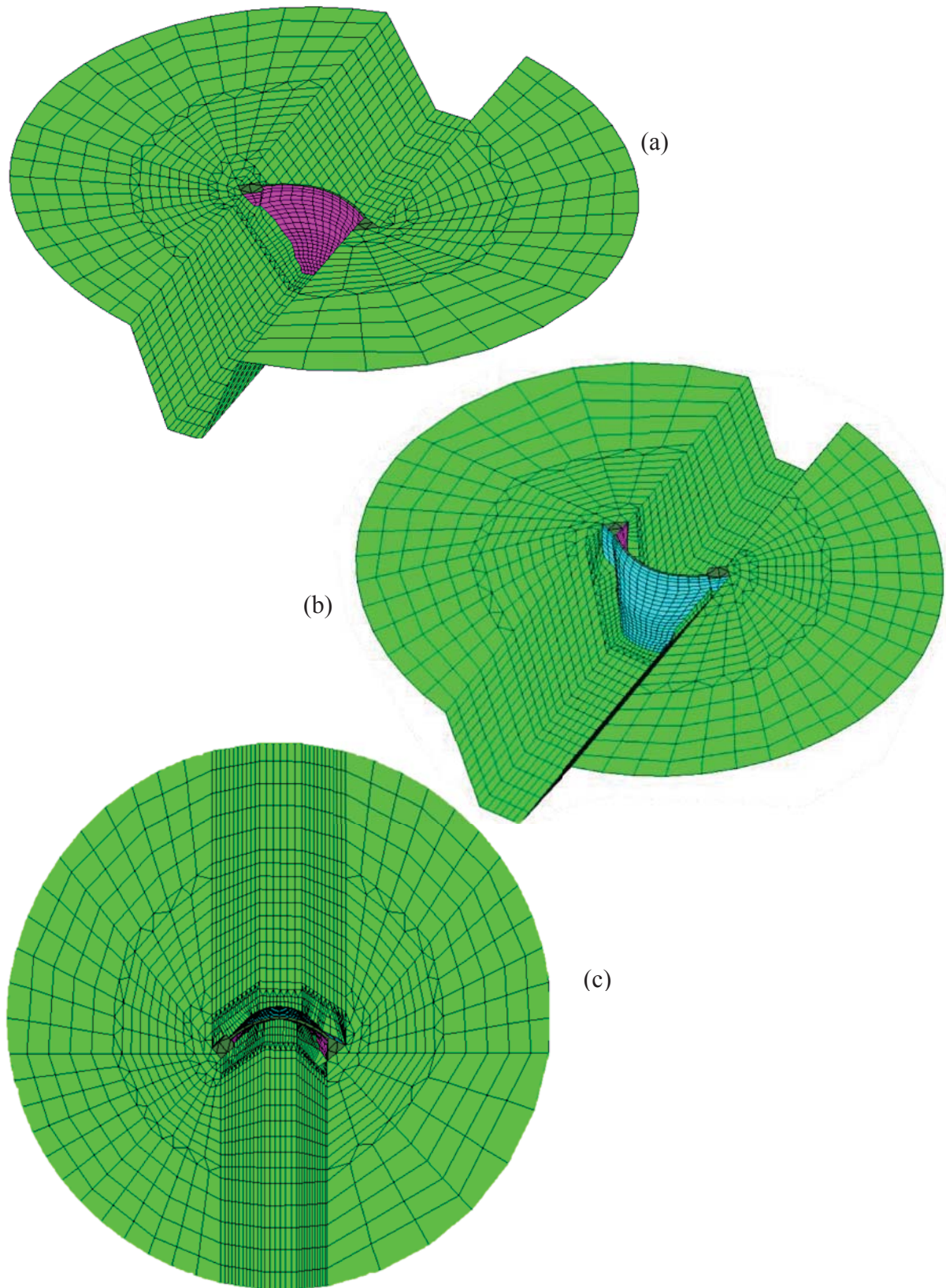
**Figure 4:** 3D mesh used for the BEM analysis of the dam wall. (a) Downstream side view, (b) up-stream side view and (c) top view.

BEM models	Number of nodes	Number of elements
Fixed base	3228	733
Compliant base. Prismatic canyon (R=240 m)	8168	2023
Compliant base. Topographic canyon (R=240 m)	10397	2739
Compliant base. Prismatic canyon (R=360 m)	10408	2631

Table 1: Number of nodes and elements in BEM models.

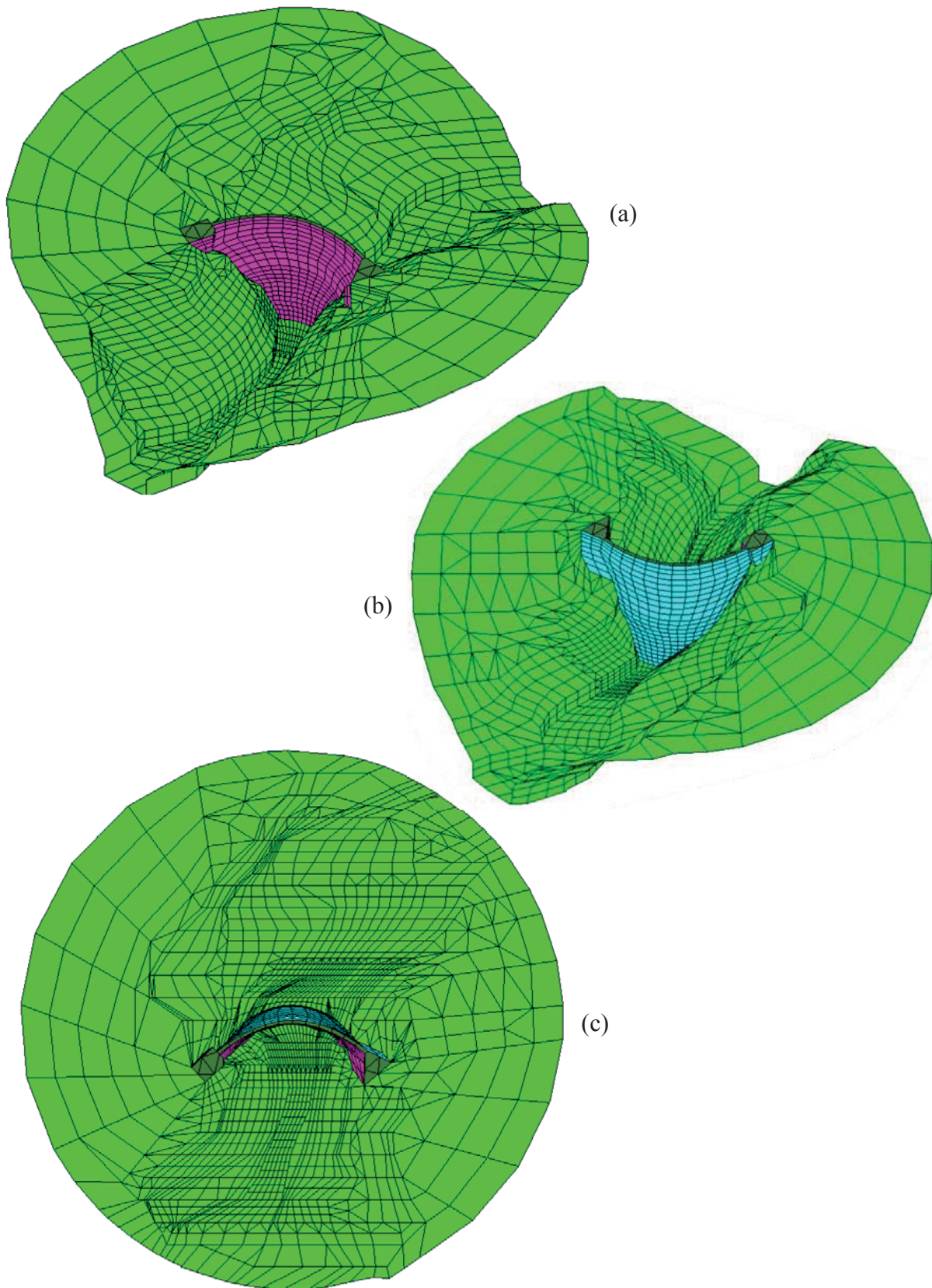


**Figure 5:** BE model, prismatic canyon. Extension of the free-field discretization: 240 m. (a) Downstream side view, (b) up-stream side view and (c) top view.



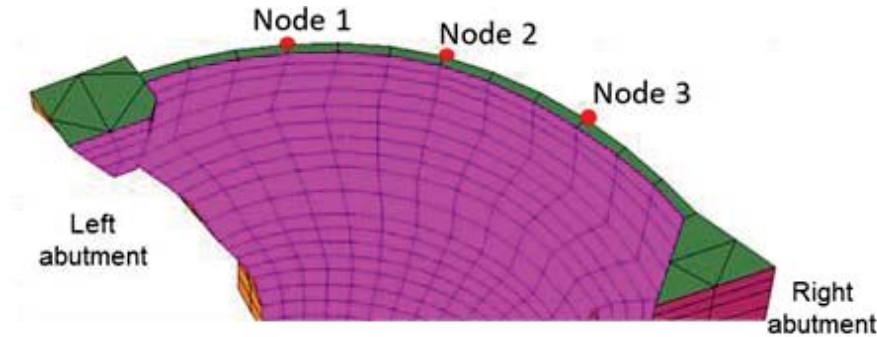
**Figure 6:** BE model, prismatic canyon. Extension of the free-field discretization: 360 m. (a) Downstream side view, (b) up-stream side view and (c) top view.





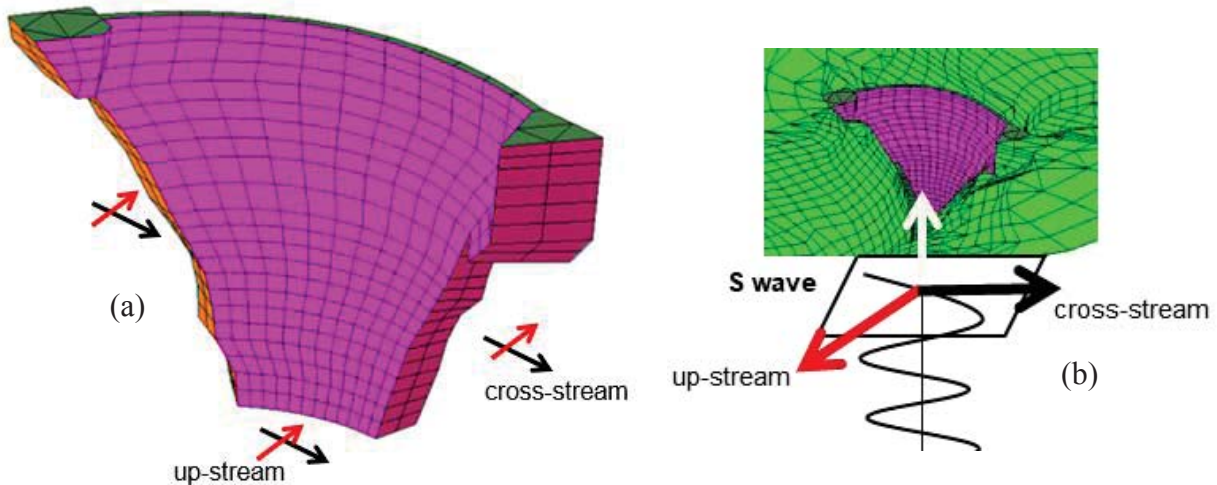
**Figure 7:** BE model. Approximation of the actual topography of the canyon. Extension of the free-field discretization: 240 m. (a) Downstream side view, (b) upstream side view and (c) top view.

The nodes studied are node 1, node 2 and node 3 which are located approximately at 1/4, 1/2 and 3/4 of the dam crest, measured from left to right abutment, respectively (Figure 8). Frequency response functions obtained by BE method in these nodes will be plotted for 4 cases: Fixed-base and compliant-base with different geometries (Figures 5, 6 and 7).



**Figure 8:** Nodes studied.

On the one hand, in the fixed-base analysis, a unit harmonic horizontal displacement along the up-stream and cross-stream direction was prescribed at the abutments and base of the dam wall (Figure 9.a) ; on the another, for the compliant analysis, the system is assumed to be impinged by seismic time-harmonic plane waves. For this analysis, it was assumed that the incident wave field consists solely of plane S waves propagating vertically with a horizontal up-stream and cross-stream free-field ground surface motion [7] (Figure 9.b).



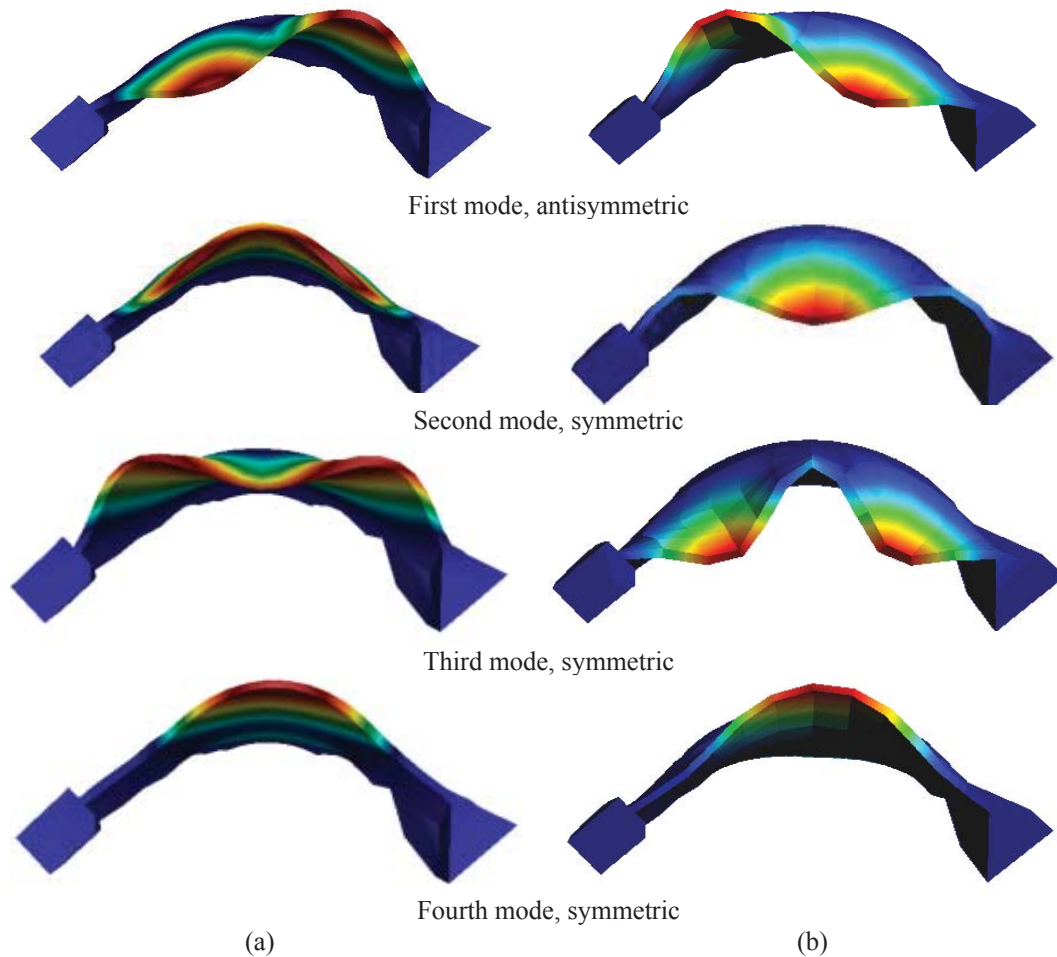
**Figure 9:** Boundary conditions used in harmonic analyses. (a) Fixed and (b) compliant base.

As mentioned, the concrete dam wall is assumed to be viscoelastic solid with the following properties: density,  $\rho = 2300 \text{ kg/m}^3$ ; Poisson's ratio,  $\nu = 0.2$ ; shear modulus,  $G = 8167 \text{ MPa}$  and internal damping,  $\xi = 0.01$ ; the foundation rock material is also assumed to be viscoelastic media with a density,  $\rho = 2143 \text{ kg/m}^3$ ; Poisson's ratio,  $\nu = 0.2$ ; shear modulus,  $G = 12083 \text{ MPa}$  and internal damping,  $\xi = 0.01$  [1, 7].



### 3 ANALYSIS OF RESULTS

The first four mode shapes and natural vibration frequencies obtained with the finite element modal analysis (FEM) with the fixed-base model, together with the modes inferred from the harmonic analysis with the fixed-base model using boundary element method (BEM) are shown in Figure 9 and table 2, respectively.



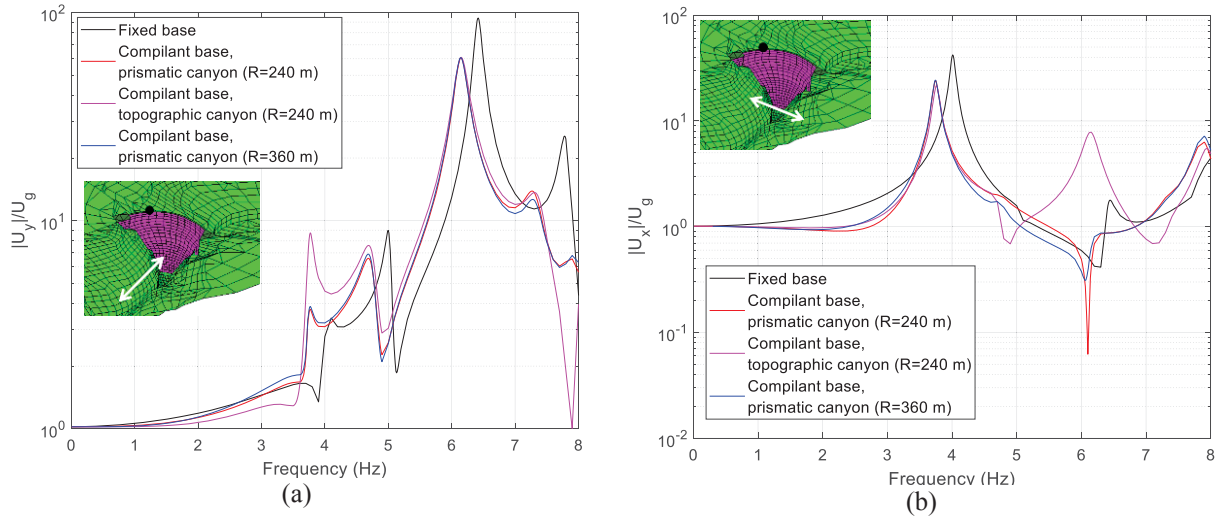
**Figure 9:** Mode shapes of vibration: (a) FEM ; (b) BEM.

Mode shapes	FEM	BEM
First mode	3,99 Hz	4,00 Hz
Second mode	4,99 Hz	5,00 Hz
Third mode	6,37 Hz	6,40 Hz
Fourth mode	7,80 Hz	7,80 Hz

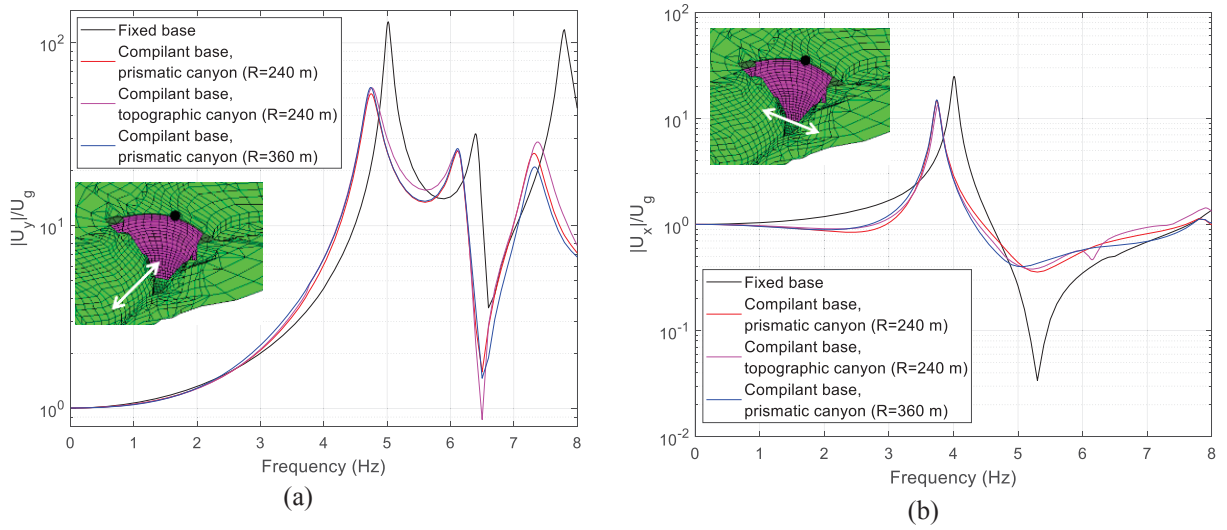
Table 2: Fundamental frequencies: FEM and BEM models.

As can be seen, a very good agreement is observed between the two sets of results, in terms of both mode shapes (Figure 8) and fundamental frequencies (table 2) which contributes to validate the BE wall mesh used below in the fixed and compliant-base harmonic analyses.

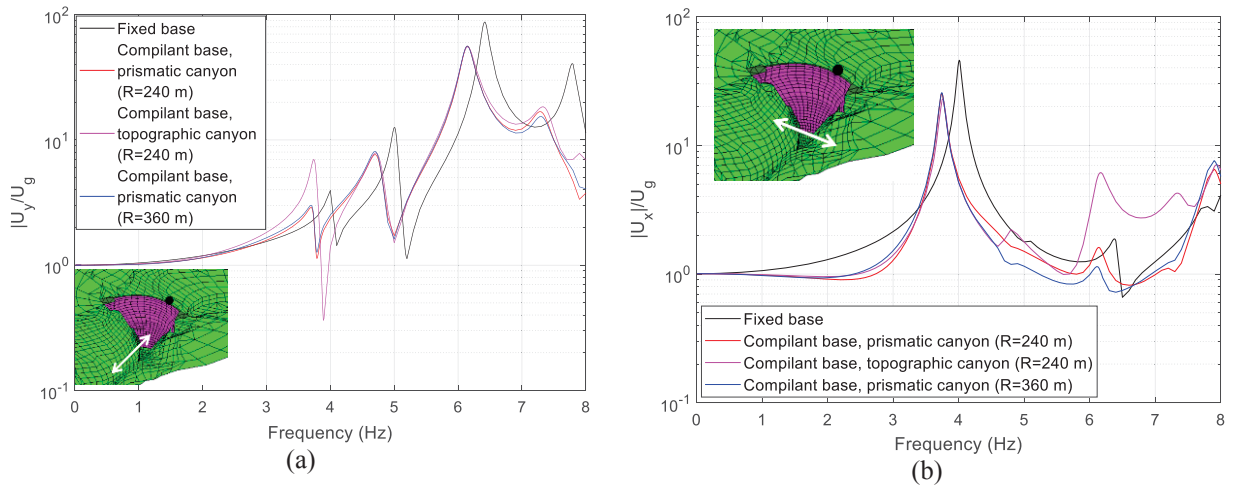
The frequency response functions computed for the fixed-base and compliant-base models with different geometries at the nodes studied are plotted in Figures 10 and 11.



**Figure 10:** FRFs. (a) Longitudinal and (b) transversal response of node 1.



**Figure 11:** FRFs. (a) Longitudinal and (b) transversal response of node 2.



**Figure 12:** FRFs. (a) Longitudinal and (b) transversal response of node 3.

BEM models	First frequency	Second frequency	Third frequency	Fourth frequency
Fixed base	4.01 Hz	5.00 Hz	6.44 Hz	7.80 Hz
Compilant base, prismatic canyon (R=240 m)	3.74 Hz	4.75 Hz	6.10 Hz	7.32 Hz
Compilant base, topographic canyon (R=240 m)	3.76Hz	4.76 Hz	6.14 Hz	7.38 Hz
Compilant base, prismatic canyon (R=360 m)	3.74 Hz	4.74 Hz	6.11 Hz	7.33 Hz

Table 3: Fundamental frequencies obtained with harmonic analyses.

As expected, the frequency-domain analyses carried out show that the soil—structure interaction has an important influence on the dynamic response of the dam wall both in amplitude and frequency (Figures 10, 11 and 12, table 3) due to damping character of the soil; as can be observed in table 4, the vibration frequencies on compliant base are between 4.5-6.5% lower than in fixed base.

Models	First frequency	Second frequency	Third frequency	Fourth frequency
Compilant base, prismatic canyon (R=240 m)	- 6.50%	- 5.00%	- 4.53%	- 6.15%
Compilant base, topographic canyon (R=240 m)	- 6.00%	- 4.80%	- 4.53%	- 5.38%
Compilant base, prismatic canyon (R=360 m)	- 6.50%	- 5.20%	- 4.53%	- 6.02%

Table 4: Fundamental frequencies reduction %. Compliant base versus to fixed base.

On the other hand, regarding the seismic response of the compliant-base models with different geometrical models of the canyon, it can be seen that while the response of the central node (Figure 11) is mostly unaffected by the level of accuracy of the representation of the topography of the area around the dam wall, the response computed for the most accurate geometrical model for the nodes placed at 1/4 (Figure 10) and 3/4 (Figure 12) of the length of the dam crest show a larger response of the first mode (which is mostly asymmetrical) for the upstream excitation (Figures 10.a and 12.a) and larger response of the third mode (which is mostly symmetrical) for the cross-stream excitation (Figures 10.b and 12.b). This is clearly due to the asymmetry of the topographical representation of the canyon, not present in the first two simplified models of the canyon.

#### 4 CONCLUSIONS

In this paper, a boundary element model for the dynamic analysis of coupled systems consisting of solid viscoelastic regions have been applied to the study of the dynamic response of a concrete arch dam taking into account soil-structure interaction.

The frequency-domain analyses carried out show that the soil—structure interaction has an important influence on the seismic response of the dam wall (the vibration frequencies on compliant base are up to 6.50% lower than in fixed base). It has also been found that the asymmetry of the canyon might affect significantly the seismic response of the dam wall.

In future studies, numerical models involving structure-soil-water interaction with different reservoir levels will be studied in order to analyze the influence of this interaction on the dam crest, moreover an experimental modal analysis is also planned in order to obtain information for the calibration of the numerical model.

## REFERENCES

- [1] Jaime J. González. Presa de Soria. Una historia de proyectos, informes y notas informativas. Gran Canaria 1935-1972. Depósito Legal: GC.562-2010.
- [2] INPROES, S.A. and Hermanos Garrote de Marcos, S.A. Documento XYZT de la presa de Soria, 1991.
- [3] Infraestructura de Datos Espaciales de Canarias. [www.idecanarias.es](http://www.idecanarias.es). 2017.
- [4] EDF R&D, Code\_Aster software: Analysis of Structures and Thermomechanics for Studies & Research, 2017.
- [5] O. Maeso, J.J. Aznárez, J. Domínguez. Three-dimensional models of reservoir sediment and effects on seismic response of arch dams. Earthquake Engineering and Structural Dynamics, 33, pp. 1103-1123, 08/2004.
- [6] O. Maeso, J.J. Aznárez, J. Domínguez. Effects of space distribution of excitation on seismic response of arch dams. Journal of Engineering Mechanics (ASCE), 128, pp. 759-768, 07/2002.
- [7] J. Domínguez, "Boundary elements in dynamics", Southampton, New York, Computational Mechanics Publications & Elsevier Applied Science; 1993.
- [8] Instituto Eduardo Torroja de la construcción - Ministerio de Vivienda (España). Catálogo de Elementos constructivos del Código Técnico de la Edificación, 2010. Disponible en: [https://www.codigotecnico.org/images/stories/pdf/aplicaciones/nCatalog\\_infoEConstr/CAT-EC-v06.3\\_marzo\\_10.pdf](https://www.codigotecnico.org/images/stories/pdf/aplicaciones/nCatalog_infoEConstr/CAT-EC-v06.3_marzo_10.pdf)

## SOIL-CAISSON-BRIDGE PIER-DECK DYNAMIC INTERACTION UNDER STRONG EARTHQUAKES: THE INFLUENCE OF PRIMARY AND SECONDARY SOIL NONLINEARITIES

D. Gaudio<sup>1</sup> and S. Rampello<sup>1</sup>

<sup>1</sup> Sapienza University of Rome  
via Eudossiana 18, 00184, Rome, Italy  
e-mail: domenico.gaudio@uniroma1.it  
e-mail: sebastiano.rampello@uniroma1.it

---

### Abstract

*In the last few years, the ever-increasing computing power of personal computers has allowed to explore beyond the assumption of linear viscous-elastic behaviour usually made for foundation soils, even when subjected to strong seismic excitations. In this context, [Gaudio and Rampello \[1\]](#) performed a parametric study focusing on the seismic performance of massive caisson foundations supporting bridge piers subjected to strong one-directional earthquakes, capable of triggering the nonlinear and inelastic soil behaviour. 3D dynamic Finite Element (FE) analyses were performed twice in the time domain, once assuming the soil to behave as an elastic-plastic and once as a linear viscous-elastic medium: through the comparison of results, the observed reduction of inertial forces transmitted to the superstructure was mainly attributed to the energy dissipation occurring in the foundation soils, due to the attainment of their inelastic behaviour. These nonlinearities can be classified as “primary”, developing in the free-field soil, and “secondary”, resulting from the oscillating foundation [2]: these were not distinguished in the parametric study.*

*In this paper a step further is made, as the relative influence of the “primary” and “secondary” nonlinearities is evaluated. A simple 3-degree-of-freedom plane-strain model simulating the soil-foundation-bridge pier-deck system is subjected to the horizontal acceleration time histories computed at the depth of the foundation centroid from preliminary 1D inelastic ground response analyses performed in free-field conditions. The influence of “primary” nonlinearities is assessed by comparing these results with those obtained after applying seismic inputs coming from 1D nonlinear viscous-elastic free-field analyses. The comparison is performed in terms of some performance indexes, such as the deck drift and the bending moment acting at the base of the pier. A fair estimate of the influence of “secondary” nonlinearities is finally provided comparing the results obtained applying the 1D inelastic free-field motion with those computed in the 3D nonlinear dynamic FE analyses.*

**Keywords:** Soil Nonlinearities, Caisson Foundation, Bridge Pier, Earthquake, Dynamic Soil-Structure Interaction, Finite Element Analysis.

---



## 1 INTRODUCTION

Role of soils on the seismic performance of superstructure such as buildings and bridges has been being explored with increasing accuracy for the last 50 years. However, its influence has been often condensed in the increase of flexibility of the soil-foundation-structure system seen as a whole and of the damping with respect to the fixed-base case, thanks to the introduction of the foundation-soil finite stiffness and of the geometric and material damping [3, 4]. This change in the dynamic properties is even more pronounced when the system is hit by high-intensity earthquakes, as a result of the decreasing shear modulus and growing damping ratio as a function of the shear strain experienced by the foundation soils during the seismic event. The increase of the period of the equivalent system can be easily evaluated even through analytical relationships, provided that at least a preliminary 1D ground response analysis is performed in free-field conditions via the Linear Equivalent (*LE*) method [5], so that the magnitude of the shear strain to be expected is properly evaluated. Although this approach allows the user to account for the nonlinear behaviour of foundation soils, it does not permit any evaluation of the effects of their inelastic behaviour, the latter implying the accumulation of permanent deformations until the end of the seismic shaking. Indeed, this aspect can strongly affect the seismic performance of structures subjected to strong ground motions and should be carefully assessed.

In the above-mentioned context, Gaudio and Rampello [1] recently performed a parametric study through 3D nonlinear dynamic FE analyses on caisson foundations of bridge piers subjected to strong ground motions, clearly showing that the influence of soil inelastic behaviour is to be considered when assessing their seismic performance, especially when the fundamental period of the whole soil-caisson-pier-deck system (i.e. considering lengthening of the period due to soil-structure interaction),  $T_{eq}$ , approaches the period of the free-field 1D soil column,  $T_0$ . They also discussed the influence of *Foundation Input Motion (FIM)* and compared it with that of irreversible soil behaviour. Although the study [1] provides some useful empirical relationships that can be used to get the overestimation of peak displacements and forces that is typically obtained when irreversible and hysteretic soil behaviour is neglected, as a function of the period ratio  $T_{eq}/T_0$  and of the significant duration of the earthquake,  $T_D^{inp}$  [6], it does not detail the contribution of the so-called “primary” and “secondary” soil nonlinearities (even if “nonlinearities” should be replaced with “plasticity” in this context, more properly). The term “primary” stands for the development of permanent deformations and dissipation of energy in the free-field soil column, whereas “secondary” indicates the same but caused by the oscillating foundation and by the structure as a whole.

In this paper, the relative influence of the primary and secondary nonlinearities is evaluated, following the work that can be found in [1]. Specifically, a 3-degree-of-freedom (3DoF) plane-strain model representing several soil-foundation-bridge pier-deck systems is subjected to the horizontal acceleration time histories computed at the depth of the foundation centroid from preliminary 1D inelastic free-field ground response analyses. The influence of “primary” nonlinearities is first assessed by comparing these results with those computed applying at the node representing the foundation the input motions retrieved from 1D nonlinear viscous-elastic free-field analyses. The comparison is performed in terms of the deck drift and the bending moment acting at the base of the pier. A fair estimate of the influence of “secondary” nonlinearities is then provided through the comparison of the results obtained applying the 1D inelastic free-field motion with those computed in the 3D nonlinear dynamic FE analyses in which the soil-foundation-pier-deck system is described. Although not rigorous, this procedure permits clearly understanding, for the cases at hand, of the relative contribution of soil far and close to the structure.

## 2 PROBLEM SETTING

The problem layout considered in the parametric study is depicted in Figure 1a. The transversal section of a bridge is considered, where the cylindrical caisson foundation of height  $H$  and diameter  $D$  is embedded in a 5-m-thick gravelly sand layer underlain by a 55-m-thick layer of silty clay, this being representative of an alluvial deposit. The infinitely-rigid bedrock is located at depth  $Z = 60$  m, where the seismic input motion is applied in the  $x$  direction in terms of horizontal acceleration time histories. Water table is placed at the interface between the sand and the clay layers ( $z_w = 5$  m), with a hydrostatic pore water pressure regime. The pier is modelled through a linear viscous-elastic Single-Degree-of-Freedom System (*SDoF*) characterized by a stiffness  $k_s$ , simulating the flexural stiffness of the pier, a damping ratio  $\xi_s = 5\%$  and a lumped mass  $m_s = m_{\text{deck}} + 0.5 \cdot m_{\text{pier}}$ , where  $m_{\text{deck}}$  and  $0.5 \cdot m_{\text{pier}}$  are the mass of the deck and of the upper half of the pier, respectively. The mass of the lower half of the pier is applied to the top of the caisson via a uniform distribution of vertical stresses  $\sigma_{z(0.5\text{pier})}$ .

Mechanical properties of the foundation soils are given in Table 1, where  $\gamma$  is the unit weight,  $c'$  and  $\phi'$  are the effective cohesion and the angle of shearing resistance,  $OCR$  is the overconsolidation ratio and  $k_0$  is the earth pressure coefficient at rest [7]. The profile assumed for the small-strain shear modulus  $G_0$  was obtained using the empirical relations proposed by Hardin and Richart [8] for the gravelly sand and by Rampello *et al.* [9] for the silty clay, and

Soil	$\gamma$ (kN/m <sup>3</sup> )	$c'$ (kPa)	$\phi'$ (°)	$OCR$ (-)	$k_0$ (-)	$G_0^{\text{rel}}$ (MPa)	$m$ (-)	$\gamma_{0.7}$ (%)	$E_{\text{ur}}^{\text{rel}}$ (MPa)	$\nu_{\text{ur}}$ (-)	$E_{50}^{\text{rel}}$ (MPa)	$E_{\text{oed}}^{\text{rel}}$ (MPa)
Gravelly sand	20	0	30	1.0	0.5	145.7	0.61	0.024	174.9	0.2	58.3	58.3
Silty clay	20	20	23	4.4÷1.5	1.1÷0.7	65.7	0.75	0.045	58.2	0.2	19.4	19.4

Table 1: Mechanical properties assumed for soils and adopted in the *HS small* model.

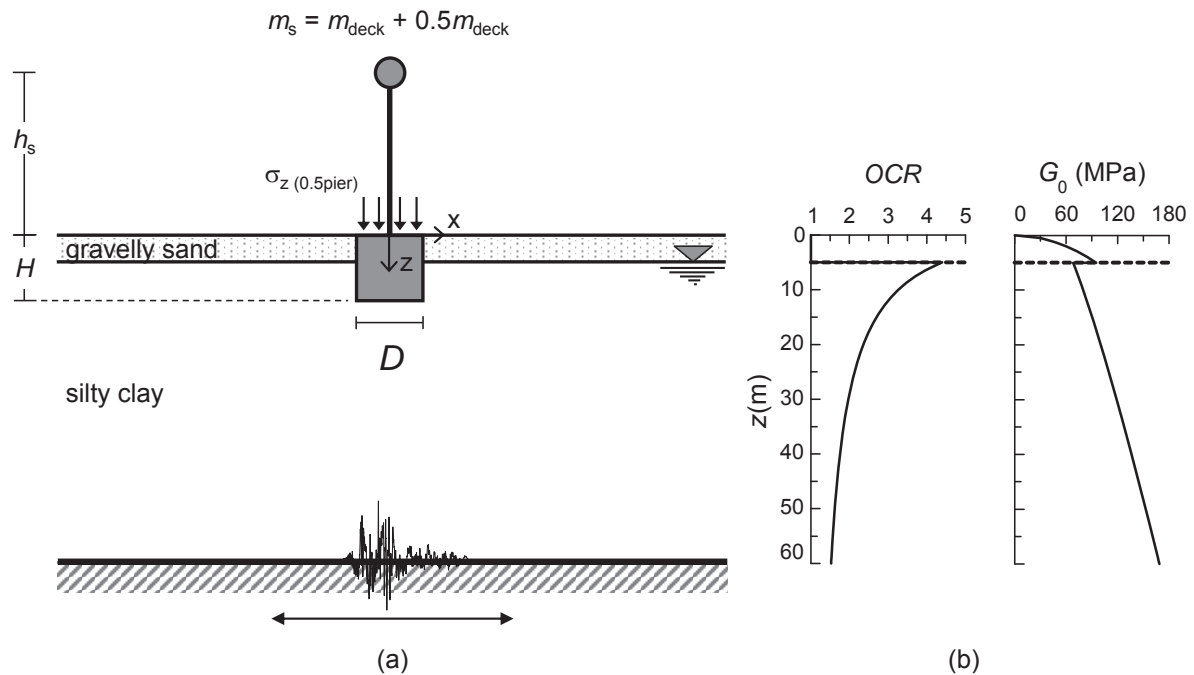


Figure 1: (a) layout considered in the parametric study; (b) profiles assumed for the overconsolidation ratio and the small-strain shear modulus (modified from [10]).

$D$ (m)	$H/D$ (-)	$h_s$ (m)	$k_s$ (MN/m)	$m_{\text{deck}}$ (Mg)	$m_{\text{pier}}$ (Mg)	$m_s$ (Mg)
8	0.5	15	10.1	1278.0	196.7	1376.4
	1	30	11.8	1500.3	217.2	1608.9
		60	6.2	698.6	1018.9	1208.1
	2	15	102.4	2115.4	112.0	2171.4
		30	46.9	1804.8	422.6	2016.1
		60	20.8	1162.4	1065.0	1694.9
12	0.5	15	106.4	3445.1	113.2	3501.7
		30	37.7	3173.5	384.8	3365.9
		60	19.8	2159.0	1399.3	2858.6
	1	15	169.3	4160.5	134.6	4227.8
		30	78.7	3806.0	489.2	4050.6
		60	29.9	2841.1	1454.0	3568.1
	2	30	411.2	4986.9	904.2	5439.0
		60	192.3	2374.3	3156.8	4132.7

Table 2: Properties of the systems considered in the parametric study.

is plotted in [Figure 1b](#) together with that of *OCR*.

In the parametric study fourteen deck-pier-caisson-soil systems were considered, differing in caisson diameter ( $D = 8$  and  $12$  m), caisson slenderness ratio ( $H/D = 0.5$ ,  $1$  and  $2$ ), and pier height ( $h_s = 15$ ,  $30$  and  $60$  m). Here it is worth noting that some extreme cases were excluded as they were deemed not realistic (i.e. pier of height  $h_s = 15$  m over a  $24$ -m-deep caisson). Values of the pier flexural stiffness  $k_s$  and masses  $m_{\text{deck}}$ ,  $m_{\text{pier}}$  and  $m_s$  were selected to represent span lengths ranging between  $40$  and  $110$  m and to return fixed values of the safety factor against bearing capacity under static and pseudo-static conditions,  $F_{\text{sv}} = 5.5$  and  $F_{\text{se}} = 0.7$ , respectively. More details about this methodology are given in [\[11, 12\]](#); the main characteristics of the systems are reported in [Table 2](#).

### 3 FINITE ELEMENT MODELLING

The dynamic analyses were first performed using the FE code PLAXIS 3D [\[13\]](#) with the numerical domain shown in [Figure 2a](#) [\[1\]](#). Each analysis was performed twice, adopting two different constitutive models for foundation soils: the elastic-plastic constitutive model *Hardening Soil with Small-Strain Stiffness* (*HS small*, [\[14\]](#)) and a linear viscous-elastic model, the former with the mechanical parameters given in [Table 1](#), the latter with “mobilised” values of shear modulus  $G$  and of damping ratio  $\xi$  resulting from preliminary 1D free-field analyses carried out with the *LE* method. Here it is worth mentioning that the same curves reproducing shear modulus decay and damping ratio increase with the shear strain,  $G/G_0$  and  $\xi = f(\gamma)$ , were assumed in the 3D analyses with *HS small* and in the 1D free-field analyses with the *LE* method, namely that proposed by [Seed and Idriss](#) [\[15\]](#) for the sand and by [Vucetic and Dobry](#) [\[16\]](#) for the clay (plasticity index  $I_p = 25$  %). In the dynamic calculation phase, the systems were subjected to six different acceleration time histories, intense enough to trigger the bearing capacity of the caisson foundations: for the sake of brevity, only three of them are considered in the following ([Fig. 3a-b](#)).

Comparison of results permitted to better understand the role of soil plasticity on the seismic performance of the systems at hand. Albeit these analyses were useful in achieving the proposed objective, they did not allow to properly distinguish in between primary and secondary nonlinearities, as summarised in [Table 3](#). Therefore, a simplified plane-strain *3DoF*

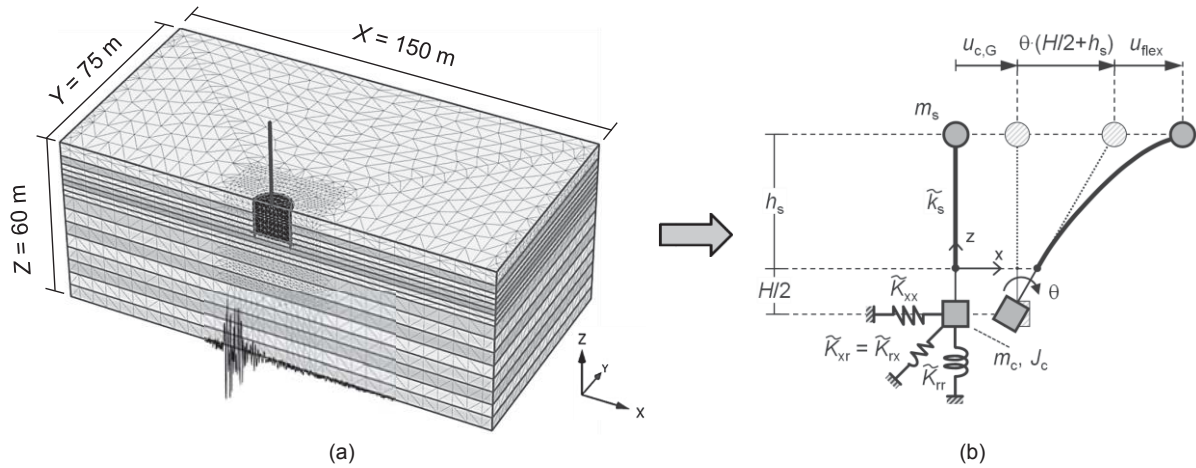


Figure 2: (a) numerical domain modelled in Plaxis 3D; (b) 3DoF model (modified from [1]).

model was implemented in the FE code SAP2000 v.20 [17], where the three independent degrees of freedom are: the horizontal displacement of the foundation relative to the motion applied to the fixed end of the horizontal impedance  $\tilde{K}_{xx}$ ,  $u_{c,G}$ , the angle of caisson rigid rotation  $\theta$  and the flexural displacement of the pier column,  $u_{flex}$  (Fig. 2b). This model turned out to be reliable in reproducing the results obtained in the 3D FE linear viscous-elastic analyses, provided that the *FIM* is applied, that the dynamic impedance matrix is computed referring to the “mobilised” values of  $G$  and  $\xi$  and that the coupled terms  $\tilde{K}_{xr} = \tilde{K}_{rx}$  are considered [1]. This 3DoF model was also adopted to understand the relative influence of the “primary” and “secondary” soil nonlinearities. To this end, the free-field motion (*FFM*) computed at the depth of the caisson centroid,  $z = z_G$ , from preliminary 1D ground response analyses was applied at the fixed end of the pure-translational dynamic impedance,  $\tilde{K}_{xx}$ : following what already done for the 3D FE analyses, these free-field analyses were performed twice, once adopting *HS small* and once through the *LE* method, already implemented in the code MARTA [18] (Tab. 3). Albeit not being rigorous, this procedure permitted to catch the role of primary nonlinearities on the seismic performance of bridge piers over caisson foundations, as it will be clarified in the following section.

#### 4 1D FREE-FIELD GROUND RESPONSE ANALYSES

The input motions applied at the base of the 3DoF model were preliminary computed at

#	model	soil const. model	seismic input	nonlinearities
1	3D	elastic-plastic	bedrock at $z = Z$	$G/G_0$ and $\xi = f(\gamma)$ , primary, secondary
2	3D	linear viscous-elastic	bedrock at $z = Z$	$G/G_0$ and $\xi = f(\gamma)$
3	3DoF	nonlinear viscous-elastic	from 1D free-field analyses with <i>HS small</i> at $z = z_G$	$G/G_0$ and $\xi = f(\gamma)$ , primary
4	3DoF	nonlinear viscous-elastic	from 1D free-field analyses with nonlinear viscous-elastic model at $z = z_G$	$G/G_0$ and $\xi = f(\gamma)$

Table 3: FE analyses carried out to assess the influence of the nonlinear and irreversible soil behaviour.

Record	$F$ (-)	$a_{\max}^{\text{inp}}$ (g)	$I_A^{\text{inp}}$ (m/s)	$T_m^{\text{inp}}$ (s)	$T_D^{\text{inp}}$ (s)
Tolmezzo E-W	1.00	0.316	1.17	0.50	5.220
Assisi E-W	2.00	0.332	1.12	0.24	4.295
Adana E-W	1.05	0.292	1.17	0.62	12.990

Table 4: Parameters of the scaled seismic input motions.

the depth  $z = z_G = H/2$  of the caissons' centroid by performing the above-mentioned 1D ground response analyses in free-field conditions twice, once with the elastic-plastic *HS small* and once with the nonlinear viscous-elastic soil constitutive models. The analyses were carried out imposing at the base of the soil column ( $z = Z = 60$  m) six different high-intensity seismic inputs: for the sake of brevity, only three of them are considered in this paper, whose horizontal acceleration time histories and elastic acceleration spectra are plotted in Figure 3a and b, respectively. The main characteristics of these seismic inputs are listed in Table 4, where  $F$  is the amplification factor adopted to reach the desired level of Arias intensity,  $a_{\max}^{\text{inp}}$  is the peak horizontal acceleration,  $I_A^{\text{inp}}$  is the Arias intensity [19],  $T_m^{\text{inp}}$  is the mean period [20] and  $T_D^{\text{inp}}$  is the strong-motion duration. All the records are characterised by about the same  $I_A^{\text{inp}}$ : moreover, the Assisi record (second line) differs from the Tolmezzo one (first line) in its frequency content ( $T_m^{\text{inp}}$ ), having the same strong-motion duration, while the Adana record (third line) differs from Tolmezzo in  $T_D^{\text{inp}}$ , having about the same frequency content.

The average spectrum resulting from all six records is also plotted in Figure 3b for a damping ratio  $\xi = 5\%$  (equal to that of the bridge pier,  $\xi_s$ ), together with the one resulting from the Italian Building Code [21] for a return period  $T_R = 1424$  years, taken as a reference to check spectrum compatibility in the entire parametric study.

The inputs applied at the base of the *3DoF* models were extracted from the 1D soil column at the depth of the caissons' centroid, as represented in Figure 3c, where the soil column modelled in Plaxis 3D for the elastic-plastic analyses (*HS small*) is given. The results of the free-field ground response analyses are discussed in the following section.

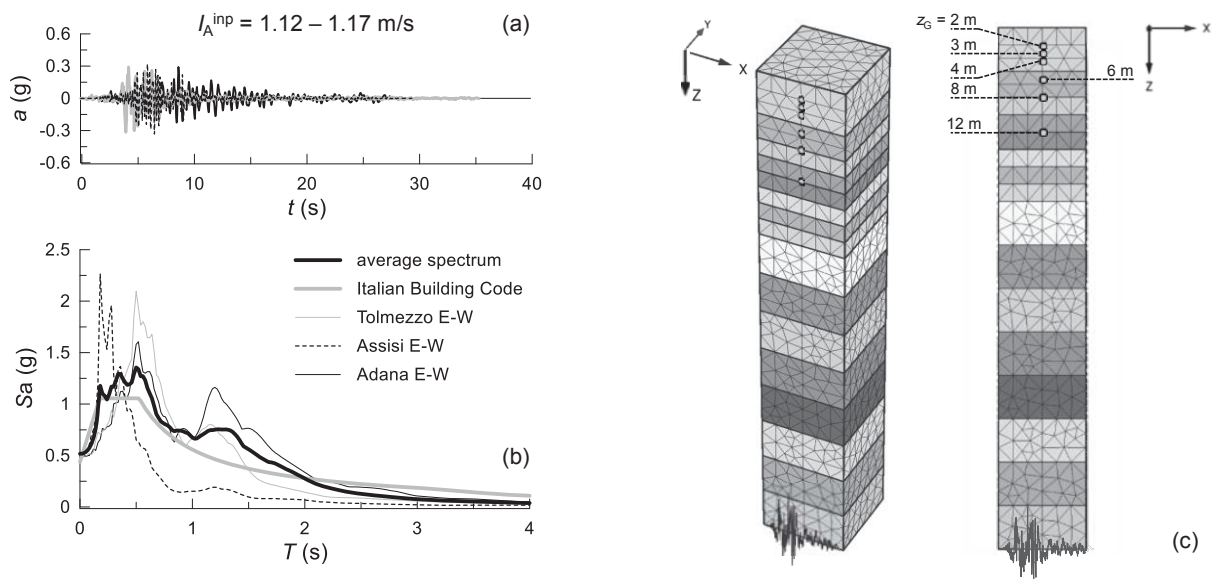


Figure 3: (a) Time histories and (b) elastic spectra of horizontal acceleration of the adopted input motions; (c) soil column modelled in Plaxis for the 1D ground response analysis with *HS small* and depths at which seismic outputs were extracted.



## 5 INFLUENCE OF PRIMARY SOIL NONLINEARITIES ON THE SEISMIC PERFORMANCE

The influence of primary soil nonlinearities was assessed by comparing the seismic performance obtained applying to the *3DoF* model the horizontal acceleration time histories computed at  $z = z_G = H/2$  in the elastic-plastic and the nonlinear viscous-elastic free-field analyses. Hence, a comparison of free-field results only is first made (§ 5.1); then, the seismic performance obtained with the *3DoF* model is assessed (§ 5.2).

### 5.1 Comparison of results in free-field conditions

A sample of results obtained for the soil column is given in Figure 4 referring to the Tolmezzo record, where profiles of the peak horizontal acceleration (a) and shear strain (b) are plotted, together with the contours of the plastic deviatoric strain  $\varepsilon_s^p$  obtained at the end of the earthquake when adopting the *HS small* constitutive model (elastic-plastic analyses, (c)). The deviatoric strain is the second invariant of the strain tensor, defined as follows:

$$\varepsilon_s = \sqrt{\frac{2}{3} \left[ \left( \varepsilon_{xx} - \frac{\varepsilon_v}{3} \right)^2 + \left( \varepsilon_{yy} - \frac{\varepsilon_v}{3} \right)^2 + \left( \varepsilon_{zz} - \frac{\varepsilon_v}{3} \right)^2 + \frac{1}{2} (\gamma_{xy}^2 + \gamma_{yz}^2 + \gamma_{zx}^2) \right]} \quad (1)$$

where  $\varepsilon_{ii}$  and  $\gamma_{ij}$ , for  $i \neq j$  and  $i, j = x, y, z$  are the components of the strain tensor along the three cartesian directions and  $\varepsilon_v = \varepsilon_{xx} + \varepsilon_{yy} + \varepsilon_{zz}$  is the volumetric strain.

The profile of peak horizontal acceleration (Fig. 4a) clearly shows almost overlapping elastic and elastic-plastic profiles from the base of the soil column ( $z = Z = 60$  m) up to a depth  $z \approx 17.5$  m: in this range of depths both constitutive assumptions predict a slight reduction of the peak acceleration with respect to the input one ( $a_{\max}^{\text{inp}} = 0.316$  g). This result is consistent with what observed for the peak shear strain  $\gamma_{\max}$ : indeed, similar trends are computed, with slightly higher  $\gamma_{\max}$  computed when adopting the nonlinear viscous-elastic soil model. Both analyses provide the same maximum peak shear strain  $\gamma_{\max} \approx 0.3\%$  at depth  $z \approx 17.5$  m, above

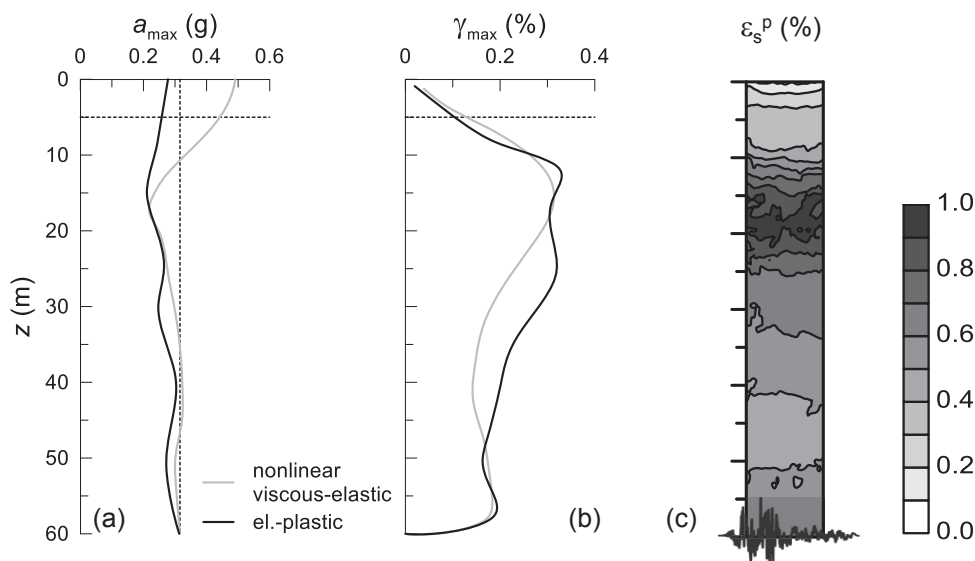


Figure 4: Comparison of 1D free-field ground response analyses when applying the Tolmezzo record: (a) peak acceleration; (b) peak shear strain; (c) contours of the plastic deviatoric strain at the end of the seismic shaking.

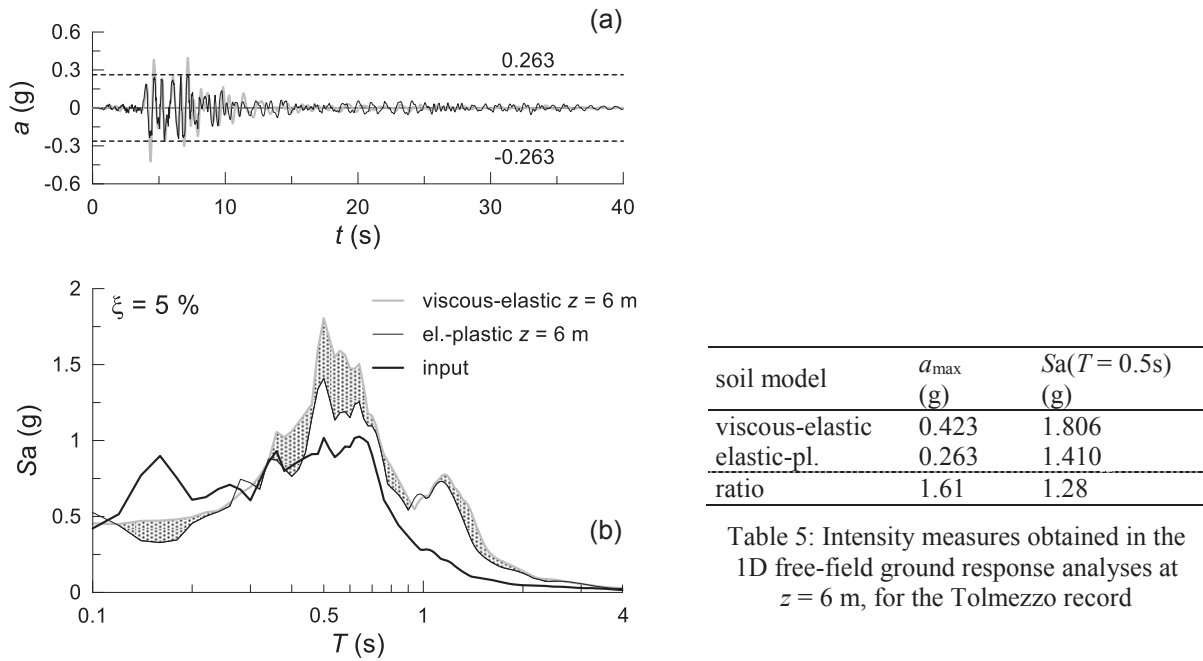


Figure 5: a) Time histories and (b) elastic spectra of horizontal accelerations computed at depth  $z = 6$  m in the viscous-elastic and elastic-plastic 1D free-field ground response analyses, together with the Tolmezzo record applied at the base of the column.

which shear strains still go overlapping with the two models. Due to this high distress experienced by the soil, peak horizontal accelerations  $a_{\max}$  start diverging when approaching the ground surface, with an almost constant peak acceleration in the elastic-plastic analyses ( $a_{\max} \approx 0.28g$  at  $z = 0$ ) whereas a strong amplification of motion is predicted by the elastic analysis ( $a_{\max} \approx 0.50g$  at  $z = 0$ ). This result may be attributed to the nonlinear and irreversible behaviour of foundation soils, mostly triggered at  $z \approx 20$  m, where dissipation of energy occurs, as it is clearly shown by the contours of plastic deviatoric strain  $\varepsilon_s^p$  plotted in Figure 4c, that attains its maximum value of about 1% at the end of the seismic shaking.

The influence of soil dissipating energy introduced by the seismic record on the free-field motion is shown in Figure 5 as well, where the horizontal acceleration time histories (a) and elastic acceleration spectra (b) computed at depth  $z = 6$  m are plotted for the Tolmezzo record. These results are the input motions applied at the node representing the foundation in the 3DoF model when caisson foundations with  $D = 12$  m and  $H/D = 1$  (i.e.  $z_G = 6$  m) are considered. The decrease of horizontal accelerations can be recognised in Figure 5a, where the time history computed with *HS small* shows a cut-off at  $a_{\max} = 0.263$  g, while that obtained with the linear viscous-elastic model attain its peak value  $a_{\max} = 0.423$  g.

Energy dissipation caused by irreversible soil behaviour turned out to be mainly located around the eigenperiods of the free-field soil column, provided that they are effectively activated by the frequency content of the seismic input. Shaded area plotted in Figure 5b indicates the range of periods where elastic acceleration spectrum obtained with the nonlinear viscous-elastic constitutive model is higher than the elastic-plastic one, this pointing out where dissipation of energy occurs. Main reduction of amplitude is located at  $T = 0.5$  s, this being the second eigenperiod of the soil column; less-intense reduction is observed close to  $T = T_0 \approx 1.0$  s, that is the fundamental period of the soil column.

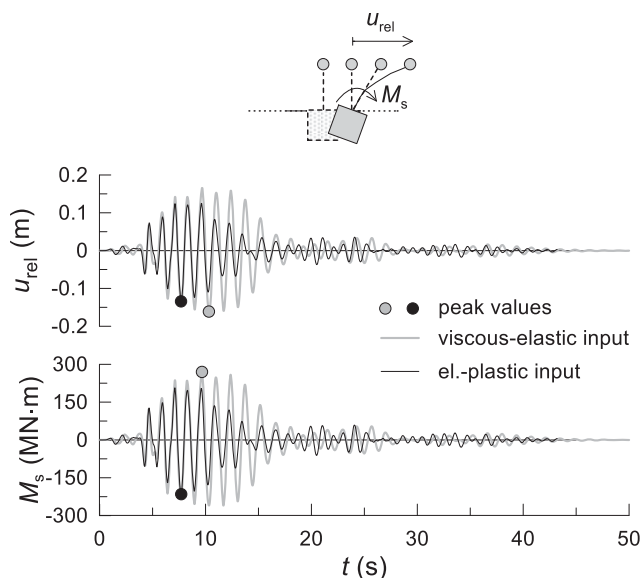
A summary of the obtained values of  $a_{\max}$  and  $Sa(T = 0.5$  s) is given in Table 5.

## 5.2 Seismic performance of the system

The influence of primary nonlinearities on the seismic performance of the whole system was evaluated through the comparison of results obtained applying at the base of the *3DoF* model the free-field motions computed with the *HS small* and the nonlinear viscous-elastic soil models (Fig. 2b). With the three above-mentioned records (Tab. 4) and the fourteen systems considered in the parametric study (Tab. 2), 42 linear dynamic analyses were performed twice in the time domain, this returning a total amount of 84 analyses. A comparison of results is given in Figure 6, where the time histories of deck drift  $u_{rel}$  and bending moment acting at the pier base  $M_s$  are plotted, for the system with  $D = 12$  m,  $H/D = 1$  and  $h_s = 15$  m, subjected to the free-field motions shown in Figure 5a. As it could have been anticipated from the free-field results, peak values  $u_{rel, max}$  and  $M_{s, max}$ , here assumed as seismic performance indexes, attain lower values when considering elastic-plastic soil behaviour. Specifically, an overestimation of about 20% is computed when ignoring soil plasticity, as summarised in Table 6, whereas a quite similar frequency content is obtained for both time histories. Therefore, primary nonlinearities do affect the seismic performance of the system. This contribution is compared to secondary nonlinearities in the following section.

## 6 INFLUENCE OF SECONDARY SOIL NONLINEARITIES ON THE SEISMIC PERFORMANCE

The influence of secondary soil nonlinearities was finally assessed comparing the seismic performance indexes  $u_{rel, max}$  and  $M_{s, max}$  obtained in the proper 3D elastic-plastic analyses of the whole system carried out through the Plaxis numerical model (Fig. 2a and first line of Tab. 3) with the relevant results computed through the *3DoF* model when applying the elastic-plastic (i.e. *HS small*, third line of Tab. 3) 1D free-field motion. Figure 7 shows that the vast majority of results lay above the 1:1 line for both the deck drift (a) and the bending moment at the pier base (b), this indicating that soil irreversible strains developing close to the oscillating foundation during the seismic event play a remarkable role in improving the seis-



input from	$u_{rel, max}$ (m)	$M_{s, max}$ (MN·m)
viscous-elastic 1D	0.166	267.49
elastic-pl. 1D	0.134	220.40
ratio	1.24	1.21

Table 6: Seismic performance indexes computed for the system with  $D = 12$  m,  $H/D = 1$  and  $h_s = 15$  m, Tolmezzo record

Figure 6: Time histories of (a) deck drift and (b) bending moment computed for the system with  $D = 12$  m,  $H/D = 1$  and  $h_s = 15$  m through the *3DoF* model by applying at  $z_G$  the acceleration time histories computed with the viscous-elastic and elastic-plastic 1D free-field ground response analyses.

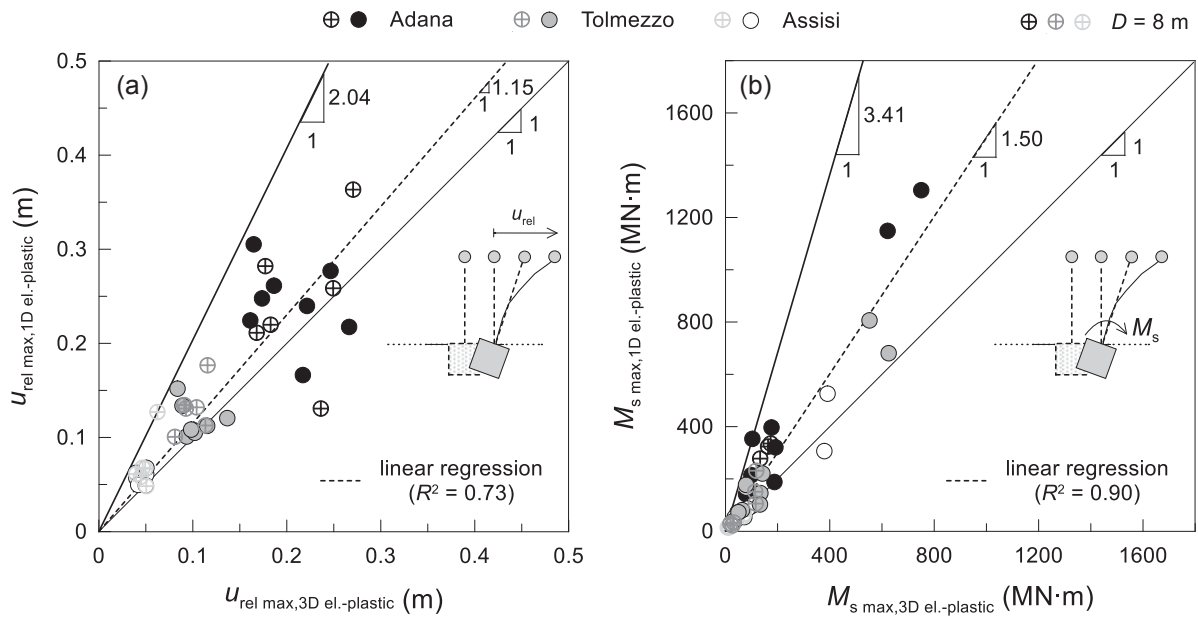


Figure 7: Comparison of results of the 3D elastic-plastic analyses of the whole system with those computed with the 3DoF model applying as input motion the 1D elastic-plastic free-field motion: peak values of (a) deck drift and (b) bending moment.

mic performance of the systems at hand, together with some kinematic interaction effects. In order to quantify the average overestimation of the peak values  $u_{rel, max}$  and  $M_{s, max}$  when performing the analyses with the 3DoF model subjected to the 1D elastic-plastic free-field motion, the slope of a standard linear regression was computed. Values equal to 1.15 and 1.50 were obtained for the deck drift and the bending moment, respectively, while a maximum overestimation of about 2.0 and 3.4 times was obtained, this clearly showing that the influence of secondary soil nonlinearities is stronger in reducing the inertial forces transmitted to the superstructure than the displacements. The role of the applied seismic inputs and of the caisson diameter on the contribution of secondary nonlinearities is not clear enough to draw any conclusion.

Graphs similar to those commented above are given in Figure 8, where the seismic performance computed in the 3D elastic-plastic analyses of the whole system is compared with the one obtained applying the nonlinear viscous-elastic 1D free-field motion to the base of the 3DoF model. As expected, higher slopes are obtained in Figure 8, as now the results include both the effects of primary and secondary nonlinearities: specifically, slopes equal to 1.25 and 1.63 were obtained for  $u_{rel, max}$  and  $M_{s, max}$ , with a maximum overestimation of about 2.73 and 3.87, respectively. The ratio between the slopes of linear regressions shown in Figures 7 and 8 allows to get a quick estimate of the relative influence of the primary and secondary soil nonlinearities: with reference to the average overestimation, about the same ratio is obtained for the deck drift and the bending moment, equal to about 9% ( $1.25/1.15 \approx 1.63/1.50 \approx 1.09$ ). This result suggests that, on average, neglecting primary nonlinearities would imply overestimating the peak values of the deck drift and bending moment of about 9%, whereas disregarding secondary nonlinearities would entail overestimating the seismic performance indexes of about 15 and 50%, respectively for  $u_{rel, max}$  and  $M_{s, max}$ , this proving the bigger role of soil plasticity developed close to the oscillating foundation than the one already triggered in free-field conditions for the cases at hand.

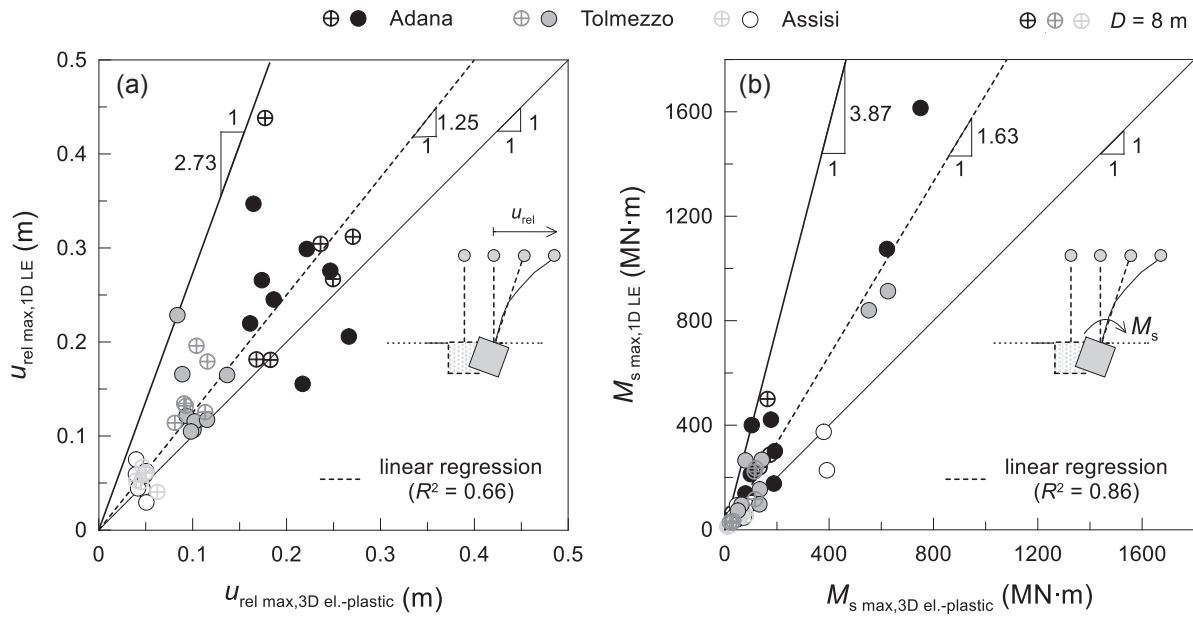


Figure 8: Comparison of results of the 3D elastic-plastic analyses with those computed with the 3DoF model applying as input motion the 1D LE free-field motion: peak values of (a) deck drift and (b) bending moment.

## 7 CONCLUSIONS

In this paper, the influence of irreversible and hysteretic soil behaviour occurring far (primary) and close (secondary) to oscillating caisson foundations supporting bridge piers has been assessed. To this end, free-field motion acting at the depth of the caisson centroids has been evaluated through 1D nonlinear viscous-elastic and elastic-plastic ground response analyses performed applying strong ground motions, capable of activating plastic soil behaviour. Then, the computed acceleration time histories have been applied to the node representing the soil-caisson system in a simple plain-strain 3-degree-of-freedom linear viscous-elastic structural model. The results have been compared with those obtained from a parametric study carried out on the whole soil-caisson-pier-deck system through 3D nonlinear dynamic FE analyses, using the peak deck drift and the bending moment at the base of the pier as performance indexes.

The comparison clearly indicates that, as it could be anticipated, primary soil nonlinearities imply a reduction of both  $u_{rel,max}$  and  $M_{s,max}$ , but only of about 9%, which might be deemed negligible. Conversely, the role of secondary nonlinearities is more pronounced, as this entailed a reduction approaching 15% for the deck drift and even 50% for the bending moment, this clearly indicating the major role of irreversible and hysteretic soil behaviour developing close to the foundation when hit by strong earthquakes.

Two main limitations arise in the study: first, there is the underlying assumption for which the effects of primary and secondary soil nonlinearities can be added. Clearly, this is a strong approximation, as in the inelastic regime the superposition principle does not hold: nonetheless, the discussed results may still shed some light on the relative influence of primary and secondary soil nonlinearities. Second, analyses may need some extension in terms of amount of systems and seismic inputs to be adopted, so as to make the study gain more generality and applicability to cases that have not been directly considered in the analyses, although the discussed results can be deemed suitable to soils whose stiffness linearly increases with depth. However, adopted systems and records already cover a wide range of cases typically encountered in the common practice and are representative of a large variety of input characteristics.



## REFERENCES

- [1] D. Gaudio, S. Rampello, On the assessment of seismic performance of bridge piers on caisson foundations subjected to strong ground motions. *Earthquake Engineering and Structural Dynamics*, **50** (5), 1429-1450, 2021. DOI: <https://doi.org/10.1002/eqe.3407>
- [2] G. Mylonakis, S. Nikolaou, G. Gazetas, Footings under seismic loading: Analysis and design issues with emphasis on bridge foundations, *Soil Dynamics and Earthquake Engineering*, **26**, 824-853, 2006.
- [3] A.S. Veletsos, J.W. Meek, Dynamic behaviour of building-foundation systems, *Earthquake Engineering and Structural Dynamics*, **3**, 121-138, 1974.
- [4] J.P. Wolf, *Dynamic soil-structure interaction*, Prentice-Hall, 1985.
- [5] I.M. Idriss, H.M. Seed, Response of horizontal soil layers during earthquakes, *Journal of the Soil Mechanics and Foundation Division*, ASCE, **94** (SM4) 1003-1031, 1968.
- [6] M.D. Trifunac, A.G. Brady, A study on the duration of strong earthquake ground motion. *Bulletin of the Seismological Society of America*, **65** (3), 581-626, 1975.
- [7] P.W. Mayne, F.H. Kulhawy,  $K_0$  - OCR relationships in soil. *Journal of the Geotechnical Engineering Division*, ASCE, **108** (GT6) 851-872, 1982.
- [8] B.O. Hardin, F.E. Richart, Elastic wave velocities in granular soils. *Journal of the Soil Mechanics and Foundation Division*, ASCE, **89** (SM1) 33-65, 1963.
- [9] S. Rampello, F. Silvestri, G. Viggiani, The dependence of  $G_0$  on stress state and history in cohesive soils. Balkema ed. *1<sup>st</sup> International Symposium on Pre-Failure Deformation Characteristics of Geomaterials – Measurements and Applications*, **2**, 1155-1160, Sapporo, Japan, 1994.
- [10] D. Gaudio, S. Rampello, Equivalent seismic coefficients for caisson foundations supporting bridge piers. *Soil Dynamics and Earthquake Engineering*, **129**, 105955, 2020. DOI: <https://doi.org/10.1016/j.soildyn.2019.105955>
- [11] D. Gaudio, S. Rampello, The influence of soil plasticity on the seismic performance of bridge piers on caisson foundations. *Soil Dynamics and Earthquake Engineering*, **118**, 120-133, 2019. DOI: <https://doi.org/10.1016/j.soildyn.2018.12.007>
- [12] D. Gaudio, S. Rampello, The role of soil constitutive modelling on the assessment of seismic performance of caisson foundations. Silvestri & Moraci eds. *7<sup>th</sup> International Conference on Geotechnical Earthquake Engineering*, Rome, Italy, June 17-20, 2019, pp. 2574-2582.
- [13] R.B.J. Brinkgreve, E. Engine, W.M. Swolfs, *PLAXIS 3D. Reference Manual*, 2013.
- [14] T. Benz, P.A. Vermeer, R. Schwab, A small-strain overlay model. *International Journal for Numerical and Analytical Methods in Geomechanics*, **33** (1), 25-44, 2009.
- [15] H.B. Seed, I.M. Idriss, *Soil moduli and damping factors for dynamic response analyses*, Report No. EERC 70-10. Earthquake Engineering Research Centre, University of California, Berkeley, California, 1970.
- [16] M. Vucetic, R. Dobry, Effect of soil plasticity on cyclic response. *Journal of Geotechnical Engineering*, **117** (1), 89-107, 1991.

- [17] CSI (Computer and Structures Inc.), *SAP2000: integrated finite element analysis and design of structures*, 2017.
- [18] L. Callisto, *MARTA v. 1.1: a computer program for the site response analysis of a layered soil deposit*, 2015.
- [19] A. Arias, *A measure of earthquake intensity. Seismic design for nuclear power plants*. Cambridge MA: Massachusetts Institute of Technology Press, Hansen RJ ed., pp. 438-483, 1970.
- [20] E.M. Rathje, N. Abrahamson, J.D. Bray, Simplified frequency content estimates of earthquake ground motions. *Journal of Geotechnical and Geoenvironmental Engineering*, ASCE, **124** (2), 150-159, 1998.
- [21] Ministero delle Infrastrutture. *Norme tecniche per le Costruzioni*, Gazzetta Ufficiale della Repubblica Italiana 42, Decreto Ministero Infrastrutture 17.01.2018, Rome (in Italian), 2018.

## INFLUENCE OF SCOUR ON DYNAMIC IMPEDANCES OF BRIDGE SHALLOW FOUNDATIONS

C. Antonopoulos<sup>1</sup>, E. Tubaldi<sup>1</sup>, S. Carbonari<sup>2</sup>, F. Gara<sup>2</sup>, and F. Dezi<sup>3</sup>

<sup>1</sup> Department of Civil and Environmental Engineering  
University of Strathclyde  
Glasgow, Scotland  
e-mail: {christos.antonopoulos,enrico.tubaldi}@strath.ac.uk

<sup>2</sup> Department of Construction, Civil Engineering and Architecture (DICEA)  
Università Politecnica delle Marche  
Ancona, Italy  
{s.carbonari,f.gara}@staff.univpm.it

<sup>3</sup> Department of Economics, Science and Law (DESD)  
University of the Republic of San Marino  
Republic of San Marino  
francesca.dezi@unirmsm.sm

---

### Abstract

*Many bridges in earthquake-prone countries cross waterways and have foundations in riverbeds, and thus are exposed to flood, which may cause scour and a change of the bridge dynamics. The present study illustrates a modeling strategy for investigating numerically the influence of scour on the dynamic behaviour of bridges with scoured shallow foundations. The proposed strategy is based on the evaluation of the impedance functions of a massless rigid foundation resting on an elastic half-space under increasing depths of scour. The derived impedance functions are used to evaluate the effects of scour on the dynamic behaviour of a Soil-Foundation-Structure system representative of a bridge pier. In particular, the changes in the fundamental vibration period due to scour are investigated. The results of the study can be used for developing vibration-based scour detection techniques and for investigating the seismic response of scoured bridges.*

**Keywords:** Scour, Bridges, Soil-structure Interaction, Foundation Impedances

---

## 1 INTRODUCTION

Scour is the first cause of bridge failure worldwide [1-3], inducing not only traffic disruption but also significant socio-economic losses and fatalities [4-6]. Bridge scour is the erosion of sediments around bridge piers and abutments due to flowing water. Scour can be classified into natural, contraction and local scour, being the latter the most critical one. Particularly, local scour is formed due to local features, such as bridge piers and abutments, that obstruct the flow, leading to increased local flow velocities and turbulence levels that result in vortices and thus in local sediment movements and erosion around underwater foundations [7]. Scour may cause a significant loss of foundation carrying capacity [8, 9] and a reduction of the stiffness of bridges [10-16]. A great number of bridges worldwide, such as masonry-arch bridges, has shallow foundations that are more vulnerable to scour in comparison with those with deep foundations. Interestingly, the majority of the studies in the literature focus on the effects of scour on bridges with deep foundations, whereas studies related to bridges with shallow foundations are quite limited. Only recently, some research efforts have aimed at filling this knowledge gap [17-19].

Scour causes a change of the global stiffness of bridges, and thus a different response to dynamic loadings, such as earthquakes. In particular, scour can alter dramatically both the kinematic and the inertial soil-structure interaction, resulting in a reduction of the fundamental vibration frequency. There are several studies about the combined effect of scour and earthquake hazard on the dynamic properties of bridges [20-22], however most of them focus on bridges with deep foundations. To account for soil-foundation-structure (SFS) interaction effects, the sub-structure approach is usually employed, simulating the soil-foundation system in inertial interaction analyses through impedance functions [23-25]. These functions represent the frequency dependent stiffness and damping characteristics of soil-foundation system and govern relationships between forces and displacements of the compliant restraints at the foundation level. To the author's knowledge, only Guo [18] investigated the seismic response of bridges with scoured shallow foundations. Specifically, the foundation impedance functions were calculated under scour hazard, which led to a reduction of the foundation stiffness and radiation damping. It was found that scour reduces seismic force demands but may increase the displacement demands. Given the existence of a great number of bridge footings on shallow foundations in earthquake-prone countries and the current frequent occurrence of extreme weather events, further research on the effects of scour on the dynamic response of bridges is imperative.

This study investigates numerically the impact of scour on the dynamic response of bridges with shallow foundations. For this purpose, the case of a massless rigid strip foundation resting on a homogenous elastic half-space is modelled in Abaqus [26] under various scour scenarios to estimate the impedance functions of the soil-foundation system. Subsequently, the derived impedance functions are used to evaluate the dynamic behavior of a SFS systems, representative of a bridge pier, with particular focus on the fundamental vibration frequency.

## 2 NUMERICAL ESTIMATION OF FOUNDATIONS IMPEDANCES

In this section, a massless rigid strip foundation resting on a homogenous elastic soil domain is investigated. For the sake of simplification, a plane-strain problem assumption is made, based on taking into account the aspect ratios of masonry bridge's piers characterized by a slender rectangular shape. The model developed in Abaqus is firstly validated with numerical analytical solutions provided by Hryniewicz [23] and then adopted for the estimation of the impedance functions considering various scour profiles.

## 2.1 Finite element model

The modelling strategy developed in Abaqus for the estimation of impedance functions of the studied strip foundation is described in this subsection. The impedance functions can be expressed in non-dimensional form as a function of the non-dimensional frequency  $a_0 = \frac{\omega b_f}{V_s}$ , where  $\omega$  is the circular frequency of the excitation,  $b_f$  the half width of the foundation, and  $V_s$  the shear wave velocity.

The dimensions of the finite soil domain are assumed to be 125 x 62.5 m, while infinite elements are placed at the boundaries in order to satisfy the radiation condition preventing wave reflections (Figure 1i). These infinite elements are long strips with width equal to the half width of the soil domain, i.e. 62.5 m. Since a plane-strain assumption is made, the soil domain consists of four node plane-strain elements (CPE4), whereas the boundaries consists of plane-strain solid continuum infinite elements (CINPE4). The soil is characterized by a Young modulus ( $E$ ), Poisson's ratio ( $\nu$ ) and density ( $\rho$ ) equal to 162.41 MPa, 0.25 and 1600 kg/m<sup>3</sup>, respectively. The rigid strip foundation with width  $2b_f = 1$  m is simulated through a rigid-body constrain applied to the set of nodes belonging to the soil-foundation interface (at the ground surface). Considering that the estimated impedance functions are presented in a non-dimensional form, the selected values for the characteristics of the soil and foundation do not affect the results but are herein indicated because they have to comply with the adopted mesh for convergence issues. Indeed, in order to accurately capture the wave propagation, the mesh size of the soil domain should satisfy the following relation [27, 28]:

$$l_{max} \leq \frac{\lambda_{min}}{10} \leq \frac{V_{s,min}}{10 f_{max}} \quad (1)$$

where  $l_{max}$  is the maximum element size,  $\lambda_{min}$  is the shear wavelength and  $f_{max}$  is the maximum frequency of interest, which, for seismic applications, is typically within the range 0-15 Hz. For a given element size, the maximum dimensionless excitation frequency  $a_0$  satisfies:

$$a_0 \leq \frac{2\pi b_f}{10 l_{max}} \quad (2)$$

It is worth noting that a 1% damping ratio is added with a Rayleigh model to the soil domain in order to lessen the numerical fluctuation of the results. Considering above requirements, a refined mesh around the foundation is employed. Specifically, a square mesh 0.005 x 0.005 (m) and 0.025 x 0.025 (m) is used nearby the left and right sides of the foundation, respectively. The different mesh sizes at each part of the foundation aim at reducing the computational cost and facilitating the removal of elements at the next stages for the various scour simulations (see Section 2.4.). In the rest of the soil domain, a bias mesh towards to the boundaries is used with maximum element size  $l_{max} = 0.3$  m.

## 2.2 Methodology

The impedance functions are estimated by means of steady-state analyses by applying harmonic unit amplitude displacements at the centroid of the foundation (master node) and by measuring the corresponding harmonic reaction forces (Figure 1ii). The harmonic motion of the master node can be expressed with the following equation:



$$\begin{bmatrix} P(\omega) \\ Q(\omega) \\ M(\omega)/b_f \end{bmatrix} = \begin{bmatrix} k_{zz} + id_{zz} & 0 & 0 \\ 0 & k_{xx} + id_{xx} & k_{xr_y} + id_{xr_y} \\ 0 & k_{xr_y} + id_{xr_y} & k_{r_y r_y} + id_{r_y r_y} \end{bmatrix} \begin{bmatrix} w_0(\omega) \\ u_0(\omega) \\ \varphi_0(\omega)b_f \end{bmatrix} \quad (3)$$

where  $w_0$ ,  $u_0$  are the displacement amplitudes along the  $z$  and  $x$  directions, respectively,  $\varphi_0$  is the rotation amplitude, and  $k_{ij}$ ,  $d_{ij}=c_{ij}\omega$  are frequency-dependent quantities describing the real and the imaginary parts of the impedance functions, respectively, for the foundation response in the  $i$ -th direction due to the excitation in the  $j$ -th direction. Figure 2 illustrates forces and displacements along the various directions. The coefficients  $k_{ij}$  and  $d_{ij}$  evaluated numerically are presented as a function of the dimensionless frequency  $a_0$  and compared with the analytical estimates obtained by Hryniewicz [23]. This procedure will be also repeated for two scour layouts, characterized by different geometries (see Section 2.4.).

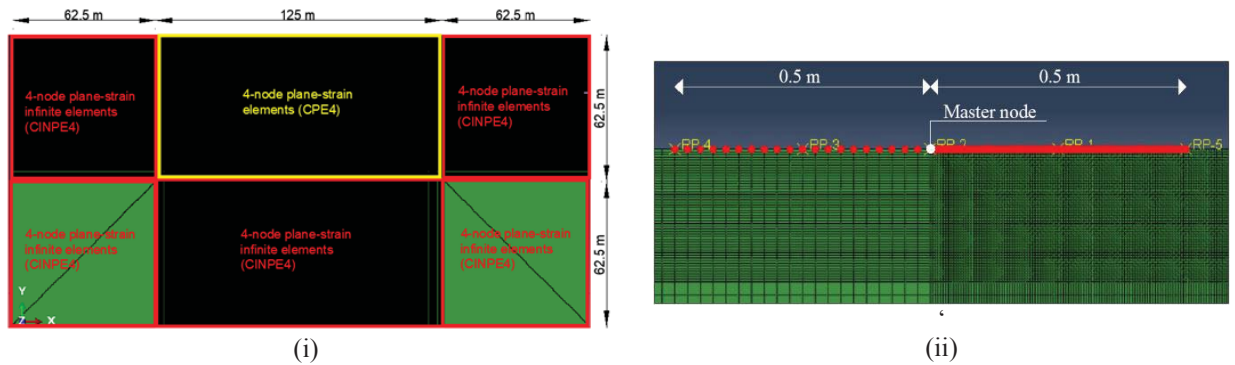


Figure 1: (i) FE model of the soil domain with infinite elements at boundaries, (ii) Rigid-body constraint used to simulate the massless rigid strip foundation.

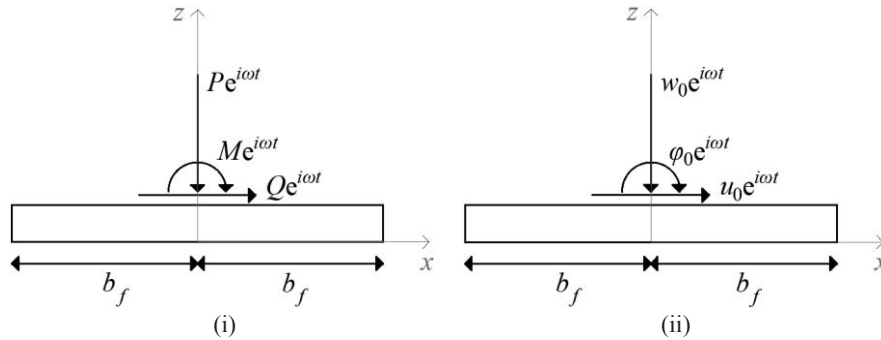


Figure 2: (i) Forces and (ii) displacements of the strip foundation.

### 2.3 Validation of numerical model

In this subsection, the previously described numerical model is validated by comparing the derived impedance functions with those obtained by Hryniewicz [23]. It is noteworthy that in Hryniewicz [23] the coupling between the horizontal and rotational response of the foundation is neglected (i.e.  $k_{xr_y} = 0$ ,  $d_{xr_y} = 0$ ). However, this effect is expected to be not significant and for this reason in the numerical study the rotation of the master node is restrained when a unit horizontal displacement is applied and vice-versa. The harmonic analyses are carried out for frequencies in the range between 3.2 Hz and 200 Hz, corresponding to values of the dimensionless frequency  $a_0$  between 0.05 and 3.11. The derived impedance functions (NS-IC)

are depicted and compared with Hryniewicz's ones in Figure 3. The acronym NS stands for the case of "No Scour".

In general, the derived real and imaginary parts of the impedance functions converge with the analytically estimated ones. Nevertheless, some differences are observed for the real part of the rotational behaviour ( $k_{r_y r_y}$ ), which may be due to the approximation introduced by Hryniewicz [23] for deriving the problem solution. As mentioned before, the maximum element size of the finite soil domain is  $l_{max} = 0.3$  m, which, according to Eq. 2, leads to a maximum dimensionless frequency  $a_0 = 1.05$ . However, the application of a biased mesh around the foundation with element size significantly smaller than  $l_{max}$  results in a satisfactory agreement between the derived and analytical data also for higher frequencies (up to  $a_{0,max} = 3.11$ ).

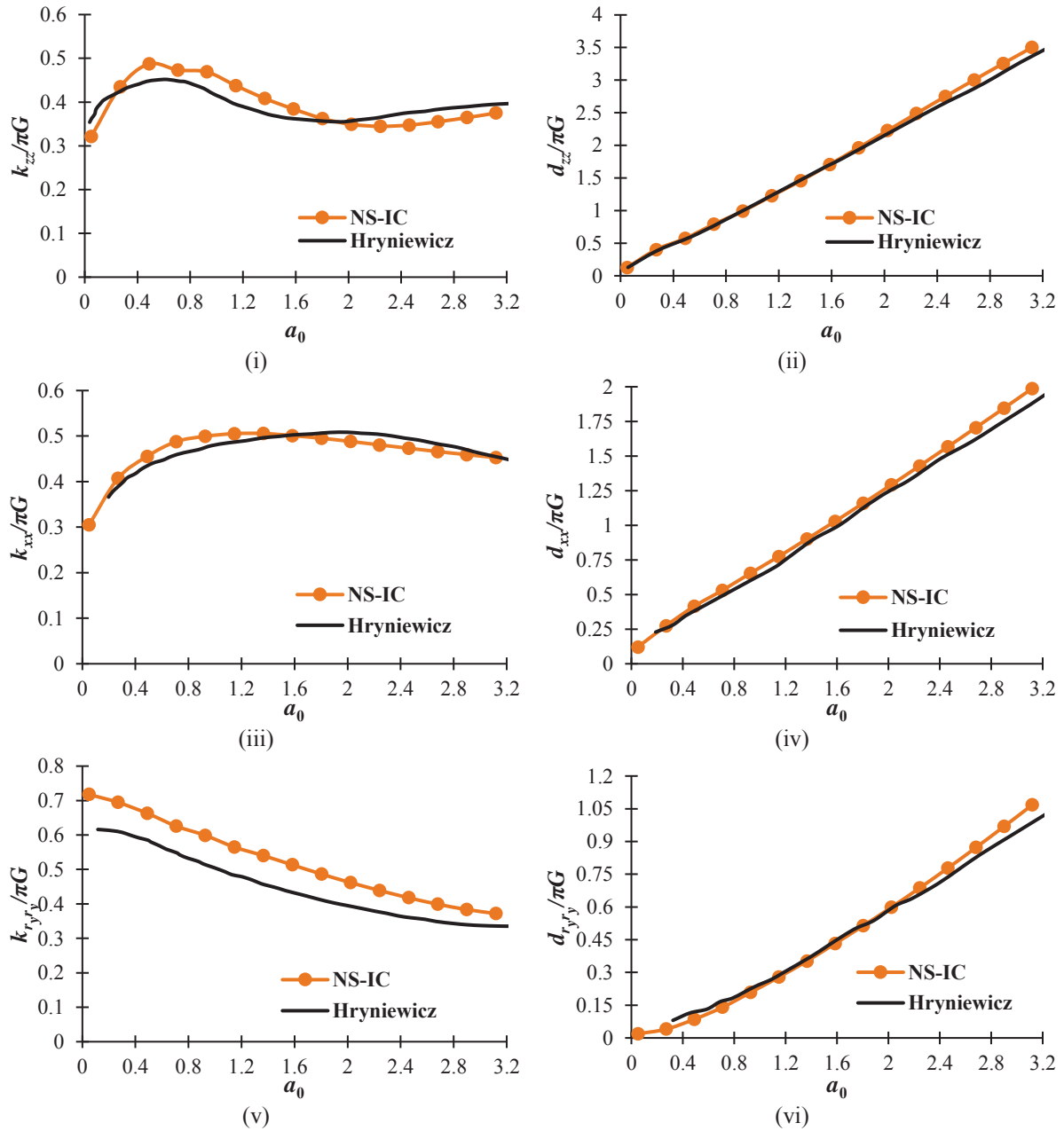


Figure 3: Comparisons of impedance functions obtained numerically (NS-IC) with those developed by Hryniewicz (i)  $k_{zz}$ , (ii)  $d_{zz}$ , (iii)  $k_{xx}$ , (iv)  $d_{xx}$ , (v)  $k_{r_y r_y}$ , (vi)  $d_{r_y r_y}$ .

## 2.4 Impact of scour on the foundation impedances

This subsection investigates the changes of the impedance functions of the foundation due to scour. Specifically, two triangular shaped scour scenarios with different widths and depths are considered, corresponding to one fourth (denoted as TS1/4) and three eighth (denoted as TS3/8) of the width of the foundation subjected to scour (Figure 4), respectively. Moreover, the upstream scour hole slope is assumed equal to  $\varphi=30^\circ$ , whereas the downstream scour slope is approximately half of the upstream slope [29].

The impedance functions of the foundation under the various scour scenarios are derived by removing the corresponding finite elements from the soil domain beneath the foundation and rerunning the harmonic analyses. It must be mentioned that the results are obtained by taking the coupling phenomenon between the horizontal and rotation response of the foundation into account (Figure 5). In general, it can be noticed that increasing the scour hole dimensions leads to a reduction of both real and imaginary components of the impedance functions for low frequencies. On the other hand, for high values of  $\alpha_0$ , increasing the scour depth and width results in an increase of the real part of the impedance functions. Moreover, it is remarkable that the values of the vertical real component ( $k_{zz}$ ) are higher than the case of no scour for higher frequencies.

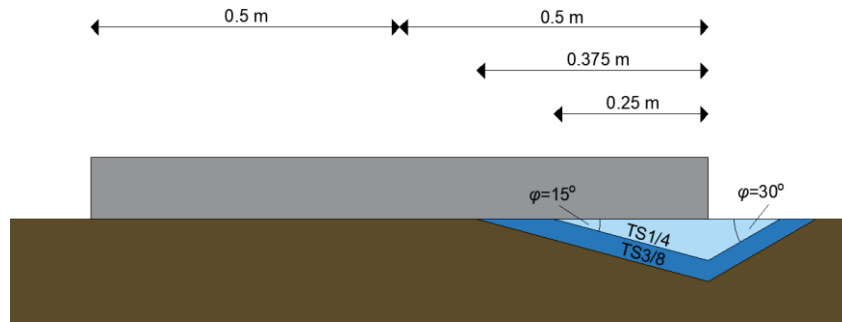


Figure 4: Geometry of the 3 different scour hole scenarios investigated.

## 3 IMPACT OF SCOUR ON FUNDAMENTAL VIBRATION FREQUENCY OF A SFS SYSTEM

The foundation impedance functions for various scour scenarios estimated in Section 2, are herein used to investigate the impact of scour on the fundamental vibration frequency of a SFS system, representative of a bridge pier. Initially, the formulation of the dynamic problem is presented, and then the fundamental vibration frequency of the SFS system is calculated solving the eigenvalue problem for different levels of scour.

### 3.1 Problem formulation for SFS system with scoured foundations

The considered SFS model consists of a superstructure with lumped mass  $m_s$ , lateral stiffness  $k_s$ , height  $h_s$ , and a foundation with mass  $m_f$ , height  $2h_f$ , width  $2b_f$  and mass moment of Inertia  $I_f$  (Figure 6). The foundation rests on a soil domain with shear modulus  $G$ , mass density  $\rho$  and Poisson's ratio  $\nu$ , while the soil-foundation compliance is expressed through the already calculated impedance functions (see Section 2.4.). The system has three degrees of freedom, namely the foundation translation ( $u_f$ ) and rotation ( $\theta_f$ ), and the relative displacement  $u_s$  of mass  $m_s$  with respect to the base.

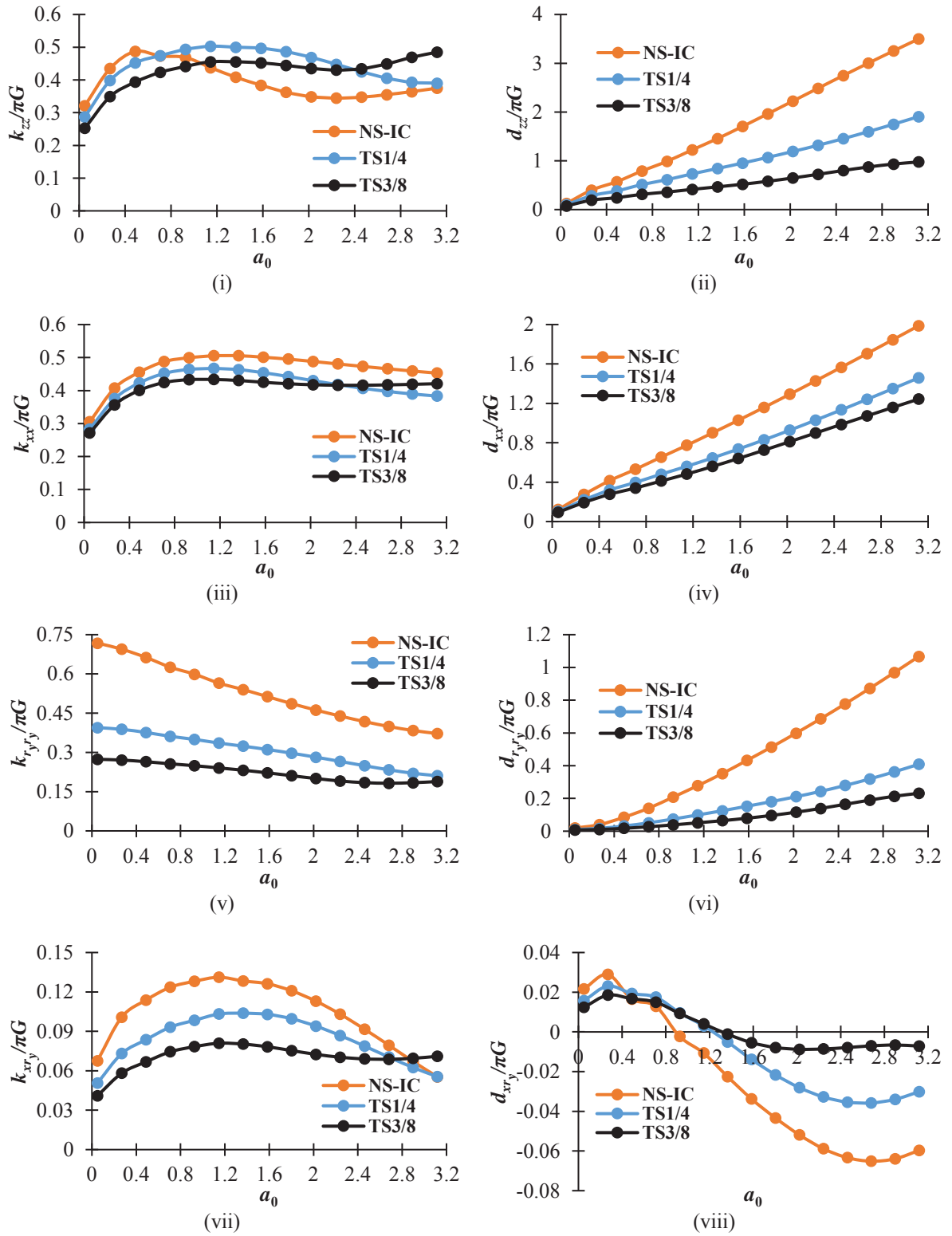


Figure 5: Comparisons of the calculated impedance functions for different scour scenarios (i)  $k_{zz}$ , (ii)  $c_{zz}$ , (iii)  $k_{xx}$ , (iv)  $c_{xx}$ , (v)  $k_{yy}$ , (vi)  $c_{yy}$ , (vii)  $k_{xy}$ , (viii)  $c_{xy}$

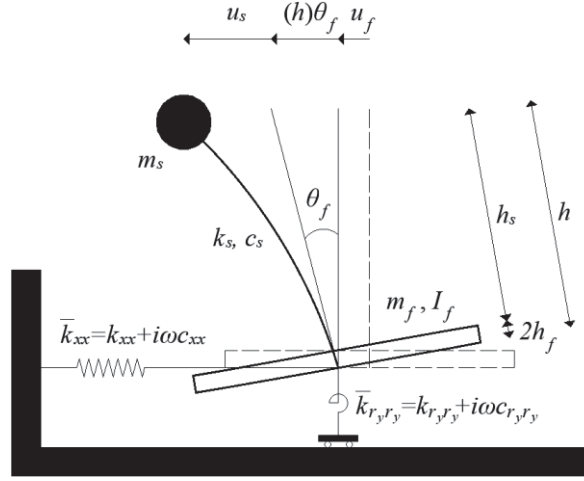


Figure 6: Model of the SFS system (coupling terms are not illustrated).

The equation of motion of the free vibrations for the above described SFS system can be expressed in the frequency domain in a vector form as:

$$-\omega^2 \mathbf{M} \bar{\mathbf{U}} + i\omega \mathbf{C}(\omega) \bar{\mathbf{U}} + \mathbf{K}(\omega) \bar{\mathbf{U}} = 0 \quad (4)$$

where  $\bar{\mathbf{U}}$  denotes the Fourier transform of the vector collecting the system translational and rotational degrees of freedom, while  $\mathbf{M}$ ,  $\mathbf{C}$  and  $\mathbf{K}$  are the mass, damping and stiffness matrices of the system, respectively. Vector and matrices appearing in Eq. 4 are expressed as follows [30]:

$$\mathbf{U} = \begin{bmatrix} u_f & \theta_f & u_s \end{bmatrix}^T \quad (5)$$

$$\mathbf{M} = \begin{bmatrix} m_f + m_s & m_f h_f + m_s h & m_s \\ m_f h_f + m_s h & I_f + m_f h_f^2 + m_s h^2 & m_s h \\ m_s & m_s h & m_s \end{bmatrix} \quad (6)$$

$$\mathbf{C}(\omega) = \begin{bmatrix} c_{xx}(\omega) & b_f c_{xr_y}(\omega) & 0 \\ b_f c_{xr_y}(\omega) & b_f^2 c_{r_yr_y}(\omega) & 0 \\ 0 & 0 & c_s \end{bmatrix} \quad (7)$$

$$\mathbf{K}(\omega) = \begin{bmatrix} k_{xx}(\omega) & b_f k_{xr_y}(\omega) & 0 \\ b_f k_{xr_y}(\omega) & b_f^2 k_{r_yr_y}(\omega) & 0 \\ 0 & 0 & k_s \end{bmatrix} \quad (8)$$

For the sake of simplicity, the damping of the system is neglected by assuming the imaginary parts of the impedance functions to be zero. Therefore, the fundamental vibration frequency of the system can be found by solving the eigenvalue problem of Eq. 4, which can be rewritten as follows:

$$\begin{aligned} -\omega^2 m_s (\bar{u}_f + h \bar{\theta}_f + \bar{u}_s) - \omega^2 m_f (\bar{u}_f + h_f \bar{\theta}_f) + \bar{k}_{xx} \bar{u}_f + b_f \bar{k}_{xr_y} \bar{\theta}_f &= 0 \\ -\omega^2 m_s h (\bar{u}_f + h \bar{\theta}_f + \bar{u}_s) - \omega^2 I_f \bar{\theta}_f - \omega^2 m_f h_f (\bar{u}_f + h_f \bar{\theta}_f) + b_f \bar{k}_{xr_y} \bar{u}_f + b_f^2 \bar{k}_{r_yr_y} \bar{\theta}_f &= 0 \\ -\omega^2 m_s (\bar{u}_f + h \bar{\theta}_f + \bar{u}_s) + \bar{k}_s \bar{u}_s &= 0 \end{aligned} \quad (9)$$



where  $\bar{k}$  contains both the real and imaginary part of the impedances ( $\bar{k}_{ij}=k_{ij}+i\omega c_{ij}$ ).

Eq. 9i and Eq. 9iii can be written as:

$$\bar{\theta}_f = -\frac{\omega^2 m_s (\bar{u}_f + \bar{u}_s) - \bar{k}_{xx} \bar{u}_f + \omega^2 m_f \bar{u}_f}{-b_f \bar{k}_{xry} + h\omega^2 m_s + h_f \omega^2 m_f} \quad (10)$$

$$\bar{\theta}_f = \frac{\bar{k}_s \bar{u}_s - \omega^2 m_s (\bar{u}_f + \bar{u}_s)}{h\omega^2 m_s} \quad (11)$$

Equating Eq. 10 and Eq. 11 one obtains:

$$\bar{u}_f = \frac{\frac{\bar{k}_s \bar{u}_s - \omega^2 m_s \bar{u}_s}{h\omega^2 m_s} + \frac{\omega^2 m_s \bar{u}_s}{-b_f \bar{k}_{xry} + h\omega^2 m_s + h_f \omega^2 m_f}}{\frac{1}{h} - \frac{\omega^2 m_f - \bar{k}_{xx} + \omega^2 m_s}{-b_f \bar{k}_{xry} + h\omega^2 m_s + h_f \omega^2 m_f}} \quad (12)$$

Entering Eq. 12 into Eq. 11 yields:

$$\bar{\theta}_f = \frac{\bar{k}_s \bar{u}_s - \omega^2 m_s \left( \bar{u}_s + \frac{\frac{\bar{k}_s \bar{u}_s - \omega^2 m_s \bar{u}_s}{h\omega^2 m_s} + \frac{\omega^2 m_s \bar{u}_s}{-b_f \bar{k}_{xry} + h\omega^2 m_s + h_f \omega^2 m_f}}{\frac{1}{h} - \frac{\omega^2 m_f - \bar{k}_{xx} + \omega^2 m_s}{-b_f \bar{k}_{xry} + h\omega^2 m_s + h_f \omega^2 m_f}} \right)}{h\omega^2 m_s} \quad (13)$$

Entering Eq. 12 and Eq. 13 into Eq. 9ii finally gives the following homogeneous equation:

$$(\alpha + \beta + \gamma) \bar{u}_s = 0 \quad (14)$$

where:

$$\alpha = (-b_f \bar{k}_{xry} + h_f m_f \omega^2 + h m_s \omega^2) \delta \quad (15)$$

$$\beta = \left( b_f^2 \bar{k}_{r_y r_y} - h^2 m_s \omega^2 - h_f^2 m_f \omega^2 - I_f \omega^2 \right) \frac{\bar{k}_s - m_s \omega^2 (1 - \delta)}{h m_s \omega^2} \quad (16)$$

$$\gamma = -h m_s \omega^2 \quad (17)$$

$$\delta = \frac{\frac{\bar{k}_s - m_s \omega^2}{h m_s \omega^2} - \frac{m_s \omega^2}{b_f \bar{k}_{xry} - h m_s \omega^2 - h_f m_f \omega^2}}{\frac{\bar{k}_{xx} - m_f \omega^2 - m_s \omega^2}{b_f \bar{k}_{xry} - h m_s \omega^2 - h_f m_f \omega^2} - \frac{1}{h}} \quad (18)$$

The solution of the eigenvalue problem described by Eq. 14 is elaborate, since impedances  $k_{xx}$ ,  $k_{xry}$ ,  $k_{ryry}$  are functions of the excitation frequency and depend on  $G$ ,  $V_s$ ,  $b_f$ . In literature there are various approaches for solving this eigenvalue problem, and thus to evaluate the system resonance frequency  $\tilde{\omega}$  (see e.g. [31, 32]). In this paper, the resonance frequency is derived by solving repeatedly Eq. 14. In more detail, each time Eq. 14 is solved for the values

of the impedance function  $k_{xx}$ ,  $k_{xy}$ ,  $k_{ry}$ , which correspond to a specific excitation of frequency  $\omega$ . The one for which  $\omega = \tilde{\omega}$  is the solution of the problem.

The above described procedure is implemented considering a SFS whose properties are consistent with the the EuroProteas' prototype [33]. The superstructure is characterised by a height  $h_s = 4.2$  m, lateral stiffness  $k_s = 2672.16$  kN/m<sup>2</sup>, mass  $m_s = 6.11$  ton/m and it is based on a strip foundation with width  $2b_f = 3$  m, thickness  $2h_f = 0.4$  m mass  $m_f = 3.05$  ton/m and moment of inertia  $I_f = 2.33$  ton·m<sup>2</sup>/m. The soil beneath the foundation is described by a shear modulus  $G = 31.47$  MPa and shear wave velocity  $V_s = 130$  m/s. Figure 7 illustrates the values of the fundamental frequency of the system for different levels of scour, calculated using the impedance functions of Section 2. It can be observed that the natural frequency of the system decreases linearly for increasing widths and thus depths of scour. The reduction of frequency is of the order of 30% when the width of the scour hole beneath the foundation is about 1/3 of the foundation total width.

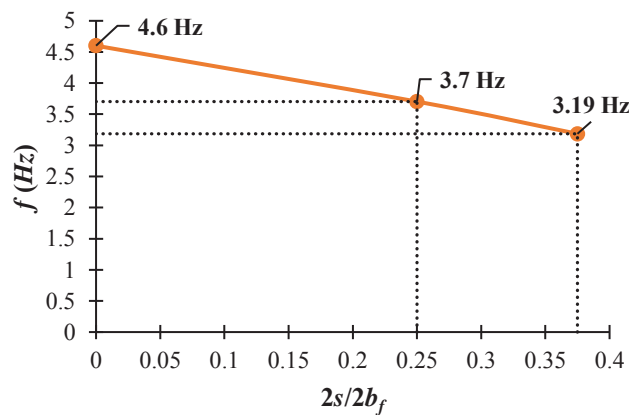


Figure 7: Fundamental vibration frequency of the SFS system for four different scour scenarios.

## 4 CONCLUSIONS

The impact of scour on the dynamic behaviour of bridges has been studied in this paper, by considering a soil-foundation-structure (SFS) system representative of a bridge pier. This SFS system consists of a single degree of freedom superstructure on a rigid strip foundation resting on an elastic soil domain. Initially, a massless rigid strip foundation is simulated in Abaqus to calculate its impedance functions in the case of no scour. Subsequently, the model is validated by comparing the derived impedance functions with the analytical estimates obtained by Hryniewicz [23]. Consequently, the model is used for a numerical investigation of the effects of scour on impedances, considering two scour scenarios with increasing width and depth. Based on the results of this study, the following conclusions can be drawn:

- In general, the foundation impedances are affected differently by scour, depending on the scour hole size and excitation frequency.
- The values of both the real and imaginary parts of the impedance functions decrease for increasing scour width (and thus depth) at low frequencies. On the other hand, for high frequencies a clear general trend cannot be identified, since scour affects the various components differently.

In the second part of the paper, the derived impedance functions are used to investigate the impact of scour on the fundamental vibration frequency of a SFS system, representative of a bridge pier. A linear decrease of the vibration frequency of the system is observed for increasing widths of scour. The variations of frequency are quite significant.

The results of this study can be used to develop inverse techniques for evaluating the extent of scour beneath bridge foundations based on an estimation of the changes of the vibration frequency of SFS systems. Future studies will consider a wider range of SFS systems and also three-dimensional models for the bridges and the soil domain.

## ACKNOWLEDGEMENTS

This work was supported by funding from the National Centre for Resilience (project title “Evaluating the benefit of structural health monitoring for improving bridge resilience against scour”) and by the Scottish Road Research Board (project title “Decision Support System based on “adaptive” Flood Level Markers”).

## REFERENCES

- [1] A.M. Shirole, R.C. Holt, *Planning for a Comprehensive Bridge Safety Assurance Program. Transportation Research Record*, 1290, 39-50, 1991.
- [2] J.L. Briaud, C.F.K. Ting, H.C. Chen, R. Gudavalli, S. Perugu, G. Wei, SRICOS: Prediction of Scour Rate in Cohesive Soils at Bridge Piers. *Journal of Geotechnical and Geoenvironmental Engineering*, **125**(4), 237-246, 1999.
- [3] K. Wardhana, F.C. Hadipriono, Analysis of Recent Bridge Failures in the United States. *Journal of Performance of Constructed Facilities*, **17**(3), 144-150, 2003.  
[https://doi.org/10.1061/\(ASCE\)0887-3828\(2003\)17:3\(144\)](https://doi.org/10.1061/(ASCE)0887-3828(2003)17:3(144))
- [4] P.F. Lagasse, P.E. Clopper, L.W. Zevenberge, L.G. Giraldo, Countermeasures to protect bridge piers from scour. NCHRP Report 593, Transportation research board, National research council, 2007.
- [5] R. Lamb, P. Garside, P. Raghav, J.W. Hall, A Probabilistic Model of the Economic Risk to Britain’s Railway Network from Bridge Scour During Floods. *Risk Analysis*, **39**(11), 2457–2478, 2019. <https://doi.org/10.1111/risa.13370>
- [6] A. Pizarro, S. Manfreda, E. Tubaldi, The science behind scour at bridge foundations: A review. *Water*, **12**(2), 374, 2020.
- [7] A.M. Kirby, M. Roca, A. Kitchen, M. Escameia, O.J. Chesterton, *Manual on Scour at Bridges and Other Hydraulic Structures - Second Edition*. CIRIA742, 2015.
- [8] Y.N. Kishore, S.N. Rao, J.S. Mani, The Behavior of Laterally Loaded Piles Subjected to Scour in Marine Environment. *KSCE Journal of Civil Engineering*, **13**(6), 403–406, 2009.  
<https://doi.org/10.1007/s12205-009-0403-2>
- [9] F. Li, T. Peisan, W. Lixian, C. Mingsheng, Investigation on Lateral Bearing Capacity of Monopile under Combined Vertical-Lateral Loads and Scouring Condition. *Marine Georesources and Geotechnology*, 1521-0618, 2020.  
<https://doi.org/10.1080/1064119X.2020.1719562>
- [10] S. Foti, D. Sabia, Influence of Foundation Scour on the Dynamic Response of an Existing Bridge. *Journal of Bridge Engineering*, **16**(2), 295–304, 2011.  
[https://doi.org/10.1061/\(ASCE\)BE.1943-5592.0000146](https://doi.org/10.1061/(ASCE)BE.1943-5592.0000146)

- [11] A. Zarafshan, A. Iranmanesh, F. Ansari, Vibration-Based Method and Sensor for Monitoring of Bridge Scour. *Journal of Bridge Engineering*, **17**(6), 829–838, 2012.  
[https://doi.org/10.1061/\(ASCE\)BE.1943-5592.0000362](https://doi.org/10.1061/(ASCE)BE.1943-5592.0000362)
- [12] T. Bao, R.A. Swartz, S. Vitton, Y. Sun, C. Zhang, Z. Liu, Critical Insights for Advanced Bridge Scour Detection Using the Natural Frequency. *Journal of Sound and Vibration*, **386**, 116-133, 2017. <https://doi.org/10.1016/j.jsv.2016.06.039>
- [13] L.J. Prendergast, K. Gavin, D. Hester, Isolating the Location of Scour-Induced Stiffness Loss in Bridges Using Local Modal Behaviour. *Journal of Civil Structural Health Monitoring*, **7**, 483-503, 2017. <https://doi.org/10.1007/s13349-017-0238-3>
- [14] K.K.G.K.D. Kariyawasam, P.R.A Fidler, J.P. Talbot, C.R. Middleton, Field Deployment of an Ambient Vibration - Based Scour Monitoring System at Baildon Bridge, UK. *International Conference on Smart Infrastructure and Construction*, Cambridge, England, 711–719, July 8-10, 2019. <https://doi.org/10.1680/icsic.64669.711>
- [15] F. Gara, M. Regni, D. Roia, S. Carbonari, F. Dezi, Evidence of coupled soil-structure interaction and site response in continuous viaducts from ambient vibration tests. *Soil Dynamics And Earthquake Engineering*, **120**, 408-422, 2019.
- [16] V. Nicoletti, D. Arezzo, S. Carbonari, F. Dezi, F. Gara. Measurements of ambient vibrations for a cable-stayed bridge including the soil-foundation system. *XI International Conference on Structural Dynamics (EURODYN)*, Athens, Greece, November 23-26, 2020. <https://doi.org/10.47964/1120.9138.20136>
- [17] E. Tubaldi, R. Lupo, S. Mitoulis, S. Argyroudis, F. Gara, L. Ragni, S. Carbonari, F. Dezi, Field tests on a soil-foundation-structure system subjected to scour. *XVII CONVEGNO ANIDIS*, Ascoli Piceno, September 15 – October 19, 2019.
- [18] X. Guo, Seismic Vulnerability Analysis of Scoured Bridge Systems. Doctoral dissertation. University of Missouri, Kansas City, 2014.
- [19] P. Zampieri, M.A. Zanini, F. Faleschini, L. Hofer, C. Pellegrino, Failure Analysis of Masonry Arch Bridges Subject to Local Pier Scour. *Engineering Failure Analysis*, **79**, 371-384, 2017. <https://doi.org/10.1016/j.engfailanal.2017.05.028>
- [20] A. Alipour, B. Shafei, Performance Assessment of Highway Bridges Under Earthquake and Scour Effects. *15th World Conference of Earthquake Engineering*, Lisbon, Portugal, September 24-28, 2012.
- [21] S. Banerjee, G.G. Prasad, Seismic Risk Assessment of Reinforced Concrete Bridges in Flood-Prone Regions. *Structure and Infrastructure Engineering*, **9**(9), 952-968, 2013.  
<https://doi.org/10.1080/15732479.2011.649292>
- [22] B. Zhu, X. Wu, Y. Wang, Y. Chen, Centrifuge Modeling for Seismic Response of Fixed-End Model Piles Considering Local Scour. *Journal of Waterway, Port, Coastal, and Ocean Engineering*, **146**(6), 04020041, 2020.  
[https://doi.org/10.1061/\(ASCE\)WW.1943-5460.0000604](https://doi.org/10.1061/(ASCE)WW.1943-5460.0000604)
- [23] Z. Hryniewicz, Dynamic Response of a Rigid Strip on an Elastic Half-Space. *Computer Methods in Applied Mechanics and Engineering*, **25**(3), 355–64, 1981.  
[https://doi.org/10.1016/0045-7825\(81\)90038-4](https://doi.org/10.1016/0045-7825(81)90038-4)

- [24] G. Gazetas. Formulas and Charts for Impedances of Surface and Embedded Foundations. *Journal of Geotechnical Engineering*, **117**(9), 1363-1381, 1991.  
[https://doi.org/10.1061/\(ASCE\)0733-9410\(1991\)117:9\(1363\)](https://doi.org/10.1061/(ASCE)0733-9410(1991)117:9(1363))
- [25] J. Zhang, Y. Tang, Evaluating Radiation Damping of Shallow Foundations on Nonlinear Soil Medium for Soil-Structure Interaction Analysis of Bridges. *22<sup>nd</sup> US-Japan Bridge Engineering Workshop*, Seattle, WA, October 23-28, 2006.
- [26] Dassault Systèmes Simulia. Abaqus 2018.
- [27] R.L. Kuhlemeyer, J. Lysmer, Finite Element Method Accuracy for Wave Propagation Problems. *Journal of the Soil Mechanics and Foundations Division*, **99**(5):421-7, 1973.
- [28] C. Volpini, J. Douglas, A.H. Nielsen, Guidance on Conducting 2D Linear Viscoelastic Site Response Analysis Using a Finite Element Code. *Journal of Earthquake Engineering*, 2019.  
<https://doi.org/10.1080/13632469.2019.1568931>
- [29] G.J.C.M. Hoffmans, H.J. Verheij, Scour Manual. Balkema, Rotterdam, Netherlands, 1997.  
<https://doi.org/10.1201/9780203740132>
- [30] S. Tileylioglu, J.P. Stewart, R.L. Nigbor. Dynamic Stiffness and Damping of a Shallow Foundation from Forced Vibration of a Field Test Structure. *Journal of Geotechnical and Geoenvironmental Engineering*, **137**(4), 344–53, 2011.  
[https://doi.org/10.1061/\(ASCE\)GT.1943-5606.0000430](https://doi.org/10.1061/(ASCE)GT.1943-5606.0000430)
- [31] A. Maravas, G. Mylonakis, D.L. Karabalis, Simplified Discrete Systems for Dynamic Analysis of Structures on Footings and Piles. *Soil Dynamics and Earthquake Engineering*, 61–62, 29–39, 2014. <https://doi.org/10.1016/j.soildyn.2014.01.016>
- [32] J. Fu, J. Liang, M. Todorovska, M. Trifunac, Soil-Structure System Frequency and Damping: Estimation from Eigenvalues and Results for a 2D Model in Layered Half-Space. *Earthquake Engineering and Structural Dynamics*, **47**, 2055-2075, 2018.  
<https://doi.org/10.1002/eqe.3055>
- [33] D. Pitilakis, E. Rovithis, A. Anastasiadis, A. Vratsikidis, M. Manakou. Field Evidence of SSI from Full-Scale Structure Testing. *Soil Dynamics and Earthquake Engineering*, **112**, 89-106, 2018. <https://doi.org/10.1016/j.soildyn.2018.04.024>



## KINEMATIC PILE-HEAD BENDING UNDER LARGE EARTHQUAKE-INDUCED SHEAR STRAINS

Stefano Stacul<sup>1</sup>, Emmanouil Rovithis<sup>2</sup> and Raffaele Di Laora<sup>3</sup>

<sup>1</sup> Università di Pisa, Pisa, Italy  
[stefano.stacul@ing.unipi.it](mailto:stefano.stacul@ing.unipi.it)

<sup>2</sup> Institute of Engineering Seismology and Earthquake Engineering, ITSAK – EPPO  
Thessaloniki, Greece  
[rovithis@itsak.gr](mailto:rovithis@itsak.gr)

<sup>3</sup> Università degli Studi della Campania “Luigi Vanvitelli”  
Aversa, Italy  
[raffaele.dilaora@unicampania.it](mailto:raffaele.dilaora@unicampania.it)

### Abstract

*The problem of kinematic bending moments imposed at the head of a single pile during the passage of seismic waves is explored under large shear strains in the surrounding soil. To this end, non-linear soil response at free-field conditions is derived numerically by a freely-available 1D code and then utilized to calibrate the constitutive law of soil introduced in a rigorous 3D Finite-Difference (FD) model of the soil-pile system employed to obtain pile's head bending moments. The pile is considered embedded to a normally-consolidated clay and seven earthquake records with different amplitude and frequency content are imposed as input motions at the base of the soil layer, thus allowing the investigation of pile kinematic bending with increasing levels of shear strains in the soil, exceeding the limit of equivalent-linear soil behavior. The performance of a simple analytical expression for predicting the kinematic bending moment at the pile-head is compared to the rigorous FD solution. It is concluded that this simple solution is still applicable, with slight modifications, for high shear strains related to non-linear soil behavior close to shear failure, provided that the proper mobilized soil properties from 1D soil response analysis are introduced.*

**Keywords:** soil-pile interaction, 3D Finite-Difference, soil response, kinematic pile bending.

---

## 1 INTRODUCTION

Piles in earthquake-prone areas are traditionally designed to withstand inertial forces and moments coming from the oscillation of the superstructure. However, during the passage of seismic waves in the soil, an additional loading source is generated due kinematic interaction between pile and soil, which forces the pile to deform along its whole length, thus imposing additional bending on the pile. In some cases, this kinematic bending induced at the pile-head or at deeper elevations close to interfaces of soil layers with sharp stiffness contrast may be larger than pile bending due to inertial forces. Empirical evidence on this critical aspect of pile bending has been provided by post-earthquake observations in non-liquefiable soils [1–3]. The above field surveys recognized pile failures at depths where inertial forces from the superstructure are negligible. Thus, a reliable prediction of pile-head kinematic bending should follow a proper modelling of soil behavior at free-field conditions to estimate the deformation demand which the soil tries to impose on the pile.

To this end, the Equivalent Linear (EL) method is widely employed to derive free-field soil response when shear strains in the soil do not exceed a threshold value being around 0.2% [4]. In this case, soil response is far from failure and the EL approximation allows a reliable prediction of soil response by considering soil stiffness degradation and hysteretic damping increase with increasing strain. Under these conditions and upon considering for example a continuously inhomogeneous soil, a simplified analytical expression that is available in the literature [5] may be employed to assess kinematic pile-head bending moments by utilizing the mobilized stiffness of the soil which is compatible to the induced shear strains in free-field conditions.

On the other hand, under larger shear strains that may be generated when a soft soil is subjected to strong earthquake shaking, the assumption of soil response being controlled only by soil stiffness is no longer appropriate, since the shear strength of the soil plays a dominant role and, therefore, soil response cannot be captured by considering its stiffness degradation alone [6]. In this case, free-field ground response may be derived by a pertinent 1D analysis with a freely-available software like DEEPSOIL [7] once soil stiffness and strength properties are known. On the contrary, the prediction of pile kinematic bending under large shear strains in the soil seems to be possible only by numerical analyses of complex soil-pile models with advanced constitutive laws at least for the soil.

Upon considering that such type of analyses are excessively demanding for pile design practice, this paper explores the applicability of the abovementioned analytical formula by properly adapting its input parameters in the presence of shear strains close to soil failure. For this reason, a series of Finite-Difference (FD) analyses are performed by employing experimentally validated constitutive models for the case of a normally-consolidated clay. Rigorous analyses results in terms of kinematic pile-head bending are compared with the predictions of a proposed analytical expression including frequency effects.

## 2 SOIL-PILE SYSTEM UNDER STUDY

The system under investigation refers to a single fixed-head pile embedded in a 30m thick soil layer resting on a rigid base (Figure 1). The pile is a linear elastic cylindrical solid beam of diameter  $d = 1$  m, length  $L = 20$  m, Poisson's ratio  $\nu_p = 0.15$ , unit weight  $\rho_p = 24$  kN/m<sup>3</sup> and elastic modulus  $E_p = 25$  GPa. A soft normally-consolidated clay layer is considered the low-strain stiffness and strength properties of which are described in the ensuing.

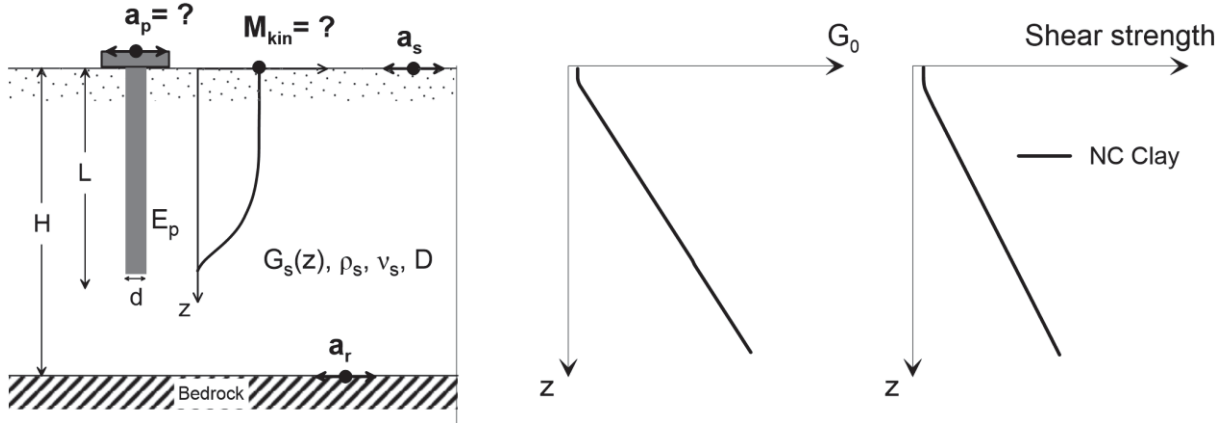


Figure 1: Single elastic fixed-head pile in a normally-consolidated (NC) clay soil.

## 2.1 Normally-consolidated (NC) Clay properties

A fine-grained, fully saturated normally-consolidated (NC) clay having a unit weight  $\gamma_{\text{sat}} = 17.9 \text{ kN/m}^3$  and a plasticity index  $I_p = 40\%$  is considered. The ratio  $s_u / \sigma'_{v0}$  of the undrained shear strength ( $s_u$ ) over the vertical effective geostatic stress for a NC clay can be derived by [8]:

$$\frac{s_u}{\sigma'_{v0}} = 0.11 + 0.0037 I_p \quad (1)$$

with  $I_p$  expressed in percentage. For  $I_p = 40\%$  the above expression yields:

$$s_u (\text{kPa}) = 2.1z \quad (2)$$

where  $z$  is the depth from the ground surface. Upon considering that the low-strain shear modulus  $G_0$  is proportional to depth through a multiplier of the associated shear strength profile (i.e.  $G_0 = 800s_u$ ) the following distribution of  $G_0$  with depth is obtained:

$$G_0 (\text{MPa}) = 1.7z \quad (3)$$

which corresponds to a shear wave propagation velocity profile in the form:

$$V_{s0} = 30z^{0.5} \quad (4)$$

and a  $V_{s,30}$  value at 100 m/s, referring to soil type D according to EC8. The above expression was also adopted by Travasarou and Gazetas [9] to describe the  $V_{s0}$  profile of a particularly soft normally consolidated clay in a real site. The above low-strain stiffness and the strength profiles are plotted in Figure 1.

## 2.2 Input motions

A set of seven earthquake recordings selected from the PEER Strong Motion Database [10] were imposed at the base of the soil layer, in the form of vertically propagating SH waves, to investigate pile-head kinematic bending under seismic loading. The selected records were acquired from stations resting on soil type A or B of the USGS classification system. The 5%-damped acceleration response spectra of the selected motions normalized by the peak rock acceleration (PRA) are plotted in Figure 2. Three levels of increasing intensity of the input motion were examined by scaling the records to three levels of Peak Rock Acceleration (PRA) considered at 0.10g, 0.15g and 0.25g.

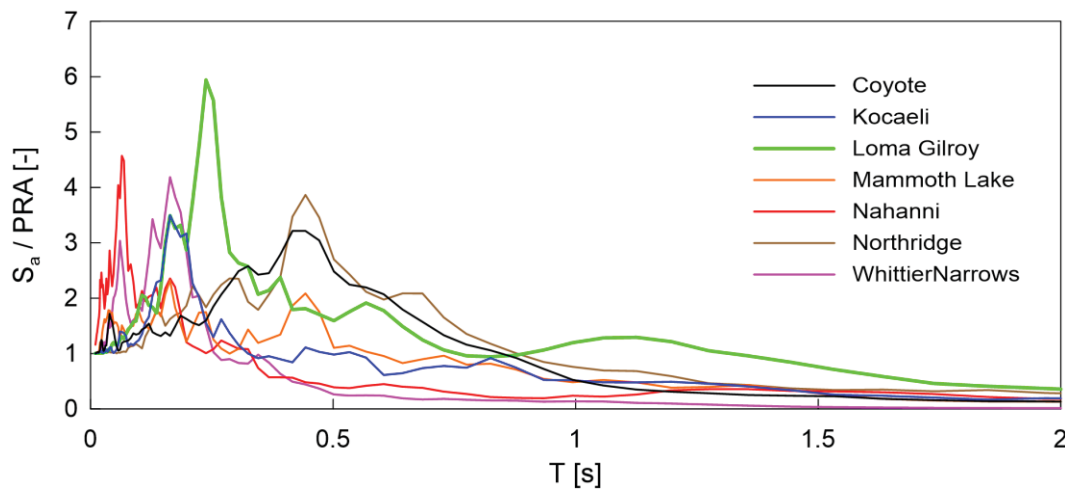


Figure 2: Normalized elastic response acceleration spectra of the selected input motions.

### 3 NUMERICAL ANALYSES

First, a one-dimensional free-field soil response analysis was performed with the DEEPSOIL code [7], by considering equivalent linear (EL) and non-linear (NL) soil behaviour. The Finite-Difference (FD) code FLAC3D [11] was then employed to perform non-linear time history analyses by implementing a rigorous 3D model of the soil-pile system with pertinent constitutive models to describe soil behaviour.

#### 3.1 DEEPSOIL non-linear soil model

The General Quadratic/Hyperbolic (GQ/H) model [12] was adopted to model the backbone curve of the shear stress-strain relationship for the non-linear (NL) analyses in time domain performed with DEEPSOIL. The GQ/H model allows the shear strength of the soil to be directly introduced as an input parameter, contrary to the Modified Kondner Zelasko (MKZ) model [13], which may overestimate the shear strength of the soil depending on the values of the curve-fitting parameters [14]. For the hysteretic soil behaviour during unloading and re-loading, the associated stress-strain loops were defined on the basis of the non-Masing Modulus Reduction and Damping with reduction Factor (MRDF) formulation proposed in Phillips and Hashash [15], to avoid damping overestimation at large shear strains when Masing rules are adopted [16].

#### 3.2 FLAC3D soil-pile model

Following a sensitivity analysis on critical modelling aspects such as model size, discretization scheme, pile and pile-soil interface, the final 3D FD soil – pile model (Figure 3) implemented in FLAC3D code, has a base, width, and height equal to 30m, 30m, and 31m, respectively. The one-meter-thick bottom layer models the elastic bedrock with a shear wave velocity at 800 m/s and the same unit weight like the soil layers above. The grid-element size in the vertical direction (z-axis) was selected according to the indications provided in Kuhlemeyer and Lysmer [17]. The first 20 m were discretized with 80 layers of 0.25 m thickness each, while 20 layers of 0.50 m thickness each were adopted to discretize the soil profile between 20 and 30 m.

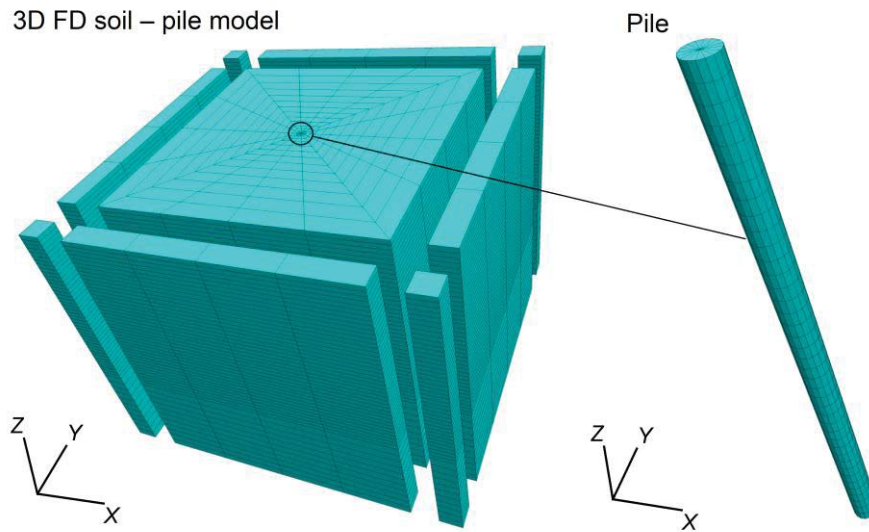


Figure 3: 3D Finite-Difference (FD) soil – pile model employed in FLAC3D code.

The same discretization was adopted in the DEEPSOIL code, satisfying the criterion of a frequency  $f_{\max,i}$  ( $= V_{s0,i} / 4H_i$ ), that a layer of thickness  $H_i$  and shear wave velocity  $V_{s0,i}$  can propagate, above 25 Hz [7]. A linear elastic behavior of the pile material and a bonded connection between soil and pile elements were assumed. The latter was based on the fact that soil-pile contact stresses under kinematic loading are negligible compared to those induced by forces or moments applied at the pile-head [18].

Nonlinear soil response in dynamic analyses was accounted for by means of the UCSDCLAY model [19]. The UCSDCLAY model is a pressure-independent 3D elasto-plastic material model, which enables reproducing nonlinear hysteric shear behavior, and it allows the shear strength of the soil to be introduced as a direct input. Rayleigh damping, which is commonly applied to take into account small strain (viscous) damping or to remove high frequency noise, was found to be unnecessary.

### 3.3 UCSDClay model calibration

A recursive calibration procedure was followed to obtain similar non-linear behavior between the GQ/H and USCDClay models. In this regard, the following steps were performed: (Figure 4): (i) first, the GQ/H model was calibrated by the Vucetic and Dobry [20] curves for  $I_p = 40\%$  (noted in Figure 4 as “DS fit.1”), (ii) the fitted DEEPSOIL curves were employed to calibrate the USCDClay model introduced in FLAC3D and (iii) the fitted FLAC3D-based curves were employed to calibrate again the GQ/H model (noted in Figure 4 as “DS fit.2”). In this manner, it was possible to derive comparable  $\tau - \gamma$  backbone curves between the two models (Figure 4c) at the expense of higher hysteretic damping at large strains with respect to the experimental data (Figure 4b).



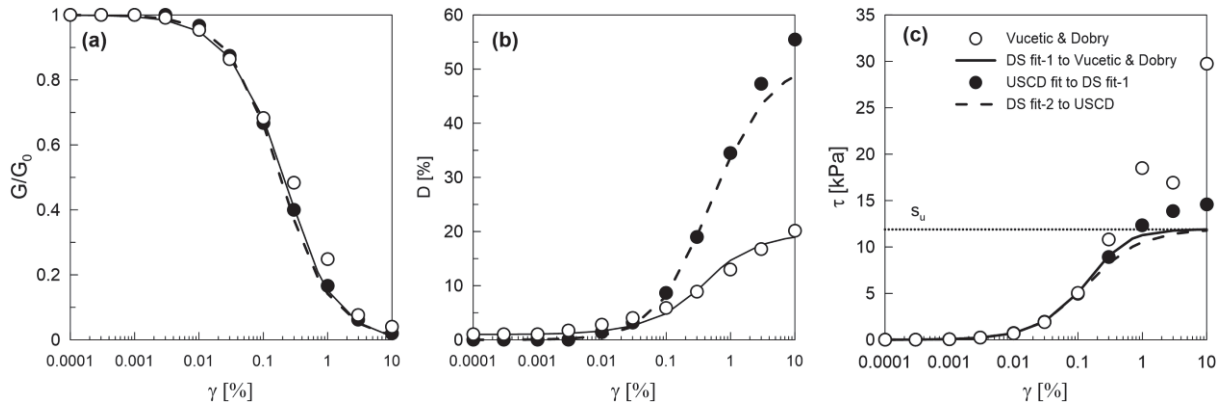


Figure 4: Calibration of DEEPSOIL and FLAC3D soil models for the NC Clay case based on Vucetic and Dobry [20]  $G/G_0 - \gamma - D(\%)$  curves for  $I_p = 40\%$  regarding: (a) Stiffness degradation, (b) Hysteretic damping increase and (c) Shear stress-strain backbone curve at the depth of 4.375m (the implied shear strength derived in DEEPSOIL is also mentioned).

#### 4 SOIL RESPONSE AT FREE-FIELD CONDITIONS

Non-linear analyses results of the free-field ground response derived with DEEPSOIL code under the prescribed input motions is shown in Figure 5, in terms of peak ground acceleration (Figure 5a), maximum shear strain (Figure 5b) and maximum shear stress (Figure 5c) profiles, referring to average values between those computed separately for each one of the seven base excitations. An effective shear strain profile was then computed as 0.65 times the maximum strain developed at any depth and was then employed to obtain the corresponding mobilized shear modulus and damping profiles based on the calibrated  $G/G_0 - \gamma - D(\%)$  curves. In this manner, a single mobilized stiffness and damping profile was derived for each one of the seven input motions. An average mobilized  $G$  profile obtained by averaging these seven profiles is shown in Figure 5d. All the results shown in Figure 5 correspond to the maximum PRA at 0.25g. The same analyses results obtained with DEEPSOIL by implementing this time the Equivalent Linear (LE) approximation to model soil behavior are also plotted in Figure 5. In this case, a frequency independent expression [i.e.  $G^* = G(1+2iD)$ ] was adopted for the complex formulation of the shear modulus while the effective shear strain ratio was set at 0.65. The degradation of the shear modulus and the increase of the hysteretic damping of the soil with increasing shear strain were modeled by implementing the  $G/G_0 - \gamma - D(\%)$  curves proposed in Vucetic and Dobry [20] for the plasticity index under consideration ( $I_p = 40\%$ ). It is noted that for the first 1.5 m of the soft NC clay profile, the low-strain shear modulus ( $G_0$ ) and the undrained shear strength ( $s_u$ ) were considered constant at 2.55 MPa and 6.2 kPa, respectively, due to a numerical issue observed in DEEPSOIL when very low values of the above parameters are introduced. Below 1.5m, the  $s_u$  and the  $G_0$  profiles follow the linear variation with depth described by Equations 2 and 3, respectively.

It is observed that under the EL assumption, a sudden increase of the peak ground acceleration is observed close to the ground surface, being in qualitative agreement with analytical elasto-dynamic investigations reported in Rovithis et al. [21] for a similar shear wave velocity profile. On the contrary, when the non-linear behavior of soil is modeled by the rigorous GQ/H model, ground acceleration is de-amplified as it propagates through the soil due to the low shear strength of the soft clay, which limits the transmission of shear stresses. Such a behavior has also been reported in experimental studies of the seismic behavior of soft clays [22]. This indicates that the EL approximation is not able to capture the complex soil behavior, which is also reflected in the  $\tau$ - $\gamma$  loops derived at two depths close to the ground surface (Figure 6) for PRA = 0.25g. The strong non-linear behavior of the soil generates large inelastic

strains on the order of 1%, while the developed shear stresses are bounded by the low shear strength  $s_u$  of the soft clay. Apparently, the above soil response cannot be reproduced by the linear elastic  $\tau$ - $\gamma$  relationship under the EL assumption (Figure 6). This does not mean absence of energy dissipation through the hysteretic behavior of the soil, as the latter is taken into account through the complex shear modulus during each iteration of an EL analysis.

The corresponding average profiles of free-field ground response obtained with FLAC3D are also plotted in Figure 5. The agreement between DEEPSOIL NL and FLAC3D analysis indicates that critical trends of ground response may be reproduced in a similar manner, which provides confidence that the adopted model in FLAC3D is able to reproduce highly non-linear ground response and, therefore, kinematic soil-pile interaction over a wide range of shear strains.

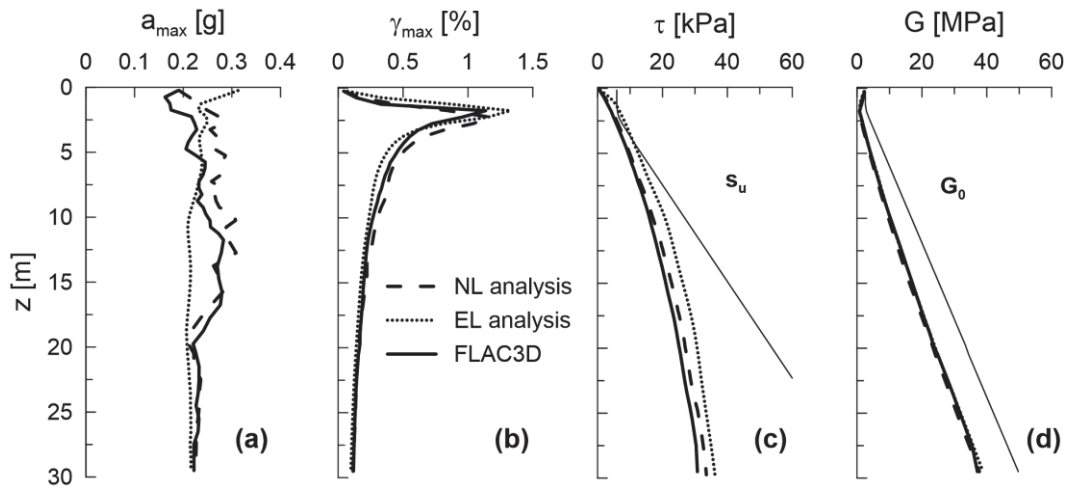


Figure 5: Comparison of free-field ground response analysis results between DEEPSOIL (EL and NL analysis) and FLAC3D for the NC clay profile in terms of: (a) PGA profile (b) average maximum shear strain profile (c) average shear stress and (d) mobilized shear modulus  $G$  with depth. All plots refer to  $PRA = 0.25g$ .

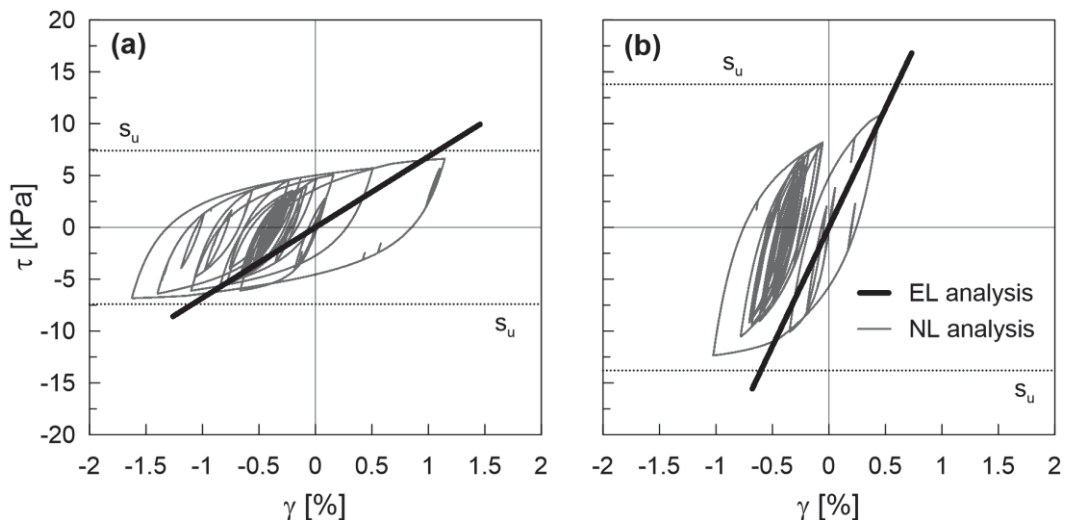


Figure 6: Comparison of EL and NL soil response analysis with DEEPSOIL for the NC clay profile in terms of  $\tau$  -  $\gamma$  loops at the depth of: (a) 2.625 m and (b) 5.125 m. All plots refer to  $PRA = 0.25g$ .

## 5 PILE-HEAD KINEMATIC BENDING

In the general case of an inhomogeneous soil profile with shear stiffness varying continuously with depth according to the law:

$$G_s(z) = G_{sd} \left[ a + (1-a) \frac{z}{d} \right]^n \quad (5)$$

where  $G_s(z)$  is the depth-varying soil shear modulus,  $G_{sd}$  is the shear modulus at the depth of one pile diameter (i.e., at  $z = d$ ) and  $a, n$  are dimensionless factors controlling the stiffness profile, the active length ( $L_a$ ) of the pile may be calculated by the expression [5, 23, 24]:

$$L_a = \frac{d}{1-a} \left\{ \left[ a^{\frac{n+4}{4}} + \frac{5}{16} (n+4) (1-a) \left( \frac{\pi E_p}{2 E_{sd}} \right)^{\frac{1}{4}} \right]^{\frac{4}{n+4}} - a \right\} \quad (6)$$

where  $E_{sd}$  is the Young's modulus of elasticity of the soil at one pile diameter depth.

### 5.1 Constant ground acceleration

Upon considering that there is an effective portion of the soil controlling pile-head bending, which is proportional to a characteristic wavelength of the soil-pile system, Di Laora and Rovithis [5] introduced the notion of an effective soil curvature  $[(1/R)_{s,eff}]$  as the ratio of the shear strain  $\gamma_s(z_{eff})$  at an effective depth  $z_{eff}$  over  $z_{eff}$  [i.e.  $(1/R)_{s,eff} = \gamma_s(z_{eff}) / z_{eff}$ ] to derive a simple analytical expression for the kinematic bending moment at the head of a pile in a continuously inhomogeneous soil, such as that described by Equation 5, and proved that under constant ground acceleration,  $a_s$ , the ratio of the pile-head curvature  $(1/R)_p$  over  $(1/R)_{s,eff}$  for long piles is equal to 1, which allows calculation of pile-head kinematic bending by the formula:

$$M_{kin} = E_p I_p (1/R)_p = E_p I_p (1/R)_{s,eff} = E_p I_p \frac{\gamma_s(z_{eff})}{z_{eff}} \quad (7)$$

where the depth  $z_{eff}$  is considered as one half of the pile's active length  $L_a$ :

$$z_{eff} = \frac{L_a}{2} \quad (8)$$

The equilibrium of a 1D soil column with constant mass density  $\rho_s$  and variable shear modulus  $G(z)$  with depth yields that in static conditions  $\gamma(z_{eff})$  may be expressed as:

$$\gamma_s(z_{eff}) = \frac{a_s \rho_s z_{eff}}{G_s(z_{eff})} \quad (9)$$

where  $G(z_{eff})$  is the mobilized shear modulus of the soil at  $z_{eff}$ . Thus, Equation 7 may be re-written as:

$$M_{kin} = E_p I_p \frac{a_s \rho_s}{G_s(z_{eff})} \quad (10)$$

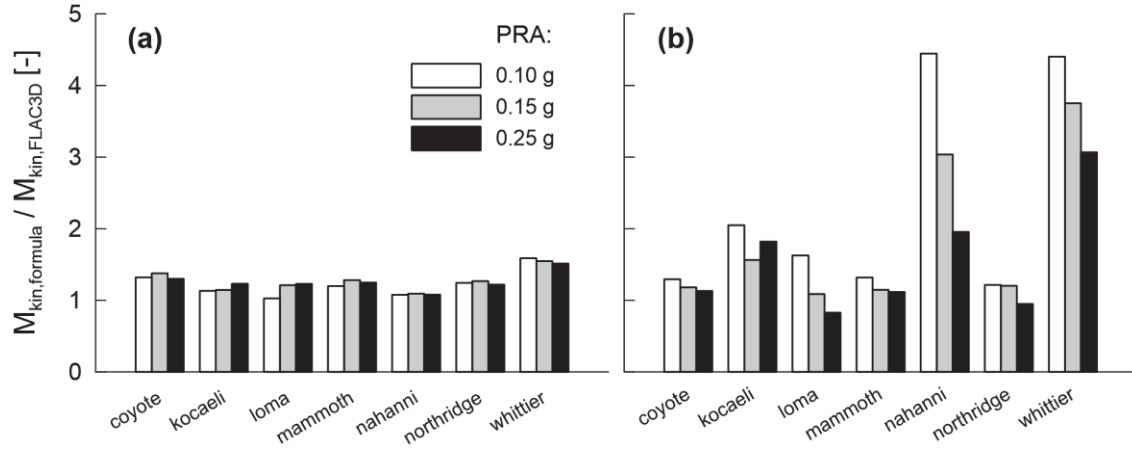


Figure 7: Ratios of kinematic pile-head bending moment between 3D FD analyses (FLAC3D) and the predictions of (a) Equation 7 and (b) Equation 10.

In order to apply the above formulae, one has fit the mobilized shear modulus profile derived from 1D ground response analysis, to the formula of  $G_s(z)$  in Equation 5 in order to obtain the parameters  $G_{sd}$ ,  $a$  and  $n$  and then calculate  $L_a$  and  $z_{eff}$  from Equations 6 and 8, respectively. As the above parameters are interrelated, an iterative procedure may be followed by considering the value of  $L_a = 10d$  as a starting point and employing a least square linear (i.e.  $n = 1$ ) fit. A single iteration leads to quite accurate results.

The performance of Equations 7 and 10 is compared to the rigorous 3D Finite-Difference model response in Figure 7, in the form of  $(M_{kin,formula} / M_{kin,FLAC3D})$  ratio for all the examined input motions scaled to 0.10g, 0.15g and 0.25g. Each group of bars refers to a different base excitation noted in the abscissa of the plots. To this end, the maximum shear strain  $\gamma_{max,s}(z_{eff})$  at  $z_{eff}$  was introduced in Equation 7, while the peak ground acceleration at soil surface was employed to derive  $M_{kin,formula}$  in Equation 10. Both of these parameters were obtained by the FLAC3D analyses for the purpose of this comparison.

It is observed that for the particularly soft NC Clay under consideration, where the maximum shear strain at  $z_{eff}$  attains considerably large values up to 0.8 - 1 % (Figure 5b), the kinematic pile-head bending predicted by Equation 7 is much closer to the rigorous FD solution (Figure 7a), denoting that the maximum shear strain at  $z_{eff}$  is a better indicator of the developed pile-head bending compared to the peak ground acceleration at surface (Figure 7b), when soil behavior is close to failure (Figure 5c). However, despite its better performance, Equation 7 may still be quite conservative for certain base excitations, like in the case of the Whittier base motion where an overestimation of 50% is attained.

## 5.2 Frequency effects: Proposed analytical expression

The above over-prediction of kinematic bending is explainable, though, as it follows the original conservative assumption of constant ground acceleration to derive Equation 7, implying low-frequency excitations. This is valid if the frequency content of the time variant parameter  $\gamma_s(z_{eff})$  controlling the kinematic demand is low enough to be considered as almost statically applied. Otherwise, the bending moment attains lower values as the shear strain (and the corresponding effective soil curvature) is a decreasing function of the excitation frequency regardless of the soil properties [5].

In this case, frequency effects in kinematic bending may be accounted for by implementing the expression of the dynamic  $(1/R)_{p,dyn}$  over the static  $(1/R)_{p,static}$  pile curvature ratio proposed in Di Laora and Rovithis [5]:

$$\frac{(1/R)_{p,dyn.}}{(1/R)_{p,static}} = \left[ 1 + 0.02 a_{eff,La}^3 \right]^{-1} \quad (11)$$

In the above expression,  $a_{eff,La}$  is a dimensionless frequency which controls the kinematic response of the pile in the dynamic regime [5, 24]:

$$a_{eff,La} = \frac{\omega L_a}{V_{s,av}} \quad (12)$$

where  $\omega$  is the cyclic frequency of the excitation,  $L_a$  is the active length of the pile (Equation 6) and  $V_{s,av}$  refers to an average shear wave velocity along  $z_{eff}$  given by:

$$V_{s,av} = V_{s,d} \frac{L_a (a-1)(n-2)}{4d} \left[ \left( a + (1-a) \frac{L_a}{d} \right)^{1-n/2} - a^{1-n/2} \right]^{-1} \quad (13)$$

where  $V_{sd}$  is the mobilized shear wave at one pile diameter depth which may be derived by the corresponding value of  $G_{sd}$  once the mobilized shear modulus profile is fitted to a linear function as mentioned above.

Obviously, Equation 11 is a continuous function of  $\omega$ . In order to obtain a single-valued prediction of the kinematic pile-head moments in the dynamic regime, a mean cyclic frequency  $\omega_{m,\gamma}$  is considered as an index of the frequency content of the shear strain time history at  $z_{eff}$ . Following the definition of the mean period ( $T_m$ ) of an acceleration time history introduced in Rathje et al. [25],  $\omega_{m,\gamma}$  may be computed from:

$$\omega_{m,\gamma} = 2\pi \frac{\sum_i c_{i,\gamma}^2}{\sum_i c_{i,\gamma}^2 \left( \frac{1}{f_i} \right)} \quad (14)$$

where  $C_{i,\gamma}$  refer to the Fourier amplitudes of the shear strain time history at  $z_{eff}$  and  $f_i$  are the discrete Fourier transform frequencies between 0.25 Hz and 20 Hz. In this manner, a mean dimensionless frequency  $a_{eff,m,La}$  of the shear strain demand at  $z_{eff}$  may be defined by introducing  $\omega_{m,\gamma}$  in Equation 12:

$$a_{eff,m,La} = \frac{\omega_{m,\gamma} L_a}{V_{s,av}} \quad (15)$$

Upon introducing  $a_{eff,m,La}$  in Equation 11, a single value of the  $(1/R)_{p,dyn} / (1/R)_{p,static}$  ratio may be computed for each base excitation according to the associated value of  $a_{eff,m,La}$ . Taking also into account that for long piles  $(1/R)_{p,static} = (1/R)_{s,eff}$ , the kinematic pile-head bending moment including frequency effects may be derived by the expression:

$$M_{kin} = E_p I_p \frac{\gamma_{max,s}(z_{eff})}{z_{eff}} \left[ 1 + 0.02 a_{eff,m,La}^3 \right]^{-1} \quad (16)$$

The performance of the above expression against the rigorous FD solution is compared in Figure 8. The improvement of the agreement between the two solutions with respect to that shown in Figure 7a cannot be overstated, denoting maximum deviations of less than 10%.



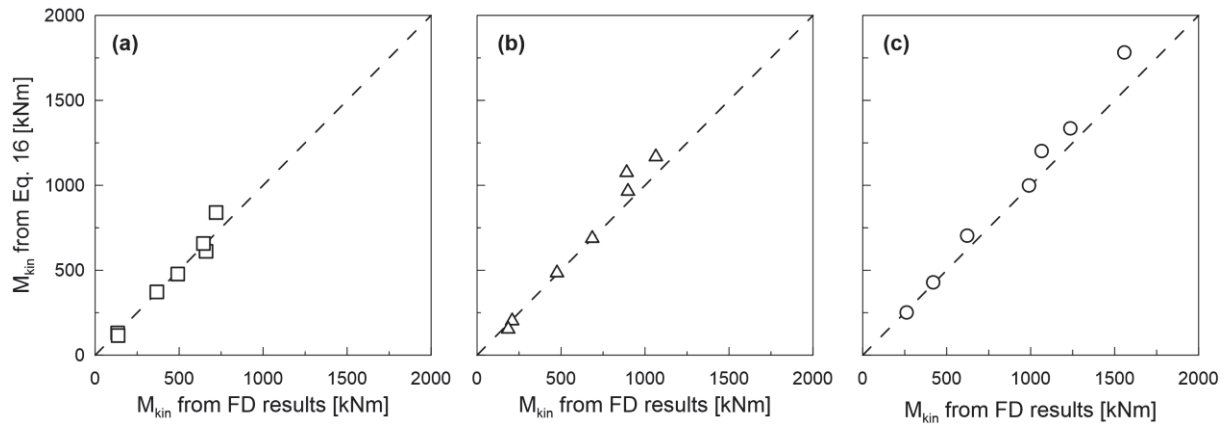


Figure 8: Comparison of kinematic pile-head bending moments between Equation 16 and FD results for PRA at (a) 0.10g (b) 0.15g and (c) 0.25g. Each point in the plots refers to a different input motion.

This suggests that the simple analytical formula in Equation 16 is applicable even in the highly nonlinear range of soil response close to failure, provided that the associated shear strain demand induced by the surrounding soil and the corresponding mobilized stiffness profile are introduced. It may thus be asserted that dynamic effects result in modifying solely soil deformations at free-field conditions while soil-pile kinematic interaction mechanism remains static. The latter was first discussed by Di Laora et al. [26] for homogeneous soils and confirmed further in Di Laora and Rovithis [5] for nonhomogeneous soils. The results of this study extend, therefore, the validity of the simple analytical solutions to the non-linear range of soil response, denoting that kinematic soil-pile interaction is controlled by the soil stiffness even if the response of the soil is controlled by its strength. The above finding generalizes earlier indications [27–30] of the controlling role of the mobilized soil stiffness on pile kinematic bending.

## 6 CONCLUSIONS

Kinematic pile-head bending moments were explored under increasing earthquake-induced shear strains in the soil, by means of a rigorous 3D Finite Difference model of the soil-pile system, taking into account both stiffness degradation and strength of the soil. The numerical results were compared to the predictions of a proposed simple formula properly adapted for the non-linear regime of soil response over an earlier publication of the Authors. The main conclusions can be summarized as follows:

- While in the linear and static regime Equations 7 and 10 return identical predictions of pile-head bending moments, in the non-linear regime the use of ground surface acceleration is no longer reliable and the maximum shear strain at an effective depth equal to one half of the pile's active length becomes the dominant soil response parameter controlling kinematic bending at the pile-head.
- The simplified formula in Equation 16 may be employed to derive kinematic pile-head bending in the non-linear dynamic range of soil response. In this regard, a 1D free-field non-linear soil response analysis, which properly considers both stiffness degradation and soil strength, should be performed to derive the necessary input parameters in the formula.
- A mean cyclic frequency was suggested (Equation 14) as a single index of the frequency content of the shear strain time history at one half of the pile's active length. Such an in-

terpretation of the frequency content of a shear strain time history has not been previously explored in the kinematic bending of piles.

- It was proven that dynamic and non-linear effects result in modifying solely soil deformations at free-field conditions, while soil-pile kinematic interaction mechanism remains static and linear. This shed lights to the actual nature of kinematic soil-pile interaction mechanism which may be considered as stiffness-controlled even if free-field soil response is strength-controlled.

## ACKNOWLEDGEMENTS

The authors wish to thank ITASCA for a loan of software within the Itasca Education Partnership (IEP).

## REFERENCES

- [1] T. Tazoh, K. Shimizu, T. Wakahara, Seismic Observations and Analysis of Grouped Piles. *Dynamic Response of Pile Foundations—Experiment, Analysis and Observation*, ASCE, Geotechnical Special Publication, **11**, 1-20, 1987.
- [2] H. Mizuno, Pile damage during earthquake in Japan. T. Nogami, editor. *Dynamic Response of Pile Foundations*, ASCE, Geotechnical Special Publication, **11**, 53-78, 1987.
- [3] S. Nikolaou, G. Mylonakis, G. Gazetas, T. Tazoh, Kinematic pile bending during earthquakes: analysis and field measurements. *Géotechnique*, **51**(5), 425-440, 2001.
- [4] J. Kaklamanos, B.A. Bradley, E.M. Thompson, L.G. Baise, Critical parameters affecting bias and variability in site - response analyses using KiK - net downhole array data. *Bulletin of the Seismological Society of America*, **103**(3), 1733-1749, 2013.
- [5] R. Di Laora, E. Rovithis, Kinematic bending of fixed-head piles in nonhomogeneous soil. *Journal of Geotechnical and Geoenvironmental Engineering*, **141**(4), 04014126, 2015.
- [6] J. Shi, D. Asimaki, From stiffness to strength: Formulation and validation of a hybrid hyperbolic nonlinear soil model for site - response analyses. *Bulletin of the Seismological Society of America*, **107**(3), 1336-1355, 2017.
- [7] Y.M.A. Hashash, M.I. Musgrove, J.A. Harmon, D.R. Groholski, C.A. Phillips, D. Park, *DEEPSOIL 6.1, User Manual*. Urbana, IL, Board of Trustees of University of Illinois at Urbana-Champaign, 2016.
- [8] A.W. Skempton, Discussion: Further data on the c/p ratio in normally consolidated clays. *Proceedings of the Institution of Civil Engineers*, **7**, 305-307, 1957.
- [9] T. Travasarou, G. Gazetas, On the linear seismic response of soils with modulus varying as a power of depth: the Maliakos marine clay. *Soils and Foundations*, **44**(5), 85-93, 2004.
- [10] T. Ancheta, R. Darragh, J.P. Stewart, E. Seyhan, W. Silva, B. Chiou, K. Wooddell, R. Graves, A. Kottke, D. Boore, T. Kishida, J. Donahue, *PEER NGA-West2 Database*,

- PEER Report 2013/03 Pacific Earthquake Engineering Research Center Headquarters at the University of California, Berkeley, 2013.
- [11] Itasca, Fast Lagrangian Analysis of Continua (FLAC3D 6.00). Itasca Consulting Group Inc, Minneapolis, USA, 2017.
  - [12] D. R. Groholski, Y.M.A. Hashash, M. Musgrove, J. Harmon, B. Kim, Evaluation of 1-D Non-linear site response analysis using a general quadratic/hyperbolic strength-controlled constitutive model. *Proceedings of the 6th International Conference on Earthquake Geotechnical Engineering*, Christchurch, New Zealand, 2015.
  - [13] N. Matasovic, *Seismic response of composite horizontally-layered soil deposits*. Ph.D. Thesis, University of California, Los Angeles, 1993.
  - [14] D.R. Groholski, Y.M.A. Hashash, B. Kim, M. Musgrove, J. Harmon, J.P. Stewart, Simplified model for small-strain nonlinearity and strength in 1D seismic response analysis. *Journal of Geotechnical and Geoenvironmental Engineering*, **142**(9): 04016042, 2016.
  - [15] C. Phillips, Y.M.A. Hashash, Damping formulation for non-linear 1D site response analyses. *Soil Dynamics and Earthquake Engineering*, **29**, 1143-1158, 2009.
  - [16] A.O. Kwok, J.P. Stewart, Y.M. Hashash, N. Matasovic, R. Pyke, Z. Wang, Z. Yang, Use of exact solutions of wave propagation problems to guide implementation of non-linear seismic ground response analysis procedures. *Journal of Geotechnical and Geoenvironmental Engineering*, **133**(11), 1385-1398, 2007.
  - [17] R.L. Kuhlemeyer, J. Lysmer, Finite element method accuracy for wave propagation problems. *Journal of the Soil Dynamics Division*, **99**, 421-427, 1973.
  - [18] R. Di Laora, G. Mylonakis, A. Mandolini, Size limitations for piles in seismic regions. *Earthquake Spectra*, **33**(2), 729-756, 2017.
  - [19] A. Elgamal, L. Yan, Z. Yang, J.P. Conte, Three-dimensional seismic response of Humboldt Bay bridge foundation-ground System, *Journal of Structural Engineering*, ASCE, **134**(7), 1165-1176, 2008.
  - [20] M. Vucetic, R. Dobry, Effect of soil plasticity on cyclic response. *Journal of Geotechnical Engineering*, **17**, 89-107, 1991.
  - [21] E. Rovithis, C. Parashakis, G. Mylonakis, 1D harmonic response of layered inhomogeneous soil: Analytical investigation, *Soil Dynamics and Earthquake Engineering*, **31**, 879-890, 2011.
  - [22] T.K. Garala, G.S.P. Madabhushi, Seismic behaviour of soft clay and its influence on the response of friction pile foundations, *Bulletin of Earthquake Engineering*, **17**, 1919–1939, 2019.
  - [23] X. Karatzia, G. Mylonakis, Discussion of kinematic bending of fixed-head piles in non-homogeneous soil by Raffaele Di Laora and Emmanouil Rovithis, *Journal of Geotechnical and Geoenvironmental Engineering*, **142**(2), 07015042, 2016.
  - [24] M. Iovino, R. Di Laora, E. Rovithis, L. de Sanctis, The beneficial role of piles on the seismic loading of structures, *Earthquake Spectra*, **35**(3), 1141-1162, 2019.
  - [25] E.M. Rathje, N.A. Abrahamson, J.D. Bray, Simplified frequency contents estimates of earthquake ground motions. *Journal of Geotechnical and Geoenvironmental Engineering*, **124**(2), 150-158, 1998.

- [26] R. Di Laora, A. Mandolini, G. Mylonakis, Insight on kinematic bending of flexible piles in layered soil. *Soil Dynamics and Earthquake Engineering*, **43**, 309-322, 2012.
- [27] M. Mucciacciaro, S. Sica, Nonlinear soil and pile behaviour on kinematic bending response of flexible piles. *Soil Dynamics and Earthquake Engineering*, **107**, 195-213, 2018.
- [28] S. Stacul, A. Franceschi, N. Squeglia, Effect of non-linear soil response and pile post-cracking behavior on seismically induced bending moments in fixed-head long piles. In *7th International Conference on Earthquake Geotechnical Engineering (ICEGE 2019)*, CRC Press/Balkema, Rome, Italy, June 17-20, 2019.
- [29] S. Stacul, N. Squeglia, Simplified assessment of pile-head kinematic demand in layered soil. *Soil Dynamics and Earthquake Engineering*, **130**, 105975, 2020.
- [30] T.K. Garala, G.S. Madabhushi, R. Di Laora, Experimental investigation of kinematic pile bending in layered soils using dynamic centrifuge modelling. *Géotechnique*, 1-16, 2020.

## ASPECTS OF SEISMIC SOIL-PILE-STRUCTURE INTERACTION IN SOFT CLAY BY CENTRIFUGE TESTING

Maria Iovino<sup>1</sup>, Emmanouil Rovithis<sup>2</sup>, Raffaele Di Laora<sup>3</sup>, Cristiano D'Alterio<sup>3</sup>, Luca de Sanctis<sup>1</sup>, Thejesh K. Garala<sup>4</sup>, Stuart Haigh<sup>5</sup>, Gopal S. Madabhushi<sup>5</sup>

<sup>1</sup> Università degli Studi di Napoli 'Parthenope'  
Napoli (Italy)

[maria.iovino@uniparthenope.it](mailto:maria.iovino@uniparthenope.it), [luca.desanctis@uniparthenope.it](mailto:luca.desanctis@uniparthenope.it)

<sup>2</sup> Institute of Engineering Seismology and Earthquake Engineering EPPO-ITSAK  
Thessaloniki (Greece)  
[rovithis@itsak.gr](mailto:rovithis@itsak.gr)

<sup>3</sup> Università della Campania 'Luigi Vanvitelli'  
Aversa (Italy)

[raffaele.dilaora@unicampania.it](mailto:raffaele.dilaora@unicampania.it), [cristiano.dalterio@studenti.unicampania.it](mailto:cristiano.dalterio@studenti.unicampania.it)

<sup>4</sup> University of Nottingham  
Nottingham (UK)

[thejesh.garala@nottingham.ac.uk](mailto:thejesh.garala@nottingham.ac.uk)

<sup>5</sup> University of Cambridge  
Cambridge (UK)

[skh20@cam.ac.uk](mailto:skh20@cam.ac.uk), [mshg1@cam.ac.uk](mailto:mshg1@cam.ac.uk)

### Abstract

*This paper presents experimental data from two series of centrifuge tests on pile foundations embedded in a kaolin clay under earthquake excitation. A single pile and two pile-group configurations were tested in the centrifuge at 50g. In the first test series (flight 1) the seismic response of the soil-pile system was monitored, allowing experimentally-driven insights on the kinematic interaction between soil and pile. In the second series of tests (flight 2), a superstructure mass was attached to each foundation model, allowing investigation of the seismic behaviour of the coupled soil-foundation-structure (SFS) system. Two earthquake excitations were analysed during each flight having similar frequency and amplitude characteristics. Results are presented in terms of soil response along a vertical array, pile-caps spectral acceleration and superstructure top-to-ground surface response ratio. Experimental data suggests that for soft soils such as those employed in this experimental campaign, piles may amplify the motion with respect to the one at ground surface, while the natural period of the SFS system may be largely increased compared to its fixed-base counterpart, indicating a strong effect of soil compliance.*

**Keywords:** centrifuge, kaolin clay, kinematic soil-pile interaction, coupled soil-structure system.

---



## 1 INTRODUCTION

Seismic analysis of structures supported on piles is conventionally performed by considering the structure fixed at its base and excited under the free-field motion at ground surface. The above considerations which are normally followed in design practice disregard the interaction between soil, piles and structures that takes place during earthquake shaking and may affect both the actual motion which is imposed at the base of the superstructure and the vibrational characteristics of the structure compared to its fixed-base counterpart, especially in the case of soft soils, where piles represent the most common design option. With reference to the modification of the free-field soil motion, the associated physical mechanism is related to the fact that, during the passage of seismic waves, piles, due to their flexural stiffness, are progressively unable to follow the wavy pattern of the soil with increasing frequency of excitation, which is referred to as kinematic soil-pile interaction [1-6]. Relevant empirical evidence has been documented by field measurements on instrumented pile-supported structures [7-9], indicating that piles may filter out the high frequency components of the free-field motion. Under certain conditions, such a filtering action may be particularly important. For example, Di Laora and de Sanctis [5] reported that in the case of large-diameter piles in soft soil, the seismic demand on a low-period structure may be up to 50% - 70% with respect to the demand imposed by the free-field motion. A holistic interpretation of the filtering action of piles has been very recently suggested in [10-11] by considering that piles average the non-uniform profile of displacement imposed by the surrounding soil along a fraction of the pile's active length.

On the other hand, the effect of soil compliance on the vibrational characteristics of a flexible-base structure, consisting of the elongation of the natural period and the modification of the energy dissipation mechanism with respect to the fixed-base case, has been well-established since the early 70s [12-19] and supported by relevant experimental data [20-23]. This phenomenon is due to soil hysteresis and radiation of seismic waves emanating from the foundation. Soil-foundation-structure interaction may have a detrimental or beneficial effect on the seismic loading imposed to the superstructure depending on the soil-foundation configuration and the characteristics of the earthquake excitation [24], especially, again, in the case of soft soils. The issue has been recognized by modern seismic codes that specify conditions where soil-pile-structure interaction should be taken into account.

Along these lines, a large centrifuge testing campaign was performed in the framework of the Transnational Access (TA) project COSMO funded by the SERA research program to explore the above aspects of soil-pile-structure interaction (SPSI) in a soft clay under earthquake loading. Part of the experimental data is presented in this paper, referring to the kinematic response of single piles and pile groups (i.e. in the absence of a supporting structure) and to the seismic response of the coupled soil-piles-structure (SPS) system, with the same pile layouts supporting a single degree of freedom (SDOF) structure. Experimental data are elaborated in terms of soil response along a vertical array, pile-cap spectral accelerations and superstructure top-to-ground surface response spectral ratio, following a detailed description of the centrifuge models preparation and testing procedure.

## 2 CENTRIFUGE MODELS AND TESTING PROCEDURE

The experiments were carried out at 50g in the Turner Beam centrifuge [25] at the Schofield Centre of the University of Cambridge. The foundation models reported herein consisted of a single pile (SP) and two 3x1 pile groups (PG1 and PG2) (Figure 1) installed in a kaolin clay. All piles were aluminum tubes of length  $L = 200$  mm, diameter  $d = 15$  mm and thickness  $t = 1$  mm, so that, in terms of flexural stiffness, they are equivalent to 0.75 m diame-

ter and high-strength concrete piles. In model scale dimensions, pile spacing in PG1 and PG2 configurations was considered at  $s = 64$  mm. The different heights of the pile groups' caps,  $D_1 = 20$  mm (mass = 90 g) and  $D_2 = 40$  mm (mass = 170 g), represented two different foundation embedment depths.

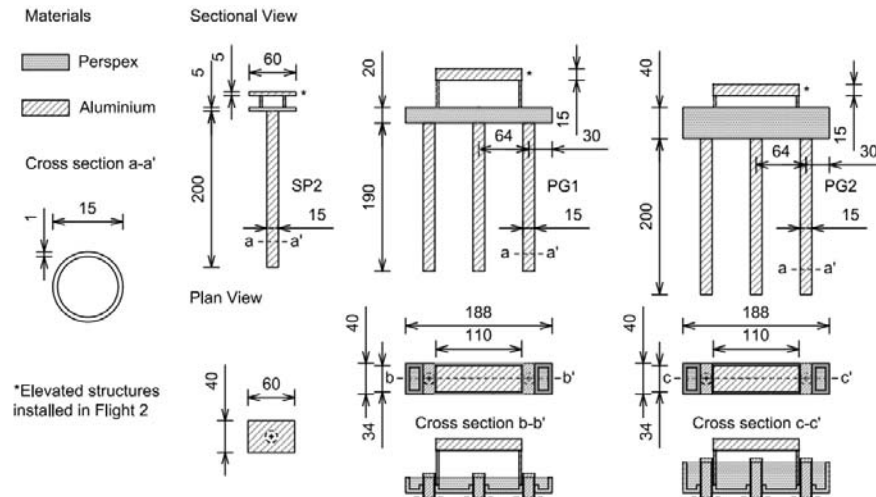


Figure 1: Model pile foundations and superstructures. Model (prototype) dimensions are in mm (m).

## 2.1 Centrifuge flights 1 and 2

Two centrifuge flights were successively performed (Table 1). In the first flight only the piled foundations embedded in the kaolin clay were tested to investigate kinematic soil-pile interaction under earthquake loading. Hollow Perspex caps were installed on model foundations to accommodate instruments and, with regard to the pile groups, to rigidly connect the piles' heads. Mass of the Perspex caps for the SP, PG1 and PG2 are 11 g, 90 g and 170 g, respectively, being thus negligible in comparison to the self-weight of the piles. Hence, the accelerations during flight 1 can be considered as the effect of kinematic interaction.

In the second flight, elevated aluminum caps were added to each foundation configuration to model a SDOF structure, thus allowing the experimental investigation of the seismic response of the coupled SPS system. It is noted that the fixed-base natural period of the SDOF was measured at 0.2 s in prototype scale.

Centrifuge flights	Foundation models	SDOF model on piles
flight 1	SP, PG1, PG2	No
flight 2	SP, PG1, PG2	Yes

Table 1: Model configurations included in centrifuge flights 1 and 2

## 2.2 Model preparation and soil properties

The model was prepared inside an Equivalent Shear Box (ESB) [26] (Schofield and Zeng 1992), in order to simulate field conditions accurately. It is a 645×230×400 mm rectangular box having alternate layers of rubber and aluminum rings (of width 75 mm), in order to reproduce the  $K_0$  conditions (zero lateral strains) and to match the shear deformation of the soil layer for a given earthquake. The bottom of ESB box was covered with a thin layer of filter

material and its inner surface was coated with silicone grease to minimize friction against the clay.

Laboratory grade Speswhite kaolin, whose mechanical behaviour has been extensively studied in Cambridge for many experimental campaigns [27-32] was used in the tests. Its properties are listed in Table 2. The kaolin clay powder was first mixed with de-aired water in 1:1.25 ratio under vacuum for two-three hours using the clay-mixer available in the Schofield Centre. The Clay slurry was then transferred into the ESB, once the instruments were fixed with utmost care. Under normal gravity (1g) conditions, the clay was allowed to consolidate on its self-weight for 24 hours and then the ESB box was placed under a computer controlled hydraulic press to consolidate under a vertical stress of 14.10 kPa. Simultaneously, the model was subjected to a suction of -90 kPa at the base. The purpose of a combination of vertical stress and suction-induced seepage consolidation is explained in detail in [32]. Once the clay was consolidated to stress level needed to achieve the desired undrained shear strength profile, the sample was unloaded and taken out from the consolidation chamber. At this stage, the model depth,  $H$ , and density,  $\rho_s$ , of the clay were 290 mm and 1.623 Mg/m<sup>3</sup>, respectively. Piles were then installed by gentle push into the clay layer at 1g.

Property	Value
Plastic limit, $PL$ [%]	30
Liquid limit, $LL$ [%]	63
Plasticity index, $I_P$ [%]	33
Specific gravity, $G_s$	2.60
Slope of critical state limit (CSL) in $q'$ - $p$ plane	0.90
Intercept of an unload-reload line, $\kappa$	0.039
Intercept of CSL at $p' = 1$ kPa, $\Gamma$	3.31
Slope of normal consolidation line, $\lambda$	0.22

Table 2: Properties of Speswhite kaolin clay (from Lau 2015 [29]).

### 2.3 Centrifuge models instrumentation

In order to capture the response of clay and pile foundations during the test, the model was equipped with (a) 11 Piezo-electric Accelerometers (PAs), to record the seismic accelerations developed in the clay; (b) 20 Micro-Electro-Mechanical System accelerometers (MEMSs), to measure both horizontal and vertical accelerations of pile foundations; (c) 6 Linearly Variable Differential Transformers (LVDTs), to monitor the settlement of clay, single piles and pile groups at different phases of testing; (d) 4 Pore Pressure Transducers (PPTs), to measure the pore pressure within the soil model; (e) an air hammer device (AHD), to determine soil stiffness. In order to fix the location of the instruments inside the box, five horizontal aluminum wires were settled in it and the clay slurry was transferred into the ESB box, once the instruments were fixed with utmost care. Figure 2 shows the schematic plan view and section of the model along with the exact locations of the instrumentation scheme.

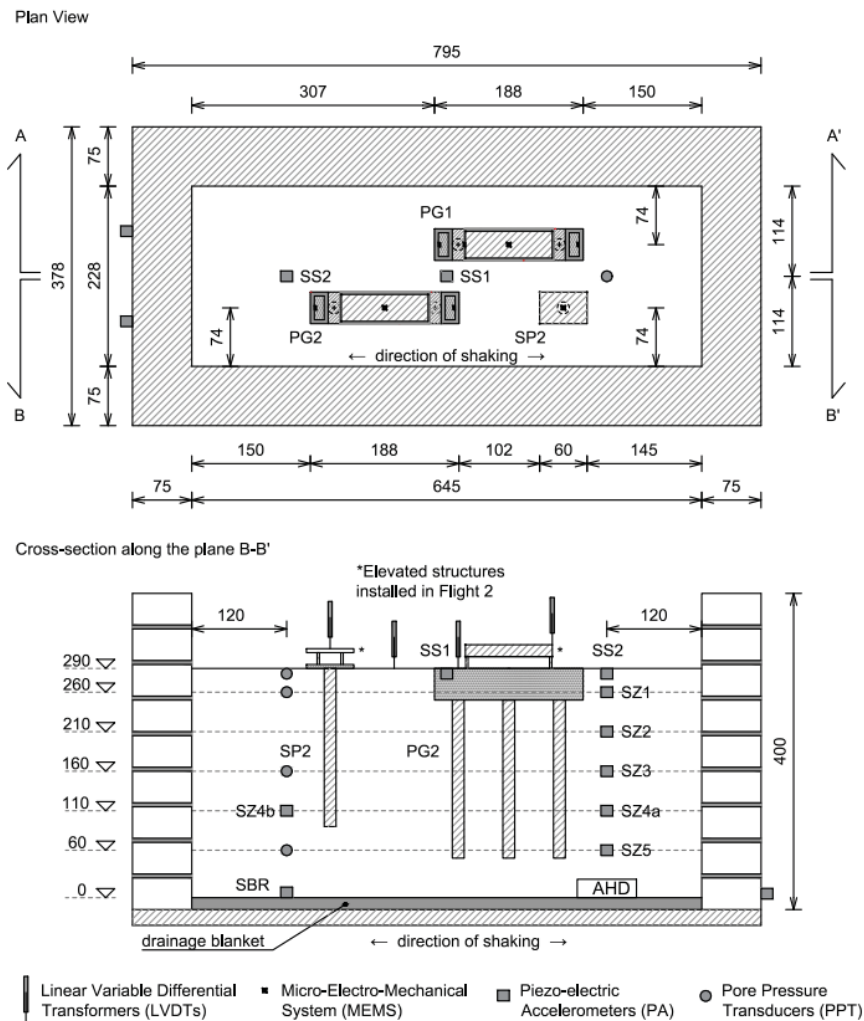


Figure 2: Plan view and cross-section of the model showing instruments locations. Model dimensions are in mm.

## 2.4 Input motions

The model was swung up to 50g in the centrifuge, with gradual increments of 10g. Once the clay model attained equilibrium, it was subjected to a sequence of quasi-sinusoidal waves and real earthquakes (nine signals in total). Quasi-sinusoidal waves with different amplitude and predominant frequency and real earthquakes were applied throughout the servo-hydraulic shaker recently developed at the Schofield Centre [33]. Some results from the centrifuge experiments are discussed in the following sections, with reference to two real earthquakes, EQ1 and EQ2 (Figure 3) with similar peak acceleration close to 0.1g. The Fourier amplitude spectra and the response spectra of the two input motions are also shown in Figure 3. Soil response under a sine sweep input signal, with a maximum amplitude of 0.08g and frequency varying from 30 up to 150 Hz, was also elaborated as reported in the ensuing.

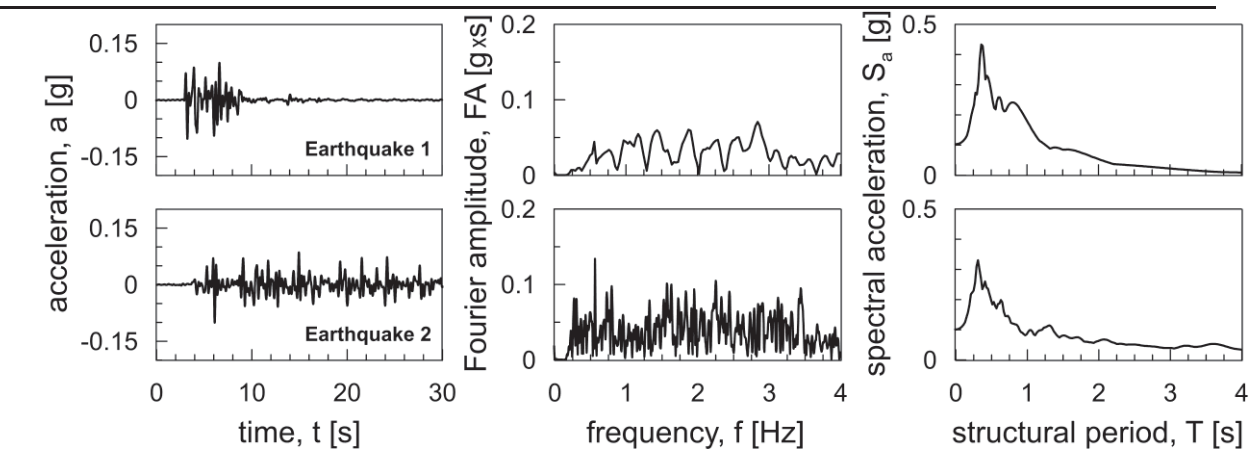


Figure 3: Earthquakes considered in the study (prototype scale).

### 3 SEISMIC BEHAVIOUR OF CLAY

Figures 4 (a) and (b) shows the maximum ground acceleration,  $a_{\max}$ , with depth for earthquakes 1 and 2, respectively. Accelerations in the soil are quite similar during flights 1 and 2 (Figure 4). This also suggests that soil stiffness and strength do not change significantly between the two flights and that superstructure has a minor effect on soil accelerations, even nearby the foundation.

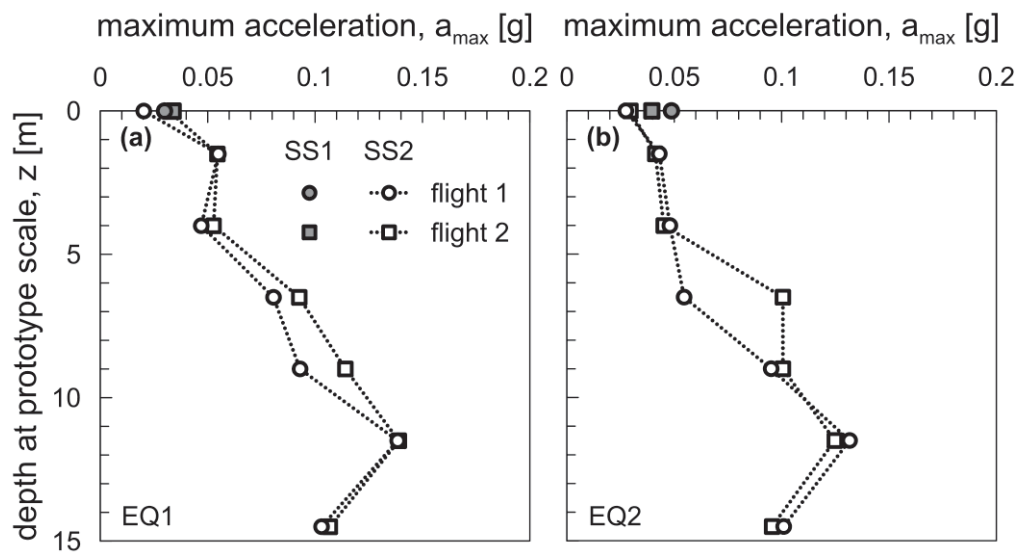


Figure 4: Maximum ground acceleration profile for (a) earthquake EQ1 and (b) earthquake EQ2. The location of SS1 and SS2 is shown in Figure 2.

For both earthquakes, an attenuation of maximum ground acceleration when approaching surface is observed. This suggests that soil may have reached close-to-failure shear stresses. Acceleration response spectra at different depths are plotted in Figure 5, showing that the high frequency components are filtered out by the layers either near the surface or nearby the base while low frequencies are still amplified.

The main intention behind the adoption of the sine-sweep excitation with a maximum amplitude of 0.08g and frequency varying from 30 up to 150 Hz was to determine the natural frequencies of soil layer and soil-foundations systems.



The measurements by the accelerometers on the surface and at the bottom of the model allow to estimate the soil layer amplification function (Figure 6).

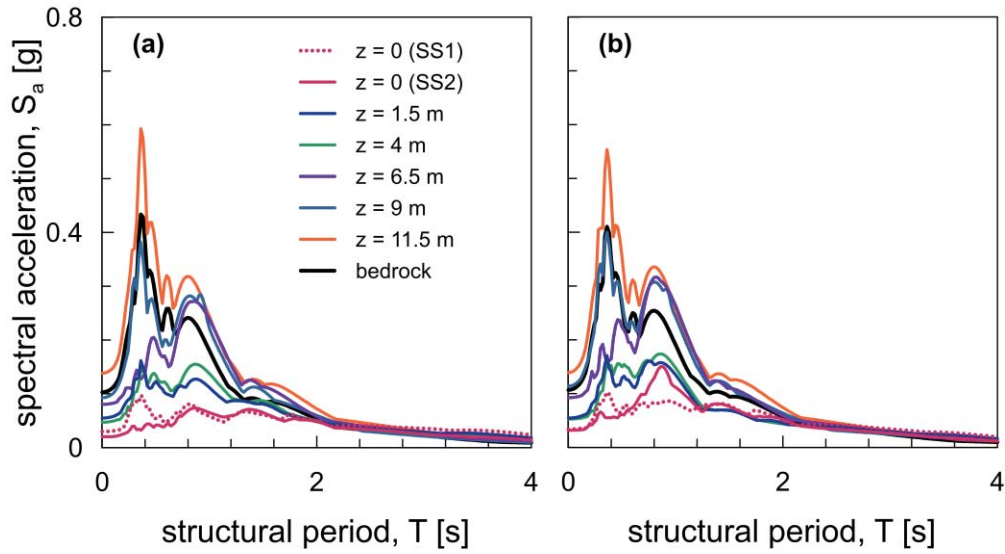


Figure 5: Response spectra along the vertical array for earthquake EQ1 in (a) flight 1 and (b) flight 2.

The top-to-base Fourier amplitude ratio obtained considering both signals at the ground surface are quite similar for both flights 1 and 2, indicating a natural frequency of about 0.2 Hz. Differences in the amplitude of the first peak in flights 1 and 2 reflects the influence of the superstructure in the dynamic response of the system.

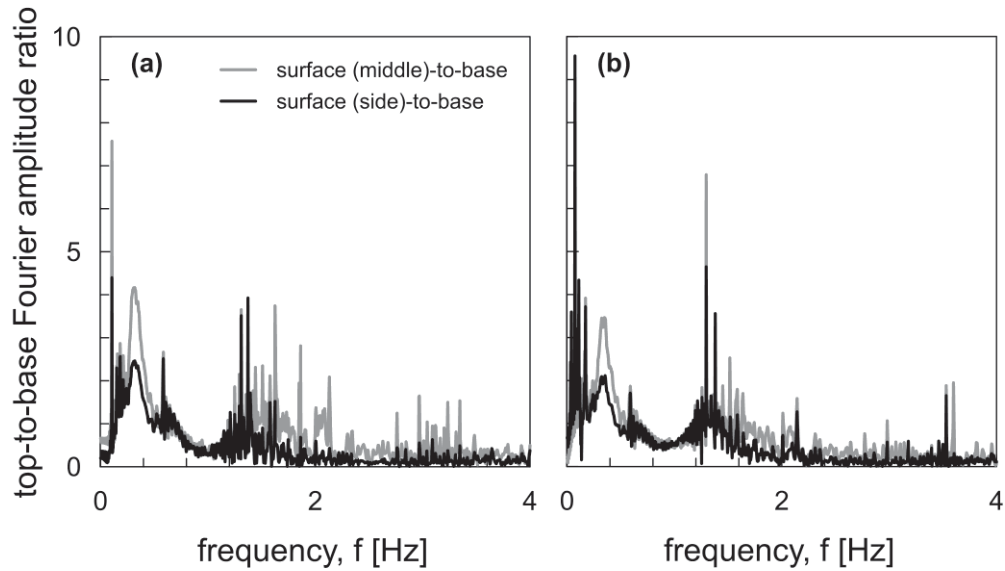


Figure 6: Top-to-base Fourier amplitude ratio obtained under the sine sweep input motion in (a) flight 1 and (b) flight 2.

#### 4 KINEMATIC EFFECTS ON PILE-HEAD RESPONSE

Kinematic soil-pile interaction effects were then explored on pile-head response as recorded during flight 1. To this end, acceleration response spectra computed at the head of the SP or at the cap of the PG1 and PG2 models are compared in Figures 7a and 7b for EQ1 and EQ2, respectively. The corresponding response spectrum at the ground surface (SS2 in Figure 2) is

also plotted. Contrary to the usual belief of a beneficial effect of a fixed-head pile in reducing the amplitude of high-frequency components of the ground surface motion at free-field conditions, the response spectra plotted in Figure 7 show a reversed trend where spectral ordinates at the level of the pile-head are above those of the ground surface motion. Such a behaviour imply that in this particular case of a very soft soil, the actual amplitude of motion imposed at the base of a pile-supported structure may be higher with respect to the amplitude of motion at soil surface, which is traditionally employed in design practice, highlighting a possibly detrimental effect of pile foundations. This observation could possibly be associated to the interpretation given in Iovino et al. [10] that piles average the non-uniform deformation of the surrounding soil along an effective depth which is a fraction of the pile active length. In the case where the non-uniform soil deformation is de-amplified between this effective depth and ground surface (Figure 4) then the averaging action of piles may lead larger amplitudes of motion. However, further elaboration is needed to understand the interaction mechanism in such cases, taking also into account the contribution of the rotational component of the pile-head motion.

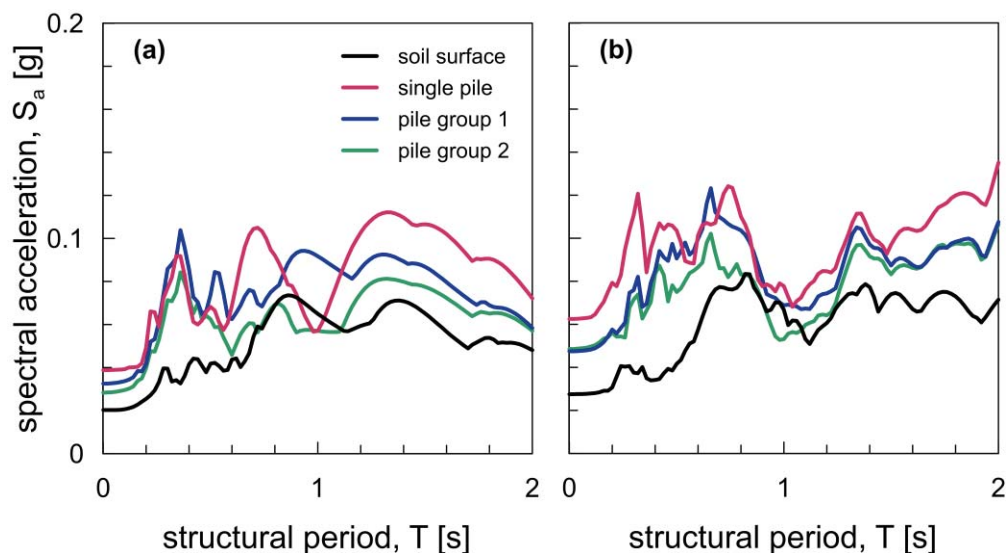


Figure 7: Response spectra for flight 1 during (a) earthquake EQ1 and (b) earthquake EQ2.

## 5 SSI PERIOD OF THE COUPLED SPS SYSTEMS

Mention has already been made that soil compliance may affect considerably the vibrational characteristics of a structure, referring to an elongation of its natural period with respect to the fixed-base case, that may be important in the case of soft soils such as the one employed in the centrifuge tests at hand. In order to identify this aspect by means of the centrifuge records acquired from flight 2, we derived structural top-to-ground surface acceleration response spectra ratios for each coupled system included in the centrifuge apparatus. Results are plotted in Figures 8a and 8b for EQ1 and EQ2, respectively, referring to the SDOF structure supported by the SP, the PG1 and the PG2 foundation models. The period at which this ratio achieves its peak value corresponds to the natural period of the coupled system ( $T_{ssi}$ ), including the effect of soil compliance. It is reiterated that the fixed-base period ( $T_{fixed}$ ) of the SDOF oscillator was measured at 0.2 sec.

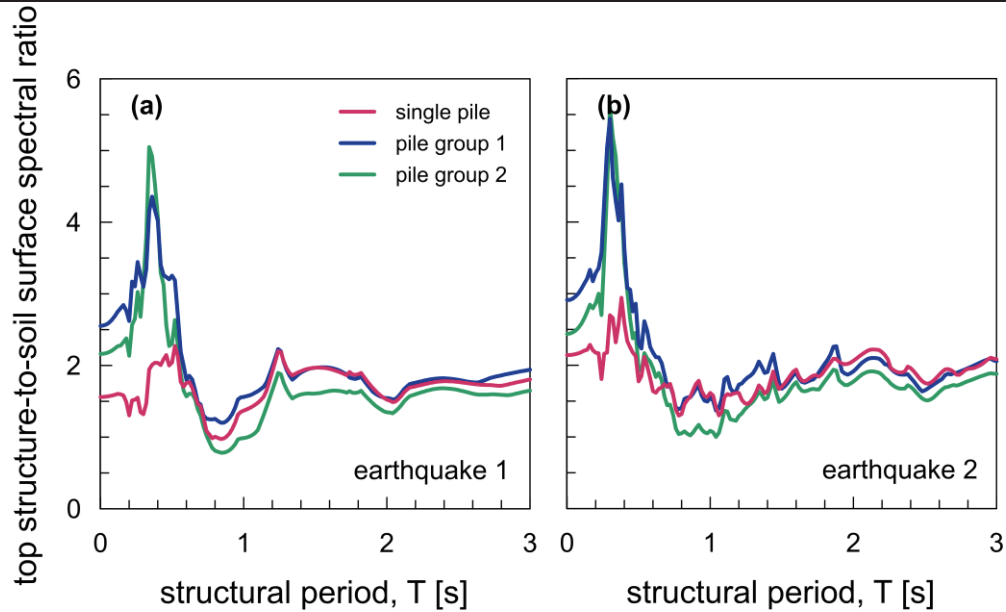


Figure 8: Top structure-to-soil surface spectral ratio obtained from Flight 2 for (a) earthquake EQ1 and (b) earthquake EQ2.

The experimentally-derived values of  $T_{ssi}$  and the corresponding ratios of  $T_{ssi}/T_{fixed}$  are summarized in Table 3 for each case under consideration. It is observed that for both input motions, the role of such a soft soil in controlling the dynamic characteristics of the flexible-supported structures is dominant, as reflected in the large values of the computed  $T_{ssi}/T_{fixed}$  ratios. The effect is understandably more pronounced for the SDOF oscillator supported by the SP foundation model. In this case, the  $T_{ssi}/T_{fixed}$  ratio reaches or even exceeds 2, denoting a very strong effect of soil flexibility on the system period. When the SDOF structure is supported by the pile groups the effect of soil compliance is less pronounced but still quite important, leading to  $T_{ssi}/T_{fixed}$  ratios at 1.5 or higher, which denote a 50% or more of increase of the SSI period with respect to the fixed-base case. It is also noteworthy that the SSI period is almost the same between SDOF-PG1 and SDOF-PG2 systems, indicating a negligible effect of pile cap embedment on  $T_{ssi}$ .

Input motion	Coupled system	$T_{ssi}$ (sec)	$T_{ssi} / T_{fixed}$
EQ1	SDOF on SP	0.46	2.3
	SDOF on PG1	0.36	1.8
	SDOF on PG2	0.34	1.7
EQ2	SDOF on SP	0.38	1.9
	SDOF on PG1	0.30	1.5
	SDOF on PG2	0.30	1.5

Table 3:  $T_{ssi}$  period and ratios of  $T_{ssi}/T_{fixed}$  identified from centrifuge data elaboration of flight 2.

## 6 CONCLUSIONS

Critical aspects of soil-pile-structure interaction in a soft kaolin clay soil were explored under earthquake loading in centrifuge tests carried out at 50g aboard the Turner Beam centrifuge at the Schofield Centre of the University of Cambridge. A single pile and two 3x1 pile groups were modeled in the centrifuge to explore kinematic soil-pile interaction effects on the modification of the soil motion and soil compliance effects on the vibrational characteristics of a SDOF structure. Preliminary analysis of the experimental data revealed the following trends:

- A remarkable attenuation of maximum ground acceleration between base and surface of the soil layer was recorded, showing a substantial filtering effect of soil on the high-frequency components of motion. Such a de-amplification can be attributed to large earthquake-induced shear stresses close to the low shear strength of the particular soft clay, a condition which limits the transmission of the propagating wave field.
- A strong amplification of the motion at the pile-head with respect to that at ground surface was recorded for both earthquake excitations considered in this study, providing evidence that the actual seismic loading imposed at the base of the supporting structure may be higher with respect to the one induced by ground surface motion, which is usually employed in design practice. Further analysis of the centrifuge data is needed to obtain insight on such a behaviour, including the possibly important contribution of the rotational component of the pile motion.
- The experimentally-obtained natural period of the examined SSI systems was increased substantially with respect to the fixed-base case, denoting a dominant effect of the soil compliance in the case of the examined soft clay. For the foundation layouts modeled in the centrifuge, ratios of flexible- over fixed-base period exceeded 1.5, being more pronounced in the case of the single pile with respect to the pile-groups. In the latter case, the effect of the embedment depth on the SSI period was minor.

## ACKNOWLEDGEMENTS

This research has been developed under SERA project COSMO 'Change of Seismic motion due to pile-soil-kinematic interaction' funded within the framework of European Union's Horizon 2020 research and innovation program Transnational Access to SERA, Seismology and Earthquake Engineering Infrastructure Alliance for Europe, Grant Agreement No. 730900.

## REFERENCES

- [1] R. Flores-Berrones, R. V. Whitman. Seismic Response of End-Bearing Piles. *Journal of Geotechnical Engineering*, **109**(5), 781-781, 1983.
- [2] A. Kaynia, E. Kausel. Dynamics of piles and pile groups in layered soil media. *Soil Dynamics and Earthquake Engineering*, **10.8**: 386-401, 1991.
- [3] S. Nikolaou, G. Mylonakis, G. Gazetas, T. Tazoh. Kinematic pile bending during earthquakes: analysis and field measurements. *Géotechnique*, **51**(5), 425-440, 2001.

- 
- [4] G. Anoyatis, R. Di Laora, A. Mandolini, G. Mylonakis. Kinematic response of single piles for different boundary conditions: Analytical solutions and normalization scheme. *Soil Dynamics and Earthquake Engineering*, **44**, 183-195, 2013.
  - [5] R. Di Laora, L. de Sanctis. Piles-induced filtering effect on the foundation input motion. *Soil Dynamics and Earthquake Engineering*, **46**, 52-63, 2013.
  - [6] E. Rovithis, G. Mylonakis, K. Pitilakis. Dynamic stiffness and kinematic response of single piles in inhomogeneous soil. *Bulletin of Earthquake Engineering*, **11(6)**, 1949-1972, 2013.
  - [7] S. Kawamura, S. H. Umemura, Y. Osawa. Earthquake motion measurement of a pile supported building on reclaimed ground. *Proceedings of 6th WCEE*, India, 1977.
  - [8] T. Ohta, S. Uchiyama, M. Niwa, K. Ueno. Earthquake response characteristics of structure with pile foundation on soft subsoil layer and its simulation analysis, *Proceedings of the 7th World Conference on Earthquake Engineering*, Vol. 3. Istanbul, Turkey, 1980.
  - [9] G. Gazetas. Seismic response of end-bearing single piles. *International Journal of Soil Dynamics and Earthquake Engineering*, **3(2)**, 82-93, 1984.
  - [10] M. Iovino, R. Di Laora, E. Rovithis, L. de Sanctis L. The Beneficial Role of Piles on the Seismic Loading of Structures. *Earthquake Spectra*, **35(3)**, 1141-1162, 2019.
  - [11] R. Di Laora, E. Rovithis. Design of piles under seismic loading, In *Pile Foundations Under Static and Dynamic Loads* (A. Kaynia ed), ISBN 9780367374167 (in press), 2021.
  - [12] R. A. Parmelee RA. Building-foundation interaction effects. *Journal Engineering Mech Div, ASCE*, **93(EM2)**, 131-162, 1967.
  - [13] P. C. Jennings, J. Bielak. Dynamics of building-soil interaction. *Bulletin of the seismological society of America*, **63(1)**, 9-48, 1973.
  - [14] A. S. Veletsos, J. W. Meek. Dynamic behaviour of building-foundation systems. *Earthquake Engineering & Structural Dynamics*, **3(2)**, 121-138, 1974.
  - [15] A. S. Veletsos, V. V. Nair. Seismic interaction of structures on hysteretic foundations. *Journal of the Structural Division, ASCE*, **101(1)**, 109-129, 1975.
  - [16] J. P. Wolf. Soil-structure interaction. *Prentice Hall Inc., Englewood Cliffs, New Jersey* ISBN 0 13, 221565(9), 01, 1985.
  - [17] A. Maravas, G. Mylonakis, D. L. Karabalis. Dynamic soil-structure interaction for SDOF structures on footings and piles. In *Geotechnical Earthquake Engineering and Soil Dynamics IV* (pp. 1-10), 2008.
  - [18] A. Maravas, G. Mylonakis, D. L. Karabalis. Simplified discrete systems for dynamic analysis of structures on footings and piles. *Soil Dynamics and Earthquake Engineering*, **61**, 29-39, 2014.
  - [19] V. Zania. Natural vibration frequency and damping of slender structures founded on monopiles. *Soil dynamics and Earthquake engineering*, **59**, 8-20, 2014.
  - [20] K. Weissman, J. H. Prevost. A Study of Radiation Damping and Soil-structure Interaction Effects in the Centrifuge. National Center for Earthquake Engineering Research, 1988.



- 
- [21] R. W. Boulanger, C. J. Curras, B. L. Kutter, D. W. Wilson, A. Abghari. Seismic soil-pile-structure interaction experiments and analyses. *Journal of Geotechnical and Geoenvironmental Engineering*, **125**(9), 750-759, 1999.
  - [22] M. N. Hussien, T. Tobita, S. Iai, M. Karray. Soil-pile-structure kinematic and inertial interaction observed in geotechnical centrifuge experiments. *Soil Dynamics and Earthquake Engineering*, **89**, 75-84, 2016.
  - [23] P. Martakis, D. Taeseri, E. Chatzi, J. Laue, J. A centrifuge-based experimental verification of Soil-Structure Interaction effects. *Soil Dynamics and Earthquake Engineering*, **103**, 1-14, 2017.
  - [24] G. Mylonakis, G. Gazetas. Seismic soil-structure interaction: beneficial or detrimental?. *Journal of earthquake engineering*, **4**(3), 277-301, 2020.
  - [25] A. N. Schofield. Cambridge geotechnical centrifuge operations. *Géotechnique*, **30**(3), 227-268, 1980.
  - [26] A. N. Schofield, X. Zeng. Design and performance of an equivalent-shear-beam (ESB) container for earthquake centrifuge modelling. University of Cambridge, Department of Engineering, 1992.
  - [27] W. A. Take. The influence of seasonal moisture cycles on clay slopes. PhD dissertation, University of Cambridge, UK, 2003.
  - [28] S. S. Y. Lam. Ground movements due to excavation in clay: physical and analytical models. PhD dissertation, University of Cambridge, UK, 2010.
  - [29] B. H. Lau. Cyclic behaviour of monopile foundations for offshore wind turbines in clay. PhD dissertation, University of Cambridge, UK, 2015.
  - [30] T. K. Garala. Seismic response of pile foundations in soft clays and layered soils. PhD dissertation, University of Cambridge, UK, 2020.
  - [31] T. K. Garala, S. P. G. Madabhushi. Seismic behaviour of soft clay and its influence on the response of friction pile foundations. *Bulletin of Earthquake Engineering*, **17**(4), 1919–1939, 2019.
  - [32] T. K. Garala, S. P. G. Madabhushi, R. Di Laora. Experimental investigation of kinematic pile bending in layered soils using dynamic centrifuge modelling. *Géotechnique*, 1-16, 2020.
  - [33] S. P. G. Madabhushi, S. K. Haigh, N. Houghton, E. Gould. Development of a servo-hydraulic earthquake actuator for the Cambridge Turner beam centrifuge. *International Journal of Physical Modelling in Geotechnics*, **12**(2), 77-88, 2012.

## LONG TERM MONITORING OF THE SANTA MARIA DI COLLEMAGGIO BASILICA

A. Aloisio<sup>1</sup>, R. Cirella<sup>2</sup>, A. Elena<sup>2</sup>, and R. Alaggio<sup>2</sup>

<sup>1</sup> e-mail: angelo.aloisio1@uni vaq.it

<sup>2</sup> e-mail: {riccardo.cirella, elena.antonacci, rocco.alaggio }@uni vaq.it

**Keywords:** Structural Heath Monitoring; Automatic Operational Modal Analysis; Environmental effects; Static monitoring; Frequency veering.

**Abstract.** *The Santa Maria di Collemaggio basilica is a 13th-century masonry masterpiece. The restoration works following the 2009 earthquake in L'Aquila included the installation of a permanent monitoring system. Crack gauges monitor a few significant cracks that appeared during the 2009 earthquake. Force-Balance accelerometers record the dynamic response of the entire structure. The dynamic response to ambient excitation leads to the estimation of the modal parameters. The current paper reports the outcomes of two years of static and dynamic monitoring from 1/1/2018 to 31/12/2019. The authors correlated the outdoor temperature and relative humidity to both the amplitude of the cracks and the modal parameters. The temperature deeply affects the static and dynamic response of the basilica. However, the linear correlations between the temperature and the structural response are diverse. There are cracks which stretch when the temperature rises and cracks which act oppositely. Natural frequencies lower when the temperature rises, while the same modes exhibit modal interaction phenomena. Furthermore, the natural frequencies of the basilica are not stationary but are moderately declining across the years. The basilica is a complex structure, where the different constitutive behaviour of three different materials, masonry, steel and timber may yield a varied structural response. The authors attempt to provide a qualitative interpretation of the observed behaviour, namely the detected correlations to the outdoor temperature, the lowering of the natural frequencies across the years and mode interaction phenomena.*

## 1 INTRODUCTION

Long term monitoring of civil structures belongs to almost thirty years of practice [1, 2, 3]. However, the long term monitoring of large masonry structures has almost ten years of history. After the work by Ramos et al. [4], a few other scholars investigated the static and dynamic behaviour of historical masonry structures: towers [5, 6, 7], cathedrals [4] and palaces [8].

A few research groups, mainly concentrated in the Mediterranean area, dedicated their research efforts to this topic. Concerning the masonry churches, L.F. Ramos et al. [4] and Masciotta et al. [9, 10] monitored the Church of Monastery of Jeronimos. Elyamani et al. [11] monitored the Mallorca cathedral (Mallorca Island, Spain) under ambient sources of vibration and seismic events. A few months ago, Gentile et al. [12] reported on the long-term monitoring of the Milan cathedral, which hosts the most extensive monitoring system ever installed in a cultural heritage monument.

The current paper illustrates the static and dynamic monitoring of the Santa Maria di Collemaggio basilica. Differently from the considered cases, the Church of Monastery of Jeronimos, the Mallorca cathedral and the Milan cathedral, the Santa Maria di Collemaggio basilica suffered the structural consequences of a destructive earthquake in 2009. The monitoring system will allow understanding, not just the correlation of the modal parameters to environmental effects, but the effects of the retrofit interventions.

The University of L'Aquila began the study of the dynamics of the Santa Maria di Collemaggio basilica in 1989. Dozens of scholars studied the basilica from historical [13], archaeological [14], architectural [15, 16, 17, 18], structural [19, 20, 21, 22, 23, 24, 3, 25, 26, 27], geotechnical [28, 29] and even energetic [30] perspectives. The dynamics of the Basilica was investigated by the University of L'Aquila [31, 32, 33, 34, 35, 36]. So far, no study presented the results of long-term monitoring of the Santa Maria di Collemaggio basilica.

After the 2009 earthquake in L'Aquila, the University of L'Aquila, the University La Sapienza in Rome and the Politecnico in Milan supported the design phase of the restoration, supervised by the *Soprintendenza ai Beni Architettonici e Paesaggistici per l'Abruzzo*. A funding agreement, signed by Eni and the municipality of L'Aquila, pointed at developing a paradigmatic model in the panorama of restoration of monumental architectural heritage, based on a multidisciplinary plan. The University of L'Aquila was further commissioned to conceive a monitoring system, which could operate during and after the rehabilitation. In the first working phase, the monitoring system provided the construction manager with a survey tool about structural interventions. After the rehabilitation, the monitoring system was fully-fledged – an essential instrument for the implementation of the conservation plan. The conservation plan aims at assessing the conservation state of the basilica, based on its intrinsic vulnerability and the regional seismic risk.

Moreover, the permanent monitoring system, installed in 2017, aims at supporting research activities which will possibly lead to the assessment of reliability thresholds, damage detection and damage localization. The significant number of accelerometers allows a refined resolution of the mode shapes and may give enough information to reliably estimate the evolution of the structural condition of the basilica, especially after seismic events. The definition of the reliability thresholds is essential in assessing the structural safety based on dynamic data after seismic events.

The paper presents selected results from the long-term monitoring of the Santa Maria di Collemaggio basilica extracted from [37].

## 2 The basilica

Santa Maria di Collemaggio, built at the end of the 13th century, is a large medieval church in L'Aquila, central Italy. It is a world-famous church for its significance in religious history [38]. The elegant Romanesque façade has the appearance of a wall, with a central door, embellished in the 15th century, and two smaller flanking doors; The interior follows the standard plan of a nave and two side aisles, each one divided from it by a row of columns, from which arches support a tall wooden ceiling. The Basilica has a masonry structure typical of ancient buildings in L'Aquila [39], with varied, but prevalently regular, masonry textures [38, 40, 41, 42]. On the lateral wall stands the Holy Door (Fig.1(c)), opened on 28th and 29th of August every year in occasion of the annual jubilee.

The Basilica has a middle nave (61 m long and 11.3 m wide) and two side naves (approx 8 m wide). The central and side naves reach a maximum height of 20.4 m and 15 m respectively, while the facade is 29.5 m wide and 21.3 m high.

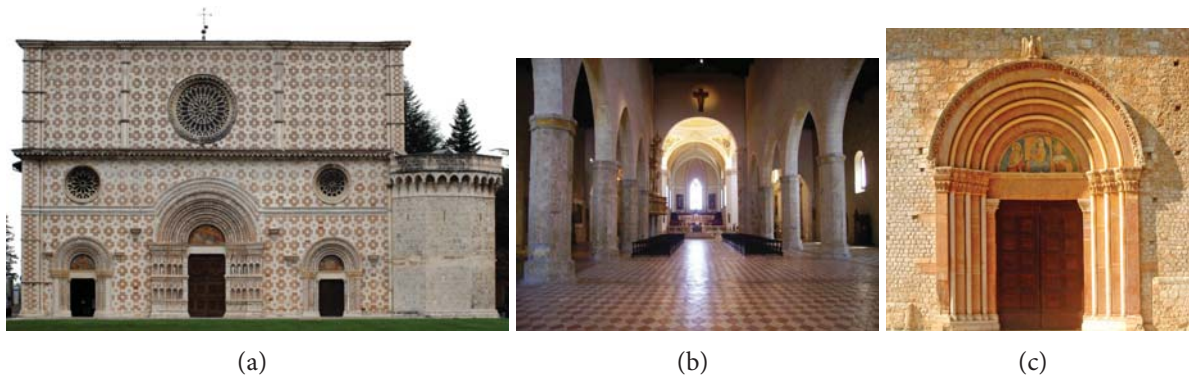


Figure 1: (a) Facade, (b) interior, (c) Holy Door, (d) plan of the basilica, (e) prospect of the apse, (f) and the Holy Door wall.

The permanent monitoring system consists of nine crack measurement devices, 78 Force-balance accelerometers (2 triaxial 12 biaxial and 48 monoaxial), and five temperature/humidity sensors.

The crack measurement devices are high precision triangulation lasers with a 25mm measuring range, 0.03mm linearity and  $2.5\mu\text{m}$  reproducibility. The FBA accelerometers are characterized by a 2.5V/g sensitivity. The details of the monitoring system are presented in [37]

## 3 Long term static monitoring

The monitoring devices, placed over significant cracks, have acquired every hour since 31/08/2018. The authors report selected results from 31/08/2018 to 21/12/2019. The behaviour of the cracks suggests the following coarse classification see Tab.1:

- FP2, FP3 and FP7 (Fig.2(b),(c),(g)): The amplitude is almost constant with oscillation between the maximum and minimum amplitudes equal to 0.03 mm, 0.04 mm and 0.06mm respectively.  
FP2 and FP7 are the sole devices which monitor the cracks on the intrados of the ogival arches in the central nave. The amplitude rests constant, likely meaning that the ogival arches are stable against static forces and environmental parameters. FP3 reveals the stability of a crack below a pavilion vault on the right side of the apse.

Table 1: Statistical description of the amplitude of the instrumented cracks from 31/08/2018 to 21/12/2019

Instrument	Crack measurement [mm]			
	Mean	Variance	Maximum	Minimum
FP1	0.11	$7.50 \times 10^{-4}$	0.18	0.06
FP2	0.07	$9.10 \times 10^{-5}$	0.09	0.06
FP3	15.68	$3.67 \times 10^{-5}$	15.69	15.65
FP4	0.71	$5.15 \times 10^{-3}$	0.86	0.57
FP5	1.02	$9.00 \times 10^{-3}$	1.17	0.81
FP6	0.10	$5.21 \times 10^{-4}$	0.16	0.06
FP7	5.73	$1.88 \times 10^{-4}$	5.75	5.69
FP8	0.22	$1.34 \times 10^{-3}$	0.31	0.16
FP8	6.19	$1.99 \times 10^{-2}$	6.42	6.18

- FP1, FP4, FP6, FP8 and FP9 (Fig.2(a),(d),(f),(h),(i)) show higher discrepancies between the minimum and maximum amplitudes, equal to 0.12 mm, 0.29 mm, 0.10 mm and 0.24 mm respectively. The amplitude of these cracks increases during spring and summer and decreases in the cold seasons. These devices measure the amplitude of the cracks in the presbiterion: the right chapel (FP4 and FP8), the apse (FP5, FP8 and FP9) and the left chapel (FP1).
- FP5 (Fig.2(e)) yields a 0.36 mm discrepancy between the two extreme values. However, the amplitude decreases during the cold season and vice versa. FP5 monitors a crack on the intrados of the apse vault.

### 3.1 Environmental effects

The evolution of the amplitudes suggests a season-driven behaviour: the environmental parameters mainly determine the observed oscillations. Unfortunately, the thermoigrometers suffered functioning discontinuities due to the difficulty in promptly replacing the batteries by the owner of the basilica. For this reason, the authors adopted as correlation parameters the outdoor temperature and relative humidity recorded by the CETEMPS, (the Centre of Excellence on Telesensing of Environment and Model Prediction Severe events, see <http://cetemps.aquila.infn.it/>) in L'Aquila. Fig.3(a)-(b) show the minute by minute evolution of the temperature and relative humidity from 1/1/2018 to 31/12/2019. The relative humidity has a scattered behaviour; a red line follows the averaged trend obtained from a moving average over a thousand samples. Fig.4 illustrates the correlation between the crack amplitudes and the temperature. The correlations to temperature confirm three trends, already remarked in the previous paragraphs. (i) An almost stationary behaviour in FP2, FP3 and FP7; (ii) A positive rate in FP1, FP4, FP6, FP8 and FP9; (iii) A negative rate in FP5.

The two opposite trends may descend from opposing kinematic mechanisms, which can determine the closing or stretching of the cracks when the masonry swells from thermal expansion. Except for FP9, which is placed outside the apse, the other devices are inside the basilica. Two kinematic mechanisms may stand behind the identified correlations.

The temperature is not constant across the wall thickness. During summer, the outer layers have higher temperature values than the inside ones, and vice versa during winter: likely, a 15°C temperature difference between the outer and inner wall layers occurs during summer and an opposite 15°C difference during winter. The thermal gradient may yield the curvature of the wall, see Fig.5: the external crack stretches ( $l_1$ ), while the internal one reduces ( $l_2$ ). By assuming a thermal expansion coefficient equal to  $\alpha = 5 \times 10^{-6} [^\circ\text{C}^{-1}]$ , and a  $\Delta T = 30^\circ\text{C}$  gradient,



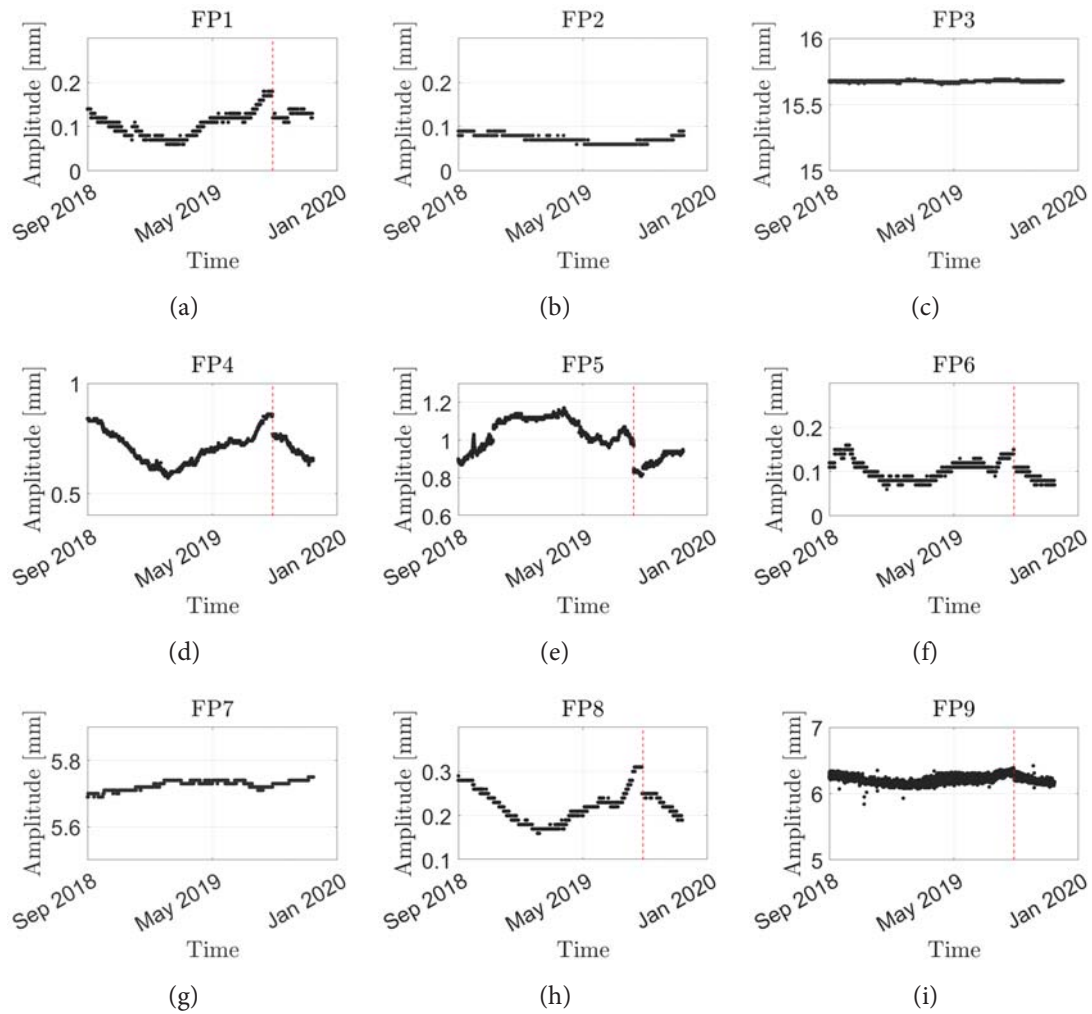


Figure 2: Variation of the cracks amplitudes measured from 31/08/2018 to 21/12/2019. The drops in FP1, FP4, FP5 and FP8 derive from almost one month interruption, indicated by a dashed vertical line.

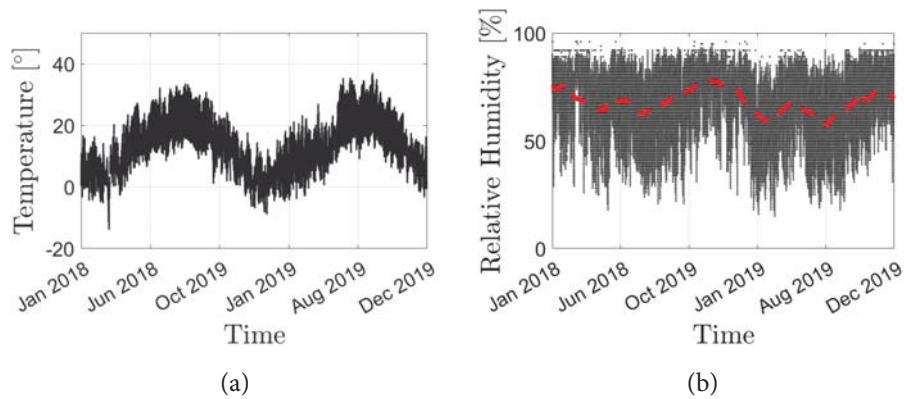


Figure 3: Variation of the environmental parameters measured from 1/01/2018 to 31/12/2019: (a) Outdoor temperature; (b) Outdoor Relative Humidity; The red line is the moving average over a thousand samples.

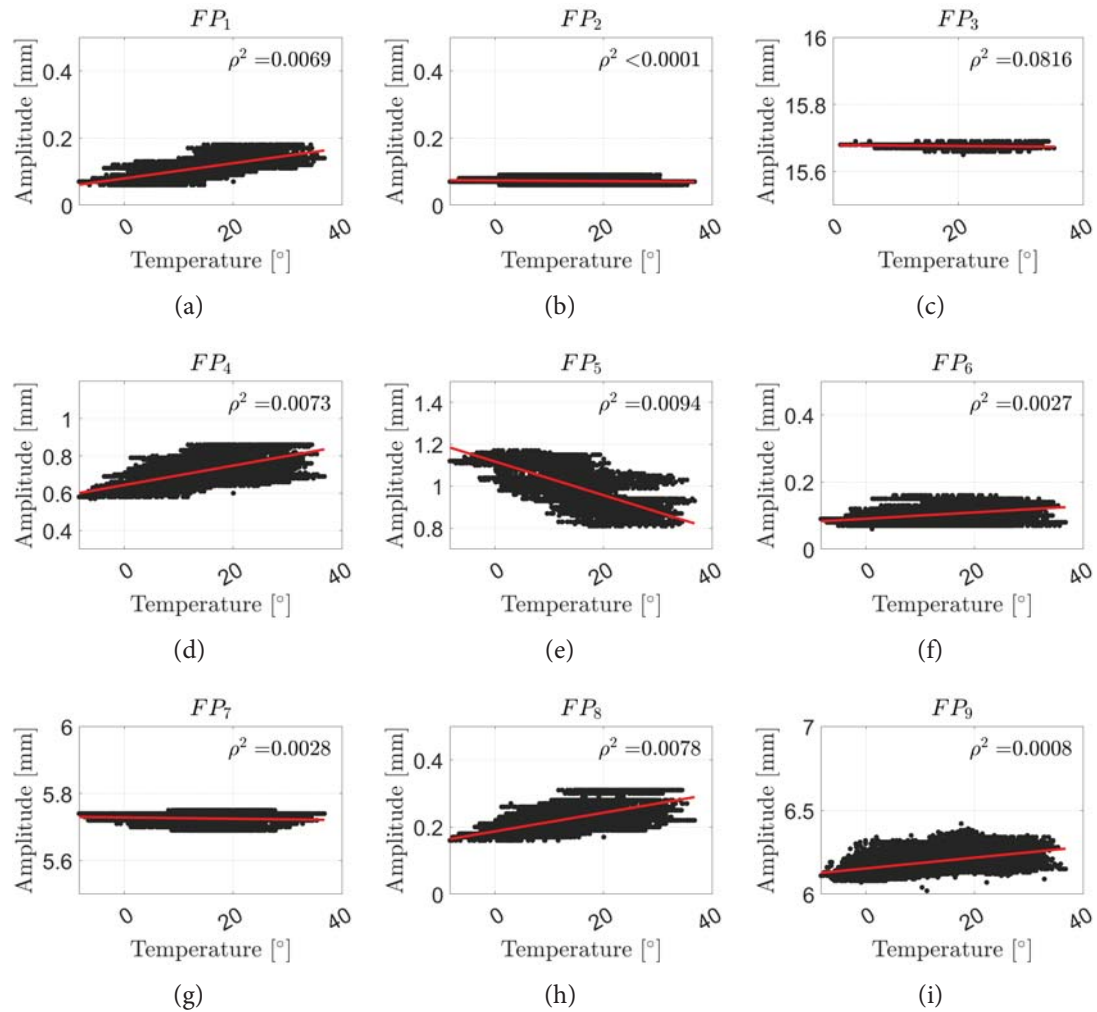


Figure 4: Correlation between the crack amplitude and the outdoor temperature (from 31/08/2018 to 21/12/2019).

obtained by summing the absolute gradients of summer ( $\Delta T_s = 15^\circ\text{C}$ ) and winter ( $\Delta T_w = -15^\circ\text{C}$ ), the equivalent thickness  $t_{eq}$  associated to the maximum drifts are approximately between 0.8m and 2m, see Tab.2, according to the following equations:

$$|\Delta x|_{max} = |\Delta x_s| + |\Delta x_w| = t_{eq} \alpha (|\Delta T_s| + |\Delta T_w|) \quad (1)$$

$$t_{eq} = \frac{\Delta x_{max}}{\alpha \Delta T} \quad (2)$$

where  $t_{eq}$  is the equivalent thickness,  $\Delta x_{max}$  the relative movement of the crack during the year, obtained by summing the effects of summer  $\Delta x_s$  and winter  $\Delta x_w$ ,  $\alpha$  the thermal expansion coefficient and  $\Delta T$  difference between the outdoor temperature during summer and the indoor temperature during winter. Tab.2 reports the equivalent thickness related to the devices which

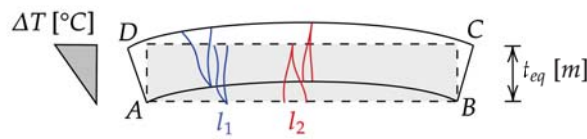


Figure 5: kinematic mechanism possibly associated to the crack behaviour.

measured relative displacements higher than 0.1mm. The identified values match with the wall

Table 2: Estimate of the equivalent wall thickness associated to the maximum relative displacement measured by the crack monitoring devices.

Instrument	Max displ. [mm]	$\alpha$ [ $^\circ\text{C}^{-1}$ ]	$\Delta T$ [ $^\circ\text{C}$ ]	Equiv. Thickness [m]
FP1	0.12	$5 \times 10^{-6}$	30	0.80
FP4	0.29	$5 \times 10^{-6}$	30	1.93
FP5	0.36	$5 \times 10^{-6}$	30	2.40
FP8	0.15	$5 \times 10^{-6}$	30	1.00
FP9	0.24	$5 \times 10^{-6}$	30	1.60

thicknesses corresponding to the measurement devices and possibly validate the elementary kinematic mechanism assumed in Fig.5.

The simple calculations in the above paragraphs have the sole objective of a crude understanding of the results. The equivalent thickness is not the physical thickness of the wall. Besides, the real thickness of masonry is not constant, since most of the cracks stand in the vaults, which were reinforced and filled with expanded clay during the retrofitting interventions: the thickness of the vaults depends on the collaboration between the structure and the filling material. For this reason, the authors preferred to check the amounts of the obtained results, which are on average compatible with the actual masonry thicknesses and, consequently, they possibly descend from the sole thermal effects, rather than other phenomena.

#### 4 Dynamic monitoring

The section presents the outcomes of long-term dynamic monitoring. The first part introduces the results of dynamic identification in terms of mode shapes, natural frequencies and viscous damping. The following parts collect the natural frequencies and MAC (Modal Assurance Criterion) values identified from all time-series and relate them to the outdoor environmental parameters: temperature and relative humidity.

#### 4.1 Dynamic identification

The authors developed an automatic processing algorithm, implemented in MATLAB, based on the Stochastic Subspace Identification (SSI)-cov method [43, 44, 45, 46, 47]. The method yields an estimate of the modal parameters from the acceleration time-series recorded in operational condition.

A factor  $N_d=20$  decimates the initial sampling frequency equal to 250Hz. [37] details the automatic identification algorithm.

#### 5 The dynamics of the nave walls

The dynamic identification of the nave walls returns four stable modes. The authors report the averaged natural frequencies values up to the first decimal place. The higher decimal places will be discussed in light of long-term monitoring. The first mode at 2.09Hz (Fig.6(a)) interests the displacement of all measurement points in the same direction. The displacement is consistently low in the apse comparing to the nave walls motion: the apse is very rigid compared to other parts of the basilica. The particular mode shape possibly originates from the Cross Laminated Timber (CLT) ceiling, behaving like a rigid diaphragm which imposes the same displacement to the nave walls summits.

The higher modes affect the bending of the nave walls. The second mode at 3.11 Hz (Fig.6(b)) mainly regards the change of direction along the vertical: the measurement points by the top of the columns move oppositely to those by the CLT ceiling. Moreover, the phases of the two nave walls are opposite. The third mode at 3.27 Hz (Fig.6(c)) mainly concerns the change of direction of the measurement points along the x-direction, like a second bending mode. The fourth mode at 3.82 Hz (Fig.6(d)) is quite twisted: it is a sort of third bending mode shape. Tab.3 reports the cross MAC between the identified modes in Fig.6. The terms out of the main diagonal are shallow: the mode shapes are dissimilar between each other and distinctly identifiable.

The apse is quite massive, and participate to the identified mode shapes with much lower deformation than the other structural members due to its significant stiffness. The investigation of the apse dynamics requires dedicated efforts and will be the object of future studies by the authors. The dynamic identification carried out before the restoration by [31] evidenced four modes (see

Table 3: Cross MAC between the identified mode shapes.

	2.09	3.11	3.27	3.82
2.09	<b>1</b>	0.04	0.009	0.004
3.11	0.04	<b>1</b>	0.006	0.004
3.27	0.009	0.006	<b>1</b>	0.151
3.82	0.004	0.004	0.151	<b>1</b>

Tab.4), resembling the ones in Fig.6 with the following natural frequencies: 1.25, 1.72, 2.35

Table 4: Evolution of the natural frequencies, before and after the 2009 earthquake and, after the restoration.

	Before 2009 [31]	Since 2017
1st mode [Hz]	1.25	2.09
2nd mode [Hz]	1.72	3.11
3rd mode [Hz]	2.35	3.27
4th mode [Hz]	2.44	3.82

Tab.4), resembling the ones in Fig.6 with the following natural frequencies: 1.25, 1.72, 2.35

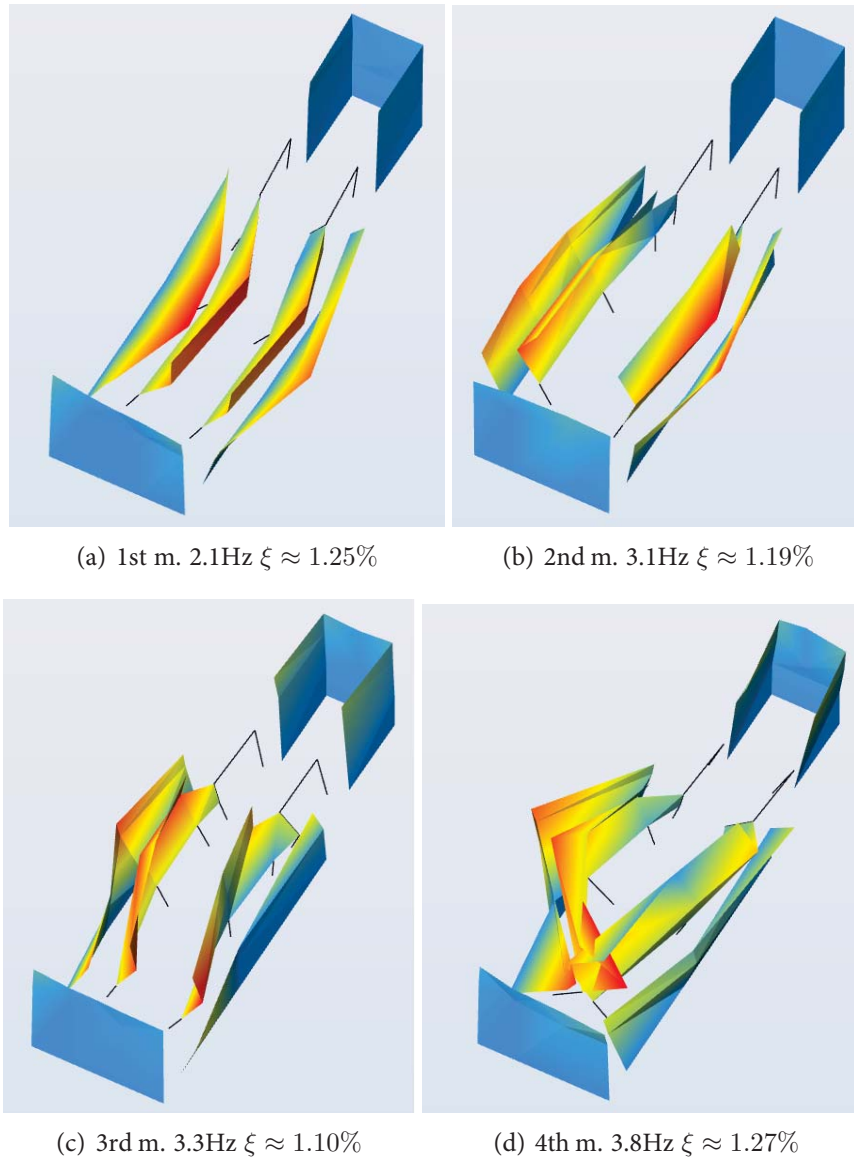


Figure 6: Illustration of the mode shapes of the nave walls, where m. stands for mode and  $\xi$  is the average modal damping.



and 2.44 Hz. The structural interventions following the 2009 earthquake produced meaningful differences on the corresponding natural frequencies, which have increased of 66.80%, 80.99%, 39.15% and 59.35% respectively; the average increment of the current four natural frequencies is approximately 60.82%, compared to the structural behaviour before the 2009 earthquake. The identification in operational condition, based on the current measurement set-up, marks a significant localization in the mode shapes, i.e. many mode shapes show significantly higher displacement in some parts rather than in others. As illustrated in Fig.6, the modes between the 1st and the 4th (2.1 – 3.8 Hz) affect almost exclusively nave walls. Although the basilica can be considered as an elastic continuum, the localization of deformation produces the potential uncoupling of the macroelement responses, which are the facade and the nave walls. The localization of deformation might encourage the implementation of predictive reduced-order models for the facade and the nave walls.

### 5.1 Long-term monitoring

The natural frequencies identified from each set of time-series are concatenated and reported in Fig.7. Tab.7 evidences two concurring trends: the natural frequency oscillates between seasons; The natural frequencies are lightly decreasing in the entire period. The first observation is in full line with the finding by [4, 10, 7, 48]: the environmental parameters sensibly affect the natural frequencies. However, to the authors' knowledge, the second aspect does not occur in any case study. Tab.6 shows the maximum and minimum values of the linear correlation

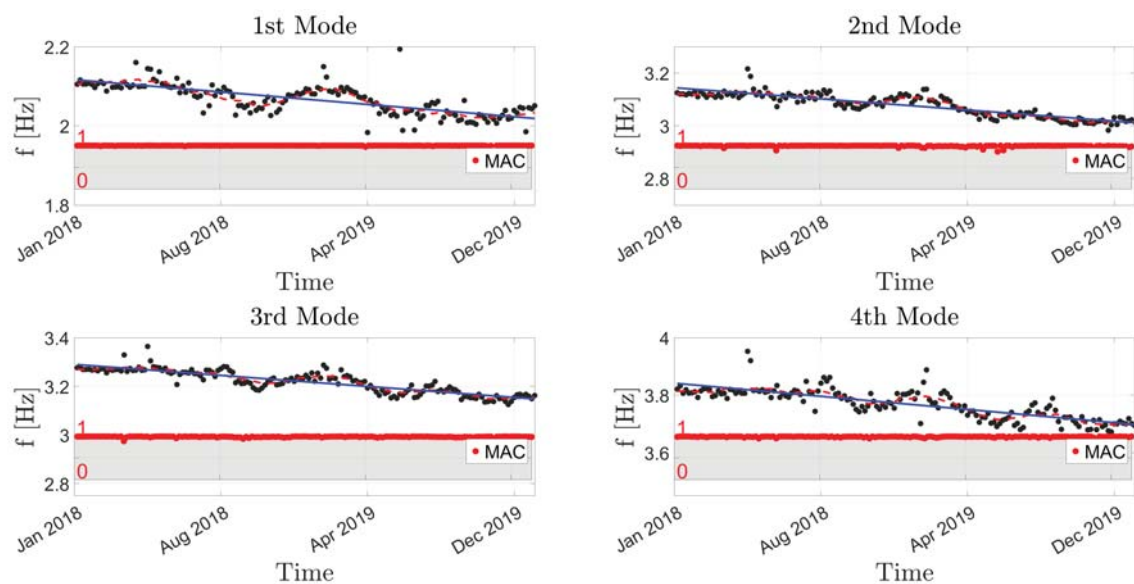


Figure 7: Variation of the natural frequencies and MAC of the detected modes during the investigated period. Red dashed line represents the moving mean of the samples, reflecting frequencies seasonal variation, blue straight interpolating line indicates its general decrease over time. The MAC values refer to a fixed set of modes corresponding to the recordings of 1/1/18.

reported as a solid line in Fig.7. The natural frequencies of the nave walls exhibited a 0.1 Hz decrement. There are no detectable variations of the mode shapes: the MAC values, estimated to a reference set of mode shapes, stand approximately constant and close to 1, see Fig.7. The nave walls, which are bound together by the top CLT roof, are anchored to the nave walls and the facade by threaded steel bars.

The reason of this decrement may derive from the behaviour exhibited by the constituent mate-

Table 5: Statistical description of the frequency and MAC values.

Mode	Frequency [Hz]		MAC	
	Mean	Variance	Mean	Variance
1st	2.07	0.002	0.99	$5.793 \times 10^{-4}$
2nd	3.08	0.002	0.99	$4.408 \times 10^{-4}$
3rd	3.22	0.002	0.99	$1.502 \times 10^{-4}$
4th	3.77	0.002	0.99	$1.046 \times 10^{-4}$

Table 6: Decrease of the natural frequency according to the linear regressions in Fig.7.

Mode	$f_{in}$ [Hz]	$f_{fin}$ [Hz]	$\Delta f$
1st	2.12	2.02	-0.10
2nd	3.14	3.01	-0.13
3rd	3.29	3.15	-0.14
4th	3.84	3.69	-0.15

rials over time. While masonry and steel do not exhibit a sensible decaying of their mechanical properties (especially in two years), it is more likely that the mechanical properties of the Cross-Lam Timber (CLT) roof are stabilizing. In the authors' opinion, the effect which may justify the observed phenomenon is microcracking due to wood drying and thermal expansion constrained by the steel anchoring [49].

## 5.2 Environmental effects

The natural frequencies are correlated to the outdoor temperature and the relative humidity. As already noticed in the long-term static monitoring, the relative humidity does not yield significant correlations, see Fig.9. Conversely, the temperature values return good correlations, evidenced by the linear fitting in Fig.8.

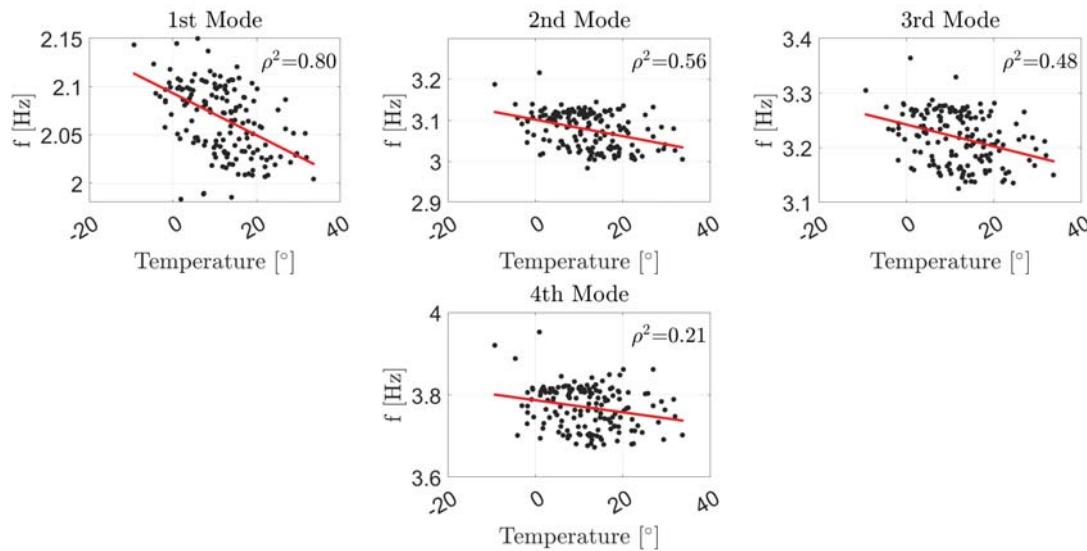


Figure 8: Correlation between the natural frequencies of the identified modes and the outdoor temperature (from 1/01/2018 to 31/12/2019).

To the authors' knowledge, the negative dependence of the natural frequencies to the outdoor temperature was observed in two sole cases: the Milan cathedral [12] and the Consoli Palace

in Gubbio [8]. According to Gentile et al. [12], the negative frequency-temperature correlation in the Milan Cathedral originates from the structural arrangement, consisting of double vault system constrained by an extended net of metallic tie-rods.

Kita et al. noticed a negative correlation [8] between natural frequencies and temperature in the Consoli Palace. The marked increase in natural frequencies of the global vibration modes of the Palace with decreasing ambient temperature has been attributed to an increase in global structural stiffness due to strengthening effects of metallic reinforcements (tie rods shortening at lower temperatures) and the presence of a moderate structural damage state in the Palace.

In the current case, the Santa Maria di Collemaggio basilica has a CLT roof which likely experiences significant thermal expansions and contractions. It acts bonding together the nave walls and provides a significant in-plane stiffness to the roof. The negative frequency-temperature correlations could originate from a decrease in global structural stiffness due to the expansion of the CLT roof at higher temperatures.

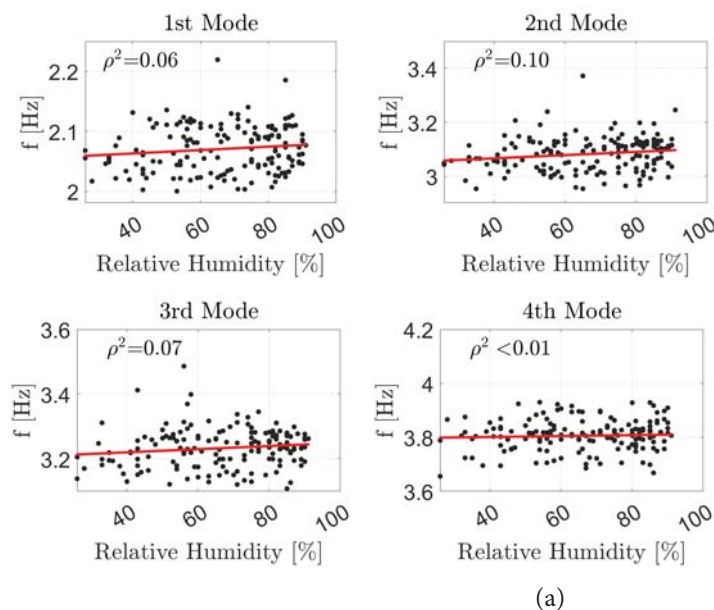


Figure 9: Correlation between the natural frequencies of the identified modes and the outdoor Relative Humidity (from 1/01/2018 to 31/12/2019).

The authors further estimated the temperature effects on the mode shapes. Accurately, the cross MAC between the mode shapes identified from all recordings are related to the outdoor temperature, as illustrated in Fig.10. The inspection of Fig.10 proves the substantial time invariance of the mode shapes. The crack amplitude was not correlated to the natural frequencies. The sole cracks on the nave walls do not change significantly, see Fig.2. The other cracks mainly gather in the apse and the vaults chapels, which, as remarked, participate with lower deformation to the monitored mode shapes.

### 5.3 Discussion

The most significant result regards the moderate but continuous decay of the natural frequencies over time. Likely, the observed decay will converge towards a stationary value, although the experimental data acquired so far are insufficient to formulate a reliable forecast. Data collected during the years will gradually enhance the reliability of the forecast and allow thoughtful

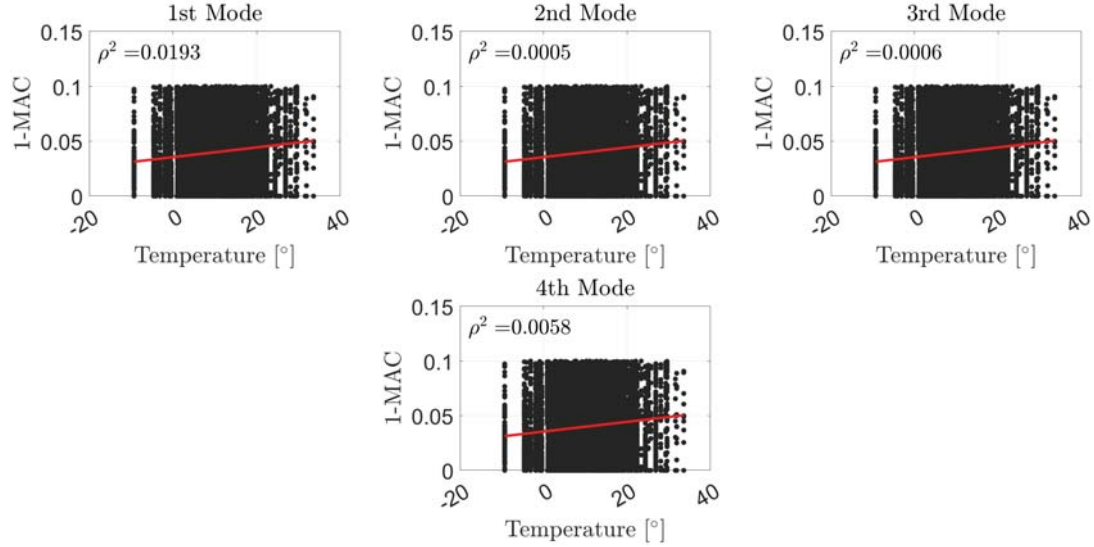


Figure 10: Correlation between outdoor temperature and (1-MAC) of identified modes (from 1/01/2018 to 31/12/2019).

judgment.

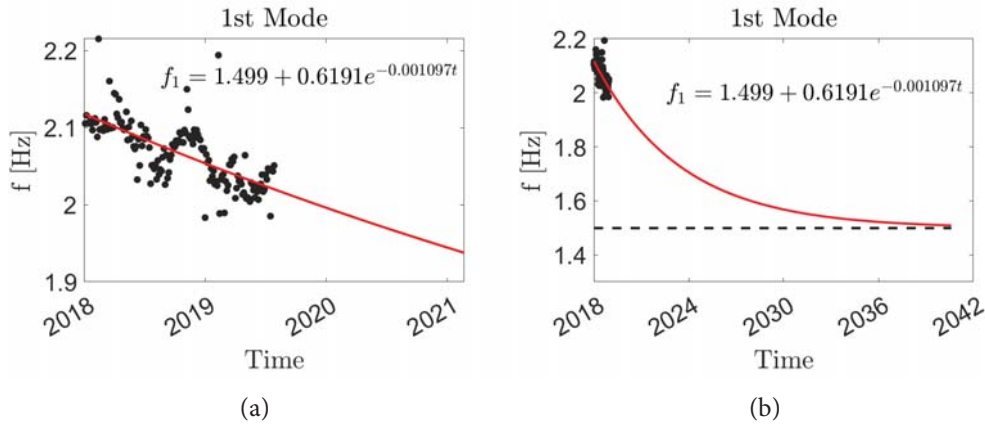


Figure 11: (a) Detail of the exponential fitting of the first natural frequency; (b) Exponential fitting of the first natural frequency extrapolated to a 24 years period.

The authors estimated the optimum exponential fitting of the first natural frequency using the Lovemberg-Marquardt algorithm [50], see (Fig.11):

$$f_1 = 1.499 + 0.6191e^{-0.001097t} \quad (3)$$

The sole material, among those used in the restoration, which has time-dependent mechanical properties in the first life period is timber [51, 52, 53]. The mechanical properties of the CLT roof may be stabilizing due to the actual environmental conditions: the CLT roof was installed in 2017. The considered two-years period is too short to derive plausible convergence values. The analysis has a qualitative and illustrative character, aiming at explaining the possible future scenarios. The reported exponential decay suggests that this effect will extinguish in an almost 20 years period since the CLT installation in 2017.

However, a mechanical interpretation of the obtained results requires a numerical model of the basilica, which allows determining the possible percentage decrease of the CLT roof stiffness congruous with the experimental findings. Further, additional instrumentation of the roof would enlighten on the structural behaviour of the timber members.

## 6 The dynamics of the facade

### 6.1 Modal identification and long-term monitoring

The fifth sixth and seventh modes mainly involve the facade, rather than the nave walls (Fig.12). They are all characterized by out-of-plane displacements most visible in the upper part, free, at their rear, from the nave walls constraints.

The fifth mode, at 4.5 Hz (Fig.12(a)), shows the bending of the facade by the rose window, while the modal components given by the sensors at the top edges have the same directions.

The sixth mode at 4.8 Hz highlights the phase opposition of the displacement of the two upper edges of the facade and a deflection above the portal (Fig.12(b)).

The last identified mode is similar to the fifth. The main difference lies in a shallow deflection occurring by the middle of the facade.

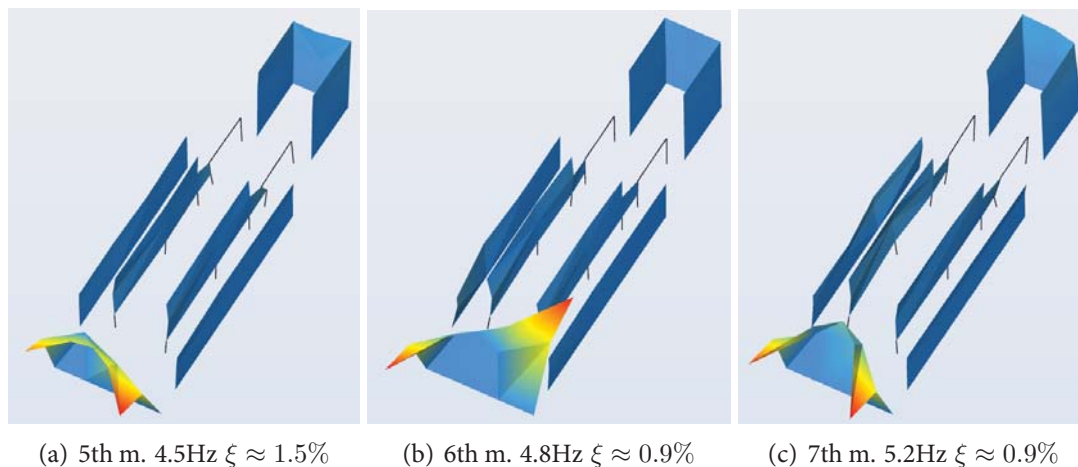


Figure 12: Illustration of the facade mode shapes, where m. stands for mode and  $\xi$  is the averaged modal damping.

Fig.13 presents the results of the modal tracking of the modes associated with the facade. The authors found the same trends found in the previous modes: the seasonal fluctuation of frequencies and their slight decreasing over time. However, the seasonal fluctuations are more marked than those in the previous modes.

Tab.8 shows the maximum and minimum values of the linear correlation reported as a solid

Table 7: Statistical description of the frequency and MAC values.

Mode	Frequency [Hz]		MAC	
	Mean	Variance	Mean	Variance
5th	4.38	0.016	0.92	$6.30 \times 10^{-3}$
6th	4.78	0.018	0.94	$2.63 \times 10^{-3}$
7th	5.14	0.036	0.89	0.031

line in Fig.13.



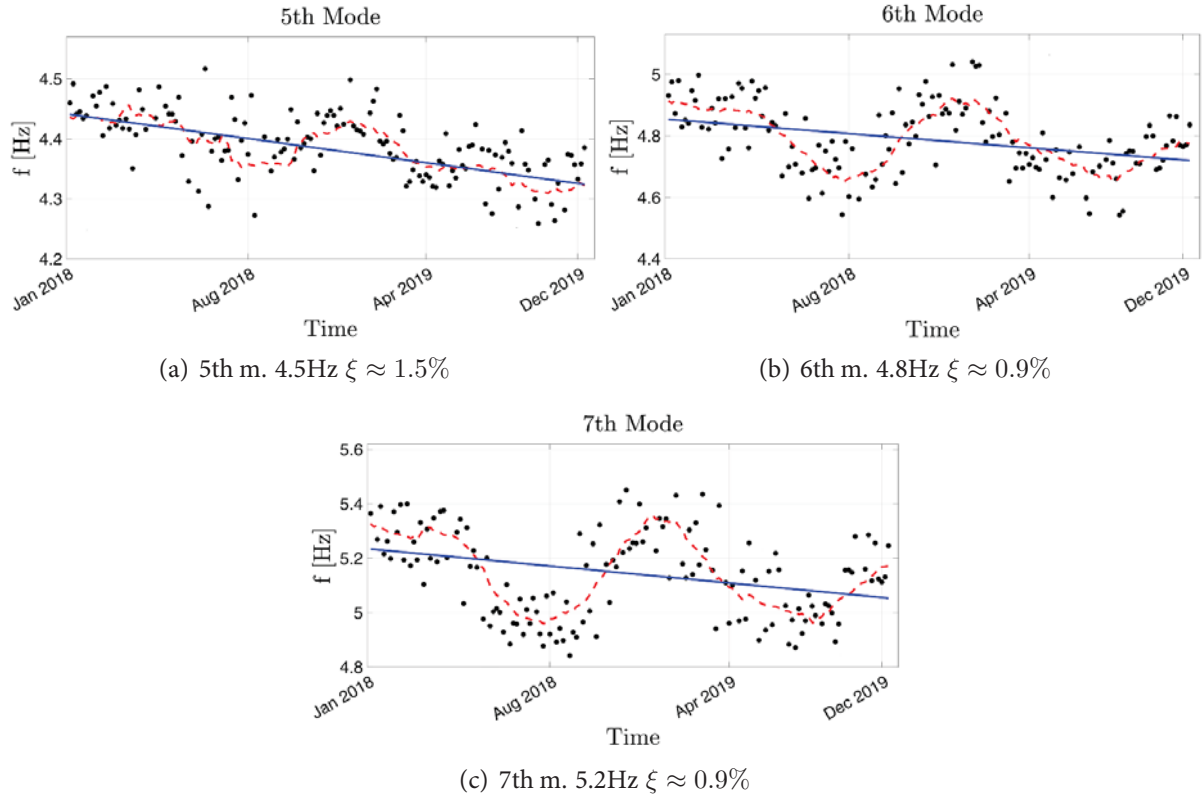


Figure 13: Variation of the natural frequencies during the year. The red dashed line represents the moving mean of the samples, the blue straight interpolating line indicates its general decrease over time.

Table 8: Decrease of the natural frequency according to the linear regressions in Fig.13.

Mode	$f_{in}[Hz]$	$f_{fin}[Hz]$	$\Delta f$
5th	4.44	4.32	-0.12
6th	3.14	3.01	-0.13
7th	3.29	3.15	-0.18

## 6.2 Modal interaction

An impressive phenomenon affects the fifth and seventh modes: not solely their natural frequencies decrease during the hot season, but their shape and the mutual distance between the frequencies do change during the year, almost cyclically in both the years under investigation. In order to better understand what happens, dates belonging to two different seasons have been compared: as evidenced by Tab.9, the frequencies vary between 3% and 8% among January and September.

The MAC between modal shapes proves a similarity between the 5th mode of September and

Table 9: The identified frequencies in January and September, 2019.

Mode	Jan	Sept	$\Delta f$ (%)
5th	4.43	4.28	-3.3
6th	4.82	4.43	-8.0
7th	5.14	4.85	-5.6

the 7th mode of January and vice versa (Tab.10). The sixth mode does not seem to be affected by changes in shape.

Fig.14 shows the one-year variations of the 5th and 7th natural frequencies, adimensionalized

Table 10: MAC evaluated between the modes of the facade identified in January and in September, 2019.

Mode	5th <sub>Jan</sub>	6th <sub>Jan</sub>	7th <sub>Jan</sub>
5th <sub>Sept</sub>	0.685	0.002	<b>0.901</b>
6th <sub>Sept</sub>	0.130	<b>0.905</b>	0.150
7th <sub>Sept</sub>	<b>0.689</b>	0.266	0.567

to the fifth mode, compared to the temperature values. The increase in temperature, typical of the summer season, leads the frequencies to approach each other.

The mode shapes change during the year: the two mode shapes mutate until reaching the

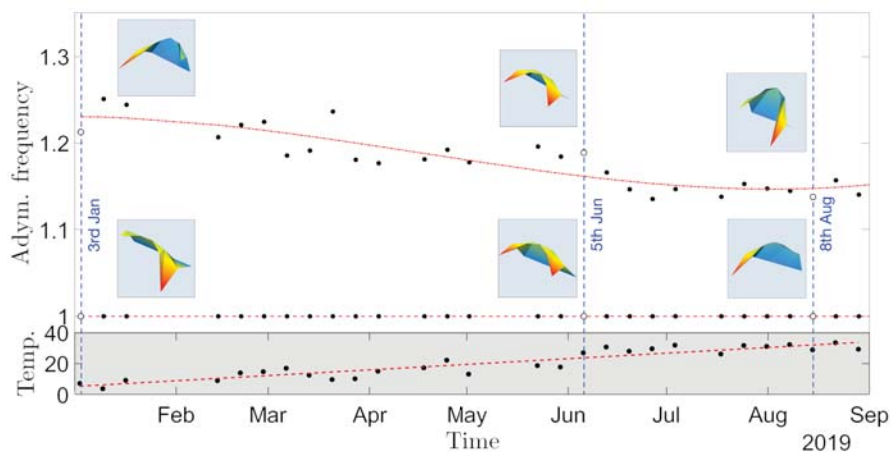


Figure 14: Evolution of the fifth and seventh natural frequency, adimensionalized to the fifth. The dash-dot line interpolates the data associated with the seventh mode. The pictures of the mode shapes correspond to the dates indicated. Below, the trend of temperatures in the same period. Data correspond to acquisitions recorded at the same hour (2 pm) between January and September, when temperature progressively rises.

maximum similarity in June, and then they exhibit the complete shape inversion between August

and September, in which temperature attains the highest values.

Subsequently, the arrival of the cold season determines the reversed process: both the mode shapes return to their starting states.

The phenomenon is strongly related to temperature: the variation of the two mode shapes is synthetically described by introducing the  $R$  parameter, defined as

$$R = \frac{d_{F9}}{d_{F5}} \quad (4)$$

The parameter represents the ratio between the out-of-plane mode components in points  $F9$ , on the left top of the facade, and  $F5$  on the opposite side. Fig.15 shows the value of the  $R$  param-

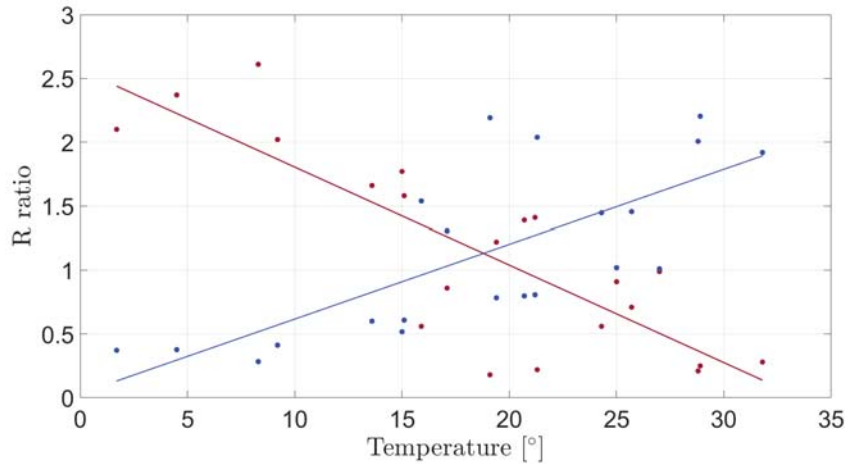


Figure 15:  $R$  Ratio evaluated for both the 5th mode (blue) and the 7th (red).

eter associated with the 5th and the 7th modes, which have opposite temperature correlations. The intersection of the two interpolating lines identifies a value of  $R$  approximately equal to one, meaning that the modal displacements of the two upper edges of the facade coincide, for both modes. The abscissa of the intersection point marks a temperature of about 20 degrees, attributable to that recorded in June.

The trend of frequencies of the 7th mode evidences a slight increase at the end of August, while the temperature still increases.

Although samples recorded in this month are too scarce to yield a sound validation, the overall phenomenon partially resembles that of mode interaction typical of frequency veering, well known in structural dynamics [54].

In the authors' opinion, this particular behaviour could be due to local effects related to the influence of temperature on the elastic parameters of the structure.

## 7 Conclusions

The paper presents the results of two years (2018-2019) static and dynamic monitoring of the Santa Maria di Collemaggio basilica. The masonry structure, severely damaged by the 2009 earthquake in L'Aquila, was rehabilitated and reopened in 2017. The restoration included the installation of a monitoring system consisting of 78 Force Balance accelerometers and nine crack monitoring devices. The authors mainly focused on the estimate of the modal properties and the effect of the environmental parameters. Here follow the main results of this study:

1. Seven modes have been detected in the frequency range 0-5.5 Hz, identified in operational condition using the SSI-cov algorithm [43]. The identification based on the current measurement set-up, denotes a notable localization in the mode shapes, i.e. many mode shapes show significantly higher displacement in some parts rather than in others. The first four modes (2.1 – 3.8 Hz) affect almost exclusively nave walls. Conversely, the following modes (4.5 - 5.3 Hz) affect the facade and negligibly the nave walls.
2. The authors implemented an automatic algorithm to identify the modal parameters and track their evolution over time. The natural frequencies are decreasing over time: In two years, there has been an almost 0.1 Hz frequency decrement. It possibly derived from the moderate in-plane stiffness decaying of the Cross Lam timber roof due to superficial microcracking (wood drying and constrained thermal expansion, e.g.).
3. The modal tracking process of the modes mainly affecting the facade evidenced a phenomenon resembling frequency veering and mode interaction. It strongly depends on temperature: the frequencies of the two modes approach to each other with increasing temperature and their shapes interchange cyclically over time. Despite this, the algorithm was able to perform the tracking process. Other mode shapes do not experience meaningful seasonal variations and are substantially time-invariant.
4. The outdoor temperature drives the observed fluctuation of the natural frequencies. The first four modes have negative temperature-frequency correlations. This effect could arise from a decrease in the global structural stiffness due to the expansion of the CLT roof at higher temperatures. For modes mainly involving the facade, frequency variation due to temperature is amplified by the phenomenon of frequency veering.
5. The outdoor temperature mainly drives the crack evolution. In most cases, the devices revealed positive temperature-amplitude correlations. In a single case, the authors noted the opposite trend. The two behaviours possibly originate from the difference between the outdoor and indoor temperature. The thermal gradient enhances the curvature of the wall, yielding stretching or closing of the cracks depending on their position across the wall thickness.

This paper mainly focuses on the dynamic monitoring of the nave walls and the facade. Future developments will deal with the dynamics of the apse and transept. The present analyses are preliminary to the developing of a probabilistic model of the modal response of the basilica within a Structural Health Monitoring program.

## 8 Acknowledgments

The authors thank Eni, for having financed the restoration of the basilica and the monitoring system, Prof. Dante Galeota as Representative of the University of L'Aquila in the restoration committee, Dr Felice Fusco for his contribution in the design phase of the monitoring system, Prof. Roberto Aloisio to be intermediary with the CETEMPS, and the CETEMPS itself, the centre of excellence on telesensing of environment and model prediction severe events (<http://cetemps.aquila.infn.it/>) of the University of L'Aquila, which provided us with the environmental parameters. The authors further acknowledge the availability of the SolGeo s.r.l. for the maintenance needs.

## REFERENCES

- [1] C. R. Farrar, W. Baker, T. Bell, K. Cone, T. Darling, T. Duffey, A. Eklund, and A. Migliori, "Dynamic characterization and damage detection in the i-40 bridge over the rio grande," tech. rep., Los Alamos National Lab., NM (United States), 1994.
- [2] S. Quqa, L. Landi, and P. P. Diotallevi, "Instantaneous modal identification under varying structural characteristics: A decentralized algorithm," *Mechanical Systems and Signal Processing*, vol. 142, p. 106750, 2020.
- [3] A. Aloisio, A. Di Pasquale, R. Alaggio, and M. Fragiaco, "Assessment of seismic retrofitting interventions of a masonry palace using operational modal analysis," *International Journal of Architectural Heritage*, pp. 1–13, 2020.
- [4] L. F. Ramos, L. Marques, P. B. Lourenço, G. De Roeck, A. Campos-Costa, and J. Roque, "Monitoring historical masonry structures with operational modal analysis: two case studies," *Mechanical systems and signal processing*, vol. 24, no. 5, pp. 1291–1305, 2010.
- [5] F. Ubertini, G. Comanducci, N. Cavalagli, A. L. Pisello, A. L. Materazzi, and F. Cotana, "Environmental effects on natural frequencies of the san pietro bell tower in perugia, italy, and their removal for structural performance assessment," *Mechanical Systems and Signal Processing*, vol. 82, pp. 307–322, 2017.
- [6] A. Saisi, C. Gentile, and M. Guidobaldi, "Post-earthquake continuous dynamic monitoring of the gabbia tower in mantua, italy," *Construction and Building Materials*, vol. 81, pp. 101–112, 2015.
- [7] R. M. Azzara, G. De Roeck, M. Girardi, C. Padovani, D. Pellegrini, and E. Reynders, "The influence of environmental parameters on the dynamic behaviour of the san frediano bell tower in lucca," *Engineering Structures*, vol. 156, pp. 175–187, 2018.
- [8] A. Kita, N. Cavalagli, and F. Ubertini, "Temperature effects on static and dynamic behavior of consoli palace in gubbio, italy," *Mechanical Systems and Signal Processing*, vol. 120, pp. 180–202, 2019.
- [9] M.-G. Masciotta, J. C. Roque, L. F. Ramos, and P. B. Lourenço, "A multidisciplinary approach to assess the health state of heritage structures: The case study of the church of monastery of jerónimos in lisbon," *Construction and Building Materials*, vol. 116, pp. 169–187, 2016.
- [10] M.-G. Masciotta, L. F. Ramos, and P. B. Lourenço, "The importance of structural monitoring as a diagnosis and control tool in the restoration process of heritage structures: a case study in portugal," *Journal of Cultural Heritage*, vol. 27, pp. 36–47, 2017.
- [11] A. Elyamani, O. Caselles, P. Roca, and J. Clapes, "Dynamic investigation of a large historical cathedral," *Structural Control and Health Monitoring*, vol. 24, no. 3, p. e1885, 2017.
- [12] C. Gentile, A. Ruccolo, and F. Canali, "Long-term monitoring for the condition-based structural maintenance of the milan cathedral," *Construction and Building Materials*, vol. 228, p. 117101, 2019.



- [13] M. G. Lopardi, *I templari ed il colle magico di Celestino*. Idea libri, 2002.
- [14] F. Redi, “Santa maria di collemaggio. archeologia di un monumento,” *Celestino V e la sua Basilica*, pp. 71–133, 2006.
- [15] M. Moretti, *Collemaggio*. De Luca, 1972.
- [16] D. Oreni, R. Brumana, S. Della Torre, F. Banfi and M. Previtali, “Survey turned into hbim: the restoration and the work involved concerning the basilica di collemaggio after the earthquake (l’aquila),” *ISPRS annals of the photogrammetry, remote sensing and spatial information sciences*, vol. 2, no. 5, p. 267, 2014.
- [17] V. Baiocchi, V. Giammarresi, R. Ialongo, C. Piccaro, M. Allegra, and D. Dominici, “The survey of the basilica di collemaggio in l’aquila with a system of terrestrial imaging and most proven techniques,” *European Journal of Remote Sensing*, vol. 50, no. 1, pp. 237–253, 2017.
- [18] R. Brumana, S. Della Torre, M. Previtali, L. Barazzetti, L. Cantini, D. Oreni, and F. Banfi “Generative hbim modelling to embody complexity (lod, log, loa, loi): surveying, preservation, site intervention—the basilica di collemaggio (l’aquila),” *Applied geomatics*, vol. 10, no. 4, pp. 545–567, 2018.
- [19] E. Antonacci, G. Beolchini, and F. D. F. V. Gattulli, “Retrofitting effects on the dynamic behaviour of s. maria di collemaggio,” *WIT Transactions on Modelling and Simulation*, vol. 30, 2001.
- [20] D. Ranalli, M. Scozzafava, and M. Tallini, “Ground penetrating radar investigations for the restoration of historic buildings: the case study of the collemaggio basilica (l’aquila, italy),” *Journal of cultural heritage*, vol. 5, no. 1, pp. 91–99, 2004.
- [21] E. Antonacci, V. Gattulli, A. Martinelli, and F. Vestroni, “Il crollo del transetto della basilica di collemaggio: analisi di vulnerabilità e meccanismo di collasso,” in *Atti del workshop: Sicurezza e conservazione dei beni culturali colpiti da sisma: Strategie e tecniche di ricostruzione ad un anno dal terremoto abruzzese*, pp. 8–9, 2010.
- [22] S. Sfarra, A. Bendada, C. Ibarra-Castaneda, D. Ambrosini, D. Paoletti, and X. Maldague, “Santa maria di collemaggio church (l’aquila, italy): historical reconstruction by non-destructive testing techniques,” *International Journal of Architectural Heritage*, vol. 9, no. 4, pp. 367–390, 2015.
- [23] P. Crespi, A. Franchi, N. Giordano, M. Scamardo, and P. Ronca, “Structural analysis of stone masonry columns of the basilica s. maria di collemaggio,” *Engineering structures*, vol. 129, pp. 81–90, 2016.
- [24] M. Zucca, A. Franchi, P. Crespi, N. Longarini, and P. Ronca, “The new foundation system for the transept reconstruction of the basilica di collemaggio,” in *10th IMC-Proceedings of the 10th International Masonry Conference*, pp. 2441–2450, 2018.
- [25] A. Aloisio, R. Alaggio, and M. Fragiaco, “Dynamic identification of a masonry façade from seismic response data based on an elementary ordinary least squares approach,” *Engineering Structures*, vol. 197, p. 109415, 2019.

- [26] E. Antonacci, A. Aloisio, D. Galeota, and R. Alaggio, “The s. maria di collemaggio basilica: from vulnerability assessment to first results of shm,” *Journal of Architectural Engineering*, vol. In press, 2020.
- [27] A. Aloisio, L. Di Battista, R. Alaggio, and M. Fragiaco, “Analysis of the forced dynamics of a masonry facade by means of input-output techniques and a linear regression model,” in *COMPDYN, 2019, 7th International Conference on Computational Methods in Structural Dynamics and Earthquake Engineering*, 2019.
- [28] S. Amoroso, I. Gaudiosi, M. Tallini, G. Di Giulio, and G. Milana, “2d site response analysis of a cultural heritage: the case study of the site of santa maria di collemaggio basilica (l’aquila, italy),” *Bulletin of Earthquake Engineering*, vol. 16, no. 10, pp. 4443–4466, 2018.
- [29] G. Totani, P. Monaco, F. Totani, G. Lanzo, A. Pagliaroli, S. Amoroso, and D. Marchetti, “Site characterization and seismic response analysis in the area of collemaggio, l’aquila (italy),” in *Proc., 5th International Conf on Geotechnical and Geophysical Site Characterization, Australian Geomechanics Society, Gold Coast, Australia*, vol. 2, pp. 1051–1056, 2016.
- [30] N. Aste, S. Della Torre, R. S. Adhikari, M. Buzzetti, C. Del Pero, F. Leonforte, and M. Manfren, “Sustainable church heating: The basilica di collemaggio case-study,” *Energy and Buildings*, vol. 116, pp. 218–231, 2016.
- [31] E. Antonacci, G. Beolchini, F. Di Fabio, and V. Gattulli, “The dynamic behaviour of the basilica s. maria di collemaggio,” in *Proc. of 2nd Int. Congress on Studies in Ancient Structures, SAS2001*, 2001.
- [32] E. Antonacci and G. Beolchini, “The dynamic behaviour of the façade of the basilica s. maria di collemaggio,” *Structural analysis of historical constructions*, pp. 469–476, 2005.
- [33] F. Potenza, F. Federici, M. Lepidi, V. Gattulli, F. Graziosi, and A. Colarieti, “Long-term structural monitoring of the damaged basilica s. maria di collemaggio through a low-cost wireless sensor network,” *Journal of Civil Structural Health Monitoring*, vol. 5, no. 5, pp. 655–676, 2015.
- [34] D. Galeota, G. Sforza, and L. Sbaraglia, “Dynamic characterization of the basilica of s. maria di collemaggio after the earthquake of 2009 by means of operational modal analysis,” *Computational Methods and Experimental Measurements XVII*, vol. 59, p. 357, 2015.
- [35] D. Galeota, E. Antonacci, A. Aloisio, and R. Alaggio, “The s. maria di collemaggio basilica: from the vulnerability assessment to the first results of shm,” in *Proceedings of the XVII National Conference ANIDIS, 13–17 September 2019, Ascoli Piceno, Italy*, vol. 17, ANIDIS, 2019.
- [36] A. Aloisio, E. Antonacci, M. Fragiaco, and R. Alaggio, “The recorded seismic response of the santa maria di collemaggio basilica to low-intensity earthquakes,” *International Journal of Architectural Heritage*, 2020.

- [37] R. Alaggio, A. Aloisio, E. Antonacci, and R. Cirella, “Two-years static and dynamic monitoring of the santa maria di collemaggio basilica,” *Construction and Building Materials*, p. 121069, 2020.
- [38] C. Bartolomucci, *Santa Maria di Collemaggio: interpretazione critica e problemi di conservazione*. Palombi, 2004.
- [39] M. Angiolilli, A. Gregori, M. Pathirage, and G. Cusatis, “Fiber reinforced cementitious matrix (frcm) for strengthening historical stone masonry structures: Experiments and computations,” *Engineering Structures*, vol. 224, p. 111102, 2020.
- [40] A. Aloisio, M. Fragiaco, and G. D’Alò, “Traditional masonries in the city centre of l’aquila—the baraccato aquilano,” *International Journal of Architectural Heritage*, pp. 1–18, 2019.
- [41] A. Aloisio, M. Fragiaco, and G. D’Alò, “The 18th-century baraccato of l’aquila,” *International Journal of Architectural Heritage*, pp. 1–15, 2019.
- [42] A. Aloisio, I. Capanna, R. Cirella, R. Alaggio, and M. Fragiaco, “The san silvestro belfry: dynamic identification and model updating via numerical and analytical modelling,” *Buildings*, 2020.
- [43] B. Peeters and G. De Roeck, “Reference-based stochastic subspace identification for output-only modal analysis,” *Mechanical systems and signal processing*, vol. 13, no. 6, pp. 855–878, 1999.
- [44] A. Aloisio, D. Pasca, R. Tomasi, and M. Fragiaco, “Dynamic identification and model updating of an eight-storey clt building,” *Engineering Structures*, vol. 213, p. 110593, 2020.
- [45] A. Aloisio, L. Di Battista, R. Alaggio, and M. Fragiaco, “Sensitivity analysis of subspace-based damage indicators under changes in ambient excitation covariance, severity and location of damage,” *Engineering Structures*, vol. 208, p. 110235, 2020.
- [46] A. Aloisio, R. Alaggio, and M. Fragiaco, “Time-domain identification of elastic modulus of simply supported box girders under moving loads: method and full-scale validation,” *Engineering Structures*, 2020.
- [47] A. Aloisio, R. Alaggio, and M. Fragiaco, “Dynamic identification and model updating of full-scale concrete box girders based on the experimental torsional response,” *Construction and Building Materials*, vol. 264, p. 120146, 2020.
- [48] C. Gentile and A. Saisi, “Ambient vibration testing of historic masonry towers for structural identification and damage assessment,” *Construction and building materials*, vol. 21, no. 6, pp. 1311–1321, 2007.
- [49] M. Piazza, R. Modena, and R. Tomasi, *Strutture in legno. Materiale, calcolo e progetto secondo le nuove normative europee*. Hoepli Editore, 2005.
- [50] J. J. Moré, “The levenberg-marquardt algorithm: implementation and theory,” in *Numerical analysis*, pp. 105–116, Springer, 1978.

- [51] Z. Chen, C. Ni, C. Dagenais, and S. Kuan, “Woodst: a temperature-dependent plastic-damage constitutive model used for numerical simulation of wood-based materials and connections,” *Journal of Structural Engineering*, vol. 146, no. 3, p. 04019225, 2020.
- [52] A. Aloisio, R. Alaggio, and M. Fragiaco, “Equivalent viscous damping of cross-laminated timber structural archetypes,” *Journal of Structural Engineering*, vol. 147, no. 4, p. 04021012, 2021.
- [53] A. Aloisio, R. Alaggio, and M. Fragiaco, “Fragility functions and behavior factors estimation of multi-story cross-laminated timber structures characterized by an energy-dependent hysteretic model,” *Earthquake Spectra*, p. 8755293020936696, 2020.
- [54] F. Benedettini, D. Zulli, and R. Alaggio, “Frequency-veering and mode hybridization in arch bridges,” in *Proceedings of the 27th International Modal Analysis Conference*, 2009.

## AMBIENT VIBRATION TEST ON AN EXISTING PRESTRESSED CONCRETE BRIDGE

A. De Angelis<sup>1</sup>, G. Esposito<sup>1</sup>, G. Maddaloni<sup>1</sup>, E. Cosenza<sup>2</sup> and M. Pecce<sup>1</sup>

<sup>1</sup> Department of Engineering, University of Sannio  
Piazza Roma, 21, Benevento-Italy

e-mail: {adeangelis, g.maddaloni, pecce}@unisannio.it; giac9593@gmail.com

<sup>2</sup> Department of Structures for Engineering and Architecture, University of Naples Federico II,  
Via Claudio 21, Naples (80125), Italy  
{edoardo.cosenza}@unina.it

---

### Abstract

*The dynamic test in situ of existing bridges is a very promising solution for assessing a reliable model, since it is more convenient than a load test requiring to organize the trucks and close the use of the infrastructure for a longer time. However its effectiveness depends on the test technique, the number, type and location of the sensors, but also on the numerical model that have to allow the introduction of the real boundary conditions. Clearly the dynamic identification of the structural behavior can be also the first step of a monitoring process to check the health of the construction during the time, therefore its effectiveness is fundamental.*

*In this paper the first results of the structural identification based on an ambient vibration test of an existing prestressed concrete bridge are presented. The selected case study is a bridge designed by Riccardo Morandi in 1952-1955 with the emerging technique of Prestressed Concrete (PC).*

*An important step of the process is the developing of the model through a survey and a wide investigation campaign, but also the role of the knowledge of the original design is highlighted due the complexity of the structure.*

**Keywords:** Prestressed bridge, Dynamic test, Model updating, Finite element analysis, Operational Modal Analysis.

---



## 1 INTRODUCTION

Structural identification for assessing and ensuring the safety and integrity of bridge structures is gaining much attention among researchers, due to the more frequent failure of bridges [1, 2], and also considering the existing heritage, in many countries near to the end of its service life.

Currently the dynamic tests are gaining increasing importance and efficiency especially to calibrate reliable numerical models [3-4] useful for a structural analysis, or to start a damage monitoring by two approaches. In one case the monitoring is carried out by the numerical model upgrading [5-7] in the other case a direct analysis of the signals [8-9].

It is noted that the first procedure is certainly more efficient and of great potential since a numerical model allows to investigate in detail the causes of a possible variation of the structural response [10-11], and then can be used to investigate the load-bearing capacity [12-13], its structural behavior under traffic [14] or seismic excitation and the efficiency of a prospective reinforcement interventions. However, the type and uncertainties of the model influence the process and the computational work is heavy.

In this paper the procedure of the structural identification is proposed underlining the various steps that contribute to individuate the real in-situ boundary conditions and the degradation of the construction through the variation of the elastic dynamic response [15-16]. The ambient vibration test (AVT) is carried out due to the simple applicability, albeit it is generally less effective than harmonically forced tests [17]. A brief review of testing methods for bridges explaining their advantages and limitations was presented by Salawu and Williams [18].

Moreover many researchers demonstrated that the environmental actions are able to excite the most significant modes of vibration in the low range of frequencies for flexible systems like cable-stayed bridges [19-20], large span arch bridges [21-22] and suspension bridges [23]. The bridge considered herein is particularly interesting because the static scheme and the technology adopted by Riccardo Morandi in his design was innovative and ambitious at the time but still currently the construction is complex and its analysis requires a detailed finite element model (FEM) that is useful to assess through tests in situ. Furthermore the real boundary conditions have to be assessed to better address the future design of strengthening interventions.

## 2 OVERVIEW OF THE BRIDGE

The case study bridge (Fig. 1), erected in Benevento and designed by Riccardo Morandi in early '50, although not so large, has a great importance since it connects two parts of the city crossing the creek San Nicola that goes through a valley with instable hillsides.



Figure 1: Current lateral view of San Nicola bridge.

A detailed analysis of its conceptual design is reported in [24] evidencing a careful process of optimization by adopting an innovative method of construction with pre-casted segments.

The deck of San Nicola bridge is made of prestressed concrete cast in site with piers and foundations made of reinforced concrete. The static scheme is a portal frame composed by one main span 80.0 m long and two cantilevers of 20.0 m long as shown in Fig. 2.

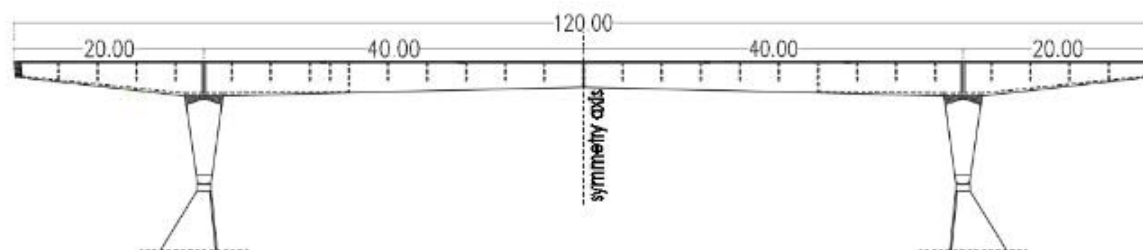


Fig. 2: Longitudinal scheme of the bridge.

The bridge deck is supported by two piers 9.40 m high; each pier, as shown in Fig. 3, was realized by eight columns of rectangular section, 40.0 cm thick and variable width from 1.50 m at the base to 4.00 m at the top, that are transversally connected at the base and top by a transverse beam.

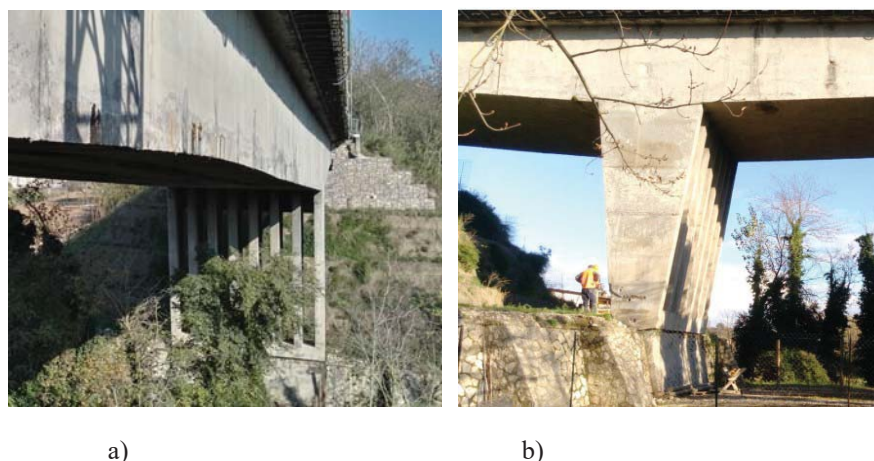


Figure 3: Transversal and frontal view of the pier.

The piers are linked to the foundations underneath by hinges made of steel rebars to avoid bending moments on the foundation that have to also contain the thrust; in fact, the foundations also act as abutments.

The deck consists of a multicellular caisson whose webs vary in thickness, from a minimum of 13 cm at the midspan, to a maximum of 30 cm at the supports (see Fig. 4). Moreover, the deck shows varying-depth through the spans (beam with curved intrados), which characterizes an approximately linear shape giving also a beneficial arch effect. The depth of the deck cross section varies from a maximum of 3.60 m at the pier supports, to a minimum of 1.60 m at the ends of cantilevers and 2.70 m at the midspan.

The deck is characterized by internal tendons, symmetrical about midspan. The prestressing steel cables are composed of 27 aligned wires with diameter of 5mm and are placed along a straight line in the top slab where the bending moment shows negative values and in the bottom slab in the midspan, but also curved cables are installed along the entire bridge. A portion of the original drawing with the prestressing cables is reported in Fig. 5.

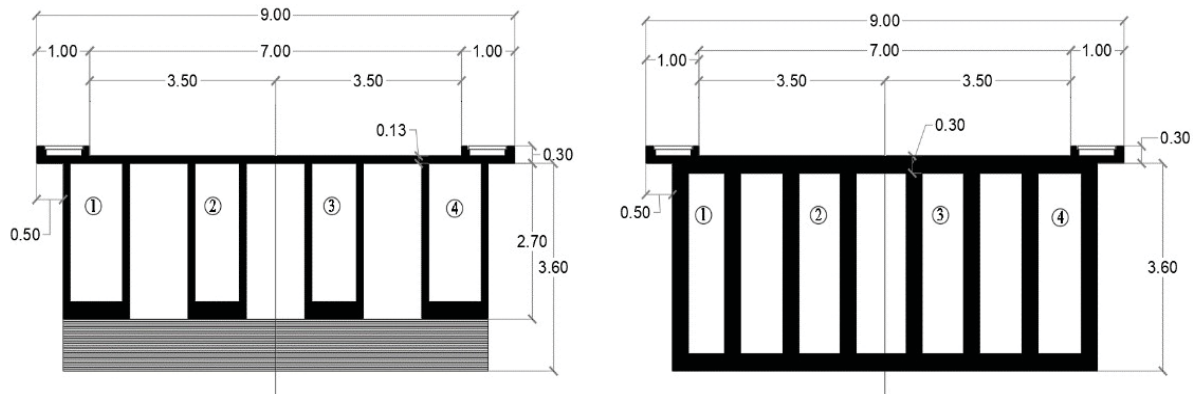


Figure 4: Cross sections of caissons at the midspan (left) and the supports (right).

The upper slab is 9.00 m width and consists of two traffic lanes, 7.00 m width, and two sidewalks 1.00 m width each one. Also the thickness is variable from 13 cm (in the area of the central span where there are no top cables) to 20 cm.

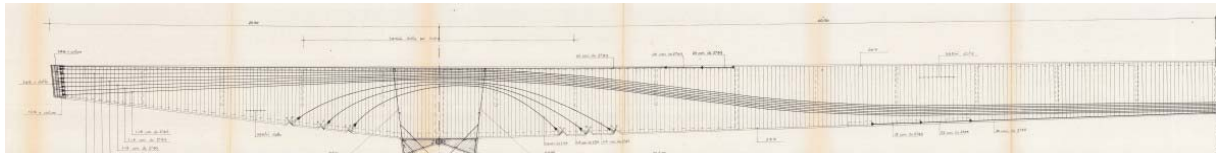


Figure 5: Original drawing with the prestressing cables

### 3 SURVEY AND MATERIAL CHARACTERIZATION

An extensive survey campaign, including surveys, essays and destructive tests on materials, i.e., concrete, steel reinforcement and prestressing steel cable, was carried out.

The geometric survey of the elements forming the deck and the piers shows that the structure was realized quite as designed.

Several essays were carried out on the deck highlighting the concrete cover degradation due to the disposal of the water, especially inside the multicellular caisson, however, no cracking is visible. The good conditions of the ducts and cables were detected except in specific parts where water stagnates. Pier and abutments concrete and reinforcements were also investigated pointing out a concrete surface degradation but limited corrosion of the steel re-bars.

Regarding the materials, 14 cores were taken for the assessment of the compressive strength of the concrete. An average cubic compression strength ( $R_{cm}$ ) of 39.21 MPa and 54.21 MPa have been obtained for pier and deck, respectively. These average values were used to calculate the elastic modulus adopted in the model, described in section 4.

Also samples of prestressing steel cables were taken and tested in the laboratory but the elastic modulus of the steel is assumed from the literature.

### 4 THE IN-SITU DYNAMIC TEST

The AVT was chosen as dynamic test because it doesn't require any additive equipment and affects the use of the bridge for few time.

The dynamic behavior of the bridge has been analyzed by means of a preliminary numerical finite element model, described in the next section to establish the layout of the sensors shown in Fig. 6 that involved the choice of 30 measuring points.

In order to identify both the bending, in plane and out-of-plane, and torsional modes, sensors were arranged in pairs at the long sides of the roadway with a distance of 6 m along the cantilever and 10-12 m along the center span.

The adopted instrumentation consists of five triaxial piezoelectric accelerometers with MEMS technology, characterized by an integrated 24-bit A/D converter of the Sigmadelta type. The sensors sample at a preset frequency of 1024 Hz, transmitting the acquired signal directly to an acquisition unit, characterized by an industrial PC with a preinstalled Linux system.

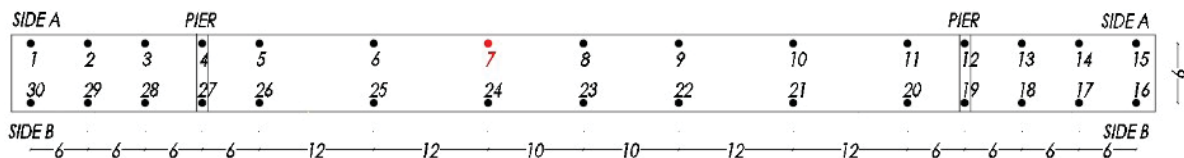


Figure 6: The layout of sensors in the dynamic test

Since only 5 accelerometers were available during the test, more test setups were performed, considering one sensor, indicated as n. 7 in Fig. 6, as reference transducer which was kept at the same location in all the setups. In each setup the accelerations were acquired in the presence of environmental actions (wind, passage of persons) [25] for a duration of 15 minutes at a frequency of 1024 Hz.

The environmental records carried out at the points of measurement have been inspected and validated. Subsequently, each recording was filtered by the application of a Butterworth-type bandwidth filter of order 6 in the range 0.2-20 Hz. Subsequently, the time series were decimated to obtain a final sampling frequency of 20 Hz. It is worth to note that filtering performed before decimation ensures the absence of aliasing problems in the frequency range of interest.

The data processing and the extraction of modal shapes were carried out with the commercial program ARTEMIS [26] both in the frequency and time domain to obtain the natural frequencies, damping ratios and modal shapes of different modes of vibration of the structure. In particular the Enhanced Frequency Domain Decomposition (EFDD) [27] and the data driven Stochastic Subspace Identification (SSI) [28] were used as output-only techniques.

The analysis of the data and the comparison of the results provided by the various methods allowed the identification of the fundamental modes of the structure and the validation of the data obtained. Specifically, the comparison of the estimates provided by the different methods (EFDD, SSI) showed a maximum frequency deviation of 0.6 % and CROSS-MAC values not less than 0.87 for all identified modal shapes.

Fig. 7 shows the modal shapes and values of natural frequencies and damping ratios for each of the identified modes. The latter can be classified as follows:

1. Transversal bending mode;
2. Vertical bending mode;
3. Vertical torsional mode.

In addition, the identified modes are all normal modes, as can be seen from the examination of the complexity plots shown in Fig. 8. It is hardly necessary to point out that the imaginary components present in some modes are minimal, clearly attributable to the effects of the measuring noise.



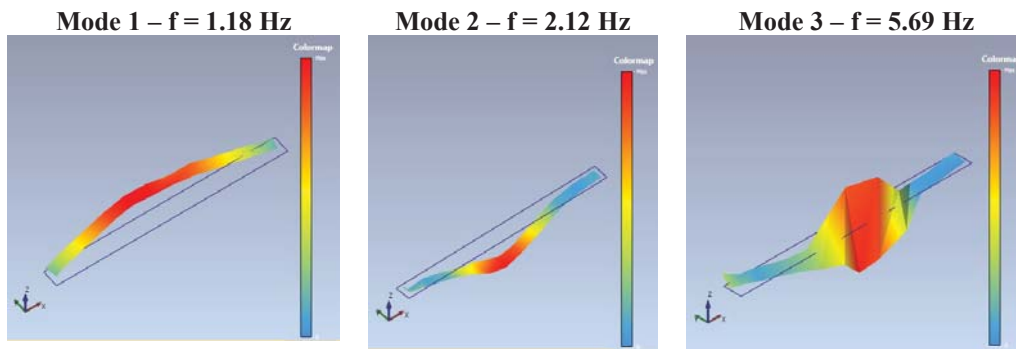


Figure 7: Experimental mode shapes.

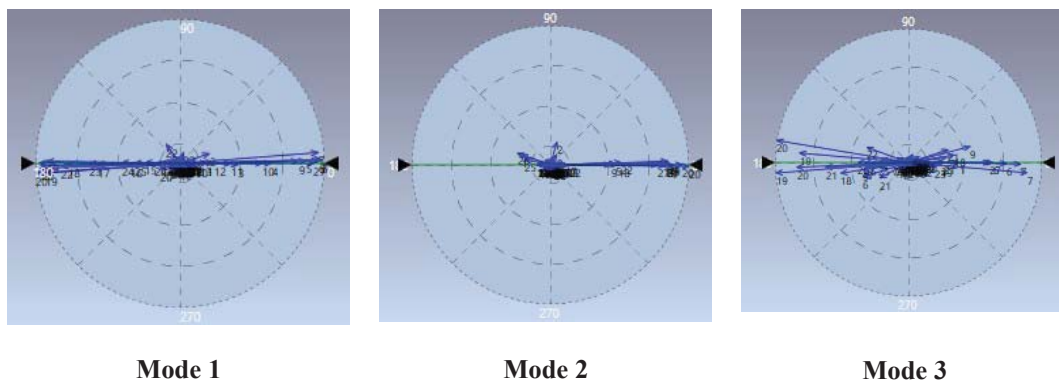


Figure 8: Complexity plots of the experimental mode shapes.

## 5 THE NUMERICAL MODEL OF BRIDGE

The FE model of the bridge assumed as case study was developed by the software SAP2000 [29]. The various components of the structure were modeled considering their real geometry with mono-dimensional (frame) and bi-dimensional (shell) finite elements, getting a three-dimensional model including deck and piers restrained at the base by hinges.

The concrete section was considered entirely reactive assuming prestressing effect efficient. The deck was modeled by thin "shell" elements, with 4 nodes and a formulation that combines membrane and plate-bending behavior. Stress and strain are evaluated in the local coordinate system of the elements in 2x2 Gaussian integration points and are extrapolated in the connection nodes between the elements. The nodes of discretization of the deck are approximately 4600 with a mesh of 1 x 0.7 m for the upper slab.

The piers were modeled using frame elements for the 8 pillars and shell elements for the transverse elements at the top and the bottom. Moreover, tendon elements were added in the model to simulate the presence of prestressed cables. Tendon elements are an object type that can be inserted into other objects (Frame, Shell, Plane, Asolid, and Solid) to simulate the effects of pre-stressing but in this dynamic analysis their effect is the stiffness and mass contribution.

**Errore. L'origine riferimento non è stata trovata.** 9 shows the view of the model implemented by the software SAP2000 [29].

The elastic modulus of concrete was evaluated by the Eurocode 2 formulation [30] using the mean concrete strength measured by the in situ tests, and resulted of 34700 MPa and 32700 for the concrete of piers and deck respectively. Furthermore a value of 196500 MPa from literature was adopted for the steel cables.



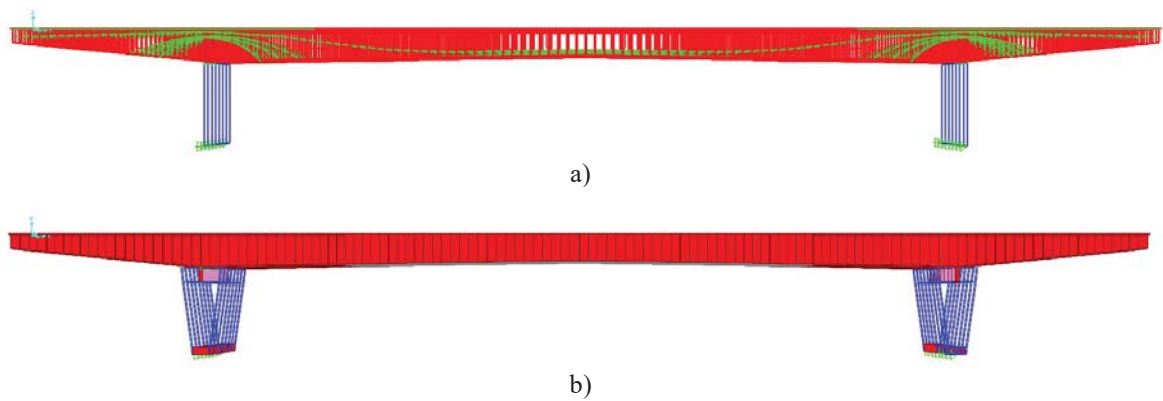


Figure 9: a) FEM model of the bridge including prestressed cables; b) extruded view of the model.

Fig 10 shows the deformed shapes of the first nine numerical modes that involve always the deck structure of the bridge and the piers for the modes that have horizontal components.

Mode I (f= 1.06 Hz)	Mode II (f=1.09 Hz)	Mode III (f=1.21 Hz)
Mode IV (f=1.74 Hz)	Mode V (f=2.14 Hz)	Mode VI (f=3.66 Hz)
Mode VII (f=4.36 Hz)	Mode VIII (f=4.45 Hz)	Mode IX (f= 4.71 Hz)

Figure 10: Numerical mode shapes of the bridge.

## 6. FIRST RESULTS OF THE STRUCTURAL IDENTIFICATION

Once the model was specialized on the basis of the in site detected geometry and the collected values of material mass and stiffness, a first comparison between the numerical and experimental results was carried out in terms of frequencies and mode shapes. The consistency of

the latter comparison was measured with the MAC index - Modal Assurance Criterion - which provides a measure of the degree of linearity between the vectors of the mode shapes [31]. A MAC index value close to unity indicate a high level of correspondence between the compared mode shapes. The results are reported in Table 1. The numerical model provides, among the first nine mode shapes, the experimental mode shapes identified with the dynamic test. In particular, the experimental modes correspond respectively to the fourth, fifth and ninth numerical ones as can be observed in Fig. 10.

Table 1. Theoretical-experimental comparison

Experimental		Numerical		
Mode N.	$f_{exp}$ [Hz]	Mode N.	$f_{FEM}$ [Hz]	MAC
1	1.18	1	1.19	0.86
2	2.12	5	2.12	0.98
3	5.69	9	4.72	0.76

As can be noted from Table 1 the assessment between numerical and experimental returns, with reference to the fundamental modes of the structure, a good agreement in terms of frequency and MAC for the two first experimental modes. Otherwise mode 3 shows a slightly lower correlation between the experimental mode shape and the corresponding numerical data, with a low MAC index of 0.76.

It is worth to note that the numerical model provides many in-plane and out of-plane bending modes of the deck that have not been detected by the dynamic test. Thus, the model needs to be calibrated to identify the actual conditions of the bridge, especially in terms of constraints, that avoid or reduce the movement of the bridge in the deck plane. Therefore, in the paper a first manually updating of the model was performed changing the following prominent items in agreement with physical phenomena due to real conditions observed during the investigation:

1) A fixed support was assigned to the base of the piers in the transverse direction (short dimension of the deck) because the hinge at the base of the pier may not be activated in the transverse direction for the environmental vibrations due to friction between the concrete of the pier and the foundation.

2) Fixed supports in transversal and longitudinal direction were inserted at the edges of the cantilevered spans to take in account that the longitudinal and transverse displacements are prevented because the gap between the bridge and the road has been filled with cement.

3) elastic supports were adopted at the longitudinal edges in vertical direction to take into account that gap below the bridge is not enough to avoid the support effect of the gabions and reinforced soil. A first calibration of the restraints stiffness has been made but this aspect needs of further study.

4) A rectangular beam was arranged along the two longitudinal sides of the bridge to consider the stiffness effect along the transverse direction due to the sidewalk added in 1982 by a steel structure bolted to the bridge. equivalent to.

5) The elastic modulus of the concrete for the piers (24000 MPa) was reduced to take account of the degradation phenomena of concrete cover evidenced during the in-situ survey. The above considerations, properly introduced in the numerical model modified the mode shapes of the model, and led to the correspondence of the order between experimental and numerical modes. In Table 2 the comparison of numerical and experimental modes after the updating is shown. An improvement of the correspondence between numeric and experimental behavior is also confirmed by the increment of MAC, after the first manual updating

of the model, that was necessary to introduce the correct boundary conditions that correspond to real circumstances and not to numerical optimization. Clearly a further step is necessary in the updating process in order to reduce the difference in frequency between experimental and numerical modes by a better assessment of the parameters values as the elastic modulus of the materials, the restraints conditions and the elasticity of the constraints.

Table 2. Theoretical-experimental comparison after updating

Experimental		Numerical		
Mode N.	$f_{\text{exp}}$ [Hz]	Mode N.	$f_{\text{FEM}}$ [Hz]	MAC
1	1.18	1	1.91	0.97
2	2.12	2	2.16	0.97
3	5.69	3	4.16	0.80

## 6 CONCLUSIONS

The study presents the complete procedure of structural identification of an existing bridge and the first results of the consequent model updating. The selected case study, that is a complex, even if not large, structure designed by Riccardo Morandi in '50 years, evidenced the following general aspects:

- The AVT is a suitable procedure to define the experimental behavior of a structure in the linear field because it doesn't require the time and organization for application of actions; however a reliable numerical elaboration of the results is necessary with more than a technique. A few number of sensors can be used applying more than one setup and combining the results by a suitable technique. In the case study 5 sensors were available but 8 setup allowed to have experimental results of 30 points along the bridge.
- The numerical model has to be developed considering the aspects that is necessary to update by the identification process. The basic model has to be developed considering the results of a detailed in situ investigation on geometry, materials and boundary conditions of the structure.
- A first updating process addressed by physical considerations of the conditions that can bring the numerical model near to the experimental behavior is important to avoid that a numerical optimization process can use other properties to attain the final results. In the case proposed herein some constraints are due to real in situ conditions (filling of the gaps between the road and the bridge not considered in the design) that influence the linear elastic response, therefore their presence have to be introduced before starting an update process of the elastic properties of the construction.

The strategy of carrying out a dynamic experimental test to calibrate a reliable model provides a good structural identification, allowing to accurately identify the real boundary conditions of the structure, not always possible without in situ tests. The presented work is in progress to complete the model updating and compare the behavior of the structure evidenced by the dynamic test with the one obtained by a load in situ test.

## REFERENCES

- [1] J. Scheer, *Failed Bridges, Case Studies, Causes and Consequences*. Ernst & Sohn, 2010.

- [2] Calvi, G. M., Moratti, M., O'Reilly, G. J., Scattarreggia, N., Monteiro, R., Malomo, D., Calvi, P. M., Pinho, R., (2019). Once upon a time in Italy: The tale of the Morandi Bridge. *Struct. Eng. Int.* 29 (2): 198–217.
- [3] Altunisik, A.C., Bayraktar, A., (2017). Manual model updating of highway bridges under operational condition. *Journal of Structures and Systems*, 19: 39-46.
- [4] A. Morassi, S. Tonon, Dynamic testing for structural identification of a bridge, *J. Bridge Eng.* ASCE 13 (6) (2008) 573–585.
- [5] Van der Auweraer H, Peeters B. International research projects on structural health monitoring: an overview. *Struct Health Monit* 2003;2:341–58.
- [6] Ko JM, Ni YQ. Technology developments in structural health monitoring of large-scale bridges. *Eng Struct* 2005; 27:1715–25.
- [7] Hsieh KH, Halling MW, Barr PJ. Overview of vibrational structural health monitoring with representative case studies. *J Bridge Eng* 2006;11(6):707–15.
- [8] Caetano E, Cunha A, Magalhães F. Studies for controlling human-induced vibration of the Pedro e Ins footbridge, Portugal. Part 2: implementation of tuned mass dampers. *Eng Struct* 2010;32:1082–91.
- [9] Chen WH, Lu ZR, Lin W, Chen SH, Ni YQ, Xia Y, Liao WY. Theoretical and experimental modal analysis of the Guangzhou new tv tower. *Eng Struct* 2011;33:3628–46.
- [10] Dilella M, Morassi A, Perin M. Dynamic identification of a reinforced concrete damaged bridge. *Mech Syst Signal Pr* 2011;25:2990–3009.
- [11] Alvandi A, Cremona C. Assessment of vibration-based damage identification techniques. *J Sound Vib* 2006;292:179–202.
- [12] Askegaard, V. and Lanso, H.E. Correlation between Changes in Dynamic Properties and Remaining Carrying Capacity, *Materiaux et Constructions*, Vol. 19, No. 109, 11–20 (1986).
- [13] Marefat, M.S., Ghahremani-Gargary, E. and Ataei, S. (2004), “Load test of a plain concrete arch railway bridge of 20-m span”, *Constr. Build. Mater.*, 18, 661-667.
- [14] Frýba, L. and Pirner, M. (2001), “Load tests and modal analysis of bridges”, *Eng. Struct.*, 23, 102-109.
- [15] Mottershead JE, Friswell MI. Model updating in structural dynamics: a survey. *J Sound Vib* 1993;167:347–75.
- [16] Zàrate BA, Caicedo JM. Finite element model updating: multiple alternatives. *Eng Struct* 2008;30:3724–30.
- [17] Salawu O. S., and Williams C., Bridge assessment using forced vibration testing, *J. Struct. Eng.*, 121(2), 161–173, 1995.
- [18] Salawu, O.S. and Williams, C. Review of full-scale dynamic testing of bridge structures, *Engineering Structures*, 17, 2,113–12, Elsevier Science, (1995).
- [19] Wilson JC, Liu T. Ambient vibration measurements on a cable-stayed bridge. *Earthquake Eng Struct Dyn* 1991;20:723–47.
- [20] Gentile C, Martinez y Cabrera F. Dynamic investigation of a repaired cable stayed bridge. *Earthquake Eng Struct Dyn* 1997;26(1):41–59.

- [21] Calçada R, Cunha A, Delgado R. Dynamic analysis of metallic arch railway bridge. *J Bridge Eng*, ASCE 2000;7(4):214–22.
- [22] Magalhães F, Cunha A, Caetano E. Dynamic monitoring of a long span arch bridge. *Eng Struct* 2008;30(10):3034–44.
- [23] Brownjohn JMW, Dumanoglu AA, Severn RT. Ambient vibration survey of the Faith Sultan Mehmet (second Bosphorus) suspension bridge. *Earthquake Eng Struct Dyn* 1992;21:907–24.
- [24] M.R. Pecce, F. Santamato, E. Ciampa, E. Cosenza, The design approach of a Prestressed Concrete bridge constructed in 1950s in Italy. *Proc. of the International fib Symposium on Conceptual Design of Structures*, Instituto de Ciencias de la Construcción Eduardo Torroja, Madrid, Spain, Sept 26-28, 2019.
- [25] Rainieri C. & Fabbrocino G., Learning operational modal analysis in four steps. 6<sup>th</sup> IOMAC International Conference on Operational Modal Analysis, Gjøen, 2015.
- [26] SVS 2010. ARTeMIS extractor 2010 release 5.0. <http://www.svibs.com/>.
- [27] Brincker R, Ventura CE, Andersen P. Damping estimation by Frequency Domain Decomposition. In: *Proc. 19th int. modal analysis conf. IMAC-XIX*. 2001.
- [28] van Overschee P, De Moor B. Subspace identification for linear systems: theory, implementation, applications. Boston (London, Dordrecht): Kluwer; 1996.
- [29] Computers and Structures. *SAP2000 Version 18*; Computers and Structures: Walnut Creek, CA, USA, 2016.
- [30] EN 1992-1-1, Design of concrete structures – General rules and rules for buildings, European Committee for Standardization, CEN, Brussels (2004).
- [31] Allemang R. J., The Modal Assurance Criterion –Twenty Years of Use and Abuse, *Sound And Vibration*, 2003.



## MODAL ANALYSIS OF THE HISTORICAL SS FILIPPO E GIACOMO MASONRY ARCH BRIDGE IN ASCOLI PICENO (ITALY)

F. Gara<sup>1</sup>, G. Leoni<sup>2</sup>, M. Morici<sup>2</sup>

<sup>1</sup> Università Politecnica delle Marche, Department of Construction, Civil Engineering and Architecture  
60131 Ancona, Italy  
[f.gara@univpm.it](mailto:f.gara@univpm.it)

<sup>2</sup> University of Camerino, School of Architecture and Design  
63100 Ascoli Piceno, Italy  
e-mail: {graziano.leoni, michele.morici}@unicam.it

---

### Abstract

*This paper presents the experimental test campaign to calibrate a finite element model intended to evaluate the seismic vulnerability of the SS Filippo e Giacomo historical masonry arch bridge in Ascoli Piceno (Italy).*

*The bridge was built in 14<sup>th</sup> century and had undergone very complex vicissitudes related mainly to exceptional floods; it was partially rebuilt twice and other strengthening works were carried out over the time. The bridge, which is almost completely built with travertine blocks, has a total length of 146 m and follows a slightly curved path. Six arches, the main of which is semi-circular with span of 25 m and the others are lancet arches with span of about 8 m, support the carriageway that is about 8 m wide. The piers and abutments are founded on the bedrock and consequently some piers are deeply embedded in the sandy gravel deposit.*

*A campaign of experimental tests was executed encompassing onsite measurements of stresses and modulus of elasticity as well as laboratory measurements on specimens taken from the structures. Vibration tests were also carried out to evaluate the modal properties of the bridge. The acquired experimental data were used to calibrate a 3D model that has been developed also including the soil deposit. A very good consistency was achieved between experimental and theoretical behaviors.*

**Keywords:** Stone Masonry Bridges, Finite Element Models, Modal Analysis, Ambient Vibrations, Experimental In-Situ Tests.

---

## 1 INTRODUCTION

Evaluation of a historical masonry structure is a difficult task because of many uncertainties associated with the knowledge of the structure in its current conditions (original structure and structural changes due to repair enlargement and retrofit works, different construction systems and different materials, structural and material degradation and damages, soil and foundation modifications) and also due to modelling techniques complexity as well as to analysis methods. In this sense, after a deep historical analysis and a complete geometrical and structural survey, sophisticated measurement techniques are necessary to catch the real behaviour of the structure, especially the mechanical properties of the structural materials and the global dynamic behaviour.

About the material survey, both traditional techniques and innovative methods are available but non destructive techniques are generally preferred when dealing with historic and valuable structures. An extensive test campaign on material may permit to fix a large part of the most important parameters in the definition of the structural finite element model. The global dynamic behaviour of the structure can be experimentally determined by means of several kinds of test such as forced, impulse, release or ambient vibration tests, by using modal identification methods [1], [2], [3]. In the last decades ambient vibration test, with the relevant output-only modal identification methods, has become the preferred test typology for evaluating the modal parameters of full scale structures and especially for historic structures since no artificial excitation is required and the test can be carried out in operational conditions without interrupting the use of the structure and causing a minimum interference with it [4]. The experimental modal parameters can then be used to update refined finite element models able to describe the real behaviour of structures, which can be required for structural verifications and for designing repair and retrofit works [5], [6], [7].

This paper presents the experimental test campaign and the finite element model updating of the SS. Filippo and Giacomo Bridge over the Tronto river at Ascoli Piceno, in the centre of Italy. The bridge was built in the XIV century and was then subjected to many changes for repair, strengthening, retrofit, and enlargement works. This results in a large complexity of the structural organism, due to interaction between parts of different age which are made of materials with different mechanical properties. Due to these uncertainties and considering the importance of the bridge an accurate analysis of its current conditions was deemed essential to obtain a reliable predictive finite element model to be used for the design of seismic retrofit. First of all a historic study and geometric survey of the bridge were developed. For the material properties in-situ tests, both destructive and non destructive, were carried out, to evaluate the quality of the travertine block masonry. These information were used to develop a refined 3D finite element model that was tuned based on the experimental modal parameters; in particular, the Young's modulus of some materials initially defined according to standard values suggested by codes, was calibrated to fit the dynamic behaviour obtained experimentally.

## 2 “SS. FILIPPO AND GIACOMO” BRIDGE

“SS. Filippo and Giacomo” Bridge rises in a less urbanized area of Ascoli Piceno town and crosses the Tronto River in a short straight section comprised between two loops. It was partially rebuilt twice and other strengthening works were carried out over the time.

It has a total length of 146 m and maximum height over 20 m. The bridge is built between two rock escarpments; one of which is characterized by an important slope (Figure 1).

Six arches constitute the bridge. The main arch crosses the river during its regular flow and has a semicircular shape with span of about 25 m. The arch barrel has the minimum thickness of 0.90 m at the crown and increases up to 1.40 m at the imposts.

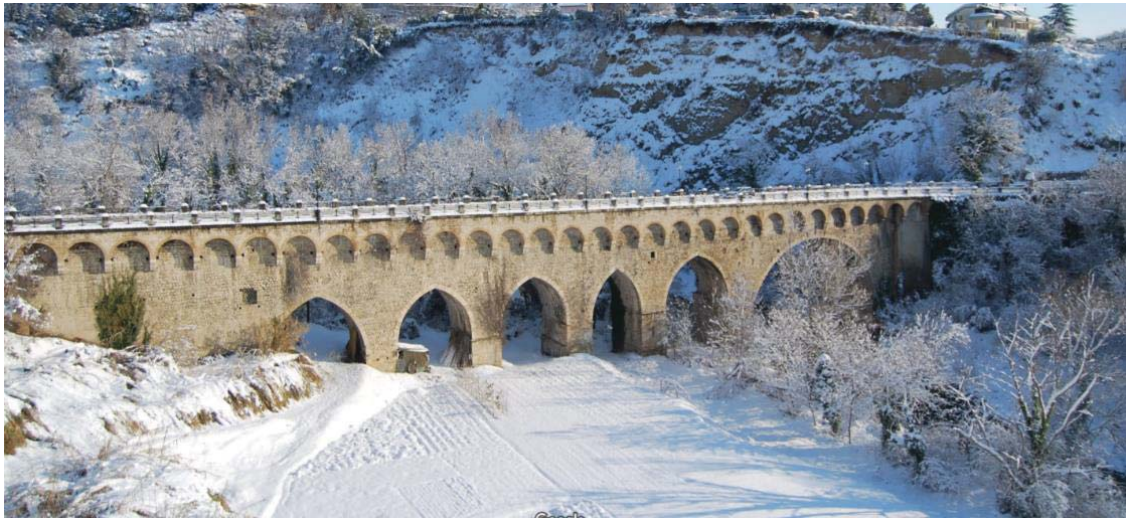


Figure 1: Aerial photogrammetric bridge view.

The other five arches are lancet shaped with span of about 8 m. The depth of the fill at the crowns of arches is variable from about 6.0 to 7.5 m. The spandrel walls have thickness of about 1.0 m. All the piers are placed at the right bank occupied by the river during exceptional floods. The plan path is mostly rectilinear with a bend in proximity of the left abutment.

The two-lane road is almost 6 m wide and is flanked by two about 1 m wide sidewalks that were realized in the first half of the 20th century by enlarging the bridge with a double series of pensile semicircular small arches, with spans of about 4 m, sustained by stone corbels.

The bridge, is completely built with travertine blocks with exception of the twentieth-century pensile arches and of inner lightening rooms that are realized with brick masonry.

## 2.1 Geometrical, material and geological survey

The range-based survey used to acquire geometrical/metric data was made by means of a 3D-TOF laser scanner technique. Both the external geometry and the geometry of the various internal vaulted rooms over the main arch, at the pier top and at the abutments, were surveyed. Wooden and steel ties, placed to avoid the spandrel wall overturning toward outside were also surveyed in the accessible zones. The acquired dataset was then processed to obtain a refined 3D geometrical model that was later used to generate a structural model with very precise geometry and rigorous mass distributions. Such a kind of survey revealed to be extremely useful in the case under consideration characterized by a very complex geometry.

Piers is characterized by an external curtain, having variable thickness and realized with Ascoli Piceno travertine squared blocks, and an important internal, rather irregular, rubble stone infill characterized by the presence of water in the lower parts. For what concerns the masonry of the interior vaulted rooms, it was built with a good quality brick masonry. Nevertheless, it is worth noticing that such components are not expected to give a significant contribution to the overall behavior of the structure excepting for the mass.

The bridge rises between two rock escarpments produced by erosion of Tronto River (Figure 2). The left escarpment has a rather high slope ( $52^\circ$ ) whereas the right one is less sloping ( $31^\circ$ ). The gorge is characterized by a sandy gravel deposit on the right riverbank, with variable thickness up to 10 m, whereas the sandstone bedrock is outcropping at the left riverbank. Investigations carried out in correspondence of piers P1, P2 and P3 demonstrated that foundations are placed at the sandstone bedrock which is horizontal; despite other specific analyses were not carried out for the other piers (P4 and P5) there is no evidence (e.g. vertical settlements) that these are founded over the deposit; the sandy gravel deposit is thus placed around the pier but not under the foundation layer.

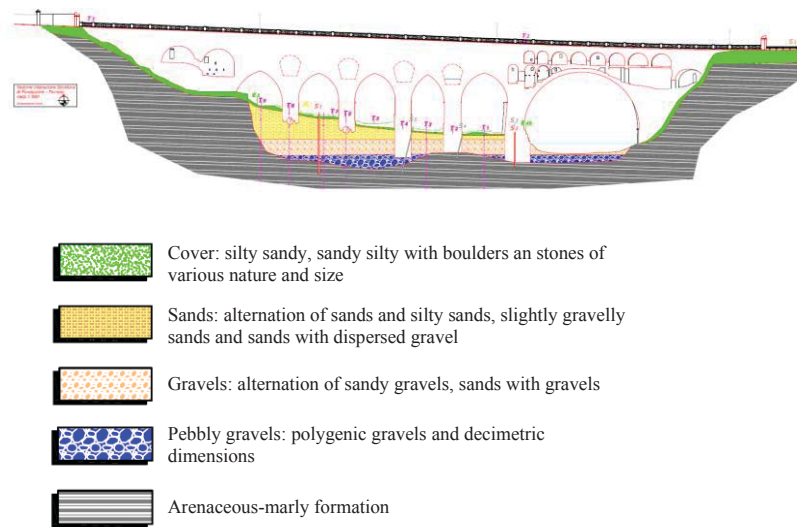


Figure 2: Geological configuration and foundation level.

### 3 OPERATIONAL MODAL TESTING

#### 3.1 Instrumentation and tests

The modal parameters of the bridge, i.e. natural frequencies, damping ratios and mode shapes, are experimentally estimated by means of operational modal analysis starting from the accelerations of the deck recorded during ambient vibration measurements which are mainly due to traffic, wind and microtremors. The tests are performed by using 8 low noise piezoelectric uniaxial accelerometers, a 24-bit data acquisition system, and coaxial cables (Figure 3). Different configurations are adopted in order to identify the global behaviour of the bridge; in this paper only that useful to investigate the transversal behaviour is reported and analysed.

Two configurations were considered in order to capture transversal and vertical-torsional behavior of the bridge (Figure 4). In order to capture the transversal behavior, 8 accelerometers aligned throughout the longitudinal axis of the bridge and oriented in transverse direction were installed (Configuration 1), while to capture the flexural-torsional response, 8 accelerometers lined up in pairs and oriented in vertical direction were installed (Configuration 2).

Time histories 1000 seconds long, sampled at a rate of 2048 Hz (the minimum sampling rate for the used data acquisition system), were acquired. This time length provides enough data to obtain modal parameters with a good accuracy, as reported in [8] where an acquisition time longer than about 1000-2000 times the fundamental period, is recommended (in this case a value of about 2.5 Hz was obtained from preliminary measurements that leads to 400-800 s).

Before performing the operational modal analysis all the recorded data were processed by means of suitable signal processing techniques: trend removal, low-pass filtering (to eliminate the contribution of high frequencies and to avoid aliasing phenomena) and down-sampling at 51.2 Hz, in order to decrease the amount of data and make faster the successive analyses.



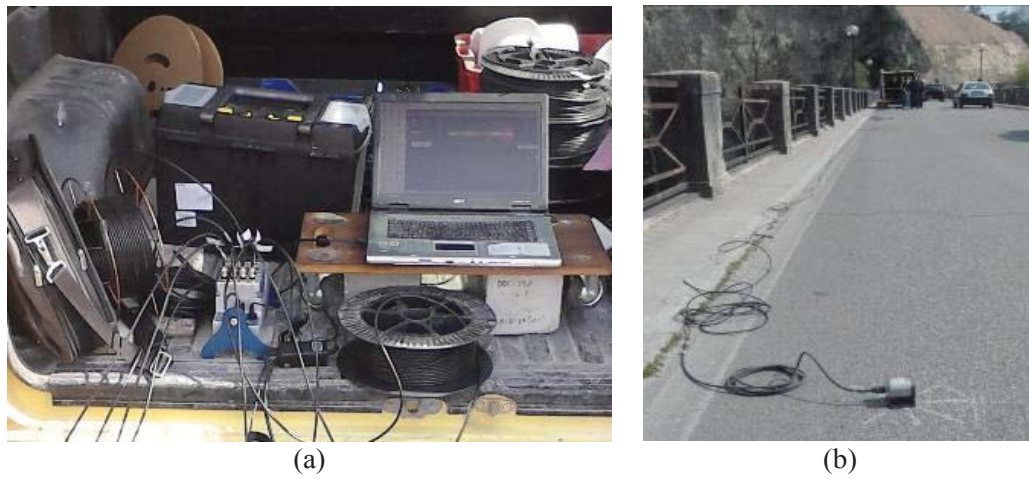


Figure 3. Instrumentation and uniaxial accelerometers.

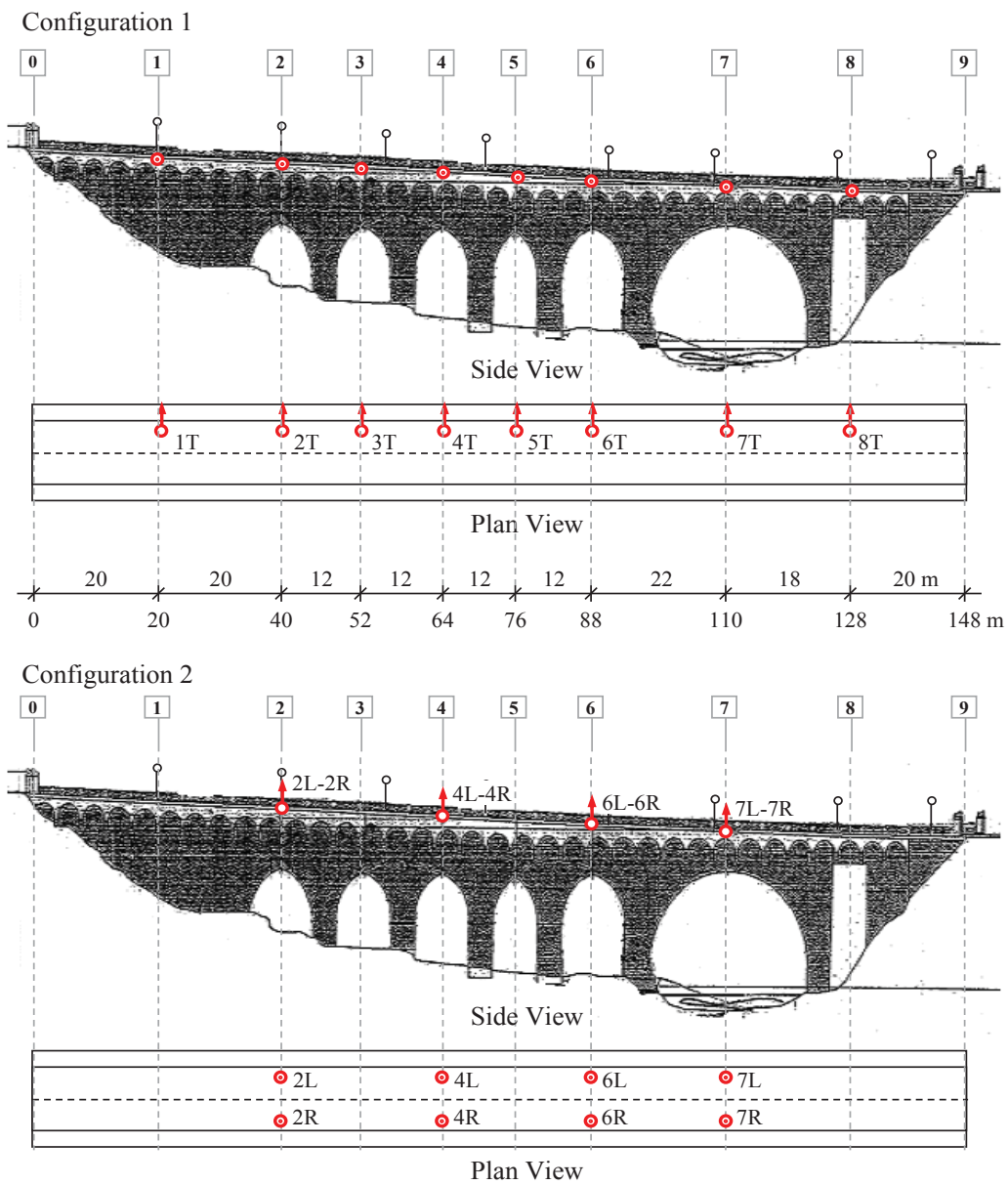


Figure 4. Location of accelerometers for the two configurations



### 3.2 Operational modal analysis (methods and results)

The Covariance-Driven Stochastic Subspace Identification (SSI-Cov) is used to estimate the modal parameters on the basis of the accelerations recorded during the ambient vibration test. This method uses a stochastic state-space model, simplifying the second-order system of differential equation that describes the dynamic problem into a first-order system. Starting from the recorded data sampled at discrete interval, the stochastic state-space model is represented by [9]

$$\mathbf{x}_{k+1} = \mathbf{A}\mathbf{x}_k + \mathbf{w}_k \quad (1)$$

$$\mathbf{y}_k = \mathbf{C}\mathbf{x}_k + \mathbf{v}_k \quad (2)$$

where  $\mathbf{x}_k$  is the discrete-time state vector at time instant  $k$ ,  $\mathbf{y}_k$  is the vector of the output,  $\mathbf{A}$  is the discrete state matrix,  $\mathbf{C}$  is the discrete output matrix, and  $\mathbf{w}_k$  and  $\mathbf{v}_k$  represent the process and measurement noise respectively. The Toeplitz matrix containing the covariance matrices of measured accelerations is used to extract  $\mathbf{A}$  and  $\mathbf{C}$  matrices by means of a Singular Value Decomposition and a least square procedure [10]. The modal parameters are obtained by the two matrices characterizing the state-space model. The SSI-Cov permits the estimation of a number of modes depending on the model order used in the state-space model. The physical modes are separated by the spurious ones by means of the stabilization diagram which allows the identification of (y-axis) the stable modes (x-axis) i.e. the modes presenting modal parameters (natural frequencies, damping ratios and mode shapes) which remain similar as the model order increases (Figure 5). In this work models with up to 40 order are used and the modes are considered to be consistent if, when increasing the model order one by one: (i) natural frequency variation is less than 1%, (ii) damping ratio variation is less than 2%, and (iii) Modal Assurance Criterion (MAC) between the modes is greater than 98%.

Table 2 reports the natural frequencies with the relevant damping ratios obtained with the operational modal analysis in the frequency range 2-6 Hz from Configuration 1, while Figure 6 shows the normalized modal shapes obtained with SSI-Cov method. The modes identified are the transversal modes typical for such a masonry bridge. The modal parameters estimated experimentally are crucial to evaluate the reliability of the model and to calibrate some important parameters. Table 3 reports the natural frequencies with the relevant damping ratios obtained with the operational modal analysis from Configuration 2, while Figure 7 shows the normalized modal shapes obtained with SSI-Cov method.

In this case the natural frequencies and mode shapes estimated in Configuration 1 are used in the sequel to calibrate the mass distribution along the bridge length (based on some assumption in absence of experimental survey) and the elastic modulus of the travertine masonry.

Mode	$f$ (Hz)	$\xi$ (%)	Mode shape
1	2.46	2.11	1 <sup>st</sup> transverse
2	3.30	2.97	2 <sup>nd</sup> transverse
3	4.54	2.54	3 <sup>rd</sup> transverse
4	5.61	2.50	4 <sup>th</sup> transverse

Table 2: Modal parameters from Configuration 1.

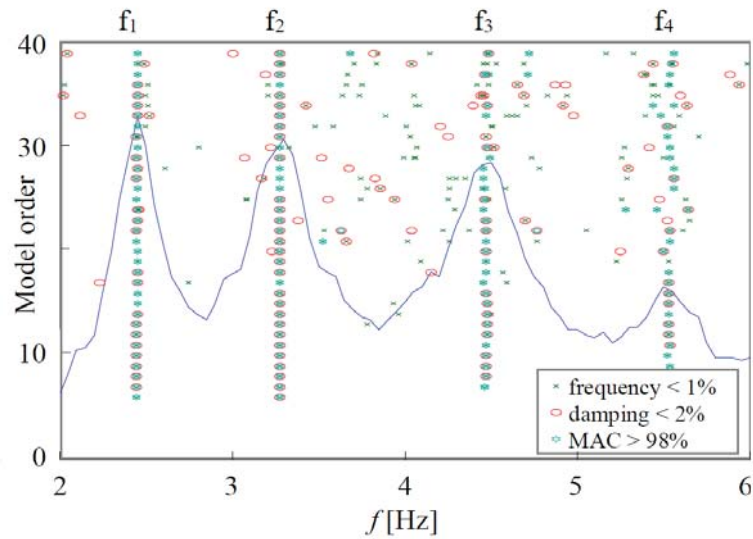


Figure 5. Stabilization diagram

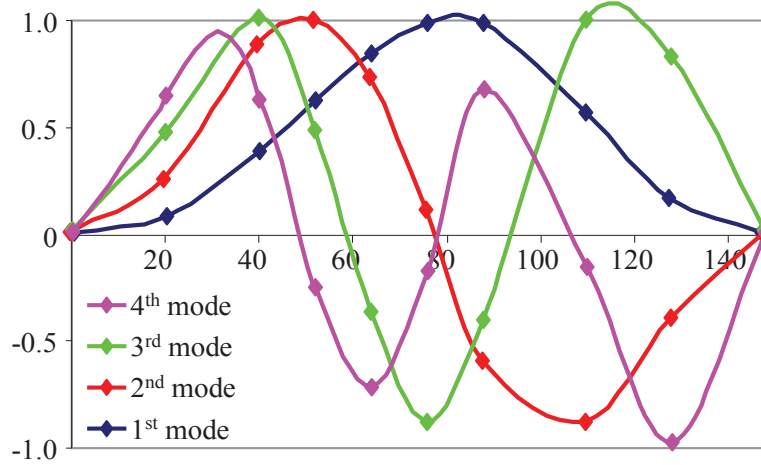


Figure 6. Experimental transverse mode shapes.

Mode	$f$ (Hz)	$\xi$ (%)	Mode shape
1°	6.27	3.88	Flexural mode
2°	8.55	1.67	Flexural mode
3°	9.68	5.27	Flexural mode
4°	12.40	3.54	Flexural mode
5°	14.07	2.02	Torsional mode

Table 3: Modal parameters from Configuration 2.

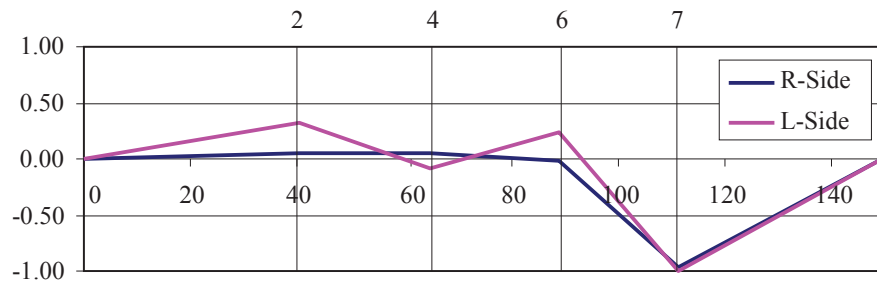
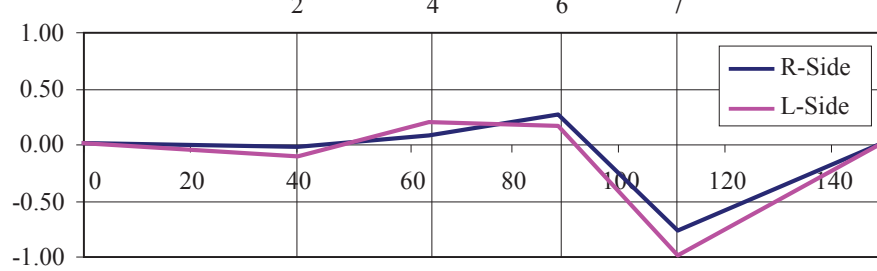
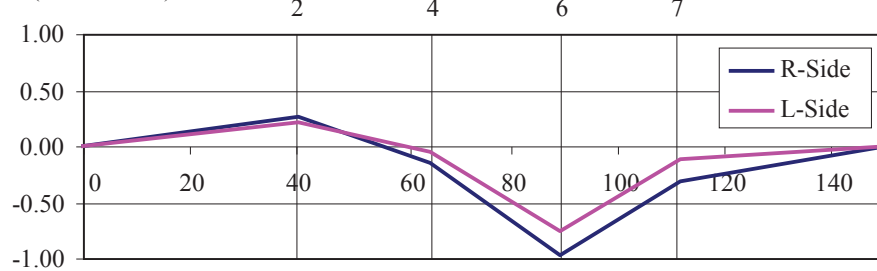
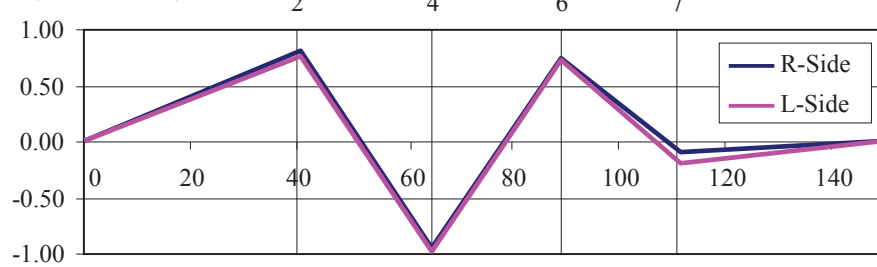
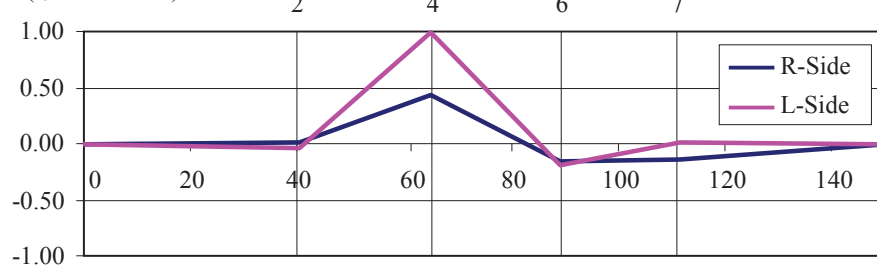
1<sup>st</sup> MODE ( $f_1 = 6.27$  Hz)2<sup>nd</sup> MODE ( $f_2 = 8.55$  Hz)3<sup>rd</sup> MODE ( $f_3 = 9.68$  Hz)4<sup>th</sup> MODE ( $f_4 = 12.40$  Hz)5<sup>th</sup> MODE ( $f_5 = 14.07$  Hz)

Figure 7. Experimental vertical mode shapes.

## 4 STRUCTURAL MODEL OF THE BRIDGE

### 4.1 Finite element model

Model for the overall structural analysis is developed in Straus7 [11] by integrating data available from the laser scanner survey. In particular, the 3D model (Figure 8a) encompasses a suitable portion of the soil deposit with variable depth in order to account for the particular geological configuration and to capture effects of soil-pier interaction.

The finite element model is obtained with a mesh of 4-node tetrahedral elements with linear interpolation shape functions (Tetra4). The mesh is generated by importing a closed poly-surface constructed by approximating the geometry obtained with the laser scanner survey.

For such a purpose the geometry is simplified in order to avoid excessive refinement of the mesh due to details that do not actually affect the overall behavior of the bridge; at the same time all internal rooms and the earth fill are modelled in order to capture the real stiffness and mass distribution of the structure. Maximum length imposed to the element edge is 1.0 m for the bridge structure whereas it is increased up to 4.5 m for the elements of the soil deposit (Figure 8b). Fixity restraint are placed at the deposit base and at the structure sections interacting with the sand stone formation. The model is constituted by 120,545 elements for a total of 75,204 degrees of freedom. All the materials, including earth fills and the soil deposit, are considered to be linear elastic and isotropic.

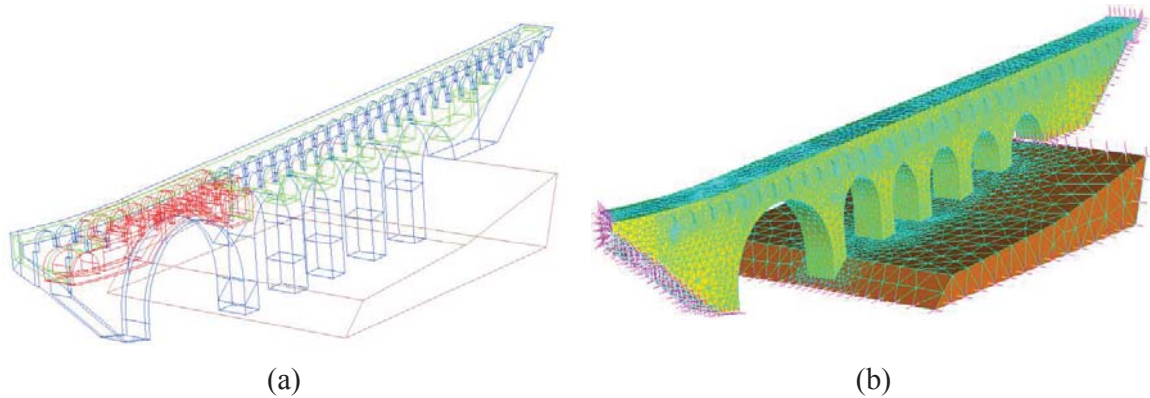


Figure 8. (a) Geometrical model; (b) Finite element model.

### 4.2 Model tuning

The mechanical parameters of the finite element model are calibrated by fitting the experimental modal parameters with numerical ones relevant to the finite element model previously discussed. Initial value of the parameters are selected according to the valued reported in the Italian standard [12-13].

Figure 9a shows the first four mode shapes obtained by means of model calibration changing only the elastic modulus of the travertine masonry constituting the main structure. In Figure 9b the comparison among the first four experimental and numerical mode shapes is reported, while Table 4 reports the percentage errors relevant to the frequencies and the approximation of the mode shapes by means of the MAC

$$MAC = 100 \times \frac{(\boldsymbol{\varphi}_i \cdot \tilde{\boldsymbol{\varphi}}_i)^2}{(\boldsymbol{\varphi}_i \cdot \boldsymbol{\varphi}_i)(\tilde{\boldsymbol{\varphi}}_i \cdot \tilde{\boldsymbol{\varphi}}_i)} \quad (3)$$

which tends to 100 when the theoretical  $(\boldsymbol{\varphi}_i)$  and experimental  $(\tilde{\boldsymbol{\varphi}}_i)$  modes tends to be equal.

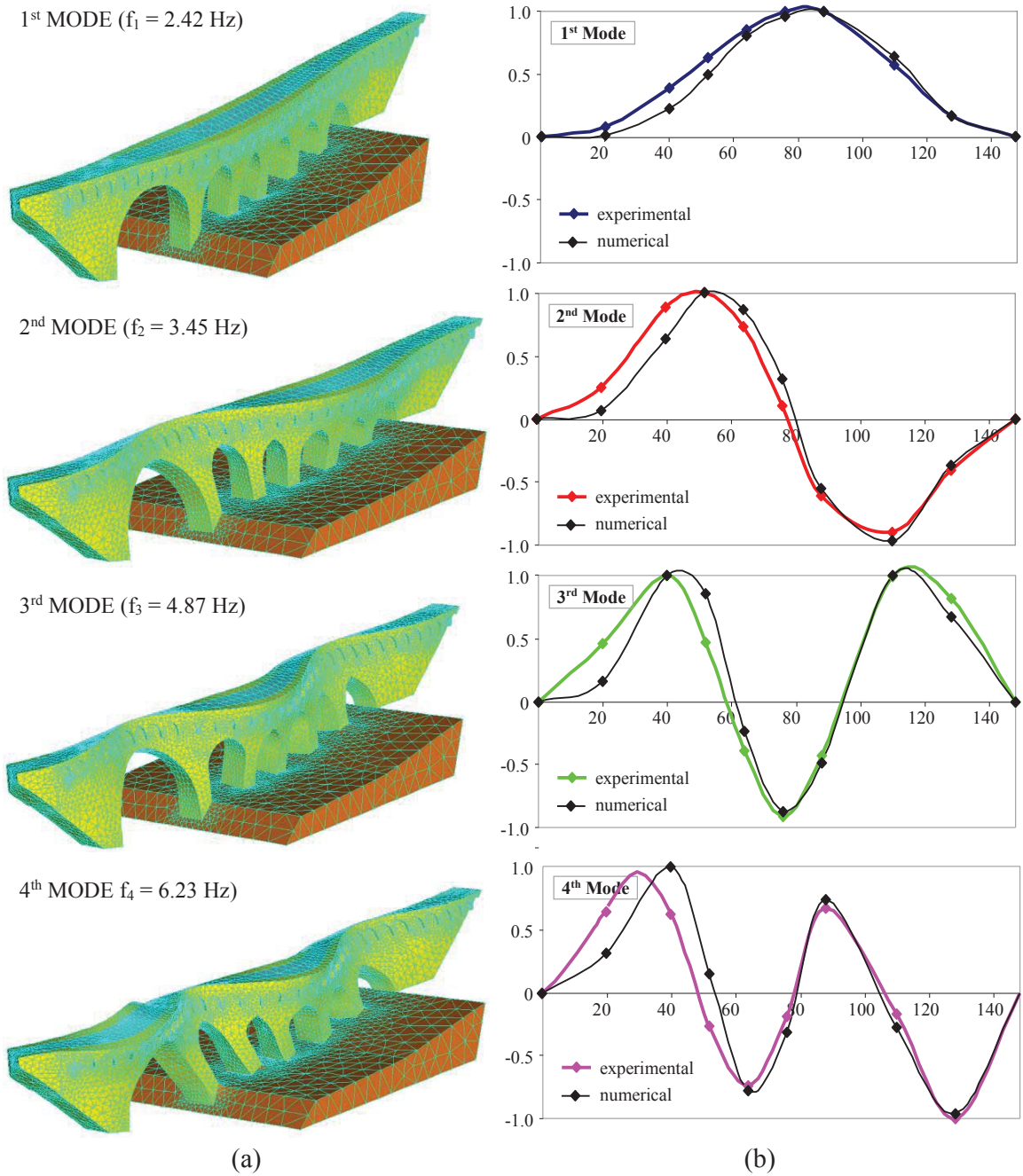


Figure 9. (a) First four transverse vibration modes; (b) Comparison between experimental and numerical modes

Mode	Frequency (Hz)		Error (%)	MAC (%)
	Experimental	Numerical		
1	2.46	2.42	1.55	98.58
2	3.30	3.45	-4.67	95.43
3	4.54	4.87	-7.34	93.37
4	5.61	6.23	-10.99	86.45

Table 4. Comparison between experimental and numerical results



The parameters used in the model are reported in Table 5. The soil parameters are derived from geotechnical tests while infill materials are hypothesized.

Material	E (N/mm <sup>2</sup> )	G (N/mm <sup>2</sup> )	w (kN/m <sup>3</sup> )
Travertine masonry	7000	2414	22
Brick masonry	1282	427	18
Earth fill	666	238	18
Soil deposit	666	243	19

Table 5. Mechanical parameters of materials

## 5 CONCLUSIONS

An experimental test campaign aimed at calibrating the finite element model of a historical masonry bridge, characterized by an unusual geometry deriving by very complex historical vicissitudes, has been presented. The bridge rises in a gorge and is founded on a sand-stone deposit that is outcropping at the abutments. The bridge is constituted by six different arches whose piers are founded on the sand-stone formation and are embedded for significant sections (up to 10 m) into the fluvial deposit constituted by sandy-gravel soil.

A laser scanner survey was crucial to obtain a model encompassing all main features of the real structure such as the inner lightening rooms, with very irregular geometry, as well as the pensile arches constructed to enlarge the carriageway.

The onsite tests permitted the evaluation of the main mechanical characteristics of the materials and the estimation of the stress state in critical sections of the piers.

The operational modal analysis, used to detect the dynamic behavior of the bridge, was decisive for tuning a finite element model capable of predicting the overall behavior of the bridge.

## REFERENCES

- [1] F.Aras, L. Krstevska, L. Tashkov. Experimental and numerical modal analyses of a historical masonry palace. *Constr Build Mater*, 25(1): 81-91, 2011.
- [2] G.C. Beolchini, F. Vestroni. Experimental and analytical study of dynamic behaviour of a bridge. *J Struct Eng ASCE*, 123(11): 1506-1511, 1997.
- [3] D. Benedetti, C. Gentile. Identification of modal quantities from two earthquake responses. *Earthquake Eng Struct Dynam*, 23(4): 447-462, 1994.
- [4] G. Gentile, A. Saisi. Ambient vibration testing of historic masonry towers for structural identification and damage assessment. *Constr Build Mater*, 21(6): 1311-1321, 2007.
- [5] A. De Sortis, E. Antonacci, F. Vestroni. Dynamic identification of a masonry building using forced vibration tests. *Eng Struct*, 27(2): 155-165, 2005.
- [6] H. Ahmadian, G.M. Gladwell, F. Ismail. Finite element model identification using modal data. *J Sound Vib*, 172(5): 657-669, 1994.
- [7] J.E. Mottershead, M.I. Friswell. Model updating in structural dynamics: a survey. *J Sound Vib*, 167(2): 347-375, 1993.

- [8] Cantieni, R. Experimental methods used in system identification of civil engineering structures. *Proc. 1<sup>st</sup> Int. Operational Modal Analysis Conf.*, Copenhagen, Denmark, pp. 249-260, 2005.
- [9] J.-N. Juang. Applied System Identification. Prentice-Hall Englewood Cliffs, New Jersey, USA, 1994.
- [10] P. Van Overschee, B. De Moor. Subspace identification for linear systems: theory–implementation–applications. Dordrecht, The Netherlands: Kluwer Academic Publishers, 1996.
- [11] Straus7, G+D Computing Pty Limited, <http://www.straus7.com>
- [12] *Norme tecniche per le costruzioni. D.M. Ministero Infrastrutture e Trasporti 2018*, Supplemento ordinario alla “Gazzetta Ufficiale n. 42 del 20 febbraio 2018 - Serie generale (In italian), 2018
- [13] *Istruzioni per l'applicazione delle Nuove norme tecniche per le costruzioni di cui al decreto ministeriale 14 gennaio 2018*. Ministero delle Infrastrutture e dei Trasporti e Consiglio Superiore dei Lavori Pubblici, Circolare 21 gennaio 2019, n. 7. Gazzetta Ufficiale n. 35 del 11 febbraio 2019 - supplemento ordinario n. 5 (in Italian), 2019.

## THE TRACKING OF MODAL PARAMETERS FOR A REINFORCED CONCRETE BUILDING DURING LOW-MEDIUM INTENSITY EARTHQUAKES

Davide Arezzo<sup>1</sup>, Vanni Nicoletti<sup>1</sup>, Sandro Carbonari<sup>1</sup>, and Fabrizio Gara<sup>1</sup>

<sup>1</sup> Dept. ICEA, Università Politecnica delle Marche  
Via Brece Bianche, 60131, Ancona, Italy

e-mail: d.arezzo@pm.univpm.it, v.nicoletti@pm.univpm.it, s.carbonari@univpm.it, f.gara@univpm.it

---

### Abstract

*This paper presents the results of the dynamic monitoring carried out on a school building in central Italy during the seismic sequence following the first main shock of the 2016 Central Italy earthquake. The building is located in the historical centre of Camerino and consists of a reinforced concrete frame structure with masonry infill walls. The school, dating back to the 60s, underwent seismic retrofit in 2013 through the construction of 2 dissipative towers, a recent patented system for seismic protection of buildings.*

*In August 2016 a dynamic monitoring system was installed on the building, positioning an array of accelerometers both on the top two floors of the structure and on the foundation level; this made it possible to record the building response to the aftershocks that occurred during the monitoring period, and the corresponding seismic input. The dynamic characteristics of the structure during the monitoring period are identified starting from the response of the structure subjected to the seismic swarm following the main event, and to the environmental vibrations between two subsequent events.*

*Although during the monitoring days the building did not suffer any damage, the response of the structure proved to be nonlinear and strongly dependent on the amplitude of the accelerations to which it was subjected; in this work, a procedure to linearize the structural response and carry out the dynamic identification in terms of modal parameters starting from the non-stationary response of the structure is proposed.*

**Keywords:** Structural Health Monitoring; Infilled RC frame building; Ambient vibrations; Seismic monitoring; Earthquake swarm; Dynamic system identification; Time-varying systems.

---

## 1 INTRODUCTION

There has been a progressive increase in attention in recent years to the usefulness and advantages of permanent monitoring systems in the field of civil engineering. Recording the dynamic response of structures during seismic events can ensure significant benefits: on one hand, it provides useful information for damage detection and post-earthquake emergency management and, on the other hand, it can allow the improvement of the seismic risk assessment through the decrease of uncertainties relevant to both the hazard estimation and structural vulnerability. The reduction of uncertainties relevant to the structural vulnerability can derive from the validation of structural models based on the registration of the structural response subjected to low-medium intensity events while the reduction of uncertainties relevant to the hazard requires the monitoring of the soil-foundation system through which the validation of soil and source models can be attempted.

With respect to low-medium intensity earthquakes, an interesting aspect that emerges from the monitoring is the well-known variability of the dynamic properties of structures during shaking in absence of damage producing a "wandering" of the modal parameters of the construction that can be attributed to minor nonlinearities of the response [1] such as the light cracking of infills or frictions relevant to the interactions between structural and non-structural components. The latter issue, in addition to the well-known dependence of structural frequencies on the environmental conditions [2, 3, 4], makes the identification of structural damage from records obtained from continuous monitoring systems particularly problematic. In the literature it is possible to find several works that address the problem with reference to historical masonry buildings [5, 6, 7], but a limited number of works refer to reinforced concrete structures.

With the aim of providing a contribution in this research area, this paper presents an approach for tracking the fundamental frequencies of monitored buildings accounting for their nonlinear response, triggered by low-medium intensity earthquakes. The procedure is applied to a record extracted from the monitoring of a school building, the Liceo Varano located in Camerino in the province of Macerata (Italy), during the seismic swarm following the earthquake in central Italy in August 2016.

## 2 DESCRIPTION OF THE BUILDING

The building at hand dates back to the 60's and was born from the decision to enlarge and rehabilitate the old masonry building constituting the Liceo Ginnasio Napoleonico since 1833 and, before, the Convent of Santa Elisabetta. Part of the new building is founded on the old convent, while the other part rests on the ground. The building has an L-shaped plan formed by two wings, indicated in Fig. 1a and Fig. 1b with "A" and "B". The structure consists of reinforced concrete frames; beams have a rectangular section, excepting those on the perimeter, which are characterized by cross-sections with a tapered articulated geometry (i.e. with variable height and width) (Fig. 1c). All columns have a square cross-section rotated by  $45^\circ$  with respect to the direction of the frames for architectural reasons, with dimensions equal to 35x35 cm, excepting two inner columns of body "A" that have a 42x42 cm cross-section.

In 2013 the building was seismically retrofitted through the construction of two Dissipative Towers [8] (Fig. 1d), one connected both to body "A" and to body "B" (Tower A) and the other only to body "B" (Tower B). The towers rest on a thick reinforced concrete plate connected by a central spherical hinge to a second slab founded on piles. Simplifying as much as possible the description of the retrofit, it can be stated that the Towers have the twofold aim (i) to regularize the horizontal displacements of the building, favoring a linear deflection (i.e. constant inter-story drifts), and (ii) to increase the dissipation of the seismic input energy through viscous

dissipative devices that exploit the relative velocities between the two reinforced concrete plates at the base of each Tower.

During the seismic retrofit, dynamic ambient vibration tests were performed to identify the modal parameters of the building. A first dynamic identification was conducted in 2012, before the intervention, and a second one was carried out in 2013 upon completion of the upgrading work. The purpose of the investigations carried out was twofold: on one hand, the preliminary identification tests allowed to obtain information on the global dynamic behavior of the building to support the design of the intervention and the calibration of a finite element model; on the other hand, the investigations in the post-operam situation allowed to verify that the modal parameters of the retrofitted structure matched those predicted by the numerical model. More details on the intervention, which is heavily constrained by technical requirements, can be found in Balducci et al. (2015) [9], while a more extensive description of the tests and the relevant results can be found in Gara et al. (2021) [10].

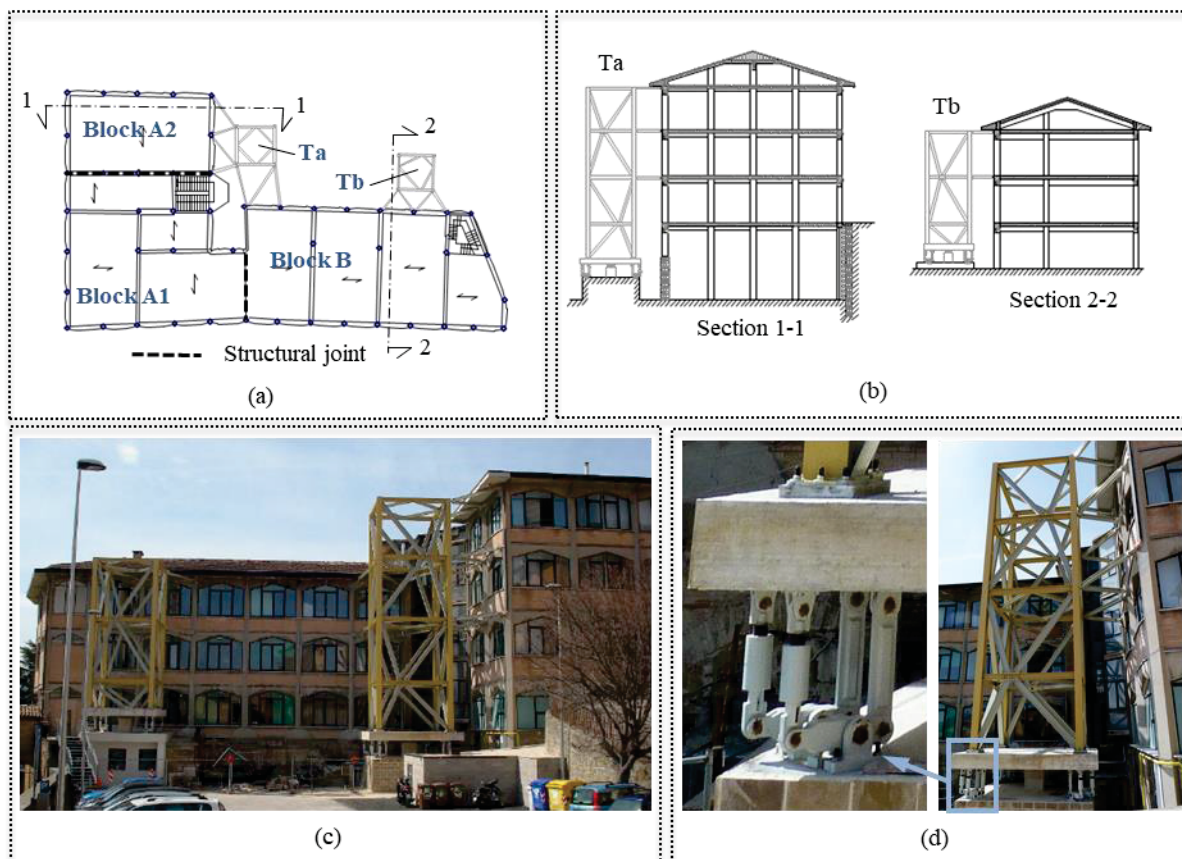


Figure 1: The Costanza da Varano high school: (a) plan view; (b) cross-section; (c) photo of the building; (d) photo of the Dissipative Towers with details of the dampers.

### 3 DESCRIPTION OF THE DYNAMIC MONITORING

After the seismic event of magnitude 6.0 occurred on August 24, 2016, a new ambient vibration test was performed on August 27, 2016, with the purpose of verifying the health of the structure. Fig. 2a shows the sensor configuration adopted for each floor of the building while Fig. 2b shows a photo of the acquisition system. As for the instrumentation, PCB 393B31 piezoelectric sensors with a sensitivity of 10 V/g, NI 9234 analog-to-digital conversion boards with a resolution of 24 bits, a cDAQ 9178 chassis, and a notebook for data acquisition and



storage have been used. A sampling rate of 2048 Hz has been used for the acquisitions. Fig. 2c shows the frequency content of the recordings carried out while Fig. 2d and Fig. 2e show the results of the dynamic identification performed using the SSI-COV algorithm and the MAC (Modal Assurance Criterion) matrix. It is worth to specify that the building dynamics after the event of August 2016 remained unchanged from that identified after the retrofitting in 2013.

Following this test, a continuous dynamic monitoring system has been installed on the structure for three days; the system was composed by the same instrumentation adopted to perform the benchmark tests but additional accelerometers were installed at the foundation level in order to record the seismic input. Ambient vibration tests at the beginning of the monitoring allowed the identification of modal parameters that were subsequently traced via the continuous monitoring system. During the monitoring days (from August 27 to 29, 2017) several earthquakes occurred; the event with the highest intensity of magnitude 4.2 was registered on August 28 and occurred approximately 37 km away from the building.

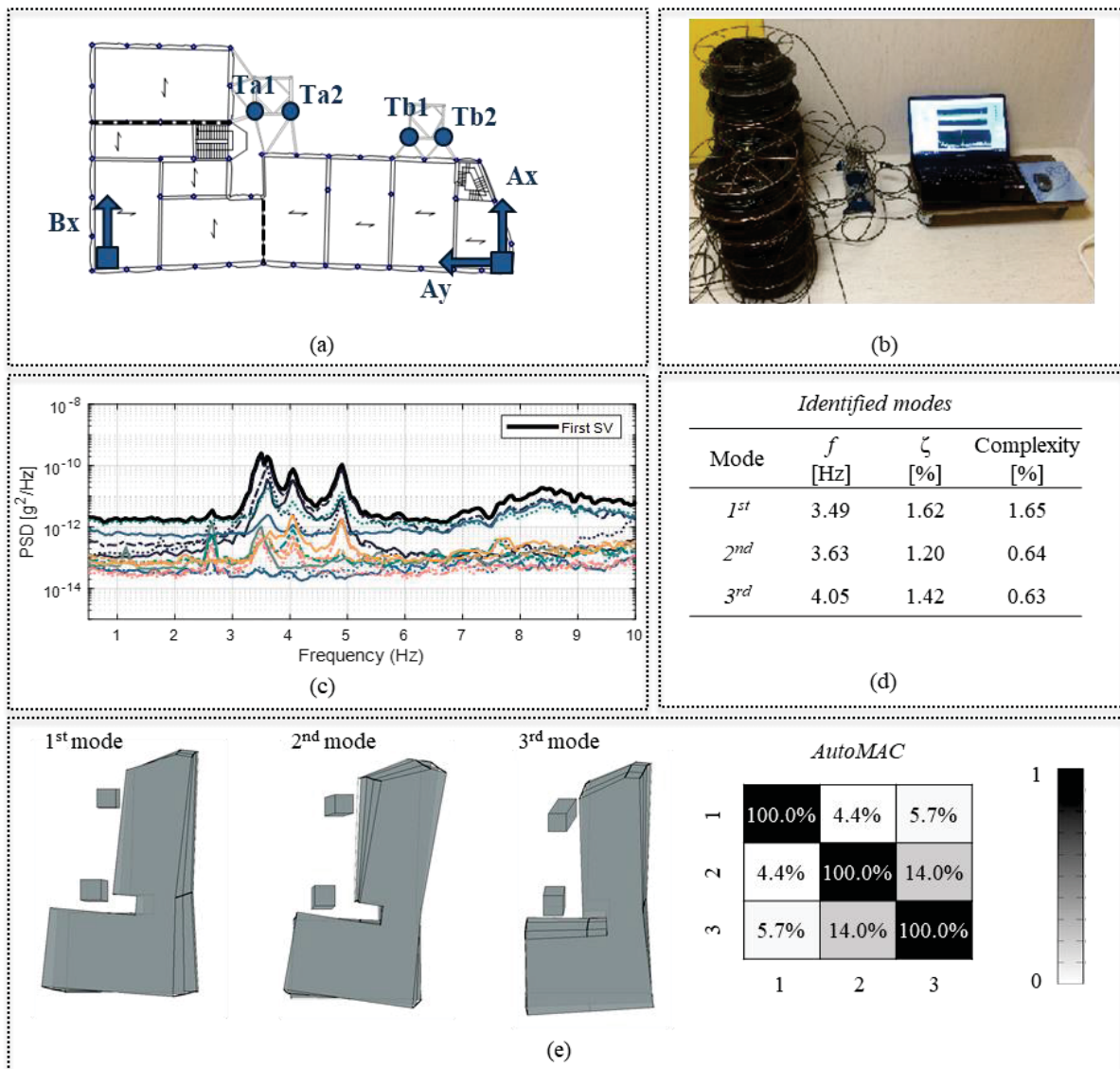


Figure 2: a) Sensors configuration adopted for each floor; b) acquisition system; c) frequency content from measurements during ambient vibration test; d) results of the dynamic identification; e) identified modal shapes and relevant AutoMAC matrix.

#### 4 DESCRIPTION OF THE LINEARIZATION PROCEDURE

For all the registered events, the structure exhibited a nonlinear response that made it difficult to identify its modal parameters from the seismic response. Fig. 3 shows a time-frequency analysis, performed using the Short Time Fourier Transform (STFT), performed on the measurement of the magnitude 4.2 event for the sensor on the top floor (location Ay). From Fig. 3, it is possible to observe the non-stationarity of the structural response, which leads the need of implementing a method to linearize the structural response.

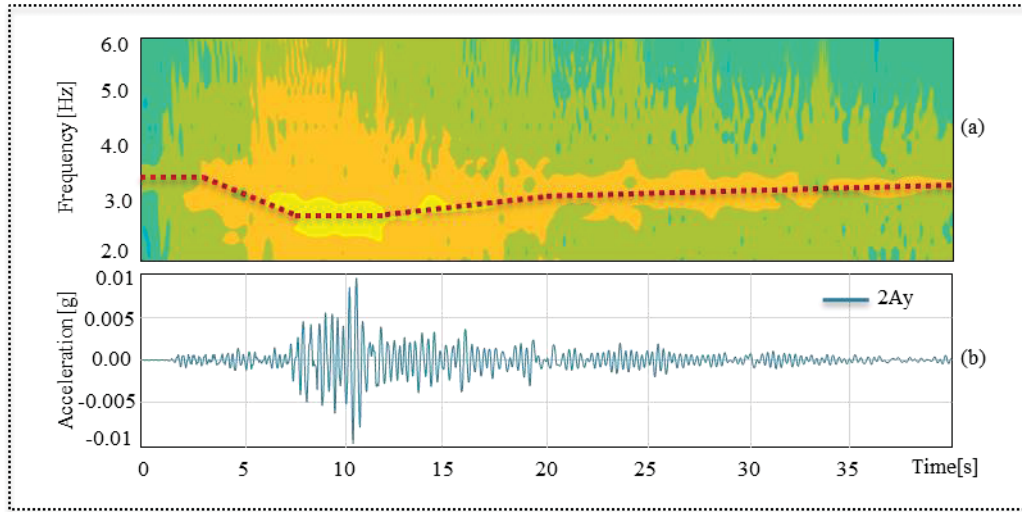


Figure 3: Short Time Fourier Transform carried out on a record made during the magnitude 4.2 event.

The proposed algorithm takes advantage of the subspace identification methods; the latter are well established in the civil engineering field and are considered as robust and reliable algorithms. The recurrent algorithms in the literature, for the identification of MIMO systems are the Multivariable Output Error State Space (MOESP) [11] and the numerical algorithm for Subspace State Space System IDentification (N4SID) [12]. Many works can be found in which above algorithms have been successfully used for dynamic identification of full-scale case studies during seismic events [13, 14, 15, 16]. The first step in using the subspace identification algorithms is to write the dynamical system in the state space, through a state equation (Eq. 1) and an output equation (Eq. 2):

$$\mathbf{x}_{k+1} = \mathbf{A}\mathbf{x}_k + \mathbf{B}\mathbf{u}_k + \mathbf{w}_k \quad (1)$$

$$\mathbf{y}_k = \mathbf{C}\mathbf{x}_k + \mathbf{D}\mathbf{u}_k + \mathbf{v}_k \quad (2)$$

where  $\mathbf{u}_k \in \mathbb{R}^m$  and  $\mathbf{y}_k \in \mathbb{R}^l$  denote the input and output signals, respectively, at a certain time  $k$ , while  $\mathbf{x}_k \in \mathbb{R}^n$  is the state vector. In addition,  $\mathbf{A} \in \mathbb{R}^{n \times n}$  is the dynamical system matrix,  $\mathbf{B} \in \mathbb{R}^{n \times m}$  is the input matrix that describes how the deterministic inputs influence the next state,  $\mathbf{C} \in \mathbb{R}^{l \times n}$  is the output matrix that characterizes how the internal state influences the outputs and  $\mathbf{D} \in \mathbb{R}^{l \times m}$  is the direct transition matrix. For a linear time-invariant system above matrices are constant. Furthermore,  $\mathbf{w}_k \in \mathbb{R}^n$  and  $\mathbf{v}_k \in \mathbb{R}^l$  are unmeasurable vector signals, which are assumed to be normally distributed, zero mean, white noise signals.

For the case study under investigation, the structural response to seismic events of the building at hand is clearly time-varying, and it can therefore be assumed that the system matrices of the state space model change with time  $k$ . Several works in the literature deal with methods for

the identification of time-varying systems; in particular, some interesting algorithms are the MOESP-VAR [17], the N4SID-VAR [18], and the one proposed in Loh and Chen [19].

In this paper, an iterative procedure for the identification of the time-varying dynamical system is proposed, based on the optimization of the number of samples, and thus the length of the signal windows, in which the dynamics of the system can be described as a linear time-invariant process. The length of the first window is selected from the results of the time-frequency analysis and varied until the identified dynamic model accurately reproduces the experimental response starting from the measured input. The steps of the optimization procedure are summarized in the flowchart of Fig. 4; the identification within each window was done through the "robust combined algorithm" proposed by Van Overschee and De Moor in [12]. The accuracy of the identified model in reproducing the building response is evaluated comparing the predicted and measured time histories of accelerations through the comparison metrics proposed by Kavrakov et al. [20], which consider several signal properties such as phase, peak, root mean square, and frequency contents. A detailed explanation of the approach can be found in Gara et al. (2021) [21].

Fig. 5 shows the results obtained by applying the proposed procedure on the seismic response of the building to the magnitude 4.4 event. In particular, Fig. 5a shows the comparison between the signal recorded at the measurement point Ay at the top floor and the response estimated by the identified time-varying dynamical system. Figs. 5b and 5c show the results in terms of modal parameters (resonant frequencies and damping ratios) and reveal how the first three frequencies of the structure decrease during the strong motion and then gradually come back to the initial values at the end of the event; an opposite trend is observed for the damping ratios. The explanation is probably to be sought in the nonlinear phenomena, e.g. light infill cracking, frictions, and interaction phenomena between structural and non-structural members that are triggered above a certain level of excitation provided to the structure.

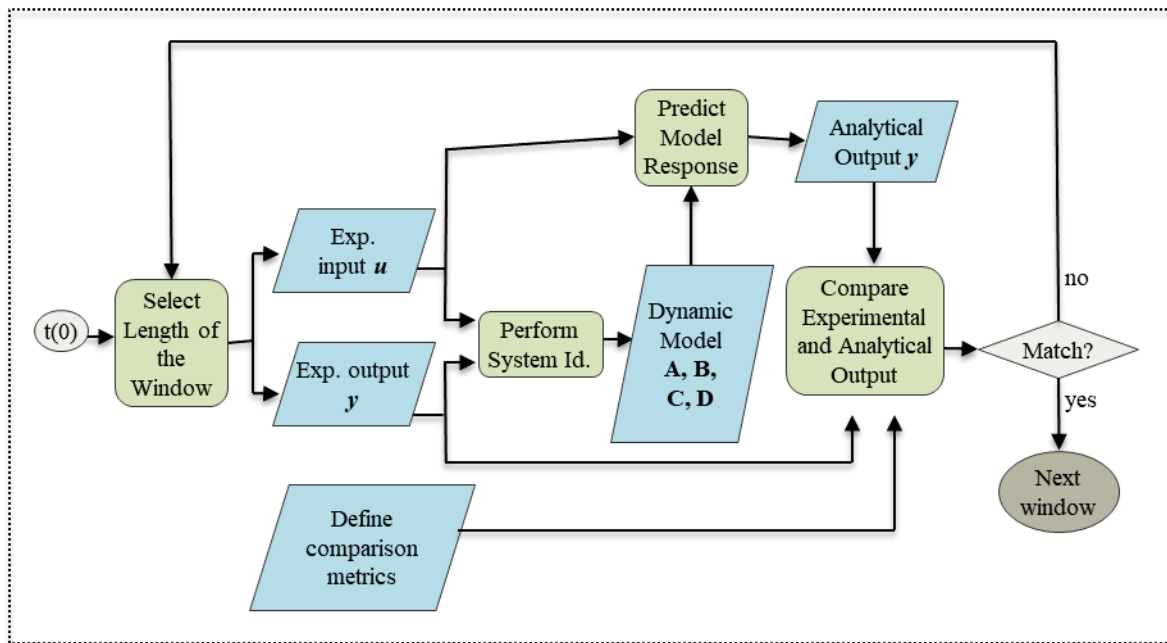


Figure 4: Flow chart of the proposed identification algorithm.

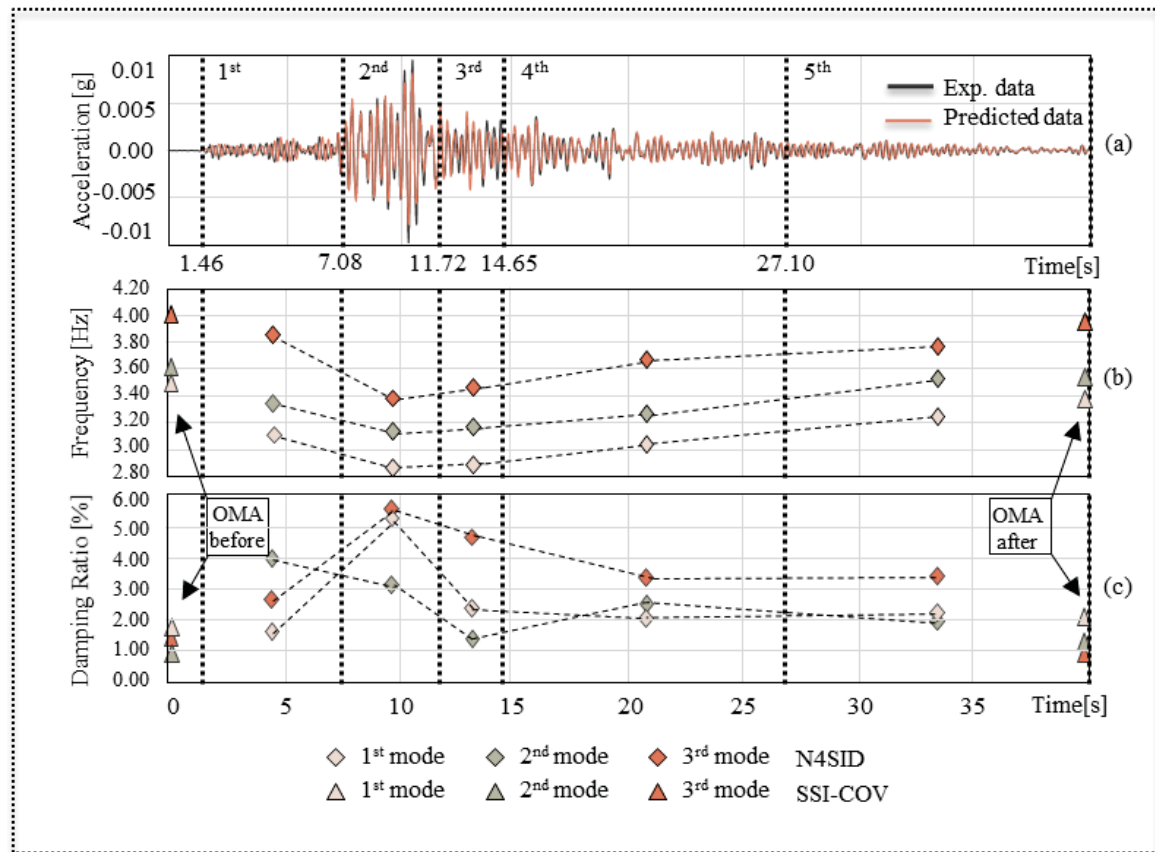


Figure 5: Laboratory mock-up case study.

## 5 CONCLUSIONS

An approach for tracking the fundamental frequencies of monitored buildings accounting for their nonlinear response triggered by low-medium intensity earthquakes has been presented in this paper. The procedure, consisting of an iterative algorithm aimed at identifying signal windows in which the dynamics of the system can be described as a linear time-invariant process, is applied to a record extracted from the monitoring of a school building located in Camerino during the seismic swarm that followed the August 2016 Central Italy earthquake. The results highlighted the nonlinearity of the building seismic response even in the absence of damage, providing a useful tool for the interpretation of accelerometric data in structural health monitoring.

## REFERENCES

- [1] Clinton, J. F., Bradford, S. C., Heaton, H. T., and Favela, J. (2006). "The Observed Wander of the Natural Frequencies in a Structure." *Bulletin of the Seismological Society of America* 96 (1): 237–57. <https://doi.org/10.1785/0120050052>.
- [2] Regni, M., Arezzo, D., Carbonari, S., Gara, F., and Zonta, D. (2018). "Effect of Environmental Conditions on the Modal Response of a 10-Story Reinforced Concrete Tower." *Shock and Vibration* 2018 (July): 1–16. <https://doi.org/10.1155/2018/9476146>.

- [3] Rainieri, C., Magalhaes, F., Gargaro, D., Fabbrocino, G., and Cunha, A. (2018). "Predicting the Variability of Natural Frequencies and Its Causes by Second-Order Blind Identification." *Structural Health Monitoring* 18 (2): 486–507. <https://doi.org/10.1177/1475921718758629>.
- [4] Rainieri, C., Gargaro, D., and Fabbrocino, G. (2019). "Hardware and Software Solutions for Seismic SHM of Hospitals." In *Seismic Structural Health Monitoring*, edited by Maria Pina Limongelli and Mehmet Çelebi, 279–300. Springer Tracts in Civil Engineering. Cham: Springer International Publishing. [https://doi.org/10.1007/978-3-030-13976-6\\_12](https://doi.org/10.1007/978-3-030-13976-6_12).
- [5] Gentile, C., Antonello, R., and Saisi, A. (2019). "Continuous Dynamic Monitoring to Enhance the Knowledge of a Historic Bell-Tower." *International Journal of Architectural Heritage* 13 (7): 992–1004. <https://doi.org/10.1080/15583058.2019.1605552>.
- [6] Cavalagli, N., Comanducci, G., and Ubertini, F. (2018). "Earthquake-Induced Damage Detection in a Monumental Masonry Bell-Tower Using Long-Term Dynamic Monitoring Data." *Journal of Earthquake Engineering* 22 (sup1): 96–119. <https://doi.org/10.1080/13632469.2017.1323048>.
- [7] Ubertini, F., Cavalagli, N., Kita, A., and Comanducci, G. (2018). "Assessment of a Monumental Masonry Bell-Tower after 2016 Central Italy Seismic Sequence by Long-Term SHM." *Bulletin of Earthquake Engineering* 16 (2): 775–801. <https://doi.org/10.1007/s10518-017-0222-7>.
- [8] Balducci, A., 2005. "Dissipative Towers". Application n. EP20100747238, PCT n. WO2010EP62748 20100831, International and European classification E04H9/02 – Italian concession n° 0001395591.
- [9] Balducci, A., and Castellano, M. G. (2015). "Adeguamento sismico del liceo Varano di Camerino mediante sistema a torri dissipative." *Progettazione Sismica*, no. 01: 69–91. <https://doi.org/10.7414/PS.6.1.69-91>.
- [10] Gara, F., Carbonari, S., Roia, D., Balducci, A., and Dezi L. (2021). "Seismic retrofit assessment of a school building through operational modal analysis and f.e. modelling". *J. Struct. Eng. (ASCE)*. doi:10.1061/(ASCE)ST.1943-541X.0002865.
- [11] Verhaegen, M. (1994). "Identification of the Deterministic Part of MIMO State Space Models given in Innovations Form from Input-Output Data." *Automatica* 30 (1): 61–74. [https://doi.org/10.1016/0005-1098\(94\)90229-1](https://doi.org/10.1016/0005-1098(94)90229-1).
- [12] Van Overschee, P., and De Moor, B. (1996). *Subspace Identification for Linear Systems*. Boston, MA: Springer US. <https://doi.org/10.1007/978-1-4613-0465-4>.
- [13] Ceravolo, R., Matta, E., Quattrone, A., and Zanolli Fragonara, L. (2017). "Amplitude Dependence of Equivalent Modal Parameters in Monitored Buildings during Earthquake Swarms: Amplitude Dependence of Modal Parameters in Monitored Structure." *Earthquake Engineering & Structural Dynamics* 46 (14): 2399–2417. <https://doi.org/10.1002/eqe.2910>
- [14] Skolnik, D., Lei, Y. Yu, E., and Wallace., J. W. (2006). "Identification, Model Updating, and Response Prediction of an Instrumented 15-Story Steel-Frame Building." *Earthquake Spectra* 22 (3): 781–802. <https://doi.org/10.1193/1.2219487>.
- [15] García-Illescas, M. Á., Murià-Vila, D., and Alvarez-Icaza, L. (2019). "Monitoring and Identification of Vibration Frequencies on a Portion of México City Metro Line 12." *Advances in Civil Engineering* 2019 (July): 1–13. <https://doi.org/10.1155/2019/4128320>.



- [16] Boroschek, R. L. (2013). "Structural Health Monitoring Performance During the 2010 Gigantic Chile Earthquake." In *Earthquakes and Health Monitoring of Civil Structures*, edited by Mihail Garevski, 197–216. Springer Environmental Science and Engineering. Dordrecht: Springer Netherlands. [https://doi.org/10.1007/978-94-007-5182-8\\_8](https://doi.org/10.1007/978-94-007-5182-8_8).
- [17] Tamariz, A.D.R., Bottura, C.P., and Barreto, G. (2005). "Iterative MOESP Type Algorithm for Discrete Time Variant System Identification." In *Proceedings of the 2005 IEEE International Symposium on, Mediterrean Conference on Control and Automation Intelligent Control*, 2005., 399–404. Limassol, Cyprus: IEEE. <https://doi.org/10.1109/2005.1467048>.
- [18] Robles, A. E., and Giesbrecht, M. (2018). "N4SID-VAR Method for Multivariable Discrete Linear Time-Variant System Identification." In *Proceedings of the 15th International Conference on Informatics in Control, Automation and Robotics*, 502–9. Porto, Portugal: SCITEPRESS - Science and Technology Publications. <https://doi.org/10.5220/0006907505020509>.
- [19] Loh, C., and Chen, J. (2017). "Tracking Modal Parameters from Building Seismic Response Data Using Recursive Subspace Identification Algorithm: Tracking Modal Parameters Using Recursive Subspace Identification." *Earthquake Engineering & Structural Dynamics* 46 (13): 2163–83. <https://doi.org/10.1002/eqe.2900>.
- [20] Kavrakov, I., Ahsan K., and Morgenthal, G. (2020). "Comparison Metrics for Time-Histories: Application to Bridge Aerodynamics." *Journal of Engineering Mechanics* 146 (9): 04020093. [https://doi.org/10.1061/\(ASCE\)EM.1943-7889.0001811](https://doi.org/10.1061/(ASCE)EM.1943-7889.0001811).
- [21] Gara F., Arezzo D., Nicoletti V., Carbonari S. "Monitoring of the Modal Properties of a RC School Building During the Central Italy Seismic Swarm." *Journal of Structural Engineering (ASCE)* 147(7):05021002. [https://doi.org/10.1061/\(ASCE\)ST.1943-541X.0003025](https://doi.org/10.1061/(ASCE)ST.1943-541X.0003025).

## FIRST RESULTS OF LONG-TERM MONITORING OF PORTICO VARANO IN THE CAMERINO DUCAL PALACE (ITALY)

Leonardo Cipriani, Andrea Dall'Asta, Graziano Leoni,  
Michele Morici, Alessandro Zona

University of Camerino, School of Architecture and Design  
Viale della Rimembranza 3, 63100 Ascoli Piceno, Italy  
{leonardo.cipriani, andrea.dallasta, graziano.leoni, michele.morici, alessandro.zona}@unicam.it

---

### Abstract

*Portico Varano in the Ducal Palace of Camerino (Italy) is a Renaissance monumental quadriporticus that was severely damaged by the Central Italy earthquakes in 2016. Within the field activities for saving cultural heritage foreseen within a recent European research project, a long-term static and dynamic monitoring system was installed in October 2020. Through a series of accelerometers, the monitoring system allows to track the evolution of the modal parameters of the structure, namely frequency, damping ratio and modal shapes, and investigate the effects of environmental conditions on the building dynamics. Furthermore, a series of displacement transducers installed on the vaults of the courtyard allows controlling the evolution of the crack patterns. In this paper, the design and installation of the monitoring system as well as some first results are presented and discussed.*

**Keywords:** Operational Modal Analysis, Structural Health Monitoring, Cultural Heritage Buildings, Ambient Vibrations, Dynamic System Identification.

---

## 1 INTRODUCTION

The Italian architectural heritage is constituted by a wide number of historical masonry constructions such as churches, towers, buildings, and fortresses, characterized by both structural and typological vulnerabilities, which are often responsible for their poor seismic performance, e.g. [1-3]. Such situation is unfortunately periodically confirmed by the damage observed after the occurrence of seismic events, inevitable reminders of the high seismic risk of the Italian peninsula.

The analysis of the seismic vulnerability of architectural heritage requires an integrated approach where different disciplines provide indispensable contributions: historic investigations of the construction evolution; survey of the construction; in situ experimental testing and characterization of the materials; structural modelling and seismic analysis. Such contributions do not necessarily have a predetermined chronological sequence, given that the results of one of them influence the development of the investigations of the other three [4]. Among the various possibilities for experimental testing, dynamic testing under service conditions, commonly referred as Operational Modal Analysis (OMA), e.g. [5], constitute a very effective tool for structural identification and model updating, essential tools to support model-based simulation for the prediction of the seismic response of heritage constructions as well as for the calibrations of advanced seismic upgrading interventions, e.g. [6]. Examples of recent structural monitoring studies in the Italian architectural heritage include: the Consoli Palace in Gubbio [7], the church of Santa Maria in Collemaggio in L'Aquila [8], the San Pietro bell-tower in Perugia [9], the Milan Cathedral [10], the San Vittore bell-tower in Arcisate [11], and the Rubbianello Bridge [12].

This paper adds to the above list and presents the first results from a structural monitoring system installed in the quadriporticus of the Ducal Palace in Camerino, within the field activities planned in the European research project named ARCH (Advancing resilience of historic areas against climate-related and other hazards - <https://savingculturalheritage.eu/>) funded in the Horizon 2020 framework for the years 2019-2022. The objective of the ARCH project is the evaluation of the resilience of the historical centres and the risk management related to climate change and other natural disasters.

## 2 THE DUCAL PALACE IN CAMERINO

The Ducal Palace (Figure 1) is one of the main Renaissance monuments of the city of Camerino, located in Central Italy in the inner Apennine area of the Marche Region, about 65 km from the Adriatic Coast, 70 km from the city of Perugia and 190 km from Rome. The building hosted the headquarters of the University of Camerino before the 2016 Central Italy seismic events. The nucleus has ancient origins, remodelled at the end of the XIV century and completed in the second half of the XV century under Giulio Cesare da Varano. Over the centuries, the layout of the Palace underwent many modifications thanks to acquisitions that led to the incorporation of other surrounding buildings. These caused a continuous structural reorganization and maintenance works, resulting in a very complex and densely stratified palace. Continuous interactions between the building and the city led to architecture and urban spaces that were mutually conditioned. For this reason, the Ducal Palace is also defined as “part of the city”.

The quadriporticus courtyard (Figure 1a,e), also called Portico Varano or Sottocorte, probably designed by the great military architect Baccio Pontelli, is the central architectural element around which the palace is organized. Before the damages following the 2016 Central Italy earthquakes, the quadriporticus courtyard played a key role in the social life of the academic community of the University of Camerino.

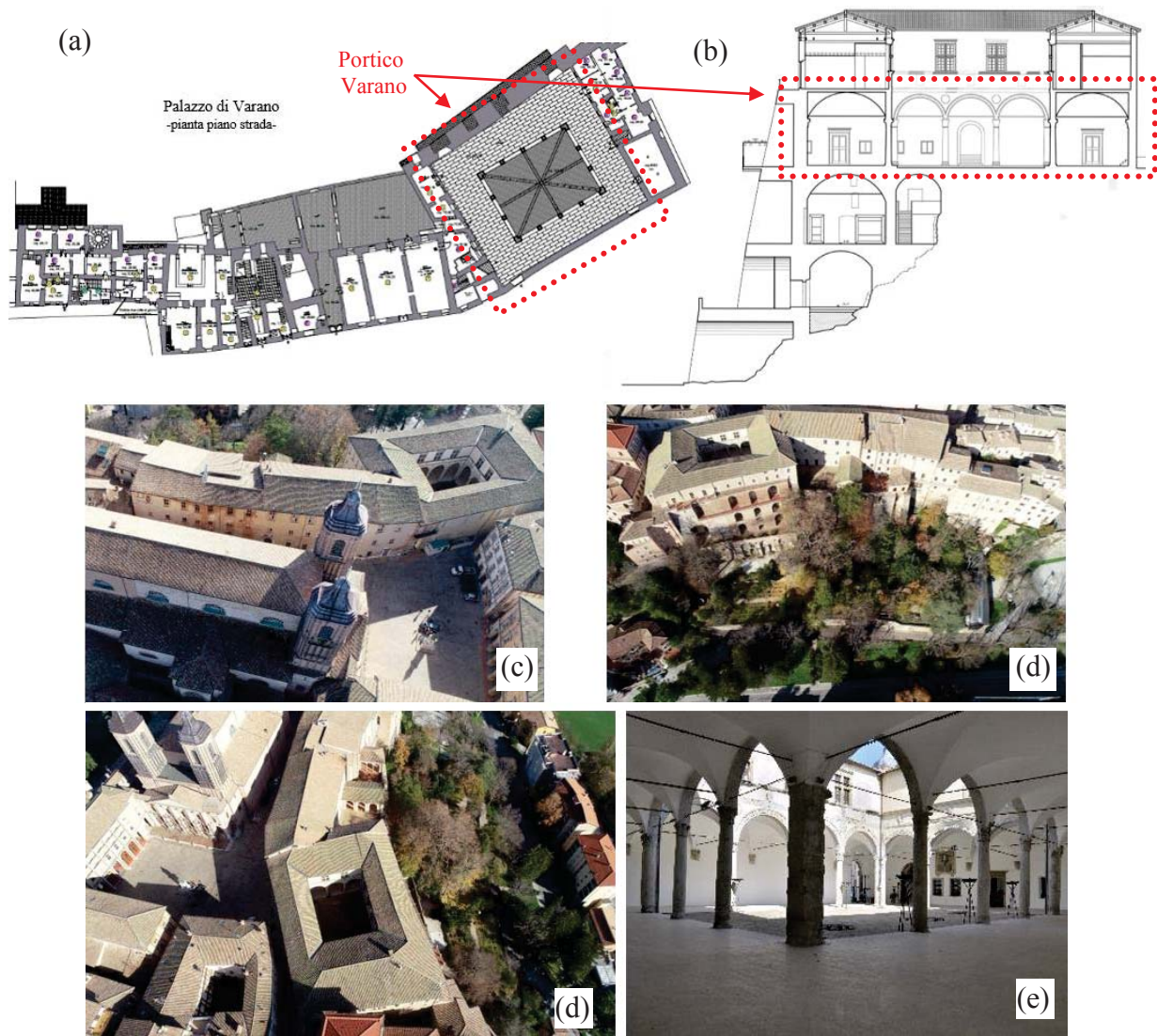


Figure 1: Ducal Palace Camerino, Italy (a) layout at the street level; (b) vertical section; (c) aerial view from the North-West side (d) aerial view from South-East; (d) aerial view from South-West; (e) view of the inner courtyard from the North corner of the quadriporticus.

After the latest seismic sequence that hit central Italy from August 2016 to January 2017, the structural vulnerabilities of the Ducal Palace were exposed, with damage observed both in the elevation structures and in the floors (for example some sample photos are shown in Figure 2). Damages in the vault of the quadriporticus, and in the perimeter walls interdicted the public access to the Ducal Palace and required safety measures (Figure 2). In addition, important damages concerned non-structural element with detachment of internal plaster and cracks in the “camorcanna” ceilings, some of them decorated with fresco paintings.





Figure 2: Examples of the damages in “Portico Varano” after the 2016 Central Italy earthquakes.

### 3 MONITORING SYSTEM AND FIRST RESULTS

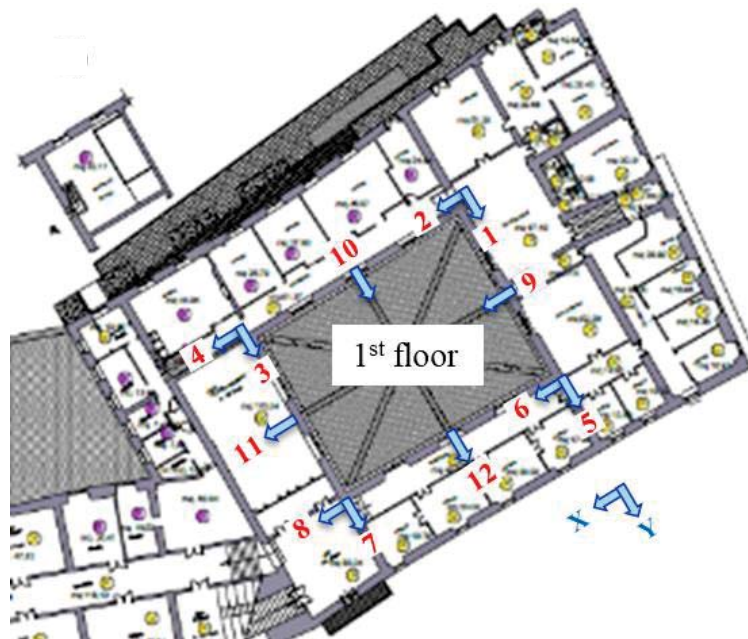
#### 3.1 Preliminary monitoring system and dynamic characterization

The Ducal Palace is a very complex case study and reliable structural models were not available in the first stage of the field activities foreseen in the ARCH project. For this reason, preliminary structural monitoring tests were made in June 2020 in order to provide a characterization of the dynamic behaviour of the quadriporticus under ambient-induced vibrations to support the first evaluations on its structural behaviour.

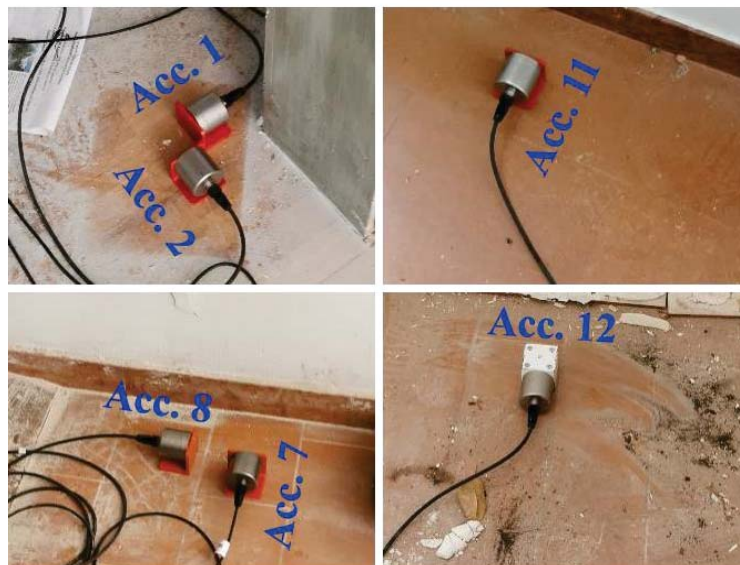
The instrumentation adopted during this preliminary experimental campaign consisted of 12 uniaxial high sensitivity piezoelectric accelerometers (PCB model 393B31) connected through high-quality shielded coaxial cables to the acquisition system (National Instruments cDAQ-9178 installed with NI 9234 analogue-to-digital converters) controlled through a Dell Precision 7540 laptop running National Instruments Signal Express software. The accelerometers were placed on the first floor as depicted in Figure 3 in order to provide a comprehensive description of its horizontal motion, given that such floor cannot be realistically modelled as a rigid diaphragm due to its geometry and materials. The adopted configuration was possible given that the interested portions of the first floor were safely accessible. Other configurations keeping some of the accelerometers as fixed (reference sensors) and the other as roving sensors, e.g. [5], were not explored given the major difficulties in a safe accessing other areas of the same floor and the impossibility of a safe access to the roof level just above the first floor. Data acquisition was performed at 2048 Hz for about 30 minutes. This duration corresponds to more than 4000 times the fundamental period of the building, as suggested in [7]. Afterwards, the signals were pre-processed to remove the linear trend by subtracting the logged signal with a zero-degree polynomial, filtering with a low-pass filter with a cut-off frequency



of 49 Hz, and a resampling at a frequency of 102.4 Hz to reduce the amount of data and to make subsequent analyses faster.



(a)



(b)

Figure 3: Configuration of the installed 12 accelerometers in preliminary monitoring: (a) position of sensors; (b) example of installations.

The identification of the modal parameters (frequencies and damping ratios) was carried out by the Covariance data driven - Stochastic Subspace Identification (SSI/Cov) [5][14]. Figure 4 shows the stabilization diagram obtained from the tests, where the identification of the stable modes indicated on the graph by a solid black circle, was carried out considering a difference less than 1% in frequency and a MAC greater than 95% on mode shape. The first mode is essentially a translational mode along the X-direction and has an estimated frequency 3.36 Hz (period 0.298 s) and damping ratio 1.86%. The second mode is essentially a transla-

tional mode along the Y-direction and has an estimated frequency 4.52 Hz (period 0.221 s) and damping ratio 3.71%.

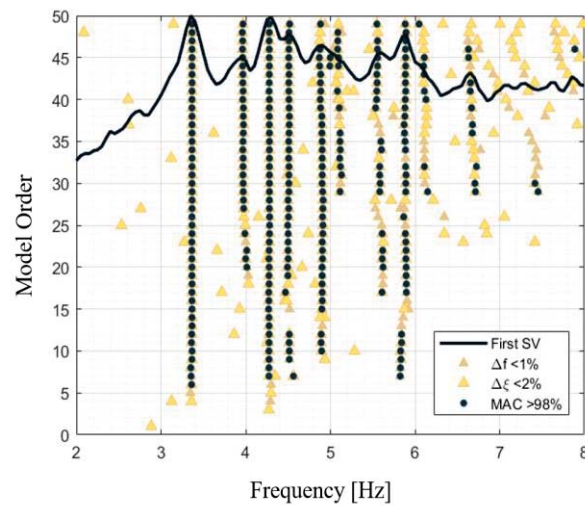


Figure 4: Results of preliminary monitoring (June 2020): Stabilization diagram.

### 3.2 Long-term monitoring system and first results of continuous monitoring

The results of the preliminary structural monitoring made in June 2020 provided the support for the definition of a simpler configuration using a limited number of accelerometers in order to reduce the data to be stored and processed. Given that the larger accelerations were measured in points 9, 10, 11 and 12 (according to Figure 3) and that such sensors were able to identify the first modes, the selected configuration for long-term monitoring uses four accelerometers located as depicted in Figure 5a. The adopted accelerometers are uniaxial high sensitivity piezoelectric accelerometers (PCB model 393B31). Environmental parameters are monitored using an independent system comprising two wireless sensors for internal temperature and relative humidity (Elitech RC-51H) as well as a weather station for temperature, relative humidity, wind speed and direction (WatchDog 2700) located just outside the Ducal Palace (Figure 5b). In addition, a triplet of linear potentiometers (Gefran model PZ67-A) were installed across the cracks in the cross vaults in order to measure their movements (Figure 5a). The configuration of the displacement transducers is composed by three linear potentiometers placed across the vaults connected by two galvanised metal sheets (2 mm thickness) to follow the curvature of the vaulting. Each pair of linear potentiometers forms an angle of 60 degrees. Such configuration permits to evaluate every motion of the cracks, such as side scrolling or stretching movements leading to an opening of the crack itself (Figure 6). Besides, image-based monitoring, e.g. [15], is being evaluated to possibly complement contact sensors.

Both accelerometers and linear potentiometers were connected through high-quality shielded cables to the acquisition system (National Instruments cRIO 9045 installed with NI 9234 analogue-to-digital converters for acquiring accelerometers and NI 9209 for acquiring potentiometers). The acquisition procedure was developed in the cRIO 9045 using the programming environment National Instruments LabView to control the entire process, i.e., 30-minute time logging every 2 hours, local data storage, data transfer on cloud storage accessible for remote verifications. The procedure is characterized by a continuous data acquisition of the data and a timing control that activate the logging data; within the logging cycle there is another timing control that stops the logging procedure when the assigned time elapsed. To optimize the accelerometers and linear potentiometers acquisition, the physical channels defi-

nition were divided into two parallel cycles with specific sample clock to synchronize the analogue to digital converters modules (Figure 7).

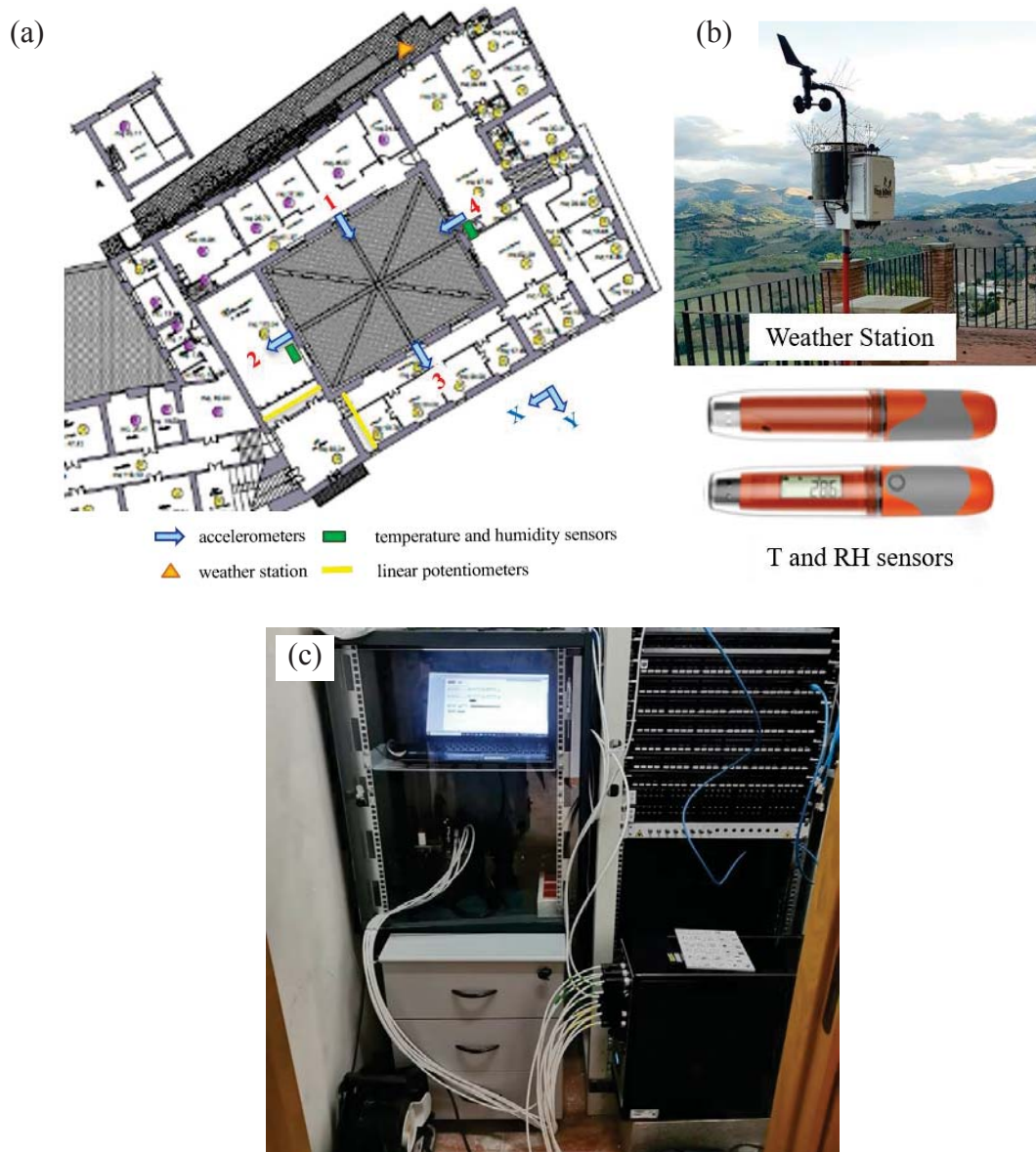


Figure 5: (a) configuration of the sensors position; (b) environmental sensors; (c) acquisition system (laptop, data acquisition module with AD converters, and signal conditioner for linear potentiometers).

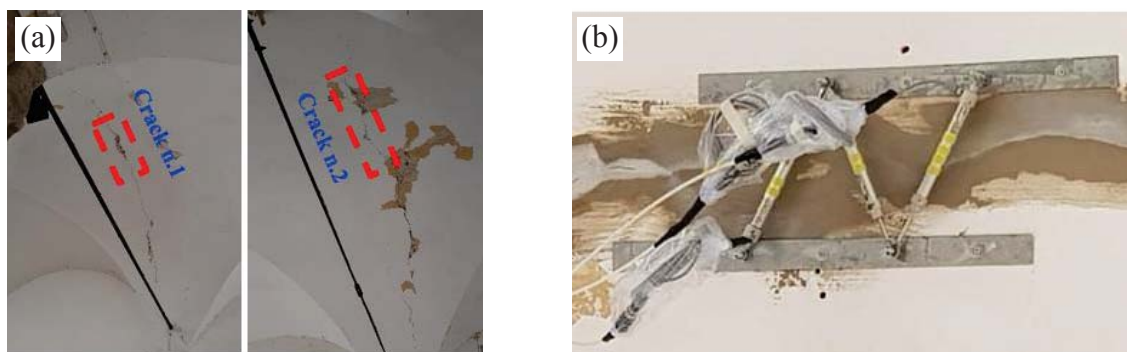


Figure 6: (a) survey of the monitored cracks; (b) arrangement of the triplet of linear potentiometers.



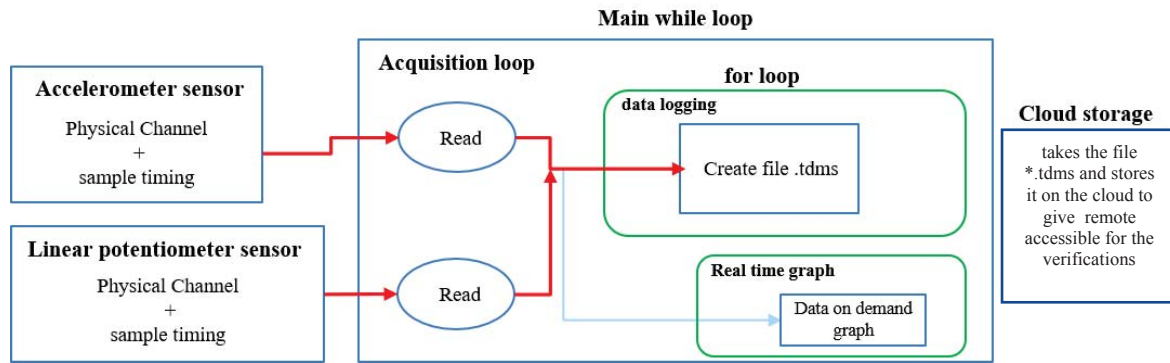


Figure 7: Schematization of the acquisition procedure.

The analysis of the first results is based only on the first month (October 2020) of acquisition of the long-term monitoring system. If attention is focused on the two translation modes identified in the preliminary monitoring described in the previous paragraph, then the results indicate a rather stable trend of the frequencies (Figure 8) with some points missing when the instrument noise was comparable with the background environmental accelerations, making the results of post-processing unreliable. In fact, it should be remarked that the historical centre of Camerino is still a restricted area following the major damages after the 2016 Central Italy earthquakes; this condition makes the area characterized by very low level of environmental noise during the day (a condition possibly exacerbated by the current pandemic restrictions) and even more during the night. At this regard, Figure 9 compares the power spectral density of the signal provided by the same accelerometer in the evening and daytime this highlights the large variation of the signal intensity over the day. Some recordings were excluded in the post-processing because instrument noise was comparable with the environmental accelerations.

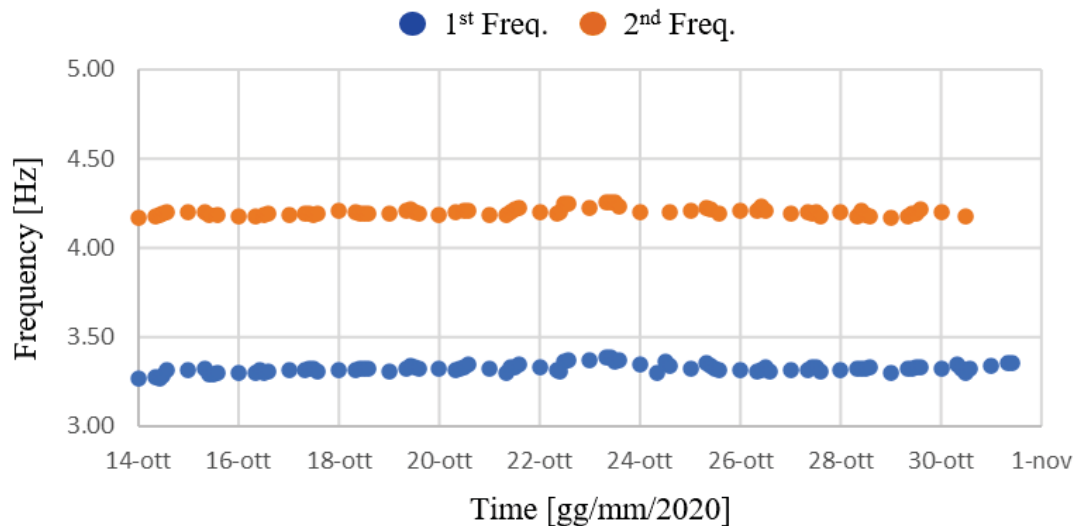


Figure 8: Monitored eigenfrequencies in the first month (October 2020).

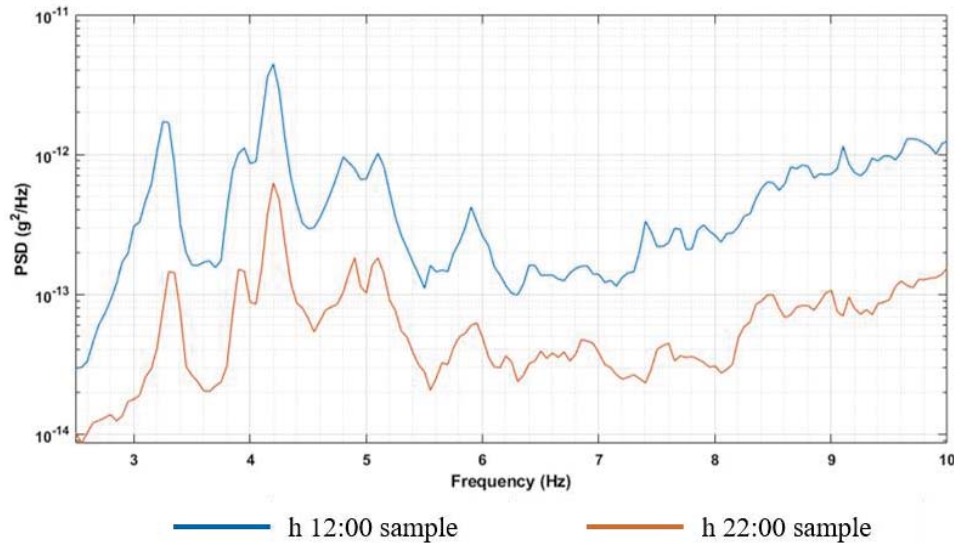


Figure 9: Comparisons of Power Spectral Densities during daylight and at night.

#### 4 CONCLUSION

This paper described the long-term monitoring system designed and installed in the Portico Varano, the quadriporticus of the Ducal Palace in Camerino (Italy), damaged after the 2016 central Italy earthquakes. The system comprises four high sensitivity accelerometers (whose position was selected after preliminary vibration monitoring tests using twelve accelerometers), a triplet of linear potentiometers installed across the most critical crack in the most damaged cross vault, and environmental sensors (temperature, relative humidity, wind speed and direction). The accelerometers permits to observe the natural frequencies of vibration and relevant mode shapes and damping, providing essential information on the evolution over time of the main structural properties and their variation that can be correlated to the level of damage. The displacement transducers complement the information gained through the accelerometer with a direct measure of the variations of the width of the cracks. The environmental sensors allows to separate the contribution caused by the changes in the temperature and humidity to those related to structural damages as well as the relations between wind intensity and induced structural vibrations. Data recording started in October 2020 and some initial results were discussed. It is observed that the low level of measured vibrations due to restricted access to the Camerino city centre (given the safety concerns after the occurred seismic damages and possibly exacerbated by the current pandemic crisis) poses major challenges to long-term monitoring and enforces the use of high-quality and high-sensitivity sensors connected using highly shielded wires. Nevertheless, stable results were observed during the monitoring time window, constituting a first set of data that could be an essential tool to support model-based simulation for the prediction of the seismic response of the Ducal Palace as well as for the optimal calibrations of the required seismic upgrading interventions.

#### ACKNOWLEDGEMENTS

This work is a part of the ARCH project. ARCH has received funding from the European Union's Framework Programme for Research and Innovation (Horizon 2020) under grant agreement No 820999. The contents of this publication are the sole responsibility of University of Camerino and do not necessarily reflect the opinion of the European Union.



## REFERENCES

- [1] V. Despotaki, V. Silva, S. Lagomarsino, I. Pavlova, J. Torres, Evaluation of Seismic Risk on UNESCO Cultural Heritage sites in Europe. *International Journal of Architectural Heritage*, **12**, 1231-1244, 2018.
- [2] F. Doglioni, A. Moretti, V. Petrini, P. Angeletti, *Le Chiese e il Terremoti: Dalla Vulnerabilità Constatata nel Terremoto del Friuli al Miglioramento Antisismico nel Restauro, Verso una Politica di Prevenzione*. Edizioni Lint, Trieste, Italy, 1994.
- [3] C. Canuti, S. Carbonari, A. Dall'Asta, L. Dezi, F. Gara, G. Leoni, M. Morici, E. Petrucci, A. Prota, A. Zona, Post-earthquake damage and vulnerability assessment of churches in the Marche region struck by the 2016 Central Italy seismic sequence. *International Journal of Architectural Heritage* 2019. DOI: 10.1080/15583058.2019.1653403
- [4] A. Dall'Asta, G. Leoni, A. Meschini, E. Petrucci, A. Zona, Integrated approach for seismic vulnerability analysis of historic massive defensive structures. *Journal of Cultural Heritage* **35**(1), 86-98, 2019.
- [5] R. Brincker, C. Ventura, *Introduction to operational modal analysis*. Wiley, 2015.
- [6] A. Pavia, F. Scozzese, E. Petrucci, A. Zona, Seismic upgrading of a historical masonry bell tower through an internal dissipative steel structure. *Buildings*, **11**(1), 24, 2021.
- [7] A. Kita, N. Cavalagli, F. Ubertini. Temperature effects on static dynamic behaviour of Consoli Palace in Gubbio, Italy. *Mechanical Systems and Signal Processing*, **120**, 180-202, 2019.
- [8] F. Potenza, F. Federici, M. Lepidi, V. Gattulli, F. Graziosi, A. Colarieti, Long-term structural monitoring of damaged Basilica S. Maria di Collemaggio through a low-cost wireless sensor network. *Journal of Civil Structural Health Monitoring*, **5**(5), 655-676, 2015.
- [9] F. Ubertini, G. Comanducci, N. Cavalagli, Vibration-based structural health monitoring of a historic bell-tower using output-only measurements and multivariate statistical analysis. *Structural Health Monitoring*, **15**(4), 438-457, 2016.
- [10] C. Gentile, A. Ruccolo, F. Canali, Continuous monitoring of the Milan Cathedral: dynamic characteristics and vibration-based SHM. *Journal of Civil Structural Health Monitoring*, **9**(5), 671-688, 2019.
- [11] A. Cabboi, C. Gentile, A. Saisi, From continuous vibration monitoring to FEM-based damage assessment: application on a stone-masonry tower. *Construction and Building Materials*, **156**, 252-265, 2017.
- [12] F. Scozzese, L. Ragni, E. Tubaldi, F. Gara, Modal properties variation and collapse assessment of masonry arch bridges under scour action. *Engineering Structures*, **199**, 109665, 2019.
- [13] L. Ragni, F. Scozzese, F. Gara, Dynamic identification and collapse assessment of Rubbianello Bridge. *IABSE Symposium: Towards a Resilient Built Environment Risk and Asset Management*. Guimaraes, Portugal, 27-29 March 2019.
- [14] B. Peeters, G. De Roeck, Reference-based stochastic subspace identification for output-only modal analysis. *Mechanical systems and signal processing*, **13**(6), 855-878, 1999.
- [15] A. Zona, Vision-based vibration monitoring of structures and infrastructures: an overview of recent applications. *Infrastructures*, **6**(1), 4, 2021.

## DEVELOPMENT OF LOW COST SENSORS FOR MONITORING OF STRUCTURES

**Giuseppe Maddaloni<sup>1</sup>, Alessandra De Angelis<sup>1</sup>, Francesco Minicozzi<sup>1</sup>, Claudio Martino<sup>2</sup> and Maria R. Pecce<sup>1</sup>**

1. Department of Engineering, University of Sannio  
Piazza Roma 21, Benevento-Italy  
e-mail: {maddaloni, adeangelis, francesco.minicozzi, pecce}@unisannio.it

2. Istituto Nazionale di Geofisica e Vulcanologia (INGV)  
Osservatorio Vesuviano, via Diocleziano 328, Naples-Italy  
e-mail: martino.claudio@gmail.com

---

### Abstract

*In the last years, in Italy, due to the recent catastrophic collapses, an increasing amount of resources has been invested in the maintenance of existing infrastructures. In particular, the monitoring of the structural “health” has assumed a crucial role in the assessment of structures and infrastructures. The technological advancement obtained in the field of informatics and electronic has allowed to move from a discrete and partial control of the structural conditions to a continuous and complete Structural Health Monitoring (SHM). Different techniques may be applied and the Operational Modal Analysis (OMA), among others, aims at identifying the health status of the structure by the modal properties when is under its operating conditions. This paper compares the results of OMA technique using the vibration data obtained by two different sensors equipment applied to an existing bridge located in Benevento, Italy. A dynamic test was performed in 2020 by using a low cost experimental equipment specially designed and developed by the University of Sannio. The tests results have been compared with the data obtained on the same bridge in 2018 by using a commercial and more expensive sensors equipment. The main purpose of the comparison is to support the “homemade” equipment development identifying the aspects on which to improve the same.*

**Keywords:** SHM, OMA, low cost sensors, data processing.

---

## 1 INTRODUCTION

A large number of road infrastructures has widely overcome 50 years of service design life and need urgent prevention and control measures. Following the critical events occurred in the last years to several highway infrastructures, the issue of their maintenance has assumed a primary role [1]. The interest is very significant since they are not single punctual elements but are part of a more extensive network. Hence, the potential disruption could have exceptional consequences in both the economic and social sides, proportionally to the importance of the infrastructure itself. Structural damage depends on several elements as, among others, quality and type of materials, age, construction techniques, loads level and environmental conditions. Generally, degradation or damaging phenomena can be responsible to modify the mechanical properties of the materials [2]. In reinforced concrete elements, the corrosion of the steel bars is the main cause of degradation phenomena. Due to the porosity of concrete, some chemicals including carbon dioxide, oxygen and water, can penetrate the material triggering the carbonation process. Chloride ions, if passing a critical concentration threshold [3], perforate the protective oxide film surrounding the rebars, starting the corrosion phenomena. The latter case is typical of bridges that are subjected to winter frosts and are generally kept operational using de-icing salts. The same is true for all those structures located in coastal areas or directly exposed to seawater [4].

From here, the necessity of checking the “structures health” by using effective monitoring systems. The most appropriate monitoring system depends on many factors. Traditional checking and monitoring methods for infrastructures rely on visual inspections, but they often lead to a temporary interruption of use and must be carried out by highly qualified personnel. Furthermore, mainly due to the subjectivity of the evaluation, it is difficult, using this technique, to obtain an effective monitoring over time [5]. Hence, with the main target to provide automatic tools useful for observing the evolution of degradation phenomena in support of traditional techniques, many others elaborate methods were developed [6, 7]. When the devices that allow the loading and damaging condition of a structure to be recorded, analyzed, localized and predicted, become an integral part of the structure, the monitoring approach is called Structural Health Monitoring (SHM) [8]. The SHM is a process based on a series of axioms [9] and phases [10] widely applied in various engineering sectors due to its ability to respond to adverse structural changes, improving structural reliability and life cycle management. To implement a SHM system, several components, such as sensors, data acquisition, transmission system and software for data processing, are needed. By analyzing data collected from sensors, it is possible to identify any damaging in progress and evaluate the structural performance both in operating and in exceptional (e.g. earthquakes or after earthquakes) conditions. The number of sensors to use depends on the structural dimension. For long structure as a bridge, it can represent a very expansive cost. For this reason, the development of low cost and easy to install sensors can be a fundamental target in the SHM applications. This work shows the results obtained by applying a network of nine prototype accelerometer sensors with these characteristics to an existing RC bridge located in south Italy.

## 2 OPERATIONAL MODAL ANALYSIS

The dynamic behavior of a structure depends on mass, stiffness, damping and nevertheless by external and internal constraints. These properties give information about the free vibration response, therefore, if they do not change (e.g., as a result of structural damages), the dynamic characteristics remain the same. Generally speaking, the analysis of the dynamic behavior of a structure can be addressed using analytical or experimental approaches. For bridges, the most used technique in experimental approaches is the Operational Modal Analysis (OMA). It allows to identify the modal parameters of the structures [11, 12, 13] based on vibration data collected when the structure is under its operating conditions, i.e., vehicular traffic, wind, etc. It relies on a series of basic assumptions such as linearity, stationarity, observability [14, 15]. OMA test is a suitable technique for SHM because interruption of the structure use is not required. Sensors can be permanently installed to identify changes in the dynamic properties. On the other hand, unknown load conditions can make it more difficult for the processing phase. Over the last few decades, several mathematical methods have been developed to determine the modal parameters of the structure by OMA methodology (time or frequency domain, SDOF or MDOF methods, etc.).

In frequency domain, the Frequency Domain Decomposition (FDD) consists of the identification of the peaks of the Power Spectral Density (PSD) matrix of output. The basic assumption is that the resonance response is dominated by the contribution of the mode whose natural frequency is closest [16]. The contribute of the other modes is negligible, and therefore, FDD is classified as SDOF method. This method gives good results for structures having well-separated modes and with non-negligible damping. FDD method relies on the Singular Value Decomposition (SVD) of the PSD matrix at a specific frequency  $f$  [17] and allows to define resonance frequencies and mode shapes, but not modal damping. Modal damping ratio can be found by using the so-called Enhanced Frequency Domain Decomposition (EFDD) method. It is an improvement of the FDD method that uses the singular vector defined in FDD application but relies on the so-called Modal Assurance Criterion (MAC) that allow to compare the modes shape  $\{\phi_r\}$ . The MAC number is defined as:

$$MAC(\{u_j\}; \{\phi_r\}) = \frac{|\{u_j\}^H \{\phi_r\}|^2}{(\{u_j\}^H \{u_j\}) (\{\phi_r\}^H \{\phi_r\})} \quad (1)$$

where  $\{u_j\}$  is the generic singular vector closed to the peak response corresponding to the  $r$ -th mode  $\{\phi_r\}$  and  $H$  is the symbol to indicates the conjugate and transpose operator. MAC is a useful statistical indicator for the quantitative comparison between modal vectors. It ranges between 0, namely the modes are completely unrelated and 1 which means that the modes perfectly match [18]. Finally, the Curve-Fitting Frequency Domain Decomposition (CFDD) is a parametric technique that relies on the curve-fitting of the PSD function in the frequency domain. Consequently, a more accurate estimation of frequencies and damping ratios is obtained [19].

Time-domain methods are based on the analysis of time histories or correlation functions. The most used is the Stochastic Subspace Identification (SSI) which most common declinations are the Unweighted Principal Component (SSI-UPC) and the Principal Component (SSI-PC). The difference between the SSI approaches is the weight matrixes to use for the determination of the observability matrix. Indeed, in SSI method the projection of the future unto the past (respectively the lower and the upper part of the Block Hankel matrix) defines a matrix so called "O" which columns represent a stacked free decay of the system to a set of unknown initial conditions. Since the observability matrix is unknown it is necessary to pre and post-multiply the matrix O by the so-called weight matrixes and then to apply the SVD to it [20].



### 3 THE CASE STUDY

The results of OMA technique using the vibration data obtained by two different experimental sensors equipment applied to an existing bridge located in Benevento (Italy), are herein proposed and compared. The case study is the so-called San Nicola Bridge, located in Benevento as part of the main street S.S. 90 bis and spans river San Nicola (Figure 1).



Figure 1 – *San Nicola Bridge. Global (left) and street (right) views*

The bridge was designed by the famous engineer Riccardo Morandi between 1952 and 1955 and built between 1955 and 1956. The static scheme is a portal frame composed by one main span 80.0 m long and two cantilevers of 20.0 m (Figure 2). The deck consists of four prestressed box-girders, whose webs vary in thickness, from a minimum of 13 cm at the midspan, to a maximum of 30 cm at the supports, and it is supported by two piers 9.40 m high and linked to the foundations underneath by hinges made of steel rebars. Each pier consists of eight columns of rectangular section, 40.0 cm thick and variable width from 1.50 m at the base to 4.00 m at the top, that are connected at the base and top by a transverse beam. The width of the upper slab is 9.00 m and consists of two traffic lanes, 7.00 m width, and two sidewalks 1.00 m width on both sides. Plan and prospectus of the bridge are reported in Figure 3.



Figure 2 – *Bridge pier (left), bridge deck (right)*



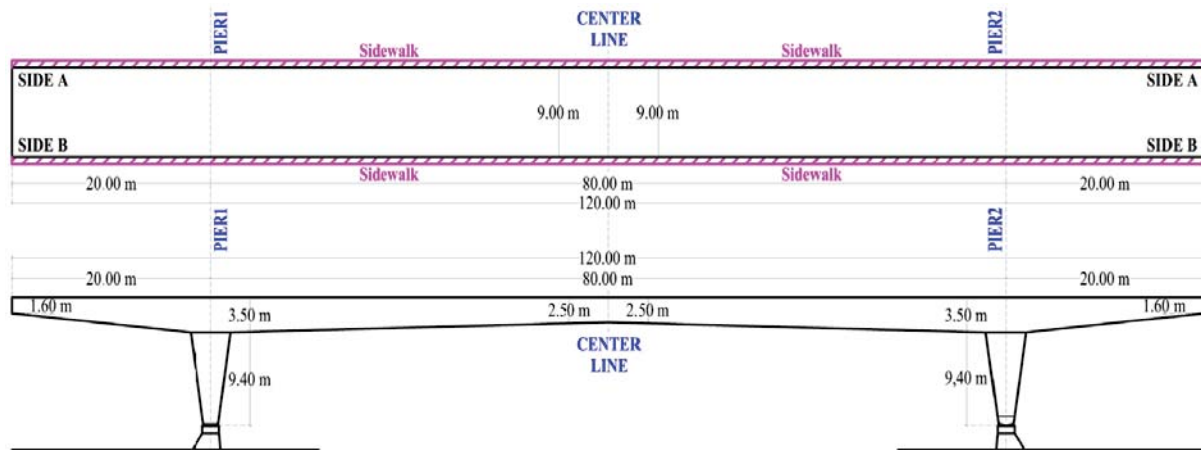


Figure 3 – San Nicola bridge plan and prospectus view

Following the collapse of the Polcevera viaduct (designed by the same engineer Riccardo Morandi) occurs in Genoa (Italy) on 14 August 2018, the bridge was closed as a preventive measure from August to December 2018. To determine the health status of the bridge, a series of tests were carried out by the Department of Engineering of the University of Sannio. In particular, a dynamic test to identify fundamental frequencies and mode shapes of the bridge was performed in 2018 and subsequently replicate in 2020. A finite element model has been also developed by CSiBridge software [21] using shell elements for the deck, frame elements for the piers and modelling the prestressing cables as tendon. Model calibration using the results coming from the experimental campaign was performed in [22]. Modal analysis results are reported in Figure 4. As evident, the first mode is transversal, with frequency 1.91 Hz, the second vertical (2.16 Hz) and the third torsional (4.16 Hz).

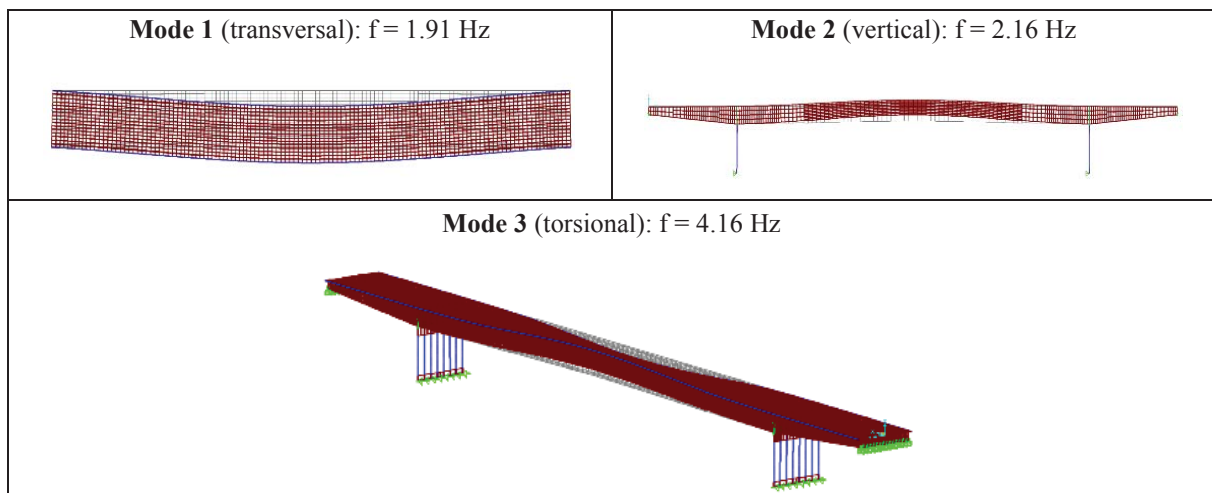


Figure 4 – Mode shapes and frequencies analysis results

#### 4 EXPERIMENTAL TESTS DESCRIPTION

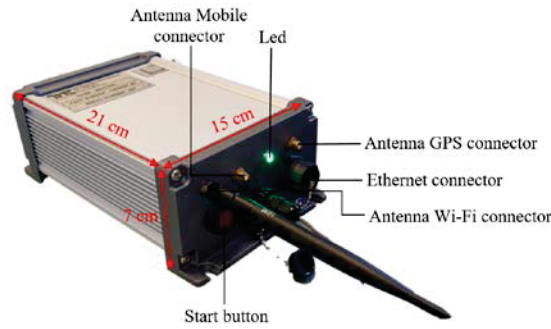
In 2018 and 2020, dynamic tests were performed on San Nicola Bridge by using a commercial and prototype experimental equipment respectively. For safety, in both cases the bridge was closed to traffic, that means vibrations were caused just by environmental noise. The recorded row data have been pre-processed by filtering and resampling operations by MATLAB [23] and subsequently analyzed by the specific software ARTeMIS [24] to find the modal parameters of the structure.

In particular, on December 2018, the test was performed by the commercial and certified equipment of SEQUOIA manufacturing [25]. The system consists of a network of five sensors (called GEA II sensor) connected by cables to a data acquisition device (DAQ) (Figure 5). Designed to permanent or semi-permanent installations, its size is about 60x30x40 cm for the DAQ device and about 11 cm of diameter for the sensors (Figure 5). The commercial cost of the equipment is about 50'000 euros.



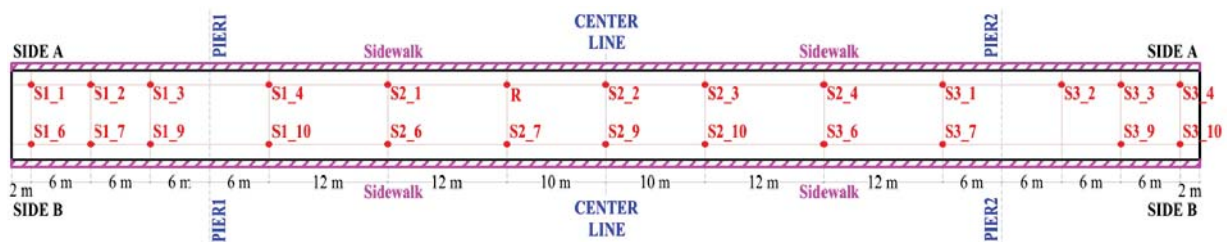
Figure 5 – GEA II sensors and DAQ

On September 2020, the dynamic test on the same bridge has been replicated by a prototype low-cost and no wired system (Figure 6) called SENTINEL properly developed by the Department of Engineering of the University of Sannio. The system consisted of a network of nine high sensitivity accelerometers capable to record structural vibrations. No data acquisition (DAQ) has been used: each device already has on board all that is needed to be an independent accelerometric station. The devices allow to set specific technical parameters as the sampling frequency (choosing between 125, 250, 500 and 1000 Hz), the full-scale range (choosing between 1, 2, 4 and 8 g), the file duration recording (the interval of data storing). The sensors are equipped with an internal battery, a micro-sd card slot, a router UMTS/WIFI, a GPS receiver, a microprocessor and a MEMS accelerometer (Figure 7). An autonomy of 24 hours recording time is guaranteed. The small size (21x15x7 cm) and the low weight (about 2 kg) of the device makes it very easy to manage. The assumed commercial cost for each prototype device is about 500 euros (a total cost equipment of about 5'000 euros is estimated).

Figure 6 – *SENTINEL* deviceFigure 7 – *SENTINEL* device components

The devices have been fixed to the deck of the bridge by two screws (Figure 8). Three different setups were performed modifying their position except for the reference sensor (R) that remained in the same position for the entire experimental campaign. In Figure 9, the position of the sensors for each setup is reported. To note that S means sensor, the first number indicates the setup, the second the id of the sensor; the reference sensor is identified by the letter R. The total number of the recorded points is 25. The spacing among sensor positions is from a minimum of 6 to a maximum of 12 meters for both sides of the bridge (A and B).

The signals have been recorded for 30 minutes for each setup at 125 Hz sampling rate.

Figure 8 – *Installation: device detail (left) and global view (right)*Figure 9 – *Position of sensors for each setup in the 2020 experimental campaign*

## 5 RESULTS OF THE EXPERIMENTAL CAMPAIGN USING PROTOTYPE EQUIPMENT

The dynamic characteristics of the bridge obtained by the experimental campaign performed in 2020 using the prototype equipment have been evaluated by the software ARTeMIS. In particular, the mode shapes associated with the first two modes (transversal and vertical modes respectively), obtained applying the FDD method and normalize to one magnitude, are represented in Figures 10 and 11 for both sides A and B of the bridge separately. The black and the red continues lines, indicated the undeformed and the mode shapes respectively. Specifically, mode shapes represented by the dashed red lines are the first result of the row data elaboration. As evident the mode shapes are not clearly defined that is are not well-separated from each others. This is due to the absence of a DAQ device with the specific assignment to synchronize starting record of a system with multiply measure points. This problem has been partially solved by knowing the instant of time at which the last sensor has started the recording and manually cutting all the data stored by the other stations before this time. Furthermore, due to hardware problems, the sampling frequency was not constant. Specifically, even if the sampling rate has been set the same for all devices (i.e. 125 Hz), the effective values have been different. Hence a resampling has been applied. The new mode shapes obtained after the synchronization procedure are represented as red continue lines in Figures 10 and 11. As evident, a good improvement was obtained for the first mode (transversal), especially for side A. Some discrepancies are still present at side B, that is two vectors have an opposite direction than expected (Figure 10). The same good results were found for the second modal (vertical) shape for side B while for side A some vectors have an unexpected direction (Figure 11).

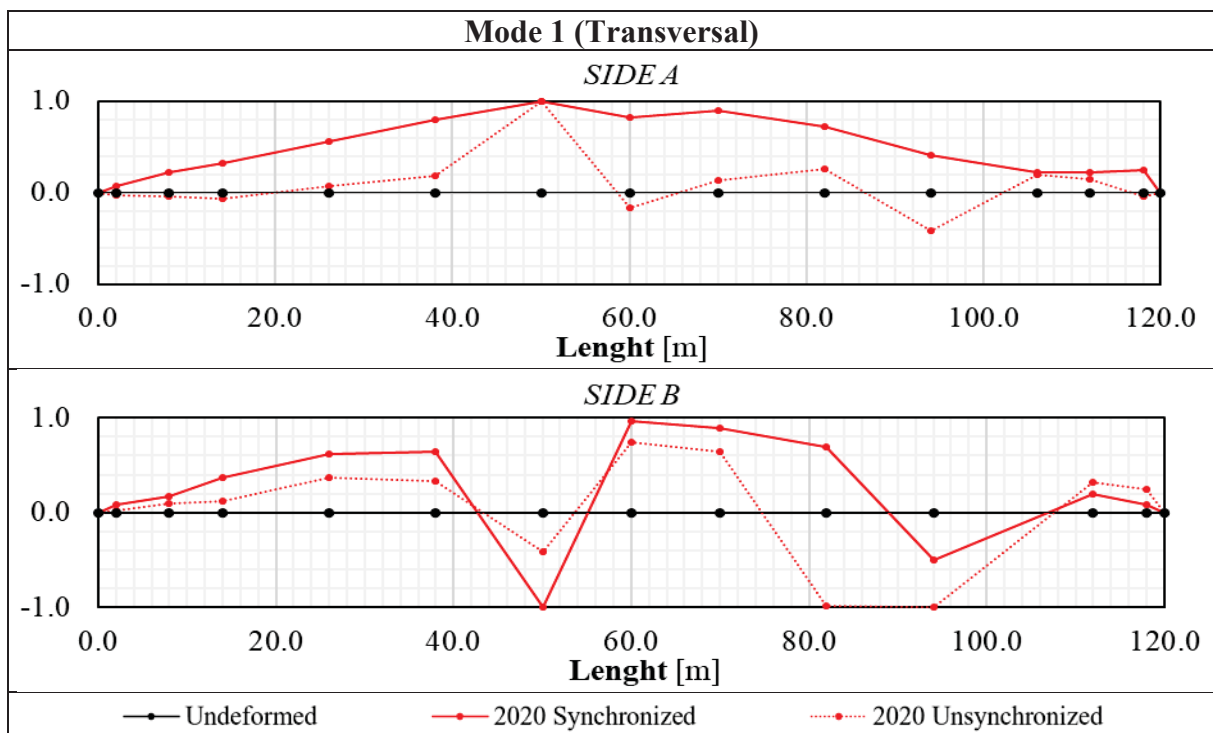


Figure 10 – Mode 1 (transversal): Comparison between unsynchronized (dashed red line) and synchronized (red line) mode shapes obtained applying FDD method

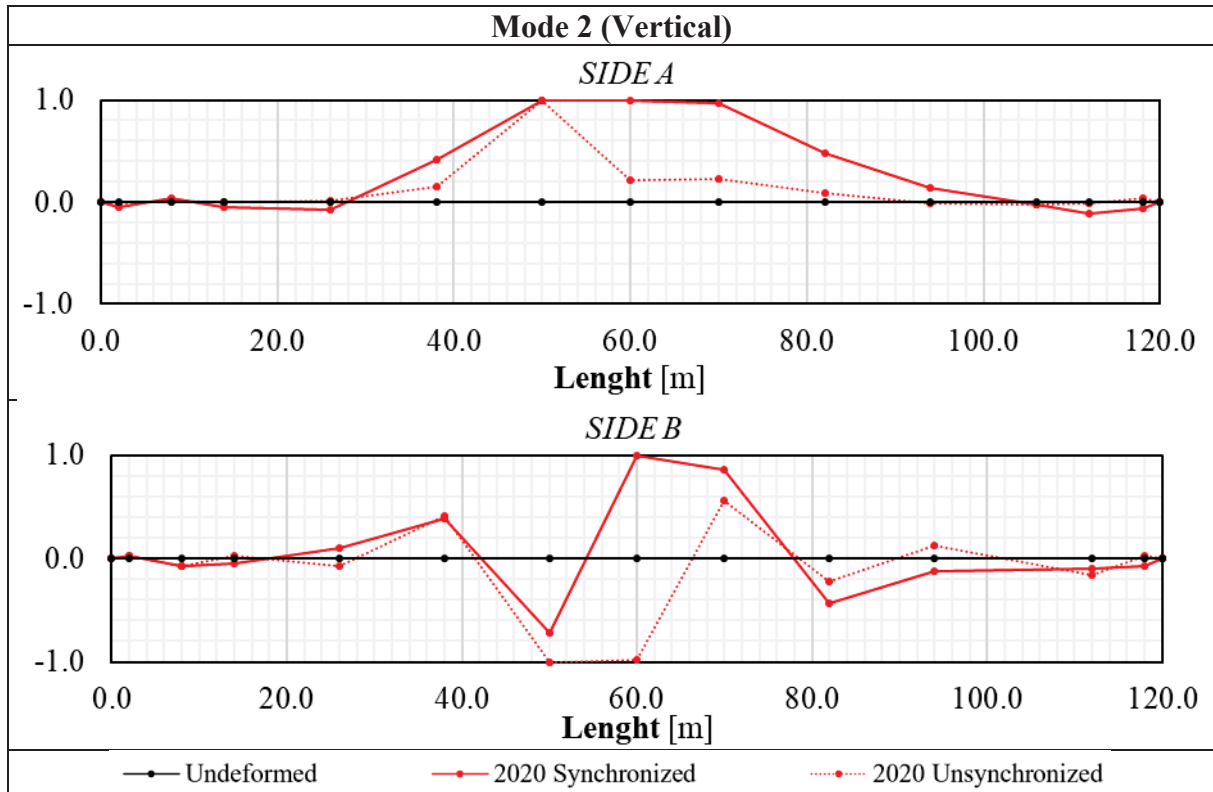


Figure 11 – Mode 2 (vertical): comparison between unsynchronized (dashed red line) and synchronized (red line) mode shapes obtained applying FDD method

For different frequency-domain methods applied (FDD, EFDD, CFDD), transversal mode frequency values are very similar (1.26, 1.27 and 1.26 Hz respectively) and closed to analytical result (1.91 Hz). However, applying time-domain methods no transversal mode have been founded. A maximum difference about 10% has been obtained for frequency values associated with the vertical mode (2.23-2.45 Hz). Finally, frequency values related to the torsional mode show modest difference (5.23-5.65 Hz) but are quite far from analytical value (4.16 Hz). Table 1 summarizes these results.

OMA method	Mode 1 (transversal)	Mode 2 (vertical)	Mode 3 (torsional)
<i>FDD</i> [Hz]	1.26	2.23	5.46
<i>EFDD</i> [Hz]	1.27	2.23	5.46
<i>CFDD</i> [Hz]	1.26	2.22	5.46
<i>SSI-UPC</i> [Hz]	-	2.37	5.24
<i>SSI-PC</i> [Hz]	-	2.45	5.23
<b>Max variation [%]</b>	<b>0.08</b>	<b>10.16</b>	<b>4.38</b>
<i>Analytical results</i> [Hz]	1.91	2.16	4.16

Table 1 - Results of 2020 experimental campaign in terms of frequencies



Modal forms obtained using frequency domain (FDD, EFDD, CFDD) and time domain (SSI-UPC, SSI-PC) methods are compared in Figures 12 and 13. As shown, all the methods have given, as first mode, the same results. Small differences were found in the vertical mode. For the third mode, as expected, the methods failed to provide a unique solution.

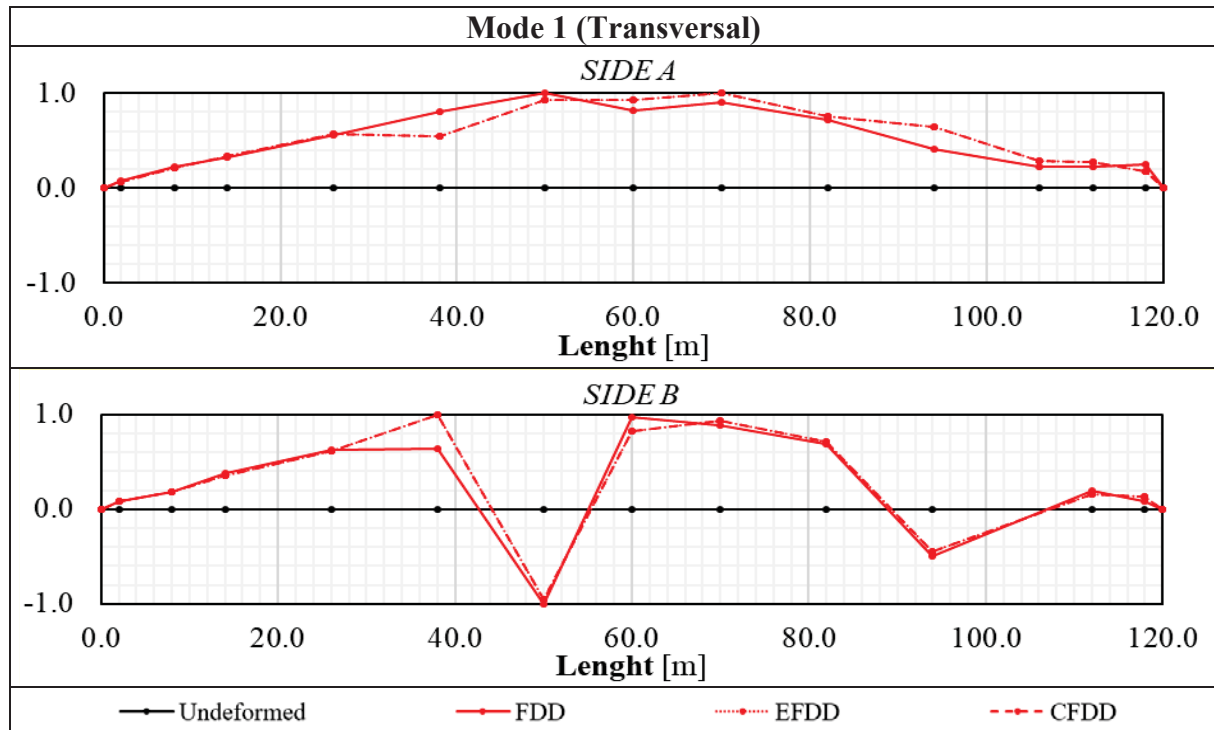


Figure 12 – Mode 1 (transversal): comparison of mode shapes obtained applying different OMA methods

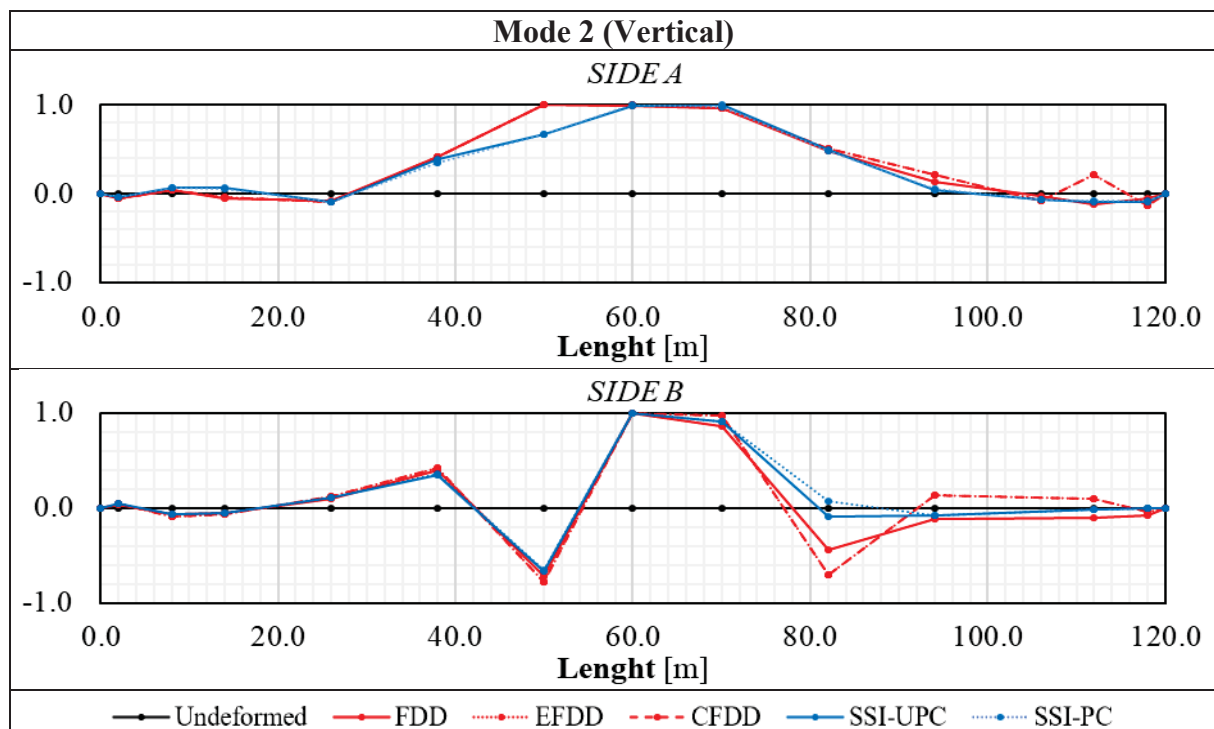


Figure 13 – Mode 2 (vertical): comparison of mode shapes obtained applying different OMA methods

The validation of the obtained results has been carried out by the MAC number, already described in section 2. First of all, a comparison between all the combinations of mode shape pairs calculated using a single technique is made (AutoMAC criterion). As shown in the left part of Figure 14, second and third unsynchronized mode shapes are not well-separated from each other (MAC values outside the main diagonal are about 0.5 for all techniques). After the synchronization procedure, an important improvement was obtained: the MAC values outside the main diagonal are very close to zero (right part of Figure 14) except for the SSI-PC method, where second and third modes remain very similar to each other despite the synchronization procedure.

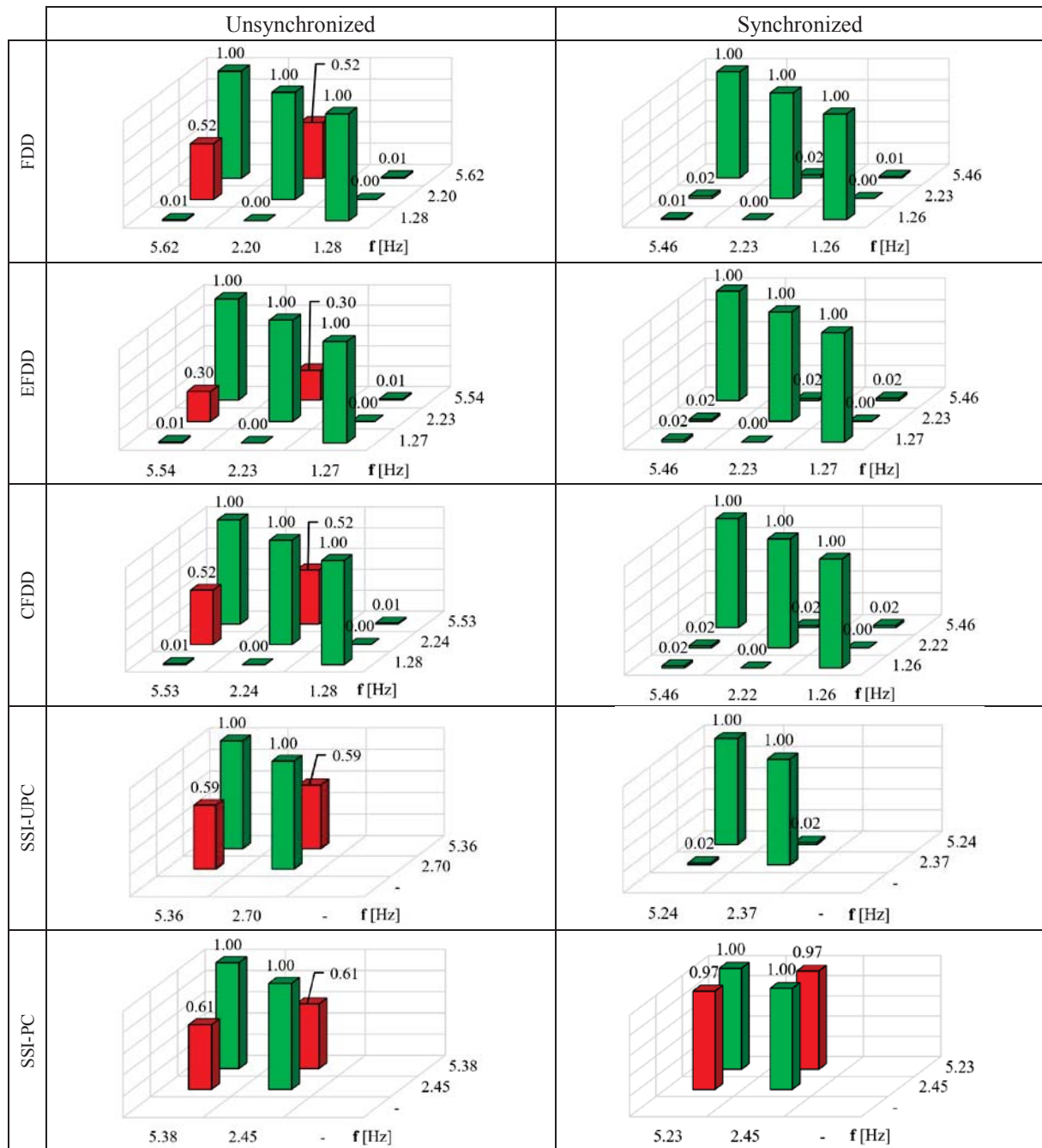


Figure 14 – Validation: comparison between MAC numbers for unsynchronized (left) and synchronized (right) mode shapes (data labels indicate the MAC numbers)

In Figure 15 the “CrossMAC” criterion results are reported for synchronized mode shapes. It consists of comparing sets of modes calculated by different OMA techniques. High values mean a good estimation for the mode shapes. As evident, the results are good since MAC values are very high with a limited range 0.87 – 1.00, except for the third mode in SSI technique (values close to 0).

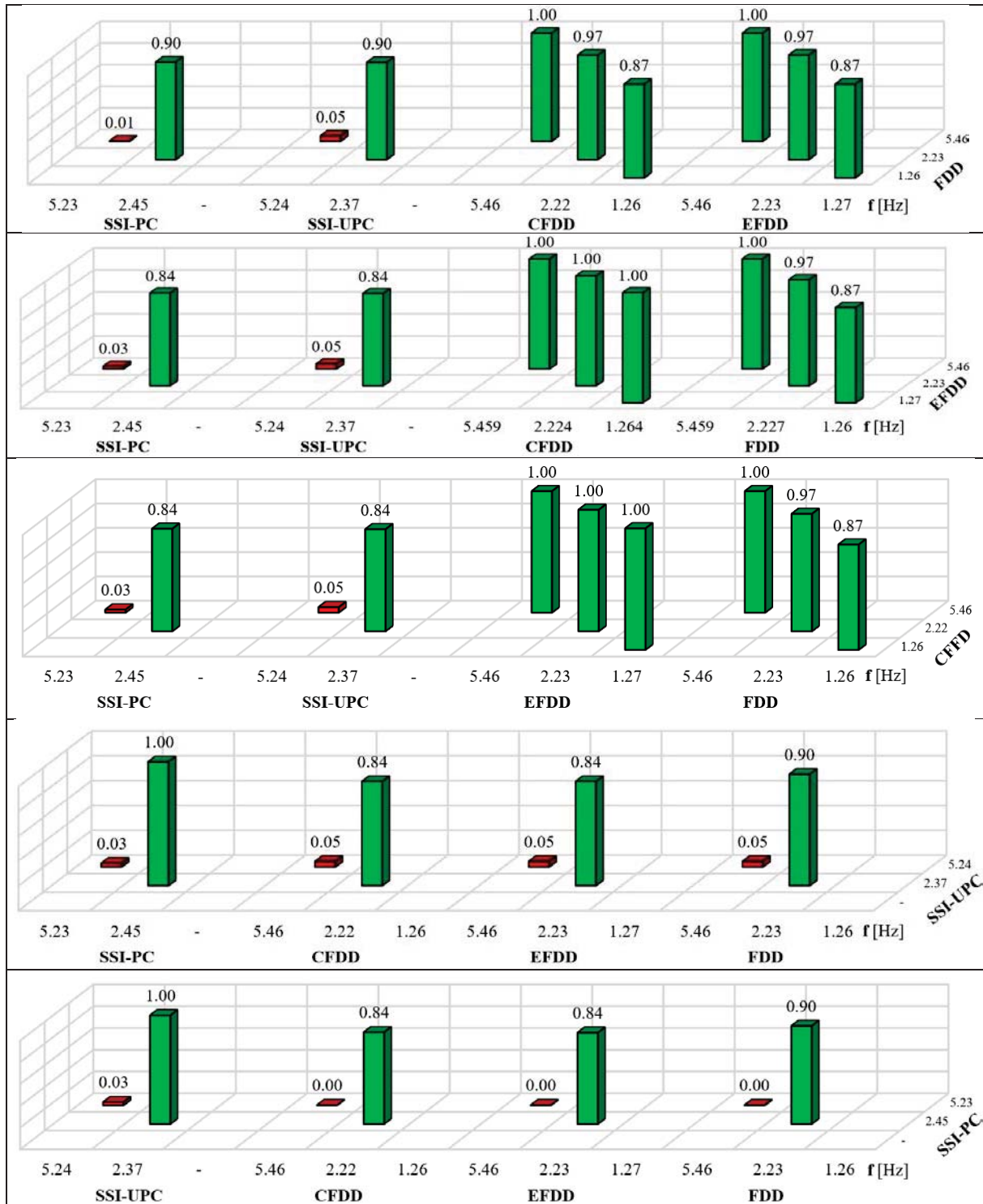


Figure 15 – Comparison between MAC numbers using different techniques for synchronized mode shapes (data labels indicate the MAC numbers)

## 6 COMPARISON BETWEEN COMMERCIAL AND PROTOTYPE EQUIPMENT TEST RESULTS

The results of the test performed by using the prototype equipment in 2020 have been compared with those obtained on the same bridge in 2018 by using a commercial sensors equipment. In terms of frequencies, a good correlation has been found for all the OMA techniques (a difference lower than 7% is appreciated) except for the SSI-UPC method, where an important difference of about 25% is noted for the second (vertical) mode (Table 2).

OMA method	Mode 1 (trasversal)			Mode 2 (vertical)			Mode 3 (torsional)		
	$f_{\text{prototype}}$	$f_{\text{commercial}}$	Variation	$f_{\text{prototype}}$	$f_{\text{commercial}}$	Variation	$f_{\text{prototype}}$	$f_{\text{commercial}}$	Variation
	[Hz]	[Hz]	[%]	[Hz]	[Hz]	[%]	[Hz]	[Hz]	[%]
FDD	1.26	1.18	6.60	2.23	2.16	3.20	5.46	5.65	5.46
EFDD	1.27	1.18	6.93	2.23	2.12	5.00	5.46	5.65	5.46
CFDD	1.26	1.18	6.85	2.22	2.12	4.81	5.46	5.65	5.46
SSI-UPC	-	-	-	2.37	1.89	25.44	5.24	5.65	5.24
SSI-PC	-	-	-	2.45	2.32	5.47	5.23	5.67	5.23
Analytical result	1.91			2.16			4.16		

Table 2 - Comparison between modal frequencies obtained by prototype and commercial equipment

A comparison between modes defined using prototype (red line) and commercial (blue line) equipment and analytical predictions (dashed blue line) is reported in Figures 16 and 17. For the first mode, except for some points, the shapes are completely overlapping (especially for the side A). For the second mode, the results are very good for the side A, while for the side B, no good result was obtained: the vectors have a direction that is opposite than expected.

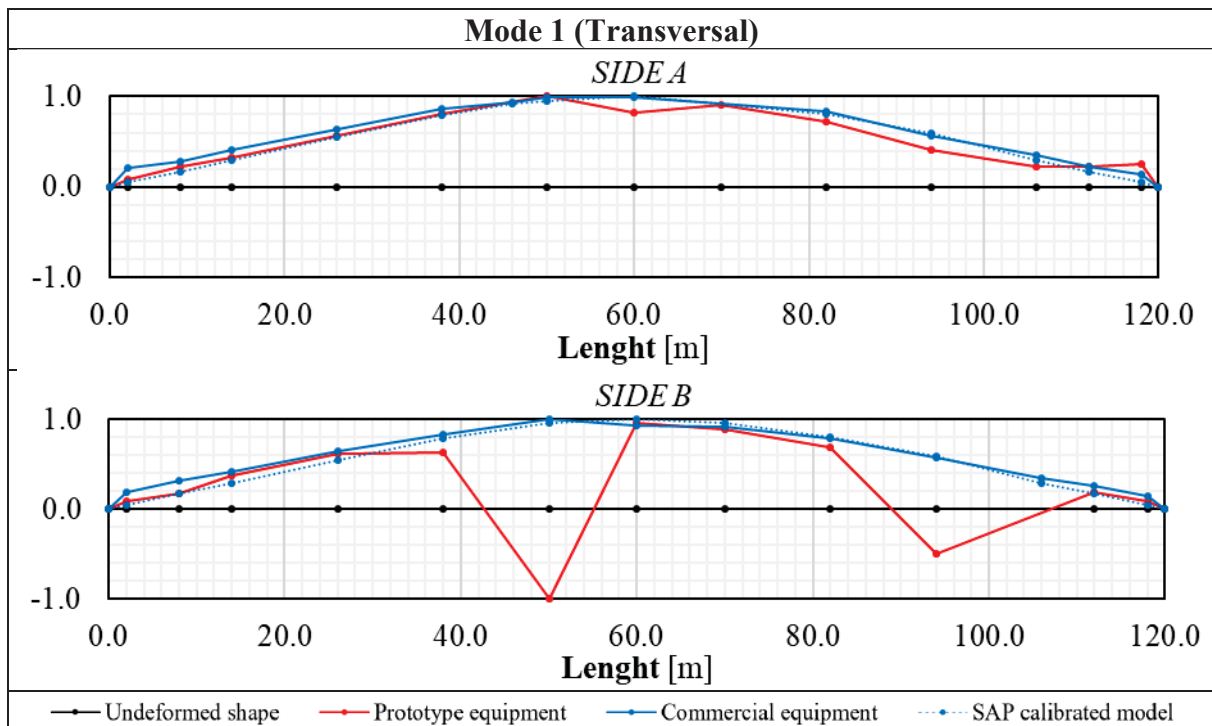


Figure 16 – Mode 1 (transversal): comparison between mode shapes defined using prototype equipment (red line), commercial sensors (blue line) and analytical calculation (dashed blue line)

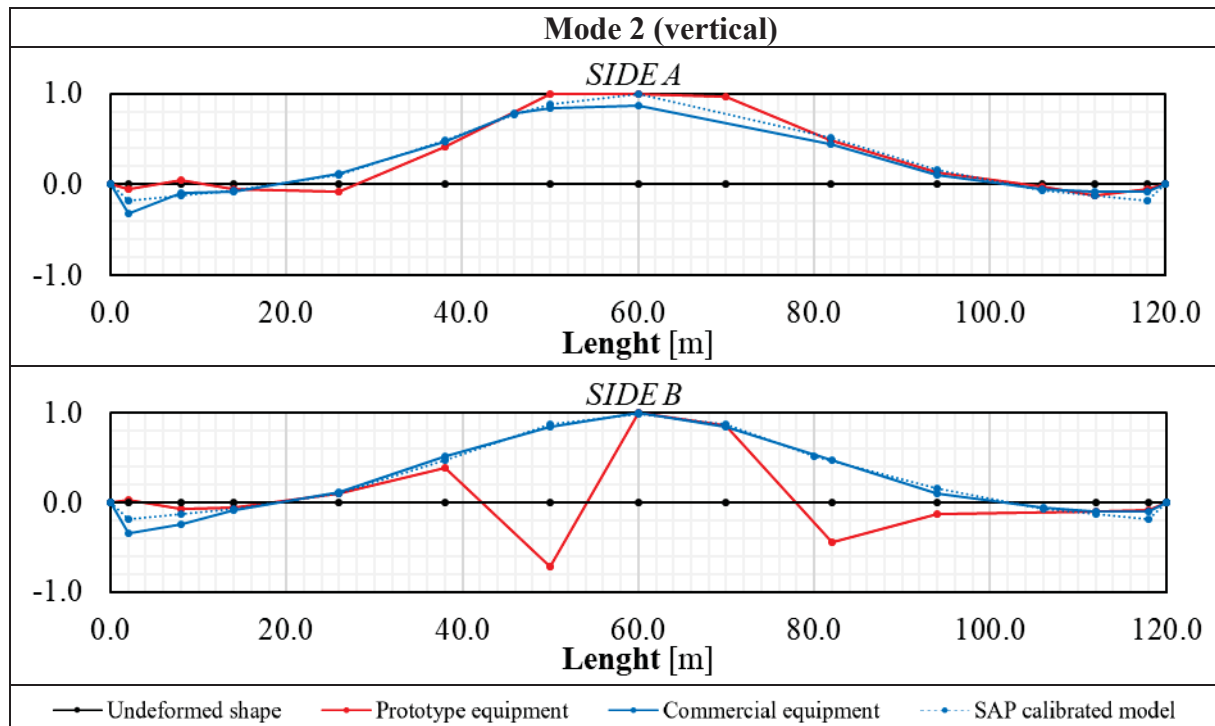


Figure 17 – Mode 2 (vertical): comparison between mode shapes defined using prototype equipment (red line), commercial sensors (blue line) and analytical calculation (dashed blue line)

## 7 DISCUSSION AND CONCLUSIONS

In this paper, the effectiveness of a wireless, low-cost and easy to install monitoring system, is evaluated. The system is a prototype consisting of nine accelerometric sensors developed by the Department of Engineering of the University of Sannio. Specific problems due to the synchronization among the devices have been addressed and solved. The equipment was tested by performing a dynamic identification test on an existing bridge located in Benevento, Italy. Two experimental mode shapes were found and validated using MAC number. The tests results have been compared with the data obtained on the same bridge in 2018 by using a commercial sensors equipment. Results demonstrate the effectiveness of the prototype system. Future developments concerning the modification of the hardware apparatus in order to solve some occurred problems have been already addressed.



## 8 REFERENCES

- [1] V. Barrile, G. Candela, A. Fotia, E. Bernardo, *UAV Survey of Bridges and Viaduct: Workflow and application*, ICCSA 2019 (International Conference on Computational Science and its Applications), 269-284, 2019.
- [2] M. Sanchez-Silva, J. Riascos-Ochoa, *Seismic risk models for aging and deteriorating buildings and civil infrastructure*, Handbook of seismic risk analysis, 387-409, Doi: 10.1533/9780857098986.3.387, 2013.
- [3] C.L. Page, J. Havdahl, *Electrochemical monitoring of corrosion of steel in microsilica cement pastes*, Materials and Structures, 18, 41-47, 1985.
- [4] R.D. Browne, *Mechanism of corrosion of steel in concrete in relation to design, inspection and repairs of offshore and coastal structures*, ACI (American Concrete Institute) Symposium Paper, 65, 169–204, 1980.
- [5] B.A. Graybeal, B.M. Phares, D.D. Rolander, M. Moor, G. Washer, *Visual Inspection of Highway Bridges*, Journal of Nondestructive Evaluation, Vol. 21, No. 3, September 2002.
- [6] ACI 228.2R-98 (American Concrete Institute committee 228), *Nondestructive test methods for evaluation of concrete in structures*, Farmington Hills, Michigan, 1998, reapproved 2004.
- [7] D.M. McCann, M.C. Forde, *Review of NDT methods in the assessment of concrete and masonry structures*, NDT&E International Vol. 34, No. 2, 71-84, Doi: 10.1016/s0963-8695(00)00032-3, 2001.
- [8] C. Boller, *Chapter 1: Structural Health Monitoring – An Introduction and Definitions*, Encyclopedia of structural health monitoring, 2009.
- [9] K. Worden, C.R. Farrar, G. Manson, G. Park, *The fundamental axioms of structural health monitoring*, Proceedings of the Royal Society A, 463, 1639-1664, Doi: 10.1098/rspa.2007.1834, April 2007.
- [10] C.R. Farrar, S.W. Doebling, D.A. Nix, *Vibration-based structural damage identification*, Proceedings of the Royal Society A, 359, 131-149, Doi: 10.1098/rsta.2000.0717, 2001.
- [11] A. Bayraktar, T. Turker, A.C. Altunisik, *Experimental frequencies and damping ratios for historical masonry arch bridges*, Construction and Building Material, 75, 234-241, 2015.
- [12] A. Cabboi, C. Gentile, A. Saisi, *Vibration-based SHM of a centenary bridge: a comparative study between two different automated OMA techniques*, Proceedings of the 9<sup>th</sup> International Conference on Structural Dynamic, EUROLYN 2014, Porto, 2014.
- [13] G.W. Chen, P. Omenzetter, S. Beskhyroun, *Operational modal analysis of an eleven-span bridge subjected to weak ambient excitations*, Engineering Structures, 151, 839-860, 2017.
- [14] C. Ranieri, G. Fabbrocino, *Operational Modal Analysis of Civil Engineering Structures – An introduction and Guide for Applications*, Springer, 2014.
- [15] M. Ghalishooyan, A. Shooshtari, *Operational Modal Analysis techniques and their theoretical and practical aspects: a comprehensive review and introduction*, IOMAC15 (International Operational Model Analysis Conference, May 2015), 2015.
- [16] D. J. Ewins, *Modal Testing: Theory and Practice*, Research Studies Press, 2000.

- [17] R. Aguilar, D. Torrealva, L.F. Ramos, P.B. Lourenço, *Operational Modal Analysis Tests on Peruvian Historical Buildings: The Case Study of the 19<sup>th</sup> Century Hotel Comercio*, 15<sup>th</sup> World Conference on Earthquake Engineering (WCEE), 2012.
- [18] M. Pastor, M. Binda, T. Hancarik, *Modal Assurance Criterion*, Procedia Engineering, 48, 543-548, doi: 10.1016/j.proeng.2012.09.551, 2012.
- [19] N-J. Jacobsen, P. Andersen, *Operational Modal Analysis on Structures with Rotating Parts*, ISMA International Conference on Noise and Vibration Engineering, 2008.
- [20] R. Brincker, P. Andersen, *Understanding Stochastic Subspace Identification*, Conference Proceedings: IMACXXIV - A Conference & Exposition on Structural Dynamics Society for Experimental Mechanics, 2006.
- [21] CSiBridge 23.0.0, 1978-2016 Computers & Structures, Inc.
- [22] A. De Angelis, G. Esposito, G. Maddaloni, E. Cosenza, M.R. Pecce, *Ambient vibration test on an existing prestressed concrete bridge*, COMPDYN 2021.8<sup>th</sup> ECCOMAS Thematic Conference on Computational Methods in Structural Dynamics and Earthquake Engineering. M. Papadrakakis, M. Fragiadakis (eds.). Streamed from Athens, Greece, 27–30 June 2021.
- [23] MATLAB R2020b, © 1994-2021 The MathWorks, Inc.
- [24] ARTeMIS Modal 6.0 © 1999-2019 Structural Vibration Solutions A/S.
- [25] Sequoia, vibration monitoring: <https://en.sequoia-vibrationmonitoring.com/gea-line/>

## CALIBRATION OF NUMERICAL MODELS TO SUPPORT SHM: THE CONSOLI PALACE OF GUBBIO, ITALY

Serena Cattari<sup>1</sup>, Daniele Sivori<sup>1\*</sup>, Sara Alfano<sup>1</sup>, Laura Ierimonti<sup>2</sup>,  
Nicola Cavalagli<sup>2</sup>, Ilaria Venanzi<sup>2</sup>, Filippo Ubertini<sup>2</sup>

<sup>1</sup> University of Genoa, DICCA, Dept. of Civil, Chemical and Environmental Engineering  
Via Montallegro 1, 16145, Genoa  
serena.cattari@unige.it, daniele.sivori@dicca.unige.it, asara94@gmail.com

<sup>2</sup> University of Perugia, DICA, Dept. of Civil and Environmental Engineering  
Via G. Duranti 93, 06125, Perugia  
laura.ierimonti@unipg.it, nicola.cavalagli@unipg.it, ilaria.venanzi@unipg.it, filippo.ubertini@unipg.it

---

### Abstract

*Historical masonry structures constitute a fundamental part of the built cultural heritage but are characterized by an intrinsic vulnerability to ageing and natural hazards, in particular to earthquakes. The related need to assess their current health condition and to ensure their future conservation is giving rise to increasing efforts in scientific research. The combined employment of health monitoring systems and structural modelling is widely adopted in this field, either to better interpret the effects of age-related degradation or to reliably predict the structural response to earthquakes. Both scenarios can leverage experimental measurements for the model calibration, thus reducing epistemic and aleatory uncertainties in the assessment phase. Among the available modelling strategies, refined Finite Element (FE) models represent the most common choice in the SHM perspective for monumental URM structures. Nonetheless, the computational effort required by the assessments in the nonlinear field – unavoidable in seismic evaluations – is often unfeasible, especially in practice engineering. In the case of palaces, an alternative is the employment of more computationally efficient formulations such as Equivalent Frame (EF) models. Within this framework, the paper firstly deals with the equivalent-frame modelling and model updating of the Consoli Palace, a historic masonry building in Gubbio (Italy) investigated through ambient vibration tests. The peculiar aspects of the building – e.g. the unusually high inter-storey height, the presence of vaulted floors, the irregular distribution of the openings – make the equivalent-frame idealization a challenging task. The comparison with a detailed finite element model developed in previous research points out the differences and limits of the two approaches, providing some suggestions to benefit from their integrated use.*

**Keywords:** historical masonry buildings, Structural Health Monitoring, Equivalent Frame models.

---

## 1 INTRODUCTION

Masonry structures constitute probably the largest part of the worldwide built heritage. Being masonry one of the oldest materials employed to build by humankind, this structural typology is commonly characterized by exceptional historical, cultural and architectural value. For these reasons, structural health assessment, conservation and rehabilitation of the built masonry heritage are crucial responsibilities of today's society. The statement is relevant both from a social and an economic point of view, urging for the efforts of the scientific community to address these tasks. Indeed, because of their age, old masonry structures suffer today the effects of ageing and deterioration over the past centuries, together with the succession of countless anthropic modifications and the constant acting of natural phenomena. These aspects, considering the intrinsic complexity of old masonry structures, make their structural health assessment a challenging goal.

In this context, the employment of non-destructive experimental techniques is leading the Structural Health Monitoring (SHM) research field, aimed at supporting the engineering judgment through experimental evidence. Together with the measurement of environmental factors, a primary role is played by dynamic testing through permanent monitoring systems, allowing for real-time identification and tracking of the dynamic properties of existing structures. Dynamic properties, indeed, are those commonly assumed as the *proxy* of structural health, so that detection of their variations corresponds to the potential – such as the occurrence of damage.

If the main trends of the research [1] follow the employment of *data-driven* statistical methodologies aimed at unsupervised evaluations, not less important is the complementary employment of engineering-based *model-driven* approaches, relying on accurate mechanical models for the simulation of the structural behaviour. In the case of historical masonry structures, among the possible modelling strategies (reviewed in [2][3] and discussed in [4] from a seismic engineering perspective), the common approach relies on refined Finite Element (FE) models, allowing for a detailed idealization of the structure. Such a potential, commonly, comes at the cost of (i) a large set of input parameters and (ii) high computational requirements, which often makes the employment of FE models unfeasible – for example, in nonlinear seismic analyses.

In the case of palaces, on the other hand, an alternative option is provided by Equivalent Frame (EF) models, specifically addressed to the analysis of the global seismic response of ordinary masonry buildings. This modelling technique discretizes the masonry continuum as an assemblage of macroscopic structural elements. Being governed by few mechanical parameters and a limited number of elements, EF models are an attractive choice thanks to their computational efficiency [5]. Nonetheless, as discussed in the following Sections, the common simplifying assumptions of this approach challenge its applicability in the case of monumental masonry palaces.

Based on the above presented motivations, the paper addresses the employment of EF models to support the SHM in the case of masonry palaces, proposing some preliminary considerations through the comparison with more refined FE models. In particular, the historical *Consoli Palace* of Gubbio, Italy, is chosen as the suited case study (§2). The three-dimensional FE of the palace, previously developed and dynamically calibrated by the University of Perugia research group, is assumed as the reference result (§3.2). An EF formulation of the palace is proposed, highlighting some possible issues related to common modelling assumptions (§4.1). The model is dynamically calibrated based on the results of AVTs employing a global search algorithm, taking into account the uncertainties related to the limited knowledge of the mechanical properties of the existing structure, as well as those produced by the EF idealization (§4.2). The dynamics of the updated model is satisfyingly close to the experimental evidence and the set of optimal parameter points out the importance of the out-of-plane stiffness contribution of



masonry walls (§4.3). A final comparison between the updated models shows good accordance in terms of dynamic and seismic properties (§4.4), confirming the possibility of their integrated use in the SHM perspective and pointing out interesting developments of the research (§5).

## 2 THE CONSOLI PALACE OF GUBBIO, ITALY

The Consoli Palace (Figure 1a), located in the medieval town of Gubbio (Central Italy) is a monumental palace built between 1332 and 1349 according to different architectural building styles. The whole structure (Figure 1b) is mainly made of calcareous stone masonry also in the newest parts, as the staircase of the main façade, which is characterized, in the upper part, by coupled round-arched windows separated by *lesenes*. Above them, merlons enclose the rooftop and the bell tower. The lower part of the main façade is characterized by mullioned windows, a Gothic-style portal and the main staircase.

The palace has a 40x20 m rectangular plan and an elevation of about 60 m. The structure is arranged on different floors: two levels on the foundation system; the *Arengo hall* at a height of 4.64 m, accessible from the principal staircase (Figure 1c); the *Nobili hall* at a height of 18.89 m (Figure 1d); the rooftop at a height of about 30 m. The Arengo hall, in particular, develops seamlessly – i.e. without intermediate walls – thanks to the huge structural thickness of the perimetral walls, which support a huge barrel vault. The Southside of the Palace is characterized by the *loggia*, a not-in-built architectural portion.

A recent in situ survey has allowed identifying different connection degrees between structural elements (walls-to-walls, walls-to-vaults) standing from interlocking to simply leaning elements. Moreover, the external stones of the Palace exhibit an apparent state of degradation, possibly attributed to exposition to environmental stresses and pollutants, such as biological patina, black crust, presence of vegetation, spalling, reintegration and encrustation.

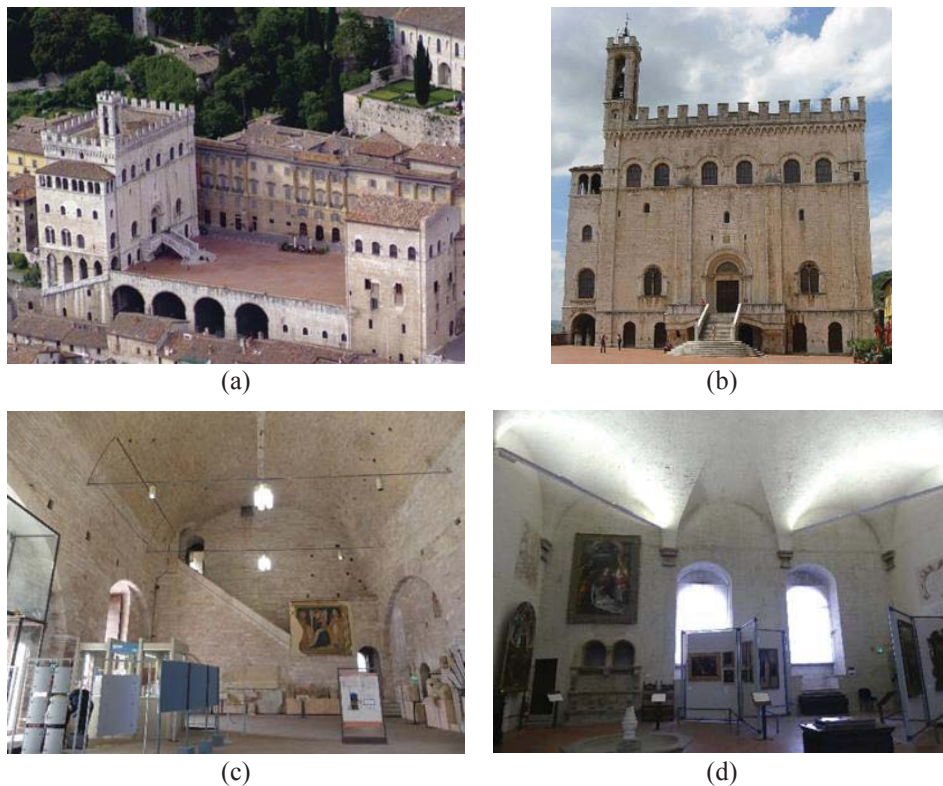


Figure 1: The Consoli Palace of Gubbio, Italy. (a) Aerial view of the Consoli Palace and the main square “Piazza Grande”, (b) main façade, (c) Arengo hall and (d) Nobili hall.



### 3 TARGET DYNAMIC DATA AVAILABLE FOR MODELS' CALIBRATION AND COMPARISON

#### 3.1 Dynamic identification from Ambient Vibration Tests (AVTs)

The dynamic properties of the Consoli Palace were investigated through Ambient Vibration Tests (AVTs) carried out on May 4<sup>th</sup>, 2017. The main purpose of the AVTs was the identification of the elastic dynamic properties of the structure, i.e., natural frequencies, mode shapes and damping ratios, for structural monitoring and finite element model calibration purposes.

According to the hypothesis of in-plane rigid behaviour of the horizontal floor diaphragms, a network of 9 uni-axial high sensitivity piezoelectric accelerometers – model PCB 393B12, capable of measuring maximum accelerations of  $\pm 0.50$  g with a sensitivity of 10 V/g – were deployed on the three main floors of the Palace (rooftop, Arengo hall, Nobili hall, Figure 2).

The AVT was conducted by using a multi-channel data acquisition system characterized by 24-bit resolution, 102 dB dynamic range and anti-aliasing filters.

The modal identification of Consoli Palace was performed by considering accelerations induced by micro-tremors, mainly due to wind and weak traffic excitation coming from the neighbouring area around the Palace. Consecutive time windows of 1800 s were collected, corresponding to more than 4000 times the fundamental period of the building.

The acceleration responses of the palace were recorded with the hardware own sampling frequency of 1652 Hz. Then, since the dominant natural frequencies were expected to lay below 10 Hz, signals were down-sampled to 40 Hz after low-pass filtering, with a Nyquist frequency of 20 Hz.

The acquired signals were affected by anomalous peaks due to the bells-dependent non-stationary excitation, produced by the bell tower playing all day and night long with a 15-minute step interval. To remove this effect, an automated simple pre-processing tool has been implemented and applied to the data enabling to identify portions of the signals containing peak response accelerations overcoming a prescribed threshold (assumed as ten times the root mean square value of the signal) and to remove these portions – after application of half Hanning windows to the tails of the signals to be concatenated.

Finally, the dynamic identification was performed employing the Stochastic Subspace Identification (SSI) technique. To briefly introduce the SSI methods, it is convenient to consider a time-invariant  $n$ -dof structural system, whose state-space equations of motion can be written as

$$\begin{aligned} \mathbf{x}(k+1) &= \mathbf{A}\mathbf{x}(k) + \mathbf{w}(k) \\ \mathbf{y}(k) &= \mathbf{C}\mathbf{x}(k) + \mathbf{v}(k) \end{aligned} \quad (1)$$

where  $k$  denotes the time step;  $\mathbf{x} \in \mathbb{R}^n$  is the state vector;  $\mathbf{y} \in \mathbb{R}^l$  is the vector of the  $l$  output measurements;  $\mathbf{w} \in \mathbb{R}^n$  is the external input, modelled as a white noise process vector;  $\mathbf{v} \in \mathbb{R}^l$  is a white noise affecting the measurements;  $\mathbf{A} \in \mathbb{R}^{n \times n}$  is the system matrix;  $\mathbf{C} \in \mathbb{R}^{l \times n}$  is the output matrix. Then, thanks to a transformation of the state-space system, rewritten in the frequency domain by its transfer function through the so-called Canonical Variate Analysis (CVA) algorithm, the modal features can be extracted. More extensive details on this modal identification tool are reported in [6]. Table 1 summarizes the AVT-based fundamental vibration modes, where directions  $x$  and  $y$  are defined along the larger and the smaller dimension of the rectangular plan, respectively. The global mode shapes, i.e., 1-2-5, identified by the adopted SSI procedure are presented in Figure 3.

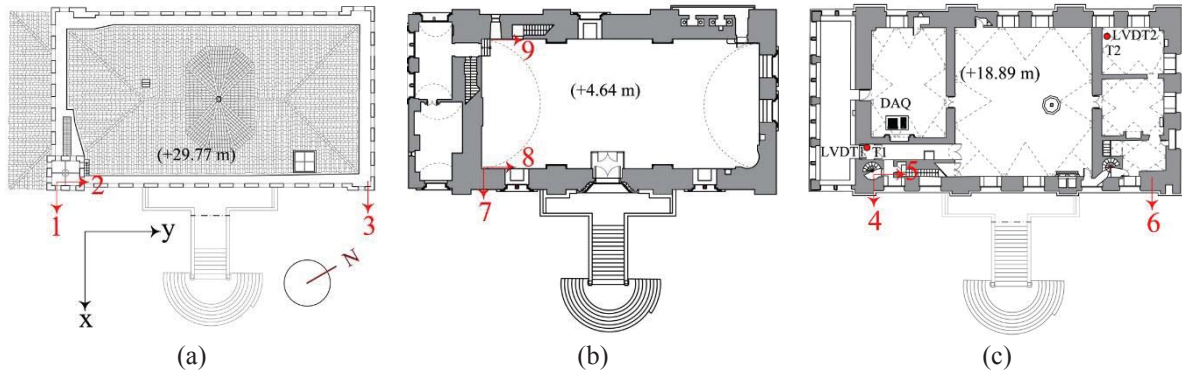


Figure 2: Configuration of 9 accelerometers and data acquisition system adopted in the AVT (a) at the top of the building (channels 1, 2, 3), (b) in the Arengo hall (channels 7, 8, 9), (c) in the Nobili hall (channels 4, 5, 6).

Mode	Type	Description	$f_e$ (Hz)	$\xi_e$ (%)
1	global	flexural along $x$ -direction	2.296	1.121
2	global	flexural along $y$ -direction	2.989	0.751
3	local	flexural of the bell tower	3.508	0.779
4	local	flexural of the bell tower	3.743	2.477
5	global	torsional	4.172	1.104
6	local	torsional of the bell tower	7.035	1.089

Table 1: Identified natural frequencies ( $f_e$ ) and damping ratios ( $\xi_e$ ) of the Palace, estimated by SSI of the AVTs carried out on May 4th 2017.

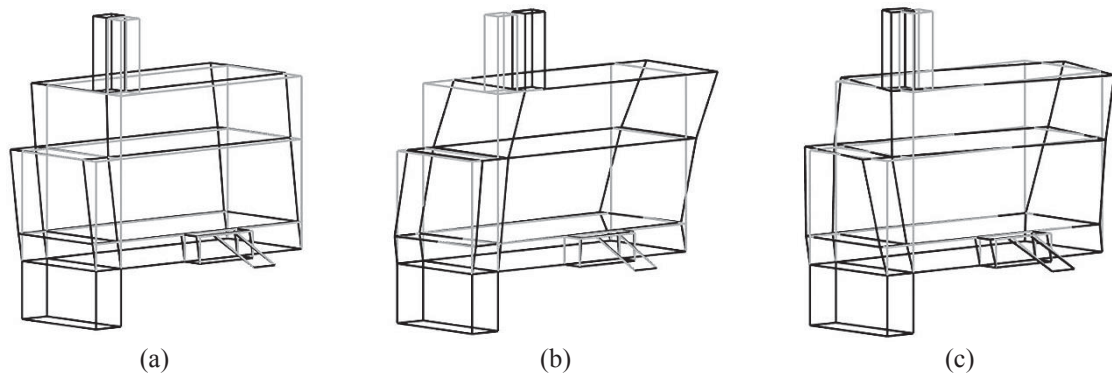


Figure 3: Global mode shapes of Consoli Palace identified from AVT acceleration records by automated SSI. (a) Mode 1, (b) mode 2 and (c) mode 5.

### 3.2 Updated Finite Element (FE) model of the palace

To perform a consistent interpretation of the identified vibration modes, a 3D numerical Finite Element (FE) model of the structure has been built in the ABAQUS environment [7]. The mesh of the model is composed of a dense grid of tetrahedral elements (see Figure 5a in §4.1). Based on the principal architectural portions identified within the building (as described in §2), the model has been subdivided into four homogenous parts characterized by different values of Young's modulus of the masonry: the foundation level, the Arengo level, the Nobili level and the bell-tower. Hence, Young's moduli are assumed as uncertain parameters and their values have been adjusted in the calibration process to minimize the average relative difference

between numerically predicted and experimentally identified natural frequencies. On the contrary, the same values of Poisson's coefficient and material density have been considered in the whole building.

The updated values of Young's moduli are summarized in Table 2. The relative difference  $\Delta f$  between experimentally identified ( $f_e$ ) and numerically predicted ( $f_{n,FE}$ ) natural frequencies is highlighted in Table 3. Extensive details on the FE model calibration can be found in [8].

Part	Initial value (MPa)	Updated value (MPa)
Foundation level	2440	3327
Arengo level	2440	3510
Nobili level	2440	3327
Bell tower	2440	3450

Table 2: Updated values of Young's moduli.

Mode	$f_e$ (Hz)	$f_{n,FE}$ (Hz)	$\Delta_f$
1	2.296	2.352	0.024
2	2.989	3.047	0.019
3	3.508	3.460	-0.014
4	3.743	3.544	-0.053
5	4.172	4.171	<0.001
6	7.035	7.09	0.008

Table 3: Comparison between experimentally identified ( $f_e$ ) and numerically predicted ( $f_{n,FE}$ ) natural frequencies, where  $\Delta_f = (f_n - f_e)/f_e$  represents the relative frequency difference.

## 4 FORMULATION AND CALIBRATION OF THE EQUIVALENT FRAME (EF) MODEL

### 4.1 Equivalent-frame modelling assumptions and related issues

The structural model of the Consoli Palace, based on the Equivalent Frame (EF) modelling approach, is built with the commercial software 3Muri (Release 11.5.7) distributed by S.T.A. Data. In the EF approach, as known, the deformability and the nonlinearity are concentrated in specific parts of the masonry walls, i.e. piers and spandrels. These are the portions in which seismic damage tends to concentrate, as widely testified by in situ observations of existing buildings hit by recent earthquakes (for example, in Italy [9][10][11][12]). According to this idealization, the *piers* – vertical portions of masonry between horizontally aligned openings – resist both vertical and horizontal loads, whereas the *spandrels* – horizontal portions of masonry between vertically aligned openings – play a primary role in piers coupling. The remaining portions of the walls are idealized as *rigid nodes*.

The EF approach, thus, is commonly employed to simulate the global seismic response of ordinary masonry buildings. Some of the simplifying assumptions adopted by EF models, on the other hand, make their application more involved – and sometimes unsuitable – for historical monumental buildings. This is the case of the Consoli Palace, for which the EF approach requires particular caution and poses interesting engineering challenges. The following paragraphs address some of the issues faced in the synthetic EF description of the palace, highlighting the differences with more detailed FE approaches and proposing some possible modelling solutions.

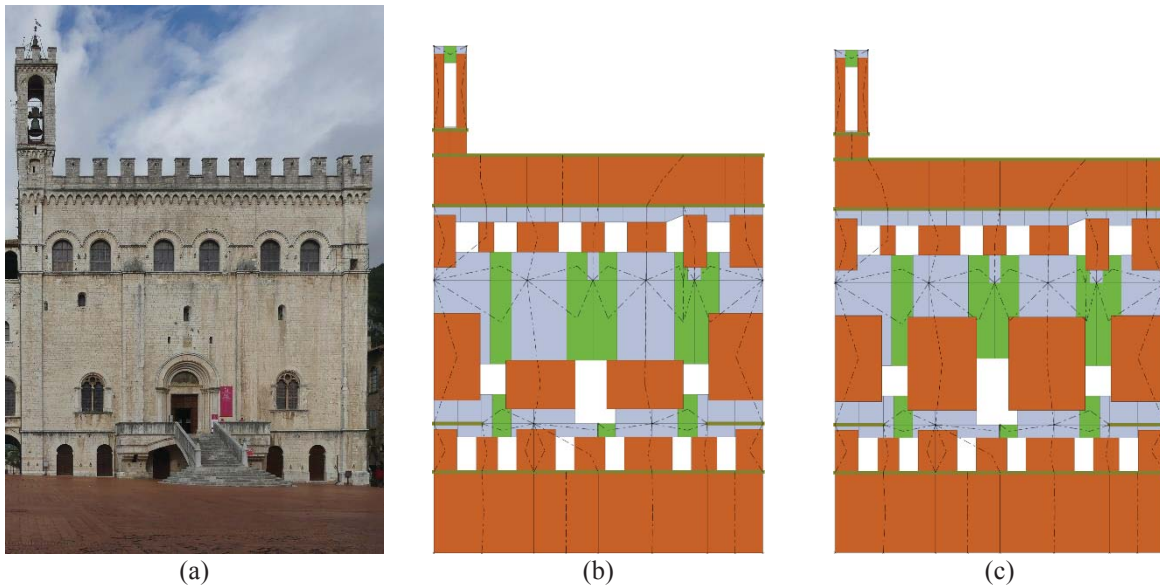


Figure 4: (a) Rectified picture of the Consoli Palace façade. Corresponding EF mesh according to (b) the criteria implemented in 3Muri and (c) after manual modification. The colours orange, green and light blue represents respectively piers, spandrels and rigid nodes.

The definition of the geometry of the vertical structural elements (Figure 4), mainly depends on the number and arrangement of openings. This procedure is straightforward when openings are aligned and regularly distributed. Conversely, in the case of irregularly shaped and sparse openings, the EF modelling becomes non-trivial and requires expert engineering judgment – due to the potential source of large dispersion in the simulation of the seismic response [13][14]. Indeed, the structural mesh significantly influences the static and dynamic behaviour of the structure in the linear and nonlinear regime, so that appropriate criteria for its definition are crucial to obtain reliable simulations.

Several contributions of the literature address this task, providing various indications [15][16][17][18] for the definition of the EF mesh geometry. Nonetheless, most of the rules have been developed based on a regular arrangement of the openings. Among those, recent research [19] and detailed comparisons with cracking patterns of damaged buildings [14] suggest the criterion implemented by 3Muri software to be reliable. Defining the effective height of piers is particularly challenging when the layout of the openings is irregular, which unfortunately represents a recurrent situation in existing buildings. In recent years, many researchers have focused their efforts to overcome this issue (see for example [20][21][22][23][24][25]). However, no shared consensus in the scientific community and standardized rules have been established yet.

The openings of the Consoli Palace are often irregularly arranged on the walls, without systematic horizontal and vertical alignments. In this case, according to the criterion adopted by 3Muri software, large portions of the walls would be idealized as rigid nodes due to the unusually large interstorey heights (such as those of the Arengo hall, §2). In light of these issues, firstly, some very small openings on the perimeter of the palace have been neglected to enhance the quality of the meshing. As shown by recent studies [25][26], this simplification is acceptable when the opening is sufficiently smaller than the masonry panel. Secondly, the software-generated mesh (Figure 4b) has been carefully revised and manually edited, to define deformable masonry portions more consistent with physical expectations (Figure 4c).

For what concerns the floor diaphragms, they are modelled as rectangular orthotropic membranes [15]. Their elastic mechanical properties are identified by the axial Young's moduli of



the two main directions of in-plane deformation and, more importantly, by the shear modulus  $G_d$ . This parameter, depending on the diaphragm thickness, governs the equivalent shear stiffness provided by floor diaphragms to the coupled walls, determining the redistribution of horizontal seismic actions as well. As previously highlighted (§2), the Consoli Palace is mainly characterized by vaulted floors of different typologies. Their geometric characteristics are peculiar, especially those regarding the huge barrel vault covering the Arengo hall, in which narrow and long vaulted rooms have been built within the volume of the vault itself. This complex system of rooms has not been explicitly described in the EF model, coherently with its simplified nature. Nevertheless, the dynamic calibration of the model considers wider uncertainties in the masses and horizontal stiffness contributions provided by this floor (see §4.2).

With similar reasoning and due to its complexity, the roofing system has been modelled only through its mass contribution. It should be remarked that the proper and additional masses of floors, in the EF model, are distributed to the diaphragm perimeter nodes. In the case of the Consoli Palace, these masses are relevant, accounting for 30% of the total mass of the structure.

Another important aspect of the three-dimensional EF assembling regards the degree of connection between walls and horizontal diaphragms and between walls. The first is governed by the stiffness properties of the diaphragms themselves. The second, on the other hand, must reproduce the quality of the anchoring between intersecting walls, depending on the mechanical properties of masonry and the stone arrangement at the walls joint. Different effectiveness of the wall-to-wall connection may be achieved by different modelling strategies in EF models, as discussed in [27], among which the use of connecting beams is particularly effective.

The recent in situ survey (§2) allowed identifying those walls in which the so-called *flange effect* is guaranteed, so to be equivalently described by stiff coupling beams. In other cases, walls are not intersecting but simply leaning against each other, so that the flange effect is negligible. The intermediate cases are reproduced in the model through appropriate connecting beams, whose stiffness properties determine the degree of coupling between intersecting masonry walls.

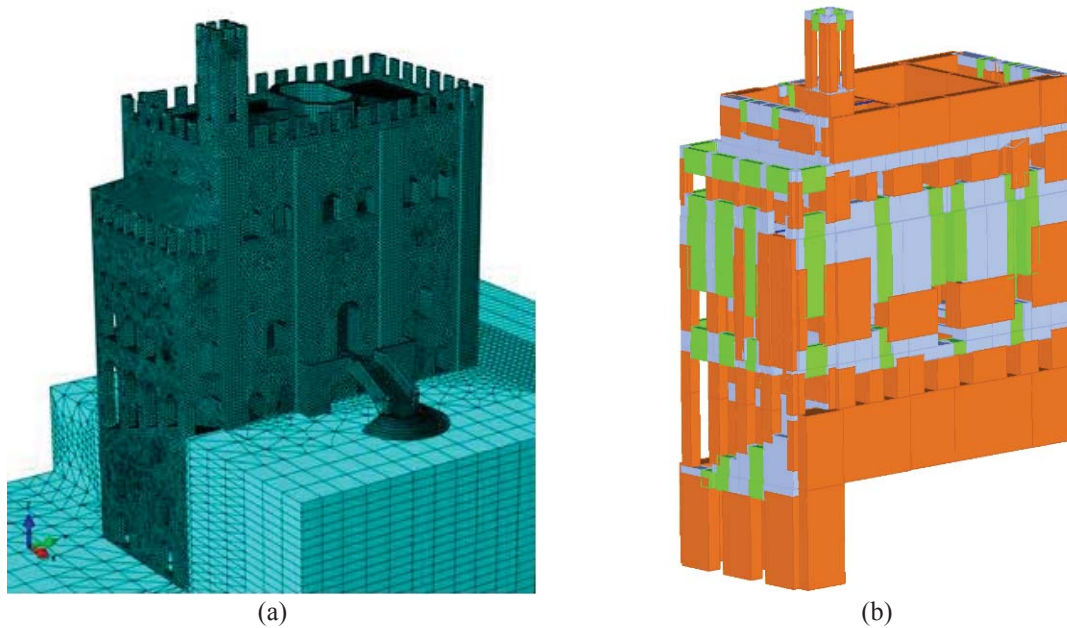


Figure 5: (a) Finite element (FE) model and (b) Equivalent Frame (EF) model of the Consoli Palace.



Finally, the three-dimensional structure is assembled from bi-dimensional elements, walls elements and floor diaphragms, neglecting their out-of-plane stiffness contributions. This assumption is reasonable and widely adopted in the analysis of ordinary masonry buildings. In the case of Consoli Palace, however, the thicknesses of bearing walls are much larger – sometimes comparable with the in-plane extension, see §2 and Figure 3 – than those found in ordinary buildings. As a consequence, their out-of-plane stiffness is expected to influence significantly the global dynamic behaviour of the structure. This effect has been properly accounted for in the calibration process (see §4.2).

In light of these premises, the resulting three-dimensional EF model (Figure 5b) faithfully reproduces the geometric and structural characteristics of the palace, derived from the available documentation and refined following the on-site investigations. If compared to the FE model (Figure 5a), indeed, the biggest simplification lies in the impossibility to explicitly model the volume of the subsoil at the foundation level. In the EF model, this limitation is overcome by employing proper node constraints.

#### 4.2 Uncertainties and updating technique

The model updating process is formulated as a constrained global optimization problem, in which uncertain mechanical parameters characterizing the structural model are calibrated to minimize the differences between the numerical simulations and the experimental results. Considering the availability of three reliable experimental modes – identified from AVTs in §3.1 and employed for the calibration of the FE model of the palace in §3.2 – resulting in three target frequencies and as many mode shapes, the dimensions of the problem (i.e. the number of free parameters) are limited to a maximum of six unknowns.

The extension of the parameter space, i.e. allowed range of variation of each parameter, reflects (i) the related degree of uncertainty deriving from the limited knowledge of the existing structure and (ii) as thoroughly discussed in the following, some limitations of the EF in modelling such a complex masonry structure (§4.1). Based on this premise, in a preliminary phase, five mechanical parameters – expected to influence the undamped free vibrations of the structure in the investigated range of frequencies – are assumed as the problem unknowns. Their reference values and ranges of variation are synthetically reported in Table 4.

The parameter  $E_m$  represents the masonry Young's modulus of the whole body of the palace. According to the EF idealization, this quantity governs the in-plane flexural response of the vertical structural elements (i.e. piers and spandrels). In this respect, this parameter is expected to have a primary influence on the natural frequencies of the global (in this case, translational and rotational) modes. Since no experimental tests are available to directly characterize the mechanical properties of the palace masonry, the reference elastic modulus is assumed as the average value of the range proposed by the Italian Circular No. 7/2019 [28] for massive stone (Table C8.5.I) – which characterizes most of the palace bearing walls – taking into account the good quality of the mortar joint observed during the in situ surveys (Table C8.5.II). Similarly, concerning the lowest acceptable value, the range of variation is constrained according to the same code provision. Conversely, the less stringent upper bound is mainly aimed at an indirect in-plane compensation of the unmodeled out-of-plane stiffness of the vertical elements (§4.1). This statement should not be surprising, observing the significant out-of-plane thickness of the bearing walls (§2). The in-plane shear contribution, governed by the shear modulus of the masonry  $G_m$ , is derived assuming a Poisson ratio equal to 0.2 – as in the FE calibration (§3.2) – leading to  $G_m = E_m/1.4$ .

Parameter	Description	Reference value	Lower bound	Upper bound
$E_m$ (MPa)	Young's modulus of palace masonry	3420	2400	12000
$E_{mt}$ (MPa)	Young's modulus of bell tower masonry	3420	2400	12000
$\rho_m$ (kg/m <sup>3</sup> )	Mass density of palace masonry	2200	1800	2400
$c_{Md}$	Relative variation of floor masses (Arengo and roof level)	1	0.5	1.5
$c_{Gd}$	Relative variation of floor diaphragms in-plane shear stiffness (vaults)	1	0.5	25
$c_{oop}$	Relative variation of $E_m$ along the $y$ direction	1	0.5	1.5

Table 4: Reference values and variation boundaries of the parameters calibrated in the updating process.

The Young's modulus of bell tower masonry  $E_{mt}$  governs the frequency of the local modes of the bell tower, in particular those involving its flexural behaviour. From the mechanical point of view, no significant differences are expected between the palace and tower masonries – sharing the same typology, see §4.1. Choosing this parameter as a separate variable, nevertheless, allows decoupling the effects of the unmodeled out-of-plane stiffness belonging to the main building from those belonging to the tower itself. This parameter is expected to be overestimated from the updating procedure as well, due to the significant thickness of the pillars supporting the bell tower.

The variation of the mass density  $\rho_m$  of the palace masonry is constrained according to a limited uncertainty related to the building material properties. It should be remarked, in this regard, that the wall mass contribution is around 70% of the total mass of the building, making the calibration process quite sensitive even to small variations of this parameter.

The relative weighting factor  $c_{Md}$  takes into account the uncertainty in the definition of the proper and added masses insisting on the Arengo vault and the roof level. This parameter addresses the vertical loads contribution (i) the complex system of rooms rising above the Arengo vault and of (ii) the roofing, none of which being explicitly described by the model (§4.1). Such masses are estimated to be around 2000 ton each, making up around 60% of the floor masses and 15% of the total mass of the palace. According to the EF modelling assumptions, the diaphragms masses are lumped to the nodes located on the supporting perimeter walls, so that their variation is expected to influence the torsional inertia of the floors.

The coefficient  $c_{Gd}$  allows tuning the equivalent in-plane shear stiffness  $G_d$  provided by horizontal diaphragms, in particular by those representing vaulted floors. This choice is justified by the unusually large dimensions of the Arengo vault (§2), which make analytical estimations – such as those presented in [29] and employed to estimate reference values – less reliable. A recent contribution of the literature allows to quantitatively identify the actual shear stiffness of floor diaphragms from ambient vibration data [30]. Nevertheless, in this specific case, the limited number of sensors and their suboptimal location prevent a successful identification [31]. For these reasons, a finer calibration of this parameter is delegated to the updating process.

Finally, the factor  $c_{oop}$  characterizes the masonry Young's modulus of the bearing walls aligned with the  $y$  axis, according to the expression  $E_{m,y} = c_{oop}E_m$ . This parameter addresses the potential unbalance between the global out-of-plane stiffness provided by each direction. Based on simple geometric considerations, observing the huge thickness and length of the two perimeter walls developing along  $x$ , the out-of-plane contribution is expected to be prominent along  $y$  (i.e.  $c_{oop} > 1$ ).

The simplifying assumptions of the 3Muri EF implementation – discussed in detail in §4.1 – and, more in general, those of the equivalent frame formulation, surely make the modelling of a complex structure such as the Consoli Palace a challenging task. On the other hand, if compared to FE modelling, the synthetic EF formulation ensures much lower computational requirements. Taking advantage of this feature, the inverse updating problem is approached from a *global search* perspective, aimed at the extensive exploration of the parameter space.

In particular, a genetic algorithm is chosen among the several global optimization approaches suitable to carry out the updating process. This metaheuristic search, belonging to the larger class of evolutionary algorithms, mimics the natural selection process relying on biologically inspired operators such as *selection*, *crossover* and *mutation*. The initial population size is set to 200 members, sampled uniformly from the bounded parameter space. *Parents* are selected among the members of each population with the lowest objective values. To ensure diversity, each subsequent generation is composed of (i) ten *elite* members, those with the highest ranking from the previous generation, (ii) 80% of the remaining members generated from parents *crossover* – mixing different *genes*, i.e. parameters – and (iii) 20% generated from parents *mutations* – applying random Gaussian noise to their parameters.

The single objective function  $\Pi$  to be minimized is representative of the relative differences between simulated and experimental modes, according to the expression

$$\Pi = w_f \Pi_f + w_s \Pi_s, \quad w_f + w_s = 1$$

$$\Pi_f = \sum_k \left( \frac{f_{n,k} - f_{e,k}}{f_{e,k}} \right)^2, \quad \Pi_s = \sum_k \frac{(1 - \sqrt{\text{MAC}_{ne,kk}})^2}{\text{MAC}_{ne,kk}} \quad (2)$$

where  $\Pi_f, \Pi_s$  measure respectively the differences in natural *frequencies* and mode *shapes* [32] – whose relative importance is governed by the weighting factors  $w_f, w_s$  – over the  $k$  selected modes. The expressions of  $\Pi_f$  and  $\Pi_s$  are balanced in their relative magnitudes, so that the updating process is penalizing frequency differences when MAC [33] values are greater than 0.7. Based on this consideration, intrinsically addressing the higher robustness of experimentally identified frequencies compared to mode shapes, the weights  $w_f, w_s$  are initially assumed to be both equal to 0.5.

### 4.3 Dynamic calibration based on experimental results

Few are the contributions of the literature addressing the use of AVTs results to dynamically calibrate EF models, aimed at reducing the aforementioned epistemic and aleatory uncertainties intrinsic to the modelling process [34].

Considering the set of experimental modes identified by AVTs (§3.1) and following the approach followed by the FE model calibration (§3.2), the first, second and fifth identified modes (Table 1, Figure 3) are selected as the target of the updating process. Convergence – as an average relative variation in the best objective function lower than 10% – is obtained at the eleventh generation, corresponding to 2300 function evaluations (modal analyses solved with the TreMuri research version [15]). The solution is achieved in around 40 minutes, exploiting the multiprocessing capabilities of a modern quad-core CPU. This time is comparable with the one employed by the corresponding FE model to solve a single modal analysis.

A first calibration is pursued employing a synthetic EF model in which the bell tower is not explicitly modelled, i.e. addressing its inertial contribution only. The corresponding label *w/oT* stands for “*without tower*”. The set of reference parameter, named *w/oT0* (Table 5), produces (i) large underestimates of natural frequencies and (ii) for the second mode, a poor mode shape correlation (Table 6). In particular, the relative frequency differences  $\Delta_f = (f_n - f_e)/f_e$  range

from -30% to -50%. This outcome was expected, given the importance of the unmodeled out-of-plane stiffness of the bearing walls (§4.1). The calibration results (referred to as w/oT1) show that, despite significant improvements in the objective function, frequency differences remain large. Indeed, a better agreement could be achieved – for example, setting  $w_f, w_s$  equal to 0.8 and 0.2 respectively – at the cost of completely losing the mode shape correlation of the second mode. Conversely, no set of parameters manages to improve such a correlation, due to the torsional component not observed in experimental results (Figure 6a).

If the explicit introduction of the bell tower – label  $T$  – does not improve significantly the reference configuration T0, better results are obtained from the calibration of the tower stiffness properties. The calibration T1 achieves (i) frequency differences lower than 5% for the first two modes and lower than 10% for the fifth mode and (ii) good mode shapes accordance, resulting in a reduction of the objective function of one order of magnitude (Table 7). Remarkably, the second mode shows a pure translational behaviour along the  $x$ -direction (Figure 6b), significantly improving the agreement with experimental observations. This outcome seems to confirm the primary role played by the bell tower and its non-negligible influence on the global dynamics of the palace.

The corresponding set of updated parameters, compared with their reference values, shows a large increase in Young's moduli of both the palace and bell tower masonries. In the case of tower's pillars, a simple manual estimation of the unmodeled out-of-plane stiffness – ranging from 1.25 to 1.5 times the corresponding in-plane stiffness for the cantilever and double-clamped schemes – yields physically reasonable estimates of the elastic moduli. The parameters governing the wall and diaphragms masses show a reasonable decrease, compatible with the initial underestimation of natural frequencies. The coefficient governing the in-plane shear stiffness of floor diaphragms, close to its upper bound, suggest the underestimation of the stiffness properties of vaults (§4.2).

Parameter	w/oT0	w/oT1	T0	T1	T2
$E_m$ (MPa)	3420	6450	3420	11960	7650
$E_{mt}$ (MPa)	//	//	3420	7000	9100
$\rho_m$ (kg/m <sup>3</sup> )	2200	1810	2200	1970	1893
$c_{Md}$	1	1.29	1	0.5	0.5
$c_{Gd}$	1	24.8	1	24.9	24.4
$c_{oop}$	//	//	//	//	1.5

Table 5: Reference and updated values of the parameters calibrated by the updating process.

w/oT0 - $\Pi = 0.4628$					w/oT1 - $\Pi = 0.1723$		
Mode	$f_e$ (Hz)	Mode	$f_{n,EF}$ (Hz)	$\Delta_f$ MAC	$f_{n,EF}$ (Hz)	$\Delta_f$	MAC
1	2.296	1	1.19	-0.482 0.97	1.63	-0.290	0.98
2	2.989	2	1.93	-0.354 0.42	2.63	-0.120	0.53
5	4.172	3	2.02	-0.516 0.85	2.83	-0.322	0.87

Table 6: Comparison between the experimental results, the reference and the updated EF model w/oT.

T0 - $\Pi = 0.3999$					T1 - $\Pi = 0.0200$			T2 - $\Pi = 0.0164$		
Mode	$f_e$ (Hz)	Mode	$f_{n,EF}$ (Hz)	$\Delta_f$ MAC	$f_{n,EF}$ (Hz)	$\Delta_f$	MAC	$f_{n,EF}$ (Hz)	$\Delta_f$	MAC
1	2.296	1	1.19	-0.482 0.97	2.34	0.019	0.99	2.25	-0.020	0.99
2	2.989	2	1.89	-0.368 0.47	3.06	0.024	0.80	3.19	0.067	0.80
5	4.172	5	2.27	-0.456 0.78	3.83	-0.082	0.77	3.87	-0.072	0.84

Table 7: Comparison between the experimental results and the updated EF model T.

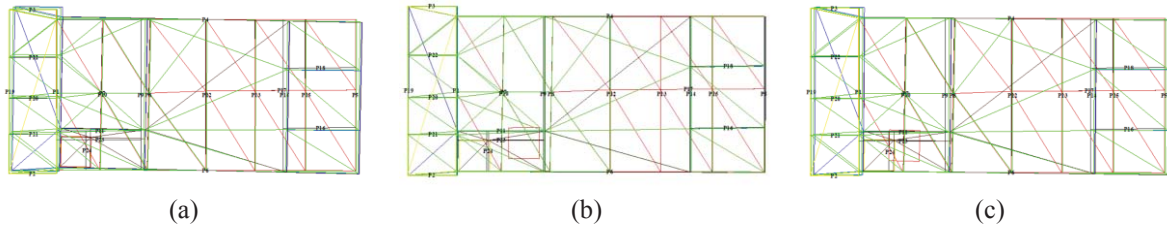


Figure 6: Shape of mode 2 in the (a) w/oT1, (b) T1 and (c) T2 updated EF models.

Introducing the coefficient  $c_{oop}$ , accounting for the directional effects of the unmodeled out-of-plane stiffness (see §4.2), does not bring improvements to the updating process. Nevertheless, solution T2 gives some further insights into the model dynamic behaviour. Comparing T2 with T1, neglecting the small variations in mass density, a lower stiffness along the  $x$ -direction allows obtaining equally satisfying results. Conversely, a much higher stiffness along the  $y$ -direction – 1.5 times greater than that of  $x$  – forms the optimal solution, confirming the expectations regarding the unbalance between the out-of-plane contributions provided by each direction.

#### 4.4 Comparison with the updated FE model

The results of the model update process (§4.2) show the ability of the calibrated EF model to correctly reproduce the experimental dynamics of the Consoli Palace. The unusual complexity of the structure, in this case, highlights the limitations introduced by common assumptions in the EF modelling of masonry structures as well. In the following, a detailed dynamic comparison with the updated FE model of the palace (§3.2) gives further insights on the suitability of these two formulations in supporting the SHM of historical masonry structures. Since the update of both structural models targeted the same experimental modes, the comparison is extended to the entire set of the first five modes (regardless of their employment in the updating process). Moreover, to overcome some issues faced with experimental mode shapes – mainly related to spatial aliasing and due to the absence of sensors on the bell tower, §3.1 – the two models are compared accounting for an increased number of nodes.

From a dynamic point of view, the two models show a similar ability to reproduce the ambient behaviour of the palace (see Table 3 and Table 7). Indeed, the FE model does not suffer from critical modelling simplifications (such as those related to the out-of-plane stiffness) which makes the EF updating process less straightforward. For these reasons, rather than looking at the constitutive parameters, it seems more interesting to compare directly the models' dynamic response.

For what concerns the calibration T1, the EF model does not correctly reproduce some modes of the FE model (Table 8), in particular the third mode – involving the flexural behaviour of the bell tower, Figure 3. This result is not unexpected, considering that this mode has not been included in the updating procedure. Undoubtedly, the most important difference between the two models lies in the second natural mode. In the EF model, mode 2 is mainly characterized by a *local* flexural behaviour of the bell tower in the  $x$ -direction. From a seismic point of view, this causes the activation of only a small fraction  $m_x$  of the total dynamic mass. In the FE model, on the other hand, the mode *globally* involves both the main body of the palace and the bell tower, so that a significant portion of the total dynamic mass is activated.

Calibration T2 appears to overcome most of these drawbacks. First, there is a remarkably good agreement in frequencies and an acceptable correlation in mode shapes – even for modes 3 and 4, excluded from the updating. Second, and more importantly, mode 2 configures itself



as a global mode, with a participant mass ratio comparable with the FE one. This finding emphasizes, again, the influence of the bell tower on the global dynamic behaviour of the structure, calling for further experimental investigations specifically aimed at identifying such an interaction.

Mode	FE (26000 ton)		EF – T1 (25800 ton)				EF – T2 (25000 ton)			
	$m_x$	$m_y$	$m_x$	$m_y$	$\Delta_f$	MAC	$m_x$	$m_y$	$\Delta_f$	MAC
1	0	0.80	0	0.57	-0.011	0.98	0	0.58	-0.044	0.98
2	0.52	0	0.05	0	0.003	0.79	0.45	0	0.046	0.73
3	0.10	0.01	0	0.02	-0.105	0.37	0.01	0	-0.031	0.65
4	0.18	0	0	0	-0.025	0.69	0.11	0.01	0.022	0.91
5	0.01	0.02	0.28	0	-0.082	0.68	0.08	0	-0.073	0.74

Table 8: Comparison between the updated FE model and the updated EF model T (with bell tower).

## 5 CONCLUSIONS AND FUTURE PERSPECTIVES

The paper proposes an uncommon application of the equivalent frame (EF) technique to the structural modelling of a historical masonry palace, the Consoli Palace of Gubbio, Italy. The EF modelling of such a complex and heterogeneous structure poses some challenging issues, which are discussed and specifically addressed in the work. The computational efficiency of the model allows the employment of a global search updating strategy, aimed at minimizing the differences with the experimental modal properties of the structure identified from ambient vibration tests. The results show the capability of the EF approach in describing the elastic dynamic behaviour of the structure and the need, for this structural typology, to overcome some limitations arising from simplifying modelling assumptions. The most relevant, in this case, proves to be the out-of-plane stiffness of the bearing walls, which is implicitly incorporated by the in-plane stiffness in the calibration process. The good accordance with the refined and updated Finite Element (FE) model of the structure confirms the possibility to employ the simplified EF formulation to support the model-based health monitoring of the palace. The comparison highlights, finally, the primary role played by the bell tower in determining the global dynamics of the structure. This outcome calls for further experimental investigations, which are being addressed within the Italian PRIN 2017 project *DETECT-AGING* through an extended dynamic, static and environmental monitoring system that has been recently deployed. The future developments will tackle the employment of both the EF and FE in the statistical simulations of post-seismic scenarios, supporting the localization and quantification of damage from vibration measurements through *metamodelling*. Further refinements of the EF model, aimed at the explicit description of the out-of-plane stiffness contributions of walls, are currently ongoing.

## 6 ACKNOWLEDGEMENT

This research has been supported by the Italian Ministry of Education, University and Research (MIUR) thanks to the funded project of national interest *DETECT-AGING* – “Degradation Effects on sTructural safEty of Cultural heriTAGE constructions through simulation and health monitorING” (Protocol No. 201747Y73L).

## REFERENCES

- [1] F. Clementi, A. Formisano, G. Milani, F. Ubertini, Structural Health Monitoring of Architectural Heritage: From the past to the Future Advances. *International Journal of Architectural Heritage*, **15**(1), 2021.
- [2] P. Roca, M. Cervera, G. Gariup, L. Pelà, Structural analysis of masonry historical constructions. Classical and advanced approaches. *Archives of Computational Methods in Engineering*, **17**(3), 299-325, 2010.
- [3] A.M. D’Altri, V. Sarhosis, G. Milani, J. Rots, S. Cattari, S. Lagomarsino, E. Sacco, A. Tralli, G. Castellazzi, S. de Miranda, Modeling strategies for the computational analysis of unreinforced masonry structures: review and classification. *Archives of Computational Methods in Engineering*, **27**, 1153-1185, 2019.
- [4] S. Lagomarsino, S. Cattari, PERPETUATE guidelines for seismic performance-based assessment of cultural heritage masonry structures. *Bulletin of Earthquake Engineering*, **13**, 13-47, 2015.
- [5] E. Quagliarini, G. Maracchini, F. Clementi, Uses and limits of the Equivalent Frame Model on existing unreinforced masonry buildings for assessing their seismic risk: A review. *Journal of Building Engineering*, **10**, 166-182, 2017.
- [6] F. Ubertini, C. Gentile, A.L. Materazzi, Automated modal identification in operational conditions and its application to bridges. *Engineering Structures*, **46**, 264-278, 2013.
- [7] Simulia, Abaqus Analysis User's Manual. Volume III: Materials, Dessault Systèmes, USA, 2010.
- [8] A. Kita, N. Cavalagli, F. Ubertini, Temperature effects on static and dynamic behavior of the Consoli Palace in Gubbio, Italy. *Mechanical Systems and Signal Processing*, **120**, 180-202, 2019.
- [9] N. Augenti, F. Parisi, Learning from construction failures due to the 2009 L’Aquila, Italy, earthquake. *Journal of Performance of Constructed Facilities*, **24**(6), 536-555, 2010.
- [10] S. Cattari, S. Degli Abbati, D. Ferretti, S. Lagomarsino, D. Ottonelli, A. Tralli, The seismic behaviour of ancient masonry buildings after the earthquake in Emilia (Italy) on May 20<sup>th</sup> and 29<sup>th</sup>, 2012. *Ingegneria Sismica*, **29**(2-3), 87-119, 2012.
- [11] A. Penna, P. Morandi, M. Rota, C.F. Manzini, F. Da Porto, G. Magenes, Performance of masonry buildings during the Emilia 2012 earthquake. *Bulletin of Earthquake Engineering*, **12**(5), 2255-2273, 2014.
- [12] L. Sorrentino, S. Cattari, F. Da Porto, G. Magenes, A. Penna, Seismic behaviour of ordinary masonry buildings during the 2016 central Italy earthquakes. *Bulletin of Earthquake Engineering*, **17**(10), 5583-5607, 2019.
- [13] S. Bracchi, M. Rota, A. Penna, G. Magenes, Consideration of modelling uncertainties in the seismic assessment of masonry buildings by equivalent-frame approach. *Bulletin of Earthquake Engineering*, **13**(11), 3423-3448, 2015.
- [14] D. Ottonelli, C. Marano, C. Manzini, B. Calderoni, S. Cattari, A comparative study on a complex URM building. Part I: sensitivity of the seismic response to different modelling options in the equivalent frame models. *Bulletin of Earthquake Engineering*, 2021. Submitted to the S.I.: URM nonlinear modelling - Benchmark project.

- [15] S. Lagomarsino, A. Penna, A. Galasco, S. Cattari, TREMURI program: an equivalent frame model for the nonlinear seismic analysis of masonry buildings. *Engineering structures*, **56**, 1787-1799, 2013.
- [16] N. Augenti, Seismic behaviour of irregular masonry walls. *Proceedings of the 1st European Conference on Earthquake Engineering and Seismology (ECEES)*, Geneva, Switzerland, 3-8 September, 2006.
- [17] M. Dolce, Schematizzazione e modellazione degli edifici in muratura soggetti ad azioni sismiche. *Industria delle costruzioni*, **25**(242), 44-57, 1991 (in Italian).
- [18] F.L. Moon, T. Yi, R.T. Leon, L.F. Kahn, Recommendations for seismic evaluation and retrofit of low-rise URM structures. *Journal of Structural Engineering*, **132**(5), 663-672, 2006.
- [19] S. Cattari, D. Camilletti, A.M. D'Altri, S. Lagomarsino, On the use of continuum Finite Element and Equivalent Frame models for the seismic assessment of masonry walls, *Journal of Building Engineering*, 2021. <https://doi.org/10.1016/j.jobbe.2021.102519>
- [20] F. Parisi, N. Augenti, Seismic capacity of irregular unreinforced masonry walls with openings, *Earthquake Engineering and Structural Dynamics*, **42**(1), 101-121, 2013.
- [21] M. Berti, L. Salvatori, M. Orlando, P. Spinelli, Unreinforced masonry walls with irregular opening layouts: reliability of equivalent-frame modelling for seismic vulnerability assessment. *Bulletin of Earthquake Engineering*, **15**(3), 1213-1239, 2017.
- [22] R. Siano, V. Sepe, G. Camata, E. Spacone, P. Roca, L. Pelà, Analysis of the performance in the linear field of equivalent-frame models for regular and irregular masonry walls. *Engineering Structures*, **145**, 190-210, 2017.
- [23] B. Calderoni, E.A. Cordasco, C. Musella, A. Sandoli, La modellazione delle pareti murarie in relazione alle irregolarità geometriche: problemi aperti. *Proceedings of XVII ANIDIS Conference*, Pistoia, Italy, 17-21 September, 2017. (in Italian)
- [24] R. Siano, P. Roca, G. Camata, L. Pelà, V. Sepe, E. Spacone, M. Petracca, Numerical investigation of non-linear equivalent-frame models for regular masonry walls. *Engineering Structures*, **173**, 512-529, 2018.
- [25] D. Camilletti, S. Cattari, S. Lagomarsino, In plane seismic response of irregular URM walls through Equivalent Frame and Finite Element models, *Proceedings of 16<sup>th</sup> European Conference on Earthquake Engineering (ECEE)*, Thessaloniki, Greece, 18-21 June, 2018.
- [26] D. Camilletti, Equivalent Frame modelling of URM buildings: numerical validation and rules. PhD thesis, University of Genoa, Genoa, Italy, 2019.
- [27] S. Cattari, G. Magenes, Benchmarking the software packages to model and assess the seismic response of unreinforced masonry existing buildings through nonlinear static analyses. *Bulletin of Earthquake Engineering*, 2021. <https://doi.org/10.1007/s10518-021-01078-0>
- [28] MIT 2019, Ministry of Infrastructures and Transportation, Circ. C.S.LL.PP. No. 7 of 21/1/2019. Istruzioni per l'applicazione dell'aggiornamento delle norme tecniche per le costruzioni di cui al Decreto Ministeriale 17 Gennaio 2018. G.U.S.O. No. 35 of 11/2/2019. (in Italian)

- [29] S. Cattari, S. Resemini, S. Lagomarsino, Modelling of vaults as equivalent diaphragms in 3D seismic analysis of masonry buildings. In *Structural analysis of historic construction: preserving safety and significance*, Two Volume Set, 537-544, 2008. CRC press.
- [30] D. Sivori, M. Lepidi, S. Cattari, Structural identification of the dynamic behavior of floor diaphragms in existing buildings. *Smart Structures and Systems*, **27**(2), 173, 2021.
- [31] D. Sivori, M. Lepidi, S. Cattari, Ambient vibration tools to validate the rigid diaphragm assumption in the seismic assessment of buildings. *Earthquake Engineering and Structural Dynamics*, **49**(2), 194-211, 2020.
- [32] B. Jaishi, W.X. Ren, Structural finite element model updating using ambient vibration test results. *Journal of structural engineering*, **131**(4), 617-628, 2005.
- [33] R.J. Allemang, The modal assurance criterion—twenty years of use and abuse. *Sound and vibration*, **37**(8), 14-23, 2003.
- [34] S. Cattari, S. Degli Abbatì, S. Alfano, A. Brunelli, F. Lorenzoni, F. Da Porto, Dynamic calibration and seismic validation of numerical models of URM buildings through permanent monitoring data. *Earthquake Engineering and Structural Dynamics*, 2021. Accepted for publication.

## RAPID DESIGN OF R/C COLUMNS USING MACHINE LEARNING TECHNIQUES

Vassilis K. Papanikolaou<sup>1</sup>, and Aristotelis E. Charalampakis<sup>2</sup>

<sup>1</sup> School of Civil Engineering  
Aristotle University of Thessaloniki  
Thessaloniki, 54124, Greece  
billy@civil.auth.gr

<sup>2</sup> Department of Civil Engineering  
University of West Attica  
Athens, 12244, Greece  
achar@uniwa.gr

---

### Abstract

*The development of Machine Learning, which is deemed to be the path to Artificial Intelligence, has changed tremendously the way many computationally intensive tasks are treated nowadays. Regarding the design of R/C columns and bridge piers, the results of a recent project which proposes a number of design functions are examined and discussed in this work. Both rectangular and circular as well as solid and hollow sections are treated. The proposed design functions are naturally immune to numerical instabilities and achieve more than adequate accuracy for design. They are also, by nature, orders of magnitude faster than any design algorithm based on iterative equilibrium procedures. The error estimation for each function is described in detail based on extensive test sets. Certain method pitfalls, which were encountered and successfully treated, are also discussed.*

**Keywords:** Machine Learning; Artificial Neural Networks; Big Data; Reinforced Concrete; Design; Columns; Bridge piers.

---



## 1 INTRODUCTION

Reinforced concrete (R/C) vertical members (e.g., columns, bridge piers, structural walls) are generally subjected to a combined action comprising two perpendicular planes of flexure (biaxial bending) and a usually compressive axial load. The magnitude and ratio between these three actions ( $N$ ,  $M_x$ ,  $M_y$ ) mainly depends on the stiffness and position of the member within the structure and the applied loading combination (e.g., gravity, seismic, wind). The design of critical sections for these vertical members, i.e., the calculation of required reinforcement, is normally carried out either by use of traditional design charts (e.g., [1]) or by more rigorous algorithmic solutions that require modern computational resources (e.g., [2,3]). Numerous repetitions of the above design process are usually required at structural level; therefore, its computational efficiency is of prime importance.

In this paper, a fundamentally different approach to the design of R/C vertical members is suggested; instead of applying design data (e.g., section dimensions, material properties, etc.) and computational rules (e.g., stress integration, section equilibrium, etc.) to produce answers to the design problem (i.e., the required reinforcement), the exact inverse procedure is applied; using a robust section analysis algorithm, an extensive set (tens of millions) of sample solutions to the problem is first compiled. Then, large Artificial Neural Networks (ANNs) are trained to predict the solution, i.e., the required reinforcement. The obvious reward of this approach is that the forward-propagation can be transformed into closed-form design functions which are by orders of magnitude faster than any iterative schemes. They are also immune to any numerical instability issues.

## 2 MACHINE LEARNING

Machine learning (ML) provides the technical background of data mining, i.e., extraction of information from large datasets, focused on predictions based on known data properties [4]. This is not something new; simple regression analyses based on experimental data can be considered to be early ML applications in engineering. However, regarding the R/C design problem investigated herein, such attempts have not gained much recognition due to the limited amount of experimental data, which may lead to overfitting and eventually inaccurate predictions. Contrarily, the proposed approach operates directly on a huge amount of pre-calculated results which are based on structural mechanics principles and Code regulations [e.g., 5]. It is true that the structure of the produced design functions is obscure; yet, when utilized as a black-box, their results are easily verifiable by comparing them to the results of classic iterative computational methods.

The objective of this work is to produce the simplest possible algorithm (function) that yields an acceptable level of accuracy for practical design purposes. In this context, the initial goal for the calculation of mechanical reinforcement ratio ( $\omega$ ) was to produce a maximum absolute error of 0.01, corresponding to an actual reinforcement area error as low as 0.3 % (in a typical R/C column design). Experimentation with various ML implementations showed that only relatively large Artificial Neural Networks (ANNs) have the adequate complexity to address the high nonlinearities inherent in the data. Moreover, data overfitting can be avoided effectively by using extremely large training sets. These training sets were evenly spaced within a standard range of values for each design parameter. Also, additional engineered parameters were applied to assist the learning process. In order to validate of the applied procedure, new testing sets, unknown to the trained ANN, of double the size of their training counterparts were also compiled. The final measure to ensure the robustness of the proposed method was to apply auxiliary ANN-based functions to screen out unreasonable user input that may cause false output due to extrapolation.

### 3 ANN TRAINING & TESTING

For training and testing the ANN-based design functions, extensive sets were pre-calculated using a robust derivative-free algorithm for section analysis under biaxial bending and axial load [3]. Four section types were considered (**R**ectangular / **C**ircular, **S**olid / **H**ollow) using normalized input parameters, similar to traditional design charts [1]. Two notable novelties were the inclusion of the actual concrete cover ( $c$ ) instead of cover ratios and the consideration of uniformly distributed reinforcement along the section perimeter (constant  $A_s$  per unit length – subscript ‘d’), additional to the standard equal amount per side ( $A_s/4$  – subscript ‘e’) for rectangular sections. Fig. 1 shows the considered section parameters for the various section types.

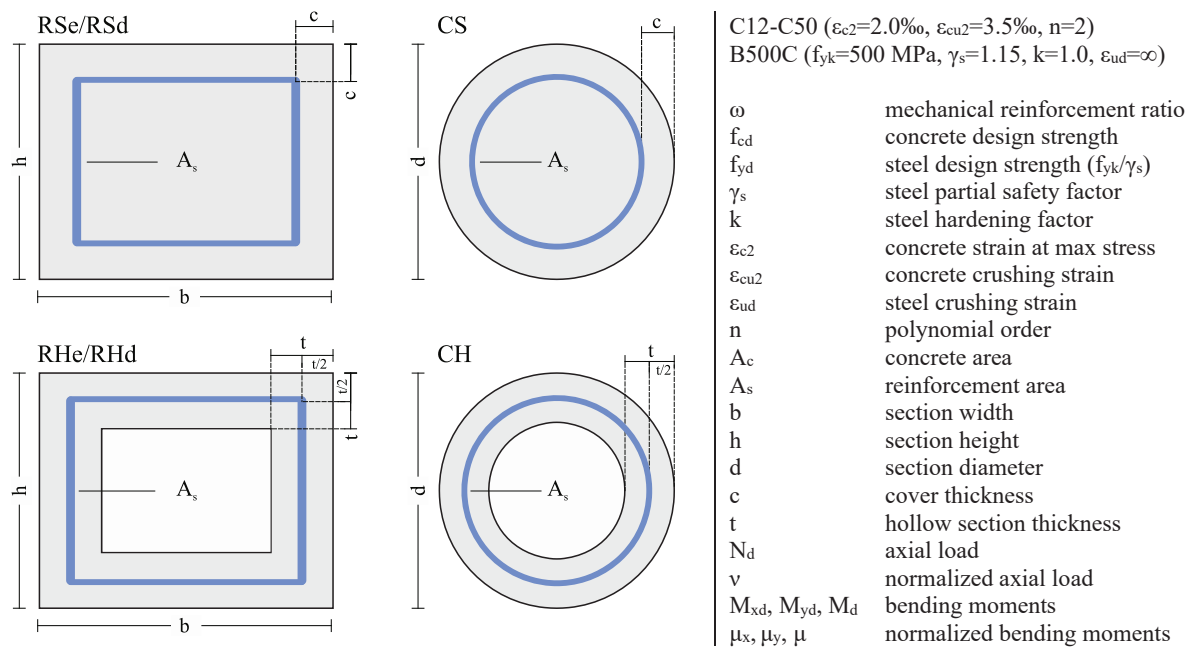


Fig. 1: Section design parameters

Normal strength concrete (C12/15 to C50/60) with parabolic ( $n=2$ ) stress-strain relationship and standard B500C steel grade (no hardening, no strain limit) was considered, according to the provisions of the latest draft of Eurocode 2 (EN1992-1-1 [6]). Typical ranges for section parameters were (i) a normalized axial load ( $v$ ) from  $-0.6$  to  $0.1$  (compression negative), (ii) rectangular section aspect ratios ( $b/h$ ) from  $1.0$  (square) to  $2.0$ , (iii) hollow section width to size ( $t/b$  or  $t/d$ ) from  $0.05$  to  $2.0$ , (iv) concrete cover to section size ratios ( $c/b$  or  $c/d$ ) from  $0.01$  to  $0.15$  and (v) mechanical reinforcement ratios from zero (no reinforcement) to  $0.7$ , which is deemed a sufficient upper limit for practical design purposes. More details on the ANN setup and the compilation of training/testing sets can be found in [6]. Table 1 shows the set sizes (number of instances) that were finally processed in the present ANN implementation.

Solid section	Training	Test	Hollow section	Training	Test
CS	88,394	177,675	CH	176,823	355,385
RSe	37,009,460	75,131,088	RHe	41,637,616	84,032,253
RSd	37,009,459	75,131,295	RHd	41,637,623	84,032,269

Table 1: Training/test set sizes

## 4 RESULTS

The training procedure ran for several days on a modern PC with 128 GB of RAM and produced six closed form design functions for the considered section types. All analyses presented herein have been carried out using Python/TensorFlow. Table 2 shows a detailed overview of these functions, together with the ANN configuration (nodes in the input/inner/output layers). Moreover, it includes the mean absolute error (MAE) and the maximum positive and negative errors (MPE/MNE), in terms of calculated mechanical reinforcement ratio ( $\omega$ ), when tested against independent sets of double the training size. It is apparent that in all cases, the maximum error is well below the initial target of  $\omega = 0.01$ .

Section	Function	ANN size	MAE	MPE/MNE
CS	$\omega = f(c/d, v, \mu)$	3-15-15-1	0.000125	0.000947/-0.001123
CH	$\omega = f(t/d, v, \mu)$	3-15-15-1	0.000117	0.000902/-0.000858
RSe	$\omega = f(b/h, c/b, v, \mu_x, \mu_y)$	9-35-35-1	0.000186	0.006404/-0.004423
RSd	$\omega = f(b/h, c/b, v, \mu_x, \mu_y)$	9-35-35-1	0.000207	0.005233/-0.005694
RHe	$\omega = f(b/h, t/b, v, \mu_x, \mu_y)$	9-35-35-1	0.000170	0.004691/-0.003494
RHd	$\omega = f(b/h, t/b, v, \mu_x, \mu_y)$	9-35-35-1	0.000203	0.005037/-0.006202

Table 2: Design functions and ANN performance

The above functions are provided in various programming languages (C#, C++, Delphi, Fortran, Java, MATLAB, Python, VB.NET, VBA) in the following GitHub repository:

<https://github.com/rcslab-auth/Project-Omega>

Fig. 2 shows the typical source code of one of these functions, together with a provided spreadsheet that facilitates their use in everyday practice.

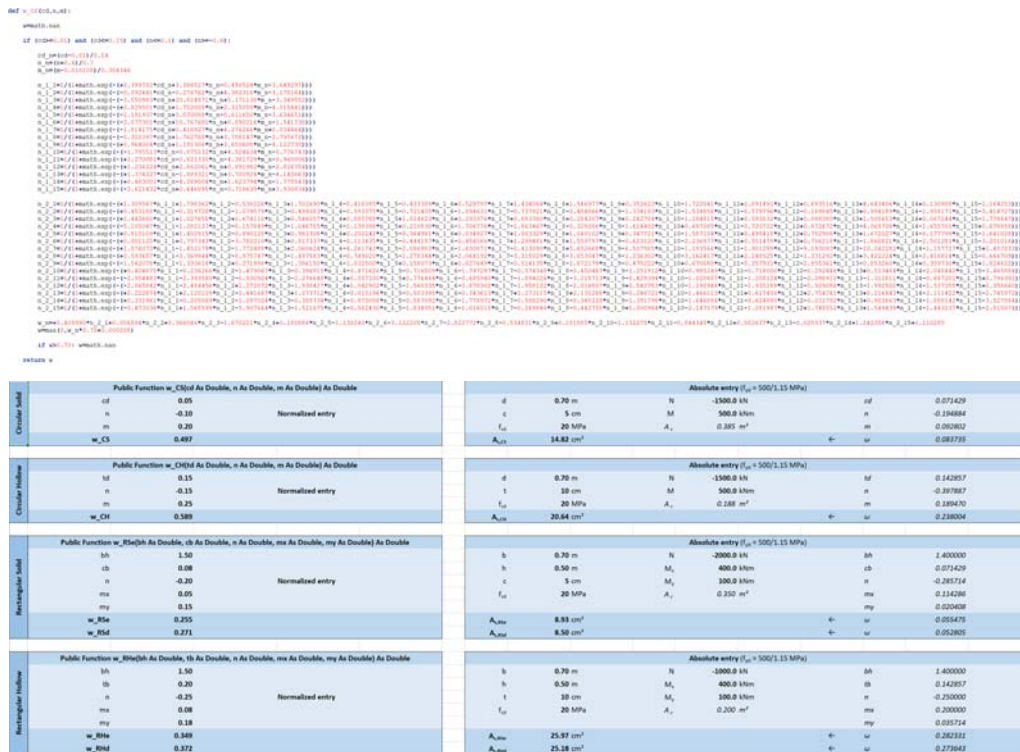


Fig. 2: Function code (Python) and spreadsheet format (Excel)

## 5 ISSUES / VALIDATION / BENCHMARK

In order to prevent invalid user input, all input variables were limited to the aforementioned ranges on which the respective functions were trained for; however, this could not be applied for normalized bending moments ( $\mu_x$ ,  $\mu_y$ ), since their limit values were not known in advance, depending mainly on the axial load level ( $v$ ). This led to unpredictable function behavior for unreasonably high user input for bending moments, which, due to the high nonlinearity of design functions, may wrongly predict values for ( $\omega$ ) in the valid range of  $[0, 0.7]$  (extrapolation issues, Fig. 3a). To remedy this problem, suitable boundary functions were introduced using small ANNs trained on a fixed value of  $\omega = 0.75$ , in order to successfully control invalid user input (Fig. 3b). A detailed description of this procedure can be found in [6].

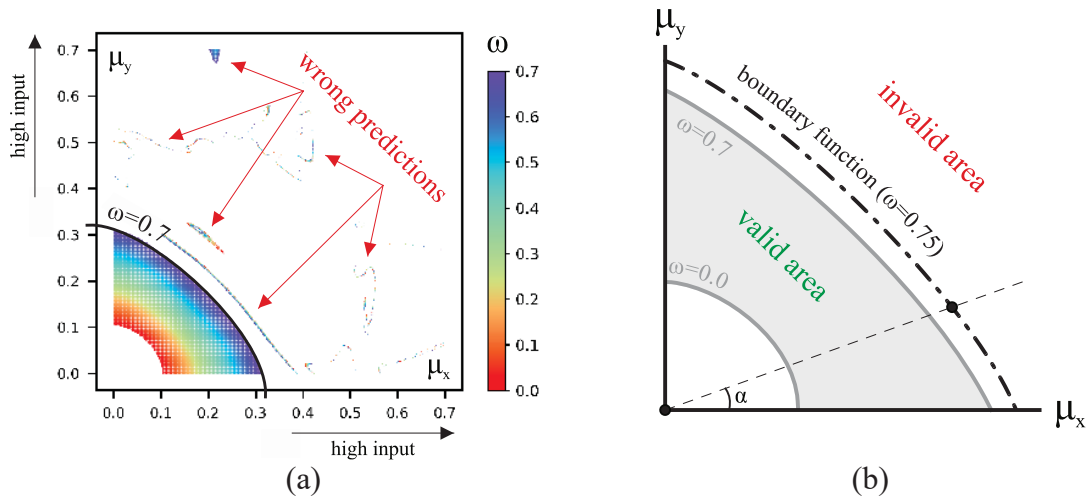


Fig. 3 Extrapolation issues and boundary functions

The accuracy of the suggested design functions was further tested against well-established uniaxial and biaxial design charts [7,1] using millions of moment and axial load combinations that were directly overlaid on charts together with the calculated mechanical reinforcement ratio ( $\omega$ ), as shown in Fig. 4. In all cases, correlation was excellent.

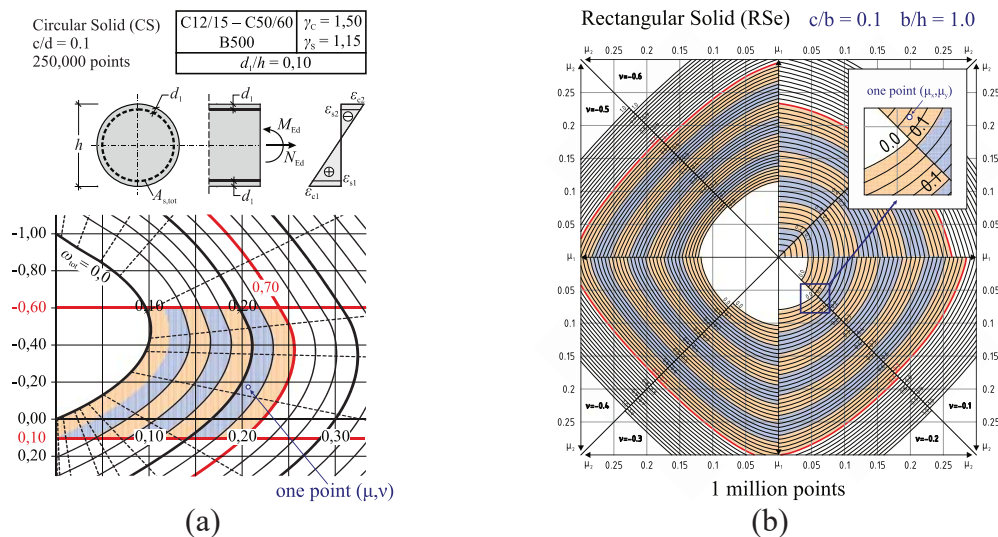


Fig. 4 Design function tests against (a) uniaxial [7] and (b) biaxial design charts [1]

Finally, for evaluating the computational performance of the proposed design functions, one million rectangular solid section configurations were calculated, and execution time was compared against an identical run with a classic fast biaxial design iterative algorithm [8]. It was measured that the execution time for the ML-based functions was about *120 times faster* (5 s compared to 600 s on an average PC). Since the proposed design functions produce closed form (i.e., non-iterative) solutions, it is claimed that these will always outperform by a large margin any iterative design method based on stress integration.

## 6 CONCLUSIONS

In this paper, novel closed-form design functions are proposed for the rapid and accurate design of R/C columns and bridge piers under biaxial bending with axial load, based on relatively large Artificial Neural Networks. The use of these functions outperforms any known iterative design methods by orders of magnitude and it is immune to any numerical instabilities. Moreover, improved features not available in classic design charts, such as constant concrete cover thickness, hollow rectangular sections and constant reinforcement per unit length along the perimeter have been implemented.

All functions are available in a public repository in multiple programming languages, ready to be integrated into design software with minimal effort. It is believed that similar ANN-based regression procedures can effectively substitute traditional programming approaches in many engineering problems, providing the desired accuracy with unprecedented computational performance.

## REFERENCES

- [1] Papanikolaou VK, Sextos AG. Design charts for rectangular R/C columns under biaxial bending: A historical review toward a Eurocode-2 compliant update. *Eng Struct* 2016;115:196–206. doi:10.1016/j.engstruct.2016.02.033.
- [2] Charalampakis AE, Koumousis VK. Ultimate strength analysis of composite sections under biaxial bending and axial load. *Adv Eng Softw* 2008;39:923–36. doi:10.1016/j.advengsoft.2008.01.007.
- [3] Papanikolaou VK, Analysis of arbitrary composite sections in biaxial bending and axial load. *Comput Struct* 2012;98–99:33–54. doi:10.1016/j.compstruc.2012.02.004.
- [4] Witten IH, Frank E, Hall MA, Pal CJ. Data mining : practical machine learning tools and techniques. 4th ed. Morgan Kaufmann; 2016.
- [5] CEN Eurocode 2: Design of concrete structures - Part 1-1: general rules and rules for buildings 2004:EN 1992-1-1.
- [6] Charalampakis, A.E. and Papanikolaou, V.K. Machine learning design of R/C columns. *Eng Struct* 2021;226:111412.doi:10.1016/j.engstruct.2020.111412.
- [7] Holschemacher K, Müller T, Lobisch F. Bemessungshilfsmittel für Betonbauteile nach Eurocode 2. Weinheim, Germany: Wiley-VCH Verlag GmbH & Co. KGaA; 2012. doi:10.1002/9783433602102
- [8] Penelis GG. Analytical investigation of the biaxial bending problem of R/C sections using plasticity theory (in Greek). Aristotle University of Thessaloniki, 1969.



## DEVELOPMENT OF A NEW FUNDAMENTAL PERIOD FORMULA BY CONSIDERING SOIL-STRUCTURE INTERACTION WITH THE USE OF MACHINE LEARNING ALGORITHMS

Vicky-Lee Taljaard<sup>1</sup>, Dewald Z. Gravett<sup>1</sup>, Christos Mourlas<sup>2</sup>, George Markou<sup>1</sup>, Nikolaos Bakas<sup>3</sup> and Manolis Papadrakakis<sup>2</sup>

<sup>1</sup> Department of Civil Engineering, University of Pretoria, South Africa  
e-mail: [u17078882@tuks.co.za](mailto:u17078882@tuks.co.za); [u16004664@tuks.co.za](mailto:u16004664@tuks.co.za); [George.markou@up.ac.za](mailto:George.markou@up.ac.za)

<sup>2</sup> Institute of Structural Analysis & Seismic Research, National Technical University of Athens, 9  
Iroon Polytechniou Str., Zografou Campus, GR-15780 Athens, Greece  
e-mail: {mourlasch, [mpapadra](mailto:mpapadra}@central.ntua.gr)}@central.ntua.gr

<sup>3</sup> Scientific Coordinator, Computation-based Science and Technology Research Center, The Cyprus  
Institute, Nicosia, Cyprus  
e-mail: [n.bakas@cyi.ac.cy](mailto:n.bakas@cyi.ac.cy)

---

### Abstract

*The fundamental period of a structure is one of the key parameters utilized in the design phase to compute the seismic-resistant forces. Although the importance of seismic-resistant buildings is well understood it has been found that the current design code formulae, which are used to predict the fundamental period of reinforced concrete (RC) buildings are quite simplistic, failing to accurately predict the natural frequency, raising many concerns with regards to their reliability. The primary objective of this research project was to develop a formula that has the ability to compute the fundamental period of an RC structure, while taking into account the soil-structure interaction phenomenon. This was achieved by using a computationally efficient and robust 3D detailed modelling approach for modal analysis obtaining the numerically predicted fundamental period of 475 models, producing a dataset with numerical results. This dataset was then used to train a machine learning algorithm to formulate three fundamental period formulae using a higher-order, nonlinear regression modelling framework. The three newly proposed formulae were evaluated during the validation phase to investigate their performance using 60 new out-of-sample modal results, where, in this work, additional validation models are created and used to test the predictive abilities of the proposed fundamental period formulae. The findings of this research report suggest that the proposed fundamental period formulae exhibit exceptional predictive capabilities for the under-study RC multi-storey buildings, where they outperform all existing de-sign code fundamental period formulae currently in effect.*

**Keywords:** Fundamental Period Formula, Soil-Structure Interaction, Machine Learning Algorithms, Modal Analysis, Finite Element Method, Reinforced Concrete.

---

## 1 INTRODUCTION

The importance of seismic resistant design of structures and the ability thereof to capture the dynamic response of structures is crucial, especially in areas prone to seismic activity. One of the most important dynamic characteristics is the fundamental period, as it has a significant influence on the calculation of the seismic loads. During a seismic excitation, the interaction between the superstructure (building) and the substructure (soil) can become important as it starts to affect the stress-strain distribution within the superstructure, altering the initial expected results [1-3]. In general, it has been found that soil-structure interaction (SSI) can increase the fundamental period and the overall damping of the system, thus it is important to consider it in order to eliminate unsafe designs and unexpected damage development [4-5] during an earthquake excitation.

Numerous codes worldwide foresee their own methodology of computing the fundamental period of reinforced concrete (RC) structures. However, it is well documented that the current design codes all fail to consider the effect that SSI has on the fundamental period of a structure [3]. There are also some shortfalls with respect to the stiffness distribution of the structure, as the effect of the shear walls is not properly taken into considerations especially in the current Eurocode 8 [6], amongst others as presented in [1]. Thus, establishing design tools that would be able to predict the dynamic properties of RC buildings is of significant importance.

The methodology foresees the use of a computationally efficient and robust 3D modelling technique known as the HYMOD approach [7-9] in order to perform modal analysis to investigate the effect that SSI has on the fundamental period of RC structures. The overall approach foresaw the creation of a dataset comprising out of all the modal analysis results obtained from the various numerical models [1].

Thereafter this research work foresaw [1] the development of fundamental period formulae that were validated through an out-of-plane dataset and were found to have high accuracy. A number of machine learning (ML) and artificial intelligence (AI) algorithms were used to develop predictive models (including closed-form formulae), where it was found that the ability to predict the fundamental period of RC structures through a validation out-of-sample dataset was significantly high. This research work aims to further validate the proposed fundamental period formulae [1] through the use of additional fundamental period results that were developed for the needs of this manuscript.

## 2 MACHINE LEARNING ALGORITHM

The fundamental principles of the ML model are based on the formation of nonlinear terms consisting of various combinations of independent variables, up to the third degree [10]. The algorithm is able to automatically select nonlinear features, corresponding to the minimum prediction error. The data is normalized by subtracting the mean value from it as to eliminate any irregular outliers.

The algorithm was programmed to use 85% of the data to analyse the trends, by identifying relative relationships used to train the algorithm. The remaining 15% of the data is then used to evaluate the proposed fundamental period formulae. The algorithm presented in the next page represents the procedure for the generation of the formula which is developed by the various authors of Julia programming language [11]. Based on the numerical investigation performed for the needs of this work, it was confirmed that the proposed algorithm is efficient providing with the necessary tools in developing the predictive formulae.

---

**Algorithm: Higher Order Regression**


---

**Input:**  $XX^1$ ,  $YY^2$ ,  $nlf^3$ **Output:** Prediction Formulae

1. Create all nonlinear features<sup>4</sup> ( $anlf$ )
2. For  $i=1:nlf$  do
3.     For  $j=1:anlf$  do
4.         Add  $j$  to the model
5.         Calculate Prediction Error
6.     End
7.     Keep in the model the  $j^{\text{th}}$  feature which yields the minimum prediction error
5. End

**Return:** Prediction Formula

---

<sup>1</sup>Independent Variables, <sup>2</sup>Dependent Variable, <sup>3</sup>desired number of nonlinear features, <sup>4</sup>with all combinations up to the 3<sup>rd</sup> degree.

---

### 3 NUMERICAL MODELS AND DATASET DEVELOPMENT

To develop a design formula through training, requires a relatively large number of models that will be analyzed under a modal analysis thereof. The HYMOD approach was used to generate models of RC structures founded on soft, medium and hard soil. This was achieved by extending the work performed by Gravett et al. [7] to add more models to the existing database that was used for the investigation of the SSI effect on RC buildings [1].

The models all originated from the 4-storey RC building studied by Markou et al. [12] with two parallel frames connected by four out-of-plane central beams and a continuous slab of 150mm resulting in a plan area consisting of 3 bays (see Fig. 1). The total span of each parallel frame was 8.9m and had a perpendicular distance of 6.25m between the two frames. Each floor is vertically spaced 3m center-to-center with the central bay infilled with an RC shear wall of 2.9 x 0.25 m section as shown in Fig. 2. It should be noted that the frame of the RC building was designed based on the old Cyprus code [13] and then retrofitted with RC infill shear walls. The reinforcement details for the in-plane beams, columns and shear walls are shown in Fig. 2.

The 475 modal results were generated from models that were modified geometrically, where different soil domains were also assumed. Table 1 shows the minimum and maximum dimensions of the models based on the research work presented in [1]. Fig. 3 shows the case of a 2-storey RC frame with multiple openings, which was then modified to 4, 6, 8 and 10-storey buildings. For more information related to the models' geometries, one may refer to [1].

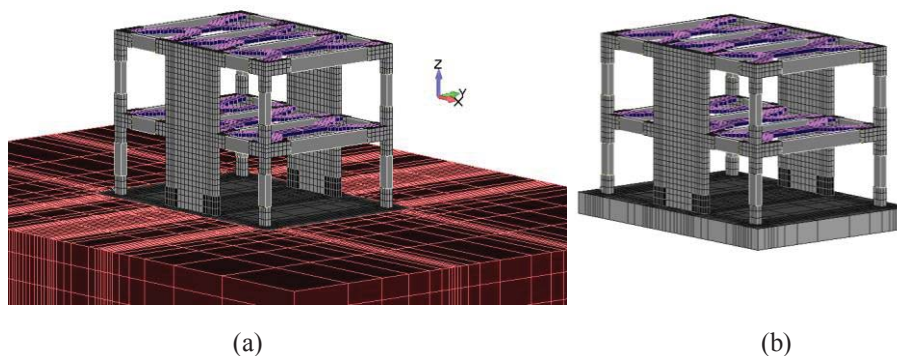


Figure 1. Single span RC mesh of a 2-storey structure with shear walls (a) flexible-base SSI mesh (b) fixed-base with raft foundation mesh.

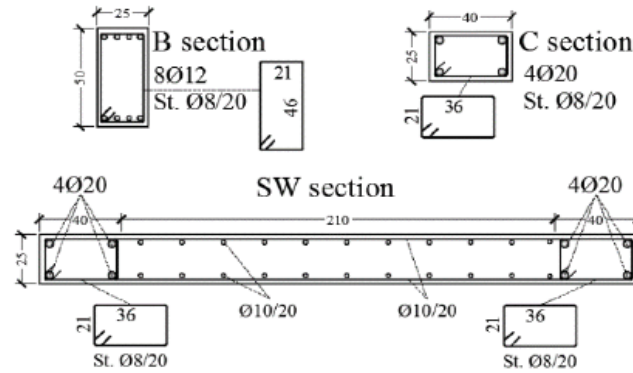


Figure 2. Reinforcement details of the (B)eam section, (C)olumn section and (SW) Shear Wall section respectively [9].

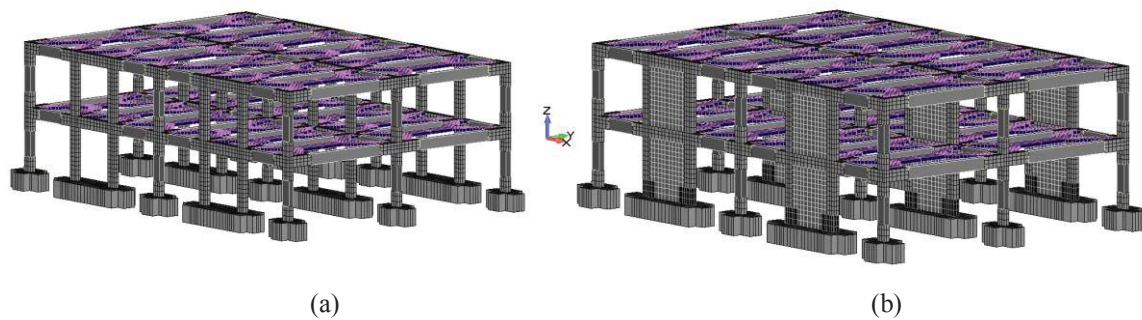


Figure 3. Double span mesh of a 2-storey RC structure without SSI (a) with shear walls (b) without shear walls.

Variables	Minimum	Maximum
Soil Depth (m)	3	60
Soil E (kPa)	65 000	700 000
H (m)	6	30
L (m)	6.25	18.25
B (m)	6.25	18.25
$\rho$ (%)	0	82.9

Table 1: Minimum and maximum values of the HYMOD meshes.

In order to further investigate the performance of the proposed formulae, a new set of additional validation models were created for the needs of this paper. A diverse set of 15 random models were created which yielded a total of 30 numerically derived fundamental periods. The aim of this validation set was to create random models that have geometries that significantly deviate from the typical geometries used to generate the dataset which was used to extract the proposed formulae.

These models were analyzed by assuming a fixed or flexible base (with and without considering the effect of SSI), which then yielded a total of 15 new models. This was done in order to investigate the proposed formulae to predict the fundamental mode of out-of-sample models since these additional models differ substantially from those in the original validation set [1]. It is important to note that all of the additional validation models fall within the range of values as set out in Table 1. Fig. 4 shows the layout of the five additional validation models, where the model in Figs 4d and 4e foresee the analysis of asymmetric frames in-terms of the shear wall positioning. This type of geometries was not assumed within the dataset that was used to train the models and derive the proposed fundamental period formulae. It is also important to note



here that, the newly developed models foresaw the discretization of a 5m deep soil when the SSI was accounted for, where the soil Young modulus was equal to 300 and 700 MPa. Therefore, 5 fixed models, 5 models with 300 MPa soil and another 5 with 700 MPa soil.

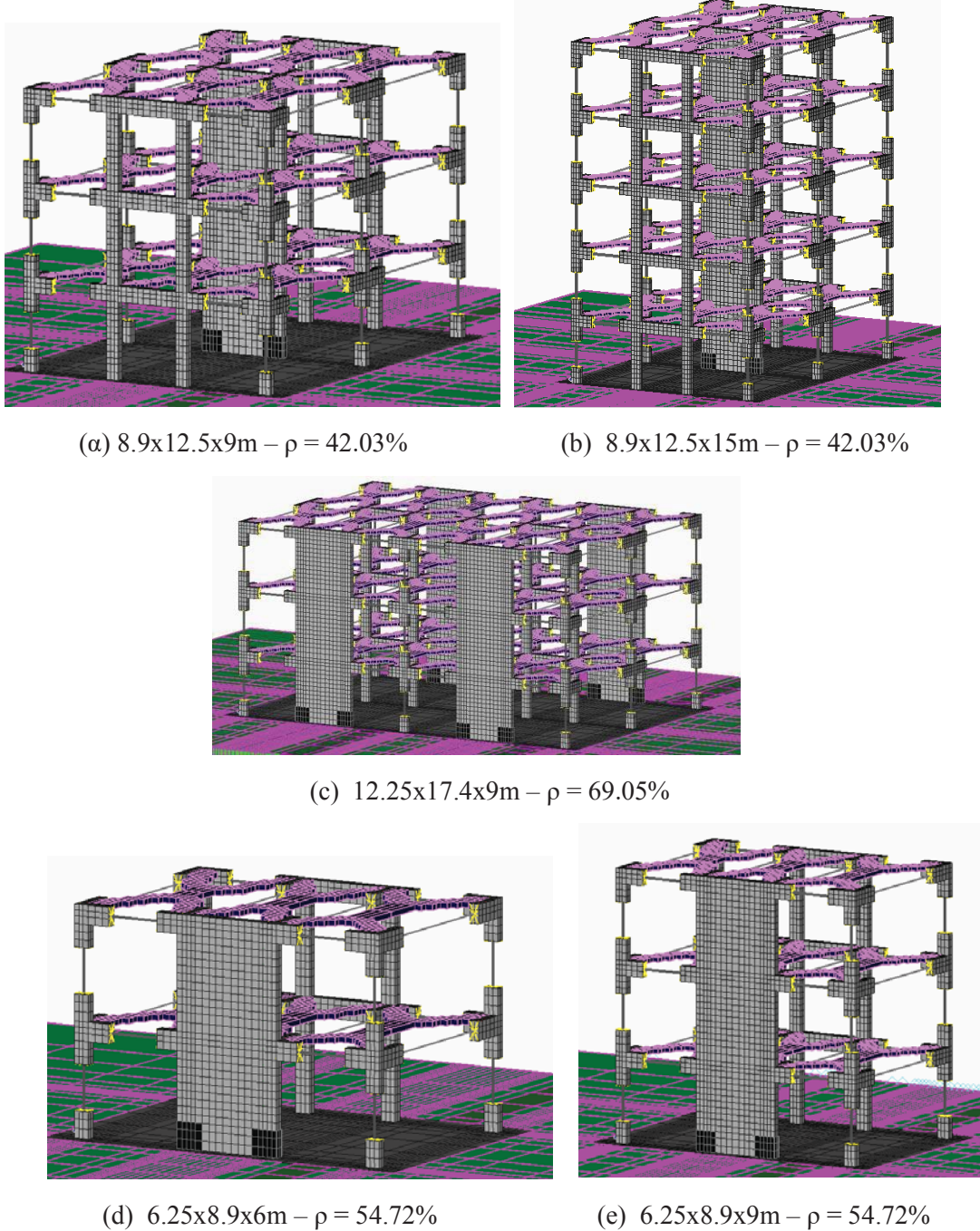


Figure 4. RC building models with soil. (a) 3-storey and (b) 5-storey with a shear wall in the middle, (c) 3-storey shear walls at the perimeter and (d) 2-storey and (e) 3-storey with a single shear wall (asymmetric cases).

#### 4 PROPOSED FUNDAMENTAL PERIOD FORMULAE

Upon successful completion of the ML implementation, three design formulae were generated. The proposed formulae are currently only valid for the range of values shown in Table 1,



as previously discussed. The accuracy of the design formulae is directly related to the correlation between the numerically predicted period and those of the formulae. This in return depends on the number of features used within the design formulae.

Therefore, three individual features were considered (3, 5, and 20) to develop and parametrically investigate the numerical response of the developed formulae. It is important to note herein that the building features that were accounted for, during the training process are the following:

**H** the building's height (m)

**$\rho$**  the percentage of shear walls (%)

**L** the length of building parallel to the oscillating direction (m)

**B** the width of the building perpendicular to the oscillating direction (m)

**$E_s$**  the soils' modulus of elasticity (kPa)

**D** the soil depth (m)

The three different assumptions in terms of the number of features within each formula yielded three different formulae as shown below:

3-Features Formula:

$$T = (0.0332205 \cdot H) - (0.000123101 \cdot \rho \cdot H) + (16.726 \times 10^{-6} \cdot L \cdot B^2) - 0.0275279 \quad (1)$$

5-Features Formula:

$$T = (0.0324913 \cdot H) - (86.048 \times 10^{-6} \cdot \rho \cdot H) + (20.105 \times 10^{-6} \cdot L \cdot B^2) - (28.11 \times 10^{-14} \cdot \rho \cdot L \cdot E_s) - (53.766 \times 10^{-6} \cdot \rho \cdot L) - 0.0173241 \quad (2)$$

20-Features Formula:

$$\begin{aligned} T = & (0.0328677 \cdot H) - (143.475 \times 10^{-6} \cdot \rho \cdot H) - (79.921 \times 10^{-8} \cdot L \cdot B^2) \\ & - (10.458 \times 10^{-14} \cdot \rho \cdot L \cdot E_s) - (55.061 \times 10^{-6} \cdot \rho \cdot L) \\ & - (71.214 \times 10^{-12} \cdot E_s \cdot D^2) + (5.016 \times 10^{-6} \cdot L \cdot H \cdot D) \\ & - (2.93 \times 10^{-18} \cdot B \cdot E_s^2) + (7.121 \times 10^{-10} \cdot B \cdot E_s) + (8.702 \times 10^{-6} \cdot L \cdot H^2) \\ & + (93.621 \times 10^{-8} \cdot L \cdot \rho^2) - (6.093 \times 10^{-6} \cdot L \cdot H \cdot \rho) + (3.351 \times 10^{-6} \cdot \rho \cdot H^2) \\ & + (60.549 \times 10^{-12} \cdot B \cdot E_s \cdot D) + (16.982 \times 10^{-5} \cdot B^2) - (64.89 \times 10^{-6} \cdot H^2) \\ & - (9.776 \times 10^{-12} \cdot H \cdot E_s \cdot D) + (1.477 \times 10^{-17} \cdot H \cdot E_s^2) \\ & - (44.111 \times 10^{-10} \cdot H \cdot E_s) - (2.891 \times 10^{-6} \cdot H \cdot D \cdot B) + 3.8476 \times 10^{-4} \quad (3) \end{aligned}$$

Each formula was compared against the numerical results from the modal analysis in order to evaluate the average absolute error which resulted in 9.04%, 7.86% and 5.35% for the 3-, 5- and 20-feature period formulae, respectively [1]. An additional set of 60 out-of-sample modal results were developed [1], where the proposed formulae managed to predict the results with a high accuracy and outperform any existing fundamental period formula that can be found in the international literature. However, the ability of these formulae to predict out-of-sample cases should be further investigated through the use of more unconventional in-terms of geometry buildings as it is going to be presented in the next section.

## 5 ADDITIONAL VALIDATION RESULTS

Numerically computed periods derived from the additional validation models that were developed herein (30 additional modal results) were compared against those obtained from the formulae for each case. The numerically predicted periods were plotted against those obtained from the formulae for each case along with their correlation as can be seen in Figs 5 – 7.

By evaluating the correlation between the relationships of the numerically calculated periods against those obtained from the formulae for each case, it is easy to observe that a high correlation was achieved for each formula. The relationship obtained from the 20-feature correlation

indicates that the formula yields a very good prediction deriving a prediction error of 8.5% (see Table 2). The 5- and 3-feature formulae have less accuracy given that their complexity and ability to account for the contribution of each feature of the building and its soil is not as high as that of the 20-feature formula. It is also interesting to note at this point that even though the newly developed validation models vary substantially from the original models used to train the formulae [1], the proposed formulae were still able to accurately predict the fundamental periods (Figs 5 – 7) demonstrating their ability to predict out-of-sample results.

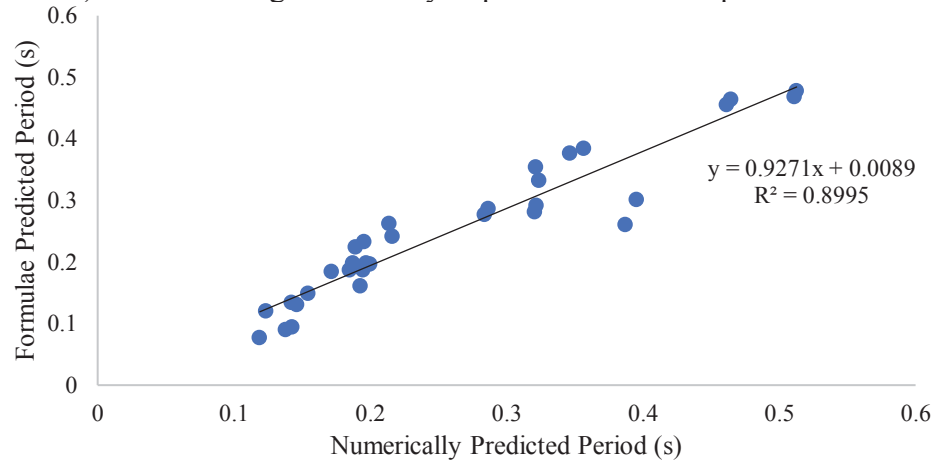


Figure 5. Extra validation data. Correlation of the 3-feature formula.

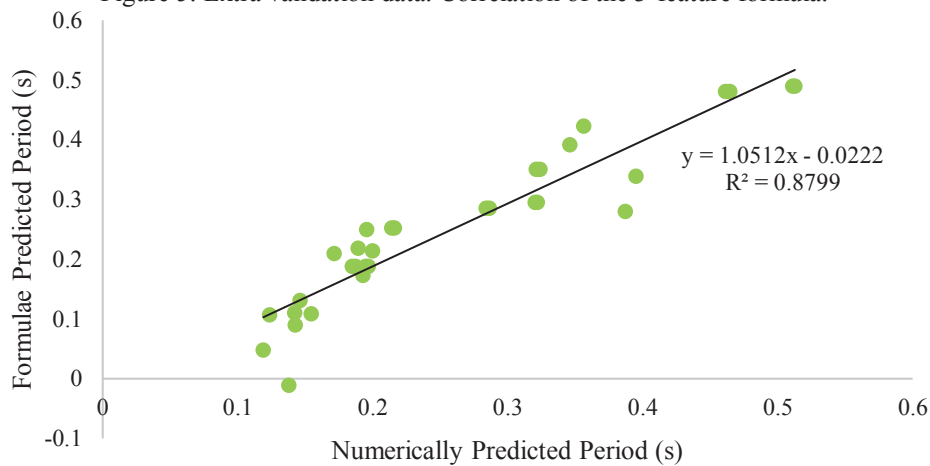


Figure 6. Extra validation data. Correlation of the 5-feature formula.

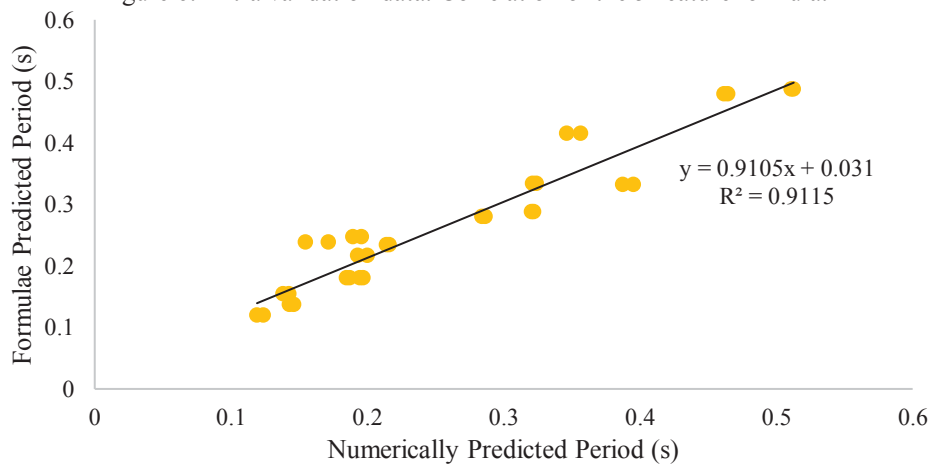


Figure 7. Extra validation data. Correlation of the 20-feature formula.

Table 2 shows the comparison between the proposed formulae and the design formulae of Eurocode [6] and NEAK [14]. It is easy to observe that the Eurocode 8 formula derives the highest mean absolute error, while the 20-feature formula the lowest, which is a finding further supporting the research findings of [1].

Description	Formula	Mean Absolute Error
3-Feature Formula	Eq. 1	13.0%
5-Feature Formula	Eq. 2	11.4%
20-Feature Formula	Eq. 3	<b>8.5%</b>
NEAK	$T_{NEAK} = 0.09 \frac{H}{\sqrt{L}} \sqrt{\frac{H}{H + \rho L}}$	17.7%
EC 8	$T_{EC} = C_T H^{0.75}$ , with: $C_T = 0.075$	62.0%

Table 2: Fundamental Period Formulae predictions on the additional validation data.

## 6 CONCLUSIONS

The parametric investigation of three newly proposed fundamental period formulae was performed on 30 additional out-of-sample modal results and their ability to predict the fundamental period of RC buildings was performed. The 3-, 5- and 20-feature formulae displayed minimal errors when compared to the validation sets, concluding in very promising results thus verifying the findings reported in [1].

It was also found that the 20-feature formula exhibited a higher overall accuracy due to its high number of features, a finding that is in line with the work presented in [1]. The 3-feature formula had the highest error as it was not able to include the SSI related parameters, where the 5-feature formula was found to provide an improved predictive ability. It was also observed that, even though the out-of-sample models that were used to generate the additional validation modal results were dissimilar to the models used to generate the training dataset in-terms of geometry, the proposed formulae managed to derive good predictions with high accuracy. This highlights the extendibility of the proposed fundamental period formulae.

It is also interesting to note at this point that the 20-feature formula is not “elegant”, consisting of numerous features, but according to the authors’ foresight, this will be the future of Civil Engineering design, where ML and AI-generated models will be directly integrated within software tools that will be used to design our structures. Finally, future work foresees the development of additional models that will extend the spectrum in terms of the geometry of RC buildings, developing new formulae that will be able to predict the fundamental period of structures of various shapes. The case of steel structures will also be investigated in a similar project that is currently active.

## REFERENCES

- [1] Z.D. Gravett, C. Mourlas, V. Taljaard, P.N. Bakas, G. Markou, and M. Papadrakakis (2021), New Fundamental Period Formulae for Soil-Reinforced Concrete Structures Interaction Using Machine Learning Algorithms and ANNs, *Soil Dynamics and Earthquake Engineering*, 144 (2021) 106656.

- [2] Z.D. Gravett, and G. Markou, (2021), State-of-the-art Investigation of Wind Turbine Structures Founded on Soft Clay by Considering the Soil-Foundation-Structure Interaction Phenomenon – Optimization of Battered RC Piles, *Engineering Structures*, Volume 235, 112013.
- [3] C. Mourlas, Z.D. Gravett, G. Markou, and P. Manolis, 2019. Investigation of the soil structure interaction effect on the dynamic behavior of multistorey RC buildings. *COUPLED PROBLEMS*. VII International Conference on Computational Methods for Coupled Problems in Science and Engineering, 3-5 June 2019. Spain.
- [4] C. Mourlas, G. Markou, and M. Papadrakakis, 2019. Accurate and computationally efficient nonlinear static and dynamic analysis of reinforced concrete structures considering damage factors. *Engineering Structures*, Vol 178, Jan, pp 258–285.
- [5] C. Mourlas, G. Markou, and M. Papadrakakis, 2019. 3D Detailed Modeling of Reinforced Concrete Frames Considering accumulated damage during static cyclic and dynamic analysis – new validation case studies. *COMPDYN 2019*, 7th ICCMSDEE. 24-26 June 2019, Crete, Greece.
- [6] CEN. Eurocode 8: Design of structures for earthquake resistance. Part 1: general rules, seismic actions and rules for buildings. *European Standard EN 1998-1:2004*, Comit'e Erop'een de Normalisation, Brussels, Belgium, 2004.
- [7] Z.D. Gravett, C. Mourlas, G. Markou, and M. Papadrakakis, 2019. Numerical Performance of a New Algorithm for Performing Modal Analysis of Full-Scale Reinforced Concrete Structures that are Discretized with the HYMOD Approach, *COMPDYN 2019*, 7th ICCMSDEE. 24-26, June. Crete. Greece.
- [8] G. Markou, and M. Papadrakakis, 2015. A Simplified and Efficient Hybrid Finite Element Model (HYMOD) for Non-Linear 3D Simulation of RC Structures, *Engineering Computations*, 32 (5), pp. 1477-1524.
- [9] G. Markou, C. Mourlas, H. Bark, and M. Papadrakakis, 2018. Simplified HYMOD non-linear simulations of a full-scale multistorey retrofitted RC structure that undergoes multiple cyclic excitations – An infill RC wall retrofitting study. *Engineering Structures*, Vol 176, pp. 892–916.
- [10] T. Dimopoulos, H. Tyrallis, N.P. Bakas, and D.G. Hadjimitsis, 2018. Accuracy measurement of Random Forests and Linear Regression for mass appraisal models that estimate the prices of residential apartments in Nicosia, Cyprus. *Advances in Geosciences*, Vol 45, Nov, pp 377-382.
- [11] J. Bezanson, A. Edelman, S. Karpinski, and V.B. Shah, 2017. Julia: A fresh approach to numerical computing. *SIAM Rev*, Vol 59, No 1, pp 65–98.
- [12] G. Markou, C. Mourlas, H. Bark, and M. Papadrakakis, 2018, Simplified HYMOD Non-Linear Simulations of a Full-Scale Multistory Retrofitted RC Structure that Undergoes Multiple Cyclic Excitations – An infill RC Wall Retrofitting Study, *Engineering Structures*, Vol 176 (2018), pp. 892–916.
- [13] Cyprus earthquake resistant design code 1991, Cyprus
- [14] New Greek Seismic Code (NEAK), Athens. 2000.

## PREDICTING THE SHEAR CAPACITY OF REINFORCED CONCRETE SLENDER BEAMS WITHOUT STIRRUPS BY APPLYING ARTIFICIAL INTELLIGENCE ALGORITHMS

Zelda Spijkerman<sup>1</sup>, Nikolaos Bakas<sup>2</sup>, George Markou<sup>1</sup>, Manolis Papadrakakis<sup>3</sup>

<sup>1</sup> Department of Civil Engineering, University of Pretoria, South Africa

e-mail: [u17056757@tuks.co.za](mailto:u17056757@tuks.co.za); [george.markou@up.ac.za](mailto:george.markou@up.ac.za)

<sup>2</sup> Scientific Coordinator, Computation-based Science and Technology Research Center, The Cyprus  
Institute, Nicosia, Cyprus  
e-mail: [n.bakas@cyi.ac.cy](mailto:n.bakas@cyi.ac.cy)

<sup>3</sup> Institute of Structural Analysis & Seismic Research, National Technical University of Athens, 9  
Iroon Polytechniou Str., Zografou Campus, GR-15780 Athens, Greece  
e-mail: [mpapadra@central.ntua.gr](mailto:mpapadra@central.ntua.gr)

---

### Abstract

*This paper focusses on the ongoing discussion of developing a single relationship that can accurately predict the shear capacity of slender, reinforced concrete (RC) beams without stirrups. To date, the main approach used to predict the shear capacity of RC beams, has been based on the derivation of a formula from experimental data. In this study, the approach uses the development of RC FEM models without stirrups, where the beam width is larger or equal to the section height and tested under three-point bending. The models were created and analysed by using Reconan FEA software, where the obtained results from the nonlinear analyses were used to construct a large database of 10,000 beams with varying material and geometric properties. Artificial Intelligence (AI) training was performed by using machine learning algorithms on the numerically generated database to develop predictive models and to develop an improved formula for predicting the shear capacity of RC beams without stirrups. The proposed predictive formula was validated against an available ACI database of RC beams that were assembled by using experimentally tested, physical beams without stirrups. The predictive formula was also compared with the design code formulae proposed by ACI 318-19 and Eurocode 2. According to the numerical findings of this research work, the proposed formula outperformed both design formulae demonstrating significant potential in replacing the current design approach.*

**Keywords:** Shear Strength Prediction, Artificial Intelligence Algorithms, Design Formulae, Finite Element Method, Reinforced Concrete.

---



## 1 INTRODUCTION

Shear failure of Reinforced Concrete (RC) beams takes place due to insufficient shear resistance in the web of the beams. It is important to sufficiently understand the shear capacity of beams in civil engineering applications to avoid catastrophic, brittle failures that occur suddenly, with little to no warning.

The behaviour of RC in shear has been a topic of discussion for numerous years, but the challenge of accurately predicting the shear capacity of RC beams remains an unresolved problem. The main approach so far has been to derive formulae using physical experiments and extrapolating the relevant values. This method is unfavourable, as a major disadvantage is insufficient available experimental data. It is impractical and infeasible to conduct enough physical experiments to cover all possible beam geometries, concrete and steel reinforcement properties, load cases and boundary conditions. The existing formulae are based on a limited number of physical experiments and do not consider other cases, such as the use of deep beams experiencing arc action, or different material types of reinforcement rebars. Therefore, the use of the current design formulae is in need of improvement and expansion.

With the rise of Artificial Intelligence (AI) and Machine Learning (ML) in the past 20 years, researchers and engineers have explored the use of ML algorithms on experimental data sets to predict the shear capacity of beams more accurately. To an extent, this method improved the predictive abilities for certain geometries of RC beams, but the restriction of available experimental data sets still limits the prediction capabilities. These studies were also numerically constrained and the accuracy of predicting the shear capacity of beams is unsatisfactory.

In this research paper, the approach originally introduced by Bakas et al. [1] is extended. Instead of using the results obtained from limited experimental data sets, this newly developed procedure focusses on generating a large numerical database by using Finite Element Method (FEM) software and then using these models to train ML algorithms in order to predict the shear capacity of slender RC beams with no shear reinforcement. The proposed new formula will therefore solely be based on 3D nonlinear Finite Element Analysis (FEA). It is important to note that no physical experiments were used to generate or train the developed formulae. The physical experiments were used for validation purposes only.

This paper aims to more accurately predict the shear capacity of RC beams without stirrups that have smaller geometries, when compared to existing design formulae.

## 2 NUMERICAL INVESTIGATION

A numerical procedure was developed for a database of twenty different geometrical RC beams. The characteristics for each of these beams were then increased by a random generation of 500 material property combinations to produce a database containing 10,000 unique beams. The 3D approach presented in [2-4], was used in the modeling and nonlinear analysis of the beams.

### 2.1 Development of Numerical Campaign

The simply supported, slender, RC beams that were generated for the purpose of this research project used 20-noded isoparametric hexahedral finite elements to model the concrete and the steel plates that act at the supports, as well as 2-noded rod elements for the steel reinforcement bars.

Fig. 1 depicts how the typical generated model looked like. The simply supported, slender RC beam had the smallest mesh of all the constructed beams and spans 1,500 mm. The beam has a 300x150 mm rectangular cross-section that was discretized by using hexahedral elements that are 150x150x75 mm in the x, y and z directions, respectively.

A total of 76 hexahedral elements were used of which 4 were for the steel base plates at the supports, 48 for the concrete hexahedral elements and 24 for the steel reinforcement bars. In Fig. 2 the tensile longitudinal reinforcement bars at the bottom of the beam are embedded rod elements and the applied force at midspan is also visible.

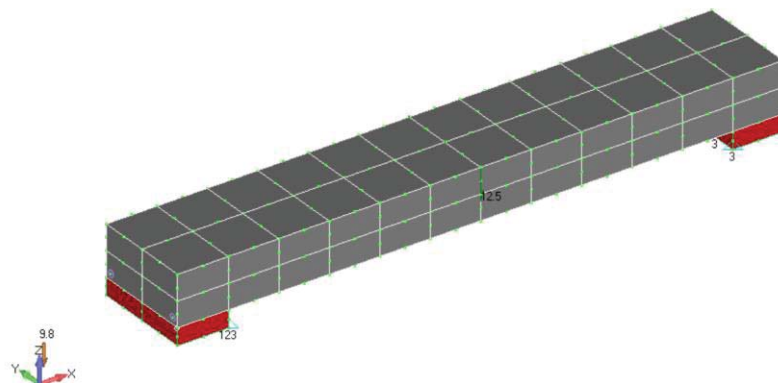


Figure 1. Hexahedral element mesh of a simply supported slender RC beam that has a net span of 1,500 mm and a 300x150 mm cross section.

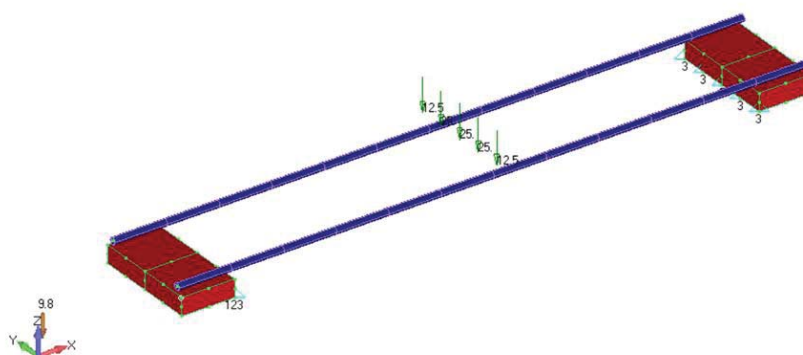


Figure 2. Embedded rod element mesh of a simply supported RC beam that has a net span of 1,500 mm and a 300x150 mm cross section with loads shown.

The largest mesh that was developed for this research project consisted of 450 hexahedral elements, where 10 elements were used for the steel support plates, 400 for the hexahedral elements and 40 for the steel rebars. The beam has a geometry of 750x350 mm and spans 2,700 mm. The concrete cover for all the beams depended on the height of the section. Beams with a height smaller or equal to 250 mm had a concrete cover of 20 mm and beams with a height larger than 250 mm were modelled to have a concrete cover of 30 mm.

Parameter	Minimum	Maximum
L (mm)	1,500	2,700
b (mm)	300	750
h (mm)	150	350
L/h	6	10.8
h/b	0.33	0.83

Table 1: Minimum and maximum beam geometries used in generating the 20 new models.

Twenty new beam geometries were constructed to generate the database. Only beam geometries where the width is greater or equal to the height were constructed. Table 1 shows a

summary of the constructed models. The first model was generated with the minimum span, height and width values from Table 1 as can be seen in Fig. 1 and the subsequent models were generated by modifying the first model to get the needed geometries and spans. The span values start at a minimum of 1,500 mm and increase with 300 mm up until 2700 mm. Span over section height ( $L/h$ ) and the section height over the width ( $h/b$ ) is also given in Table 1 with minimum and maximum values of 6 and 0.33 as well as 10.8 and 0.83, respectively.

## 2.2 Analysing Multiple Finite Element Beams

To generate a database with sufficient input files, a certain level of automation is needed. Without automation, the required time to generate and analyse the input data would be a major disadvantage. The manual effort required to create the data would reduce the possible scope and negatively impact the resulting benefit of the research project. It was thus important to use automation code for data creation and entry. To minimise the time spent on producing and analysing the various FE models it was advantageous to use the previously developed automation tools from [1], Reconan Multirun v1.00.

A random generation of material properties combinations, consisting of  $f_c$  (kPa),  $E_c$  (kPa),  $f_t$ ,  $\beta$ ,  $E_s$  (kPa),  $f_y$  (kPa) and  $A_s$  ( $m^2$ ), was performed and used to generate the corresponding input file for each individual model. Each model's parameter input file included the node ID that had to be monitored, the direction in which the deflection was monitored, maximum deformation, the beam span as well as the section geometry with section height and section width. In all the generated models the node that was identified for monitoring was chosen as the nodal point at the centre of the total span, at the bottom of the beam's height and in the middle of the width.

The Reconan Multirun software was developed to modify each of the 20 model meshes that were generated to have the required material property assumptions and reinforcement ratios as described herein. The Reconan FEA [5], which was also algorithmically modified to read and analyse these FE input files to return the maximum capacity of the beam as well as the maximum deflection. It must be noted that, Reconan Multirun can also read the generated output files with the purpose of continuing the analyses if it was interrupted. This is a useful feature as unplanned power failures or system interruptions, such as operating system up-dates, would otherwise result in substantial delays and rework.

For each of the 20 models constructed as described in section 2.1, 500 different material properties and reinforcement ratio combinations were used, thus resulting in 10,000 analysis results that were used in training the AI algorithm.

The personal computer (PC) used for this research project had a 12-core i7-8700K CPU @ 3.70 GHz and 64.0 GB RAM and had the capability to run 10 Multirun analyses at the same time. As the model meshes became larger, with a larger span and geometry, the computational time to run the analyses increased. The entire analyses of all 10,000 models completed in roughly 36 hours, highlighting the computational efficiency of Reconan FEA [5] in performing nonlinear analysis using 3D detail models.

## 3 DEVELOPMENT OF THE PROPOSED FORMULA

For the second phase, the data was prepared by selecting, pre-processing and transforming the data to apply ML algorithms. The AI training proceeded by extracting the material features and predicting the shear strength of the beams. ML algorithms learn from data, so it was crucial that the right, quality data is fed into the system. The results achieved by the ML algorithms are directly related to the quality and volume of data used during the training stage.

Data selection for this project entailed generating a database that consisted of ten independent variables, which were split into two groups. The first group involved the variables that were

used during the meshing of the models. These variables included the net span,  $L$  (mm), effective depth,  $d$  (mm) and width,  $b$  (mm). The second group of variables were strength-and material related properties and consisted of: uniaxial compressive strength of a cylindrical specimen ( $f_c$  in MPa), concrete tensile strength ratio ( $f_t$ ), steel yielding stress ( $f_y$  in MPa), Young's modulus of steel ( $E_s$  in MPa), Young's modulus of concrete ( $E_c$  in MPa), remaining shear capacity strength factor ( $\beta$ ) and the tensile longitudinal reinforcement ratio ( $\rho$ ).

The above-mentioned independent variables are presented in Table 2 with the statistical characteristics and minimum and maximum values of the database.

	$L$	$d$	$b$	$f_c$	$f_t$	$f_y$	$E_s$	$E_c$	$\beta$	$\rho$
$\bar{X}$	2100	242	537.5	41	0.061	500.8	200045.8	30024.9	0.034	0.0110
$\sigma$	424.3	59.5	170.2	11.3	0.023	58.5	5602.2	2952.9	0.008	0.0053
Median	2100	230	500	40.9	0.061	499.2	200070.1	30072.1	0.034	0.0111
Minimum	1500	130	300	20.1	0.02	401.2	190000	25000	0.02	0.0016
Maximum	2700	320	750	59.9	0.1	598.5	210000	35000	0.05	0.0199
$c_v$	0.202	0.246	0.317	0.277	0.377	0.1117	0.028	0.098	0.247	0.479

Table 2: Statistical values of independent variables.

### 3.1 Model Training

The training process of any ML algorithm model can be split into 3 major phases: Pre-processing, Feature Selection and Extraction and Prediction.

Pre-processing of the assembled dataset was conducted by normalising the data by dividing each variable in the set by the standard deviation. The normalisation of the dataset was required because the features of the set have different ranges and consists of some outliers. The ranges were however not distorted, and the values of the different variables were changed to fit to a shared scale. Normalisation reduces duplicates in the database and increases the validation accuracy of the model. It also allows the optimization of the ML model to be more robust, as the convergence rate of the gradient descent is reduced.

Feature (or variable) selection then uses a process of dimensionality reduction to decrease the initial set of normalised data to more manageable groups. It greatly improves the ML algorithm's performance and reduces the computational power needed to perform the training. Following on from the feature selection is feature extraction. When a number of features in a dataset become similar or too large, the ML model can suffer from overfitting where the model fits the data too well and is no longer able to fit additional data or predict future observations in a consistent way. Feature extraction is the method for combining certain variables into features, reducing the number of values in the dataset without losing an accurate representation of the original data. The relevance and optimisation of the ML model is also considered during feature selection and extraction.

The algorithm chosen for the prediction phase of the ML and AI process is the NLR (non-linear regression) model. Regression models are used to predict unknown values which are gathered from continuous (regression) variables and the NLR model is consequently beneficial to the research project and produces a closed-form solution. The prediction developed by the NLR model is presented as a formula in section 3.2 of this manuscript.

It is important to note that 85% of the generated database was used to train the algorithm, and the remaining 15% used for testing purposes. The test data proved that the prediction model that was created is accurate. The robustness of the model will be discussed in the next section. In addition, a set of physical RC beams was used for validation purposes, after the testing was performed. This step, which is considered to be the most important, was performed so as to

check whether the proposed formula is able to predict the shear capacity of real beams that were experimentally tested.

### 3.2 Proposed Predictive Equation

The formula developed during this research project, used to predict the ultimate characteristic shear strength  $V_c$ , utilized the NLR ML algorithm and was mainly dependent on  $L$ ,  $d$ ,  $b$ ,  $f_c$  and  $\rho$ . Formulae using 10, 100 and 500 terms were generated and investigated for robustness and accuracy. The higher order NLR that was implemented in this research project consists of a combination of variables that were created up to 3<sup>rd</sup> order. The methodology uses the RF-algorithm (random forests) and the analyses was run on the Julia programming language as written by Dimopoulos and Bakas [6].

During the comparison of the three initially developed formulae, the mean absolute error (MAE) of the ten-term formula was 5.1% higher than the 100 and 500 term formulae, and the MAE for the 100 and 500 term formulae was the same and equal to 6.89%.

The proposed formula to calculate  $V_c$ , was obtained as output from the ML algorithm. The formula with ten-terms and the variables  $L$ ,  $d$ ,  $b$ ,  $f_c$ ,  $f_t$ ,  $\rho$ ,  $\beta$ ,  $E_s$  and corresponding weights are given in Eq. 1. The 10, 100 and 500 term formulae have been validated against the experimental data to determine the most accurate formula.

$$\begin{aligned}
 V_c = & 0.253939 * \rho * d^2 - 0.0571682 * d * L * \rho + 0.0967954 * \rho * b * d \\
 & + 0.0000000193334 * E_s * f_c * d - 0.000000234107 * f_c * L^2 + 0.003624 \\
 & * \rho * L^2 - 0.00809799 * \rho * L * b + 0.00000538644 * f_c * b * d + 343643 \\
 & * \rho * f_t * \beta - 387.761 * \rho^2 * d + 0.950862
 \end{aligned} \tag{1}$$

## 4 VALIDATION OF PROPOSED EQUATION THROUGH EXPERIMENTAL DATA

The validation of the predictive model was conducted using 36 experimentally tested beams that were taken from the ACI database [7] of shear tests on slender reinforced concrete beams without stirrups. The 36 beams were specifically selected to fall within the range of the 20 different beam geometries that were developed for the needs of this research project. The material properties were also within the boundaries of the generated database of the 10,000 models. Any experimental results from the ACI database that had incomplete data, were removed and not included in the validation beams.

It is necessary to mention that the ACI experimental database did not include values for  $f_t$  and  $\beta$ . To include these parameters, the average value of  $f_t$  of the training set was taken.  $\beta$  was chosen as a random percentage of less than 5%. This selection was made to optimise the results from the predictive model and to enhance the performance and accuracy. It is also important to note that all the validation beams were out-of-sample cases, given that the values of material properties and geometrical features differed in comparison to the values adopted for the generation of the 10,000 numerical results.

An additional observation related to the validation data is that, from the 36 beams in the ACI database [7] of experimentally tested beams, there were instances where beams with exactly the same beam geometry, reinforcement ratio and material properties resulted in different ultimate shear capacities. This finding highlights the level of uncertainty when discussing the physically tested beams and confirms that experimental results typically include noise because of uncontrolled factors during the testing phase.

It is noteworthy that the predictive model was successfully constructed without the use of any physical experimental data. By removing the dependency on physical beam data, it was



possible to work with a much larger data set and avoid the inconsistencies inherent in physically collected data. The predictive formula, and the resulting accuracy, is purely based on the results obtained from the FEA. The experimental data used in this section was for validation purposes only.

Two industry-standard formulae were compared with the new proposed model, namely the ACI 318-19 [8] and Eurocode 2 [9]. The data in the experimental data set, with 36 RC beams without stirrups, were used to calculate a predicted shear capacity strength using the industry-standard formulae. The same data were used with the new model and the results were compared against the standard design formulae.

The ACI formula is expressed in imperial units so the data were first converted to the correct metric unit before calculations were made. Eq. 2 is the newly developed ACI 318-19 predictive formula that was published in 2019 and it is more similar to the design code suggested by Eurocode 2 [9]. In the case of this research project, no axial force was present, and  $Nu$  is irrelevant ( $Nu = 0$ ). In the ACI formula, the beam geometry and concrete strength plays an important role. The reinforcement ratio ( $\rho$ ) also has an impact on the shear capacity of the RC beam. The formula in Eurocode 2 (Eq. 3), depends on the reinforcement ratio, strength of concrete and the beam geometry.

$$V_c = \left[ 8\lambda_s \lambda(\rho_w)^{1/3} \sqrt{f'_c} + \frac{N_u}{6A_g} \right] b_w d \quad (2)$$

$$V_{Rk,c} = C_{Rk,c} k (100\rho f_{ck})^{1/3} b_w d \quad (3)$$

$$\text{with } k = 1 + \sqrt{\frac{200}{d}} \leq 2.0 \text{ (d in mm) and } \rho = \frac{A_{sl}}{b_w d}$$

Both formulae were developed based on the results obtained from physically constructing and testing several beams, therefore, they are both semiempirical. The obtained results are graphically displayed in Fig. 3 to 5. In each figure, the physically tested, experimental results are displayed on the horizontal x-axis and the shear capacity at which the beams were predicted to fail, using different formulae and models, is displayed on the vertical y-axis.

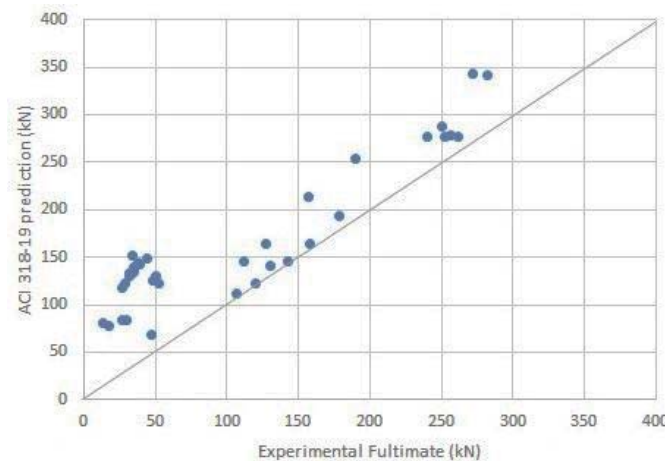


Figure 3. Experimental Shear Strength vs ACI 318-19 Prediction.

The influence of the longitudinal reinforcement ratio,  $\rho$ , impacts the outcome of the shear capacity, providing the ACI 318-19 formula with some accuracy. However, the ACI formula

tends to over-predict the ultimate shear capacity of the beams, meaning that a much higher shear strength was calculated than the actual shear strength that the beam could resist.

The accuracy of the Eurocode 2 prediction of the ultimate shear strength of RC beams without stirrups is higher than the ACI formula, with a MAE of 1.1298, thus it is considered more accurate than the 2019 version of the ACI code when implemented on the validation set of beams. From Fig. 4 it is seen that for experimental values of  $V_c$  less than 50 kN, the prediction calculates a much larger value and is less accurate, whereas values of  $V_c$  larger than 50 kN are close to the predicted values.

Fig. 5 compares the experimental shear strength of the RC beams with the new, improved predictive ten-term formula developed by using NLR. When compared to Figs 3 and 4, and looking at the newly calculated MAE, the new ten-term formula is found to be more accurate and best predicts the shear capacity of the beams which fail at a higher ultimate force.

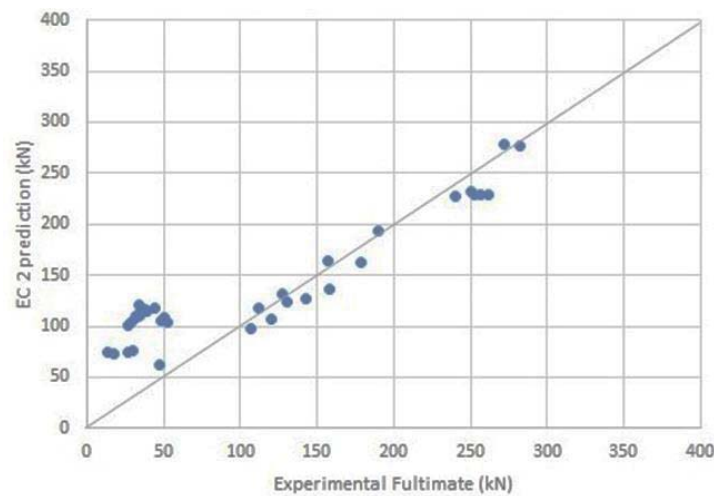


Figure 4. Experimental Shear Strength vs EC 2 Prediction.

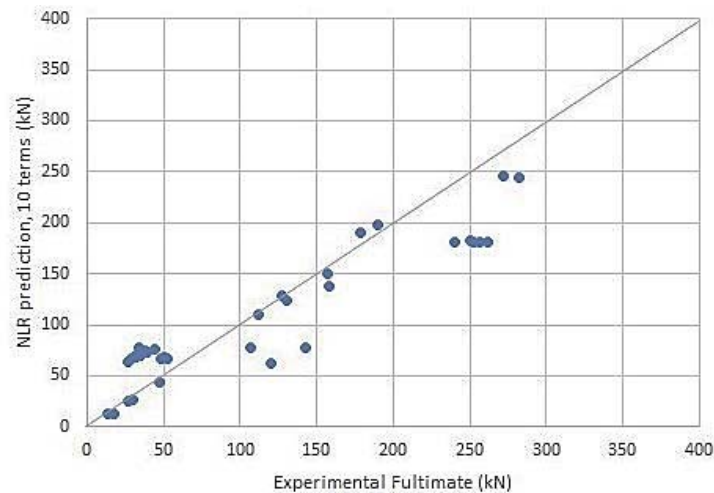


Figure 5: Experimental Shear Strength vs NLR prediction formula with ten-terms.

For the new formula the overall distribution of the datapoints is closer to the  $x = y$  line, when compared to the ACI 318 and Eurocode 2 predictions. The proposed predictive formula results look visually similar to those presented in Figs 3 and 4, however, there is a closer and more accurate prediction when looking at ultimate forces smaller than 50 kN.

The forces larger and equal to 50 kN appear slightly less accurate when compared to the Eurocode formula predictions in Fig. 4. The proposed formula yields a more conservative numerical response to the problem by predicting forces smaller than the actual force at which the RC experimental beams fail.

The new 10-, 100- and 500-term formulae were compared by looking at their respective MAEs. The new 10-term formula was the most accurate by far, with a MAE of only 0.4703. Thereafter the 100-term formula with a MAE of 0.6408 and the 500-term formula follows closely with a MAE value of 0.6616. The MAEs of the different predictive models are shown in Table 3, with the lowest error resulting from the new 10-term NLR predictive model generated in this study.

Interestingly, although the model was trained on a dataset with different beams' width-height ratios, it exhibited high accuracy, compared to the Eurocode and ACI building codes. All three of the new NLR formulae composed in this study yield more accurate results than the existing industry-standard design formulae when used to predict the shear capacity of the 36 validation RC beams. The ten-term formula provides the best fit and has the lowest error. Although overfitting is present with both the 100- and 500-term formulae they also provide a lower MAE when compared to the existing industry-standard formulae.

Predictive Model	MAE (%)	Accuracy
10-term NLR	47.03	Best
100-term NLR	64.08	
500-term NLR	66.16	
Eurocode 2	112.98	
ACI318-19	145.51	Worst

Table 3: MAE of predictive models.

## 5 CONCLUSIONS

Non-linear regression algorithms were used to train and test a database that consisted of 10,000 shear strength results. Removing the requirement for physical beam data enabled the creation of a much larger data set, which made it possible to use Machine Learning techniques. The shear strength results from the physical experimental data were only used to validate the results obtained from the combination of the FEA and ML algorithms.

The proposed predictive formula with 10-terms for computing the shear capacity of slender RC beams without stirrups presented in this research project outperformed the existing available design code formulae (ACI 318-19 and Eurocode 2). The new formula was shown to be more accurate and better predicted the shear capacity of RC slender beams without shear reinforcement. FEA used in conjunction with advanced ML was shown to provide a reliable approach in developing a predictive formula for estimating the capacity of RC beams without stirrups.

The proposed predictive formula can be further improved by extending the current generated database with a larger variety of beam geometries, spans, and material properties that fall outside of the current range. Further research can be done on different design codes, such as the Canadian code, and formulae used around the world to compare the accuracy of currently used design formulae.

Furthermore, it is recommended to build on this research by looking at slender beams with shear reinforcement, beams with compressive longitudinal reinforcement bars, deep beams, slabs and RC beams with fibre reinforced polymer rebar as well as RC beams with fibres. Additionally, columns, shear walls and joints should be investigated under monotonic and cyclic loading conditions.

## REFERENCES

- [1] N. Bakas, G. Markou, D. Charmpis and K. Hadjiyiannakou, “Performance and scalability of deep learning models trained on a hybrid supercomputer: Application in the prediction of the shear strength of reinforced concrete slender beams without stirrups”, COMPDYN 2021, 27-30 June 2021, Streamed from Athens, Greece.
- [2] G. Markou, N.P. Bakas, Computationally efficient 3D finite element modelling of RC structures, *Computers and Concrete*, Vol 12, No 4, May, pp 443-447, 2013.
- [3] G. Markou and F. Genco, Seismic Assessment of Small Modular Reactors: NuScale Case Study for the 8.8 Mw Earthquake in Chile, *Nuclear Engineering and Design*, 342(2019), pp. 176-204, 2019.
- [4] C. Mourlas, G. Markou and M. Papadrakakis, Accurate and Computationally Efficient Nonlinear Static and Dynamic Analysis of Reinforced Concrete Structures Considering Damage Factors, *Engineering Structures*, 178 (2019), pp. 258–285, 2019.
- [5] Reconan FEA v2.00, User’s Manual, 2020.  
[https://www.researchgate.net/publication/342361609\\_ReConAn\\_v200\\_Finite\\_Element\\_Analysis\\_Software\\_User's\\_Manual](https://www.researchgate.net/publication/342361609_ReConAn_v200_Finite_Element_Analysis_Software_User's_Manual)
- [6] T. Dimpoulos and N. Bakas, Sensitivity analysis of machine learning models for the mass appraisal of real estate. Case study of residential units in Nicosia, Cyprus, *Remote Sensing*, vol. 11, no. 24, p. 3047, 2019.
- [7] K.-H. Reineck, E.C. Bentz, B. Fitik, D.A. Kuchma and O. Bayrak, ACI-DAFSTB database of shear tests on slender reinforced concrete beams without stirrups, *ACI Structural Journal*, 110 (5), 2013.
- [8] A.C. Institute, Building Code Requirements for Structural Concrete (ACI 318-19): Commentary on Building Code Requirements for Structural Concrete (ACI 318R-19): an ACI Report, American Concrete Institute. ACI, 2019.
- [9] EN1992-1-1, Eurocode 2 (2004), Design of concrete structures.

## STRUCTURAL DAMAGE PREDICTION UNDER SEISMIC SEQUENCE USING NEURAL NETWORKS

Petros C. Lazaridis<sup>1</sup>, Ioannis E. Kavvadias<sup>1</sup>, Konstantinos Demertzis<sup>1</sup>, Lazaros Iliadis<sup>1</sup>,  
Antonios Papaleonidas<sup>1</sup>, Lazaros K. Vasiliadis<sup>1</sup>, Anaxagoras Elenas<sup>1</sup>

<sup>1</sup>Department of Civil Engineering, Democritus University of Thrace, Campus of Kimmeria, 67100  
Xanthi, Greece

e-mail: {petrlaza1@civil, ikavvadi@civil, kdemertz@fmenr, liliadis@civil, papaleon@civil,  
lvasilia@civil, elenas@civil}.duth.gr

**Keywords:** Seismic Sequence, Neural Networks, Repeated Earthquakes, Structural Damage Prediction, Artificial Intelligence, Intensity Measures

**Abstract.** *Advanced machine learning algorithms, such as neural networks, have the potential to be successfully applied to many areas of system modelling. Several studies have been already conducted on forecasting structural damage due to individual earthquakes, ignoring the influence of seismic sequences, using neural networks. In the present study, an ensemble neural network approach is applied to predict the final structural damage of an 8-storey reinforced concrete frame under real and artificial ground motion sequences. Successive earthquakes consisted of two seismic events are utilised. We considered 16 well-known ground motion intensity measures and the structural damage that occurred by the first earthquake as the features of the machine-learning problem, while the final structural damage was the target. After the first seismic events and after the seismic sequences, both actual values of damage indices are calculated through nonlinear time history analysis. The machine-learning model is trained using the dataset generated from artificial sequences. Finally, the predictive capacity of the fitted neural network is accessed using the natural seismic sequences as a test set.*



## 1 INTRODUCTION

In recent years advanced Machine Learning (ML) algorithms, such as Artificial Neural Networks (ANN), has been successfully applied to many areas of system modelling. Their success is based on the thorough processing of data that captures the behaviour of a system. By detecting patterns in the collected data, valuable information can be extracted and predictions can be made that automate the decision-making process. That fact arrives ML as an advanced tool in modern engineering modelling.

The object of the present research is the application of neural networks to predict the structural damage under seismic sequences. The recent disaster held on March 2021 in Tyrnavos-Elassona region, Thessaly of Greece due to a pair of compatible magnitude ( $M_w=6.3$ ,  $M_w=6.1$ ) [1, 2] shallow earthquakes with more than 1800 damaged or non-serviceable buildings, indicate the critical role of seismic sequences in the final damage state of buildings again. In the field of seismic sequences have been conducted many kinds of research to access the contribution of repeated ground motions on the post-seismic performance state of a building so far, which concluded that aftershocks increase the ductility demands. Amadio et al. [3] studied the influence of repeated shocks on the response of nonlinear Single Degree of Freedom (SDOF) systems using different hysteretic models. Hatzigeorgiou and Beskos [4] conducted an exhausting parametric study on SDOF systems and proposed an empirical relation to calculate inelastic displacement ratio under repeated earthquakes. Hatzigeorgiou and Liolios [5] examined the nonlinear behaviour of Reinforced Concrete (RC) frames subjected to multiple shocks considering a set of eight frames that varied both at height regularity and dimensioning practice. Hatzivassiliou and Hatzigeorgiou [6] studied the accumulation of damage and ductility demands due to seismic sequence on three dimensional RC structures. Hosseinpour and Abdelnaby [7] studied the impact of different aspects, as earthquake direction, aftershock polarity and the influence of the vertical component, on the nonlinear response of RC frames under successive earthquakes. Also, more recently, Kavvadias et al. [8] and Zhou et al. [9] investigated the correlation between aftershock related Intensity Measures (IMs) and final structural damage indices.

Previous several studies have been conducted on forecasting of structural damage due to individual earthquakes, ignoring the influence of seismic sequences. De Latour and Omenzetter [10] investigated the efficiency of ANNs on the prediction of seismic damage on numerous RC frames, Alvanitopoulos et al. [11] also examined regular RC structures and, they incorporate fuzzy layers in ANN configuration (architecture). Later, Morfidis and Kostinakis [12] used feature selection methods in a dataset of 3 dimensional RC buildings to found the more damage correlated set of seismic IMs. More recently, the same authors [13] examined the effectiveness of ANNs on the prediction of damage of non-regular at height structures. Applications of Recurrent Neural Networks (RNNs) on Earthquake Engineering made by González et al. [14] and Mangalathu and Burton [15], also Zhang et al. [16] developed a LSTM (Long-Short Term Memory) network to predict structural response. Convolutional Neural Networks (CNNs) applied by Li et al. [17] and Oh et al. [18] for the same purpose.

In the present study, ANNs are applied, considering real and artificial sequences of double seismic shocks, to predict the amount of final structural damage on an already damaged 8-storey RC frame after a first shock. We use 16 well-known ground motion IMs and the established damage from the first earthquake as the features of the ML problem, while the final structural damage (after sequence) employed as the target. Both damage indices after the first seismic event and after the sequence are calculated through Nonlinear Time History Analysis (NTHA).

## 2 SELECTION OF PRIMITIVE DATA

In this section, the primitive data of the problem is described. Specifically, the selection of the ground motion records and the examined RC frame is presented.

### 2.1 Ground motion records

Both artificial and natural seismic sequences are considered to take into account, the phenomenon of multiple shocks. After the random combination from a suite of 318 acceleration records from several earthquakes, the set of artificial sequences determined. More specifically, every record of the above 318 records suite is combined randomly three times with another record from the same dataset. As a result, 954 pairs of first and second shock are constructed, which are utilised as a training set for the specific ML problem. As a test set, we employed 119 natural pairs of sequential shocks, which occurred from 1972 to 2020. The training and test sets are completely independent with no common record. Both sequential and individual records are selected and downloaded from ESM [19] and PEER NGA West [20] databases. The criteria according to the selection of natural sequences conducted are the time gap between the occurrences of successive shocks which are considered smaller than three months and that the sequential events are recorded by the same station. As a result of this process collected 119 pairs of successive ground motion acceleration records from 41 real seismic sequences, recorded by 65 stations. The occurrences time and Peak Ground Acceleration (PGA) data of the natural sequences listed in Table 1. Every pair concatenated in the same array to compose the sequential ground acceleration time history. In addition, an intermediate zero ceasing time gap of 20 seconds added to eliminate the overlap between the building oscillations due to successive earthquakes. This process is implemented in Python [21], and the new files containing the seismic sequence acceleration signals are exported.

### 2.2 Reinforced concrete structure

Existing buildings designed and constructed without earthquake provisions comprise the majority of structures both in Greece and worldwide, which causes particular concern about their response to a potential earthquake. As an example, in this study we examined an 8-storey planar regular RC frame (Figure 1) designed only for gravity loads by Hatzigeorgiou and Liolios [5], with mean compressive strength of concrete equal to 28 MPa and steel grade S500s. The finite element simulation of the frame held in IDARC 2D [22], using spread plasticity concept and three-parameter Park hysteretic model [23]. Every floor considered to have only one horizontal degree of freedom to into account the huge plane stiffness of RC slab as a rigid diaphragm. Sparsely placed stirrups with poor anchor details are assumed in order to be in accordance with obsolete design codes. Thus, a nonlinear deformation-stress model for concrete without confinement is adopted. As a result, the corresponding concrete curve defined by the initial modulus of elasticity ( $E_0 = 31.42 \text{ GPa}$ ), the strain at the maximum stress ( $\epsilon_{c0} = 2\text{‰}$ ), the ultimate strain in compression ( $\epsilon_{cu} = 3.5\text{‰}$ ), the stress at tension cracking  $\sigma_t = 0.0022 \text{ GPa}$ , and the slope of the post-peak falling branch ( $E_{fb} = -6.2 \text{ GPa}$ ). Also, the bilinear curve with hardening employed for steel with yield and ultimate strengths equal to 550 MPa and 660 MPa respectively and the corresponding strains equal to 2.75‰ and 45‰, according to Eurocode-2 [24] provisions. The initial elastic fundamental period of the structure is equal to 1.27 seconds.

### 2.3 Technicalities

The generation of IDARC 2D input files and the extraction of responses from output files implemented through GNU Octave [25, 26] code. Using the same high-level programming language we automated the multiple analysis process and computed the IMs, which are described in the next section, for the overall dataset of first and second seismic shocks.

Region	1st Sh. Date	2nd Sh. Date	Station Code / Name	Stream	PGA 1st $\frac{cm}{s^2}$	PGA 2nd $\frac{cm}{s^2}$
Ancona	1972-06-14	1972-06-21	ANP	N-S	216.17	402.88
				E-W	206.15	208.0
Friuli	1976-09-11	1976-09-15	BUI	N-S	229.04	108.53
				E-W	106.41	91.37
			GMN	N-S	322.02	318.58
				E-W	293.6	632.0
Northwestern Balkan Peninsula	1979-04-15	1979-04-15	PETO	E-W	298.18	87.4
		1979-05-24	BAR	N-S	364.69	197.33
				E-W	353.28	262.19
			HRZ	N-S	211.32	65.68
				E-W	249.49	75.05
			ULO	N-S	277.13	32.9
				E-W	232.34	30.13
Imperial Valley	1979-10-15	1979-10-15	Holtville Post Office	315	217.24	250.07
Mammoth Lakes	1980-05-25	1980-05-25	Convict Creek	90	411.49	364.47
Irpinia	1980-11-23	1980-11-24	BGI	N-S	126.96	30.71
				E-W	185.88	33.32
			STR	N-S	220.44	18.37
				E-W	314.41	31.41
Greece	1981-02-24	1981-02-25	KORA	Trans	290.82	119.32
				Logn	235.91	118.72
Coalinga	1983-07-22	1983-07-25	Elm (Old CHP)	90	509.27	664.53
				0	334.97	472.1
Southern Greece	1986-09-13	1986-09-15	KAL1	Trans	264.6	138.13
				Logn	227.84	232.78
			KALA	Trans	290.91	149.6
				Logn	212.21	327.68
Spitak	1988-01-07	1988-01-07	GUK	N-S	178.23	142.0
				E-W	178.81	97.63
Western Caucasus	1989-01-08	1989-01-08	NAB	N-S	188.92	192.91
				E-W	202.05	213.12
Greece	1990-05-17	1995-06-15	AIGA	Trans	198.1	510.79
				Logn	116.29	488.87
Western Caucasus	1991-05-03	1991-05-03	SAMB	N-S	347.84	204.3
				E-W	494.46	120.01
Turkey	1992-03-13	1992-03-15	AI 178 ERC MET	N-S	403.55	32.15
				E-W	478.36	39.11
Southern Greece	1993-03-26	1993-03-26	PYR1	Trans	218.77	117.3
				Logn	107.23	98.62
Northridge	1994-01-17	1994-01-17	Moorpark - Fire Sta	90	189.38	136.86
				180	286.27	180.75
			Pacoima Kagel Canyon	360	424.6	52.45
		1994-03-20	Rinaldi Receiving Sta	228	857.45	519.21
			Sepulveda Hospital	270	738.22	100.1
			Sylmar - Olive Med	90	593.39	178.32
Umbria Marche	1997-09-26	1997-09-26	CLF	N-S	271.52	193.84
				E-W	251.78	223.46
			NCR	N-S	387.53	492.33
				E-W	251.0	415.1
Southern Greece	1997-10-13	1997-11-18	KRN1	Trans	117.43	70.44
				Logn	116.52	90.77
Bovec	1998-04-12	1998-08-31	FAGG	N-S	24.08	23.0
				E-W	23.32	26.16
Azores Islands	1998-07-09	1998-07-11	HOR	N-S	397.33	80.57
				E-W	362.48	90.37
Izmit	1999-08-17	1999-11-12	ARC	N-S	206.54	7.39

Continued on next page

Region	1st Sh. Date	2nd Sh. Date	Station Code / Name	Stream	PGA 1st $\frac{cm}{s^2}$	PGA 2nd $\frac{cm}{s^2}$
Greece	1999-09-07	1999-09-07	ATK	E-W	130.42	7.55
				N-S	100.31	16.25
			DHM	E-W	164.3	16.01
				N-S	88.28	17.03
			FAT	E-W	82.92	17.24
				N-S	178.45	34.32
			KMP	E-W	158.58	23.77
				N-S	100.59	14.43
			ZYT	E-W	125.13	17.21
				N-S	116.96	21.41
			ATHENS-SEPOLIA B	E-W	107.05	28.88
				Trans	317.98	58.14
			TCU071	Logn	335.1	69.79
				N-S	638.91	375.02
Chi-Chi Taiwan	1999-09-20	1999-09-20	TCU129	E-W	518.53	189.69
				N-S	390.42	612.17
			TCU078	E-W	929.28	985.77
				N-S	301.13	379.95
			TCU079	E-W	438.81	261.21
				N-S	416.3	614.35
Duzce Turkey	1999-11-12 2003-05-01	1999-11-12 2003-05-01	AI 010 BOL	E-W	580.9	761.01
				N-S	804.95	59.27
			AI 049 BNG	E-W	509.25	144.45
				N-S	286.03	67.56
L Aquila	2009-04-06	2009-04-07	AQK	E-W	346.9	80.4
				N-S	323.84	88.45
			AQV	E-W	535.39	144.13
				N-S	644.47	127.22
			AVZ	E-W	67.71	21.44
				N-S	434.0	56.85
Darfield New Zealand	2010-09-03	2009-04-09 2011-02-21	AQA	N-S	434.0	56.85
				S01W	186.4	443.68
			Botanical Gardens	N89W	152.43	542.17
				S80E	246.32	342.41
			Cashmere High School	N26W	190.79	376.79
				N64E	228.91	469.24
			Cathedral College	N01W	205.41	339.41
				S89W	149.4	356.74
			Christchurch Hospital	N-S	258.89	288.73
				E-W	257.32	218.65
Emilia	2012-05-20	2012-05-29	MRN	N-S	481.11	574.06
				E-W	258.35	230.4
Northern Italy	2012-06-03	2012-06-12	T0827	E-W	49.54	10.59
				N-S	368.51	329.9
Central Italy	2016-08-24	2016-08-24 2016-08-26	AQK	E-W	851.09	318.84
				N-S	334.88	302.66
			AMT	E-W	707.04	638.53
				N-S	545.76	527.19
			CMI	E-W	49.29	384.83
				N-S	88.35	426.01
	2016-10-26	2016-10-26	CNE	E-W	51.02	209.24
				N-S	90.49	319.58
			ACC	E-W	189.45	571.62
				N-S	180.02	418.76
			CIT	E-W	373.26	288.38
				N-S	164.82	185.15
	2016-10-30	2016-10-30	CLO	E-W	166.99	185.39
				N-S	210.87	305.85
			CNE	E-W	210.87	305.85
				N-S	850.26	182.16
			MMO	E-W	779.54	207.93
				N-S	575.2	550.63
Near The Coast Of Western Turkey	2017-01-18	2017-01-18	PCB	E-W	400.57	380.9
				N-S	441.94	882.26
	2019-08-08	2020-10-30	GMLD	E-W	660.9	748.75
				N-S	441.94	882.26
				E-W	660.9	748.75
				N-S	441.94	882.26

Table 1: Seismic Metadata for Natural Sequences (Test Set).

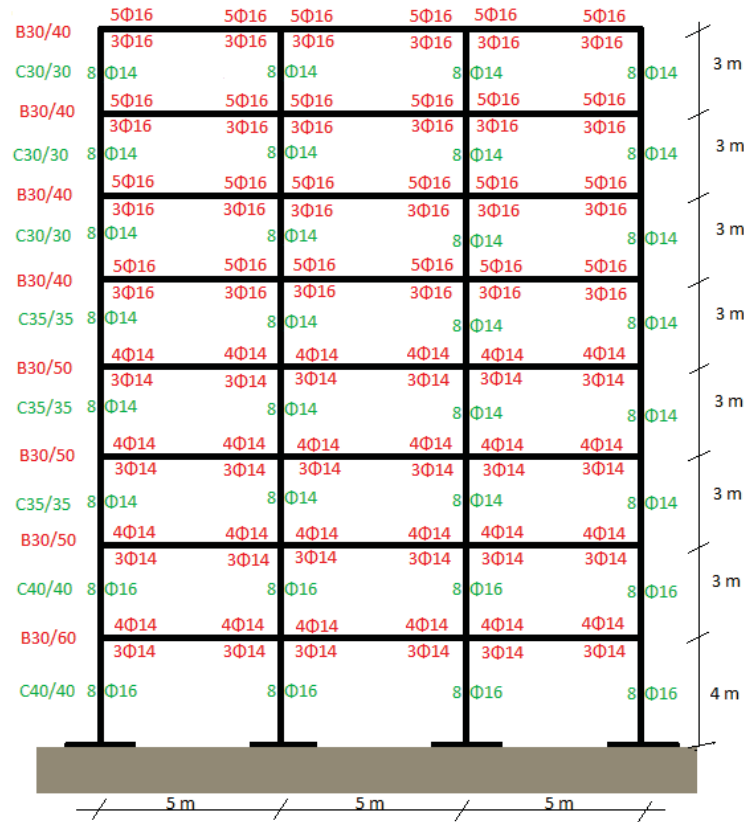


Figure 1: Reinforced Concrete Frame designed by Hatzigeorgiou and Liolios [5].

### 3 FEATURES AND TARGET OF THE ML PROBLEM

This work examined a reinforced concrete planar frame subjected to both artificial and natural sequential acceleration records. The ground motion intensity is evaluated, through scalar measures which are proposed in the literature. The structural damage is accessed in terms of well-known overall damage indices. These features are presented and explained below.

#### 3.1 Ground motion IMs

As previous studies in the prediction of seismic damage amount, we use as features well-known ground motion IMs. The simplest of these are the maximum absolute values of ground accelerations ( $a_g(t)$ ), velocities ( $v_g(t)$ ), and displacements ( $d_g(t)$ ) signals, which referenced as PGA, PGV, and PGD [27], respectively. Widely used IMs are the Intensity Arias ( $I_A$ ) [28] and the Cumulative Absolute Velocity (CAV) [29]. Based on the evolution of Intensity Arias over time the Husid Diagram ( $H_d$ ) [30] is constructed from which duration parameters calculated.

An inherent feature of signals is the frequency content which varies dynamically against the time in the case of ground motion records. However, it is often quantified using the equivalent frequency  $PGA/PGV$  [27] as if it was a sinusoid signal. Another quantity that has been proposed and related to the frequency is the Potential Destructiveness Measure after Araya and Saragoni ( $I_{AS}$ ) [31], resulting from the zero crossings number of the acceleration signal ( $u_o$ ) per unit of time.

Various definitions have been given in the past for the strong motion duration of a seismic excitation, in order to identify the time interval of the signal in which the vast amount of its total intensity is released. In this work, the strong motion durations defined by Trifunac and



Num	Name	Expression	Ref.	Num	Name	Expression	Ref.
1	$PGA$	$\max a_g(t) $	[27]	9	$SMD_{ROG}$	$t(H_d = 97.5\%) - t(H_d = 2.5\%)$	[33]
2	$PGV$	$\max v_g(t) $	[27]	10	$SMD_{Bolt}$	$\Delta t(a > 0.05g)$	[34]
3	$PGD$	$\max d_g(t) $	[27]	11	$P_{90}$	$\frac{I_A(H_d=95\%) - I_A(H_d=5\%)}{SMD_{TB}}$	[27]
4	$I_A$	$\frac{\pi}{2g} \int_0^{t_{end}} a_g^2(t) dt$	[28]	12	$a_{rms}$	$\sqrt{\frac{1}{SMD_{TB}} \int_{5\%}^{95\%} a(t)^2 dt}$	[27]
5	$CAV$	$\int_0^{t_{end}}  a(t)  dt$	[27]	13	$I_c$	$a_{rms}^{1.5} \cdot SMD_{TB}^{0.5}$	[27]
6	$PGA/PGV$	$\frac{PGA}{PGV}$	[27]	14	$I_{FVF}$	$PGV \cdot SMD_{TB}^{0.25}$	[35]
7	$I_{AS}$	$\frac{I_A}{u_o}$	[31]	15	$I_{RG}$	$PGD \cdot SMD_{TB}^{\frac{1}{3}}$	[36]
8	$SMD_{TB}$	$t(H_d = 95\%) - t(H_d = 5\%)$	[32]	16	$SI_H$	$\int_{0.1}^{2.5} PSV(T, \xi = 0.05) dT$	[37]

Table 2: Mathematical Expressions of IMs.

	$SMD$															
	$PGA$	$PGV$	$PGD$	$I_A$	$CAV$	$\frac{PGA}{PGV}$	$I_{AS}$	$TB$	$ROG$	$Bolt$	$P_{90}$	$a_{rms}$	$I_c$	$I_{FVF}$	$I_{RG}$	$SI_H$
	$\frac{cm}{s^2}$	$\frac{cm}{s}$	$cm$	$\frac{cm}{s}$	$\frac{cm}{s}$	$s^{-1}$	$\frac{cm}{s}$	$s$	$s$	$s$	$\frac{cm}{s^2}$	$\frac{cm}{s^2}$	$\frac{cm^{1.5}}{s^{2.5}}$	$cm \cdot s^{-0.75}$	$cm \cdot s^{\frac{1}{3}}$	$cm$
mean	305.0	29.5	55.5	135.6	747.7	13.1	3.5	13.6	17.0	11.9	16.3	77.1	2320.5	53.2	152.2	91.5
std	254.0	24.9	132.0	190.4	519.3	8.8	5.2	10.0	11.2	10.1	26.8	65.3	2516.4	42.8	417.5	73.5
min	32.7	1.2	0.1	0.7	28.0	1.7	0.0	0.6	1.9	0.0	0.1	7.4	55.3	1.4	0.1	2.1
25%	124.7	10.5	2.7	20.6	325.2	7.2	0.3	6.1	8.6	4.8	1.5	30.9	639.9	18.6	5.6	31.5
50%	218.8	23.8	10.5	81.1	693.1	11.3	1.5	10.4	13.6	10.2	4.7	54.2	1544.1	43.2	21.5	76.5
75%	414.2	41.5	40.5	157.2	1008.6	16.6	4.9	18.0	22.8	14.8	16.9	102.8	2916.0	77.3	98.2	134.0
max	1465.2	130.4	1314.2	1332.4	3119.3	75.5	41.5	46.8	55.5	58.6	131.1	286.3	13323.4	201.8	4625.5	387.1

Table 3: Descriptive Statistics of 2nd Seismic Shock IMs (Train Set-837 examples).

Brady ( $SMD_{TB}$ ) [32], and by Reinoso, Ordaz and Guerrero ( $SMD_{ROG}$ ) [33] are assumed. Both of these are based on the time evolution of Arias Intensity according to Husid Diagram. Also, the bracketed duration as described by Bolt ( $SMD_{Bolt}$ ) [34], which is defined by the first and last exceedance of the 5 percent of  $g$ , is employed.

Combining the above parameters results in more complex measures such as Power  $P_{90}$  [27],  $a_{rms}$  [27], Characteristic Intensity ( $I_c$ ) [27], the potential damage measure according to Fajfar, Vidic and Fischinger ( $I_{FVF}$ ) [35] and the IM after Riddell and Garcia ( $I_{RG}$ ) [36].

Also, we did not use seismic parameters that depend on the fundamental period, like individual spectral values of the structure due to the elongation of the initial elastic period before the start of the second seismic event. Instead, we employed Housner Intensity [37] ( $SI_H$ ) which accumulate spectral pseudo-velocities to a constant range of possible eigenperiods and presents a high correlation with the structural damage [38, 12, 39]. The calculation of spectrums for the above purpose implemented using OpenSeismoMatlab [40].

All of the mathematical expressions for employed IMs summarised in Table 2. Tables 3 and 4 present the descriptive statistics of the IMs corresponding to the second seismic shocks of the training and test datasets, respectively. We observed that the training set covers the major range of the test set values. From the initially 954 artificially generated sequences, finally we hold 837 of them, which the NTHAs did not present convergence problems.

	PGA	PGV	PGD	$I_A$	CAV	$\frac{PGA}{PGV}$	SMD					$P_{90}$	$a_{rms}$	$I_c$	$I_{FVF}$	$I_{RG}$	$SI_H$
	$\frac{cm}{s^2}$	$\frac{cm}{s}$	cm	$\frac{cm}{s}$	$\frac{cm}{s}$	$s^{-1}$	$I_{AS}$	TB	ROG	Bolt		$\frac{cm}{s^2}$	$\frac{cm}{s^2}$	$\frac{cm^{1.5}}{s^{2.5}}$	$cm \cdot s^{-0.75}$	$cm \cdot s^{\frac{1}{3}}$	cm
mean	239.2	19.4	15.8	91.4	448.5	16.0	2.5	9.2	11.9	5.2	14.6	69.0	1690.4	31.5	34.1	62.8	
std	212.3	20.9	42.4	184.8	571.7	10.0	5.8	7.7	9.3	7.1	26.1	66.3	2240.4	37.3	99.2	75.7	
min	7.4	0.8	0.0	0.2	29.3	2.9	0.0	0.5	0.7	0.0	0.0	1.8	12.5	1.4	0.1	1.5	
25%	68.7	4.5	0.7	3.4	133.3	9.2	0.1	3.9	5.5	0.2	0.5	17.7	189.3	7.8	1.3	12.5	
50%	185.4	10.8	2.6	15.4	234.9	13.3	0.2	7.0	9.7	2.5	2.8	42.2	616.8	16.2	4.6	31.7	
75%	369.7	30.1	9.4	99.5	588.2	20.6	1.2	11.0	14.3	7.8	18.9	108.7	2527.0	42.0	20.1	80.7	
max	985.8	91.8	277.5	1165.6	3354.8	53.0	32.3	37.4	44.2	42.7	170.7	326.2	11393.9	185.6	737.3	304.0	

Table 4: Descriptive Statistics of 2nd Seismic Shock IMs (Test Set-119 examples).

### 3.2 Damage indicators

In the present section, the damage indices considered in this study are described. The structural damage is used both as an input feature to take into account the existing damage due to the first seismic shock and as a target of the ML problem to describe the accumulated damage after the occurrence of the second earthquake.

#### 3.2.1 Damage index after Park and Ang ( $DI_{PA}$ )

The damage index, proposed by Park and Ang [41], results from summing the contributions of the maximum flexural responses and the hysteretic energy consumed in the plastic hinges areas and is calculated by Equation (1) modified by Kunnath et al. (Equation (2)) [42]. The total damage index [22] is calculated as a weighted average of the sub-factors, weighted by the percentages of the total energy consumed by each member of the construction, according to Equation (3). The overall damage index  $DI_{G,PA}$  as close to zero as possible implies a complete damage-free structural system with an elastic response but when tends to unit characterises a near collapse structure. For abbreviation reason in the next sections  $DI_{G,PA}$  referred to simple as  $DI_{PA}$ .

$$DI_{PA} = \frac{\delta_m}{\delta_u} + \frac{\beta}{Q_y \delta_u} \int dE \quad (1)$$

$$DI_{PA,component} = \frac{\theta_m - \theta_r}{\theta_u - \theta_r} + \frac{\beta}{\theta_u M_y} E_h \quad (2)$$

$$DI_{G,PA} = \frac{\sum E_i DI_{PA,component}}{\sum E_i} \quad (3)$$

where  $\delta_m$  is the maximum element displacement response,  $\delta_u$  is the ultimate element displacement,  $\beta$  is the model constant parameter for strength deterioration proposed by Park et al. [43],  $\int dE$  is the cumulative hysteretic energy consumed by the element during its response,  $Q_y$  is the yield strength of the element,  $\theta_m$  is the maximum element rotation during the time history response,  $\theta_u$  is the ultimate capacity of the element,  $\theta_r$  is the recoverable element rotation during unloading.

### 3.2.2 Damage index after DiPasquale and Cakmak ( $DI_{DC}$ )

During high-intensity seismic events, it is known that the cross-sections in plastic hinges areas of a building can be severely cracked or even present steel yielding, resulting in a stiffness reduction and consequently degradation of the overall stiffness of the structure. Therefore, it is expected that the building will become more flexible and its fundamental period increase. On the above mentioned increasing of the fundamental period due to inelastic dynamic response of a building, based the DiPasquale and Cakmak [44] damage index, calculated according to (4):

$$DI_{DC} = 1 - \frac{T_{0_{initial}}}{T_{0_{equivalent}}} \quad (4)$$

$T_{0_{initial}}$  : The fundamental period before the starting of analysis.

$T_{0_{equivalent}}$  : The fundamental period at the end of the analysis.

### 3.2.3 Max Inter-Storey Drift Ratio (MIDR)

The Max Inter-Storey Drift Ratio [45] during the seismic response of the construction can be used as a measure of the performance it has shown against the earthquake it has hit. The increase in the relative displacements results in an increase of the required floor ductility with similar effects for the rotation and curvature ductility in the areas of the plastic hinges of each component and their cross-sections respectively. So estimating the magnitude of generalised displacements such as MIDR can indirectly aggregate local damages and quantify the total degree of structural damage define by (5).

$$MIDR = \frac{|u|_{max}}{h} 100\% \quad (5)$$

$|u|_{max}$ : Max absolute interstorey deformation recorded during the time history response

$h$ : Storey height

### 3.2.4 Residual Max Inter-Storey Drift Ratio (RMIDR)

Residual displacements cause an important role in the post-seismic performance state of a building to indicate the established damage. Also, consist a critical variable for the reparability of seismic damaged structures [45]. We included it in the problem and evaluate it as the residual maximum inter-storey drift ratio in the post-seismic state, after the end of building oscillation.

## 4 APPLICATION OF NEURAL NETWORKS

The most conventional used Neural Network configuration is the Multi-Layer Perceptron (MLP) [46], which is considered as the simpler learning architecture, consisted from of a few linear layers which are interconnected successively. Each of them receive input from the previous layer, which is multiplied matricially by appropriate weights, subsequently a vector of biases is added. Finally, in every element of the previously defined vector, a nonlinear function is applied to produce the activations of the following layer. This forward process continues until the regression is completed by concluding with the target value from the output layer. The final output values are compared with the real ones, and the regression error is calculated using an

appropriate loss function. The weights of all layers are updated one by one using Stochastic Gradient Descent to minimise the cost function. Data scientists, based on their assumptions and experience, tune their numerous parameters by relating them to the specific problems they need to solve, making use of the available training datasets. Thus, the application of MLP to realistic problems is still challenging and specialised for each problem.

#### 4.1 Gaussian kernel functions

Since the problem under consideration essentially involves the prediction of values based on similar training data samples, kernel function modelling was chosen, which is an appropriate solution as it allows for accurate modelling of data with complex dependencies between input features and target data. They are essentially representations of the input vectors  $x$  in  $\mathfrak{R}$ , which have specific form and properties and are highly generalisable. The appropriate transformation of the input vectors in order to achieve a more easily generalisable solution to the regression problem first requires the transformation of the input space into a transformed feature space with a higher dimension and with a nonlinear representation. The transfer of the problem in a higher dimensional feature space is achieved by the kernel method. In this work, the Gaussian Radial Basis Function kernel (GRBFk) was used, which is appropriate in cases where the identification or manipulation of real values, which tend to cluster around an average value, is required.

#### 4.2 Extreme learning machines

In this paper, a holistic Single-hidden Layer Feed Forward Network (ShLFFN) shallow architecture approach with  $N$  neurons in the hidden layer, randomly chosen input weights and random values of bias constants on the hidden layer neurons, while the output weights are computed by a single matrix multiplication, which automates and optimally solves the problem, was used. These ShLFFN architectures, called Extreme Learning Machines (ELMs) [47], used in complex problems, due to their ability to access any continuous function. Also, the networks in question can learn  $N$  samples with accuracy, while their learning speed can be even thousands of times faster than conventional Feed Forward Network Networks, as their training is not based on time-consuming repetitive processes such as the algorithm. Back Propagation, which changes the weights of the neural network by estimating the quadratic error between the target vectors and the actual network outputs, for all training samples, which are entered into the network in a random serial manner and for many repetitions (epochs)

Driven by the observation that the first stage of the algorithm can be considered as a process of mapping the training vectors into a higher dimensional vector space, in the hidden layer we chose a sufficiently large number of neurons (at least twice the input parameters) so that the algorithm has the property of a universal approximator and can train ShLFFN efficiently. More specifically, the input data are mapped to a random  $\tilde{N}$ -dimensional space with a discrete training set  $N$  where  $(x_i, t_i)$  with  $i \in [1, N]$   $x_i \in \mathfrak{R}^d$  and  $t_i \in \mathfrak{R}^c$ . The output of the network presented in Equation (6).

$$f_L(x) = \sum_{i=1}^{\tilde{N}} \beta_i h_i(x) = \mathbf{h}(x)\beta, \quad i \in [i, N] \quad (6)$$

where  $\beta = [\beta_1, \dots, \beta_{\tilde{N}}]^T$  is the weight matrix between hidden and output neurons  $h(x) = [g(x_1), \dots, g(x_2)]$  is the output of hidden neurons for the input  $x$ , and  $g(x_i)$  is the output of  $i^{th}$  hidden node. Based on  $N$  length training set  $\{(x_i, t_i)\}_{i=1}^N$ , the ELM can solve the learning problem  $\mathbf{H}\beta = \mathbf{T}$ , where  $\mathbf{T} = [t_1, \dots, t_N]^T$  are the target labels and the output matrix of the hidden layer

output presented in Equation (7).

$$\mathbf{H}(\mathbf{W}, \mathbf{b}, \mathbf{X}) = \begin{bmatrix} g(\mathbf{w}_1 \cdot \mathbf{x}_1 + b_1) & \cdots & g(\mathbf{w}_{\tilde{N}} \cdot \mathbf{x}_1 + b_{\tilde{N}}) \\ \vdots & \ddots & \vdots \\ g(\mathbf{w}_1 \cdot \mathbf{x}_N + b_1) & \cdots & g(\mathbf{w}_{\tilde{N}} \cdot \mathbf{x}_N + b_{\tilde{N}}) \end{bmatrix}_{N \times \tilde{N}} \quad (7)$$

Before the training, the weight matrix  $\mathbf{W}$  and the bias vectors  $\mathbf{b}$  initialised randomly in the interval  $[-1, 1]$ , given  $\mathbf{w}_j = [w_{j1}, w_{j2}, \dots, w_{jm}]^T$  and  $\beta_j = [\beta_{j1}, \beta_{j2}, \dots, \beta_{jm}]^T$ . The output weight matrix of the hidden layer  $\mathbf{H}$  came up from Equation (8), given the training data and the activation function  $g$ .

$$\mathbf{H} = g(\mathbf{W}\mathbf{x} + \mathbf{b}) \quad (8)$$

The hidden layer (Figure 2) is responsible for transforming the input data into a different representation. The transformation is achieved in two steps:

- First Step. The input data is input to the hidden layer using the weights and corresponding values of the input layer.
- Second Step. The data is transformed based on a nonlinear transformation function.

Finally, the output weights  $\beta$  could compute from Equation (9).

$$\beta = \mathbf{H}^* \mathbf{T} \quad (9)$$

where  $\mathbf{H}^*$  is the Moore-Penrose generalised inverse matrix for  $\mathbf{H}$ .

### 4.3 Bootstrap sampling and ensemble technique

Bootstrap sampling [48] is adopted so that different subsets of the dataset can train the model in the most fruitful way, to increase the efficiency of the method. Bootstrap sampling is the process of applying progressively larger random samples until the accuracy of the neural network is improved. Every sample is used to train an individual model and the results of each model are summarised by “voting”, i.e. for any input vector, each classifier predicts the output variable and finally, for every variable the value with the most “votes” is chosen. This methodology, which belongs to the Ensemble methods, is called Bagging and has many advantages, such as reducing covariance. The Ensemble technique [49] is used due to the fact that in the specific problem, the prediction results show multivariability, which can be attributed to the sensitivity of the correlation models to the data and the complex relationship that describes them. Also, an important advantage gained by the proposed system is focused on the fact that it offers more efficient and stable prediction model, since the overall behaviour of multiple MLP ANNs is less noisy than a single one, and in any case reduces the overall risk of a particularly inaccurate values. Finally, in order to evaluate the reliability of the implemented bagging method, the variance of the expected error is checked to be around the mean error value.

## 5 RESULTS

This section presents both the results from NTHAs in terms of overall seismic damage indices and the neural network testing in terms of correlations between real and predicted values. In the case of structural damage indices we present both the results of the first shocks NTHAs adopted between the inputs of the ML problem (Figure 2) and the corresponding after the second shocks which employed as targets of the problem.



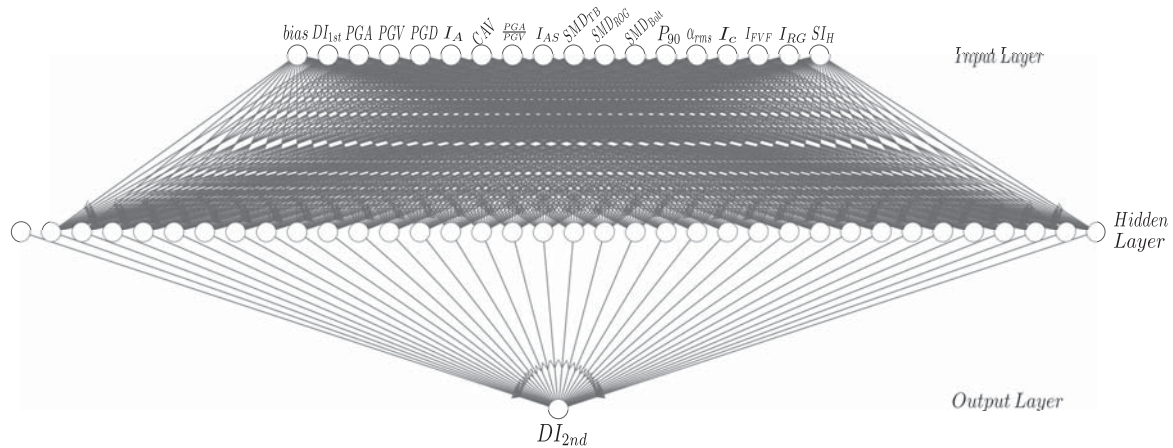


Figure 2: An ELM neural network architecture uses as input arguments both damage index from the first seismic event and the IMs of the second event to predict the final damage index (after second event).

### 5.1 Results of NTHAs

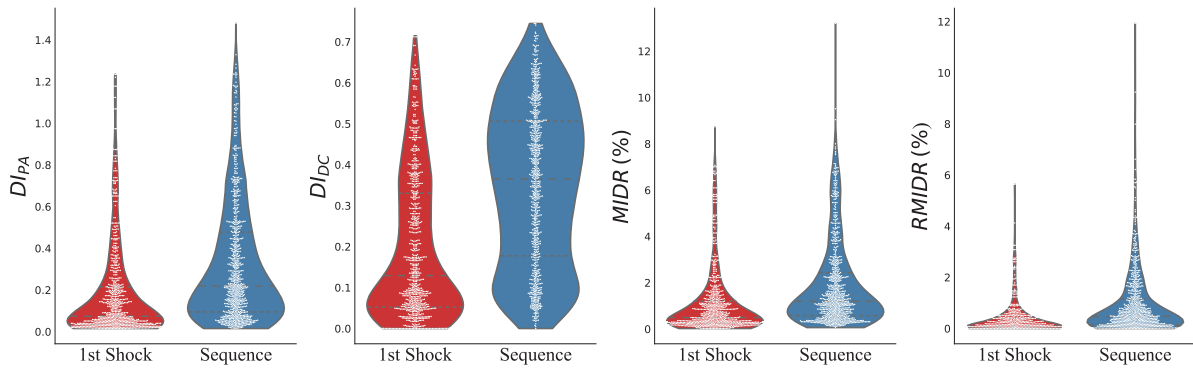
The results of NTHAs represented in terms of damage indices after the occurrence of the first shocks and after the sequences (Figure 3). As we compare the distributions of damage indices after the first and second shock, we see a clear increase after the second shock, both in the training and test set. The increase is higher in the case of  $DI_{DC}$ . The maximum value of this damage index seems to be constant around 0.7 both in the training and test set. The other damage indices have a smaller increase but a clear offset of the upper-end value both to training and test set as we shown in Figures 3a and 3b respectively.

### 5.2 Results of ANN testing

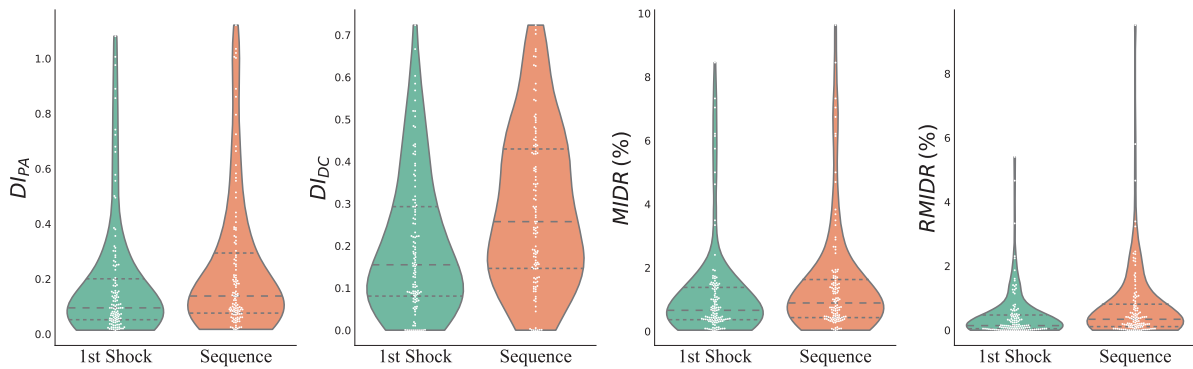
Since the model described in Section 4, trained using the dataset generated from artificial sequences, several correlation coefficients calculated between predicted and actual values of the targets on the test set (natural sequences) to evaluate the effectiveness of the fitted ML model. The results of three correlation coefficients (Pearson, Kendall and Spearman) and two error metrics, Mean Absolute Error (MAE) and Root Mean Square Error (RMSE), for the final fitted model are presented in Table 5. We can observe that the damage indices with the best predictive behaviour are the  $MIDR$  and  $DI_{PA}$  which display the higher values of Pearson, Kendall and Spearman coefficients. The relation between predicted and the actual values of  $DI_{DC}$  looks to be quite linear since the values of Pearson and Spearman coefficients are similar and quite high.

	Pearson	Kendall	Spearman	MAE	RMSE
$DI_{PA}$	0.9104	0.7956	0.9366	0.0574	0.1059
$DI_{DC}$	0.8875	0.7140	0.8898	0.0648	0.0867
$MIDR$	0.8960	0.8277	0.9582	0.3542	0.7933
$RMIDR$	0.8316	0.7488	0.9146	0.2956	0.6870

Table 5: Results of correlation between actual and predicted values on the test set.



(a) Violin plots of damage indicators distributions of the training set (837 artificial sequences).



(b) Violin plots of damage indicators distributions of the test set (119 natural seismic sequences).

Figure 3: Violin plots of damage indicators distributions.

## 6 CONCLUSIONS

In the present study, we used an ensemble neural network methodology to predict the final damage of an 8-storey RC frame under successive earthquakes. For this purpose, we employed a training dataset of 837 artificial seismic sequences and a test set of 119 natural seismic sequences. Finally, the main conclusions are summarised as follows:

- In both training and test sets, the structural damage under the sequences is increased in comparison with the corresponding damage that occurred after the initial shocks.
- In general, the predictive capacity of the configured Ensemble Neural Network seems to be quite satisfactory.
- The Ensemble Neural Network presents a higher performance in forecasting the final structural damage in terms of  $DI_{PA}$  (damage index after Park-Ang) and  $MIDR$  (Maximum Inter-storey Drift Ratio).

For future machine learning applications in structural damage prediction due to successive earthquakes enriched dataset of natural seismic sequences may be considered. Moreover, a wide range of structural systems should be examined in order to incorporate structural attributes as ML problem input features.

## REFERENCES

- [1] C. Karakostas, N. Klimis, V. Lekidis, K. Makra, B. Margaris, K. Morfidis, C. Papaioannou, E. Rovithis, T. Salonikios, D. Sotiriadis, and N. Theodoulidis, Thessaly Earthquakes M6.3, 03/03/2021 and M6.1, 04/03/2021 – Preliminary Report, tech. rep., Research Unit ITSAK, EPPO and Department of Civil Engineering, DUTH, Mar. 2021.
- [2] E. Lekkas, K. Agorastos, S. Mavroulis, H. Kranis, E. Skourtsos, P. Carydis, M. Gogou, K.N. Katsetsiadou, G.A. Papadopoulos, I. Triantafyllou, A. Agalos, M. Sotiris, E. Stamati, D. Psarris, G. Kaviris, V. Kapetanidis, P. Papadimitriou, A. Karakostas, I. Spingos, V. Kouskouna, I. Kassaras, K. Pavlou, N. Voulgaris, M. Mavrouli, S. Pavlides, A. Chatzipetros, S. Sboras, E. Kremastas, A. Chatziioannou, A.A. Kiratzi, C. Papazachos, N. Chatzis, V. Karakostas, E. Papadimitriou, I. Koukouvelas, K. Nikolakopoulos, A. Kyriou, D. Apostolopoulos, V. Zygouri, S. Verroios, A. Belesis, I. Tsentzos, P. Krasakis, K. Lymperopoulos, A. Karavias, D. Bafi, T. Gatsios, M. Karatzia, I. Gkougkoustamos, T. Falaras, I. Parcharidis, G. Papathanassiou, C. Evangelidis, V. Karastathis, A. Tselentis, A. Ganas, V. Tsironi, I. Karasante, S. Valkaniotis, D. Galanakis, G. Konstantopoulou, N. Papadopoulos, A. Kourou, M. Manousaki, and T. Thoma, The early March 2021 Thessaly (Greece) earthquake sequence, *Newsletter of Environmental, Disaster and Crises Management Strategies*.
- [3] C. Amadio, M. Fragiaco, and S. Rajgelj, The effects of repeated earthquake ground motions on the non-linear response of SDOF systems, *Earthquake Engineering & Structural Dynamics*, **32**(2), 291–308, 2003.
- [4] G.D. Hatzigeorgiou and D.E. Beskos, Inelastic displacement ratios for SDOF structures subjected to repeated earthquakes, *Engineering Structures*, **31**(11), 2744–2755, 2009.
- [5] G.D. Hatzigeorgiou and A.A. Liolios, Nonlinear behaviour of RC frames under repeated strong ground motions, *Soil Dynamics and Earthquake Engineering*, **30**(10), 1010–1025, 2010.
- [6] M. Hatzivassiliou and G.D. Hatzigeorgiou, Seismic sequence effects on three-dimensional reinforced concrete buildings, *Soil Dynamics and Earthquake Engineering*, **72**, 77–88, 2015.
- [7] F. Hosseinpour and A. Abdelnaby, Effect of different aspects of multiple earthquakes on the nonlinear behavior of RC structures, *Soil Dynamics and Earthquake Engineering*, **92**, 706–725, 2017.
- [8] I.E. Kavvadias, P.Z. Rovithis, L.K. Vasiliadis, and A. Elenas, Effect of the aftershock intensity characteristics on the seismic response of RC frame buildings, in *Proceedings of the 16th European Conference on Earthquake Engineering, Thessaloniki, Greece*, 18–21, 2018.
- [9] Z. Zhou, X. Yu, and D. Lu, Identifying Optimal Intensity Measures for Predicting Damage Potential of Mainshock–Aftershock Sequences, *Applied Sciences*, **10**(19), 6795, 2020.
- [10] O.R. De Lautour and P. Omenzetter, Prediction of seismic-induced structural damage using artificial neural networks, *Engineering Structures*, **31**(2), 600–606, 2009.

- [11] P. Alvanitopoulos, I. Andreadis, and A. Elenas, Neuro-fuzzy techniques for the classification of earthquake damages in buildings, *Measurement*, **43**(6), 797–809, 2010.
- [12] K. Morfidis and K. Kostinakis, Seismic parameters' combinations for the optimum prediction of the damage state of R/C buildings using neural networks, *Advances in Engineering Software*, **106**, 1–16, 2017.
- [13] K. Kostinakis and K. Morfidis, Application of Artificial Neural Networks for the Assessment of the Seismic Damage of Buildings with Irregular Infills' Distribution, in *Seismic Behaviour and Design of Irregular and Complex Civil Structures III*, 291–306, Springer, 2020.
- [14] J. González, W. Yu, and L. Telesca, Earthquake Magnitude Prediction Using Recurrent Neural Networks, in *Multidisciplinary Digital Publishing Institute Proceedings*, **24**(1), 22, 2019.
- [15] S. Mangalathu and H.V. Burton, Deep learning-based classification of earthquake-impacted buildings using textual damage descriptions, *International Journal of Disaster Risk Reduction*, **36**, 101111, 2019.
- [16] R. Zhang, Z. Chen, S. Chen, J. Zheng, O. Büyüköztürk, and H. Sun, Deep long short-term memory networks for nonlinear structural seismic response prediction, *Computers & Structures*, **220**, 55–68, 2019.
- [17] J. Li, Z. He, and X. Zhao, A data-driven building's seismic response estimation method using a deep convolutional neural network, *IEEE Access*, 1, Mar 2021.
- [18] B.K. Oh, Y. Park, and H.S. Park, Seismic response prediction method for building structures using convolutional neural network, *Structural Control and Health Monitoring*, **27**(5), e2519, 2020.
- [19] L. Luzi, G. Lanzano, C. Felicetta, M. D'Amico, E. Russo, S. Sgobba, F. Pacor, and ORFEUS Working Group 5, Engineering Strong Motion Database (ESM) (Version 2.0), *Istituto Nazionale di Geofisica e Vulcanologia (INGV), Rome, Italy*, 2020.
- [20] T.D. Ancheta, R.B. Darragh, J.P. Stewart, E. Seyhan, W.J. Silva, B.S. Chiou, K.E. Wooddell, R.W. Graves, A.R. Kottke, D.M. Boore, *et al.*, Peer NGA-West2 database, tech. rep., Pacific Earthquake Engineering Research Center Berkeley, CA, 2013.
- [21] G. Rossum, Python reference manual, 1995.
- [22] R. Valles, A.M. Reinhorn, S.K. Kunnath, C. Li, and A. Madan, IDARC2D version 4.0: A computer program for the inelastic damage analysis of buildings, tech. rep., US National Center for Earthquake Engineering Research (NCEER), 1996.
- [23] Y.J. Park, A.M. Reinhorn, and S.K. Kunnath, *IDARC: Inelastic Damage Analysis of Reinforced Concrete Frame-Shear-Wall Structures*, National Center for Earthquake Engineering Research Buffalo, NY, 1987.
- [24] CEN, EN 1992-1-1 Eurocode 2: Design of concrete structures - Part 1-1: General rules and rules for buildings, *Brussels: European Committee for Standardization*, 2005.

- [25] J.W. Eaton, GNU Octave and reproducible research, *Journal of Process Control*, **22**(8), 1433–1438, 2012.
- [26] J.W. Eaton, D. Bateman, S. Hauberg, and R. Wehbring, *GNU Octave version 6.2.0 manual: a high-level interactive language for numerical computations*, 2021.
- [27] S.L. Kramer, *Geotechnical earthquake engineering*, Pearson Education India, 1996.
- [28] A. Arias, A measure of earthquake intensity. Seismic Design for Nuclear Power Plants, *Massachusetts Institute of Technology*, 1970.
- [29] A. EPRI, Criterion for determining exceedance of the operating basis earthquake. Rapport NP-5930 2848-16, *Electric Power Research Institute, USA*, 1988.
- [30] R. Husid, Características de terremotos. Análisis general, *Revista IDIEM*, **8**(1), ág–21, 1969.
- [31] R. Araya, Earthquake accelerogram destructiveness potential factor, in *Proc. 8th World Conference on Earthquake Engineering*, 1985. 7, **11**, 835–843, 1985.
- [32] M.D. Trifunac and A.G. Brady, A study on the duration of strong earthquake ground motion, *Bulletin of the Seismological Society of America*, **65**(3), 581–626, 1975.
- [33] E. Reinoso, M. Ordaz, and R. Guerrero, Influence of strong ground-motion duration in seismic design of structures, in *Proceedings, 12th World Conference on Earthquake Engineering*, **1151**, 2000.
- [34] B.A. Bolt, Duration of strong ground motion, in *5th World Conference on Earthquake Engineering*, **292**, 25–29, 1973.
- [35] P. Fajfar, T. Vidic, and M. Fischinger, A measure of earthquake motion capacity to damage medium-period structures, *Soil Dynamics and Earthquake Engineering*, **9**(5), 236–242, 1990.
- [36] R. Riddell and J.E. Garcia, Hysteretic energy spectrum and damage control, *Earthquake Engineering & Structural Dynamics*, **30**(12), 1791–1816, 2001.
- [37] G. Housner, Spectrum intensities of strong-motion earthquakes, 1952.
- [38] A. Masi, M. Vona, and M. Mucciarelli, Selection of Natural and Synthetic Accelerograms for Seismic Vulnerability Studies on Reinforced Concrete Frames, *Journal of Structural Engineering*, **137**(3), 367–378, 2011.
- [39] P.C. Lazaridis, I.E. Kavvadias, and L.K. Vasiliadis, Correlation between Seismic Parameters and Damage Indices of Reinforced Concrete Structures, 2019.
- [40] G. Papazafeiropoulos and V. Plevris, OpenSeismoMatlab: A new open-source software for strong ground motion data processing, *Heliyon*, **4**(9), e00784, 2018.
- [41] Y.J. Park and A.H.S. Ang, Mechanistic seismic damage model for reinforced concrete, *Journal of Structural Engineering*, **111**(4), 722–739, 1985.



- [42] S.K. Kunnath, A.M. Reinhorn, and R. Lobo, IDARC Version 3.0: A program for the inelastic damage analysis of reinforced concrete structures, tech. rep., US National Center for Earthquake Engineering Research (NCEER), 1992.
- [43] Y.J. Park, A.H. Ang, and Y.K. Wen, Damage-limiting aseismic design of buildings, *Earthquake Spectra*, **3**(1), 1–26, 1987.
- [44] E. DiPasquale and A. Çakmak, Detection of seismic structural damage using parameter-based global damage indices, *Probabilistic Engineering Mechanics*, **5**(2), 60–65, 1990.
- [45] FEMA, P58–1 Seismic performance assessment of buildings (volume 1-Methodology), *Federal Emergency Management Agency, Washington*, **1**, 2012.
- [46] M. Minsky and S.A. Papert, *Perceptrons: An introduction to computational geometry*, MIT Press, 2017.
- [47] G.B. Huang, Q.Y. Zhu, and C.K. Siew, Extreme learning machine: theory and applications, *Neurocomputing*, **70**(1-3), 489–501, 2006.
- [48] T.H. Lee, A. Ullah, and R. Wang, Bootstrap aggregating and random forest, in *Macroeconomic Forecasting in the Era of Big Data*, 389–429, Springer, 2020.
- [49] L.K. Hansen and P. Salamon, Neural network ensembles, *IEEE Transactions on Pattern Analysis and Machine Intelligence*, **12**(10), 993–1001, 1990.

## AUTOMATED ESTIMATION OF BUILDING HEIGHT THROUGH IMAGE PROCESSING

Pietro Carpanese<sup>1</sup>, Marco Donà<sup>1,2</sup>, and Francesca da Porto<sup>1</sup>

<sup>1</sup> Depart. of Geosciences - University of Padova  
Via G. Gradenigo, 6, 35131 Padova (IT)  
pietro.carpanese@phd.unipd.it, francesca.daporto@unipd.it

<sup>2</sup> Earthquake Engineering Research & Test Center – Guangzhou University  
Guang Yuan Zhong Rd. 248, 510405 Guangzhou, China  
dona\_marco@gzhu.edu.cn

---

### Abstract

*Seismic risk is one of the main problems in highly urbanized countries with a considerable seismic hazard like Italy. To assess seismic risk of the built heritage, it is necessary to deepen the knowledge of its components, vulnerability in particular. Vulnerability can be evaluated through mechanical methods, which require detailed information on parameters that may affect the seismic response. The implementation of such methods often results in time-consuming and expensive investigations, thus making the risk assessment analysis very cumbersome.*

*In order to make this process easier and faster, remote sensing algorithms can be taken into consideration. In this work, satellite images of areas of interest are automatically extracted via open source online maps, as well as some preliminary information about the buildings detected in the pictures. Afterwards, a filter is set in order to visualize only targeted building typologies (e.g., residential buildings), and street view images are obtained for each selected building. The images are then processed through feature extraction techniques, in order to predict the number of stories of the buildings.*

*The remote and automated retrieval of this feature, along with other meaningful parameters, could allow the association of a specific vulnerability level for each building, thus making on-site surveys unnecessary, with a remarkable reduction in time and costs.*

**Keywords:** Remote Sensing, Satellite Images, Street View, Image Processing, Building Height, Seismic Vulnerability

---

## 1 INTRODUCTION

Seismic risk is one of the main problems in highly urbanized countries with a considerable seismic hazard like Italy. Even more, seismic risk mitigation represents a major challenge to reduce socio-economic impact of future earthquakes. To carry out seismic risk assessments, it is necessary to deepen the knowledge of the different components of this risk.

Seismic risk is defined as the combination of seismic hazard (probability that a particular earthquake occurs), exposure (number of people, quantity and value of buildings and goods) and seismic vulnerability. The latter can be described as the propensity of a building to suffer a certain level of damage after a seismic event. [1]

In order to assess seismic vulnerability of buildings, it can be useful to define fragility curves, which correlate ground motion with the damage suffered by the buildings. In literature, many approaches allow the calibration of fragility curves. Among others, analytical-mechanical approaches define fragility based on structural models in order to simulate the seismic behavior of buildings. [2-6]. However, when implementing mechanical methods to properly characterize the behavior of buildings at a territorial scale, it is always necessary to collect a big amount of structural data, such as material, construction period, height, as well as some more detailed geometric features. Especially when dealing with large districts or even entire towns, the investigation of these essential parameters often results in time-consuming and expensive surveys, making the risk assessment analysis very cumbersome [7-8].

In order to make this investigation process faster and easier, artificial intelligence techniques may be taken into consideration. For example, instance classification methods have already been used to classify buildings and some of their features using street view images [9-10]. Further information such as building age and category has also been obtained by analyzing morphology, neighborhood characteristics and urban patterns from topographic maps [11-16]. Some works have employed shadow detection techniques in satellite images, in order to estimate building heights [17-19], while others combine maps and street level images to perform the same task [20-23]. In general, it has become evident how artificial intelligence can be useful for elaborating models that extract building information, and consequently for carrying out risk management assessments [24].

In this paper, particular attention is paid to the retrieval of building footprints from satellite images of areas of different sizes, as well as some preliminary geometric and typological features. Subsequently, a methodology for estimating building heights (in terms of number of stories) from street view images is presented, where image processing and feature extraction techniques are used. The main steps of the algorithm are commented, along with the resolution of the main obstacles that can be encountered when analyzing street view pictures.

## 2 AUTOMATED RETRIEVAL OF BUILDING FOOTPRINTS

When seismic risk analyses are to be carried out at a territorial scale, an important element to assess is building exposure. This first step is necessary to understand how urbanized the area is (how many buildings there are), as well as to identify the building typologies. A good estimate of exposure, indeed, takes into account the different usages of buildings, as well as their construction material, construction period, etc.

For this aim, a Python code was developed, in order to retrieve building footprints given a specific satellite image.

To retrieve the desired satellite image, the script provides two input possibilities: the user can search a place by town/municipality, or can enter a pair of coordinates (latitude and longitude) and distance radius  $R$ . In the first case, the program will also return the centroid of the chosen town (in terms of latitude and longitude); in the second case, the program will extract

the name of the municipality, region and country to which the chosen area belongs. The code performs this task through the Static Maps service from the Mapbox API. Figure 1 shows two example of satellite images: Figure 1a shows an image extracted for an entire town (Padova), while Figure 1b displays an area centered in the point (45.409605, 11.888727) with a radius  $R$  of 300 meters.

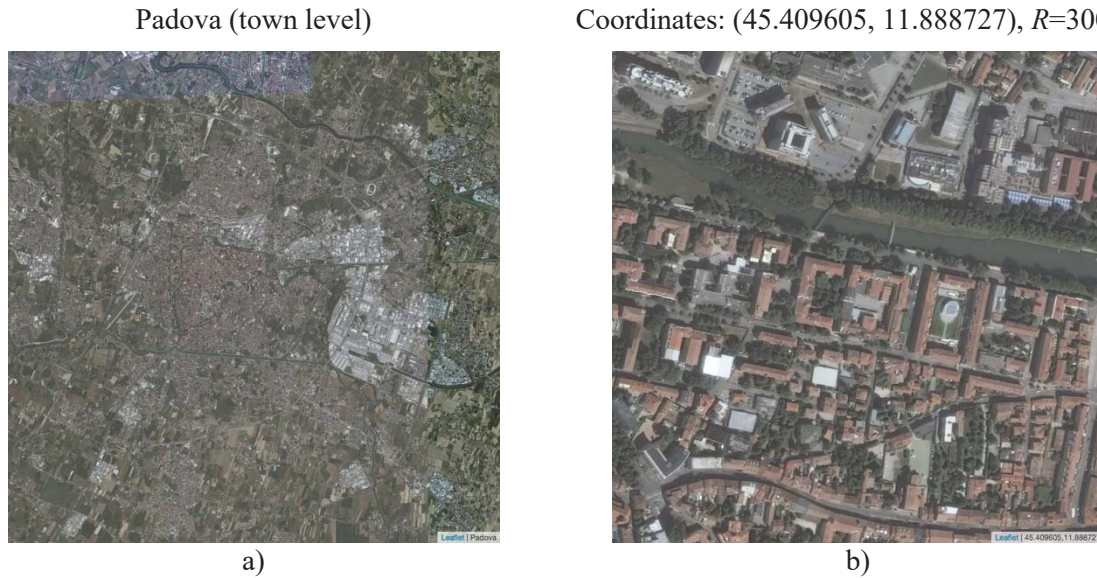


Figure 1: Satellite images for a) the town of Padova, b) an area centered in the point of coordinates (45.409605, 11.888727) with a radius of 300 meters

The second step of the code involves the acquisition of the building footprints that can be found in the satellite images. To do so, the OSM dependency is utilized, which provides access to OpenStreetMap services. Particularly, the key “building” is selected, in order to extract only this type of objects from the map. The two maps in Figure 2 show the building footprints related to the satellite images shown in Figure 1.

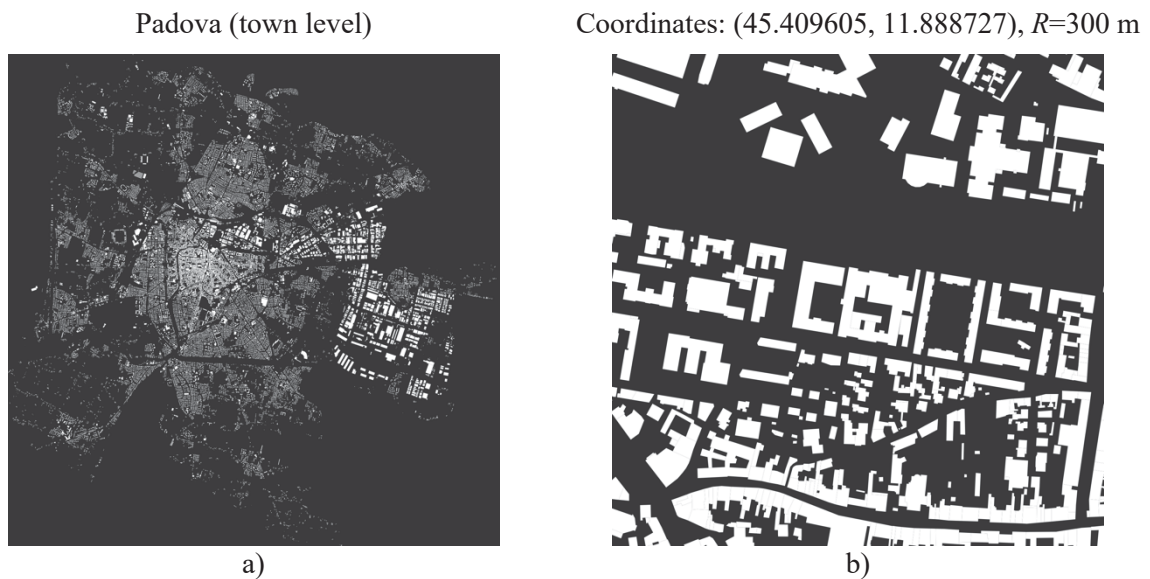


Figure 2: Building footprints for a) the town of Padova, b) an area centered in the point of coordinates (45.409605, 11.888727) with a radius of 300 meters



This section of the code not only retrieves the building footprints, but also retains their floor area, their centroid (latitude-longitude) and the labels of each building (such as “accommodation”, “commercial”, “religious”, etc). All the data obtained are stored in a DataFrame, where each row represents a building; they can be accessed and edited via GeoPandas, an open source project that helps manage geospatial data in Python. Figure 3 shows the building footprints from Figure 2b, with different colors according to their label.



Figure 3: Building footprints and their labels

In addition, the way in which data are stored makes it easy to filter them. As an example, only residential buildings and their outbuildings are shown in colors in Figure 4, while other building typologies are plotted in gray.



Figure 4: Building footprints and their labels, where only residential buildings and outbuildings are kept

As said before, for each building the centroid is known. Thanks to the Google Street View API, it is possible to automatically obtain the façade picture of a desired building, given its centroid coordinates. The user can select the size of the output picture, the pitch (vertical angle) and the heading (horizontal angle). In this work, the default size was chosen, i.e., 640x640 pixels. Also, no heading was specified: each time, a value is calculated that directs the camera towards the specified location, from the point at which the closest photograph was taken. For what concerns the pitch, an angle of 5° was selected, so that even taller buildings can fit in the



image taken (the default value would be  $0^\circ$ , which means flat horizontal). In Figure 5, some examples of street view images associated to the area under consideration are shown. The code could easily acquire the street view pictures for all the building footprints in the image, in a fairly short computation time.



Figure 5: Examples of street view images obtained from the coordinates of the building footprints

### 3 AUTOMATED ESTIMATION OF BUILDING HEIGHTS

The workflow described in §2 leads to a good estimate of building exposure in a specific area, in terms of number of buildings, building typology and total built-up area.

As said before, however, such information is not sufficient to predict the seismic vulnerability and risk level of a urban district, since more building parameters should be evaluated. In particular, previous works have shown that a good estimate of vulnerability can be obtained by knowing at least the number of stories, the material and the construction period of the buildings examined [5].

In this paper, the variable “number of stories” is examined. Specifically, an algorithm that automatically retrieves the number of floors of buildings from street view images was developed. Image processing and feature extraction techniques were implemented in this algorithm.

#### 3.1 Building detection with bounding boxes

The first step in this algorithm is the correct identification of buildings in the street view image. To perform this task, other works have used Convolutional Neural Networks (CNNs) that are able to detect and classify façade structures from street view pictures [9].

In this specific case, however, a complete detection of buildings is not necessary. In fact, to estimate the number of stories, only a single vertical strip of windows could be sufficient. For this reason, a script that selects the appropriate bounding box was developed. A bounding box is a rectangle that fully encloses an object in a digital image; in this case, the bounding box is set to include one or two vertical strips of windows (optionally including the door), going from the bottom of the building (e.g pavement line) to the rooftop (e.g skyline). In this way, the rest of the code will only have to deal with a smaller portion of the detected building, thus reducing the computation time and possible overlapping errors.

The method used to detect a bounding box relies on the Hough transform. The Hough transform is a feature extraction technique often used in digital image processing, whose main purpose is the identification of lines in the image [25].

Firstly, only the vertical Hough lines are taken into consideration, with a range of slopes between  $-15^\circ$  and  $+15^\circ$ , where a  $0^\circ$  represents a perfectly vertical line (green lines in Figure 6b). By doing so, vertical strips of windows can be easily defined.

Secondly, the ground and the sky must be detected. Also in this step, the Hough transform is utilized, keeping only the lines whose slope is between  $60^\circ$  and  $90^\circ$  (both positive or negative). These values were chosen to make it possible to detect the base and the rooftop of a building, even when the street view image is not perfectly frontal. For detecting the skyline (blue line in Figure 6b), only the top half of the street view image is considered, while for the bottom line of the building (red line in Figure 6b) only the bottom half is kept. The fact that the street view images are acquired with pitch angles of  $5^\circ$  helps to remove part of the pavement, which is an irrelevant element for creating the bounding box.

The code was written in MATLAB, and more information about the parametric representation of lines with the Hough transform can be found in the algorithms section of the mathworks page.

In Figure 6c, it can be seen that from a rather complex street view image (with more than one building, a car, a gate, trees), the algorithm is able to crop only the part of the picture that will be useful for the estimation of the number of stories.

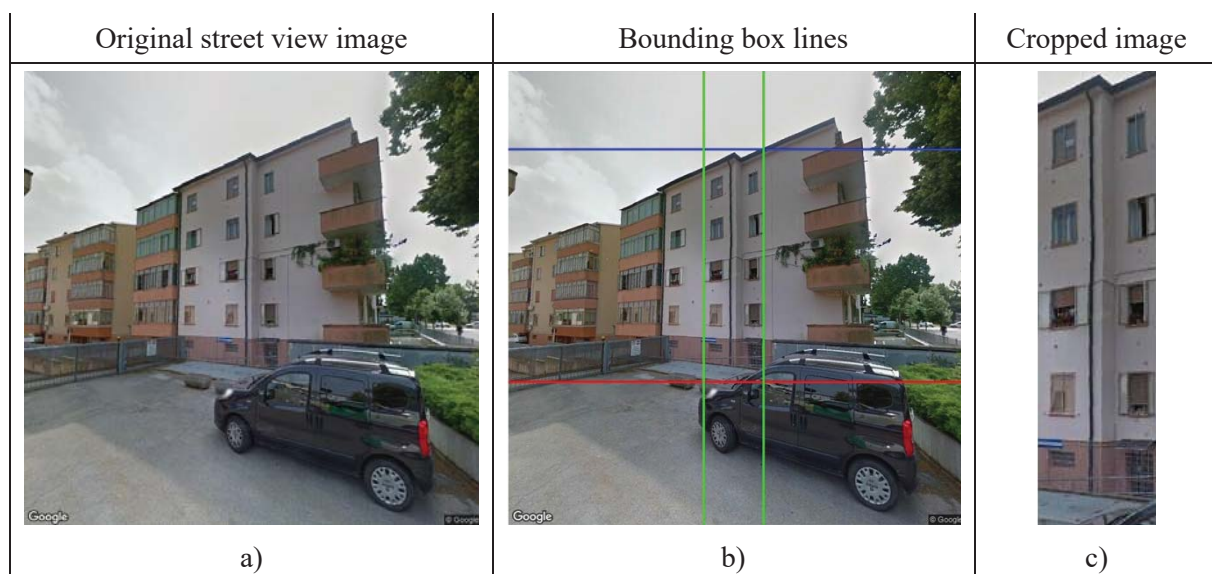


Figure 6: Example of a bounding box

### 3.2 Feature extraction for estimating the number of stories

Now that only a meaningful part of the street view image has been selected, the algorithm can proceed with the estimation of the number of stories. The key concept of this step is that the top and bottom of every door and window (or row of windows) must be detected, so that they can be associated with the presence of a floor.

To begin with, the raw Google Street View image has to be processed. Firstly, the original picture is turned into a grayscale image, and then an edge detection method is implemented. Edge detection is an image processing technique for finding the boundaries of objects within images, which works by detecting discontinuities in brightness. This technique is commonly used for image segmentation and data extraction. In this work, a Canny edge detection method

is implemented [26]. This method finds edges by looking for local maxima of the gradient of the grayscale image, which is calculated using the derivative of a Gaussian filter. The Canny method is one of the most suitable to detect true edges. The result is a binary (black and white) image, as shown in the example of Figure 7c for a bounding box image.

Secondly, morphological operations are applied to the binary image. These operations can process images based on shapes, so that each pixel in the image is adjusted based on the value of other pixels in its neighborhood. In particular, the following morphological operations are used: *skeleton*, which removes pixels on the boundaries of objects but does not allow objects to break apart; *thin*, which thins objects to lines; *spur*, which removes pixels starting from the end of any branch as well as the two ends of the main skeleton; and lastly *clean*, which removes isolated pixels. Essentially, all these operations allow a simplification of the binary image, where only the main lines are kept (as can be seen in Figure 7d).

The final step is the window (and consequently floor) detection. Once again, the Hough transform was used to detect horizontal lines, as described in §3.1. Out of all the lines that are found, the ones that are too close to each other (i.e., at a distance of less than 20 pixels) are grouped together, and only one of them is kept. This solution was adopted in order to avoid detecting the same line twice, since the border of a window may be associated with multiple Hough lines. In addition, the script eliminates intersecting lines, which are usually caused by obstacles in front of the actual window or door, such as the branches of a tree.

Figure 7 shows the general workflow that has just been explained. In Figure 7a, the original street view image is shown, as obtained from Google Street View. Figure 7b shows the bounding box that selects only the main door and one strip of windows. Figure 7c shows the result of applying the Canny Edge method to the bounding box image, while in Figure 7d morphological operations are applied to the binary image. Lastly, Figure 7e represents the feature extraction step, where the Hough transform technique is used to identify the lines delimiting doors and windows.

Looking at Figure 7e, the estimation of number of stories is immediate, since every couple of lines represents a different floor. Moreover, the code automatically computes this parameter, by taking into account the final number of lines, dividing it by two and rounding this value down.






Original street view image	Step 1: Bounding box	Step 2: Canny edge detector	Step 3: Morphological operations	Step 4: Hough lines (stories)
				
a)	b)	c)	d)	e)

Figure 7: Main steps of the algorithm to estimate the number of stories of a building from street view images



### 3.3 Particular case: bounding box for hidden buildings

The code described in §3.2 works with a good degree of accuracy when the building is completely visible, and the façade can be seen from a frontal or near-frontal perspective. However, many Google Street View images contain pictures of buildings that are partially hidden or covered by obstacles. In order to cope with this problem, some adjustments were made in the algorithm. Here, the case where a tree blocks part of the picture is commented.

In the example provided in Figure 8a, tree branches and leaves occupy almost the entire top half of the picture. When applying the Canny edge detector to this type of images, a lot of noise (in terms of blobs and irregular shapes) is generated in association with these objects, as can be seen in Figure 8b. This may affect the performance of the code, since the Hough transform method may mistake lines belonging to the branches for window lines.

Fortunately, the building that has to be detected (the one in the middle) is not concealed, and the base and rooftop are both visible behind the tree, as well as the door and the windows. For this reason, some specific morphological operations can be performed, so that the lines and dots belonging to the leaves are deleted, and the algorithm is able to operate only with lines associated to the actual building. In particular, the operation called *branchpoints* is used, which finds lines connected to the main objects of the image. Subsequently, the branchpoints are enlarged, in order to really separate the lines. Then, the branchpoints are erased from the original binary image to leave just the single, unbranched lines, as shown in Figure 8c. Lastly, the blobs that are formed by less than  $n$  pixels can be deleted (in this work, a value of 30 pixels was chosen), and the result is shown in Figure 8d. In this last image, it is clear how the noise due to the tree can be almost completely removed, maintaining only the main lines of the building under consideration. Figure 8e shows the bounding box related to the building, and it can be noticed how the algorithm can detect the façade without being influenced by the tree or other elements.

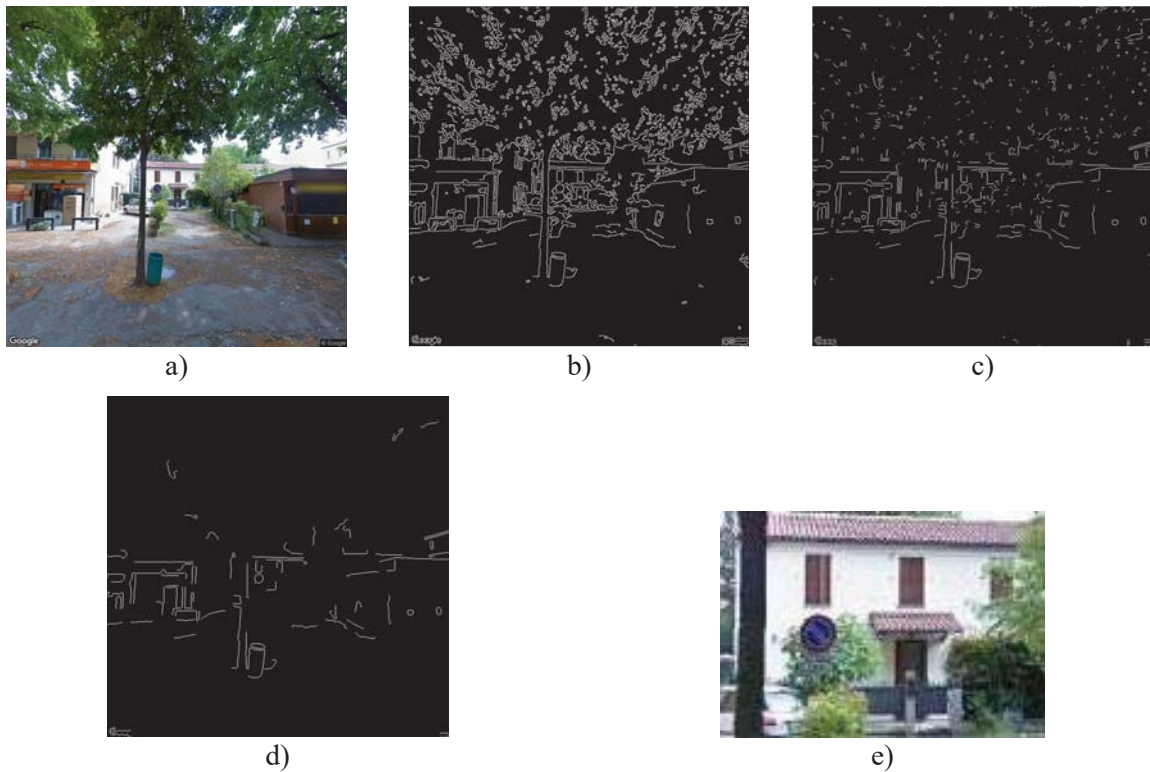


Figure 8: Example of bounding box for a street view image with an obstacle (tree)

## 4 CONCLUSIONS

- An algorithm that automatically retrieves satellite images from a pair of coordinates or a town name was discussed. The code also returns the building footprints that can be found in the image, together with their coordinates, areas, and labels. These data can be edited, and the resulting map can be filtered. The following part of the algorithm uses the coordinates of the buildings found in the area to acquire street view images.
- A second algorithm was presented, to estimate the number of stories of the buildings found from the previous code. The street view images obtained before are the input of this algorithm. Firstly, the code creates a bounding box that selects only the part of the building that is sufficient to estimate its number of stories. Secondly, the number of stories is evaluated through image processing and feature extraction techniques, particularly the Canny edge detection method, morphological operations and the Hough transform. In addition, some particular cases where the building is hidden by obstacles were treated.
- The work presented in this paper is in phase of validation. The code works best for buildings that can be seen from a frontal perspective, although some expedients were adopted for images that do not have the same characteristics. However, a more systematic validation should be carried out, involving different areas, different territorial scales, and different building typologies.
- This work fits into the wider context of automated seismic risk assessment. In order to carry out risk analysis, the estimation of the height parameter is not sufficient to achieve an acceptable level of accuracy. Other variables will have to be evaluated, first of all construction period and material. Once all these parameters are known, it will be possible to estimate seismic vulnerability more accurately and automatically at a territorial scale. Therefore, this algorithm could represent a useful tool for authorities in the field of seismic risk management, and it could make on-site surveys unnecessary, with a remarkable reduction in time and costs.

## ACKNOWLEDGMENTS

This work is part of the European project BESTOFRAC. The authors would like to offer special thanks to the Institut für Strukturmechanik (ISM) of the Bauhaus-Universität in Weimar (Germany).

## REFERENCES

- [1] M. Dolce, A. Prota, B. Borzi, F. da Porto, S. Lagomarsino, G. Magenes, C. Moroni, A. Penna, M. Polese, E. Speranza, G.M. Verderame, G.Zuccaro, Seismic risk assessment of residential buildings in Italy. *Bulletin of Earthquake Engineering*, 2020.
- [2] M. Donà, P. Carpanese, V. Follador, F. da Porto, Derivation of mechanical fragility curves for macro-typologies of Italian masonry buildings. M. Papadrakakis, M. Fragiadakis eds. *7th ECCOMAS Thematic Conference on Computational Methods in Structural Dynamics and Earthquake Engineering (COMPDYN 2019)*, Crete, Greece, June 24-26, 2019.



- [3] S. Lagomarsino, S. Cattari, Fragility functions of masonry buildings, (Chapter 5), K. Pitilakis, H. Crowley, A.M. Kaynia eds. *SYNER-G: Typology Definition and Fragility Functions for Physical Elements at Seismic Risk, Vol. 27*, 111–156, Springer 2014.
- [4] B. Borzi, M. Faravelli, A. Di Meo, Application of the SP-BELA methodology to RC residential buildings in Italy to produce seismic risk maps for the national risk assessment. *Bulletin of Earthquake Engineering*, 2020.
- [5] M. Donà, P. Carpanese, V. Follador, L. Sbrogio, F. da Porto, Mechanics-based fragility curves for Italian residential URM buildings. *Bulletin of Earthquake Engineering*, 2020.
- [6] F. da Porto, M. Donà, A. Rosti, M. Rota, S. Lagomarsino, S. Cattari, B. Borzi, M. Onida, D. De Gregorio, F.L. Perelli, C. Del Gaudio, P. Ricci, E. Speranza. Comparative analysis of the fragility curves for Italian residential masonry and RC buildings. *Bulletin of Earthquake Engineering, Special Issue: Seismic Risk Assessment in Italy*, 2021.
- [7] M. Vettore, M. Donà, P. Carpanese, V. Follador, F. da Porto, M.R. Valluzzi, A Multilevel Procedure at Urban Scale to Assess the Vulnerability and the Exposure of Residential Masonry Buildings: The Case Study of Pordenone, Northeast Italy. *Heritage*, **3**(4), 1433–1468, 2020.
- [8] G.P. Campostrini, S. Taffarel, G. Bettiol, M.R. Valluzzi, F. da Porto, C. Modena, A Bayesian approach to rapid seismic vulnerability assessment at urban scale, *International Journal of Architectural Heritage*, **12**, 36-46, 2017.
- [9] J. Kang, M. Körner, Y. Wang, H. Taubenböck, X.X. Zhu, Building instance classification using street view images. *ISPRS Journal of Photogrammetry and Remote Sensing*, **145**, 44–59, 2018.
- [10] J. Castagno, E. Atkin, Roof shape classification from LiDAR and satellite image data fusion using supervised learning. *Sensors (Switzerland)*, **18**(11), 2018.
- [11] J.F. Rosser, D.S. Boyd, G. Long, S. Zakhary, Y. Mao, D. Robinson, Predicting residential building age from map data. *Computers, Environment and Urban Systems*, **73**, 56–67, 2019.
- [12] R. Hecht, G. Meinel, M. Buchroithner, Automatic identification of building types based on topographic databases – a comparison of different data sources. *International Journal of Cartography*, **1**(1), 18–31, 2015.
- [13] M. Fleischmann, A. Feliciotti, O. Romice, S. Porta, Morphological tessellation as a way of partitioning space: Improving consistency in urban morphology at the plot scale. *Computers, Environment and Urban Systems*, **80**, 2020.
- [14] G. Boeing, Spatial information and the legibility of urban form: Big data in urban morphology. *International Journal of Information Management*, **56**, 2021.
- [15] M. Wieland, M. Pittore, Performance evaluation of machine learning algorithms for urban pattern recognition from multi-spectral satellite images. *Remote Sensing*, **6**(4), 2912–2939, 2014.
- [16] S. Steiniger, T. Lange, D. Burghardt, R. Weibel, An approach for the classification of urban building structures based on discriminant analysis techniques. *Transactions in GIS*, **12**(1), 31–59, 2008.
- [17] G. Liasis, S. Stavrou, Satellite images analysis for shadow detection and building height estimation. *ISPRS Journal of Photogrammetry and Remote Sensing*, **119**, 437–450, 2016.

- [18] A. Comber, M. Umezaki, R. Zhou, Y. Ding, Y. Li, H. Fu, H. Jiang, A. Tewkesbury, Using shadows in high-resolution imagery to determine building height. *Remote Sensing Letters*, **3**(7), 551–556, 2012.
- [19] P.L.N. Raju, H. Chaudhary, A.K. Jha, Shadow analysis technique for extraction of building height using high resolution satellite single image and accuracy assessment. *International Archives of the Photogrammetry, Remote Sensing and Spatial Information Sciences - ISPRS Archives*, **40**(8), 1185–1192, 2014.
- [20] J. Yuan, A.M. Cheriyyadat, Combining maps and street level images for building height and facade estimation. *Proceedings of the 2nd ACM SIGSPATIAL Workshop on Smart Cities and Urban Analytics, UrbanGIS 2016*, Burlingame, California, United States, October 2016.
- [21] E.D. Diaz Plata, H Arguello, An algorithm to estimate building heights from Google street-view imagery using single view metrology across a representational state transfer system. *Proceedings of the SPIE, Volume 9868*, Baltimore, Maryland, United States, April 2016.
- [22] G.C. Iannelli, F. Dell’Acqua, Extensive exposure mapping in urban areas through deep analysis of street-level pictures for floor count determination. *Urban Science*, **1**(2):16, 2017.
- [23] Y. Zhano, J. Qi, R. Zhang, CBHE: Corner-based building height estimation for complex street scene images. *WWW '19: The World Wide Web Conference*, 2436-2447, San Francisco, California, United States, May 2019.
- [24] C. Wang, Q. Yu, K.H. Law, F. McKenna, S.X. Yu, E. Taciroglu, A. Zsarnóczyay, W. Elhaddad, B. Cetiner, Machine learning-based regional scale intelligent modeling of building information for natural hazard risk management. *Automation in Construction*, **122**, 2021.
- [25] R.O. Duda, P.E. Hart, Use of the Hough transformation to detect lines and curves in pictures. *Communication of the ACM*, **15**(1), 1972.
- [26] J.F. Canny. A computational approach to edge detection. *IEEE Trans. Pattern Analysis and Machine Intelligence*, **8**(6), 679-698, 1986.

## MACHINE LEARNING TECHNIQUES FOR THE ESTIMATION OF LIMIT STATE THRESHOLDS AND BRIDGE-SPECIFIC FRAGILITY ANALYSIS OF R/C BRIDGES

Sotiria P. Stefanidou<sup>1</sup>, Vassilis K. Papanikolaou<sup>2</sup>,  
Elias A. Paraskevopoulos<sup>1</sup>, Andreas J. Kappos<sup>3</sup>

<sup>1</sup>Postdoctoral Researcher, School of Civil Engineering, Aristotle University of Thessaloniki  
Thessaloniki, 54124, Greece  
e-mail: [ssotiria@civil.auth.gr](mailto:ssotiria@civil.auth.gr), [eapcivil@gmail.com](mailto:eapcivil@gmail.com)

<sup>2</sup>Assistant Professor, School of Civil Engineering, Aristotle University of Thessaloniki  
Thessaloniki, 54124, Greece  
e-mail: [billy@civil.auth.gr](mailto:billy@civil.auth.gr)

<sup>3</sup> Professor, Department of Civil Infrastructure and Environmental Engineering, Khalifa University  
Abu Dhabi, United Arab Emirates; formerly, Professor, School of Civil Engineering,  
Aristotle University of Thessaloniki, Thessaloniki, 54124, Greece  
e-mail: [andreas.kappos@ku.ac.ae](mailto:andreas.kappos@ku.ac.ae)

---

### Abstract

*Based on past earthquake events, bridges are the most critical and usually the most vulnerable components of road and rail transport systems, while bridge damage is related to substantial direct and indirect losses. In view of this, the need for direct and reliable assessment of bridge vulnerability has emerged, and several methodologies have been developed using probabilistic analysis for the derivation of fragility curves. A new framework for the derivation of bridge-specific fragility curves is proposed herein, introducing machine learning techniques for a reliable estimation of limit state thresholds of the most critical component of the bridge system (which in standard -ductility based- design is the piers), in terms of a widely used engineering demand parameter, i.e. displacement of control point. A set of parameters affecting the seismic capacity and the failure modes of bridge piers is selected, including geometry, material properties, and reinforcement ratios for cylindrical piers. Training and test sets are generated from multiple inelastic pushover analyses of the pier component, and Artificial Neural Networks (ANN) analysis is performed to derive closed-form relationships for the estimation of limit state thresholds. The latter are compared with closed-form relationships available in the literature, highlighting the effect of machine learning techniques on the reliable estimation of bridge fragility curves for all damage states.*

**Keywords:** Bridge fragility curves, Limit state thresholds, Machine learning techniques, ANN

---

## 1 INTRODUCTION

There is an increasing trend for assessment and retrofit prioritization of existing infrastructure in earthquake-prone areas, as well as investment planning, to be based on reliability analysis results. In this context, numerous methodologies have been proposed during the last 30 years for the derivation of bridge fragility curves, with increasing accuracy and efficiency over the years, introducing the use of advanced computational methods and probabilistic framework for the estimation of the probability of damage for different levels of earthquake intensity and limit states. The majority of the methodologies proposed are analytical, differing mainly in the quantitative definition of limit states (LS), i.e., the threshold values of LS considered, the type of analysis, the uncertainty treatment, and the probabilistic model used for the fragility analysis (probabilistic seismic demand model, response surface models, meta-models) [1, 2]. Both generic and bridge-specific fragility curves have been proposed, accounting for the various uncertainties in seismic capacity and demand estimation of critical components, and a few of them for the effect of case-specific properties on the results.

Very recently [3], the potential exploitation of Artificial Intelligence algorithms and Machine Learning (ML) techniques in earthquake engineering, (i.e., seismic hazard analysis, system identification and damage detection, seismic fragility assessment, and structural control for earthquake mitigation) has been explored; it is still at a rather early stage, but a promising development. ML algorithms can be classified into supervised learning and unsupervised learning type. Supervised learning uses prior knowledge of the labeled data set to learn a function that best approximates the relationship between input and labeled output in the data. In contrast, unsupervised learning aims to infer the natural structure from a set of data points that have no target labels [3].

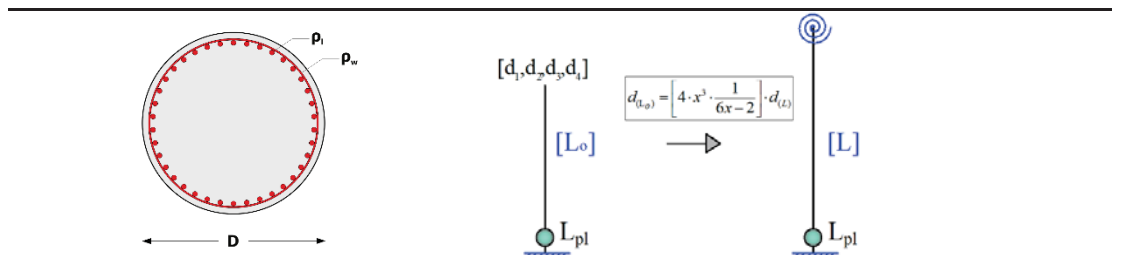
Several machine learning tools (i.e., classification-based tools like random forest, neural networks, etc.) have been proposed and applied to assess bridges and derive fragility curves. The efficiency of ML techniques for the derivation of fragility curves for different bridge classes and the identification of the effect of parameter uncertainties on the results have been studied for different bridge types and structural systems [4], [5]. Furthermore, the capabilities of machine learning techniques have been used to check the validity of assumptions during fragility analysis of bridges (e.g., the assumption of lognormal distribution of the demand model, etc.) [6]. Rapid damage assessment of bridges has been proposed based on analysis of selected bridge classes using the prediction model established via the training set and evaluating the performance of the model using the test set, as proposed in [5]. Based on the above, it is clear that the use of ML algorithms in the frame of fragility analysis of bridges is a new, promising approach that could eventually drastically reduce the computational effort and increase the accuracy and the efficiency of fragility analysis. However, since fragility analysis includes multiple steps and calculations (i.e., capacity, demand, uncertainty, etc.), the use of ML techniques at several stages should be properly addressed.

In view of the above, a methodology for the derivation of bridge-specific fragility curves that has recently been proposed by the authors [7], and is applicable to bridge stocks will serve as the starting point for setting up a ML procedure. The aim of this paper is to develop and apply ML algorithms (Artificial Neural Networks (ANN)) for a more reliable estimation of bridge pier capacity and limit state thresholds for all limit states (minor damage to collapse) considered in fragility analysis. A set of parameters affecting the seismic capacity and the failure modes of cylindrical bridge piers is initially selected, including geometry, material properties, axial load and reinforcement ratios. The range of parameters is selected with a view to representing realistic cases and resulting in training and tests of sufficient size. Analysis at local level (pier section) and global level (inelastic pushover analysis of bridge compo-

nents) is performed and the results in terms of a widely used engineering demand parameter (EDP: displacement of control point/drift) are recorded. Test and training sets are generated from the results of numerous inelastic pushover analyses, and Artificial Neural Networks (ANN) analysis is performed, resulting in closed-form relationships for the estimation of limit state thresholds. The latter are compared with closed-form relationships derived through ‘standard’ regression analysis, in the frame of the methodology described in [7], to study the effect of ML techniques on the accuracy of the limit state threshold definition and, eventually, its potential for estimating bridge fragility curves for all limit states.

## 2 COMPONENT-SPECIFIC LIMIT STATE THRESHOLDS AND PROPOSED CLOSED-FORM RELATIONSHIPS

Utilising the methodology described in [7], component-specific limit state thresholds are estimated for bridge piers in terms of displacement at the component control point (pier top). Closed-form relationships relating  $d/h$  to the parameters affecting the seismic performance and ductility of bridge piers, namely geometry, material properties, longitudinal and transverse reinforcement ratios, and axial load, are derived for all limit states (minor damage to collapse). Limit state thresholds are initially defined qualitatively and subsequently quantitatively at local (section) and global (component) level.



Parameters	Values for Parametric Analysis						NoPar.
D (m)	1.5	1.6	1.8	2	2.25	–	[5]
$\rho_l$	0.005	0.01	0.015	0.02	0.025	0.030	[6]
$\rho_w$	0.0025	0.008	0.010	0.015	–	–	[4]
$f_c$ (MPa)	16	20	25	30	35	–	[5]
$f_y$ (MPa)	220	400	500	–	–	–	[3]
$\nu$	0.15	0.2	0.25	0.35	–	–	[4]
H (m)	2.5	5.0	10.0	15.0	20		[5]
<i>Inelastic Pushover Analyses Performed</i>							<b>36,000</b>

Table 1: Cylindrical pier section and component parameters considered.

A broad range of different pier section properties described in Table 1 are considered, and section analysis is performed using an in-house developed software that provides bilinearised moment-curvature ( $M-\phi$ ) curves [8]. Damage is initially quantified in terms of material strain limit values, namely  $\varepsilon_c$  and  $\varepsilon_s$  corresponding to experimentally observed crack widths, and moment corresponding to loss of bearing capacity for limit state 4 (post-peak  $M=0.9 \cdot M_{\max}$ ). More details regarding local limit state definition are available in [7]. Based on cross section analysis, moment-curvature curves are derived (and bilinearised) and curvature values corresponding to the aforementioned material strains are defined. Hence, damage is initially quan-



tified in curvature terms (*local* EDPs  $\phi_1, \phi_2, \phi_3, \phi_4$ ), and  $M-\phi$  curves, as well as effective stiffnesses  $EI_{\text{eff}}$  ( $M_y/\phi_y$ , needed for pushover analysis) are defined. Section analysis results for all possible parameter combinations (7,200 section analyses), are obtained; a sufficiently broad range of heights is considered, and parametric setup of an inelastic cantilever model (Fig.1) is performed in order to perform inelastic pushover component analysis (36,000 pushover analyses, see Table 1). Plastic hinge formation is considered at the pier base (lumped plasticity model), while the bilinear  $M-\phi$  curve is used as input. Inelastic pushover analysis is performed for all sections considered paired with all different pier heights, and the global engineering demand parameter values ( $d_1, d_2, d_3, d_4$ ) are recorded at the analysis step that the relevant local values ( $\phi_1, \phi_2, \phi_3, \phi_4$ ) are exceeded. Check for shear failure, calculating the displacement ( $d_v$ ) when shear strength  $V_u$  is exceeded is performed, considering reduced concrete contribution in the inelastic range [1];  $d_v$  is compared to the displacement at flexural failure ( $d_{fl}$ ) and the minimum value is considered as threshold value for the limit state (Fig.1).

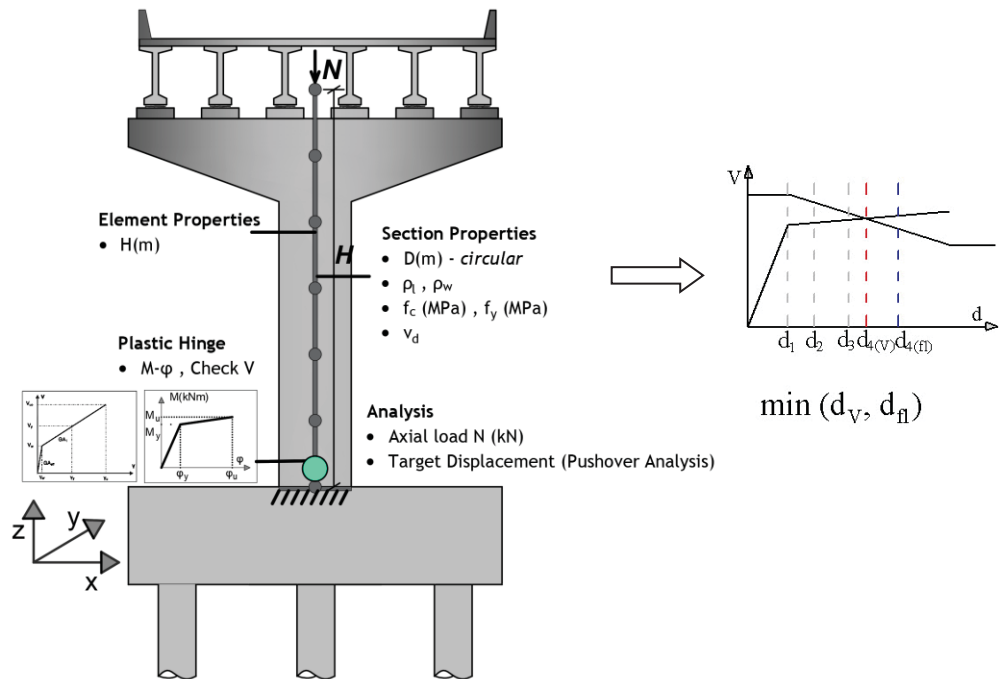


Figure 1: – Inelastic Pushover Analysis of the cantilever model and limit state threshold estimation

$\delta/H = \exp[\beta_0 + \beta_1 \cdot \ln(D/H) + \beta_2 \cdot \ln(v) + \beta_3 \cdot \ln(f_c / f_y) + \beta_4 \cdot \ln \rho_w + \beta_5 \cdot \ln \rho_l]$						
	$\beta_0$	$\beta_1$	$\beta_2$	$\beta_3$	$\beta_4$	$\beta_5$
$\delta_1/H$	-6.524	-0.876	-0.018	-0.688	+0.086	+0.292
$\delta_2/H$	-6.016	-0.674	-0.265	-0.076	+0.030	-0.072
$\delta_3/H$	-3.872	-0.572	-0.238	-0.470	+0.505	-0.108
$\delta_4/H$	-3.663	-0.542	-0.381	-0.518	+0.439	+0.001

Table 2: Closed-form relationships based on regression of analysis results.

The pushover analysis results ( $d_1/h \sim d_4/h$ ) of the extensive parametric study are obtained, and regression analysis (considering the parameters in logarithmic form and performing nonlinear

fit) is carried out to derive closed-form relationships for cylindrical piers. The proposed closed-form relationships for the estimation of limit state thresholds ( $d_1 \sim d_4$ ) and, eventually, of seismic capacity, are provided in Table 2.

### 3 METHODOLOGY FOR THE DERIVATION OF LIMIT STATE THRESHOLDS USING ML TECHNIQUES (ANN)

An alternative method for the estimation of pier LS threshold values in the context of bridge-specific fragility analysis is introduced herein, entailing the use of ML techniques, i.e., Artificial Neural Networks (ANNs), trained to predict  $d_1 \sim d_4$  values calculated from inelastic pushover component analysis. The use of ANNs in engineering problems is common; however issues like high bias (i.e., not enough complexity to describe the input data) and high variance (i.e., overfitting), should be avoided, as described in [9], where additional information regarding ANNs is provided.

The first part of the methodology is the same as the one proposed in [7] and described in §2, i.e. a range of parameters is selected and paired in order to perform section and component analyses and estimate limit state thresholds in displacement terms. The range of parameters, selected in order to represent realistic cases and result in training and tests of sufficient size, is presented in Table 3.

Parameters	Training & Test Sets		Number of Param.
	Range	Step	
D (m)	1.5 - 2.3	0.1	[9]
$\rho_l$	0.005 - 0.03	0.0025	[11]
$\rho_w$	0.0025 - 0.015	0.0025	[6]
$\nu$	0.1 - 0.3	0.02	[11]
$f_c$ (MPa)	16 , 20 , 25 , 30		[4]
$f_y$ (MPa)	220 , 400 , 500		[3]
H (m)	2.5 , 5 , 10 , 15		[4]
	Analyses Performed		<b>313,632</b>

Table 3: Parameters considered for section and inelastic pushover analyses for training and test of ANNs

```

D_H_n = (D_H-0.1)/0.82
v_n = (v-0.1)/0.2
fc_fy_n = (fc_fy-0.043636)/0.113388
rw_n = (rw-0.0025)/0.0125
rl_n = (rl-0.005)/0.025

n_1_1 = 1/(1+math.exp(-(11.059100*D_H_n+0.023165*v_n+0.193476*fc_fy_n+0.158260*rw_n+0.611629*rl_n-1.547203)))
n_1_2 = 1/(1+math.exp(-(11.011895*D_H_n+0.148311*v_n+0.429360*fc_fy_n+0.264461*rw_n+0.371765*rl_n-0.250965)))
n_1_3 = 1/(1+math.exp(-(31.650587*D_H_n+0.090764*v_n+1.587679*fc_fy_n+0.443491*rw_n+0.264063*rl_n-1.026917)))
n_1_4 = 1/(1+math.exp(-(1.671041*D_H_n+0.275991*v_n+12.922011*fc_fy_n+0.442604*rw_n+0.170544*rl_n-1.979497)))
n_1_5 = 1/(1+math.exp(-(6.602409*D_H_n+0.138811*v_n+1.346275*fc_fy_n+0.613021*rw_n+0.060748*rl_n-0.466473)))
n_1_6 = 1/(1+math.exp(-(1.671076*D_H_n+0.027800*v_n+13.501011*fc_fy_n+0.414039*rw_n+0.151114*rl_n+14.957344)))
n_1_7 = 1/(1+math.exp(-(1.024661*D_H_n+0.838350*v_n+1.253191*fc_fy_n+0.107657*rw_n+6.005546*rl_n-2.095468)))
n_1_8 = 1/(1+math.exp(-(12.569545*D_H_n+2.183519*v_n+1.833650*fc_fy_n+0.322950*rw_n+1.923378*rl_n-1.395455)))
n_1_9 = 1/(1+math.exp(-(0.423730*D_H_n+0.488681*v_n+1.481968*fc_fy_n+0.896061*rw_n+1.149639*rl_n-1.160453)))
n_1_10 = 1/(1+math.exp(-(6.425603*D_H_n+1.649814*v_n+5.440611*fc_fy_n+1.454577*rw_n+2.548596*rl_n-2.198821)))

n_2_1 = 1/(1+math.exp(-(1.040010*n_1_1+0.241425*n_1_2+1.368039*n_1_3+0.815847*n_1_4+1.061105*n_1_5-0.108867*n_1_6-2.644435*n_1_7-0.774115*n_1_8-0.654877*n_1_9-0.914445*n_1_10-1.782937)))
n_2_2 = 1/(1+math.exp(-(1.325656*n_1_1+0.367361*n_1_2+1.822595*n_1_3+1.899550*n_1_4+1.111754*n_1_5+0.104057*n_1_6-2.707503*n_1_7-0.075872*n_1_8-0.220614*n_1_9-0.357537*n_1_10-1.673762)))
n_2_3 = 1/(1+math.exp(-(1.545985*n_1_1+0.239986*n_1_2+0.546221*n_1_3+1.164940*n_1_4+1.249297*n_1_5+0.548552*n_1_6-3.974099*n_1_7-1.445585*n_1_8-0.018756*n_1_9+0.286338*n_1_10-2.090533)))
n_2_4 = 1/(1+math.exp(-(1.354308*n_1_1+0.397205*n_1_2+1.728741*n_1_3+0.423011*n_1_4+1.618606*n_1_5+1.631244*n_1_6+0.648620*n_1_7+0.733911*n_1_8+1.601784*n_1_9+0.776338*n_1_10+0.471690)))
n_2_5 = 1/(1+math.exp(-(1.946454*n_1_1+2.221021*n_1_2+0.082987*n_1_3+1.836011*n_1_4+1.209192*n_1_5+1.639505*n_1_6+1.231661*n_1_7+1.833758*n_1_8+1.590040*n_1_9+1.119379*n_1_10+1.164780)))
n_2_6 = 1/(1+math.exp(-(1.045790*n_1_1+0.756806*n_1_2+1.251676*n_1_3+0.779314*n_1_4+1.286562*n_1_5+1.125247*n_1_6+0.991301*n_1_7+0.008884*n_1_8+0.956591*n_1_9+0.705963*n_1_10+2.111532)))
n_2_7 = 1/(1+math.exp(-(1.422576*n_1_1+1.753205*n_1_2+5.186595*n_1_3+0.718055*n_1_4+0.850791*n_1_5+1.296244*n_1_6+2.091144*n_1_7+3.200664*n_1_8+1.136181*n_1_9+3.237728*n_1_10+0.322711)))
n_2_8 = 1/(1+math.exp(-(1.214805*n_1_1+0.418039*n_1_2+1.592729*n_1_3+0.999137*n_1_4+0.956148*n_1_5+0.052541*n_1_6+2.681390*n_1_7+0.329333*n_1_8+0.166920*n_1_9+0.254368*n_1_10+1.484156)))
n_2_9 = 1/(1+math.exp(-(1.061953*n_1_1+0.414086*n_1_2+1.145767*n_1_3+0.738611*n_1_4+0.838389*n_1_5+0.127846*n_1_6+0.057216*n_1_7+0.468345*n_1_8+0.198377*n_1_9+0.499662*n_1_10+1.516249)))
n_2_10 = 1/(1+math.exp(-(1.033302*n_1_1+0.046616*n_1_2+0.324727*n_1_3+0.680325*n_1_4+1.293348*n_1_5+0.541086*n_1_6+2.788825*n_1_7+0.690458*n_1_8+1.071435*n_1_9+2.725996*n_1_10+2.172316)))

d1_H_n = 0.232127*n_2_1+0.380543*n_2_2+0.739785*n_2_3+0.661344*n_2_4+0.122474*n_2_5-0.179927*n_2_6+0.559195*n_2_7+0.335794*n_2_8+0.246601*n_2_9+0.155497*n_2_10+0.321322

return max(0, d1_H_n*0.0232+0.006600000000000000)

```

Figure 2: Function code (python) for  $d_1$  closed-form relationship

A total of 313,632 pushover analyses were performed and used for training and testing of ANNs (half of the total set size used for training and the other half for testing). Different ANN sizes were examined (i.e. 5-5-5-1, 5-5-5-5, 5-10-10-1, 5-15-15-1) to select the most efficient in terms of recorded MAE (mean absolute error) and MPE/MNE (maximum positive and negative errors). The 5-10-10-1 (two inner layers of 10 nodes each) was found the most appropriate ANN size, since the recorded errors did not differ significantly from the ones of 5-15-15-1 size and were apparently lower than those recorded when 5-5-5-5 was applied. The training procedure produced four closed-form relationships (functions) for the considered pier type (cylindrical pier) and all limit states. All analyses presented herein have been carried out using Python / TensorFlow 2.5 and a typical format of the relationship proposed for  $d_1$  is provided in Figure 2. Testing of the relationships for  $d_1 \sim d_4$  was performed using the test set described above, estimating the errors to establish the accuracy of the proposed relationships and their efficiency towards limit state thresholds estimation.

#### 4 COMPARISON

To evaluate and compare the closed-form relationships proposed herein based on the training/testing of ANNs, with those proposed in [7], derived from regression analysis, the diagrams of drift  $(d/h)_{\text{analysis}}$  values and the error resulting from the proposed relationships  $((d/h)_{\text{predicted}} - (d/h)_{\text{analysis}})$  are calculated for both cases, providing the relevant plots and the fit indicators, i.e. the MAE, MPE, MNE and the RMSE (Root Mean Squared Error) and  $R^2$  (Root Mean Squared Error).

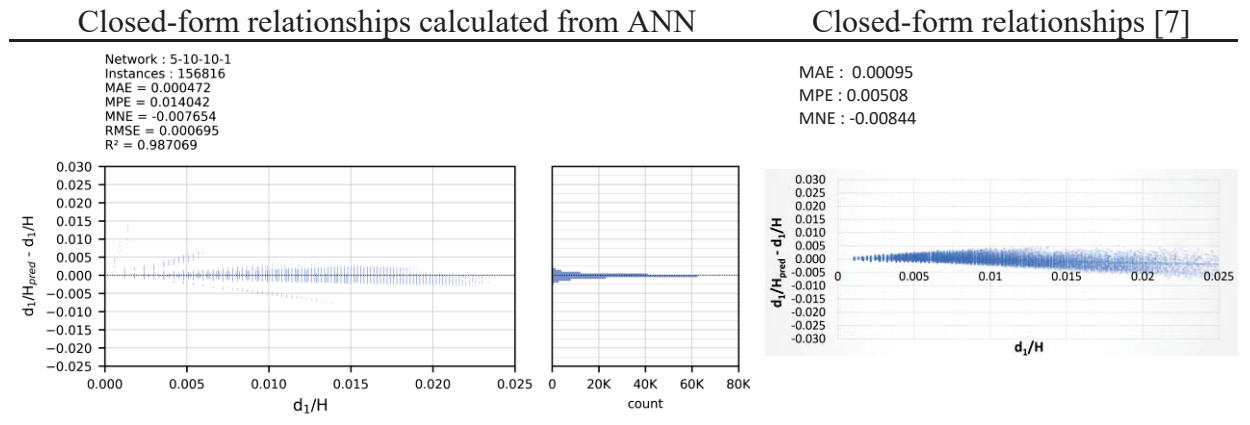


Figure 3: Comparison of  $d_1$  prediction error of the closed-form relationships proposed in [7] and application of ML techniques (ANN)

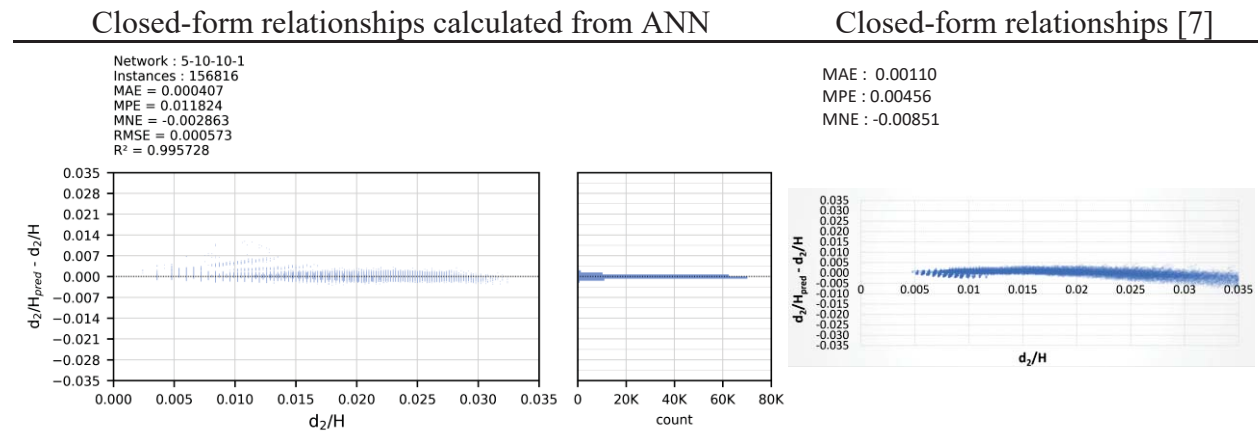
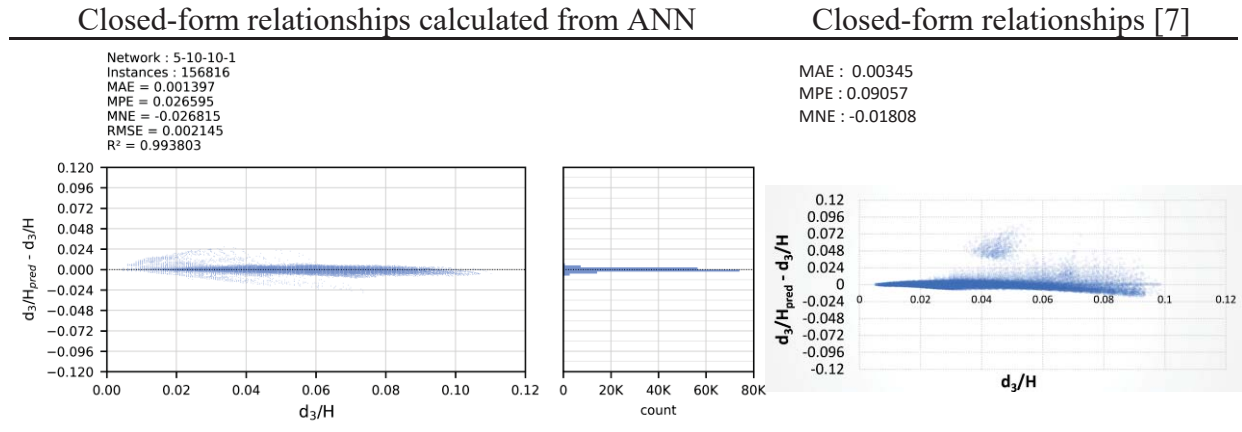
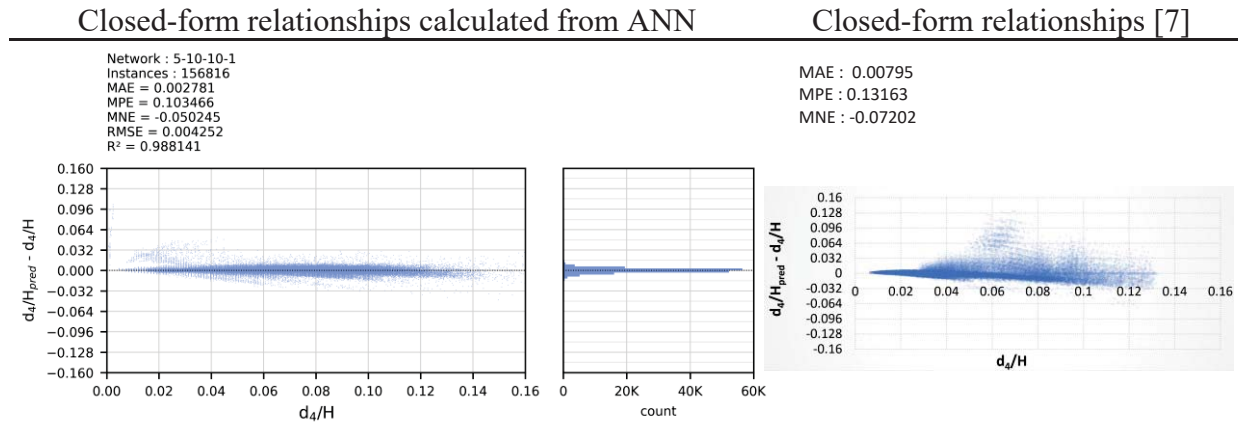


Figure 4: Comparison of  $d_2$  prediction error of the closed-form relationships proposed in [7] and application of ML techniques (ANN)Figure 5: Comparison of  $d_3$  prediction error of the closed-form relationships proposed in [7] and application of ML techniques (ANN)Figure 6: Comparison of  $d_4$  prediction error of the closed-form relationships proposed in [7] and application of ML techniques (ANN)

From Figures 3 to 6 it is clear that the values of MAE, MPE, MNE are lower in the case of the relationships proposed herein based on ANN training, compared to the ones proposed in [7]. The new relationships show a better fit of data, on the basis of the low RMSE and high R<sup>2</sup> values (0.987~0.996 instead of 0.75~0.80 of the new relationships), i.e. better prediction of the LS thresholds for all LS. The reduction of the prediction to analysis mean absolute error (MAE) ranges from 2 to 2.85 times, while it is obvious that the error reduction is larger for the higher limit states ( $d_3$  &  $d_4$ ), wherein the data fit based on regression analysis proposed in [7] was found inadequate.

## 5 CONCLUSIONS

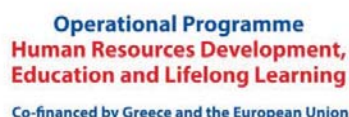
The effectiveness of ML algorithms (ANN) for the quantitative estimation of limit state thresholds and the derivation of closed-form relationships (functions) used for seismic capacity estimation in the frame of a bridge-specific methodology proposed by the authors [7] was investigated herein. The closed-form relationships proposed within the methodology described in [7] which are based on regression of parametric inelastic analysis results of bridge piers are compared with those estimated based on extensive parametric analysis results used

for training and testing of ANNs. The parameters considered for both cases are the same (geometry, material properties, axial load and reinforcement ratios), however the approach proposed herein is differentiated regarding the number of parametric analysis performed for the development of training and test sets and the application of ANNs, instead of typical regression analysis. The most important findings related to the effectiveness of ML techniques and the increased accuracy achieved during the quantitative limit state threshold definition and, eventually, the estimation of bridge fragility curves for all damage states, are:

- The relationships derived herein based on ANN training, have lower error (MAE, MPE, MNE) and high  $R^2$  values, indicating better fit of data; i.e. better prediction of the LS thresholds for all LS, compared to those proposed in [7] derived from regression analysis.
- The reduction of the prediction to analysis mean absolute error (MAE) ranges from 50% to 65% when ANNs are used for closed-form relationship estimation.
- The error reduction is larger for the higher limit states ( $d_3$  &  $d_4$ ), where the data fit based on regression analysis proposed in [7] was found inadequate. The latter is due to the increased sample size used and the training/testing of ANNs.
- The relationships proposed herein for the estimation of limit state thresholds for cylindrical piers ( $d_1 \sim d_4$ ) indicate in general better fit to analysis data, hence providing more accurate and reliable prediction of component capacity and, eventually, seismic fragility.

## ACKNOWLEDGEMENTS

“This research was co-financed by Greece and the European Union (European Social Fund-ESF) through the Operational Programme «Human Resources Development, Education and Lifelong Learning 2014- 2020» in the context of the project “Online database for the development of fragility curves for as-built and retrofitted RC bridges using machine learning techniques” (MIS 5047878).



## REFERENCES

- [1] S.P. Stefanidou, & A. J. Kappos. Bridge Specific Fragility Analysis: When is it really necessary? *Bulletin of Earthquake Engineering*, **17**(4), 2245–2280, 2019.
- [2] S.P. Stefanidou & A.J. Kappos. Fragility-informed selection of bridge retrofit scheme based on performance criteria. *Engineering Structures*, **234**, 111976, 2021
- [3] Y. Xie, M. Ebad Sichani, J. E. Padgett, & R. DesRoches. The promise of implementing machine learning in earthquake engineering: A state-of-the-art review. *Earthquake Spectra*, **36**(4), 1769–1801, 2020



- [4] S. Mangalathu, G. Heo, & J.S. Jeon. Artificial neural network based multi-dimensional fragility development of skewed concrete bridge classes. *Engineering Structures*, **162**, 166–176, 2018.
- [5] S. Mangalathu, S.H. Hwang, E. Choi & J.S. Jeon. Rapid seismic damage evaluation of bridge portfolios using machine learning techniques. *Engineering Structures*, **201**, 109785, 2019.
- [6] S. Mangalathu & J.S. Jeon. Stripe-based fragility analysis of multispan concrete bridge classes using machine learning techniques. *Earthquake Engineering and Structural Dynamics*, **48(11)**, 1238–1255, 2019.
- [7] S.P. Stefanidou & A.J. Kappos. Methodology for the development of bridge-specific fragility curves. *Earthquake Engineering & Structural Dynamics*, **46**, 73–93, 2017.
- [8] V.K. Papanikolaou, Analysis of arbitrary composite sections in biaxial bending and axial load. *Computers & Structures*, **98–99**, 33–54, 2012.
- [9] A.E. Charalampakis & V.K. Papanikolaou. Machine learning design of R/C columns. *Engineering Structures*, **226**, 111412, 2021.

## LINKS OF AESTHETIC VALUE OF MULTI-CURVATURE ARTIFACTS, WITH THEIR STRUCTURAL BEHAVIOR, UTILIZING MACHINE LEARNING ALGORITHMS

Nikolaos P. Bakas<sup>1\*</sup>, Neofytos Christofi<sup>2</sup>, John Bellos<sup>2</sup>, Dimitris Antoniou<sup>3</sup>, George Markou<sup>4</sup>

<sup>1</sup>Computation-based Science and Technology Research Center, The Cyprus Institute, Nicosia, Cyprus.  
e-mail: n.bakas@cyi.ac.cy

<sup>2</sup>School of Architecture, Engineering, Land and Environmental Sciences, Neapolis University Pafos,  
Danais 2, 8042, Pafos, Cyprus. emails: {n.christofi,j.bellos}@nup.ac.cy

<sup>3</sup>Department of Architecture, University of Patras, University Campus, 265 00 Rio, Patras, Greece,  
email: antonioud@upatras.gr

<sup>4</sup>Department of Civil Engineering, University of Pretoria, South Africa

e-mail: george.markou@up.ac.za

---

### Abstract

*In this work, quantitative evidence on whether the aesthetic value of architectural design is associated with its structural response is investigated. The procedure for this study was based on 170 parametric projects, as well as their structural analysis results. The aesthetic value of an architectural project is an ambiguous concept, as it is based on each individual's perception of beauty. This is highlighted in the corresponding literature on parametric design, form-finding, and aesthetics, as well as in an extensive bibliometric analysis of several hundreds of research papers with respect to aesthetics and structures. Henceforth, a questionnaire was developed and given for vote to 23 persons from a variety of disciplines such as architects, engineers, as well as people with profession irrelevant to structures and/or aesthetics. The mean value of the votes of the questionnaire was considered as the dependent variable of the mathematical model, while the structural response parameters, internal forces and nodal displacements, were set as the Independent variables of the model. The obtained data were analyzed with regression analysis, utilizing linear and machine learning models, revealing a significant link between structural response and aesthetics.*

**Keywords:** Building Aesthetics, Structural Behaviour, Structural Analysis, Machine Learning, Regression Analysis.

---

## 1 INTRODUCTION

Architectural design is highly dependent on structural behaviour and a variety of studies exist in the corresponding literature. Monedero [1] has performed an analysis of the existing literature on parametric design, stating that in the last few years there has been an evolution in technology, while architects have started using it to their advantage. In particular, parametric design is a process of mathematical and programming algorithms, which creates multiple components and operations, assisting the designer to create any complex artifact from simple lines and curves to a composite project which is usually difficult to understand, but it's beautiful aesthetically. By utilizing structural plugins such as Katamba 3D [2]–[6], the creator can investigate the structural analysis results during the architectural design, and change the project so as the structural configuration will be adequate. Shells have been a frequent object of research [7] as it is often seen in nature. Santiago Huerta [8], explains that Gaudi had been using physical models and graphic methods to support his designs. Accordingly, huge columns support the domes of the Sagrada Familia which bring to mind trees. Similarly, by utilizing computer algorithms, Miloš Dimčić [9] demonstrates that by using the same surface and the same number of points, which can be structural objects, you can create a number of different batches that have better structural behaviour than other ordinary objects. Furthermore, at the Post Rotterdam, which has been refurbished [10], the redesign of the building had been done with the aid of Grasshopper3d [3], a software capable for parametric design, in combination with other software in order to find the optimum structural response based on form-finding. The author concludes that these types of tools in design help a lot in finding an ideal figure and furthermore performs excellently in regards to the structural part of the design by making calculations in a short period of time.

In a review paper [11], John S. Gero refers to the fact that after the 19th century, architecture is not considered only as art but also as a science-based on its evolution at its current stage. As a conclusion, he states that architecture combines science that doesn't only create forms and objects but also adjusts them with reference to the human factor in combination with its structural analysis. Natural forms are not drawn or created based on aesthetics but on their structural behaviour in combination with different types of materials [12]. Famous architects like Antonio Gaudi, and to some extent Luigi Nevri and Frei Otto have studied these natural forms in order for them to conclude and create a more natural and organic architecture. The conclusion of this study is that if an architect studies organic designs, he discovers a new world, says the author. To achieve this, one needs a lot of different trials, with different methods, considering environmental issues, materials, engineering and often he refers to pure luck. Michela Turrin [13], refers to the advantages that arise from the parametric design and how easy one can find different forms with the same rationale. She continues by explaining that this is key in the architectural form. Paolo Basso [14] explains that all organic geometric forms that exist are arranged and can be configured based on the NURBS curves, concluding that in the fields of both architecture and engineering new methods need to be found in regards to research, analysis and resolution. The approach of parametric design or other software that use NURBS curves gives the user full control over the smoothness of the object that is being created.

In a statement on Frei Otto [15], Boho Rasch mentions that Frei Otto is fascinated by organic, physical forms (the same happens when we minimize the inclination forces), and lightweight construction. He also states that the architect uses computer-aided means and the vast potential they have in order to specify the shape and behaviour of such organic forms. He concludes that Otto believes in the organic, lightweight form as he believes that it improves the human health and mood, but also nature itself. Renaud Aleis Pierre Emile [16] refers to

the current tools of design and analysis, as being highly powerful and that they can allow someone to produce and analyze any structural form. However, most of them are not allowed to use such means in the pure design stage of a project. The parametric design allows for a rapid study of complex geometric shapes and can be combined with an algorithmic analysis and optimization to design with performance as a parameter as well as objective. In his conclusions, he states that his work reflects that parametric design can be extended by using ground breaking computer-based ideas in the research for design with an epicenter to perform in creative ways.

Neri Oxman [17], mentions that the recent development of computer-based geometry and the expansion of the CAD software packages that support geometrical model design, combined with the research on design, lead to the evolution of analysis tools. Such tools have now been expanded in order to include complex computerized methods for non-Euclidean geometries, such as the B-spline curves and the NURBS surface. Hence, there will be a new model that studies the form and the implementation of design at the same time. If such an emersion is possible, then this knowledge that computerized geometry offers will be one of the most important forms of disciplined knowledge in computerized design software in architecture. Allen Carlson [18], mentions that aesthetics and nature are directly linked and that the relationship between science and nature is controversial. He also supports the environment and the nature we live in has led us to each one of our own aesthetics. The need of nature is to create something functional and at the same time light [19]; which is a result of constant optimization, that has been going on for millions of years, and which will continue to be as long as this world exists. Accordingly, the concept of form-finding is a process of optimizing the static equilibrium of the structure, finding the corresponding structural form, and architectural synthesis at the same time. The theory of evolution of the species in nature has inspired computer scientists, to develop the so-called evolutionary optimization algorithms [20], [21]. The purpose of this work was to investigate whether the structural behaviour of an architectural artifact is linked with the beauty of the design. It was attained, by utilizing 170 parametric structures, and their structural analysis results, via machine learning techniques.

## 2 BIBLIOMETRIC LITERATURE REVIEW

In order to investigate the literature related to architecture, computational design and structural analysis, the following bibliometric techniques were implemented. Initially, the Google Books database [22], based on 25 million books was searched using Architectural design, parametric design, computational design and form-finding. In Figure 1, it is depicted that in the last few years, and in particular since 1960, more people have begun to look for and learn about parametric design and have also begun to deal with computational design and form-finding as well. Additionally, from Figure 1, it is derived there is a proportion in the world looking for architecture after parametric design and then for form-finding. Interestingly, these are the steps that an architect can follow to design an organic form.

Growth rates of scientific knowledge correspond to a doubling every 9 years [22]. Hence, a vast amount of research papers were investigated with respect to their keywords associations, utilizing a procedure developed in [23], [24]. Figure 2, is the bibliometric map for the keywords of the 1414 documents, obtained from a search in Scopus database [25], comprising the term aesthetics. The frequency of its keyword is indicated with a number before the text, while the size of the corresponding circle is proportional to this frequency. Furthermore, the distances between the circles indicate the number of co-occurrences of these keywords in the papers' database. Utilizing this clustering technique, two major clusters are constructed, one with aesthetics in the center, near with the perception, architecture design and innovation keywords.

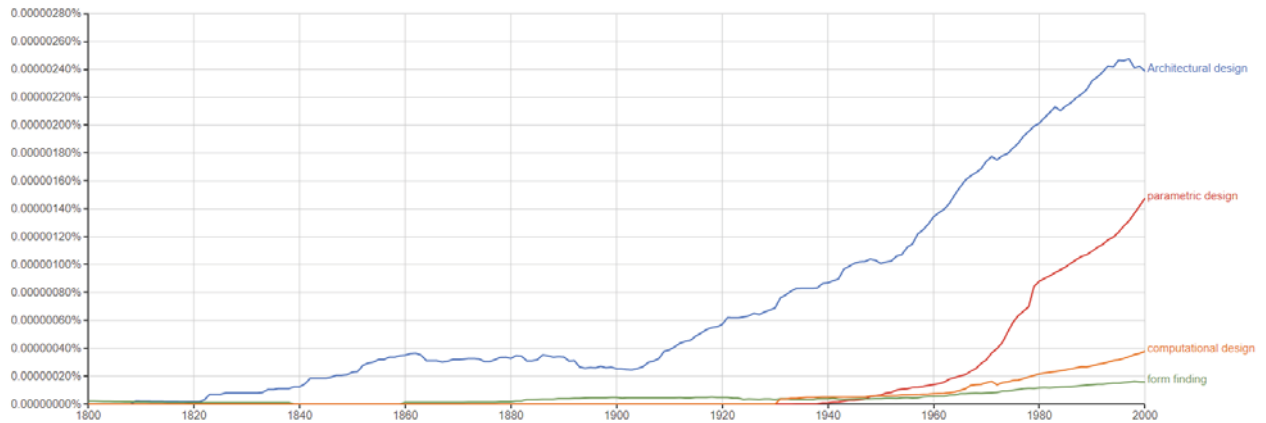


Figure 1: Google Books results of search terms

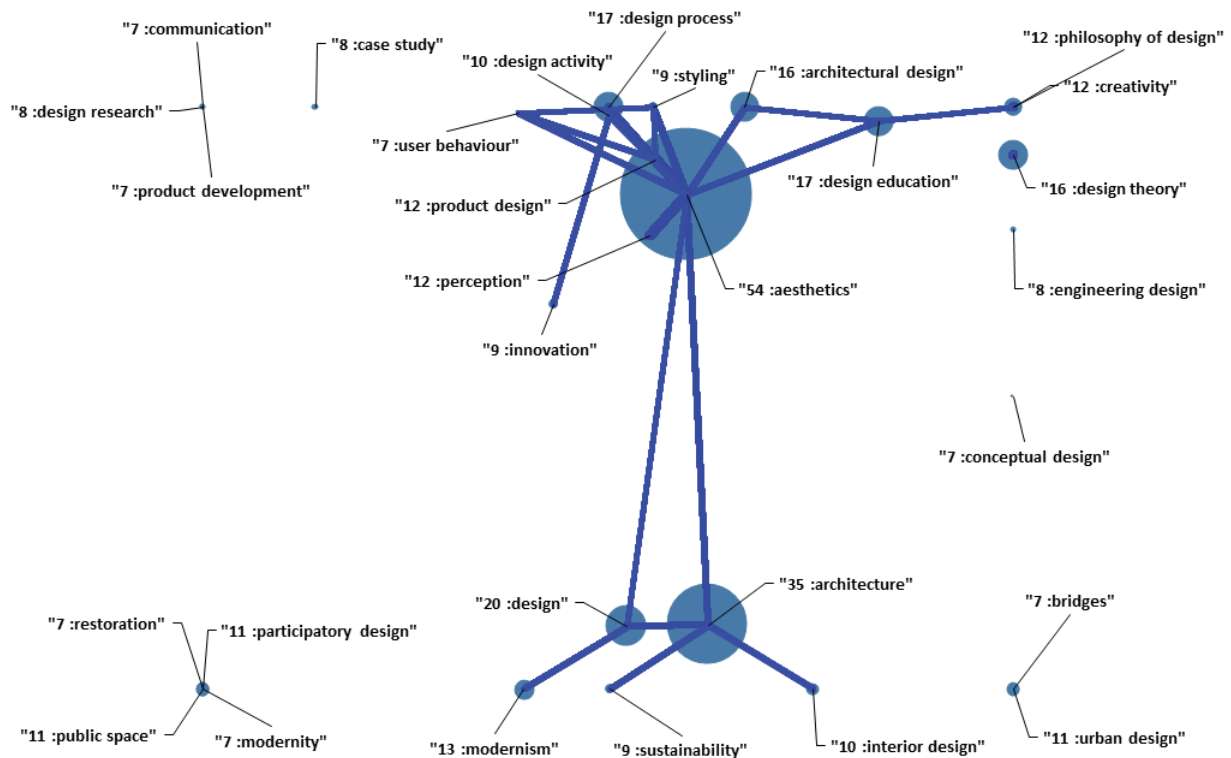


Figure 2: Scopus search for aesthetics

Accordingly, Figure 3, was created, by narrowing the search with the specific keywords of Table 1, as well as limiting the results with the generic keyword stuctur\*. Accordingly, tow clusters are developed, one at the bottom left side relative to the engineering literature with keywords structural engineering, engineering design, structural design- and another at the top right region of the map with keywords such as aesthetics, design process, perception etc.



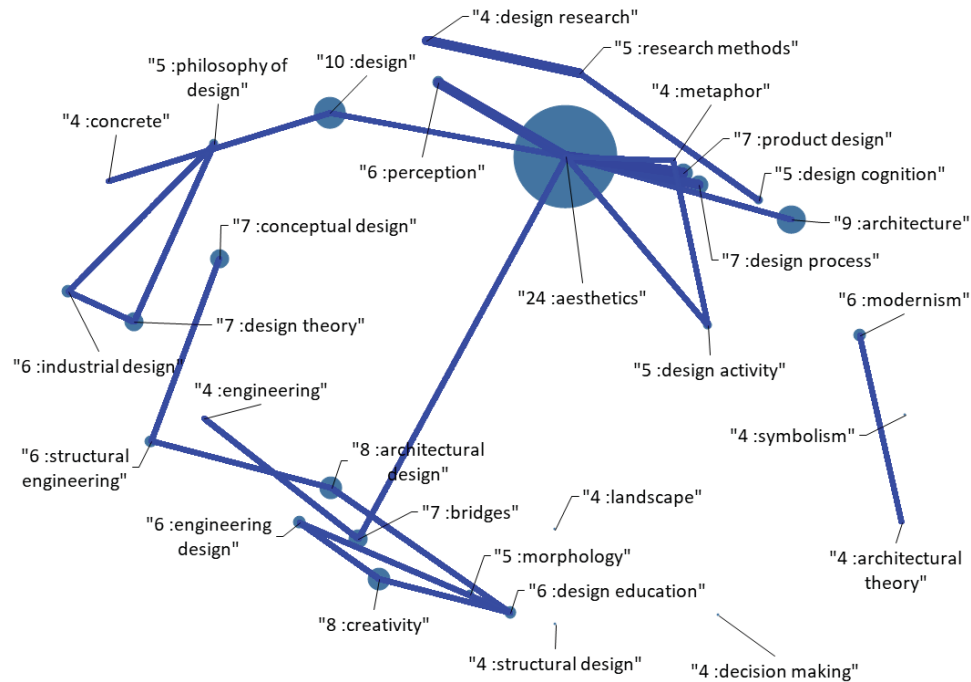


Figure 3: Scopus search for aesthetics with specific keywords

"Design"	"Design Cognition"	"Concretes"
"Architectural Design"	"Esthetic Property"	"Culture"
"Aesthetics"	"Morphology"	"Design Models"
"Structural Design"	"Optimization"	"Design Problems"
"Architecture"	"Philosophy Of Design"	"Design Processes"
"Engineering"	"Symbolism"	"Earthquake Resistance"
"Bridges"	"Tall Buildings"	"Efficiency"
"Design Process"	"Arches"	"Empirical Studies"
"Esthetics"	"Architects"	"Exploratory Studies"
"Architectural Textile"	"Architectural Theory"	"Form"
"Buildings"	"Cables"	"Heritage"
"Conceptual Design"	"Concept Selection"	"Historic Building"
"Roofs"	"Concrete"	"History"
"Computer Aided Design"	"Design Practice"	"Housing"
"Creativity"	"Engineers"	"Imagination"
"Engineering Design"	"Footbridges"	"Innovation"
"Structural Analysis"	"Geometry"	"Istanbul"
"Timber"	"Masonry Construction"	"Masonry"
"Design Theory"	"Metaphor"	"Mathematical Models"
"Structural Systems"	"Philosophy"	"Membrane"
"Cultural Heritage"	"Steel"	"Mortar"
"Design Research"	"Structural Loads"	"Problem Solving"
"Historic Preservation"	"Symmetry"	"Semantics"
"Modernism"	"Topology"	"Space Syntax"
"Reinforced Concrete"	"Brick"	
"Restoration"	"Bridge"	
"Structural Engineering"	"Bridge Decks"	
"Building"	"Bridge Design"	
"Civil Engineering"	"Building Materials"	
"Design Activity"	"Case Studies"	
"Design And Construction"	"Case Study"	

Table 1: Special keywords for the final database construction

### 3 STUDIED DATABASE

Seventeen projects have been used, of which all had ten different, parametric variations, by changing the slider components in the software [2], [3], and have been created mainly by the third-year students of the school of architecture at Neapolis University Pafos, in their modules, Computational Design and Advanced Structural Systems. From these ten alterations, we get sixteen structural analysis results, regarding the maximum and minimum displacements, nodal rotations, internal axial forces and bending moments. All these results are included in Appendix II, while indicative results are demonstrated in Table 2. These sixteen output values from each variation of the projects, in combination with a questionnaire which was completed by architects, engineers and other people, not related to this profession, will be analyzed statistically in order to investigate the hypothesis that structural response is correlated with the aesthetic value of each project. The aesthetic value was considered as the mean value (for each project) of the participants to this research. The questionnaire was filled by 23 people and the mean value of the responses was used as the dependent variable, representing an unbiased indicator for aesthetic value.

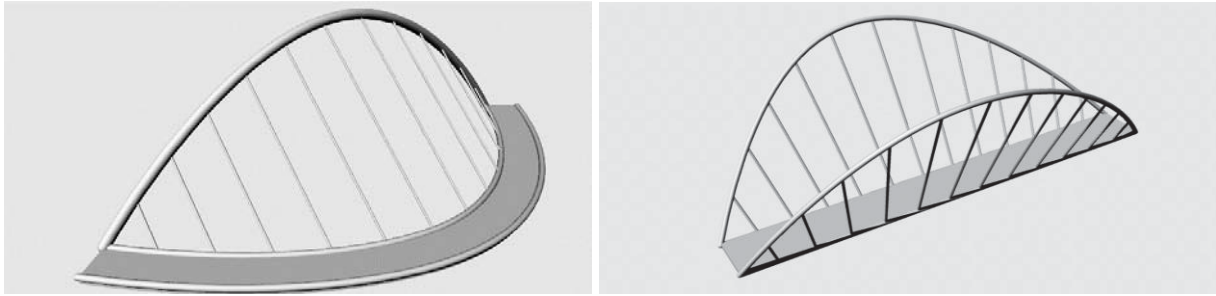
	N (max)	N (avg)	M (max)	M (avg)	Tx (max)	Tx (avg)	Ty (max)	Tz (avg)	Rx (max)	Rx (avg)	Ry (max)	Ry (avg)	Rz (avg)	aesthetics
001	1.6E+00	5.2E-01	2.9E-01	7.8E-02	1.7E-04	4.0E-05	5.5E-05	4.8E-05	6.3E-05	1.4E-05	1.9E-04	5.7E-05	9.3E-06	4.2E+00
002	1.5E+00	4.6E-01	2.4E-01	7.1E-02	1.2E-04	3.7E-05	3.0E-05	4.6E-05	5.0E-05	1.2E-05	1.6E-04	5.5E-05	9.8E-06	3.9E+00
003	1.7E+00	5.3E-01	3.0E-01	7.1E-02	1.7E-04	3.4E-05	6.9E-05	4.2E-05	7.5E-05	1.5E-05	1.9E-04	4.9E-05	1.1E-05	3.9E+00
004	1.7E+00	5.4E-01	3.1E-01	8.2E-02	2.0E-04	4.5E-05	5.1E-05	5.4E-05	9.2E-05	1.5E-05	2.1E-04	6.1E-05	8.8E-06	3.8E+00
005	1.5E+00	4.8E-01	2.6E-01	7.1E-02	1.2E-04	3.2E-05	3.1E-05	3.9E-05	4.2E-05	8.6E-06	1.6E-04	5.1E-05	6.3E-06	3.8E+00
006	1.5E+00	4.4E-01	2.4E-01	5.6E-02	1.0E-04	2.1E-05	3.7E-05	2.6E-05	5.3E-05	8.8E-06	1.4E-04	3.6E-05	8.0E-06	3.8E+00
007	1.4E+00	4.2E-01	1.9E-01	5.1E-02	7.0E-05	1.5E-05	3.1E-05	1.9E-05	3.4E-05	7.6E-06	8.6E-05	2.8E-05	6.5E-06	3.8E+00
008	1.4E+00	4.3E-01	1.9E-01	5.5E-02	6.7E-05	1.8E-05	3.0E-05	2.2E-05	3.1E-05	8.0E-06	8.7E-05	3.2E-05	6.4E-06	3.8E+00
009	1.3E+00	4.0E-01	1.7E-01	5.0E-02	6.2E-05	1.7E-05	2.8E-05	2.1E-05	2.8E-05	8.1E-06	7.9E-05	2.9E-05	6.4E-06	3.7E+00
010	1.5E+00	4.5E-01	2.4E-01	5.9E-02	1.5E-04	2.5E-05	1.1E-04	3.1E-05	7.2E-05	1.7E-05	1.4E-04	3.8E-05	1.5E-05	3.7E+00

Table 2: Structural analysis results for structure 001-010

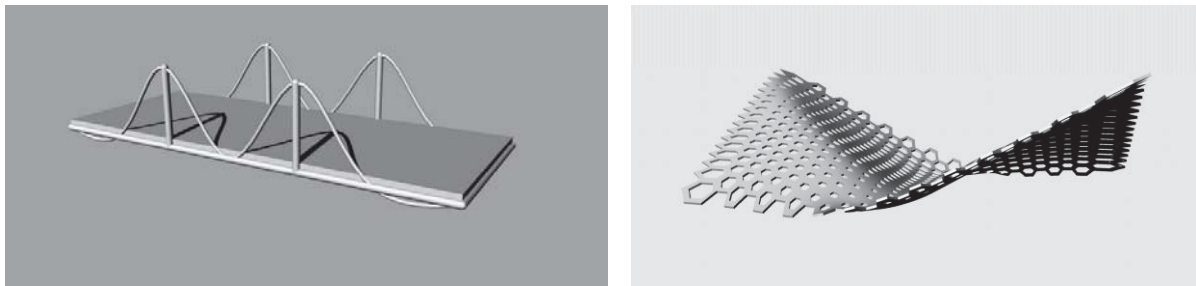
The numerical procedure was started by creating ten versions of each project by using the software Rhino [4], and its plugin Grasshopper3d [3] and then save ten renders from a different viewing point of each alteration. For the static solution of these projects the plugin Karamba3d [2], [5] was used, in which we came up with the maximum and minimum internal forces and also the maximum and minimum displacements. Furthermore, a questioner on Google docs (Appendix I), was created with all the images, which are included in Appendix III, in order for people to vote. From this feedback, an excel file was created so as to be analyzed with regression analysis. Furthermore, the top five projects that were voted, are demonstrated in Figure 7. Finally, two examples of the code that was used in Grasshopper3d, and one example code from Karamba3d are depicted in Appendix III.

In Figure 7 - A, which is a curved hanging bridge, the concept is to rotate around from its vertical axis to pass the ships under the bridge. Figure 7 - B, is a hanging bridge in a straight line similar to the previous one. In Figure 7 - C, we still demonstrate a hanging bridge of similar structural rationale, in the simplest form. In Figure 7 - D, we show a parametric shell with polygonal openings on the roof. Finally, in Figure 7 - E a large-scale enclosure is demonstrated. Accordingly, in, Figure10, the corresponding code in the Grasshopper3d [3] program and the congruent code is for the project of Figure 7-B. Then the code for the project of Figure 7-A is demonstrated in Figure 11 with an optimization tool to the right in order to find a place where the bridge has the minimum bending moments. Finally, for the same project, we see the

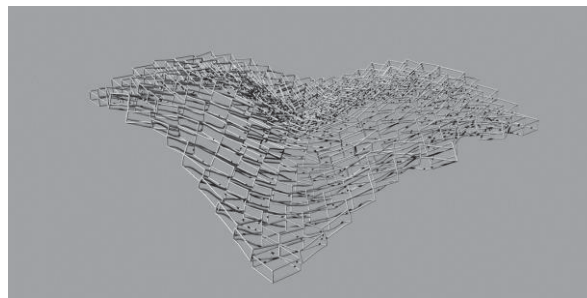
Karamba3d [2] code and the various values we output for moments and displacements (see Figure 12 in Appendix II).



A-B: Parametric projects 215, 226



C-D: Parametric projects 081, 236



E: Parametric project 107

Figure 4: Highest rated projects

## 4 HEADINGS

In order to perform the regression analysis, the results of each project were normalized to have zero mean and unit standard deviation, so as to utilize the same range for the Karamba3d results for its project and the statistical analysis to be more representative. The projects with irrational values of internal forces were excluded from the database via anomaly detection software [26], as they probably had errors in the connectivity of the model. We used three Machine Learning simulations, in order to construct prediction models, and in particular, Linear Regression [27], Random Forests [28], [29], and Gradient Boosting [30], [31], as developed in Julia [32] programming language. In Table 3, the accuracy metrics indicate a strong link among the structural analysis results, with the aesthetic value, as computed by the questionnaires. Afterwards, sensitivity analysis [33], [34] was conducted in order to investigate the influence of each independent variable to the dependent, by keeping all other variables constant at their Median value. In Figure 8, the corresponding results for Aesthetic value vs Bending Moments over Axial Forces are depicted, exhibiting a decreasing pattern. This is in accordance with the rationale of Antonio Gaudi [7] and the minimum bending moments of arches and domes.

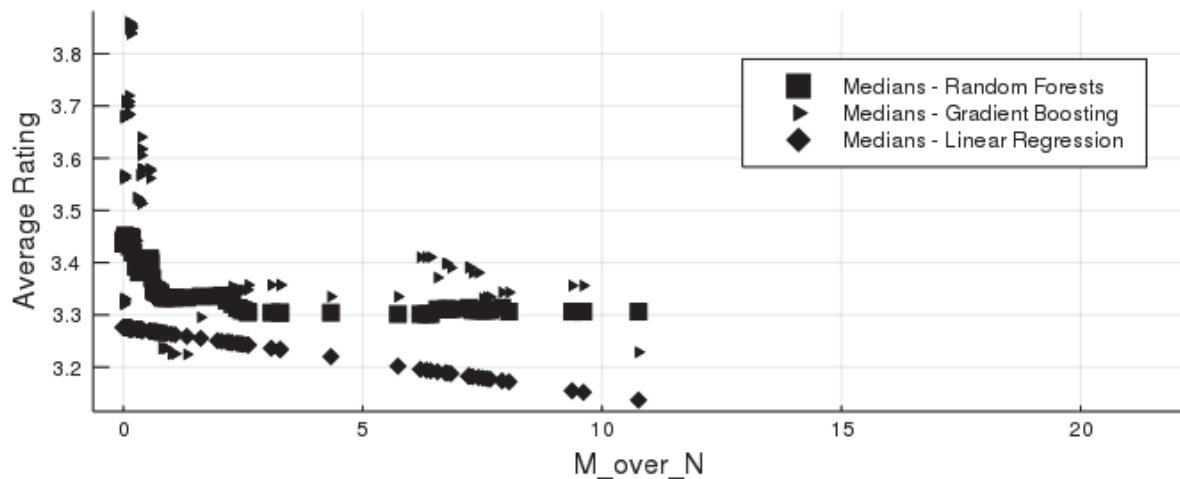


Figure 5: Sensitivity analysis

Methods	Pears. Corr.	MAE	RMSE	MAPE	MAXPE	Alpha
Random Forests	0.8156	0.1460	0.1980	0.0466	0.2065	0.5704
Gradient Boosting	0.9732	0.0183	0.0771	0.0055	0.1761	0.9469
Linear Regression	0.3769	0.2449	0.3155	0.0800	0.3533	0.1154

Table 3: Accuracy Metrics of Machine Learning Models

## 5 CONCLUSIONS

This research was an attempt to contribute to the question of many architects and civil engineers on whether the structural response of a structure is useful to the stability of the building, or it has another utilization on the architectural synthesis as well. The literature regarding parametric design and form-finding, although indirectly refer to the aesthetics of the structure, lack any identification of a numerical link between the structural response and aesthetics of the structure. This was farther investigated and confirmed with bibliometric analysis of the literature regarding aesthetics and structural response, where the clusters of the aesthetic related keywords were separated from the engineering related keywords. An adequate amount of projects (170) were developed and studied in order to construct a database for such an investigation. The regression analysis confirmed numerically that there exists a link between structural response and aesthetics.

## 6 ACKNOWLEDGEMENTS

Special thanks to the students which participated in this study, by offering their studio projects:

Mais-Wakid Abbas, Theodoros Antoniou, Christina Georgiou, Rafaella Georgiou, Maria Giannaka, Panagiotis Kontopyrakis, Iuliia Logacheva, Maria-Pavlina Pavloudaki, Elina-Stergia Pieri, Demetris Socratous, Elenos Tsigkis, Maria-Evangelia Tzouveleki.

## REFERENCES

- [1] J. Monedero, Parametric design: A review and some experiences, *Autom. Constr.*, 2000.
- [2] C. Preisinger and others, *Karamba3D, Version*, vol. 1, no. 2, p. 25, 2015.

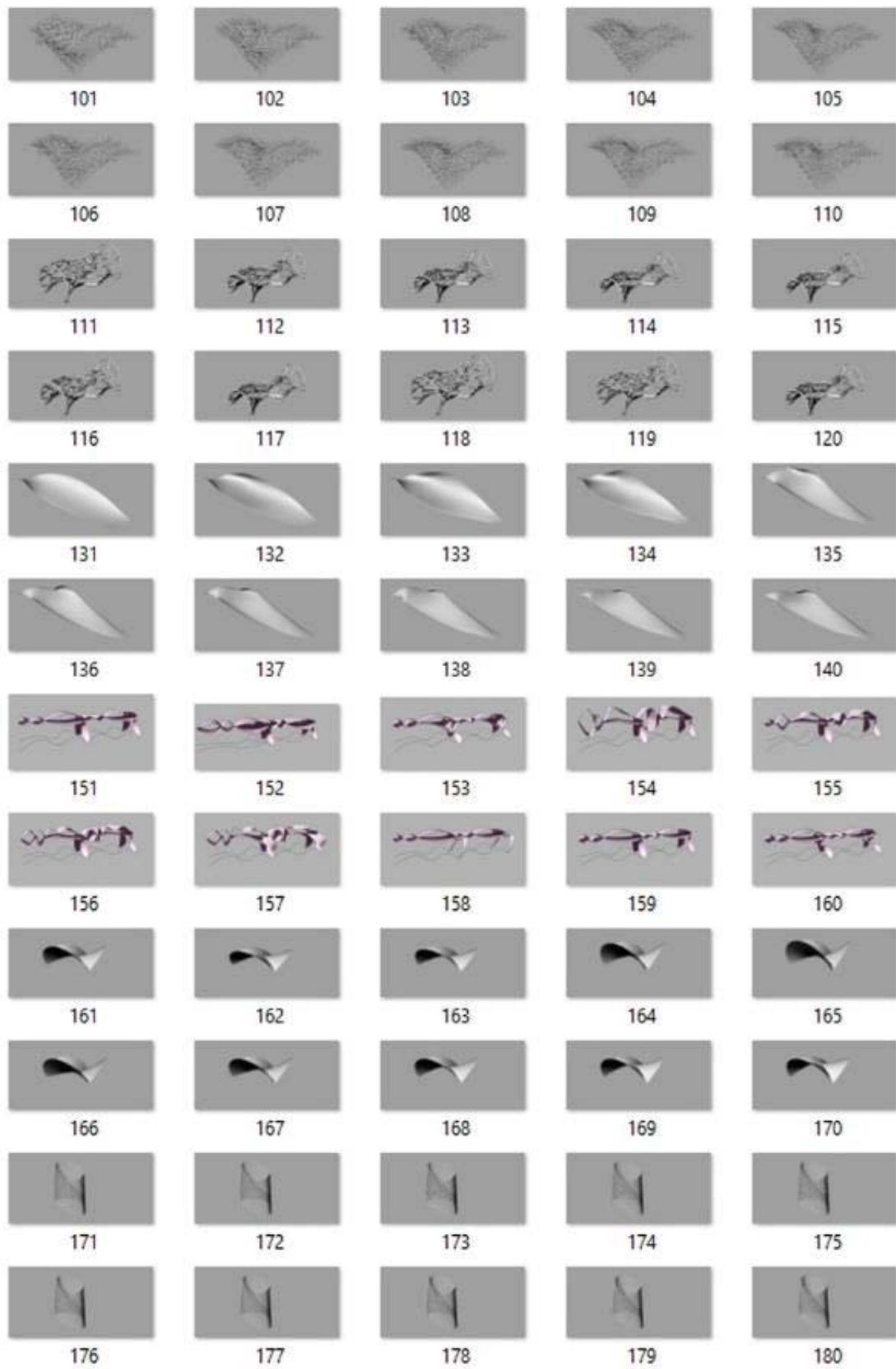
- [3] Grasshopper3d. 2019.
- [4] Rhino3d. Robert McNeel & Associates, 2019.
- [5] C. Preisinger, Linking structure and parametric geometry, *Archit. Des.*, 2013.
- [6] C. Preisinger, Karamba3D User Manual (Version 1.3.2). 2019.
- [7] A. Pugnale and M. Sassone, Morphogenesis and structural optimization of shell structures with the aid of a genetic algorithm, in *Journal of the International Association for Shell and Spatial Structures*, 2007.
- [8] S. Huerta, Structural design in the work of gaudí, *Archit. Sci. Rev.*, 2006.
- [9] M. Dimcic, *Structural Optimization of Grid Shells Based on Genetic Algorithms*. 2011.
- [10] S. Schoina, Performance-based form-finding and material distribution of free form roof structures: Implementation in the Post Rotterdam Case Study, 2016.
- [11] J. S. GERO, Architectural Optimization-A Review, *Eng. Optim.*, vol. 1, no. 3, pp. 189–199, 1975.
- [12] A. J. Isaacs, Self-Organisational Architecture: Design Through Form-Finding Methods, *J. Chem. Inf. Model.*, 2013.
- [13] M. Turrin, P. Von Buelow, and R. Stouffs, Design explorations of performance driven geometry in architectural design using parametric modeling and genetic algorithms, *Adv. Eng. Informatics*, vol. 25, no. 4, pp. 656–675, 2011.
- [14] P. Basso, A. E. Del Grosso, A. Pugnale, and M. Sassone, Computational morphogenesis in architecture: Cost optimization of free-form grid shells, in *Journal of the International Association for Shell and Spatial Structures*, 2009.
- [15] F. Otto, B. Rasch, D. W. Bayern, K. V. Stuck, and A. anlässlich der Preisverleihung des Deutschen Werkbundes Bayern an Frei Otto und Bodo Rasch, *Frei Otto, Bodo Rasch: Finding form: towards on architecture of the minimal; the Werkbund shows Frei Otto, Frei Otto shows Bodo Rasch; exhibition in the Villa Stuck, Munich, on the occasion of the award of the 1992 Deutscher Werkbund Bayern Prize to Frei .* Ed. Menges, 2006.
- [16] R. A. P. E. Danhaive, Integrating interactive evolutionary exploration and parametric structural design, Massachusetts Institute of Technology, 2015.
- [17] N. Oxman, Get Real towards Performance-Driven Computational Geometry, *Int. J. Archit. Comput.*, 2007.
- [18] A. Carlson, *Aesthetics and the environment: The appreciation of nature, art and architecture*. Routledge, 2005.
- [19] S. Adriaenssens, P. Block, D. Veenendaal, and C. Williams, *Shell structures for architecture: Form finding and optimization*. 2014.
- [20] N. D. Lagaros, M. Papadrakakis, and N. P. Bakas, Automatic minimization of the rigidity eccentricity of 3D reinforced concrete buildings, *J. Earthq. Eng.*, vol. 10, no. 4, pp. 533–564, Jul. 2006.
- [21] N. D. Lagaros, N. Bakas, and M. Papadrakakis, Optimum Design Approaches for Improving the Seismic Performance of 3D RC Buildings, *J. Earthq. Eng.*, vol. 13, no. 3, pp. 345–363, Mar. 2009.
- [22] S. Heyman, Google Books: a Complex and Controversial Experiment, *New York Times*, 2015.
- [23] V. Plevris, N. Bakas, G. Markeset, and J. Bellos, Literature review of masonry structures under earthquake excitation utilizing machine learning algorithms, in *Proceedings of the 6th International Conference on Computational Methods in Structural Dynamics and Earthquake Engineering (COMPDYN 2015)*, 2017, pp. 2685–2694.
- [24] T. Dimopoulos and N. Bakas, An artificial intelligence algorithm analyzing 30 years of

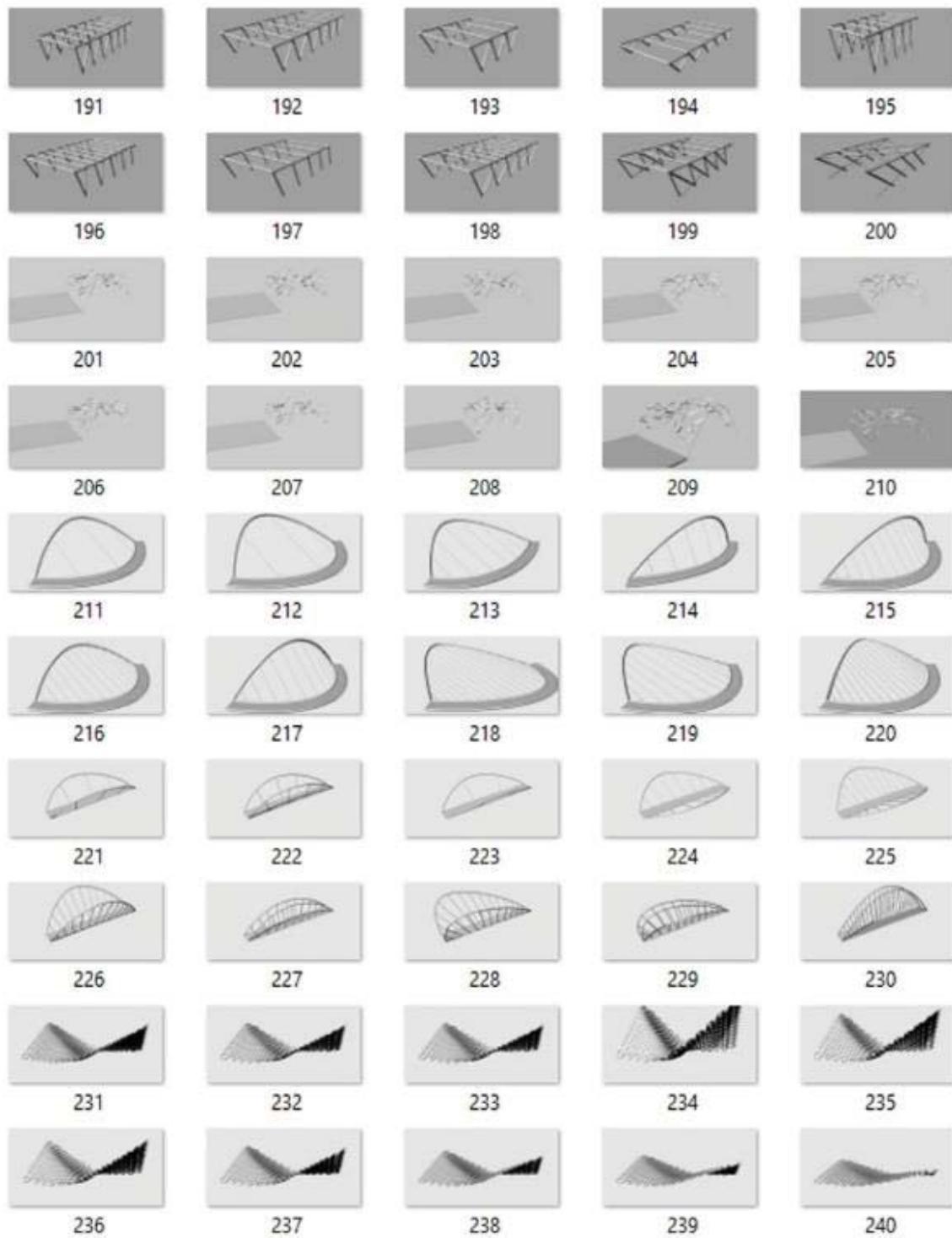


- research in mass appraisals, *Rel. Int. J. Real Estate L. Plan.*, vol. 2, no. 0, pp. 10–27, 2019.
- [25] Scopus. [Online]. Available: <https://scopus.com/home.uri>.
- [26] N. P. Bakas, NOESYS-AI Regression: A generic framework for predictive modeling and sensitivity analysis. 2018.
- [27] T. Dimopoulos, H. Tyrallis, N. P. Bakas, and D. Hadjimitsis, Accuracy measurement of Random Forests and Linear Regression for mass appraisal models that estimate the prices of residential apartments in Nicosia, Cyprus, *Adv. Geosci.*, vol. 45, pp. 377–382, Nov. 2018.
- [28] L. Breiman, Random Forreests, *Mach. Learn.*, 2001.
- [29] Luis Pedro Coelho, MILK: Machine Learning Toolkit - DecisionTree.jl. .
- [30] B. XU and T. CHEN, XGBoost.jl. 2014.
- [31] T. Chen and C. Guestrin, XGBoost: A scalable tree boosting system, in *Proceedings of the ACM SIGKDD International Conference on Knowledge Discovery and Data Mining*, 2016.
- [32] J. Bezanson, A. Edelman, S. Karpinski, and V. B. Shah, Julia: A fresh approach to numerical computing, *SIAM Rev.*, vol. 59, no. 1, pp. 65–98, 2017.
- [33] J. D. Olden and D. A. Jackson, Illuminating the ‘black box’: A randomization approach for understanding variable contributions in artificial neural networks, *Ecol. Modell.*, 2002.
- [34] M. Gevrey, I. Dimopoulos, and S. Lek, Review and comparison of methods to study the contribution of variables in artificial neural network models, in *Ecological Modelling*, 2003.

## Appendix I: Figures, of the studied projects







## Appendix II: Example Codes

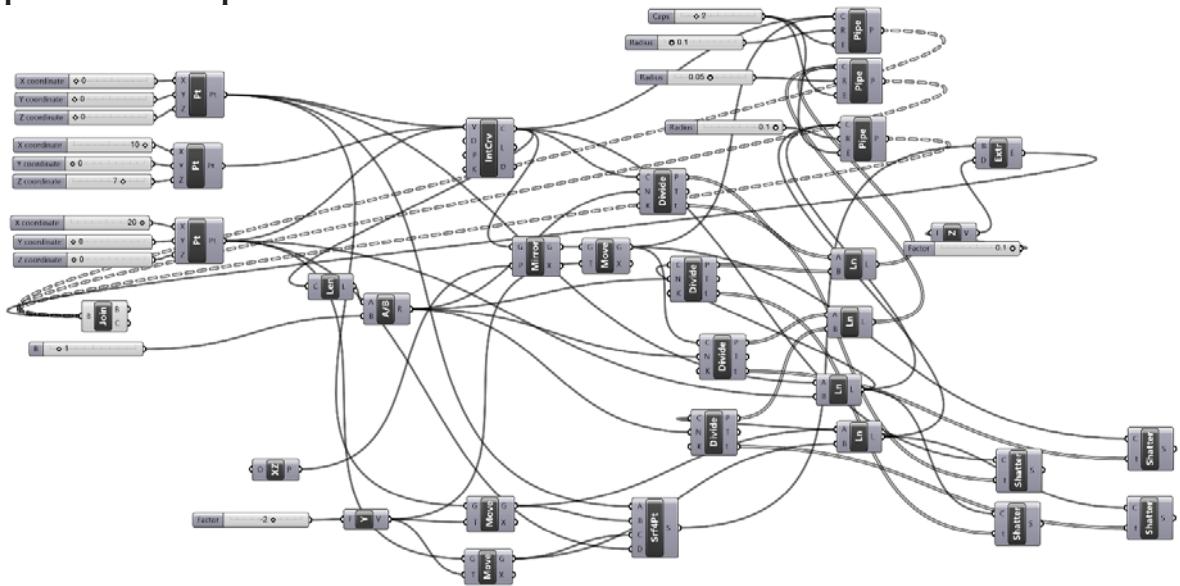


Figure 6: Parametric code 226

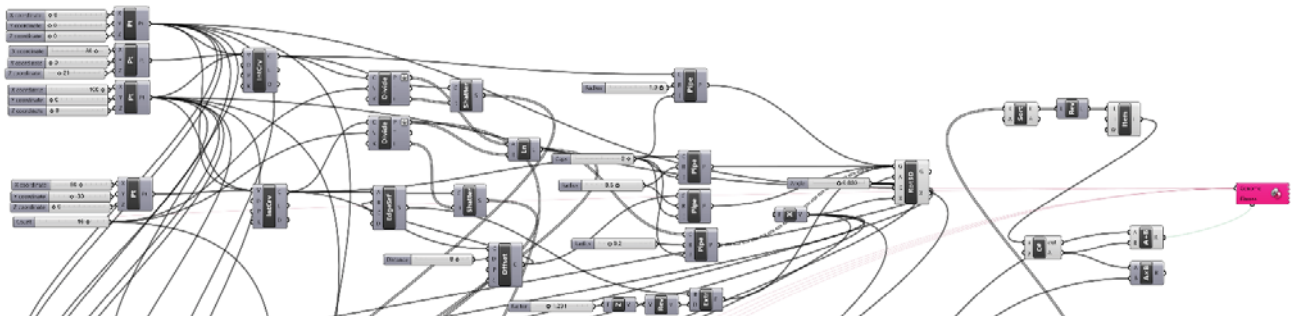


Figure 7: Parametric code 215

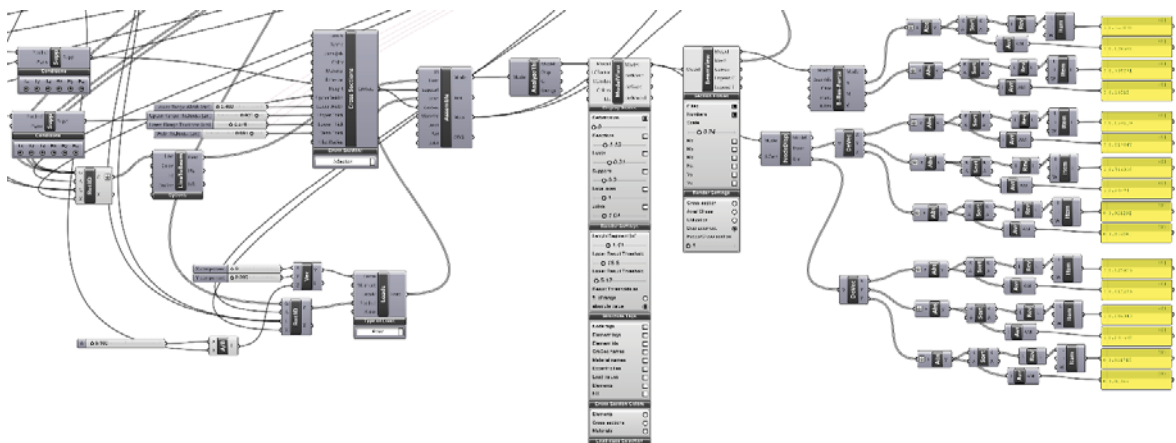


Figure 12: Karamba3d code 215



Appendix III: Tables, of the studied projects

	N (max)	N (avg)	M (max)	M (avg)	Tx (max)	Tx (avg)	Ty (max)	Ty (avg)	Tz (max)	Tz (avg)	Rx (max)	Rx (avg)	Ry (max)	Ry (avg)	Rz (max)	Rz (avg)	type (beams=L, shells=0)	aesthet- ics
001	1.6E+0 0	5.2E+01	2.9E+01	7.8E+02	1.7E+04	4.0E+05	5.5E+05	1.3E+05	2.7E+04	4.8E+05	6.3E+05	1.4E+05	1.9E+04	5.7E+05	4.4E+05	9.3E+06	1	4.2E+00
002	1.5E+0 0	4.6E+01	2.4E+01	7.1E+02	1.2E+04	3.7E+05	3.0E+05	9.4E+06	2.1E+04	4.6E+05	5.0E+05	1.2E+05	1.6E+04	5.5E+05	3.2E+05	9.8E+06	1	3.9E+00
003	1.7E+0 0	5.3E+01	3.0E+01	7.1E+02	1.7E+04	3.4E+05	6.9E+05	1.7E+05	2.8E+04	4.2E+05	7.5E+05	1.5E+05	1.9E+04	4.9E+05	5.3E+05	1.1E+05	1	3.9E+00
004	1.7E+0 0	5.4E+01	3.1E+01	8.2E+02	2.0E+04	4.5E+05	5.1E+05	1.0E+05	3.2E+04	5.4E+05	9.2E+05	1.5E+05	2.1E+04	6.1E+05	5.9E+05	8.8E+06	1	3.8E+00
005	1.5E+0 0	4.8E+01	2.6E+01	7.1E+02	1.2E+04	3.2E+05	3.1E+05	7.1E+06	1.9E+04	3.9E+05	4.2E+05	8.6E+06	1.6E+04	5.1E+05	2.8E+05	6.3E+06	1	3.8E+00
006	1.5E+0 0	4.4E+01	2.4E+01	5.6E+02	1.0E+04	2.1E+05	3.7E+05	8.4E+06	1.7E+04	2.6E+05	5.3E+05	8.8E+06	1.4E+04	3.6E+05	3.5E+05	8.0E+06	1	3.8E+00
007	1.4E+0 0	4.2E+01	1.9E+01	5.1E+02	7.0E+05	1.5E+05	3.1E+05	5.7E+06	1.2E+04	1.9E+05	3.4E+05	7.6E+06	8.6E+05	2.8E+05	3.2E+05	6.5E+06	1	3.8E+00
008	1.4E+0 0	4.3E+01	1.9E+01	5.5E+02	6.7E+05	1.8E+05	3.0E+05	6.8E+06	1.1E+04	2.2E+05	3.1E+05	8.0E+06	8.7E+05	3.2E+05	2.9E+05	6.4E+06	1	3.8E+00
009	1.3E+0 0	4.0E+01	1.7E+01	5.0E+02	6.2E+05	1.7E+05	2.8E+05	6.8E+06	1.0E+04	2.1E+05	2.8E+05	8.1E+06	7.9E+05	2.9E+05	2.8E+05	6.4E+06	1	3.7E+00
010	1.5E+0 0	4.5E+01	2.4E+01	5.9E+02	1.5E+04	2.5E+05	1.1E+04	1.8E+05	2.4E+04	3.1E+05	7.2E+05	1.7E+05	1.4E+04	3.8E+05	7.7E+05	1.5E+05	1	3.7E+00
011	5.4E+0 2	2.1E+0 2	5.7E+0 1	2.3E+0 1	1.3E+06	2.7E+07	2.3E+06	6.7E+07	1.1E+05	2.9E+06	1.3E+06	3.7E+07	3.2E+06	8.6E+07	4.1E+07	1.1E+07	0	3.7E+00
012	5.5E+0 2	2.0E+0 2	6.0E+0 1	2.2E+0 1	1.4E+06	2.5E+07	2.5E+06	7.4E+07	1.1E+05	2.6E+06	1.5E+06	4.5E+07	3.4E+06	7.7E+07	4.4E+07	1.2E+07	0	3.7E+00
013	5.1E+0 2	1.9E+0 2	5.3E+0 1	2.1E+0 1	1.2E+06	2.1E+07	2.7E+06	6.8E+07	1.0E+05	2.3E+06	1.4E+06	4.5E+07	3.1E+06	7.2E+07	4.2E+07	1.1E+07	0	3.7E+00
014	5.4E+0 2	2.2E+0 2	6.2E+0 1	2.6E+0 1	2.7E+06	3.9E+07	6.5E+06	1.3E+06	1.7E+05	3.3E+06	3.0E+06	8.2E+07	4.9E+06	9.9E+07	1.3E+06	2.6E+07	0	3.7E+00
015	4.3E+0 2	2.0E+0 2	4.2E+0 1	1.9E+0 1	1.5E+06	2.6E+06	5.7E+06	9.6E+07	1.2E+05	2.6E+06	2.5E+06	6.6E+07	2.7E+06	7.3E+07	9.8E+07	2.0E+07	0	3.7E+00
016	5.1E+0 2	2.3E+0 2	5.5E+0 1	2.6E+0 1	1.7E+06	3.7E+07	2.7E+06	8.7E+07	1.0E+05	3.5E+06	1.7E+06	5.0E+07	3.8E+06	9.6E+07	6.6E+07	1.5E+07	0	3.6E+00
017	6.2E+0 2	2.6E+0 2	7.4E+0 1	3.4E+0 1	3.6E+06	7.0E+07	4.7E+06	2.0E+06	2.0E+05	5.3E+06	2.3E+06	7.1E+07	5.8E+06	1.6E+06	9.2E+07	2.8E+07	0	3.6E+00
018	5.2E+0 2	1.9E+0 2	5.5E+0 1	2.2E+0 1	2.5E+06	3.0E+07	8.4E+06	1.3E+06	1.7E+05	2.8E+06	3.9E+06	8.3E+07	4.5E+06	8.5E+07	1.4E+06	2.4E+07	0	3.6E+00
019	6.2E+0 2	2.2E+0 2	7.6E+0 1	2.6E+0 1	3.6E+06	4.3E+07	7.2E+06	1.5E+06	2.0E+05	3.3E+06	3.4E+06	9.1E+07	5.5E+06	1.0E+06	1.5E+06	2.8E+07	0	3.5E+00
020	4.4E+0 2	1.8E+0 2	4.5E+0 1	1.9E+0 1	6.9E+07	1.5E+07	1.7E+06	4.9E+07	7.3E+06	1.9E+06	1.2E+06	3.4E+07	2.4E+06	5.7E+07	2.9E+07	7.2E+08	0	3.5E+00
041	5.1E+0 2	7.7E+0 2	1.8E+0 1	1.5E+0 1	7.0E+0 0	3.7E+0 0	7.6E+0 0	2.5E+0 0	1.5E+0 1	6.2E+0 0	9.6E+01	3.4E+01	6.2E+01	2.2E+01	4.7E+01	1.4E+01	1	3.5E+00
042	4.5E+0 2	9.9E+0 2	1.6E+0 2	1.5E+0 1	7.0E+0 0	2.9E+0 0	7.4E+0 0	1.6E+0 0	1.9E+0 1	6.5E+0 0	1.0E+0 0	3.4E+01	6.5E+01	2.6E+01	4.4E+01	1.3E+01	1	3.5E+00
043	4.5E+0 2	6.3E+0 1	5.9E+0 1	1.1E+0 1	2.9E+0 0	1.7E+0 0	2.4E+0 0	8.3E+01	7.0E+0 0	2.9E+0 0	3.7E+01	9.9E+02	4.0E+01	1.5E+01	1.7E+01	2.7E+02	1	3.5E+00
044	3.8E+0 2	5.8E+0 1	5.6E+0 1	6.1E+0 0	2.0E+0 0	5.2E+01	1.3E+0 0	4.7E+01	4.7E+0 0	1.2E+0 0	2.0E+01	6.0E+02	3.1E+01	8.4E+02	8.3E+02	3.5E+02	1	3.5E+00

045	2.8E+0 2	4.1E+0 1	4.2E+0 1	7.0E+0 0	1.9E+0 0	1.1E+0 0	7.3E-01	3.0E-01	3.3E+0 0	1.3E+0 0	2.7E-01	5.2E-02	2.7E-01	8.1E-02	8.5E-02	1.7E-02	1	3.5E+00
046	2.8E+0 2	3.6E+0	5.5E+0 1	9.8E+0 0	1.5E+0 0	5.7E-01	2.3E+0	1.0E+0 0	5.5E+0 0	1.9E+0 0	1.8E-01	5.4E-02	3.0E-01	1.3E-01	1.6E-01	5.5E-02	1	3.5E+00
047	2.1E+0 2	2.5E+0 1	3.4E+0 1	8.2E+0 0	2.2E+0 0	3.4E-01	7.7E-01	2.0E-01	3.9E+0 0	1.2E+0 0	2.0E-01	8.7E-02	3.1E-01	9.8E-02	1.4E-01	3.1E-02	1	3.5E+00
048	1.3E+0 2	2.1E+0 1	4.0E+0 1	6.0E+0 0	6.7E-01	1.6E-01	6.5E-01	2.6E-01	2.2E+0 0	7.1E-01	1.6E-01	6.8E-02	1.4E-01	6.1E-02	5.6E-02	2.1E-02	1	3.5E+00
049	4.7E+0 2	5.3E+0 1	1.2E+0 2	1.0E+0 1	4.4E+0 0	1.7E+0 0	4.2E+0 0	6.3E-01	1.1E+0 1	3.5E+0 0	4.5E-01	2.4E-01	4.7E-01	1.3E-01	1.7E-01	8.2E-02	1	3.5E+00
050	7.9E+0 2	7.8E+0	4.9E+0 2	3.3E+0 1	2.6E+0 1	1.1E+0 1	8.7E+0 0	2.0E+0 0	5.7E+0 1	2.2E+0 1	1.7E+0 0	3.8E-01	2.3E+0 0	9.1E-01	6.4E-01	2.0E-01	1	3.5E+00
051	3.7E+0 0	1.9E+0 0	6.0E+0 0	1.6E+0 0	0.0E+0 0	0.0E+0 0	3.5E-01	5.0E-02	4.2E-01	7.0E-02	6.3E-02	1.2E-02	0.0E+0 0	0.0E+0 0	0.0E+0 0	0.0E+0 0	1	3.5E+00
052	6.2E+0 0	3.9E+0 0	4.9E+0 0	1.3E+0 0	0.0E+0 0	0.0E+0 0	7.1E-02	1.0E-02	2.8E-01	4.6E-02	3.9E-02	7.8E-03	0.0E+0 0	0.0E+0 0	0.0E+0 0	0.0E+0 0	1	3.4E+00
053	3.8E+0 0	1.7E+0 0	6.1E+0 0	1.4E+0 0	0.0E+0 0	0.0E+0 0	4.1E-01	4.6E-02	4.6E-01	6.1E-02	6.5E-02	1.1E-02	0.0E+0 0	0.0E+0 0	0.0E+0 0	0.0E+0 0	1	3.4E+00
054	2.9E+0 0	8.5E-01	6.6E-01	9.2E-02	0.0E+0 0	0.0E+0 0	4.2E-03	3.2E-04	3.8E-03	3.6E-04	1.5E-03	1.8E-04	0.0E+0 0	0.0E+0 0	0.0E+0 0	0.0E+0 0	1	3.4E+00
055	3.9E+0 0	2.1E+0 0	5.4E+0 0	1.5E+0 0	0.0E+0 0	0.0E+0 0	2.1E-01	3.1E-02	3.5E-01	5.8E-02	5.1E-02	1.0E-02	0.0E+0 0	0.0E+0 0	0.0E+0 0	0.0E+0 0	1	3.4E+00
056	3.8E+0 0	1.7E+0 0	6.2E+0 0	1.2E+0 0	0.0E+0 0	0.0E+0 0	4.1E-01	4.0E-02	4.7E-01	5.2E-02	6.4E-02	9.4E-03	0.0E+0 0	0.0E+0 0	0.0E+0 0	0.0E+0 0	1	3.4E+00
057	7.1E+0 0	4.6E+0 0	4.9E+0 0	1.3E+0 0	0.0E+0 0	0.0E+0 0	5.8E-02	8.3E-03	2.8E-01	4.5E-02	3.8E-02	7.7E-03	0.0E+0 0	0.0E+0 0	0.0E+0 0	0.0E+0 0	1	3.4E+00
058	4.1E+0 0	2.3E+0 0	5.2E+0 0	1.4E+0 0	0.0E+0 0	0.0E+0 0	1.7E-01	2.4E-02	3.3E-01	5.3E-02	4.7E-02	9.2E-03	0.0E+0 0	0.0E+0 0	0.0E+0 0	0.0E+0 0	1	3.4E+00
059	3.8E+0 0	1.8E+0 0	6.2E+0 0	1.7E+0 0	0.0E+0 0	0.0E+0 0	3.8E-01	5.6E-02	4.4E-01	7.3E-02	6.6E-02	1.3E-02	0.0E+0 0	0.0E+0 0	0.0E+0 0	0.0E+0 0	1	3.4E+00
060	3.8E+0 0	1.9E+0 0	5.8E+0 0	1.6E+0 0	0.0E+0 0	0.0E+0 0	2.9E-01	4.2E-02	3.9E-01	6.5E-02	5.8E-02	1.1E-02	0.0E+0 0	0.0E+0 0	0.0E+0 0	0.0E+0 0	1	3.4E+00
081	4.2E+0 0	1.2E+0 0	1.8E+0 1	2.0E+0 0	1.2E-01	3.0E-02	2.6E-01	7.7E-02	4.9E+0 0	2.5E-01	1.2E-01	3.0E-02	2.6E-01	7.7E-02	4.9E+0 0	2.5E-01	1	3.4E+00
082	4.2E+0 0	1.2E+0 0	6.3E+0 1	4.3E+0 0	9.6E-02	1.5E-02	1.5E-01	3.1E-02	1.3E+1 4	1.0E+1 3	9.6E-02	1.5E-02	1.5E-01	3.1E-02	1.3E+1 4	1.0E+1 3	1	3.3E+00
083	5.1E+0 0	9.5E-01	6.3E+0 1	3.6E+0 0	3.1E-01	4.3E-02	2.9E-01	6.7E-02	1.7E+1 4	1.3E+1 3	3.1E-01	4.3E-02	2.9E-01	6.7E-02	1.7E+1 4	1.3E+1 3	1	3.3E+00
084	3.5E+0 1	3.5E+0 0	2.5E+0 2	2.4E+0 1	2.9E+0 0	8.0E-01	3.6E+0 1	1.0E+0 1	2.7E+0 3	2.7E+0 2	2.9E+0 0	8.0E-01	3.6E+0 1	1.0E+0 1	2.7E+0 3	2.7E+0 2	1	3.3E+00
085	7.7E+0 0	1.3E+0 0	1.0E+0 3	2.7E+0 1	8.3E+0 0	4.0E-01	6.1E+0 0	5.4E-01	1.2E+1 4	1.3E+1 3	8.3E+0 0	4.0E-01	6.1E+0 0	5.4E-01	1.2E+1 4	1.3E+1 3	1	3.3E+00
086	1.1E+0 1	1.5E+0 0	6.2E+0 2	4.2E+0 1	4.8E+0 0	8.1E-01	3.2E+0 0	4.1E-01	4.7E+1 3	6.0E+1 2	4.8E+0 0	8.1E-01	3.2E+0 0	4.1E-01	4.7E+1 3	6.0E+1 2	1	3.3E+00
087	1.1E+0 1	1.9E+0 0	8.4E+0 1	1.2E+0 1	1.6E+0 1	3.1E+0 0	3.7E+0 1	7.6E+0 0	1.5E+0 2	1.6E+0 1	1.6E+0 1	3.1E+0 0	3.7E+0 1	7.6E+0 0	1.5E+0 2	1.6E+0 1	1	3.3E+00
088	1.2E+0 1	2.6E+0 2	1.1E+0 2	2.0E+0 1	1.4E+0 1	1.0E+0 0	4.2E+0 1	1.6E+0 1	1.7E+0 2	3.3E+0 3	1.4E+0 1	1.0E+0 0	4.2E+0 1	1.6E+0 1	1.7E+0 2	3.3E+0 1	1	3.3E+00
089	5.6E+0 0	1.0E+0 0	1.8E+0 1	2.7E+0 0	3.5E-01	5.4E-02	3.9E-01	9.4E-02	1.6E+1 3	1.0E+1 2	3.5E-01	5.4E-02	3.9E-01	9.4E-02	1.6E+1 3	1.0E+1 2	1	3.3E+00
090	6.8E+0 0	6.8E+0 0	6.8E+0 0	6.8E+0 0	6.8E+0 0	6.8E+0 0	6.8E+0 0	6.8E+0 0	6.8E+0 0	6.8E+0 0	6.8E+0 0	6.8E+0 0	6.8E+0 0	6.8E+0 0	6.8E+0 0	6.8E+0 0	1	3.3E+00
091	1.2E+0 6	3.5E+0 5	1.1E+0 7	2.1E+0 6	1.6E+0 3	1.7E-01	2.0E-01	3.1E-02	1.9E+0 3	1.8E-01	3.5E-02	5.0E-03	8.5E-02	1.1E-02	2.4E-02	2.0E-03	1	3.3E+00
092	1.3E+0 6	3.5E+0 5	1.3E+0 7	2.5E+0 6	2.2E+0 3	2.6E-01	2.4E-01	3.5E-02	2.6E+0 3	2.5E-01	4.2E-02	5.0E-03	1.1E-01	1.6E-02	3.1E-02	3.0E-03	1	3.3E+00

093	1.3E+0 6	3.5E+0 5	1.3E+0 7	2.5E+0 6	2.3E+0 3	2.5E+01	2.4E-01	3.7E-02	2.7E+0 3	2.5E-01	4.3E-02	5.0E-03	1.1E-01	1.5E-02	3.2E-02	3.0E-03	1	3.3E+00
094	1.4E+0 6	3.9E+0 5	1.3E+0 7	2.6E+0 6	2.7E+0 3	2.9E+01	2.6E-01	3.7E-02	3.0E+0 3	2.7E-01	4.5E-02	5.0E-03	1.2E-01	1.6E-02	3.5E-02	3.0E-03	1	3.2E+00
095	1.7E+0 6	4.1E+0 5	1.4E+0 7	2.7E+0 6	3.0E+0 3	3.2E+01	1.6E-01	3.0E-02	3.4E+0 3	3.0E-01	4.6E-02	5.0E-03	1.3E-01	1.9E-02	3.8E-02	4.0E-03	1	3.2E+00
096	2.1E+0 6	4.2E+0 5	1.5E+0 7	2.8E+0 6	3.1E+0 3	3.3E+01	1.3E-01	2.4E-02	3.5E+0 3	3.2E-01	4.8E-02	5.0E-03	1.3E-01	1.9E-02	4.0E-02	4.0E-03	1	3.2E+00
097	1.5E+0 6	3.7E+0 5	1.6E+0 7	2.8E+0 6	2.6E+0 3	2.6E+01	3.0E-01	3.7E-02	4.0E+0 3	3.7E-01	6.0E-02	7.0E-03	1.4E-01	1.9E-02	3.3E-02	4.0E-03	1	3.2E+00
098	1.6E+0 6	4.3E+0 5	1.2E+0 7	2.5E+0 6	1.6E-01	4.5E-02	4.9E-01	5.6E-02	1.3E+0 3	1.6E-01	2.5E-02	3.0E-03	3.6E-02	5.0E-03	1.3E-02	1.0E-03	1	3.2E+00
099	2.1E+0 6	4.0E+0 5	9.1E+0 6	2.1E+0 6	4.6E-01	5.0E-02	5.4E-01	5.0E-02	1.4E+0 3	1.3E-01	3.2E-02	4.0E-03	4.2E-02	5.0E-03	1.8E-02	2.0E-03	1	3.2E+00
100	1.5E+0 6	4.5E+0 5	7.7E+0 6	2.3E+0 6	8.4E-01	1.2E+01	9.4E-01	9.8E-02	1.9E+0 3	1.5E-01	4.2E-02	5.0E-03	6.8E-02	7.0E-03	2.0E-02	2.0E-03	1	3.2E+00
101	4.6E+0 1	4.9E+0 0	1.8E+0 1	2.7E+0 0	3.4E-01	5.5E-03	2.2E-02	5.8E-03	1.1E-01	4.4E-02	1.3E-02	3.4E-03	1.2E-02	2.8E-03	7.2E-03	1.6E-02	1	3.2E+00
102	3.6E+0 1	4.8E+0 0	1.3E+0 1	2.6E+0 0	2.9E-02	4.2E-03	2.2E-01	5.5E-03	9.6E-01	3.9E-02	1.2E-02	3.0E-03	9.6E-03	2.5E-03	4.5E-03	1.3E-03	1	3.2E+00
103	3.8E+0 1	4.7E+0 0	1.4E+0 1	2.6E+0 0	2.5E-03	4.6E-03	2.3E-03	5.2E-03	1.0E-01	3.8E-02	9.2E-03	2.9E-03	1.1E-02	2.6E-03	5.9E-03	1.3E-03	1	3.2E+00
104	4.9E+0 1	4.6E+0 0	1.4E+0 1	2.6E+0 0	2.4E-02	4.6E-03	2.4E-02	4.7E-03	9.6E-02	3.8E-02	1.1E-02	2.8E-03	8.4E-03	2.7E-03	5.2E-03	1.3E-03	1	3.2E+00
105	5.6E+0 1	4.6E+0 0	1.4E+0 1	2.5E+0 0	2.2E-02	4.4E-03	2.3E-02	4.7E-03	9.4E-01	3.7E-01	9.3E-03	2.7E-03	8.4E-03	2.6E-03	6.8E-03	1.2E-03	1	3.2E+00
106	4.3E+0 1	4.6E+0 0	1.4E+0 1	2.6E+0 0	2.5E-02	4.5E-03	2.3E-02	4.7E-03	9.5E-02	3.9E-02	1.0E-02	2.8E-03	8.6E-03	2.7E-03	6.1E-03	1.4E-03	1	3.2E+00
107	4.2E+0 1	4.5E+0 0	1.3E+0 1	2.5E+0 0	1.9E-02	4.4E-03	2.4E-02	4.4E-03	8.6E-02	3.7E-02	9.2E-03	2.6E-03	7.9E-03	2.5E-03	5.5E-03	1.3E-03	1	3.2E+00
108	5.0E+0 1	4.7E+0 0	1.3E+0 1	2.6E+0 0	2.1E-02	4.7E-03	2.5E-02	4.4E-03	9.5E-02	3.8E-02	1.2E-02	2.5E-03	9.6E-03	2.6E-03	5.9E-03	1.3E-03	1	3.2E+00
109	4.8E+0 1	4.7E+0 0	1.3E+0 1	2.6E+0 0	2.0E-02	4.5E-03	2.4E-02	4.9E-03	8.8E-02	3.7E-02	9.3E-03	2.7E-03	7.9E-03	2.6E-03	5.6E-03	1.3E-03	1	3.2E+00
110	3.5E+0 1	4.7E+0 0	1.3E+0 1	2.6E+0 0	2.1E-02	4.4E-03	2.3E-02	4.0E-03	9.6E-02	3.9E-02	1.1E-02	2.5E-03	9.4E-03	2.5E-03	5.0E-03	1.3E-03	1	3.2E+00
111	1.2E+0 1	1.9E+0 0	4.6E+0 0	1.4E+0 0	1.8E-02	4.9E-03	3.7E-02	8.0E-03	6.6E-02	2.1E-02	1.1E-02	2.9E-03	7.1E-03	1.9E-03	4.7E-03	9.4E-04	1	3.2E+00
112	1.2E+0 1	1.7E+0 0	3.9E+0 0	1.2E+0 0	1.3E-02	2.9E-03	2.1E-02	4.0E-03	4.8E-02	1.6E-02	6.2E-03	2.1E-03	5.0E-03	1.6E-03	3.8E-03	7.9E-04	1	3.2E+00
113	1.3E+0 1	1.8E+0 0	3.8E+0 0	1.2E+0 0	1.4E-02	2.7E-03	2.2E-02	3.8E-03	4.6E-02	1.6E-02	5.8E-03	2.1E-03	5.0E-03	1.6E-03	3.7E-03	7.9E-04	1	3.2E+00
114	1.7E+0 1	1.8E+0 0	3.9E+0 0	1.2E+0 0	1.6E-02	2.6E-03	2.3E-02	3.6E-03	4.5E-02	1.5E-02	5.9E-03	2.2E-03	5.4E-03	1.9E-03	3.2E-03	7.5E-04	1	3.2E+00
115	1.9E+0 1	1.9E+0 0	4.1E+0 0	1.2E+0 0	1.7E-02	2.6E-03	2.3E-02	3.6E-03	4.5E-02	1.6E-02	6.3E-03	2.4E-03	5.9E-03	2.0E-03	3.0E-03	7.4E-04	1	3.2E+00
116	1.1E+0 1	1.7E+0 0	4.1E+0 0	1.3E+0 0	1.2E-02	3.3E-03	2.2E-02	5.1E-03	5.3E-02	1.7E-02	7.2E-03	2.3E-03	5.6E-03	1.6E-03	4.0E-03	8.3E-04	1	3.2E+00
117	1.6E+0 1	1.8E+0 0	3.9E+0 0	1.2E+0 0	1.6E-02	2.6E-03	2.3E-02	3.6E-03	4.5E-02	1.5E-02	5.9E-03	2.2E-03	5.4E-03	1.8E-03	3.2E-03	7.6E-04	1	3.2E+00
118	1.2E+0 1	1.9E+0 0	4.8E+0 0	1.5E+0 0	2.0E-02	5.4E-03	4.0E-02	8.8E-03	7.0E-02	2.2E-02	1.1E-02	3.1E-03	7.6E-03	2.0E-03	4.8E-03	9.6E-04	1	3.2E+00
119	1.2E+0 1	1.8E+0 0	4.4E+0 0	1.4E+0 0	1.6E-02	4.6E-03	3.3E-02	7.3E-03	6.3E-02	2.0E-02	9.9E-03	2.8E-03	6.8E-03	1.8E-03	4.6E-03	9.1E-04	1	3.2E+00
120	1.5E+0 1	1.8E+0 0	3.8E+0 0	1.2E+0 0	1.6E-02	2.6E-03	2.2E-02	3.6E-03	4.5E-02	1.5E-02	5.7E-03	2.2E-03	5.2E-03	1.8E-03	3.3E-03	7.6E-04	1	3.2E+00

131	8.1E+0 5	5.3E+0 4	1.1E+0 4	2.2E+0 3	1.5E+1 1	3.8E+1 0	2.5E+0 1	6.6E+0 0	1.6E+1 2	8.0E+1 1	1.0E+0 1	5.5E+0 0	2.6E+1 0	2.6E+1 0	9.0E+01	3.4E+01	0	3.2E+00
132	1.4E+0 5	6.7E+0 3	2.4E+0 3	3.0E+0 2	1.5E+0 9	2.9E+0 8	4.5E+0 0	7.3E+01	1.6E+1 0	8.1E+0 9	1.1E+0 0	7.3E+01	2.7E+0 8	2.7E+0 8	1.1E+01	5.3E+02	0	3.2E+00
133	6.2E+0 4	3.7E+0 3	1.3E+0 3	2.1E+0 2	2.0E+0 8	3.5E+0 7	4.7E+0 0	6.4E+01	1.6E+0 9	7.5E+0 8	9.2E+01	5.3E+01	2.6E+0 7	2.6E+0 7	8.4E+02	2.0E+02	0	3.1E+00
134	5.1E+0 4	4.2E+0 3	8.2E+0 2	1.5E+0 2	4.1E+0 9	7.3E+0 8	9.0E+01	2.4E+01	3.3E+1 0	1.5E+1 0	2.3E+01	6.0E+02	5.4E+0 8	5.4E+0 8	3.5E+02	1.4E+02	0	3.1E+00
135	4.4E+0 5	1.7E+0 4	6.9E+0 3	7.7E+0 2	6.5E+0 7	3.2E+0 7	2.8E+0 1	1.0E+0 1	5.3E+0 8	2.3E+0 8	3.6E+0 0	1.4E+0 0	8.8E+0 6	8.8E+0 6	7.0E+01	3.6E+01	0	3.1E+00
136	4.4E+0 5	1.7E+0 4	7.0E+0 3	7.8E+0 2	6.6E+0 7	3.1E+0 7	2.7E+0 1	9.5E+0 8	5.5E+0 8	2.4E+0 8	3.6E+0 0	1.4E+0 0	9.1E+0 6	9.1E+0 6	6.7E+01	3.6E+01	0	3.1E+00
137	1.4E+0 5	8.2E+0 3	3.6E+0 3	3.7E+0 2	2.5E+0 6	1.4E+0 6	1.2E+0 1	4.2E+0 0	2.6E+0 7	1.1E+0 7	1.6E+0 0	6.5E+01	4.3E+0 5	4.3E+0 5	2.8E+01	1.5E+01	0	3.1E+00
138	1.1E+0 6	3.5E+0 4	1.4E+0 4	1.3E+0 3	7.0E+0 7	3.7E+0 7	4.4E+0 1	1.7E+0 1	7.8E+0 8	3.4E+0 8	5.9E+0 0	2.4E+0 0	1.3E+0 7	1.3E+0 7	1.1E+0 0	6.1E+01	0	3.1E+00
139	5.3E+0 5	3.2E+0 4	1.2E+0 4	1.4E+0 3	7.5E+0 7	3.6E+0 7	4.2E+0 1	1.5E+0 1	8.6E+0 8	3.9E+0 8	6.4E+0 0	3.1E+0 0	1.4E+0 7	1.4E+0 7	1.1E+0 0	6.0E+01	0	3.1E+00
140	4.3E+0 5	1.9E+0 4	6.7E+0 3	7.8E+0 2	3.5E+0 9	1.5E+0 9	2.1E+0 1	7.4E+0 0	4.0E+1 0	1.8E+1 0	3.5E+0 0	1.7E+0 0	6.6E+0 8	6.6E+0 8	5.9E+01	3.2E+01	0	3.1E+00
151	5.5E+0 3	1.8E+0 2	9.7E+0 1	4.7E+0 0	3.2E+0 0	2.5E+01	1.1E+0 1	6.8E+0 0	4.8E+0 1	1.5E+0 1	4.7E+0 0	1.8E+0 0	2.6E+0 0	2.6E+0 0	1.9E+0 0	8.2E+02	1	3.1E+00
152	9.6E+0 4	7.8E+0 2	1.0E+0 3	1.5E+0 1	5.4E+0 1	2.2E+0 1	4.3E+0 2	3.3E+0 2	1.2E+0 3	4.8E+0 2	7.7E+0 1	7.1E+0 1	1.3E+0 1	2.8E+0 0	1.5E+0 1	3.4E+0 0	1	3.1E+00
153	1.1E+0 4	2.5E+0 2	1.2E+0 2	3.8E+0 0	2.1E+0 0	4.4E+01	8.4E+0 0	5.9E+0 0	2.8E+0 1	8.6E+0 0	2.7E+0 0	1.5E+0 0	1.7E+0 0	5.3E+01	1.3E+0 0	8.2E+02	1	3.1E+00
154	1.6E+0 4	4.7E+0 2	4.4E+0 2	1.2E+0 1	1.8E+0 1	6.0E+0 0	1.2E+0 2	4.8E+0 1	2.8E+0 2	8.2E+0 1	2.6E+0 1	1.2E+0 1	5.5E+0 0	1.6E+0 0	3.3E+0 0	8.8E+01	1	3.0E+00
155	6.5E+0 3	2.3E+0 2	1.2E+0 2	6.1E+0 0	3.2E+0 0	4.2E+01	2.2E+0 1	1.1E+0 1	8.6E+0 1	2.5E+0 1	7.8E+0 0	3.6E+0 0	2.8E+0 0	7.0E+02	1.6E+0 0	8.5E+02	1	3.0E+00
156	7.4E+0 3	1.8E+0 2	1.2E+0 2	7.1E+0 0	3.8E+0 0	6.0E+01	2.7E+0 1	1.4E+0 1	1.0E+0 2	2.9E+0 1	9.0E+0 0	3.9E+0 0	3.2E+0 0	1.1E+01	1.9E+0 0	1.1E+01	1	3.0E+00
157	9.8E+0 3	3.6E+0 2	1.9E+0 2	7.3E+0 0	1.6E+0 1	3.7E+0 0	3.4E+0 1	1.3E+0 1	1.1E+0 2	2.5E+0 1	1.1E+0 1	4.4E+0 0	1.9E+0 0	5.2E+01	1.8E+0 0	5.7E+01	1	3.0E+00
158	3.0E+0 4	6.5E+0 2	7.2E+0 2	1.2E+0 1	3.5E+0 0	1.1E+0 0	1.6E+0 1	3.6E+0 0	1.6E+0 2	4.9E+0 1	1.2E+0 1	6.0E+0 0	5.8E+0 0	2.6E+01	1.1E+0 1	3.7E+01	1	3.0E+00
159	5.4E+0 3	1.7E+0 2	1.1E+0 2	4.3E+0 0	4.0E+0 0	4.9E+01	1.3E+0 1	8.0E+0 0	5.5E+0 1	1.8E+0 1	5.2E+0 0	2.1E+0 0	3.0E+0 0	2.5E+01	2.1E+0 0	8.5E+02	1	3.0E+00
160	1.1E+0 4	3.3E+0 2	1.9E+0 2	4.4E+0 0	3.4E+0 0	6.1E+01	1.1E+0 1	8.4E+0 0	3.1E+0 1	1.2E+0 1	3.7E+0 0	1.5E+0 0	2.8E+0 0	3.2E+01	2.6E+0 0	1.5E+01	1	3.0E+00
161	8.9E+0 4	2.0E+0 3	2.7E+0 4	7.4E+0 2	1.6E+0 0	3.1E+01	1.6E+0 0	2.9E+01	2.0E+0 0	5.9E+01	1.1E+01	3.0E+02	1.1E+01	2.8E+02	4.7E+02	2.1E+02	1	3.0E+00
162	9.6E+0 4	2.0E+0 3	2.7E+0 4	7.3E+0 2	1.5E+0 0	2.9E+01	1.4E+0 0	2.7E+01	1.9E+0 0	5.7E+01	1.1E+01	3.0E+02	1.1E+01	2.8E+02	4.4E+02	2.0E+02	1	3.0E+00
163	9.1E+0 4	1.9E+0 3	2.7E+0 4	7.3E+0 2	1.6E+0 0	3.0E+01	1.5E+0 0	2.8E+01	1.9E+0 0	5.8E+01	1.1E+01	3.0E+02	1.1E+01	2.8E+02	4.6E+02	2.0E+02	1	3.0E+00
164	8.8E+0 4	2.0E+0 3	2.7E+0 4	7.5E+0 2	1.7E+0 0	3.2E+01	1.6E+0 0	3.0E+01	2.0E+0 0	5.9E+01	1.2E+01	3.0E+02	1.2E+01	2.8E+02	4.9E+02	2.1E+02	1	3.0E+00
165	8.7E+0 4	1.9E+0 3	3.1E+0 4	6.9E+0 2	1.7E+0 0	3.2E+01	1.6E+0 0	2.9E+01	2.0E+0 0	6.0E+01	1.2E+01	2.4E+02	1.2E+01	7.8E+03	5.0E+02	1.3E+03	1	3.0E+00
166	7.4E+0 4	1.9E+0 3	2.5E+0 4	7.0E+0 2	1.6E+0 0	3.0E+01	1.5E+0 0	2.8E+01	1.9E+0 0	6.1E+01	1.1E+01	3.8E+02	1.1E+01	2.7E+02	4.8E+02	1.9E+02	1	3.0E+00
167	8.0E+0 3	1.9E+0 4	2.6E+0 4	7.2E+0 2	1.6E+0 0	3.0E+01	1.5E+0 0	2.9E+01	2.0E+0 0	6.0E+01	1.1E+01	2.9E+02	1.1E+01	2.8E+02	4.7E+02	2.0E+02	1	3.0E+00
168	9.2E+0 4	2.0E+0 3	2.7E+0 4	7.5E+0 2	1.6E+0 0	3.2E+01	1.6E+0 0	3.0E+01	2.0E+0 0	5.9E+01	1.2E+01	3.1E+02	1.1E+01	8.9E+02	4.7E+02	2.1E+02	1	3.0E+00

169	9.1E+0 4	2.0E+0 3	2.8E+0 4	7.7E+0 2	1.7E+0 0	3.2E+01	1.6E+0 0	3.1E+01	2.0E+0 0	6.0E+01	1.2E+01	3.1E+02	1.1E+01	3.0E+02	4.7E+02	2.1E+02	1	3.0E+00
170	9.1E+0 4	2.0E+0 3	2.8E+0 4	7.8E+0 2	1.7E+0 0	3.3E+01	1.6E+0 0	3.1E+01	2.1E+0 0	6.2E+01	1.2E+01	3.2E+02	1.2E+01	3.1E+01	4.7E+02	2.1E+02	1	3.0E+00
171	2.1E+0 2	2.4E+0 1	2.0E+0 0	4.8E+01	7.4E+01	8.3E+02	2.8E+01	5.3E+02	8.2E+02	1.6E+02	8.6E+03	1.8E+03	2.2E+02	3.4E+03	4.3E+02	7.4E+03	1	3.0E+00
172	2.1E+0 2	2.4E+0 1	2.1E+0 0	4.9E+01	7.5E+01	8.4E+02	2.9E+01	5.4E+03	8.7E+02	1.6E+02	8.5E+03	1.9E+03	2.2E+01	3.5E+03	4.4E+02	7.5E+03	1	3.0E+00
173	2.1E+0 2	2.4E+0 1	2.2E+0 0	5.0E+01	7.7E+01	8.6E+02	3.0E+01	5.4E+02	9.2E+02	1.7E+02	8.4E+03	1.9E+03	2.3E+02	3.6E+03	4.6E+02	7.7E+03	1	3.0E+00
174	2.2E+0 2	2.5E+0 1	2.3E+0 0	5.1E+01	7.8E+01	8.8E+02	3.1E+01	5.5E+02	9.7E+02	1.8E+02	8.3E+03	2.0E+03	2.3E+02	3.7E+03	4.7E+02	7.8E+03	1	2.9E+00
175	2.2E+0 2	2.5E+0 1	2.4E+0 0	5.2E+01	8.0E+01	9.1E+02	3.2E+01	5.5E+02	1.0E+01	1.8E+02	8.9E+03	2.0E+03	2.3E+02	3.7E+03	4.8E+02	8.0E+03	1	2.9E+00
176	2.2E+0 2	2.5E+0 1	2.5E+0 0	5.2E+01	8.1E+01	9.3E+02	3.2E+01	5.6E+02	1.1E+01	1.9E+02	9.5E+03	2.1E+03	2.3E+02	3.8E+03	4.9E+02	8.2E+03	1	2.9E+00
177	2.2E+0 2	2.6E+0 1	2.8E+0 0	5.4E+01	8.4E+01	9.8E+02	3.4E+01	5.7E+02	1.2E+01	2.0E+02	1.1E+02	2.2E+03	2.3E+02	4.1E+03	5.2E+02	8.6E+03	1	2.9E+00
178	2.2E+0 2	2.6E+0 1	2.9E+0 0	5.5E+01	8.5E+01	1.0E+01	3.5E+01	5.7E+02	1.3E+01	2.1E+02	1.2E+02	2.3E+03	3.2E+02	4.2E+03	5.3E+02	8.8E+03	1	2.9E+00
179	2.2E+0 2	2.6E+0 1	3.0E+0 0	5.6E+01	8.7E+01	1.0E+01	3.5E+01	5.8E+02	1.3E+01	2.2E+02	1.3E+02	2.4E+03	2.3E+02	4.3E+03	5.4E+02	9.0E+03	1	2.9E+00
180	2.2E+0 2	2.6E+0 1	3.2E+0 0	5.7E+01	8.8E+01	1.0E+01	3.6E+01	5.9E+02	1.4E+01	2.3E+02	1.3E+02	2.4E+03	2.4E+02	4.4E+03	5.5E+02	9.2E+03	1	2.9E+00
191	1.9E+0 2	6.7E+0 2	3.4E+0 2	5.0E+0 1	3.0E+0 0	6.1E+0 0	3.0E+0 0	1.5E+0 1	1.3E+0 2	3.4E+0 0	8.9E+0 0	4.9E+0 0	4.3E+0 0	1.7E+0 0	1.0E+0 0	3.5E+01	1	2.9E+00
192	2.3E+0 2	1.1E+0 1	7.0E+0 2	1.0E+0 2	7.1E+0 1	1.4E+0 1	6.8E+0 1	3.6E+0 1	4.9E+0 2	1.3E+0 2	2.2E+0 1	1.2E+0 1	1.1E+0 1	4.3E+0 0	1.9E+0 0	5.0E+01	1	2.9E+00
193	5.5E+0 1	4.7E+0 0	1.9E+0 2	5.0E+0 1	2.0E+0 1	4.2E+0 0	2.2E+0 1	1.4E+0 1	1.1E+0 2	4.1E+0 1	6.6E+0 0	4.8E+0 0	2.8E+0 0	1.1E+0 0	6.4E+01	1.9E+01	1	2.9E+00
194	1.5E+0 2	1.4E+0 1	4.6E+0 2	8.7E+0 1	2.0E+0 1	3.6E+0 0	3.2E+0 1	1.4E+0 1	3.0E+0 2	8.4E+0 1	1.6E+0 1	9.3E+0 0	6.9E+0 0	2.5E+0 0	1.0E+0 0	1.6E+01	1	2.9E+00
195	1.5E+0 2	5.8E+0 2	2.7E+0 2	4.4E+0 1	3.8E+0 1	7.7E+0 0	3.7E+0 1	2.1E+0 1	1.2E+0 2	3.4E+0 0	8.9E+0 0	5.4E+0 0	4.1E+0 0	1.6E+0 0	1.3E+0 0	4.7E+01	1	2.9E+00
196	1.2E+0 2	1.3E+0 2	7.8E+0 2	9.8E+0 1	5.0E+0 2	1.0E+0 2	1.5E+0 3	2.1E+0 2	2.2E+0 3	3.1E+0 2	1.4E+0 2	3.7E+0 1	7.6E+0 1	2.3E+0 1	3.5E+0 1	1.2E+0 1	1	2.9E+00
197	3.3E+0 1	1.7E+0 0	6.0E+0 2	5.4E+0 1	4.3E+0 3	1.9E+0 3	6.8E+0 3	2.4E+0 3	4.9E+0 3	1.3E+0 3	2.9E+0 2	1.6E+0 2	1.1E+0 2	3.3E+0 1	2.5E+0 2	2.3E+0 2	1	2.9E+00
198	1.5E+0 2	1.6E+0 2	8.1E+0 2	1.0E+0 2	1.4E+0 2	3.1E+0 2	5.0E+0 2	7.8E+0 1	1.1E+0 3	2.0E+0 2	6.5E+0 1	2.3E+0 1	3.0E+0 1	9.0E+0 0	1.1E+0 1	3.2E+0 0	1	2.9E+00
199	2.4E+0 2	1.6E+0 1	1.1E+0 3	1.1E+0 2	3.2E+0 2	1.1E+0 2	4.6E+0 2	1.4E+0 2	7.9E+0 2	2.4E+0 2	4.9E+0 1	2.7E+0 1	1.6E+0 1	5.2E+0 0	1.7E+0 1	1.3E+0 1	1	2.8E+00
200	3.3E+0 1	1.5E+0 0	8.8E+0 2	9.9E+0 1	1.3E+0 4	5.6E+0 3	2.6E+0 4	8.1E+0 3	5.9E+0 4	1.3E+0 4	3.9E+0 3	1.6E+0 3	7.7E+0 1	2.1E+0 1	8.5E+0 2	7.1E+0 2	1	2.8E+00
201	2.9E+0 2	1.6E+0 1	3.1E+0 2	3.6E+0 1	1.5E+0 1	6.9E+0 0	2.9E+0 1	1.4E+0 1	4.8E+0 1	2.9E+0 1	2.7E+0 0	4.2E+01	1.7E+0 0	2.9E+01	1.2E+0 0	1.7E+01	1	2.8E+00
202	1.5E+0 2	1.3E+0 2	3.6E+0 2	3.2E+0 1	4.6E+0 1	2.2E+0 1	2.6E+0 1	1.1E+0 1	7.3E+0 1	4.6E+0 0	3.5E+0 0	6.8E+01	2.4E+0 0	5.7E+01	1.4E+0 0	1.5E+01	1	2.8E+00
203	4.8E+0 2	2.3E+0 2	3.2E+0 2	5.0E+0 1	6.3E+0 1	1.2E+0 1	5.5E+0 1	2.7E+0 1	1.0E+0 2	5.6E+0 1	2.9E+0 0	5.9E+01	2.3E+0 0	9.1E+01	2.1E+0 0	4.4E+01	1	2.8E+00
204	1.3E+0 2	1.4E+0 2	2.8E+0 2	3.6E+0 1	2.4E+0 1	7.2E+0 0	7.8E+0 0	2.6E+0 1	7.8E+0 1	3.8E+0 1	4.0E+0 0	7.6E+01	4.6E+0 0	4.9E+01	2.3E+0 0	4.3E+01	1	2.8E+00
205	9.2E+0 1	1.5E+0 2	2.2E+0 2	3.5E+0 1	2.4E+0 1	1.3E+0 1	4.9E+0 1	1.3E+0 1	7.1E+0 1	2.4E+0 0	2.1E+0 0	3.6E+01	1.9E+0 0	5.0E+01	1.5E+0 0	4.0E+01	1	2.8E+00
206	1.0E+0 2	1.5E+0 1	3.0E+0 2	3.7E+0 1	3.9E+0 1	1.1E+0 1	8.6E+0 1	2.4E+0 1	1.0E+0 2	3.8E+0 1	2.7E+0 0	7.9E+01	3.9E+0 0	6.2E+01	2.7E+0 0	7.9E+01	1	2.8E+00



207	2.3E+0 2	1.4E+0 1	4.2E+0 2	3.5E+0 1	4.4E+0 1	1.9E+0 1	3.0E+0 1	1.7E+0 1	9.1E+0 1	4.0E+0 1	1.6E+0 0	5.0E-01 0	4.4E+0 0	6.4E-01 0	2.9E+0 0	2.6E-01 0	1	2.8E+00
208	3.6E+0 3	9.7E+0 1	1.5E+0 4	5.6E+0 2	2.0E+0 4	7.6E+0 3	2.7E+0 4	1.4E+0 4	1.0E+0 5	4.4E+0 4	6.3E+0 2	5.5E+0 2	5.4E+0 2	4.6E+0 2	9.5E+0 1	7.4E+0 1	1	2.8E+00
209	1.1E+0 2	1.7E+0 2	9.4E+0 2	1.3E+0 2	8.9E+1 1	6.6E+0 9	8.9E+1 1	5.3E+0 9	2.7E+1 2	2.5E+1 0	8.4E+1 1	8.5E+0 9	2.9E+1 0	2.9E+0 8	1.5E+1 2	1.5E+1 0	1	2.8E+00
210	1.3E+0 2	1.6E+0 1	4.5E+0 2	5.4E+0 1	1.3E+0 2	4.5E+0 1	1.2E+0 2	2.1E+0 1	3.0E+0 2	6.8E+0 1	4.7E+0 0	1.2E+0 0	4.7E+0 0	1.4E+0 0	3.3E+0 0	6.2E-01 0	1	2.8E+00
211	7.0E-02 0	4.8E-02 0	5.9E-01 0	3.0E-01 0	1.7E-02 0	6.2E-03 0	1.1E+0 0	2.7E-01 0	1.1E+0 0	5.4E-01 0	4.9E-02 0	2.8E-02 0	1.3E-02 0	6.3E-03 0	1.0E-02 0	3.0E-03 0	1	2.7E+00
212	7.1E-02 0	4.5E-02 0	6.5E-01 0	3.1E-01 0	3.5E-02 0	1.4E-02 0	1.2E+0 0	3.0E-01 0	1.3E+0 0	6.2E-01 0	5.1E-02 0	2.8E-02 0	1.6E-02 0	7.7E-03 0	1.2E-02 0	3.9E-03 0	1	2.7E+00
213	1.6E-01 0	7.6E-02 0	5.2E-01 0	1.7E-01 0	3.9E-02 0	1.6E-02 0	6.0E-01 0	1.7E-01 0	1.3E+0 0	5.1E-01 0	3.7E-02 0	2.2E-02 0	2.0E-02 0	8.6E-03 0	1.1E-02 0	2.9E-03 0	1	2.7E+00
214	6.5E-02 0	2.1E-02 0	5.8E-01 0	2.0E-01 0	2.6E-02 0	1.1E-02 0	8.9E-01 0	2.5E-01 0	5.6E-01 0	1.6E-01 0	3.6E-02 0	2.3E-02 0	7.4E-03 0	2.7E-03 0	1.4E-02 0	4.1E-03 0	1	2.7E+00
215	1.5E-01 0	2.7E-02 0	8.0E-01 0	1.8E-01 0	5.4E-02 0	1.8E-02 0	7.2E-01 0	2.1E-01 0	8.0E-01 0	2.2E-01 0	2.9E-02 0	1.9E-02 0	9.3E-03 0	3.7E-03 0	1.2E-01 0	3.9E-03 0	1	2.7E+00
216	1.2E-01 0	4.4E-02 0	7.0E-01 0	1.9E-01 0	2.3E-02 0	1.0E-02 0	7.7E-01 0	2.1E-01 0	1.1E+0 0	5.2E-01 0	3.9E-02 0	2.6E-02 0	1.5E-02 0	8.7E-03 0	9.3E-03 0	3.5E-03 0	1	2.7E+00
217	1.3E-01 0	2.5E-02 0	7.8E-01 0	2.0E-01 0	3.2E-02 0	1.2E-02 0	8.6E-01 0	2.4E-01 0	8.7E-01 0	2.4E-01 0	3.1E-02 0	2.1E-02 0	1.0E-02 0	3.8E-03 0	9.1E-03 0	3.8E-03 0	1	2.7E+00
218	1.5E-01 0	6.3E-02 0	1.1E+0 0	2.1E-01 0	2.7E-01 0	8.7E-03 0	1.7E-01 0	6.4E-02 0	2.7E+0 0	1.2E+0 0	4.5E-02 0	2.6E-02 0	6.4E-02 0	2.1E-02 0	7.2E-03 0	3.0E-03 0	1	2.7E+00
219	3.2E-01 0	1.6E-01 0	9.2E-01 0	2.2E-01 0	2.8E-01 0	7.3E-02 0	2.0E-01 0	7.4E-02 0	3.2E+0 0	1.2E+0 0	4.6E-02 0	2.7E-02 0	3.7E-02 0	1.9E-02 0	7.6E-03 0	3.3E-03 0	1	2.7E+00
220	2.6E-01 0	8.8E-02 0	1.0E+0 0	1.9E-01 0	2.5E-01 0	8.3E-02 0	2.9E-01 0	9.4E-02 0	2.9E+0 0	1.1E+0 0	4.6E-02 0	2.5E-02 0	5.4E-02 0	1.9E-02 0	8.0E-03 0	2.9E-03 0	1	2.7E+00
221	1.6E+0 0	4.8E-01 0	6.0E+0 0	1.5E+0 0	1.6E-03 0	5.5E-04 0	1.9E-01 0	5.3E-02 0	1.3E-01 0	3.5E-02 0	5.3E-02 0	3.2E-02 0	8.5E-03 0	2.5E-03 0	1.3E-02 0	3.7E-03 0	1	2.7E+00
222	2.8E+0 0	8.9E-01 0	3.9E+0 0	9.6E-01 0	1.7E-03 0	6.0E-04 0	1.8E-01 0	5.1E-02 0	5.9E-02 0	1.7E-02 0	4.7E-02 0	3.0E-02 0	4.2E-03 0	1.4E-03 0	1.4E-02 0	4.0E-03 0	1	2.7E+00
223	8.9E-01 0	2.8E-01 0	6.0E+0 0	1.6E+0 0	7.5E-04 0	2.2E-04 0	1.3E-01 0	4.3E-02 0	1.3E-01 0	4.3E-02 0	4.6E-02 0	2.9E-02 0	5.5E-03 0	2.0E-03 0	5.4E-03 0	1.9E-03 0	1	2.7E+00
224	1.7E+0 0	4.4E-01 0	1.8E+0 1	3.6E+0 0	1.3E-03 0	4.6E-04 0	3.5E-01 0	9.2E-02 0	5.9E-01 0	1.5E-01 0	1.2E-01 0	7.5E-02 0	4.0E-02 0	1.2E-02 0	2.4E-02 0	7.5E-03 0	1	2.6E+00
225	3.1E+0 0	7.4E-01 0	3.2E+0 1	5.3E+0 0	2.5E-03 0	8.3E-04 0	7.8E-01 0	2.0E-01 0	1.2E+0 0	3.0E-01 0	2.0E-01 0	1.3E-01 0	7.7E-02 0	2.4E-02 0	5.2E-02 0	1.6E-02 0	1	2.6E+00
226	5.9E+0 0	1.4E+0 0	1.8E+0 1	2.9E+0 0	3.6E-03 0	1.2E-03 0	8.4E-01 0	2.2E-01 0	4.2E-01 0	1.1E-01 0	1.4E-01 0	9.4E-02 0	2.8E-02 0	8.8E-03 0	5.7E-02 0	1.8E-02 0	1	2.6E+00
227	7.7E+0 0	2.4E+0 0	4.1E-01 0	1.9E-01 0	8.0E-04 0	2.6E-04 0	0.0E+0 0	0.0E+0 0	1.6E-03 0	7.2E-04 0	0.0E+0 0	0.0E+0 0	3.5E-04 0	1.8E-04 0	0.0E+0 0	0.0E+0 0	1	2.6E+00
228	5.7E+0 0	1.7E+0 0	1.6E+0 1	3.4E+0 0	9.1E-03 0	3.0E-03 0	8.1E-01 0	2.2E-01 0	4.2E-01 0	1.2E-01 0	1.6E-01 0	1.0E-01 0	3.6E-02 0	1.2E-02 0	7.5E-02 0	2.2E-02 0	1	2.5E+00
229	7.9E+0 0	2.8E+0 0	2.0E+0 0	9.7E-01 0	4.6E-03 0	1.7E-03 0	0.0E+0 0	0.0E+0 0	1.1E-02 0	4.9E-03 0	0.0E+0 0	0.0E+0 0	1.9E-03 0	9.9E-04 0	0.0E+0 0	0.0E+0 0	1	2.5E+00
230	1.4E+0 1	3.7E+0 0	4.9E-01 0	1.4E-01 0	5.9E-04 0	1.6E-04 0	0.0E+0 0	0.0E+0 0	8.3E-04 0	4.2E-04 0	0.0E+0 0	0.0E+0 0	2.7E-04 0	1.6E-04 0	0.0E+0 0	0.0E+0 0	1	2.5E+00
231	2.2E+0 5	1.8E+0 3	2.4E+0 4	2.2E+0 2	3.7E-04 2	7.4E-05 2	2.9E-04 2	7.1E-05 2	1.0E-03 2	3.6E-04 2	8.8E-05 2	3.2E-05 2	1.3E-04 2	3.5E-05 2	7.8E-05 2	1.7E-05 2	1	2.5E+00
232	7.4E+0 4	3.7E+0 3	2.8E+0 4	1.0E+0 3	2.0E-03 3	3.4E-04 3	6.7E-03 3	1.2E-03 3	1.6E-02 3	3.2E-03 3	1.2E-03 3	4.8E-04 3	7.7E-04 3	1.8E-04 3	3.1E-04 3	6.5E-05 3	1	2.5E+00
233	1.8E+0 5	2.0E+0 3	1.7E+0 4	3.4E+0 2	4.2E-04 2	6.5E-05 2	1.5E-03 2	2.2E-04 2	2.8E-03 2	5.4E-04 2	3.0E-04 2	7.4E-05 2	1.3E-04 2	3.2E-05 2	1.1E-04 2	2.2E-05 2	1	2.4E+00
234	1.7E+0 0	4.4E-01 0	1.8E+0 1	3.6E+0 0	1.3E-03 0	4.6E-04 0	3.5E-01 0	9.2E-02 0	5.9E-01 0	1.5E-01 0	1.2E-01 0	7.5E-02 0	4.0E-02 0	1.2E-02 0	2.4E-02 0	7.5E-03 0	1	2.4E+00

225	3.1E+0 0	7.4E-01	3.2E+0 1	5.3E+0 0	2.5E-03	8.3E-04	7.8E-01	2.0E-01	1.2E+0 0	3.0E-01	2.0E-01	1.3E-01	7.7E-02	2.4E-02	5.2E-02	1.6E-02	1	2.4E+00
226	5.9E+0 0	1.4E+0 0	1.8E+0 1	2.9E+0 0	3.6E-03	1.2E-03	8.4E-01	2.2E-01	4.2E-01	1.1E-01	1.4E-01	9.4E-02	2.8E-02	8.8E-03	5.7E-02	1.8E-02	1	2.4E+00
227	7.7E+0 0	2.4E+0 0	4.1E-01	1.9E-01	8.0E-04	2.6E-04	0.0E+0 0	0.0E+0 0	1.6E-03	7.2E-04	0.0E+0 0	0.0E+0 0	3.5E-04	1.8E-04	0.0E+0 0	0.0E+0 0	1	2.4E+00
228	5.7E+0 0	1.7E+0 0	1.6E+0 1	3.4E+0 0	9.1E-03	3.0E-03	8.1E-01	2.2E-01	4.2E-01	1.2E-01	1.6E-01	1.0E-01	3.6E-02	1.2E-02	7.5E-02	2.2E-02	1	2.3E+00
229	7.9E+0 0	2.8E+0 0	2.0E+0 0	9.7E-01	4.6E-03	1.7E-03	0.0E+0 0	0.0E+0 0	1.1E-02	4.9E-03	0.0E+0 0	0.0E+0 0	1.9E-03	9.9E-04	0.0E+0 0	0.0E+0 0	1	2.2E+00
230	1.4E+0 1	3.7E+0 0	4.9E-01	1.4E-01	5.9E-04	1.6E-04	0.0E+0 0	0.0E+0 0	8.3E-04	4.2E-04	0.0E+0 0	0.0E+0 0	2.7E-04	1.6E-04	0.0E+0 0	0.0E+0 0	1	2.1E+00

## PERFORMANCE AND SCALABILITY OF DEEP LEARNING MODELS TRAINED ON A HYBRID SUPERCOMPUTER: APPLICATION IN THE PREDICTION OF THE SHEAR STRENGTH OF SLENDER RC BEAMS

Nikolaos Bakas<sup>1</sup>, George Markou<sup>2</sup>, Dimos C. Charmpis<sup>3</sup> and Kyriakos  
Hadjiyiannakou<sup>4,1</sup>

<sup>1</sup>Computation-based Science and Technology Research Center, The Cyprus Institute  
20 Konstantinou Kavafi Street, 2121, Aglantzia Nicosia, Cyprus.  
e-mail: n.bakas@cyi.ac.cy

<sup>2</sup> Structures Division, Civil Engineering Department, University of Pretoria  
Hatfield Campus, 0028 Pretoria, South Africa.  
e-mail: george.markou@up.ac.za

<sup>3</sup> Department of Civil and Environmental Engineering, University of Cyprus  
75 Kallipoleos Str., P.O. Box 20537, 1678 Nicosia, Cyprus  
e-mail: charmpis@ucy.ac.cy

<sup>4</sup> University of Cyprus, Department of Physics  
e-mail: k.hadjiyiannakou@cyi.ac.cy

**Keywords:** High-Performance Computing, Deep Learning, Artificial Neural Network, Finite Elements, Nonlinear Analysis, Reinforced Concrete, Slender Beams.

**Abstract.** *Data-driven models employing artificial intelligence approaches have been increasingly utilized in structural analysis and design problems over the past two decades. The main applications involve the processing of datasets, which are gathered from experimentally derived records or obtained numerically, in order to develop closed-form formulae or numerical tools predicting quantities related to structural response and mechanical behaviour. Given that datasets are difficult to assemble due to the limited available information and the high cost entailed to enrich them, exhaustively processing the available data to produce the best possible prediction models is an essential task of particular interest. For specific applications, this exhaustive computing task involves large numbers of iterations performed to train detailed prediction models with large numbers of parameters. Despite the intense computational demands of such problems, limited research work exists on the scaling-up of the utilized algorithms on supercomputers. In this work, a distributed training and hyperparameter tuning algorithm is proposed for the modelling of the shear strength of slender beams without stirrups. The training dataset comprises results obtained from the detailed modelling and analysis of several beams with non-linear finite elements using the Reconan software. The results presented in this research work highlight the importance of optimally utilizing computational power for the solution of such problems. The developed computer code is available on GitHub.*

## 1 INTRODUCTION

Artificial intelligence techniques have emerged over the last decades as an effective and efficient tool to predict analysis outputs for computationally demanding engineering problems. Application areas requiring multiple analysis runs (design optimization, structural reliability, etc.) have largely benefited from various computational approaches eliminating the need for performing actual analyses by providing adequate estimations for the outputs of interest (e.g. [1, 2, 3, 4]).

The training process of an Artificial Intelligence model is itself a demanding task in terms of computational resources. Particularly, an Artificial Neural Network can comprise millions of parameters to train via iterative procedures, such as the stochastic gradient descent algorithm. These algorithms yield data structures that frequently cannot fit in the GPU (graphics processing unit) accelerators' RAM; hence parallelization is vital for the accomplishment of the training task, and obtaining accurate results. The optimization algorithms employed during the training process of a deep network can be parallelized by following either of two main routes. The first one is data parallelism [5, 6, 7], which foresees the splitting of the "batch of samples" (utilized in each iteration) into a number of smaller mini-batches, which are processed in parallel, depending on the number of available resources (GPUs). Alternatively, we may use model parallelism [8], by partitioning the deep learning model on distributed GPUs.

Despite the fast-pacing growth of deep learning, along with the vast need for computational resources, there are rather limited relevant engineering applications reported in the literature [9, 10, 11, 12, 13], none of which concerns reinforced concrete (RC) structures or slender beams. The purpose of this work is to investigate deep-learning algorithms for the prediction of the shear strength of RC beams. For the needs of this research work, detailed 3D finite element (FE) modelling of RC structures is adopted [14, 15, 16, 17, 18], in order to develop a large database of results on slender RC beams without stirrups. The numerically generated data set is then used to train models to predict the beams' shear strength. A new algorithm is designed and programmed, in order to be able to develop multiple input files (FE models) and efficiently analyze them through the use of the software Reconan FEA [19]. The newly developed algorithm (Reconan Multirun) and Reconan FEA were used to generate and analyse approximately 36,000 slender RC beams without stirrups; the obtained results were used for the training of the predictive models.

## 2 DATABASE ASSEMBLY

For each beam considered, 10 independent variables (input) and one dependent variable, which is the load corresponding to the ultimate strength (output), are varied. Particularly, the basic geometric variables are varied for each beam: the net span  $L$  (mm), the width  $b$  (mm), and the effective depth  $d$  (mm) of the beam. Apart from these variables that affect the FE meshing of the beams, strength and material related variables are also varied, and, particularly,  $f_c$  (uniaxial compressive strength of a cylindrical specimen in MPa),  $E_c$  (concrete Young modulus in MPa),  $f_t$  (concrete tensile strength ratio),  $\beta$  (remaining shear capacity strength factor),  $E_s$  (steel Young modulus in MPa),  $f_y$  (steel yielding stress in MPa), and  $\rho$  (tensile longitudinal reinforcement ratio).

Sampling for the 10 independent variables was performed uniformly as per Table 1, with the variables' coefficient of variation  $c_v = \frac{\sigma}{m}$  (standard deviation over mean) being kept within the range 0.2 to 0.5 [20]. Hence, for each group of beams, different values for geometric and strength variables were generated, and the overall database is finally constituted of 35,849

Table 1: Statistical metrics of independent variables.

	$L$	$d$	$b$	$f_c$	$E_c$	$f_t$	$\beta$	$E_s$	$f_y$	$\rho$
Minimum	1500.0	260.0	200.0	20.0	25000.0	0.020	0.020	$1.90 \times 10^5$	400.0	0.0010
Maximum	8700.0	1310.0	600.0	60.0	35000.0	0.100	0.050	$2.10 \times 10^5$	600.0	0.0200
$c_v$	0.416	0.406	0.228	0.305	0.097	0.404	0.252	0.029	0.115	0.627

observations in total. Out of the total database population, 85% was used as a training set and the remaining 15% was used for testing.

### 3 BASELINE AND MACHINE LEARNING MODELS

The predictive modelling of the database was implemented by utilizing four machine learning (ML) methods, and in particular Linear Regression (LR), Non Linear - higher order Regression (NLR) [21], Random Forests (RF) [22] as implemented in [23], and Gradient Boosting [24] (GB) as implemented in [25]. The performance of each ML method varies, and the Mean Absolute Percentage Error (MAPE) [26] was used as a meaningful metric for engineering applications. The MAPE in the test set for the four methods was 10.843 (RF), 12.178 (GB), 22.036 (NLR), and 32.211 (LR). Random forests exhibit the lowest MAPE for the test set, while LR the highest, which was expected as it is the simplest (linear) model used. Nonlinear regression (NLR) exhibits higher error than RF and GB, however, the NLR model is useful due to the closed-form formula that it generates. The distribution of ML models' residuals exhibited a shape close to the Gaussian, for all methods except the linear regression, which was skewed. This is due to its inability to capture the non-linear behaviour of the variables included in the model, highlighting the need for more complex ML models.

### 4 DISTRIBUTED DEEP LEARNING

PyTorch was used herein which is an “imperative style, high-performance deep learning library” [27], distinguished for scientific as well as industrial projects, due to a straightforward yet efficient implementation of an automatic differentiation algorithm [28]. For multi-GPU training, the Horovod [29] was implemented, a library that has been developed at Uber. Particularly, by using Horovod, one may take a single-GPU training script and efficiently scale it to run across many GPUs in parallel. With MPI commands [30], each process is initialized and is assigned its MPI rank in a straightforward manner, which is achieved with fewer code changes compared to other approaches. Ultimately, Horovod scripts can run on a single-GPU, multiple-GPUs, or even multiple hosts without any further code changes. Algorithms on various experiments were tested for the needs of this research work on the Cyclone Supercomputer<sup>1</sup>, utilizing PyTorch for computer vision as well as regression tasks<sup>2</sup>, highlighting the efficiency of data parallelism, as well as the scaling-up capabilities compared with standard ML platforms, such as Kaggle and Google Colab.

#### 4.1 Parallel Stochastic Gradient Descent

In Stochastic Gradient Descent, at each iteration, a random data-point  $i$  is selected, the Loss Function for this data-point is differentiated, and then the weights for the entire network are

<sup>1</sup><https://hpcf.cyi.ac.cy/>

<sup>2</sup><https://github.com/CaSToRC-CyI/artificial-intelligence-hpc>



updated. In mini-batch Stochastic Gradient Descent,  $i$  is the current “batch” of data, which is a subset of all dataset indices. The parallelization is performed at this point, by updating the weights for all batches in parallel. Hence, in Parallel Stochastic Gradient Descent, for each GPU (in parallel) a random data-point is selected, for which the gradient is computed and the weights are mixed. The average for the mixing of the weights can be implemented for this purpose, or other methods, such as ensembles, AdaSum, etc. Afterwards, the update of the weights for all GPUs takes place. In order to perform this operation in parallel, the utilization of MPI<sup>3</sup> framework is required, so as to gather the results among all GPUs, reduce, and broadcast them across all available GPUs again. This algorithmic procedure is described in Figure 1.

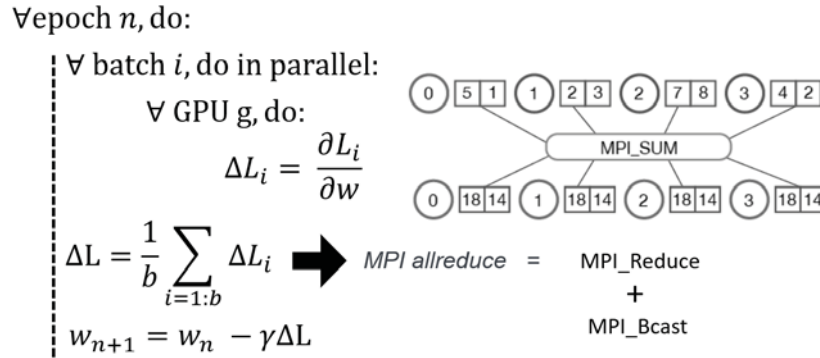


Figure 1: Parallel Stochastic Gradient Descent.

In general, it applies that, when using larger batch sizes the procedure becomes faster, and when adopting smaller batch sizes it becomes more accurate. In any case, the batch must fit into the relevant hardware memory, so the utilization of a larger number of nodes is required when a GPU cannot handle the batch size. Furthermore, in practice, the weights’ mix causes some accuracy losses. However, all these aspects regarding the computational behaviour of the Parallel Stochastic Gradient Descent procedure are not always absolutely valid, as the loss function is a highly non-linear function of the Artificial Neural Network’s (ANN’s) weights and depends on the dataset’s particular features, thus the computational procedure’s behaviour cannot be predicted. Therefore, the training of the network has to be performed by investigating a variety of architectures. In order to effectively treat this issue, hyperparameter tuning is adopted in the present work, and, ultimately, the training of a very large network on Cyclone supercomputer is attempted.

## 4.2 Hyperparameter tuning

In order to investigate the effect of the network’s hyperparameters, the Ray-Tune<sup>4</sup> module of PyTorch is implemented. Particularly, a number of ANNs are constructed by varying the batch size, the drop-out ratio, the number of Epochs and neurons, as well as the learning rate. Subsequently, the training of the networks is conducted. Accordingly, for each training example, the time for the training is recorded, while the final loss function and the ratio among the validation and train loss *Ratio V-T* are computed. The results obtained are presented in the Appendix. This

<sup>3</sup><https://mpitutorial.com/tutorials/mpi-reduce-and-allreduce/>

<sup>4</sup>[https://pytorch.org/tutorials/beginner/hyperparameter\\_tuning\\_tutorial.html](https://pytorch.org/tutorials/beginner/hyperparameter_tuning_tutorial.html)

is a time-consuming procedure, therefore, it was found useful to identify an optimal drop-out region of ratios [31]. As depicted in Figure 2, it can be concluded that, for lower drop-out values, the corresponding values of the loss function are also lower. However, as will be explained below, the drop-out could not be zero.

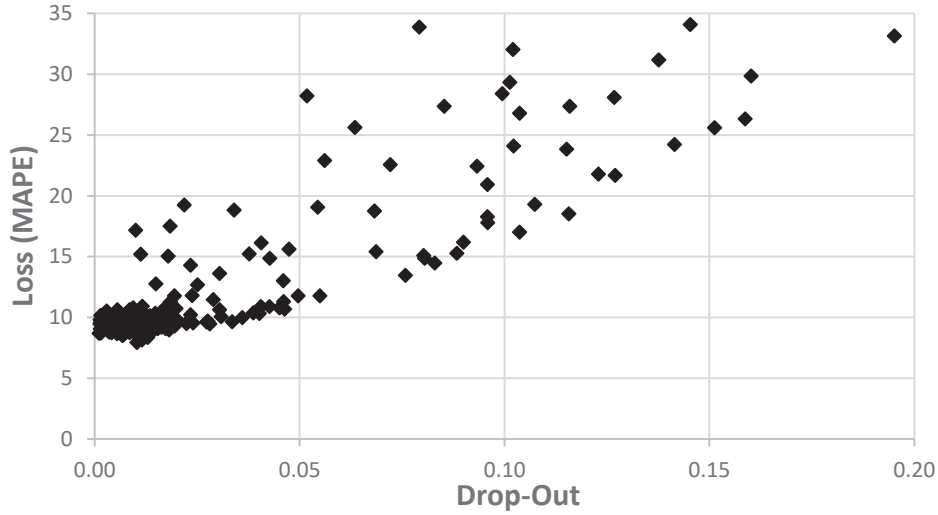


Figure 2: Ray-Tune results.

### 4.3 Combination of MPI & Horovod

During the training of an ANN, the loss function is automatically recorded, as loss is the core function that is differentiated to update the weights. In engineering applications, the Mean Squared Error (MSE) does not offer meaningful information, and the MAPE is being utilized as a more practical metric. Accordingly, as the best ANN's architecture is not known in advance, and given that multiple experiments must be performed, it is necessary to record the MAPE during training in real-time. However, as the data are split and reside at many GPUs, an operator should be implemented that gathers the individual predictions to obtain an aggregated metric for the dataset as a whole.

For this purpose, a mix of Horovod with MPI is proposed. In Figure 3, three code snippets are depicted describing the implementation of such an operation. The overall operation starts with the initialisation of vector *pred* in the code at the upper right part of Figure 3, which is used later as a container of all results. The code at the upper left part imports the MPI module from *mpi4py* and gets the rank of each GPU. Afterwards, as shown in the code at the bottom-left part of Figure 3, after each step of the optimizer, a barrier is set to wait for all GPUs to finish with their numerical processes. Then, the responses *y\_train\_pred* of each GPU are stored in vector *pred\_i* and, with the *comm.gather* command, all results are placed in *pred\_i*. Finally, an additional barrier is introduced to wait for all GPUs to finish and concatenate the results in vector *pred* only for rank 0. At this stage, vector *pred* holds the concatenated predictions and can be utilized to calculate the MAPE.

```
from mpi4py import MPI
comm = MPI.COMM_WORLD
rank = comm.Get_rank()
torch.manual_seed(0)
```

```
for e in tqdm(range(1, EPOCHS+1)):
    if rank == 0:
        t1=time()
        pred = np.empty(0)
        predV = np.empty(0)
    else:
        pred = None
        predV = None
```

```
optimizer.step()
comm.Barrier()
pred_i = copy(y_train_pred[:,0])
pred_i = comm.gather(pred_i, root=0)
comm.Barrier()
if rank == 0:
    for ii in range(len(pred_i)):
        pred = np.concatenate((pred, pred_i[ii].detach().cpu().numpy()), axis=0)
comm.Barrier()
```

Figure 3: Combination of MPI and Horovod.

#### 4.4 Parallel training

Figure 4 demonstrates the learning curves for the model without using a drop-out and with a 10% drop-out. In the case of no drop-out (Figure 4, left), even though there is in general a decreasing tendency in MAPE with the number of epochs, a number of significant peaks are evident. This can be interpreted as an effect of the averaging of the weights in parallel, which is a source of error. However, with the utilisation of a 10% drop-out (Figure 4, right), smoother learning curves are achieved and the aforementioned phenomenon seems to be not activated. Furthermore, it should be stressed that the validation curve for 10% drop-out is lower than the training curve, which is very important for the generalisation of the results.

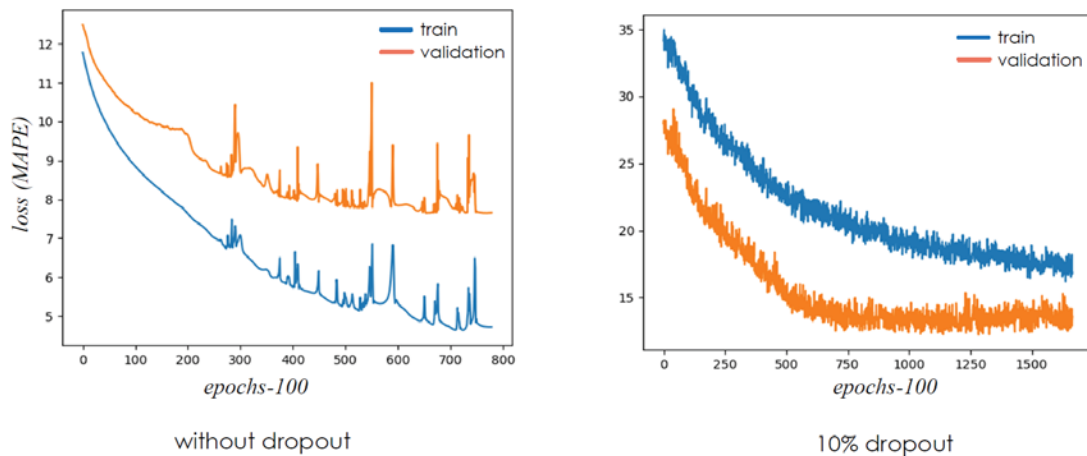


Figure 4: Drop-out effect on the loss function during training in parallel. The model with drop-out exhibits a validation loss history with lower values than the corresponding train curve.

It is noteworthy to state that a variety of experiments was performed to attain an optimal drop-out ratio. Figure 5 presents results for a drop-out equal to 0.01. As can be seen at the right part of Figure 5, when the validation curve is higher than the training curve, it practically stabilizes around a constant value. This is helpful during training, as over-training of the network will not cause over-fitting of the derived predictive model.

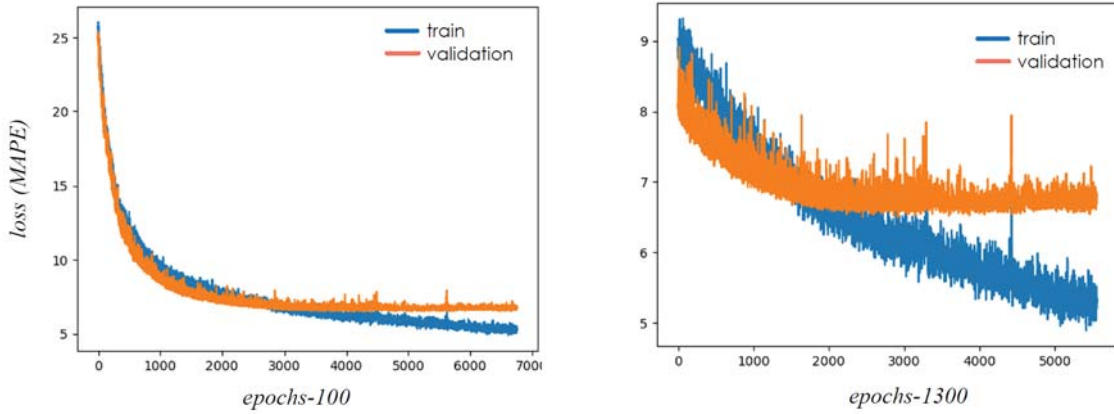


Figure 5: Results for low drop-out=0.01.

## 5 CONCLUSIONS

The numerical experiments performed in the present work comprised networks with large numbers of neurons, and thus, weights. For example, a network with 1000 neurons per layer and 10 layers corresponds to approximately 10 million weights to be optimised. As the most suitable network architecture is not known a-priori, several experiments need to be performed towards establishing the minimum possible error. Hence, computational power is vital for the best possible accuracy of the predictions.

It was also found that using PyTorch and Horovod as a functional solution for running deep-learning models on Cyclone Supercomputer is a very efficient approach. Furthermore, according to the parametric investigation performed in this research work, deep learning exhibited high accuracy in comparison to other ML methods. The best loss attained (MAPE) was 5.94%, while with Random Forests the corresponding loss was 10.7%, with Gradient Boosting 12.7%, Non-Linear Regression 24.0%, while Linear Regression had the worst numerical response with 32.3% loss.

The dataset under study comprised values with an increment of 10 kN and an average of 98.22 kN, thus an error  $\frac{10/2}{98.22} = 5.091$  inevitably occurs on average. Henceforth, any improvement of the 5.94% loss attained would be trivial. This highlights the power of deep learning on one hand, however, the computational demand for training as well as optimising the architecture of such networks is very expensive. Distributed training made these operations possible herein, achieving both efficient and accurate results.

## ACKNOWLEDGEMENTS

This work used resources from Cyclone Supercomputer<sup>5</sup> and was funded by the EuroCC project GA 951732. The use of computer resources under project Ispre519s1 of The Cyprus Institute is also acknowledged.

## REFERENCES

- [1] N. D. Lagaros, D. C. Charmpis, and M. Papadrakakis, “An adaptive neural network strategy for improving the computational performance of evolutionary structural

<sup>5</sup><https://hpcf.cyi.ac.cy/>

- optimization,” *Computer Methods in Applied Mechanics and Engineering*, vol. 194, no. 30, pp. 3374–3393, 2005. [Online]. Available: <https://doi.org/10.1016/j.cma.2004.12.023>
- [2] V. Sundar and M. D. Shields, “Surrogate-enhanced stochastic search algorithms to identify implicitly defined functions for reliability analysis,” *Structural Safety*, vol. 62, pp. 1–11, 2016. [Online]. Available: <https://doi.org/10.1016/j.strusafe.2016.05.001>
- [3] A. Roy, R. Manna, and S. Chakraborty, “Support vector regression based metamodeling for structural reliability analysis,” *Probabilistic Engineering Mechanics*, vol. 55, pp. 78–89, 2019. [Online]. Available: <https://doi.org/10.1016/j.probengmech.2018.11.001>
- [4] K. Singh and R. Kapania, “Alga: Active learning-based genetic algorithm for accelerating structural optimization,” *AIAA Journal*, vol. 59, no. 1, pp. 330–344, 2021. [Online]. Available: <https://doi.org/10.2514/1.J059240>
- [5] H. Li, A. Kadav, E. Kruus, and C. Ungureanu, “Malt: distributed data-parallelism for existing ml applications,” in *Proceedings of the Tenth European Conference on Computer Systems*, 2015, pp. 1–16.
- [6] C.-C. Chen, C.-L. Yang, and H.-Y. Cheng, “Efficient and robust parallel dnn training through model parallelism on multi-gpu platform,” *arXiv preprint arXiv:1809.02839*, 2018.
- [7] C. J. Shallue, J. Lee, J. Antognini, J. Sohl-Dickstein, R. Frostig, and G. E. Dahl, “Measuring the effects of data parallelism on neural network training,” *arXiv preprint arXiv:1811.03600*, 2018.
- [8] J. H. Park, G. Yun, M. Y. Chang, N. T. Nguyen, S. Lee, J. Choi, S. H. Noh, and Y.-r. Choi, “Hetpipe: Enabling large dnn training on (whimpy) heterogeneous gpu clusters through integration of pipelined model parallelism and data parallelism,” in *2020 USENIX Annual Technical Conference (USENIX ATC 20)*, 2020, pp. 307–321.
- [9] D. Abueidda, S. Koric, and N. Sobh, “Topology optimization of 2d structures with nonlinearities using deep learning,” *Computers and Structures*, vol. 237, 2020.
- [10] A. Gorshenin and V. Kuzmin, “Analysis of configurations of lstm networks for medium-term vector forecasting,” *Informatika i ee Primeneniya*, vol. 14, no. 1, pp. 10–16, 2020.
- [11] N. Do, A. Taberner, and B. Ruddy, “Design of a linear permanent magnet transverse flux motor for needle-free jet injection,” 2019.
- [12] R. Miller, B. Moore, H. Viswanathan, and G. Srinivasan, “Image analysis using convolutional neural networks for modeling 2d fracture propagation,” vol. 2017-November, 2017, pp. 979–982.
- [13] A. Oishi and G. Yagawa, “Computational mechanics enhanced by deep learning,” *Computer Methods in Applied Mechanics and Engineering*, vol. 327, pp. 327–351, 2017, advances in Computational Mechanics and Scientific Computation—the Cutting Edge. [Online]. Available: <https://doi.org/10.1016/j.cma.2017.08.040>



- [14] G. Markou and M. Papadrakakis, “Accurate and computationally efficient 3d finite element modeling of rc structures,” *Computers & Concrete*, vol. 12, 2013.
- [15] C. Mourlas, M. Papadrakakis, and G. Markou, “A computationally efficient model for the cyclic behavior of reinforced concrete structural members,” *Engineering Structures*, vol. 141, 2017.
- [16] G. Markou, C. Mourlas, H. Bark, and M. Papadrakakis, “Simplified hysteresis non-linear simulations of a full-scale multistory retrofitted rc structure that undergoes multiple cyclic excitations – an infill rc wall retrofitting study,” *Engineering Structures*, vol. 176, 2018.
- [17] G. Markou, C. Mourlas, and M. Papadrakakis, “A hybrid finite element model (hysteresis) for the non-linear 3d cyclic simulation of rc structure,” *International Journal of computational Methods*, vol. 16, 2019.
- [18] G. Markou and W. Roeloffze, “Finite element modelling of plain and reinforced concrete specimens with the kotsovos and pavlovic material model, smeared crack approach and fine meshes,” *International Journal of Damage Mechanics*, 2021.
- [19] G. Markou, “v2.00,” *Reconan, F.E.A. - User’s Manual*, 2020.
- [20] L. H. Koopmans, D. B. Owen, and J. I. Rosenblatt, “Confidence Intervals for the Coefficient of Variation for the Normal and Log Normal Distributions,” *Biometrika*, 2006.
- [21] N. P. Bakas, “NOESYS-AI Regression: A generic framework for predictive modeling and sensitivity analysis,” 2018. [Online]. Available: <https://noesys.net/regression-and-sensitivity-analysis/>
- [22] L. Breiman, “Random Forests,” *Machine learning*, vol. 45, no. 1, pp. 5–32, 2001.
- [23] B. Sadeghi, “DecisionTree.jl,” 2013. [Online]. Available: <https://github.com/bensadeghi/DecisionTree.jl>
- [24] J. H. Friedman, “Stochastic gradient boosting,” *Computational statistics & data analysis*, vol. 38, no. 4, pp. 367–378, 2002.
- [25] B. Xu and T. Chen, “Xgboost.jl,” 2014. [Online]. Available: <https://github.com/dmlc/XGBoost.jl>
- [26] T. Dimopoulos, H. Tyralis, N. P. Bakas, and D. Hadjimitsis, “Accuracy measurement of Random Forests and Linear Regression for mass appraisal models that estimate the prices of residential apartments in Nicosia, Cyprus,” *Advances in Geosciences*, vol. 45, pp. 377–382, 2018.
- [27] A. Paszke, S. Gross, F. Massa, A. Lerer, J. Bradbury, G. Chanan, T. Killeen, Z. Lin, N. Gimelshein, L. Antiga *et al.*, “Pytorch: An imperative style, high-performance deep learning library,” *arXiv preprint arXiv:1912.01703*, 2019.
- [28] A. Paszke, S. Gross, S. Chintala, G. Chanan, E. Yang, Z. DeVito, Z. Lin, A. Desmaison, L. Antiga, and A. Lerer, “Automatic differentiation in pytorch,” 2017.

- [29] A. Sergeev and M. D. Balso, “Horovod: fast and easy distributed deep learning in TensorFlow,” *arXiv preprint arXiv:1802.05799*, 2018.
- [30] L. Clarke, I. Glendinning, and R. Hempel, “The mpi message passing interface standard,” in *Programming environments for massively parallel distributed systems*. Springer, 1994, pp. 213–218.
- [31] N. Srivastava, G. Hinton, A. Krizhevsky, I. Sutskever, and R. Salakhutdinov, “Dropout: a simple way to prevent neural networks from overfitting,” *The journal of machine learning research*, vol. 15, no. 1, pp. 1929–1958, 2014.

# APPENDIX: HYPERPARAMETER TUNING RESULTS

Loss	Batch size	Drop-out	Epochs	#neurons	Learning Rate	Ratio V-T	Time
7.92	4096	0.0103	1418	1906	0.00086	0.849	981
8.13	256	0.0116	906	228	0.00034	0.872	679
8.35	512	0.0130	681	201	0.00035	0.755	343
8.50	2048	0.0068	677	580	0.00030	0.947	262
8.55	2048	0.0071	1193	566	0.00038	1.098	461
8.65	4096	0.0055	1065	1511	0.00072	1.092	632
8.68	256	0.0011	1358	758	0.00013	2.761	1017
8.71	512	0.0016	1047	1564	0.00021	2.313	730
8.72	1024	0.0105	1244	520	0.00015	1.009	500
8.72	2048	0.0086	1272	779	0.00096	1.077	510
8.73	256	0.0042	1570	1852	0.00075	1.652	1725
8.74	1024	0.0102	763	479	0.00055	0.992	309
8.78	512	0.0103	803	794	0.00002	0.841	415
8.79	4096	0.0036	691	1969	0.00088	0.998	490
8.83	4096	0.0094	1291	1305	0.00028	1.085	698
8.84	2048	0.0079	1318	1184	0.00064	1.022	608
8.84	4096	0.0108	1272	630	0.00090	0.933	594
8.88	4096	0.0122	1352	1110	0.00040	1.000	718
8.91	2048	0.0092	1320	1044	0.00010	1.062	565
8.92	512	0.0019	1039	596	0.00027	2.049	501
8.94	512	0.0085	683	1435	0.00096	1.071	442
8.97	512	0.0182	950	1669	0.00098	0.889	694
8.98	1024	0.0144	788	880	0.00016	0.926	317
8.99	4096	0.0137	956	1221	0.00018	0.892	527
8.99	2048	0.0095	635	1403	0.00039	1.019	328
9.00	4096	0.0146	745	744	0.00046	0.780	353
9.02	1024	0.0108	610	1465	0.00095	0.886	346
9.05	1024	0.0134	1473	530	0.00037	1.074	586
9.05	4096	0.0032	854	686	0.00035	1.202	389
9.05	2048	0.0014	796	1266	0.00014	1.784	386
9.07	512	0.0154	770	1411	0.00094	0.947	473
9.07	2048	0.0173	888	1397	0.00097	0.832	448
9.08	2048	0.0044	963	1245	0.00066	1.464	442
9.09	4096	0.0035	604	1955	0.00097	0.972	440
9.10	1024	0.0016	3177	711	0.00011	2.595	1186
9.11	1024	0.0183	1220	1471	0.00079	0.953	691
9.11	2048	0.0050	1393	1455	0.00045	1.309	737
9.13	2048	0.0112	1061	913	0.00086	1.046	434
9.13	4096	0.0103	858	1120	0.00018	0.912	438
9.15	1024	0.0137	443	680	0.00009	0.742	177
9.15	4096	0.0123	688	1887	0.00083	0.862	484
9.15	4096	0.0154	1473	1157	0.00052	0.970	786
9.17	1024	0.0030	1600	1363	0.00098	1.862	870
9.18	2048	0.0041	821	931	0.00096	1.364	330
9.18	2048	0.0149	1477	1410	0.00015	1.090	729
9.18	4096	0.0024	773	1290	0.00023	1.445	419
9.19	1024	0.0163	778	404	0.00042	0.840	324
9.19	512	0.0104	805	975	0.00010	1.137	406
9.20	4096	0.0187	1232	1076	0.00011	0.761	603
9.21	1024	0.0159	309	376	0.00074	0.701	126

9.21	2048	0.0048	568	1873	0.00027	1.101	384
9.23	2048	0.0071	807	726	0.00042	1.143	320
9.23	2048	0.0101	1059	1917	0.00091	0.950	726
9.25	1024	0.0150	788	772	0.00031	0.956	297
9.26	2048	0.0074	879	1037	0.00097	1.180	378
9.27	512	0.0195	860	723	0.00010	0.855	443
9.28	1024	0.0131	516	820	0.00003	0.719	203
9.28	4096	0.0158	1402	557	0.00013	0.776	702
9.29	512	0.0154	1304	644	0.00093	1.109	639
9.30	2048	0.0050	1129	1441	0.00071	1.366	576
9.32	256	0.0092	1905	577	0.00020	1.490	1440
9.33	2048	0.0058	993	714	0.00019	1.137	358
9.34	2048	0.0031	959	1288	0.00045	1.563	447
9.35	256	0.0196	963	589	0.00038	0.960	715
9.36	2048	0.0098	716	1195	0.00050	1.068	316
9.37	512	0.0151	652	1756	0.00087	0.973	495
9.38	512	0.0116	905	816	0.00065	1.178	447
9.39	1024	0.0148	1128	1878	0.00090	0.967	783
9.41	2048	0.0023	1413	1650	0.00072	2.149	829
9.41	512	0.0136	229	695	0.00094	0.837	115
9.41	1024	0.0102	1412	610	0.00051	1.285	538
9.43	1024	0.0175	1441	1129	0.00094	1.026	680
9.43	512	0.0046	1225	1866	0.00046	1.829	980
9.44	2048	0.0193	513	1841	0.00023	0.797	334
9.44	4096	0.0042	1369	1646	0.00027	1.487	861
9.44	512	0.0066	1341	1767	0.00060	1.586	1056
9.44	1024	0.0198	1025	1113	0.00094	0.951	474
9.45	256	0.0281	495	652	0.00048	0.763	369
9.45	512	0.0180	619	1870	0.00012	0.991	506
9.45	512	0.0019	4715	525	0.00041	2.939	2458
9.46	2048	0.0014	1230	747	0.00067	2.091	464
9.47	2048	0.0100	792	1063	0.00030	1.042	338
9.48	256	0.0225	260	533	0.00066	0.754	194
9.48	512	0.0143	1114	1061	0.00052	1.185	588
9.49	2048	0.0105	1358	946	0.00094	1.224	509
9.49	1024	0.0163	1292	1825	0.00094	0.957	913
9.49	4096	0.0189	1355	1187	0.00036	0.892	749
9.50	2048	0.0194	792	1564	0.00053	0.674	430
9.51	512	0.0133	1324	1587	0.00095	1.198	942
9.51	1024	0.0110	1042	1044	0.00053	1.262	445
9.52	512	0.0145	1324	1426	0.00021	1.253	825
9.52	1024	0.0146	1150	667	0.00063	1.073	422
9.53	2048	0.0111	1448	931	0.00046	1.231	586
9.53	2048	0.0187	1065	1837	0.00067	0.904	708
9.53	4096	0.0089	633	1181	0.00038	0.951	327
9.53	2048	0.0051	532	530	0.00039	1.109	191
9.54	2048	0.0195	941	1357	0.00039	0.938	473
9.54	1024	0.0122	1070	885	0.00082	1.195	447
9.54	1024	0.0014	3511	795	0.00024	2.938	1423
9.54	4096	0.0075	1227	1781	0.00090	0.980	841
9.54	1024	0.0025	1966	1495	0.00063	2.386	1100

9.54	512	0.0241	295	515	0.00095	0.713	151
9.54	2048	0.0115	1155	1593	0.00070	1.117	660
9.55	4096	0.0182	586	946	0.00080	0.758	284
9.56	512	0.0053	1486	1014	0.00039	1.836	760
9.57	512	0.0021	1315	1058	0.00024	2.414	714
9.58	1024	0.0028	1137	1099	0.00058	2.039	523
9.58	1024	0.0037	1351	1345	0.00034	1.902	733
9.60	1024	0.0144	923	878	0.00086	1.079	378
9.61	512	0.0098	1354	526	0.00064	1.358	679
9.61	512	0.0274	668	992	0.00059	0.843	345
9.61	1024	0.0128	905	1632	0.00060	1.183	540
9.62	2048	0.0027	503	1779	0.00053	1.337	322
9.62	512	0.0116	1232	752	0.00026	1.291	633
9.63	256	0.0046	1132	1745	0.00016	1.939	1147
9.64	512	0.0336	408	768	0.00048	0.706	215
9.65	1024	0.0141	779	1132	0.00097	1.044	347
9.65	512	0.0185	675	1059	0.00041	1.008	339
9.65	512	0.0071	1171	912	0.00042	1.557	570
9.65	512	0.0227	674	194	0.00050	0.742	341
9.68	1024	0.0176	1035	1645	0.00068	1.037	666
9.69	4096	0.0078	961	1317	0.00061	1.197	551
9.69	1024	0.0103	1147	811	0.00032	1.287	454
9.69	256	0.0277	642	449	0.00025	0.793	476
9.69	1024	0.0116	1148	1601	0.00093	1.300	705
9.69	512	0.0136	585	1259	0.00043	1.116	328
9.71	4096	0.0120	1495	987	0.00064	1.107	719
9.72	256	0.0179	977	822	0.00010	1.068	738
9.72	4096	0.0023	863	795	0.00040	1.364	418
9.73	512	0.0026	3663	829	0.00014	2.670	1876
9.76	2048	0.0056	1358	1024	0.00066	1.513	560
9.77	512	0.0118	1393	1786	0.00053	1.374	1086
9.78	256	0.0013	4018	1386	0.00040	3.475	3436
9.79	1024	0.0184	881	1673	0.00020	1.060	561
9.79	4096	0.0117	1145	1912	0.00097	0.797	801
9.79	4096	0.0176	646	1405	0.00058	0.825	350
9.80	4096	0.0091	1292	1126	0.00060	1.154	647
9.80	4096	0.0120	631	1236	0.00092	0.920	325
9.81	512	0.0056	971	1278	0.00040	1.645	559
9.81	4096	0.0186	734	1985	0.00054	0.809	544
9.82	1024	0.0019	3403	672	0.00096	2.983	1390
9.83	512	0.0061	703	1132	0.00082	1.529	368
9.85	4096	0.0189	1478	1977	0.00049	0.951	1087
9.85	512	0.0130	828	1039	0.00060	1.196	426
9.85	1024	0.0147	1320	1253	0.00070	1.227	687
9.85	512	0.0149	519	894	0.00057	1.043	269
9.85	1024	0.0127	931	1211	0.00036	1.190	470
9.87	1024	0.0122	651	1545	0.00073	1.147	384
9.88	1024	0.0084	1342	1357	0.00022	1.567	724
9.88	512	0.0200	1300	1481	0.00076	1.102	858
9.89	1024	0.0125	831	977	0.00039	1.173	356
9.90	256	0.0177	103	945	0.00042	0.724	78



9.94	1024	0.0157	1420	1706	0.00020	1.268	918
9.95	1024	0.0185	875	1198	0.00075	1.024	453
9.95	1024	0.0047	1308	1208	0.00066	1.799	645
9.97	1024	0.0141	1351	1964	0.00012	1.315	1034
9.97	256	0.0361	656	638	0.00005	0.674	484
9.98	4096	0.0125	524	1680	0.00036	0.913	337
10.02	2048	0.0049	503	1808	0.00076	1.022	321
10.05	512	0.0309	607	225	0.00016	0.649	315
10.05	2048	0.0130	952	1242	0.00075	1.044	456
10.06	2048	0.0111	827	1697	0.00058	1.077	499
10.07	4096	0.0052	1105	1057	0.00063	1.295	572
10.08	1024	0.0164	1327	1600	0.00021	1.228	800
10.11	512	0.0116	1463	1972	0.00016	1.490	1317
10.12	4096	0.0077	923	1549	0.00065	1.135	572
10.13	256	0.0135	2635	1221	0.00044	1.477	2121
10.14	4096	0.0109	1227	1867	0.00058	1.175	845
10.14	4096	0.0185	822	1897	0.00081	0.786	574
10.14	2048	0.0127	923	1464	0.00073	1.030	501
10.15	1024	0.0162	1479	1675	0.00063	1.244	960
10.16	512	0.0015	4397	1666	0.00040	3.699	3244
10.18	512	0.0148	509	382	0.00003	0.680	251
10.22	256	0.0234	150	413	0.00014	0.648	113
10.22	1024	0.0165	3996	826	0.00018	1.489	1564
10.28	4096	0.0166	806	1132	0.00085	0.926	394
10.31	256	0.0402	222	794	0.00015	0.627	165
10.34	1024	0.0148	1329	1465	0.00034	1.316	750
10.36	256	0.0388	205	591	0.00088	0.653	156
10.46	1024	0.0182	240	422	0.00016	0.680	99
10.48	512	0.0174	1486	1345	0.00027	1.304	913
10.51	256	0.0029	4573	1540	0.00027	2.930	4303
10.60	1024	0.0190	1268	1809	0.00018	1.227	865
10.62	512	0.0305	978	766	0.00002	0.728	496
10.62	4096	0.0086	724	1294	0.00082	1.021	393
10.63	1024	0.0056	4784	1079	0.00043	2.569	2007
10.66	1024	0.0181	2242	1607	0.00024	1.465	1365
10.68	1024	0.0169	771	1243	0.00094	0.888	402
10.69	1024	0.0464	960	423	0.00021	0.664	380
10.72	4096	0.0199	543	1776	0.00082	0.832	351
10.75	256	0.0173	594	366	0.00001	0.679	458
10.78	512	0.0451	425	533	0.00087	0.690	216
10.79	2048	0.0095	650	1369	0.00081	1.079	331
10.88	4096	0.0185	586	752	0.00096	0.889	260
10.89	1024	0.0427	924	938	0.00058	0.795	404
10.90	512	0.0406	663	935	0.00037	0.780	344
10.91	1024	0.0116	607	527	0.00002	0.746	237
11.27	512	0.0185	3795	1472	0.00030	1.817	2587
11.30	512	0.0461	877	702	0.00007	0.703	457
11.46	1024	0.0290	285	875	0.00006	0.668	123
11.76	512	0.0550	810	627	0.00029	0.734	407
11.76	512	0.0496	455	443	0.00020	0.670	226
11.78	2048	0.0195	764	1965	0.00070	0.938	550

11.79	1024	0.0238	156	691	0.00054	0.741	61
12.68	1024	0.0252	639	193	0.00021	0.811	244
12.76	1024	0.0149	289	681	0.00003	0.762	111
13.01	1024	0.0460	666	992	0.00003	0.709	289
13.46	256	0.0758	477	662	0.00019	0.681	375
13.61	1024	0.0305	817	140	0.00057	0.903	323
14.29	256	0.0234	520	129	0.00005	0.797	388
14.46	256	0.0830	368	408	0.00016	0.650	284
14.84	256	0.0427	295	350	0.00003	0.668	222
14.86	512	0.0805	203	525	0.00044	0.641	103
15.04	1024	0.0180	181	779	0.00003	0.773	70
15.09	512	0.0803	819	763	0.00026	0.791	427
15.18	1024	0.0113	149	326	0.00009	0.809	61
15.22	256	0.0377	766	309	0.00001	0.702	568
15.27	512	0.0884	399	984	0.00018	0.700	212
15.39	1024	0.0687	925	645	0.00007	0.759	366
15.61	1024	0.0474	377	646	0.00003	0.693	146
16.12	1024	0.0407	673	161	0.00015	0.831	258
16.17	1024	0.0900	488	829	0.00024	0.724	203
17.00	256	0.1037	213	582	0.00073	0.701	160
17.16	256	0.0100	470	102	0.00002	0.816	352
17.49	1024	0.0184	241	193	0.00007	0.800	94
17.77	512	0.0959	868	401	0.00009	0.754	409
18.28	256	0.0959	846	368	0.00006	0.768	619
18.50	1024	0.1157	773	556	0.00086	0.783	317
18.74	1024	0.0683	646	183	0.00036	0.869	249
18.82	256	0.0340	585	156	0.00002	0.770	443
19.07	256	0.0544	156	726	0.00002	0.738	117
19.24	1024	0.0219	833	125	0.00003	0.772	323
19.28	256	0.1074	404	514	0.00049	0.819	302
20.93	1024	0.0958	284	529	0.00010	0.739	113
21.68	1024	0.1270	564	803	0.00044	0.848	225
21.77	256	0.1230	555	257	0.00043	0.866	424
22.42	1024	0.0933	701	205	0.00009	0.807	269
22.55	512	0.0722	934	313	0.00001	0.801	478
22.89	512	0.0562	421	119	0.00009	0.869	207
23.82	512	0.1151	504	410	0.00007	0.842	251
24.10	256	0.1023	852	166	0.00005	0.875	645
24.22	256	0.1415	203	560	0.00055	0.843	152
25.58	1024	0.1513	748	312	0.00041	0.894	294
25.61	256	0.0635	532	213	0.00001	0.802	391
26.32	256	0.1588	565	926	0.00008	0.907	433
26.78	1024	0.1037	604	202	0.00008	0.874	244
27.34	1024	0.1159	805	797	0.00002	0.906	332
27.36	256	0.0853	532	272	0.00001	0.836	390
28.08	1024	0.1268	922	199	0.00011	0.941	362
28.22	512	0.0518	100	393	0.00001	0.791	51
28.39	1024	0.0995	864	322	0.00002	0.867	351
29.32	1024	0.1013	561	507	0.00002	0.886	220
29.84	512	0.1602	219	827	0.00009	0.875	115
31.17	512	0.1376	187	413	0.00005	0.826	90

32.02	1024	0.1021	235	100	0.00017	0.889	91
33.13	256	0.1951	225	929	0.00007	0.928	170
33.86	1024	0.0792	200	217	0.00001	0.814	79
34.07	1024	0.1454	880	648	0.00002	1.037	358
35.30	512	0.1691	222	367	0.00007	0.892	110
35.33	512	0.1899	866	311	0.00062	1.143	429
36.68	1024	0.1930	415	791	0.00007	0.994	168
39.03	256	0.0016	3444	1917	0.00017	0.546	1
40.97	1024	0.1668	108	463	0.00002	0.889	43
87.95	2048	0.0031	1422	1241	0.00044	0.757	1

## PREDICTION OF THE EIGENPERIODS OF MDOF SHEAR BUILDINGS USING NEURAL NETWORKS

Vagelis Plevris<sup>1</sup> and German Solorzano<sup>2</sup>

<sup>1</sup> Department of Civil and Architectural Engineering, Qatar University  
P.O. Box: 2713, Doha, Qatar  
e-mail: [vplevris@qu.edu.qa](mailto:vplevris@qu.edu.qa)

<sup>2</sup> Department of Civil Engineering and Energy Technology, OsloMet–Oslo Metropolitan University  
Pilestredet 35, Oslo 0166, Norway  
e-mail: [germanso@oslomet.no](mailto:germanso@oslomet.no)

---

### Abstract

*The study of multi-degree of freedom (MDOF) systems is essential to evaluate and understand the seismic response of buildings. Through a MDOF idealization, the dynamic properties of the building such as its natural frequencies and modal shapes can be approximated. These properties are then used to determine the final design of the structural system of the building. A shear building MDOF system consists of an idealized model of the building in which the masses are concentrated at the floor levels and each floor is connected to other adjacent floors with elements that provide stiffness and only allow horizontal displacements. The dynamic properties of the idealized system are obtained by numerically solving a generalized eigenvalue problem which is a computationally expensive operation. In this paper, we propose a methodology to replace the required solution of the generalized eigenvalue problem with a Machine Learning NN-based approach. Two shear building models with 3 and 5 stories are considered, where the mass and the stiffness are held constant for every story. For every model, a database with the solution of several idealized models with varying mass and stiffness is created using a small number of samples ( $m$ ,  $k$  pairs). Finally, an Artificial Neural Network is trained with the database to predict the eigenperiods of other similar models avoiding the computation of the eigenvalue problem. The results show a high level of accuracy in the predictions and a significant reduction of the computational time compared to the hard-computing mathematical approach. Furthermore, the approach demonstrated in this study can be easily expanded to be applied to more complex dynamic systems for future research.*

**Keywords:** Structural Dynamics, MDOF system, Eigenperiod, Natural frequency, NN, prediction.

---

## 1 INTRODUCTION

The field of structural dynamics covers the behavior of structures subjected to dynamic loading. Such loads include wind, waves, traffic, earthquake, blasts and others. In practice, the dynamic response of buildings is obtained by applying a series of assumptions and simplifications that attempt to capture the most relevant dynamical properties of the system. In structural engineering, it is common to use the finite element method (FEM) to perform this kind of analysis [1]. In this case, the structure, which is essentially a continuous system, is idealized into a series of lumped masses interconnected by elements acting as springs and providing stiffness.

Using FEM, there are various methodologies that can be used to perform the dynamic analysis of a building against earthquake loading, such as explicit step-by-step integration of the coupled equations of motion [2], explicit step-by-step integration of the full (or a partial) set of uncoupled equations, response spectrum modal analysis (RSMA) [3] and the simplified equivalent lateral force (ELF) method [4]. Although RSMA and ELF are both approximate methods, they can give good results that can be used in engineering practice, especially if certain conditions are met. RSMA is widely used today as the standard procedure for designing earthquake resistant structures.

Both RSMA and ELF require the calculation of the natural periods (or eigenperiods) of the structure, i.e. the periods at which it will naturally resonate. These periods of vibration are very important in earthquake engineering and in structural dynamics in general. In structural design against earthquake loading, it is imperative that the natural frequency of the building does not match the frequency of expected earthquakes in the region the building is to be constructed. If the two frequencies match, resonance will occur, and the structure can experience severe damage. Determining the natural frequencies, or equivalently the eigenperiods of buildings, is of great importance in earthquake engineering.

The types of equations arising in FEM-based modal analysis are those seen in algebraic eigensystems. The physical interpretation of the eigenvalues and eigenvectors which come from solving the system is that they represent the frequencies and the corresponding mode shapes of the structure. In practical applications, the main desired modes are the lowest frequencies (or highest eigenperiods) because they represent the most prominent modes at which the structure will vibrate, dominating all higher frequency modes. In other words, the first (greatest) eigenperiods are the most important for determining the dynamic response of a structure. The ELF method is particularly based on the very first eigenperiod and the corresponding first eigenmode, only, while RSMA usually takes into account a limited number of eigenperiods and eigenmodes.

ANNs have been successfully employed in the structural engineering field to replace complex and time-consuming mathematical procedures and give predictions of analysis results, among others. Plevris and Asteris [5, 6] proposed a novel method with applying ANNs to approximate the failure surface for brittle anisotropic materials. Afaq et al. [7] created a novel knowledge-based structural analysis system based on ANN to predict the load-carrying capacity of RC members, reducing substantially the computational time compared to traditional Nonlinear finite element analysis. ANNs have also been used for the dynamic analysis of structures. Oh et al. [8] proposed a model to predict the seismic response of buildings based on the correlation of the ground motion and the structure using ANN. Worden and Green [9] developed a machine learning approach for the inversion of the modal transformation in nonlinear modal analysis. Gu and Oyadiji [10] presented an innovative approach using diagonal recurrent neural networks for the control of vibration in structural systems overperforming conventional control strategies such as the linear quadratic regulator for linear MDOF systems.



Bojórquez et. al [11] employed a Neural Network approach to obtain the transformation factors from single-degree of freedom (SDOF) to multi-degree of freedom (MDOF) to predict the seismic response of steel framed buildings, reducing considerably the computational effort. Payán-Serrano et al. [12] investigated the prediction of maximum story drift of MDOF structures subjected to dynamic wind load using ANNs through the combination of several structural and turbulent wind parameters. Chakraverty et al. [13] used ANNs to simulate and estimate the structural response of a two-story shear building by training the model for a particular earthquake. Lagaros and Papadrakakis [14] proposed a new adaptive scheme to predict the structural non-linear behavior when earthquake actions of increased severity are considered.

In this paper, a methodology is developed to replace the numerical procedure used for the calculation of the eigenperiods of MDOF shear buildings with an Artificial Neural Network (ANN). Two models with 3 and 5 stories are examined, where the mass and the stiffness are held constant for every story. For every model, a database with the solution of several idealized models with varying mass ( $m$ ) and stiffness ( $k$ ) is created using a number of ( $m, k$ ) pairs. Finally, an ANN is trained with the database to predict the eigenperiods of other similar models avoiding the direct computation of the eigenvalue problem. The remaining of this paper is organized as follows: In Section 2, a brief description of dynamic modal analysis is given with the definitions of SDOF and MDOF systems and the relevant equations. In section 3, the concept of ANNs for regression problems is explained, together with the introduction of some error metrics that can be used for NN predictions. Section 4 presents the methodology and the numerical results followed by section 5 where the conclusions and future research directions are discussed.

## 2 DYNAMIC MODAL ANALYSIS

Modal analysis is based on using the mass and stiffness of a structure to find the various periods at which it will naturally resonate. The RSMA method requires the calculation of the natural mode shapes and frequencies of a structure during free vibration as the method is based on the superposition of the responses of the structure and the use of a response spectrum. Instead of solving the time history problem for each mode, the method uses the response spectrum to compute the maximum response in each mode. Then the maximum modal responses are combined using some statistical technique, such as square root of the sum of the squares (SRSS) or complete quadratic combination (CQC).

### 2.1 Single-degree of Freedom System

An idealized shear building resulting in a SDOF system is depicted in Figure 1, where  $m$  is the mass of the system and  $k$  is its stiffness, provided by the column(s).

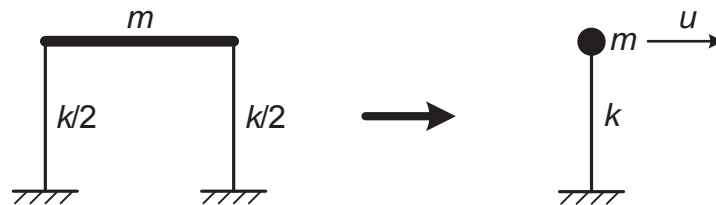


Figure 1: A SDOF dynamic system.

The dynamic equilibrium of the system at any instant of time  $t$  can be expressed as follows:

$$m\ddot{u}(t) + c\dot{u}(t) + ku(t) = F(t) \quad (1)$$

where  $\ddot{u}$ ,  $\dot{u}$  and  $u$  are the acceleration, velocity, and displacement, respectively,  $c$  is the damping of the system and  $F$  is the externally imposed dynamic loading. Eq. (1) is referred as the equation of motion and its solution is a well-known problem that has been studied thoroughly by many authors [15]. For a SDOF system without damping ( $c=0$ ), the circular frequency  $\omega$  of the system is given by the formula

$$\omega = \sqrt{\frac{k}{m}} \quad (2)$$

The cyclic frequency  $f$  is given by

$$f = \frac{\omega}{2\pi} \quad (3)$$

and the natural period of vibration, or eigenperiod  $T$ , is given by

$$T = \frac{1}{f} = \frac{2\pi}{\omega} = 2\pi\sqrt{\frac{m}{k}} \quad (4)$$

## 2.2 Multi-degree of Freedom System

The number of degrees of freedom for a vibrating system depends on the number of inertial elements (masses or rigid bodies) and the number of constraints imposed on the motion. A shear building idealized into a MDOF system with 3 degrees of freedom is depicted in Figure 2.

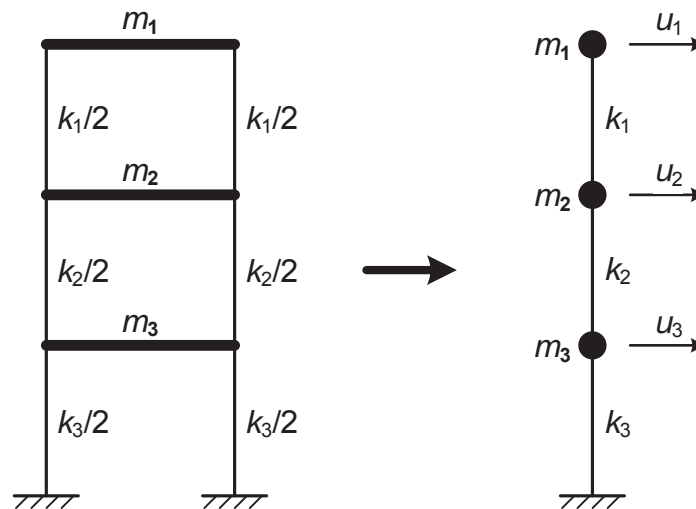


Figure 2: A MDOF dynamic system with 3 degrees of freedom (shear building).

The dynamic equilibrium of a MDOF structure at any instant of time  $t$  can be expressed with the following equation of motion:

$$\mathbf{M}\ddot{\mathbf{u}}(t) + \mathbf{C}\dot{\mathbf{u}}(t) + \mathbf{K}\mathbf{u}(t) = \mathbf{F}(t) \quad (5)$$

where  $\mathbf{M}$  is the mass matrix;  $\mathbf{K}$  is the stiffness matrix;  $\mathbf{C}$  represents the damping matrix,  $\ddot{\mathbf{u}}$ ,  $\dot{\mathbf{u}}$  and  $\mathbf{u}$  are the acceleration, velocity and displacement vectors, respectively, and  $\mathbf{F}$  is the external force vector.

In the case of free vibration without damping, Eq. (5) becomes

$$\mathbf{M}\ddot{\mathbf{u}}(t) + \mathbf{K}\mathbf{u}(t) = \mathbf{0} \quad (6)$$

In free vibration without damping, the system will oscillate in a steady-state harmonic manner. The resulting motion will be a mixture of modes, each having its own circular frequency  $\omega_i$  so that

$$\ddot{\mathbf{u}}(t) = -\omega_i^2 \mathbf{u}(t) \quad (7)$$

By substituting Eq. (7) on Eq. (6), the following expression is obtained

$$(\mathbf{K} - \omega_i^2 \mathbf{M}) \cdot \mathbf{u}(t) = \mathbf{0} \quad (8)$$

The  $n$  circular frequencies  $\omega_i$  ( $i=1, 2, \dots, n$ ) of the system can be found using Eq. (8), where the trivial solution is obtained when  $\mathbf{u}(t)=\mathbf{0}$ . For a non-trivial solution, the term inside the first parenthesis in Eq. (8) must be equal to zero, such that

$$|\mathbf{K} - \omega_i^2 \mathbf{M}| = 0 \quad (9)$$

After having found the circular frequencies  $\omega_i$ , we can now substitute those values back into Eq. (8) and solve for the vector  $\mathbf{u}$  which corresponds to the  $i$ -th modal shape. Each modal shape or eigenvector is denoted as  $\Phi_i$  ( $n \times 1$ ) so that Eq. (8) can be rewritten as

$$(\mathbf{K} - \omega_i^2 \mathbf{M}) \cdot \Phi_i = \mathbf{0} \quad (10)$$

Eq. (10) represents a classic problem in Mathematics referred as generalized eigenvalue problem [16] and its solution involves a series of matrix decompositions which can be computationally expensive, especially for large systems.

For the special case of a MDOF shear building with  $n$  degrees of freedom (stories), like the one of Figure 2 (shown there for the case  $n=3$ ), the mass matrix  $\mathbf{M}$  is a  $n \times n$  diagonal matrix given by

$$\mathbf{M} = \begin{bmatrix} m_1 & 0 & 0 & 0 \\ 0 & m_2 & 0 & 0 \\ 0 & 0 & \ddots & 0 \\ 0 & 0 & 0 & m_n \end{bmatrix} \quad (11)$$

where  $m_i$  is the mass of every story starting numbering from the top to the bottom, according to the notation used in this manuscript. The stiffness matrix  $\mathbf{K}$  is a  $n \times n$  square matrix calculated as

$$\mathbf{K} = \begin{bmatrix} k_1 & -k_1 & 0 & 0 \\ -k_1 & k_1 + k_2 & -k_2 & 0 \\ 0 & -k_2 & \ddots & -k_{n-1} \\ 0 & 0 & -k_{n-1} & k_{n-1} + k_n \end{bmatrix} \quad (12)$$

where  $k_i$  is the stiffness of each story, with numbering again from top to bottom.

### 3 ARTIFICIAL NEURAL NETWORKS

An Artificial Neural Network is a collection of interconnected units referred as artificial neurons that resembles the basic structure of biological neurons that constitute animal and human brains. It is known that when a biological brain receives an input signal such as the desire to move a limb, the signal is processed through the interconnected neurons inside the brain to produce a corresponding output signal as a response [17]. In the case of moving a

limb, the response is a signal that contracts the required muscles to move it. The connectivity of the neurons inside the brain is the fundamental key to make that happen. Through the experiences of the individual, the connections of the neurons are constantly self-adjusting to improve the quality of the response. This process is what we, humans, know as learning.

An ANN tries to mimic the functionality of biological brains using an analogous but much more simplistic model. The ANN receives a set of numeric input values that are processed by the artificial neurons to produce a numeric response. To obtain the desired or “correct” response, the ANN is trained with known data containing numerous examples of inputs with their matching output values. Then, by using a mathematical optimization algorithm, the network parameters are adjusted so that the ANN learns to map the inputs to their corresponding outputs. Therefore, a properly trained ANN can be used to accurately predict the output values of new inputs that were not used in the training data [18].

### 3.1 Back Propagation Neural Networks

For this study, the selected ANN type is a backpropagation neural network (BPNN). The BPNN is composed of several layers and each layer has a specific number of neurons. The neurons of the first layer are connected to the neurons of the second layer, which in turn are connected to the neurons of the third layer, and so on. The very first layer and the last layer are known as the input and output layers respectively, while the other layers are called “hidden layers”. The notation used to denote the layer composition is generally as follows:

$$N - H_1 - H_2 - \dots - H_{L-1} - M,$$

where  $N$  denotes the number of neurons in the input layer (number of inputs),  $H_i$  stands for the number of neurons in the  $i$ -th hidden layer,  $M$  is the number of neurons in the output layer, and  $L$  is the total number of layers, including the output layer but excluding the input layer. For example, a 2-3-3-2 BPNN consists of an input layer with 2 neuron, 2 hidden layers with 3 neurons each, and an output layer with 2 neurons, as shown in Figure 3.

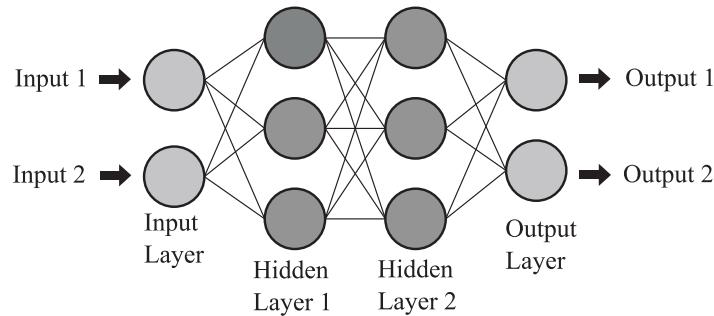


Figure 3: A 2-3-3-2 BPNN.

To obtain the output values from the ANN, the input values are fed to the network by a feedforward process. It starts by setting the input values at the first layer  $N$ , and then, moving forward to the next layer, the values of all the neurons at that layer are computed. The process is repeated until the output layer  $M$  is reached and the output values are obtained. At each neuron, a weighted summation of the values coming from the other connected neurons and an additional bias neuron is performed, see Figure 4.

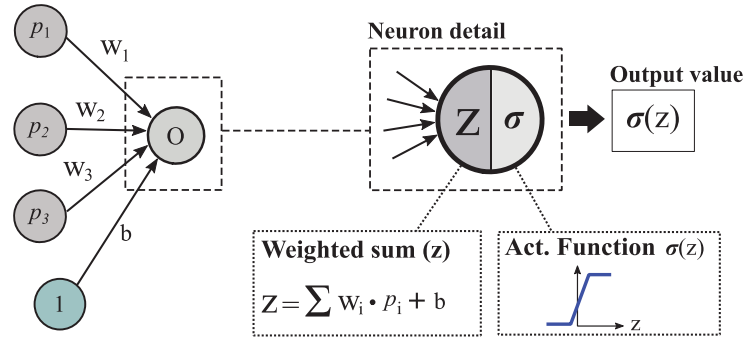


Figure 4: Detail of a single neuron connected to 3 other neurons from the previous layer. The picture shows the process on how the numerical output value is obtained in a neuron.

For the case of Figure 4, the operation can be written in matrix form as follows

$$z = \mathbf{W} \cdot \mathbf{p} + b \quad (13)$$

$$\mathbf{W} = \begin{bmatrix} w_1 & w_2 & w_3 \end{bmatrix} \quad (14)$$

$$\mathbf{p} = \begin{bmatrix} p_1 & p_2 & p_3 \end{bmatrix}^T \quad (15)$$

$$O = \sigma(z) = \sigma(\mathbf{W} \cdot \mathbf{p} + b) \quad (16)$$

where  $O$  is the output of the output neuron,  $\mathbf{p}$  is a column vector with the values of the neurons at the previous layer;  $\mathbf{W}$  is the weight row vector that connects this output neuron with the previous layer; and  $b$  is a bias neuron that is added to the weighted summation to form the input for the activation function  $\sigma$ .

Activation functions are used to add non-linearity into the neural network and to facilitate the training process in which the gradient of the model parameters is computed. Additionally, they help to restrict the neuron values to a certain limit providing stability to the network. Therefore, the activation functions are usually simple, continuous, and differentiable. Among the most commonly used are the Linear, ReLu and Sigmoid activation functions. Figure 5 presents the Relu and the Sigmoid activation functions.

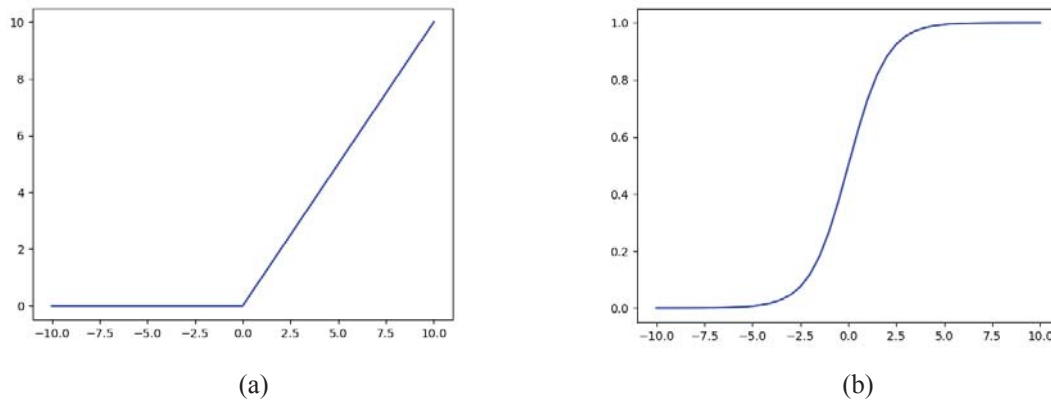


Figure 5: ReLu (a) and Sigmoid (b) activation functions, plotted from -10 to 10.

### 3.2 Training Process

The training process consists of adjusting the initial random weights of the network to fit the given training data. The weight updating process starts by feeding a set of input values



through the network and obtaining the corresponding outputs. The obtained values are then compared with their known values from the training dataset and an error is estimated using a predefined error function. The idea is to determine the gradient or the rate of change of the error function with respect to the model parameters (i.e. all the weights). Thanks to the network architecture, the computation of the gradient is possible using a chain rule of partial derivatives with the known quantities. Then, by using the back propagation scheme, the gradients computed at the output neurons are propagated back through the hidden layers so that a gradient value is defined at each one of the weights in the model. Finally, the weights of the model are updated by a small quantity obtained by multiplying the gradients with a factor called *learning rate*. This weight-update scheme is an optimization method known as gradient decent (GD) which attempts to minimize the error function.

To properly train the BPNN, the full training dataset must be processed by the network multiple times. In other words, the weights must be updated with the GD scheme for every data point in the training set. Every time that the full training set has been processed with the GD scheme is called an Epoch. However, at every Epoch, the data must be fed in different order as it turns out that if the full training data is presented multiple times in a random order, the overall fluctuations of the gradient update path will average out and converge to a good solution. Such random reordering of the training dataset at every Epoch is known as stochastic gradient decent (SGD) and it is one of the most popular weight-optimization schemes for ANNs.

The training process can be quite demanding in terms of computational effort for large NN models with large training data sets. Nevertheless, in this paper that is not the case as the investigated problem can be solved with a relatively simple BPNN architecture and a small amount of training data. The stopping criteria of the training process is usually monitored by having a separated validation set of data which is not used for training. At every Epoch, the error of both the training and the validation sets are measured. Naturally, the error of the training set reduces with every Epoch due to the optimization scheme. However, if the error on the validation set suddenly starts to increase, while the training set error keeps reducing, it is a clear indication of an unwanted characteristic called overfitting in which the NN loses its generality. Therefore, the stopping criteria is set to the last Epoch before the overfitting was detected. Alternatively, the stopping criterion can be set for a fixed number of Epochs.

### 3.3 Prediction error metrics

The NN predictions are never completely accurate as each prediction always contains a small error. There are various metrics that can be used to measure the prediction error. Let  $\mathbf{p}$  ( $N \times 1$  vector) be the predicted values and  $\mathbf{x}$  ( $N \times 1$  vector) be the real values of a quantity calculated (or measured) a number  $N$  of times. For example, for predicting the fundamental period of a MDOF system, we ask the NN to predict it  $N$  times using different pairs of  $m$  and  $k$  parameters. The following metrics can be defined for calculating the prediction error.

The prediction error values **Err** (or residuals) can be expressed as the difference between the predicted values and the real values, as follows:

$$\mathbf{Err} = \mathbf{p} - \mathbf{x} \quad (17)$$

The absolute value of the residuals (or absolute error) **AbsErr** is a measure of how far from the regression line data points are. Each element  $AbsErr_i$  of the vector **AbsErr** is given by

$$AbsErr_i = |Err_i| = |p_i - x_i| \quad (18)$$

The mean absolute error (**MAE**) is the average value of the absolute error, given as

$$MAE = \frac{\sum_{i=1}^N AbsErr_i}{N} = \frac{\sum_{i=1}^N |p_i - x_i|}{N} \quad (19)$$

The squared error **SqErr** is the squared value of the error, with its elements given by

$$SqErr_i = (p_i - x_i)^2 \quad (20)$$

The mean squared error (**MSE**) is the average value of the squared errors, given by

$$MSE = \frac{1}{N} \sum_{i=1}^N SqErr_i = \frac{1}{N} \sum_{i=1}^N (p_i - x_i)^2 \quad (21)$$

The root mean squared error (**RMSE**) is the square root of **MSE**, given by

$$RMSE = \sqrt{MSE} \quad (22)$$

The relative error values **RelErr** is the absolute error divided by the real value, provided that the real value is not equal to zero. It is given by

$$RelErr_i = \frac{|Err_i|}{x_i} = \frac{|p_i - x_i|}{x_i} \quad (23)$$

The mean relative error (**MRE**) is the average value of the relative errors, given by

$$MRE = \frac{1}{N} \sum_{i=1}^N RelErr_i = \frac{1}{N} \sum_{i=1}^N \frac{|p_i - x_i|}{x_i} \quad (24)$$

The Pearson correlation coefficient (**R**) is a measure of linear correlation between two sets of data, in our case the predicted values and the real values. It is the covariance of two variables, divided by the product of their standard deviations. Thus, it is essentially a normalized measurement of the covariance, such that the result always has a value between  $-1$  and  $1$ . If there is no error in the prediction, then the predicted values coincide with the real values and  $R=1$ . **R** is given by the formula

$$R = \frac{\sum_{i=1}^N (p_i - \bar{p})(x_i - \bar{x})}{\sqrt{\sum_{i=1}^N (p_i - \bar{p})^2} \sqrt{\sum_{i=1}^N (x_i - \bar{x})^2}} \quad (25)$$

In the above formula,  $\bar{p}$  and  $\bar{x}$  are the mean values of **p** and **x**, respectively:

$$\bar{p} = \frac{1}{N} \sum_{i=1}^N p_i \quad (26)$$

$$\bar{x} = \frac{1}{N} \sum_{i=1}^N x_i \quad (27)$$

## 4 NUMERICAL RESULTS

Two models have been examined, a 3-DOF shear building and a 5-DOF shear building. For both models, the parameters *m* (mass) and *k* (stiffness) are the same for all stories, as shown in Figure 6. This limits the input parameters of the Neural Network to 2 in every case.

The output parameters are the eigenperiods of the system, which are 3 for the 3-DOF system and 5 for the 5-DOF system. The mass  $m$  varies from  $m_{\min}=2$  ton to  $m_{\max}=20$  ton while the stiffness  $k$  varies from  $k_{\min}=20,000$  kN/m to  $k_{\max}=200,000$  kN/m.

We use standard intervals of  $m$  and  $k$  for the generation of the data used for training. The mass and stiffness intervals are set to 6, which means that we have 7 values of mass and 7 values of stiffness which makes  $7 \times 7 = 49$  pairs of  $(m, k)$  for each structure. 70% of the database is used for training (35 pairs), while the rest (30%) of the database is used for validation (15%, 7 pairs) and testing (15%, 7 pairs).

For both cases, we use a simple NN architecture of one hidden layer with 10 neurons. In the 3-DOF system, the network architecture is 2-10-3 while for the 5-DOF system, the network architecture is 2-10-5.

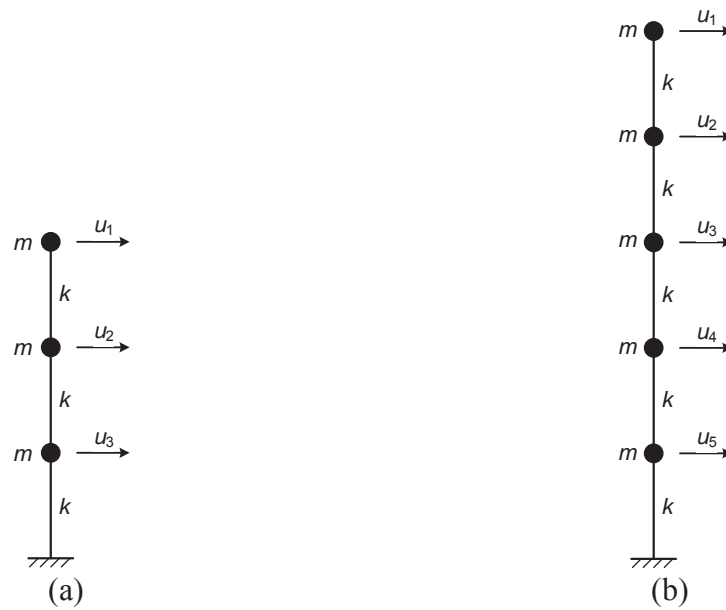


Figure 6: (a) 3-DOF shear building, (b) 5-DOF shear building.

#### 4.1 Three DOF system

The first numerical example is a 3-DOF system where the NN is asked to predict the three eigenperiods of the system, i.e.  $T_1, T_2, T_3$  where  $T_1 > T_2 > T_3$ . The NN architecture used is 2-10-3. The maximum number of validation increases is set to 6, i.e. if the error in the validation set increases for 6 times then the training is stopped. Given this criterion, training is stopped in Epoch 110, as shown in Figure 7.

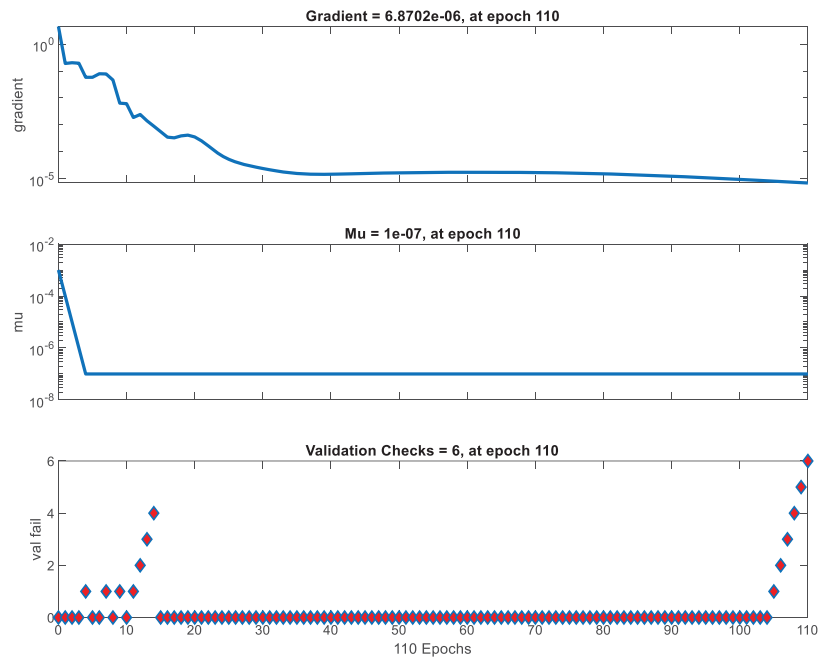


Figure 7: Example 1, Final NN Train State.

The performance of the NN is depicted in Figure 8, where the three lines show the error obtained for the training set (blue line), the validation set (green line) and the test set (red line).

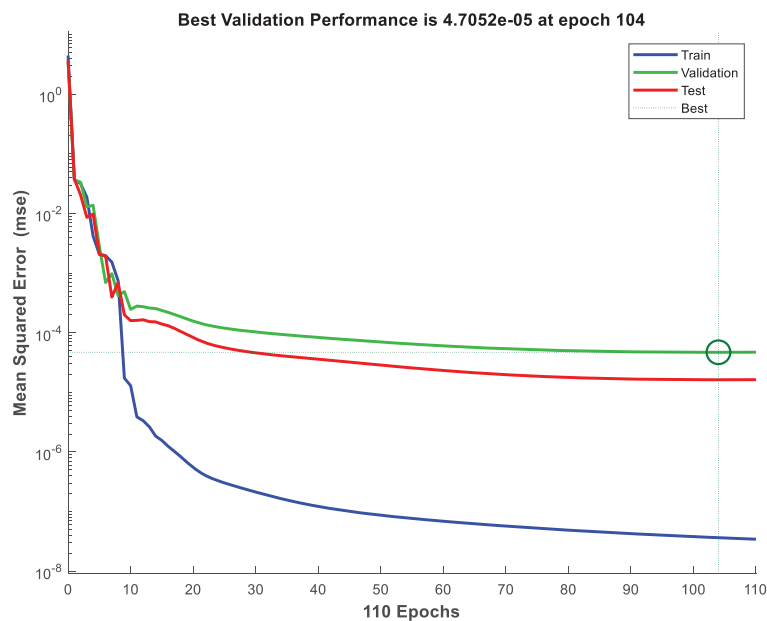


Figure 8: Example 1, NN Training Performance.

The training regression of the NN data is depicted in Figure 8, where the three colored lines correspond again to the three different sets and the fourth black line contains all the data sets together. The  $R$  values reported correspond to the normalized data.

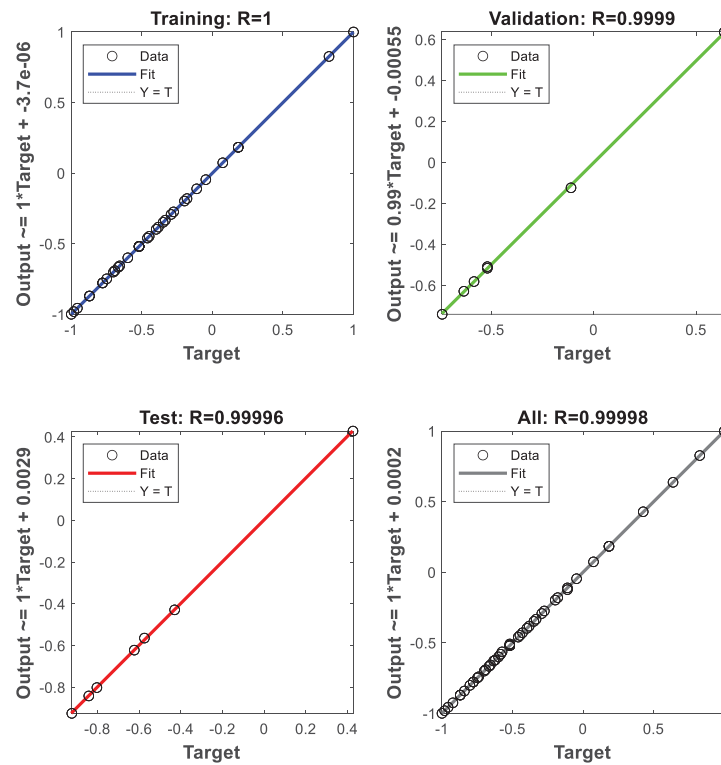


Figure 9: Example 1, NN Training Regression (for the Normalized Data).

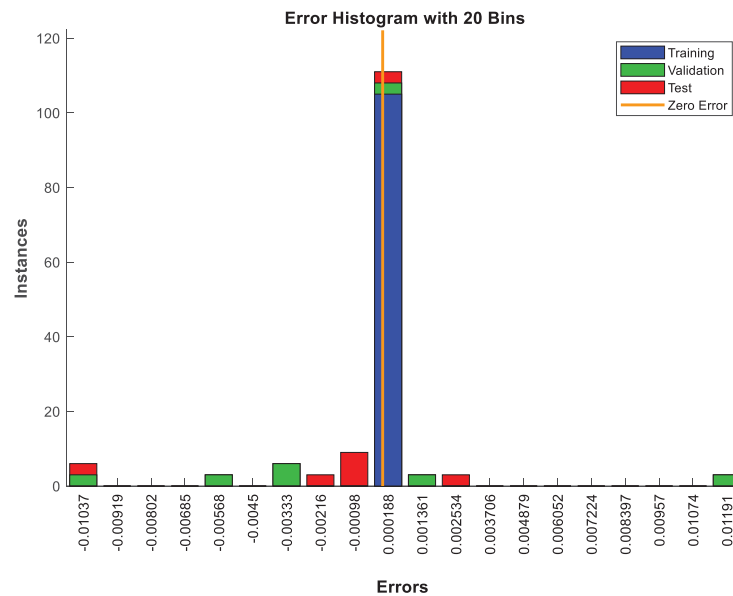


Figure 10: Example 1, NN Error Histogram (for the Normalized Data).

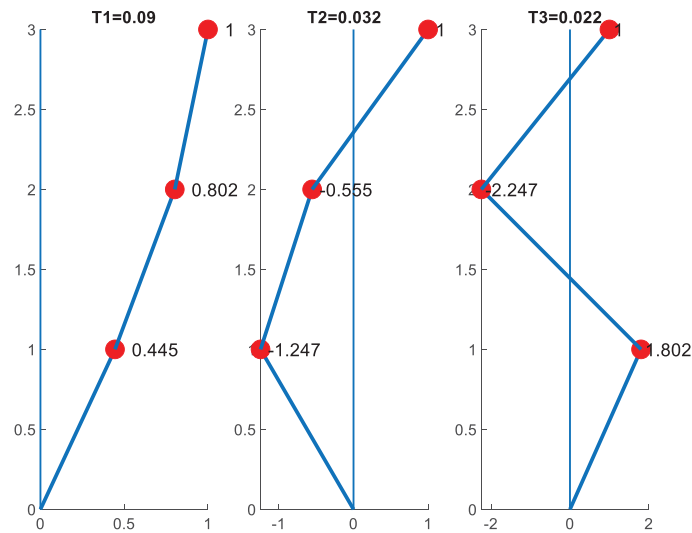
In order to test the NN results, we generated 100 random  $(m, k)$  pairs within the training region and we calculated the errors in the NN predictions. The results are presented in Table 1.



<b>Metric</b>	<b><math>T_1</math></b>	<b><math>T_2</math></b>	<b><math>T_3</math></b>	<b>All periods</b>
<i>MSE</i>	4.33E-06	5.52E-07	2.64E-07	1.72E-06
<i>RMSE</i>	2.08E-03	7.43E-04	5.14E-04	1.31E-03
<i>MAE</i>	8.46E-04	3.02E-04	2.09E-04	4.52E-04
<i>MRE</i>	4.10E-03	4.10E-03	4.10E-03	4.10E-03
<i>R</i>	0.999745	0.999745	0.999745	0.99986

Table 1: Example 1, Error metrics for the independent test with 100 random  $(m, k)$  pairs..

It is shown that the error of the NN predictions is very small. The mean relative error is only 0.41% for all the NN predictions together ( $T_1$ ,  $T_2$  and  $T_3$ ). As an example, for  $m=5.52$  ton and  $k=137,000$  kN/m, the real values of the eigenperiods are  $T_1=0.0896$  s,  $T_2=0.0320$  s and  $T_3=0.0221$  s, as shown in Figure 11 together with the three corresponding eigenmodes. The corresponding NN predictions are  $T_1=0.0898$  s,  $T_2=0.0320$  s and  $T_3=0.0222$  s. The NN manages to give very accurate results, although the data set used contains only 49  $(m, k)$  pairs, of which only 35 (70%) have been used for the NN training itself.

Figure 11: Eigenmodes of a 3-DOF shear building with  $m=5.52$  ton and  $k=137,000$  kN/m (uniformly, at every story).

#### 4.2 Five DOF system

The second numerical example is a 5-DOF system where the NN is asked to predict the five eigenperiods of the system, i.e.  $T_1$  to  $T_5$ , where  $T_1 > T_2 > T_3 > T_4 > T_5$ . The NN architecture used is 2-10-5, with 10 neurons in the hidden layer. The maximum number of validation increases is again set to 6. This time training stops earlier, in Epoch 30, as shown in Figure 12.

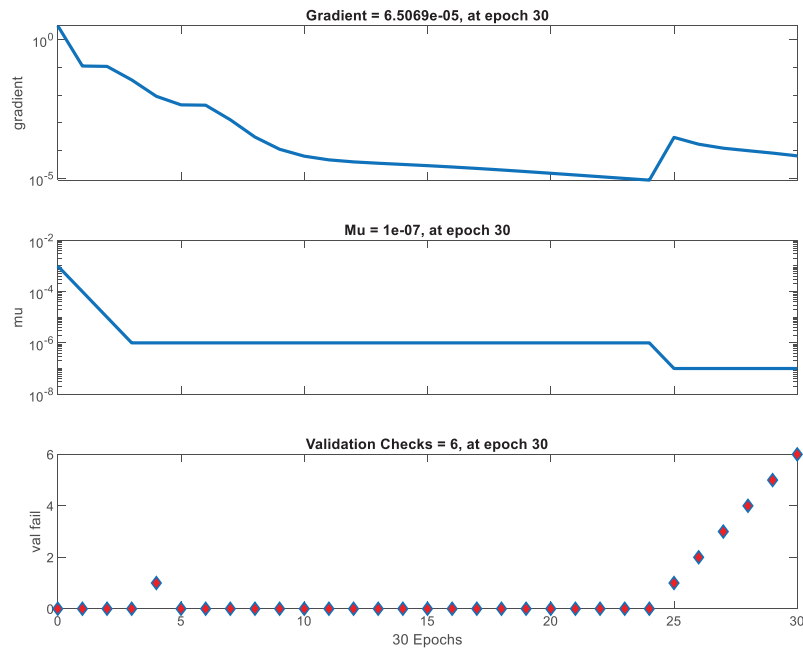


Figure 12: Example 2, Final NN Train State.

The performance of the NN is depicted in Figure 13, where the three lines show the error obtained for the training set (blue line), the validation set (green line) and the test set (red line).

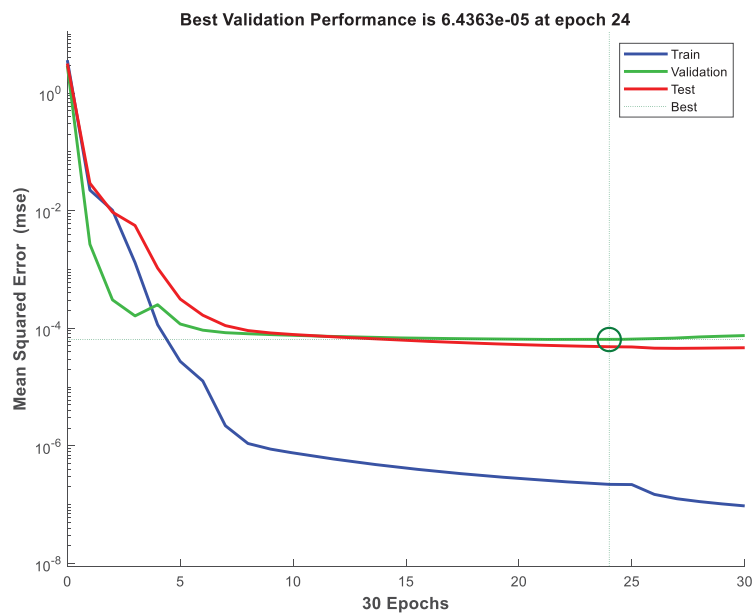


Figure 13: Example 2, NN Training Performance.

The training regression of the NN data is depicted in Figure 14, where the three colored lines correspond again to the three different sets and the fourth black line contains all the data sets together. The  $R$  values reported correspond to the normalized data.

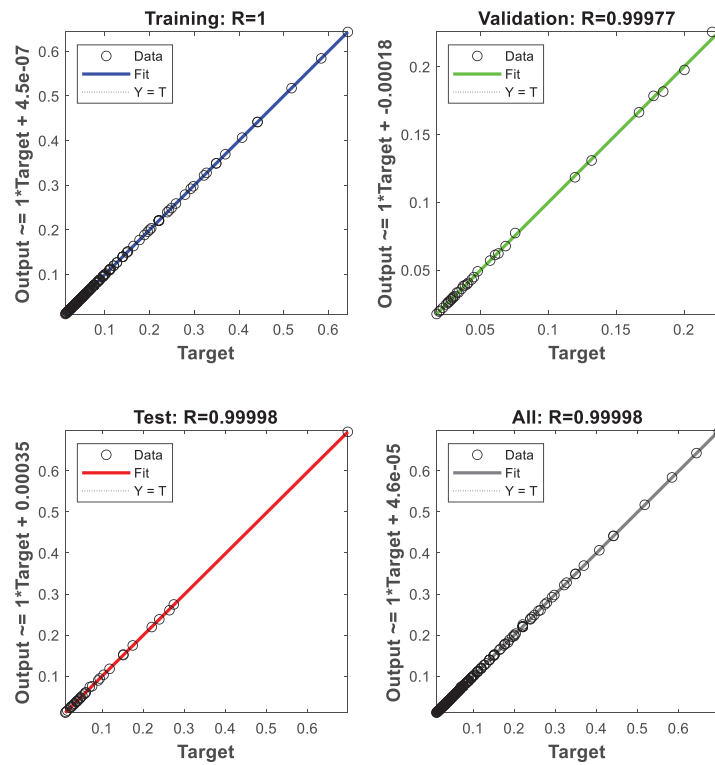


Figure 14: Example 2, NN Training Regression (for the Normalized Data).

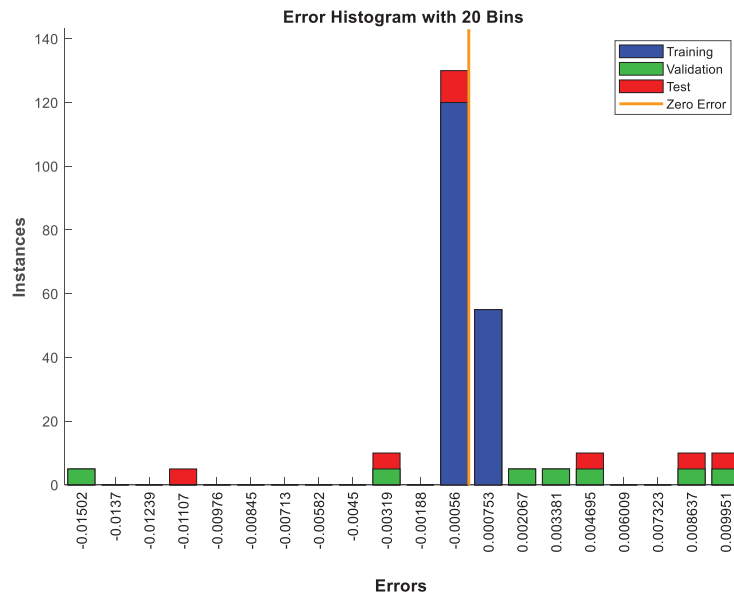


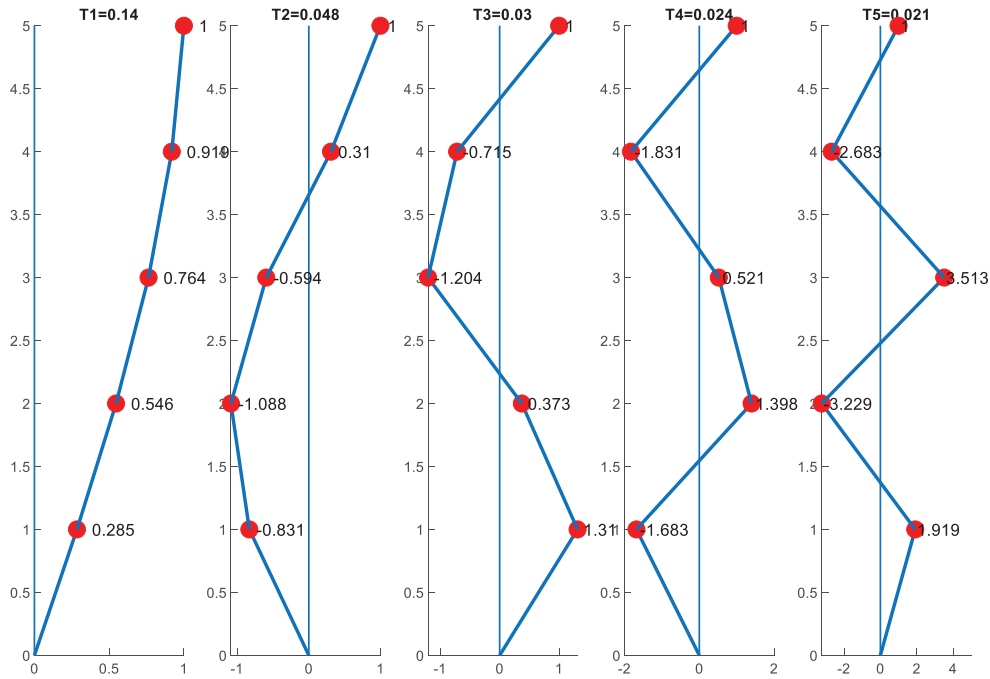
Figure 15: Example 2, NN Error Histogram (for the Normalized Data).

In order to test the NN results, we generated 100 random  $(m, k)$  pairs within the training region and we calculated the errors in the NN predictions. The results are presented in Table 1.

Metric	$T_1$	$T_2$	$T_3$	$T_4$	$T_5$	All periods
$MSE$	1.52E-05	1.78E-06	7.18E-07	4.35E-07	3.34E-07	3.69E-06
$RMSE$	3.90E-03	1.34E-03	8.47E-04	6.60E-04	5.78E-04	1.92E-03
$MAE$	2.02E-03	6.94E-04	4.40E-04	3.43E-04	3.00E-04	7.60E-04
$MRE$	7.95E-03	7.95E-03	7.95E-03	7.95E-03	7.95E-03	7.95E-03
$R$	0.999678	0.999678	0.999678	0.999678	0.999678	0.999859

Table 2: Example 2, Error metrics for the independent test with 100 random  $(m, k)$  pairs.

It is shown that the error of the NN predictions is again very small. The mean relative error is only 0.79% for all the NN predictions together ( $T_1$  to  $T_5$ ). As an example, for  $m=5.52$  ton and  $k=137,000$  kN/m, the real values of the eigenperiods are  $T_1=0.1401$  s,  $T_2=0.0480$  s,  $T_3=0.0305$  s,  $T_4=0.0237$  s,  $T_5=0.0208$  s, as shown in Figure 16. The corresponding NN predictions are  $T_1=0.1384$  s,  $T_2=0.0474$  s,  $T_3=0.0301$  s,  $T_4=0.0234$  s,  $T_5=0.0205$  s. The NN manages to give very accurate results for all five eigenperiods.

Figure 16: Eigenmodes of a 5-DOF shear building with  $m=5.52$  ton and  $k=137,000$  kN/m (uniformly, at every story).

## 5 CONCLUSIONS

In the present study, a methodology to predict the dynamic properties of a MDOF idealized model using a machine learning oriented strategy is implemented. An Artificial Neural Network is trained to accurately predict all the eigenperiods of MDOF shear buildings with a uniform distribution of mass and stiffness at every story. The goal of the study has been to reduce the computational effort of the complex mathematical process that is required to solve the generalized eigenvalue problem that arises from the modal analysis. It is noted that to train the ANN, a training database of previously solved eigenvalue problems is required, which is itself also a computationally expensive operation. However, the creating of the training set and the

training procedure are one-time processes, only. After the ANN is trained, it can be used to predict the behavior of any system (within the domain of the training data) with a very low computational effort.

The methodology has been tested for two different MDOF models, a 3-DOF system and a 5-DOF system. The results show highly accurate predictions reaching mean relative error values of 0.41% and 0.79%, respectively. All the error metrics used show a highly accurate prediction. This research has shown that for this type of problems, a relatively small database can be used to train highly accurate BPNNs. The developed framework is going to serve as a base for further research into more complex dynamic systems, for example systems with more degrees of freedom and also multi-story shear buildings with independent values of  $m$  and  $k$  for every single story. Having independent values of mass and stiffness at each story dramatically increases the complexity of the problem as the input parameters increase from 2 to  $3 \times 2 = 6$  and  $5 \times 2 = 10$  for the 3-DOF and the 5-DOF system, respectively.

## REFERENCES

- [1] Plevris, V. and G. Markeset, *Educational Challenges in Computer-based Finite Element Analysis and Design of Structures*. Journal of Computer Science, 2018. **14**(10): p. 1351-1362.
- [2] Papazafeiropoulos, G. and V. Plevris, *OpenSeismoMatlab: A new open-source software for strong ground motion data processing*. Heliyon, 2018. **4**(9): p. 1-39.
- [3] Arias, H. and J.D. Jaramillo, *Base shear determination using response-spectrum modal analysis of multi-degree-of-freedom systems with soil-structure interaction*. Bulletin of Earthquake Engineering, 2019. **17**(7): p. 3801-3814 DOI: 10.1007/s10518-019-00612-5.
- [4] Yenidogan, C. and M. Erdik, *A comparative evaluation of design provisions for seismically isolated buildings*. Soil Dynamics and Earthquake Engineering, 2016. **90**: p. 265-286 DOI: <https://doi.org/10.1016/j.soildyn.2016.08.016>.
- [5] Plevris, V. and P.G. Asteris, *Modeling of Masonry Failure Surface under Biaxial Compressive Stress Using Neural Networks*. Construction and Building Materials, 2014. **55**: p. 447-461 DOI: 10.1016/j.conbuildmat.2014.01.041.
- [6] Asteris, P.G. and V. Plevris, *Anisotropic masonry failure criterion using artificial neural networks*. Neural Computing and Applications, 2017. **28**(8): p. 2207-2229 DOI: 10.1007/s00521-016-2181-3.
- [7] Ahmad, A., D.M. Cotsovos, and N.D. Lagaros, *Framework for the development of artificial neural networks for predicting the load carrying capacity of RC members*. SN Applied Sciences, 2020. **2**(4): p. 1-21.
- [8] Oh, B.K., et al., *Neural network-based seismic response prediction model for building structures using artificial earthquakes*. Journal of Sound and Vibration, 2020. **468**: p. 115109 DOI: <https://doi.org/10.1016/j.jsv.2019.115109>.
- [9] Worden, K. and P.L. Green, *A machine learning approach to nonlinear modal analysis*. Mechanical Systems and Signal Processing, 2017. **84**: p. 34-53 DOI: <https://doi.org/10.1016/j.ymssp.2016.04.029>.
- [10] Gu, Z.Q. and S.O. Oyadiji, *Diagonal Recurrent Neural Networks for MDOF Structural Vibration Control*. Journal of Vibration and Acoustics, 2008. **130**(6) DOI: 10.1115/1.2948369.



- [11] Bojórquez, J., et al., *Probabilistic seismic response transformation factors between SDOF and MDOF systems using artificial neural networks*. Journal of Vibroengineering, 2016. **18**(4): p. 2248-2262 DOI: 10.21595/jve.2016.16506.
- [12] Payán-Serrano, O., et al., *Prediction of Maximum Story Drift of MDOF Structures under Simulated Wind Loads Using Artificial Neural Networks*. Applied Sciences, 2017. **7**(6): p. 563.
- [13] Chakraverty, S., P. Gupta, and S. Sharma, *Neural network-based simulation for response identification of two-storey shear building subject to earthquake motion*. Neural Computing and Applications, 2010. **19**(3): p. 367-375 DOI: 10.1007/s00521-009-0279-6.
- [14] Lagaros, N.D. and M. Papadrakakis, *Neural network based prediction schemes of the non-linear seismic response of 3D buildings*. Advances in Engineering Software, 2012. **44**(1): p. 92-115 DOI: <https://doi.org/10.1016/j.advengsoft.2011.05.033>.
- [15] Chopra, A.K., *Dynamics of structures. theory and applications to Earthquake Engineering*. 2017.
- [16] Ghojogh, B., F. Karray, and M. Crowley, *Eigenvalue and Generalized Eigenvalue Problems: Tutorial*. ArXiv e-prints, 2019(arXiv:1903.11240v1): p. 8 DOI: <https://arxiv.org/abs/1903.11240v1>.
- [17] Rickert, J., et al., *Dynamic Encoding of Movement Direction in Motor Cortical Neurons*. The Journal of Neuroscience, 2009. **29**(44): p. 13870-13882 DOI: 10.1523/jneurosci.5441-08.2009.
- [18] Plevris, V., *Innovative computational techniques for the optimum structural design considering uncertainties*. 2009, National Technical University of Athens: Athens, Greece. p. 312.

## SEISMIC PERFORMANCE OF STRUCTURES EQUIPPED WITH BRB

P. Castaldo<sup>1</sup>, E. Tubaldi<sup>2</sup>, and L. Gioiella<sup>3</sup>

<sup>1</sup> Department of Structural, Geotechnical and Building Engineering (DISEG),  
Politecnico di Torino, Turin, Italy  
paolo.castaldo@polito.it

<sup>2</sup> Department of Civil and Environmental Engineering,  
University of Strathclyde, Glasgow, Scotland  
enrico.tubaldi@strath.ac.uk

<sup>3</sup> School of Architecture and Design SAAD,  
University of Camerino, Ascoli Piceno, Italy,  
laura.gioiella@unicam.it

---

### Abstract

*Over the years, the buckling restrained braces (BRBs) have more and more become one of the best solutions for retrofitting or upgrading many existing reinforced concrete framed buildings located in areas with a high seismic hazard. The present investigation studies the effectiveness of BRBs used to seismically retrofit a reinforced concrete (RC) building in L'Aquila defining an advanced non-linear 3D model in OpenSees. The seismic performance of the investigated building is assessed developing the following comparisons: before and after the retrofit through BRBs. Adopting a hysteretic model specific for the BRBs, both non-linear static analyses and incremental dynamic analyses under a set of real ground motion records are carried out to build the seismic demand hazard curves. The numerical results highlighted the influence of the BRBs on the seismic performance of the system components also in relation to the effectiveness of the retrofit.*

**Keywords:** Seismic Demand Hazard Curves, Buckling Restrained Braces, Capacity, Reinforced Concrete Frame, Masonry Infill Walls.

---

## 1 INTRODUCTION

Among the different solutions available to enhance the performance of existing structures, a great variety of passive energy dissipation systems [1]-[3] have been proposed in the last decades. These systems are usually classified as hysteretic dampers, viscoelastic dampers, viscous fluid dampers [4] and friction dampers [5]. Buckling restrained braces (BRBs) are hysteretic dampers that constitute one of the most efficient system for adding stiffness, strength and energy dissipation capacity to a structure [6]-[8]. The effectiveness of these devices has been proven by many experimental tests and numerical simulations, and numerous applications to existing buildings have been documented in the literature (e.g., [9]-[12]). BRBs consist of a steel core placed inside a steel tube filled with a concrete material [13]-[14]. According to numerous experimental tests, BRBs exhibit a stable hysteretic behaviour with a high-energy dissipation capacity, up to ductility levels higher than 20 [15]-[16].

Many studies in the literature have proposed methodologies for the design of BRBs for retrofitting existing frames and have evaluated the performance of the retrofit with deterministic approaches (e.g., [17]-[19]). However, very few works have analyzed the performance of buildings retrofitted with BRBs by employing probabilistic approaches accounting for the effect of the uncertainties inherent to the seismic input. Among these, Guneyisi [20] investigated the application of BRBs for seismic retrofitting of steel moment resisting framed buildings. Fragility curves were developed using the maximum interstorey drift ratio as engineering demand parameter (EDP), and were used to compare the performances of the bare frame, the frame retrofitted with conventional braces, and the frame retrofitted with BRBs. Freddi et al. [7] proposed a probabilistic framework, based on the use of component and system fragility curves, to evaluate the effectiveness of BRBs for retrofitting reinforced concrete (RC) frames with low ductility capacity. Moreover, important EDPs, such as the absolute accelerations, were disregarded. Adding stiffness and strength to a frame through the BRBs often leads to an increase rather than a decrease of absolute accelerations, due to the reduction of the vibration period, and this may affect the performance of acceleration-sensitive non-structural building components. Furthermore, it is widely acknowledged that the main drawback of BRBs is their low post-yield stiffness, which may result in excessive residual inter-storey drifts in structures equipped with them [21]-[23]. Thus, an assessment of the effectiveness of the retrofit should also account for the response in terms of these two EDPs.

Finally, previous studies on the performance of buildings retrofitted with BRBs have employed simplified models of the BRBs with essentially elasto-plastic behaviour and kinematic hardening. However, more sophisticated constitutive models should be considered to properly account for the specific features of the behaviour of these devices that emerged in numerous experimental tests [13], [24]-[25]. These include the significant role of isotropic hardening and the asymmetry in the yield force in compression with respect to that in tension [13], [24]. The cumulative plastic deformations in the BRBs, that may control the failure of these devices due to low-cycle fatigue, need also to be monitored [26]-[31].

The aim of this work is to evaluate the effectiveness of buckling restrained braces for retrofitting an existing RC building, by employing an advanced model of BRBs and a wide range of EDPs for monitoring the performance of the building components and of the BRBs. For this purpose, an existing RC building located in L'Aquila, damaged by the 2009 earthquake, is used as case study. First, a non-linear three-dimensional model of the existing RC building is defined in OpenSees [32]. A widely employed procedure based on pushover analyses and N2 method [33] is employed to design the braces. Specifically, the bracing system is designed by disregarding the effect of infill walls and with the target objective of achieving a maximum interstorey drift ratio of 1.5% under the life safety limit state design seismic action [34] for the

site (return period of 475 years). Successively, the seismic performance of the retrofitted building is evaluated by performing both non-linear static analyses and incremental dynamic analyses under a set of real ground motion records. Seismic fragility and demand hazard curves of the building are derived considering multiple EDPs. These include the maximum interstorey drifts together with the absolute accelerations.

The capability of the dissipative bracing system in enhancing the performance of structural and non-structural components of the frame is assessed by evaluating the results in terms of seismic demand hazard curves, providing the annual rate exceeding different demand levels.

## 2 CASE STUDY: DESCRIPTION AND MODELLING

The case study (Figure 1) is a reinforced concrete frame built in 1984 that is representative of many RC structures built in Italy before the introduction of modern seismic codes and designed for gravity loads only, without any seismic detailing. The building is composed of five stories with a height of 2.8 m at the ground storey and of 3 m at the other storeys. Figure 1 describes the plan configuration of the frame, with an overall length of 25.30x10.85 m along the horizontal (X) and vertical (Y) directions, respectively. A reinforced concrete staircase is located centrally in the lower part of the building. The frame columns have a rectangular cross section with dimensions 35x60 cm at the ground floor and 30x60 cm at the other floors, whereas the columns that support the stair landing have the same rectangular cross section of 25x60 cm at each floor. The beams along the Y direction are deep beams with various rectangular sections: 35x50 cm, 30x50 cm and 25x50 cm. The properties of materials used for the structural components of the frame have been evaluated via a campaign of destructive in-situ tests. In particular, the concrete material behavior was evaluated based on 16 compressive tests on concrete cores extracted from the RC frame elements, while the steel properties were evaluated based on tensile strength tests executed on rebar samples. Table 1 reports the average mechanical properties for unconfined concrete and reinforcement steel. With regards to concrete,  $f_c$  denotes the compressive strength,  $E_c$  the elastic modulus,  $\varepsilon_c$  and  $\varepsilon_{cu}$  the peak and ultimate deformations, and  $f_{cu}$  the ultimate strength. With regards to steel,  $f_{sy}$  is the yield stress,  $E_s$  the elastic modulus, and  $b$  the post-elastic to elastic stiffness hardening ratio.

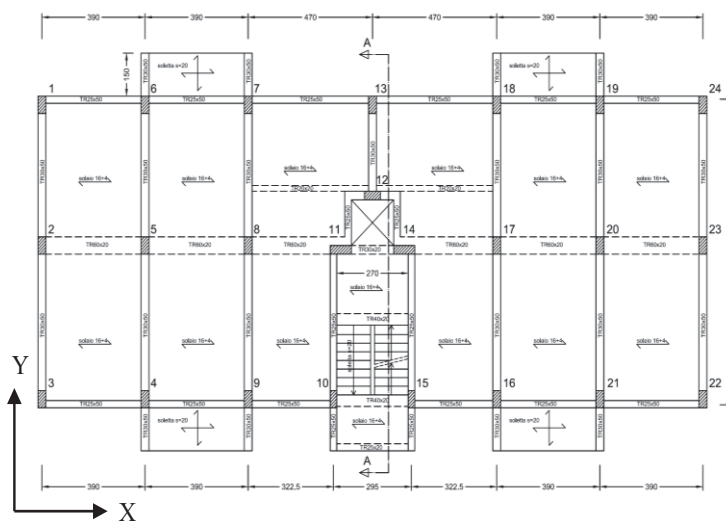


Figure 1. Schematic plan configuration of the building. (Dimensions in cm)

Unconfined concrete					Steel		
$f_{cm}$ [N/mm <sup>2</sup> ]	$\varepsilon_c$ [-]	$f_{cu}$ [N/mm <sup>2</sup> ]	$\varepsilon_{cu}$ [N/mm <sup>2</sup> ]	$E_c$ [N/mm <sup>2</sup> ]	$f_{sy}$ [N/mm <sup>2</sup> ]	$E_s$ [N/mm <sup>2</sup> ]	$b$ [-]
21.6	0.018	21.6	0.0035	27717.8	430.7	206000	0.01

Table 1. Mechanical properties of unconfined concrete and steel reinforcement.

The building is located in L'Aquila (Italy), with geographical coordinates Lon. = 13.394° and Lat. = 42.36°, on a soil of class D and topographical category T1, according to [34]. Figure 2 shows the code elastic response spectra in terms of accelerations and displacements for different limit states and relevant return periods (i.e., Operational – 30 years, Damage – 50 years, Life Safety – 475 years, Near Collapse - 975 years) assuming an inherent damping factor of 5%, respectively.

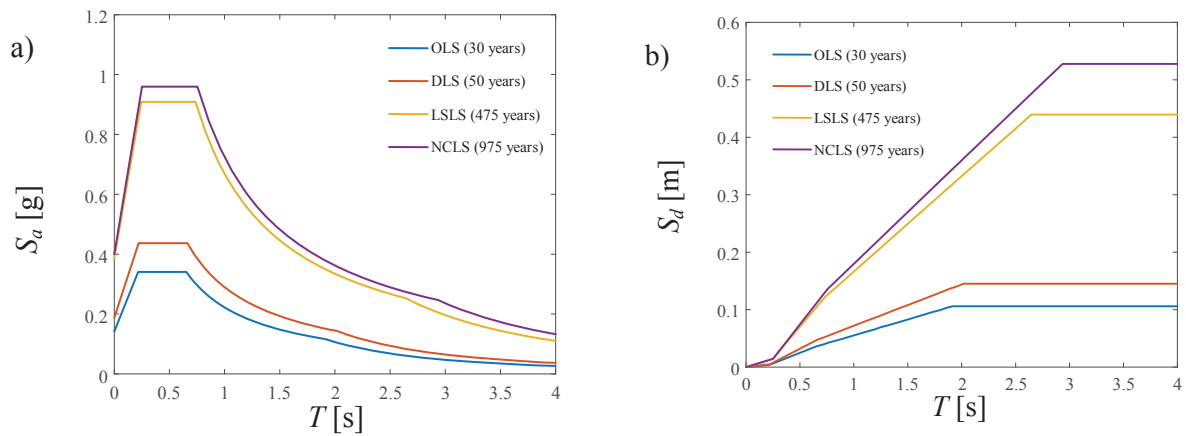


Figure 2. Code elastic response spectra in terms of accelerations a) and displacements b).

Figure 3 shows the numerical model of the RC frame developed in OpenSees [32], which employs “beam with hinges” elements [35] to describe the nonlinear hysteretic response of beams and columns. The beam-column joints are described by beam elements with very high stiffness whereas the in-plane rigid floor slab is described by a diaphragm constraint at each floor. In the “beam with hinges” elements, the inelastic behaviour is concentrated over specified hinge lengths  $L_{pi}$  and  $L_{pj}$  at the two element ends while, a linear elastic behaviour is assigned to the central portion. The lengths of the plastic hinges are defined as a function of the shear span  $L_v$ , assumed equal to the half element length, and of the product between the bar yield strength and diameter  $f_{sy}d_b$  [36]:

$$L_p = 0.12L_v + 0.014\alpha_{sl}f_{sy}d_b \quad (1)$$

where  $\alpha_{sl}$  is a variable that can assume the value 1 if the slippage of the reinforcement bars from the anchorage zone beyond the end section is possible or 0 if is not.

In the plastic hinge zone, the behaviour of concrete is described by the nonlinear degrading Concrete02 material model [32], with tensile strength set to  $0.1f_{cm}$  and a linear tension softening.

The effect of the confinement of the concrete core fibers of beams and columns is taken into account by modifying the concrete constitutive law as suggested by [37]. The compressive



strength of the confined concrete increases thanks to the compressive effect provided by the stirrups and the longitudinal reinforcement and can be evaluated as:

$$f'_{cc} = f_{cm} \left( -1.254 + 2.254 \sqrt{1 + \frac{7.94 f'_l}{f_{cm}}} - 2 \frac{f'_l}{f_{cm}} \right) \quad (2)$$

where  $f_{cm}$  is the compressive strength of the unconfined concrete (Table 1) and  $f'_l$  depends on the geometry of the section and of the reinforcements as explained in [37]. The ultimate compressive strain,  $\varepsilon_{cu}$ , corresponds to the rupture of the first hoop and can be found based on an energy balance approach [37]. The confinement differs for each section, since it depends on the dimensions, and amount of longitudinal bars and stirrups. Thus, different values of  $f'_{cc}$ , crushing strength and  $\varepsilon_{cu}$  are obtained for the various sections.

The behaviour of steel reinforcement is described by using a uniaxial bilinear constitutive law with kinematic hardening (Steel01 in OpenSees [32]). Concrete cracking is taken into account by considering an effective flexural stiffness for the elastic part of each beam and column element. This stiffness is evaluated by means of moment-curvature analysis of the sections at the extremes of the elements, for the axial force level induced by the dead loads (zero axial load in case of beams).

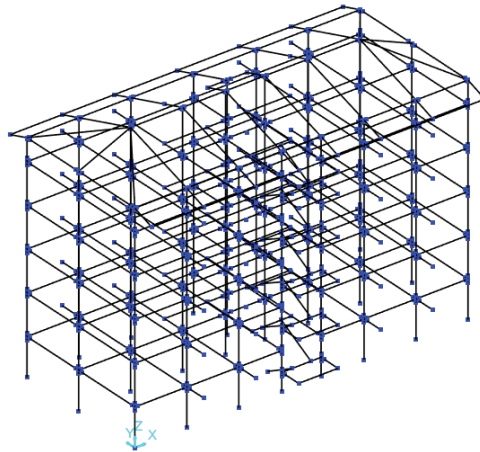


Figure 3. Numerical model of the RC building in OpenSees (with no infills).

Using the function “MinMax material” of OpenSees [32], material failure can be simulated in the fibers of the RC sections by setting the stresses to zero once a prefixed strain threshold value is attained. Conservatively, the same threshold of  $\varepsilon_{cu}$  equal to -0.012 is set for all the concrete fibers with the confined properties. For the unconfined concrete of the cover of the cross sections, the strain threshold was set to -0.0035. The rupture of the reinforcement bars, with a drop of the stress to zero, is assumed to occur at a strain of 0.075. The system nonlinear geometrical behaviour is taken into account by considering second-order P-delta effects.

### 3 DESIGN AND MODELLING OF THE HYSTERETIC DEVICES (BRBS)

The method proposed by Dall'Asta et al. [17] is employed in this study to design the dissipative bracing system. According to this method, the dissipative bracing system and the existing frame are described as two elastic-perfectly plastic single-degree-of-freedom (SDOF) systems acting in parallel. The properties of the SDOF system equivalent to the existing frame

are derived by performing a pushover analysis under a distribution of forces corresponding to its first vibration mode [33]. The capacity curve of the frame is replaced by an elastic perfectly-plastic one, which is obtained based on an energy equivalence criterion and is described by the initial stiffness  $K_f$ , the base shear capacity  $V_f$ , and the ductility capacity  $\mu_{fc}$  (Figure 4a).

The properties of the bracing system depend on the properties of the diagonal braces at each storey. It is worth to recall that the diagonal dissipative braces considered here consist of two members in series, namely the BRB device and the over-strengthened brace. Only the first one undergoes plastic deformations, whereas the second is designed to remain elastic.

The distribution of the stiffness of the braces along the building height is assumed equal to the one of the frame in order to obtain a coupled system with the same first mode shape. Moreover, the braces are assumed to yield simultaneously when the structure vibrates according to the first mode.

The design ultimate displacement of the diagonal brace system can be assumed equal to that of the frame, in order to ensure simultaneous failure of both the frame and the braces. The capacity curve of the bracing system is idealized as an elastic-perfectly plastic curve, and described by few parameters that are the design variables: the initial stiffness  $K_d$ , the base shear capacity  $V_d$ , and ductility capacity  $\mu_{dc}$ , equal to that of the diagonal braces under the assumption of simultaneous yielding of the diagonal braces at all the storeys. It is noteworthy that the BRBs, and thus the bracing system, exhibit a more complicated behaviour, which however is simplified in the design stage.

In this study, only the retrofit of the frame along the X direction is considered, since this corresponds to the weak direction of the bare frame. The results from the modal analysis of the bare frame for the first five vibration modes are summarized in Table 2. The coupling between the modal responses along the two directions is very low, and the mass participation factor of the first mode along the X direction is very high (i.e., 80.8%).

Mode	Type	$\omega$ [rad/s]	$T$ [s]
1	Translational X	7.388	0.850
2	Rotational	9.371	0.670
3	Translational Y	9.496	0.662
4	Translational X	23.432	0.268
5	Rotational	30.300	0.207

Table 2. Vibration modes of the bare frame.

The design procedure of the bracing system requires the evaluation of the bare frame capacity curve along the X direction by means of a nonlinear static (pushover) analysis. The lateral load pattern for the pushover analysis is determined for a distribution of the loads proportional to the first vibration mode of the structure. The control node is the centre of mass of the top floor. Figure 4a shows the capacity curve of the equivalent SDOF system and its bilinearization according to the Italian code [34]. These curves are expressed in terms of  $d^*$  and  $V^*$ , which are obtained dividing the displacement of the control node and the base shear of the MDOF system by the modal participation factor  $\Gamma = \sum m_i u_i / \sum m_i u_i^2$  of the first vibration mode. The ductility capacity of the frame is  $\mu_{fc} = 3.73$ , corresponding to a maximum inter-storey drift ratio of 2.3%.

Figure 4b compares, in the acceleration-displacement plane, the elasto-plastic capacity curve of the bare frame and the seismic demand for the life safety limit state according to the N2 method. The values of the acceleration  $a^*$  of the capacity curve are obtained by dividing the forces  $V^*$  by the equivalent mass  $m^* = \sum m_i u_i$  of the SDOF system. It can be seen that the ductility demand  $\mu_f=3.55$  is quite close to the ductility capacity of the structure. Thus, the structure needs to undergo significant plastic deformations to withstand the seismic demand, leading to extended damage.

In order to reduce the seismic damage, the bracing system is added in parallel to the frame, and the target ductility demand of the frame under the design seismic input is assumed equal to  $\mu_f=2.64$ , corresponding to a maximum interstorey drift ratio (IDR) of 1.5%.

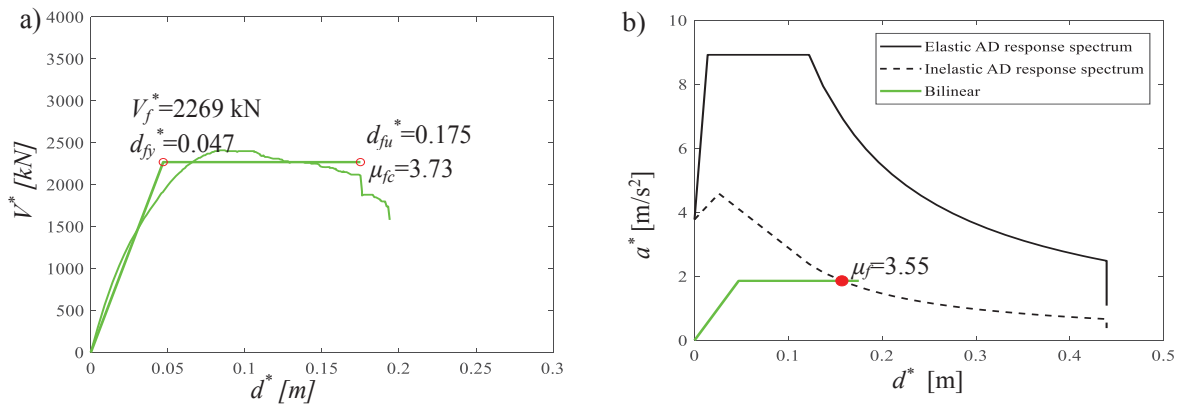


Figure 4. a) Capacity curve of the SDOF system equivalent to the bare frame and its bi-linearization and b) comparison between the seismic demand and capacity for the bare frame.

The ductility capacity of the BRB devices and of the dissipative system are assumed respectively equal to  $\mu_{0c}=15$  and  $\mu_{dc}=10$ . It is noteworthy that the value of  $\mu_{dc}$  is less than the value of  $\mu_{0c}$  due to the flexibility of the brace placed in series with the BRB device ([6], [17]). The base shear capacity of the BRB system must be equal to  $V_d=900$  kN to obtain a design capacity curve of the coupled system (frame and BRBs system) that intersects the inelastic demand spectrum (Figure 5a-b). It is noteworthy that the base shear of the bracing system is only 39% of the base shear of the bare frame. Although a higher value could be chosen, by reducing the ductility demand of the frame, this would result in excessive forces transmitted to the columns adjacent to the bracing system, and an increase of their vulnerability [6]. Moreover, higher values of this ratio are generally associated with excessive interstorey residual drift levels, impairing reparability after major earthquake events.

Given the properties of the bracing system, the characteristics of the BRB devices and of the elastic braces at each storey can be determined by following the procedure described in Dall'Asta et al. [17] and they are reported in Table 3. It is worth to recall that the design properties of the braces (initial stiffness  $K_d^i$ , yielding force  $F_d^i$  and ductility capacity  $\mu_{dc}^i$  where  $i$  denotes the storey number) depend on the properties of the BRB device (initial stiffness  $K_0^i$ , yield force  $F_0^i$  and ductility capacity  $\mu_{0c}^i$ ) and on the properties of the elastic brace (length  $L_b^i$  and stiffness  $K_b^i$ ). The brace length  $L_d^i$  is equal to the sum of the BRB length  $L_0^i$  and the elastic brace length  $L_b^i$ .

In order to limit the axial forces transmitted to the columns adjacent to the braces, four diagonal braces are employed at each storey. The brace arrangement is shown in Figure 6.

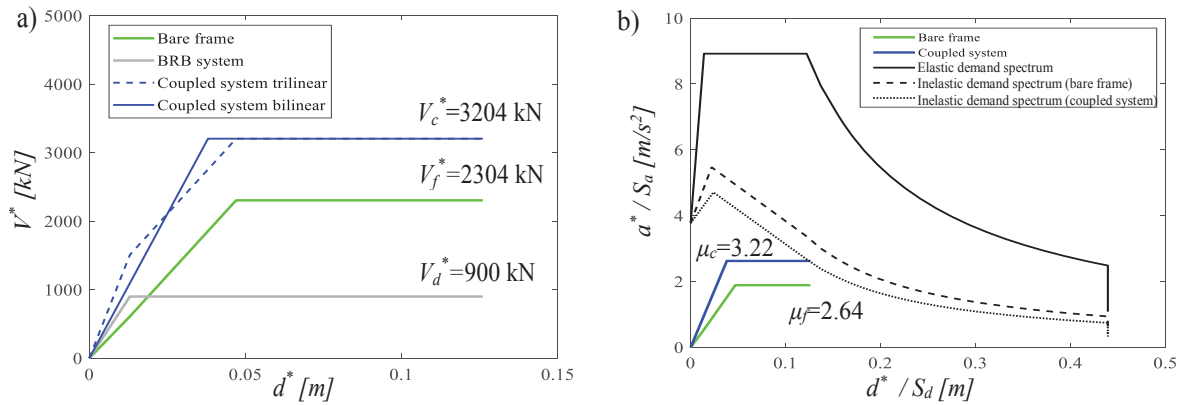


Figure 5. a) Design bilinear capacity curve of the SDOF system equivalent to the retrofitted frame and b) comparison between the seismic demand and capacity for the retrofitted frame.

Storey	Braces		BRBs				Elastic braces				
	$F_c^i$	$K_c^i$	$K_0^i$	$F_0^i$	$A_0^i$	$L_0^i$	$K_b^i$	$F_b^i$	$A_b^i$	$t_b^i$	$L_b^i$
[-]	[kN]	[kN/m]	[kN]	[kN/m]	[m <sup>2</sup> ]	[m]	[kN]	[kN/m]	[m <sup>2</sup> ]	[mm]	[m]
4	152	91404	142.18	152.05	608.19	898.3	142.18	152.05	608.19	10	898.3
3	235.6	91793	142.79	235.56	942.23	1385.7	142.79	235.56	942.23	10	1385.7
2	299	95200	148.09	299.04	1196.14	1696.2	148.09	299.04	1196.14	10	1696.2
1	338	105238	163.7	337.99	1351.97	1734.3	163.7	337.99	1351.97	10	1734.3
0	343.8	188593	293.37	343.78	1375.14	984.4	293.37	343.78	1375.14	10	984.4

Table 3. Dissipative braces, BRBs and elastic brace properties at each storey.

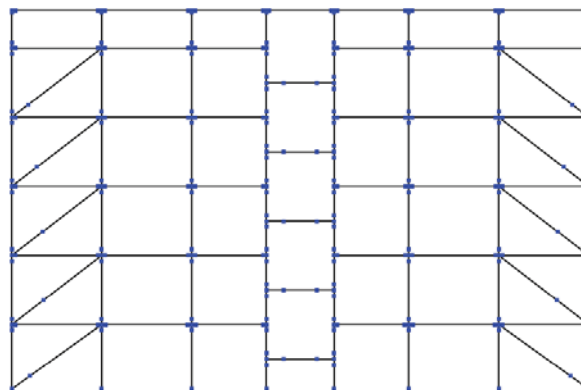


Figure 6. Modelling of the BRB by means of two elements (truss + elastic beam).

The dissipative braces are modelled by using two elements (Figure 6): an elastic beam element for the elastic brace and a truss element for the BRB. The BRB is assigned the constitutive law of Zona et al. [30]. The parameters that influence the hardening and hysteresis of the elasto-plastic model can be calibrated based on experimental characterization tests carried out on BRB prototypes. In this study, the parameters reported in Zona et al. [30] and calibrated on

the experimental tests of Tremblay et al. [38] are considered. Figure 7 shows the capacity curve evaluated by performing the nonlinear static analysis of the retrofitted structure, and the corresponding equivalent bilinear curve. The capacity curve is truncated at a value of the displacement equal to 0.15 m, corresponding to an IDR of 1.5% for the frame and a ductility capacity  $\mu_c=3.22$ . The ductility of the coupled system is much higher than that of the frame ( $\mu_f=2.64$ ), thanks to the addition of the BRBs. Figure 7b compares the elastic and inelastic seismic demand with the capacity of the coupled system. The seismic design action induces a ductility demand of 3.13 (Figure 7b) in the system.

It is noteworthy that the design of the dissipative bracing system has been carried out disregarding the contribution of the infill walls.

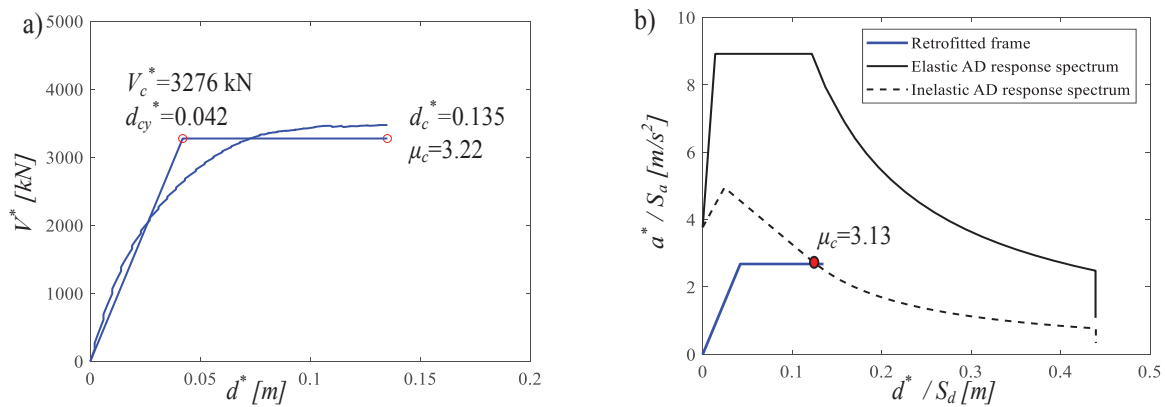


Figure 7. a) Capacity curve of the SDOF system equivalent to the retrofitted system and its bi-linearization and b) comparison between the seismic demand and capacity for the retrofitted frame.

#### 4 SEISMIC PERFORMANCE AND RETROFIT EFFECTIVENESS EVALUATION

The seismic performance assessment of the system and the evaluation of the effectiveness of BRBs for the retrofit are based on the development and comparison of seismic demand hazard curves for different EDPs describing the seismic response of structural and non-structural components, as well as of the BRBs. Coherently with the performance-based earthquake engineering (PBEE) approach [39]-[41], the uncertainties related to the seismic input intensity are separated from those related to the characteristics of the record (i.e., record-to-record variability) by introducing an intensity measure ( $IM$ ). In particular, the randomness in the seismic intensity is described by a hazard curve, whereas the record-to-record variability for a fixed intensity level is modelled by selecting a set of natural ground motion records characterized by a different duration and frequency content, scaled to the assumed intensity level [42].

It is worth to note that, in general, the  $IM$ 's choice should be driven by criteria of efficiency, sufficiency and hazard computability [43]-[45]. In this study, the spectral acceleration,  $S_a(\xi, T)$ , at the fundamental period of the system,  $T = 2\pi / \omega$  and for the damping ratio  $\xi = 5\%$ , is assumed as intensity measure. This is a structural dependent  $IM$  that changes with the structural model. Table 4 reports the periods of the four models considered, together with the corresponding  $IM$  values at the life safety limit state (LFLS) and near collapse limit state (CLS).

Incremental dynamic analysis (IDA) [46] are carried out to investigate the response of the different systems for increasing intensity levels. The set of 30 ground motion records employed in IDA are derived from 19 different seismic natural events, selected within the ground motion database of PEER (Pacific Earthquake Engineering Research Center) [47], of ITACA



(Italian Accelerometric Archive) [48] and of ISESD (Internet-Site for European Strong-Motion Data) [49]. The characteristics of the selected ground motion records are reported in Table 5. Their source-to-site distance,  $R_s$ , is greater than 8.7 km, and their moment magnitude,  $M$ , is in the range between 6 and 7.6. Figure 8 shows the acceleration elastic response spectra of the unscaled records of Table 5.

	Bare frame	Retrofitted frame	Infilled frame	Inf. retrofitted frame
$T$ [s]	0.850	0.637	0.836	0.632
$S_{a,LSLS}$ [g]	0.787	0.909	0.799	0.909
$S_{a,NCLS}$ [g]	0.851	0.959	0.865	0.959

Table 4. Periods of the four models.

#	Year	Earthquake Name	Recording Station Name	$V_{s30}$ [m/s]	Fault Type	$M$ [-]	$R_s$ [km]	PGA [g]
1	1994	Northridge	Beverly Hills - Mulhol	356	Thrust	6.7	13.3	0.52
2	1994	Northridge	Canyon Country-WLC	309	Thrust	6.7	26.5	0.48
3	1994	Northridge	LA-Hollywood Stor	316	Thrust	6.7	22.9	0.36
4	1999	Duzce, Turkey	Bolu	326	Strike-slip	7.1	41.3	0.82
5	1999	Hector Mine	Hector	685	Strike-slip	7.1	26.5	0.34
6	1979	Imperial Valley	Delta	275	Strike-slip	6.5	33.7	0.35
7	1979	Imperial Valley	El Centro Array #11	196	Strike-slip	6.5	29.4	0.38
8	1995	Kobe, Japan	Nishi-Akashi	609	Strike-slip	6.9	8.7	0.51
9	1995	Kobe, Japan	Shin-Osaka	256	Strike-slip	6.9	46.0	0.24
10	1999	Kocaeli, Turkey	Duzce	276	Strike-slip	7.5	98.2	0.36
11	1999	Kocaeli, Turkey	Arcelik	523	Strike-slip	7.5	53.7	0.22
12	1992	Landers	Yermo Fire Station	354	Strike-slip	7.3	86.0	0.24
13	1992	Landers	Coolwater	271	Strike-slip	7.3	82.1	0.42
14	1989	Loma Prieta	Capitola	289	Strike-slip	6.9	9.8	0.53
15	1989	Loma Prieta	Gilroy Array #3	350	Strike-slip	6.9	31.4	0.56
16	1990	Manjil, Iran	Abbar	724	Strike-slip	7.4	40.4	0.51
17	1987	Superstition Hills	El Centro Imp. Co.	192	Strike-slip	6.5	35.8	0.36
18	1987	Superstition Hills	Poe Road (temp)	208	Strike-slip	6.5	11.2	0.45
19	1987	Superstition Hills	Westmorland Fire Stat.	194	Strike Slip	6.5	15.1	0.21
20	1992	Cape Mendocino	Rio Dell Overpass	312	Thrust	7.0	22.7	0.55
21	1999	Chi-Chi, Taiwan	CHY101	259	Thrust	7.6	32	0.44
22	1999	Chi-Chi, Taiwan	TCU045	705	Thrust	7.6	77.5	0.51
23	1971	San Fernando	LA - Hollywood Stor	316	Thrust	6.6	39.5	0.21
24	1976	Friuli, Italy	Tolmezzo	425	Thrust	6.5	20.2	0.35
25	1980	Irpinia	Bisaccia	496		6.9	21.3	0.94
26	1979	Montenegro	ST64	1083	Thrust	6.9	21.0	0.18
27	1997	Umbria Marche	ST238	n/a	Normal	6.0	21.5	0.19
28	2000	South Iceland	ST2487	n/a	Strike Slip	6.5	13	0.16
29	2000	South Iceland (a.s.)	ST2557	n/a	Strike Slip	6.4	15.0	0.13
30	2003	Bingol	ST539	806	Strike Slip	6.3	14.0	0.30

Table 5. Selected ground motions for the time history analyses.

The EDPs considered for monitoring the seismic response are the peak values, among the various storeys, of the interstorey drift ratio (IDR) and the absolute acceleration (ACC).

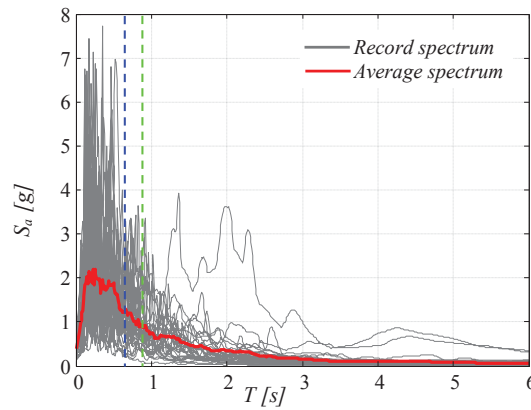


Figure 8. Acceleration elastic response spectra for the seismic records. The dashed lines indicate the structural periods of the various models.

Figure 9 shows the IDA curves in terms of IDR obtained for the various models considered. It is noteworthy that for high  $IM$  values, some convergence issues arise due to the failure of some fibers in critical sections and nonlinear geometrical behaviour of the model. Thus, plotted in the figure are only the numerically-converging dynamic analysis points. It can be observed in the plot that in the case of the bare frame, the IDR of 1.5% is reached at an  $IM = 0.3g$  for the bare frame model and at  $0.7g$  for the retrofitted model. This results already shows the benefit of the use of the BRBs in terms of drift reduction, which is only partially impaired by the seismic demand increase due to period reduction (see Table 4).

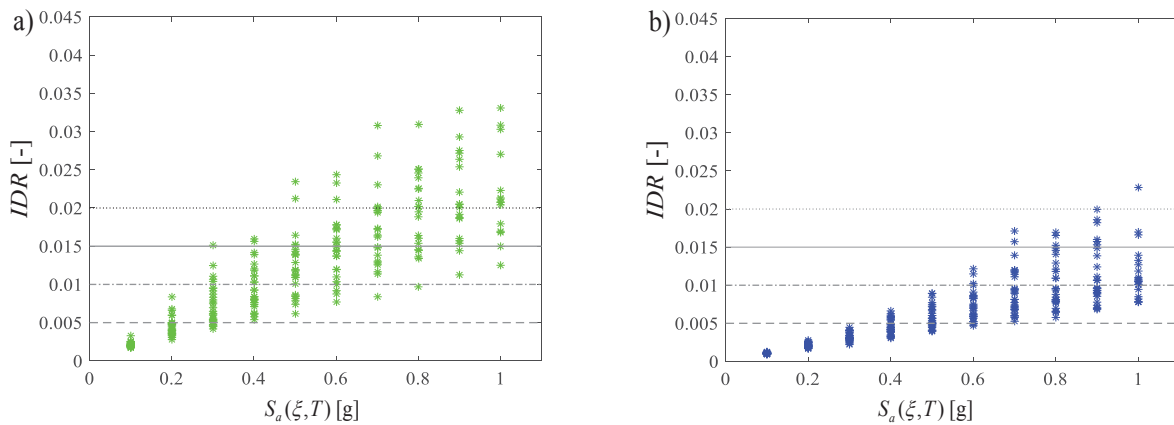


Figure 9. IDA results in terms of IDR: a) Bare frame; b) Bare frame with BRBs.

For each EDP considered, the conditional exceeding probability  $G_{EDP|IM}(d|im)$  is evaluated for the different models at the various  $IM$  levels considered. Both the collapse (and convergence) and not-collapse results are taken into account by applying the total probability theorem [50]-[53], according to the following expression:

$$G_{EDP|IM}(edp|im) = G_{EDP|IM}(edp|im, NC)(1 - P[C|IM]) + P[C|IM] \quad (3)$$

where  $G_{EDP|IM}(edp|im, NC)$  is the probability of exceedance of the EDP conditional to the  $IM$  and to not-collapse, the probability of collapse  $P[C|IM]$  is evaluated numerically for each  $IM$  level by dividing the number of analyses for which collapse occur by the total number of analyses.

Figure 10 shows the conditional exceedance curves for the IDRs, which are fitted by means of lognormal distributions. Five different demand thresholds are considered, namely 0.5%, 1%, 1.5%, 2% and 2.5%. These values correspond to increasing levels of seismic damage of the frame [50], [51], [54]. Obviously, the median value of the spectral acceleration corresponding to the threshold of 1.5% increases due to the retrofit and slightly decreases if the infill frames are considered in the models.

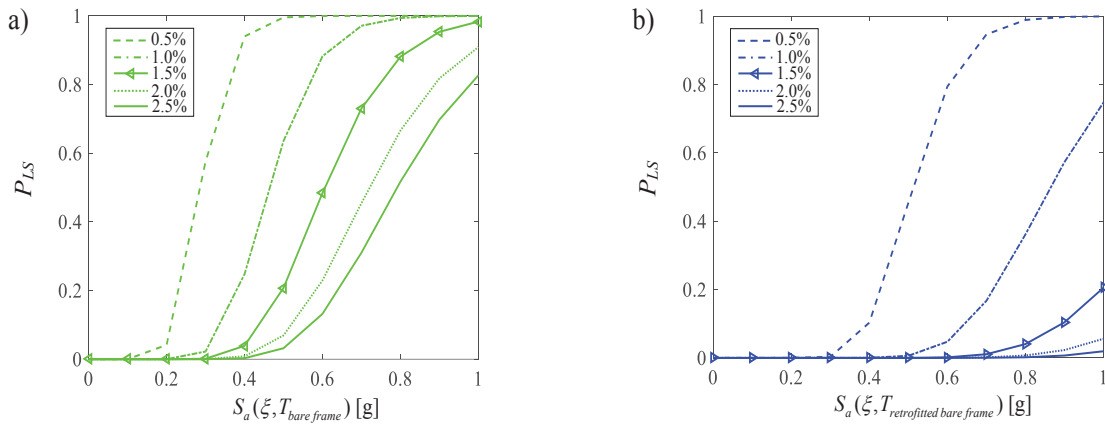


Figure 10. Conditional probability of exceedance vs. IM for the IDR: a) Bare frame; b) Bare frame with BRBs.

Figure 11 illustrates the conditional exceedance curves for the other EDP. In general, the exceeding probabilities decrease for increasing values of the threshold and increase for higher  $IM$  levels, as expected. The systems with added BRBs exhibit lower conditional probabilities compared to the ones without BRBs, for the same  $IM$  and threshold levels, for all the monitored EDPs. Quite interestingly, also the probability of exceedance of the absolute accelerations slightly reduces due to the addition of the BRBs, whereas the infills have a minor effect on this probability.

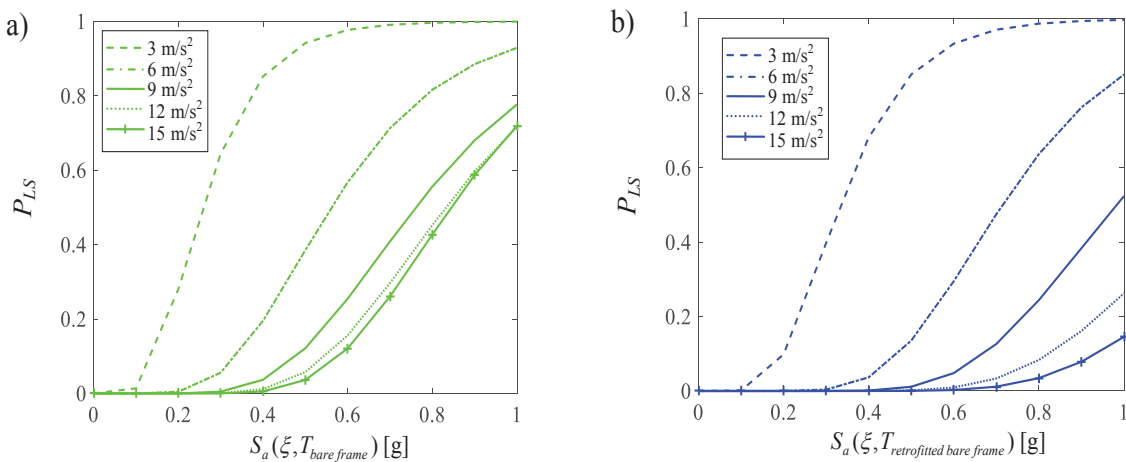


Figure 11. Conditional probability of exceedance vs. IM for the ACCs: a) Bare frame; b) Bare frame with BRBs.

It is noteworthy that the curves plotted in Figure 10-Figure 11 have been derived by considering different  $IM$ s for each of the models analysed. Thus, they could not be directly compared to each other. While in Freddi et al. [7] the concept of safety margin is used to compare fragility curves developed for a RC frame before and after the retrofit with BRBs, in this study seismic demand hazard curves, that are not conditional to the  $IM$ , are employed.

## 5 SEISMIC DEMAND HAZARD CURVES

Figure 12 shows the seismic hazard curves, expressing the mean annual rate (MAF) of exceedance  $\lambda$  of the various  $IM$ s considered in this study. These curves, plotted in semi-logarithmic scale, have been derived for the site in L'Aquila, where the structure is located, by following the procedure described in [34]. It can be observed that for the same level of the MAF of exceedance, the spectral acceleration is higher for the retrofitted frame than for the unretrofitted frame.

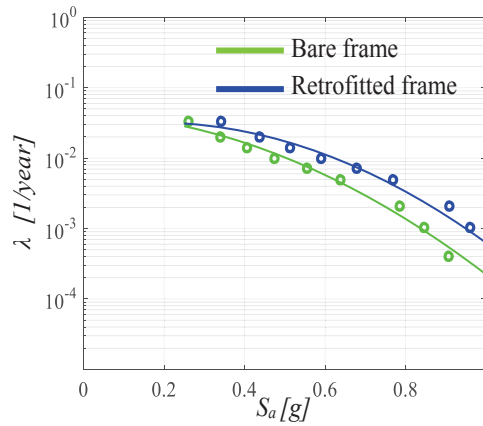


Figure 12. Seismic hazard curves for the unretrofitted frame and the frame retrofitted with BRBs obtained by neglecting the infill wall contribution.

The seismic demand hazard curves for the various systems and EDPs of interest are obtained by convolution of the conditional probability of exceedance (Figure 10 to Figure 11) with the relevant seismic hazard curve (Figure 12). The demand hazard curve for the generic EDP can be estimated as follows:

$$\lambda_{EDP}(edp) = \int_0^{\infty} G_{EDP|IM}(edp|im) \left| \frac{d\lambda_{IM}(im)}{d(im)} \right| d(im) \quad (4)$$

where  $d(\cdot)$  denotes the differential operator.

Figure 13 shows the demand hazard curves of the various EDPs of interest obtained for the structural models considered.

With regard to the  $IDR$ , it can be observed that the BRBs are effective to reduce the seismic demand to more acceptable values. In particular, the MAF of exceedance of the 0.5% threshold, commonly associated to onset of nonlinear behaviour of the frame, reduces from 0.0164 1/year to 0.0249 1/year, whereas the MAF of exceedance of the 2% threshold, associated to significant damage to the frame, reduces from 0.0037 1/year to 0.0001 1/year. Thus, the performance improvement is higher for high drift levels. It is also interesting to observe that the MAF of exceedance of the 1.5% limit, which is considered for the design of the BRBs, is equal to  $6 \cdot 10^{-4}$  1/year for the case of the retrofitted frame. This value is lower than the MAF

of exceedance of the design seismic input, which is  $2.1 \cdot 10^{-3}$  1/year. The discrepancy may be due to the simplifying assumptions of the design procedure, particularly the fact that the isotropic hardening behavior of the BRBs is neglected when evaluating the pushover curve of the retrofitted frame. Nevertheless, the MAF of exceedance is higher than the reference MAF of collapse that is targeted by the risk-based design approaches in the US [55]. In Europe, lower values of the MAF of collapse are sought for new structures, (about  $10^{-5}$ - $10^{-6}$  1/year [51], [55]).

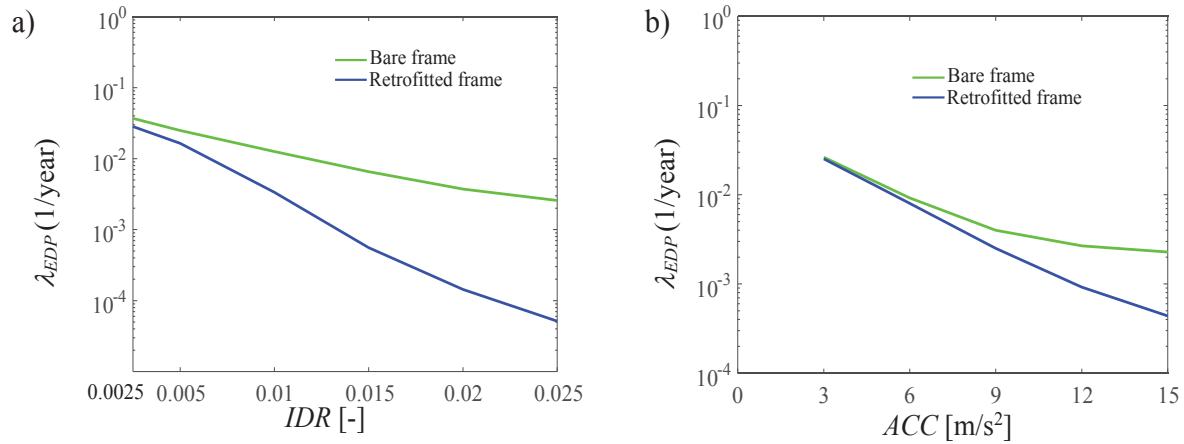


Figure 13. Demand hazard curves of the EDPs for the different structural models considered.

In Figure 13b, it is interesting to observe that the curve of the MAF of exceedance of the absolute accelerations is very similar for all the models for low acceleration values, below  $9 m/s^2$ . This is because adding the BRBs and the infills to the frame results both in a decrease of period, which would increase the acceleration demand, but also in an increase of energy dissipation, which on the other hand reduces the acceleration demand. Thus, this type of retrofit is not very effective in improving the performance of acceleration-sensitive non-structural components. Some improvements in terms of acceleration demand reduction can be observed for acceleration value higher than  $9 m/s^2$ . More details may be found in [56].

## 6 CONCLUSIONS

In this work, a performance-based approach is employed to evaluate the efficiency of the retrofitting of an existing RC building with buckling restrained braces (BRBs). In particular, an existing reinforced concrete building located in L'Aquila is used as case study. An advanced non-linear three-dimensional model of the existing RC building is defined in OpenSees, and a widely employed procedure based on pushover analyses is used to design the braces. Specifically, the bracing system is designed to obtain a retrofitted bare structure that is able to withstand the seismic demand associated to the life safety limit state design spectrum (return period of 475 years) experiencing a maximum absolute interstorey drift index of 1.5%. Successively, the seismic performance of the retrofitted bare building is evaluated by performing both non-linear static analyses and incremental dynamic analyses under a set of real ground motion records scaled to increasing seismic intensity levels. Seismic demand hazard curves are estimated for the interstorey drifts and other engineering demand parameters. The spectral acceleration at the fundamental period of the bare or infilled structure for a damping factor of 5% is used as intensity measure.

Based on the study results, the following conclusions can be drawn:

- Adding a relatively light BRB brace system to the existing frame results in notable performance improvements. In fact the use of the BRBs provides not only an increased ductility



capacity to the system, but also a reduction of the softening behavior following the attainment of the peak resistance, as shown by the capacity curves of the analysed models. The benefit in terms drift reduction due to the use of BRBs are also evident by observing the demand hazard curves for the IDRs. The MAF of exceedance of the 1.5% limit, which is considered for the design of the BRBs, is equal to  $6 \cdot 10^{-4}$  1/year for the case of the retrofitted frame with no infills, and it is about 1/10 of the corresponding MAF level for the case of the bare frame with no BRBs.

- The retrofit with BRBs does not reduce significantly the risk of exceeding absolute acceleration demands less than  $9 \text{ m/s}^2$ , but it more effective for higher acceleration levels. Thus, alternative retrofit measures may have to be employed if the seismic performance of acceleration-sensitive non-structural components has to be minimized.

## REFERENCES

- [1] Soong T.T., Dargush G.F. Passive Energy Dissipation Systems in Structural Engineering. Wiley & Sons, 1997.
- [2] De Iuliis, M., & Castaldo, P. (2012). An energy-based approach to the seismic control of one-way asymmetrical structural systems using semi-active devices. *Ingegneria Sismica-International Journal of Earthquake Engineering*, 29(4), 31-42.
- [3] Soong T.T., Constantinou M.C. Passive and Active Structural Vibration Control in Civil Engineering. Springer-Verlag: Wien-New York, 1994.
- [4] Castaldo P., De Iuliis M. Optimal integrated seismic design of structural and viscoelastic bracing-damper systems. *Earthquake Engineering and Structural Dynamics*. 2014; **43**(12): 1809-1827.
- [5] Soong T.T., Spencer B.F. Jr. Supplemental energy dissipation: state of the art and state of the practice. *Engineering Structures*. 2002; **24**: 243-259.
- [6] Di Sarno L., Manfredi G. Seismic retrofitting of existing RC frames with buckling restrained braces. ATC & SEI 2009 Conference on Improving the Seismic Performance of Existing Buildings and Other Structures.
- [7] Freddi F., Tubaldi E., Ragni L., Dall'Asta A. Probabilistic performance assessment of low-ductility reinforced concrete frames retrofitted with dissipative braces. *Earthquake Engineering & Structural Dynamics*. 2013; **42**(7): 993-1011.
- [8] Sadeghi S., Rofooei F.R. Improving the seismic performance of diagrid structures using buckling restrained braces. *Journal of Construction Steel Research*, 2020, <https://doi.org/10.1016/j.jcsr.2019.105905>.
- [9] Brown A.P., Aiken I.D., Jafarzadeh F.J. Buckling Restrained Braces Provide the Key to the Seismic Retrofit of the Wallace F. Bennett Federal Building. Modern Steel construction, AISC, 2001.
- [10] Tremblay R., Degrange G., Blouin J. Seismic rehabilitation of a four-storey building with a stiffened bracing system. Proceedings of the 8<sup>th</sup> Canadian Conference on Earthquake Engineering, Vancouver, Canada 1999.
- [11] Di Sarno L, Elnashai AS. Bracing systems for seismic retrofitting of steel frames. *J Construct Steel Res* 2009;65(2):452–65. <http://dx.doi.org/10.1016/j.jcsr.2008.02.013>.

- [12] De Domenico, D., Impollonia, N., and Ricciardi, G. (2019a). Seismic retrofitting of confined masonry-RC buildings: The case study of the university hall of residence in Messina, Italy. *Ingegneria Sismica* 36, 54–85.
- [13] Bozorgnia Y., Bertero V.V. Earthquake Engineering: From Engineering Seismology to Performance-Based Engineering. ICC-CRC Press, Boca Raton, Florida, USA 2004.
- [14] Watanabe A., Hitomi Y., Saeki E., Wada A., Fujimoto M. Properties of Brace Eneased in Concrete-Filled Steel Tube. Proceedings of the 9<sup>th</sup> World Conference on Earthquake Engineering, Tokyo-Kyoto, Japan, 1988.
- [15] Iwata M., Kato T., Wada A. Buckling-restrained braces as hysteretic dampers. Proc. STESSA 2000 Conf., 33-38, Montreal, Canada, August 2000.
- [16] Black C., Makris N., Aiken I. Component Testing, Stability Analysis and Characterization of Buckling-Restrained Unbonded Braces. Report No. PEER 2002/08, Univ. of California, Berkeley, CA, 2002.
- [17] Dall'Asta A., Ragni L., Tubaldi E., Freddi F. Design methods for existing r.c. frames equipped with elasto-plastic or viscoelastic dissipative braces. Conference: XIII National Conference ANIDIS: L'Ingegneria sismica in Italia, 2009.
- [18] Di Sarno L., Manfredi G. Seismic retrofitting with buckling restrained braces: Application to an existing non-ductile RC framed building. *Soil Dynamics and Earthquake Engineering*. 2010; **30**(11): 1279-1297.
- [19] Sutcu F., Takeuchi T., Matsui, R. Seismic retrofit design method for RC buildings using buckling-restrained braces and steel frames. *Journal of Constructional Steel Research*. 2014; **101**: 304-313.
- [20] Güneyisi EM. Seismic reliability of steel moment resisting framed buildings retrofitted with buckling restrained braces. *Earthquake Engineering and Structural Dynamics*. 2012; **41**(5): 853–874.
- [21] Sabelli R, Mahin SA, Chang C. Seismic demands on steel braced-frame buildings with buckling-restrained braces. *Engineering Structures*. 2003; **25**: 655-666.
- [22] Erochko J., Christopoulos C., Tremblay R., and Choi, H. Residual drift response of SMRFs and BRB frames in steel buildings designed according to ASCE 7-05. *Journal of Structural Engineering*. 2011; **137**(5): 589–599.
- [23] Kiggins S., Uang, C. M. Reducing residual interstory drift of buckling-restrained braced frames as a dual system. *Engineering Structures*. 2006; **28**(11): 1525–1532.
- [24] Uang C.M., Nakashima M., Tsai K.C. Research and application of buckling restrained braced frames. *International Journal of Steel Structures*. 2004; **4**(4):301-13.
- [25] Xie Q. State of the art of buckling-restrained braces in Asia. *Journal of constructional steel research*. 2005; **61**(6): 727-48.
- [26] Takeuchi T., Ida M., Yamada S., Suzuki K. Estimation of cumulative deformation capacity of buckling restrained braces. *Journal of Structural Engineering*. 2008; **134**(5): 822-31.
- [27] Andrews B.M., Fahnestock L.A. Song J. Ductility capacity models for buckling restrained braces. *Journal of Constructional Steel Research*. 2009; **65**(8-9): 1712-20.

- [28] Fahnestock L. A., Ricles J. M., Sause R. Experimental evaluation of a large scale buckling-restrained braced frame. *Journal of Structural Engineering*. 2007; **133**(9): 1205-1214.
- [29] Merritt S., Uang C. M., Benzoni G. Subassemblage testing of Star Seismic buckling-restrained braces. Structural Systems Research Project, Rep. No. TR-2003/04, Univ. of California at San Diego, San Diego, 2003.
- [30] Zona A., Dall'Asta A. Elastoplastic model for steel buckling-restrained braces. *Journal of Constructional Steel Research*. 2012; **68**(1): 118-125.
- [31] Gu, Q., Zona, A., Peng, Y., & Dall'Asta, A. (2014). Effect of buckling-restrained brace model parameters on seismic structural response. *Journal of Constructional Steel Research*, 98, 100-113.
- [32] McKenna F., Fenves G.L., Scott M.H. OpenSees: Open system for earthquake engineering simulation. Pacific Earthquake Engineering Research Center, University of California, Berkeley, CA, 2006.
- [33] Fajfar P. A nonlinear analysis method for performance-based seismic design. *Earthquake Spectra*. 2000; **16**(3): 573-592.
- [34] Ministero delle Infrastrutture e dei Trasporti (2018). Aggiornamento delle “Norme tecniche per le costruzioni” (NTC 2018). Gazzetta Ufficiale 20/02/2017, n. 42 - Suppl. Ord. n. 8.
- [35] Scott MH, Fenves GL. Plastic hinge integration methods for force-based beam-column elements. *Journal of Structural Engineering*. 2006; **132**(2): 244–252.
- [36] Panagiotakos T. B., Fardis M. N. Deformations of Reinforced Concrete Members at Yielding and Ultimate. *ACI Structural Journal*, 2001; **98**(2): 135-148.
- [37] Mander J. B., Priestley M. J., Park R. Theoretical Stress-Strain Model for Confined Concrete. *Journal of Structural Engineering*. 1988; **114**(8).
- [38] Tremblay R., Poncet L., Bolduc P., Neville R., DeVall R. (2004). Testing and design of buckling restrained braces for Canadian application. Proceeding of the 13<sup>th</sup> World Conference on Earthquake Engineering, Vancouver, Canada.
- [39] Cornell C.A., Krawinkler H. Progress and challenges in seismic performance assessment. *PEER Center News*. 2000; **4**(1): 1-3.
- [40] Aslani H, Miranda E. Probability-based seismic response analysis. *Engineering Structures* 2005; **27**(8): 1151-1163.
- [41] Porter KA. (2003). An overview of PEER's performance-based earthquake engineering methodology. Proceedings of the 9<sup>th</sup> International Conference on Application of Statistics and Probability in Civil Engineering (ICASP9), San Francisco, California.
- [42] Iervolino I., Cornell C.A. Record Selection for Nonlinear Seismic Analysis of Structures. *Earthquake Spectra*. 2005; **21**(3): 685–713.
- [43] Shome N, Cornell C.A., Bazzurro P., Carballo J.E. Earthquake, records, and nonlinear responses. *Earthquake Spectra*. 1998; **14**(3): 469-500.
- [44] Luco N., Cornell C.A. Structure-specific scalar intensity measures for near-source and ordinary earthquake ground motions. *Earthquake Spectra*. 2007; **23**(2): 357-92.

- [45] Pinto P.E., Giannini R., Franchin P. Seismic Reliability Analysis of Structures, IUSS Press, Pavia, Italy, 2003.
- [46] Vamvatsikos D., Cornell CA. Incremental dynamic analysis. *Earthquake Engineering and Structural Dynamics*. 2002; **31**(3): 491–514.
- [47] PEER, Pacific Earthquake Engineering Research Center <http://peer.berkeley.edu/>
- [48] ITACA, Italian Accelerometric Archive  
[http://itaca.mi.ingv.it/ItacaNet/itaca10\\_links.htm](http://itaca.mi.ingv.it/ItacaNet/itaca10_links.htm)
- [49] ISED, Internet-Site for European Strong-Motion Data  
[http://www.isesd.hi.is/ESD\\_Local/frameset.htm](http://www.isesd.hi.is/ESD_Local/frameset.htm)
- [50] Bazzurro P., Cornell C.A., Shome N, Carballo J.E. Three proposals for characterizing MDOF nonlinear seismic response. *Journal of Structural Engineering*. 1998, **124**(11), 1281-1289.
- [51] Castaldo P., Palazzo B., Della Vecchia P. Life-cycle cost and seismic reliability analysis of 3D systems equipped with FPS for different isolation degrees. *Engineering Structures*. 2016; **125**: 349–363.
- [52] Palazzo, B., Castaldo, P., & Della Vecchia, P. (2014, September). Seismic reliability analysis of base-isolated structures with friction pendulum system. In 2014 IEEE Workshop on Environmental, Energy, and Structural Monitoring Systems Proceedings (pp. 1-6). IEEE.
- [53] Castaldo P., Alfano G. Seismic reliability-based design of hardening and softening structures isolated by double concave sliding devices, *Soil Dynamics and Earthquake Engineering*, 2020, **129**,105930.
- [54] Bertero RD, Bertero VV. Performance-based seismic engineering: the need for a reliable conceptual comprehensive approach. *Earthquake Engineering and Structural Dynamics*. 2002; **31**: 627–652.
- [55] Gkimprxis A., Tubaldi E., Douglas, J. Comparison of methods to develop risk-targeted seismic design maps. *Bulletin of Earthquake Engineering*. 2019; 1-26.
- [56] Castaldo P., Tubaldi E., Selvi F., Gioiella L. Seismic performance of an existing RC structure retrofitted with buckling restrained braces. *Journal of Building Engineering*, 2021, 33, 101688.

## EFFECT OF LEAD RUBBER BEARING (LRB) MODELING TECHNIQUE ON THE SEISMIC RESPONSE OF BASE-ISOLATED BRIDGES

Vahid Aghaeidoost<sup>1\*</sup>, AHM Muntasir Billah<sup>2</sup>

<sup>1\*</sup> Lakehead University  
955 Oliver Road, Thunder Bay, ON, P7B5E1, Canada  
e-mail: vaghaei@lakeheadu.ca

<sup>2</sup> Lakehead University  
955 Oliver Road, Thunder Bay, ON, P7B5E1, Canada  
muntasir.billah@lakeheadu.ca

---

### Abstract

*Seismic isolation bearings are one of the most widely used seismic protection systems for bridges. Taking advantage of improved energy dissipation and flexibility, Lead Rubber Bearings (LRB) have emerged as a popular solution for seismic protection of bridges. Over the last few decades, LRBs have been studied significantly both experimentally and numerically, resulting in different numerical modeling approaches of LRB. Since the seismic response of a base-isolated bridge largely depends on the modeling technique adopted for the bearing element, it is essential to identify an appropriate modeling scheme for LRBs. The objective of this study is to investigate the seismic response sensitivity of an isolated bridge when different LRB modeling techniques are adopted. In this study, a three-span curved steel girder bridge isolated with LRB is considered as the reference bridge that was tested in a shake table at the University of Nevada, Reno. The validated numerical model of the reference bridge is first developed using OpenSees. Three different LRB modeling techniques available in OpenSees are used to model the isolation bearings. Using the ElastomericX, LeadRubberX, and KikuchiAikenLRB modeling techniques, the seismic response of the bridge is compared against the experimental results. The performance of the isolated bridge is evaluated in terms of isolator force-deformation relationship and fragility curves. The analysis results show that LRB modeling approach has a noteworthy impact on the seismic response of base-isolated bridge and requires careful selection of modeling parameters.*

**Keywords:** Lead rubber bearing, Seismic response, Curved Bridge, Numerical modeling, Dynamic analysis.

---



## 1 INTRODUCTION

Bridges are one of the vital infrastructures of any country's transportation network. Bridge damage due to a strong earthquake leads to the cessation of the function of these vital infrastructures at critical times, which are needed to provide emergency services or help evacuating a damaged area. The use of seismic isolators is one of the effective methods to improve the seismic performance of bridges. With seismic isolators, ductility increases, and forces applied to the bridge structure due to earthquakes decrease. The behavior and performance of seismic isolation systems are highly nonlinear and more complex than other structural elements (such as girders, cap beams, columns) and can be affected by several factors.

Behavioral characteristics of nonlinear seismic isolators are a function of the dynamic responses of seismic isolators during an earthquake, and this poses severe challenges for modeling the response of these seismic isolators. To overcome these challenges, several main aspects of isolation bearing modeling, are: (a) bidirectional motion coupling in the horizontal plane, (b) the relationship of vertical and horizontal motion of the seismic isolator, (c) cavitation behavior and post-cavity seismic isolator in tension, (d) decrease in tensile cyclic loading resistance during cavitation behavior, (e) changes in critical buckling load capacity due to lateral displacement [1].

The flexibility of seismic isolators increases the fundamental period of base-isolated bridges and reduces the seismic forces applied to them. Although this reduction may be associated with large horizontal displacements of the seismic isolators, lateral flexibility plus horizontal displacements result in a significant reduction in the critical buckling load capacity of the seismic isolator [2-5].

An experimental study by Buckle et al. [6] on a set of seismic isolators showed that the critical loading capacity decreases with an increasing horizontal displacement or shear strain, and the horizontal stiffness decreases with increasing axial load and horizontal displacement [2]. Recent studies and experience of past earthquakes have shown that the impact of considering the vertical component of ground motions is significant for the analysis and design of structures.

Shekar et al. [7] investigated the effect of dampers and design standards on the response of highway bridges. They developed a three-dimensional model for this purpose. A significant vulnerability of the non-seismic bridge designed with a bearing could be observed because of the bridge pier's non-ductile failure. With the modern seismic design, the vulnerability of the bridge was significantly reduced.

The objective of this study is to investigate the seismic response sensitivity of an isolated bridge when different LRB modeling techniques are adopted. In this study, a three-span curved steel girder bridge isolated with LRB is considered as the reference bridge that was tested in a shake table at the University of Nevada, Reno [8]. The distinguishing feature of this study is that conventional simplifications are not used in seismic isolator modeling techniques, and instead, the main aspects of modeling and the factors affecting the behavior of isolators are fully included in the modeling. For this purpose, Lead Rubber Bearing (LRB) is studied using different modeling techniques available in OpenSees, and by performing Incremental Dynamic Analysis (IDA) and fragility analysis, different bridge responses under near-fault ground motions are studied.

## 2 MODEL OF BRIDGE

### 2.1 Description

The bridge considered in this study was designed and experimentally tested at the University of Nevada, Reno [8]. The bridge is a three-span composite steel I-girder bridge. Fig.1 indicates the plan of the bridge model and shows the location of abutments and piers. The design and geometric details of the scaled bridge can be found in [8]. This bridge superstructure has three composite steel I-girders with an 83mm concrete deck. The lengths of the spans are 12.8, 18.6, and 12.8 m, respectively (total length 44.2 meters), and the centerline radius is 24.4 m. The width of the deck is 3.66 m and the distance between the girders is 1.37 m. The height of the columns and their diameters are 2.44 and 0.61 m, respectively.

Fig.2 shows the detailed numerical model of the bridge used in this study. The piers are mono-column with 1% longitudinal and transverse steel rebar ratios. The concrete compressive strength is 44 MPa and the steel reinforcement is A706 grade with a yield strength of 490 MPa. The total bridge model weight is 1486 kN that is spread along with the longitudinal nodes of the deck.

In the numerical simulation with OpenSees, the confined and unconfined concrete behavior is considered and calculated according to the Chang and Manders [28] model (Concrete07). The reinforcing steel properties are simulated using steel02 model. The superstructure elements are assumed as elastic element and the piers and LRB are considered as nonlinear elements. The effect of soil-structure interaction is ignored in this study.

### 2.2 Lead rubber bearing systems

Three modeling techniques are used for modeling LRB as a seismic base isolation system. The LRB characteristics such as, shear modulus, modulus of elasticity, and characteristic strength are 0.41 MPa, 1.24 MPa, and 6.27 (Abutment), 9.03 (Pier) kN, respectively. More details about designing the LRB can be found in [8]. Three techniques are used for modeling LRB in Opensees: (a) KikuchiAikenLRB material with the zero-length element, (b) ElastomericX element, and (c) LeadRubberX element. The fundamental period of the base-isolated bridge with three LRB modeling techniques is found to be 0.66, 0.68, and 0.68 sec, respectively.

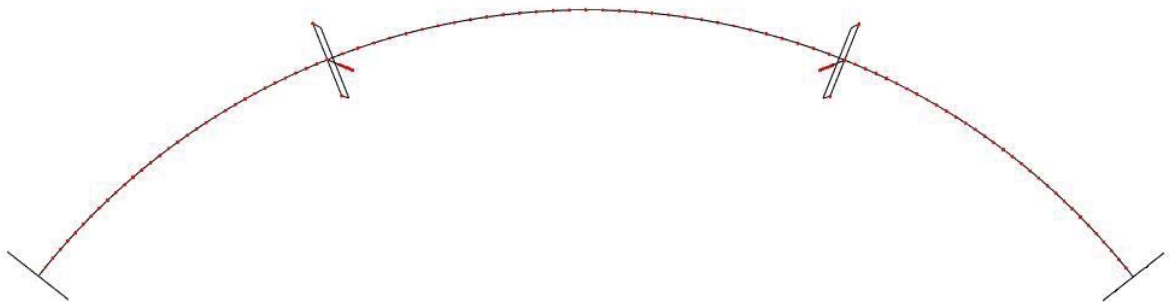


Figure 1: Bridge Plan.

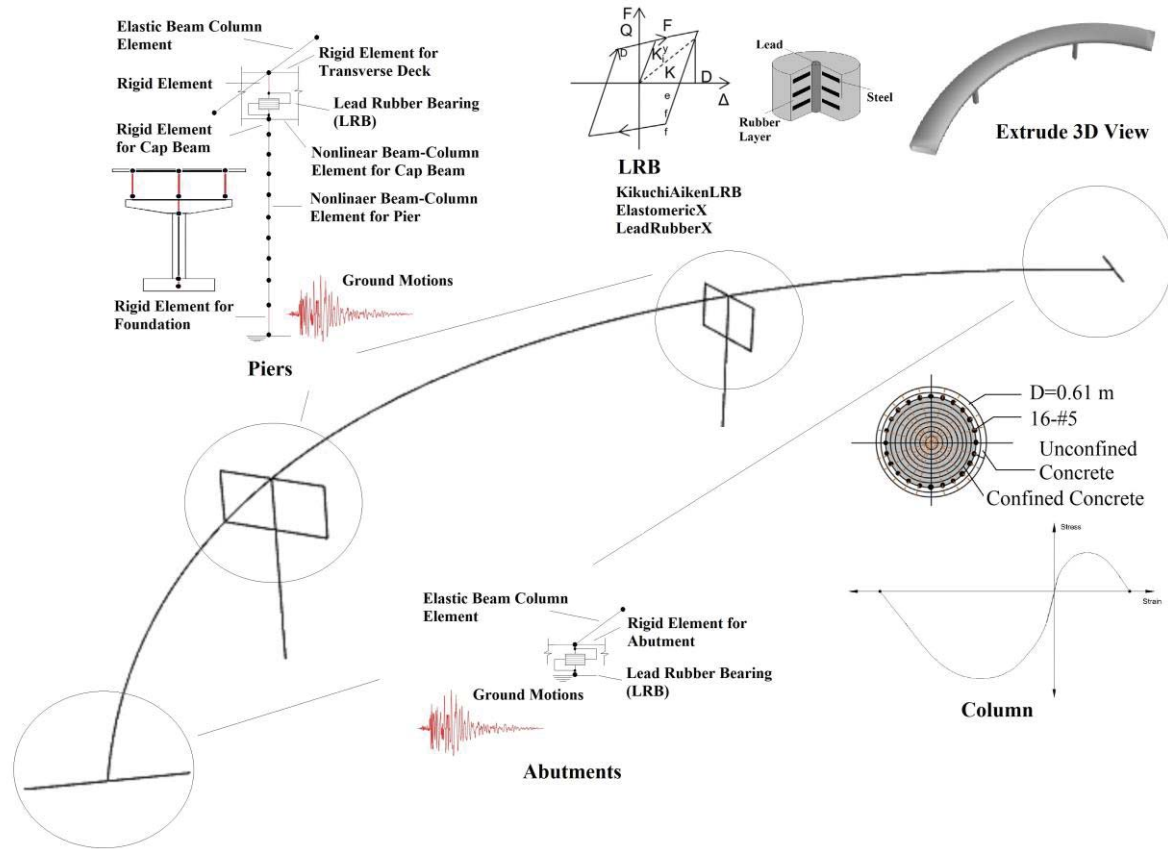


Figure 2: Numerical model of the bridge details.

### 3 MODEL VERIFICATION

The 2/5<sup>th</sup> scale bridge model was tested in shake table at the University of Nevada, Reno under the Sylmar station motion from the 1940 Imperial Valley earthquake as the Design Earthquake (DE). The tests were conducted at increments of 10% to 300% of the DE. To validate the numerical modeling approach adopted in this study, the test results obtained from the 100% DE is considered in this study. The hysteretic response of the LRB obtained from the shake table results are verified with the KikuchiAikenLRB, ElastomericX, and LeadRubberX modeling techniques. Fig.3 shows the hysteresis curves of the LRB at the pier location. According to this figure, the shape of the hysteresis curves is similar to the experimental hysteresis curve. In Table 1, the experimental responses in terms of the maximum shear force, displacement along the x-direction, both in positive and negative, and the energy dissipation are compared with the three mentioned techniques. For maximum shear force, all three models over predicted the force in the positive direction while under predicted in the negative direction. Similar observation can be made from the comparison of maximum bearing deformation. In terms of energy dissipation, the difference between the experimental and numerical results using KikuchiAikenLRB, ElastomericX, and LeadRubberX modeling techniques are 13%, 14%, and 9%, respectively.

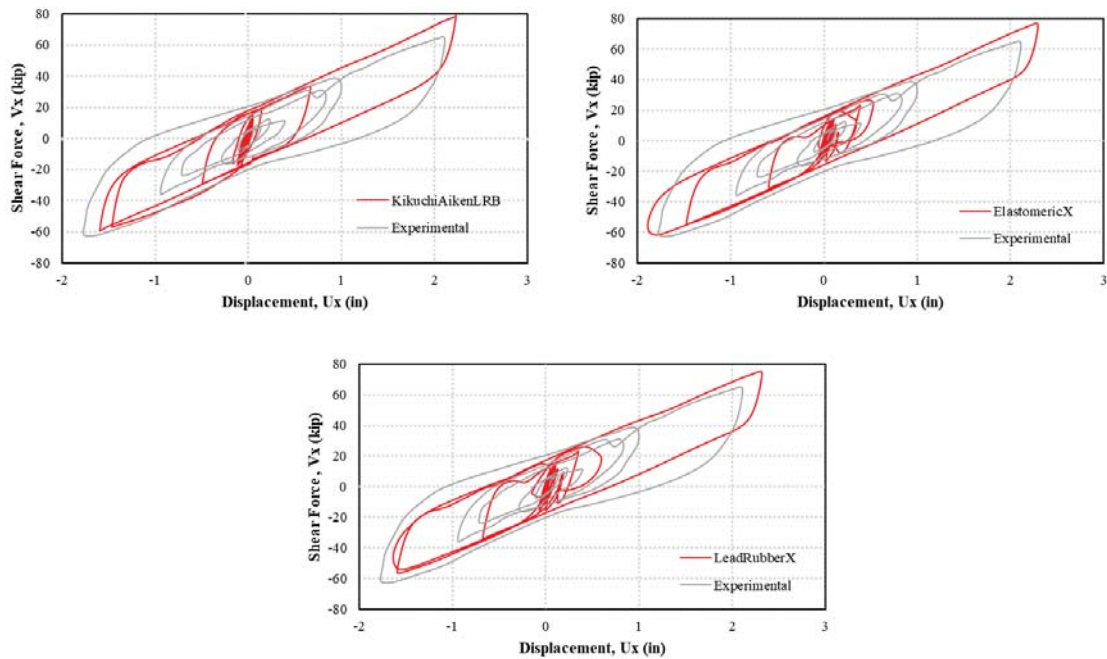


Figure 3: Hysteresis curve verification for LRB modeling techniques (a) KikuchiAikenLRB, (b) ElastomericX, and (c) LeadRubberX with Experimental result.

Parameters		Experimental	KikuchiAikenLRB	ElastomericX	LeadRubberX
Max. Shear force (kip)	+	64.89	78.80	76.86	75.24
	-	-62.67	-59.33	-61.75	-56.41
Max. Displacement (in)	+	2.10	2.23	2.29	2.32
	-	-1.78	-1.59	-1.89	-1.63
Energy Dissipation (kip.in <sup>2</sup> /s <sup>2</sup> )		243.18	212.36	210.12	222.04

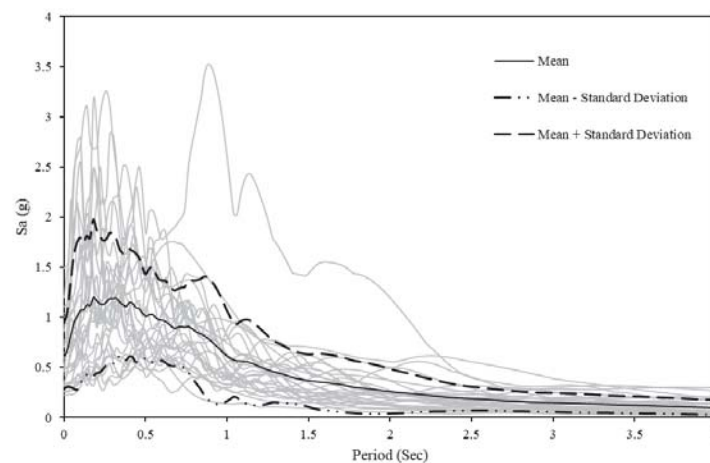
Table 1: Verification of LRB techniques with Experimental results.

#### 4 GROUND MOTION SELECTION

After validating the numerical models, the sensitivity of the three modeling techniques is compared by conducting seismic fragility analysis of the isolated bridges. To develop fragility curves, appropriate ground motions according to FEMA P695 [29] are selected. Table 2 shows the characteristics of the selected 14 non pulse near-field ground motions for increment dynamic analysis (IDA). The ground motions are extracted from the Pacific Earthquake Engineering Research (PEER) earthquake database [9]. The recorded primary orientations (provided by PEER (NGA)) of selected ground motions are rotated to strike-parallel and strike-normal orientations. Individual response spectrum variation of selected records and mean and mean  $\pm$  standard deviation are illustrated in Figure 4.

ID No.	Earthquake			Recording Station		R <sub>rup</sub> (km)
	M	Year	Name	Name	PGA (g)	
	No Pulse Records Subset					
1	6.8	1976	Gazli, USSR	Karakyr	0.864	5.460
2	6.5	1979	Imperial Valley-06	Bonds Corner	0.777	2.660
3	6.5	1979	Imperial Valley-06	Chihuahua	0.270	7.290
4	6.8	1985	Nahanni, Canada	Site 1	1.201	9.600
5	6.8	1985	Nahanni, Canada	Site 2	0.519	4.930
6	6.9	1989	Loma Prieta	BRAN	0.502	10.72
7	6.9	1989	Loma Prieta	Corralitos	0.645	3.850
8	7.0	1992	Cape Mendocino	Cape Mendocino	1.494	6.960
9	6.7	1994	Northridge-01	LA – Sepulveda VA	0.932	8.440
10	6.7	1994	Northridge-01	Northridge – Saticoy	0.459	12.09
11	7.5	1999	Kocaeli, Turkey	Yarimca	0.322	4.830
12	7.6	1999	Chi-Chi, Taiwan	TCU067	0.499	0.620
13	7.6	1999	Chi-Chi, Taiwan	TCU084	1.009	11.48
14	7.9	2002	Denali, Alaska	TAPS Pump Sta #10	0.333	2.740

Table 2: Selected non-pulse ground motions according to FEMA P695.


Figure 4: Response spectra of selected non-pulse ground motions, also, to mean and mean  $\pm$  standard deviation.

## 5 ENGINEERING DEMAND PARAMETES (EDPs)

Bridge piers and base-isolation systems of the bridge typically govern the response of the bridge system over other elements. Diverse sorts of EDPs such as pier displacement, bridge pier ductility, isolation bearing displacement, bearing shear strain (%), etc., have been used by different researchers to quantify the damage in bridge pier and isolation bearing. Shear strain (%) or bearing displacement is usually used to define the damage states [10, 11] for the base-isolation system. In this research, damage states are defined in terms of base-isolation system shear strain (%) and bridge pier displacement ductility ( $\mu_d$ ). The experimental observations are considered to determine the damage states for the base-isolators resulting in pounding and unseating. Lead rubber bearing can take shear strain up to 400% before failure. Total deformation of bridge deck-girders and unseating issues in the whole bridge system are raised from such high strain. So this value is limited to 250% [12]. Limiting values for different damage



states are taken from Hwang et al. [13] and Zhang and Huo [14]. Outline of distinctive damage states' physical appearance and criteria are displayed in Table 3.

Damage State	→	Slight	Moderate	Extensive	Collapse	Ref
Bridge components	Physical phenomenon →	Cracking and spalling	Moderate cracking and spalling	Degradation without collapse	Failure leading to collapse	FEMA [15]
Bridge pier	Displacement ductility $\mu_d$	$\mu_d > 1.0$	$\mu_d > 1.2$	$\mu_d > 1.76$	$\mu_d > 4.76$	Hwang et al [13]
LRB	Shear strain $\gamma$ (%)	$\gamma > 100$	$\gamma > 150$	$\gamma > 200$	$\gamma > 250$	Zhang and Huo [14]

Table 3: Damage states of bridge components.

## 6 SEISMIC FRAGILITY ANALYSIS

The fragility curve expresses the probability of damage corresponding to a given damage state at several levels of seismic events. In fact, the fragility curve describes the relation between the intensity measure and the level of possible seismic damage. In order to accurately develop fragility curves, it is important to choose an appropriate earthquake intensity measure for structure under study. Intensity measures that indicate the severity of the earthquake as appropriate for fragility analysis include  $S_a$ , PGA, PGV, and PGD. Fragility curves can be obtained from logical regression analysis of real or simulated damage information or numerical solution methods.

Fragility curves distribute the failure between slight, moderate, extensive, and collapse states according to HAZUS-MH [15]. These curves are plotted separately for each damage state for a set of ground motions and are used as input to the structural damage calculation.

Researchers have previously used various methods to obtain fragility curves [16]. Billah and Alam [16] have surveyed diverse methods and proposed a technique to obtaining a hybrid fragility curve. The research examined the preferences, shortcomings, and imperatives of all the strategies in assessing seismic vulnerability of bridges. The fragility function is a probabilistic method that portrays the probability of damaging a structure beyond a specific damage level for a certain ground motion intensity [17]. The fragility of a structure, is expressed as the conditional probability of a damage state (DS) occurring given a specific intensity measure (IM), which can be expressed mathematically as [18]:

$$Fragility_{DS}(y) = P[DM \geq DS | IM = y] \quad (1)$$

The relationship of the engineering demand parameter (EDP) and the IM is set up by a probabilistic seismic demand model (PSDM) in this research. By utilizing the incremental dynamic analysis (IDA) on the bridge system, the PSDM is formed. There are two methods to create the PSDM: the scaling approach [10, 14] and the cloud approach [19, 20, 21, 22]. The cloud method is utilized in assessing the seismic fragility function of the bridge piers and lead rubber bearing systems in this study.

The shear strain (%) of the LRB and pier displacement ductility are selected as the EDPs, and the spectral acceleration at the fundamental period of the bridge ( $S_a$ , T1) of each ground motion is taken as the IM. Regression analysis is performed to obtain the mean and standard deviation of each damage condition by assuming the power-law function [23] in the cloud method. The logarithmic relationship between IM and median EDP is expressed as follows.

$$EDP = a(IM)^b \text{ or, } \ln(EDP) = \ln(a) + b \ln(IM) \quad (2)$$

In this correlation,  $a$  and  $b$  are coefficients that can be estimated from a regression. The lognormal distribution is recommended for the EDPs by Gradoni et al. [24]. In order to obtain adequate data for the cloud approach, IDA is carried out rather than the nonlinear time history analysis. The ground motions are scaled from a very low IM to a high IM for the IDA. The time history analysis and scaling are repeated until dynamic instability in the shape of large drifts occurs, demonstrating structural collapse. This reduced the computational time and provided adequate damage data for generating fragility curves. Each intensity level of a specific ground motion can be considered as a one-time history analysis. Hence, it was possible to generate adequate damage data corresponding to a diverse ground motion intensity levels. The logarithmic standard deviation (dispersion) of the demand parameters,  $\beta_{EDP|IM}$  conditioned upon the IM is estimated using the following equation [25].

$$\beta_{EDP|IM} = \sqrt{\frac{\sum_{i=1}^N (\ln(EDP) - \ln(aIM^b))^2}{N-2}} \quad (3)$$

In this equation,  $N$  is the number of simulation cases.

Fragility curves are created utilizing the following equation from Padgett [26].

$$P[DS|IM] = \Phi \left[ \frac{\ln(IM) - \ln(IM_n)}{\beta_{comp}} \right] \quad (4)$$

In this equation,  $\Phi [ ]$  is the standard normal cumulative distribution function and

$$\ln(IM_n) = \frac{\ln(S_c) - \ln(a)}{b} \quad (5)$$

$IM_n$  is characterized as the median value of the intensity measure for the chosen damage states. The following equation presents the dispersion [26].

$$\beta_{comp} = \frac{\sqrt{\beta_{EDP|IM}^2 + \beta_c^2}}{b} \quad (6)$$

In this equation,  $S_c$  and  $\beta_c$  are the median and dispersion values for a specific damage state of the bridge components (bridge pier and isolation bearing), respectively. The coefficient of variation (COV) is related to each damage state for related uncertainties. COV is assumed to be 0.25 for slight and moderate damage states and 0.5 for the extensive and collapse damage states [18]. The following equation is used to calculate the dispersion value [27].

$$\beta_c = \sqrt{\ln(1 + COV^2)} \quad (7)$$

The total bridge system fragility function is more conceivable than the individual component fragility function [14, 19, 21, 22]. The global damage likelihood can be simply assessed utilizing the series system and first-order reliability theory. Moreover, the upper and lower bound of failure likelihood of the bridge can be determined utilizing Eq. (8). Both bounds present a conservative and un-conservative estimation of damage likelihoods, respectively.

$$\max_{i=1}^n [P(F_i)] \leq P(F_{system}) \leq 1 - \prod_{i=1}^n [1 - P(F_i)] \quad (8)$$

In this equation,  $P(F_i)$  represents the probability of exceeding the prescribed bound of the component's actual damage state. Moreover,  $P(F_{\text{system}})$  is for the whole bridge system.

## 7 RESULTS

Fragility functions are developed for the based-isolated curved bridge considering the fragilities of the pier and LRB for various modeling techniques. The fragility functions, assuming a lognormal distribution with respect to the median of seismic intensity ( $S_a$ ,  $T_1$ ), are generated using Eq. (4), and calibrated with the damage states as shown in Table 3. To evaluate the effect of LRB modeling techniques on the relative fragility of each component, fragility curves are developed for the piers and isolation bearings at abutments and piers. However, the fragilities of the pier and abutment bearings are not provided here due to space limitations. Fig. 5 compares the fragility curves for the LRB at four damage states. Fig. 5 shows that when LRB is modeled using KikuchiAikenLRB technique, independent of the considered damage level, LRB is less vulnerable during a seismic event. As the damage level changes from slight to collapse, the contrast between the relative vulnerability of KikuchiAikenLRB and other techniques increase and become more visible. This interpretation is also accurate for the LeadRubberX and ElastomericX techniques, but its value is less obvious.

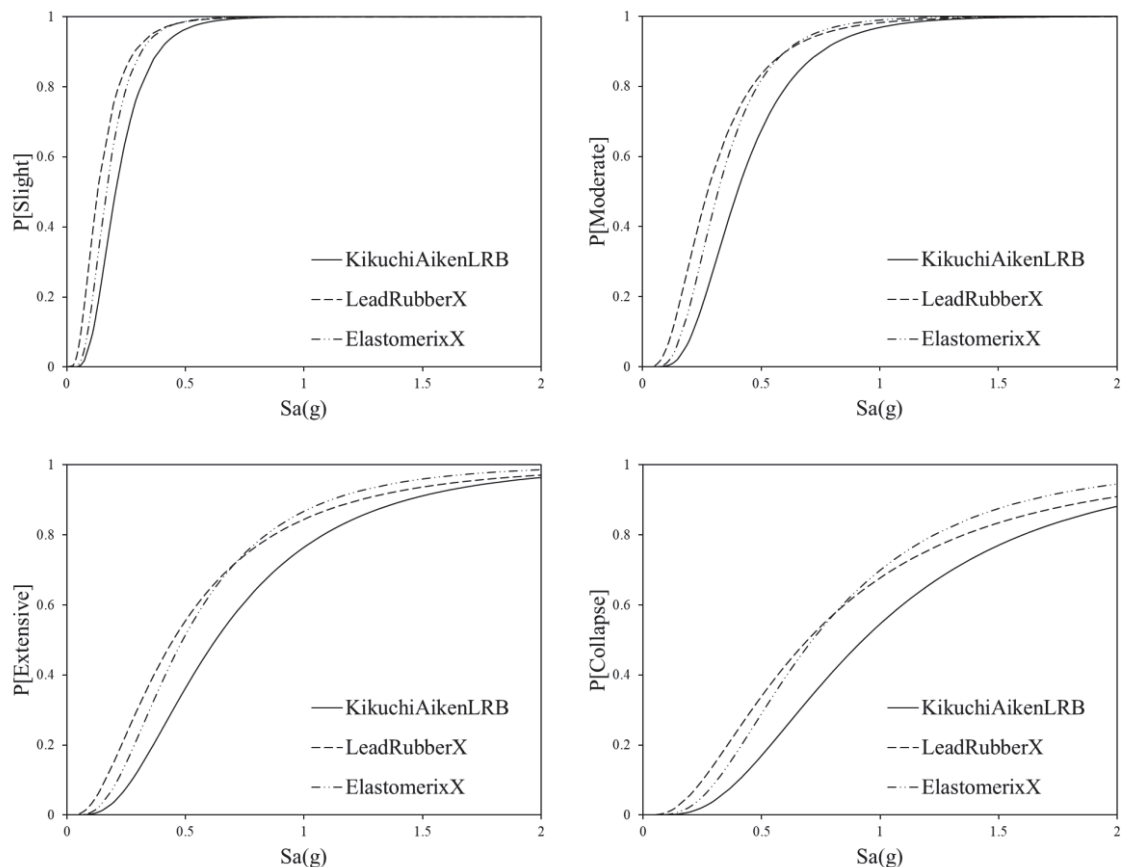


Figure 5: Comparison of fragility curves of LRB.

As the collapse of bridge components (column and/or bearing) will lead to the collapse of the bridge, the fragility curves of each component should be combined to get a system fragility curve. After obtaining the bridge component fragility curves, the bridge system fragility

curves are determined according to Eq. (8). Fig. 6 shows the system fragility curves of the bridge with various modeling techniques. The same observation can be seen as a bearing isolation system for the bridge system, as utilizing KikuchiAikenLRB can lead to a reduced damage compared to the other techniques. The bridge fragility curves of ElastomericX and LeadRubberX techniques are very similar. The bridge system fragility demonstrates that system fragility is generally influenced at the extensive and collapse damage level due to the using KikuchiAikenLRB techniques. It is also observed that the ElastomericX and LeadRubberX have almost identical fragility curves.

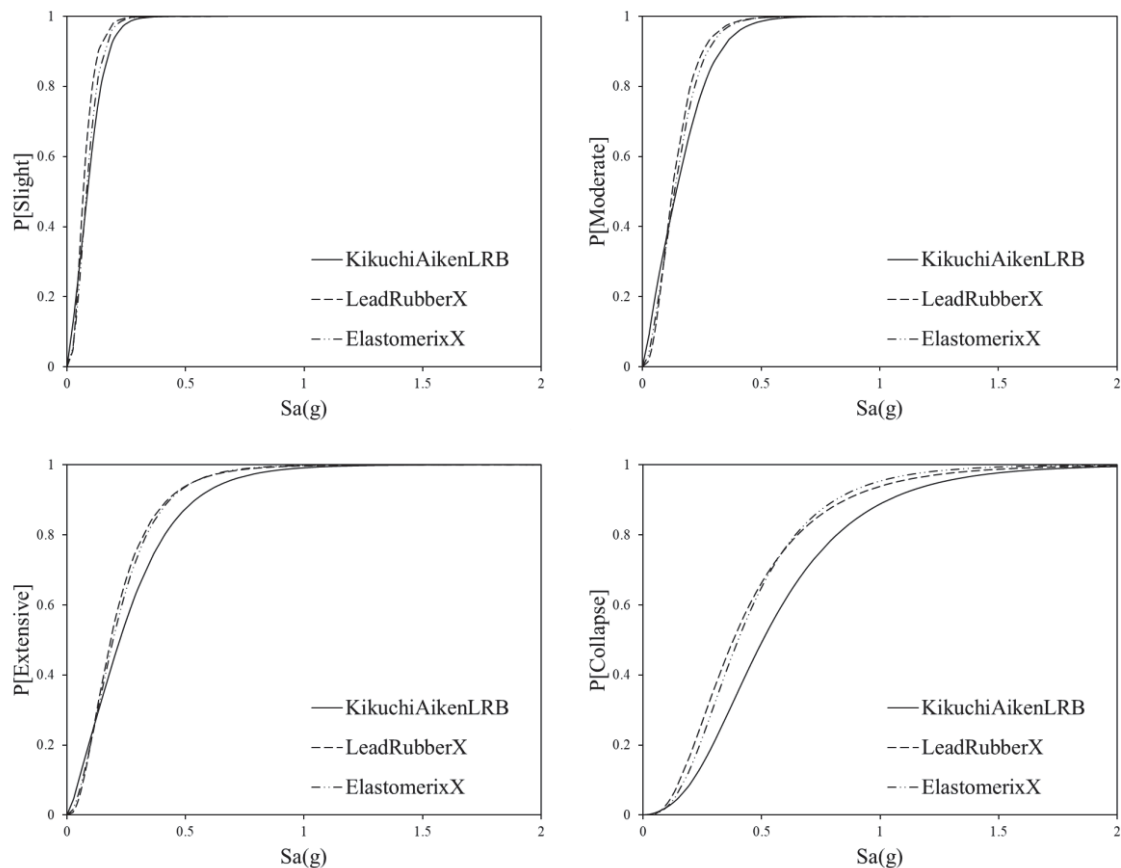


Figure 6: Comparison of fragility curves of Bridge System.

## 8 CONCLUSIONS

In this paper, various bearing isolation modeling techniques are assessed in terms of pier displacement and LRB deformation. Increment dynamic analysis is implemented to derive the appropriate data for fragility analysis. Then, seismic fragility curves are obtained for each bridge component as well as the bridge system. According to the results of the numerical analysis, the following conclusions are drawn:

- KikuchiAikenLRB is susceptible to lower shear force as compared to ElastomericX and LeadRubberX significantly.
- The influence of modeling techniques on the fragility of LRB shows increased susceptibility of exceeding different damage states in ElastomericX and LeadRubberX techniques compared to the KikuchiAikenLRB technique.

- Extensive and collapse damage states of the bridge system fragility considering the KikuchiAikenLRB technique is mostly affected than the other two techniques.
- The likelihood of an isolated bridge exceeding collapse damage level is highly dependent on the adopted modeling techniques. The higher probability of the bridge experiencing collapse is mainly attributable to the fragility of the bearings arising from the LeadRubberX and ElastomericX LRB modeling techniques.

### Acknowledgment

The Natural Sciences and Engineering Research Council (NSERC) of Canada supported this study through the Discovery Grant. The financial support is highly appreciated.

### REFERENCES

- [1] M. Kumar, A.S. Whittaker, M.C. Constantinou, An advanced numerical model of elastomeric seismic isolation bearings, *Earthquake Engineering & Structural Dynamics*, 43(13), 1955-1974, 2014.
- [2] I. Buckle, S. Nagarajaiah, K. Ferrell, Stability of elastomeric isolation bearings: Experimental study, *Journal of Structural Engineering*, 128(1), 3-11, 2002.
- [3] I.G. Buckle, J.M. Kelly, Properties of slender elastomeric isolation bearings during shake table studies of a large-scale model bridge deck, *Special Publication*, 94, 247-270, 1986.
- [4] I. Buckle, H. Liu, Experimental determination of critical loads of elastomeric isolators at high shear strain, *NCEER Bull*, 8(3), 1-5, 1994.
- [5] C.G. Koh, J.M. Kelly, Effects of axial load on elastomeric isolation bearings, *Earthquake Engineering Research Center, University of California: Berkeley*, United States, 1987.
- [6] A. Elgamal, L. He, Vertical earthquake ground motion records: an overview, *Journal of Earthquake Engineering*, 8(05), 663-697, 2004.
- [7] S. Shekhar, J. Ghosh, S. Ghosh, Influence of bearing types and design code advances on seismic vulnerability of simply supported highway bridges, *Journal of Earthquake Engineering*, 1-27, 2003.
- [8] Monzon, E.V, Seismic Performance of Curved Steel Plate Girder Bridges with Seismic Isolation (Dissertation), *Nevada: University of Nevada, Reno*, 2013.
- [9] PEER (Pacific Earthquake Engineering Research), new ground motion selection procedures and selected motions for the PEER transportation research program, *PEER report 2011/03. Berkeley, CA: University of California*, 2011.
- [10] Alam MS, Bhuiyan AR, Billah AHMM, Seismic fragility assessment of SMA- bar restrained multi-span continuous highway bridge isolated with laminated rubber bearing in medium to strong seismic risk zones, *Bulletin of Earthquake Engineering*, 10, 1885-1909, 2012.
- [11] Bhuiyan MAR, Alam MS, Seismic vulnerability assessment of a multi-span continuous highway bridge fitted with shape memory alloy bars and laminated rubber bearings, *Earthquake Spectra*, 28, 1379-1404, 2012.



- [12] JRA. Specifications for highway bridges-part V: Seismic design. Tokyo, *Japan: Japan Road Association*, 2002.
- [13] Hwang H, Liu JB, Chiu YH, Seismic fragility analysis of highway bridges, *MAEC RR-4. Urbana: Mid America Earthquake Center*, 2001.
- [14] Zhang J, Huo Y, Evaluating effectiveness and optimum design of isolation devices for highway bridges using the fragility function method, *Engineering Structures*, 31, 1648-1660, 2009.
- [15] Federal Emergency Management Agency (FEMA), *HAZUS-MH software*, Washington DC, 2003.
- [16] Billah AHMM, Alam MS, Seismic fragility assessment of highway bridges: a state-of the- art review, *Structure and Infrastructure Engineering*, 11, 804-832, 2015.
- [17] Billah AHMM, Alam MS, Seismic fragility assessment of concrete bridge pier reinforced with super-elastic shape memory alloy, *Earthq. Spectra*, 31, 1515-1541, 2014.
- [18] Porter K, Kennedy R, Bachman R, Creating fragility functions for performance based earthquake engineering, *Earthquake Spectra*, 23(2), 471-489, 2007.
- [19] Choi E, DesRoches R, Nielson BG, Seismic fragility of typical bridges in moderate seismic zones, *Engineering Structures*, 26, 187-199, 2004.
- [20] Mackie KR, Stojadinović B, Fragility curves for reinforced concrete highway overpass bridges, *13th world conference on earthquake engineering*, Vancouver, B.C., Canada, August 2004.
- [21] Nielson BG, DesRoches R, Seismic fragility curves for typical highway bridge classes in the central and southeastern United States, *Earthquake Spectra*, 23, 615–633, 2007.
- [22] Nielson BG, DesRoches R, Seismic fragility methodology for highway bridges using a component level approach, *Earthq. Engr. and Structural Dynamics*, 36, 823–839, 2007.
- [23] Cornell AC, Jalayer F, Hamburger RO, Probabilistic basis for 2000 SAC federal emergency management agency steel moment frame guidelines, *Journal of Engineering Structure*, 128, 526–532, 2002.
- [24] Gardoni P, Mosalam KM, Der Kiureghian A, Probabilistic seismic demand models and fragility estimates for RC bridges, *.of Earthquake Engineering*, 7(1), 79–106, 2003.
- [25] Baker JW, Cornell CA, Vector-valued ground motion intensity measures for probabilistic seismic demand analysis, *Pacific earthquake engineering research report 2006/08. University of California Berkeley: PEER Centre*, 2006.
- [26] Padgett JE, Seismic vulnerability assessment of retrofitted bridges using probabilistic methods (Dissertation), *Atlanta: Georgia Institute of Technology*, 2007.
- [27] Nielson BG, Analytical fragility curves for highway bridges in moderate seismic zones (Dissertation), *Atlanta: Georgia Institute of Technology*, 2005.
- [28] Chang, G.A., and Mander, J.B., Seismic Energy Based Fatigue Damage Analysis of Bridge Columns: Part 1 – Evaluation of Seismic Capacity, *NCEER Technical Report No. NCEER-94-0006 State University of New York, Buffalo, N.Y*, 1994.
- [29] Applied Technology Council, Quantification of building seismic performance factors. Redwood City, USA: FEMA; 2009:P695.

## AN ADVANCED MODEL FOR THE FLUID VISCOUS DAMPER BRITTLE FAILURE

L. Gioiella<sup>1</sup>, F. Scozzese<sup>1</sup>, E. Tubaldi<sup>2</sup>, L. Ragni<sup>3</sup>, and A. Dall'Asta<sup>1</sup>

<sup>1</sup> SAAD, University of Camerino  
Viale della Rimembranza 3, 63100 Ascoli Piceno (AP), Italy  
{laura.gioiella, fabrizio.scozzese, andrea.dallasta}@unicam.it

<sup>2</sup> Department of Civil and Environmental Engineering, University of Strathclyde  
75 Montrose Street, Glasgow G1 1XJ, Scotland, UK  
enrico.tubaldi@strath.ac.uk

Department of Civil and Building Engineering and Architecture, Università Politecnica delle  
Marche  
Via Breccie Bianche Ancona, Italy  
laura.ragni@univpm.it

---

### Abstract

*Fluid viscous dampers have proven to be a very efficient solution for reducing the seismic demand on structural and non-structural components, for both new and existing structures. Nowadays, the topics, which need to be further investigated, deal with the reliability and robustness of such kind of energy dissipating devices. Damper failures are generally brittle mechanisms, which can compromise the capacity of the structure to withstand the seismic action, leading to a lack of robustness of the overall system.*

*In this study, an advanced model, which is able to describe the fluid viscous damper brittle failure, has been developed in OpenSees and is discussed. The failure of a damper is related to the exceedance of its strength capacity and can be attained because of the forces arising related to the end-stroke impact or can be due to excessive piston velocity (over-velocity). The effect of damper failure on the seismic performance of the structural system is investigated by performing multi-stripe analyses and monitoring different global and local demand parameters. The proposed model for the damper is applied to a benchmark structure, consisting on a 3-storey steel moment resisting frame.*

**Keywords:** Viscous Dampers; End-stroke; Over-velocity; Brittle Failure; Seismic Risk; Reliability.

---

## 1 INTRODUCTION

Fluid viscous dampers (FVDs) are devices widely used for seismic passive protection of both new and existing structures. They are widely employed for reducing displacements and interstorey drift demands in newly-designed structures as well as in existing ones by using both external and internal configurations [1]-[8].

Several approaches are to date available for designing both size and location of viscous dampers within a building frame based on direct procedures [1][9][10][11][12] or optimization methods [13][14]. These design approaches generally allow to control the seismic performance of buildings under the design seismic intensity level. However, the reliability under extreme, low-probability earthquake events may be characterized by low robustness and inadequate safety levels because dampers usually exhibit a brittle collapse behaviour and their failure may trigger the collapse of the whole system. As a consequence, more accurate studies simulating the effect of the device failure should be carried out to provide a better evaluation of the structural reliability under strong earthquakes.

In order to shed light on this aspect, the present paper introduces a model able at describing the brittle failure of FVD devices and its influence on the structural reliability. The collapse is due to the attainment of the force capacity of the damper, related to the over-velocity or to the achievement of the end-stroke. In particular, it is assumed that a brittle failure occurs in the device once the maximum force is attained, consistently with the viscous damper numerical model proposed in [15]. This way, the proposed model can be suitable to describe the consequences of the failure of the devices on the seismic performance of structural systems and also to evaluating the probability of collapse of structures equipped with dampers, through risk analyses performed by using probabilistic approaches [16]-[24].

Recent probabilistic analyses, indeed, have already investigated some specific issues, such as the effect of ground motion variability on the response of systems equipped with either linear and nonlinear viscous dampers [19][20][21]; the influence of the degree of nonlinearity of the dampers [20][22], and the effect of the damper parameters variability [22][23][24] stemming from the device manufacturing process, as acknowledged by the main international Standards for seismic structural design [25][26][27][28]. However, in these studies the device failure was not explicitly taken into account.

The proposed model is firstly described in the following section and then it is applied to a three-storey steel building case study, already considered as benchmark structure in previous studies (SAC Phase II Steel Project, [29]). For consistency with the adopted benchmark case study, the seismic hazard is also assumed equal to the one of [29]. The dissipative system is dimensioned to provide an added damping equal to 30%, using both linear and nonlinear devices, by varying their degree of nonlinearity among two boundary values. The capacity of the dampers (stroke and strength) is evaluated at the design condition, corresponding to a seismic action with Mean Annual Frequency (MAF) of exceeding equal to  $2 \cdot 10^{-3}$ .

Some preliminary results under increasing harmonic load histories are reported to illustrate the model capabilities and the sequence of failures triggered by the damper failure. Subsequently, few selected results from Multi Stripe Analysis (MSA) are also presented to illustrate overall the problem of damper failure and related effects on the structural performance of the case study. Finally, a preliminary evaluation of the overall probabilistic response is provided. Results obtained by considering the failure of the dampers are compared with those achieved with two limit cases, that is the condition of no failure, where no damper's failure is permitted and the bare frame, which represents the building without FVDs.

Further details regarding fragility curves and demand hazard curves, where the structural performance is analysed considering MAF of exceeding up to  $10^{-5}$  1/yr, can be found in [30].

## 2 FLUID VISCOUS DAMPERS MODELLING

The constitutive law of a fluid viscous damper (FVD) can be described through the following relationship [15][31]:

$$F_d(v) = c|v|^\alpha \text{sgn}(v) \quad (1)$$

where  $v$  is the relative velocity between the device ends,  $F_d$  is the damper resisting force,  $|v|$  is the absolute value of  $v$ ,  $\text{sgn}$  is the sign operator,  $c$  and  $\alpha$  are two constitutive parameters: the former is an amplification factor, while the latter describes the damper nonlinear behaviour.

It is worth noting that viscous dampers can be produced with  $\alpha$  values ranging from 0.1 and 2. Devices with  $\alpha > 1$  are not dissipative and are used as shock transmitters. Devices with  $0.1 \leq \alpha \leq 1.0$  are all potentially suitable for seismic energy dissipation, among these values, the range  $0.3 \leq \alpha \leq 1.0$  is the most widespread [32][33][34][35].

A fluid viscous damper generally consists of a steel cylinder filled of a silicone fluid, within which a steel piston with small orifices on its head can move. In case of seismic events, the fluid is forced to pass through the orifices, moving from one side to the opposite side of the cylinder, thus dissipating into heat the input mechanical energy. The higher is the velocity of the movement, the greater is the dissipated energy. The cylinder is equipped with spherical hinges at its ends to avoid device bending. FVDs are generally connected to the structure by a stiff connection, consisting in a driver brace, dimensioned using an over-strength factor with respect to the viscous device. The stiffness of the driver brace is an important feature, because it needs to be sufficiently high to allow the device to be effective in dissipating energy. Further details on the damper components and their behaviour can be found in [15].

The failure of a damper is related to the exceedance of its strength capacity and can be attained because of the forces related to the end-stroke impact or can be due to excessive piston velocity. According to the described behaviour, dampers are generally classified and tested with reference to two characteristic parameters: the maximum values of stroke  $\Delta_{d,max}$ , and the maximum transmissible force  $F_{d,max}$ .

The end-stroke can be attained both in tension (maximum elongation of the device) and in compression (maximum shortening of the device). During a seismic event with an intensity higher than the design level of the device, it may happen that the device exploits the entire available stroke, resulting in an impact. At the instant of the impact, the velocity becomes null and the force notably increases, however, the attainment of the impact does not strictly imply the damper failure because the impact force may be lower than the device strength.

The second mechanism refers to the attainment of the maximum viscous force due to an excessive value of the velocity of the piston (over-velocity with respect to the design value). This extreme value of the force can induce a leak of the fluid or can damage the damper components, resulting in the failure of the device. It is noteworthy that once the maximum capacity ( $F_{d,max}$ ) is attained, the resulting failure mechanisms is brittle, thus making the device ineffective, with no residual ability to sustain loads or dissipate energy.

The model, proposed hereinafter, aims to describe the two aforesaid mechanisms using the damper model, depicted in Figure 1. It is composed of three elements: a dashpot, describing the dissipative behaviour; a hook and gap element, set in parallel to the dissipative device, which simulate the impact due to either excessive shortening ( $-\Delta_{d,max}$ ) or elongation ( $+\Delta_{d,max}$ ); and a third element, set in series with the others, simulating the failure due to the attainment of the force capacity. In this paper, the strength capacity is assumed to be the same in traction and in compression and the failure occurs when the modulus of damper force attains the limit value  $F_{d,max}$ .

The damper model discussed above is implemented in OpenSees [36] using two-node link elements simulating each of the three components, while various material properties are used to describe the different behaviours. A “Viscous material” is used for the dissipative element, by assigning the values of the constitutive parameters  $c$  and  $\alpha$ . An “ElasticMultilinear material” depicts the force-displacement relationship related to impacts occurring both for elongation and shortening. Finally, a “MinMax material” is used to simulate the brittle failure, assigning the value of the strength capacity  $F_{d,max}$ . The stiffness of the “MinMax material” can be used to model the overall deformability of damper, connections, and brace. However, once the strength capacity is reached, the element fails and does not provide any more contribution in terms of reaction force.

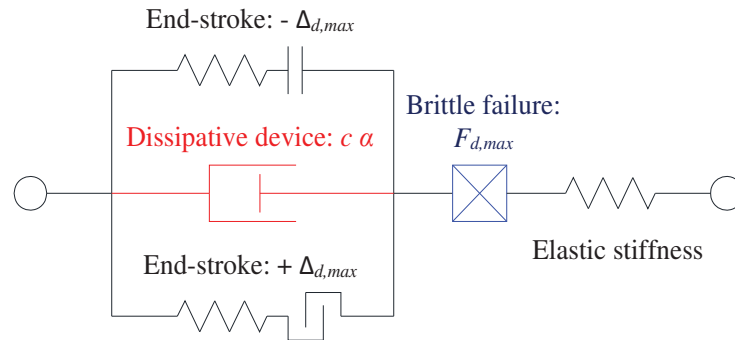


Figure 1: Dissipative device model encompassing the failure mechanisms.

### 3 CASE STUDY

In this section, the case study, dealing with a steel moment-resisting frame structure representative of low-rise buildings is introduced together with the considered seismic scenario. The frame is equipped with FVDs with both linear and non-linear behaviour that is values of the damper exponent  $\alpha$  corresponding to 1.0 and 0.3.

#### 3.1 Benchmark structure and hazard scenario

The three-storey building selected as case study is a steel moment resisting frame designed within the SAC-FEMA project with reference to gravity, wind and seismic load in compliance to the code requirement. It has been also widely used as benchmark structure in several studies concerning structural response control (e.g., [2][29][20]). The structural system of the building consists of perimeter moment-resisting frames and internal gravity frames with shear connections. The finite element model of the building (Figure 2) is a two-dimensional model representative of the weak and short direction of the building and has been developed in OpenSees following a non-linear fiber distributed approach, whose details can be found in [30].

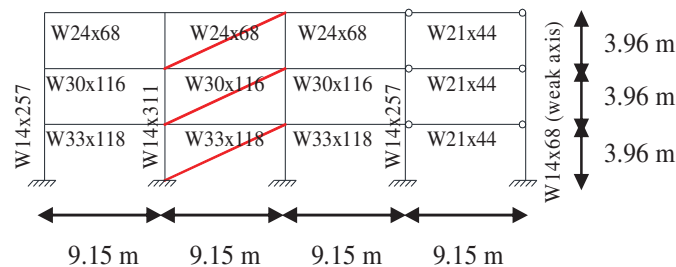


Figure 2: Building model descriptions: locations of the dampers (in red) and cross-sections of the members.



For consistency with the adopted benchmark case study, the hazard model and the related IM hazard curves are taken from [29]; however, the curves have been slightly extrapolated to make sure that the system failure probabilities can be accurately estimated, by following the recommendation of [37] about the optimal IM curve truncation for an accurate risk estimation via MSA analysis. The spectral pseudo-acceleration  $S_a(T_1)$  of a linear elastic SDOF system with 2% damping ratio and fundamental vibration period equal to that of the structure  $T_1$  is considered as intensity measure (IM). MSA is performed at 20 IM levels, with a set of 30 ground motions per each intensity level taken from the 60 records used in the SAC project [2].

For what concerns the FVDs design, this is carried out by considering the set of 30 records corresponding to a MAF of exceedance  $\nu_{design} = \nu_{IM}(im_{design}) = 0.0021$  1/yr. Further details and features of these records can be found in [30].

### 3.2 Damping system

The design of the FVDs is carried out to enhance the performance of the building under a seismic scenario with a 10% probability of exceedance in 50 years (ULS scenario according to Eurocode 8). To this aim, a target value  $\xi_{add} = 30\%$  has been chosen for supplemental damping. In the present study, the damping coefficients of the linear devices have been distributed proportionally to the storey shear of the first mode of the bare frame.

Once determined the damping coefficients of the devices for the linear case, the viscous coefficients for the nonlinear FVDs corresponding to given value of the exponent  $\alpha$ , are evaluated following the approach outlined in [9][38][39] and based on the equivalence of the energies dissipated by the linear and nonlinear FVDs. It is noteworthy that the maximum interstorey drift along the building height without dampers, averaged over the 30 records considered, is equal to 3%, while with the addition of the dampers, it becomes 1.2%.

Table 1 and Table 2 report, respectively, the damping properties and the design parameters of the FVDs of the three elevations of the building for both the values of the constitutive parameter  $\alpha$ . Further details concerning the dissipative devices design can be found in [30].

$\alpha$	$c_1$	$c_2$	$c_3$
	$[kNs^\alpha/m^\alpha]$		
1	13,780	11,914	7428
0.3	4669	4037	2517

Table 1: Damping properties for different levels of damper nonlinearity.

$\alpha$	$\Delta_{d,1}$	$\Delta_{d,2}$	$\Delta_{d,3}$	$F_{d,1}$	$F_{d,2}$	$F_{d,3}$
	$[mm]$	$[mm]$	$[mm]$	$[kN]$	$[kN]$	$[kN]$
1.0	35.4	44.5	37.1	3109	3336	1956
0.3	29.6	39.7	35.7	3044	2796	1712

Table 2: FVD design parameter at the design condition.

### 3.3 Amplification factors for the FVD control parameters

Modern seismic codes prescribe that anti-seismic devices shall be dimensioned starting from the values of the control parameters evaluated for seismic design actions having an assigned probability of exceedance. Then, the capacities of the devices are assigned amplifying these

control parameters, which are stroke and force for the FVDs, by means of amplification factors, or reliability factors, in order to ensure a target level of safety.

The amplification factors proposed by Codes are two and aim to control the two failure mechanisms discussed above. The former, here denoted by  $\gamma_\Delta$ , amplifies the maximum stroke measured at design condition. The amplified stroke must not exceed the damper capacity  $\Delta_{d,max}$ . The latter, here denoted by  $\gamma_v$ , amplifies the maximum velocity measured at design condition. Damper force is obtained by Eqn. (1) and must not exceed the damper capacity  $F_{d,max}$ .

Per each value of the constitutive parameter  $\alpha$ , five combinations of amplification factors relevant to damper stroke and strength are considered, ranging from 1.0 up to 3.0, considering also, the prescriptions of European codes [26][27] and American Standards [28]. Moreover, for comparison purposes, two more limit cases are considered: “No Failure” that is the case where no dampers’ failures are permitted, and “Bare Model”, which represents the frame without FVDs. Further details concerning the combinations of amplification factors can be found in [30].

#### 4 SYSTEM RESPONSE UNDER AN INCREASING SINUSOIDAL INPUT

In this section, the results obtained for a sinusoidal ground motion of increasing intensity are presented. The FVDs response parameters at the design condition refer to linear devices ( $\alpha = 1$ ) without amplification factors, that is  $\gamma_v = \gamma_\Delta = 1.0$ .

The choice of an increasing harmonic input motion is motivated by the fact that it allows to easily identify the attainment of the damper strength capacity through one of the two mechanisms, impact and over-velocity and the related consequences on the frame undergoing a more general time-history input motion.

Figure 3 shows the sinusoidal input having a period of 0.9 seconds and an initial magnitude of  $1 \text{ m/s}^2$ . The amplitude of the motion is constant for five cycles, after that it is increased with a coefficient equal to 1.5 and remains again constant for five cycles. The magnification of the motion amplitude is repeated four times, resulting in a motion that has five different amplitudes, with a maximum equal to  $5 \text{ m/s}^2$ , and that lasts 22.5 seconds. At the end of the input, there are few seconds, which are useful to understand how the case study restores its rest condition.

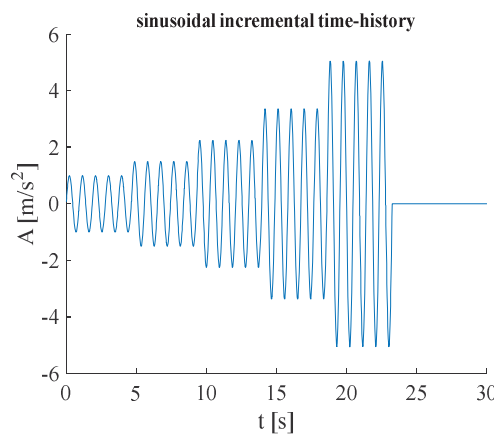


Figure 3: Sinusoidal incremental dynamic input.

Figure 4 a) and b) illustrate the time-history of the damper forces  $F_{d,i}$  recorded along the height of the building. The black solid line refers to the device installed between the ground and the first floor, the red one refers to the intermediate device at the second storey, while the blue one represents the damper at the top storey. At the beginning of the third increment of the

sinusoidal input (between 14.4 and 14.5 seconds), graphs show some small ripples, which are more evident for the intermediate and top-storey devices (Figure 4 b), and they are caused by small impacts due to the end-stroke attainment. In this case, the impact occurs but it does not lead to the attainment of the damper strength capacity. At the time instant 14.6 s the damper placed at the first level reaches its force capacity due to over-velocity and its force drops to zero. Few instants later, also the other devices fail for over-velocity.

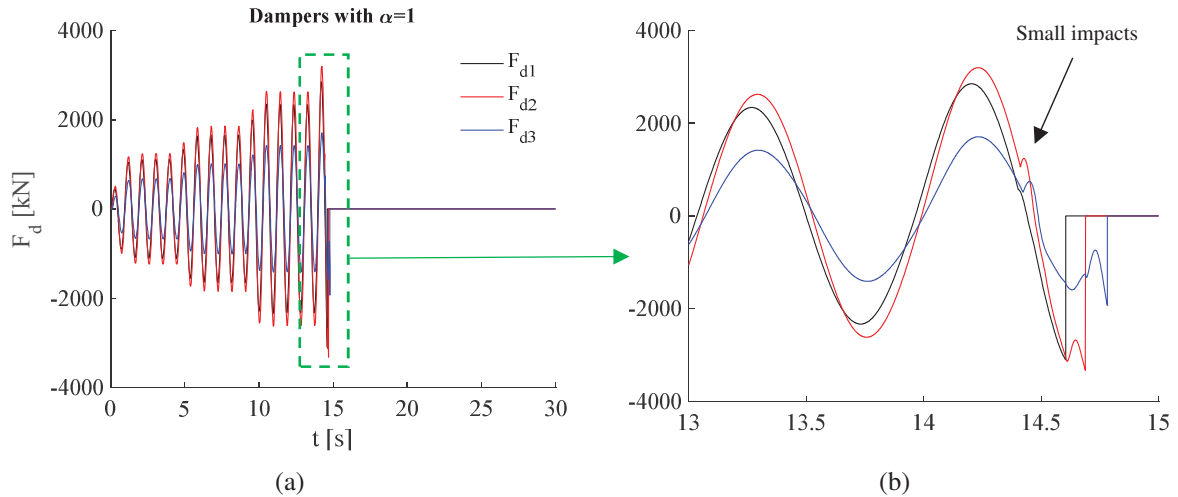


Figure 4: Time-history of the damper forces along the height of the building.

The effects of the damper failure can be deeper investigated through Figure 5 a) - c), where the stroke-force relationship ( $\Delta_{d,i}-F_{d,i}$ ) of each device is shown. In particular, by observing these stroke-force relationships it is evident that at the beginning of the third increment of the input motion, all the three dampers experience the end-stroke attainment without failure, with impacts that are more evident for the intermediate and top-storey devices. After these impacts, occurred without consequences, the FVDs restore their behaviour as pure dissipative devices. Few instants later, suddenly, the damper located at the ground floor fails due to over-velocity (Figure 5 a), triggering the sequence of damper failures at the upper elevations. The sequence is highlighted by a series of ripples in the stroke-force relationship of the intermediate (Figure 5 b) and especially top-storey device (Figure 5 c). The ripples begin when the first device fails and last until all the devices fail for over-velocity.

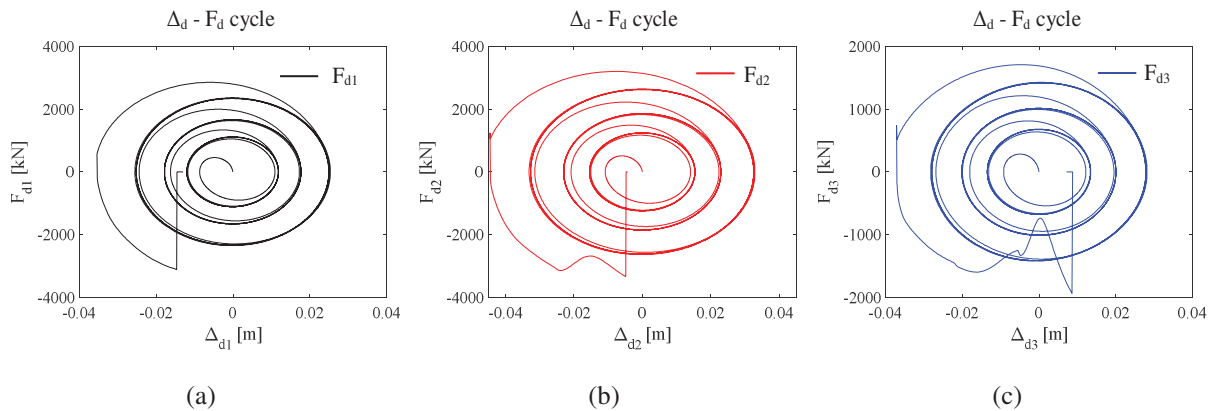


Figure 5: Stroke-force relationships of the devices.

Figure 6 a) - c) shows the time-histories of the parameters strictly related to the frame response, that is floor displacements  $u_i$ , floor relative velocities  $v_{r,i}$  and floor absolute accelerations  $A_i$ , highlighting the consequences of the damper failures on the frame itself. Generally, all the responses are significantly amplified by the impacts occurring in the dampers and by their failure. The absolute accelerations (Figure 6 c) are more affected than the displacements (Figure 6 a). It is worth to note that the peaks in terms of absolute accelerations, recorded between 14 and 15 seconds, are mainly related to the impacts experimented by the devices before their failure.

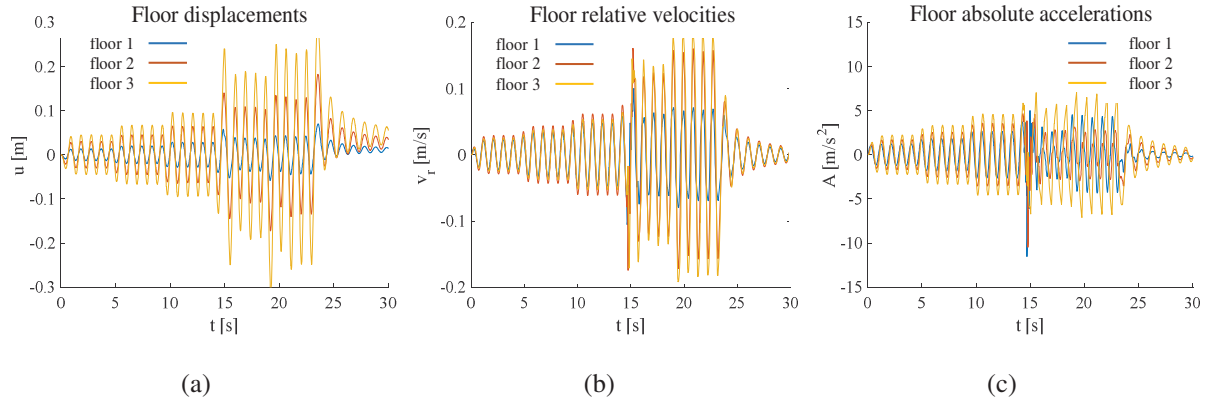


Figure 6: Time-histories of the response parameters of the frame.

## 5 SYSTEM SEISMIC RESPONSE

To shed further light on the consequences of FVDs failure, this subsection shows few selected information from MSA analyses to illustrate overall the problem of damper failure and related effects on the structural performance of the case study. The results refer to both low (*IM* level 5) and high (*IM* level 15) seismic intensities and for a single time-history (TH) analysis (TH 25).

Figure 7 a) and b) compares the time-histories of the interstorey-drift ratio (IDR) response of the bare model and of the system with linear and nonlinear dampers designed without amplification factors ( $\gamma_v = \gamma_\Delta = \gamma = 1.0$ ) at both the seismic intensity levels. The response in terms of IDR at floor 1 is only discussed, given the high similarity of the response at all floors.

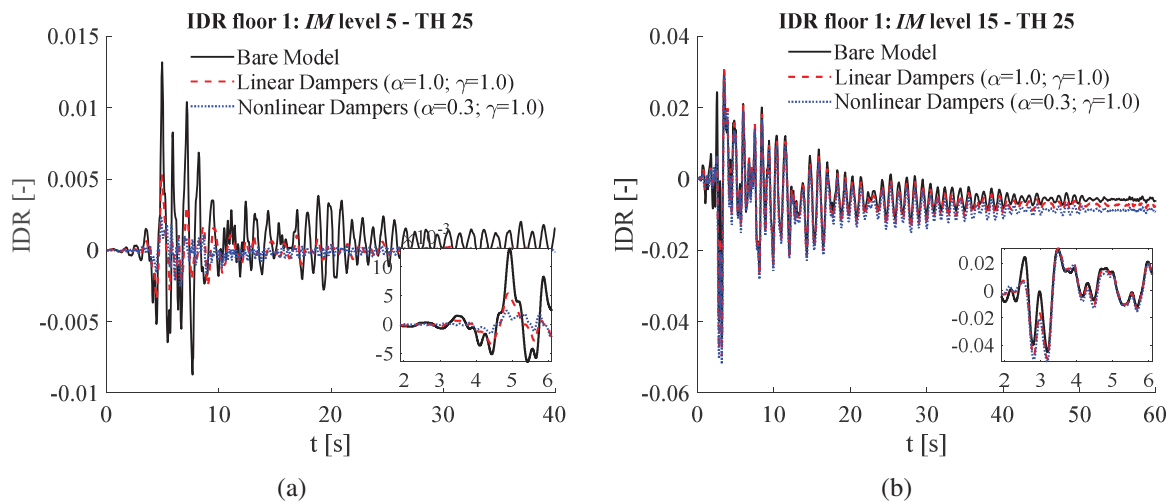


Figure 7: Time histories of the IDR at *IM* level n. 5 (a) and (b) *IM* n. 15. Comparison between the bare model and the model with linear and nonlinear dampers (without amplification factors).

As already shown for the incremental harmonic input, it is confirmed that at lower seismic intensities FVDs are effective in damping the response, while the beneficial mitigation of the response provided by the dampers vanishes at higher *IMs*, due to their failure. At *IM* level 5, indeed, the response of the frame with FVDs is damped over the whole earthquake duration, since no device failure is observed at this intensity level. From the inset of Figure 7 (b), instead, it can be observed that dampers fail at around 2.5 seconds since the beginning of the time-history of *IM* level 15, therefore the IDR response is damped until that time instant, while later on the response tends towards the bare-frame response.

To deeply understand the FVDs behaviour along the height of the building, Figure 8 compares the time histories selected from the *IM* level 15 (higher intensity) of the force on dampers at all the three elevations of the building. Here dampers failure occurs quite simultaneously at 2.5 s, when the forces suddenly drop to zero and the dampers become ineffective.

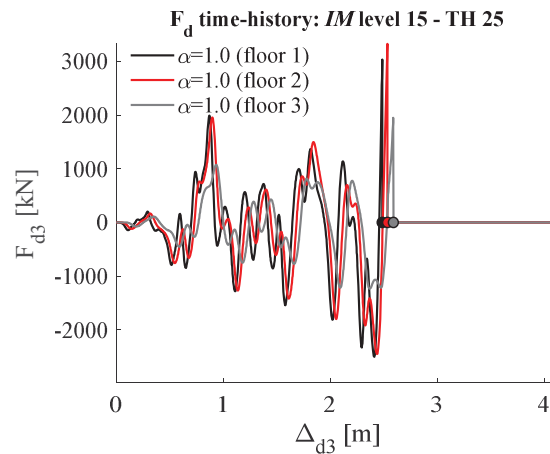


Figure 8: Failure time-lag among dampers at different floors.

For sake of completeness, the dampers force-stroke cyclic responses corresponding to the cases plotted in Figure 7 are shown in Figure 9 (*IM* level 5) and Figure 10 (*IM* level 15). In each figure a comparison is made between the responses of the linear (red dashed line) and nonlinear dampers (blue dotted line) at the first (figure a) and third storey (figure b). It is worth to observe that at *IM* level 5 (Figure 9 a) and b) there is no evidence of impact and the failure is never attained, thus complete cycles can be observed.

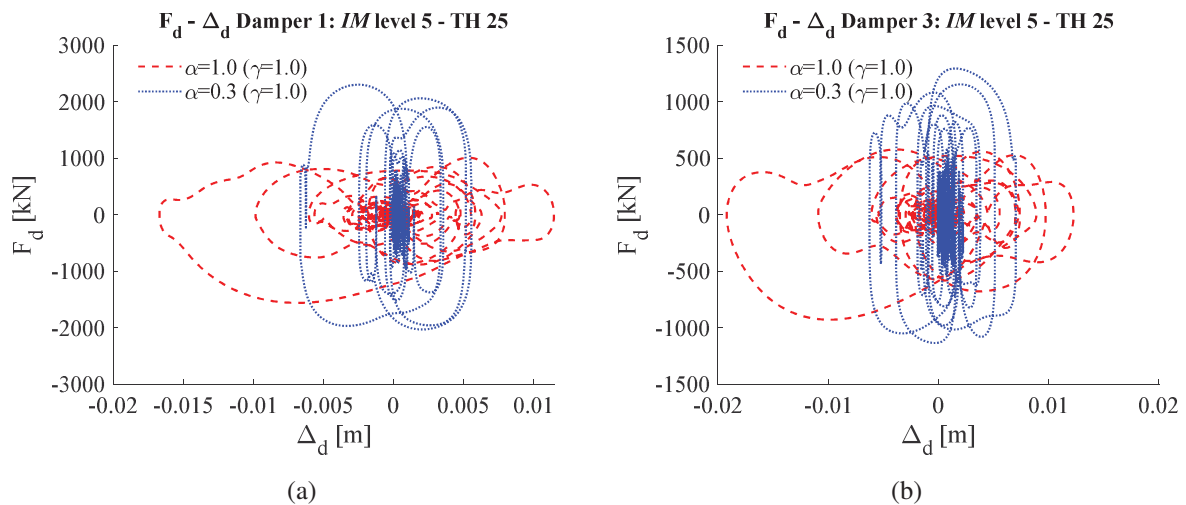


Figure 9: Damper response at *IM* levels 15. Comparison between linear and nonlinear dampers (without amplification factors) at (a) first and (b) third floor



In Figure 10 a) and b), instead, the attainment of the maximum force capacity (hence the failure), for both linear and nonlinear dampers, is due to over-velocity because the force suddenly becomes null and the hysteretic cycle is suddenly interrupted, without any impact.

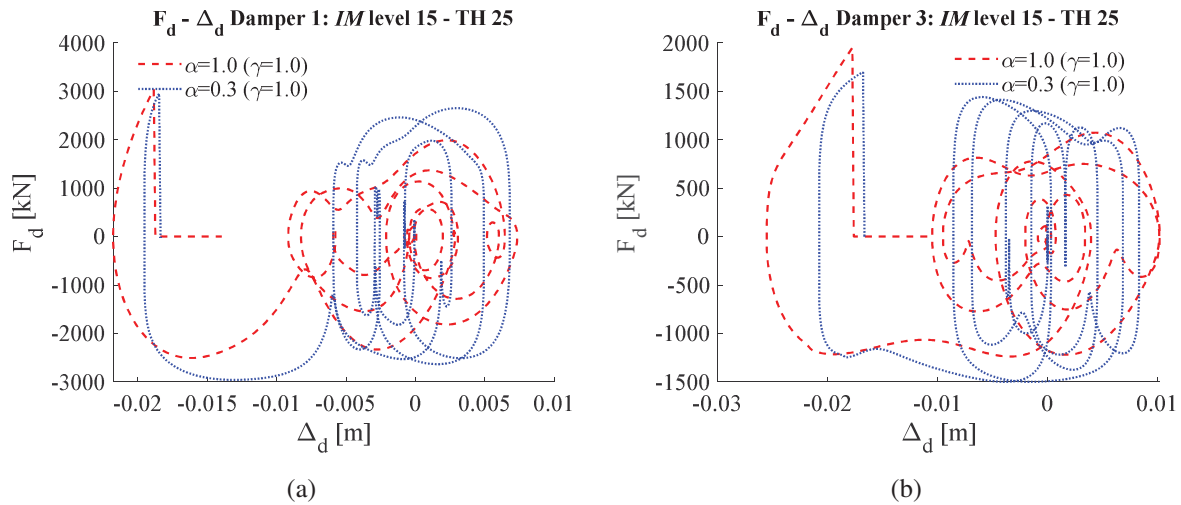


Figure 10: Damper response at *IM* levels 15. Comparison between linear and nonlinear dampers (without amplification factors) at (a) first and (b) third floor.

### 5.1 Preliminary evaluation of the overall probabilistic response

This section provides a preliminary evaluation of the overall probabilistic response of the analysed case study in terms of global engineering demand parameters (EDPs). First, the median response of the building at different *IM* levels is presented, then the demand hazard curves, with respect to the mean annual rate of exceedance,  $\nu_D$ , of the same EDPs are introduced. The monitored parameters are the maximum interstorey drift (IDR) and the maximum absolute acceleration (A) recorded among the various storeys.

The median response of the building at different seismic intensities for the case of linear dampers ( $\alpha = 1.0$ ) is compared in Figure 11. The comparison involves the following three cases: 1) bare model (black line); 2) building with dampers designed without amplification factors ( $\gamma_v = \gamma_\Delta = 1$ ) (blue line); 3) building with no dampers' failure permitted ( $\gamma_v = \gamma_\Delta = \infty$ ) (red line).

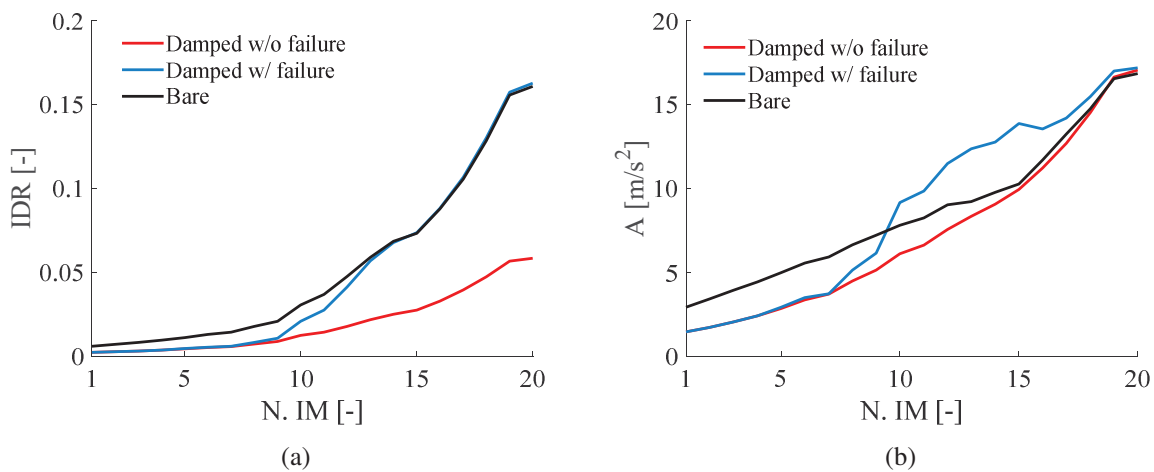


Figure 11: Building response at different *IM* levels for the case with linear dampers ( $\alpha=1.0$ ) in terms of (a) IDR and (b) A. Comparison between damped (with and without failure) and bare model.

Based on the results depicted in Figure 11 a) and b), it can be observed that the case of FVDs without failure notably reduces the response in terms of IDR up to the highest seismic intensities, while the beneficial effect in terms of acceleration mitigation is lower. On the other hand, in the case of FVDs that can fail, the IDR response of the damped systems tends to be almost that of the bare building once the devices are no longer effective (for  $IM$  levels higher than 10). The response in acceleration  $A$ , instead, shows peaks higher than the undamped frame system, due to the impacts induced by the devices end-stroke attainment.

Finally, Figure 12 a) and b) provides a first insight regarding the demand hazard curves of the maxima IDR and  $A$  among the storeys, with respect to the mean annual rate of exceedance  $\nu_D$ , for the linear dampers only ( $\alpha = 1.0$ ).

The demand hazard curves compare the results achieved when accounting for different values of the amplification factors, previously introduced in section 3.3. The analysed cases are: dampers without amplification factors ( $\gamma_v = \gamma_\Delta = 1.0$ ) (blue solid line) and dampers designed with different  $\gamma$  factors, that is  $\gamma_v = 1.5$  and  $\gamma_\Delta = 1.0$  (brown solid line);  $\gamma_v = \gamma_\Delta = 1.5$  (yellow solid line);  $\gamma_v = \gamma_\Delta = 2.0$  (violet solid line);  $\gamma_v = \gamma_\Delta = 3.0$  (green solid line). Moreover, the two limit cases of the bare frame model (black dashed line) and the damped model without damper failure (i.e., with  $\gamma_\Delta = \gamma_v = \infty$ ) (red solid line) are also analysed for comparison purposes. Two horizontal dotted lines are also depicted in the charts, one identifying the design hazard level  $0.0021 \text{ yr}^{-1}$  (black dotted line) and the other (red dotted line) denoting the target risk level desired for the structural systems ( $2 \times 10^{-4} \text{ yr}^{-1}$ ) [40][41].

With reference to Figure 12 a), it is worth to observe that when the dampers are designed with amplification factors larger than 1.0, the rate of exceeding of the target drift performance ( $IDR=0.012$ ) is around  $0.0021 \text{ yr}^{-1}$ , the hazard level of the design action, with some slight deviations that can be justified by the probabilistic nature of the analysis. Once damper rupture is attained, the building response tends to that of the bare model (black dashed line) and the magnitude of the amplification factors governs the “rapidity” of the transition from the damped to the bare frame curve.

For what concerns the response in terms of absolute accelerations, instead, (Figure 12 b) they are lower than those of the bare frame until the dampers are effective, while they become even higher than that of the bare frame due to end-strokes impacts experienced by the dampers, before their failures for almost all the values of the amplification factors higher than 1.0. In this case also, the magnitude of the amplification factors determines the annual rate probability at which the response tends to become higher than that of the bare frame. Further details concerning the probabilistic analyses results can be found in [30].

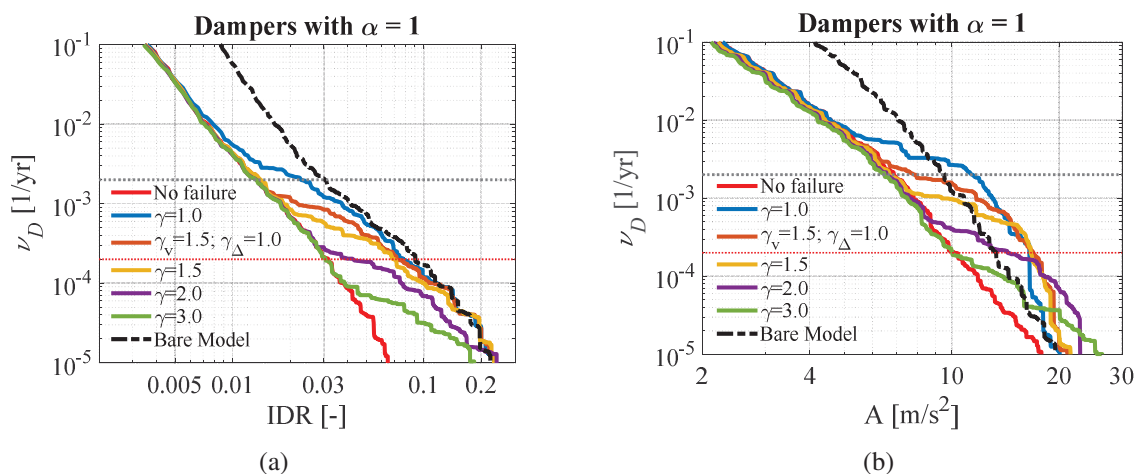


Figure 12: Demand hazard curves of (a) IDR and (b)  $A$  for different damper amplification factors. Case of building with linear dampers ( $\alpha = 1.0$ ).

## 6 CONCLUSIONS

The present paper introduces an advanced model which is able to describe the brittle failure of FVDs. Such kind of collapse occurs when the internal force of the device attains its strength capacity and this may occur for two reasons: impact when end-stroke is attained, or attainment of excessive velocity. Both these failure modalities are considered in the analyses.

As a general result, it is observed that combined effects of impacts and extreme velocities may induce a global brittle behaviour that cannot be perceived by models neglecting these phenomena. More specifically, the following conclusions can be drawn:

- The consequences of the damper failure on the performance of a structural system depend on the number of dampers remained active. If all dampers fail together, then the system response in terms of IDR tends to that of the bare building, while the one regarding absolute accelerations may be higher or even worse than that of the bare frame, as a consequence of impacts and dissipation concentrated at some storeys only.
- The magnitude of the amplification factors ( $\gamma_\Delta, \gamma_v$ ) adopted for damper stroke and velocity, governs the “rapidity” of the response transition from damped, or partially damped.
- If no amplification is provided ( $\gamma_v = \gamma_\Delta = 1.0$ ), the dampers probability of failure is higher than the design hazard level (assumed in this work equal to  $0.0021 \text{ yr}^{-1}$ ), thus, dampers experience failure at intensity levels lower than the design one.
- The use of amplification factors higher than 1.0 allows attaining lower failure probabilities, and this beneficial effect is more significant for larger  $\gamma$ -factors.

## REFERENCES

- [1] Tubaldi, E., Gioiella, L., Scozzese, F., Ragni, L., & Dall'Asta, A. (2020). A design method for viscous dampers connecting adjacent structures. *Frontiers in Built Environment*, 6, 25.
- [2] Barroso LR. Performance evaluation of vibration controlled steel structures under seismic loads. PhD thesis, Stanford University, California, US, 1999.
- [3] Pavlou, E, Constantinou, M.C., 2006. Response of Nonstructural Components in Structures with Damping Systems, *Journal of Structural Engineering*, **132**(7), 1108-1117.
- [4] Lavan, O, Dargush, G.F., 2009. Multi-Objective Evolutionary Seismic Design with Passive Energy Dissipation Systems, *Journal of Earthquake Engineering*, **13**(6), 758-790.
- [5] Gioiella, L., Tubaldi, E., Gara, F., Dezi, L., Dall'Asta, A. (2018). Modal properties and seismic behaviour of buildings equipped with external dissipative pinned rocking braced frames. *Engineering Structures*, 172. <https://doi.org/10.1016/j.engstruct.2018.06.043>
- [6] Pavia, A., Scozzese, F., Petrucci, E., & Zona, A. (2021). Seismic Upgrading of a Historical Masonry Bell Tower through an Internal Dissipative Steel Structure. *Buildings*, 11(1), 24.
- [7] Gioiella, L., Tubaldi, E., Gara, F., Dezi, L., Dall'Asta, A. (2018). Stochastic Seismic Analysis and Comparison of Alternative External Dissipative Systems. *Shock and Vibrations*, 47. <https://doi.org/10.1155/2018/5403737>
- [8] Tubaldi, E. (2015). Dynamic behavior of adjacent buildings connected by linear viscous/viscoelastic dampers. *Structural Control and Health Monitoring*, **22**(8), 1086-1102.

- [9] Hwang, J.S., Lin, W.C., Wu, N.J. (2010). Comparison of distribution methods for viscous damping coefficients to building. *Structure and Infrastructure Engineering: Maintenance, Management, Life-Cycle Design and Performance*, 9(1), 28-41. <http://dx.doi.org/10.1080/15732479.2010.513713>
- [10] Silvestri, S., Palermo, M., & Trombetti, T. (2018). A direct procedure for the seismic design of frame structures with added viscous dampers. *Seismic Resistant Structures*, 37.
- [11] Tubaldi, E., Barbato, M., Dall'Asta, A., 2015. Efficient approach for the reliability-based design of linear damping devices for seismic protection of buildings. *ASCE-ASME Journal of Risk and Uncertainty in Engineering Systems, Part A: Civil Engineering*, 2(2), C4015009. DOI: 10.1061/AJRUA6.0000858.
- [12] Palermo, M., Silvestri, S., Landi, L., Gasparini, G., & Trombetti, T. (2018). A “direct five-step procedure” for the preliminary seismic design of buildings with added viscous dampers. *Engineering Structures*, 173, 933-950.
- [13] Altieri, D., Tubaldi, E., De Angelis, M., Patelli, E., & Dall'Asta, A. (2018). Reliability-based optimal design of nonlinear viscous dampers for the seismic protection of structural systems. *Bulletin of Earthquake Engineering*, 16(2), 963-982.
- [14] Pollini, N., Lavan, O., & Amir, O. (2018). Optimization-based minimum-cost seismic retrofitting of hysteretic frames with nonlinear fluid viscous dampers. *Earthquake Engineering & Structural Dynamics*, 47(15), 2985-3005.
- [15] Miyamoto, H. K., Gilani, A. S., Wada, A., & Ariyaratana, C. (2010). Limit states and failure mechanisms of viscous dampers and the implications for large earthquakes. *Earthquake Engineering & Structural Dynamics*, 39, 1279-1297.
- [16] Seo, C.Y., Karavasilis, T.L., Ricles, J.M, Sause, R., 2014. Seismic performance and probabilistic collapse resistance assessment of steel moment resisting frames with fluid viscous dampers, *Earthquake Engineering and Structural Dynamics*, 43(14), 2135-2154.
- [17] Gidaris, I., Taflanidis, A.A., 2015. Performance assessment and optimization of fluid viscous dampers through life-cycle cost criteria and comparison to alternative design approaches. *Bulletin of Earthquake Engineering*, 13, 1003-1028.
- [18] Tubaldi, E., Barbato, M., Dall'Asta, A., 2014. Performance-based seismic risk assessment for buildings equipped with linear and nonlinear viscous dampers. *Engineering Structures*, 78, 90-99.
- [19] Tubaldi, E., Kougioumtzoglou, I.A., 2015. Nonstationary stochastic response of structural systems equipped with nonlinear viscous dampers under seismic excitation. *Earthquake Engineering and Structural Dynamics*, 44(1): 121–138.
- [20] Dall'Asta, A., Tubaldi, E., Ragni, L., 2016. Influence of the nonlinear behaviour of viscous dampers on the seismic demand hazard of building frames. *Earthquake Engineering and Structural Dynamics*, 45(1), 149-169.
- [21] Tubaldi, E., Ragni, L., Dall'Asta, A., 2015. Probabilistic seismic response assessment of linear systems equipped with nonlinear viscous dampers. *Earthquake Engineering & Structural Dynamics*, 44 (1), 101-120. DOI: 10.1002/eqe.2461
- [22] Dall'Asta, A., Scozzese, F., Ragni, L., Tubaldi, E., 2017. Effect of the damper property variability on the seismic reliability of linear systems equipped with viscous dampers.

- Bulletin of Earthquake Engineering, 15(11), 5025-5053. DOI 10.1007/s10518-017-0169-8
- [23] Lavan, O., Avishur, M., 2013. Seismic behavior of viscously damped yielding frames under structural and damping uncertainties. *Bulletin of Earthquake Engineering*, 11(6), 2309–2332.
  - [24] Scozzese, F., Dall'Asta, A., Tubaldi, E., 2019. Seismic risk sensitivity of structures equipped with anti-seismic devices with uncertain properties, *Structural Safety*, 77, 30-47.
  - [25] American Society of Civil Engineers. Seismic Evaluation and Retrofit of Existing Buildings: ASCE Standard ASCE/SEI 41-17. American Society of Civil Engineers, 2017.
  - [26] European Committee for Standardization. EN 15129:2010 - Antiseismic devices, Brussels, Belgium, 2010
  - [27] European Committee for Standardization. Eurocode 8-Design of Structures for Earthquake Resistance. Part 1: General Rules, Seismic Actions and Rules for Buildings, Brussels, Belgium, 2004.
  - [28] ASCE (American Society of Civil Engineers). (2010). Minimum design loads for buildings and other structures. *Standard ASCE/SEI 7-10*.
  - [29] Barroso LR, Winterstein S. Probabilistic seismic demand analysis of controlled steel moment-resisting frame structures. *Earthquake Engineering and Structural Dynamics* 2002; 31(12):2049–2066.
  - [30] Scozzese, F., Gioiella, L., Tubaldi, E., Ragni, L., Dall'Asta, A., 2021. Influence of viscous dampers ultimate capacity on the seismic reliability of building structures. *Structural Safety* 2021. <https://doi.org/10.1016/j.strusafe.2021.102096>
  - [31] Constantinou, M. C., & Symans, M. D. (1992). Experimental and analytical investigation of seismic response of structures with supplemental fluid viscous dampers. Buffalo, NY: National Center for earthquake engineering research.
  - [32] Lee, D., & Taylor, D. P. (2001). Viscous damper development and future trends. *The Structural Design of Tall Buildings*, 10(5), 311-320.
  - [33] Agrawal, A. K., & Amjadian, M. (2016). Seismic component devices. In *Innovative bridge design handbook* (pp. 531-553). Butterworth-Heinemann.
  - [34] Filiatrault, A., & Christopoulos, C. (2006). Principles of passive supplemental damping and seismic isolation.
  - [35] Impollonia, N., & Palmeri, A. (2018). Seismic performance of buildings retrofitted with nonlinear viscous dampers and adjacent reaction towers. *Earthquake Engineering & Structural Dynamics*, 47(5), 1329-1351.
  - [36] McKenna, F. (2011). OpenSees: a framework for earthquake engineering simulation. *Computing in Science & Engineering*, 13(4), 58-66.
  - [37] Scozzese, F., Tubaldi, E., & Dall'Asta, A. (2020). Assessment of the effectiveness of Multiple-Stripe Analysis by using a stochastic earthquake input model. *Bulletin of Earthquake Engineering*, 1-37.
  - [38] Seleemah, A.A. and Constantinou, M.C. (1997). *Investigation of seismic response of buildings with linear and nonlinear fluid viscous dampers*. Report No. NCEER-97-0004.



New York: National Center for Earthquake Engineering Research, State University of New York at Buffalo.

- [39] Hanson, R.D. and Song, T.T. (2001). *Seismic design with supplemental energy dissipation devices*. Oakland, California: Earthquake Engineering Research Institute.
- [40] Fajfar, P. (2018). Analysis in seismic provisions for buildings: past, present and future. *Bulletin of Earthquake Engineering*, **16**, 2567-2608. DOI:°10.1007/s10518-017-0290-8
- [41] Gkimprxis, A., Tubaldi, E., & Douglas, J. (2019). Comparison of methods to develop risk-targeted seismic design maps. *Bulletin of earthquake engineering*, 17(7), 3727-3752.

## SEISMIC PERFORMANCE OF STEEL MRFs RETROFITTED WITH BRBS: INFLUENCE OF THE DESIGN DECISIONS FOR THE DEVICES

Fernando Gutiérrez-Urzúa<sup>1</sup> and Fabio Freddi<sup>1</sup>

<sup>1</sup> Dept. of Civil, Environmental & Geomatic Engineering, University College London  
Gower St., London, WC1E 6BT, U.K.  
{f.urzua,f.freddi}@ucl.ac.uk

---

### Abstract

*Buckling Restrained Braces (BRBs) represent an effective strategy for the seismic retrofit of existing steel Moment Resisting Frames (MRFs), as they contribute to increase the strength, stiffness and energy dissipation capacity of the frame. Nonetheless, the design choices made during the retrofit process have a significant impact on the performance of the structure. For example, the inclusion of 'large' BRBs (i.e., high yielding strength and stiffness) may contribute to limit the deformation demands in the MRF; nonetheless, it may also induce large forces in the beams and columns of the existing structure. On the other hand, the inclusion of 'smaller' BRBs (i.e., low yielding force and stiffness), while allowing reaching the required safety requirements, may not be able to protect the MRF from damage. Additionally, the sizing of the BRB elements has an influence on the seismic demand parameters affecting the global performance of structural and non-structural components (i.e., peak and residual drifts, as well as storey accelerations). The present study investigates the impact of the design choices in the seismic performance of a retrofitted three-storey case-study frame by considering three retrofit options. The case-study MRF for the bare frame and the three retrofit configurations are modelled and numerically investigated in Opensees by monitoring local damage states (e.g., damage in BRBs, beams, columns, panel zones). First, a comparison is made in terms of non-linear static analyses to identify the deficiencies of the structures. Then, a fragility analysis is carried out through Incremental Dynamic Analyses (IDAs) accounting for the influence of the record-to-record variability. Finally, a comparison is made in terms of local and global Engineering Demand Parameters, by developing fragility curves for the components, for storey drifts and accelerations.*

**Keywords:** Buckling-restrained braces; Seismic retrofit; Design strategy; Local engineering demand parameters; Fragility curves.

---

## 1 INTRODUCTION

Buckling Restrained Braces (BRBs) have proven to be effective in improving the seismic performance of existing and new Moment Resisting Frames (MRFs) [1–3]. Such devices can be included within diagonal steel bracing connected to the existing frame contributing to the strength and stiffness of the existing structures by providing a parallel truss-like force path for the seismic lateral load imposed on the building hence forming a dual system [4]. In addition, the stable hysteretic behaviour provided by the BRBs largely contributes towards the increase of the energy dissipation capacity of the structure [2,5]. Similarly to other yielding devices, BRBs rely on the passive dissipation of elasto-plastic energy through the yielding of a steel core, which is surrounded by an unbonded buckling-restraining sleeve that allows the development of significant compression capacity, thus generating nearly symmetrical hysteretic loops [6,7]. In addition, BRBs require low maintenance and can be easily replaced after a strong earthquake, if required.

Regardless of the multiple advantages of BRBs, several aspects require further investigation. For example, the use of BRBs as a retrofit measure for existing steel MRF is followed by a redistribution of load paths and deformation mechanisms, which may induce larger seismic demands on the existing elements [2]. In addition, while the high ductility of BRBs may provide the structure with large energy dissipation capacity, their low post-yielding stiffness may result in large Residual Inter-storey Drift Ratios (RIDRs) [8], hence jeopardising the operativity and repairability of such structures [9–11]. Besides, residual deformations, together with the device's cumulative damage, may also increase the collapse risk under future earthquakes [12].

When properly designed, the MRF can provide restoring forces to counteract the residual drifts related to the yielding of BRBs [4]. Additionally, the Buckling Restrained Braced Frame (BRBF) can contribute towards the reduction of the floor accelerations arising from higher modes effects [4,13] and can limit the damage in the MRF [8]. Nonetheless, the efficiency of this dual system (*i.e.*, MRF + BRBF) is function of the relative properties of the MRF and the BRBF; therefore, the sizing of the bracing system plays a significant role in the effectiveness of the retrofitting scheme.

The present study aims at evaluating the influence of the design choices in the fragility of steel MRFs retrofitted by means of BRBs. First, the assessment of the un-retrofitted case-study structure is performed by comparing deformation-based local Engineering Demand Parameters (EDPs) (*i.e.*, rotations in beams and columns, distortion in panel zones and ductility demand in the BRBs), with the Acceptance Criteria (AC) corresponding to Performance Levels (PLs) as outlined in the ASCE 41-17 [14]. Successively, the design of three retrofitting schemes is carried out considering different design objectives. Then, the bare and retrofitted structures' seismic response is compared by performing both non-linear static and dynamic analysis in an Incremental Dynamic Analyses (IDAs) [15] fashion. The IDAs are performed considering 30 Ground Motion (GM) records allowing the definition of fragility curves. A few preliminary considerations and insights are provided on the influence of the design objectives in the different parameters characterising the seismic performance of structures retrofitted with BRBs.

## 2 CASE-STUDY STRUCTURE AND RETROFITTING SCHEMES

The Boston 3-storey, pre-Northridge MRF designed within the SAC Steel Project [16] has been selected for case-study purposes. This structure is representative of low-code pre-Northridge steel MRFs, as it was designed according to the 12<sup>th</sup> edition of the National Building Code. In this study, the structure is considered to be representative of buildings designed for low seismic demands, which often require retrofitting due to an update in the structural design regulations (*i.e.*, their performance does not comply with new regulations) or those structures

located in regions where design seismic demand was increased as a result of new data on the seismic hazard of the site. The case-study structure was designed assuming stiff soil (Soil Class D in modern standards, *e.g.*, [14,17]), office occupancy, and regular plan distribution and with no considerable irregularities along with the height. In addition, only the perimeter frames are considered to withstand lateral loads (*i.e.*, internal frames are connected as gravity frames only), as it was a common practice in the early 1990s in the United States. Details of the case-study frame are shown in Figure 1.

A 2-D non-linear Finite Element (FE) model of the north-south direction frames is developed in OpenSees [18]. Only this frame is considered in the present study, as the structure is fully symmetric (*i.e.*, torsional effects are negligible). Additional details on the modelling strategy are extensively detailed in Gutiérrez-Urzúa *et al.* [19].

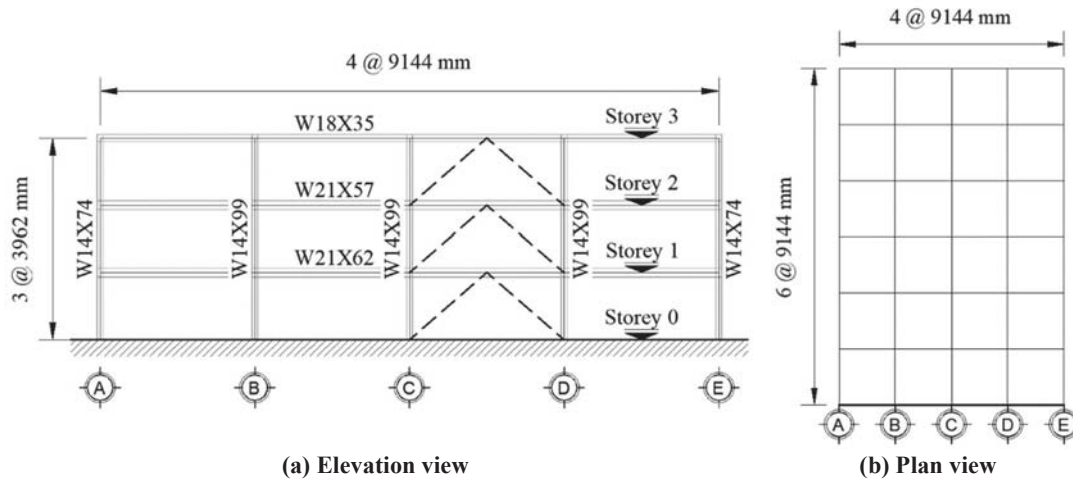


Figure 1: Description of the case-study structure: (a) elevation view of the MRF and location of braces in the retrofitting schemes; (b) plan view of the typical storey floor.

## 2.1 Assessment of the case-study structure

The first and second periods of vibration are  $T_1 = 1.88$  sec and  $T_2 = 0.52$  sec, which is in agreement with previous studies (*i.e.*, [16]). The mode-shape corresponding to the first mode (*i.e.*, [0.29 0.66 1.00]) shows a relatively uniform distribution of mass and stiffness along with the height. Non-linear static analyses, with lateral loads proportional to the first mode-shape and story mass distribution, are performed to evaluate the local components' capacity hierarchy for each PL and to identify the structure's deficiencies. Figure 2 shows the pushover curves for the Inter-storey Drift Ratios (IDRs), including markers for each local component type (*i.e.*, columns, beams and panel zones), to indicate at which points each AC is overpassed. The PLs and AC used in the present study are those defined in the ASCE 41-17 [14]. The green, yellow and red symbols in Figure 2 are related to the Immediate Occupancy (IO), Life Safety (LS) and Collapse Prevention (CP) PLs, respectively. As observed in Figure 2, the failure of the panel zones (square markers in Figure 2) is the first mechanism to occur at all storeys and PLs. For the IO PL the failure of the panel zones is followed by the columns (circle markers in Figure 2) at the first storey and the beams (triangle markers in Figure 2) at the third storey. The system overpasses the IO PL at a roof drift of 0.11 m (corresponding to IDRs of 0.82%, 1.04% and 0.94% for the first, second and third storeys, respectively). Similarly, the LS and CP PLs are reached simultaneously at a roof drift of 0.44 m (corresponding to IDR of 3.61%, 3.96% and 3.46% for the first, second and third storeys, respectively), as the AC for the panel zones is the same in the LS and CP PLs.

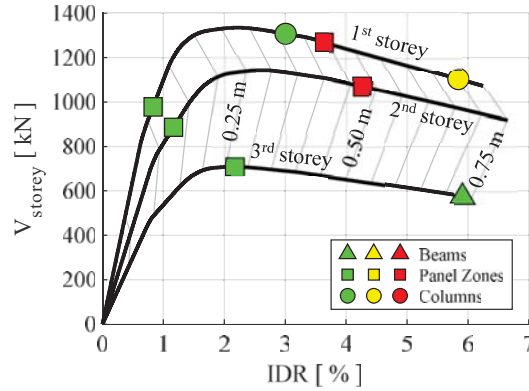


Figure 2: Pushover curves for the un-retrofitted structure. Grey lines relate the IDR at each storey to the roof displacement at every 0.05 m.

## 2.2 Buckling Restrained Braces (BRBs) retrofitting design

Three retrofit schemes are designed to comply with different design objectives, expressed in terms of target roof displacements ( $d_u$ ). The first retrofit scheme (R-A) is designed to match the roof displacement at which the first element reaches the CP PL in the MRF structure (panel zones in the first storey, as observed in Figure 2). This represents the design choice where all the resources of the structure are exploited to satisfy the CP requirements. The second retrofit scheme (R-B) is designed based on the roof displacement at which the IDR reaches 2% in any of the storeys, as this is one of the prescribed design limit established by the AISC 341-16 [20] for BRBFs. Finally, the third retrofit scheme (R-C) aims at avoiding damage in the MRF; therefore, the roof displacement is limited to the step at which any of the MRF elements overpasses the IO PL, based on the AC defined by the ASCE 41-17 [14]. Nowadays, there is considerable interest in the definition of seismic-resilient structures (*e.g.*, [11,21,22]) and this third retrofit option aims at limiting the damage to the BRBs only at the CP PL hence allowing an easy and quick reparability of the structure. Table 1 summarises the design limits for the three retrofitting schemes.

Retrofit scheme	Design objective	Target roof displacement, $d_u$
R-A	Avoid the CP PL in the MRF (according to ASCE 41-17 [14])	0.44 m
R-B	Limiting the IDR to 2% in all storeys (according to AISC 341-16 [20])	0.21 m
R-C	Avoid the IO PL in the MRF (according to ASCE 41-17 [14])	0.11 m

Table 1: Target roof displacements ( $d_u$ ) for the considered design objectives.

The design process is carried out by considering an equivalent Single-Degree-of-Freedom (SDoF) system approximation [23], based on the bi-linearised (system base shear vs. roof displacement) capacity curves from the original bare frame, with an initial stiffness ( $k_0$ ) equivalent to the ratio between the 60% of the maximum base shear ( $F_u$ ), and its corresponding roof displacement. The yielding force and displacement ( $F_y$ ,  $d_y$ ) are calculated by considering an equal energy approach (*i.e.*, equal areas under the pushover curves; therefore, defined consistently



with  $k_0$  and  $d_u$ ), and the equivalent SDoF capacity curves are compared to the seismic demands in the acceleration-displacement response spectrum (ADRS) plane.

The seismic demands are calculated considering Seattle as case-study region (corresponding to a moderate seismic region) and following the approach suggested by the ASCE 41-17 [14]. Seismic Risk Category II and stiff soil (Type D) are considered. All the retrofit schemes are designed by considering the BSE-2E hazard provisions (*i.e.*, 5% probability of exceedance in 50 years); nonetheless, the BSE-2N hazard is also considered, as the code requires to use this hazard level as an upper boundary in those cases in which BSE-2E results in higher demands. The response spectra are built aided by the SEAOC's online tool [24], and further modified to consider a 3% damping ratio (*i.e.*, spectra are multiplied by a factor  $B_1$  for BSE-2E and  $B_{SI}$  for BSE-2N, as specified in ASCE 41-17 [14] and ASCE 7-16 [25], respectively). Figure 3 shows the response spectra for the BSE-2E and BSE-2N hazard levels for the 3% damping ratio. As it can be observed, BSE-2N results in lower demands in all periods; therefore, this spectrum is used for the retrofit design in the present study.

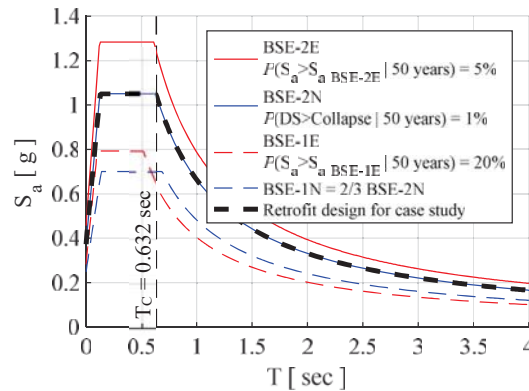


Figure 3: Elastic response spectra for the design of retrofit schemes, corresponding to the BSE-2E and BSE-2N hazard levels. BSE-1E and BSE-1N hazards shown for reference purposes.

Figure 4 shows the comparisons between the seismic demand and capacity for the MRF (*i.e.*, the red lines) by considering the three target roof displacements. The comparison shows the inadequacy of the bare frame and hence the need for retrofitting. At the same time, the figures show the seismic demand and capacity for the retrofitted frames (*i.e.*, the dual system) designed such that the capacity is able to meet the demand (*i.e.*, the blue lines). The retrofitted capacity line is the bilinearised form of the trilinear curve composed by the addition of the MRF capacity line and the BRBF capacity line (*i.e.*, the purple line). The ductility-reduced demands [23] are obtained after bi-linearisation of the systems.

The MRF ductility ( $\mu_{MRF}$ ) is equal to 3.32, 1.74 and 1.17 for the R-A, R-B and R-C schemes, respectively, while the BRBF ductility ( $\mu_{BRBF}$ ) is designed as 18, 14 and 8. The resulting system ductility ( $\mu_{DS}$ ), defined as the ratio between the ultimate and yielding displacements in the dual system bilinearised curve ( $d_u/d_y$ ), is equal to 4.74, 4.28 and 4.40. In order to match the BRBF stiffness and ductility requirements, the SDoF is de-coupled by considering the original mode shape of the structure, therefore, defining the design requirements at each storey. Finally, the area and length of the BRBs is defined in accordance to the force and ductility requirements for the storey, while the area in the complementing elastic brace is defined in accordance with the stiffness requirements of the storey (*i.e.*, with the elastic brace and BRB working in series). For a more in-depth discussion on the design method, the reader is referred to Freddi *et al.* [26].

The nominal material yield strength ( $f_y$ ) considered for the BRBs, correspond to steel ASTM A36 ( $f_y = 248$  MPa), which is further increased by 30% for the design, to represent the expected

yield strength ( $f_{ye}$ ) of the material, based on the ratios provided by the AISC 341-16 [20]. The design ductility ( $\mu_{BRB}$ ) of the BRB material is 20, which is within (and consistent with) the ranges observed in previous experimental work [27]. The elastic braces are made in steel ASTM A500 Grade C ( $f_y = 317$  MPa).

The BRBs are modelled in Opensees [18] by using the *SteelBRB* material [5], while the elastic braces are modelled by considering the *Elastic* material, as they are not expected to yield at any point due to the lower strength in the connected BRBs. Table 2 shows a summary of the BRB properties for each retrofitting scheme.

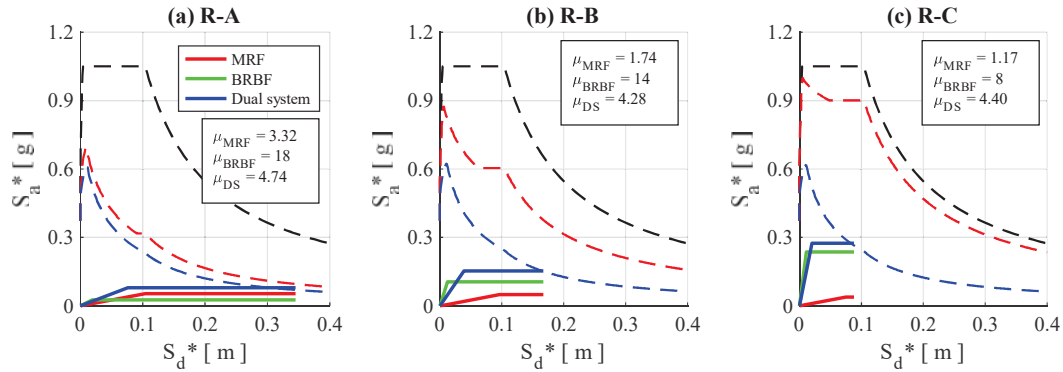


Figure 4: Bi-linearised pushover curves of the equivalent SDOF bare and retrofitted structures, in comparison with the demands, presented in the displacement-acceleration response spectrum (ADRS) plane.

Model	Storey	BRB device		Elastic brace	
		Area [mm <sup>2</sup> ]	Length [m]	Area [mm <sup>2</sup> ]	Length [m]
R-A	1	1301	2.96	11542	3.09
	2	1115	3.75	5813	2.30
	3	693	3.47	4385	2.58
R-B	1	5204	1.41	37167	4.64
	2	4460	1.78	23109	4.27
	3	2771	1.08	16017	4.97
R-C	1	11710	0.70	52383	5.35
	2	10034	0.58	34204	5.47
	3	6236	0.54	23280	5.51

Table 2: Characteristics of the BRBs and elastic braces in the different retrofitting schemes.

### 3 ASSESSMENT OF THE RETROFITTED CASE-STUDY STRUCTURES

After the retrofitting of the case-study building, the structure's fundamental period is reduced from 1.88 s, for the bare frame, to 1.06 s, 0.60 s and 0.50 s for R-A, R-B and R-C, respectively. Non-linear static analyses are performed on the retrofitted structures, and the AC thresholds for all the structural PLs established in ASCE 41-17 [14] are monitored and shown in Figure 5. For BRBs, the AC is expressed in terms of plastic deformations and the CP PL is increased from 13.3 to 19 times the yielding deformation, as this value is consistent with the design ductility of 20.

In the case of R-A, shown in Figure 5a, the structure's improvement allows reaching base shear values over 2000 kN, with PLs that are first overpassed by the BRBs at all storeys. However, the PLs for the panel zones in the IO and CP PLs, closely follows, highlighting the

adequacy of the design strategy in terms of the distribution of the devices stiffness and strength. In addition, when the structure reaches a CP PL, columns in the bottom storey are considered to experience structural damage, as their IO PL is overpassed. In the case of R-B, shown in Figure 5b, the pushover curves show higher post-yielding stiffness due to the hardening of the BRBs, which provide a larger base shear contribution in this configuration. BRBs control the system failure for all PLs; nonetheless, panel zones reach the IO PL when the BRBs overpass the LS PL, which suggests that the MRF exhibits damage whenever the BRBs overpass this PL. Finally, the case R-C, is shown in Figure 5c. In this case the strength and stiffness contribution of the BRBs is significantly higher, while the BRBs reach the CP LS almost as the panel zones reach the IO LS, which suggests that the MRF remains undamaged while the BRBs reaches its considered failure. It is worth mentioning that the damage scenario observed is consistent with the design objectives which are also represented by the lines for the design displacement  $d_u$  (*i.e.*, the blue dotted lines) in Figure 5.

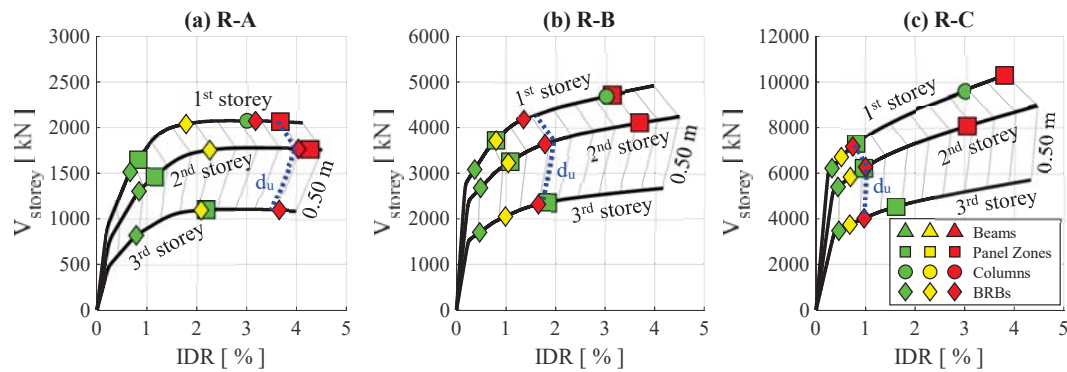


Figure 5: Pushover curves for the retrofitted structures. Grey lines relate the IDR at each storey to the roof displacement at every 0.05 m.

### 3.1 Fragility of the case-study structure and retrofitting schemes

The fragility of the bare and retrofitted structures is derived based on IDAs [15] by considering a set of 30 GM records selected from the PEER NGA-West2 database [28]. These GMs are selected to be in agreement with the BSE-2N spectrum (see Figure 3), with no further discrimination (all types, with no distinction for distances, wave velocities nor significant duration). Only the acceleration in the  $x$ -direction is considered.

Based on the results of the IDAs, fragility curves are derived. These provide the probability of the Damage State (DS) exceeding a specific PL in a component (or in the system), conditional to the value of the intensity measure (IM), *i.e.*,  $P(DS \geq PL | IM)$ . DSs are defined by the the seismic deformation demands and compared to the capacity (*i.e.*, the element-based AC related to a PL) for all the considered components. The spectral acceleration corresponding to the structure's fundamental period  $S_a(T_1)$  is considered as IM [29] in the present study.

The fragility curves for the bare and retrofitted case-study structures are shown in Figure 6. These curves are derived for each element type (*e.g.*, BRBs, columns, beams and panel zones), while the system fragility is defined by considering a series arrangement of the components, *i.e.*, corresponds to the first element (of any kind) to overpass the AC for the considered PL. In addition, fragility curves are built for those cases in which the numerical model does not reach convergence due to excessive deformation (*i.e.*, collapse cases, as defined by Jalayer *et al.*) [30]. Nonetheless, these cases occur once the element-based AC is overpassed in all PLs, therefore, they are simply treated as collapse cases.

Consistently with the observations from the pushover analyses, the panel zones define the system fragility for the bare frame, while the BRBs define the system fragility in the retrofitted cases, *i.e.*, they represent the most fragile components for the whole range of IM values. The direct comparison of fragility curves for the different retrofitting schemes allows to synthetically contrast the capacity of the retrofitting schemes, however, it should be noted that it does not allow to consider the demand changes due to the period shifting, therefore, a comprehensive comparison requires site-dependent hazard considerations.

As it can be observed, the increase of capacity is reflected in the shifting of the fragility curves to higher IM values, accordingly with the retrofitting level. The median intensity values ( $IM_{50}$ ) of the retrofitted structures are increased by 136%, 255% and 445% for the R-A, R-B and R-C retrofitting schemes for the IO PL; by 54%, 80% and 100% for the LS PL; and by 159%, 184% and 207% for the CP LS. The effect of the record-to-record variability is more noticeable in the retrofitting scheme R-A when compared to R-B and R-C, as reflected by the lognormal standard deviation  $\beta$  values. This effect may be related to the larger ductility of the BRBF in the R-A retrofitting scheme, as highlighted by Freddi *et al.* [4]. It is relevant to highlight that all force-controlled failures (*e.g.*, compression/tension in columns, shear in beams) occur after all the PLs are overpassed, therefore, they do not influence the fragility curves.

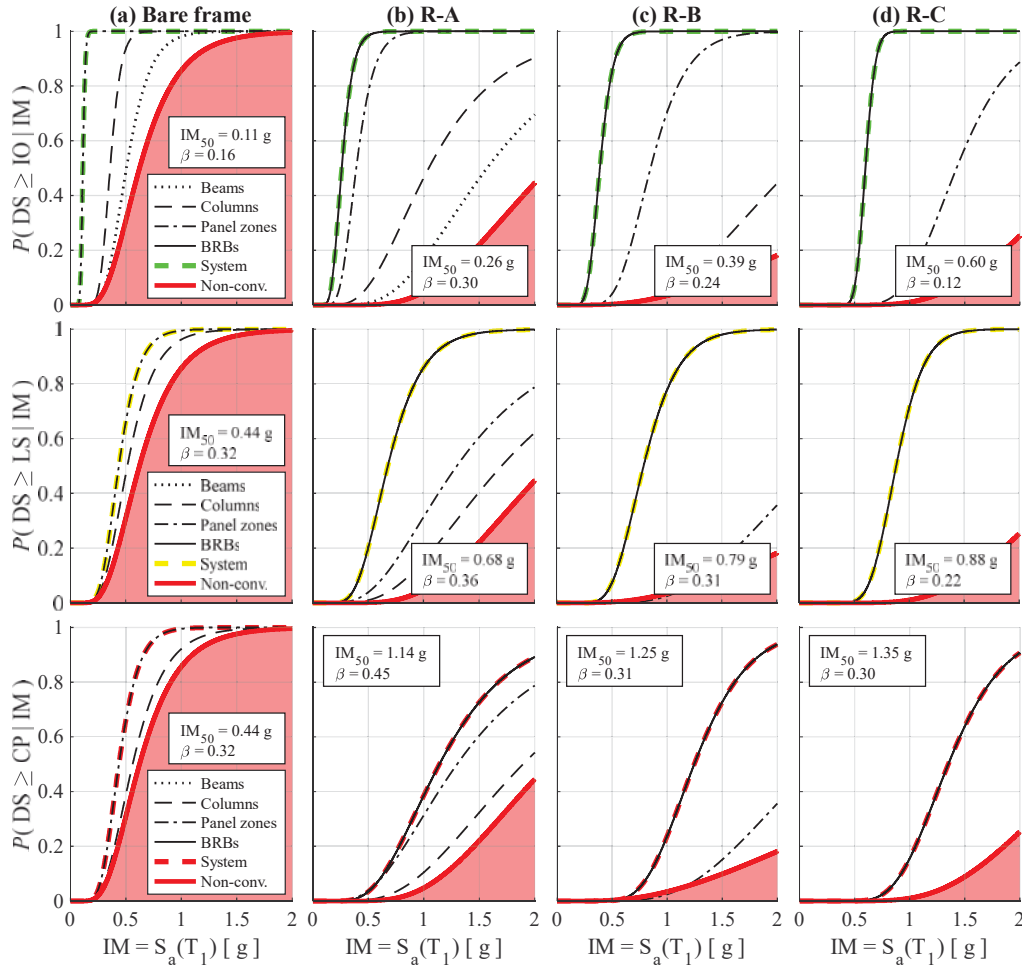


Figure 6: Element-based fragility curves for the IO, LS and CP PLs. The parameters  $IM_{50}$  and  $\beta$  are shown for each system fragility curve.

Finally, for comparison purposes only, Figure 7 shows the fragility curves for the monitored global EDPs, which include the Peak Inter-storey Drift Ratios (PIDRs), the Residual Inter-storey Drift Ratios (RIDRs) and Peak Storey Accelerations (PSAs). The AC thresholds for the PIDR of 0.5%, 1.5%, and 2%, suggested by the ASCE 41-06 [31] for braced frames, respectively for IO, LS and CP PLs have been assumed in this study. For the RIDR, an AC thresholds of 0.5% is used, in accordance with McCormick *et al.* [9], which was defined with the aim of controlling building reparability. Finally, the AC thresholds for PSA have been assumed based on the limits used by the Hazus-MH MR4 Technical Manual [32] for moderate-code structures, corresponding to 0.5g, 1.0g and 2.0g for the Moderate, Extensive and Complete PLs.

As shown in Figure 7, the median (*i.e.*,  $IM_{50}$ ) values for the PIDR and the RIDR fragility curves are increased as the stiffness of the structure is increased, as expected. In the case of the  $IM_{50}$  for the PSA fragility curves, all the retrofitting schemes exhibit similar values for the first two thresholds (*i.e.*, 0.5g, 1.0g); however, when the largest acceleration threshold (*i.e.*, 2.0g) is considered, the stiffest structures exhibit larger  $IM_{50}$  values. Similarly to the element-based fragility curves, the  $\beta$  parameter is larger in the retrofitting schemes with larger ductility in the BRBF. Also, the dispersion is observed to be larger for the RIDR and PSA fragility curves.

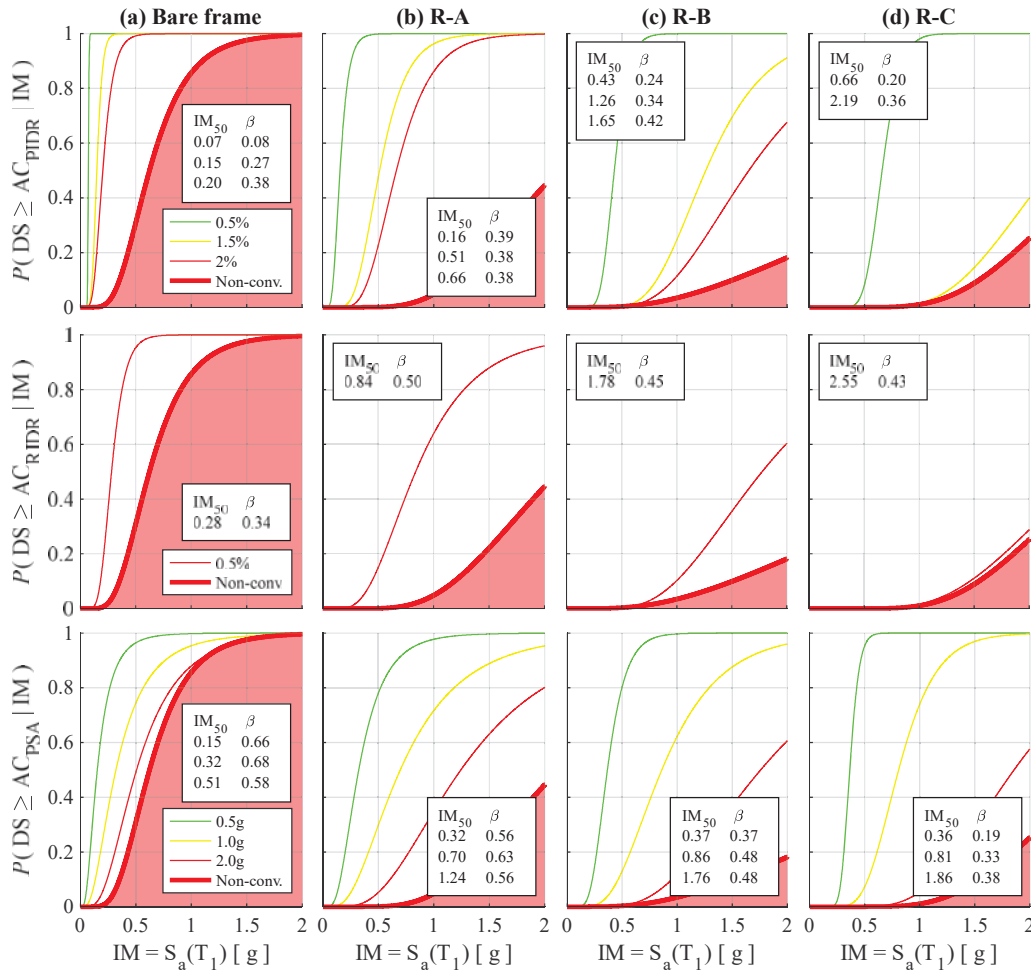


Figure 7: Global fragility curves for the peak inter-storey drift ratios -PIDR- (top), residual inter-storey drift ratios -RIDR- (middle) and peak storey accelerations -PSA- (bottom), for different performance limits (PLs).



#### 4 CONCLUSIONS

This paper presented the fragility assessment of a case-study steel Moment Resisting Frame (MRF) retrofitted with Buckling Restrained Braces (BRBs). Three retrofit configurations were considered which aimed at achieving different performance levels (PLs): R-A was designed to protect the MRF elements from reaching the Collapse Prevention (CP) Performance Limit (PL); R-B was designed to avoid a Peak Inter-storey Drift Ratio larger than 2% at any storey; while R-C was designed to protect the MRF elements from reaching the Immediate Occupancy (IO) PL. The assessment of the bare frame and of the three retrofitting solutions was carried out both by pushover analyses and by Incremental Dynamic Analyses (IDAs). IDAs were performed by using a set of 30 Ground Motion (GM) records, and fragility curves were successively derived by considering limits for element-based and global Engineering Demand Parameters (EDPs).

The following conclusions can be drawn:

- The R-A fragility was controlled by the BRBs in all PLs, closely followed by the panel zones in the IO and CP PLs. In the R-B scheme, the BRBs were capable of protecting the MRF from damage (*i.e.*, overpassing the IO PL) up to a Life Safety (LS) PL in the BRBs. Finally, the R-C scheme was capable of protecting the MRF from damage up to a CP PL, as originally intended during the retrofitting design. These observations are made based on both the non-linear static and the fragility assessments.
- In the case of the global EDPs, the retrofitted structures exhibited a lower probability of exceeding the PLs for all the values of intensity measure (IM), when compared to the bare frame. The stiffer retrofitting schemes were capable of reducing the Peak and Residual Inter-storey Drift Ratios (PIDR and RIDR) for all the values of IM. Conversely, for Peak Storey Acceleration (PSA), the fragility curves derived by considering low acceleration limits (*e.g.*, 0.5g and 1.0g) is similar for all retrofitting schemes. For larger limits of acceleration (*e.g.*, 2.0g), the probability of exceedance is reduced for all values of IM in the stiffer retrofitting schemes (*i.e.*, R-B and R-C).
- In all fragility curves, the dispersion of the distribution (represented by the lognormal standard deviation,  $\beta$ ) is increased in structures with larger ductility (*e.g.*, R-A) while it is reduced in structures with lower ductility (*e.g.*, R-C). In all cases, the fragility curves for the RIDR and the PSA exhibit larger  $\beta$  values, in comparison to other EDPs. This is consistent with other studies present in the literature.
- Despite the increase of axial demands in the column and beam elements due to the trussing effects provided by the braces, none of the retrofitting schemes exhibited force-controlled failures in these elements earlier than any of the deformation-controlled acceptance criteria (AC) defined.
- In general, the median capacity (represented by  $IM_{50}$ ) of the retrofitted structures was benefited from larger retrofitting options, in particular, when large PLs are considered as limits (*e.g.*, CP). The dispersion of the fragility distribution ( $\beta$ ) generally increased when considering higher PLs, as well as when considering the RIDR and PSA in comparison with other EDPs. In addition, larger values of  $\beta$  were observed when the Buckling Restrained Braced Frames (BRBFs) within the dual systems were designed for larger ductility targets (*e.g.* R-A).

It is noteworthy that the comparison in terms of fragility only does not provide information on the retrofit's effectiveness, as it considers the variation of the capacity alone. Future work is required toward the inclusions of considerations related to the seismic demand variation for the different retrofit options (*e.g.*, risk definition).

## REFERENCES

- [1] F.M. Mazzolani, G. Della Corte, M. D’Aniello, Experimental analysis of steel dissipative bracing systems for seismic upgrading, *J. Civ. Eng. Manag.* 15 (2009) 7–19. <https://doi.org/10.3846/1392-3730.2009.15.7-19>.
- [2] F. Freddi, E. Tubaldi, L. Ragni, A. Dall’Asta, Probabilistic performance assessment of low-ductility reinforced concrete frames retrofitted with dissipative braces, *Earthq. Eng. Struct. Dyn.* 42 (2013) 993–1011. <https://doi.org/10.1002/eqe.2255>.
- [3] L. Di Sarno, G. Manfredi, Seismic retrofitting with buckling restrained braces: Application to an existing non-ductile RC framed building, *Soil Dyn. Earthq. Eng.* 30 (2010) 1279–1297. <https://doi.org/10.1016/j.soildyn.2010.06.001>.
- [4] F. Freddi, E. Tubaldi, A. Zona, A. Dall’Asta, Seismic performance of dual systems coupling moment-resisting and buckling-restrained braced frames, *Earthq. Eng. Struct. Dyn.* (2020) 1–25. <https://doi.org/10.1002/eqe.3332>.
- [5] A. Zona, A. Dall’Asta, Elastoplastic model for steel buckling-restrained braces, *J. Constr. Steel Res.* 68 (2012) 118–125. <https://doi.org/10.1016/j.jcsr.2011.07.017>.
- [6] T.T. Soong, B.F. Spencer, Supplemental energy dissipation: State-of-the-art and state-of-the-practice, *Eng. Struct.* 24 (2002) 243–259. [https://doi.org/10.1016/S0141-0296\(01\)00092-X](https://doi.org/10.1016/S0141-0296(01)00092-X).
- [7] R. Tremblay, L. Poncet, P. Bolduc, R. Neville, R. DeVall, Testing and design of buckling restrained braces for canadian application, 13th World Conf. Earthq. Eng. (2004).
- [8] J. Erochko, C. Christopoulos, R. Tremblay, H. Choi, Residual Drift Response of SMRFs and BRB Frames in Steel Buildings Designed according to ASCE 7-05, *J. Struct. Eng.* 137 (2011) 589–599. [https://doi.org/10.1061/\(asce\)st.1943-541x.0000296](https://doi.org/10.1061/(asce)st.1943-541x.0000296).
- [9] J. McCormick, H. Aburano, M. Ikenaga, M. Nakashima, Permissible Residual Deformation Levels for Building Structures Considering both Safety and Human Elements, 14th World Conf. Earthq. Eng. (2008) 8.
- [10] Y. Iwata, H. Sugimoto, H. Kuwamura, Reparability limit of steel structural buildings : Study on performance based design of steel structural buildings, Part 2, *J. Struct. Constr. Eng.* 70 (2005) 165–172. [https://doi.org/10.3130/aijs.70.165\\_1](https://doi.org/10.3130/aijs.70.165_1).
- [11] E. Elettore, F. Freddi, M. Latour, G. Rizzano, Design and analysis of a seismic resilient steel moment resisting frame equipped with damage-free self-centering column bases, *J. Constr. Steel Res.* 179 (2021) 106543. <https://doi.org/10.1016/j.jcsr.2021.106543>.
- [12] F. Morfuni, F. Freddi, C. Galasso, Seismic performance of dual systems with BRBs under mainshock-aftershock sequences, 13th Int. Conf. Appl. Stat. Probab. Civ. Eng. ICASP 2019. (2019) 1–8.
- [13] H. Choi, J. Erochko, C. Christopoulos, R. Tremblay, Comparison of the seismic response of steel buildings incorporating self-centering energy-dissipative braces, buckling restrained braces and moment-resisting frames, *Res. Rep.* 05-2008. (2008).
- [14] American Society of Civil Engineers, Seismic Evaluation and Retrofit of Existing Buildings, ASCE/SEI 41-17. (2017). <https://doi.org/10.1061/9780784414859>.
- [15] D. Vamvatsikos, C. Allin Cornell, Incremental dynamic analysis, *Earthq. Eng. Struct. Dyn.* 24 (1998) 1–25.

- Dyn. 31 (2002) 491–514. <https://doi.org/10.1002/eqe.141>.
- [16] A. Gupta, H. Krawinkler, Behavior of Ductile SMRFs at Various Seismic Hazard Levels, *J. Struct. Eng.* 126 (2000) 98–107.
  - [17] G. Teng, J. Baker, Evaluation of SCEC cybershake ground motions for engineering practice, *Earthq. Spectra.* 35 (2019) 1311–1328. <https://doi.org/10.1193/100918EQS230M>.
  - [18] F. McKenna, G.L. Fenves, M.H. Scott, Open system for earthquake engineering simulation (OpenSees), (2000).
  - [19] F. Gutiérrez-Urzúa, F. Freddi, L. Di Sarno, Comparative analysis of code-based approaches for seismic assessment of existing steel moment resisting frames, *J. Constr. Steel Res.* 181 (2021) 106589. <https://doi.org/10.1016/j.jcsr.2021.106589>.
  - [20] American Institute of Steel Construction, Seismic Provisions for Structural Steel Buildings, 2016. <https://doi.org/10.1201/b11248-8>.
  - [21] F. Freddi, C.A. Dimopoulos, T.L. Karavasilis, Experimental Evaluation of a Rocking Damage-Free Steel Column Base with Friction Devices, *J. Struct. Eng.* 146 (2020) 04020217. [https://doi.org/10.1061/\(asce\)st.1943-541x.0002779](https://doi.org/10.1061/(asce)st.1943-541x.0002779).
  - [22] M. Latour, M. D’Aniello, M. Zimbru, G. Rizzano, V. Piluso, R. Landolfo, Removable friction dampers for low-damage steel beam-to-column joints, *Soil Dyn. Earthq. Eng.* 115 (2018) 66–81. <https://doi.org/10.1016/j.soildyn.2018.08.002>.
  - [23] P. Fajfar, A Nonlinear Analysis Method for Performance-Based Seismic Design, *Earthq. Spectra.* 16 (2000) 573–592. <https://doi.org/10.1193/1.1586128>.
  - [24] Structural Engineers Association of California (SEAOC), California’s Office of Statewide Health Planning and Development (OSHPD), U.S. Seismic Design Maps, (2020). <https://seismicmaps.org>.
  - [25] American Society of Civil Engineers, Minimum Design Loads and Associated Criteria for Buildings and Other Structures, ASCE/SEI 7-16. (2017). <https://doi.org/10.1061/9780784414248>.
  - [26] F. Freddi, J. Ghosh, N. Kotoky, M. Raghunandan, Device Uncertainty Propagation in Low-Ductility RC Frames Retrofitted with BRBs for Seismic Risk Mitigation, *Earthq. Eng. Struct. Dyn.* (2021). <https://doi.org/10.1002/eqe.3456>.
  - [27] L.A. Fahnestock, R. Sause, J.M. Ricles, L.-W. Lu, Ductility demands on buckling-restrained braced frames under earthquake loading, *Earthq. Eng. Eng. Vib.* 2 (2003) 255–268. <https://doi.org/10.1007/s11803-003-0009-5>.
  - [28] Y. Bozorgnia, N.A. Abrahamson, L. Al Atik, T.D. Ancheta, G.M. Atkinson, J.W. Baker, A. Baltay, D.M. Boore, K.W. Campbell, B.S.-J. Chiou, R. Darragh, S. Day, J. Donahue, R.W. Graves, N. Gregor, T. Hanks, I.M. Idriss, R. Kamai, T. Kishida, A. Kottke, S.A. Mahin, S. Rezaeian, B. Rowshandel, E. Seyhan, S. Shahi, T. Shantz, W. Silva, P. Spudich, J.P. Stewart, J. Watson-Lamprey, K. Wooddell, R. Youngs, NGA-West2 Research Project, *Earthq. Spectra.* 30 (2014) 973–987. <https://doi.org/10.1193/072113EQS209M>.
  - [29] F. Freddi, J.E. Padgett, A. Dall’Asta, Probabilistic seismic demand modeling of local level response parameters of an RC frame, *Bull. Earthq. Eng.* 15 (2017). <https://doi.org/10.1007/s10518-016-9948-x>.

- [30] F. Jalayer, H. Ebrahimian, A. Miano, G. Manfredi, H. Sezen, Analytical fragility assessment using unscaled ground motion records, *Earthq. Eng. Struct. Dyn.* 46 (2017) 2639–2663. <https://doi.org/10.1002/eqe.2922>.
- [31] American Society of Civil Engineers, *Seismic Rehabilitation of Existing Buildings*, ASCE/SEI 41-06. (2007). <https://doi.org/10.1061/9780784408841>.
- [32] Federal Emergency Management Agency, *HAZUS-MH MR4 Technical Manual*, Natl. Inst. Build. Sci. Fed. Emerg. Manag. Agency (NIBS FEMA). (2003) 712.

## EXPERIMENTAL INVESTIGATION OF SPHERICAL RUBBER SEISMIC ISOLATION BEARINGS

Antonios A. Katsamakas<sup>1</sup>, Gabriel Belser<sup>2</sup>, M.F. Vassiliou<sup>3</sup>, M. Blondet<sup>4</sup>, B. Stojadinovic<sup>5</sup>

<sup>1</sup>PhD Candidate, Chair of Seismic Design and Analysis, IBK, ETH Zurich  
e-mail: katsamakas@ibk.baug.ethz.ch

<sup>2</sup> MSc student, IBK, ETH Zurich <sup>3</sup> Assistant Professor, Chair of Seismic Design and Analysis, IBK, ETH Zurich <sup>4</sup> Professor, Pontificia Universidad Católica del Perú <sup>5</sup> Professor, Chair of Structural Dynamics and Earthquake Engineering, IBK, ETH Zurich  
{belserg,vassiliou,stojaadinovic}@ibk.baug.ethz.ch  
mblondet@pucp.edu.pe}

---

### Abstract

*Seismic isolation is a mature and effective method of reducing earthquake-induced building damage. However, applications of this technology are limited to special and important structures, predominantly in the developed world, due to the associated high costs.*

*An experimental study of a spherical rubber seismic isolator is presented herein. The cost of these devices is sufficiently low that their wide-spread application in low-income countries seems economically viable. Using a closely spaced grid of such spheres may require only a thin, lightly-reinforced diaphragm slab above the isolation level, further reducing construction costs. Avoiding the cost of this extra slab is crucial to make seismically isolated low-rise buildings economically feasible in poor regions of the globe.*

*The examined seismic isolation bearings are based on rolling, with rubber spheres rolling on concave (spherical) or flat concrete surfaces. Concave concrete surfaces provide restoring force to the isolated structure through gravity. In contrast, in the case of flat concrete surfaces, no restoring force is applied. Rubber spheres offer increased damping and better stress distribution in the contact areas than spheres made using stiffer materials. This work investigated the effects of the geometry of the rolling surface (i.e., flat or concave), the diameter of the rolling sphere (i.e., 50 or 100 mm), and the applied compressive load on the seismic behavior of these isolation bearings. Initially, the rubber isolators were subjected to monotonic uniaxial compression to examine their behavior under vertical loading. Subsequently, cyclic tests were performed to obtain the lateral force-displacement diagram of the isolation system. It was found that the coefficient of rolling friction depends on the axial load, and the diameter of the spheres. The governing parameter for the design of the rubber spheres is not material failure, but excessive compressive deformation that leads to undesirably high rolling friction. Overall, experimental results proved the efficiency of the investigated system in terms of decreasing the inertia forces transmitted to the superstructure.*

**Keywords:** seismic isolation, rolling bearings, cyclic testing, low-cost construction, rubber bearings

---



## 1 INTRODUCTION

Seismic isolation [1,2] is a seismic response modification technique, which uncouples the motion of the structure from the ground shaking. This is achieved by placing a low-stiffness or slippery layer at the base of the structure. This elongates the dominant eigenperiod of the structure, reducing the applied accelerations and, thus, the inertial forces. The main drawback is that it leads to increased displacements; however, these displacements are localized at the isolation level, with the interstory drifts maintaining low values. The three key concepts that a seismic isolation scheme should fulfill are: i) Sufficient bearing capacity under vertical (gravity) loads, ii) sufficient flexibility in the horizontal direction to uncouple the motion of the structure from the ground motion, iii) energy dissipation [3]. An important design consideration is that, when seismic isolation is used, the superstructure should be designed to remain essentially elastic. Previous studies [4,5] proved that this is not a conservative design, but a necessity, emerging from the dynamics of base-isolated structures.

Modern applications of rolling seismic isolation systems focused on isolation of precious equipment, where the supported mass is expected to be low. The rolling spheres were mainly made of steel or rubber, and the supporting plates were made of concrete or steel [6-10]. The geometry of the supporting plates was either conical or concave, providing restoring force through gravity. Even though the efficiency of isolation devices is acknowledged, the implementation of these technologies is limited due to the associated high cost. The high cost originates from a) the cost of the isolation devices and b) the cost of the extra slab required at the isolation level. Finally, the high weight of these devices (can reach 1 ton per device) demands the use of lifting equipment, further increasing the complexity of the construction [11]. There have been numerous attempts to reduce the cost of seismic isolation devices [12-27, among others].

This work focuses on the recently published work by Cilsalar and Constantinou [28-30], who essentially suggested a Friction Pendulum System (FPS bearing) based on rolling instead of sliding (Figure 1). It comprises two concrete surfaces and a stiff rubber sphere (with or without a steel core) that rolls in between. The system is indeed low-cost, as the rubber balls can be obtained for low price. However, it still requires an extra slab above the isolation devices – hence, the overall cost still remains prohibitive for low-rise buildings in low-income countries. This paper suggests the use of a grid of closely-spaced rubber spheres. Using a grid could allow the construction of a thin, lightly reinforced diaphragm, reducing the construction cost (Figure 2). Moreover, since several spheres are used, each sphere supports a lower vertical force (weight); therefore, one could use spheres with smaller diameter, made of rubber material of lower stiffness, and without a steel core.

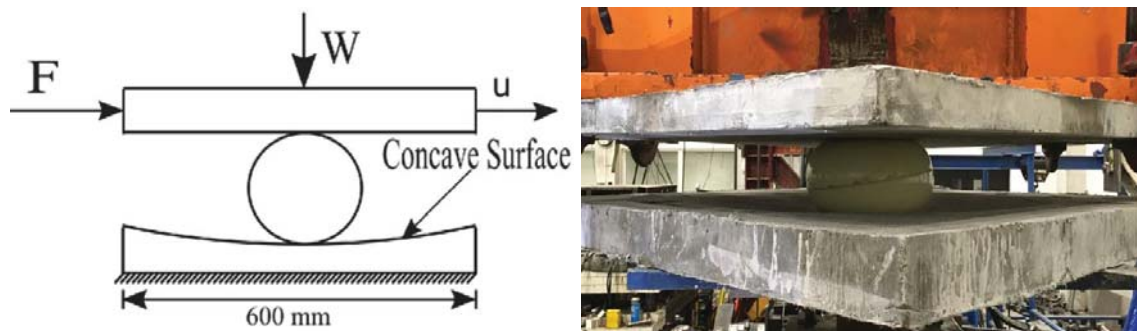


Figure 1: Low-cost rubber rolling isolator, tested by Cilsalar and Constantinou [28-30].

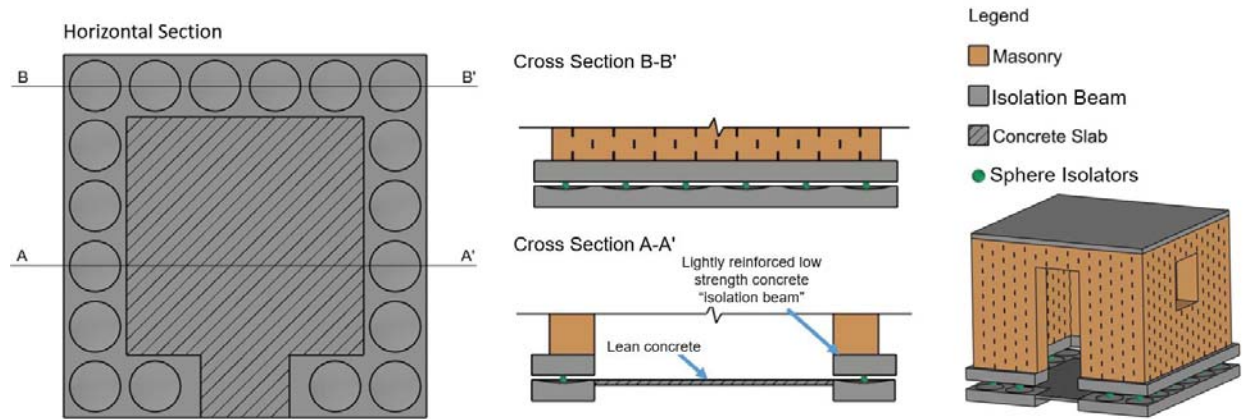


Figure 2: Schematic representation of the low-cost seismic isolation proposed in the present study.

This study presents the compressive and cyclic behavior of low-cost rolling rubber isolators. The cyclic behavior is quantified using a half-scale system of four isolators, capped with a slab. Parameters of investigation are the diameter of the rubber sphere (i.e., 50 mm or 100 mm), the geometry of the concrete plate (i.e., flat or concave), and the supported weight (i.e., 2.08 kN, 3.23 kN or 4.74 kN).

## 2 EXPERIMENTAL SETUP

### 2.1 Testing equipment and instrumentation

Cyclic tests were performed using the shake table of the ETH [31] as an actuator. The shake table is a stiff steel box with dimensions of 1 x 2 m, operated by a servo-hydraulic actuator of 100 kN, which acts only in one direction. The stroke, maximum velocity, and maximum payload is 240 mm, 220 mm/second, and 7.5 tons, respectively. Before testing, the accuracy of the shake table was assessed by performing preliminary tests and comparing the applied to the expected motion, with the two being closely correlated.

The experimental setup is shown in Figures 3 and 4. Four isolators (i.e., four pairs of concrete plates) were placed on top of the shake table. A 30mm-thick steel slab was mounted on the top plates, and weight was placed on top of it. The slab was connected to a stiff column via two rigid struts to constrain its motion along the table axis ( $x$ ) and around the vertical axis ( $z$ ). Side stoppers and a rail in the middle prevented the slab from moving out of plane. Variable weight in the form of steel beams was placed on top of the structure to apply vertical load on the bearings. In all configurations, the bottom concrete plates were flat. In some configurations, hereafter characterized as “concave,” the top rolling surfaces were spherical.

The plates were made of unreinforced concrete with fine aggregate since steel reinforcement increases cost and construction time, making implementation harder in developing countries. The geometry of the plates is shown in Figure 5.

The radius of curvature of the concave concrete plates ( $R$ ) was  $R = 750$  mm. In plan view, the diameter of the concave concrete plate was 350mm. A commercial low-cost M15 concrete mix was selected, with a maximum aggregate size of 4 mm. The mean compressive and flexural strength was equal to 27.62 MPa, and 4.63 MPa, respectively, tested according to EN 1015-11 (1993) [32]. The utilized rubber spheres were made of natural rubber (NR), with a

shore hardness of 85A. The cost of the 50 mm and 100 mm diameter spheres was 3 \$ and 17\$, respectively [33].

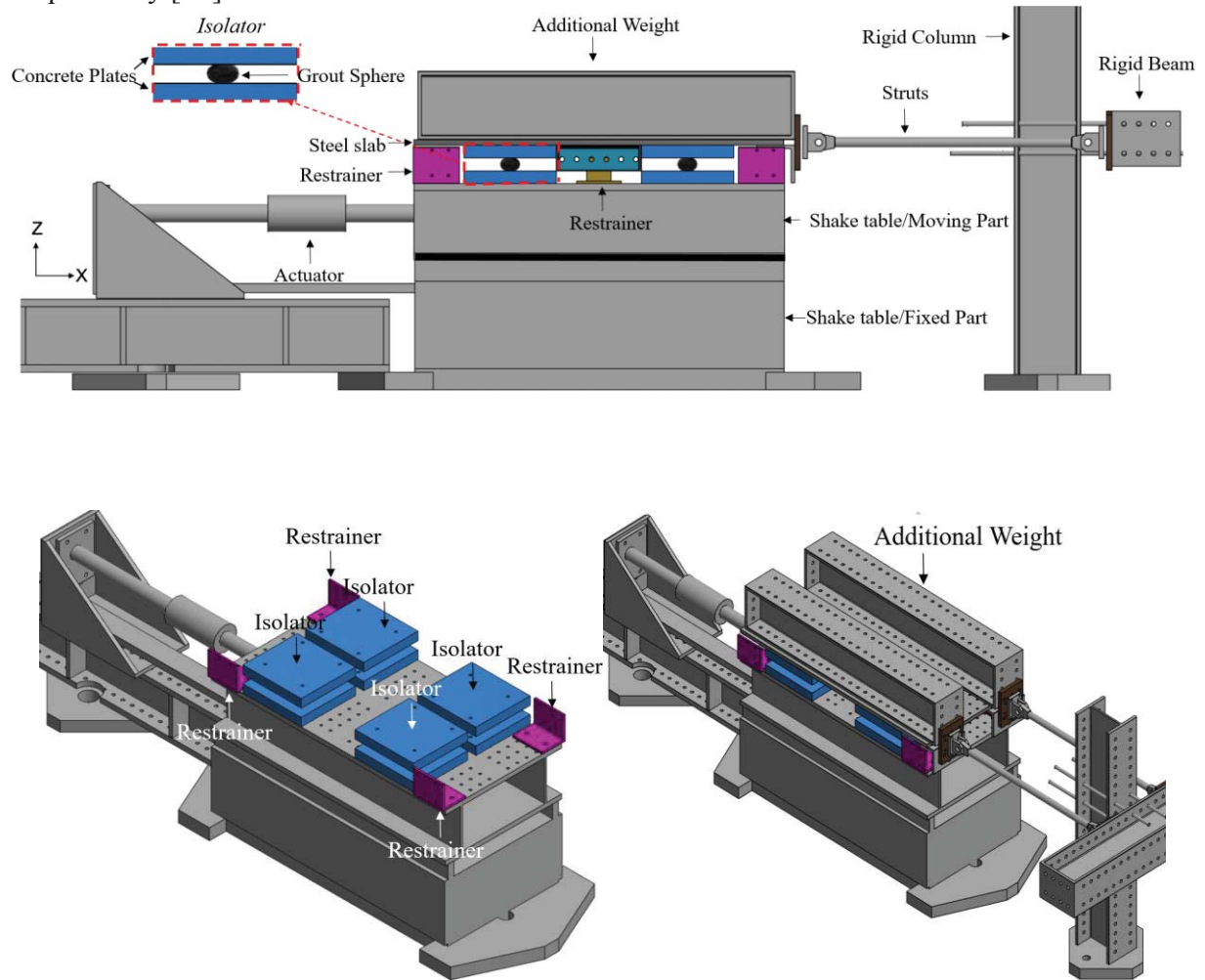


Figure 3: Schematic representation of the utilized experimental setup

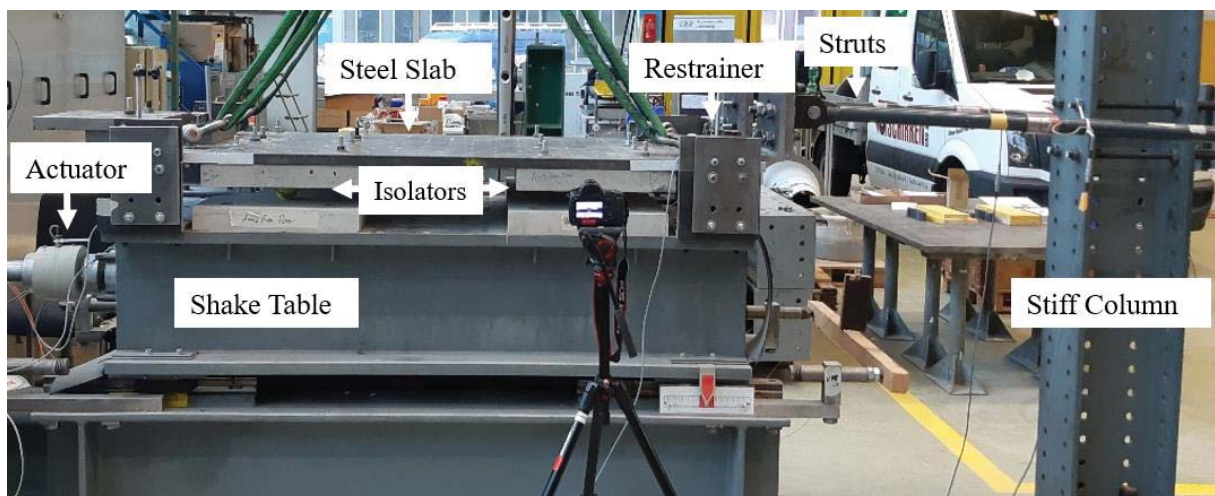


Figure 4: View of the experimental setup

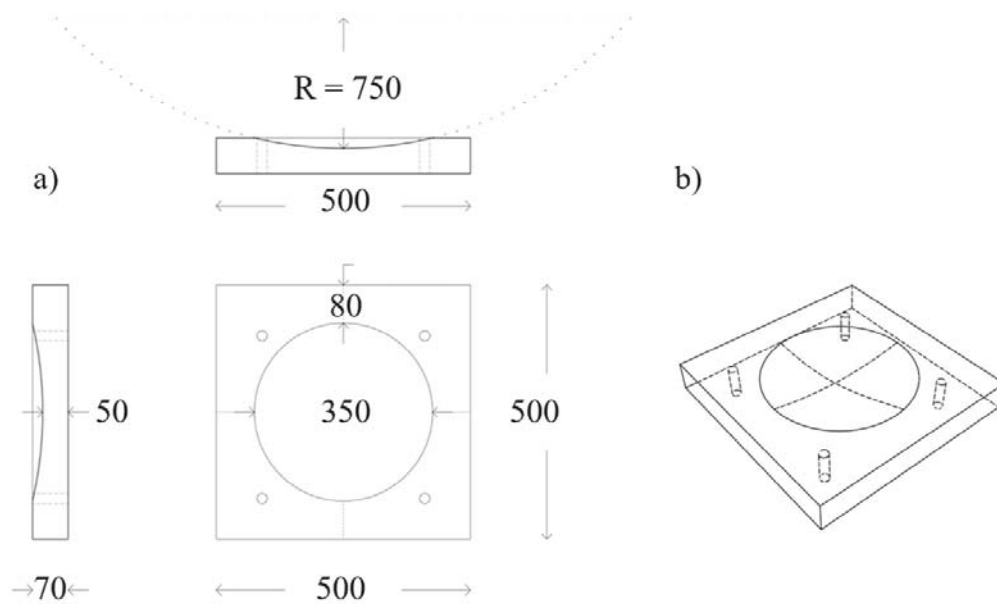


Figure 5: Schematic representation of the utilized concave concrete plates (dimensions in mm); a) Plan and side views, b) 3D view

## 2.2 Tested configurations and similitude laws

Walls of modern unconfined masonry houses in Cuba weight  $2.80 \text{ kN/m}^2$ . Assuming a wall height of 2.8m, gives an unfactored weight of the masonry wall of  $7.8 \text{ kN/m}$ . A 10 cm roof slab at a typical  $5 \times 5 \text{ m}$  room would add  $3 \text{ kN/m}$  to each wall, giving a total weight of  $11 \text{ kN/m}$ . Assuming isolators placed every 1 m, the vertical load of each isolator is  $11 \text{ kN}$ .

The tests were designed assuming a geometrical scaling of  $S_L = 1:2 = 0.5$ . Therefore, to preserve similitude of stresses the force scaling factor is  $S_F = S_L^{-2} = 4$  [34].

Rubber spheres of 50 and 100mm diameter were tested. Three compressive loads (2.08 kN, 3.23 kN or 4.74 kN per sphere in the model scale) under 2 rolling surface geometries (flat/flat and flat/concave) were planned. This corresponds to a total number of 12 configurations. However, due to a limitation of the experimental setup, the spheres with a diameter of 50 mm were tested only with flat concrete plates and with the lower two weight configurations (2.08 kN and 3.23 kN per sphere). A summary of the tested configurations appears in Table 1. Table 2 summarizes the relevant quantities in the model and prototype scale.

Weight per sphere (kN)	Geometry of Concrete Plates	Diameter of Rubber Spheres (mm)	
		100	50
2.08	Flat	Tested	Tested
	Concave	Tested	Not tested
3.23	Flat	Tested	Tested
	Concave	Tested	Not tested
4.74	Flat	Tested	Not tested
	Concave	Tested	Not tested

Table 1: Summary of the tested configurations



Quantity	Model Scale	Prototype Scale
Radius of concave concrete plates	750 mm	1500 mm
Eigenperiod of concave concrete plates	1.74 sec	2.46 sec
Plan view diameter of the concave isolator	350 mm	700 mm
Diameter of large rubber spheres	100 mm	200 mm
Diameter of small rubber spheres	50 mm	100 mm
Vertical load	2.08, 3.23, 4.74 kN	8.32, 12.92, 18.96 kN
Amplitude of cyclic test	$\pm 100$ mm	$\pm 200$ mm

Table 2: Summary of the main quantities of the experimental model and the corresponding prototype structure

### 3 TEST RESULTS

#### 3.1 COMPRESSION TESTS

The first part of the experimental investigation comprised monotonic uniaxial compression tests to characterize the response of the rubber spheres under vertical loading (Figure 6). The compression tests were conducted using displacement control. This corresponds to a displacement rate of 0.33 mm/sec and 0.167 mm/sec for the rubber spheres with a diameter of 100 mm and 50 mm, respectively. The compression tests revealed that material failure is not a critical design parameter, since the utilized spheres can sustain very high vertical load, without material failure. The critical design parameter is expected to be the excessive deformation and the associated shape change. Under high vertical loading, the shape of the rolling rubber isolators is no longer spherical; thus, the rolling friction coefficient (i.e., the ratio of horizontal-to-vertical force to initiate rolling) reaches high values.

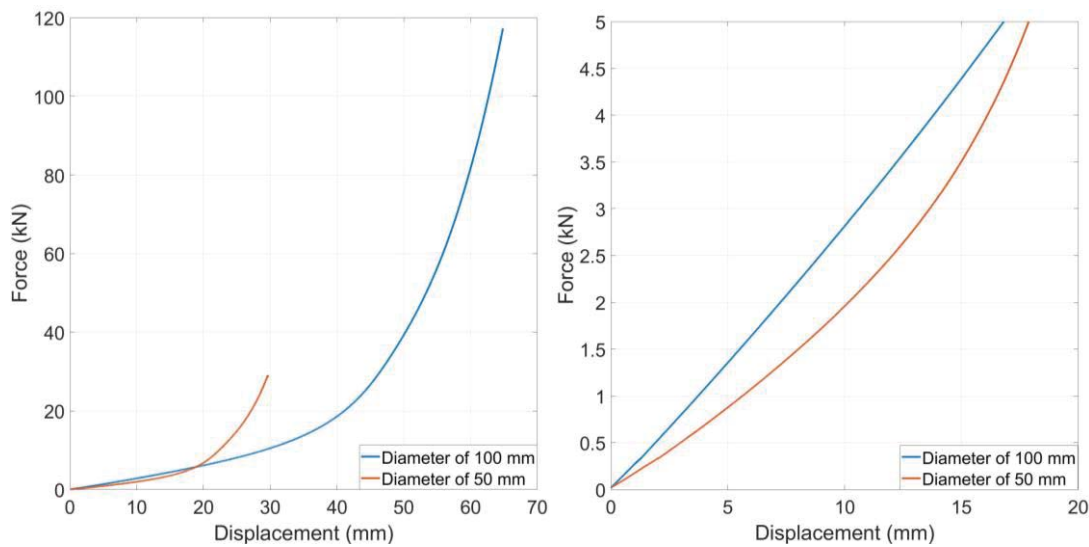


Figure 6. Results of the compression tests of rubber spheres; Left: full view of the tests; Right: Detailed view for the load levels that correspond to the configurations tested in the cyclic tests

#### 3.2 CYCLIC TESTS

The second part of the experimental procedure comprised cyclic testing of the various configurations of rolling isolators. All configurations were subjected to sinusoidal displacement, with an amplitude of 100 mm and a frequency of 0.2 Hz. The isolators were subjected to at



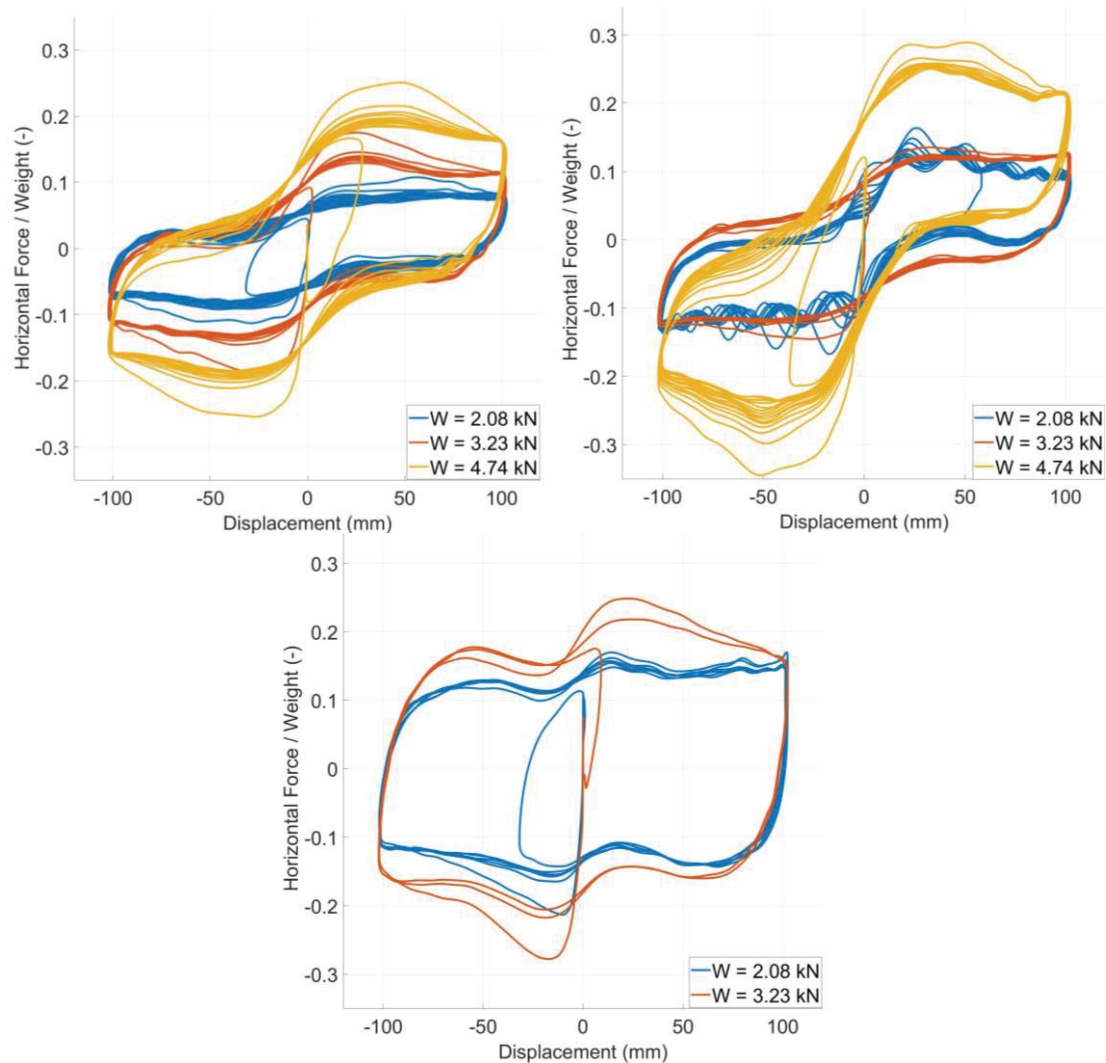


Figure 7. Influence of the vertical load on the cyclic response. Top-left: Spheres with a diameter of 100 mm and flat concrete plates, Top-right: Spheres with a diameter of 100 mm and one concave concrete plate, Bottom: Spheres with a diameter of 50 mm and flat concrete plates

least three cyclic loops, whereas in some cases, more cycles were applied to investigate the possible deterioration of the rolling spheres. All spheres were preloaded for seven days before testing with a load equal to the load they supported during cyclic testing, so that much of their creep is completed.

Figures 7 and 8 present normalized force – deformation loops for different vertical loads. The rolling friction coefficient is defined as  $\mu = Q/W$ , where  $Q$  is the force at zero displacement and  $W$  is the weight carried by the bearings. An increase of the vertical load or a reduction of the diameter of the sphere leads to an increased rolling friction coefficient. Moreover, the ratio of the horizontal-to-vertical force increases for all levels of displacement, with the isolation system dissipating more energy (i.e., larger area included in the cyclic loops).

During the first cycle, the spheres exhibit slightly stiffer behavior, whereas after the second cycle, the loop becomes stable, and no further softening is observed. Figure 9 compares the response of flat and concave bearings. Unexpectedly, they exhibit a similar behavior. A possible explanation is that 7 days of creep have resulted in the rubber spheres taking an oval shape that is maintained for the loading rate of the tests. Stiffness originates from the rise of the top plates as the isolator is sheared. It seems that the rise due to the oval shape of the rubber is more important than the one because of the spherical shape of one of the plates. Note,

that the applied displacements cause rotations equal to only  $57.3^\circ$  and  $114.6^\circ$  on the 100mm and 50mm spheres respectively, that is they do not make even half of a full turn. Hence, to explore the behavior at larger displacements, an extrapolation cannot be performed and more tests are needed.

It is worth noting that some cyclic plots include negative-stiffness branches, which are either monotonic or alternating with positive-stiffness branches. These observations are consistent with the observations of Cui et al [6], who tested similar isolators under lower vertical load levels.

Finally, one of the cyclic plots ( $W = 2.08$  kN,  $D = 100$  mm, Flat concrete plates) demonstrated significant fluctuations, with these fluctuations being consistent over the cycles. Similar behavior has been observed by Nikfar and Konstantinidis [35] in tests of equipment supported on caster tires and is called “flat spotting” and they require further study.

In all cases, the rolling friction coefficient maintained low values, sufficient for seismic isolation applications. A summary of the rolling friction coefficient for each case appears in table 3. The coefficient of friction will be reduced if harder rubber is used.

## 4 CONCLUSIONS

This paper presents an experimental study on the cyclic and compressive response of low-cost bearings comprising balls rolling on concrete surfaces. Placing the spheres below the walls of the structure at a dense grid would only require the construction of a thin, lightly-reinforced isolation diaphragm, instead of the massive slab that is now required. This is crucial to make seismic isolation affordable in low-income countries.

A half-scale model of prototype bearings was tested, comprising four isolators capped with a slab. Parameters of investigation were the vertical force on each rolling isolator (i.e., 2.08 kN, 3.23 kN, or 4.74 kN), the geometry of the rolling surface (i.e., flat or concave) and the diameter of the rolling sphere (i.e., 50 mm or 100 mm).

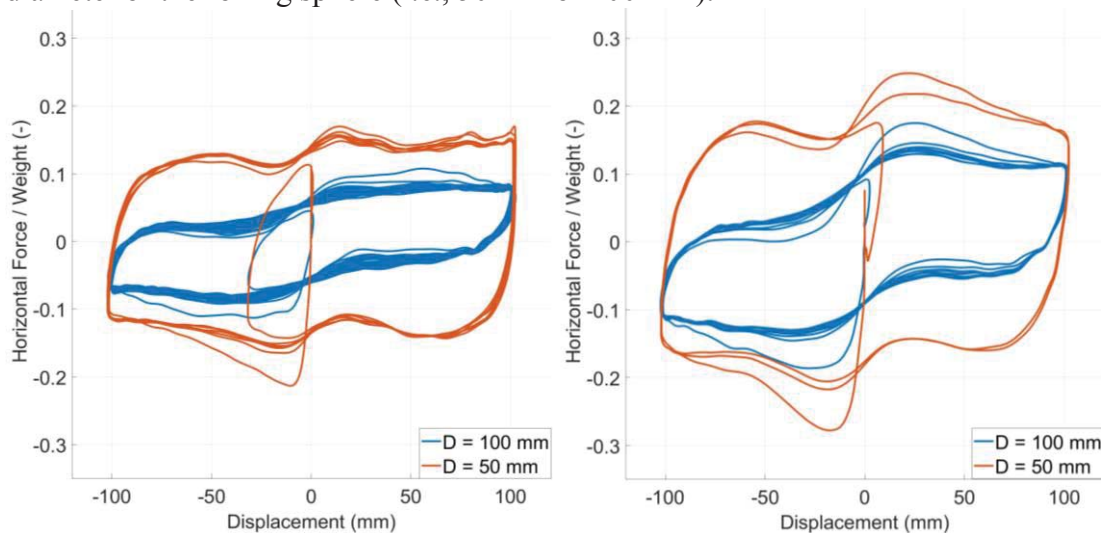


Figure 8. Influence of the diameter of the spheres on the cyclic response, using flat concrete plates. Left: Vertical load of 2.08 kN, Right: Vertical load of 3.23 kN

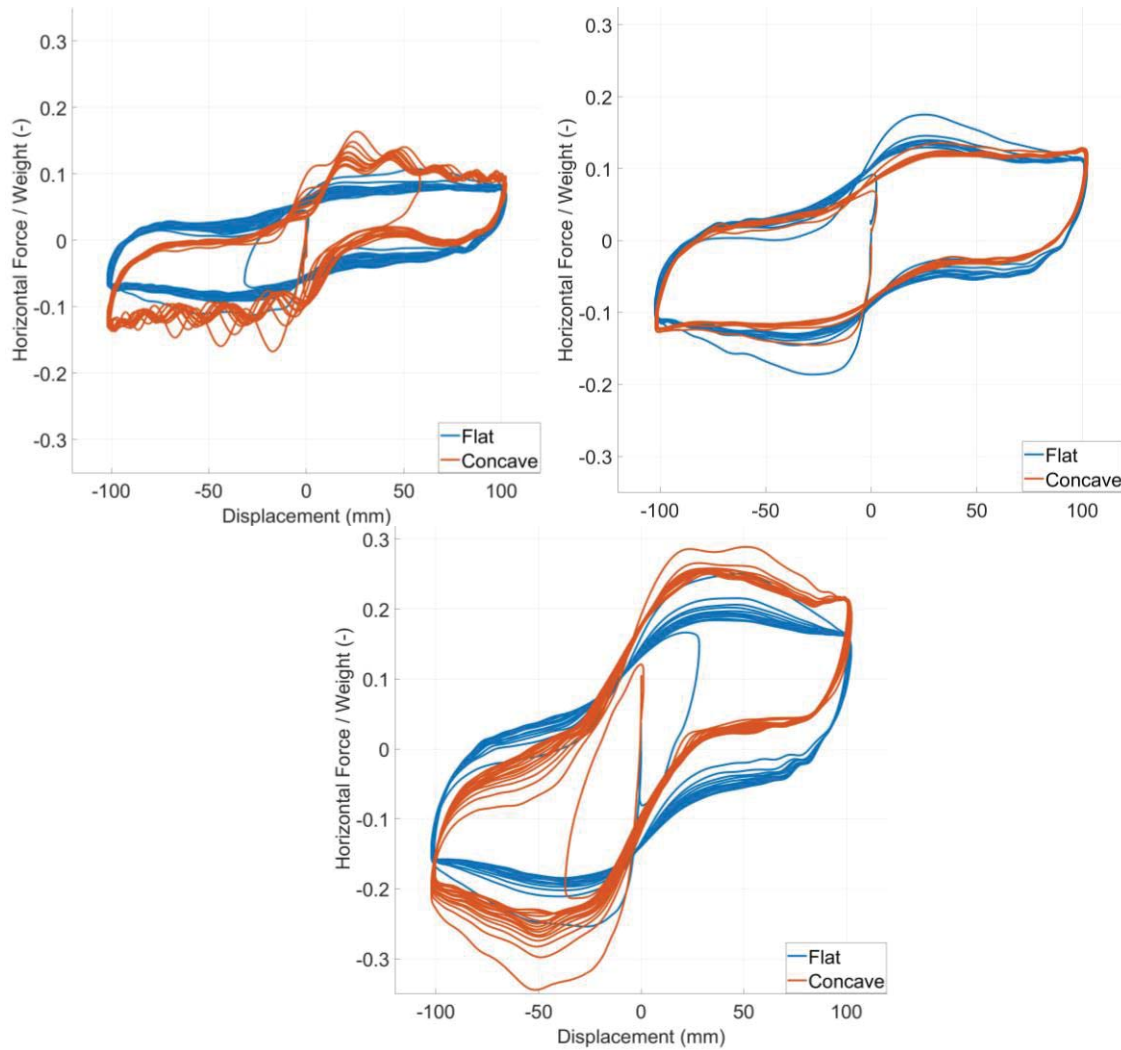


Figure 9. Influence of the geometry of the concrete plates on the cyclic response of spheres with a diameter of 100mm. Top-left: Vertical load of 2.08 kN, Top-right: Vertical load of 3.23 kN, Bottom: Vertical load of 4.74 kN

Diameter of Rubber Sphere (mm)	Vertical Load (kN)	Concrete Plate	Rolling Friction Coefficient (%)
100	2.08	Flat	6.1
		Concave	7.1
	3.23	Flat	8.9
		Concave	8.2
	4.74	Flat	13.7
		Concave	10.7
50	2.08	Flat	13.2
	3.23	Flat	17.6

Table 3: Summary of the rolling friction coefficient of the various tested configurations

Vertical loads up to a representative value for low-rise masonry building in the developing world were applied. Experimental results proved the efficiency of the investigated system in reducing the inertia forces transmitted to the superstructure, with the rolling friction coeffi-

cient (i.e., the ratio of horizontal to vertical force at zero displacement) being in the range of 6.1-17.6 %, thus, suitable for seismic isolation applications.

An increase in the vertical load or a reduction of the size of the sphere leads to a more deformed shape of the isolator, hence, to an increased rolling friction coefficient.

For the displacements considered, the influence of the concrete plate (i.e., flat or concave) is marginal since the deformed shape of the rolling isolator dominates the response. More tests are needed to understand the behavior of the system at larger displacements.

## 5 ACKNOWLEDGMENT

Support to the first and third author was provided by the European Research Council (ERC) under Starting Grant 803908. The methods, results, opinions, findings, and conclusions presented in this report are those of the authors and do not necessarily reflect the views of the funding agency.

## REFERENCES

- [1] Naeim, F., Kelly, J.M. (1999). Design of Seismic Isolated Structures: From theory to practice. John Wiley & Sons
- [2] Kelly, J.M., Konstantinidis, D.A. (2011) Mechanics of Rubber Bearings for Seismic and Vibration Isolation. Wiley
- [3] Makris, N. Seismic isolation: Early history. *Earthquake Engng Struct Dyn.* 2019; 48: 269– 283. <https://doi.org/10.1002/eqe.3124>
- [4] Vassiliou, M.F., Tsiavos, A. and Stojadinović, B. (2013), Dynamics of inelastic base-isolated structures subjected to analytical pulse ground motions. *Earthquake Engng Struct. Dyn.*, 42: 2043-2060. <https://doi.org/10.1002/eqe.2311>
- [5] Tsiavos, A., Mackie, K.R., Vassiliou, M.F., Stojadinovic, B. (2017). Dynamics of inelastic base-isolated structures subjected to recorded ground motions *Bull Earthquake Eng* (2017) 15:1807–1830, DOI 10.1007/s10518-016-0022-5
- [6] Cui, S., Bruneau, M., Constantinou, M.C. (2012) Integrated Design Methodology for Isolated Floor Systems in Single-Degree-of-Freedom Structural Fuse Systems, Technical Report MCEER-12-0004
- [7] Harvey, P.S., Jr., Zéhil, G.-P. and Gavin, H.P. (2014), Experimental validation of a simplified model for rolling isolation systems. *Earthquake Engng Struct. Dyn.*, 43: 1067-1088. <https://doi.org/10.1002/eqe.2387>
- [8] Harvey, P.S., Kelly, K.C. (2016), A review of rolling-type seismic isolation: Historical development and future directions. *Engineering Structures*, Volume 125, 15 October 2016, Pages 521-531, <https://doi.org/10.1016/j.engstruct.2016.07.031>
- [9] Cui S., Bruneau M. (2008) Experimental study of isolated floor systems. *14<sup>th</sup> World Conference on Earthquake Engineering*
- [10] Foti, D., & Kelly, J. M. (1996). Experimental study of a reduced scale model seismically base isolated with Rubber-Layer Roller Bearings (RLRB). Centre Internacional de Mètodes Numèrics en Enginyeria (CIMNE).

- [11] Kelly JM. (2002) Seismic Isolation Systems for Developing Countries. *Earthquake Spectra*. 2002;18(3):385-406. doi:[10.1193/1.1503339](https://doi.org/10.1193/1.1503339)
- [12] Osgoodei, P.M., Van Engelen, N.C., Konstantinidis, D., Tait, M.J. (2015) Experimental and finite element study on the lateral response of modified rectangular fiber-reinforced elastomeric isolators (MR-FREIs). *Engineering Structures*, <https://doi.org/10.1016/j.engstruct.2014.11.037>
- [13] Osgoodei, P.M., Tait, M.J., Konstantinidis, D. (2014) Three-dimensional finite element analysis of circular fiber-reinforced elastomeric bearings under compression. *Composite Structures*, <https://doi.org/10.1016/j.compstruct.2013.09.008>
- [14] Van Engelen, N. C., Konstantinidis, D., & Tait, M. J. (2016). Structural and nonstructural performance of a seismically isolated building using stable unbonded fiber-reinforced elastomeric isolators. *Earthquake Engineering & Structural Dynamics*, 45(3), 421-439.
- [15] Strauss, A., Apostolidi, E., Zimmermann, T., Gerhaher, U., & Dritsos, S. (2014). Experimental investigations of fiber and steel reinforced elastomeric bearings: Shear modulus and damping coefficient. *Engineering structures*, 75, 402-413.
- [16] Montella, G., Calabrese, A., & Serino, G. (2014). Mechanical characterization of a Tire Derived Material: Experiments, hyperelastic modeling and numerical validation. *Construction and Building Materials*, 66, 336-347.
- [17] Calabrese, A., Spizzuoco, M., Serino, G., Della Corte, G., & Maddaloni, G. (2015). Shaking table investigation of a novel, low-cost, base isolation technology using recycled rubber. *Structural Control and Health Monitoring*, 22(1), 107-122.
- [18] Swensen, S., 2014. Seismically Enhanced Light-Frame Residential Structures, Ph.D. Thesis, Stanford University, Stanford, CA.
- [19] Osgoodei, P.M., Tait, M.J., Konstantinidis, D. (2014) Finite element analysis of unbonded square fiber-reinforced elastomeric isolators (FREIs) under lateral loading in different directions. *Composite Structures*, <https://doi.org/10.1016/j.compstruct.2014.02.033>
- [20] Tran, C., Calabrese, A., Vassiliou, MF., Galano, S. (2020) A simple strategy to tune the lateral response of unbonded Fiber Reinforced Elastomeric Isolators (FREIs). *Engineering Structures*, <https://doi.org/10.1016/j.engstruct.2020.111128>
- [21] Nanda, R.P., Shrikhande. M., Agarwal. P. (2015), Low-cost base-isolation system for seismic protection of rural buildings, Practice Periodical on Structural Design and Construction (ASCE) DOI: 10.1061/(ASCE)SC.1943-5576.0000254
- [22] Tsiavos A, Sextos A, Stavridis A, Dietz M, Dihoru L, Alexander NA. (2020) Large-scale experimental investigation of a low-cost PVC ‘sand-wich’ (PVC-s) seismic isolation for developing countries. *Earthquake Spectra*. 2020;36(4):1886-1911. doi:[10.1177/8755293020935149](https://doi.org/10.1177/8755293020935149)
- [23] Tsiavos, A., Alexander, N. A., Diambra, A., Ibraim, E., Vardanega, P. J., Gonzalez-Buelga, A., & Sextos, A. (2019). A sand-rubber deformable granular layer as a low-cost seismic isolation strategy in developing countries: Experimental investigation. *Soil Dynamics and Earthquake Engineering*, 125, 105731.



- [24] Jampole E, Deierlein G, Miranda E, Fell B, Swensen S, Acevedo C. (2016) Full-Scale Dynamic Testing of a Sliding Seismically Isolated Unibody House. *Earthquake Spectra*. 2016;32(4):2245-2270. doi:[10.1193/010616EQS003M](https://doi.org/10.1193/010616EQS003M)
- [25] Das, A., Deb, S. K., & Dutta, A. (2016a). Shake table testing of un-reinforced brick masonry building test model isolated by U-FREI. *Earthquake Engineering & Structural Dynamics*, 45(2), 253-272.
- [26] Van Ngo, T., Dutta, A., & Deb, S. K. (2017). Evaluation of horizontal stiffness of fibre-reinforced elastomeric isolators. *Earthquake Engineering & Structural Dynamics*, 46(11), 1747-1767.
- [27] Das, A., Deb, S. K., & Dutta, A. (2016b). Comparison of Numerical and Experimental Seismic Responses of FREI-Supported Un-reinforced Brick Masonry Model Building. *Journal of Earthquake Engineering*, 20(8), 1239-1262.
- [28] Cilsalar, H., Constantinou, M.C. (2019) Behavior of a spherical deformable rolling seismic isolator for lightweight residential construction. *Bull Earthquake Eng* **17**, 4321–4345 (2019). <https://doi.org/10.1007/s10518-019-00626-z>
- [29] Cilsalar, H., Constantinou, M.C. (2019) Parametric study of seismic collapse performance of lightweight buildings with spherical deformable rolling isolation system. *Bull Earthquake Eng* **18**, 1475–1498 (2020). <https://doi.org/10.1007/s10518-019-00753-7>
- [30] Cilsalar, H., Constantinou, M.C. (2019) Development and Validation of a Seismic Isolation System for Lightweight Residential Construction, Technical Report MCEER-19-0001
- [31] Bachmann H, Wenk T, Baumann M, Lestuzzi P. Der neue ETH-Erdbebensimulator. *Schweizer Ingenieur und Architekt*. 1999;4:63-67.
- [32] EN 1015-11, (1993), “Methods of test for mortar for masonry – Part 11: Determination of flexural and compressive strength of hardened mortar”, European Committee for Standardization, Brussels.
- [33] Xiamen Neway Rubber & Plastic Products Co., Ltd, China, Quotation, February 2020
- [34] Makris, N., & Vassiliou, M. F. (2011). The existence of ‘complete similarities’ in the response of seismic isolated structures subjected to pulse-like ground motions and their implications in analysis. *Earthquake Engineering & Structural Dynamics*, 40(10), 1103-1121.
- [35] Nikfar, F., and Konstantinidis, D. (2017) Shake table investigation on the seismic performance of hospital equipment supported on wheels/casters. *Earthquake Engng Struct. Dyn.*, 46: 243– 266. doi: [10.1002/eqe.2789](https://doi.org/10.1002/eqe.2789).

## EXPERIMENTAL SEISMIC POST-TENSIONING PERFORMANCE AND LONG-TERM EFFECTS OF A POST-TENSIONED TIMBER FRAMED MODEL WITH DISSIPATIVE SYSTEMS

A. Di Cesare<sup>1</sup>, F. C. Ponzo<sup>1</sup>, N. Lamarucciola<sup>1</sup> and D. Nigro<sup>1</sup>

<sup>1</sup> School of Engineering, University of Basilicata  
Viale dell'Ateneo Lucano, 10 - 85100 Potenza  
{antonio.dicesare, felice.ponzo, nicla.lamarucciola, domenico.nigro}@unibas.it

---

### Abstract

*In recent years, post-tensioned timber framed buildings, recognized as one of the most effective sustainable and anti-seismic solutions, are developing throughout the world. Post-tensioning (PT) loss in timber framed buildings with post-tensioned beam to column joints is a crucial aspect which governs the moment capacity of the connection and the global seismic performance of the frame.*

*This paper investigates on the variations of the post-tensioning force of a 2/3 scaled, three-storey, post-tensioned timber frame experimental model investigated in three different configurations: bare frame; with dissipative rocking mechanism; with dissipative bracing system. The variation of post-tensioning during shaking table testing a set of seven spectra-compatible earthquakes at increasing PGA levels has been evaluated and the long-term losses over about four years have been investigated.*

**Keywords:** Post-tensioned timber framed buildings, Energy dissipation systems, Shaking table tests, Post-tensioning variation.

---

## 1 INTRODUCTION

In recent years, Europe Union strategies and worldwide policies are moving towards the reduction of greenhouse gas emissions and there is an increased trend to reconsider timber as construction material for multi-storey buildings optimizing the structural concept and the seismic design, with the dual purpose to obtain more sustainable and anti-seismic constructions. In order to mitigate seismic risk and significantly reduce structural and non-structural damage avoiding high economic loss, in the last decades research studies focused on low damage design and technologies.

Recent advancement in earthquake engineering have led to the development of a pre-stressed laminated (Pres-Lam) technology for timber constructions. The system, originally conceived by Priestley et al. (PRESSS) [1] for precast concrete frame and wall constructions, was successfully applied to create timber jointed ductile connections [2]. It consists in the use of high strength unbounded steel cables or bars to connect timber beams and columns, or walls to their foundations, providing self-centering capability to the frame. In order to increase the seismic performance additional internal or external dampers could be added to the joints, to provide additional strength and energy dissipation capability. During the rocking motion due to earthquake or other horizontal loads, a gap opening (and connection rotation  $\theta$ ) is produced, as shown in Figure 1 for the beam-column joint, activating the elongation of the unbounded post-tensioned bar ( $F_{PT} + \Delta F_{PT}$ ) and the yielding of the additional hysteretic dissipation devices ( $F_y$ ). The introduction of external metallic yielding dampers represents an optimal low-cost solution requiring a little maintenance and easily replaceable in case of damage. The combination of the moment capacity due to post-tensioning  $M_{PT}$  (bilinear elastic response) and to yielding of steel devices  $M_s$  (hysteretic response), provide the total moment capacity  $M_t = M_{PT} + M_s$ . This hybrid system allows to obtain damage-avoiding structures characterized by the typical flag-shaped response with the capability to absorb energy in a major earthquake while rocking back to an undamaged position after the shaking, resulting in negligible residual drift.

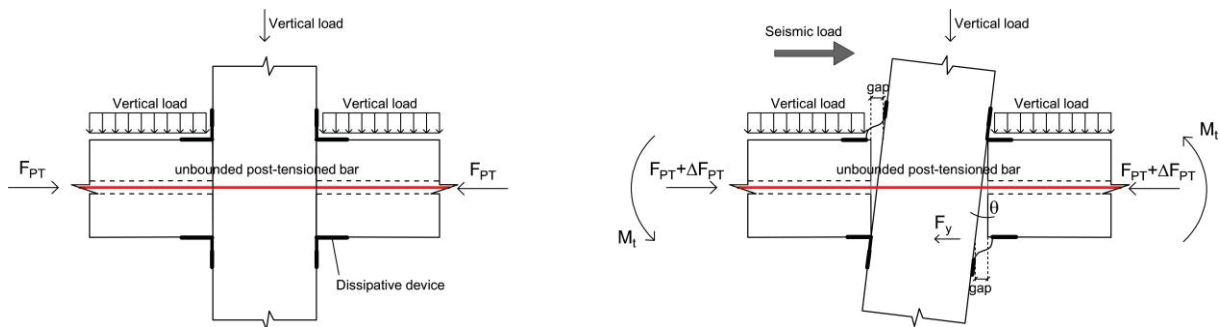


Figure 1: Undeformed configuration and post-tensioning stresses during the seismic motion of the beam-column joint.

A crucial aspect in timber building is represented by the long term rheological effects, such as creep phenomena due to permanent loads, which can affect serviceability and structural integrity of the building. The long-term performance of post-tensioned timber systems is of interest, particularly regarding tension loss in the steel cables or bars, which can lead to reduction of the moment capacity of the connection, affecting recentering capabilities and the global seismic performance of the frame [3]. Moreover, the relationship with environmental loads and creep behavior of the timber elements contribute to post-tensioning loss [4] and the horizontal motions of timber buildings can be monitored to detect residual drifts after a seismic event. To date, few research study on the post-tensioning losses of this

recent timber construction system are available in literature. Recent experimental and analytical studies [5]-[6] on post-tensioning loss deriving from creep phenomena in compressed timber elements were performed in New Zealand and Switzerland. The results showed expected losses in the range of 6-50% in 50 years in various real monitored building, such as the Trimble Navigation Offices (NZ) and the House of Natural Resources (Switzerland), mainly depending on the ratio between post-tensioning steel and timber and on the amount of timber loaded perpendicular to the grain [7].

This paper focuses on seismic post-tensioning variations and on long-term losses evaluated on a 2/3 scaled, three-storey, post-tensioned timber frame experimental model tested at the structural laboratory of University of Basilicata (Italy), in collaboration with University of Canterbury (New Zealand) [8]. The experimental model was investigated in different testing configuration with increasing amount of energy dissipation and the tension losses were monitored over about four years.

## 2 EXPERIMENTAL MODEL

A three-storey post-tensioned timber frame model was designed and dynamically tested at the structural laboratory of the University of Basilicata. The prototype model was a 3D, three-storey glulam timber frame, characterized by single bays in both directions. The frame was designed according to European code [9] for office use at first and second floors (live load of  $Q = 3$  kPa) and considering a rooftop garden load ( $Q = 2$  kPa). A scale factor of 2/3 was applied to the experimental model obtaining an inter-storey height of 2 m and a scaled footprint of 4 m x 3 m (Figure 2). Suitable scale factors were used observing mass similitude related to the Cauchy-Froude similitude laws [10]. The additional masses due to scaling of dead load and live load were made up of concrete blocks and steel hold downs. The beam-column connection (see Figure 1) was realized by a single unbounded post-tensioned steel bar (of 26.5 mm diameter) crossing the beam. Based on MMBA [11] procedure the tension loading of the steel bar was 100 kN and 50 kN for the longitudinal and transversal direction, respectively.

The three following testing configurations, with different amount of energy dissipation [8][12][13], were considered: i) bare post-tensioned frame (F) shown in Figure 3a, representing the free rocking condition with post-tensioning only without energy dissipation; ii) dissipative frame (DF), representing the bare frame (F) with additional dissipative rocking at the beam-column joints and at the column-foundation connection; and iii) braced frame (BF) shown in Figure 3b, representing the bare frame (F) with dissipative braces.

The seismic response of the frame was recorded by more than 50 acquisition channels. Different types of sensors were installed on the test frame, providing measurements of horizontal and vertical accelerations, absolute displacements, strain and force. Among various monitored parameters, the tendon's load was recorded by 6 load cells placed at the beam-column joints (see Figure 2), in both longitudinal and transversal directions of the experimental model in all configurations. For more information about the experimental model and data acquisition please refer to Di Cesare et al. [8]. In this study, seismic post-tensioning losses during shaking table tests and the long-term post-tensioning losses among the various configurations have been investigated.



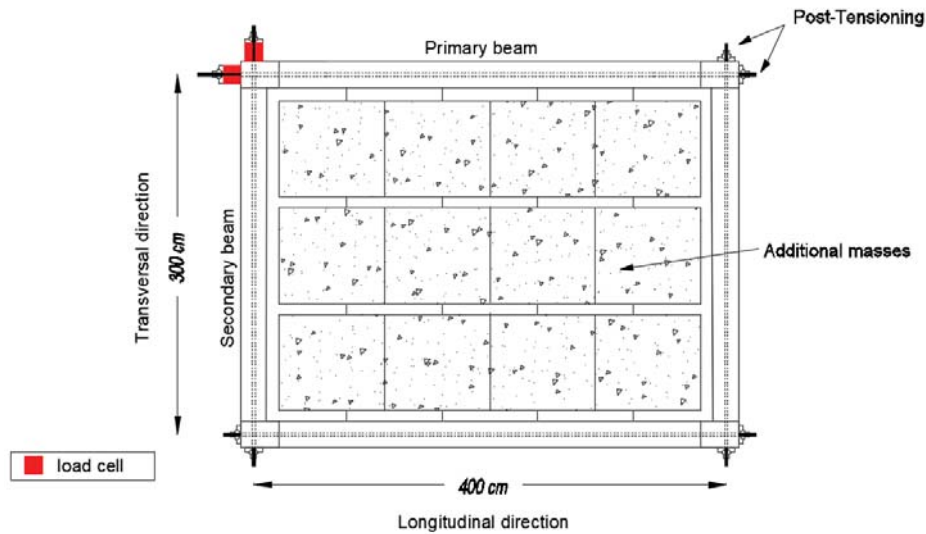


Figure 2: Plan view of timber frame with location of post-tensioned bars.

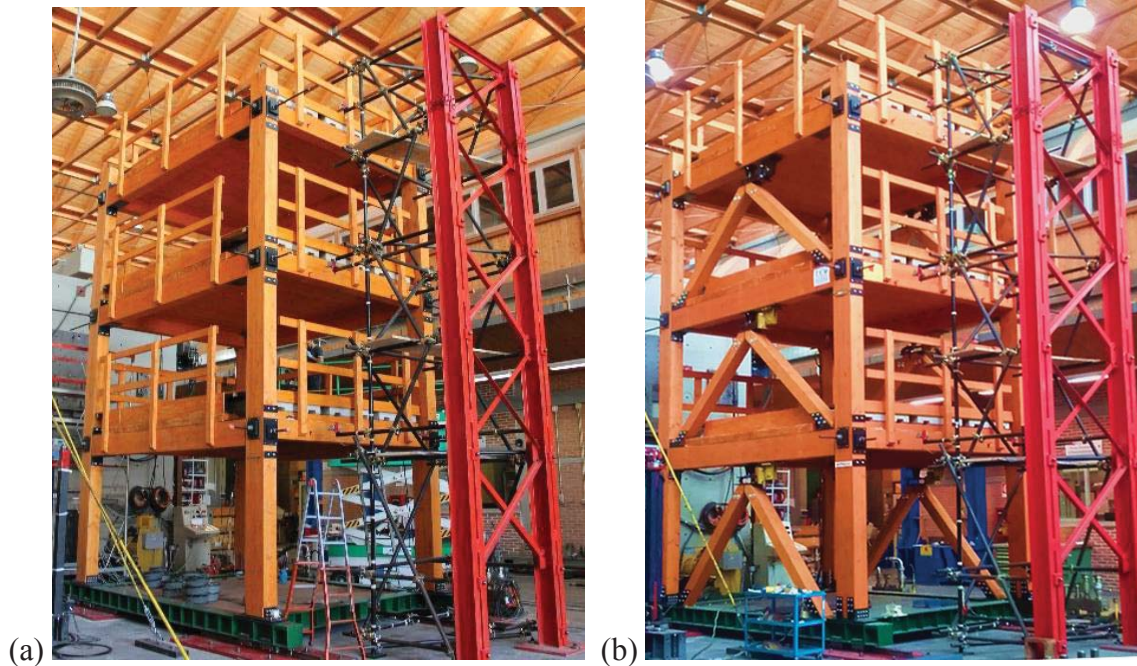


Figure 3: General views of experimental model at the structural laboratory of University of Basilicata: (a) post-tensioned timber bare frame (F configuration); (b) post-tensioned model with dissipative bracing systems (BF configuration).

### 3 POST-TENSIONING VARIATIONS

#### 3.1 Variations due to seismic motion

The experimental campaign was performed using a set of seven natural earthquake records, selected from the European strong motion database. The spectra-compatible records were defined according to the current Eurocode [9] considering a peak ground acceleration PGA of 0.44 g and medium soil class (type B) in high seismic zone. To ensure consistency with the scale of the experimental model, all input accelerations were scaled down in duration by a



factor of  $1/\sqrt{(3/2)}$ . In order to match the real acceleration inputs to the Eurocode response spectrum it was necessary to scale some earthquakes by means of an appropriate scale factor.

The reduced set of three spectra-compatible earthquakes selected in this paper and the shake table testing program of all experimental configurations are summarized in Figure 4. The intensity of the ground motion was progressively increased in acceleration for earthquake cases 1228, 196, 535 from 10% to 100% of average PGA for DF and BF configurations, in order to provide additional information regarding the frame response at varying damage levels.

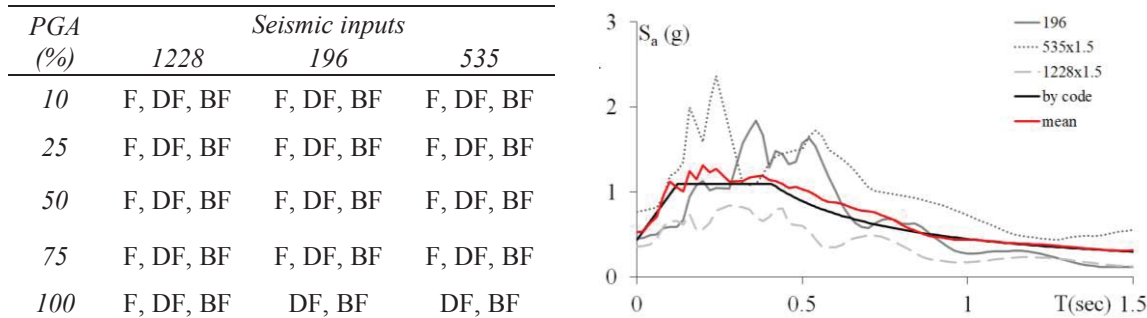


Figure 4: Testing program for selected seismic inputs of the experimental model and selected seismic inputs.

During shaking table tests the tension load has been recorded and the post-tensioning variation  $\Delta F_{PT} = (F_{PT,max} - F_{PT,initial})$  for the three testing configurations (F, DF and BF) has been evaluated. The maximum and mean variation of post-tensioning force  $\Delta P_T$  are shown in Figure 5 for all configurations at increasing PGA levels. As can be observed, the introduction of the bracing system was effective in reducing the post-tensioning of over 50% than F configuration.

Figure 6 shows the time histories of the post-tensioning variation  $\Delta F_{PT}$  of the first storey beam-column connection and Figure 7 and Figure 8 show  $\Delta F_{PT}$  versus drift for the three selected seismic inputs at 25% and 75% of PGA level of all testing configurations. As can be observed at low PGA level of all seismic inputs the PT bar was slightly activated with a maximum PT variation of 12 kN in F model configuration due to the elastic response of the frame model. At PGA 75% the re-centering effect due to the post-tensioning is more evident in all configurations. It can be observed that increasing amount of energy dissipation introduced in the frame (from F to DF and to BF configurations) led to a significant reduction of drift and of post-tensioning force variation demonstrating the effectiveness of the design procedure. In all cases a complete re-centering of the connection is observed without damages on the structural elements in all configurations tested.

Seismic post-tensioning losses due to subsequent earthquakes have been also investigated, considering the complete sequence of shaking table testing at all PGA levels (from 10% to 100%). The post-tensioned bars were tensioned to the design PT force of 100 kN in the test direction only at the beginning of each test configuration (F, DF and BF model). Figure 9 shows the post-tensioning loss at the end of seismic sequence, defined as the variation between the initial and the final value of the post-tensioning force recorded within the complete set of ground motion for each testing configuration at all levels both in longitudinal and transversal direction. It results negligible for the cases of bare frame F and of braced frame BF models and slightly higher than 2% for the dissipative frame DF model along the longitudinal direction due to the strengthening effect of dissipative angles of the post-tensioned beam-column joints. Results highlight the capability of the building to withstand multiple consecutive strong earthquakes. During the experimental campaign over than 100 tests were performed for each configuration without observing any structural damage.

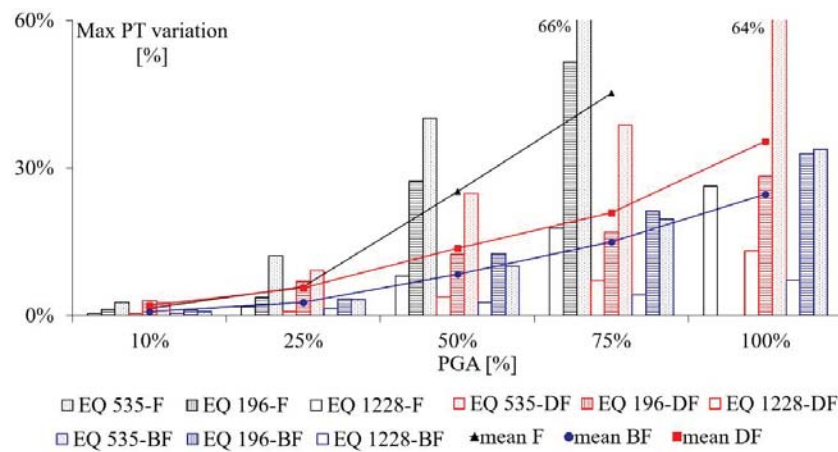


Figure 5: Maximum post-tensioning force variation profiles at increasing PGA levels for the three selected seismic inputs.

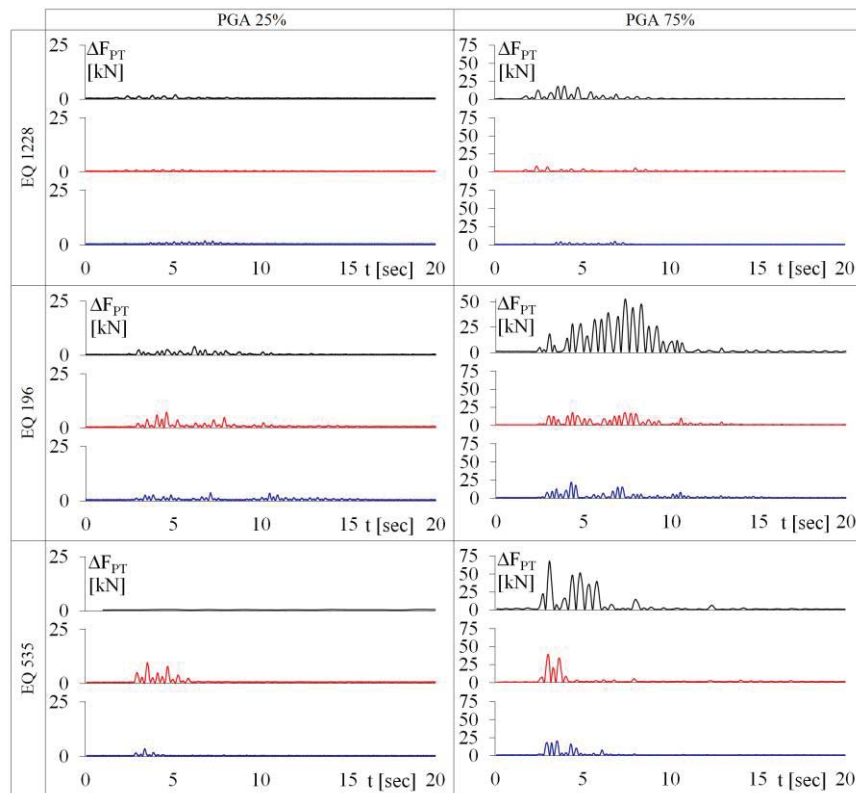


Figure 6: Post-tensioning variation time histories at the first storey beam-column connection for seismic inputs 1228, 196 and 535 at 25% and 75% of PGA levels.

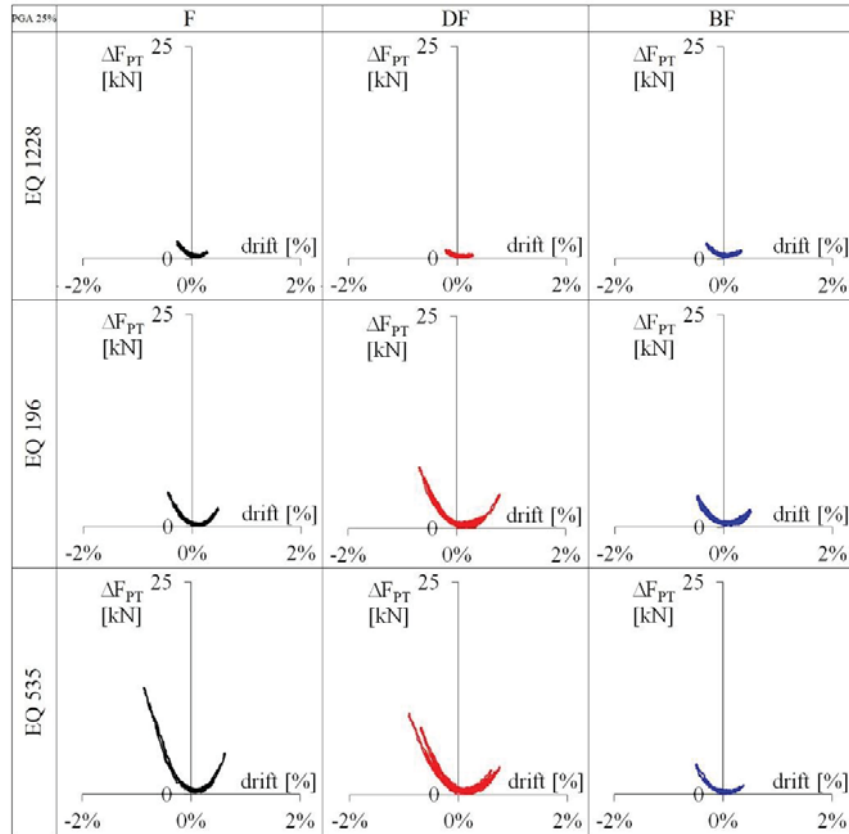


Figure 7: Post-tensioning variation versus drift for the three selected seismic inputs at 25% of PGA.

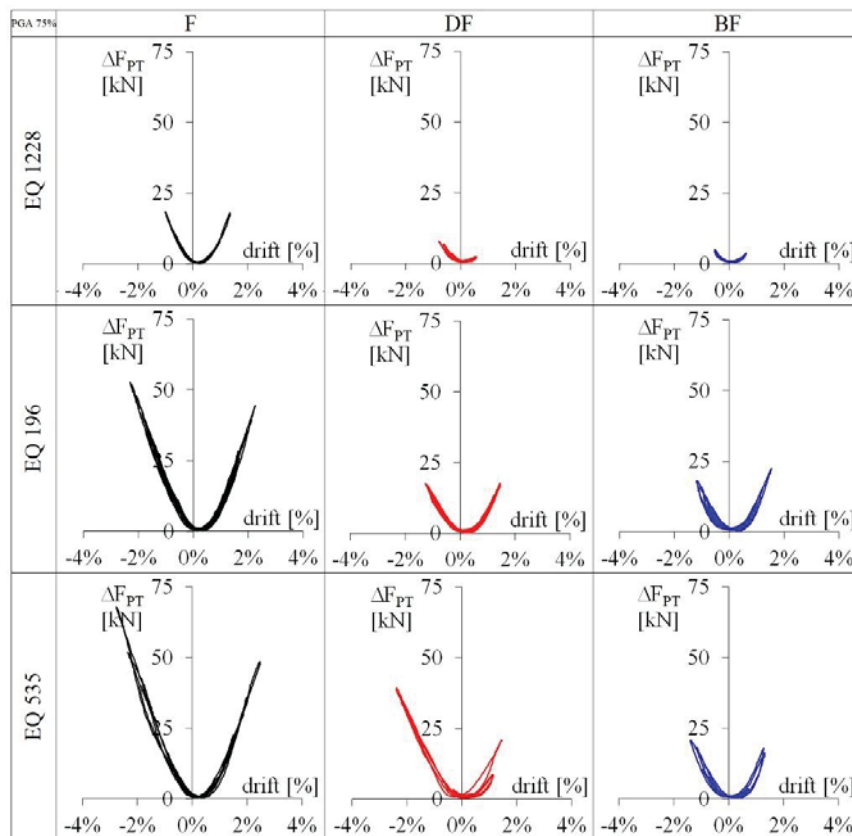


Figure 8: Post-tensioning variation versus drift for the three selected seismic inputs at 75% of PGA.

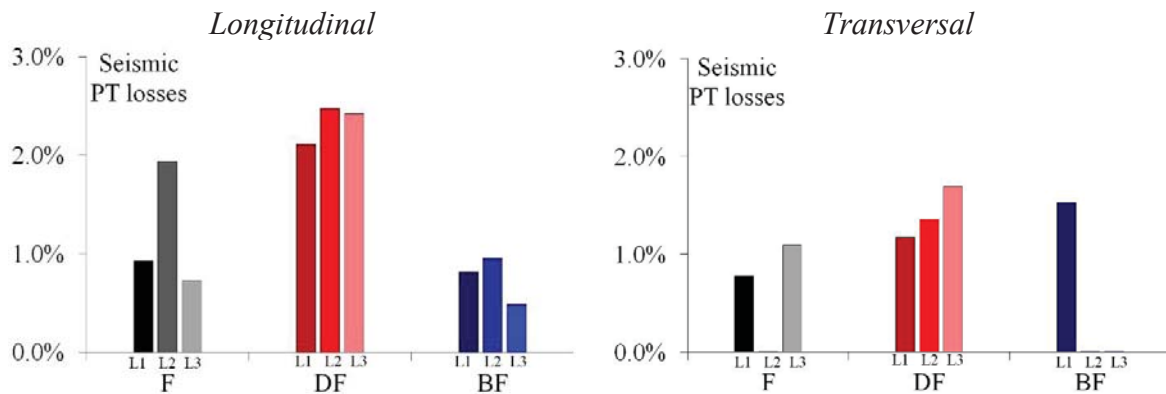


Figure 9: Seismic post-tensioning losses recorded for the three testing configurations at the three levels in longitudinal and transversal direction.

### 3.2 Variations due to long term effects

The long-term post-tensioning losses at all levels both in longitudinal and transversal direction of bare frame F and dissipative frame DF configurations are shown in Figure 10 in terms of post-tensioning force ( $F_{PT}$ ) recording over a time period of about one year after testing of F configuration and over about three years after testing of DF configuration. Percentages values of post-tensioning losses are reported in Table 1.

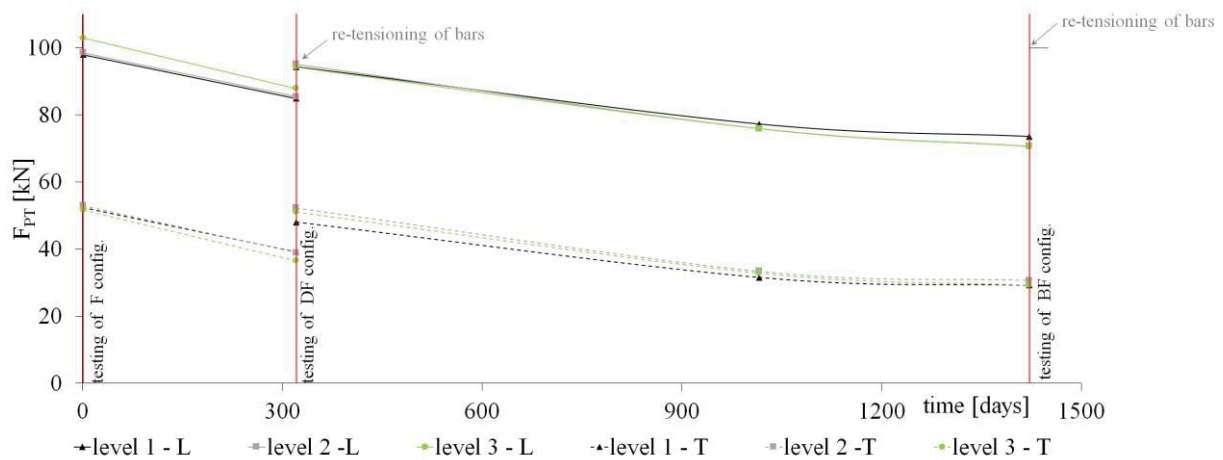


Figure 10. Post-tensioning losses over time for F and DF configurations at all storey in longitudinal (L) and transversal (T) directions.

Model Config.	$\Delta t$ [days]	Post tensioning losses [%]					
		Longitudinal			Transversal		
		1 <sup>st</sup> storey	2 <sup>nd</sup> storey	3 <sup>rd</sup> storey	1 <sup>st</sup> storey	2 <sup>nd</sup> storey	3 <sup>rd</sup> storey
F	321	15%	13%	13%	29%	27%	25%
DF	1101	25%	26%	22%	43%	41%	39%

Table 1. Post-tensioning losses recorded over time at all storey for the F and DF configurations.

As expected, a decreasing trend of post-tensioning force was observed in both F and DF configurations. It can be pointed out that in case of DF configuration after a period of about 2 years the post-tensioning losses stabilized at around 25% in the longitudinal direction. Highest post-tensioning losses were recorded for both F and DF in the transversal direction. Moreover, by comparing the trend of post-tensioning force recorded for F and DF specimens during the first year both in the longitudinal and transversal direction, lower post-tensioning losses were observed in the frame with dissipative rocking mechanism at the beam-column connections. During each configuration the bars were not re-tensioned over time and post-tensioning losses can be significant when the PT connection is left to transfer the post-tensioning load. However, in case of operative timber structures the effect of long-term losses can be contrasted by using disc springs designed for the initial PT force, characterized by high load capacity with a small spring deflection, and periodically monitored and/or re-tensioned.

#### **4 CONCLUSIONS**

This paper investigates on the long-term and seismic post-tensioning losses of a 3D, three storey, 2/3 scaled post-tensioned timber framed building designed and tested at the structural laboratory of Basilicata. The extensive shaking table testing campaign was performed in three different configurations, considering the bare frame with post-tensioning only, with dissipative rocking mechanisms and with dissipative bracing systems, subjected to different seismic inputs at increasing PGA levels. During each testing configuration the frame was not re-tensioned.

The results showed that during the seismic motion, the variation of post-tensioning force at due to the rocking at the beam-column joints and the gap opening reduced with the introduction of dissipative systems, in DF and BF configurations. Moreover, the post-tensioning losses recorded within the complete set of ground motions for each testing configuration at all levels both in longitudinal and transversal direction were negligible. The maximum recorded value was of about 2% in DF configuration due to the strengthening effect of dissipative angles. The long term the post-tensioning force decreased linearly in the first two 2 years, reaching a 25% of losses, after that responded almost constant.

#### **ACKNOWLEDGEMENTS**

Authors would like to acknowledge financial support from RELUIS 2019-2021 project ([www.reluis.it](http://www.reluis.it)) funded by the Italian Civil Protection Department.

#### **REFERENCES**

- [1] Priestley M.J.N., Sritharan S., Conley J.R., Pampanin S. (1999). Preliminary Results and Conclusions from the PRESSS Five-Story Precast Concrete Test Building. *PCI Journal*, 44.
- [2] Palermo A., Pampanin S., Buchanan A. and Newcombe M.P., (2005) Seismic Design of Multi-Storey Buildings using Laminated Veneer Lumber (LVL), NZSEE Conference, Taupo, New Zealand.



- [3] Baas, E. J., Riggio, M., & Barbosa, A. R. (2021). A methodological approach for structural health monitoring of mass-timber buildings under construction. *Construction and Building Materials*, 268, 121153.
- [4] Granello, G., Palermo, A., Pampanin, S., Smith, T., & Sarti, F. (2018). The implications of post-tensioning losses on the seismic response of Pres-Lam frames. *Bulletin of the New Zealand Society for Earthquake Engineering*, 51(2), 57-69.
- [5] Wanninger, F., Frangi, A., & Fragiacomio, M. (2015). Long-term behavior of post-tensioned timber connections. *Journal of Structural Engineering*, 141(6), 04014155.
- [6] Granello, G., Leyder, C., Frangi, A., Palermo, A., & Chatzi, E. (2019). Long-term performance assessment of an operative post-tensioned timber frame structure. *Journal of Structural Engineering*, 145(5), 04019034.
- [7] Granello, G., & Palermo, A. (2020). Monitoring Dynamic Properties of a Pres-Lam Structure: Trimble Navigation Office. *Journal of Performance of Constructed Facilities*, 34(1), 04019087.
- [8] Di Cesare, A.; Ponzo, F.C.; Lamarucciola, N.; Nigro, D. (2020) Dynamic Seismic Response of Nonlinear Displacement Dependent Devices Versus Testing Required by Codes: Experimental Case Studies. *Applied Science*, 10, 8857.
- [9] UNI EN 1998-1 (2013) EUROCODE 8: design of structures for earthquake resistance-part 1: general rules, seismic actions and rules for buildings. European Committee for Standardization, Brussels, Belgium.
- [10] Krawinkler H., and Moncarz P. D. (1981) Theory and Application of Experimental Model Analysis in Earthquake Engineering. Stanford, CA: NASA STI/Recon Technical Report N 82.
- [11] Newcombe, M. P., Pampanin, S., A.Buchanan, and Palermo, A. (2008). "Section Analysis and Cyclic Behavior of Post-Tensioned Jointed Ductile Connections for Multi-Story Timber Buildings." *Journal of Earthquake Engineering*, 12(1), 83-110.
- [12] Ponzo, F.C.; Di Cesare, A.; Lamarucciola, N.; Nigro, D., Pampanin S. (2017). Modeling of post-tensioned timber-framed buildings with seismic rocking mechanism at the column-foundation connections. *International Journal of Computational Methods and Experimental Measurements*, Vol. 5, Issue 6, Pages 966-978.
- [13] Ponzo, F.C.; Di Cesare, A.; Lamarucciola, N.; Nigro, D. (2019). Seismic design and testing of post-tensioned timber buildings with dissipative bracing systems. *Front. Built Environ.*, 5, 104, doi:10.3389/fbuil.2019.00104.

## EXPERIMENTAL COMPARISON BETWEEN FLAT AND CURVED SLIDING CONDITIONS FOR THE RESPONSE EVALUATION OF CURVED SURFACE SLIDER DEVICES

Alberto Pavese<sup>1</sup>, and Marco Furinghetti<sup>1,2</sup>

<sup>1</sup> University of Pavia  
Via Ferrata 3, 27100 Pavia (Italy)  
a.pavese@unipv.it  
marco.furinghetti@unipv.it

<sup>2</sup> EUCENTRE  
Via Ferrata 1, 27100 Pavia (Italy)  
marco.furinghetti@eucentre.it

---

### Abstract

*Curved Surface Slider devices have been widely used in last years for the protection of both building and structural systems. The spherical shape of the implemented sliding surfaces provide a certain recentering capability, which is generally combined to significant amount of energy dissipation, due to the frictional characteristics of the adopted sliding material. Since both behaviors act simultaneously during motion, experimental tests could return significantly high force values, especially if large bearings are considered. In some of those cases, the maximum force capacity of the testing equipment can be even overcome, and consequently experimental tests can not be performed.*

*The scope of the present work is to provide experimental evidence of the comparison between flat and curved sliding motions. Precisely, the outcomes of bi-directional tests performed on on full-scale Double Curved Surface Slider and Flat Slider devices have been analyzed. On the former typology the frictional and the recentering behaviors have been numerically decoupled, in order to compare the obtained results to the frictional response of the latter device. Results have shown a good agreement between the considered sliding motions, which seems to suggest that the experimental evaluation of flat sliding characteristics could be representative of curved sliding motions.*

**Keywords:** Curved Surface Slider, Flat slider, base isolation, Experimental campaign, friction coefficient.

---

## 1 INTRODUCTION

In last years the research about Curved Surface Slider devices has shown good performance in reducing the structural vulnerability of both buildings and bridge structures ([5] , [4] , [12] , [13] ). The overall response can be significantly mitigated, through the energy dissipation induced by the frictional behavior of the sliding motion, together with potentially low residual displacements, thanks to a properly designed recentering characteristics. In addition, the growing interest in investigating the experimental response of such devices have highlighted a number of important aspects to account for, such as some dependencies of the friction coefficient with respect to specific response parameters, in terms of sliding velocity, vertical load/contact pressure and cyclic effect ([6] , [11] ). These dependencies have been detected, by analyzing the force response of both flat and curved sliding motions, and consequently a certain correlation between these different loading conditions is expected, regardless the applied loading conditions ([7] , [9] , [2] ). From a theoretical perspective, the lateral force of a Curved slider can be computed as the summation of a recentering behavior, modeled as a linear spring with respect to displacements and a frictional response ([3] , [10] ). This relationship can be used to compare the frictional response of flat and curved sliding motions. If results between the aforementioned sliding conditions were actually comparable, testing possibility of curved devices would increase, since it would be possible to perform tests on the flat sliding material only, rather than the full curved isolator, and consequently much lower force demands could be achieved. In this work the outcomes of a wide experimental campaign on full-scale flat and curved sliders are analyzed, in terms of comparison of the resulting frictional properties. The considered dynamic tests have been performed at the Laboratory of EUCENTRE Foundation in Pavia, by adopting a special testing setup, in order to apply bidirectional motions.

## 2 TESTED DEVICES

In order to analyze the differences between flat and curved sliding motions, two individual typologies of sliding devices have been adopted. Precisely, full-scale isolators have been adopted, aiming at obtaining more realistic experimental results, as representative of the proper loading conditions of the devices ([6] ).

The former device consists of a Flat Slider, which returns the pure frictional behavior: it consists of a stainless steel flat sliding surface, which has been polished to mirror finish, by considering a roughness index  $R_a$  0.2, and a slider with a circular sliding pad. Such a device can be subjected to bidirectional displacements up to 250mm.

The latter isolator is a Double Curved Surface Slider, which represents one of the most common technology for isolation bearings. Two spherical sliding surfaces with the same curvature radius have been implemented, both polished to mirror finish in order to achieve the same roughness index of the Flat Slider: consequently, same frictional properties can be ensured; in addition, since the same radius of curvature has been designed for both the upper and the lower spherical surfaces, the global horizontal motion applied to the device can be considered as halved in two opposite sliding motions at the sliding interfaces. Within the equal sliding surfaces, a non-articulated slider is installed, which is made up of a unique steel block (material S355JR): such an element houses two circular sliding pads, having same diameter (260mm) and same material composition, aiming at considering the same contact pressure and the same frictional properties at both the sliding interfaces. Both the radii of curvature of the spherical surfaces are 1600mm each, with internal slider height of 120mm: consequently, the equivalent radius of curvature of the device is approximately equal to 3080mm.

In Figure 1 both the adopted isolation devices are shown.

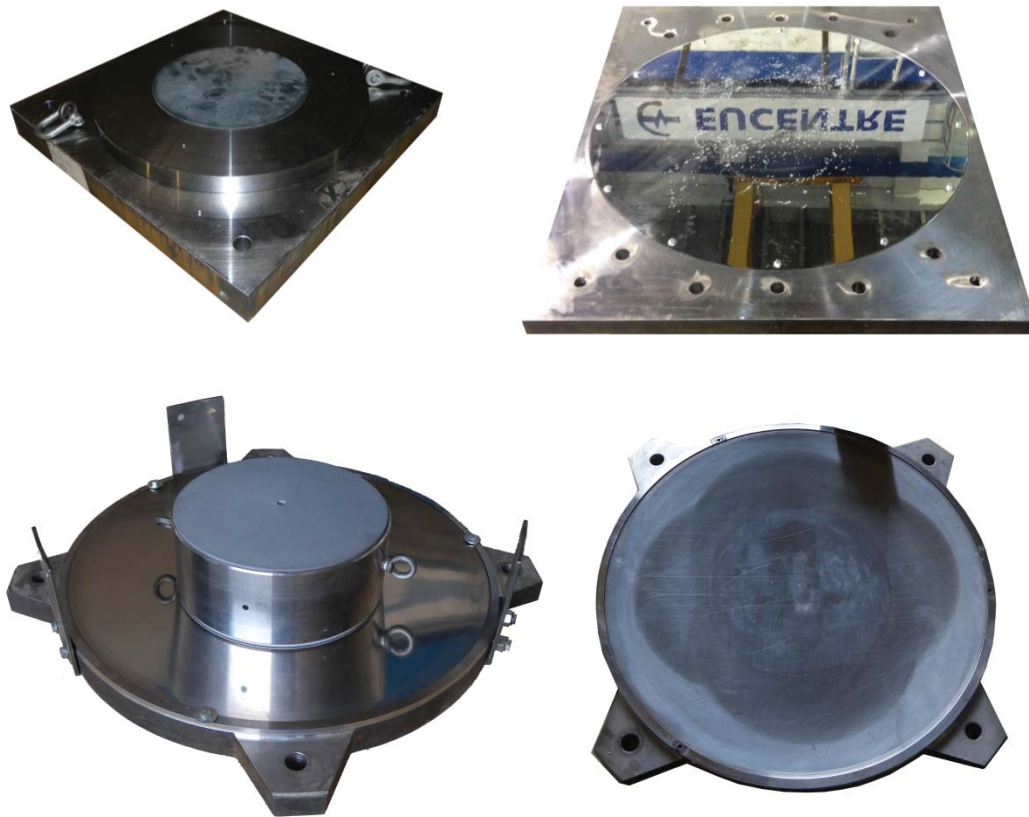


Figure 1: Full-scale Flat (top) & Concave (bottom) Surface Slider devices (FS & DCSS)

Isolation devices have been equipped with an innovative sliding material, which returns a controlled frictional response. Precisely, a pigmented graded PTFE filled with carbon fibres has been considered. The chemical formulation, such a material results in a much stiffer material in comparison to ordinary PTFE compositions. For both the typologies of isolation devices, three different sliding pad sizes have been considered, as shown in Figure 2.

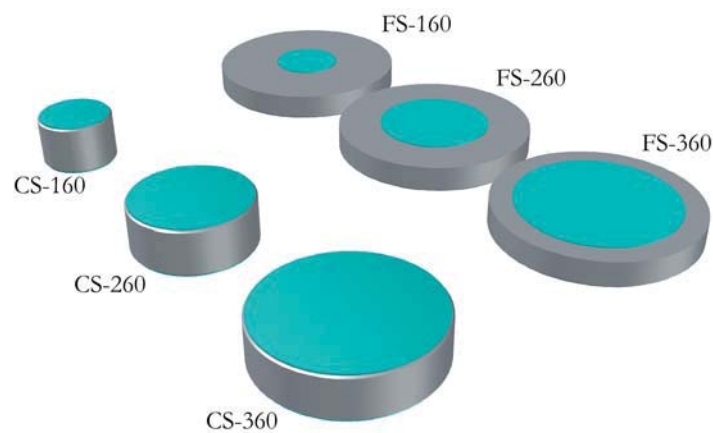


Figure 2: Internal sliders for Flat and Curved devices

Thanks to the adopted sliders it is possible to analyze the comparison between flat and curved sliding conditions also for different sizes of the sliding pads, which may influence the distribution of the contact stresses at each interface and, consequently, the frictional response.

### 3 BIDIRECTIONAL TESTING PROTOCOL

The testing protocol has been defined, by considering bidirectional tests, according to the cloverleaf orbit, which is ruled by the European standard code UNI:EN15129:2009 for anti-seismic devices ([1]). Tests have been carried out through the Bearing Tester System at the Laboratory of the EUCENTRE Foundation in Pavia ([8]), which provides a special equipment for the application of bidirectional horizontal motions to isolation devices. Specifically, the time series of horizontal displacement along both x and y directions for the cloverleaf orbits can be returned by the following expressions:

$$\begin{aligned} x(t) &= \frac{D_{\max}}{\sqrt{2}} \cdot \sin(4\pi ft) \cdot [\sin(2\pi ft) + \cos(2\pi ft)] \\ y(t) &= \frac{D_{\max}}{\sqrt{2}} \cdot \sin(4\pi ft) \cdot [\sin(2\pi ft) - \cos(2\pi ft)] \end{aligned} \quad (1)$$

Such displacement time series have to be applied simultaneously to the device, which is consequently subjected to a bidirectional motion.

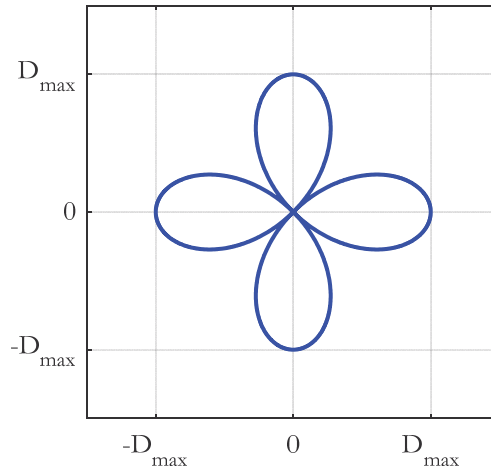


Figure 3: Cloverleaf bidirectional orbit

The aforementioned analytical definition of the displacement input leads to the following expression of the peak vectorial velocity of the test.

$$V_{\max} = 4 \cdot \pi \cdot f \cdot D_{\max} \quad (2)$$

In order to better characterize the frictional properties of all the investigated devices, by ensuring a constant value of vectorial sliding velocity, input signals for bidirectional tests have been modified. Precisely, according to the aforementioned analytical definition of motion, the tangent velocity modulus varies between 50% and 100% of the peak value of the test, variations which may induce unexpected discrepancies in the overall frictional behavior of the considered device. Thus, a special resampling procedure has been applied to all tests, in order to obtain a constant modulus of the tangent velocity for the whole duration of motion. In Fig-



Figure 4 a comparison of the input signals for ordinary and CTV (Constant Tangent Velocity) orbits is provided.

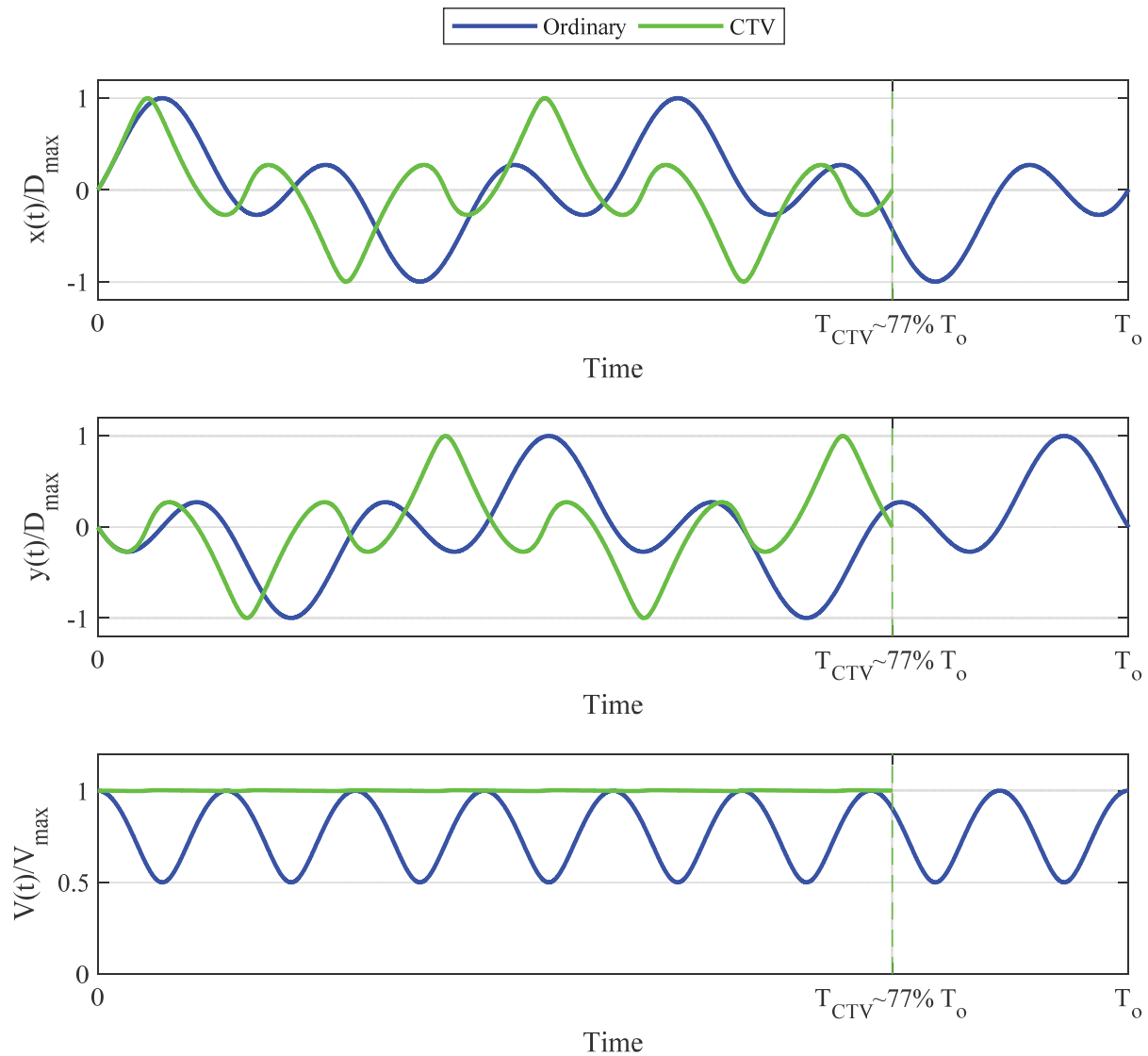


Figure 4: Comparison between ordinary and CTV bidirectional orbits

The aim of the present research work is to directly compare the frictional response of both flat and curved sliding motions, by adopting different diameters of the implemented sliding pads, under bidirectional motions. In order to obtain to apply to the flat slider the effective motion of a single sliding interface of the curved isolator, the geometrical characteristics of the adopted spherical surfaces and the internal slider have been studied. Precisely, since the Curved Slider has the same radius of curvature for both the sliding surfaces, each sliding interface of the internal slider is subjected to 50% of the global displacement applied to the curved device; consequently, the velocity at the sliding interface is also halved. Hence, the testing protocol of the Flat Slider (FS) is obtained by halving peak values of both maximum displacement and velocity of the curved device.

In Table 1 the testing protocol for all the devices is summarized.

Table 1. Bidirectional testing protocol for DCSS devices

Test #	Trajectory	Maximum Displacement [mm]			$V_{\max}$ [mm/s]	P [MPa]
		$\Phi 160$	$\Phi 260$	$\Phi 360$		
1	Cloverleaf CTV (2 repetitions)	150	200	120	20	15
2					80	
3					300	
4	Cloverleaf CTV (2 repetitions)	150	200	90	20	33
5					80	
6					300	
7	Cloverleaf CTV (2 repetitions)	150	200	-	20	45
8					80	
9					300	

The vertical load of each test has been computed, by applying 15MPa, 33MPa and 45MPa contact pressures for each sliding pad diameter, and by considering two repetitions of bidirectional CTV cloverleaf orbit for all tests. It has to be noted that 45MPa pressure level has not been applied to the 360mm sliding pad, due to the high resulting vertical load value.

#### 4 DEFINITION OF THE HYBRID FORCE RESPONSE

The force response of a Concave Surface Slider (CSS) device is generally computed as the summation of the restoring force, provided by the stepwise projection of the applied vertical load along the tangent line to the sliding surface, and the curved frictional force, originated at the sliding interfaces. Thus, in order to compare the force response of the flat and the curved sliders, a hybrid force signal has been computed for both x and y directions, in terms of summation of an experimental flat frictional force, provided by tests carried out on the Flat Slider, and a numerical recenetring force, modeled as a linear spring with respect to displacements along x and y directions.

$$F_{Hybrid} = F_{f-Flat} + F_{rec-num} = F_{f-Flat} + \frac{W}{R_{eq}} \begin{bmatrix} x \\ y \end{bmatrix} \quad (3)$$

The obtained hybrid forces can be directly compared to the force response of the curved device, and resulting frictional properties can be studied. To this aim, the same diameter of the implemented sliding pads for both the tested devices has been considered, and a proper scaled flat testing protocol has been defined, in order to apply same loading conditions to all the sliding interfaces.

#### 5 AVERAGE FRICTION COEFFICIENT PER CYCLE

The cyclic behavior of the frictional response has been studied in terms of decay of the friction coefficient value, by applying an ad hoc analytical definition of the Average Friction Coefficient per cycle, comparable to the one ruled by the code UNI:EN15129:2009. In order

to do so, a proper “bi-directional cycle” has to be defined for the adopted cloverleaf orbit, similarly to what is considered when unidirectional motions are applied. Under radial tests, sinusoidal waveforms are applied, and consequently the device within a single cycle has to reach the maximum and the minimum displacements respectively starting from the centred position (the maximum value of the displacement is reached twice along two opposite directions). Consequently, if two lobes of the cloverleaf trajectory are considered, the maximum vectorial displacement is reached twice along two different (and orthogonal) directions as well. Thus, a set of two lobes of the bidirectional cloverleaf orbit can be fairly considered as a bidirectional cycle, as shown in Figure 5.

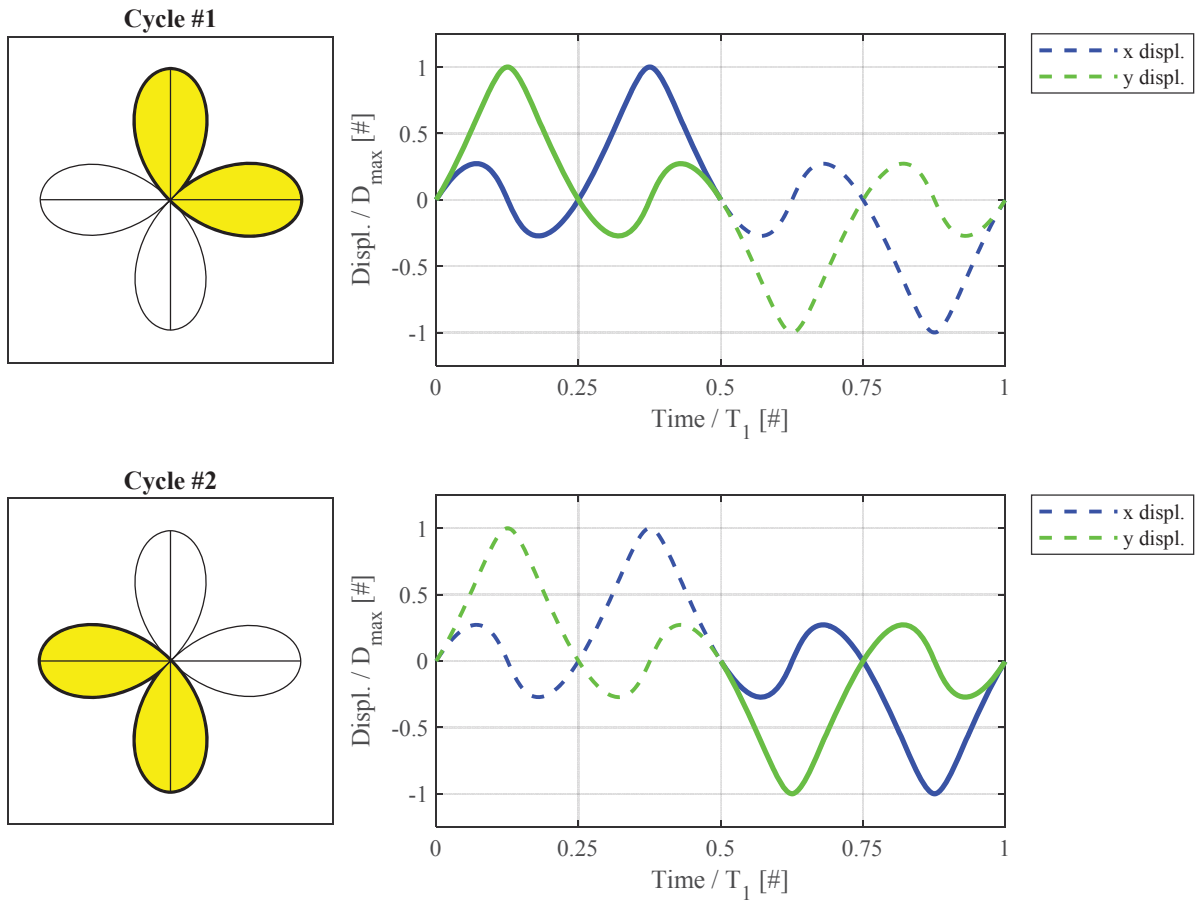


Figure 5: Definition of the bidirectional cycle

Thanks to this definition of the bidirectional cycle, for each test of the testing protocol of all devices four individual values of average friction coefficient per cycle can be computed, since the cloverleaf orbit has been repeated twice (8 lobes). The numerical value of the average friction coefficient per cycle can be computed, as a function of the Energy Dissipated per Cycle (EDC) and the product between the applied vertical load  $W$  and the total length of the bidirectional travelled path along two lobes ( $4,844 D_{max}$ ).

$$\mu_{EDC} = \frac{EDC}{4,844 D_{max} W} \quad (4)$$

The EDC value can be computed through the evaluation of the total work, in terms of integral of the scalar product between the force and the differential displacement vectors.

$$EDC = \int \vec{F} \cdot d\vec{s} \quad (5)$$

The computed average friction coefficient per cycle has to be referred to the dissipated energy value which occurs at half cycle point, which corresponds to the zero displacement point (undeformed configuration), between the achievement of the maximum displacement along the orthogonal directions (i.e. at the end of the first lobe of the bidirectional cycle).

## 6 EXPERIMENTAL RESULTS

In Figure 6, Figure 7 and Figure 8 results are shown for all the velocity levels, with a contact pressure equal to 15MPa, 33MPa and 45MPa respectively.

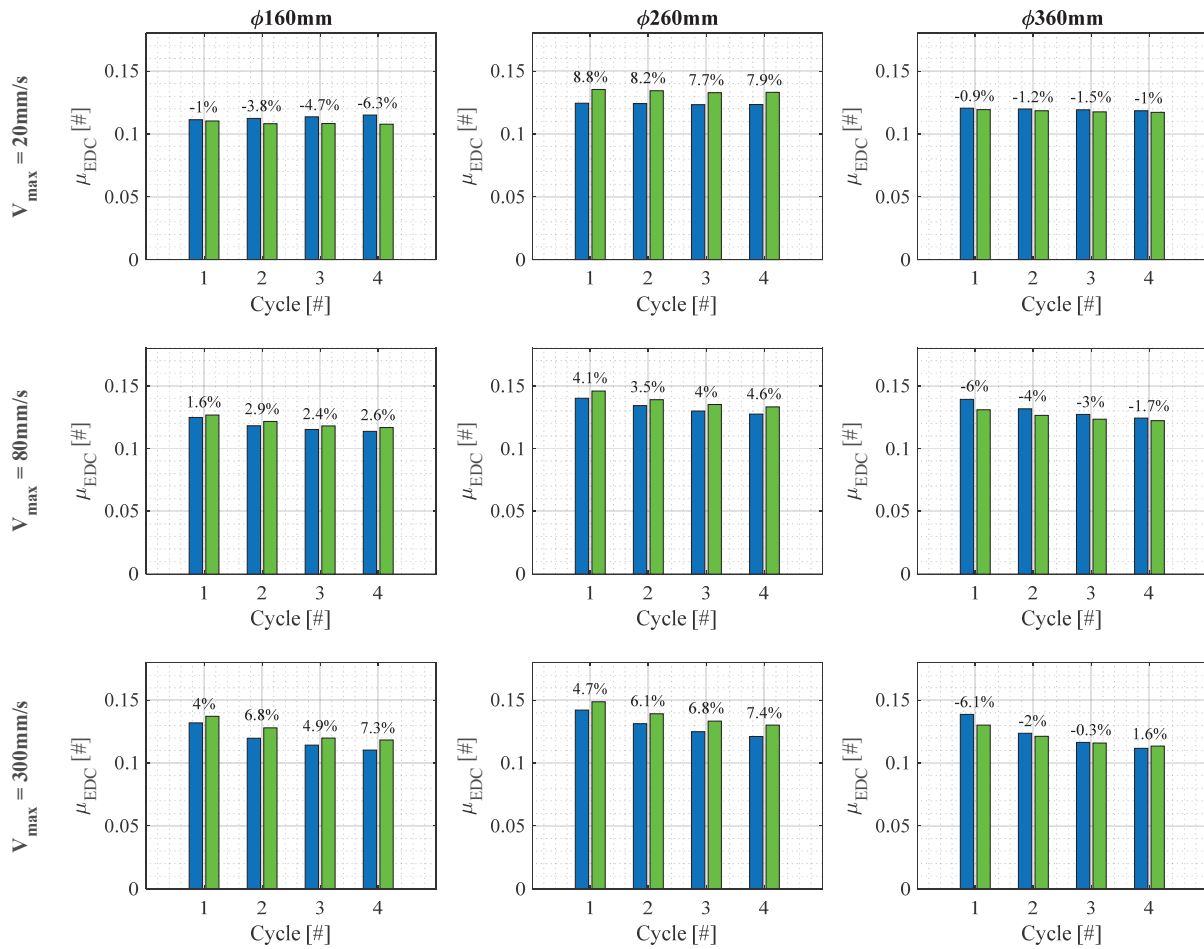
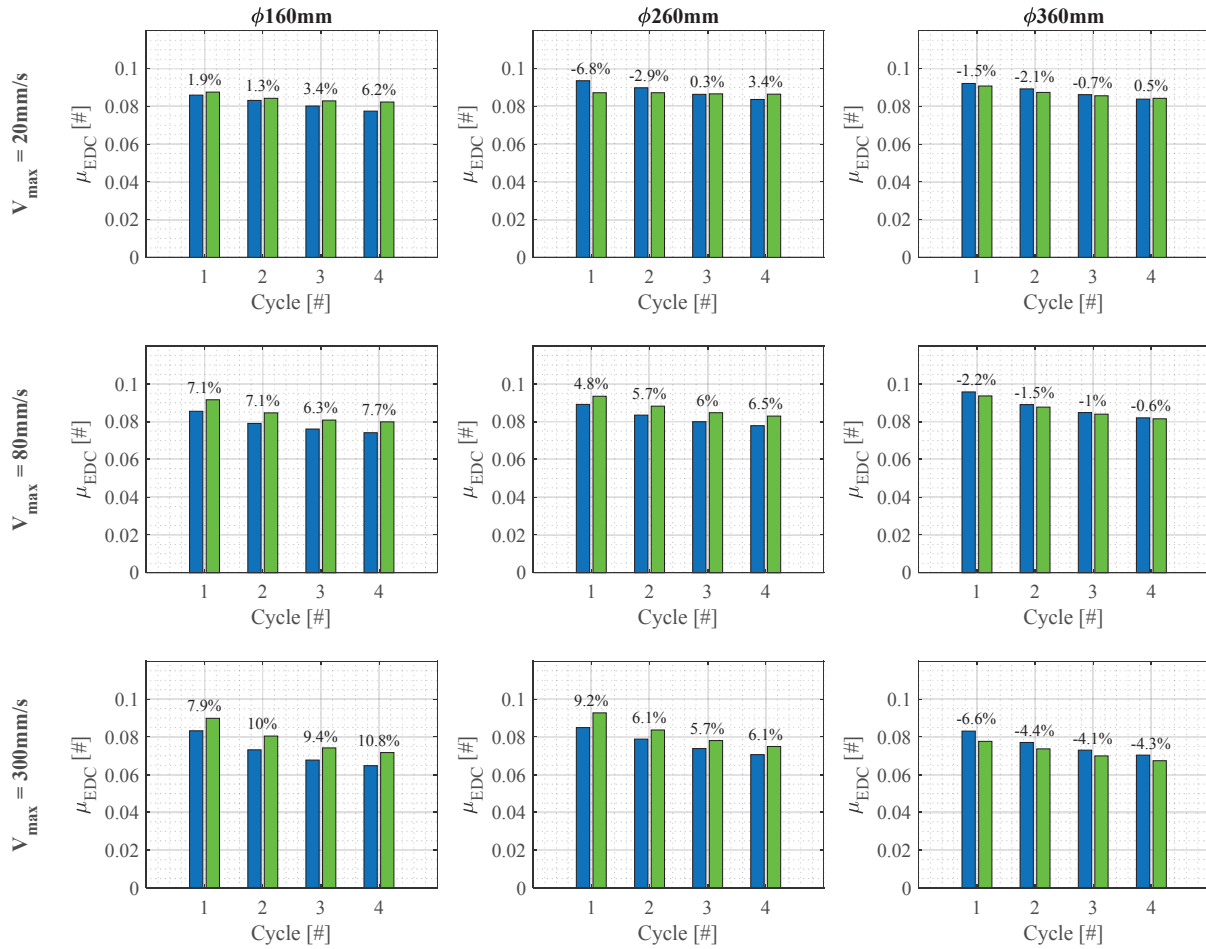
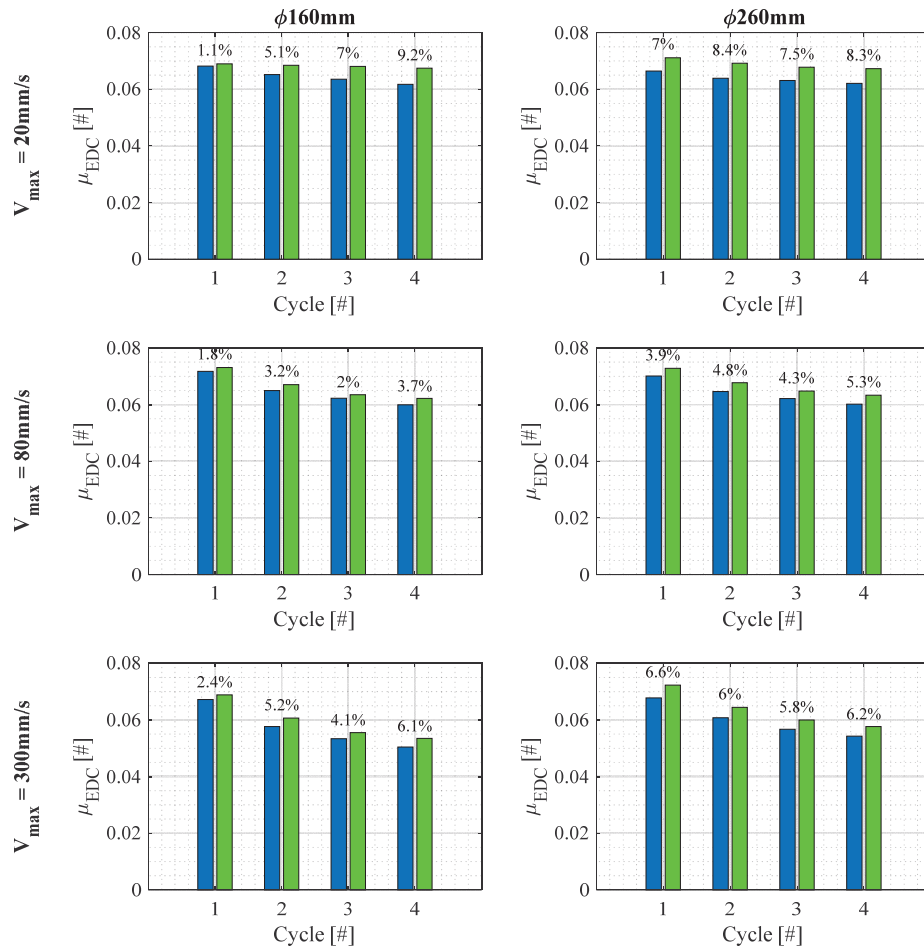


Figure 6: Average friction coefficient per cycle for **Curved** and **Flat** sliders,  $P = 15\text{MPa}$ .


 Figure 7: Average friction coefficient per cycle for **Curved** and **Flat** sliders,  $P = 33\text{MPa}$ .

Results are presented as values of average friction coefficient per each applied bidirectional cycle, which means four cycles for all the tests. More specifically, values have been computed, by considering the outcomes of tests performed on the Double Curved Surface Slider devices and the hybrid lateral response, computed as a combination of a numerical restoring force and the experimental flat frictional force. For the evaluation of the hybrid frictional characteristics, the displacement time series has been doubled, in order to consider the proper analogy with respect to the curved device. Results show a very good agreement between the frictional responses of the DCSS device and hybrid force related to the flat slider. Precisely, it can be assessed that for small-to-medium diameters of the sliding pad (160mm and 260mm) the hybrid friction coefficient is generally higher than the corresponding value related to the curved device, whereas for large diameters (360mm) flat motions lead to lower friction coefficient values, in comparison to curved isolators, especially for high velocity. In all figures variation values are reported, in terms of variation of the friction coefficient returned by the hybrid response, with respect to the value related to the curved device. As can be noted, such variation values are less than 10%, which highlight that the proposed method for frictional characterization provides a very good estimate of the real properties of the DCSS isolator.




 Figure 8: Average friction coefficient per cycle for **Curved** and **Flat** sliders,  $P = 45\text{MPa}$ .

Another aspect which can be noticed by analyzing graphical results is related to the frictional decay and the actual numerical values of the average friction coefficient per cycle. Precisely, it can be assessed that numerical values returned by the different sliding pad diameters are comparable, and approximately the same decay trend can be detected for all the velocity and contact pressure levels. This is a very important experimental evidence, which seems to prove that different diameters of the sliding pad actually lead to the same frictional properties, characterized by the same cyclic effect, if the proper motion is applied.

## 7 CONCLUSIONS

The presented experimental research provides the comparison between the frictional response returned by both flat and curved sliding motions. A large number of bidirectional dynamic tests have been performed at the Laboratory of EUCENTRE Foundation in Italy, by applying different loading conditions (i.e. contact pressure and sliding velocity) to ad hoc designed and realized full-scale devices, in order to provide results more comparable to applications commonly developed in the real practice. Precisely, Flat Sliders (FS) and Double Curved Surface Sliders (DCSS) have been adopted, by considering three individual sliding pad diameters. The testing program of the flat devices has been computed, by halving the peak displacement and velocity of the tests performed on the curved isolators, since both the

spherical sliding surfaces have the same radius of curvature, and consequently the same sliding motion is originated at each sliding interface. Both the typologies of tested devices have been equipped with an innovative sliding material, which consists of a graded PTFE filled with carbon fibres. In order to carry out bidirectional tests, the cloverleaf orbit has been adopted, as ruled by the European standard code for anti-seismic devices UNI:EN15129:2009; in addition, displacement time series along both  $x$  and  $y$  directions have been resampled, in order to obtain a constant tangent velocity modulus for the whole duration of all tests. Average friction coefficient per cycle values have been computed, according to a proper definition of bidirectional cycle for the adopted orbit, and Flat and Curved frictional properties have been compared, by means of a hybrid response: such a force response can be computed as the summation between the experimental frictional force of the Flat Slider device and a numerical recentering force, modeled as a linear spring with respect to displacements (displacement time series have been doubled, in order to consider the actual motion of the curved devices). Results have been analyzed, in terms of average friction coefficient per each bidirectional cycle (four full cycles for each tests).

According to the presented results, it can be assessed that:

- The proposed hybrid response, computed as a function of the flat slider outcomes, leads to a very good estimate of the frictional properties of the corresponding curved device;
- The variation between the hybrid and the curved responses is bounded between  $\pm 10\%$ , and in most of cases the average friction coefficient per cycle achieves higher values, when the hybrid force is adopted, especially for small-to-medium diameters of the sliding pads, and for high velocities;
- Different sliding pad diameters seems to lead to approximately same frictional properties, from both numerical values and cyclic effects (decay trend of the friction coefficient) points of view.

The obtained results look extremely promising, since curved sliding motions for the considered devices can be actually represented by equivalent flat responses, with small variations of the correspondent frictional behavior. The importance of such a conclusion can be noticed from both an economic and a technical standpoints: if the recentering contribution can be actually numerically modeled and the frictional response can be tested by considering an equivalent flat device, the behavior of Curved Surface Slider (CSS) devices can be easily captured by the definition of the hybrid response, and consequently large devices can be fully characterized, even though large force demands are experienced. Consequently, if the testing equipment is able to perform tests on the flat slider, the response of the curved isolator can still be obtained; nonetheless, if the capacity of the testing equipment is not enough to perform tests on the full-scale flat slider, a scaled sliding pad can be considered. Such results may need further experimental investigations, by analyzing different diameters of the sliders, rather than other sliding materials, commonly adopted in real practice applications.

## ACKNOWLEDGMENTS

Part of the current work has been carried out under the financial support Italian Civil Protection, within the framework of the Executive Project DPC-EUCENTRE 2014–2016 (Project S2.0 – Seismic isolation and supplemental damping systems: evaluation of the seismic response of devices and structures) and ReLUI project 2019-2021 (WP15, Task 15.1).

## REFERENCES

- [1] CEN (2009): Comité Européen de Normalisation TC 340, European Code UNI EN 15129:2009 Anti-seismic devices, European Committee for Standardization. Brussels, Belgium.
- [2] Dolce M, Cardone D, Croatto F (2005). Frictional behavior of steel-PTFE interfaces for seismic isolation. *Bulletin of Earthquake Engineering*, **3**, pp. 75-99.
- [3] Fenz D, Constantinou MC (2006). Behaviour of the double concave friction pendulum bearing. *Earthquake Engineering And Structural Dynamics*, **35**, pp. 1403-1424.
- [4] Furinghetti M., Lanese I., Pavese A. (2020) Experimental assessment of the seismic response of a base isolated building through hybrid simulation technique, *Frontiers in Built Environment*, DOI: 10.3389/fbuil.2020.00033.
- [5] Furinghetti M., Pavese A. (2020) Definition of a Simplified Design Procedure of Seismic Isolation Systems for Bridges, *Structural Engineering International*, DOI: 10.1080/10168664.2020.1775535.
- [6] Furinghetti M., Pavese A., Quaglini V., Dubini P. (2019) Experimental Investigation Of The Cyclic Response Of Double Curved Surface Sliders Subjected To Radial And Bidirectional Sliding Motions, *Soil Dynamics and Earthquake Engineering*, DOI: 10.1016/j.soildyn.2018.11.020.
- [7] Lomiento G, Bonessio N, Benzoni G (2013): Concave sliding isolator's performance under multi-directional excitation. *Ingegneria Sismica*, 30 (3), 17-32.
- [8] Peloso S, Pavese A, Casarotti C (2012): EUCENTRE TREES lab: Laboratory for training and research in earthquake engineering and seismology. *Geotechnical, Geological and Earthquake Engineering*, 20, 65-81.
- [9] Quaglini V, Bocciarelli M, Gandelli E, Dubini P (2014): Numerical Assessment of Frictional Heating in Sliding Bearings for Seismic Isolation. *Journal of Earthquake Engineering*, 18 (8), 1198-1216.
- [10] Quaglini V, Gandelli E, Dubini P (2017). Experimental investigation of the re-centring capability of curved surface sliders. *Structural Control and Health Monitoring*, **24**, Issue 2, DOI: 10.1002/stc.1870.
- [11] Quaglini V., Dubini P., Furinghetti M., Pavese A. (2019). Assessment of Scale Effects in the Experimental Evaluation of the Coefficient of Friction of Sliding Isolators. *Journal of Earthquake Engineering*, DOI: 10.1080/13632469.2019.1687054.
- [12] Tsiavos A, Schlatter D, Markic T, Stojadinovic B. (2017). Experimental and analytical investigation of the inelastic behavior of structures isolated using friction pendulum bearings. *Procedia engineering*, **199**:465–70.

- [13] Tsiavos A, Schlatter D, Markic T, Stojadinovic B. (2021) Shaking table investigation of inelastic deformation demand for a structure isolated using friction-pendulum sliding bearings. *Structures*, **31**, 1041-1052.

## THE NEW CAMERINO UNIVERSITY RESEARCH CENTER: DESIGN OF THE BASE-ISOLATED BUILDING AND DYNAMIC TESTING

A. Dall'Asta<sup>1</sup>, G. Leoni<sup>1</sup>, F. Micozzi<sup>1</sup>, L. Gioiella<sup>1</sup>, N. Ceccolini<sup>1</sup> and L. Ragni<sup>2</sup>

<sup>1</sup> SAAD, University of Camerino  
Viale della Rimembranza 3, 63100 Ascoli Piceno (AP), Italy  
{andrea.dallasta, graziano.leoni, fabio.micozzi, laura.gioiella, nicola.ceccolini}@unicam.it

<sup>2</sup> Department of Civil and Building Engineering and Architecture,  
Università Politecnica delle Marche  
Via Brecce Bianche Ancona, Italy  
laura.ragni@univpm.it

---

### Abstract

*This paper deals with the new Research Centre designed for the University of Camerino and entirely financed by the national Civil Protection Department (DPC), following the seismic events in Central Italy in 2016. The building consists of a base-isolated steel braced super-structure and r.c. sub-structures able to adapt to the complex morphology of the area. In particular, the first part of the paper illustrates the design choices made to achieve a high level of resilience and robustness of the building, i.e. to limit damage to structural and non-structural components and equipment under moderate and design seismic actions and to avoid disproportionate consequences in the event of extreme actions, larger than the design ones. The second part of the paper is focused on static and dynamic tests performed during the construction phase of the building. At the end of the structural system construction (including sub-structures, the isolation system composed by elastomeric bearings and flat sliders and the steel super-structure), the building has been tested by means of static and dynamic (snap-back) in-field tests up to a displacement of the isolation system of 280mm and 220mm, respectively. Displacements have been imposed by means of a properly designed testing mechanism and different measure instruments have been placed in the building to register the structural response.*

**Keywords:** Hybrid base-isolation system; elastomeric bearings; seismic reliability; seismic robustness; in-field tests; in-field snap-back tests.

---



## 1 INTRODUCTION

The new Research Centre of the University of Camerino, called Chemistry Interdisciplinary Project (*CHIP*), is a strategic building intended for high-risk activities of the chemistry and physics laboratories, whose construction started after the 2016 seismic sequences in the Central Italy [1]. The building has been entirely financed by the national Civil Protection Department (*DPC*) and it will be also used as coordination center for civil protection post-earthquake activities in the case of possible future seismic events. Due to its use destinations, the building has been conceived by adopting a structural solution able to guarantee a high level of safety, especially with regard to seismic actions, and, at the same time, the speed of execution (and possible dismantling). To this purpose a base-isolated steel braced structure with pinned joints has been conceived with r.c. sub-structures able to adapt to the complex morphology of the area. In particular, a hybrid isolation system has been adopted, comprising High Damping Rubber Bearings (*HDRBs*) and low-friction Flat Sliding Bearings (*FSBs*) able to provide a high period of isolation and a moderate damping [2]. This solution is suitable in providing both resilience and robustness to the building. In fact, the hazard of the site does not lead to excessive displacements for strong earthquakes, which can be faced with a moderate damping. Moreover, for lower displacements the stiffness and damping of this kind of bearings only slightly increase, resulting in low accelerations of the super-structures and thus no damage (and downtime) of non-structural elements and interior contents. In addition, two complementary strategies have been adopted to also ensure adequate structural robustness against extreme actions, larger than the design ones. The first consists of a safety margin adopted for the displacement capacity of both the devices composing the isolation system and the seismic gaps on the upstream side of the building. For both of them a capacity limit greater than the maximum design displacement at the Collapse Limit State (*CLS*, characterized by a return period of  $R_P = 950$  years) has been required to avoid anomalous behaviours, such as the exit of the sliders out of the sliding surface or the impact of the building with neighbouring structures. The second strategy consists of adopting a steel super-structure equipped with elasto-plastic braces characterized by a proper over-strength, which is important in the case of extreme horizontal actions causing an increase in the stiffness of the *HDR* bearings (due to their hardening behaviour for large shear strains) or the closure of the gaps. Moreover, the robustness under exceptional scenario (such as fire events or explosions) leading to the loss of vertical bearing of isolators is ensured by adopting safety supports around the devices. Finally, with the aim of increasing also the reliability of the building, an in-field experimental campaign has been planned during the design phase of the building. Many similar tests have been carried out in the past on isolated structure in Italy [3][4][5][6]. Some of them adopted a releasing device based on a quadrilateral articulated strut structure with a central fuse [7][8][9], as also used in this work.

In this paper a description of the building is first presented, successively the main design aspects of the base isolation hybrid system and of the in-field tests (testing device as well as reaction structure for the contrast) are illustrated in detail. The last part of the paper describes the static and dynamic in-field tests carried out at the end of the structural system construction (including sub-structures, the isolation system and the steel super-structure). Preliminary results are illustrated even in the light of tests carried out during the bearings production. For the interested reader a video description of the video can be found in [10].

## 2 BUILDING DESCRIPTION AND DESIGN

The upper part of the building (super-structure) is made of steel elements and it is developed by assuming a 7.2 m x 7.2 m modular system, for a total of 7 modules along each direction, plus a cantilever zone, which spans 1.9 m, along the entire perimeter of the building (Figure 1).

The steel elements have been optimized in terms of dimensions and connection systems based on the single module, resulting in a significant saving on materials and an important reduction in construction time. The isolation system has been placed at the horizontal level above the r.c. elements of the sub-structure; this latter has been designed to adapt itself to the ground profile characterized by a remarkable slope. The characteristics of the soil and the variability of the thickness of the deformable layer led to the adoption of deep foundations (Figure 1).

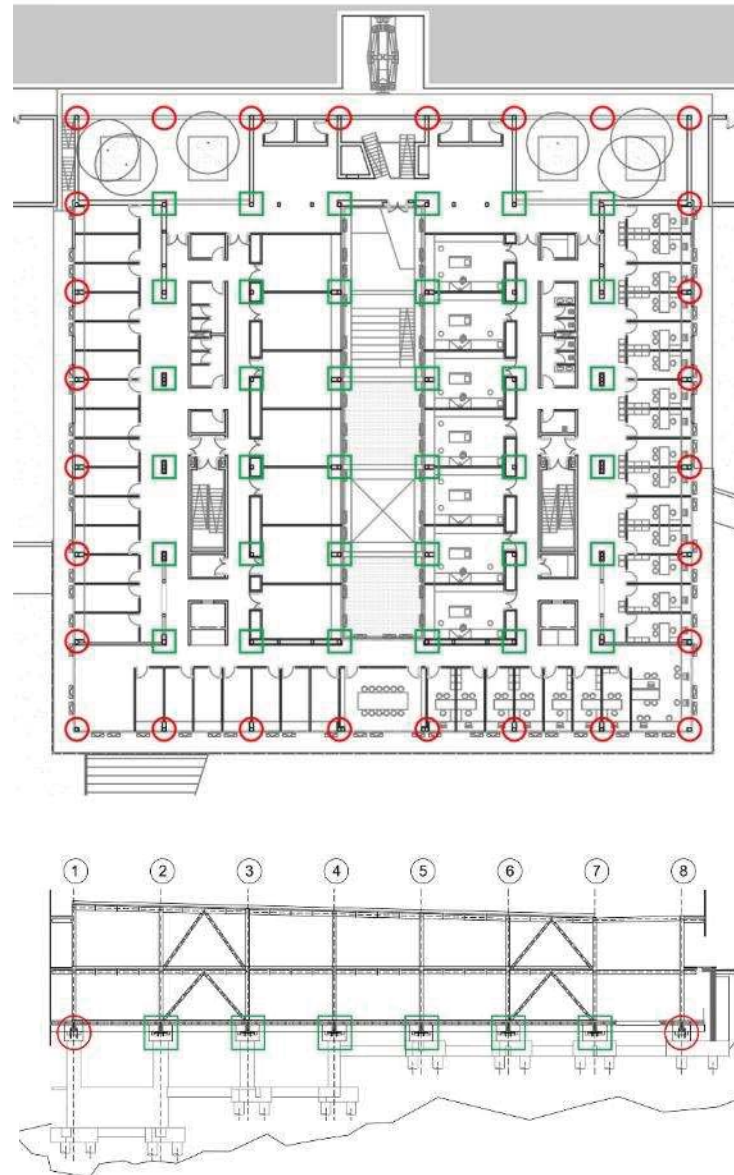


Figure 1: Plan view and longitudinal section of the building (red circles represent *HDRBs* and green squares represent *FSBs*).

## 2.1 Design of the base-isolated building

The isolation system has been designed considering a target period of  $T_{is} = 3.5$  s at the design intensity earthquake (having an exceedance probability of 2.5% in 50 years), to be able to guarantee a significant reduction of the actions transferred to the super-structure in the case of a seismic event. The solution adopted to achieve the desired period involves the use of a hybrid isolation system with *HDRBs* arranged on the perimeter, in order to maximize torsional stiffness,

and *FSBs* in the central part to support higher vertical loads. *HDRBs* commonly used in Italy have a damping ratio ranging from 10% to 15% [11]. However, for the design of the isolation system, the lower limit of 10% of damping and a shear stiffness equal to 0.4 MPa (soft rubber) were assumed in the design phase, in order to deal with different producers. For what concerns the *FSBs*, a dynamic friction coefficient less than 1% was required, to reduce the activation force and possible activation of superior modes and consequently higher accelerations [2]. In a preliminary phase, the bearings were dimensioned by assuming rigid both the super-structure and the sub-structures to obtain a 1-DOF (single degree of freedom system) and by neglecting the slider friction. Thus, the elastic response spectra have been used, reduced for all the periods in the range  $T \geq 0.8T_{is}$  by the equivalent damping of the *HDRBs*. Figure 2 shows the elastic displacement and pseudo-acceleration spectra for the considered site (Camerino, soil type B) at the different limit states, that is the Operational Limit State (*OLS*), the Damage Limit State (*DLS*), the Ultimate Limit State (*ULS*) and the Collapse Limit State (*CLS*), characterized by return periods respectively equal to  $R_P = 60$  years,  $R_P = 100$  years,  $R_P = 950$  years and  $R_P = 1950$  years, according to the national seismic code NTC 2018 [12] for the use class IV. The design was carried out by deriving the maximum displacement of the isolators from the displacement spectrum at the *CLS* corresponding to the isolation period of 3.5 s, which is about 0.27 m. An average design shear strain equal to 1.5 is assumed, ensuring a significant safety margin against possible shear failure, even in the presence of accidental torsional effects, because significantly lower than the maximum value allowed by the European standard on anti-seismic devices EN15129 [13], which establishes a value equal to 2.5.

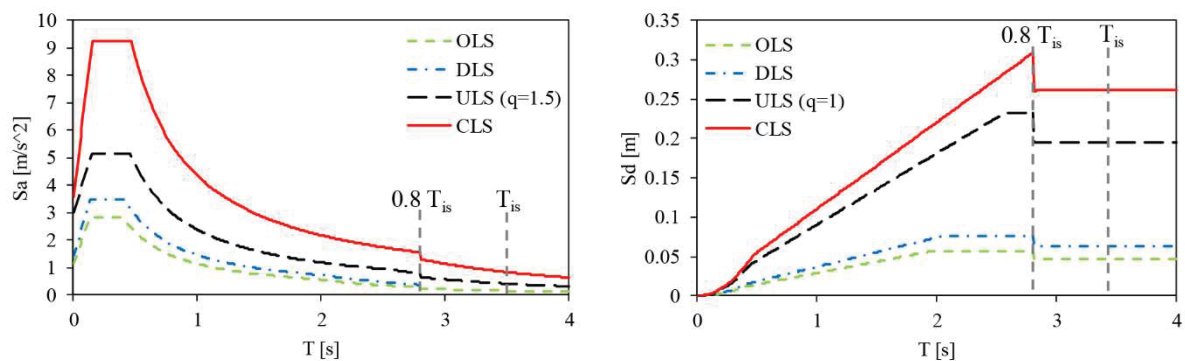


Figure 2: Elastic pseudo-acceleration and displacement spectra at the different limit states

Based on the total rubber area obtained and on the devices generally available on the national market, the following types of devices have been chosen: (i) elastomeric isolators with a diameter of 600 mm, total height of rubber 184 mm, with horizontal rigidity 0.62 kN/mm and maximum displacement 350 mm, (ii) sliding supports with a maximum displacement of 400 mm and friction coefficient lower than 1%. The final choice of devices led to a slightly higher isolation period equal to  $T_{is} = 3.60$  s. It should be noted that the displacement capacity of both the devices is larger than the maximum displacement at the *CLS* accounting also for torsional effects, which can be estimated as  $270 \cdot 1.2 = 324$  mm. As already highlighted in the introduction, larger safety assumption guarantees the absence of anomalous behaviours due, for example, to the exit of the sliders for actions greater than those considered in the design. The higher value chosen for the *FSBs* with respect to the *HDRBs* is related to the lower robustness of the former because displacements higher than the sliding surface dimension suddenly lead to a loss of bearing capacity. On the contrary, rubber isolators can usually sustain displacements larger than their nominal capacity without a significant loss of performance. An adequate dimension (350

During the building construction, in-field dynamic “snap-back” test and static tests have been performed in order to verify the actual behaviour and the characteristic of the isolation system. With this purpose, the design of the releasing device and relevant contrasting structures has been conducted during the design phase of the building. In particular, a “reaction box” made by r.c. walls and founded on piles has been arranged in the upstream part of the building to place the releasing device, as depicted in Figure 1. Figure 3 reports a plan view and a longitudinal cross section of the “reaction box” and of the releasing device. It is worth to note that the estimated maximum reaction force is about 5000 kN and all the nine piles of the box base slab collaborate in contrasting it. Moreover, the reinforcements of the building slab, where the releasing device is attached, has been properly designed and detailed according to a strut-and-tie tall beam model (Figure 4 and Figure 5 a). Similarly, proper steel reinforcement bars have been located in the r.c. walls, especially near the location of the hydraulic jacks in order to avoid local punching shear mechanism (Figure 5 b).

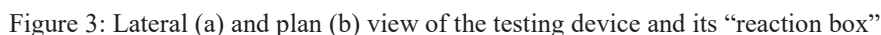




Figure 4: Reinforcement details of the tall beam on the building side (a) and strut-and-tie main mechanism (strut=grey zones, tie=red solid lines, nodes=dark grey zones) (b).

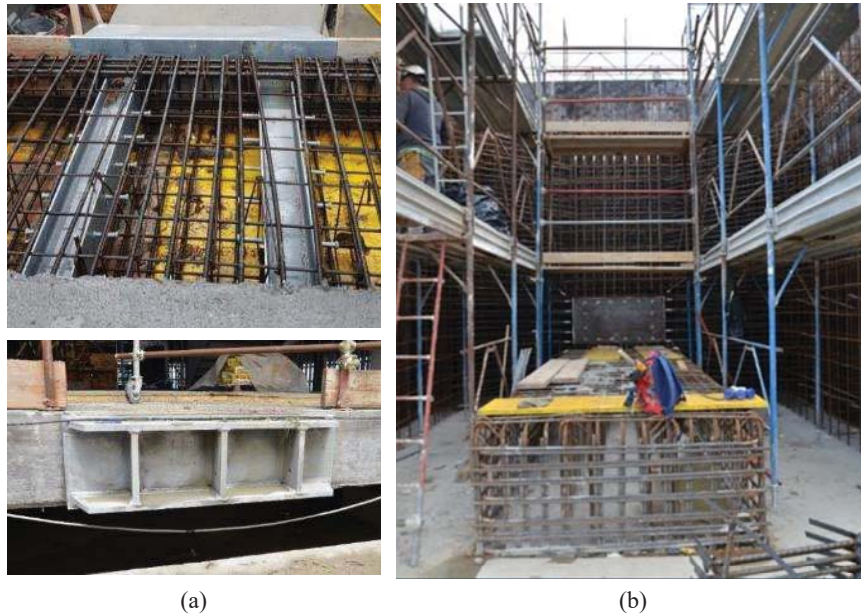


Figure 5: Reinforcement details of the building tall beam (a) and the reaction walls (b).

The tests are carried out using two hydraulic jacks (a maximum force of 5000 kN each and a maximum stroke of 300 mm) in series with the releasing device and two load cells on the opposite side (Figure 6 a). This latter is conceptually a quadrilateral articulated steel strut blocked by the central tie and supported by steel wheels on rails to ensure the longitudinal displacement with the lowest friction force. A fuse element made of high strength turned rod (Figure 6 b) is lodged in the middle of the tie element. The strut angle respect to the pushing direction defines the ratio between the pushing force and the tension force applied to the tie. The turning geometry and the low plastic deformation of high strength steel used for the fuse ensure a brittle rupture of the rod and a high accuracy of the release force. A friction dissipative device (Figure 6 c), similar to the ones used for falling rock protection barrier, have been installed in parallel with the tie element.

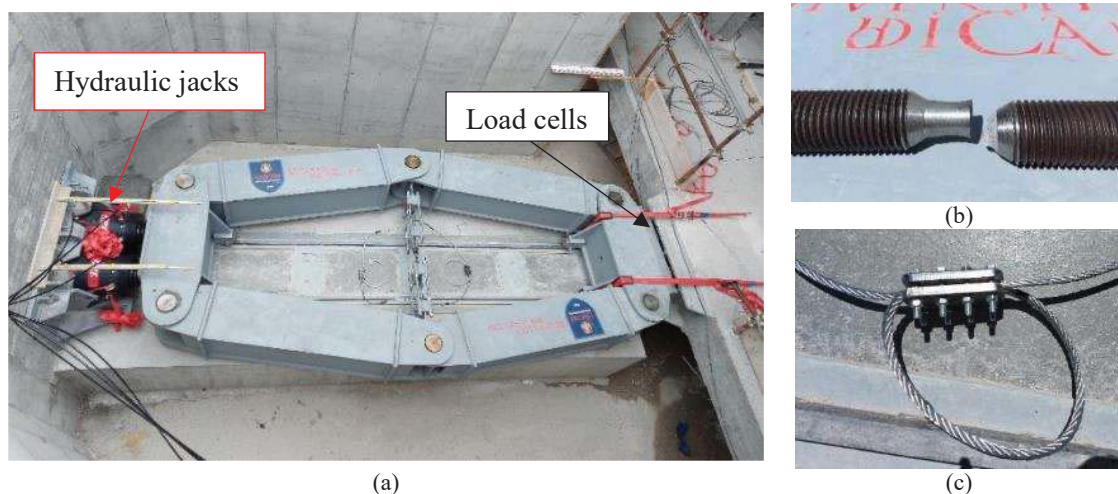


Figure 6: Releasing device equipped with hydraulic jacks and load cells (a) and high strength turned rod fuse after the rupture (b), after the rupture and friction dissipative device (c).



After the fuse rupture, the elastic energy stored in the device is partially dissipated by the friction dissipative device (Figure 6 c), avoiding damages to both the cylindrical articulations and the strut elements. The dissipating mechanism is based on a friction clamp applying a calibrated force (controlled by belleville washers) to the looped cable [14]. The loop ensures an end-stroke of the rope sliding. Finally, to further secure the cell loads from possible impacts during the release phase, the releasing device was anchored on the building side using ratchet belts. It is worth to note that both the device mass and the device friction force are negligible with respect to the building mass and response.

### 3 STATIC AND DYNAMIC IN-FIELD TESTS

The isolation system of the CHIP building has been tested during the construction phase, when the structures were completed and no partition, nor external walls, neither equipment were installed. In particular, a series of Dynamic Snap-Back (*DSB*) tests and Quasi Static (*QS*) tests have been performed, during two different days (3<sup>rd</sup> and 6<sup>th</sup> July 2020). The equipment used to move the building during the *QS* tests and the first part of the *DSB* tests has been described in section 2.2, while some measurement instrumentations are illustrated in Figure 7.

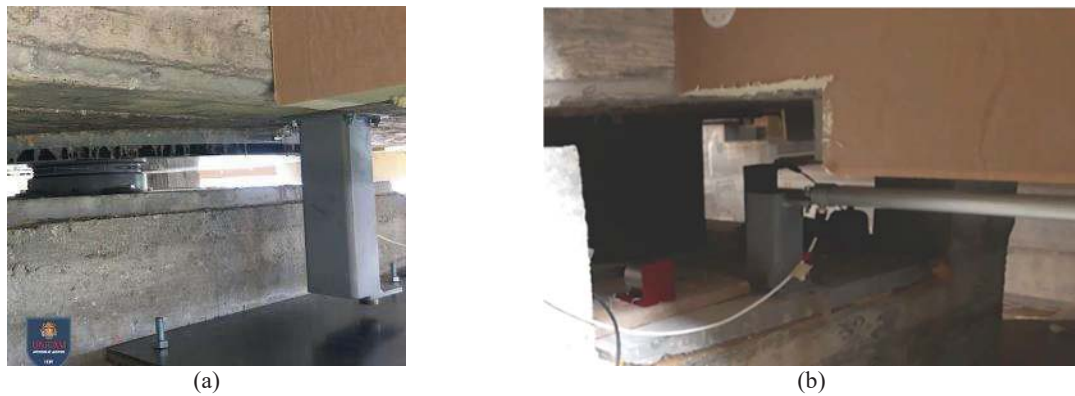


Figure 7: Sensors for recording vertical (a) and horizontal (b) displacements.

The sequence of the tests, the maximum applied displacements and thrust forces are reported in Table 1. Residual displacements at long time (immediately before the subsequent test) are also reported in the last column of the table. The last test (*QS7*), in which the maximum displacement has been imposed, showed the largest residual drift (31.4 mm) but a large part of it was recovered after few days from the test (final residual displacement equal to 25 mm).

Test	Date	max displacement [mm]	max Force [kN]	Residual displacement [mm]
<i>Pre-test1</i>	3 <sup>rd</sup> July	0.0	518	0.0
<i>DSB2</i>	3 <sup>rd</sup> July	177.3	2729	15.2
<i>QS3</i>	3 <sup>rd</sup> July	232.4	3206	22.1
<i>DSB4</i>	6 <sup>th</sup> July	109.4	1756	22.1
<i>DSB5</i>	6 <sup>th</sup> July	226.9	3122	22.0
<i>DSB6</i>	6 <sup>th</sup> July	121.8	1786	22.4
<i>QS7</i>	6 <sup>th</sup> July	284.6	3834	31.4→25

Table 1: Tests sequence

Figure 8 (a) reports results in terms of response curves, i.e. loading force-displacement curves of some *DSBs* and the loading and unloading force-displacement curves of the two *QS*

tests, showing some characteristic behaviours of hybrid isolation systems composed by *HDRBs* and *FSBs*. The first one is the breakaway friction force of the system. During *DSB2* test the structure is moved for the first time from its initial position and starts to move after reaching a force of 700 kN, which is higher than the breakaway friction force observed during all the subsequent tests. The reason is that the trajectory followed by all the tests is almost the same, thus the lubrication of the sliding surfaces increases at each test. Furthermore, from the unloading branch, the dynamic friction force can be estimated since the vertical drop at the maximum force is theoretically 2 times this force. The obtained values, highlighted in Figure 8 (a), are approximately equal to 400 kN for both the *QS* tests, thus the dynamic friction force is estimated to be nearly 200 kN, which is significantly lower than static friction force. Both the reduction of the friction due to repeated cycles and the difference between static and dynamic friction are phenomena already known in specific technical literature [15]. However, it can be noted that after the tests the building does not restore its initial position, thus the initial force measured to start the movement is not only related to the friction of *FSBs* but also to the residual force of *HDRBs*. From Figure 8 (a) it is clear that after having performed the *DSB2* test, the succeeding *QS3* test starts in a displaced configuration equal to 15 mm and equal to 23 mm for all the following tests, resulting in a horizontal shifting of the responses.

Another characteristic aspect that can be observed from the tests deals with the viscous behaviour of *HDRBs* (i.e. the influence of the displacement rate on the response). To better explain this point the response curves of Figure 8 (a), once deduced the dynamic friction force previously estimated and scaled with respect to a single *HDRB*, have been compared in Figure 8 (b) with the response curves of two type tests, carried out according to [13] before the bearings production. Specifically, such tests are the Horizontal Cyclic test at 150% shear deformation at third cycle (*HC* in Figure 8 b) and One Side Ramp test (*OSR* in Figure 8 b). It can be observed that the *HC* test (performed at 0.5 Hz, with a mean speed of 550 mm/s) is stiffer and more dissipative than all the other tests, which have been carried out with a significantly lower displacement rate (about 5 mm/s the *OSR* type test and 0.2 mm/s the load branch of in-field *QS* tests). A further remark involves the in-field *QS* tests, whose loading branch is very close to the *OSR* test, even though the speed is different. On the contrary, the unloading branches are significantly different due to the different unloading modalities, resulting in a lower energy dissipation and a higher recentring capacity of the *QS* in-field tests. For what concerns the loading phase of the *DSB2* in-field test, the response significantly differs from the other tests because it is affected by the first breakaway friction force and by the first cycle effect of the “virgin” rubber, i.e. the first time that all the *HDRBs* reach this level of strain [16][17].

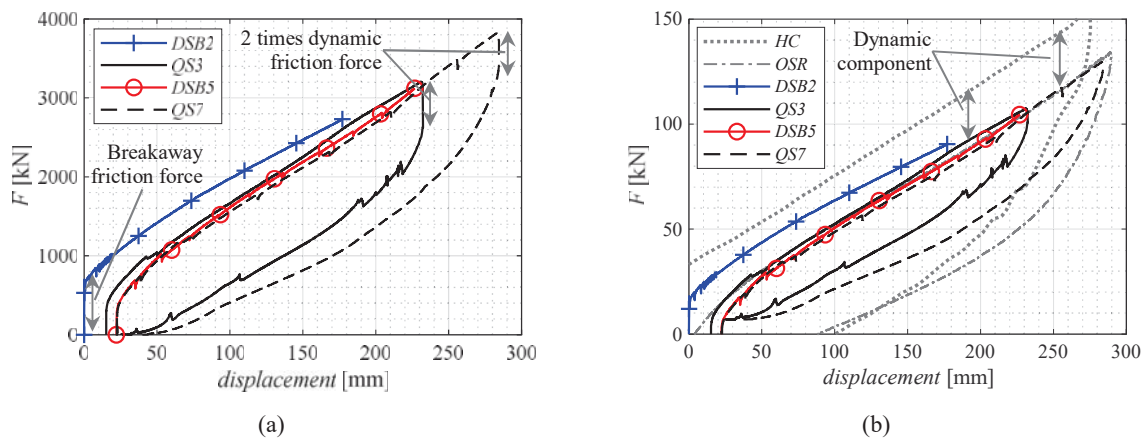


Figure 8: Force-displacement curves of the in-field tests (a) and their comparison with type tests with reference to a single *HDRB* (b).

Finally, Figure 9 summarizes the displacement time-histories observed during the *DSB* tests. It is worth to note that the isolation period, ranging between 2.5 s and 3.12 s, is lower than the design period due to the lower mass of the isolated building during the tests with respect to the design one. Furthermore, it can be observed that the free vibration of the building oscillates between a non-zero displacement configuration, but a slow recentring displacement can be recognized by looking at the response after 4 s from the release. This confirms the importance of the viscous component of *HDRBs* response, which leads to a final residual displacement of around 22-25 mm (see Table 1).

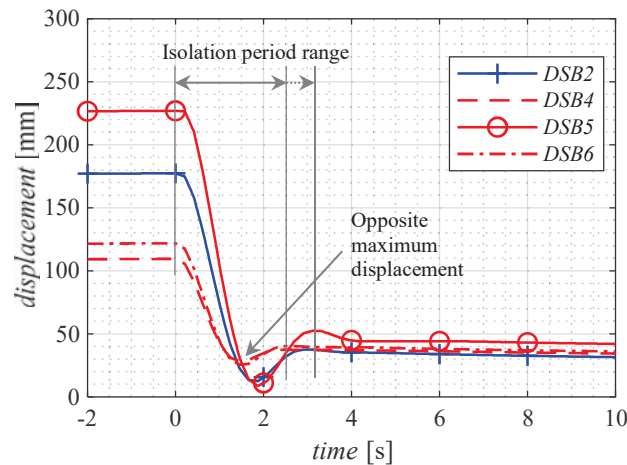


Figure 9: Displacements time-histories of in-field *DSB* tests.

#### 4 CONCLUSIONS

This paper describes the isolated-building of the new Research Centre of the Camerino University, called *CHIP* (Chemistry Interdisciplinary Project), with particular focus on dynamic and static in-field tests carried out during the building construction to characterize the isolation system response. The design of the in-field experiment campaign has been developed in parallel with the design of the building. In particular, a quadrilateral articulated steel strut element has been designed and used as releasing device, furthermore a reaction box has been designed close to the building and properly dimensioned. A pair of hydraulic jacks, whose force has been monitored through load cells, has been used for the pushing phase, while the displacements of the isolation system has been recorded thanks to horizontal and vertical transducers. Preliminary results, in terms of force-displacement response curves of quasi-static tests and displacement time-histories of dynamic snap-back tests have been showed and discussed. By analysing the force-displacement response curves of the quasi-static tests, both the static and dynamic friction force of *FSBs* has been estimated. The response of *HDRBs* has been also identified and compared with type tests carried on single bearing devices. Finally, the displacement time-histories of the snap-back tests have been analysed by estimating the isolation period range and the recentring capacity of the isolation system.

#### REFERENCES

- [1] A. Dall'Asta, G. Leoni, F. Micozzi, L. Gioiella and L. Ragni, A Resilience and Robustness Oriented Design of Base-Isolated Structures: The New Camerino University Research Center. *Front. Built Environ.* 6:50. 2020. doi: 10.3389/fbuil.2020.00050

- [2] Ragni L, Micozzi F, Tubaldi E and Dall'Asta A. Seismic behaviour of a rc frame isolated by hdnr bearings under increasing intensity levels. 7th ECCOMAS Thematic Conference COMPDYN 2019. Crete, Greece, 24–26 June 2019
- [3] F. Bettinali, M. Forni, M. Indirli, A. Martelli, P. Masoni, G. Bonacina, On site dynamic tests of a large seismically isolated building. Proceedings of International Meeting on Earthquake Protection of Buildings, Ancona, Italy. 1991, p. 145.
- [4] M. Forni, A. Martelli, B. Spadoni, E. Casalini, G. Bonacina, G. Pucci, Dynamic tests on seismically isolated structure mockups and validation of numerical models. Proceedings of International Meeting on Earthquake Protection of Buildings, Ancona, Italy. 1991, p. 169.
- [5] A.R. Bixio, M. Dolce, D. Nigro, F.C. Ponzo, F. Braga, M. Nicoletti, Repeatable dynamic re-lease tests on a base-isolated building. *Journal of Earthquake Engineering* 2001;5(3):369–93.
- [6] F. Braga, M. Laterza. Field testing of low-rise base isolated building. *Engineering Structures*, 2004; 26(11): 1599–1610. DOI: 10.1016/j.engstruct.2004.06.002.
- [7] N.D. Oliveto, G. Scalia G, G. Oliveto. Time domain identification of hybrid base isolation systems using free vibration tests. *Earthquake Engineering & Structural Dynamics* 2010: DOI: 10.1002/eqe.984.
- [8] F.C. Ponzo, R. Ditommaso, D. Nigro, R. Romaniello, D. Cardone, Analysis of dynamic behaviour of a base isolated building: a release test in Augusta (SI), 2nd European conference on earthquake engineering and seismology, Istanbul, 2014
- [9] M.F. Ferrotto, L. Cavaleri, F. Di Trapani, P. Castaldo. Full scale tests of the base-isolation system for an emergency hospital, 7th ECCOMAS Thematic Conference COMPDYN 2019. Crete, Greece.
- [10] Web site URL: [https://youtu.be/Ou95s6\\_Jcws](https://youtu.be/Ou95s6_Jcws)
- [11] FIP, S02-Isolatori Elastomerici Serie SI (italian), 2016. Available online at: [www.fipindustriale.it](http://www.fipindustriale.it) (October, 2019).
- [12] NTC 2018 (2018). Aggiornamento delle “Norme Tecniche per le costruzioni” (in italian). D:M: 17/01/2018 Ministry of Infrastructure and Transport.
- [13] European Committee for Standardization. EN 15129:2010 - Antiseismic devices, Brussels, Belgium, 2010.
- [14] L. Castanon-Jano, E. Blanco-Fernandez, D. Castro-Fresno, F. Ballester-Muñoz, Energy Dissipating Devices in Falling Rock Protection Barriers. *Rock Mechanics and Rock Engineering* 2017; 50(3): 603–619. DOI: 10.1007/s00603-016-1130-x.
- [15] M. Dolce, D. Cardone, F. Croatto, Frictional Behavior of Steel-PTFE Interfaces for Seismic Isolation. *Bulletin of Earthquake Engineering*, 3:75–99, 2005
- [16] E. Tubaldi, L. Ragni, A. Dall'Asta, H. Ahmadi, A. Muhr, Stress softening behaviour of HDNR bearings: modelling and influence on the seismic response of isolated structures. *Earthquake Engineering & Structural Dynamics*, 2017. DOI: 10.1002/eqe.2897.
- [17] L. Ragni, F. Micozzi, E. Tubaldi and A. Dall'Asta (2020): Behaviour of Structures Isolated by HDNR Bearings at Design and Service Conditions, *Journal of Earthquake Engineering*, DOI: 10.1080/13632469.2020.1776792

## VARIATION IN RESPONSE OF A BRIDGE SEISMICALLY ISOLATED WITH LRBS UNDER THE EFFECT OF LOW AMBIENT TEMPERATURE

E. Cavdar<sup>1</sup>, V. Karuk<sup>1</sup>, G. Ozdemir<sup>1</sup>

<sup>1</sup>ESQUAKE Seismic Isolator Test Laboratory, Eskisehir Technical University  
Eskisehir, Turkey  
e-mail: esengulcavdar@eskisehir.edu.tr

{volkankaruk, gokhan\_ozdemir}@eskisehir.edu.tr

---

### Abstract

*In this paper, the change in response parameters of a seismically isolated bridge, namely maximum isolator displacement (MID) and shear force (MSF), is studied when the ambient temperatures drops to (-30°C) from 20°C. Isolation system of the analyzed bridge is assumed to be composed of lead rubber bearings (LRBs). First, the LRB was subjected to cyclic loading after a conditioning period of 24 hours at both temperatures. Test results were used to validate the success of analytical model used to idealize the deteriorating hysteretic behavior of the LRB. Then, verified analytical representation of LRB was utilized in nonlinear response history analyses in order to measure the variation in MID and MSF in the bridge model under the effect of bidirectional seismic excitations at 20°C and -30°C. Two distinct group of ground motions, that constitute characteristics of both near-field and large-magnitude-small-distance records, were used in the analyses. Results showed that MIDs obtained for LRB properties of 20°C are about 20% larger than the ones obtained for -30°C, in an average sense. Furthermore, average MSF obtained for near-field ground motions at 20°C and -30°C are identical. However, for large-magnitude-small-distance ground motions, MSF of -30°C is almost 25% larger than that of 20°C.*

**Keywords:** Seismic Isolation, Ambient Temperature, Nonlinear Analysis, Lead Rubber Bearing, Strength Deterioration.

---



## 1 INTRODUCTION

Seismic isolation is an earthquake protection system which is used for new and retrofit construction in many countries such as Japan, Italy, United State and Turkey. Its low horizontal stiffness enables the natural period of the structure lengthening, hence, in case of maximum earthquake shaking isolation systems are reduce the force demands and superstructure remain elastic behavior. Among broad classes of seismic isolation systems, lead rubber bearing (LRB) is the most popular used seismic isolator type. In these units, rubber layers reinforced by steel plates and a lead core placed at the center passes through the height of the bearing. The use of steel plates responsible for reducing the bulge and increasing the vertical stiffness of the bearing whereas lead core supplies the required strength in horizontal direction.

The usage area of LRB has been extensively increase around the world since it was invented, such as bridge, hospital, residential building, data centers. In parallel, several research has been conducted to understand the change in mechanical properties of LRB isolators, namely post yield stiffness and characteristic strength, under the effect of different parameters [1-7]. One of these parameters is the change in ambient temperature in which either affects rigidity of rubber [8-14] or needs to modify of LRB properties at low temperatures [15-17] under the effect of cyclic loading. In particular, Hasegawa et al. [15] tested a LRB which is 250 mm in diameter with a lead core diameter of 38 mm. Displacement controlled LRB tests were conducted at temperatures of 40, 20, 0 and -20°C for a shear strain of 100% at 0.3 Hz. Similarly, Constantinou et al. [4] conducted tests with an LRB having rubber and lead core diameters of 381 mm and 70 mm, respectively. On the other hand, rather than displacement-controlled test results, seismic performance of bridges, isolated by LRBs, under the effects of both ground motion excitations and low temperature have also been investigated. For instance, Billah and Todorov [18] investigated the seismic response of an LRB isolated bridge in case of subfreezing temperature. Authors performed nonlinear response history analyses (NRHA) using a bridge model subjected to different ground motions representative of earthquakes in Eastern Canada. In their study, LRBs were modeled with two different non-deteriorating bilinear force-displacement curves to idealize hysteretic behavior of LRBs at “summer” (25°C) and “winter” (-30°C) with properties provided by manufacturer. Another study that has focused on seismic response of LRB isolated bridge under low temperature was conducted by Deng et al. [19]. Similarly, in the analytical model, they used a non-deteriorating hysteretic representation for LRBs where stiffness and strength of LRB was modified in accordance with an empirical formulation. LRB properties used in the analyses were computed for temperatures changing from -30°C to 40°C. However, it is to be mentioned that both Billah and Todorov [18] and Deng et al. [19] neglected the deterioration in strength of LRBs due to temperature rise in the lead core under cyclic motion. Thus, presented results are based on bounding analyses where hysteretic properties such as strength and stiffness of LRB do not change during the applied motion.

Detailed review of the literature for seismic response of LRB isolated bridges at low temperatures revealed that (i) results regarding the variation in mechanical properties of LRB isolators are based on either small- or moderate-size bearings (ii) analytical models for isolator behavior at low temperature do not address the deteriorating hysteretic behavior of LRBs. Thus, there is a need to revisit the performance of LRB isolated bridges subjected to ground motion excitations at low temperature.

The objective of this study is to determine the variation in seismic performance of an LRB isolated bridge considering the change in mechanical properties of LRB when exposed to low temperature. For this purpose, first, a large-size LRB was tested at both room (20°C) and low

(-30°C) temperatures under dynamic conditions. Change in mechanical properties of tested LRB was reported. Then, experimental data is used to verify the success of analytical model employed to idealize hysteretic response of LRBs. Accordingly, deteriorating hysteretic behaviors of the LRB obtained from both experiments and analytical models were compared with each other. Once the use of analytical model to idealize nonlinear hysteretic behavior of LRBs has been shown to be appropriate for both room and low temperature conditions, a representative bridge seismically isolated by LRBs, was analyzed under the effect of both near-field and large-magnitude small-distance ground motions. In the analyses, both horizontal components of selected ground motions were subjected to structural model simultaneously. Maximum isolator displacements (MIDs), and maximum isolator forces (MIFs) were the response quantities used to quantify the variation in seismic performance of LRB isolated bridge at low temperature.

## 2 EXPERIMENT OF A LARGE-SIZE LEAD RUBBER BEARING

### 2.1 Specimen

The bearing tested in this study is a large-size LRB with rubber and lead core diameters of 1020 mm and 190 mm, respectively. Height of the bearing is 436 mm including the top and bottom plates together with the end shim at the top. It is composed of 28 layers of rubber each of which has 10 mm thickness with a total rubber height of 280 mm. Geometrical properties of the tested LRB is presented in Figure 1.

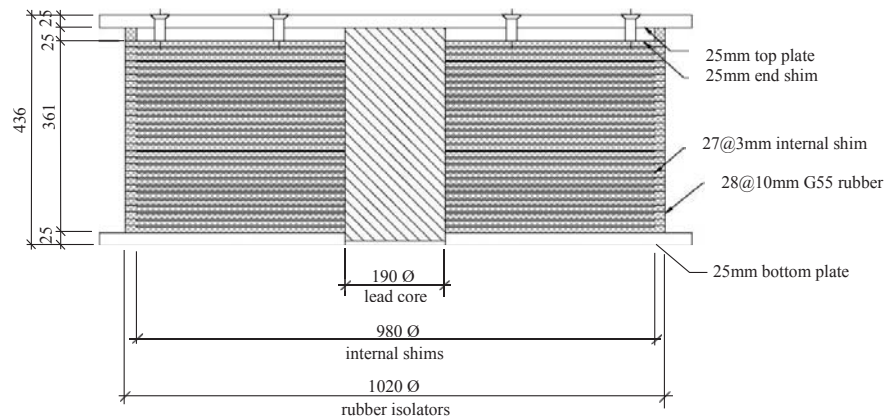


Figure 1- Section cut of test specimen

### 2.2 Loading Device

Tests were conducted at ESQUAKE Seismic Isolator Test Laboratory of Eskisehir Technical University. Figure 2.a, b shows the air-conditioned room and test setup used in the experiment, respectively. The temperature capacity of the air conditioning room is between -40°C and +50°C. In the loading device, vertical actuator has the maximum capacity of 20000kN load. In the horizontal actuator, the maximum capacity of 2000kN load and  $\pm 600$  mm stroke with 1000mm/s velocity.

### 2.3 Loading Method

In order to determine the mechanical properties of the specimen, its hysteretic response in shear was recorded under a constant compressive load. Accordingly, the LRB was subjected to three cycles of sinusoidal motion with amplitude equals to 280 mm that corresponds to

100% shear strain. Frequency of the motion was 0.1 Hz where the maximum velocity is 176 mm/s. The LRB was first tested at a temperature of 20°C after conditioning for 24 hours inside the laboratory and tested again at a temperature of -30°C after conditioning for 24 hours inside the air-conditioned room (Figure 2.a). In all experiments described in this paper, vertical load is equal to 4500kN (6MPa normal stress).



Figure 2 - (a) Air-conditioned room and (b) seismic isolator test setup of ESQUAKE

## 2.4 Test Results

Mechanical properties of the tested LRB such as post-yield stiffness ( $K_d$ ), characteristic strength ( $Q_d$ ), effective stiffness ( $K_{eff}$ ), energy dissipation capacity ( $EDC$ ) and effective damping ratio ( $\xi_{eff}$ ) are computed by means of Equations (1)-(4) provided by ISO 22762-1 [20]. In Equations (1) and (2),  $Q_1'$ ,  $Q_1''$ ,  $Q_2'$  and  $Q_2''$  are the isolator forces at 50% of the maximum positive and negative horizontal displacements  $d_{max}$  and  $d_{min}$ .  $Q_1$  and  $Q_2$  of Equation (3) are the isolator forces at  $d_{max}$  and  $d_{min}$ , respectively (see Figure 3). The calculated test results of LRB isolator are presented in Table 1 for temperatures of 20°C and -30°C.

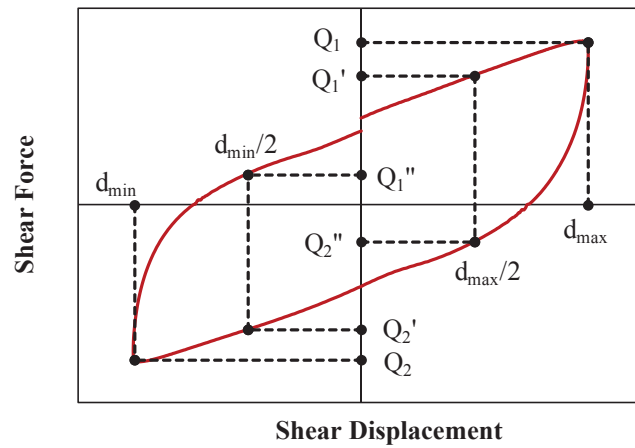


Figure 3 - Force-displacement definitions for LRBs.

$$Q_d = \left[ \frac{Q_1'' d_{max}/2 - Q_1' d_{min}/2}{(d_{max} - d_{min})/2} - \frac{Q_2' d_{max}/2 - Q_2'' d_{min}/2}{(d_{max} - d_{min})/2} \right] / 2 \quad (1)$$

$$K_d = \left[ \frac{Q_1' - Q_1''}{(d_{\max} - d_{\min})/2} + \frac{Q_2'' - Q_2'}{(d_{\max} - d_{\min})/2} \right] / 2 \quad (2)$$

$$K_{eff} = \left[ \frac{Q_1 - Q_2}{d_{\max} - d_{\min}} \right] \quad (3)$$

$$\xi = \left[ \frac{EDC}{\pi(F_{\max} D_{\max} + F_{\min} D_{\min})} \right] \quad (4)$$

Temperature	Cycle	$Q_d$ (kN)	$K_d$ (kN/m)	$K_{eff}$ (kN/m)	$EDC$ (kN·m)	$\xi_{eff}$ (%)
-30°C	1	489	2020	3441	504	0.29
	2	414	1919	3100	433	0.28
	3	372	1864	2913	382	0.26
20°C	1	324	1833	2706	335	0.25
	2	286	1796	2510	297	0.24
	3	260	1766	2392	264	0.22

Table 1: Mechanical properties of LRB at 20°C and -30°C.

According to the test results, it can be revealed that characteristic strength  $Q_d$  of the tested LRB increases when the temperature drops down to -30°C. The amount of amplification in  $Q_d$  is 50% for the first cycle whereas it is 45% and 43% for the second and third cycles, respectively. Similarly, post-yield stiffness  $K_d$  of the LRB increases 10% as the temperature decreases for first cycle. On the other hand, energy dissipation capacity (EDC), increases as the temperature decreases. In parallel, reducing the temperature from 20°C to -30°C contributes to an increase in effective damping ratio  $\xi_{eff}$  equal to 17% for the first cycle. Considering the obtained results, it can be noted that variation in mechanical properties of LRB is not constant while different air temperatures expose to the bearing.

### 3 ANALYTICAL REPRESENTATION OF LRB ISOLATED BRIDGE MODEL

#### 3.1 Hysteretic Response of LRB

The analytical representation of the tested LRB were performed by means of OpenSees [21] structural analysis program. Force-displacement curves obtained from experiments are compared with the analytical ones for both 20°C and -30°C. Figure 4 shows that hysteretic response of the tested LRB can be idealized realistically with great success in the analyses regardless of the ambient temperature. During the LRB model, mathematical representation proposed by Kalpakidis and Constantinou [22] can be considered to modify the initial strength of lead as a function of lead core temperature. Their model considers the instantaneous temperature rise in the lead core and allows calculating the reduction in strength of isolator via reducing the initial yield stress of the lead, instantly. For detailed information please refer to Kalpakidis and Constantinou [22].

#### 3.2 Bridge Model

Analyzed bridge model is a cast-in-place concrete box girder bridge with a 30-degree skew. The length of the bridge is 97.5m and has three spans with lengths of 30.5m, 36.5m and

30.5m. Intermediate bents consist of two 1.22m circular columns and a cap beam with dimensions of 1.22m x 1.83m. The total weight of the bridge above the isolation level is 24956 kN (box girder and each diaphragm weigh 229 kN/m and 657 kN, respectively). The section at one of the intermediate bents is presented in Figure 5.a.

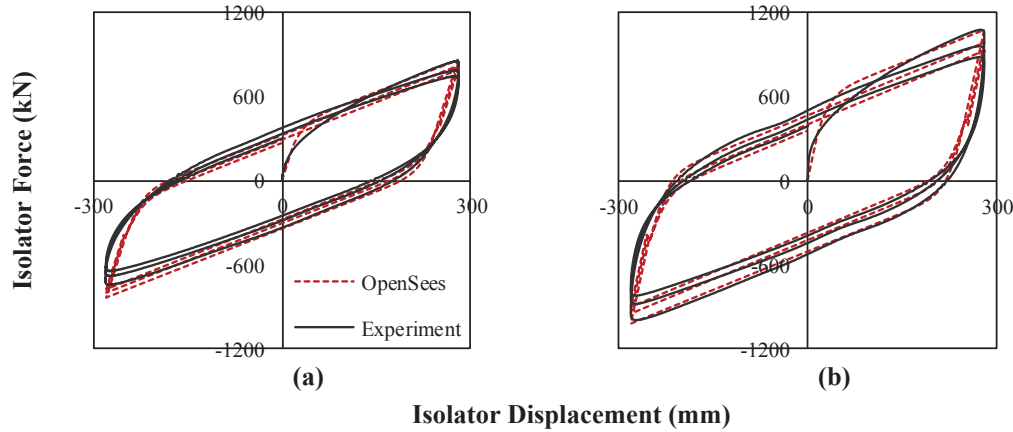


Figure 4: Comparison of experimental and analytical hysteretic curves of LRB tested at a) 20°C and b) -30°C.

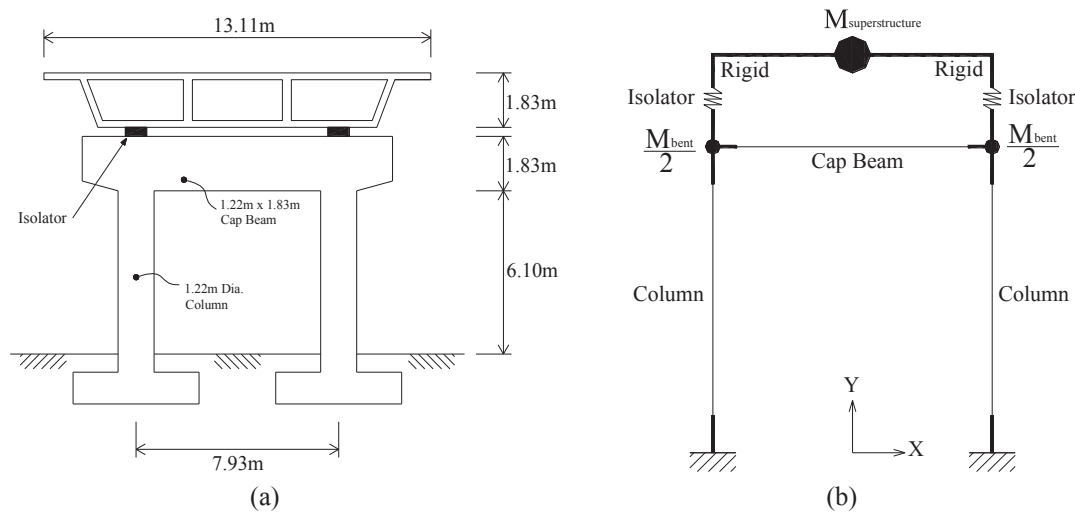


Figure 5: (a) bent geometry and (b) analytical model of the bent.

As shown in Figure 5.a, seismic isolation system is composed of two LRBs at each abutment and pier with a total of eight isolators. They are modeled by deteriorating hysteretic behavior. In order to consider nonlinear bidirectional interaction of LRBs in case of simultaneous excitations of ground motions in both horizontal directions, bidirectional hysteretic model developed by Park et al [23] was employed in the model.

The bridge superstructure was assumed to have infinite in-plane rigidity [24-25]. Analytical representation of the bridge bent is given in Figure 5.b where  $M_{\text{superstructure}}$  is defined based on the tributary weight of the superstructure + the additional weight of the diaphragm and equals to 850t (isolation period based on the post-yield stiffness of the tested LRB at 20°C is 3s). Total mass of the bent components,  $M_{\text{bent}}$ , is lumped equally at the column tops. In the analytical model, member rigid end zone matter is also taken into account to represent the bent stiffness properly. The bridge superstructure and columns are modeled as elastic based on the assumption that structure remains within the elastic range due to seismic isolation by means of *elasticbeamcolumn* element of OpenSees [21]. Accordingly, the elastic



modulus of concrete is taken as 24820 MPa. Bridge structure is assumed to be fixed at the foundation level.

#### 4 GROUND MOTIONS

Two sets of ground motions previously used by Warn and Whittaker [24], were considered in the analyses. Each ground motion set is composed of 10 pairs of record. They were clustered to represent characteristics of near-field (NF) and large-magnitude small-distance (LMSD) records. The magnitudes of ground motions grouped as near-field are in between 6.7 and 7.6 with closest distances to the fault rupture less than 10 km. On the other hand, large-magnitude small-distance ground motions have magnitudes greater than 6.5 while closest distances to fault rupture are in between 10 km and 30 km. Tables 2 and 3 give the characteristics of the considered ground motions where PGA, PGV and PGD stands for peak ground acceleration, peak ground velocity and peak ground displacement, respectively.

#	Event	Station	M <sub>w</sub>	Comp.	PGA	PGV	PGD	Distance
1	Tabas, Iran	Tabas	7.4	FN FP	0.90 0.98	109.7 105.8	55.5 74.9	1.2
2	Loma, Prieta	Lex Dam	7.0	FN FP	0.69 0.37	178.7 68.7	56.6 25.4	6.3
3	Cape Mendocino	Petrolia	7.1	FN FP	0.64 0.65	62.9 46.5	14.1 10.3	8.5
4	Erzincan, Turkey	Erzincan	6.7	FN FP	0.43 0.46	119.1 58.1	42.1 29.5	2.0
5	Landers	Lucerne	7.3	FN FP	0.71 0.80	136.1 70.3	11.2 184.3	1.1
6	Northridge	Rinaldi	6.7	FN FP	0.89 0.39	174.2 60.9	38.3 17.3	7.5
7	Northridge	Olive View	6.7	FN FP	0.73 0.60	122.1 53.9	30.7 9.1	6.4
8	Kobe	JMA	6.9	FN FP	1.09 0.57	160.2 72.4	40.1 15.9	3.4
9	Chi-Chi, Taiwan	TCU065	7.	West North	0.81 0.60	126.2 78.8	92.6 60.8	1.0
10	Chi-Chi, Taiwan	TCU075	7.6	West North	0.33 0.26	88.3 38.2	86.5 33.2	1.5

Table 2 - Characteristics of selected near-field ground motions.

#	Event	Station	M <sub>w</sub>	Comp.	PGA	PGV	PGD	Distance
1	Loma Prieta	Gilroy Array #1	6.9	0 90	0.41 0.47	31.6 33.9	6.4 8.5	11.2
2	Kocaeli, Turkey	Gebze	7.4	0 270	0.24 0.14	50.3 29.7	42.8 27.6	17.0
3	Loma Prieta	Saratoga Aloha Ave	6.9	0 90	0.51 0.32	41.2 42.6	16.3 27.6	13.0
4	Cape Mendocino	Rio Dell Over Pass FF	7.1	270 360	0.39 0.55	43.8 41.9	21.7 19.5	18.5
5	Landers	Joshua Tree	7.3	0 90	0.27 0.28	27.5 43.1	9.5 14.3	11.6
6	Loma Prieta	Gilroy Array #2	6.9	0 90	0.37 0.32	32.9 39.1	7.2 12.1	12.7
7	Landers	Yermo Fire Station	7.3	270 360	0.25 0.15	51.4 29.7	43.9 24.6	24.9
8	Kobe	Abeno	6.9	0 90	0.22 0.24	20.7 24.2	9.1 10.0	23.8
9	Duzce, Turkey	Bolu	7.1	0 90	0.73 0.82	56.4 62.1	23.1 13.6	17.6
10	Northridge	Canoga Park Topanga Can	6.7	106 196	0.36 0.42	32.1 60.7	9.1 20.3	15.8

Table 3: Characteristics of selected large-magnitude small-distance ground motions.

## 5 DYNAMIC ANALYSES RESULTS

Nonlinear response history analyses were performed in OpenSees [21] with due consideration of deteriorating hysteretic representation of LRBs under bidirectional excitations of ground motions given Tables 2 and 3 in order to evaluate the variation in response quantities of the SIB due to change in environmental temperature. Accordingly, maximum isolator displacements (MIDs) and base shears in the pier are presented in a comparative manner for 20°C and -30°C.

### 5.1 Maximum Isolator Displacement

This section presents the observations related to variation of MID of the analyzed structural system due to change in ambient temperature. Figure 6 shows the comparison of MIDs obtained for 20°C and -30°C for both ground motion sets of NF and LMSD. Averages of MIDs recorded for all of the considered ground motion records are also given in Figure 6

where MIDs were calculated by taking the maxima of  $\sqrt{(D_x^2 + D_y^2)}$ . Here,  $D_x$  and  $D_y$  are the isolator displacements in horizontal x- and y-directions, respectively. Figure 6.a, at which MIDs for NF ground motions are presented, reveals that MID reduces significantly when the ambient temperature drops down from 20°C to -30°C. The amount of reductions in MID ranges from 8% to 53% with an average value of 19%. Similar comparison for LMSD ground motions is given in Figure 6.b. In this case, the amounts of change in MIDs for individual ground motion records range from 33% to -52% with an average of -16%.

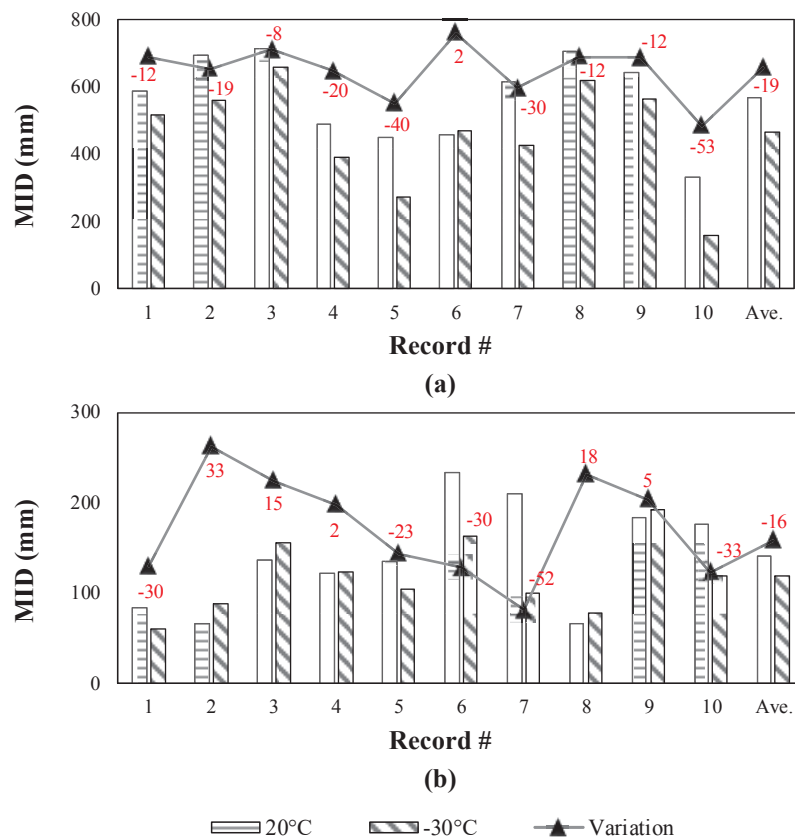


Figure 6: Comparison of MIDs for (a) NF and (b) LMSD ground motions at 20°C and -30°C.

## 5.2 Maximum Base Shear in the Piers

In this section, variation of base shears acting on each column of the bridge is presented in Figure 7 as a function of ambient temperature and seismicity level. For near field ground motions, Figure 7.a shows that the amounts of variation in isolator force are in between -13% to 20% when temperature decreases from 20°C to -30°C. However, it is interesting to observe that when the averages of base shears are of concern, they are identical for both 20°C to -30°C with a magnitude of 1248 kN. Although the initial strength and stiffness of isolator increases due to reduced ambient temperature, the average shear force does not change for both 20°C to -30°C. Figure 7.b is depicted to investigate the variation of isolator force for large-magnitude small-distance ground motion set when temperature is reduced from 20°C to -30°C. Figure 7.b reveals that although the average value of amplification in isolator force is calculated as 23%, for the selected ground motions it may be up to 60%, individually.

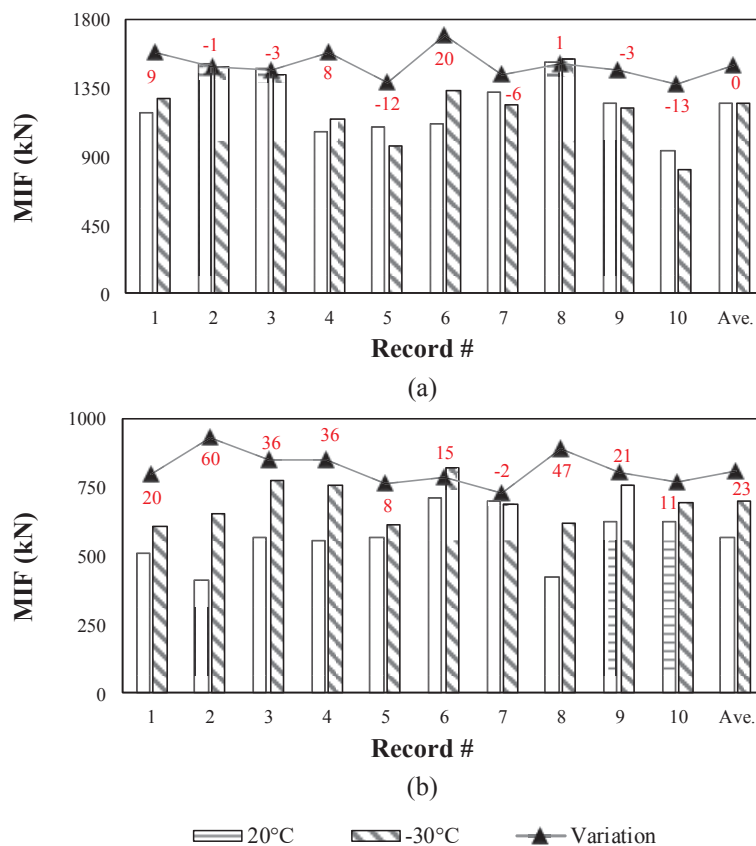


Figure 7: Comparison of MIFs for (a) NF and (b) LMSD ground motions at 20°C and -30°C.

## 6 CONCLUSIONS

In this paper, variation in response parameters of a seismically isolated bridge is studied under the effect of low (-30°C) and air temperature (20°C). The major findings showed that MIDs obtained for LRB properties of 20°C are about 20% larger than the ones obtained for -30°C, in an average sense. Furthermore, average MSF obtained for near-field ground motions at 20°C and -30°C are identical. However, for large-magnitude-small-distance ground motions, MSF of -30°C is almost 25% larger than that of 20°C.

## REFERENCES

- [1] W.H. Robinson, Lead Rubber Hysteretic Bearings Suitable for Protecting Structures During Earthquake, *Earthquake Engineering and Structural Dynamics*, 10(4), 593–604, 1982.
- [2] S. Nagarajaiah, X. Sun, Response of Base Isolated USC Hospital Building in Northridge Earthquake, *Journal of Structural Engineering (ASCE)*, 126(10), 1177–1186, 2000.
- [3] C.W. Roeder, Proposed Design Method for Thermal Bridge Movements, *Journal of Bridge Engineering*, 8(1), 12–19, 2003.
- [4] M.C. Constantinou, A.S. Whittaker, Y. Kalpakidis, D.M. Fenz, G.P. Warn, Performance of Seismic Isolation Hardware Under Service and Seismic Loading, *Technical report, NY: MCEER=07-2012*, Buffalo, 2007.
- [5] G. Benzonì, C. Casarotti, Effects of Vertical Load, Strain Rate and Cycling on The Response of Lead-Rubber Seismic Isolators, *Journal of Earthquake Engineering*, 13(3), 293–312, 2009.
- [6] H. Erdoğan, E. Çavdar, G. Özdemir, Türk Deprem Yönetmelikleri (DBYBHY ve TBDY) Spektrum Tanımlarının Deprem Yalıtım Sistemi Tasarımı Özelinde Karşılaştırılması, *Teknik Dergi*, 32(5), 2021.
- [7] S. Pinarbasi, U. Akyuz, Sismik İzolasyon ve Elastomerik Yastık Deneyleri. *İMO Teknik Dergi*, 237, 3581–3598, 2005.
- [8] C.W. Roeder, J.F. Stanto, A.W. Taylor, *Performance of Elastomeric Bearings* (No. 298). Washington, DC: National Cooperative Highway Research Program, Transportation Research Board, 1987.
- [9] D.F. Ritchie, *Neoprene Bridge Bearing Pads, Gaskets and Seals*. Rubber World, Lippincott & Petto Inc. 200(2), 27–31, 1989.
- [10] R. Eyre, A. Stevenson, Performance of Elastomeric Bridge Bearings at Low Temperatures, *Proceedings 3rd World Congress on Joint Sealing and Bearing Systems for Concrete Structures*, 736–762. Toronto, Canada, 1991.
- [11] A. Yakut, J.A. Yura, Evaluation of Low-Temperature Test Methods for Elastomeric Bridge Bearings, *Journal of Bridge Engineering*, 7(1), 50–56, 2002(a).
- [12] A. Yakut, J.A. Yura, Parameters Influencing Performance of Elastomeric Bearings at Low Temperatures, *Journal of Structural Engineering*, 128(8), 986–994., 2002(b).
- [13] K.N.G. Fuller, J. Gough, A.G. Thomas, The Effect of Low-Temperature Crystallization on The Mechanical Behavior of Rubber, *Journal of Polymer Science: Part B: Polymer Physics*, 42(11), 2181–2190, 2004.
- [14] D. Cardone, G. Gesualdi, D. Nigro, Effects of Air Temperature on The Cyclic Behavior of Elastomeric Seismic Isolators, *Bulletin of Earthquake Engineering*, 9(4), 1227–55, 2011.
- [15] O. Hasegawa, I. Shimoda, M. Ikenaga, Characteristic of Lead Rubber Bearing by Temperature. *Summaries of Technical Papers of Annual Meeting Architectural Institute of Japan*, B-2, Structures II, Structural Dynamics Nuclear Power Plants, Architectural Institute of Japan, pp: 511–512, 1997.

- [16] C.B. Cho, I.J. Kwahk, Y.J. Kim, An Experimental Study for The Shear Property and The Temperature Dependency of Seismic Isolation Bearings, *Journal of the Earthquake Engineering Society of Korea*, 12(1), 67-77, 2008.
- [17] J.Y. Park, K.S. Jang, H.P. Lee, Y.H. Lee, H. Kim, Experimental Study on The Temperature Dependency of Full-Scale Low Hardness Lead Rubber Bearing, *Journal of Computational Structural Engineering*, 25(6), 533-540, 2012.
- [18] M. Billah, B. Todorov, Effects of Subfreezing Temperature on The Seismic Response of Lead Rubber Bearing Isolated Bridge, *Soil Dynamics and Earthquake Engineering*, 126, 1-13, 2019.
- [19] P. Deng, Z. Gan, T. Hayashikawa, T. Matsumoto, Seismic Response of Highway Viaducts Equipped with Lead-Rubber Bearings Under Low Temperature, *Engineering Structures*, 209:110008, 2019.
- [20] ISO (International Organization for Standardization). ISO 22762-1:2005: Elastomeric seismic-protection isolators – Part 1: Test methods, 2005.
- [21] OpenSees, Open System for Earthquake Engineering Simulation; Version: 2.1.0, University of California, Pacific Earthquake Engineering Research Center, Berkeley, California, 2001.
- [22] I.V. Kalpakidis, M.C. Constantinou, Effects of Heating on The Behavior of Lead-Rubber Bearings. I: Theory, *Journal of Structural Engineering*, 135(12), 1440–1449, 2009a.
- [23] Y.J. Park, Y.K. Wen, A.H. Ang, Random Vibration of Hysteretic Systems Under Bi-Directional Ground Motions, *Earthquake Engineering and Structural Dynamics*, 14(4), 543-557, 1986.
- [24] G.P. Warn, A.S. Whittaker, Performance Estimates in Seismically Isolated Bridge Structures, *Engineering Structures*, 26(9), 1261–78, 2004.
- [25] M. Dicleli, Performance of Seismic-Isolated Bridges in Relation to Near-Fault Ground-Motion and Isolator Characteristics, *Earthquake Spectra*, 22(4), 887-907, 2006.



## SEISMIC PROTECTION OF MULTI-STORY STRUCTURES WITH NOVEL VIBRATION ABSORPTION DEVICES COMBINING NEGATIVE STIFFNESS AND INERTER

Konstantinos A. Kapasakalis<sup>1</sup>, Georgios I. Florakis<sup>1</sup>, Ioannis A. Antoniadis<sup>2</sup>,  
and Evangelos J. Sapountzakis<sup>1</sup>

<sup>1</sup> Institute of Structural Analysis and Antiseismic Research, School Civil Engineering  
National Technical University of Athens  
Zografou Campus, GR-157 80 Athens, Greece  
kapasakalis@mail.ntua.gr, giorgosfls@mail.ntua.gr, cvsapoun@central.ntua.gr

<sup>2</sup> Mechanical Design and Control Systems Section, Mechanical Engineering Department  
National Technical University of Athens  
Zografou Campus, GR-157 80 Athens, Greece  
antogian@central.ntua.gr

---

### Abstract

*This paper proposes a Stiff Seismic Base Absorber (SBA). An inerter is first implemented, connecting directly the structure to the ground. This results to the decrease of the natural frequency of the structure, without the decrease of the structural stiffness. Parallel, an extension of the KDamper is used, in order to increase the apparent damping behavior of the inerter. A negative stiffness (NS) element connects the additional mass of the SBA to the structure and a positive stiffness element the additional mass to the base. Also, an artificial damper is placed in parallel with each stiffness element. The design of the SBA is based on an appropriate optimization approach, which includes the following novel features: i) the SBA foresees variation in all stiffness elements, ii) the optimal system parameters are selected based on engineering criteria with proper constraints and limitations to the system dynamic responses, iii) the earthquake input motion is selected according to the seismic design codes, iv) for the NS element, a displacement-dependent non-linear mechanism is proposed realized by a pre-compressed leaf spring instead of conventional coil springs. Compared to other vibration absorbers, the SBA presents a number of advantages. An improved superstructure dynamic behavior is observed combined with small base displacements, in the order of a few centimeters. The drastically reduced base displacements render the implementation of the SBA feasible using conventional structural elements. As a result, the SBA is a possible retrofitting option for seismic protection.*

**Keywords:** Inerter, Negative Stiffness, KDamper, Seismic Protection, Damping.

---

## 1 INTRODUCTION

In recent years, seismic codes have been significantly modified with the intention to lead to robust structures that perform better under seismic loading. To this end, the reduction of structural responses induced by environmental excitations has become a subject of intensive research. Many structural control concepts have been evolved for this purpose, and quite a few of them have been implemented in practice. They include the mitigation of vibrations in structures due to unexpected large environmental hazards, the retrofitting of existing structures, the protection of seismic equipment and important secondary systems and the provision of new principles for structural design against environmental loading. These structural control systems can be broadly classified into active, passive, semi-active and hybrid control systems.

Seismic base isolation is considered perhaps the most efficient design approach of anti-seismic protection because it relies on reducing the seismic demand rather than increasing the structure's rigidity by adding shear walls or braced frames. It has led to earthquake-resistant design of building structures [1, 2], bridges [3] and industrial facilities [4-6]. The seismic isolation system is installed between the foundation and the upper structure providing horizontal isolation and reducing seismic wave propagation into the structure. This way, the fundamental period of the system is significantly longer and thus the structural peak accelerations are reduced. Over the years, a number of isolation devices such as elastomeric bearings, frictional/sliding bearings and roller bearings have been developed [7-10]. However, this type of isolation is inefficient for high rise structures, cannot be applied partially to structures unlike other retrofitting and is not suitable for buildings rested on soft soil. Also, under long-period ground motions large displacements are produced to the base isolated building that can provoke structural pounding leading to a serious risk of damage or even collapse of the building.

Due to these disadvantages, alternative vibration control methods have been developed that combine the conventional base isolation (BI) scheme with other active or passive control systems, including: (i) Tuned Mass Dampers (TMDs), (ii) Inerters, (iii) Negative Stiffness Devices (NSD) and "Quazi Zero Stiffness" (QZS) oscillators and (iv) Mechanisms combining Negative Stiffness and Absorbers/KDampers.

A Tuned Mass Damper (TMD) is a device consisting of a mass, a stiffness element and a damper that is attached to the structure in order to reduce its dynamic response. The natural frequency of the TMD is tuned in resonance with the fundamental mode of the primary structure, so that when that frequency is excited, the damper will resonate out of phase with the structural motion. Thus, a large amount of the structural vibrating energy induced by wind and earthquake loads is transferred to the TMD and then dissipated by damping. TMDs have been installed in a great number of tall buildings [11-13] in order to reduce vibrations caused by seismic or wind loading in main systems. Also, during last years a novel control strategy combining BI and TMD [14-18] has been developed. Although TMDs are effective and reliable, their usage presents a number of drawbacks, including: (i) detuning, caused by environmental influences, which can lead to a significant loss of system's performance [19], (ii) the requirement for large additional mass or large space for their installation, (iii) the restriction of the maximum weight that can be practically placed on the top of the structure and (iv) the large TMD displacements [20], which in some cases exceed even the base displacements.

A more efficient alternative is a new passive BI control strategy combining the TMD with an inerter (TMDI) [21, 22]. In this concept, the additional mass of the TMD is connected to the supporting ground by an inerter device [23]. The inerter is a two terminal element which has the property that force generated at its ends is proportional to the relative acceleration between them. The TMDI takes advantage of the "mass amplification effect" of the inerter to achieve enhanced performance compared to the classical TMD. As a result, the proposed

TMDI configuration can either replace part of the TMD vibrating mass to achieve lightweight passive vibration control solutions, or improve the performance of the classical TMD for a given additional mass. Still, to work effectively, all considered devices have to be precisely calibrated which can be challenging or even impossible in some cases. Moreover, proposed TMDs with inerters suffer from susceptibility to detuning.

A parallel direction to the various TMD approaches is the concept of negative stiffness (NS) vibration isolation devices. These devices, due to their promising potentials into the field of vibration control, they have attracted a significant amount of attention in research areas. They use a passive mechanical system to generate negative stiffness without the need of any external power supply. Negative stiffness is defined as a force that assists motion instead of opposing it. The concept of negative stiffness elements (or “anti-springs”) for vibration isolation was first introduced in the pioneering publications of Molyneaux [24] and later on, in the milestone developments of Platus [25]. The main feature of these approaches is the significant reduction of the isolator’s stiffness, which consequently leads to the decrease of the natural frequency of the system (the system’s natural period is increased) even at almost zero levels, resulting in configurations called “Quasi-Zero Stiffness” (QZS) oscillators [26]. In the field of seismic protection of structures, QZS oscillators have a wide variety of applications [27–30]. The primary disadvantage of these devices is their requirement for a drastic reduction of the structure’s stiffness almost to zero levels, limiting its static load capacity.

In an effort to exploit the advantages of TMDs and QZS oscillators, a novel passive vibration isolation, and damping concept, termed as KDamper, has been first introduced in Antoniadis et al. [31]. This device consists of an additional mass, a damper, a spring and is characterized by the incorporation of a negative stiffness element. The force produced from this NS element during excitations, increase indirectly the inertia effect of the additional mass, abolishing the need of a large additional mass unlike TMD in order to work efficiently. The presence of this mass serves in mitigating the effects of a vibrating load, operating as an energy dissipation mechanism. This oscillator exhibits extraordinary damping properties and is designed to maintain the same overall static stiffness as a traditional reference original oscillator, contrary to the QZS mechanism. Also it overcomes the sensitivity problems of TMDs as the tuning is mainly controlled by the negative stiffness element’s parameters. The KDamper has been examined for the seismic protection of several structural systems, such as bridges [32–36], wind turbines [37, 38] and buildings [39, 40]. In addition, it has effectively implemented as an Absorption Base (KDAB) in the bases of structures [41–46].

In this paper a Stiff Seismic Base Absorber (SBA) is proposed, that combines an extension of the KDamper and an inerter, connected in parallel. The Extension of the KDamper, termed as EKD [47] is an alternative configuration based on the initial design, and aims to further improve its dynamic behavior. The purpose of the EKD is to increase the damping behavior of the inerter and to further reduce the structural relative displacements under seismic loading. In section 2 of this paper, a novel negative stiffness mechanism is proposed for the realization of the NS element, which includes a pre-compressed leaf spring instead of conventional stiffness elements. The properties, parameters and nonlinear equations of motion of the SBA implemented in a multi-story building are presented in section 3. However, the complexity of the SBA renders the conventional min-max approaches ineffective for the determination of the optimal parameters of the device. Therefore, section 4 presents the proposed optimization procedure of the SBA based on engineering criteria with proper geometrical and constructional limitations. In section 5, the effectiveness of the SBA is compared with a conventional and a highly damped base isolated structure, through a numerical example of a building subjected to artificial accelerograms designed to match the EC8 acceleration response spectra. Finally, an indicative design is proposed for the examined configuration.

## 2 REALIZATION OF THE NEGATIVE STIFFNESS MECHANISM

Negative stiffness in applications concerning vibration isolation is mainly achieved by appropriate mechanical designs involving positive stiffness pre-stressed elastic components, such as post-buckled beams, plates, shells and pre-compressed springs arranged in specific geometrical configurations [48-50]. Alternatively to elastic forces, the negative stiffness effect can also be produced by gravitational [51], magnetic [52] or electromagnetic forces [53]. However, elastic forces tend to be the only viable option when dealing with seismic effects mitigation on buildings or bridges, where the required values of negative stiffness are very high.

In this chapter, the proposed configuration for the realization of the negative stiffness is presented. The novelty of this mechanism is that a pre-compressed leaf spring is involved, which can withstand huge vertical loads compared to conventional springs. It is an effective mechanism with simple design and has the ability to easily control the negative stiffness value.

### 2.1 Proposed configuration

The negative stiffness mechanism under consideration is depicted in Figure (1), where any other part of the EKD device is excluded. The system comprises a vertical stiffness element (spring), one end of which is fixed and the other is hinged to a metal rod. The rod has length  $a$  and its upper end is connected with a roller support which allows the horizontal displacement  $u$  during the earthquake.

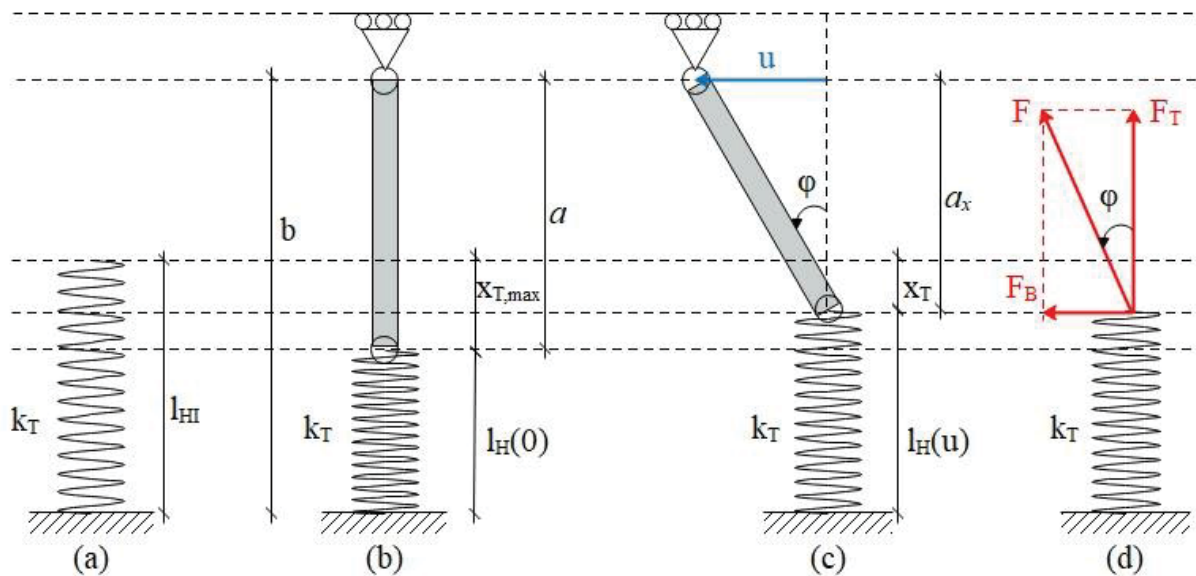


Figure 1: Schematic representation of the negative stiffness mechanism of the Extended KDamper.

The vertical stiffness element has initial length  $l_{HI}$  (Figure (1a)), stiffness  $k_T$  and reaches its maximum compression when it's collinear with the rod (Figure (1b)). This position, termed as undeformed configuration, is also the unstable equilibrium position where the equivalent negative stiffness value  $k_N$  is maximized. When the mechanism deforms in one direction, the rod rotates and creates a force that assists motion (Figure (1d)), generating thereby the negative stiffness mechanism. In this position the value of the equivalent negative stiffness is decreased and reaches its minimum value when  $u=u_{max}$ . The perturbed position is depicted in Figure (1), along with the necessary notation concerning the various displacements and dimensions of the system.

From the length  $a$  of the rod, the total height  $b$  of the mechanism, the initial free length  $l_{HI}$  of the spring and for maximum horizontal displacement  $u=u_{\max}$ , a dimensionless parameter is defined as:

$$c_I = \frac{b-l_{HI}}{a} \quad (1)$$

From the geometry of the mechanism results:

$$a_x = \sqrt{a^2 - u^2} \quad (2)$$

$$\varphi = \arctan(u / a_x) \quad (3)$$

$$l_H(u) = b - a_x \quad (4)$$

where  $l_H(u)$  is the varying length of the vertical stiffness element during the oscillation of the mechanism. The potential energy, the exerted force and the equivalent negative stiffness of the system respectively are given by:

$$U_N(u) = \frac{1}{2} k_T [l_H(u) - l_{HI}]^2 \quad (5)$$

$$f_N(u) = \frac{dU_N}{du} = -k_T \left[ 1 - c_I \frac{1}{\sqrt{1 - (u/a)^2}} \right] u \quad (6)$$

$$k_N(u) = \frac{df_N}{du} = -k_T \left[ 1 - c_I \frac{1}{[1 - (u/a)^2]^{3/2}} \right] \quad (7)$$

The maximized value of the equivalent negative stiffness which occurs at the equilibrium position of the mechanism ( $u=0$ ) and which corresponds to the desired value of  $k_N$  as calculated from the dimensioning of the Extended KDamper is:

$$k_N(u=0) = -k_T (1 - c_I) \quad (8)$$

The term  $(1 - c_I)$  by exploiting Eq. (1) becomes

$$1 - c_I = 1 - \frac{b - l_{HI}}{a} = \frac{l_{HI} - (b - a)}{a} = \frac{x_{T,\max}}{a} \Rightarrow c_I = 1 - \frac{x_{T,\max}}{a} \quad (9)$$

where  $x_{T,\max}$  is the maximum deformation of the vertical stiffness element. Therefore Eq. (8) becomes:

$$k_N(u=0) = -k_T \frac{x_{T,\max}}{a} \quad (10)$$

By dividing Eq. (7) and Eq. (10) and by using Eq. (9), the negative stiffness ratio is defined as:

$$r_k = \frac{k_N(u)}{k_N(u=0)} = \frac{1 - \left( 1 - \frac{x_{T,\max}}{a} \right) \frac{1}{[1 - (u/a)^2]^{3/2}}}{x_{T,\max} / a} \quad (11)$$



This ratio expresses the variation in the value of the negative stiffness during the motion from the position  $u=0$  up to position  $u=u_{\max}$ . Optimally we aim this ratio to be larger than 0.75.

The vertical and horizontal forces applied to the rod due the oscillation of the system are given respectively as:

$$F_T = k_T x_T \quad (12)$$

$$F_B = F_T \tan \varphi \quad (13)$$

where  $x_T$  is the deformation of the spring from its initial free length. The vertical force  $F_T$  becomes maximum when  $x_T = x_{T,\max}$ , while the horizontal force  $F_B$  becomes maximum when  $u = u_{\max}$ .

## 2.2 Vertical stiffness element of the proposed configuration

The vertical stiffness element of the mechanism with stiffness  $k_T$  is realized by a leaf spring which is composed of several parallel metal leaves (sheets) mounted on top of each other in multiple layers and groups. These leaves have rectangular section and they held together by metal clips attached at the center and at either end. Due to sheer amount of metal layered together, the leaf spring can take huge vertical loads due to its tight-knit structure.

Each layer of the leaf spring consists of two metal sheets with length  $L$  and can be approximated by a center loaded beam fixed at both ends as depicted in Figure (2).

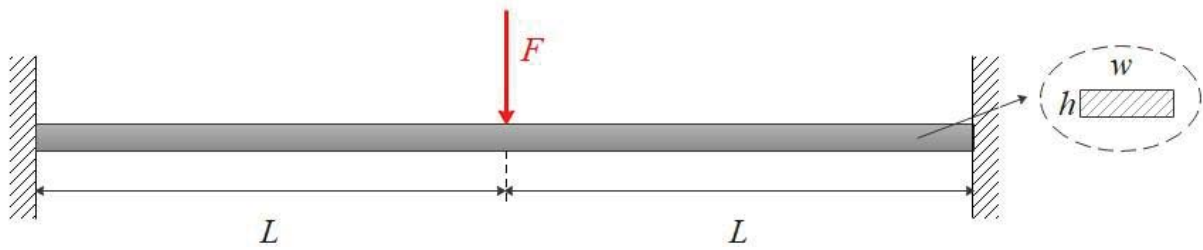


Figure 2: Center loaded fixed-fixed beam.

The bending area moment of inertia, of the beam's cross section  $A = wh$  is defined as:

$$I = \frac{wh^3}{12} \quad (14)$$

The bending stiffness of the beam can be expressed as:

$$k_B = \frac{24EI}{L^3} \quad (15)$$

or by substituting Eq. (14):

$$k_B = 2Ew \left( \frac{h}{L} \right)^3 \quad (16)$$

From Hooke's Law,  $F = k_B \cdot x_B$ , the bending deflection at the center of the beam is calculated as:

$$x_B = \frac{FL^3}{24EI} \quad (17)$$

The maximum stress ( $y = h/2$ ) due to the bending moment  $M = FL/4$  resulting from the application of the center loading ( $x = L$ ) is calculated as:

$$\sigma_{\max} = \frac{3Eh}{L^2} x_B \quad (18)$$

which must be lower than the yield stress  $\sigma_y$  of the leaf spring material.

The overall stiffness of the leaf spring consisting of such leafs/beams connected in various configurations is defined as:

$$k_T = \frac{N_B}{2N_G} k_B \quad (19)$$

where  $N_B$  is the number of parallel leaves/beams and  $N_G$  is the number of groups connected in series as depicted in Figure (3). Simultaneously, the resulting range of motion comes as:

$$x_T = 2N_G x_B \quad (20)$$

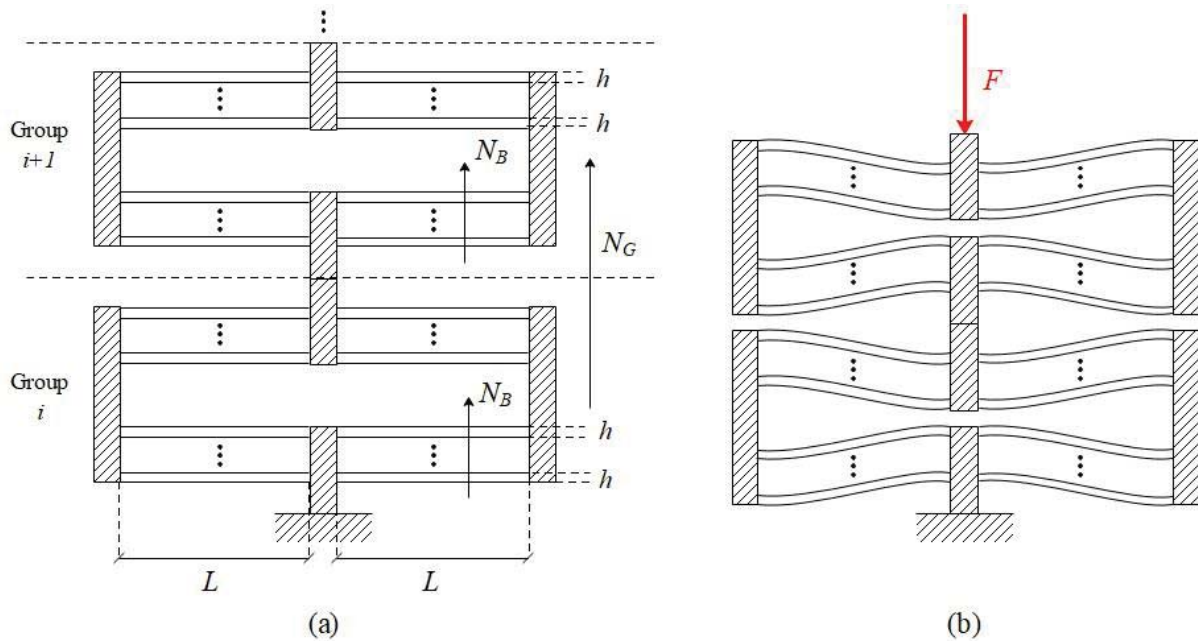


Figure 3: Schematic representation of a leaf spring configuration (a) undeformed and (b) deformed.

### 2.3 Implementation example

A theoretical implementation example of this NS mechanism is presented in this subsection. The general purpose of the proposed SBA is the seismic protection of multi-story building structures. Therefore, a reference mass of 50 tn (structural mass) is assumed for the design of the SBA mechanism. This way, multiple SBA device can be implemented with respect to the total superstructure mass, as SBAs can operate in parallel. The reference values of the NS the dynamic responses relative to the operation of the SBA used in this example, are obtained from [47]. Figure (4a) presents the equivalent NS ratio ( $k_N/k_N(u=0)$ ) over the dimensionless relative displacement between the two terminals of the NS configuration ( $u/u_{\max}$ ), obtained by the proposed mechanism presented previously. It is observed that this mechanism is sufficient in keeping the NS in acceptable levels ( $>0.75$ ) for all the operating range. Figure (4b) presents the ratio of the vertical deformation of the leaf spring, as a function of  $u/u_{\max}$ . It is observed that substantial vertical load can be supported due to the properties of the leaf spring.

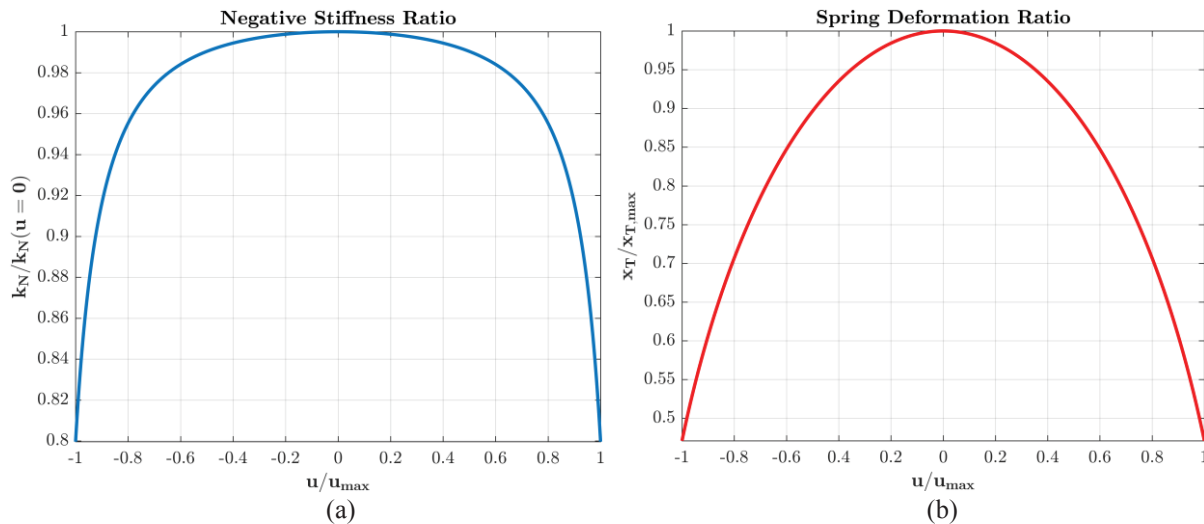


Figure 4: Numerical analysis of the NS element: (a) equivalent NS, (b) vertical deformation of the leaf spring.

### 3 SEISMIC BASE ABSORBER CONFIGURATION

In this section the proposed Seismic Base Absorber (SBA) configuration is presented. The SBA is a seismic isolation device implemented in the base of the structure, composed of an Extended KDamper (EKD) and an inerter connected in parallel. The EKD is an extension of the already developed KDamper [32–46], which in previous studies has indicated a significant improvement in the dynamic behavior of a structure both in terms of absolute accelerations and relative displacements compared to other base isolation scenarios (rubber bearings, QZS oscillators, TMDs, etc.). The proposed extension exhibits even a better performance, while it foresees variation in all stiffness elements, while in the KDamper concept only the negative stiffness variation is taken into consideration. Furthermore, the negative stiffness element stroke, which is critical for the design of the whole configuration is dramatically reduced. Concerning the proposed SBA design, the EKD is used in order to increase the damping behavior of the inerter.

The basic idea behind the proposed SBA configuration is the decreasing of the nominal frequency of the system achieved with inerter and subsequently the control of the structural relative displacements with the extraordinary damping properties that EKD offers. Also, the small base displacements and NS element stroke, render the implementation of the proposed control system feasible, using conventional structural elements, making it the more efficient retrofitting option for horizontal seismic protection.

#### 3.1 Parameters of the SBA

The implementation of the SBA in the base of a multi-story building structure for horizontal seismic protection is depicted in Figure (5a). In the next sections, the performance of the SBA in seismic isolation will be compared with the performance of Lead Rubber Bearings (LRB) implemented in the base of the structure (Figure (5b)), which is the most commonly used seismic isolation system. As depicted in Figure (5a), the SBA consists of a negative stiffness (NS) element  $k_{NS}$ , a positive stiffness (PS) element  $k_{PS}$  and two artificial dampers with damping coefficients  $c_{NS}$ ,  $c_{PS}$  placed in parallel to  $k_{NS}$  and  $k_{PS}$  respectively. Compared to the KDamper, the NS element connects the additional mass  $m_D$  to the structure, instead of the PS element, which now connects the  $m_D$  to the ground. The inerter with constant  $b_I$  (measured in kilograms), is parallel to the EKD. Finally, the positive stiffness  $k_R$  works independent from the other parts of the device and there are numerous alternatives for its realization.

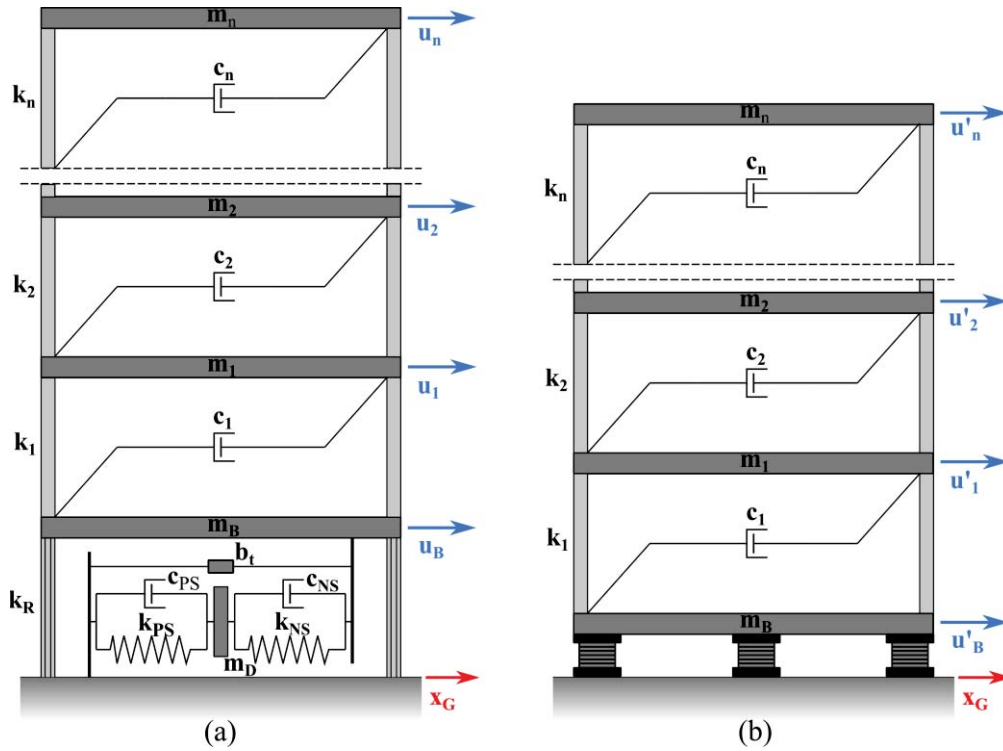


Figure 5: Multi-story building structure with (a) the proposed SBA configuration and (b) the conventional LRB, implemented in its base.

The basic requirement of the proposed configuration of the SBA is that the overall stiffness of the system is maintained:

$$k_R + \frac{k_{PS}k_{NS}}{k_{PS} + k_{NS}} = k_0 = (2\pi f_0)^2 m_{total} \quad (21)$$

where  $k_0$  is the equivalent static stiffness of the SBA,  $f_0$  the nominal frequency of the SBA and  $m_{total}$  the overall mass of the structure including the base and the additional mass. This requirement overcomes the fundamental disadvantage of QZS oscillators, in which the overall stiffness of the system is reduced, limiting its static load capacity. Theoretically the values of  $k_{NS}$ ,  $k_{PS}$  and  $k_R$ , are selected according to Eq. (21) in order to ensure the static stability of the system. Nevertheless, these values may present significant variations in practice due to a number of reasons (temperature fluctuations, manufacturing tolerances or non-linear behavior) which must be taken into account. As a consequence, a simultaneous increase of the absolute value of  $k_{NS}$  by a factor of  $\varepsilon_{NS}$  and a decrease of the values of  $k_{PS}$  or  $k_R$  by a factor of  $\varepsilon_{PS}$  and  $\varepsilon_R$ , respectively, may result in an unstable system. This occurs when:

$$R \times k_R + \frac{P \times k_{PS} \times N \times k_{NS}}{P \times k_{PS} + N \times k_{NS}} = 0 \quad (22)$$

where  $R=1-\varepsilon_R$ ,  $P=1-\varepsilon_{PS}$  and  $N=1+\varepsilon_{NS}$ . Assuming the negative stiffness ratio as  $kn=k_{NS}/k_0$ , or the absolute value of  $k_{NS}$  known, the rest of the stiffness elements result from Eq. (21), (22) as:

$$\begin{aligned} kr &= \frac{-b - \sqrt{b^2 - 4 \times a \times c}}{2a} \Rightarrow k_R = kr \times k_0 \\ kp &= \frac{kn - kr \times kn}{kr + kn - 1} \Rightarrow k_{PS} = kp \times k_0 \end{aligned} \quad (23)$$

where the parameters  $a$ ,  $b$  and  $c$  are defined as:

$$\begin{aligned} a &= R(P - N) \\ b &= kn \times N(P - R) + R(N - P) \\ c &= -P \times N \times kn \end{aligned} \quad (24)$$

Finally, assuming that the additional mass,  $m_D$ , and the variations  $\varepsilon_{NS}$ ,  $\varepsilon_{PS}$  and  $\varepsilon_R$  of the stiffness elements are known, the unknown parameters of the system are: i) the nominal KDamper frequency  $f_0$ , ii) the negative stiffness ratio  $kn$  or the value of the negative stiffness element  $k_N$  iii) the damping coefficients  $c_{NS}$  and  $c_{PS}$  and iv) the coefficient  $b_t$  of the inerter.

### 3.2 Equations of motion of the system

The structure illustrated in Figure (5) is based on the following assumptions: (i) the total building's mass is concentrated at floor level, (ii) the slabs and girders on the floors are rigid compared to the columns, (iii) the columns are weightless and their axial deformation is neglected providing only lateral stiffness, (iv) the SSI effects are not accounted. Consequently, the superstructure has  $n$  dynamic DOFs, represented by the relative base displacements ( $u_i$ ) of the  $n$ -stories. The structure has 2 more DOFs due to the relative to the ground displacement of the base ( $u_B$ ) and the additional mass ( $u_D$ ). The vector of displacements is defined as:

$$[u(t)]_{(n+2) \times 1}^T = \left[ [u_s(t)]_n^T \quad u_B(t) \quad u_D(t) \right]_{(n+2) \times 1}^T \quad (25)$$

where  $[u_s(t)]_n^T = [u_1 \quad u_2 \quad \dots \quad u_n]_{n \times 1}^T$ . The equations of motion of the system depicted in Figure 5a for ground displacement  $x_G$  are expressed in a matrix form as:

$$[M][\ddot{u}] + [C][\dot{u}] + [K][u] = -[\tau]\ddot{x}_G \quad (26)$$

where:

$$\begin{aligned} [M]_{(n+2) \times (n+2)} &= \begin{bmatrix} [M_S]_{n \times n} & [0]_{n \times 1} & [0]_{n \times 1} \\ [0]_{1 \times n} & m_B + b_t & 0 \\ [0]_{1 \times n} & 0 & m_D \end{bmatrix}_{(n+2) \times (n+2)} \\ [K]_{(n+2) \times (n+2)} &= \begin{bmatrix} [K_S]_{n \times n} & [0]_{n \times 1} & [0]_{n \times 1} \\ [0]_{1 \times n} & k_{NS} + k_R & -k_{NS} \\ [0]_{1 \times n} & -k_{NS} & k_{NS} + k_{PS} \end{bmatrix}_{(n+2) \times (n+2)} \\ [C]_{(n+2) \times (n+2)} &= \begin{bmatrix} [C_S]_{n \times n} & [0]_{n \times 1} & [0]_{n \times 1} \\ [0]_{1 \times n} & c_{PS} & -c_{PS} \\ [0]_{1 \times n} & -c_{PS} & c_{PS} + c_{NS} \end{bmatrix}_{(n+2) \times (n+2)} \\ [\tau]_{(n+2) \times 1} &= \begin{bmatrix} [M][1]_{n \times 1} \\ m_B \\ m_D \end{bmatrix}_{(n+2) \times 1} \end{aligned} \quad (27)$$

The terms  $[M_S]$ ,  $[C_S]$  and  $[K_S]$  are the  $n$ -dimensional matrices of mass, damping and stiffness of the superstructure, respectively.



## 4 OPTIMIZATION OF THE PROPOSED SBA

Having established the nonlinear equations of motion Eq. (26), the next objective is to determine the optimal SBA parameters in order to attain the best possible vibration control strategy. Conventional min-max approaches ( $H_\infty$ ) [54] are rendered ineffective, due to the complexity of the SBA configuration, and the limitations imposed by the examined structural system and NS configuration (e.g., the one proposed in section 2). In this paper, the SBA is designed based on an engineering-criteria driven optimization procedure. This way, the geometrical and constructional limitations (e.g., large NS element stroke) imposed by the respective structural system are taken into account and the values of its individual components are retained in reasonable ranges. The optimal parameters of the SBA are evaluated using Harmony Search (HS), a novel metaheuristic algorithm [55], and the excitation input is selected according to the provisions of the EC8.

### 4.1 Artificial earthquake motion

In this section, a presentation of the details regarding the generation of artificial accelerograms based on the design response spectra is undertaken. For the purposes of this study, the approach followed is based on generating a sample of artificial accelerograms with acceleration response spectra in accordance with the EC8 design response spectra. Artificial, spectrum-compatible accelerograms are generated using the SeismoArtif Software [56]. In this paper, the artificial accelerograms are designed to match the EC8 response spectra with the following seismic properties: ground type C, spectral acceleration 0.36 g, spectrum type I and importance class II. A sample of 30 artificial accelerograms, with a mean PGA of 5.19  $m/sec^2$  is generated and plotted in Figure (6), and is compared to the EC8 response spectrum. An accurate match is observed (percentage deviation less than 10%) in the range of periods from 0.2 to 2 sec, which are considered relevant for the structural performance.

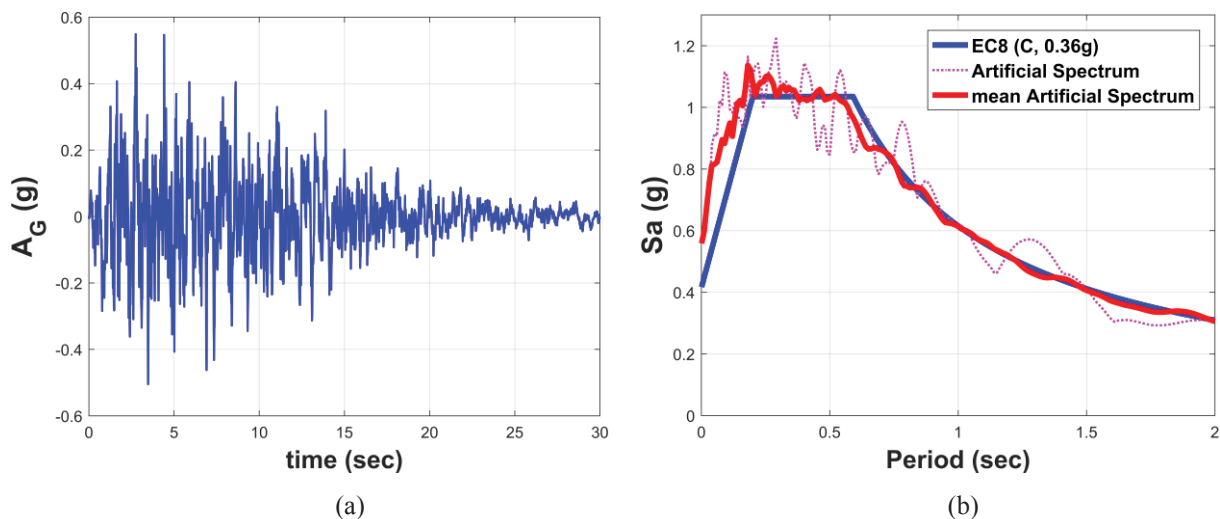


Figure 6: Generation of artificial spectrum compatible accelerograms. (a) Excitation sample, (b) mean acceleration response spectrum of 30 artificial samples compared to the EC8. Table 1

### 4.2 Optimization constraints and limitations based on engineering criteria

As stated in section 3.1, the independent design variables of the SBA are: i) the nominal SBA frequency  $f_0$ , the value of the NS element  $k_{NS}$ , the artificial dampers  $c_{NS}$ ,  $c_{PS}$ , and the interter coefficient  $b_t$ , assuming that the additional oscillating mass  $m_D$  and the variations of the stiffness elements  $\varepsilon_{NS}$ ,  $\varepsilon_{PS}$  and  $\varepsilon_R$  are known. The optimization problem is formed for the mean

of the maximum dynamic responses for the 30 artificial records of the database. The objective function and the constraints are selected from the geometrically non-linear time domain responses, as described below:

- i. Assign values to the known parameters (initial guess).
  - a) According to previous work of KDamper [46], an additional mass of 5% is efficient. In this paper, in an effort to drastically reduce the additional mass,  $m_D$  is selected as 0.1%.
  - b) The stability factors of the positive stiffness elements  $k_{PS}$ ,  $k_R$  are conservatively selected as 10%. The variation of the NS element  $k_{NS}$ , is selected according to the proposed configuration presented in section 2.1. 25% is a realistic value.

- ii. Set the objective function (OF) as the minimization of the mean of the maximum relative to the ground base displacements of the structure.

$$\min : \text{mean}[\max[abs(u_B)]] \quad (\text{OF}) \quad (28)$$

- iii. Set an acceleration filter (AF) as a constraint for the structure floors' absolute acceleration, expressed as a percentage of the mean PGA.

$$\text{mean}[\max[abs(a_i)]] \leq AF \times \text{mean}(PGA) \quad (i = 1, \dots, n) \quad (\text{Constraint 1}) \quad (29)$$

- iv. The NS element value and stroke are set as constraints, indicated from the proposed design of the NS configuration presented in section 2.3:

$$|k_{NS}| \leq 30 \text{ kN} / \text{m} / \text{tn} \quad (\text{Constraint 2}) \quad (30)$$

$$\text{mean}[\max[abs(u_B - u_D)]] \leq 0.07 \text{ m} \quad (\text{Constrain 3}) \quad (31)$$

- v. Set an upper limit for the damping coefficients  $c_{NS}$ ,  $c_{PS}$  with respect to the superstructure mass. This constraint is based on previous works [47] as well as on manufacturing restrictions:

$$c_{NS} \leq 1000 \text{ kNs} / \text{m} \quad (\text{Constraint 4}) \quad (32)$$

$$c_{PS} \leq 1000 \text{ kNs} / \text{m} \quad (\text{Constraint 5})$$

- vi. The nominal frequency  $f_0$  of the SBA varies in the range  $[0.1 \text{ } 5] \text{ Hz}$ , (Constraint 6).

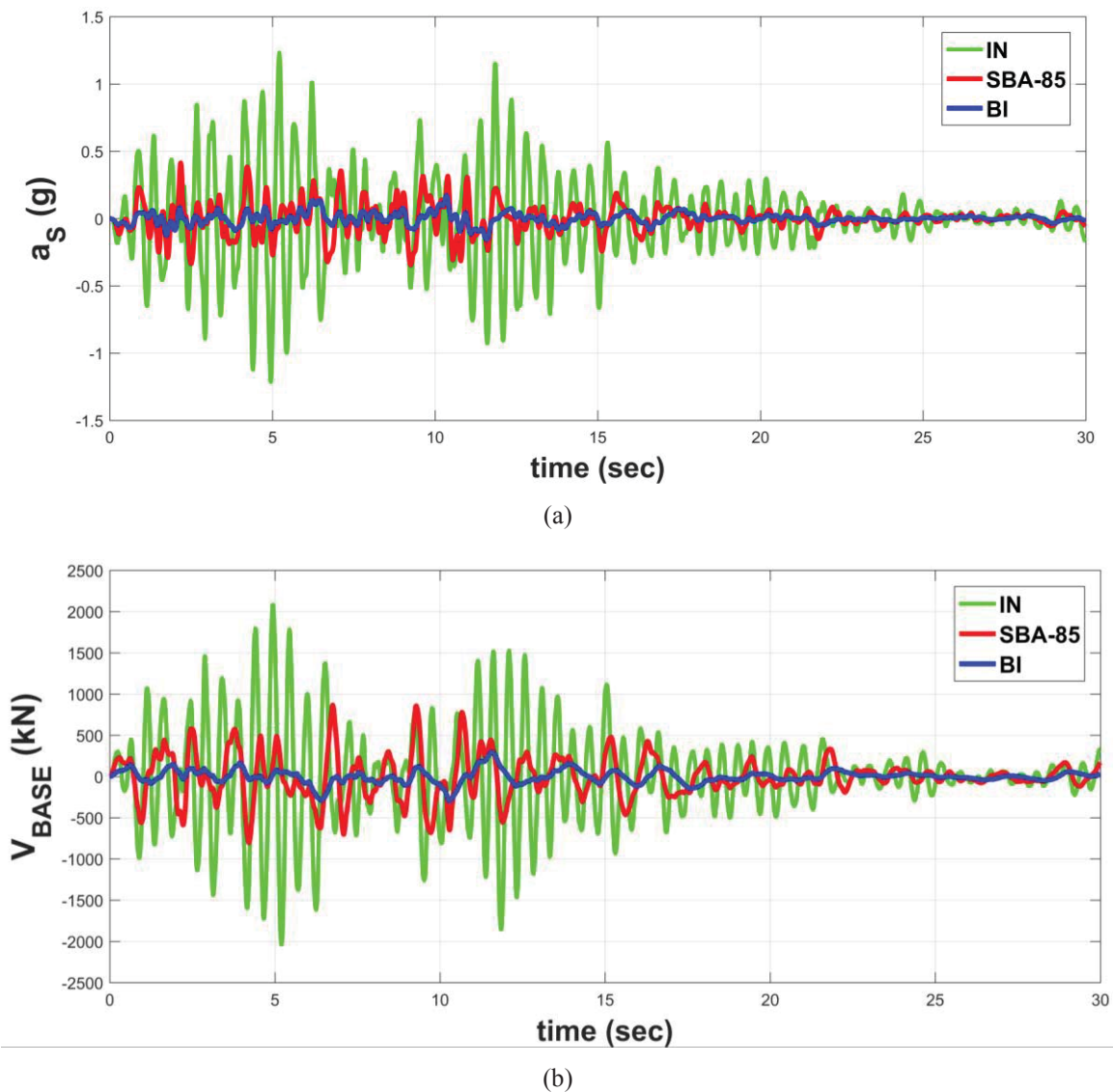
## 5 NUMERICAL APPLICATION

A numerical case study has been conducted considering a 3-story typical residential building. The elastic modulus of reinforced concrete (assuming long-term cracked conditions) is equal to  $E=26 \text{ GPa}$ . The mass of the building is considered to be concentrated at the floor levels, with  $m_i=80 \text{ tn}$  denoting the mass of each one of the 3 stories, while the columns are assumed to be weightless. Rayleigh damping is assumed (mass and stiffness proportional) with  $\zeta_{Si}=0.02$ . A  $15 \times 15 \text{ m}$  floor plan-view has been considered with  $0.3 \times 0.3 \text{ m}$  square columns. According to performed modal analysis, the natural periods of the original structure are:  $T_{Si} [\text{sec}] = [0.495, 0.177, 0.122]$ . The mass of the base is equal to  $60 \text{ tn}$  and thus the superstructure total mass is equal to  $300 \text{ tn}$ . The optimal SBA parameters obtained from the optimization procedure described in section 4.2 with acceleration filter (AF) equal to 85%, and realized with the proposed nonlinear configuration presented in section 2, are presented in Table (1).

Fix parameters		Independent design variables					Resulting stiffnesses	
$m_D$ (% $m_{tot}$ )	$\varepsilon_{NS}, \varepsilon_{PS}, \varepsilon_R$ (%)	$k_{NS}$ (kN/m)	$c_{NS}$ (kNs/m)	$c_{PS}$ (kNs/m)	$b_t$ (% $m_{tot}$ )	$f_0$ (Hz)	$k_{PS}$ (kN/m)	$k_R$ (kN/m)
5	25, 10, 10	-9000	789	667	0.135	0.808	22243	23237

Table 1: SBA set of optimized parameters for AF=70%.

In order to observe the efficiency of the proposed system, SBA, the results of the controlled structure are compared to other seismically protected structures. In particular: 1) a conventional base isolated structure with  $\zeta_B=5\%$  and  $f_B=0.4$  Hz (BI), and 2) a highly damped base isolated structure with an increased damping ratio of 20% (BI-HD). Table 2 presents the main dynamic responses of all the considered structural systems (initial, BI, BI-HD, SBA) for all the artificial accelerograms of the database (mean of max). It is observed that the SBA-85 manages to greatly improve the superstructure dynamic behavior, retaining the base displacement drastically low (few centimeters). Comparative results: a) of the top floor absolute acceleration, b) the total base shear and c) the base relative displacement between the initial, the BI and the SBA-85, are presented in Figure 7 for an artificial sample.



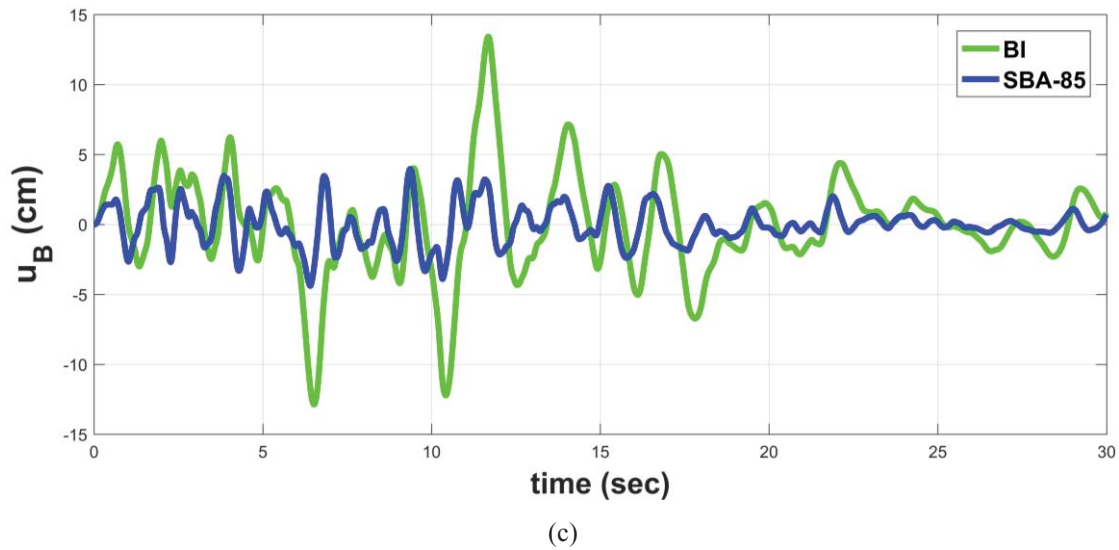


Figure 7: Comparative results, in terms of (a) superstructure absolute acceleration (top floor), (b) total base shear, and (c) base relative displacement between the initial, a conventional base isolated structure and the SBA-85 system implemented in the base of the structure.

		Initial	BI (5%)	BI-HD (20%)	SBA (AF=85)
1 <sup>st</sup> floor drift (cm)	mean(max)	3.42	0.36	0.32	1.15
	reduction (%)	-	<b>89.5</b>	<b>90.6</b>	<b>66.4</b>
3 <sup>rd</sup> floor abs. acc. (m/sec <sup>2</sup> )	mean(max)	12.45	1.312	1.566	4.539
	reduction (%)	-	<b>89.5</b>	<b>87.4</b>	<b>63.5</b>
Vbase (kN)	mean(max)	2220.4	281.86	258.3	953.64
	reduction (%)	-	<b>87.3</b>	<b>88.4</b>	<b>57.1</b>
Base displace- ment (cm)	mean(max)	-	14.67	11.6	4.97
	reduction (%)	-	-	<b>20.9</b>	<b>66.1</b>
NS stroke (cm)	mean(max)	-	-	-	6.77
u <sub>D</sub> (cm)	mean(max)	-	-	-	3.05

Table 2: Main dynamic responses of the initial, BI, BI-HD and SBA systems, for all the artificial samples in the database (mean of maximum values).

### 5.1 Indicative design of the implemented SBA device

For the seismic isolation of the considered 3-story building with total mass of 300 tn, 6 SBAs are used in total, each supporting a mass of 50 tn. The devices are placed uniformly under the base of the superstructure connecting it with the foundation. In order to design the components of the SBA, the maximum dynamic responses as emerged from this section are required. Specifically, the NS element  $k_{NS}$  is designed according to the maximum NS element stroke which is  $\max|u_{NS}|=7\text{cm}$ , the PS element  $k_{PS}$  according to the maximum relative displacement of the additional mass which is  $\max|u_D|=3.38\text{cm}$  and the  $k_R$  according to the maximum relative displacement of the base, which is  $\max|u_B|=4.95\text{cm}$ .

The negative stiffness for each one of the 6 SBAs in the equilibrium position is  $k_{NSi}=-9000/6=-1500\text{kN/m}$ . Considering the values of  $k_{NSi}$ ,  $\max|u_{NS}|$ , the requirement of NS ratio to

be  $r > 0.75$  and by following the procedure described in section 2, the vertical stiffness element  $k_T$  of the NS mechanism (Figure 1) is selected to be realized with a leaf spring. The leaves of the spring along with its clips are made of steel with elastic modulus  $E=210\text{GPa}$ , shear modulus  $G=80\text{GPa}$  and yielding strength  $\sigma_y=250\text{MPa}$ . In Table 3 are summarized the parameters of the leaf spring, where  $h$ ,  $w$  and  $L$  are the dimensions of each metal leaf,  $x_T$  is the maximum deformation and  $H_S$  is the total height of the spring including the gaps between each leaf and between each group. In Figure 8 is depicted the realistic representation of the proposed spring along with its dimensions. Also, from the analysis of the NS mechanism is derived the value of the dimensionless parameter is  $c_f=0.025$  and the length of the rod is  $a=80\text{mm}$ .

Metal Leaf			Total Configuration				
$h$ (mm)	$w$ (mm)	$L$ (mm)	$N_B$	$N_G$	$k_T$ (kN/m)	$x_T$ (mm)	$H_S$ (mm)
11	760	556	5	4	1544.89	78	808

Table 3: Parameters of Leaf Spring

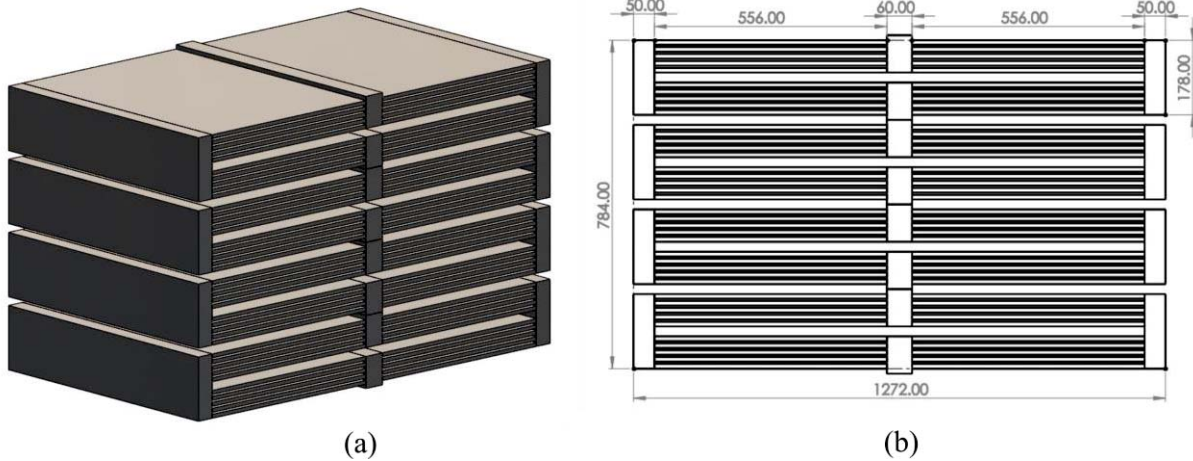


Figure 8: Representation of the proposed Leaf Spring (a) 3D design, (b) design drawing

For the realization of the positive stiffness elements, 4 heavy duty compression springs are implemented in each device. These types of springs are used to undergo some considerable amounts of load and are usually manufactured with large wire diameters along with the rest of its dimensions. For  $k_{PSi}=22243/(6 \times 4)=926.8\text{kN/m}$  and for maximum deformation  $\max|u_D|$  the dimensions of the each spring are summarized in Table 4. The springs are made of Hard Drawn ASTM A227 steel and have closed and squared type of ends.

Wire Diameter (mm)	Outer Diameter (mm)	Free Length (mm)	Number of active coils	Number of total coils	Solid Length (mm)	Spring Index	Pitch (mm)
30	150	300	5	7	240	4	42

Table 4: Physical dimensions of the compression spring  $k_{PSi}$ 

The artificial dampers are realized with four parallel dampers implemented per device. The damping values are low,  $c_{NS}=789/(6 \times 4)=32.875\text{ kNs/m}$  and  $c_{PS}=667/(6 \times 4)=27.8\text{ kNs/m}$ , therefore linear damping devices are used, LD1110 from ITT Infrastructure catalog. The realization of  $k_R=23237\text{ kN/m}$  is possible with 8 simple elastomeric bearings such as SI-N 500/54 ( $k_H=2910 \times 8=23280\text{ kN/m}$ ) from the FIP Industriale elastomeric isolators catalog.



## 6 CONCLUSIONS

In this paper, a stiff seismic base absorber (SBA) is proposed, that combines an extension of the KDamper concept with an inerter device, and is implemented in the base of a multi-story building for seismic protection. A novel mechanism is proposed for the realization of the NS element with leaf springs. The design of the SBA is realistic and its optimal parameters are selected based on engineering criteria. Proper constraints and limitations are posed on the independent design variables and the system nonlinear dynamic responses. The input ground motions are artificial ground motions generated to be compatible with the EC8 response spectra. In order to verify the effectiveness of the SBA, a comparison is made with a conventional and a highly damped base isolated structure. Based on the dynamic analysis and the results obtained, the following concluding remarks can be made:

1. The leaf spring is a simple, cost-efficient and robust solution to carry not only heavy vertical structural loads but also transversal forces derived by ground motions.
2. The proposed negative stiffness mechanism is capable of supporting an oscillating mass of 50tn retaining the negative stiffness ratio to acceptable levels ( $>0.75$ ).
3. The SBA is realistically designed. A small additional mass of 5% is employed, a variation in all stiffness elements is foreseen (10-25%), and the optimal system parameters are obtained by a constrained optimization procedure.
4. The superstructure dynamic behavior of the examined multi-story building controlled with SBA is greatly improved. More specifically, the floor accelerations and the inter-story drifts are significantly reduced (60-70%), and at the same time, the base displacement is dramatically low, as compared to other base isolation approaches (reductions 65-70%).
5. The design of the SBA devices is realistic and within reasonable technological capabilities.

## 7 ACKNOWLEDGMENTS

This research has been co-financed by the European Union and Greek national funds through the Operational Program Competitiveness, Entrepreneurship and Innovation, under the call RESEARCH – CREATE – INNOVATE (project code: T1EDK-02827).



Co-financed by Greece and the European Union

## REFERENCES

- [1] G.P. Warn, K.L. Ryan, A Review of Seismic Isolation for Buildings: Historical Development and Research Needs. *Buildings*, **2**(3), 300–325, 2012.
- [2] A. Reggio, M. De Angelis, Optimal energy-based seismic design of non-conventional Tuned Mass Damper (TMD) implemented via inter-story isolation. *Earth Engineering Structural Dynamics*, **44**, 1623–1642, 2015.
- [3] M.C. Kunde, R.S. Jangid, Seismic behavior of isolated bridges: A-state-of-the-art review. *Electronic Journal of Structural Engineering*, **3**, 2003.

- [4] M. De Angelis, R. Giannini, F. Paolacci, Experimental investigation on the seismic response of a steel liquid storage tank equipped with floating roof by shaking table tests. *Earthquake Engineering & Structural Dynamics*, **39**, 377-396, 2009.
- [5] F. Paolacci, R. Giannini, M. De Angelis, Seismic response mitigation of chemical plant components by passive control techniques. *Journal of Loss Prevention in the Process Industries*, **26**, 924-935, 2013.
- [6] A. Whittaker, M. Kumar, M. Kumar, Seismic isolation of nuclear power plants. *Nuclear Engineering and Technology*, **45**, 569-580, 2014.
- [7] M. Farag, S.s.F. Mehanny, M.M. Bakhoun, Establishing optimal gap size for precast beam bridges with a buffer-gap-elastomeric bearings system. *Earthquake and Structures*, **9**, 195-219, 2015.
- [8] G. Wu, K. Wang, P. Zhang, G. Lu, Effect of mechanical degradation of laminated elastomeric bearings and shear keys upon seismic behaviors of small-to-medium-span highway bridges in transverse direction. *Earthquake Engineering and Engineering Vibration*, **17**, 205-220, 2018.
- [9] T. Peng, X. Yu, Z. Wang, L. Han, Study of the seismic performance of expansion double spherical seismic isolation bearings for continuous girder bridges. *Earthquake Engineering and Engineering Vibration*, **11**, 163-172, 2012.
- [10] C. Wang, J. Zhao, L. Zhu, Y. Bao, Effects of vertical excitation on the seismic performance of a seismically isolated bridge with sliding friction bearings. *Earthquake Engineering and Engineering Vibration*, **15**, 187-196, 2016.
- [11] L. Qin, W. Yan, Y. Li, Design of frictional pendulum TMD and its wind control effectiveness. *Earthquake Engineering and Engineering Vibration*, **29**, 153-157, 2009.
- [12] R.J. McNamara, Tuned Mass Dampers for Buildings. *Journal of the Structural Division*, **103**, 1785-1798, 1977.
- [13] R.W. Luft, Optimal Tuned Mass Dampers for Buildings. *Journal of Structural Division*, **105**, 2766-2772, 1979.
- [14] H.C. Tsai, The effect of tuned-mass dampers on the seismic response of base-isolated structures. *International Journal of Solids and Structures*, **32**, 1195-1210, 1995.
- [15] B. Palazzo, L. Petti, M. de Ligo. Response of base isolated systems equipped with tuned mass dampers to random excitations. *Journal of Structural Control*, **4**, 9-22, 2006.
- [16] T. Taniguchi, A. Der Kiureghian, M. Melkumyan, Effect of tuned mass damper on displacement demand of base-isolated structures. *Engineering Structures*, **30**, 3478-3488, 2008.
- [17] P. Xiang, A. Nishitani, Optimum design for more effective tuned mass damper system and its application to base-isolated buildings. *Structural Control and Health Monitoring*, **21**, 98-114, 2013.
- [18] T. Hashimoto, K. Fujita, M. Tsuji, I. Takewaki, Innovative base-isolated building with large mass-ratio TMD at basement for greater earthquake resilience. *Future Cities and Environment*, **1**, 2015.
- [19] B. Weber, G. Feltrin, Assessment of long-term behavior of tuned mass dampers by system identification. *Engineering Structures*, **32**, 3670-3682, 2010.

- [20] J.-F. Wang, C.-C. Lin, C.-H. Lian, Two-stage optimum design of tuned mass dampers with consideration of stroke. *Structural Control and Health Monitoring*, **16**, 55-72, 2009.
- [21] D. De Domenico, G. Ricciardi, An enhanced base isolation system equipped with optimal tuned mass damper inerter (TMDI). *Earthquake Engineering & Structural Dynamics*, **47**, 1169-1192, 2017.
- [22] I.F. Lazar, S.A. Neild, D.J. Wagg, Using an inerter-based device for structural vibration suppression. *Earthquake Engineering & Structural Dynamics*, **43**, 1129-1147, 2013.
- [23] M.C. Smith, Synthesis of Mechanical Networks: *The Inerter*. *IEEE Transactions on Automatic Control*, **47**, 1648-1662, 2002.
- [24] W.G. Molyneaux, Supports for Vibration Isolation. *Aeronautical Research Council Current Papers*, 1957.
- [25] D.L. Platus, Negative-stiffness-mechanism vibration isolation systems. C.G. Gordon. eds. *Vibration Control in Microelectronics, Optics, and Metrology*, San Jose, California, United States, November 1-30, 1991.
- [26] A. Carrella, M.J. Brennan, T.P. Waters, Static analysis of a passive vibration isolator with quasi-zero-stiffness characteristic. *Journal of Sound and Vibration*, **301**, 678-689, 2007.
- [27] D.T.R. Pasala, A.A.S. Sarlis, S. Nagarajaiah, A.M. Reinhorn, M.C. Constantinou, D. Taylor, Adaptive Negative Stiffness: A New Structural Modification Approach for Seismic Protection. *Advanced Materials Research*, **639-640**, 54-66, 2013.
- [28] R. DeSalvo, Passive, Nonlinear, Mechanical Structures for Seismic Attenuation. *Journal of Computation and Nonlinear Dynamics*, **2(4)**, 290-298, 2007.
- [29] H. Iemura, M.H. Pradono, Advances in the development of pseudo-negative-stiffness dampers for seismic response control. *Structural Control and Health Monitoring*, **16**, 784-799, 2009.
- [30] A.A. Sarlis, D.T.R. Pasala, M.C. Constantinou, A.M. Reinhorn, S. Nagarajaiah, D. P. Taylor, Negative Stiffness Device for Seismic Protection of Structures. *Journal of Structural Engineering*, **139**, 1124-1133, 2013.
- [31] I.A. Antoniadis, S.A. Kanarachos, K. Gryllias, I.E. Sapountzakis, KDamping: A stiffness based vibration absorption concept. *Journal of Vibration and Control*, **24**, 588-606, 2016.
- [32] I.A. Antoniadis, K.A. Kapasakalis, E.J. Sapountzakis, Isolation or Damping? A Soil-dependent approach based on the KDamper concept. G. Gazetas, I. Anastasopoulos eds. *2<sup>nd</sup> International Conference on Natural Hazards & Infrastructures (ICONHIC 2019)*, Chania, Crete, Greece, June 23-26, 2019.
- [33] E.J. Sapountzakis, K.A. Kapasakalis, I.A. Antoniadis, Negative Stiffness Elements in Seismic Isolation of Bridges. G. Gazetas, I. Anastasopoulos eds. *2<sup>nd</sup> International Conference on Natural Hazards & Infrastructures (ICONHIC 2019)*, Chania, Crete, Greece, June 23-26, 2019.
- [34] K.A. Kapasakalis, C.H.T. Alamir, I.A. Antoniadis, E.J. Sapountzakis, Frequency Base Design of the KDamper Concept for Seismic Isolation of Bridges. E.J. Sapountzakis, M.

- Banerjee, P. Biswas, E. Inan eds. *14<sup>th</sup> International Conference on Vibration Problems (ICOVP 2019)*, Hersonissos, Crete, Greece, September 1-4, 2019.
- [35] P.-O.N. Bollano, K.A. Kapasakalis, E.J. Sapountzakis, I.A. Antoniadis, Design and Optimization of the KDamper Concept for Seismic Protection of Bridges. E.J. Sapountzakis, M. Banerjee, P. Biswas, E. Inan eds. *14<sup>th</sup> International Conference on Vibration Problems (ICOVP 2019)*, Hersonissos, Crete, Greece, September 1-4, 2019.
- [36] K.A. Kapasakalis, I.A. Antoniadis, A.E. Sapountzaki, Implementation of the KDamper Concept for Seismic Protection of Bridges. E.J. Sapountzakis, M. Banerjee, P. Biswas, E. Inan eds. *14<sup>th</sup> International Conference on Vibration Problems (ICOVP 2019)*, Hersonissos, Crete, Greece, September 1-4, 2019.
- [37] K.A. Kapasakalis, E.J. Sapountzakis, I.A. Antoniadis, Implementation of the KDamper Concept to Wind Turbine Towers. M. Papadrakakis, M. Fragiadakis, eds. *6<sup>th</sup> International Conference on Computational Methods in Structural Dynamics and Earthquake Engineering (COMPDYN 2017)*, Rhodes Island, Greece, June 15-17, 2017.
- [38] K.A. Kapasakalis, E.J. Sapountzakis, I.A. Antoniadis, Optimal Design of the KDamper Concept for Structures on Compliant Supports. K. Pitilakis eds. *16<sup>th</sup> European Conference on Earthquake Engineering (16ECEE 2018)*, Thessaloniki, Greece, June 18-21, 2018.
- [39] K.A. Kapasakalis, E.J. Sapountzakis, I.A. Antoniadis, KDamper Concept in Seismic Isolation of Multi Storey Building Structures. M. Papadrakakis, G.E. Stavroulakis eds. *9<sup>th</sup> International Congress on Computational Mechanics (9GRACM 2018)*, Chania, Crete, Greece, June 4-6, 2018.
- [40] K.A. Kapasakalis, E.J. Sapountzakis, I.A. Antoniadis, Kdamper concept in seismic isolation of building structures with soil structure interaction. *13<sup>th</sup> International Conference on Computational Structures Technology (CTS 2018)*, Sitges, Spain, September 4-6, 2018.
- [41] K.A. Kapasakalis, I.A. Antoniadis, E.J. Sapountzakis, Control of Multi Storey Building Structures with a New Passive Vibration Control System Combining Base Isolation with KDamper. M. Papadrakakis, M. Fragiadakis eds. *7<sup>th</sup> International Conference on Computational Methods in Structural Dynamics and Earthquake Engineering (COMPDYN 2019)*, Hersonissos, Crete, Greece, June 24-26, 2019.
- [42] K.A. Kapasakalis, I.A. Antoniadis, E.J. Sapountzakis, Implementation of the KDamper Concept for Base Isolation to a Typical Concrete Building Structure. *12<sup>th</sup> International Congress on Mechanics (12HSTAM 2019)*, Thessaloniki, Greece, September 22-25, 2019.
- [43] K.A. Kapasakalis, I.A. Antoniadis, E.J. Sapountzakis, KDamper Concept for Base Isolation and Damping of High-Rise Building Structures. E.J. Sapountzakis, M. Banerjee, P. Biswas, E. Inan eds. *14<sup>th</sup> International Conference on Vibration Problems (ICOVP 2019)*, Hersonissos, Crete, Greece, September 1-4, 2019.
- [44] I.A. Antoniadis, K.A. Kapasakalis, E.J. Sapountzakis, Advanced Negative Stiffness Absorbers for the Seismic Protection of Structures. I.U. Ahad, I. Gaidan, eds. *International Conference on Key Enabling Technologies (KEYTECH 2019)*, Istanbul, Turkey, April 24-26, 2019.

- [45] K.A. Kapasakalis, I.A. Antoniadis, E.J. Sapountzakis, Novel Vibration Absorption Systems with Negative Stiffness Elements for the Seismic Protection of Structures. *4<sup>th</sup> National Conference on Earthquake Engineering and Engineering Seismology (Hellenic Association for Earthquake Engineering - HAEE / ETAM 2019)*, Athens, Greece, 2019.
- [46] K.A. Kapasakalis, I.A. Antoniadis, E.J. Sapountzakis, Performance Assessment of the KDamper as a Seismic Absorption Base. *Structural Control and Health Monitoring*, **27**, 2019.
- [47] K.A. Kapasakalis, I.A. Antoniadis, E.J. Sapountzakis, Constrained Optimal Design of Seismic Base Absorbers Based on an Extended KDamper Concept. *Engineering Structures*, **226**, 2021.
- [48] Ibrahim RA (2008) Recent advances in nonlinear passive vibration isolators. *Journal of Sound and Vibration* 314(3–5): 371–452. DOI: 10.1016/j.jsv.2008.01.014.
- [49] J. Winterflood, D. Blair, B. Slagmolen, High performance vibration isolation using springs in Euler column buckling mode. *Physics Letters A*, **300**, 122–130, 2002.
- [50] L.N. Virgin, S.T. Santillan, R.H. Plaut, Vibration isolation using extreme geometric nonlinearity. *Journal of Sound and Vibration*, **315**, 721–731, 2008.
- [51] A.V. Dyskin, E. Pasternak, Mechanical effect of rotating non-spherical particles on failure in compression. *Philosophical Magazine*, **92**, 3451–3473, 2012.
- [52] W.S. Robertson, M.R.F. Kidner, B.S. Cazzolato, A.C. Zander, Theoretical design parameters for a quasi-zero stiffness magnetic spring for vibration isolation. *Journal of Sound and Vibration*, **326**, 88–103, 2009.
- [53] C. Han, X. Liu, M. Wu, W. Liang, A New Approach to Achieve Variable Negative Stiffness by Using an Electromagnetic Asymmetric Tooth Structure. *Shock and Vibration*, **2018**, 1–11, 2018.
- [54] J.P. Den Hartog, *Mechanical Vibrations, 4th Edition*. McGraw Hill, 1956.
- [55] Z.W. Geem, J.H. Kim, G.V. Loganathan, A New Heuristic Optimization Algorithm: Harmony Search. *Simulation*, **76**, 60–68, 2001.
- [56] Seismosoft [2018]. SeismoArtif - A computer program for generating artificial earthquake accelerograms matched to a specific target response spectrum 2018. <http://www.seismosoft.com>.



## MULTI-LEVEL OPTIMISATION OF NONLINEAR VISCOUS DAMPERS FOR SEISMIC RETROFIT OF SUBSTANDARD STEEL FRAMES

Dario De Domenico<sup>1</sup>, Iman Hajirasouliha<sup>2</sup>

<sup>1</sup> Department of Engineering, University of Messina  
Contrada Di Dio, 98166 Messina, Italy  
e-mail: [dario.dedomenico@unime.it](mailto:dario.dedomenico@unime.it)

<sup>2</sup> Department of Civil and Structural Engineering, The University of Sheffield  
Mappin Street, Sheffield S1 3JD, UK  
[i.hajirasouliha@sheffield.ac.uk](mailto:i.hajirasouliha@sheffield.ac.uk)

---

### Abstract

*This contribution presents a multi-level optimization procedure of nonlinear viscous dampers (NVDs) for the seismic retrofit of existing substandard steel frames. The procedure is based on the concept of uniform damage distribution (UDD) and aims to identify the best characteristics of NVDs to satisfy pre-assigned design requirements. The damper-brace elements are simulated with a Maxwell model comprising a dashpot with power law force-velocity behavior in series with a linear spring simulating the stiffness of the brace-damper system. The beam and column members of the steel frames are modelled with a distributed-plasticity fiber-based section approach. The optimization procedure is based on iterative nonlinear time-history analyses performed in OpenSees interfaced with an external subroutine written in MATLAB that governs the adjustment of the damper properties. The method is developed with reference to a set of synthetic and natural earthquakes compatible with the Eurocode 8 response spectrum. The effectiveness of the design procedure is illustrated through examples on 3-, 7- and 12-storey substandard steel frames. It is demonstrated that the proposed procedure leads to frames with reduced maximum inter-story drift, maximum plastic rotation and global damage index compared to an equal-cost uniform damping distribution. A slight variant of the procedure is also capable to comply with multiple performance objectives at different intensity levels of the earthquake excitation, thus realizing a multi-level optimization of the nonlinear viscous dampers. This is of practical importance in view of current performance-based design guidelines of seismic standards.*

**Keywords:** Optimization; Nonlinear viscous damper; Seismic performance; Performance-based design; Steel frames; Energy dissipation.

---

## 1 INTRODUCTION

Many existing structures do not comply with seismic regulations in force today and need seismic retrofitting interventions. A convenient strategy to increase the seismic performance of substandard structures while simultaneously reducing the need (and cost) of extensive interventions or localized repairing actions is to install passive energy dissipation devices [1]. These supplemental devices increase the energy dissipation capability of the structure, thus absorbing a significant portion of the earthquake input energy. In this way, the vibrational energy transferred from the ground shaking to the structure is considerably reduced, and the structure itself can remain in an elastic (or at the most quasi-elastic) range of behavior under the seismic design loads [2]. Among the most popular passive energy dissipation systems, fluid viscous dampers (FVDs) proved to be efficient devices for seismic retrofitting purposes. Some of the advantages of FVDs include the generation of velocity-dependent forces, whose peak values occur out of phase with respect to the occurrence of maximum displacements in the parent frame, and the possibility of increasing the damping features of the structure without affecting the stiffness of the structure. The latter characteristic is a major advantage compared to other hysteretic (e.g., metallic) dampers and, in general, to any displacement-dependent device as defined in the UNI EN15129 regulations. Moreover, this characteristic drastically simplifies the design procedure and the topology optimization of the devices.

The seismic performance of a structure equipped with added FVDs is reasonably affected by the choice of an appropriate size and position of the dampers. A plethora of analytical and numerical procedures for the optimal design and placement of FVDs have been proposed in the literature, as overviewed by De Domenico et al. [3], which range from sequential search algorithms [4] to gradient-based techniques [5], from evolutionary algorithms [6] to a fully stressed analysis/redesign procedure [7], stochastic-based approaches [8]-[10] or response-spectrum related procedures [11], [12]. Some of the methodologies presented in the literature assumed a simplified model of the structure (e.g., linear elastic shear-type behavior [13]) and of the FVDs (e.g., linear viscous dashpots with a force linearly proportional to the relative velocity at the two terminals [14]). Nevertheless, existing substandard frames requiring seismic retrofitting interventions may exceed the elastic threshold when subjected to severe earthquake excitations, so that incorporation of material nonlinearity in the model seems more appropriate for the correct design and optimal placement of FVDs. Additionally, the constitutive behavior of FVDs, particularly of dampers available in the market, is more faithfully described by the following nonlinear power law force-velocity expression [15]:

$$F_d = c_d |\dot{u}_d|^\alpha \operatorname{sgn}(\dot{u}_d) \quad (1)$$

where  $c_d$  is the damping coefficient;  $\dot{u}_d$  is the relative velocity between the two terminals of the device projected along the axis of the damper;  $\alpha$  is a velocity exponent related to the hydraulic circuit used, which ranges from 0.1 to 0.5 for commonly used dampers ( $\alpha=1$  for the case of linear damper);  $\operatorname{sgn}(\cdot)$  represents the signum function. For a fixed hydraulic circuit, the exponent  $\alpha$  is fixed, therefore the design of the dampers reduces to the selection of the damper size expressed by the damping coefficient  $c_d$ .

In this contribution, a multi-level optimization procedure of FVDs for the seismic retrofit of existing substandard steel frames is presented. The proposed procedure addresses nonlinear viscous dampers (NVDs) and incorporates the nonlinearity of the parent steel frame through a distributed-plasticity fiber-based section approach. The design methodology aims at achieving a state of uniform damage distribution (UDD) in the frame, thus avoiding localized damage (here quantified by the value of the inter-story drift). The state of UDD is achieved through

iterative nonlinear time-history analyses performed in OpenSees and interfaced with an external subroutine written in MATLAB that controls the adjustment of the damper properties depending on the profile of inter-story drifts at the current iteration. The proposed procedure is simple and can be applied to satisfy multiple performance objectives at different intensity levels of the seismic input, thus complying with modern performance-based design guidelines of seismic standards.

## 2 REFERENCE STEEL FRAMES AND SEISMIC INPUT

The effectiveness of the proposed design procedure is illustrated through examples on 3-, 7- and 12-storey substandard steel frames. More specifically, 3-bay planar steel frames made of steel S275 are considered, with bay width of 5.0m and story height equal to 3.2m, designed according to Eurocode 8. Dead loads and live loads equal to 5.0 and 2.5 kN/m<sup>2</sup> are considered for each story except for the roof level where the values are reduced to 3.5 and 1.0 kN/m<sup>2</sup>, respectively. For the beams, wide flange profiles (HEA types) are adopted, whereas for columns square hollow sections are used (as an example, 180x17.5 denotes a square section with thickness 17.5mm and side equal to 180mm) as listed in Table 1. Plan view and front view of a representative frame (specifically, the 7-story steel frame) are illustrated in Fig. 1.

Story level	3-story frame		7-story frame		12-story frame	
	beam	column	beam	column	beam	column
1	HE260A	180x17.5	HE300A	260x17.5	HE360A	340x17.5
2	HE260A	160x17.5	HE300A	240x17.5	HE360A	340x17.5
3	HE220A	140x17.5	HE280A	220x17.5	HE280A	340x17.5
4			HE280A	200x17.5	HE280A	340x17.5
5			HE260A	180x17.5	HE280A	340x17.5
6			HE260A	160x17.5	HE260A	320x17.5
7			HE220A	140x14.2	HE260A	280x17.5
8					HE260A	220x17.5
9					HE260A	220x17.5
10					HE260A	200x17.5
11					HE260A	160x17.5
12					HE220A	140x14.2

Table 1: Steel profiles of 3-story, 7-story, and 12-story substandard steel frames to be retrofitted with NVDs.

The finite element model of the steel frames is realized with the software OpenSees [16], using force-based *nonlinearBeamColumn* elements with five Gauss-Lobatto integration points per element, and discretizing the cross section with a number of fibers ranging from 40 to 52. Geometric nonlinearity (P-Delta effects) is incorporated in the columns, and the Rayleigh damping formulation is adopted for the steel frame (damping ratio equal to 5% is assumed for the first mode and for the mode corresponding to a cumulative participating mass equal to 95% of the total mass). The steel frames are retrofitted with NVDs mounted on diagonal braces in the central bay as depicted in Fig. 1. The NVDs are modeled in OpenSees through *twoNodeLink* elements with a *ViscousDamper* material governed by a Maxwell model (i.e., nonlinear dashpot with power law nonlinearity expressed by Eq. (1) in series with a linear spring, representing an equivalent stiffness coefficient of the damper-brace system). Throughout the examples of the paper, the exponent factor is assumed as  $\alpha = 0.3$ .

Nonlinear time-history analyses are performed under a suite of synthetic and natural spectrum-compatible records. The design response spectrum is assumed as the Eurocode 8 elastic

design spectrum with peak ground acceleration (PGA) equal to 0.4g (g being the gravity acceleration), soil type C. Fifteen natural records and six synthetic records (nomenclature SIM01 – SIM06) are selected to match the EC8 target response spectrum, as illustrated in Fig. 2 where the natural periods of the three steel frames are also marked as  $T_3, T_7, T_{12}$ .

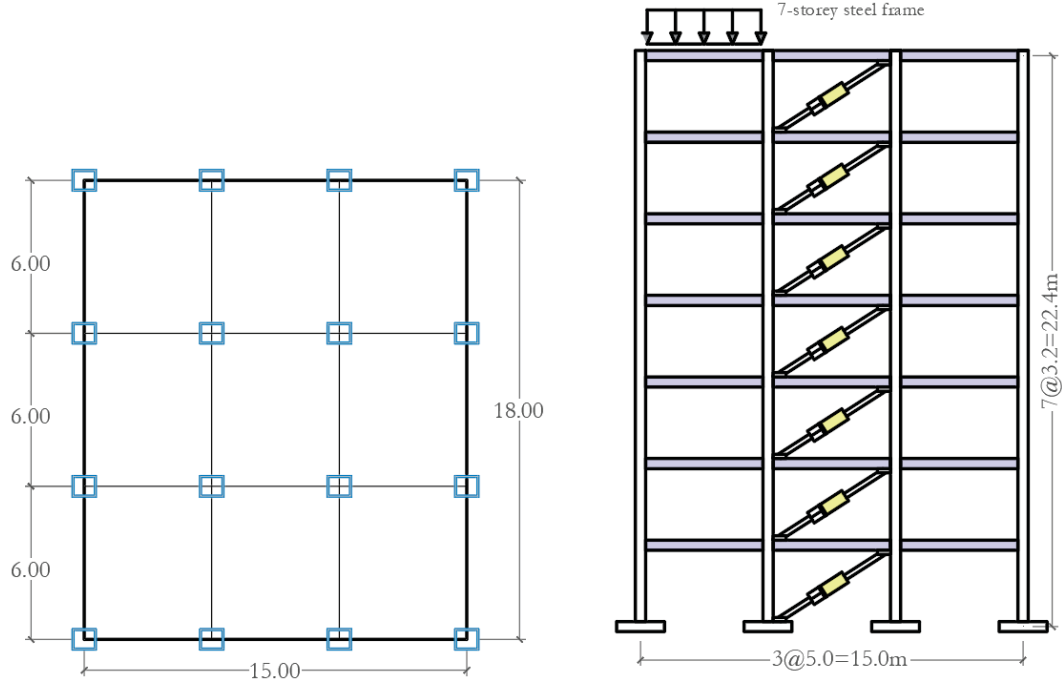


Figure 1: Plan view (left) and front view (right) of reference 7-story steel frame (steel profiles listed in Table 1).

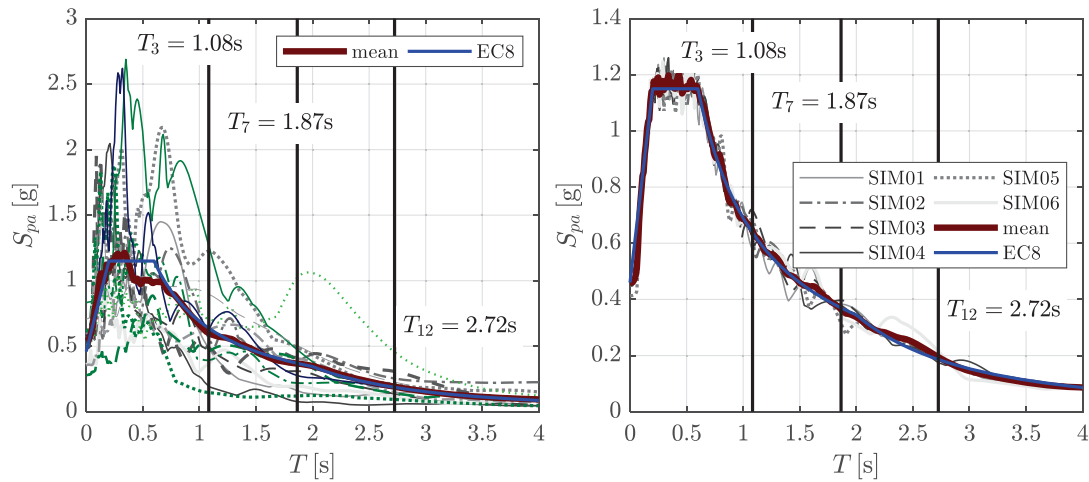


Figure 2: Acceleration response spectra of natural (left) and synthetic records (right) versus EC8 target spectrum.

### 3 UNIFORM DAMAGE DISTRIBUTION (UDD) DESIGN APPROACH

The proposed design approach aims at achieving a state of UDD in the retrofitted structure, thus avoiding localized damage. The genesis of the UDD method dates back to around fifteen years ago, and was extensively applied to performance-based optimization of different structural systems, including steel braced frames [17], truss like structures [18], shear buildings [19], reinforced concrete structures [20], [21], friction walls [22] and buckling restrained dampers [23].

To achieve the status of UDD in a structure equipped with NVDs, the damping coefficients of NVDs are increased in those story levels in which the inter-story drift (damage indicator) is higher, and are reduced in those story levels that, in contrast, are associated with a modest deformation demand (damage) according to the following sequential updating/adjustment expression:

$$c_{d,i}^{n+1} = c_{d,i}^n \times \left( \frac{\Delta_{\max,i}^n}{\Delta_{\text{target}}} \right)^\gamma \quad (2)$$

where  $c_{d,i}^n$  and  $c_{d,i}^{n+1}$  indicate the damping coefficients of NVDs at the  $i^{\text{th}}$  story level relevant to iteration  $n$  and  $n+1$ , respectively,  $\Delta_{\max,i}^n$  and  $\Delta_{\text{target}}$  represent the maximum inter-story drift ratio at the  $i^{\text{th}}$  story level calculated at the  $n^{\text{th}}$  iteration and the target value (depending on the performance requirement), respectively, while  $\gamma$  denotes a scalar parameter that affects the rate of convergence of the iterative procedure, which is assumed equal to 2.0 in this study. The sequential adjustment of the damping coefficient distribution controlled by Eq. (2) is carried on until the inter-story drift ratios tend to a uniform distribution, that is, the value of the coefficient of variation (CoV) of the inter-story drift values is lower than a fixed threshold.

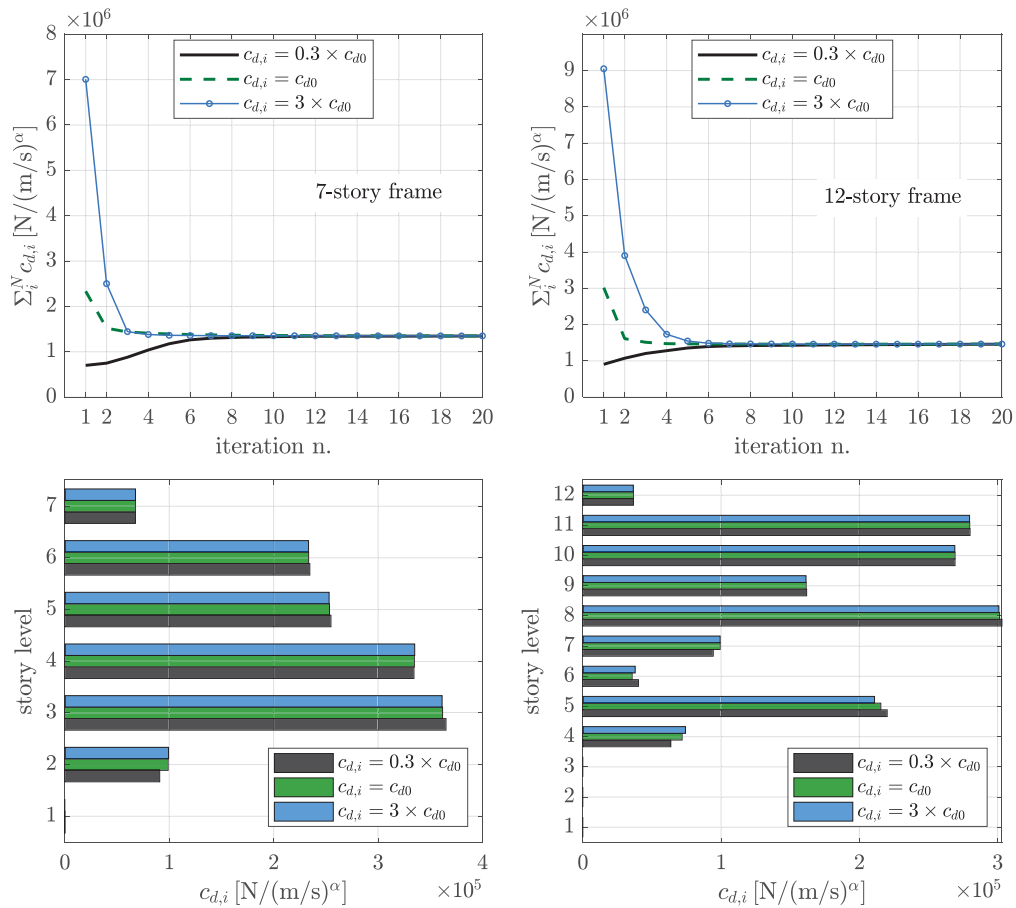


Figure 3: Effect of different initial damping distributions on convergence rate of total damping coefficient (top) and final height-wise damping distribution after 20 iterations (bottom) for 7-story and 12-story steel frames.

The application of Eq. (2) to the 7-story and 12-story is illustrated in Fig. 3 with reference to one synthetic record (SIM01). As initial step (step 0) a uniform damping distribution



$c_{d,i}^0 = c_{d0} = \text{cost}$ . is assumed, where  $c_{d0}$  is the minimum value of damping coefficient satisfying a pre-defined performance requirement (that is, the damping coefficient such that  $\Delta_{\max,i}^n \leq \Delta_{\text{target}}$  for all story levels  $i$ ). In this case, the target drift ratio is assumed as  $\Delta_{\text{target}} = 1.5\%$ , which is consistent with the FEMA life safety performance level for braced steel frames [24].

It is worth noting that assuming a different initial distribution does not lead to a local optimum solution, but to the same global solution. Indeed, to demonstrate the convergence rate and the efficiency of the proposed methodology, in addition to the uniform distribution, two alternative uniform damping distributions are analyzed as initial solutions, namely  $c_{d,i}^0 = 0.3 \times c_{d0}$  and  $c_{d,i}^0 = 3 \times c_{d0}$ . In all cases, the same final height-wise distribution of damping coefficient is obtained after 20 iterations, which confirms that the final optimum solution is basically independent from the initial choice of the damping coefficient distribution at the beginning of the sequential procedure. It is also worth noting that assuming  $\gamma = 2.0$  ensures a rapid convergence of the procedure, as the total damping coefficient tends to stabilize after just 6-8 iterations.

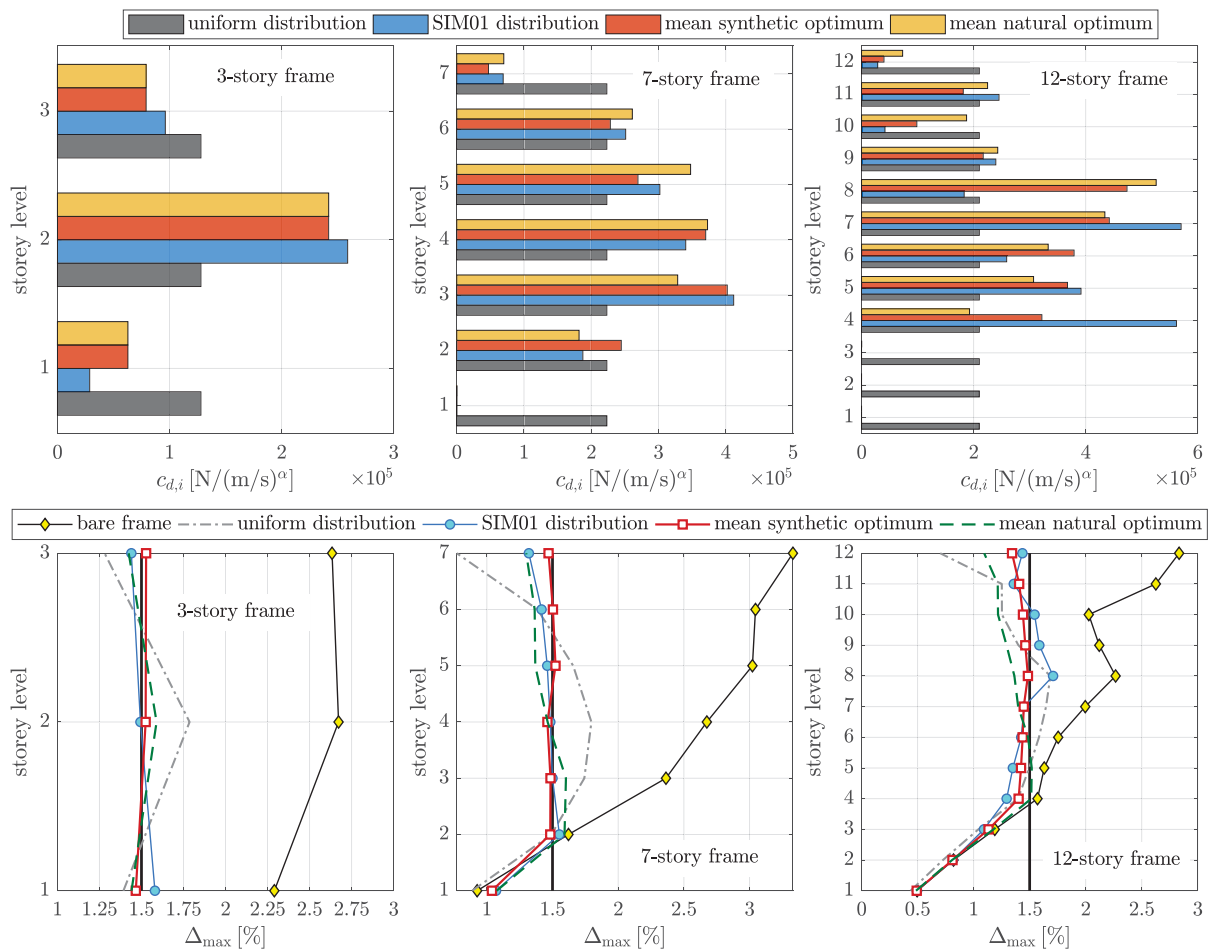


Figure 4: Comparison of four damping distributions considering different seismic input.

Another interesting point concerns the seismic input considered in the application of the proposed UDD design approach. Indeed, the optimum damping coefficient distribution is strictly related to the choice of the earthquake excitation used in the iterative nonlinear time-

history analyses. To scrutinize this effect and the sensitivity of the optimum solution to the choice of the earthquake record, in Fig. 4 four damping distributions are compared, namely: uniform distribution, UDD optimum distribution obtained by considering only the first synthetic record (SIM01 distribution), UDD optimum distribution in which the damping distribution is obtained as mean of the six distributions relevant to each of the six synthetic spectrum-compatible records (mean synthetic optimum) and of the fifteen distributions relevant to each of the fifteen natural spectrum-compatible records (mean natural optimum).

The four damping distributions compared in Fig. 4 are associated with the same total damping coefficient  $\sum c_{d,i} = \Sigma_{\text{target}}$ . This can be obtained by scaling (at each iteration) the damping distribution obtained by the iterative application of Eq. (2) according to:

$$[c_{d,i}^{n+1}]_{\text{scaled}} = c_{d,i}^{n+1} \times \left( \frac{\Sigma_{\text{target}}}{\sum_i^N c_{d,i}^{n+1}} \right) \quad (3)$$

so that the sum of the damping coefficient  $\sum c_{d,i} = \Sigma_{\text{target}}$  remains unchanged during the iterations and for every distribution analyzed. In the specific case, the value  $\Sigma_{\text{target}}$  is assumed to be that of the mean synthetic optimum distribution. The results shown in Fig. 4 demonstrate that the optimum damping distribution obtained by the proposed UDD procedure considering only one synthetic record (SIM01 distribution) represents a reasonable approximation of the optimum damping distribution obtained by considering a set of spectrum-compatible records (mean synthetic and mean natural optimum distribution). However, this is more evident in the case of 3-story and 7-story steel frames, whereas in the case of 12-story frame higher-order modes make the optimum damping distribution slightly more dependent upon the considered seismic input. In other words, the use of a single synthetic records leads to acceptable results for short-to-medium rise structures in the proposed UDD design procedure but may lead to higher approximations in the case of taller buildings.

#### 4 SEISMIC PERFORMANCE ASSESSMENT OF FRAMES EQUIPPED WITH OPTIMUM NVDS

Once the optimum damping distribution of NVDs is identified through the proposed UDD design methodology, the seismic performance can be assessed by performing nonlinear time-history analyses of the steel frames equipped with NVDs under the selected fifteen natural spectrum-compatible records. Hereafter only average max results of some selected response indicators are reported to quantify the seismic performance of the structure equipped with different distribution of NVDs, namely: NVDs uniformly distributed along the building height (called “uniform distribution”); NVDs designed according to the proposed UDD methodology considering a single synthetic record (called “SIM01 distribution”) and the mean of the damping distributions considering the six synthetic optimum distribution (simply called “optimum”). The three distributions share the same total damping coefficient, so that the different seismic performance of the three structures is uniquely related to the different height-wise distribution of the NVDs. This aims to quantify the effectiveness of the proposed UDD design philosophy against the uniform (equal cost) damping distribution in terms of seismic performance. Relevant results, in terms of average maximum values of plastic rotation, global damage index (quantified as indicated by Nabid et al. [22]), base shear and floor acceleration are depicted in Fig. 5 in a normalized fashion, scaled to bare frame results, with standard devia-

tion values being reported in the superimposed error bars. It can be observed that the proposed UDD design philosophy leads to frames with reduced maximum inter-story drift, maximum plastic rotation and global damage index compared to an equal-cost uniform damping distribution. A marked difference is noted in the values of the local (plastic rotation) and global damage indices, whereas the response in terms of base shear and floor acceleration is rather comparable in the three analyzed damping distributions, which is reasonable in view of the fact that the three damping distributions share the same total damping coefficient.

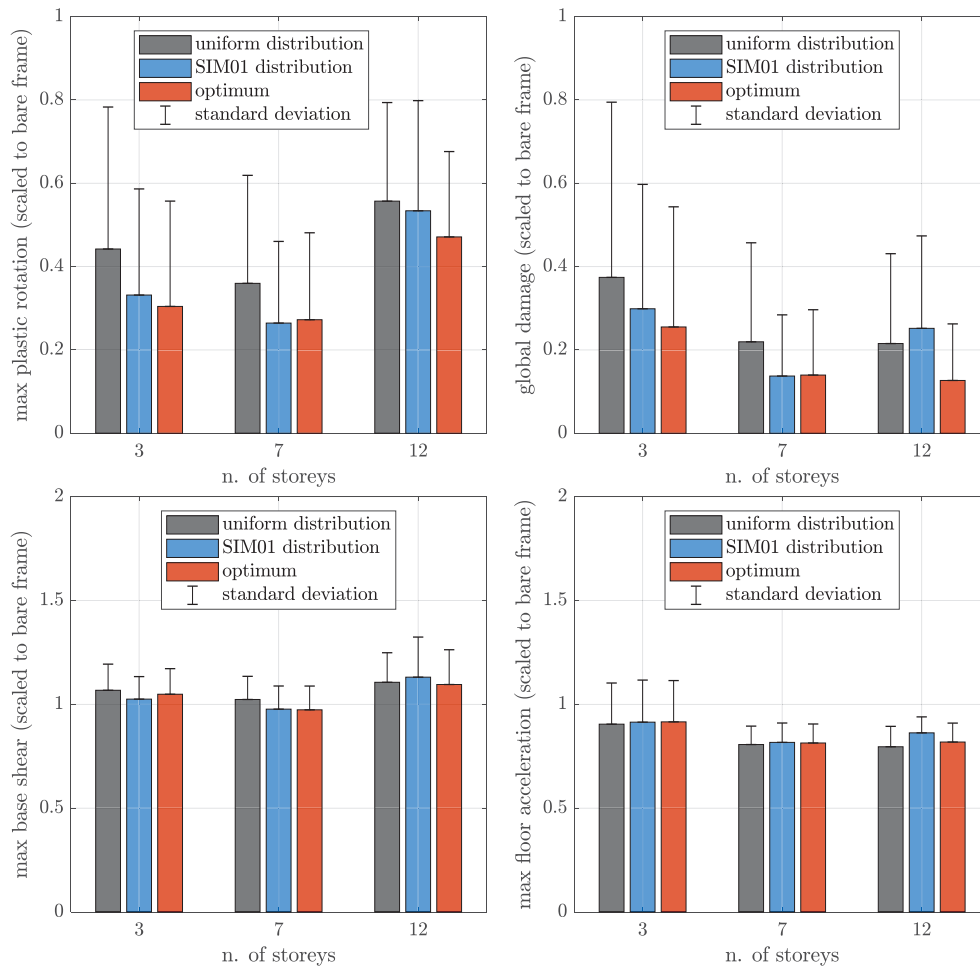


Figure 5: Seismic performance assessment of structures equipped with different distributions of NVDs.

## 5 MULTI-LEVEL PERFORMANCE-BASED OPTIMIZATION OF NVDS

It has been noted that the proposed methodology is of simple application and requires few iterations to converge. It is rather easy to incorporate the nonlinearity of the parent frame and that of the damper behavior. As an additional potential of the proposed approach, a slightly variant of the proposed UDD methodology makes it possible to address multiple performance objectives at different intensity levels of the seismic excitation. To this aim, a simple and conservative way to accomplish this objective is to generalize the sequential updating expression given in Eq. (2) as follows:

$$c_{d,i}^{n+1} = c_{d,i}^n \times \max \left[ \left( \frac{\Delta_{\max,i}^{n,I}}{\Delta_{\text{target}}^I} \right); \left( \frac{\Delta_{\max,i}^{n,II}}{\Delta_{\text{target}}^{II}} \right); \dots; \left( \frac{\Delta_{\max,i}^{n,K}}{\Delta_{\text{target}}^K} \right) \right]^\gamma \quad (4)$$

where  $\Delta_{\max,i}^{n,K}$  and  $\Delta_{\text{target}}^K$  represent the maximum and target inter-story drift ratio at the  $i^{\text{th}}$  story level, for the  $n^{\text{th}}$  iteration, and the  $K^{\text{th}}$  performance objective, respectively, with  $K = I, II, \dots$  including all the performance levels of interest.

To demonstrate the application of the proposed multi-level UDD design methodology, we extend the procedure previously illustrated for a single performance objective to two (rather than one) performance levels, namely:  $I$  = life safety (LS) performance level under the design basis earthquake (DBE) (corresponding to a 10% probability of exceedance during the reference life of the structure) and  $II$  = collapse prevention (CP) performance level under the maximum credible earthquake (MCE) (corresponding to a 2% probability of exceedance). In this paper, DBE is defined by  $\text{PGA} = 0.4g$ , whereas MCE is defined by  $\text{PGA} = 0.56g$  (that is,  $\text{MCE} = 1.4 \text{ DBE}$ ). The target inter-story drift ratio is set equal to  $\Delta_{\text{target}}^I = 1.5\%$  and  $\Delta_{\text{target}}^{II} = 2.0\%$  for DBE and MCE, in accordance with FEMA guidelines for LS and CP performance levels in braced steel frames [24].

Fig. 6 illustrates the maximum drift ratio along the building height (average results under the six synthetic records) comparing the UDD design methodology in its single-level and multi-level variant. It is clearly observed that the multi-level UDD methodology satisfies all the performance requirements on the maximum drift ratios for both DBE (LS) and MCE (CP). In contrast, the single-level UDD methodology leads to maximum drift ratios exceeding the MCE limitations for all the steel frames, in a more marked way in the case of the 3-story and 7-story steel frames, and in a less evident way for the 12-story steel frame. This example demonstrates that it is rather simple to incorporate different performance requirements in the proposed UDD design methodology through the adoption of the sequential formula (4).

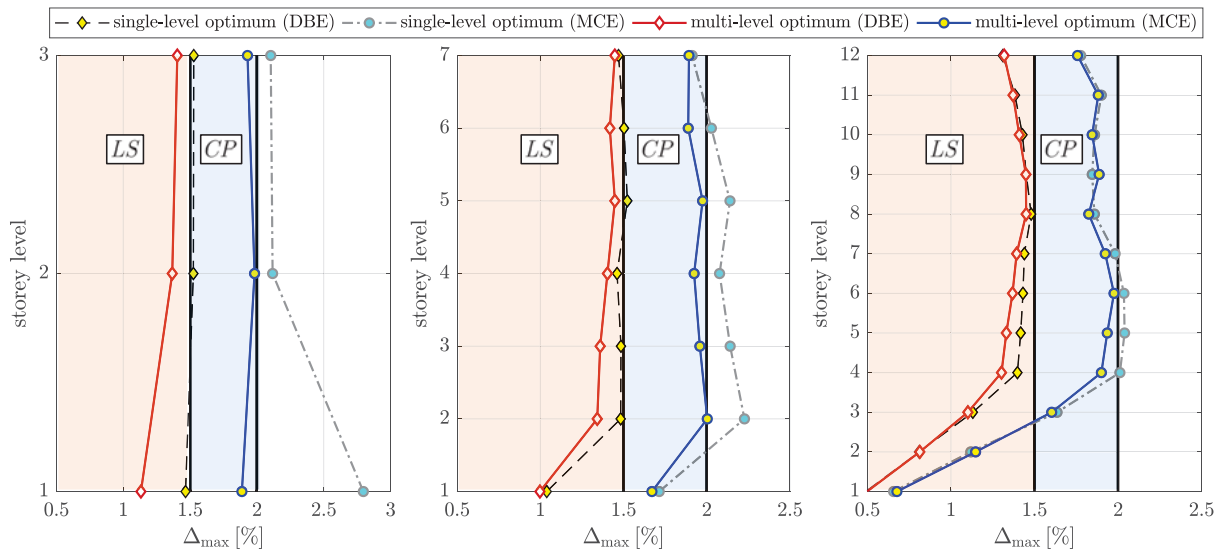


Figure 6: Maximum drift ratios  $\Delta_{\max}$  for single-level and multi-level UDD design procedure under DBE-MCE.

## 6 CONCLUSIONS

A simple yet efficient performance-based methodology for the optimum design of NVDs for the seismic retrofit of existing substandard steel frames has been presented. The proposed methodology invokes a UDD design philosophy and assumes, for simplicity, that the level of damage at a specific story is directly related to the value of the drift ratio associated with that story level. However, the generality of the formulation makes it possible to address other damage-related measures in a similar fashion and using a similar implementation approach. The core of the design procedure is based on an iterative adjustment of the damping coefficients of NVDs along the building height in order to achieve a status of uniform damage. In particular, the damping coefficients of the story levels undergoing larger extent of damage are increased, whereas the damping coefficients related to those story levels experiencing modest deformation demand are decreased iteratively. The design procedure entails a sequence of nonlinear time-history analyses, performed in OpenSees, and interfaced with an external MATLAB subroutine that governs the iterative updating of the damping coefficients. The procedure is general and easily incorporates the nonlinearity of the parent steel frame (through a distributed plasticity fiber-based section approach) and of the damper behavior (through a Maxwell model comprising a linear spring in series with a nonlinear, power law, dashpot element). The efficiency of the proposed design procedure has been illustrated with reference to three benchmark structures, namely 3-story, 7-story and 12-story substandard steel frames. The convergence of the proposed procedure has been investigated with reference to the initial damping distribution (set at the beginning of the iterations) as well as by considering different natural or synthetic records (belonging to the same class of spectrum-compatible records) as representative seismic input. It has been found that the proposed UDD design philosophy leads to steel frames with reduced maximum inter-story drift, maximum plastic rotation and global damage index compared to an equal-cost uniform damping distribution. A slight variant of the procedure has also been proposed to comply with multiple performance objectives at different intensity levels of the earthquake excitation, thus realizing a multi-level optimization of the nonlinear viscous dampers, in line with current performance-based design guidelines of seismic standards.

## REFERENCES

- [1] S. Ishida, I. Takewaki, Optimal seismic design of stiffness and gap of hysteretic-viscous hybrid damper system in nonlinear building frames for simultaneous reduction of inter-story drift and acceleration, *Frontiers in Built Environment*, **7**, 22, 2021.
- [2] S. Sorace, G. Terenzi, Fluid viscous damped-based seismic retrofit strategies of steel structures: General concepts and design applications, *Advanced Steel Construction*, **5**(3), 322-339, 2009.
- [3] D. De Domenico, G. Ricciardi, I. Takewaki, Design strategies of viscous dampers for seismic protection of building structures: a review, *Soil Dynamics and Earthquake Engineering*, **118**, 144-165, 2019.



- [4] R.H. Zhang, T.T. Soong, Seismic design of viscoelastic dampers for structural applications. *Journal of Structural Engineering*, **118**(5), 1375-1392, 1992.
- [5] I. Takewaki, Optimal damper placement for minimum transfer functions, *Earthquake Engineering and Structural Dynamics*, **26**, 1113–24, 1997.
- [6] G. Apostolakis, Optimal evolutionary seismic design of three-dimensional multistory structures with damping devices, *Journal of Structural Engineering*, **146**(10), 04020205, 2020.
- [7] R. Levy, O. Lavan, Fully stressed design of passive controllers in framed structures for seismic loadings, *Structural and Multidisciplinary Optimization*, **32**(6), 485-498, 2006.
- [8] E. Tubaldi, I.A. Kougioumtzoglou, Nonstationary stochastic response of structural systems equipped with nonlinear viscous dampers under seismic excitation, *Earthquake Engineering and Structural Dynamics*, **44**(1), 121–138, 2015.
- [9] D. De Domenico, G. Ricciardi, Earthquake protection of structures with nonlinear viscous dampers optimized through an energy-based stochastic approach, *Engineering Structures*, **179**, 523–39, 2019.
- [10] D. De Domenico, G. Ricciardi, Improved stochastic linearization technique for structures with nonlinear viscous dampers, *Soil Dynamics and Earthquake Engineering*, **113**, 415-419, 2018.
- [11] A. Moslehi Tabar, D. De Domenico, Nonlinear response spectrum analysis of structures equipped with nonlinear power law viscous dampers, *Engineering Structures*, **219**, 110857, 2020.
- [12] A. Moslehi Tabar, D. De Domenico, H. Dindari, Seismic Rehabilitation of Steel Arch Bridges Using Nonlinear Viscous Dampers: Application to a Case Study, *Practice Periodical on Structural Design and Construction*, **26**(3), 04021012, 2021.
- [13] H. Cetin, E. Aydin, B. Ozturk, Optimal design and distribution of viscous dampers for shear building structures under seismic excitations, *Frontiers in Built Environment*, **5**(90), 1–13, 2019.
- [14] G.M. Del Gobbo, A. Blakeborough, M.S. Williams, Improving total-building seismic performance using linear fluid viscous dampers, *Bulletin of Earthquake Engineering*, **16**(9), 4249–4272, 2018.
- [15] E. Tubaldi, M. Barbato, A. Dall'Asta, Performance-based seismic risk assessment for buildings equipped with linear and nonlinear viscous dampers, *Engineering Structures*, **126**, 90–99, 2014.
- [16] F. McKenna, G. Fenves, M. Scott, *Computer program OpenSees: open system for earthquake engineering simulation*, 2006, <https://opensees.berkeley.edu>.
- [17] H. Moghaddam, I. Hajirasouliha, A. Doostan, Optimum seismic design of concentrically braced steel frames: concepts and design procedures, *Journal of Constructional Steel Research*, **61**(2), 151-166, 2005.
- [18] I. Hajirasouliha, K. Pilakoutas, H. Moghaddam, Topology optimization for the seismic design of truss-like structures. *Computers & structures*, **89**(7-8), 702-711, 2011.

- [19] I. Hajirasouliha, K. Pilakoutas, General seismic load distribution for optimum performance-based design of shear-buildings, *Journal of Earthquake Engineering*, **16**(4), 443-462, 2012.
- [20] I. Hajirasouliha, P. Asadi, K. Pilakoutas, An efficient performance-based seismic design method for reinforced concrete frames, *Earthquake engineering & structural dynamics*, **41**(4), 663-679, 2012.
- [21] P. Asadi, I. Hajirasouliha, A practical methodology for optimum seismic design of RC frames for minimum damage and life-cycle cost, *Engineering Structures*, **202**, 109896, 2020.
- [22] N. Nabid, I. Hajirasouliha, M. Petkovski, Performance-based optimisation of RC frames with friction wall dampers using a low-cost optimisation method, *Bulletin of Earthquake Engineering*, **16**(10), 5017–5040, 2018.
- [23] R.K. Mohammadi, M.R. Garoosi, I. Hajirasouliha, Practical method for optimal rehabilitation of steel frame buildings using buckling restrained brace dampers, *Soil Dynamics and Earthquake Engineering*, **123**, 242-251, 2019.
- [24] FEMA-356. Prestandard and Commentary for the Seismic Rehabilitation of Buildings. Report FEMA-356. Federal Emergency Management Agency, Washington DC; 2000.

## SEISMIC RETROFIT OF EXISTING PRECAST RC BUILDINGS WITH DISSIPATIVE DEVICES BASED ON CARBON WRAPPED STEEL TUBES

Lucia Praticò<sup>1</sup>, Andrea Vittorio Pollini<sup>2</sup>, Devis Sonda<sup>2</sup> and Nicola Buratti<sup>1</sup>

<sup>1</sup> University of Bologna, DICAM Department  
Viale Risorgimento 2, 40136 Bologna - Italy  
{lucia.pratico3, nicola.buratti}@unibo.it

<sup>2</sup> Sismo Solution s.r.l.  
Viale Carlo Pepoli 82, 40123 Bologna - Italy  
{apollini, dsonda}@sismosolution.com

---

### Abstract

*The seismic vulnerability of existing precast RC buildings not designed against seismic actions is a well-known issue nowadays, as emerged from the aftermath of the seismic events that affected many productive areas in the Emilia region (north Italy) in 2012. This is a consequence of the lack of structural redundancy and the widespread adoption of friction-based connections, which can lead to collapses and significant damage to contents. Thus, the necessity of identifying suitable intervention strategies has been widely recognized by researchers, which proposed different retrofit techniques. One of the most diffused approaches is to introduce mechanical connectors between columns and roof elements, resulting in an increase of the base shear and the need to strengthen the columns. To prevent this phenomenon, dissipative devices based on Carbon-Wrapped Steel Tubes (CWST) are introduced herein for the retrofit of existing precast RC structures, aiming at reducing the forces transmitted to columns, and providing a suitable connection between columns and beams. To this regard, this paper discusses the seismic retrofit of an existing precast building equipped with CWSTs. Linear and non-linear time history analyses have been conducted on two different models of the structure, one with hinged beam-column connections, and on the one with CWSTs. The yielding and the ultimate rotations of the plastic hinges at the base of the columns as well as the cyclic shear resistance depending on the ductility demand on each element, are defined according to Eurocode 8 prescriptions. The paper discusses the effects of the introduction of the CWSTs in the connections in terms of forces and proposes equivalent behavior factor values for the two structures.*

**Keywords:** Precast RC buildings, Dissipative devices, Seismic retrofitting, NLTH analysis, Behavior factor

---

## 1 INTRODUCTION

Since the 1970s, precast Reinforced Concrete (RC) structures have been widely used in many countries for one-story industrial buildings such as warehouses and factories. The seismic vulnerability of existing precast RC buildings built without seismic-design criteria is a well-known issue nowadays, as highlighted by damage occurred after the 2012 Northern Italy earthquakes that affected many productive areas [1, 2, 3, 4, 5]. The main source of vulnerability of these structures is the lack of effective mechanical connectors between their structural elements, indeed friction-based connections were widespread [6, 7, 8, 9, 10]. Friction-based connections are not able to guarantee an effective shear force transmission, causing loss of support failures and collapses; moreover, the simultaneous effect of the horizontal and vertical components of the seismic action can increase the probability of occurrence of this type of failure [11]. The vulnerability of structures characterized by these frictional connections has been confirmed by numerous numerical simulations [8, 10, 12, 13, 14, 15]. In addition, the failure of beam-column connections based on friction only, can frequently occur before the development of plastic hinges at the base of columns, causing undesired non-ductile failure modes, as reported in Deyanova et al. [16].

Given the high vulnerability of friction-based connections and the economic significance of prefabricated RC structures, many strengthening solutions have been proposed in the literature [6, 8, 17, 18, 19]. The reduction of damage and collapses due to seismic events for this type of structures, becomes even more strategical since a high economic impact due to industrial business interruption has to be taken in account, in addition to the direct economic losses [20, 21, 22]. All the strengthening solutions are typically based on the introduction of steel ties, plates, or cable restraints, to avoid sliding of the beams and therefore unseating failures. Most of these solutions aim only at converting friction-based connections into hinged connections with no focus on energy dissipation, and therefore they often require the strengthening of the base of columns.

Thus, *ad hoc* solutions based on different energy dissipation mechanisms have been proposed. For instance, Dal Lago et al. [23, 24, 25] proposed to concentrate energy dissipation in simple and rather inexpensive elements, such as steel angles connectors. Scotta et al. [26] focused on the dissipative role of cladding panels acting as shear walls; Belleri et al. [27] introduced energy dissipation in hinged connection, suggesting a re-centering dissipative devices based on rotary friction; Martinelli and Mulas [28] proposed a similar solution involving the insertion of devices dissipating energy through rotary friction, with no re-centering capacity. Alternative solutions are based on the introduction of dampers, as suggested by Marinini et al. [29].

In this context, the present paper refers to a low-damage solution for the retrofit of beam-column connections of existing precast RC structures, proposing the introduction of dissipative fuse devices based on Carbon-Wrapped Steel Tubes (CWST), introduced in Pollini et al. [30, 31]. Pollini et al. [32] presented an analytical simplified approach to estimate an equivalent behavior factor to be used in design applications with these devices, validated by comparison with a large number of incremental dynamic analyses (IDAs).

In this paper, the evaluation of the improvement in the seismic behavior of an existing precast RC building retrofitted with CWST devices is proposed, through comparative considerations on the behavior factor calculated for the existing structure, and for the one after the intervention. The first part of the paper presents the properties of the dissipative fuse devices adopted for the retrofit intervention of the main frame of the building. Thus, the modelling strategies are described in detail, as well as the development of the non-linear time history analyses. Finally, the results in terms of behavior factor quantification, for the current structure and

for the retrofitted one, are proposed and discussed with the aim of evaluating the effects of the CWSTs in the reduction of the seismic vulnerability of the building.

## 2 CWST DISSIPATIVE DEVICES

The dissipative fuse devices based on CWSTs [31, 32] considered in the present paper have two main purposes: (i) to connect beam-column joints in order to prevent the possible unseating failure of beams, and (ii) to act as dissipative fuses, thus reducing the effects of seismic actions on structural elements. Specific studies in automotive engineering on structural crashworthiness [33, 34] showed that metals, combined with composite materials in thin-walled circular tubes, have excellent capacities of energy absorption under axial compressive loads. From these, the CWST devices were developed, and an example of a real application can be seen in Figure 1a.

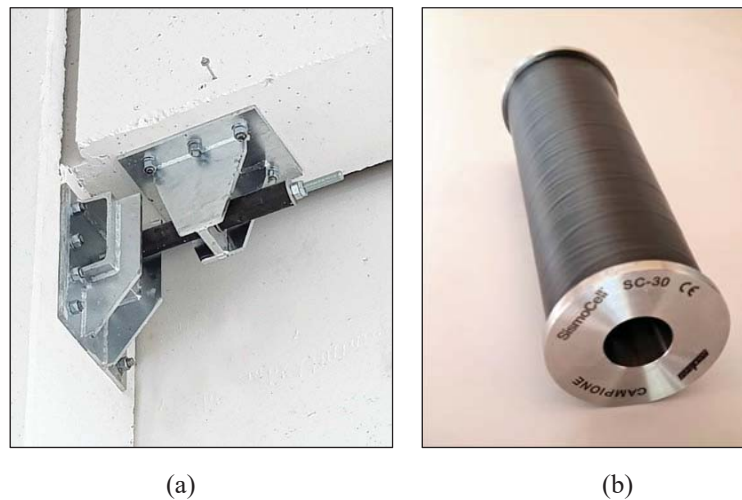


Figure 1: (a) Example of a beam-column connection provided with coupled CWST dissipative devices; (b) single fuse device made of carbon-wrapped steel tubes.

It is worth noticing that, since each CWST (Figure 1b) dissipates energy only under compressive loading, two devices must be positioned at each beam-column joint. A threaded bar is placed through the CWSTs in order to guide their displacement, and also to ease their connection to structural elements. In this way, standard steel anchoring elements can be used to fix the threaded bar to the column. Moreover, the anchorage on the beam is guaranteed by a significantly stiff and strong steel element, able to transfer forces from beams to the CWSTs.

The CWST device works firstly in the elastic range, like a fuse restraint avoiding relative displacement between two structural components, below a certain pre-established force threshold. Above this threshold, the plastic deformation of the device begins (plasticization phase), as well as the energy dissipation.

In order to understand the behavior of the devices, in Figure 2a the force-deformation diagram of a single CWST in compression is proposed [31]. In the Figure,  $F_{eq}$  is the equivalent plastic force threshold, and  $S_{max}$  is the maximum deformation capacity. The behavior of a connection with a CWST device can be described within three main steps. In the initial branch O-A the device remains elastic, and the lateral seismic force is fully taken by the column. As soon as the force overcome  $F_{eq}$  (branch A-B of the curve), the device starts to buckle and the plastic deformation develops, while a constant value of the force is transmitted to the column. After point B, when the device attains its maximum deformation capacity, the stiffness boosts significantly. At this step, the device performs as a displacement-limiter between beams and columns,



thanks to the aforementioned threaded bar, thus, from this point, the columns fully bears the seismic load and start to deform and yield (typically at the base).

In case of ground motions, and in general under cyclic loading, the two CWSTs positioned in one joint, work alternatively. Figure 2b represents the force-deformation law of a couple of devices in case of cyclic loads. In the picture, the red path shows that, when a load reversal occurs after entering the plastic branch of one of the devices, the connection slides with no force until the recovery of the entire deformation.

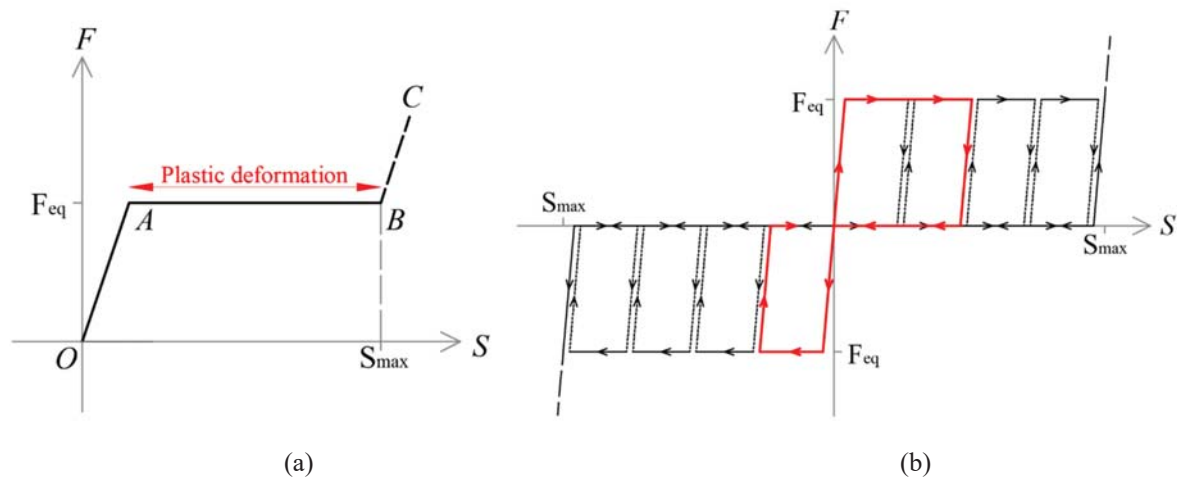


Figure 2: Force-deformation behavior of the CWST device: (a) single device behavior under compression; (b) hysteretic behavior of two devices under cyclic loading.

### 3 FEM MODELS OF THE PRECAST RC FRAME

The seismic retrofit with CWST devices is herein applied to an existing precast RC building located in Carpi (MO), in the Emilia Romagna region (Italy). The building was built in the '70, and features double span main frames constituted by I-shaped precast beams, simply supported on rectangular precast columns. After the seismic events of May 2012, the building was subjected to a temporary retrofit solution with steel plates applied at the beam-column joints, aimed to prevent the unseating of the precast elements. It is worth noticing that the retrofit with CWSTs discussed in this work, has the purpose of improving the seismic behavior of the building with respect to the current condition.

The roof slab is made by simply supported hollow-clay elements, without a rigid concrete slab, thus, the structural scheme lacks structural redundancy, consisting in simply supported beams and cantilever columns [35, 36]. Since the building is simple and regular in plan, and there is not a rigid diaphragm at the roof level, the seismic behavior of the entire building can be approximated with the 2D model of one of the internal main frames, in the direction of the beams. In the orthogonal direction, a different retrofit solution was adopted.

In order to evaluate the effects of the retrofit intervention, two different frames are modelled with finite elements, with the software Midas GEN [37]:

- A) main frame of the building with hinged beam-column connections, representing the structure in the current condition with the temporary retrofit solution (Figure 3a);
- B) main frame of the building with CWST devices placed at the beam-column joints, representing the retrofitted structure (Figure 3b). In this last model, appropriate *link* elements, i.e. nonlinear springs, are used in order to model the behavior of the dissipative devices, as explained in the following sections.

The frames are subjected to seven horizontal recorded ground-motion accelerograms, according to Eurocodes prescriptions for safety verifications of existing buildings with non-linear analyses [38, 39], as furtherly described in Section 4.1. The vertical seismic action is not considered in this work.

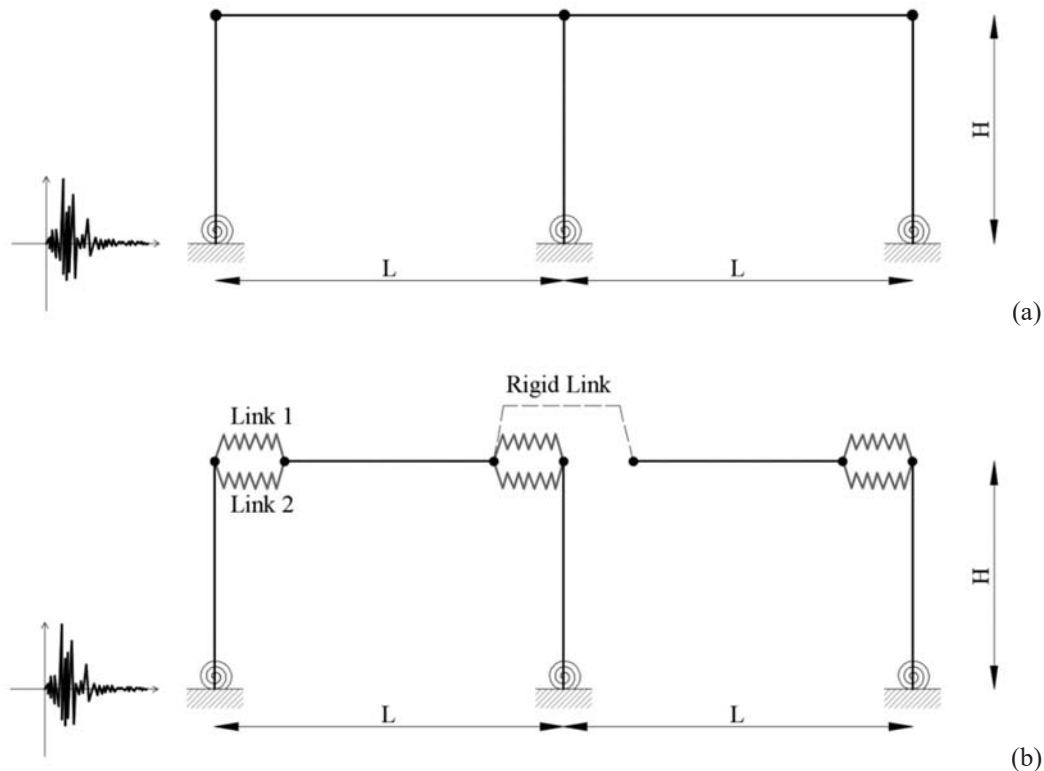


Figure 3: Structural FEM models adopted in the analyses: a) model A representing the existing structure; b) model B representing the frame retrofitted with CWSTs.

The main frame illustrated features two spans of 21.8 m, with precast main beams characterized by sections with depth spanning from 0.8 m at their ends to 1.6 m at mid-span. The three columns are 5.5 m high, with a rectangular section of 40 x 54 cm. Mechanical steel connectors are present between beams and columns, allowing to consider a rigid hinged connection between the elements in the existing condition.

The gravity loads are computed in the seismic combination of actions [38] according to the influence area of each element, and transformed into lumped masses for the dynamic analyses. The axial load ratio, computed in the seismic combination of loads, is 0.033 for the two external columns, and 0.063 for the internal. The material properties have been estimated according to in-situ testing reports, showing a concrete class C32/40 and a steel class FeB44k for the column reinforcement.

Since the building was built before the introduction of seismic design criteria in the region, the columns exhibit low seismic detailing and in particular poor transverse reinforcement. Indeed, the columns are reinforced with 4 $\Phi$ 14 ribbed bars with 2.5 cm concrete cover, and 2 additional  $\Phi$ 6 located along the height of the section, confined with transversal stirrups  $\Phi$ 6 spaced 20 cm. The columns are modelled clamped at their base, since, due to the presence of a rigid industrial floor, the interaction with the foundation is not under analysis in this work. At the base of columns, non-linear lumped plastic hinges are modelled adopting trilinear moment-rotation relationships, defined according to Eurocode 8 formulations for reinforced concrete structures [39]. The shear resistance of the columns is computed following the expression for

cyclic shear resistance calculation in Eurocode 8 [39], depending on the ductility demand of each element. It is worth noticing that, in all models, beams have a linear behavior since no damage is expected to occur in these elements.

### 3.1 Properties of the plastic hinges

The non-linear flexural behavior of columns is taken into account by means of plastic hinges at their base. Trilinear moment-rotation rules are implemented, considering the cracking point  $(\theta_{cr}, M_{cr})$ , the yielding point  $(\theta_y, M_y)$ , and the ultimate point  $(\theta_u, M_u)$ , with a perfectly plastic post-yielding behavior. The hysteresis model considered is a symmetric Takeda rule [40] able to represent the stiffness degradation of the elements, with an exponent in unloading stiffness equal to 0.4, and an inner loop unloading stiffness reduction factor equal to 1.

The value of the chord rotation at cracking is calculated as the ratio between the cracking moment and the elastic stiffness of a cantilever column with a fully reacting section. The yielding and the ultimate rotations at the life safety limit state are defined according to Biskinis and Fardis formulations [41, 42] adopted in Part 3 of Eurocode 8. The formulas are reported in Equations (1) and (2), respectively:

$$\theta_y = \phi_y \frac{L_V}{3} + 0.0013 \left( 1 + 1.5 \frac{h}{L_V} \right) + 0.13 \phi_y \frac{d_{bL} f_y}{\sqrt{f_c}} \quad (1)$$

$$\theta_{u,SLV} = \frac{3}{4} \frac{1}{\gamma_{el}} 0.016 (0.3^v) \left[ \frac{\max(0.01; \omega')}{\max(0.01; \omega)} f_c \right]^{0.225} \left( \frac{L_V}{h} \right)^{0.35} 25^{(\alpha \rho_{sx} \frac{f_{yw}}{f_c})} (1.25^{100} \rho_d) \quad (2)$$

where:  $\phi_y$  is the yield curvature at the end section,  $L_V$  is the ratio moment/shear at the end section,  $h$  is the depth of the cross-section,  $d_{bL}$  is the mean diameter of the tension reinforcement,  $f_y$  and  $f_c$  are the steel yield stress and the concrete strength, respectively,  $\gamma_{el}$  is equal to 1.5 for primary seismic elements,  $v$  is the axial load ratio,  $\omega$  and  $\omega'$  are the mechanical reinforcement ratios of the tension and compression, respectively, longitudinal reinforcements,  $\alpha$  is the confinement effectiveness factor,  $\rho_{sx}$  is the ratio of transverse steel parallel to the direction of loading,  $f_{yw}$  is the stirrup yield strength,  $\rho_d$  is the steel ratio of diagonal reinforcement, if any, in each diagonal direction. It is worth noticing that the same materials and sections characterize the three columns, which differ only because of the axial load. Mean values of the material properties are adopted to calculate moments and rotations. Moreover, the shear span  $L_V$  is equal to the full column height. The coordinates of the characteristic points of the trilinear plastic hinges are reported in Table 1.

It is important to highlight that the expression used for the calculation of  $\theta_u$  is defined for elements with ribbed bars and seismic detailing. The formula can be also adopted for elements that are not conforming to seismic codes, by applying reduction factors. In particular, empirical scaling factors are defined based on whether a member i) does not conform to modern seismic codes (22.9% reduction); ii) is not provided with properly anchored stirrups providing effective confinement (1.6% reduction); iii) has laps of longitudinal bars inside the plastic hinge region (from 15% to 66% reduction). This last factor significantly influences the calculation of the ultimate rotation [43], resulting in a reduction coefficient which increases if the lap is less than 40 diameters (in case of ribbed bars). For the case study frame, the first two empirical reduction coefficients are taken into account for the determination of  $\theta_u$ . Since the columns are prefabricated, with continuous longitudinal bars, it is not possible to consider the third correcting coefficient. All this enhances the necessity to evaluate other types of significant reduction

coefficients to be proposed in this formula for the specific case of existing prefabricated elements not designed with anti-seismic standards, for which additional research may be required [44, 45].

In this work, in order to analyse the sensitivity of the results depending on the value of ultimate chord rotation considered, the authors consider the adoption of two alternative values corresponding to 80% and 60% of  $\theta_u$ . Thus, the dynamic analyses are conducted with three different threshold values of rotations for both the models (i.e. model A and B), in order to evaluate the influence of this parameter on the estimation of the behavior factor. The values calculated for the case study frame are presented in Table 1.

	$M_{cr}$ (kNm)	$M_y$ (kNm)	$M_u$ (kNm)	$\theta_{cr}$ (rad)	$\theta_y$ (rad)	$\theta_u$ (rad)	80% $\theta_u$ (rad)	60% $\theta_u$ (rad)
External column	70.5	236.6	236.6	0.00074	0.01412	0.03232	0.02586	0.01939
Internal column	70.5	297.5	297.5	0.00074	0.01462	0.03118	0.02495	0.01871

Table 1: Characteristic points of the moment-rotation relationships adopted for the external and the internal columns of the precast frame.

### 3.2 Shear resistance

The shear in columns is checked at each step of the analysis with respect to the shear resistance, as prescribed by Eurocode 8, avoiding the modelling of non-linear shear hinges. The formula adopted for the verification is given in Eurocode 8, part 3 [39]. It accounts for the cyclic shear resistance which decreases with the increase of the plastic ductility demand  $\mu_{\Delta}^{pl}$ . This last parameter is calculated as the plastic part of the chord rotation normalized to the yielding chord rotation  $\theta_y$ . The adopted shear strength formula is reported in Equation (3).

$$V_R = \frac{1}{\gamma_{el}} \left[ \frac{h-x}{2L_V} \min(N; 0.55A_c f_c) + (1 - 0.05 \min(5; \mu_{\Delta}^{pl})) \cdot \left[ 0.16 \max(0.5; 100\rho_{tot}) \left( 1 - 0.16 \min\left(5; \frac{L_V}{h}\right) \right) \sqrt{f_c} A_c + V_W \right] \right] \quad (3)$$

where:  $\gamma_{el}$  is equal to 1.15 for primary seismic elements,  $h$  is the depth of the cross-section,  $x$  is the compression zone depth,  $L_V$  is the ratio moment/shear at the end section,  $N$  is the compressive axial force,  $A_c$  is the cross-section area,  $f_c$  is the concrete strength,  $\mu_{\Delta}^{pl}$  is the plastic part of the chord rotation normalized to the yielding chord rotation,  $\rho_{tot}$  is the total longitudinal reinforcement ratio,  $V_W$  is the contribution of transverse reinforcement to shear resistance.

In this formula, mean values of the material properties divided by the partial factors are considered to calculate the shear resistance, in accordance with Eurocode criteria for safety verifications of brittle failure modes. Moreover, the resistance is updated at each step of the analysis depending on the actual ductility demand. In addition, if the ductility demand is lower than 1, the value of shear resistance is calculated with the expression defined for members not requiring shear reinforcement, given in Eurocode 2, part 1-1 [46].

### 3.3 CWSTs dissipative devices

The CWST dissipative devices are introduced in frame B (see Figure 3), i.e. the retrofitted one. The devices are modelled in Midas GEN through the use of two *link* elements working in parallel:

- a non-linear symmetric element with property type *SLIP bilinear* (link 1 element in Figure 3b) which simulates the cyclic behavior of the devices before the attainment of

the maximum deformation capacity. A yielding strength  $F_{eq}$  equal to 30 kN and an initial stiffness is 30'000 kN/m are considered. This element works symmetrically in order to represent the presence of two CWSTs equipped at each beam-column node;

- a non-linear symmetric element with *SLIP bilinear* property defined with an initial gap of 7.5 cm (link 2 element in Figure 3b), which simulates the behavior of the devices after the attainment of the maximum deformation  $S_{max}$  capacity. It is modelled with a symmetric behavior in order to consider the maximum displacement of both tubes. The yielding strength and the stiffness of this element are set with significantly high values, so that to model a rigid hinged connection between beams and columns.

A couple of link elements with the aforementioned properties is modelled at the top of each column, connecting beams to columns, to represent a set of seismic devices working in the horizontal direction of the ground-motion. At the top of the internal column, an additional horizontal rigid link is modelled in order to connect the seismic devices to both beam ends, as shown in Figure 3. It is worth saying that a vertical support is guaranteed for each node of the beams through appropriate settings in the software.

Friction was not implemented in the models because of the uncertainty in the determination of the parameters that control this mechanism, i.e. the definition of the coefficient of friction, the combination of horizontal and vertical components of the seismic action, and the energy dissipation related to friction. Considering a frictional mechanism in the model would imply to admit the benefits of friction energy dissipation that cannot be considered to be constant, and on which it is not always possible to rely because of the variations of the axial load in columns, due to the vertical component of the ground-motion. Furthermore, standard provisions do not allow to consider friction in the seismic response of structures.

Nevertheless, the contribution of friction in terms of maximum force transferred to columns, has been taken into account in the selection of the yielding strength capacity of the dissipative devices adopted in this case study. Indeed, the value of the equivalent force of plasticization  $F_{eq}$  (see Section 2) for the CWSTs, was selected to be lower than the maximum value of force that could be transferred to the top of the columns without yielding their base sections.

Consequently, the column exhibits a certain degree of overstrength in order to guarantee that the sum of friction threshold force and of forces transmitted by the CWST devices, is lower than the force that would lead to the formation of a plastic hinge at the base. This is in accordance with the design criterion of this retrofit intervention, aimed at having columns performing linear elastic until the devices reach their maximum deformation capacity. Therefore,  $F_{eq}$  plus the contribution of frictional forces, has to be lower than the force activating yielding in columns, i.e. about 43 kN in for the external columns, and 54 kN for the central column, for the frame under analysis.

#### 4 TIME-HISTORY ANALYSES

The first step of this Section consists in performing linear modal analysis to estimate the first period of vibration of the existing frame. For this purpose, model A is implemented in a linear model without the three plastic hinges at the base of the columns, but considering the cracked stiffness of the columns, following Eurocode 8 prescriptions [38]. In particular, a reduction coefficient for the moment of inertia of each column has been evaluated, so that to consider the secant lateral stiffness at yielding of each column. The result of this analysis is a first period of vibration  $T_1$  of 1.561 seconds, for which almost the entire modal mass of the structure is participating. Indeed, precast RC structures are typically simple and strongly dominated by one vibrating mode [31].



#### 4.1 Selection of the records

The seismic input adopted for the non-linear dynamic analyses is a set of 7 spectrum-compatible ground acceleration time histories. The target spectrum for the selection is the life safety limit state elastic response spectrum, defined by the Italian building code [47] for the site of Carpi (MO) in Italy. This spectrum has a return period of 712 years, corresponding, to a nominal life equal to 50 years and importance class III. Ground type C with no topographic amplification effects is assumed. The 7 accelerograms used in the analyses were selected from the NGA-West database developed by PEER [48], with the following *ad hoc* algorithm: i) only earthquakes with moment magnitude between 4 and 6 and recording stations with source-to-site shorter than 30 km are considered; ii) pulse-like ground-motions are excluded; iii) recordings not usable for periods up to 3.0 s are excluded [49]; iv) all spectra of the remaining accelerograms are scaled to the PGA of the target spectrum; v) response spectra with scaling factors higher than 3.0 or lower than 0.4 are excluded; vi) the scaled spectra are sorted based on ascending values of the average root-mean-square deviation of the observed spectrum from the target (DRMS) [49] in a range of periods from 1.0 s to 3.0 s; vii) all the possible combinations of 7 spectra are considered among the 10 scaled spectra with the lowest DRMS values; viii) for each combination of 7 spectra the DRMS value for the mean spectrum is computed; ix) the 7 spectra with the mean spectrum with the lowest DRMS value are identified.

The selected scaled spectra are plotted in Figure 4, and the corresponding ground-motion data are reported in Table 2. In particular, the earthquake name and year are indicated, together with the name of the recording station, the Joyner-Boore source-to-site distance  $R_{JB}$ , the moment magnitude ( $M_w$ ), the direction of the horizontal component with reference to the NGA classification [48], the peak ground acceleration PGA, and the scaling factor  $SF^0$ .

Following Eurocode 8 recommendations [38] when seven ground motions are used, the average result of the response quantities from the analyses is adopted to compute the value of the action effect.

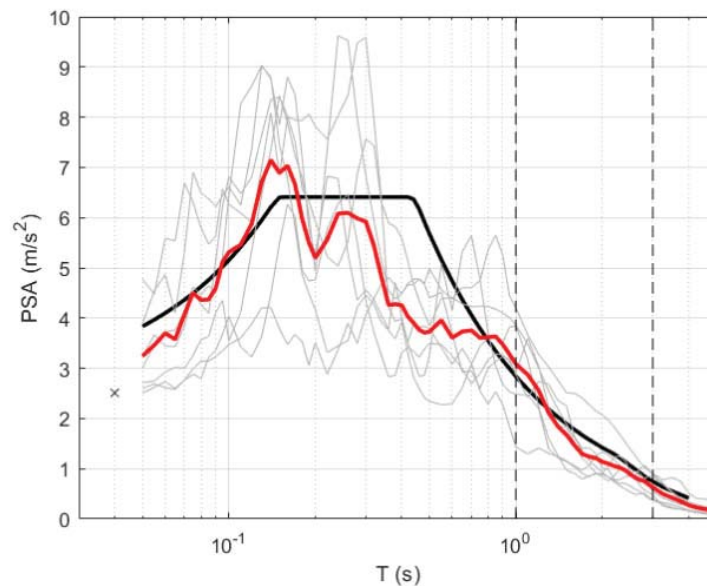


Figure 4: Scaled response rectum for each of the 7 accelerograms selected (gray lines), average spectrum (red), and target code spectrum for spectral compatibility in the range of periods spanning from 1.0 s to 3.0 s. The PGA is indicated with the symbol  $\times$ . All the accelerograms are scaled to the same PGA.

N°	Earthquake name, Year [-]	Station name [-]	$R_{JB}$ distance [km]	$M_w$ [-]	Component [-]	PGA [m/s <sup>2</sup> ]	SF <sup>0</sup> [-]
TH1	Chalfant Valley-01, 1986	Bishop - LADWP South St	23.38	5.77	H1	1.270	1.982
TH2	Chalfant Valley-01, 1986	Bishop - LADWP South St	23.38	5.77	H2	0.926	2.717
TH3	Westmorland, 1981	Brawley Airport	15.28	5.90	H1	1.660	1.516
TH4	Westmorland, 1981	Salton Sea Wildlife Refuge	7.57	5.90	H2	1.729	1.455
TH5	Coyote Lake, 1979	Gilroy Array #3	6.75	5.74	H2	2.242	1.122
TH6	San Salvador, 1986	National Geografical Inst	3.71	5.80	H1	3.987	0.631
TH7	Coyote Lake, 1979	Gilroy Array #3	6.75	5.74	H1	2.673	0.941

Table 2: Main parameters of the seven accelerograms selected.

#### 4.2 Non-linear analyses

Non-linear time history analyses have been performed on both model A (frame with hinged connections) and model B (frame retrofitted with CWSTs), with the purpose of estimating, for each accelerogram, the scaling factor that leads to the attainment of one of the ultimate conditions of the structure. In particular, each record is gradually scaled until one of these collapse conditions is reached: (i) ultimate chord rotation in one of the three columns; (ii) cyclic shear resistance in one of the three columns. It is worth saying that the scaling of the time-histories is performed with factors SF<sup>1</sup> on the records already scaled with the SF<sup>0</sup> introduced for the spectra compatibility. The scaling factors SF<sup>1</sup> are reported up to the first decimal digit. Therefore, the  $i$ -th accelerogram is actually scaled by  $SF_i = SF_i^0 \cdot SF_i^1$ .

The non-linear analyses are carried out with Rayleigh damping, calculated based on the first and the second periods of vibration (see Section 4.1), considering 5% damping ratio. P-Delta effects are also taken into account in the analyses, even if not particularly significant for this frame, since the columns are characterized by low axial loads.

For each analysis, the time histories of the following response parameters are evaluated: the shear in columns, the displacements at the top of columns, the chord rotations of columns, the hysteretic behavior of the CWSTs and of the plastic hinges. As mentioned before, the analyses are conducted considering three different values of the ultimate chord rotations:

- Rotation Limit RL1 - Ultimate chord rotations calculated with Equation (2);
- Rotation Limit RL2 - 80% of the values of the ultimate chord rotations adopted in RL1;
- Rotation Limit RL3 - 60% of the values of the ultimate chord rotations adopted in RL1.

As an example, some significant results are proposed for models A and B, referring to the accelerogram TH6, for a scaling factor SF<sup>1</sup> equal to 1, for the ultimate chord rotations capacity RL1. Figure 5 shows moment-rotation plots for the left and the central column of the frame, for the model A (black line) and the model B (red line). In the model A, the rotation in all plastic hinges exceeds the yielding point, while in the model B, all columns remain elastic. Moreover, in model B, one of the CWST devices in each couple at the top of the three columns, reaches the maximum deformation capacity  $S_{max}$ . Therefore, the three link 2 elements (see Section 3.3) are activated, transferring the full effect of seismic actions from beams to columns. This effect is visible in Figure 6, which shows the non-linear force-deformation cyclic behaviors of the three devices in model B. The cyclic behavior link 1 elements are shown in Figure 6a, these have a deformation capacity  $S_{max}$  equal to 7.5 cm, then the link 2 elements are activated (Figure 6b).

With the subsequent increase of the scaling factor SF<sup>1</sup> of time history TH6, the yielding of the plastic hinges of columns gradually occurs also in model B. However, the three columns in

model A reach the ultimate rotation values for a  $SF^1$  equal to 1.30, lower than the one corresponding to model B, which is equal to 1.70. Furthermore, for all time histories, it can be observed that the plastic hinges of the columns in model B remain elastic until the CWST devices attain their ultimate deformation capacity. This confirms that the CWSTs in model B, allow to guarantee a higher performance against the ultimate rotation capacity of columns.

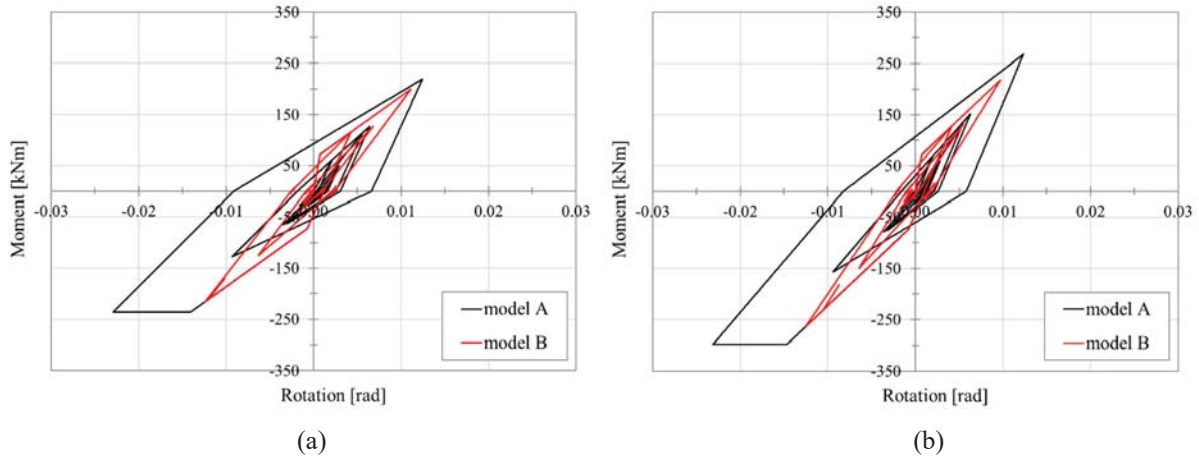


Figure 5: Cyclic behavior of columns plastic hinges for model A (black line) and model B (red line), for time history TH6 and  $SF^1 = 1$ : a) left column the frame; b) central column of the frame.

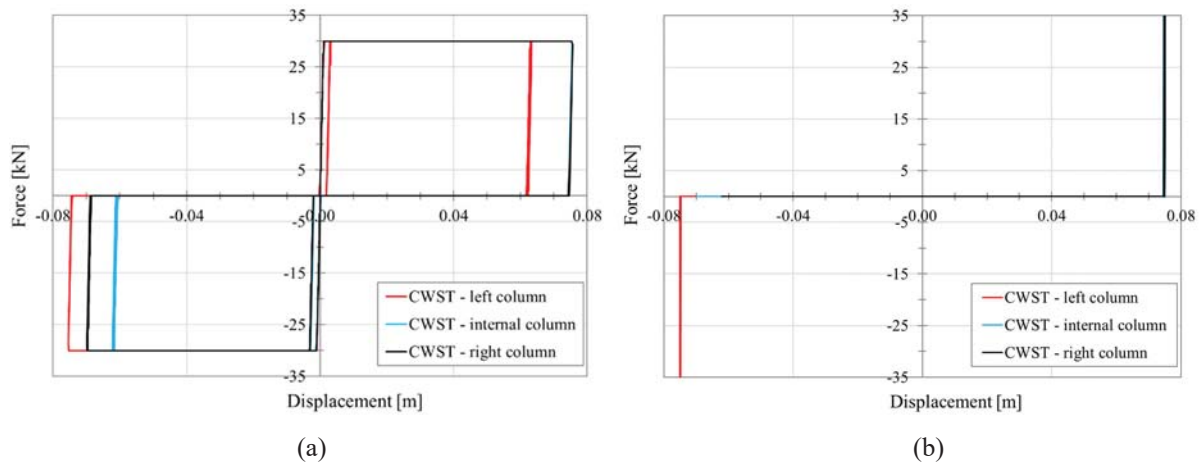


Figure 6: Cyclic behavior of the three CWSTs at the beam-column nodes in model B, for time history TH6 and  $SF^1 = 1$ : a) cyclic behavior of link 1 (see Section 3.3); b) cyclic behavior of link 2 (see Section 3.3).

In order to further evaluate the influence of the CWSTs, the time-histories of the deformations in the plastic hinge, and the shear in the left column of the frame, are proposed in Figure 7 and 8, for the accelerogram TH2 and the rotation limit RL1. Figure 7a and 8a refer to a scaling factor  $SF^1 = 1.5$  for both models, while Figure 7b and 8b refer to a scaling factor  $SF^1 = 2$ . In Figure 7, the positive effect of the devices can be observed in terms of lower deformations in model B compared to model A. Figure 8a shows that the left column in model A reaches a value of shear that corresponds to the yielding of the plastic hinge (about 43 kN), while the left column in model B has lower shear values. Indeed, for a scaling factor  $SF^1 = 1.5$ , all the columns in model A are yielded, while all the columns in model B are still elastic.

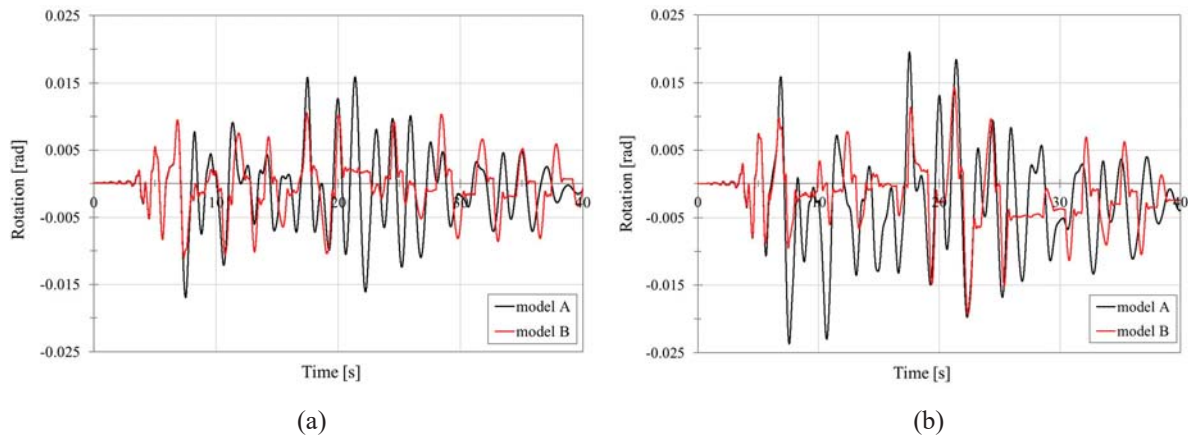


Figure 7: Time-histories of the chord rotation of the left column for TH2, for model A (black line) and model B (red line): a)  $SF^I = 1.5$ ; b)  $SF^I = 2.0$ .

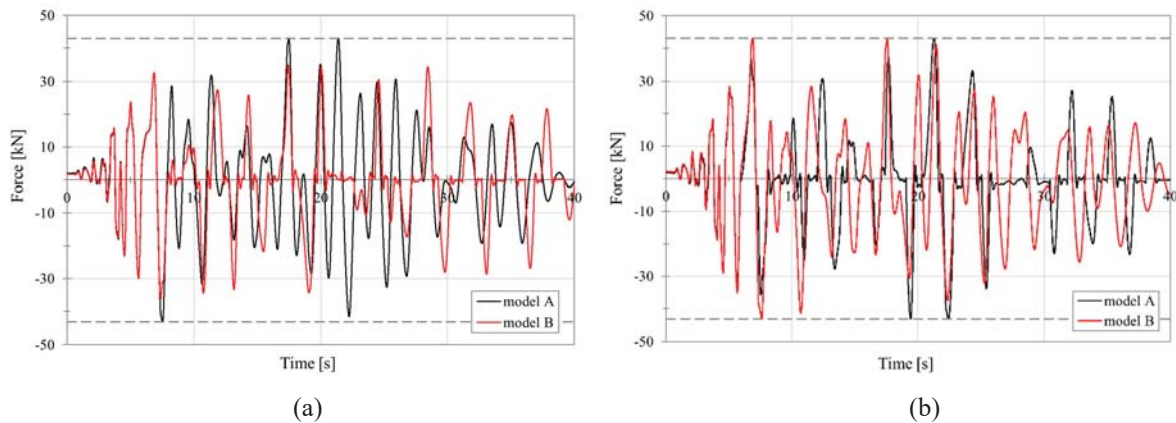


Figure 8: Time-histories of the base shear for the left column for TH2, for model A (black line) and model B (red line): a)  $SF^I = 1.5$ ; b)  $SF^I = 2.0$ .

For  $SF^I = 2$ , Figure 8b, it is possible to observe that the left column reaches the yielding force both in model A and B. However, in Figure 7b it can be noticed that, even if the left column is yielded in both models, the deformation of the plastic hinge in model B is lower than in model A. This is the positive effect of the activation of the CWSTs in the non-linear model B.

As mentioned before, the different values of chord rotations influence also the calculation of the resistance against cyclic shear. For the left column of the frame with  $SF^I = 2$ , that is equal to 82.3 kN for model A and 135.7 kN for model B. Whereas, for  $SF^I = 1.5$ , they decrease to 80.6 kN and 81.7 kN, respectively. Indeed, due to the fact that the ductility demand is higher in model A, the shear resistance is lower than the one found for model B, for both scaling factors. In any case, the shear strength of columns is always higher than the shear value corresponding to the maximum flexural capacity of the plastic hinges, therefore no shear failure is predicted by the analyses. Therefore, the base shear at the ultimate condition is equal for systems with and without CWSTs, so the verifications depend on the value of chord rotations only.

Table 3 summarizes the scaling factors to be used in models A and B in order to achieve the ultimate rotation of the plastic hinges at the base of columns, considering the three different rotation limits RL defined at the beginning of the present section. The positive effect of the CWSTs is generally visible, since the model B reaches the collapse condition for higher scaling factors compared to model A. However, ground-motion record TH1 has an opposite behavior for the rotation limit RL1. Anyway, this effect is not observed considering all the other cases.

This particular behavior can be attributed to the insurgence of dynamic amplifying effects in model B for this specific record, at scaling factors  $SF^1$  higher than 2.8. Indeed, for lower scaling factors, the positive action of the CWSTs is again evident in model B. As expected, the lowest scaling factors for both models A and B among the three thresholds considered, are found for RL3, corresponding to 60% reduction of the ultimate chord rotations.

N°	$SF^0$	RL1: $\theta_u$		RL2: 80% $\theta_u$		RL3: 60% $\theta_u$	
		$SF^1$	$SF^1$	$SF^1$	$SF^1$	$SF^1$	$SF^1$
		model A	model B	model A	model B	model A	model B
TH1	1.982	3.20	2.90	2.70	2.80	2.00	2.30
TH2	2.717	2.80	3.20	2.40	2.80	1.60	2.00
TH3	1.516	3.10	3.90	2.70	3.50	2.10	2.30
TH4	1.455	3.80	5.20	3.40	4.40	2.20	3.00
TH5	1.122	1.80	3.10	1.50	2.30	1.10	1.80
TH6	0.631	1.30	1.70	1.10	1.50	0.90	1.30
TH7	0.941	3.60	6.20	3.00	5.10	2.40	3.60

Table 3: Scaling factors  $SF^1$  for each of the seven accelerograms adopted in the time-history analyses, for model A and model B, corresponding to the three chord rotation limits considered.

## 5 BEHAVIOR FACTOR ESTIMATION

The evaluation of the behavior factor for the existing structure (Model A), and for the structure equipped with CWSTs (Model B), is discussed out in this section. The behavior factor  $q$  is calculated as:

$$q = \frac{V_{b,el}}{V_{b,nl}} \quad (4)$$

where  $V_{b,nl}$  is the maximum base shear calculated from the non-linear analyses described in Section 4.2, with a ground-motion scaling factor bringing each model to the ultimate chord rotation, and  $V_{b,el}$  is the maximum base shear in an equivalent elastic structure with the same base acceleration. For all the limits of ultimate chord rotation considered,  $V_{b,nl}$  is constant and equal to 140 kN while the corresponding scaling factor for each accelerogram is reported in Table 3, with reference to the three different rotation limits RL. The absolute values of  $V_{b,el}$  obtained from the equivalent elastic model are reported Table 4. This model is similar to model A, but it does not have plastic hinges at the base of columns.

N°	$V_{b,nl}$ [kN]	RL1: $\theta_u$		RL2: 80% $\theta_u$		RL3: 60% $\theta_u$	
		$V_{b,el}$ [kN]	$V_{b,el}$ [kN]	$V_{b,el}$ [kN]	$V_{b,el}$ [kN]	$V_{b,el}$ [kN]	$V_{b,el}$ [kN]
		model A	model B	model A	model B	model A	model B
TH1	140	483	441	412	427	309	354
TH2	140	493	558	427	493	289	359
TH3	140	375	466	328	421	257	281
TH4	140	440	591	395	506	258	350
TH5	140	318	528	267	401	197	318
TH6	140	371	471	318	422	263	371
TH7	140	341	543	289	460	234	341

Table 4: Absolute values of the base shear calculated in the time-history analyses of the linear frame model. See Table 3 for the corresponding scaling factors for the accelerograms.



As an example, the time histories of the base shear for the equivalent linear model are reported in Figure 9, for TH7. In particular, Figure 9a concerns RL1 and shows with a black line the base shear  $V_{b,el}$ , calculated with a scaling factor  $SF^1 = 3.6$  obtained from model A, and with a red line  $V_{b,el}$  calculated with  $SF^1 = 6.2$ , obtained from model B. The value of  $V_{b,nl}$  is also reported with a dashed line. Clearly, since the model is fully linear, the time histories are simply scaled. Figure 9b illustrates the same results for RL3, corresponding to the 60% reduction of the ultimate chord rotation thresholds. The plots correspond to  $SF^1 = 2.4$  for frame A, and  $SF^1 = 3.6$  for frame B. In this case, with a lower threshold for the ultimate condition compared to the previously discussed case, the gap between the results of frames A and B is lower. This is probably due to the aforementioned amplifying dynamic effects observed at higher values of the scaling factors.

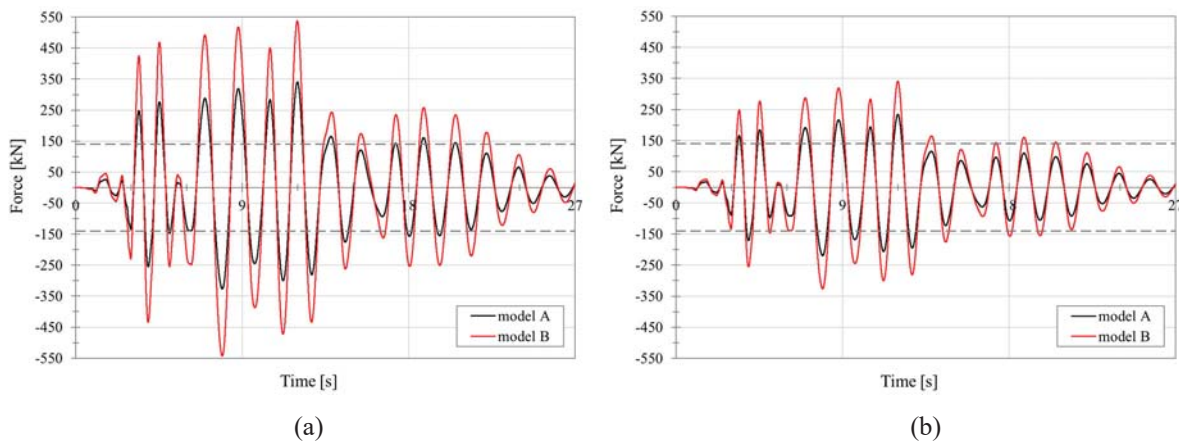


Figure 9: Time-histories of the base shear  $V_{b,el}$  for record TH7, for model A (black line) and model B (red line): a) results for RL1 with threshold  $\theta_u$ ; b) results for RL3 with threshold 60%  $\theta_u$ .

Table 5 reports the behavior factor values calculated with Equation (4) for each RL, and the corresponding average values in the bottom row. The same values are plotted in Figure 10, showing the variability of  $q$  for the seven accelerograms adopted, for each model. On average, the variability of  $q$  is consistent with the values observed for the precast buildings analyzed in Pollini et al. [32].

It is worth noticing that the same behavior factors are obtained for TH5, TH6 and TH7, both for model A for RL1, and for model B for RL3. These results for the two models are not correlated, and they are probably due to the fact the scaling factors  $SF^1$  are calculated up to the first decimal digit. If additional analyses were performed, considering more refined scaling factors, the results would likely differ for the two models.

As expected, the adoption of different ultimate chord rotations in columns affect significantly the results, since in RL2 and RL3 there is a consistent reduction in the behavior factors with respect to RL1. In particular for what concerns the model A, the average behavior factors for RL2 and 3 are 14% and 36% lower than the value obtained for RL1, respectively. Similarly for the model B, the behavior factors are 13% and 34% smaller compared to RL1 results.

Eurocode 8 part 1 [38], would recommend to adopt a behavior factor lower than 1.5 for a newly designed precast structure without seismic detailing. Moreover, Eurocode 8 part 3 [39] suggests to adopt a behavior factor not higher than 1.5 for an existing reinforced concrete structure for which the available ductility is not specifically justified. Since the columns of the existing frame under analysis are characterized by poor transversal reinforcement and are not designed against seismic actions, the average behavior factor of 2.88 obtained for model A is

deemed to have a certain degree of overestimation. The result is considered to be more realistic for this case study, when a reduction of the ultimate chord rotation is introduced. In particular,  $q$  decreases from 2.88, to 2.49 with a collapse limit 80% of  $\theta_u$ , and to 1.84 with a collapse limit 60% of  $\theta_u$ . These results clearly depend on the ultimate rotation limits predicted by Equation (2), which are not specific for existing precast columns, therefore, additional research is necessary in order to find more suitable formulations to be applied to this structural typologies, as recognized also by Magliulo et al. [45].

N°	RL1: $\theta_u$		RL2: 80% $\theta_u$		RL3: 60% $\theta_u$	
	$q$ model A	$q$ model B	$q$ model A	$q$ model B	$q$ model A	$q$ model B
TH1	3.45	3.15	2.94	3.05	2.21	2.53
TH2	3.52	3.98	3.05	3.52	2.06	2.56
TH3	2.68	3.33	2.34	3.01	1.83	2.00
TH4	3.14	4.22	2.82	3.61	1.84	2.50
TH5	2.27	3.77	1.90	2.87	1.41	2.27
TH6	2.65	3.36	2.27	3.01	1.88	2.65
TH7	2.44	3.88	2.06	3.29	1.67	2.44
Average values	<b>2.88</b>	<b>3.67</b>	<b>2.49</b>	<b>3.19</b>	<b>1.84</b>	<b>2.42</b>

Table 5: Behavior factors estimated for model A and model B, for the seven records adopted in the time-history analyses, for the three ultimate Rotation Limits considered.

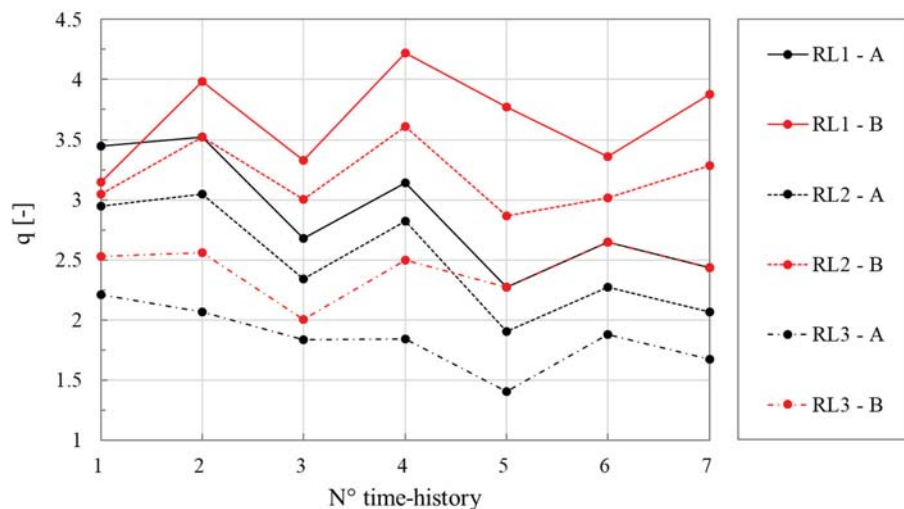


Figure 10: Behavior factor calculated for model A and B, for the three RL scenarios considered.

## 6 CONCLUSIONS

The paper discusses the seismic retrofit of an existing precast RC building equipped with CWSTs at beam-column joints. Non-linear time-history analyses have been conducted on two different models of the main frame of the structure, one with hinged beam-column connections representing the existing condition (model A), and on the one with CWST devices (model B). The effects of the introduction of the CWSTs in the connections is evaluated in terms of chord rotations demand on the columns and base shear forces, and equivalent behavior factors are proposed for the two structures. The sensitivity of the outcomes depending on the ultimate

chord rotations of columns is analyzed considering three rotation limits. On the basis of the results of the numerical simulations, the following conclusions can be drawn:

- In general, the maximum chord rotations of columns observed in the frame model with CWSTs are lower than the maximum values observed in the frame model with hinged connections, at the same scaling factor of the records, i.e. under the same seismic action;
- The damage mechanism of columns is in fully agreement with the design criteria adopted for the intervention, since, in all the analyses, the columns in model B do not yield until the attainment of the maximum deformation of the devices;
- Equivalent behavior factors are calculated for model A and model B, for three threshold values of ultimate chord rotations;
- The behavior factors estimated for model B are always higher than the ones estimated for model A, featuring simple hinged connections: the increase of the mean values of behavior factor is about 30% for model B with dissipative devices;
- The behavior factor depends on the ultimate chord rotation of columns considered, showing that the behavior factor significantly decreases with the decrease of  $\theta_u$ ;
- Additional analyses adopting other formulations for the calculation of  $\theta_u$  are required in order to find realistic results for the specific case of evaluating existing precast columns; moreover, further research may be necessary for the modelling of the non-linear flexural behavior of precast elements;
- CWST devices are deemed to be a good solution for maintaining a low level of stress and deformation in the existing columns of the frame, since frame model B is less vulnerable than frame model A, under the same seismic actions.

## ACKNOWLEDGEMENTS

The support of Sismocell - Sismo Solution s.r.l., is gratefully acknowledged.

## REFERENCES

- [1] A. Belleri, E. Brunesi, R. Nascimbene, M. Pagani, P. Riva, Seismic performance of precast industrial facilities following major earthquakes in the Italian territory. *Journal of Performance of Constructed Facilities*, **29**(5): 04014135, 2014. [https://doi.org/10.1061/\(ASCE\)CF.1943-5509.0000617](https://doi.org/10.1061/(ASCE)CF.1943-5509.0000617)
- [2] M. Savoia, N. Buratti, L. Vincenzi, Damage and collapses in industrial precast buildings after the 2012 Emilia earthquake. *Engineering Structures*, **137**, 162-180, 2017. <https://doi.org/10.1016/j.engstruct.2017.01.059>
- [3] N. Buratti, F. Minghini, E. Ongaretto, M. Savoia, N. Tullini, Empirical seismic fragility for the precast RC industrial buildings damaged by the 2012 Emilia (Italy) earthquakes. *Earthquake Engineering & Structural Dynamics*, **46**, 2317-2335, 2017. <https://doi.org/10.1002/eqe.2906>

- [4] F. Minghini, E. Ongaretto, V. Ligabue, M. Savoia, N. Tullini, Observational failure analysis of precast buildings after the 2012 Emilia earthquakes. *Earthquake Structures*, **11**(2), 327-346, 2016. <https://doi.org/10.12989/eas.2016.11.2.327>
- [5] N. Batalha, H. Rodrigues, H. Varum, Seismic performance of RC precast industrial buildings—learning with the past earthquakes. *Innovative Infrastructure Solutions*, **4**(4), 2019. <https://doi.org/10.1007/s41062-018-0191-y>
- [6] D.A. Bournas, P. Negro, F.F. Taucer, Performance of industrial buildings during the Emilia earthquakes in Northern Italy and recommendations for their strengthening. *Bulletin of Earthquake Engineering*, **12**, 2383-2404, 2013. <https://doi.org/10.1007/s10518-013-9466-z>
- [7] L. Liberatore, L. Sorrentino, D. Liberatore, L.D. Decanini, Failure of industrial structures induced by the Emilia (Italy) 2012 earthquakes. *Engineering Failure Analysis*, **34**, 629-647, 2013. <https://doi.org/10.1016/j.engfailanal.2013.02.009>
- [8] G. Magliulo, M. Ercolino, C. Petrone, O. Coppola, G. Manfredi, The Emilia earthquake: seismic performance of precast reinforced concrete buildings. *Earthquake Spectra*, **30**, 891-912, 2014. <https://doi.org/10.1193/091012EQS285M>
- [9] A. Babič, M. Dolšek, Seismic fragility functions of industrial precast building classes. *Engineering Structures*, **118**, 357-370, 2016. <https://doi.org/10.1016/j.engstruct.2016.03.069>
- [10] C. Demartino, I. Vanzi, G. Monti, C. Sulpizio, Precast industrial buildings in Southern Europe: loss of support at frictional beam-to-column connections under seismic actions. *Bulletin of Earthquake Engineering*, **16**, 259-294, 2018. <https://doi.org/10.1007/s10518-017-0196-5>
- [11] M. Bovo, M. Savoia, Evaluation of force fluctuations induced by vertical seismic component on reinforced concrete precast structures. *Engineering Structures*, **179**, 70-87, 2019. <https://doi.org/10.1016/j.engstruct.2018.10.018>
- [12] A. Titi, F. Biondini, G. Toniolo, Seismic assessment of existing precast structures with dry-friction beam-to-column joints. *Bulletin of Earthquake Engineering*, **16**, 2067-2086, 2018. <https://doi.org/10.1007/s10518-017-0271-y>
- [13] F. Biondini, A. Titi, G. Toniolo. Biondini F, Titi A, Toniolo G, Prestazioni sismiche di strutture prefabbricate con connessioni trave - pilastro ad attrito (in Italian). *Proceedings of the XV Conference of the Italian Association of Seismic Engineering (ANIDIS)*, Padua, Italy, 30 June-4 July, 2013.
- [14] M. Ercolino, G. Magliulo, G. Manfredi, Failure of a precast RC building due to Emilia-Romagna earthquakes. *Engineering Structures*, **118**, 262-273, 2016. <http://dx.doi.org/10.1016/j.engstruct.2016.03.054>
- [15] M. Bovo, M. Savoia, Numerical simulation of seismic-induced failure of a precast structure during the Emilia earthquake. *Journal of Performance of Constructed Facilities*, **32**(1): 04017119, 2018. [https://doi.org/10.1061/\(ASCE\)CF.1943-5509.0001086](https://doi.org/10.1061/(ASCE)CF.1943-5509.0001086)
- [16] M.G. Deyanova, S. Pampanin, R. Nascimbene, Assessment of single-storey precast concrete industrial buildings with hinged beam-column connections with and without dowels. *Second European conference on earthquake engineering and seismology*, Istanbul, Turkey, 25-29 August, 2014.

- [17] V. Ligabue, M. Bovo, M. Savoia, Connessioni tegolo-trave: studio sperimentale e numerico del comportamento di angolari di collegamento (in Italian). *Proceedings of workshop "Tecniche innovative per il miglioramento sismico di edifici prefabbricati"*, Bologna, Italy, 22 October, 2014.
- [18] G. Muciaccia, M. Cervio, M. Franzoso, M. Veneziano, Utilizzo di ancoraggi post-inseriti in interventi di recupero di capannoni industriali in zona sismica (in Italian). *Proceedings of Workshop "Tecniche innovative per il miglioramento sismico di edifici prefabbricati"*, Bologna, Italy, 22 October, 2014.
- [19] E. Nastri, M. Vergato, M. Latour, Performance evaluation of a seismic retrofitted R.C. precast industrial building. *Earthquake and Structures*, **12**(1), 13-21, 2017. <https://doi.org/10.12989/eas.2017.12.1.013>
- [20] L. Rossi, M. Stupazzini, D. Parisi, B. Holtschoppen, G. Ruggieri, C. Butenweg, Empirical fragility functions and loss curves for Italian business facilities based on the 2012 Emilia-Romagna earthquake official database. *Bulletin of Earthquake Engineering*, **18**, 1693-1721, 2020. <https://doi.org/10.1007/s10518-019-00759-1>
- [21] D. Rodrigues, H. Crowley, V. Silva, Earthquake loss assessment of precast RC industrial structures in Tuscany (Italy). *Bulletin of Earthquake Engineering*, **16**, 203-228, 2017. <https://doi.org/10.1007/s10518-017-0195-6>
- [22] M. Bosio, A. Belleri, P. Riva, A. Marini, Displacement-based simplified seismic loss assessment of Italian precast buildings. *Journal of Earthquake Engineering*, **24**(1), 60-81, 2020. <https://doi.org/10.1080/13632469.2020.1724215>
- [23] B. Dal Lago, F. Biondini, G. Toniolo, Friction-based dissipative devices for precast concrete panels. *Engineering Structures*, **147**, 356-371, 2017. <https://doi.org/10.1016/J.ENGSTRUCT.2017.05.050>
- [24] B. Dal Lago, F. Biondini, G. Toniolo, Experimental investigation on steel W-shaped folded plate dissipative connectors for horizontal precast concrete cladding panels. *Journal of Earthquake Engineering*, **22**(5), 778-800, 2017. <https://doi.org/10.1080/13632469.2016.1264333>
- [25] B. Dal Lago, G. Toniolo, R. Felicetti, M. Lamperti Tornaghi, End support connection of precast roof elements by bolted steel angles. *Structural Concrete*, **18**(5), 755-767, 2017. <https://doi.org/10.1002/suco.201600218>
- [26] R. Scotta, L. De Stefani, R. Vitaliani, Passive control of precast building response using cladding panels as dissipative shear walls. *Bulletin of Earthquake Engineering*, **13**, 3527-3552, 2015. <https://doi.org/10.1007/s10518-015-9763-9>
- [27] A. Belleri, A. Marini, P. Riva, R. Nascimbene, Dissipating and re-centring devices for portal-frame precast structures. *Engineering Structures*, **150**, 736-745, 2017. <https://doi.org/10.1016/j.engstruct.2017.07.072>
- [28] P. Martinelli, M.G. Mulas, An innovative passive control technique for industrial precast frames. *Engineering Structures*, **32**, 1123-1132, 2010. <https://doi.org/10.1016/j.engstruct.2009.12.038>
- [29] L. Marinini, P. Spatti, P. Riva, R. Nascimbene, Strutture prefabbricate: moderni sistemi di protezione antisismica (in Italian). *Progettazione sismica*, **3**, 23-44, 2011.



- [30] A.V. Pollini, N. Buratti, C. Mazzotti, Effectiveness of a dissipative beam-column connection based on carbon-wrapped steel tubes. *Second European conference on earthquake engineering and seismology*, Istanbul, Turkey, 25-29 August, 2014.
- [31] A.V. Pollini, N. Buratti, C. Mazzotti, Experimental and numerical behaviour of dissipative devices based on carbon-wrapped steel tubes for the retrofitting of existing precast RC structures. *Earthquake Engineering & Structural Dynamics*, 1-21, 2018. <https://doi.org/10.1002/eqe.3017>
- [32] A.V. Pollini, N. Buratti, C. Mazzotti, Behavior factor of concrete portal frames with dissipative devices based on carbon-wrapped steel tubes. *Bulletin of Earthquake Engineering*, **19**, 553-578, 2021. <https://doi.org/10.1007/s10518-020-00977-y>
- [33] H-W. Song, Z-M. Wan, Z-M. Xie, X-W. Du, Axial impact behavior and energy absorption efficiency of composite wrapped metal tubes. *International Journal of Impact Engineering*, **24**(4), 385-401, 2000. [https://doi.org/10.1016/S0734-743X\(99\)00165-7](https://doi.org/10.1016/S0734-743X(99)00165-7)
- [34] R.M. Lima, Z.N. Ismarrubie, E.S. Zainudin, S.H. Tang, Axial behavior of steel tube wrapped by composite as energy absorber under compressive load, *IEEE Symposium on Business, Engineering and Industrial Applications (ISBEIA)*, Langkawi, Malaysia, 2011.
- [35] M. Savoia, C. Mazzotti, N. Buratti, B. Ferracuti, M. Bovo, V. Ligabue, L. Vincenzi, Damages and collapses in industrial precast buildings after the Emilia earthquake (in Italian). *Ingegneria Sismica*, **29**(2), 120-131, 2012.
- [36] D. Bellotti, C. Casotto, H. Crowley, M.G. Deyanova, F. Germagnoli, G. Fianchisti, E. Lucarelli, S. Riva, R. Nascimbene, Single-storey precast buildings: probabilistic distribution of structural systems and subsystems from the sixties (in Italian). *Progettazione Sismica*, **5**(3), 41-70, 2014.
- [37] <https://www.cspfea.net/prodotti/midas-gen/>. Accessed 21 March 2021.
- [38] CEN (European Committee for Standardization), Design of structures for earthquake resistance – Part 1: General rules, seismic actions and rules for building. *Eurocode 8*, Brussels, 2005.
- [39] CEN (European Committee for Standardization), Design of structures for earthquake resistance – Part 3: Assessment and retrofitting of buildings. *Eurocode 8*, Brussels, 2005.
- [40] T. Takeda, M.A. Sozen, N.N. Nielsen, Reinforced concrete response to simulated earthquake. *Journal of the structural division*, **96**(12), 2557-2573, 1970.
- [41] D.E Biskinis, M.N. Fardis, Cyclic strength and deformation capacity of RC members, including members retrofitted for earthquake resistance. *Proceedings of the 5th International Ph.D Symposium in Civil Engineering*, Delft, Balkema, 1125-1133, 2004.
- [42] D.E. Biskinis, M.N. Fardis, Cyclic deformation capacity, resistance and effective stiffness of RC members with or without retrofitting. *Proceedings of the 14<sup>th</sup> World conference on Earthquake Engineering*, Beijing, China, 12-17 October, 2008.
- [43] G.M. Verderame, P. Ricci, G. Manfredi, E. Cosenza, Ultimate chord rotation of RC columns with smooth bars: some considerations about EC8 prescriptions. *Bulletin of Earthquake Engineering*, **8**, 1351-1373, 2010. <https://doi.org/10.1007/s10518-010-9190-x>
- [44] M. Bovo, N. Buratti, Evaluation of the variability contribution due to epistemic uncertainty on constitutive models in the definition of fragility curves of RC frames. *Engineering Structures*, **188**, 700-716, 2019. <https://doi.org/10.1016/j.engstruct.2019.03.064>

- [45] G. Magliulo, D. Bellotti, C. Di Salvatore, F. Cavalieri, RINTC-E project: towards the seismic risk of low and pre-code single-story RC precast buildings in Italy. *Proceedings of the 7<sup>th</sup> ECCOMAS Thematic Conference on Computational Methods in Structural Dynamics and Earthquake Engineering (COMPDYN)*, Crete, Greece, 24-26 June, 2019.
- [46] CEN (European Committee for Standardization), Design of concrete structures – Part 1-1: General rules and rules for buildings. *Eurocode 2*, Brussels, 2004.
- [47] D.M. 20/02/2018, Norme tecniche per le costruzioni (in Italian). Decreto ministeriale del Ministero delle Infrastrutture e dei trasporti, 2018.
- [48] <https://peer.berkeley.edu/nga-west>. Accessed 21 March 2021.
- [49] J.J. Boomer, A.B. Acevedo, The use of real earthquake accelerograms as input to dynamic analysis. *Journal of Earthquake Engineering*, **8**(1), 43-91, 2004.

## METAMODELING CHOICES FOR SEISMIC VULNERABILITY ASSESSMENT OF BRB-RETROFITTED LOW-DUCTILITY RC FRAMES

J. Ghosh<sup>1</sup>, F. Freddi<sup>2</sup>

<sup>1</sup> Department of Civil Engineering, Indian Institute of Technology Bombay, Mumbai, India  
e-mail: [jghosh@iitb.ac.in](mailto:jghosh@iitb.ac.in)

<sup>2</sup> Dept. of Civil, Environmental & Geomatic Engineering, University College London, London, UK  
e-mail: [f.freddi@ucl.ac.uk](mailto:f.freddi@ucl.ac.uk)

---

### Abstract

*Damage incurred in low-ductility reinforced concrete (RC) buildings during recent earthquakes continues to underline their structural vulnerability under seismic shaking. Among the viable seismic retrofitting procedures, passive control systems such as buckling-restrained braces (BRBs) have emerged as an efficient strategy for structural damage mitigation through stable energy dissipation while providing additional strength and stiffness to low-ductility buildings. Although quantifying the beneficial effects of BRBs for vulnerability reduction through seismic fragility curves has been suitably investigated in literature, almost all such studies consider a deterministic description of the BRB device. This study illustrates a meta-modeling framework rooted in statistical learning techniques for efficient seismic vulnerability assessment of BRB-retrofitted low-ductility RC frames. The framework develops multidimensional probabilistic seismic demand models for response prediction of a case study retrofitted frames as a function of ground motion characteristics as well as the design parameters of the BRB device. These demand models when compared against damage states capacity estimates subsequently yields vector-based seismic fragility functions that provide notable advantages over unidimensional fragility curves in terms of efficiency as well as generality. Additionally, uncertainties stemming from a multitude of sources can also be conveniently captured and propagated through the different stages of statistical model development. The proposed study aims to help researchers, stakeholders, and even device manufactures by providing a convenient tool for vulnerability evaluation of retrofitted structures with reasonable accuracy and enhanced efficiency of computation.*

**Keywords:** Buckling-Restrained Braces, Reinforced Concrete Frames, Seismic Retrofit, Seismic Devices Uncertainty, Metamodeling.

---

## 1 INTRODUCTION

Many recent earthquakes worldwide have continued to underline the substantial seismic vulnerability of existing reinforced concrete (RC) buildings (*e.g.*, [1][2]) and the urgent need for reliable retrofit strategies to effectively increase their seismic safety and resilience.

Among the many retrofit strategies available, the use of passive control systems [3] such as buckling-restrained braces (BRBs) have emerged as an efficient strategy for structural damage mitigation through stable energy dissipation while providing additional strength and stiffness to low-ductility buildings (*e.g.*, [4][5][7][6][8][9][10]). BRBs are a type of yielding device where a sleeve provides buckling resistance to an unbonded core that resists the axial stress. As buckling is prevented, the BRB's core can develop axial yielding in both tension as well as compression, with an almost symmetric hysteretic behaviour and the development of large and stable hysteretic loops, providing significant energy dissipation capacity [11].

The use of BRBs for seismic retrofitting has been widely investigated in the last few years, however, while the effect of some uncertain parameters, such as the ground motion record-to-record variability, is often investigated (*e.g.*, [7][8][10]), only a deterministic description of the dampers' properties is usually considered.

The seismic reliability assessment of a structural system should consider all the uncertainties related to the seismic input, the geometry, the mechanical properties of the structure, as well as the dissipative devices contributing to the lateral load resisting system. Previous studies have shown that, in conventional structures, the effect of model parameter uncertainty is usually negligible with respect to the record-to-record variability [12]; however, this is not the case for structures equipped with dampers since their seismic response heavily depends on the properties of a few numbers of devices (*e.g.*, [13][14][15][16]).

Dampers are produced by the manufacturer in order to meet the design values of some parameters and successively assessed by quality-control tests considering tolerance limits established by seismic and qualification codes (*e.g.*, [17][18][19]). Codes worldwide provide varying tolerance limits for different types of devices, considering different device properties and the influence of multiple factors, such as, imperfections related to the manufacturing process, temperature variation, and aging. For example, the EN 15129 [17] requires the control of the devices' variation with respect to the nominal values introducing upper and lower limits of the devices' properties, defined by a tolerance. For 'displacement dependent devices', such as BRBs, the EN 15129 [17] requires performing qualification tests to show that the effective (*i.e.*, secant) stiffness  $K_{eff,b}$ , and effective damping  $\xi_{eff,b}$  evaluated in correspondence to the design displacement are in good agreement with the prescribed nominal design values. Tolerances are set to  $\pm 15\%$  to account for variation during the manufacturing process. These two control parameters ( $K_{eff,b}$  and  $\xi_{eff,b}$ ) exhaustively identify the primary characteristics of the device behaviour. Therefore, the code-based tolerance limits are also implicitly applied to other related parameters, such as the associated device forces and displacement capacity values. Similar recommendations exist within the ASCE/SEI 7-16 [18] and other seismic codes worldwide. In particular, the ASCE/SEI 7-16 [18] allows for tolerances that could go up to  $\pm 20\%$  from nominal design values and controlling the variation in terms of device's force  $F_b$  and area of the hysteretic loop  $E_{loop,b}$  measured during the tests wherein the latter parameter allows the control dissipation capacity variation of the devices.

In a recent study, Freddi *et al.* [16] investigated the influence of the BRBs' uncertainty related to tolerance limits used in device qualification control tests by considering a three-story three-bay RC moment-resisting frame (MRF) as case study. BRBs' uncertainty was implemented through a two-level factorial design strategy and Latin-Hypercube Sampling technique. Cloud analysis and probabilistic seismic demand models were used to develop fragility

functions for the bare and retrofitted frame for four damage states while also accounting for the uncertainty in the property of BRBs. Risk estimates were successively evaluated for three case-study regions. The results showed that, for the considered case-study structure, these uncertainties could lead to an increase of fragility up to 21% and a variation in seismic risk estimates up to 56%. The obtained results underlined the impact of the BRBs' uncertainty and the need for appropriate safety coefficients for their design as functions of the tolerance limits adopted. Also, additional studies are required to investigate the influence of BRB device variability on different case study structures, considering different retrofit levels (*i.e.*, different proportions of the base shear between the MRF and the BRBs) and the influence of different tolerance limits. This would require modelling a large number of case study structures and performing a large number of numerical analysis while considering the influence of all the above-mentioned parameters.

However, advanced probabilistic tools allow the study of the influence several parameters in a simplified and efficient way. In this direction, the present study investigates the use of a metamodeling framework rooted in statistical learning techniques for efficient seismic vulnerability assessment of BRB-retrofitted low-ductility RC frames accounting for different tolerance limits adopted during qualification tests of BRB devices. The framework develops multidimensional probabilistic seismic demand models for response prediction of a case study retrofitted frames as a function of: a) ground motion characteristics, and b) design parameters of the BRB device. These demand models when compared against damage states capacity estimates subsequently yields vector-based seismic fragility functions that provide notable advantages over unidimensional fragility curves in terms of efficiency as well as generality. The present study demonstrates the adequacy of such advanced probabilistic tool for vulnerability evaluation of retrofitted structures with reasonable accuracy and enhanced efficiency of computation and establishes a framework for the inclusion of uncertainties stemming from additional sources.

## 2 CASE-STUDY RETROFITTED LOW-DUCTILITY FRAME

### 2.1 Frame Description

The present study selects a benchmark three-story three-bays RC MRF, representative of non-seismically designed (low-ductility) low-rise RC buildings. This structure is representative of typical constructions designed before the introduction of modern seismic design codes in several areas of the mid-west of the USA, many countries in Europe, and several regions in Asia. Moreover, the availability of laboratory experimental test results from a 1:3 reduced scale model of the case-study frame [20], as well as frame-subassemblages [21], makes the selected reference structure as an ideal choice for this study. FE model validation against experimental results helps in gaining confidence in the numerical approach as well as predicted building response at both the global- and local-level.

Figure 1 shows the frame layout including the placement of the BRBs. The dissipative braces (BRBs) employed in RC MRFs are typically made by a series arrangement the BRB device and an elastic steel brace exhibiting adequate over-strength (see Figure 1). The case-study frame has an inter-story height of 3.66 m, a total building height of 10.75 m, and constant bay width of 5.49 m. The building is designed for gravity loads only, without any seismic detailing provisions following the pre-seismic design rules of the ACI 318-89 [22]. Furthermore, negligible wind loads for low-rise structures, such as the case-study frame, leads to a complete lack of accounting for lateral loads in the frame design. The building columns are constant square sections of 300 mm  $\times$  300 mm, while beams dimensions are 230 mm  $\times$  460 mm at each floor. The concrete compressive cube strength is  $f_c = 24$  MPa, and the reinforcing bars are Grade 40 steel with a yield strength of  $f_y = 276$  MPa. Further details on the case-study structure and



reinforcement configurations within beams, columns, and beam-column joints can be found in Bracci *et al.* [20] and Aycardi *et al.* [21].

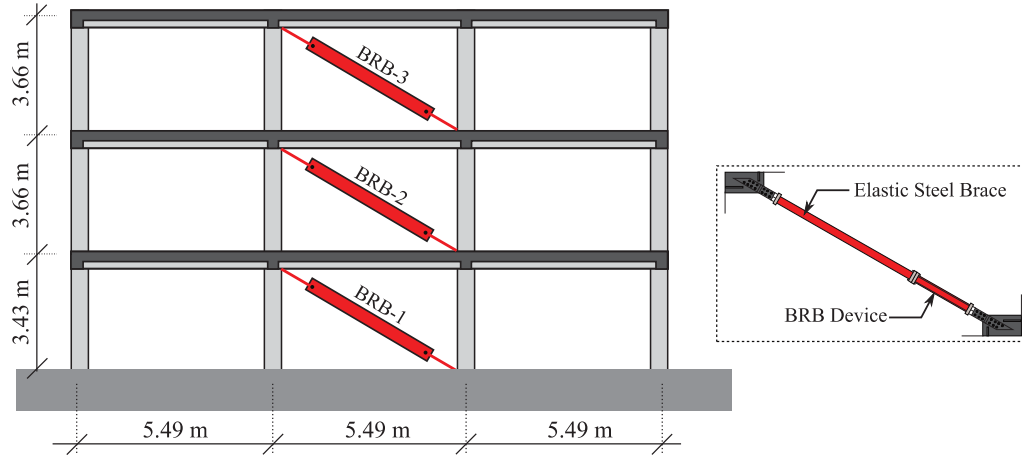


Figure 1: Case-study bare-frame layout (adapted from Bracci *et al.* [20]), placement and arrangement of BRBs.

The design of the BRBs is based on the methodology described in Freddi *et al.* [8]. The BRB design procedure is based on the displacement distribution of the first vibration mode and uses non-linear static analysis of the bare frame and a Single-Degree-of-Freedom (SDoF) simplification for the definition of some design parameters which are related to the retrofit objectives, such as the design displacement ( $d_u$ ); the target ductility of the dissipative braces ( $\mu_d$ ) and the base shear capacity of the dissipative system ( $V_{d,1}$ ).

As shown in Figure 1, the retrofitting is performed by introducing the BRBs in the central bay at each story of the case-study frame. The base shear and the design displacement of the bare frame, defined based on the pushover analysis, are respectively  $V_{f,1} = 180.72$  kN and  $d_u = 0.308$  m where  $d_u$  is selected as the maximum lateral displacement capacity of the bare frame corresponding to the Complete Damage State.

In the present study, the retrofitted configuration investigated is the one where the base shear of the dissipative system ( $V_{d,1}$ ) is selected equal to the base shear of the bare frame ( $V_{f,1}$ ), or in other words, the strength proportion coefficient  $\alpha = V_{d,1}/V_{f,1}$  is assumed equal to 1 [10], hence doubling the base shear resistance of the retrofitted frame. The ductility of the dissipative braces, *i.e.*, dissipative device plus elastic brace ( $\mu_d$ ) is assumed equal to 15. The design method provides properties such as strength  $F_{d,i}$  and stiffness  $K_{d,i}$  of the dissipative braces at each story. Assuming the ductility of the BRB devices ( $\mu_{BRB} = 20$ ), the yielding resistance of the materials for BRB devices ( $f_{y,BRB} = 250$  MPa) and elastic braces ( $f_{y,eb} = 355$  MPa), and based on strength  $F_{d,i}$ , and stiffness  $K_{d,i}$  of the dissipative braces, the properties of the components can be easily derived.

## 2.2 Modelling Strategy

The FE package OpenSees [23] is used to develop a state-of-the-art two-dimensional model of the case-study frame. The non-linear flexural hysteretic response of beams and columns is simulated using the 'beamWithHinges' element that consists of a central elastic element and two plastic hinge regions at the elements ends defined by fiber sections [24]. The effective flexural stiffness of the elastic portion of the element is evaluated by the ratio of the moment and the curvature corresponding to the yielding of the first rebar of the section. The plastic hinge lengths for both beams and columns are evaluated based on Panagiotakos and Fardis [25].

In these regions, fiber sections are defined that consider the spread of plasticity within unconfined (cover) concrete, confined (core) concrete, and layers of longitudinal reinforcement. While the core and cover concrete within the fiber sections are modelled using the non-linear degrading ‘Concrete02’ material model, the ‘Hysteretic’ material model is used to model the longitudinal reinforcements. For this material, the parameters controlling pinching, damage, and degraded unloading stiffness are calibrated such that close agreements are attained between the numerical and experimental results for model validation. The slab is modelled using unconfined concrete material model with an effective width equal to four times the beam's width, as recommended in the ACI 318-89 [22]. The rigid-floor diaphragm is modelled by assigning high axial stiffness to the beams. Gravity loads are distributed on the beams while masses are concentrated at the beam-column intersections.

‘ZeroLength’ shear and axial springs are introduced at the top of each column, by assigning them the ‘LimitState’ uniaxial material accounting for possible brittle failure mechanisms typical of low-ductility RC MRFs. Moreover, a two-node ‘zeroLength’ rotational joint spring and four rigid offsets are used to model the joint behaviour, including the influence of short embedment lengths of bottom reinforcements of beams within the beam-column joints as done in Jeon *et al.* [26]. In this model, beams and columns are continuous, while the joint model controls their relative rotation. The ‘Pinching4’ material model is used to define the beam-column joint response.

The dissipative braces are modelled by two elements in series representing respectively the BRB device and the elastic brace. The ‘steelBRB’ material model [11] is used to describes the hysteretic behaviour of the BRBs while capturing the kinematic and isotropic hardening, along with the tension-compression asymmetry that typically characterizes these devices.

The model both at component- and at global-level has been validated against the experimental results provided by Aycardi *et al.* [21] and Bracci *et al.* [20]. For the BRB devices a calibration has been conducted based on the results of the experimental qualification tests performed by a manufacturer. For additional details on the modelling and validation please refer to Freddi *et al.* [8][16][27].

### 2.3 Uncertain Parameters

The present paper investigates the influence of the uncertainty stemming from device-to-device variation by the definition of story- and system-level fragility curves. As previously discussed, for ‘Displacement-dependent devices’, such as BRBs, the EN 15129 [17] requires quality-control tests to show that the effective (secant) stiffness  $K_{eff,b}$ , and effective damping  $\xi_{eff,b}$  are in good agreement with the prescribed nominal design values and within prescribed tolerance limits. Alternatively, the ASCE/SEI 7-16 [18] controls the variation in terms of device’s force  $F_b$  and area of the hysteretic loop  $E_{loop,b}$  measured during the tests. In both approaches, the two control parameters exhaustively identify the main characteristics of the device behaviour. Therefore, the code-based tolerance limits are implicitly applied to other related parameters.

In the present study, stiffness, force and dissipation capacity variations are numerically reflected within the model by accounting for variations in the area of the BRB devices ( $A_{BRB}$ ) while keeping the material yield strength ( $f_{y,BRB}$ ) as constant. Variation in the BRB device area ( $A_{BRB}$ ) has been chosen as opposed to the material yield strength ( $f_{y,BRB}$ ) as it induces the highest variation in the device response since alteration of the BRB area affects both stiffness, strength and the hysteretic energy dissipated. Device-to-device variation is assumed within the limits set by the codes (*i.e.*,  $\pm 15\%$  in accordance with the EN 15129 [17] and ASCE/SEI 7-16 [18]) and applied independently among the devices at the different stories. The study considers different

values of the tolerance limits assumed and investigates their influence in terms of fragility estimates.

### 3 SURROGATE MODELLING AND PARAMETERIZED FRAGILITY DEVELOPMENT

This section of the paper focuses on the development of parameterized seismic fragility functions for the retrofitted frame that are conditioned on the ground motion intensity measure ( $IM$ ), and the BRB areas across the different stories. The following subsections outline the fragility development procedure that comprises of first constructing an experimental design matrix with uncertain model parameters, metamodel fitting to the response parameter, and eventual parameterized model development using logistic regression.

#### 3.1 Modelling design of experiments

This study adopts a Latin Hypercube Design of experiments that initiates with discretizing the domain of each of the input variables  $A_{BRB1}$ ,  $A_{BRB2}$ , and  $A_{BRB3}$  to  $k$  intervals, where  $k$  is the number of Latin Hypercube samples to be selected for each variable and eventually resulting in an experimental design matrix of  $n \times k$ . Following the discretization, the set of all possible Cartesian products of these discretized intervals constitutes the partitioning of the  $n$ -dimensional sample space to  $k^n$  cells. Consequently, a set of  $k$  cells are chosen of the possible  $k^n$  cells such that the projection of the center of each cell on the respective axes of each parameter generates  $k$  unique points. Consequently, choosing a random point within each selected cell generates a Latin Hypercube Design.

It is noted that the above procedure to generate sample points may still not guarantee an efficient exploration of the sample space. This study adopts a *maximin based Latin Hypercube Design* which selects design points after maximizing the minimum distance between the sample points ensuring that two points are not located too close together. For instance, if  $l$  is a measure of distance (based on the  $L1$  or  $L2$  norm), and  $\mathbb{S}$  is a  $k$ -point design, the smallest distance between any two points  $A_{BRBi}$  and  $A_{BRBj}$  may be given by:

$$\min_{A_{BRBi}, A_{BRBj} \in \mathbb{S}, i \neq j} l(A_{BRBi}, A_{BRBj}) \quad (1)$$

Consequently, a maximin distance design maximizes the minimum distance given in Equation (1) to generate another  $k$ -point design  $\mathbb{S}_M$  such that the minimum distance between the points  $A_{BRBi}$  and  $A_{BRBj}$  now becomes:

$$\min_{A_{BRBi}, A_{BRBj} \in \mathbb{S}_M, i \neq j} l(A_{BRBi}, A_{BRBj}) = \max_{\mathbb{S} \subset \Theta} \left[ \min_{A_{BRBi}, A_{BRBj} \in \mathbb{S}, i \neq j} l(A_{BRBi}, A_{BRBj}) \right] \quad (2)$$

where,  $\Theta$  constitutes the  $n$ -dimensional design sample space. In addition to the maximin based Latin Hypercube design, this study also considers experimental design based on quasi-random sampling. A typical experimental design  $D$  of size  $k \times n$  generate by the Latin Hypercube Design can be represented as shown in Equation (3):

$$D = \begin{bmatrix} A_{BRB1,1} & A_{BRB2,1} & A_{BRB3,1} \\ A_{BRB1,2} & A_{BRB2,2} & A_{BRB3,2} \\ \vdots & \vdots & \vdots \\ A_{BRB1,k} & A_{BRB2,k} & A_{BRB3,k} \end{bmatrix} \quad (3)$$

where each row of the design matrix provides a unique combination of BRB areas within the tolerance limits. In addition to these parameters, a critical parameter of interest is the ground motion intensity  $IM$ . Due to the inherent randomness in ground motion time-histories,  $IM$  is treated as an uncontrollable parameter in the experimental design. The uncertainty associated with ground motions is propagated in this study by pairing each row of the design matrix with a random time-history record and conducting nonlinear dynamic analysis of  $k$ -statistically similar but characteristically different retrofitted building samples. The peak interstory drift ratios for the overall frame are used next to fit multivariate probabilistic seismic demand models and fragility functions as described in the next step.

In the present study, the uncertainty affecting the seismic input in terms of variability in duration, frequency content, and other characteristics of the input expected to act on the system, is taken into account by considering the set of 240 natural records selected by Baker *et al.* [28].

### 3.2 Metamodel fitting to storey level response

Among the various metamodeling strategies, this study adopts the polynomial response surface models to approximate the maximum story and system level response as a function of the ground motion intensity measure and BRB areas. Polynomial response surface models were first developed by Box and Wilson [29] and have been widely adopted for predicting the response of complex engineering systems, such as buildings and bridges. The most widely used response surface models consist of low order polynomial functions. Simpson *et al.* [30] recommended that first order polynomials shall suffice for responses characterized by low curvatures: an assumption that is valid for the present case at hand. Consequently, first order response surface polynomials of the form shown in Equation (4) are adopted because of enhanced goodness-of-fit measures in comparison to first order polynomial models.

$$\hat{y} = \beta_0 + \beta_{IM} + \sum_{i=1}^3 \beta_i A_{BRBi} \quad (4)$$

In this equation,  $\hat{y}$  represents the predicted value of the maximum interstory drift ratio (story level:  $IDR_{max,i}$  or system level:  $IDR_{max}$ ), and  $\beta_0$ ,  $\beta_{IM}$ , and  $\beta_i$  are the regression coefficients obtained using least square principles after fitting the response surface to the response data from nonlinear time history analyses of the retrofitted frame. Table 1 shows the regression coefficients for the polynomial response surface model for each of the three stories as well as the overall frame along with the  $R^2$  goodness of fit measure indicative of the satisfactory response prediction at the story as well as system level.

	Story 1	Story 2	Story 3	Whole Frame
$\beta_0$	0.802	0.800	0.343	0.951
$\beta_{IM}$	1.023	0.978	0.877	1.005
$\beta_1$	-0.079	0.021	0.040	-0.001
$\beta_2$	-0.039	-0.099	-0.013	-0.091
$\beta_3$	0.075	-0.001	-0.192	0.012
$R^2$	0.831	0.891	0.895	0.860

Table 1: Regression coefficients and  $R^2$  estimates corresponding to the polynomial response surface model for the three stories and the overall frame.

The polynomial response surface model utilized in this study also aids in the identification of the critical variables other than  $IM$  that most affect the interstory drift ratios. These are shown in Figure 2(a) through (b) using Pareto charts corresponding to maximum interstory drift ratios

for the individual stories as well as for the overall frame. The left vertical axis of the Pareto charts represents the absolute  $t$ -statistic ratios for the parameters arranged in decreasing order of importance. This statistic is computed as the ratio between the parameter estimate and the corresponding standard error. The right vertical axis represents the cumulative sum of the absolute values of the  $t$ -ratio (in percentage) and elucidates the aggregated explanatory power of variables when jointly considered in succession. As Figure 2 reveals, while  $IM$  emerges as the most critical variable across all stories, the story-level BRB areas affect the response of specific individual stories. In other words, among the three different BRB areas,  $A_{BRBi}$  most affects the response of the  $i^{\text{th}}$  story. This finding is intuitive and also aligns with the seismic design strategy used for the BRBs. For the overall frame, the maximum interstory drift ratio ( $IDR_{\max}$ ) is most dependent on  $A_{BRB2}$  at the second story as shown in Figure 2(d).

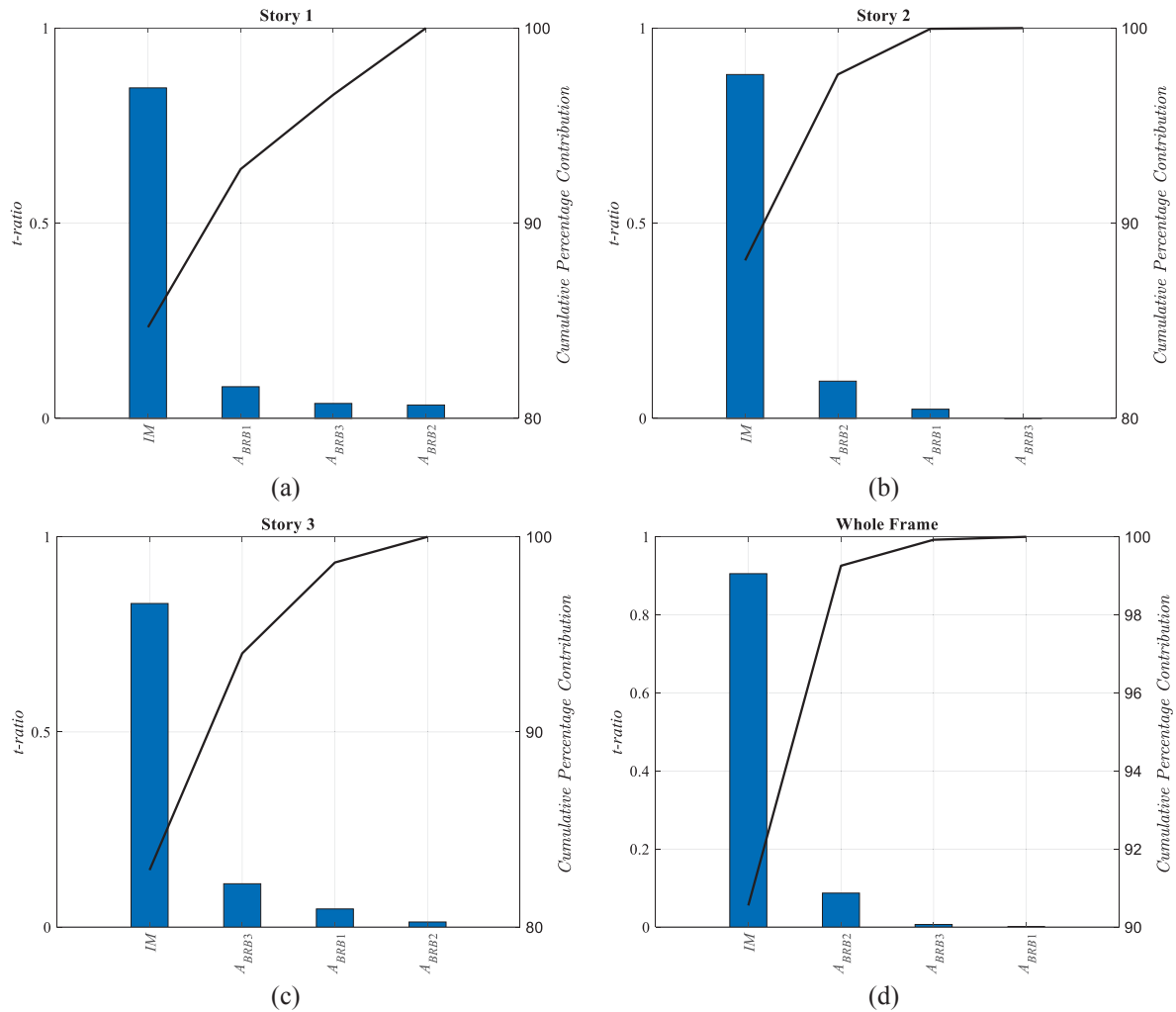


Figure 2: Pareto Charts depicting the contribution of the ground motion intensity measure and BRB areas on the maximum interstory drift ratios for a) Story 1, b) Story 2, c) Story 3, and d) Overall frame.

### 3.3 Parameterized fragility function development

The multidimensional story and system level seismic demand models developed in the previous section are utilized in this stage to develop parameterized seismic fragility functions after comparing with the capacity estimates. The capacity distributions for the individual stories as well as the overall frame are obtained using nonlinear static pushover analysis and are directly adopted from Freddi *et al.* [16]. Comparison between large number of seismic demand and



capacity samples help generate binary survive-failure vectors. These binary vectors are then used to develop time-evolving seismic fragility functions by using the logistic regression approach. Note that other techniques such as naïve Bayes classifier, Probit model, Support vector machines, among others may be also utilized for fragility development. A brief description of the steps involved to develop fragility functions using logistic regression is provided herein [31][32]:

**Step 1:** For a particular building story or the overall frame, sample a large number ( $N_{MC}$ ) of demand estimates from the probabilistic seismic demand models of the maximum interstory drift ratios as elaborated in the previous step. These samples should ideally reflect substantially distinct combinations of the ground motion  $IM$  and the BRB areas ( $A_{BRB1}$ ,  $A_{BRB2}$ , and  $A_{BRB3}$ ).

**Step 2:** Generate  $N_{MC}$  capacity estimates from the capacity distribution of individual stories or the overall frame for the four considered damage states (*i.e.*, Slight, Moderate, Extensive and Complete).

**Step 3:** Compare the demand estimates against the capacity samples and generate a binary vector  $\{\mathbf{bin}\}$  consisting of 1's and 0's, where, 1's represent a story or system-level failure (demand greater than capacity) and 0's represent a story or system-level survival (demand less than capacity).

**Step 4:** Conduct logistic regression using the binary survival–failure vector to determine the story or system-level failure probability for particular damage state  $ds$  as:

$$Pf_{ds|IM, A_{BRB1}, A_{BRB2}, A_{BRB3}} = \frac{e^{\theta_0 + \theta_{IM} \ln(IM) + \sum_{i=1}^3 \theta_{BRBi} A_{BRBi}}}{1 + e^{\theta_0 + \theta_{IM} \ln(IM) + \sum_{i=1}^3 \theta_{BRBi} A_{BRBi}}} \quad (5)$$

where,  $\theta_0$ ,  $\theta_{IM}$ , and  $\theta_{BRBi}$  ( $i = 1$  to 3) are the story or system-level logistic regression coefficients for damage state  $ds$ . Table 2 below enlists the logistic regression coefficients that are utilized in the next section of the paper to derive seismic fragility curves for nominal BRB areas as well as quantify the effect of uncertainty on fragility estimates.

	Story 1	Story 2	Story 3	Whole Frame
$\theta_0$	8.140	2.071	0.405	-3.013
$\theta_{IM}$	6.102	6.014	6.739	11.942
$\theta_{BRBi}$	-0.023	-0.062	-0.010	0.038
$\theta_{BRBi}$	-0.582	-0.526	-0.595	-0.538
$\theta_{BRBi}$	0.072	0.187	0.133	0.052

Table 2: Logistic regression coefficients at story and system level for seismic fragility development.

## 4 RESULTS AND DISCUSSIONS

Unlike unidimensional seismic fragility functions as typically adopted for seismic vulnerability assessment of retrofitted frames, the parameterized fragility models developed in the earlier section offers several advantages. Firstly, for the nominal BRB areas, these fragility functions provide prompt estimates of individual story and system-level fragilities. For instance, Figure 3(a) depicts the individual story fragilities, as well for the whole frame corresponding to the design BRB areas. As expected, the fragility curve for the overall frame emerges

predominantly more fragile than the individual stories. Additionally, among the different stories, the second story emerge as the most fragile and lies in close proximity to the system-level vulnerability curve. Secondly, without the need of additional computationally expensive finite element model runs, the parameterized fragility functions help investigate the influence of BRBs' property variation on retrofitted frame fragility. While Section 3 earlier showed that  $A_{BRB2}$  emerge as a critical parameter affecting the system-level frame response ( $IDR_{max}$ ), Figure 3(b) depicts the variation of retrofitted frame fragility as a function of  $A_{BRB2}$  variation within  $\pm 20\%$  of design estimates for moderate damage state, while holding other BRB areas ( $A_{BRB1}$  and  $A_{BRB3}$ ) constant at nominal values. As expected, the figure shows that higher  $A_{BRB2}$  areas tend to reduce the retrofitted frame fragility, however high BRB areas may not be optimal from the design perspective.

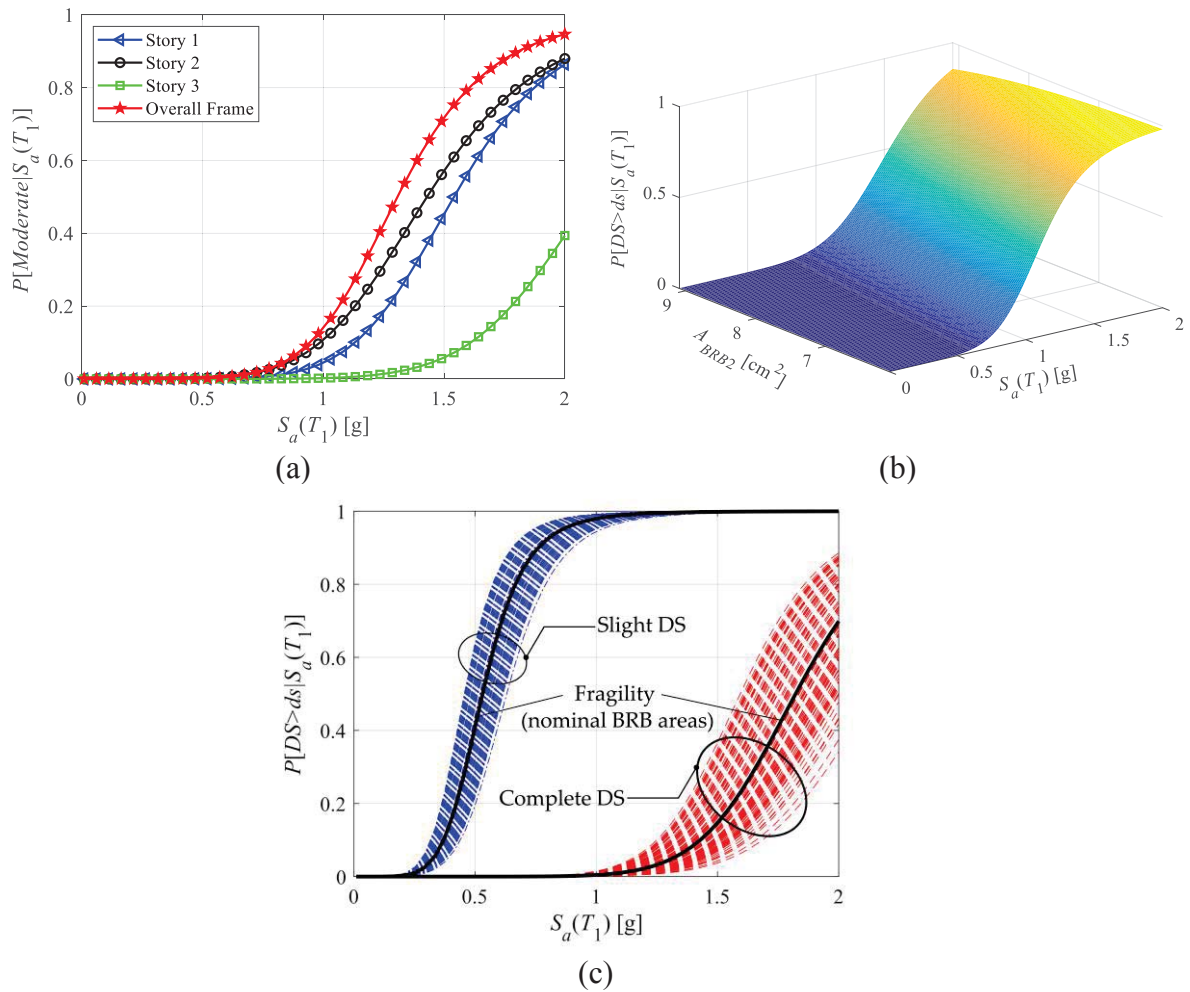


Figure 3: a) Seismic fragility curves for different stories as well as the retrofitted frame corresponding to the moderate damage state for nominal BRB areas, b) variation of retrofitted frame vulnerability with  $\pm 20\%$  variation of  $A_{BRB2}$ , and c) fragility bands depicting the uncertainty in retrofitted frame fragility for the slight and complete damage states due to variations in  $A_{BRB1}$ ,  $A_{BRB2}$ , and  $A_{BRB3}$  within  $\pm 20\%$  of design limits.

The parameterized seismic fragility functions also help estimate the bounds of fragility estimates corresponding to independent variation of the BRB areas across the three stories. Figure 3(c) shows the departures from the “mean” fragility estimates of the retrofitted frame for the slight and complete damage states due to variations in  $A_{BRB1}$ ,  $A_{BRB2}$ , and  $A_{BRB3}$  within  $\pm 20\%$  of design estimates. These fragility bounds also underline the wide variability in retrofitted frame fragilities as a consequence of potential randomness in the BRB areas within the prescribed

code limits. The upper and lower values of the median estimates are observed to range from 0.45 g to 0.62 g for the slight, 1.10 g to 1.51 g for moderate, 1.41 g to 1.91 g for extensive, and 1.53 g to 2.10 g for the complete damage states respectively.

## 5 CONCLUSIONS

Seismic fragility assessment of retrofitted structures typically uses conventional techniques for vulnerability evaluation that may often emerge as tedious in terms of computer run-time. Moreover, to ascertain the influence of parameter variation on building fragility one may need to resort to costly re-analysis under dynamic loads. This study focuses on a computationally efficient technique to assess the impact of variation in BRB device parameters on story level as well as overall retrofitted frame fragility.

To achieve the above objective, first an experimental design matrix is constructed that provides an optimum combination of BRB device areas (chosen as the parameter of interest) within  $\pm 20\%$  of nominal estimates while offering an efficient exploration of the sample space. Next through the results obtained from the nonlinear dynamic analysis of statistically different yet nominally identical frame models polynomial response relationships are developed between the story and system level maximum interstory drift ratios. Comparison of t-statistic ratios indicate that other than the ground motion intensity measure, individual story level BRB device areas emerge most critical for response prediction for that specific story. For the overall frame, the device area at the second story has the most controlling effect. Next, the developed polynomial demand models are compared with capacity estimates to derive parameterized fragility functions using logistic regression techniques. These functions offer significant advantages over traditional intensity-measure-only dependent fragility curves and helps prompt assessment of a) individual and overall frame fragility for nominal BRB area estimates, b) influence of parameter variation on story and system level fragility, and c) development of uncertainty bands to estimate the departures from “average” fragility estimates when variations in device areas are taken into consideration. For the retrofitted case-study frame, the upper and lower values of the median estimates are observed to range from 0.45 g to 0.62 g for the slight, 1.10 g to 1.51 g for moderate, 1.41 g to 1.91 g for extensive, and 1.53 g to 2.10 g for the complete damage states respectively.

Future work on this topic will investigate the influence of BRB device variability on different case study structures and will consider different retrofit levels (*i.e.*, different proportions of the base shear between the MRF and the BRBs). In these cases, due to the variation of the structural vibration period, an alternative intensity measure needs to be evaluated, this representing one of the main challenges for the extension of the proposed methodology.

## REFERENCES

- [1] A. Rao, D. Dutta, P. Kalita, N. Ackerley, V. Silva, M. Raghunandan, J. Ghosh, S. Ghosh, S. Brzev, K. Dasgupta, Probabilistic seismic risk assessment of India. *Earthquake Spectra*, **36**(S1): 345–371, 2020.
- [2] F. Freddi, V. Novelli, R. Gentile, E. Velu, A. Andonov, S. Andreev, F. Greco, E. Zhuleku, Observations from the 26<sup>th</sup> November 2019 Albania Earthquake: the Earthquake Engineering Field Investigation Team (EEFIT) mission. *Bulletin of Earthquake Engineering*, **19**(5), 2013-2044, 2020.
- [3] T.T. Soong, B.F. Spencer, Supplemental energy dissipation: State-of-the-art and state-of-the-practice, *Engineering Structures*, **24**, 243–259, 2002.

- [4] L.A. Fahnestock, R. Sause, J.M. Ricles, L.-W. Lu, Ductility demands on buckling-restrained braced frames under earthquake loading, *Earthquake Engineering and Engineering Vibration*, **2**, 255–268, 2003.
- [5] F.M. Mazzolani, G. Della Corte, M. D’Aniello, Experimental analysis of steel dissipative bracing systems for seismic upgrading, *Journal of Civil Engineering and Management*, **15**, 7–19, 2009.
- [6] L. Di Sarno, G. Manfredi, Experimental tests on full-scale RC unretrofitted frame and retrofitted with buckling-restrained braces. *Earthquake Engineering and Structural Dynamics*, **41**(2), 315–333, 2012.
- [7] E.M. Güneysi, Seismic reliability of steel moment resisting framed buildings retrofitted with buckling restrained braces, *Earthquake Engineering and Structural Dynamics*, **41**(5), 853–874, 2012.
- [8] F. Freddi, E. Tubaldi, L. Ragni, A. Dall’Asta, Probabilistic performance assessment of low-ductility reinforced concrete frames retrofitted with dissipative braces. *Earthquake Engineering and Structural Dynamics*, **42**(7), 993–1011, 2013.
- [9] G. Della Corte, M. D’Aniello, R. Landolfo, Field testing of all-steel buckling-restrained braces applied to a damaged reinforced concrete building. *Journal of Structural Engineering (United States)*, **141**(1), D4014004, 2015.
- [10] F. Freddi, E. Tubaldi, A. Zona, A. Dall’Asta, Seismic performance of dual systems coupling moment-resisting frames and buckling-restrained braced frames. *Earthquake Engineering and Structural Dynamics*, **50**(2), 329–353, 2021.
- [11] A. Zona, A. Dall’Asta. Elastoplastic model for steel buckling-restrained braces. *Journal of Constructional Steel Research*, **68**(1), 118–125, 2012.
- [12] E. Tubaldi, M. Barbato, A. Dall’Asta, Influence of model parameter uncertainty on seismic transverse response and vulnerability of steel-concrete composite bridges with dual load path. *Journal of Structural Engineering*, **138**(3), 363–374, 2012.
- [13] A. Dall’Asta, F. Scozzese, L. Ragni, E. Tubaldi, Effect of the damper property variability on the seismic reliability of linear systems equipped with viscous dampers. *Bulletin of Earthquake Engineering*, **15**(11), 5025–5053, 2017.
- [14] F. Scozzese, A. Dall’Asta, E. Tubaldi, Seismic risk sensitivity of structures equipped with anti-seismic devices with uncertain properties. *Structural Safety*, **77**, 30–47, 2019.
- [15] N. Kotoky, F. Freddi, J. Ghosh, M. Raghunandan, BRBs uncertainty propagation in seismic retrofit of RC structures. *13<sup>th</sup> International Conference on Applications of Statistics and Probability in Civil Engineering (ICASP13)*, Seoul, South Korea, 26–30 May 2019.
- [16] F. Freddi, J. Ghosh, N. Kotoky, M. Raghunandan, Device Uncertainty Propagation in Low-Ductility RC Frames Retrofitted with BRBs for Seismic Risk Mitigation. *Earthquake Engineering & Structural Dynamics*, 2021. DOI: [10.1002/eqe.3456](https://doi.org/10.1002/eqe.3456)
- [17] EN 15129. Anti-seismic devices. European Committee for Standardization 2018; Brussels, Belgium.
- [18] ASCE/SEI 7-16. Minimum design loads and associated criteria for buildings and other structures. American Society of Civil Engineers 2016, Reston, VA.

- [19] ASCE 41-13. Seismic Evaluation and Retrofit Rehabilitation of Existing Buildings. American Society of Civil Engineers 2013, Reston, VA.
- [20] J.M. Bracci, A.M. Reinhorn, J.B. Mander, Seismic resistance of reinforced concrete frame structures designed for gravity loads: performance of structural system. *ACI Structural Journal*, **92**(5), 597–608, 1995.
- [21] L.E. Aycardi, J.B. Mander, A.M. Reinhorn, Seismic resistance of reinforced concrete frame structures designed only for gravity loads: experimental performance of subassemblages. *ACI Structural Journal*, **91**(5), 552–563, 1994.
- [22] ACI Committee 318. Building code requirements for reinforced concrete and commentary (ACI 318-89/ACI 318R-89). American Concrete Institute, Detroit, 1989.
- [23] McKenna F, Fenves GL, Scott MH. Open system for earthquake engineering simulation. University of California 2006, Berkeley, CA.
- [24] M.H. Scott, G.L. Fenves, Plastic hinge integration methods for force-based beam-column elements. *Journal of Structural Engineering*, **132**(2), 244–252, 2006.
- [25] T.B. Panagiotakos, M.N. Fardis, Deformation of reinforced concrete members at yielding and ultimate. *ACI Structural Journal*, **98**(2), 135–148, 2001.
- [26] J.S. Jeon, L.N. Lowes, R. DesRoches, I. Brilakis. Fragility curves for non-ductile reinforced concrete frames that exhibit different component response mechanisms. *Engineering Structures*, **85**, 127–143, 2015.
- [27] F. Freddi, J.E. Padgett, A. Dall'Asta, Probabilistic seismic demand modeling of local level response parameters of an RC frame. *Bulletin of Earthquake Engineering*, **15**, 1–23, 2017.
- [28] J.W. Baker, N. Jayaram, S. Shahi, New ground motion selection procedures and selected motions for the PEER transportation research program. *PEER Technical Report* 2011/03, Berkeley, CA, 2011.
- [29] G.E.P. Box, K.B. Wilson, On the Experimental Attainment of Optimum Conditions, *Journal of the Royal Statistical Society. Series B (Methodological)*, **13**(1), 1–45, 1951.
- [30] T.W. Simpson, J.D. Poplinski, P.N. Koch, J.K. Allen, Metamodels for computer-based engineering design: survey and recommendations, *Engineering with computers*, **17**(2), 129–150, 2001.
- [31] D.W. Hosmer, L. Stanley, R.X. Sturdivant, Applied logistic regression. *Wiley, Hoboken, N.J.*, 2013.
- [32] P.S. Koutsourelakis, Assessing structural vulnerability against earthquakes using multi-dimensional fragility surfaces: A Bayesian framework. *Probabilistic Engineering Mechanics*, **25**(1), 49–60, 2010.



## NUMERICAL INVESTIGATION OF RUBBER BEARINGS WITH LOW SHAPE FACTOR UNDER SEISMIC EXCITATION

A. Orfeo<sup>1</sup>, E. Tubaldi<sup>1</sup>, A. Muhr<sup>2</sup>, D. Losanno<sup>3</sup>

<sup>1</sup> Department of Civil and Environmental Engineering, University of Strathclyde  
Glasgow, UK  
{alessandra.orfeo, enrico.tubaldi}@strath.ac.uk

<sup>2</sup> Tun Abdul Razak Research Centre-TARRC  
Hertford, UK  
amuhr@tarrrc.co.uk

<sup>3</sup> Department of Structures for Engineering and Architecture, University of Naples Federico II  
Napoli, Italy  
daniele.losanno@unina.it

---

### Abstract

*This study illustrates the development of a modeling strategy for simulating the seismic response of structures mounted on elastomeric bearings with a low shape factor (LSF). These bearings can be employed to achieve a three-dimensional seismic isolation of structures, due to their low vertical and horizontal stiffness. The first part of this work investigates the mechanical behaviour of LSF bearings by means of three-dimensional Finite Element (FE) analysis in Abaqus. The FE results provide a numerical evaluation of the horizontal, vertical, and rotational stiffness of the bearings. These are used in the second part of the study to develop in SAP2000 a simplified model of a structure with LSF bearings tested experimentally on the shaking table at University of Naples Federico II. The study results show that the developed model can be effectively used to simulate the response of the isolated structure under different earthquake inputs.*

**Keywords:** Isolation system, low shape factor bearing, FE simulation, hyperelastic material.

---

## 1 INTRODUCTION

Elastomeric bearings are among the most common types of isolation system for protecting structures from earthquakes. They consist of multiple layers of rubber vulcanized to steel reinforcing layers that produce a combination of vertical stiffness and horizontal flexibility [1]. The geometry of these bearing is characterized by the primary shape factor,  $S$ , which defines the ratio of the loaded area to the area free to bulge for an individual rubber layer [2]–[4]. Shape factor values of 10–20 are typically used to guarantee high critical load capacities while keeping a low horizontal stiffness. On the other hand, bearings with high  $S$  values are significantly heavy due to the large number of steel plates and consequently expensive in terms of production and installation. Moreover, superstructures isolated with high vertical stiffness bearings are characterized by low vibration periods in the vertical direction, causing problems for critical facilities such as nuclear power plants or hospitals hosting sensitive equipment needing protection against the effects of vertical component of earthquake inputs.

The concept of low shape factor (LSF) rubber bearings as a way to achieve an economic 3D isolation has been investigated by other researchers [5] [6]. Recently, it has also been the object of an extensive experimental campaign carried out by Cilento et al. [7] to demonstrate the effectiveness of isolating a structure with a very LSF.

The aim of this paper is to present a finite element (FE) modelling strategy for simulating the seismic response of structures equipped with LSF bearings. The proposed strategy is validated considering the results of the experimental campaign carried out by Tun Abdul Razak Research Center (TARRC) and University of Naples Federico II on a structural prototype with LSF rubber bearings made with lightly filled natural rubber [8]. The first part of the paper focuses on the simulation of the bearing behaviour in Abaqus [9], using a three-dimensional modelling approach for the LSF bearings, with a hyperelastic constitutive law for the rubber calibrated using the double shear test results. In the second part of the paper, a simplified model based on a linearized description of the bearing mechanical behaviour is developed in SAP2000 [10]. This model is validated by simulating the shaking table tests performed on a structure isolated with LSF bearings. The numerical results of the analyses shed light on the possibility of using simplified device models for the preliminary seismic assessment of isolated structures mounted on LSF bearings.

## 2 NUMERICAL SIMULATIONS OF MATERIAL AND BEARING TESTS

This section describes the three-dimensional (3D) numerical models developed in Abaqus [9] to simulate the tests on the double shear testpieces and the elastomeric bearings carried out at TARRC [7]. The double shear cylindrical testpieces consisted of two rubber layers bonded to metal parts, as shown in Figure 1a, and were subjected to sinusoidal shear displacement histories. Figure 1b illustrates the laminated bearing considered in the test, which consists of three layers of rubber 19mm thick and sides 100x100 mm, designed to achieve a shape factor  $S = 1.32$ . The bearing was subjected simultaneously to static compression and dynamic shear loading in a double shear configuration. The testing sequence consisted of two cycles of sinusoidal displacement at increasing shear strain amplitudes [8] [11].

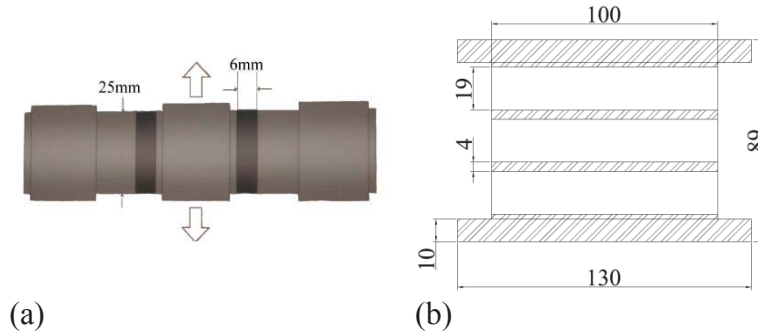


Figure 1: (a) Double shear test piece geometry, (b) Elastomeric bearing geometry

In the numerical models, the rubber is described using a hyperelastic constitutive material. Hyperelastic materials are defined by the strain energy potential  $W$ , the strain energy stored in the material per unit of reference volume, as a function of the strain at that point in the material. Yeoh constitutive relationship is used in this study and the strain energy potential is derived from the reduced polynomial strain energy potential that is a function of only the deviatoric strain invariant  $I_1$  and has the following expression:

$$W = \sum_{i=1}^N C_{i0} (I_1 - 3)^i \quad (1)$$

where  $C_{i0}$  are material parameters. The Yeoh form is obtained for a number of terms  $N$  equal to 3. The values of material parameters  $C_{i0}$  in the equation (1) can be obtained from the double shear experiments and are shown in Table 1.

Model parameters	C10 [MPa]	C20 [MPa]	C30 [MPa]
Yeoh	0.3	-0.005	0.000311

Table 1 Material parameters for Yeoh hyperelastic material model

Rayleigh damping is used in the numerical analysis to describe the damping property of the rubber material. The coefficients for the Rayleigh damping are calculated using a damping ratio of 1% for the first and second modes of the isolated system described in section 3. The coefficient  $\alpha$  for the mass matrix and the coefficient  $\beta$  for the elastic initial stiffness matrix are calculated to be 0.067926 and 0.00080, respectively.

The shear stiffness values obtained numerically for different maximum shear strain have been compared with the experimental data, as shown in Figure 2a. A good agreement between simulations and the test is found for all the investigated shear deformation amplitudes, apart from low values of shear strains.

The estimates of the equivalent damping ratio of the rubber block from FE analysis results for different levels of strain amplitude are shown in Figure 2b, where they are compared with the corresponding values obtained experimentally. Although a simple description of the damping is used, a good agreement is found between numerical and experimental results. It is noteworthy that more advanced description of the damping, e.g. using a Prony series approach [13] or the Bergstrom Boyce model [14], would require further tests in order to calibrate the higher number of model parameters.

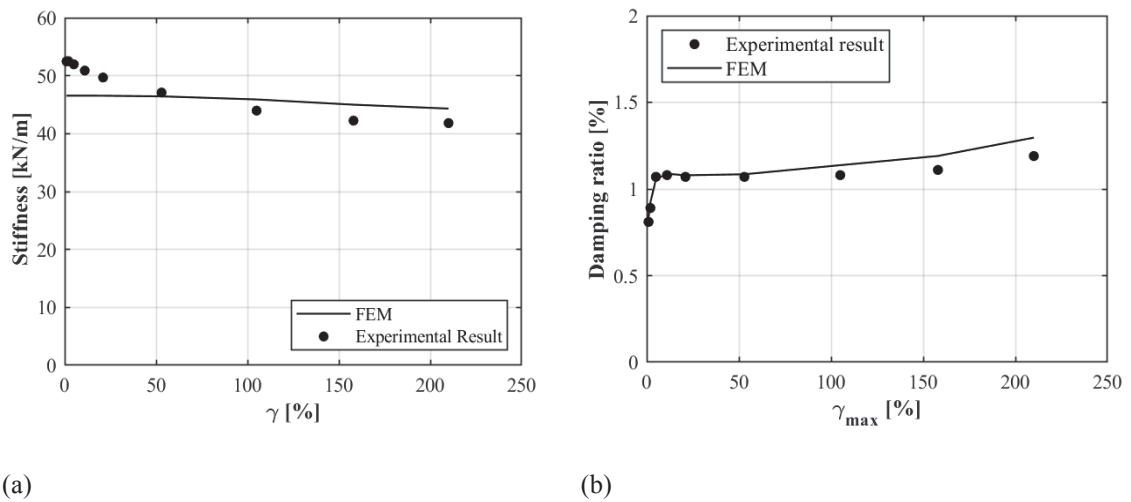


Figure 2: Experimental and numerical values of (a) Shear stiffness for different maximum shear strains (b) Equivalent damping ratio for different maximum shear strains

The LSF bearing FEM model is illustrated in Figure 3. The rubber layers, the intermediate steel shim plates and end plates are modelled using C3D8H elements that are available in the Abaqus library [9]. The tie contact between steel and rubber layers of the bearing is expressed by contact pair option available in Abaqus. The displacement boundary conditions are applied to the top end plate while performing compression and shearing tests, whereas the bottom anchor plate is fixed in all degrees of freedom.

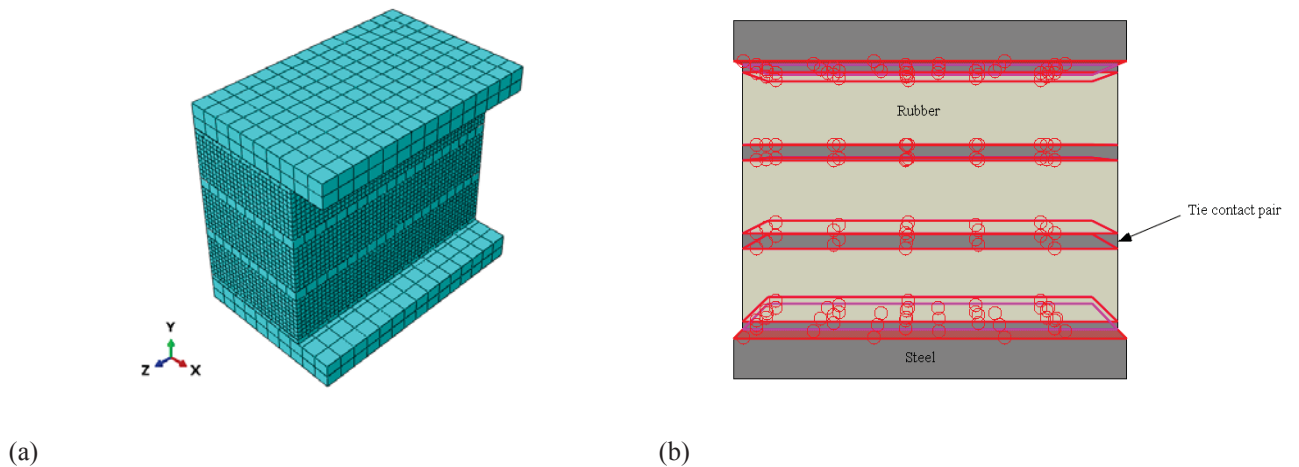


Figure 3: Elastomeric Bearing: (a) Meshing, (b) Details of connections between various layers.

A vertical downward displacement was first imposed at the top plate, until a compressive load of 19kN is achieved, being the gravity load in the shaking table tests, described in the next section. Subsequently, two cycles of sinusoidal displacements are applied while preventing vertical motion and rotation of the top plate.

Figure 4a shows the changes with the maximum amplitude of average shear deformation of the horizontal secant stiffness of the bearing. These have been evaluated both numerically and experimentally as the ratio of base shear force to the maximum displacement at each incremental step. In general, the experimental and numerical values are very close, except for low shear strains, for which the numerical model is more flexible. The bearing equivalent viscous damping has been evaluated numerically and compared with the experimental results, as

shown in Figure 4b. Both experiment and numerical results show that with the increase of shear strains, the damping decreases.

Figure 4c compares the estimates of the initial shear stiffness at zero shear displacement for increasing values of the applied vertical displacement according to the numerical FE model and the experimental results.

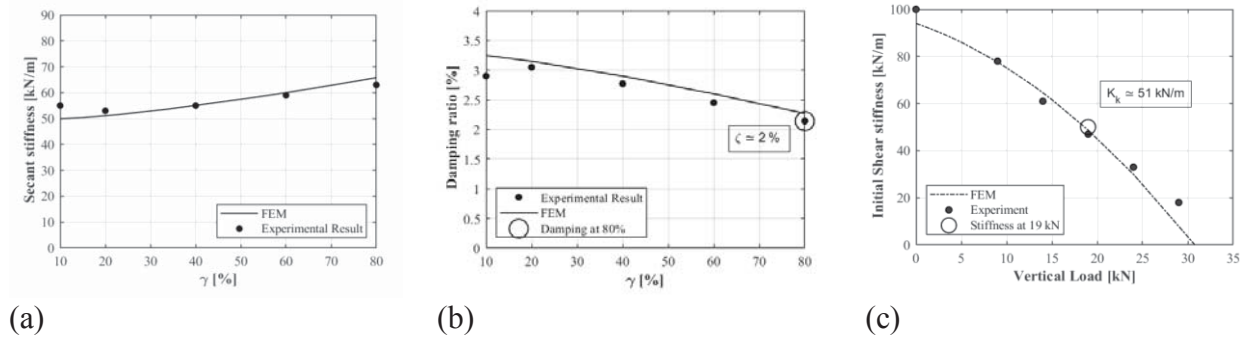


Figure 4: (a) Secant shear stiffness-average shear strain relation (b) Equivalent damping ratio at different levels of shear strain (c) Stiffness vs vertical displacement. Experimental values taken from [11].

The numerical model provides an overall good estimate of the shear stiffness for increasing of compression levels. In general, the horizontal stiffness reduces with the increase of the vertical load, and the condition of instability is attained when it becomes zero. It is noteworthy that the observed buckling load is 50% higher than the applied compression load of 19kN and it is also 3 times higher than the critical load evaluated according to the theory of Gent and of Koh and Kelly [15] [16]. It is also interesting to observe that the ratio between the initial horizontal and vertical stiffness is about 43, which is significantly lower than the values typical of high shape factor bearings ([1], e.g. about 800 for  $S=12$  in Tubaldi et al. [17], which deals with isolation bearings for bridges).

### 3 SHAKING TABLE TESTS

#### 3.1 Prototype and test description

This subsection describes the shaking table tests carried out at the Department of Structures for Engineering and Architecture of University of Naples Federico II on a prototype base-isolated building with LSF bearings [8]. The steel superstructure is composed of one level and has a total height of 2900mm. The plan dimensions of the structure are 2500x2000mm with concrete slab placed on the roof of the structure, having a depth of 25mm, and concrete blocks added to the base level to achieve a total mass  $M_{tot} = 7.7$  tons. The columns have a box section 150x150x15mm. The beams of the top floor are pinned to the columns and are hot-formed square hollow sections 120x120x12.5mm. The four perimetric beams at the base of the frame have HEM 160 profile. The bearings are identical to those tested at TARRC. The same mock-up has been recently used for bi-directional tests on recycled rubber and fibre-reinforced unbounded isolators [18][19]. Ground motions were applied along the direction in which the frame span is 2500 mm. The vibration period of the fixed-base structure is  $T_s = 0.24$  s. The isolation system of the scaled prototype was designed to achieve a horizontal vibration period  $T_{is} = 0.92$  s, estimated from an assumed value of the rubber shear modulus of 0.5MPa and considering the superstructure as rigid and the bearings as infinitely stiff in the vertical direction. Under these simplifying assumptions, the isolation period can be expressed as  $T_{is} = 2\pi\sqrt{(M_{tot}/K_{is})}$ , where  $K_{is}$  is the total stiffness of the bearings in the horizontal direction. It is noteworthy that the system was designed considering a geometry scale factor of



1/3 and an elastic modulus scale factor of 1. Therefore, according to the dynamic similitude rule, the equivalent period of the full-scale structure is  $T_{fs} = 1.59$  s, (i.e.  $T_{fs} = \sqrt{3}T_{is}$ ). A set of seven waveforms was selected from the European strong-motion database, whose main characteristics are described in Table 2.

Waveform ID	Earthquake Name	Earthquake Country	Mw	PGA (m/s <sup>2</sup> )	PGV (cm/s)	PGD (cm)
7142	Bingol	Turkey	6.3	2.55	18.29	3.25
55	Friuli	Italy	6.5	2.55	15.25	9.29
200	Montenegro	Montenegro	6.9	2.55	12.87	9.60
428	Etolia	Greece	5.3	2.55	12.46	6.06
372	Lazio Abruzzo	Italy	5.9	2.55	15.02	6.80
290	Campano Lucano	Italy	6.9	2.55	44.10	16.20
287	Campano Lucano	Italy	6.9	2.55	43.90	14.00

Table 2: Ground motion characteristics (Mw=Magnitude, PGA=Peak ground acceleration, PGV= Peak ground velocity, PGD= Peak ground displacement)

### 3.2 Simulation of shaking table tests

Figure 5 shows the simplified FEM model of the isolated structure developed in SAP2000 [10]. The steel columns and beams of the frame are assumed to remain elastic and are modelled with beam elements assigning a Young's modulus of 210000MPa, a Poisson's ratio of 0.3, and mass density of 7.8E-09 ton/mm<sup>3</sup>. The mass at top and bottom level is 2.05 and 1.8 tons respectively, so that the vertical load applied to the bearing is 19kN. The isolators are modelled using the two-node link linear elements [10] connecting the bottom of the base beam to the ground (Figure 5).

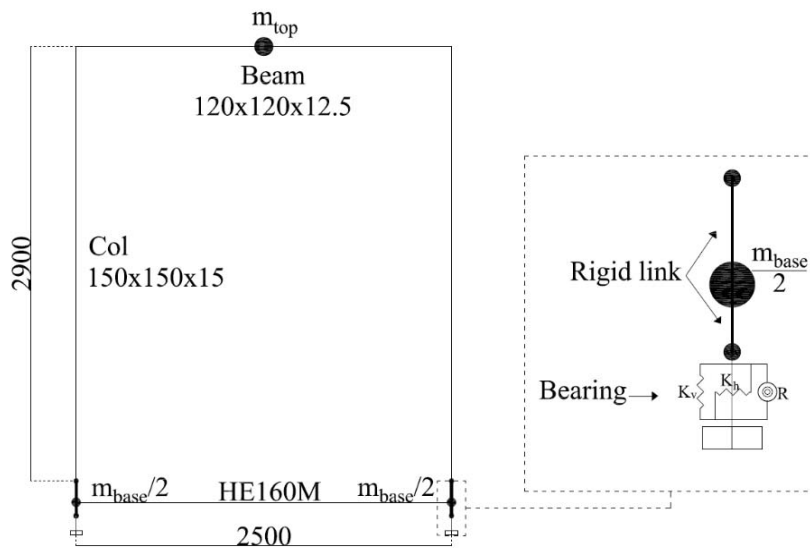


Figure 5: Front view of the base isolated structure configuration and detail of the isolation system

Table 3 shows the values of the stiffness assigned to the two-node link elements, where  $K_v$ ,  $K_h$  and  $K_r$  are the vertical, shear and rotational stiffnesses, respectively. These values are de-

terminated by considering the bearing model developed in Abaqus and applying a small axial displacement, shear displacement and rotation on the bearings compressed by a vertical load of 19 kN.

$K_v$	$K_h$	$K_r$
N/mm	N/mm	Nmm
2209	51	1180000

Table 3: Link Element Properties

A Rayleigh damping model has been assumed and the damping ratio of the first two modes of the base isolated structure has been set equal to  $\zeta = 0.02$ . In contrast to the definition of damping on a 3D numerical model, that is related to the material property, the damping ratio in this case needs to be specified to the whole bearing. The adopted value of  $\zeta$  refers to the equivalent damping ratio of bearing correspondent to 80% of shear strain, shown in Figure 4b. Seismic analyses are performed using the developed model. Displacement history of isolator and top structure horizontal accelerations resulting from numerical model are compared to the recorded ones for Etolia earthquake input, as shown in Figure 6a-b. In general, it can be observed that assuming a linearized behaviour of the bearings superimposed on the finite strains induced by the vertical static loading on the bearing provides a good approximation of the response in the case of Etolia earthquake input.

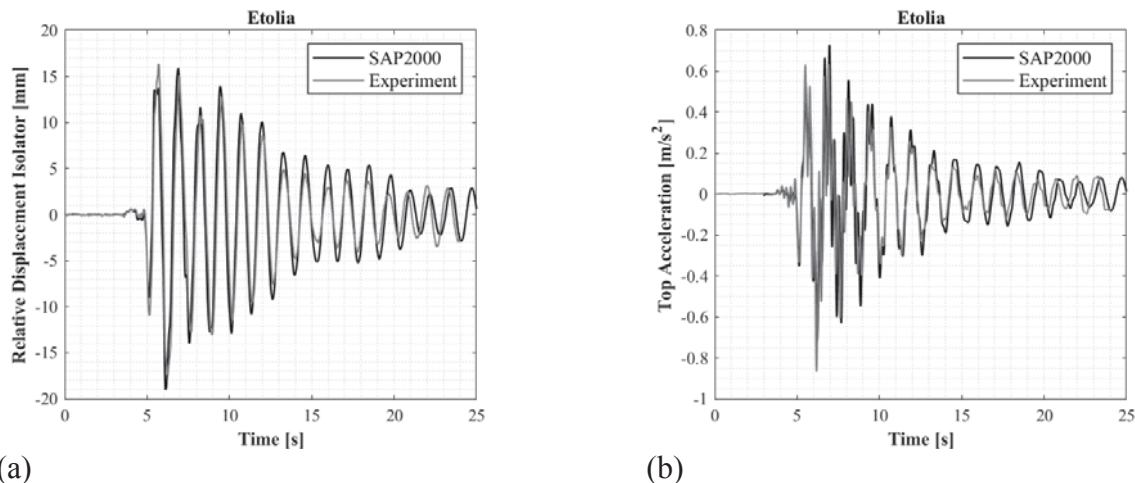


Figure 6: (a) Relative Displacement Isolator time history (b) Acceleration at the top of the superstructure

Table 4 shows the numerical-experimental comparisons in terms of maximum absolute values of the isolator deflection, interstorey drift and acceleration at the top of the structure. The response of the superstructure is slightly underestimated, and this may be due to the assumption of a rigid connection between the columns and the base.

Earthquake Name	Max Displacement Isolator [mm]			Max Drift Structure [%]			Max Top Acceleration [m/s²]		
	Exp	SAP 2000	Relative error %	Exp	SAP 2000	Relative error %	Exp	SAP 2000	Relative error %
<b>Bingol</b>	45.88	36.37	-20.73	0.30	0.30	0.56	1.22	1.22	-0.16
<b>Friuli</b>	17.24	16.08	-6.73	0.17	0.13	-24.49	0.87	0.68	-21.68
<b>Montenegro</b>	17.29	18.88	9.20	0.17	0.14	-20.08	0.86	0.72	-16.47
<b>Etolia</b>	17.41	19.03	9.30	0.17	0.14	-17.71	0.86	0.73	-15.87

Earthquake Name	Max Displacement Isolator [mm]			Max Drift Structure [%]			Max Top Acceleration [m/s <sup>2</sup> ]		
	Exp	SAP 2000	Relative error %	Exp	SAP 2000	Relative error %	Exp	SAP 2000	Relative error %
<b>Bingol</b>	45.88	36.37	-20.73	0.30	0.30	0.56	1.22	1.22	-0.16
<b>Friuli</b>	17.24	16.08	-6.73	0.17	0.13	-24.49	0.87	0.68	-21.68
<b>Lazio/Abruzzo</b>	17.55	19.03	8.43	0.16	0.14	-14.33	0.87	0.73	-16.01
<b>ID 290</b>	17.57	18.95	7.85	0.16	0.14	-16.85	0.87	0.73	-15.61
<b>ID 287</b>	17.33	18.94	9.29	0.17	0.14	-20.24	0.86	0.72	-16.02

Table 4 Maximum absolute values of various response parameters according to experimental test and numerical model.

#### 4 CONCLUSION AND FUTURE RESEARCH NEEDS

This study investigates numerically the mechanical behaviour of elastomeric bearings with low shape factor (LSF) under compressive and shear loading, and the dynamic behaviour of structures mounted on them. The first part of the paper illustrates the development of a three-dimensional (3D) numerical model in Abaqus for simulating the experimental tests conducted at Tun Abdul Razak Research Center (TARRC) rubber research center on LSF rubber bearings with low damping. It is shown that the Yeoh hyperelastic material model, calibrated against material double-shear tests, can be used to accurately describe the complex nonlinear shear response of compressed LSF bearings.

In the second part of the paper, the shaking table tests carried out on a model isolated structure on LSF bearings performed at University of Naples Federico II are simulated using a simplified numerical model. The prototype isolated structure is analyzed using SAP2000 under different earthquake loadings and the numerical estimates of the response are compared with the experimental ones. The isolators are described using two-node links with linear elastic behaviour and vertical, shear and rotational stiffnesses are estimated by performing numerical analyses of the LSF bearing in Abaqus. In general, it is observed that the development of simple FEM model for the tested prototype isolated structure can be used for preliminary assessment and design purposes due to the good agreement between numerical responses and experimental results.

Further studies will include the development of advanced numerical models to evaluate the behaviour of LSF bearings and their capability of providing full three-dimensional isolation. Moreover, the response of LSF bearing made with high damping rubber compounds, characterized by more complex behaviour, will be investigated.

#### REFERENCES

- [1] J. M. Kelly and D. A. Konstantinidis, *Mechanics of Rubber Bearings for Seismic and Vibration Isolation*. 2011.
- [2] M. C. Constantinou, A. Kartoum, and J. M. Kelly, "Analysis of compression of hollow circular elastomeric bearings," *Eng. Struct.*, vol. 14, no. 2, pp. 103–111, 1992.
- [3] G. M. Montuori, E. Mele, G. Marrazzo, G. Brandonisio, and A. De Luca, "Stability issues and pressure–shear interaction in elastomeric bearings: the primary role of the secondary shape factor," *Bull. Earthq. Eng.*, vol. 14, no. 2, pp. 569–597, 2016.

- [4] E. Tubaldi, S. A. Mitoulis, H. Ahmadi, and A. Muhr, “A parametric study on the axial behaviour of elastomeric isolators in multi-span bridges subjected to horizontal seismic excitations,” *Bull. Earthq. Eng.*, vol. 14, no. 4, pp. 1285–1310, 2016.
- [5] J. M. Kelly, “Base Isolation in Japan,” no. December, p. 100, 1988.
- [6] I. D. Aiken, J. M. Kelly, and F. F. Tajirian, “Mechanics of Low Shape Factor Elastomeric Seismic Isolation.”
- [7] F. Cilento, R. Vitale, M. Spizzuoco, G. Serino, and A. H. Muhr, “Analysis of the Experimental Behaviour of Low Shape Factor Isolation Rubber Bearings by Shaking Table Investigation,” 2017.
- [8] F. Cilento, R. Vitale, M. Spizzuoco, G. Serino, and A. Muhr, “Dynamic behaviour in compression and shear of low shape factor rubber blocks,” *Ing. Sismica*, vol. 36, no. 2, pp. 86–102, 2017.
- [9] “Dassault Systèmes, Abaqus Analysis User’s Manual Version 2018.”
- [10] C. CSI, “SAP2000 Integrated Software for Structural Analysis and Design,” Computers and Structures Inc., Berkeley, “No Title.”
- [11] G. Cuomo, “Design, development and experimental validation of multilayer modular laminated natural rubber isolators.,” 2014.
- [12] R. . Ogden, “Dover Civil and Mechanical Engineering R. W. Ogden - Non-Linear Elastic Deformations.” 1984.
- [13] H. R. Ahmadi, J. G. R. Kingston, and A. H. Muhr, “Dynamic Properties of Filled Rubber — Part I: Simple Model, Experimental Data and Simulated Results,” *Rubber Chem. Technol.*, vol. 81, no. 1, pp. 1–18, 2008.
- [14] J. Bergstrom, “Constitutive modeling of the large strain time-dependent behavior of elastomers,” vol. 46, no. 5, p. 931, 1998.
- [15] C. G. Koh and J. M. Kelly, “Modelling of seismic isolation bearings including shear deformation and stability effects,” *Appl. Mech. Rev.*, vol. 42, no. 11, pp. 113–120, 1989.
- [16] A. N. Gent, “Elastic Stability of Rubber Compression Springs,” *Rubber Chem. Technol.*, vol. 38, no. 2, pp. 415–430, 1965.
- [17] E. Tubaldi, S. A. Mitoulis, and H. Ahmadi, “Comparison of different models for high damping rubber bearings in seismically isolated bridges,” *Soil Dyn. Earthq. Eng.*, vol. 104, no. May 2017, pp. 329–345, 2018.
- [18] D. Losanno, M. Spizzuoco, and A. Calabrese, “Bidirectional shaking-table tests of unbonded recycled-rubber fiber-reinforced bearings (RR-FRBs),” *Struct. Control Heal. Monit.*, vol. 26, no. 9, 2019.
- [19] D. Losanno, I. E. Madera Sierra, M. Spizzuoco, J. Marulanda, and P. Thomson, “Experimental performance of unbonded polyester and carbon fiber reinforced elastomeric isolators under bidirectional seismic excitation,” *Eng. Struct.*, vol. 209, no. November 2019, p. 110003, 2020.

## INELASTIC RESPONSE MODES OF SEISMICALLY ISOLATED STRUCTURES: FAILURE OF THE ISOLATORS OR DAMAGE IN THE ISOLATED STRUCTURE?

Anastasios Tsiavos<sup>1</sup>, Tomislav Markic<sup>2</sup>, David Schlatter<sup>3</sup> and Bozidar Stojadinovic<sup>4</sup>

<sup>1</sup> Lecturer, Department of Civil, Environmental and Geomatic Engineering, ETH Zurich, Switzerland  
e-mail: [tsiavos@ibk.baug.ethz.ch](mailto:tsiavos@ibk.baug.ethz.ch)

<sup>2</sup> PhD Student, Department of Civil, Environmental and Geomatic Engineering, ETH Zurich, Switzerland  
e-mail: [markic@ibk.baug.ethz.ch](mailto:markic@ibk.baug.ethz.ch)

<sup>3</sup> Master Student, Department of Civil, Environmental and Geomatic Engineering, ETH Zurich, Switzerland  
e-mail: [dschlatter@student.ethz.ch](mailto:dschlatter@student.ethz.ch)

<sup>4</sup> Professor, Department of Civil, Environmental and Geomatic Engineering, ETH Zurich, Switzerland  
e-mail: [stojadinovic@ibk.baug.ethz.ch](mailto:stojadinovic@ibk.baug.ethz.ch)

---

### Abstract

The goal of this study is to determine experimentally the inelastic response modes of seismically isolated structures. A steel specimen is designed and constructed to simulate the dynamic behavior of a Single-Degree-Of-Freedom (SDOF) system. The specimen is seismically isolated with four friction pendulum bearings and excited by a group of earthquake ground motion records using the shaking table of ETH Zurich Laboratory. A mechanical clevis connection consisting of two hinges and two replaceable steel coupons is designed and constructed to facilitate the parametric investigation of the inelastic response of the isolated structure for varying values of its strength. Two fundamentally different inelastic response modes have been observed during the excitation of the structure: A response mode dominated by large sliding displacement demand in the isolators and a response mode characterized by large displacement ductility demand in the isolated structure. This paper shows the effect of the design parameters of the isolation system and the isolated structure on the manifestation of these two response modes, thus paving the way for the understanding of the inelastic response of seismically isolated structures subjected to extreme earthquake ground motions.

**Keywords:** seismic isolation, shaking table tests, friction pendulum bearings, inelastic behavior of seismically isolated structures

---



## 1 INTRODUCTION

The attractive characteristics of seismic isolation on the seismic protection of structures through the use of frictional or elastomeric devices have been demonstrated by many researchers in the past [1-3]. The current seismic code provisions prescribe the elastic design of these structures for a design-basis earthquake event. In view of these provisions, most of the existing studies investigating the dynamic response of seismically isolated structures use an elastic dynamic model for the simulation of the seismic response of the isolated structure.

However, seismically isolated structures can be subjected to inelastic behavior and damage, when they are excited by earthquake ground motion with intensities exceeding the design seismic hazard level. Furthermore, seismically isolated structures can manifest inelastic behavior even for ground motion intensities corresponding to the design hazard level, when they are unintentionally constructed with lower strength than the value prescribed by the code provisions [4-7]. The investigation of such behavior of existing seismically isolated structures sheds light on their reliability and robustness compared to fixed-based structures, as defined by Castaldo et al. [8, 9], Tsang [10] and Peng et al. [11].

In view of these challenges, the inelastic behavior of seismically isolated structures has been investigated in several studies in the past. Kikuchi et al. [12] and Cardone et al. [13] investigated analytically the inelastic behavior of seismically isolated structures, concluding that the behavior of these structures after they yield is substantially different from the corresponding fixed-based structures. Ragni et al. [14] presented the seismic damage and collapse risk of seismically isolated buildings, designed according to the Italian seismic code provisions. Tsiavos et al. [15] determined analytically and verified experimentally [16, 17] the relations between the strength reduction factor  $R_y$ , the ductility demand  $\mu$  and the fixed-based vibration period  $T_n$  of seismically isolated structures.

Nevertheless, these studies did not focus on the two different failure types that characterize the inelastic behavior of seismically isolated structures: The failure of the isolators and the occurrence of damage in the isolated structure.

Along these lines, the present study aims to illustrate experimentally the design parameters that lead to the two different failure types of seismically isolated structures. A steel structure is seismically isolated with four friction pendulum bearings and subjected to an ensemble of recorded, unidirectional earthquake ground motion excitations. The design and construction of a mechanical clevis connection allows the variation of the strength of the isolated structure.

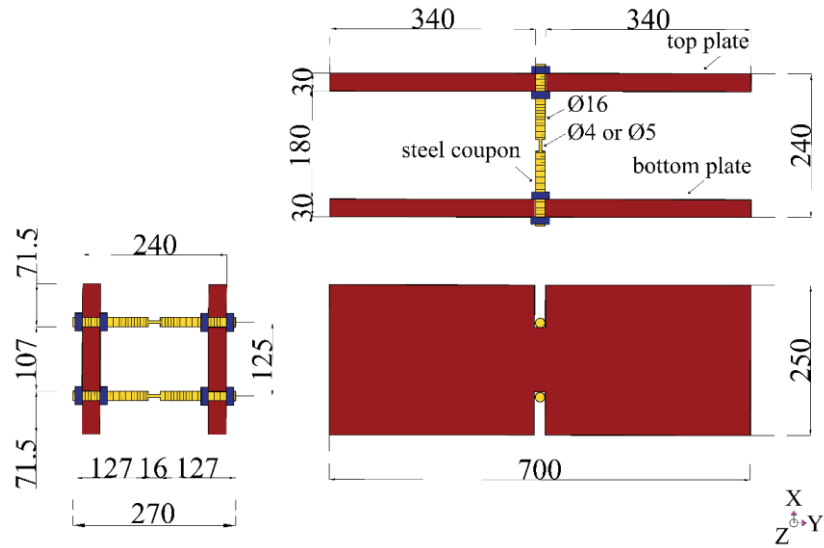
## 2 EXPERIMENTAL CONFIGURATION

### 2.1 Design of the experimental setup

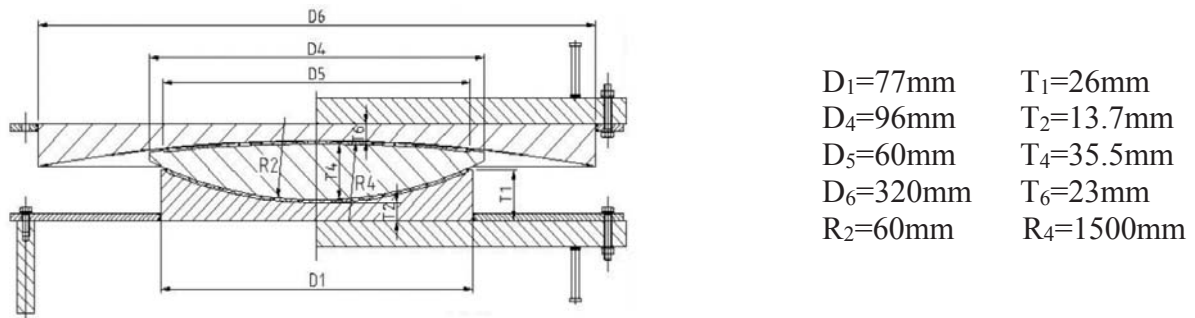
The experimental setup shown in Fig. 1 entails a 1.9m tall steel structure, which is seismically isolated using four friction pendulum bearings. The seismically isolated structure is excited by an ensemble of earthquake ground motion excitations using the 2m x 1m unidirectional shaking table of the ETH Laboratory.

The steel structure was designed with a fixed-base vibration period  $T_n=0.5s$ , similar to the one of a 2-4 story building. The structure comprises a steel frame with a lumped mass  $m_s=250kg$  rigidly fixed on top. The frame consists of two hollow rectangular columns connected at regular intervals by seven horizontal struts. A mechanical clevis connection consisting of two hinge elements and a couple of replaceable steel coupons was designed to enable a





**Fig. 2.** Top view and cross sections of the mechanical configuration comprising two replaceable steel coupons (Dimensions in mm).



**Fig. 3.** Drawing of the friction pendulum bearings used in the experimental setup, as designed by the company Mageba SA.



**Fig. 4.** Constructed experimental setup at the ETH Structures Laboratory.

## 2.2 Ground motion ensemble

The seismically isolated structure shown in Fig. 1 was excited by 8 different ground motion records obtained from the PEER Strong Ground Motion Database. The characteristics of the applied records are shown in Table 1. The recorded motions, scaled to different Peak Ground Acceleration (PGA) levels, are applied in the X-direction of the experimental setup shown in Fig. 1, using the unidirectional shaking table of the ETH Structures Laboratory with a stroke  $d_{max}=240\text{mm}$ . Each ground motion record was applied twice to the seismically isolated structure, characterized by two different strength values: First, a seismically isolated structure with strength reduction factor  $R_y=1.5$ , engineered through the use of steel coupons with reduced section (Fig. 2) of diameter  $D_{red}=5\text{mm}$ , was subjected to the ground motion record. Second, a seismically isolated structure with strength reduction factor  $R_y=2$ , engineered through the use of steel coupons with reduced section (Fig. 2) of diameter  $D_{red}=4\text{mm}$ , was subjected to the same ground motion record.

## 2.3 Instrumentation

The attachment of 6 uniaxial accelerometers and 6 displacement markers to the experimentally investigated structure shown in Fig. 1 enables the continuous monitoring of the acceleration and the displacement time history response of the structure during the shaking table motion.

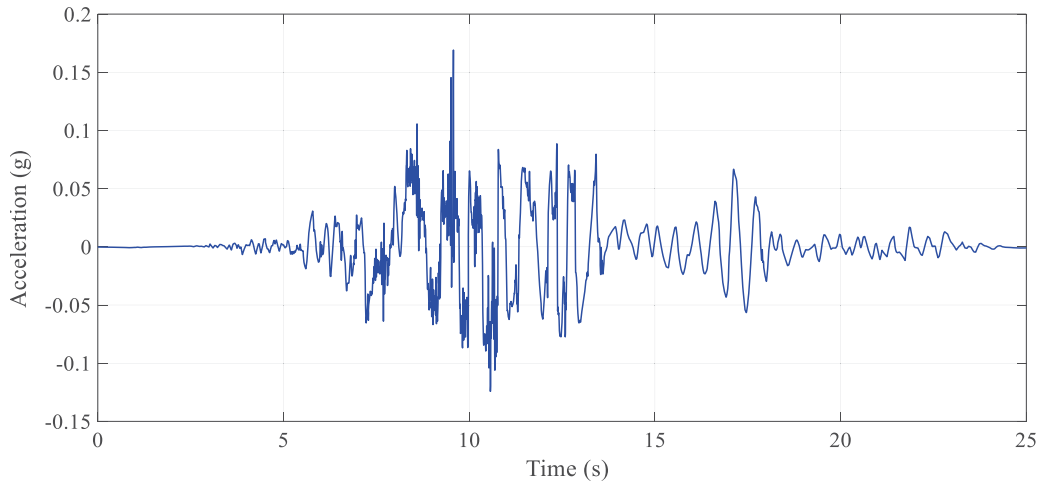
**Table 1.** List of recorded earthquake ground motions used for the excitation of the steel structure (PEER NGA Database, 2019 [18]).

No.	Date	Earthquake and Station	PGA of the original motion (g)	Amplitude scaling of the original motion	PGA of the scaled motion (g)
1	9/2/1971	San Fernando, 279 Pacoima Dam	1.23	35%	0.43
2	17/1/1994	Northridge, USGS/VA 637 LA-Sepulveda VA Hospital	0.75	75%	0.56
3	02/5/1982	Coalinga, 1651 Transmitter Hill station	0.84	100%	0.84
4	16/9/1978	Tabas, 9101	0.84	32.5%	0.27
5	20/9/1999	Chi-Chi, CHY 080	0.97	40%	0.39
6	16/01/1995	Kobe, KJMA	0.82	65%	0.53
7	18/10/1989	Loma Prieta, UCSC 16 LGPC	0.97	17.5%	0.17
8	24/04/1984	Morgan Hill, 57217 Coyote Lake Dam	0.71	100%	0.71

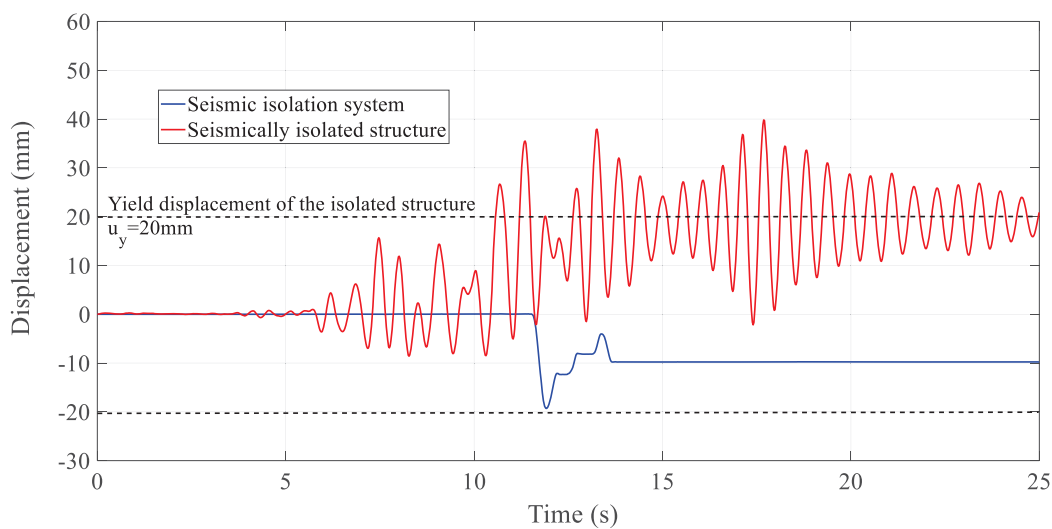
### 3 SHAKING TABLE INVESTIGATION

#### 3.1 Response dominated by inelastic behaviour of the seismically isolated structure

The presented structure (Fig. 1) was first excited by the 17.5% scaled-down 1989 Loma Prieta ground motion acceleration record (No. 7 in Table 1), shown in Fig. 5. The experimentally derived displacement time history response of the isolated structure designed with a strength reduction factor  $R_y=1.5$  relative to the isolators is shown in Fig. 6. The experimentally observed displacement time history response of the seismic isolation system relative to the shaking table motion is shown in the same Figure.



**Fig. 5.** 17.5%-scaled Loma Prieta ground motion acceleration record.



**Fig. 6.** Displacement time history response of the seismically isolated structure with a strength reduction factor  $R_y=1.5$  and the seismic isolation system subjected to the 17.5%-scaled Loma Prieta ground motion.

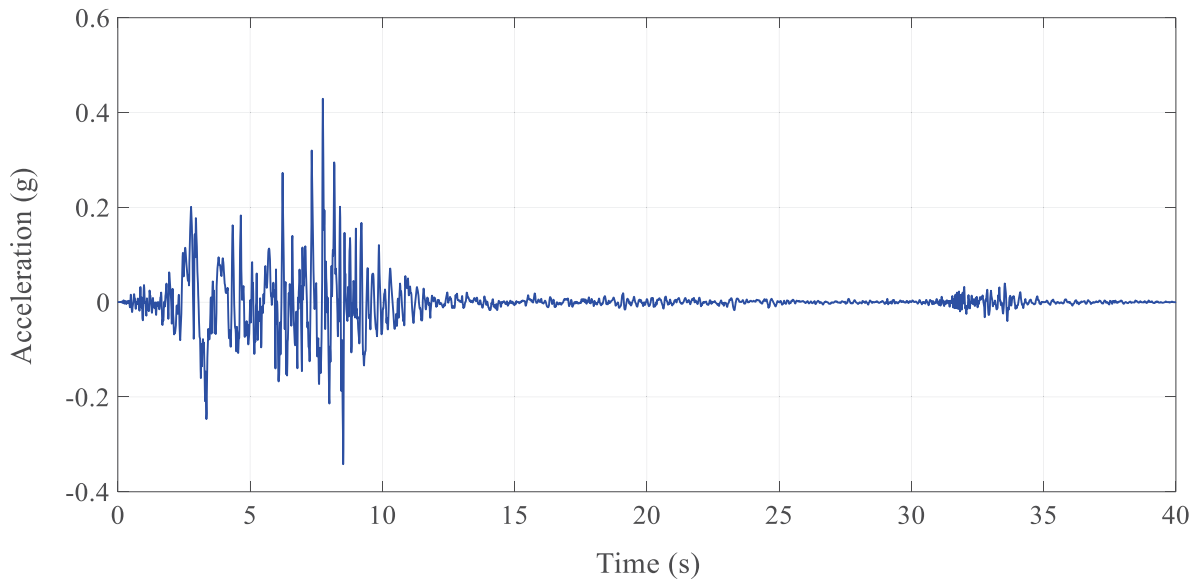
After the initiation of yielding, the isolated structure manifested significant inelastic behavior, leading to a maximum inelastic displacement  $u_{max}=40.2\text{mm}$  and a ductility demand  $\mu=u_{max}/u_y=40.2\text{mm}/20\text{mm}=2.01$ . The maximum sliding displacement of the seismic isolation



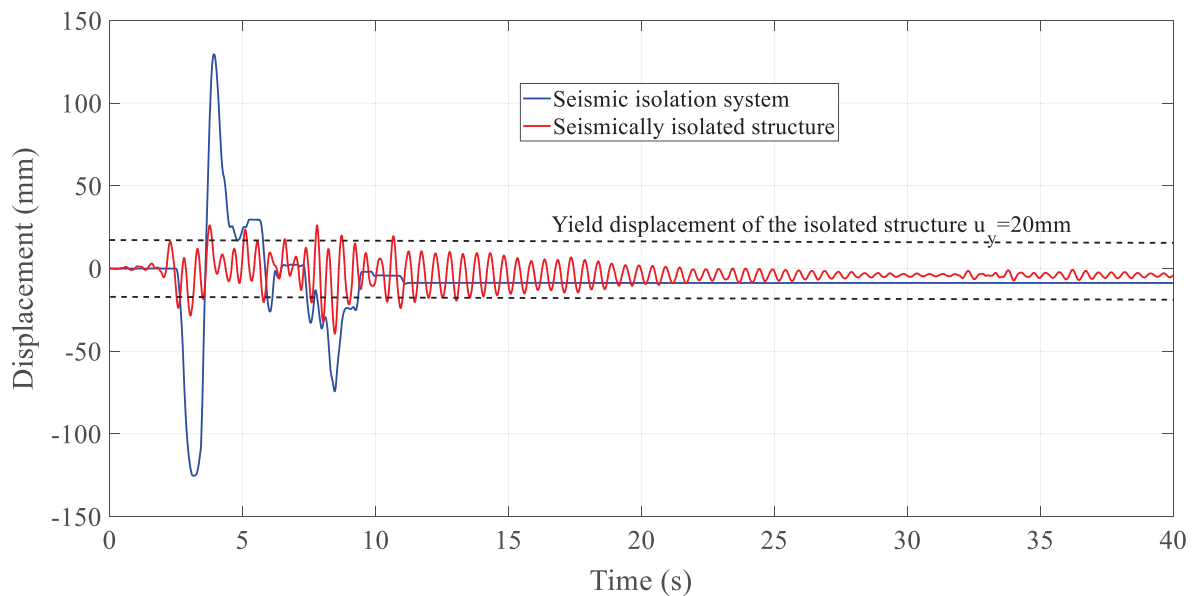
system was not significant for this ground motion excitation, reaching a maximum value of 19.8mm for a dimensionless friction ratio  $\Pi_2 = \mu_f g / \text{PGA} = 0.62$ , as defined by Tsiavos et al. [15].

### 3.2 Response dominated by the sliding displacement of the seismic isolation system

The experimentally derived response of the seismic isolation system was substantially different when the seismically isolated structure (Fig. 1) was subjected to the 35% scaled-down San Fernando ground motion acceleration record (No. 1 in Table 2), shown in Fig. 7.



**Fig. 7.** 35%-scaled San Fernando ground motion acceleration record.



**Fig. 8.** Displacement time history response of the seismically isolated structure with a strength reduction factor  $R_y = 1.5$  and the seismic isolation system subjected to the 35%-scaled San Fernando ground motion.

As shown in the displacement time history response of Fig. 8, the isolated structure manifested significant inelastic behavior in this case as well, despite the earlier and more pronounced activation of the seismic isolation system. The emerging ductility demand in this case (for the same strength reduction factor  $R_y=1.5$ ) in the isolated structure was  $\mu=u_{max}/u_y=37.4\text{mm}/20\text{mm}=1.87$ . Furthermore, the maximum sliding displacement of the seismic isolation system relative to the shaking table was in this case 125mm, much higher than the corresponding sliding displacement of 19.8mm observed for the Loma Prieta ground motion. This large sliding displacements usually manifest themselves during excitations of the seismically isolated structure by long-period ground motion records, as observed by Tsiavos et al. [19, 20], Banovic et al. [21], De Domenico et al. [22] and Gandelli et al. [23].

### 3.3 Damage Type

Two different limit states have been identified in this study to quantify the potential occurrence of damage in a seismically isolated structures: The exceedance of a predetermined ductility demand level in the seismically isolated structure indicating damage in the structure; and the exceedance of a predefined isolator displacement, which is related to a potential damage in the isolators.

The exceedance of the ductility demand level  $\mu=2$  was chosen to quantify the manifestation of severe damage in the isolated structure. As the current code provisions for seismically isolated structures prescribe the elastic design of these structures, the detailing of these structures is usually not sufficient to facilitate high ductility capacity in the isolated structure.

The exceedance of an isolator displacement corresponding to 90% of the isolator displacement capacity  $d=150\text{mm}$  was chosen to quantify the occurrence of damage in the seismic isolation system. Furinghetti et al. [5] have experimentally evaluated and determined the extra-stroke displacement capacity of curved surface slider devices, which is limited by the maximum contact pressure that can be tolerated by the installed sliding material. This extra-stroke displacement capacity was not considered in this study, but it can be further investigated by future studies on the same topic.

As shown in Tables 2 and 3, the value of the dimensionless friction ratio  $\Pi_2=\mu g/\text{PGA}$ , as defined by [15], indicated the predominant response and damage mode of the system for the case of a strength reduction factor of the isolated structure  $R_y=1.5$ : Values of  $\Pi_2$  smaller than 20% were correlated with high sliding displacement and potential damage in the seismic isolation system. Nevertheless, values of  $\Pi_2$  greater than 30% led to high ductility demand and damage concentrated in the seismically isolated structure. This variability in the response modes of the system for  $R_y=1.5$  indicates that the response is also influenced by the frequency content of the ground motion characteristics.

However, the design of a weaker isolated structure with  $R_y=2$  led to high ductility demand and concentration of damage in the seismically isolated structure for all the ground motion records used in this study. The sliding displacement of the seismic isolation system was substantially lower in this case, indicating that the response mode of the isolated structure subjected to extreme earthquake events is significantly influenced by the strength of the isolated structure: The reduction of the strength of the isolated structure leads to higher amount of damage in the isolated structure, which is not influenced by the ground motion characteristics.

**Table 2.** Experimentally and analytically derived response for  $R_y=1.5$ .

No.	Strength reduction factor $R_y$	Experimentally observed ductility demand $\mu$	Dimensionless friction ratio $\Pi_2$ (%)	Experimentally observed maximum sliding displacement of the seismic isolation system (mm)	Damage type
1	1.5	1.87	24	125	-
2	1.5	1.96	19	148.3	Seismic isolation system
3	1.5	1.78	13	147.4	Seismic isolation system
4	1.5	2.03	39	56.9	Isolated structure
5	1.5	2.23	30	77.6	Isolated structure
6	1.5	1.81	20	150	Seismic isolation system
7	1.5	2.01	62	19.8	Isolated structure
8	1.5	1.82	15	143	Seismic isolation system

**Table 3.** Experimentally and analytically derived response for  $R_y=2$ .

No.	Strength reduction factor $R_y$	Experimentally observed ductility demand $\mu$	Dimensionless friction ratio $\Pi_2$ (%)	Experimentally observed maximum sliding displacement of the seismic isolation system (mm)	Damage type
1	2.0	2.92	24	117.3	Isolated structure
2	2.0	2.81	19	135.8	Isolated structure
3	2.0	2.77	13	139.2	Isolated structure
4	2.0	3.08	39	55.1	Isolated structure
5	2.0	3.17	30	72.4	Isolated structure
6	2.0	2.45	20	131.2	Isolated structure
7	2.0	3.38	62	16.7	Isolated structure
8	2.0	2.76	15	129.5	Isolated structure

#### 4 CONCLUSIONS

This study shows experimentally the effect of the design parameters of the seismic isolation system and the seismically isolated structure on the response modes of seismically isolated structures subjected to extreme earthquake events. This effect is demonstrated through a shaking table investigation of the response of a seismically isolated steel structure, subjected to a strong earthquake ground motion excitation ensemble. The tested steel structure was seismically isolated with four friction pendulum bearings. The steel structure was equipped with a mechanical clevis connection comprising two hinges and a pair of replaceable steel coupons. The coupons are designed to yield before the other components of the structure and can be replaced after every shaking table test, thus allowing the experimental seismic fragility analysis of structures.

The shaking table investigation demonstrated the two different fundamental response modes of seismically isolated structures, subjected to above-design earthquake ground motion excitation: A mode characterized by excessive damage of the seismically isolated structure but limited damage in the isolators and a mode dominated by excessive isolator displacement and less damage in the isolated structure.

The two different seismic damage modes of a seismically isolated structure emerging from these two response modes were quantified based on two selected limit states. For the case of a seismically isolated structure designed with a strength reduction factor  $R_y=1.5$ , both damage modes were observed. These modes were strongly correlated with the value of the dimensionless friction ratio  $\Pi_2$ : Values of  $\Pi_2$  smaller than 20% were correlated with damage in the seismic isolation system, while values of  $\Pi_2$  bigger than 30% led to damage concentrated in the seismically isolated structure. However, the weaker seismically isolated structure designed with  $R_y=2$  manifested only damage in the isolated structure and lower sliding displacement of the isolation system, when subjected to the same ground motion excitation ensemble.

## REFERENCES

- [1] S. Kitayama, M.C. Constantinou, Implications of strong earthquake ground motion duration on the response and testing of seismic isolation systems. *Earthquake Engineering and Structural Dynamics*, **50** (2), 290-308, 2021.
- [2] S. Kitayama, M.C. Constantinou, Effect of superstructure modeling assumptions on the seismic performance of seismically isolated buildings. *Earthquake Engineering and Structural Dynamics*, 2021, DOI: <https://doi.org/10.1002/eqe.3427>
- [3] K. Gkatzogias, A. Kappos, Direct estimation of seismic response in reduced degree of freedom isolation and energy dissipation systems. *Earthquake Engineering and Structural Dynamics*, **48** (10), 1112-1133, 2019, DOI: <https://doi.org/10.1002/eqe.3169>
- [4] M. Furinghetti, I. Lanese, A. Pavese, Experimental assessment of the seismic response of a base-isolated building through a hybrid simulation. *Recent Advances and Applications of Seismic Isolation, Frontiers in Built Environment*, **6** (33), 2021, DOI: <https://doi.org/10.3389/fbuil.2020.00033>.
- [5] M. Furinghetti, T. Yang, P.M. Calvi, A. Pavese, Experimental evaluation of extra-stroke displacement capacity for curved surface slider devices. *Soil Dynamics and Earthquake Engineering*, 2021, DOI: <https://doi.org/10.1016/j.soildyn.2021.106752>.
- [6] M. Furinghetti, A. Pavese. Definition of a Simplified Design Procedure of Seismic Isolation Systems for Bridges, *Structural Engineering International*, 2020, DOI: 10.1080/10168664.2020.1775535.
- [7] A. Tsiavos, B. Stojadinovic, A probabilistic approach towards and evaluation of existing code provisions for seismically isolated structures, European Congress on Computational Methods in Applied Sciences and Engineering (ECCOMAS), Crete Island, Greece, 5–10 June 2016.
- [8] P. Castaldo, B. Palazzo, P. Della Vecchia, Seismic reliability of base-isolated structures with friction pendulum bearings. *Engineering Structures*, **95**, 80–93, 2015.
- [9] P. Castaldo, M. Ripani, R.L. Priore, Influence of soil conditions on the optimal sliding friction coefficient for isolated bridges. *Soil Dynamics and Earthquake Engineering*, 111, 131-148. 2018.

- [10] H.H. Tsang, Seismic isolation by rubber–soil mixtures for developing countries. *Earthquake Engineering and Structural Dynamics*, **37**, 283–303, 2008.
- [11] Y.B. Peng, Y.Y. Ma, T.C. Huang, D. De Domenico, Reliability-based design optimization of adaptive sliding base isolation system for improving seismic performance of structures. *Reliability Engineering and System Safety*, **205**, 107167, 2021.
- [12] M. Kikuchi, C.J. Black, I.D. Aiken, On the response of yielding seismically isolated structures. *Earthquake Engineering and Structural Dynamics*, **37**, 659–679, 2008.
- [13] D. Cardone, A. Flora, G. Guesualdi, Inelastic response of RC frame buildings with seismic isolation. *Earthquake Engineering and Structural Dynamics*, **42**, 871–889, 2013. doi:10.1002/eqe.2250
- [14] L. Ragni, D. Cardone, N. Conte, A. Dall'Asta, A. Di Cesare, A. Flora, G. Leccese, F. Micozzi, C. Ponzo, Modelling and Seismic Response Analysis of Italian Code Conforming Base-Isolated Buildings. *Journal of Earthquake Engineering*, **22** (2), 198–230, 2018, DOI: 10.1080/13632469.2018.1527263.
- [15] A. Tsiavos, K.R. Mackie, M.F. Vassiliou, B. Stojadinovic, Dynamics of inelastic base-isolated structures subjected to recorded ground motions. *Bulletin of Earthquake Engineering*, **15**(4), 1807–1830, 2017.
- [16] A. Tsiavos, D. Schlatter, T. Markic, B. Stojadinovic, Experimental and analytical investigation of the inelastic behavior of structures isolated using friction pendulum bearings. *Procedia engineering*, **199**, 465–70, 2017.
- [17] A. Tsiavos, D. Schlatter, T. Markic, B. Stojadinovic, Shaking table investigation of inelastic deformation demand for a structure isolated using friction-pendulum sliding bearings. *Structures*, **31**, 1041–1052, 2021. DOI: <https://doi.org/10.1016/j.istruc.2021.02.040>
- [18] PEER NGA Strong Motion Database (2018) Pacific Earthquake Engineering Research Center, University of California, Berkeley, available at. <https://ngawest2.berkeley.edu/>.
- [19] A. Tsiavos, A. Sextos, A. Stavridis, M. Dietz, L. Dihoru, N. Alexander. Large-scale experimental investigation of a low-cost PVC ‘sand-wich’ (PVC-s) seismic isolation for developing countries. *Earthquake Spectra*, **36**(4), 1886–911, 2020.
- [20] A. Tsiavos, P. Haladij, A. Sextos, N. Alexander, Analytical investigation of the effect of a deformable sliding layer on the dynamic response of seismically isolated structures *Structures*, **27**, 2426–2436, 2020.
- [21] I. Banovic, J. Radnić, N. Grgić. Foundation size effect on the efficiency of seismic base isolation using a layer of stone pebbles. *Earthquakes and Structures*, **19** (2), 2020.
- [22] D. De Domenico, E. Gandelli, V. Quaglini, Adaptive isolation system combining low friction sliding pendulum bearings and SMA-based gap dampers. *Engineering Structures*, **212**, 2020.
- [23] E. Gandelli, D. De Domenico, P. Dubini, M. Besio, E. Bruschi, V. Quaglini. Influence of the breakaway friction on the seismic response of buildings isolated with curved surface sliders: parametric study and design recommendations. *Structures*, **27**, 788–81, 2020.



## A NEW PARALLEL ALGORITHM FOR THE OPTIMUM EMBEDDED REBAR MESH GENERATION FOR LARGE-SCALE REINFORCED CONCRETE STRUCTURES

Dewald Z. Gravett<sup>1</sup> and George Markou<sup>1</sup>

<sup>1</sup> Department of Civil Engineering, University of Pretoria, South Africa  
e-mail: u16004664@tuks.co.za; George.markou@up.ac.za

---

### Abstract

*The modeling of large-scale reinforced concrete (RC) structures through 3D detailed modeling is not feasible due to the excessive computational demand that is required during different phases of the analysis. Especially when the overall objective is to perform nonlinear dynamic analysis of RC structures that also take into account the soil-structure interaction effect by discretizing the soil domain with hexahedral elements. These large-scale models have a significant computational demand when analysed, where the use of high-performance computing and parallel solution algorithms is currently the only solution in achieving reasonable computational times. One of the computationally demanding processes during this type of analysis, is the embedded rebar mesh generation, where millions of elements have to be created. This research work proposes a new load distribution algorithm that optimizes the numerical response of a previous parallel embedded rebar mesh generation algorithm incorporated in Reconan FEA. After the implementation of the proposed parallel algorithm, it was found that the computational time was decreased by an average of 57.48% compared to the performance of the old parallel algorithm.*

**Keywords:** Parallel Processing, Embedded Rebars, Reinforced Concrete Structures, Large-Scale Models, Finite Element Method

---

## 1 INTRODUCTION

The finite element (FE) method is widely used to solve and optimize any type of engineering problem. Computationally demanding and complex engineering problems composed of several thousand degrees of freedom are not uncommon anymore, especially when performing assessments with nonlinear dynamic analysis of reinforced concrete (RC) structures such as bridges, nuclear reactor and high-rise buildings that foresee the discretization of the concrete domain through isoparametric hexahedral elements and the reinforcement mesh with embedded rod or beam FEs. This modeling approach is known as 3D detailed approach [1-2], where embedded rebar macro-elements are found within the hexahedral mesh.

A search procedure is required to be performed to find the intersection of the macro-elements [3] with the hexahedral mesh (Fig. 1), to allocate the embedded rebar elements found within each hexahedral element. This procedure can be time consuming for large-scale models that consist of millions of embedded rebar elements. An efficient method for the generation of embedded reinforcement mesh was proposed by Markou and Papadrakakis [4] and parallelized in [5]. This work extends the algorithm proposed in [5], where the computational distribution is optimized.

## 2 EMBEDDED REBAR MESH GENERATION

Barzegar and Maddipudi [6] proposed the numerical method for the allocation and generation of embedded rebars inside hexahedral elements, which was an extension of the work performed by Elwi and Hrudey [7]. According to the hexahedral mesh, the standard Barzegar and Maddipudi [6] method is performed for cases of non-prismatic hexahedral elements, to allocate the natural coordinates of the corresponding virtual node. A point P1 with global coordinates  $(x, y, z)_{P1}$  on the initial rebar mesh (Fig. 1), is contained in a given concrete element if its natural coordinates  $\xi_{P1}, \eta_{P1}, \zeta_{P1}$  satisfy the following constraint:

$$|\xi_{P1}, \eta_{P1}, \zeta_{P1}| \leq 1 \quad (1)$$

In this formulation the global coordinates  $(x, y, z)$  of a common point within a solid element can be expressed as:

$$\begin{Bmatrix} x \\ y \\ z \end{Bmatrix} = \begin{bmatrix} N & 0 & 0 \\ 0 & N & 0 \\ 0 & 0 & N \end{bmatrix} \begin{Bmatrix} x_i \\ y_i \\ z_i \end{Bmatrix} \quad (2)$$

where  $x_i, y_i, z_i$  are the global coordinate vectors of the hexahedral nodes and  $N$  represents the row vector of the displacement-shape functions.

$$\begin{Bmatrix} x \\ y \\ z \end{Bmatrix}_{P1} - \begin{bmatrix} N & 0 & 0 \\ 0 & N & 0 \\ 0 & 0 & N \end{bmatrix} \begin{Bmatrix} x \\ y \\ z \end{Bmatrix} = 0 \quad (3)$$

Given that the natural coordinates  $(\xi, \eta, \zeta)_{P1}$  are the roots of Eq. 3, a Newton-Raphson iterative procedure is required in order to compute the solution of the above equation as follows:

$$\begin{Bmatrix} \xi \\ \eta \\ \zeta \end{Bmatrix}_{P_1}^{n+1} = \begin{Bmatrix} \xi \\ \eta \\ \zeta \end{Bmatrix}_{P_1}^n + \begin{Bmatrix} \Delta \xi \\ \Delta \eta \\ \Delta \zeta \end{Bmatrix}_{P_1}^{n+1} \quad (4)$$

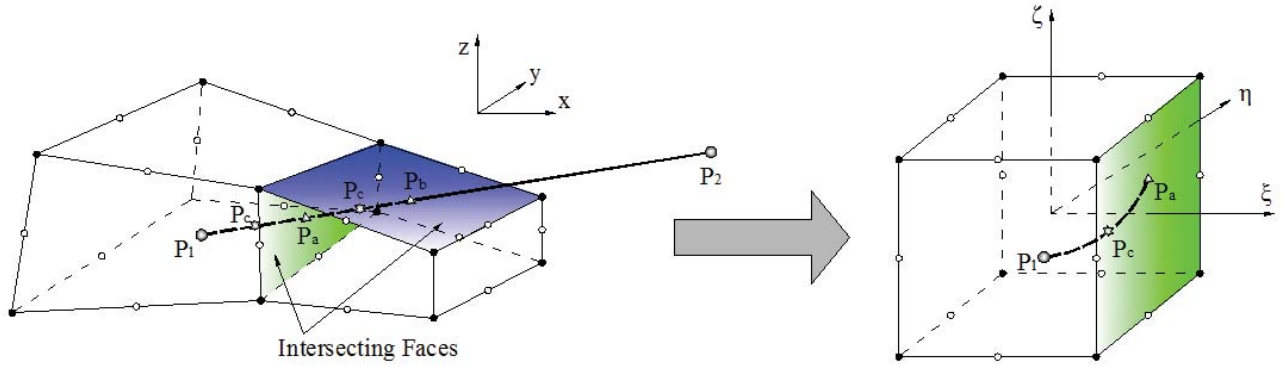


Figure 1. Embedded reinforcement in hexahedral concrete element [3].

Since,

$$\begin{Bmatrix} d\xi \\ d\eta \\ d\zeta \end{Bmatrix} = (\mathbf{J}^T)^{-1} \begin{Bmatrix} dx \\ dy \\ dz \end{Bmatrix} \quad (5)$$

where  $\mathbf{J}$  is the Jacobian matrix, the incremental natural coordinates can then be computed from Eq. 6.

$$\begin{Bmatrix} \Delta \xi \\ \Delta \eta \\ \Delta \zeta \end{Bmatrix}_{P_1}^{n+1} = (\mathbf{J}^{nT})^{-1} \left[ \begin{Bmatrix} x \\ y \\ z \end{Bmatrix}_{P_1} - \begin{bmatrix} N^n & \mathbf{0} & \mathbf{0} \\ \mathbf{0} & N^n & \mathbf{0} \\ \mathbf{0} & \mathbf{0} & N^n \end{bmatrix} \begin{Bmatrix} x \\ y \\ z \end{Bmatrix} \right] \quad (6)$$

with

$$\mathbf{J}^n = \mathbf{J}(\xi^n, \eta^n, \zeta^n); \quad N^n = N(\xi^n, \eta^n, \zeta^n).$$

The mesh generation method proposed by Barzegar and Maddipudi [6] was found to be hindered with additional computational demand, however, this computational demand was reduced and optimized within [3] by implementing a geometric constraint that decreases unnecessary searches of intersection points. Furthermore, the algorithm was further integrated by determining if a hexahedral element is a parallelepiped or not. The proposed mesh generation procedure [3] was then parallelized in [5] as shown in Fig. 2.

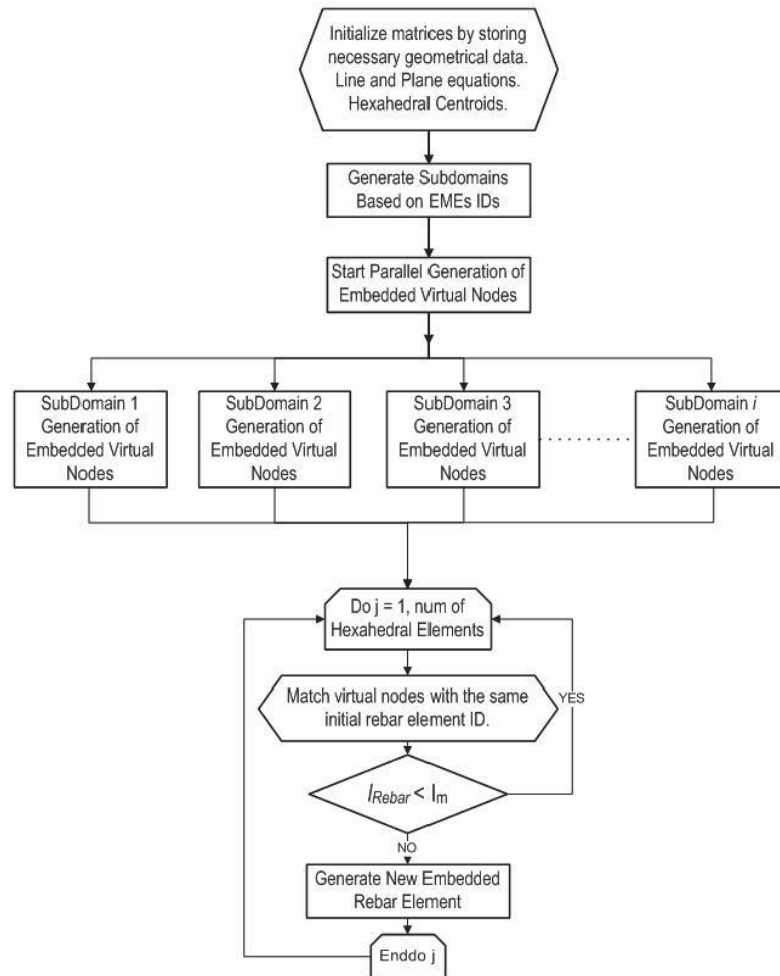


Figure 2. Flow chart of the embedded rebar mesh generation procedure [5].

This research work foresees the development of a parallel algorithm to improve the computational performance and efficiency of the algorithm shown in Fig. 2 for the large-scale embedded rebar mesh generation process.

### 3 PARALLEL PROCESSING METHODS AND TECHNIQUES

Engineering and scientific computing methods have significantly evolved over the past two decades, with the use of graphic processing units (GPU) in cooperation with a central processing unit (CPU). GPU-accelerated computing has become more popular due to its advanced features related to its parallel architecture, as well as, its capabilities on handling multiple problems simultaneously. Nevertheless, the use of GPUs is constrained from the need of customizing the build according to the hardware at hand. Furthermore, the appearance of the multicore processors brings about an important turning point in programming practices, especially with FE applications.

Fernández et al. [8] presented a new alternate way to formulate the finite element method (FEM) for parallel processing based on the solution of single mesh elements called FEM-SES. This method decouples the solution of a single element from the whole mesh, therefore, exposing parallelism at the element level. Each element solution is then superimposed node-wise using a weighted sum over the concurrent nodes. The research study performed by Fernández et al. [8] showed results up to 111 times faster than the results obtained on classic FEM problems.

Stavroulakis et al. [9] investigated a GPU domain decomposition solution for the spectral stochastic FEM. Within this research work they demonstrate the benefits achieved with the exploitation of the GPU capabilities, where they addressed problems where the solution of the FE algebraic equations was performed with the dual domain decomposition method by implementing specifically tailored preconditioners. This research concluded a significant enhancement of the spectral stochastic FEM, as well as the consumed energy efficiency achieved by this methodology.

Several other researchers [10-14] used parallel processing methods, introducing the basics of implementing parallel processing algorithms enhancing the efficiency and decrease the computational demand of FE software. The only research work found on parallel embedded rebar mesh generation was presented by [5] which is the work that will be used herein in proposing an improved parallel embedded rebar mesh generation framework. The main objective is to significantly improve the scalability and overall computational efficiency of the parallel embedded rebar mesh generation procedure.

#### 4 PROPOSED PARALLEL ALGORITHM

The proposed parallel algorithm is implemented within the research software, Reconan FEA [15]. The initial parallel framework was discussed and tested within [5], by analysing a NuScale reactor building that was investigated in Markou and Filippo [16]. This RC building was discretized with 8-noded hexahedral elements as it is going to be discussed in the next section.

The proposed parallel algorithm suggests a new computational load distribution process that calculates the computational load that will be assigned to each core prior to the mesh generation. The initial parallel algorithm foresaw the division of the number of embedded macro-elements into equal numbers based on their ID. This caused the unequal computational load distribution not allowing the embedded rebar mesh generation procedure to be performed in a computationally optimum manner, especially in cases where the macro-element lengths had significant differences within the model.

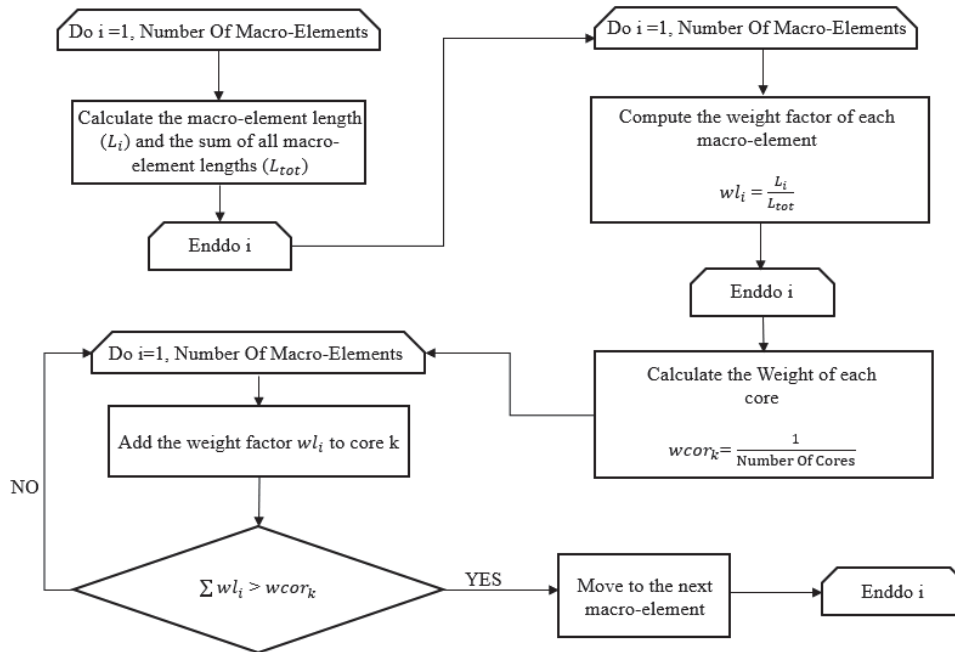


Figure 3. Flowchart for the proposed parallel algorithm.



An improved computational load distribution algorithm was developed for the needs of this research study that is performed based on the geometrical features of the embedded macro-elements found within the mesh. As it can be seen in Fig. 3, the proposed algorithm foresees the computation of the length of each macro-element  $L_i$ , while computing the total length of all macro-elements  $L_{tot}$  found within the mesh. A weight factor  $wl_i$  is computed for each macro-element, which equals to the length of the macro-element  $L_i$  divided by the total macro-elements' length:

$$L_{tot} = \sum_{j=1}^{num.elem.} L_j \quad (7)$$

$$wl_i = L_j / L_{tot} \quad (8)$$

Following the calculation of the weight factor  $wl_i$ , the computation of the weight factor  $wcor_k$  is computed for each core as shown in Fig. 3. This weight factor determines the total length of macro-elements that will be assigned to core  $k$ . Therefore, the macro-elements are divided and assigned to each core according to the overall length of the macro-elements that is directly connected to the performed calculations during the search of embedded rebar elements. The longer the macro-element is, the larger the number of hexahedral intersections, thus the larger the calculations required for the allocation of the virtual embedded rebar nodes.

## 5 REINFORCED CONCRETE MODEL

The NuScale reactor building, developed and studied in [16] is analysed for the needs of investigating the numerical response of the proposed parallel algorithm. This RC model shown in Fig. 4 has a total length of 75.25 m, a width of 30 m and a maximum height of 39.55 m. The FE framing system of the NuScale model was discretized with 181,076 8-noded isoparametric hexahedral elements as it can be seen in Fig. 4. Additionally, to decrease the mesh construction procedure, very long embedded macro-elements were used (up to 75 m in length, where the shortest macro-elements had 0.5 m length). The embedded macro-element mesh can be seen in Fig. 5 as it was developed by Markou and Filippo [16]. It should be noted that this structure has a total of 177,504 embedded macro-elements, where after the execution of the embedded rebar mesh generation procedure, a total of 2,703,251 embedded rebar finite elements are created within the final FE numerical model.

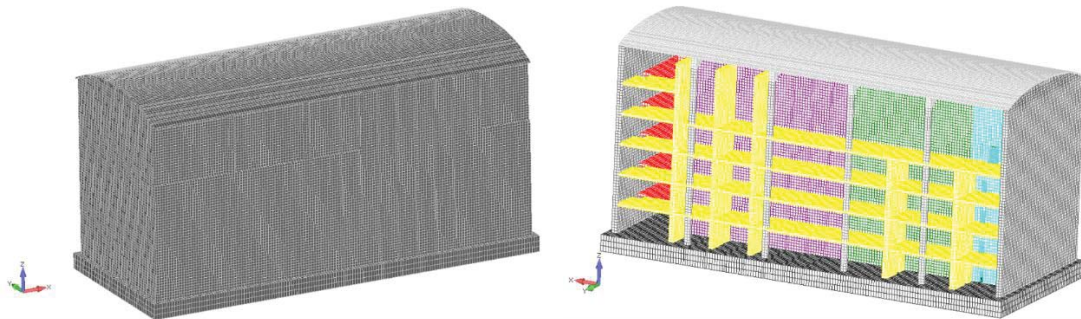


Figure 4: NuScale reactor building discretized with 8-noded isoperimetric hexahedral FEs.

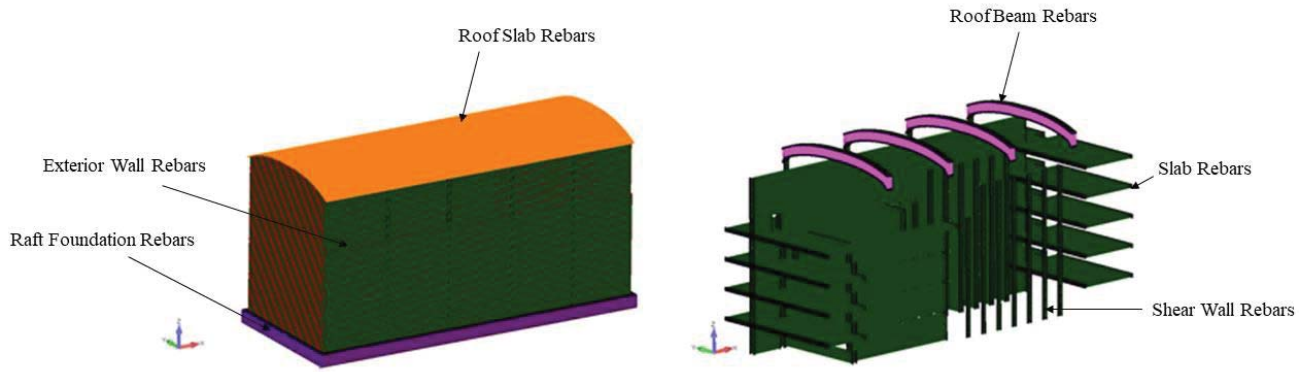


Figure 5. Macro-elements of the NuScale reactor building.

## 6 NUMERICAL INVESTIGATION OF THE PROPOSED ALGORITHM

The numerical performance of the proposed algorithm was investigated through the use of a 12-core computer, with 4.2 GHz per core computational processing unit. This investigation foresaw the execution of 66 analyses of the NuScale reactor building presented above, in generating the embedded rebar elements. It should be noted at this point that 3 analyses were performed for each solution case using the proposed and the old parallel algorithms by assuming different number of cores, ranging from 2 to 12. When performing the analysis in a serial manner (1 core), the rebar generation computational time equals to 176.93 min. The results obtained from the parallel embedded rebar mesh generations can be seen in Fig. 6.

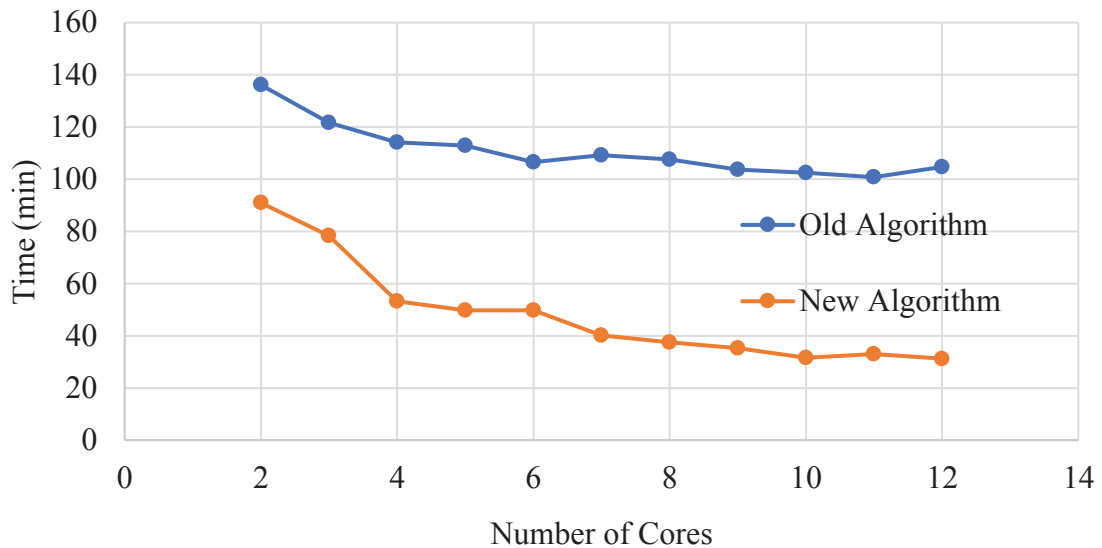


Figure 6: Algorithmic performance results for different number of cores when using the old and new algorithm.

As it can be depicted from Fig. 6, the computational time decreases as the number of cores increases, where the proposed distribution algorithm significantly improved the efficiency of the embedded rebar mesh generation procedure. When the number of cores used to solve the problem is set to 2, the proposed algorithm manages to achieve a 33.2% computational time decrease compared to the old algorithm. Furthermore, it is easy to observe that the new proposed algorithm decreased the computational demand from 104.69 minutes to 31.22 minutes when using 12 cores (see Table 1), which makes the proposed algorithm 3.4 times faster than the old one. As shown in Table 1, the scalability also improves when the number of cores used to solve this problem increases, when the proposed and the old algorithms are compared. In

addition to that, the proposed algorithm manages to decrease the total embedded rebar mesh generation time by 5.7 times when using 12 cores compared to the solution with 1 core.

Table 1: Computational time for each parallel analysis with the old and new algorithm.

	Number of cores										
	2	3	4	5	6	7	8	9	10	11	12
Old Algorithm parallel time (min)	136.10	121.63	114.14	112.81	106.44	109.15	107.59	103.72	102.39	100.76	104.69
New Algorithm parallel time (min)	90.91	78.37	53.26	49.82	49.80	40.11	37.56	35.25	31.52	32.91	31.22
Computational Time Decrease (%)	33.20	35.57	53.34	55.84	53.22	63.26	65.09	66.02	69.21	67.33	70.18

## 7 CONCLUSIONS

A newly developed and improved distribution load algorithm for parallel processing was presented and numerically investigated through the use of a NuScale reactor building model, consisting a total of 2,703,251 embedded rebar elements. The proposed algorithm took into account the length of each embedded macro-element utilizing a macro-element weight factor to distribute the computational load evenly to each core. Therefore, the distribution of the computational demand was performed based on the total macro-element length sent to each core and not based on the number of embedded macro-elements assigned to each core.

According to the numerical findings obtained from 66 analyses that foresaw the use of different number of cores, it was concluded that the proposed algorithm yielded a significant computational efficiency, allowing the embedded rebar mesh generation procedure to become up to 3.4 times faster compared to the performance of the older parallel algorithm [5].

Currently, the proposed algorithm is parametrically investigated through the use of more large-scale models, such as wind turbine structures, high-rise buildings and bridges. Furthermore, Reconan FEA has been integrated and is now been tested on a high-performance computer which has 40 cores per node. Future research work will investigate more computational load distribution approaches that will further optimize the numerical performance and scalability of the developed embedded rebar mesh generation procedure.

## REFERENCES

- [1] Mourlas, C., Markou, G. and Papadrakakis, M., Accurate and Computationally Efficient Nonlinear Static and Dynamic Analysis of Reinforced Concrete Structures Considering Damage Factors, *Engineering Structures*, 178 (2019), pp. 258–285, 2019.
- [2] Mourlas, Ch., Khabele, N., Bark, H.A., Karamitros, D., Taddei, F., Markou, G. and Papadrakakis, M., The Effect of Soil-Structure Interaction on the Nonlinear Dynamic Response of Reinforced Concrete Structures, *International Journal of Structural Stability and Dynamics*, 2020, <https://doi.org/10.1142/S0219455420410138>.
- [3] Markou, G., Computational Performance of an Embedded Reinforcement Mesh Generation Method for Large-Scale RC Simulations, *International Journal of Computational Methods*, 12(3): 1550019-1:48, 2015.
- [4] Markou, G. and Papadrakakis, M., An efficient generation method of embedded reinforcement in hexahedral elements for reinforced concrete simulations, *Advances in Engineering Software ADES*, Vol. 45(1), Pp 175-187, 2012.

- [5] Markou, G., A Parallel Algorithm for the Embedded Reinforcement Mesh Generation of Large-Scale Reinforced Concrete Models, *9<sup>th</sup> GRACM International Congress on Computational Mechanics*, Chania. Markou G. (2015). Computational Performance of an Embedded Reinforcement Mesh Generation Method for Large-Scale RC Simulations, *International Journal of Computational Methods*, 12(3): 1550019-1:48, 2018.
- [6] Barzegar, F. and Maddipudi, S., Generating reinforcement in FE modeling of concrete structures, *Journal of Structural Engineering*, 120, pp.1656 –1662, 1994
- [7] Elwi, A.E. and Hrudey, T.M., Finite element model for curved embedded reinforcement, *Journal of Engineering Mechanics*, 115:740 –754, 1989.
- [8] Fernández, D.M., Mehri Dehnavi, M., Gross, W.J. and Giannacopoulos, D., Alternate Parallel Processing Approach for FEM, *IEEE Transactions on Magnetics*, VOL. 48, NO. 2, pp 399-402, 2012.
- [9] Stravroulakis, G., Giovanis, D.G., Papadopoulos, V. and Papadrakakis, M., A GPU domain decomposition solution for spectral stochastic finite element method, *Comput. Methods Appl. Mech. Engrg.* 327, pp 392-410, 2017.
- [10] Carey, G. F., Barragy, E., McLay, R. and Sharma, M., Element-by-element vector and parallel computations, *Commun. Appl. Numer. Methods*, VOL. 4, no. 3, pp. 299-307, 1988.
- [11] Okimura, T., Sasayama, T., Takahashi, N. and Ikuno, S., Parallelization of Finite Element Analysis of Nonlinear Magnetic Fields Using GPU, *IEEE Transactions on Magnetics*, vol. 49, no. 5, pp. 1557-1560, 2013.
- [12] Jimack, P.K. and Touheed, N., Developing Parallel Finite Element Software Using MPI, School of Computer studies, University of Leeds, UK, 2014.
- [13] Mpong, S.M., de Montleau, P., Godinas, A. and Habraken, A.M., A Parallel Computing Model for the Acceleration of a Finite Element Software, *PDPTA '02 International Conference*, 2002.
- [14] Cave, W.C., Wassmer, R.E., Ledgard, H.F., Salisbury, A.B., Irvine, K.T. and Mulshine, M.A., A New Approach to Parallel Processing, *IEEE Access*, Vol 8, 2020.
- [15] Reconan FEA v2.0, User's Manual, 2020.  
[https://www.researchgate.net/publication/342361609\\_ReConAn\\_v200\\_Finite\\_Element\\_Analysis\\_Software\\_User%27s\\_Manual](https://www.researchgate.net/publication/342361609_ReConAn_v200_Finite_Element_Analysis_Software_User%27s_Manual)
- [16] Markou, G. and Genco, F., Seismic Assessment of Small Modular Reactors: NuScale Case Study for the 8.8 Mw Earthquake in Chile, *Nuclear Engineering and Design*, 342(2019), pp. 176-204, 2019.

## ON THE APPLICATION OF GENERALISED SCHUR COMPLEMENTS TO SUBSYSTEM-LEVEL VARIABILITY QUANTIFICATION

Vladimir V. Yotov<sup>1</sup>

<sup>1</sup>Independent researcher  
München, Germany  
e-mail: v.v.yotov@gmail.com

**Keywords:** Structural Dynamics, Random Matrices, Uncertainty Modelling, Component Mode Synthesis, Finite Element Method, Monte Carlo Simulation

**Abstract.** *Representation of random uncertainties in the context of reduced order models is addressed in this article. Traditional strategies are generally based on the description of non-deterministic features by random fields or parameters. Extraction of statistical properties of interest is achieved via a costly direct Monte Carlo simulation (MCS). While dynamic substructuring and reduction techniques can alleviate the impractical computational requirements of these methods, propagation of the physical space uncertainty characterisation into a condensed model is nontrivial. An explicit definition of random reduced substructural mass and stiffness poses an alternative. However, such a technique must yield samples that preserve certain mathematical properties of the nominal matrices. Following this paradigm, a recent approach, permitting the robust construction of  $2 \times 2$  block-partitioned, nonnegative definite Hermitian matrices is adopted herein. It employs a formulation relying on generalised Schur complements and random unitary matrices. Unlike other existing schemes, the sampling of component-level off-diagonal matrix blocks is an inherent feature of this method. Thus, it also preserves the blockwise mass and stiffness sparsity pattern of the global component mode synthesis (CMS) model. In this paper, an improved formulation allowing strict rank preservation and more efficient sampling is laid out. The proposed technique is compared against parametric MCS for the case of a satellite structure subjected to a non-uniform pressure excitation. A simulation speed-up of approximately 3 orders of magnitude is achieved, while a solid agreement with the benchmark solution is observed for the prediction of structural response variability.*



## 1 INTRODUCTION

Irrespectively of the level of detail of a mechanical system's mathematical model, deterministic descriptions are bound to provide only a partial insight into its actual physical behaviour. Uncertainty is introduced through various paths, such as non-ideal materials, geometric approximations and random boundary conditions. The description and quantification of such non-deterministic behaviour is central to the field of stochastic structural mechanics, reviewed in [1, 2, 3]. Contemporary techniques fall into a few major categories, as follows.

Probabilistic structural analysis (PSA) treats uncertain model properties as independent random variables, whose mean and variance are estimated a priori. Barring perturbation theory, which is not well-suited to representing high coefficients of variation (COVs) [2], MCS is traditionally performed [4]. Upon generating a sufficiently large number of realisations of the random structure, each resultant deterministic case is solved. Quantities of interest are then computed by statistical manipulation of the results. Direct MCS application is comparatively straightforward, and its predictions tend capture the real structure's stochastic behaviour well. Thus other schemes are often validated against PSA, e.g. for spacecraft design and analysis [5, 6].

The parameter space characterisation of PSA is often viewed as oversimplified. Logically, an uncertain physical quantity would not deviate uniformly from some mean value over its whole domain. The basis of the stochastic finite element method (SFEM) [7, 8] is formed by the inclusion of spatial variability, which gives rise to random fields. They are expressed via field variables that represent spatial fluctuation and probabilistic behaviour. A challenging aspect of SFEM is that a discrete computational domain has to be prescribed for the random fields over the application geometry. In contrast to SFEM's academic popularity, utilisation in commercial software remains currently limited, with notable exceptions discussed in [9, 10].

A solid practical argument against the aforesaid techniques is the estimation of a system failure probability  $p_F$ . Conventional MCS demands a number of analyses of order  $1/p_F$ , such that very low-probability samples containing failure events can be extracted from the population. With the exception of simple problems, MCS is clearly infeasible. The issue is addressed by a class of so-called variance reduction methods, comprised of two prominent advancements - subset simulation [11] and line sampling [12]. Both exhibit comparable performance for certain high-complexity problems, with the evaluation of  $p_F$  taking hundreds of samples, instead of millions for the direct MCS [13, 5, 6].

In contrast to other methods, the popular nonparametric probabilistic approach of Soize [14] constructs a non-deterministic model without random variables or fields. It relies on random matrix theory and the maximum entropy principle, which stems from information theory. The objective is to build a stochastic model that maximises uncertainty within available constraints. Random structural matrices are obtained from known deterministic ones, with only a single parameter responsible for specifying their dispersion. Statistical moments of the responses are calculated by standard MCS. An updated version of the approach [15] permits the separate treatment of modelling errors and system parameter uncertainties.

Shifting the perspective to practicality of analysis and computational efficiency, splitting complex FE representations into smaller parts is commonplace [16], c.f. Figure 1. In CMS, each component is projected onto a suitable basis in a generalised degree of freedom (DOF) space, yielding greatly reduced problem dimensions. The condensed system is then synthesised, i.e. reassembled. Unsurprisingly, CMS is widely adopted in the space industry, where FE models can surpass millions of DOFs, becoming impractical to handle. The classic Craig-Bampton

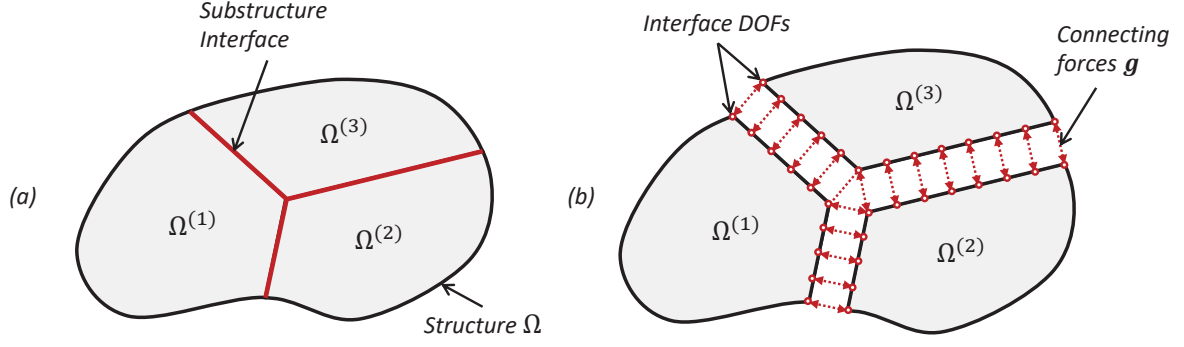


Figure 1: Substructuring visualisation: (a) partitioning, (b) definition of component interface connections

(CB) method [17] remains the prevalent CMS technique, with multiple improved versions also available [18, 19]. Additional modern contributions to the field include automated substructuring [20], exploring non-standard projection bases, different interface reduction schemes and combinations thereof [21, 22, 23].

As the ongoing growth in computing resources has been matched by FE model complexity, closing the gap between stochastic analysis and reduction techniques remains highly desirable. Some modal approaches such as [24] have been delineated, normally restricted to a CB reduction [25, 26]. However, a distinct lack of methods appropriate for dealing with random uncertainties on a substructural level in a generic CMS setting is observed. The nonparametric probabilistic approach marks a partial exception, but it does not preserve the blockwise sparsity of CMS representations. In brief, robustly constructing individual random blocks of substructural matrices is not tractable with existing methods, especially for off-diagonal partitions.

In the present article, these issues are dealt with by a mathematical formulation specifically derived for the construction of blockwise random  $2 \times 2$  nonnegative definite matrices of given rank. An early rendition of the method was presented in [27], indicating promising efficiency and accuracy. Here, an amended version is laid out, benefiting from a simpler, yet mathematically more rigorous definition. Verification against direct MCS for a practical benchmark case of a Craig-Bampton reduced spacecraft is demonstrated.

## 2 STOCHASTIC CMS THEORETICAL FORMULATION

### 2.1 General notation

Let us first establish the notation employed throughout the rest of the article. Boldface upper and lower case letters are used for matrices and vectors, respectively. We denote the conjugate transpose of a matrix  $\mathbf{A} \in \mathbb{C}^{m \times n}$  by  $\mathbf{A}^*$  and its pseudoinverse by  $\mathbf{A}^+$ . For better readability, the shorthand style  $\mathbf{A}^{+*}$  is used in place of the compound operation  $(\mathbf{A}^+)^*$ , equivalent to  $(\mathbf{A}^*)^+$ . The (possibly generalised) Schur complement of  $\mathbf{X}$  in  $\mathbf{A}$  is denoted by  $\mathbf{A}/\mathbf{X}$ . We further use  $\mathbf{A} \succ \mathbf{0}$  and  $\mathbf{A} \succeq \mathbf{0}$  to specify that  $\mathbf{A} \in \mathbb{C}^{n \times n}$  is strictly positive definite or positive semi-definite (PSD), respectively.

The  $i$ -th eigenvalue of  $\mathbf{A} \in \mathbb{C}^{n \times n}$  is written as  $\lambda_i(\mathbf{A})$ , with ordering  $\lambda_1 \geq \dots \geq \lambda_n$ . Analogously,  $\sigma_i(\mathbf{A})$  is  $i$ -th singular value of  $\mathbf{A} \in \mathbb{C}^{m \times n}$ , where  $\sigma_1 \geq \dots \geq \sigma_{\min\{m,n\}}$ . Lastly, the tilde accent indicates non-deterministic quantities, e.g.  $\tilde{x}$  is a random variable  $x$ . The topics in linear algebra relevant to this paper are covered in [28, 29].

## 2.2 Prerequisites

Consider the generalised eigenvalue problem (GEP):

$$(\mathbf{K} - \lambda_i \mathbf{M})\phi_i = 0, \quad i = \{1, \dots, n\} \quad (1)$$

with  $i$ -th structural mode  $\phi_i$  and discrete stiffness and mass  $\mathbf{K}$ ,  $\mathbf{M}$ , typically both real in FEM. Unless  $\mathbf{K}$ ,  $\mathbf{M} \succeq \mathbf{0}$ , i.e. they are at least positive semi-definite, the GEP can be shown to have negative eigenvalues. This translates to complex structural natural frequencies, which are given by  $\omega_i^2 = \lambda_i(\mathbf{K}, \mathbf{M})$ . Consequentially,  $\phi_i \in \mathbb{R}$  does not hold either. In order to circumvent this issue, the random matrices  $\tilde{\mathbf{K}}$ ,  $\tilde{\mathbf{M}}$  that we will construct must be strictly PSD.

To avoid superfluous notation, let us introduce an  $n \times n$  Hermitian matrix  $\mathbf{G}$  and its random counterpart  $\tilde{\mathbf{G}}$ , with their  $2 \times 2$  block partitioning

$$\mathbf{G} = \begin{bmatrix} \mathbf{A} & \mathbf{B} \\ \mathbf{B}^* & \mathbf{D} \end{bmatrix}, \quad \tilde{\mathbf{G}} = \begin{bmatrix} \tilde{\mathbf{A}} & \tilde{\mathbf{B}} \\ \tilde{\mathbf{B}}^* & \tilde{\mathbf{D}} \end{bmatrix} \quad (2)$$

as placeholders for any substructural or global  $\mathbf{M}$  or  $\mathbf{K}$ . Usually, free-free configuration FE models' mass and stiffness matrices have nonempty nullspaces. These correspond to the rigid body modes of the structure, thus are normally subspaces whose dimension is 6, i.e. equal to the number of global spatial degrees of freedom in 3D. The nullspace dimension of  $\tilde{\mathbf{G}}$  with respect to  $\mathbf{G}$  is therefore a further mathematical feature that should be respected. Altering the number of rigid body modes in realisations of the random structure would clearly be unphysical.

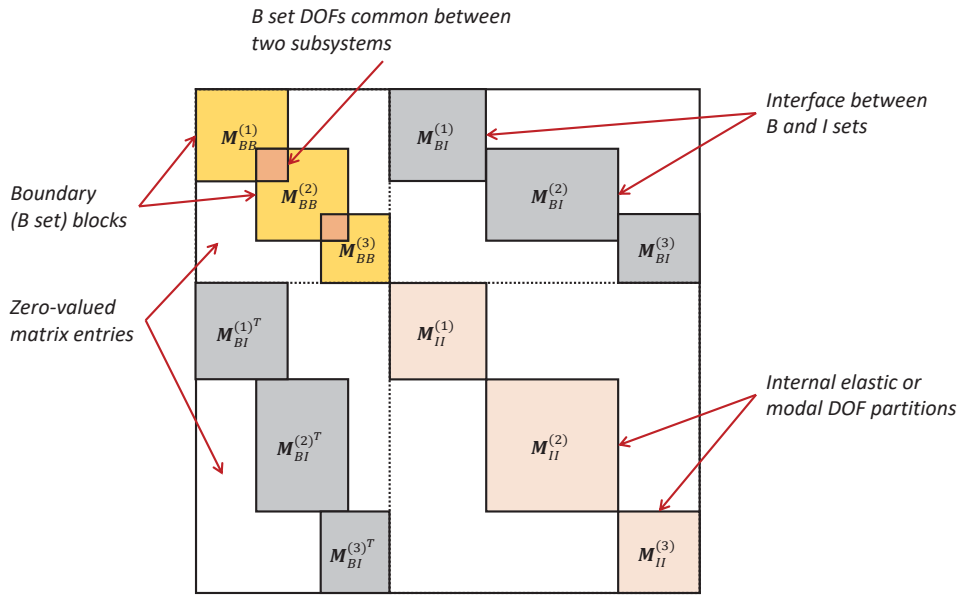


Figure 2: Form of a partitioned and DOF-ordered mass matrix for 3 subsystems

## 2.3 Mathematical framework

In dynamic substructuring problems the  $2 \times 2$  block matrix format naturally occurs on both local and global system levels, owed to the separation of boundary and internal elastic DOFs. This is illustrated on Figure 2, which depicts the blockwise sparse structure of a mass matrix in primal assembly. Exploiting this logical division would be particularly attractive for describing

subcomponent variability, especially in a reduced model context. The main obstacle lies in finding an interdependency within the global matrix structure, such that the permissible range of values for any of its blocks can be specified as some function of the remaining ones. For instance, how can the random partition  $\tilde{\mathbf{B}}$  be characterised by the submatrices  $\mathbf{A}$  and  $\mathbf{D}$ , such that for any possible realisation of  $\tilde{\mathbf{B}}$ , the conditions of Section 2.2 are met.

Note that the detailed proofs of ensuing key statements are fairly lengthy and thus beyond the scope of this paper. It is possible to derive the following fundamental result:

**Theorem 1** (Nonnegative definiteness). *For a Hermitian matrix  $\mathbf{G} = \begin{pmatrix} \mathbf{A} & \mathbf{B} \\ \mathbf{B}^* & \mathbf{D} \end{pmatrix}$ ,  $\mathbf{G} \succeq \mathbf{0}$  if and only if*

- (a) *all singular values  $\sigma_i(\mathbf{L}_A^+ \mathbf{B} \mathbf{L}_D^{+*}) \leq 1$ , where  $\mathbf{A} = \mathbf{L}_A \mathbf{L}_A^*$  and  $\mathbf{D} = \mathbf{L}_D \mathbf{L}_D^*$*
- (b)  *$\text{range}(\mathbf{B}) \subseteq \text{range}(\mathbf{A})$*
- (c)  *$\text{range}(\mathbf{B}^*) \subseteq \text{range}(\mathbf{D}^*)$*

Broadly speaking, Theorem 1 can be proven by calling upon the generalised Schur complement condition, which states that  $\mathbf{G} \succeq \mathbf{0}$  if and only if

$$\mathbf{A} \succeq \mathbf{0}, \mathbf{D} - \mathbf{B}^* \mathbf{A}^+ \mathbf{B} \succeq \mathbf{0}, (\mathbf{I} - \mathbf{A} \mathbf{A}^+) \mathbf{B} = \mathbf{0} \quad (3)$$

in conjunction with a technical lemma

**Lemma 2.** *For a Hermitian  $\mathbf{T}$  a necessary but not sufficient condition for  $\mathbf{S} \mathbf{T} \mathbf{S}^* \succeq \mathbf{0}$  is  $\text{range}(\mathbf{V}_n) \cap \text{range}(\mathbf{S}^*) = \{\mathbf{0}\}$ , where  $\mathbf{V}_n$  is the matrix of eigenvectors of  $\mathbf{T}$  with negative associated eigenvalues.*

For the strict case, which corresponds to a matrix  $\mathbf{G}$  with a trivial nullspace, e.g. the mass or stiffness of a FE model constrained in space, we have

**Corollary 3.** *Given a Hermitian matrix  $\mathbf{G} = \begin{pmatrix} \mathbf{A} & \mathbf{B} \\ \mathbf{B}^* & \mathbf{D} \end{pmatrix}$ ,  $\mathbf{G} \succ \mathbf{0}$  if and only if  $\sigma_i(\mathbf{L}_A^{-1} \mathbf{B} \mathbf{L}_D^{-*}) < 1$ , where  $\mathbf{A} = \mathbf{L}_A \mathbf{L}_A^*$  and  $\mathbf{D} = \mathbf{L}_D \mathbf{L}_D^*$ .*

Attention is drawn to the fact  $\mathbf{L}_A$  and  $\mathbf{L}_D$  may be any possible factors of the diagonal blocks of  $\mathbf{G}$ . For a strictly positive definite block, a Cholesky decomposition can be taken. Generally, at least one of  $\mathbf{A}$ ,  $\mathbf{D}$  may be singular. We can use the singular value decompositions (SVDs)

$$\mathbf{L}_A = \mathbf{Q}_A \Sigma_A^{1/2} \mathbf{X}_A^*, \quad \mathbf{L}_D = \mathbf{Q}_D \Sigma_D^{1/2} \mathbf{X}_D^* \quad (4)$$

where  $\mathbf{L}_A \mathbf{L}_A^* = \mathbf{Q}_A \Sigma_A \mathbf{Q}_A^*$  is the spectral decomposition of  $\mathbf{A}$ ,  $\mathbf{X}_A^*$  is an arbitrary unitary matrix, and  $\mathbf{L}_D$  is obtained analogously.

We turn our attention to the construction of blockwise stochastic matrices. Initially, we consider only the off-diagonal partitions  $\mathbf{B}$  of  $\mathbf{G}$ . Using Eq. (4), let  $\mathbf{Z}$  and its SVD be given by

$$\mathbf{Z} = \mathbf{L}_A^+ \mathbf{B} \mathbf{L}_D^{+*} = \mathbf{U}_Z \Sigma_Z \mathbf{V}_Z^* \quad (5)$$

Now, take  $\tilde{\Sigma}_Z \in \mathbb{R}$  to be a random diagonal matrix of the size and rank of  $\Sigma_Z$ , with nonzero elements not exceeding unity. Then

$$\tilde{\mathbf{Z}} = \tilde{\mathbf{U}}_Z \tilde{\Sigma}_Z \tilde{\mathbf{V}}_Z^* \quad (6a)$$

$$\tilde{\mathbf{B}} = \mathbf{L}_A \tilde{\mathbf{Z}} \mathbf{L}_D^* = \mathbf{L}_A \tilde{\mathbf{U}}_Z \tilde{\Sigma}_Z \tilde{\mathbf{V}}_Z^* \mathbf{L}_D^* \quad (6b)$$

where  $\tilde{\mathbf{U}}_Z$  and  $\tilde{\mathbf{V}}_Z$  are completely unrestricted random unitary matrices. Crucially, it holds that

**Proposition 4.** Let  $\mathbf{G} = \begin{pmatrix} \mathbf{A} & \mathbf{B} \\ \mathbf{B}^* & \mathbf{D} \end{pmatrix}$  be a Hermitian PSD matrix,  $\tilde{\mathbf{B}} = \mathbf{L}_A \tilde{\mathbf{Z}} \mathbf{L}_D^*$  be random blocks, as per Eq. (6), and  $\tilde{\mathbf{Z}}$  be any possible matrix abiding to Eq. (5) whose singular values do not exceed unity. Then the domain of  $\tilde{\mathbf{G}} = \begin{pmatrix} \mathbf{A} & \tilde{\mathbf{B}} \\ \tilde{\mathbf{B}}^* & \mathbf{D} \end{pmatrix}$  coincides with the set of all nonnegative definite matrices with constant diagonal blocks  $\mathbf{A}$ ,  $\mathbf{D}$ .

A proof of Proposition 4 hinges on the assertion that swapping  $\mathbf{B}$  with its random counterpart still fulfils all conditions of Theorem 1. Provided that  $\mathbf{A}$  and  $\mathbf{D}$  are kept fixed, the transition from  $\mathbf{Z}$  to  $\tilde{\mathbf{Z}}$  is facilitated entirely by  $\tilde{\mathbf{B}}$ . The construction of  $\tilde{\mathbf{B}}$  is hence 'uncoupled' from that of  $\tilde{\mathbf{A}}$ ,  $\tilde{\mathbf{D}}$ . Regarding these partitions, which are square and PSD, methods such as eigenvalue perturbation or the nonparametric variability approach can be applied. Thereby only the more involved case of  $\tilde{\mathbf{B}}$  was discussed here. Evaluating realisations of  $\tilde{\mathbf{G}}$  can be done by sampling  $\tilde{\mathbf{A}}$ ,  $\tilde{\mathbf{D}}$ , then  $\tilde{\mathbf{B}}$  sequentially.

So far we have shown that Eq. (6) describes all possible matrices  $\tilde{\mathbf{B}}$  that satisfy Theorem 1 for given  $\mathbf{A}$ ,  $\mathbf{D}$ . Now, nullspace dimension controllability can be addressed

**Theorem 5 (Rank).** The rank of  $\tilde{\mathbf{G}}$  is invariant with respect to unitary transformations of  $\mathbf{L}_A^+ \mathbf{B} \mathbf{L}_D^{+*}$  and if  $\text{null}(\mathbf{L}_A) = \text{null}(\mathbf{L}_D) = \{\mathbf{0}\}$  it is exactly equal to  $\text{rank}(\mathbf{I} - \tilde{\Sigma}_Z^* \tilde{\Sigma}_Z)$ .

Rephrasing Theorem 5, any unitary transformation of  $\mathbf{L}_A^+ \mathbf{B} \mathbf{L}_D^{+*}$  is, both mathematically and for all pragmatic intents and purposes, equivalent to sampling  $\tilde{\mathbf{U}}_Z$  and  $\tilde{\mathbf{V}}_Z$  in Eq. (6a). Furthermore,  $\mathbf{L}_A$  and  $\mathbf{L}_D$  can be ensured to have a trivial nullspace by taking a standard truncated SVD in Eq. (4), by discarding all singular vectors corresponding to zero singular values. In practice if, for instance,  $\mathbf{A}$  is degenerate,  $\mathbf{L}_A$  would be rectangular, with as many 'missing' columns as is the rank deficiency of  $\mathbf{A}$ . Of course,  $\text{rank}(\mathbf{A}) = \text{rank}(\mathbf{L}_A)$  still holds. Note that the validity of all preceding assertions only requires the existence of  $\mathbf{L}_A$ ,  $\mathbf{L}_D$ , and is invariant with their shape.

Finally,  $\text{rank}(\tilde{\mathbf{G}}) = \text{rank}(\mathbf{I} - \tilde{\Sigma}_Z^* \tilde{\Sigma}_Z)$  postulates that retaining the number of ones on the diagonal of  $\Sigma_Z$  unaltered when sampling  $\tilde{\Sigma}_Z$  is necessary and sufficient to ensure  $\dim(\text{null}(\mathbf{G})) = \dim(\text{null}(\tilde{\mathbf{G}}))$ .

## 2.4 An appropriate model for the random unitary matrices

A sensible definition of  $\tilde{\mathbf{U}}_Z$  and  $\tilde{\mathbf{V}}_Z$  through which the dispersion of  $\tilde{\mathbf{B}}$  is constrained and can be regulated is vital. Throughout Section 2.3,  $\mathbf{G}$  was assumed complex, but all arguments made trivially ensue for the special case  $\mathbf{G} \in \mathbb{R}$ , pertinent to structural FEM. Thereby we seek to construct stochastic orthogonal  $\tilde{\mathbf{U}}_Z, \tilde{\mathbf{V}}_Z \in \mathbb{R}$ . The approach suggested here is to compute their eigendecompositions

$$\mathbf{U}_Z = \mathbf{Q}_U \mathbf{\Lambda}_U \mathbf{Q}_U^*, \quad \mathbf{V}_Z = \mathbf{Q}_V \mathbf{\Lambda}_V \mathbf{Q}_V^* \quad (7)$$

and retain the bases  $\mathbf{Q}_U, \mathbf{Q}_V$ , resulting in

$$\tilde{\mathbf{U}}_Z = \mathbf{Q}_U \tilde{\mathbf{\Lambda}}_U \mathbf{Q}_U^*, \quad \tilde{\mathbf{V}}_Z = \mathbf{Q}_V \tilde{\mathbf{\Lambda}}_V \mathbf{Q}_V^* \quad (8)$$

The eigenvalues of orthogonal matrices lie on the unit circle and appear in either complex conjugate pairs or are equal to one. The diagonal matrices  $\tilde{\mathbf{\Lambda}}_U, \tilde{\mathbf{\Lambda}}_V$  in Eq. (8) therefore adhere to the form

$$\tilde{\mathbf{\Lambda}}_U = \text{diag}(e^{i\tilde{\theta}_U}), \quad \tilde{\mathbf{\Lambda}}_V = \text{diag}(e^{i\tilde{\theta}_V}) \quad (9)$$

where  $i$  is the imaginary unit,  $\tilde{\theta}_U, \tilde{\theta}_V$  are random angle vectors. It can be validated that realisations of  $\tilde{\mathbf{U}}_Z, \tilde{\mathbf{V}}_Z$  are real and orthogonal, provided the complex conjugate pairs in  $\tilde{\theta}_U, \tilde{\theta}_V$  are kept unmodified with respect to  $\theta_U, \theta_V$ . Consequentially, for a non-deterministic orthogonal matrix



$\tilde{U}_Z$  of size  $n$ , only a random vector  $\tilde{\varphi}_U$  of length  $\lfloor \frac{n}{2} \rfloor$  needs to be sampled in order to evaluate a realisation of the corresponding  $\tilde{\theta}_U$ .

Observe that now  $\tilde{B}$ , as defined in Eq. (6b), is fully specified by  $\tilde{\theta}_U$ ,  $\tilde{\theta}_V$  (through  $\tilde{\varphi}_U$ ,  $\tilde{\varphi}_V$ ), and  $\tilde{\Sigma}_Z$  by

$$\begin{aligned}\tilde{B} &= L_A \tilde{U}_Z \tilde{\Sigma}_Z \tilde{V}_Z^* L_D^* \\ &= L_A Q_U \tilde{\Lambda}_U Q_U^* \tilde{\Sigma}_Z Q_V \tilde{\Lambda}_V^* Q_V^* L_D^*\end{aligned}\quad (10)$$

This construction poses several key benefits. Firstly, rank preservation of  $\tilde{G}$ , thus  $\tilde{M}$  or  $\tilde{K}$  is always guaranteed. Secondly, computation of realisations is easy, as only random vectors need to be sampled. Vectorised code implementations are also straightforward to write.

## 2.5 Comparison to the original technique and algorithmic complexity

In comparison to theory outlined above, the prototype of the random block matrix method, i.e. [27], employed

$$\tilde{U}_Z = \tilde{R}_A U_Z, \quad \tilde{V}_Z = \tilde{R}_D V_Z \quad (11)$$

where  $\tilde{R}_A$ ,  $\tilde{R}_D$  are sparse non-deterministic rotation matrices, composed of random Givens rotations. While it performed well in test cases, it is feasible to strictly prove that rank preservation, thus nullspace dimension of random mass and stiffness, is not guaranteed under certain conditions. The issue is solved in the present paper by the rank/shape constraints imposed on  $L_A$ ,  $L_D$  in Theorem 5. In fact, the original definition of  $\tilde{B}$  in Eq. (11) is now generalised by Eq. (6). Furthermore, Eqns. (8)-(10) provide means of prescribing  $\tilde{B}$  without introducing any auxiliary matrices that do not emerge naturally from decompositions of partitions of  $G$ .

Sampling submatrices of  $\tilde{G}$  is evidently of cubic complexity. The cost incurred by the updated Eq. (10) is very similar to the original method, c.f. [27]. It is worth pointing out that the decompositions  $L_K^{(k)}$  or  $L_M^{(k)}$  for the  $k$ -th component need to be computed only once. In addition, the number of DOFs in a subsystem's boundary or modal representations would typically be small, namely of order not exceeding  $10^3$ , either by design or due to the use of interface reduction. Due to the minimal size of the random blocks,  $O(n^3)$  complexity of the stochastic block matrix sampling does not impair overall efficiency. Per realisation, it is in-line with the cost of a plain CMS modal solution.

Referring to Figure 2, eqns. (8)-(10) would facilitate generation of non-deterministic interface blocks  $\tilde{M}_{BI}^{(k)}$  from factorisations of  $M_{BB}^{(k)}$  and  $M_{II}^{(k)}$ . Note that in this example, subsystems 1 and 3 do not share common DOFs.

## 3 METHOD VALIDATION

The methodology outlined in Section 2 was implemented in Matlab and benchmarked with a realistic test case, based on the SSTL300 spacecraft, shown in Figure 3. It is designed and built by Surrey Satellite Technology Limited (SSTL) and has external dimensions of 1370 mm  $\times$  850 mm  $\times$  1200 mm and mass of 300 kg.

A mock-up surface load was obtained from 50 superimposed plane wave sources, evenly distributed over a unit sphere, whose centre coincides with the geometric centre of the model. A diffuse sound field was emulated by sampling the wave phases from a uniform distribution between  $-\pi$  and  $\pi$ . Their amplitudes were extracted from a Gaussian distribution truncated to the interval  $[0, 2]$ , whose mean and variance were 1 and 0.5, respectively. The incident field

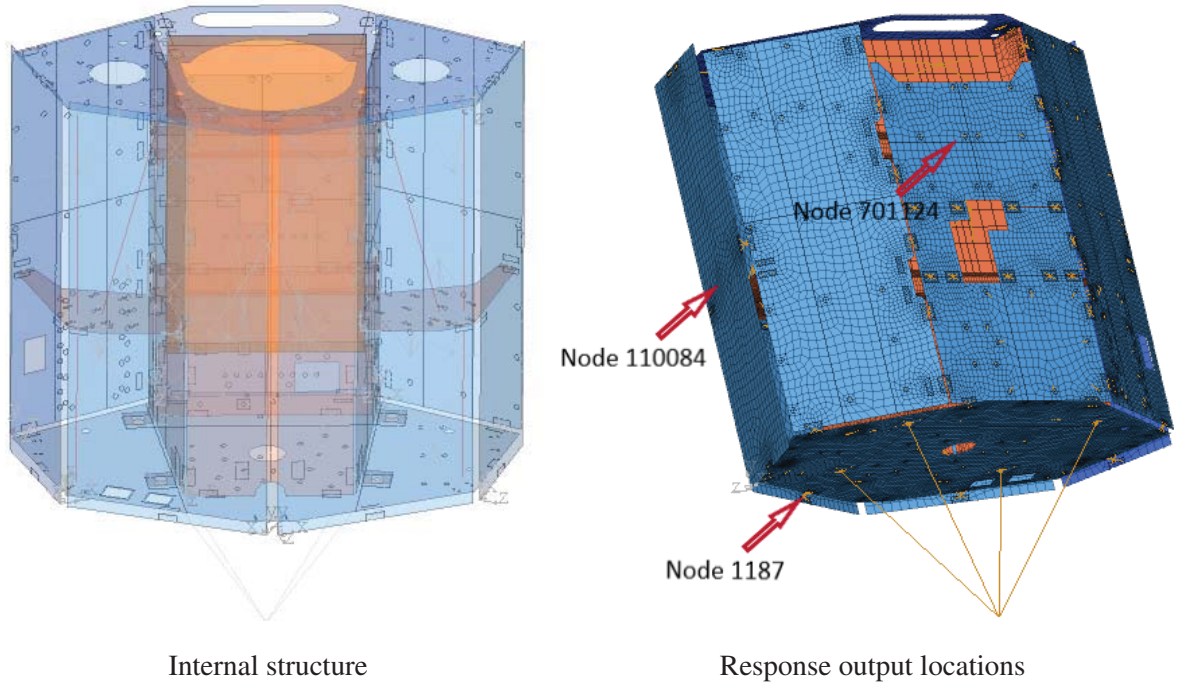


Figure 3: Stochastic CMS realistic test case: SSTL300 spacecraft

was evaluated at 200 frequency points, spaced logarithmically between 1 Hz and 1.5 kHz. It was subsequently used as direct excitation to the structure. Normally, elasto-acoustic coupling would be accounted for. Nevertheless, the aim of this test was solely to compare the stochastic CMS against a well-established numerical scheme for a complex model. Provided a good agreement between the two methods is observed, either would be similarly representative of any data acquired from physical tests.

Firstly, a direct Monte Carlo simulation was set up. Uncertain parameters in the model were approximated as normally distributed random variables. The concrete values used are given in Table 1, expressed in terms of COV, with  $\mu$  being the distribution mean. The selection of appropriate COVs has been thoroughly studied. Such investigations are widely available in literature, for instance in [5]. 500 realisations were sampled and solved for the MCS.

From a CMS perspective, the formulation delineated in Section 2 was applied to a standard Craig-Bampton reduction. The spacecraft was split into 10 subsystems, 9 of which were its main external panels. The latter were subjected to the aforesaid pressure excitation, whereas no loads were directly applied to the internal structure. An example is depicted in Figure 4. All component condensations included modes up to 2.5 kHz. As a preprocessing step, MSC Nastran was employed for producing the physical space structural and CB transformation matrices. It was further utilised for the modal solution of MCS realisations. The stochastic CMS was executed fully on in-house Matlab code.

Detailed component and global DOF set data is presented in Table 2. The equilibrium equation for the  $k$ -th condensed substructure is

$$\begin{bmatrix} \mathbf{M}_{bb}^{(k)} & \widetilde{\mathbf{M}}_{bm}^{(k)} \\ \widetilde{\mathbf{M}}_{mb}^{(k)} & \mathbf{I}_{mm}^{(k)} \end{bmatrix} \begin{bmatrix} \ddot{\mathbf{u}}_b^{(k)} \\ \ddot{\mathbf{u}}_m^{(k)} \end{bmatrix} + \begin{bmatrix} \mathbf{K}_{bb}^{(k)} & \mathbf{0} \\ \mathbf{0} & \widetilde{\mathbf{\Lambda}}_{mm}^{(k)} \end{bmatrix} \begin{bmatrix} \mathbf{u}_b^{(k)} \\ \mathbf{u}_m^{(k)} \end{bmatrix} = \begin{bmatrix} \mathbf{f}_B^{(k)} + \mathbf{\Phi}_B^{(k)T} \mathbf{f}_I^{(k)} \\ \mathbf{\Phi}_I^{(k)T} \mathbf{f}_I^{(k)} \end{bmatrix} \quad (12)$$

where subscripts  $b$  and  $m$ , respectively, refer to the reduced boundary and internal elastic DOF sets and  $\mathbf{u}$  denotes displacements. The physical space forces are given by  $\mathbf{f}_B$  and  $\mathbf{f}_I$ . They are

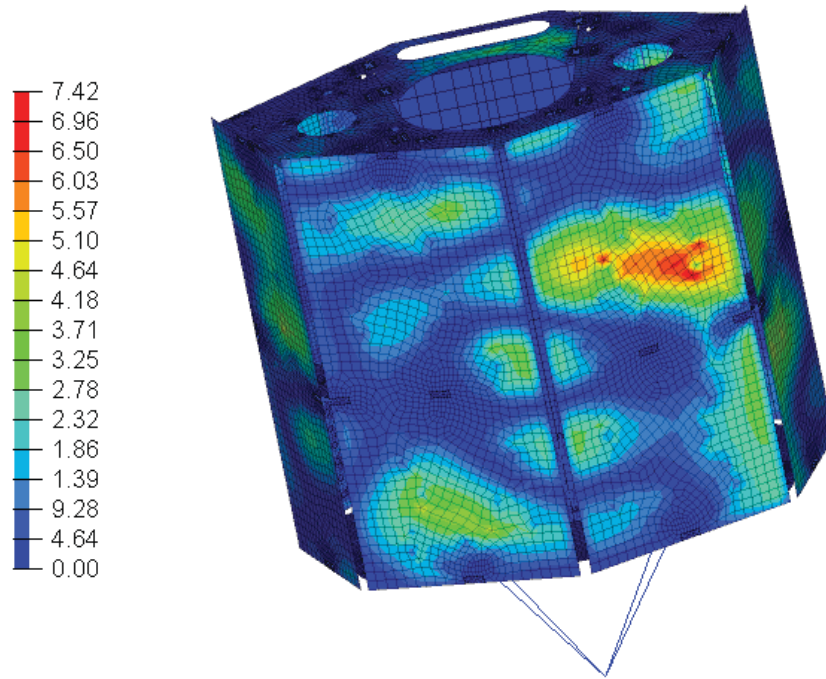


Figure 4: Applied acoustic pressure field at 100 Hz, magnitude, [Pa]

Table 1: Coefficients of variation for the variables in the SSTL300 parametric model

Type	Property	Symbol	St. deviation
Isotropic material	Young's modulus	$E$	$0.07\mu$
	Poisson's ratio	$\nu$	$0.03\mu$
	Shear modulus	$G$	$0.11\mu^a$
	Density	$\rho$	$0.04\mu$
Solid element	Property matrix	$G_{ij}$	$0.10\mu$
	Density	$\rho$	$0.04\mu$
Simple beam	Section dimension	$L$	$0.05\mu$
	Non-structural mass	NSM	$0.12\mu^a$
Composite laminate	Ply thickness	$t_i$	$0.10\mu$
	Fibre orientation	$\Theta_i$	$1.0^\circ$
	Non-structural mass	NSM	$0.12\mu$
Thin shell	Thickness	$t$	$0.10\mu$
	Non-structural mass	NSM	$0.10\mu$
Spring	Stiffness	$k_i$	$0.05\mu$
Point mass	Mass	$m$	$0.06\mu$
Damping	Modal value		const.

<sup>a</sup> Not applicable to the test case, or is described as a function of already defined values, e.g.  $G = \frac{E}{2+2\nu}$

projected onto Craig-Bampton mixed physical-modal coordinates through the typical transformation matrices  $\Phi_B$  and  $\Phi_I$ . The latter are a constraint mode matrix and a truncated eigenbasis, respectively. Conforming to the widely accepted normalisation, the modal mass is scaled to the identity matrix  $I_{mm}$ , hence modal stiffness  $\Lambda_{mm}$  is given by the square of each mode's respective natural frequency.

Table 2: DOFs per subsystem for the Craig-Bampton reduced and physical coordinate SSTL300 model

Subsystem	CB Reduction		Full model
	modal	boundary	physical
1	92	114	23202
2	97	114	15732
3	118	186	38066
4	79	72	19566
5	98	114	25488
6	37	24	6870
7	56	30	9714
8	37	24	6870
9	56	30	9714
10	359	366	82829
Total	1029	1074	244812
Reassembled	1029	540	243738

The stochastic off-diagonal mass terms,  $\widetilde{M}_{mb}^{(k)}$  were modelled and sampled according to Eqns. (8)-(10). Gaussian distributions with standard deviation of 0.3 radians and mean  $\varphi$  were assigned to the random angles  $\widetilde{\varphi}$ , whereas  $\widetilde{\Sigma}_z$  was kept constant. The component modal stiffnesses  $\widetilde{\Lambda}_{mm}^{(k)}$  were also normally distributed, with COVs of 0.1. A remark should be made that in general, the  $\widetilde{\Sigma}_z$  term exerts a relatively minor influence on the variance of the computed global solutions. Similarly to the direct MCS, 500 random model realisations were evaluated. This number was deemed reasonable for acceptable convergence of the first two statistical moments to be attained.

The results collected from the new stochastic CMS are plotted and compared against the direct MCS in Figure 5. The mean and  $\mu + 3\sigma$  response curves, equivalent to a 99.7% confidence interval, are plotted for either numeric scheme, along with the baseline deterministic solution. Overall, the predictions of the reduced-order stochastic method conform to the ones obtained by direct MCS. Examining the plots closely, it can be seen that the low-frequency range uncertainty is predicted to have slightly smaller variance compared to the MCS. However, the COVs chosen for this work were not based on an extensive parameter survey. It is expected that even better correlation against the MCS could be observed under some optimised strategy for designating variability level to the random substructures.

As a measure of the overall uncertainty prediction quality, a global linear correlation coefficient was computed for the statistical moments estimated by the new method against the MCS. This was done by averaging solution correlations over all output DOFs for the full frequency range. Coefficients of 0.95 and 0.93 were calculated for the mean and variance of the solutions,

respectively. Figure 5 is representative of these values.

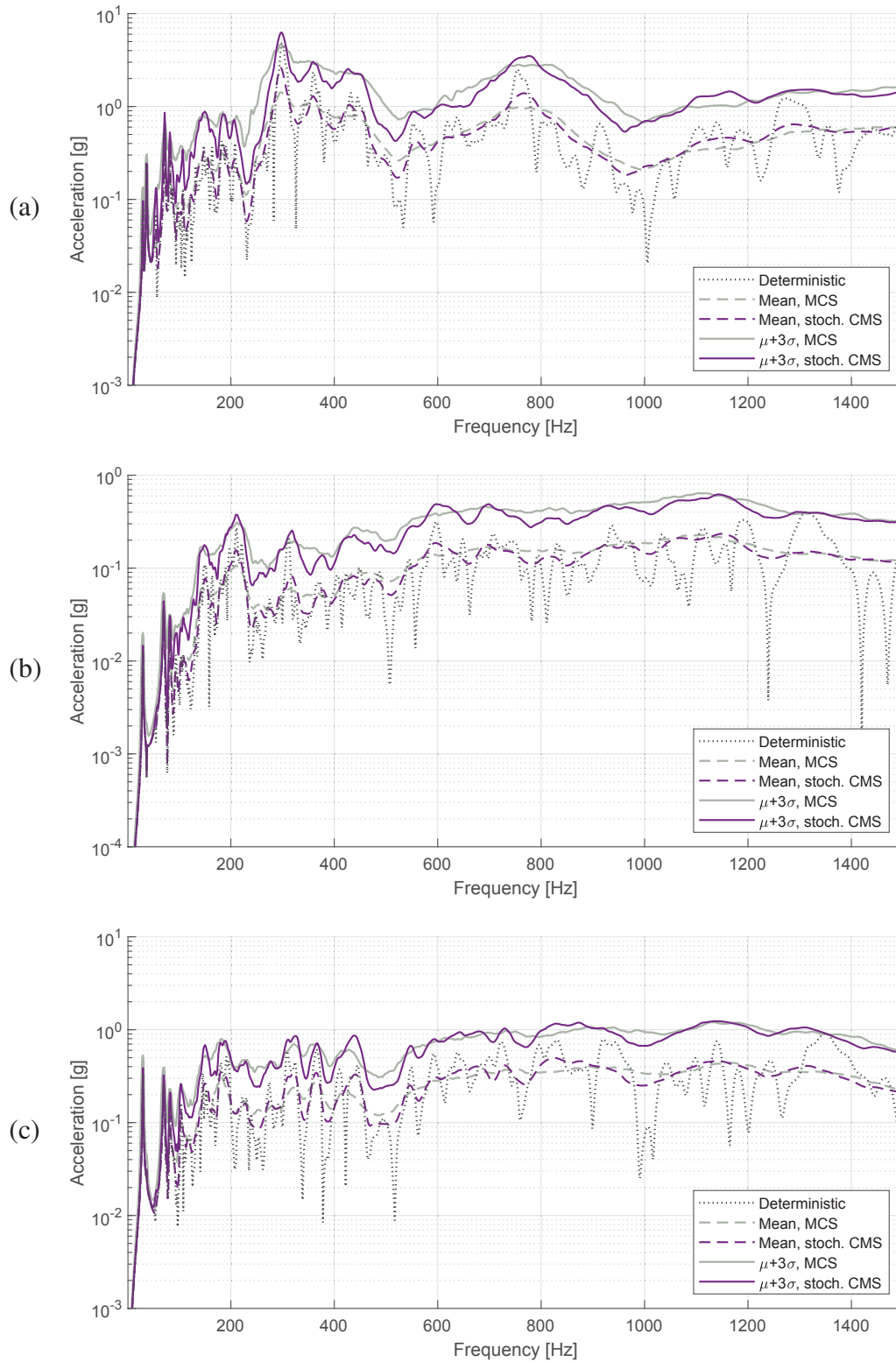


Figure 5: Acceleration magnitude: (a) node 1187, z-axis,  $B$  set physical interface between two subsystems, (b) node 701124, x-axis,  $B$  set output location, not used as CMS subsystem connector, (c) node 1100884, y-axis,  $I$  set, response recovered from the CB solution



Regarding computational efficiency, the reduced-order scheme exhibited a clear advantage by taking approximately 0.8 s per realisation, against 302 s for the parametric approach. Note that the latter is pure solver CPU time and comprises less than half the wall-clock time per realisation when I/O operations are taken into account. In practice, this translates to an improvement factor of over 750. Furthermore, while a commercial solver was used for the direct MCS, the stochastic CMS was solved on code that could benefit from further optimisation. Overall, the new method provided nodal acceleration estimations close to the baseline solution, but with greatly improved performance and arguably ease of implementation.

## 4 CONCLUSIONS

Modelling of random uncertainties on a subsystem-level is addressed in this article. To that end, a method circumventing many of the usual restrictions associated with nonparametric techniques in a reduced-order model context was proposed. Namely, the component-level matrix structure naturally arising in CMS can be exploited to robustly define and sample random local mass and stiffness partitions. The foundation for the technique's mathematical definition was derived from the generalised Schur complement condition for nonnegative definiteness. Further extending the concept, a framework was provided for individual block sampling of  $2 \times 2$  random Hermitian matrices of fixed rank. A construction to adapt this theoretical basis to FEM structural matrices was provided. The proposed stochastic CMS technique was applied to a spacecraft structure subjected to acoustic excitation, and compared against parametric MCS. Reliable response predictions were recorded, whereas computational cost was reduced by close to 3 orders of magnitude.

## ACKNOWLEDGEMENTS

The author would like to thank Surrey Satellite Technology Limited for providing the spacecraft model used for this work.

## REFERENCES

- [1] Hurtado, J. E. and Barbat, A. H. Monte Carlo techniques in computational stochastic mechanics, *Archives of Computational Methods in Engineering*, **5** (1), 3–30, (1998).
- [2] Schuëller, G. I. Developments in stochastic structural mechanics, *Archive of Applied Mechanics*, **75** (10-12), 755–773, (2006).
- [3] Soize, C. Stochastic modeling of uncertainties in computational structural dynamics - Recent theoretical advances, *Journal of Sound and Vibration*, **332** (10), 2379–2395, (2013).
- [4] Calvi, A. Uncertainty-based loads analysis for spacecraft: Finite element model validation and dynamic responses, *Computers & Structures*, **83** (14), 1103–1112, (2005).
- [5] Pradlwarter, H. J., Pellissetti, M. F., Schenk, C. A., Schuëller, G. I., Kreis, A., Fransen, S., Calvi, A. and Klein, M. Realistic and efficient reliability estimation for aerospace structures, *Computer Methods in Applied Mechanics and Engineering*, **194** (12-16), 1597–1617, (2005).
- [6] Pellissetti, M., Schuëller, G. I., Pradlwarter, H. J., Calvi, A., Fransen, S. and Klein, M. Reliability analysis of spacecraft structures under static and dynamic loading, *Computers & Structures*, **84** (21), 1313–1325, (2006).

- 
- [7] Vanmarcke, E., Shinozuka, M., Nakagiri, S., Schuëller, G. I. and Grigoriu, M. Random fields and stochastic finite elements, *Structural Safety*, **3** (3-4), 143–166, (1986).
- [8] Arregui-Mena, J. D., Margetts, L. and Mummery, P. M. Practical application of the stochastic finite element method, *Archives of Computational Methods in Engineering*, **23** (1), 171–190, (2016).
- [9] Shang, S. and Yun, G. J. Stochastic finite element with material uncertainties: Implementation in a general purpose simulation program, *Finite Elements in Analysis and Design*, **64** (65-78), (2013).
- [10] Stefanou, G. The stochastic finite element method: Past, present and future, *Computer Methods in Applied Mechanics and Engineering*, **198** (9-12), 1031–1051, (2009).
- [11] Au, S.-K. and Beck, J. L. Estimation of small failure probabilities in high dimensions by subset simulation, *Probabilistic Engineering Mechanics*, **16** (4), 263–277, (2001).
- [12] Koutsourelakis, P. S., Pradlwarter, H. J. and Schuëller, G. I. Reliability of structures in high dimensions, part I: algorithms and applications, *Probabilistic Engineering Mechanics*, **19** (4), 409–417, (2004).
- [13] Pradlwarter, H. J., Schuëller, G. I., Koutsourelakis, P. S. and Charmpis, D. C. Application of line sampling simulation method to reliability benchmark problems, *Structural Safety*, **29** (3), (2007).
- [14] Soize, C. A nonparametric model of random uncertainties for reduced matrix models in structural dynamics, *Probabilistic Engineering Mechanics*, **15** (3), 277–294, (2000).
- [15] Soize, C. Generalized probabilistic approach of uncertainties in computational dynamics using random matrices and polynomial chaos decompositions, *International Journal for Numerical Methods in Engineering*, **81** (8), 939–970, (2010).
- [16] de Klerk, D., Rixen, D. J. and Voormeeren, S. N. General framework for dynamic substructuring: History, review and classification of techniques, *AIAA Journal*, **46** (5), 1169–1181, (2008).
- [17] Craig, R. R. and Bampton, M. C. C. Coupling of substructures for dynamic analysis, *AIAA Journal*, **6** (7), 1313–1319, (1968).
- [18] Rixen, D. J. A dual Craig-Bampton method for dynamic substructuring, *Journal of Computational and Applied Mathematics*, **168** (1-2), 383–391, (2004).
- [19] Kim, J.-G. and Lee, P.-S. An enhanced Craig-Bampton method, *International Journal for Numerical Methods in Engineering*, **103**, 79–93, (2015).
- [20] Bennighof, J. K. and Lehoucq, R. B. An automated multilevel substructuring method for eigenspace computation in linear elastodynamics, *SIAM Journal on Scientific Computing*, **25** (6), 2084–2106, (2004).
- [21] Tournaire, H., Renaud, F. and Dion, J. L. Using singular value decomposition of component eigenmodes for interface reduction, *Journal of Sound and Vibration*, **414**, 1–14, (2018).

- [22] Junge, M., Brunner, D., Becker, J. and Gaul, L. Interface reduction for the Craig-Bampton and Rubin method applied to FE-BE coupling with a large fluid-structure interface, *International Journal for Numerical Methods in Engineering*, **77** (12), 1731–1752, (2009).
- [23] Holzwarth, P. and Eberhard, P. SVD-based improvements for component mode synthesis in elastic multibody systems, *European Journal of Mechanics - A/Solids*, **49**, 408–418, (2015).
- [24] Van den Nieuwenhof, B. and Coyette, J.-P. Modal approaches for the stochastic finite element analysis of structures with material and geometric uncertainties, *Computer Methods in Applied Mechanics and Engineering*, **192** (33-34), 3705–3729, (2003).
- [25] Mace, B. R. and Shorter, P. J. A local/modal perturbational method for estimating frequency response statistics of built-up structures with uncertain properties, *Journal of Sound and Vibration*, **242** (5), 793–811, (2001).
- [26] Yotov, V. V., Remedias, M., Aglietti, G. S. and Richardson, G. Improved Craig–Bampton stochastic method for spacecraft vibroacoustic analysis, *Acta Astronautica*, **178**, 556–570, (2021).
- [27] Yotov, V. V., Remedias, M., Aglietti, G. S. and Richardson, G. Non-parametric stochastic FEM/hierarchical matrix BEM for efficient mid-frequency vibroacoustic response estimation, *25<sup>th</sup> International Congress on Sound and Vibration*.
- [28] Zhang, F., *The Schur complement and its applications*, Numerical Methods and Algorithms, Springer, Boston, MA (2005).
- [29] Golub, G. H. and Van Loan, C. F., *Matrix computations*, The Johns Hopkins University Press, Baltimore, Maryland, 4 edn. (2013).

## BEHAVIOUR OF LAP SHEAR RIVETED CONNECTIONS WITH CONSTRUCTIONAL IMPERFECTIONS

A. Milone<sup>1</sup>, A. De Martino<sup>2</sup>

<sup>1</sup>Department of Structures for Engineering and Architecture, University of Naples “Federico II”, Via  
Forno Vecchio 36, 80134 Naples, Italy; aldo.milone@unina.it

<sup>2</sup>Department of Structures for Engineering and Architecture, University of Naples “Federico II”, Via  
Forno Vecchio 36, 80134 Naples, Italy; attilio.demartino@unina.it

---

### Abstract

*Riveted connections are the most common structural details of existing steel bridges. Due to the increase of traffic loads as respect to the conditions at their erection time, existing riveted bridges are usually characterized by structural deficiencies and prone to fatigue damages. Moreover, the structural inadequacies are often magnified by the presence of peculiar constructional defects (i.e. shank misalignment, forged head distortion), which induce local stress concentrations that further reduce the service life.*

*In this paper, the behaviour of riveted lap shear connections under static and cyclic actions is investigated by means of finite element (FE) simulations. The investigated connections are representative of typical geometries of the details of actual existing railway bridges. FE models were calibrated against the results of former tests drawn from literature. In addition, the FE models allowed at investigating the influence of constructional imperfections on the ultimate static and fatigue resistance and of the connections. In order to widen the parametric study, the following parameters are varied, namely: (i) number of rivets, (ii) diameter of rivet shank, (iii) thickness and width of the plates.*

**Keywords:** Lap shear connections, Fatigue, Riveted connections, Existing Steel Bridges, Finite Element Analysis.

---

## 1 INTRODUCTION

Riveted steel bridges represent the most common type of existing railway bridges in Italy [1]. The diffusion of this structural typology mainly developed between the XIX<sup>th</sup> century and the first half of the XX<sup>th</sup> century, after which the usage of hot-driven rivets gradually diminished owing to the introduction of high-strength bolts [2]. Therefore, existing riveted railway bridges in Italy are often characterized by an exceptionally long service life. This condition, in conjunction with the increase of traffic loads through the years, inevitably exposes such kind of structures to critical fatigue issues.

Moreover, the adopted technology for the implementation of hot-driven rivets (i.e. heat forging) can lead to peculiar structural imperfections which further reduce the structural service life. Indeed, the heating process brings the rivet base material to a plastic state which enables the realization of an on-field head by means of a pneumatic hammer. This semifluid consistency also leads to a diameter dilatation due to the hammering, leaving no gaps among the rivet shank and the relative plate holes, differently from bolted connections. However, if involved plates are not correctly aligned, the forging operation will result in a distorted shank which presents several superficial discontinuities acting as critical stress amplifiers.

It should be remarked that current provisions for fatigue design of steel structures (EN:1993-1-9 [3]) only provide a single detail category for riveted connections ( $\Delta\sigma_c = 71$  MPa) which does not account for the actual riveted joint, although the influence of joints detailing on the cyclic behavior of steel structures is widely recognized in literature [4-16]. Moreover, the presence of the aforementioned structural imperfections is completely overlooked.

Therefore, in this paper the actual static and fatigue behavior of common types of riveted connections is parametrically investigated by means of numerical analyses.

The present work is divided in three parts. In the first section, the main features of investigated riveted connections are presented; the most relevant modeling assumptions are reported in the second part, with particular attention to damage modeling and fatigue load protocol derivation. Finally, the results of numerical analyses are discussed, highlighting the influence of the investigated parameters on both the static and cyclic response of considered riveted joints.

## 2 DESCRIPTION OF INVESTIGATED RIVETED CONNECTIONS

Four different types of lap shear riveted connections were tested in order to evaluate the influence of (i) rivet diameter, (ii) plates width and thickness and (iii) number of rivets on both static and fatigue behavior of these joints. Each adopted configuration is representative of typical details adopted in existing railway bridges.

Among the different typologies of possible constructional imperfections, in this paper only the shank distortion due to plates misalignment is considered. According to the Sustainable Bridges report [17], such kind of misalignment is considered acceptable for an existing riveted connection (i.e. connection repair or substitution is not required) if the ratio between the shank eccentricity  $e$  and the rivet diameter  $d$  does not exceed 0.15.

In order to account for possible difficulties in on-field eccentricity measuring, a maximum value of  $e/d$  equal to 0.20 was considered.

A proper nomenclature  $L-D-T-N-E$  was introduced to label each investigated joint, where:

$L$  is the considered load condition;

$D$  is the rivet diameter;

$T$  is the plate thickness;

$N$  is the number of rivets;

$E$  is the shank eccentricity.



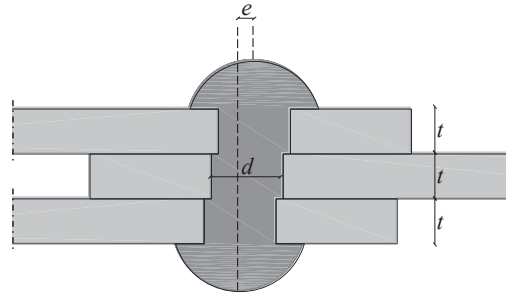


Figure 1: Relevant geometrical parameters for the investigated rivets in presence of constructional defects.

In order to reproduce the actual technique for on-field eccentricity measuring, the parameter  $e$  has been defined as the distance between the shop head and the heat forged head of the rivet in the direction of the applied loads, as depicted in Figure 1. A total of 40 finite element analyses (FEAs) were conducted accounting for the variation of each introduced parameter (see Tab. 1).

Joint Typology	Load Conditions	Rivet Diameter D [mm]	Plate Thickness T [mm]	Number of Rivets N	Eccentricity E [e/d]
L-16-10-1-E	S (Static) or F (Fatigue Cyclic)	16	10	1	0.00 (No Imperfections) to 0.20
L-19-10-1-E		19	10	1	
L-19-12-1-E		19	12	1	
L-19-10-2-E		19	10	2	

Table 1: Main features of investigated joint configurations.

### 3 MODELLING ASSUMPTION

Finite element models (FEMs) were developed using ABAQUS 6.14 [18]. In order to reduce the computational effort, riveted connections have been modelled considering their geometrical and mechanical symmetry. Static and fatigue behavior of each connection has been investigated imposing monotonic and cyclic displacement histories at the plates tip, respectively. The adopted boundary conditions are reported in Figure 2.

All elements were discretized using solid C3D8 element type (i.e. 8-node linear brick). The mesh density was defined on the basis of preliminary sensitivity analyses; therefore, a mesh size of 1 mm was set for the connection zone, while a value of 20 mm was adopted for the plates ends, which were expected to remain in their elastic range.

Steel yielding was modelled using the Von Mises criterion. Yield stress for both rivets and plates was calibrated against experimental trials carried out by D’Aniello et al. [2]. Both kinematic and isotropic hardening were implemented by means of material parameters. Ductile damage formulation was introduced to reproduce the material degradation due to plasticization under triaxial stresses. According to Yang et al. [19], the following analytical expression for triaxiality curves was considered:

$$\varepsilon_{pl,eq,\eta} = \bar{\varepsilon}_{pl,eq} \exp(-3/2(\eta - 1/3)) \quad (1)$$

where  $\varepsilon_{pl,eq,\eta}$  is the equivalent plastic strain (PEEQ) at damage initiation for a given stress triaxiality,  $\bar{\varepsilon}_{pl,eq}$  is the equivalent plastic strain at damage initiation under uniaxial stress and  $\eta$  is the stress triaxiality, defined as the ratio between the mean pressure  $\sigma_m$  and the equivalent Von Mises stress  $\sigma_{eq,VM}$  at a given point. Adopted values of  $\bar{\varepsilon}_{pl,eq}$  were calibrated against the aforementioned experimental tests on real riveted joints. The assumed values of mechanical parameters are reported in Table 2. “Surface-to-Surface” interactions were introduced to model contact among rivets and plates.

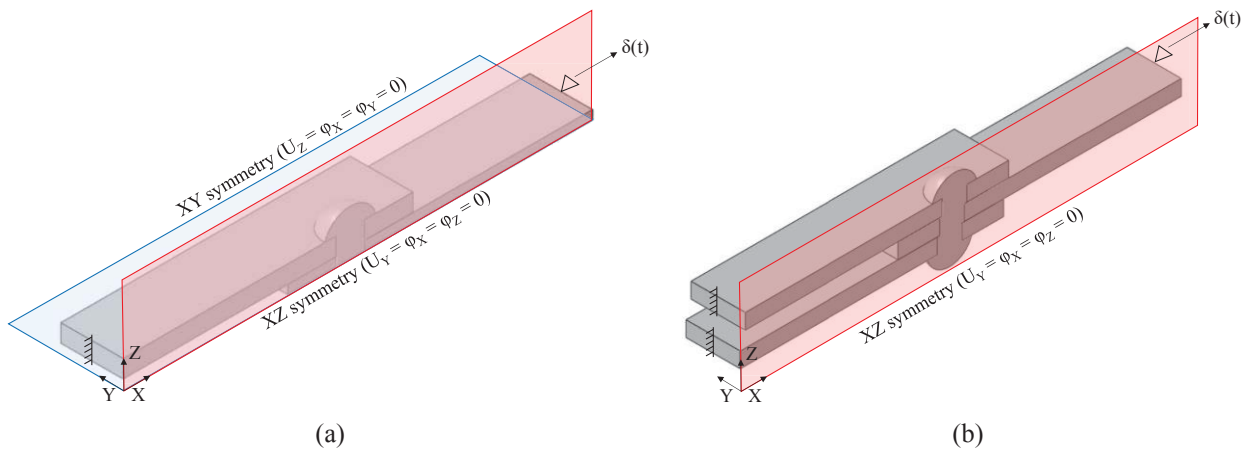


Figure 2: Boundary condition adopted for investigated riveted joints in absence (a) and presence (b) of constructional defects.

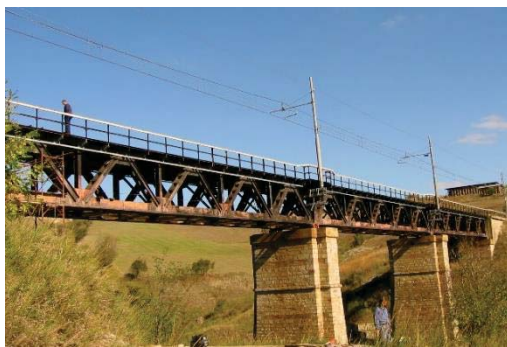
An “Hard Contact” formulation was considered for the normal contact behavior, while a penalty formulation was used to model the tangential behavior (with friction coeff. = 0.30).

Investigated Joint	Plate Yield Stress [MPa]	Rivet Yield Stress [MPa]	Rivet Damage Strain [-]
L-16-10-1-E	298	385	0.54
L-19-10-1-E	298	461	0.53
L-19-12-1-E	298	414	0.60
L-19-10-2-E	298	350	0.32

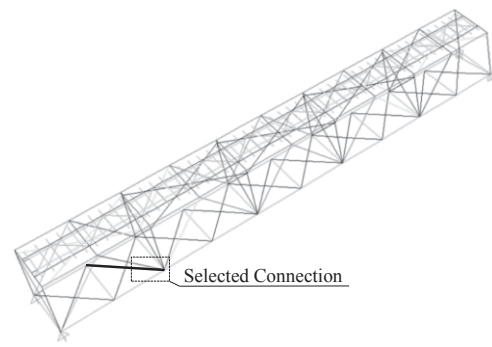
Table 2: Adopted material parameters for the investigated riveted joints.

### 3.1 Derivation of the fatigue load protocol

In order to reproduce fatigue loads which could affect real riveted connections comparable with the investigated ones during their service life, a cyclic protocol was developed starting from the structural analysis of an existing railway riveted bridge situated in Italy (Bridge over Gesso Torrent, see Figure 3a). The investigated bridge, which is composed by three identical simply-supported spans, has a reticular structure with two main external longitudinal trusses and two supplementary internal girders supporting the overlying embankment. Longitudinal trusses are connected by means of X-shaped braces in both the transversal and horizontal direction [1]. The whole structure was modeled using SAP2000 v.21 [20] (see Figure 3b) and subjected to fatigue load trains borrowed from current Italian provisions for fatigue design of railway bridges [21]. The main features of the load models considered are reported in Table 3.



(a)



(b)

Figure 3: Overall view of riveted bridge over Gesso Torrent (a) and relative structural model made with SAP2000 (b).

“Moving Load” command was used to reproduce the effect of transient train loads, thus obtaining the variation of nodal actions through time. Among the various existing connections, the one linking the most stressed diagonal to the tension side of the truss was chosen.

The resulting loads history relative to a single rivet was finally used as load protocol for the fatigue analysis of investigated riveted connections (see Figure 4).

Load Train	Total Load [kN]	Number of Axles [-]	Train Length [m]	Daily Passages [-]
3	9400	60	385.5	7
4	5100	30	237.6	6
8	10350	46	212.5	1
9	2960	24	134.8	1

Table 3: Main features of the load trains adopted according to [21].

## 4 RESULTS OF NUMERICAL ANALYSES

### 4.1 Static behavior of investigated joints

The static behavior of each investigated joint in terms of shear strength-eccentricity and ultimate displacement-eccentricity is reported in Table 4. One can notice that the peak resistance of each investigated joint does not change significantly as the shank eccentricity  $e/d$  increases. This outcome is consistent with the failure mechanism related to all analyzed specimens (i.e. rivet shear failure for each investigated joint). Indeed, the shear resisting section of the distorted rivets is not actually influenced by the holes misalignment due to the diameter dilatation.

However, the effect of shank distortion can be appreciated in terms of both ultimate displacement and damage concentration. Due to the loss of in-plane symmetry, the material damage develops unevenly among the shear planes, as depicted in Figure 5. This leads to a reduction of joint ductility which becomes more consistent with increasing eccentricity  $e/d$ .

Moreover, this tendency is more pronounced for low values of “rivet slenderness” ratio  $t/d$ . (i.e. S-19-10-1-E specimen,  $t/d = 0.53$ ) due to the higher influence of second order bending moments caused by distorted geometry. Nevertheless, the influence of these effects on the static behavior of examined riveted joints can be considered negligible within the investigated range of defects amplitude. Indeed, as reported in Table 4, the loss of shear resistance with respect to undistorted specimens is extremely low. This outcome is in consistency with tolerances on eccentricity suggested by Sustainable Bridges Report [17].

### 4.2 Fatigue behavior of investigated joints

The fatigue behavior of each investigated joint in terms of maximum damage initiation parameter-eccentricity is reported in Table 5.

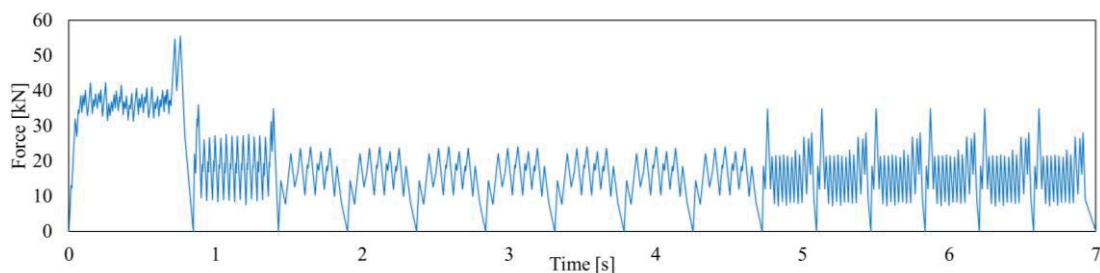


Figure 4: Cyclic protocol adopted for the fatigue analysis of the investigated riveted connections.

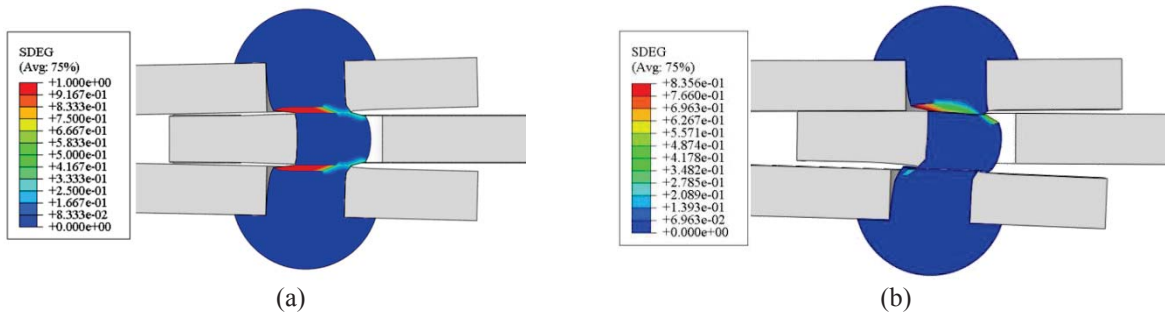


Figure 5: Distribution of scalar damage parameter at failure in absence (S-16-10-1-0.00, a) and presence (S-16-10-1-0.20, b) of imperfections.

Investigated Joint	Shear Strength [kN]					Ultimate Displacement [mm]				
	$e/d$ [%]					$e/d$ [%]				
	0	5	10	15	20	0	5	10	15	20
S-16-10-1-E	149.6	149.2	148.0	145.9	144.1	7.1	6.9	6.6	6.2	6.1
S-19-10-1-E	211.9	203.0	202.9	202.4	200.4	14.0	10.7	10.6	10.5	10.3
S-19-12-1-E	215.9	215.8	215.4	213.9	210.9	7.7	7.5	7.5	7.4	7.1
S-19-10-2-E	354.1	340.0	337.5	332.8	327.8	15.9	12.1	11.7	11.0	10.5

Table 4: Shear strength and ultimate displacement for all investigated joints in static conditions.

In all cases a sharp increase in damage parameter can be noticed for increasing values of shank eccentricity. Moreover, for higher values of  $e/d$  fracture spots relocate nearby shank discontinuities, while rivet heads are the most damaged components for undistorted specimens (see Fig. 6). In analogy with static analyses, joints with low “rivet slenderness”  $t/d$  (i.e. F-19-10-1-E specimens) are the most affected from constructional imperfections. The worst scenario is represented by F-19-10-2-E specimens in which have low  $t/d$  ratio and are further penalized by the presence of two distorted shanks, which both act as stress and damage amplifiers. Indeed, the maximum damage parameter for  $e/d = 0.20$  is 8.6 times higher with respect to undistorted joint.

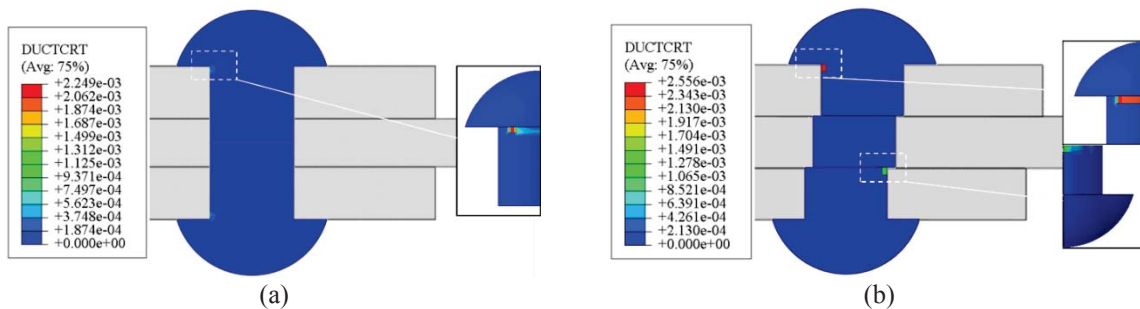


Figure 6: Distribution of damage initiation parameter after the cyclic protocol in absence (F-16-10-1-0.00, a) and presence (F-16-10-1-0.20, b) of imperfections.

Investigated Joint	Damage initiation Par. ( $\cdot 10^3$ ) [-]				
	$e/d$ [%]				
	0	5	10	15	20
F-16-10-1-E	2.25	2.38	2.47	2.51	2.56
F-19-10-1-E	0.71	1.03	1.72	2.67	2.83
F-19-12-1-E	1.17	1.63	2.04	2.10	2.12
F-19-10-2-E	0.59	1.04	3.81	4.74	5.09

Table 5: Damage initiation parameter for all investigated joints under cyclic actions.

## 5 CONCLUSIONS

The static and fatigue behavior of four different kinds of lap shear riveted joints has been studied by means of numerical analyses. The influence of constructional imperfections on the joint's response was investigated introducing hole misalignments up to 20% of rivet diameters. A proper cyclic load protocol was derived from the structural analysis of an existing riveted railway bridge situated in Italy.

From results of FEAs the following conclusions can be drawn:

- The static behavior of each investigated joint is not consistently influenced by the presence of constructional imperfections, with a maximum shear strength loss of about 5% with respect to undistorted specimens.
- However, a small difference can be noticed in terms of ultimate displacements, which decrease with increasing values of shank eccentricity; a modification of the damage mechanism is also observed due to distorted geometry.
- Ductility reduction increases for low values of “rivet slenderness”  $t/d$  due to higher second order stresses which promote damage evolution.
- The fatigue behavior of joints is highly dependent from shank eccentricity; increasing values of  $e/d$  lead to higher damages and develop of fracture spots nearby shank discontinuities.
- Similarly to the static scenario, low “rivet slenderness”  $t/d$  has a consistent influence on fatigue damage as well.
- The parametrical study will be further extended considering unsymmetrical joints, different kinds of imperfections and using standard cyclic protocols provided by EN:1993-1-9 [3].

## REFERENCES

- [1] R. Landolfo, L. Cascini, M. D’Aniello, F. Portioli, The effects of fatigue and corrosion deterioration on the metalworking of railway bridges: An integrated approach for the evaluation of remanent life. *Rivista Italiana della Saldatura*, **63**, 367-377, 2011. [in Italian].
- [2] M. D’Aniello, F. Portioli, L. Fiorino, R. Landolfo. Experimental investigation on shear capacity of riveted connections in steel structures. *Engineering Structures*, **33**, 516-531, 2011.
- [3] EN 1993-1-9, Design of Steel Structures - Part 1-9: Fatigue, CEN, 2005.
- [4] R. Tartaglia, M. D’Aniello, M. Zimbru, Experimental and numerical study on the T-Stub behaviour with preloaded bolts under large deformations. *Structures*, **27**, 2137-2155, 2020.
- [5] R. Tartaglia, M. D’Aniello, M. Andreini, S. la Mendola, The performance of preloaded bolts in seismically prequalified steel joints in a fire scenario. *Materials*, **13**(22), 1-14, 2020.
- [6] R. Tartaglia, M. D’Aniello, R. Landolfo, Numerical simulations to predict the seismic performance of a 2-story steel moment-resisting frame. *Materials*, **13**(21), 1-17, 2020.
- [7] R. Tartaglia, M. D’Aniello, Influence of Transverse Beams on the Ultimate Behaviour of Seismic Resistant Partial Strength Beam-To-Column Joints. *Ingegneria Sismica*, **37**(3), 50-65, 2020.
- [8] M. D’Aniello, R. Tartaglia, D. Cassiano, Experimental investigation of the inelastic tensile behaviour of non-preloadable grade 8.8 bolts. *Ingegneria Sismica*, **37**(2), 92-109, 2020.



- [9] R. Tartaglia, M. D’Aniello, G.A. Rassati, Proposal of AISC-compliant seismic design criteria for ductile partially-restrained end-plate bolted joints. *Journal of Constructional Steel Research*, **159**, 364–383, 2019.
- [10] S. Costanzo, R. Tartaglia, G. Di Lorenzo, A. de Martino, Seismic behaviour of EC8-compliant moment resisting and concentrically braced frames. *Buildings*, **9**(9), 196, 2019.
- [11] R. Tartaglia, M. D’Aniello, Nonlinear performance of extended stiffened end plate bolted beam-to-column joints subjected to column removal. *Open Civil Engineering Journal*, **11**(M6), 369–383, 2017.
- [12] R. Tartaglia, M. D’Aniello, A. de Martino, Ultimate performance of external end-plate bolted joints under column loss scenario accounting for the influence of the transverse beam. *Open Construction and Building Technology Journal*, **12**, 132–139, 2018.
- [13] R. Tartaglia, M. D’Aniello, G. Di Lorenzo, A. de Martino, Influence of EC8 rules on p-delta effects on the design and response of steel MRF. *Ingegneria Sismica*, **35**(3), 104–120, 2018.
- [14] R. Tartaglia, M. D’Aniello, G.A. Rassati, J.A. Swanson, R. Landolfo, Full strength extended stiffened end-plate joints: AISC vs recent European design criteria. *Engineering Structures*, **159**, 155–171, 2018.
- [15] A.F. Santos, A. Santiago, M. Latour, G. Rizzano, Analytical assessment of the friction dampers behaviour under different loading rates, *Journal of Constructional Steel Research*, **158**, 443–459, 2019.
- [16] M. D’Antimo, M. Latour, G. Rizzano, J.F. Demonceau, Experimental and numerical assessment of steel beams under impact loadings. *Journal of Constructional Steel Research*, **158**, 230–247, 2019.
- [17] Sustainable Bridges – European research project under the EU 6<sup>th</sup> framework programme, 2006. <http://www.sustainablebridges.net/>.
- [18] Dassault, Abaqus 6.14 User’s Manual, Dassault Systèmes Simulia Corp, 2014.
- [19] F. Yang, M. Veljkovic, Damage model calibration for s275 and s690 steels. *ce/papers*, **3**, 262–271, 2019.
- [20] CSI, SAP2000 v.21 User’s Manual, Computer and Structures Inc., 2019.
- [21] RFI (Italian National Railways Network), RFI\_DTC\_INC\_PO\_SP\_IFS\_003\_A\_2011: Specifica per la verifica a fatica dei ponti ferroviari, 2011 [in Italian].

## BEHAVIOR OF INNO3D JOINTS UNDER MONOTONIC AND CYCLIC LOADING

A. Poursadrollah<sup>1</sup>, A. De Martino<sup>2</sup>

<sup>1</sup> Ph.D. candidate

University of Naples Federico II, Department of Civil Engineering, Naples, Italy  
arash.poursadrollah@unina.it

<sup>2</sup>Professor

University of Naples Federico II, Department of Civil Engineering, Naples, Italy  
attilio.demartino@unina.it

---

### Abstract

*Hybrid structures are highly efficient and economical. In particular, modular solutions with tubular columns combined with horizontal light-weight girders made of cold-formed steel sections may provide a cheap and efficient system. In order to simplify the on-site erection phases, a novel plug and play joint has been proposed within the RFCS INNO3D joints project to enable industrialized and modular solutions that ensure fast-track construction and increase the quality of the finished product. The aim of this paper is the investigation of both the monotonic and cyclic behavior of this type of joint by finite element analyses. Thus, an advanced numerical model was developed and validated against experimental results performed within the INNO3D research project. The results show for a large rotational value and increase of the joint stiffness due by the contact between the joint components.*

**Keywords:** INNO3D joints, Finite element model, Abaqus, Plug and play joint

---

## 1 INTRODUCTION

Nowadays increasing attention is given in the design of steel structures located seismic area to avoid brittle failure concentrating all the plastic deformation within the ductile elements [1-17]. In particular, in steel market there is a growing interest in developing new design and construction approaches that could results more efficient, safer, environmentally friendly, less labor-intensive, and can lead to buildings that are of higher standards and can be constructed in a compressed schedule [17-22]. Shortage of skilled workers, low productivity, and increasingly stringent client requirements are the incentives behind developing innovative approaches. The construction industry has been dominated by conventional construction practices which are less efficient and economical. Modular constructions provide several advantages. The economy of modular systems depends on several variables, namely: resistance to lateral load and the type of connections which plays a major role in stability and robustness of the system.

To meet the needs of clients and communities of the future it is required to rethink the design and construction processes and develop appropriate responsive strategies. A few modular construction systems are available using light-weight steel solutions, which are easily assembled in panels and delivered on site. The European project DRYCONDIS summarizes the capabilities of light-weight steel dry construction building systems [23]. Several research projects have dealt with light-weight steel systems for prefabricated steel buildings and their integration with the steel skeletal system (e.g. ETHICS; InFaSo; FrameUp; PRECASTEEL, [24-27]). However, in only a few of them, the execution phase was a main parameter considered in the development and optimization of the system.

In the light of these considerations, innovative modular constructions with hybrid systems made of lightweight steel truss girders connected to tubular columns by means of plug-and-play joints have been developed within the recent INNO3DJOINTS (acronym of “Innovative 3D joints for robust and economical hybrid tubular construction”) project in order to ensure fast-track construction and increase the quality of the finished product. This paper aims to provide a preliminary investigation of the joint under monotonic loading.

## 2 DEFENITION OF THE INNO3DJOINTS

Figure 1 (a) illustrates the main elements of the system and the details of the plug-and-play connection (b). Columns could have cold-formed rectangular, square, or circular hollow structural section, while the beams are truss girders composed of light-gauge cold-formed profiles which provides the main lateral resistance of the system. The joint is a plug and play joint which guarantee a fast and safe on-site execution. As showed in Figure 1b, the joint is connected to the column at two different levels. It is noteworthy to mention that, due to the cold-formed characteristics of the cross section, the joint is connected to the column at the end of the corner radius; these details improve the connectivity of the joint to the column, since the welding procedure of this this type of profiles could show some local imperfections. The main components are the socket and the plug: the former is made of two S-shape plates that are welded to the column's face at one end, while serves as a host for the plug on the other end. The plug is made of a T-shape and U-shape plates, and it is reinforced by stiffeners at both sides. In addition, the plug is connected to the truss on one end, and it will be locked in the socket on the other side. During fabrication of the structure in a steel workshop, the T-plug with Y-fork are assembled to the truss girder and the socket is welded to column.

The slab in this system is constructed using CLT panels, providing both the necessary gravity load-bearing capacity and enough in plane rigidity to act as a rigid plane diaphragm.

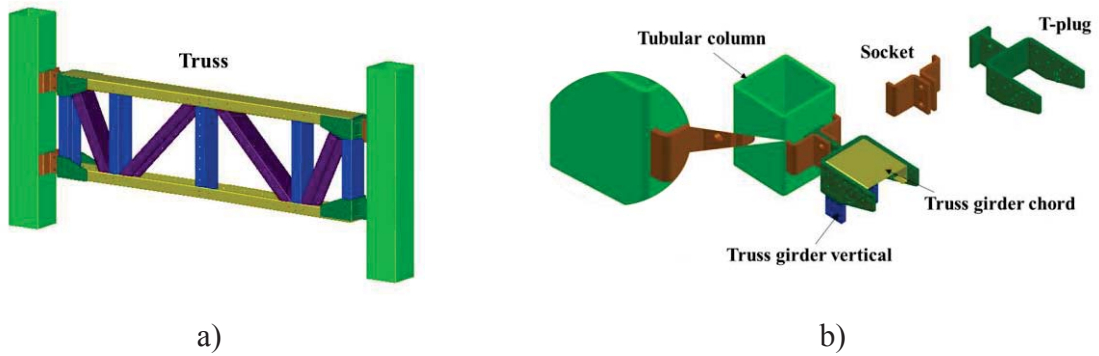


Figure 1 Structural system (a); Details of the plug-and-play connection (b)

### 3 FINITE ELEMENT MODELING OF THE JOINT

A 3D model of the test specimens was developed based on the experimental set-up as shown in Figure 2. The model was developed by means of Abaqus software [28] and all the main modelling assumptions are in line with the models developed by Tartaglia et al. [29-34]. Due to the large number of contacts, the bolts and the material nonlinearity, the full 3D model is difficult to construct and is computationally intensive. Thus, considering some simplification is necessary for the model; in this case proper boundary condition were introduced to reproduce the symmetry of the connection. A mesh transition technique is used to mesh the model. The fine mesh was used in a critical area or anywhere that the behavior of the model is important. A coarser mesh is used in areas further away from the critical zones by using a wedge element between two zones. A general contact is defined for the model. For general contact interactions, the discretization, tracking approach, and surface role assignments are selected automatically by Abaqus/Standard. A contact property that has tangential and normal behavior is assigned to the contact. The penalty method is selected for enforcing the contract. It enforces the contact by use of springs without adding a degree of freedom to the matrix structure.

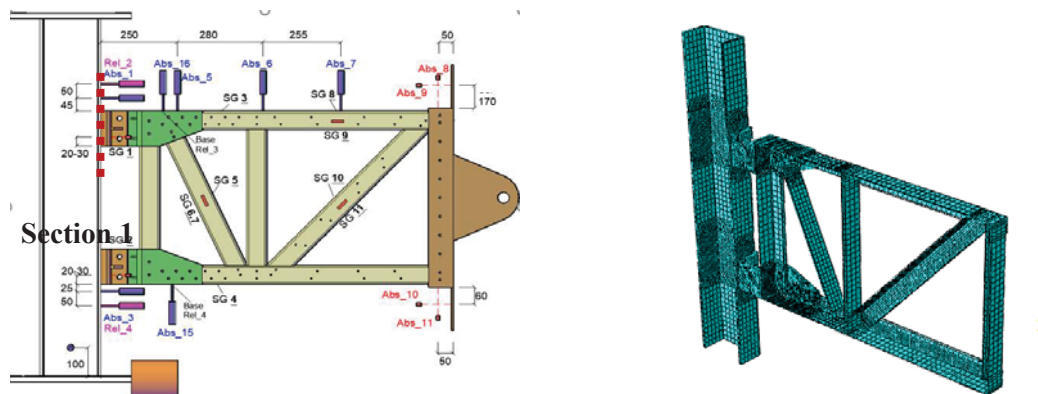


Figure 2 Left: the test set-up Right: the FEM

Figure 3a shows the comparison between the numerical simulation and the experimental test in terms of force versus the displacement curve. The force is measured by the load cell while the vertical displacement is extracted from the LDTV ABS\_11 (see Figure 2). After an initial decrease, the joint shows an increase of stiffness. This additional source of stiffness is due to the contact between the T-plug and the socket.

The Von-mises stress are also depicted in Figure 3b where a large concentration of tensions can be observed at the joint location.

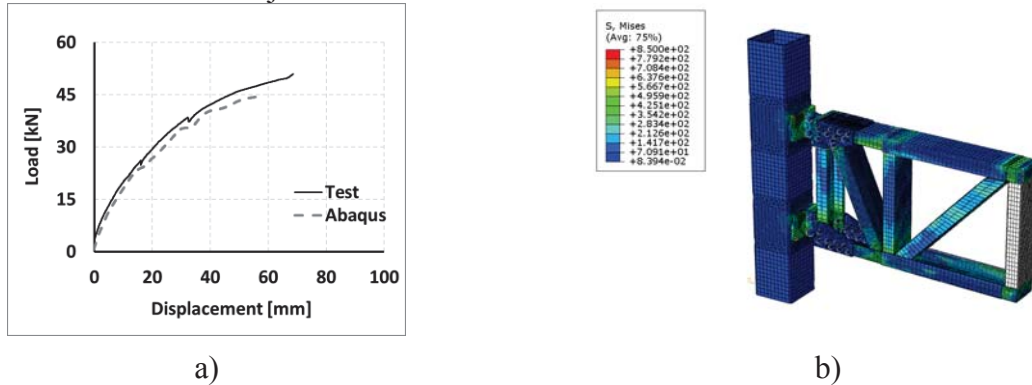


Figure 3 Force-displacement from the FEM and available experimental data.

The top joint is isolated from the system to investigate the cyclic response of the joint as shown in Figure 4a. The cyclic behavior of the joint is investigated under the ECCS loading protocol. First, a monotonically increasing displacement load (rotation) was applied to the reference point that is highlighted in yellow. From the recorded force (moment) – displacement (rotation) curve, the conventional limit of the elastic range and the corresponding displacement (rotation) were deduced based on ECCS prescriptions. The reaction forces and moments are extracted from section-1 (see Figure 2).

The cyclic behavior of the joint is evaluated and shown in Figure 4 in terms of bending moment, shear and axial force. The curves are normalized with respect to the axial, shear and bending yielding resistance evaluated from the monotonic response. The hysteretic behavior shows a fair amount of pinching which is mainly due to the opening and closing of the bolts or contact and separation of different plates in the joint.

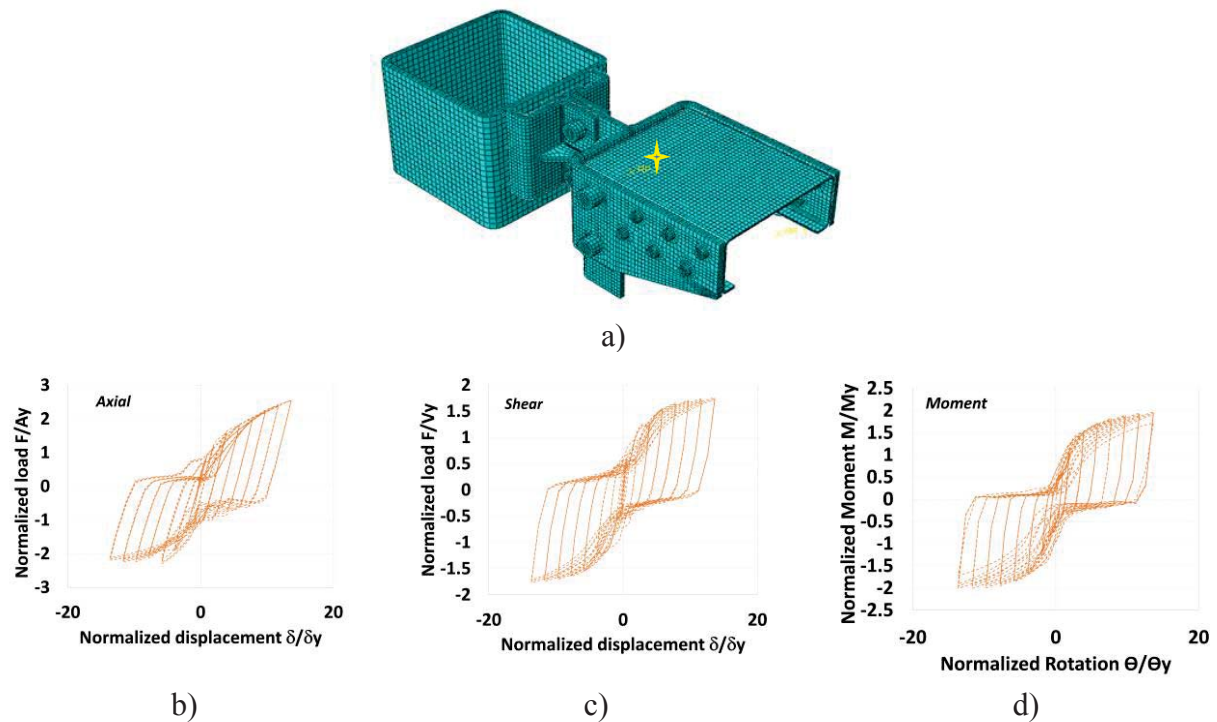


Figure 4: The cyclic behavior of the inno3Djoint



#### 4 SUMMARY AND CONCLUSIONS

INNO3DJOINTS joint is an innovative plug-and-play joint for hybrid tubular construction, whereby tubular columns are combined with cold-formed lightweight steel profiles to provide a highly efficient structural system. A finite element model of the joint was developed based and validated against the experimental test. Under monotonic loads an initial loss of stiffness due to contact between the T-plug and the socket can be observed; contrariwise for increasing value of rotation an increase of stiffness was observed. This discontinuity can be observed also when the joint is subjected to cyclic action; indeed, as observed the joint cyclic behavior is characterized by a pinching behavior.

#### REFERENCES

- [1] L. Fiorino, T. Pali, R. Landolfo, Out-of-plane seismic design by testing of non-structural lightweight steel drywall partition walls. *Thin-Walled Structures*, **130**, 213-230, 2018.
- [2] V. Macillo, S. Shakeel, L. Fiorino, R. Landolfo, Development and Calibration of Hysteretic Model for CFS Strap braced stud walls. *International Journal of Advanced Steel Construction*, **14(3)**, 337-360, 2018.
- [3] L. Fiorino, O. Iuorio, V. Macillo, M.T. Terracciano, T. Pali, R. Landolfo, Seismic Design Method for CFS Diagonal Strap-Braced Stud Walls: Experimental Validation. *Journal of Structural Engineering*, **142(3)**, 1-12, 2016.
- [4] A. Campiche, Numerical modelling of cfs three-story strap-braced building under shaking-table excitations. *Materials*, **14(1)**, 1–13, 2021
- [5] L. Fiorino, O. Iuorio, R. Landolfo, Seismic analysis of sheathing-braced cold-formed steel structures. *Engineering Structures*, **34**, 538-547, 2012.
- [6] V. Macillo, A. Campiche, S. Shakeel, B. Bucciero, T. Pali, M.T. Terracciano, L. Fiorino, R. Landolfo, Seismic Behaviour of Sheathed CFS Buildings: Shake-Table Testing and Numerical Modelling, *Key Eng. Mater.* **763**, 584–591, 2018.
- [7] A. Campiche, L. Fiorino, R. Landolfo, Numerical modelling of CFS two-storey sheathing-braced building under shaking-table excitations, *J. Constr. Steel Res.* **170**, 2020
- [8] A. Campiche, S. Shakeel, V. Macillo, M.T. Terracciano, B. Bucciero, T. Pali, L. Fiorino, R. Landolfo, Seismic behaviour of sheathed CFS buildings: Shake table tests and numerical modelling, 2018. *Ingegneria sismica-International Journal of Earthquake Engineering*, **35**, 106-123, 2018.
- [9] A.C. Faralli, M. Latour, P.J. Tan, G. Rizzano, P. Wrobel, Experimental investigation and modelling of T-stubs undergoing large displacements. *Journal of Constructional Steel Research*, **180**, 2021
- [10] V. Giordano, C. Chisari, G. Rizzano, M. Latour, Prediction of seismic response of moment resistant steel frames using different hysteretic models for dissipative zones. *Ingegneria Sismica*, **34 (4)**, 42-56, 2017
- [11] R. Tartaglia, M. D’Aniello, G. Di Lorenzo, A. de Martino, Influence of EC8 rules on p-delta effects on the design and response of steel MRF. *Ingegneria Sismica*, **35(3)**, 104-120, 2018.

- [12] R. Montuori, E. Nastri, V. Piluso, S. Streppone, M. D’Aniello, M. Zimbru, R. Landolfo, Comparison between different design strategies for freedom frames: Push-overs and IDA analyses. *Open Construction and Building Technology Journal*, **12**,140-153, 2018
- [13] S. Costanzo, R. Tartaglia, G. Di Lorenzo, A. de Martino, Seismic behaviour of EC8-compliant moment resisting and concentrically braced frames. *Buildings*, **9(9)**, 196, 2019.
- [14] G. Dell’Aglia, R. Montuori, E. Nastri, V. Piluso, Consideration of second-order effects on plastic design of steel moment resisting frames. *Bulletin of Earthquake Engineering*, **17 (6)**, 3041-3070, 2019.
- [15] E. Nastri, M. D’Aniello, M. Zimbru, S. Streppone, R. Landolfo, R. Montuori, V. Piluso, Seismic response of steel Moment Resisting Frames equipped with friction beam-to-column joints. *Soil Dynamics and Earthquake Engineering*, **119**, 144-157, 2049.
- [16] R. Montuori, E. Nastri, V. Piluso, Preliminary analysis on the influence of the link configuration on seismic performances of MRF-EBF dual systems designed by TPMC. *Ingegneria Sismica*, **33 (3)**, 52-64, 2016.
- [17] R. Montuori, E. Nastri, V. Piluso, Seismic response of EB-frames with inverted Y-scheme: TPMC versus eurocode provisions. *Earthquake and Structures*, **8 (5)**, 1191-1214, 2015.
- [18] A.B. Francavilla, M. Latour, V. Piluso, G. Rizzano, Design criteria for beam-to-column connections equipped with friction devices. *Journal of Constructional Steel Research*, **172**, 2020.
- [19] E. Elettore, F. Freddi, M. Latour, G. Rizzano, Design and analysis of a seismic resilient steel moment resisting frame equipped with damage-free self-centering column bases. *Journal of Constructional Steel Research*, **179**, 2021.
- [20] M. Latour, G. Rizzano, Seismic behavior of cross-laminated timber panel buildings equipped with traditional and innovative connectors. *Archives of Civil and Mechanical Engineering*, **17(2)**, 382-399, (2017).
- [21] A.F. Santos, A. Santiago, M. Latour, G. Rizzano, L. Simões da Silva, Response of friction joints under different velocity rates. *Journal of Constructional Steel Research*, **168**, 2020.
- [22] M. D’Antimo, M. Latour, G.F. Cavallaro, J.P. Jaspart, S. Ramhormozian, J.F. Demonceau, Short- and long-term loss of preloading in slotted bolted connections. *Journal of Constructional Steel Research*, **167**, 2020.
- [23] R. Tartaglia, M. D’Aniello, G.A. Rassati, Proposal of AISC-compliant seismic design criteria for ductile partially-restrained end-plate bolted joints. *Journal of Constructional Steel Research*, **159**, 364–383, 2019.
- [24] J J. Kesti, et al. Dissemination of knowledge in the use of steel-intensive dry construction systems in housing. Final Report, Research Fund for Coal and Steel, European Commission (2008)
- [25] Optimization of frames for effective assembling, FRAMEUP, RFSR-CT-2011-00035, final report.
- [26] New market chances for steel structures by innovative fastening solutions, INFASO, RFSR-CT-2007-00051, final report.

- [27] Energy and thermal improvements for construction in steel, ETHICS, RFSR-CT-2008-00038, final report.
- [28] Prefabricated steel structures for low-rise buildings in seismic areas, PRECASTEEL, RFSR-CT-2007-00038, final report.
- [29] Dassault (2014), Abaqus 6.14 User's Manual, Dassault Systèmes Simulia Corp.
- [30] R. Tartaglia, M. D'Aniello, M. Zimbru, Experimental and numerical study on the T-Stub behaviour with preloaded bolts under large deformations. *Structures*, **27**, 2137-2155, 2020.
- [31] R. Tartaglia, M. D'Aniello, M. Andreini, S. la Mendola, The performance of preloaded bolts in seismically prequalified steel joints in a fire scenario. *Materials*, **13(22)**, 1-14, 2020.
- [32] R. Tartaglia, M. D'Aniello, R. Landolfo, Numerical simulations to predict the seismic performance of a 2-story steel moment-resisting frame. *Materials*, **13(21)**, 1-17, 2020.
- [33] R. Tartaglia, M. D'Aniello, Influence of Transverse Beams On the Ultimate Behaviour of Seismic Resistant Partial Strength Beam-To-Column Joints. *Ingegneria Sismica*, **37(3)**, 50-65, 2020.
- [34] M. D'Aniello, R. Tartaglia, D. Cassiano, Experimental investigation of the inelastic tensile behaviour of non-preloadable grade 8.8 bolts. *Ingegneria Sismica*, **37(2)**, 92-109, 2020.
- [35] R. Tartaglia, M. D'Aniello, Nonlinear performance of extended stiffened end plate bolted beam-to-column joints subjected to column removal. *Open Civil Engineering Journal*, **11(M6)**, 369–383, 2017.

## DESIGN AND ANALYSIS OF FREEDAM FRAMES: COMPARISON WITH TRADITIONAL CONNECTIONS

**Maria Maglio, Camilla Naddei, Elide Nastri, Rosaria Russo, Paolo Todisco**

Department of Civil Engineering, University of Salerno  
Via Giovanni Paolo II, 132, 84084, Fisciano (SA), Italy  
e-mail: enastri@unisa.it

---

### Abstract

*The aim of this work is to present the results of the design of Moment Resisting Frames and Dual-Concentrically Braced Frames (D-CBFs) according to the Theory of Plastic Mechanism Control. These frames are equipped with both haunched connections, analysed in the framework of the RFCS founded EqualJoints Plus research project, and FREEDAM joints analysed in the framework of the RFCS founded FREEDAM Plus. The seismic performances of the structures are investigated by both pushover and nonlinear dynamic analyses.*

**Keywords:** Prequalified connections, Concentrically Braced Frames, TPMC, Dual Systems, seismic response, FREEDAM Plus.

---

## 1 INTRODUCTION

The design of modern seismic resistant structures is based on a preliminary selection of the so-called dissipative zones which must be designed to assure, by means of their plastic engagement, the dissipation of the earthquake input energy. It is well known that Moment Resisting Frames (MRFs) [1]-[4] are characterized by a limited lateral stiffness and high ductility linked to the possibility of forming many plastic hinges. The location of such dissipative zones at the beam ends is commonly preferred by designing full-strength beam-to-column joints. It is recommended that beam-to-column joints are designed with sufficient over-strength with respect to the connected beams to assure their yielding accounting for the influence of random material variability and for strain-hardening occurring before the complete development of the ultimate flexural resistance of plastic hinges.

Dual Concentrically Braced Frames (D-CBFs) [6]-[7] constitute an appealing structural scheme because they combine the advantages of MRFs, which are characterized by high global ductility due to the high number of dissipative zones, and CBF, which are characterized by high lateral stiffness due to the exploitation of the axial stiffness of diagonal members. In fact, thanks to bracing members, providing additional lateral stiffness, D-CBFs allow respecting serviceability code requirements. However, they are penalized by the occurrence of buckling of bracing members in compression which governs the shape of the hysteresis loops of such dissipative zones [8]-[14]. D-CBFs are also attractive for collapse prevention requirements because they allow exploiting the local ductility supply of the MR part thus giving to the diagonal members only the stiffening task. This observation suggests a design approach where the braced frame is dimensioned to satisfy serviceability requirements while the moment resisting part is designed to satisfy ultimate limit state requirements.

It is known that, to prevent catastrophic collapses, the structural system and members should have enough strength and ductility to resist to earthquakes [15]-[23]. Therefore, a stable and reliable capacity for energy dissipation should be provided through proper design and detailing of the system, members, and joints. These latter attracted much attention because an improper design or fabrication of the connections may lead to the collapse failure of the whole structure.

In this paper, reference is made to the use of full-strength joints [24]-[30] that has been always considered the best way to dissipate the seismic input energy. In particular, the joint typology herein investigated is the so-called “haunched” connections which are characterized by a haunch at the lower flange of the beam having the aim of increasing the connection stiffness thus allowing the yielding in the beam ends. As regards code provisions, UNI EN 1993-1-8 [31] provides design rules and analytical models to predict the mechanical behavior of the joints; while UNI EN 1998-1 [32] provides additional design rules for seismic resistant joints. From the existing scientific literature, a wide data base of experimental results on beam-to-column joints is available [33]. Moreover, several research projects have been developed and devoted to investigating the beam-to-column joints behavior under both seismic and non-seismic loadings. Even though these projects have provided a large amount of data dealing with steel beam-to-column connections, none of the existing European studies has been aimed at prequalifying specific configurations for seismic areas based on parametric experimental investigations. In order to fill these gaps, the recently finished European research project EQUALJOINTS [34] was aimed at providing prequalification criteria of steel joints for the next version of UNI EN 1998-1 [32]. The following dissemination project EQUALJOINTS-PLUS [35]-[38], had the scope to promote the valorisation and dissemination of the technical knowledge and the design tools developed within the EQUALJOINTS project. The goal is to reach a wider and easier use of dissipative beam-to-column connections in steel seismic resist-



ing systems in Europe. The joint typologies selected for prequalification procedure are representative of those most adopted in European practice. In the context of the research project EQUALJOINTS [34], four types of prequalified connections are considered. In particular, three types of prequalified bolted beam-to-column joints (Figure 1 a, b and c) will be considered, as well as welded dog-bone beam-to-column joint made of heavy sections (Figure 1 d). In this paper, reference is made to “haunched” connections (Figure 1 a).

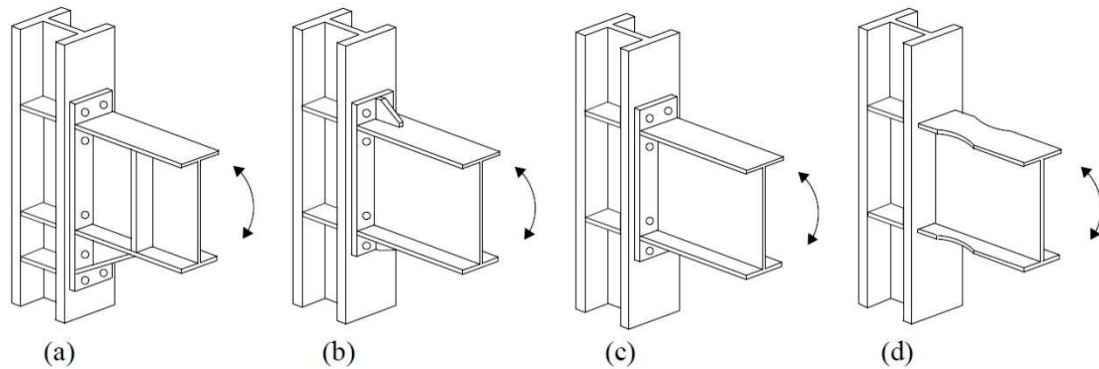


Figure 1: Beam-to-column joints investigated in the framework of EQUALJOINTS project: a) Bolted haunched joints; b) Bolted extended stiffened end-plate joint; c) Bolted extended unstiffened end-plate joint; d) Welded dog-bone joint

However, independently of the use of either full-strength or partial-strength beam-to-column joints, the main drawback of the traditional seismic resistant design strategy is intrinsic in the strategy itself. The structural damage is essential to dissipate the earthquake input energy but, on the other hand, it is the main source of direct and indirect losses. For this reason, many researchers have focused their attention on the strategy of supplementary energy dissipation with the aim to reduce the structural damage under destructive seismic events and, therefore, the direct and indirect losses. This strategy is based on the use of specific energy dissipation devices which have to be inserted between couples of points of the structural scheme for which high relative displacements or velocities are expected under the action of severe ground motions. In this work, reference is made to beam-to-column FREEDAM [39] connections that have been widely tested at the Laboratory of Materials and Structures of University of Salerno and to FREEDAM connections equipping the intersection between the diagonals of chevron brace frames (CBFs) when the structure is not a simple Moment resisting frame (MRF) but dual systems given by the combination of MRFs and CBFs.

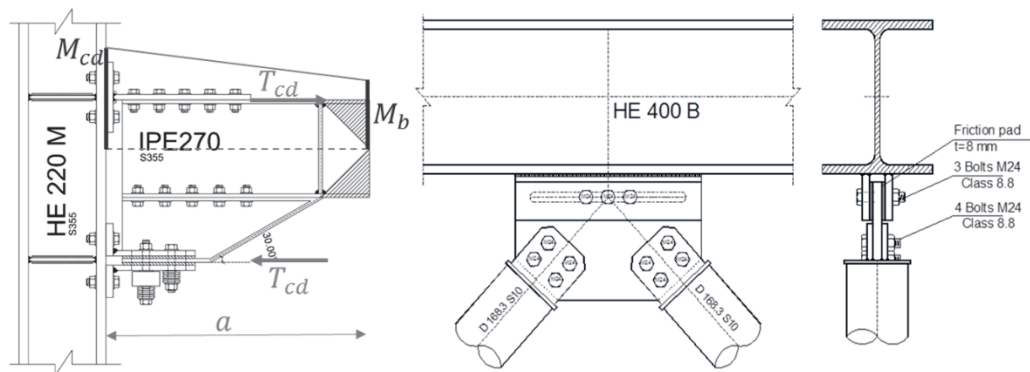


Figure 2: Beam-to-column joints investigated in the framework of FREEDAM plus project: a) MRF FREEDAM joint; b) FREEDAM friction damper to chevron brace.

The scope of the paper is investigating the influence of both the mentioned connection typologies in the seismic response of MRFs and D-CBFs. To this scope, medium-rise structures have been designed according to the Theory of Plastic Mechanism Control (TPMC) design approach [40]-[49], which is a powerful design. The structural response was analysed by means of both non-linear static and dynamic analyses. All the activities described in this work are performed in the framework of the RFCS Project FREEDAM Plus [50] aimed at the valorisation and dissemination of the technical knowledge and the design tools developed within FREEDAM project, to reach a wider and easier use of dissipative beam-to-column connections in steel seismic resisting systems.

## 2 HAUNCHED CONNECTIONS VS FREEDAM CONNECTIONS

Bolted joints are very interesting for practice in steel buildings, owing to their inherent advantages not only in terms of high-quality execution (e.g. shop welding and bolting on site), but also highly productive erection (less time-consuming). Full strength joints are designed to guarantee the formation of all plastic deformations into the beam, which is consistent with EN 1998 strong column-weak beam capacity design rules (i.e. non-dissipative joint).

“Haunched” connections [51] increasing the web depth also makes an increase of the height of panel zone, which reduces the panel zone yielding. In that case a greater beam plastic rotation is needed to achieve an equivalent seismic energy dissipation. Application of the haunches assures that plastic hinges form in the beams which increases the global seismic performance of steel moment resisting frames. Appropriate detailing and use of “haunched” joints could be an effective way for ductile design of steel frames. The haunched connection used in this paper is described in Figure 3 where  $M_{j,Rd}^n$  is the joint resistance,  $M_{pl,b,cf,Rd}^e$  is the beam resistance. All the prequalifying requirements reported in Figure 3 are finalized to the stiffening of the panel zone whose strength is also calibrated not to yield in case of destructive seismic events.

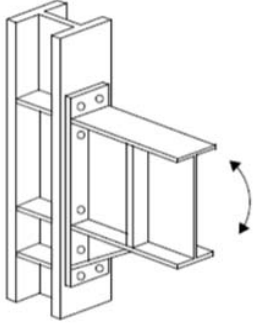
					
Joint Type	Geometry	Strength		Stiffness	
		Connection:	Panel Zone:	Connection:	Panel Zone:
<b>EH-S:</b> Full-strength with strong panel zone	$\frac{h_h}{h_b} = 0.45$  $\frac{s_h}{h_b} = 0.65$ $z_{wp} = h_b + h_h$	$\frac{M_{j,Rd}^n}{M_{pl,b,cf,Rd}^e} = 1.3$	External nodes: $\frac{V_{wp,Rd}^n \cdot z_{wp}}{M_{pl,b,cf,Rd}^e} = 1.65$	$\frac{s_{con,ini}}{s_b} = 80$	External nodes: $\frac{s_{wp,ini}}{s_h} = 55$
			Internal nodes: $\frac{V_{wp,Rd}^n \cdot z_{wp}}{2 \cdot M_{pl,b,cf,Rd}^e} = 1.65$		Internal nodes: $\frac{s_{wp,ini}}{2 \cdot s_h} = 55$

Figure 3: Details of “Haunched” connections

FREEDAM connections, studied in the framework of the recently accomplished homonymous project (RFSR-CT-2015-00022) have a wide-ranging use because it is a technology that

can be used both in the construction of new buildings and for the seismic rehabilitation of existing buildings. From the technological point of view, the innovation regards the conception of beam-to-column connections. In fact, beam-to-column connections are equipped with friction dampers which can be located either at the bottom flange level or at the levels of both the flanges. Such friction dampers must be designed to assure the transmission of the beam bending moment required to fulfil serviceability limit state requirements and to withstand without slippage the gravity loads. In addition, they must be designed to assure the dissipation of the earthquake input energy, corresponding to the collapse prevention limit state, without any damage. FREEDAM joints are extremely robust, because they are characterized by a first phase of the response corresponding to the damper slippage and by a second phase in which a secondary resisting mechanism is activated with the bolts acting in shear and the plate elements subjected to bearing. The added value to what has already been achieved at both European and worldwide level is the increase the safety buildings and reduction of the direct and indirect costs related to the development of structural damage in case of rare seismic events or exceptional loads. The friction resistance is calibrated by acting on the number and diameter of bolts and their tightening torque governing the preloading. The flexural resistance results from the product between the damper friction resistance and the lever arm. Such connections exhibit wide and stable hysteresis loops without any damage to the connection steel plate elements, so that they can be referred as “Free from Damage Connections”.

FREEDAM joints can be designed according to the following equation:

$$M_{f.Ed} \leq M_{f.Rd} = \frac{\mu_{st} n_b n_s P_f}{\gamma_{F2}} h_f \quad (1)$$

where  $\mu_{st}$  is the average value of the static friction coefficient equal to 0.76,  $n_b$  is the number of bolts,  $n_s$  is the number of the contact surfaces equal to 2,  $h_f$  is the lever arm given as the sum of  $H$  (Figure 14) and  $h_b$  (height of the beam),  $\gamma_{F2}$  is the partial safety factor accounting for the randomness of friction and bolt preload, and it is equal to 1.26,  $P_f$  is the preloading force that has to be calibrated to assure that the FREEDAM connection resistance is as much close as possible to the design moment  $M_{f.Ed}$  at the column face resulting from the seismic load combination. Therefore:

$$P_f \cong \frac{M_{f.Ed} \gamma_{F2}}{\mu_{st} n_b n_s h_f} \quad (2)$$

The bolt preloading should be between 40% and 100% of the maximum bolt preloading allowed by code provisions (EN 1993-1-8).

The number of bolts changes according to the standardised devices (Table 1). The friction damper to be adopted must be selected in function of the beam height  $h_b$  and of the increase of the lever arm due to the haunch resulting from the damper geometry (Figure 4).

Device	Number of bolts $n_b$
D1	4
D2	4
D3	6
D4	8
D5	8

Table 1: Number of bolts of the prequalified devices

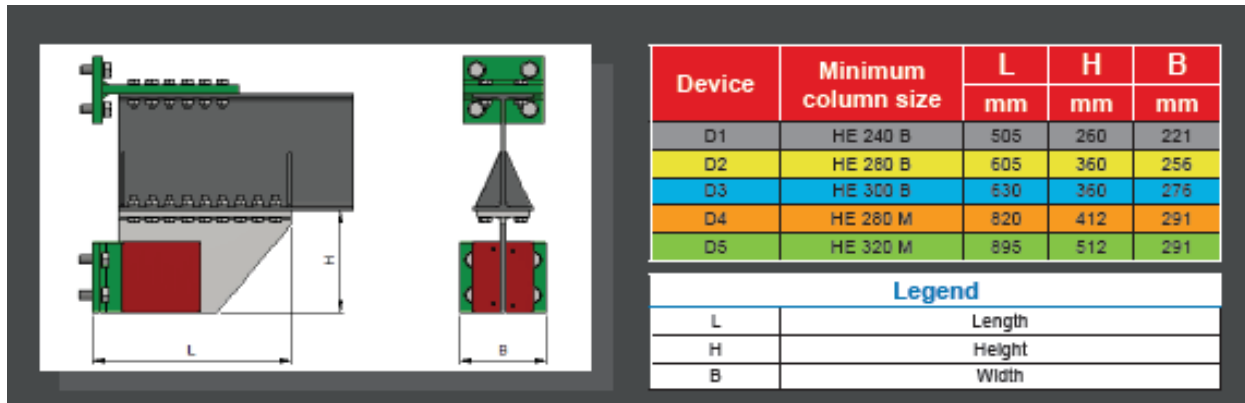


Figure 4: Dimension of prequalified FREEDAM connections

It is important underlining the need to perform a local hierarchy criterion to prevent the beam yielding that can be expressed as follows:

$$M_{b,Rd} \geq \gamma_{rm} M_{f,Rd} \left( \frac{l-L}{l} \right)$$

where  $\gamma_{rm} = 1.60$  [52],  $M_{b,Rd}$  is the beam plastic moment,  $M_{f,Rd}$  is the FREEDAM joint resistance (Eq. (1)),  $l$  is the beam length and  $L$  is the device dimension as reported in Figure 4.

### 3 DESIGN APPROACH

The design approaches herein proposed regard the Theory of Plastic Mechanism Control [40], [53]-[56]. The Theory of Plastic Mechanism Control is a design approach based on a rigorous theoretical background. It assures the development at collapse of a mechanism of global type. TPMC exploits the kinematic theorem of plastic collapse extended to the concept of mechanism equilibrium curve:

$$\alpha = \alpha_0 - \gamma \delta \quad (3)$$

where, following the theory of rigid-plastic analysis,  $\alpha_0$  is the first order collapse multiplier of horizontal forces,  $\gamma$  is the slope of the linearized mechanism equilibrium curve due to second order effects and  $\delta$  is the plastic top sway displacement. It means that in the case of the global mechanism Eq. (3) becomes:

$$\alpha^{(g)} = \alpha_0^{(g)} - \gamma^{(g)} \delta \quad (4)$$

while in the case of undesired mechanism becomes:

$$\alpha_{i_m}^{(t)} = \alpha_{0.i_m}^{(t)} - \gamma_{i_m}^{(t)} \delta \quad (5)$$

where  $\alpha_0^{(g)}$  and  $\alpha_{0.i_m}^{(t)}$  are the first order collapse mechanism multipliers for global and undesired mechanism, respectively;  $\alpha^{(g)}$  and  $\alpha_{i_m}^{(t)}$  are the collapse multiplier of horizontal force for the global and undesired mechanism, respectively and  $\gamma^{(g)}$  and  $\gamma_{i_m}^{(t)}$  are the slope of mechanism equilibrium curve for the global and undesired mechanism, respectively. TPMC states that the mechanism equilibrium curve corresponding to the global mechanism (Eq. (4)) has to be located below those corresponding to all the undesired mechanisms (Eq. (5)) until a design displacement  $\delta_u$  compatible with the local ductility supply (Figure 5). The column sections at each storey that guarantee a global collapse mechanism are the unknowns of the design problem, while the dissipative zones are preliminarily designed according to the first principle of capacity design. In this paper, the ultimate design displacement  $\delta_u$  is computed as:

$$\delta_u = \theta h_{ns} \quad (6)$$

where  $\theta$  is the target rotation of the plastic hinge that is assumed equal to 0.04 rad neglecting the higher stiffness of braces, and  $h_{ns}$  is the building height. The plastic hinge rotation is set equal to the interstorey drift ratio, since the idealized behavior of the structure is rigid-plastic. It is worth noting that P-Delta second order effects are taken into account using the TPMC design approach and, as a consequence, does not deeply affect the design as the use of the  $\theta$  [57] factor proposed in the framework of Eurocode 8 [32], thus allowing to optimize the design overstrength of the structure and the non-linear response as well.

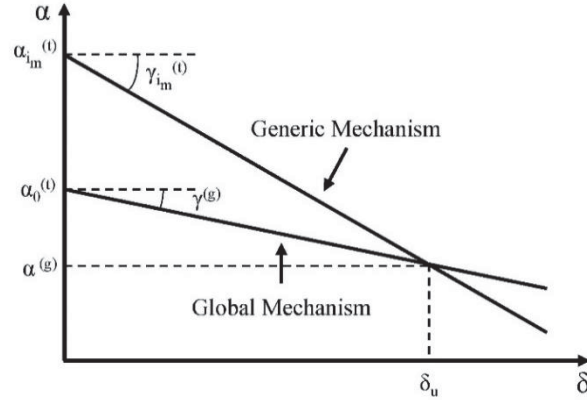


Figure 5: TPMC statement.

#### 4 STUDY CASE

The seismic resistant structural system is a perimeter seismic resistant system. The inner bays are pinned and designed for gravity loads only. The building has 4 storeys and 4 bays. The bay span is equal to 6.00 m; the interstorey height is equal to 3.50 m. Stairs are located outside the analysed building by means of an independent structure as the same as the elevator. The seismic resistant scheme of the building is depicted in Figure 6 for X direction. The elevation configuration is reported in Figure 7. The material adopted for the structure is steel grade S355 using a partial safety factor equal to 1, so the nominal yield stress is 355 MPa for beams and for columns. The following permanent loads are considered:

- Permanent loads on floors and roof:  $3,25 + 0,75 = 4,0 \text{ kN/m}^2$
- Permanent loads of external walls:  $1,0 \text{ kN/m}^2$

while the live loads are equal to  $3.50 \text{ kN/m}^2$  for current floors and  $3.00 \text{ kN/m}^2$  for the roof.

The design horizontal forces have been determined according to the new Eurocode 8 draft [58] spectra assuming a reference spectral acceleration at plateau of  $8.5 \text{ m/s}^2$ , a behaviour factor equal to 6.5 for MRFs and D-CBFs with FREEDAM joints and 4.8 for D-CBFs with traditional haunched connections.

Serviceability requirements have been checked by response spectrum analysis to compute the elastic displacements and to derive the interstorey drift values to be compared with the corresponding limits according to:

$$d_r = 0.020 h \quad (7)$$

where  $d_r$  is the relative displacement increased by the behaviour factor and  $h$  is the interstorey height. The limitation is the one reported into the new Eurocode 8 draft [59].



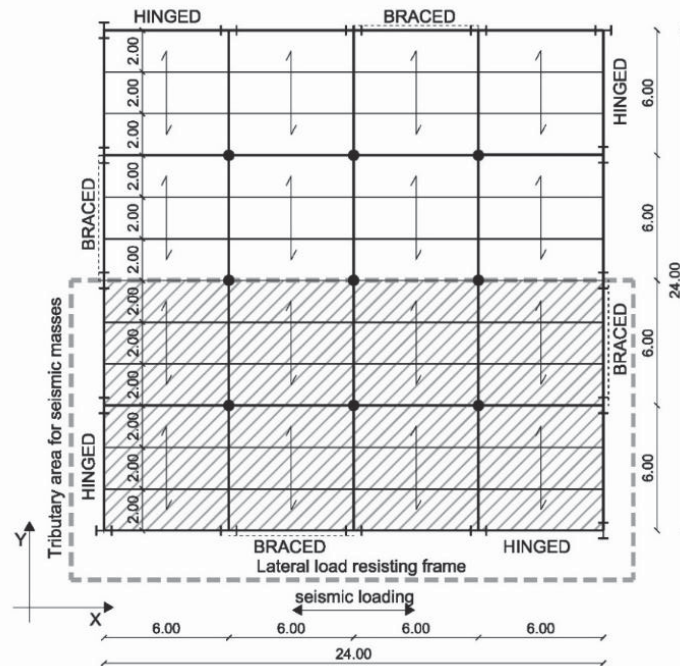


Figure 6: Plan configuration of the building with identification of the lateral load resisting system

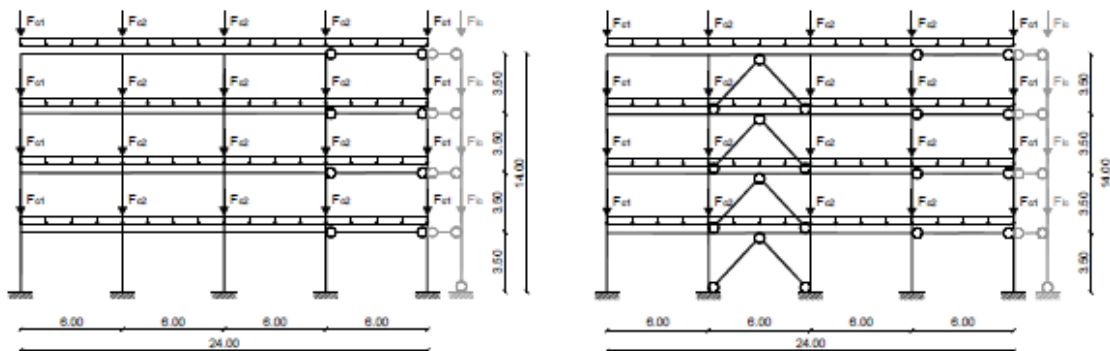


Figure 7: Elevation configuration of the building (MRFs and D-CBFs)

## 5 DESIGNED STRUCTURES

This section summarizes the description of the MRFs and Dual-CBFs designed according to TPMC and equipped with both haunched and FREEDAM connections.

Storey	Bay 1	Bay 2	Bay 3	Bay 4 (pinned)
1-2	IPE 330 haunched	IPE 330 haunched	IPE 330 haunched	IPE 220
3-4	IPE 300 haunched	IPE 300 haunched	IPE 300 haunched	IPE 220
Storey	Column 1-5	Column 2	Column 3	Column 4
1-2	HE 340 B	HE 340 B	HE 340 B	HE 340 B
3-4	HE 320 B	HE 320 B	HE 320 B	HE 320 B

Weight of structural elements: 12876 kg

Table 2: Beam and column sections for 4 St\_DC3\_MRFs\_X\_TRADITIONAL

Storey	Bay 1	Bay 2	Bay 3	Bay 4 (pinned)
1-2	IPE 330 FREEDAM	IPE 330 FREEDAM	IPE 330 FREEDAM	IPE 220

3-4	IPE 300 FREEDAM	IPE 300 FREEDAM	IPE 300 FREEDAM	IPE 220
Storey	Column 1-5	Column 2	Column 3	Column 4
1-2	HE 300 B	HE 300 B	HE 300 B	HE 300 B
3-4	HE 260 B	HE 260 B	HE 260 B	HE 260 B

Weight of structural elements: 11500 kg

Table 3: Beam and column sections for 4 St\_DC3\_MRFs\_X\_FREEDAM

Storey	Bay 1	Bay 2	Bay 3	Bay 4 (pinned)
1-2	IPE 330 haunched	IPE 270 haunched	IPE 330 haunched	IPE 220
3-4	IPE 330 haunched	IPE 270 haunched	IPE 330 haunched	IPE 220
Storey	Column 1-5	Column 2	Column 3	Column 4
1-2	HE 360 B	HE 450 B	HE 450 B	HE 450 B
3-4	HE 320 B	HE 450 B	HE 450 B	HE 450 B
Storey	Diagonal			
1-2	CHS 88.9x5			
3-4	CHS 88.9x4			

Weight of structural elements: 14951.8 kg

Table 4: Beam, diagonal and column sections for 4 St\_DC3\_D-CBFs\_X\_TRADITIONAL

Storey	Bay 1	Bay 2	Bay 3	Bay 4 (pinned)
1-2	IPE 360 FREEDAM	IPE 360 FREEDAM	IPE 360 FREEDAM	IPE 220
3-4	IPE 330 FREEDAM	IPE 330 FREEDAM	IPE 330 FREEDAM	IPE 220
Storey	Column 1-5	Column 2	Column 3	Column 4
1-2	HE 300 B	HE 300 B	HE 300 B	HE 300 B
3-4	HE 260 B	HE 260 B	HE 260 B	HE 260 B
Storey	Diagonal			
1	CHS 114.3x6.3			
2	CHS 114.3x5			
3	CHS 114.3x4			
4	CHS 88.9x5			

Weight of structural elements: 12486 kg

Table 5: Beam, diagonal and column sections for 4 St\_DC3\_D-CBFs\_X\_FREEDAM

Figure 8 shows the comparison in terms of weight among MRFs and D-CBFs equipped with haunched and FREEDAM connections. It is evident that in both cases the structures with traditional connections leads to heavier structures.

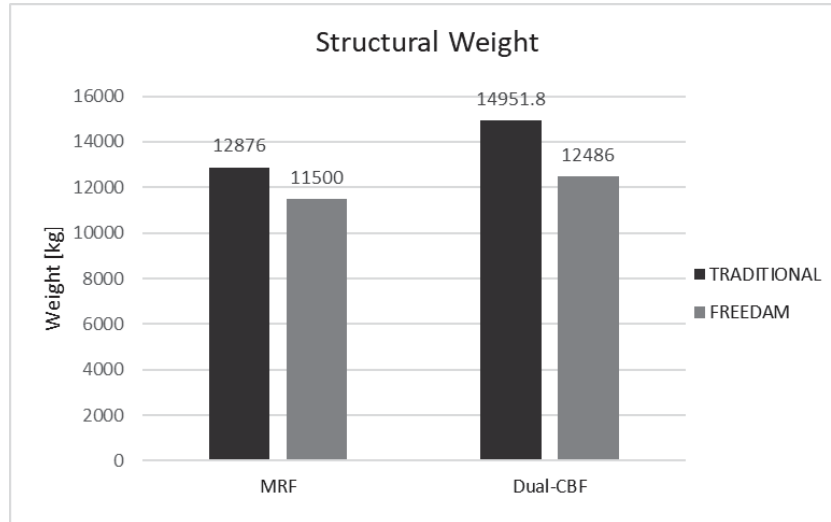


Figure 8: Comparison in terms of weight among MRFs and D-CBFs equipped with haunched and FREEDAM connections designed according to TPMC.

## 6 MODELING ASSUMPTIONS

The modelling of these structures is carried out in SAP 2000 ambience [60] according to the scheme reported in Figure 7. The leaning column (Figure 7) is used to consider the vertical loads acting on the frame (including masses) and the second order effects. The material steel grade is S355 where the coefficients 1.20 and 1.10 are the overstrength factor due to random material variability according to the Probabilistic TPMC [49] and the strain hardening, respectively. [61]-[66]. The plastic behaviour of members has been modelled in terms of lumped plasticity by P-hinge properties.

### 6.1 Structures with traditional joints

Beams and columns have been modelled by means of beam-column elements, whose non linearities have been concentrated in plastic hinges (“Moment M3” elements). On the beams, hinges are at the end of haunched connection, namely at a distance  $s_h$ , from the face of the column; while on the columns they are assigned with a relative distance of 0 and 1. Of fundamental importance are the demand for plastic rotation during the development of the kinematic mechanism and the capacity for plastic rotation. In the case of columns with dimensionless normal stress lower than 0.30 and beams in flexure, the plastic deformation capacity is expressed as a multiple of the chord rotation at yielding  $\vartheta$ , defined as a property of the member itself.

In particular, for columns arranged strong axis and for beams, the rotation of the member is:

$$\theta_y = \frac{\gamma_{rm} M_{pl,y} l_m}{6EI_m} \quad (8)$$

For columns arranged weak axis, the rotation of the member is:

$$\theta_z = \frac{\gamma_{rm} M_{pl,z} l_m}{6EI_m} \quad (9)$$

where  $M_{pl,y}$  and  $M_{pl,z}$  are the plastic moment of the member for y and z axis respectively;  $l_m$  is the length of the member;  $I_m$  is the moment of inertia; E is the elastic modulus and  $\gamma_{rm}$  is the material overstrength coefficient place equal to 1.25. Plastic rotation capacity at the end of

beams or columns with dimensionless axial load  $v$  not greater than 0.30 in Table B.1 of EC8-3 [67] are reported, as shown in Figure 6. The hysteresis type is kinematic.

Point	Moment/SF	Rotation/SF
E-	-0.67	$0.075/v$
D-	-1.2	$0.028/v$
C-	-1.2	$0.016/v$
B-	-1	0
A	0	0
B	1	0
C	1.2	$0.016/v$
D	1.2	$0.028/v$
E	0.67	$0.075/v$

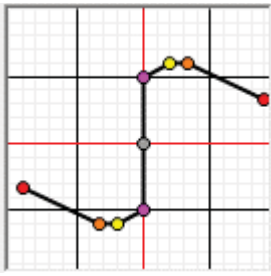


Table 6: Beams and columns hinge model.

To model the plastic hinge of the bracing diagonals in Sap2000 we start from the Georgescu model [68] generally used for cyclic analysis (Figure 9) [67].

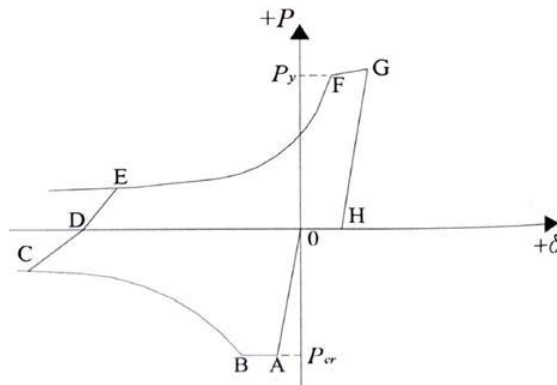


Figure 9: Georgescu model for cyclic analysis

The model used for the pushover analyzes starts from a first simplification of the Georgescu model (Figure 10) that exploits the OA, AB and BC traits for compression. On the other hand, in traction the behavior is defined with a Perfectly Plastic Elastic bound (EPP).

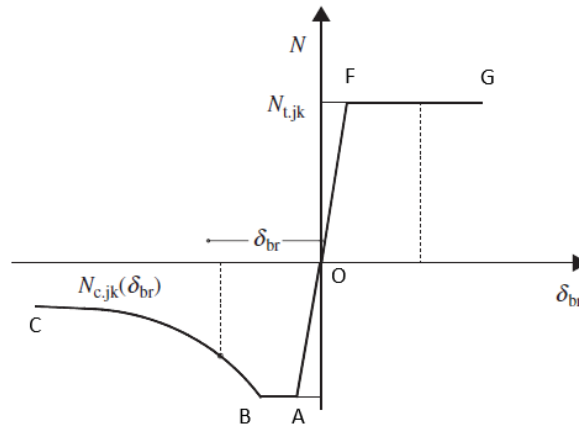


Figure 10: First simplification of the Georgescu model for pushover analysis

The equations of model branches are reported in the following:

- Initial imperfection

$$f_0 = \frac{W}{A} \alpha (\bar{\lambda}^2 - 0.04) \quad \text{with } \alpha = 0.21, \bar{\lambda} = \frac{\lambda}{\lambda_y} \quad (10)$$

- OA branch:

$$P = \frac{EA}{L} \delta_{OA} = K_d \delta_{OA} \quad \text{with } P \text{ limited to } P_{crit}; \quad \delta_A = \frac{P_{crit}}{K_d} \quad (11)$$

- AB branch:

$$f_{tB} = \frac{M_{pl}}{P_{crit}} \left( 1 - \frac{P_{crit}}{P_y} \right) \quad (12)$$

$$\delta_B = -\frac{P_{crit}L}{EA} + \frac{\pi^2}{4L} (f_{tB}^2 - f_0^2) \quad (13)$$

- BC branch:

$$f_t = \frac{M_{pl}}{P} \left( 1 - \frac{P}{P_y} \right) \quad \text{with } P \text{ generic } < P_{crit} \quad (14)$$

$$f_0 = \delta_{BC} = -\frac{PL}{EA} + \frac{\pi^2}{4L} (f_t^2 - f_0^2) \quad (15)$$

- OF branch:

$$P = \frac{EA}{L} \delta_{OF} = K_d \delta_{OF} \quad \text{with } P \text{ limited to } P_y; \quad \delta_F = \frac{P_y}{K_d} \quad (16)$$

- FG branch:

$$P = P_y \quad \forall \delta_{FG} \quad (17)$$

A second simplification adopted in the Sap2000 model consist in considering the OA and OF sections as rigid, while the BC section is represented with bilinear approximation (Figure 11). The elastic behaviour is demanded to the beam-column element representing the diagonal section.

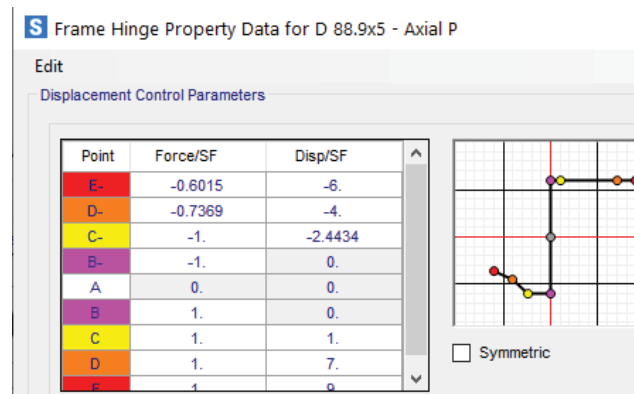


Figure 11: Second simplification of the Georgescu model for pushover analysis, in Sap2000

The bilinear approximation of the BC section was obtained by considering two points of the curve, or those corresponding to the limit displacements provided by Eurocode for the compressed diagonals. These points were also identified in traction (on the horizontal branch) according to the limits given for taut diagonals.



For braces in compression the inelastic deformation capacity should be expressed in terms of the axial deformation of the brace, as a multiple of the axial deformation of the brace at buckling load,  $\Delta_c$ . For braces in compression (except for braces of eccentric braced frames) the inelastic deformation capacities at the three LSs may be taken in accordance with Table B.2 of EC8-3 [67]. For braces in tension the inelastic deformation capacity should be expressed in terms of the axial deformation of the brace, as a multiple of the axial deformation of the brace at tensile yielding load,  $\Delta_t$ . For braces in tension (except for braces of eccentric braced frames) with cross section class 1 or 2, the inelastic deformation capacities at the three LSs may be taken in accordance with Table B.3 in EC8-3 [67]. To allow the diagonal buckling and therefore, their cyclic behaviour the diagonal must be split into two parts and the middle node must be put out of plane with an initial imperfection.

## 6.2 Structures with FREEDAM joints

In the structures with FREEDAM connections the beams and columns have the same plastic hinge described above. The P-hinge properties representing the FREEDAM connections are rigid perfectly plastic, and they are located at the column face, i.e. where it is expected the device rotation. The rotation depends on the level arm of the device used. Under the bending action, the node is forced to rotate around the center of rotation, located at the base of the upper T-stub, and the dissipated energy is guaranteed by the alternating sliding of the bolts on the vertical stainless-steel plate (Figure 12).

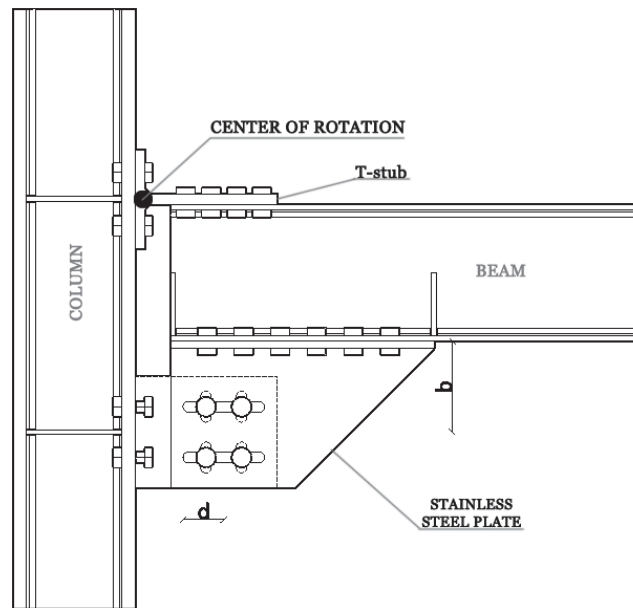


Figure 12: Center of rotation of FREEDAM hinge

In particular, the FREEDAM rotation is:

$$\vartheta_y = \frac{d}{H} \quad \text{with } H = h_b + b \quad (18)$$

where  $d$  is the distance between the bolt and the slot,  $h_b$  is the beam height,  $b$  is the distance between the center of gravity of the bolts and the lower flange of the beam.

As already mentioned, the bracing diagonals of the D-CBFs structures equipped with FREEDAM dampers do not suffer any damage in the case of a seismic event as the energy dissipation occurs through the friction dampers placed at the chevron braces intersection.

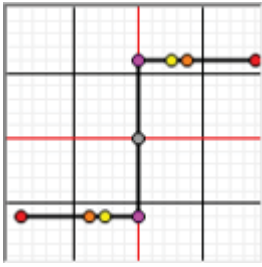
Point	Moment/SF	Rotation/SF	
E-	-1	$-\vartheta_y$	
D-	-1	-0.06	
C-	-1	-0.04	
B-	-1	0	
A	0	0	
B	1	0	
C	1	0.04	
D	1	0.06	
E	1	$\vartheta_y$	

Table 7: FREEDAM hinges model.

For the sole purpose of carrying out pushover and non-linear dynamic analyses, this friction device was modeled as a “short link” with a cross-section equal to the diagonals it joins and a cross section axial area of zero. The length of the link is:  $l_{link} = h_b/2 + 260$ ; in other words, it has been set equal to half the height of the beam plus the height of device D1.

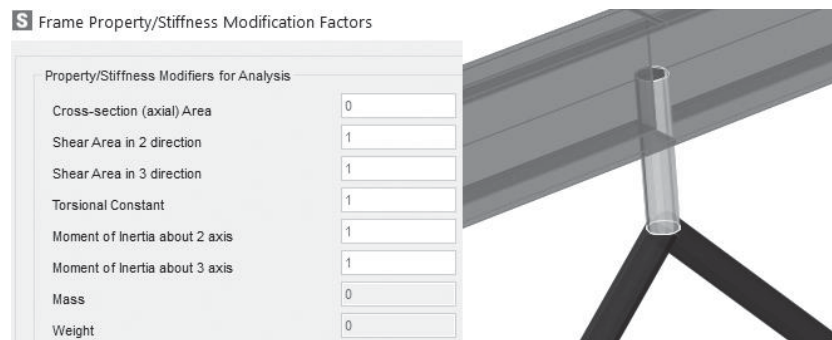


Figure 13 – Friction dampers model for pushover and non-linear dynamic analyses

A rigid plastic frame hinge “Shear V2” behaviour is assigned to “link” members with a max displacement equal to:  $d_{max} = 0.04 \cdot h_i = 0.04 \cdot 3.50 = 0.14$  m; where  $h_i$  is the inter-storey height of the structure. In the definition of FREEDAM hinges, the bending and shear strength of the beam-column and diagonal intersection devices was amplified with the coefficient  $\gamma_{rm}$  equal to 1.6 [52].

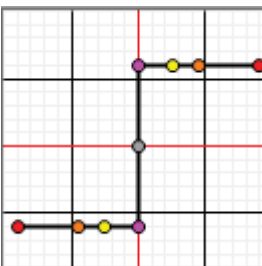
Point	Moment/SF	Rotation/SF	
E-	-1	$-d_{max}$	
D-	-1	-0.07	
C-	-1	-0.04	
B-	-1	0	
A	0	0	
B	1	0	
C	1	0.04	
D	1	0.07	
E	1	$d_{max}$	

Table 8: – FREEDAM hinges “Shear V2” model

## 7 PUSHOVER ANALYSES

Pushover analyses are led in displacement control considering both geometrical and mechanical nonlinearities under two lateral load patterns, as suggested by EC8: a load distribution corresponding to the fundamental mode shape and a uniform distribution proportional to seismic masses at each floor. The response parameters monitored by the performed pushover analyses are illustrated in Figure 14. Pushover analyses are carried out on SAP2000 computer program.

In particular,  $V_u$  is the base shear at maximum plastic capacity of the structure,  $V_1$  is the base shear at first plastic event;  $\delta_1$  and  $\delta_{max}$  are the roof displacements corresponding to the formation of the first plastic hinge and to the first occurrence of the structural collapse corresponding to the achievement of the ultimate rotation.

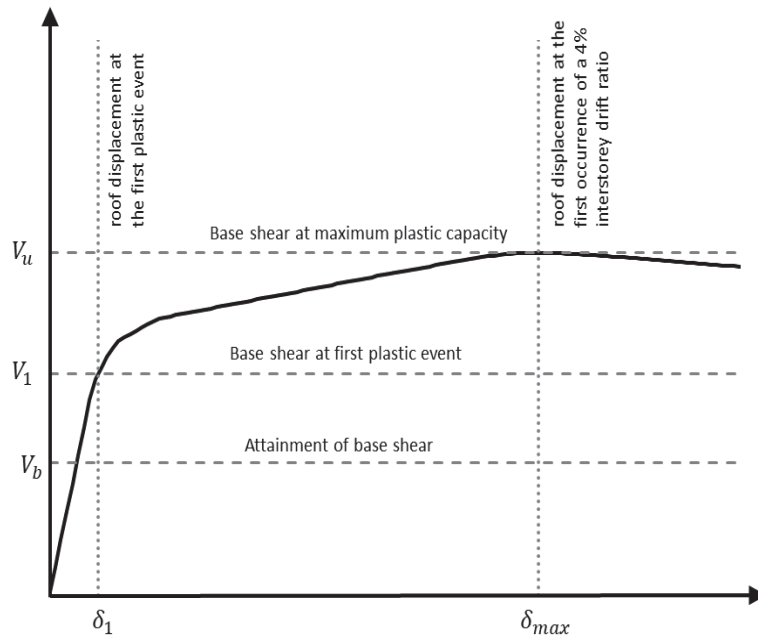


Figure 14: Monitored parameters in capacity curves.

Among the strength parameters monitored the base shear  $V_u$  is a measure of the overall overstrength of the structure. In addition, the ratio  $V_u/V_1$  is a measure of redundancy. This value depends on the frame configuration, formation of the collapse mechanism, redistribution capacity and gravity loading. Conversely,  $V_1$  can be considered as an overdesign factor related to aspects of the design procedure such as differences between actual and nominal material strength, member oversizing due to choices of commercial cross section and design governed by deformation and/or non-seismic loading. The  $\mu$  factor is defined as:

$$\mu = \frac{\delta_{max}}{\delta_1} \quad (19)$$

where  $\delta_{max}$  is the roof displacement at structural collapse and  $\delta_1$  is the roof displacement associated to formation of the first plastic hinge. From the comparison of pushover response curves (from Figure 15 to Figure 18) it is observed that the D-CBF designed according to EC8 are characterized by larger overstrength than the corresponding structures designed according to TPMC. Moreover, EC8 rules induce overdesigning the braces to satisfy both slenderness limits and the variation of brace overstrength along the building height, while TPMC do not have such requirements. In general, the differences among the different “haunched” connections are negligible.

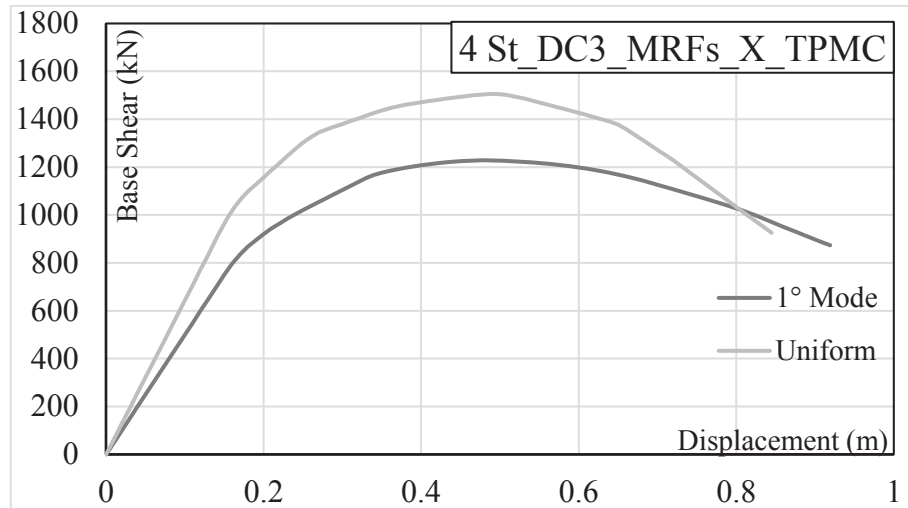


Figure 15: Push-over curves for 4 Storey MRFs with traditional connections

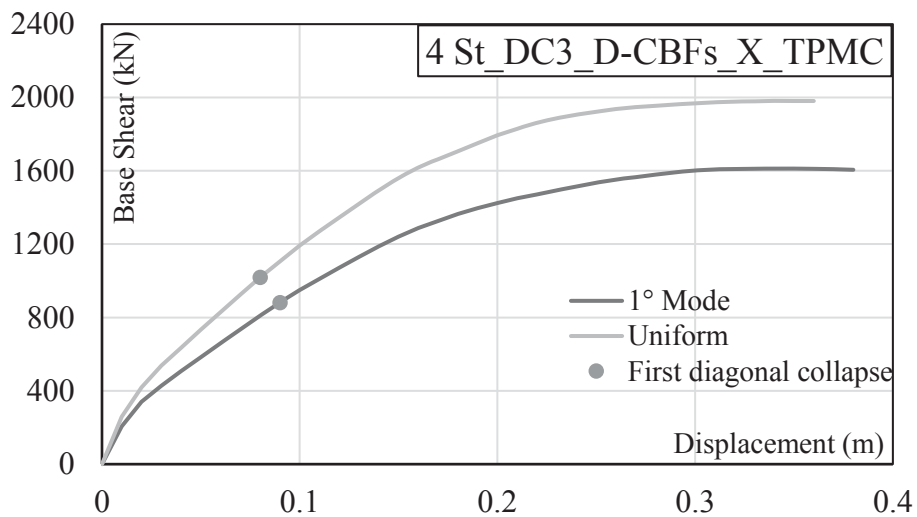


Figure 16: Push-over curves for 4 Storey D-CBFs with traditional connections

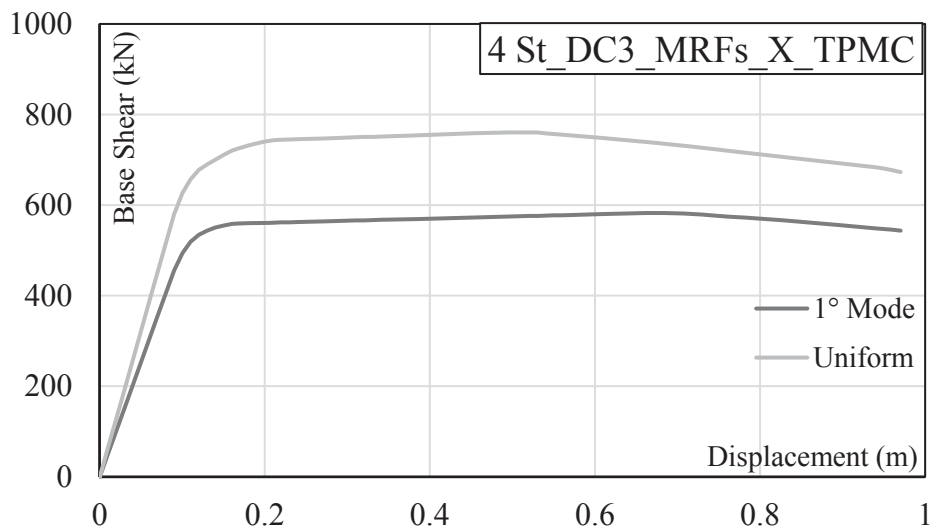


Figure 17: Push-over curves for 4 Storey MRFs with FREEDAM connections

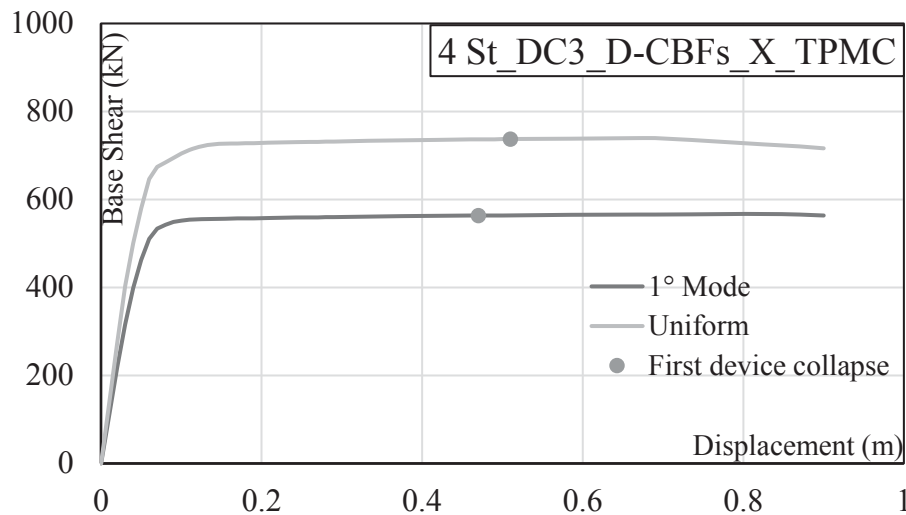


Figure 18: Push-over curves for 4 Storey D-CBFs with FREEDAM connections

In Figure 19 and Figure 21 the redundancy and the ductility of the structures are reported, respectively. It is observed that the highest values of redundancy and ductility are exhibited by the structures designed by EC8. The presence of the “haunched” connections seems to affect not too much the seismic performances of the structures while the effect of balanced panel zone is easy pointed out because of higher values of the ductility.

About global ductility (Figure 19-Figure 20), it can be noted that the MRFs\_FREEDAM and D-CBFs\_FREEDAM structures have a higher ductility if compared with structures equipped with traditional joints.

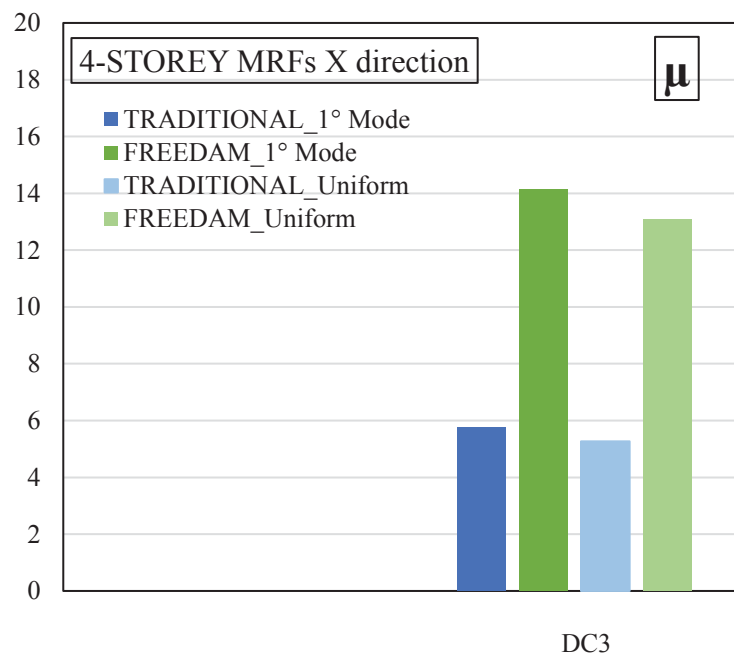


Figure 19: Ductility for MRFs with traditional and FREEDAM connections



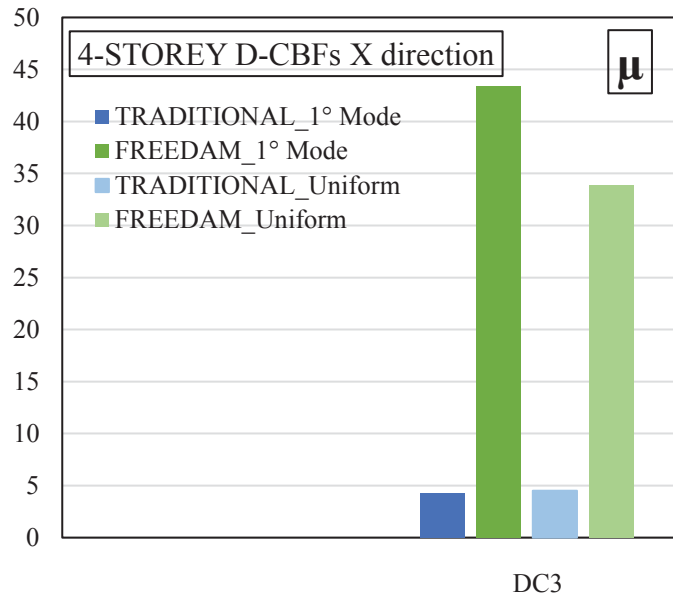


Figure 20: Ductility for D-CBFs with traditional and FREEDAM connections

About the system overstrength (Figure 21-Figure 22), it can be observed that in traditional structures it is higher than the FREEDAM ones. However, this redundancy is higher than the one suggested by the new Eurocode draft [59].

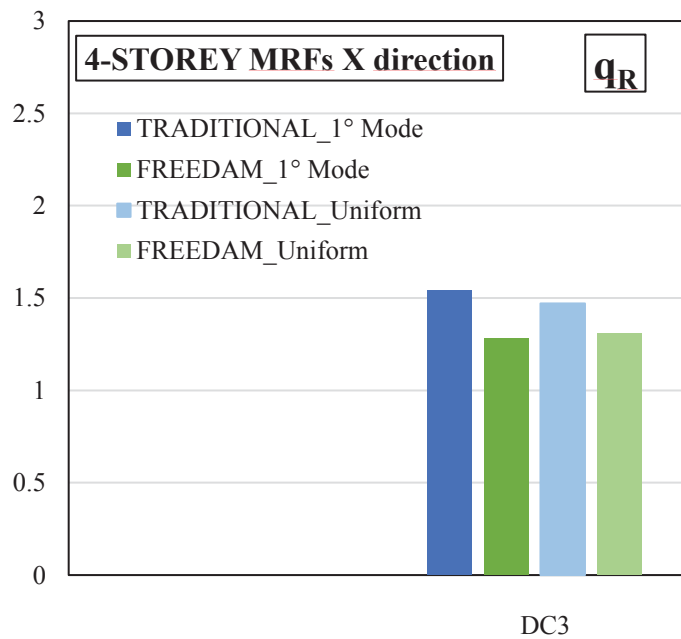


Figure 21: Redundancy for MRFs with traditional and FREEDAM connections

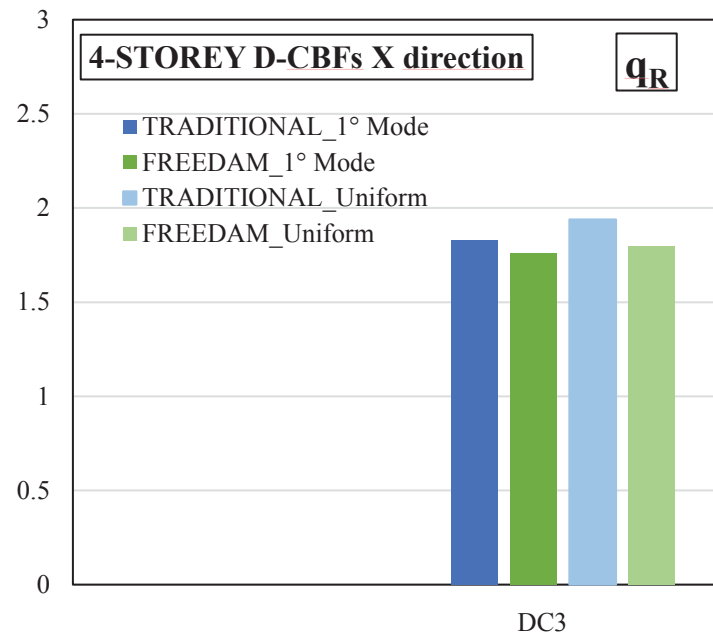


Figure 22: Redundancy for D-CBFs with traditional and FREEDAM connections

## 8 DYNAMIC NON-LINEAR ANALYSES

Non-linear Dynamic Analyses [69] are also performed to investigate the structural performance for the 3 limit states defined in EN1998-3 [67], namely damage limitation (DL), significant damage (SD) and collapse prevention (CP). EN1998-3 [67] associates a seismic intensity with each limit states and establishes performance limits related to global and local damage. The IDA analyses have been carried out for three increasing values of PGA value corresponding to the following limit state Damage limitation (DL), Severe Damage (SD) and Near Collapse (NC). The values of the multiplier of accelerograms are assumed equal to 0.59, 1 and 1.73 for DL, SD and NC [67], respectively. The non-linear dynamic analyses are carried out using the same structural model adopted for pushover analyses. Rayleigh formulation for a 5% damping has been assumed with the proportional factors computed with reference to the first and second mode of vibration. In addition, first  $T_1$  and second  $T_2$  periods of vibration are required and reported in Table 10. Record-to-record variability has been accounted for by considering 10 recorded accelerograms selected from ESM [70]. In Table 9 the analyzed records (Earthquake name, Date, Duration, Station name, Station Country, moment magnitude (MW), local magnitude (ML) and Fault mechanism) have been reported.

Station Code	Station Name	Earthquake name	Date	Network	Mw
BAR	Bar-Skupstina	NW_Balkan_Peninsula	15.04.1979	EU	6.9
CSO1	CARSOLI1	L'Aquila	06.04.2009	IT	6.1
KAL1	KAL1	Southern_Greece	13.09.1986	HI	5.9
MCT	Macerata	Central_Italy	26.10.2016	IT	5.9
MZ12	Amatrice	Central_Italy	26.10.2016	3A	5.9
MZ102	Accumoli	Central_Italy	30.10.2016	3A	6.5

Table 9: Analyzed ground motion records

These recorded accelerograms have been selected to approximately match the code elastic response spectrum [58]. In other words, the spectra of the 7 recorded accelerograms have been properly scaled to let their average value to be compatible with the design EC8 spectrum. The accelerogram multipliers are reported in the Table 11.

Scheme	TPMC	
	$T_1$ (s)	$T_2$ (s)
MRFs TRADITIONAL	1.62	0.48
MRFs FREEDAM	1.63	0.52
MRFs TRADITIONAL	0.84	0.27
MRFs FREEDAM	0.77	0.27

Table 10: First and second vibration periods

Station Code	Length (s)	Step recording (s)	Scale Factor (-)
BAR	47.83	0.01	1.11
CSO1	99.80	0.01	11.7
KAL1	30.02	0.01	1.3
MCT	96.38	0.01	5.85
MZ12	82.67	0.01	3.64
MZ102	77.15	0.01	1.04
PZI1	63.45	0.01	9.75

Table 11: Accelerogram multipliers, length and step recording

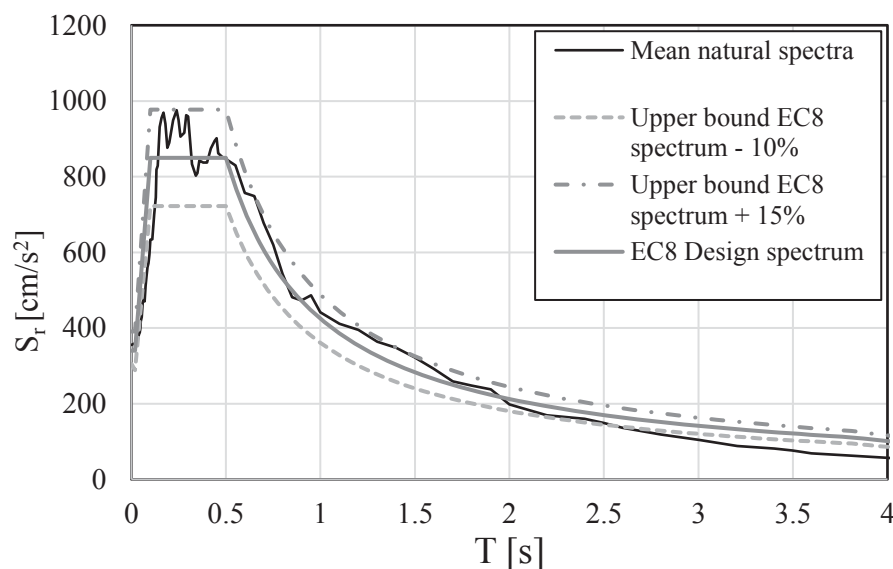
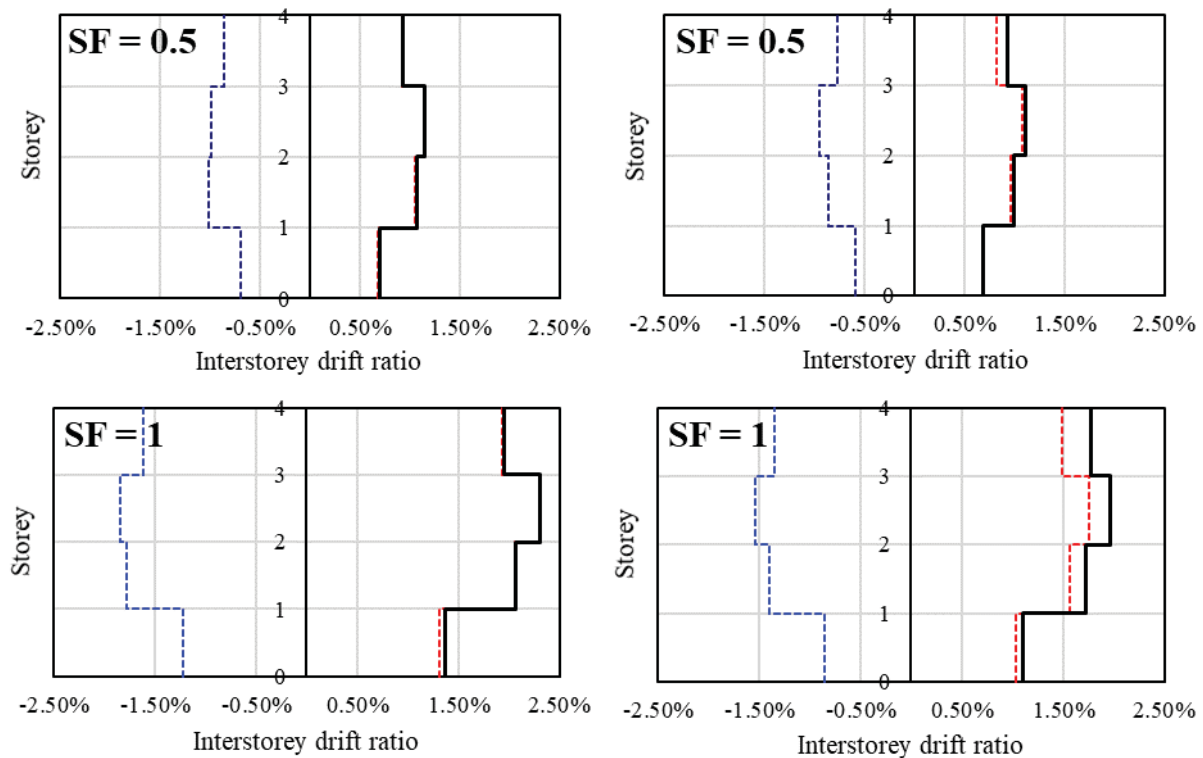


Figure 23: Comparison between natural signals average spectrum and EC8 design spectrum

From dynamic analyses it can be observed that the soft-storey mechanism does not develop, but the collapse mechanism is almost global, i.e. it develops a pattern of hinge compatible with the global mechanism.

From a comparison between the seismic performance of the structures with traditional connections and the same structures equipped with FREEDAM connections given in terms of Maximum Interstorey Drift, it is possible to observe that the structure equipped with FREEDAM connections at beam-to-column joint show, on average, better performances if compared with full strength joint ones. It is due to the high dissipative capacity of FREEDAM connections which do not present relevant degradation under cyclic loading. In addition, it is important observing that the performances of the structures equipped with FREEDAM connections can be higher if the involvement of bolt in shear is considered after the achievement of the ultimate stroke of dampers. However, the maximum stroke is never achieved even at Near Collapse limit state. The average maximum absolute peak interstorey drift of FREEDAM structures is lower than the structures with traditional full-strength joints for MRFs. In particular this happens for increasing values of PGA corresponding to the multipliers 1 and 1.5. Conversely, for the D-CBFs structures the opposite occurs, this is probably due to the insertion of the friction device at the top of chevron braces which guarantees a maximum displacement that can be reached of 14 cm. In Figure 24 and Figure 25 the comparison between MRFs and D-CBFs in terms of peak interstorey drift for each limit state is reported.



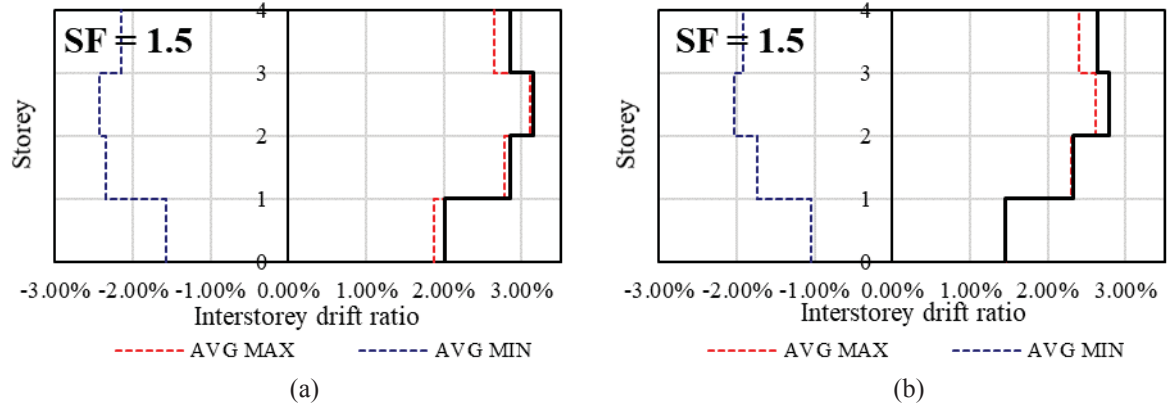


Figure 24: Peak interstorey drift curves for MRFs equipped with both traditional haunched connections and FREEDAM connections

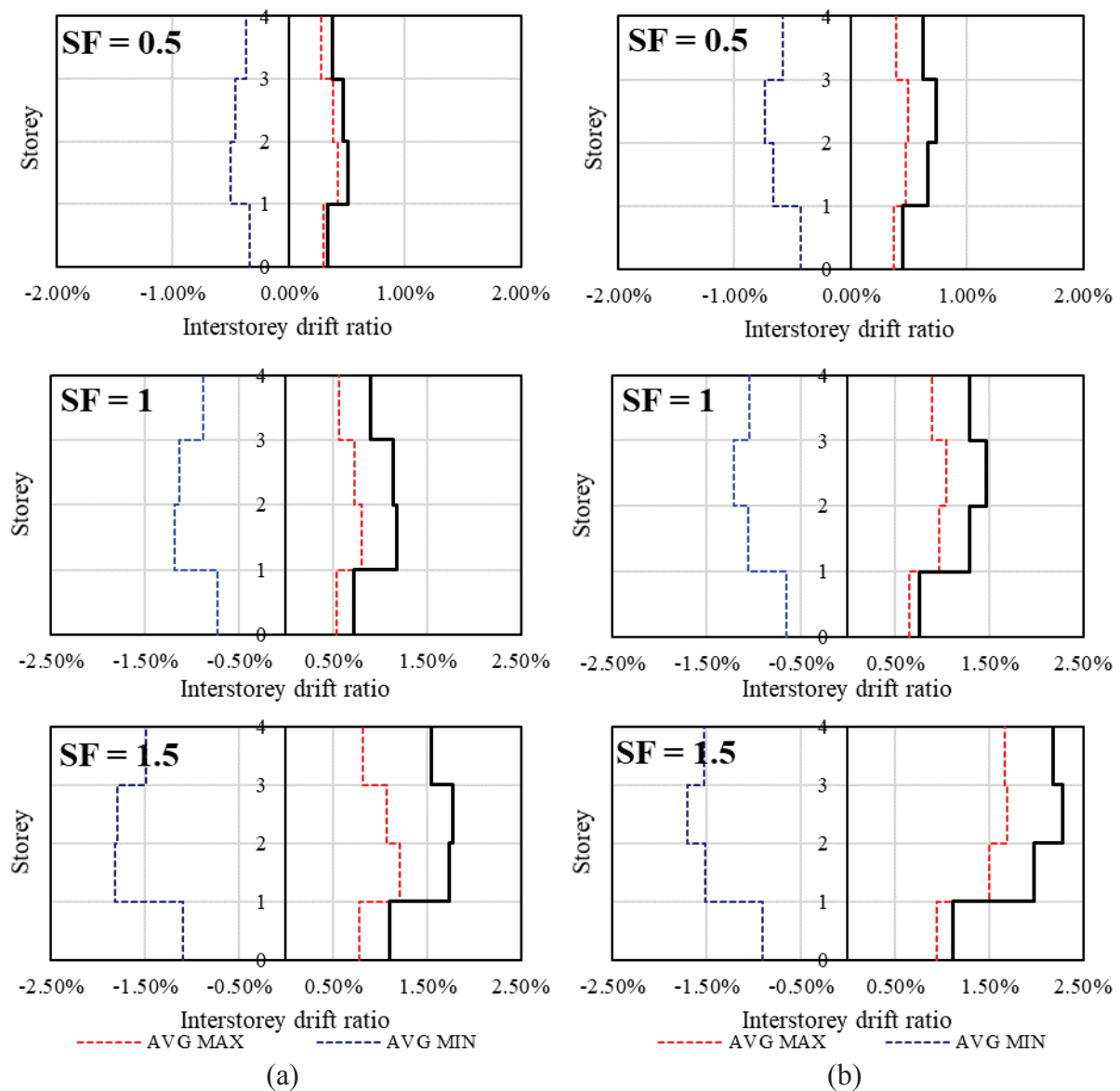


Figure 25: Peak interstorey drift curves for D-CBFs equipped with both traditional haunched connections (a) and FREEDAM connections (b)



## 9 ACKNOWLEDGEMENTS

The research leading to the results presented in this paper has received funding from the European Union's Research Fund for Coal and Steel (RFCS) research program under grant agreement n° RFCS-AM-2019-899321. The support of the European Commission within RFCS Research & Innovation is gratefully acknowledged.

## 10 CONCLUSIONS

- The work herein presented, developed in the contest of the RFCS Project FREEDAM Plus.
- Both Dual CBFs and MRFs low rise structures are designed considering traditional connections and FREEDAM connections.
- The design methodology adopted is the Theory of Plastic Mechanism Control (TPMC).
- The comparison in terms of weight among MRFs and D-CBFs equipped with haunched and FREEDAM connections shows that in both cases the use of traditional connections leads to heavier structures.
- From the pushover it is observed that the redundancy is higher for the structure with traditional connections
- Conversely, the ductility is higher for the structures equipped with FREEDAM connections.
- From the Dynamic Analysis point of view it is possible to observe that structures equipped with FREEDAM connections have better seismic performance than structures equipped with traditional connections.
- The TPMC has proved to be an excellent design tool for both traditional and FREEDAM structures assuring that columns sections are not involved in plastic range.

## REFERENCES

- [1] S. Avgerinou, X. Lignos, P. Thanopoulos, A. Spiliopoulos, I. Vayas, "Moment-resisting-frames under cyclic loading: Large scale tests and validation of plasticity and damage numerical models", *Soil Dynamics and Earthquake Engineering*, **115**, pp. 564-577, (2018).
- [2] C. Bernuzzi, D. Rodigari, M. Simoncelli, "Incremental dynamic analysis for assessing the seismic performance of moment resisting steel frames" (2020) *Ingegneria Sismica*, (4), pp. 23-44.
- [3] A. Sandoli, B. Calderoni, G. Brandonisio, Effect of panel zone on non-linear behaviour of mrfs in the light of seismic codes (2019) *Ingegneria Sismica*, 36 (4), pp. 100-119.
- [4] C. Bernuzzi, C. Chesi, D. Rodigari, R. De Col, "Remarks on the approaches for seismic design of moment-resisting steel frames", *Ingegneria Sismica*, **35** (2), pp. 37-47. (2018).
- [5] R. Montuori, E. Nastri, P. Todisco, "Influence of the seismic shear proportioning factor on steel MRFs seismic performances", *Soil Dynamics and Earthquake Engineering*, 2020, 106498, ISSN 0267-7261, <https://doi.org/10.1016/j.soildyn.2020.106498>.

- [6] V. Piluso, R. Montuori, E. Nastri, A. Paciello, “Seismic response of MRF-CBF dual systems equipped with low damage friction connections” *Journal of Constructional Steel Research*, **154**, pp. 263-277, (2019).
- [7] S. Streppone, R. Montuori, “Design and Seismic Assessment of MRFs and DUAL CBFs equipped with friction dampers”, *Compdyn 2019, 7th International Conference on Computational Methods in Structural Dynamics and Earthquake Engineering*, 24-26 June 2019.
- [8] B.V. Fell, A.T. Myers, G.G. Deierlein, and A.M. Kanvinde, A. “Testing and simulation in steel braces”, Paper presented at the 8th U.S. national conference on Earthquake Engineering, San Francisco, CA. (2006, April).
- [9] K. Ikeda, S.A. Mahin, “A refined physical theory model for predicting the seismic behaviour of braced frames” (Report UMEE 77R3). MI: Department of Civil Engineering, University of Michigan, (1984).
- [10] A.K. Jain, S.C. Goel, R.D. Hanson, “Hysteresis behaviour of bracing members and seismic response of braced frames with different proportions” (Report UMEE 78R3). Ann Arbor, MI: Department of Civil Engineering, University of Michigan, (1978).
- [11] K. Lee, M. Bruneau, “Review of energy dissipation compression members in concentrically braced frames” (Report MCEER-02-0005). Buffalo, NY: Department of Civil Engineering, The University of Buffalo. (2002).
- [12] R. Sabelli, S. Mahin, C. Chang, “Seismic demands on steel braced frame buildings with buckling-restrained braces”, *Engineering Structures*, **25**, 655–666. (2003).
- [13] X. Tang, S.C. Goel, “Brace fractures and analysis of phase I structure” *ASCE Journal of Structural Engineering*, **102**, 1960–1976. (1989).
- [14] R. Tremblay, “Inelastic seismic response of steel bracing members”, *Journal of Constructional Steel Research*, **58**, 665–701. (2002).
- [15] L. Fiorino, V. Macillo, R. Landolfo, “Shake table tests of a full-scale two-story sheathing-braced cold-formed steel building” *Engineering Structures*, **151**, pp. 633–647, (2017).
- [16] L. Fiorino, M.T. Terracciano, R. Landolfo, “Experimental investigation of seismic behaviour of low dissipative CFS strap-braced stud walls” *Journal of Constructional Steel Research*, Vol. **127**, pp. 92-107, (2016).
- [17] V. Macillo, L. Fiorino, R. Landolfo, “Seismic response of CFS shear walls sheathed with nailed gypsum panels: Experimental tests” *Thin-Walled Structures*, Vol. **120**, pp. 161-171, (2017).
- [18] S. Shakeel, L. Fiorino, R. Landolfo, Behavior factor evaluation of CFS wood sheathed shear walls according to FEMA P695 for Eurocodes. *Engineering Structures*, 2020, 221, 111042
- [19] L. Fiorino, S. Shakeel, R. Landolfo, Seismic behaviour of a bracing system for LWS suspended ceilings: Preliminary experimental evaluation through cyclic tests. *Thin-Walled Structures*, 2020, 155, 106956
- [20] A. Campiche, L. Fiorino, R. Landolfo, Numerical modelling of CFS two-storey sheathing-braced building under shaking-table excitations. *Journal of Constructional Steel Research*, 2020, 170, 106110

- [21] A. Campiche, Numerical modelling of cfs three-story strap-braced building under shaking-table excitations. *Materials*, 2021, 14(1), pp. 1–13, 118
- [22] V. Macillo, O. Iuorio, M.T. Terracciano, L. Fiorino, R. Landolfo, “Seismic response of Cfs strap-braced stud walls: Theoretical study” *Thin-Walled Structures*, Vol. **85**, pp. 301-312, (2014).
- [23] M.T. Giugliano, A. Longo, R. Montuori, V. Piluso, “Influence of homoschedasticity hypothesis of structural response parameters on seismic reliability of CB-frames” *Georisk*, **5** (2), pp. 120-131, (2011).
- [24] R. Tartaglia, M. D’Aniello, G.A. Rassati, (2019). Proposal of AISC-compliant seismic design criteria for ductile partially-restrained end-plate bolted joints. *Journal of Constructional Steel Research* Volume 159, August 2019, Pages 364-383
- [25] R. Tartaglia, M. D’Aniello, M. Zimbru, R. Landolfo, (2018). Finite element simulations on the ultimate response of extended stiffened end-plate joints. *Steel and Composite Structures*, An International Journal Vol. 27 No. 6, June25 2018. pages 727-745. DOI: 10.12989/scs.2018.27.6.727
- [26] R. Tartaglia, M. D’Aniello, R. Landolfo, (2018). The influence of rib stiffeners on the response of extended end-plate joints. *Journal of Constructional Steel Research* 148 (2018) 669–690.
- [27] M. D’Aniello, R. Tartaglia, D. Cassiano, (2020) Experimental Investigation of The Inelastic Tensile Behaviour of Non-Preloadable Grade 8.8 Bolts. *Ingegneria Sismica: International Journal of Earthquake Engineering*, Volume 37, Issue 2, 2020, Pages 92-110
- [28] R. Tartaglia, M. D’Aniello, M. Zimbru, (2020). Experimental and numerical study on the T-Stub behaviour with preloaded bolts under large Deformations. *Structures* Volume 27, October 2020, Pages 2137-2155 <https://doi.org/10.1016/j.istruc.2020.08.039>
- [29] M. Pongiglione, C. Calderini, M. D’Aniello, R. Landolfo, “Novel Reversible Seismic-Resistant Joint for Sustainable and Deconstructable Steel Structures” (2021) *Journal of Building Engineering*, **35**, 101989, <https://doi.org/10.1016/j.jobbe.2020.101989>
- [30] R. Tartaglia, M. D’Aniello, R. Landolfo, (2020). Numerical Simulations to Predict the Seismic Performance of a 2-Story Steel Moment-Resisting Frame. *Materials* 2020, 13(21), 4831; doi:10.3390/ma13214831
- [31] UNI EN 1993-1: “Eurocode 3: Design of steel constructions”. CEN, 2005.
- [32] UNI EN 1998-1: “Eurocode 8: Design of structures for earthquake resistance-Part 1: General rules, seismic sections and rules for buildings”. CEN, 2004.
- [33] K. Weynand, M. Huter, P. Kirby, L. Simões da Silva, P. Cruz: “SERICON – A Data-bank for tests on semi-rigid joints”. In Proc. of the COST C1 Inter. Conf. on Control of the Semi-Rigid Behaviour of Civil Engineering Structural Connections, pp. 217-228, Liège, Belgium (1998).
- [34] RFCS research project European pre-qualified steel joints (EQUALJOINTS - RFSR-CT-2013-00021), 2013.07.1-2016.06.31.
- [35] RFCS-2016 Valorisation of knowledge for European pre-qualified steel JOINTS (EQUALJOINTS-PLUS - RFSR-AM-02-2016-754048).

- [36] G. D. Porta, I. Russo, E. Nistri, "Preliminary comparison on MRFs and dual systems equipped with extended stiffened connections" (2019) *AIP Conference Proceedings*, **2116**, art. no. 260023.
- [37] E. Nistri, P. Tsarpalis, "Seismic analyses of dual concentrically braced frames accounting for the presence of haunched connections" (2019) *COMPDYN Proceedings*, **1**, pp. 73-95.
- [38] A. Catapano, E. Nistri, S. Streppone, "Design and analysis of dual EBFs equipped with prequalified connections" (2019) *COMPDYN Proceedings*, **1**, pp. 96-130.
- [39] RFCS-2015 FREEDAM Project, (RFSR-CT-2015-00022)
- [40] F.M. Mazzolani, V. Piluso, "Theory and Design of Seismic Resistant Steel Frames". E&FN Spon, E&FN Spon, an Imprint of Chapman & Hall, 1996.
- [41] F.M. Mazzolani, "Moment Resistant Connections of Steel Frames in Seismic Areas, Design and Reliability". E&FN Spoon, 2000.
- [42] V. Piluso, E. Nistri, R. Montuori, "Advances in Theory of Plastic Mechanism Control: Closed Form Solution for MR-Frames", *Earthquake Engineering and Structural Dynamics*, **44**, Issue 7, pp.1035-1054, (2015).
- [43] R. Montuori, E. Nistri, V. Piluso, P. Todisco, "A simplified performance based approach for the evaluation of seismic performances of steel frames", (2020) *Engineering Structures*, **224**, art. no. 111222,.
- [44] R. Montuori, E. Nistri, V. Piluso, P. Todisco, "Evaluation of the seismic capacity of existing moment resisting frames by a simplified approach: Examples and numerical application" (2021) *Applied Sciences (Switzerland)*, **11**(6), art. no. 2594.
- [45] R. Montuori, R. Muscatia, "Plastic design of seismic resistant reinforced concrete frame" *Earthquake and Structures*, **8** (1), pp. 205-224, (2015).
- [46] G. Dell'Aglia, R. Montuori, E. Nistri, V. Piluso, "A critical review of plastic design approaches for failure mode control of steel moment resisting frames" *Ingegneria Sismica*, **34** (4), pp. 82-102, (2017).
- [47] R. Montuori, E. Nistri, V. Piluso, M. Troisi, "Influence of connection typology on seismic response of MR-Frames with and without 'set-backs'" *Earthquake Engineering and Structural Dynamics*, **46** (1), pp. 5-25, (2017).
- [48] R. Montuori, V. Sagarese, "The use of steel rbs to increase ductility of wooden beams" *Engineering Structures*, **169**, pp. 154-161, (2018).
- [49] V. Piluso, A. Pisapia, P. Castaldo, E. Nistri, "Probabilistic Theory of Plastic Mechanism Control for Steel Moment Resisting Frames" *Structural Safety*, **76**, pp. 95-107(2019).
- [50] RFCS-2020 Valorisation of knowledge for FREE from DAMage steel connections (FREEDAM PLUS - RFSR-AM-02-2019-899321).
- [51] K. Lee, C. Vulcu "Numerical investigation on seismic behaviors of steel haunch connections". Study Program: SUSCOS\_M, Universitatea Politehnica Timișoara, Romania. 2015/2016

- [52] F. Di Lauro, R. Montuori, E. Nastri, V. Piluso, “Partial safety factors and overstrength coefficient evaluation for the design of connections equipped with friction dampers” (2019) *Engineering Structures*, **178**, pp. 645-655.
- [53] A. Longo, R. Montuori, V. Piluso, “Moment frames – concentrically braced frames dual systems: analysis of different design criteria” *Structure and Infrastructure Engineering*, **12** (1), pp. 122-141, (2016).
- [54] A. Longo, R. Montuori, V. Piluso, “Seismic design of chevron braces cupled with MRF fail safe systems” *Earthquake and Structures*, **8** (5), pp. 1215-1239, (2015).
- [55] A. Longo, R. Montuori, V. Piluso, “Theory of plastic mechanism control for MRF–CBF dual systems and its validation” *Bulletin of Earthquake Engineering*, **12** (6), pp. 2745-2775, (2014).
- [56] A. Longo, R. Montuori, E. Nastri, V. Piluso, “On the use of HSS in seismic-resistant structures”, *Journal of Constructional Steel Research*, **103**, pp. 1-12, (2014).
- [57] R. Tartaglia, M. D'Aniello, G. Di Lorenzo, A. De Martino, “Influence of EC8 rules on P-delta effects on the design and response of steel MRF” (2018) *Ingegneria Sismica*, **35** (3), pp. 104-120.
- [58] CEN, Eurocode 8, draft. "Design of structures for earthquake resistance - Part 1-1: General rules and seismic action", 2020a.
- [59] CEN, Eurocode 8 draft: "Design of structures for earthquake resistance - Part 1-2: Rules for new buildings", 2020.
- [60] CSI 2007. SAP 2000, "Integrated Finite Element Analysis and Design of Structures. Analysis Reference.," Computer and Structure Inc. University of California, Bekerley.
- [61] M. D’Aniello, G. La Manna Ambrosino, F. Portioli, R. Landolfo, “Modelling aspects of the seismic response of steel concentric braced frames” *Steel and Composite Structures, An International Journal*, **15**(5), pp. 539-566, (2013).
- [62] S. Costanzo, M. D'Aniello, R. Landolfo, “The influence of moment resisting beam-to-column connections on seismic behavior of chevron concentrically braced frames”, *Soil Dynamics and Earthquake Engineering*, **113**, pp. 136-147, (2018).
- [63] S. Costanzo, M. D'Aniello, R. Landolfo, “Seismic design criteria for chevron CBFs: Proposals for the next EC8 (part-2)” *Journal of Constructional Steel Research*, **138**, pp. 17-37, (2017).
- [64] S. Costanzo, M. D’Aniello, R. Landolfo, “Seismic design criteria for Chevron CBFs: European vs North American codes (Part-1)” *Journal of Constructional Steel Research*, **135**, pp. 83-96, (2017).
- [65] S. Costanzo, M. D'Aniello, R. Landolfo, “Critical review of seismic design criteria for chevron concentrically braced frames: The role of the brace-intercepted beam” *Ingegneria Sismica*, **33** (1-2), pp. 72-89, (2016).
- [66] S. Costanzo, M. D'Aniello, R. Landolfo, “The influence of beam stiffness on seismic response of chevron concentric bracings” *Journal of Constructional Steel Research*, **112**, pp. 305-324, (2015).
- [67] UNI EN 1998-3: “Eurocode 8: Design of Structures for Earthquake Resistance-Part 3: Evaluation and adaptation of buildings”, CEN, 2004.



- [68] D. Georgescu “Earthquake-Recent developments in theoretical and experimental results in steel structures”, Seismic resistant braced frames, 1996.
- [69] D. Vamvatsikos, C.A. Cornell, “Incremental dynamic analyses”. Earthquake Engineering and Structural Dynamics, 2002.
- [70] L. Luzi, R. Puglia, E. Russo & ORFEUS WG5 (2016). Engineering Strong Motion database (ESM), version 1.0. Istituto Nazionale di Geofisica e Vulcanologia. Observatories & Research Facilities for European Seismology. doi: 10.13127/ESM, FEMA-355F: “State of Art Report on Performance Prediction and Evaluation of Steel Moment-Frame Buildings”. Federal Emergency Management Agency/September, 2000, 4 – 25-30.

## COMPONENT MODELLING OF CONNECTIONS BETWEEN CIRCULAR-HOLLOW-SECTIONS AND THROUGH-ALL MEMBERS

A. Saldutti<sup>1</sup>, S. Di Benedetto<sup>2</sup>, M. Latour<sup>3</sup>, G. Rizzano<sup>4</sup>

<sup>1</sup> Master Student, <sup>2</sup> PhD Student, <sup>3</sup> Professor, <sup>4</sup> Professor  
University of Salerno, Italy  
a.saldutti3@studenti.unisa.it, sdibenedetto@unisa.it, mlatour@unisa.it, g.rizzano@unisa.it

---

### Abstract

*The recent use of the 3D Laser Cutting Technology in the field of civil engineering has led to the development of novel typologies of steel beam-to-column connections made by welding circular hollow section columns (CHS) to through-all members. The main feature of these joints is that they are able to provide higher flexural strength, stiffness and energy dissipation capacity compared to the corresponding joints with elements simply welded to the external surface of the hollow section. Currently, there are no codified rules for such a type of structural details and, consequently, the design of these joints implies the development of complex FE models. Aiming at filling the knowledge gap regarding the structural flexural behaviour of CHS through I-beam joints, a research activity is currently ongoing at the STRENGTH laboratory of the University of Salerno with the objective to provide simple analytical tools for the design and modelling of such connections through the component method, both under monotonic and cyclic loading conditions.*

*This paper deals with the preliminary study of the behaviour of one of the elementary components characterising the response of beam-to-column joints composed by CHS columns and I-beams, which is the "plate transversally welded to the column in tension/compression". This component is meant to model the local behaviour exhibited by the CHS tube at the upper/lower beam flange level. This component is very important because it governs the deformability of the connection and may limit the resistance of the joint due to the local failure of the CHS tube. In the performed work, monotonic and cyclic tests on specimens representative of realistic geometric configurations of beam-to-column joints have been carried out. Subsequently, a finite element (FE) model, representative of the analysed connection, has been developed and validated against the experimental results.*

**Keywords:** component method, laser cutting technology (LCT), experimental activity, FEM.

---

## 1 INTRODUCTION

In the last decades, the 3D-Laser Cutting Technology (3D-LCT) has proved to be very useful in many applicative fields since it allows to manufacture a mass production with high accuracy. The only exception regards the field of civil engineering because of the relevant cost of large-scale structural components. Nevertheless, the 3D-LCT is a good solution when very complex geometrical components have to be manufactured; an example of such a case is represented by steel beam-to-column connections between circular hollow section (CHS) columns and double-tee beams. In fact, until now, except for the study of the behaviour of tubular profiles ([1]-[4]), some different solutions for coupling the aforementioned profiles have been conceived: i) the beam is simply welded to the external surface of the column [5]; ii) plates, welded to the flanges of the double-tee profile, intersect the column [6]; iii) the beam is welded to collar plates externally welded or bolted to the column [7]; iv) the connection is filled with concrete, while the beam is welded to the external surface of the column [8]. The first solution is very easy to manufacture, but the obtained connection provides low stiffness and resistance such that it can be adopted only in the case of pinned or semi-continuous frames [9]. The second and the third solution, instead, are good alternatives but the need of conceiving complex special elements [10] represents a relevant drawback. The fourth approach, instead, induces the slowdown of the construction process due to the pouring of concrete on-site [11].

The briefly above summarised existing solutions well clarify the possibilities offered by the beam-to-column connection between CHS columns and through-all beams obtained by adopting the 3D-LCT. In fact, the cut of the tubular profile according to the shape of the double-tee section guarantees the beam to cross the CHS before welding both the members, increasing, in such a way, both the stiffness and the resistance of the joint without appealing to additional plates or concrete. Because of these benefits, a relevant interest in the technological aspects [10] and mechanical behaviour exhibited by the aforementioned beam-to-column connection recently arose. In particular, at the University of Salerno, experimental, numerical and theoretical activities have been carried out in order to study the resistance and the stiffness of the analysed joint. As results of the first step of the study, formulations to predict the flexural strength and initial stiffness of CHS columns to through-all I-beam connections have been proposed ([12]-[14]). These equations have been analytically derived starting from the behaviour of the easiest components in which the connection could be simplistically divided: the hollow section subjected to the transverse tension/compression of the flanges of the double-tee profile and the beam web and column under shear actions. Because of the complexity of the obtained theoretical formulations, it has been necessary to derive simplified equations whose coefficients have been calibrated against the overall response of the numerically simulated connections. Basing on such statements, it is clear that, even though the proposed equations allow to have a reliable prediction of the flexural strength and initial stiffness of the studied connection nevertheless, they do not allow to really account for the local behaviour of the single nodal components. This is the reason why one of the steps of the research activity consists of studying singularly all the components of the CHS to through-all double-tee connections aiming at assembling all the components to foresee the behaviour of the whole joint.

Within this framework, this paper deals with the study of the component consisting of the "plate transversally welded to the column in tension/compression". Such a topic is not a novelty since Voth [15] has already investigated it, also proposing a formulation for the strength prediction. Nevertheless, his approach consisted of calibration against experimental and numerical results of regression coefficients of an existing formula ([16], [17]) for tubes with

plates externally welded to the column, without adapting the theoretical approach to the specificities exhibited by the connection with through plate.

The present study is a preliminary work for characterizing the behaviour of the nodal component between CHS profiles and through-all plates under tension/compression forces and it is composed of experimental and numerical activities. The experimental campaign consisted of performing three monotonic and three cyclic tests on CHS to through-all plates specimens differing for the geometric properties of the connected elements. Afterwards, numerical models of the tested specimens have been modelled thanks to finite element software and have been validated against the experimental results. As future developments, the validated numerical models will be exploited to perform parametric analyses to investigate a wide range of geometrical properties of the studied CHS to through-all plate connections, aiming at proposing design equations meant to predict the strength and stiffness of the analysed component.

## 2 EXPERIMENTAL ACTIVITY

Aiming at studying the component highlighted in the introduction, three monotonic and three cyclic tests have been performed on specimens having as members circular hollow section profiles and through-all plates (Figure 1).

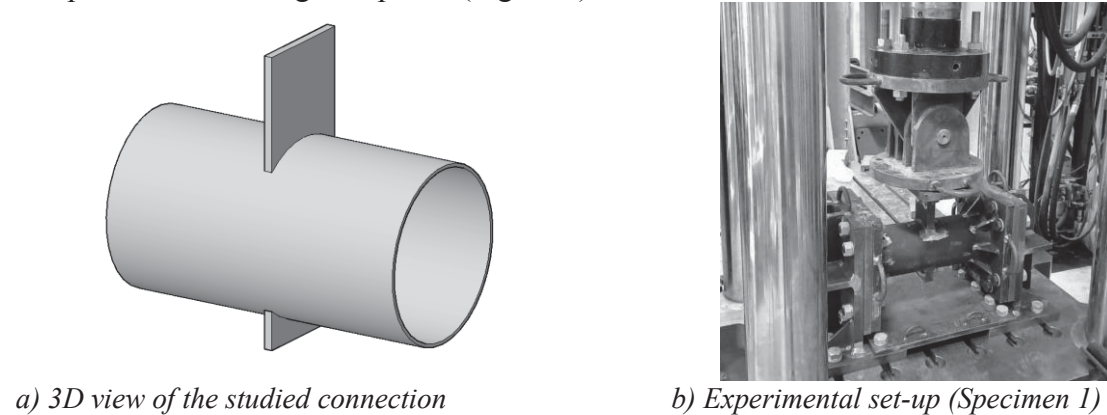


Figure 1: Analysed connection and experimental set-up

The examined specimens differ for the geometric properties of the connected profiles: the first connection is characterised by a tubular member with a diameter equal to 168 mm, thickness 6 mm, length 450 mm and by a 100 mm width, 30 mm thick and 350 mm length through-all plate; the second specimen is characterised by a CHS with a diameter equal to 219.1 mm, thickness 5 mm, length 500 mm and by a through-all plate with a width of 150 mm, the thickness of 20 mm and length of 350 mm; the third specimen has a tubular member with a diameter equal to 273 mm, thickness 6 mm, length 500 mm and a 160 mm width, 20 mm thick through-all plate with length equal to 400 mm. The plates have been properly selected in order to be ideally representative of the flanges of double-tee profiles (IPE200, IPE300 and IPE330 for the three specimens, respectively) of a CHS to through-all -beam connection.

In order to ensure the plates could pass through the CHSs, the tubular members have been cut with a tolerance of 2 mm around the imprint of the shape of the plates, while the welds consist of single-sided full-penetration butt welds chamfered with an angle equal to 30° adopting the Metal Inert Gas (MIG) welding technique, as suggested by EN 4063-131 provision [18].

The basic material properties of the steel members, characterised by a S275JR steel grade, have been defined by tension coupon tests obtained by the base metal of the specimens.

The testing rig has been conceived in such a way to apply the force at the upper end of the plate employing a vertical actuator (load capacity of 2000 kN in tension and 3000 kN in compression) which is fixed to a rigid steel reaction frame constrained at its base to the strong laboratory floor.

In the test layout, the CHS has been placed horizontally, and its ends have been restrained thanks to steel supports conceived to fix all the degrees of freedom and bolted to the rigid floor of the ITALSIGMA machine (Figure 1). The monotonic and cyclic tests consisted of applying displacements at a rate of 0.5 mm/min until 10 mm displacement, 1 mm/min between a displacement of 10 mm and 20 mm, and 2 mm/min for displacements higher than 20 mm. The specimens have been equipped with 5 LVDTs to monitor not only the vertical displacements but also the horizontal displacements of the supports in order to prove they behave as fixed supports.

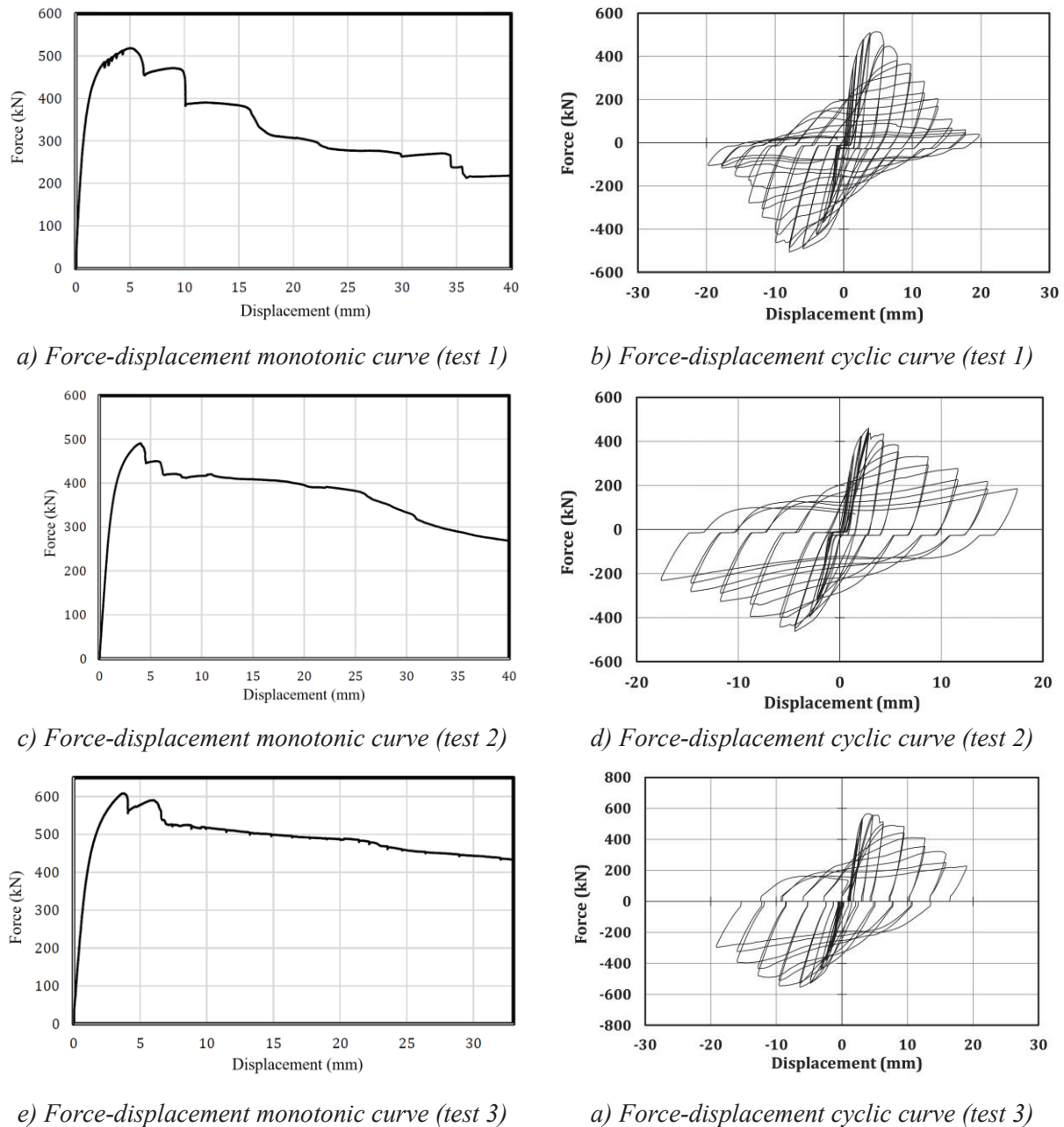


Figure 2: Experimental tests



In Figure 2 the force-displacement curves of the specimens are presented. The maximum forces withstood by the monotonically loaded connections are equal to 518 kN, 491 kN and 608 kN, respectively, for the three specimens, and in all the cases, the maximum strength capacity has been achieved for displacements lower than 5 mm. Instead, the maximum strength experienced by the connections subjected to the cyclic histories are equal to 521 kN, 466 kN and 570 kN, respectively, for the three specimens.

All the specimens collapsed because of the transverse crushing of the tube consistently with the deformed configuration analysed by [12].

### 3 NUMERICAL ACTIVITY

This paragraph is devoted to validating the numerical models of the tested specimens thanks to the finite element (FE) software Abaqus [19].

The geometric characteristics of the specimens have been properly modelled, except for the welds, which have been substituted by Tie contacts between the plate and the tubular profile. Instead, the definition of the mechanical properties has been based on the tension coupon tests; for the sake of clarity, the stress-strain laws have been modelled according to the quadri-linear relationship proposed by Faella [20] with Young's modulus of 210000 MPa and a Poisson's ratio equal to 0.30.

In the FE software, the specimens have been modelled together with the rigid floor of the testing rig and the fixed supports, as given in Figure 3a.

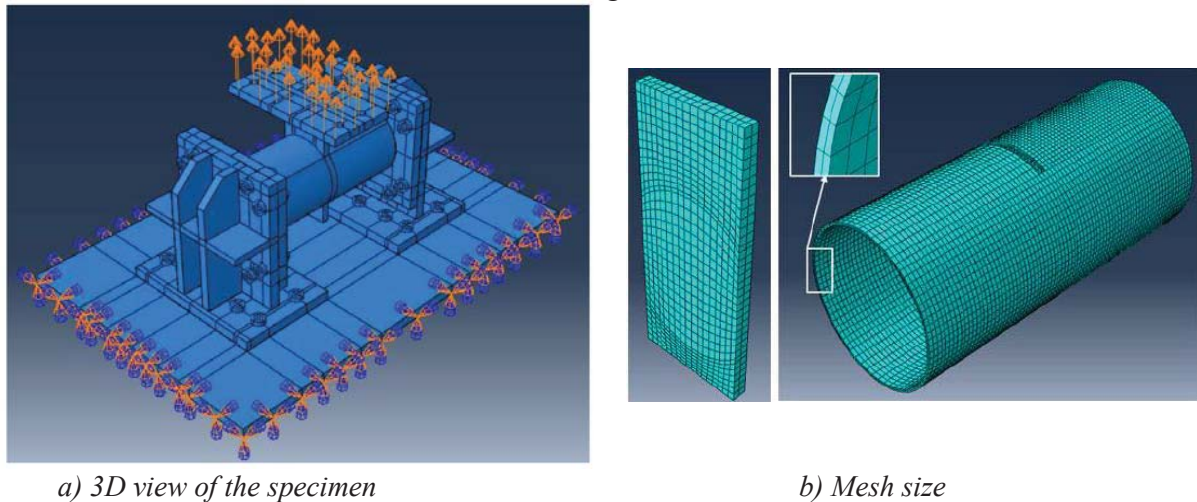


Figure 3: FE model

"Hard" contacts for normal behaviour and frictionless contacts for the tangential behaviour have been applied among the bolts and the plates to which they are connected with; Tie contacts have been employed to model not only the welds between the through-plate and the CHS profile, but also the welds among the plates of the fixed supports. In order to account for the damage evolution, in the numerical model, an equivalent plastic displacement at fracture equal to 4.8 mm has been considered according to the suggestions of [21], [22].

C3D8-type (8-node linear brick) elements with a size equal to 5 mm have been used to mesh the members (Figure 3b).

Referring to Eurocode 3 part 1.5 [23] and according to the construction tolerances provided by EN10034 [24], the imperfection related to the beam-plate attachment, which promotes the local buckling of the tubular profile, has been embedded in the numerical model.

The numerical model has been validated against the experimental results by loading the end of the plate with the same monotonic displacement histories to which the real-scale spec-

imens were subjected. At the end of the simulations, carried out by adopting a static solver, it has been possible to observe the consistency of the failure modes exhibited by the FE models with the experimental observations and also the good prediction of the force-displacement curves, as shown in Figure 4.

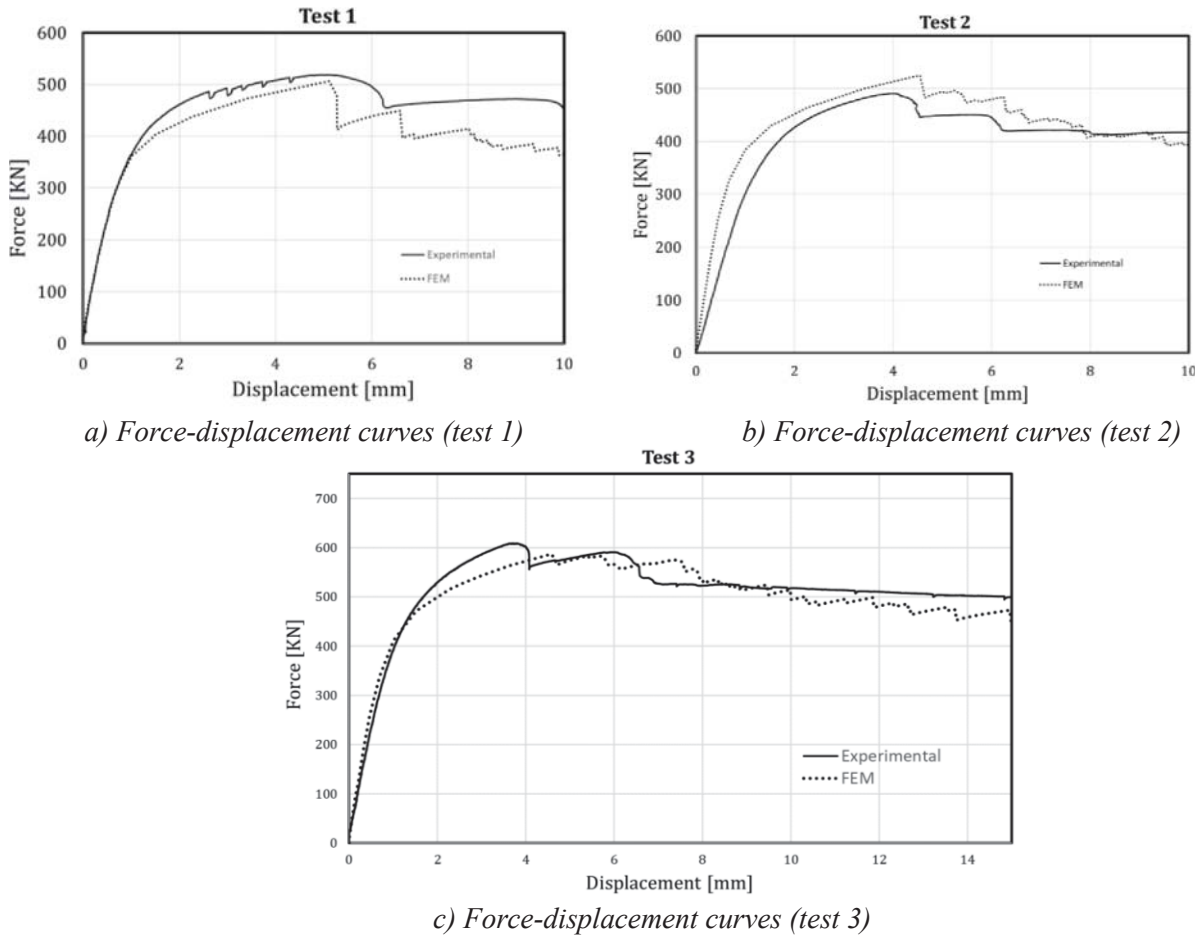


Figure 4: Experimental versus FE results

## 4 CONCLUSIONS

The present work is devoted to studying one of the components of CHS to through-all I-beam connections; in fact, the attention has been focused on the analysis of the plate transversally welded to the circular tubular profile in tension/compression since this component is supposed to behave as the flanges of the double-tee beam welded to the CHS member.

The research efforts consisted in performing experimental tests and numerical simulations. The main conclusions are:

1. the experimental activity has shown that the developed collapse mechanism exhibited by the analysed component is consistent with the supposed theoretical mechanism proposed by [12];
2. a numerical model of the tested specimens has been validated against the experimental results.

Starting from the validated numerical model, the future research efforts will be devoted to the study of a wider range of CHS to through-all plate connections characterized by different geometrical properties. The ultimate aim of the present research activity is to propose design formulations able to foresee the strength and stiffness of the analysed component.

## ACKNOWLEDGEMENTS

The authors want to express their gratitude to Dr. Eng. Francesco Perri and Eng. Ciro Esposito for the help provided during the experimental activity.

## REFERENCES

- [1] M. D'Aniello, E.M. Güneyisi, R. Landolfo, K. Mermerdaş, Predictive models of the flexural overstrength factor for steel thin-walled circular hollow section beams. *Thin-Walled Structures*, 94:67-78. 10.1016/j.tws.2015.03.020, 2015.
- [2] A. Poursadrollah, M. D'Aniello, R. Landolfo, A. De Martino, PRELIMINARY STUDY ON THE SEISMIC PERFORMANCE OF HYBRID STEEL STRUCTURES WITH TRUSS LIGHTWEIGHT GIRDERS AND PLUG-AND-PLAY CONNECTIONS. *Ingegneria Sismica: International Journal of Earthquake Engineering*, Volume 37, Issue 1, 2020, Pages 103-113, 2020.
- [3] M. Pongiglione, C. Calderini, M. D'Aniello, R. Landolfo, NOVEL REVERSIBLE SEISMIC-RESISTANT JOINT FOR SUSTAINABLE AND DECONSTRUCTABLE STEEL STRUCTURES, *Journal of Building Engineering*, 35, 101989 <https://doi.org/10.1016/j.jobbe.2020.101989>, 2021.
- [4] L.S. da Silva, L.C. Silva, T. Tankova, H.D. Craveiro, R. Simões, R. Costa, M. D'Aniello, R. Landolfo, Performance of modular hybrid cold-formed/tubular structural system. *Structures*, Volume 30, Pages 1006-1019. <https://doi.org/10.1016/j.istruc.2021.01.066>, 2021.
- [5] EN 1993-1-8, Eurocode 3: Design of Steel Structures. Part 1-8: Design of Joints. CEN, European Committee for Standardization, 2005.
- [6] AIJ, Recommendations for the design and fabrication of tubular truss structures in steel. *Architectural Institute of Japan*, 2002.
- [7] Y. Sawada, S. Idogaki, K. Skeia, Static and fatigue tests on T-joints stiffened by an internal ring. *Proceedings of the Offshore Technology Conference OTC 3422*, Houston, USA, 1979.
- [8] X.L. Zhao, J.A. Packer, Tests and design of concrete-filled elliptical hollow section stub columns. *Thin-Walled Structures*, Vol. 47, Np. 6/7, pp. 617-628, 2009.
- [9] A. Voth, J.A. Packer, Branch Plate-to-Circular Hollow Structural Section Connections. I: Experimental Investigation and Finite-Element Modelling. *Journal of Structural Engineering*, ASCE, 2012.
- [10] A. Kanyilmaz, C. Castiglioni, G. Brambilla, K. Gjoka, A. Galazzi, S. Raso, A. Valli, M. Brugnolli, R. Hojda, Experimental assessment of tolerances for the fabrication of laser-cut steel joints. *ce/papers*. 1. 776-785. 10.1002/cepa.117, 2017.
- [11] A. Voth, Branch Plate-to-Circular Hollow Structural Section Connections. *Ph. D. Thesis*, Toronto, 2010.
- [12] S. Di Benedetto, M. Latour, G. Rizzano, Chord failure resistance of 3D cut welded connections with CHS columns and through I-BEAMS. *Thin Walled Struct.* 2020, 154, 106821, doi:10.1016/j.tws.2020.106821.

- [13] S. Di Benedetto, M. Latour, G. Rizzano, Assessment of the stiffness of 3D cut welded connections with CHS columns and through I-BEAMS. *Structures* 2020, 27, 247–258, doi:10.1016/j.istruc.2020.05.043.
- [14] S. Di Benedetto, M. Latour, G. Rizzano, Stiffness Prediction of Connections between CHS Tubes and Externally Welded I-Beams: FE Analyses and Analytical Study. *Materials* 13, 2020, no. 13: 3030. <https://doi.org/10.3390/ma13133030>.
- [15] A. Voth, J.A. Packer, Circular Hollow Through Plate Connections. *Steel Construction* (9), 2016.
- [16] T. Togo, Experimental study on mechanical behavior of tubular joints. *D. Eng. Thesis*, Osaka University, Osaka, Japan, 1967.
- [17] J. Wardenier, J.A. Packer, X.L. Zhao, G.J. van der Vegte, Hollow section in structural applications, 2nd Edition. *CIDECT and Bowen met Staal*, Rotterdam, The Netherlands, 2010.
- [18] EN 4063, Welding and allied processes - Nomenclature of processes and reference numbers, 2011.
- [19] Abaqus, Analysis user's manual version 6.17, *Abaqus Inc*, 2017.
- [20] C. Faella, V. Piluso, G. Rizzano, Structural Steel Semirigid Connections. *CRC Press*, Boca Raton, FL, 2000.
- [21] M. Pavlovic, Z. Markovic, M. Veljkovic, D. Budevack, Bolted shear connectors vs. headed studs behaviour in push-out tests. *J. Constr. Steel Res.*, 88:134-149, 2013.
- [22] A.C. Faralli, Large deformation of T-stub connection in bolted steel joints. *Ph. D. Thesis*, University College of London, 2019.
- [23] EN 1993-1-5, Eurocode 3: Design of steel structures. Part 1-5: Piling. *CEN European Committee for Standardization*, 2006.
- [24] EN 10034, Structural Steel I and H sections. Tolerances on shape and dimensions, 1995.

## SEISMIC RESPONSE OF INNOVATIVE CFS WALLS BRACED WITH UHS STEEL BARS: EXPERIMENTAL INVESTIGATION

Alessia Campiche<sup>1</sup>

<sup>1</sup> Department of Structures for Engineering and Architecture, University of Naples “Federico II”, Italy

e-mail: alessia.campiche@unina.it

---

### Abstract

*Advantages of Cold Formed Steel (CFS) structures are now well known all over the world. The new goal is represented by the improvement of structural performances, in order to build higher and safer constructions in seismic area. To this aim, in the framework of an Italian project in cooperation with Lamieredil S.p.A. company, the University of Naples “Federico II” developed a new Lateral Force Resisting System (LFRS), made of CFS frame braced by Ultra High Strength (UHS) steel bars in “V” configuration. Three different configurations of the LFRS, with increasing lateral capacities, were designed, and tested under monotonic and reversed cyclic load protocols at the Lab of the Department of Structures for Engineering and Architecture. In total, five tests on full scale 2400x2800 mm<sub>2</sub> (length x height) were carried out. The paper provides all the details on the full-scale wall tests and discusses the obtained results. Moreover, a test-based evaluation of behaviour factor is presented.*

**Keywords:** LWS system, CFS structure, Seismic behaviour, Full-scale test, Behaviour factor.

---



## 1 INTRODUCTION

Many Italian research projects, numerical and analytical studies demonstrated the ability of steel systems to show very good structural [1-16].

The increasing market demand for high-performance and low-cost constructions oriented the choice of the last decades to a competitive and eco-friendly solution: Lightweight Steel (LWS) systems made of Cold-Formed Steel (CFS). In this field the University of Naples “Federico II” was really active [17-25] and in this perspective an Italian Research Project, named as ECCEISA [1], has recently finished, in which the main aim was the development of an innovative LWS system with higher structural, energetic and environmental performances. The core of the project was the evaluation of seismic and thermal performances of a wall system braced with pre-tensioned Ultra-High-Strength (UHS) steel bars.

The innovative wall system is mainly composed of: (1) UHS steel bracing; (2) pre-tensioning devices; (3) chord studs; (4) tracks; (5) hold-downs; (6) blocking profiles and flat straps.

The UHS steel bracing consists of two diagonal braces, which are pre-tensioned dog bone shaped round bars having thread ends to allow their connection and pre-tensioning. For the chord studs, a back-to-back C section was selected, while for tracks a box section was chosen. The pre-tensioning device is a U shape profile connected to the hold-down through a cylindrical hinge, which allows the rotation in the plane of the wall.

A UHS steel ( $f_y=1300$  MPa,  $f_u=1450$  MPa) is adopted for the diagonal braces, while chord studs, tracks, blocking and flat straps are made of S280 GD+ Z steel grade, and devices for pre-tensioning and hold-downs are made of S355 steel grade ( $f_y=355$  MPa,  $f_u=470$  MPa). More details about the innovative wall and the design phase are available in [26].

The effectiveness and the limitations of the innovative wall system were validated through an extensive experimental campaign carried out at Laboratory of the Department of Structures for Engineering and Architecture of University of Naples “Federico II”, which consisted of small-scale tests on materials and nut-bar assemblies and full-scale wall tests. This paper describes in details the full-scale wall tests and the obtained results.

## 2 EXPERIMENTAL TESTS

The main core of the research project was the evaluation of seismic behaviour of the innovative wall system. To this purpose, five tests, including three monotonic tests and two cyclic tests, were carried out on full-scale 2400 mm long and 2800 mm high wall specimens. Two configurations of the innovative wall system have been investigated, which were representative of Light (L) and Medium (M) configurations developed. The label defines the specimen typology. Namely, the first letter indicates the test typology (M for monotonic test and C for reversed cyclic test), the second letter is referred to the wall specimen (L for specimen representative of Light configuration and M for specimen representative of Medium configuration) and the number represents the test number; e.g. M\_L1 means the monotonic test no. 1 carried out on the specimen representative of the Light wall configuration. Both configura-

ration specimens are represented in Figure 1. In both configurations and for both protocols used, the bars were pre-tensioned before starting the test via a torque wrench.

The test program is summarized in Table 1, in which the load type, loading protocol and number of tests are shown.



L Configuration wall tested



M Configuration wall tested

Figure 1 Specimen tested

Table 1 Test matrix for the monotonic and cyclic tests on full-scale walls

Test Label	Wall type	Load Type	Protocol	Number of tests
M L	Light	Monotonic	-	2
M M	Medium	Monotonic	-	1
C L	Light	Cyclic	CUREE	1
C M	Medium	Cyclic	CUREE	1

An available steel frame set-up for in-plane wall tests was modified and used for the experimental activity (Figure 2). The wall prototype was restrained to the laboratory strong floor by the bottom beam, which has a  $300 \times 180 \times 30$  (width  $\times$  height  $\times$  thickness) rectangular hollow section. Horizontal loads were transmitted to the wall through the loading beam, which has a  $200 \times 120 \times 10$  mm (width  $\times$  height  $\times$  thickness) rectangular hollow section. The out-of-plane displacements of the wall were restrained by two steel portal frames equipped with roller wheels. The tests were performed by using a hydraulic actuator having a stroke displacement of 500 mm and a load capacity of 500 kN. A sliding-hinge was placed between the loading actuator and the loading beam, in order to avoid vertical load components.

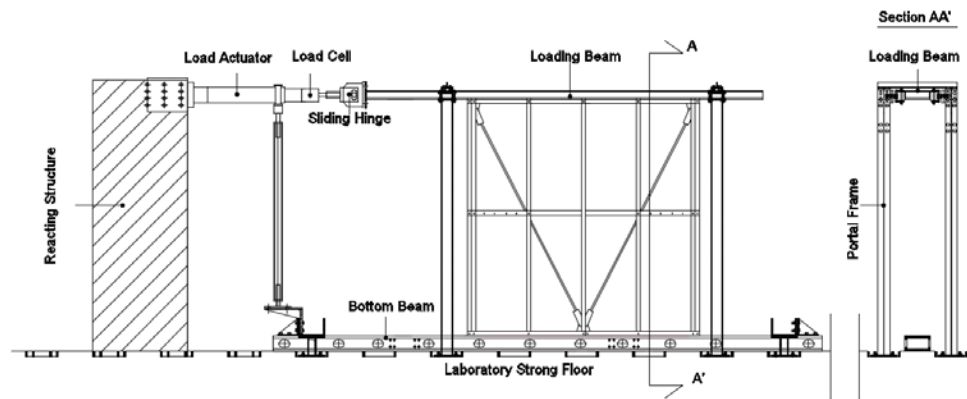


Figure 2 Wall test set-up

Six LVDTs and two potentiometers were used to measure the specimen displacements. In particular, three LVDTs (L1, L2 and L3) were installed to record hold-down horizontal and vertical displacements, two LVDTs (L4 and L5) for the upper beam vertical displacements, one LVDT (L6) for wall vertical displacements and two potentiometers (P1 and P2) for wall horizontal displacements. The strains in selected points of the diagonal bars and studs were recorded by means of fourteen strain-gauges. Two strain-gauges were installed on each diagonal (SG1 and SG2 placed near the middle section, where the diameter is reduced, and SG3 and SG4 placed where the section is maximum), four strain gauges were placed on the intermediate stud in two sections (SG5 and SG6 placed on the upper section, SG7 and SG8 on the lower section) and six strain gauges were placed on the right chord stud (SG9, SG10 and SG11 placed on the upper section and SG12, SG13 and SG14 placed on the lower section). The instrumentation pictures are shown in Figure 3. A load cell was used to measure the applied loads.



Figure 3 Photographs of wall test instrumentation

## 2.1 Monotonic tests

Monotonic tests were carried out with displacements imposed at a rate of 0.10 mm/s until the collapse of specimens occurred. The data were recorded with a sampling frequency equal to 10 Hz.

Three monotonic tests were carried out on two L and one M walls. Results for M\_L2 and M\_L1 specimens are provided in **Errore. L'origine riferimento non è stata trovata.**, in term of load (H) vs. inter-storey drift ratio (dr) curves. The displacements used for the evaluation of inter-storey drifts were measured by potentiometer P1, whereas load was provided by load cell.

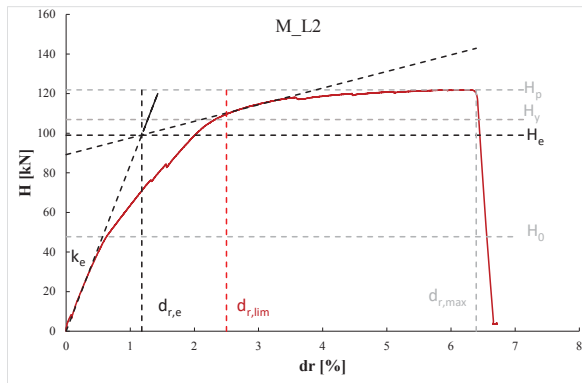
Numerical values are provided in Table 2, according to the following parameters:

- $H_0$ : wall strength corresponding to the end of the Phase (1);
- $H_e$ : wall conventional yield strength evaluated according to ECCS procedure [9];
- $H_y$ : wall strength corresponding to the end of the Phase (2);
- $H_p$ : maximum recorded load corresponding to the end of the Phase (3);
- $d_e$ : yield displacement evaluated according to ECCS procedure [27];
- $d_{max}$ : maximum displacement, evaluated in correspondence of  $H_p$
- $d_{r,e}$ : yield inter-storey drift ratio, equal to  $d_e/h$ ;
- $d_{r,max}$ : maximum inter-storeydrift ratio, equal to  $d_{max}/h$ ;
- $k_e$ : initial elastic stiffness corresponding to the tangent to initial part of the response curve, equal to  $H_e/d_e$ ;
- $\mu$ : ductility, equal to the ratio between the conventional ultimate displacement and displacement at conventional elastic limit load  $d_{max}/d_e$  or equally  $d_{r,max}/d_{r,e}$ .

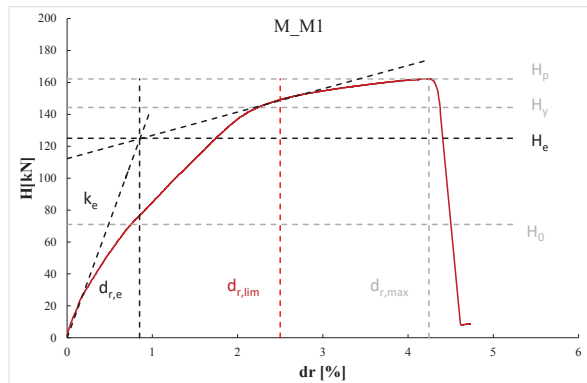
Globally, for all the specimens the monotonic response showed a three-phase lateral behaviour. In particular, the curves are characterized by three different branches: (1) the first linear branch with a stiffness  $k_e$ ; (2) once achieved  $H_0$ , the second branch characterised by a linear response having a stiffness smaller than  $k_e$ ; (3) once achieved  $H_y$ , the third branch characterised by a nonlinear response.

M\_L2 and M\_M1 specimens showed the same collapse due to the tension failure of the bar, whereas in M\_L1 specimen, during the phase (3), nut failure happened, since only one 12 property Class nut was employed. The collapse mechanism observed in M\_L2 test is provided in Figure 5. Comparing the results of two nominal identical tests, M\_L1 and M\_L2, can be noticed that:

- small differences in terms of  $H_y$  and  $H_p$  were revealed, equal to about 3% and 1%, respectively;
- high differences in term of inter-storey drift ratios achieved were registered, equal to about 19 and 51% for  $d_{r,e}$  and  $d_{r,max}$ , respectively, since the M\_L1 showed a brittle nut failure.



Results of M\_L2 test



Results of M\_M1 test

Figure 4 Results of M\_L2 and M\_M1 tests



Figure 5 M\_L2 test: collapse mechanism

Table 2 Monotonic test results

Test	M_L1	M_L2	M_M1
$H_0$ [kN]	37.99	47.73	71.01
$H_e$ [kN]	100.0	99.00	125.00
$H_y$ [kN]	103.9	106.90	144.32
$H_p$ [kN]	120.5	121.89	162.18
$d_e$ [mm]	26.60	33.04	23.80
$d_{max}$ [mm]	87.21	179.01	118.86
$d_{r,e}$ [%]	0.95	1.18	0.85
$d_{r,max}$ [%]	3.11	6.39	4.25
$k_e$ [kN/mm]	3.76	3.00	5.25
$\mu$ [-]	3.28	5.42	4.99



## 2.2 Reversed cyclic tests

Cyclic tests were carried out by adopting a loading protocol known as “CUREE ordinary ground motions reversed cyclic load protocol” developed for wood walls by Krawinkler et al. [28], modified according to the prescription given in Velchev et al. [29]). The general cyclic protocol is summarized in Figure 6. Since  $\Delta$  obtained from monotonic results was not really different between L and M configuration, the same specific protocol was adopted for both C\_L1 and C\_M1 tests.

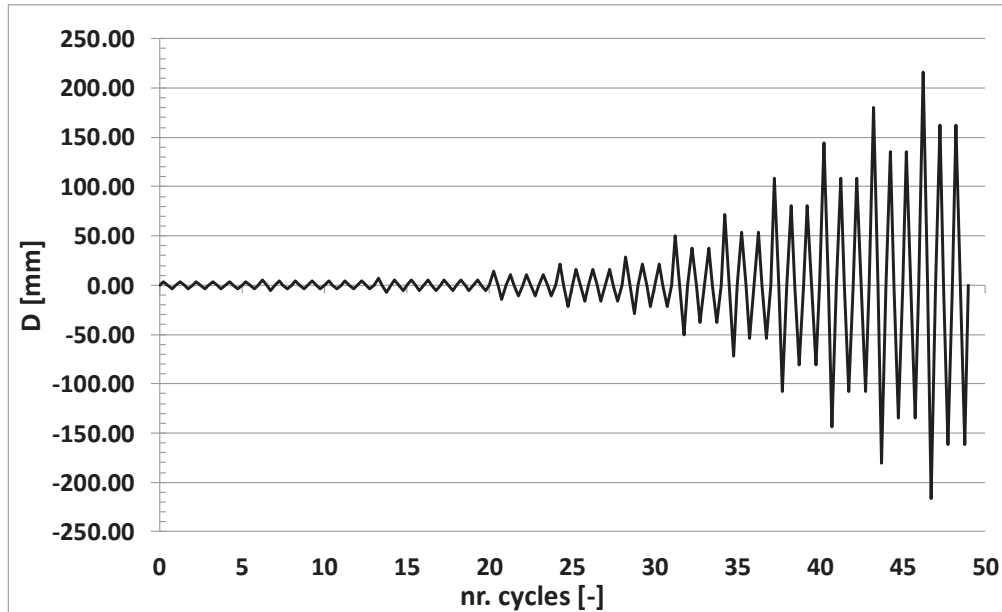
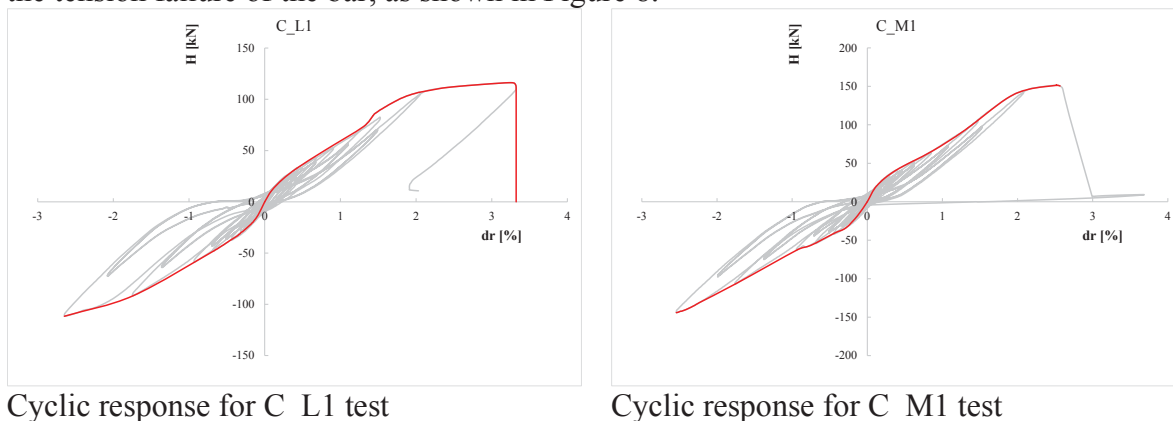


Figure 6 CUREE cyclic protocol adopted for C\_L1 and C\_M1 tests

The cyclic curves obtained (Figure 7) showed a behaviour rather symmetrical. The three-phase behaviour also characterized the cyclic response, but only in pushing. In fact, for both specimens collapse happened immediately reached the Phase (3) in pushing (positive range), whereas in pulling (negative range) the Phase (3) was not reached. Table 3 summarizes numerical results obtained. Both C\_L1 and C\_M1 specimens had the same collapse due to the tension failure of the bar, as shown in Figure 8.



Cyclic response for C\_L1 test

Cyclic response for C\_M1 test

Figure 7 Cyclic responses obtained

Table 3 Cyclic test results

Test	C <sub>-</sub> L1	C <sub>-</sub> M1
	22.	21.
H <sub>0</sub> [kN]	00	00
H <sub>e</sub> [kN]	90.	12
H <sub>y</sub> [kN]	00	8.00
H <sub>p</sub> [kN]	86.	14
d <sub>e</sub> [mm]	75	6.22
d <sub>max</sub> [mm]	11	15
d <sub>r,e</sub> [%]	6.24	1.40
d <sub>r,max</sub> [%]	25.	24.
k <sub>e</sub> [kN/mm]	76	36
μ [-]	70.	71.
	60	84
	0.9	0.8
	2	7
	3.3	2.5
	2	7
	3.4	5.2
	9	5
	3.6	2.9
	1	5



Figure 8 C\_M1 test: collapse mechanism

### 2.3 Discussion of results

The global behaviour of the innovative wall was evaluated through the measurements obtained during monotonic and cyclic tests. Thanks to potentiometers P1 and P2 the wall lateral behaviour was individuated. More considerations can be done, if a comparison between monotonic and cyclic results of nominally identical specimens (Figure 9) is conducted and, in particular, considering M\_L2 and M\_M1 as monotonic tests and C\_L1 and C\_M1 as cyclic

tests. Results of M\_L1 were not considered, since it showed nut failure, instead of tension collapse of bar. It can be observed that:

- Cyclic protocol does not affect greatly the resistance of wall, in fact, monotonic and cyclic  $H_p$  difference is equal to about 5% and 7% for L and M configuration, respectively;
- Cyclic protocol greatly affects the displacement capacity of wall, indeed the ductility of wall. In fact, difference in term of  $d_{r,max}$  is equal to about 92% and 65% for L and M configuration, respectively;
- Monotonic and cyclic elastic stiffness exhibited similar values for both L and M configurations (3.00 and 3.49 kN/mm for L configuration and 5.25 and 5.25 for M configuration).

The data obtained from LVDTs make possible the evaluation of hold-down stiffness and, in particular, three stiffnesses were evaluated: vertical stiffness  $k_v$ , horizontal stiffness  $k_h$  and rotational stiffness  $k_r$ . The adding source of deformability  $1/k_{tot}$  produced by hold-downs was evaluated, according to Equation 1, and it was in the range  $2-3 \times 10^{-5}$ .

Equation 1

$$\frac{1}{k_{tot}} = \frac{1}{k_1 + k_2 + 2k_h}$$

Where  $k_1$  and  $k_2$  are the adding source of global stiffnesses to vertical translation and rotation offered by hold-downs and are evaluated with Equation 2 and Equation 3.

Equation 2

$$k_1 = \frac{k_r}{h^2}$$

Equation 3

$$k_2 = \frac{L^2}{h^2} k_v$$

Therefore, from the results, it can be assumed that hold-downs are rigid and offer a perfectly rigid restrain to the system.

Furthermore, through the local measurements given by SG, it was possible to evaluate the distribution of stresses and quantify the horizontal load absorbed by the frame and by the bracing. According to results, the contribution offered by the frame is really important, absorbing 50% of total horizontal load applied to the wall.

As far as inter-storey drift ratios are concerned, experimental values achieved were in the range 2.6%-6.8% and were always higher than design limit drift ratio considered (2.5%).

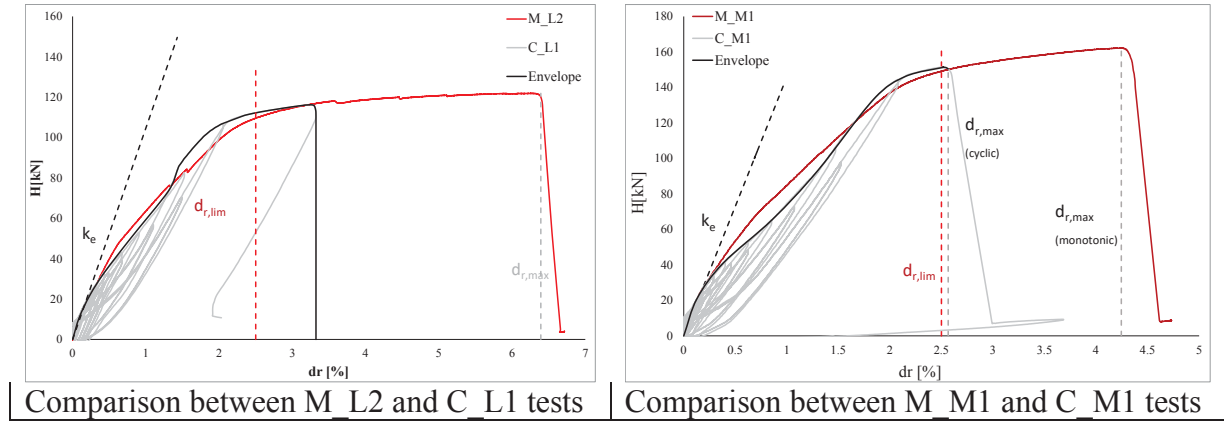


Figure 9 Comparison between monotonic and cyclic results

### 3 TEST-BASED BEHAVIOUR FACTOR EVALUATION

A preliminary experimentally based evaluation of behaviour factor was conducted. The behaviour factor ( $q$ ) was defined by the ductility-related ( $R_d$ ) and overstrength-related ( $R_0$ ) modification factors.

In particular, the ductility-related modification factor  $R_d$  represents the ability of the structural system to dissipate seismic energy, whereas the overstrength-related modification factor  $R_0$  represents the reserve of strength of the designed structure. The behaviour factor ( $q$ ) can be estimated using Equation 4, as given in Uang [56]:

Equation 4

$$q = R_d \cdot R_0$$

Since fundamental periods for this structural system is generally in the range 0.1-0.5 s, the ductility-related force modification factor  $R_d$  can be evaluated according to the principle of equal energy (Equation 5):

Equation 5

$$R_d = \sqrt{2\mu - 1}$$

where  $\mu$  is the ductility.

The  $R_0$  factor can be evaluated through the formulation provided by Mitchell et al. [57]:

Equation 6

$$R_0 = R_{sd} \cdot R_\phi \cdot R_{yield} \cdot R_{sh}$$

where  $R_{sd} = H_c/H_d$ , with  $H_c$  and  $H_d$  design wall resistance and seismic demand, respectively;

$R_\phi = H_{yn}/H_c$ , with  $H_{yn}$  design resistance associated by yielding of the braces multiplied by the safety factor  $\gamma_{M0}$ ;

$R_{yield} = H_y/H_{yn}$ , with  $H_y$  experimental yielding resistance;

$R_{sh} = H_p/H_y$ , with  $H_p$  experimental wall strength.

In order to neglect the design overstrength, in this study the assumption of  $R_{sd} = H_c/H_d = 1$  has been made. Therefore, the  $R_0$  factor can be evaluated through Equation 7:

Equation 7

$$R_0 = \frac{H_{yn}}{H_c} \cdot \frac{H_y}{H_{yn}} \cdot \frac{H_p}{H_y} = \frac{H_p}{H_c}$$

Table 4 shows the values of the behaviour factors obtained by the test-based evaluation. For the cyclic tests  $R_0$ ,  $R_d$  and  $q$  were evaluated considering the average values in pushing and pulling phases. The test M\_L1 was not considered since it showed a brittle premature failure. The average test-based values of behaviour factors are in the range of 3.09- 4.07 for the L Configuration and 3.67- 4.07 for the M Configuration. On the safe side, it can be concluded that a value of behaviour factor equal to 3 can be assumed for the L configuration and a value equal to 2.5 for the M Configuration.

Table 4 Test-based evaluation of behaviour factor

Test	M_L2	M_M1	C_L1	C_M1
$\mu$	5,42	4,99	3,61	2,95
$R_d$	3,14	3,00	2,49	2,21
$R_0$	1,30	1,22	1,24	1,14
$q$	4,07	3,67	<b>3,09</b>	<b>2,53</b>

#### 4 CONCLUSIONS

In the framework of an Italian research project, developed in cooperation with Lamieredil S.p.A. Company, an innovative wall system was developed and tested. The experimental tests were performed at the Laboratory of DIST (Department of Structures for Engineering and Architecture) of the University of Naples “Federico II”. The experimental results showed satisfactory seismic responses, in line with the theoretical previsions, if all the prescriptions are followed. In particular, if not well designed, the nut used for the bar pre-tensioning can cause a premature failure of the system and the displacement capacity is strongly reduced. The walls, in which all the design prescriptions were respected, exhibited satisfactory force and displacement capacity.

#### REFERENCES

- [1] R. Tartaglia, M. D’Aniello, M. Zimbru, Experimental and numerical study on the T-Stub behaviour with preloaded bolts under large deformations. *Structures*, **27**, 2137-2155, 2020.
- [2] R. Tartaglia, M. D’Aniello, M. Andreini, S. la Mendola, The performance of preloaded bolts in seismically prequalified steel joints in a fire scenario. *Materials*, **13(22)**, 1-14, 2020.
- [3] R. Tartaglia, M. D’Aniello, R. Landolfo, Numerical simulations to predict the seismic performance of a 2-story steel moment-resisting frame. *Materials*, **13(21)**, 1-17, 2020.



- [4] R. Tartaglia, M. D’Aniello, Influence of Transverse Beams On the Ultimate Behaviour of Seismic Resistant Partial Strength Beam-To-Column Joints. *Ingegneria Sismica*, **37(3)**, 50-65, 2020.
- [5] M. D’Aniello, R. Tartaglia, D. Cassiano, Experimental investigation of the inelastic tensile behaviour of non-preloadable grade 8.8 bolts. *Ingegneria Sismica*, **37(2)**, 92-109, 2020.
- [6] R. Tartaglia, M. D’Aniello, G.A. Rassati, Proposal of AISC-compliant seismic design criteria for ductile partially-restrained end-plate bolted joints. *Journal of Constructional Steel Research*, **159**, 364–383, 2019.
- [7] S. Costanzo, R. Tartaglia, G. Di Lorenzo, A. de Martino, Seismic behaviour of EC8-compliant moment resisting and concentrically braced frames. *Buildings*, **9(9)**, 196, 2019.
- [8] R. Tartaglia, M. D’Aniello, Nonlinear performance of extended stiffened end plate bolted beam-to-column joints subjected to column removal. *Open Civil Engineering Journal*, **11(M6)**, 369–383, 2017.
- [9] R. Tartaglia, M. D’Aniello, A. de Martino, Ultimate performance of external end-plate bolted joints under column loss scenario accounting for the influence of the transverse beam. *Open Construction and Building Technology Journal*, **12**, 132–139, 2018.
- [10] R. Tartaglia, M. D’Aniello, G. Di Lorenzo, A. de Martino, Influence of EC8 rules on p-delta effects on the design and response of steel MRF. *Ingegneria Sismica*, **35(3)**, 104-120, 2018.
- [11] R. Tartaglia, M. D’Aniello, G.A. Rassati, J.A. Swanson, R. Landolfo, Full strength extended stiffened end-plate joints: AISC vs recent European design criteria. *Engineering Structures*, **159**, 155-171, 2018.
- [12] G. Dell’Aglio, R. Montuori, E. Nastri, V. Piluso, Consideration of second-order effects on plastic design of steel moment resisting frames, *Bulletin of Earthquake Engineering*, **17 (6)**, 3041-3070, 2019
- [13] V. Piluso, A. Pisapia, E. Nastri, R. Montuori, "Ultimate resistance and rotation capacity of low yielding high hardening aluminium alloy beams under non-uniform bending", *Thin-Walled Structures*, **135**, 123-136, 2019.
- [14] R. Montuori, E. Nastri, V. Piluso, "Problems of modeling for the analysis of the seismic vulnerability of existing buildings", *Ingegneria Sismica*, **36 (2)**, 53-85, 2019.
- [15] R. Montuori, G. Gabbianelli, E. Nastri, M. Simoncelli, Rigid plastic analysis for the seismic performance evaluation of steel storage racks, *Steel and Composite Structures*, **32 (1)**, 1-19, 2019.
- [16] F. Di Lauro, R. Montuori, E. Nastri, V. Piluso, Partial safety factors and overstrength coefficient evaluation for the design of connections equipped with friction dampers, *Engineering Structures*, **178**, 645-655, 2019.

- [17] L. Fiorino, T. Pali, R. Landolfo. Out-of-plane seismic design by testing of non-structural lightweight steel drywall partition walls. *Thin-Walled Structures*, **130**, 213-230, 2018. doi: 10.1016/j.tws.2018.03.032
- [18] V. Macillo, S. Shakeel, L. Fiorino, R. Landolfo Development and Calibration of Hysteretic Model for CFS Strap braced stud walls. *International Journal of Advanced Steel Construction, Hong Kong Institute of Steel Construction*, **14(3)**, 337-360. 2018. doi: 10.18057/IJASC.2018.14.3.2
- [19] L. Fiorino, V. Macillo, R. Landolfo, Experimental characterization of quick mechanical connecting systems for cold-formed steel structures. *Advances in Structural Engineering, Multi-Science*. ISSN 1369-4332, **20 (7)**, 1098-1110, 2017. doi:10.1177/1369433216671318
- [20] L. Fiorino, O. Iuorio, V. Macillo, M.T. Terracciano, T. Pali, R. Landolfo. Seismic Design Method for CFS Diagonal Strap-Braced Stud Walls: Experimental Validation. *Journal of Structural Engineering*. ASCE. ISSN 0733-9445. **142(3)**, 04015154-1- 04015154-12: doi:10.1061/(ASCE)ST.1943-541X.0001408, 2016
- [21] O. Iuorio, L. Fiorino, R. Landolfo. Testing CFS structures: The new school BFS in Naples. *Thin-Walled Structures*, Elsevier Science. ISSN 0263-8231. **84**, 275-288, 2014. doi: 10.1016/j.tws.2014.06.006
- [22] R. Landolfo, L. Fiorino, O. Iuorio.. A specific procedure for seismic design of cold-formed steel housing. *Advanced Steel Construction*, **6(1)**, 603-618, 2010.
- [23] L. Fiorino, O. Iuorio, V. Macillo, R. Landolfo, Performance-based design of sheathed CFS buildings in seismic area, *Thin-Walled Structures*, **61**, 248-257, 2012.
- [24] L. Fiorino, O. Iuorio, R. Landolfo Seismic analysis of sheathing-braced cold-formed steel structures, *Engineering Structures*, **34**, 538-547, 2012.
- [25] L. Fiorino, O. Iuorio, R. Landolfo Sheathed cold-formed steel housing: A seismic design procedure. *Thin-Walled Structures*, **47(8-9)**, 919-930, 2009.
- [26] A. Campiche, Innovative UHS steel material for tension-only braced CFS walls, *Key Engineering Materials*, **873**, 25–31, 2021.
- [27] ECCS. Recommended Testing Procedure for Assessing the Behaviour of Structural Steel Elements under Cyclic Loads, P045, ECCS Technical Committee 1 – Structural Safety and Loadings, Technical Working Group 1.3 – Seismic Design, European Convention fo, 1986.
- [28] H. Krawinkler, P. Francisco, L. Ibarra, A. Ayoub, R. Medina, CUREE publication No. W-02 Development of a Testing Protocol for Woodframe Structures, 2001.

- [29] K. Velchev, G. Comeau, N. Balh, C.A. Rogers, Evaluation of the AISI S213 seismic design procedures through testing of strap braced cold-formed steel walls, *Thin-Walled Struct.* **48**, 846–856, 2010. <https://doi.org/10.1016/j.tws.2010.01.003>.
- [30] C. Uang, Establishing R (or  $R_w$ ) and Cd Factors for Building Seismic Provisions, *J. Struct. Eng.*, **117**, 19–28, 1991. [https://doi.org/10.1061/\(ASCE\)0733-9445\(1991\)117:1\(19\)](https://doi.org/10.1061/(ASCE)0733-9445(1991)117:1(19)).
- [31] D. Mitchell, R. Tremblay, E. Karacabeyli, P. Paultre, M. Saatcioglu, D.L. Anderson, Seismic force modification factors for the proposed 2005 edition of the National Building Code of Canada, *Can. J. Civ. Eng.*, **30** () 308–327, 2003. <https://doi.org/10.1139/102-111>.
- [32]

## VALIDATION OF NOVEL SEISMIC DESIGN CRITERIA FOR LIGHTWEIGHT STEEL BUILDING IN EUROPE

Sarmad Shakeel<sup>1</sup>, Marica Navarra<sup>2</sup>, and Alessia Campiche<sup>2</sup>

<sup>1</sup> NUST Institute of Civil Engineering, School of Civil and Environmental Engineering, National University of Science and Technology (NUST), H-12, Islamabad, Pakistan  
e-mail: sshakil@nice.nust.edu.pk

<sup>2</sup> Department for Structures for Engineering and Architecture, University of Naples Federico II, Piazzale Techio 80, Naples, Italy  
marica.navarra@gmail.com, alessia.campich@unina.it

---

### Abstract

*Lightweight Steel (LWS) buildings fabricated with cold-formed steel profiles are a viable alternative to traditional reinforced concrete or masonry buildings for low to mid-rise constructions. The current edition of Eurocode 8 does not provide seismic design guidelines for them in Europe. This paper presents a new seismic design criterion for these buildings, which is proposed to be added in the next edition of Eurocode 8. The criteria include design guidelines for lateral force resisting systems that are most common to LWS buildings. These systems include: CFS strap braced walls and CFS shear walls with steel sheets, wood, or gypsum sheathing. A brief overview of these guidelines and the relevant background information is provided in this paper. Then these guidelines are validated with a numerical study on several building archetypes. Archetypes are designed following the proposed seismic design criteria and analyzed under the suite of forty-four earthquake records. Archetypes are analyzed using both nonlinear pushover analysis and incremental dynamic analysis. Based on the analysis results, their collapse probability is gauged to judge the level of protection against seismic hazard provided by the proposed design criteria.*

**Keywords:** Eurocode 8, seismic design criteria, lightweight steel structures, lateral force resisting systems, cold-formed steel

---

## 1 INTRODUCTION

Lightweight Steel (LWS) buildings are low to mid-rise constructions fabricated with cold-formed steel (CFS) frames. In Europe, the use of these buildings is limited in regions with medium-to-high seismic hazard. This is mainly due to the absence of seismic design guidelines for these types of building in European building codes: Eurocodes. In particular, the Eurocode 8 part 1: EN 1998-1 [1] deals with the seismic design of building structures. The current edition of EN 1998-1 was published back in 2004 and it does not provide a specific seismic design criterion for LWS buildings, which can utilize their energy dissipation potential. Therefore, the main crux of this paper is the proposal of the seismic design criterion for the LWS buildings, which could be included in the upcoming second edition of EN 1998-1.

Design rules for LWS buildings are already available in North American Standard for seismic design of cold-formed steel structures: AISI S400 [2] for use in the USA, Canada, and Mexico. Apart from this, no other building code in the world provides seismic design guidelines for LWS buildings, which can utilize their energy dissipation potential. The design rules given by AISI S400 follow the capacity design approach. For all LFRS covered by AISI S400, it defines energy dissipation mechanisms of dissipative components, provides overstrength requirements concerning non-dissipative components and gives a value of response modification factor accounting for system inherent overstrength and ductility. LWS buildings are not explicitly covered by current edition of EN 1998-1 and only LWS buildings braced with strap braced walls could be designed as common Low dissipative steel structures belonging to Ductility class low (DCL) structures made of Class 4 cross-section profiles, for which EN 1998-1 allows a behavior factor of 1.5 to be used in the design.

The main aim of the paper is to enlighten the readers and users of Eurocodes about the background information on the research works [3–4, 13–22, 5, 23–27–6–12] and the reference design standards, already being used in some parts of the world, which formed the basis of proposed seismic design guidelines for LWS buildings. The design guidelines are explained and its validation through a numerical study on several LWS building archetypes is shown. The second edition of EN 1998-1 will provide rules for LWS buildings laterally braced with four different types of LFRS's: CFS strap braced walls (Figure 1); CFS shear walls with steel sheet sheathing (Figure 2), or wood sheathing, or gypsum sheathing.

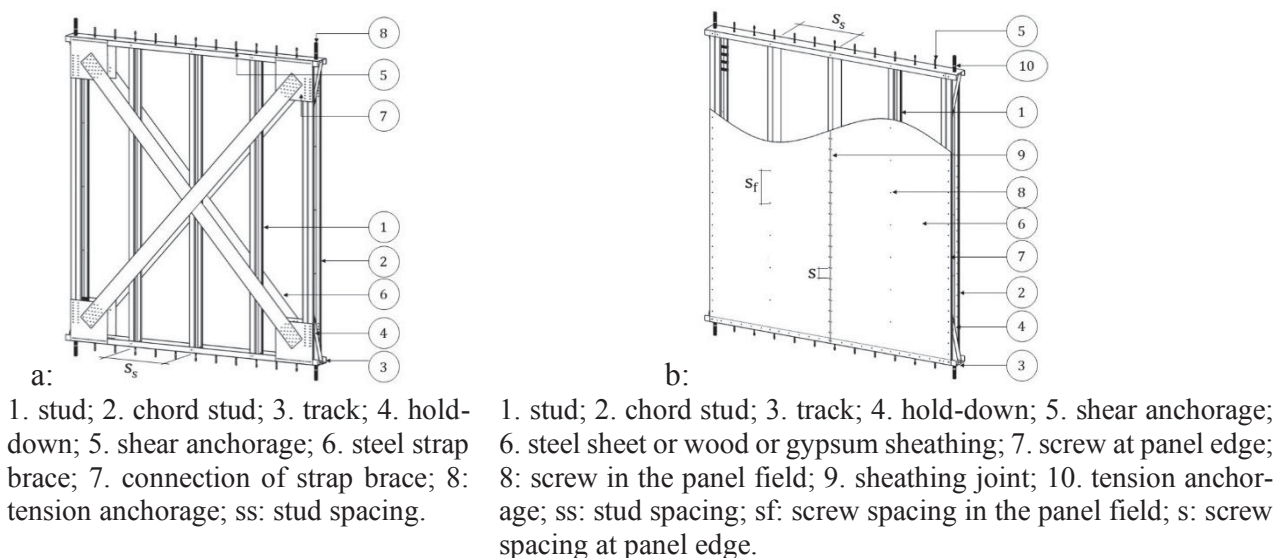


Figure 1 a: CFS strap braced wall; b: CFS Shear walls



## 2 DESIGN FRAMEWORK OF 2ND EDITION OF EN 1998-1

The second editions of Eurocode 8: EN 1998-1 would allow achieving three levels of ductility in building structures equipped with a certain type of LFRS. These levels include:

1. DC1: Low Dissipative structural behavior.
2. DC2: Medium Dissipative structural behavior.
3. DC3: High Dissipative structural behavior.

A structure cannot be designed beyond a certain limit of seismic load in the case of DC1 and DC2 Class structures while in the case of DC3 Class structures, there is no limit on the seismic action. In DC2 and DC3 Class structures, the capability of parts of the LFRS (dissipative components) to resist the seismic actions through plastic behavior in dissipative components is taken into consideration during the design process. To ensure the development of plastic mechanisms and subsequent energy dissipation in the dissipative components, specific design requirements are provided for them. For non-dissipative components of LFRS, design requirements ensure an overstrength in them to safeguard against failure. The overall design process of the second edition of EN 1998-1 would be a capacity design process. The design requirements for the dissipative components of CFS LFRS's belonging to both DC2 and DC3 Class structures would be the same. On the other hand, overstrength requirements for the non-dissipative components would be different for DC2 and DC3 Class structures.

In contrast to the DC2 and DC3 Class structures, the DC1 Class structures would not be required to follow any specific design and overstrength requirements. The design of individual components of DC1 class structure can be carried out according to EN 1993-1-3 [28], and other relevant European building standards [29–30]. Therefore, DC1 class structures would have a limited ductility capacity, and a lower value of behavior factor ( $q$ ) equal to 1.5 is proposed for them. Meanwhile, in the case of DC2 and DC3 class structures, the ability of structures to dissipate energy through their plastic behavior is accounted for, therefore higher values of  $q$  are proposed for them. The values of the behavior factor for DC2 and DC3 Class structures are derived from the studies [31–32] conducted following the FEMA P695 methodology [33].

Apart from providing special design requirements for DC2 and DC3 Class structures, the second edition of EN 1998-1 will also provide some general rules. These general rules include the limitation on the aspect ratio (height-to-length ratio) of the walls, which is fixed equal to 2.0 for all types of LFRS's. To have a sufficient deformation capacity of connections in the walls, the new version of EN 1998-1 would require the design shear resistance of the screws to be greater than 1.2 times the design bearing resistance of the steel structural member, or the design embedment resistance of wood or gypsum panels (in case of shear walls with panels), or the design net area resistance of the strap brace (in case of strap brace walls). This rule has been derived from the already existing guidelines in EN 1993-1-3 [28] for the shear design of connections made with screws.

## 3 DESIGN REQUIREMENTS FOR DISSIPATIVE COMPONENTS

The second edition of EN 1998-1 would provide specific rules to calculate the design strength of the LFRS in the case of DC2 and DC3 class structures. In addition to these design rules, the code will also provide geometrical and mechanical requirements for the components and parts of the shear walls, which must also be fulfilled to achieve the desired energy dissipation response in the walls. The requirements are defined based on the already existing geometrical and mechanical limitations on the permitted wall configurations given in AISI S400 [2].

For strap braced walls, the yield resistance ( $N_{pl, Rd}$ ) of the gross cross-section of the strap braces should be greater than the design value of the axial force in the strap brace in the seismic design situation and the design net area resistance ( $N_{u, Rd}$ ) of the strap brace. This requirement

ensures the formation of plastic mechanism in steel straps before the net section failure happens in strap connection to the wall frame. The values of  $N_{pl,Rd}$  and  $N_{u,Rd}$  can be obtained from other relevant parts of Eurocode 3 [30].

In case of shear walls with steel sheet sheathing, the in-plane lateral resistance ( $R_{c,Rd}$ ) corresponding to the strength of the sheathing connection within the effective sheathing strip should be greater than the design value of the lateral force acting on the shear wall in the seismic design situation, but it should be less than, the design yielding resistance of the effective sheathing strip ( $R_{y,Rd}$ ).  $R_{c,Rd}$  and  $R_{y,Rd}$  are evaluated based on the effective strip method (ESM) proposed in [31]. ESM was calibrated based on the large amount of steel sheathed shear walls tested in USA and Canada over recent years. In the original proposed ESM [31],  $R_{c,Rd}$  is calculated according to Eq. (1), which relies on the formulation of North American specification for the design of CFS structural members AISI S100 [32] for the calculation of single sheathing connection bearing strength ( $F_{b,Rd}$ ).

$$R_{c,Rd} = 1.33nF_{b,Rd} \cos \left( \text{Arctan} \left( \frac{h}{w} \right) \right) \quad (1)$$

where  $F_{b,Rd}$  is the bearing resistance of the sheathing connection,  $n$  is the number of sheathing connections in the effective width,  $h$  is the height of wall and  $w$  is the length of wall. AISI S100 provides a different relationships for  $F_{b,Rd}$  than the one provided in Eurocode 3 [28]. Eq. (2) and (3) gives the formulations of  $F_{b,Rd}$  given by AISI S400. If  $t_1/t \leq 1.0$ , then Eq. (2) is used or if  $t_1/t \geq 2.5$ , then Eq. (3) is used else  $F_{b,Rd}$  can be linearly interpolated between the values obtained from Eq. (2) and (3).

$$F_{b,Rd} = \min(2(t_1^3 d)^{\frac{1}{2}} f_{u,1}; 2.7 t_1 d f_{u,1}) / \gamma_{M2} \quad (2)$$

$$F_{b,Rd} = \min(2.7 t_1 d f_{u,1}) / \gamma_{M2} \quad (3)$$

where  $f_{u,1}$  and  $f_u$  are the ultimate tensile strength of the framing elements and the sheathing, respectively;  $t_1$  is the thickness of stud or track;  $d$  is the nominal diameter of screws and  $\gamma_{M2}$  is the partial safety factor equal to 1.25. Contrarily in the European standard for cold-formed steel design (EN1993-1-3 [28]), a different formula is proposed. Authors in their recent study [34] checked the validity of the ESM with  $F_{b,Rd}$  evaluated according to equation given by EN 1993-1-3. The use of the value of  $F_{b,Rd}$  evaluated from equation by EN 1993-1-3 results in underestimation of the wall strength. Therefore, the second edition of EN 1998-1 would require the strength of sheathing connections ( $F_{b,Rd}$ ) to be calculated according to equation (2) and (3), that are taken from AISI S100.

For CFS shear walls with wood or gypsum sheathing, the in-plane lateral resistance ( $R_{c,Rd}$ ) corresponding to the strength of the sheathing connection should be greater than the design value of the lateral force acting on the shear wall in the seismic design situation.

## 4 OVERSTRENGTH REQUIREMENTS

To guard the non-dissipative components of the LFRS's against the failure, an overstrength would be provided in them for use in DC2 and DC3 class structures according to the second edition of EN 1998-1.

### 4.1 DC2 class structure

The overstrength requirements for the DC2 Class structures ensure the formation of the desired energy dissipation mechanism in the dissipative components of LFRS through an overstrength in the non-dissipative components. The overstrength factors are applied using Equation (4) on the non-dissipative components of the LFRS of a DC2 Class structure to verify their strength and stability against the most unfavorable combination of the axial force  $N_{Ed}$ .

$$N_{Ed} = N_{Ed,G} + \Omega N_{Ed,E} \quad (4)$$

where:  $N_{Ed,G}$ , is the axial force in the non-dissipative member due to the non-seismic actions included in the combination of actions for the seismic design situation; and  $N_{Ed,E}$ , is the axial force in the non-dissipative member due to the design seismic action. The overstrength factor for different types of LFRS's is listed in Table 1 along with their behavior factor.

LFRS	q	$\Omega$
Strap braced walls	2.0	1.5
Shear walls with steel sheet sheathing	2.0	1.5
Shear walls with wood sheathing	2.0	1.5
Shear walls with gypsum sheathing	1.7	1.35

Table 1 Behavior and overstrength factors for DC2 Class structures

#### 4.2 DC3 class structures

The overstrength requirements for DC3 class structure are different for each type of LFRS in the second edition of EN-1998-1. For strap braced walls, the brittle components listed in Section 2.1 should be designed with an overstrength computed according to (5).

$$R_d \geq F_{Ed,G} + \gamma_{rm} \gamma_{sh} R_{fy} \quad (5)$$

where,  $R_d$  is the design resistance of the non-dissipative brittle component;  $F_{Ed,G}$  is the design action in the component due to the non-seismic actions included in the combination of actions for the seismic design situation;  $\gamma_{rm}$  is the overstrength factor accounting for the variability of the steel yield strength in the dissipative zones, i.e., ratio between the expected (average) and nominal yield strength, and ranges from 1.20 to 1.45 for lower to higher steel grades,  $\gamma_{sh}$  is the overstrength factor accounting for the hardening in the dissipative zones and is equal to 1.1;  $R_{fy}$  is the plastic resistance of the gross cross-section of the strap braces based on the nominal yield stress of the material as defined in Eurocode 3 [35].

For shear walls with steel sheet sheathing, equation (6) is proposed, which ensures the overstrength in their brittle components.

$$R_d \geq F_{Ed,G} + \gamma_{rm} R_{c,Rd} \quad (6)$$

where  $\gamma_{rm}$  is the overstrength factor, i.e., ratio between the expected (average) and design in-plane lateral resistance of the shear wall, equal to 1.40, and  $R_{c,Rd}$  is the design in-plane lateral resistance of the shear wall evaluated based on sheathing connection strength calculated according to equation (1).

For CFS shear walls with gypsum or wood sheathing, equation (7) is used to provide overstrength in their brittle components.

$$R_d \geq F_{Ed,G} + \gamma_{rm} R_{c,k} \quad (7)$$

where  $\gamma_{rm}$  is the overstrength factor, i.e., ratio between the expected (average) and characteristic in-plane lateral resistance of the shear wall, equal to 1.50, and  $R_{c,k}$  is the characteristic in-plane lateral resistance of the shear wall. Table 2 summarizes the values of  $\gamma_{rm}$  used for the overstrength of DC3 Class structures along with the values of the behavior factor for different LFRS's.

LFRS	q	$\gamma_{rm}$
Strap braced walls	2.5	1.20 to 1.45
Shear walls with steel sheet sheathing	2.5	1.40
Shear walls with wood sheathing	2.5	1.50
Shear walls with gypsum sheathing	2.0	1.50

Table 2 Behavior and overstrength factors for DC3 Class structures

## 5 VALIDATION OF DESIGN CRITERIA

To validate the design rules listed in previous sections, proposed for inclusion in the second edition EN1998-1, a numerical study considering several building archetypes was performed. LWS building archetypes braced with all four types of seismic force-resisting systems were designed as both DC2 and DC3 class structures. Nonlinear FE models for the archetypes were developed in OpenSees software [36]. The seismic performance of the models is evaluated following the FEMA P695 methodology [33].

### 5.1 Building archetypes

A total of eight double-storey residential building archetypes designed as DC2 or DC3 class structures and braced with the four types of LFRS's were selected. The archetypes were assumed to be situated on a soil type C in a medium seismic intensity zone having reference PGA (Peak Ground Acceleration),  $a_{g,R}$ , of 0.2g, which has a 10% probability of exceedance in 50 years. The live load due to residential occupancy was 2.0 kN/m<sup>2</sup>. In addition to permanent loads and live loads, a 1.00 kN/m<sup>2</sup> snow load and 0.35 kN/m<sup>2</sup> wind load were also considered to be acting.

EN 1993-1-3 [28] was used to design the gravity load resisting elements of the archetypes. Current in practice edition of Eurocode 8: EN 1998-1 [1] was used to define the seismic actions on the buildings. The lateral force method was used to obtain the building design base shear ( $F_b$ ), which is mainly the function of building design response spectrum and mass.

The seismic design process of LWS buildings involves the selection of configurations of strap braced or shear walls, that can be used to resist the lateral actions, evaluating the design strength of the wall configurations, and then eventually the total number of the required walls are obtained by dividing the design base shear with the design strength of a single wall. Table 3 lists the design base shear of the archetypes ( $F_b$ ), design strength of the walls ( $R_d$ ), and the number of the walls provided in each planar direction of the archetype.

Archetype Ductility class	Wall name	w x h <sup>1</sup> [m]	q [-]	Fb kN	Rd kN	No. of walls required <sup>2</sup> [-]	No. of walls provided [-]	C/D <sup>3</sup> [-]	D/C <sup>4</sup> [-]
<b>Strap braced walls</b>									
DC2	WLD mod	2.4 x 2.7	2	212.3	43.7	4.9	6	1.235	0.81
DC3	WLD	2.4 x 2.7	2.5	170.8	43.7	3.9	4	1.024	0.97
<b>Shear walls with steel sheet sheathing</b>									
DC2	ST1-c mod	1.22 x 2.44	2	212.3	14.6	14.6	16	1.098	0.91
DC3	ST1-c	1.22 x 2.44	2.5	170.8	14.6	11.7	12	1.024	0.97
<b>Shear walls with wood sheathing</b>									
DC2	wall 14	2.44 x 2.74	2	212.3	34.3	6.2	8	1.291	0.77
DC3	wall 4	1.22 x 2.74	2.5	170.8	17.1	10.0	10	1.003	0.99
<b>Shear walls with gypsum sheathing</b>									
DC2	S_2400C mod	2.4 x 2.3	1.7	248.9	29.2	8.5	10	1.174	0.85
DC3	S_2400C	2.4 x 2.3	2	212.3	29.2	7.3	8	1.101	0.90

<sup>1</sup> Width x Height of the shear wall

<sup>2</sup> No of walls required= $F_b/R_d$

<sup>3</sup> Building archetype design capacity to design demand ratio

<sup>4</sup> Building archetype design demand to design capacity ratio

Table 3 Seismic design details of building archetypes

The selected configuration for strap braced walls in the DC3 building archetype has been already tested in an Italian research project [32]. On the other hand, no reference test results were found for the wall, which can only meet the criteria of the DC2 ductility class. Therefore, it was decided to downgrade the DC3 walls in a way that it would become DC2. For this purpose, the chord studs and the hold-down devices have been modified. In this way, the new wall named as WDL mod does not satisfy the design criteria required for the DC3 ductility class but guarantees the fulfillment of the criteria for the DC2.

In the case of steel sheathed shear walls, the selected wall configuration belonging to the DC3 class has already been tested at McGill University in Canada [37] and was named as ST1 -c in the referenced research. On the other hand, DC2 wall configuration is obtained for steel sheathed shear walls similarly to strap braced walls. Likewise, gypsum sheathed shear wall configuration to be used in a DC3 class building is selected from the series of tests carried out at the University of Naples Federico II, Italy within the ELISSA project [32]. The DC3 wall selected from the referenced research was named S\_2400C. While DC2 wall configuration is obtained by modifying the chord studs of the DC3 wall configuration in the case of gypsum sheathed shear walls. The wood sheathed shear wall configuration to be used in a DC3 and DC2 class building archetypes were selected from the series of tests carried out in the USA within the CFS NEES project [38]. The tested wall configuration 14 and 4 in the reference research are used as DC2 and DC3 class walls, respectively.

## 5.2 Numerical modeling and analysis

A three-dimensional numerical model was developed for each archetype in OpenSees software [36]. The nonlinear behavior of building archetypes was represented in the lateral load resisting walls. Thus, the simulation of seismic response of the walls is the single most significant consideration in the modeling of LWS building analyzed under the seismic design situation.

A simplified diagonal truss model was used to simulate the in-plane force-displacement hysteretic response of the walls. More detail on the modeling of walls can be found in [32]. Pinching4 material [39] is used for the diagonal truss elements. The values of pinching 4 material properties are selected from the studies in the literature [32], in which numerical models of selected wall configurations have been developed.

The development of wall models was followed by the development of 3D building models for the archetypes. The model included only the main structural elements: LFRS walls, gravity load-bearing studs, floor representations, and a P-delta frame. The gravity load resisting studs are modeled as the truss elements. The floor was modeled using the rigid elastic beam-column elements. To capture the lateral displacement arising from the P-delta effect, a rigid frame made of axially rigid elastic beam-column elements with low flexure stiffness having a co-rotational coordinate transformation is connected to the building in the direction of seismic action. Gravity load is applied to the P-delta columns at floor levels. More information on the modeling of CFS archetypes is given in [32]. Moreover, a 2% damping ratio defined based on the Rayleigh damping model is also used in dynamic analysis. These values of damping ratio reflect the values measured during the shake-table tests [32] on LWS building specimens.

## 5.3 Analysis, results, and discussion

To investigate the building performance, pushover analysis and incremental dynamic analysis were performed on the archetypes. The analysis was performed following the framework of the FEMA P695 methodology [33]. More details about the FEMA P695 approach can be found in [32]. Figure 2 show the capacity curves of all archetypes, in which the model base



shear ( $V_b$ ) was normalized by the design base shear ( $F_b$ ) and the design overstrength ( $C/D$  ratio), and the top displacement ( $\Delta$ ) was normalized by building height ( $H$ ).

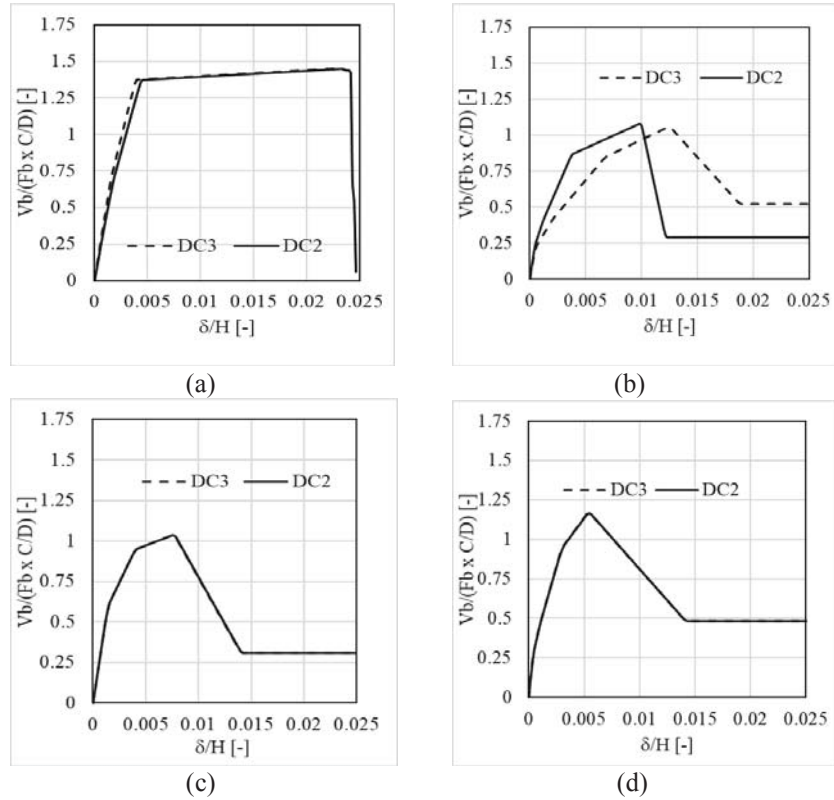


Figure 2: Pushover curves building archetype models braced with: a) CFS strap braced walls; b) CFS shear walls with wood sheathing; c) CFS shear walls with steel sheathing; d) CFS shear walls with gypsum sheathing.

The pushover curves shown in Figure 3 do not highlight any differences among DC2 and DC3 archetypes in terms of building peak strengths, while small differences were observed in the case of building ductility. During the pushover analysis, no brittle failure mechanism was observed. All the archetypes depicted a failure (inter-storey drifts accumulation) at a particular storey.

To better interpret the results, Incremental Dynamic Analysis (IDA) of all archetypes was performed. The analysis was performed using pair of 22 earthquake records provided by FEMA P695 [33]. The collapse performance of archetypes was gauged using Collapse Margin Ratio (CMR). CMR is defined as the ratio between median collapse intensity ( $S_{CT}$ ) to the maximum considered earthquake intensity ( $S_{MT}$ ).  $S_{CT}$  is defined as the intensity at which half of the ground motions in the record set used during the IDA cause collapse of an archetype model. The archetype collapse was represented by the exceedance of the threshold value of an inter-storey drift ratio. The threshold value of inter-storey drift ratio was the level of the drift until which the individual units of lateral load resisting walls did not experience collapse during the tests [32–37–38]. A value of 5%, 2%, and 4% inter-storey drift level was used for archetypes with CFS strap braced, steel sheathed shear, and wood or gypsum sheathed shear wall, respectively.

During IDA, all 44 records (22 records x 2 orthogonal directions) were applied separately to the archetype models in both planar directions. Records were applied in an increment of 20% in their intensity. IDA started with all the earthquake records have an intensity of 20 % (Scaling factor = 0.2) and was continued up to an intensity of 300% or 600% (Scaling factor = 6.0) with increments of 20%, until a failure is not observed. The Scaling factor of 1.0 represents a design

earthquake (DE) level because the median of all the records was matched with the building design response spectrum as explained earlier. The scaling factor of 1.5 can be considered as MCE (Maximum Considered Earthquake) intensity earthquake. This is due to the fact that the MCE is 1.5 times the DE [40]. Figure 3 shows the results of IDA results for the DC2 Class building archetype braced with CFS steel sheathed shear wall.

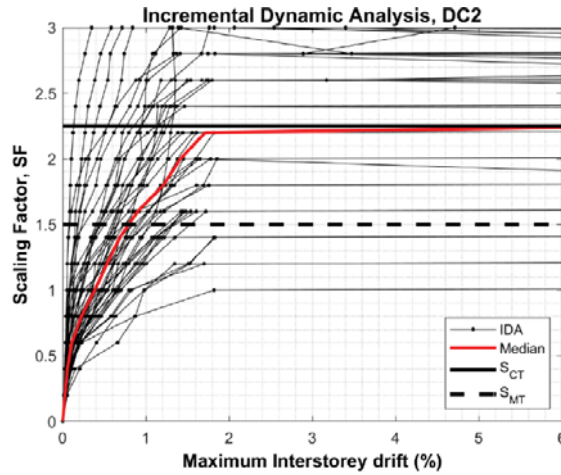


Figure 3: IDA curves for DC2 class building archetype braced with CFS steel sheathed shear wall.

The CMR obtained from IDA is multiplied with the spectral shape factor (SSF) to obtain Adjusted Collapse Margin Ratio (ACMR). SSF is provided in the FEMA P695 document [33] as a function of period-based ductility ( $\mu_T$ ), numerical fundamental vibration period ( $T_1$ ) and seismic design category of an archetype [41]. FEMA P695 methodology also outlines a performance evaluation process for the archetypes. In particular, it outlines two performance goals: the average value of ACMR,  $ACMR_{avg}$ , for each performance group should be greater than  $ACMR_{10\%}$ , and the individual values of the  $ACMR_i$ , for each archetype should be greater than  $ACMR_{20\%}$ .  $ACMR_{10\%}$  and  $ACMR_{20\%}$  are values of acceptable collapse probability, taken as 10% and 20%, respectively, and are given in Table 7-3 of FEMA P695., which lists them as a function of the total collapse uncertainty  $\beta_{TOT}$ . In this study, the archetypes are not categorized into performance groups due to different lateral force resisting systems, therefore the performance against the second goal  $ACMR_{20\%}$  is only measured.

$\beta_{TOT}$  merges various sources of uncertainty including record to record uncertainty ( $\beta_{RTR}$ ), design requirements uncertainty ( $\beta_{DR}$ ), test data uncertainty ( $\beta_{TD}$ ); and modeling uncertainty ( $\beta_{MDL}$ ) using Equation (8).

$$\beta_{TOT} = \sqrt{\beta_{RTR}^2 + \beta_{DR}^2 + \beta_{TD}^2 + \beta_{MDL}^2} \quad (8)$$

Record to record uncertainty ( $\beta_{RTR}$ ) represents the variability in archetypes response model due to the application of various ground motion records, that could have different dynamic characteristics and frequency content.  $\beta_{RTR}$  is computed using Equation (9).

$$\beta_{RTR} = 0.1 + 0.1 \cdot \mu_T, \text{ with } \beta_{RTR} > 0.2 \text{ and } \beta_{RTR} \leq 0.4 \quad (9)$$

All of the archetypes had  $\beta_{RTR}$  of 0.40. The rest of the parameters in Equation (11) are qualitative indicators provided by FEMA P695 [33] on the basis of the following scale: (a) Superior,  $\beta = 0.10$ ; (b) Good,  $\beta = 0.20$ ; (c) Fair,  $\beta = 0.35$ ; and (d) Poor,  $\beta = 0.50$ . The design process used in this study ensures the formation of ductile mechanism in the walls, while protecting against brittle failure mechanisms happening in wall components. The design method is also able to predict the design strength of the shear wall in a close match to the test results. Therefore, the design requirements used to design the archetypes are rated as “Good” ( $\beta_{DR} = 0.2$ ). In authors opinion, the rating can only be excellent, if the seismic design guidelines for LFRS are

already given in building standards. The available experimental data on LFRS performance is rated as “Superior” ( $\beta_{TD} = 0.1$ ) for CFS shear walls, because different wall components and walls themselves have been tested, [38] and the seismic performance of the building with LFRS has also been investigated via shake-table tests [42]. For strap braced walls, a rating of “Good” ( $\beta_{TD} = 0.2$ ) was utilized because there was no shake table data available on their performance. For DC2 building archetypes braced with the walls, which were obtained by modifying respective DC3 walls, rating of test data was taken as poor ( $\beta_{TD} = 0.5$ ) due to unavailability of test results. Modelling of building archetypes was rated as “Good” ( $\beta_{MDL} = 0.2$ ) due to their ability to simulate brittle failure mechanisms and post peak deterioration of shear strength. Table 5 shows the performance evaluation results of all archetypes.

Archetype		T (sec)	$\mu_T$	S <sub>CT</sub>	S <sub>MT</sub>	SSF	$\beta_{TOT}$	CMR	ACMR	ACMR 20%	ACMR / ACMR 20%
Strap braced	DC2	0.30	13.0	5.40	1.50	1.14	0.70	3.60	4.10	1.80	2.28
	DC3	0.35	13.6	4.20	1.50	1.14	0.50	2.80	3.19	1.56	2.04
Steel Sheathed	DC2	0.28	8.6	2.40	1.50	1.14	0.70	1.60	1.82	1.80	1.01
	DC3	0.31	9.9	1.80	1.50	1.14	0.50	1.20	1.37	1.52	0.90
Wood Sheathed	DC2	0.33	6.0	2.80	1.50	1.12	0.50	1.87	2.09	1.52	1.38
	DC3	0.48	6.4	2.20	1.50	1.12	0.50	1.47	1.65	1.52	1.09
Gypsum Sheathed	DC2	0.29	5.1	2.60	1.50	1.10	0.70	1.73	1.92	1.80	1.07
	DC3	0.30	5.9	2.60	1.50	1.11	0.50	1.73	1.94	1.52	1.28

Table 4 Performance evaluation of building archetypes based on IDA results.

From the results shown in Table 4, it is evident that the proposed design guidelines provide a significant margin of safety (CMR) against collapse. All the archetypes have also ACMR greater than ACMR<sub>20%</sub> except in the case of the DC3 archetype with CFS steel sheathed shear wall.

## 6 CONCLUSIONS

This paper presents the seismic design criteria for LWS buildings. The design criteria cover four different types of LFRS's: CFS strap braced walls, CFS shear walls with steel sheet or wood or gypsum sheathing, which can be used to achieve three levels of ductility classes in LWS building. Special capacity design rules and limitations on the geometrical and mechanical properties are required to be followed for DC2 and DC3 Class structures, while DC1 Class structures require no specific capacity design rules and limitations. Different values of the behavior factors are also proposed for DC2 and DC3 Class structures. Overstrength rules will be provided separately for DC2 and DC3 class structures to safeguard against the brittle failure mechanism in the non-dissipative components. Furthermore, formulations to predict the design strength of the wall would also be provided.

To validate the proposed design criteria, a numerical study was performed considering several building archetypes. Archetypes were designed following the proposed design criteria and modeled in OpenSees. Pushover analysis on archetypes indicated the redundancy of models against the brittle failure mechanism as they were not observed. Through incremental dynamic analysis, the collapse performance of archetypes was evaluated. All of the archetypes passed the FEMA P695 performance evaluation criteria with a good margin except one, in which the performance goal was not met by the close margin. To conclude, based on the numerical results, it can be asserted that the design criteria allow guaranteeing wide margins of safety against collapse and the desired hierarchy of resistances in the LFRS's.

## 7 REFERENCES

- [1]. CEN, *EN 1998-1 Eurocode 8: Design of Structures for earthquake resistance-Part 1: General rules, seismic actions and rules for buildings* (Brussels: European Committee for Standardization, 2004).
- [2]. AISI, *S400-15 North American Standard for Seismic Design of Cold formed Steel Structural Systems* (American Iron and Steel Institute (AISI), 2015).
- [3]. Fiorino, L., Pali, T., and Landolfo, R., Out-of-plane seismic design by testing of non-structural lightweight steel drywall partition walls. *Thin-Walled Structures*, 130, 213–230, 2018.
- [4]. Fiorino, L., Bucciero, B., and Landolfo, R., Shake table tests of three storey cold-formed steel structures with strap-braced walls. *Bulletin of Earthquake Engineering*, 2019.
- [5]. Fiorino, L., Macillo, V., and Landolfo, R., Experimental characterization of quick mechanical connecting systems for cold-formed steel structures. *Advances in Structural Engineering*, 20, 1098–1110, 2017.
- [6]. Fiorino, L., Iuorio, O., Macillo, V., Terracciano, M. T., Pali, T., and Landolfo, R., Seismic Design Method for CFS Diagonal Strap-Braced Stud Walls: Experimental Validation. *Journal of Structural Engineering*, 142, 04015154, 2016.
- [7]. Iuorio, O., Fiorino, L., and Landolfo, R., Testing CFS structures: The new school BFS in Naples. *Thin-Walled Structures*, 84, 275–288, 2014.
- [8]. Fiorino, L., Iuorio, O., and Landolfo, L., A Specific Procedure for the Seismic Design of Cold-Formed Steel Housing. *Proc. 5th Int. Conf. Adv. Steel Struct. (ICASS 2007)* (Singapore, 2007), pp. 298–305.
- [9]. Fiorino, L., Iuorio, O., Macillo, V., and Landolfo, R., Performance-based design of sheathed CFS buildings in seismic area. *Thin-Walled Structures*, 61, 248–257, 2012.
- [10]. Fiorino, L., Iuorio, O., and Landolfo, R., Seismic analysis of sheathing-braced cold-formed steel structures. *Engineering Structures*, 34, 538–547, 2012.
- [11]. Fiorino, L., Iuorio, O., and Landolfo, R., Sheathed cold-formed steel housing: A seismic design procedure. *Thin-Walled Structures*, 47, 919–930, 2009.
- [12]. Tartaglia, R., D’Aniello, M., and Zimbru, M., Experimental and numerical study on the T-Stub behaviour with preloaded bolts under large deformations. *Structures*, 27, 2137–2155, 2020.
- [13]. Tartaglia, R., D’Aniello, M., Andreini, M., and La Mendola, S., The Performance of Preloaded Bolts in Seismically Prequalified Steel Joints in a Fire Scenario. *Materials*, 13, 5079, 2020.
- [14]. Tartaglia, R., D’Aniello, M., and Landolfo, R., Numerical Simulations to Predict the Seismic Performance of a 2-Story Steel Moment-Resisting Frame. *Materials*, 13, 4831, 2020.
- [15]. Tartaglia, R. and D’Aniello, M., Influence of Transverse Beams On the Ultimate Behaviour of Seismic Resistant Partial Strength Beam-To-Column Joints. *Ingegneria Sismica*, 37, 50–65, 2020.
- [16]. Mario D’Aniello, Tartaglia, R., and Cassiano, D., Experimental investigation of the

- inelastic tensile behaviour of non-preloadable grade 8.8 bolts. *Ingegneria Sismica*, 37, 92-109, 2020.
- [17]. Tartaglia, R., D’Aniello, M., and Rassati, G. A., Proposal of AISC-compliant seismic design criteria for ductile partially-restrained end-plate bolted joints. *Journal of Constructional Steel Research*, 159, 364–383, 2019.
  - [18]. Costanzo, S., Tartaglia, R., Di Lorenzo, G., and De Martino, A., Seismic Behaviour of EC8-Compliant Moment Resisting and Concentrically Braced Frames. *Buildings*, 9, 196, 2019.
  - [19]. Tartaglia, R. and D’Aniello, M., Nonlinear Performance of Extended Stiffened End Plate Bolted Beam-to-column Joints Subjected to Column Removal. *The Open Civil Engineering Journal*, 11, 369–383, 2017.
  - [20]. Tartaglia, R., D’Aniello, M., and De Martino, A., Ultimate Performance of External End-plate Bolted Joints Under Column Loss Scenario Accounting for the Influence of the Transverse Beam. *The Open Construction and Building Technology Journal*, 12, 132–139, 2018.
  - [21]. Tartaglia, R., D’Aniello, M., Gianmaria, D. L., and Attilio De Martino, D. M., Influence of EC8 rules on P-Delta effects on the design and response of steel MRF. *Ingegneria Sismica: International Journal of Earthquake Engineering*, 13, 104–120, 2018.
  - [22]. Tartaglia, R., D’Aniello, M., Rassati, G. A., Swanson, J. A., and Landolfo, R., Full strength extended stiffened end-plate joints: AISC vs recent European design criteria. *Engineering Structures*, 159, 155–171, 2018.
  - [23]. Montuori, R., Nastri, E., Piluso, V., Streppone, S., D’Aniello, M., Zimbru, M., and Landolfo, R., Comparison Between Different Design Strategies For Freedom Frames: Push-Overs and Ida Analyses. *The Open Construction and Building Technology Journal*, 12, 140–153, 2018.
  - [24]. Castaldo, P., Nastri, E., and Piluso, V., Ultimate behaviour of RHS temper T6 aluminium alloy beams subjected to non-uniform bending: Parametric analysis. *Thin-Walled Structures*, 115, 129–141, 2017.
  - [25]. Castaldo, P., Nastri, E., and Piluso, V., FEM simulations and rotation capacity evaluation for RHS temper T4 aluminium alloy beams. *Composites Part B: Engineering*, 2017.
  - [26]. Montuori, R., Nastri, E., and Piluso, V., Modelling of floor joists contribution to the lateral stiffness of RC buildings designed for gravity loads. *Engineering Structures*, 121, 85–96, 2016.
  - [27]. Nastri, E., Vergato, M., and Latour, M., Performance evaluation of a seismic retrofitted R.C. precast industrial building. *Earthquakes and Structures*, 12, 13–21, 2017.
  - [28]. CEN, *EN 1993-1-3 Eurocode 3: Design of steel structures-Part 1-3: General rules-Supplementary rules for cold-formed members and sheeting* (Brussels: European Committee for Standardization, 2006).
  - [29]. CEN, *EN 1994-1-1 Eurocode 4: Design of composite steel and concrete structures - Part 1-1: General rules and rules for buildings* (Brussels: European Committee for Standardization, 2004).



- [30]. CEN, *EN 1995-1-1 Eurocode 5: Design of timber structures Part 1-1: general - Common rules and rules for buildings* (Brussels: European Committee for Standardization, 2005).
- [31]. Shamim, I. and Rogers, C. A., Numerical evaluation: AISI S400 steel-sheathed CFS framed shear wall seismic design method. *Thin-Walled Structures*, 95, 48–59, 2015.
- [32]. Landolfo, R., Lightweight steel framed systems in seismic areas: Current achievements and future challenges. *Thin-Walled Structures*, 140, 114–131, 2019.
- [33]. FEMA, *FEMA P695: Quantification of Building Seismic Performance Factors* (Washington, DC, USA, 2009).
- [34]. Campiche, A., Shakeel, S., Fiorino, L., and Landolfo, R., Seismic design criteria for CFS steel-sheathed shear walls. *Stab. Ductility Steel Struct. - Proc. Int. Colloq. Stab. Ductility Steel Struct. 2019* (2019).
- [35]. CEN, *EN 1993-1-1 Eurocode 3: Design of steel structures-Part 1-1: General rules and rules for buildings* (Brussels: European Committee for Standardization, 2005).
- [36]. Mazzoni, S., McKenna, F., Scott, M. H., and Fenves, G. L., OpenSees. 2009.
- [37]. Shamim, I., DaBreo, J., and Rogers, C. A., Dynamic Testing of Single- and Double-Story Steel-Sheathed Cold-Formed Steel-Framed Shear Walls. *Journal of Structural Engineering*, 139, 807–817, 2013.
- [38]. Liu, P., Peterman, K. D., and Schafer, B. W., Impact of construction details on OSB-sheathed cold-formed steel framed shear walls. *Journal of Constructional Steel Research*, 101, 114–123, 2014.
- [39]. Mazzoni, S., McKenna, F., Scott, M. H., and Fenves, G. L., Open System for Earthquake Engineering (OpenSees). 2009.
- [40]. Leyendecker, E. V., Hunt, R. J., Frankel, A. D., and Rukstales, K. S., Development of Maximum Considered Earthquake Ground Motion Maps. *Earthquake Spectra*, 16, 21–40, 2000.
- [41]. SEI/ASCE, *ASCE 7-16 Minimum Design Loads for Buildings and Other Structures* (Reston, Virginia: American Society of Civil Engineers, 2016).
- [42]. Peterman, K. D., Stehman, M. J. J., Madsen, R. L., Buonopane, S. G., Nakata, N., and Schafer, B. W., Experimental Seismic Response of a Full-Scale Cold-Formed Steel-Framed Building. II: Subsystem-Level Response. *Journal of Structural Engineering*, 142, 04016128, 2016.

## BEHAVIOUR OF T-STUB UNDER MODE 2 AND 3 WITH HV AND HR BOLTS

Roberto Tartaglia<sup>1</sup>, Mario D’Aniello<sup>2</sup>

<sup>1</sup> Department of Structures for Engineering and Architecture  
University of Naples Federico II  
via Forno Vecchio 34, 80136 Naples (Italy)  
e-mail: [roberto.tartaglia@unina.it](mailto:roberto.tartaglia@unina.it)

<sup>2</sup> Department of Structures for Engineering and Architecture  
University of Naples Federico II  
via Forno Vecchio 34, 80136 Naples (Italy)  
e-mail: [mdaniel@unina.it](mailto:mdaniel@unina.it)

---

### Abstract

*The behavior of the bolts can strongly influence stiffness, strength, and ductility of joints. The current Eurocodes allows using both HV (German type with failure by nut stripping) and HR (British-French type with failure by necking of the shank) bolts without making any distinction between them. However, recent studies showed that these two types of pre-loadable bolts are characterized by different ultimate tensile behavior that could lead different joint ductility. The aim of this work is to investigate the influence of the type of pre-loadable bolts on the behavior of T-stubs when it is subjected to mode 2 and 3. To this end, analytical and numerical analyses were carried out. The results show that only in case of the failure mode 3 some differences can be observed between HV and HR.*

**Keywords:** T-Stub, Seismic behavior, Bolt behavior, experimental tests, ductility.

---

## 1 INTRODUCTION

The steel structures represent a viable solution in seismic areas providing a very good performance in terms of stiffness resistance and ductility [1-16]. Among them, in the recent years particular attention was given to the bolted connections that are widely used for steel structures due to both their lower constructional costs performance in terms of both resistance and ductility [8-10]. To describe the mechanical characteristics of bolted connections following the code methodology the design relies on the behavior of sub-components. Those representing the end-plate and column flange in bending are analytically modelled with equivalent T-stub connections.

The behavior of T-stubs was widely investigated [17-26] prior to the implementation of the Component method in EN1993-1-8 [1].

The tensile behavior of the bolts plays an important role in the performance of T-stubs. Zhu et al [27] observed two additional failure modes (aside from the three currently considered in [1]) due to nut stripping in the threaded part of the bolt shank. Also D'Aniello et al. [28-29] studied the tensile behavior of European HR and HV preloaded bolts under both monotonic and cyclic loading, showing the significant difference in terms of failure mode and residual resistance. In particular, the failure mode under pure tension of HR bolts is the shank necking, while HV bolts fail under nut stripping with premature loss of strength but larger displacement capacity as respect to the corresponding HR bolts. This aspect may highly affect the T-stub ductility, which can change in function of the type of bolt, while current EN1993-1-8 that allows the indifferent use of both HV or HR bolts.

Therefore, in this paper the influence of the type of preloaded bolts (i.e. either HV or HR) and the effectiveness of the component method in the definition of the T-stub resistance are also experimentally investigated.

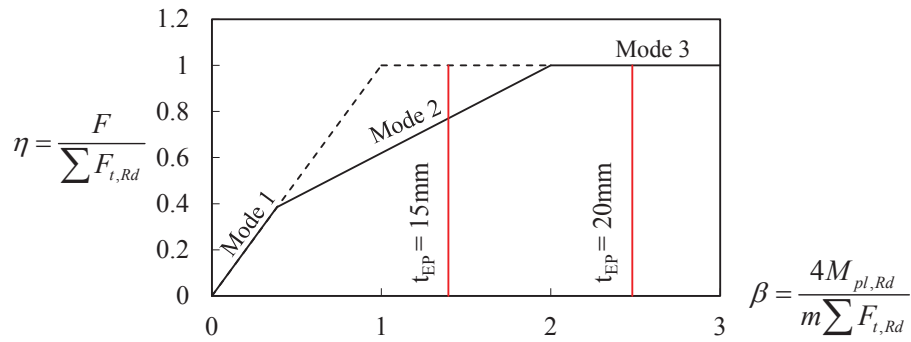
The work is organized in four main parts: in the first the design procedure, the experimental setup and the tests results are presented. The second part is focused on the comparison between the experimental results with the analytical model prescribed by the EN1993-1-8.

## 2 DESIGN OF T-STUB SPECIMENS

The geometrical and mechanical features of the T-stub specimens were designed to investigate the behavior under failure mode 2 and failure mode 3 (see Figure 1).

To achieve this purpose the geometry of the specimens was varied on the basis of the relation depicted in Figure 1, which shows that the T-Stub failure modes theoretically vary in function of the ratio  $\beta$  between the tensile resistance of the bolts and sign flexural the strength related to a failure mode 1 of the connected plate ( $4M_{pl,Rd}/m$ ) and the ratio  $\eta$  is the ratio between the T-stub strength ( $F$ ) and the bolt tensile design resistance ( $F_{t,Rd}$ ).

Each region identified in the graph corresponds to the range of features to which one failure mode is associated. As it can be observed, the normalized strength for mode 1 in case of non-circular patterns depends on the ratio  $v = e/m$  (where  $m$  is the distance between the bolt axis and the web of Tee, and  $e$  is the distance between the bolt axis and the plate edge).

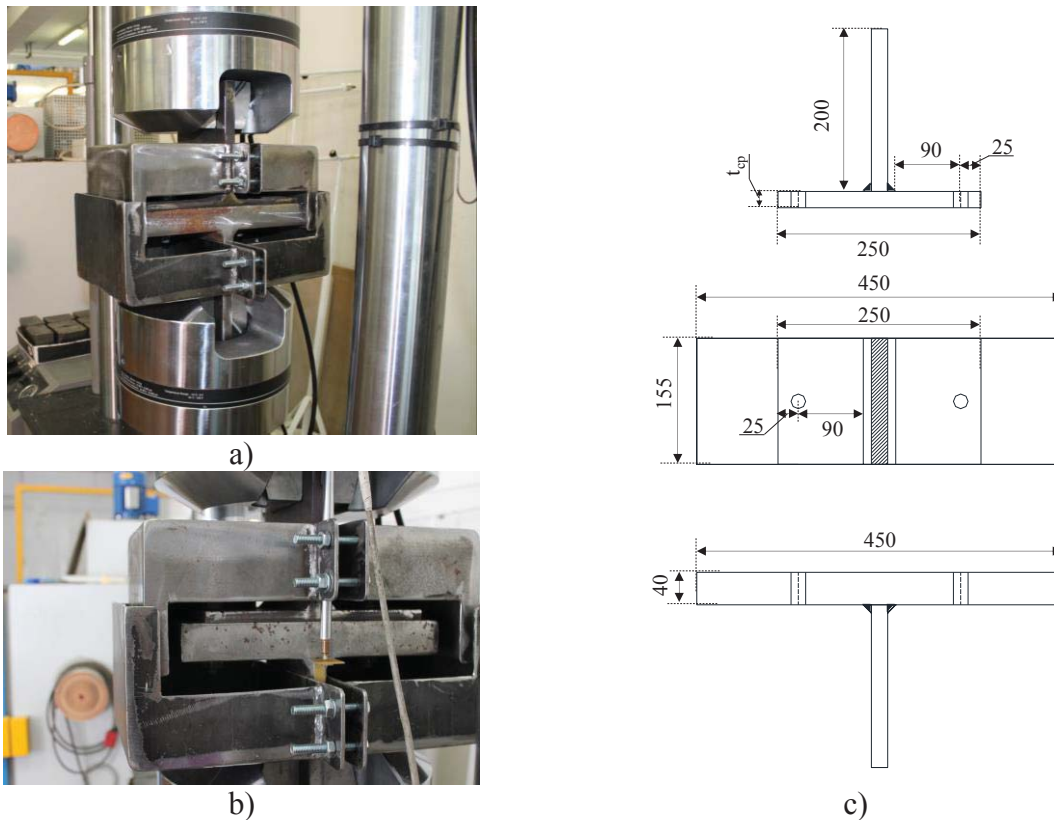


**Figure 1** T-stub resistance and corresponding mechanism according to EN1993:1-8

Table 1 summarizes the experimental tests performed on the four specimens varying both the plate thickness and the bolt typologies (i.e. HR or HV). Each specimen is univocally identified by a label code with four parts that is derived from the main feature of the connection, namely:

- the first letter T stands for T-Stub connection;
- the second part identifies the type of preloaded bolt (i.e. HV or HR).
- the last part stands for the thickness of the flange.

The monotonic tensile tests on T-stub specimens were carried out using a universal electro-mechanical MTS testing machine. Tests were carried out under displacement control until failure. To prevent any damage to the test equipment that might have been induced by bolts following their failure, an encasing steel box was mounted on the web of each specimen as shown in Figure 2a and b.



**Figure 2** Description of the experimental setup

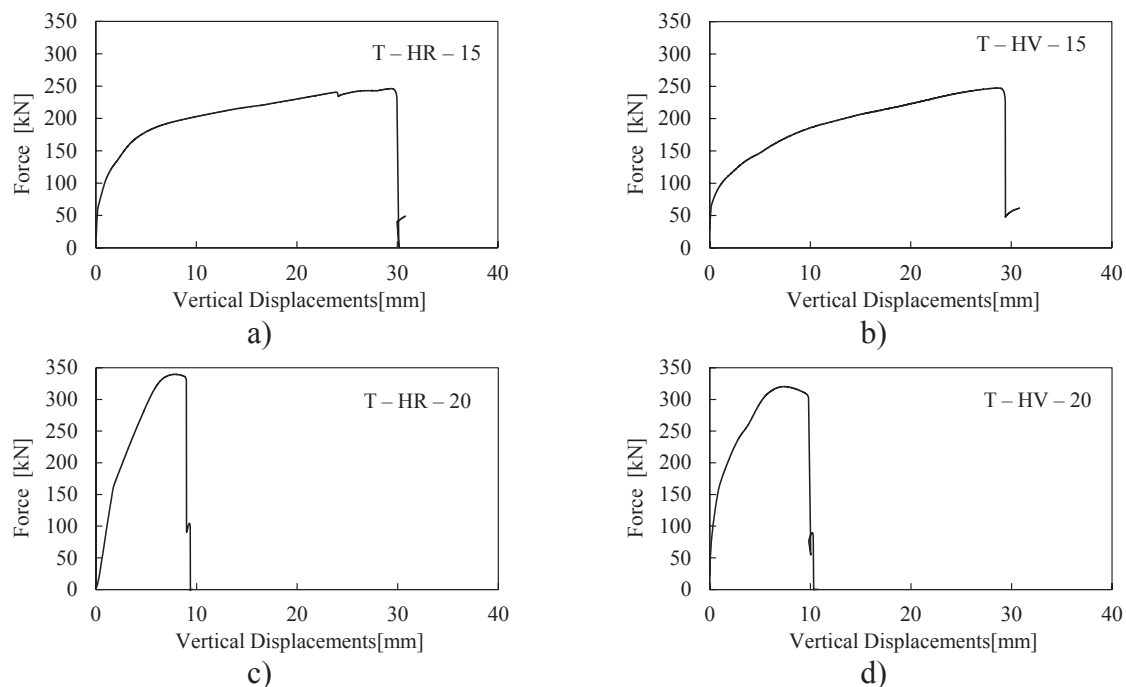
Label [-]	Specimen [-]	Flange thickness $t_f$ [mm]	Bolt type [HR or HV]
T-HR-15	T-15	15	HR
T-HR-20	T-20	20	HR
T-HV-15	T-15	15	HV
T-HV-20	T-20	20	HV

**Table 1** Experimental specimens and relative flange thickness and bolt type

### 3 EXPERIMENTAL TESTS

The experimental results are reported in terms of force-displacement curves (see Figure 3) and in terms of overall failure modes (see Figure 4). In line with the design assumptions, it can be trivially observed that increasing the thickness of the connected plate, the resistance of the specimens increases, and the failure mode moves from the flange to the bolts and ductility decreases accordingly. When a failure mode 2 is observed (e.g. see T-S-HV/HR-15), the plastic deformations are balance between the flange and the bolts; in these cases indeed large plastic deformations can be observed in the plates (see Figure 4 a and b) and in the bolts independently from the their typologies (i.e. HR or HV). The test was stopped only at very large displacements, where the fracture in the bolts was observed (see Figure 4 a and b); it is important to observe that in both the investigated cases, all the bolts show the same failure mode due to a fracture in the shank.

Indeed, when large displacements are reached a membrane action develops in the flange, thus the bolts are not subjected only to the tensile action but also to shear. This mechanism is clearly observable in the specimens T-S-HR/HV-15, where the ovalization of bolt-holes is shown in Figure 4 a and b.

**Figure 3** T-stub results in terms of force displacement curve

Contrariwise, increasing the flange thickness imply a larger demand in the bolts that are mainly subjected to the tensile action without developing significant prying forces. In these cases,



despite no appreciable differences can be observed in terms of force displacements curve, the failure of the two family of bolts is different and it is function of their typologies.



**Figure 4** Failure mode and bolts rupture of the investigated T-Stub

#### 4 CONCLUSIONS

The influence of the type of preloaded high-strength bolts on the T-stub behaviour were investigated by means of four experimental tests.

Although the tensile failure modes of HV and HR bolts are significantly different (i.e. nut stripping and shank necking, respectively), the experimental tests showed that the mode 2 response of T-Stub connections is not affected by the different types of preloaded bolts. This result is mainly due to the type of failure exhibited by bolts that is never under pure tension, but it occurs for a combination of bending moment, axial force and shear force. Hence, HV and HR bolts can be used without any distinction when T-Stub connections are designed to experience mode 1 and 2.

Of course, in the case of very thick flange (i.e. when the resistance of mode 3 is about 3 times or more the resistance of mode 1) the different types of tensile failure mode of the bolts influence the residual resistance of the connection.

## REFERENCES

- [1] CEN 2005. CEN (European Committee for Standardization), Design of steel structures, part 1.8: Design of joints. EN 1993:1-8, Brussels, 2005
- [2] G. Dell’Aglia, R. Montuori, E. Nistri, V. Piluso, Consideration of second-order effects on plastic design of steel moment resisting frames. *Bulletin of Earthquake Engineering*, **17**(6), 3041-3070, 2019.
- [3] P. Castaldo, E. Nistri, V. Piluso, Ultimate behaviour of RHS temper T6 aluminium alloy beams subjected to non-uniform bending: Parametric analysis, *Thin-Walled Structures*, **115**, 129-141, 2017.
- [4] P. Castaldo, E. Nistri, V. Piluso, FEM simulations and rotation capacity evaluation for RHS temper T4 aluminium alloy beams, *Composites Part B: Engineering*, **115**, 124-137, 2017.
- [5] V. Piluso, A. Pisapia, E. Nistri, R. Montuori, Ultimate resistance and rotation capacity of low yielding high hardening aluminium alloy beams under non-uniform bending, *Thin-Walled Structures*, **135**, 123-136, 2019.
- [6] V. Macillo, S. Shakeel, L. Fiorino, R. Landolfo, Development and Calibration of Hysteretic Model for CFS Strap braced stud walls, *International Journal of Advanced Steel Construction, Hong Kong Institute of Steel Construction. ISSN 1816-112X*, **14**(3), 337-360, 2018.
- [7] A. Campiche, L. Fiorino, R. Landolfo, Numerical modelling of CFS two-storey sheathing-braced building under shaking-table excitations, *J. Constr. Steel Res.*, **170**, 2020.
- [8] S. Shakeel, L. Fiorino, R. Landolfo, Behavior factor evaluation of CFS wood sheathed shear walls according to FEMA P695 for Eurocodes, *Engineering Structures*, **221**(15) 2000.
- [9] L. Fiorino, O. Iuorio, V. Macillo, R. Landolfo, Performance-based design of sheathed CFS buildings in seismic area, *Thin-Walled Structures*, **61**, 248-257, 2012.
- [10] V. Macillo, A. Campiche, S. Shakeel, B. Bucciero, T. Pali, M.T. Terracciano, L. Fiorino, R. Landolfo, Seismic Behaviour of Sheathed CFS Buildings: Shake-Table Testing and Numerical Modelling, *Key Eng. Mater.* **763**, 584–591, 2018.
- [11] A. Campiche, Numerical modelling of cfs three-story strap-braced building under shaking-table excitations, *Materials*, **14**(1), pp. 1–13, 118, 2021.
- [12] A. Campiche, S. Shakeel, V. Macillo, M.T. Terracciano, B. Bucciero, T. Pali, L. Fiorino, R. Landolfo, Seismic behaviour of sheathed CFS buildings: Shake table tests and numerical modelling, *Ingegneria sismica-International Journal of Earthquake Engineering*, **35**, 106-123, 2018.
- [13] R. Tartaglia, M. D’Aniello, M. Andreini, S. la Mendola, The performance of preloaded bolts in seismically prequalified steel joints in a fire scenario. *Materials*, **13**(22), 1-14, 2020.

- 
- [14] R. Tartaglia, M. D’Aniello, R. Landolfo, Numerical simulations to predict the seismic performance of a 2-story steel moment-resisting frame. *Materials*, **13**(21), 1-17, 2020.
- [15] R. Tartaglia, M. D’Aniello, Influence of Transverse Beams On the Ultimate Behaviour of Seismic Resistant Partial Strength Beam-To-Column Joints. *Ingegneria Sismica*, **37**(3), 50-65, 2020.
- [16] M. D’Aniello, R. Tartaglia, D. Cassiano, Experimental investigation of the inelastic tensile behaviour of non-preloadable grade 8.8 bolts. *Ingegneria Sismica*, **37**(2), 92-109, 2020.
- [17] R. Tartaglia, M. D’Aniello, M. Zimbru, Experimental and numerical study on the T-Stub behaviour with preloaded bolts under large deformations. *Structures*, **27**, 2137-2155, 2020.
- [18] EL Minas, JG Charlis, An incremental model for predicting the mechanical characteristics of T-stub steel connections. *J Mech Mater Struct*, **1**(7), 1135–59, 2006.
- [19] A. Francavilla, M. Latour, V. Piluso, G. Rizzano, Bolted T-stubs: A refined model for flange and bolt fracture modes. *Steel and Composite Structures*, **20**, 267-293, 2016.
- [20] C. Faella, V. Piluso, G. Rizzano, Experimental analysis of bolted connections: Snug versus preloaded bolts, *J. Struct. Eng.*, **124**(7), 765-774, 1998.
- [21] J.A. Swanson, R.T. Leon, Bolted steel connections: Tests on T-stub components, *J. Struct. Engrg.*, ASCE, **126**(1), 50–56, 2000.
- [22] J.A. Swanson, R.T. Leon, Stiffness modeling of bolted T-stub connection components, *Journal of Structural Engineering*, 127, 2001.
- [23] M. Latour, G. Rizzano, Experimental Behavior and Mechanical Modeling of Dissipative T-Stub Connections, *J. Struct. Eng.*, **138**(2), 170-182, 2012.
- [24] J. Ribeiro, A. Santiago, C. Rigueiro, L.S. Da Silva, Analytical model for the response of T-stub joint component under impact loading, *Journal of Constructional Steel Research*, **106**, 23-34, 2015.
- [25] M. Latour, G. Rizzano, A. Santiago, L.S. Da Silva, Experimental analysis and mechanical modeling of T-stubs with four bolts per row, *Journal of Constructional Steel Research*, **101**, 158-174, 2014.
- [26] A.B. Francavilla, M. Latour, V. Piluso, G. Rizzano, Simplified finite element analysis of bolted T-stub connection components, *Engineering Structures*, **100**, 656-664, 2015.
- [27] Xulin Zhu, Peijun Wang, Mei Liu, Wulan Tuoya, Shuqing Hu, Behaviors of one-side bolted T-stub through thread holes under tension strengthened with backing plate, *Journal of Constructional Steel Research*, **134**: 53-65, 2017.
- [28] M. D’Aniello, D. Cassiano, R. Landolfo, Monotonic and cyclic inelastic tensile response of European preloadable GR10.9 bolt assemblies, *Journal of Constructional Steel Research*, **124**: 77–90, 2016.
- [29] M. D’Aniello, D. Cassiano, R. Landolfo, Simplified criteria for finite element modelling of European preloadable bolts, *Steel and Composite Structures*, **24**(6), 643-658, 2017.

## INFLUENCE OF THE JOINT BEHAVIOUR ON THE PERFORMANCE OF ORTHOGONAL EXOSKELETONS FOR SEISMIC RETROFIT

R. Tartaglia<sup>1</sup>, G. Di Lorenzo<sup>2</sup>, A. Formisano<sup>2</sup>, R. Landolfo<sup>2</sup>

<sup>1</sup> Department of Structures for Engineering and Architecture  
University of Naples Federico II  
via Forno Vecchio 34, 80136 Naples (Italy)  
e-mail: [roberto.tartaglia@unina.it](mailto:roberto.tartaglia@unina.it)

<sup>2</sup> Department of Structures for Engineering and Architecture  
University of Naples Federico II  
via Forno Vecchio 34, 80136 Naples (Italy)

---

### Abstract

*The orthogonal exoskeletons can be used in seismic application to retrofit an existing building without interfere with the structure operativity. These types of structures are usually placed on the external perimeter of the existing structures and contribute to absorb the horizontal action in case of seismic events. The exoskeletons should be designed in function of the design target and depending on the lateral stiffness of the existing structures. Therefore, the exoskeletons lateral stiffness represents one of the key parameters in the design procedure; however, their structural stiffness is influenced by the joint features. In this work, the influence of the geometrical and mechanical characteristics of the joint on the global exoskeleton's performance is investigated. Non-linear numerical analyses were performed in order to investigate the performance of the exoskeletons accounting for the presence of the joints by the introduction of a no-dimensional local spring. The results show that the local response of the exoskeletons is affected by the joints features, and that in the design phase it is important to take into account the real exoskeletons lateral stiffness.*

**Keywords:** Existing structures, Seismic retrofit, Orthogonal exoskeletal, Joint behavior, Numerical analyses.

---

## 1 INTRODUCTION

Exoskeletons are shear walls composed by steel members. Such kind of resisting systems can be located on the perimeter of an existing building to increasing its lateral stiffness, thus improving the seismic response of the structure [1-5]. Exoskeletons can exhibit a 3-dimensional or 2-dimensional lateral behaviour; with reference to 2-D systems, a further distinction can be made between parallel and orthogonal exoskeletons, in dependence from their orientation with respect to the existing building facades. The present work concerns with 2-D orthogonal exoskeletons (EXO-2D- $\perp$ ), which can represent a competitive strategy for the seismic retrofit of existing structures; indeed, no interruption of productive activities within the building is required for the installation of these systems, which are also suitable for serial production.

Exoskeletons design is mainly governed by the global analysis of the existing structure in presence of lateral loads. However, a considerable influence on the actual structural behaviour is also played by geometrical and mechanical features of the joints, which can modify the whole exoskeleton lateral stiffness in dependence from their local flexural response.

Therefore, in the present paper the influence of joint detailing on the global exoskeleton performance is investigated by means of non-linear numerical analyses. For this purpose an existing reinforced concrete school building located in Italy has been selected as case study.

This work is divided in three parts. In the first section the description of the investigated structure is presented, paying particular attention to its structural deficiencies; the main features of adopted exoskeletons and the different configurations investigated for the relative joints are described in the second part. Finally results of non-linear numerical analyses are presented and commented in the last section.

## 2 DESCRIPTION OF THE CASE STUDY

The selected structure, which is located in province of Macerata, was realized during 1965 to serve as a school building. In analogy with other constructions built in the same period in Italy, the resisting structure has been made using reinforced concrete (RC) and designed only to withstand gravity loads, neglecting any seismic action. The building is articulated on three levels (with a total height of 10.9 m) and has an almost squared footprint of 22 x 17.9 m<sup>2</sup>.

In Figure 1 are depicted an overall view of the case study and its relative building plan.

It can be noticed that RC moment resisting frames are basically unidirectional; indeed, while four main frames are disposed along X direction, only two frames are arranged along the Y direction to act as edge closures, although the presence of a pair of concrete shear walls oriented in the vertical direction (functioning as stairwell) has to be remarked.

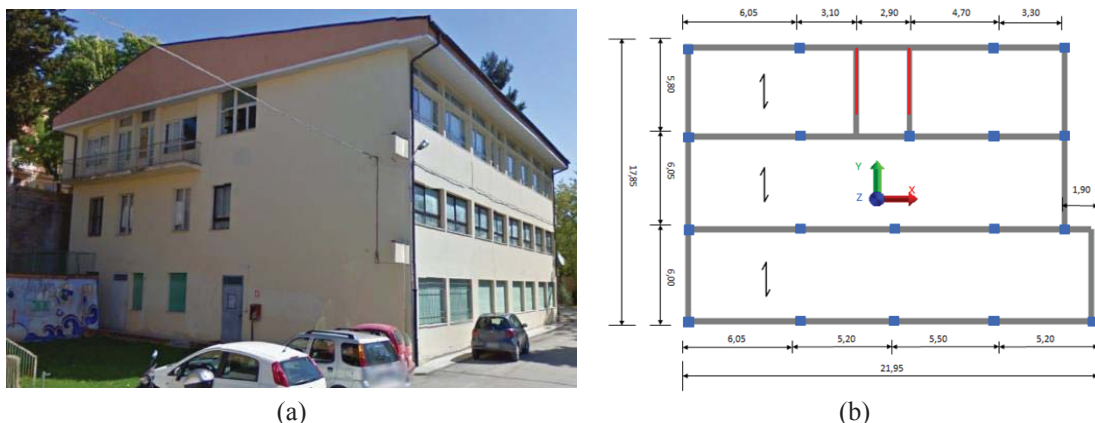


Figure 1: Overall view of the selected school building (a) and relative building plan (b)



A preliminary analysis of the structure has been carried out by the Authors to highlight its critical structural deficiencies, which can be summarized as follows:

- The lack of RC moment resisting frames in the vertical direction, which is a direct consequence of a non-seismic structural conception, leads to the absence of a 2-dimensional structural grid which is necessary to resist seismic actions;
- Both beams and columns are characterized by a large spacing among the steel stirrups, exposing the members to fragile shear mechanisms and reducing the confinement efficiency;
- Since the first two floors are partially underground, inter-story height is inhomogeneous, thus the structure cannot be considered regular along its elevation;
- Testing of materials showed that concrete has poor mechanical characteristics (i.e. its mean compressive strength is lower than 10 N/mm<sup>2</sup>).

### 3 DESCRIPTION OF EXOSKELETONS AND JOINTS

#### 3.1 Description of adopted exoskeletons

The structural criticalities which emerged from the preliminary analysis of the case study made EXO-2D- $\perp$  a viable strategy for the seismic retrofit of the building. Exoskeletons have been designed in accordance to Italian seismic provisions currently in force to allow the structure to resist the full seismic demand expected in the edification site (PGA = 0.202 g for life-safety limit state, considering a service life equal to 75 years), thus restoring a seismic safety factor IS-V equal to 1.

Moreover, although in general exoskeletons can be designed as dissipative systems, in this application EXO-2D- $\perp$  have been proportioned in order to always remain in their elastic range. Among the different possible configurations, a tapered Y-shaped concentrically braced (CBF) solution (see Figure 2a) has been chosen in order to maximize the lateral stiffness incrementation without obstructing the passage in correspondence of the steel frames.

As depicted in Figure 2b, orthogonal exoskeletons have been placed in correspondence of all existing RC frames and nearby the concrete shear walls. Therefore, in order to minimize eccentricity between centre of mass and centre of stiffness two additional systems have been placed in the Y direction on the lower facade.

S355 Circular hollow sections (CHS) have been used for all steel members. The designed cross-sections of all different structural elements (i.e. chords, vertical struts and diagonals) are reported in Table 1.

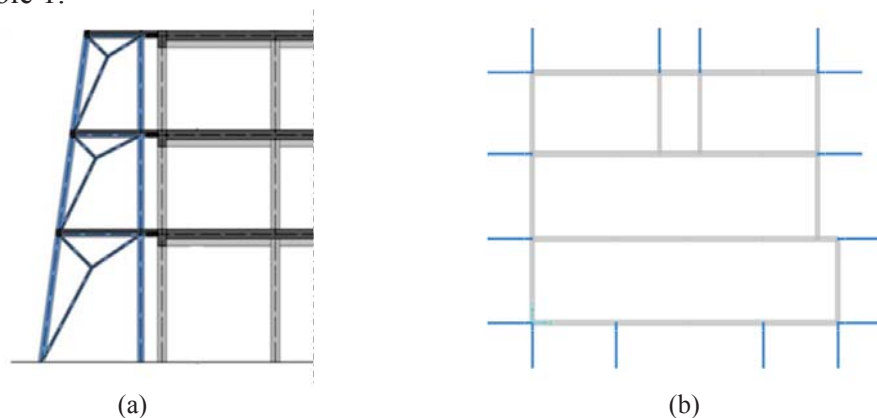


Figure 2: Morphology of adopted orthogonal exoskeletons (a) and relative disposition in plan (b)

Structural member	Diameter [mm]	Thickness [mm]
Chords	244.5	12.5
Vertical Struts	177.8	12.0
Diagonals	139.7	10.0

Table 1: Geometrical features of designed structural members.

### 3.2 Description of investigated joint configurations

Figure 3 depicts the different kinds of considered joint configurations. According to EN1993:1-8 (EC3-1-8), the three investigated alternatives can be identified as rigid (Fig. 3a), semirigid (Fig 3b) and nominally pinned joint (Fig. 3c), respectively. Pinned configuration is made with bolted pins connected to a gusset plate which is in turn fillet-welded to the vertical strut, which subsequently is the only structural member preserving its flexural continuity. In case of semirigid joints all steel members are directly connected to each other by means of fillet welds. To fulfil the EC3-1-8 requirements for a rigid joint the addition of stiffening plates was needed. The effect of local flexural stiffness of the joints has been investigated using SAP2000 v.21 by means of non-dimensional and non-linear spring elements. Constitutive parameters of these elements have been evaluated by means of preliminary finite element analyses. Plasticization in RC elements has been simulated introducing concentrated plastic hinges modelled in accordance with ASCE 41-13 provisions (see Figure 4).

## 4 RESULTS OF NUMERICAL ANALYSES

In order to investigate the influence of joint detailing on the global response of designed EXO-2D- $\perp$ , a total of 24 non-linear static analyses (Pushover) have been conducted on both a singular exoskeleton and on the whole retrofitted structure.

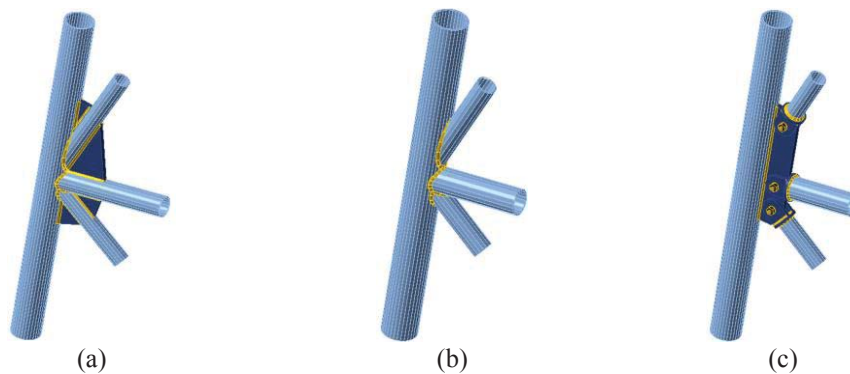


Figure 3: Representation of investigated joint configurations: rigid joint (a), semirigid joint (b) and nominally pinned joint (c).

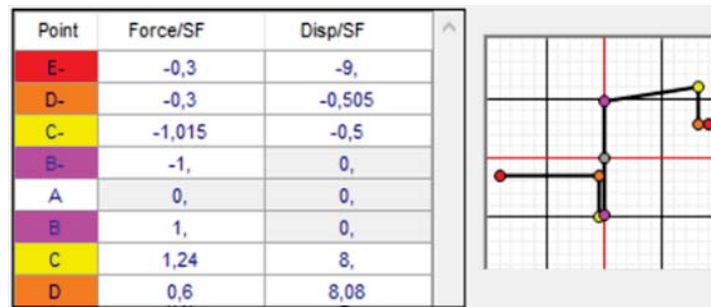


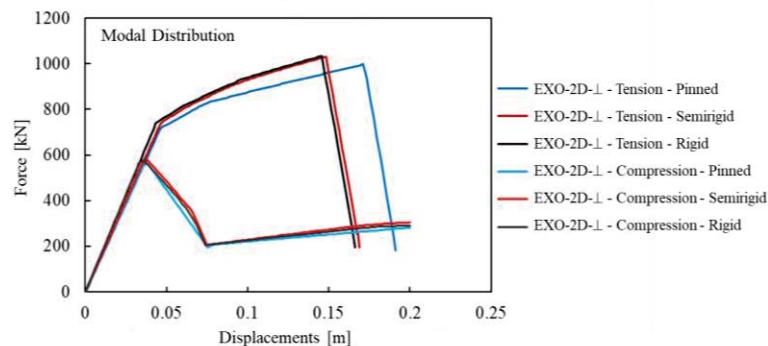
Figure 4: Constitutive relation adopted for plastic hinges.



Figure 5: Structural scheme of a single exoskeleton implemented in SAP2000 v. 21

Both modal and mass proportional force distributions were considered; the seismic actions was applied on both the principal directions of the building. The structural scheme of an exoskeleton as implemented in SAP2000 v.21 is depicted in Figure 5.

Pushover curves for a single EXO-2D- $\perp$ , which are reported in Figure 6, display the influence of joints flexural stiffness on the global response of the system. Indeed, the structural behavior is slightly different when pinned joints are used in place of rigid or semirigid connections. This difference is most noticeable if the exoskeleton is subjected to tension; indeed, after the first yielding the pinned solution displays a more ductile behavior accompanied by a lower value of base shear force. No significant variation can be appreciated while the exoskeleton is in its elastic range. This evidence also explains the almost equivalent behavior of EXO-2D- $\perp$  in compression for all different joints configurations, since in this case the collapse mechanism is governed by global buckling of the first floor diagonal, which causes a sudden loss of capacity without any plasticization phenomenon. Figure 7 reports pushover analyses for the whole retrofitted structure in function of the adopted joints configuration.



(a)

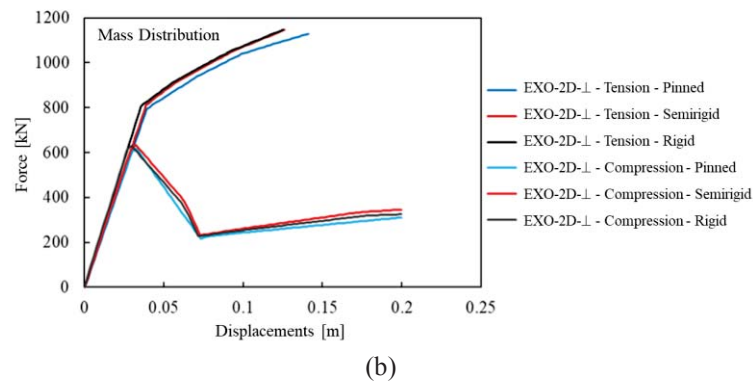


Figure 6: Pushover curves for a single exoskeleton in case of modal (a) and mass (b) force distributions.

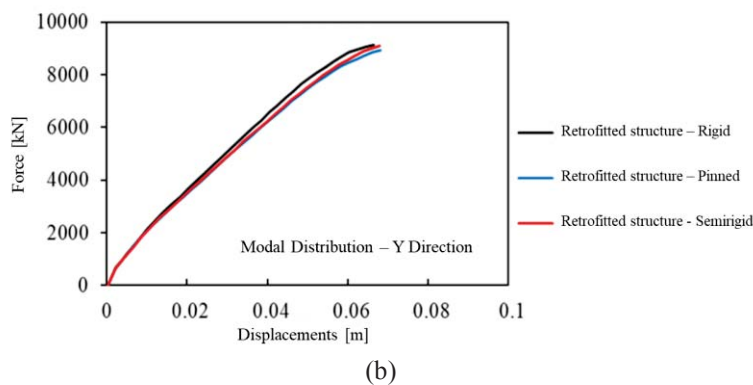
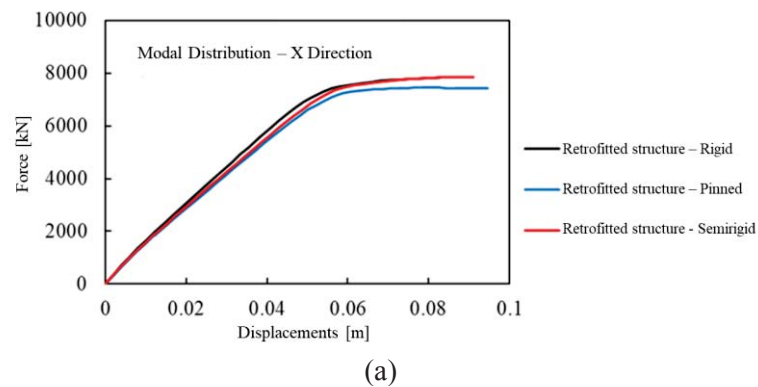


Figure 6: Pushover curves for the retrofitted structure in case of modal distribution forces applied along the X direction (a) and Y direction (b).

One can notice that all investigated solutions display almost the same global response. This outcome is consistent with results relative to a single EXO-2D-⊥.

Indeed, while the influence of joint detailing becomes appreciable in the post-elastic range, it should be remarked that the proposed exoskeletons were all designed to always behave elastically. Moreover, these kind of exoskeletons are prevalently subjected to an axial regime, thus reducing the importance of flexural stiffness on their overall response. Nevertheless, X direction pushover analyses display a more ductile global behavior with respect to Y direction ones. This outcome depends from the disposition of resisting RC systems in the existing structures. Indeed, since all EXO-2D-⊥ remain elastic, the plasticization is concentrated in the RC beams ends, which are almost absent along the Y direction. Therefore, in the vertical direction the structural performance is highly influenced by exoskeletons response, resulting in a more brittle behavior.

## 5 CONCLUSIONS

The influence of joint detailing on the global behavior of 2-D orthogonal exoskeletons has been investigated by means of non-linear numerical analyses. For this purpose an existing school building located in Italy has been selected as case study. From analyses results the following conclusions can be pointed out:

- The influence of joint flexural stiffness on EXO-2D- $\perp$  global behavior is most noticeable in the post-elastic range;
- In post-elastic range pinned solutions display a more ductile behavior with a lower base shear with respect to semirigid or rigid configurations;
- Since the retrofitting of the case study involved exoskeletons designed to remain in their elastic range, there is a minimum difference among the considered solutions;
- Further studies will be conducted considering dissipative exoskeletons to investigate more widely the influence of joint flexural behavior on the structural response when EXO-2D- $\perp$  are in the post-elastic range.

## REFERENCES

- [1] Dell’Aglio, G., Montuori, R., Nastri, E., Piluso, V. Consideration of second-order effects on plastic design of steel moment resisting frames (2019) *Bulletin of Earthquake Engineering*, 17 (6), pp. 3041-3070.
- [2] R. Tartaglia, M. D’Aniello, M. Andreini, S. la Mendola, The performance of preloaded bolts in seismically prequalified steel joints in a fire scenario. *Materials*, **13**(22), 1-14, 2020.
- [3] R. Tartaglia, M. D’Aniello, R. Landolfo, Numerical simulations to predict the seismic performance of a 2-story steel moment-resisting frame. *Materials*, **13**(21), 1-17, 2020.
- [4] R. Tartaglia, M. D’Aniello, Influence of Transverse Beams On the Ultimate Behaviour of Seismic Resistant Partial Strength Beam-To-Column Joints. *Ingegneria Sismica*, **37**(3), 50-65, 2020.
- [5] M. D’Aniello, R. Tartaglia, D. Cassiano, Experimental investigation of the inelastic tensile behaviour of non-preloadable grade 8.8 bolts. *Ingegneria Sismica*, **37**(2), 92-109, 2020.



## EVALUATION OF THE SEISMIC BEHAVIOR OF HISTORICAL CHURCHES REINFORCED BY CROSS-LAM ROOF-STRUCTURE

N. Longarini<sup>1</sup>, P. Crespi<sup>2</sup>, and M. Zucca<sup>2</sup>

<sup>1</sup> Department of Architecture, Built Environment and Construction Engineering, Politecnico di Milano  
e-mail: nicola.longarini@polimi.it

<sup>2</sup> Department of Architecture, Built Environment and Construction Engineering, Politecnico di Milano  
{pietro.crespi,marco.zucca}@polimi.it

---

### Abstract

*Many typical historical masonry churches, with one nave and wooden roofs, have shown high seismic vulnerability in the recent seismic events, especially under transverse earthquakes. In fact, the nave transverse response of this kind of constructions is influenced both by the materials features and the geometrical characteristics. In order to improve the seismic response, the box behavior strategy basing on dissipative roof-diaphragm, can be pursued by adopting cross laminated timber panels (CLT). In this paper, for five historical masonry churches, the effectiveness of different CLT panels solutions is investigated by performing comparative non-linear dynamic analyses adopting equivalent finite element models. The CLT solutions differ themselves for the panels thickness (6mm and 10mm) and the number of the connections (8, 16 and 32 crews in one linear meter). The results are shown in terms of dimensionless transverse displacement (drift) and shear occurred at the base of the façade. Therefore, the influence of the most important geometrical features (as slenderness of the perimeter walls, the width and the length of the churches) in the seismic response is pointed out for each church equipped by different CLT roof-diaphragm solutions.*

**Keywords:** Historical Churches, Seismic Vulnerability, Roof-Diaphragm, Time-History analysis.

---

## 1 INTRODUCTION

In the historical masonry churches the observation of post-earthquake damages allowed the identification of several recurring collapse mechanisms [1, 2, 3]. In the nave transversal response [4] an excessive rocking of the perimeter walls can lead to: (i) out-of-plane mechanisms with a consequent collapse of the roof structure supports [5, 6, 7] or (ii) in-plane excessive stress in the walls in parallel located with respect to the earthquake. On the other hand, the historical masonry churches with wooden roof structures, realized in several configurations in according to the traditional construction techniques of the location site [8, 9], were originally designed to withstand static loads even if the constructions are in regions nowadays classified as seismic [10-15]. To preserve the cultural heritage, the seismic strengthening of historical churches represents a mandatory issue achieving by retrofitting strategies able to provide the “global box behavior” to the construction. Therefore, after accurate analyses about (i) the conservation status of the masonry and wooden elements, (ii) the clamping between the head and perimeter walls and (iii) the wall-to-roof connections, the retrofitting operations can be chosen in order to avoid both out-of-plane and in-plane collapse mechanisms.

Comparative analyses among churches with same configuration can be useful to predict the structural failure in seismic response and to orient the retrofitting techniques [16-20] according to the conservative restoration criteria satisfying, as far as possible, the original material compatibility without changing the authenticity of the constructions [21, 22, 23]. Among these techniques the realization of dissipative wooden based roof-diaphragm represents a valid option because the out-of-plane rocking of the longitudinal walls can be reduced limiting the in-plane shear actions transferred to the head walls [24]. Several wooden based roof-diaphragm configurations can be realized [25, 26, 27]. One of these is based on the use of Cross Laminated Timber (CLT) panels characterized by an alternated sequence of glued timber layers [28, 29, 30]. This kind of panels have been initially adopted in new timber buildings [31-34] but, in several experimental tests and numerical analyses, they have shown enough in-plane stiffness able to guarantee the floor diaphragm effect especially if the panels are over-placed on the existing wooden beams or planks creating wood-to-wood composite sections [35, 36, 37]. Under the seismic actions, the energy dissipation in the timber roof-diaphragm must be occurred in the panel-to-panel and wall-to-panel connections, as a consequence the roof diaphragm should be designed in terms of strength, stiffness and ductility [13, 38]. In fact, if the connection resistance exceeding the seismic demand an elastic response without energy dissipation can be occurred, vice versa an excessive stiffness can increase the shear in the folded CLT panels with a consequent thickness increase.

Considering the previous issues, the present work is aimed to evaluate the influence of the geometrical and material features on the nave transverse response for different one nave configuration churches, reinforced by CLT roof structures, under the same seismic action. An adequate representation of the non-linear behavior of the masonry and roof-diaphragm (CLT panels with steel connections) is required to investigate the seismic response under the transverse earthquake [19, 39, 40]. In this way, several methods with different level of accuracy and computational costs should be considered [41], e.g. simplified method [42], limit analysis [43], macro-modelling based on finite element method [44] and equivalent models [25]. These methods are generally based on the discretization of the structure by macro-elements, with concentrated non-linear properties. In the present work, the macro-elements approach is used by equivalent models implementation with vertical mono-dimensional elements representing the masonry elements and horizontal ones representing the roof diaphragm [45]. Non-linear dynamic analyses are performed by introducing the seismic action as time histories in order to simulate the damped rocking mechanism pursued by the dissipative roof-diaphragm.

## 2 EQUIVALENT MODEL

The non-linear dynamic analyses have been performed considering an equivalent finite element model where the structural elements involved in the seismic response of the church are schematized with mono-dimensional macro-elements. In fact, the church was subdivided into  $n$ -seismic resistant systems transversally disposed with respect to the nave: façade, lateral walls coupled themselves, triumphal arches and head wall (Figure 1). The non-linear properties of the perimeter masonry walls and the CLT roof diaphragm are assigned to the related equivalent elements according to [25].

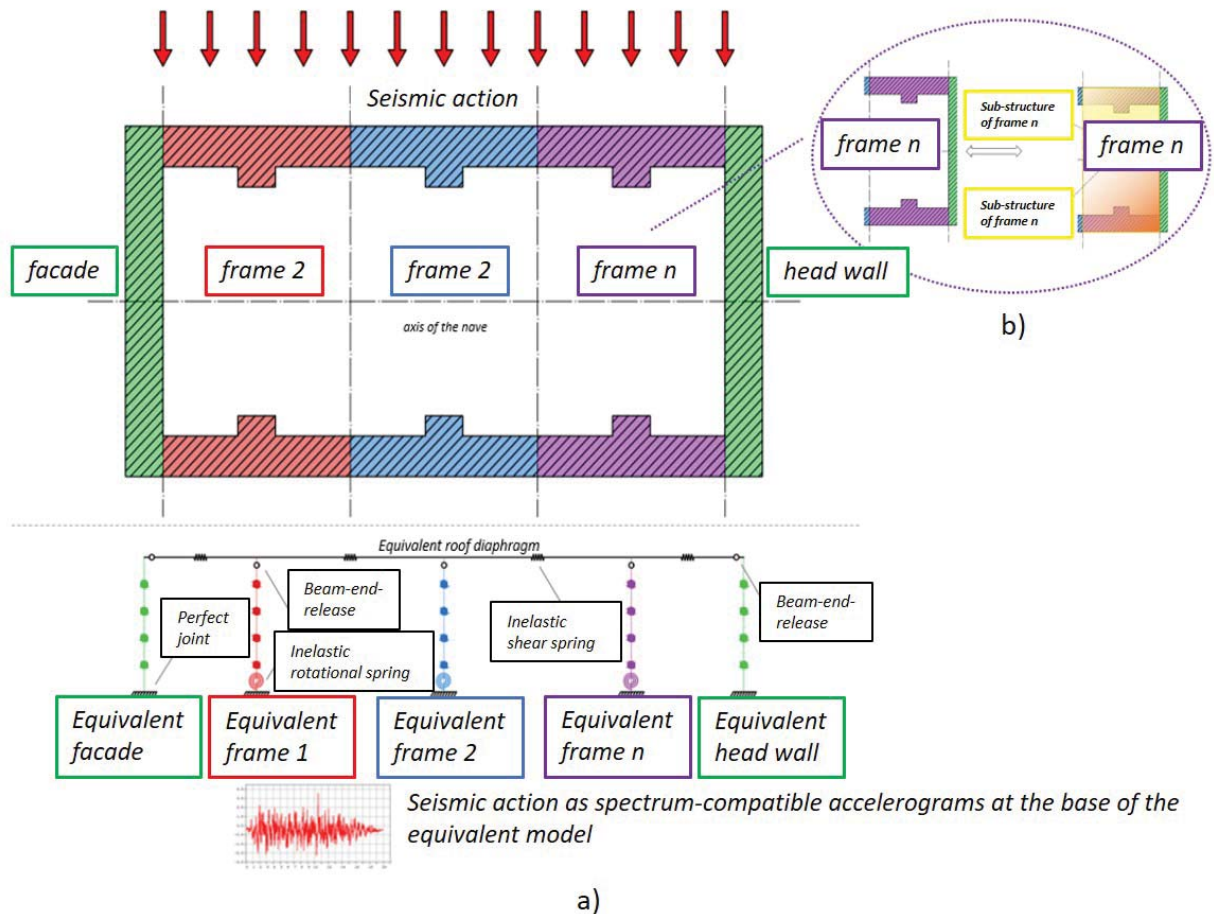


Figure 1: a) Identification of seismic resistant frame in the one nave configuration church (plan view) and related equivalent finite element model representation (longitudinal view) and b) plan view of the sub-structures characterizing the  $n$ -seismic resistant frame.

To implement the equivalent finite element model, three main steps are considered. In the first step, pushover analyses are performed considering the sub-structures schematizing the single parts of the  $n$ -seismic resistant systems as the piers of the longitudinal walls included within the openings or the abutments (Figure 1 and 2a). Each sub-structure is subdivided in section with fibers discretization where the non-linear characteristics are calculated considering a trilinear constitutive law with tensile strength equal to 0 or concrete damaged elasticity model [46, 47] in which tensile cracking and compressive crushing as main failure modes.

In the second step, the yielding and ultimate values obtained by the  $M$ - $\chi$  diagrams calculated through the pushover analyses performed in the first step, are used to implement the inelastic rotational springs assigned at the base of the seismic resistant elements considering a bi-linear constitutive law. Pushover analyses are again carried out in order to obtain the base

shear-top displacement ( $V-\delta$ ) curves of the transversal resistant system and the  $M-\chi$  which characterizes each system is evaluated considering the related shear length (Figure 2b).

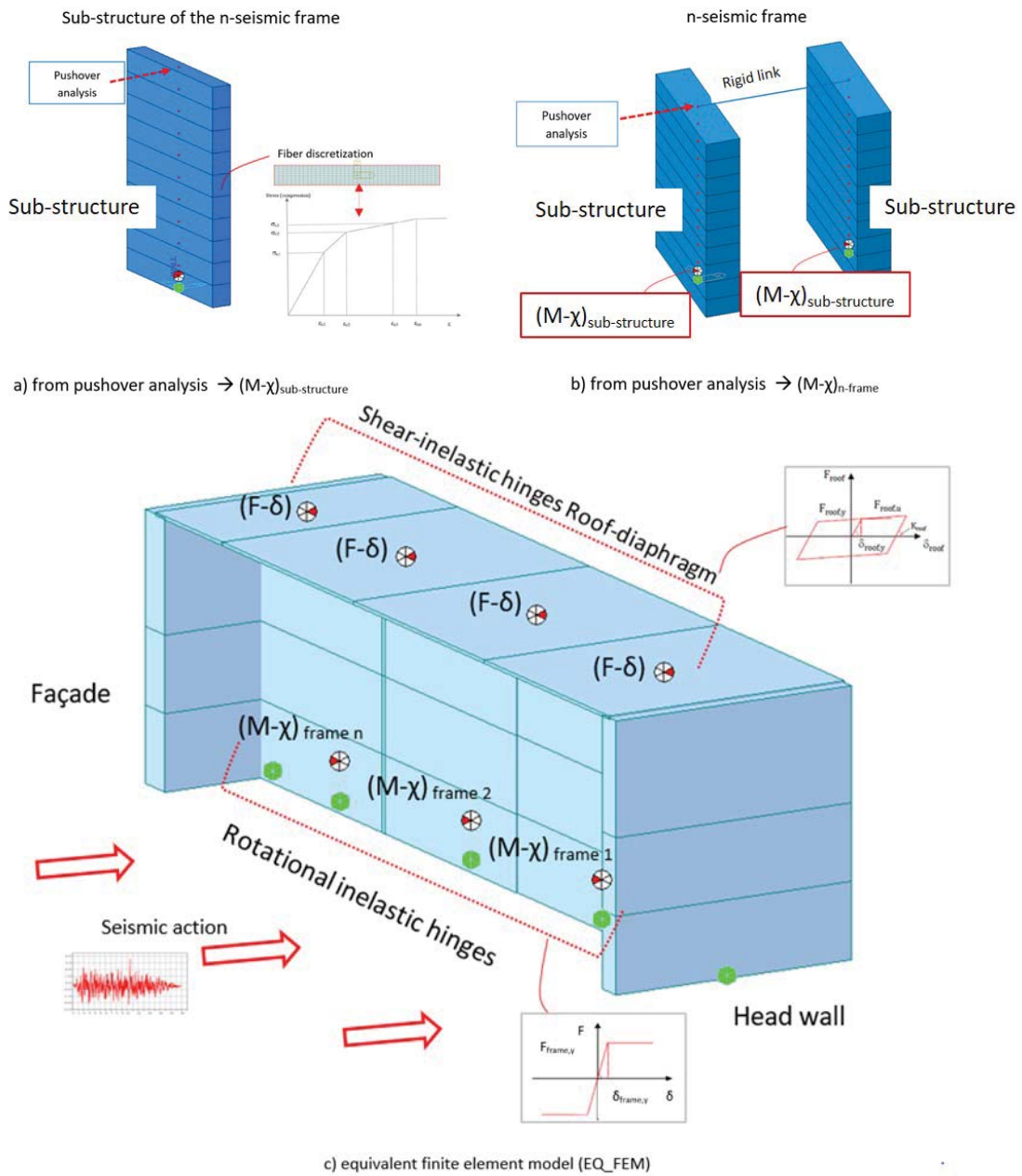


Figure 2: a) pushover analyses on sub-structures, b) pushover analyses on seismic resistant frame with inelastic rotational springs having  $M-\chi$  detected in step a) and c) equivalent finite element model under seven spectrum-compatible accelerograms.

In the third step, the head wall, the façade and the transversal frames are schematized through mono-dimensional equivalent elements. Furthermore, the façade and the head wall are implemented by equivalent elastic mono-dimensional elements fully restrained at the base, considering that their in-plane strength and stiffness are greater than the longitudinal walls [25, 48]. The transversal frames are characterized by the presence of concentrated inelastic rotational springs located at the base and obtained from the above-mentioned  $M-\chi$  diagrams calculated during the second step (Figure 2c). The equivalent finite element model (EQ\_FEM) is

completed through the application of horizontal mono-dimensional equivalent elements representing the roof-diaphragm. The elements of the roof are linked to the vertical ones by hinges located at the end of the vertical elements in order to trigger the rocking and it allows to not transfer the bending moment to the roof. The equivalent elements of the roof are also pinned with respect to the head wall and façade. The shear deformability that characterizes the roof and the non-linear behavior of the connections are implemented to consider the dissipative response of the roof diaphragm through elasto-plastic shear hinges. The shear roof springs are implemented considering a trilinear degrading model [49] or Clough model [28, 50, 51] where the unloading stiffness is calculated considering the reduction of the elastic one with the following relation:

$$K_R = K_0 |D_y / D_m|^\alpha \leq K_0 \quad (1)$$

where  $K_R$  is the unloading stiffness,  $K_0$  is the elastic stiffness,  $D_y$  is the yield displacement,  $D_m$  is the maximum displacement and  $\alpha$  is the unloading stiffness degradation parameter, in this case equal to 0.4. The unloading stiffness gradually reduces when the deformation increases. The seismic action is applied considering a set of spectrum-compatible accelerograms acting transversely to the nave.

### 3 DAMPED ROCKING RESPONSE

The CLT panels, the wall-to-roof and wall-to-wall connections represent a deformable diaphragm which allow the rocking trigger of the perimeter walls but limiting either the drift in a fixed design range and the seismic loads on the rigid head walls (thanks to the energy dissipation occurred in the steel connections). The dissipative roof-diaphragm represents a damper located at the top of the constructions with a behavior analogous to one of a top located damper [4]. By the dissipative roof-diaphragm, the nave transverse response of one nave historical church, usually characterized by high percentage of the total mass involved in the first vibrational mode, can be represented by flag-shaped diagram (Figure 3c) obtained from the bi-linear free rocking behavior of the masonry seismic resistant systems (Figure 3a) [45] and the (ii) the dissipative hysteretic behavior of the roof-diaphragm (Figure 3b) [52, 53].

It is possible to represent the bi-linear behavior of the free rocking through the yielding ( $F_{frame,y}$ ) and ultimate ( $F_{frame,u}$ ) force related to the yielding ( $\delta_{frame,y}$ ) and ultimate ( $\delta_{frame,u}$ ) displacement of the generic resistant seismic frame, obtained by the pushover analyses performed during the second step and mentioned in Section 2. The frame stiffness is calculated considering the following relation:

$$k_{frame} = F_{frame,y} / \delta_{frame,y} \quad (2)$$

Furthermore, it is possible to schematize the dissipative behavior of the roof considering the yielding ( $F_{roof,y}$ ) and ultimate ( $F_{roof,u}$ ) force related to the yielding ( $\delta_{roof,y}$ ) and ultimate ( $\delta_{roof,u}$ ) displacement that characterizes the roof. These values are obtained by the experimental tests on the connector chosen for the connections [28, 54]. Similarly, the roof stiffness is evaluated as follow:

$$k_{frame} = F_{roof,y} / \delta_{roof,y} \quad (3)$$

The flag shaped diagram, shown in Figure 3c, is based on two fundamental hysteretic variables  $\zeta$  and  $\beta$ , defined as follow:



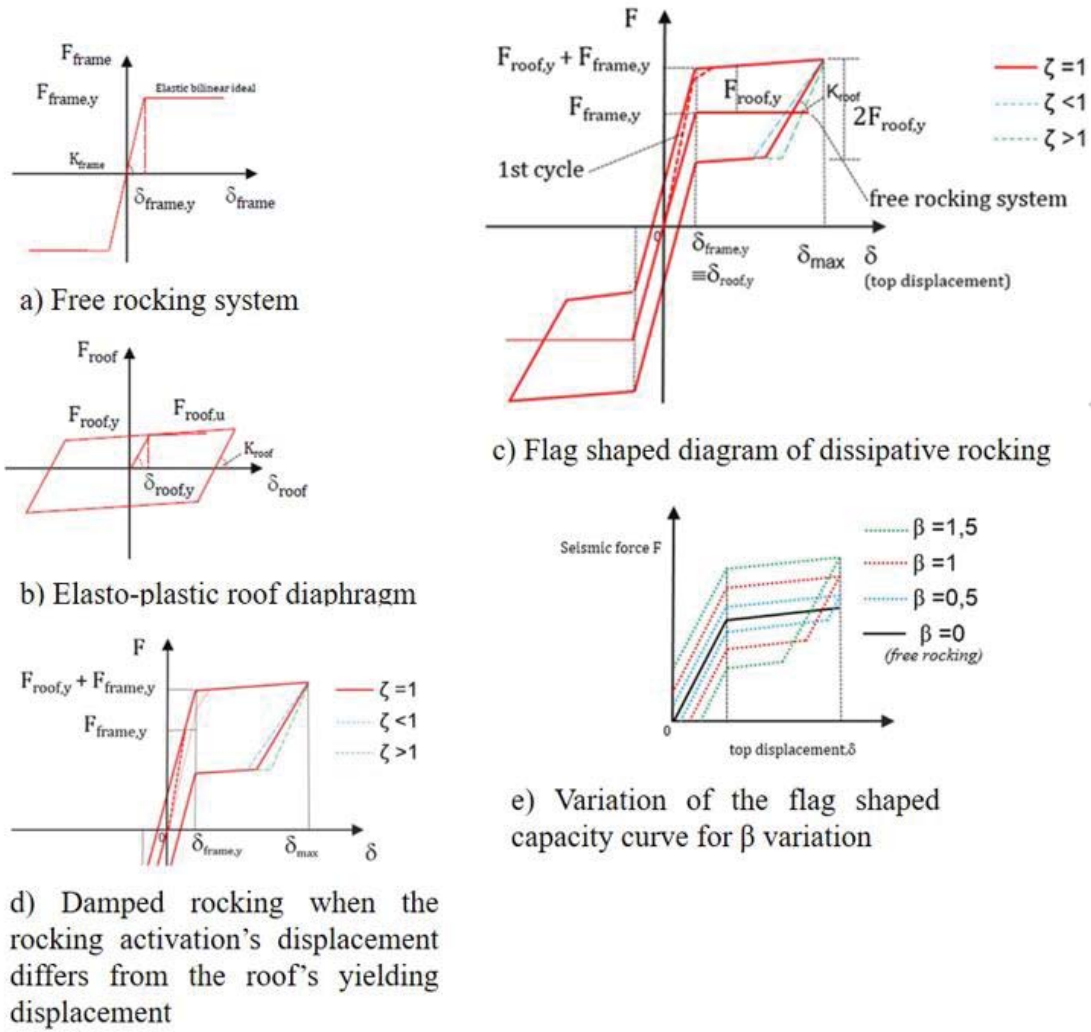


Figure 3: damped rocking diagram.

$$\zeta = (F_{\text{roof},y} \cdot k_{\text{frame}}) / (k_{\text{roof}} \cdot F_{\text{frame},u}) \quad (4)$$

$$\beta = 2 F_{\text{roof},y} / F_{\text{frame},y} \quad (5)$$

It is possible to define the yielding force of the roof in terms of  $\beta$ :

$$F_{\text{roof},y} = (F_{\text{frame},y} \cdot \beta) / 2 \quad (6)$$

while the roof stiffness can be calculated considering both  $\zeta$  and  $\beta$  parameters:

$$k_{\text{roof},y} = (k_{\text{frame}} \cdot F_{\text{roof},y}) / (\zeta \cdot F_{\text{frame},y}) \quad (7)$$

$$k_{\text{roof},y} = k_{\text{frame},y} \cdot [(\beta \cdot \delta_{\text{frame},y}) / (2 \cdot \delta_{\text{roof},y})] \quad (8)$$

It possible to notice that  $\zeta$  can be described through the ratio between the yielding displacement of the roof and the yielding displacements of the frame ( $\zeta = \delta_{\text{roof-y}} / \delta_{\text{frame-y}}$ ) and pro-

vides a measure of the roof diaphragm. As shown in Figure 3d,  $\zeta$  is indirectly proportional to  $k_{\text{roof}}$  because if  $\zeta$  increases, lower energy dissipation occurs.

The  $\beta$  parameter is fundamental for the correct intervention design because it is an index of the energy dissipated by the roof: if  $\beta$  increases, the damping effect increases (Figure 3e). Usually, the  $\beta$  value is between 0 and 1.5. In fact,  $\beta < 2$  is preferable because it allows the self-centering rocking behavior whereas for  $\beta > 2$  there-centering functioning is partially inhibited having a flag-shaped diagram with significant residual displacement, as shown in Figure 3e where the diagram changes from blue line to green one.

The roof diaphragm stiffness, related to the wood elements and the steel connections, is evaluated considering the bending stiffness  $k_{\text{df}}$  and the shear stiffness  $k_{\text{dt}}$ :

$$k_{\text{roof}} = (1/k_{\text{df}} - 1/k_{\text{dt}})^{-1} = [(5/6) \cdot (L^3/E_w^* \cdot J_{\text{id}}) \cdot (\chi L/G_w^* A^*)]^{-1} \quad (9)$$

where  $E_w^*$  is the equivalent elastic modulus,  $G_w^*$  is the equivalent shear modulus and  $J_{\text{id}}$  is the ideal inertia moment of the section:

$$E_w^* = [(Lk_n/n_s)/(2 \cdot ((t_w L_y / \cos \alpha)/n_n) + ((k_n(L/n_s))/E_w))] \quad (10)$$

$$G_w^*(n_n, n_s) = [(Lk_n/n_s)/(2 \cdot ((t_w L_y / \cos \alpha)/n_n) + ((k_n(L/n_s))/G_w))] \quad (11)$$

$$J_{\text{id}}(n_n, n_s) = (t_w L^3 / 12 \cos \alpha) + n_{\text{ws}} \cdot [2A_s (L_y/2)^2] \quad (12)$$

considering that  $n_{\text{ws}}$  is the homogenization coefficient of the steel connection to the wooden diaphragm ( $n_{\text{ws}} = E_s/E_w^*$  where  $E_s$  is the Young modulus of the steel),  $L$  is the distance between the transversal seismic resistant elements and the central nave,  $L_y$  is the roof width,  $k_n$  is the stiffness of the single connector,  $t_w$  is the panels thickness,  $n_s$  is the number of the connections stripes for each span,  $n_n$  is the number of connectors for each connections stripe equal to the ratio between the inter-axis of the seismic elements and the inter-axis of the connectors.

The initial value of  $k_{\text{roof}}$  depends on the geometrical characteristics and the material properties of the CLT panels and on the connections details, calculated according to [24, 25]. This value of  $k_{\text{roof}}$  can be used in the non-linear dynamic analyses even if the optimum roof stiffness ( $k_{\text{roof-opt}}$ ) could be consequently evaluated in correspondence to optimal  $\beta$  ( $\beta_{\text{opt}}$ ) able to limit the drift under the design value  $\delta_{\text{design}} \leq 0.005h_w$ , where  $h_w$  is the height of the perimeter walls [25].  $k_{\text{roof-opt}}$  is evaluated according to the following relation:

$$k_{\text{roof-opt}} = (\beta_{\text{opt}} \cdot k_{\text{frame}})/2\Delta \quad (13)$$

where  $\Delta$  is the ratio between the yielding displacement ( $\delta_{\text{roof,y}}$ ) of the roof and the yielding displacement of the frame ( $\delta_{\text{frame,y}}$ ). The approach is valid because the drift limitation is the first step towards the evaluation of the roof-diaphragm effectiveness. Furthermore, the stiffness of the roof-diaphragm does not influence the intensity of the seismic action on the structure, vice-versa it affects the maximum drift.

## 4 CASE STUDIES

The parametric non-linear dynamic analysis is carried out considering some of the fundamental geometrical features that characterize the five existing one nave historical churches under study (Figure 4) strengthened by four different CLT panels roof structure configurations,

varying the value of  $\beta$  between 0.1 and 1.5. Table 1 shows the values of the geometrical and material characteristics of the above-mentioned churches under study, where  $C$  is the number of spans,  $l_c$  is the length of the church,  $l_f$  is the width of the church,  $t_w$  is the average thickness of the lateral walls,  $h_w$  is the height of the lateral walls,  $\lambda_w$  is the geometrical slenderness of the walls given by the ratio  $\lambda_w = h_w / t_w$ ,  $h_f$  is the height of the façade,  $\lambda_f$  is the geometrical slenderness of the façade given by the ratio  $\lambda_f = h_f / l_f$ ,  $S_F$  is the shape factor ( $S_F = l_c / l_f$ ),  $E_m$  is the elastic modulus of the masonry,  $G_m$  is the shear modulus of the masonry and  $w_m$  is the weight density of the masonry while Figure 5 reports the value of the geometrical characteristics of the churches.

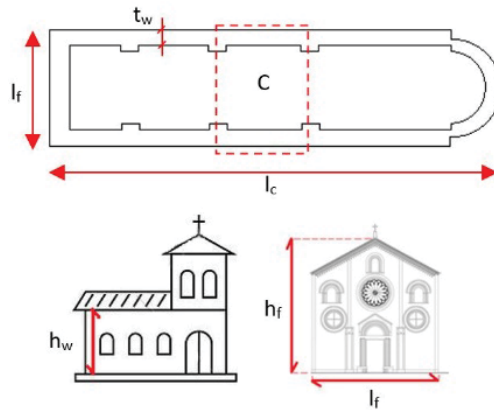


Figure 4: main geometrical characteristics of the churches considered in this work.

church	C	$l_c$ [m]	$l_f$ [m]	$t_w$ [m]	$h_w$ [m]	$\lambda_w$ [-]	$\lambda_f$ [-]	$S_F$ [-]	$E_m$ [MPa]	$G_m$ [MPa]	$w_m$ [kN/m <sup>3</sup> ]
San Pietro Felizzano	7	25	8.50	1.35	10.7	7.92	1.25	2.94	1500	500	18
San Pietro Celestino	4	24	8.75	1.50	11.10	7.40	1.26	2.74	1230	410	20
Santa Maria del Parco	6	33	10.00	1.50	11.75	9.79	1.18	3.30	1080	360	16
Santa Maria del Carmelo	5	32	9.36	1.65	16.00	9.70	1.70	3.42	1230	410	20
San Lorenzo	3	16	4.80	1.65	5.00	7.14	1.04	3.33	1050	350	18

Table 1: geometrical and material characteristics of the churches under study.

Table 3 summarizes the CLT panels roof structure configurations considered in this study which are characterized by the same type of connectors with Ø10 diameter steel screws and stiffness  $k_c = 6500$  N/mm but different panels thickness ( $t$ ), connectors number in the strips present for each span ( $n_s$ ) and mutual distance between the connectors ( $i$ ) (Figure 6).

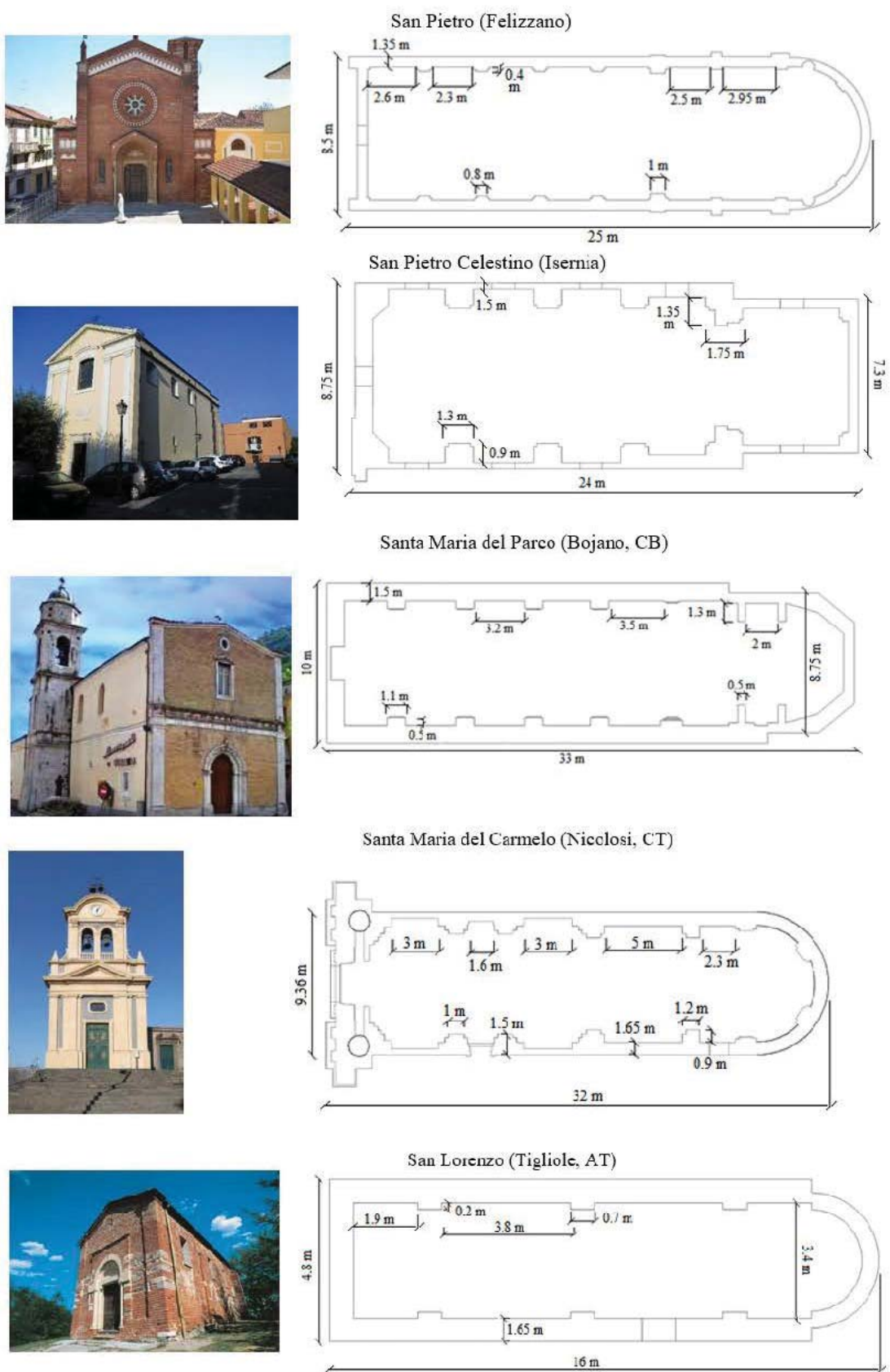


Figure 5: churches under study.

configurations	t [mm]	i [mm]	$k_c$ [N/mm]	$n_s$	Code of the roof diaphragm configuration
a	100	250	6500	272	CLT_t10_i250
b	80	125	6500	136	CLT_t8_i125
c	60	125	6500	136	CLT_t6_i125
d	60	250	6500	68	CLT_t6_i250

Table 2: roof diaphragm configurations.

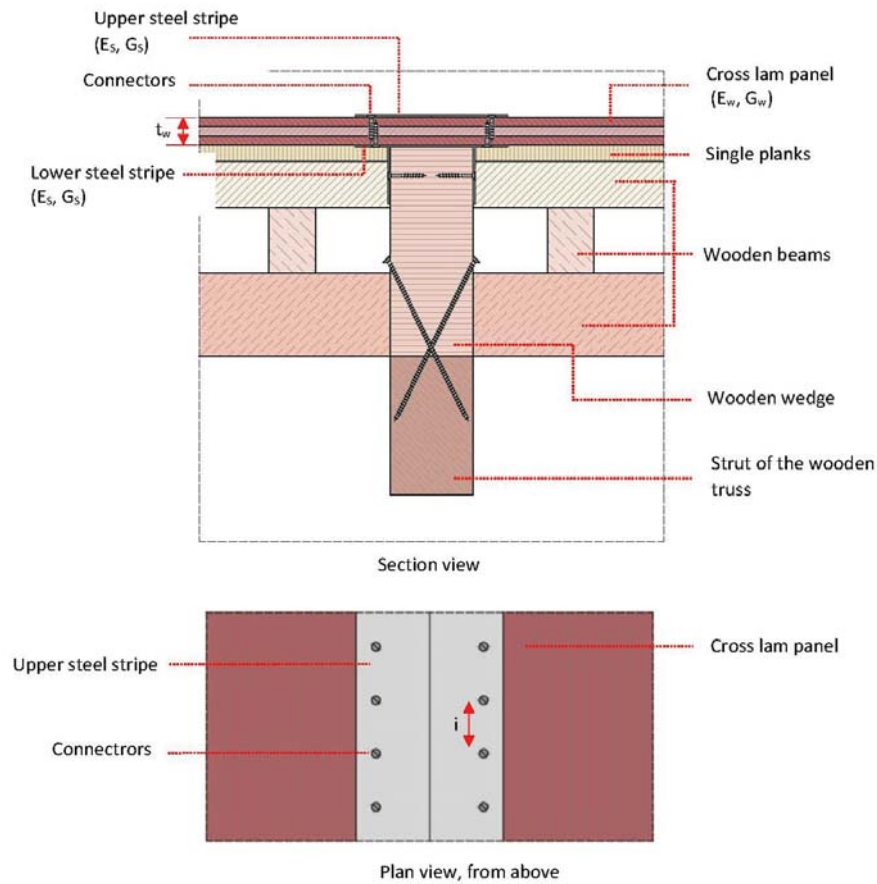


Figure 6: example of CLT panels roof-structure configuration.

Table 3 reports the values of  $k_{\text{roof}}$  obtained by considering the different CLT panels roof-structure configurations for each historical church under study. As mentioned before, the seismic action implemented in the equivalent FEM through seven spectrum-compatible accelerograms detected by Roxel 3.5 software [55] considering the response spectrum of L'Aquila [56] with return period equal to 475 years [57].



San Pietro Felizzano			
configuration	$k_{\text{roof}}$ between façade and element 1 [N/mm]	$k_{\text{roof}}$ between elements 1-2-3-4-5-6-7 [N/mm]	$k_{\text{roof}}$ between element 7 and head wall [N/mm]
CLT_t10_i250	103785.845	79185.243	63681.799
CLT_t8_i125	74517.507	57924.992	46760.372
CLT_t6_i125	59071.713	46441.943	37786.878
CLT_t6_i250	48313.279	38964.366	31792.958
San Pietro Celestino			
configuration	$k_{\text{roof}}$ between façade and element 1 and elements 2-3 [N/mm]	$k_{\text{roof}}$ between elements 1-2 and elements 3-4 [N/mm]	$k_{\text{roof}}$ between element 4 and head wall [N/mm]
CLT_t10_i250	115051.513	98762.181	123290.462
CLT_t8_i125	81589.723	71596.946	83110.602
CLT_t6_i125	64852.888	56999.118	67643.925
CLT_t6_i250	51976.794	47253.905	49976.935
Santa Maria del Parco			
configuration	$k_{\text{roof}}$ between façade and element 1 [N/mm]	$k_{\text{roof}}$ between elements 1-2-3-4-5-6 [N/mm]	$k_{\text{roof}}$ between element 6 and head wall [N/mm]
CLT_t10_i250	136821.131	118930.143	101482.358
CLT_t8_i125	97442.883	86152.975	74129.488
CLT_t6_i125	78098.949	68970.534	59572.859
CLT_t6_i250	62771.455	56959.427	49797.593
Santa Maria del Carmelo			
configuration	$k_{\text{roof}}$ between façade and element 1, [N/mm]	$k_{\text{roof}}$ between elements 1-2-3-4-5 [N/mm]	$k_{\text{roof}}$ between element 5 and head wall [N/mm]
CLT_t10_i250	130395.453	104761.866	119531.499
CLT_t8_i125	91760.781	76103.294	85715.572
CLT_t6_i125	73477.534	60818.342	68348.094
CLT_t6_i250	58032.417	50501.171	55642.081
San Lorenzo			
configuration	$k_{\text{roof}}$ between façade and element 1, between elements 1-2-3, between element 3 and head wall [N/mm]		
CLT_t10_i250	49074.997		
CLT_t8_i125	34984.088		
CLT_t6_i125	26330.719		
CLT_t6_i250	21840.971		

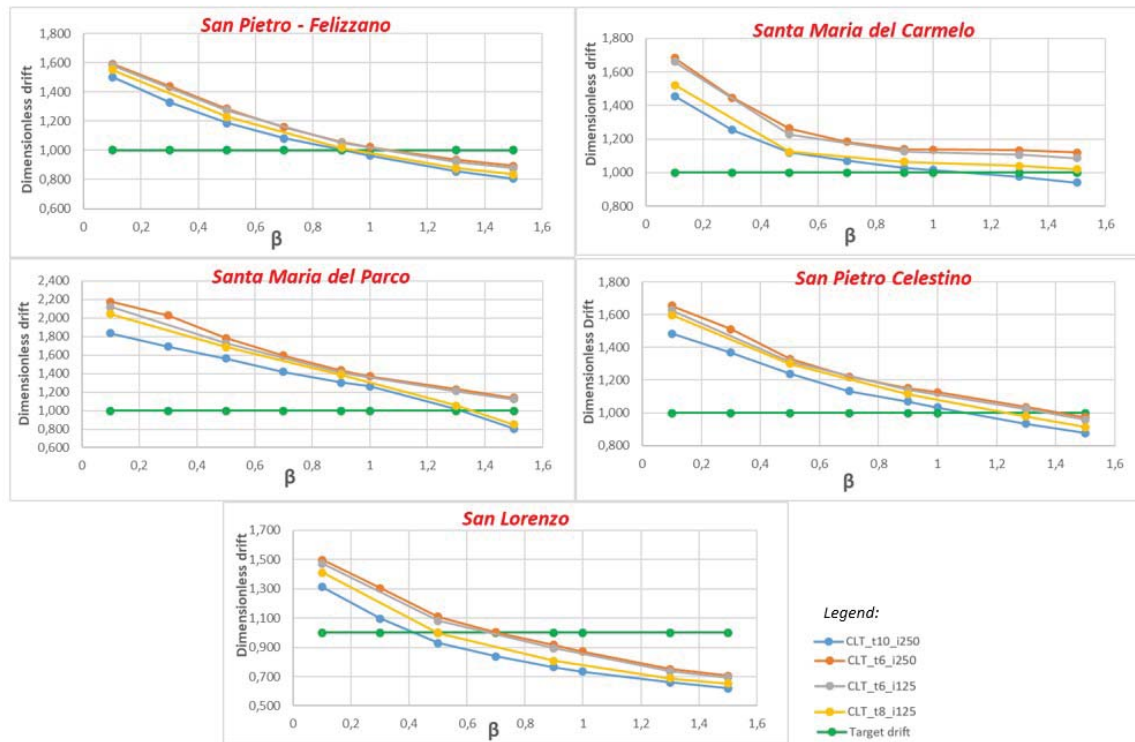
Table 3:  $k_{\text{roof}}$  values.

## 5 RESULTS

The results of the parametric analysis, considering a  $\beta$  value ranging between 0.1 and 1.5, are discussed in terms of two parameters: (i) the ratio between the drift and the height of the lateral walls (dimensionless drift) and (ii) the ratio between the base shear and the axial force on the same equivalent element (dimensionless base shear) taking into account the geometrical slenderness of the walls ( $\lambda_w = h_w/t_w$ ), the geometrical slenderness of the façade ( $\lambda_f = h_f/t_f$ ) and the shape factor ( $S_F = l_c/l_f$ ).

The drift, the base shear and the axial force are evaluated, considering the results obtained by the equivalent element models, as the average values of the maximum ones under the seven spectrum-compatible accelerograms.

The first step of the parametric analysis regards the choice of the optimum  $\beta$  value for each church under study, considering the different roof diaphragm configurations. Figure 7 shows the results obtained from the numerical analyses where the design drift is taken equal to 5% of the height of the lateral walls (green line).

Figure 7: dimensionless drift –  $\beta$  trend.

It is possible to notice that the drift decreases for high values of  $\beta$  parameter because a higher energy dissipation occurs in the connections, according to as reports in Figure 3. Furthermore, the panels thickness influences the seismic response. In fact, considering the same church, when the thickness panels increases the target drift is achieved for lower value of  $\beta$ .

Another important aspect regards the percentage variation of the dimensionless drift ( $\Delta\eta$ ) for each church and the four roof diaphragm configurations by varying  $\beta$  with respect to the single plank roof-configuration (taken as zero condition). Figure 8 shows the  $\Delta\eta$ - $\beta$  trend evaluated for each church under study which are useful to understand the drift improvements as a function of  $\beta$ . It is possible to notice that considering the same church, the variations are more evident for panels with higher thickness. Furthermore, for the same panels thickness, the number of connections slightly influences the variations.

The third consideration regards the variations of the dimensionless base shear of the central equivalent elements and the dimensionless base shear of the façade (Figures 9 and 10). In this case, the results show that the dimensionless shear variations for the central equivalent element and for the façade are in opposite themselves. When  $\beta$  increases, the base shear of the central equivalent element decreases considering that this seismic resistant element is located in the area in which the top displacement is maximum. Consequently, in the central part of the church, the drift and the base shear are in opposite themselves. Similar consideration can be made for the façade. Considering the thickness panels of the roof diaphragm, when this increases the base shear of the central equivalent element decreases. On the contrary, the façade base shear is lower for minor thickness panels.

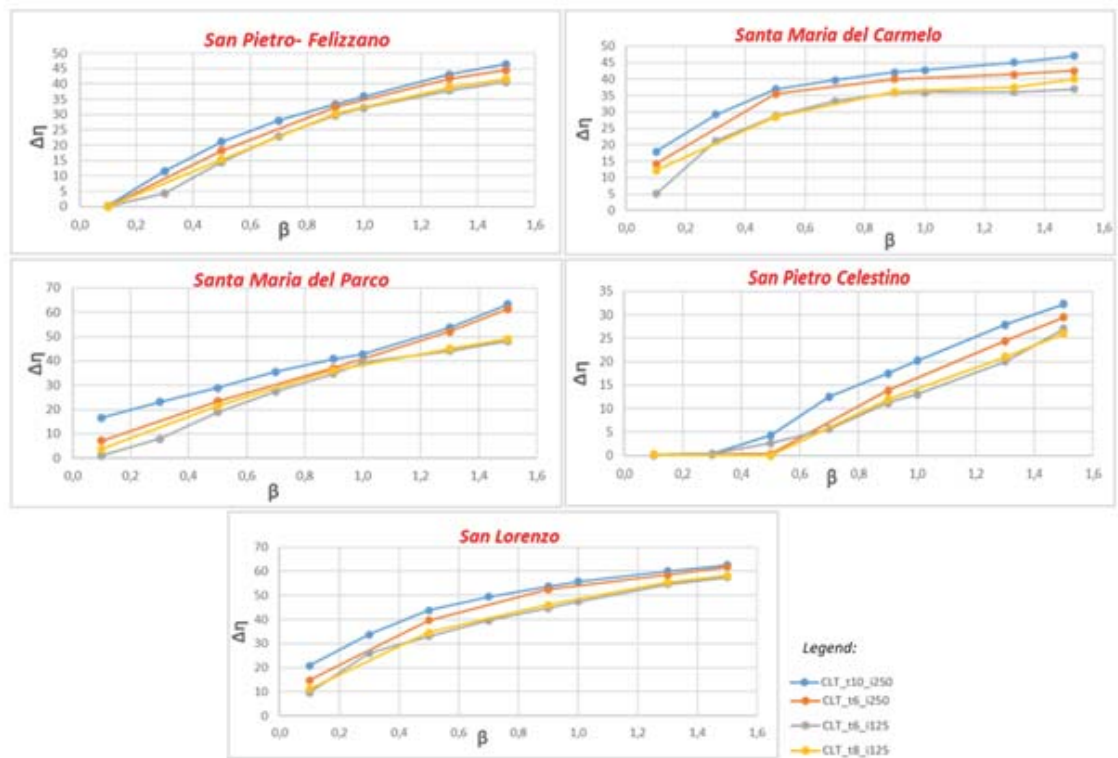


Figure 8:  $\Delta\eta$ - $\beta$  trend.

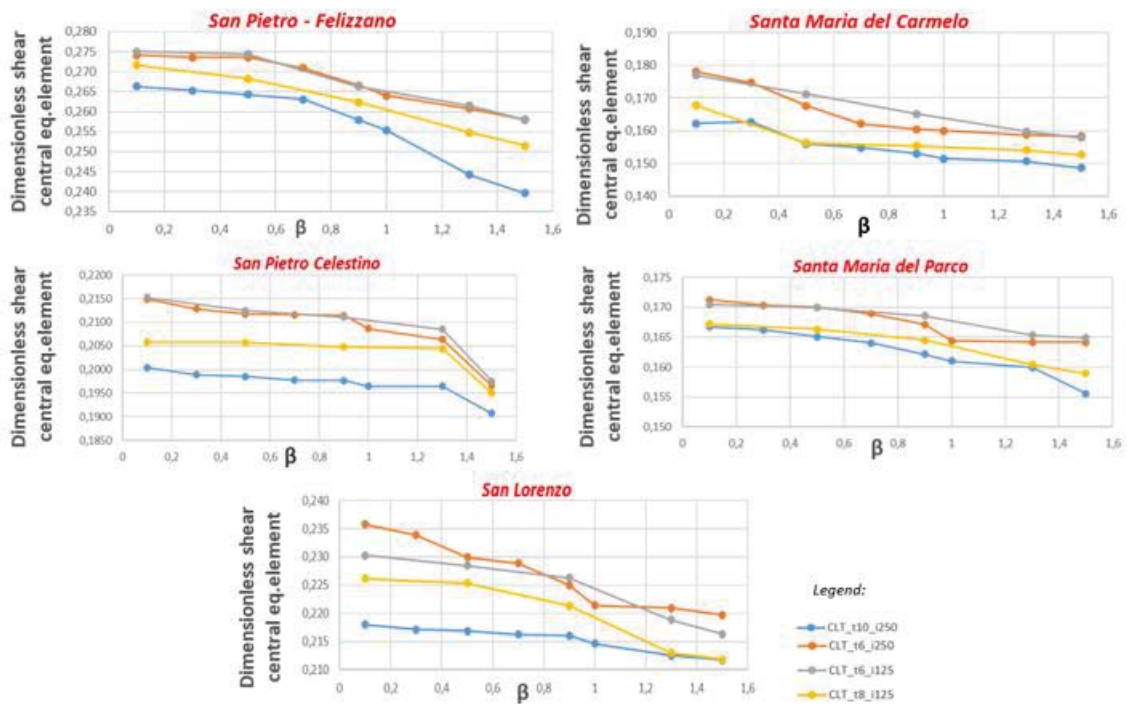


Figure 9: variation of the dimensionless base shear for the central equivalent element as a function of  $\beta$ .

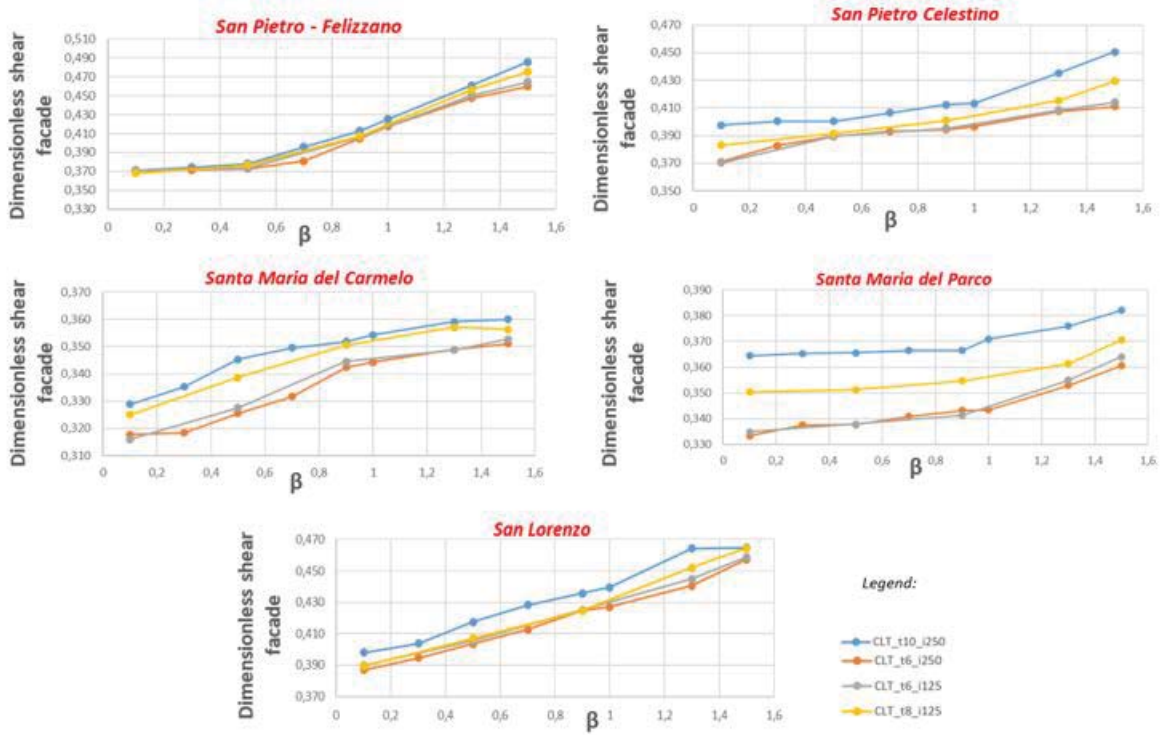


Figure 10: variation of the dimensionless base shear for the façade as a function of  $\beta$ .

The influence of the geometrical slenderness of the walls ( $\lambda_w$ ) and the façade ( $\lambda_f$ ) on the seismic response of the churches under study are analyzed considering the different roof diaphragm configurations. Figures 11 and 12 summarize the results obtained by the numerical analyses.

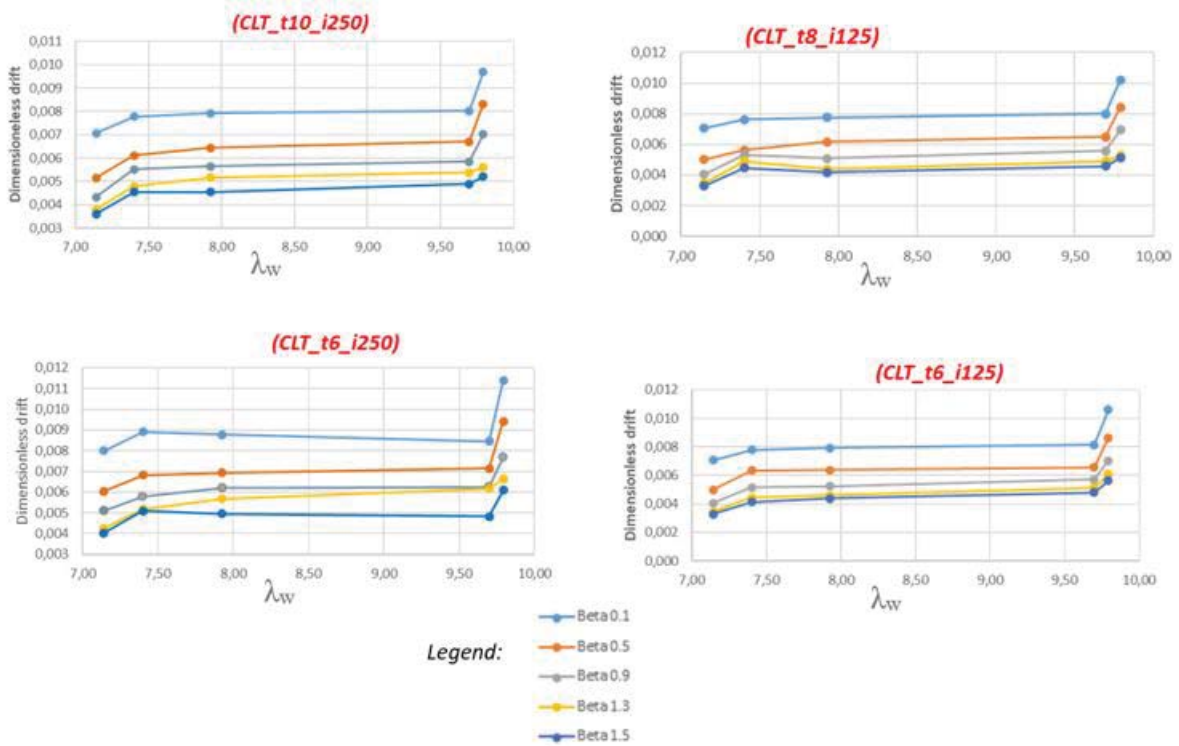


Figure 11: dimensionless drift in comparison to the geometrical slenderness of the lateral walls ( $\lambda_w$ ).



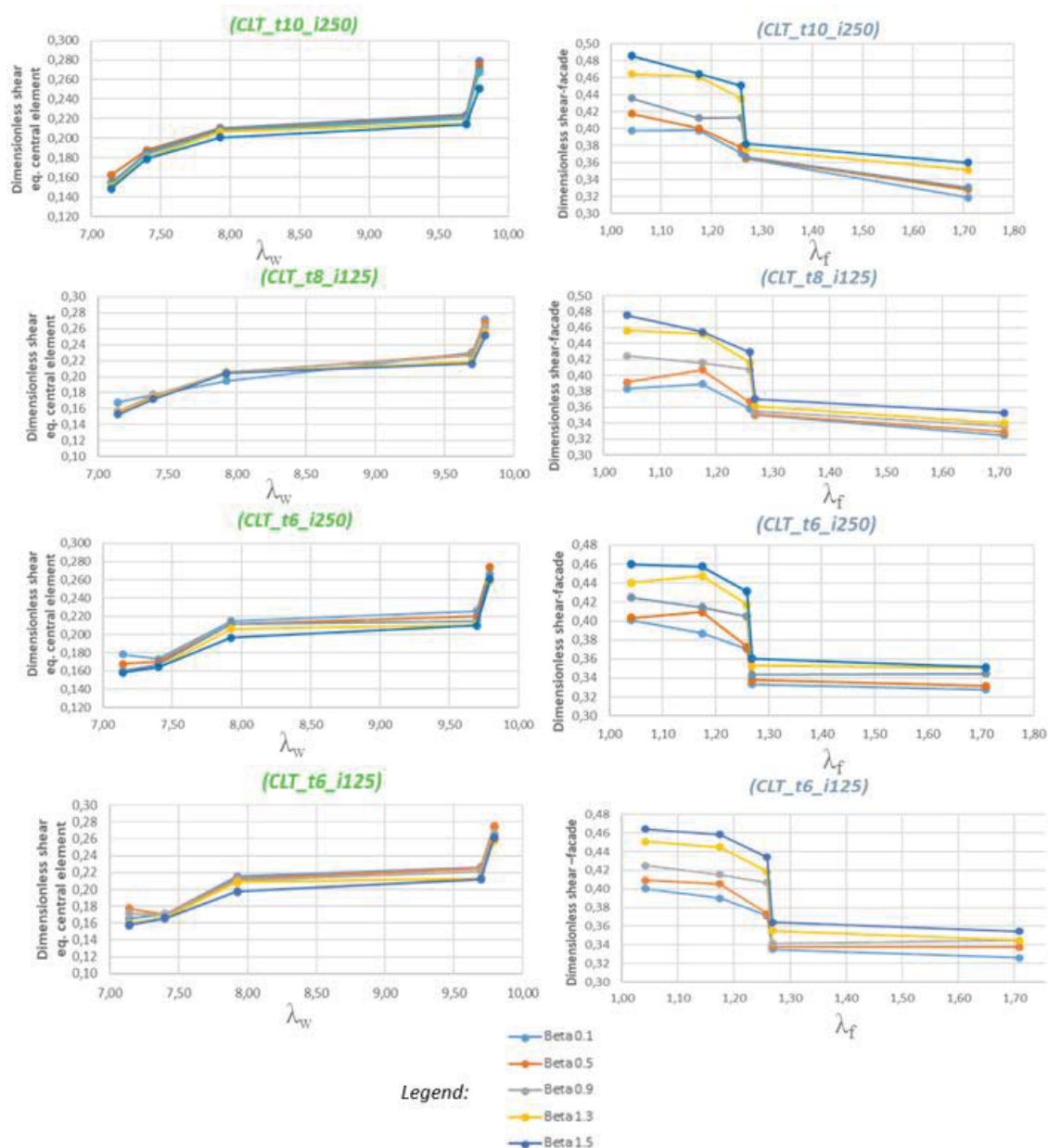


Figure 12: dimensionless base shear in comparison to the geometrical slenderness of the lateral walls ( $\lambda_w$ ) and the geometrical slenderness of the façade ( $\lambda_f$ ).

The results show that a slightly increases of the drift and the base shear acting on the central equivalent element occurs in correspondence to high value of lateral walls slenderness. On the contrary, the dimensionless base shear decreases when the façade slenderness increases.

Considering the trend of the drift and shear of the central equivalent element in relation to the lateral walls slenderness, abrupt variations are obtained when  $9.5 \leq \lambda_w \leq 10$ . It is important to highlight that two churches (Santa Maria del Carmelo and Santa Maria del Parco) characterized by a similar value of lateral walls slenderness were built with different materials and, consequently, different inertia forces are involved during the seismic action. Similar consideration can be made for San Pietro Felizzano and San Pietro Celestino church, analyzing the trend of the base shear related to façade slenderness  $\lambda_f$ . Furthermore, the shapes of the trends appear not be afflicted by the thickness of the panels or the number of the connections.



Figures 13 and 14 summarize the results obtained considering the shape factor ( $S_F$ ) parameter.

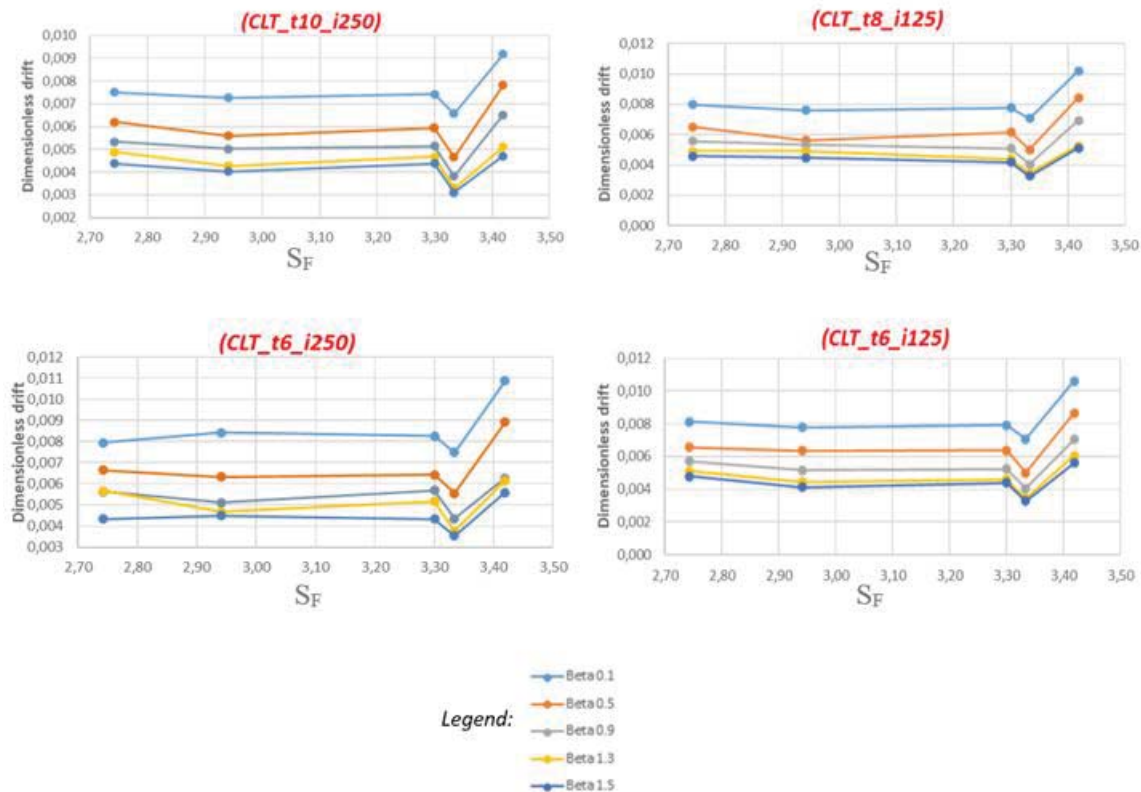


Figure 13: dimensionless drift in comparison to the shape factor  $S_F$ .

It is possible to notice that the dimensionless drift is generally constant with a slight increase for higher shape factor  $S_F$ . Considering the base shear acting on the central equivalent element, the trend obtained is opposite to that calculated for the façade.

Referring to the base shear of the façade, the most evident decrease occurred around  $S_F = 3,30$  for the churches Santa Maria del Parco and San Lorenzo. This fact is due to the very different geometrical characteristics that characterize the two churches (spans, total length and width). Also in this case, the shapes of the trends appear not be afflicted by the thickness of the panels or the number of the connections

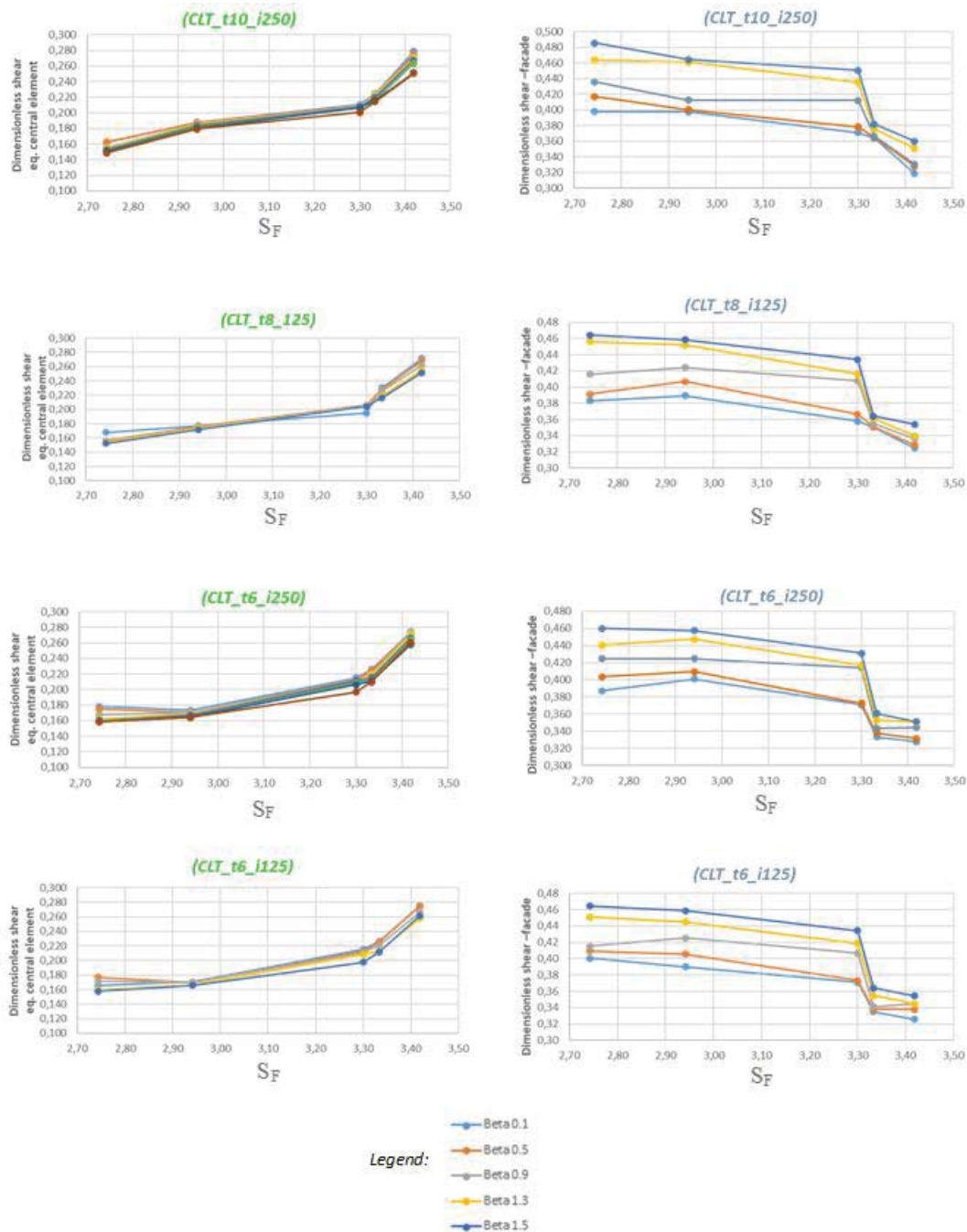


Figure 14: dimensionless base shear (central element and façade) in comparison to the shape factor ( $S_F$ ).

## 6 CONCLUSIONS

In this paper, the influence of the geometrical characteristics on the nave transverse response under seismic action of five historical churches, strengthen by different configurations of CLT panels roof structure, is studied through the execution of a series of non-linear dynamic analyses. The effects of the dissipative roof-diaphragm obtained by the CLT panels and connections are appreciable, especially in terms of dimensionless top displacement (drift) and dimensionless shear evaluated either at the base of the façade and the central part of the perimeter walls.

From the obtained results, the following main observations can be drawn.

- The CLT panels roof-structure in seismic restoration of historical churches can be considered as a valid solution either for the structural benefits in the nave transverse response and the satisfaction of the conservative restoration criteria.
- The equivalent finite element model with calibrated concentrated non-linear material properties (for the masonry and the roof-diaphragm) allows to evaluate the global response of historical churches with low calculation effort.
- The damped rocking mechanism pursued by the dissipative roof-structure is mainly ruled by the variations of the hysteretic variable  $\beta$  that gives a measure of the energy dissipation; the calibration of  $\beta$  is preferable in the range  $0 \div 1.5$  in order to limit the drift under the design drift value guaranteeing the self re-centering rocking behavior and limiting acceptable actions in the head and perimeter walls with respect to the masonry properties.
- The trends of the drift are in according to the shear: when the drift increases the façade base shear increases (while the shear at the base of the central part of the perimeter walls decreases).
- The drift and base shear variations depend more on the thickness of the CLT panels with respect to the connectors numerosity.
- The geometrical slenderness of the perimeter walls ( $\lambda_w$ ) influences the nave transverse response especially beyond  $\lambda_w > 9.5$  even if the seismic behavior cannot uniquely determine only by the geometrical slenderness because it is also influenced by the masonry properties (weight density and elastic modulus) and other geometrical features.
- The drift and the base shears are slightly afflicted by the shape factor.

## REFERENCES

- [1] N. Augenti, F. Parisi. Learning from construction failures due to the 2009 L'Aquila, Italy, earthquake. *Journal of Performance of Constructed Facilities*, **24(6)**, 2016.
- [2] S. Lagomarsino. Damage assessment of churches after L'Aquila earthquake (2009). *Bulletin of Earthquake Engineering*, **10**, 73-92, 2012.
- [3] M. Zucca, P. Crespi, N. Longarini, M.A. Scamardo. The new foundation system of the Basilica di Collemaggio's transept. *International Journal of Masonry Research and Innovation*, **5(1)**, 67-84, 2020.
- [4] V. Bolis, M. Preti, A. Marini, E. Giuriani. Experimental cyclic and dynamic in-plane rocking response of a masonry transverse arch typical of historical churches. *Engineering Structures*, **147**, 285-296, 2017.
- [5] E. Giuriani, A. Marini, M. Preti. Thin-folded shell for the renewal of existing wooden roofs. *International Journal of Architectural Heritage*, **10(6)**, 797-816, 2016.
- [6] G. Brandonisio, E. Mele, R. Santianiello, A. De Luca. Seismic safety of basilica churches: analysis of ten case studies. *6<sup>th</sup> International Conference of Structural Analysis of Historic Construction*, Bath, United Kingdom, July 2-4, 2008.
- [7] M. Valente, G. Milani. Damage survey, simplified assessment, and advanced seismic analyses of two masonry churches after the 2012 Emilia earthquake. *International Journal of Architectural Heritage*, **13(6)**, 901-924, 2019.

- [8] S. Galassi, L. Dipasquale, N. Ruggerini, G. Tempesta. Andalusian timber roof structure in Chefchaouen, Northern Morocco: construction technique and structural behavior. *Journal of Architectural Engineering*, **24(3)**, 2018.
- [9] N. Longarini, P. Crespi, M. Zucca. Dissipative cross lam roof structure for seismic restoration of historical churches. *7<sup>th</sup> Euro-American Congress on Construction Pathology, Rehabilitation Technology and Heritage Management, REHABEND 2018*, Caceres, Spain, May 15-18, 2018.
- [10] N. Augenti, F. Parisi. Learning from construction failures due to the 2009 L'Aquila, Italy, earthquake. *Journal of Performance of Constructed Facilities*, **24(6)**, 2016.
- [11] D.F. D'Ayala, S. Paganoni. Assessment and analysis of damage in L'Aquila historic city centre after 6th April 2009. *Bulletin of Earthquake Engineering*, **9**, 81-104, 2011.
- [12] A. Penna, P. Morandi, M. Rota, C.F. Manzini, F. da Porto, G. Magenes. Performance of masonry buildings during the Emilia 2012 earthquake. *Bulletin of Earthquake Engineering*, **12**, 2255-2273, 2014.
- [13] A. Dal Cin, S. Russo. Annex and rigid diaphragm effects on the failure analysis and earthquake damages of historic churches. *Engineering Failure Analysis*, **59**, 122-139, 2016.
- [14] D. Liberatore, C. Doglioni, O. AlShawa, S. Atzori, L. Sorrentino. Effects of coseismic ground vertical motion on masonry constructions damage during the 2016 Amatrice-Norcia (Central Italy) earthquakes. *Soil Dynamics and Earthquake Engineering*, **120**, 423-435, 2019.
- [15] M. Zucca, A. Franchi, P. Crespi, N. Longarini, P. Ronca. The new foundation system for the transept reconstruction of the basilica di collemaggio. *10<sup>th</sup> International Masonry Conference, IMC 2018*, Milan, Italy, July 9-11, 2018.
- [16] P. Roca, R. Clemente. Studies on the origin of deformation and damage in long-span historical structures. *11<sup>th</sup> International Conference on Fracture, ICF11*, Turin, Italy, March 20-25, 2005.
- [17] G. Lucibello, G. Brandonisio, E. Mele, A. De Luca. Seismic behavior of some Basilica churches after L'Aquila 2009 earthquake. *Advanced Materials Research*, **133-134**, 801-806.
- [18] M. Valente, G. Barbieri, L. Biolzi. Damage assessment of three medieval churches after the 2012 Emilia earthquake. *Bulletin of Earthquake Engineering*, **15**, 2939-2980, 2017.
- [19] M. Betti, A. Vignoli. Numerical assessment of the static and seismic behaviour of the basilica of Santa Maria all'Impruneta (Italy). *Construction and Building Materials*, **25(12)**, 4308-4324, 2011.
- [20] M. Betti, L. Galano, A. Vignoli. Comparative analysis on the seismic behaviour of unreinforced masonry buildings with flexible diaphragms. *Engineering Structures*, **6(1)**, 195-208, 2014.
- [21] N. Gattesco, I. Boem. Numerical study on the reduction of the seismic vulnerability of historical industrial buildings with wide timber roofs. *Procedia Structural Integrity*, **11**, 298-305, 2018.
- [22] M. Zucca, P. Crespi, R. Mendoza, L. Ruggeri. Seismic assessment and retrofitting of an old masonry barrack. *8<sup>th</sup> Euro-American Congress on Construction Pathology, Rehabil-*

- itation Technology and Heritage Management, REHABEND 2020*, Granada, Spain, March 24-27, 2020.
- [23] N. Gattesco, L. Macorini. High reversibility technique for in-plane stiffening of wooden floors. *VI International Conference on Structural Analysis of Historic Construction, SAHC08*, Bath, United Kingdom, July 2-4, 2008.
  - [24] V. Bolis, M. Preti, A. Marini, E. Giuriani. Experimental cyclic and dynamic in-plane rocking response of a masonry transverse arch typical of historical churches. *Engineering Structures*, **147**, 285-296, 2013.
  - [25] E. Giuriani, A. Marini. Wooden roof box structure for the anti-seismic strengthening of historic buildings. *International Journal of Architectural Heritage*, **2(3)**, 226-246, 2008.
  - [26] M.A. Parisi, M. Piazza. Seismic strengthening and seismic improvement of timber structures. *Construction and Building Materials*, **97**, 55-66, 2015.
  - [27] E. Ongaretto, L. Pozza, M. Savoia. Wood-based solutions to improve quality and safety against seismic events in conservation of historical buildings. *International Journal for Quality Research*, **10**, 17-46, 2016.
  - [28] I. Gavric, M. Fragiaco, A. Ceccotti. Cyclic behaviour of typical metal connectors for cross-laminated (CLT) structures. *Materials and Structures*, **48**, 1841-1847, 2015.
  - [29] N. Longarini, P. Crespi, M.A. Scamardo. Numerical approaches for cross-laminated timber roof structure optimization in seismic retrofitting of a historical masonry church. *Bulletin of Earthquake Engineering*, **18**, 487-512, 2020.
  - [30] B. Roensmaens, L. Van Parys, T. Descamps. Proposal of a CLT reinforcement of old timber floors. In: Aguilar R., Torrealva D., Moreira S., Pando M.A., Ramos L.F. (eds) *Structural Analysis of Historical Constructions*. RILEM Bookseries, vol 18. Springer, Cham.
  - [31] A. Ceccotti, M. Follesa, E. Karacabeyli. 3D seismic analysis of multi-storey wood frame construction. *6<sup>th</sup> world conference on timber engineering*, Whistler resort, British Columbia, Canada, July 31-August 3, 2000.
  - [32] M. Follesa, I.P. Christovasilis, D. Vassallo, M. Fragiaco, A. Ceccotti. Seismic design of multi-storey cross laminated timber buildings according to Eurocode 8. *Ingegneria Sismica*, **30(4)**, 27-53, 2013.
  - [33] M. Popovski, I. Gravic, J. Schneider. Performance of two-storey CLT house subjected to lateral loads. *13<sup>th</sup> world conference on timber engineering*, Quebec City, Canada, August 10-14, 2014.
  - [34] P. Ronca, P. Crespi, D. Bonardi, A. Palermo, S. Pampanin. High performance wooden building subjected to seismic action. *International Journal for Housing Science and its Application*, 161-172, 2014.
  - [35] A. Gubana. State-of-the-Art Report on high reversible timber to timber strengthening interventions on wooden floors. *Construction and Building Materials*, **97**, 25-33, 2015.
  - [36] A. Gubana. Experimental tests on timber-to-cross lam composite section beams. *10<sup>th</sup> world conference on timber engineering*, Riva del Garda, Trento, Italy, June 20-24, 2010.



- [37] A. Gubana, M. Melotto. Experimental tests on wooden-based in-plane strengthening solutions for the seismic retrofit of traditional timber floors. *Construction and Building Materials*, **191**, 290-299, 2018.
- [38] M. Piazza, C. Baldessari, R. Tomasi. The role of in-plane floor stiffness in the seismic behaviour of traditional buildings. *14<sup>th</sup> World Conference on Earthquake Engineering*, Beijing, China, October 12-17, 2008.
- [39] G. Milani, R. Shehu, M. Valente. Possibilities and limitations of innovative retrofitting for masonry churches: Advanced computations on three case studies. *Construction and Building Materials*, **147**, 239-263, 2017.
- [40] M. Valente, G. Barbieri, L. Biolzi. Seismic assessment of two masonry Baroque churches damaged by the 2012 Emilia earthquake. *Engineering Failure Analysis*, **79**, 773-802, 2017.
- [41] P. Roca, M. Cervera, G. Gariup, L. Pelà. Structural analysis of masonry historical constructions. classical and advanced approaches. *Archives of Computational Methods in Engineering*, **17**, 299-325, 2010.
- [42] S. Lagomarsino, A. Penna, A. Galasco, S. Cattari. TREMURI program: an equivalent frame model for the nonlinear seismic analysis of masonry buildings. *Engineering Structures*, **56**, 1787-1799, 2013.
- [43] G. Milani. Lesson learned after the Emilia-Romagna, Italy, 20–29 May 2012 earthquakes: a limit analysis insight on three masonry churches. *Engineering Failure Analysis*, **34**, 761-778, 2013.
- [44] P.B. Lourenco, J.G. Rots, J. Blaauwendraad. Two approaches for the analysis of masonry structures: micro and macro-modeling. *Heron*, **40**(4), 1995.
- [45] M. Preti, S. Loda, V. Bolis, S. Cominelli, A. Marini, E. Giuriani. Dissipative roof diaphragm for the seismic retrofit of listed masonry churches. *Journal of Earthquake Engineering*, **23**(8), 1241-1261, 2019.
- [46] J. Lubliner, J. Oliver, S. Oller, E. Onate. A plastic-damage model for concrete. *International Journal of Solids and Structures*, **25**(3), 299-326, 1989.
- [47] J. Lee, G.L. Fenves. Plastic-damage model for cyclic loading of concrete structures. *Journal of Engineering Mechanics*, **124**(8), 1998.
- [48] M. Preti, V. Bolis, A. Marini, E. Giuriani. Example of the benefits of a dissipative roof diaphragm in the seismic response of masonry buildings. *9<sup>th</sup> International Conference on Structural Analysis of Historical Constructions, SAHC2014*, Mexico City, Mexico, October 14-17, 2014.
- [49] T.M. Ferreira, V. Romeu, A.A. Costa, H. Varum. Application of the trilinear model for the analytical study of the out-of-plane behaviour of unreinforced stone masonry walls. *9<sup>th</sup> International Masonry Conference*, Guimaraes, Portugal, July 7-9, 2014.
- [50] T. Genshu, Z. Yongfeng. Seismic force modification factors for modified-Clough hysteretic model. *Engineering Structures*, **29**, 3053-3070, 2007.
- [51] G. Rinaldin, C. Amadio, M. Fragiaco. A component approach for the hysteretic behaviour of connections in cross - laminated wooden structures. *Earthquake Engineering and Structural Dynamics*, **42**(13), 2023-2042, 2013.

- [52] K.W. Johansen. Theory of timber connections. *IABSE Publications*, **9**, 249-262, 1949.
- [53] H.J.K.W. Larsen. Johansen's nail tests. *Bygningssstatistiske meddelelser*, **48**, 9-30, 1977.
- [54] C. Sandhass, J.W.G. van de Kuilen. Strength and stiffness of timber joints with very high strength steel dowels. *Engineering Structures*, **131**, 394-404, 2017.
- [55] I. Iervolino, C. Galasso, E. Cosenza. REXEL: Computer aided record selection for code-based seismic structural analysis. *Bulletin of Earthquake Engineering*, **8**, 339-362, 2010.
- [56] Ministerial Decree (NTC2018). Updating of Technical Codes for Constructions (in Italian). Rome: Official Gazette n°42 of 20/02/2018, Ordinary Supplement n°8.
- [57] G. Totani, P. Monaco, F. Totani, G. Lanzo, A. Pagliaroli, S. Amoroso, D. Marchetti. Site characterization and seismic response analysis in the area of Collemaggio, L'Aquila (Italy). *5<sup>th</sup> International Conference on Geotechnical and Geophysical Site Characterization*, Gold Coast, Queensland, Australia, September 5-9, 2016.

# SEISMIC RESPONSE OF SEVEN EXISTING REINFORCED CONCRETE CHIMNEYS EQUIPPED WITH TUNED MASS DAMPERS UNDER FIVE STRONG SEISMIC EVENTS

P.Crespi<sup>1</sup>, N. Longarini<sup>1</sup>, M. Valente<sup>1</sup>, M.Zucca<sup>1</sup>

<sup>1</sup> Department of Architecture, Built Environment and Construction Engineering  
Politecnico di Milano, Milano, Italy

{pietro.crespi, nicola.longarini, marco.valente, marco.zucca} @polimi.it

---

## Abstract

*The seismic response of seven existing reinforced concrete chimneys equipped with optimized Tuned Mass Dampers (TMDs) are investigated under five acceleration time histories recorded during different important European seismic events. For each chimney, the features of the TMDs are detected by nonlinear dynamic analyses, starting from the investigation about the optimum mass ratio (between the optimum mass of the TMD and the mass of the chimney without the TMD involved in the most representative vibrational modes). By the application of sinusoidal forces, the contribute of the TMDs are evaluated by the estimation of the equivalent damping ratio.*

**Keywords:** Tuned Mass Damper, RC chimney, Seismic Response, Non-linear analysis.

---

## 1 INTRODUCTION

All over the world many industrial plants are characterized by the presence of chimneys. Starting from the '50 of the 20th century, in the new manufacturing and chemical plants reinforced concrete (RC) chimneys were built instead of the masonry traditional ones, due to plants requirements derived from the industrial developments and environmental reasons. From the middle of the 20th century, thanks to the new concrete techniques in use, it was possible to satisfy the new industrial processes requirements by reducing the environmental impacts with a significant height increasing (up to about 400 m), thus defining a wide range of possible heights from 100 m to 400 m. It is remarkable many RC chimneys were designed without specific earthquake-resistant provisions, considering only the wind as horizontal force [1] even if in some European countries, e.g. in Italy, many chimneys were built in areas only nowadays considered as seismic regions [2]. It represents an evident structural negligence for the seismic performance of many existing RC chimneys in terms of resistance and ductility and for economic aspects. Under seismic loads, the chimneys are characterized by an inelastic response, different from the elastic behavior. The domain of higher modes vibration and large natural period vibration consistently drives to a complex global dynamic response during earthquake events, reporting extremely increase of structural stress states, possible brittle collapse [3–10].

A recent study [11] has pointed out 6 major chimney failures causes, from 739 study cases, statistically summarized. The damage of these RC chimneys was mainly caused by seismic and wind action, temperature stress and construction defect [9].

Several researches have made relevant considerations in the earthquake engineering field [12,13] which revealed a sort of crack pattern of these slender constructions. In particular, they identified a failure-prone region at  $1/3$  to  $2/3$  also  $0.8$  of the height of a standard designed chimney, which concentrates inelastic deformations. It may occur when remarkable inertial force takes place in hazard earthquake, observing fractures in the horizontal, vertical, and inclined directions depicted after the strong motion. A predominance of cracks with 20–30 mm widths according to [11] was noticeable in many seismic events. It was observed the specific wind design cannot allow an adequate seismic response [12] in particular in terms of concrete stiffness with respect the concrete strength [14]. The increase of the height over 130 m exposes chimneys to large displacements wreaking cracks which demand extensive rehabilitation. Moreover, the radius-thickness ratio feature has also relevant influence in the dynamic response that decreases the displacement with the growth of the radius-thickness. It can be observed in chimney tapered from bottom to top lesser displacement values than chimneys which are tapered from the bottom then becomes uniform at one-third height. Shell stress as well decreases with the increase of radius thickness ratio in a fully tapered chimney in respect of partially tapered chimney. Chimneys with heights ranging from 325 m to 350 m are vulnerable against seismic forces especially in case of elliptical cross-section. However circular chimneys have higher displacement than the elliptical section ones with higher accelerations under the seismic events. For improving the seismic response an adequate representation of the chimneys and the earthquakes is mandatory as it is explained in [9,10]. In these studies, the efficiency of passive tuned mass dampers is also proposed as a valid cost-benefits solution [15]. In several cases, the use of a single TMD represents a valid solution in terms of structural and economic convenience. The contribute of the single TMD can be described by shifting period coupled to the damping increase characterized the new system represented by the chimney with the TMD are easily detected.

## 2 STRUCTURE OF THE PAPER

In Section 3, starting from the features of the chimneys (3.1) and the ones of the seismic actions (3.2), for each chimney the parameters of the Tuned Mass Dampers (TMDs) are detected (3.3). In the Section 4 the contribute of the TMDs in terms of equivalent damping is evaluated whereas the energetic contributions are shown in Section 5 (where a comparison between the cases chimneys without TMDs and chimneys with TMDs is shown as well). Finally, Section 6 contains the remarks about the results characterized Section 4 and Section 5,

## 3 IDENTIFICATION OF THE TUNED MASS DAMPERS FEATURES

### 3.1 Chimneys

The seven RC chimneys here investigated were built from the '60 to the first half of the '80 years. They are classified considering four main geometrical features: the height (H), the geometrical slenderness  $\lambda = H/D_{\text{base}}$ , the taper ratio  $t_d = D_{\text{top}}/D_{\text{base}}$  and the mass distributed along the height ( $q_h$ ), depending on the chimney materials and the structural configuration and where  $D_{\text{top}}$  represents the external diameter at the top of the structure while  $D_{\text{base}}$  indicates the external diameter at the base of the structure. In Table 1 the main information about the chimneys are shown.

Chimney	$D_{\text{base}}$ [m]	$D_{\text{top}}$ [m]	H [m]	$t_d$	$\lambda$	$t_h$ [cm]	$q_h$ [kN/m]
CH_1	4.8	2.5	60	0.52	12.50	30	76.50
CH_2	16.1	13.6	100	0.85	6.21	40-30	100.00
CH_3	10.3	6.6	115	0.64	11.17	45-20	71.00
CH_4	15.0	14.8	120	0.99	8.00	35-26.5	29.00
CH_5	15.7	9.4	183	0.60	11.66	60-30	56.00
CH_6	16.0	8.5	220	0.53	13.75	76-20	76.50
CH_7	26.0	16.8	245	0.65	9.42	70-35	80.00

Table 1. Main characteristics of the seven chimneys. Note:  $D_{\text{base}}$ =diameter at the base;  $D_{\text{top}}$ =diameter at the top; H=height;  $t_d$ =taper ratio;  $\lambda$ =slenderness;  $t_h$ =thickness of the circular hollow section;  $q_k$ =distributed mass along the height.

The finite element model (FEM) of each chimney is implemented by MIDAS Gen software [16]. Each FEM has beam elements with a perfect restrain at the base. The self-weight and the dead loads are converted to mass in order to carry out the eigenvalue analyses for evaluating the periods, the related modal participation mass and the deformed shapes. The nonlinear material property of the concrete is attributed by Kent-Park property [17] and the ones attributed to the steel rebars is described in [18]. Eigenvalue results are shown in Table 2.

Chimney	$T_1$ [s]	$M_1$ [%]
CH_1	1.63	58.48
CH_2	0.90	66.51
CH_3	1.77	54.24
CH_4	1.33	63.82
CH_5	2.55	53.87
CH_6	3.21	48.02
CH_7	3.79	45.23

Table 2. Eigenvalue analysis results. Note:  $T_1$  is the first fundamental period and  $M_1$  is the related involved mass



### 3.2 Seismic actions

The seismic actions are represented by five acceleration times histories recorded during different European seismic events (Greece, Amatrice, L'Aquila, Friuli and Montenegro), included in the European Strong-Motion Database. The features of the seismic inputs are shown in Table 3. The seismic inputs have been selected in order to obtain Magnitude between 6 and 6.9 and a PGA value between 0.35 g and 0.53 g: however, they are characterized by different integral parameters values, gaining a large variability of the ground motion characteristics , [19,20].

Event	Event id	Stat.	Year	PGA	PGV	PGD	M <sub>w</sub>	Arias Int.
[-]	[-]	[-]	[-]	[g]	[cm/s]	[cm]	[-]	[cm/s]
Friuli (Acc1)	IT-1976-0030	FRC	1976	0.35	23.7	5.3	6	84.5
Montenegro (Acc2)	ME-1979-0003	PETO	1979	0.45	38.5	6.9	6.9	455.7
Amatrice (Acc3)	EMSC-20161030_0000029	AMT	2016	0.53	37.9	7.5	6.5	156.4
Greece (Acc4)	GR-1995-0047	AIGA	1995	0.52	51.3	8.3	6.5	117.1
L'Aquila (Acc5)	IT-2009-0009	AQG	2009	0.49	35.8	6.0	6.1	132.4

Table 3. Characteristics of the seismic inputs.

### 3.3 Tuned mass dampers parameters

Once the vibration mode shapes and the main frequencies of the structures are known, the features of the TMDs can be evaluated according to [21,22] and the seismic response can be analyzed by introducing the TMDs in the FEMs of each chimney (system 2). The TMD is implemented through a nodal mass connected to the chimney with a spring and linear dashpot characterized by horizontal stiffness ( $k_{TMD}$ ) and damping coefficient ( $C_{TMD}$ ). The boundary conditions of the node representing the TMD are set to allow only the horizontal displacements of the mass. The horizontal stiffness ( $k_{TMD}$ ) and the related damping coefficient ( $C_{TMD}$ ) are evaluated considering the following relations [23]:

$$k_{TMD} = m \cdot \alpha_{opt}^2 \cdot \omega_s^2 \quad (1)$$

$$C_{TMD} = 2 \cdot \xi_{opt} \cdot \sqrt{(k_{TMD} \cdot m_d)} \quad (2)$$

From [24] the values of  $k_{TMD}$  and  $C_{TMD}$  are obtained starting from the definition of the ratio ( $\mu$ ) given by the ratio of the mass of TMD ( $m_d$ ) and the mass of the chimney ( $m$ ) involved in the main vibrational mode (already explained in Phase A) and  $\omega_s$  defined as the pulsation depending by the main frequency ( $f_1$  corresponding to the frequency value of the first and second mode shapes of the chimney without TMD) by the equation (3):

$$\omega_s = 2\pi \cdot f_1 \quad (3)$$

The TMD mass ratio is given by the Eq.4 to obtain concerning the fundamental mode ( $\mu_1$ ) is given by:

$$\mu_1 = \frac{m_d}{\alpha_1 \cdot m} \quad (4)$$

where  $\alpha_1$  is the participant mass ratio of the fundamental mode of the structure without the TMD. The general mass ratio  $\mu$  is expressed as:

$$\mu = \frac{m_d}{m} = \frac{\mu_1 \cdot \alpha_1 \cdot m}{m} = \mu_1 \cdot \alpha_1 \quad (5)$$

In order to define  $k_{TMD}$  and  $C_{TMD}$ , the optimal coefficient for the frequencies ( $\alpha_{opt}$ ) and the optimal equivalent viscous damping ratio ( $\xi_{opt}$ ) are evaluated as it comes out from the following expressions, where  $\xi$  is the equivalent damping ratio for the structure:

$$\alpha_{opt} = \left( \frac{\sqrt{1 - 0.5\mu}}{1 + \mu} + \sqrt{1 - 2\xi^2} - 1 \right) - (2.375 - 1.034\sqrt{\mu} - 0.426\mu) \cdot \xi \cdot \mu - (3.730 - 16.903 + 20.496\mu) \cdot \xi^2 \cdot \sqrt{\mu} \quad (6)$$

$$\xi_{opt} = \sqrt{\left( \frac{\sqrt{3\mu}}{8(1 + \mu)(1 - 0.5\mu)} \right) + (0.151\xi - 0.175\xi^2) + (0.163\xi + 4.98\xi^2) \cdot \mu} \quad (7)$$

Basing on the previous relations the values of mass the TMD can be taken in the range 1%÷5% of the mass of the chimney excited in correspondence of the main frequency (related to the first and second mode shapes). Testing different values of the TMD's mass, the related values of  $k_{TMD}$  and  $C_{TMD}$  (see relation (1) and (2)) can be detected and the different seismic response of “chimney with TMD” (system 2) can be evaluated in the FEMs where displacement, shear and moment variations are graphically shown in Figure 1. Once the average trends are detected for each chimney, the mass ratios optimizing the sizes of the TMDs are evaluated. The optimized size must minimize the mass of the damper but it must allow to reduce as far as possible the displacements, the base shear and base bending moment [4,25]. Therefore, for each chimney when the optimum mass ratio ( $\mu_{OPT}$ ) is chosen, the features of each TMD are evaluated as well in terms of horizontal stiffness ( $k_{TMD}$ ) damping coefficient ( $C_{TMD}$ ) and pulsation ( $\omega_s$ ) by the previous equations (1÷3), see Table 4.

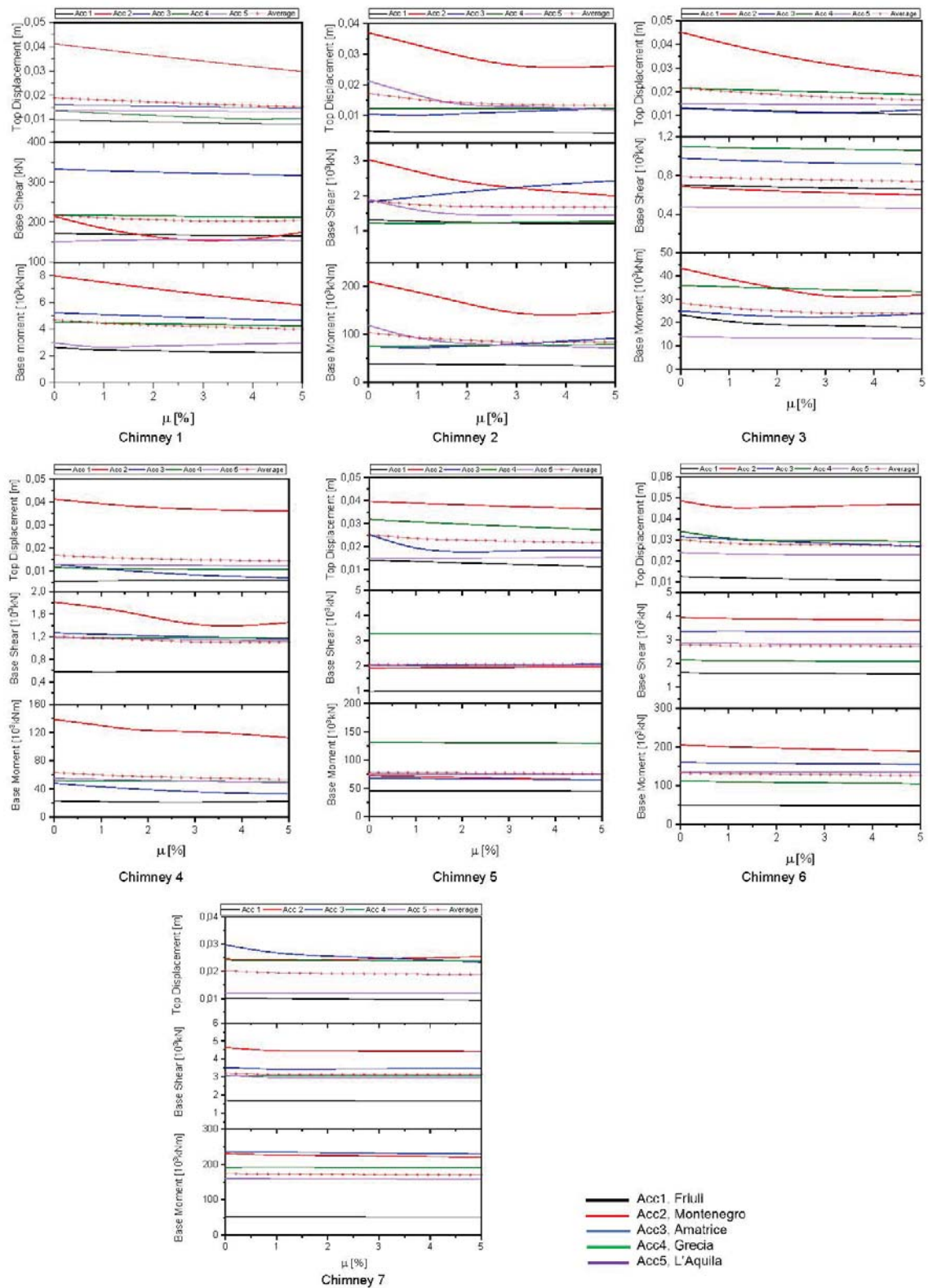


Figure 1. Optimization of the TMDs features in terms of top displacement, base shear and base moment in relation to the mass ratio for the seven existing chimneys

Optimum TMD Properties	CH_1	CH_2	CH_3	CH_4	CH_5	CH_6	CH_7
$\mu_{\text{opt}}$	4%	1.5%	3%	3%	3%	5%	3%
$\omega_{\text{TMD}}$	0.58	1.08	0.54	0.72	0.38	0.29	0.26
$m_{\text{TMD}}$ [kN/g]	22.19	48.53	53.17	88.96	148.81	344.61	233.33
$k_{\text{TMD}}$ [kN/m]	293.22	2224.90	613.50	1812.41	828.56	1148.62	589.11
$c_{\text{TMD}}$ [kNs/m]	20.47	52.56	40.00	88.92	77.77	177.43	82.11

Table 4. Properties of the optimum tuned mass dampers selected for the seven chimneys (CH\_ identifies the chimneys).

#### 4 EQUIVALENT DAMPING EVALUATION

The contribution of the mass dampers of each chimney in terms of equivalent damping ( $\xi_e$ ) is here estimated starting from the dynamic amplification factor (H) given by the ratio between  $X_s$  and  $X_d$ , where  $X_s$  is the top displacement under seismic action and  $X_d$  is the dynamic top displacement under forces with frequencies included in the range  $(0.8 \div 1.2) \cdot f_l$  where  $f_l$  corresponds to the frequency to smooth (this value is obviously different for each chimney). The ratio between the frequencies of the forces and the frequency to smooth is called  $\rho$  (the variation of H by  $\rho$  is shown in Figure 2). The equivalent damping ( $\xi_e$ ) due to the TMDs can be detected as well from H because  $\xi_e$  is given by the relation (7) and it can be plotted once again in relation to  $\rho$ . The final value of the equivalent damping corresponds to the average one of the two lower peaks of the diagrams  $\xi_e$ - $\rho$  (Figure 3):

$$\xi_e = \frac{H}{2} \quad (7)$$

It is worth nothing the influence of the main frequency of the chimney in the TMD's contribution in terms of equivalent damping given to the main structure. The results plotted in the Figure 2 and Figure 3, respectively in terms of dynamic amplification factor (H) and equivalent damping ( $\xi_e$ ), are useful in order to appreciate the smooth effects given by the TMDs for each chimney under the five seismic events. The equivalent damping values are summarized in Table 5; the variation of the equivalent damping in relation to the frequencies of the chimneys is shown in Figure 4.

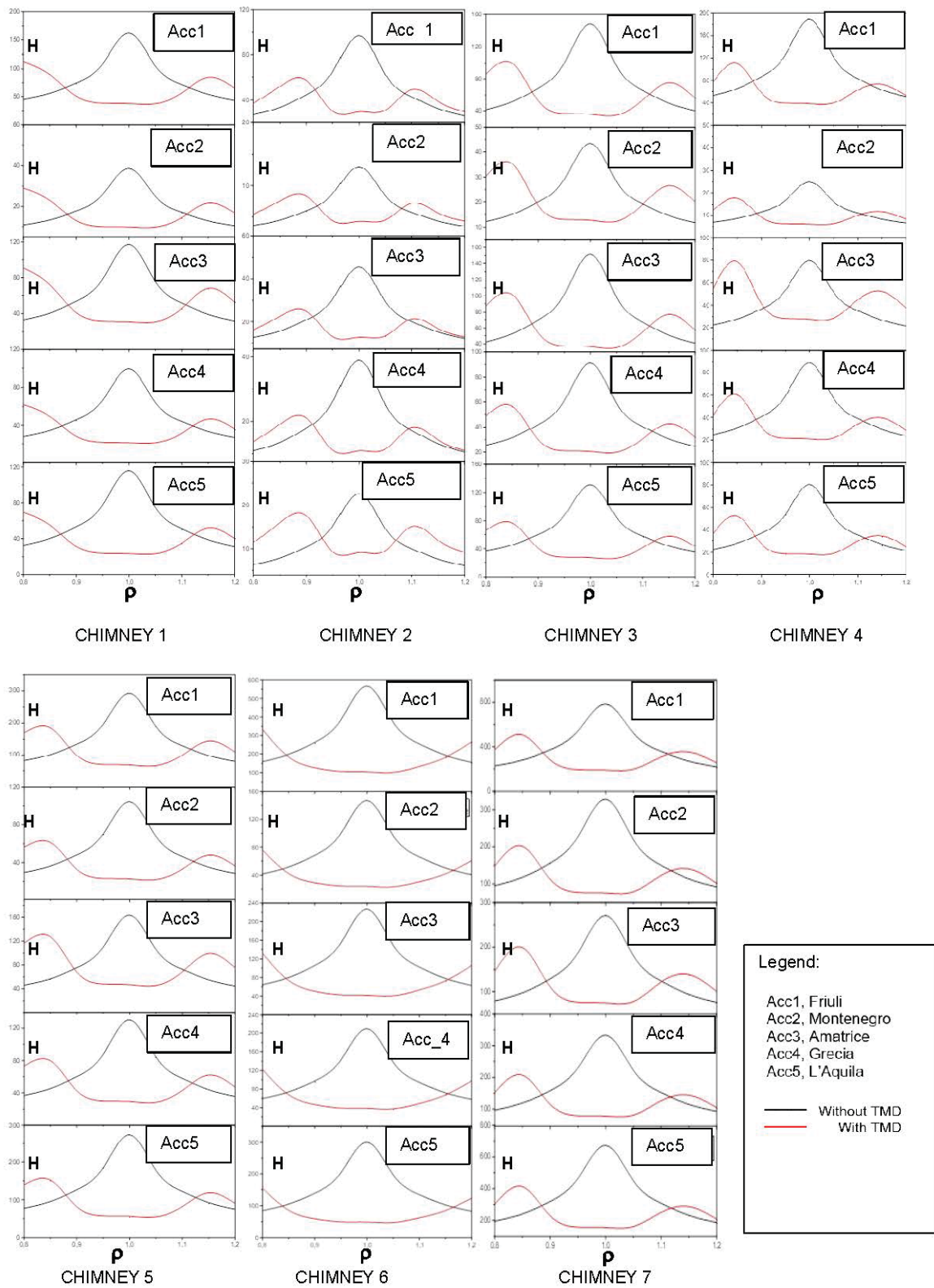


Figure 2. Dynamic Amplification Factor (H) in relation to the frequency ratio ( $\rho$ )



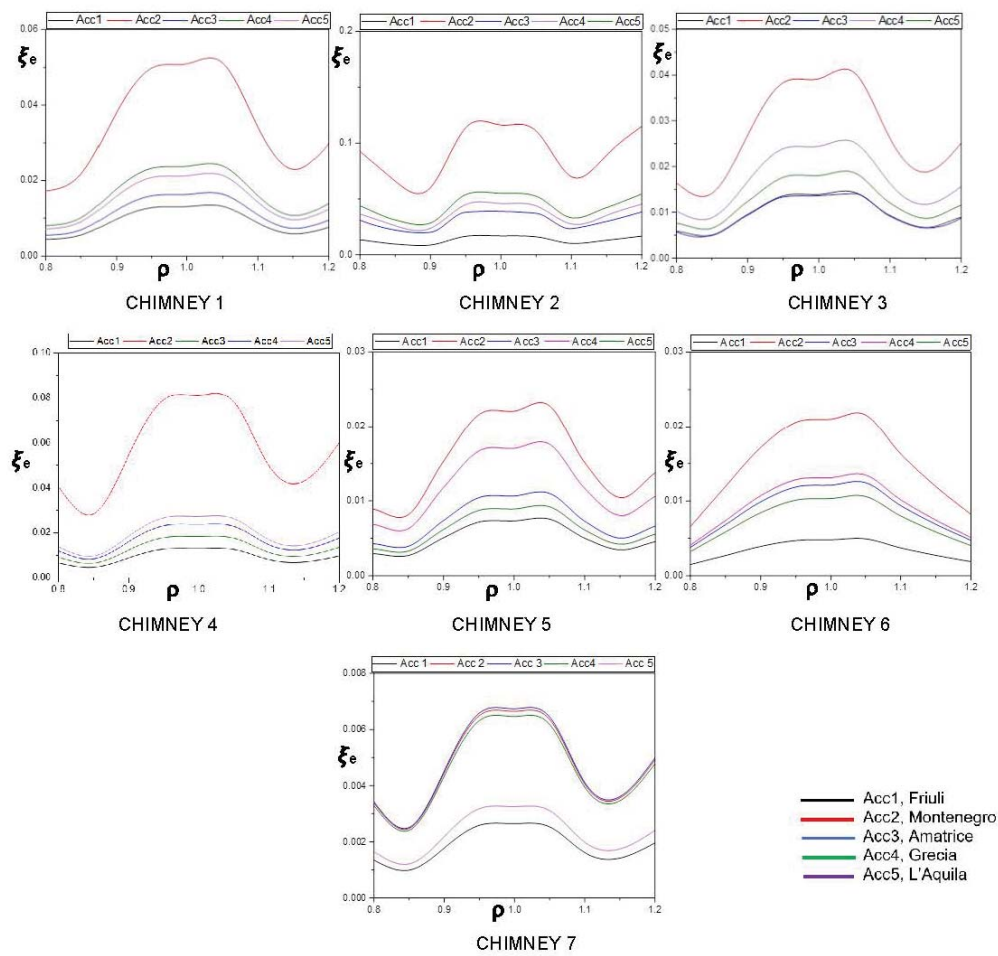


Figure 3. Equivalent Damping ( $\xi_e$ ) in relation to the frequency ratio ( $\rho$ ) for the five earthquakes

	Chimney 1	Chimney 2	Chimney 3	Chimney 4	Chimney 5	Chimney 6	Chimney 7
Acc	$\xi_e$	$\xi_e$	$\xi_e$	$\xi_e$	$\xi_e$	$\xi_e$	$\xi_e$
1	0.0076	0.011	0.008	0.007	0.004	0.003	0.001
2	0.0309	0.077	0.026	0.047	0.012	0.010	0.004
3	0.0101	0.023	0.008	0.013	0.007	0.007	0.004
4	0.0128	0.027	0.013	0.013	0.009	0.007	0.004
5	0.0112	0.041	0.009	0.015	0.005	0.005	0.002

Table 5. Equivalent damping  $\xi_e$  for the seven chimneys in correspondence of the five seismic events

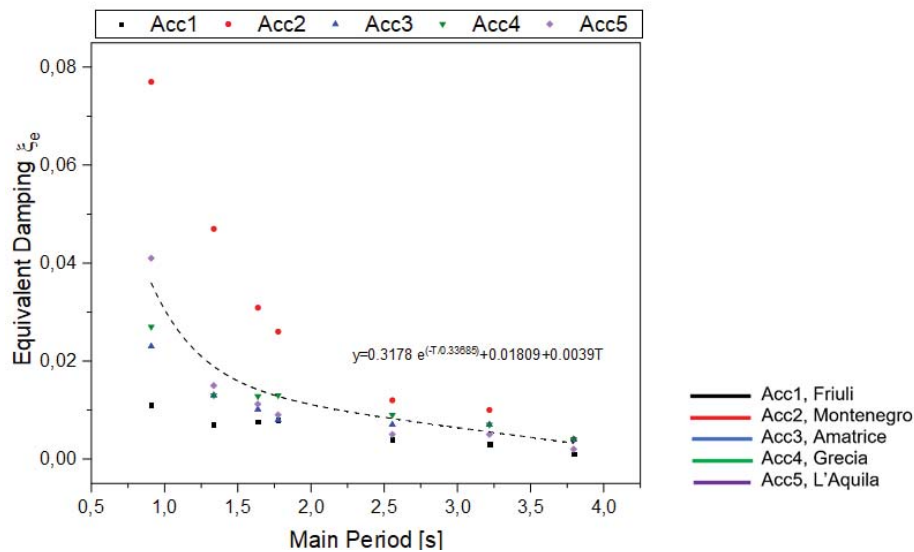


Figure 4. Variation of the equivalent damping with respect to the main periods of the seven chimneys.

## 5 ENERGETIC CONTRIBUTION OF THE TUNED MASS DAMPERS

In the present phase the dynamic behavior of the five case studies (chimneys with TMDs) is deepened in terms of energy damping starting from the assumption that for the generic chimney the input energy ( $E_i$ ) due to the seismic action is the work done by the ground motion on the construction. Considering the time dependent conservation of the energy, ( $E_i$ ) is given by the summation of the kinetic energy ( $E_k$ ), the elastic strain energy ( $E_s$ ), the energy dissipated by the structure throughout the inelastic features ( $E_h$ ) and the damped dissipative energy of the building and the mass damper if present ( $E_d$ ). Formulations about the energies are present in [26,27]. The aim of this phase is the evaluation of the damping energy during each seismic event for the seven chimneys either in the case chimneys without TMD and chimneys with TMDs. In Figure 5, for each chimney, the damping energy ( $E_d$ ) is plotted for the five accelerograms. The output of the energetic analyses represents the variation of the damping energy during the seismic events therefore the results of this kind of analysis is plotted by time histories in both cases (chimneys without and with TMDs). Each time history represents the percentage of the damping energy with respect to the input energy.

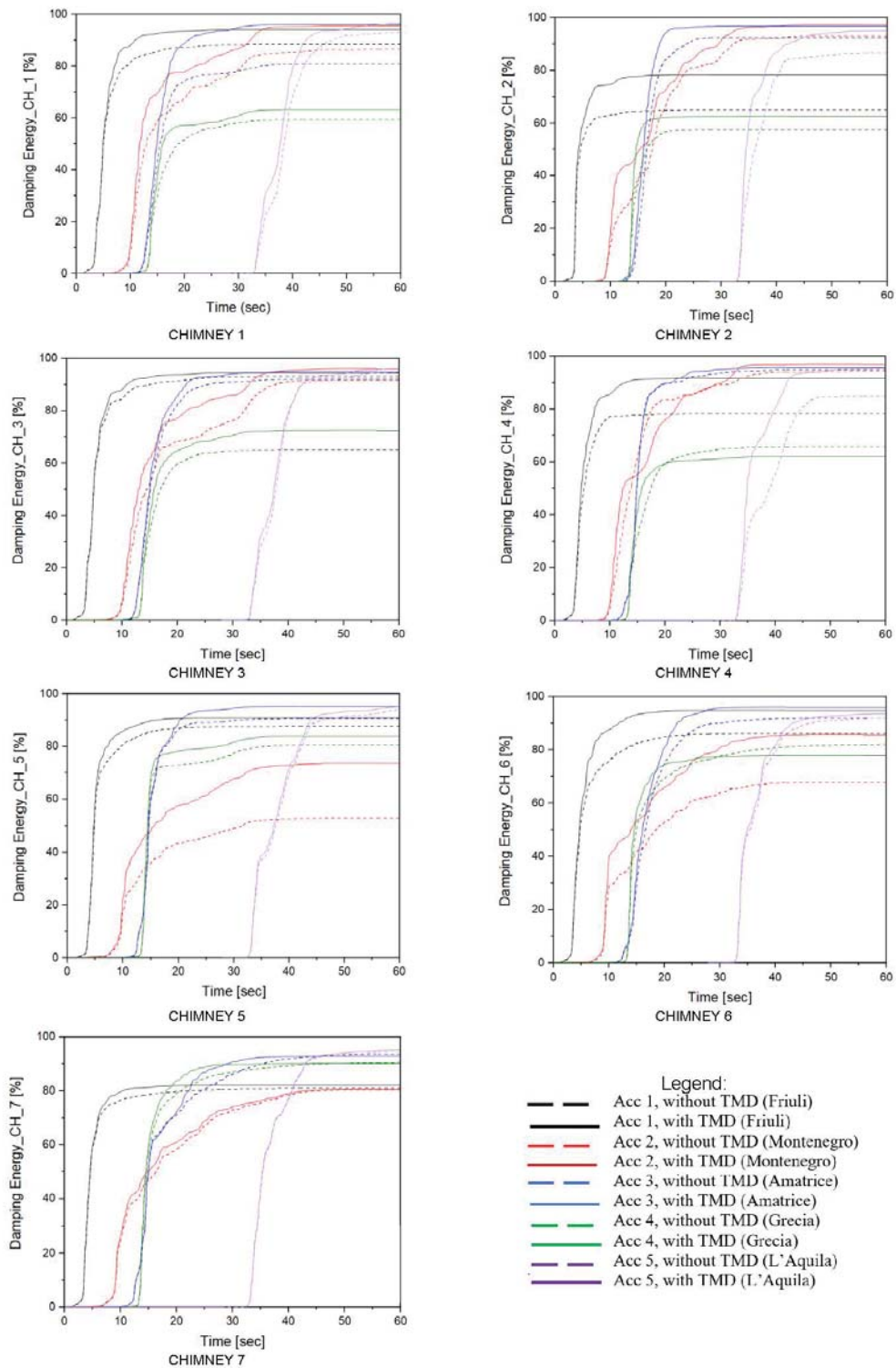


Figure 5. Evaluation of the percentage of the damping energy ( $E_d$ ) with respect the input energy ( $E_i$ )

## 6 REMARKS

- The use of the Tuned Mass Dampers for existent Reinforced Concrete chimneys represents a valid solution for improving the seismic response of this kind of construction especially if originally built in areas only nowadays classified as seismic areas;
- The size of the TMD is influenced by the geometrical features of the chimneys: in fact, chimneys with high slenderness values need TMD with optimum mass ratio  $\mu_{opt}$  higher than the ones with low slenderness. For slenderness value around  $\lambda = 10$  the optimum mass ratio  $\mu_{opt}$  is around 3% but for higher slenderness values, as it is for CH\_6 with  $\lambda_{CH\_6} = 13.75$ , higher mass ratio  $\mu_{opt-CH\_6} = 5\%$  is adopted; vice versa CH\_2 with slenderness  $\lambda_{CH\_2} = 6.21$  needs lower mass ratio  $\mu_{opt-CH\_2} = 1.5\%$ ; similar consideration may not be valid about the effect of the taper ratio  $td$  on the size of the TMD because chimneys with different  $td$ , as CH\_1 with  $td = 0.52$  and CH\_4 with  $td = 0.99$ , are characterized by mass ratio values very close themselves (e.g.  $\mu_{opt-CH\_1} = 4\%$  and  $\mu_{opt-CH\_4} = 3\%$ );
- In the seismic events here adopted, the most important variations with the TMDs occur in terms of top displacement for each chimney; although, the base shear variation is not appreciable for each chimney especially in comparison to the displacements and moment variations;
- the equivalent damping does not appear dependent by the individual features of the chimneys (even if for high value of the geometrical slenderness - as it is for chimneys 1, 5 and 6 respectively with  $\lambda_{CH\_1} = 12.5$ ,  $\lambda_{CH\_5} = 11.66$  and  $\lambda_{CH\_6} = 13.75$  - the equivalent damping values are very similar themselves); it is worth nothing the equivalent damping due to the TMD depends on the characteristics of the seismic event combined to the natural frequency of each single chimney, thus the seismic response is a correlation between the chimney's features (as the height, taper ratio, slenderness and dead loads) and the ones of each seismic event shaking the construction. A relation between the equivalent damping and the main periods of the chimneys ( $T$ ) is expressed in the relation shown in Figure 4 where the equivalent damping  $\xi_e$  here estimated exhibits exponential variation growing for the lower values of  $T$ ; vice versa, the intensity of the strong motion becomes irrelevant when the main period increases.

$$\xi_e = 0.3178 \cdot e^{-\frac{T}{0.33683}} + 0.01809 + 0.0039T \quad (8)$$

- under the five earthquakes the damping energy for the seven chimneys increases thanks to the TMDs; the contribution of TMDs is much evident in the asymptotic branch of the curves, especially under accelerograms 1 and 2 (drawn by black and red lines. In the case chimneys with TMDs, the damping energy increases. Generally, the dissipation of the input energy due to the seismic event occurs for damping contribute whereas the one due to the strain energy is practically zero. At the same time the TMD slightly reduces the contribute of kinetic energy in the dissipation of the input energy.

## REFERENCES

- [1] DIVER M. CALCUL PRATIQUE DES CHEMINEES EN BETON ARME. Inst Tech Batim Des Trav Publics-Annales 1969.

- [2] NTC2018. Norme Tecniche per le Costruzioni. 2018.
- [3] Elias S, Matsagar V, Datta TK. Distributed Multiple Tuned Mass Dampers for Wind Response Control of Chimney with Flexible Foundation. *Procedia Eng.*, 2017. <https://doi.org/10.1016/j.proeng.2017.09.087>.
- [4] Elias S, Matsagar V. Research developments in vibration control of structures using passive tuned mass dampers. *Annu Rev Control* 2017. <https://doi.org/10.1016/j.arcontrol.2017.09.015>.
- [5] Elias S, Rupakhety R, Ólafsson S. Tuned Mass Dampers for Response Reduction of a Reinforced Concrete Chimney Under Near-Fault Pulse-Like Ground Motions. *Front Built Environ* 2020. <https://doi.org/10.3389/fbuil.2020.00092>.
- [6] Elias S, Matsagar V, Datta TK. Effectiveness of distributed tuned mass dampers for multi-mode control of chimney under earthquakes. *Eng Struct* 2016. <https://doi.org/10.1016/j.engstruct.2016.06.006>.
- [7] Longarini N, Cabras L, Zucca M, Chapain S, Aly AM. Structural Improvements for Tall Buildings under Wind Loads: Comparative Study. *Shock Vib* 2017;2017. <https://doi.org/10.1155/2017/2031248>.
- [8] Longarini N, Zucca M, Silvestro G. The constructions vibration control by tuned mass dumper. *IABSE Conf. Geneva 2015 Struct. Eng. Provid. Solut. to Glob. Challenges - Rep.*, 2015.
- [9] Wilson JL. Earthquake response of tall reinforced concrete chimneys. *Eng Struct* 2003. [https://doi.org/10.1016/S0141-0296\(02\)00098-6](https://doi.org/10.1016/S0141-0296(02)00098-6).
- [10] Wilson JL. The cyclic behaviour of reinforced concrete chimney sections with and without openings. *Adv Struct Eng* 2009. <https://doi.org/10.1260/136943309788708329>.
- [11] Wang L, Fan X yan. Failure cases of high chimneys: A review. *Eng Fail Anal* 2019. <https://doi.org/10.1016/j.engfailanal.2019.07.032>.
- [12] Bońkowski PA, Zembaty Z, Minch MY. Seismic effects on leaning slender structures and tall buildings. *Eng Struct* 2019. <https://doi.org/10.1016/j.engstruct.2019.109518>.
- [13] Tabeshpour MR. Nonlinear dynamic analysis of chimney-like towers. *Asian J Civ Eng* 2012.
- [14] Bońkowski P, Zembaty Z, Minch MY. Nonlinear interaction of initial leaning of r/c slender tower with its seismic response. *Insights Innov. Struct. Eng. Mech. Comput. - Proc. 6th Int. Conf. Struct. Eng. Mech. Comput. SEMC 2016*, 2016. <https://doi.org/10.1201/9781315641645-50>.
- [15] Akyürek O, Suksawang N, Go TH, Tekeli H. Performance evaluation of a reinforced concrete building strengthened respectively by the infill wall, active and passive tuned mass damper under seismic load. *Comput Struct* 2019. <https://doi.org/10.1016/j.compstruc.2019.07.006>.
- [16] Midas. Midas GEN FX Program - General structure design system n.d.
- [17] Park R, Kent DC, Sampson RA. REINFORCED CONCRETE MEMBERS WITH CYCLIC LOADING. *ASCE J Struct Div* 1972.
- [18] Scott BD, Park R, Priestley MJN. STRESS-STRAIN BEHAVIOR OF CONCRETE CONFINED BY OVERLAPPING HOOPS AT LOW AND HIGH STRAIN RATES. *J*



- Am Concr Inst 1982. <https://doi.org/10.14359/10875>.
- [19] Zucca M, Tropeano G, Erbi E, Crespi P. Evaluation of the seismic behavior of multi-propped shallow underground structures embedded in granular soils: A comparison between coupled and decoupled approaches. *Earthq. Geotech. Eng. Prot. Dev. Environ. Constr. Proc. 7th Int. Conf. Earthq. Geotech. Eng.* 2019, 2019.
- [20] Zucca M, Valente M. On the limitations of decoupled approach for the seismic behaviour evaluation of shallow multi-propped underground structures embedded in granular soils. *Eng Struct* 2020. <https://doi.org/10.1016/j.engstruct.2020.110497>.
- [21] Tsai H -C, Lin G -C. Optimum tuned-mass dampers for minimizing steady-state response of support-excited and damped systems. *Earthq Eng Struct Dyn* 1993. <https://doi.org/10.1002/eqe.4290221104>.
- [22] Ormondroyd J, Den Hartog JP. The theory of the dynamic vibration absorber. *Trans Am Soc Mech Eng* 1928.
- [23] Li C, Qu W. Optimum properties of multiple tuned mass dampers for reduction of translational and torsional response of structures subject to ground acceleration. *Eng Struct* 2006. <https://doi.org/10.1016/j.engstruct.2005.09.003>.
- [24] Hoang N, Fujino Y, Warnitchai P. Optimal tuned mass damper for seismic applications and practical design formulas. *Eng Struct* 2008. <https://doi.org/10.1016/j.engstruct.2007.05.007>.
- [25] Longarini N, Zucca M. A chimney's seismic assessment by a tuned mass damper. *Eng Struct* 2014;79. <https://doi.org/10.1016/j.engstruct.2014.05.020>.
- [26] Elias S. Seismic energy assessment of buildings with tuned vibration absorbers. *Shock Vib* 2018. <https://doi.org/10.1155/2018/2051687>.
- [27] Anam I, Manju F, Khan F. Seismic vibration control of nonlinear RC structures. *Wind Earthq. Eng. - Proc. 10th East Asia-Pacific Conf. Struct. Eng. Constr. EASEC* 2010, 2006.

## SHAKING TABLE TEST ON THE EFFECTS OF SHEAR WALLS FOR LONG-SPAN KOREAN TRADITIONAL TIMBER STRUCTURE

Yeong-Min. Kim<sup>1</sup>

<sup>1</sup> Professor, College of Architecture, Myongji University  
116 Myongji-ro, Cheoin-gu, Yongin, Gyeonggi-do, 17058, Republic of Korea  
e-mail: ymkim@mju.ac.kr

---

### Abstract

*In this research, the dynamic characteristics and effects of shear walls in lateral stiffness of long-span Hanok have been studied by shaking table test. The 1/20 scale experimental model for the long-span test-bed Hanok has been built for shaking table test. The shaking table test was done on two cases, that is, full or no shear wall. The shaking table test was done on a 1/20 scale experimental model for the previous two cases. The experiment was done sequentially, first for full shear wall model, and then no shear wall model. The shaking table was actuated sequentially by four types of input gain, that is, from random gain 1 to random gain 4 with increasing scenario. The maximum displacement of experimental model on its roof top was measured for both full and no shear wall cases for four random gains. Full shear wall case showed much less displacement for all random gains compared to the no shear wall case. The average displacement reduction ratio for four random gains is 64.4%, which shows the significant effect of shear wall in lateral load resisting capability. The natural vibration frequency of full shear wall is 11.28Hz compared to the no shear wall of 5.5Hz, which shows stiffness is about 4 times.*

**Keywords:** Long-span Hanok, Shaking Table Test, Shear Wall, Lateral Stiffness.

---

## 1 INTRODUCTION

The Korean traditional timber structure, especially used as residential is called Hanok. Hanok has history of more than two thousand years. The structure of Hanok as shown in Fig. 1(a) is characterized as a post and beam structure. The vertical load is supported mainly by post and beam as shown in Fig. 1(b), and the lateral load is supported mainly by walls incorporated with peripheral timber frame. In a very rare case, truss is used as lateral load resisting system as shown in Fig. 1(c).



(a) Korean Traditional Timber Structure



(b) Load paths of through post and beam in Hanok



(c) Trussed wall used as a lateral load resisting system in Hanok

Figure 1: Korean traditional timber structure and its load paths

The main characteristic of Hanok is in its joints. The joint of Hanok is mostly mortise and tenon joint of only wood as shown in Fig. 2. It rarely uses steel connector or steel nails. The

heavy roof weight of Hanok helps the joint have somewhat rotational rigidity against lateral load. Generally, the span of traditional Hanok between columns is about 2.4~4.8 meters. This short span does not matter as a residential use. Nowadays, long span, which is about 10~20 meters, is required to accommodate various modern life style of people and to enlarge the use of Hanok as a public usage. As the span is longer various problems should be solved in structural point of view.



Figure 2: Traditional mortise and tenon joint of Hanok

As the span of Hanok becomes longer, new load carrying paths and new joint types should be carefully planned and designed to support increased load and unfamiliar large inner space. Timber structure in East Asia and the West has much in common in their skeleton and construction method. So, various researches on the timber structures have been carried out extensively around the world. Seo et al. [1] studied the structural characteristics of wooden frames with tenon joints under lateral static and cyclic load, Han et al. [2] studied mechanical performance of tenon joints to enhance traditional wooden house, Kang et al. [3] studied the static performance of mortise and tenon joint in Chinese traditional timber structure, Lee et al. [4], [5] studied both the longitudinal and transversal load carrying capacity of Korean traditional timber structure, and Kim et al. [6] evaluated rotational stiffness of steel joints used in a new-styled Hanok by static experiment on a 1/4 scale model.

Fang et al. [7] performed dynamic test on traditional Chinese timber structure and verified its structural characteristics, Hwang et al. [8] performed shaking table test on Korean traditional timber structure and showed the variation of natural frequency according to vibration amplitude, and Lee et al. [9] compared dynamic characteristics of both traditional and new-styled Hanok according to excitation amplitude. Ozsev et al. [10] conducted small scale hands-on experiments on a model wooden frame structure under dynamic effects.

As a design aid to the Korean traditional timber structures, section tables and structural design software for the design of main structural members of Hanok has been developed [11],[12],[13],[14] and these design tools were used in making Korean design standard on Hanok. Recently, evaluation tool on the torsional irregularity of Hanok has been developed to aid seismic design of Hanok [15].

In this study, the dynamic characteristics of long-span Hanok and the effects of shear walls in lateral stiffness have been studied by shaking table test and the results are analyzed.

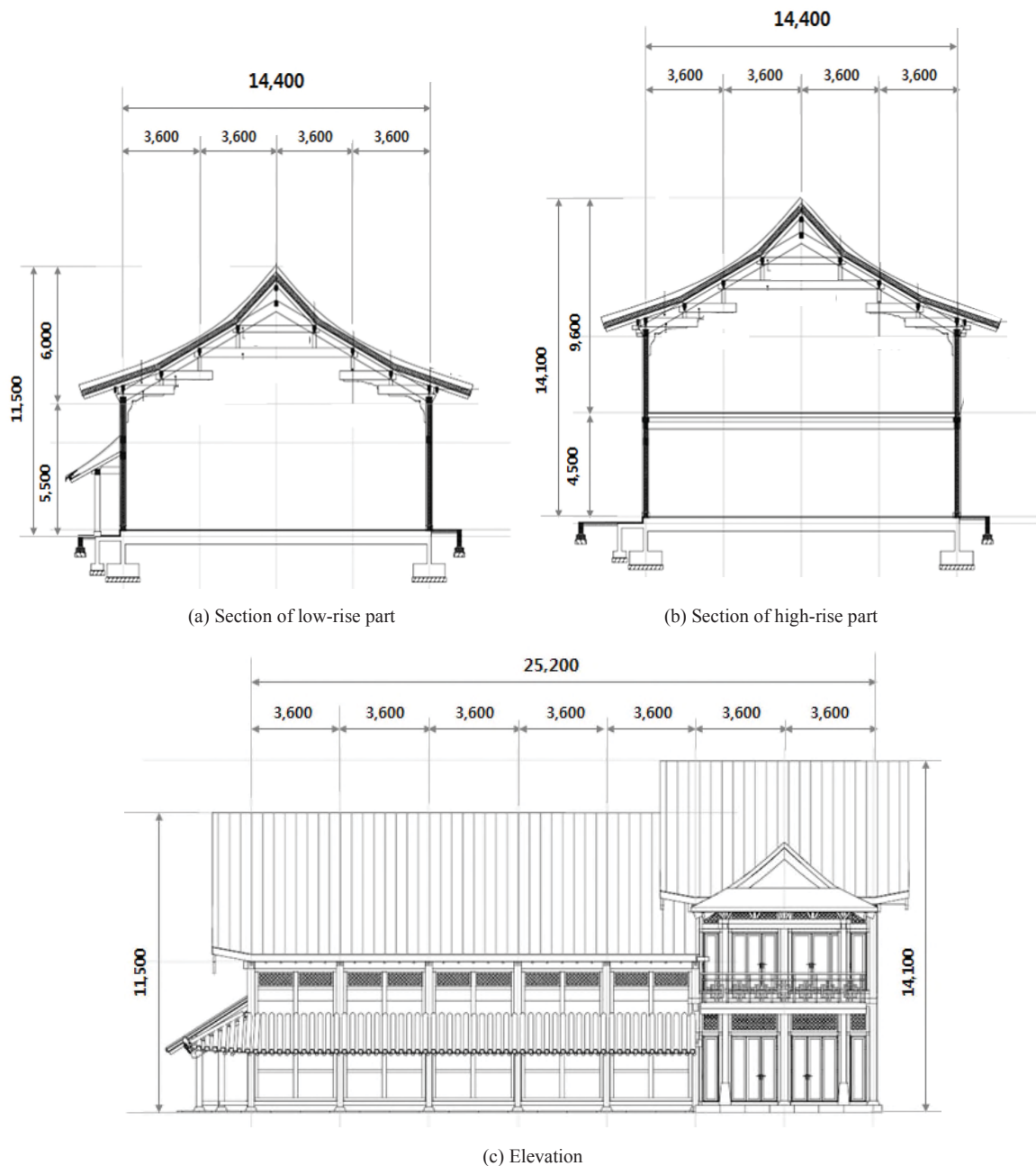
## 2 EXPERIMENTAL MODEL FOR SHAKING TABLE TEST

The long-span test-bed Hanok with its transversal span of 14.4meter and longitudinal span of 25.2meter has been designed as shown in Fig. 3. This long-span test-bed Hanok is scheduled to be built in Yongin, Korea, 2021. The 1/20 scale experimental model for this long-span test-bed Hanok has been built for shaking table test as shown in Fig. 4(a). The vertical load

was imposed on the roof and floor of the experimental model with steel plate as shown in Fig. 4(b). The total weight is 87.24kg.

The shaking table test was done on two cases, that is, Case A and Case B as shown in Table 1. Case A has full shear wall, that is, no opening, whereas, Case B has no shear wall, that is, full opening. Fig. 5(a) shows the location of shear wall in plan, and Fig. 5(b) and Fig. 5(c) show the front and rear view of test model of Case A.

The motor of shaking table is operated by real-time displacement control method using Labview program of NI corporation. The velocity, corresponding to input acceleration was numerically integrated and this was used as the input signal of motor. Four accelerometers were used to measure both X and Y directional movement. The sampling rate for data is 3200Hz. The relative displacement of the model compared to the base was measured by laser displacement equipment by measuring both the roof and base displacement of the model.





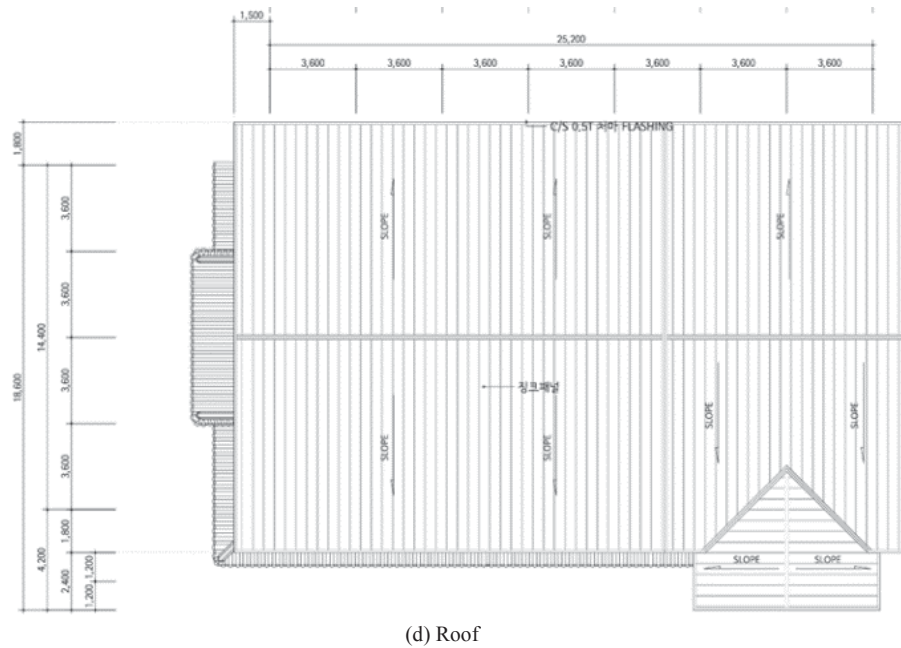


Figure 3: Section, elevation and roof plan of actual building

Model Case	Shear walls	Opening ratio
Case A	Full shear walls (No opening)	0%
Case B	No shear walls (Full opening)	100%

Table 1: Opening ratio of each cases.



(a) 1/20 scale experimental model for shaking table test



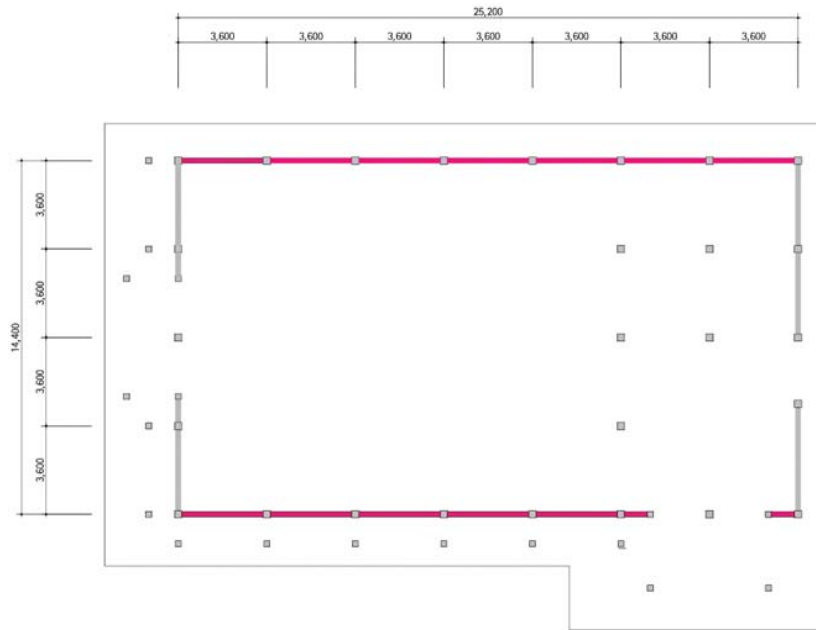
(b) Imposition of vertical load by steel plate

Figure 4: . 1/20 scale experimental model and imposition of vertical load

### 3 SHAKING TABLE TEST ON EXPERIMENTAL MODEL

The shaking table is one-directional as shown in Fig. 6. The experiment was done sequentially. First, shaking table experiment was done for Case A with full shear wall as shown in Fig. 7(a), and then shear wall was removed and the same shaking table experiment was done, which is for Case B as shown in Fig. 7(b). There are four types of input gain to the shaking

table as shown in Fig. 8, that is, from random gain 1 to random gain 4 with sequentially increasing scenario.



(a) Location of shear wall in plan



(b) Front view and location of shear wall



(c) Rear view and location of shear wall

Figure 5: Location of shear wall in plan and 1/20 scale test model

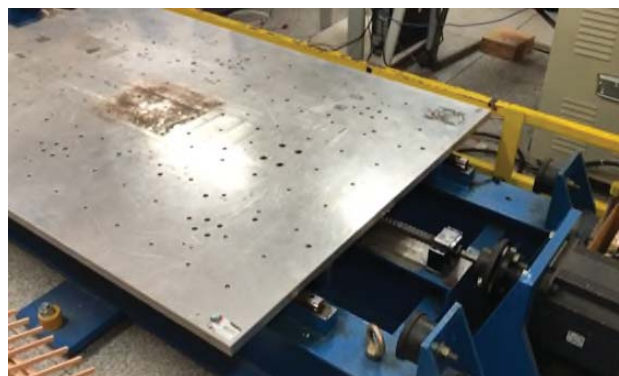


Figure 6: Shaking Table



(a) Case A : full shear wall with no opening



(b) Case B : no shear wall with full opening

Figure 7: Two experimental models, Case A and Case B

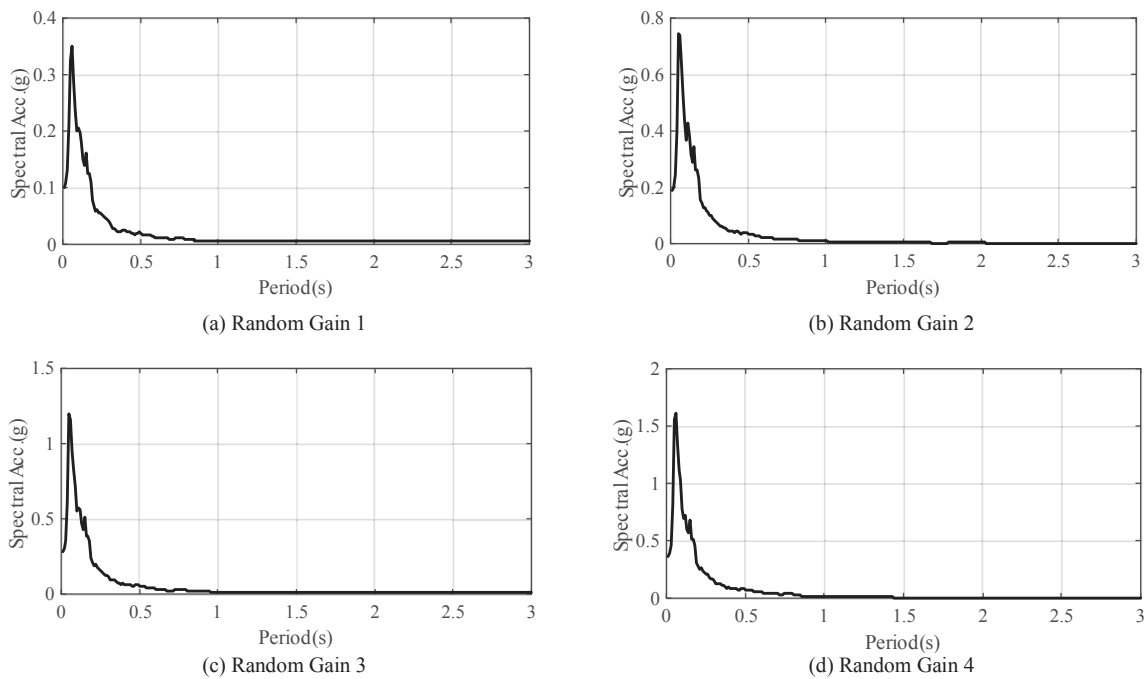


Figure 8: Response spectrum of four types of random gain

#### 4 RESULTS OF SHAKING TABLE TEST

The maximum displacement of experimental model on its roof top was measured for Case A and Case B for each random gain. The results are shown in Table 2. Compared to Case B, which has no shear wall, Case A showed much less displacement for all random gains. The

average displacement reduction ratio for four random gains is 64.4%. Here we can deduce that, the shear wall shows significant effect in lateral load resisting capability.

The natural vibration frequency of Case A is 11.28Hz compared to the Case B of 5.5Hz. As the vibration frequency is about two times larger, we can deduce that the stiffness is about 4 times larger. Here we only compared the maximum displacement and natural vibration frequency only for preliminary test. The other dynamic characteristics including torsional effect are scheduled to be studied in the coming paper.

Input load	Maximum displacement (mm)		Displacement reduction ratio (%)
	Case A (No opening)	Case B (Full opening)	
Ran. Gain 1	0.44	1.43	69.2
Ran. Gain 2	0.80	2.61	69.3
Ran. Gain 3	1.25	3.22	61.2
Ran. Gain 4	1.56	3.71	58.0

Table 2: Displacement Reduction Ratio According to Shear Wall

## 5 CONCLUSIONS

In this research, the dynamic characteristics of long-span Hanok and the effects of shear walls in lateral stiffness have been studied by shaking table test and the results are analyzed. The 1/20 scale experimental model for the long-span test-bed Hanok has been built for shaking table test. The shaking table test was done on two cases, that is, full or no shear wall. The shaking table test was done on a 1/20 scale experimental model for the previous two cases.

The experiment was done sequentially, first for full shear wall model, and then no shear wall model. The shaking table was actuated sequentially by four types of input gain, that is, from random gain 1 to random gain 4 with increasing scenario. The maximum displacement of experimental model on its roof top was measured for both full and no shear wall cases for four random gains. Full shear wall case showed much less displacement for all random gains compared to the no shear wall case.

The average displacement reduction ratio for four random gains is 64.4%, which shows the significant effect of shear wall in lateral load resisting capability. The natural vibration frequency of full shear wall is 11.28Hz compared to 5.5Hz for no shear wall, which shows stiffness is about 4 times larger in the former. In the coming paper, we are going to study the natural vibration period and other dynamic characteristics of long-span Hanok.

## 6 ACKNOWLEDGEMENTS

This work was supported by a grant (21AUDP-B128638-05) from Urban and Architecture Research Program funded by Ministry of Land, Infrastructure and Transport Affairs of Korean Government.

## REFERENCES

- [1] J.M. Seo, I.K. Choi, J.R. Lee, Static and Cyclic Behavior of Wooden Frames with Tenon Joints Under Lateral Load, *Journal of Structural Engineering*, Vol. 125, No. 3, 344-349, 1999.
- [2] J.S. Han, C.J. Kim, An Experimental Study on Mechanical Performance of Tenon for Analysis of Structural System and Modernization of Traditional Wooden Architecture, *Journal of the Architectural Institute of Korea: Planning & Design*, Vol. 21, No. 4, 121-128, 2005.
- [3] M. Kang, N. Yang, Q. Cha, Studies on Static Performance of Mortise and Tenon Joint in Traditional Column and Tie Construction Timber Structure, *Electric Technology and Civil Engineering (ICETCE), 2011 International Conference*, 6197-6200, 2001.
- [4] Y.W. Lee, B.S. Bae, S.G. Hong, J.G. Hwang, N.H. Kim, S.J. Jung, An Analytical Modelling of the Beam-Direction Frame of Traditional Wood Structure System, *Journal of the Architectural Institute of Korea : Structure & Construction*, Vol. 22, No. 3, 29-36, 2006.
- [5] Y.W. Lee, S.G. Hong, J.G. Hwang, B.S. Bae, Capacity of Lateral Load Resistance of Dori-Directional Frame with Jangbu-connection in Traditional Wood Structure System, *Journal of the Architectural Institute of Korea : Structure & Construction*, Vol. 23, No. 2, 35-42, 2007.
- [6] Y.M. Kim, S.G. Lee, Evaluation of Connection Stiffness of Test-bed Hanok Using a 1/4 Scale Two-Storied Model, *Journal of the Architectural Institute of Korea: Structure & Construction*, Vol. 29, No. 12, 73-80, 2013.
- [7] D.P. Fang, S. Iwasaki, M.H. Yu, Q.P. Shen, Y. Miyamoto, H. Hikosaka, Ancient Chinese Timber Architecture II: Dynamic Characteristics, *Journal of Structural Engineering*, Vol. 127, No. 11, 1358-1364, 2001.
- [8] J.G. Hwang, S.G. Hong, Y.W. Lee, S.J. Jung, Natural Frequency Characteristics of Traditional Wooden Structure for Vibration Amplitude, *Journal of the Architectural Institute of Korea : Structure & Construction*, Vol. 25, No. 5, 3-10, 2009.
- [9] S.G. Lee, Y.M. Kim, J.E. Roh, S.H. Lee, S.S. Woo, Dynamic Characteristics of Traditional and New Korean-style Houses According to Excitation Amplitude. *Journal of the Architectural Institute of Korea : Structure & Construction*, Vol. 29, No. 1, 49-58, 2013.
- [10] A.E. Ozsoy, H. Ozkaynak, Structural and Earthquake Engineering Applications of a Model Wooden Structure. *Civil Engineering and Architecture*, Vol. 5, No. 1, 18-25, 2017.
- [11] Y.M. Kim, J.H. Kim, A Study on the Development of Section Tables for Lateral Members of Hanok. *Journal of the Architectural Institute of Korea: Structure & Construction*, Vol. 30, No. 2, 37-44, 2014.
- [12] Y.M. Kim, Structural Check Schemes for the Initial Design of Columns of Hanok for Vertical Loads. *Journal of the Architectural Institute of Korea: Structure & Construction*, Vol. 31, No. 11, 21-28, 2015.



- [13] Y.M. Kim, Development of Automated Structural Design Tool for Horizontal Members of Hanok, *Journal of the Architectural Institute of Korea: Structure & Construction Section*, Vol. 33, No. 4, 21-28, 2017.
- [14] Y.M. Kim, Development of Structural Design Tool of Hanok Columns Considering Rotational Stiffness, *Journal of the Architectural Institute of Korea: Structure & Construction Section*, Vol. 33, No. 8, 29-36, 2017.
- [15] Y.M. Kim, An Evaluation Scheme of Torsional Irregularity for Seismic Design of Hanok, *Journal of the Architectural Institute of Korea: Structure & Construction Section*, Vol. 35, No. 10, 191-198, 2019

## INVESTIGATION OF THE IMPACT OF SEISMIC ZONE TO THE COST OF CONSTRUCTION OF A 5-STOREY R/C BUILDING

Theodoros A. Chrysanidis<sup>1</sup>, Nikolaos O. Alamanis<sup>2</sup>, Grigorios P. Papageorgiou<sup>3</sup>, Georgia Kaouri<sup>1</sup>

<sup>1</sup> Hellenic Open University  
Parodos Aristotelous 18, P.C. 26335, Patra, Greece  
theodoros\_gr@yahoo.com

<sup>2</sup> University of Thessaly  
P.C. 41110, Larissa, Greece  
alam@teilar.gr

<sup>3</sup> University of Thessaly  
V. Griva 11, P.C. 41300, Karditsa, Greece  
gpapageor@uth.gr

---

### Abstract

*Residing in a country like Greece, where the earthquake is a common phenomenon in most of its areas, the need for constructing earthquake resistant buildings that will provide security and functionality to their residents is imperative. For this reason, the present study estimates the cost of constructing the same five-storey building in three different seismic hazard zones. Initially, this building is studied, in accordance with the provisions of Eurocode 8, for seismic zones I, II and III. The dimensioning and calculation of the weight of the required steel and the volume of the required concrete is carried out. The results from the three seismic zones are presented in detail, both for each structural element of the construction separately and for the whole construction, and a comparison is made between them.*

**Keywords:** Seismic hazard zones, Multi-storey building, Construction's cost, Reinforcement

---

## 1 INTRODUCTION

In modern times, various materials are used for the construction of high-rise buildings. The choice of these materials can be made depending on the use of the building, the area in which it is located, the architectural and static study, the cost of construction [1]–[5]. However, in Greece, for the majority of buildings, reinforced concrete is used as a construction material. A reinforced concrete building is made of concrete and steels in the form of rebars or ties. These two materials are harmoniously combined in order, on the one hand, the concrete to receive the compressive forces and on the other hand, the steel to receive the tensile stresses [6], [7]. Greece is an intensely seismic country and as earthquake action is a dangerous and destructive natural phenomenon, the buildings, whether they are new constructions or older, must deal with it effectively. This effective response comes through the design and construction of anti-seismic buildings, but also the strengthening of existing ones [8]–[18].

Nowadays, more and more high-rise buildings are being constructed, with many floors, which are quite sensitive, not only to large earthquakes, but also to less intense ones, if they are not built properly. One of the main problems of these buildings is that, during the earthquake, probably some of their floors move in one direction, while at the same time the other floors move in the opposite direction [19], [20]. Therefore, the engineer should take very seriously the seismic zone in which each building is constructed. The seismic zone significantly affects the dimensioning of the structure, the cross sections of its structural elements and their reinforcement, thus affecting its cost. The engineer has the ability, if for some reason he deems it necessary, to dimension his building in a higher seismic zone than the one to which the building belongs. However, he should not forget that his choice will increase the final construction cost.

The present study presents the simulation and dimensioning, based on modern regulations, of three buildings which have the same standard floor plan, the number of floors (five floors), but are located in different seismic zones. The cost comparisons for the same building between the three different seismic zones leads to useful and interesting conclusions.

## 2 ANALYTICAL RESEARCH

### 2.1 Construction description

The floor plan of the building has dimensions 25 x 25 m, therefore the total area of the floor plan is equal to  $E = 625.00 \text{ m}^2$  (Figure 1). The height of the floors is  $h = 3.00 \text{ m}$ , except for the height of the first floor (ground floor) which is  $h = 4.50 \text{ m}$ . Therefore, the total height of the building is  $h_{\text{tot}} = 16.5 \text{ m}$ . Rigid supports are used and the effect of soil is neglected [21], [22].

The main element of the load-bearing structure can be characterized as the main core, which is located in the center of the building and includes the elevators and stairwells. Regarding the dimensions of the structural elements, there are some small differences from floor to floor. There are also some structural walls in the building. These are the structural walls  $T_3$  and  $T_{10}$  at the two sides of the building's plan. Finally, in terms of beams, they are divided into perimeter and internal. The dimensions of the perimetric beams and the beams of the core are 25 x 70 cm and the internal ones have dimensions 25 x 60 cm. The cross-sections of the structural elements are shown in Table 1.

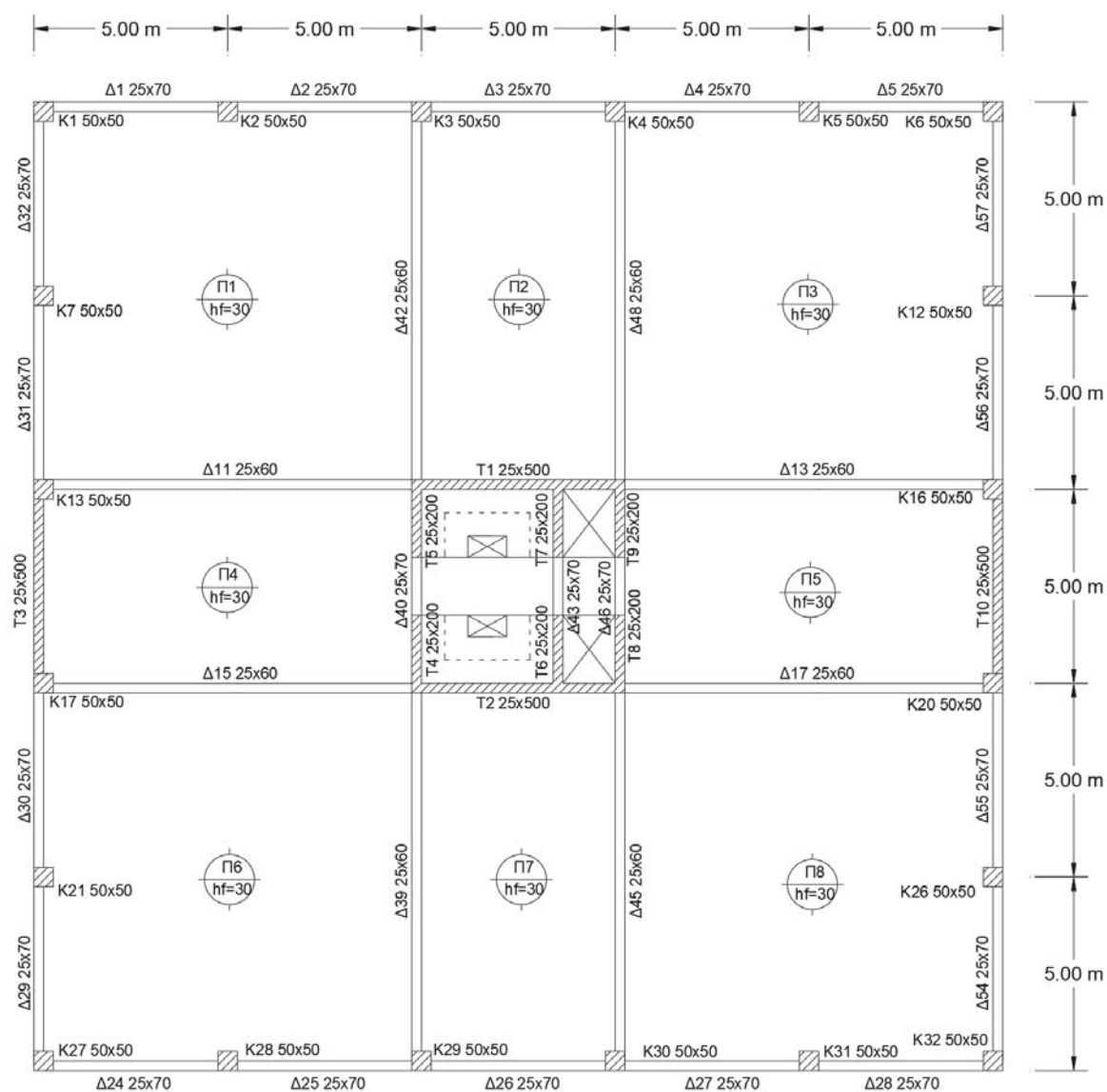


Figure 1: Typical floor plan.

Floor	Height (m)	Beam dimensions (cm)		Wall thickness (cm)	Column dimensions (cm)
		Perimetric	Internal		
1 <sup>st</sup> (Ground floor)	4.50	25x70	25x60	25	50x50
2	3.00	25x70	25x60	25	50x50
3	3.00	25x70	25x60	25	45x45
4	3.00	25x70	25x60	25	40x40
5	3.00	25x70	25x60	25	35x35

Table 1: Dimensions of the structural elements.

## 2.2 Materials

For all the load-bearing structural elements of the construction, concrete quality C30/37 and steel quality B500C were used for the reinforcement bars. According to Eurocode 2 [23], for concrete quality C30/37, the modulus of elasticity is given equal to  $E_{cm} = 32$  GPa. The Poisson ratio is considered equal to zero ( $\nu = 0$ ) for cracked. The steel quality B500C has a characteristic strength equal to  $f_{yk} = 500$  MPa.

## 2.3 Analysis method

The building was analyzed for the vertical loads applied under the combination of  $1.35G + 1.50Q$ , as well as for the seismic actions under the combination of  $G + \psi_2Q \pm E$ . The dynamic spectral method was used for the dynamic analysis of the building. The building was analyzed and examined in three different seismic hazard zones. In zone I with maximum seismic horizontal ground acceleration  $a_g = 0.16g$ , in zone II with  $a_g = 0.24g$  and in zone III with  $a_g = 0.36g$  (where  $g$  is the acceleration of gravity and is equal to  $9.81 \text{ m/sec}^2$ ). Also, the design spectrum was used, according to Eurocode 8 [24], for soil category B and spectrum type 1. Spectrum data used according to EC8 are displayed in Table 2:

SPECTRUM DATA EC8		
N/A	Type	Data
1	Spectrum type	Horizontal design spectrum type 1
2	Soil category	B
3	Factor $\beta$	0.20
4	Seismic acceleration factor $\alpha$	For the three categories: $\alpha = 0.16, 0.24, 0.36$
5	Gravity acceleration $g$	$9.81 \text{ m/sec}^2$
6	Coefficient behavior $q$	Calculation based on EC8

Table 2: Spectrum data used for the dynamic analysis.

## 2.4 Gravity loads

The weight of the reinforced concrete is considered equal to  $25.00 \text{ kN/m}^3$ . The load of the partition masonry is considered to be evenly distributed over the entire surface of the floor plan and the load of the perimeter masonry is applied only on the perimeter beams and directly on them. Also, on the roof, all around the perimeter is considered to be a parapet with a height equal to  $0.90 \text{ m}$ . Flooring is considered to be equal to  $1.40 \text{ kN/m}^2$ . The permanent load for the masonry structures is taken equal to  $1.00 \text{ kN/m}^2$  for the internal brick structures used as partitions and equal to  $8.00 \text{ kN/m}$  for the masonry structures at the perimeter of the slab of the building. The roofing is considered equal to  $3.50 \text{ kN/m}^2$  and the load for the parapet which is at the perimeter of the roof is assumed as equal to  $3.60 \text{ kN/m}^2$ . Live loads are considered equal to  $2.00 \text{ kN/m}^2$  at every floor slab; meaning for the ground floor, the other typical floors and the roof. Permanent and live loads are shown at Table 3.

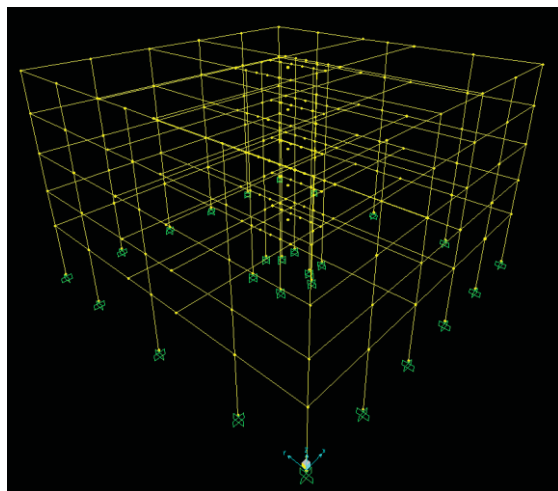


PERMANENT LOADS		
N/A	Type	Value
1	Flooring	1.40 kN/m <sup>2</sup>
2	Partition brick structures	1.00 kN/m <sup>2</sup>
3	Perimeter brick structures	8.00 kN/m
4	Roofing	3.50 kN/m <sup>2</sup>
5	Parapet roof load	3.60 kN/m <sup>2</sup>
LIVE LOADS		
N/A	Type	Value
1	Ground floor	2.00 kN/m <sup>2</sup>
2	Typical floors	2.00 kN/m <sup>2</sup>
3	Roof	2.00 kN/m <sup>2</sup>

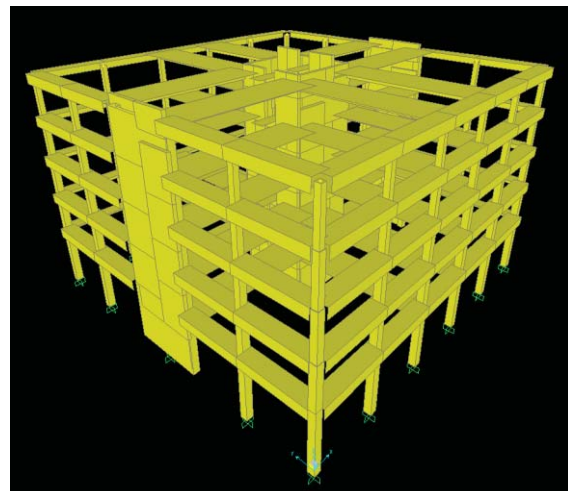
Table 3: Permanent and live loads.

## 2.5 Modelling and dimensioning

Some assumptions were used in the design of the model of the five-storey building. Stiffness for cracked sections is considered equal to 0.5. Torsional stiffness is considered equal to 0.1. For the calculation of the masses of each floor, half the masses of the vertical structural elements of the underneath floor and half the masses of the vertical structural elements of the upper floor were used. In the context of this study, the dimensioning of the individual structural elements was carried out exclusively for the first floor (ground floor) of the five-storey building, for each of the three seismic zones. Figure 2 shows the 3D model of the building. Figure 3 displays the methodology with which the slab loads are transferred to the beams.



(a)



(b)

Figure 2: Views of the 3D building model: (a) Linear finite elements (b) Sections.

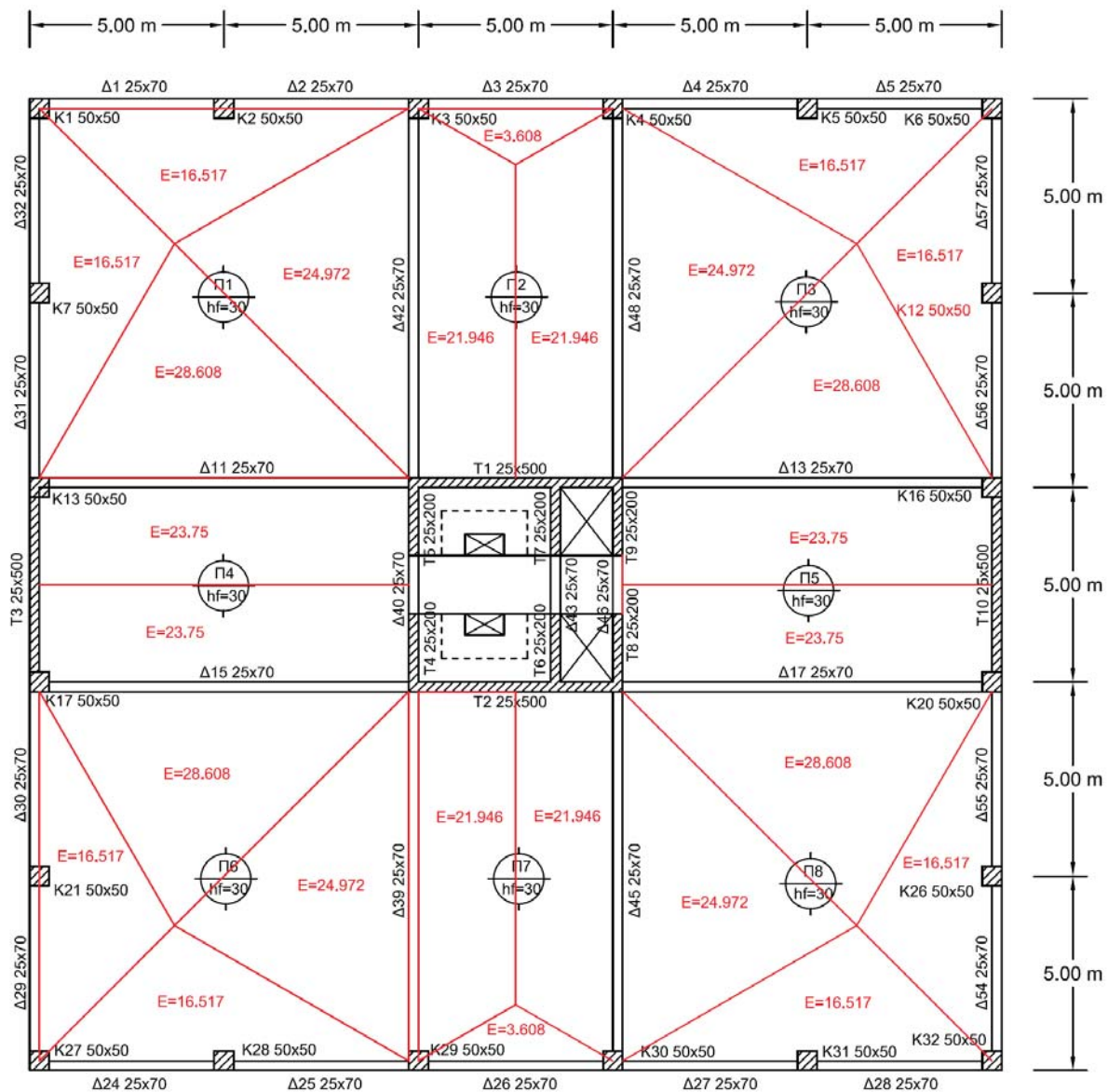


Figure 3: Methodology of calculating beam loads.

### 3 MEASUREMENTS OF MATERIALS

#### 3.1 Concrete and steel measurements for the ground floor

Concrete and steel used for the reinforcement of the structural elements are measured for the ground floor. Concrete is measured in terms of volume and reinforcement steel is measured in terms of weight. Table 4 displays the amount of concrete occupied by the structural elements of the load-bearing structure for all three seismic zones. Also, the same table displays the weight of steel used for all three seismic zones, too. Furthermore, the steel over concrete ratio is calculated and the increase of the steel weight is given in terms of percentages, again for all three seismic hazard zones.

GROUND FLOOR					
Seismic zone	Concrete volume (m <sup>3</sup> )	Steel weight (kg)	Steel / concrete ratio (kg/m <sup>3</sup> )	Increase of steel weight (%)	
Zone I	248.325	19721.91	79.42	-	
Zone II	248.325	21202.56	85.38	7.51	
Zone III	248.325	22360.64	90.05	13.38	5.46

Table 4: Concrete and steel measurements for ground floor.

### 3.2 Concrete and steel measurements for the whole building

The measurements of the materials calculated for the ground floor are used for the estimation of the quantities of the concrete and steel needed for the whole load-bearing structure of the building. Table 5 shows the results for the quantities of concrete and steel for the whole building structure.

BUILDING					
Seismic zone	Concrete volume (m <sup>3</sup> )	Steel weight (kg)	Steel / concrete ratio (kg/m <sup>3</sup> )	Increase of steel weight (%)	
Zone I	1151.58	93636.64	81.31	-	
Zone II	1151.58	99738.59	86.61	6.52	
Zone III	1151.58	105118.39	91.28	12.26	5.39

Table 5: Concrete and steel measurements for building.

## 4 ANALYSIS OF RESULTS

### 4.1 Concrete and steel measurements for the ground floor

The ratio of reinforcement steel used for the rebars over the concrete volume used for concreting the structural elements of the load-bearing structure is calculated for all three seismic hazard zones both for ground floor and for the whole building (Figure 4). Moreover, the reinforcement steel weight increment when changing seismic zone is calculated, too. This calculation takes place for changing from zone I to zone II, from zone I to zone III and from zone II to zone III both for the ground floor, as well as, for the whole building (Figure 5).

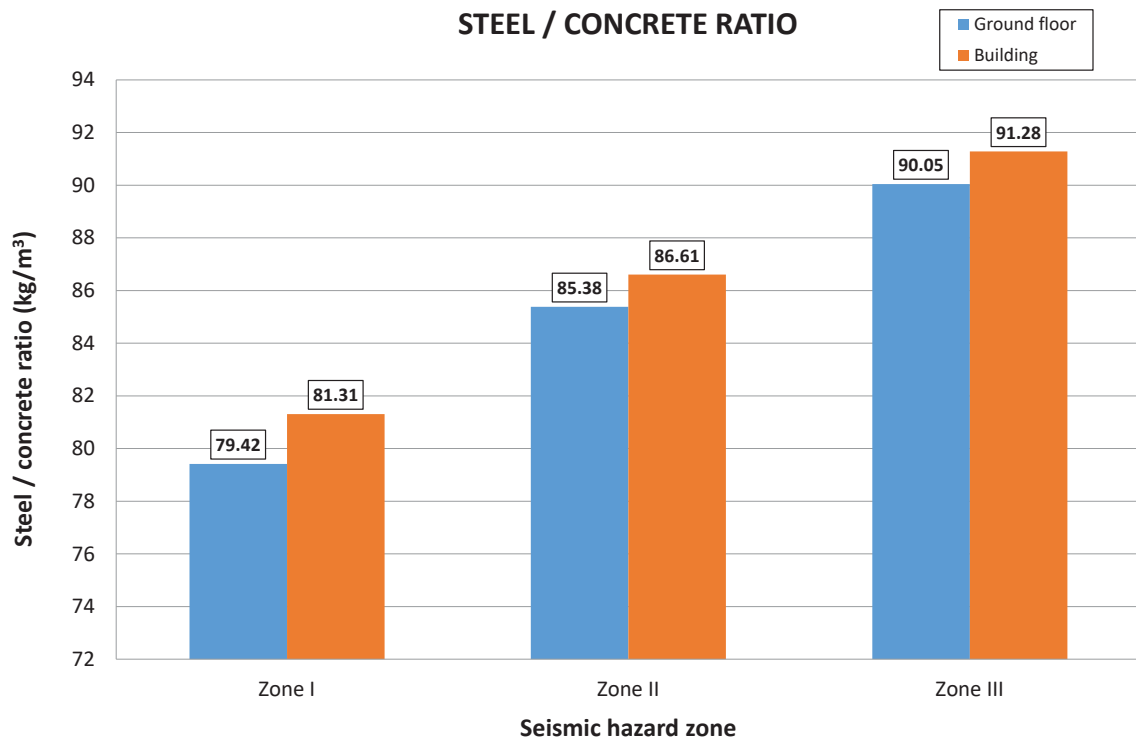


Figure 4: Steel / concrete ratio diagram for the ground floor and the whole building.

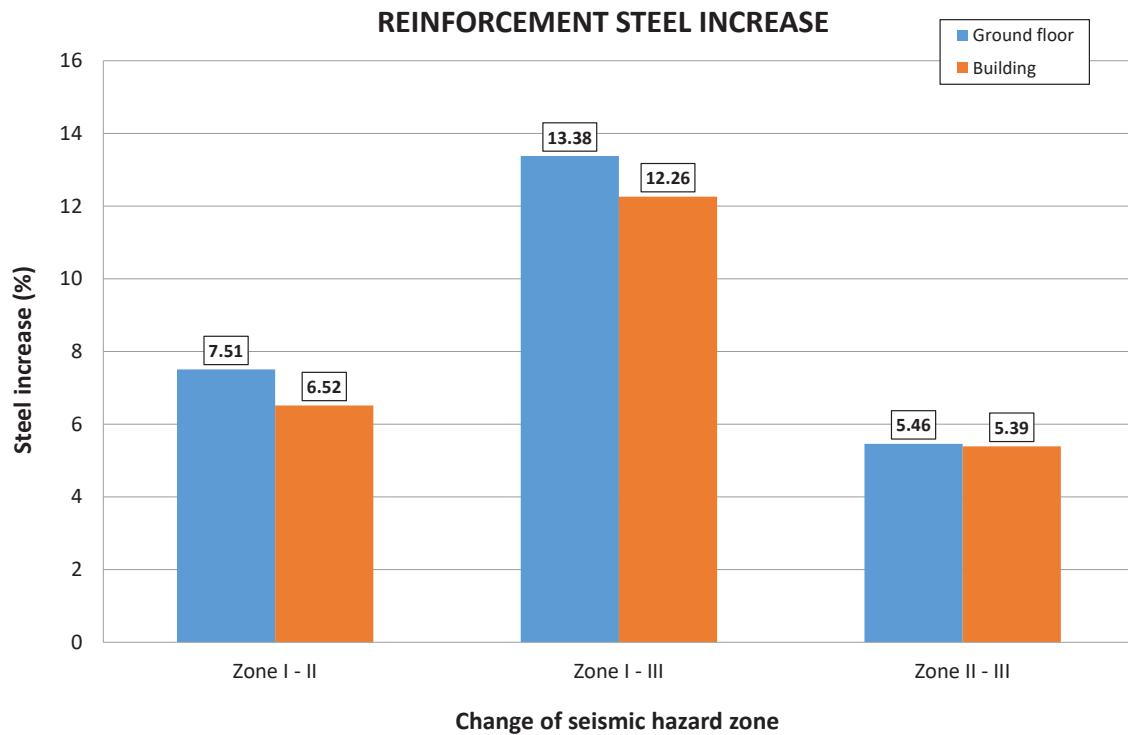


Figure 5: Diagram of steel increase when changing seismic zone for the ground floor and the whole building.

## 4.2 Analysis of results

The analysis of the previous results leads to the following:

1. As far as the floor slabs are concerned, both the volume of their concrete and the weight of their steel do not change in the three seismic hazard zones.
2. Collectively, in terms of reinforcement steel weight, there is an increase of 6.52% from seismic zone I to II and 5.39% from seismic zone II to III (Figure 5). The increase rates of the steel weight for the ground floor of the building are similar, 7.51% and 5.46% respectively (Figure 5).
3. Also, Table 5 and Figure 4 show that the requirement of the five-storey building in reinforcement in seismic zone I is 94 tn with steel to concrete ratio equal to  $81.31 \text{ kg/m}^3$ , while for zone III the weight of reinforcement reaches 105 tn with a ratio of steel to concrete equal to  $91.28 \text{ kg/m}^3$ .

## 5 CONCLUSIONS

The observation of the measurement tables of the concrete volume and those of the steel weight of the various structural elements of the building in question, as well as the tables and the various diagrams concerning the steel/concrete ratio and the percentage increase of the weight of steel leads to some conclusions that mainly concern the behavior of the structural elements but also the whole construction in the three seismic hazard zones and consequently the cost that will be spent for this construction.

1. From seismic zone I to zone II, there is an increase in seismic acceleration of 50%, from I to III 125% and from II to III 50%. These percentages should be compared mainly with the percentages of increase in the weight of steel, in order to prove if the construction cost of the building is within reasonable limits.
2. The sizing of the slabs, whether it concerns the reinforcement (steel weight) or the cross sections (volume of concrete) remains constant in all three seismic zones. Therefore, the ratio of steel to concrete in the slabs also remains constant for all floors and finally throughout the construction.
3. Regarding the whole construction, as it is logical, as the weight of the reinforcement increases separately for each structural element, moving from one seismic zone to another, the same increases for the whole construction. This change plays a very important role, as with the increase of the weight of the reinforcement, there is a corresponding increase of the cost of the structure. However, the total increase in the quantity of materials and consequently the construction cost from seismic zone I to II is only of the order of 6.52%, i.e., 8 times less than the increase in seismic acceleration in the respective zones. Also, the increase in the amount of materials from seismic zone I to III is of the order of 12.26%, i.e., 10 times less than the increase in seismic acceleration in these zones. Finally, the increase in the amount of materials from seismic zone II to III is of the order of 5.39%, i.e., 9 times smaller than the increase in seismic acceleration in the respective zones.
4. In conclusion, observing the results obtained for all the structural elements in the three seismic zones, it can be said that the rate of increase of construction costs from one zone to another is quite small in relation to the rate of increase of seismic acceleration in the respective seismic hazard zones. Thus, if the engineer wishes, for reasons of greater safety, to dimension a construction, using the immediately larger seismic zone than the one in which the construction is actually located, he can do so without significantly increasing the cost of materials (6.52% from seismic zone I to II and 5.39% from seismic zone II to III). The same could be said for the case where the building is



located in the seismic hazard zone I and the engineer wishes to dimension it in zone III. The rate of increase of the cost of materials (12.26%) is less than the safety that thus ensures the engineer for the relevant structure.

## REFERENCES

- [1] T. Chrysanidis and I. Tegos, "Cost Comparison and Parametrical Investigation of the R/C Shear Wall Core of a Tall Building," *International Journal of Engineering Research and Technology*, vol. 5, no. 09, pp. 592–595, 2016.
- [2] T. Chrysanidis, V. Panoskaltsis, and I. Tegos, "Parametrical cost analysis of an ultra high-rise building: Detailed design," *International Journal of Applied Engineering Research*, vol. 11, no. 18, pp. 9644–9650, 2016.
- [3] G. Papageorgiou, E. Papadimitriou, N. Alamanis, N. Xafoulis, I. Chouliaras, and K. Lazogiannis, "Construction cost comparative analysis of highways in Greece," *PRIME International Journal Practical Research in Innovative Management & Entrepreneurship*, vol. 12, no. 1, pp. 68–85, 2019.
- [4] G. Papageorgiou, "Economic assessment of pavement maintenance and strengthening techniques in view of implementation cost," *European Transport*, no. 78, p. Article 5, 2020.
- [5] A. Tsiknas, A. Athanasopoulou, and G. Papageorgiou, "Evaluation of flexible pavement construction cost according to the design method," *Proceedings of the Institution of Civil Engineers (ICE) - Transport*, vol. 173, no. 1, pp. 3–12, 2020.
- [6] G. G. Penelis and A. J. Kappos, *Earthquake-resistant Concrete Structures*. London, UK: E & F N SPON (Chapman & Hall), 1996.
- [7] G. Penelis, K. Stylianidis, A. Kappos, and C. Ignatakis, *Reinforced Concrete Structures*. Thessaloniki, Greece: A.U.Th. Press, 1995.
- [8] T. Chrysanidis, "Evaluation of Out-of-Plane Response of R/C Structural Wall Boundary Edges Detailed with Maximum Code-Prescribed Longitudinal Reinforcement Ratio," *International Journal of Concrete Structures and Materials*, vol. 14, no. 1. 2020, doi: 10.1186/s40069-019-0378-4.
- [9] T. Chrysanidis and I. Tegos, "Axial and transverse strengthening of R/C circular columns: Conventional and new type of steel and hybrid jackets using high-strength mortar," *Journal of Building Engineering*, vol. 30, no. January, p. 101236, 2020, doi: 10.1016/j.jobbe.2020.101236.
- [10] S. Raza, M. Khan, S. Menegon, H.-H. Tsang, and J. Wilson, "Strengthening and repair of reinforced concrete columns by jacketing: State-of-the-art review," *Sustainability (Switzerland)*, vol. 11, no. 11, pp. 1–31, 2019, doi: 10.3390/su11113208.
- [11] T. Chrysanidis, "Influence of elongation degree on transverse buckling of confined boundary regions of R/C seismic walls," *Construction and Building Materials*, vol. 211, pp. 703–720, Jun. 2019, doi: 10.1016/J.CONBUILDMAT.2019.03.271.
- [12] I. Tegos, N. Giannakas, and T. Chrysanidis, "Cross-correlation of stresses in the transverse reinforcement under shear load and confinement," in *Proceedings of the 2013 International Van Earthquake Symposium*, 2013.

- [13] I. Tegos, T. Chrysanidis, and M. Tsitotas, "Seismic behaviour of R/C columns and beams with interlocking spirals," *International Journal of Scientific and Engineering Research*, vol. 5, no. 8, pp. 310–319, 2014.
- [14] I. Tegos and T. Chrysanidis, "Spare Additional Confinement in Spiral Arrangements," *International Journal of Scientific Research*, vol. 3, no. 9, pp. 110–113, 2014.
- [15] I. Tegos and T. Chrysanidis, "Columns With Spiral Reinforcement Under Concentric Compression," *International Journal of Research in Engineering and Technology*, vol. 03, no. 08, pp. 125–132, 2014, doi: 10.15623/ijret.2014.0308020.
- [16] G. Minafò and M. Papia, "Concrete softening effects on the axial capacity of RC jacketed circular columns," *Engineering Structures*, vol. 128, pp. 215–224, 2016, doi: 10.1016/j.engstruct.2016.09.043.
- [17] G. Minafò, "A practical approach for the strength evaluation of RC columns reinforced with RC jackets," *Engineering Structures*, vol. 85, pp. 162–169, 2015, doi: 10.1016/j.engstruct.2014.12.025.
- [18] A. Takeuti, J. de Hanai, and A. Mirmiran, "Preloaded RC columns strengthened with high-strength concrete jackets under uniaxial compression," *Materials and Structures*, vol. 41, no. 7, pp. 1251–1262, 2008, doi: 10.1617/s11527-007-9323-0.
- [19] S. Taghavi and E. Miranda, "Approximate Floor Acceleration Demands in Multistory Buildings. II: Applications," *Journal of Structural Engineering*, vol. 131, no. 2, pp. 212–220, 2005, doi: 10.1061/(asce)0733-9445(2005)131:2(212).
- [20] S. Otani, T. Kabeyasawa, H. Shlohara, and H. Aoyama, "Analysis of the full scale seven story reinforced concrete test structure," *Symposium Paper*, vol. 84, no., pp. 203–239, 1984.
- [21] N. Alamanis and P. Dakoulas, "Investigation on the effect of spatial variability of soil properties on permanent seismic displacements of slopes in load," in *14th Baltic Sea Geotechnical Conference 2020*, 2020.
- [22] N. Alamanis and P. Dakoulas, "Vulnerability of soil slopes against seismic damage based on the effect of spatial variability of soil properties on the development of permanent seismic displacements," in *International Conference on Research in Engineering, Technology and Science*, 2019.
- [23] European Committee for Standardization, "EN 1992-1-1:2004, Eurocode 2: Design of concrete structures - Part 1-1: General rules and rules for buildings," Brussels, Belgium, 2004.
- [24] European Committee for Standardization, "EN 1998-1:2004, Eurocode 8: Design of structures for earthquake resistance - Part 1: General rules, seismic actions and rules for buildings," Brussels, Belgium, 2004.

## **FLEXURAL PERFORMANCE OF CONCRETE BEAMS UNDER CYCLIC LOADING**

**Waseem Khan<sup>1</sup>, Saleem Akhtar<sup>2</sup>, Aruna Rawat<sup>3</sup> and Anindya Basu<sup>4</sup>**

<sup>1</sup> Research Scholar, Department of Civil Engineering, University Institute of Technology (UIT), RGPV, Bhopal - 462 033, Madhya Pradesh, India.  
e-mail: wkrgpv@gmail.com

<sup>2</sup> Professor, Department of Civil Engineering, University Institute of Technology (UIT), RGPV, Bhopal - 462 033, Madhya Pradesh, India.  
e-mail: sargpv@gmail.com

<sup>3</sup> Assistant Professor, Department of Civil Engineering, University Institute of Technology (UIT), RGPV, Bhopal - 462 033, Madhya Pradesh, India.  
e-mail: augupta2001@gmail.com

<sup>4</sup> UGC-Assistant Professor, School of Pharmaceutical Science Engineering, RGPV, Bhopal - 462 033, Madhya Pradesh, India.  
e-mail: anindya@rgtu.net

---

### **Abstract**

*A large portion of the civil concrete structures get damaged during an earthquake event, hence structures required some substitution and restoration. In the present study, the flexural performance of concrete beams under variation of magnitude on cyclic loading is investigated. ABAQUS finite element (FE) program is used to numerically perform a parametric study for five different depths of beams varying from 250 to 750 mm under cyclic loading. The finite element (FE) beams are modeled using Concrete Damaged Plasticity model (CDP) model. The effect of beam depth on the flexural strength of concrete beam is investigated. The effect of cyclic loading on strength and deformation behavior, yielding, ultimate, failure strengths as well as on displacements are evaluated. The load-deflection curves are obtained for different beams and are compared to static loading.*

**Keywords:** Concrete damage plasticity, Cyclic load, Finite element model, Flexural strength.

---

## 1 INTRODUCTION

A large portion of the civil concrete structures get damaged during an earthquake event, hence structures required some substitution and restoration. A wide range of tests have been conducted to understand the effect of cyclic load on reinforced concrete structural members during the earthquake. The failure of reinforced concrete (RC) beam is a progressive process of micro crack initiation and propagation leading to micro cracks that grow to a stage in which failure occurs. Under the repeated cyclic loading, the mechanical properties of concrete changes, thus strain increases permanently, whereas the modulus of elasticity decreases. In the case of a reinforcing bar, cyclic load causes micro- cracking that initiates a stress concentration at the bar surface. As the cyclic stress continues, the crack propagates, leading to sudden fracture crack that grow to a stage in which failure occurs.

In the present study, the flexural performance of three-dimensional nonlinear RC beams under cyclic and static loading are analyzed using concrete damaged-plasticity (CDP) [10] model available in the software ABAQUS [11].

### 1.2 Furthermore work has been done on cyclic load

Yonezawa et al., 2020 [1] investigated the effect of cyclic load on welded joints and measured the residual stress at the ultrasonic impact treatment groove using X-ray diffraction method. Ftaikhan et al., 2019 [2] studied the effect of FRP and CFRP bar embedded in RC frame subjected to dynamic loading using ABAQUS and ARCS3D finite element softwares. Tsutsumi et al., 2019 [3] analyzed the cyclic response of steel bridged pier and also evaluate the load-carrying capacity of steel bridge pier. Jamadin et al., 2019 [4] investigated the natural frequencies, mode shapes and damping ratios for bridge reinforced concrete deck slabs under cyclic and static loads. Koltsida et al., 2019 [5] tested brick masonry prisms under compressive cyclic loading at different maximum stress levels until failure and developed three mathematical equations to predict the three characteristic stages of fatigue of brick masonry. Haris and Roszevák, 2019 [6] analyzed RC frame joint under monotonic increasing quasi-static and cyclic changing loads. Xiao et al., 2018 [7] studied the effect change in loading rate on the dynamic behavior of reinforced concrete beams under cyclic loading. Harba and Abdulridha, 2017 [8] studied the effect of five different cyclic loads on RC hunched beam. Parvez and Foster, 2015 [9] showed that steel-fiber-reinforced concrete under constant amplitude cyclic loading has low smaller deflections and smaller crack widths than that of control specimens and reducing the stress level in the tensile reinforcement.

Based on the observations from the literature review and gaps, the following are the objectives of the present work:

- (i) A parametric study of five different depths of rectangular beams (having width 200 mm and length 1500 mm constant) varying from 250 to 750 mm under static and cyclic loading is carried out.
- (ii) To study the effect of increasing depth of beam on load-deflection curve of RC beams under cyclic loading and also compared it with static loading.
- (iii) To determine plastic strain, principal stress and mid span deflection under cyclic and static loadings.

## 2 PROPOSED METHODOLOGY

A rectangular RC beam having constant width 200 mm and length 1500 mm. the beam is having varying depths of 250 mm, 350 mm, 500 mm, 600 mm and 750 mm is analysed as given in Table 1. A FE element model of RC beam using C3D8 brick element has been created and analysed in FE software package ABAQUS. The material properties of RC beam are

given in Table 2. The nonlinear behavior of concrete is modeled using CDP model [10] can define the compression load behavior and tension load behavior. Figure 1 shows the cyclic loading considered in the present study having load of 2000 N to 3000 N. Figure 2 shows the FE model of RC beam. The steel reinforcement is embedded in to the concrete beam. The mesh size adopted in the present work is 50 mm.

Beam Designation	Width (mm)	Depth (mm)	Effective length (mm)	Width/Depth ratio
B-1	200	250	1500	0.8
B-2	200	350	1500	0.57
B-3	200	500	1500	0.4
B-4	200	600	1500	0.33
B-5	200	750	1500	0.27

Table 1: Beam dimensions.

Beam	Concrete mix	$f_{ck}$ (Mpa)	$f_{tk}$ (MPa)	$E_c$ (MPa)	$E_s$ (GPa)	Main Reinforcement	Stirrups	Effective cover
B-1 to B-5	M60	61.8	4.6	39306.49	2.1	4#20 mm dia.	10 mm dia. @ 140 mm c/c	20 mm

Table 2: Material properties.

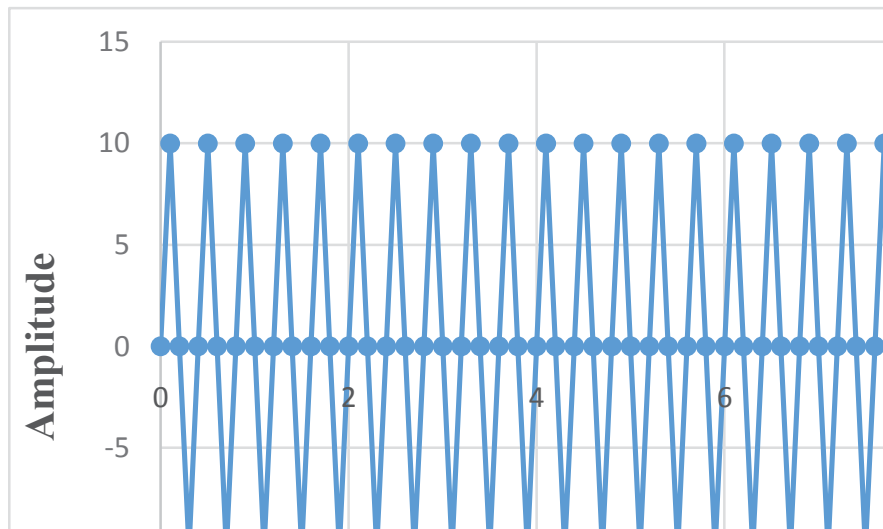


Figure 1: Cyclic loading.



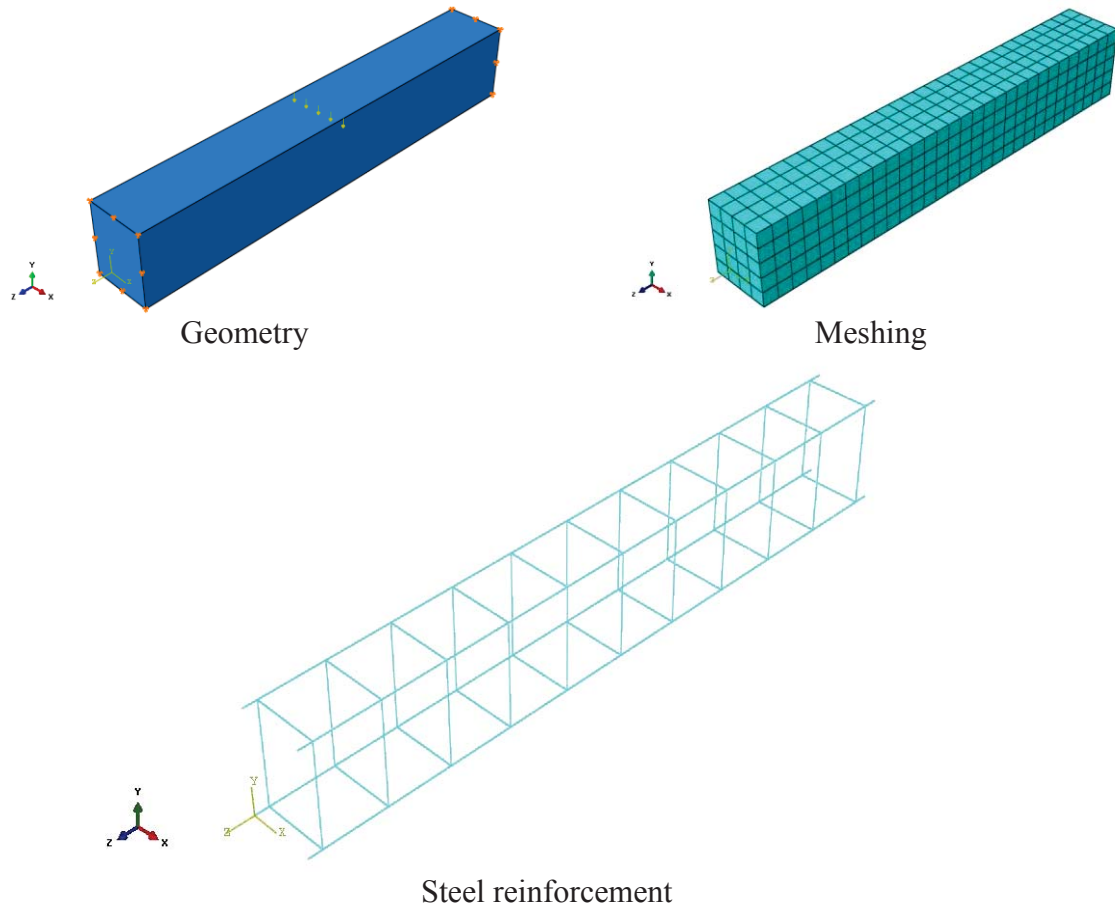


Figure 2: FE model of RC beam.

### 3 RESULTS AND DISCUSSIONS

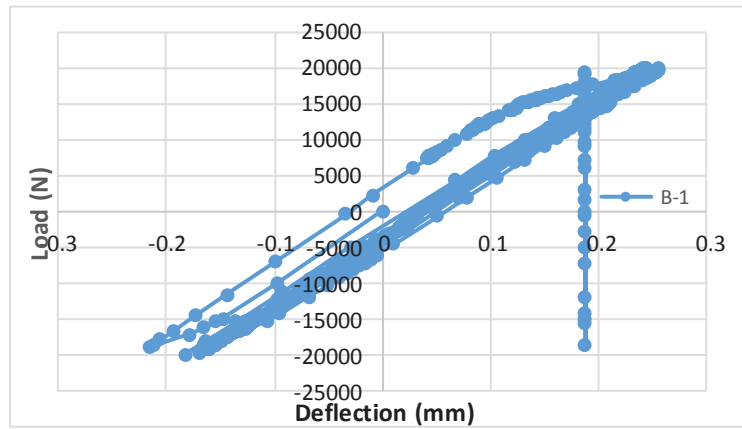
Total five RC beams (B-1 to B-5) has been analyzed. The results prevail to the objectives of the study are presented and discussed in this section. Table 3 gives the initial plastic load and deflection for B-1 to B-5 beams under cyclic loading. Table 4 gives the load and deflection values under static loading of 50000 N. Figure 3 shows the load-deflection curves for B-1 to B-5 RC beams under cyclic loading. It can be observed that as the depth of beam increases the deflection decrease in the beams. Figure 4 shows the load-deflection curve for the RC beams under static loading. It can be observed from the figure that as the depth of beam increases the deflection reduces. It is observed that deflection is less in B-5 beam having a depth of 750 mm.

Beam Designation	Initial Plastic Load (N)	Initial Plastic deflection (mm)
B-1	19987.2	0.26
B-2	24932.6	0.15
B-3	29768.3	0.05
B-4	29586.4	0.03
B-5	25000	0.02

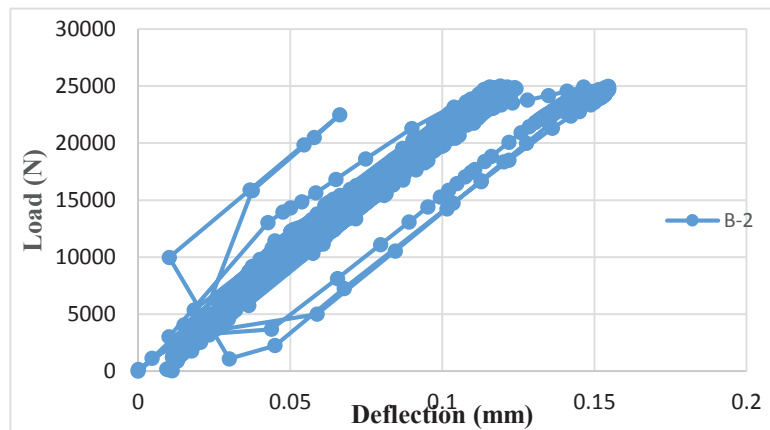
Table 3: Initial plastic load and deflection under cyclic loading.

Beam Designation	Load (N)	Deflection (mm)
B-1	50000	1.42
B-2	50000	0.70
B-3	50000	0.50
B-4	50000	0.47
B-5	50000	0.45

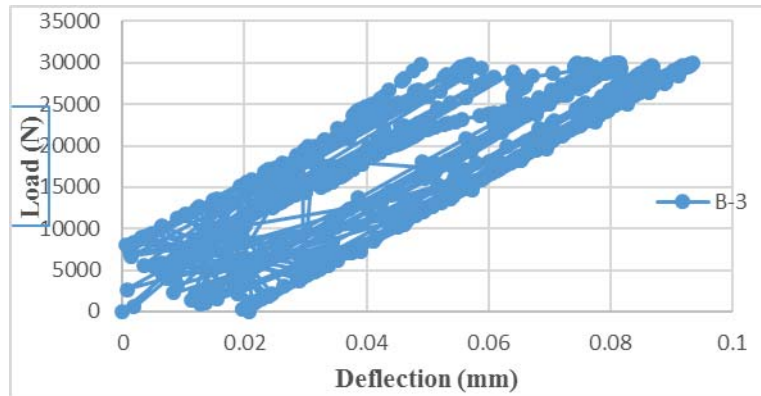
Table 4: Load and deflection under static load.



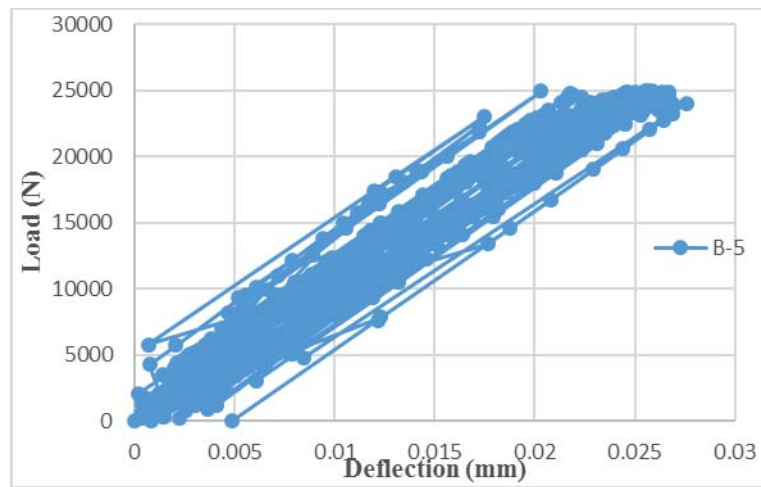
(a) B-1 RC beam



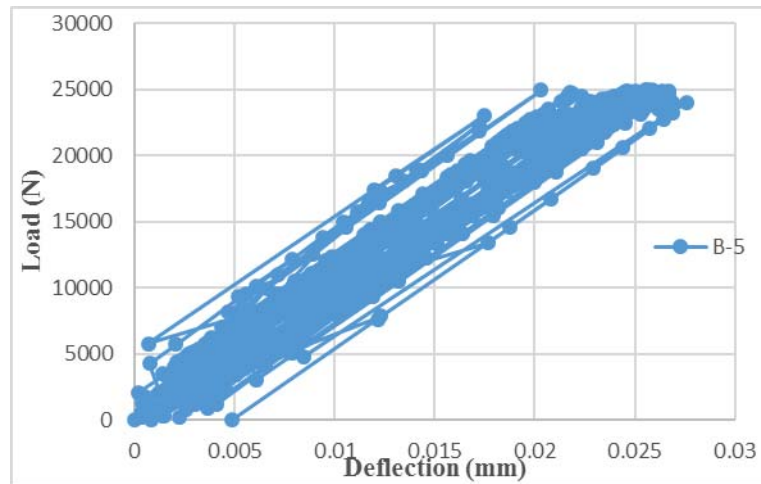
(b) B-2 RC beam



(c) B-3 RC beam



(d) B-4 RC beam



(e) B-5 RC beam

Figure 3: Load-deflection curves RC beams under cyclic loading.

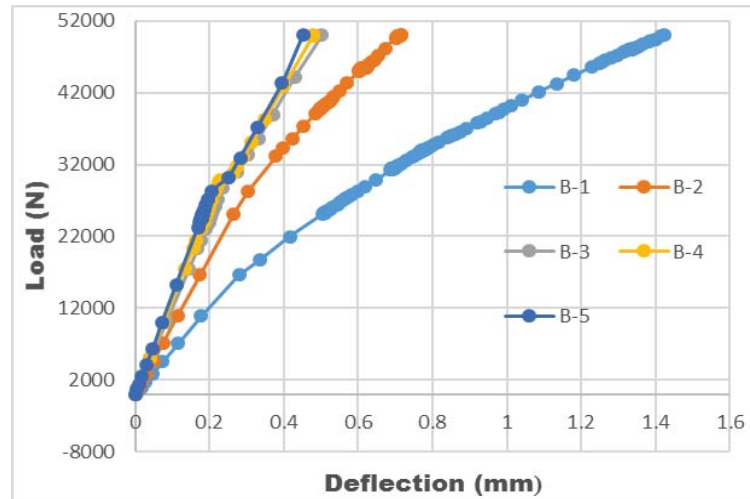
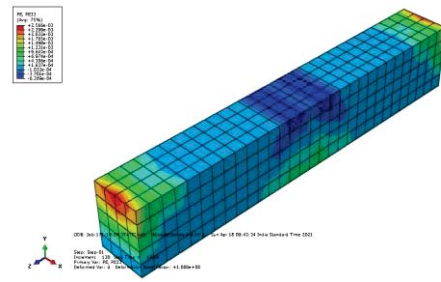
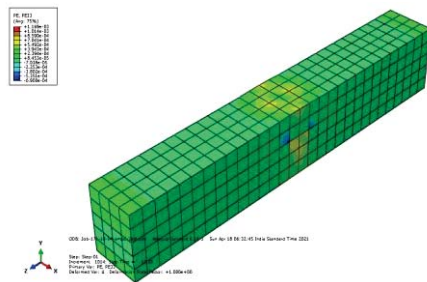
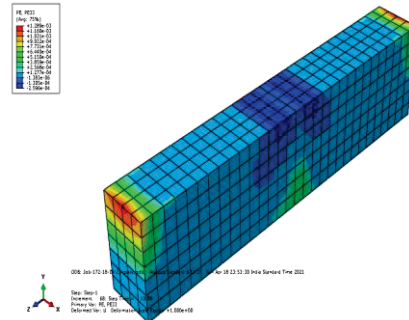
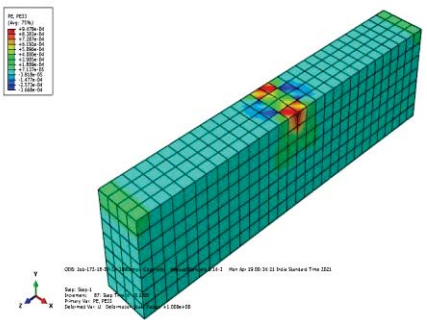


Figure 4: Load-deflection curves RC beams under static loading.

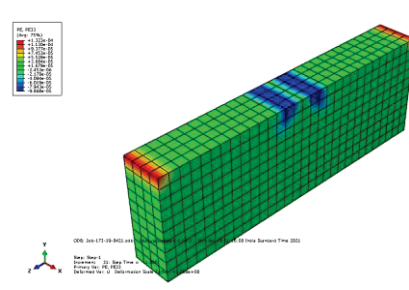
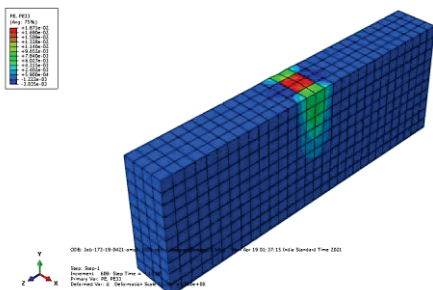
B-1



B-2



B-3



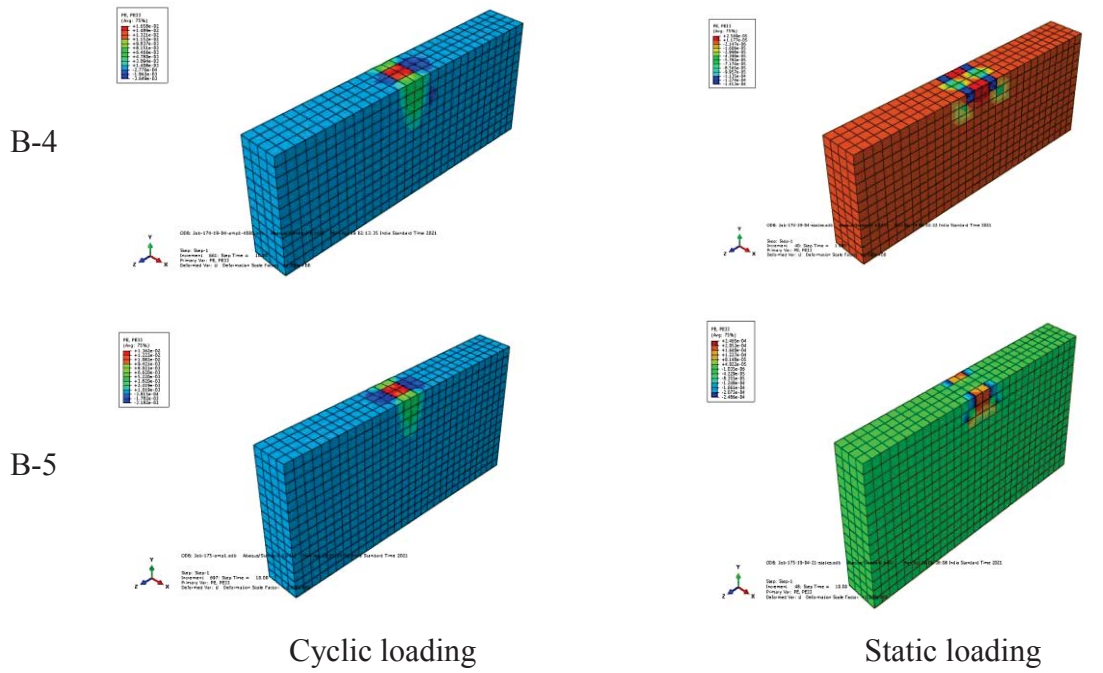
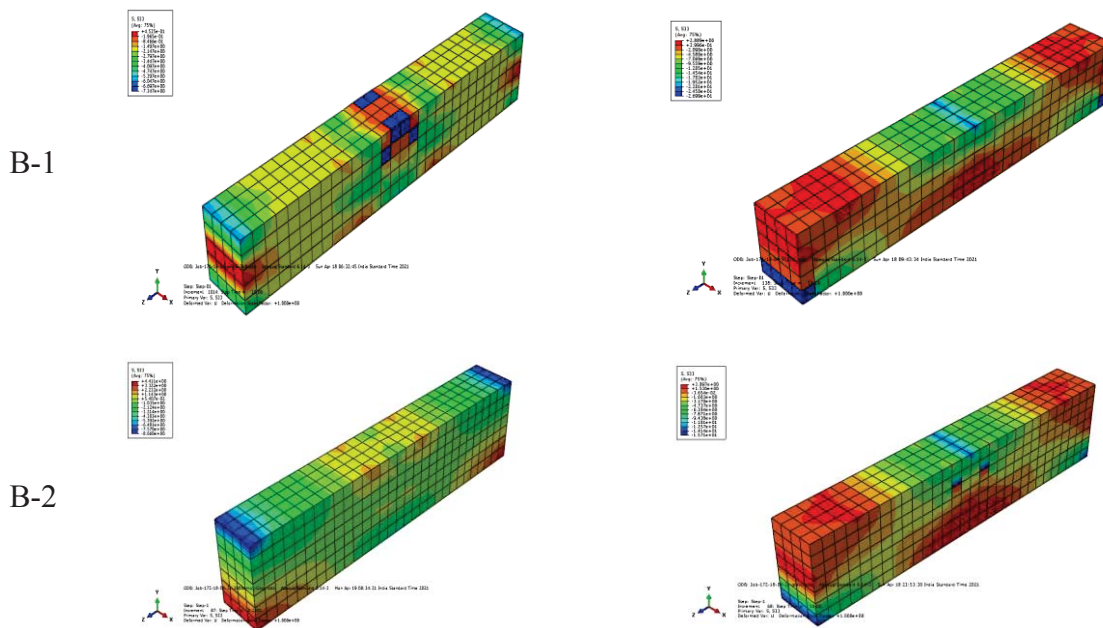


Figure 5: Plastic strain for RC beams under cyclic and static loading.





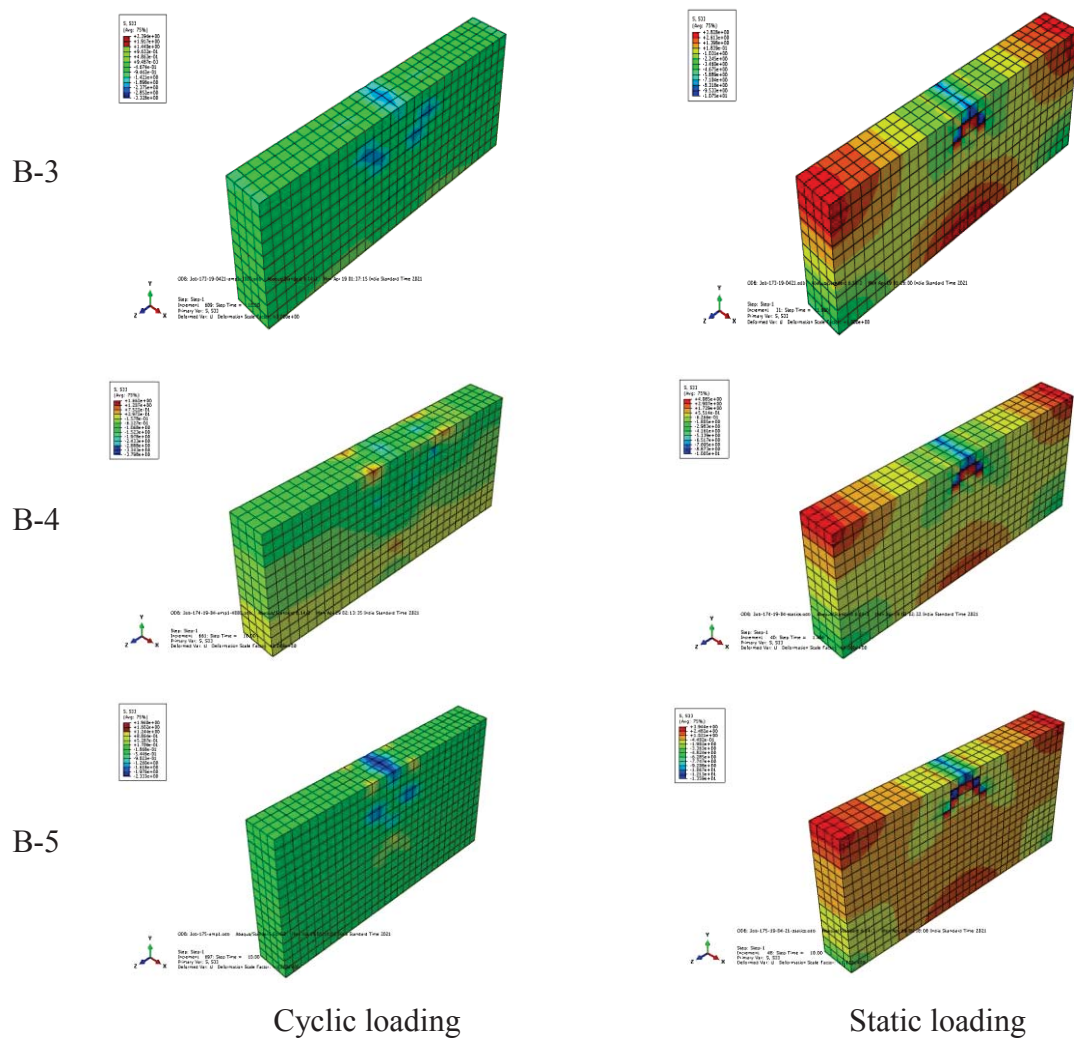
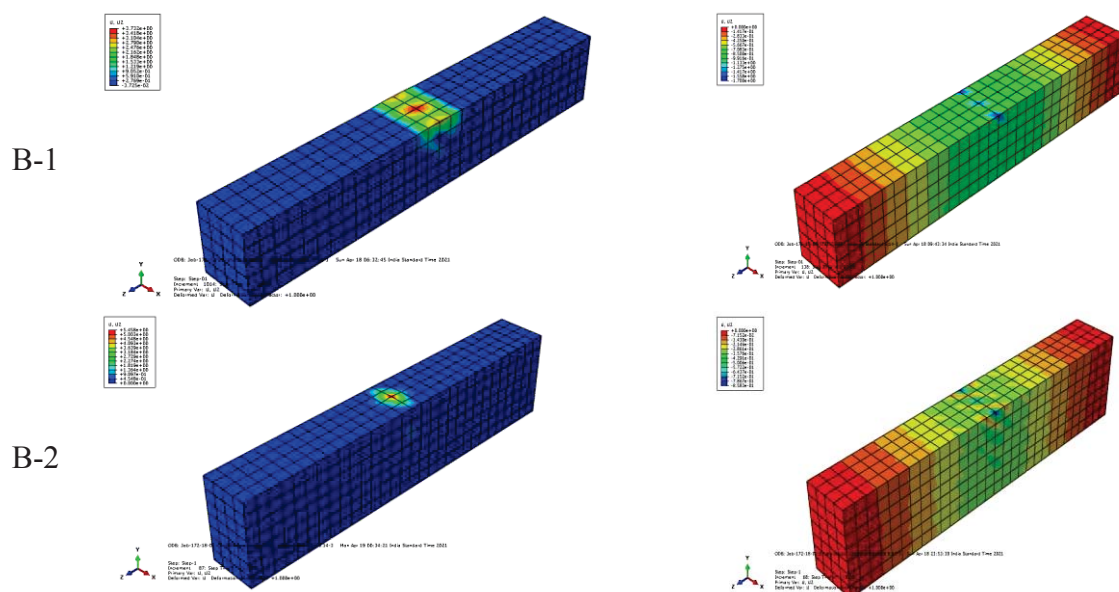


Figure 6: Principal stress for RC beams under cyclic and static loading.



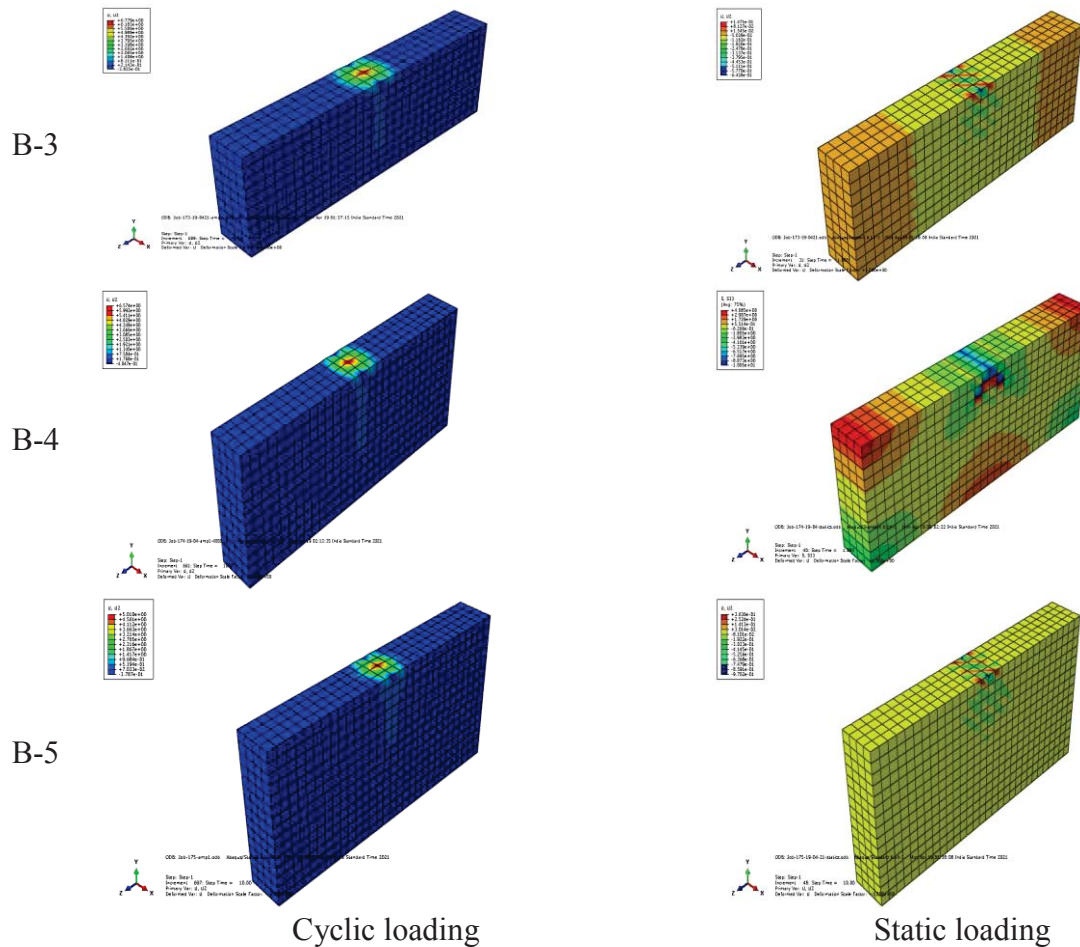


Figure 7: Mid span deflection for RC beams under cyclic and static loading.

Figures 5, 6 and 7 shows the plastic strain, principal stress and mid span deflection for RC beams under cyclic and static loading, respectively. The plastic strain, principal stress and deflection are observed less in the case of B-5 RC beam having a depth of 750 mm for cyclic load and static load.

#### 4 CONCLUSIONS

In the present study, the flexural performance of three-dimensional nonlinear RC beams under cyclic and static loading are analyzed using concrete damaged-plasticity (CDP) model. A parametric study of five different depths of rectangular beams (having width 200 mm and length 1500 mm constant) varying from 250 to 750 mm under static and cyclic loading is carried out. The effect of increasing depth of beam on load-deflection curve of RC beams under cyclic loading and also compared it with static loading are studied. The plastic strain, principal stress and mid span deflection under cyclic and static loadings are investigated. On the basis of FE analysis of RC beams the following conclusions are drawn:

- (i) By increasing the depth of beam that is width to depth ratio the load carrying capacity of beam increases for both cyclic and static loadings.
- (ii) In cyclic loading it is observed that as the load amplitude is high the damage observed is more as compared to static loading.

## REFERENCES

- [1] T. Yonezawa, H. Shimanuki, and T. Mori, Influence of cyclic loading on the relaxation behavior of compressive residual stress induced by UIT. *Welding in the World*, **64**(1), 171-178, 2020.
- [2] A. Abdulrahman Ftaikhan, F. Hejazi, R.S.M. Rashid, and N. Ostovar, Performance of reinforced-concrete frame with embedded FRP rod. *IOP Conf. Ser. Earth Environ. Sci.*, **357**, no. 1, 2019.
- [3] S. Tsutsumi, R. Fincato, and H. Momii, Effect of tangential plasticity on structural response under non-proportional cyclic loading. *Acta Mech.*, **58**(10), 8-19, 2019.
- [4] A. Jamadin, Z. Ibrahim, M. Z. Jumaat and E.S.A. Wahab, Effect of high-cyclic loads on dynamic response of reinforced concrete slabs. *KSCE Journal of Civil Engineering*, **23**(3), 1293-301, 2019.
- [5] I. S. Koltsida, A. K. Tomor, and C. A. Booth, Strain evolution of brick masonry under cyclic compressive loading. *Mater. Struct. Constr.*, **52**(4), 2019.
- [6] I. Haris and Z. Roszevák, Finite element analysis of cast-in-situ RC frame corner joints under quasi-static and cyclic loading. *Rev. la Constr.*, **18**(3), 579-594, 2019.
- [7] S. Xiao, J. Li, and Y. L. Mo, Effect of loading rate on cyclic behavior of reinforced concrete beams. *Adv. Struct. Eng.*, **21**(7), 990-1001, 2018.
- [8] I. S. I. Harba and A. J. Abdulridha, Finite element analysis of RC tapered beams under cyclic loading. *Al-Nahrain J. Eng. Sci.*, **20**(2), 378-396, 2017.
- [9] A. Parvez and S. J. Foster, Fatigue behavior of steel-fiber-reinforced concrete beams. *J. Struct. Eng.*, **141**(4), 04014117-01, 2015.
- [10] Ł. Polus, and M. Szumigała, Laboratory tests vs. FE analysis of concrete cylinders subjected to compression. *AIP Conference Proceedings*, 2078, 2019.
- [11] ABAQUS Version 6.14 Documentation- ABAQUS Theory Guide, Dassault Systems Simulia Corporation, 2014.

## A MULTILAYER SHELL ELEMENT FOR NONLINEAR ANALYSIS OF R/C SHEAR WALLS

Vassilis K. Papanikolaou<sup>1</sup>, Christos Z. Karakostas<sup>2</sup>, Konstantinos E. Morfidis<sup>2</sup>  
and Emmanouil Baboukas<sup>3</sup>

<sup>1</sup> School of Civil Engineering  
Aristotle University of Thessaloniki  
Thessaloniki, 54124, Greece  
billy@civil.auth.gr

<sup>2</sup> ITSAK-EPPO  
Dasylliou Str., Elaiones Pylaias, Thessaloniki, 55535, Greece  
christos@itsak.gr, kmorfidis@itsak.gr

<sup>3</sup>TOL – Technical Software House  
60 Karterou Str., Heraklion, 71201, Greece  
man@tol.com.gr

---

### Abstract

*The objective of this study is the development of a multilayer shell element for the nonlinear finite element analysis of reinforced concrete shear walls. The nonlinear shell element is based on a composite formulation for each integration (material) point, comprised of a number of layers with different thicknesses and material properties. For the analysis of R/C structural walls, concrete and steel nonlinear cyclic constitutive laws are assigned to each layer with isotropic plane-stress conditions for concrete and orthotropic conditions for smeared steel reinforcement, depending on their longitudinal or transverse direction. Strains at each individual layer are first derived from trial strains and curvatures of the respective integration point and then stresses are calculated by the respective layer material law. Forces and bending moments for each integration point are finally derived by numerical integration across all layers. At the present development stage, the above formulation is validated using a constitutive driver for various monotonic and cyclic strain histories, aiming eventually to its full integration into a commercial finite element code.*

**Keywords:** Reinforced concrete; shear walls; finite elements; constitutive laws; nonlinear analysis; software

---

## 1 INTRODUCTION

Reinforced concrete (R/C) shear walls are one of the most important lateral load resisting elements in mid- and high-rise structures, providing adequate stiffness, strength and deformation capacity, primarily against extreme earthquake and wind loading. Considering that (i) reinforced concrete is a highly nonlinear material, even under moderate loading (ii) nonlinear analysis at structural level with complex geometry is far more computationally demanding than at element level (iii) nonlinear static or dynamic (especially cyclic) loading conditions often impose convergence issues in practical applications (e.g. performance-based design or response assessment of existing structures), it is evident that providing solutions of improved accuracy, robustness and numerical efficiency for shear wall modeling is a challenging task.

In order to maintain a balance between accuracy and computational cost for nonlinear modeling of shear walls at structural level, the usual practice is to use linear elements (e.g. lumped or distributed plasticity) of equivalent section, together with rigid links or numerical constraints to provide displacement compatibility with the rest of the structure. Extending the wall element dimension to its natural planar type (e.g. membrane or shell elements), incorporating features such as plane stress conditions, out of plane response and cracking visualization, requires sophisticated element formulations and material constitutive laws. In this regard, the objective of this study is the development of a multilayer shell element for the nonlinear finite element analysis of reinforced concrete shear walls, aiming to be fully integrated into an existing commercial finite element software [1].

## 2 LITERATURE REVIEW

Over the years, a large number of numerical formulations for modeling planar R/C elements have been suggested in the literature, aiming to capture the inherent properties of concrete and steel materials under uniaxial, biaxial and triaxial stress states. From early nonlinear elasticity formulations, research has subsequently focused on plasticity and total-strain theory, fracture mechanics and (more recently) damage continuum mechanics, as well as hybrid formulations, blending more than one of the above categories. However, only a handful of the suggested solutions have managed to deploy themselves into finite element software (open source or proprietary) and therefore applied to real structural models. Reference is herein made to (i) VecTor and DIANA software, mainly including (total-strain) modified compression field theory (MCFT) [2] models, (ii) ATENA [3] software, including nonlinear elasticity as well as fracture-plasticity models, (iii) ABAQUS [4] software, with models based on damage-plasticity formulations and finally (iv) OpenSees [5], an open-source platform that accepts user contributions from the academic and engineering community. In this regard, a number of material models are available for two-dimensional modeling of shear walls, mainly based on a multilayered shell formulation, where both concrete and steel reinforcement models are attached, according to the wall section geometry. For concrete, a number of damage continuum mechanics models have been proposed, known for their simple, non-iterative formulation and computational efficiency in large, structural-level analyses: (i) the PSUMAT model by Lu et al. [6,7], using damage evolution curves under tension, as recommended by Løland [8] and under compression, as suggested by Mazars [9], (ii) the Mazars scalar elastic-damage model [9], implemented by Ramirez [10] and (iii) the two-scalar elastic-damage PRM [11] and “ $\mu$ ” [12] models, implemented by Lopez [13]. It is noted that materials (ii) and (iii) have not yet been included in the official OpenSees repository. By evaluating the performance and limitations of the above models, in the present study it was decided to adopt the layered shell formulation together with the Lu et al. concrete damage model, which has proved its numerical efficiency and robustness under large-scale structural analysis applications [6,7].



### 3 MATERIAL MODEL FORMULATION

This section describes the theoretical background and the necessary additions and modifications for integrating a nonlinear multilayer shell element into the commercial finite element software RAF [1]; a suite capable of both linear and nonlinear analysis and design of building structures, adherent to various seismic codes, including Eurocodes (e.g. [14,15]) and the Greek Code for Interventions (KANEPE) [16].

A graphical overview of a typical shear wall modeling process is depicted in Fig. 1; it comprises two boundary regions (typically 15 % of wall length each [15]) with dense longitudinal and transverse reinforcement that resist flexure and a web with two parallel grids of coarse reinforcement, designed for shear actions. These regions are usually modeled with 4-node isoparametric shell elements (MITC4), combining membrane and plate response, in order to simulate both in-plane and out-of-plane stress states. The shell mesh is characterized by a global tangent stiffness matrix ( $\mathbf{K}_T$ ) assembled by individual element contributions, while force ( $\mathbf{P}$ ) and displacement ( $\mathbf{U}$ ) vectors follow either static (Eq. 1) or dynamic (Eq. 2) equilibrium during loading.

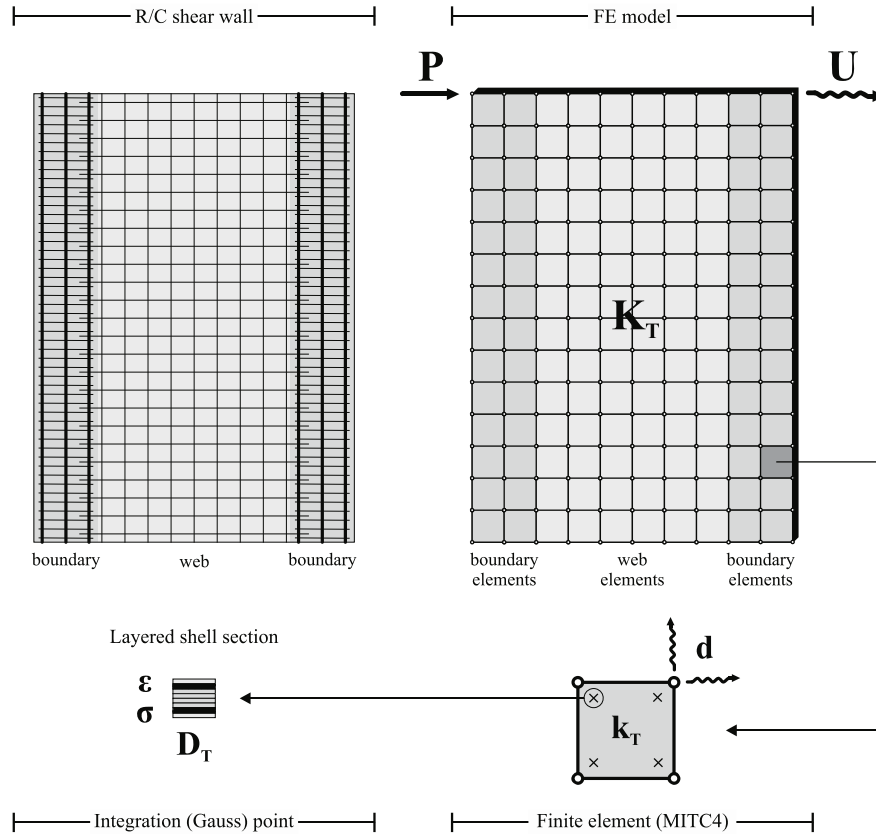


Figure 1: Overview of shear wall modeling process.

$$\mathbf{K}_T \mathbf{U} = \mathbf{P} \quad (1)$$

$$\mathbf{M} \frac{d^2 \mathbf{U}}{dt^2} + \mathbf{C} \frac{d \mathbf{U}}{dt} + \mathbf{K}_T \mathbf{U} = -\mathbf{M} \frac{d^2 \mathbf{U}_g}{dt^2} \quad (2)$$

where  $\mathbf{M}$ ,  $\mathbf{C}$  and  $\mathbf{U}_g$  are the global mass, damping and ground displacement matrices, respectively.

In the standard nonlinear finite element method, for every new load / time increment, an iterative solution algorithm (e.g. Newton-Raphson) imposes a vector of elastic trial strains ( $\boldsymbol{\varepsilon}_{tr}$ ) on each element:

$$\boldsymbol{\varepsilon}_{tr} = \mathbf{B}\mathbf{d} \quad (3)$$

where  $\mathbf{d}$  is the element nodal displacement vector and  $\mathbf{B}$  is the strain-displacement matrix. Trial strains are inserted into the nonlinear material constitutive law that updates the *material* stress vector ( $\boldsymbol{\sigma}_{n+1}$ ) and tangent stiffness matrix ( $\mathbf{D}_T$ ):

$$\boldsymbol{\sigma}_{n+1}, \mathbf{D}_T = f(\boldsymbol{\varepsilon}_{tr}, \boldsymbol{\sigma}_n) \quad (4)$$

The *element* tangent stiffness matrix ( $\mathbf{k}_T$ ) and force vector ( $\mathbf{r}$ ) are subsequently derived by integration over the element volume (using a number of integration (Gauss) points):

$$\mathbf{k}_T = \int_V \mathbf{B}^T \mathbf{D}_T \mathbf{B} dv \quad (5)$$

$$\mathbf{r} = \int_V \mathbf{B}^T \boldsymbol{\sigma}_{n+1} dv \quad (6)$$

Finally, the updated global stiffness matrix ( $\mathbf{K}_T$ ) and force vector ( $\mathbf{R}$ ) are assembled from individual element contributions.

Since the employed software [1] already features 4-node isoparametric shell elements (MITC4) for elastic analysis, the present development focuses on the inclusion of a nonlinear material constitutive law (Eq. 4) and the subsequent volume integrations (Eqs. 5-6). The material law is based on a layered shell approach [6,7] applied to each element Gauss point (Fig. 1), as is outlined in more detail in Fig. 2. Specifically, the element section is represented by a stack of ( $n$ ) individual material layers of different thicknesses ( $t_n$ ), material angles ( $\alpha_n$ ) and constitutive laws  $\{\sigma = f(\varepsilon)\}_n$ . Trial strains ( $\boldsymbol{\varepsilon}_{tr}$ ), assumed at the section midplane, are decomposed to the individual layers assuming plane-section conditions. The updated stress state for each layer is calculated by the corresponding material law and finally the updated stress state ( $\boldsymbol{\sigma}_{n+1}$ ) and tangent stiffness ( $\mathbf{D}_T$ ) for the whole section are derived using numerical integration over the total section thickness.

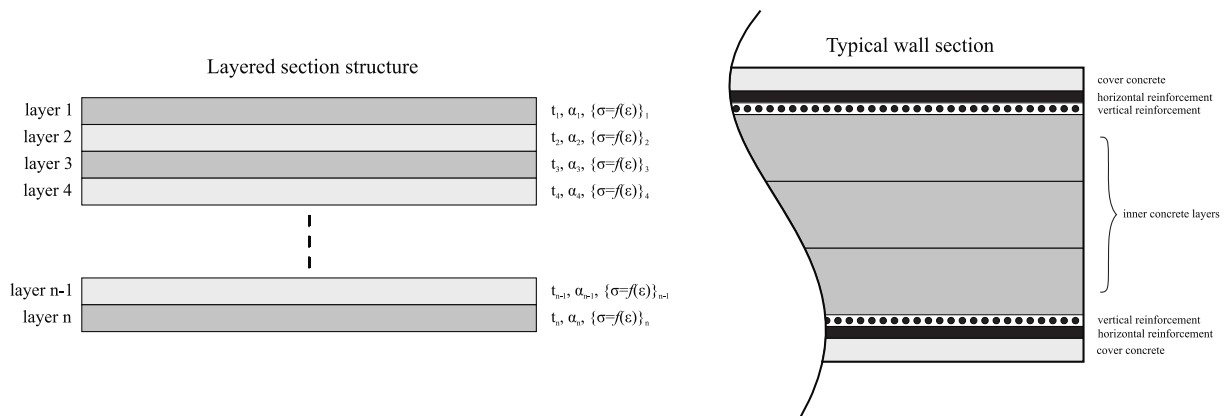


Figure 2: Layered shell formulation

In the case of a typical wall section, a layered decomposition may be simulated by two outer cover concrete layers and a number of inner concrete layers, separated by two reinforcement grids, each comprising a horizontal ( $\alpha = 0^\circ$ ) and a vertical ( $\alpha = 90^\circ$ ) smeared rein-

forcement layer. For concrete layers, the damage model by Lu et al. [6,7] is employed, with parameters derived by the characteristic concrete compressive strength ( $f_{ck}$ ), according to EN1992-1-1 [14]. For steel layers, the uniaxial Giuffr -Menegotto-Pinto model is employed [17], with parameters derived by the characteristic steel yield strength ( $f_{yk}$ ) and layer equivalent thicknesses by the corresponding steel reinforcement ratios. Fig. 3 shows the concrete, steel and layered section strain and stress states, as derived by respective constitutive laws and section integration, respectively. Eq. 7 describes the section strain decomposition to individual layers and Eq. 8 the section membrane force ( $f$ ), moment ( $m$ ) and shear force ( $q$ ) integration from layer contributions ( $z_k$  is the distance between the layer ( $k$ ) and section midplane).

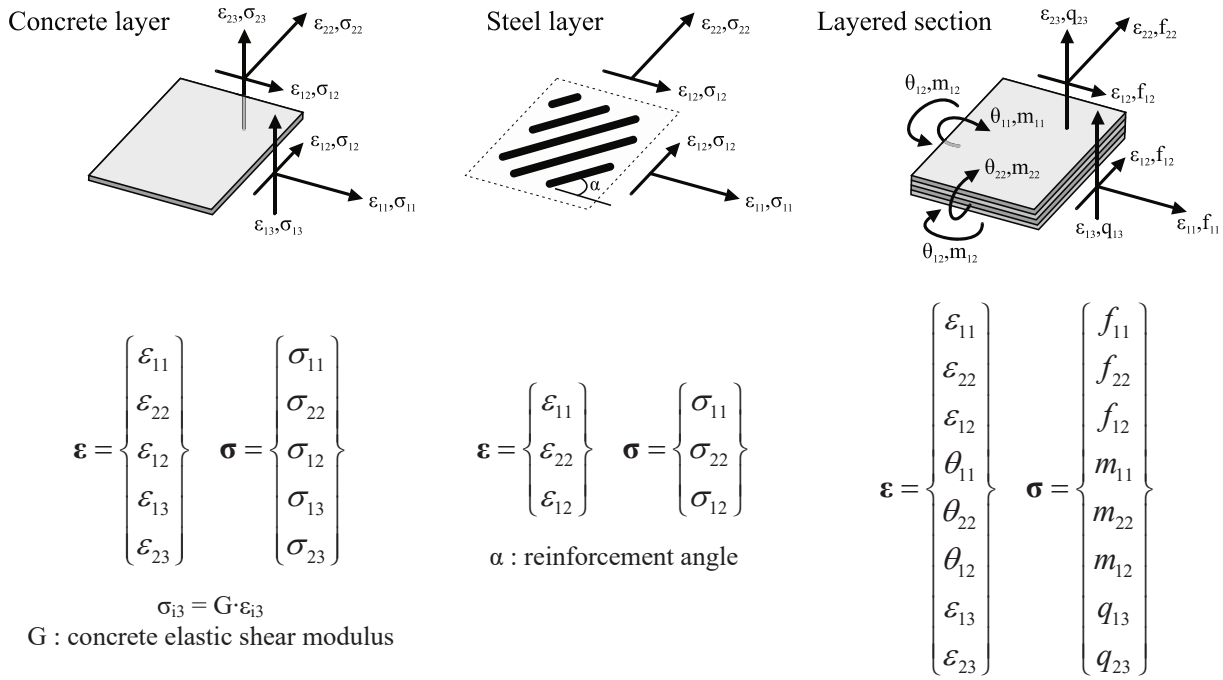


Figure 3: Layer and section strain/stress states

$$\epsilon_{ij,layer\ k} = \epsilon_{ij,section} - z_k \cdot \theta_{ij,section} \quad (7)$$

$$\gamma_{ij,layer\ k} = \gamma_{ij,section}$$

$$\begin{aligned} f_{ij,section} &= \sum_{k=1}^n \sigma_{ij,layer\ k} \cdot t_k \\ m_{ij,section} &= \sum_{k=1}^n z_k \cdot \sigma_{ij,layer\ k} \cdot t_k \\ q_{ij,section} &= \sum_{k=1}^n q_{ij,layer\ k} \cdot t_k \end{aligned} \quad (8)$$

The above formulations were implemented in the form of several FORTRAN subroutines, operating on a single one-dimensional dynamic array that contains the required information (layer structure, material properties, stress states etc.) for all Gauss points corresponding to the nonlinear shell elements. Fig. 4 shows a simplified form of the developed code structure toward its integration in the commercial finite element program [1].

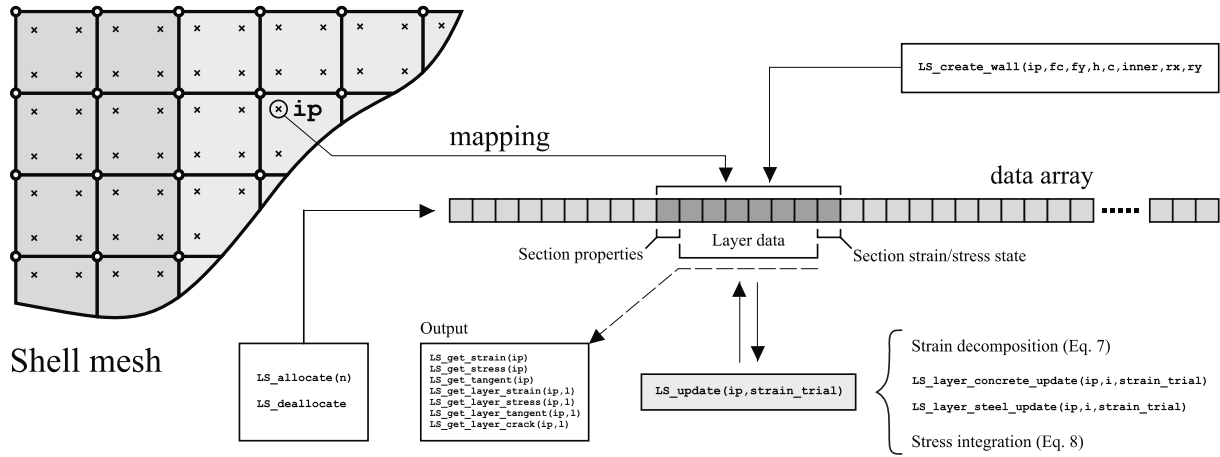


Figure 4: Simplified code structure

#### 4 VERIFICATION

Following the code development, a set of primary verification tests was performed on the material and section level, for a single element integration point. Material parameters were based on typical C20/25 ( $f_{ck} = 20$  MPa) and B500C ( $f_{yk} = 500$  MPa) concrete and steel grades, respectively, according to EN1992-1-1 [14]. Wall section width was set equal 0.2 m with three inner concrete layers, and steel reinforcement ratios equal to 5.0 ‰ and 2.0 ‰ for horizontal and vertical grid directions, respectively. Fig. 5 shows the uniaxial stress-strain response for concrete and steel layers under various monotonic and cyclic strain loading histories. It is observed that the employed constitutive models reproduce well the expected response.

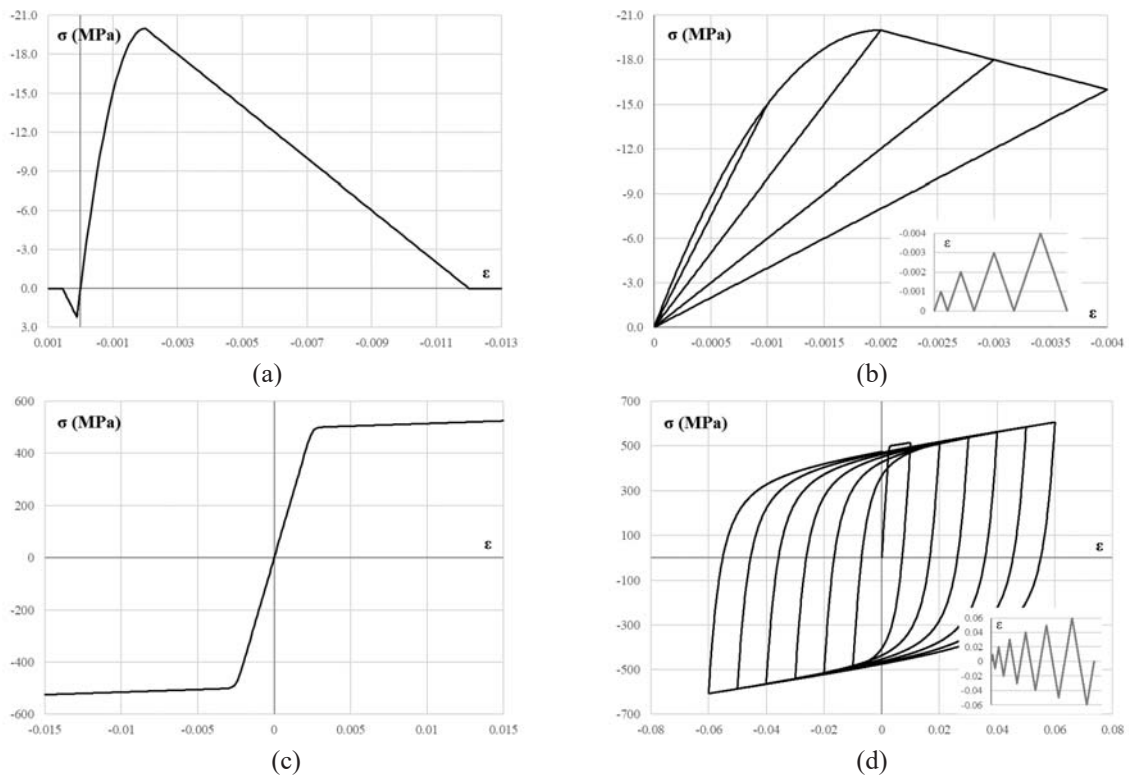


Figure 5: Uniaxial material response: (a) concrete monotonic (b) concrete cyclic (c) steel monotonic (d) steel cyclic

Fig. 6 shows the wall section response in membrane force vs. strain terms, derived by layer integration (Eq. 8) for (a) uniaxial tension in the horizontal direction followed by unloading and reloading in compression, (b) for equibiaxial compression ( $\varepsilon_1 = \varepsilon_2$ ) and (c) for compression in the vertical direction together with tension in the horizontal direction ( $\varepsilon_1 = -0.1\varepsilon_2$ ).

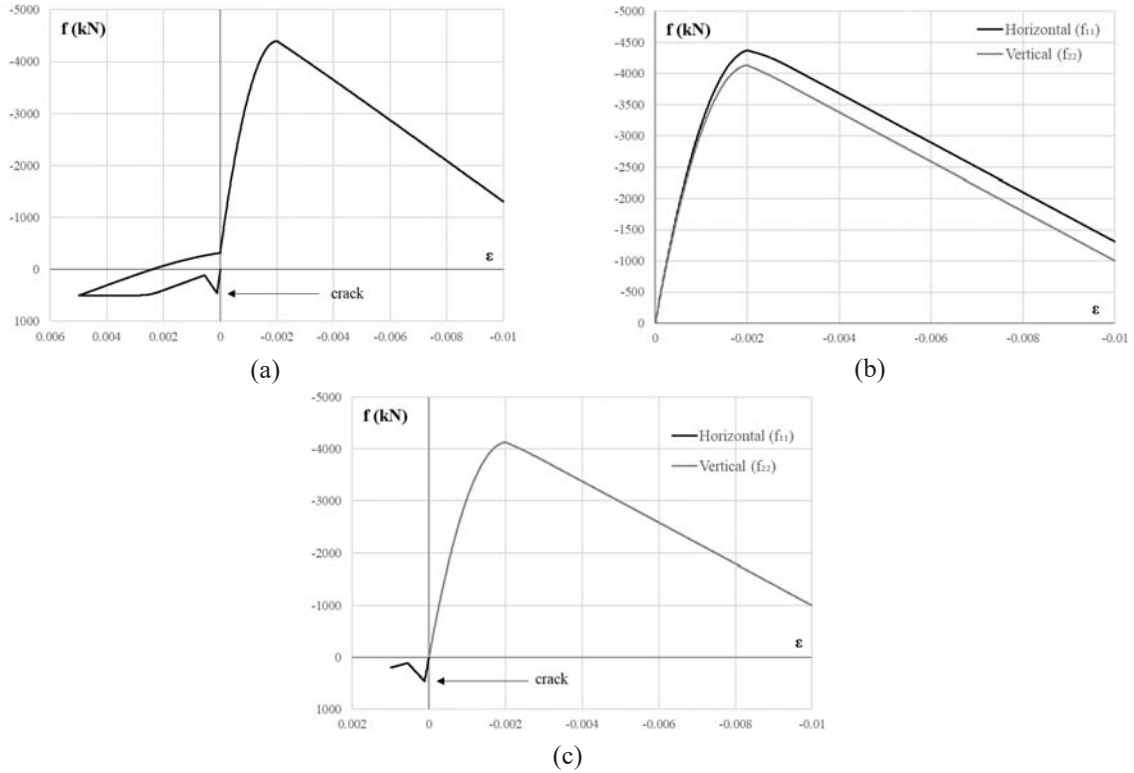


Figure 6: Membrane force vs. strain response for wall layered section

## 5 CLOSURE

In this ongoing study, a multilayer shell element for the nonlinear finite element analysis of reinforced concrete shear walls was developed, for integration into an existing commercial structural analysis software [1]. A new, modular FORTRAN-based code, operating at integration point level and based on existing formulations and inelastic constitutive models from the literature was compiled. Primary validation tests against simple loading histories at element (Gauss point) level demonstrated a satisfactory performance. This section material model will be subsequently mapped to MITC4 shell finite elements and will be further validated, for finally assembling structural models ready for nonlinear static and dynamic analysis.

## ACKNOWLEDGMENT

This research has been co-financed by the European Regional Development Fund of the European Union and Greek national funds through the Operational Program ‘Competitiveness, Entrepreneurship and Innovation’, under the call RESEARCH CREATE INNOVATE (project code: T1EDK-01800).



## REFERENCES

- [1] TOL. RAF, Structural Analysis and Design Software v.2021.0. *Technical Software House*, Iraklion, Crete, Greece, 2021.
- [2] F. Vecchio, M. Collins. The Modified Compression-Field Theory for Reinforced Concrete Elements Subjected to Shear. *ACI Structural Journal*, **83**, 219-231, 1986.
- [3] V. Červenka, L. Jendele, J. Červenka. ATENA Program Documentation Part 1 – Theory. *Červenka Consulting*, Prague, Czech Republic, 2020.
- [4] M. Smith. ABAQUS/Standard User's Manual, Version 6.9. *Dassault Systèmes Simulia Corp.*, 2009.
- [5] F. McKenna, M.H. Scott, G.L. Fenves. Nonlinear finite-element analysis software architecture using object composition. *Journal of Computing in Civil Engineering*, **24**(1), 95-107, 2010.
- [6] X.Z. Lu, L.L. Xie, H. Guan, Y.L. Huang, X. Lu. A shear wall element for nonlinear seismic analysis of super tall buildings using OpenSees. *Finite Elements in Analysis & Design*, **98**, 14-25, 2015.
- [7] X.Z. Lu, H. Guan. Earthquake Disaster Simulation of Civil Infrastructures: From Tall Buildings to Urban Areas, 2<sup>nd</sup> Edition. *Science Press & Springer*, Beijing, 2021.
- [8] K.E. Løland. Continuous damage model for load-response estimation of concrete. *Cement and Concrete Research*, **10**, 395-402, 1980.
- [9] J. Mazars. A description of micro- and macroscale damage of concrete structures. *Engineering Fracture Mechanics*, **25**, 729-737, 1986.
- [10] B.G. Ramirez. Implementation of a Simple Biaxial Concrete Model for Reinforced Concrete Membranes. Master Thesis, *Dept. of Civil and Environmental Engineering*, University of Alberta, Canada, 2017.
- [11] C. Pontiroli, A. Rouquand, J. Mazars. Predicting Concrete Behaviour From Quasi-static Loading to Hypervelocity Impact. *European Journal of Environmental and Civil Engineering*, **14**, 703-727, 2010.
- [12] J. Mazars, F. Hamon, S. Grange. A New 3D Damage Model for Concrete. *Materials and Structures*, **48**, 3779-3793, 2015.
- [13] J.R.S. Lopez. Implementation and Verification of Simple Concrete Biaxial Models Under Monotonic, Cyclic, and Dynamic Loading. Master Thesis, *Dept. of Civil and Environmental Engineering*, University of Alberta, Canada, 2019.
- [14] CEN. Eurocode 2. Design of concrete structures – Part 1–1: General rules and rules for buildings (EN 1992-1-1). *European Committee for Standardization*, Brussels, 2004.
- [15] CEN. Eurocode 8: Design of structures for earthquake resistance - Part 1: General rules, seismic actions and rules for buildings (EN1998-1) . *European Committee for Standardization*, Brussels, 2004.
- [16] EPPO. Greek Code for Interventions (KANEPE), 2<sup>nd</sup> revision. *Earthquake Planning and Protection Organization*, Athens, 2017.
- [17] F.C. Filippou, E.P. Popov, V.V. Bertero. Effects of Bond Deterioration on Hysteretic Behavior of Reinforced Concrete Joints. Report EERC 83-19, *Earthquake Engineering Research Center*, University of California, Berkeley, 1983.

## COMPARISON OF THE EFFICIENCY OF MINIMUM-THICKNESS CIRCULAR AND PARABOLIC ARCHES FOR VARIOUS GRAVITY CONDITIONS

Nicos Kalapodis<sup>1</sup>, Georgios Kampas<sup>1\*</sup>, Thomas McLean<sup>2</sup>, Christian Malaga-Chuquitaype<sup>2</sup>

<sup>1</sup> University of Greenwich  
ME4 4TB Chatham, United Kingdom  
g.kampas@greenwich.ac.uk, n.kalapodis@greenwich.ac.uk

<sup>2</sup> Imperial College London  
South Kensington Campus London SW7 2AZ, UK  
thomas.mclean16@imperial.ac.uk, c.malaga@imperial.ac.uk

---

### Abstract

*Arches are structural forms that have been used for thousands of years and rely on gravity for their inherent stability. Currently, given the space race for lunar and martian exploration, it has become apparent that soon enough, there will be a need to design and build the first resilient shielding structures on the Moon and Mars against extreme radiation. Arches represent an ideal option for such structures given that they are durable and can be easily built. This paper is based on previous work of the authors and focuses on the stability of circular and parabolic arches with different embrace angles subjected to different levels of equivalent inertial loading in low-gravity conditions. More specifically, it reveals that although parabolic arches can be much more efficient than the corresponding circular for gravitational-only loading, this is not the case for different combinations of inertial loading and embrace angles where the opposite can be true. It highlights the dominant effect of low-gravity conditions on the minimum thickness requirements for both types of arches and considers the effect of a potential additional infill for radiation shielding. Furthermore, this study reveals a self-similar behavior and introduces a “universal” inertial loading.*

**Keywords:** Seismic analysis, Low-gravity conditions, Minimum thickness, Failure mechanism, Extraterrestrial structures.

---

## 1 INTRODUCTION

Since ancient times, arches and vaulted structures constituted widespread structural forms, due to their inherent advantage to secure a smooth transition of the compressive internal forces from the crown to the springing. Masonry structures, were constructed during the classical period in ancient Greece. Some of those structures were vaults used as entrances to stadiums (Olympia, Nemea). Subsequently, that structural style was further advanced within the Roman period through the construction of bridges, aqueducts and tunnels [1]. In modern history, great engineers had studied the stability of arches beginning with Robert Hooke [2] who was the first to introduce the inverted chain concept with the purpose of describing the path of the compressive resultant force through a catenary (alysoid) shape. Then, Couplet [3] was the first who published his research on the evaluation of the minimum thickness of a semi-circular arch of constant thickness, subjected to its self-weight. However, for the same arch geometry, Milankovitch [4] managed to analytically calculate its minimum thickness and detect the exact locations of the hinges right after the formation of the hinge mechanism. Also, Milankovitch developed an analytical expression for the thrust line and proved that it is not an admissible catenary thrust line. Makris and Alexakis [1] not only verified Milankovitch's results, but also found out that different stereotomies can slightly affect the shape of the thrust line and thus, the minimum required thickness in order for the arch to withstand the applied loading. Additionally, based on Clemente's [5] and Oschendorf's [6] innovative research, Alexakis and Makris [7] extended their research with the evaluation of the minimum thickness of circular arches subjected to both their self-weight and horizontal acceleration that lead to a characteristic four-hinge failure mechanism.

Due to their ability to bridge long spans and their inherent strength, they are considered as suitable structural forms for creating ample space available for the storage of valuable assets or even to provide shelter to future habitable modules in extreme environments. Aiming to create a new space age, various space agencies (NASA, ESA, ISRO, etc) and private firms (SpaceX, Virgin Galactic, Blue Origin, etc) are investing in challenging missions such as "Artemis" amongst others towards the potential human settlement in other planetary bodies starting from the Moon and later on Mars. Thus, there is fertile ground for start conceptualising, designing and then, building the first extra-terrestrial habitats [8] within the coming decades. In their work Kalapodis et al., [9] present a plethora of structural concepts about the design of the prospective extra-terrestrial human habitats. The most predominant such concepts and ideas emphasise the need for an external resilient shielding structure in order to secure valuable assets (energy fuel tanks, robotic elements, future inflatable modules, etc) against harsh conditions like extreme temperature fluctuations[10] and solar radiation [11].

Such extra-terrestrial structures can be made from local soil called regolith [12] in keeping with the In-Situ Resource Utilisation (ISRU) framework [13]. This is proposed to be an arch-like structure in order to be used as storage facility and act mainly in compression since regolith, as structural material, is not expected to develop substantial tensile strength [14], while it will be able to provide the necessary compressive strength [15]. Even so, such structures will need to be durable against strong ground motions that, may be generated by shallow moonquakes [16] and marsquakes with epicentres close to the structure or generated by meteoroid impacts [17]. Since the self-weight is reduced due to the reduced gravitational acceleration (although the inertia of the structure remains constant), the structural response will change accordingly [18, 19]. This research is based on the work of [28] and deals with the limit-state analysis of both circular and parabolic monolithic arches subjected to different levels of horizontal acceleration, for regular gravity and low-gravity conditions, by assuming lower gravitational accelerations,  $a_g = \{0.17; 0.38\}g$  in accordance with the lunar and martian gravitational fields

respectively. Furthermore, a comparison of the efficiency between arches of circular and parabolic geometries is presented.

## 2 BACKGROUND OF THE PROBLEM

Except of the case of semicircular arches, various researchers dealt with the investigation of other arch geometries such as parabolic [20, 28], elliptical [21], pointed/gothic [20, 22, 23] and catenary arches [23, 24]. Most of the works mentioned above, are referred to the static behaviour and stability of the arches through determining their corresponding upper and lower bound thrust lines. According to [25], there are infinite states of equilibrium in an arch; nevertheless, the upper and lower limits for all the associated admissible thrust lines of any arch is indicated by the maximum and minimum thrust transferred to the springing (horizontal component of the reaction force) and are related to a statically determinate three-hinge arch (Fig. 1). [20] Analytically calculated the thrust line of a semicircular arch subjected to both vertical and horizontal loading. Also they proceed with the numerical estimation, through Point Collocation Method [26] and constrained optimisation, of the upper and lower limits of semicircular, parabolic and pointed (statically determinate) arches. Furthermore, [1, 4] estimated the minimum thickness of circular arches that suffices for a specific loading through limit-state analysis. Specifically, [1] confirmed the results of [4] about the dimensionless minimum thickness of semicircular arches that equals  $t/R = 0.1075$  ( $t$ : thickness,  $R$ : radius) utilising radial cuts and  $t/R = 0.1095$  by implementing vertical cuts when subjected to self-weight. The above was achieved by the calculation of the limit thrust line associated with a five-hinge mechanism (a four-hinge mechanism would not be possible due to symmetry) as shown in Fig. 2a. Subsequently, [7] determined the minimum thickness of circular arches with different embrace angles ( $\beta$ ) subjected to their self-weight combined with inertial loading. The dimensionless minimum thickness was found through a variational formulation and the application of the principle of potential energy that allowed the evaluation of the minimum horizontal acceleration levels that turn the arch into a four-hinge mechanism (Fig. 2b). Furthermore, [22] estimated the minimum dimensionless thickness of pointed/gothic arches under self-weight, on the verge of becoming a five-hinge mechanism, via the thrust-line method. After Hooke [2], the catenary shape symbolised the perfect arch shape as it represented the optimal thrust line. [24] Highlighted the deviation of the resulting thrust line from the catenary centerline of a catenary arch, although he admitted that there is no minimum thickness for a two-dimensional catenary arch under self-weight. The justification is that, as the thickness of a catenary arch tends to zero (one-dimensional arch), the thrust line tends to follow a purely catenary shape and hence, it will always be confined within the arch's geometry (intrados and extrados). The above indicates that two-dimensional arches of catenary geometry, which are subjected only to their self-weight, may constitute the best option among all the other arches of known geometries. Consequently, this work is based on [28] and aims to apply limit-state analysis to parabolic arches, since they bear great resemblance and also are more commonly used than catenary arches, for both self-weight and inertial loads. Since there is a need to provide useful observations and solid knowledge about the strength and stability of "extraterrestrial" arches serving as shielding mechanisms for valuable assets on the Moon and Mars [9, 12], the research will be applied to low-gravity fields as well. These regolith-based arches are believed to function monolithically, regardless of the construction process (additive manufacturing, interlocking bricks, etc.). Furthermore, no material shear failure (including slipping at the base) is taken into consideration, so only the development of radial cuts is permissible everywhere along the arch geometry. The impact of stereotomy is outside the reach of this paper.

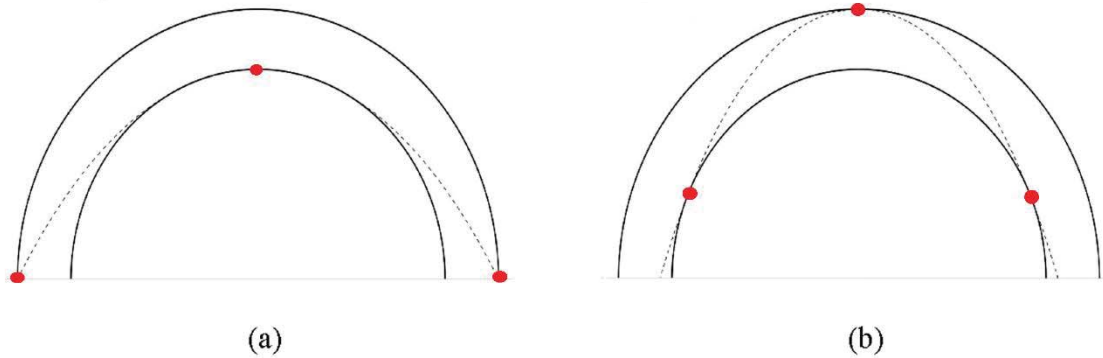


Figure 1: Statically determinate semicircular arch under its self-weight, with its (a) maximum and (b) minimum thrust line.

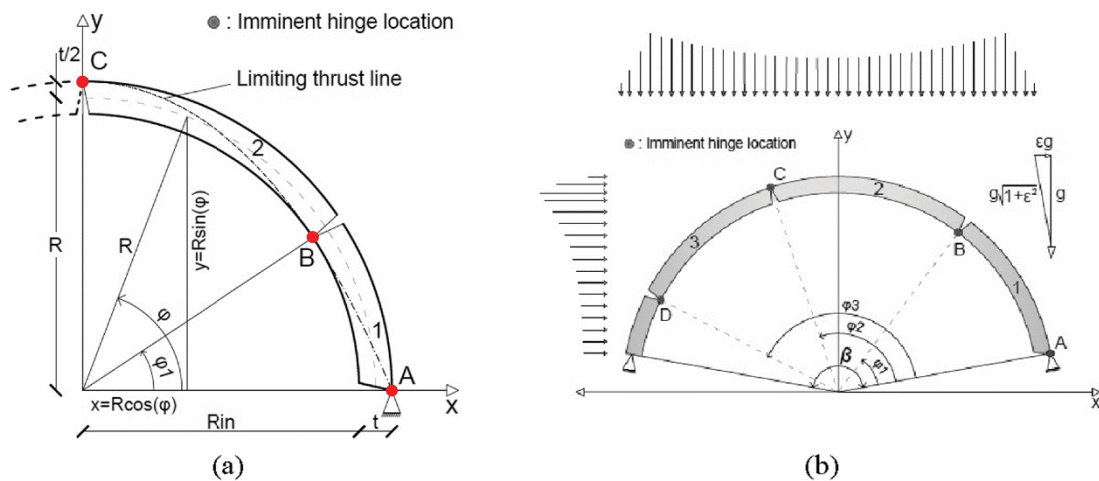


Figure 2: Statically determinate semicircular arch under its self-weight, with its (a) maximum and (b) minimum thrust line.

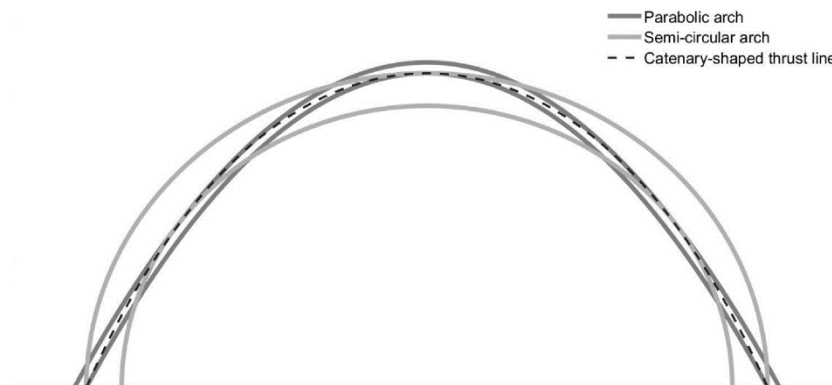


Figure 3: Qualitative illustration presenting the distinctions between the symmetric five hinge mechanism of a semi-circular and a parabolic arch under self-weight. The thrust line is represented by a catenary (black dashed line) and the two optimal arches with continuous grey-scaled lines.

This study also aims to contrast the findings of the parabolic arch with those of circular arches, which are the most typical. Within Figure 3 lies the source of motivation for the qualitative identification of the failure mechanism for parabolic arches. Under self-weight only, the same thrust line (black dotted line) is marginally fitted inside both a semicircular and a parabolic (grey-scaled lines) arch with a catenary form (that bears a great resemblance to the actual thrust



lines, even though it is not an admissible one). Clearly, there are two major points to be taken from Figure 3: a) The parabolic arch's five-hinge mechanism is essentially opposite than that of the semicircular, and b) the parabolic arch is substantially thinner than the semicircular. The reference structure is a parabolic arch with an aspect ratio of  $c = 1/2$ . (as shown in Fig. 4a). Since it is closely analogous to semicircular arches, this aspect ratio is of special importance.

### 3. ANALYTICAL FORMULATION

The analytical formulation of the symmetric five-hinge mechanism owing to self-weight for the parabolic arch is presented (see Fig. 4a). One may find details about the analytical procedure and the derivation of the pertinent equations in [28] however, selective parts of the analytical procedure are presented herein for reasons of better understanding.

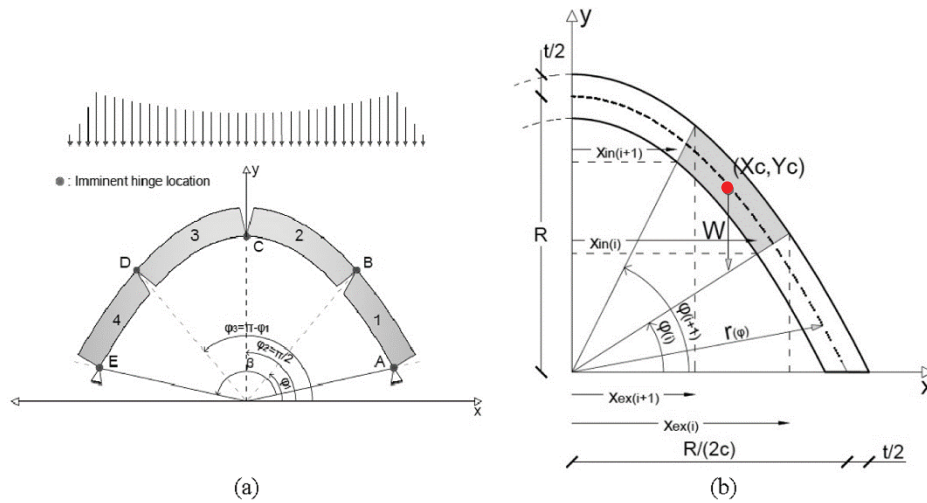


Figure 4: Parabolic arch: (a) symmetric five-hinge mechanism of the arch with  $c = 1/2$  and embrace angle  $\beta$ , when subjected to its self-weight and (b) reference system used in this study.

#### 3.1 Equations of the parabolic arch

The generic equation that describes a parabola is:

$$y = \alpha - bx^2 \quad (1)$$

The Cartesian coordinates of a parabolic arch can be represented using the following equation, assuming  $c$ : rise over span ratio (this is true only for an embrace angle of  $180^\circ$ ) and  $R$ : rise of a parabolic arch.

$$y = R - \frac{4c^2}{R}x^2 \quad (2)$$

Finally, after applying simple calculus, the Cartesian coordinates have been converted to polar and the geometry of the parabolic arch (see Fig. 4b) is expressed as follows:

$$\begin{cases} r_{(\varphi_i)} = \left\{ \frac{-\sin(\varphi_i) + \sqrt{\sin^2(\varphi_i) + 16c^2 \cos^2(\varphi_i)}}{8c^2 \cos^2(\varphi_i)} \right\} R \\ r_{(\varphi_i)} = R \end{cases} \quad \forall \varphi_i \in \left[0, \frac{\pi}{2}\right) \cup \left(\frac{\pi}{2}, \pi\right] \quad (3)$$

for  $\varphi_i = \frac{\pi}{2}$

### 3.2 Moment equilibrium at the onset of the five-hinge mechanism

The imminent hinges (at a state of equilibrium) of the collapse mechanism of the parabolic arch will appear at the intrados, where they would appear at the extrados for a semicircular arch and vice versa (Figs. 2a and 4a). The symmetric right part of the collapse mechanism is depicted in Figure 5. The gravitational multiplier,  $\alpha = \frac{g'}{g}$ , is defined as the ratio of the gravitational acceleration on other planetary surfaces,  $g'$ , over the terrestrial acceleration,  $g = 9.81 \frac{m}{s^2}$ , in order to describe different gravitational environments. Additionally, the factor,  $L = \frac{m_{total}}{m_{inertial}}$  is measured as the ratio of the structure's total mass and the additional infill mass ( $m_{total} = m_{structure} + m_{infill}$ ), over the mass that corresponds to the inertial loading ( $m_{inertial}$ ) which is a ratio of the  $m_{total}$ . For terrestrial applications where  $\alpha = 1$ , it is assumed that there is no extra infill and thus, the total mass fully participates to the inertial loads ( $m_{total} = m_{structure} = m_{inertial}$ ) and  $L = 1$ .

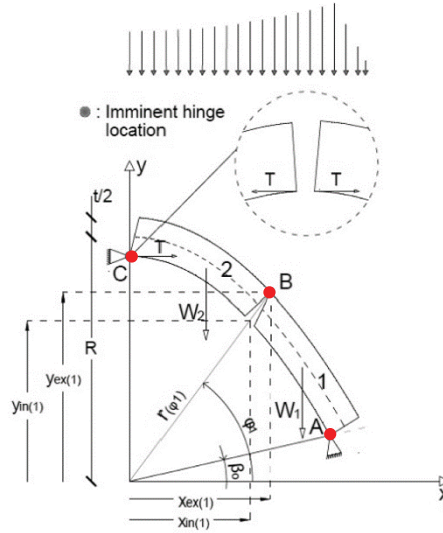


Figure 5: System of reference of the right symmetric part of the collapse mechanism of a parabolic arch subjected only to its self-weight.

Regarding the half right part (Fig. 5) of the arch, after applying a moment equilibrium about the point A, the minimum horizontal thrust at the intrados of the crown,  $T$ , is calculated. Considering the low gravity effect ( $\alpha$ ) and the additional vertical (shielding) loading ( $L$ ), the weight of the segment (1–2) is taken equal to  $\alpha L W_{12}$ . The moment equilibrium is represented by the following equation:

$$\begin{aligned} \text{Segment}(1-2): T \left( \left\{ R - \frac{t}{2} \right\} - \sin(\beta_0) \left\{ r_0 - \frac{t}{2} \right\} \right) - \alpha L W_{12} \left( \cos(\beta_0) \left\{ r_0 - \frac{t}{2} \right\} - x_{c12} \right) &= 0 \\ \Rightarrow T = \frac{\alpha L W_{12} \left( \cos(\beta_0) \left\{ r_0 - \frac{t}{2} \right\} - x_{c12} \right)}{\left\{ R - \frac{t}{2} \right\} - \sin(\beta_0) \left\{ r_0 - \frac{t}{2} \right\}} , \quad \beta_0 \neq \frac{\pi}{2} \end{aligned} \quad (4)$$

where:  $W_{12}$  represents the weight of half the arch

$x_{c12}$  is the abscissa of the center of gravity of the half arch

$r_0$  is the radius at an angle  $\beta_0$

After assuming a radial cut as seen in Fig. 5, moment equilibrium of the arch's upper portion (segment 2) over hinge B gives,

Segment(2):

$$\begin{aligned} -\alpha L W_2 \left( \cos(\varphi_1) \left\{ r_{(\varphi_1)} + \frac{t}{2} \right\} - x_{c2} \right) + T \left( \sin(\varphi_2) \left\{ r_{(\varphi_2)} - \frac{t}{2} \right\} - \sin(\varphi_1) \left\{ r_{(\varphi_1)} + \frac{t}{2} \right\} \right) &= 0 \\ \Rightarrow -\alpha L W_2 \left( \cos(\varphi_1) \left\{ r_{(\varphi_1)} + \frac{t}{2} \right\} - x_{c2} \right) & \\ + \frac{\alpha L W_{12} \left( \cos(\beta_0) \left\{ r_0 - \frac{t}{2} \right\} - x_{c12} \right)}{\left\{ R - \frac{t}{2} \right\} - \sin(\beta_0) \left\{ r_0 - \frac{t}{2} \right\}} \left( \left\{ R - \frac{t}{2} \right\} - \sin(\varphi_1) \left\{ r_{(\varphi_1)} + \frac{t}{2} \right\} \right) &= 0 \end{aligned} \quad (5)$$

where  $W_2$  is the weight of the segment 2

$x_{c2}$  is the abscissa of the center of gravity of the segment 2

$r_{(\varphi_1)}$  represents the radius at an angle  $\varphi_1$

As Eq. 5 is solved with respect to  $t$  (arch thickness), a transcendental equation is obtained that links the unknown rupture angle  $\varphi_1$  with the unknown minimum thickness  $t$ . The following is the general representation of this equation:

$$t = f(\varphi_1) \quad (6)$$

If adopt the horizontal axis  $x$  ( $y = 0$ ) as a level of reference, the potential energy of the parabolic arch following an embrace angle  $\beta$  (Fig. 7b) will be,

$$V = W_{arch} \cdot y_0 \quad (7)$$

where  $W_{arch}$  represents the weight of the parabolic arch and  $y_0$  is the ordinate of the center of gravity of the parabolic arch. By substituting Eq. 6 in Eq. 7, we have,

$$V(\varphi_1) = W_{arch} \cdot y_0 \quad (8)$$

Based on the theoreme of stationary potential energy, the geometrically admissible hinge mechanism (Fig. 4a) is in a state of equilibrium if and only if the total potential energy is stationary, i.e.,

$$\delta V(\varphi_1) = 0 \Rightarrow \frac{dV(\varphi_1)}{d\varphi_1} \delta\varphi_1 = 0 \Rightarrow \frac{dV(\varphi_1)}{d\varphi_1} = 0 \quad (9)$$

After solving the system of Eqs. (6) and (9) one may evaluate the unknown location of the rupture angle  $\varphi_1$  along with the minimum width  $t$  of a parabolic arch for a given embrace angle  $\beta$ .

### 3.3 Results – considering self-weight for terrestrial gravity

Figure 6 contrasts the limit thrust lines regarding semicircular and parabolic arches with embrace angle  $\beta = 180^\circ$  subjected to their self-weight. As it is expected, the collapse mechanisms are exactly opposite. Specifically, in the case of the semi-circular arch, the thrust line starts at the extrados of the base, it touches the intrados at  $35.52^\circ$  and then the extrados at the

crown, while for the parabolic arches the limit thrust line initiates at the intrados at the base, then touches the extrados at  $43.81^\circ$  and the intrados at the crown. Most importantly, the minimum thickness of parabolic arches is  $\frac{t}{R} = 0.0239$ , while the corresponding minimum thickness for semicircular arches is  $\frac{t}{R} = 0.1075$ .

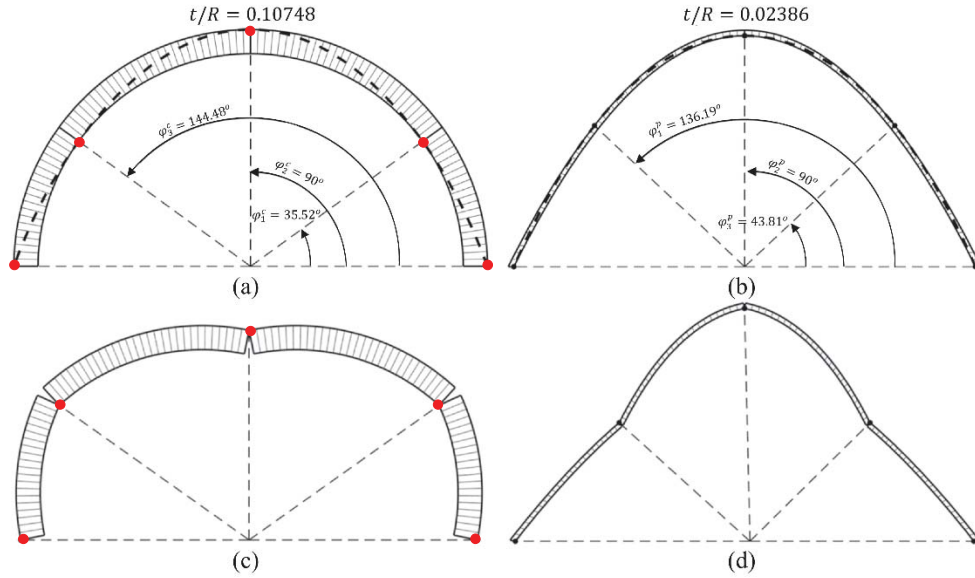


Figure 6: Limit thrust line for (a) semicircular and (b) parabolic arches; symmetric five-hinge mechanism of (c) semicircular and (d) parabolic arches when subjected to their self-weight.

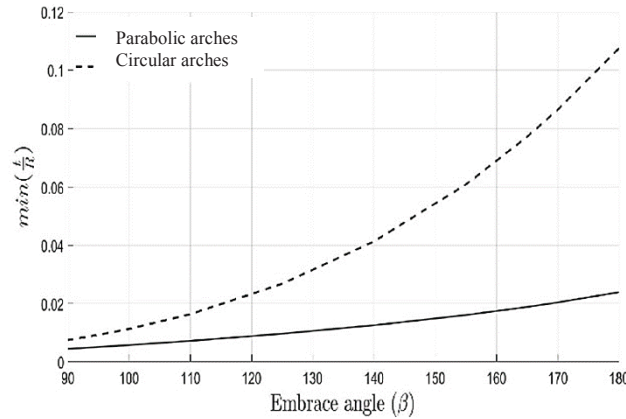


Figure 7: Minimum  $t/R$  and versus various embrace angles ( $\beta$ ) for circular (solid line) and parabolic arches (dashed line) subjected only to their self-weight.

Also, figure 7 compares the minimum dimensionless thickness of circular to parabolic arches for various embrace angles,  $\beta$ . Evidently, the parabolic arches (with  $c = \frac{1}{2}$ ), always require thinner geometries to support their self-weight than their circular counterparts, regardless of  $\beta$ . Moreover, the difference between the  $\min(\frac{t}{R})$  of a circular and parabolic arch decreases for smaller values of  $\beta$  (Fig. 7).

#### 4. IDENTIFICATION OF THE FOUR-HINGE MECHANISM

When an arch is subjected to horizontal acceleration ( $\varepsilon$ ), it exhibits a four-hinge non-symmetric mechanism [7, 28]. As in the case of the five-hinge mechanism, the failure mechanisms

are exactly opposite. To facilitate comparisons between the different failure mechanisms of the two arch geometries examined in this work, the following assumptions regarding the rupture angles have been made. In the case of circular geometry,  $\varphi_1 = \varphi_1^C$ ,  $\varphi_2 = \varphi_2^C$  and  $\varphi_3 = \varphi_3^C$  while for the parabolic geometry,  $\varphi_1 = \pi - \varphi_1^P$ ,  $\varphi_2 = \pi - \varphi_2^P$  and  $\varphi_3 = \pi - \varphi_3^P$ .

#### 4.1 Moment equilibrium at the onset of the four-hinge mechanism

Following similar procedure with that of the five-hinge mechanism and after implementing moment equilibrium, one may end up to the following equation that links the lateral acceleration level ( $\varepsilon$ ) with the three rupture angles ( $\varphi_1, \varphi_2, \varphi_3$ ) and the minimum thickness ( $t$ ) [28].

$$\varepsilon = f(\varphi_1, \varphi_2, \varphi_3, t) \quad (10)$$

To calculate the rupture angles,  $\varphi_1, \varphi_2, \varphi_3$  referring to a minimum  $t/R$  and a given horizontal acceleration level,  $\varepsilon$ , the principle of potential energy is applied. Thus, the total energy of the system is expressed as the work of all forces acting on the structure with reference  $y = 0$ . The loading on a parabolic arch subjected to a horizontal acceleration,  $\varepsilon g$ , is equivalent to the gravity loading on the same parabolic arch when it is rotated by an angle,  $\omega = \tan^{-1} \frac{\varepsilon}{\alpha}$  from the vertical under a new gravitational field,  $\hat{g} = g\sqrt{\alpha^2 + \varepsilon^2}$ . The resultant gravitational field is  $\hat{g}$  and the potential energy can be expressed as

$$\begin{aligned} \hat{V} &= \hat{W} \cdot \hat{y} = \sqrt{\alpha^2 + \varepsilon^2} W \hat{y} \neq V \quad \text{or} \\ V(\varphi_1, \varphi_2, \varphi_3, \varepsilon) &= \sqrt{1 + f(\varphi_1, \varphi_2, \varphi_3, t)^2} W \hat{y} \end{aligned} \quad (11)$$

According to potential energy principle, the four-hinge mechanism is in equilibrium if, and only if, the variational work increment vanishes for arbitrary geometrically admissible variations. Therefore, the potential energy of the system needs to be stationary,  $\delta V = 0$ . The potential energy is stationary when

$$\delta V = V(\varphi_i \pm \delta \varphi_i) - V(\varphi_i) = \frac{\partial V(\varphi_i, \varepsilon)}{\partial \varphi_i} \delta \varphi_i = 0 \Rightarrow \frac{\partial V(\varphi_i, \varepsilon)}{\partial \varphi_i} = 0$$

This leads to the following expressions:

$$\frac{\partial V(\varphi_1, \varphi_2, \varphi_3, \varepsilon)}{\partial \varphi_1} = 0 \quad (12)$$

$$\frac{\partial V(\varphi_1, \varphi_2, \varphi_3, \varepsilon)}{\partial \varphi_2} = 0 \quad (13)$$

$$\frac{\partial V(\varphi_1, \varphi_2, \varphi_3, \varepsilon)}{\partial \varphi_3} = 0 \quad (14)$$

Where by substituting Eq. 11 to Eqs. 12, 13, 14

$$\frac{\partial V(\varphi_1, \varphi_2, \varphi_3, \varepsilon)}{\partial \varphi_i} = \frac{\partial f(\varphi_1, \varphi_2, \varphi_3, t)}{\partial \varphi_i} W \hat{y} \frac{f(\varphi_1, \varphi_2, \varphi_3, t)}{\sqrt{1 + f(\varphi_1, \varphi_2, \varphi_3, t)^2}} = 0 \quad i \in [1, 2, 3] \quad (15)$$



Since the horizontal acceleration is not zero,  $\varepsilon = f(\varphi_1, \varphi_2, \varphi_3, t) \neq 0$ , and that  $\hat{y}$  is nonzero as well, equation (15) yields

$$\frac{\partial f(\varphi_1, \varphi_2, \varphi_3, t)}{\partial \varphi_i} = \frac{\partial \varepsilon}{\partial \varphi_i} = 0 \quad (16)$$

Equation (10) combined with Eq. (16) for  $i \in [1, 2, 3]$  yield to a  $4 \times 4$  system of equations that can be solved in order to compute the four unknowns  $\varphi_1, \varphi_2, \varphi_3$  and  $t$  for a certain acceleration level and embrace angle  $\beta$ .

#### 4.2 Results – considering self-weight and inertial acceleration for terrestrial gravity

The minimum dimensionless thickness of the parabolic and circular arches are presented in figure 8 for terrestrial gravitational conditions ( $\alpha = 1$ ) and assuming that the whole mass contributes to inertial forces ( $L = 1$ ). As anticipated, Fig. 8 highlights i) the need for thicker geometries as the lateral inertial load increases and ii) the need for thinner geometries as the embrace angle decreases, for both the circular and parabolic case. In spite of the self-weight consideration where the parabolic arches have been proved more optimal than the corresponding circular ones, figure 8 indicates that after a certain value of embrace angle ( $\beta$ ) and lateral inertial load ( $\varepsilon g$ ), the circular arches tend to be more efficient.

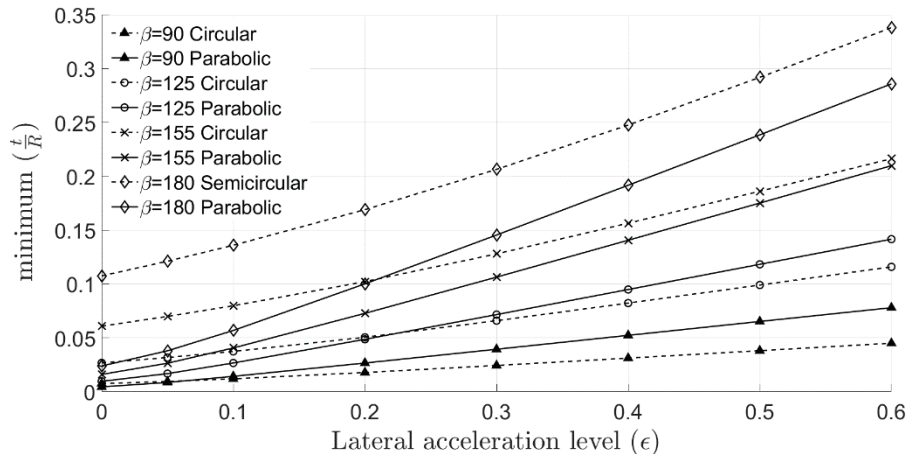


Figure 8: Minimum  $\frac{t}{R}$  versus horizontal acceleration for circular and parabolic arches with embrace angles  $\{\beta = 90^\circ, 125^\circ, 155^\circ \text{ and } 180^\circ\}$ .

Figure 9 shows the different limit thrust lines for semicircular and parabolic arches under terrestrial gravity ( $g = 9.81 \frac{m}{s^2}$ ) and horizontal accelerations,  $\varepsilon g = \{0.1; 0.2; 0.4; 0.6\}g$  together with the corresponding rupture angles. Regarding the parabolic arches, given a horizontal acceleration directed from left to right, the failure mechanism always starts from the intrados at the left springing, then there is  $\varphi_1$  at the extrados,  $\varphi_2$  at the intrados and  $\varphi_3$  at the extrados of the right springing.

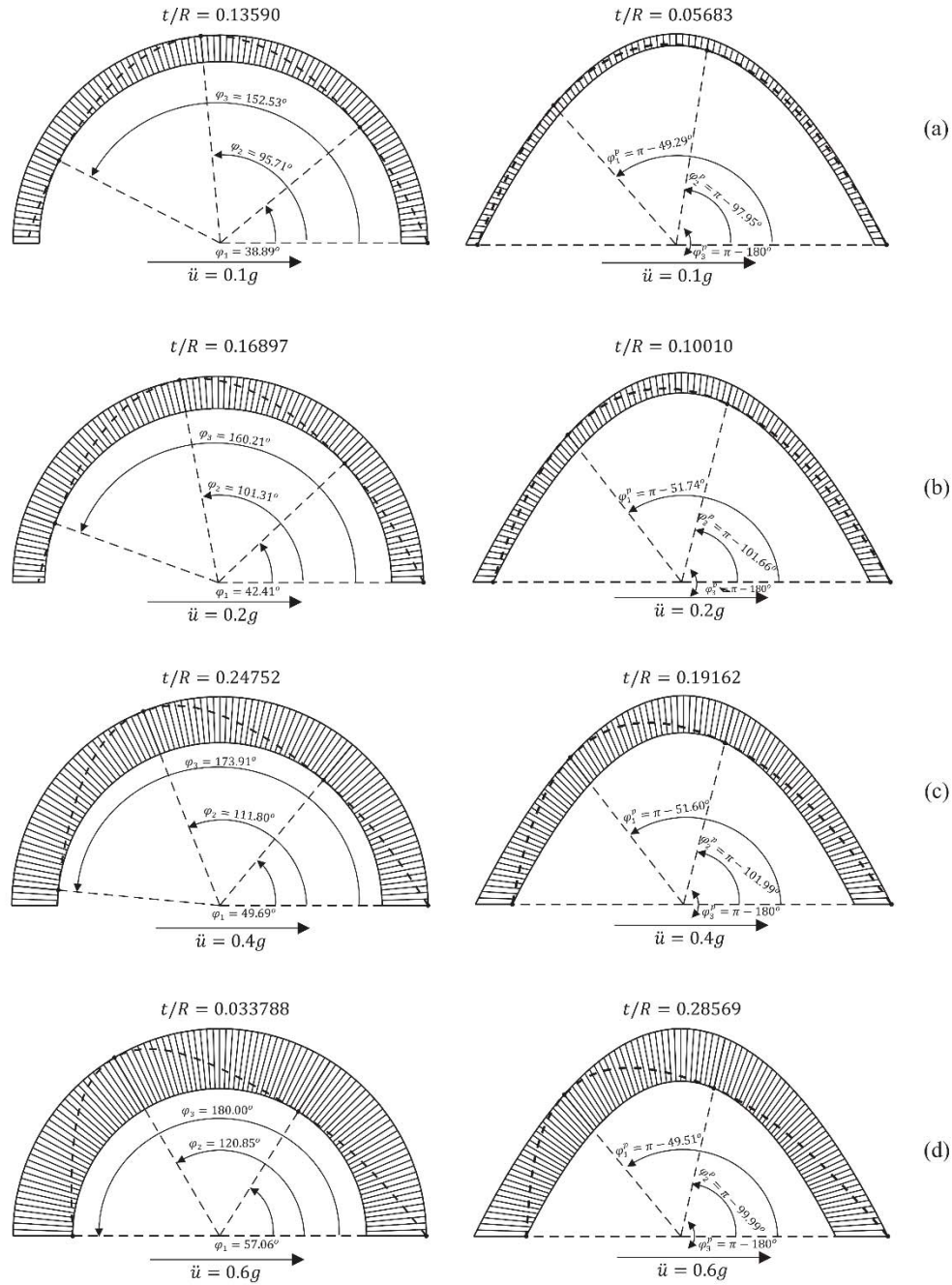


Figure 9: Contrast of the limit thrust lines for semicircular and parabolic arches under their self-weight and horizontal acceleration (from left to right) of (a)  $\varepsilon g = 0.1g$ ; (b)  $\varepsilon g = 0.2g$ ; (c)  $\varepsilon g = 0.4g$  and (d)  $\varepsilon g = 0.6g$ .

## 5. ARCHES IN LOW-GRAVITY CONDITIONS

The effects of low gravity on the stability of parabolic and circular arches are discussed in this section. The gravitational multiplier,  $\alpha = \frac{g'}{g}$ , is used to account for the influence of low gravity, with values of 0.38 and 0.17 with respect to the martian and lunar gravitational fields. Given that these arches might be used as possible shielding structures against radiation and intense temperature fluctuations, loose regolith material at the top could be needed to achieve a safe thickness of about 250 cm [27].

$L = \frac{m_{total}}{m_{inertia}} = \frac{m_{structure} + m_{infill}}{m_{inertia}}$ , in this case the factor  $L$  takes the additional mass due loose regolith infill into consideration ( $m_{infill} \neq 0$ ) and since not all of it contributes to inertial loading,  $L$  may take the values higher than 1. Specifically,  $L = 1, 2, 3, 4$  is considered herewith, where  $L = 1$  signifies that the entire mass contributes to inertia,  $m_{total} = m_{inertia}$ . Figure 10 roughly depicts the loose regolith infill atop a parabolic arch. As the structure is exposed to more regular, low-impact ground motions, (Fig. 10a), the infill remains intact (similarly to Serviceability Limit State, SLS). Thus, in this case  $L = 1$  since the infill participates entirely to the inertial loading. However, when the structure is exposed to more intense ground motions, it is highly possible that the infill will yield and then partially collapse, as it is shown in figure 10b (similarly to the Ultimate Limit State, ULS). In this case, the infill contributes only partially to the inertia of the structure, as it is not monolithically attached to it and therefore  $L > 1$ . The intensity of ground motion, the geometry of the arch, how the loose material has been connected to the arch, the coherence between the loose and the structural material, the gravitational conditions, among other considerations, all play a significant role in this partial collapse, and further analysis is required before designing such structures.

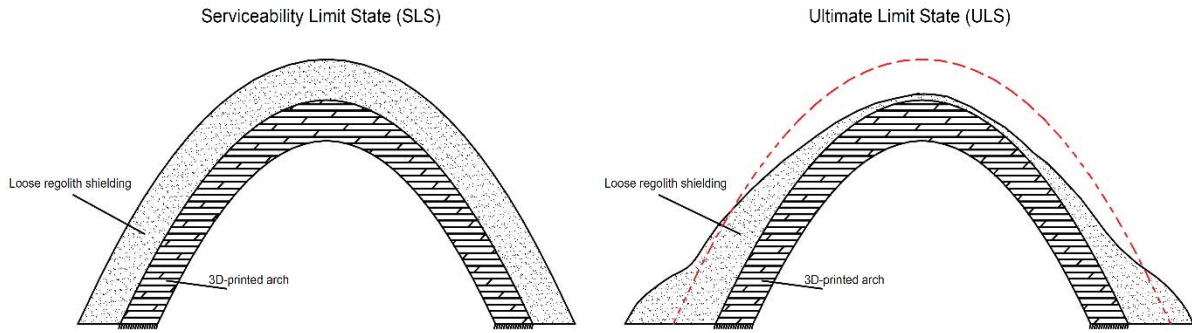


Figure 10: Minimum  $\frac{t}{R}$  versus horizontal acceleration for circular and parabolic arches with embrace angles  $\{\beta = 90^\circ, 125^\circ, 155^\circ \text{ and } 180^\circ\}$ .

Intriguingly, for both parabolic and circular arches, the phenomenon develops a self-similar behaviour portrayed by the master curves of the minimum  $\frac{t}{R}$  and rupture angles versus the dimensionless horizontal acceleration,  $\frac{\varepsilon}{\alpha L}$  in figures 11. In particular, each pair of  $\beta$  and minimum  $\frac{t}{R}$  corresponds to a unique vector of  $\left\{\frac{\varepsilon}{\alpha L}, \varphi_1, \varphi_2, \varphi_3\right\}$ . After observing figure 11 one may notice that for high values of  $\frac{\varepsilon}{\alpha L}$  (which translates to either substantial inertial loads or low-gravity conditions and no additional vertical loading) the parabolic arch is always thinner than the circular arch for  $\beta = 180^\circ$ . Nevertheless, for smaller embrace angles, there is a certain value of  $\frac{\varepsilon}{\alpha L}$  after which the circular arch becomes more efficient (in terms of material usage) than the parabolic. A more thorough investigation of the self-similar behavior phenomenon mentioned above is presented in [28].

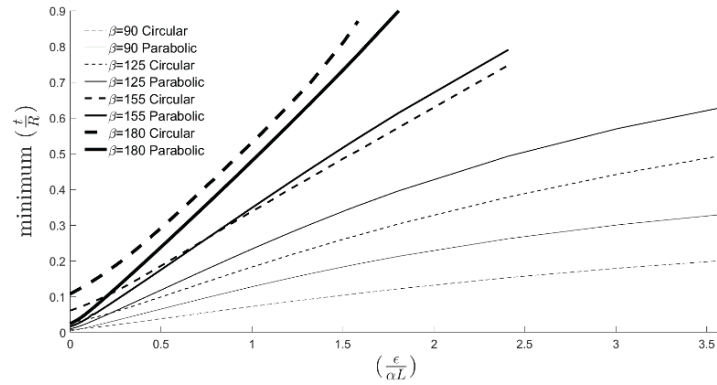


Figure 11: Master curves of the minimum required  $\frac{t}{R}$  versus the dimensionless inertial loading,  $\frac{\epsilon}{\alpha L}$ , for both circular and parabolic arches.

## 6. CONCLUSIONS

This work is based on that of [28] and has investigated via limit-state analysis the structural behavior of circular and parabolic arches when they are subjected to self-weight, additional vertical weight and inertial loading in low-gravity conditions. More specifically, this research uses a variational formulation to evaluate the minimum necessary thickness of the various arches in order for them to avoid becoming a mechanism under various load combinations and gravitational fields. The findings indicate that contrary to circular arches, parabolic arches need a far lower minimum thickness to withstand their own weight and display the symmetrically opposite five-hinge mechanism. This manifests the “geometrical superiority” among structures that resemble the catenary shape (parabolic) under self-weight. It is observed that larger inertial loading results in higher minimum thickness, smaller embrace angles lead to thinner arches.

Interestingly, both the symmetrical five hinge mechanism formed due to the effect of self-weight and the asymmetrical four-hinge mechanism developed due to the horizontal loading are opposite for the two types of arches. Nevertheless, regarding the four-hinge mechanism, the mechanism pattern shows a significant similarity between these two arch geometries, in the sense that as the inertial loading increases, in all cases, the mechanism tends to move “upstream” against the horizontal load in order for the arches to accommodate their limit thrust lines.

Moreover, a self-similar behaviour has been observed, revealing that every arch of a certain geometry type and embrace angle ( $\beta$ ) that is subjected to a “universal” dimensionless inertial load  $\frac{\epsilon}{\alpha L}$ , always results in the same minimum thickness and rupture angles  $\{\frac{t}{R}, \varphi_1, \varphi_2, \varphi_3\}$ . One may refer to [28] for further information about the analytical procedure, the justification of the self-similarity and the conditions under which the parabolic geometry is more efficient than the corresponding circular and vice versa.

Given all the above, the need to optimise the arch geometry becomes apparent in low-gravity conditions, as shown in Section 5, since the required minimum thickness can become prohibitively large.

## REFERENCES

- [1] N. Makris and H. Alexakis. The effect of stereotomy on the shape of the thrust-line and the minimum thickness of semicircular masonry arches. *Archive of Applied Mechanics*, **83**(10),1511-1533, 2013.

- [2] R. Hooke. A description of helioscopes, and some other instruments. London, 1675.
- [3] Couplet P. De la pouss'ee des voûtes. Histoire de l'Acad'emie Royale des Sciences, Paris (1731, 1732), pp. 79–117 and pp. 117–141 (1729, 1730).
- [4] M. Milankovitch. Beitrag zur Theorie der Druckkurven. Dissertation zur Erlangung der Doktorwürde, K.K. technische Hochschule, Vienna, 1904.
- [5] P. Clemente. Introduction to dynamics of stone arches. *Earthquake Engineering and Structural Dynamics*, **27**,513–522, 1998.
- [6] J. Ochsendorf. Collapse of masonry structures. PhD Dissertation. Cambridge: Department of Engineering, University of Cambridge, 2002.
- [7] H. Alexakis, N. Makris. Limit equilibrium analysis and the minimum thickness of circular masonry arches to withstand lateral inertial loading. *Archive of Applied Mechanics*, **84**(5),757-772, 2014.
- [8] M. Trial. Some effects of declining US university civil engineering enrollments on the space enterprise. ASCE, 7<sup>th</sup> *International Conference and Exposition on Engineering, Construction, Operations, and Business in Space (Space 2000)*, Albuquerque, New Mexico, United States, February 27-March 2, 2000.
- [9] N. Kalapodis, G. Kampas, O-J. Ktenidou. A review towards the design of extraterrestrial structures: from regolith to human outposts. *Acta Astronautica*, **175**, 540-569, 2020.
- [10] AM. Jablonski, KA. Ogden. Technical requirements for lunar structures. *Journal of Aerospace Engineering*, **21**(2),72–90, 2008.
- [11] G. Reitz, T. Berger, D. Matthiae. Radiation exposure in the moon environment. *Planetary and Space Science*, **74**(1),78–83, 2012.
- [12] S. Wilkinson, J. Musil, J. Dierckx, I. Gallou, X. De Kestelier. Autonomous Additive Construction on Mars. Earth and space 2016: engineering for extreme environments – proceedings of the 15th biennial international conference on engineering, science, construction and operations in challenging environments, p.343–53, 2016.
- [13] D. Rapp. Use of extraterrestrial resources for human space missions to moon or mars; 2018.
- [14] BJ. Chow, T. Chen, Y. Zhong, Y. Qiao. Direct formation of structural components using a Martian soil simulant. *Scientific Reports*, **7**(1), 1151, 2017.
- [15] A. Goulas, JGP. Binner, RA. Harris, RJ. Friel. Assessing extraterrestrial regolith material simulants for in-situ resource utilisation based 3D printing. *Applied Materials Today*, **6**,54-61, 2017.
- [16] Y. Nakamura, GV. Latham, HJ. Dorman. How we processed Apollo Lunar seismic data. *Physics of the Earth and Planetary Interiors*, **21**(2-3), 218-224, 1980.
- [17] F. Duennebier, J. Dorman, D. Lammlein, G. Latham, Y. Nakamura. Meteoroid flux from passive seismic experiment data. In: Proceedings. lunar science conference, 6<sup>th</sup>, p. 2417-2426, 1975.
- [18] N. Kalapodis, G. Kampas, O-J. Ktenidou. Revisiting the fundamental structural dynamic systems: the effect of low gravity. *Archive of Applied Mechanics*, **10**, 1861-1884, 2019.



- [19] N. Kalapodis, G. Kampas, J. Webb, O-J. Ktenidou. The effect of self-weight on free-standing blocks. In: 2nd International Conference on Natural Hazards & Infrastructures (ICONHIC), 2019.
- [20] E. Ricci, A. Fraddosio, MD. Piccioni, E. Sacco. A new numerical approach for determining optimal thrust curves of masonry arches. *European Journal of Mechanics-A/Solids*, **75**, 426-442, 2019.
- [21] H. Alexakis, N. Makris. Minimum thickness of elliptical masonry arches. *Acta Mechanica*, **224**(12), 2977-2991, 2013.
- [22] D. Nikolić. Thrust line analysis and the minimum thickness of pointed masonry arches. *Acta Mechanica*, **228**(6), 2219-2236, 2017.
- [23] G. Tempesta, S. Galassi. Safety evaluation of masonry arches. A numerical procedure based on the thrust line closest to the geometrical axis. *International Journal of Mechanical Science*, **155**, 206-221, 2019.
- [24] D. Nikolić. Catenary arch of finite thickness as the optimal arch shape. *Structural and Multidisciplinary Optimization*, **60**(5), 1957-1966, 2019.
- [25] P. Block, M. DeJong, J. Ochsendorf. As hangs the flexible line: equilibrium of masonry arches. *Nexus Network Journal*, **8**(2), 13-24, 2006.
- [26] A. Iserles. A first course in the numerical analysis of differential equations. Cambridge University Press; 2008.
- [27] H. Benaroya, L. Bernold, KM. Chua. Engineering, design and construction of lunar bases. *Journal of Aerospace Engineering*, **15**(2), 33-45, 2002.
- [28] Kampas, G., Kalapodis, N., McLean, T., Málaga-Chuquitaype, C. Limit-state analysis of parabolic arches subjected to inertial loading in different gravitational fields using a variational formulation. *Engineering Structures*, **228**, 111501, 2021.

# **LARGE-DISPLACEMENT RESPONSE OF UNREINFORCED MASONRY STRUCTURES: COMPARISON BETWEEN ANALYTICAL SOLUTIONS AND DEM MODELS INCLUDING OPEN-SOURCE SOFTWARE**

**Igor Bouckaert<sup>1\*</sup>, Michele Godio<sup>2</sup>, João Pacheco de Almeida<sup>1</sup>**

<sup>1</sup>Institute of Mechanics, Materials and Civil Engineering, UCLouvain  
Louvain-la-Neuve, Belgium  
{igor.bouckaert, joao.almieda}@uclouvain.be

<sup>2</sup>RISE Research Institutes of Sweden  
Brinellgatan 4, 504 62 Borås, Sweden  
michele.godio@ri.se

**Keywords:** Masonry, Structural Dynamics, Discrete Element Methods, Open source

**Abstract.** *Unreinforced masonry (URM) has been the most widespread construction material for centuries and is widely used in many countries. Accurate numerical models for this material are required when designing new structures, and, even more importantly, for assessing or renovating the existing stock. However, an accurate modelling of URM structures remains a challenge due to its highly non-linear mechanical behaviour involving, among other features, large out-of-plane displacements, the variability of the material properties, and the influence of construction details. The discrete element method (DEM), for which applications to masonry structures appeared in the 1990s, has gained in popularity due to its capacity to accurately capture masonry-specific phenomena; in particular, as it represents the structure as an assembly of distinct blocks, deformations are concentrated at the interfaces with low or zero tension strength, and the effect of large displacements. Unfortunately, the majority of computer programs for structural analysis based on the DEM are proprietary software, which limits its spread among practitioners and researchers. The aim of this work is to evaluate the open-source software package LMGC90, which implements the Non-Smooth Contact Dynamics Method, as a tool for modelling masonry structures.*

## 1 INTRODUCTION

Recently, the region of Wallonia (Belgium), along with the neighbouring parts of France, Germany and Holland, was indicated as one of the locations in Europe with potential for largest economic losses, because of their very large exposure and vulnerability to earthquakes [3]. Recent exposure studies have shown that the most earthquake-prone cities in Belgium have an absolutely predominant stock of URM buildings [4, 13]. One example is the city of Liège - struck by an earthquake in 1983 damaging around 16'000 houses - for which 95% of their buildings are in masonry [2]. A good understanding of the structural behaviour of typical Belgian masonry houses is therefore required to predict and best prevent the occurrence of potential damage in future low- to medium-intensity earthquakes.

In this paper, we investigate the open source software *LMGC90* [12] as a tool for modeling masonry structures subjected to earthquakes. This software was originally developed for spherical elements, simulating rapid granular flows [14]. Eventually, it was adapted to polyhedral elements and its relevance for URM modeling has been growing ever since [11]. This software has been used to study the seismic behaviour of historical masonry structures such as the Roman amphitheatre in Nîmes [15], a medieval church in Portuno [10], or the reassessment of a wall in the Prince of Wales's Fort [9]. In the last decade, some specific features relative to the modeling of URM buildings have been added to *LMGC90* and the software becomes more and more interesting for the URM community [16]. The aim of this paper is to evaluate the suitability of the software for masonry modeling. The results of the examples presented in the current study are benchmarked against analytical solutions and numerical results obtained with another well-known proprietary DEM software, namely *UDEC* [5, 6]. The examples presented in this study address several issues encountered when modeling the large-displacement response of masonry structures subjected to earthquakes, like the effect of rocking, contact stiffness and imperfections between the blocks. Two benchmark problems are presented and discussed in this paper. the first one addresses the rocking response of masonry columns, and the second one addresses the in-plane behaviour of masonry panels. In Section 2, a masonry column and a masonry arch are submitted to a horizontal impulse acceleration at the base and the failure domain is computed in terms of impulse amplitude and duration. The results are compared with those of a *UDEC* model reported in the literature [7]. In Section 3, the in-plane behaviour of a series of panels is analysed through up-to-collapse quasi-static simulations. The results are shown in terms of collapse mechanism and force capacity for each wall and compared with existing solutions extracted from the literature [8] as well as with the results of ad-hoc *UDEC* simulations.

## 2 RESPONSE OF COLUMNS AND ARCHES TO IMPULSE BASE ACCELERATION

### 2.1 Description of the benchmark

The aim of this benchmark is to explore the ability of *LMGC90* to capture the rocking mechanism of masonry structures. Moreover, the construction of non-convex shapes — with the associated difficulties of contact determination — is addressed in the second part of the example.

Firstly, the dynamic behaviour of a URM column (dimensions shown in Figure 1a) subjected to a two-sided horizontal base impulse acceleration represented in Figure 2 is analysed. A parametric study is carried out on the column by increasing the acceleration amplitude  $a$  for a range of impulse duration  $t_p$  varying between 0.1 and 1.0 s. This is done in order to obtain the failure domain of the column, i.e. the couples of values  $(a, t_p)$  which lead to the collapse of the column. The column modelled in this example is inspired from the 9<sup>th</sup> column of the eastern

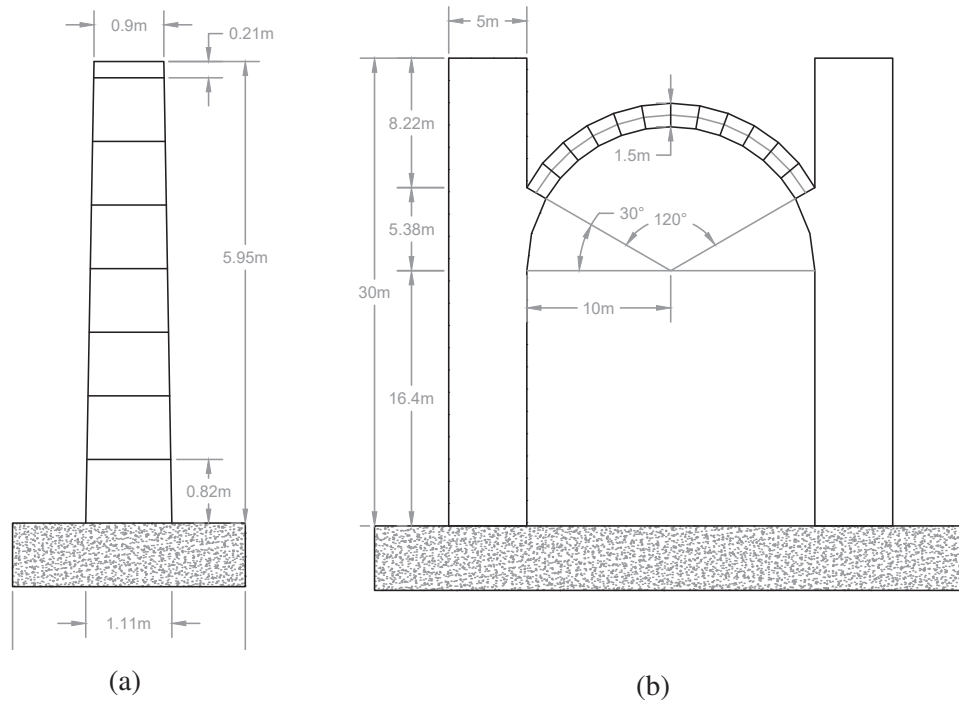


Figure 1: Geometry of the analysed column (a) and arch (b)

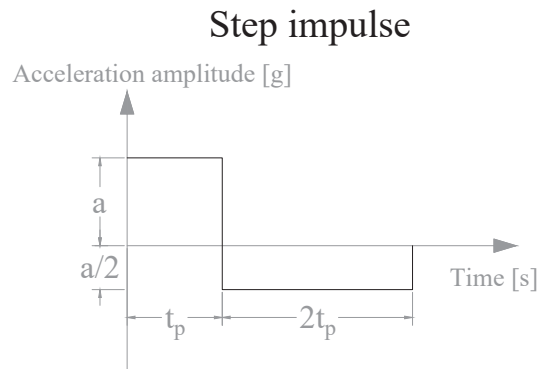


Figure 2: Acceleration step impulse applied to the base of the column [7]

flank of the temple of Apollo at Bassae, Greece. It is composed of 8 drums and has a total height of 5.95 m, a base width of 1.11 m and a top width of 0.9 m. The model implemented in *LMGC90* is in two dimensions with rigid blocks with a density of  $2620 \text{ kg/m}^3$ . The contact between the blocks is a Coulomb friction law with a friction angle of  $35^\circ$ , which is equivalent to a coefficient of friction  $\mu = 0.7$ . The simulation is run for 20 s in order to observe the response of the column after the application of the step impulse. The failure domain obtained with this model is compared with the one obtained by the implementation of the same problem using UDEC, by Dimitri et al. [7]. The *UDEC* model is implemented without damping while the damping model used in *LMGC90* is the default model of the program. The definition of the damping model and damping parameters in *LMGC90* will be explored in future studies.

A similar study is then carried out for a circular arch supported on buttresses. The dimen-

sions of the problem are shown in Figure 1b. The arch consists of 12 voussoirs, while each buttress is modelled as one monolithic block. The base of the buttresses is subjected to the same two-sided impulse acceleration used in the previous example. In particular, the acceleration is progressively increased until the failure of the arch is attained. Moreover, the position of the hinges that form in the collapse mechanism at specific values of  $a$  and  $t_p$  is compared with the results obtained with UDEC [7].

## 2.2 Results and discussion

The results obtained with *LMGC90* are summarised in this section. The plots were generated with the open-source multiple-platform application for interactive scientific visualisation *ParaView* [1].

Figure 3a shows that the failure domain obtained with the model implemented in *LMGC90* agrees well with the failure domain obtained with *UDEC* in the work by Dimitri et al. [7]. As the value of  $t_p$  increases, the acceleration amplitude causing the collapse of the column comes closer to the value of 0.19g, which is the magnitude necessary to put the column in motion according to the equilibrium static analysis. Acceleration amplitudes below that value are not going to initiate any rocking or sliding of the column [7]. The graph also hints at a change in the failure mode at around  $t_p = 0.34$ s: below that value, the columns tilts to the left and only a portion of the blocks is involved in the failure mechanism, whereas the full column tilts to the right for impulse duration above this threshold value. The failure modes obtained at  $t_p = 0.2$ s and  $t_p = 0.8$ s are displayed in Figures 3b and 3c. This could be explained by the fact that, below this threshold value, the column collapses during the first part of the impulse (positive acceleration  $a$ ) whereas for longer impulses the collapse occurs in the second part of the impulse (negative acceleration  $a/2$ ). In addition, for shorter impulses, higher rocking 'modes' are activated. As the impulse duration decreases, the results from *LMGC90* and from Dimitri et al. [7] seem to match a little bit less. This difference is probably due to definition of the damping parameters in *LMGC90*, which will be analysed in future studies.

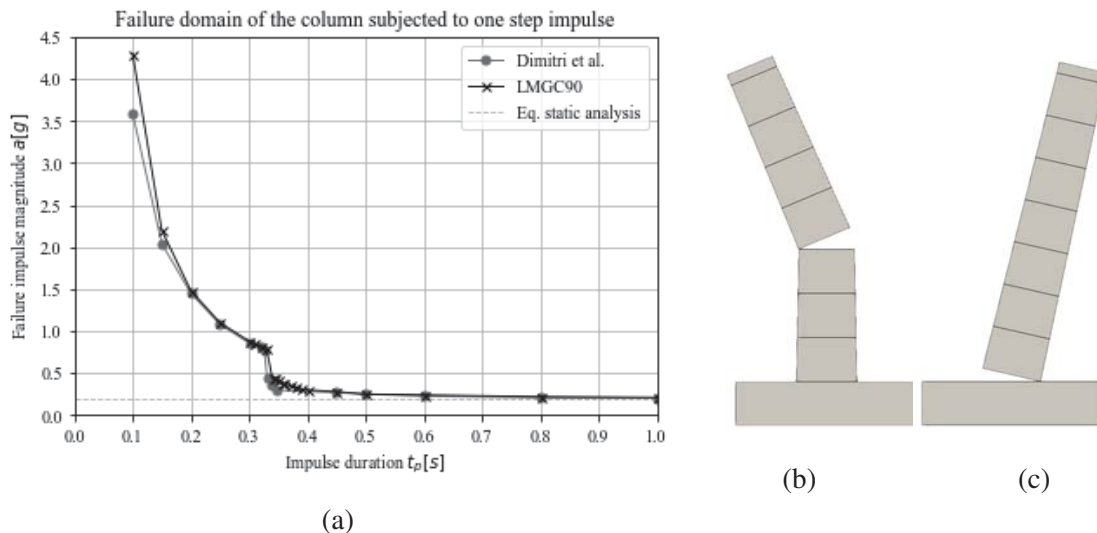


Figure 3: (a) Failure domain of the column subjected to the step impulse (b) Failure mode at  $t_p=0.2$ s and (c) Failure mode at  $t_p=0.8$ s

Figure 4 shows the results obtained for the arch of Figure 1b. Also in this case the results



obtained with *LMGC90* match very satisfactorily those obtained by Dimitri et al. [7]. Moreover, the collapse mechanisms produced by both software at two different acceleration amplitudes were compared and are in good agreement in terms of the position and number of hinges that form at collapse, see Figures 6a and 6b.

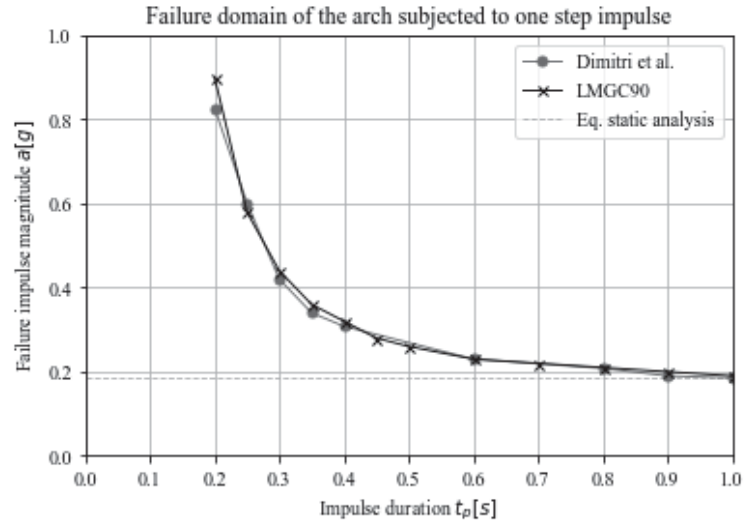


Figure 4: Failure domain of the circular arch subjected to the step impulse

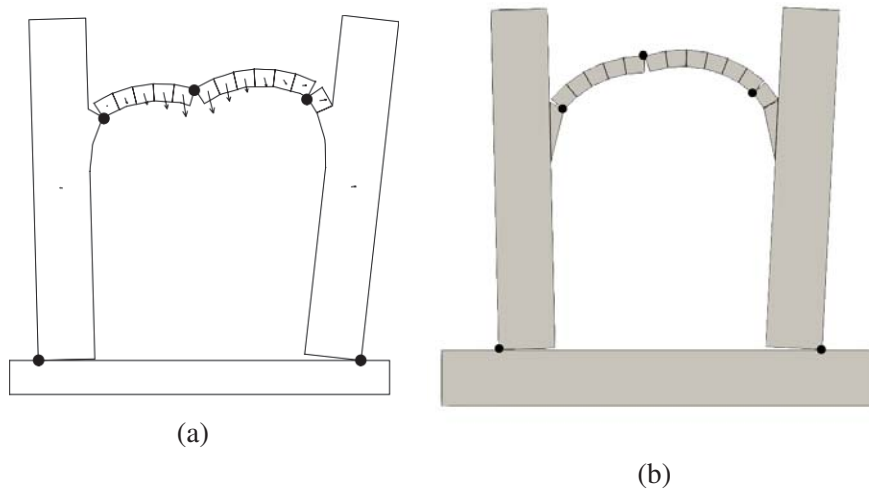


Figure 5: Failure mode of the arch at  $t_p = 0.2s$ ,  $a = 0.82g$ , from (a) *UDEC* [7] and (b) *LMGC90*

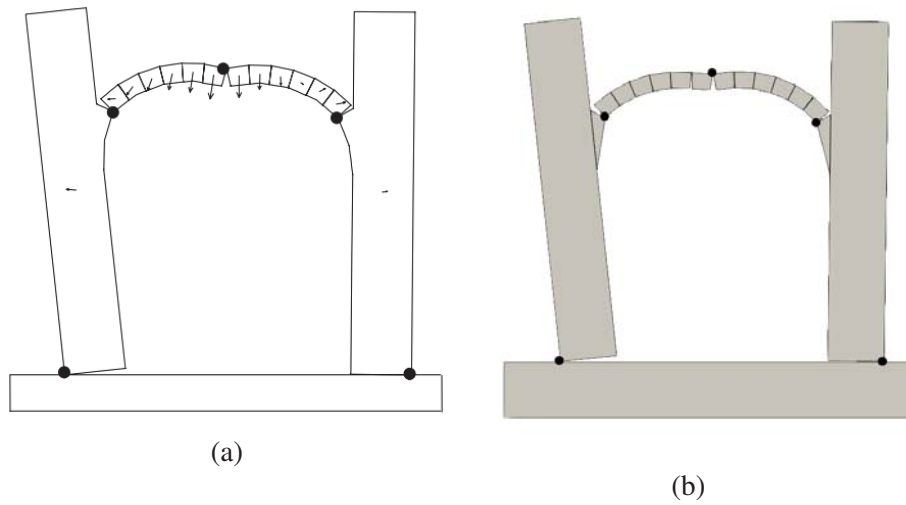


Figure 6: Failure mode of the arch at  $t_p = 1s$ ,  $a = 0.2g$ , from (a) *UDEC* [7] and (b) *LMGC90*

### 3 IN-PLANE BEHAVIOUR OF MASONRY WALLS SUBJECTED TO STATIC LATERAL LOAD

#### 3.1 Description of the benchmark

In this benchmark, quasi-static analyses are performed on a series of six wall configurations. Each wall is composed of bricks of size  $0.4\text{ m} \times 0.175\text{ m}$  with sharp or rounded edges, as depicted in Figure 7. The walls have different geometries, four of which include openings, as depicted in Figures 8 to 13. During the analysis, each block is subjected to its self-weight  $W$ , being the unit weight of the blocks equal to  $10\text{ kN/m}^3$ , and to a horizontal force  $\alpha W$  applied at its centre of gravity (Figure 7a). This configuration allows the seismic loading to be simulated as an equivalent static lateral force distribution proportional to the blocks mass [8].

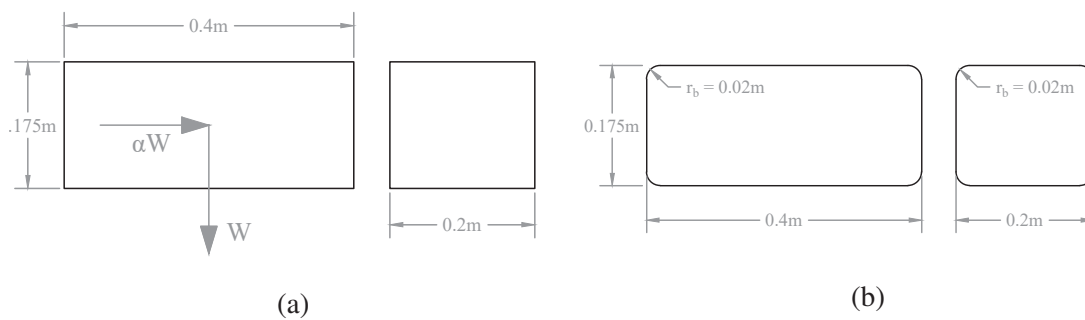


Figure 7: (a) Block and half-block with sharp edges (applied forces shown on the full block) for comparison with [8] (b) Block and half-block with rounded edges for comparison with *UDEC*

The objective of this example is to find the maximal in-plane capacity of the wall, which, according to the load pattern described above, is expressed in terms of maximum collapse load multiplier  $\alpha_{max}$  and corresponds to the maximum value of  $\alpha$  that the wall can sustain.

### 3.2 Comparison between solutions from limit analysis and *LMGC90*

First, the benchmark is implemented in *LMGC90* with rigid blocks with sharp edges as shown in Figure 7a. The contact law between the blocks is defined by a rigid-plastic law, and failure between the blocks is described by a Coulomb friction criterion with friction coefficient  $\mu=0.65$  and zero tensile strength. During the first 10 s of the simulation, the bricks are only subjected to their self-weight. Next, the value of the load multiplier  $\alpha$  is linearly increased at a rate of  $5 \times 10^{-4}/s$  which is assumed to be low enough to keep the system in quasi-static conditions until the collapse mechanism forms. The value of  $\alpha_{max}$  selected as the collapse load multiplier is the maximal horizontal reaction observed at the support divided by the total weight of the wall. Indeed, a decrease in the horizontal reaction while the total applied horizontal force keeps increasing linearly can only mean that equilibrium is no longer satisfied and that part of the applied horizontal force is converted into kinetic energy.

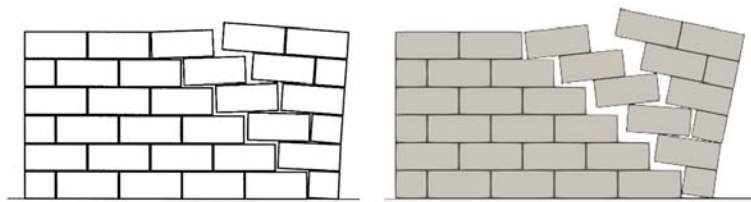


Figure 8: Mechanism of wall 1 (sharp edges) from limit analysis [8] (left) and *LMGC90* (right)

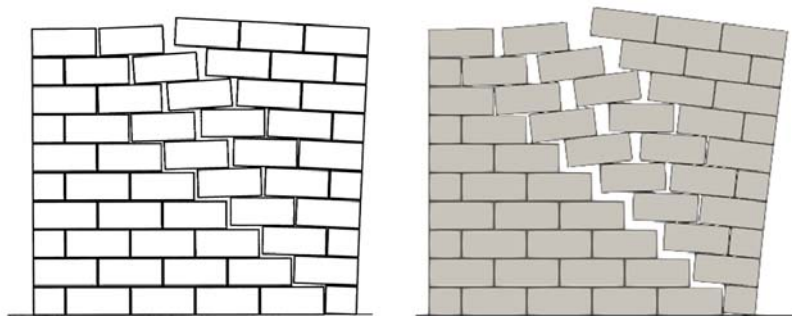


Figure 9: Mechanism of wall 2 (sharp edges) from limit analysis [8] (left) and *LMGC90* (right)

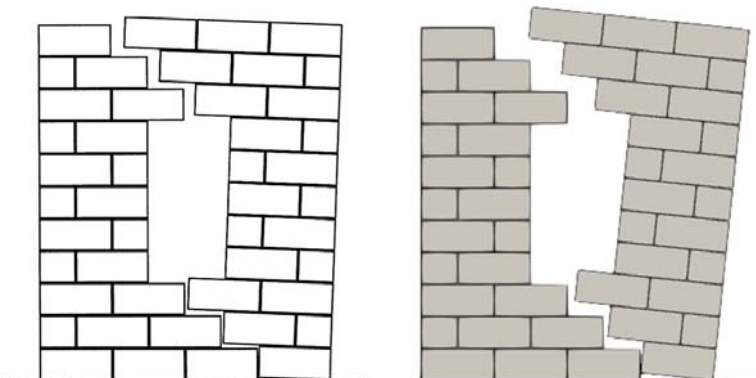


Figure 10: Mechanism of wall 3 (sharp edges) from limit analysis [8] (left) and *LMGC90* (right)

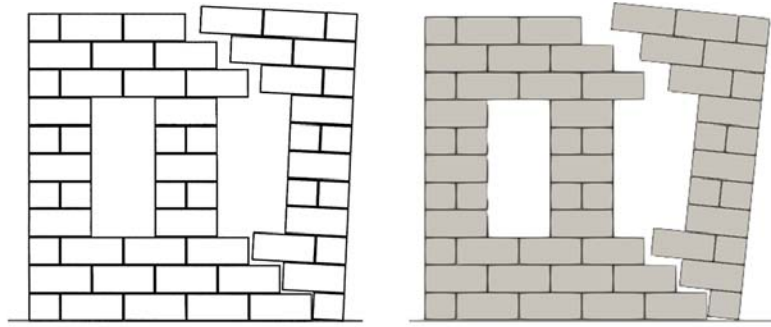


Figure 11: Mechanism of wall 4 (sharp edges) from limit analysis [8] (left) and *LMGC90* (right)

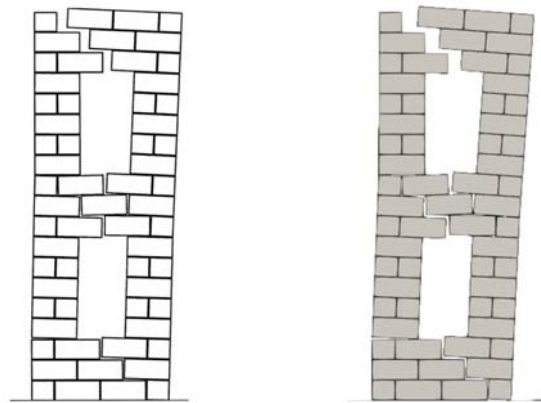


Figure 12: Mechanism of wall 5 (sharp edges) from limit analysis [8] (left) and *LMGC90* (right)

The values of  $\alpha_{max}$  are compared with the collapse load multipliers calculated by means of a limit analysis of the walls formulated as a special optimisation problem known as Mathematical Program with Equilibrium Constraints (MPEC) described by Ferris and Tin-Loi [8]. The results are summarized in Table 1. The collapse mechanisms obtained with *LMGC90* are compared with those shown by Ferris and Tin-Loi [8] in Figures 8 to 13. The figures obtained by *LMGC90* are plotted when the displacement of the upper right corner of the wall was equal to 0.2m. The value of this displacement is not specified in [8] but the figures clearly display very similar cracking patterns.

	$\alpha_{max}$ Sharp edges		% Error
	Ferris [8]	<i>LMGC90</i>	
Wall 1	0.643	0.640	-0.5
Wall 2	0.564	0.565	+0.2
Wall 3	0.359	0.358	+0.3
Wall 4	0.264	0.266	+0.8
Wall 5	0.216	0.216	+0.0
Wall 6	0.297	0.295	-0.7

Table 1: Collapse load multipliers computed in [8] and with *LMGC90*

The results obtained with *LMGC90* are very close to the ones obtained by limit analysis [8], both in terms of collapse load multiplier (with a maximal difference of 0.8%) and in terms of

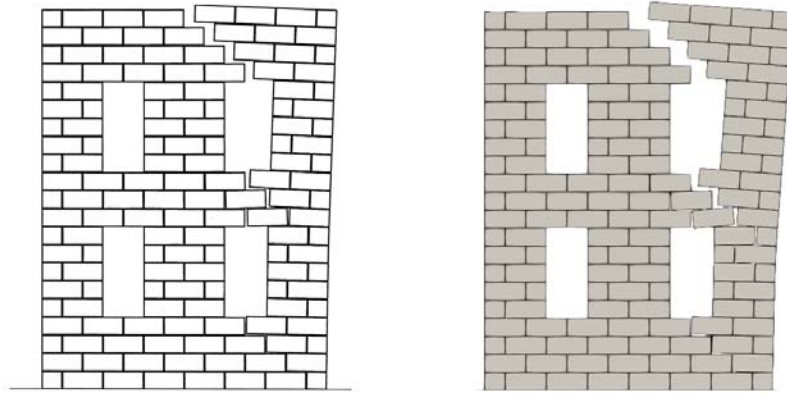


Figure 13: Mechanism of wall 6 (sharp edges) from limit analysis [8] (left) and *LMGC90* (right)

collapse mechanism.

### 3.3 Comparison between solutions from *UDEC* and *LMGC90*

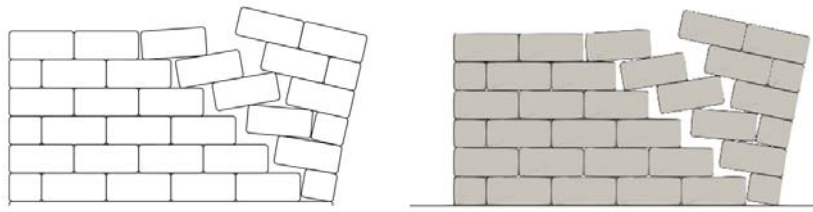
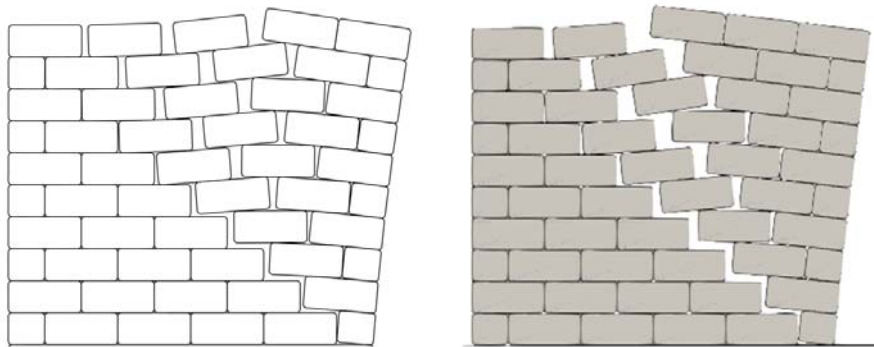
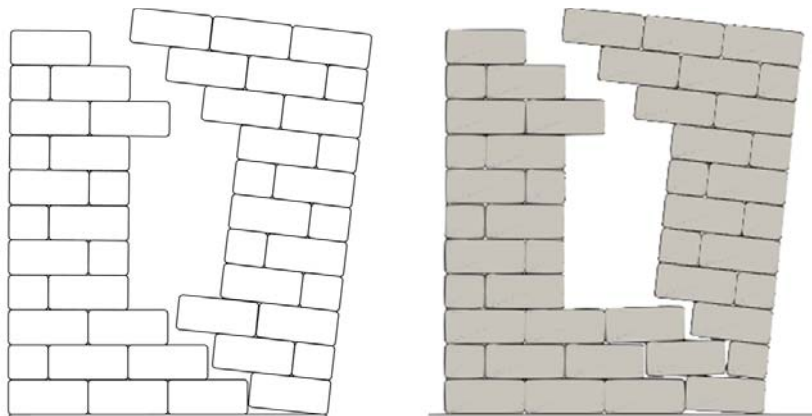
Since neither the limit analysis carried out by Ferris and Tin-Loi [8], neither the *LMGC90* implementation described above take into account any axial stiffness of the bed and head joints, the deformations of the wall before reaching collapse will be zero. Another model has been implemented in two different DEM software, the proprietary software *UDEC* and the aforementioned open source software *LMGC90*. This was also done in order to consider the effect of imperfections in the brick corners. This is assumed to be closer to reality than the implementation in section 3.2 where contact was perfectly plastic and blocks had sharp corners.

The bricks implemented in both software are rigid, 2D and have the same dimensions as previously but this time the corners are rounded with a rounding radius  $r_b$  of 0.02 m, as shown in Figure 7b. Moreover, the contact law is different than in Section 3.2 in order to take into account the stiffness of the joints. In *UDEC*, the user can define the friction coefficient between the blocks ( $\mu = 0.65$ , as previously), the normal stiffness which was set to  $k_n = 10^8$  Pa/m, the dilatancy angle and the tangential stiffness. Regarding the two latter parameters, since *LMGC90* does not allow to define a tangential stiffness nor a dilatancy angle, those parameters have been set to a very high value and to zero, respectively, to allow a valid comparison with the model implemented in *LMGC90*. Therefore, in the *UDEC* model  $k_t = 10^{14}$  Pa/m and  $\psi = 0^\circ$ . Since the axial stiffness parameter  $K_n$  defined in *LMGC90* must be expressed in N/m, the contact stiffness from the model implemented in *UDEC* must be multiplied by the surface associated to each contact point, namely  $0.1m^2$  for the bed joints (4 contact points for each brick's bed joint) and  $0.0875m^2$  for the head joints (2 contact points for each brick's head joint).

Table 2 summarises the results obtained for the six walls with rounded blocks, both with *UDEC* and *LMGC90*. The collapse load multiplier of the walls with rounded edges is a little lower than its equivalent with sharp edges.



	$\alpha_{max}$		% Error	Sharp edges [8]	% Difference between sharp and rounded edges
	UDEC	LMGC90			
Wall 1	0.577	0.578	+0.2	0.643	-10.1
Wall 2	0.495	0.512	+3.46	0.564	-9.2
Wall 3	0.325	0.321	-1.24	0.359	-10.6
Wall 4	0.236	0.242	+2.7	0.264	-8.3
Wall 5	0.157	0.175	+11.2	0.216	-19
Wall 6	0.219	0.216	+1.6	0.297	-27.2

Table 2: Collapse load multipliers computed with *UDEC* and *LMGC90*Figure 14: Mechanism of wall 1 (rounded edges) from *UDEC* (left) and *LMGC90* (right)Figure 15: Mechanism of wall 2 (rounded edges) from *UDEC* (left) and *LMGC90*Figure 16: Mechanism of wall 3 (rounded edges) from *UDEC* (left) and *LMGC90*

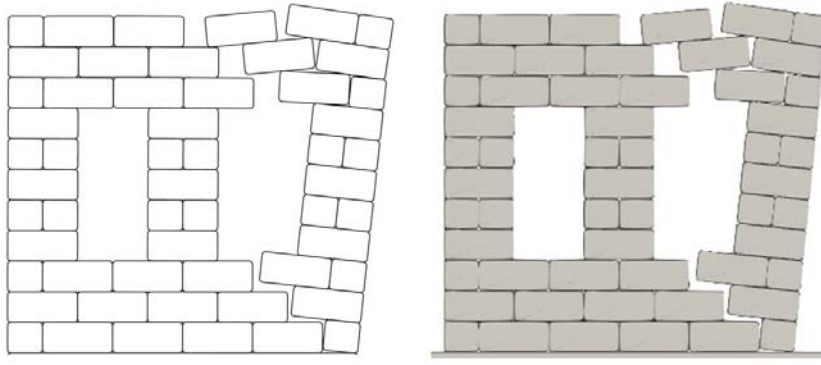


Figure 17: Mechanism of wall 4 (rounded edges) from *UDEC* (left) and *LMGC90*

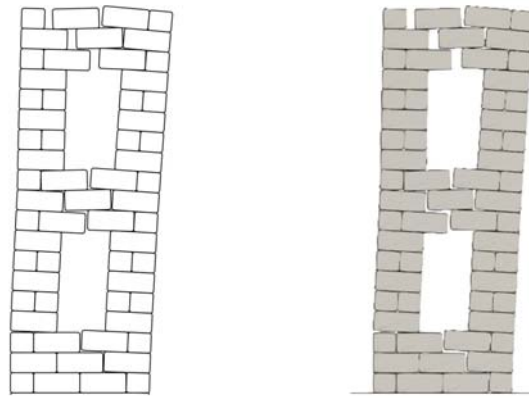


Figure 18: Mechanism of wall 5 (rounded edges) from *UDEC* (left) and *LMGC90*

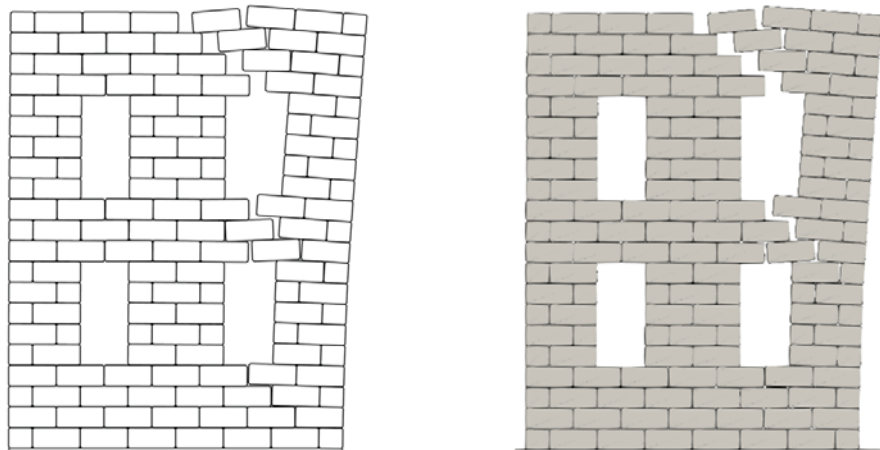


Figure 19: Mechanism of wall 6 (rounded edges) from *UDEC* (left) and *LMGC90*

The collapse mechanisms of the six walls with rounded edges are displayed in Figures 14 to 19. Both for *UDEC* and *LMGC90*, the collapse mechanism is displayed when the upper right corner of the upper right brick reaches a displacement of 0.2 m. In general, the two solutions are very close to each other in terms of collapse mechanisms. The exception is in the mechanism

of the third wall, where a bigger macro-block detaches from the structure in the mechanism obtained in *UDEC*, see Figure 16.

The values of the collapse load multipliers obtained with *LMGC90* are always higher than the values obtained with *UDEC* with a maximal error right above 10% for the fifth wall, with the exception of the third wall, which can be explained by the difference in the collapse mechanisms. When comparing the full displacement - load factor curves (not represented herein), the results obtained with *LMGC90* always seem to indicate that the walls are slightly stiffer than in *UDEC*, except for the stiffness in the elastic range which is identical in both software. This difference in stiffness, which could be a consequence of the distinct definition of the normal stiffness discussed above, could explain why the collapse load multipliers obtained with *LMGC90* are always higher than the ones obtained with *UDEC*. This matter will be explored in future works.

The comparison between both software is still limited by the impossibility in *LMGC90* to use a contact law between the blocks that includes parameters such as dilatancy or tangential stiffness, which are very common when working with *UDEC*. Inversely, the impossibility to define sharp edges when using *UDEC* makes it difficult to compare the results obtained with this software with the limit analysis carried out in [8].

## 4 CONCLUSION

Different benchmark problems have been implemented in the open-source DEM software *LMGC90* and the results were compared with the literature or with an implementation of the same benchmark problem in the proprietary software *UDEC*. These examples were chosen in order to address some of the most important aspects such as rocking, the joint stiffness and the block imperfections. Overall, the results obtained with the open-source software showed satisfactory resemblance with the literature and with the implementations in *UDEC*. Familiarisation with the interface of *LMGC90* can be time-consuming, and the choice of the tolerance and time step parameters of a simulation requires some experience, but once the user is familiar with the Python interface proposed by *LMGC90* and with the structure of the software, it opens up many possibilities for either static or dynamic analyses. The results shown in this paper confirm the applicability and validity of this open-source software in simulating large-displacement response of masonry structures. Future investigations into the possibilities offered by the *LMGC90* software regarding modeling of URM could include in-and-out-of-plane interaction of masonry walls, definition of more parameters such as dilatancy, tangential contact stiffness and damping.

## 5 Acknowledgements

Computational resources have been provided by the supercomputing facilities of the Université catholique de Louvain (CISM/UCL) and the Consortium des Équipements de Calcul Intensif en Fédération Wallonie Bruxelles (CÉCI) funded by the Fond de la Recherche Scientifique de Belgique (F.R.S.-FNRS) under convention 2.5020.11 and by the Walloon Region

## REFERENCES

- [1] J. Ahrens, B. Geveci, and C. Law. *ParaView: An End-User Tool for Large Data Visualization*. Visualization Handbook. 2005.

- [2] A. A. Costa, J. Pirmez, and J. Pacheco de Almeida. Desenvolvimento de curvas de fragilidade à acção sísmica para construções tradicionais de liège, b lgica. In *Congresso da Reabilita  o*, page 11.
- [3] H. Crowley. Preliminary european seismic risk results. In *European Seismic Risk Workshop*, 2019.
- [4] H. Crowley, V. Despotaki, D. Rodrigues, V. Silva, D. Toma-Danila, E. Riga, A. Karatzet-zou, S. Fotopoulou, Z. Zugic, L. Sousa, S. Ozcebe, and P. Gamba. Exposure model for european seismic risk assessment. *Earthquake Spectra*, 36(1 suppl):252–273, 2020.
- [5] P. A. Cundall. A computer model for simulating progressive large scale movements in blocky rock systems. In *Symposium of the International Society for Rock Mechanics*, volume II-8. Society for Rock Mechanics (ISRM).
- [6] P. A. Cundall. Formulation of a three-dimensional distinct element model—part i. a scheme to detect and represent contacts in a system composed of many polyhedral blocks. *International Journal of Rock Mechanics and Mining Sciences Geomechanics Abstracts*, 25(3):107–116, 1988.
- [7] R. Dimitri, L. De Lorenzis, and G. Zavarise. Numerical study on the dynamic behavior of masonry columns and arches on buttresses with the discrete element method. *Engineering Structures*, 33(12):3172–3188, 2011.
- [8] M. C. Ferris and F. Tin-Loi. Limit analysis of frictional block assemblies as a mathematical program with complementarity constraints. *International Journal of Mechanical Sciences*, 43(1):209–224, 2001.
- [9] A. Isfeld and N. Shrive. Discrete Element Modeling of Stone Masonry Walls With Varying Core Conditions: Prince of Wales Fort Case Study. *International Journal of Architectural Heritage*, 9(5):564–580, 2015.
- [10] G. Lancioni, S. Lenci, Q. Piattoni, and E. Quagliarini. Dynamics and failure mechanisms of ancient masonry churches subjected to seismic actions by using the NSCD method: The case of the medieval church of S. Maria in Portuno. *Engineering Structures*, 56:1527–1546, 2013.
- [11] J. V. Lemos. Discrete element modeling of masonry structures. *International Journal of Architectural Heritage*, 1(2):190–213, 2007.
- [12] F. Perales, F. Dubois, Y. Monerie, B. Piar, and L. Stainier. A nonsmooth contact dynamics-based multi-domain solver. *European Journal of Computational Mechanics*, 19(4):389–417, 2010.
- [13] A. Plumier, C. Doneux, T. Camelbeeck, G. Van Rompaey, D. Jongmans, M. Wathélet, H. Teerlynck, and F. Nguyen. Seismic risk assessment and mitigation for belgium in the frame of eurocode 8 : Final report. *Brussels : Federal Science Policy*, 2008.
- [14] F. Radjai and F. Dubois. *Mod lisation num rique discr te des mat riaux granulaires*. Hermes Sciences, Lavoisier, 2010.

- [15] A. Rafiee, M. Vinches, and C. Bohatier. Modelling and analysis of the Nîmes arena and the Arles aqueduct subjected to a seismic loading, using the Non-Smooth Contact Dynamics method. *Engineering Structures*, 30(12):3457–3467, 2008.
- [16] P. Taforel. *Apport de la Méthode des Eléments Discrets à la Modélisation des Maçonneries en Contexte Sismique : Vers une Nouvelle Approche Numérique de la Vulnérabilité Sismique*. Thesis, 2012.



## NONLINEAR FINITE ELEMENT MODELS FOR EMBEDDED BASE CONNECTIONS

Nicolas Mora-Bowen<sup>1</sup>, Pablo Torres-Rodas<sup>2</sup>

<sup>1</sup> Universidad San Francisco de Quito  
Diego de Robles  
e-mail: nmorabowen@estud.usfq.edu.ec

<sup>2</sup> Universidad San Francisco de Quito  
Diego de Robles  
e-mail: patorresr@usfq.edu.ec

---

### Abstract

Column base connections are one of the most critical components in Steel Moment Frames (SMFs) since these connections transfer the loads (i.e., gravity, seismic, wind) from the entire superstructure into the concrete-foundation, being an interface between them. Typically, exposed base plates are preferred for low-and mid-rise buildings, while embedded base connections are the norm for tall buildings. This latter base configuration response is controlled by complex interactions between the column flange and the bottom base plate with the concrete foundation, where the mechanisms to transfer internal forces are idealized to underpin the current strength design methods. These mechanisms include horizontal bearing stresses between the column flange and the surrounding concrete and vertical bearing stresses of the base plate and the concrete foundation. Current methods to estimate the strength of these connections are validated against a limited number of experimental tests complicating their generalization for the different configurations that have not been tested. Although the results from these methods show good agreement with test data, the assumptions that underpin these methods have not been verified through sophisticated nonlinear finite element models. Motivated by this issue, this paper presents a series of nonlinear finite element models developed to provide insights into the behavior of embedded base connections for SMFs. These models incorporate the essential aspects that control the connection behavior, including constitutive material modeling and contacts among the connection components. Possible design implications are discussed, while the limitations of the current work and future lines of research are outlined.

**Keywords:** Column Base Connections, Embedded Base Connections, Finite Element Models.

---

## 1 INTRODUCTION

Column Base Connections are one of the most important components of Steel Moment Frames (SMFs). Several researchers [1-6] have demonstrated their significant influence on the seismic performance of SMFs systems. Because of this, these connections have been extensively studied over the last decade in different programs [7-11]. Typically, base connections can be broadly classified as exposed base plates (EBPs) and embedded base connections (EmBCs). The former type is the preferred detail for low to mid-rise buildings, while the latter is the norm for tall buildings.

EmBCs consist of a column welded to a bottom base plate (Refer to Fig. 1) and embedded into a concrete foundation. The applied forces, i.e., Axial Load, Bending Moment, and Shear, are resisted by a combination of the bearing stresses developed by the contact between the column flange and the foundation and by the vertical stresses at the bottom base plate. Grilli and Kanvinde [7] conducted a large-scale experimental program to study the seismic response of EmBCs. This program's focus was the flexural capacity of these connections and the development of a strength method based on the insights gained from the tests. A total of five tests were evaluated. The difference among them was the embedded length (510 and 760mm), column size, and axial load level.

Grilli and Kanvinde [7] postulated an internal stress distribution to idealize the mechanism that resists the applied loads. Figure 1 illustrates this mechanism which consists of horizontal bearing stresses accompanied by joint shear in the panel zone and vertical stresses at the bottom base plate. However, this idealized mechanism relies on pre-defined stress distribution (rectangular) on the bottom base plate as well as in the column flange against the foundation. It is well-known that the real stress distribution might differ from the assumed one due to the complex interactions between the components.

The behavior of EmBCs has been studied in the past from different perspectives. Grilli and Kanvinde [7] suggested a strength method to estimate their flexural strength. Torres-Rodas [12] proposed a procedure to estimate their rotational stiffness by aggregating the deformations within the components. The hysteretic characteristics of these connections were explored by Torres-Rodas [13] through a hinged model, which was validated experimentally and capture the force transfer mechanisms observed at [7]. Recently, Inamasu et al., [14] developed Finite Element (FE) models to explore the behavior of EmBCs further and suggest design recommendations. These models consist of shell elements with two rotational springs. Results indicate that current methods for the design of EmBCs are nonconservative.

Motivated by the preceding discussion, this paper presents a study with 3D sophisticated FE models to investigate further the seismic behavior of EmBCs. These models provide insights into the internal stress distribution and patterns of deformation of these connections. The models intend to capture phenomena such as the multi-axial constitutive response of the materials (steel and concrete), large deformations, and the contact between the column flange and the foundation. The paper starts by describing the models developed herein, and then the main findings are presented. Finally, the limitations of the study are discussed, and recommendations for future research are presented.

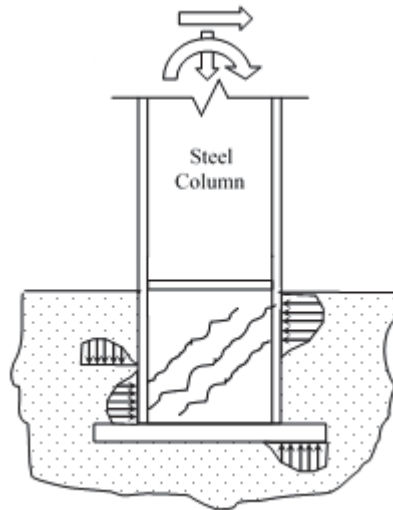


Figure 1: EmBC detail and internal force mechanism (from [7,12])

## 2 EXPERIMENTAL DATA

In this study, for the purposes of model validation, the experimental program conducted by Grilli and Kanvinde [7] at the University of California Davis was used. Thus, in this section of the paper, the details of the experimental program are briefly summarized. All tests consist of a steel column welded to a bottom base plate. The column height was about 3m, and it was embedded into a concrete foundation. All the specimens were subjected to the cyclic loading protocol ATC-SAC (Krawinkler et al. 2000 [15]). The parameters that changed among the tests are the embedded depth, the level of Axial Load (Tensile forces were used in one test), and the column size. Table 1 shows a summary of the test parameters, while Figure 2 a schematic representation of the test setup at UC Davis.

Based on the insights obtained from the mentioned experimental program, Grilli and Kanvinde [7] presented a strength method to characterize the flexural capacity of EmBCs. Key aspects of this method are detailed here. The applied Moment is resisted by a combination of horizontal bearing stresses developed by the contact between the column flange and the concrete foundation and vertical bearing stresses at the bottom base plate. Shear forces in the panel zone complement the horizontal bearing stresses. Thus, the Moment is resisted by these two mechanisms, i.e., horizontal and vertical stresses, with the implication that a fraction of the total applied Moment is distributed to each mechanism. This idealization entails an indeterminate problem, which is solved by the introduction of an empirically calibrated equation that considers the relative stiffness of the embedded column and the surrounding media.

In this manner, the connection strength may be calculated based on the associated limit states to each force transfer mechanism. For the horizontal bearing stresses, two limit states can take place 1) concrete bearing failure and 2) joint shear failure. On the other hand, in the vertical bearing mechanisms, four possible modes of failure are identified 1) base plate yielding, 2) concrete breakout under the base plate, 3) concrete breakout above the base plate, and 4) bearing failure of the concrete around the base plate. The connection strength is calculated by combining the Moment capacity associated with both mechanisms ( $M_{HB}^{capacity}$  and  $M_{VB}^{capacity}$ ). Grilli and Kanvinde [7] concluded that the capacity estimated with the preceding procedure must be reduced by 30% for design purposes.

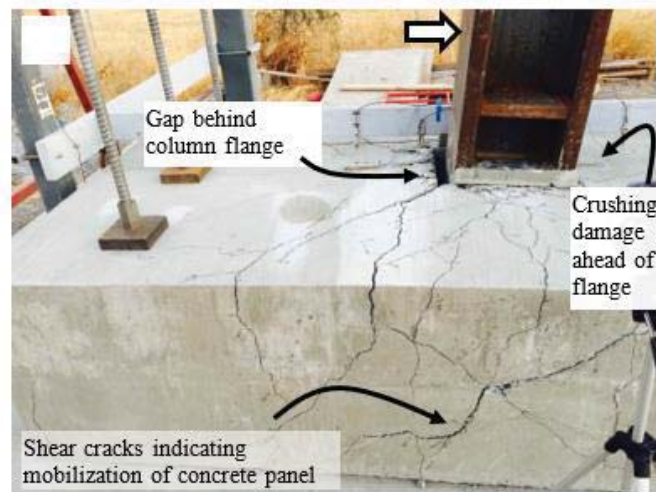


Figure 2: UC Davis experimental test (from [7,12])

### 3 FINITE ELEMENT MODELS

A total of four FE models have been developed to study the seismic behavior of EmBCs using the ABAQUS [16] simulation platform. Figure 3 illustrates a representative model built in this investigation. The models are composed of 3D Hex-structured elements. The meshes were refined in places where concentrations of stress are anticipated. As described in the previous section, the strength of the connection may be explained due to the contacts between the column flange and the base plate with the concrete foundation. Thus, the contacts are an essential feature of these models. These contacts are simulated with a finite sliding formulation with Normal and Tangential interaction properties. The former property was defined as hard contact, while the latter with a frictional formulation following the penalty method. A friction coefficient of 0.45 is adopted as recommended by Gomez et al. [11]. In contrast, welded elements inside the connection are assigned the tie constraint (i.e., steel column and base plate, steel column, and stiffeners) since welds are detailed to resist fracture even at large deformations.

Geometric nonlinearities, including large deformations formulations, are included in the models. The steel column and base plate are modeled with the Von-Mises surface with isotropic hardening. On the other hand, for concrete modeling, it is common to assume that this material behaves as an elastoplastic material in compression and brittle in tension. In this investigation, the concrete damaged constitutive plasticity (CDP) model was employed since it provides a general capability for modeling concrete and other quasi-brittle materials. Some of the details of this constitutive model provided by [16] are discussed. The CDP model uses concepts of isotropic damaged elasticity in combination with isotropic tensile and compressive plasticity to represent the inelastic behavior of concrete. It assumes that the main two failure mechanisms are tensile cracking and compressive crushing of the concrete material. Two hardening parameters control the evolution of the yield surface,  $\epsilon_t^{-pl}$  and  $\epsilon_c^{-pl}$  associated to failure mechanisms under tension and compression loading, respectively [16]. The material properties are obtained from the ancillary tests from [7], and true stresses and strains were assumed in the material formulation.

The FE models were subjected to the SAC load protocol [15] in the Axial Load presence. In order to avoid the interference of P-delta effects in the connection response, the Axial Load was

applied strategically at the bottom of the base plate. Thus, the Moment-Rotation response was recorded from the simulations and compared to validate the models with the associate experimental test. Figure 4 illustrates the results of the simulations and the corresponding validation against the experimental data. As per this Figure, the essential aspects of the hysteretic response are capture by the numerical results. Specifically, the simulations are able to capture the pinching behavior observed in the tests. Cyclic deterioration of the strength and the unloading stiffness are identified in these connections and well-represented in the simulations. The parameters that define the response's backbone curve are the Moment at First Yield, the Initial Rotational Stiffness, the Peak Moment Strength, and the Rotation Associate to the Peak Strength. A visual inspection of Figure 4 indicates that the differences between the simulations' parameters to the experimental tests' corresponding values are neglectable. Consequently, in the authors' opinion, the FE models are able to capture the key features of the connection response and are appropriate to investigate the behavior of EmBCs.

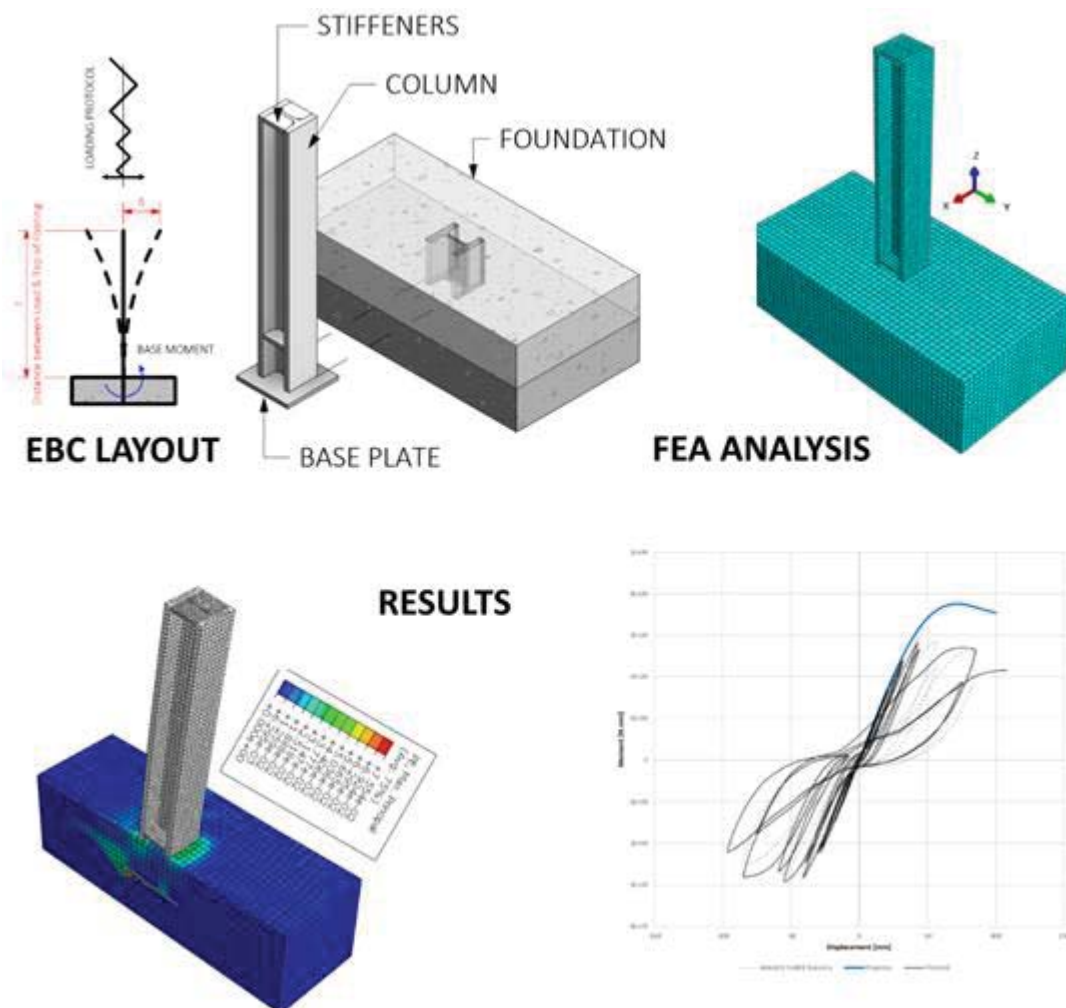


Figure 3: a) EmBC layout, b) representative 3D FE model, c) example of the distribution of Stresses of a simulation, d) example of a hysteretic response



Test #	Column Size	$P$	$d_{embedded}$	Base Plate			
				$t_p$	$N$	$B$	$Z$
		[kN]	[mm]	[mm]	[mm]	[mm]	[mm]
1	W14x370	445 [C]	510	50	760	760	2850
2	W18x311	445 [C]	510	50	865	710	2850
3	W14x370	0	760	50	760	760	3100
4	W14x370	445 [C]	760	50	760	760	3100

Table 1: Test Matrix Geometry and applied Axial Loads

#### 4 DISCUSSION OF THE RESULTS

This section discusses the key findings from the FE simulations. Referring to Figure 4, all simulations show a well-defined linear-elastic branch up to the point where nonlinear behavior starts, which corresponds to rotations close to 0.005rad. This observation is consistent with the experimental evidence reported by [7] that indicates that after 0.005rads, small cracks on the tension column flange start to open, entailing a gradual nonlinear response. These small cracks are accompanied by diagonal cracks, which start to grow near the steel column corners. Figure 5 shows a schematic representation of the crack propagation obtained from the simulation of test 1 once the deformation progresses.

As deformation progresses in all simulations, an appreciable loss of stiffness is observed because the concrete reaches its peak strength. At this point, the gap formed in the foundation in the tension flange side grows, which is consistent with the experimental tests [7]. This gap entails the pinching behavior observed in all the tests since it causes a relatively unconstrained rotation of the steel column as it moves back to the vertical position and goes in the reverse direction (following the cyclic loading protocol). A closer inspection of Figure 4 reveals that tests with higher embedment depths (760mm) present a more gradual stiffness decrease. This phenomenon may be attributed to the fact that higher embedment lengths imply a great fraction of the total Moment carried by the horizontal bearing stresses. Thus, when this latter mechanism starts to deteriorate, the force transfer to the vertical stresses seems to be more gradual.

Finally, in this section, the distribution of the horizontal bearing stresses is discussed. Figure 6 shows the stress distribution along the steel column flange of test 1 in two stages of the response, i.e., at the Moment associated with the First Yield and Peak Strength. As per Figure 6, for the first condition (i.e.,  $M_y$ ), the "real" stress distribution is closer to a triangular shape. This observation is not surprising since at this level of deformation, the connection starts to incursion in the nonlinear regime, and a triangular shape is consistent with an elastic behavior. In contrast, once the connection has reached its peak, it is observed in the simulations a more uniform stress distribution along a certain length of the flange. This finding is consistent with the rectangular stress block assumed by Grilli and Kanvinde [7] in their strength method. Although these findings may be used in the future to refine the strength, this topic deserves further scrutiny.

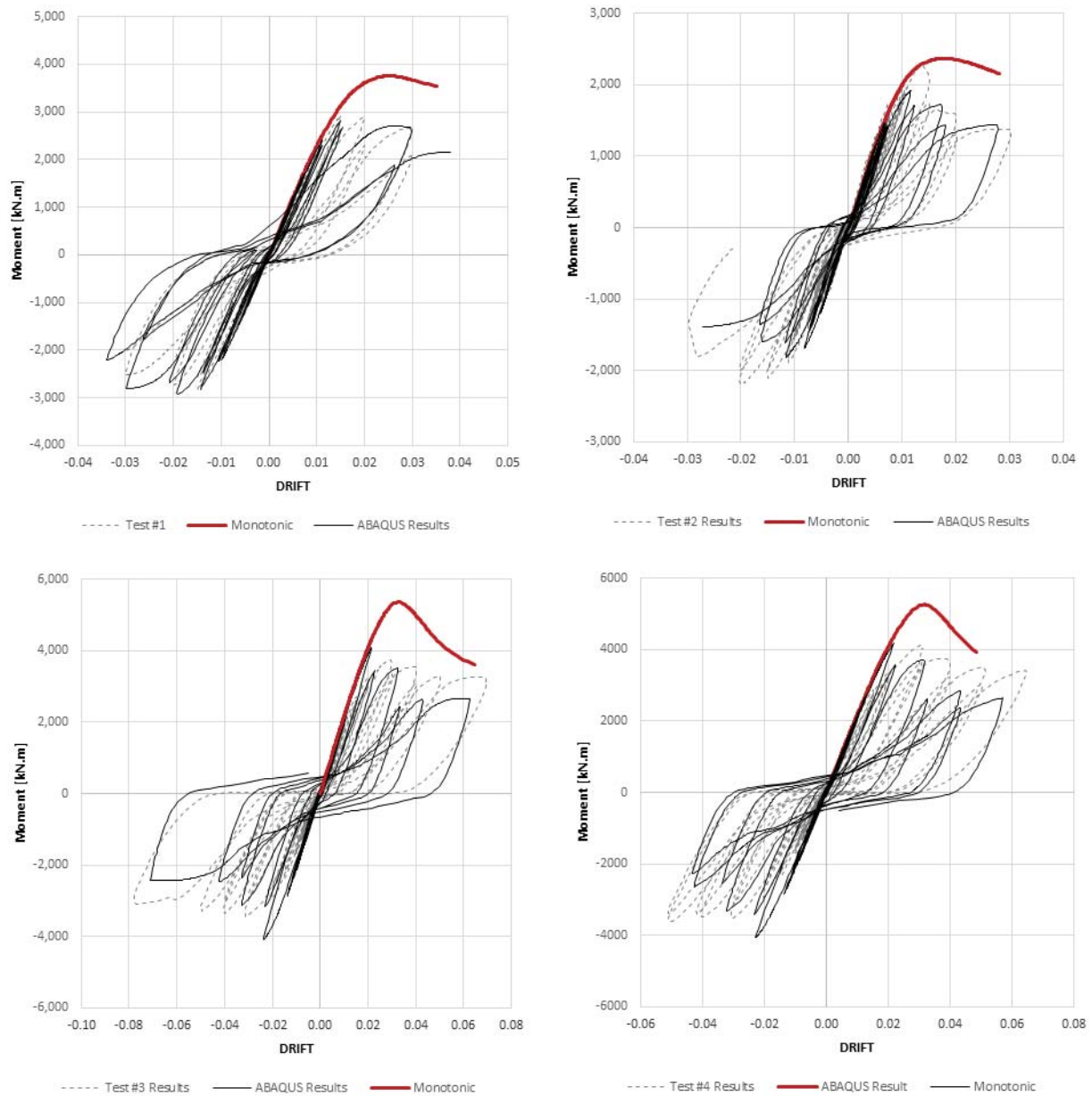


Figure 4: Hysteretic response of all FE simulations vs. Experimental data from [7]

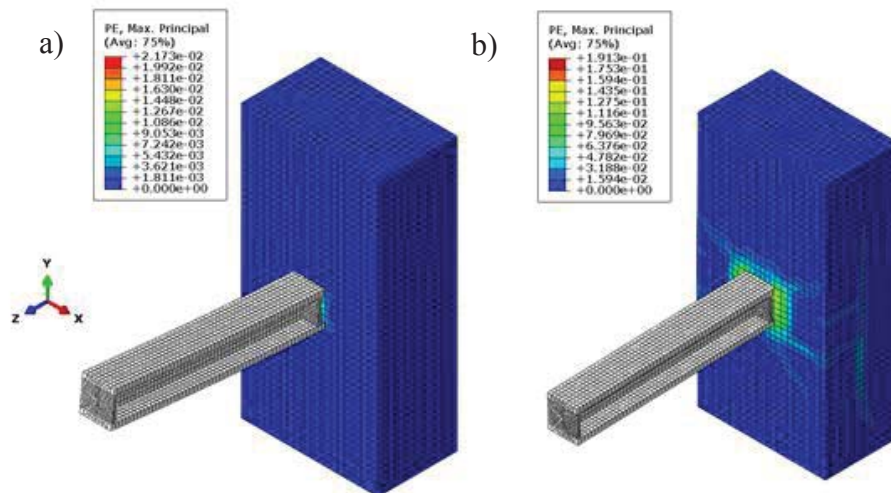


Figure 5: plastic strain distribution on the concrete at a) first yield, b) peak strength

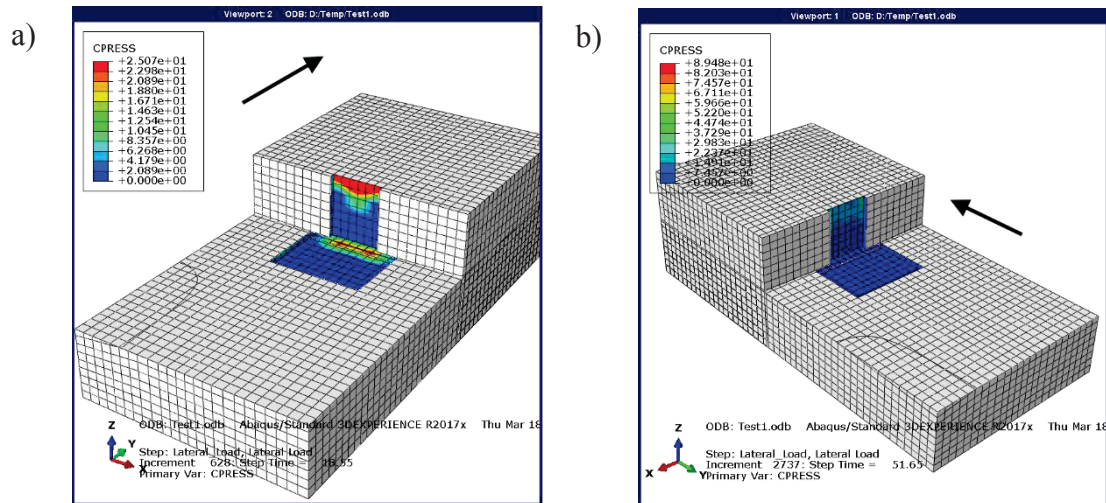


Figure 6: stress distribution on the concrete foundation due to column flange contact at rotations associated with  
a) first yield, b) peak strength

## 5 SUMMARY, LIMITATIONS, AND RECOMMENDATIONS

This paper presents a numerical study conducted on a critical component of SMFs such as EmBCs. A total of four FE models were developed in the ABAQUS platform [16] to explore the seismic behavior of these connections. Specifically, in this study, the internal force distribution and the patterns of deformation were identified from the simulations with the intention to gain insights aimed to improve the current design methods (e.g., [7]). All the models were validated against the experimental program conducted by Grilli and Kanvinde [7]. The goodness of the fit (i.e., the difference between the experimental and the numerical results) was considered an indicator of the reliability of the models.

The simulations indicate that at rotation levels close to the "first" yield of the connection, the stresses are not uniform along the column flange; instead, a triangular shape can be assumed. In contrast, at higher rotations, the stresses tend to become relatively uniform. Thus, when the connection reaches its peak strength, it seems that the rectangular block assumption is appropriate. However, this issue deserves a further look.

The paper has several limitations that should be addressed in a new study in order to generalize the conclusions. For example, the number of simulations (four in total) is limited. Moreover, the experimental program by [7] is the only testbed used. It is recommended to build more FE models from other experimental programs available to assess different configurations' behavior (e.g., column size, embedment length, the influence of shear studs). Besides, this study does not address issues related to the seismic demands on the EmBCs, or a reliability analysis to assess if the strength resistance factors adopted are adequate or not. These topics have been addressed for exposed-based plates by [17,18,19] and should be conducted for EmBCs.

## 6 REFERENCES

- [1] Torres-Rodas, P., Flores, F., & Zareian, F. (2018). Seismic response of steel moment frame considering gravity system and column base flexibility. In Proc. 11th US Natl. Conf. Earthq. Eng., June 25–29, Los Angeles, USA.
- [2] Falborski, T., Torres-Rodas, P., Zareian, F., & Kanvinde, A. (2020). Effect of base-connection strength and ductility on the seismic performance of steel moment-resisting frames. *Journal of Structural Engineering*, 146(5), 04020054.
- [3] Torres-Rodas, P., Flores, F., Astudillo, B.X., Pozo, S. (2020). Sensitivity of special steel moment frames to the influence of column-base hysteretic behavior including gravity framing system. *Proceedings of the International Conference on Structural Dynamic , EURODDYN*, 2020, 2, pp. 3629–3642
- [4] Inamasu, H., de Castro e Sousa, A., Güell, G., & Lignos, D. G. (2020). Anchor-yield exposed column bases for minimizing residual deformations in seismic-resistant steel moment frames. *Earthquake Engineering & Structural Dynamics*.
- [5] Y. Cui, F. Wang, S. Yamada, Effect of Column Base Behavior on Seismic Performance of Multi-Story Steel Moment Resisting Frames, *International Journal of Structural Stability and Dynamics*. 19 (2019) 1940007. <https://doi.org/10.1142/S0219455419400078>.
- [6] Torres-Rodas, P., Flores, F., Pozo, S., & Astudillo, B. X. (2021). Seismic performance of steel moment frames considering the effects of column-base hysteretic behavior and gravity framing system. *Soil Dynamics and Earthquake Engineering*, 144, 106654.
- [7] Grilli, D.A. and Kanvinde, A.M. (2015). "Embedded Column Based Connections subjected to Flexure and Axial loads," Report 3-11 submitted to the Charles Pankow Foundation.
- [8] DeWolf J.T., and Sarisley, E.F. (1980), "Column Base Plates with Axial Loads and Moments," *Journal of the Structural Division, ASCE*, Vol. 106, No. 11, November 1980, pp. 2167-2184
- [9] Astaneh, A., Bergsma, G., and Shen J.H. (1992). "Behavior and Design of Base Plates for Gravity, Wind and Seismic Loads," *Proceedings of the National Steel Construction Conference*, Las Vegas, Nevada, AISC, Chicago, Illinois.
- [10] Burda, J.J., and Itani, A.M. (1999). "Studies of Seismic Behavior of Steel Base Plates," Report No. CCEER 99-7, Reno (NV): Center of Civil Engineers Earthquake Research, Department of Civil and Environmental Engineering, University of Nevada, NV.
- [11] Gomez I.R., Kanvinde A.M. and Deierlein G.G. (2010). "Exposed Column Base Connections Subjected to Axial Compression and Flexure," Report Submitted to the American Institute of Steel Construction (AISC), Chicago, IL.
- [12] Rodas, P. T., Zareian, F., & Kanvinde, A. (2017). Rotational stiffness of deeply embedded column–base connections. *Journal of structural engineering*, 143(8), 04017064.
- [13] Torres-Rodas, P., Zareian, F., & Kanvinde, A. (2018). A hysteretic model for the rotational response of embedded column base connections. *Soil Dynamics and Earthquake Engineering*, 115, 55-65.

- [14] Inamasu, H., Kanvinde, A. M., & Lignos, D. G. (2021). Seismic design of non-dissipative embedded column base connections. *Journal of Constructional Steel Research*, 177, 106417.
- [15] Gupta, A., & Krawinkler, H. (2002). Prediction of Seismic Demands for SMRF's with Ductile Connections and Elements. SAC Joint Venture.
- [16] ABAQUS, ABAQUS Analysis User's Manual Version 6.14–1, Dassault Systems Simulia Corp, RI, USA, 2014.
- [17] Torres-Rodas, P., Zareian, F., & Kanvinde, A. (2018). Seismic demands in column base connections of steel moment frames. *Earthquake Spectra*, 34(3), 1383-1403.
- [18] Torres-Rodas, P., Fayaz, J., & Zareian, F. (2020). Strength resistance factors for seismic design of exposed based plate connections in special steel moment resisting frames. *Earthquake Spectra*, 36(2), 537-553.
- [19] Song, B., Galasso, C., & Kanvinde, A. (2021). Reliability Analysis and Design Considerations for Exposed Column Base Plate Connections Subjected to Flexure and Axial Compression. *Journal of Structural Engineering*, 147(2), 04020328.



## LOCAL SCALE DAMPING MODEL FOR REINFORCED CONCRETE ELEMENTS

Clotilde Chambreuil<sup>1</sup>, Cédric Giry<sup>1</sup>, Frédéric Ragueneau<sup>1</sup>, and Pierre Léger<sup>2</sup>

<sup>1</sup>Université Paris-Saclay, ENS Paris-Saclay, CNRS, LMT - Laboratoire de Mécanique et Technologie, 91190, Gif-sur-Yvette, France.

e-mail: {clotilde.chambreuil,cedric.giry,frederic.ragueneau}@ens-paris-saclay.fr

<sup>2</sup> École Polytechnique de Montréal, Department of Civil, Geological and Mining Engineering, C.P. 6079, succ. Centre-Ville, Montréal, Québec, Canada, H3C 3A7.

e-mail: pierre.leger@polymtl.ca

**Keywords:** Damping, Reinforced Concrete, Dynamic, Nonlinear Model, Energy Balances.

**Abstract.** Reinforced concrete (RC) structures dissipate energy when subjected to seismic excitations. Modeling seismic energy dissipations on a rational basis still represents challenging issues. At local scale, dissipative constitutive RC models are developed to take into consideration different phenomena, such as cracks opening, friction, plasticity, and their couplings or rebar bond slip. Practically some of those dissipative mechanisms are modeled by equivalent Rayleigh viscous damping at the global structural level. However, Rayleigh damping lacks a physical basis leading sometimes to an uncontrolled evolution of energy dissipation when non linearities occur [1]. This paper provides the basis of an updated local damping model based on parameters modeling concrete dissipative phenomenon, to reduce the need for arbitrary equivalent viscous damping as much as possible and thus better model energy dissipations on a rational physical basis. Using shake table experimental results on prismatic RC beams [2], a numerical study is presented to assess the performance of sixteen different global damping formulations to represent physical energy dissipation mechanisms. Energy balance analyses are used to evaluate dissipative phenomena at the local concrete level and to demonstrate that friction is the most significant local dissipative phenomenon. In addition, an equivalent viscous damping identification method is developed to determine transient damping ratio evolution during dynamic computations as a function of damage parameters, like stiffness degradation. An exponential function is found suitable to take into consideration global viscous damping adjustment as a function of local damage occurring during dynamic nonlinear analyses.

## 1 INTRODUCTION

Earthquake events in recent years lead to the need to evaluate structural vulnerability and to quantify related safety margins. Particularly, the combination of critical infrastructures presence on territories and more stringent seismic regulations represent a current challenge. Nuclear power plants are representing such critical structures. In the aim of increasing their lifespan, analyses are required to ensure their safety under current and evolving standards. For example, after a moderate earthquake excitation, the nuclear containment vessel still need to demonstrate airtightness. But, the difficulty with reinforced concrete structures is related to the lack of knowledge about concrete cracking damage and about the ability of the material to dissipate seismic energy.

To improve dynamic non-linear computations of complex structures under earthquake excitations, rational physical models need to be developed. To model dissipations during earthquake events, different scales are considered. First, at local scale, physical phenomena can be described through material constitutive laws. Then, at global scale, energy dissipations are also occurring because of the structure interaction with its environment. The impossibility to model all phenomena at local and structural scales leads to the use of equivalent viscous damping. Following Rayleigh's works [3], a large amount of viscous damping matrix formulations have been developed in the literature. However, those formulations still lack a sound physical basis.

Based on a shake table experimental campaign performed by Heitz [2] to characterize seismic energy dissipation in reinforced concrete beams, a numerical study is presented herein. It aims at evaluating the performances of existing local as well as global (Rayleigh) damping formulations in representing the experimental data. The focus is put in dissipative evolutions at local and global scales. An identification method is also developed to study evolution of the equivalent viscous damping ratio during non-linear computations.

## 2 REINFORCED CONCRETE BEAM UNDER EARTHQUAKE EXCITATION

The experimental campaign performed by [2] at the French Alternative Energies and Atomic Energy Commission (CEA) Saclay represents a huge amount of data that can be used as a reference to validate numerical analyses. Experiments were performed with different material properties, structural configurations and excitation characteristics on reinforced concrete beam. The main objective was to evaluate seismic energy dissipations mechanisms.

### 2.1 Beam model



Figure 1: Dynamic experimental setup

Based on information about the experimental setup (fig. 1), a numerical model of the tested reinforced concrete beams has been developed using Cast3m, a finite-element software. The main advantages of using a multi-fiber models are: (i) to avoid solid 3D models, limiting the number of degrees-of-freedom and so to save computational time, (ii) to consider 1D constitutive material models, which are easier to implement and unable to model local behaviors, and (iii) its usability for results interpretation [4, 5, 6]. Multi-fiber beam elements are based on Timoshenko beam the-

ory in Cast3m.

A typical model geometry is presented in figure 2. Along the beam, sections are considered at each Gauss point of the beam elements (fig. 2a). Then, each section is decomposed in fiber elements. Figure 2b shows the section model with concrete and steel elements. Those elements are 2D linear quadrangle elements.

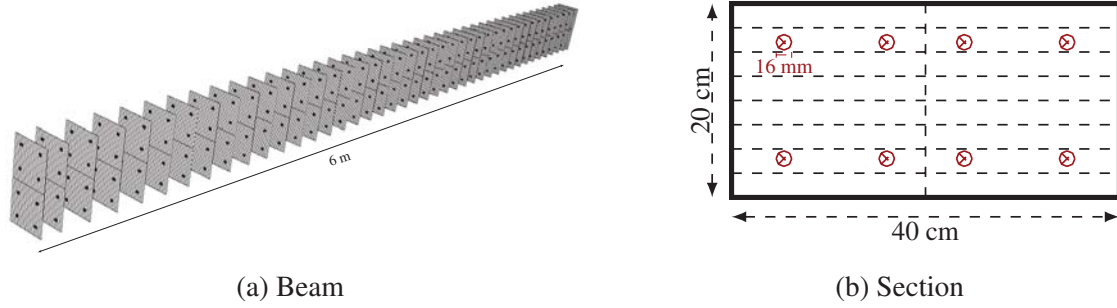


Figure 2: Beam geometry and discretization

To match experimental boundary conditions and beam undamaged properties, spring elastic supports are considered. Spring rotational and translational stiffnesses are calibrated from modal analyses performed on undamaged beam, considering a global symmetrical problem. The aim is to match the two first numerical eigen-frequencies with those deduced from experimental hammer shock tests. Finally, additional masses are added at the quarter and three-quarter beam span, and vertical displacements are blocked at those nodes. For quasi-static analyses, displacements are imposed at additional masses positions, and for dynamic computations, a force equivalent loading is derived from measured table accelerations.

## 2.2 Material constitutive models

**Concrete model** Two hysteretic models developed in Cast3m are compared in numerical studies. First a simple model, named BARFRA, was proposed by Crambuer [7]: the only dissipative phenomena considered is concrete cracking. The second model, named RICBET and developed by Richard [8] is more complex because it considers four dissipative phenomena: (i) cracking and (ii) friction in tension, (iii) plasticity in compression, as well as (iv) the unilateral effect dissipating energy upon crack closing. Thermodynamic potentials of both models are respectively expressed in equations 1 and 2. Computations of energy dissipations in section 3.1 of the paper will be deduced from those equations.

$$\rho\psi = \frac{1}{2}(1 - d_+)\langle\varepsilon_{ij}\rangle_+ C_{ijkl} \langle\varepsilon_{kl}\rangle_+ + H_+(z_+) + \frac{1}{2}(1 - d_-)\langle\varepsilon_{ij}\rangle_- C_{ijkl} \langle\varepsilon_{kl}\rangle_- + H_-(z_-) \quad (1)$$

with  $\langle\varepsilon_{ij}\rangle_+$  and  $\langle\varepsilon_{ij}\rangle_-$  respectively the positive and negative parts of the strain tensor,  $C_{ijkl}$  the elastic tensor,  $d_+$  and  $d_-$  the damage index representing concrete cracking respectively for positive and negative strains and  $H_+(z_+)$  and  $H_-(z_-)$  the functions representing isotropic work

hardening respectively for positive and negative strains.

$$\begin{aligned} \rho\Psi = & \frac{1}{2} \left\{ (1 - D) (\varepsilon_{ij} - \varepsilon_{ij}^p) C_{ijkl} (\varepsilon_{kl} - \varepsilon_{kl}^p) \right\} + \frac{1}{2} \left\{ D (\varepsilon_{ij} - \eta \varepsilon_{ij}^\pi - \varepsilon_{ij}^p) C_{ijkl} (\varepsilon_{kl} - \eta \varepsilon_{kl}^\pi - \varepsilon_{kl}^p) \right\} \\ & + \frac{1}{2} \left\{ \gamma \alpha_{ij} \alpha_{ij} \right\} + H(z) + G(p) \end{aligned} \quad (2)$$

with  $D$  the damage index representing concrete tensile cracking,  $\varepsilon_{ij}^p$  the plastic strain tensor,  $\eta$  the variable associated to unilateral effect,  $\varepsilon_{ij}^\pi$  the strain tensor associated to friction,  $\gamma$  a parameter characterizing friction,  $\alpha_{ij}$  the tensor of kinematic work hardening (friction phenomenon) and  $H(z)$  and  $G(p)$  the functions representing isotropic work hardening (damage and plasticity phenomena).

Both models are calibrated on the experimental data obtained from quasi-static tests. The advantage of using the most complex model is to better represent hysteresis cycles.

**Steel model** For steel reinforcements a classical elastoplastic model is used. Typical parameter values are considered. Indeed, experimental tests were developed to avoid reaching nonlinearities in steel reinforcements, to represent what happens to structures subjected to moderate earthquake accelerations.

### 2.3 Dynamic problem

**General equation** After calibrating the model with quasi-static tests, non-linear dynamic computations can be performed. Dynamic equilibrium equation for a multi-degree-of-freedom (MDOF) nonlinear damped system is:

$$\mathbb{M} \cdot \ddot{\mathbf{U}} + \mathbb{C} \cdot \dot{\mathbf{U}} + \mathbf{f}_{int}(\mathbf{U}) = -\mathbb{M} \cdot \underline{\Gamma} \cdot \ddot{\mathbf{U}}_s \quad (3)$$

with  $\mathbb{M}$  the mass matrix,  $\mathbb{C}$  the damping matrix,  $\ddot{\mathbf{U}}$ ,  $\dot{\mathbf{U}}$  and  $\mathbf{U}$  respectively the acceleration, velocity and displacement of beam nodes,  $\mathbf{f}_{int}(\mathbf{U})$  the internal force characterizing the non-linear constitutive model,  $\ddot{\mathbf{U}}_s$  the seismic accelerations and  $\underline{\Gamma}$  is the influence vector given the direction of seismic excitation. So, only the damping matrix  $\mathbb{C}$  is unknown if  $\mathbf{f}_{int}$  can be assessed with confidence.

**Focus on damping matrix formulations** The most frequently used formulation for the damping matrix derived from Rayleigh's work [3]. It consists in a linear combination of mass and initial stiffness matrices. Mathematically, this model leads to a decoupled problem using the undamped modal basis enabling its solving. However, numerous papers present the limits of this damping model, synthesized by Hall [1]. That is why, the literature presents different alternative for Rayleigh damping formulation that improve computations by minimizing some Rayleigh damping limitations. Particularly, we can find the use of tangent or secant stiffness matrix instead of initial ones [9]. This requires recomputing the damping matrix several time during analysis, increasing computational time. But it is a way to consider non-linear behavior in Rayleigh damping. On the other hand, it was demonstrated that the mass proportional part leads to unrealistic damping forces because higher modes are very lightly undamped. So, some papers propose to remove the mass matrix to keep only the stiffness proportional part given a linear correlation between the damping ratio of each mode and its frequency [10].

In addition to Rayleigh-type formulations, modal damping formulations are often used in the literature. In those cases, the  $\mathbb{C}$  matrix is computed from modes determined from a modal analysis. For example, Wilson & Penzien [11] proposed such a formulation, as well as Chopra & McKenna [12] based on the choice of a damping ratio for  $N$  modes.

Herein, sixteen equivalent viscous damping formulations have been studied and compared in relation to each other, but also with different damping ratios, and with or without parameters updating. When parameters are updated during computation, modal analyses are performed at each time step and the new frequencies are considered to compute the damping matrix. Table 1 presents the classification and name of all studied Rayleigh type and modal damping formulations.

	Formulation	Modes*	Parameter updating		Formulation	Modes*	Parameter updating
<b>RD</b>	Classical Rayleigh damping	1 and 2	✗	<b>CRD</b>	Commit-stiffness Rayleigh damping	1 and 2	✗
<b>RD_ACT</b>	Classical Rayleigh damping	1 and 2	✓	<b>CRD_ACT</b>	Commit-stiffness Rayleigh damping	1 and 2	✓
<b>MPD</b>	Mass proportional damping	1	✗	<b>SRD</b>	Secant-stiffness Rayleigh damping	1 and 2	✗
<b>MPD_ACT</b>	Mass proportional damping	1	✓	<b>MD</b>	Modal damping	1 to 6	✗
<b>KPD</b>	Initial-stiffness proportional damping	1	✗	<b>MD_ACT</b>	Modal damping	1 to 6	✓
<b>KPD_ACT</b>	Initial-stiffness proportional damping	1	✓	<b>WPD</b>	Wilson-Penzien damping	1 to 6	✗
<b>CKPD</b>	Commit-stiffness proportional damping	1	✗	<b>CWPD</b>	Commit-stiffness Wilson-Penzien damping	1 and 2	✗
<b>SKPD</b>	Secant-stiffness proportional damping	1	✗	<b>SWPD</b>	Secant-stiffness Wilson-Penzien damping	1 and 2	✗

\* Modes 1 and 2 represents 89.6% of the beam effective modal mass.

Table 1: Global damping matrices ( $\mathbb{C}$ ) nomenclature

### 3 THEORETICAL DEVELOPMENTS

Using the developed multi-fiber model, the aim of this section is to focus on seismic energy dissipation-computations and transient damping evolution.

#### 3.1 Energy analyses

**Structural level** Energy balance is deduced from the integration of dynamic equations (eq. 4) [13], corresponding to equation 5, in absolute formalism:

$$\frac{1}{2} (\mathbb{M} \cdot \dot{\mathbf{U}}_a) \cdot \dot{\mathbf{U}}_a + \int (\mathbb{C} \cdot \dot{\mathbf{U}}) \cdot \dot{\mathbf{U}} dt + \int \mathbf{f}_{int}(\mathbf{U}) \cdot d\mathbf{U} = \int (\mathbb{M} \cdot \ddot{\mathbf{U}}_a) \cdot d\mathbf{U}_s \quad (4)$$

$$E_{k,a} + E_d + E_a = E_{i,a} \quad (5)$$

where  $E_{k,a}$ ,  $E_d$ ,  $E_a$  and  $E_{i,a}$  are respectively the absolute kinematic energy, the viscous damping energy, the absorbed energy (or internal energy) and the absolute injected energy. In the case of a linear behavior, the three left terms are easily computed respectively from mass, damping and stiffness matrices. However, when a nonlinear constitutive model is considered, the absorbed energy is decomposed between the strain energy (corresponding to the elastic part) and the hysteretic energy deduced from thermodynamical approach. The right energy balance term, the injected energy, corresponds to the energy induced by the seismic acceleration.



**Local level** At material level, the hysteretic energy is now defined for both constitutive models in Table 2, with phenomenon and associated variables presented in Table 3 for BARFRA model and in Table 4 for RICBET model.

Name	Symbol	Equation	
		BARFRA	RICBET
<b>Hysteretic energy</b>	$E_h$	$\int_{\mathcal{V}} (Y.\dot{d}) d\mathcal{V}$	$\int_{\mathcal{V}} (\sigma_c.\dot{\varepsilon}_c^p + \sigma^\pi.\dot{\varepsilon}^\pi + Y.\dot{d} + \zeta.\dot{\eta}) d\mathcal{V}$
<b>Concrete strain energy</b> (elastic recoverable)	$E_{s,c}$	$\int_{\mathcal{V}} (\sigma_c.\dot{\varepsilon}_c - Y.\dot{d}) d\mathcal{V}$	$\int_{\mathcal{V}} (\sigma_c.\dot{\varepsilon}_c - \sigma_c.\dot{\varepsilon}_c^p - \sigma^\pi.\dot{\varepsilon}^\pi - Y.\dot{d} + \zeta.\dot{\eta}) d\mathcal{V}$
<b>Steel strain energy</b> (elastic recoverable)	$E_{s,s}$	$\int_{\mathcal{V}} (\sigma_s.\dot{\varepsilon}_s^e) d\mathcal{V}$	$\int_{\mathcal{V}} (\sigma_s.\dot{\varepsilon}_s^e) d\mathcal{V}$
<b>Work hardening</b>	$W_h$	$\int_{\mathcal{V}} (Z.\dot{z}) d\mathcal{V}$	$\int_{\mathcal{V}} (R.\dot{p} + X.\dot{\alpha} + Z.\dot{z}) d\mathcal{V}$
<b>Dissipated energy</b>	$E_{dis}$	$\int_{\mathcal{V}} (Y.\dot{d} - Z.\dot{z}) d\mathcal{V}$	$\int_{\mathcal{V}} (\sigma_c.\dot{\varepsilon}_c^p + \sigma^\pi.\dot{\varepsilon}^\pi + Y.\dot{d} + \zeta.\dot{\eta} - R.\dot{p} - X.\dot{\alpha} - Z.\dot{z}) d\mathcal{V}$

Table 2: Absorbed energy decomposition

Observable	Internal	Associated forces	Phenomena
$\varepsilon$	$\longrightarrow$	$\sigma$	Elasticity
	$d_+ \longrightarrow$	$Y_+$	Damage ( $\varepsilon > 0$ )
	$d_- \longrightarrow$	$Y_-$	Damage ( $\varepsilon < 0$ )
	$z_+ \longrightarrow$	$Z_+$	Damage ( $\varepsilon > 0$ )
	$z_- \longrightarrow$	$Z_-$	Damage ( $\varepsilon < 0$ )

Table 3: BARFRA model variables

Observable	Internal	Associated forces	Phenomena
$\varepsilon$	$\longrightarrow$	$\sigma$	Elasticity
	$\varepsilon^\pi \longrightarrow$	$\sigma^\pi$	Friction
	$\varepsilon^p \longrightarrow$	$\sigma$	Plasticity
	$\alpha \longrightarrow$	$X$	Friction
	$d \longrightarrow$	$Y$	Damage
	$z \longrightarrow$	$Z$	Damage
	$\eta \longrightarrow$	$\xi$	Unilateral effect
	$p \longrightarrow$	$R$	Plasticity

Table 4: RICBET model variables

### 3.2 Viscous damping identification method

To study the evolution of viscous damping during nonlinear dynamic computations, an identification method using a single degree-of-freedom model, equivalent to the global structural beam, is developed.

**Coupling of modes** When the projection on a modal basis is used to solve a dynamic problem, orthogonality of mode is implemented. But, if the damping matrix evolves during computation,

for example by considering the tangent stiffness matrix, the orthogonality can be altered. So, to evaluate the evolution of modes orthogonality along computation, the matrix  $\mathbb{C}^{mod}$  is computed at different time steps. This matrix is composed by the terms  $C_{ij}^{mod}$  in equation 6.

$$C_{ij}^{mod} = \underline{\phi}_i \cdot \mathbb{C} \cdot \underline{\phi}_j \quad \forall (i, j) \in \llbracket 1; N \rrbracket^2 \quad (6)$$

where  $\{\underline{\phi}_i\}_{i \in \llbracket 1; N \rrbracket}$  are the modes determined by a modal analysis on a linear system. So, only matrix  $\mathbb{C}$  is evolving during computation in equation 6. By computing  $\mathbb{C}^{mod}$  at different damage levels during dynamic computations, we did not observe significant coupling development. So the resolution of dynamic equation on modal basis remains herein acceptable, even when the tangent stiffness matrix is used.

**Modal basis projection** Equivalent model of structural element is obtained using a projection of dynamic equation (eq. 3) on modal basis  $\mathcal{B} = \{\underline{\phi}_i\}_{i \in \llbracket 1; N \rrbracket}$ . Displacement vector is defined as a linear combination of modes:  $\mathbf{U} = \sum_{i=1}^N a_i \cdot \underline{\phi}_i$  with orthogonal modes:  $\underline{\phi}_i \cdot \mathbb{M} \cdot \underline{\phi}_j = \delta_{ij} \cdot m_i$  and  $\underline{\phi}_i \cdot \mathbb{K} \cdot \underline{\phi}_j = \delta_{ij} \cdot k_i$  where  $\delta_{ij}$  is Kronecker index, and  $m_i$  and  $k_i$  are respectively the mass and the stiffness associated to mode  $i$ . Generally, the basis is mass-normalized, so  $m_i = 1$  and  $k_i = \omega_i^2$  where  $\omega_i = 2\pi f_i$  with  $f_i$  the frequency associated to mode  $i$ .

The first mode is representing more than 90% of modal mass, therefore the projection will be done on the first mode only. The displacement is expressed as  $\mathbf{U} = a_1 \cdot \underline{\phi}_1$  where  $a_1$  is time dependent. So, equation 3 in a linear case, and projected on the first mode, becomes equation 7, and then equation 8 on a normalized format:

$$\ddot{a}_1 \cdot \underline{\phi}_1 \cdot \mathbb{M} \cdot \underline{\phi}_1 + \dot{a}_1 \cdot \underline{\phi}_1 \cdot \mathbb{C} \cdot \underline{\phi}_1 + a_1 \cdot \underline{\phi}_1 \cdot \mathbb{K} \cdot \underline{\phi}_1 = -\underline{\phi}_1 \cdot \mathbb{M} \cdot \underline{\Gamma} \cdot \ddot{\mathbf{U}}_s \quad (7)$$

$$\ddot{a}_1 + 2\xi\omega_0 \cdot \dot{a}_1 + \omega_D^2 \cdot a_1 = -\frac{\kappa_1}{m_1} \cdot \ddot{u}_s \quad (8)$$

where  $\xi$  is the viscous damping ratio,  $\omega_0$  the initial eigen-frequency,  $\omega_D$  represents a "damaged" eigen-frequency,  $\kappa_1 = \underline{\phi}_1 \cdot \mathbb{M} \cdot \underline{\Gamma}$  is the projection coefficient and  $\ddot{u}_s$  is the seismic acceleration.

**Method presentation** Demarie & Sabia [15] proposed a non-linear and non-parametric method to identify non-linear damping and frequency of damaged reinforced concrete elements. The method developed herein is based on this approach. Despite the non-linearity in the studied time responses, we consider that it is possible to decompose the signal in  $n_w$  windows, such that in each time window the system response can be considered linear. That is to say that, in each window, we are able to evaluate a viscous damping ratio  $\xi_w$  and a damage eigen-frequency  $\omega_{D,w}$  from equation 8 reduced to the window  $w$ .

After having projected data on the modal basis, a function to identify  $f_{id}$  has to be defined, as well as windows characteristics. On each window, a minimization algorithm is performed to find the best pair of parameters  $(\xi_w, \omega_{D,w})$  using the objective function in equation 9:

$$\varepsilon_w = \frac{\int_{t=0}^{t_w} (f_{id,w} - f_{c,w})^2 dt}{\int_{t=0}^{t_w} (f_{id,w})^2 dt} \quad (9)$$

where  $f_{id,w}$  and  $f_{c,w}$  are, respectively, the function to identify and the computed function, reduced to the window  $w$ . Finally, by applying the minimization algorithm in all windows, we obtain the evolution of identified parameters all along the computation.

## 4 STUDIES ON DAMPING MODELS

### 4.1 Dynamic response of the beam

**Comparison of classical damping matrix** The first dynamic signal has a very low amplitude. Experimentally, this white-noise signal was performed to characterize the undamaged modal properties of the beam. Numerical responses are well matching experimental ones and we found a first mode eigen-frequency with less than 3% of error with almost all tested damping formulations. A damping ratio around 0.5% is required to compute Rayleigh-type matrices.

Then, non-linearities development is studied by applying a high amplitude decreasing sine sweep signal (fig. 3). Damping matrix formulations are compared with experimental data in terms of displacement, acceleration and from constitutive law responses. Viscous damping ratios varying between 0.5% and 5% have also been studied. On the contrary to the first linear test, viscous damping ratios around 2% are most appropriate. This value is smaller than the 5% often recommended in engineering codes because of the dissipative model used at local scale, the no-yielding of steel reinforcements and the modest strains and stresses responses. It appears that the viscous damping ratio is strongly dependent on input signal, damping formulations and levels of stress, strain and damage. So, it is impossible to propose a general viscous damping ratio working for all experimental vs numerical simulations. This represents a very significant limitation of viscous damping models computed from classical matrices.

To compare damping matrix formulations, figure 4 synthesizes different results as (i) the error between experimental and numerical data for displacements, accelerations and force responses and (ii) the error in the evolution of eigen-frequencies, and (iii) energy criteria. The best damping formulations are the one given the largest area in spider diagrams. Some formulations are better for some criteria than others. We are still able to say that the most appropriate damping formulations are Rayleigh damping (CRD) and stiffness proportional damping (CKPD) both with the use of tangent stiffness.

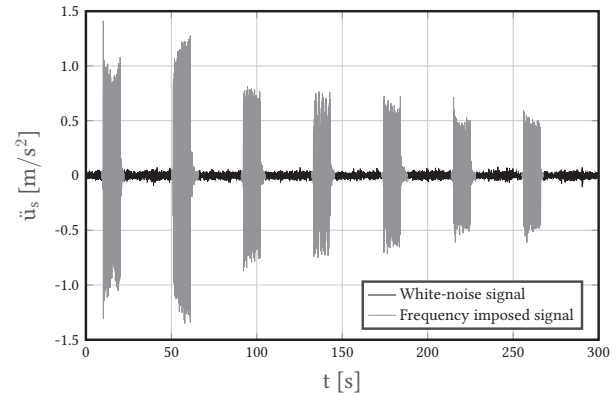


Figure 3: Decreasing sinus sweep - DSS85b

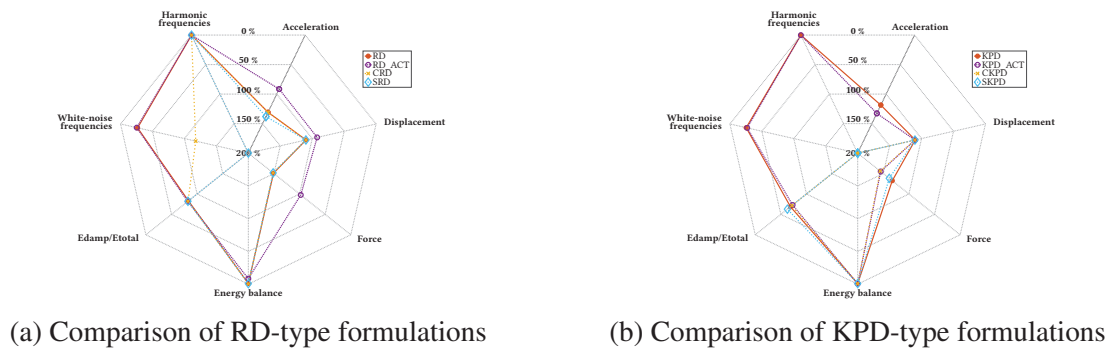


Figure 4: General comparison of damping formulations

**Energy dissipations** Energies presented in equation 5 are plotted in figure 5a for CKPD damping matrix formulation with a viscous damping ratio of 2% in case of a damageable (cracking) test (DSS) and with RICBET constitutive model. What is of interest, in this figure, is the distribution of energy between viscous damping and internal local material mechanisms. Indeed, kinematic energy represents a very small part of total energy and is recoverable, so it is null at the end. Generally, viscous damping energy dissipates the most energy. Only stiffness proportional damping matrix leads to a distribution almost 50%/50%. This demonstrates that even with a complex material model, a large amount of energy lacks to be dissipated at material level and has to be dissipated by equivalent viscous damping. Undoubtedly, decreasing the viscous damping ratio leads to a most equal distribution of the two dissipative energy but we saw in dynamic responses that a very small viscous damping ratio does not allow to match experimental data. Finally, to be able to reduce the requirement of viscous damping, we have to dissipate more energy at the material level.

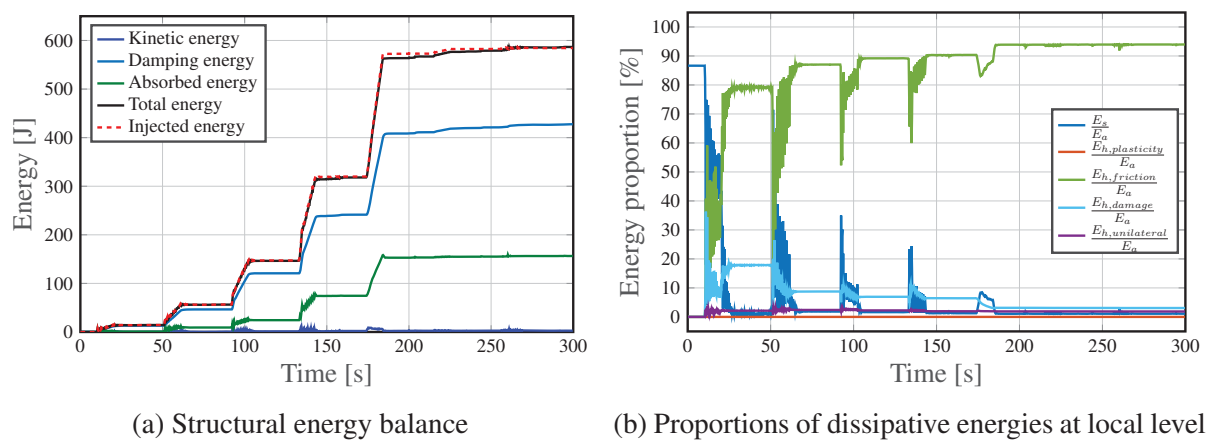


Figure 5: Energy analyses

The RICBET model takes into consideration four dissipative phenomena. Figure 5b focuses on hysteretic and strain energies, at local scale. In the beginning, the beam behaves linearly, so no dissipation occurs and strain energy is dominating. Then, cracks open and damage associated energy is dissipated. As soon as cracks open, because they are submitted to an oscillating signal, friction between crack lips develops. We observe that friction fast becomes dominating. When, a mono-harmonic signal segment excites the beams more strongly, cracks pattern evolves leading to an increase in the cracking associated energy proportion (crack propagation) at the expense of friction energy. Finally, plasticity is not dissipating energy because we do not reach concrete compressive non-linearities. Unilateral effect dissipates a small amount of energy during all computation after development of non-linearities.

As a conclusion, we can say that viscous energy is still representing a major part of all dissipative energies demonstrating again the lack of knowledge around the physical representation of local dissipative mechanisms. And, in the case of linear response of steel reinforcements, but nonlinear concrete behavior, the main concrete local dissipative phenomena is the friction, so works should focus on that phenomenon.

## 4.2 Damping coefficient evolution

Identification method can be applied on experimental or numerical data. Figure 6 particularly focuses on experimental data of two tests. Green data correspond to the lowest amplitude signal (with a maximum acceleration of  $1.25 \text{ m/s}^2$ ) while blue data correspond to the strongest signal (with a maximum acceleration of  $2.25 \text{ m/s}^2$ ). The first test leads to a maximal damage index (modelling the stiffness reduction due to cracking) around 0.6 what we also observed in identification of numerical data. But, in terms of viscous damping ratio, green data are staying around 5% experimentally while much stronger values are obtained with numerical identification. This demonstrates that the multi-fiber numerical model is not able to dissipate enough energy at the local scale and that a stronger influence has to be given to viscous damping in numerical computations. This is a huge limitation for the use of viscous damping in non-linear structural analyses.

To conclude on experimental data, the combination of the two more damageable tests shows that the viscous damping ratio can be defined as an exponential (eq. 10) or a polynomial (eq. 11) function of the cracking damage index.

$$\xi_{expon} = (2.96 \times 10^{-3}) \times \exp(4.75 \cdot d) \quad (10)$$

$$\xi_{ratio} = \frac{-62.1 \cdot d + 385}{d^2 - 1.36 \times 10^4 \cdot d + 1.41 \times 10^4} \quad (11)$$

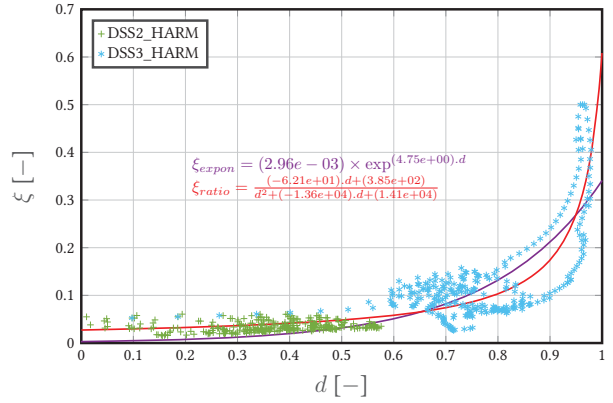


Figure 6: Experimental evolution of identified damping coefficient



## 5 CONCLUSIONS

The modeling of damping in structural non-linear dynamic computations was discussed in this paper using different analyses. First, an exhaustive numerical campaign was performed to characterize dissipations in reinforced concrete elements submitted to earthquake excitations and tested on a shake table. Particularly, sixteen classical damping matrix formulations proposed in literature have been compared. Results demonstrate that it is difficult to determine one type of damping working for all signal intensities. The damping formulation has to be selected depending on input signal intensity. However, using tangent stiffness matrix in Rayleigh damping formulation with or without the mass proportional part appears the best choice herein to represent the dynamic experimental responses. Rayleigh damping matrix evaluation requires to impose damping ratios for some modes frequencies. Analyses performed on multi-fiber model as well as on identification studies with a 1D model show that a constant value of damping ratio all along computation does not give accurate results when non-linearities occur. Exponential evolutions of damping coefficient as a function of internal damage characterized by stiffness degradation due to concrete cracking seems to better model physical phenomena and so to improve correlation with experimental data.

The works to follow will propose a new formulation of damping matrix based on local variables. The aim is to increase physical basis of the damping matrix. Preliminary results are showing good accuracy in comparisons with experimental data. But some developments still remain to compare local variables associated to different phenomena, like friction, and determine predictive functions to compute damping matrix.

## ACKNOWLEDGMENTS

- The authors wish to thank SEISM Institute for financing a part of the research and development performed at École Polytechnique of Montréal.
- This work was performed using HPC resources from the "Mésocentre" computing center of CentraleSupélec and École Normale Supérieure Paris-Saclay supported by CNRS and Région Île-de-France (<http://mesocentre.centralesupelec.fr>).

## REFERENCES

- [1] J. F. Hall, Problems encountered from the use (or misuse) of Rayleigh damping. *Earthquake Engineering and Structural Dynamics*, **35**:525–545, 2005.
- [2] T. Heitz, A. Le Maout, B. Richard, C. Giry, F. Ragueneau, Dissipations in reinforced concrete components: Static and dynamic experimental identification strategy. *Engineering Structures*, **163**:436–451, 2018.
- [3] J. W. S. B. Rayleigh, The theory of sound - Volume II. *Macmillan*, 1896.
- [4] E. Spacone, F. C. Filippou, F. F. Taucer, Fiber beam-column model for non-linear analysis of R/C frames: Part I. Formulation. *Earthquake Engineering & Structural Dynamics*, **25**(7):711-725, 1996.
- [5] S. Moulin, Code\_Aster : Élément de poutre multifibre (droite). Manuel de Référence R3.08.08, 2010.
- [6] S. Capdevielle, Comportement des grands ouvrages de Génie Civil - Modélisation par éléments poutres multifibres. PhD thesis, 2017.
- [7] R. Crambuer, Contribution à l'identification de l'amortissement : Approches expérimentales et numériques. PhD thesis, 2013.
- [8] B. Richard, F. Ragueneau, Continuum damage mechanics based model for quasi brittle materials subjected to cyclic loadings: Formulation, numerical implementation and applications. *Engineering Fracture Mechanics*, **98**:383-406, 2013.
- [9] M. J. N. Priestley, D. N. Grant, Viscous damping in seismic design and analysis. *Journal of Earthquake Engineering*, **09**(2):229-255, 2005.
- [10] L. Petrini, C. Maggi, M J. N. Priestley, G. M. Calvi, Experimental verification of viscous damping modelling for inelastic time history analyzes. *Journal of Earthquake Engineering*, **12**(1):125-145, 2008.
- [11] E. L. Wilson, J. Penzien, Evaluation of orthogonal damping matrices. *International Journal for Numerical Methods in Engineering*, **4**(1):5-10, 1972.
- [12] A. Chopra, F. McKenna, Modelling viscous damping in nonlinear response history analysis of buildings for earthquake excitations: Modal damping. *Earthquake Engineering & Structural Dynamics*, **45**(2):193-211, 2016.
- [13] C.-M. Uang, V. V. Bertero, Evaluation of seismic energy in structures. *Earthquake Engineering & Structural Dynamics*, **19**(1):77-90, 1990.
- [14] K. Low, A modified Dunkerley formula for eigenfrequencies of beams carrying concentrated masses. *International Journal of Mechanical Sciences*, **42**(7):1287-1305, 2000.
- [15] G. V. Demarie, D. Sabia, Non-linear damping and frequency identification in a progressively damaged R.C. element. *Experimental Mechanics*, **51**(2):229-245, 2011.
- [16] T. Heitz, C. Giry, B. Richard, F. Ragueneau, Identification of an equivalent viscous damping function depending on engineering demand parameters. *Engineering Structures*, **188**:637-649, 2019.

## NUMERICAL STUDY ON THE DAMPING CHARACTERISTICS OF A SHOCK ABSORBER VALVE UTILIZING DIFFERENT VELOCITIES THROUGH CFD ANALYSIS

Yousif Badri<sup>1</sup>, Thaer Syam<sup>1</sup>, Sadok Sassi<sup>1\*</sup>, Mohammed Hussein<sup>2</sup>, Jamil Renno<sup>1</sup>,  
Saud Ghani<sup>1</sup>

<sup>1</sup>Department of Mechanical and Industrial Engineering, College of Engineering, Qatar University,  
Doha, Qatar

<sup>2</sup>Department of Civil and Architectural Engineering, College of Engineering, Qatar University,  
Doha, Qatar

<sup>1\*</sup>Corresponding author

**E-mail:** <sup>1</sup>yb1903174@qu.edu.qa, <sup>1</sup>thaer@qu.edu.qa, <sup>1\*</sup>sadok.sassi@qu.edu.qa,  
<sup>2</sup>mhusein@qu.edu.qa, <sup>1</sup>jamil.renno@qu.edu.qa, <sup>1</sup>s.ghani@qu.edu.qa

**Abstract.** Shock absorbers or hydraulic dampers are power dissipating devices. The fluid flow inside the damper is governed by predefined passages. The damping effect is accomplished by the resistance of oil to flow through the restrictions. The impact of the viscosity and the velocity of the oil determines the fluid flow behaviour and hence, the resulting damping effect. The piston inside the damper has various orifices or piston valves that cause different flow losses. These losses are observed during the extension and compression strokes of the damper. In the compression and extension strokes, rebound and compression pressures are developed at the damper orifice. In this work, Computational Fluid Dynamics (CFD) analysis is carried out on a rear side two-wheeler automobile mono tube damper to investigate the variation of the damping properties using viscous oils. Averaged Navier-Stokes equations are solved by the SIMPLE method and the RNG  $k-\epsilon$  is used to model turbulence. The piston contains eight orifices which separate the rebound and compression chambers of the damper. The numerical analysis used four values of velocity; 0.8, 1, 1.2, and 1.5 m/s. The viscous fluid model was SVI2.5, having viscosity value of 0.009 Pa.s. The damping coefficient values for rebound and compression sides were obtained based on their pressure values showed in the CFD contour plots. It was noticed that the increasing trend of damping coefficient is linearly for two velocity's intervals; (0.8-1) m/s and (1.2-1.5) m/s, and nonlinearly for velocity interval of (1-1.2) m/s.

**Keywords:** Hydraulic damper, viscosity, CFD, damping characteristics, orifice, and pressure contours.

## 1 INTRODUCTION

A shock absorber, or viscous damper, is mainly functioning to dampen body/suspension motions, control tire force variation, and dissipate impact energy. Hydraulic oil is passed between two chambers via a system of pressure sensitive flow restrictions. The damping effect is accomplished by the resistance of oil to flow through the restrictions. Most vehicular shock absorbers are either twin-tube or mono-tube types with some variations on these themes as shown in Fig. 1. Twin tube shock absorber consists of two nested cylindrical tubes, an inner tube that is called the "working tube" or the "pressure tube", and an outer tube called the "reserve tube". At the bottom of the device on the inside is a compression valve or base valve. When the piston is forced up or down, hydraulic fluid moves between different chambers via small holes or "orifices" in the piston and via the valve. The fluid movement converts the "shock" energy into heat which must then be dissipated. The mono-tube shock, which is a gas-pressurized shock and also comes in a coil over format, consists of only one tube, the pressure tube, though it has two pistons. The two pistons separate the shock's fluid and gas components. Mono tube shocks are typically found in trucks, vans, or vehicles used for hauling or transportation or driven in areas where harsh road conditions are common. While twin tube is found in cars and smaller SUVs, twin-tube shocks have a second cylinder specifically for internal fluid (Shams et al. [1]).

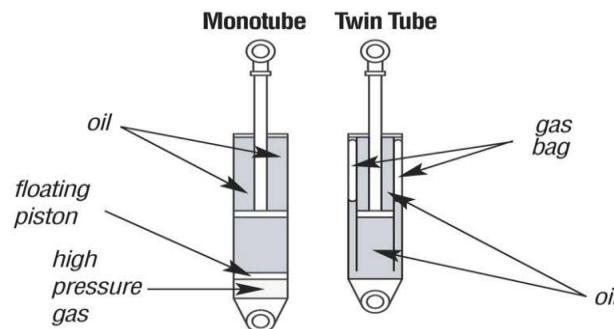


Fig. 1. Types of shock absorbers [1].

Generally, two main analytical models describe the viscous shock absorber behaviour; linear model, and generalized viscous damper model [2]. In linear model the damping force increases linearly as the velocity increases. On the other hand, generalized viscous model include the nonlinear behaviour of the damper force with respect to the change in velocity. The nonlinear behaviour provides a high damping force for the small vibration amplitudes (velocity). In viscous dampers, the linearity behaviour is governed by; orifice and damper geometry, fluid characteristics, and velocity of the vibrating structure. Many experimental studies were carried out to investigate the behaviour of fluid damper [3],[4]. For example, a recent experimental study conducted by Badri et al. [5] to investigate the effect of increasing velocity (increasing frequency) of mono tube damper in the damping coefficient value. In addition, numerical models are also used to characterize the viscous damper's damping effect. A physical model for a shock absorber was developed by Surace et al. [6]. This model provided a more realistic representation of the stiffness characteristics than previous simple models. Reybrouk et al. [7] presented a nonlinear physical model for predicting shock absorber performance. Dyum et al. [8] studied the mechanism of shock absorber rattling noise by valve behaviour analysis and CFD simulation. Herr et al. [9] identified valve parameters from several simple dynamometer tests and an additional incompressible model. These parameters

were then used to analytically determine valve flows for given pressure drops in the main model. Purdy et al. [10] evaluated the flow and performance of an automotive shock absorber by coupling a Computational Fluid Dynamics method with a dynamic modelling technique. They evaluated the pressure flow characteristics of the differing valve components using Computational Fluid Dynamics (CFD). Disk deformation information from finite element analysis simulations are incorporated into the calculation of blow-off valve opening. They obtained the damping force versus piston velocity curves. The radial flow of magnetic fluid under the piston of a magneto fluid shock absorber was studied by Tallec et al. [11]. Lee et al. [12] developed a non-linear model that includes the compressibility of the fluid, trapped gas and expansion of the cylinder. The performance of the shock absorber model was examined as the parameters were varied. Interaction of fluid and deformable structural parts in the shock absorber caused difficulties such as; compelling the kinematic compatibility at the fluid-structure interface and updating the geometry of the domain. Maikulal et al. [13] investigated the damping characteristics when the number of orifice holes changed using CFD. The numerical model results showed a nonlinear increase in the damping force with respect to the velocity increase.

In this paper, CFD simulations using ANSYS Fluent software is used to model a fluid flow inside the cylinder of a mono tube shock absorber. The damper's damping characteristics are investigated by changing the flow velocity using Rock Oil Rear shock fluid SVI2.5 oil as a viscous oil of the damper

This paper is outlined as follows; Section 1 introduces the topic and provides a literature review. Section 2 shows the methodology followed for the CFD starting from the governing equations and ending with the boundary conditions. Section 3 discusses the results and the main findings of this work. Finally, this paper ends at Section 4 which concludes and summarize the scope of this work as well as the main findings.

## **2 METHODOLOGY**

This work will follow a methodology used by Maikulal et al. [13], when a CFD model simulates the flow inside a viscous damper. Following the same approach, a mono tube damper with new orifice design will be characterized over different velocities. The model is characterizing the viscous damper by calculating the damping coefficient at compression and rebound side based on their damping forces. Damping forces when using SIV-2.5 oil is analysed for different velocities and the variation of damping coefficient value will be investigated. In this section, the internal damper's chambers will be discussed, followed by the equations used to obtain the damping forces regarding constant velocities.

### **2.1 Damping characteristics of a damper**

The scope of this work for the hydraulic damper is by identifying the damping action by allowing the hydraulic fluid (mainly a viscous fluid) to throttle through orifice in the piston (piston valve). The flow will be governed by the physical properties of the fluid such as viscosity and density, and the geometry of the piston valve (orifice). Mainly, the damper modelled for the CFD analysis is a piston cylinder system representing a mono tube shock absorber containing a hydraulic fluid as shown in Fig. 2 (a). The piston consists of; a rod and an orifice plate which connects two chambers (Chamber 1 and Chamber 2) showed in Fig. 2. The orifice plate has a small orifice which exposed to both piston sides and chambers of the



cylinder as shown in Fig. 2 (b). Chamber 1 represents the rebound piston side and chamber 2 represents the compression piston side.

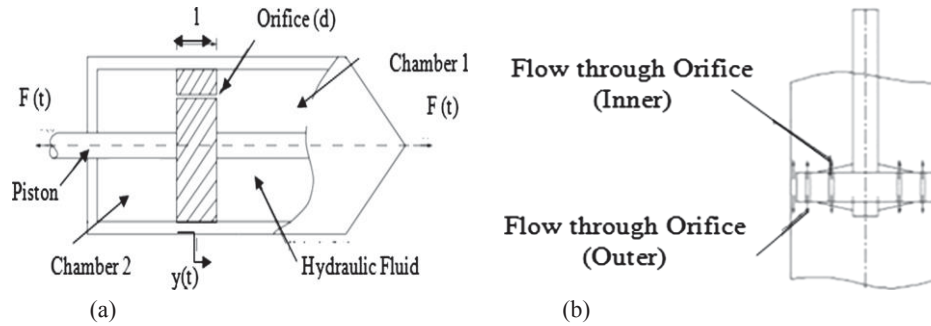


Fig. 2. Hydraulic fluid flow through orifices [13].

The damping force is proportional to the velocity, as for a linear viscous damper, the damping force ( $F_d$ ) may be related to the piston velocity ( $v$ ) by Leea et al. [14]

$$F_d = c \times v \quad (1)$$

where  $F_d$  = damping Force (N),  $c$  = Damping Coefficient (N.s/m),  $v$  = velocity of the piston (m/s).

The force of the piston in the two chambers is found by obtaining the pressure and the area on each piston side (compression and rebound). The force of the compression piston side is expressed by Guan et al. [15]

$$F_c = P_c \times A_c \quad (2)$$

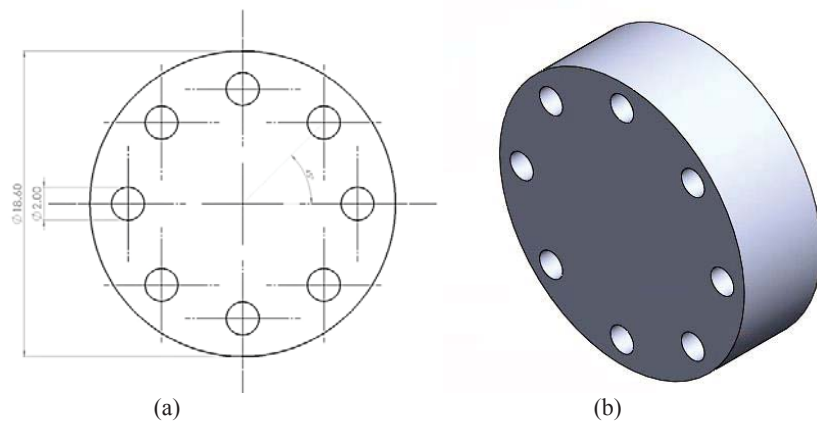
$$F_r = P_r \times A_r \quad (3)$$

where  $F_c$  and  $F_r$  are piston forces on compression and rebound side, respectively.  $P_c$  and  $P_r$  are the pressure on compression and rebound side (Pa),  $A_c$  and  $A_r$  are the area of piston on compression and rebound sides ( $m^2$ ).

### 3 NUMERICAL ANALYSIS

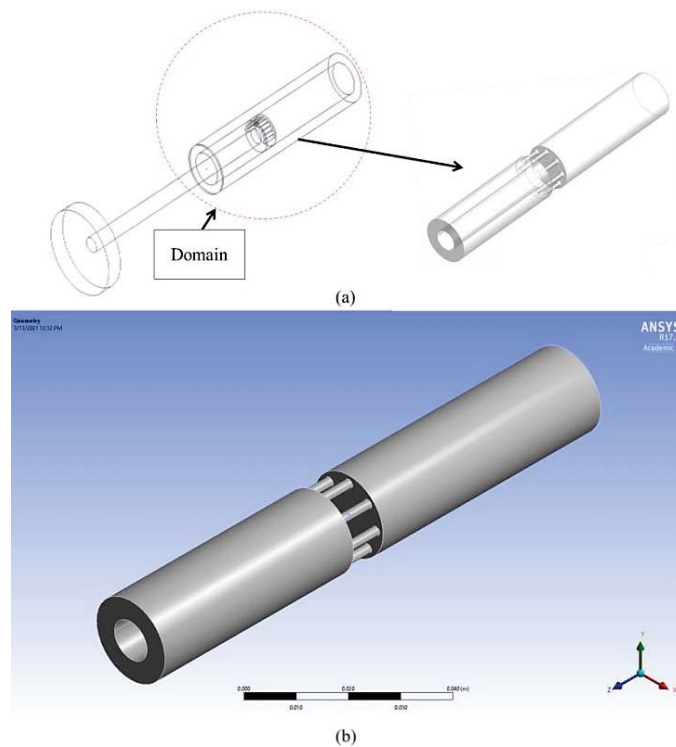
#### 3.1 3D CAD modeling

In this study the orifice geometry was reproduced from dimensions used in Maikulal et al. [13]. The orifices plate was redesigned by modifying the number, and location of the orifice holes. 8 orifice holes are placed near the edge of the plate separated by an angle ( $45^\circ$ ). Top view of the orifice plate is shown in Fig. 3 (a). Fig. 3 (b) shows the 3D CAD drawing of the plate.



**Fig. 3.** Orifice's geometry and orientation.

Fig. 4 shows the 3D drawing of the damper. The idea behind this model is that CFD simulation will be done inside the cylinder of the damper. This can be explained as the domain as shown in Fig. 4 (a); where the viscous oil will be moving through the orifice plate between the chambers at a specific velocity. Fig. 4 shows the 3D CAD model of the damper with 8 orifices in ANSYS.



**Fig. 4.** 3D CAD drawings of the damper.

The CFD analysis will be based on throttling the viscous oil through the orifice of the three different cases. This will require the drawing of the inside domain of the cylinder. The oil will be throttled between the two chambers. Therefore, the domain will appear as a solid, but it will be considered as fluid in the CFD simulations. The orifice plate is placed at the midpoint of the length of the cylinder which is 118 mm. The volume of the orifice plate and the rod

(piston) is subtracted so that the domain is only fluid throttling through the orifice for the different three cases.

### 3.2. Mesh generation and quality

Unstructured automatic fine meshing with 3D tetrahedral cells was used. The meshing smoothing chooses to be high, while having a normal curvature angle of  $15^\circ$ . The mesh responded to high gradient and curvature areas by providing more cells to those areas. By increasing the number of cells at the throttling area, while having fewer elements at areas near the inlet, and the outlet ensure accurate results with less computational time. The grid is then generated having 445076 elements with 87552 nodes, as shown in Fig. 5.

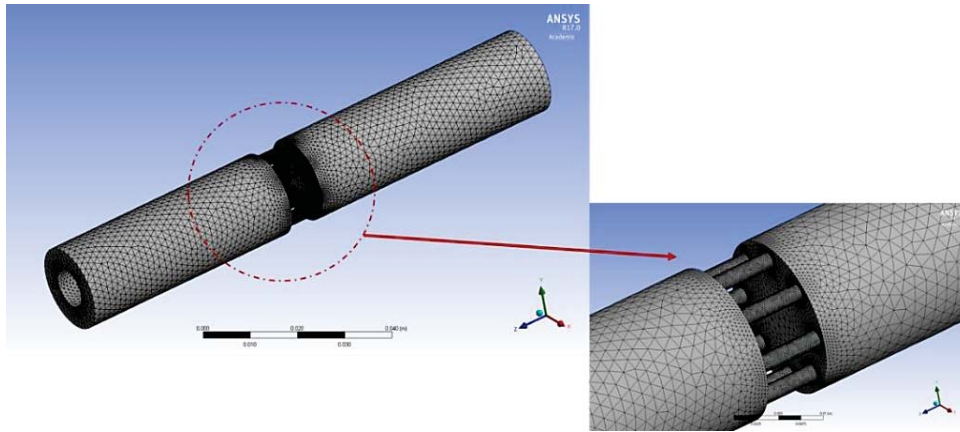


Fig. 5. Meshing.

### 3.3 CFD methodology, boundary conditions and simulation studies

The CFD modelling involves the numerical solution of the conservation equations in the laminar and turbulent fluid flow regimes. Therefore, the theoretical predictions were obtained by simultaneous solution of the continuity and the Reynolds averaged Navier-Stokes (RANS) equations. The governing equations for an incompressible flow are [16]

Conservation of mass:

$$\vec{\nabla} \cdot (\vec{v}) = 0 \quad (4)$$

Conservation of momentum:

$$\rho \left[ \frac{\partial(\vec{v})}{\partial t} + (\vec{v} \cdot \vec{\nabla}) \vec{v} \right] = \rho g - \nabla P + \mu \nabla^2 \vec{v} \quad (5)$$

Since the flow in the shock absorber is in a state of turbulent motion, it is important to use an appropriate turbulence model for evaluating the flow field. The standard  $k-\epsilon$  model is a semi-empirical model based on transport equations for the turbulent kinetic energy ( $k$ ) and its dissipation rate ( $\epsilon$ ). Improvements have been made to the model to improve its performance by the Realizable  $k-\epsilon$  model [20]. Realizable  $k-\epsilon$  model have shown substantial improvements over the standard  $k-\epsilon$  model where the flow features include strong streamline curvature, vortices and rotation. The flow governing equations are solved with ANSYS FLUENT 17R. A standard wall functions is used in order for wall treatment since the most focus is on

the orifice plate. The velocity and pressure coupling used the SIMPLE algorithm with a second order upwind spatial discretization for a pressure-based study.

#### 4. RESULTS AND DISCUSSION

Static pressure contours are required to identify the forces on the two orifice sides (rebound, compression). The pressure contours for the compression and rebound piston sides for one case are presented in Fig. 7 (velocity of 0.8 m/s and using SVI-25 oil; 0.009 Pa.s).

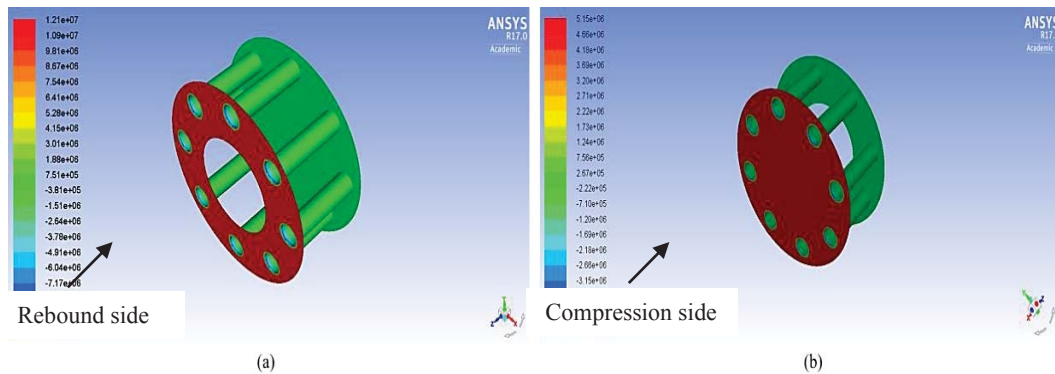
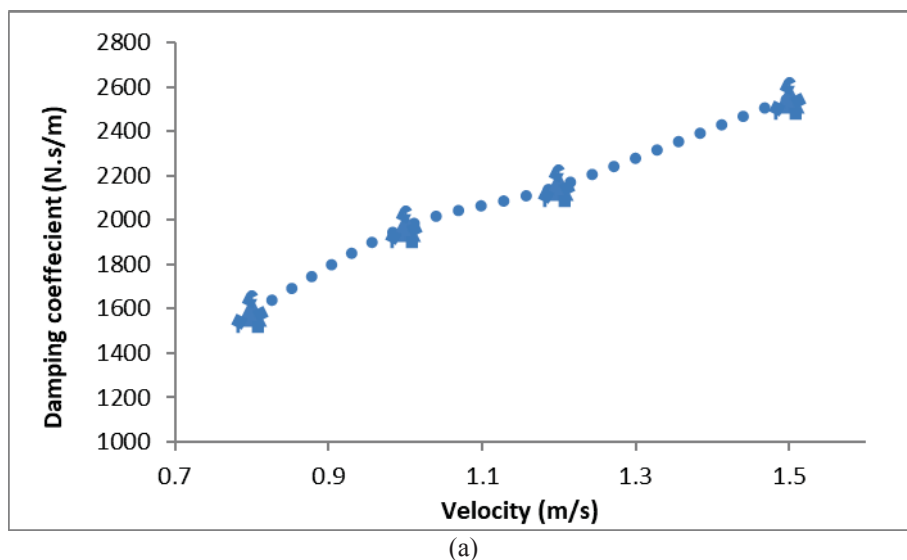


Fig. 6. Pressure contour for (a) rebound piston side, and (b) compression piston side.

The rebound-compression forces are calculated with respect to the maximum pressure value observed at the contour plot range. These forces are also related to the piston side surface areas. The compression side area is  $1.8569 \times 10^{-4} \text{ m}^2$ , and the rebound surface area is  $2.4649 \times 10^{-4} \text{ m}^2$ . The forces acting on small area (rebound) is greater than the forces acting on bigger area (compression) due to the pressure and area differences.



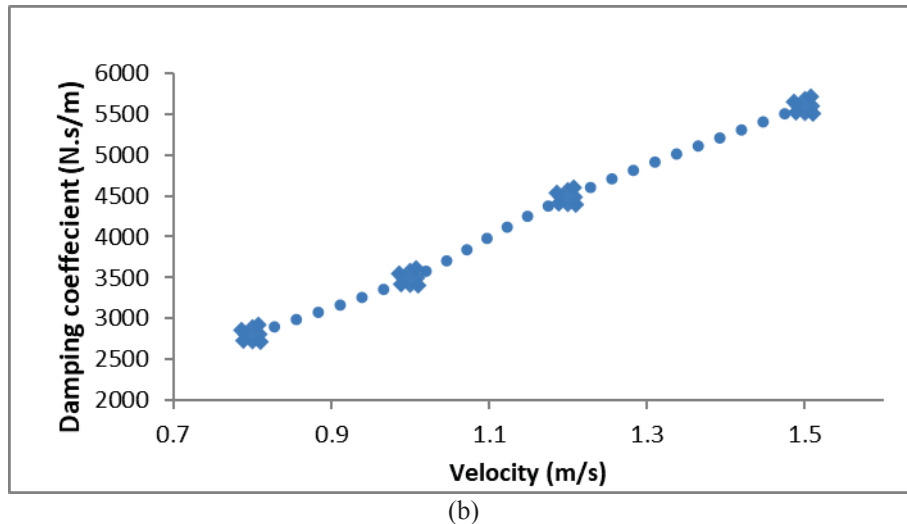


Fig. 7. Damping coefficient vs velocity (a) at the compression stroke (b) at the rebound stroke.

Damping values results are shown in Fig. 7 for the range of velocity of 0.8 m/s, 1 m/s, 1.2 m/s, and 1.5 m/s. Fig. 7 (a) shows the damping coefficient variation inside the compression chamber which was found to be; 1.59kN.s/m, 1.97kN.s/m, 2.15kN.s/m, 2.55kN.s/m, respectively. The damping coefficient inside the rebound chamber is shown in Fig. 7(b). The damping constant values with respect to the velocity range was found to be; 2.81kN.s/m, 3.5kN.s/m, 4.5kN.s/m, 5.6kN.s/m.

## 5 CONCLUSION

In this study, a CFD model was used to characterize a mono tube damper filled with SIV-2.5 oil over a range of velocity using Ansys 17 Fluent. The CFD model only takes into consideration the fluid chamber compressibility. However, the contribution of the internal friction in the damping force was omitted. Based on the obtained numerical damping coefficient values parametric the following was concluded:

- 1- Increasing the velocity tend to contribute in increasing the damping force, and hence the damping coefficient.
- 2- The damping values in both compression and rebound strokes are increasing linearly with the increase of velocity for two ranges; (0.8 - 1) m/s and (1.2 - 1.5) m/s. The damper is experiencing a nonlinear increase of the damping constant at the middle range of velocity of (1 - 1.3) m/s.
- 3- Using oil with low viscosity value (0.009 Pa.s) combines the linear-nonlinear behavior.

## REFERENCES

- [1] M. Shams and E. Reza (2007), "CFD-FEA analysis of hydraulic shock absorber valve behavior CFD-FEA ANALYSIS OF HYDRAULIC SHOCK ABSORBER VALVE,".



- [2] R. Greco and G. C. Marano, "A comparative study on parameter identification of fluid viscous dampers with different models," no. August, 2014.
- [3] D. I. Narkhede and R. Sinha, "Behavior of nonlinear fluid viscous dampers for control of shock vibrations," *J. Sound Vib.*, vol. 333, no. 1, pp. 80–98, 2014.
- [4] P. Torino, "Experimental determination of viscous damper parameters in low velocity ranges," no. July, 2017.
- [5] Y. Badri, M. Hussein, S. Sassi, and J. Renno, "Investigation of the Effect of the Force-Frequency on the Behaviour of a New Viscous Damper for Railway Applications," no. Cic, pp. 666–671, 2020.
- [6] Surace, C., Worden, K. and Tomlinson, G. R. (1992). An improved nonlinear model for an automotive shock absorber. *Nonlinear Dynamics* 3, 6, 413–429.
- [7] Reybrouck, K. (1994). A nonlinear parametric model of an automotive shock absorber. *SAE Paper No. 9400869*.
- [8] Morinaga, H., Kuboto, M. and Kume, H. (1997). Mechanism analysis of shock absorber rattling noise. *J. SAE Review* 18, 2, 198-198.
- [9] Reybrouck, K. and Duym, S. (1998). A physical and parametric model for nonlinear dynamic and temperature dependant behaviour of automotive shock absorbers. *Proc. 11th ADAMS Users Conf.*, Frankfurt.
- [10] Herr, F., Mallin, T., Lane, J. and Roth, S. (1999). A shock absorber model using CFD analysis and easy 5. *SAE Steering and Suspension Technology Symp.*, Detroit, Michigan, 267-281.
- [11] Krakov, M. S. (1999). Influence of rheological properties of magnetic fluid on damping ability of magnetic fluid shock absorber. *J. Magnetism and Magnetic Materials*, 201, 368-371.
- [12] Purdy, D. J. (2000). Theoretical and experimental investigation into an adjustable automotive damper. *Proc. Institution of Mechanical Engineers, Part D, J. Automobile Engineering* 214, 3, 265-283.
- [13] L. Maikulal, S. Singh, and S. M. Sawant (2016), "Fluid flow modeling and experimental investigation on automobile damper," *Constr. Build. Mater.*, vol. 121, pp. 760–772.
- [14] Choon-Tae Leea, Byung-Young Moonb (2004), Simulation and experimental validation of vehicle dynamic characteristics for displacement-sensitive shock absorber using fluid-flow modeling, *Proceeding of Mechanical Systems and Signal Processing*, vol. 20(2), Elsevier, pp. 373–388.

- [15] Changbin Guan, Zongxia Jiao, Shouzhan He (2014), Theoretical study of flow ripple for an aviation axial-piston pump with damping holes in the valve plate, *J. Aeronaut.* 27 (1) 169–181.
- [16] Gabriel J. DeSalvo and John A. Swanson. (1985). ANSYS engineering analysis system user's manual. Houston, Pa. :*Swanson Analysis Systems*,

## ENERGY HARVESTING FROM RAILWAY VIBRATIONS – A NUMERICAL STUDY BASED ON BEAM-ON-ELASTIC-FOUNDATION UNDER QUASI-STATIC LOADING

Shahd Elshafei<sup>1</sup>, Mohammed Hussein<sup>1</sup>, Jamil Renno<sup>2</sup>, and Asan Muthalif<sup>2</sup>

<sup>1</sup>Department of Civil & Architectural Engineering  
Qatar University, Doha 2713, Qatar  
e-mail: mhussein@qu.edu.qa

<sup>2</sup> Department of Mechanical & Industrial Engineering  
Qatar University, Doha 2713, Qatar  
e-mail: {jamil.renno,drasan}@qu.edu.qa

**Keywords:** energy harvesting, vibration energy harvester, stack harvester, ballasted track, passenger trains

**Abstract.** *The objective of this paper is to investigate energy harvesting of train-induced rail vibrations and to provide a comparison between various feasible harvesting locations based on the expected electrical power output. The vibrations of the railway track are modelled using the beam-on-elastic-foundation model under quasi-static loading. The loading applied is from a passenger train moving at a constant velocity. The vibrations of the railway track are then used to determine the energy harvested at each location using one-degree-of-freedom models. The numerical study concludes that the optimal configuration of the harvester is on the rail for the vibration harvester and as a harvesting rail pad between the sleeper and the rail for the compression harvester. The harvested energy with each configurations is  $\mathcal{O}(\sim 10^{-6})$  and  $\mathcal{O}(1)$  J/kg of harvester, respectively.*

## 1 Introduction

The use of energy harvesting systems has been explored in a wide array of systems ranging from biomedical application to condition monitoring systems. Zurbuchen et al. [1] developed a customized pacemaker which was tested to harvest energy from heartbeats while pacing the heart. Research in embedding piezoelectric harvesters into knee implants showed potential in improving patient experience and enhancing motion post-surgery [2]. Yip et al. [3] presented a fully-implantable cochlea for acoustic sensing of the middle ear. Akkaya and Özdemir [4] designed and tested a cost-effective piezoelectric energy harvester that converts wind energy into useful electric energy. Mekid et al. [5] even investigated the worthiness of energy harvesting from ambient radio frequency.

To optimize the operational life of a helicopter blade, Jong et al. [6] recommended a compression (stack-type) harvester designed to monitor blade health and transmit information to the aircraft using mechanical energy. A compression harvesting system under pavements was developed by Jiang et al. [7] to investigate the feasibility of powering transport infrastructure using traffic-induced vibrations. Zhang et al. [8] conducted comprehensive simulations of various bridge properties under different loading conditions and analysed their impact on vibration-based energy harvesting. Recently, Bendine et al. [9] proposed using a vibration energy harvester in the form of a cantilever beam to harvest vibration energy from a bridge subjected to time-dependent moving loads.

This paper targets promoting energy harvesters by proposing five suitable energy harvesting configurations using vibration and stack harvesting technologies. In this paper, energy harvesting from five locations on a ballasted track using two different harvesters is investigated. The two harvesters are: vibration harvesters and compression harvesters. The vibration harvester is studied at two locations: (a) attached to the rail and (b) attached to the sleeper. The compression harvester is studied at three locations: (a) between the rail and rail pad, (b) between the rail pad and sleeper and (c) as a rail pad.

The remainder of this paper is organized as follows. In Section 2, a numerical model for the vibration of the train loading, the vibration of the track and the dynamics of the energy harvesters are presented. The models adopted for describing rail vibration and energy harvesting are described in section 2 and section 3, respectively. Section 4 presents the simulation results and analyses the energy harvesting capability of each of the five configurations for various train speeds. Conclusions for this work are drawn in section 5.

## 2 Rail Vibration and Energy Harvesting

In this section, a model for the vibration of a railway track is presented. Then, approaches to harvest energy from rail vibration will be briefly reviewed.

### 2.1 Railway Track Model

The loading applied on the rail is determined based on a typical passenger train. This choice is arbitrary and is only used for the purpose of advocating the adoption of energy harvesting capabilities in the railway sector. The developed model allows for adjustments that can later be made to accommodate for any train type. For simplification, this study considers a train made of four passenger cars of equal geometry and weight.

To calculate the loading applied by each passenger car the following is assumed:

1. The maximum seating and standing capacity is 376 passengers and thus the total weight observed accounts for the difference in the tare weight of each car type.

2. The weight of the train is equally distributed between the cars and the weight of each car is equally distributed between eight wheels.
3. The load is transmitted to the rail as vertical point loads.

Four train speeds will be considered in the numerical simulations: 20, 40, 80 and 160 km/h. The mathematical model used to establish the train-induced vibrations of a ballasted track is the Winkler mathematical model. In order to conform to this model, the two rails in a typical track system are modelled as a single continuously-supported infinite elastic beam. The loading applied by two parallel wheels on the rail is combined to produce a single quasi-static, vertical load. Superposition is enforced to take into account the influence of successive wheels on an arbitrary location of the track, i.e., the harvester's location  $z$  as shown in Figure 1.

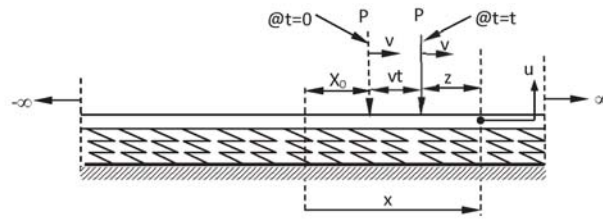


Figure 1: A beam on Elastic Foundation (Winkler model) subjected to a point load.

The vertical rail displacement  $u_r$  at any location  $z$  is given by:

$$u_r(t) = -\frac{P}{8EI\lambda^3}e^{-\lambda|z|}[\cos(\lambda|z|) + \sin(\lambda|z|)] \quad \text{with} \quad \lambda = \sqrt[4]{\frac{k}{4EI}} \quad (1)$$

where  $EI$  is the bending stiffness of the beam representing the two rails and  $k$  is the stiffness of foundation per unit length.

For a load  $P$  moving with a constant velocity  $v$  that is lower than the critical wave velocity of the track (i.e., quasi-static), and given that the load is at position  $x_0$  at time  $t = 0$  (see Figure 1), the response of the beam at point  $x$  and time  $t$  can be calculated by substituting  $z = x - x_0 - vt$  in Equation 1.

The direct differentiation of Equation 1, the velocity and acceleration of the rail are numerically evaluated in preparation for the dynamic analysis in Section 3. The velocity and acceleration of the track can be obtained as:

$$v_r(t) = \begin{cases} -\frac{Pv}{4EI\lambda^2}e^{-\lambda z}[\sin(\lambda z)] & \forall z \geq 0 \\ -\frac{Pv}{4EI\lambda^2}e^{\lambda z}[\sin(\lambda z)] & \forall z \leq 0 \end{cases} \quad (2)$$

$$a_r(t) = \begin{cases} \frac{Pv^2}{8EI\lambda}e^{-\lambda z}[\cos(\lambda z) - \sin(\lambda z)] & z \geq 0 \\ \frac{Pv^2}{8EI\lambda}e^{\lambda z}[\cos(\lambda z) + \sin(\lambda z)] & z \leq 0 \end{cases} \quad (3)$$

## 2.2 Rail Stiffness

Due to the variation in the components and their respective characteristics, in order to simulate the track as a whole system the stiffness of the various components were combined. In the simulated cases, the track components from top to bottom consist of the rail (denoted by



subscript  $r$ ), rail pads (denoted by subscript  $rp$ ), sleepers (denoted by subscript  $s$ ), ballast foundation (denoted by subscript  $b$ ) and the ground (denoted by subscript  $g$ ). As the rail displacement considered is at the web of the rail, the equivalent stiffness ( $k_e$ ) of the track system is determined using the stiffness of the components in series.

$$\frac{1}{k_e} = \frac{1}{k_{rp}} + \frac{1}{k_s} + \frac{1}{k_b} + \frac{1}{k_g} \approx \frac{1}{k_{rp}} + \frac{1}{k_b}$$

Since the stiffness of both the sleeper  $k_s$  and ground  $k_g$  are significantly larger than that of the ballast and rail pad, then

$$\frac{1}{k_e} \approx \frac{1}{k_{rp}} + \frac{1}{k_b}$$

In the following simulations, the following numerical values will be used: the bending stiffness  $EI$  is assumed to be  $2.52 \times 10^7 \text{ Nm}^2$  and the equivalent stiffness  $k_e$  is  $1.66 \times 10^8 \text{ N/m}$  as per the work of Cleante et al. [17].

### 2.3 Base-Excitation Energy Harvesters

The first systems that were developed to harvest energy from rail vibration were track-mounted [18]. Such harvesters rely on base-excitation ensuing from the track to convert the mechanical energy to electric energy. However, the base excitation of the track will depend on the exact mounting location (e.g. sleeper vs rail). With loading applied to the rails being directly transferred to the sleepers ( $k_s$ ), the following relationship can be used to represent the train-induced vibration of the sleeper as a factor of the rail vibration:

$$u_s(t) = \frac{k_s k_r}{k_s + k_g} u_r(t) \approx 0.53 u_r \quad (4)$$

where  $u_h$  is the displacement of the harvester  $m_h$ . From Equation 2 and 3 and the rail-sleeper relationship prescribed above, it is inferred that the sleeper velocity and acceleration can be determined as a fraction of the rail velocity and acceleration, respectively as

$$v_s(t) = \frac{d}{dt} \left[ \frac{k_s k_r}{k_s + k_g} u_r(t) \right] \approx 0.53 v_r \quad \text{and} \quad a_s(t) = \frac{d^2}{dt^2} \left[ \frac{k_s k_r}{k_s + k_g} u_r(t) \right] \approx 0.53 a_r \quad (5)$$

where  $v_r(t)$  and  $a_r(t)$  were obtained in Equations 2 and 3.

Previous literature utilized vibrations at the sleeper to produce energy rather than the rail due to ease of access. This energy harvesting configuration generated an optimal electrical output in the order of mW which is sufficient for low-power applications such as warning signals, switches and health monitoring sensors [19]. The linear power equation adopted in many energy harvesting works:

$$P_h = c_h v_h^2 \quad (6)$$

where subscript  $h$  denotes the harvester,  $P$  is the electrical energy harvested,  $c$  is the damping and  $v$  is the velocity induced by the mechanical vibrations of the rail.

### 2.4 Compression-Based Energy Harvester

Compression-based harvesters (also known as stack harvesters) are composed of two surface electrodes with opposing polarities inducing a voltage in the piezoelectric material sandwiched between them [20, 21]. Throughout this section it is assumed that the strains are uni-directional and in the direction of the applied loading only.

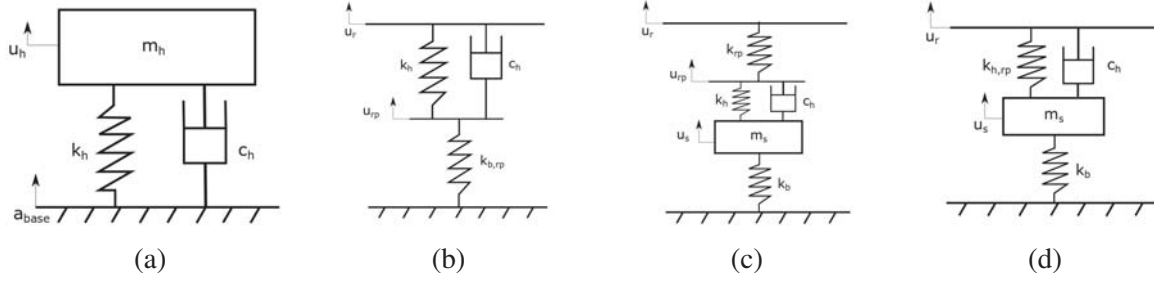


Figure 2: (a) SDOF harvester model mounted on rail (Configuration 1) or on sleeper (Configuration 2), (b) Stack harvester between the rail pad and the rail – Configuration 3, (c) Stack harvester between the rail pad and the sleeper – Configuration 4, (d) Stack harvester is used as rail pad – Configuration 5.

### 3 Harvester Models

In [10, 21], track-mounted harvesters were represented as single-degree-of-freedom (SDOF) systems. This methodology will be adopted here to study the performance of vibration energy harvesters and compression energy harvesters.

#### 3.1 Vibration Energy Harvesters

The model shown in Figure 2a is adopted herein in two configurations: (a) the SDOF harvester is mounted on the rail (Configuration 1) or (b) mounted on the sleeper (Configuration 2).

These models can be used to determine the optimal electrical power output at each train speed. It must be noted that the dynamic model applied to both configurations is identical, the only difference is the base excitation  $a_{base}$  applied to the system is dependent on the mounting location of the harvester. The governing equation of the harvester in this case is

$$m_h a_h + c_h v_h + k_h u_h = m_h a_{base} \quad (7)$$

where  $m$  is mass in kg,  $a$  is acceleration in  $m/s^2$ ,  $c$  is the damping constant,  $k$  is the stiffness in  $N/m$ ,  $v$  is the velocity in  $m/s$ ,  $u$  is the displacement and  $a_{base}$  is the base acceleration in  $m/s^2$ . In the forthcoming simulations, the following values will be used:  $m_h = 1$ ,  $k_h = 1.5$  and three values of the damping ratio will be used  $\zeta_h = c_h / \sqrt{k_h m_h} = 10^{-3}$ ,  $5.5 \times 10^{-3}$  and  $10^{-2}$ . The appropriate base acceleration  $a_{base}$  is obtained from the Winkler model.

#### 3.2 Compression Energy Harvesters

The compression harvester has three configurations: (a) the harvester is placed between the rail and the rail pad (Configuration 3 in Figure 2b), (b) the harvester is placed between the rail pad and the sleeper (Configuration 4 in Figure 2c) and (c) the rail pad itself is a compression harvester (Configuration 5 in Figure 2d). The mass of the compression harvester is assumed to be only 0.004% of the sleeper's mass; therefore, the harvester is presented as a point mass for the three aforementioned configurations. The governing equations of these three configurations are presented below:

The governing equations of Configuration 3 (Figure 2b) is

$$c_h(v_r - v_{rp}) + k_h(u_r - u_{rp}) - k_{b,rp}u_r = 0 \quad \text{with} \quad k_{b,rp} = \frac{k_b}{1 + \frac{k_b}{k_{rp}}} \quad (8)$$

Table 1: Modelled compression harvester parameters

Component	Mass, $m$ [kg]	Damping values $\zeta$ [dimensionless]	Stiffness $k$ [N/m]
Rail pad, $rp$	0	0	$2.1 \times 10^8$
Sleeper, $s$	192	0	$\infty$
Harvester, $h$	$7.5 \times 10^{-3}$	$10^{-3}, 5.5 \times 10^{-3}, 10^{-2}$	$7.8 \times 10^8$

Configuration 4 (Figure 2c) is governed by the following equation

$$m_s a_s - c_h(v_{rp} - v_s) - k_h(u_{rp} - u_s) + k_b u_s = 0 \quad (9)$$

The governing equation of Configuration 5 (Figure 2d) is

$$m_s a_s - c_h(v_r - v_s) - k_{h,rp}(u_r - u_s) + k_b u_s = 0 \quad \text{with} \quad k_{h,rp} = \frac{k_{rp}}{1 + \frac{k_h}{k_{rp}}} \quad (10)$$

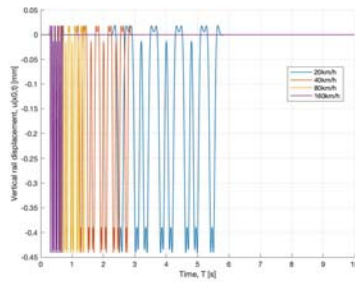
where  $k_{h,rp}$  is equivalent stiffness of the the harvester and rail pad.

Numerical values for the parameters of Equation 8 through Equation 10 are provided in Table 1.

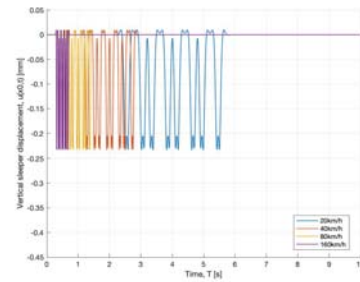
The stiffness of the rail pad and the sleeper are extracted from [20]. The sleepers are introduced into the model also undamped with negligible stiffness. As for the compression harvester, a cuboid structure of dimensions  $10^{-2} \times 10^{-2} \times 10^{-2} \text{ m}^3$  was adopted. The modelled stack harvester is purely made of piezoceramic material with a density of  $7500 \text{ kg/m}^3$ . Based on an averaged Young's modulus value for piezoceramic material and the set dimensions mentioned earlier, the axial stiffness of the harvester was obtained as listed in Table 1.

#### 4 Results and Discussion

The simulation was run for all velocities under consideration ( $v = 20, 40, 80, 160 \text{ km/h}$ ). Figure 3a and 3b shows the response of the rail under a moving passenger train at speeds 20, 40, 80 and 160 km/h. It can be noted that the sleeper displacement is 53% of the rail displacement as a result of the relationship employed in Section 2.2.



(a) Rail displacement,  $u_r(t)$ .

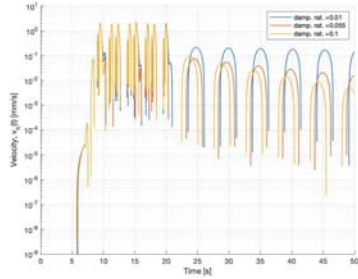


(b) Sleeper displacement,  $u_s(t)$ .

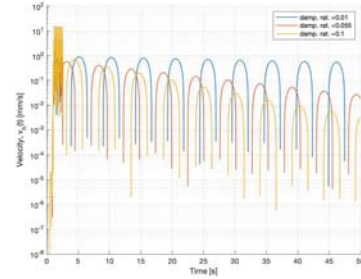
Figure 3: Vertical displacement for various train speeds,  $v$ , using the Winkler model.

Determining the vibration harvester velocity required the numerical integration of Equation 2a using simultaneously state representation of the 2<sup>nd</sup> order ODE. It can be observed from Figure 5a between 8 and 20 s that the vibration harvester is in a transient state. The transient

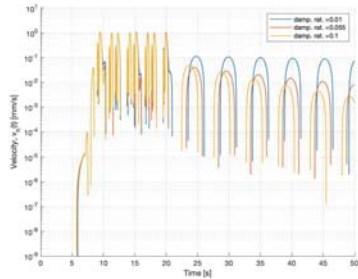
state in Figure 5b is between 1 and 3s, far shorter and much sooner than Figure 5a. It is evident from Figures 4a-4d that with increased harvester damping, the time it takes for the harvesting system to reach rest decreases. It must be noted from Figures 4a-4d that despite the train having passed, the harvester continues to oscillate and hence producing electrical output at both velocities for  $t \rightarrow \infty$ .



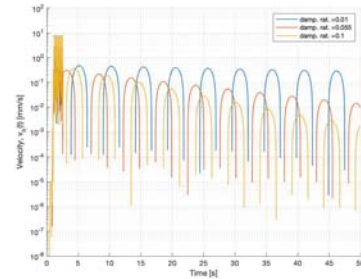
(a) Configuration 1,  $v = 20$  km/h.



(b) Configuration 1,  $v = 160$  km/h.



(c) Configuration 2,  $v = 20$  km/h.



(d) Configuration 1,  $v = 160$  km/h.

Figure 4: Vertical harvester velocity,  $v_h(t)$ , for different configurations and train speeds.

From Figures 5a-5d it is observed that the peaks of power generated by the harvester correspond with the peaks in velocity from Figures 4a-4d. Thus, the majority of the electrical energy provided by the harvester is extracted during the transient-state. For forcing frequencies not equal to the harvester natural frequency, a larger damping is beneficial. However, greater damping of the system does not necessarily guarantee optimal power generation. This is attributed to larger damping having a detrimental affect on the oscillations of the harvester when not under resonance [14]. Table 2 presents the results of the the five investigated configurations.

Table 2: Energy harvested  $E$  in J/kg

Configuration	Optimal Damping, $\zeta_h$	Train speed $v$ in km/h			
		20	40	80	160
1	$10^{-2}$	$2.85 \times 10^{-6}$	$5.15 \times 10^{-6}$	$9.92 \times 10^{-6}$	$2.00 \times 10^{-5}$
2	$10^{-2}$	$7.90 \times 10^{-7}$	$1.43 \times 10^{-8}$	$2.75 \times 10^{-6}$	$5.53 \times 10^{-6}$
3	$10^{-3}$	$1.45 \times 10^6$	$3.82 \times 10^5$	$1.84 \times 10^5$	$9.13 \times 10^4$
4	$10^{-3}$	$5.38 \times 10^4$	$1.45 \times 10^2$	$3.00 \times 10^1$	$3.93 \times 10^{10}$
5	$10^{-2}$	$7.18 \times 10^{-2}$	$1.36 \times 10^{-1}$	$2.71 \times 10^{-1}$	5.19

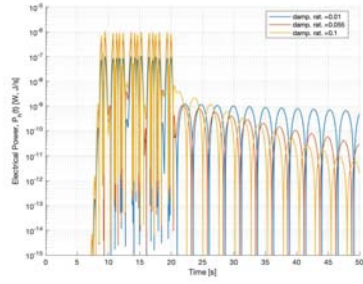
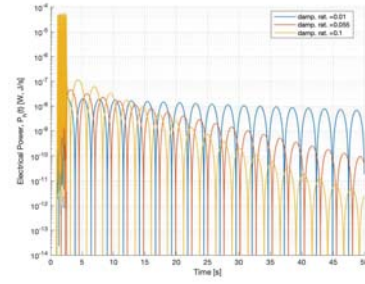
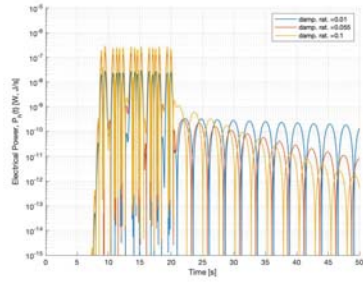
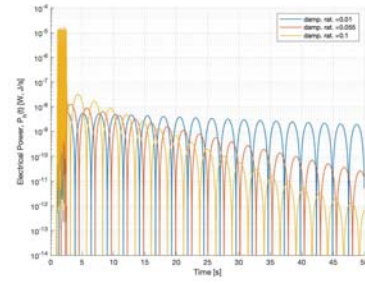
(a) Configuration 1,  $v = 20$  km/h.(b) Configuration 1,  $v = 160$  km/h.(c) Configuration 2,  $v = 20$  km/h.(d) Configuration 2,  $v = 160$  km/h.

Figure 5: Harvested electric power,  $P_h(t)$ , for different harvester configuration and at different train velocities.

## 5 Conclusions

To articulate the potential of harvester technology in providing reliable, safe and green energy to power and monitor appliances in industry, this paper proceeded in utilizing preliminary dynamic models and a typical passenger train to propose an optimal harvesting configuration for railway application. Current literature on railway harvesting are limited to vibration energy harvesting from sleepers due to ease of access and installation in comparison to alternative locations. This paper aspires to numerically model multiple harvesting configurations using MATLAB and determining an optimal harvesting location and corresponding harvester properties based on performance. Firstly the beam-on-elastic-foundation model for a continuously-supported infinite beam on ballast foundation was employed to determine the rail responses under train-induced quasi-static loading. The train modelled was a typical passenger train. Simplified mass-spring damper models were used to represent five different configurations of energy harvesters. The five configurations considered are labelled 1-5 are in the following order: Electromagnetic harvester placed on the rails, Electromagnetic harvester placed on the sleeper, Stack of harvesters above the rail pads, Stack of harvesters between rail pads and sleepers, Stack harvesting rail pad. The energy harvested at each configuration for a number of train speeds was evaluated. It was concluded that Configuration 1 is the most favourable for vibration harvester for all train speeds. As for the stack harvester, the more advantageous configuration is a variable of the train speed. Overall, Configuration 3 and 4 are better at generating electrical energy under the same conditions than Configuration 5.



## 6 Acknowledgment

This paper has been carried out under a research project entitled “Framework for Research on Railway Engineering” which is supported by a grant sponsored by Qatar Rail and managed by Qatar University under reference number: QUEx-CENG-Rail 17/18.

## REFERENCES

- [1] A. Zurbuchen, A. Haeberlin, L. Bereuter, J. Wagner, A. Pfenniger, S. Omari, J. Schaerer, F. Jutzi, C. Huber, J. Fuhrer, and R. Vogel. The swiss approach for a heartbeat-driven lead- and batteryless pacemaker. *Heart Rhythm*, 14(2):294–299, 2017.
- [2] M. Safaei, R.M. Meneghini, and S.R. Anton. Energy harvesting and sensing with embedded piezoelectric ceramics in knee implants. *IEEE/ASME Transactions on Mechatronics*, 23(2):864–874, 2018.
- [3] M. Yip, R. Jin, H.H. Nakajima, K.M. Stankovic, and A.P. Chandrakasan. A fully-implantable cochlear implant soc with piezoelectric middle-ear sensor and arbitrary waveform neural stimulation. *IEEE Journal of Solid-State Circuits*, 50(1):214–229, 2015.
- [4] S. Akkaya Oy and A.E. Özdemir. Piezoelectric-based low-power wind generator design and testing. *Arabian Journal for Science and Engineering*, 43(6):2759–2767, 2018.
- [5] S. Mekid, A. Qureshi, and U. Baroudi. Energy harvesting from ambient radio frequency: Is it worth it? *Arabian Journal for Science and Engineering*, 42(7):2673–2683, 2017.
- [6] P.H. De Jong, A. De Boer, R. Loendersloot, and P.J.M. Van Der Hoogt. Power harvesting in a helicopter rotor using a piezo stack in the lag damper. *Journal of Intelligent Material Systems and Structures*, 24(11):1392–1404, 2013.
- [7] X. Jiang, Y. Li, J. Li, J. Wang, and J. Yao. Piezoelectric energy harvesting from traffic-induced pavement vibrations. *Journal of Renewable and Sustainable Energy*, 6(4), 2014.
- [8] Y. Zhang, S.C.S. Cai, and L. Deng. Piezoelectric-based energy harvesting in bridge systems. *Journal of Intelligent Material Systems and Structures*, 25(12):1414–1428, 2014.
- [9] K. Bendine, M. Hamdaoui, and B.F. Boukhoulda. Piezoelectric energy harvesting from a bridge subjected to time-dependent moving loads using finite elements. *Arabian Journal for Science and Engineering*, 44(6):5743–5763, 2019.
- [10] T. Lin, J.J. Wang, and L. Zuo. Efficient electromagnetic energy harvester for railroad transportation. *Mechatronics*, 53:277–286, 2018.
- [11] M. Gao, P. Wang, Y. Cao, R. Chen, and D. Cai. Design and verification of a rail-borne energy harvester for powering wireless sensor networks in the railway industry. *IEEE Transactions on Intelligent Transportation Systems*, 18(6):1596–1609, 2017.
- [12] V.G. Cleante, M.J. Brennan, G. Gatti, and D.J. Thompson. On the target frequency for harvesting energy from track vibrations due to passing trains. *Mechanical Systems and Signal Processing*, 114:212–223, 2019.

- [13] J. Ortiz, P.M. Monje, N. Zabala, M. Arsuaga, J. Etxaniz, and G. Aranguren. New proposal for bogie-mounted sensors using energy harvesting and wireless communications. *Proceedings of the Institution of Mechanical Engineers, Part F: Journal of Rail and Rapid Transit*, 228(7):807–820, 2014.
- [14] G. Gatti, M.J. Brennan, M.G. Tehrani, and D.J. Thompson. Harvesting energy from the vibration of a passing train using a single-degree-of-freedom oscillator. *Mechanical Systems and Signal Processing*, 66-67:785–792, 2016.
- [15] C.A. Nelson, A. Pourghodrat, and M. Fateh. Energy harvesting from vertical deflection of railroad track using a hydraulic system for improving railroad track safety. In *ASME 2011 International Mechanical Engineering Congress and Exposition, IMECE 2011*, volume 3, pages 259–266, 2011.
- [16] J. Wang, Z. Shi, H. Xiang, and G. Song. Modeling on energy harvesting from a railway system using piezoelectric transducers. *Smart Materials and Structures*, 24(10), 2015.
- [17] V.G. Cleante, M.J. Brennan, G. Gatti, and D.J. Thompson. Energy harvesting from the vibrations of a passing train: Effect of speed variability. In *Journal of Physics: Conference Series*, volume 744, 2016.
- [18] C.A. Nelson, S.R. Platt, S.E. Hansena, and M. Fateh. Power harvesting for railroad track safety enhancement using vertical track displacement. In *Proceedings of SPIE - The International Society for Optical Engineering*, volume 7288, 2009.
- [19] J.J. Wang, G.P. Penamalli, and L. Zuo. Electromagnetic energy harvesting from train induced railway track vibrations. In *Proceedings of 2012 8th IEEE/ASME International Conference on Mechatronic and Embedded Systems and Applications, MESA 2012*, pages 29–34, 2012.
- [20] B. C. Kok, Saleh Gareh, H. H. Goh, and C. Uttraphan. Electromechanical-traffic model of compression-based piezoelectric energy harvesting. In *International Conference on Manufacturing and Industrial Technologies*, volume 70, 2016.
- [21] D.R.M. Milne, L.M. Le Pen, D.J. Thompson, and W. Powrie. Properties of train load frequencies and their applications. *Journal of Sound and Vibration*, 397:123–140, 2017.

## IMPACT FACTORS DERIVED FROM INTERNAL FORCES IN TIMOSHENKO BEAMS SUBJECTED TO CONCENTRATED MOVING LOADS

Benjamín Pinazo<sup>1</sup>, Salvador Monleón<sup>2</sup>, Carlos Lázaro<sup>3</sup>, and Pedro Museros<sup>4</sup>

Affiliation of authors

Universitat Politècnica de València  
Dpt. of Continuum Mechanics and Theory of Structures  
Camino de Vera s/n, 46022 Valencia, Spain

e-mail: <sup>1</sup> bpinazo@doctor.upv.es,  
<sup>2</sup> smonleon@mes.upv.es,  
<sup>3</sup> carlafer@mes.upv.es,  
<sup>4</sup> pmuseros@mes.upv.es

**Keywords:** Structural Dynamics, Moving Loads, Impact Factors, Continuous Beams.

**Abstract.** *The aim of this work is to analyse the impact factors in the Timoshenko beams response under moving loads in terms of both displacements and internal forces, particularly bending moments. The dynamic response is determined by modal analysis, which consist in representing the absolute displacement field by means of a weighted combination of the undamped system eigenfunctions. This paper presents a finite-element based approach that can be used to compute the dynamic internal forces, both in Bernoulli–Euler and Timoshenko beams models under moving loads. Firstly, this methodology has been validated against an analytical solution for a single-span bridge. Afterwards, the impact factors in a real four-span bridge are presented with a discussion of several issues which come up with the resolution of this kind of problems, such as the damping level and the difference between positive and negative bending moments. Finally, conclusions about the similarities in the dynamic amplification factors for different magnitudes are discussed, including one case of visible resonant behaviour.*

## 1 INTRODUCTION

The idea of substituting the dynamic analysis of structures under moving loads by static analyses where the results are amplified by an *impact factor* is as old as the moving load problem itself. Certainly, static analysis is more amenable to practical application by engineers who may be specialists in various aspects of structural analysis and design, but with no particular background in dynamics. Moreover, before the speeds of trains were high enough to raise concerns about resonance problems, carrying out full dynamic analyses with the sole purpose of obtaining a certain percentage of increase in structural displacements and internal forces was not justified: a simple amplification coefficient is generally perceived as sufficient in that case, also because vibrations levels (accelerations) are not of importance. With the advent of high-speeds railways, the perspective has changed noticeably.

Presently this issue is tackled in some building codes in a way that leaves margin for interpretation. We consider EN 1991-2 [1] as a reference standard for railway bridge design. Under certain conditions, an impact coefficient or *dynamic enhancement*  $\varphi'$  is to be calculated according to EN 1991-2, as a function of the “maximum dynamic response” and “maximum static response”, where the meaning of the term “response” is not unambiguous. If the designer is to provide a solution that complies with the standard employing the least effort, “response” can be interpreted as “displacement”—particularly, “vertical displacement” when the deformation is characterised by such type of motion, as it is the case during bending of beam-like structures.

Therefore, the question can be set forth as follows: is it possible to obtain a good approximation to the dynamic enhancement of internal forces (bending moments, shear force, etc.) by using the dynamic enhancement corresponding to displacements?

Since the computation of dynamic displacements is simpler than for internal forces, an affirmative answer to this question would have certain advantages: a coarser mesh could be used and, principally, less modes are needed for a good convergence to the dynamic displacements than to internal forces. The difficulties of convergence can be circumvented by using solution methods that combine *quasi-static* analysis plus a *dynamic increment* with respect to the quasi-static solution, as González *et al.* employed for the shear forces in [2]. However, this approach is not usually available in commercial Finite Element (FEM) codes. Additionally, less information is generated and manipulated if only displacements are postprocessed to obtain the impact factors, which results in faster analyses and reduced possibilities of unnoticed errors.

For these reasons, this paper explores the possibility of approximating impact coefficients for internal forces by means of displacement-based coefficients. The problem is addressed for bending moments in continuous beams, which is a structural type of great interest in bridge engineering. Timoshenko beam theory is used as a basis. While this theory is not expected to produce results significantly different from Bernoulli–Euler (B-E) theory for maximum resonant response of railway bridges—due to the usual slenderness of such structures—, there are other applications of interest where Timoshenko beam theory could be required, as for instance Hyperloop™ tubes of large diameter and small thickness, recently analysed by the authors under the main expected design loads [3].

The dynamic response of continuous beams is determined here by modal analysis. The paper presents a systematic, finite-element based approach to compute the dynamic internal forces, both in B-E and Timoshenko beams models under moving loads. In section 2 the closed-form solution is presented for the vertical displacements and rotations according to Timoshenko’s theory. Subsequently, the FEM approach is described in section 3. Section 4 presents a validation example of the FEM modal solution against the closed-form version. From there, obtaining

the internal forces is straightforward. Section 5 shows an application to the computation of impact factors in a real four-span continuous bridge; the results are presented with a discussion of several issues that come up with the resolution of this kind of problems, such as the poor convergence of some magnitudes and damping modelisation. Finally, conclusions about the similarities in the dynamic amplification factors for different magnitudes are discussed.

## 2 CLOSED-FORM SOLUTION

Analytical methods for dynamic response of one-span Bernoulli-Euler beam under concentrated moving loads has been extensively developed in the last few decades. Regarding the solution to this problem in the framework of Timoshenko's beam theory, current existing publications address the question employing several methods such as modal expansion, integral transforms or wave propagation functions to name just a few. A complete treatment is given in the work of Kim *et al.* [4].

For the sake of completeness, the essential aspects of the solution corresponding to Timoshenko's beam theory are summarised in this section. Classical modal expansion approach is adopted here, in which the complete displacement field is represented by means of a weighted combination of the undamped system eigenfunctions, typically truncated for computational efficiency.

Aside from the beam model selected, as is well known, a deflection function convergence is achieved with relatively low modes whereas bending moment and shear forces require far more terms to attain a reasonable accuracy. Since conventional methods are not able to capture well the discontinuities in shear diagram and bending moment slope generated at the concentrated moving load location, some attempts has been made to overcome this limitations, see [5]. For our purpose, the accuracy achieved with the modal superposition technique is enough to gain insight into the impact factor properties for the bending moments.

Consider the governing differential equations of a Timoshenko beam model:

$$\begin{aligned} m \frac{\partial^2 w}{\partial t^2} - k_s G A \left( \frac{\partial \theta_y}{\partial x} + \frac{\partial^2 w}{\partial x^2} \right) &= q_z \\ m r_y^2 \frac{\partial^2 \theta_y}{\partial t^2} + k_s G A \left( \theta_y + \frac{\partial w}{\partial x} \right) - E I_y \frac{\partial^2 \theta_y}{\partial x^2} &= m_y \end{aligned} \quad (1)$$

Once the separation of variables has been imposed  $w(x, t) = W(x)e^{i\omega t}$ ,  $\theta_y(x, t) = \Psi(x)e^{i\omega t}$  on the related homogeneous equation, the spatial displacement function  $W(x)$  will be the solution of the following compact equation,

$$W^{IV}(x) + \frac{m(\omega r)^2}{EI} \left( 1 + \frac{E}{k_s G} \right) W^{II}(x) - \frac{m\omega^2}{EI} \left( 1 - \frac{m(\omega r)^2}{k_s G A} \right) W(x) = 0 \quad (2)$$

being the roots of this spatial differential equation,

$$r_{1,2,3,4} = \pm \frac{\bar{\omega}}{\sqrt{2}\lambda} \sqrt{\sqrt{\left(1 - \frac{\eta}{12}\lambda^2\right)^2 + \left(\frac{2\lambda^2}{\bar{\omega}}\right)^2} \pm \left(1 + \frac{\eta}{12}\lambda^2\right)} \quad (3)$$



where the following dimensionless parameters has been defined,

$$\begin{aligned}\lambda &= \frac{L}{\sqrt{I/A}} && \text{slenderness ratio} \\ \bar{\omega} &= \omega \sqrt{m/EI} L^2 && \text{adimensional frequency} \\ \eta &= \frac{12EI}{k_s GAL^2} && \text{bending to shear stiffness ratio}\end{aligned}$$

Except for the critical frequency  $\bar{\omega}_c = \sqrt{12/\eta} \lambda$  the general solution is in the form,

$$W(x) = A_1 e^{r_1 x/L} + A_2 e^{r_2 x/L} + A_3 e^{r_3 x/L} + A_4 e^{r_4 x/L} \quad (4)$$

which in turn can be reformulated in terms of trigonometric and hyperbolic functions,

$$W(x) = C_1 \sin(ax) + C_2 \cos(ax) + C_3 \sinh(bx) + C_4 \cosh(ax) \quad (5)$$

being,

$$\begin{aligned}a &= \frac{\bar{\omega}}{\sqrt{2}\lambda L} \sqrt{\sqrt{\left(1 - \frac{\eta}{12}\lambda^2\right)^2 + \left(\frac{2\lambda^2}{\bar{\omega}}\right)^2} - \left(1 + \frac{\eta}{12}\lambda^2\right)} \\ b &= \frac{\bar{\omega}}{\sqrt{2}\lambda L} \sqrt{\sqrt{\left(1 - \frac{\eta}{12}\lambda^2\right)^2 + \left(\frac{2\lambda^2}{\bar{\omega}}\right)^2} + \left(1 + \frac{\eta}{12}\lambda^2\right)}\end{aligned}$$

Additionally, taking into account the boundary conditions of a simply supported beam, these coefficients  $C_i$  can be established as a function of  $\bar{\omega}$  except for a constant of proportionality. In order to let exist a non-trivial solution, the frequency equation for frequencies lower than  $\bar{\omega}_c$  is as follows,

$$\sin(aL) = 0 \quad \longrightarrow \quad aL = h_k \pi \quad (6)$$

Sorting the eigenvalues in increasing order ( $w_k$ ;  $k = 1, n$ ) and preserving the number of its spatial half-waves  $h_k$  (wave number), their associate eigenfuctions turn out to be,

$$\begin{aligned}W_k(x) &= \sin\left(h_k \pi \frac{x}{L}\right) \\ \Psi_k(x) &= \frac{-h_k \pi}{L} \left[1 - \frac{\eta}{12} \left(\frac{\bar{\omega}_k}{h_k \pi}\right)^2\right] \cos\left(h_k \pi \frac{x}{L}\right)\end{aligned} \quad (7)$$

in virtue of the orthogonality property of modes, the projection onto the modal space with the displacement vector  $N_k(x) = (W_k(x) \ \Psi_k(x))^T$  results in a set of independent non-homogeneous second order differential equation.

$$\ddot{q}_k(t) + 2\zeta_k \omega_k \dot{q}_k(t) + \omega_k^2 q_k(t) = \frac{P \sin\left(h_k \pi \frac{x}{L}\right)}{\frac{mL}{2} M_{eq_k}} \quad (8)$$

with the equivalent modal mass

$$M_{eq_k} = m \int_0^L N_k^T \begin{pmatrix} 1 & 0 \\ 0 & \left(\frac{L}{\lambda}\right)^2 \end{pmatrix} N_k dx \quad (9)$$

its solution for an underdamped system will be,

$$q_k(t) = \begin{cases} \frac{1}{\omega_{d_k}} \int_0^t e^{-\omega_k \zeta_k (t-\tilde{t})} \sin(\omega_{d_k} (t-\tilde{t})) \frac{P \sin(h_k \pi \frac{v \tilde{t}}{L})}{\frac{mL}{2} M e q_k} d\tilde{t}, & \text{if } t \leq t_e \\ e^{-\omega_k \zeta_k (t-t_e)} \left( \frac{\dot{q}_k(t_e) + \omega_k \zeta_k q_k(t_e)}{\omega_{d_k}} \sin(\omega_{d_k} (t-t_e)) + q_k(t_e) \cos(\omega_{d_k} (t-t_e)) \right), & \text{otherwise.} \end{cases} \quad (10)$$

where,

$$\begin{aligned} \omega_{d_k} &= \omega_k \sqrt{1 - \zeta^2} && \text{damped angular frequency} \\ v &&& \text{load constant velocity} \\ t_e &= L/v && \text{time when the load leaves the bridge} \end{aligned}$$

Adding up the contribution of all retained modes, the displacement and rotation response will be respectively,

$$\begin{aligned} w(x, t) &= \sum_{k=1}^n q_k(t) W_k(x) \\ \theta_y(x, t) &= \sum_{k=1}^n q_k(t) \Psi_k(x) \end{aligned} \quad (11)$$

### 3 FINITE ELEMENT IMPLEMENTATION

An analytical formulation for a one-span simple supported beam has been presented in previous section. However, analytical solution for multiple-span bridges with general boundary conditions is so arduous and cumbersome to obtain analytically that it is of common use to employ numerical methods like, in most cases, the Finite Element Method [6]. The FEM permits a systematic implementation to solve general problems, so the implementation to solve the moving load problem is particularly presented here in this section.

A Timoshenko beam element has been adopted to model the bridge behaviour, as well as the Bernoulli-Euler to allow a comparison of results. Element mass and stiffness matrices follow the formulation in [7], while the concentrated moving loads are assembled as equivalent nodal loads to obtain the global matrices. The equation of motion of the bridge is given in terms of the displacement vector  $\mathbf{x}$ , and its derivatives  $\dot{\mathbf{x}}$ ,  $\ddot{\mathbf{x}}$ , the force vector  $\mathbf{f}$ , mass matrix  $\mathbf{M}$  and stiffness matrix  $\mathbf{K}$  as

$$\mathbf{M} \ddot{\mathbf{x}} + \mathbf{K} \mathbf{x} = \mathbf{f} \quad (12)$$

As well as in the analytical formulation, displacements are represented by a truncated base of eigenvectors  $\Phi_k$ , previously determined by a modal analysis.

$$\mathbf{x}(t) = \sum_{k=1}^k q_k(t) \Phi_k \quad \begin{cases} |\omega^2 \mathbf{M} - \mathbf{K}| = 0 \\ [\omega_k^2 \mathbf{M} - \mathbf{K}] \Phi_k = \mathbf{0} \end{cases} \quad (13)$$

The orthogonality property of the undamped eigenvectors permit the projection of the global matrix equation onto the modal space turning into a set of independent second order differential equations in which viscous modal damping  $\zeta_k$  is then assigned.

$$\ddot{q}_k(t) + 2 \zeta_k \omega_k \dot{q}_k(t) + \omega_k^2 q_k(t) = \frac{\Phi_k^T \mathbf{f}}{\Phi_k^T \mathbf{M} \Phi_k} \quad (14)$$

After each mode coordinate  $q_k(t)$  is obtained, the displacements are expanded as previously stated 13. Internal forces, namely bending moment and shear force, are afterwards recovered by means of the element stiffness matrices  $\mathbf{K}^e$  and the displacement vector  $\mathbf{u}^e$  of their related nodes.

$$\mathbf{F}^e = \mathbf{K}^e \mathbf{u}^e \quad (15)$$

Actually, element nodal loads consist of a contribution of stiffness, damping and inertial forces. Inertial loads at nodes are a result of the space discretization and tends to vanish with the mesh refinement. Internal damping forces depends on the physical phenomena from which they are originated. Introducing modal damping leaves the distribution of that forces undetermined and a hypothesis on how they are generated is required to define damping forces. In any case, for a conventional structure damping  $\zeta$  is usually below 3%, which would represent a negligible contribution to the total internal force. Thus, if the mesh is refined enough, the stiffness part

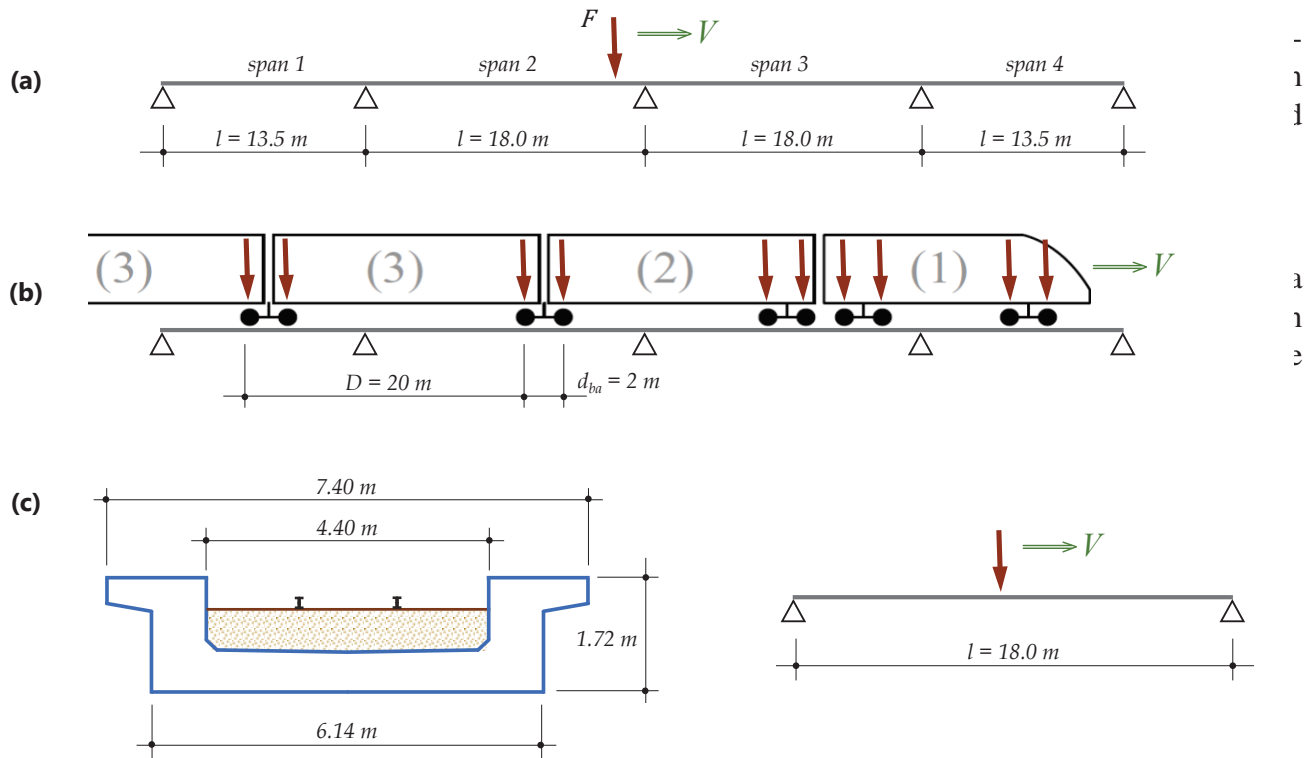


Figure 1: Bridge Section and one-span moving load model.

Figuras Artículo HL

1

Section properties are as follows: cross-section area  $A = 6.46 \text{ m}^2$ , second moment of area about an horizontal axis passing through the c.o.g.  $I = 1.69 \text{ m}^4$  with a linear mass density  $m = 21400 \text{ kg/m}$  including self and dead weight. Flexural to shear stiffness factor is estimated in  $k_s = 0.461$  to be used in the Timoshenko beam model. Material properties are  $E = 36.0 \text{ GPa}$ ,  $\nu = 0.3$  with a viscous critical damping ratio of  $\zeta = 1.14\%$  for prestressed structures according to [1].

## 4.2 FEM RESULTS vs. CLOSED-FORM SOLUTION

In a single-span SS beam the firsts few lower modes are the major contributors to the displacement response, with a fast convergence to the complete solution. Therefore, in this section both analytical and FEM displacement variables are expanded with the contribution of the first five modes.

As can be seen in Table 1, with a mesh of 100 elements, relative error of FEM compared to the analytical solution is negligible. Even with 0.75m element length (24 elem) is enough to accurately capture up to 5 modes with a relative error less than 1.0%.

An interesting fact is that the first two eigenfrequencies from B-E theory are quite similar to that of Timoshenko theory, while higher modes are appreciably stiffer with the B-E modelisation.

Mode no.	Timoshenko			Bernoulli-Euler		
	Analytic	FEM	$\epsilon_r(\%)$	Analytic <sup>1</sup>	FEM	$\epsilon_r(\%)$
1	7.968	7.968	0.000%	$\pi^2 k$	8.175	0.000%
2	29.76	29.76	0.000%	$(2\pi)^2 k$	32.70	0.000%
3	60.97	60.97	0.000%	$(3\pi)^2 k$	73.57	0.000%
4	97.62	97.62	0.001%	$(4\pi)^2 k$	130.8	0.000%
5	137.1	137.1	0.002%	$(5\pi)^2 k$	204.4	0.000%

<sup>1</sup> Conversion factor from dimensionless frequency to the angular frequency  $k = \sqrt{EI/m}/(2\pi L^2)=0.828\text{Hz}$

Table 1: Timoshenko vs Bernoulli-Euler eigenvalues.

Figure 2 illustrates the displacement transient response of the mid-span section when the beam is traversed by a concentrated load of 100 kN. An excellent agreement of the FEM solutions compared with the analytical one is obtained with a 100 elements mesh for two different load velocities in a one-span simple supported bridge. Changes to the spatial discretisation show that even with a coarse mesh of 4 elements reasonable accuracy is achieved. The use of different beam models arise some perceivable differences in the transient response, but the maximum response is quite similar in this example.

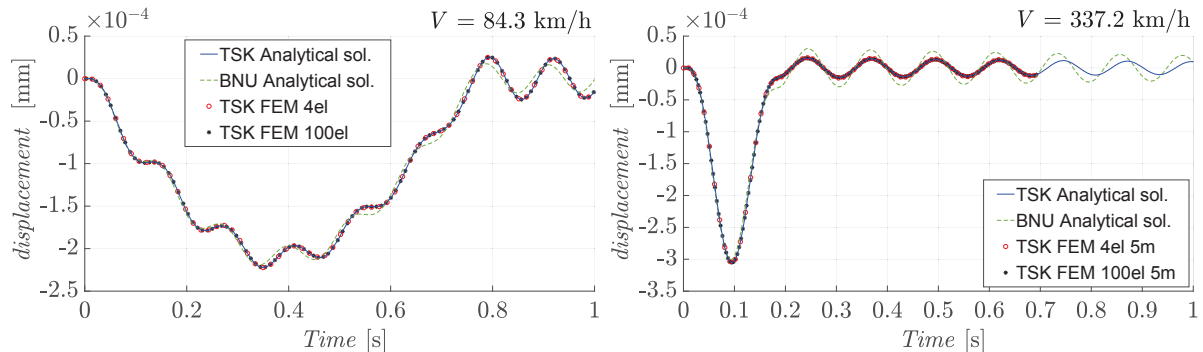


Figure 2: Analytical and FEM displacements (TSK - Timoshenko; BNU - Bernoulli-Euler beam model).

## 5 REAL CASE STUDY. FOUR-SPAN BRIDGE

As mentioned before, one four-span continuous bridge from the Swedish railway network has been selected as a real case study. Figure 3 shows the spans length and Figure 1 depicts the beam section dimensions whose properties has been described in Section 4.1

### 5.1 LOAD CASES

Two cases of constant velocity moving loads are considered, and presented in Figure 3. Case (a) is a single concentrated moving load 100 kN, while (b) is an articulated train (HSLM-A Train A-3, as defined in [1]) comprising a series of coaches with axle loads of 180 kN.

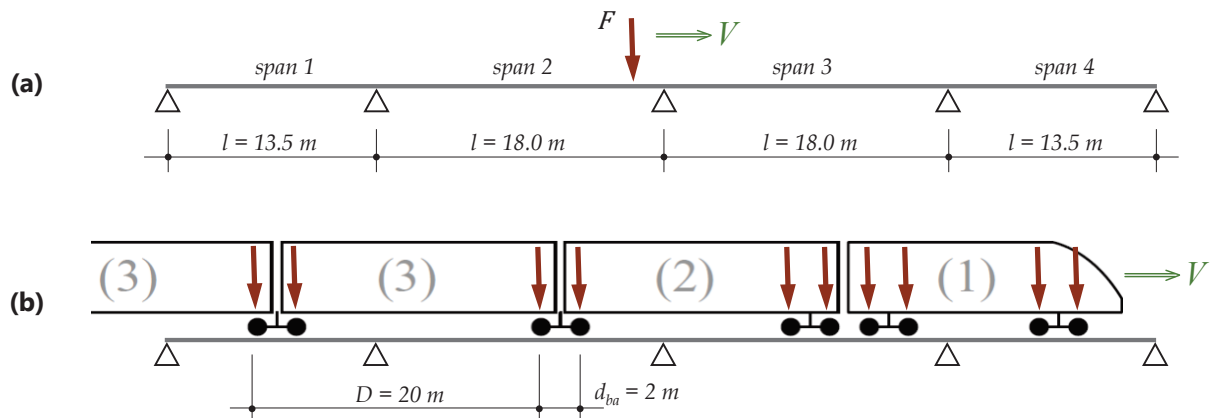


Figure 3: Bridge dimensions, support conditions and load set (a) single load, (b) HSLM-A3 trainset.

### 5.2 IMPACT FACTORS

In order to compare the impact factors (IF) of displacements and bending moments, both are evaluated at the mid-span sections. The IF is defined simply as the ratio between the maximum dynamic effect divided by the maximum static effect. First, positive bending moments at mid-span are compared with downward displacements in order to analyse possible similarities. Later, negative bending moments will be also discussed. A 0.75m mesh element length has been used and response variables are expanded with the contribution of 5 clusters of modes. A cluster is considered as group of (similar) frequencies equal to the number of spans, which is typical in continuous beams.

IFs for a single load, Figure 4, does not display too prominent peaks, and values remain lower than 1.2 in the analysed velocity range. Its aspect reminds of the classical dynamic influence lines, obtained for one load in a single span [8]. While for central spans maximum value appears at 300-350 km/h, outer spans seems to increase their level at velocities higher than 400 km/h. Also, the curves for spans 1-2 are smoother than for spans 3-4. Of great interest is that IFs for positive bending moment follow in general the same tendency than the displacement ones for each span, with somewhat lower values.

When a train of loads is considered, the system can be expected to develop resonance at certain speeds. Figure 5 presents a noticeable peak around 340 km/h that is more prominent in spans 1-2-3. Interestingly, as it happened for the single concentrated load, positive bending moment IFs follow the same tendency than the displacement ones, being slightly lower.



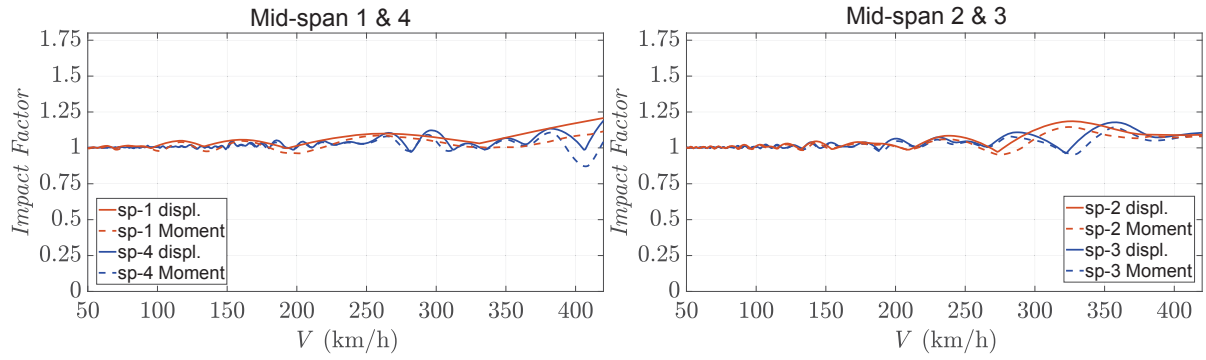


Figure 4: IF for a single concentrated moving load,  $\zeta = 1.14\%$ , outer spans (left) and inner spans (right).

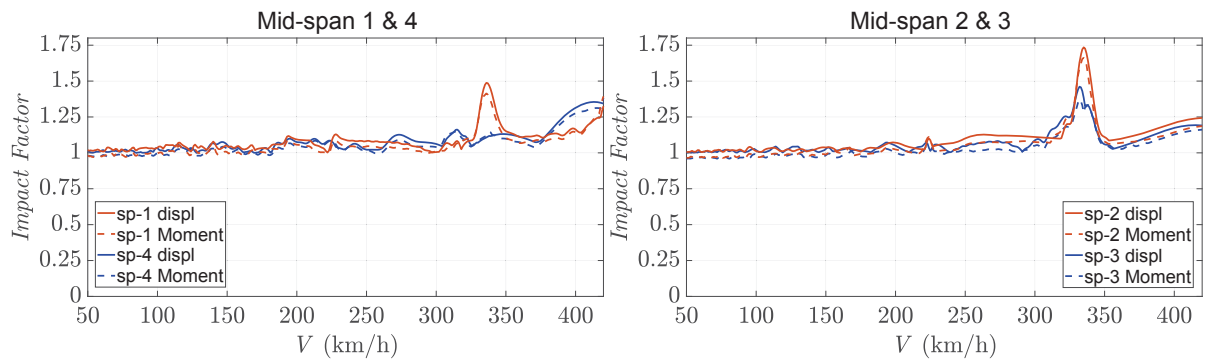


Figure 5: IF for HSLM-A3 train,  $\zeta = 1.14\%$ , outer spans (left) and inner spans (right).

As it was expected, a decrement in the damping factor produce a higher amplification of the IF as can be seen in Figure 6. All the conclusions from the previous analyses are applicable to this case as well.

In this case, the fact that IFs for positive bending moment follow the trends of the displacement IF, being slightly lower, is in accordance with the usual procedure followed in many technical offices, in which the displacement IF is also applied for the strength verification at ULS, as it was mentioned in the introductory section.

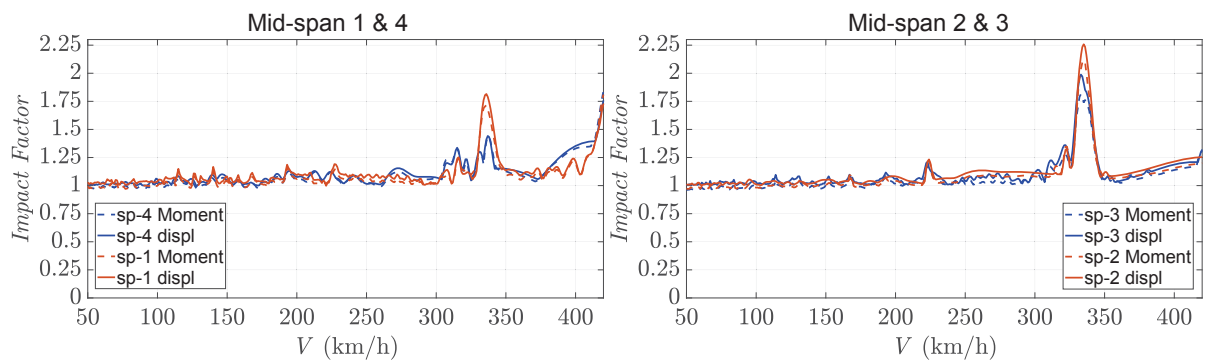


Figure 6: IF for HSLM-A3 train,  $\zeta = 0.50\%$ , outer spans (left) and inner spans (right).

However, the situation is not so clear when negative bending moments at the supports are analysed. Figures 7 to 9 show the IF for the negative moment in all three supports, along with the IFs corresponding, in each case, to the mid-span sections of both adjacent spans, as well

as the average displacement IF of both mid spans. We designate *support 2* the one located at the left end of *span 2*, according to Figure 3, and similarly for supports 3 and 4. Focussing on the resonant speed determinant for the bridge design, one first conclusion is that IFs for negative bending moments are lower compared to positive bending moments. Moreover, the approximation via displacement IFs is not satisfactory: in supports 2 and 3 the displacement coefficients overestimate the negative bending moment impact, see Figures 7 and 8; besides, in support 4 the correlation of the peak is good with the average of the displacements, but the curves are irregular in that speed range and no clear trend can be established (Figure 9).

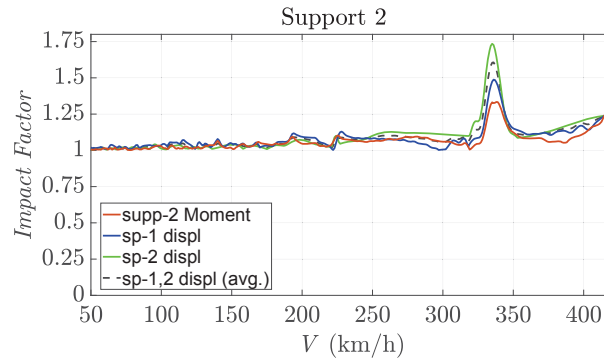


Figure 7: IF for HSLM-A3 train,  $\zeta = 1.14\%$ , support 2.

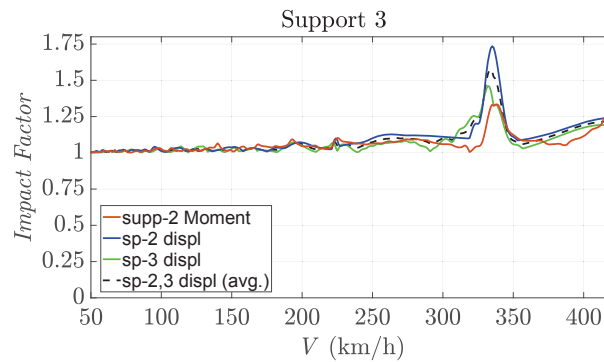


Figure 8: IF for HSLM-A3 train,  $\zeta = 1.14\%$ , support 3.

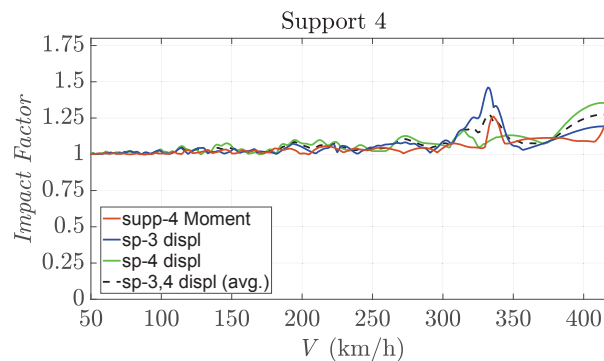


Figure 9: IF for HSLM-A3 train,  $\zeta = 1.14\%$ , support 4.

These findings suggest that using displacement-based impact factors to amplify static negative bending moments may be less accurate than for positive bending moments. Nevertheless,

such conclusion is based in the analysis of one representative example and needs further verification.

## 6 CONCLUSIONS

In this paper a Finite Element approach based on Timoshenko beam theory for the calculation of dynamic impact factors in continuous beams has been presented. The time-varying amplitudes of the modal coordinates have been validated against a closed-form solution of the equations of motion. The influence of mesh refinement has been discussed.

Subsequently, the impact factors for positive bending moments at mid-span have been compared with those of downwards displacements. Impact factors for negative bending moments have been scrutinised as well. First, a single travelling load has been considered; secondly, the effects of a high-speed train capable of producing resonance have been analysed for an actual four-span, single-track, continuous railway bridge. In light of the outcomes of these analyses it can be concluded that:

- Though it is sometimes believed that continuous bridges are largely immune to resonance, results for the four-span bridge studied here under the HSLM-A3 train display a prominent peak around 340 km/h, with impact factors as high as 1.6 (for damping  $\zeta = 1.14\%$ ), or 2.1 (for damping  $\zeta = 0.5\%$ ).
- Inner spans present higher resonant peaks than the end spans.
- Impact factors for positive bending moment follow the same tendencies of the displacement ones for each span, with slightly lower values.
- The preceding conclusions related to the impact factors are valid for different levels of structural damping.
- The use of displacement-based impact factors to amplify static negative bending moments may be less accurate than for positive bending moments.
- As it is known, Bernoulli-Euler beam theory overestimates natural frequencies with respect to the Timoshenko beam model. Particularly, the first two natural frequencies of a single-span railway bridge have been found to be quite similar—specially the first one. The difference increases noticeably for the higher modes.

## 7 ACKNOWLEDGMENTS

The authors gratefully acknowledge the financial support of the *Generalitat Valenciana*, through grant AICO/2019/025 for the project “Análisis Dinámico aplicado al Diseño de Viaductos para Hyperloop: Vibraciones de Flexión, Torsión y Límites Normativos”, within research funding program AICO2019: *Subvenciones para grupos de investigación consolidables*.

## REFERENCES

- [1] European Committee for Standardisation (CEN), *EN 1991-2 – Eurocode 1: Actions on structures. Part 2: General Actions – Traffic Loads on Bridges*. September 2003.
- [2] A. González, D. Cantero, E.J. O'Brien, Dynamic increment for shear force due to heavy vehicles crossing a highway bridge. *Computers and Structures*, **89**, 2261–2272, 2011. DOI: 10.1016/j.compstruc.2011.08.009

- [3] P. Museros, C. Lázaro, B. Pinazo, S. Monleón, Key aspects in the analysis and design of Hyperloop<sup>TM</sup> infrastructure under static, dynamic and thermal loads. *Engineering Structures*, **In Press**.
- [4] T. Kim, I. Park, U. Lee, Forced vibration of a Timoshenko beam subjected to stationary and moving loads using the modal analysis method. *Shock and Vibration*, Article ID 3924921, 2017. DOI: 10.1155/2017/3924921
- [5] M. Zehsaz, M.H. Sadeghi and A. Ziaei Asl, Dynamics Response of Railway Under a Moving Load. *Journal of Applied Sciences*, **9(8)**, 1474–1481, 2009. DOI: 10.3923/jas.2009.1474.1481
- [6] P. Lou and F.T.K. Au, Finite element formulae for internal forces of Bernoulli-Euler beams under moving vehicles. *Journal of Sound and Vibration*, **332**, 1533–1552, 2013. DOI: 10.1016/j.jsv.2012.11.011
- [7] J. S. Przemieniecki, *Theory of Matrix Structural Analysis*. Dover Publications, inc. New York 1968.
- [8] P. Museros, E. Moliner and L. Martínez-Rodrigo, Free vibrations of simply-supported beam bridges under moving loads: Maximum resonance, cancellation and resonant vertical acceleration. *J Sound Vib*, **332**, 326–346, 2013. DOI: 10.1016/j.jsv.2012.08.008

## ON THE DEVELOPMENT OF A NOVEL APPROACH FOR SIMULATING ELASTIC BEAMS IN DUALSPHYSICS WITH THE USE OF THE PROJECT CHRONO LIBRARY

Salvatore Capasso<sup>1\*</sup>, Bonaventura Tagliaferro<sup>1</sup>, Iván Martínez-Estévez<sup>2</sup>, José M. Domínguez<sup>2</sup>, Joe El Rahi<sup>3</sup>, Vasiliki Stratigaki<sup>3</sup>, Alejandro J.C. Crespo<sup>2</sup>, Rosario Montuori<sup>1</sup>, Peter Troch<sup>3</sup>, Moncho Gómez-Gesteira<sup>2</sup>, Giacomo Viccione<sup>1</sup>

<sup>1</sup>University of Salerno  
Via Giovanni Paolo II, 132, 84084 Fisciano, Italy  
capassosalva7@gmail.com, btagliaferro@unisa.it, gviccione@unisa.it, r.montuori@unisa.it

<sup>2</sup>Universidade de Vigo  
Campus As Lagoas s/n, 32004, Ourense, Spain  
ivan.martinez.estevez@uvigo.es, jmdominguez@uvigo.es, alexbexe@uvigo.es, mggesteira@uvigo.es

<sup>3</sup>Ghent University  
Department of Civil Engineering, 9000 Belgium  
Joe.ElRahi@ugent.be, Vasiliki.stratigaki@ugent.be, Peter.Troch@UGent.be

**Keywords:** SPH, Euler-Bernoulli, Linear Elasticity, FSI, CFD, DualSPHysics, Project Chrono.

**Abstract.** *This work presents a novel numerical framework for dynamic analyses of structure systems within the meshless approach Smoothed Particle Hydrodynamics (SPH) method. The Lagrangian solver DualSPHysics presents several advantages over the widely used Eulerian solvers, dealing with nonlinearities and multiphase phenomena with reasonable numerical stability and reliability. The proposed procedure exploits the mechanical features provided by the Project Chrono library to simulate elastic beams. The modelling procedure is of interest for studying complex soil-, solid-, fluid-structure interactions, involving a system that includes all of the aforementioned phases in a unitary context. The analytical formulation to pass information over to the SPH solver for generating a sub-assembly of rigid stubs and elastic hinges, that will mimic the behavior of a Euler-Bernoulli flexible beam, is presented. The approach is validated against theoretical Euler-Bernoulli solutions: the agreement between the theoretical solutions for the behavior of the flexible beams and the presented model is very good and increases when the number of elements that make up the beam,  $N$ , increases. In addition, the behavior of the flexible beam thus created in the SPH environment is validated considering a sensitivity analysis based on several parameters, such as the model resolution (initial interparticle distance) and the number of elements.*



## 1 INTRODUCTION

The Meshfree Particle Methods (MPMs) present several advantages over mesh-based methods, like the natural ability to solve multi-mechanics problems: the Lagrangian nature of this family of numerical methods allows to compute, with relative ease, multi-mechanics problems involving complex interfaces and moving boundaries. In particular, the Smoothed Particle Hydrodynamics (SPH) method, is, by now, well established in the Computational Fluid Dynamics (CFD) discipline, and its effectiveness has been proven in several works, especially when dealing with free-surfaces flows and large deformations [1].

The DualSPHysics code has been applied to several multiphysics phenomena, for example in coastal engineering simulations: to compute forces exerted by large waves on the urban furniture of a realistic promenade [2], to study the run-up on a real armour block coastal breakwater [3, 4] and to simulate large waves generated by land-slide events [5]. Other successful applications of DualSPHysics are performed in the field of renewable energies, for example the simulation of Wave Energy Converters (WECs) in several contexts: from the study of the moorings and floatings dynamics [6, 7, 8, 9], to the efficiency [10] and survivability [11] analysis when combined with closed loops [12, 13], PTO systems [4, 14] or non linear mechanical constraints [15]. These works present first attempts of reproducing the effects of power take-off systems through simplified, although reliable, approaches. Specific validation of Fluid Structure Interactions (FSI) in DualSPHysics are provided by [16]. However, an option to model flexible objects is not yet available.

In this work, the potentiality of an SPH-based solver, DualSPHysics [17], augmented with the Project Chrono library [18], developed as a general purpose simulation framework for multi-body problems, are utilized to simulate the flexural behavior of one-dimensional beams. Other approaches to this issue, with the SPH formulation, can be found in several works (for example, [19, 20, 21, 22]). Rigid bodies and mutual constraints allow developing an alternative framework for the dynamics analysis of structural systems, able to reproduce extremely high deformations of flexible elements, under complex and time-variant load conditions, or impacts - useful for simulating the response of engineered structures under the menaces of hazardous natural events. The aforementioned numerical architecture, in fact, provides a robust and reliable framework for studying fluid-solid interaction, handling arbitrarily defined fluid-structure-structure coupled systems, consenting to specify mutual and/or absolute constraints, such as joints and sliders. SPH is a suitable method for modelling water-related natural hazards due to its characteristics [23, 24].

The proposed beam model relies on a lumped elasticity formulation, in which the only deformation allowed is represented by the relative rotation between consecutive trunks. A similar representation can be found in [25], while a valid application of this formulation to structure collapse is presented in [26]. To improve this work, following [25] and [26], the interactions between the rigid bodies, modelled as mutual constraints, can be characterized by elastic, then plastic behavior, up to a threshold value of stress that determines the collapse. For the peculiarities of the Lagrangian-based method here presented, the latter situation is reproducible with relative ease, encouraging further investigations. In the SPH-based framework, the dynamics of the trunks, and so of the beam as a whole, depends on the Newton's equations for rigid bodies, computed taking into account the mutual constraints and the interaction with external forces. A numerical algorithm developed from classical static theories is here proposed (i.e. Euler-Bernoulli (EB) beam theory), and implemented in DualSPHysics to simulate linear elasticity, using the features provided by the coupling with Project Chrono. In the following, after the

presentation of the SPH formulation implemented in the DualSPHysics code, and its coupling with Project Chrono, the theoretical approach is formulated and validated against EB solutions. Then, the proposed approach is reproduced in DualSPHysics by combining hinges and rigid bodies and their response in investigated.

## 2 SPH FORMULATION

MPMs in general refers to the class of meshfree methods that employ a set of finite number of discrete particles to represent the state of a system and to record its movement. Each particle can either be directly associated with one discrete physical object, or be generated to represent a part of the continuum problem domain. For CFD problems, each particle possesses a set of field variables such as mass, momentum, energy, positions etc., and other variables (vorticity, etc.) related to the specific problem. The advantages of the MPMs methods over conventional grid-based numerical methods can be roughly summarized as follows:

- the problem domain is discretized with particles without a fixed connectivity, so treatment of large deformation is relatively easier;
- discretization of complex geometry is simpler as only an initial discretization is required;
- it is easy to obtain the features of the entire physical system through tracing the motion of the particles, therefore, identifying free surfaces, moving interfaces and deformable boundaries, is no longer a tough task.

Among the MPMs, the Smoothed Particle Hydrodynamics (SPH) method is employed in the present work.

### 2.1 Principles of the SPH method

The strategy in SPH is to discretize the physical domain (fluid and/or solid objects) into a set of particles, where the physical quantities (position, velocity, density and pressure) are obtained as an interpolation of the corresponding quantities of the surrounding particles. The contribution of those particles is weighted using a kernel function, with an area of influence that is defined using a characteristic smoothing length. This discretization process is divided into two key steps [27].

The first step is the integral representation or the so-called kernel approximation of field functions, consisting in the integration of a multiplication of an arbitrary function and a smoothing kernel function. The integral representation of a generic spatial function  $f(\mathbf{r})$  within an integral volume  $\Omega$ , is given by:

$$\langle f(\mathbf{r}) \rangle = \int_{\Omega} f(\mathbf{r}') W(\mathbf{r} - \mathbf{r}', h) d\mathbf{r}' \quad (1)$$

where  $W$  is the so-called smoothing kernel function or kernel. In the smoothing function,  $h$  is the smoothing length defining the influence area of  $W$  (Figure 1).

The second step is the particle approximation. The integral representation is approximated by summing up the values of the nearest neighbor particles, which yields the particle approximation of the function at a discrete point (particle). The position  $\mathbf{r}_b$  is defined as the position of a particle having a fixed mass  $m_b$  and a finite volume  $V_b$ , related by

$$V_b = \frac{m_b}{\rho_b} \quad (2)$$

where  $\rho_b$  is the density of particle  $b = 1, \dots, N_p$  in which  $N_p$  is the number of particles within the support domain of particle  $a$ . The integral representation can be written in a discrete form for a particle  $a$ ,  $b$  being part of its support domain:

$$\langle f(\mathbf{r}_a) \rangle = \sum_{b=1}^{N_p} \frac{m_b}{\rho_b} f(\mathbf{r}_b) W_{ab} \quad (3)$$

where:

$$W_{ab} = W(\mathbf{r}_a - \mathbf{r}_b, h) \quad (4)$$

The kernel function, hence, plays a fundamental role in the SPH method. In DualSPHysics the Wendland [28] quintic kernel function is utilized:

$$W(r, h) = \alpha_{D,n} \begin{cases} \left(1 - \frac{q}{2}\right)^4 (1 + 2q) & 0 \leq q \leq 2 \\ 0 & 2 < q \end{cases} \quad (5)$$

where:

$$q = \frac{r}{h} = \frac{|\mathbf{r} - \mathbf{r}'|}{h} \quad (6)$$

and  $\alpha_{D,n}$  is a constant depending on the dimension of the problem.

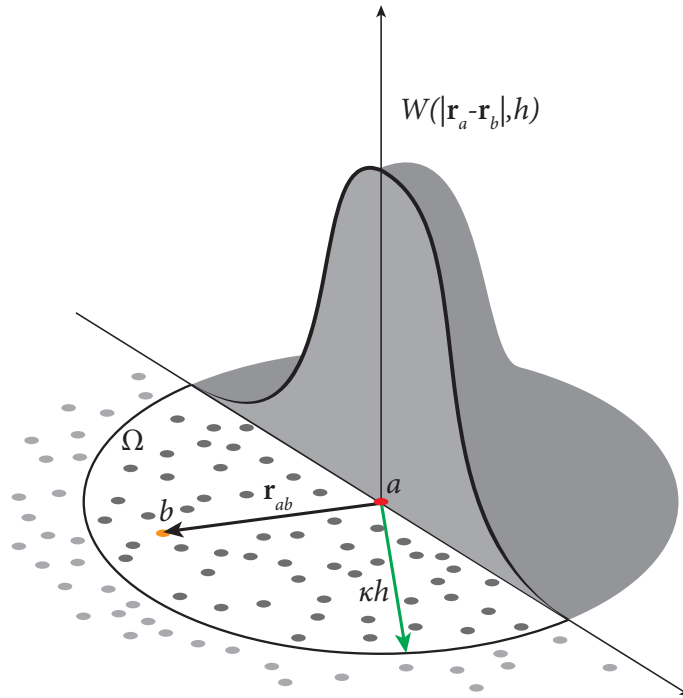


Figure 1: Smoothing kernel function.

## 2.2 Governing equations for rigid bodies

Rigid bodies are sub-sets of SPH particles, the variables of which are integrated in time with the Newton's equations for rigid body dynamics, in the domain frame reference.

The equations of motion are:

$$\begin{aligned} M \frac{d\mathbf{V}}{dt} &= \mathbf{F}_\Omega \\ \mathbf{J} \frac{d\boldsymbol{\Omega}}{dt} &= \mathbf{F}_\Omega \end{aligned} \quad (7)$$

where  $\mathbf{F}_\Omega$  is the *total moment* with respect to the center of mass, and they assume the following aspect in particle approximation:

$$\begin{aligned} M_I \frac{d\mathbf{V}_I}{dt} &= \sum_{k \in I} m_k \frac{d\mathbf{u}_k}{dt} \\ \mathbf{J}_I \frac{d\boldsymbol{\Omega}_I}{dt} &= \sum_{k \in I} m_k (\mathbf{r}_k - \mathbf{R}_I) \times \frac{d\mathbf{u}_k}{dt} \end{aligned} \quad (8)$$

where the body  $I$  posses a mass  $M_I$ , velocity  $\mathbf{V}_I$ , inertia tensor  $\mathbf{J}_I$ , angular velocity  $\boldsymbol{\Omega}_I$  and center of gravity  $\mathbf{R}_I$ . The vectorial quantities are computed at every time step (discretizing the temporal derivative  $\frac{d}{dt}$ ). The force by unit mass applied to the particle  $k$  belonging to  $I$  is expressed as  $m_k \frac{d\mathbf{u}_k}{dt}$ , encompassing body forces (gravity) and external loads resultants. The net force on each boundary particle is computed according to the sum of the contributions of all surrounding fluid particles according to the designated kernel function and smoothing length. It is clear that every particle within the body has a velocity given by:

$$\mathbf{u}_k = \mathbf{V} + \boldsymbol{\Omega}_I \times (\mathbf{r}_k - \mathbf{R}_I) \quad (9)$$

These equations are integrated in times over a staggered interval, in DualSPHysics, using a computationally simple Verlet based scheme that guarantees a second order spatial accuracy. For more details about rigid bodies in DualSPHysics, [29] is suggested.

### 2.3 Coupling scheme

Mechanisms involving contacts and impacts between parts can be modeled in terms of multi-body systems with unilateral constraints. Considering the success of SPH for fluid descriptions and non-smooth multi-body solvers for mechanical systems, attempting to couple both under a generalized framework should provide new simulation possibilities, by leveraging the strengths of both methods. Project Chrono is able to simulate a wide range of physical problems, but at the moment, DualSPHysics uses the rigid body, constraints and collision detection parts of the library. This allows to use a set of bodies described in meshes, define restrictions applied to the bodies (from the implemented list of joints, hinges and springs) and compute interactions between bodies, in a similar fashion of the DEM implementation, but in a more stable manner.

The implementation strategy is to couple both models with a message passing interface. Once quantities from the rigid bodies are computed by DualSPHysics (Equation (8)), the time step, along with the linear and angular accelerations from each body, are sent to the Project Chrono module [16]. For that time step, Chrono returns the linear and angular velocities, as well as centres of mass position, computed by integrating the fluid contributions with the dynamic or kinematic restrictions of the system, including collisions.

## 3 LUMPED ELASTICITY FORMULATION

The developed approach is based on the discretization of a one-dimensional element (Figure 2) defined under the assumptions of the EB theory, which are here briefly recalled. Being  $x$  the abscissa that identifies the beam axis:

- the longitudinal axis of the unloaded, undeformed beam, is rectilinear;
- small shifts;
- inalterability of the cross section, i.e. always planar;
- the generic cross section  $\Sigma(x)$  is always orthogonal to the axis, also in the deformed configuration;
- isotropic elastic material;
- $x$  dimension predominant with respect to  $y, z$ .

As a consequence of these assumptions, considering the behavior of the beam to be only flexural, the function which uniquely describes its deformation is the *vertical displacement function*  $v = v(z)$ , namely the *elastic line equation* (Figure 2). Furthermore, every cross section is characterized by infinitesimal rigid displacements, expressible as a summation of a translation ( $v$ ) and a rotation ( $\vartheta$ ) around its centre of mass  $G$ .

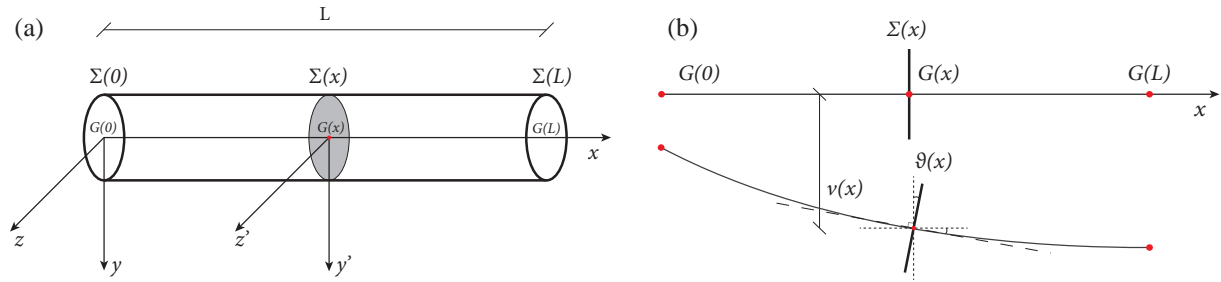


Figure 2: Representation of a beam with rectilinear axis (a), and relative kinematic parameters (b).

Following these considerations, it is possible to reproduce the displacement function with the finite element representation, in which the elements assume a physical dimension, and thus the latter are governed by the rigid body kinematics. In fact, a generic derivable function, in this case  $v = v(x)$ , can be replaced with a series of local defined low-order functions  $\psi_i$ , which interpolate between the  $v(x_i) = v_i$  values:

$$v(z) \approx \sum_i \psi_i v_i \quad (10)$$

In case  $\psi_i$  is a first order polynomial, the approximation is linear, which can be materially represented by rigid elements, from now on *trunks*. The numerical properties of the interpolation polynomials are physically the positions and the lengths of the trunks, whose ending cross section are equipped with rotational hinges. The hinge positions, related to a generic trunk, identified respectively as  $i$  and  $i + 1$ , are expressible with a single rotational parameter, namely  $\vartheta_i$  (Figure 3). The displacement of the point  $i + 1$  is known, once the the angle  $\vartheta_i$  (rotation in  $i$ ) is note; from the Equation (9) we have:

$$\mathbf{u}_{i+1} = \mathbf{\Omega}_i \times \mathbf{r}_{i,i+1} \quad (11)$$

which becomes in a two-dimensional EB framework, being  $r_{i,i+1} = r_{i+1} - r_i \doteq \Delta x$ , and assuming  $\mathbf{\Omega} = \{0, 0, \vartheta_i\}$ :

$$v_{i+1} = \sin \vartheta_i \Delta x \quad (12)$$



The proposed numerical model is elaborated for a cantilever, but its approximations can be extended to any kind of Boundary Conditions (BC). This particular static scheme was chosen because several FSI problems present models akin to this one, and also various validation processes are based on cantilevers (see [30, 31]). The cantilever, hence, is discretized as a set of rigid trunks and rotational hinges [25]. The hinge is characterized by a proper value of *rotational stiffness*  $K_{\vartheta,i}$ , constant with the length of the trunk  $\Delta x$ , that is deduced from the geometrical e mechanical properties of the section.

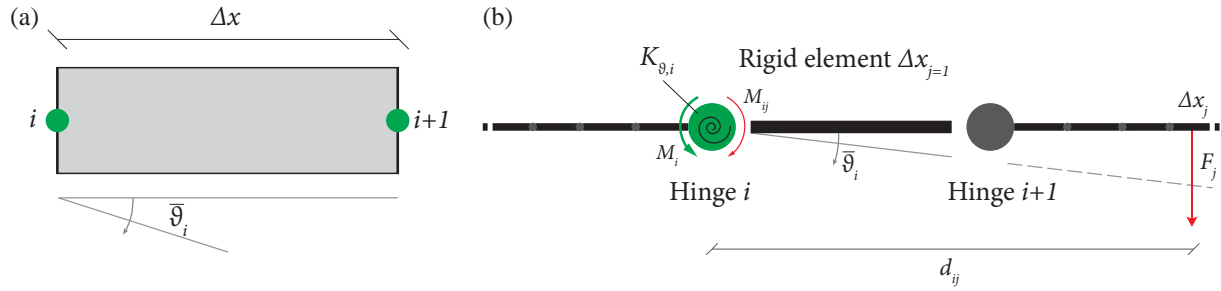


Figure 3: Vertical displacement of the end of a rigid trunk (a), and discretization scheme (b).

### 3.1 Numerical discretization

Let us consider the cantilever section in the plane  $\{x, y\}$ , of length  $L_s$  and thickness  $h_b$ , the beam axis being axis of symmetry and coincident with  $x$ . Let  $A_s = h_s b_s$  be the area of the cross section, assumed rectangular and constant,  $b_s$  being the base, aligned with  $x$ ,  $I_s$  the moment of inertia,  $E_s$  and  $\rho_s$  respectively the Young's modulus and density of the material. The beam is arbitrarily divided in  $N$  (identified with the subscript  $j$ ) trunks  $\Delta x$ , linked with  $N$  (identified with the subscript  $i$ ) hinges (Figure 5). In case of constant spatial discretization, we can define:

$$\Delta x = \frac{L_s}{N} \quad (13)$$

and the generic abscissa is  $x(i) \doteq x_i$ . Within this framework, following the assumption that the behavior of the beam is only flexural, as visible in the elastic line equation:

$$\frac{d^2 v(x)}{dx^2} = -\frac{M(x)}{E_s I_s} \quad (14)$$

the moment is the only components of tension to be dealt with. The *moment*  $M_{ij}$  is defined as the moment created by the  $j$ -th resultant with respect to the  $i$ -th hinge:

$$M_{ij} = d_{ij} F_j \quad (15)$$

where  $d_{ij}$  is the *lever arm* of the force  $F_j$ , applied in the center of mass  $G_j$  of the trunk, with  $G_j > x_i$ . The *total moment* referred to the  $i$ -th hinge is:

$$M_i \doteq \sum_{k=j}^N M_{ik} = \sum_{k=j}^N d_{ik} F_k \quad (16)$$

The *local rotation*  $\bar{\vartheta}_i$  of the  $i$ -th hinge is proportional to the total moment calculated in the section  $x_i$ , by the rotational stiffness, following the theory of linear elasticity:

$$\bar{\vartheta}_i = \frac{M_i}{K_{\vartheta,i}} \quad (17)$$

This value, which characterizes the flexural behavior of each trunk, can be computed once the external load is known. To secure a correct numerical result for a cantilever scheme, the rotational stiffness of the bearing (first section) has to be doubled with respect to the generic stiffness value, since the first trunk can be considered semi-fixed. Thanks to rigid body kinematics is possible, then, to obtain the complete displacement function of the beam; let

$$\vartheta_i = \sum_{k=1}^i \bar{\vartheta}_k \quad (18)$$

be the *total rotation* of the  $i - th$  hinge;

$$\bar{v}_{i+1} = \Delta x_{j=i} \sin \vartheta_i \quad (19)$$

is, hence, the *local vertical displacement* of the section  $x_{i+1}$ , and

$$v_i = \sum_{k=1}^i \bar{v}_k \quad (20)$$

is the *total vertical displacement*.

This numerical approach, being based on an equilibrium (Equation (17)), can be naturally extended in the dynamic framework of DualSPHysics and Project Chrono, once defined the governing parameters to be transmitted: number and dimensions of the trunks and the stiffness related to each hinge. To complete the implementation of the one-dimensional elastic element in DualSPHysics, the resolution parameter  $dp$  has to be defined, namely the initial inter-particle distance, as function of the beam thickness  $h_s$ :

$$dp \doteq \frac{h_s}{pp(h_s)} \quad (21)$$

where  $pp(h_s)$  is the number of particles per straight section.

#### 4 Validation

The use of the SPH formulation to discretize one-dimensional flexible elements has two main, and consequential, objectives:

1. demonstrate that a fixed set of particles is able to reproduce, properly, the behavior of a rigid element, subject to active (force  $\frac{d\mathbf{u}_k}{dt}$  applied to the  $k - th$  particle, computed with Equation (8) by DualSPHysics) and reactive (forces exerted by the mutual and absolute constraints, computed by the Project Chrono module) forces, and that several rigid elements and links can be combined to mimic one-dimensional flexible beams;
2. proved the first statement, the potentialities of the SPH method can be exploited: due to the use of rigid body dynamics, high order elasticity formulations are not required to compute extremely high deformations; the natural ability to reproduce free-surface flows, impacts, complex interfaces, can be used, then, to investigate fluid elastic-structure interactions (for example [20, 32, 33]).

The validation is based on a static comparison between the analytical and numerical displacement function of a cantilever: being the DualSPHysics framework dynamic, the results of

a static case can be generalized with ease to a wide field of dynamic conditions. The potentialities of this approach in the SPH framework are, then, shown in several works, which represent various possible physical contests, like interaction with free-surfaces flows or dynamics impacts with fluid mass (reproducing a dambreak flow impacting a flexible obstacle [31, 33]).

#### 4.1 Cantilever test case: static validation

Here the graphics of the statical deflection of the beam, compared against the EB solution, are exposed. The elastic line equation for a cantilever gives:

$$v_{an}(x) = \frac{q_s L_s^2 x^2}{4E_s I_s} - \frac{q_s L_s x^3}{6E_s I_s} + \frac{q_s x^4}{24E_s I_s} \quad (22)$$

where  $q_s = q_s(x)$  is the *vertical load* (only gravitational load, in this case).

The sensitivity analysis on the model is conducted with variable number of trunks ( $N$ ) and with different values of resolution. The displacement function in the DualSPHysics dynamic framework is obtained by adding a linear spring element at the free end of the cantilever, as schematized in Figure 4. The circles in Figure 4(b) represent the hinges, that mutually link the trunks, identified with the color bar and a number  $mk$ .

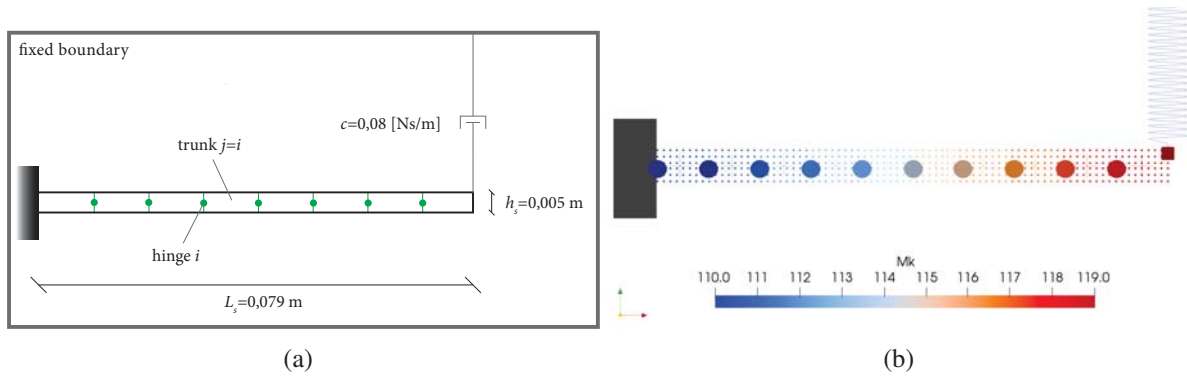


Figure 4: Simulation set-up (a) and relative SPH model (b).

The ulterior constraint works uniquely as a liner damper, being the stiffness value set to zero, thus affecting only the velocity of the oscillation and yielding to the steady state for the system. In the two-dimensional  $\{O, x, z\}$  space of our simulations, the force exerted by the additional constraint is:

$$F_{ls} = cu_{v,z} \quad (23)$$

where  $c$  is the damping, considering the cantilever axis parallel to  $x$  axis.

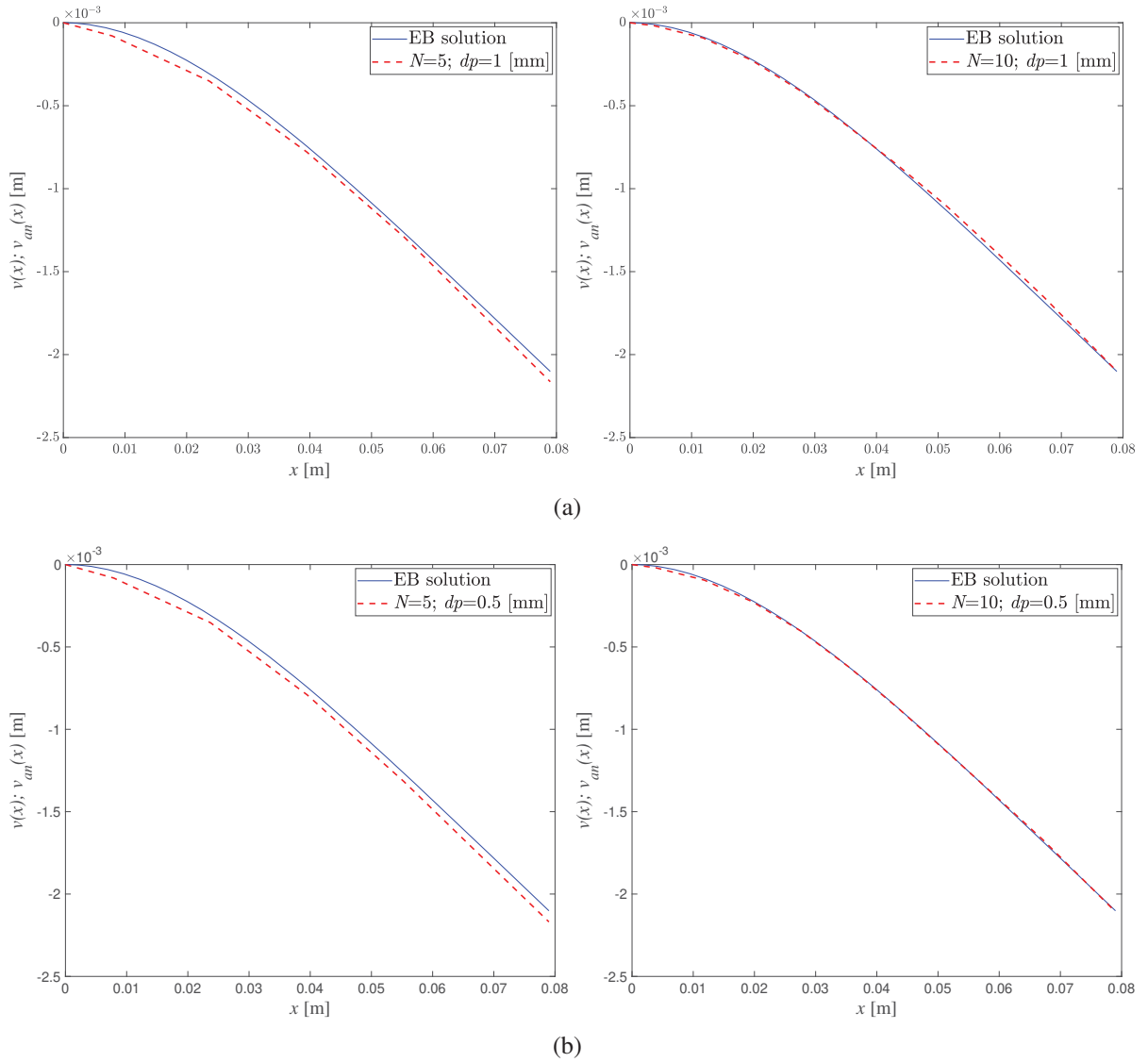
In the Table 4.1, the model information necessary for the DualSPHysics simulations is recalled, with clear significance of the nomenclature. The simulation shows the rising agreement, in the SPH framework, depending on the number of trunks. The agreement is good, and the model can be considered effective with the first value of resolution,

$$dp = \frac{0.005}{5} = 0.001 \text{ [m]} \quad (24)$$

the displacement function being properly fitted (Figure 5(a)), despite a small deviation around the centerline, regardless of the number of trunks. This is highlighted in the zoom (Figure 6(a)). By doubling the resolution, instead, the numerical solution is perfectly reproduced (Figure 5(b)).

Dimensions	
$L_s$ [m]	0.079
$b_s$ [m]	0.005
$h_s$ [m]	0.005
Physical characteristics	
$\rho_s$ [kg/m <sup>3</sup> ]	1100
$E_s$ [N/m <sup>2</sup> ]	1.2E+7
$g$ [m/s <sup>2</sup> ]	9.81
$c$ [Ns/m]	0.08

Table 1: Dimension and physical characteristics of the cantilever.

Figure 5: Comparison between the DualSPHysics results and the analytic solution: first value of resolution ( $dp = 1$  [mm]) (a), and second value of resolution ( $dp = 0.5$  [mm]) (b).

It is safe to say, after this test, that the software is able to simulate the static displacement function of an EB cantilever, and the model converges with the analytical solution as the number

of trunks increases, as visible in Figure 6. With a higher number of particles the precision is very high (Figure 6(b)), but more costly in terms of computation, since the resolution value is unique for all the simulated domain. The particle analysis on the beam model shows that beyond a certain value of particles per cross section, the agreement remains unchanged. These two values, the number of trunks and the number of particles, influence the computational effort: the former by increasing the number of interactions to be computed by the Project Chrono module, the latter by increasing the number of discrete entities where the field variables have to be calculated by DualSPHysics, with more neighbors within each support domain. With  $N = 10$ , as seen in Figure 5, the model is already effective in simulating one-dimensional beams; for what concerns the resolution value, an adequate value of  $pp(h_s)$  is enough to guarantee the numerical stability. It means that, in complex simulation involving fluid domains, the resolution needed for the beam constitutes the lower limit, which could be increased if required by other relevant conditions, just as the number of trunks, which can be raised if there are particular situations or a very high precision is required.

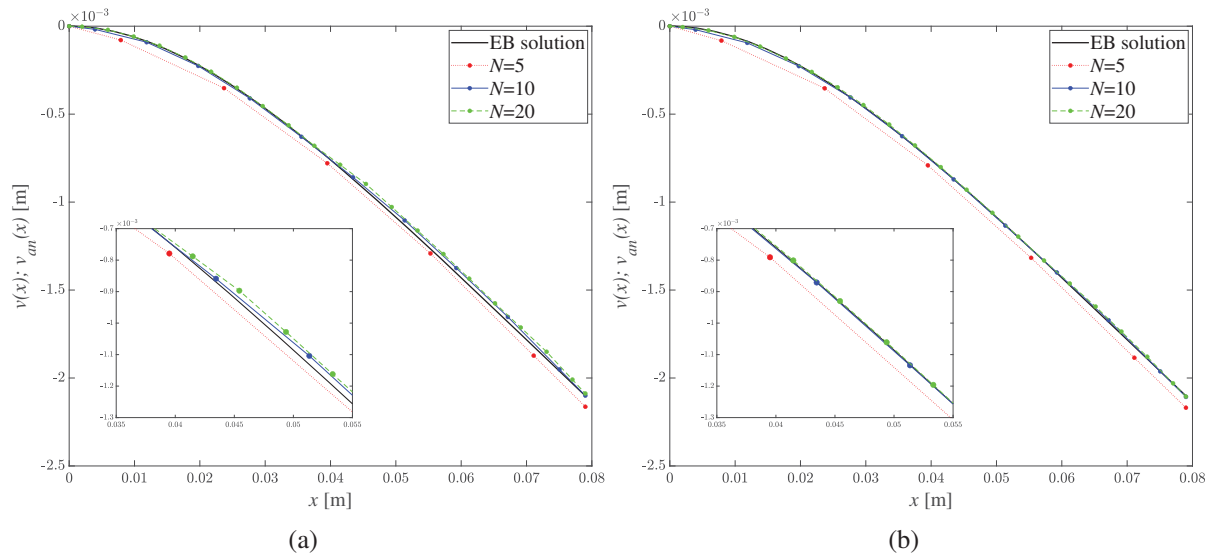


Figure 6: Convergence analysis of DualSPHysics results: first value of resolution ( $dp = 1$  [mm]) (a), and second value of resolution ( $dp = 0.5$  [mm]) (b).

## 5 CONCLUSIONS AND FUTURE WORK

The results show very good agreement between the analytic solutions and the presented model, highlighting its applicability to elastic cantilevers, or comparable static schemes, interacting with fluid or, in general, subject to dynamic impacts, time-variant load conditions, causing extreme deformations and high order effects. The numerous advantages of the SPH formulation, hence, allow thorough investigation of structure models, based on the proposed lumped elasticity discretization.

The solid framework of DualSPHysics and Project Chrono, moreover, offers the possibility to simulate complex multiphysics problems, making it suit to real-world engineering problems. Possible application fields are:

- flow-structure interactions of coastal vegetation;
- swinging of wind turbine columns subject to waves or seismic action;



- modelling of vibrations of one-dimensional structures interacting with Newtonian or non-Newtonian fluids; and
- structure collapse.

In conclusion, the simplicity, the effectiveness and the wide possibilities of implementation, in several fields, make this model a valuable starting point to investigate fluid elastic-structure interactions, or, more widely, elastic structure dynamics.

## REFERENCES

- [1] D. Violeau and B.D. Rogers. Smoothed particle hydrodynamics (sph) for free-surface flows: past, present and future. *Journal of Hydraulic Research*, 54(1):1–26, 2016. doi: 10.1080/00221686.2015.1119209.
- [2] A. Barreiro, A.J.C. Crespo, J.M. Domínguez, and M. Gómez-Gesteira. Smoothed particle hydrodynamics for coastal engineering problems. *Computers & Structures*, 120:96–106, 2013. ISSN 0045-7949. doi: <https://doi.org/10.1016/j.compstruc.2013.02.010>. URL <https://www.sciencedirect.com/science/article/pii/S0045794913000588>.
- [3] C. Altomare, A.J.C. Crespo, B.D. Rogers, J.M. Dominguez, X. Gironella, and M. Gómez-Gesteira. Numerical modelling of armour block sea breakwater with smoothed particle hydrodynamics. *Computers & Structures*, 130:34–45, 2014. ISSN 0045-7949. doi: <https://doi.org/10.1016/j.compstruc.2013.10.011>. URL <https://www.sciencedirect.com/science/article/pii/S0045794913002824>.
- [4] Z. Zang, Q. Zhang, Y. Qi, and X. Fu. Hydrodynamic responses and efficiency analyses of a heaving-buoy wave energy converter with pto damping in regular and irregular waves. *Renewable Energy*, 116:527 – 542, 2018. ISSN 0960-1481. doi: <https://doi.org/10.1016/j.renene.2017.09.057>.
- [5] Renato Vacondio, Benedict Rogers, P.K. Stansby, Paolo Mignosa, and Jon Feldman. Variable resolution for sph: A dynamic particle coalescing and splitting scheme. *Computer Methods in Applied Mechanics and Engineering*, 256:132–148, 04 2013. doi: 10.1016/j.cma.2012.12.014.
- [6] Minghao Wu, Vicky Stratigaki, Tim Verbrugghe, Peter Troch, Corrado Altomare, Alejandro Crespo, Dogan Kisacik, Lorenzo Cappiotti, José Dominguez, Matthew Hall, Moncho Gómez-Gesteira, Peter Stanstby, Ricarod Birjukovs Canelas, and Rui Ferreira. Experimental study of motion and mooring behavior of a floating oscillating water column wave energy converter. 2018.
- [7] Minghao Wu, Vasiliki Stratigaki, Peter Troch, Corrado Altomare, Tim Verbrugghe, Alejandro Crespo, Lorenzo Cappiotti, Matthew Hall, and Moncho Gómez-Gesteira. Experimental study of a moored floating oscillating water column wave-energy converter and of a moored cubic box. *Energies*, 12(10), 2019. ISSN 1996-1073. doi: 10.3390/en12101834.
- [8] J.M. Domínguez, A.J.C. Crespo, M. Hall, C. Altomare, M. Wu, V. Stratigaki, P. Troch, L. Cappiotti, and M. Gómez-Gesteira. Sph simulation of floating structures with moorings. *Coastal Engineering*, 153:103560, 2019. ISSN 0378-3839. doi: <https://doi.org/10.1016/j.coastaleng.2019.103560>.

- [9] Alejandro Crespo, Matthew Hall, J.M. Domínguez, Corrado Altomare, Minghao Wu, Tim Verbrugghe, Vasiliki Stratigaki, Peter Troch, and Moncho Gómez-Gesteira. Floating moored oscillating water column with meshless sph method. pages 11–53, 06 2018. doi: 10.1115/OMAE2018-77313.
- [10] N. Quartier, P. Ropero-Giralda, J.M. Domínguez, V. Stratigaki, and P. Troch. Influence of the drag force on the average absorbed power of heaving wave energy converters using smoothed particle hydrodynamics. *Water (Switzerland)*, 13(3), 2021. doi: 10.3390/w13030384.
- [11] D. Kisacik, V. Stratigaki, M. Wu, L. Cappiotti, I. Simonetti, P. Troch, A. Crespo, C. Altomare, J.M. Domínguez, M. Hall, M. Gómez-Gesteira, R. Canelas, and P.K. Stansby. Efficiency and survivability of a floating oscillating water column wave energy converter moored to the seabed: An overview of the esflowc marinet2 database. *Water*, 12:992, 04 2020. doi: 10.3390/w12040992.
- [12] Pablo Ropero-Giralda, Alejandro J.C. Crespo, Bonaventura Tagliaferro, Corrado Altomare, José M. Domínguez, Moncho Gómez-Gesteira, and Giacomo Viccione. Efficiency and survivability analysis of a point-absorber wave energy converter using dual-physics. *Renewable Energy*, 162:1763 – 1776, 2020. ISSN 0960-1481. doi: <https://doi.org/10.1016/j.renene.2020.10.012>. URL <http://www.sciencedirect.com/science/article/pii/S0960148120315780>.
- [13] Pablo Ropero-Giralda, Alejandro J. C. Crespo, Ryan G. Coe, Bonaventura Tagliaferro, José M. Domínguez, Giorgio Bacelli, and Moncho Gómez-Gesteira. Modelling a heaving point-absorber with a closed-loop control system using the dualphysics code. *Energies*, 14(3), 2021. ISSN 1996-1073. doi: 10.3390/en14030760. URL <https://www.mdpi.com/1996-1073/14/3/760>.
- [14] Bonaventura Tagliaferro, Rosario Montuori, Ioannis Vayas, Pablo Ropero-Giralda, Alejandro Crespo, José Domínguez, Corrado Altomare, Giacomo Viccione, and Moncho Gómez-Gesteira. A new open source solver for modelling fluid-structure interaction: case study of a point-absorber wave energy converter with a power take-off unit. In *Proceedings of the 11<sup>th</sup> International Conference on Structural Dynamics, Athens, Greece*, 11 2020. doi: 10.47964/1120.9052.21578.
- [15] M. Brito, R.B. Canelas, O. García-Feal, J.M. Domínguez, A.J.C. Crespo, R.M.L. Ferreira, M.G. Neves, and L. Teixeira. A numerical tool for modelling oscillating wave surge converter with nonlinear mechanical constraints. *Renewable Energy*, 146:2024 – 2043, 2020. ISSN 0960-1481. doi: <https://doi.org/10.1016/j.renene.2019.08.034>.
- [16] R.B. Canelas, M. Brito, O.G. Feal, J.M. Domínguez, and A.J.C. Crespo. Extending dualphysics with a differential variational inequality: modeling fluid-mechanism interaction. *Applied Ocean Research*, 76:88 – 97, 2018. ISSN 0141-1187. doi: <https://doi.org/10.1016/j.apor.2018.04.015>.
- [17] J.M. Domínguez, G. Fourtakas, Corrado Altomare, Ricardo Canelas, Angelo Tafuni, Orlando García Feal, Iván Martínez-Estévez, A. Mokos, Renato Vacondio, Alejandro Crespo, Benedict Rogers, P.K. Stansby, and M. Gómez-Gesteira. Dualphysics: from fluid

- dynamics to multiphysics problems. *Computational Particle Mechanics*, 03 2021. doi: 10.1007/s40571-021-00404-2.
- [18] Alessandro Tasora, Radu Serban, Hammad Mazhar, Arman Pazouki, Daniel Melanz, Jonathan Fleischmann, Michael Taylor, Hiroyuki Sugiyama, and Dan Negrut. Chrono: An open source multi-physics dynamics engine. pages 19–49, 06 2016. ISBN 978-3-319-40360-1. doi: 10.1007/978-3-319-40361-8\_2.
- [19] Carla Antoci, Mario Gallati, and Stefano Sibilla. Numerical simulation of fluid–structure interaction by sph. *Computers Structures*, 85(11):879–890, 2007. ISSN 0045-7949. doi: <https://doi.org/10.1016/j.compstruc.2007.01.002>. URL <https://www.sciencedirect.com/science/article/pii/S0045794907000132>. Fourth MIT Conference on Computational Fluid and Solid Mechanics.
- [20] G. Fourey, C. Hermange, D. Le Touzé, and G. Oger. An efficient fsi coupling strategy between smoothed particle hydrodynamics and finite element methods. *Computer Physics Communications*, 217:66–81, 2017. ISSN 0010-4655. doi: <https://doi.org/10.1016/j.cpc.2017.04.005>. URL <https://www.sciencedirect.com/science/article/pii/S0010465517301194>.
- [21] Abbas Khayyer, Hitoshi Gotoh, Hosein Falahaty, and Yuma Shimizu. An enhanced isph-sph coupled method for simulation of incompressible fluid-elastic structure interactions. *Computer Physics Communications*, 232, 06 2018. doi: 10.1016/j.cpc.2018.05.012.
- [22] Abbas Khayyer, Yuma Shimizu, Hitoshi Gotoh, and Shunsuke Hattori. Multi-resolution isph-sph for accurate and efficient simulation of hydroelastic fluid-structure interactions in ocean engineering. *Ocean Engineering*, 226:108652, 2021. ISSN 0029-8018. doi: <https://doi.org/10.1016/j.oceaneng.2021.108652>. URL <https://www.sciencedirect.com/science/article/pii/S0029801821000871>.
- [23] Sauro Manenti, Dong Wang, J.M. Domínguez, S. Li, Andrea Amicarelli, and Raffaele Albano. Sph modeling of water-related natural hazards. *Water*, 11:1875, 09 2019. doi: 10.3390/w11091875.
- [24] A. Amicarelli, S. Manenti, R. Albano, G. Agate, M. Paggi, L. Longoni, D. Mirauda, L. Ziane, G. Viccione, S. Todeschini, A. Sole, L.M. Baldini, D. Brambilla, M. Papini, M.C. Khellaf, B. Tagliaferro, L. Sarno, and G. Pirovano. Sphera v.9.0.0: A computational fluid dynamics research code, based on the smoothed particle hydrodynamics mesh-less method. *Computer Physics Communications*, 250:107157, 2020. ISSN 0010-4655. doi: <https://doi.org/10.1016/j.cpc.2020.107157>.
- [25] Piseth Heng, Anas Alhasawi, Jean-Marc Battini, and Mohammed Hjiij. Co-rotating rigid beam with generalized plastic hinges for the nonlinear dynamic analysis of planar framed structures subjected to impact loading. *Finite Elements in Analysis and Design*, 157:38–49, 2019. ISSN 0168-874X. doi: <https://doi.org/10.1016/j.finel.2018.11.003>. URL <https://www.sciencedirect.com/science/article/pii/S0168874X17305966>.

- [26] Dan Dubina, Ioan Marginean, and Florea Dinu. Impact modelling for progressive collapse assessment of selective rack systems. *Thin-Walled Structures*, 143:106201, 2019. ISSN 0263-8231. doi: <https://doi.org/10.1016/j.tws.2019.106201>. URL <https://www.sciencedirect.com/science/article/pii/S0263823118316021>.
- [27] G.R. Liu and M.B. Liu. *Smoothed Particle Hydrodynamics: A Meshfree Particle Method*. 01 2003. doi: 10.1142/5340.
- [28] H. Wendland. Piecewise polynomial, positive definite and compactly supported radial basis functions of minimal degree. *Advances in Computational Mathematics*, 4(1):389–396, December 1995. doi: 10.1007/BF02123482. URL <http://sro.sussex.ac.uk/id/eprint/24323/>.
- [29] Ricardo B. Canelas, Jose M. Domínguez, Alejandro J.C. Crespo, Moncho Gómez-Gesteira, and Rui M.L. Ferreira. A smooth particle hydrodynamics discretization for the modelling of free surface flows and rigid body dynamics. *International Journal for Numerical Methods in Fluids*, 78(9):581–593, 2015. doi: <https://doi.org/10.1002/fld.4031>.
- [30] Stefan Turek and Jaroslav Hron. *Proposal for Numerical Benchmarking of Fluid–Structure Interaction Between an Elastic Object and Laminar Incompressible Flow*, volume 53, pages 371–385. 06 2007. ISBN 978-3-540-34595-4. doi: 10.1007/3-540-34596-5.15.
- [31] Kangping Liao, Changhong Hu, and Makoto Sueyoshi. Free surface flow impacting on an elastic structure: Experiment versus numerical simulation. *Applied Ocean Research*, 50:192–208, 2015. ISSN 0141-1187. doi: <https://doi.org/10.1016/j.apor.2015.02.002>. URL <https://www.sciencedirect.com/science/article/pii/S0141118715000231>.
- [32] Peng-Nan Sun, David Le Touzé, Guillaume Oger, and A-Man Zhang. An accurate fsi-sph modeling of challenging fluid-structure interaction problems in two and three dimensions. *Ocean Engineering*, 221:108552, 2021. ISSN 0029-8018. doi: <https://doi.org/10.1016/j.oceaneng.2020.108552>. URL <https://www.sciencedirect.com/science/article/pii/S0029801820314608>.
- [33] P.N. Sun, D. Le Touzé, and A.-M. Zhang. Study of a complex fluid-structure dam-breaking benchmark problem using a multi-phase sph method with apr. *Engineering Analysis with Boundary Elements*, 104:240–258, 2019. ISSN 0955-7997. doi: <https://doi.org/10.1016/j.enganabound.2019.03.033>. URL <https://www.sciencedirect.com/science/article/pii/S0955799719300943>.

## DIGITAL SIMULATION OF WIND FIELD VELOCITY FOR EVALUATING PROPER STIFFNESS INDICATORS OF WINDOW MULLIONS

Gian Felice Giaccu<sup>1</sup>, and Antonio Cazzani<sup>2</sup>

<sup>1</sup> Department of Architecture, Design and Urban Planning, University of Sassari, Alghero, Sassari,

Italy  
e-mail: gf.giaccu@uniss.it

<sup>2</sup> Department of Civil, Environmental Engineering and Architecture, University of Cagliari, Cagliari,  
Italy

e-mail: antonio.cazzani@unica.it

---

### Abstract

*Mullions are important structural windows elements that provide their resistance to wind forces. These elements are of fundamental importance for the energy balance of the building since their structural behavior deeply affects its energy losses. A proper structural design of the windows mullions is therefore important for evaluating a suitable stiffness indicator of the mullions to avoid energy losses. In the present paper, a parametric study aiming to investigate the wind-induced displacements of the window mullions and their compatibility with their thermal barrier has been conducted. The proposed study aims to evaluate a proper moment of inertia of the aluminum profiles forming the mullions as a function of the windows exposition for different wind forces depending on the elevation of the building in which the window has been installed.*

**Keywords:** wind induced effects, window mullions, stiffness indicators.

---



## 1 INTRODUCTION

The This paper discusses the turbulent wind effects on the window mullions for different wind window expositions and different wind velocities. A proper design of the window mullions is of paramount importance for the energy balance of the building since their structural behavior deeply affects the energy losses of the building [1].

At present, it is always a big challenge for architects and planning engineers to design new buildings with different shapes with respect to the fact that the wind load is an important input parameter in the design of the windows. Wind forces acting on windows are strongly dependent on the building shape, on the environment and by the orographic in which the building has been built, such forces are usually determined by using Computational Fluid Dynamics (CFD) techniques or wind tunnel experiments [2].

In the present paper, a parametric study aimed to investigate the wind-induced displacements of the mullions and their compatibility with the energy losses of the building has been conducted, the study aims to assess a proper stiffness indicator of the mullions as a function of the window elevation.

## 2 DIGITAL SIMULATION OF WIND FIELD VELOCITY

Wind load simulation has been studied acting on the mullions through spatial discretization of the wind field using an idealized grid. At each node of the grid partially correlated wind turbulence time histories of the along-wind field (primary) load component are synthetically generated by the standard wave superposition method [2, 3]. The turbulent wind load, generated by assuming the validity of the quasi-steady formulation for pressures and equivalent forces (based on tributary areas), has been imposed for a duration equal to 600s, with a time step  $\Delta t = 0.01$ s and evaluated for elevation of the idealized grid (Fig.1).

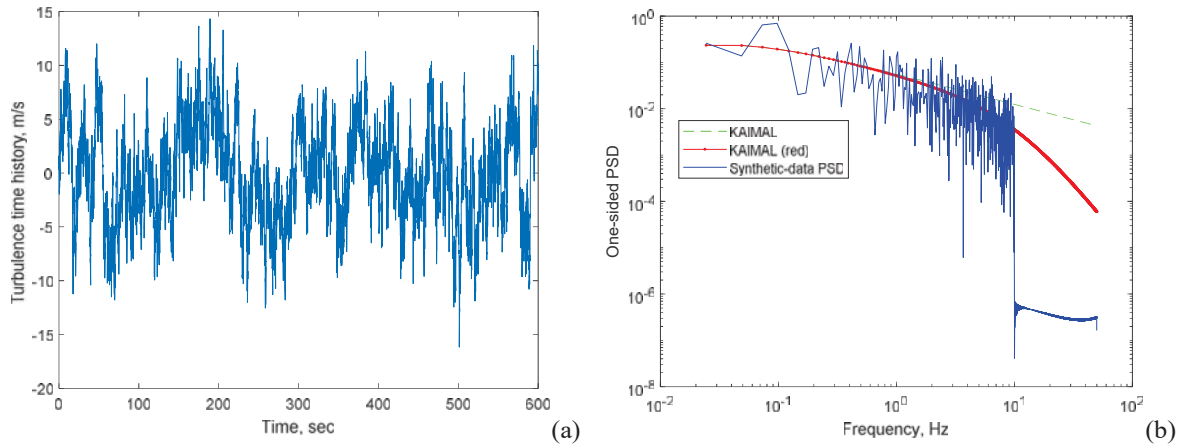
The pressure coefficients of the surface window  $C_p$  have been obtained and adapted from the results by Hubova et al. [4] in the present case has been prudentially taken  $C_p=1$ . Mean wind velocity  $\bar{U}(H)$  can be found through the following relation according to the reference wind speed  $U_{ref}$ , and the constants  $k_T$  and  $z_0$  provided by the Eurocode 1 [5]:

$$\bar{U}(H) = U_{ref} k_T \ln \frac{H}{z_0} \quad (1)$$

Accounting on the turbulent component of  $V_{turb}$  of the wind, the time varying wind speed at the altitude  $H$  can be expressed as:

$$V(t) = \bar{U}(H) + V_{turb}(t) \quad (2)$$

Figure 1 shows an example of the wind velocity simulated time history and its spectral compatibility.



**Figure 1.** Wind speed simulation for elevation  $H=30\text{m}$ ,  $U_{bar}=28\text{m/s}$  at  $H_{ref}=10\text{m}$ ; (a) Turbulent wind speed time history in one point of the idealized; (b) comparison between the employed synthetic data, Kaimal reduced and Kaimal power spectral density function.

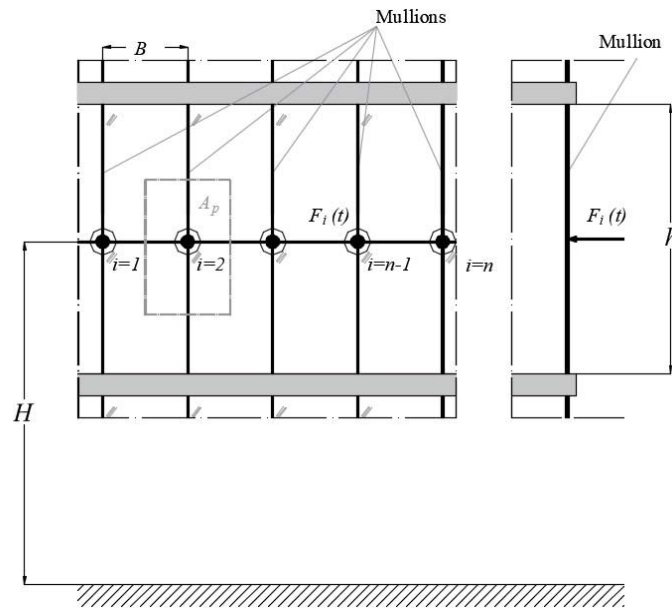
According to the above formulated hypothesis, dynamic force  $F_i(t)$  acting on the mullion can be written as:

$$F_i(t) = \frac{1}{2} C_p A_p V^2(t) \quad (3)$$

Wind force simulation has been performed through a concentrated load force acting on the center of the span of the elements accounting of an aerodynamic admittance function of rectangular plates, with “projected area”  $A_p$  (Fig. 2) orthogonal to the flow direction [6]. The loads have been evaluated for different “elevation”  $H$  and for a constant width  $B$  (mullion distance) of the idealized grid.

### 3 BACKGROUND MATHEMATICAL MODELS AND BENCHMARK SYSTEM

The present approach is based on the dynamic equilibrium equations of a discretized uncoupled Single Degree of Freedom (SDOF) lumped masse system [1] comparable to the one described by Giaccu in [7], in this treatment, structural interaction between mullion and glass has been conservatively neglected, it must be noted that this interaction is not often fully defined because of the uncertainties due to the assembly of the glass window. Geometrical properties of the glass window are described in Table 1.



**Figure 2.** Benchmark model employed for the simulations of wind forces on facade.

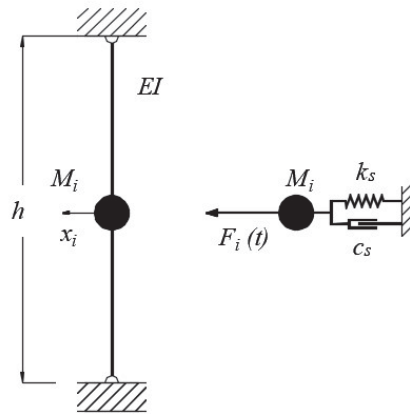
Structural properties of the dynamic system have been calculated accounting of the geometrical features of the glass window illustrated in Fig.2 and in Table 1, which include the mass per unit area of the glass  $\rho_{glass}$ , the mullion span  $h$ , the modulus of elasticity of the aluminum  $E$  and its specific mass  $\rho_{al}$ , the a cross section area of the mullion  $A_{mul}$  and the mass of unit of length of the mullion  $\rho_{mul}$ .

$h$ (m)	$B$ (m)	$A_p$ (m <sup>2</sup> )	$E$ (MPa)	$A_{mul}$ (m <sup>2</sup> )	$\rho_{glass}$ (kg/ m <sup>2</sup> )	$\rho_{al}$ (kg/m <sup>3</sup> )	$\rho_{mul}$ (kg/m)	$M$ (kg)	$\zeta_s$ (%)	$E$ (MPa)
3.00	1.50	4.5	$6.9 \times 10^{10}$	$2.24 \times 10^{-3}$	20.00	2699	6.05	98.60	5.0	$6.9 \times 10^{10}$

Table 1: Geometrical and Mechanical properties of the glass window and of the lumped mass model.

Tributary area of the window can be therefore found as  $A_p = Bh/2$ , mechanical properties of the lumped mass model can be obtained, accounting of the halved mass of the mullion, as  $M = \rho_{wind} A_p + \rho_{al} h/2$  and the stiffness of the spring which can be obtained as  $k_s = 48EI/h^3$ .

The moment of inertia of the profile can be written, accounting of the the radius of gyration of the mullion  $r_G$ , as  $I = A_{mul} r_G^2$  and damping constant can be written as  $c = 2\zeta_s(kM)^{0.5}$ , considering a conventional structural damping  $\zeta_s = 5\%$ .



**Figure 3.** Schematic representation of the mathematical model employed for the simulations.

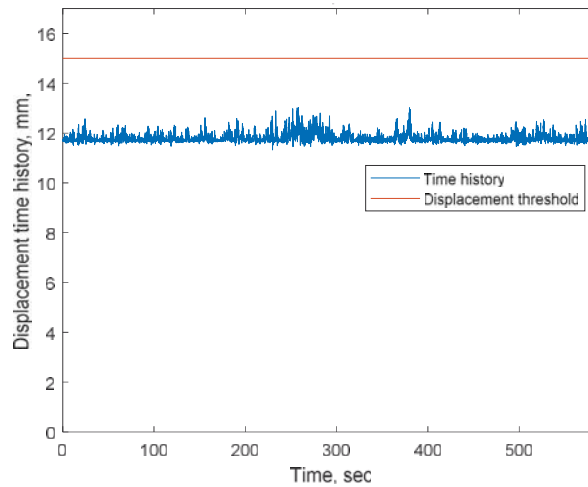
#### 4 PARAMETRIC STUDY

The parametric study has been conducted according to Eq. 1 for the mean wind speed  $U_{ref}=28\text{m/s}$  at reference altitude  $H_{ref}=10\text{m}$ , with  $k_T=0.17$  and for a roughness length  $z_0=0.03$  (m). The maximum displacement for different elevation  $H$  of the glass window has been detected.

For simplicity, the considered moments of inertia correspond to the same cross section  $A_{mul}$  for different slenderness  $\lambda$  of the mullion. Moment of inertia  $I$  of the mullion, can be therefore obtained as function of the slenderness  $\lambda$  through the following relation:

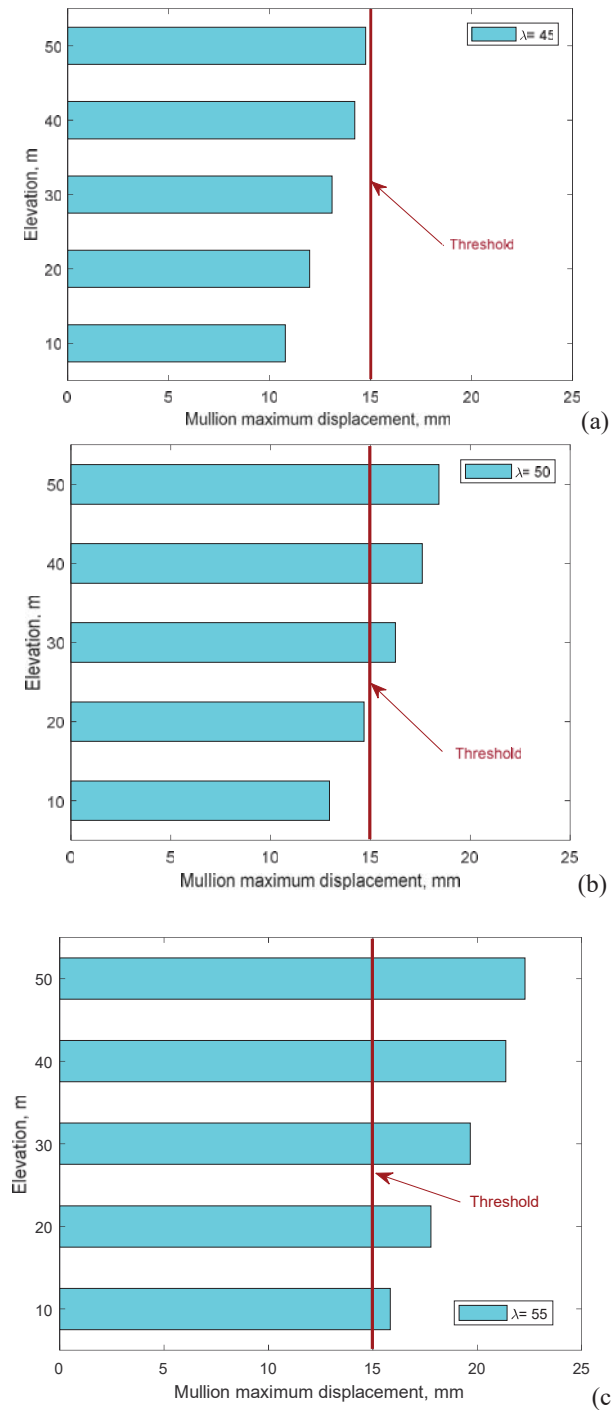
$$I = A_{mul} \left( \frac{h}{\lambda} \right)^2 \quad (4)$$

Deflections of the aluminum profiles have been compared with the conventional limit deflection indicator discussed in [1] ( $1/200$  of the span  $h$ ) which indicates the threshold beyond which the thermal barrier rigidity is necessary. The number of mullions considered in the idealized grid is  $n=6$ .



**Figure 4.** Displacement time history for  $H=40\text{m}$ ,  $U_{ref}=28\text{m/s}$  at  $H_{ref}=10\text{m}$  and  $\lambda=45$  in comparison with the displacement threshold  $h/200$ .

Results have been illustrated in Fig.5 as function of the elevation  $H$  of the window for different slenderness  $\lambda$ . Three different slenderness have been considered for the proposed simulation  $\lambda=45, 50$  and  $55$ .



**Figure 5.** Maximum displacement of the mullion in case of  $U_{bar}=28\text{m/s}$  at  $H_{ref}=10\text{m}$  for different elevation  $H$ , in comparison with the displacement threshold  $h/200$  for different slenderness  $\lambda$  of the mullion cross section: (a)  $\lambda=45$ , (b)  $\lambda=50$  and (c)  $\lambda=55$ .

From an examination of the results illustrated in Fig.5, it can be inferred that, slenderness of the mullion plays an important role in the wind induced deflections, in particular, for the considered case, a slenderness of the aluminum profile  $\lambda>55$  leads to crossing the



threshold limit ( $1/200$  of the span  $h$ ) for all the considered altitudes, whereas profile with slenderness  $\lambda=50$  can be utilized up to heights of 30 m, finally the slenderness  $\lambda=45$  can be utilized up to heights of 50 m without crossing the threshold.

## 5 CONCLUSIONS

The comparison of the data obtained during the performed simulations allowed to study different cases of buildings accounting of different expositions and different wind loading, a parametric study has been conducted for the considered cases assessing proper stiffness indicators of the mullions for different window properties and for different window expositions. A parametric study aimed to investigate the wind-induced displacements and of their compatibility with the windows' thermal barrier has been conducted. Results indicate that slenderness of the mullions plays an important role in limiting the wind-induced displacements in the mullion of the window since displacements are in turn directly related to the energy losses of the building. Suitable stiffness indicators of the mullions were indicated for all considered cases.

## REFERENCES

- [1] A. Konstantinov, E. Leontev, Remizova. A., Rigidity of the aluminum window profiles with thermal barrier, *Advances in Intelligent Systems and Computing* 982, 26-34, 2020.
- [2] M. Di Paola, Digital simulation of wind field velocity, *Journal of Wind Engineering and Industrial Aerodynamics* 74-76, 91-109, 1998.
- [3] M. Di Paola, I. Gullo, Digital generation of multivariate wind field processes, *Probabilistic Engineering Mechanics* 16, 1-10, 2001.
- [4] O. Hubova, M. Macak, L. Konecna, G. Ciglan, External Pressure Coefficients on the Atypical High-Rise Building – Computing Simulation and Measurements in Wind Tunnel, *Procedia Engineering* 190, 488-495, 2017.
- [5] Eurocode 1: Actions on Structures - General Action - Part 1-4: Wind Actions, Brussels, 2005.
- [6] B.J. Vickery, A model of atmospheric turbulence for studies of wind load on buildings, *Proceedings of the Proceedings of 2nd Australasian Conference on Hydraulics and Fluid Mechanics*, Auckland, New Zealand, 1965.
- [7] G.F. Giaccu, An equivalent frequency approach for determining non-linear effects on pre-tensioned-cable cross-braced structures *Journal of Sound and Vibration* 422, 62-78, 2018

# ANALYTICAL/NUMERICAL SOLUTIONS TO THE PROBLEM OF THE DYNAMIC RESPONSE OF AN ELASTIC PLATE ON A CONTINUOUSLY NON-HOMOGENEOUS CROSS-ANISOTROPIC VISCOELASTIC SOIL TO A MOVING LOAD

Niki D. Beskou<sup>1</sup> and Edmond V. Muho<sup>2</sup>

<sup>1</sup>Department of Civil Engineering, University of the Peloponnese  
Patras 26334, Greece  
email: nikidiane@gmail.com

<sup>2</sup>Department of Disaster Mitigation for Structures, College of Civil Engineering, Tongji University  
200092 Shanghai, China  
email: edmondmuho@gmail.com

---

## Abstract

*In this work the problem of the dynamic response of a flexural elastic plate on a continuously non-homogeneous viscoelastic cross-anisotropic half-plane or half-space soil medium to a line or rectangular load moving with constant speed is determined analytically/numerically. Soil non-homogeneity is associated with elastic moduli increasing with depth. Plate viscous damping is considered, and the viscoelastic effects of the soil are introduced via hysteric damping. The solution of the problem is obtained with the aid of the complex Fourier series method involving the horizontal coordinates and the time. Employment of this method reduces the partial differential equations of motion for the soil and the plate to ordinary differential equations with variable coefficients and an algebraic equation, respectively. Those ordinary differential equations are solved by the method of Frobenius. Verification of the solutions is done by means of comparisons with known existing analytical solutions for the special cases of isotropy and homogeneity with or without the plate.*

**Keywords:** Moving loads, dynamic response, elastic plate, soil non-homogeneity, Soil cross-anisotropy.

---

## 1 INTRODUCTION

In this work, the dynamic response of a flexural elastic plate to a distributed load moving with constant speed is determined analytically. The plate is supported by a cross-anisotropic, non-homogeneous, viscoelastic half-plane or half-space soil medium. Soil viscoelasticity is considered in order to take into account dissipation of energy [1]. In the context of linear dynamic analysis, viscoelastic material behavior is usually modeled in the frequency domain by replacing the elastic moduli by their complex counterparts, which are functions of hysteretic damping [2]. Soil anisotropy is considered in order to take into account different moduli values along different directions. In soils, the simple but realistic model of transverse isotropy (or cross-anisotropy) is considered with elastic moduli being different in horizontal and vertical planes due to the soil layers deposition process [3-5]. Soil nonhomogeneity is characterized by different physical properties (density, elastic moduli) at different depths because of the soil overburden. It can be modeled in a discrete manner by layers or in a continuous manner by assuming density and/or elastic moduli to vary continuously with depth. In the latter case, it is usually assumed that density is constant and the elastic moduli vary non-linearly with depth [6-12].

Use is made of the complex Fourier series method involving the horizontal coordinate and the time to reduce the governing equations of motion of the plate-soil system to algebraic and ordinary differential equations, respectively. The latter equations because they have variable coefficients are solved by the method of Frobenius.

The following literature review is restricted to analytical works closely related to the present work. One can place those works in the following categories:

- 1) Works associated with a homogeneous or layered, isotropic elastic half-space under point or distributed, constant or time harmonic loads moving with constant speed, e.g., [13-22].
- 2) Works associated with elastic beams or plates on a homogeneous or layered, isotropic half-space under point or distributed, constant or time harmonic loads moving with constants speed, e.g., [23-26].
- 3) Works associated with or without plates on a homogeneous or layered, transversely isotropic (or cross-anisotropic) elastic half-spaces under point or distributed, constant or time harmonic loads moving with constant speed, e.g., [27-28].
- 4) Works associated with homogeneous, transversely isotropic (or cross-anisotropic) elastic half-spaces under dynamic but stationary loads, e.g. [29-31].
- 5) Works associated with an isotropic, continuously non-homogeneous elastic half-space or half-plane under dynamic stationary or moving with constant speed [32-34].
- 6) Works associated with a transversely isotropic (or cross-anisotropic), continuously non-homogeneous, viscoelastic half-space [35,36] under stationary dynamic.

From the above, one can easily conclude that the only works dealing with all three features of soil behavior (viscoelasticity, anisotropy and continuous nonhomogeneity) are [35, 36] and the present work. However, works [35, 36] are associated with stationary and not moving loads as it is the case with the present work. In addition, no plate effect is considered in [35, 36] as in the present work. Furthermore, use is made here of the complex Fourier series method, which is able, because the load speed is constant, to handle both the horizontal coordinate and the time using a single summation and provide a closed form solution in series form. Most of all the other methods used in the aforementioned works employ integral transform methods (mainly Fourier and Hankel transforms) and this requires numerical integration or complicated analytical inversion techniques instead of simple series evaluation in the present case. This complex Fourier series method has

been successfully used by Siddharthan et al [37] and Theodorakopoulos [38] in connection with moving loads on poroelastic half-planes and Beskou et al [39] and Muho and Beskou [40] in connection with moving loads on anisotropic homogeneous half-plane and isotropic nonhomogeneous half-plane, respectively.

The obtained analytical solution of the problem considered here is first verified against other existing analytical solutions pertaining to simpler special cases.

## 2 PROBLEM DESCRIPTION

Consider a homogeneous isotropic, elastic, thin flexural plate, supported by a cross-anisotropic (or transversely isotropic) nonhomogeneous viscoelastic half-plane or half-space soil medium under conditions of plane strain, as depicted in Fig. 1 in the framework of a Cartesian system  $x$  and  $z$  or  $x, y, z$ , respectively. On the surface of the plate, a uniformly distributed load of intensity  $F$  over a rectangle with sides  $2l_1$  along the  $x$  direction or  $2l_1$  and  $2l_2$  along the  $x$  and  $y$  directions, respectively, is assumed to move with constant velocity  $V$  along the  $x$ -direction, as shown in Fig. 1.

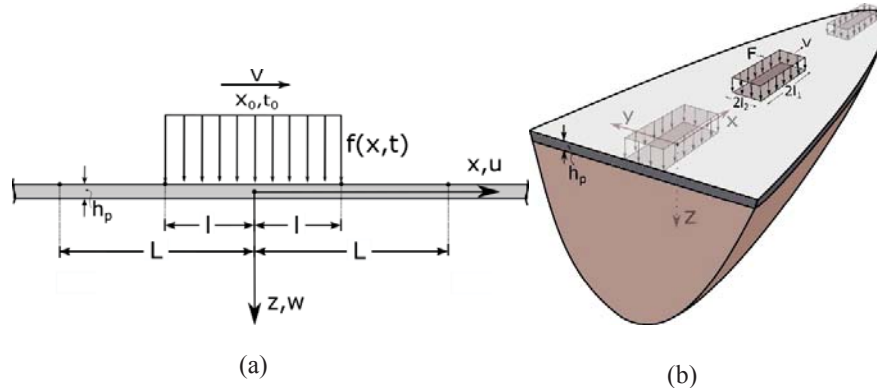


Figure 1: A rectangular distributed load moving with constant speed  $V$  on a plate resting on a transversely isotropic viscoelastic (a) half-plane or (b) half-space with variable with depth moduli.

The equations of motion of the half-plane soil medium read as [41]

$$\frac{\partial \sigma_{xx}}{\partial x} + \frac{\partial \sigma_{xz}}{\partial z} = \rho \ddot{u} \quad (1)$$

$$\frac{\partial \sigma_{xz}}{\partial x} + \frac{\partial \sigma_{zz}}{\partial z} = \rho \ddot{w} \quad (2)$$

and for the half-space as [34]

$$\frac{\partial \sigma_{xx}}{\partial x} + \frac{\partial \sigma_{xy}}{\partial y} + \frac{\partial \sigma_{xz}}{\partial z} = \rho \ddot{u} \quad (3)$$

$$\frac{\partial \sigma_{yy}}{\partial y} + \frac{\partial \sigma_{yx}}{\partial x} + \frac{\partial \sigma_{yz}}{\partial z} = \rho \ddot{v} \quad (4)$$

$$\frac{\partial \sigma_{zz}}{\partial z} + \frac{\partial \sigma_{zx}}{\partial x} + \frac{\partial \sigma_{zy}}{\partial y} = \rho \ddot{w} \quad (5)$$

where,  $\rho$  is the soil mass density,  $u = u(x, y, z, t)$ ,  $v = v(x, y, z, t)$  and  $w = w(x, y, z, t)$  are the soil displacements along the  $x$ ,  $y$  and  $z$  directions, respectively, and overdots denote differentiation with respect to time  $t$ .

The equation of lateral motion of the plate for the half-plane case has the form [42]

$$D \frac{\partial^4 w_p}{\partial x^4} + m_p \frac{\partial^2 w_p}{\partial t^2} + c_p \frac{\partial w_p}{\partial t} = f(x, t) - q(x, t) \quad (6)$$

where  $w_p = w_p(x, t)$  is the lateral plate deflection,  $m_p$  is the mass per unit length of the plate,  $c_p$  is the viscous damping coefficient of the plate,  $q(x, t)$  is the interaction of the soil on the plate and  $D$  is the flexural rigidity of the plate defined as

$$D = E_p h_p^3 / 12(1 - \nu_p^2) \quad (7)$$

with  $h_p$  being the thickness of the plate and  $E_p$  and  $\nu_p$  the modulus of elasticity and Poisson's ratio of the plate, respectively. For the half-space case Eq. (6) is replaced by

$$D \nabla^4 w_p + m_p \ddot{w}_p + c_p \dot{w}_p = f(x, y, t) - q(x, y, t) \quad (8)$$

where,  $\nabla^4 = \frac{\partial^4}{\partial x^4} + \frac{2 \partial^4}{\partial x^2 \partial y^2} + \frac{\partial^4}{\partial y^4}$  is the biharmonic differential operator.

The soil stresses are expressible in terms of displacements for the present anisotropic and nonhomogeneous half-plane case as [41]

$$\sigma_{xx} = c_{11}(z) \frac{\partial u}{\partial x} + c_{13}(z) \frac{\partial w}{\partial z} \quad (9)$$

$$\sigma_{zz} = c_{13}(z) \frac{\partial u}{\partial x} + c_{33}(z) \frac{\partial w}{\partial z} \quad (10)$$

$$\sigma_{xz} = c_{44}(z) \left( \frac{\partial u}{\partial z} + \frac{\partial w}{\partial x} \right) \quad (11)$$

and for the half-space as [34]

$$\sigma_{xx} = c_{11} \frac{\partial u}{\partial x} + c_{12} \frac{\partial v}{\partial y} + c_{13} \frac{\partial w}{\partial z} \quad (12)$$

$$\sigma_{yy} = c_{12} \frac{\partial u}{\partial x} + c_{11} \frac{\partial v}{\partial y} + c_{13} \frac{\partial w}{\partial z} \quad (13)$$

$$\sigma_{zz} = c_{13} \frac{\partial u}{\partial x} + c_{13} \frac{\partial v}{\partial y} + c_{33} \frac{\partial w}{\partial z} \quad (14)$$

$$\sigma_{yz} = c_{44} \left( \frac{\partial v}{\partial z} + \frac{\partial w}{\partial y} \right) \quad (15)$$

$$\sigma_{xz} = c_{44} \left( \frac{\partial u}{\partial z} + \frac{\partial w}{\partial x} \right) \quad (16)$$

$$\sigma_{xy} = c_{66} \left( \frac{\partial u}{\partial y} + \frac{\partial v}{\partial x} \right) \quad (17)$$



for the half-space soil medium [34].

In the above equations,  $c_{11}$ ,  $c_{12}$ ,  $c_{13}$ ,  $c_{33}$ ,  $c_{44}$  and  $c_{66}$  are elastic constants which are expressible in terms of the engineering constants as [34]

$$c_{11} = \frac{E(E' - E'v'^2)}{(1 + v)(E' - E'v - 2Ev'^2)} \quad (18)$$

$$c_{12} = \frac{E(E'v + Ev'^2)}{(1 + v)(E' - E'v - 2Ev'^2)} \quad (19)$$

$$c_{13} = \frac{EE'v'}{E' - E'v - 2Ev'^2} \quad (20)$$

$$c_{33} = \frac{E'^2(1 - v)}{E' - E'v - 2Ev'^2} \quad (21)$$

$$c_{44} = G' \quad (22)$$

$$c_{66} = G = \frac{c_{11} - c_{12}}{2} = \frac{E}{2(1 + v)} \quad (23)$$

where,  $E$ ,  $G$ , and  $v$  denote elastic modulus, shear modulus, and Poisson's ratio, respectively and the primes refer to the vertical axis of rotational material symmetry, which coincides with the  $z$ -axis of Fig.1. Those  $E$  and  $G$  without prime refer to the horizontal ( $x$ ,  $y$ ) plane of isotropy, while it has been assumed here that the value of the Poisson's ratio is the same along the vertical and horizontal direction.

Substitution of Eqs. (9)-(11) into Eqs. (1) and (2) for the half-plane model or Eqs. (12)-(17) into (3) and (4) for the half-space model, results in the governing equations of motion of the soil medium in terms of displacements of the form

$$c_{11} \frac{\partial^2 u}{\partial x^2} + c_{44} \frac{\partial^2 u}{\partial z^2} + c'_{44} \frac{\partial u}{\partial z} + (c_{13} + c_{44}) \frac{\partial^2 w}{\partial x \partial z} + c'_{44} \frac{\partial w}{\partial x} = \rho \ddot{u} \quad (24)$$

$$c_{33} \frac{\partial^2 w}{\partial z^2} + c_{44} \frac{\partial^2 w}{\partial x^2} + c'_{33} \frac{\partial w}{\partial z} + (c_{13} + c_{44}) \frac{\partial^2 u}{\partial x \partial z} + c'_{13} \frac{\partial u}{\partial x} = \rho \ddot{w} \quad (25)$$

for the half-plane and

$$c_{11} \frac{\partial^2 u}{\partial x^2} + c_{66} \frac{\partial^2 u}{\partial y^2} + c_{44} \frac{\partial^2 u}{\partial z^2} + c'_{44} \frac{\partial u}{\partial z} + (c_{12} + c_{66}) \frac{\partial^2 v}{\partial x \partial y} + (c_{13} + c_{44}) \frac{\partial^2 w}{\partial x \partial z} + c'_{44} \frac{\partial w}{\partial x} = \rho \ddot{u} \quad (26)$$

$$c_{66} \frac{\partial^2 v}{\partial x^2} + c_{11} \frac{\partial^2 v}{\partial y^2} + c_{44} \frac{\partial^2 v}{\partial z^2} + c'_{44} \frac{\partial v}{\partial z} + (c_{12} + c_{66}) \frac{\partial^2 u}{\partial x \partial y} + (c_{13} + c_{44}) \frac{\partial^2 w}{\partial y \partial z} + c'_{44} \frac{\partial w}{\partial y} = \rho \ddot{v} \quad (27)$$

$$c_{44} \frac{\partial^2 w}{\partial x^2} + c_{44} \frac{\partial^2 w}{\partial y^2} + c_{33} \frac{\partial^2 w}{\partial z^2} + c'_{33} \frac{\partial w}{\partial z} + (c_{13} + c_{44}) \frac{\partial^2 u}{\partial x \partial z} + (c_{13} + c_{44}) \frac{\partial^2 v}{\partial y \partial z} + c'_{13} \frac{\partial u}{\partial x} + c'_{13} \frac{\partial v}{\partial y} = \rho \ddot{w} \quad (28)$$

for the half-space, respectively, where primes on  $c_{ij} = c_{ij}(z)$  denote differentiation with respect to the depth  $z$ .

The boundary conditions of the half-plane case consist of dynamic equilibrium and compatibility at the plate-soil interface (where smooth contact is assumed) of the form

$$\sigma_{xz}(x, 0, t) = 0 \quad (29)$$

$$\sigma_{zz}(x, 0, t) = -q(x, t) \quad (30)$$

$$w(x, 0, t) = w_p(x, t) \quad (31)$$

The corresponding boundary conditions for the half-space case have the form

$$\sigma_{xz}(x, y, 0, t) = 0 \quad (32)$$

$$\sigma_{yz}(x, y, 0, t) = 0 \quad (33)$$

$$\sigma_{zz}(x, y, 0, t) = -q(x, y, t) \quad (34)$$

$$w(x, y, 0, t) = w_p(x, y, t) \quad (35)$$

Finally, at a depth  $z = H$  approaching infinity, all soil displacements become zero due to the radiation conditions at infinity and one has

$$u(x, H, t) = 0 \text{ for half-plane or } u(x, y, H, t) = 0 \text{ for half-space} \quad (36)$$

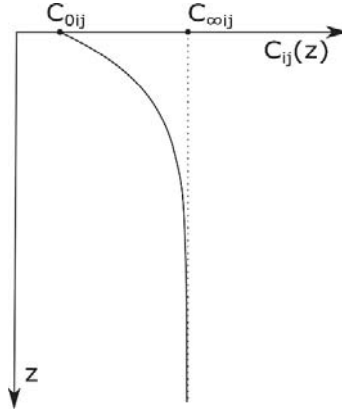
$$v(x, y, H, t) = 0 \text{ for half-space} \quad (37)$$

$$w(x, H, t) = 0 \text{ for half-plane or } w(x, y, H, t) = 0 \text{ for half-space} \quad (38)$$

Viscoelasticity in the soil medium is considered in the frequency domain, utilized during the solution procedure of the next section, by replacing the elastic constants  $c_{ij}$  by their complex counterparts  $c_{ij}^*$  according to the relation [2]

$$c_{ij}^* = c_{ij}(1 + 2i\xi) \quad (39)$$

resulting from the correspondence principle, where  $\xi$  is the hysteretic damping coefficient and  $i = \sqrt{-1}$ .


 Figure 2: Soil elastic constants  $c_{ij}$  increasing with depth  $z$ 

The nonhomogeneity of the soil is associated here only with a variability of the elastic constants with depth, i.e.,  $c_{ij} = c_{ij}(z)$ . It is assumed here that these constants increase with depth  $z$  in accordance with the relation

$$c_{ij}(z) = c_{0ij} + (c_{\infty ij} - c_{0ij})(1 - e^{-\alpha z}) \quad (40)$$

due to Vrettos [7, 8] as shown in Fig. 2, which is based on tests and provides bounded values of  $c_{ij}$  at infinity. In the above,  $c_{0ij}$ ,  $c_{\infty ij}$  and  $c_{ij}(z)$  are elastic constants at the soil surface, at an infinite depth and at depth  $z$  from the soil surface, respectively, and  $\alpha$  is a constant with dimensions of inverse length.

### 3 SOLUTION PROCEDURE

The problem to be solved consists of the governing partial differential equation of motion of the plate (Eq. (6) or Eq. (8)) and the governing partial differential equations of motion of the soil (Eqs. (24), (25) or (26)-(28)) subject to the boundary conditions (29)-(31) or (32)-(35). The solution procedure consists of two major steps: i) reduction of the partial differential equations of the plate-soil system to an algebraic and ordinary differential equations, respectively, by using the complex Fourier series approach [37-40] and ii) solution of the ordinary differential equations with variable coefficients for the soil by the method of Frobenius [43] and employment of the boundary conditions to obtain the final response of the plate-soil system to the moving load.

Thus, using the method of complex Fourier series, the load  $f(x,t)=f(x-Vt)$  is expanded in series of the form [39, 40]

$$f(x - Vt) = \text{Re} \sum_{n=0}^N F_n e^{i\lambda_n(x-Vt)} \quad (41)$$

where the load amplitude  $F_n$  is given by

$$F_n = \begin{cases} \frac{Fl}{L}, & \text{for } n = 0 \\ 2 \frac{F}{n\pi} \sin\left(\frac{n\pi l}{L}\right), & \text{for } n = 1, 2, \dots, N \rightarrow \infty \end{cases} \quad (42a)$$

for the half-plane model or

$$F_{nm} = \begin{cases} F \frac{l_1 l_2}{L_1 L_2} & \text{for } n = m = 0 \\ 2F \frac{l_2}{n\pi L_2} \sin \frac{n\pi l_1}{L_1} & \text{for } m = 0, n = 1, 2, \dots, N \\ 2F \frac{l_1}{m\pi L_1} \sin \frac{m\pi l_2}{L_2} & \text{for } n = 0, m = 1, 2, \dots, M \\ 4F \frac{1}{nm\pi^2} \sin \frac{n\pi l_1}{L_1} \sin \frac{m\pi l_2}{L_2} & \text{for } n = 1, 2, \dots, N, m = 1, 2, \dots, M \end{cases} \quad (42b)$$

for the half-space model, respectively.

In Eqs. (41) and (42) and with reference Fig.1,  $\lambda_n = n\pi/L$  are the wavenumber parameters,  $2l$  is the length of the distributed load,  $2L$  is the wavelength of the system,  $Re$  denotes the real part and  $i = \sqrt{-1}$ . Because the plate-soil system is linear, its response to the moving load  $f(x, t)$  will be of the form

$$w_p(w, t) = Re \sum_{n=0}^N W_{pn} e^{i\lambda_n(x-Vt)} \quad (43a)$$

$$u(x, z, t) = Re \sum_{n=0}^N U_n(z) e^{i\lambda_n(x-Vt)} \quad (44a)$$

$$w(x, z, t) = Re \sum_{n=0}^N W_n(z) e^{i\lambda_n(x-Vt)} \quad (45a)$$

$$q(x, z, t) = Re \sum_{n=0}^N Q_n e^{i\lambda_n(x-Vt)} \quad (46a)$$

for the half-plane model or

$$w_p(w, t) = Re \sum_{n=0}^N \sum_{m=0}^M W_{pnm} e^{i\lambda_n(x-Vt)} e^{i\mu_m y} \quad (43b)$$

$$u(x, z, t) = Re \sum_{n=0}^N \sum_{m=0}^M U_{nm} e^{i\lambda_n(x-Vt)} e^{i\mu_m y} \quad (44b)$$

$$v(x, z, t) = Re \sum_{n=0}^N \sum_{m=0}^M V_{nm} e^{i\lambda_n(x-Vt)} e^{i\mu_m y} \quad (44c)$$

$$w(x, z, t) = Re \sum_{n=0}^N \sum_{m=0}^M W_{nm} e^{i\lambda_n(x-Vt)} e^{i\mu_m y} \quad (45b)$$

$$q(x, z, t) = Re \sum_{n=0}^N \sum_{m=0}^M Q_{nm} e^{i\lambda_n(x-Vt)} e^{i\mu_m y} \quad (46b)$$

for the half-space model, respectively, where  $W_p$ ,  $U$ ,  $V$ ,  $W$  and  $Q$  denote response amplitudes to be determined and  $n, m=1, 2, \dots, N, M \rightarrow \infty$ .

In order to avoid numerical problems associated with  $n=0$  or  $m=0$  implying  $\lambda_n=0$  or  $\mu_m=0$ , respectively, solutions can be derived for each of the following four cases of the load amplitudes of Eq. (42), i.e., i)  $n=m=0$ , ii)  $m=0, n>0$ , iii)  $n=0, m>0$  and iv)  $n>0, m>0$ . Only the solution for  $n>0, m>0$  will be derived here. Solutions for the other three cases can be very easily determined following the same procedure.

Substituting Eqs. (43)-(46) in Eqs. (6), (24), (25) or (26)-(28), omitting the summation symbol and the common factors  $e^{i\lambda_n(x-Vt)}$  and introducing the proposed by Vrettos [7, 8] dimensionless parameters

$$\begin{aligned} \frac{\lambda_n^2}{a^2} &= \beta, \quad \frac{\lambda_n}{a} = -\gamma, \quad \frac{\lambda_n^2 \rho V^2}{a^2 c_{\infty 44}} = \theta \\ \frac{c_{\infty 11}}{c_{\infty 44}} &= \delta_1, \quad \frac{c_{\infty 13}}{c_{\infty 44}} = \delta_2, \quad \frac{c_{\infty 33}}{c_{\infty 44}} = \delta_3, \end{aligned} \quad (47)$$

for the half-plane or

$$\begin{aligned} \frac{\lambda_n^2}{\alpha^2} &= \beta_1, \quad \frac{\mu_m}{\alpha^2} = \beta_2, \quad \frac{\lambda_n}{\alpha} = -\gamma_1, \quad \frac{\mu_m}{\alpha} = \gamma_2 \\ \frac{\rho \lambda_n^2 V^2}{\alpha^2 c_{\infty 44}} &= \theta, \quad \frac{c_{\infty 11}}{c_{\infty 44}} = \delta_1, \quad \frac{c_{\infty 13}}{c_{\infty 44}} = \delta_2, \quad \frac{c_{\infty 33}}{c_{\infty 44}} = \delta_3, \quad \frac{c_{\infty 12}}{c_{\infty 44}} = \delta_4, \quad \frac{c_{\infty 66}}{c_{\infty 44}} = \delta_5 \end{aligned} \quad (48)$$

for the half space model, respectively, one finally receives the form

$$\zeta^2(1-\zeta)U_n'' + \zeta(1-2\zeta)U_n' + [\theta - \beta\delta_1(1-\zeta)]U_n + i\gamma\zeta(1-\zeta)(1+\delta_2)W_n' - i\gamma\zeta W_n = 0 \quad (49)$$

$$\delta_3\zeta^2(1-\zeta)W_n'' + \delta_3\zeta(1-2\zeta)W_n' + [\theta - \beta(1-\zeta)]W_n + i\gamma\zeta(1-\zeta)(1+\delta_2)U_n' - i\gamma\zeta\delta_2 U_n = 0 \quad (50)$$

for the half-plane or

$$\begin{aligned} (1-\zeta)\zeta^2 U_{nm}'' + \zeta(1-2\zeta)U_{nm}' + [\theta - (1-\zeta)(\beta_1\delta_1 + \beta_2\delta_5)]U_{nm} \\ - (\delta_4 + \delta_5)\gamma_1\gamma_2(1-\zeta)V_{nm} + (1+\delta_2)i\gamma_1\zeta(1-\zeta)W_{nm}' - i\gamma_1\zeta W_{nm} = 0 \end{aligned} \quad (51)$$

$$\begin{aligned} (1-\zeta)\zeta^2 V_{nm}'' + \zeta(1-2\zeta)V_{nm}' + [\theta - (1-\zeta)(\beta_1\delta_5 + \beta_2\delta_1)]V_{nm} \\ - (\delta_4 + \delta_5)\gamma_1\gamma_2(1-\zeta)U_{nm} + (1+\delta_2)i\gamma_2\zeta(1-\zeta)W_{nm}' - i\gamma_2\zeta W_{nm} = 0 \end{aligned} \quad (52)$$

$$\begin{aligned} \delta_3(1-\zeta)\zeta^2 W_{nm}'' + \delta_3\zeta(1-2\zeta)W_{nm}' + [\theta - (1-\zeta)(\beta_1 + \beta_2)]W_{nm} \\ + (1+\delta_5)i\gamma_1\zeta(1-\zeta)U_{nm}' - \delta_2 i\gamma_1\zeta U_{nm} + (1+\delta_2)i\gamma_2\zeta(1-\zeta)V_{nm}' \\ - \delta_2 i\gamma_2\zeta V_{nm} = 0 \end{aligned} \quad (53)$$



for the half-space model, respectively, where primes indicate differentiation with respect to  $\zeta$ .

The above system of two or three coupled ordinary differential equations with variable coefficients is solved by the method of Frobenius [43].

A power series solution is assumed of the form

$$U_n(\zeta) = \sum_{r=0}^R a_r \zeta^{r+m} \quad (54)$$

$$W_n(\zeta) = \sum_{r=0}^R b_r \zeta^{r+m} \quad (55)$$

for the half-plane or

$$U_{nm} = \sum_{r=0}^{\infty} a_r \zeta^{r+k} \quad (56)$$

$$V_{nm} = \sum_{r=0}^{\infty} b_r \zeta^{r+k} \quad (57)$$

$$W_{nm} = \sum_{r=0}^{\infty} c_r \zeta^{r+k} \quad (58)$$

for the half-space model, respectively, where  $\alpha_r$ ,  $b_r$  and  $m$  or  $a_r$ ,  $b_r$ ,  $c_r$  and  $k$  are constants to be determined and  $r=0,1,2,\dots,R \rightarrow \infty$ . Substitution of the expressions (54) and (55) for  $U_n$  and  $W_n$  or (56)-(58) for  $U_{nm}$ ,  $V_{nm}$  and  $W_{nm}$ , respectively, into Eqs. (49) and (50) or (51)-(53) after some manipulations results in the equations

$$\begin{aligned} & ([m^2 + (\theta - \beta\delta_1)]\alpha_0 + [i\gamma(1 + \delta_2)m]b_0)\zeta^m + \sum_{r=1}^R [(r+m)^2 + (\theta - \beta\delta_1)]\alpha_r \zeta^{r+m} \\ & + \sum_{r=1}^R [i\gamma(1 + \delta_2)(r+m)]b_r \zeta^{r+m} \\ & - \sum_{r=1}^R [(r+m)(r+m-1) - \beta\delta_1]\alpha_{r-1} \zeta^{r+m} \\ & - \sum_{r=1}^R [i\gamma(1 + \delta_2)(r+m-1) + i\gamma]b_{r-1} \zeta^{r+m} = 0 \end{aligned} \quad (59)$$

$$\begin{aligned}
 & ([\delta_3 m^2 + (\theta - \beta)]b_0 + [i\gamma(1 + \delta_2)m]a_0)\zeta^m + \sum_{r=1}^R [\delta_3(r + m)^2 + (\theta - \beta)]b_r \zeta^{r+m} \\
 & + \sum_{r=1}^R [i\gamma(1 + \delta_2)(r + m)]a_r \zeta^{r+m} \\
 & - \sum_{r=1}^R [\delta_3(r + m)(r + m - 1) - \beta]b_{r-1} \zeta^{r+m} \\
 & - \sum_{r=1}^R [i\gamma(1 + \delta_2)(r + m - 1) + i\gamma\delta_2]a_{r-1} \zeta^{r+m} = 0
 \end{aligned} \tag{60}$$

for the half-plane or

$$\begin{aligned}
 & ([k^2 + \theta - (\beta_1\delta_1 + \beta_2\delta_5)]a_0 - [(\delta_4 + \delta_5)\gamma_1\gamma_2]b_0 + [(1 + \delta_2)i\gamma_1k]c_0)\zeta^k \\
 & + \left( \sum_{r=1}^{\infty} [(r + k)^2 + \theta - (\beta_1\delta_1 + \beta_2\delta_5)]a_r - \sum_{r=1}^{\infty} [(\delta_4 + \delta_5)\gamma_1\gamma_2]b_r \right. \\
 & + \left. \sum_{r=1}^{\infty} [(1 + \delta_2)i\gamma_1(r + k)]c_r \right) \zeta^{r+k} \\
 & - \left( \sum_{r=1}^{\infty} [(r + k - 1)(r + k) - (\beta_1\delta_1 + \beta_2\delta_5)]a_{r-1} \right. \\
 & - \sum_{r=1}^{\infty} [(\delta_4 + \delta_5)\gamma_1\gamma_2]b_{r-1} \\
 & + \left. \sum_{r=1}^{\infty} [(1 + \delta_2)i\gamma_1(r + k - 1) + i\gamma_1]c_{r-1} \right) \zeta^{r+k} = 0
 \end{aligned} \tag{61}$$

$$\begin{aligned}
 & ([k^2 + \theta - (\beta_1\delta_5 + \beta_2\delta_1)]b_0 - [(\delta_4 + \delta_5)\gamma_1\gamma_2]a_0 + [(1 + \delta_2)i\gamma_2k]c_0)\zeta^k \\
 & + \left( \sum_{r=1}^{\infty} [(r + k)^2 + \theta - (\beta_1\delta_5 + \beta_2\delta_1)]b_r - \sum_{r=1}^{\infty} [(\delta_4 + \delta_5)\gamma_1\gamma_2]a_r \right. \\
 & + \left. \sum_{r=1}^{\infty} [(1 + \delta_2)i\gamma_2(r + k)]c_r \right) \zeta^{r+k} \\
 & - \left( \sum_{r=1}^{\infty} [(r + k - 1)(r + k) - (\beta_1\delta_5 + \beta_2\delta_1)]b_{r-1} \right. \\
 & - \sum_{r=1}^{\infty} [(\delta_4 + \delta_5)\gamma_1\gamma_2]a_{r-1} \\
 & + \left. \sum_{r=1}^{\infty} [(1 + \delta_2)i\gamma_2(r + k - 1) + i\gamma_2]c_{r-1} \right) \zeta^{r+k} = 0
 \end{aligned} \tag{62}$$

$$\begin{aligned}
 & ([\delta_3 k^2 + \theta - (\beta_1 + \beta_2)]c_0 - [(1 + \delta_2)i\gamma_1 k]a_0 + [(1 + \delta_2)i\gamma_2 k]b_0)\zeta^k \\
 & + \left( \sum_{r=1}^{\infty} [\delta_3(r+k)^2 + \theta - (\beta_1 + \beta_2)]c_r + \sum_{r=1}^{\infty} [(1 + \delta_2)i\gamma_1(r+k)]a_r \right. \\
 & \left. + \sum_{r=1}^{\infty} [(1 + \delta_2)i\gamma_2(r+k)]b_r \right) \zeta^{r+k} \\
 & - \left( \sum_{r=1}^{\infty} [\delta_3(r+k-1)(r+k) - (\beta_1 + \beta_2)]c_{r-1} \right. \\
 & - \sum_{r=1}^{\infty} i\gamma_1[(r+k)(1 + \delta_2) - 1]a_{r-1} \\
 & \left. + \sum_{r=1}^{\infty} i\gamma_2[(r+k)(1 + \delta_2) - 1]b_{r-1} \right) \zeta^{r+k} = 0
 \end{aligned} \tag{63}$$

for the half-space model, respectively.

For the case of the half-plane model, equations (59) and (60) are satisfied for all powers of  $\zeta$  and hence one obtains a system to determine  $\alpha_0$  and  $b_0$  of the form

$$[m^2 + (\theta - \beta\delta_1)]\alpha_0 + [i\gamma(1 + \delta_2)m]b_0 = 0 \tag{64}$$

$$[i\gamma(1 + \delta_2)m]\alpha_0 + [\delta_3 m^2 + (\theta - \beta)]b_0 = 0 \tag{65}$$

and a system of recursive relations to determine  $\alpha_r$  and  $b_r$  in terms of  $\alpha_{r-1}$  and  $b_{r-1}$  ( $r > 0$ ) of the form

$$[(r+m)^2 + (\theta - \beta\delta_1)]\alpha_r + [i\gamma(1 + \delta_2)(r+m)]b_r = F_1 \tag{66}$$

$$[i\gamma(1 + \delta_2)(r+m)]\alpha_r + [\delta_3(r+m)^2 + (\theta - \beta)]b_r = F_2 \tag{67}$$

where

$$F_1 = [(r+m)(r+m-1) - \beta\delta_1]\alpha_{r-1} + [i\gamma(1 + \delta_2)(r+m-1) + 1]b_{r-1} \tag{68}$$

$$F_2 = i\gamma[(1 + \delta_2)(r+m-1) + \delta_2]\alpha_{r-1} + [\delta_3(r+m)(r+m-1) - \beta]b_{r-1} \tag{69}$$

For the case of half-space model, equations (61)-(63) are satisfied for all powers of  $\zeta$  and hence one obtains a system to determine  $\alpha_0$  and  $b_0$  of the form

$$[k^2 + \theta - (\beta_1\delta_1 + \beta_2\delta_5)]a_0 - [(\delta_4 + \delta_5)\gamma_1\gamma_2]b_0 + [(1 + \delta_2)i\gamma_1 k]c_0 = 0 \tag{70}$$

$$-[(\delta_4 + \delta_5)\gamma_1\gamma_2]a_0 + [k^2 + \theta - (\beta_1\delta_5 + \beta_2\delta_1)]b_0 + [(1 + \delta_2)i\gamma_2 k]c_0 = 0 \tag{71}$$

$$[(1 + \delta_2)i\gamma_1 k]a_0 + [(1 + \delta_2)i\gamma_2 k]b_0 + [\delta_3 k^2 + \theta - (\beta_1 + \beta_2)]c_0 = 0 \tag{72}$$

and system of recursive relations to determine  $a_r$ ,  $b_r$  and  $c_r$  in terms of  $a_{r-1}$ ,  $b_{r-1}$  and  $c_{r-1}$  of the form

$$\begin{aligned}
 & [(r+k)^2 + \theta - (\beta_1\delta_1 + \beta_2\delta_5)]a_r - [(\delta_4 + \delta_5)\gamma_1\gamma_2]b_r + [(1 + \delta_2)i\gamma_1(r+k)]c_r \\
 & = F_1
 \end{aligned} \tag{73}$$

$$-[(\delta_4 + \delta_5)\gamma_1\gamma_2]a_r + [(r+k)^2 + \theta - (\beta_1\delta_5 + \beta_2\delta_1)]b_r + [(1 + \delta_2)i\gamma_2(r+k)]c_r = F_2 \quad (74)$$

$$[(1 + \delta_2)i\gamma_1k]a_r + [(1 + \delta_2)i\gamma_2(r+k)]b_r + [\delta_3(r+k)^2 + \theta - (\beta_1 + \beta_2)]c_r = F_3 \quad (75)$$

where

$$F_1 = [(r+k-1)(r+k) - (\beta_1\delta_1 + \beta_2\delta_5)]a_{r-1} - [(\delta_4 + \delta_5)\gamma_1\gamma_2]b_{r-1} + i\gamma_1[(1 + \delta_2)(r+k-1) + 1]c_{r-1} \quad (76)$$

$$F_2 = -[(\delta_4 + \delta_5)\gamma_1\gamma_2]a_{r-1} + [(r+k-1)(r+k) - (\beta_1\delta_5 + \beta_2\delta_1)]b_{r-1} + i\gamma_2[(1 + \delta_2)(r+k-1) - 1]c_{r-1} \quad (77)$$

$$F_3 = i\gamma_1[(r+k)(1 + \delta_2) - 1]a_{r-1} + i\gamma_2[(r+k)(1 + \delta_2) - 1]b_{r-1} + [\delta_3(r+k-1)(r+k) - (\beta_1 + \beta_2)]c_{r-1} \quad (78)$$

In order for the system of Eqs. (64) and (65) or (70)-(72) to have nonzero solutions, one should have

$$Am^4 + Bm^2 + C = 0 \quad (79)$$

for the half-plane or

$$A k^6 + B k^4 + C k^2 + J = 0 \quad (80)$$

for the half-space model, respectively, where A, B, C, and J are functions of the dimensionless parameters of Eq. (47) or (48). One can observe that out of the four or six roots of Eq. (79) or (80), respectively, only the two or the three positive ones are acceptable.

Thus, in view of Eqs. (54), (55) or (56)-(58), the complete solution of Eqs. (49) and (50) or Eqs. (51) – (53) has the form

$$U_n(\zeta) = A_1 U_n^{(1)}(\zeta) + A_2 U_n^{(2)}(\zeta) \quad (81)$$

$$W_n(\zeta) = A_1 W_n^{(1)}(\zeta) + A_2 W_n^{(2)}(\zeta) \quad (82)$$

for the half-plane or

$$U_{nm}(\zeta) = A_1 U_{nm}^{(1)}(\zeta) + A_2 U_{nm}^{(2)}(\zeta) + A_3 U_{nm}^{(3)}(\zeta) \quad (83)$$

$$V_{nm}(\zeta) = A_1 V_{nm}^{(1)}(\zeta) + A_2 V_{nm}^{(2)}(\zeta) + A_3 V_{nm}^{(3)}(\zeta) \quad (84)$$

$$W_{nm}(\zeta) = A_1 W_{nm}^{(1)}(\zeta) + A_2 W_{nm}^{(2)}(\zeta) + A_3 W_{nm}^{(3)}(\zeta) \quad (85)$$

for the half-space model, respectively, where  $A_1$ ,  $A_2$  and  $A_3$  are constants of integration to be determined by the boundary conditions (29)-(31) and (32)-(35) where

$$U_n^{(i)}(\zeta) = \sum_{r=0}^R a_r \zeta^{r+m_i} \quad (86)$$

$$W_n^{(i)}(\zeta) = \sum_{r=0}^R b_r \zeta^{r+m_i} \quad (87)$$

$$U_{nm}^{(i)}(\zeta) = \sum_{r=0}^{\infty} a_r \zeta^{r+k_i} \quad (88)$$

$$V_{nm}^{(i)}(\zeta) = \sum_{r=0}^{\infty} b_r \zeta^{r+k_i} \quad (89)$$

$$W_{nm}^{(i)}(\zeta) = \sum_{r=0}^{\infty} c_r \zeta^{r+k_i} \quad (90)$$

with  $i=1,2$ , (or  $i=1,2,3$ ) for the two (or three) roots of  $m$  (or  $k$ ) given by Eq. (79) or Eq. (80), the  $a_r$  and  $b_r$  and  $c_r$  given recursively from the solution of Eqs. (66) and (67) or respectively (73) – (75) and  $\alpha_0$  and  $b_0$  and  $c_0$  obtained by assuming  $\alpha_0=1$  and solving Eq. (64) for  $b_0$  or respectively the system of Eqs. (70) and (71) for  $b_0$  and  $c_0$ .

Thus, the soil response solution is given by Eqs. (44) and (45) and the plate response solution is by Eq. (43) for both the half-plane and half-space cases. Once the plate deflection  $w_p$  is known, one can obtain the plate bending moment  $M_{xx}$  and shear force  $Q_x$  from [42]

$$M_{xx} = -D \frac{\partial^2 w_p}{\partial x^2} \quad (91)$$

$$Q_x = -D \frac{\partial^3 w_p}{\partial x^3} \quad (92)$$

for the half-plane or

$$M_{xx} = -D \left( \frac{\partial^2 w_p}{\partial x^2} + \nu_p \frac{\partial^2 w_p}{\partial y^2} \right) \quad (93)$$

$$M_{yy} = -D \left( \frac{\partial^2 w_p}{\partial y^2} + \nu_p \frac{\partial^2 w_p}{\partial x^2} \right) \quad (94)$$

$$Q_x = -D \frac{\partial}{\partial x} \left( \frac{\partial^2 w_p}{\partial x^2} + \frac{\partial^2 w_p}{\partial y^2} \right) \quad (95)$$

$$Q_y = -D \frac{\partial}{\partial y} \left( \frac{\partial^2 w_p}{\partial x^2} + \frac{\partial^2 w_p}{\partial y^2} \right) \quad (96)$$

for the half-space model, respectively.

#### 4 VERIFICATION AND CONVERGENCE STUDIES

In this final section, the accuracy of the proposed method is validated through comparison with two special cases for which there exist solutions in the literature involving homogeneous soil with and without a plate on its surface. The homogeneous soil is approximated by the proposed method by assigning a very small value to  $\Xi$ , e.g.,  $\Xi = 10^{-4}$ .

For the first verification it is assumed a load  $P=80$  kN distributed on a line-length  $l=0.15$  m, which implies a value of  $F=266.66$  kN/m, moving with constant speed  $V=40$  m/s on the surface of



a half-plane isotropic soil medium. For this soil medium one has mass density  $\rho = 1816 \text{ kg/m}^3$ , Poisson's ratio  $\nu = 0.35$  and shear modulus varying with depth according to Eq. (40) with  $G_0 = 0.077 \text{ GPa}$  (or  $E_0 = 2G_0(1 + \nu)$ ) with parameters  $\Xi = 0.5$  and  $\alpha = 1 \text{ m}^{-1}$ . The absence of the plate was simulated by giving very small values to the plate parameters. Other parameters used here are  $L = 80 \text{ m}$  and  $x = L/3$ . Using the present solution, the soil surface vertical displacement  $w$  versus time  $t$  was calculated and the results are given in Fig. 3a together with those from [34]. One can clearly see in that figure that the two solutions coincide.

For the second verification, the problem of a load moving on the surface of a homogeneous cross-anisotropic half-space medium is solved by the proposed method and compared with the solution of Ba et al [27]. Thus, assuming the same values with Ba et al [27], i.e.,  $E = 5 \text{ GPa}$ ,  $E' = 2E$ ,  $\nu = \nu' = 0.25$ ,  $G = E/2(1 + \nu)$ ,  $G' = 0.3 E'$  and  $\rho = 2000 \text{ kg/m}^3$ , one can obtain the normalized vertical displacement  $\bar{w} = G_1 z / P$  at a depth  $z = 10 \text{ m}$  as a function of the normalized load speed  $\bar{V} = V / \sqrt{G' / \rho}$  as shown in Fig. 3b. The concentrated load  $P$  was modeled by the proposed method assuming a very small rectangular area of  $l_1 = l_2 = 0.015 \text{ m}$ , while the absence of the plate is approximated by the proposed method by assigning a very small value to  $h_p$ , e.g.,  $h_p = 10^{-4} \text{ m}$ . Finally, the solution is obtained assuming  $L_1 = L_2 = 75 \text{ m}$ ,  $N = M = 512$ , and  $r = 5$ . One can observe in Fig. 3b (a) that the response obtained by the proposed method coincides with the solution of Ba et al [24].

Next, a convergence study with respect to the required values of  $N$  and  $R$  in Eqs. (43a) and (55), respectively, or  $N$ ,  $M$ , and  $r$  in Eqs. (43b) and (58), respectively, is presented, where the maximum vertical displacement of the plate at the center of the load versus  $N$ ,  $M$ , and  $r$  is shown, respectively. One can observe from Figs. 4 and 5 that values of  $N$ ,  $M > 400$  are sufficient to obtain solutions with high accuracy. As far as the required maximum value of  $r$  is concerned, it should be noted here that this value depends on the non-homogeneity index  $\Xi$ . Thus, for higher values of  $\Xi$ , higher values of  $r$  are required. It has been observed that for very small values of  $\Xi$ , e.g., homogeneous soil, a value of  $r \geq 5$  is sufficient. In order to determine the highest possible required value of  $r$  in this convergence study, a very high value of non-homogeneity index is assumed, i.e.,  $\Xi = 0.99$  and as it is shown in Figs. 4b and 5c, values of  $r \geq 250$  are sufficient to obtain results of high accuracy.

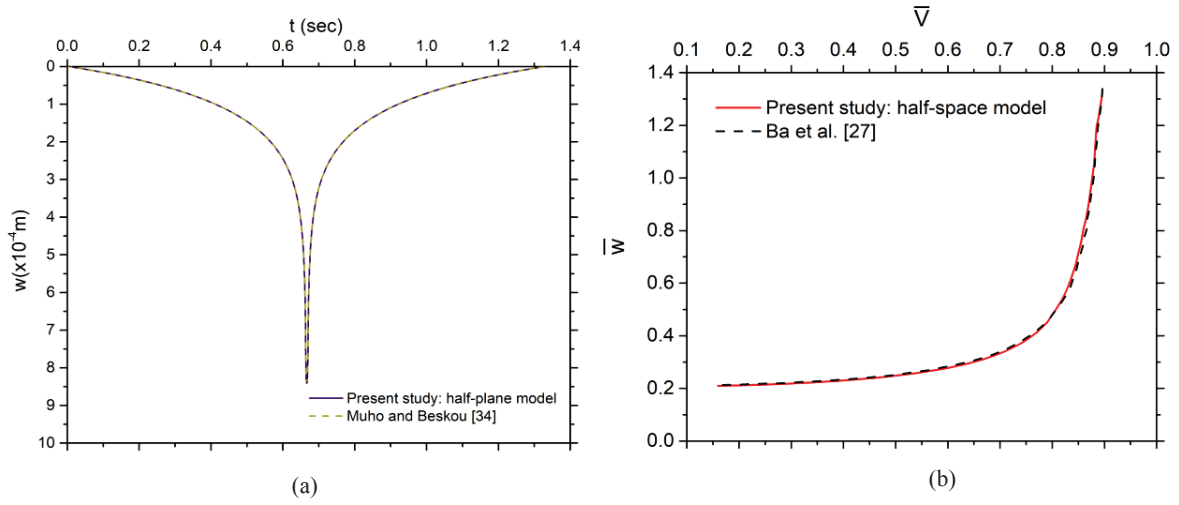


Figure 3: Use of the present solution for the special cases of (a) a nonhomogeneous isotropic half-plane without plate of [34] and (b) the homogeneous and cross-anisotropic soil of Ba et al [27].

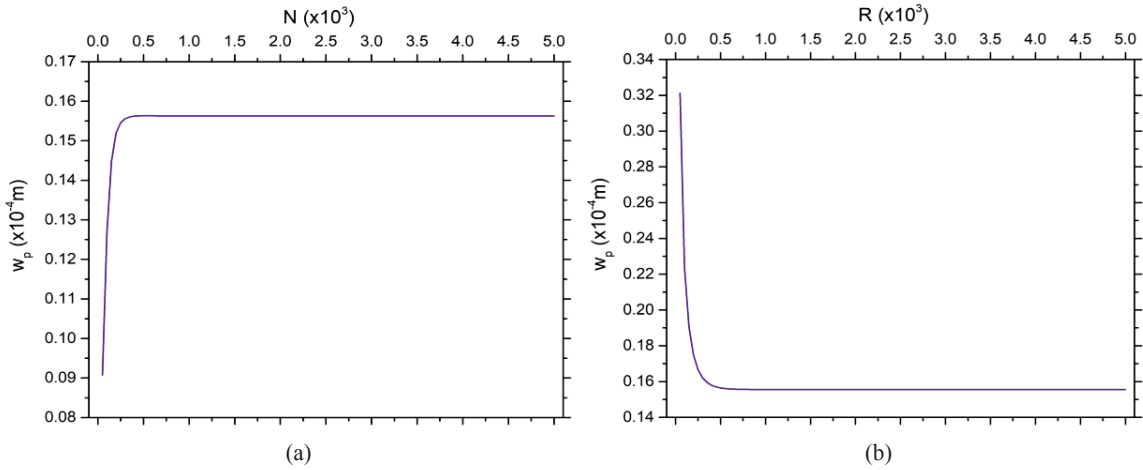


Figure 4: Convergence analysis: Maximum plate vertical displacement  $w_p$  versus (a) the number  $N$  in Eq. (43a) and (b) the number  $R$  in Eq. (55).

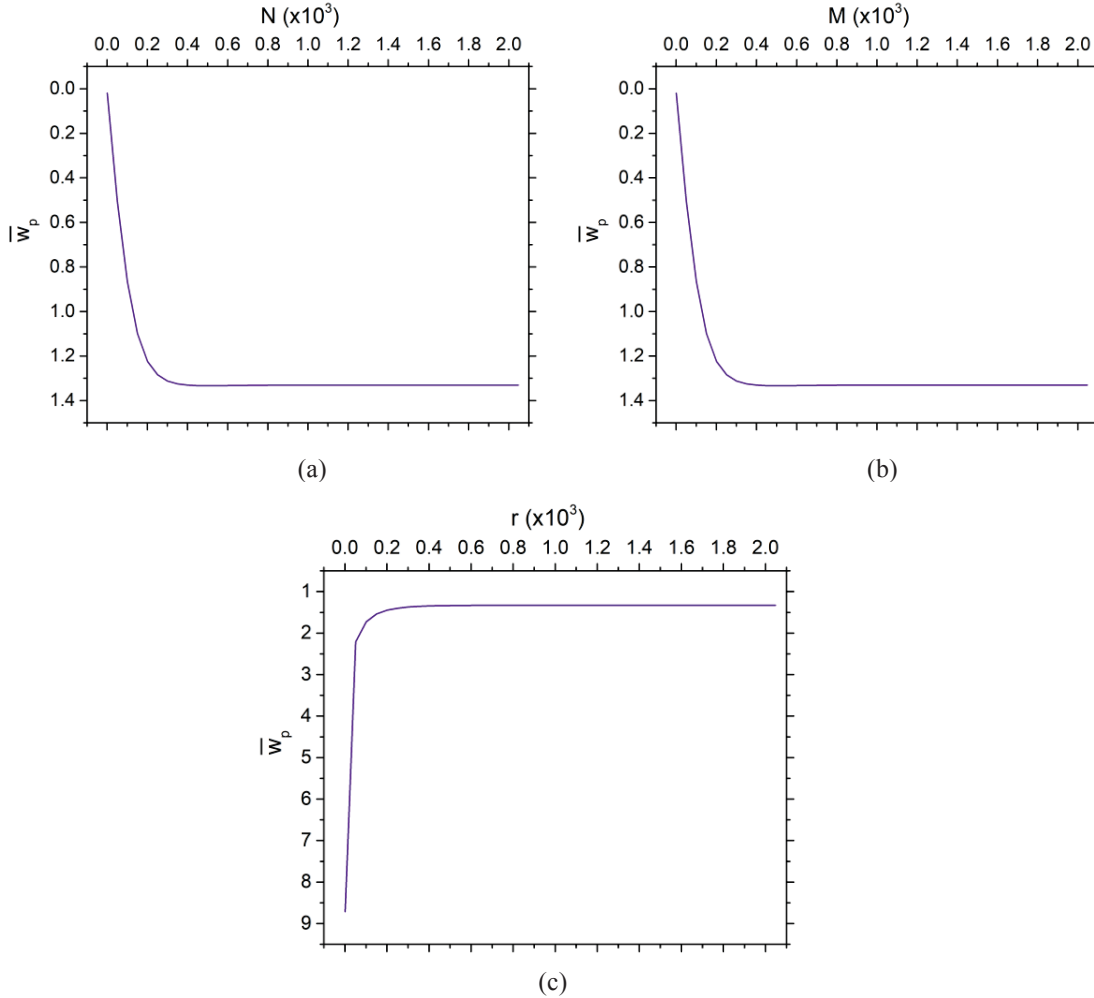


Figure 5: Convergence analysis: Maximum plate vertical displacement  $w_p$  versus (a) the number  $N$ , (b) the number  $M$  in Eq. (43b) and (c) the number  $r$  in Eq. (58).

Finally, a comparison of the results produced by the half-plane and half-space models is presented. Both models share the same material properties for the soil ( $E=0.2$  GPa,  $E'=E$ ,  $\nu=\nu'=0.35$ ,  $G'=0.30 E'$ ,  $\rho=2100$  kg/m<sup>3</sup> and  $\Xi=0.01$ ) and the plate ( $E_p=30$  GPa,  $\rho_p=2300$  kg/m<sup>3</sup>,  $\nu_p=0.2$  and  $h_p=0.2$  m) and are associated with the same data for the moving load ( $P=80$  kN,  $l_1=l_2=0.15$  m and  $V=80$  m/s). One can observe in Fig. 6 (a) that the half-space model with the plate results in much smaller maximum vertical displacement at the surface ( $z=0$  m) compared to that of the half-plane model with the plate. The same above problem is solved again assuming very small values for the plate parameters in order to model the absence of the plate and the response is shown in Fig. 6 (b). One can observe that in this case, both models provide similar maximum vertical displacement with the half-plane model resulting in a slightly higher displacement. Furthermore, it is interesting to observe that in both cases the half-plane model results in a much wider displacement-time response shape than the half-space one and clearly provides higher displacement values than those from the half-space model away from the area of the load application.

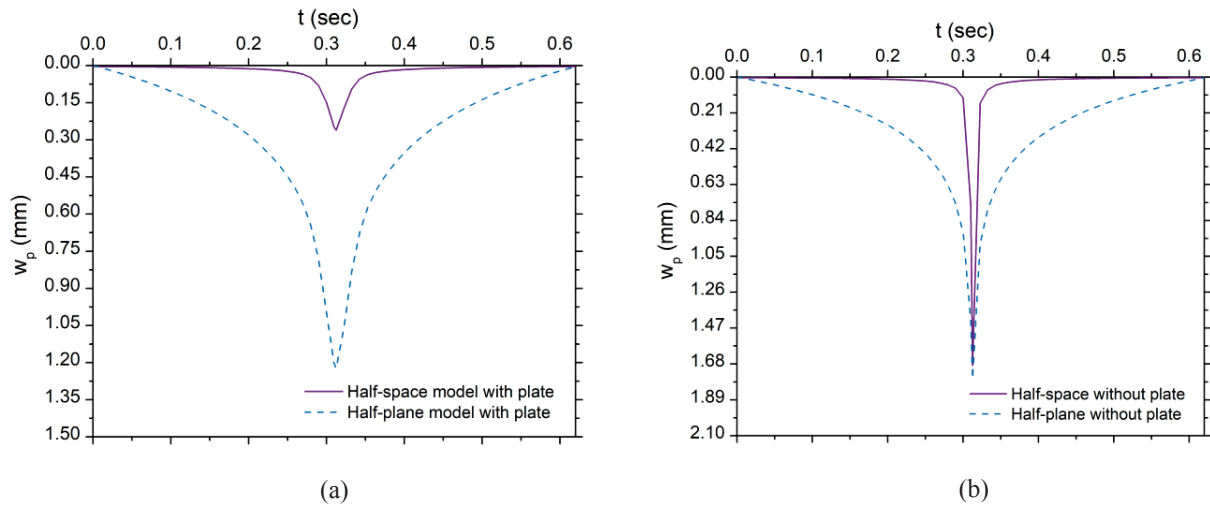


Figure 6: Comparison of the present half-space with the half-plane (a) considering the plate and (b) without the plate.

## 5 CONCLUSIONS

1. The problem of a distributed load moving with constant speed on the surface of an elastic plate resting on a non-homogeneous and cross-anisotropic viscoelastic half-plane or half-space has been analytically treated by using the complex Fourier series method.
2. The proposed solutions were verified for the two special cases of a load acting on a homogeneous cross-anisotropic elastic half-plane or half-plane.
3. A comparison of the proposed half-space and half-plane models has shown that both models result in a similar maximum vertical displacement only for the case of the half-plane model without the plate and under the load where the half-plane displacement has a slightly higher value. However, the half-plane model without the plate clearly shows higher displacements than those of the half-space far from the area of the load application. On the other hand, in case there is a plate, the half-space model results in a much lower vertical response compared to that of the half-plane one.

## ACKNOWLEDGMENTS

The second Author acknowledges with thanks the support provided to him by the National Key Research and Development Program of China (Grant No.2017YFC1500701) and the State Key Laboratory of Disaster Reduction in Civil Engineering (Grant No. SLDRCE15-B-06) for supporting this work.

## REFERENCES

- [1] R.D. Borchardt, *Viscoelastic Waves in Layered Media*, Cambridge University Press, Cambridge U.K., 2009.

- [2] S.L. Kramer, *Geotechnical Earthquake Engineering*, Prentice-Hall Pearson, Upper Saddle River, New Jersey, 1996.
- [3] G. Gazetas, *Stresses and displacements in cross-anisotropic soils*, Journal of Geotechnical Engineering Division of ASCE, 108(4): 532-553, 1982.
- [4] S.H. Kim, D.N. Little, E. Masad, R.L. Lytton, *Estimation of level of anisotropy in unbound granular layers considering aggregate physical properties*, International Journal of Pavement Engineering, 6(4): 217-227, 2005.
- [5] Y. Cai, A. Sangghaleh, E. Pan, *Effect of anisotropic base/interlayer on the mechanistic responses of layered pavements*, Computers and Geotechnics, 65: 250-257, 2015.
- [6] G. Gazetas, *Vibrational characteristics of soil deposits with variable wave velocity*, International Journal for Numerical and Analytical Methods in Geomechanics, 6: 1-20, 1982.
- [7] C. Vrettos, *In-plane vibrations of soil deposits with variable shear modulus: I surface waves*, International Journal for Numerical and Analytical Methods in Geomechanics, 14: 209-222, 1990.
- [8] C. Vrettos, *In-plane vibrations of soil deposits with variable shear modulus: II line load*, International Journal for Numerical and Analytical Methods in Geomechanics, 14: 649-662, 1990.
- [9] Vrettos C, 'Vertical and rocking impedances for rigid rectangular foundations on soils with bounded inhomogeneity', *Earthquake Engineering and Structural Dynamics* 1999; 28: 1525-1540.
- [10] G. Muravskii, *On time harmonic problem for non-homogeneous elastic half-space with shear modulus limited at infinite depth*, European Journal of Mechanics A/Solids, 16(2): 277-294, 1997.
- [11] B.B. Guzina, R.Y.S. Pak, *Vertical vibration of a circular footing on a linear-wave-velocity half-space*, Geotechnique, 48(2): 159-168, 1998.
- [12] G.D. Manolis, P.S. Divena, T.V. Rangelov, F. Wuttke, *Seismic Wave Propagation in Non-Homogeneous Elastic Media by Boundary Elements*, Springer International Publishing AG, Cham, Switzerland, 2017.
- [13] G. Eason, *The stresses produced in a semi-infinite solid by a moving surface force*, International Journal of Engineering Science, 2: 581-609, 1965.
- [14] R.G. Payton, *Transient motion of an elastic half-space due to a moving surface force*, International Journal of Engineering Science, 5: 49-79, 1967.
- [15] D.C. Gakenheimer, J. Miklowitz, *Transient excitation of an elastic half-space by a point load traveling on the surface*, Journal of Applied Mechanics of ASME, 36: 505-515, 1969.
- [16] F.C.P. De Barros, J.E. Luco, *Response of a layered viscoelastic half-space to a moving point load*, Wave Motion, 19: 189-210, 1994.
- [17] D.V. Jones, D. Le Houedec, A.D. Peplow, M. Petyt, *Ground vibration in the vicinity of a moving rectangular load on a half-space*, European Journal of Mechanics, A/Solids, 17(1): 153-166, 1998.



- [18] R.V. Siddharthan, J. Yao, P.E. Sebaaly, *Pavement strain from moving dynamic 3D load distribution*, Journal of Transportation Engineering of ASCE, 124(6): 557-566, 1998.
- [19] H. Grundmann, M. Lieb, E. Trommer, *The response of a layered half-space to traffic loads moving along its surface*, Archive of Applied Mechanics, 69: 55-67, 1999.
- [20] H.G. Georgiadis, G. Lykotrafitis, *A method based on the Radon transform for three-dimensional elastodynamic problems of moving loads*, Journal of Elasticity, 65: 87-129, 2001.
- [21] W.I. Liao, T.J. Teng, C.S. Yeh, *A method for the response of an elastic half-space to moving sub-Rayleigh point loads*, Journal of Sound and Vibration, 284: 173-188, 2005.
- [22] Y.M. Cao, H. Xia, G. Lombaert, *Solution of moving-load-induced soil vibrations based on the Betti-Rayleigh dynamic reciprocal theorem*, Soil Dynamics and Earthquake Engineering, 30: 470-480, 2010.
- [23] H.A. Dieterman, A. Metrikine, *The equivalent stiffness of a half-space interacting with a beam. Critical velocities of a moving load along the beam*, European Journal of Mechanics, A/Solids, 15: 67-90, 1996.
- [24] A.V. Kononov, R.A.M. Wolfert, *Load motion along a beam on a viscoelastic half-space*, European Journal of Mechanics, A/Solids, 19: 361-371, 2000.
- [25] C. Liu, B.F. McCullough, H.S. Oey, *Response of rigid pavements due to vehicle-road interaction*, Journal of Transportation Engineering of ASCE, 126(3): 237-242, 2000.
- [26] N.D. Beskou, E.V. Muho, J. Qian, *Dynamic analysis of an elastic plate on a cross-anisotropic elastic half-space under a rectangular moving load*, Acta Mechanica, online, 2020.
- [27] Z. Ba, J. Liang, V.W. Lee, H. Ji, *3D dynamic response of a multi-layered transversely isotropic half-space subjected to a moving point load along a horizontal straight line with constant speed*, International Journal of Solids and Structures, 100-101: 427-445, 2016.
- [28] N.D. Beskou, Y. Chen, J. Qian, *Dynamic response of an elastic plate on a cross-anisotropic elastic half-plane to a load moving on its surface*, Transportation Geotechnics, 14: 98-106, 2018.
- [29] R.G. Payton, *Epicenter motion of a transversely isotropic elastic half-space due to a suddenly applied buried point source*, International Journal of Engineering Science, 17: 879-887, 1979.
- [30] R.K.N.D. Rajapakse, Y. Wang, *Green's functions for transversely isotropic elastic half-space*, Journal of Engineering Mechanics of ASCE, 119(9): 1724-1746, 1993.
- [31] M. Eskandari-Ghadi, R.Y.S. Pak, A. Ardeshir-Behrestaghi, *Transversely isotropic elastodynamic solution of a finite layer on an infinite subgrade under surface loads*, Soil Dynamics and Earthquake Engineering, 28: 986-1003, 2008.
- [32] B.B. Guzina, R.Y.S. Pak, *Elastodynamic Green's functions for a smoothly heterogeneous half-space*, International Journal of Solids and Structures, 33(7): 1005-1021, 1996.

- [33] C. Vrettos, *Vertical and rocking impedances for rigid rectangular foundations on soils with bounded inhomogeneity*, Earthquake Engineering and Structural Dynamics, 28: 1525-1540, 1999.
- [34] E.V. Muho, N.D. Beskou, *Dynamic response of an isotropic elastic half-plane with shear modulus varying with depth to a load moving on its surface*, Transportation Geotechnics, 20, 100248, 2019.
- [35] S. Cheshmehkani, M. Eskandari-Ghadi, *Dynamic response of axisymmetric transversely isotropic viscoelastic continuously nonhomogeneous half-space*, Soil Dynamics and Earthquake Engineering, 83: 110-123, 2016.
- [36] S. Cheshmehkani, M. Eskandari-Ghadi, *Three-dimensional dynamic ring load and point load Green's functions for continuously inhomogeneous viscoelastic transversely isotropic half-space*, Engineering Analysis with Boundary Elements, 76: 10-25, 2017.
- [37] R. Siddharthan, Z. Zafir, G.M. Norris, *Moving load response of layered soil, I: formulation; II: verification and application*, Journal of Engineering Mechanics of ASCE, 119(10): 2052-2071 & 2072-2089, 1993.
- [38] D.D. Theodorakopoulos, *Dynamic analysis of a poroelastic half-plane soil medium under moving loads*, Soil Dynamics and Earthquake Engineering, 23: 521-533, 2003.
- [39] N.D. Beskou, Y. Chen, J. Qian, 'Dynamic response of an elastic plate on a cross-anisotropic elastic half-plane to a load moving on its surface', Transportation Geotechnics 2018; 14: 98-106.
- [40] E.V. Muho, N.D. Beskou, *Dynamic response of an isotropic elastic half-plane with shear modulus varying with depth to a load moving on its surface*, Transportation Geotechnics, on line 20,100248, 2019.
- [41] A.H.D. Cheng, *Poroelasticity*, Springer International Publishing AG, Cham, Switzerland, 2016.
- [42] R. Szilard, *Theory and Analysis of Plates*, Prentice-Hall, Englewood Cliffs, New Jersey, 1974.
- [43] E. Kreyszig, *Advanced Engineering Mathematics*, Wiley, New York, 1983.

## OPTIMAL DESIGN OF TID-BASED SYSTEM FOR THE CONTROL OF WIND-INDUCED VIBRATION IN TALL BUILDINGS THROUGH CULTURAL ALGORITHM

Luis Lara-Valencia<sup>1\*</sup>, Mateo Ramírez-Acevedo<sup>1</sup>, José Brito<sup>2</sup>, Daniel Caicedo<sup>1</sup> and Yosef Farbiarz<sup>1</sup>

<sup>1</sup> Universidad Nacional de Colombia  
Carrera 80 N.º 65-223, Núcleo Robledo. Medellín, Colombia.  
lualarava@unal.edu.co, maramirezac@unal.edu.co, dcaicedod@unal.edu.co, jfarbiarz@unal.edu.co

<sup>2</sup> Universidade de Brasilia  
CEP. 70910-900. Brasilia, Brasil  
jlbrito@unb.br

---

### Abstract

*Controlling wind-induced vibrations as well as aerodynamic forces is an essential part of the structural design of tall buildings in order to guarantee the serviceability limit state of the structure. This paper presents a numerical investigation focused on finding the optimal design parameters of a Tuned Inerter Damper (TID) based system for the control of wind-induced vibration in tall buildings. The control system is based on the conventional TID, with the main difference that its location is changed from the ground level to the last two story-levels of the structural system. The TID tuning procedure is based on an evolutionary cultural algorithm in which the optimum design variables defined as the frequency and damping ratios are searched according to the optimization criteria of minimizing the root mean square (RMS) response of displacements at the  $n$ th story of the structure. A Monte Carlo simulation is used to represent the dynamic action of the wind in the time domain in which a time-series derived from the Davenport spectrum using eleven harmonic functions with randomly chosen phase angles was reproduced. The above-mentioned methodology is then applied on a case-study derived from a 37-story prestressed concrete building with 144 m height, in which the wind action overcomes the seismic action. The results showed that the optimally TID is effective to reduce the RMS response of displacements up to 37.12% which demonstrates the feasibility of the system for the control of wind-induced vibrations in tall buildings.*

**Keywords:** Evolutionary Cultural Algorithm, Monte Carlo Simulation, Tuned Inerter Damper, Wind-Induced Vibrations.

---

## 1 INTRODUCTION

In recent years, the construction of high-rise buildings has increased, using lightweight and high-strength materials. Those structures are typically more flexible and exhibit lower damping values, making them more vulnerable to vibration problems induced by wind loads [12]. Consequently, interest in the field of vibration control has increased, leading to the extensive application of passive control for wind loads. According to Kwok and Samali [1], for several decades, classic devices such as Tuned Mass Damper (TMD) have been implemented, which are composed of a mass attached to the building with a system of springs and dashpots that dissipates energy as a relative movement develops between the mass and structure. In that sense, Lazar [5] proposed a novel passive control system which is called Tuned Inerter Damper (TID), similar to the TMD but with the attached mass being replaced by the inerter device. This inerter is a negligible mass device proposed by Smith [2] that induces an equivalent mass amplification effect called inertance with a 1/200 ratio between the actual mass and the inertances, as demonstrated in laboratory investigations carried out by Papageorgiou & Smith [3].

It has been shown that the use of inerter devices in control systems provides considerable improvements in controlling mechanical vibrations [7]. Different authors [14, 17, 18] have adapted the inerter device in classic TMDs, obtaining significant enhancements in the dynamic response of buildings under wind-induced vibrations. Subsequently, various authors have achieved large reductions in the vibrations of a building by applying TID as well as TMDI systems, overcoming the limitations of the large amounts of mass that have to be implemented in conventional TMDs [15, 26, 27].

This paper presents a numerical investigation focused on finding the optimal design parameters of a Tuned Inerter Damper (TID) based system for the control of wind-induced vibration in tall buildings. The control system is based on the conventional TID, with the main difference that its location is changed from the ground level to the last two story-levels of the structural system according to the recommendations provided in [15]. The TID tuning procedure is based on an evolutionary cultural algorithm in which the optimum design variables defined as the frequency and damping ratios were searched according to the optimization criteria of minimizing the root mean square (RMS) response of displacements at the  $n$ th story of the structure. A Monte Carlo simulation is used to represent the dynamic action of the wind in the time domain in which a time series derived from the Davenport spectrum is reproduced using eleven harmonic functions with randomly chosen phase angles. Effective results are expected with the implementation of optimized TID to reduce the RMS response of displacements.

## 2 MATHEMATICAL MODELS OF A MDOF STRUCTURE EQUIPPED WITH TID-BASED SYSTEM

The inerter is a two-terminal-one-port mechanical device proposed by Smith [2] with the property that the equal and opposite force applied at the terminals is proportional to the relative acceleration between the terminals.

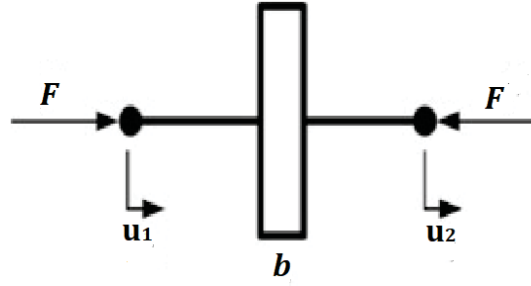


Figure 1: The symbol of inerter.

The mathematical notation corresponding to Figure 1 is:

$$F = b(\ddot{u}_2 - \ddot{u}_1) \quad (1)$$

Where  $\ddot{u}_1$  and  $\ddot{u}_2$  represents the relative acceleration between its nodes and the constant  $b$  is called the *inertance*.

The main focus of this work is to apply the variant of the TID proposed by Caicedo in [15]. Figure 2 presents a 2D shear frame with  $n$  horizontal DOF at each level of the building and wind loads applied at each level. It is observed that the TID is positioned in the last two levels with  $m_i$ ,  $k_i$  and  $c_i$  as the mass, lateral stiffness and damping coefficients of each story level ( $i = 1, 2, \dots, n$ ). Additionally,  $k_d$  and  $c_d$  are the stiffness and damping that define the behavior of the TID. These two last variables can be rewritten as:

$$k_d = \omega_s^2 f^2 b \quad (2)$$

$$c_d = 2f\xi_d\omega_sb \quad (3)$$

In equations (2) and (3),  $\omega_s$ ,  $f$  and  $\xi_d$  are the fundamental circular frequency of the structural system, the frequency and damping ratios between the structure and the TID.

The design procedure to be carried out in this work consists of finding the optimal frequency ratio and damping ratio to minimize the dynamic response of the structure.



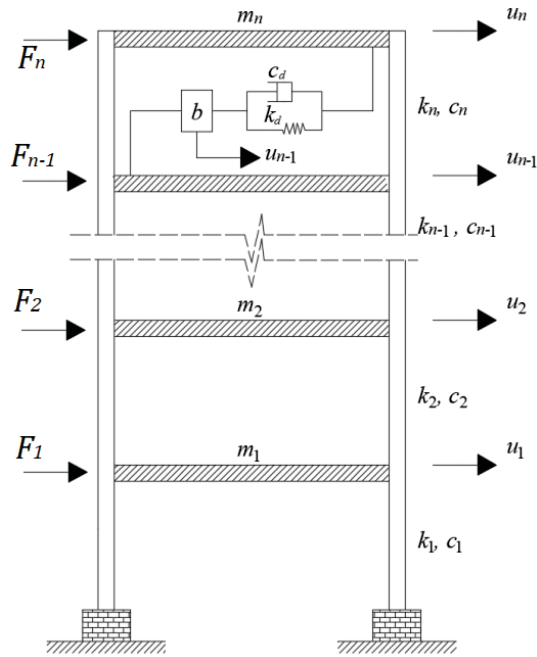


Figure 2: 2D frame equipped with a TID in the last two levels.

The following dynamic equilibrium equations describe the behavior of the  $n$  degrees of freedom of each level of the structural system, and the additional degree of freedom ( $n + 1$ ) given the possibility of horizontal movement of the TID.

$$m_1 \ddot{u}_1 + (c_1 + c_2) \dot{u}_1 - c_2 \dot{u}_2 + (k_1 + k_2) u_1 - k_2 u_2 = F_1(t) \quad (4)$$

$$m_2 \ddot{u}_2 - c_2 \dot{u}_1 + (c_2 + c_3) \dot{u}_2 - c_3 \dot{u}_3 - k_2 u_1 + (k_2 + k_3) u_2 - k_3 u_3 = F_2(t) \quad (5)$$

$$m_{n-1} \ddot{u}_{n-1} - c_{n-1} \dot{u}_{n-2} + (c_{n-1} + c_n + c_d) \dot{u}_{n-1} - c_n \dot{u}_n - c_d \dot{u}_{n+1} - k_{n-1} \dot{u}_{n-2} + (k_{n-1} + k_n + k_d) u_{n-1} - k_n u_n - k_d u_{n+1} = F_{n-1}(t) \quad (6)$$

$$m_n \ddot{u}_n - c_n \dot{u}_{n-1} + (c_n + c_d) \dot{u}_n - c_d \dot{u}_{n+1} - k_n u_{n-1} + (k_n + k_d) u_n - k_d u_{n+1} = F_n(t) \quad (7)$$

$$b \ddot{u}_{n+1} - c_d \dot{u}_{n-1} - c_d \dot{u}_n + c_d \dot{u}_{n+1} - k_d u_{n-1} - k_d u_n + k_d u_{n+1} = \frac{1}{200} b F_{n+1}(t) \quad (8)$$

Where the constant  $1/200$  denotes the ratio between the physical mass of the TID and the inertance ( $b$ ). The ratio is assumed according to Papageorgiou and Smith [3] and Papageorgiou et al. [26].

Therefore, the System of Equations can be written in matrix form, corresponding to the general equation of motion:

$$\mathbf{M} \ddot{\mathbf{U}}(t) + \mathbf{C} \dot{\mathbf{U}}(t) + \mathbf{K} \mathbf{U}(t) = \mathbf{F}(t) \quad (9)$$

$$\mathbf{M} = \begin{bmatrix} m_1 & 0 & \cdots & 0 & 0 & 0 \\ 0 & m_2 & \cdots & 0 & 0 & 0 \\ \vdots & \vdots & \ddots & \vdots & \vdots & \vdots \\ 0 & 0 & \cdots & m_{n-1} & 0 & 0 \\ 0 & 0 & \cdots & 0 & m_n & 0 \\ 0 & 0 & \cdots & 0 & 0 & b \end{bmatrix} \quad (10)$$

$$\mathbf{C} = \begin{bmatrix} c_1 + c_2 & -c_2 & \cdots & 0 & 0 & 0 \\ -c_2 & c_2 + c_3 & \cdots & 0 & 0 & 0 \\ \vdots & \vdots & \ddots & \vdots & \vdots & \vdots \\ 0 & 0 & \cdots & c_{n-1} + c_n + c_d & -c_n & -c_d \\ 0 & 0 & \cdots & -c_n & c_n + c_d & -c_d \\ 0 & 0 & \cdots & -c_d & -c_d & c_d \end{bmatrix} \quad (11)$$

$$\mathbf{K} = \begin{bmatrix} k_1 + k_2 & -k_2 & \cdots & 0 & 0 & 0 \\ -k_2 & k_2 + k_3 & \cdots & 0 & 0 & 0 \\ \vdots & \vdots & \ddots & \vdots & \vdots & \vdots \\ 0 & 0 & \cdots & k_{n-1} + k_n + k_d & -k_n & -k_d \\ 0 & 0 & \cdots & -k_n & k_n + k_d & -k_d \\ 0 & 0 & \cdots & -k_d & -k_d & k_d \end{bmatrix} \quad (12)$$

$$\mathbf{U} = \{u_1 \quad u_2 \quad \cdots \quad u_{n-1} \quad u_n \quad u_{n+1}\}^T \quad (13)$$

$$\boldsymbol{\delta} = \{1 \quad 1 \quad \cdots \quad 1 \quad 1 \quad 1/200\}^T \quad (14)$$

Where  $\mathbf{M}$ ,  $\mathbf{C}$  and  $\mathbf{K}$  are the mass, stiffness and damping matrices, and  $\mathbf{U}$  is defined as the structure displacement response.

### 3 TID DESIGN AND OPTIMIZACIÓN PROCEDURE THROUGH CULTURAL ALGORITHM

This work intends to implement a cultural algorithm for the optimal design of a TID. The cultural algorithm was first presented by Reynolds in [9] as a complementary algorithm to the evolutionary computation and natural selection algorithms. Cultural algorithms have been used for the solution and optimization of multiple engineering problems, such as the vibration control of vehicles or the design of stabilizers for power systems [10,11].

Figure 3, shows of the three components of the cultural algorithm. The first of the three components are the population space, which includes the population to be developed and the evaluation, reproduction, and modification mechanism. The second component is the belief space, representing the direction in which the population has to seek solutions. Finally, the third component of the cultural algorithm is made up of the communication protocol, through which the population and beliefs interact [9]. The functions in Figure 3 are defined as follows:

- Acceptance function: transfers individual knowledge that satisfies the aptitude value to belief space.
- Update function: adjusts the knowledge of the belief space according to the individual knowledge transferred.
- Influence function: adjusts the individual knowledge of the population space according to the knowledge of the belief space.
- Fitness function: produces the individual knowledge of the next generation according to certain rules.

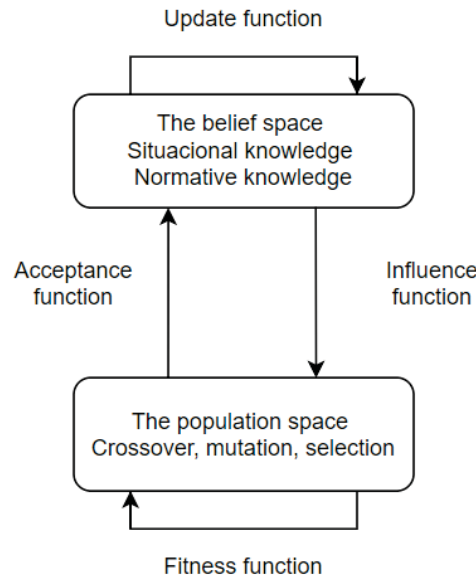


Figure 3: Framework of cultural algorithms.

The objective function defined in Eq. 15 will assess the performance of the control system applied to the case-study structure. This will be determined by means of the dynamic root mean square (RMS) response of displacements of the last floor of the structure.

$$F_{obj} = \frac{\text{RMS of the } n^{th} \text{ DOF controlled response}}{\text{RMS of the } n^{th} \text{ DOF uncontrolled response}} \quad (15)$$

#### 4 WIND EXCITATION MODEL AND FREQUENCY DOMAIN ANALYSIS FOR THE TID-EQUIPPED SYSTEM

To model the dynamic wind action, a computational simulation based on the Monte Carlo method is carried out, following the recommendations provided by Franco [21]. The procedure is based on the wind power spectrum developed by Davenport [23] through which it is possible to separate fluctuating pressure into  $m$  harmonic functions (at least 11), one of which will be resonant. The Monte Carlo method and the Fourier transform are used to reproduce the fluctuating pressures of the wind.

The building is used as case-study in this investigation. The building, which is the tallest residential tower in Medellín, with 144 m in height, distributed over 37 floors. The location and topographical characteristics of the building are used to obtain the basic parameters to be used in the Synthetic Wind Method. These parameters were taken from the Colombian code, *Reglamento Colombiano de Construcción Sismo Resistente* (NSR-10) [24]

#### 5 NUMERICAL RESULTS AND DISCUSSION

Following the procedure exposed previously and the mathematical formulation described in [19-22], it is possible to obtain the fluctuating pressures as shown in Figure 4.

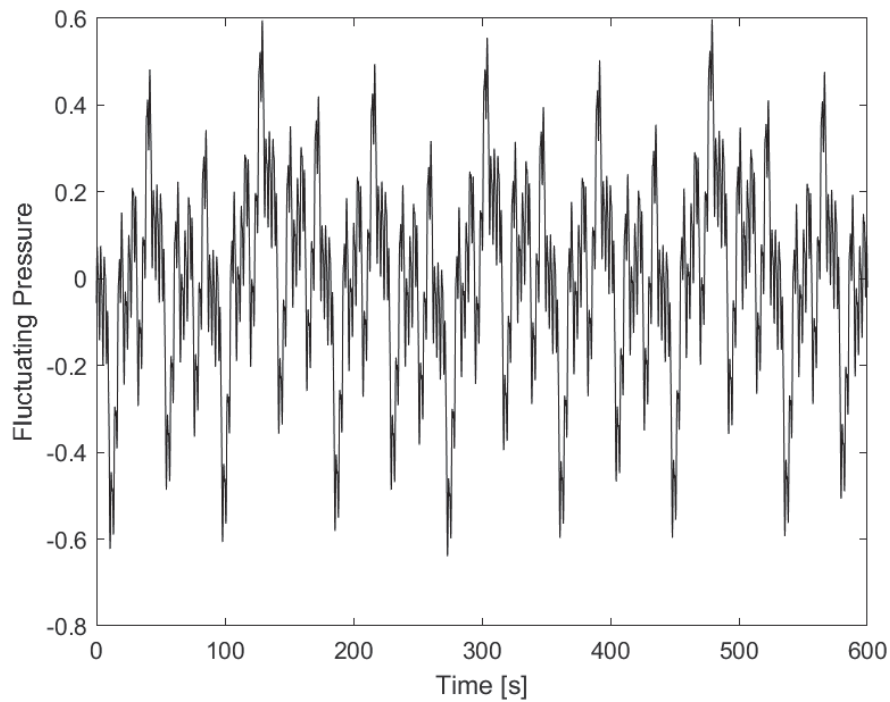


Figure 4: Fluctuating Pressure.

Now, the fluctuating forces over 600 seconds are computed from the fluctuating pressures [25]. It is worth noting that twenty simulations of fluctuating forces were performed to determine the highest displacements achieved at each simulation. Then, a unique fluctuating force is selected to generate a maximum displacement with a 95% probability of occurrence, following a Gumbel extreme value distribution. Figure 5 shows the time histories of wind loads on the 37th floor of the building.

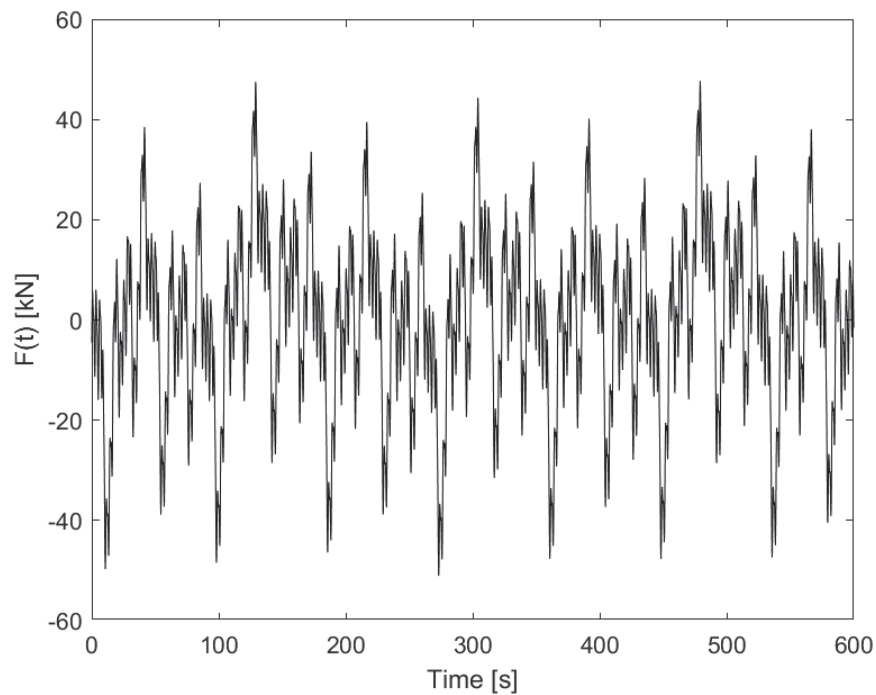


Figure 5: Time histories of wind loads on the 37<sup>th</sup> floor of the building.

Table 1 reports the design parameters optimized with the Cultural Algorithm. The optimization was carried out considering fixed  $b$  values, which represent 2%, 5% and 20% of in-ertance ratios.

$b$	$f$	$\zeta_d$	$F_{obj}$
2%	0.9882680	0.0000000	0.62616
5%	0.5000000	0.5000000	0.68861
20%	0.5000000	0.0219307	0.73547

Table 1: Optimal design parameter for the TID.

On the other hand, Table 2 reports the RMS values of the displacements for the uncontrolled and controlled structure. Furthermore, the percentage of reduction of the RMS is presented as well.

	$b$	Uncontrolled Response [m]	Controlled response [m]	% Reduction
37th RMS [m]	2%	0.17363	0.10914	37.12%
	5%	0.17363	0.11954	31.15%
	20%	0.17363	0.12770	26.45%

Table 2: Maximum RMS response of displacements of 37th story

Figure 6 shows the variation of the RMS values of the displacements of each degree of freedom considered. With these results, the efficiency of the TID is demonstrated.

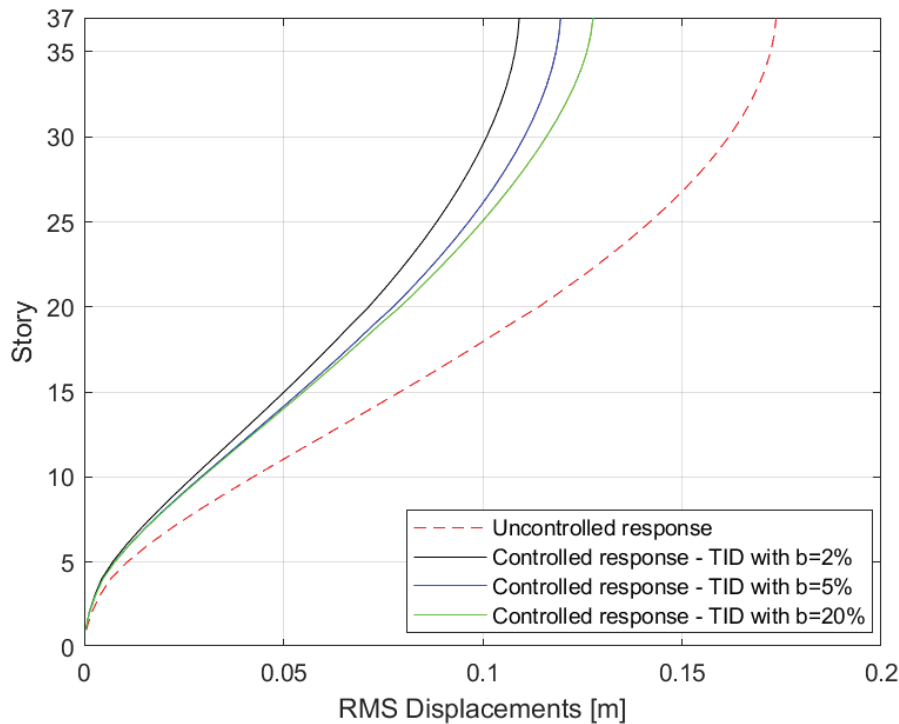


Figure 6: RMS displacement at each story level.



The maximum uncontrolled RMS response of displacement at the 37th story level in Figure 6 is 0.173 m. The reductions achieved using the optimized TID decrease between 37.12% and 26.45%, as inertance values increase. Using the  $b=2\%$  TID, the maximum RMS displacement value is 0.109 m (37.12% reduction); with  $b=5\%$ , the maximum RMS value diminish to 0.119 m (31.15% reduction); finally, with the  $b=20\%$  TID, the RMS value of displacement reduce hardly to 0.128 m (26.45% reduction). Thus, it is clear that the best reductions in the dynamic response, under wind excitations, are attained using the TID with the lowest inertance value ( $b=2\%$ ).

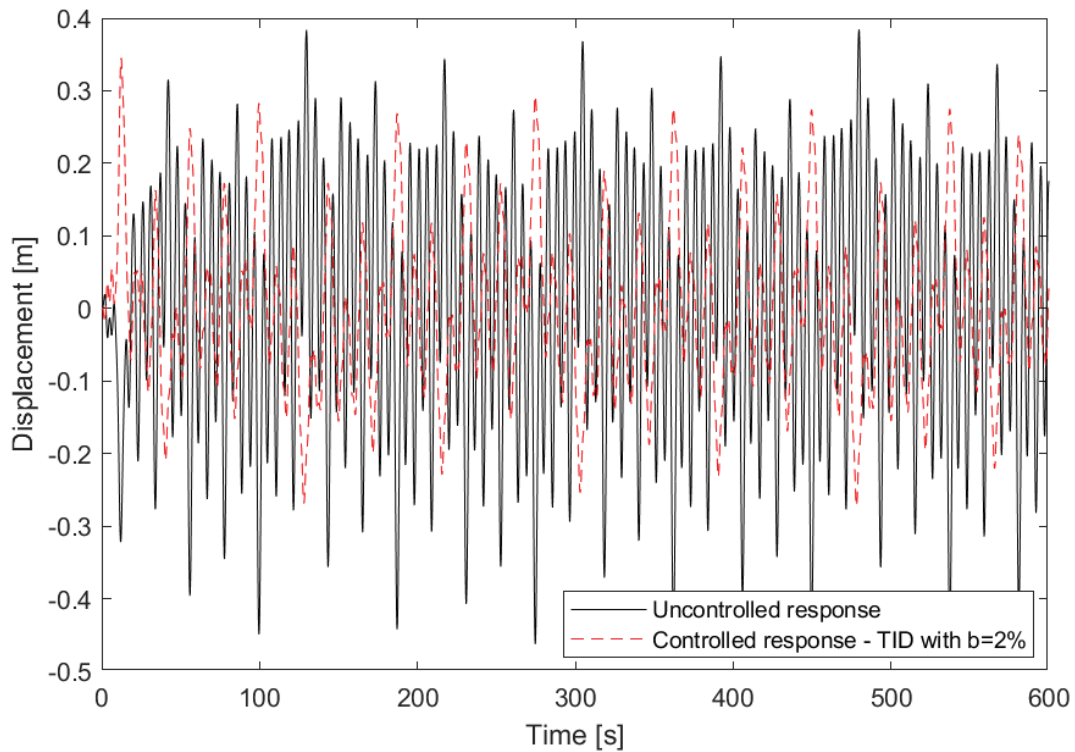


Figure 7: Time histories of controlled displacement on the 37<sup>th</sup> floor of the building.

Finally, Figure 7 shows a comparison between the uncontrolled and controlled history of displacements on the 37th floor of the structure. The peak displacement in Figure 7 was reduced from 0.463 m to 0.345 m using the  $b=2\%$  TID, which represents a 25.48% overall reduction.

## 6 CONCLUSIONS

- A numerical investigation on the optimal design parameters of a Tuned Inerter Damper (TID) based system for the control of wind-induced vibration in tall buildings was presented in this paper. The control system was inspired by the conventional TID, with the main difference that its location was changed from ground level to the last two levels of the structural system. To represent the dynamic action of the wind in the time domain, a Monte Carlo simulation was used in which a time series derived from the Davenport spectrum was re-produced using eleven harmonic functions with randomly chosen phase angles.
- The obtained results shows that TIDs with lower inertance values installed at the last floors of the building are useful to reduce the dynamic response of the structure under wind loads. Reductions up to 37.12% were achieved for RMS values of displacement us-

ing  $b=2\%$  TID. Moreover, the cultural algorithm proved to be an efficient and useful tool for determining the optimal TID de-sign parameters, and the effectiveness of modified TID systems on mitigating wind-induced vibrations in high-rise buildings was demonstrated.

## 7 ACKNOWLEDGEMENTS

The authors are grateful for the support provided by the Universidad Nacional de Colombia – Sede Medellín for the development of this work.

## 8 REFERENCES

- [1] K.C. Kwok, B. Samali, Performance of tuned mass dampers under wind loads. Vol. 17. Butterworth-Heinemann, 1995.
- [2] M.C. Smith. Synthesis of Mechanical Networks: The Inerter. *Proceedings of the 41<sup>st</sup> IEEE, Conference on Decision and Control*, Las Vegas, Nevada, USA, December, 2002.
- [3] C. Papageorgiou, M.C. Smith. Laboratory experimental testing of inerters. *In Proceedings of the 44th IEEE Conference on Decision and Control* (IEEE 2005), Seville, Spain, December 12-15, 2005.
- [4] I.F. Lazar, S.A. Neild, D.J. Wagg. Using an inerter-based device for structural vibration suppression. *Earthquake Engineering & Structural Dynamics*, 43, 1129-1147, 2014.
- [5] I.F. Lazar, S.A. Neild, D.J. Wagg. Design and Performance Analysis of Inerter-Based Vibration Control Systems. *In Dynamics of Civil Structures*, 4, 493-500. Springer, Cham, 2014.
- [6] I.F. Lazar, S.A. Neild, D.J. Wagg. Inerter-based vibration suppression systems for laterally and base-excited structures. *In Proceedings of the 9<sup>th</sup> International Conference on Structural Dynamics (EURODYN 2014)*, Porto, Portugal, 30 June – 2 July, 2014.
- [7] M.Z. Chen, Y. Hu. Inerter and Its Application in Vibration Control Systems. Springer, Singapore, 2019.
- [8] Y. Wen, Z. Chen, X. Hua. Design and evaluation of tuned inerter-based dampers for the seismic control of MDOF structures. *Journal of Structural Engineering*, 143, 2017.
- [9] R.G. Reynolds. An introduction to Cultural Algorithms. *Proceedings of the Third Annual Conference on Evolutionary Programming*, 131-139. River Edge, New Jersey, 1994.
- [10] W. Wang, Y. Song, Y. Xue, H. Jin, J. Hou, M. Zhao. An optimal vibration control strategy for a vehicle's active suspension based on improved cultural algorithm. *Applied Soft Computing*, 2014.
- [11] A. Khodabakhshian, R. Hemmati. Multi-machine power system stabilizer design by using cultural algorithms. *Electrical power and Energy Systems*, 2021.
- [12] M.Y. Liu, W.L. C, J.H. Hwang, C.R. Chu. Wind-induced vibration of high-rise building with tuned mass damper including soil-structure interaction. *Journal of Wind Engineering and Industrial Aerodynamics*, 96, 1092-1102, 2007.
- [13] A.A. Momtaz, M.A. Abdollahian. Study of Wind-induced vibrations in tall buildings with tuned mass dampers taking into account vortices effects. *International Journal of Advanced Structural Engineering*, 9, 385-395, 2017.

- [14] A. Giaralis, M. ASCE, F. Petrini. Wind-Induced Vibration Mitigation in Tall Buildings Using the Tuned Mass-Damper-Inerter. *J. Struct. Eng.*, 143: 04017127, 2017.
- [15] D.A. Caicedo. A comparative analysis on the seismic behavior of buildings using inerter-based devices: Tuned Mass Damper Inerter (TMDI) and Tuned Inerter Damper (TID). Dissertation. Medellín, Colombia, 2020.
- [16] K.C. Kwok. Perception of vibration and occupant comfort in wind-excited tall buildings. *Journal of Wind Engineering and Industrial Aerodynamics*, 97, 368-380, 2009.
- [17] A. Giaralis, F. Petrini. Optimum design of the tuned mass-damper-inerter for serviceability limit state performance in wind-excited tall buildings. *X International Conference on Structural Dynamics (EURODYN 2017)*, 199, 1773-1778, 2017.
- [18] F. Petrini, A. Giaralis, Z. Wang. Optimal tuned mass-damper-inerter (TMDI) design in wind-excited tall buildings for occupants' comfort serviceability performance and energy harvesting. *Engineering Structures*. 2019.
- [19] H.H. Barrios, N. Mosqueda, I. Huergo. Respuesta eólica de estructuras tipo punto ante viento sintético. *XXI Congreso Nacional de Ingeniería Estructural*, Sociedad Mexicana de Ingeniería Estructural. Campeche, Campeche, 2018.
- [20] M.J. Ribeiro. Análise estática e dinâmica de torres metálicas autoportantes. Dissertação de Mestrado, Publicação DM 001A/00. Departamento de Engenharia Civil e Ambiental, Universidade de Brasília, Brasília, DF, 2000.
- [21] M. Franco. Direct Along-Wind Dynamic Analysis of Tall Structures. Departamento de Engenharia de Estruturas e Fundações, Escola Politécnica da Universidade de São Paulo. São Paulo, 1993.
- [22] H.O. Sasquia. Vento sintético e a simulação de Monte Carlo - uma forma de considerar a característica aleatória e instável do carregamento dos ventos em estruturas. *Exacta*, 7, 77-85, Universidade Nove de Julho, São Paulo, Brasil, 2009.
- [23] A.G. Davenport. The spectrum of horizontal gustiness near the ground in high winds. Dept. of Civil Engineering, University of Bristol, 1961.
- [24] ASOCIACIÓN COLOMBIANA DE INGENIERÍA SÍSMICA. Normas Colombianas de Diseño y Construcción Sismo-Resistente, NSR-10, AIS, Bogotá, 2010.
- [25] Associação Brasileira de Normas Técnicas. NBR 6123 - Forças devidas ao vento nos edifícios. ABNT, Rio de Janeiro, 1988.
- [26] Z. Chang, B. Fitzgerald. Tuned mass-damper-inerter (TMDI) for suppressing edgewise vibration of wind turbine blades. *Engineering Structures*, 221, 2020.
- [27] F. Qian, Y. Luo, H. Sun, W.C. Tai, L. Zuo. Optimal tuned inerter dampers for performance enhancement of vibration isolation. *Engineering Structures*, 198, 2019.

## A PARAMETRIC ANALYSIS OF THE SEISMIC PERFORMANCE OF BRIDGES AS A FUNCTION OF THE DCFP DEVICE PROPERTIES

Paolo Castaldo<sup>1</sup>, and Guglielmo Amendola<sup>2</sup>

<sup>1</sup> Politecnico di Torino, Department of Structural, Geotechnical and Building Engineering (DISEG)  
Corso Duca degli Abruzzi 24, 10129, Turin, Italy  
e-mail: paolo.castaldo@polito.it

<sup>2</sup> Politecnico di Torino, Department of Structural, Geotechnical and Building Engineering (DISEG)  
Corso Duca degli Abruzzi 24, 10129, Turin, Italy  
guglielmo.amendola@polito.it

---

### Abstract

*The present investigation examines how the properties of the double concave friction pendulum (DCFP) devices influence the seismic performance of isolated multi-span continuous deck bridges. The numerical simulations are carried out using an eight-degree-of-freedom model to reproduce the elastic behavior of the pier, associated to the assumption of both rigid abutment and rigid deck, and the non-linear velocity-dependent behavior of the two surfaces of the double concave friction pendulum isolators, under a set of natural records with different characteristics. The results in terms of the statistics related to the relevant response parameters are computed in non-dimensional form with respect to the seismic intensity considering different properties of both DCFP isolators and bridge.*

**Keywords:** Seismic isolation, Double concave friction pendulum isolators, Multi-span continuous deck bridges, Performance-based engineering, Non-dimensional form.

---

## 1 INTRODUCTION

The seismic isolation is one of the most used and efficient techniques able to improve seismic performance of both new or existing buildings [1]-[2] and infrastructures [3]. With reference to bridges, the seismic isolation allows to uncouple the super-structure represented by the deck and the sub-structure represented by the system piers/abutments/foundations. The main benefit to the structural system relates to significant reduction of forces transmitted from the deck to the piers under seismic event.

In particular, the quantification of safety level of structures [5] and road infrastructures [6]-[8] is a relevant topic for research with special reference to areas subjected to high seismicity. In such areas, the non-linear behaviour of RC members [9]-[11] has a significant influence on structural response when structures are not provided of appropriate isolation systems. For instance, different investigations focused on the analysis of seismic response of bridges equipped with isolator devices have been performed over the years [12].

In literature, several studies have been carried out concerning seismic isolation of bridges through friction pendulum devices (FPS) [13]-[15]. The FPS bearings are able to make the natural period of the isolated bridge independent from the mass of the deck and allows significant energy dissipation under seismic motion thanks to friction on sliding surfaces [16]. The FPS bearings can be realized with single (SCFP) or multiple concave sliding surfaces [17]-[18]. In particular, the use of double concave sliding surface friction pendulum devices (DCFP) have positive influence on the seismic response of isolated bridges as demonstrated by [19].

The present study investigates the effectiveness of the use of DCFP to improve the seismic response of multi-span continuous bridges considering the interaction between piers, abutments and deck [20]. The structural response of the system under seismic excitation is analysed by means of an eight-degree-of-freedom (8-dof) model accounting for the reinforced concrete (RC) pier stiffness, the DCFP behaviour and the rigid RC abutment.

The seismic action and related uncertainties are reproduced adopting a set of natural records having different spectral characteristics. In detail, a non-dimensional parametric study is developed for several geometric configurations of the pier and of the DCFP isolators. The responses of the deck, of the pier and of each surface of the DCFP isolators are monitored to determine effectiveness of the isolation system.

## 2 DESCRIPTION OF DYNAMIC BEHAVIOUR OF DECK-ABUTMENT-PIER STRUCTURAL SYSTEM

The structural behavior of the multi-span continuous deck bridge (e.g., isolated three-span continuous deck bridge) isolated with DPCF is reproduced by means of an 8-degree-of-freedom (8-dof) system as shown by Figure 1.

In detail, 5 degrees of freedom relate to the lumped masses associated to the RC bridge pier (supposed to be elastic), 2 degrees of freedom correspond to the two sliders of the DPCF bearings and, finally, 1 degree of freedom concerns the mass of the rigid RC deck [14].

The governing equations of motion of the system can be expressed in terms of relative horizontal displacements with respect to the ground (Figure 1(a)) along the longitudinal direction as follows:



$$\begin{aligned}
 m_d [\ddot{u}_d(t) + \ddot{u}_g(t)] + F_{1a}(t) + F_{1p}(t) &= 0 \\
 m_{sa} [\ddot{u}_{sa}(t) + \ddot{u}_g(t)] - F_{1a}(t) + F_{2a}(t) &= 0 \\
 m_{sp} [\ddot{u}_{sp}(t) + \ddot{u}_g(t)] - F_{1p}(t) + F_{2p}(t) &= 0 \quad (1 \text{ a,b,c,d,e}) \\
 m_{p5} [\ddot{u}_{p5}(t) + \ddot{u}_g(t)] + c_{p5} [\dot{u}_{p5}(t) - \dot{u}_{p4}(t)] + k_{p5} [u_{p5}(t) - u_{p4}(t)] - F_{2p}(t) &= 0 \\
 m_{pi} [\ddot{u}_{pi}(t) + \ddot{u}_g(t)] + c_{pi} [\dot{u}_{pi}(t) - \dot{u}_{pi-1}(t)] + k_{pi} [u_{pi}(t) - u_{pi-1}(t)] + \\
 - c_{pi+1} [\dot{u}_{pi+1}(t) - \dot{u}_{pi}(t)] - k_{pi+1} [u_{pi+1}(t) - u_{pi}(t)] &= 0 \quad \text{for } i=1, \dots, 4
 \end{aligned}$$

where  $u_d$  denotes the displacement of the deck relative to the ground;  $u_{sp}$  is the displacement of the slider of the DCFP device located on the pier with respect to the ground;  $u_{sa}$  is the displacement of the slider of the DCFP device located on the abutment with respect to the ground,  $u_{pi}$  ( $i=1, \dots, 4, 5$ ) is the displacement relative to the ground of pier  $i$ -th mass;  $m_d$ ,  $m_{sp}$  and  $m_{sa}$  are the masses of the deck and of the two DCFP devices installed on the pier and on the abutment;  $m_{pi}$  ( $i=1, \dots, 4, 5$ ) is the  $i$ -th lumped mass of the pier segment;  $k_{pi}$  and  $c_{pi}$  ( $i=1, \dots, 5$ ) are the stiffness and associated viscous damping constant for each dof associated to the pier segments;  $t$  is the time instant;  $F_{ja}(t)$  and  $F_{jp}(t)$  denote the reaction forces of the DCFP bearings on the abutment and on the pier, respectively, for the upper ( $j=1$ ) and lower sliding surface ( $j=2$ ). With reference to the modelling of behavior of the DCFP, the device can be modelled as a serial combination of two single FPS isolators. Then, according to [17]-[18], the reaction forces at the upper ( $j=1$ ) and lower ( $j=2$ ) surface (i.e.,  $F_1$  and  $F_2$ ) are identical and can be obtained according to the following expression:

$$F = F_1 = F_2 = \frac{m_d g}{R_1 + R_2} (u) + \frac{m_d g (R_1 \mu_1 (\dot{u}_1) \text{sgn}(\dot{u}_1) + R_2 \mu_2 (\dot{u}_2) \text{sgn}(\dot{u}_2))}{R_1 + R_2} \quad (2)$$

where  $u$  is the global horizontal displacement of the DCFP isolator;  $u_1$  represents the horizontal displacement of the upper surface ( $j=1$ );  $u_2$  is the horizontal displacement of the lower surface ( $j=2$ ). The first part of Eq. (2) represents the equivalent restoring stiffness ( $k_{comb}$ ) of the DCFP device expressed as:

$$k_{comb} = \frac{m_d g}{R_1 + R_2} \quad (3)$$

from which the restoring natural period can be derived as follows:

$$T_d = 2\pi \sqrt{(R_1 + R_2) / g} = 2\pi / \omega_d \quad (4)$$

where  $g$  is the gravity constant;  $R_1$  and  $R_2$  denote the upper and lower radius of curvature of the DCFP bearing. In Eq.(2),  $\mu_j(\dot{u}_j(t))$  (with  $j=1,2$ ) represents the sliding friction coefficient, which depends on the slider slip velocity  $\dot{u}_j(t)$  along one of the two sliding surfaces and on its sign,  $\text{sgn}(\dot{u}_j)$  (for  $j=1,2$ ). The second part of Eq.(2) represents the equivalent friction coefficient of the DCFP device [17]:

$$\mu_{eqv} = \frac{\mu_1 R_1 + \mu_2 R_2}{R_1 + R_2} \quad (5)$$

Eq.(5) is valid under the assumption that the sliding occurs on the both surfaces of the device and in the same direction.

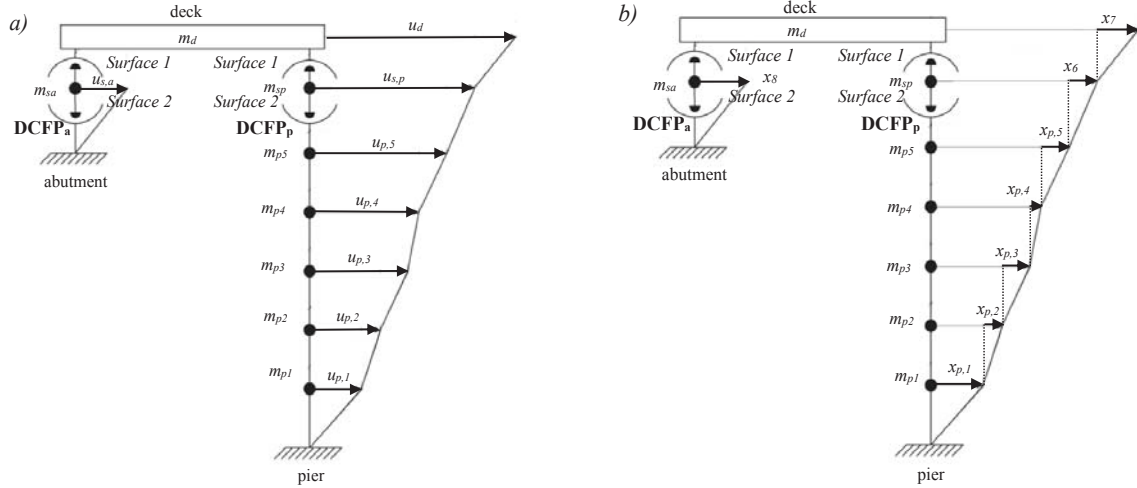


Figure 1: Representation of the 8-dof model of the bridge. Relative displacements with respect to the ground (a) and drifts between the different lumped masses (b).

The experimental investigations of [21]-[23] demonstrate that, the coefficient of friction on sliding surfaces of DCFP can be estimated according to the following expression:

$$\mu_j(\dot{u}_j) = \mu_{j,\max} - (\mu_{j,\max} - \mu_{j,\min}) \cdot \exp(-\alpha |\dot{u}_j|) \quad \text{for } j = 1, 2 \quad (6)$$

where,  $\mu_{j,\max}$  denotes the maximum value of friction coefficient at high sliding velocities;  $\mu_{j,\min}$  represents the value at near-zero sliding velocity. In the present investigation, it is assumed that  $\mu_{j,\max} = 3\mu_{j,\min}$  and  $\alpha = 30$  according to the researches of [21]-[23].

### 3 NON-DIMENSIONAL SYSTEM OF EQUATIONS

The analysis of the seismic behavior of the bridge under seismic action is performed according to non-dimensional form of the system of equations of motion, in line with previous applications [24]. In order to obtain the response of the DCFP devices along each sliding surface, Eq.(1) can be expressed in terms of drifts between the lumped masses of the structural system (Fig.1(b)), according to the following relationships:

$$\begin{aligned} & m_d \ddot{x}_7(t) + m_d \ddot{x}_6(t) + m_d \ddot{x}_{p5}(t) + m_d \ddot{x}_{p4}(t) + m_d \ddot{x}_{p3}(t) + m_d \ddot{x}_{p2}(t) + m_d \ddot{x}_{p1}(t) + \\ & + c_d \dot{x}_d(t) + F_{1a}(t) + F_{1p}(t) = -m_d \ddot{u}_g(t) \\ & m_{sp} \ddot{x}_6(t) + m_{sp} \ddot{x}_{p5}(t) + m_{sp} \ddot{x}_{p4}(t) + m_{sp} \ddot{x}_{p3}(t) + m_{sp} \ddot{x}_{p2}(t) + m_{sp} \ddot{x}_{p1}(t) - F_{1p}(t) + F_{2p}(t) = -m_{sp} \ddot{u}_g(t) \\ & m_{sa} \ddot{x}_8(t) - F_{1a}(t) + F_{2a}(t) = -m_{sa} \ddot{u}_g(t) \\ & m_{p5} \ddot{x}_{p5}(t) + m_{p5} \ddot{x}_{p4}(t) + m_{p5} \ddot{x}_{p3}(t) + m_{p5} \ddot{x}_{p2}(t) + m_{p5} \ddot{x}_{p1}(t) - c_d \dot{x}_d(t) + c_{p5} \dot{x}_{p5}(t) + \\ & + k_{p5} x_{p5}(t) - F_{2p}(t) = -m_{p5} \ddot{u}_g(t) \\ & m_{p4} \ddot{x}_{p4}(t) + m_{p4} \ddot{x}_{p3}(t) + m_{p4} \ddot{x}_{p2}(t) + m_{p4} \ddot{x}_{p1}(t) - c_{p5} \dot{x}_{p5}(t) - k_{p5} x_{p5}(t) + c_{p4} \dot{x}_{p4}(t) + k_{p4} x_{p4}(t) = -m_{p4} \ddot{u}_g(t) \\ & m_{p3} \ddot{x}_{p3}(t) + m_{p3} \ddot{x}_{p2}(t) + m_{p3} \ddot{x}_{p1}(t) - c_{p4} \dot{x}_{p4}(t) - k_{p4} x_{p4}(t) + c_{p3} \dot{x}_{p3}(t) + k_{p3} x_{p3}(t) = -m_{p3} \ddot{u}_g(t) \\ & m_{p2} \ddot{x}_{p2}(t) + m_{p2} \ddot{x}_{p1}(t) - c_{p3} \dot{x}_{p3}(t) - k_{p3} x_{p3}(t) + c_{p2} \dot{x}_{p2}(t) + k_{p2} x_{p2}(t) = -m_{p2} \ddot{u}_g(t) \\ & m_{p1} \ddot{x}_{p1}(t) - c_{p2} \dot{x}_{p2}(t) - k_{p2} x_{p2}(t) + c_{p1} \dot{x}_{p1}(t) + k_{p1} x_{p1}(t) = -m_{p1} \ddot{u}_g(t) \end{aligned} \quad (7a,b,c,d,e,f,g,h)$$

where, in line to Eq.s(2)-(6), the reactions of the DCFP bearings on the sliding surfaces are:

$$\begin{aligned}
 F_{1a} &= \frac{m_d g}{2} \left[ \frac{1}{R_{1a}} \left( \sum_{i=1}^5 x_{pi} + x_6 + x_7 - x_8 \right) + \mu_{1a}(\dot{x}_9) (\text{sgn}(\dot{x}_9)) \right] \\
 F_{2a} &= \left( \frac{m_d}{2} + m_{sa} \right) g \left[ \frac{1}{R_{2a}} (x_8) + (\mu_{2a}(\dot{x}_8)) (\text{sgn}(\dot{x}_8)) \right] \\
 F_{1p} &= \left( \frac{m_d g}{2} \right) \left[ \frac{1}{R_{1p}} (x_7) + (\mu_{1p}(\dot{x}_7)) (\text{sgn}(\dot{x}_7)) \right] \\
 F_{2p} &= \left( \frac{m_d}{2} + m_{sp} \right) g \left[ \frac{1}{R_{2p}} (x_6) + (\mu_{2p}(\dot{x}_6)) (\text{sgn}(\dot{x}_6)) \right]
 \end{aligned} \tag{8 a,b,c,d}$$

where, in detail,  $x_9 = u_d - x_8 = \sum_{i=1}^5 x_{pi} + x_6 + x_7 - x_8$ . Next, dividing all the equations by the mass  $m_d$ , the system of equation of Eq.(7) becomes:

$$\begin{aligned}
 &\ddot{x}_7(t) + \ddot{x}_6(t) + \ddot{x}_{p5}(t) + \ddot{x}_{p4}(t) + \ddot{x}_{p3}(t) + \ddot{x}_{p2}(t) + \ddot{x}_{p1}(t) + 2\xi_d \omega_d \dot{x}_d(t) + \\
 &+ \frac{g}{2} \left[ \frac{1}{R_{1a}} \left( \sum_{i=1}^5 x_{pi} + x_6 + x_7 - x_8 \right) + \mu_{1a}(v) \left( \text{sgn} \left( \sum_{i=1}^5 \dot{x}_{pi} + \dot{x}_6 + \dot{x}_7 - \dot{x}_8 = v \right) \right) \right] + \\
 &+ \frac{g}{2} \left[ \frac{1}{R_{1p}} (x_7) + (\mu_{1p}(\dot{x}_7)) (\text{sgn}(\dot{x}_7)) \right] = \ddot{u}_g(t) \\
 &\lambda_{sp} (\ddot{x}_6(t) + \ddot{x}_{p5}(t) + \ddot{x}_{p4}(t) + \ddot{x}_{p3}(t) + \ddot{x}_{p2}(t) + \ddot{x}_{p1}(t)) + \\
 &- \frac{g}{2} \left[ \frac{1}{R_{1p}} (x_7) + (\mu_{1p}(\dot{x}_7)) (\text{sgn}(\dot{x}_7)) \right] + \left( \frac{1}{2} + \lambda_{sp} \right) g \left[ \frac{1}{R_{2p}} (x_6) + (\mu_{2p}(\dot{x}_6)) (\text{sgn}(\dot{x}_6)) \right] = -\lambda_{sp} \ddot{u}_g(t) \\
 &\lambda_{sa} \ddot{x}_8(t) - \frac{g}{2} \left[ \frac{1}{R_{1a}} \left( \sum_{i=1}^5 x_{pi} + x_6 + x_7 - x_8 \right) + \mu_{1a}(v) \left( \text{sgn} \left( \sum_{i=1}^5 \dot{x}_{pi} + \dot{x}_6 + \dot{x}_7 - \dot{x}_8 = v \right) \right) \right] + \\
 &+ \left( \frac{1}{2} + \lambda_{sa} \right) g \left[ \frac{1}{R_{2a}} (x_8) + (\mu_{2a}(\dot{x}_8)) (\text{sgn}(\dot{x}_8)) \right] = -\lambda_{sa} \ddot{u}_g(t) \\
 &\lambda_{p5} (\ddot{x}_{p5}(t) + \ddot{x}_{p4}(t) + \ddot{x}_{p3}(t) + \ddot{x}_{p2}(t) + \ddot{x}_{p1}(t)) - 2\xi_d \omega_d \dot{x}_d(t) + 2\xi_{p5} \omega_{p5} \lambda_{p5} \dot{x}_{p5}(t) + \omega_{p5}^2 \lambda_{p5} x_{p5}(t) + \\
 &- \left( \frac{1}{2} + \lambda_{sp} \right) g \left[ \frac{1}{R_{2p}} (x_6) + (\mu_{2p}(\dot{x}_6)) (\text{sgn}(\dot{x}_6)) \right] = -\lambda_{p5} \ddot{u}_g(t) \\
 &\lambda_{p4} (\ddot{x}_{p4}(t) + \ddot{x}_{p3}(t) + \ddot{x}_{p2}(t) + \ddot{x}_{p1}(t)) - 2\xi_{p5} \omega_{p5} \lambda_{p5} \dot{x}_{p5}(t) - \omega_{p5}^2 \lambda_{p5} x_{p5}(t) + \\
 &+ 2\xi_{p4} \omega_{p4} \lambda_{p4} \dot{x}_{p4}(t) + \omega_{p4}^2 \lambda_{p4} x_{p4}(t) = -\lambda_{p4} \ddot{u}_g(t) \\
 &\lambda_{p3} (\ddot{x}_{p3}(t) + \ddot{x}_{p2}(t) + \ddot{x}_{p1}(t)) - 2\xi_{p4} \omega_{p4} \lambda_{p4} \dot{x}_{p4}(t) - \omega_{p4}^2 \lambda_{p4} x_{p4}(t) + 2\xi_{p3} \omega_{p3} \lambda_{p3} \dot{x}_{p3}(t) + \omega_{p3}^2 \lambda_{p3} x_{p3}(t) = -\lambda_{p3} \ddot{u}_g(t) \\
 &\lambda_{p2} (\ddot{x}_{p2}(t) + \ddot{x}_{p1}(t)) - 2\xi_{p3} \omega_{p3} \lambda_{p3} \dot{x}_{p3}(t) - \omega_{p3}^2 \lambda_{p3} x_{p3}(t) + 2\xi_{p2} \omega_{p2} \lambda_{p2} \dot{x}_{p2}(t) + \omega_{p2}^2 \lambda_{p2} x_{p2}(t) = -\lambda_{p2} \ddot{u}_g(t) \\
 &\lambda_{p1} \ddot{x}_{p1}(t) - 2\xi_{p2} \omega_{p2} \lambda_{p2} \dot{x}_{p2}(t) - \omega_{p2}^2 \lambda_{p2} x_{p2}(t) + 2\xi_{p1} \omega_{p1} \lambda_{p1} \dot{x}_{p1}(t) + \omega_{p1}^2 \lambda_{p1} x_{p1}(t) = -\lambda_{p1} \ddot{u}_g(t)
 \end{aligned} \tag{9a,b,c,d,e,f,g,h}$$

introducing the mass ratios; the circular frequency of vibration of the isolated deck and of the  $i$ -th dof of the pier; the damping coefficient of the  $i$ -th dof of the pier, as expressed in the following:

$$\lambda_{pi} = \frac{m_{pi}}{m_d}, \quad \lambda_{sa} = \frac{m_{sa}}{m_d}, \quad \lambda_{sp} = \frac{m_{sp}}{m_d}, \quad \omega_d = \sqrt{\frac{k_{comb}}{m_d}}, \quad \omega_{pi} = \sqrt{\frac{k_{pi}}{m_{pi}}}, \quad \xi_{pi} = \frac{c_{pi}}{2m_{pi}\omega_{pi}} \tag{10 a,b,c,d,e,f}$$

In line to [24], the time scale  $\tau = t\omega_d$  can be introduced together with the seismic intensity scale factor  $a_0$ , expressed as  $\ddot{u}_g(t) = a_0 \ell(\tau)$ . The function  $\ell(\tau)$  is a non-dimensional function of

time describing the time history of the seismic input. Finally, the non-dimensional system equations can be expressed as follows:

$$\begin{aligned}
 & \ddot{\psi}_7(\tau) + \ddot{\psi}_6(\tau) + \ddot{\psi}_{p5}(\tau) + \ddot{\psi}_{p4}(\tau) + \ddot{\psi}_{p3}(\tau) + \ddot{\psi}_{p2}(\tau) + \ddot{\psi}_{p1}(\tau) + 2\xi_d \dot{\psi}_7(\tau) + \frac{g}{2} \left[ \frac{1}{R_{1p}} \frac{1}{\omega_d^2} \psi_7(\tau) + \frac{\mu_{1p}(\dot{\psi}_7)}{a_0} \text{sgn}(\dot{\psi}_7) \right] + \\
 & + \frac{g}{2} \left[ \frac{1}{R_{1a}} \frac{1}{\omega_d^2} \left( \sum_{i=1}^5 \psi_{pi}(\tau) + \psi_6(\tau) + \psi_7(\tau) - \psi_8(\tau) \right) + \left( \frac{\mu_{1a}(\dot{\psi}_9)}{a_0} \right) \left( \text{sgn} \left( \sum_{i=1}^5 \dot{\psi}_{pi}(\tau) + \dot{\psi}_6(\tau) + \dot{\psi}_7(\tau) - \dot{\psi}_8(\tau) \right) \right) \right] = -\ell(\tau) \\
 \\
 & \lambda_{sp} \left[ \ddot{\psi}_6(\tau) + \ddot{\psi}_{p5}(\tau) + \ddot{\psi}_{p4}(\tau) + \ddot{\psi}_{p3}(\tau) + \ddot{\psi}_{p2}(\tau) + \ddot{\psi}_{p1}(\tau) \right] - \frac{g}{2} \left[ \frac{1}{R_{1p}} \frac{1}{\omega_d^2} \psi_7(\tau) + \frac{\mu_{1p}(\dot{\psi}_7)}{a_0} \text{sgn}(\dot{\psi}_7) \right] + \\
 & + \left( \frac{1}{2} + \lambda_{sp} \right) g \left[ \frac{1}{R_{2p}} \frac{1}{\omega_d^2} \psi_6(\tau) + \frac{\mu_{2p}(\dot{\psi}_6)}{a_0} \text{sgn}(\dot{\psi}_6) \right] = -\lambda_{sp} \ell(\tau) \\
 \\
 & \lambda_{sa} \ddot{\psi}_8(\tau) - \frac{g}{2} \left[ \frac{1}{R_{1a}} \frac{1}{\omega_d^2} \left( \sum_{i=1}^5 \psi_{pi}(\tau) + \psi_6(\tau) + \psi_7(\tau) - \psi_8(\tau) \right) + \left( \frac{\mu_{1a}(\dot{\psi}_9)}{a_0} \right) \left( \text{sgn} \left( \sum_{i=1}^5 \dot{\psi}_{pi}(\tau) + \dot{\psi}_6(\tau) + \dot{\psi}_7(\tau) - \dot{\psi}_8(\tau) \right) \right) \right] + \\
 & + \left( \frac{1}{2} + \lambda_{sa} \right) g \left[ \frac{1}{R_{2a}} \frac{1}{\omega_d^2} \psi_8(\tau) + \frac{\mu_{2a}(\dot{\psi}_8)}{a_0} \text{sgn}(\dot{\psi}_8) \right] = -\lambda_{sa} \ell(\tau) \\
 \\
 & \lambda_{p5} \left[ \ddot{\psi}_{p5}(\tau) + \ddot{\psi}_{p4}(\tau) + \ddot{\psi}_{p3}(\tau) + \ddot{\psi}_{p2}(\tau) + \ddot{\psi}_{p1}(\tau) \right] - 2\xi_d \dot{\psi}_d(\tau) + 2\xi_{p5} \lambda_{p5} \frac{\omega_{p5}}{\omega_d} \dot{\psi}_{p5}(\tau) + \frac{\lambda_{p5} \omega_{p5}^2}{\omega_d^2} \psi_{p5}(\tau) + \\
 & - \left( \frac{1}{2} + \lambda_{p5} \right) g \left[ \frac{1}{R_{2p}} \frac{1}{\omega_d^2} \psi_6(\tau) + \frac{\mu_{2p}(\dot{\psi}_6)}{a_0} \text{sgn}(\dot{\psi}_6) \right] = -\lambda_{p5} \ell(\tau) \\
 \\
 & \lambda_{p4} \left[ \ddot{\psi}_{p4}(\tau) + \ddot{\psi}_{p3}(\tau) + \ddot{\psi}_{p2}(\tau) + \ddot{\psi}_{p1}(\tau) \right] - 2\xi_{p5} \lambda_{p5} \frac{\omega_{p5}}{\omega_d} \dot{\psi}_{p5}(\tau) + \\
 & + 2\xi_{p4} \lambda_{p4} \frac{\omega_{p4}}{\omega_d} \dot{\psi}_{p4}(\tau) - \lambda_{p5} \frac{\omega_{p5}^2}{\omega_d^2} \psi_{p5}(\tau) + \lambda_{p4} \frac{\omega_{p4}^2}{\omega_d^2} \psi_{p4}(\tau) = -\lambda_{p4} \ell(\tau) \\
 \\
 & \lambda_{p3} \left[ \ddot{\psi}_{p3}(\tau) + \ddot{\psi}_{p2}(\tau) + \ddot{\psi}_{p1}(\tau) \right] - 2\xi_{p4} \lambda_{p4} \frac{\omega_{p4}}{\omega_d} \dot{\psi}_{p4}(\tau) + \\
 & + 2\xi_{p3} \lambda_{p3} \frac{\omega_{p3}}{\omega_d} \dot{\psi}_{p3}(\tau) - \lambda_{p4} \frac{\omega_{p4}^2}{\omega_d^2} \psi_{p4}(\tau) + \lambda_{p3} \frac{\omega_{p3}^2}{\omega_d^2} \psi_{p3}(\tau) = -\lambda_{p3} \ell(\tau) \\
 \\
 & \lambda_{p2} \left[ \ddot{\psi}_{p2}(\tau) + \ddot{\psi}_{p1}(\tau) \right] - 2\xi_{p3} \lambda_{p3} \frac{\omega_{p3}}{\omega_d} \dot{\psi}_{p3}(\tau) + 2\xi_{p2} \lambda_{p2} \frac{\omega_{p2}}{\omega_d} \dot{\psi}_{p2}(\tau) - \lambda_{p3} \frac{\omega_{p3}^2}{\omega_d^2} \psi_{p3}(\tau) + \\
 & + \lambda_{p2} \frac{\omega_{p2}^2}{\omega_d^2} \psi_{p2}(\tau) = -\lambda_{p2} \ell(\tau) \\
 \\
 & \lambda_{p1} \ddot{\psi}_{p1}(\tau) - 2\xi_{p2} \lambda_{p2} \frac{\omega_{p2}}{\omega_d} \dot{\psi}_{p2}(\tau) + 2\xi_{p1} \lambda_{p1} \frac{\omega_{p1}}{\omega_d} \dot{\psi}_{p1}(\tau) - \lambda_{p2} \frac{\omega_{p2}^2}{\omega_d^2} \psi_{p2}(\tau) + \lambda_{p1} \frac{\omega_{p1}^2}{\omega_d^2} \psi_{p1}(\tau) = -\lambda_{p1} \ell(\tau)
 \end{aligned}
 \tag{11 a,b,c,d,e,f,g,h}$$

with the following non-dimensional parameters:

$$\begin{aligned}
 \Pi_{oi} &= \frac{\omega_{pi}}{\omega_d} \quad , \quad \Pi_{\lambda i} = \lambda_{pi} = \frac{m_{pi}}{m_d} \quad , \quad \Pi_{\lambda sa} = \lambda_{sa} \quad , \\
 \Pi_{\lambda sp} &= \lambda_{sp} \quad , \quad \Pi_{\mu 1a}(\dot{\psi}_9) = \frac{\mu_{1a}(\dot{\psi}_9) g}{a_0} \quad , \\
 \Pi_{\mu 1p}(\dot{\psi}_7) &= \frac{\mu_{1p}(\dot{\psi}_7) g}{a_0} \quad , \quad \Pi_{\mu 2a}(\dot{\psi}_8) = \frac{\mu_{2a}(\dot{\psi}_8) g}{a_0} \quad , \\
 \Pi_{\mu 2p}(\dot{\psi}_6) &= \frac{\mu_{2p}(\dot{\psi}_6) g}{a_0} \quad , \quad \Pi_{\xi pi} = \xi_{pi}
 \end{aligned}
 \tag{12 a,b,c,d,e,f,g,h,i}$$

The non-dimensional parameters  $\Pi_{\mu 1a}$ ,  $\Pi_{\mu 1p}$ ,  $\Pi_{\mu 2a}$ ,  $\Pi_{\mu 2p}$  depend from the velocities and are used as follows:

$$\Pi_{\mu 1a}^* = \frac{\mu_{1,\max,a} g}{a_0}, \quad \Pi_{\mu 1p}^* = \frac{\mu_{1,\max,p} g}{a_0}, \quad \Pi_{\mu 2a}^* = \frac{\mu_{2,\max,a} g}{a_0}, \quad \Pi_{\mu 2p}^* = \frac{\mu_{2,\max,p} g}{a_0} \quad (13 \text{ a,b,c,d})$$

With reference to Figure 1, it can be recognized that the peak response in terms of non-dimensional parameters can be expressed as:

$$\psi_{u_d} = \frac{u_{d,\text{peak}} \omega_d^2}{a_0}, \quad \psi_{x_d} = \frac{x_{d,\text{peak}} \omega_d^2}{a_0} = \frac{(x_6 + x_7)_{\text{peak}} \omega_d^2}{a_0}, \quad \psi_{u_p} = \frac{u_{p,\text{peak}} \omega_d^2}{a_0} = \frac{\left( \sum_{i=1}^5 x_i \right)_{\text{peak}} \omega_d^2}{a_0} \quad (14 \text{ a,b,c})$$

#### 4 PARAMETRIC INVESTIGATION OF STRUCTURAL RESPONSE UNDER SEISMIC ACTIONS

Next, the results of parametric analysis of the bridge system isolated with DCFP bearings of Figure 1 are reported in non-dimensional terms. Firstly, the criteria for selection of earthquake events and the response parameters adopted to monitor the seismic performance are described.

##### 4.1 Selection of the seismic inputs

In line with the approach of performance-based earthquake engineering (PBEE) [25], the present investigation accounts for the uncertainties related to the seismic input intensity separately from the ones related to the characteristics of the record (i.e., record-to-record variability). This is possible to the introduction of an intensity measure (IM) that corresponds to the seismic intensity scale factor  $a_0$ . According to the criteria of efficiency, sufficiency and hazard compatibility [26], this study assumes that the spectral pseudo-acceleration,  $S_A$ , at the isolated period of the system,  $T_d = 2\pi / \omega_d$  (Eq.(4)), represents the adopted intensity measure IM. In the parametric analyses,  $\xi_d$  is taken equal to zero, in line to [24]. Then, the related  $IM = a_0$  is hereinafter denoted to as  $S_A(T_d)$ . The record-to-record variability is described through a set of 30 ground motion records with details in [27]-[30].

##### 4.2 Evaluation of the seismic response

In the present investigation, the peak response parameters considered are the following:

- the *peak deck response*  $u_{d,\text{peak}}$ , that corresponds to the peak isolator global response on the abutment;
- the *peak isolator global response* on the pier,  $x_{d,\text{peak}}$ ;
- the *peak displacement at the top of the pier*  $u_{p,\text{peak}}$  with respect to the ground.

According to the nondimensionalization previously introduced, the solution of Eq. (11) for the ground motions records allows to determine a set of samples of the mentioned above output variables. Next, the non-dimensional response parameters are assumed consistent with a lognormal probabilistic model as widely employed in PBEE [31] and in other studies [32]-[39]. The statistical parameters for lognormal distribution can be derived from generic response parameter  $D$  (i.e., the extreme values of  $\psi_{u_d}$ ,  $\psi_{x_p}$  and  $\psi_{u_p}$  of Eq.s (11) and (14)) by estimating the mean value  $GM(D)$  and the coefficient of variation  $\beta(D)$  of the observed samples as follows:

$$GM(D) = \sqrt[N]{d_1 \cdot \dots \cdot d_N} \quad (15)$$

$$\beta(D) = \sqrt{\frac{(\ln d_1 - \ln[GM(D)])^2 + \dots + (\ln d_N - \ln[GM(D)])^2}{N-1}} \quad (16)$$

where  $d_h$  represents the  $h$ -th sample value of  $D$  associated to the  $h$ -th accelerogram and  $N$  is the total number of samples equal to the total number of accelerograms herein adopted ( $h=1, \dots, N$ ). According to the lognormal distribution assumption, the  $k$ -th percentile of the generic response parameter  $D$  can be derived as follows:

$$d_k = GM(D) \exp[f(k)\beta(D)] \quad (17)$$

where  $f(k)$  assume the values of  $f(50) = 0$  for 50-th percentile and  $f(84) = 1$  for 84-percentile, respectively [40].

### 4.3 Outcomes from non-dimensional analyses

This section reports the results of the parametric investigation developed in line to the proposed criteria for nondimensionalization of the equations of motion. The influence of the properties of the DCFP isolators and bridge geometry on the seismic performance of the structural system under the ground motion records has been investigated. The following parametric analysis has been carried out:

- the parameters  $\Pi_{\xi_d} = \xi_d$  and  $\Pi_{\xi_p} = \xi_p$  are assumed equal to 0% and 5%;
- the isolated bridge period  $T_d$  has been assumed as 2s, 2.5s, 3s, 3.5s and 4s;
- the RC pier period  $T_p$  equal to 0.2s [19];
- the five pier lumped masses  $\Pi_{\lambda} = \lambda_p$  has been considered equal to 0.1, 0.15 and 0.2 [19];
- the two DCFP devices on the abutment and on the pier have identical properties (i.e., follows that  $\Pi_{\mu_{1a}}^* = \Pi_{\mu_{1p}}^* = \Pi_{\mu_1}^*$  as well as  $\Pi_{\lambda_{sa}} = \Pi_{\lambda_{sp}} = \Pi_{\lambda_s}$ ) and the mass ratio  $\Pi_{\lambda_s}$  is set equal to 0.005;  $R_1 / R_2$  equal to 2,  $\mu_{1,\max} / \mu_{2,\max}$  equal to 4,  $\mu_{j,\max} / \mu_{j,\min}$  (with  $j=1,2$ ) equal to 3;
- the parameter  $\Pi_{\mu_1}^*$  is assumed to vary in the range between 0 (no friction) and 2 (very high friction) (specifically, 95 values are considered).

Then, the non-dimensional parametric investigations have been carried out on 1425 different systems, defined by varying the main structural properties within the two bearing cases, assuming 30 different ground motions. For each value of the parameters of interest in the parametric study, the differential equations of motion, (i.e., Eq. (11)), have been solved for the 30 different ground motions. The Bogacki-Shampine integration algorithm available in Matlab-Simulink [41] has been adopted.

Figs 2-4 show the statistics ( $GM$  and  $\beta$  values) of the non-dimensional peak response parameters considered, obtained for different values of the system properties varying in the range of interest. Each figure contains three surface plots, corresponding to the different values of  $\Pi_{\lambda}$ .

Fig. 2 plots the results concerning the peak normalized displacement of pier top  $\psi_{u_p}$  with respect to the ground. It is noteworthy that for very low  $\Pi_{\mu_1}^*$  values,  $GM(\psi_{u_p})$  decreases by increasing  $\Pi_{\mu_1}^*$ , whereas it increases for high  $\Pi_{\mu_1}^*$  values. Thus, there exists an optimal value



of  $\Pi_{\mu 1}^*$  such that the peak displacement of pier top is minimized. This optimal value varies between 0 and 0.5 depending on the values of  $T_d$  and  $\Pi_\lambda$ . In addition,  $GM(\psi_{u_p})$  decreases significantly with increasing  $\Pi_\lambda$ . The parameter  $T_d$  has an influence on  $GM(\psi_{u_p})$  leading to a general decrease for an its increase thanks to the effectiveness of the seismic isolation. The dispersion  $\beta(\psi_{u_p})$  shows a maximum value approximatively at the same value of  $\Pi_{\mu 1}^*$  that gives the minimum  $GM(\psi_{u_p})$ . The response dispersion increases with increasing the mass ratio  $\Pi_\lambda$ . From low to high values of  $T_d$ ,  $\beta(\psi_{u_p})$  also increases.

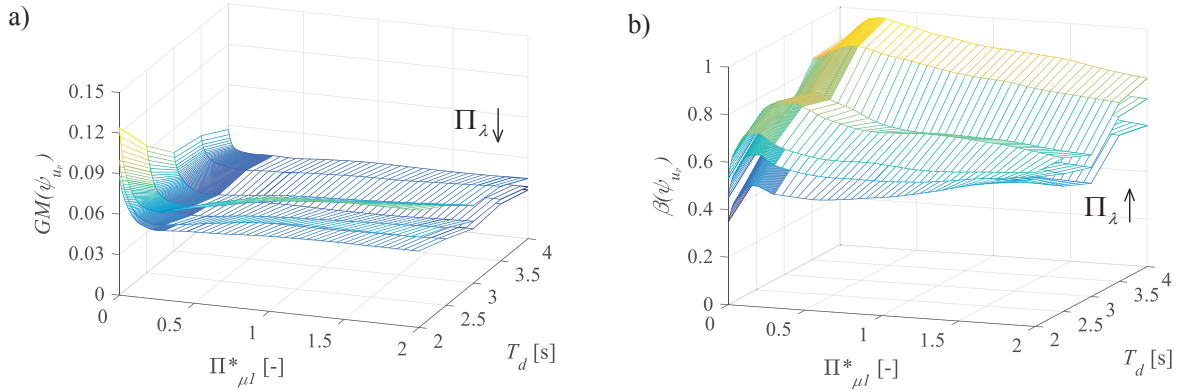


Figure 2: Normalized displacement of pier top vs.  $\Pi_{\mu 1}^*$  and  $T_d$ : median value and dispersion for  $T_p = 0.2s$  and for different values of  $\Pi_\lambda$ . The arrow denotes the increasing direction of  $\Pi_\lambda$ .

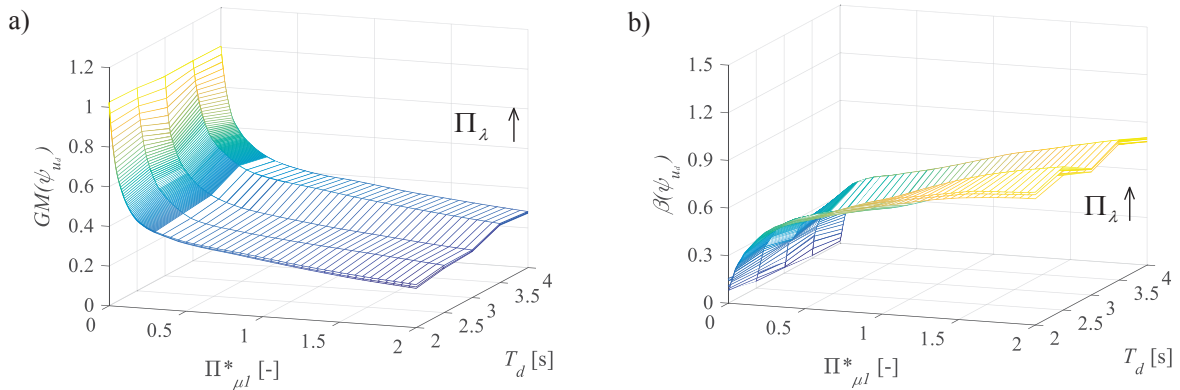


Figure 3: Normalized deck displacement vs.  $\Pi_{\mu 1}^*$  and  $T_d$ : median value and dispersion for  $T_p = 0.2s$  and for different values of  $\Pi_\lambda$ . The arrow denotes the increasing direction of  $\Pi_\lambda$ .

Fig. 3 shows the response statistics of the peak normalized deck displacement  $\psi_{u_d}$ , which also corresponds to the peak global response of the bearing placed on the abutment. Obviously,  $GM(\psi_{u_d})$  decreases significantly as  $\Pi_{\mu 1}^*$  increases. In general, the values of  $GM(\psi_{u_d})$  slightly increase for increasing values of both  $T_d$  and  $\Pi_\lambda$ . The values of the dispersion  $\beta(\psi_{u_d})$ , plotted in Fig. 3 (b), are very low for low  $\Pi_{\mu 1}^*$  values due to the high efficiency of the *IM*, and attain their maximum for high values of  $\Pi_{\mu 1}^*$ . The other system properties have a reduced influence on  $\beta(\psi_{u_d})$  compared to the influence of  $\Pi_{\mu 1}^*$ .

Fig. 4 shows the variation of the peak global response with regard to the bearing placed on the pier  $\psi_{x_d}$ . As already observed for  $GM(\psi_{u_d})$ , also  $GM(\psi_{x_d})$  tends to show a decrease

against increasing  $\Pi_{\mu 1}^*$  values. The dispersion is low in correspondence of low  $\Pi_{\mu 1}^*$  values due to the high efficiency of the *IM*, attaining its peak for high  $\Pi_{\mu 1}^*$  values. Note that the influence of  $\Pi_{\lambda}$  is slightly more marked for  $GM(\psi_{x_d})$  with respect to  $GM(\psi_{u_d})$  leading to lower values due to the flexibility of the pier.

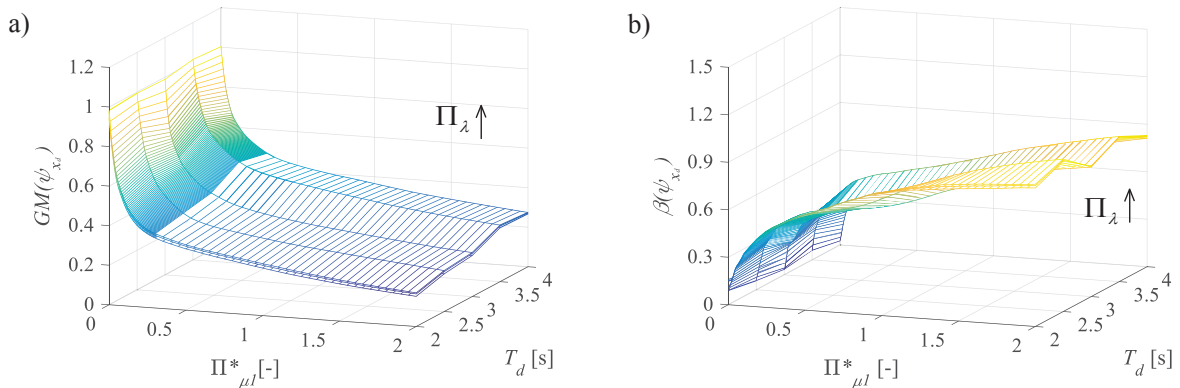


Figure 4. Normalized pier bearing global displacement vs.  $\Pi_{\mu 1}^*$  and  $T_d$ : median value and dispersion for  $T_p = 0.2s$  and for different values of  $\Pi_{\lambda}$ . The arrow denotes the increasing direction of  $\Pi_{\lambda}$ .

The existence of an optimal value of the normalised friction coefficient of the upper surface  $\Pi_{\mu 1}^*$  for the both DCFP devices able to minimize the displacement of pier top (Fig. 2) is the result of counteracting effects that occur for increasing values of the friction coefficient.

## 5 CONCLUSIONS

This paper analyzes the seismic performance of multi-span continuous deck bridges isolated with DCFP devices considering the pier-abutment-deck interaction. The results of an extensive non-dimensional parametric study encompassing a wide range of isolator and bridge properties have been illustrated monitoring various response parameters of interest related to both the isolators and the pier. Specifically, the RC pier is considered elastic, whereas the RC deck and RC abutment are assumed rigid. The results in terms of geometric mean and dispersion for each peak normalised response parameter are summarized as follows.

Regarding the pier performance, there exists an optimal value of sliding friction coefficient for each surface of the DCFP device able to minimize the pier response. This optimal value depends on the bridge and isolator properties.

Regarding the deck performance, which also corresponds to the peak global response of the bearing placed on the abutment, the response decreases significantly as the sliding friction coefficient increases. Slightly lower results are achieved for the global response of the bearing placed on the pier.

## REFERENCES

- [1] D. Gino, P. Castaldo, C. Anerdi, M. Ferrara, G. Bertagnoli, L. Giordano, Seismic upgrading of existing reinforced concrete buildings using friction pendulum Devices: A Probabilistic Evaluation. *Applied Sciences*, **10**, 8980, 2020, doi:10.3390/app10248980

- [2] P. Castaldo, G. Alfano, Seismic reliability-based design of hardening and softening structures isolated by double concave sliding devices. *Soil Dynamics and Earthquake Engineering*, **129**, 105930, 2020.
- [3] M.C. Constantinou, A. Kartoum, A.M. Reinhorn, P. Bradford, Sliding isolation system for bridges. *Experimental study, Earthquake Spectra* **8**(3), 321-344, 1992.
- [4] A. Ghobarah, H.M. Ali, Seismic performance of highway bridges. *Eng. Struct.*, **10**(3): 157-166, 1988.
- [5] G. Mancini, V.I. Carbone, G. Bertagnoli, D. Gino, Reliability-based evaluation of bond strength for tensed lapped joints and anchorages in new and existing reinforced concrete structures. *Structural Concrete*, **19**(3), 904-917, 2018. <https://doi.org/10.1002/suco.201700082>
- [6] D. Gino, P. Castaldo, G. Bertagnoli, L. Giordano, G. Mancini, Partial factor methods for existing structures according to fib Bulletin 80: Assessment of an existing prestressed concrete bridge. *Structural Concrete*, **21**, 15-31, 2020, <https://doi.org/10.1002/suco.201900231>.
- [7] Troisi R., Alfano G. 2019. Towns as Safety Organizational Fields: An Institutional Framework in Times of Emergency. *Sustainability*, **11**: 7025, 2019, doi:10.3390/su11247025.
- [8] Troisi R., Alfano G. 2020. Firms' crimes and land use in Italy. An exploratory data analysis. New Metropolitan Perspectives, International Symposium – 4th edition, 27-30 May 2020, pp 10.
- [9] D. Gino, G. Bertagnoli, D. La Mazza, G. Mancini, A quantification of model uncertainties in NLFEA of R.C. shear walls subjected to repeated loading, *Ingegneria Sismica (International journal of earthquake engineering)*, **34**(3-4), 79-91, 2017.
- [10] D. Gino, P. Castaldo, L. Giordano, G. Mancini, Model uncertainty in non-linear numerical analyses of slender reinforced concrete members. *Structural Concrete*, 1–26, 2021, <https://doi.org/10.1002/suco.202000600>.
- [11] G. Bertagnoli, D. Gino, E. Martinelli, A simplified method for predicting early-age stresses in slabs of steel-concrete composite beams in partial interaction. *Engineering Structures*, **14**, 286-297, 2017, 10.1016/j.engstruct.2017.02.058.
- [12] P. Tsopelas, M.C. Constantinou, S. Okamoto, S. Fujii, D. Ozaki, Experimental study of bridge seismic sliding isolation systems. *Eng. Struct.*, **18**(4), 301-310, 1996.
- [13] B.A. Olmos, J.M. Jara, J.M. Roeset, Effects of isolation on the seismic response of bridges designed for two different soil types. *Bulletin of Earthquake Engineering*, **9**(2), 641-656, 2011.
- [14] R.S. Jangid, Stochastic Response of Bridges Seismically Isolated by Friction Pendulum System. *J. Bridge Eng.*, **13**(4), 319, 2008.
- [15] M. Diciceli, S. Buddaram, Effect of isolator and ground motion characteristics on the performance of seismic - isolated bridges. *Earthquake engineering & structural dynamics*, **35**(2), 233-250, 2006.
- [16] V.A. Zayas, S.S. Low, S.A. Mahin, A simple pendulum technique for achieving seismic isolation. *Earthquake Spectra*, **6**, 317–33, 1990.

- [17] D.M. Fenz, M.C. Constantinou, Behaviour of the double concave friction pendulum bearing. *Earthquake Engineering and Structural Dynamics*, **35**:1403-1424, 2006.
- [18] M.C. Constantinou, Friction pendulum double concave bearings. *technical report University of Buffalo NY*, October 29, 2004.
- [19] Y.S. Kim, C.B. Yun, Seismic response characteristics of bridges using double concave friction pendulum bearings with tri-linear behavior. *Engin. Struct.*, **29**, 3082-3093, 2007.
- [20] M.C. Kunde, R.S. Jangid, Effects of pier and deck flexibility on the seismic response of isolated bridges. *Journal of Bridge Engineering*, **11**(1), 109-121, 2006.
- [21] A. Mokha , M.C. Constantinou, A.M. Reinhorn, Teflon Bearings in Base Isolation I: Testing. *J. Struct. Eng.*, **116**(2), 438-454, 1990.
- [22] M.C. Constantinou, A. Mokha, A. M. Reinhorn, Teflon Bearings in Base Isolation II: Modeling. *J. Struct. Eng.*, **116**(2), 455-474, 1990.
- [23] M.C. Constantinou, A.S. Whittaker, Y. Kalpakidis, D.M. Fenz, G.P. Warn, Performance of Seismic Isolation Hardware Under Service and Seismic Loading. *Technical Report*, 2007.
- [24] P. Castaldo, E. Tubaldi, Influence of ground motion characteristics on the optimal single concave sliding bearing properties for base-isolated structures. *Soil Dynamics and Earthquake Engineering*, **104**, 346–364, 2018.
- [25] R.D. Bertero, V.V. Bertero, Performance-based seismic engineering: the need for a reliable conceptual comprehensive approach. *Earthquake Engineering and Structural Dynamics*, **31**, 627–652, 2002.
- [26] N. Shome, C.A. Cornell, P. Bazzurro, J.E. Carballo, Earthquake, records, and nonlinear responses. *Earthquake Spectra*, **14**(3), 469-500, 1998.
- [27] P. Castaldo, B. Palazzo, T. Ferrentino T., Seismic reliability-based ductility demand evaluation for inelastic base-isolated structures with friction pendulum devices. *Earthquake Engineering and Structural Dynamics*, **46**(8): 1245-1266, 2017, DOI: 10.1002/eqe.2854.
- [28] Castaldo, P., Palazzo, B., Ferrentino, T., & Petrone, G. (2017). Influence of the strength reduction factor on the seismic reliability of structures with FPS considering intermediate PGA/PGV ratios. *Composites Part B: Engineering*, 115, 308-315.
- [29] Palazzo, B., Castaldo, P., & Della Vecchia, P. (2014, September). Seismic reliability analysis of base-isolated structures with friction pendulum system. In 2014 IEEE Workshop on Environmental, Energy, and Structural Monitoring Systems Proceedings (pp. 1-6). IEEE.
- [30] P. Castaldo, B. Palazzo, G. Alfano, M.F. Palumbo, Seismic reliability-based ductility demand for hardening and softening structures isolated by friction pendulum bearings. *Struc. Control and Health Monitoring*, e2256, 2018.
- [31] H. Aslani, E. Miranda, Probability-based seismic response analysis. *Engin. Structures*, **27**(8), 1151-1163, 2005.
- [32] Garzillo C., Troisi R. Le decisioni dell'EMA nel campo delle medicine umane. In EMA e le relazioni con le Big Pharma - I profili organizzativi della filiera del farmaco, G. Giappichelli, 85-133, 2015.

- [33] De Iuliis, M., & Castaldo, P. (2012). An energy-based approach to the seismic control of one-way asymmetrical structural systems using semi-active devices. *Ingegneria Sismica-International Journal of Earthquake Engineering*, 29(4), 31-42.
- [34] Golzio L. E., Troisi R. The value of interdisciplinary research: a model of interdisciplinarity between legal re-search and research in organizations. *Journal For Development And Leadership*, 2: 23-38, 2013.
- [35] Basone, F., Castaldo, P., Cavaleri, L., & Di Trapani, F. (2019). Response spectrum analysis of frame structures: reliability-based comparison between complete quadratic combination and damping-adjusted combination. *Bulletin of Earthquake Engineering*, 17(5), 2687-2713.
- [36] Nese A., Troisi R. Corruption among mayors: evidence from Italian Court of Cassation judgments, *Trends In Organized Crime*, 1-26, 2018. DOI:10.1007/s12117-018-9349-4.
- [37] Troisi R., Golzio, L. E. Legal studies and organization theory: a possible cooperation. *Manageable cooperation* - European Academy of Management: 16th EURAM Conference, Paris, 1-2, 1-4 June 2016.
- [38] Troisi R., Guida V. Is the Appointee Procedure a Real Selection or a Mere Political Exchange? The Case of the Italian Health-Care Chief Executive Officers. *Journal of Entrepreneurial and Organizational Diversity*, 7 (2): 19-38, 2018, DOI:10.5947/jeod.2018.008.
- [39] Troisi R. Le risorse umane nelle BCC: lavoro e motivazioni al lavoro. In *Progetto aree bianche. Il sistema del credito cooperativo in Campania*, 1: 399-417, 2012.
- [40] A.H.S. Ang, W.H. Tang, Probability Concepts in Engineering-Emphasis on Applications to Civil and Environmental Engineering. *John Wiley & Sons*, New York, USA, 2007.
- [41] Math Works Inc. MATLAB-High Performance Numeric Computation and Visualization Software. *User's Guide*. Natick: MA, USA, 1997.

## SEISMIC PERFORMANCE OF BRIDGES ISOLATED WITH FPS

P. Castaldo<sup>1</sup>, and G. Amendola<sup>2</sup>

<sup>1</sup> Department of Structural, Geotechnical and Building Engineering (DISEG), Politecnico di Torino,  
Turin, Italy  
e-mail: paolo.castaldo@polito.it ; pcastaldo@unisa.it

<sup>2</sup> Department of Structural, Geotechnical and Building Engineering (DISEG), Politecnico di Torino,  
Turin, Italy  
e-mail: guglielmo.amendola@polito.it

---

### Abstract

*The scope of the present study is focused on the evaluation of the seismic response of bridges isolated by single concave sliding pendulum isolators (FPS) for the different structural properties when the presence of the rigid abutment is considered or neglected (i.e., isolated viaducts). In this way, they have been defined two specific multi-degree-of-freedom (mdof) models to simulate the elastic behavior of the reinforced concrete pier in combination to the infinitely rigid presence of the deck and to the presence of the rigid abutment if considered. Both the numerical models also account for the non-linear velocity-dependent behavior of the FPS bearings. Considering the aleatory uncertainty in the seismic input by means of several natural records with different characteristics, a parametric analysis is developed for several structural properties. The relevant results expressed as the statistics in non-dimensional form with respect to the seismic intensity have permitted to study the differences between the two numerical models in relation to the effectiveness of the seismic isolation.*

**Keywords:** Seismic isolation, Bridge, Friction pendulum isolators, Performance-based engineering, Seismic reliability.

---



## 1 INTRODUCTION

Seismically isolated bridges permit to obtain a substantial reduction of the deck acceleration and, as consequence, of the forces transmitted to the pier in comparison to non-isolated bridges as widely demonstrated in many studies focusing with both elastomeric (LRB) and frictional (FPS) isolators [2]-[8]. This topic is in line with the issue of the infrastructure safety [9]-[10]. Tongaonkar and Jangid [11] evaluated the effects of soil-structure interaction on the peak responses of a three-span continuous deck bridge isolated by the elastomeric bearings particularly, showing their influence to assess the bearing displacements at abutment locations. Contextually, friction pendulum system (FPS) devices have been widely used for their capability to provide an isolation period mass independent and to assure high dissipation and re-centering in addition to their longevity and durability properties [12]-[14]. Several experimental and numerical researches have explored the behavior of the FPS devices [15]-[23]. The seismic response of isolated multi-span continuous deck bridges is investigated in [24] confirming the effectiveness of simplified models in relation to the flexibility of the deck and of the piers. In [25]-[26], it was carried out a large parametric analysis demonstrating the influence of the design parameters on the response of a three-dimensional multi-span continuous steel girder bridge model seismically isolated by the FPS isolators. Moreover, other works have been more oriented to develop design approaches for the isolators. In this context, the seismic reliability-based design (SRBD) approach has been proposed and widely discussed in [27]-[34] as a new methodology mainly aim to provide design solutions for seismic devices taking into account the main uncertainties relevant to the problem itself.

The main goal of this work consists in evaluating the influence of the pier-abutment-deck interaction on the seismic response of bridges isolated by single concave sliding pendulum isolators (FPS) mainly comparing the results with those coming from the seismic response of isolated bridges without considering the presence of the rigid reinforced concrete (RC) abutment (i.e., isolated viaducts). With this aim, two different multi-degree-of-freedom (mdof) models representative, respectively, of a single-column bent viaduct [22] and a multi-span continuous deck bridge [7],[13] are defined. Specifically, a six-degree-of-freedom model is used to represent the dynamic behaviour of both the isolated bridge systems. In fact, in both the mdof models, five vibrational modes are considered to describe the elastic behavior of the RC pier and an additional degree of freedom represents the response of the infinitely rigid RC deck isolated by the FPS devices. If considered, the presence of the RC abutment is assumed rigid and so no degree of freedom is related to that. The FPS isolator behavior is described through a widespread velocity-dependent model. In order to obtain a system response independent from the specific seismic source, a non-dimensional formulation of the motion equations proposed in [20] and herein extended and, in addition, a parametric analysis considering several structural properties is performed with the aim to investigate the differences between the two mdof models in relation to the relevant response parameters. The uncertainty in the seismic input is taken into account by means of a set of natural records with different characteristics. Finally, the optimum values of the sliding friction coefficient able to minimize the pier displacements relative to the ground as a function of the structural properties and of the seismic input intensity considering or neglecting the rigid presence of the abutment (i.e., single-column bent viaduct and multi-span continuous deck bridge) have been derived.

## 2 NON-DIMENSIONAL MOTION EQUATIONS

The motion equations, in terms of drifts between the different degrees of freedom, governing the seismic response when the isolated system refers to a multi-span continuous deck bridge (e.g., three-span continuous deck bridge) [7],[13], and the presence of the rigid RC abutment is considered (Figure 1(b)), subjected to the seismic input along the longitudinal direction,  $\ddot{u}_g(t)$ , are:

$$\begin{aligned}
 m_d \ddot{u}_d(t) + m_d \ddot{u}_{p5}(t) + m_d \ddot{u}_{p4}(t) + m_d \ddot{u}_{p3}(t) + m_d \ddot{u}_{p2}(t) + m_d \ddot{u}_{p1}(t) + c_d \dot{u}_d(t) + F_p(t) + F_a(t) &= -m_d \ddot{u}_g(t) \\
 m_{p5} \ddot{u}_{p5}(t) + m_{p5} \ddot{u}_{p4}(t) + m_{p5} \ddot{u}_{p3}(t) + m_{p5} \ddot{u}_{p2}(t) + m_{p5} \ddot{u}_{p1}(t) - c_{p5} \dot{u}_d(t) + c_{p5} \dot{u}_{p5}(t) + k_{p5} u_{p5}(t) - F_p(t) &= -m_{p5} \ddot{u}_g(t) \\
 m_{p4} \ddot{u}_{p4}(t) + m_{p4} \ddot{u}_{p3}(t) + m_{p4} \ddot{u}_{p2}(t) + m_{p4} \ddot{u}_{p1}(t) - c_{p5} \dot{u}_{p5}(t) - k_{p5} u_{p5}(t) + c_{p4} \dot{u}_{p4}(t) + k_{p4} u_{p4}(t) &= -m_{p4} \ddot{u}_g(t) \\
 m_{p3} \ddot{u}_{p3}(t) + m_{p3} \ddot{u}_{p2}(t) + m_{p3} \ddot{u}_{p1}(t) - c_{p4} \dot{u}_{p4}(t) - k_{p4} u_{p4}(t) + c_{p3} \dot{u}_{p3}(t) + k_{p3} u_{p3}(t) &= -m_{p3} \ddot{u}_g(t) \\
 m_{p2} \ddot{u}_{p2}(t) + m_{p2} \ddot{u}_{p1}(t) - c_{p3} \dot{u}_{p3}(t) - k_{p3} u_{p3}(t) + c_{p2} \dot{u}_{p2}(t) + k_{p2} u_{p2}(t) &= -m_{p2} \ddot{u}_g(t) \\
 m_{p1} \ddot{u}_{p1}(t) - c_{p2} \dot{u}_{p2}(t) - k_{p2} u_{p2}(t) + c_{p1} \dot{u}_{p1}(t) + k_{p1} u_{p1}(t) &= -m_{p1} \ddot{u}_g(t)
 \end{aligned} \tag{1}$$

where  $u_d$  denotes the horizontal displacement of the deck relative to pier,  $u_{p1}, u_{p2}, u_{p3}, u_{p4}, u_{p5}$  are the pier displacements relative between two consecutive dof,  $m_d, m_{p1}, m_{p2}, m_{p3}, m_{p4}, m_{p5}$  respectively the mass of the deck and of each dof of the pier,  $k_{p1}, k_{p2}, k_{p3}, k_{p4}, k_{p5}$  and  $c_{p1}, c_{p2}, c_{p3}, c_{p4}, c_{p5}$  respectively the stiffness and inherent viscous damping coefficient of each dof of the pier,  $c_d$  the bearing viscous damping factor,  $t$  the time instant, the dot differentiation over time.

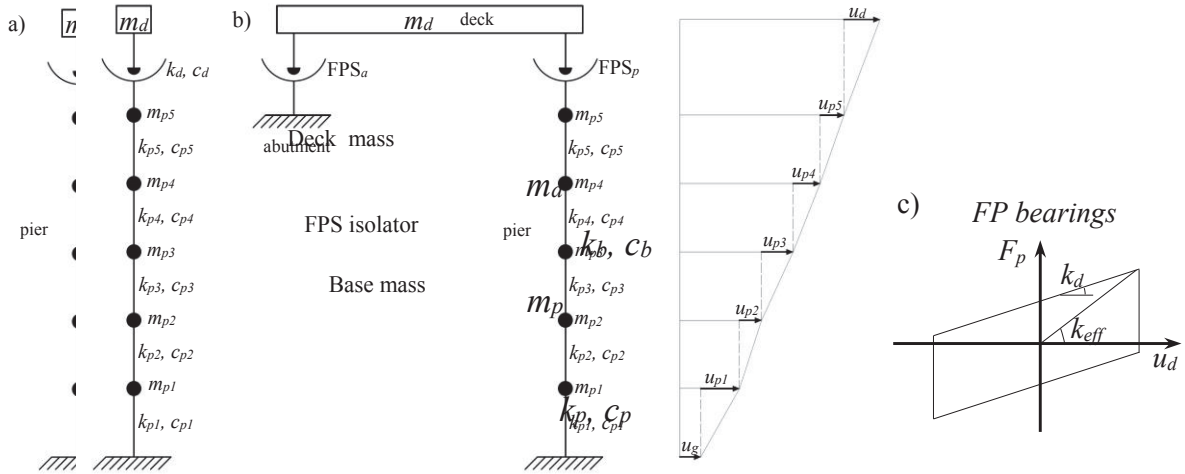


Figure 1: 6dof model of a bridge isolated by FPS bearings without pier-abutment-deck interaction (i.e., viaduct) (a); 6dof model of a bridge isolated by FPS bearings considering pier-abutment-deck interaction (b); FPS response (c).

The forces related to both the isolator device placed at the pier level  $F_p(t)$  and at the abutment level  $F_a(t)$  are the following:

$$F_p(t) = \frac{m_d g}{2} \left[ \frac{1}{R_p} u_d(t) + \mu_p (\dot{u}_d) \text{sgn}(\dot{u}_d) \right] \tag{2a}$$

$$F_a(t) = \frac{m_d g}{2} \left[ \frac{1}{R_a} \left( u_d(t) + \sum_{i=1}^5 u_{pi} \right) + \mu_a \left( \dot{u}_d(t) + \sum_{i=1}^5 \dot{u}_{pi} \right) \operatorname{sgn} \left( \dot{u}_d(t) + \sum_{i=1}^5 \dot{u}_{pi} \right) \right] \quad (2b)$$

where  $k_d = W / R = m_d g / R$ ,  $g$  is the gravity constant,  $R$  is the radius of curvature of the FPS device,  $\mu(\dot{u}_d(t))$  the sliding friction coefficient, which depends on the bearing slip horizontal velocity  $\dot{u}_d(t)$  [31], and  $\operatorname{sgn}(\cdot)$  denotes the sign function. As reported in [14], the fundamental vibration period of an isolated bridge,  $T_d = 2\pi\sqrt{R/g}$ , corresponding to the pendulum behaviour component, depends only on the radius of curvature  $R$ . According to [16]-[19], the sliding friction coefficient of teflon-steel interfaces can be expressed by the following equation:

$$\mu(\dot{u}_d) = \mu_{\max} - (\mu_{\max} - \mu_{\min}) \cdot \exp(-\alpha |\dot{u}_d|) \quad (3)$$

where  $\mu_{\max}$  and  $\mu_{\min}$  represent, respectively, the maximum value of sliding friction coefficient attained at large velocities and the value at zero velocity. In this study, it is considered that  $\mu_{\max} = 3\mu_{\min}$  with the exponent  $\alpha$  equal to 30 [20].

What is worth underlying is that, differently to the reaction force of the seismic device on the pier, the reaction force as well as the friction coefficient related to the abutment isolator depend on both the horizontal velocity and displacement [31] of the deck with respect to the ground.

By dividing Eq. (1) by the mass deck  $m_d$ , the following equation system is obtained:

$$\ddot{u}_d(t) + \ddot{u}_{p5}(t) + \ddot{u}_{p4}(t) + \ddot{u}_{p3}(t) + \ddot{u}_{p2}(t) + \ddot{u}_{p1}(t) + 2\xi_d \omega_d \dot{u}_d(t) + \frac{g}{2} \left[ \frac{1}{R_p} u_d(t) + \mu_p(\dot{u}_d) \operatorname{sgn}(\dot{u}_d) \right] + \frac{g}{2} \left[ \frac{1}{R_a} \left( u_d(t) + \sum_{i=1}^5 u_{pi} \right) + \mu_a \left( \dot{u}_d(t) + \sum_{i=1}^5 \dot{u}_{pi} \right) \operatorname{sgn} \left( \dot{u}_d(t) + \sum_{i=1}^5 \dot{u}_{pi} \right) \right] = -\ddot{u}_g(t) \quad (4a)$$

$$\lambda_{p5} [\ddot{u}_{p5}(t) + \ddot{u}_{p4}(t) + \ddot{u}_{p3}(t) + \ddot{u}_{p2}(t) + \ddot{u}_{p1}(t)] - 2\xi_d \omega_d \dot{u}_d(t) + 2\xi_{p5} \omega_{p5} \lambda_{p5} \dot{u}_{p5}(t) + \lambda_{p5} \omega_{p5}^2 u_{p5}(t) - \frac{g}{2} \left[ \frac{1}{R_p} u_d(t) + \mu_p(\dot{u}_d) \operatorname{sgn}(\dot{u}_d) \right] = -\lambda_{p5} \ddot{u}_g(t) \quad (4b)$$

$$\lambda_{p4} [\ddot{u}_{p4}(t) + \ddot{u}_{p3}(t) + \ddot{u}_{p2}(t) + \ddot{u}_{p1}(t)] - 2\xi_{p5} \omega_{p5} \lambda_{p5} \dot{u}_{p5}(t) - \lambda_{p5} \omega_{p5}^2 u_{p5}(t) + 2\xi_{p4} \omega_{p4} \lambda_{p4} \dot{u}_{p4}(t) + \lambda_{p4} \omega_{p4}^2 u_{p4}(t) = -\lambda_{p4} \ddot{u}_g(t) \quad (4c)$$

$$\lambda_{p3} [\ddot{u}_{p3}(t) + \ddot{u}_{p2}(t) + \ddot{u}_{p1}(t)] - 2\xi_{p4} \omega_{p4} \lambda_{p4} \dot{u}_{p4}(t) - \lambda_{p4} \omega_{p4}^2 u_{p4}(t) + 2\xi_{p3} \omega_{p3} \lambda_{p3} \dot{u}_{p3}(t) + \lambda_{p3} \omega_{p3}^2 u_{p3}(t) = -\lambda_{p3} \ddot{u}_g(t) \quad (4d)$$

$$\lambda_{p2} [\ddot{u}_{p2}(t) + \ddot{u}_{p1}(t)] - 2\xi_{p3} \omega_{p3} \lambda_{p3} \dot{u}_{p3}(t) - \lambda_{p3} \omega_{p3}^2 u_{p3}(t) + 2\xi_{p2} \omega_{p2} \lambda_{p2} \dot{u}_{p2}(t) + \lambda_{p2} \omega_{p2}^2 u_{p2}(t) = -\lambda_{p2} \ddot{u}_g(t) \quad (4e)$$

$$\lambda_{p1} \ddot{u}_{p1}(t) - 2\xi_{p2} \omega_{p2} \lambda_{p2} \dot{u}_{p2}(t) - \lambda_{p2} \omega_{p2}^2 u_{p2}(t) + 2\xi_{p1} \omega_{p1} \lambda_{p1} \dot{u}_{p1}(t) + \lambda_{p1} \omega_{p1}^2 u_{p1}(t) = -\lambda_{p1} \ddot{u}_g(t) \quad (4f)$$

and the following ratios are introduced:

$$\omega_d = \sqrt{\frac{k_d}{m_d}}, \quad \omega_{pi} = \sqrt{\frac{k_{pi}}{m_{pi}}}, \quad \xi_d = \frac{c_d}{2m_d \omega_d}, \quad \xi_{pi} = \frac{c_{pi}}{2m_{pi} \omega_{pi}}, \quad \lambda_{pi} = \frac{m_{pi}}{m_d} \quad \text{with } i=1, \dots, 5 \quad (5)$$

The first two terms denote, respectively, the circular frequency of vibration of the isolated deck and of the  $i$ -th lumped mass of the pier;  $\xi_d$  is the damping factor of the isolated deck,

$\xi_{pi}$  is the damping factor corresponding to the  $i$ -th dof in which the pier has been discretized. The last term represents the  $i$ -th mass ratio between the  $i$ -th lumped mass of the pier and the deck mass.

With the aim to extend the non-dimensionalization approach proposed by [20]-[21], let us introduce the time scale  $\tau = t\omega_d$ , in which  $\omega_d = \sqrt{k_d / m_d}$  is the fundamental circular frequency of the isolated system with infinitely rigid superstructure, and the seismic intensity scale  $a_0$ , so that  $\ddot{u}_g(t) = a_0 \ell(\tau)$ , where  $\ell(\tau)$  is a non-dimensional function of time describing the seismic input time-history, the following non-dimensional equations can be obtained:

$$\ddot{\psi}_d(\tau) + \ddot{\psi}_{p5}(\tau) + \ddot{\psi}_{p4}(\tau) + \ddot{\psi}_{p3}(\tau) + \ddot{\psi}_{p2}(\tau) + \ddot{\psi}_{p1}(\tau) + 2\xi_d \dot{\psi}_d(\tau) + \left[ \frac{1}{2} \psi_d(\tau) + \frac{\mu_p(\dot{\psi}_d)g}{2a_0} \text{sgn}(\dot{\psi}_d) \right] + \left[ \frac{1}{2} \left( \psi_d(\tau) + \sum_{i=1}^5 \psi_{pi}(\tau) \right) + \frac{g}{2a_0} \left( \mu_d \left( \dot{\psi}_d(\tau) + \sum_{i=1}^5 \dot{\psi}_{pi}(\tau) \right) \right) \left( \text{sgn} \left( \dot{\psi}_d(\tau) + \sum_{i=1}^5 \dot{\psi}_{pi}(\tau) \right) \right) \right] = -\ell(\tau) \quad (6a)$$

$$\lambda_{p5} \left[ \ddot{\psi}_{p5}(\tau) + \ddot{\psi}_{p4}(\tau) + \ddot{\psi}_{p3}(\tau) + \ddot{\psi}_{p2}(\tau) + \ddot{\psi}_{p1}(\tau) \right] - 2\xi_d \dot{\psi}_d(\tau) + 2\xi_{p5} \frac{\omega_{p5}^2}{\omega_d^2} \lambda_{p5} \dot{\psi}_{p5}(\tau) + \lambda_{p5} \frac{\omega_{p5}^2}{\omega_d^2} \psi_{p5}(\tau) - \left[ \frac{1}{2} \psi_d(\tau) + \frac{\mu_p(\dot{\psi}_d)g}{2a_0} \text{sgn}(\dot{\psi}_d) \right] = -\lambda_{p5} \ell(\tau) \quad (6b)$$

$$\lambda_{p4} \left[ \ddot{\psi}_{p4}(\tau) + \ddot{\psi}_{p3}(\tau) + \ddot{\psi}_{p2}(\tau) + \ddot{\psi}_{p1}(\tau) \right] - 2\xi_{p5} \frac{\omega_{p5}^2}{\omega_d^2} \lambda_{p5} \dot{\psi}_{p5}(\tau) + 2\xi_{p4} \frac{\omega_{p4}^2}{\omega_d^2} \lambda_{p4} \dot{\psi}_{p4}(\tau) - \lambda_{p5} \frac{\omega_{p5}^2}{\omega_d^2} \psi_{p5}(\tau) + \lambda_{p4} \frac{\omega_{p4}^2}{\omega_d^2} \psi_{p4}(\tau) = -\lambda_{p4} \ell(\tau) \quad (6c)$$

$$\lambda_{p3} \left[ \ddot{\psi}_{p3}(\tau) + \ddot{\psi}_{p2}(\tau) + \ddot{\psi}_{p1}(\tau) \right] - 2\xi_{p4} \frac{\omega_{p4}^2}{\omega_d^2} \lambda_{p4} \dot{\psi}_{p4}(\tau) + 2\xi_{p3} \frac{\omega_{p3}^2}{\omega_d^2} \lambda_{p3} \dot{\psi}_{p3}(\tau) - \lambda_{p4} \frac{\omega_{p4}^2}{\omega_d^2} \psi_{p4}(\tau) + \lambda_{p3} \frac{\omega_{p3}^2}{\omega_d^2} \psi_{p3}(\tau) = -\lambda_{p3} \ell(\tau) \quad (6d)$$

$$\lambda_{p2} \left[ \ddot{\psi}_{p2}(\tau) + \ddot{\psi}_{p1}(\tau) \right] - 2\xi_{p3} \frac{\omega_{p3}^2}{\omega_d^2} \lambda_{p3} \dot{\psi}_{p3}(\tau) + 2\xi_{p2} \frac{\omega_{p2}^2}{\omega_d^2} \lambda_{p2} \dot{\psi}_{p2}(\tau) - \lambda_{p3} \frac{\omega_{p3}^2}{\omega_d^2} \psi_{p3}(\tau) + \lambda_{p2} \frac{\omega_{p2}^2}{\omega_d^2} \psi_{p2}(\tau) = -\lambda_{p2} \ell(\tau) \quad (6e)$$

$$\lambda_{p1} \ddot{\psi}_{p1}(\tau) - 2\xi_{p2} \frac{\omega_{p2}^2}{\omega_d^2} \lambda_{p2} \dot{\psi}_{p2}(\tau) + 2\xi_{p1} \frac{\omega_{p1}^2}{\omega_d^2} \lambda_{p1} \dot{\psi}_{p1}(\tau) - \lambda_{p2} \frac{\omega_{p2}^2}{\omega_d^2} \psi_{p2}(\tau) + \lambda_{p1} \frac{\omega_{p1}^2}{\omega_d^2} \psi_{p1}(\tau) = -\lambda_{p1} \ell(\tau) \quad (6f)$$

The non-dimensional parameters  $\psi_{u_d} = \frac{u_{d,peak} \omega_d^2}{a_0}$  and  $\psi_{u_p} = \frac{u_{p,peak} \omega_d^2}{a_0} = \frac{\left( \sum_{i=1}^5 u_{pi} \right)_{peak} \omega_d^2}{a_0}$  describe the peak dynamic response of the deck and of pier, respectively. Moreover, from Eq.(5), it is possible to observe that the five non-dimensional  $\Pi$  terms [20]-[21],[35]-[36] that control the system non-dimensional response are:

$$\Pi_{\omega_i} = \frac{\omega_{pi}}{\omega_d}, \quad \Pi_{\lambda_{pi}} = \lambda_{pi} = \frac{m_{pi}}{m_d}, \quad \Pi_{\xi_d} = \xi_d, \quad \Pi_{\xi_{pi}} = \xi_{pi} \quad \text{with } i = 1, \dots, 5 \quad (7)$$

in particular,  $\Pi_{\omega_i}$  represents the  $i$ -th frequency ratio,  $\Pi_{\lambda_{pi}}$  is the  $i$ -th mass ratio as previously defined,  $\Pi_{\xi_{pi}}$  and  $\Pi_{\xi_d}$  are the inherent viscous damping related to the  $i$ -th dof of the pier and to the isolator/deck, respectively. Regarding the control parameters of the pier, indeed, the parameters  $\omega_{pi}$  are related to the fundamental vibration pulsation  $\omega_p$  (the first vibration mode)

as well as the sum of the mass ratios is related to the overall mass ratio  $\Pi_\lambda = \lambda_p = \sum_{i=1}^5 m_{pi} / m_d$  and, finally, all the damping factors are assumed equal to  $\Pi_{\xi_p} = \xi_p$ .

The normalized friction coefficients for the FPS devices on the pier and on the abutment are the derived, respectively:

$$\Pi_{\mu_p}(\dot{\psi}_d) = \frac{\mu_p(\dot{\psi}_d)g}{a_0}, \quad \Pi_{\mu_a}\left(\dot{\psi}_d + \sum_{i=1}^5 \dot{\psi}_{pi}\right) = \frac{\mu_a\left(\dot{\psi}_d + \sum_{i=1}^5 \dot{\psi}_{pi}\right)g}{a_0} \quad (8)$$

and since these parameters depend on the response through the corresponding velocities, each one is used in its stead as follows [20]:

$$\Pi_{\mu_p}^* = \frac{\mu_{p,\max}g}{a_0}, \quad \Pi_{\mu_a}^* = \frac{\mu_{a,\max}g}{a_0} \quad (9)$$

It is worth underlining that even if the two FPS devices are equal,  $\Pi_{\mu_p}^* = \Pi_{\mu_a}^*$ , during the dynamic response the terms of Eq.(8) depend on different velocities.

On the other hand, in the case of a single-column bent viaduct (or neglecting the presence of the abutment) [22],[37], the same 6-degree-of-freedom (dof) model presented above, having 5 degrees of freedom for the elastic RC pier and 1 degree of freedom for the rigid RC deck mass equipped with FPS devices is adopted and shown in Figure 1(a).

The main difference in the form of the equation of motion when the abutment is neglected consists in the absence of the term related to the isolator force placed on the abutment and at the beginning of the paragraph indicated as  $F_a(t)$ .

Note that cracking phenomena [38]-[42] of the RC deck are herein neglected.

### 3 GROUND MOTIONS AND INTENSITY MEASURE

#### 3.1 Seismic records

In this study, the record-to-record variability is considered using 30 seismic records selected from 19 seismic different events [43]-[45]. Table 1 reports the details of the earthquakes used for the study.

#	Year	Earthquake Name	Recording Name	Station	Vs <sub>30</sub> [m/sec]	Source (Fault Type)	M	R [km]	PGA <sub>max</sub> [g]
1	1994	Northridge	Beverly Hills - Mulhol		356	Thrust	6.7	13.3	0.52
2	1994	Northridge	Canyon Country-WLC		309	Thrust	6.7	26.5	0.48
3	1994	Northridge	LA - Hollywood Stor		316	Thrust	6.7	22.9	0.36
4	1999	Duzce, Turkey	Bolu		326	Strike-slip	7.1	41.3	0.82
5	1999	Hector Mine	Hector		685	Strike-slip	7.1	26.5	0.34
6	1979	Imperial Valley	Delta		275	Strike-slip	6.5	33.7	0.35
7	1979	Imperial Valley	El Centro Array #11		196	Strike-slip	6.5	29.4	0.38
8	1995	Kobe, Japan	Nishi-Akashi		609	Strike-slip	6.9	8.7	0.51
9	1995	Kobe, Japan	Shin-Osaka		256	Strike-slip	6.9	46	0.24
10	1999	Kocaeli, Turkey	Duzce		276	Strike-slip	7.5	98.2	0.36
11	1999	Kocaeli, Turkey	Arcelik		523	Strike-slip	7.5	53.7	0.22
12	1992	Landers	Yermo Fire Station		354	Strike-slip	7.3	86	0.24
13	1992	Landers	Coolwater		271	Strike-slip	7.3	82.1	0.42

14	1989	Loma Prieta	Capitola	289	Strike-slip	6.9	9.8	0.53
15	1989	Loma Prieta	Gilroy Array #3	350	Strike-slip	6.9	31.4	0.56
16	1990	Manjil, Iran	Abbar	724	Strike-slip	7.4	40.4	0.51
17	1987	Superstition Hills	El Centro Imp. Co.	192	Strike-slip	6.5	35.8	0.36
18	1987	Superstition Hills	Poe Road (temp)	208	Strike-slip	6.5	11.2	0.45
19	1987	Superstition Hills	Westmorland Fire Stat.	194	Strike-slip	6.5	15.1	0.21
20	1992	Cape Mendocino	Rio Dell Overpass	312	Thrust	7.0	22.7	0.55
21	1999	Chi-Chi, Taiwan	CHY101	259	Thrust	7.6	32	0.44
22	1999	Chi-Chi, Taiwan	TCU045	705	Thrust	7.6	77.5	0.51
23	1971	San Fernando	LA - Hollywood Stor	316	Thrust	6.6	39.5	0.21
24	1976	Friuli, Italy	Tolmezzo	425	Thrust	6.5	20.2	0.35
25	1980	Irpinia	Bisaccia	496		6.9	21.3	0.94
26	1979	Montenegro	ST64	1083	Thrust	6.9	21.0	0.18
27	1997	Umbria Marche	ST238	n/a	Normal	6.0	21.5	0.19
28	2000	South Iceland	ST2487	n/a	Strike-slip	6.5	13	0.16
29	2000	South Iceland (a.s.)	ST2557	n/a	Strike-slip	6.5	15.0	0.13
30	2003	Bingol	ST539	806	Strike-slip	6.3	14.0	0.30

Table 1: Seismic records used and them characteristics.

### 3.2 Intensity measure

The intensity scale factor,  $a_0$ , of Eq. (5) is the seismic intensity measure ( $IM$ ) used in this study coherently with the performance-based earthquake engineering (PBEE) [46],[47]. In this study, the abovementioned term coincides with to the spectral pseudo-acceleration,  $S_A(T_d, \xi_d)$ , corresponding to the isolated period of the bridge  $T_d = 2\pi / \omega_d$  with the damping ratio  $\Pi_{\xi_d} = \xi_d$ . As also observed in [20]-[22], since the spectral acceleration is related to the spectral displacement  $S_A(T_b, \xi_d) = \omega_d^2 S_d(T_d, \xi_d)$ , if all the records are normalized with respect to  $S_A(T_d, \xi_d)$ , the normalized displacement and force of the isolated bridge deck, in the hypothesis of both a rigid substructure (pier) and absence of the sliding friction, are equal to 1 for each record without any record-to-record variability. In the following analysis, the damping ratio  $\xi_d$  is set equal to zero [20],[34],[48] and the corresponding  $IM$  is hereinafter denoted to as  $IM=a_0=S_A(T_d)$ .

## 4 PARAMETRIC STUDY

In the analysis carried out in this study, the effects of higher order modes due to the flexibility of the elastic RC pier together with of the pier-abutment-deck interaction are investigated and the seismic performance of isolated bridges is assessed. This section describes the results of the parametric study carried out on the two systems of Figure 1 to evaluate the performance of bridge isolated with FPS bearings for different structural properties. The first subsection deals with the response parameters relevant to the seismic performance and the second subsection illustrates the parametric study results.

### 4.1 Non-dimensional response parameters examined

The following response parameters relevant to the seismic performance assessment of isolated bridges are considered: the peak deck displacement relative to the pier for the model of Figure 1(a) as well as the peak deck displacement relative to the pier or to the abutment for the model of Figure 1(b),  $u_{d,peak}$ , either important for the design of the FPS isolator and of



the seismic joint deck-abutment, the peak pier displacement  $u_{p, peak} = (\sum_{i=1}^5 u_{p_i})_{peak}$  (related to the internal forces in the bridge substructure) for the both models. All these relevant response parameters can be defined in non-dimensional form, in line with Eq.s (4) and (6), as follows:

$$\psi_{u_d} = \frac{u_{d, peak} \omega_d^2}{a_0}, \quad \psi_{u_p} = \frac{u_{p, peak} \omega_d^2}{a_0} = \frac{(\sum_{i=1}^5 u_{p_i})_{peak} \omega_d^2}{a_0} \quad (10)$$

Eq.s (4) and (6) are repeatedly and numerically solved in Matlab–Simulink [49] computing a set of samples for each response parameter for the two structural models. As also described in [20],[21],[48],[50], the response parameters are modeled in probabilistic terms [51]–[58]: the generic response parameter  $D$  (i.e., the extreme values  $\psi_{u_d}$ ,  $\psi_{u_p}$  of Eq. (10)) can be fitted by a lognormal distribution estimating the sample geometric mean,  $GM(D)$ , and dispersion,  $\beta(D)$ , defined, respectively:

$$GM(D) = \sqrt[N]{d_1 \cdot \dots \cdot d_N} \quad (11)$$

$$\beta(D) = \sigma_{\ln}(D) = \sqrt{\frac{(\ln d_1 - \ln[GM(D)])^2 + \dots + (\ln d_N - \ln[GM(D)])^2}{N-1}} \quad (12)$$

in which  $d_h$  is the  $h$ -th sample realization of  $D$ , and  $N$  represents the total number of samples (i.e., ground motions):  $h=1, \dots, N$ . The  $k$ th percentile of the response parameter  $D$  can be evaluated as:

$$d_k = GM(D) \exp[f(k)\beta(D)] \quad (13)$$

where  $f(k)$  is a function that assumes the following values  $f(50)=0$ ,  $f(84)=1$  and  $f(16)=-1$  [59], for the 50<sup>th</sup>, 16<sup>th</sup> and 84<sup>th</sup> percentile, respectively.

## 4.2 Non-dimensional results

In this section, the results of the parametric study for the two structural configurations developed on the equivalent 6dof systems, for the different structural properties and 30 ground motion records, are illustrated and commented. Specifically, in line with [2],[11],[13],[25],[60], the parameters  $\Pi_{\xi_d} = \xi_d$  and  $\Pi_{\xi_p} = \xi_p$  are assumed respectively equal to 0% and 5%, the isolation period  $T_d$  varies in the range between 2s, 2.5s, 3s, 3.5s and 4s, the elastic RC pier period  $T_p$  equal to 0.2s,  $\Pi_{\lambda} = \lambda$  between 0.1, 0.15 and 0.2,  $\Pi_{\mu}^*$  between 0 and 2. The latter one is related to the FPS device on the pier for the model without the abutment and to the FPS isolators, assumed equal, on the pier and on the abutment for the model of Figure 1(b):  $\Pi_{\mu p}^* = \Pi_{\mu a}^* = \Pi_{\mu}^*$ . For each parameter combination and for the two structural configurations, the differential motion equations (Eq.s (6) and (12)) have been repeatedly and numerically solved adopting the Bogacki-Shampine and Runge-Kutta-Fehlberg integration algorithm available in Matlab-Simulink [49]. After that, for each normalized response parameter, the geometric mean,  $GM$ , and the dispersion,  $\beta$ , have been evaluated by means of Eq.s (11) and (12) and are illustrated in Figures 2-3 for the both structural models. Each figure con-

tains different meshes as many as the values of  $\Pi_\lambda$ : the arrow indicates the increasing values of  $\Pi_\lambda$ . Note that for the configuration with the pier-abutment-deck interaction (i.e., multi-span continuous deck bridge), the peak normalized deck displacement, showed in Figures 2, has always been the one between the deck and the abutment. This is because of the elastic response of the pier that reduces the relative displacement between the deck and itself.

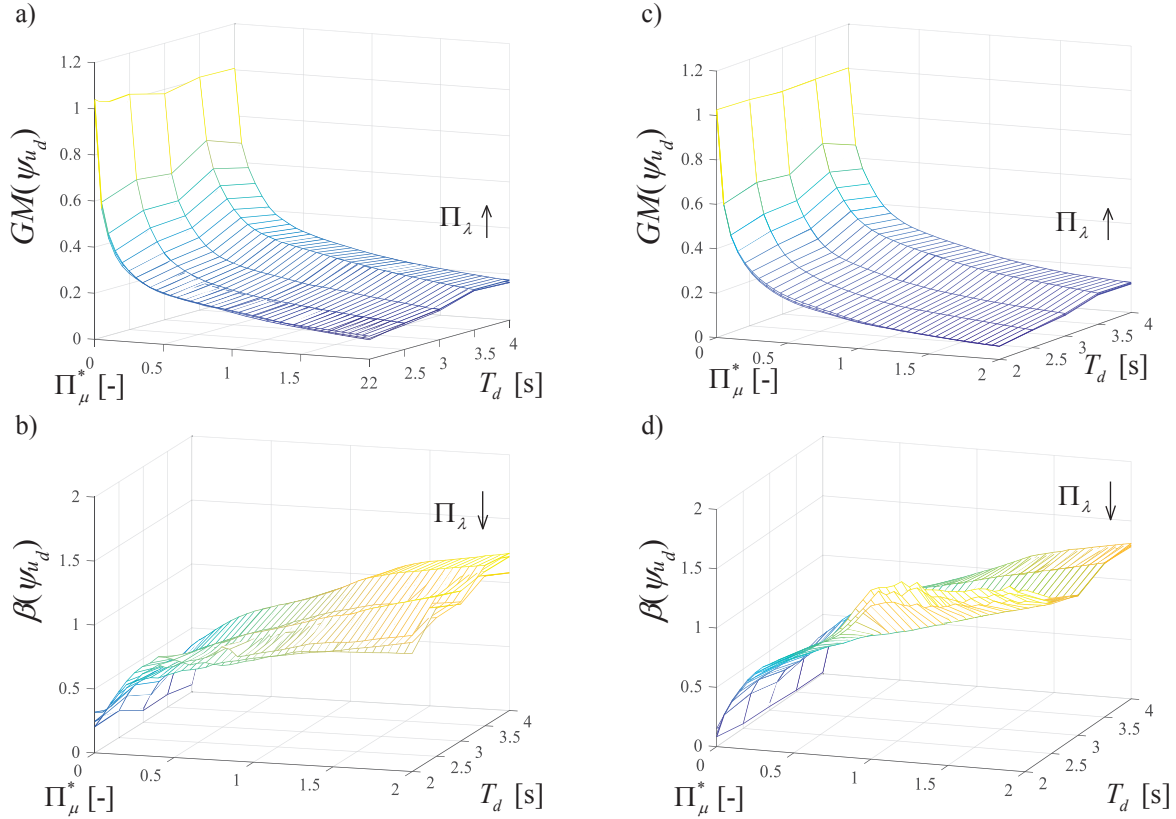


Figure 2: Normalized deck displacement vs.  $\Pi_\mu^*$  and  $T_d$ : median value ((a): analysis with only pier; (c): analysis with the pier-abutment-deck interaction) and dispersion ((b): analysis with only pier; (d): analysis with the pier-abutment-deck interaction) for  $T_p=0.2$ s and for different values of  $\Pi_\lambda$ .

In Figures 2,  $GM(\psi_{u_d})$  is quite equal to unit for  $\Pi_\mu^* = 0$ . For  $\Pi_\mu^* \neq 0$ ,  $GM(\psi_{u_d})$  increases slightly for increasing  $T_d$  because of the period elongation. Obviously,  $GM(\psi_{u_d})$  decreases significantly as  $\Pi_\mu^*$  increases showing an hyperbolic trend while it is not heavily influenced by  $\Pi_\lambda$ . The dispersion  $\beta(\psi_{u_d})$ , for high  $T_d$ , increases for increasing values of  $\Pi_\mu^*$ , as a result of the reduction of the efficiency of the IM. Obviously, in the situation corresponding to  $\Pi_\mu^* = 0$ , the dispersion is quite zero for all the values of  $T_d$  and of  $\Pi_\lambda$  considered. The mass ratio  $\Pi_\lambda$  does not affect significantly the response dispersion. Despite the trends of the both statistics are similar for the two configurations, it is possible to observe that the values of  $GM(\psi_{u_d})$  are larger in the case of the model without the pier-abutment-deck interaction. On the other hand, higher values of  $\beta(\psi_{u_d})$  are achieved for the model with the pier-abutment-deck interaction.

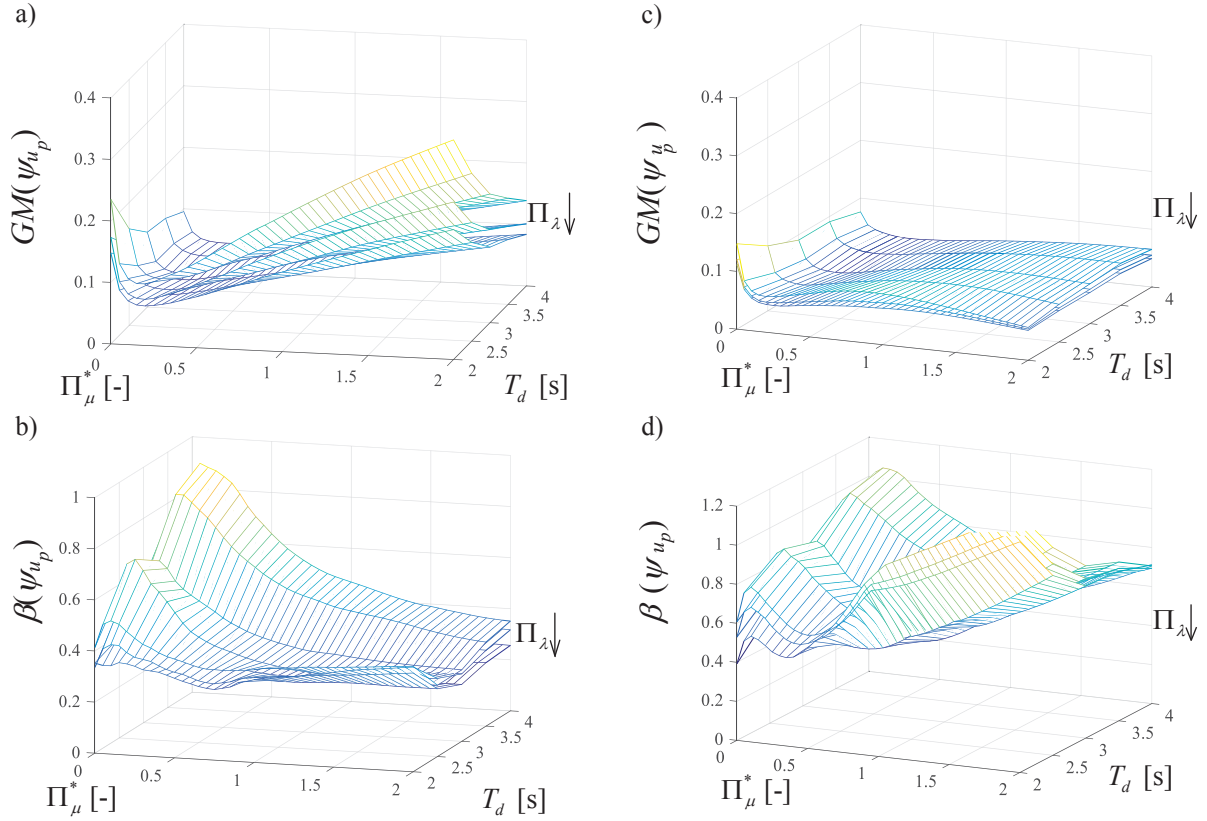


Figure 3: Normalized pier displacement vs.  $\Pi_\mu^*$  and  $T_d$ : median value ((a): analysis with only pier; (c): analysis with the pier-abutment-deck interaction) and dispersion ((b): analysis with only pier; (d): analysis with the pier-abutment-deck interaction) for  $T_p=0.2s$  and for different values of  $\Pi_\lambda$ .

Figure 3 represents the response statistics of the normalized pier displacement  $\psi_{u_p}$ . For the both structural configurations,  $GM(\psi_{u_p})$  decreases for higher values of  $T_d$  and of  $\Pi_\lambda$  as well as for decreasing values of  $T_p$ ; whereas it first decreases and then increases for increasing values of  $\Pi_\mu^*$ , meaning that there is an optimal value of  $\Pi_\mu^*$  able to minimize the geometric mean of the pier displacement. This optimal value varies in a range that depends on the values of  $T_d$  and  $\Pi_\lambda$  and on the structural configuration. Note also that for not optimal values of  $\Pi_\mu^*$ ,  $GM(\psi_{u_p})$  is not so high. Conversely,  $GM(\psi_{u_p})$  presents higher values for the structural configuration without the pier-abutment-deck interaction (i.e., single-column bent viaduct). The values of the dispersion  $\beta(\psi_{u_p})$  are very low for low  $\Pi_\mu^*$  values due to the high efficiency of the *IM* used in this work, and reach their peak for values of  $\Pi_\mu^*$  close to the optimal ones. The other system parameters have a reduced influence on  $\beta(\psi_{u_p})$  compared to the influence of  $\Pi_\mu^*$ . Higher values are achieved for the structural configuration with the pier-abutment-deck interaction (i.e., multi-span continuous deck bridge).

## 5 OPTIMAL VALUES OF THE SLIDING FRICTION COEFFICIENTS

Once the results from the analysis are obtained, for each parameter combination (i.e.,  $\Pi_\lambda$  and  $T_d$ ) and structural model (i.e., single-column bent viaduct and multi-span continuous deck bridge), the optimal values of the normalized sliding friction coefficient,  $\Pi_{\mu, \text{opt}}^*$ , that minimize the median (50<sup>th</sup> percentile) of the normalized pier displacements  $\psi_{u_p}$  have been assessed and are reported in Figure 4. Figure 4 reports the variation of  $\Pi_{\mu, \text{opt}}^*$  with  $\Pi_\lambda$  and  $T_d$  and in relation to the two structural models (Figure 4a,b). The optimal values of the sliding friction coefficient manifest a slightly increase as  $T_d$  decreases, and this is valid for the either the configurations. It is also observed that, especially for high  $T_d$  values,  $\Pi_{\mu, \text{opt}}^*$  increases by increasing  $\Pi_\lambda$  in order to dissipate more energy.

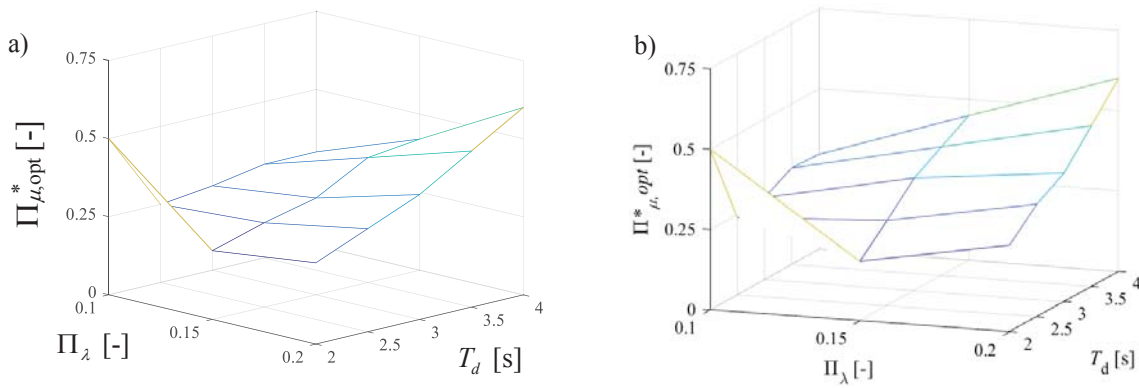


Figure 4: Optimal values of normalized friction that minimize the 50<sup>th</sup> percentile of the normalized pier displacements vs.  $\Pi_\lambda$  and  $T_d$ , for  $T_p=0.2\text{s}$ ; (a) with only pier; (b) with the pier-abutment-deck interaction.

## 6 CONCLUSIONS

This paper summarizes the seismic performance of bridges and viaducts isolated with single concave friction pendulum system bearings focusing on the influence of the pier-abutment-deck interaction on the seismic response. The analysis carried out aim to define the optimal isolator friction properties taking into account the uncertainty in the seismic input. Adopting the nondimensionalization of the motion equations, a wide parametric analysis considering several structural properties has been conducted by monitoring the response parameters of interest regarding both an isolated bridge where only the pier response is considered and an isolated bridge where the interaction between pier and abutment is taken into account (i.e., single-column bent viaduct and multi-span continuous deck bridge, respectively). The seismic response of these systems is modelled by employing a six-degree-of-freedom system mainly to capture the effects due to the higher modes of the elastic pier.

As far as the deck response is concerned, the geometric mean of the normalized deck displacement tends to slightly increase for increasing isolation period because of the period elongation and it decreases significantly as the normalized friction increases. It presents higher values in the case of the model with only pier (i.e., single-column bent viaduct). The dispersion increases for increasing both isolation period and normalised friction coefficient. It presents higher values in the case of the model with the pier-abutment-deck interaction.

With regards to the pier response, the geometric mean of the normalized displacement decreases for increasing values of isolation period and of mass ratio, whereas it first decreases

and then increases for increasing values of normalized friction. Assuming that, an optimal value of normalized friction coefficient such that the pier displacement is minimized does exist. Regarding the dispersion, higher values are observed for the pier-abutment-deck interaction model.

Finally, the optimal values of the normalized friction coefficient, able to minimize the 50<sup>th</sup> percentile of the pier response, as a function of the structural properties and for the both structural models, are estimated. Higher optimum friction coefficients are required, when the pier-abutment-deck interaction (i.e., multi-span continuous deck bridge) is taken into account.

## REFERENCES

- [1] M. C. Constantinou, A. Kartoum, A. M. Reinhorn, P. Bradford , Sliding isolation system for bridges: Experimental study, *Earthquake Spectra* 1992; 8(3): 321-344.
- [2] A. Kartoum, M. C. Constantinou, A. M. Reinhorn, Sliding isolation system for bridges: Analytical study, *J. Struct. Eng.* 1992; 8(3): 345-372.
- [3] P. Tsopelas, M. C. Constantinou, Y. S. Kim, S. Okamoto, Experimental study of FPS system in bridge seismic isolation, *Earthquake Eng. Struct. Dyn.* 1996a; 25(1): 65-78.
- [4] A. Ghobarah, H. M. Ali, Seismic performance of highway bridges, *Eng. Struct.* 1988; 10(3): 157-166
- [5] M. Dicleli, S. Buddaram, Effect of isolator and ground motion characteristics on the performance of seismic-isolated bridges. *Earth. Engin. and Struc. Dyn.* 2006; **35**(2):233-250.
- [6] P. Tsopelas, M. C. Constantinou, S. Okamoto, S. Fujii, D. Ozaki, Experimental study of bridge seismic sliding isolation systems. *Engineering Structures*, Vol. 18, No. 4, pp. 301-310, 1996.
- [7] R.S. Jangid, Seismic Response of Isolated Bridges. *J. Bridge Eng.*, 2004, 9(2): 156-166.
- [8] Jangid, R. S. (2008). Equivalent linear stochastic seismic response of isolated bridges. *Journal of Sound and Vibration*, 309(3-5), 805-822.
- [9] Troisi R., Alfano G. 2019. Towns as Safety Organizational Fields: An Institutional Framework in Times of Emergency. *Sustainability*, 11: 7025, 2019, doi:10.3390/su11247025.
- [10] Troisi R., Alfano G. 2020. Firms' crimes and land use in Italy. An exploratory data analysis. *New Metropolitan Perspectives*, International Symposium – 4th edition, 27-30 May 2020, pp 10.
- [11] N.P. Tongaonkar, R.S. Jangid, Seismic response of isolated bridges with soil–structure interaction. *Soil Dynamics and Earthquake Engineering* 23 (2003) 287–302.
- [12] L. Su, G. Ahmadi, IG. Tadjbakhsh, Comparative study of base isolation systems. *Journal of Engineering Mechanics* 1989; **115**(9):1976–92.
- [13] Yen-Po Wang, Lap-Loi Chung, Wei-Hsin Liao. Seismic response analysis of bridges isolated with friction pendulum bearings. *Earth.Eng.& Str. Dyn.*, 1998; 27, 1069-1093.
- [14] VA. Zayas, SS. Low, SA. Mahin, A simple pendulum technique for achieving seismic isolation. *Earthquake Spectra* 1990; **6**(2):317–33.



- [15] G. Mosqueda, AS. Whittaker, GL. Fenves, Characterization and modeling of Friction Pendulum bearings subjected to multiple components of excitation. *Journal of Structural Engineering* 2004; **130**(3):433-442.
- [16] A. Mokha, MC. Constantinou, AM. Reinhorn, Teflon Bearings in Base Isolation. I: Testing. *Journal of Structural Engineering* 1990; **116**(2):438-454.
- [17] MC. Constantinou, A. Mokha, AM. Reinhorn, Teflon Bearings in Base Isolation. II: Modeling. *Journal of Structural Engineering* 1990; **116**(2):455-474.
- [18] R. S. Jangid, Computational numerical models for seismic response of structures isolated by sliding systems, *Structural Control and Health Monitoring* 2005; 12:117–137.
- [19] MC. Constantinou, AS. Whittaker, Y. Kalpakidis, DM. Fenz, GP. Warn, Performance of Seismic Isolation Hardware Under Service and Seismic Loading. *Technical Report MCEER-07-0012*, 2007.
- [20] P. Castaldo, E. Tubaldi, Influence of FPS bearing properties on the seismic performance of base-isolated structures. *Earthquake Engin. and Structural Dynamics* 2015; **44**(15):2817–2836.
- [21] P. Castaldo, M. Ripani, Optimal design of friction pendulum system properties for isolated structures considering different soil conditions, *Soil Dynamics and Earthquake Engineering*, 2016, 90:74–87, DOI: 10.1016/j.soildyn.2016.08.025.
- [22] P. Castaldo, M. Ripani, R. Lo Piere, Influence of soil conditions on the optimal sliding friction coefficient for isolated bridges. *Soil Dynamics and Earth. Engineering*, 2018, 111; 131–148.
- [23] Zhang, J., & Huo, Y. (2009). Evaluating effectiveness and optimum design of isolation devices for highway bridges using the fragility function method. *Eng. Structures*, 31(8), 1648-1660.
- [24] Kunde, M. C., & Jangid, R. S. (2006). Effects of pier and deck flexibility on the seismic response of isolated bridges. *Journal of Bridge Engineering*, 11(1), 109-121.
- [25] M. Eröz, R. DesRoches. Bridge seismic response as a function of the Friction Pendulum System (FPS) modeling assumptions. *Engineering Structures*, 30 (2008) 3204–3212.
- [26] Eröz, M., & DesRoches, R. (2013). The influence of design parameters on the response of bridges seismically isolated with the friction pendulum system (FPS). *Engineering Structures*, 56, 585-599.
- [27] P. Castaldo, B. Palazzo, P. Della Vecchia, Seismic reliability of base-isolated structures with friction pendulum bearings. *Engineering Structures* 2015; **95**:80-93.
- [28] P. Castaldo, B. Palazzo, P. Della Vecchia, Life-cycle cost and seismic reliability analysis of 3D systems equipped with FPS for different isolation degrees, *Engineering Structures*, 2016; **125**:349–363, <http://dx.doi.org/10.1016/j.engstruct.2016.06.056>.
- [29] Castaldo, P., Palazzo, B., Ferrentino, T., & Petrone, G. (2017). Influence of the strength reduction factor on the seismic reliability of structures with FPS considering intermediate PGA/PGV ratios. *Composites Part B: Engineering*, 115, 308-315.
- [30] Palazzo, B., Castaldo, P., & Della Vecchia, P. (2014, September). Seismic reliability analysis of base-isolated structures with friction pendulum system. In 2014 IEEE Work-



- shop on Environmental, Energy, and Structural Monitoring Systems Proceedings (pp. 1-6). IEEE.
- [31] P. Castaldo, G. Amendola, B. Palazzo, Seismic fragility and reliability of structures isolated by friction pendulum devices: Seismic reliability-based design (SRBD), *Earthquake Engineering and Structural Dynamics*, 2017; 46(3); 425–446, DOI: 10.1002/eqe.2798.
  - [32] P. Castaldo, B. Palazzo, T. Ferrentino, Seismic reliability-based ductility demand evaluation for inelastic base-isolated structures with friction pendulum devices, *Earthquake Engineering and Structural Dynamics*, 2016; DOI: 10.1002/eqe.2854.
  - [33] P. Castaldo, G. Alfano, Seismic reliability-based design of hardening and softening structures isolated by double concave sliding devices, *Soil Dynamics and Earth. Eng.*, 129: 105930, 2020.
  - [34] P. Castaldo, B. Palazzo, G. Alfano, MF. Palumbo, Seismic reliability-based ductility demand for hardening and softening structures isolated by friction pendulum bearings, 2018, *Structural Control and Health Monitoring*, e2256. <https://doi.org/10.1002/stc.2256>.
  - [35] TL. Karavasilis, CY. Seo, N. Makris, Dimensional Response Analysis of Bilinear Systems Subjected to Non-pulse like Earthquake Ground Motions. *J. of Str. Eng.* 2011;137(5):600-606.
  - [36] M. Barbato, E. Tubaldi, A probabilistic performance-based approach for mitigating the seismic pounding risk between adjacent buildings. *Earth. Engin. & Str. Dyn.* 2013;42(8):1203-1219.
  - [37] MJN. Priestley, F. Seible, GM. Calvi, Seismic design and retrofit of bridges. *Wiley*, 1996.
  - [38] Bertagnoli, G., Mancini, G., Tondolo, F. Early age cracking of massive concrete piers, *Magazine of Concrete Research*, 2011, 63, 10, 1, 723-736.
  - [39] Bertagnoli G., Mancini G., Recupero A., Spinella N., Rotating compression field model for reinforced concrete beams under prevalent shear actions, *Structural Concrete*, 2011, 12, 3, 178-186.
  - [40] Bertagnoli G., Mancini G. Failure analysis of hollow-core slabs tested in shear. *Structural Concrete*, 2009, 10, 3, 139-152.
  - [41] Mancini G., Carbone V.I., Bertagnoli G., Gino, D. Reliability-based evaluation of bond strength for tensed lapped joints and anchorages in new and existing reinforced concrete structures, *Structural Concrete*, 2018, 19, 3, 904-917.
  - [42] Bertagnoli G., Gino D., Martinelli, E. A simplified method for predicting early-age stresses in slabs of steel-concrete composite beams in partial interaction, *Engineering Structures*, 2017, 140, 286-297.
  - [43] PEER, *Pacific Earthquake Engineering Research Center* <http://peer.berkeley.edu/>
  - [44] ITACA, *Italian Accelerometric Archive* [http://itaca.mi.ingv.it/ItacaNet/itaca10\\_links.htm](http://itaca.mi.ingv.it/ItacaNet/itaca10_links.htm)
  - [45] ISESD, *Internet-Site for European Strong-Motion Data* [http://www.isesd.hi.is/ESD\\_Local/frameset.htm](http://www.isesd.hi.is/ESD_Local/frameset.htm)

- [46] H. Aslani, E. Miranda, Probability-based seismic response analysis. *Engineering Structures* 2005;**27**(8):1151-1163.
- [47] Porter KA. An overview of PEER's performance-based earthquake engineering methodology. Proceedings, *Proceedings of the 9th International Conference on Application of Statistics and Probability in Civil Engineering (ICASP9)*, San Francisco, California, 2003.
- [48] Ryan K, Chopra A. Estimation of Seismic Demands on Isolators Based on Nonlinear Analysis. *Journal of Structural Engineering* 2004;**130**(3):392-402.
- [49] Math Works Inc. MATLAB-High Performance Numeric Computation and Visualization Software. User's Guide. Natick: MA, USA; 1997.
- [50] T. Karavasilis, C. Seo, Seismic structural and non-structural performance evaluation of highly damped self-centering and conventional systems. *Eng. Structures* 2011;**33**(8):2248-2258.
- [51] Garzillo C., Troisi R. Le decisioni dell'EMA nel campo delle medicine umane. In EMA e le relazioni con le Big Pharma - I profili organizzativi della filiera del farmaco, G. Giappichelli, 85-133, 2015.
- [52] De Iuliis, M., & Castaldo, P. (2012). An energy-based approach to the seismic control of one-way asymmetrical structural systems using semi-active devices. *Ingegneria Sismica-International Journal of Earthquake Engineering*, 29(4), 31-42.
- [53] Golzio L. E., Troisi R. The value of interdisciplinary research: a model of interdisciplinarity between legal re-search and research in organizations. *Journal For Development And Leadership*, 2: 23-38, 2013.
- [54] Basone, F., Castaldo, P., Cavaleri, L., & Di Trapani, F. (2019). Response spectrum analysis of frame structures: reliability-based comparison between complete quadratic combination and damping-adjusted combination. *Bulletin of Earthquake Engineering*, 17(5), 2687-2713.
- [55] Nese A., Troisi R. Corruption among mayors: evidence from Italian Court of Cassation judgments, *Trends In Organized Crime*, 1-26, 2018. DOI:10.1007/s12117-018-9349-4.
- [56] Troisi R., Golzio, L. E. Legal studies and organization theory: a possible cooperation. *Manageable cooperation* - European Academy of Management: 16th EURAM Conference, Paris, 1-2, 1-4 June 2016.
- [57] Troisi R., Guida V. Is the Appointee Procedure a Real Selection or a Mere Political Exchange? The Case of the Italian Health-Care Chief Executive Officers. *Journal of Entrepreneurial and Organizational Diversity*, 7 (2): 19-38, 2018, DOI:10.5947/jeod.2018.008.
- [58] Troisi R. Le risorse umane nelle BCC: lavoro e motivazioni al lavoro. In Progetto aree bianche. Il sistema del credito cooperativo in Campania, 1: 399-417, 2012.
- [59] Ang AHS, Tang WH. Probability Concepts in Engineering-Emphasis on Applications to Civil and Environmental Engineering. John Wiley & Sons, New York, USA; 2007.
- [60] Michael D. Symans, Steven W. Kelly. Fuzzy logic control of bridge structures using intelligent semi-active seismic isolation systems. *Earthquake Engng. Struct. Dyn.* 28, 37860 (1999).

## CRITICAL ACCELERATION, SEISMIC SLIDING DISPLACEMENT AND SMART DESIGN OF CANTILEVER WALLS

Loukas C. Katsenis<sup>1</sup>, Constantine A. Stamatopoulos<sup>2</sup>, Vassilis P. Panoskaltsis<sup>1</sup>

<sup>1</sup>Department of Civil Engineering, Demokritos University of Thrace,  
University Campus Xanthi-Kimmeria, 67100 Xanthi, Greece

e-mails: [katsenisloukas@yahoo.gr](mailto:katsenisloukas@yahoo.gr), [vpanoska@civil.duth.gr](mailto:vpanoska@civil.duth.gr)

<sup>2</sup> Stamatopoulos and Associates Co; Hellenic Open University; 5 Isavron str., 11471 Athens, Greece

e-mail: [k.stam@saa-geotech.gr](mailto:k.stam@saa-geotech.gr)

---

### Abstract

*Cantilever walls are a popular type of retaining system. The slip mode of failure of these retaining systems under seismic loading has recently been studied. Cantilever walls must be designed in a manner such as to minimize the seismic displacement. The "conventional" sliding-block model is the most commonly used simplified model predicting the seismic displacement of slopes for given earthquake motions. However, in dynamic analyses, usually the seismic motion is applied at the underlying bedrock and the seismic displacement along a slip surfaces depends not only on the seismic response of the slip surface, but also on the dynamic characteristics of the soil profile both above and below the slip surface. The present work proposes a cost-effective method predicting the seismic displacement of cantilever walls, and applies it for their smart design. In order to achieve the paper first proposes a method predicting the critical acceleration value of cantilever walls retaining systems by application of equations predicting the critical acceleration value for gravity walls for the slip mode of failure of these retaining systems. Then the paper proposes a method predicting the seismic displacement of cantilever walls considering the dynamic response of the underlying soil profile by applying a recently developed 1-D 2-body dynamic stick-slip method at the particular geometry of cantilever walls. Finally, based on the above, the paper proposes a cost-effective method for smart design of cantilever walls, and presents a typical example. The work illustrated that the de-amplification effect of the seismic response can be crucial if the soil underlying the wall is soft and deep and in this case a wall with a looser backfill may be preferable.*

**Keywords:** cantilever walls, sliding-block model, dynamic response, seismic displacement, slip surface, coupled analyses, smart design

---

## 1 INTRODUCTION

Engineers usually assess the seismic safety of slopes and retaining structures using the dynamic factor of safety calculated from loads. However, evaluations based on the dynamic factor of safety have the serious drawback that they do not consider the seismic displacement, which is directly related to damage and recently design of retaining structures is based on prediction of the seismic displacement along its slip surface and its comparison with the tolerable displacement that this structure can sustain [1].

Cantilever walls of L or inverted T-shape are a popular type of retaining system. The design exploits the stabilizing action of soil weight over the footing slab against both sliding and overturning. It is widely considered as advantageous over conventional gravity walls for it combines economy and ease in construction and installation [2]. Design of cantilever walls depends on its dimensions, but also the soil type used in the backfill, as well as its compaction. Cantilever walls must be designed in a manner such as to minimize the seismic displacement. The slip mode of failure of these earth structures under seismic loading has been studied by Kloukinas et al. [3]. However, the seismic displacement along a slip surface and, additionally, its dependence on the dynamic characteristics of the backfill and the soil profile below has not been studied.

The "conventional" Newmark sliding-block model [4], illustrated in Fig. 1, is the most commonly used simplified model predicting the seismic displacement of natural slopes and retaining structures for given earthquake motion [1, 5, 6]. As illustrated in Fig. 1a, a rigid block rests on an inclined plane. The resistance along the block-inclined plane boundary follows the Mohr-Coulomb law. Critical acceleration is the minimum horizontal acceleration which causes movement of the block. Every time where the applied horizontal acceleration is larger than the critical acceleration, the block slides. The total displacement is obtained by the addition of the partial slips. This model is used for the prediction of permanent seismic movement of slopes and retaining structures along a predefined slip surface, by appropriately selecting the equivalent critical and applied acceleration values of the rigid block [5]. For gravity walls, according to the Monobe-Okabe theory [7, 8], methods have been developed to determine the critical acceleration value, both by iteration [9] and analytically by first indicating the appropriate slip surface [10, 11].

In dynamic analyses, usually the seismic motion is applied at the underlying bedrock and the seismic displacement along a slip surfaces depends not only on the seismic response of the slip surface, but also on the dynamic characteristics of the soil profile both above and below the slip surface [12-14]. Katsenis et al., [13, 14] simulated the effect of the soil profile on the seismic displacement along the slip surface using a 1-D dynamic system of 2 continuous bodies separated by a horizontal slip which simulates the seismic displacement of the conventional sliding-block model.

The present work proposes a method predicting the seismic displacement of cantilever walls, and applies it for its smart design. In particular, the simplified geometry of Fig. 2 and table 1 of a cantilever wall above a soil layer is considered. In order to achieve the paper first proposes a method predicting the critical acceleration value of cantilever walls by application of equations predicting the critical acceleration value for gravity walls given by [11] for the slip mode of failure of these retaining systems identified by [3]. Then the paper proposes a method predicting the seismic displacement of cantilever walls considering the dynamic response of the soil profile be first describing the Katsenis et al. [13] model and then applying it at the particular geometry of cantilever walls. Finally, the paper proposes smart design of cantilever walls by first presenting typical results of the Katsenis et al. [13, 14] model and then applying them for cantilever walls smart design.

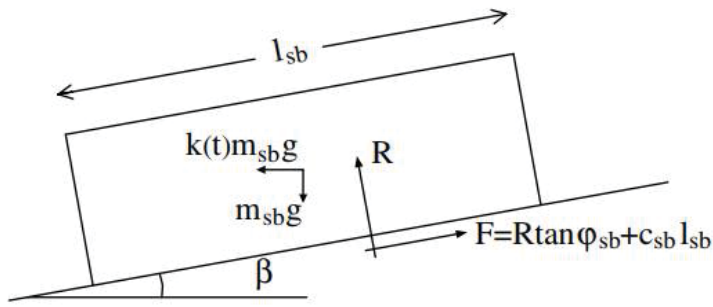


Figure 1: A block sliding in an inclined plane (the “conventional” sliding-block model)

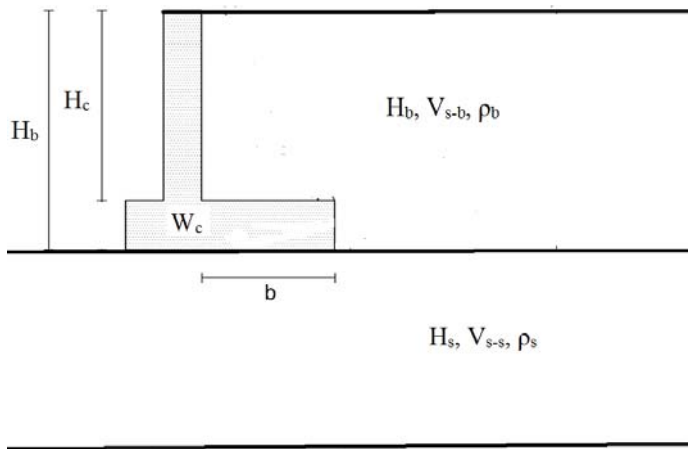


Figure 2: The problem considered: A cantilever wall above a soil layer

	Parameter	Symbol
Wall	Weight per unit length	$W_c$
	Length inside backfill	$b$
	Height above base	$H_c$
	Friction angle at base	$\phi_c$
Backfill	Height	$H_b$
	Shear Wave velocity	$V_{s-b}$
	Unit weight	$\rho_b$
	Friction angle	$\phi_b$
Soil-wall interface	Friction angle	$\phi_I = \phi_b$
Underlying soil	Height	$H_s$
	Shear Wave velocity	$V_{s-s}$
	Unit weight	$\rho_s$

Table 1: Model parameters defining the cantilever walls considered in the present study

## 2 PROPOSED METHOD PREDICTING THE CRITICAL ACCELERATION OF CANTILEVER WALLS

### 2.1 State of the art: The critical acceleration value for gravity walls

Gravity walls are relatively rigid structures walls used for supporting soil laterally so that it can be retained (Fig. 3a). The applied force in walls under a horizontal acceleration value is estimated by the Mononobe-Okabe equation [7, 8], and typically iteration is performed to estimate the estimate the critical acceleration causing failure, i.e. the value for limit equilibrium [9-11]. Furthermore, Stamatopoulos and Velgaki [10] observed that for failure of gravity walls, a wedge in the backfill behind the wall reaches an active state, and that the wall and the backfill slide outward, and thus the soil-wall system consists really of two bodies: (a) the active soil wedge that slides with the inclination of least resistance in the backfill, and (b) the wall that slides along the soil-wall boundary in the foundation (Fig. 3b).

Stamatopoulos et al. [11] developed an analytical equation predicting the critical acceleration value of the soil-wall system of Fig. 3a and table 2, by solving the force equilibrium equations assuming a geometry consisting of two rigid blocks [15]. For a horizontal wall and backfill with inclination  $\alpha_{B-i}$  and for only frictional resistance at both the backfill and the soil-wall boundaries, this equation gives

$$a_{c-i} = g AA_B / BB_B \quad (1a)$$

where  $g$  is the acceleration of gravity

$$AA_b = X G [(1 + A_i B)(1 + FD) - (B - A_i)(F - D)] - \frac{(DA_i - 1)(B - A_i)[(1 + FD) - G(F - D)]}{A_i} \quad (1b)$$

$$BB_b = X [(1 + A_i B)(1 + FD) - (B - A_i)(F - D)] - \frac{(DA_i - 1)(1 + A_i B)[(1 + FD) - G(F - D)]}{A_i} \quad (1c)$$

and

$$\begin{aligned} X &= 2 W_W / (\gamma H_o^2), & D &= \tan \delta, & B &= \tan \phi_B, \\ G &= \tan \phi_W, & F &= \tan \phi_i, & A_i &= \tan \alpha_{B-i} \end{aligned} \quad (1d)$$

where the parameters  $W_W$ ,  $\gamma$ ,  $H_o$ ,  $\delta$ , ( $\alpha_{Bcr-i}$ ) are illustrated in Fig. 3,  $\phi_B$  is the frictional resistance at the backfill,  $\phi_W$  is the frictional resistance at the foundation soil-wall boundary and  $\phi_i$  is the frictional resistance at the backfill soil-wall boundary.

The critical acceleration value  $a_c$  corresponds to the critical rupture angle  $\alpha_{Bcr-i}$  which is the value of  $\alpha_{B-i}$ , which minimizes  $a_{c-i}$  in Eq. (1). As illustrated by [10],  $a_{c-i}$  is a parabola in terms of ( $\alpha_{B-i}$ ), having a single well-defined minimum. It is inferred that estimating numerically  $A_i$ , and thus  $\alpha_{Bcr-i}$  also, is a simple matter using, for example, the bisection method [16].



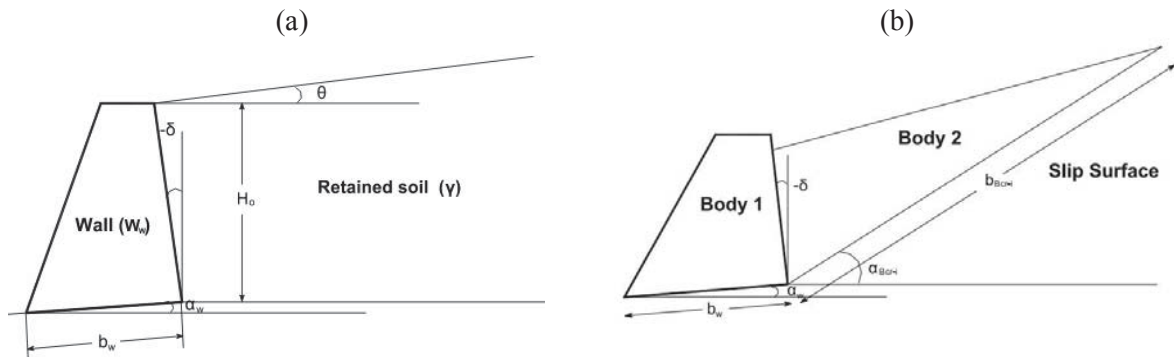


Figure 3: (a) Wall- retained soil geometry considered by [11] and (b) its simulation with a two-body model [11]

	Parameter	Symbol	For Cantilever wall
Wall	Weight	$W$	$W=W_c + \gamma_b H_c [b + H_c \tan(\alpha_i - \phi_b)]/2$
	Friction angle at base	$\phi_w$	$\phi_c$
Backfill	Height	$H$	$H_c$
	Unit density	$\gamma$	$\gamma_s$
	Friction angle	$\phi_b$	$\phi_s$
Soil-wall interface	Friction angle	$\phi_i$	$\phi_s$
	Inclination	$\delta$ (Fig. 5)	$\alpha - \phi_b$

Table 2: Parameters which define the Stamatopoulos et al. [11] model considered in section 2.1 and the corresponding values for the cantilever wall of Fig. 2.

## 2.2 The critical acceleration value of cantilever walls

Figure 4 presents the mode of failure of cantilever walls proposed by Kloukinas et al. [3], where  $\theta_2$  is related to  $\theta_1$  and the frictional resistance of the backfill ( $\phi_b$ ) as

$$\theta_2 = \theta_1 - \phi_b \quad (2)$$

Based on this mode of failure, it can be inferred that the sliding mechanism of cantilever walls can be simulated as a wall-backfill 2-body system of Fig. 3, where the first body corresponds to the cantilever wall and part of the backfill to the left of the slip segment AA' of Fig. 4, and the second body corresponds to the backfill part to the right of the slip segment AA' of Fig. 4. Table 2 gives the equivalent values of the system of Fig. 3 solving the cantilever wall of Fig. 2. A condition needed for this solution, is that the slip surface passes through the ground surface of the backfill, or that

$$\tan(\alpha_{b-i} - \phi_b) < b/H_c \quad (3)$$

It is inferred that equations (1) and the procedure outlined in section 2.1 with the values given in table 2 and the condition of equation (3) can be applied to estimate the critical acceleration value for relative motion of cantilever walls of the geometry of Fig. 2. A microsoft excel worksheet was programmed to estimate the critical acceleration value of cantilever walls of the geometry of Fig. 2, based on the procedure described above.

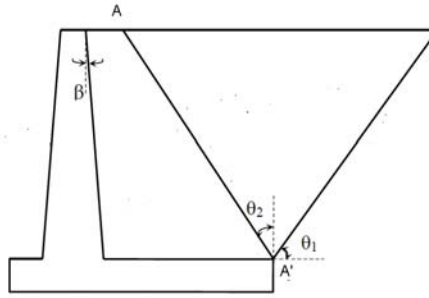


Figure 4: The mode of failure of cantilever walls proposed by Kloukinas et al. [3], where  $\theta_2$  is related to  $\theta_1$  with equation (2)

### 3 PROPOSED METHOD PREDICTING THE SEISMIC DISPLACEMENT OF CANTILEVER WALLS CONSIDERING THE DYNAMIC RESPONSE OF THE SOIL PROFILE

#### 3.1 State of the art: The Katsenis et al., [13, 14] model

Katsenis et al. [13, 14] simulated the field configuration of a slope with a slip surface where seismic displacement may accumulate as a result of a horizontal shear wave of Fig. 5a with a 1-D dynamic system of 2 continuous bodies separated by a horizontal slip element. In particular, the Katsenis et al., [13, 14] model, illustrated in Fig. 5b and table 3, considers the 1-dimensional dynamic response of a horizontal soil profile of depth  $(h_1+h_2)$  with a slip element at depth  $h_1$ . Different shear wave velocities ( $V_{s-1}$ ,  $V_{s-2}$ ), densities ( $\rho_1$ ,  $\rho_2$ ) and damping ( $\lambda_1$ ,  $\lambda_2$ ) may exist above and below the slip element. The slip element simulates the seismic displacement of the conventional sliding-block model, where its resistance is defined by the critical horizontal value ( $a_c$ ), for which relative movement in only one direction occurs.

The numerical code associated with the numerical model above is derived by extending the derivation proposed by [17]. When seismic displacement accumulates along the slip surface, the method simulates the independent movement of the two bodies, and thus the solution is “coupled”. Additional options exist in the model where (a) the rotation of the slip surface with displacement is simulated by adjusting the critical acceleration value ( $a_c$ ) in terms of the accumulated seismic displacement and (b) the non-linear shear stress-strain response of the soil profile is simulated. However, these options are not applied in the present application.

When applying the model, if the soil profile of body  $i$  is non-uniform, the average properties may be used [14]. In this respect, in the case of stratified deposit with  $M_i$  sub-layers with height  $H_{k-i}$  and shear wave velocity  $VS_{k-i}$ , it is recommended to estimate  $VS_i$  based on an equation proposed by Vijayendra et al. [18] as:

$$VS_i = \frac{h_i}{\sum_{k=1}^{M_i} \frac{H_{k-i}}{VS_{k-i}}} \quad (4)$$

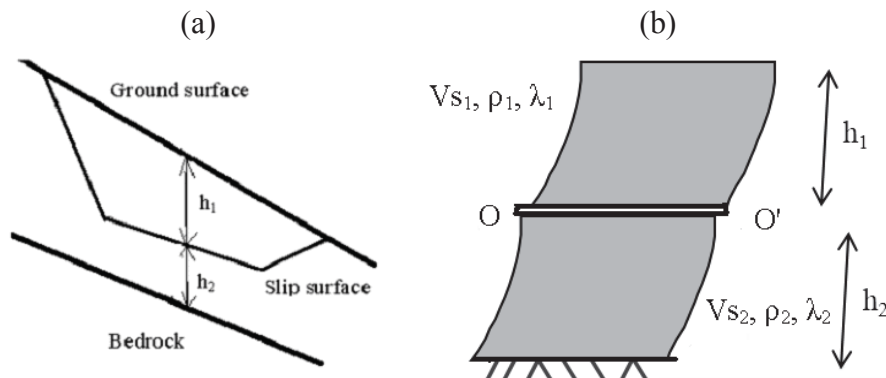


Figure 5: The Katsenis et al. [13, 14] model: (a) field configuration of a slope with a slip surface where seismic displacement may accumulate as a result of a horizontal shear wave, (b) simulation of (a) with a 1-D dynamic system of 2 continuous bodies separated by a horizontal slip element.

	Parameter	Symbol	For Cantilever wall
Upper (1) Body	Height	$h_1$	$H_b/2$
	Shear Wave velocity	$V_{s-1}$	$V_{s-b}$
	Density	$\rho_1$	$\rho_b$
Lower (2) Body	Height	$h_2$	$H_s + H_b/2$
	Shear Wave velocity	$V_{s-2}$	$(H_b/2 + H_s) / [H_b/(2 V_{s-b}) + H_s/V_{s-s}]$
	Density	$\rho_2$	$(H_b/2 + H_s) / [H_b/(2 \rho_b) + H_s/\rho_s]$
Slip surface	Critical acceleration for relative movement	$a_c$	Specified in section 2.2

Table 3: Parameters which define the Katsenis et al. [13, 14] model for the linear case. The corresponding values when this model is applied to simulate cantilever walls is also given.

### 3.2 Proposed method

In order to perform the numerical simulation of the seismic displacement of the cantilever wall of Fig. 2 considering the dynamic response of the soil profile both above and below the slip surface, we apply the 1-D coupled stick-slip dynamic model of Fig. 5b. The upper body of the dynamic system corresponds to the wall backfill above the slip plane. The lower body of the dynamic system corresponds to the wall backfill below the slip plane and the underlying soil profile. The critical acceleration of the stick-slip element for a cantilever wall was evaluated in section 3.

Based on the above, table 3 gives the corresponding when the Katsenis et al. [13, 14] model is applied to simulate the response of the cantilever wall of Fig. 2. As body 2 corresponds to both the wall backfill below the slip plane and the underlying soil profile, the average values are obtained using equation (3).

## 4 SMART DESIGN OF CANTILEVER WALLS

### 4.1 Results of the Katsenis et al. [14] model

Katsenis et al. [14] present the computed permanent seismic displacement ( $u_f$ ) for the Aegion 1995 seismic motion with  $a_c=0.5\text{m/s}^2$  and (ii) Mid-Niigata Prefecture 2004 seismic motion with

$a_c=3\text{m/s}^2$ . Table 4 gives the characteristics of the input motions considered and the critical acceleration  $a_c$  was selected as  $0.5\text{m/s}^2$  and  $3\text{m/s}^2$  for the input motions (i) and (ii) respectively, because they correspond to a rigid system having seismic displacement of about 5-10cm, which is the tolerable displacement value for typical structures.

In particular, they define

$$T_{s1}=4 h_1/V_{s-1} \quad (5a)$$

$$T_{s-ave} = 4 (h_1/V_{s-1} + h_2/V_{s-2}) \quad (5b)$$

and Fig. 6 presents the computed permanent seismic displacement ( $u_f$ ) versus (a)  $T_{s1}/T_m$  for  $h_1+h_2=30\text{m}$ ,  $\rho_1=\rho_2=2 \text{ Mg/m}^3$  and  $\lambda_1=\lambda_2=0.15$  (a) for the coupled case with  $V_{s-2}=V_{s-1}$ ,  $h_2=1\text{m}$ ,  $15\text{m}$ ,  $25\text{m}$ , (b)  $T_{s1}/T_m$  for  $h_2=15\text{m}$ ,  $V_{s-2}= 25, 75, 150, 300, 500, 5000\text{m/s}$  and (c)  $T_{s-ave}/T_m$  of the results of Figs (a), (b) for (i) the Aegion 1995 seismic motion with  $a_c=0.5\text{m/s}^2$  (ii) Mid-Niigata Prefecture 2004 seismic motion with  $a_c=3\text{m/s}^2$ . Table 4 gives the characteristics of the input motions considered.

It can be observed that if  $u_f$  is plotted in terms of the ratio  $T_{s-ave}/T_m$ , the scatter in results for different  $V_{s2}$  and  $h_2$  decreases considerably. It is inferred that the dynamic effect on  $u_f$  can partly be interpreted by relating  $u_f$  to  $T_{s-ave}$ . In particular, similarly to the response predicted by [16], but by replacing  $T_s$  with  $T_{s-ave}$ , it can be observed that the dynamic response (a) does not exist for  $T_{s-ave}=0$ , (b) as  $T_{s-ave}$  increases, it produces maximum response when  $T_{s-ave}$  approximately when  $T_{s-ave}=T_m$  and (c) as  $T_{s-ave}$  further increases, the dynamic response decreases towards zero.

No	Earthquake Title	$a_{max}$ ( $\text{m/s}^2$ )	Predominant Period ( $T_p$ ) (s)	Mean Period ( $T_m$ ) (s)	Magnitude	Arias Intensity ( $\text{cm/sec}$ )
1	Aegion, 1995	2.1	0.42	0.62	6.1	52
2	Mid-Niigata Prefecture, 2004	5.8	0.52	0.81	6.8	996

Table 4. Characteristics of the input motions considered in Fig. 6.

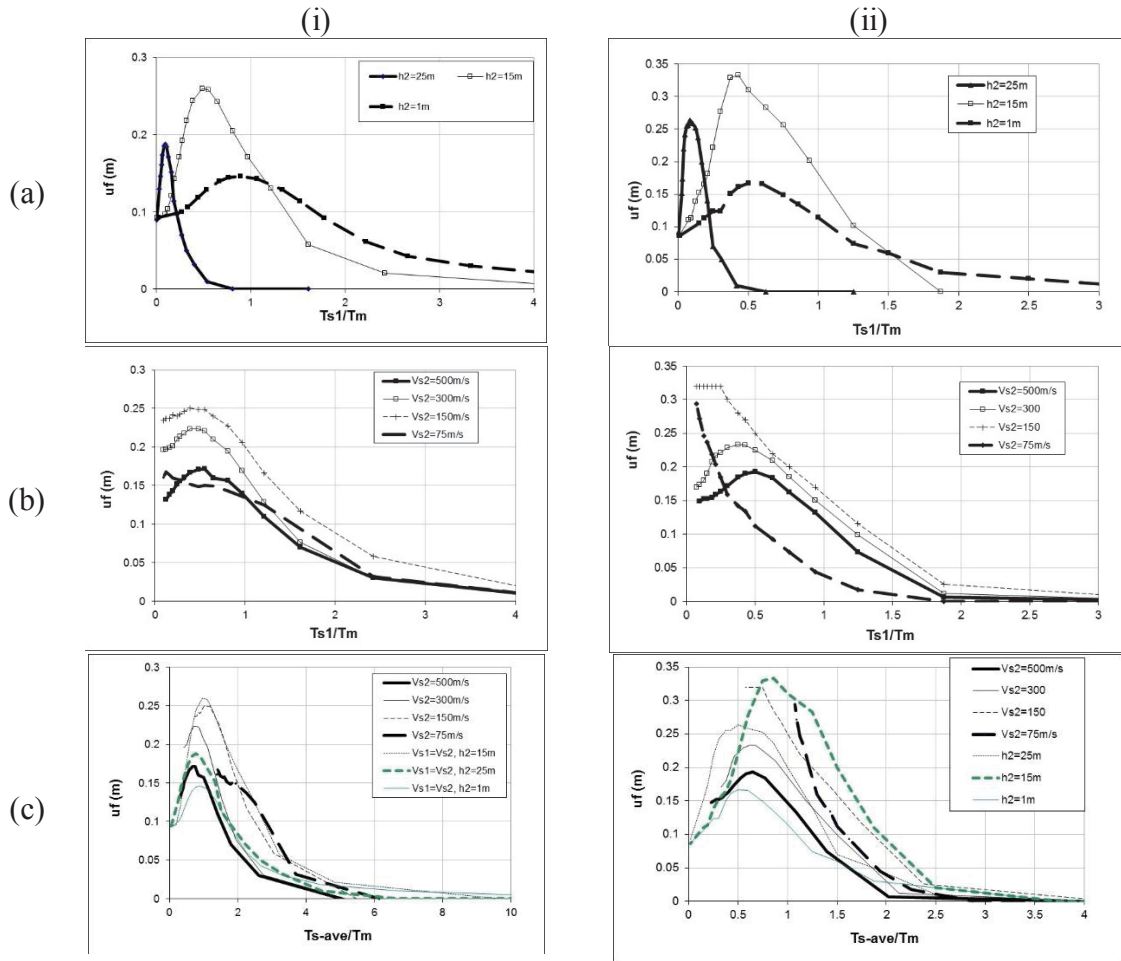


Fig. 6: The computed permanent seismic displacement ( $u_f$ ) versus (a)  $Ts_1/T_m$  for  $h_1+h_2=30m$ ,  $\rho_1=\rho_2=2 \text{ Mg/m}^3$  and  $\lambda_1=\lambda_2=0.15$  (a) for the coupled case with  $V_{s-2}=V_{s-1}$ ,  $h_2=1m, 15m, 25m$ , (b) for the coupled case with  $h_2=15m$ ,  $V_{s-2}=75, 150, 300, 500m/s$  and (c)  $u_f$  versus  $Ts\text{-ave}/T_m$  of the results of Figs (a), (b). For (i) the Aegion 1995 seismic motion with  $ac=0.5m/s^2$  (ii) Mid-Niigata Prefecture 2004 seismic motion with  $ac=3m/s^2$ . Table 4 gives the characteristics of the input motions considered.

#### 4.2 Indicative approximate criterion for de-amplification

According to Fig 6, the seismic displacement decreases and takes values less than  $0.05m$ , at large values of the ratio  $Ts\text{-ave}/T_m$ , and certainly when

$$Ts\text{-ave} / T_m > 4 \quad (6a)$$

According to Eurocode 8 [21] at rock site the dominant period is less than  $0.4 \text{ sec}$ . It is inferred that de-amplification of the seismic response occurs when

$$Ts\text{-ave} > 1.6s \quad (6b)$$

According to equations (4) and (5b), in the canteliver wall of Fig. 2,

$$T_{s-ave} = 4 (H_b/V_{s-b} + h_s/V_{s-s}) \quad (7)$$

Thus, according to eqs. (6b) and (7), for de-amplification of the seismic response

$$4 (H_b/V_{s-b} + h_s/V_{s-s}) > 1.6s \quad (8a)$$

or

$$H_b/V_{s-b} > 0.4s - H_s/V_s \quad (8c)$$

Fig. 7 presents the limit shear wave velocity of the backfill ( $V_{s-b}$ ) in terms of the height of the backfill ( $H_b$ ) and the ratio ( $H_s/V_{s-s}$ ) of the underlying soil satisfying equation (8c). Figure 7 illustrates that the de-amplification effect of the seismic response can be crucial for loose backfill and if the soil underlying the wall is soft and deep. On the other hand, for small ratios of ( $H_s/V_{s-s}$ ) of the underlying soil, smaller than 0.1, the de-amplification requires  $V_{s-b}$  values for the backfill, which are too small for practical application.

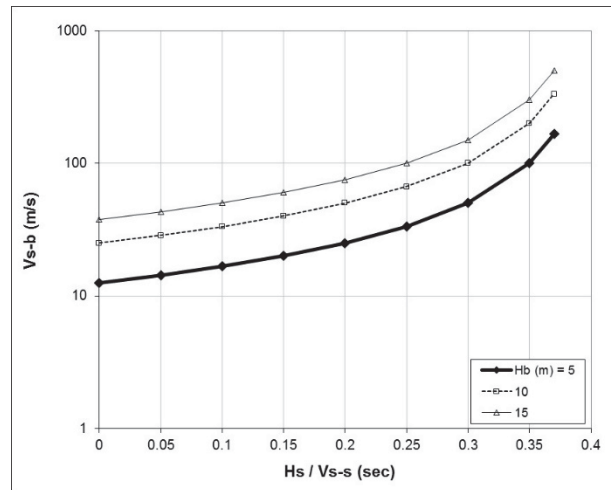


Figure 7: The limit shear wave velocity of the backfill ( $V_{s-b}$ ) in terms of the height of the backfill ( $H_b$ ) and the ratio ( $H_s/V_{s-s}$ ) of the underlying soil satisfying equation (8c).

### 4.3 Proposed smart design method

Typically, in cases where cantilever walls must be designed, the density of the backfill may be selected from loose to dense and this may affect the seismic displacement. Table 5 gives typical values of shear wave velocity [19], frictional resistance [20] and unit density in terms of soil density. Certainly dense construction is more costly and considering the soil strength along the slip surface produces less displacement. However, this may not hold in all cases: the previous section illustrated that considerable de-amplification may occur in softer layers.

The model proposed in section 3 above, which simulates in a cost-effective manner not only the mode of failure and corresponding displacement along the slip surface, but also the dynamic response of the backfill and underlying soil layer, allows the investigation and proposition of smart design of cantilever walls by performing relative parametric analyses. Such analyses are proposed to establish smart design of cantilever walls for given underlying soil conditions, and in particular the density of its backfill. Design seismic motions at the underlying bedrock, representative of the site under consideration, must be applied for this purpose.



	Loose (L)	Medium (M)	Dense (D)
$\phi$ (°)	25	35	40
$V_s$ (m/s)	100	150	350
$\gamma$ (kN/m)	18	20	22

Table 5: Typical values of shear wave velocity [19], frictional resistance [20] and unit density for loose, medium and dense sands used in the analyses.

#### 4.4 Typical example

In order to illustrate smart design of cantilever walls and its dependence to the underlying soil profile, we consider a cantilever wall with the typical properties given in table 6a above three different underlying soil profiles: C1, C1, C3 with properties given in table 6b. The backfill was considered to be in the loose, medium and dense states, with the corresponding properties of table 5. The seismic motion Mid-Niigata Prefecture 2004 was applied at the underlying rock.

##### (a) Wall

Parameter	Value
$W_c$ (kN/m)	112.5
$H_b$ (m)	6
$H_c$ (m)	5.5
$b$ (m)	3
$\phi_c$ (°)	25

##### (b) Underlying soil profile: C1, C1, C3 cases

Parameter	Value		
	C1	C2	C3
$H_s$ (m)	10	50	10
$V_{s-s}$ (m/s)	100	100	300
$\rho_s$ (T/m <sup>3</sup> )	2	2	2

Table 6: Parametric analyses: Model parameters used: (a) Wall and (b) Underlying soil profile: C1, C1, C3 cases

Table 7 presents the results of the parametric analyses and Figure 8 plots the computed ratio of the seismic displacement when the backfill is in the loose and dense states ( $u_{f-loose}/u_{f-dense}$ ), in terms of the ratio  $H_s/V_{s-s}$  of the underlying soil profile. It can be observed that if the ratio  $H_s/V_{s-s}$  is large, which corresponds to the case C2 where the soil underlying the wall is soft and deep, the loose backfill wall gives less seismic displacement and thus, for this case of seismic motion, it is recommended for optimum design.

Case	Loose	Medium	Dense
C1	0.88	0.7	0.61
C2	0.02	0.06	0.08
C3	0.7	0.65	0.36

Table 7: Results of the parametric analyses: The final seismic displacement (in m) in terms of the underlying soil type and the soil density of the backfill.

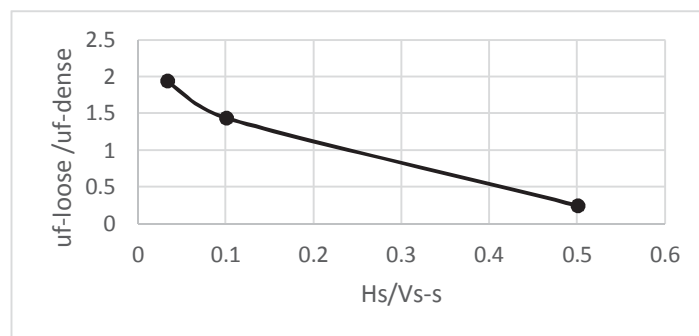


Figure 8: Results of the parametric analyses: The ratio of the seismic displacement when the backfill is in the dense and loose states in terms of the ratio  $H_s/V_{s-s}$

## 5 DISCUSSION

The analysis of the present paper are initial findings of on-going research regarding smart design of cantilever walls. The theoretical work predicting the critical acceleration of cantilever walls may be generalized considering walls of more general geometry and strength. The proposed method predicting the seismic displacement of cantilever walls considering the dynamic response of the soil profile may be (i) improved by considering the non-linear soil response [22] and (ii) verified by the comparison of predictions with results of relative elaborate numerical analyses [11]. Furthermore, smart design of cantilever walls recommendations may be established more adequately by performing extensive parametric analyses where different soil profiles are studied and more seismic motions are applied.

## 6 CONCLUSIONS

The paper considers the cantilever wall of the geometry of Fig. 2 and (a) proposes a method predicting the critical acceleration value in section 2, (b) proposes a method predicting the seismic displacement considering the dynamic response of the soil profile in section 3 and (c) studies the de-amplification effect and proposes a methodology for smart design in section 4. The work illustrated that the de-amplification effect of the seismic response may be crucial if the soil underlying the wall is soft and deep and in this case a wall with a looser backfill may be preferable.

## REFERENCES

- [1] Whitman R. V. Predicting earthquake-caused permanent deformations of earth structures, article on "Predictive Soil Mechanics", Thomas Telford, London, 729-741, 1993.
- [2] Kloukinas P., Mylonakis G. Rankine Solution for seismic earth pressures on L-shaped retaining walls, 5ICEGEAt: Santiago, Chile, January, 2011
- [3] Kloukinas P., Scotto di Santolo A., Penna A., Dietz M., Evangelista A., Simonelli L., Taylor C., Mylonakis G. Investigation of seismic response of cantilever retaining walls:

- Limit analysis vs shaking table testing. *Soil Dynamics and Earthquake Engineering*, Volume 77, October, 432-445, 2015.
- [4] Newmark, N. M. Effects of earthquakes on dams and embankments. *Geotechnique*, 55 (2), 139-159, 1965.
- [5] Ambraseys N. and Menu J. Earthquake induced ground displacements, *Earthquake engineering and structural dynamics*, 16, 7, 985-1006, 1998.
- [6] Jibson R. W. Regression models for estimating coseismic landslide displacement *Engineering Geology* 91, 209–218, 2007.
- [7] Mononobe, N. and Matsuo, H. On the determination of earth pressures during earthquakes, *Proc., World Engineering Congress*, 1929.
- [8] Okabe, S. General Theory of earth pressures. *J. of Japan Society of Civil Engineering*, 12 (1), 1926.
- [9] Richards R, Elms D. Seismic behaviour of gravity retaining walls. *J Geotech Eng Division ASCE* 105 (4), 449–464, 1979.
- [10] Stamatopoulos C. A., Velgaki E. G. Critical acceleration and seismic displacement of vertical gravity walls by a two body model. *Fourth international conference on recent advances in geotechnical earthquake engineering and soil dynamics*. San Diego, CA, March 26–31 (on CD), 2001.
- [11] Stamatopoulos C.A., Velgaki E.G., Modaressi A., Lopez-Caballero F. Seismic Displacement of Gravity Walls by a Two-body Model. *Bulletin of Earthquake Engineering* volume 4, pages 295–318, 2006.
- [12] Lin J.-S., and Whitman, R.V. Decoupling Approximation to the evaluation of earthquake-induced plastic slip in earth dams. *Earthquake Engineering and Structural Dynamics*, 11: 667–678, 1983.
- [13] Katsenis L.C., Stamatopoulos C.A., Panoskaltsis V.P. Non-linear dynamic seismic sliding movement of dry slopes, *COMPdyn 2019, 7th International Conference on Computational Methods in Structural Dynamics and Earthquake Engineering*, 24-26 June, Crete, Greece, 2019.
- [14] Katsenis L.C., Stamatopoulos C.A., Panoskaltsis V.P. Prediction of large seismic sliding movement of slopes using a 2-body non-linear dynamic model with a rotating stick-slip element, February, *Soil Dynamics and Earthquake Engineering*, 2020.
- [15] Stamatopoulos C. A., Velgaki E. and Sarma S. (2000). Sliding-block back analysis of earthquake-induced slides. *Soils and foundations*, The Japanese Geotechnical Society, Vol. 40, No. 6, Dec., 61-75, 2000.
- [16] Dahlquist G, Bjorck A, (translated by Anderson N.). *Numerical methods*. Prentice-Hall Inc., NJ, 1974.
- [17] Rathje E. M. and Bray J. D. An examination of simplified earthquake induced displacement procedures for earth structures. *Can. Geotech. J.* 36: 72–87, 1999
- [18] Vijayendra, K.V., Prasad, S.K., Nayak, S. *Computation of Fundamental Period of Soil Deposit: A Comparative Study*, Oxford, UK, second edition, Indian Geotechnical Conference, December 16-18, 2010.

- [19] Kausarian H. Rock Mass, Geotechnical and Rock Type Identification Using SASW and MASW Methods at Kajang Rock Quarry, Semenyih, Selangor Darul Ehsan. *Journal of Ocean, Mechanical and Aerospace, Science and Engineering-*, Vol.26 December 30, 2015,
- [20] Bery A. and Saad R. Tropical Clayey Sand Soil's Behaviour Analysis and Its Empirical Correlations via Geo-physics Electrical Resistivity Method and Engineering Soil Characterizations. *International Journal of Geo-sciences*, Vol. 3, No. 1, 111-116, 2012.
- [21] European Standard (2003). Eurocode 8: Design of structures for earthquake resistance, Final Draft, prEN 1998-5, December, 2003.
- [22] Vucetic M. And Dobry R. Effect of soil plasticity on cyclic response, *Journal of the Geotechnical Division, ASCE*, 117 (1), 1991.

## COMPARISON OF CONTROL ALGORITHMS APPLIED TO AN HYBRID MASS DAMPER ATTACHED TO A WIND TURBINE TOWER

Pedro H. Q. Rocha<sup>1</sup>, Suzana M. Avila<sup>1</sup>

<sup>1</sup>PPG - Integrity of Engineering Materials, University of Brasília Área Especial Indústria and Projeção  
A – UnB, 72.444-240, DF/Gama, Brasil  
e-mail: rochapedroeng@gmail.com, avilas@unb.br

---

### Abstract

*The structural control, basically, promotes a change in the damping and stiffness properties of the structure, either by the addition of external devices or by the action of external forces. It can be classified as: passive control, active control, hybrid control or semi-active control (Soong & Dargush, 1997). The hybrid mass damper (HMD) is a system that deals with the combination of a tuned mass damper (TMD) with an active control actuator. In addition to requiring lower control forces and maintaining its efficiency over a long range of frequencies, this system has a more robust and reliable control, when compared to active and passive alone (Collette & Chesné, 2016). Among the structures, the wind turbine stands out, which is supported by towers, which due to its geometry and height, are slender, flexible and can suffer excessive levels of vibration caused by the operation of the turbine, as well as by external forces (Woude & Narasimhan, 2014). In this work it is proposed the application of a structural control system, in the way of HMD, to protect a wind tower with theoretical dimensions and with a simplified as single degree of freedom model, submitted to wind and seismic loads that leads to levels of undesirable vibrations that may compromise the safety and integrity of the structure. In addition, it is proposed to compare the performances obtained from the system without control and by the Instantaneous Optimal Control (IOC), Proportional Integral Derivative (PID) and Linear Quadratic Regulator (LQR) controllers with numerical simulations performed using the MAPLESOFT, MATLAB and its Simulink control toolbox. The results obtained numerically were analyzed and compared with each other, and it was observed that HMD was efficient in reducing the dynamic response of the tower. Although it is a preliminary model, it is a basis for studies in this area to evolve into a more sophisticated model and full-scale applications.*

**Keywords:** Hybrid mass damper; Wind Turbine; Seismic; Instantaneous Optimal Control; Proportional Integral Derivative; Linear Quadratic Regulator.

---

## 1 INTRODUCTION

According to GWEC [1], despite being a pandemic year, 2020 was a record year of wind growth with an estimated 82.3 GW of new wind energy capacity globally, according to initial calculations by GWEC, which represents an increase of 36% in installations.

This expansive growth on energy generation is reflected to technological development, as well as in the development of increasingly tall and slender wind turbines, and as a consequence, these turbines can suffer severe dynamic excitations, thus reaching the service limit state for excessive vibrations [2, 3].

One way to reduce excessive vibration levels, maintain the stability and safety of systems and avoid collapse is to use the structural control solution, which can be classified into four categories, such as passive, active, hybrid and semi-active control. These four categories are based on applying external corrective forces or on the installation of external devices in order to reduce the levels of vibrations experienced by the structures and/or promoting variations in stiffness and damping properties of the main structure [4].

Each structural control category has a specific characteristic and can have more than one control method. The hybrid control has characteristics of passive control added to active control ones, always with the aim of increasing the performance of the system when compared, with a purely passive control. Making also the system less dependent on energy, when compared with the active control alone. The hybrid control uses actuators and energy dissipators [5].

According to Bhaiya [6] and Hu and He [7], the hybrid controller has a wider frequency range than the passive controller, making it more efficient and requiring less force than the active one, which reduces the cost of the system. In the case of a power failure or failure of the active control component, the passive component of the hybrid control still offers some level of protection. The hybrid mass damper (HMD) is the combination of a tuned mass damper (TMD) with an active control actuator [8, 9].

S. Xie, X. Jin, J. He et al. [10] developed a numerical model of a reduced-order offshore wind turbine, subjected to wind loads, sea waves and earthquakes for hybrid control. The authors found that the HMD system can better reduce the displacement from the top of the tower compared to the passive TMD system before and during earthquakes, although the need of high input control power and large displacements of the TMD.

D. Lima, P. López-Yáñez and M. Pereira [11] presented a vibration control device design for a 120-meter-high steel tubular tower for a wind turbine. Three types of absorbers were then studied comparatively: tuned mass damper (TMD), active mass damper (AMD) and hybrid mass damper (HMD). They used the Linear Quadratic Regulator (LQR) to obtain the optimal control variables introduced by the actuators hydraulic. It was found that the HMD achieves excellent levels of vibration reduction for the tower subjected to harmonic actions, in a transient and permanent (stationary) regime, resonant to the first mode of vibration of the structure without control.

M. Rahman, Z. Ong, Zhi Chao, W. Chong et al. [12] implements a proportional derivative integral controller (PID) designed and optimized to find the ideal required force for actuators and, therefore, reduce the vibration of the wind generator tower. The active vibration control system with an optimized PID controller in the wind turbine tower offered a higher rate of vibration reduction under different loads compared to the uncontrolled and passive control system.

Yanik [13] makes a comparison between the LQR controller and the Instantaneous Optimal Controller (IOC) using seismic forcing for a semi-active system applied in a 3-storey building and a 5-storey building.



In this work it is proposed the application of a structural control system, considering a HMD, to protect a wind tower with theoretical dimensions considering a simplified single degree of freedom model. It is submitted to wind and seismic loads that leads to levels of undesirable vibrations that may compromise the safety and reliability of the structure. In addition, it is proposed to compare the performances obtained from the system without control and with an HMD using different controllers: Instantaneous Optimal Control (IOC), Proportional Integral Derivative (PID) and Linear Quadratic Regulator (LQR) through numerical simulations.

## 2 MATHEMATICAL FORMULATION

The large wind turbine studied in this work is composed of a tall, slender and flexible tower that supports the blades and nacelle at the top. The system has infinite degrees of freedom, however, through a modal reduction technique, it is possible to model it as a discrete system with multiple degrees of freedom (MDOF) [14]. The effects of rotating the blades and their vibrations in the *flapwise* and *edgewise* directions are not considered in this preliminary model [2]. This structure can be modeled as a system having  $N$  degrees of freedom with a TMD device installed and subjected to external dynamic excitation [15]. Figure 1 represents the turbine and the system modelled as a cantilever beam with a tip mass.

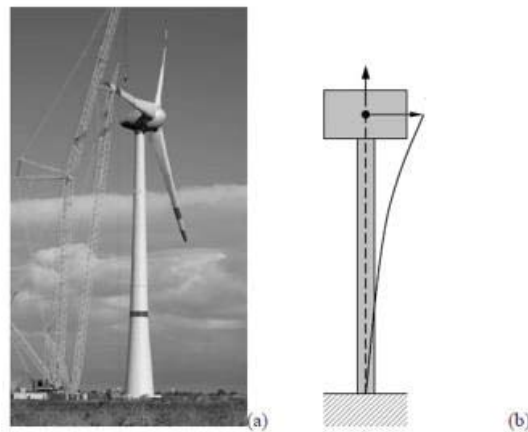


Figure 1. (a) Tubular structures of steel tower of wind turbines; (b) Schematic description of a cantilever beam with a tip mass [2].

In systems with multiple degrees of freedom, it is possible to reduce the structural response to a single degree of freedom and obtain the structural response for structural systems that vibrate mainly on a single mode, usually the first [4, 8, 14].

Although the structural model of the wind turbine has multiple degrees of freedom, the system under study was reduced to a single degree of freedom [4] and a hybrid tuned mass damper was added to the top of the turbine, which is connected to the main system with the intention of decreasing the amplitude of the structure vibration [2, 4].

The main system representing a wind turbine, reduced to a single degree of freedom associated with an HMD, shown in Figure 2, has two degrees of freedom, where  $\mathbf{M}_1$  is the mass,  $\mathbf{K}_1$  is the stiffness and  $\mathbf{C}_1$  is the damping of the main system, while  $\mathbf{M}_2$  is the upper mass of HMD,  $\mathbf{K}_2$  is the stiffness of HMD and  $\mathbf{C}_2$  is the damping of HMD,  $\mathbf{F}(t)$  is the dynamic load applied on the structure,  $\mathbf{u}(t)$  is the control force, while  $\mathbf{y}(t)$  and  $\mathbf{z}(t)$

are the horizontal displacements of the main system and the HMD, respectively.

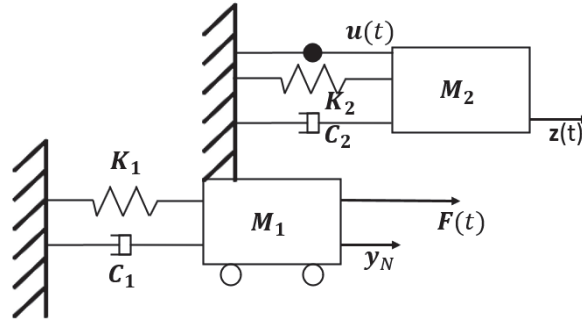


Figure 2. Two degrees of freedom model: main system + mass damper tuned with  $u(t)$  (HMD) actuator [16].

The equations of motion of the main system with a connected HMD, including the force applied to the base of the structure  $g(t)$ , and control force  $u(t)$  is given by (2):

$$M_1 \ddot{y}(t) + C_1 \dot{y}(t) + K_1 y(t) = F \quad (1)$$

$$M_2 \ddot{z}(t) + C_2 \dot{z}(t) + K_2 z(t) = -M_2 \ddot{y}(t) + g(t) + u(t) \quad (2)$$

Three control algorithms were used to calculate the control force  $u(t)$  in order to compare their performances: Linear Quadratic Regulator (LQR), Proportional, Integral, Derivative (PID) and Instantaneous Optimal Control (IOC). The Optimal Control aims to control the dynamic system at a minimum cost, the optimization process is performed through the Linear Quadratic Regulator (LQR). The LQR can be presented as a regulator that stabilizes the system's response. It is a controller capable of optimizing through control considering the constraints of a cost function and uses all states of the system for feedback, while the gain of control is selected in a way that the performance index subjected to the constraints of the system state equation is minimized [17, 18]. Although the LQR controller deals better with systems with multiple inputs and multiple outputs, on the other hand it has certain difficulties in defining the cost function and the weighting matrices [19, 20].

For modeling the LQR controller, it is necessary to represent the equations of motion of the system in state space form, according to the state equation (3) and the output equation (4) for  $n$  degrees of freedom.

Where  $A$  is the state matrix,  $B$  is the input matrix,  $C$  is the output matrix and  $D$  is the direct transmission matrix. Equations (5) and (6) represent the equations of motion of the system under study in this work in the state space.

$$\dot{x}(t) = Ax(t) + Bu(t) \quad (3)$$

$$y(t) = Cx(t) + Du(t) \quad (4)$$

$$\begin{bmatrix} \dot{X}_1 \\ \dot{X}_2 \end{bmatrix} = \begin{bmatrix} 0 & I \\ -M^{-1}K & -M^{-1}C \end{bmatrix} \begin{bmatrix} X_1 \\ X_2 \end{bmatrix} + \begin{bmatrix} 0 \\ M^{-1} \end{bmatrix} u \quad (5)$$

$$Y = [1 \quad 0 \quad 0 \quad 0] \begin{bmatrix} X_1 \\ X_2 \end{bmatrix} + \begin{bmatrix} 0 \\ 0 \end{bmatrix} \quad (6)$$

For structural control, the classical optimal control problem consists in finding the control vector  $\mathbf{u}(t)$  that minimizes the quadratic performance index [21]:

$$J = \int_{t_0}^{t_f} [\mathbf{x}^T(t) \mathbf{Q} \mathbf{x}(t) + \mathbf{u}^T(t) \mathbf{R} \mathbf{u}(t)] dt \quad (7)$$

where  $\mathbf{Q}$  is a real, symmetrical and positive semi-defined  $2n \times 2n$  real, matrix and  $\mathbf{R}$  is a real, symmetric and positive defined  $m \times m$  matrix. The matrices  $\mathbf{Q}$  and  $\mathbf{R}$  are weighting matrices, whose magnitudes are defined according to the relative importance given to the state variables and the control forces in the minimization process.

According to Meirovitch [21], in structural applications, the Riccati matrix,  $\mathbf{P}(t)$  can be approximated by a constant matrix  $\mathbf{P}$ . The minimization of the index falls on the solution of the Riccati equation.

$$\mathbf{P}\mathbf{A} - \frac{1}{2}\mathbf{P}\mathbf{B}\mathbf{R}^{-1}\mathbf{B}^T\mathbf{P} + \mathbf{A}^T\mathbf{P} + 2\mathbf{Q} = 0 \quad (8)$$

Having knowledge of the weighting matrices  $\mathbf{Q}$  and  $\mathbf{R}$ , it is possible to obtain the control gain, that is  $\mathbf{G}$  given by

$$\mathbf{G} = -\frac{1}{2}\mathbf{R}^{-1}\mathbf{B}^T\mathbf{P} \quad (9)$$

The optimal control law establishes a linear relationship of the control vector  $\mathbf{u}(t)$ .

$$\mathbf{u}(t) = \mathbf{G}\mathbf{x}(t) = -\frac{1}{2}\mathbf{R}^{-1}\mathbf{B}^T\mathbf{P}\mathbf{x}(t) \quad (10)$$

When  $\mathbf{x}(t)$  is known,  $\mathbf{u}(t)$  can be obtained through equation (10) generating a closed loop system.  $\mathbf{H}\mathbf{f}(t)$  is the portion related to external loading. The behavior of the optimally controlled structure is described by

$$\dot{\mathbf{x}}(t) = \mathbf{A}\mathbf{x}(t) + \mathbf{B}\mathbf{u}(t) + \mathbf{H}\mathbf{f}(t) \quad (11)$$

$$\dot{\mathbf{x}}(t) = (\mathbf{A} + \mathbf{B}\mathbf{G})\mathbf{x}(t) + \mathbf{H}\mathbf{f}(t) \quad (12)$$

It can be seen that the effect of closed loop control is to change the state matrix of the system from  $\mathbf{A}$  (open loop system) to  $\mathbf{A} + \mathbf{B}\mathbf{G}$  (closed loop system).

Another controller used in the comparison of the present work was the Proportional Integral Derivative (PID), this controller features the use of closed loop control loop feedback to keep the actual output of a process as close as possible to the destination output or setpoint [19].

The MATLAB control system's *Simulink* toolbox provides algorithms and applications for systematically analyze, design and adjust linear control systems. It is possible to specify a system as a transfer function, status space, zero pole gain or frequency response model.

The response of the PID controller was calculated using *Simulink* using the closed loop block diagram with the insertion of external forces such as wind and earthquake.

The transfer function of the system in relation to the HMD installed on top of the wind turbine, presents the ratio between the displacement of the main system (output) and the control force (input). Figure 3 represents a block diagram of *Simulink* with PID control under the action of external forces.

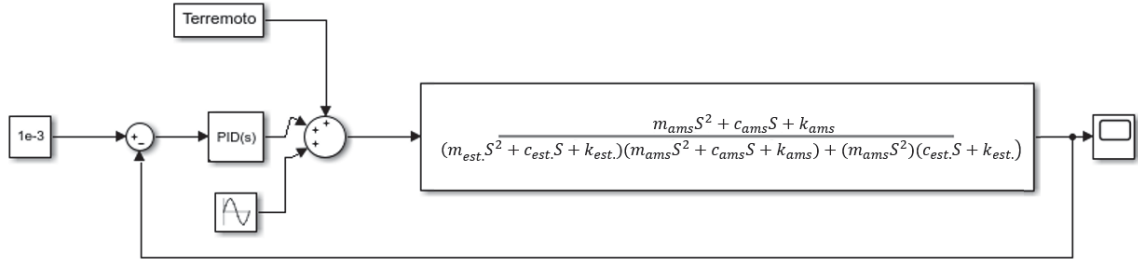


Figure 3. Closed loop block diagram with PID [16].

The instantaneous optimal control (IOC) is a variation of the classic optimal control aiming at computational cost savings since it does not require the solution of the Riccati equations [20]. For this controller, the same formulation of the equations of motion of the system was used in the form of state equations of state shown previously eq. (3) and eq. (4). This algorithm is easier to implement, since it is not necessary to calculate the Riccati matrix [8].

The quadratic performance index, represented by eq. (13), is minimized in each instant of time,

$$J(t) = \mathbf{x}^T(t) \mathbf{Q} \mathbf{x}(t) + \mathbf{u}^T(t) \mathbf{R} \mathbf{u}(t) \quad (13)$$

where  $\mathbf{T}$  is the modal matrix, whose columns are the eigenvectors of  $\mathbf{A}$ .

$$\mathbf{x}(t) = \mathbf{T} \mathbf{w}(t) \quad (14)$$

From the decoupled state equations, the diagonal matrix with the eigenvalues of  $\mathbf{A}$  is obtained.

$$\mathbf{\Lambda} = \mathbf{T}^{-1} \mathbf{A} \mathbf{T} \quad (15)$$

Over a short time step  $\Delta t$ , the modal state vector  $\mathbf{x}(t)$  can be expressed as

$$d(t - \Delta t) = \exp(\mathbf{\Lambda} \Delta t) \mathbf{T}^{-1} \left\{ \mathbf{x}(t - \Delta t) + \frac{\Delta t}{2} [\mathbf{B} \mathbf{u}(t - \Delta t) + \mathbf{H} \mathbf{f}(t - \Delta t)] \right\} \quad (16)$$

The weighting matrices  $\mathbf{Q}$  and  $\mathbf{R}$  are also arbitrarily defined in the IOC case, they influence the control force and the displacement suffered represented by equations (17) and (18), respectively.

$$\mathbf{u}(t) = -\frac{\Delta t}{2} \mathbf{R}^{-1} \mathbf{B}^T \mathbf{Q} \mathbf{x}(t) \quad (17)$$

$$\mathbf{x}(t) = \left[ \mathbf{I} + \frac{\Delta t^2}{4} \mathbf{B} \mathbf{R}^{-1} \mathbf{B}^T \mathbf{Q} \right]^{-1} \left[ \mathbf{T} d(t - \Delta t) + \frac{\Delta t}{2} \mathbf{H} \mathbf{f}(t) \right] \quad (18)$$

The optimized control force was calculated according to the procedures used by S.

Avila and P. Gonçalves [22].

### 3 RESULTS

In this, it is considered a wind turbine, previously studied by S. Avila, M. Shzu, M. Morais et al. [2]. The structure was reduced to a single degree of freedom model and subjected to the following loads: earthquake El Centro [23]; harmonic loading  $f(t) = 2500\sin(\omega t)$  applied at the top of the tower. The mass, damping and stiffness properties of the structure are, respectively,  $M_1 = 34,899,00$  kg,  $C_1 = 0,00$  Ns/m and  $K_1 = 463,671,00$  N/m. HMD properties were calculated using Den Hartog equations [24]:  $M_2 = 967,98$  kg,  $C_2 = 427,6724$  Ns/m and  $K_2 = 8,9096 \times 10^3$  N/m. The damping ratio,  $\zeta$ , is assumed to be 2% of the critical value.

Initially, the controller of the LQR type had the control force in the HMD actuator calculated and one of the factors that influence the achievement of good results through this algorithm is the choice of the weighting matrices  $Q$  and  $R$ . The values of the coefficients of the weighting matrices  $Q$  and  $R$  are defined according to the relative importance given to state variables and control forces in the minimization process [21, 22]. The weighting matrices used in the analysis were as follows:

$$Q = \begin{bmatrix} 10^{10} & 0 & 0 & 0 \\ 0 & 10^2 & 0 & 0 \\ 0 & 0 & 10^2 & 0 \\ 0 & 0 & 0 & 1 \end{bmatrix} \quad (19)$$

$$R = [1] \quad (20)$$

The LQR was performed using a function from the MATLAB library and still using a closed-loop block diagram using the Matlab Simulink toolbox. Figure 4 represents the block diagram of the LQR controller for the hybrid mass damper under the action of wind force (represented by the sinusoidal excitation) and seismic excitation (represented by the El Centro earthquake), where  $A$  is the state matrix,  $B$  is the input matrix,  $C$  is the output matrix and  $G$  is the gain.

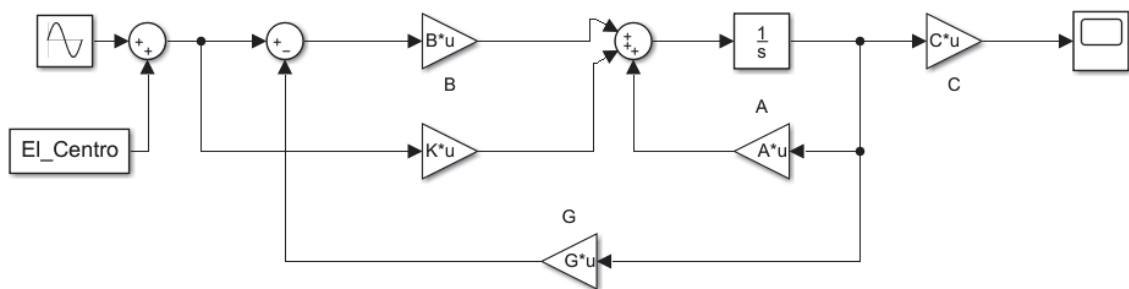


Figure 4. Block diagram of the LQR controller with HMD [16].

The displacement time history of the main structure is shown in Figure 5, comparing the use of a tuned mass damper (TMD) and an HMD, considering seismic and wind excitations with LQR controller. It can be seen that the HMD demonstrated an excellent performance, reducing, approximately, up to 6 times the amplitude of vibration presented with the passive control (TMD), when compared to the HMD.

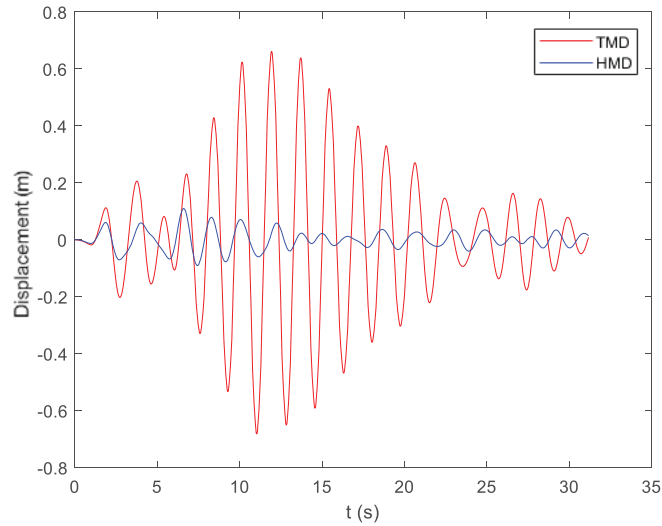


Figure 5. Time history displacement of the main system (comparative AMS x HMD) [16].

Then, numerical simulations are performed using the PID controller to obtain the HMD control force and the displacement of the main system [16]. The gains of the PID controller were obtained through the MATLAB computer package tuning tools and the Simulink toolbox. Figure 6 presents the block diagram for system analysis with HMD using the PID controller to calculate the control force. The system is subjected to the same wind and earthquake excitations, through the PID block and the transfer function of the hybrid system.

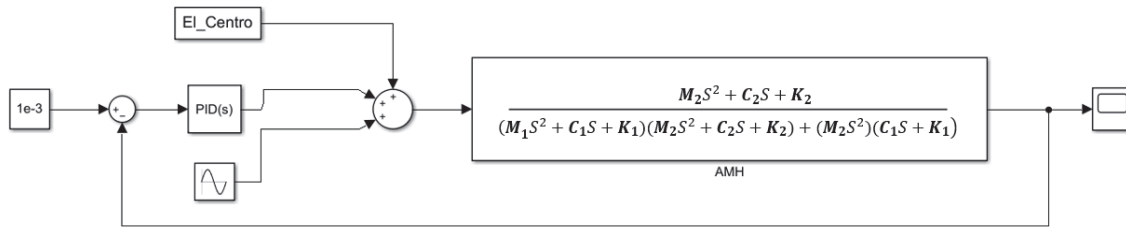


Figure 6. Block diagram of the PID controller with HMD [16].

Figure 7 shows the comparison of the response, in terms of the evolution of displacement, for the HMD, of the main system using the system without control and the LQR and PID controllers. It is possible to observe that the LQR controller has a better performance than the PID controller, with a reduction, compared to the uncontrolled system response, of approximately 63% and 43%, respectively.



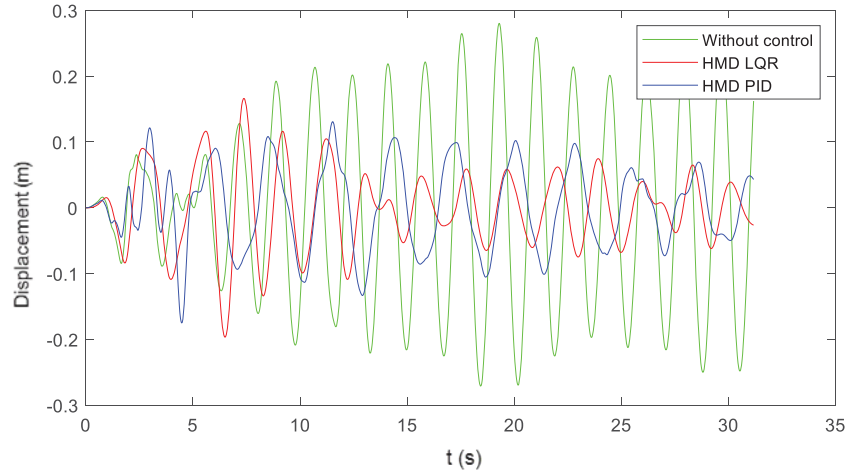


Figure 7. Time history displacement of the HMD using the LQR and PID controllers [16].

The *rms* displacement value, for the HMD, obtained for the system without control was 0.2098 m, while for the system with LQR controller, the displacement was 0.04506 m and for the PID it was 0.09592 m. For the LQR and PID controllers, there was a reduction in the *rms* response of approximately 78.5% and 54.2%, respectively.

Figure 8 presents the comparison of the evolution in time of the control force required in the LQR and PID controllers, where the maximum required force is 28030 N and 2735 N, respectively. It appears that the required control force, using the LQR, was approximately 10 times greater than the control force obtained with the PID controller.

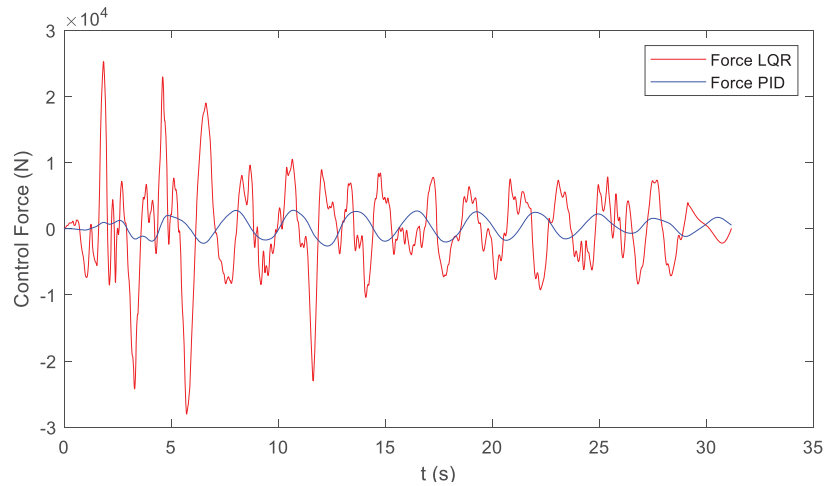


Figure 8. Time evolution of the control force required in the LQR and PID [16].

The IOC also needs an adjustment in the weighting matrices, where equations (21) and (22) present the matrices  $\mathbf{Q}$  and  $\mathbf{R}$ , respectively.

$$\mathbf{Q} = \begin{bmatrix} 0 & 0 & 0 & 0 \\ 0 & 0 & 0 & 0 \\ 6.654 * 10^3 & 0 & 0 & 0 \\ 1 * 10^{-3} & 0 & 0 & 0 \end{bmatrix} \quad (21)$$

$$\mathbf{R} = [1000000] \quad (22)$$

For the IOC algorithm, the calculations were performed using MATLAB, where it was possible to obtain the answer in a time range of 600 s. Figure 9 shows the evolution in time of the displacement of the main structure controlled by an HMD with an IOC controller. It is possible to observe that the amplitude of the response has an order of magnitude ten times smaller than those obtained in the simulations with the LQR and PID controllers.

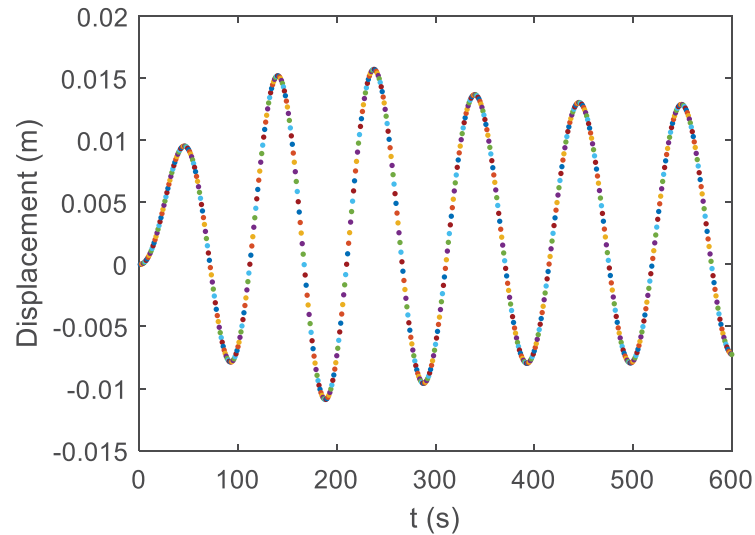


Figure 9. Time history displacement of the structure controlled by an HMD using the IOC controller.

Figure 10 represents the force response required by the IOC to control the dynamic response. It appears that the order of magnitude of the control force is a thousand times smaller compared to those corresponding to the LQR and PID controllers.

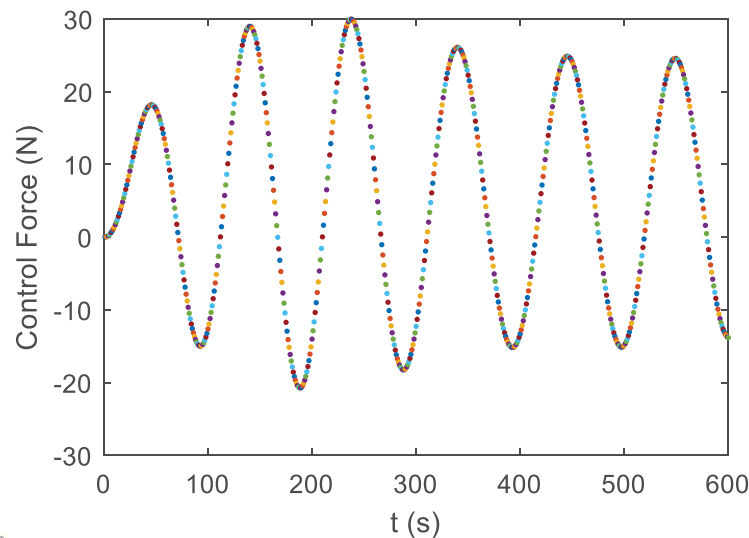


Figure 10. Time evolution of the control force required by the IOC controller.

## 4 CONCLUSION

In this work, the use of an hybrid mass damper for the analysis of the dynamic response and required control force of a wind tower model is studied. Three controllers are compared: LQR, PID and IOC. The analysis are performed using the wind turbine parameters model presented by S. Avila, M. Shzu, M. Morais et al. [2]. The results are obtained through numerical analysis considering dynamic excitations of wind and earthquake.

Although the LQR controller has a better response and a lower rms value than the PID, the two controllers reduce the system response satisfactorily. The IOC controller reduces the displacement of the system by up to 10 times and the force required to control the system is in the order of a thousand times less than the previous controllers.

It can be seen, therefore, that of the three controllers analyzed, the IOC was the one that presented the best performance, without adding computational effort. It even has the advantage of not relying on the solution of the Riccati problem, which can be computationally costly in the case of problems with a higher order. However, its efficiency is quite sensitive to the choice of suitable weighting matrices. For future work, it is interesting to carry out experimental studies using the Hardware in the Loop methodology to consolidate the comparative study.

**Acknowledgements.** The authors of this research are grateful for the financial support of the Coordination for the Improvement of Higher Education Personnel (CAPES) and the Post-Graduate Decanate of the University of Brasília (DPG-UnB).

**Authorship statement.** This section is mandatory and should be positioned immediately before the References section. The text should be exactly as follows: The authors hereby confirm that they are the sole liable persons responsible for the authorship of this work, and that all material that has been herein included as part of the present paper is either the property (and authorship) of the authors, or has the permission of the owners to be included here.

## REFERENCES

- [1] A. Pek, “A gust of growth in China makes 2020 a record year for wind energy,” 2021. <https://gwec.net/a-gust-of-growth-in-china-makes-2020-a-record-year-for-wind-energy/> (accessed Feb. 20, 2021).
- [2] S. M. Avila, M. A. M. Shzu, M. V. G. Morais, and Z. J. G. Del Prado, “Numerical modeling of the dynamic behavior of a wind turbine tower,” *J. Vib. Eng. Technol.*, vol. 4, no. 3, pp. 249–257, 2016.
- [3] P. Liu and C. Y. Barlow, “Wind turbine blade waste in 2050,” *Waste Manag.*, vol. 62, no. February, pp. 229–240, 2017, doi: 10.1016/j.wasman.2017.02.007.
- [4] T. T. Soong and G. F. Dargush, *Passive energy dissipation systems in structural engineering*. Chichester, 1997.
- [5] A. S. Ahlawat and A. Ramaswamy, “Multi-objective optimal design of FLC driven hybrid mass damper for seismically excited structures,” *Earthq. Eng. Struct. Dyn.*, vol. 31, no. 7, pp. 1459–1479, 2002, doi: 10.1002/eqe.173.

- [6] V. Bhaiya, S. D. Bharti, M. K. Shrimali, and T. K. Datta, "Hybrid seismic control of buildings using tuned mass and magnetorheological dampers," *Proc. Inst. Civ. Eng. Struct. Build.*, vol. 173, no. 7, pp. 471–487, 2018, doi: 10.1680/jstbu.18.00090.
- [7] Y. Hu and E. He, "Active structural control of a floating wind turbine with a stroke-limited hybrid mass damper," *J. Sound Vib.*, vol. 410, pp. 447–472, 2017, doi: 10.1016/j.jsv.2017.08.050.
- [8] S. M. Avila, "Controle Híbrido para Atenuação de Vibrações em Edifícios," Pontífica Universidade Católica do Rio de Janeiro, 2002.
- [9] G. B. Colherinhas, M. V. G. De Moraes, M. A. M. Shzu, and S. M. Avila, "Optimal Pendulum Tuned Mass Damper Design Applied to High Towers Using Genetic Algorithms: Two-DOF Modeling," *Int. J. Struct. Stab. Dyn.*, vol. 19, no. 10, pp. 1–17, 2019, doi: 10.1142/S0219455419501256.
- [10] S. Xie, X. Jin, J. He, J. Gao, C. Zhang, and Y. Yan, "Applying multiple tuned mass dampers to control structural loads of bottom-fixed offshore wind turbines with inclusion of soil-structure interaction," *Ocean Eng.*, vol. 205, no. September 2018, p. 107289, 2020, doi: 10.1016/j.oceaneng.2020.107289.
- [11] D. M. de Lima, P. A. López-Yáñez, and M. A. Pereira, "Vibration control device for steel tubular towers of horizontal axis wind turbines," *Lat. Am. J. Solids Struct.*, vol. 16, no. 6, pp. 1–21, 2019, doi: 10.1590/1679-78255436.
- [12] M. Rahman, Z. C. Ong, W. T. Chong, S. Julai, and X. W. Ng, "Wind Turbine Tower Modeling and Vibration Control Under Different Types of Loads Using Ant Colony Optimized PID Controller," *Arab. J. Sci. Eng.*, vol. 44, no. 2, pp. 707–720, 2019, doi: 10.1007/s13369-018-3190-6.
- [13] A. Yanik, "Seismic control performance indices for magneto-rheological dampers considering simple soil-structure interaction," *Soil Dyn. Earthq. Eng.*, vol. 129, no. November 2019, p. 105964, 2020, doi: 10.1016/j.soildyn.2019.105964.
- [14] P. J. Murtagh, B. Basu, and B. M. Broderick, "Simple models for natural frequencies and mode shapes of towers supporting utilities," *Comput. Struct.*, vol. 82, no. 20–21, pp. 1745–1750, 2004, doi: 10.1016/j.compstruc.2004.04.005.
- [15] J. A. Guimarães, "Análise Dinâmica de Torre Eólica e Dimensionamento de Amortecedor de Massa Sintonizada," Instituto Politécnico de Bragança, 2020.
- [16] P. H. Q. Rocha and S. M. Avila, "Vibration control of a wind turbine with a hybrid mass damper," *Proc. Ibero-Latin-American Congr. Comput. Methods Eng.*, p. 6, 2020.
- [17] M. Alves Melo, "Análise Comparativa de Estratégias para Suspensão Semiativa em um Modelo de 1/4 de Veículo," 2017.
- [18] K. S. Park, H. M. Koh, and S. Y. Ok, "Active control of earthquake excited structures using fuzzy supervisory technique," *Adv. Eng. Softw.*, vol. 33, no. 11–12, pp. 761–768, 2002, doi: 10.1016/S0965-9978(02)00044-3.
- [19] S. Etedali, M. R. Sohrabi, and S. Tavakoli, "An Independent Robust Modal PID Control Approach for Seismic Control of Buildings," *J. Civ. Eng. Urban.*, vol. 3, no. 5, pp. 279–291, 2013.

- [20] J. C. Wu, J. N. Yang, and W. E. Schmitendorf, “Reduced-order  $H_\infty$  and LQR control for wind-excited tall buildings,” *Eng. Struct.*, vol. 20, no. 3, pp. 222–236, 1998, doi: 10.1016/S0141-0296(97)00081-3.
- [21] L. Meirovitch, *DYNAMICS AND CONTROL OF STRUCTURES*, vol. 53, no. 9. New York, 1990.
- [22] S. M. Avila and P. B. Gonçalves, “Avaliação Do Algoritmo De Controle Ótimo Para Um Amortecedor De Massa Híbrido ( Amh ),” vol. XXIX, pp. 15–18, 2010.
- [23] A. K. Chopra, *chopra*, 4th ed., vol. 53, no. 9. California, 2012.
- [24] J. P. DEN HARTOG, *Mechanical Vibrations*. New York, 1956.

## PRELIMINARY STUDY OF AN ARDUINO CONTROLLED SHAKE TABLE TO LOW-FREQUENCY TEST

Ledymar F. Moreno<sup>1</sup>, Marcus V. G. de Moraes<sup>2</sup>, and Suzana M. Avila<sup>1</sup>

<sup>1</sup>Graduate Program in Engineering Materials Integrity, University of Brasilia  
Campus of Gama, 72444-240, Gama, DF, Brazil.  
ingfoncault@gmail.com, avila@unb.br.

<sup>2</sup>Graduate Program in Engineering Materials Integrity, University of Brasilia  
Campus of Darcy Ribeiro, 70910-900, DF, Brazil.  
mvmoraes@unb.br.

---

### Abstract

*Modernity and advances in civil design are directed at increasingly tall and slender buildings, adding vibrations to structures that generate discomfort, being necessary to mitigate the amplitudes of vibrations produced by low-frequency excitations, characterized in these buildings. In this sense, for some time, experimental studies have been developed with the objective of investigating low-cost scale models, which allow a more detailed study of this type of phenomenon. In this paper, the experimental validation of a dynamic parameterization of low-frequency periodic base motion, considering one degree of freedom, with a synchronized electrodynamic system and controlled with Arduino microcontroller boards is presented. Developed using a small-scale homemade shake table, the system was applied to case studies as a control system using a simple pendulum. The necessary tools are presented to measure the system's responses over time; the dynamic response of the vibratory system can simulate several excitation frequencies. The results obtained in the proposed experimental tests are feasible, with satisfactory precision. The documented results can support an overview of the trend in the efficiency of vibrating table tests in the study of low-frequency vibration control.*

**Keywords:** Shake Table, Arduino, Low-frequency, Control, Experimental Study.

---



## 1 INTRODUCTION

Modernity and advances in civil engineering design are directed at increasingly tall and slender buildings, causing vibrations to structures that generate discomfort, being necessary to mitigate the amplitudes of vibrations produced by low-frequency excitations, characterized in these buildings. In this sense, experimental studies have been developed aiming to investigate low-cost scale models, which allow a more detailed study of this type of phenomenon.

Shaking tables are equipments widely used in engineering laboratories, in order to analyze the behavior of structures subjected to seismic actions [1,2]. Small-scale shake tables are widely used, due to its practicality and low-cost, to study the dynamic behavior of a dynamic system. You can find several manufacturers of this equipment for commercial purchase. Or you can also design a homemade one.

Experimental studies with pendulum elements are often used in literature for experimental studies of its nonlinear behavior, to identify oscillation frequency and damping properties, for example. As well, they are always present in basic physics disciplines, teaching science, engineering, and/or technology courses.

Huang [3] and Soeiro [4] define some types of dynamic actuators (known in laboratories as shakers) as a device used to induce vibration in a system, with controlled amplitude and frequency. It may be mechanical, electromagnetic, electrodynamic or hydraulic. Oliveira [5] stated that an electrodynamic actuator is the most common excitation mechanisms in vibration laboratories to simulate controlled excitation (sinusoidal, random and mechanical shock). The electrodynamic shakers can perform tests that identify important dynamic parameters such as: resonance frequencies, resistance to fatigue and product durability. The use of these actuators is very common due to the cost-benefit ratio and their load capacity of up to 30 kN with a frequency range of 5-20 kHz [6]. At this frequency range, it can be achieved displacements up to 25 mm [7]. But these industrial solutions can reach thousands of dollars.

Damci and Şekerçi [8] compared the results of a homemade shake table with commercial ones with similar characteristics. The shake table was excited using a small-scale structure excited by a step motor actioned by *Arduino* microcontrollers, to precisely achieve the imposed base-motion. The use of small-scale shake tables is the most common way to perform vibration tests for industrial applications [9]. Liu *et al.* [10] stated that the shake table test has been increasingly used to study the dynamic responses of structures in these decades. And this device is a powerful tool for researchers and designers to examine dynamic system performance.

In this paper, the experimental validation of a dynamic parameterization of low-frequency periodic base motion, considering one degree of freedom, with a synchronized electrodynamic system and controlled with *Arduino* microcontroller boards is presented. Developed using a small-scale homemade shake table, the system was used to case studies like a control system using a simple pendulum. The necessary tools to measure the system's responses along time are presented; the dynamic response of the vibratory system can simulate several excitation frequencies. The results obtained in the proposed experimental tests are feasible, with satisfactory precision.

## 2 SHAKE TABLE

The shake table is a type of electrodynamic actuator capable of carrying out controlled displacements on a sliding table with prescribed amplitude and frequency. A schematic drawing of the shake table used in this work is shown in Figure 1.

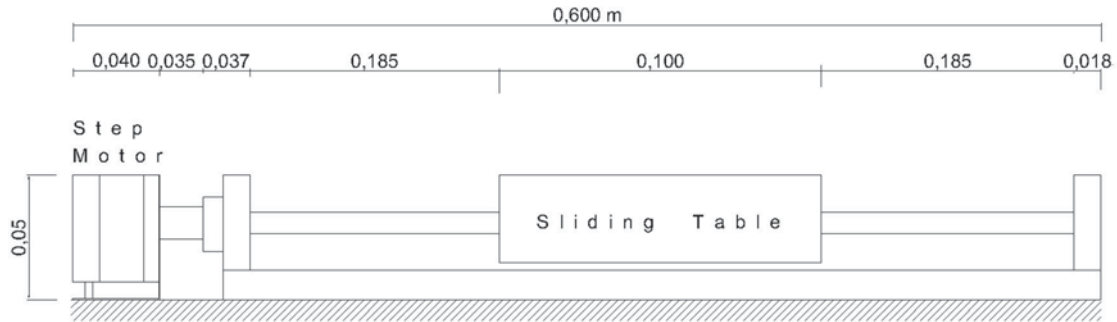


Figure 1 – Shaking Table Scheme

The shake table equipment, to generate and analyze electrodynamic excitation, is divided into two systems: movement of the mechanical system and data acquisition. For the mechanical system, a sliding platform is used to simulate the movement of seismic vibrations at low frequencies, a stepper motor as a source of mechanical force capable of generating potential energy, which allows the movement of the platform and a microcontrolled board that encodes the controlled movement to be transferred electronically to the stepper motor that transforms the force.

In this work, a handcrafted shaking table sampled was used (Figure 2). With base dimensions of 0.423 x 0.048 x 0.100 m, two axial axes (0.423 m) that serve as a guide and support, a trapezoidal spindle with 8 mm in diameter and an adaptation for the connection of the mechanical energy generator system, which is able to move the square iron base, with base dimensions of 0.100 x 0.100 m, that simulates a car.



Figure 2 – Eletro-mechanical devices of Shake Table

The electro-mechanical actuator is a bipolar stepper motor bipolar *Nema 17* to perform very precise angular movements, in discrete or fractional steps, controlled by A4988 driver module [11]. The stepper motor *Nema 17* is a high torque motor with dimensions 42 x 34 mm, the equivalent rotation angle of 1.8° for a complete lap (a spin of 360°). To know the steps taken to complete a lap or revolution, what is known as PPR (steps per revolution or pulses per revolution), the following calculation is performed:

$$PPR = \frac{360^\circ}{rotation\ angle} \quad (1)$$

$$PPR = \frac{360^\circ}{1.8^\circ} = 200 \text{ steps per revolution} \quad (2)$$

Stepper motors can be controlled in open loop, as they have a known position at all times [12] In this case the motor is connected to a microdevice controller, capable of controlling the interpolation of the flow current in stepper motors, controlling the size of the pulse. The slower the rotation, the larger the pulse size, smoothing the resulting movement of the motor. One of the main advantages of this device is being able to manually set the maximum output current, allowing the application of voltages above the motor's nominal value. The controller drive has a voltage regulator with an intelligent system that automatically adapts the decay mode, a thermal protector that shuts down allowing the temperature control and, a protection against cross currents that generates a reduced dissipation in the power and allows the immediacy in the precision.

To find the reduction in the size of the pulse, the complete cycles are divided into smaller steps, smoothing the movement of the motor, after all, the smaller the step, the greater the precision. The  $1.8^\circ$  angle can be divided up to 256 times, obtaining steps up to 0.007 degrees ( $1.8 \times 0.007$ ) or 51,200 micro steps. To establish communication with the engine it is using an Arduino Uno, which is the most popular microcontroller model and widely used for its simplicity, accessibility and low power consumption; the programming is done through the regular computer, connected by a USB port that establishes a communication link with the flash memory built into the Arduino, the USB socket also supplies power to the Arduino. The programming used is the C programming language and through execution in the integrated development environment (IDE) as explained by S. Monk [13] allowing one program to run at a time.

In Figure 3, the components of the mechanical system of the handmade vibrating table are sampled.

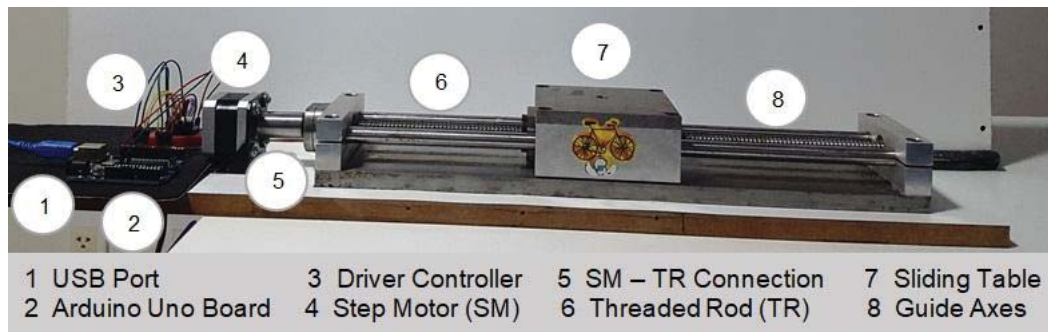


Figure 3 – Composition of the handmade shake table.

### 3 METHODOLOGY

Initially, the evaluation and behavior of the shaking table is carried out and then a simple pendulum excited by the table is analyzed.

For the movement of the vibrating table, energy is transformed using an electric motor, step-by-step, controlled by a potentiometer and a microcontroller, capable of directing the information from the programming code that allows excitation and rotation control to be carried out. Low frequencies in the range of 0.3 Hz and 2.1 Hz were considered, varying in steps of 0.2 Hz, verifying the limitations of displacement of the table in its maximum trajectory and minimum motor capacities. In order to guarantee greater reliability to the study [14], an ap-

appropriate number of repetitions were carried out for each study. In this sense, the number of repetitions of sixty-four (64) periods was considered for each operating mode of the engine in random order and in duplicate; also, it saves the life of the controller drive in function of thermodynamic capacity for the most rambling mode of the engine and the storage capacities of the data analysis program according to the resources available for the study.

The technique used in this study for data acquisition was video capture, performed using a Samsung-SM-G920A Smartphones camera, Android version 5.0.2, with resolution adapted to FHD (60fps) 1920x1080, and speed of 60 images for approximate seconds according to the instrument's specifications. Where the object of the center of analysis of differentiated color is identified that will facilitate and it was used a measuring tape that allows to carry out the necessary calibration on the screen in the data analysis software with the intention of guaranteeing the accuracy of the data under study. Figure 4 shows the image of the slide platform with the identification of the elements that allowed the object to be marked, calibrated, to locate the known points and the Cartesian axis, and to define the units considered.

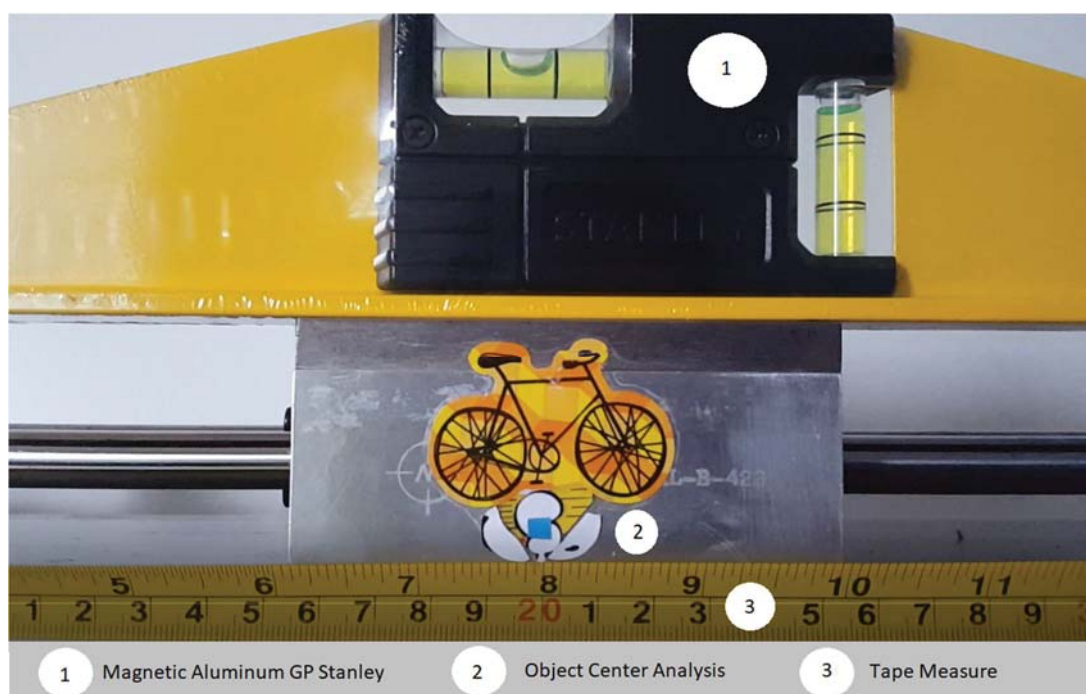


Figure 4 – Detail of sliding platform with follower point.

In this work, the free software Tracker is used to analyze the results (Figure 5), which was also used by Bezerra Jr. et al. [15] for their analysis of the results, they specified the software's capacity to measure several quantities in two-dimensional space, based on a standard established by the user. The software identifies the number of frames per second of the video in analysis, presenting the data and graphics corresponding to the study of physical phenomena, automatically and in real time, such as: displacements, velocities, accelerations, time, angular frequencies, among others, making it possible to carry out various analysis, such as comparing results, identifying discrepancies in movement patterns and analyzing performances. Bonventi Jr. and Aranha [16] describes that the software also allows you to make adjustments to various functions and even to build your own mathematical models.



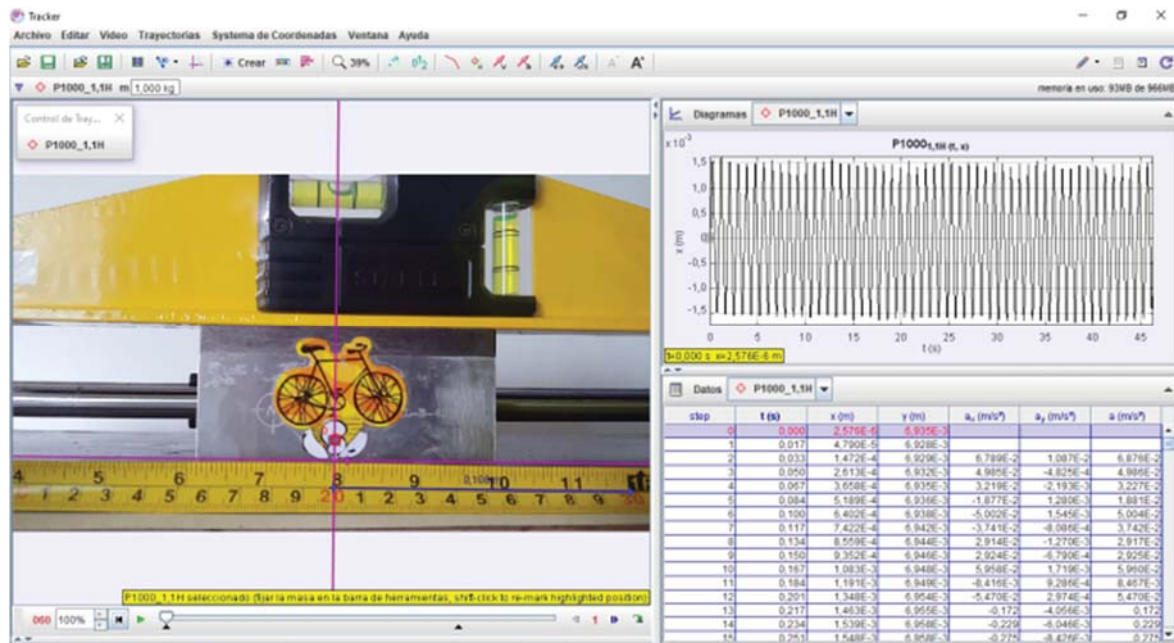


Figure 5 – Motion of sliding platform analyzed by Tracker software.

## 4 RESULTS

The results of the study consist of validating the movement of the vibratory table movement, and studying simple pendulum tests.

### 4.1 Validation of the Shake Table

The study of the motor oscillation movement for five (5) different configuration of the stepper motor + A4988 controller on the Arduino platform, Table 1, was performed.

Mode	Steps (PPRM)	Angular Speed ( $\omega$ )	Motor Deceleration (%)
Full	200	1,85	-
Half	400	1,49	(20)
1/4	800	1,07	(28)
1/8	1600	0,68	(36)
1/16	3200	0,39	(42)

Table 1 – Operating Parameters of the A4988 Controller on the NEMA motor rotational movement.

By enabling one of these operation modes of the stepper motor [11], the waveform obtained resembles the square wave, Figure 6. The precision of periodicity is observed. Figure 6 shows the experimental result of rotation of the stepper motor for modo mode, obtaining an oscillation frequency of 0.6 Hz and an average angular velocity amplitude of 2.62 rad / s, analogous to Brites, [17]. The experimental result was obtained through motion capture by video analyzed by the Tracker program.

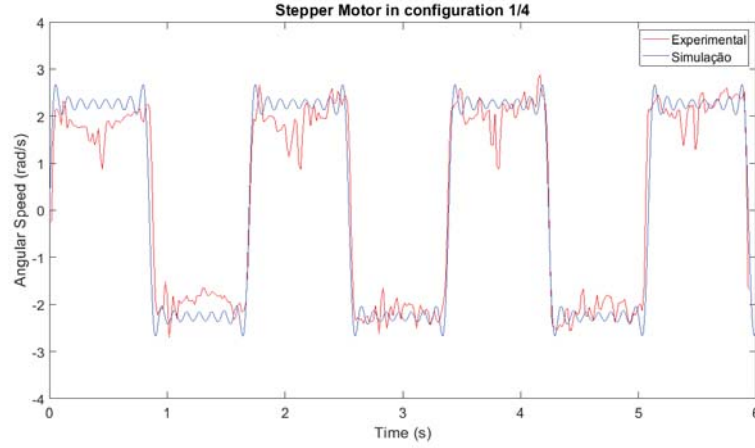


Figure 6 – Angular rotation of the stepper motor for the operation mode  $\frac{1}{4}$ .

For the validation of the movement of the shake table, the acceleration time history of the sliding platform is shown in Figure 7 showing a triangular waveform. As expected, a triangular wave-type displacement has the following shape as a series of Fourier:

$$x(t) = x_o \cdot \frac{8}{\pi^2} \sum_{i=0}^N \frac{(-1)^i}{n^2} \sin(n \cdot 2\pi f t) \quad (3)$$

where,  $n = 2i + 1 = 1, 3, 5, \dots$ . Note that from the triangular wave, the square wave is obtained with the time derivative of the expression (3) referring to the velocity of movement of the platform and similar to the angular velocity of the stepper motor.

$$\dot{x}(t) = \dot{x}_o + \frac{8}{\pi^2} \sum_{i=0}^N (n \cdot 2\pi f)^2 \cdot \frac{A(-1)^i}{(2n)^2} \sin(n \cdot 2\pi f t) \quad (4)$$

Figure 7 compares the experimental results and the simulated theoretical model regarding the acceleration of the platform. There is a gap between the experimental results and the theoretical model due to inaccuracies in the excitation frequency.

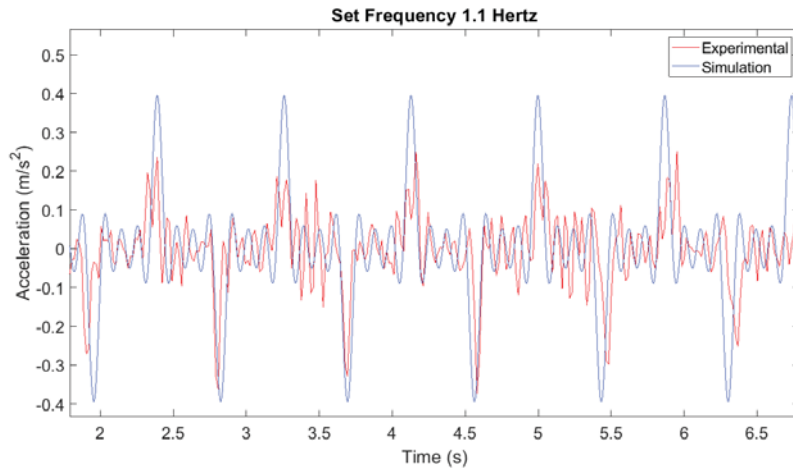


Figure 7 – Comparison of experimental data and analytical waveform of sliding platform acceleration



When analyzing the time-history acceleration of the platform in different directions, the Figure 8 shows the acceleration of the platform in the x-direction (parallel to the movement of the platform) and the y-direction (perpendicular to the movement of the platform) measured by a smartphone *Samsung-SM-G920A*, Version of *Android 5.0.2* and by the program *Tracker*. As expected, the platform response (in the x-direction) presents the expected waveform for acceleration, as Figure 8. The acceleration in the x-direction is ten times greater than the acceleration in the y-direction (perpendicular) demonstrating a good relationship signal-to-noise ratio for this frequency 1,1 Hz. These parasitic accelerations are due to noise mainly due to small clearances in the linear platform mechanism.

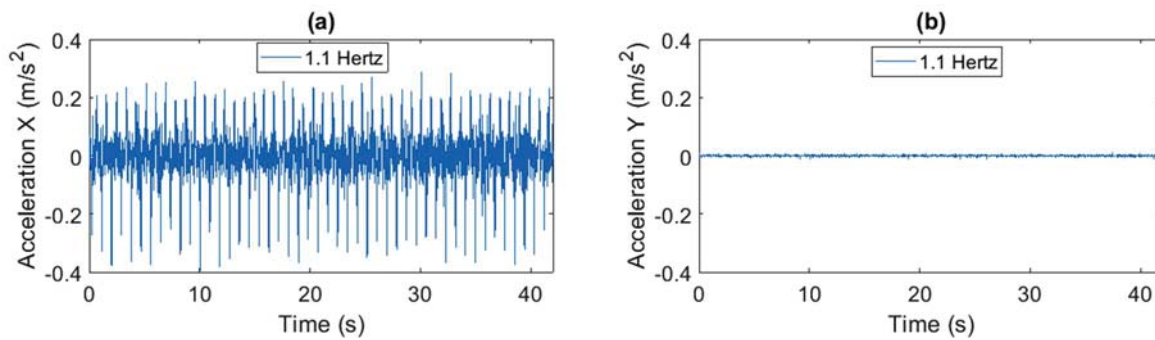


Figure 8 – Time history acceleration of the platform to the excitation frequency **1,1 Hz**.  
(a) Steering acceleration-X (b) Steering acceleration -Y.

When analyzing the experimental results for other excitation frequencies, the shake table shows signs of acceleration with different magnitudes depending on the number of steps of the stepper motor. A series of experimental measurements of the acceleration of the platform for excitation frequencies between 0,3 Hz to 2,1 Hz for a range of 0,2Hz. Only the results are presented for the frequencies of 0,3Hz (Figure 9), 0,7Hz (Figure 10) e 1,7Hz (Figure 11). The results show good signal-to-noise ratios for frequencies above 0,5Hz. Due to mechanical gaps, failures in the platform support, and inaccuracies in the stepper motor action, the acceleration signal for low frequencies is less than the noise for low frequencies ( $f \leq 0,5\text{Hz}$ ).

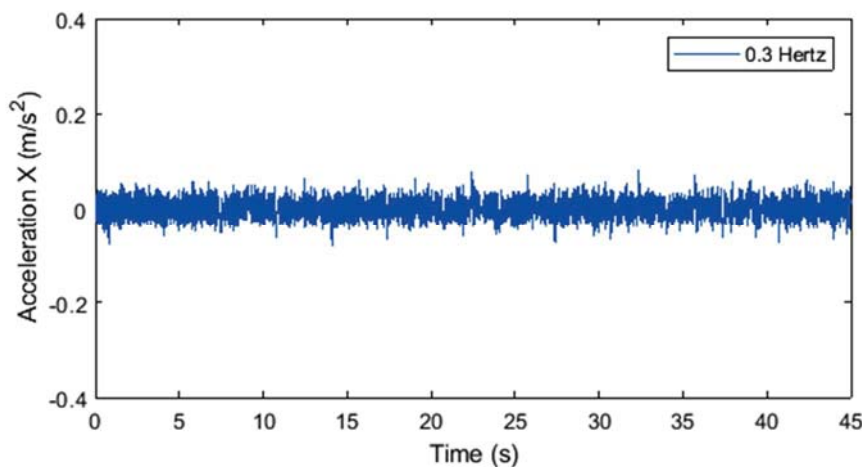


Figure 9 – Time history acceleration in the X-direction for the excitation frequency 0.3 Hz.

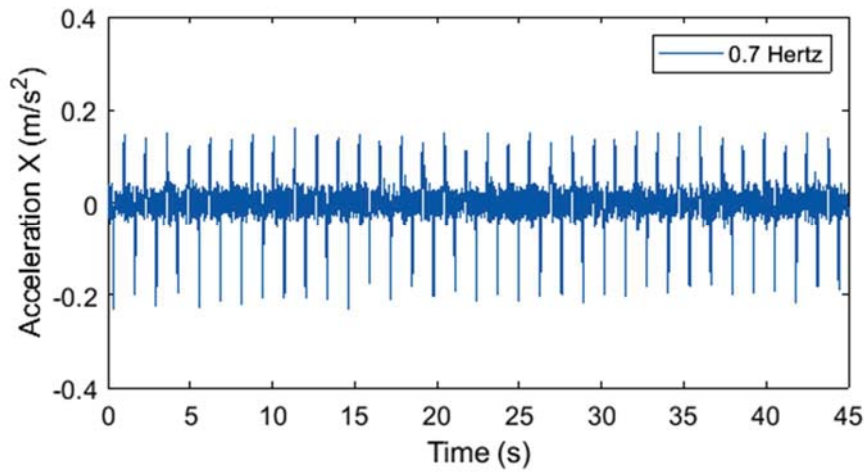


Figure 10 - Time history of acceleration in the X-direction for the excitation frequency 0.7 Hz.

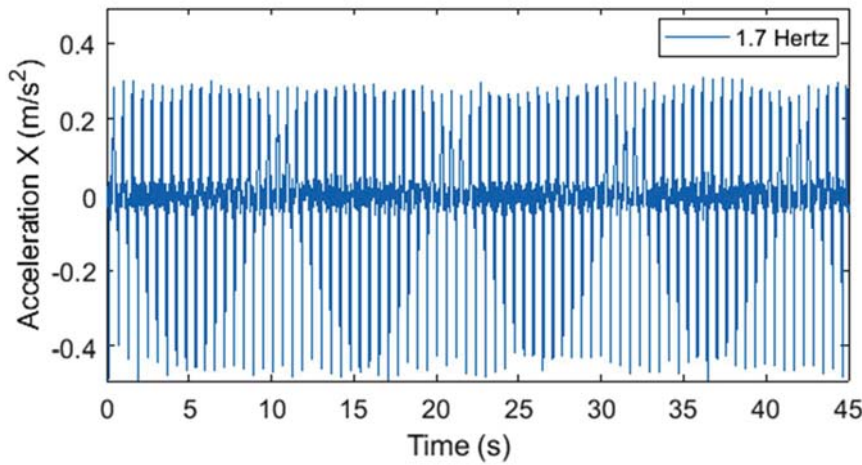


Figure 11 - Time history acceleration in the X-direction for the excitation frequency 1.7 Hz.

The analysis in the frequency domain of the temporal signals results in a spectrum of acceleration amplitudes for the excitation frequencies de 0,9 Hz (Figure 12), 1,2 Hz (Figure 13) e 2,1 Hz (Figure 14). The frequency peaks are observed for the respective fundamental frequencies  $f_n$  and its odd harmonics  $f_i = i f_n$  ( $i = 1, 3, 5, \dots$ ), accordingly the expression of the Fourier series (1).

$$f(t) = a_0 + \sum_{n=1}^{\infty} a_n \cdot \cos(n\omega_0 t) + b_n \cdot \sin(n\omega_0 t) \quad (5)$$

where, Fourier coefficients are obtained through the temporal expressions  $a_0 = \frac{1}{T_0} \int_{t_1}^{t_1+T_0} f(t) dt$ ,  $a_n = \frac{1}{T_0} \int_{t_1}^{t_1+T_0} f(t) \cdot \cos(q\omega_0 t) dt$ ,  $b_n = \frac{2}{T_0} \int_{t_1}^{t_1+T_0} f(t) \cdot \cos(q\omega_0 t) dt$ ;  $t_1$  is a temporal arbitrary instant [18]. The amplitude spectrum has even symmetry and the phase spectrum has unique symmetry. When evaluating the acceleration spectra, it is found discrete spectra containing a number of harmonics integer multiples of the signal fundamental frequency.

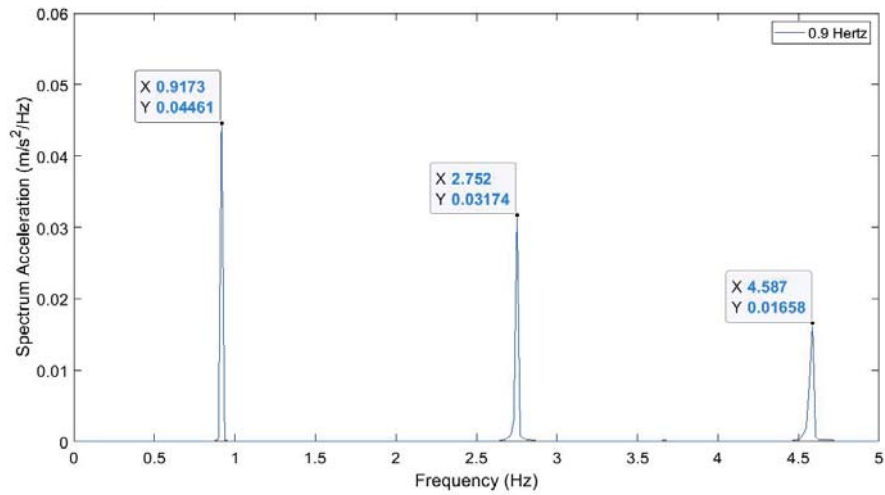


Figure 12 - Spectral response from acceleration to excitation frequency 0.9 Hz.

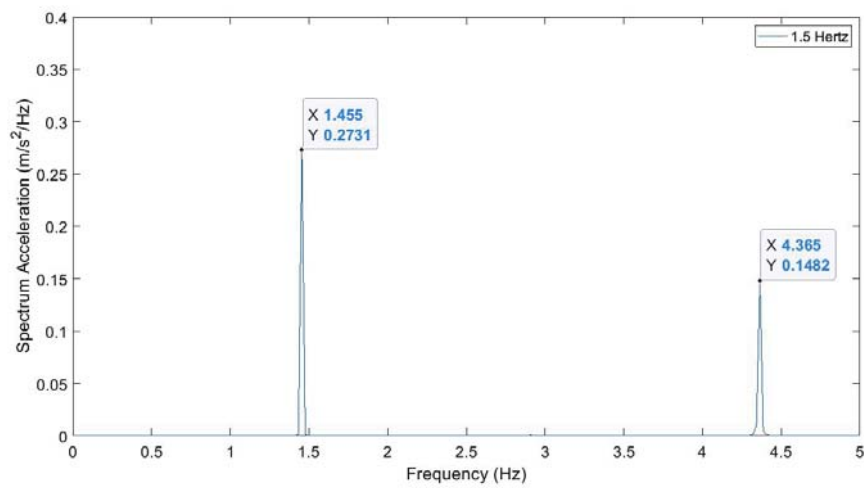


Figure 13 - Spectral response from acceleration to excitation frequency 1.5 Hz.

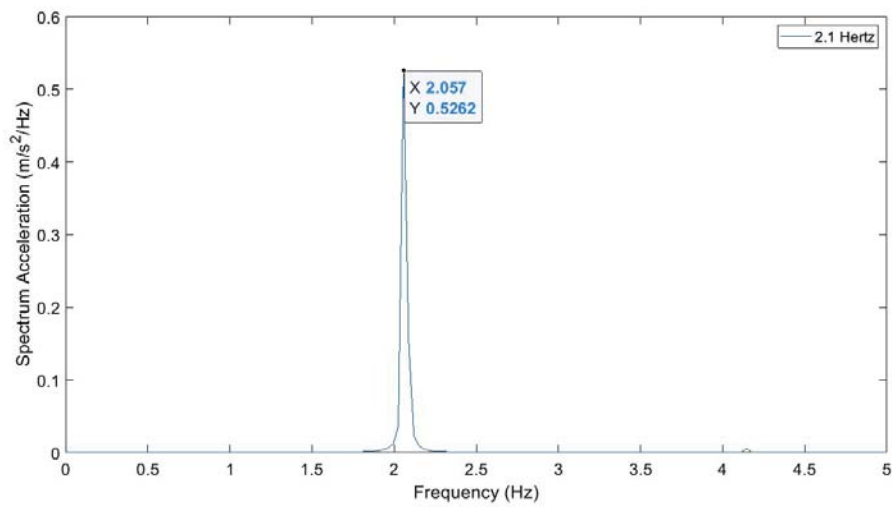


Figure 14 - Spectral response from acceleration to excitation frequency 2.1 Hz.

#### 4.2 Free Pendulum Vibration Test

In order to study a practical application of the platform, it was studied the dynamic behavior of a simple pendulum (Figure 15) with length  $l = 0,255 \text{ m}$  between the contact point and the mass center of the small sphere of mass  $m = 0,04101 \text{ g}$ , considering local gravity acceleration in Brasilia DF-Brazil ( $15^\circ 45' 43'' \text{S}$   $47^\circ 52' 25'' \text{W}$ )  $g = 9,7808439 \text{ m/s}^2$ . Using motion capture by video with the Tracker software, the dynamic behavior of the simple pendulum is studied.

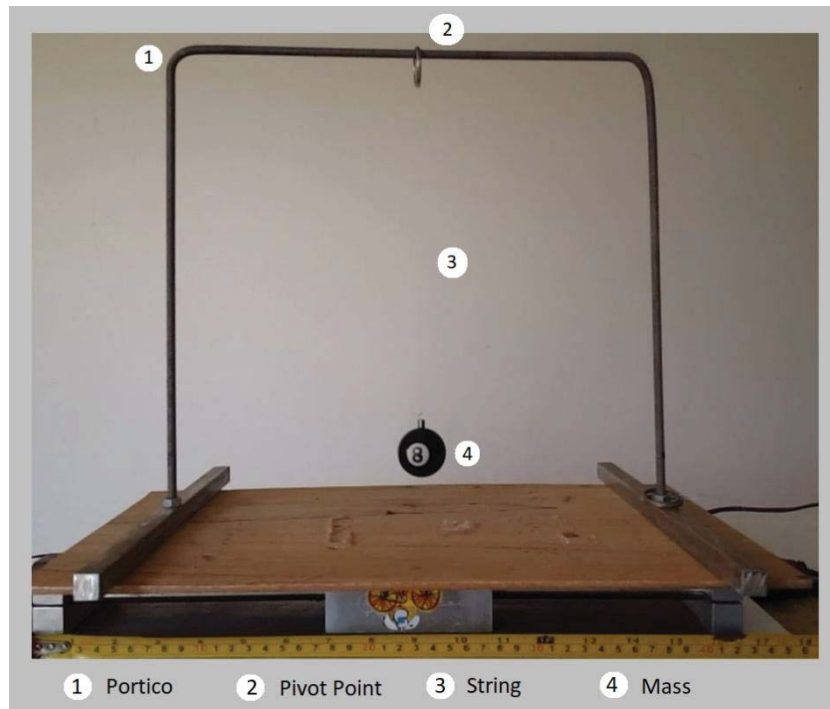


Figure 15 – Simple Pendulum

At first, the preliminary results to determine the behavior of the pendulum's amortization are presented, varying the amplitude of the sphere's displacement in small angles and considering the approximation  $\sin \theta \cong \theta$  acceptable. The initial movement is generated carefully and searching that the effects of air displacement can be minimized.

The motion equation of the pendulum can be written as:

$$\ddot{\theta} + 2\xi\omega_n\dot{\theta} + \omega_n^2 \sin \theta = 0 \quad (5)$$

where  $\theta$  is the angle of the pendulum, the period of undamped linear oscillation is  $T_0 = 2\pi/\omega_n = 2\pi\sqrt{L/g}$ , it is function of local gravity acceleration  $g$  and pendulum length  $L$ , assuming that  $\sin \theta \approx \theta$ , and the exact oscillation period  $T$  It is given by [19]:

$$T = T(\theta) \approx T_0 \left[ 1 + \frac{1}{16} \theta^2 + \frac{11}{3072} \theta^4 + \frac{173}{737280} \theta^6 + \dots \right] \quad (6)$$

Providing an initial disturbance, Figure 16 presents the comparison of the experimental response of the simple pendulum obtained by motion capture in the *Tracker* and the result of the theoretical model obtained by numerical simulation with MatLab software. In this case, the amplitude of displacement of the pendulum mass is of  $0.2094 \text{ rad}$ . There is a certain similari-

ty in the temporal results of the angular position of the mass between the theoretical models and the experimental result. The damping model needs to be improved.

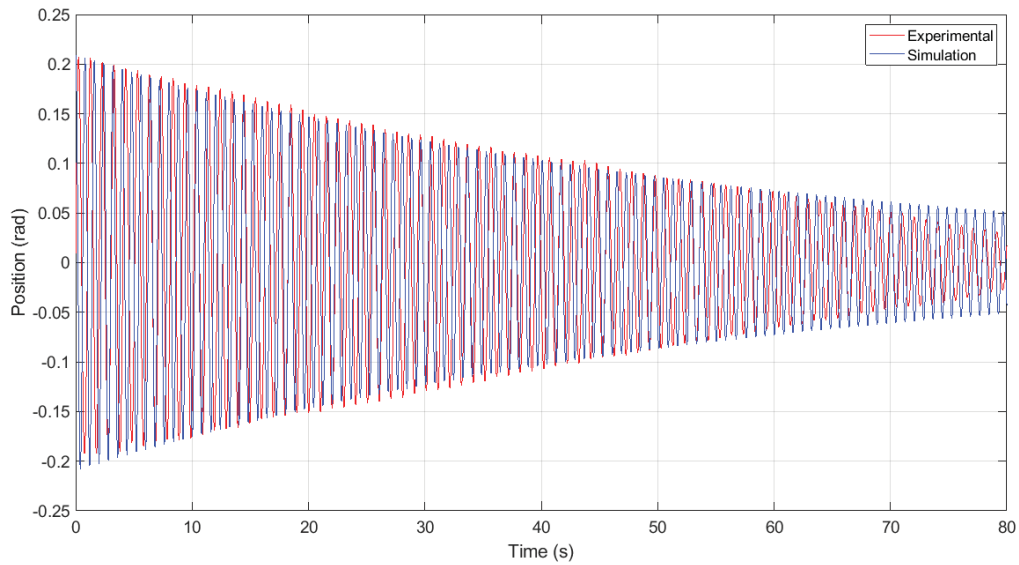


Figure 16 – Damped Response of the Simple Pendulum: Experimental results x numerical simulation.

The period of experimental oscillation is compared as a function of the angle of oscillation of the simple pendulum according to the expression (6). Figure 17 presents a comparison between the theoretical results with the experimental period extracted from the temporal response. The experimental results show an evolution close to the theoretical solution and an evolution dependent on the maximum period of oscillation angle.

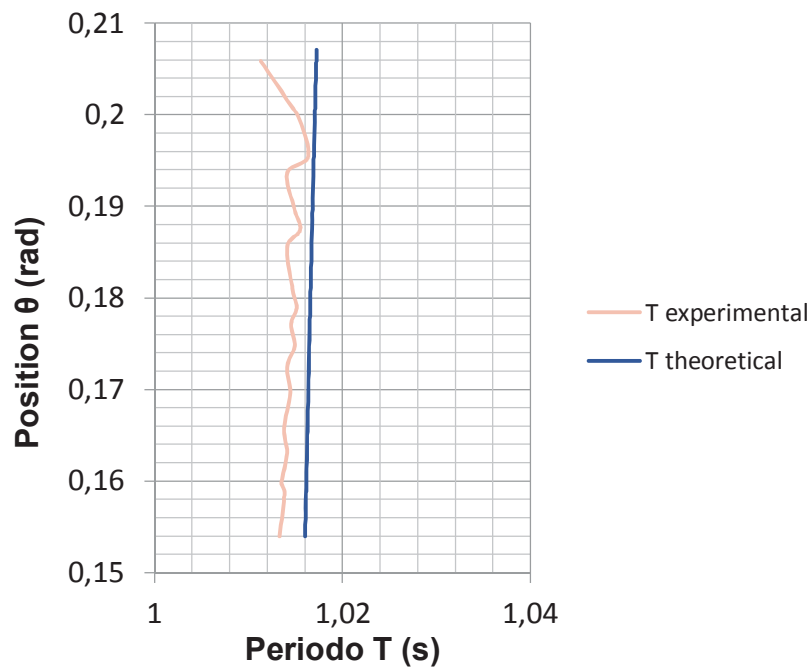


Figure 17 - Period Relationship - Position of a Simple Pendulum

## 5 CONCLUSION

This work performs an experimental study of a low-frequency handcrafted electrodynamic shake table. Initially, the validation of the shake table dynamic is done using video motion capture through Tracker software for experimental frequencies between 0.3 and 2.1 Hz. The dynamic displacement, velocity, and acceleration of the shake table platform are compared to analytical solution achieving reasonable agreement. Finally, the free vibration of a simple pendulum motion is acquired through video motion capture. The experimental data is compared to theoretical models that show a good agreement with reasonable accuracy.

The authors suggest carrying out future work to verify and adapt the study, based on the results obtained in the validation of the shake table, the study of the dynamic response of a simple pendulum, or coupled pendulums, or of a tuned liquid column damper (TLCD).

## 6 ACKNOWLEDGMENTS

The authors of this research are grateful for the financial support of the Post-Graduate Decanate of the University of Brasília (DPG-UnB), the Program of Alliances for Education and Training, the Organization of American States, the Coimbra Group of Brazilian Universities (PAEC-OEA/ GCUB) and the Coordination for the Improvement of Higher Education Personnel (CAPES).

## REFERENCES

- [1] L. A. P. Peña, University of Brasilia, UnB, Civil and Environmental Engineering, Specialization in Structures, *Dynamic response of coupled adjacent buildings: considerations on soil – structure interaction*, 240, 2017. (In Portuguese).
- [2] N. A. S. Pereira, University of Porto, FEUP, Civil Engineering Specialization in Structures. *Study of a Shake Platform for Laboratory Tests*, 104, 2015. (In Portuguese).
- [3] Â. Huang, University of Porto, FEUP, Mechanical Engineering Specialization in Automation. *Development of a Demonstration Seismic Simulation Platform for Small Models*, 101, 2018. (In Portuguese).
- [4] N. S. Soeiro, Federal University of Pará, ITEC, mechanical Engineering FEM, GVA, *Experimental modal analysis*, 74, 2001. (In Portuguese)
- [5] L. P. R. de Oliveira, University of São Paulo, Mechanical Engineering, Interaction Between *Vibration Exciters and the Structure Under Study in Tests with Multiple Excitation*, 114, 2003. (In Portuguese).
- [6] R. C. Quesada, *Vibration Control*. Educational Publisher and Distributor S.A., 2019.
- [7] N. S. Soeiro, Federal University of Pará, ITEC, mechanical Engineering FEM, GVA, *Course of Fundamentals of Vibrations and Rotor Balancing*, 125, 2008. (In Portuguese).
- [8] E. Damcı, Ç. Şekerci, Experimental Techniques. *Development of a Low-Cost Single-Axis Shake Table Based on Arduino*, 43, 179-198, 2019.
- [9] G. Hirata, J. Alvarez, R. Cuesta, Control of the Position of a Vibrating Table: Application to the Tracking of Seismic Signals. *Memories of XVI Latin American Congress of Automatic Control, (CLCA 2014)*, Cancún, Quintana Roo, México, Octubre 14-17, 2014. (In Spain).



- [10] W. Liu, C. Qin, Y. Liu, W. He, Q. Yang, Hindawi Publishing Corporation Shock and Vibration. *Shaking Table Tests on Earthquake Response Characterization of a Complex Museum Isolated Structure in High Intensity Area*, Vol. 2016, 23, 2016.
- [11] Allegro MicroSystems, LLC. 4988-DS MCO-0000827, *DMOS Microstepping Driver with Translator And Overcurrent Protection*, Rev 7, 20, 2020.
- [12] A. R. de O. Bauer, TCC - Federal University of Santa Maria - Campus Cachoeira do Sul, Electrical engineering, RS, *Development of a system to drive stepper motors for making transformer cores*, 57, 2018. (In Portuguese).
- [13] S. Monk, Movement, *Light and Sound With Arduino e Raspberry Pi*. 1st Edition. Novatec, 2016. (In Portuguese).
- [14] S. S. Rao, *Mechanical vibrations*, 4th Edition. Pearson Prentice Hall, 2008.
- [15] A. G. Bezerra Jr., L. P. de Oliveira, J.A. Lenz, N. Saavedra. Federal Technological University of Paraná Curitiba, UTFPR, Journal Cad. Bras. Ens. Fís., *Video analysis with the free software Tracker for the laboratory in physics education: parabolic motion and Newton's second law*, 29, Special 1: 469-490, 2012. (In Portuguese).
- [16] W. Bonventi Jr., N. Aranha, Journal Rev. Bras. Ens. Fís., *Study of damped oscillations of a physical pendulum with aid of "Tracker"* 37, n 2: 2504, 2015. (In Portuguese).
- [17] F. G. Brites, V. P. de A. Santos, Federal Fluminense University, PET do MEC Group PET-Tele, *Stepper Motor PET-Tele*, 15, 2008. (In Portuguese).
- [18] H. L. Soriano, *Introduction to Structural Dynamics*, Elsevier Editor, 2014. (In Portuguese).
- [19] D. Amrani, P. Paradis, M. Beaudin, Mexican Magazine of Physics. *Approximation Expressions for the Large-Angle Period of a Simple Pendulum Revisited*, E 54 (1), 59–64, 2008.

## EFFICIENT DAMPER DESIGN METHOD FOR ELASTIC-PLASTIC MDOF STRUCTURES UNDER CONSECUTIVE-LEVEL EARTHQUAKES

H. Akehashi<sup>1</sup>, I. Takewaki<sup>2</sup>

<sup>1</sup> Graduate student, Dept of Architecture and Architectural Engineering, Kyoto University  
Kyoto University, Kyoto 615-8540, Japan  
e-mail: fm-akehashi@archi.kyoto-u.ac.jp

<sup>2</sup> Professor, Dept of Architecture and Architectural Engineering, Kyoto University  
Kyoto University, Kyoto 615-8540, Japan  
takewaki@archi.kyoto-u.ac.jp

---

### Abstract

*A new optimal damper design method, called ‘consecutive design generation method (CDGM)’, is presented for elastic-plastic multi-degree-of-freedom (MDOF) building structures under multiple-level earthquake ground motions (GMs). The procedure of the proposed method is as follows: (i) Set a variety of levels of input GMs  $\{IM_1, \dots, IM_L\}$  ( $IM_1 < \dots < IM_L$ ). (ii) Obtain the optimal design under GM with  $IM = IM_1$  using an optimization method. (iii) Obtain the optimal design under GM with  $IM = IM_2$  by a local search around the optimal design under GM with  $IM = IM_1$  as the initial design. (iv) Obtain the optimal design under GM with  $IM = IM_3$  by a local search around the optimal design under GM with  $IM = IM_2$  as the initial design, and the same procedure is repeated under GMs with other IMs. By using the proposed method, all the optimal designs can be obtained with much lower computational effort than the method repeating an ordinary optimization procedure under every-level GM. The proposed method helps to understand how the distribution of added damper damping coefficients changes as the level of GMs changes. Furthermore, a simple design guideline for the problem, which design to be chosen from various optimal designs, is presented based on the ‘ideal drift response curve’, which is also a new concept. Two representative recorded ground motions are employed as a set of GMs and the proposed method is applied to these GMs. The influence of the number of GMs and the level of GMs on the optimal damper design is clarified.*

**Keywords:** Earthquake response, Elastic-plastic response, Seismic design, Viscous damping, Optimal damper placement, Robust design.

---

## 1 INTRODUCTION

Problems of optimal design of passive dampers have been tackled by many researchers (for example see [6, 11]). Zhang and Soong [15] proposed a sequential procedure to obtain the optimal placement of viscoelastic dampers. Then this method was extended to a simpler method by Garcia [5]. Takewaki [10] developed an optimality criteria-based algorithm to minimize the sum of the amplitudes of the transfer functions at the fundamental natural frequency under a constraint on the sum of the additional damping coefficients. Silvestri and Trombetti [9] demonstrated the effectiveness of mass-proportional damping systems. Some researchers compared several methods for optimal damper placement ([2, 4, 14]).

In most researches on optimal damper placement, elastic frames are treated and a limited number of researches deal with optimal damper placement problems for inelastic frames (for example, [1, 7, 12]). In the presence of yielding in a frame, the setting of the level of input ground motions (GMs) used for the optimization affects the final design. However, even in these studies, a problem how to determine the level of input GMs has not been examined. An optimal damper distribution designed under a specified-level GM may not be necessarily effective for larger-level GMs. Especially, a model optimally designed in the elastic range exhibits a large plastic deformation concentration to specific stories for larger inputs [2, 3]. Therefore, a design effective for various levels of GMs is desirable.

In this paper, a new optimal damper design method, called a ‘consecutive design generation method (CDGM)’, is presented for elastic-plastic multi-degree-of-freedom (MDOF) building structures under multiple-level GMs. The procedure of the proposed method is as follows: (i) Set a variety of levels of input GMs  $\{IM_1, \dots, IM_L\}$  ( $IM_1 < \dots < IM_L$ ). (ii) Obtain the optimal design under GM with  $IM = IM_1$  using an optimization method. (iii) Obtain the optimal design under GM with  $IM = IM_2$  by a local search around the optimal design under GM with  $IM = IM_1$  as the initial design. (iv) Obtain the optimal design under GM with  $IM = IM_3$  by a local search around the optimal design under GM with  $IM = IM_2$  as the initial design, and the same procedure is repeated under GMs with other  $IM$ s. By using the proposed method, all the optimal designs can be obtained with much lower computational effort than the method repeating an ordinary optimization procedure under every-level GM. The proposed method helps to understand how the distribution of added damper damping coefficients changes as the level of GMs changes. Furthermore, a simple design guideline for the problem, which design to be chosen from various optimal designs, is presented based on the ‘ideal drift response curve’, which is also a new concept. Two representative recorded ground motions are employed as a set of GMs and the proposed method is applied to these GMs. The influence of the number of GMs and the level of GMs on the optimal damper design is clarified.

## 2 PROBLEM OF OPTIMAL DAMPER PLACEMENT

In this section, two kinds of problems of optimal damper placement are presented. An ordinary problem of optimal damper placement (OPODP) is stated as minimizing the maximum interstory drift under the condition on the specified total quantity of added viscous damping coefficients and the specified level of input GMs. Another problem is to find the problem of optimal damper placements under consecutive-level GMs (PODPCG). The problem PODPCG is mainly dealt with in this paper. Since elastic-plastic MDOF structures are dealt with, the setting of the level of input GMs affects the final design. Therefore, solving the problem PODPCG helps to understand how the distribution of added damper damping coefficients changes as the level of GMs increases. The relation of the problems OPODP and PODPCG will be explained, and a solution algorithm will be proposed for the problem PODPCG.

## 2.1 Problem of optimal damper placement for consecutive-level ground motions

Consider first the problem OPODP.

### [Ordinary Problem of Optimal Damper Placement (OPODP)]

Find  $\mathbf{c}_{add}$   
 so as to minimize  $d_{\max} = \max_i \{d_{\max,i}\}$   
 subject to  $\mathbf{c}_{add} \cdot \mathbf{1} = W_c$  (const.)

where  $\mathbf{c}_{add}$ ,  $d_{\max,i}$ ,  $W_c$  denote the added damping coefficient vector, the maximum interstory drift in the  $i$ -th story, the sum of the added damping coefficients, respectively.

Consider next the problem PODPCG.

### [Problem of Optimal Damper Placements for Consecutive-level GMs (PODPCG)]

Obtain the  $L$  sets of damper placements  $\mathbf{c}_{add}^{opt}(IM_1), \dots, \mathbf{c}_{add}^{opt}(IM_L)$  ( $IM_1 < \dots < IM_L$ )

where  $IM, L, \mathbf{c}_{add}^{opt}(IM_j)$  denote the level of input GMs, the number of  $IM$ s, the optimal damper placement under the GMs with  $IM = IM_j$ , respectively.

All the optimal designs  $\mathbf{c}_{add}^{opt}(IM_1), \dots, \mathbf{c}_{add}^{opt}(IM_L)$  are obtained by solving the problem OPODP  $L$  times for each level of the input GMs. However, it is preferable to avoid such iteration for lower computational effort. To overcome this difficulty, a simple and efficient approach including a local search is proposed.

## 2.2 Solution algorithm: consecutive design generation method

The solution algorithm for the problem PODPCG may be described as follows.

### [Algorithm: Consecutive Design Generation Method (CDGM)]

Step 1 Set a variety of levels of input GMs  $\{IM_1, \dots, IM_L\}$  ( $IM_1 < \dots < IM_L$ ).

Step 2 Obtain  $\mathbf{c}_{add}^{opt}(IM_1)$  using an optimization method. Put  $i \rightarrow 1$ .

Step 3 Obtain  $\mathbf{c}_{add}^{opt}(IM_{i+1})$  by a local search around  $\mathbf{c}_{add}^{opt}(IM_i)$  as the initial design.

3.1 Find the story  $j$  which exhibits the largest value of  $d_{\max,j}$ .

3.2 Select the stories in which dampers are installed (exclude the stories without damper). Then find the story  $k$  which exhibits the minimum value of  $d_{\max,k}$  from those stories.

3.3 Update the damping coefficients  $c_j \rightarrow c_j + \Delta c, c_k \rightarrow c_k - \Delta c$ .

3.4 Repeat 3.1-3.3  $n_{ls}$  times.

3.5 Select the design which exhibits the minimum value of  $d_{\max}$  from  $n_{ls}$  designs.

Step 4 Put  $i \rightarrow i+1$ . If  $i = L$  is satisfied, then finalize the process. If  $i < L$  is satisfied, return to Step 3.

The overview and the flow of this algorithm are shown in Figure 1. It is noted that the sensitivity-based approach [3, 8] is adopted to obtain  $\mathbf{c}_{add}^{opt}(IM_1)$  in this paper. It is also pointed out that the local search method used in Step 3, 4 is quite simple, but it works well so far as the value of  $\Delta IM (= IM_{i+1} - IM_i)$  is small (the effectiveness of the proposed local search method is demonstrated through the numerical examples in Section 3.1 and 3.2).

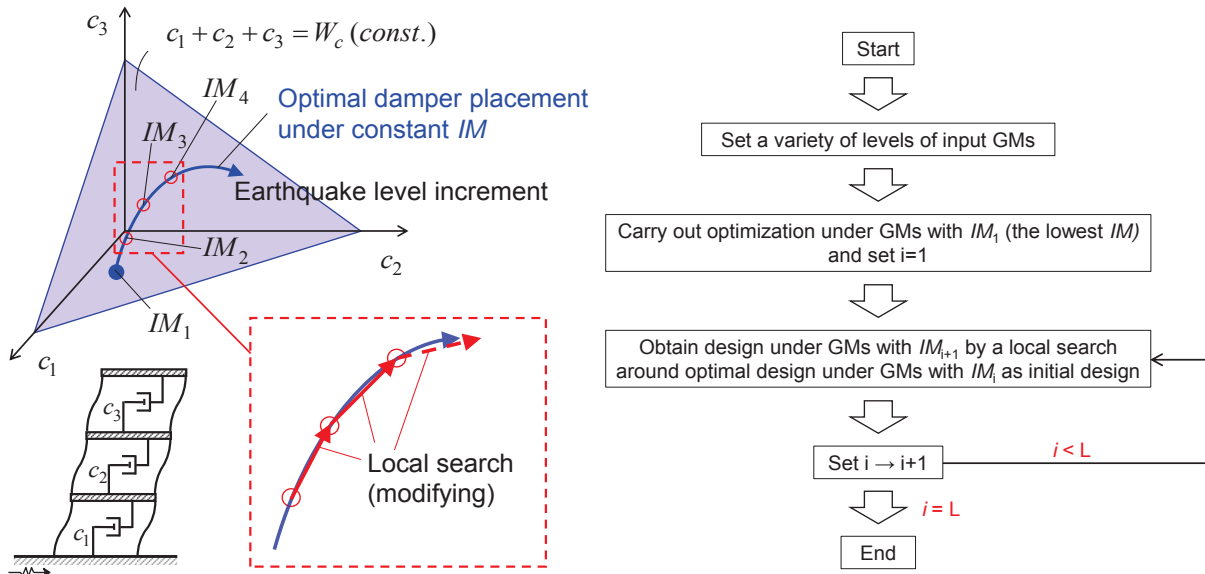


Figure 1: Overview and schematic diagram of proposed solution algorithm.

## NUMERICAL EXAMPLE

Consider two shear building models of 12 stories with different story stiffness distributions. Model 1 has a trapezoidal distribution of story stiffnesses ( $(k_1 / k_{12}) = 4$ ). Model 2 has a uniform distribution of story stiffnesses. The undamped fundamental natural period of these two models is 1.2[s] and the structural damping ratio is 0.01 (stiffness proportional type). All the floor masses have the same value. The common story height is 4[m] and the common yield interstory drift is 4/150[m]. The story shear-interstory drift relation obeys the elastic perfectly-plastic rule.

### 2.3 Influence of level of input ground motion

In this section, the influence of the level of input GMs on the final design is investigated. El Centro NS component during the Imperial Valley earthquake in 1940 is employed here. The level of the GM is adjusted by the peak ground velocities (PGV). 51 levels of the GM (from PGV = 0.5 [m/s] to PGV = 1.5 [m/s] by the increment 0.02 [m/s]) are used to obtain optimal designs. The sensitivity-based approach [3, 8] is adopted to obtain  $\mathbf{c}_{add}^{opt}$  (PGV=0.5) and the required number of time-history response analyses is about 6000 to obtain  $\mathbf{c}_{add}^{opt}$  (PGV=0.5). The targeted value of the sum of the added damping coefficients is set to  $W_c = 10 \times 10^7$  [Ns/m]. The value of  $W_c$  is given so that the final design has the fundamental-mode damping ratio of about 0.05.  $n_{ls} = 50$  and  $\Delta c = W_c / 240$  are employed for the local search. The total number of time-history response analyses is  $6000 + n_{ls} \times (51 - 1) = 8500$ .

Figures 2 and 3 show the optimal designs for Model 1 and 2. It can be observed that the proposed method certainly provides effective designs for various levels of GMs for both Model 1, 2. This means that the proposed local search method works well even though the local search method is quite simple. It can also be said that, as PGV used for the design becomes larger, the dampers concentrated to the specified stories spread around those stories and the distributions of added damping coefficients become smoother. This is because those surrounding stories without dampers tend to exhibit large deformation concentrations for larger levels of GMs. For Model 1, the added dampers are allocated only in the 6-10th stories in

the case of  $PGV < 0.7[m/s]$ . As PGV becomes larger, the dampers are allocated to the 4-5th stories. For Model 2, the dampers allocated only in the 1-3th stories for smaller PGV spread to the 4-6th stories as PGV becomes larger. Furthermore, the distribution of added damping coefficients shows a drastic change just after  $d_{\max}/d_y$  attains 1 as shown in Figures 2c and 3c. For larger levels of GMs, the distribution changes gently.

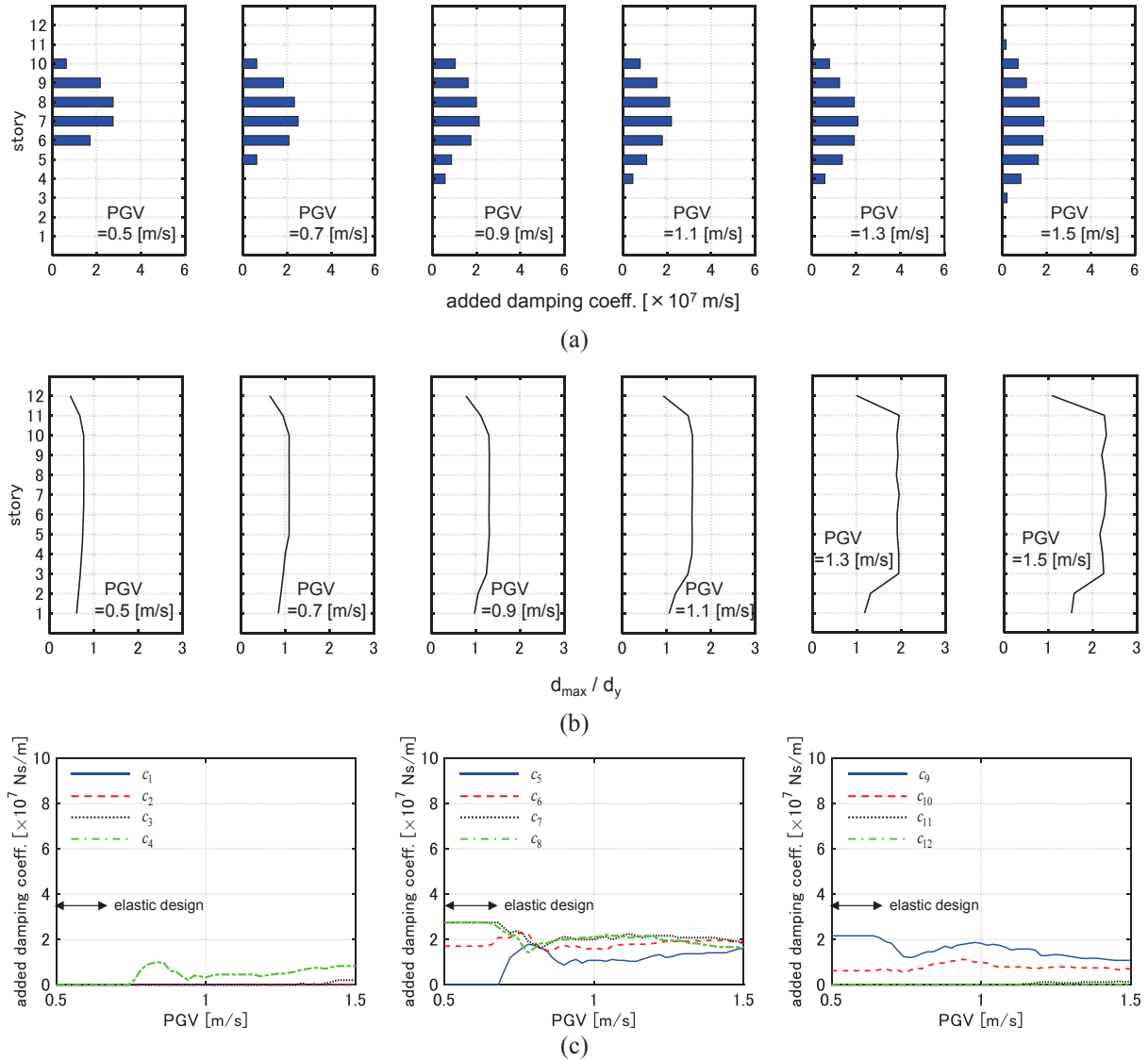


Figure 2: Optimal designs of added viscous damper for multiple-level GMs (Model 1), (a) distribution of added damping coefficient, (b) distribution of  $d_{\max,i}/d_y$ , (c) change of added damping coefficient of each story.



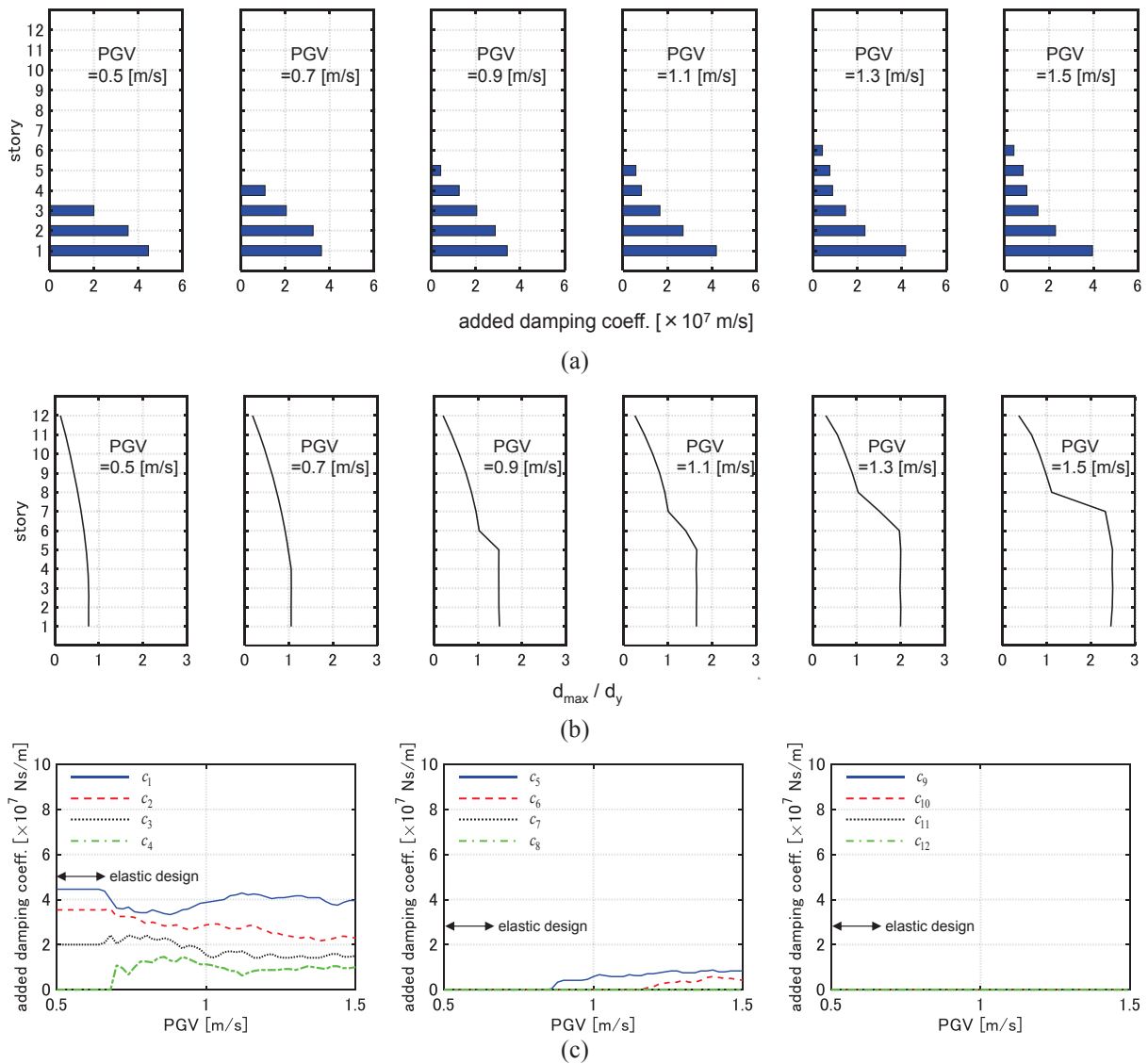


Figure 3: Optimal designs of added viscous damper for multiple-level GMs (Model 2), (a) distribution of added damping coefficient, (b) distribution of  $d_{\max,i} / d_y$ , (c) change of added damping coefficient of each story.

## 2.4 Influence of number of input ground motions

In this section, the influence of the number of input GMs on the final design is investigated. Hachinohe NS component during the Tokachi-oki earthquake in 1968 and El Centro NS component are employed. All the other parameters for the optimization are the same as those in Section 3.1. It should be noted that the predominant period of Hachinohe NS component is longer than that of El Centro NS component.

Figures 4 and 5 show the optimal designs for Model 1 and 2. It can be observed that, in the case of  $PGV \leq 0.9$  [m/s], the optimal distributions of added damping coefficients are the same as those in Section 3.1. This is because El Centro NS component provides the response envelopes. When PGV used for the design becomes larger, Hachinohe NS component is critical in the lower stories. This means that, as PGV becomes large and the plastic deformation level increases, the equivalent natural period is lengthened. For Model 1, the distributions of the

added damping coefficients are smoother than the optimal distributions designed only under El Centro NS component. For Model 2, similar to the case in Section 3.1, the added dampers are concentrated to the lower stories. This is because Model 2 has a uniform distribution of story stiffnesses and tends to exhibit plastic deformation concentration in the lower stories for large inputs. It can also be said that, while almost all the stories exhibit plastic deformations for large inputs in the case of Model 1, the upper stories remain elastic for large inputs in the case of Model 2. Therefore, the value of  $d_{\max} / d_y$  of Model 2 for larger inputs are larger than that of Model 1.

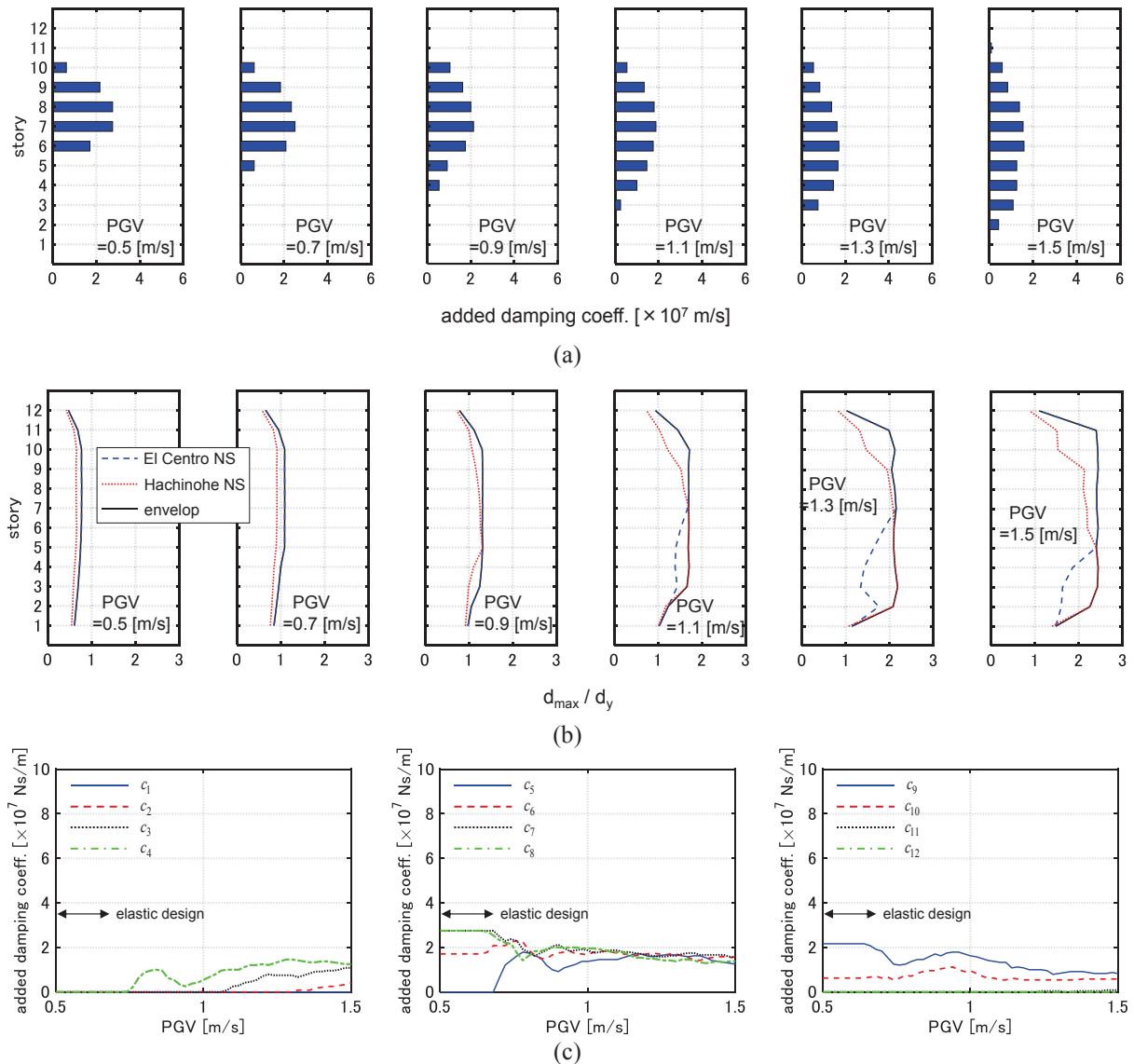


Figure 4: Optimal designs of added viscous damper for multiple-level two GMs (Model 1), (a) distribution of added damping coefficient, (b) distribution of  $d_{\max,i} / d_y$ , (c) change of added damping coefficient of each story.

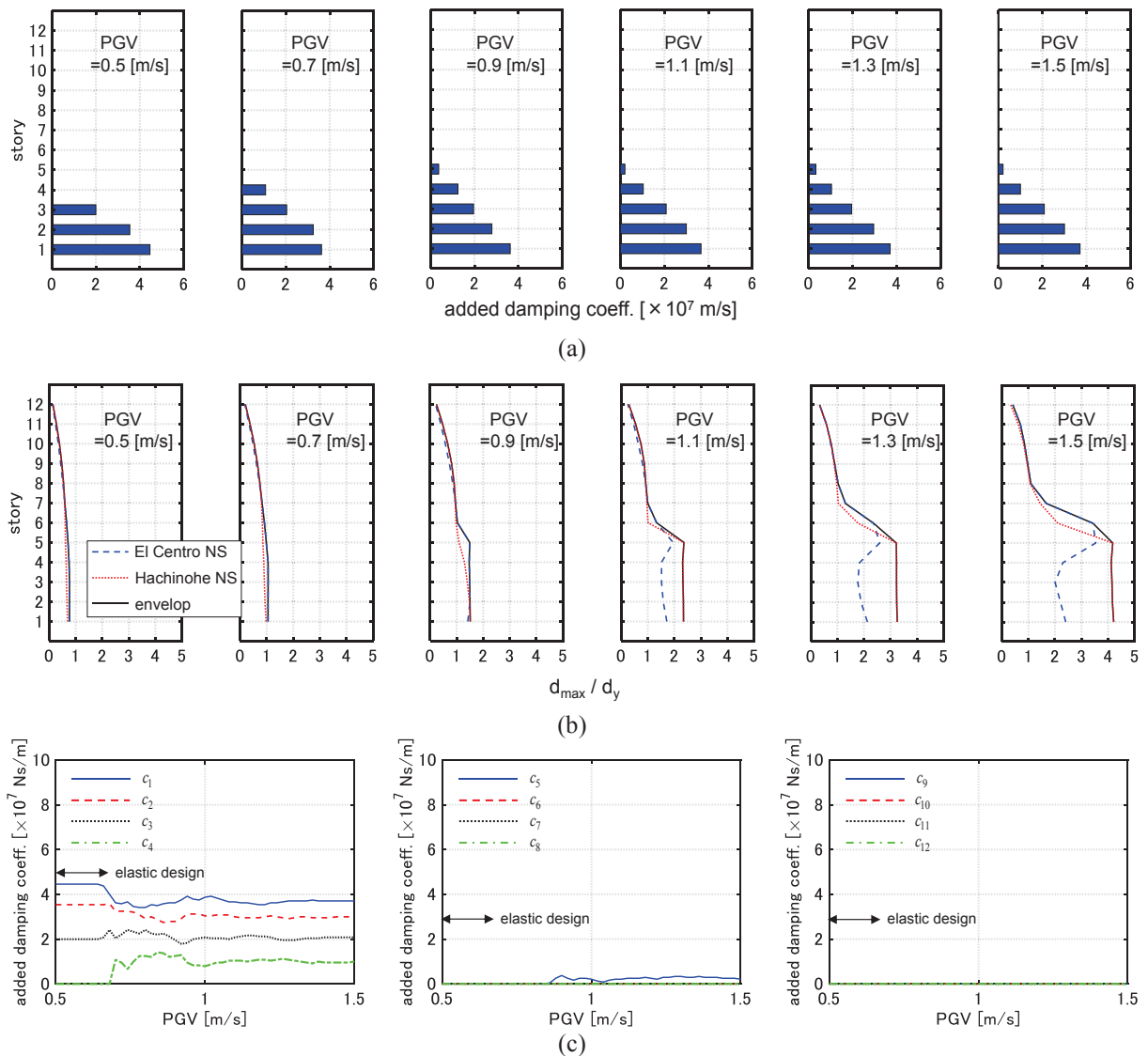


Figure 5: Optimal designs of added viscous damper for multiple-level two GMs (Model 2), (a) distribution of added damping coefficient, (b) distribution of  $d_{\max,i} / d_y$ , (c) change of added damping coefficient of each story.

## 2.5 IDA analysis and ideal drift response curve

In this section, IDA analysis [13] is conducted for the models obtained in Section 3.2. El Centro NS component and Hachinohe NS component are adopted for IDA. PGV is increased from 0.5 [m/s] to 1.5 [m/s] by 0.02 [m/s].

Figures 6a and 7a show the maximum interstory drift distributions by IDA analysis for the models designed under these two GMs with PGV=0.5, 1.0, 1.5 [m/s]. The input level PGV=0.5 corresponds to elastic design. It can be observed that the models designed for PGV=0.5, 1.0 [m/s] exhibits large deformation concentrations in specific stories for these two GMs with larger PGV. Figure 6c and 7c illustrate the critical earthquakes in the applications of IDA. El Centro NS component is critical in the lower range of PGV and Hachinohe NS component is critical in the upper range of PGV for all models since the predominant period of the latter is longer than that of the former as stated in Section 3.2.

Figures 6b and 7b show the IDA curves and the ideal drift response curves. An ideal drift response curve is a plot of the optimized maximum deformations versus design  $IM$ . The opti-

mal designs for various levels of GMs are obtained by conducting CDGM, and simultaneously the ideal drift response curve is provided. The IDA curves for all the optimal designs never cross the ideal drift response curve, and the IDA curve for each optimal design is tangent to the ideal drift response curve only at the point where  $IM$  corresponds to the design  $IM$ . It can be observed that the IDA curves for the models designed for  $PGV=1.5$  [m/s] run near the ideal drift response curves.

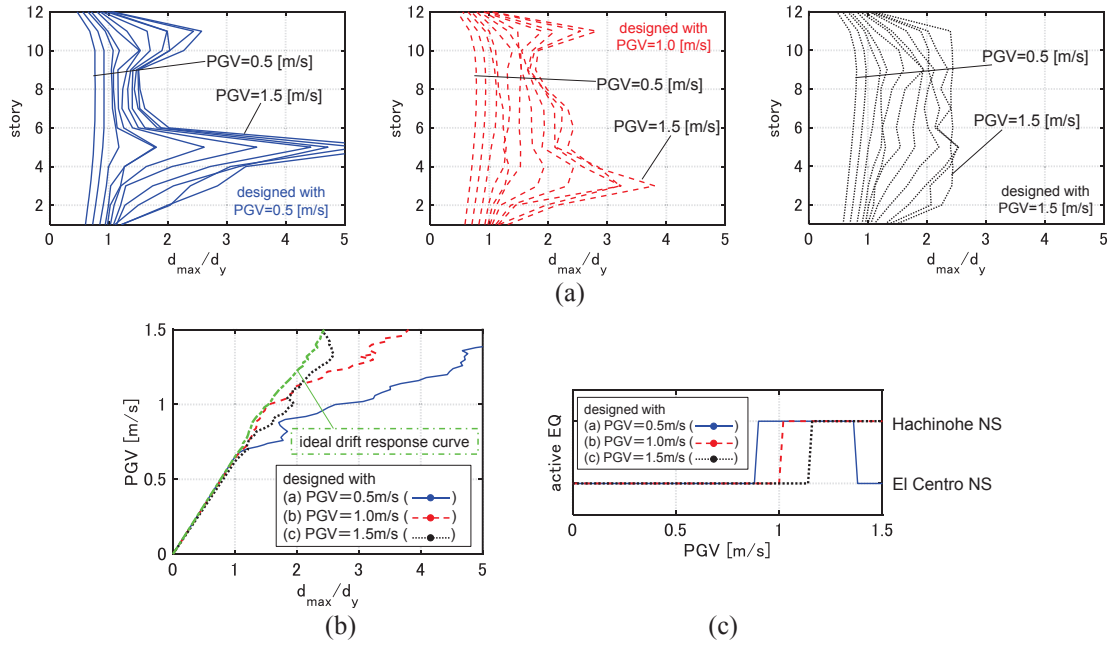


Figure 6: IDA analysis for 3 models designed under GMs with  $PGV=0.5, 1.0, 1.5$  [m/s] (Model 1), (a) distribution of  $d_{max,i} / d_y$ , (b) IDA curves and ideal drift response curve, (c) active EQ.

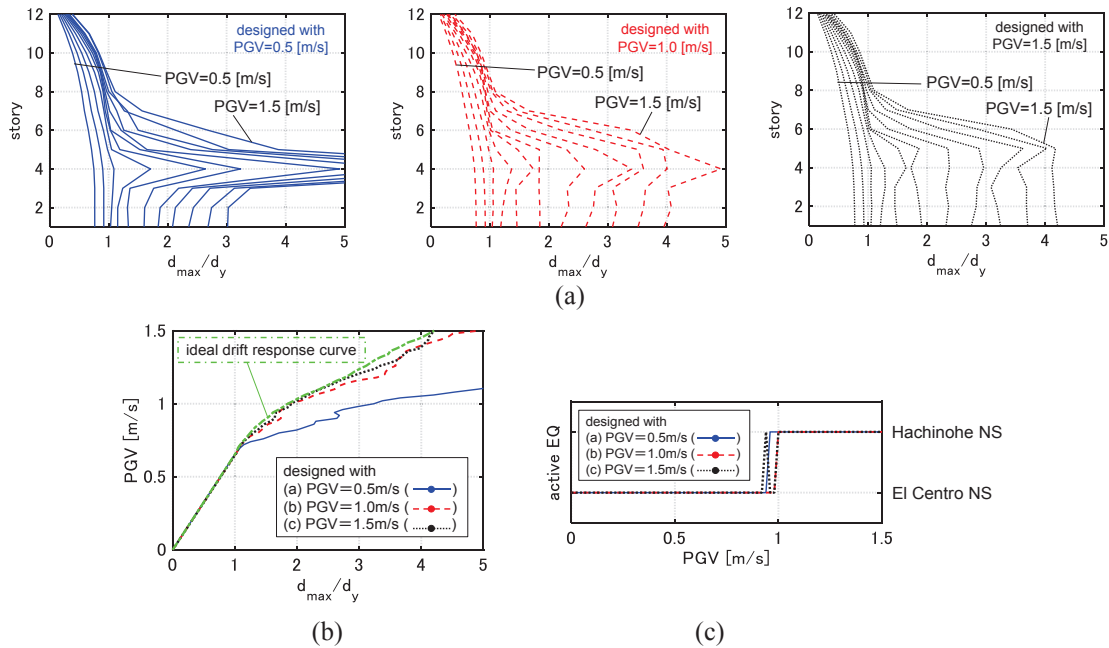


Figure 7: IDA analysis for 3 models designed under GMs with  $PGV=0.5, 1.0, 1.5$  [m/s] (Model 2), (a) distribution of  $d_{max,i} / d_y$ , (b) IDA curves and ideal drift response curve, (c) active EQ.

As shown in Figures 6 and 7, the model optimally designed for a specified-level GMs is not necessarily effective for other levels of GMs. Therefore, a design guideline for the problem, which design to be chosen from the various optimal designs, is needed. In this paper, a simple index for selection is introduced as follows,

$$\max_{IM} \{d_{\max}(IM) - \text{IDRC}(IM)\}$$

where IDRC denotes the value of the ideal drift response curve. It can be said that the design, which minimizes the proposed index, shows high robustness (effective for various levels of GMs). Figure 8 indicates the procedure for selecting such design.

Figures 9 and 10 show the values of the proposed index for the models obtained in Section 3.2 and the IDA curves for the models which minimize the proposed index. It can be observed that, as PGV used for the design becomes larger, the value of the proposed index generally decreases. It can also be said that the elastic designs provide the highest value of the index. For both Models 1 and 2, the designs, which minimize the index, are effective for various levels of the GMs. Especially for Model 2, the IDA curve for the selected design runs quite near the ideal drift response curve. This is because Model 2 tends to exhibit plastic deformation concentration in the lower stories for large inputs as stated in Section 3.2.

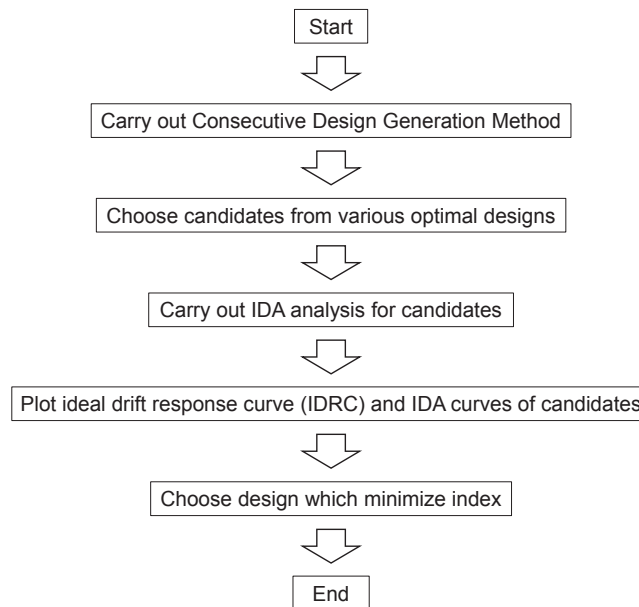


Figure 8: Schematic diagram for choosing robust design for various levels of GMs.

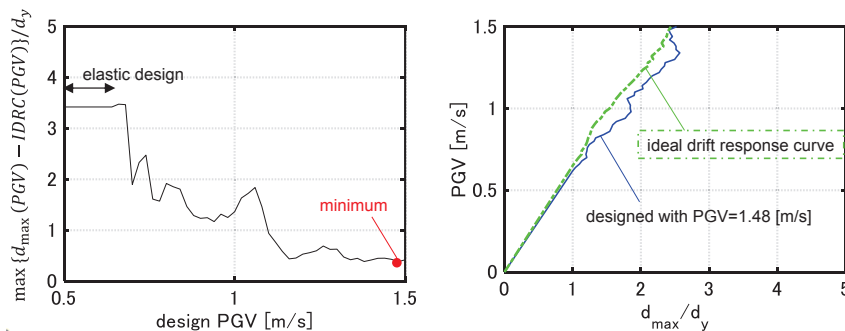


Figure 9: Proposed index and IDA curve for design with minimum index (Model 1).

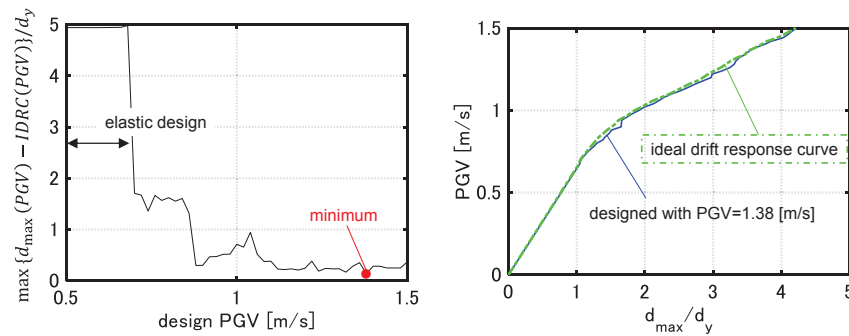


Figure 10: Proposed index and IDA curve for design with minimum index (Model 2).

### 3 CONCLUSIONS

A new optimal damper design method is presented for elastic-plastic MDOF building structures under multiple-level earthquake ground motions (GMs). The main conclusions can be summarized as follows.

- A consecutive design generation method (CDGM) was proposed for the above-mentioned problem. By using CDGM, all the optimal designs can be obtained with much lower computational effort than the method repeating an ordinary optimization procedure under every-level GM. CDGM also helps to understand how the distribution of added damper damping coefficients changes as the level of GMs changes.
- As the level of input GMs used for the design becomes larger, dampers concentrated to the specified stories spread around those stories and the distribution of the added damping coefficients becomes smoother.
- As the number of input GMs used for the design increases, the distribution of the added damping coefficients becomes smoother.
- Models designed for lower-level GMs may exhibit large plastic deformation concentrations in specific stories for larger-level GMs.
- A new concept of ‘ideal drift response curve’ was presented for selecting a robust design for various levels of GMs. This is a plot of the optimized maximum deformation versus design  $IM$  (level of input GMs). The optimal designs for various levels of GMs were obtained by conducting CDGM, and simultaneously the ideal drift response curve was provided.

### REFERENCES

- [1] Akehashi, H., and Takewaki, I. (2019). Optimal viscous damper placement for elastic-plastic MDOF structures under critical double impulse. *Frontiers in Built Environment*, 5: 20.
- [2] Akehashi, H., and Takewaki, I. (2020a). Comparative investigation on optimal viscous damper placement for elastic-plastic MDOF structures: Transfer function amplitude or double impulse. *Soil Dyn. Earthq. Eng.*, 130, 105987.
- [3] Akehashi, H., and Takewaki, I. (2020b). Simultaneous optimization of elastic-plastic building structures and viscous dampers under critical double impulse. *Frontiers in Built Environment*, 6, 211.



- [4] Cetin, H., Aydin, E., and Ozturk, B. (2019). Optimal Design and Distribution of Viscous Dampers for Shear Building Structures under Seismic Excitations. *Frontiers in Built Environment*, 5: 90.
- [5] Garcia, D.L. (2001). A simple method for the design of optimal damper configurations in MDOF structures. *Earthq. Spectra*, 17, 387-398.
- [6] Lagaros, N. D. (Ed.). (2012) *Design optimization of active and passive structural control systems.*, IGI Global.
- [7] Lavan, O., and Avishur, M. (2013). Seismic behavior of viscously damped yielding frames under structural and damping uncertainties. *Bulletin of Earthq. Eng.*, 11(6), 2309-2332.
- [8] Murakami, Y., Noshi, K., Fujita, K., Tsuji, M., and Takewaki, I. (2013). Simultaneous optimal damper placement using oil, hysteretic and inertial mass dampers, *Earthq. and Struct.*, 5(3), 261-276.
- [9] Silvestri, S., and Trombetti, T. (2007). Physical and numerical approaches for the optimal insertion of seismic viscous dampers in shear-type structures. *J. Earthq. Eng.*, 11, 787-828.
- [10] Takewaki, I. (1997). Optimal damper placement for minimum transfer functions, *Earthq. Eng. Struct. Dyn.*, 26(11), 1113-1124.
- [11] Takewaki, I. (2009). *Building Control with Passive Dampers: -Optimal Performance-based Design for Earthquakes-*, John Wiley & Sons Ltd. (Asia), Singapore.
- [12] Takewaki, I., and Akehashi, H. (2021). Comprehensive review of optimal and smart design of nonlinear building structures with and without passive dampers subjected to earthquake loading. *Frontiers in Built Environment*, 7: 631114.
- [13] Vamvatsikos, D., and Cornell, C.A. (2001). Incremental dynamic analysis. *Earthq. Eng. Struct. Dyn.*, 31(3), 491–514.
- [14] Whittle, J.K., Williams, M.S., Karavasilis, T.L., and Blakeborough, A. (2012). A comparison of viscous damper placement methods for improving seismic building design, *J. Earthq. Eng.*, 16(4), 540-560.
- [15] Zhang, R. H., and Soong, T. T. (1992). Seismic design of viscoelastic dampers for structural applications. *J. Struct. Eng.*, 118(5), 1375-1392.

## DIFFERENTIATION OF THE CONSTRUCTION COST OF A FIFTEEN-STOREY R/C BUILDING DEPENDING ON THE SEISMIC HAZARD ZONE

Paulina A. Tselempi<sup>1</sup>, Theodoros A. Chrysanidis<sup>1</sup>

<sup>1</sup> International Hellenic University  
P.O. Box 141, P.C. 57400, Sindos, Thessaloniki, Greece  
cie20160124@cie.teithe.gr, theodoros\_gr@yahoo.com

---

### Abstract

*Greece is divided into three seismic hazard zones ZI, ZII, ZIII. In the present research work, the same building in the three seismic zones of Greece is modeled, analysed and dimensioned and then the construction cost of its structural body is estimated. The building modeling was performed in SAP2000 using linear finite elements. The analysis of the building was performed by dynamic spectral analysis methods using the design spectrum of EC8. A fifteen-storey building with a standard floor plan per floor was used. The purpose of this research paper is to study the possible influence of seismicity, based on which the dimensioning takes place, on the construction cost of the load-bearing structure of a fifteen-storey building with a standard floor plan per floor. The degree of influence is studied by estimating the quantities of materials required depending on the seismic hazard zone. Interesting comparisons take place between the results for the three different seismic hazard zones. Useful conclusions are drawn regarding the influence of seismicity on the construction cost of the load-bearing structure of reinforced concrete buildings.*

**Keywords:** Seismic zone, Construction cost, Multi-storey building

---

## 1 INTRODUCTION

Greece ranks sixth in the world in the list of most seismic countries. Although it occupies 0.02 of the Earth's surface, it releases 2% of global seismic energy each year and more than 50% of the European. Therefore, Greece is challenged to face earthquake phenomenon by improving the construction of structures, taking under consideration the parameters of safety and cost. According to those factors, the earthquake resistant regulations have been evolved worldwide [1]–[3], facing with great effectiveness the safety of human life. In the seismic design of reinforced concrete structures, a key parameter is the seismic design actions, based on which the structures in each area are designed (Table 1).

The seismic design actions of the structures depend on the seismic hazard of each area and their values are determined in the Seismic Hazard Map, which is an integral part of the Earthquake Regulation [2], [3]. Seismic hazard is the maximum expected value of a seismic parameter for a given recurrence period or for a specific probability of non-overcoming and a specific period of time. The results of seismic hazard studies are given in the form of maps or curves that provide the distribution of the selected ground motion measure and the probability that it will be exceeded or not exceeded in a certain period of time (Figure 1). Usually, the probability of distribution is estimated by 10% of exceeding a defined value of land movement for the time period of 50 years or equal, an average repetition of 475 years.

The expected values of the ground acceleration are derived from seismic hazard studies, after statistical processing of seismic events that have occurred in the wider project area. Such studies are prepared for large and important projects, while for ordinary constructions the prices are given by the regulations, depending on the area in which the construction is going to take place. According to EC8 [2] and Greek Seismic Code [3], national areas are subdivided into seismic zones (Z1, Z2 and Z3) depending on the local hazard (Figure 1). By definition, it is assumed that within each zone the hazard is constant and is described by a single parameter, the value of the maximum reference ground acceleration  $\alpha_g R$ , which corresponds to soil category “A” and characterizes the seismic activity in each zone. Considering the above, the present work aims to investigate whether the design and study of a building in each seismic zone, can affect the cost of construction of its load-bearing structure. Several studies have been conducted regarding the cost, as far as various types of structures are concerned [4]–[10]. This study aims to investigate the cost in terms of the construction cost of load-bearing structure of multi-storey buildings and if and how it is affected by the seismicity of the area.

Zone of seismic risk	Ground acceleration values (g)
Z1	0,16
Z2	0,24
Z3	0,36

Table 1: Ground acceleration values [3].

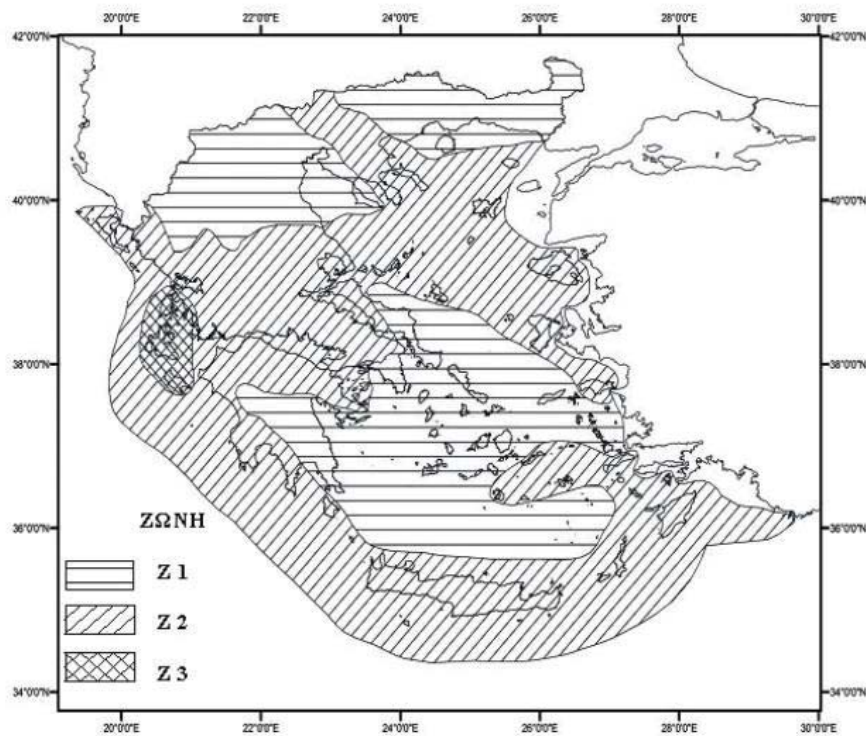


Figure 1: Seismic hazard map of Greece [3].

## 2 ANALYTICAL RESEARCH

### 2.1 Building data

The building under consideration is symmetrical, with a rectangular floor plan with dimensions of 25 x 25 m, slab thickness equal to 15 cm, total height 46.50 m (all floors are 3 m, except the 1<sup>st</sup> floor which has a height equal to 4.5 m) and will not include basement. The influence of the soil is neglected and rigid connections are used for the building's supports [11]–[16]. In the center of the floor plan, there are two symmetrical cores consisting of 8 walls with different dimensions (6 along the Y axis and 2 along the X axis), which are connected by three beams 1m long and 0.70 m high. Also, there are two walls in the perimeter of the floor plan along the Y axis, which have enlarged boundary edges at their both ends (Figure 2), in order for phenomena of lateral buckling at seismic walls to be avoided [17]–[31].

Regarding the dimensions of the cross-sections of the structural elements, the cross-sections of the columns of the building remain constant for the 1st floor (ground floor) and the 2nd, while the rest are reduced by 5 cm per floor. The cross-sections of the beams remain fixed on all floors, while the cross-sections of the walls vary in height and are reduced per 5 floors by 12.5 cm. The construction materials of the building are concrete C30/37 and steel B500C. The cross sections of the beams remain the same in every storey but the cross sections of the walls shift per floor and decrease per 5 storeys for 12.5 cm. The construction materials of the building, is C30/37 concrete and Steel B500C. Finally, below are presented the floor plan and the table of cross sections of the structural elements of the building.

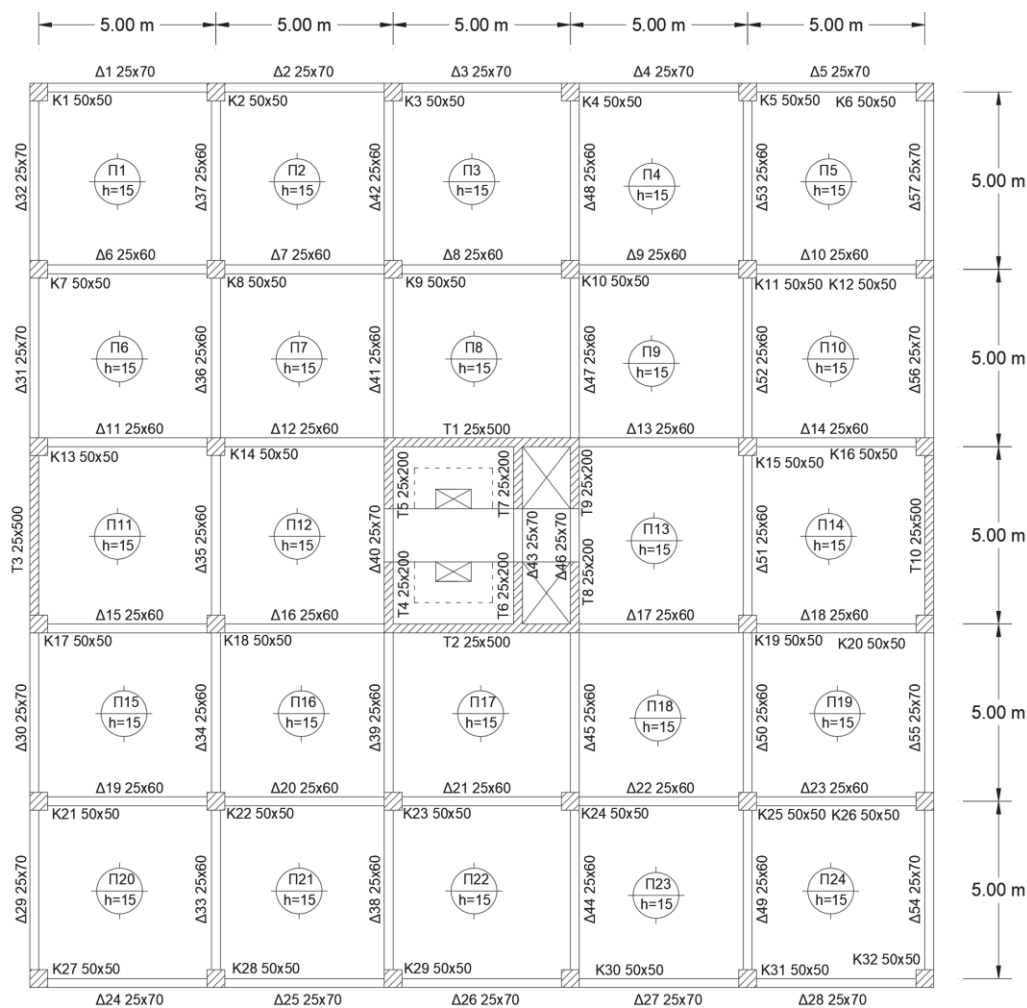


Figure 2: Typical floor plan.

Floor	Height (m)	Beam dimensions (cm)		Wall thickness (cm)	Column dimensions (cm)
		Perimetric	Internal		
<b>1<sup>st</sup> (Ground floor)</b>	4.50	25x70	25x60	50	100x100
<b>2</b>	3.00	25x70	25x60	50	100x100
<b>3</b>	3.00	25x70	25x60	50	95x95
<b>4</b>	3.00	25x70	25x60	50	90x90
<b>5</b>	3.00	25x70	25x60	50	85x85
<b>6</b>	3.00	25x70	25x60	37.5	80x80
<b>7</b>	3.00	25x70	25x60	37.5	75x75
<b>8</b>	3.00	25x70	25x60	37.5	70x70
<b>9</b>	3.00	25x70	25x60	37.5	65x65
<b>10</b>	3.00	25x70	25x60	37.5	60x60
<b>11</b>	3.00	25x70	25x60	25	55x55
<b>12</b>	3.00	25x70	25x60	25	50x50
<b>13</b>	3.00	25x70	25x60	25	45x45
<b>14</b>	3.00	25x70	25x60	25	40x40
<b>15</b>	3.00	25x70	25x60	25	35x35

Table 2: Dimensions of the structural elements.

## 2.2 Construction

The building, as a typical construction, is stressed by gravity loads which are the permanent loads (self-weight, etc.), the live loads (human load, etc.) and the seismic loads. For the building in question, the loads are shown in Table 3.

PERMANENT LOADS		
N/A	Type	Value
1	Flooring	1.40 kN/m <sup>2</sup>
2	Partition brick structures	1.00 kN/m <sup>2</sup>
3	Perimeter brick structures	8.00 kN/m
4	Roofing	3.50 kN/m <sup>2</sup>
5	Parapet roof load	3.60 kN/m <sup>2</sup>
LIVE LOADS		
N/A	Type	Value
1	Ground floor	2.00 kN/m <sup>2</sup>
2	Typical floors	2.00 kN/m <sup>2</sup>
3	Roof	2.00 kN/m <sup>2</sup>
SPECTRUM DATA EC8		
N/A	Type	Data
1	Spectrum type	Horizontal design spectrum type 1
2	Soil category	B
3	Factor $\beta$	0.20
4	Seismic acceleration factor $\alpha$	For the three categories: $\alpha = 0.16, 0.24, 0.36$
5	Gravity acceleration g	9.81 m/sec <sup>2</sup>
6	Coefficient behavior q	Calculation based on EC8

Table 3: Building loads.

## 2.3 Modelling

The modeling of the load-bearing structure of the building will be performed with the finite element software SAP2000. The individual structural elements that were modeled are the beams, the columns and the seismic walls of the building. Also, it is essential to simulate the diaphragm function of the slabs on each floor. The dynamic spectral method analysis according to the EC8 [2] will be applied for the seismic actions of the building.

In conclusion, through the simulation some results will be extracted according to which the building will be dimensioned for the three seismic hazard zones and these are the design moments of the beams, the values for N,  $M_{33}$ ,  $M_{22}$  of the vertical elements. Figure 3 presents the 3D model of the building.



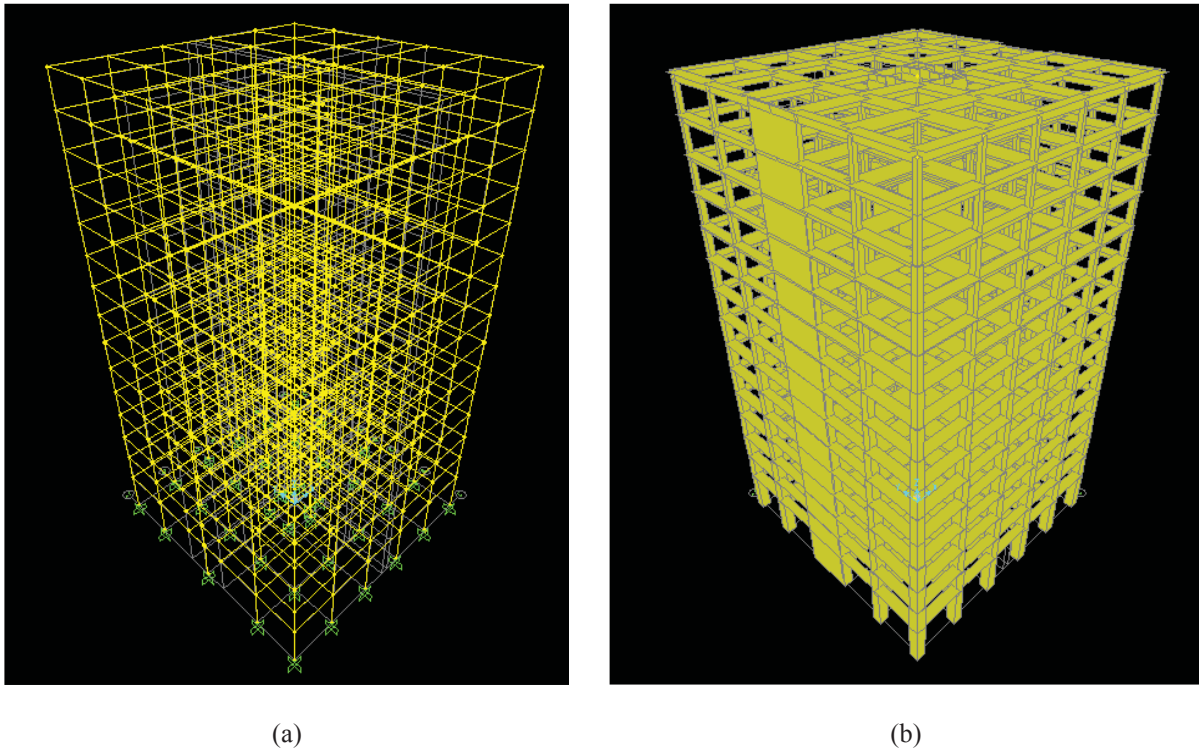


Figure 3: Views of the 3D building model: (a) Linear finite elements (b) Sections.

## 2.4 Dimensioning of the building

The dimensioning of the building will be based on EC8 [2] and EC2 [32], for each seismic hazard zone only for the 14<sup>th</sup> floor level. The horizontal structural members dimensioned are the slabs of the 14<sup>th</sup> floor and the beams of this level, while the vertical structural members are the columns and the structural walls. Figure 4 and Figure 5 present indicative reinforcement of the beam and the slab respectively resulted by the building design.

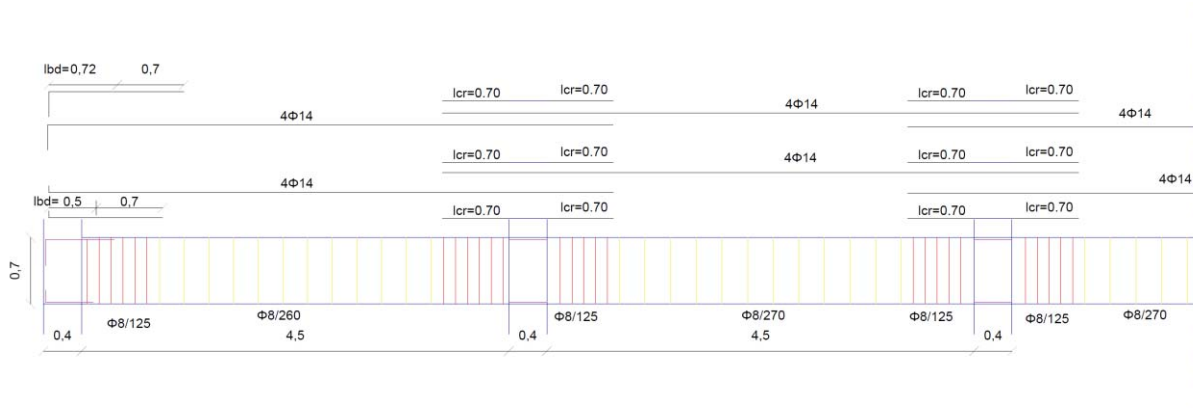
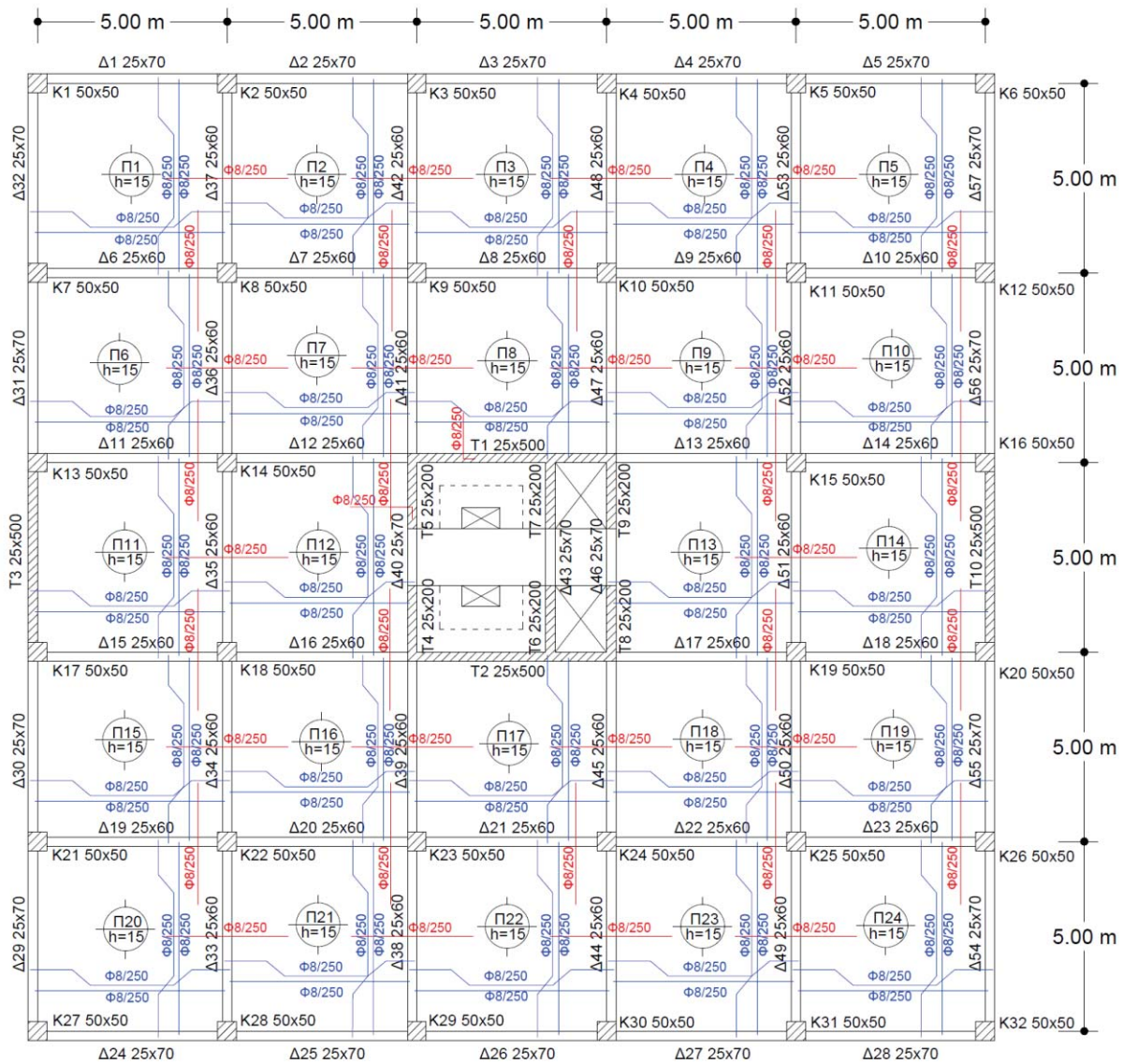


Figure 4: Beam reinforcement of the 14<sup>th</sup> floor.

Figure 5: Slab reinforcement of the 14<sup>th</sup> floor.

## 2.5 Measurements of building materials

The measurement of building materials used for the construction of the load-bearing structure (concrete and steel) for all three seismic zones will be calculated considering the results of the design. Table 4 displays the measurements for the concrete material, which remain the same for all three seismic zones. Similar calculations have taken place for the measurement of the steel material used for the concrete reinforcements.

CONCRETE MEASUREMENT					
STOREY	SLABS (m <sup>3</sup> )	BEAMS (m <sup>3</sup> )	COLUMNS (m <sup>3</sup> )	WALLS (m <sup>3</sup> )	TOTAL (STOREY) (m <sup>3</sup> )
1	90	33.08	139.2	63.08	325.36
2	90	33.08	91.20	41.33	255.61
3	90	33.92	82.31	41.61	247.84
4	90	34.72	73.87	41.90	240.49
5	90	35.55	65.89	42.18	233.62
6	90	36.35	58.37	31.85	216.57
7	90	37.19	51.30	32.06	210.55
8	90	37.99	44.69	32.28	204.96
9	90	38.82	38.53	32.49	199.84
10	90	39.62	32.83	32.70	195.15
11	90	40.46	27.59	21.95	180.00
12	90	41.26	22.80	22.09	176.15
13	90	42.09	18.47	22.23	172.79
14	90	42.89	14.59	22.37	169.85
15	90	43.69	11.17	22.52	167.38
				<b>TOTAL</b>	<b>3196.16</b>

Table 4: Concrete measurement.

### 3 RESULTS ANALYSIS

#### 3.1 Concrete measurements

Figure 6 shows the amount of concrete per floor and Figure 7 displays the amount of concrete occupied by the structural elements of the load-bearing structure.

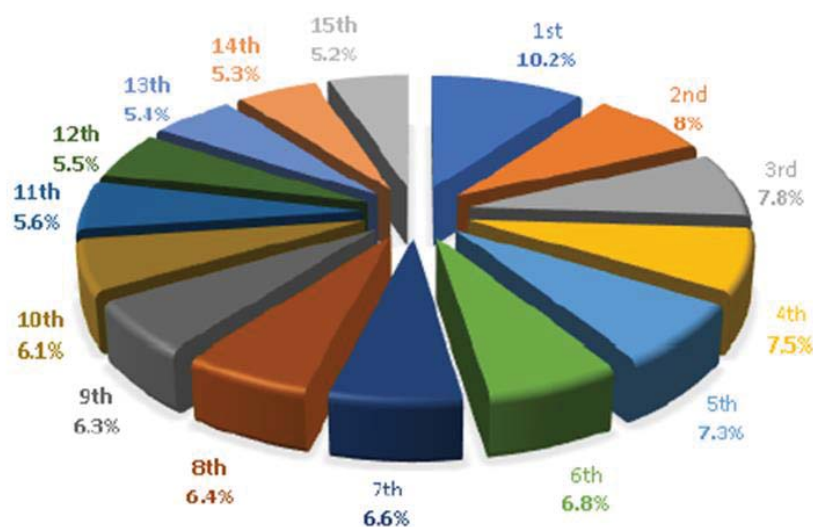


Figure 6: Percentage of concrete per floor (%).

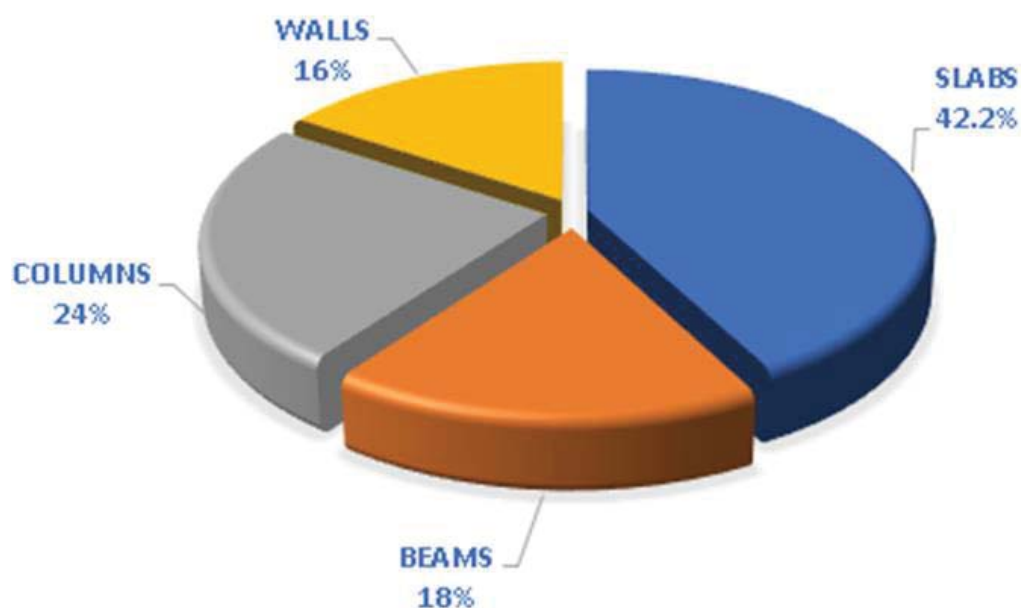


Figure 7: Percentage of structural elements in the total concrete (%).

From the previous diagrams, it is obvious that the 1<sup>st</sup> floor occupies the largest percentage of concrete in relation to the other floors, while at the same time the percentage of the other floors decreases from floor to floor. Also, the slabs occupy the largest percentage of the total concrete with 42.2%, followed by the columns with 24%, the beams with 18% and finally the walls with 16%.

### 3.2 Steel measurements

#### 3.2.1. Steel measurement per seismic zone

Table 5 presents the quantities of steel in kgr that result for the structural elements of the building, in each seismic zone. The same results are displayed in the form of a column graph in Figure 8.

REINFORCEMENT STEEL MEASUREMENT					
Seismic zone	Slabs	Beams	Columns	Walls	TOTAL
<b>I</b>	9214.32	6353.50	2615.83	2826.53	<b>21010.18</b>
<b>II</b>	9214.32	6416.78	2623.71	3019.44	<b>21274.25</b>
<b>III</b>	9214.32	6455.03	2631.59	3261.77	<b>21562.71</b>

Table 5: Structural element steel weight for the three seismic zones.

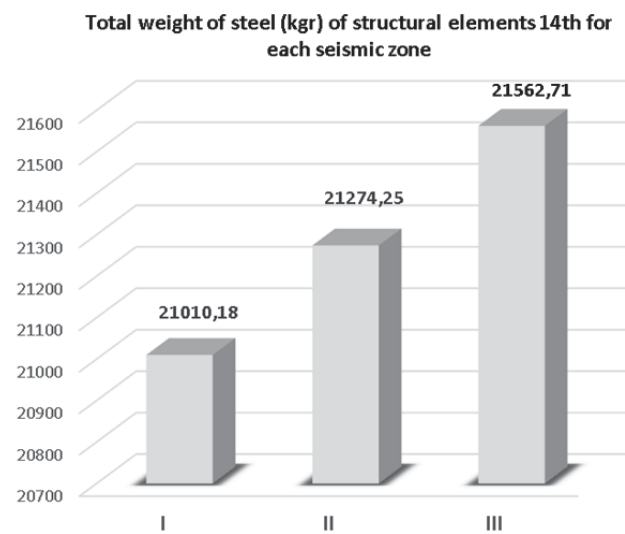


Figure 8: Total weight of reinforcement steel of structural elements of the 14<sup>th</sup> floor for each seismic zone.

### 3.2.2. Percentage change of steel weight between the seismic zones

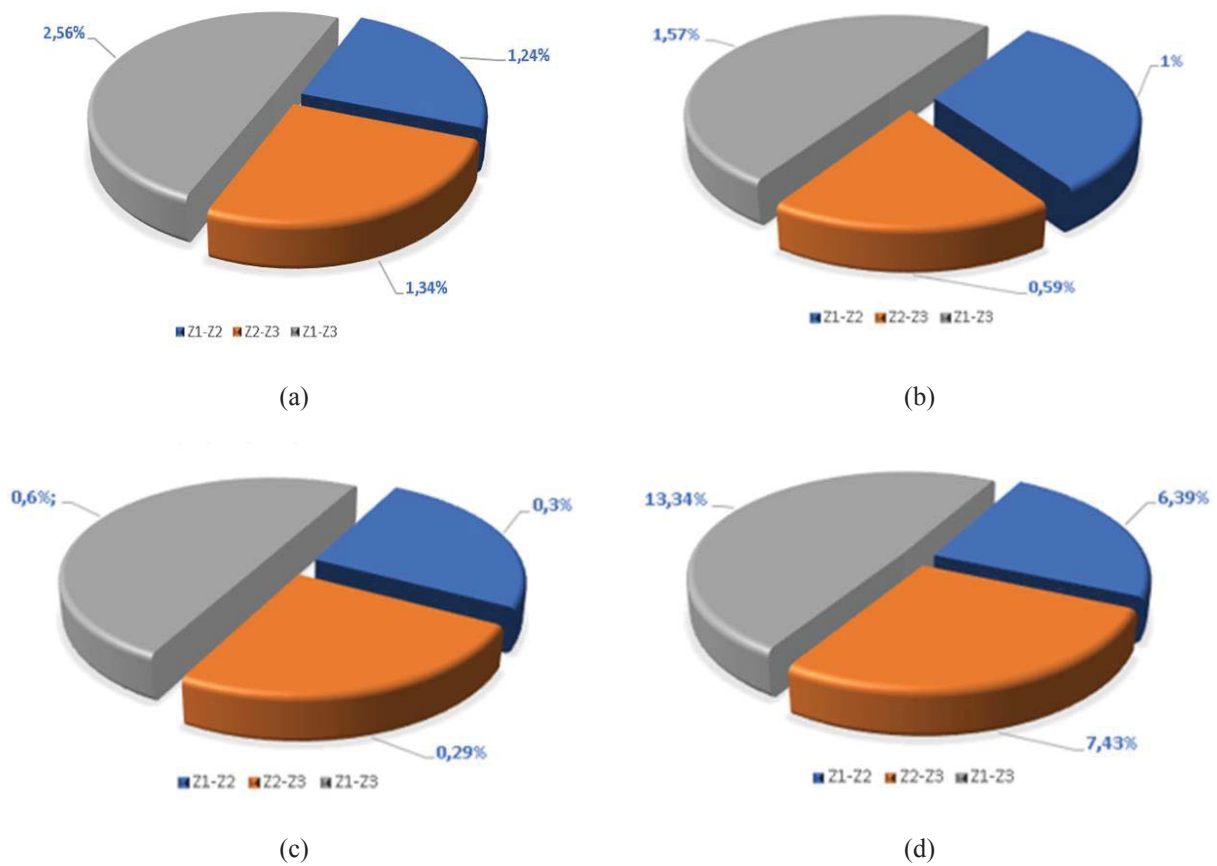


Figure 9: Percentage change of weight of steel reinforcement of the 14<sup>th</sup> floor for each seismic zone concerning:  
(a) All structural elements, (b) Beams, (c) Columns, (d) Seismic walls



From Figure 9, it appears that:

- The transition from Zone I with seismic acceleration  $\alpha_g = 0.16g$ , to Zone II with seismic acceleration  $\alpha_g = 0.24g$  causes:
  - 1.24% increase of the total steel weight for all structural elements
  - 1.00% increase of the steel weight for the beams
  - 0.3% increase of the steel weight for the columns
  - 6.39% increase of the steel weight for the structural walls
- The transition from Zone II with seismic acceleration  $\alpha_g = 0.24g$ , to Zone III with seismic acceleration  $\alpha_g = 0.36g$  causes:
  - 1.34% increase of the total steel weight for all structural elements
  - 0.59% increase of the steel weight for the beams
  - 0.29% increase of the steel weight for the columns
  - 7.43% increase of the steel weight for the structural walls
- The transition from Zone I with seismic acceleration  $\alpha_g = 0.16g$ , to Zone II with seismic acceleration  $\alpha_g = 0.36g$  causes:
  - 2.56% increase of the total steel weight for all structural elements
  - 1.57% increase of the steel weight for the beams
  - 0.60% increase of the steel weight for the columns
  - 13.34% increase of the steel weight for the structural walls

Therefore, if the weight percentage of the individual structural elements of the structure (columns, beams and structural walls) increases from Zone I to Zone II and Zone III, except for the steel weight for the slabs that remains constant in the three seismic zones, that fact results to the increase of the total steel weight of the 14<sup>th</sup> floor.

### 3.2.3. Percentage of reinforcement steel per structural element for each seismic zone

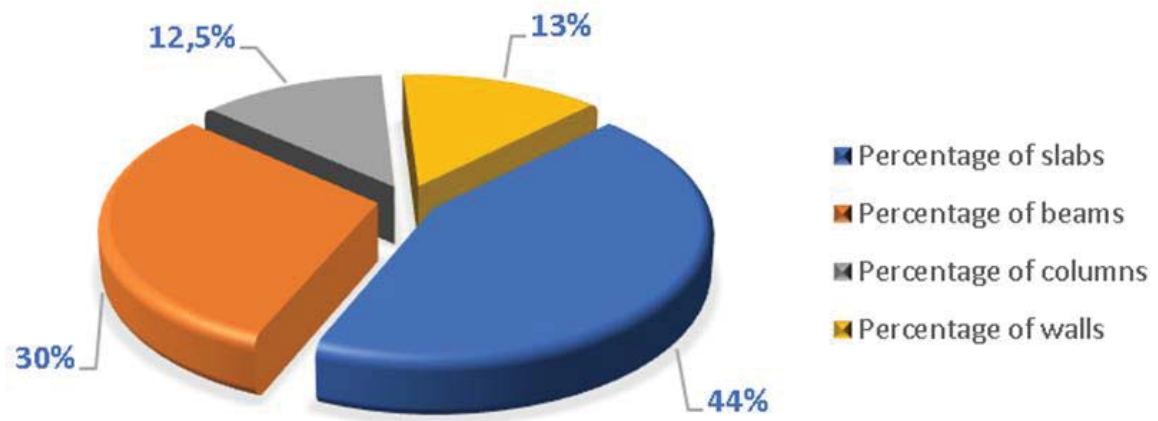
Figure 10 shows the percentage of steel weight of each structural element in all three seismic zones. According to these figure, it is concluded that:

- Slabs occupy the largest percentage of steel in Zone I: 44%, while in Zone II: 43% and in Zone III: 42.7%.
- Beams occupy the second largest percentage of steel in Zone I: 30%, while in Zone II: 30% and in Zone III: 29%.
- Structural walls occupy the third largest percentage of steel in Zone I: 13%, while in Zone II: 14.2% and in Zone III: 15.1%.
- Columns occupy the smallest percentage of steel in Zone I: 12.5%, while in Zone II: 12.3% and in Zone III: 12.2%.

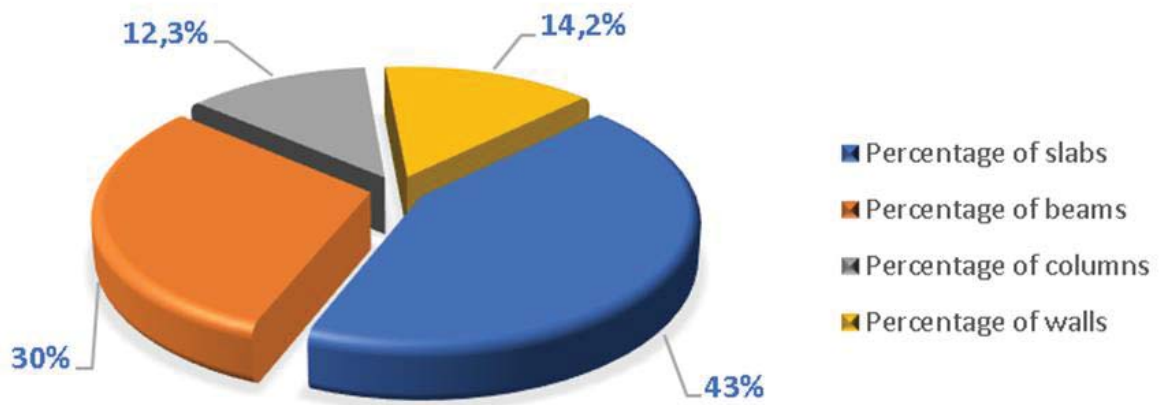
Furthermore, the design and detailing of the various structural elements has shown that during the transition from Zone I to Zone II and II:

- The beams maintain their longitudinal reinforcement constant, while the transverse reinforcement shows some increase.
- The columns also maintain their longitudinal reinforcement stable, while the transverse reinforcement shows some increase.
- Finally, the structural walls show an increase in their transverse reinforcement and the T3 and T10 structural walls (Figure 5) also show increases in their longitudinal reinforcement.

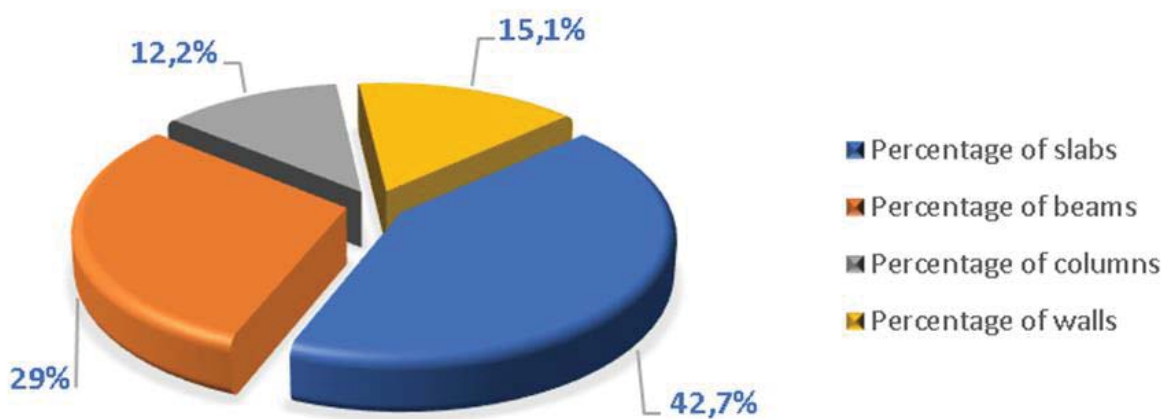




(a)



(b)



(c)

Figure 10: Percentage of steel weight per structural element for: (a) Zone I, (b) Zone II, (c) Zone III.

## 4 CONCLUSIONS

The structure studied in the present research is a fifteen-storey reinforced concrete building without a basement with rectangular conventional floor plan. It has been designed for all three seismic hazard zones Zone I, Zone II and Zone III. The resulting conclusions can be summarized as follows:

1. Walls show the largest percentage increase in steel weight with the increase of seismic acceleration.
2. At the beams, the steel weight increases much less than in seismic walls.
3. At the columns, the steel weight increases even less than the beams.
4. Therefore, the seismic walls are the dominant structural element in the building's system. Thus, it is a wall-governed system.
5. The increase of seismic acceleration  $\alpha_g$ :
  - From Zone I to Zone II is about 50%, while the percentage increase of the total amount of materials is only 1.24%.
  - From Zone II to Zone III is about 50%, while the percentage increase of the total amount of materials is only 1.34%.
  - From Zone I to Zone III is about 125%, while the percentage increase of the total amount of materials is only 2.56%.
6. Thus, the percentage increase in the total demand on steel is quite small.
7. So, we conclude that for a fifteen-storey reinforced concrete building, with a strong core wall arrangement, the influence of seismic hazard on the construction cost of the load-bearing system should not be significant because the percentage increase of materials required is much smaller than the large percentage increases of the respective seismic accelerations.

## REFERENCES

- [1] International Conference of Building Officials, "Uniform Building Code – Volume 2: Structural Engineering Design Provisions," Whittier, California, USA, 1997.
- [2] European Committee for Standardization, "EN 1998-1:2004, Eurocode 8: Design of structures for earthquake resistance - Part 1: General rules, seismic actions and rules for buildings," Brussels, Belgium, 2004.
- [3] Ministry of Environment Planning and Public Works, "Greek Earthquake Resistant Design Code," Athens, Greece, 2003, p. . (In Greek).
- [4] G. Papageorgiou, E. Papadimitriou, N. Alamanis, N. Xafoulis, I. Chouliaras, and K. Lazogiannis, "Construction cost comparative analysis of highways in Greece," *PRIME International Journal Practical Research in Innovative Management & Entrepreneurship*, vol. 12, no. 1, pp. 68–85, 2019.
- [5] G. Papageorgiou, "Economic assessment of pavement maintenance and strengthening techniques in view of implementation cost," *European Transport*, no. 78, p. Article 5, 2020.
- [6] A. Tsiknas, A. Athanasopoulou, and G. Papageorgiou, "Evaluation of flexible pavement construction cost according to the design method," *Proceedings of the Institution of Civil Engineers (ICE) - Transport*, vol. 173, no. 1, pp. 3–12, 2020.
- [7] A. Mouratidis and G. Papageorgiou, "A Rational Approach for Optimization of Road

- Upgrading,” *Canadian Journal of Civil Engineering*, vol. 37, no. 11, pp. 1462–1470, 2010.
- [8] T. Chrysanidis, V. Panoskaltsis, and I. Tegos, “Preliminary design and analysis of cost parameters of a high-rise building: Braced shear wall core system,” *International Journal of Civil Engineering and Technology*, vol. 7, no. 5, pp. 137–152, 2016.
- [9] T. Chrysanidis and I. Tegos, “Cost Comparison and Parametrical Investigation of the R/C Shear Wall Core of a Tall Building,” *International Journal of Engineering Research and Technology*, vol. 5, no. 09, pp. 592–595, 2016.
- [10] T. Chrysanidis, V. Panoskaltsis, and I. Tegos, “Parametrical cost analysis of an ultra high-rise building: Detailed design,” *International Journal of Applied Engineering Research*, vol. 11, no. 18, pp. 9644–9650, 2016.
- [11] N. Alamanis, “Influence of random soil strength properties on the earthquake vulnerability of slopes with embedded oil and natural gas pipelines,” *Energy Systems*, 2020, doi: 10.1007/s12667-020-00394-9.
- [12] N. Alamanis and I. Chouliaras, “Improvements to loose soil,” *American Scientific Research Journal for Engineering, Technology, and Sciences*, vol. 43, no. 1, pp. 190–210, 2018.
- [13] N. Alamanis, G. Papageorgiou, P. Chantzopoulou, and I. Chouliaras, “Investigation on the influence of permeability coefficient  $k$  of the soil mass on construction settlements. Cases of infrastructure settlements in Greece,” *Wseas Transactions on Environment and Development*, vol. 15, pp. 95–105, 2019.
- [14] N. Alamanis and P. Dakoulas, “Simulation of random soil properties by the Local Average Subdivision method and engineering applications,” *Energy Systems*, pp. 1–21, 2019, doi: 10.1007/s12667-019-00362-y.
- [15] G. Papageorgiou, N. Alamanis, I. Chouliaras, and P. Kapsali, “Decision making for designing infrastructure projects: The case of the city of Larissa, Greece,” *Journal of Engineering and Architecture*, vol. 7, no. 1, pp. 115–125, 2019, doi: 10.15640/jea.v7n1a13.
- [16] G. Papageorgiou, N. Alamanis, and N. Xafoulis, “Methodology for optimization of road works schedule according to local climatic data,” *International Journal of Recent Technology and Engineering*, vol. 8, no. 4, pp. 1470–1476, 2019.
- [17] T. Chrysanidis, “Evaluation of Out-of-Plane Response of R/C Structural Wall Boundary Edges Detailed with Maximum Code-Prescribed Longitudinal Reinforcement Ratio,” *International Journal of Concrete Structures and Materials*, vol. 14, no. 1. 2020, doi: 10.1186/s40069-019-0378-4.
- [18] T. Chrysanidis, “Influence of elongation degree on transverse buckling of confined boundary regions of R/C seismic walls,” *Construction and Building Materials*, vol. 211, pp. 703–720, Jun. 2019, doi: 10.1016/J.CONBUILDMAT.2019.03.271.
- [19] T. Chrysanidis and I. Tegos, “Can the diameter of longitudinal bars of extreme edges of R/C walls halt transverse buckling?,” in *Emerging Trends in Engineering Research and Technology Vol. 3*, L. Salisu, Ed. London, UK: Book Publisher International, 2020, pp. 65–72.
- [20] A. Haro, M. Kowalsky, Y. Chai, and G. Lucier, “Boundary elements of special

- reinforced concrete walls tested under different loading paths,” *Earthquake Spectra*, vol. 34, no. 3, pp. 1267–1288, 2018, doi: 10.1193/081617EQS160M.
- [21] K. Herrick and M. Kowalsky, “Out-of-plane buckling of ductile reinforced structural walls due to in-plane loads,” *Journal of Structural Engineering*, vol. 143, no. 3, pp. 1–15, 2016, doi: 10.1061/(asce)st.1943-541x.0001660.
- [22] Y. Chai and S. Kunnath, “Minimum thickness for ductile RC structural walls,” *Engineering Structures*, vol. 27, no. 7, pp. 1052–1063, Jun. 2005, doi: 10.1016/j.engstruct.2005.02.004.
- [23] T. Paulay, “The design of ductile reinforced concrete structural walls for earthquake resistance,” *Earthquake Spectra*, vol. 2, no. 4, pp. 783–823, 1986, doi: 10.1193/1.1585411.
- [24] T. Chrysanidis and I. Tegos, “Does reinforcement ratio affect displacements due to lateral buckling behavior of concrete walls?,” *International Journal of Applied Engineering Research*, vol. 12, no. 3, pp. 382–388, 2017.
- [25] T. Chrysanidis and I. Tegos, “Size of seismic tensile strain and its influence on the displacements due to transverse buckling of ultra-highly reinforced structural walls,” *ARPJ Journal of Engineering and Applied Sciences*, vol. 11, no. 23, pp. 13884–13890, 2016.
- [26] T. Chrysanidis, “Size of seismic tensile strain and its influence on the lateral buckling of highly reinforced concrete walls,” *IOSR Journal of Mechanical and Civil Engineering*, vol. 11, no. 1, pp. 18–22, 2014, doi: 10.9790/1684-11121822.
- [27] T. Chrysanidis and I. Tegos, “Influence of elongation degree on out-of-plane buckling of R/C structural walls with a medium high reinforcement ratio,” *International Journal of Civil Engineering and Technology*, vol. 7, no. 4, pp. 358–364, 2016.
- [28] T. Chrysanidis and I. Tegos, “The influence of the degree of elongation to the displacements of seismic walls with maximum code-prescribed reinforcement ratio,” *American Academic and Scholarly Research Journal*, vol. 7, no. 4, pp. 273–279, 2015.
- [29] T. Chrysanidis and I. Tegos, “The influence of the diameter of the longitudinal reinforcement of RC walls to their displacements against lateral instability,” *American Academic and Scholarly Research Journal*, vol. 6, no. 4, pp. 351–359, 2014.
- [30] T. Chrysanidis and I. Tegos, “Does the web of seismic walls play a role to their out-of-plane stability?,” in *Advanced Aspects of Engineering Research Vol. 2*, S. Gnana, Ed. London, UK: Book Publisher International, 2021, pp. 15–22.
- [31] T. Chrysanidis, “Evaluation of lateral buckling phenomenon using R/C prisms detailed with an ultra high reinforcement ratio,” in *Emerging Trends in Engineering Research and Technology Vol. 3*, L. Salisu, Ed. London, UK: Book Publisher International, 2020, pp. 55–64.
- [32] European Committee for Standardization, “EN 1992-1-1:2004, Eurocode 2: Design of concrete structures - Part 1-1: General rules and rules for buildings,” Brussels, Belgium, 2004.

## DOES THE SEISMICITY OF THE AREA HAVE AN IMPACT ON THE CONSTRUCTION COST OF THE LOAD-BEARING STRUCTURE OF R/C BUILDINGS?

Thomas-Erik N. Makris<sup>1</sup>, Theodoros A. Chrysanidis<sup>1</sup>

<sup>1</sup> International Hellenic University  
P.O. Box 141, P.C. 57400, Sindos, Thessaloniki, Greece  
thomaserikmakris14@gmail.com, theodoros\_gr@yahoo.com

---

### Abstract

*In the present research work, an attempt is made to investigate the possible influence of the seismic acceleration on the construction cost of the load-bearing anti-seismic structure of reinforced concrete (R/C) buildings. It is not uncommon for the design engineer to be confronted with the question of dimensioning a building for seismicity greater than that provided by the relevant seismic regulations. More specifically, the Greek Seismic Code (EAK 2000) provides for three different seismic hazard zones. Will the choice of the engineer, then, affect the construction cost and if so, to what extent does it influence it? A fifteen-storey building with a standard floor plan per floor was used for this study. The building simulation took place using the SAP2000 analysis and dimensioning software. The seismic regulation used is Eurocode 8. The study of the influence of seismicity takes place by measuring the quantities of concrete and steel reinforcement construction materials. Analyses of the results and comparisons between them are made for all three seismic zones. Useful conclusions are drawn regarding the influence of seismicity on the construction cost of the load-bearing structure of R/C buildings.*

**Keywords:** Cost, Seismicity, Load-bearing structure

---

## 1 INTRODUCTION

Construction cost is an issue that has troubled engineers, consultants and contractors worldwide [1], [2]. The basic problem has to do in achieving the best technical solution in terms of safety along with the best solution possible in terms of economy; meaning a techno-economical best solution for the design of a structure that should take into account the influence of the soil properties, too [3], [4]. In simple words, the goal is to achieve both safety [5]–[14] and economy at the same time when the consultant engineers design a structure. This issue has troubled engineers for all types of structures: (a) Buildings [15]–[17], (b) bridges [18], [19], (c) other types of structures [20]–[22]. Thus, this analytical study investigates the influence of seismicity to the construction cost of the load-bearing structure of reinforced concrete (R/C) buildings.

## 2 CONSTRUCTION DESCRIPTION

In the present work, the study of a load-bearing structure of a R/C building in the three seismic hazard zones is carried out. This is a fifteen-storey building, double symmetrical that has a rectangular plan with dimensions of 25 x 25 m, which corresponds to a total area of  $E=625 \text{ m}^2$ , without a basement. In the center of the floor plan, there is a strong core consisting of 8 walls of different dimensions, 6 along the Y axis and 2 along the X axis. At the perimeter of the plan, there are two walls along the Y axis, which have enlarged boundary edges at their ends. The cross-sections of the columns of the building are the same for the 1<sup>st</sup> (ground floor) and 2<sup>nd</sup> floor, while after they are gradually reduced to the other floors, except for the walls T3 and T10, whose cross-sections are reduced as they depend on the enlarged boundary edges of their ends. Below is a summary table with the geometric elements of the floor plan (Table 1), as well as a top view of the floor plan of the building (Figure 1).

FLOOR	HEIGHT (m)	BEAM DIMENSIONS		WALL THICKNESS (cm)	COLUMNS (cm)
		PERIMETER	INTERIOR		
<b>1st (Ground)</b>	4.5	25x70	25x70	50	100x100
<b>2</b>	3	25x70	25x70	50	100x100
<b>3</b>	3	25x70	25x70	50	95x95
<b>4</b>	3	25x70	25x70	50	90x90
<b>5</b>	3	25x70	25x70	50	85x85
<b>6</b>	3	25x70	25x70	37.5	80x80
<b>7</b>	3	25x70	25x70	37.5	75x75
<b>8</b>	3	25x70	25x70	37.5	70x70
<b>9</b>	3	25x70	25x70	37.5	65x65
<b>10</b>	3	25x70	25x70	37.5	60x60
<b>11</b>	3	25x70	25x70	25	55x55
<b>12</b>	3	25x70	25x70	25	50x50
<b>13</b>	3	25x70	25x70	25	45x45
<b>14</b>	3	25x70	25x70	25	40x40
<b>15</b>	3	25x70	25x70	25	35x35

Table 1: Geometric plan elements



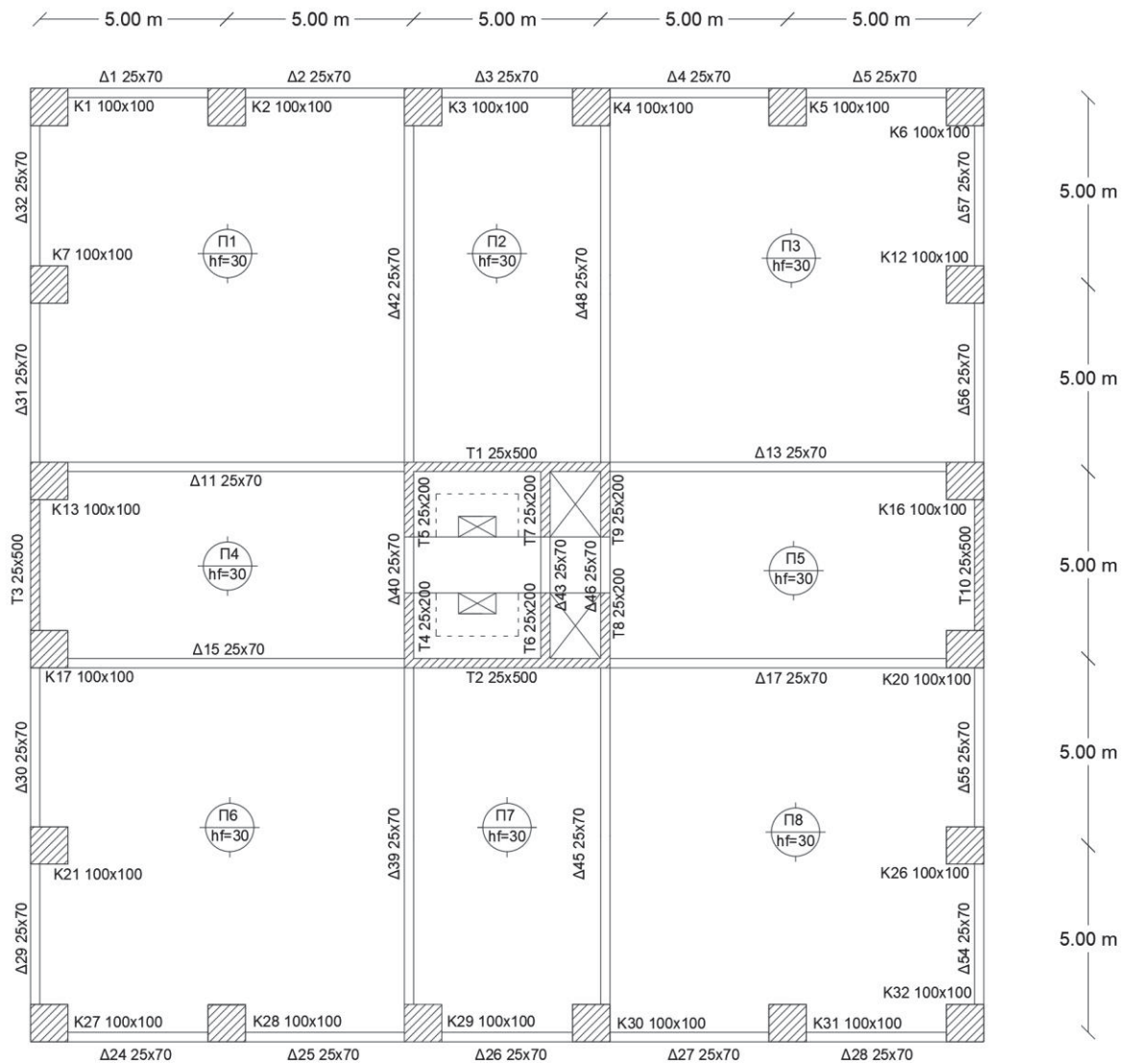


Figure 1: Floor plan of the building

### 3 BUILDING MODELING

The construction materials of the load-bearing body are:

- Concrete quality C30/37
- Steel quality B500C

According to Eurocode 2 [23] the measure of elasticity is equal to  $E_{cm} = 32$  GPa. The value of the Poisson ratio is considered to be zero, according to the specifications of the code for cracked concrete sections.

The beams are simulated using a linear finite element in space placed on the centripetal axis of the structural element. Due to the diaphragm action of the slabs, they are considered to have a T-type cross section. The columns are modeled in the same way as the beams, using linear finite elements and with reduction of their properties due to cracked concrete cross section (stage II). The modeling of the walls is done with the help of the “equivalent frame mod-

el". It has to do with the replacement at each level using a linear element that is placed on the center of gravity of the wall with reduced properties for cracked sections. The wall is connected to the neighboring beams by means of rigid bodies. The building 3D model is displayed on Figure 2.

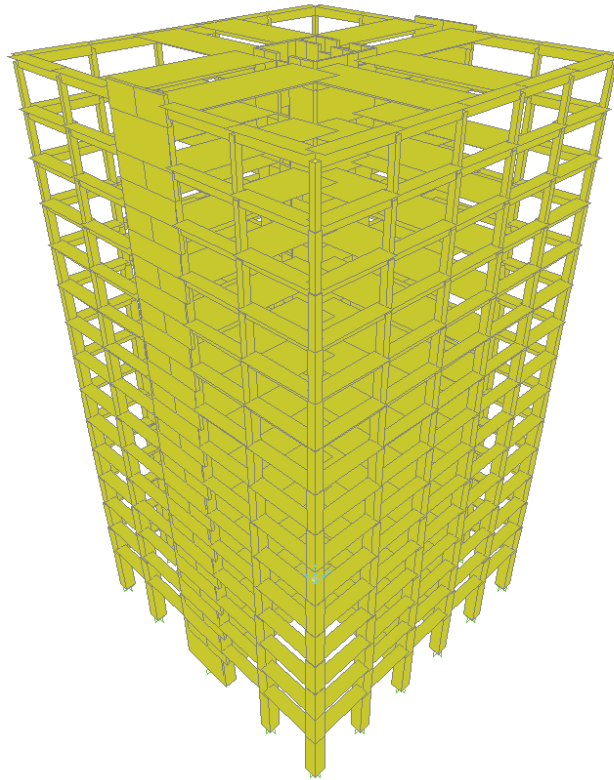


Figure 2: 3D illustration of the building

#### 4 LOADS

The dead loads of the structure according to which the building is dimensioned, are presented below in Table 2:

DEAD LOADS		
N/A	Type	Value
1	Flooring	1.40 kN/m <sup>2</sup>
2	Partition brick walls	1.00 kN/m <sup>2</sup>
3	External brick walls	8.00 kN/m
4	Roofing	3.50 kN/m <sup>2</sup>
5	Parapet roof load	3.60 kN/m <sup>2</sup>

Table 2: Dead loads

- The load of the partition brick walls is considered to be evenly distributed over the entire surface of the floor plan.
- The load of the external brick walls is applied only on the perimeter beams and directly on them.
- On the roof of the top floor around the perimeter, it is considered that there is a parapet with a height equal to 0.90 m.

Table 3 shows the live loads of the construction.

LIVE LOADS		
N/A	Type	Value
1	Ground floor	2.00 kN/m <sup>2</sup>
2	Other floors	2.00 kN/m <sup>2</sup>
3	Top roof	2.00 kN/m <sup>2</sup>

Table 3: Live loads

The spectrum data used according to Eurocode 8 [24] are shown below in Table 4:

EC8 SPECTRUM DATA		
N/A	Type	Data
1	Spectrum	Type 1
2	Soil Category	B
3	$\beta$	0.20
4	Seismic acceleration factor $a$	For all three categories i.e., $a = 0.16, 0.24, 0.36$
5	Gravity acceleration $g$	9.81 m/sec <sup>2</sup>
6	Behavior factor $q$	Calculations based on EC8

Table 4: Spectrum data

Based on the results of the dynamic analysis of the building for each seismic zone, for the two seismic combinations along the X and Y axes, the percentage of the seismic force received from the walls was determined. In this way, it is proved that the static system under consideration is a wall system in every direction and for every seismic zone.

ZONE I		
	G+0.3Q+Ex+0.3Ey	G+0.3Q+0.3Ex+Ey
Base shear force	429.76	887.01
T1, T2 (X-axis)	379.75	
T3, T10 (Y-axis)		460.21
T4, T5, T6, T7, T8, T9 (Y-axis)		415.97
Percentage of shear force by walls	88.36% > 65%	99.91% > 65%

Table 5: Indicative percentages of seismic force carried by the structural walls (Zone I)

## 5 DYNAMIC ANALYSIS

Table 6 displays the sum of mass activated in each eigenmode. According to EC8 [24], dynamic spectral analysis requires activation of a mass percentage of at least 90% of the total mass of the building per direction.

Eigenmode	Participating mass			Eigenmode	Participating mass		
	SumUX	SumUY	SumRZ		SumUX	SumUY	SumRZ
1	0.679	0.000	0.000	24	0.998	0.992	0.989
2	0.679	0.690	0.000	25	0.998	0.995	0.989
3	0.679	0.690	0.712	26	0.998	0.995	0.989
4	0.877	0.690	0.712	27	0.998	0.995	0.993
5	0.877	0.865	0.713	28	0.999	0.995	0.993
6	0.877	0.867	0.852	29	0.999	0.997	0.993
7	0.942	0.867	0.852	30	0.999	0.997	0.993
8	0.942	0.922	0.860	31	0.999	0.997	0.995
9	0.942	0.929	0.917	32	0.999	0.998	0.995
10	0.969	0.929	0.917	33	1.000	0.998	0.995
11	0.969	0.959	0.918	34	1.000	0.998	0.997
12	0.969	0.960	0.951	35	1.000	0.999	0.997
13	0.982	0.960	0.951	36	1.000	0.999	0.997
14	0.982	0.977	0.951	37	1.000	0.999	0.997
15	0.989	0.977	0.951	38	1.000	0.999	0.997
16	0.989	0.977	0.971	39	1.000	0.999	0.998
17	0.993	0.977	0.971	40	1.000	0.999	0.998
18	0.993	0.987	0.971	41	1.000	1.000	0.998
19	0.993	0.987	0.982	42	1.000	1.000	0.999
20	0.995	0.987	0.982	43	1.000	1.000	0.999
21	0.995	0.992	0.982	44	1.000	1.000	1.000
22	0.997	0.992	0.982	45	1.000	1.000	1.000
23	0.997	0.992	0.989				

Table 6: Percentage of mass activated in each eigenmode

The results of Table 6 show that:

- In the first eigenmode, 68% of the mass is activated and is translational by X.
- In the second eigenmode, 69% of the mass is activated and is translational by Y.
- In the third eigenmode, 71% of the mass is activated and a torsional result is obtained.
- The requirement of the code for 90% of the mass to be activated for movements in X and Y directions arises in the ninth eigenmode.

## 6 DIMENSIONING OF BUILDING

Building has been dimensioned for all three seismic zones based on the reinforcement calculated for the ground floor slab. Figure 3 shows the plan view of the layout and the quantity of the reinforcement of the ground floor slab which resulted based on the necessary calculations for seismic zone I.

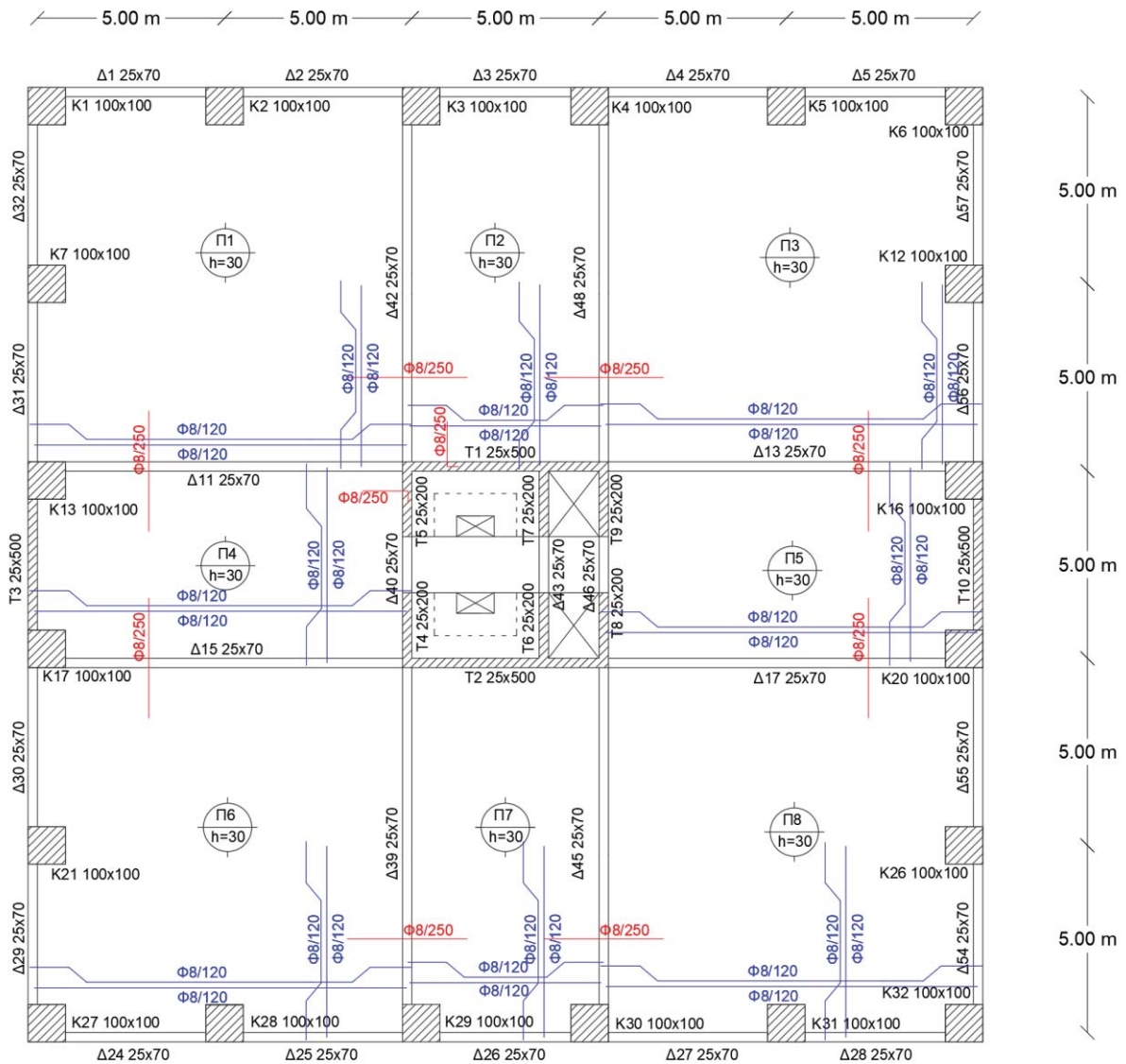


Figure 3: Ground floor slab reinforcement arrangement

## 7 CALCULATION RESULTS AND ANALYSIS

The engineering study of a building, in addition to the construction plans and the static calculations, also includes the pre-measurement of the project for the estimation of the construction costs. This section presents the measurements of the quantities of concrete and steel for the construction that has been studied, analyzed and dimensioned for all three seismic zones.

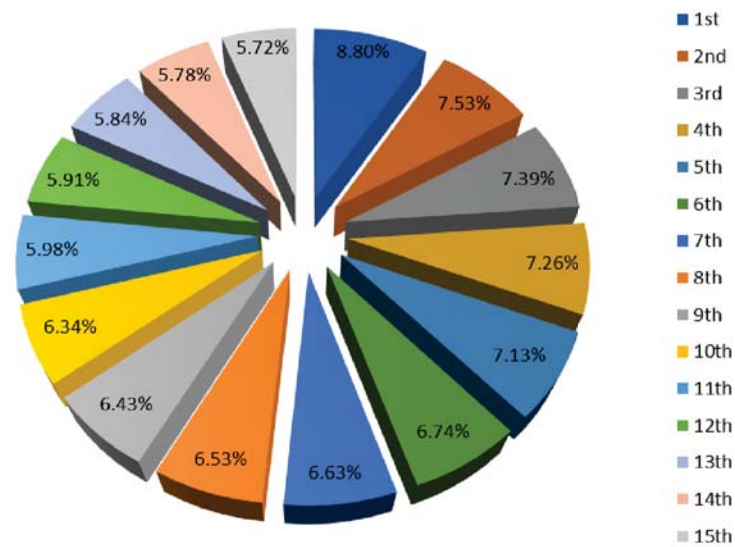


Figure 4: Percentage of concrete per floor

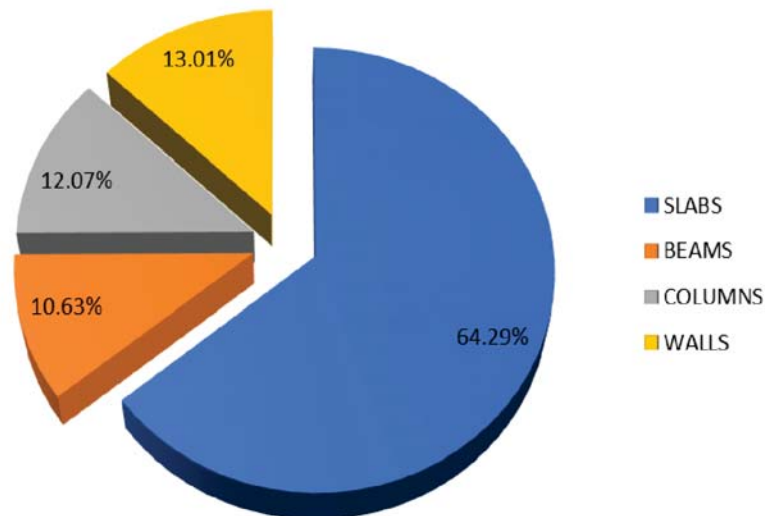


Figure 5: Percentage of total amount of concrete per structural element

It is therefore concluded that the first floor has the largest percentage of concrete while at the same time the percentage of the concrete is reduced from floor to floor (Figure 4). Also, the slabs occupy by far the largest percentage of the total amount of concrete with a percentage of 64.29%, followed by the seismic walls with 13.01%, the columns with 12.07% and finally the beams with 10.63% (Figure 5).



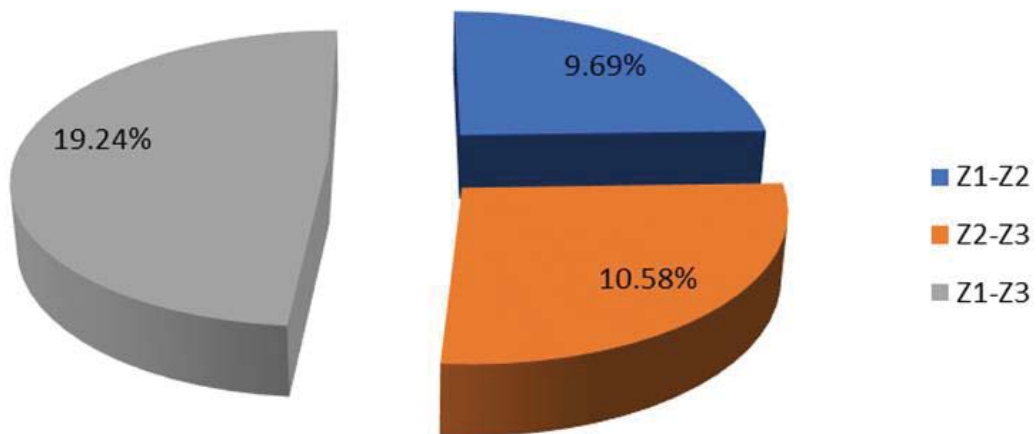


Figure 6: Percentage increase in total steel weight of ground floor seismic walls' steel (Zones I-III)

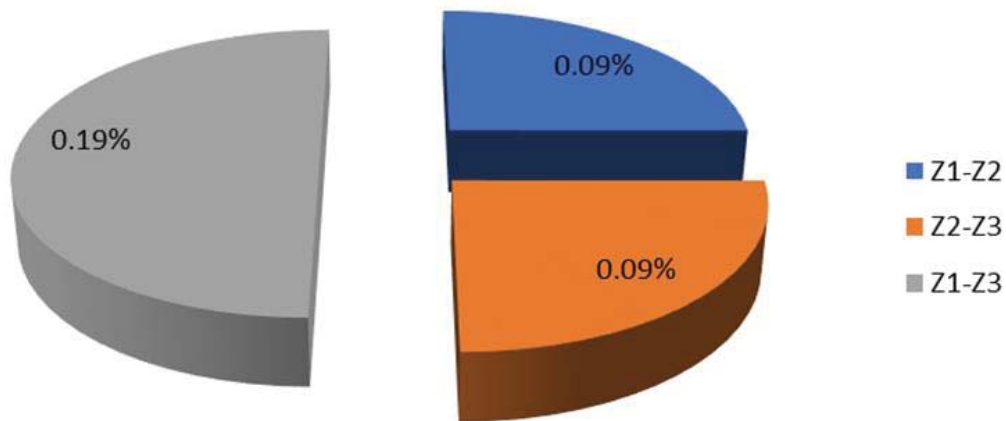


Figure 7: Percentage increase in total steel weight of ground floor beams' steel (Zones I-III)

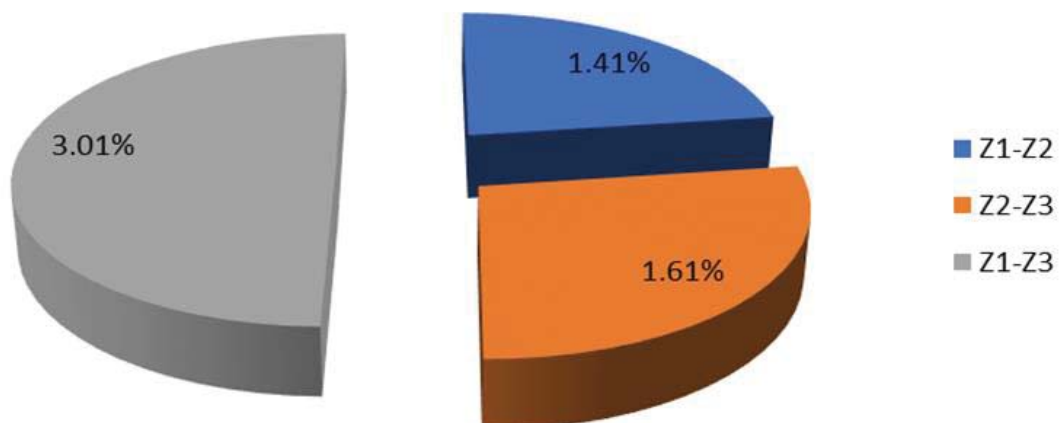


Figure 8: Percentage increase in total steel weight of ground floor structural components (Zones I-III)

From the above diagrams that emerged from the measurements of the building materials for each seismic zone, it is observed that:

1. During the increase of the seismic acceleration in the building in question, it is observed that the steel of the seismic walls has the largest percentage increase of its weight.

Specifically, during the passage from (Figure 6):

- Zone I ( $a_g = 0.16g$ )  $\rightarrow$  Zone II ( $a_g = 0.24g$ ) percentage increase of 9.69%
- Zone II ( $a_g = 0.24g$ )  $\rightarrow$  Zone III ( $a_g = 0.36g$ ) percentage increase of 10.58%
- Zone I ( $a_g = 0.16g$ )  $\rightarrow$  Zone III ( $a_g = 0.36g$ ) percentage increase of 19.24%

The steel of the beams increases by much less (Figure 7):

- Zone I ( $a_g = 0.16g$ )  $\rightarrow$  Zone II ( $a_g = 0.24g$ ) percentage increase of 0.09%
- Zone II ( $a_g = 0.24g$ )  $\rightarrow$  Zone III ( $a_g = 0.36g$ ) percentage increase of 0.09%
- Zone I ( $a_g = 0.16g$ )  $\rightarrow$  Zone III ( $a_g = 0.36g$ ) percentage increase of 0.19%

Therefore, the walls have a dominant position in the load-bearing structure, as the static system is governed by the wall behavior.

2. The increase in seismic acceleration from (Figure 8):

- Zone I to Zone II is of the order of 50% while the percentage increase in the total amount of material is only 1.41%, i.e., many times smaller.
- Zone II to Zone III is of the order of 50% while the percentage increase in the total amount of material is only 1.61%, i.e., many times smaller.
- Zone I to Zone III is of the order of 125% while the percentage increase in the total amount of material is only 3.01%, i.e., many times smaller.

## 8 CONCLUSIONS

In conclusion, in a reinforced concrete building, with strong structural walls, designed and dimensioned according to modern seismic codes, the influence of seismic hazard on the construction cost of the building is not significant, due to the small percentage increase in total material costs in comparison to the drastic percentage increases of the respective seismic accelerations.

## REFERENCES

- [1] A. Jasvi and D. Bera, "Sustainable use of low cost building materials in the rural India," *International Journal of Research in Engineering and Technology*, vol. 4, no. 13, pp. 534–547, 2015, doi: 10.15623/ijret.2015.0425077.
- [2] Ş. Atabay, "Cost optimization of three-dimensional beamless reinforced concrete shear-wall systems via genetic algorithm," *Expert Systems with Applications*, vol. 36, no. 2 PART 2, pp. 3555–3561, 2009, doi: 10.1016/j.eswa.2008.02.004.
- [3] N. Alamanis, "Influence of random soil strength properties on the earthquake vulnerability of slopes with embedded oil and natural gas pipelines," *Energy Systems*, 2020, doi: 10.1007/s12667-020-00394-9.
- [4] N. Alamanis and P. Dakoulas, "Simulation of random soil properties by the Local Average Subdivision method and engineering applications," *Energy Systems*, pp. 1–21, 2019, doi: 10.1007/s12667-019-00362-y.

- [5] F. Zareian and H. Krawinkler, "Structural System Parameter Selection Based on Collapse Potential of Buildings in Earthquakes," *Journal of Structural Engineering*, vol. 136, no. 8, pp. 933–943, 2010, doi: 10.1061/(asce)st.1943-541x.0000196.
- [6] T.-S. Eom and H.-G. Park, "Elongation of Reinforced Concrete Members Subjected to Cyclic Loading," *Journal of Structural Engineering*, vol. 136, no. 9, pp. 1044–1054, 2010, doi: 10.1061/(asce)st.1943-541x.0000201.
- [7] J. Puig, O. A. López, L. Espinosa, G. Del Re, and J. J. Hernández, "Reducing Seismic Risk of School Buildings in Venezuela," *Earthquake Spectra*, vol. 23, no. 4, pp. 771–790, 2008, doi: 10.1193/1.2791000.
- [8] T. Chrysanidis and I. Tegos, "The influence of the degree of elongation of the ultra high-reinforced end sections of R/C walls to their displacements and mode of failure," in *Proceedings of the 2013 International Van Earthquake Symposium*, 2013.
- [9] T. Chrysanidis, S. Tegou, I. Tegos, and S. Spyridonidou, "Analytical and experimental research on improvement of the ductility of buildings' R/C seismic walls through slip prevention with the use of stoppers," in *Proceedings of the 6th ECCOMAS Thematic Conference on Computational Methods in Structural Dynamics and Earthquake Engineering (COMPDYN 2017)*, 2017, doi: 10.7712/120117.5426.18266.
- [10] T. Chrysanidis and I. Tegos, "Size of seismic tensile strain and its influence on the displacements due to transverse buckling of ultra-highly reinforced structural walls," *ARPJ Journal of Engineering and Applied Sciences*, vol. 11, no. 23, pp. 13884–13890, 2016.
- [11] T. Chrysanidis, "Evaluation of Out-of-Plane Response of R/C Structural Wall Boundary Edges Detailed with Maximum Code-Prescribed Longitudinal Reinforcement Ratio," *International Journal of Concrete Structures and Materials*, vol. 14, no. 1, 2020, doi: 10.1186/s40069-019-0378-4.
- [12] T. Chrysanidis and I. Tegos, "Axial and transverse strengthening of R/C circular columns: Conventional and new type of steel and hybrid jackets using high-strength mortar," *Journal of Building Engineering*, vol. 30, no. January, p. 101236, 2020, doi: 10.1016/j.jobbe.2020.101236.
- [13] T. Chrysanidis, "Influence of elongation degree on transverse buckling of confined boundary regions of R/C seismic walls," *Construction and Building Materials*, vol. 211, pp. 703–720, Jun. 2019, doi: 10.1016/J.CONBUILDMAT.2019.03.271.
- [14] T. Chrysanidis and I. Tegos, "Influence of elongation degree on out-of-plane buckling of R/C structural walls with a medium high reinforcement ratio," *International Journal of Civil Engineering and Technology*, vol. 7, no. 4, pp. 358–364, 2016.
- [15] T. Chrysanidis and I. Tegos, "Cost Comparison and Parametrical Investigation of the R/C Shear Wall Core of a Tall Building," *International Journal of Engineering Research and Technology*, vol. 5, no. 09, pp. 592–595, 2016.
- [16] T. Chrysanidis, V. Panoskaltsis, and I. Tegos, "Preliminary design and analysis of cost parameters of a high-rise building: Braced shear wall core system," *International Journal of Civil Engineering and Technology*, vol. 7, no. 5, pp. 137–152, 2016.
- [17] T. Chrysanidis, V. Panoskaltsis, and I. Tegos, "Parametrical cost analysis of an ultra high-rise building: Detailed design," *International Journal of Applied Engineering Research*, vol. 11, no. 18, pp. 9644–9650, 2016.

- [18] I. Tegos, N. Giannakas, and T. Chrysanidis, "Serviceability cracking check of circular section piers," *Bridge Structures*, vol. 7, no. 1, pp. 43–52, 2011, doi: 10.3233/BRS-2011-018.
- [19] I. Tegos, N. Giannakas, and T. Chrysanidis, "Cross-correlation of stresses in the transverse reinforcement under shear load and confinement," in *Proceedings of the 2013 International Van Earthquake Symposium*, 2013.
- [20] G. Papageorgiou, E. Papadimitriou, N. Alamanis, N. Xafoulis, I. Chouliaras, and K. Lazogiannis, "Construction cost comparative analysis of highways in Greece," *PRIME International Journal Practical Research in Innovative Management & Entrepreneurship*, vol. 12, no. 1, pp. 68–85, 2019.
- [21] G. Papageorgiou, "Economic assessment of pavement maintenance and strengthening techniques in view of implementation cost," *European Transport*, no. 78, Article 5, 2020.
- [22] A. Mouratidis, C. Daniilidou, and G. Papageorgiou, "Evaluation of pavement maintenance and strengthening techniques," in *Bituminous Mixtures and Pavements VII, Proceedings of the 7th International Conference on Bituminous Mixtures and Pavements (ICONFBMP 2019)*, 2019, pp. 516–523.
- [23] European Committee for Standardization, "EN 1992-1-1:2004, Eurocode 2: Design of concrete structures - Part 1-1: General rules and rules for buildings," Brussels, Belgium, 2004.
- [24] European Committee for Standardization, "EN 1998-1:2004, Eurocode 8: Design of structures for earthquake resistance - Part 1: General rules, seismic actions and rules for buildings," Brussels, Belgium, 2004.

## IMPROVING ENERGY DISSIPATION CAPACITY OF NATURALLY BUCKLING BRACES UNDER LOW-CYCLE FATIGUE LOADS

Shadiya Jamshiyas<sup>1</sup>, Kazuhiro Hayashi<sup>2</sup>, Xiaopo Yang<sup>1</sup> and  
Konstantinos A. Skalomenos<sup>1</sup>

<sup>1</sup>Department of Civil Engineering, University of Birmingham  
Edgbaston, Birmingham, B15 2TT, United Kingdom  
[sxj978@student.bham.ac.uk](mailto:sxj978@student.bham.ac.uk), [xyy867@student.bham.ac.uk](mailto:xyy867@student.bham.ac.uk), [k.skalomenos@bham.ac.uk](mailto:k.skalomenos@bham.ac.uk)

<sup>2</sup>Department of Architecture, Chiba University  
1-33 Yayoicho, Inage-ku, Chiba 263-8522, Japan  
[hayashi.kazuhiro@forest.ocn.ne.jp](mailto:hayashi.kazuhiro@forest.ocn.ne.jp)

---

### Abstract

*Naturally Buckling Braces (NBBs) utilize a built-up dual material steel section given a parallel offset (i.e., eccentricity) from the normal working points of a conventional brace. NBB sections consists of a low-yield-point steel (LYS) channel and a high-strength steel (HSS) channel connected in parallel through steel battens. This new brace configuration provides a combined axial-flexural behavior that improves the buckling performance and post-yielding stiffness of braced framed structures. In this paper, on the basis of test results on a full-scale NBB specimen, a detailed computational study is performed with the aid of the finite element software ABAQUS. The specimen is subjected to a low-cycle fatigue protocol with increasing amplitudes and repeated inelastic loading cycles at the event of local buckling. The parametric study aims to evaluate partial strengthening methods for NBB sections that aim to delay local buckling initiation and local buckling growth. It was found that the energy dissipation capacity of NBBs can be enhanced up to 40% at a story drift ratio (SDR) of 2.0% by using transverse rib stiffeners at the central part of the LYS channel, while the use of thicker channel battens can provide further restrain to local buckling growth up to a 3.0% SDR.*

**Keywords:** Buckling; Dual strength; Eccentricity; Full-scale cyclic tests; FEM; Rib stiffeners.

---

## 1. INTRODUCTION

Steel braces are often used as vertical and lateral load resistant systems in multi-story buildings for dissipating large amount of input energy under damaging dynamic loads, such as strong winds and earthquakes. While the most frequently used Concentrically Braced Frames (CBFs) consisting conventional steel braces increase the lateral stiffness of steel framed structures and decrease the lateral story drift, they exhibit a marked strength deterioration under large compression loads due to sudden geometric instabilities (global and local buckling) followed by fracture [1-4]. Buckling Restrained Braced Frames (BRBFs) have been proved as reliable, more ductile alternative to CBFs providing a relatively large strength and stiffness under both tension and compression loads. However, in both CBFs and BRBFs, residual story displacements, and in a worst-case loading scenario, a soft-story failure mechanism may occur under rare earthquake events, resulted by their inherent low post-yielding stiffness [5-7].

Recently, the authors and co-workers developed an alternative brace known as Naturally Bucking Brace (NBB) [8] aiming at enhancing the poor post-yielding or post-buckling behavior of current brace design. The main advantages of NBBs are the relatively high tensile post-yielding stiffness and the delay of mid-length local buckling, thereby fracture. NBB consists of a built-up dual-material steel section made of a low-yield-point steel (LYS) channel and a high-strength steel (HSS) channel arranged in parallel and joined together through a series of battens that secure compactness of the section. An intentional eccentricity is introduced along the brace length that inherently subjects the brace to bending loads in addition to axial loads [9]. The effective combination of the two steel grades (i.e., large material contrast) and eccentricity helps the brace to develop a stable and advantageous hysteretic behavior, a concept that was recently extended in uniform circular steel cross sections [10].

Local buckling can initiate at lower drift levels in full-scale specimens compared to small scale specimens and can suddenly reduce the load carrying capacity of the member. Various studies explored the use of stiffeners to resist local buckling and it was found to be an effective method. Mulligan and Pekoz [11] who investigated the effect of edge stiffeners in lipped channel sections found a significant improvement in the local-buckling resistance. Further works suggested enhancing local-buckling resistance through selecting optimum stiffener position and proportion for web stiffeners [12] and proper configuration and sectional sizes for longitudinal stiffeners in case of bolted side plated beams [13].

In this paper, based on the experimental test results on cyclic performance of full-scale NBBs, a finite element analysis study is performed to calibrate the computational model with the experimental results, which are found to be in a good agreement. Additional finite element models with rib stiffeners and stronger channel battens are developed to perform an elaborate parametric study focusing on the effectiveness of such strengthening methods in eliminating the local buckling related failures and thereby enhancing its energy dissipation capacity. Application of rib stiffeners seemed to be a candid way of strengthening open channel sections like NBB. The effect of several parameters, such as, the number and thickness of stiffening ribs as well as the thickness of channel battens is examined.

## 2. CONFIGURATION OF NBB

NBB consists of two cold-formed LYS and HSS channels connected along the brace length at multiple points. Steel battens are welded to each channel as shown in Fig. 1. The brace-ends are free to rotate about  $x$ -axis (in-plane buckling) while are fixed to rotate about  $y$ -axis (out-of-plane buckling). LYS exhibits a low yielding stress (120~220MPa) and a high inelastic deformation capacity (30~50%) which enhances the overall ductility of NBB. On the other hand, HSS exhibits



a high yielding stress (600~800MPa) which enhances the overall strength of NBB, but emphasis needs to be given in the lower ductility (10~15%) of HSS.

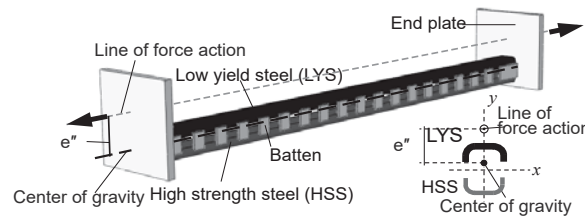


Figure 1: Overview of Naturally Buckling Brace.

The presence of eccentricity redistributes the internal stresses in a way that HSS remains elastic until very large inelastic deformations. At the same time, the very high ductility of LYS is efficiently and uniformly exhausted. This configuration and contrast of the material properties eventually contributes to the high post-yielding stiffness of NBBs. Under cyclic loading, unlike the unstable phenomenon of the axial buckling, NBB bends stably due to the combined axial-flexural behavior [8-10].

### 3. EXPERIMENTAL TEST ON NBB

#### 3.1. Overview of the test specimen

A full-scale NBB specimen denoted as SP1 was subjected to a quasi-static cyclic testing to evaluate its seismic performance. The design details of SP1 are summarized in Table 1. Japanese steels SM570 and LY225 are used for the fabrication of HSS and LYS channels, respectively. The channel battens are made of SS400 steel and are welded to the surface of each channel flanges through fillet welding.

The gusset-plate connection that accommodates in-plane member buckling is designed based on the AISC design specifications [14, 15]. A clearance distance twice the gusset-plate thickness,  $t_p$  (56mm), is considered. Assuming that a pin is formed at the middle of clearance distance, the pin-to-pin length of NBB,  $L$  is equal to 2,825mm. The actual intentional eccentricity determined based on the center of gravity is  $e''$  (see Figure 1) but as the center of gravity has been moved towards the LYS channel due to asymmetrical sections about  $x$ -axis in NBB, the measured eccentricity is denoted as  $e^\#$ . The member slenderness about  $x$ -axis is denoted as  $\lambda_x$  and thickness of steel sections as  $t_{HS}$  and  $t_{LY}$  and that of battens as  $t_{Batten}$ . The quantities  $\sigma_{y,HS}$ ,  $\sigma_{u,HS}$  and  $\sigma_{y,LY}$ ,  $\sigma_{u,LY}$  refers to the yield stress and ultimate stress of HSS and LYS channel respectively.

SPECIMEN	CROSS SECTION						HIGH-STRENGTH STEEL (HS)				LOW YIELD-POINT-STEEL (LY)			
	$B$	$D$	$e''$	$e^\#$	$t_{Ba}$ $tten$	$\lambda_x$	$t_{HS}$	$\sigma_{y,HS}$	$\sigma_{u,HS}$	$\varepsilon_{HS}$	$t_{LY}$	$\sigma_{y,LY}$	$\sigma_{u,HS}$	$\varepsilon_{LY}$
	mm	mm	mm	mm	mm	mm	mm	MPa	MPa	%	mm	MPa	MPa	%
SP1	164	166	78.7	85	6	44.0	9.13	638	690	13.4	12.1	231	308	47.2

Table 1: Dimensions and material properties of test specimens.

The loading protocol consists of two symmetric cycles laterally imposed at each load amplitude of 0.25, 0.5, 0.75, 1.0, 1.5, and 2.0% story drift ratio (SDR) except for the SDR at which local buckling occurs in compression. At this SDR, loading cycles are repeated five times

in order to evaluate the post-local buckling behavior of the brace to cumulative damage. In SP1, the local buckling initiated during 1.5% SDR. More details can be found elsewhere [16].

### 3.2. Cyclic behavior

Fig.2a shows the axial load – axial displacement relationship of SP1. A high energy dissipation capacity without any strength deterioration was observed until an axial displacement of 27.6 mm (i.e., 1.5% SDR). Fig. 2b depicts the overall deformation of brace specimen for an axial displacement of 27.6 mm (i.e., 1.5% SDR) under the 2<sup>nd</sup> compression cycle. The specimen deformed in-plane of the frame and no excessive concentration of local deformation was observed. Until 4<sup>th</sup> compression cycle of repeated loading at 1.5% SDR, a slight strength deterioration was observed. Although local buckling was more intense during the 5<sup>th</sup> repeated cycle of 1.5% SDR, the compressive strength maintained 79% of the strength that recorded in the 1<sup>st</sup> compressive cycle of this repeated loading. For an axial displacement of 36.7 mm (i.e., 2.0% SDR), local buckling increased and the compressive strength started to deteriorate but the tensile strength was further increased. During the 2<sup>nd</sup> cycle of the 2.0% SDR, the fillet welding around the steel battens was failed and battens were detached from the LYS channel during the compressive loading.

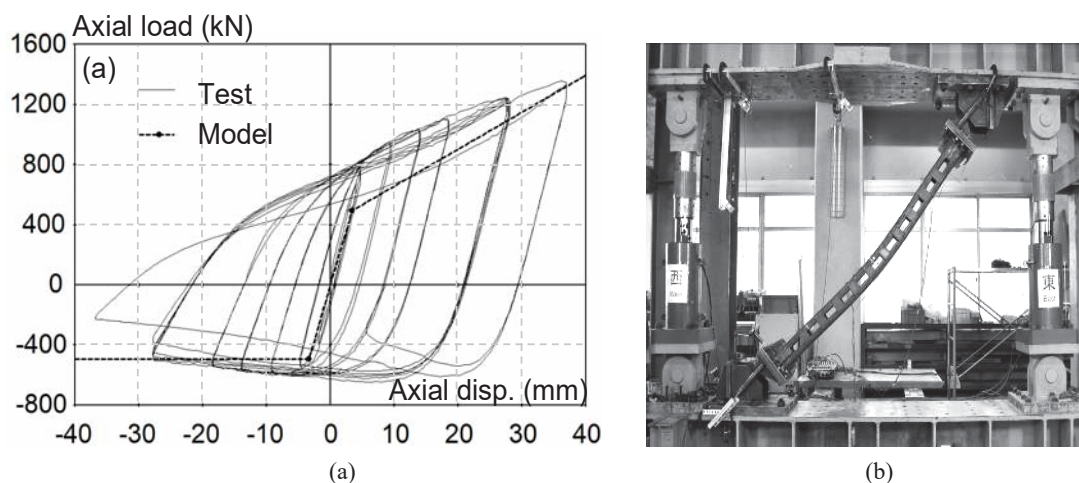


Figure 2: Test results; (a) Axial load – axial displacement relation, (b) Deformed shape at 1.5% SDR.

## 4. FINITE ELEMENT MODELING OF NBB AND PARAMETRIC STUDY

A computational study of the cyclic behavior of the NBB specimen was performed using the finite element (FE) simulation software ABAQUS [17]. To verify the reliability of the proposed detailed FE model, the computational simulation results were compared with the experimental results. The loading pattern followed for the finite element analysis is the same as the one used in experiment.

### 4.1. Finite Element Model

Fig. 3 illustrates the FE model of NBB with an HSS channel section and a LYS channel section connected through battens. The model was divided into 30 elements along the steel section and more than 100 elements along the length for each section. Fine rectangular mesh along with linear quadrilateral 4-noded S4R shell elements of reduced integration were used. Tie constraint was used to define the contact between battens and channel section surfaces. Both ends of the brace were provided with gusset plates having a  $2t_p$  clearance distance to act as

pinned connections at an eccentricity specified in Table 1. A multi-point constraint (MPC) was used to connect the gusset plates and the brace member. An incremental displacement-controlled analysis was performed to one brace end for simulation. The brace was arranged in the same angle as in the experiment.

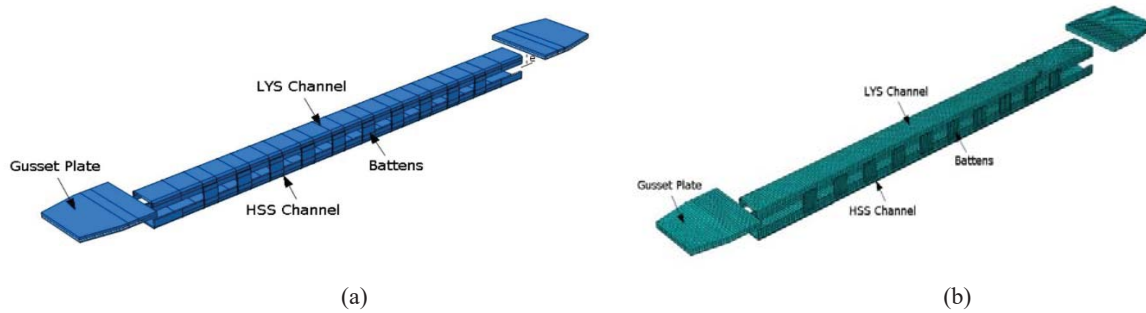


Figure 3: Finite element modeling: (a) entire FE model with gusset plates; (b) Meshed view of the model.

The properties of specimen used for the computational study are summarized in Table 2. The comparison of results from experimental and FE analysis studies are shown in Fig. 4. From the figure, one can observe that the FE model was able to simulate the test with a good accuracy. The full details of the gusset-plate connections were not modelled as a choice to reduce the computational time and complexity of the model. The FE model meticulously captured local buckling at 2% SDR as observed in the experiment. Local buckling was induced during the 1<sup>st</sup> compression cycle of 1.5% SDR and became evident at a 2% SDR. The sudden drop in strength under compression can also be observed from the FE hysteretic loop similar to test results.

SPECIMEN	$L$	$e^{\#}$	$t_{LY}$	$t_{HS}$	$\sigma_{y,LY}$	$\sigma_{y,HS}$	$t_{Batten}$	$t_{Stiffener}$	Stiffener No. ( $n$ )
	(mm)	(mm)	(mm)	(mm)	(MPa)	(MPa)	(mm)	(mm)	
SP1	2825	85	12	9	231	638	6	0	0

Table 2: Properties of different specimens used for numerical simulation.

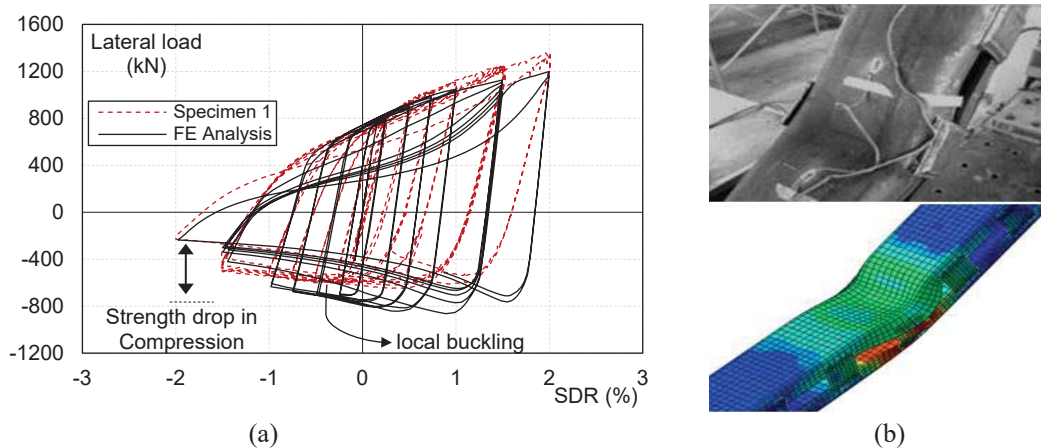


Figure 4: Test results compared with FE analysis results: (a) Lateral load - SDR relation; (b) Deformed shape at the mid-length of the LYS channel.

#### 4.2. Parametric study and performance evaluation indices

As local buckling was observed in LYS channel of NBB during the experimental study,

strengthening of NBB by utilizing stiffeners in the critical zones or by increasing the thickness of battens is explored through a parametric study. The use of stiffeners appears to be a straightforward strengthening approach as NBB consists of open channel sections. The stiffeners combined with the eccentricity distribute more evenly the local stresses in the middle area delaying the onset of local buckling. The parametric study investigated the influence of the number and thickness of stiffeners as well as the thickness of battens.

Using the hysteretic curves of each analysis model, the normalized dissipated energy is calculated to evaluate the hysteretic behavior and energy dissipation capacity of braces [18]. On the basis of this index, one can evaluate the influence local buckling has on the cyclic response and how the progress of local buckling affects the dissipative capacity of the member. More specifically, a comparison is made according to the equivalent viscous damping ratio,  $\xi_{eq}$ , by adopting the relation [19]:

$$\xi_{eq} = \frac{E_d}{2\pi F_m \Delta_m} \quad (1)$$

where  $E_d$  is the energy dissipation in each complete cycle of the force-displacement curve;  $F_m$  is the maximum force in a given cycle and  $\Delta_m$  is the corresponding displacement. The results are calculated considering a symmetrical hysteretic  $F-\Delta$  relation as obtained for chevron brace configurations (i.e., both compression and tension cycles are considered). It should be noted that  $\xi_{eq}$  accounts for the energy dissipation by nonlinear  $F-\Delta$  relations as expected during strong earthquakes.

Moreover, equivalent plastic strain (PEEQ) curves are prepared as additional performance evaluation index to  $\xi_{eq}$ , in order to identify the best brace configuration in terms of ductility capacity. PEEQ is a scalar measure of the accumulated plastic strain. For loading with reversals like cyclic loading, PEEQ will continue to increase if the plastic strain rate is non-zero (regardless of sign) and is an important index to evaluate the cumulative damage of a structural member. Higher the plastic strain, lower will be the ductility performance of the model. Effect of each parameter is discussed in the following sections.

#### 4.2.1. Effect of number of stiffeners

In order to evaluate the effect of numbers of stiffening ribs on NBB's cyclic performance, four NBB models with different numbers of stiffening ribs were developed on the basis of design details of SP1. The model properties are shown in Table 3. Nomenclature of the specimens used for the study follows the order, SP1-nSTt\_Stiffener-Bt\_Batten where ST stands for stiffeners, B for battens, 'n' for number of stiffeners, t\_Stiffener for thickness of stiffeners and t\_Batten for thickness of battens. Fig. 5a-d shows the different specimen categories along with their stiffener and numbers. Transverse rib stiffeners were placed exactly along the position of the battens and in the clearance distance between them throughout the central part of the LYS channel. Fig. 6 shows the  $\xi_{eq}$  curves and PEEQ curves. PEEQ always refers to areas prone to local buckling (i.e., usually in the middle length of the brace). In addition, Fig. 6b plots the threshold for PEEQ ( $\approx 0.58$ ). This value corresponds to the PEEQ at which local buckling occurred in FE simulations of SP1 (Fig. 4: 1<sup>st</sup> compression cycle of 1.5% SDR). It should be noted that  $\xi_{eq}$  was computed considering the complete cycles of the response at each amplitude (i.e., compression and tension). In Fig. 6b, the horizontal axis refers to the 2<sup>nd</sup> tensile loading cycle of each SDR of the low-cycle fatigue protocol considered in this study.

SPECIMEN	$L$ (mm)	$e^{\#}$ (mm)	$t_{LY}$ (mm)	$t_{HS}$ (mm)	$\sigma_{y,LY}$ (MPa)	$\sigma_{y,HS}$ (MPa)	$t_{Batten}$ (mm)	$t_{Stiffener}$ (mm)	Stiffener No. ( $n$ )
SP1	2825	85	12	9	231	638	6	0	0
SP1-1ST9-B6	2825	85	12	9	231	638	6	9	1
SP1-5ST9-B6	2825	85	12	9	231	638	6	9	5
SP1-9ST9-B6	2825	85	12	9	231	638	6	9	9
SP1-12ST9-B6	2825	85	12	9	231	638	6	9	12

Table 3: Properties of SP1 specimens with varying number of stiffening ribs.

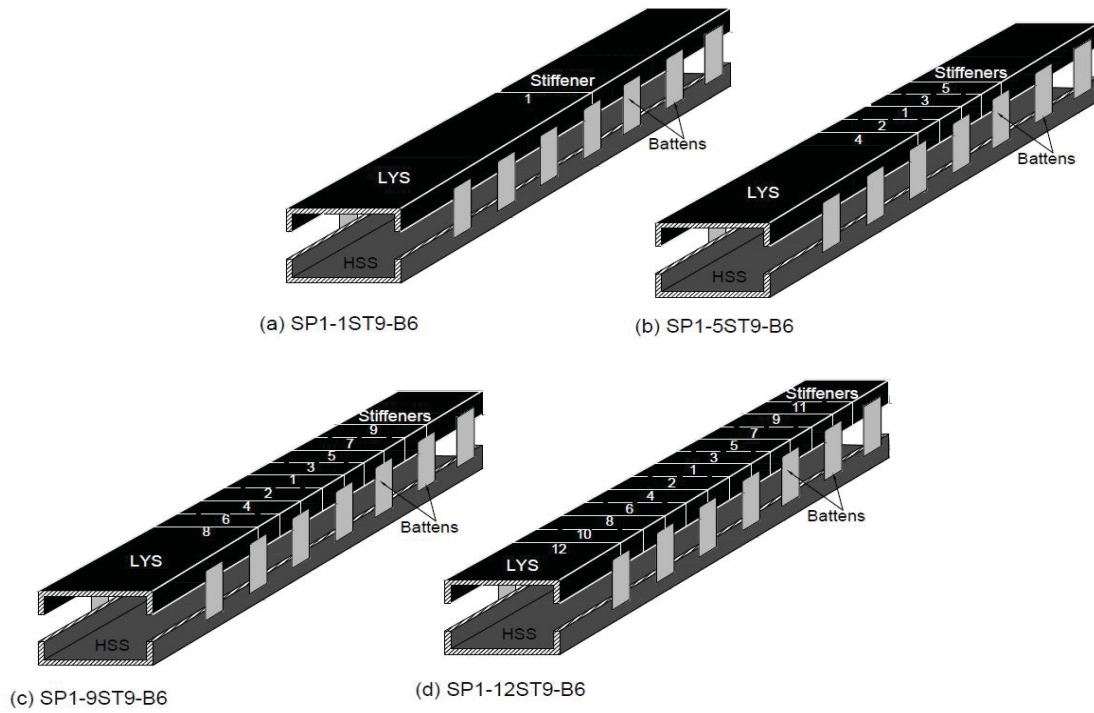


Figure 5: Specimen categories with varying specimen numbers.

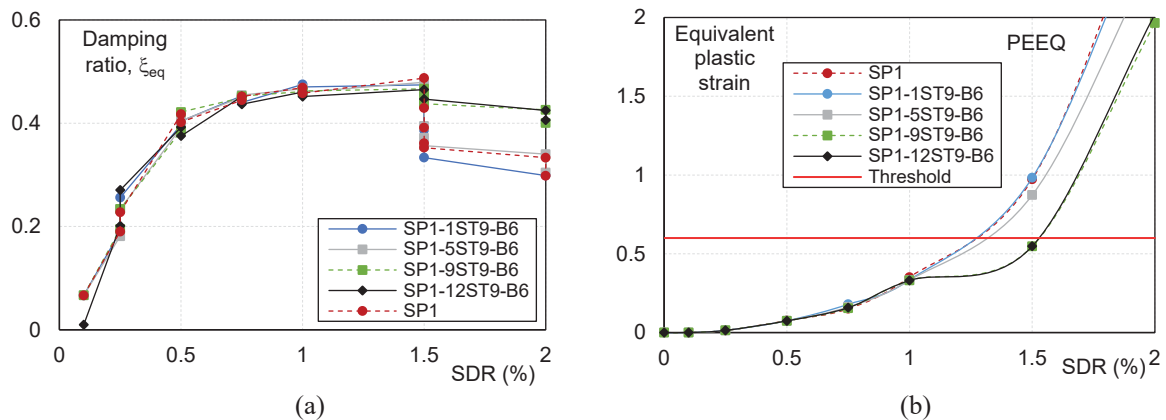


Figure 6: Relation of SDR with: (a) Equivalent damping ratio; (b) Equivalent plastic strain (PEEQ) for the FE models under the influence of varying stiffener number.

SP1 with stiffeners has an increase of 35% in its damping ratio at 2% SDR compared to SP1 without stiffeners (Fig. 6a), thereby strengthening it against local buckling. With the increase of the number of stiffening ribs in the model, its equivalent damping ratio value also increases



from 0.29 for non-strengthened model to 0.41 for model with stiffeners. It can be noted that when the number of stiffening ribs increases to 9 (SP1-9ST9-B6), the curve tends to be stable. However, when the number of stiffening ribs increases to 12 (SP1-12ST9-B6), the equivalent damping ratio curve at this point almost matches that SP1-9ST9-B6, indicating no further improvement, thus making SP1-9ST9-B6 the ideal configurations for this specimen.

In the effective strain curve of PEEQ (Fig. 6b), both SP1-9ST9-B6 and SP1-12ST9-B6 exhibit the lowest PEEQ value at 2% SDR. Moreover, for 1.5% SDR, PEEQ is lower than the threshold for both models. It should be noted that, once local buckling occurs, plastic strain accumulation takes place in the vicinity of damaged area resulting in very high values of PEEQ.

#### 4.2.2. Effect of stiffener thickness

To evaluate the effect of different thicknesses of stiffening ribs on NBB performance, three models with properties summarized in Table 4 were created. The  $\zeta_{eq}$  curves and PEEQ curves of the three models are shown in Fig. 7 in the same manner with Fig. 6.

SPECIMEN	$L$ (mm)	$e^{\#}$ (mm)	$t_{LY}$ (mm)	$t_{HS}$ (mm)	$\sigma_{y,LY}$ (MPa)	$\sigma_{y,HS}$ (MPa)	$t_{Batten}$ (mm)	$t_{Stiffener}$ (mm)	Stiffener No. ( $n$ )
SP1-9ST6-B6	2825	85	12	9	231	638	6	6	9
SP1-9ST9-B6	2825	85	12	9	231	638	6	9	9
SP1-9ST12-B6	2825	85	12	9	231	638	6	12	9

Table 4: Properties of specimens with varying stiffener thickness.

By observing Fig. 7a, the  $\zeta_{eq}$  for all FE models are not very different but takes the maximum value, i.e., 0.40 when the thickness of the rib stiffener is 12 mm (SP1-9ST12-B6) closely followed by stiffener thickness of 9 mm (SP1-9ST9-B6). On the contrary, the damping ratio is lowest, i.e., 0.37 when the rib thickness is 6 mm (SP1-9ST6-B6).

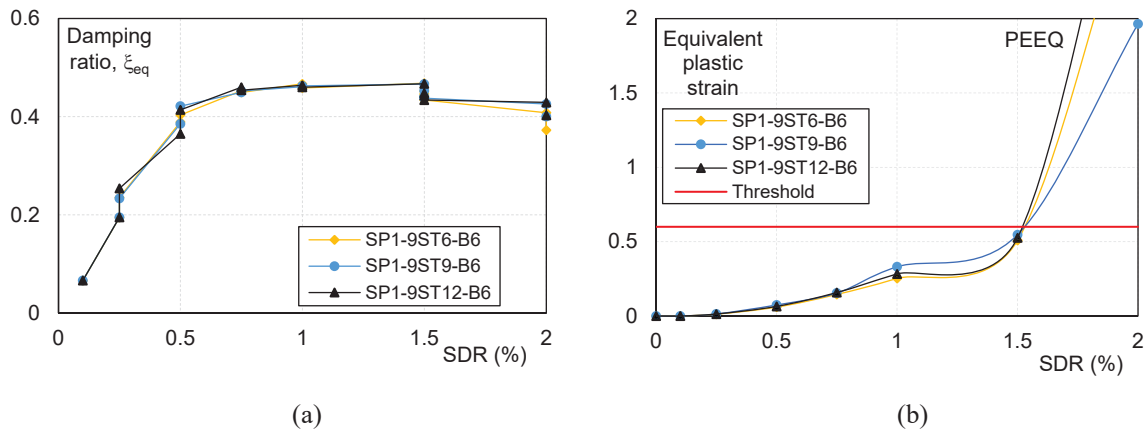


Figure 7: Relation of SDR with: (a) Equivalent damping ratio; (b) Equivalent plastic strain (PEEQ), for the FE models under the influence of varying stiffener thickness.

By observing the PEEQ curves, the model SP1-9ST9-B6 exhibits the lowest strain values indicating a higher reserved ductility capacity to tension loads. Moreover, for 1.5% SDR, PEEQ is lower than the threshold for all cases indicating that local buckling is likely to be prevented during the compression cycles of 1.5% SDR. Fig. 7b indicates that the thicker stiffeners are effective to restrain local buckling, but once local buckling occurs, they tend to increase plastic strain demands in the vicinity of damaged area more than the medium thickness ribs. As a result,



9mm stiffeners were found to be most efficient in reducing local buckling of SP1.

#### 4.2.3. Effect of batten thickness

Apart from unstiffened SP1, two models with batten thicknesses 9 mm and 12 mm were modelled without stiffeners to understand the effect of batten thickness alone. The use of thicker battens would be an alternative strengthening process to stiffening ribs. The properties of models are shown in Table 5. The  $\zeta_{eq}$  curves and PEEQ curves as obtained from the FEA are shown in Fig. 8a and b respectively.

SPECIMEN	$L$ (mm)	$e^{\#}$ (mm)	$t_{LY}$ (mm)	$t_{HS}$ (mm)	$\sigma_{y,LY}$ (MPa)	$\sigma_{y,HS}$ (MPa)	$t_{Batten}$ (mm)	$t_{Stiffener}$ (mm)	Stiffener No. ( $n$ )
SP1	2825	85	12	9	231	638	6	0	0
SP1 - B9	2825	85	12	9	231	638	9	0	0
SP1 - B12	2825	85	12	9	231	638	12	0	0

Table 5: Properties of specimens with varying batten thickness.

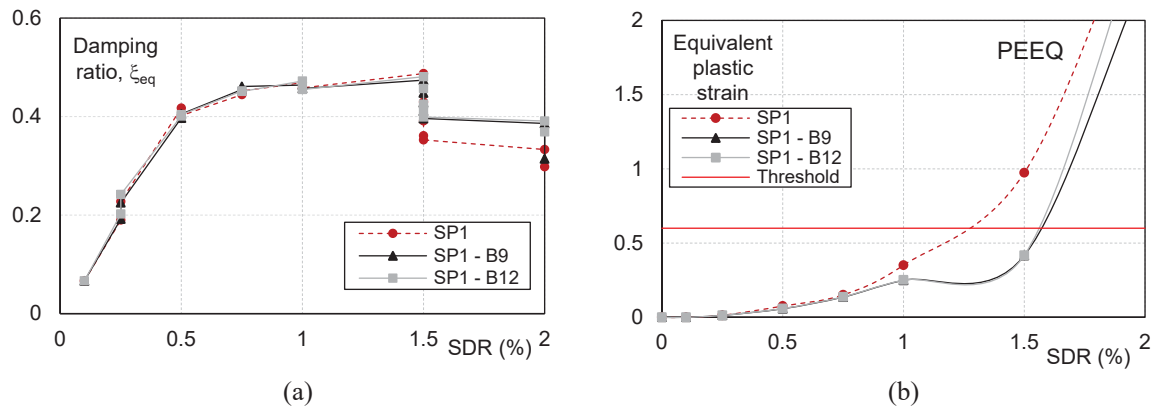


Figure 8: Relation of SDR with: (a) Equivalent damping ratio; (b) Equivalent plastic strain (PEEQ), for the FE models under the influence of varying batten thickness.

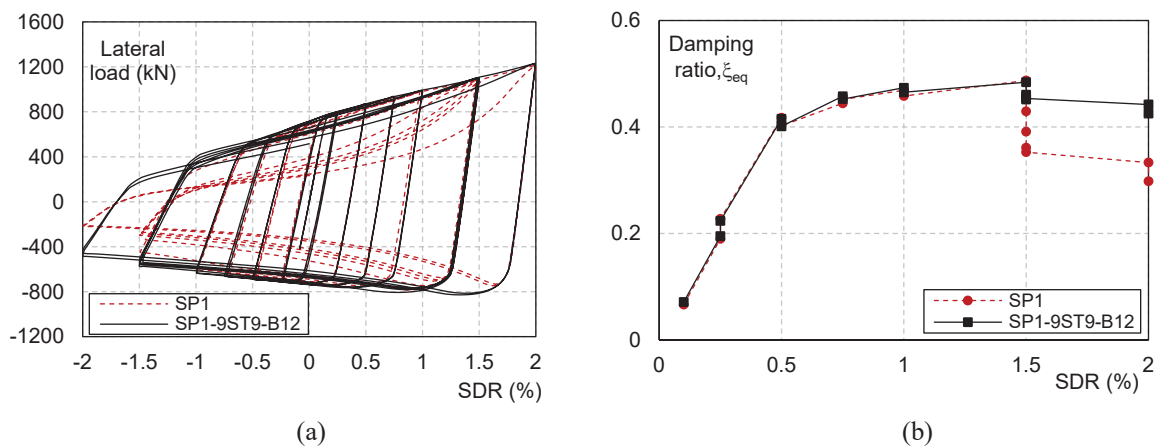


Figure 9: Comparison between SP1 and SP1-9ST9-B12 analysis results: (a) Lateral load – SDR relationship; (b) Damping ratios – SDR relation.

The difference between the  $\zeta_{eq}$  curves of the group of models in Table 5 is small, and almost coincide for models with batten thicknesses of 9 mm (SP1-B9) and 12 mm (SP1-B12),

respectively, as shown in Fig. 8a. However, for 2% SDR, the damping ratio of SP1-B9 is nearly 0.31 while that of SP1-B12 is higher and equals 0.37. This is because SP1-B9 exhibits greater strength degradation than SP1-B12 at 2% SDR but almost similar values of PEEQ at 1.5% SDR indicates a similar damage at this drift level. Based on these observations, both battens appear to be effective, but SP1-B12 can be considered as the one with the more stable cyclic behavior.

On the basis of the above parametric study, a better cyclic behavior was observed in the FE model designed to have 9 stiffeners with 9 mm thickness and channel battens with 12 mm thickness. This model is denoted as SP1-9ST9-B12 and is compared with the non-strengthened FE model SP1 in Fig. 9a and b. Overall, a 43% increase was observed in its  $\xi_{eq}$  compared to SP1 with no stiffeners at 2% SDR, while no sudden drop of compressive strength was observed until the very end of the damaging loading protocol. The use of sufficiently thick stiffeners and battens can strengthen NBB's energy dissipation capacity up to high inelastic levels. Future experimental works can validate these findings.

## 6. CONCLUSIONS

In this research, strengthening methods of Naturally Buckling Braces (NBB) against local buckling and cumulative damage were investigated through a parametric computational study using finite element (FE) analysis methods. The study proposes the use of sufficiently thick stiffeners and battens in order to enhance NBB's energy dissipation capacity up to high inelastic levels. Main conclusions are as follows:

- The application of transverse rib stiffeners in the LYS channel of NBB sections for a length equal to the two-third of the total length of the section was found to be beneficial to strengthen NBBs against local buckling failures.
- About 40% increase of the energy dissipating capacity at a 2% SDR was observed in the rib-strengthened NBBs compared to the non-strengthened NBBs. Specimen with a slenderness ratio equal to 44, requires at least 9 stiffeners and channel battens of 12 mm thickness.
- By comparing the equivalent damping ratio and the cumulative strain curves for the FE analysis models, it can be concluded that the number of rib stiffeners has the greatest impact to improve the cyclic behavior of NBB, followed by the thickness of battens. The thickness of rib stiffeners has the smallest influence on the energy dissipation capacity of NBB but rib stiffeners of at least 9 mm thickness shall be used for the NBB section with channel width-to-thickness ratio 13.6.
- Based on FE analysis results, local buckling can be reduced up to a SDR equal to 3% in strengthened full-scale NBBs.

## REFERENCES

- [1] López W.A. and Sabelli R., Seismic design of buckling-restrained braced frames. *Steel Tips Series*, Structural Steel Educational Council, USA, 2004.
- [2] Shibata M., Nakamura T., and Wakabayashi M., Mathematical expression of hysteretic behavior of braces: Part I Derivation of hysteresis functions. *Transactions of AIJ*, **316**, 18-24, 1982. (in Japanese)
- [3] Takeuchi T. and Matsui R., Cumulative cyclic deformation capacity of circular tubular braces under local buckling. *J Struct Eng ASCE*, **137(11)**, 1311-1318, 2011.
- [4] Tremblay R., Inelastic Seismic Response of Steel Bracing Members. *J Constr Steel Res*, **5-8(58)**, 665-701, 2002.
- [5] Ji X., Kato M., Wang T., Hitaka T. and Nakashima M., Effect of gravity columns on mitigation of drift concentration for braced frames. *J Constr Steel Res*, **12(65)**, 2148-2156, 2009.

- [6] Wang H., Feng Y., Wu J., Jiang Q. and Chong X., Deformation concentration effect of multistory buckling restrained braced frames. *Advances in Civil Eng*, Article ID 7164373, 2019.
- [7] Veismoradia S., Cheraghia A., Darvishan E., Probabilistic mainshock-aftershock collapse risk assessment of buckling restrained braced frames. *Soil Dyn Earth Eng*, **115**, 205-216, 2018.
- [8] Inamasu H., Skalomenos K.A., Hsiao P.C., Hayashi K., Kurata M. and Nakashima M., Gusset plate connections for naturally buckling braces. *J Struct Eng ASCE*, **8(143)**, 2017.
- [9] Skalomenos, K.A., Inamasu, H., Shimada, H., and Nakashima, M., Development of a steel brace with intentional eccentricity and experimental validation. *J Struct Eng ASCE*, **8(143)**, 2017.
- [10] Skalomenos K.A., Kurata M., and Nishiyama M., Induction-heat treated steel braces with intentional eccentricity, *Engineering Structures*, **211**, 110461, 2020.
- [11] Mulligan, G.P. and Teoman P., The influence of local buckling on the structural behavior of singly symmetric cold-formed steel columns. *Center for Cold-Formed Steel Structures Library*, **117**, 1983.
- [12] Azhari M. and Bradford M.A., Local buckling of I- Section beams with longitudinal web stiffeners. *Thin-walled structures*, **15**, 1-13, 1993
- [13] Li L.Z., Jiang C.J., Jia L.J. and Lu Z.D., Local buckling of bolted steel plates with different stiffener configuration. *Engineering Structures*, **119**, 186-197, 2016.
- [14] American Institute of Steel Construction (AISC), Seismic provisions for structural steel building. *AISC/ANSI Standard*, **341**, 16, 2016.
- [15] American Institution of Steel Construction (AISC), Specification for structural steel buildings. *AISC/ANSI Standard*, **360**, 16, 2016.
- [16] Hayashi K., Skalomenos K.A., Shadiya J., and Inamasu H., Full-scale cyclic testing of naturally buckling steel braces and evaluation of partially strengthened cross sections to repeated damage. *Soil Dynamics and Earthquake Engineering (in-press)*, 2020.
- [17] Smith M. ABAQUS/Standard User's Manual, Version 2016, *Dassault Systèmes Simulia Corp*, Providence, RI.
- [18] Hudson D.E., Equivalent viscous friction for hysteretic systems with earthquake-like excitations. *Proceedings of the 3<sup>rd</sup> World Conference on Earthquake Engineering*, vol II, 185–202, 1965.
- [19] Chopra, A.K. Dynamics of structures: *Theory and applications to earthquake engineering*, 4th Edition. Prentice Hall: Englewood Cliffs, NJ, 2012.

## NUMERICAL MODELING OF SLIP RESPONSE OF LATERALLY SWAYING BRIDGE PIERS' TENSILE REINFORCEMENT

Konstantinos G. Megalooikonomou<sup>1</sup>

<sup>1</sup> GFZ German Research Centre for Geosciences, Helmholtz Centre Potsdam, Helmholtzstraße 7,  
14467 Potsdam, Brandenburg, Germany  
e-mail: kmegal@gfz-potsdam.de

---

### Abstract

*Yield penetration occurs from the critical section towards both the shear span and the support of reinforced concrete columns; physically it refers to the extent of the nonlinear region and determines the pullout slip measured at the critical section. Contrary to the fixed design values adopted by codes of assessment, the yield penetration length is actually the only consistent definition of the notion of the plastic hinge length, whereas the latter determines the contribution of pullout rotation to column drift and column stiffness. Yield penetration in the anchored reinforcing bar inside the shear span of the column where it occurs, destroys interfacial bond between bar and concrete and reduces the strain development capacity of the reinforcement. This affects the plastic rotation of the member by increasing the contribution of bar slippage. Results obtained from the analytical procedures introduced in this paper are compared with experimental evidence from tests conducted on circular reinforced concrete bridge piers under cyclic loading designed and detailed according with Eurocode 8-II (2005). It can be seen that the produced monotonic envelope for applied shear load versus the slip of the extreme tensile reinforcing bar of the circular section of the bridge piers under study is in good agreement with the experimental results.*

**Keywords:** yield penetration, bar slippage, circular bridge piers, pull-out rotation

---

## 1 INTRODUCTION

This paper presents a unidirectional bond model and its correlation with an experimental campaign of reinforced concrete bridge piers under cyclic excitation. The prototypes that were used in this study in order to determine the details of the specimens of the experimental study were monolithic concrete bridges located along the Egnatia highway [1] in Greece. The specimens (A1-A6) were designed to represent single column-to-superstructure connections. Four connection specimens (A1-A4) modeled at 1/5 scale the geometry and actions occurring in connections swaying in the direction perpendicular to the bridge axis (Fig. 1.a,b) whereas the remaining two specimens (A5,A6) modeled connections swaying in the direction parallel to the bridge axis (Fig.1c). In the remainder of this presentation these are denoted as group A specimens (A1-A6). All connections comprised a T-joint, but joint geometry and reinforcement arrangement were parameters of investigation (Fig. 2). Specimen A1 was designed and detailed according with EN 1998-2, 2005 [2] (Fig. 2). Specimen A2 was designed with the same geometry as A1, but with part of the required joint reinforcement placed in the primary beams adjacent to the joint. This alternative placement of joint shear reinforcement is allowed in EN 1998-2, 2005 [2] and CALTRANS (2004) [3] so as to avoid reinforcement congestion (Fig.2). Specimen A3 was designed with the same dimensions as A1, but with an inspection opening in the joint body in order to evaluate this construction practice in bridge monolithic joint connections (Fig. 2). Specimen A4 was designed with reduced cap beam width, in order to check whether the increased width for cap beams required by EN 1998-2, 2005 [2] is indeed an essential requirement (Fig.2). Specimen A5 was designed also according with EN 1998-2, 2005 [2], but it was tested for force and moment transfer acting in the direction of the bridge axis. This is the first reported beam-to-column specimen designed with a hollow section of beam (Fig. 2). Moreover, it has an opening for inspector passage in the joint panel (as in the case of specimen A3), in order to evaluate the influence of the openings when force transfer occurs in the longitudinal bridge axis (Fig. 2). Specimen A6 was designed with the same dimensions as A5, but without the opening for inspector passage in the joint panel.

All steel reinforcements used for the construction of the specimens were EN 1992, 2005 [4] compliant C500 deformed bars, with a nominal yield strength of  $f_y=500\text{MPa}$ , ratio of maximum strength to yield strength between 1.15 and 1.35 ( $1.15 \leq f_u/f_y \leq 1.35$ ) and tension strain ductility at failure in excess of 7.5 ( $\epsilon_u/\epsilon_y \geq 7.5$ ). Concrete material properties were determined from standard compression tests of 150x300 mm concrete cylinders that had been cast and cured along with the test specimens (Table 1, average values at time of component testing).

Table 1: Concrete material properties for all specimens [1].

Specimen	Days of test	$f_{cm}$ (MPa)	$E_{cm,o}$ (MPa)
A1	176	27.55	9910
A2	251	29.14	12445
A3	259	29.30	11725
A4	302	29.85	10705
A5 beam	30	26.00	9440
column	28	33.95	15595
A6 beam	88	26.30	5970
column	86	45.00	14645

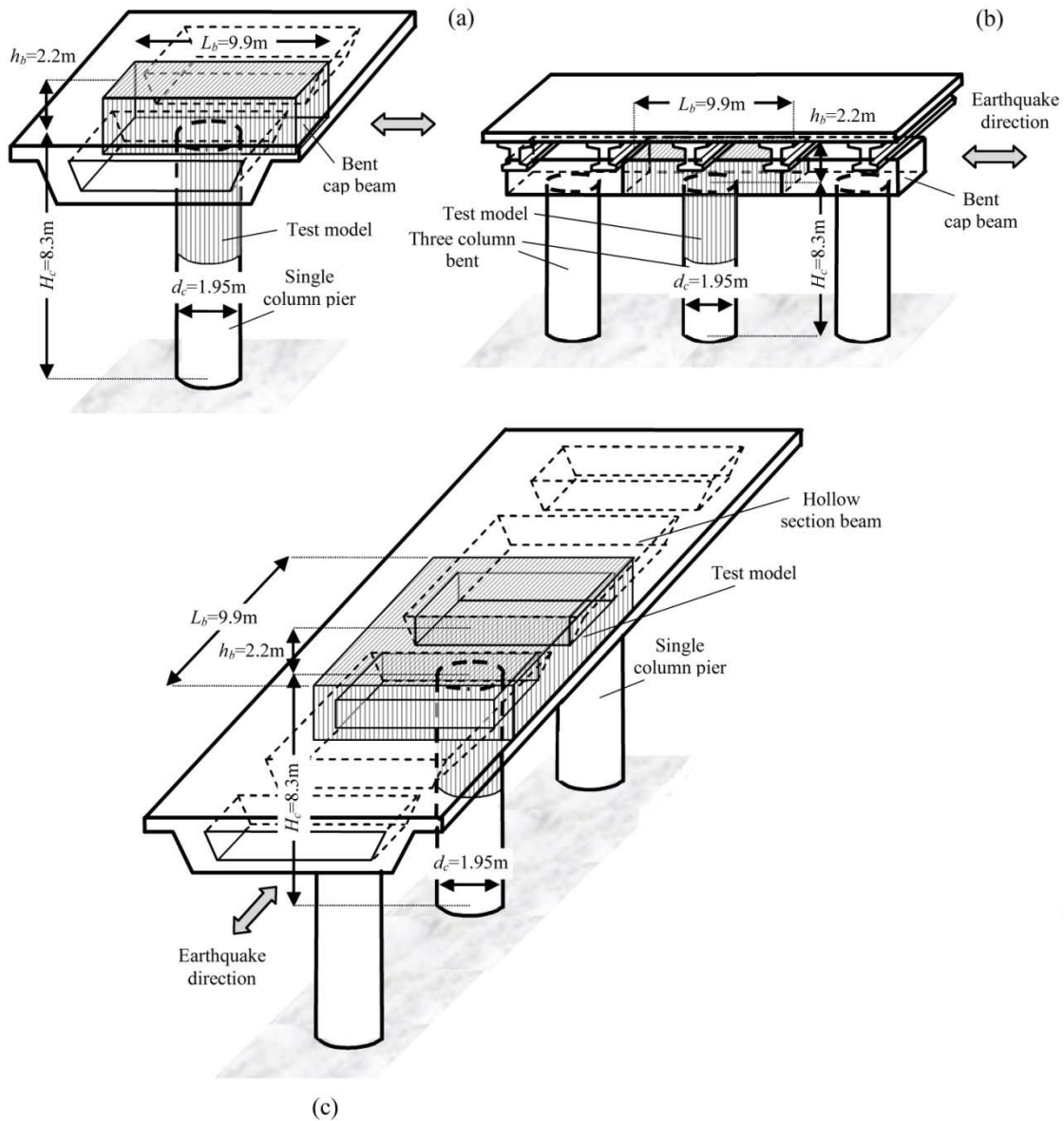


Figure 1: Representation of the prototype bridge structure commonly encountered in Egnatia Avenue and the test model for: (a-b) A1 to A4 specimens and (c) A5 and A6 specimens [1].

## 2 PROPOSED ALGORITHM OF THE UNIDIRECTIONAL BOND MODEL

The deformation capacity of frame elements comprises contributions of flexural, shear and reinforcement pullout components. The estimation of the available deformation capacity of a column is linked to the length of plastic hinges. Following an implicit assumption that all terms are additive, the flexural component of lateral displacement is obtained from the sum of an elastic component, owing to the flexural deformation occurring along the length of the member, and a plastic component that is practically owing to the inelastic rotation that occurs in the small region near the face of the support where moments may exceed the yielding limit. When comparing these deformation estimates with the experimental evidence from predominantly flexural components, it is found that there is a great disparity between measured and estimated deformation capacities characterized by notable scatter [5], [6]. Several attempts to identify the source of inaccuracy have motivated the progress made in that field, not the least



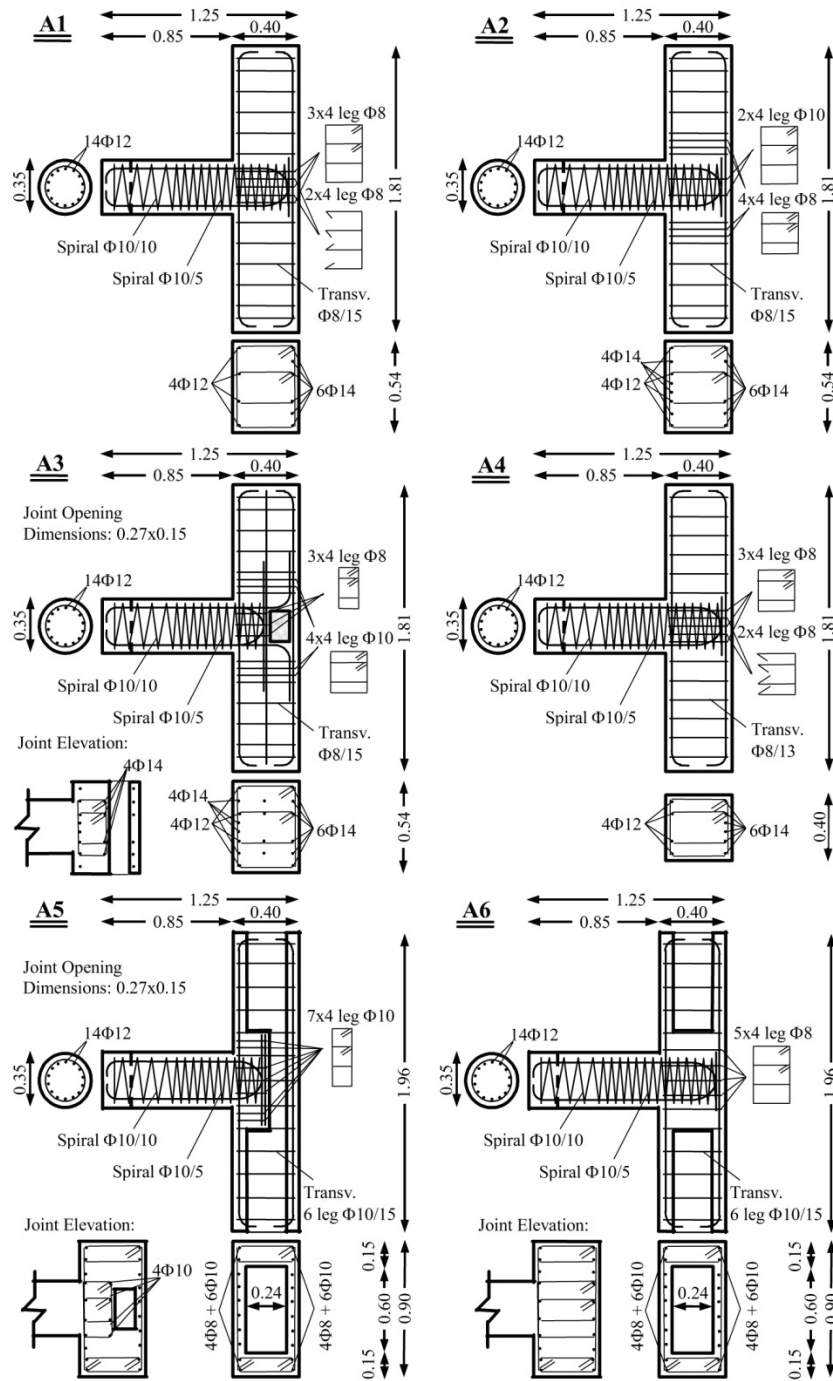


Figure 2: Geometry and reinforcement arrangement for Group A specimens [1].

the empirical expressions for deformation capacity which are included in EN 1998-3, 2005 [7] that completely bypass the requirement of calculating the plastic hinge length. Another approach, initiated by Priestley et al. (1996) [8] and then followed by several other researchers, and the approach to deformability by EN 1998-1, 2004 [9] estimates the plastic hinge length including the length of yield penetration inside the anchorage (see, for example, the detailed analysis in [8]).

In new structural design with EN 1998-1 2004 [9], the plastic hinge length is also used in reinforced concrete (RC) seismic detailing in order to determine the region where additional confinement requirements apply, this is apart from its use in seismic assessment to estimate

the flexural deformation capacity. Due to its importance in these applications as the key to understanding deformability of members, the plastic hinge has been the subject of many experimental and analytical studies and the expressions derived have been quantified and calibrated against several hundreds of tests on isolated column specimens. Still, the disconnect between observation and theory persists, and is considered a major roadblock in establishing the performance criteria for many special categories of members (e.g. walls, columns carrying a high axial load, very slender columns, etc.).

In the typical test, a cantilever column fixed at the base and carrying a constant axial load is driven to a protocol of reversed cyclic lateral load displacement history at the top. Deformation capacity of such members is usually described by the chord rotation that may be sustained by the member prior to loss of its lateral load strength. Apart from the rotation due to flexural curvature that occurs along the length of the member, lumped rotation at the critical section resulting from inelastic strain penetration into the support (e.g. footing) as well as inside the shear span adds up in the reported drift ratios at different levels of performance. This share of deformation is attributed to reinforcement pullout due to the incompatible length change between the bar and the surrounding concrete.

In columns that do not fail by web crushing, pullout rotation increases gradually with imposed drift, claiming a predominant share of the members' deformation capacity near the ultimate limit state.

The following algorithm (Fig. 3) is established in order to define the locations of primary cracks and bar strain, slip and bond distribution along the shear span  $L_s$  of a laterally loaded reinforced concrete column as well as the yield penetration length (plastic hinge length). The equations of the proposed algorithm are given in Megalooikonomou et al. 2018 [10]:

**Initial Data:** Using standard section analysis obtain  $M-\phi$  (*Moment -curvature*) and  $M-\varepsilon$  (*Moment – Tensile Strain of Reinforcement*) diagrams (or better a unified diagram  $M-\phi-\varepsilon$ ) given the Axial Load  $N$  for the typical section of the reinforced concrete column studied:

**1<sup>st</sup> Step:** Select value of bar strain,  $\varepsilon_o^{(1)} = \varepsilon_o$ , after crack formation at the support (Fig. 3).

**2<sup>nd</sup> Step:** Find the corresponding moment,  $M_o$  at the support, from moment-bar strain diagram. Solve for the length of the disturbed region [10]  $\ell_{D1}$  emanating from the first crack.

**3<sup>rd</sup> Step:** Increase strain at critical section to  $\varepsilon_o^{(2)} = \varepsilon_o^{(1)} + \Delta\varepsilon_o$ . Find the location  $x_{cr,2}$  of the second crack. Check if second crack will occur: (a) inside  $\ell_{D1}$ , or (b) in the undisturbed region  $L_s - \ell_{D1}$ .

**4<sup>th</sup> Step:** (a) If next crack forms within  $\ell_{D1}$ , repeat Step 3 for  $\varepsilon_o^{(3)} = \varepsilon_o^{(2)} + \Delta\varepsilon_o$ . (b) Otherwise, find the new disturbed region  $\ell_{D2}$  that extends beyond  $x_{cr,2}$ .

**5<sup>th</sup> Step:** Find total disturbed length,  $\ell_{Do} = x_{cr,2} + \ell_{D2}$

**6<sup>th</sup> Step:** Solve for  $\varepsilon(x)$  (*strain*),  $s(x)$  (*slip*),  $f_b(x)$  (*bond stress*) for  $x_{cr,2} \leq x \leq \ell_{Do}$ . In this phase of the solution and up to stabilization of cracking elastic bond is assumed in  $\ell_{D2}$ .

**7<sup>th</sup> Step:** Repeat steps 2 to 6 for  $\varepsilon_o^{(i)} = \varepsilon_o^{(i-1)} + \Delta\varepsilon_o$  until stabilization of cracking (i.e., no more primary cracks can develop:  $\varepsilon_o^{stbl} = \varepsilon_o^{(i)}$ ). Final length of disturbed zone is obtained from the  $n^{th}$  increment using this procedure:  $\ell_{Do} = x_{cr,n} + \ell_{D,n}$ .

**8<sup>th</sup> Step:** Increase  $\varepsilon_o^{(i)} = \varepsilon_o^{(i-1)} + \Delta\varepsilon_o > \varepsilon_o^{stbl}$ . Solve for one continuous disturbed region  $\ell_{Do} \geq x_{cr,n} + \ell_{D,n}$  allowing for bond plastification and debonding as well as bar yielding (anchorage solution) up to either (a)  $\varepsilon_o$  exhausting the ultimate strain of the  $M-\varepsilon$  diagram, or (b)  $\ell_{Do}$  exceeding the available development length of the bar in the shear span, taken here as  $(L_s + h_{hook})$ , where  $h_{hook}$  refers to the bent length of a hooked anchorage (according with *fib* Model Code (2010) [11] the contribution of a hook to the strength of an anchored bar is  $50A_{bf}f_b^{max}$ , which corresponds to an additional anchored length,  $\Delta L_b = h_{hook} = 12.5D_b$ ). If (b) controls, continue

beyond that point for higher strains using the anchorage solution presented in [10] for the entire length  $\ell_{Do}$ .

**9<sup>th</sup> Step:** The last converged value of  $l_r$  in the shear span is added to the corresponding yield penetration length into the anchorage resulting in the definition of the total plastic hinge length  $\ell_{pl}$ .

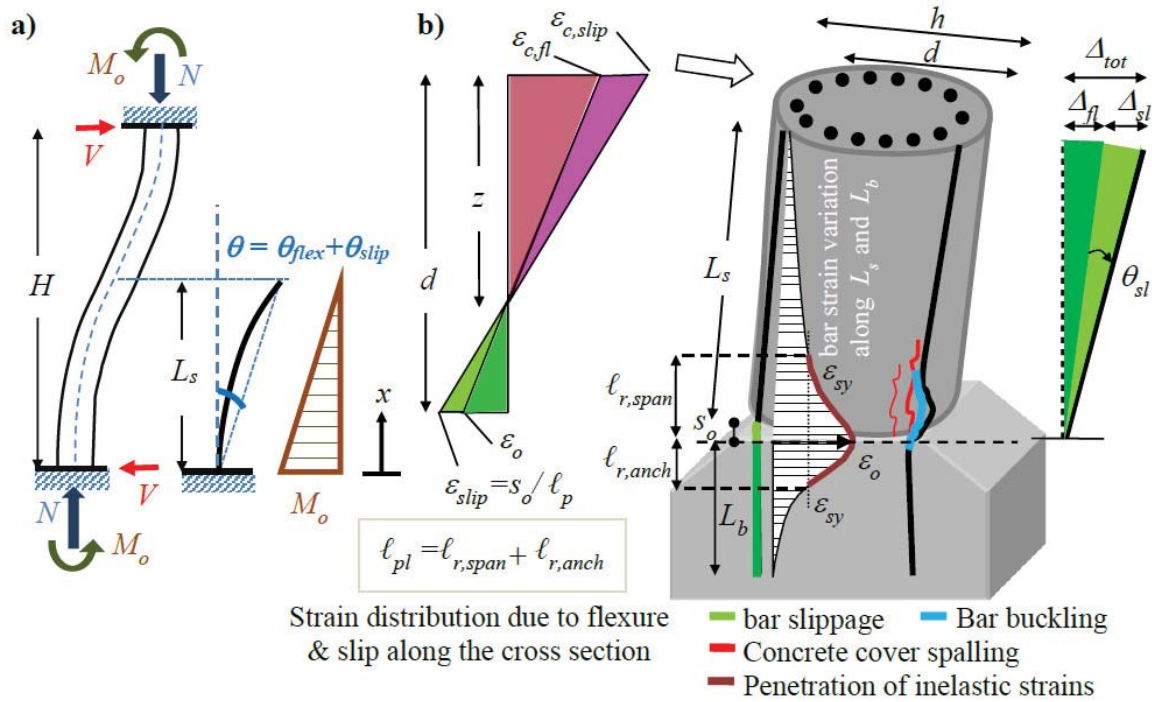


Figure 3: a) Column under lateral sway and b) cantilever model for its deformation analysis

### 3 CORRELATION WITH THE EXPERIMENTAL RESULTS

It is evident that yield penetration occurs from the critical section towards both the shear span and the support of columns; physically it refers to the extent of the nonlinear region and determines the pull-out slip measured at the critical section. Contrary to the fixed design values adopted by codes of assessment, the yield penetration length is actually the only consistent definition of the notion of the plastic hinge length, whereas the latter determines the contribution of pull-out rotation to column drift and column stiffness. When a reinforced concrete (RC) column is subjected to lateral sway as a result of earthquake action, the large strain demand in the end sections is supported by development of a strain distribution in the anchorage (Fig 3). This causes the bars to displace (or slip) relative to the anchoring concrete at the column fixed end(s). The lumped slip causes rigid-body rotation of the column, thereby alleviating partially the column deformation. This reinforcement slip is assumed to occur in the tension bars only and cause the rotation about the neutral axis. Development of flexural yielding and large rotation ductilities in the plastic hinge zones of frame members is synonymous with the spread of bar reinforcement yielding. Yield penetration in the anchored reinforcing bar inside the shear span of the column where it occurs, destroys interfacial bond between bar and concrete and reduces the strain development capacity of the reinforcement. This affects the plastic rotation of the member by increasing the contribution of bar slippage. Results obtained from the analytical procedures introduced in the previous section are compared here

with experimental evidence from the tests conducted on reinforced concrete bridge piers under cyclic loading reported previously.

In the following figures the aforementioned comparison is depicted and it can be seen that the produced monotonic envelope for applied shear load versus the slip of the extreme tensile reinforcing bar of the circular section of the bridge piers is in good agreement with the experimental evidence [1], [10].

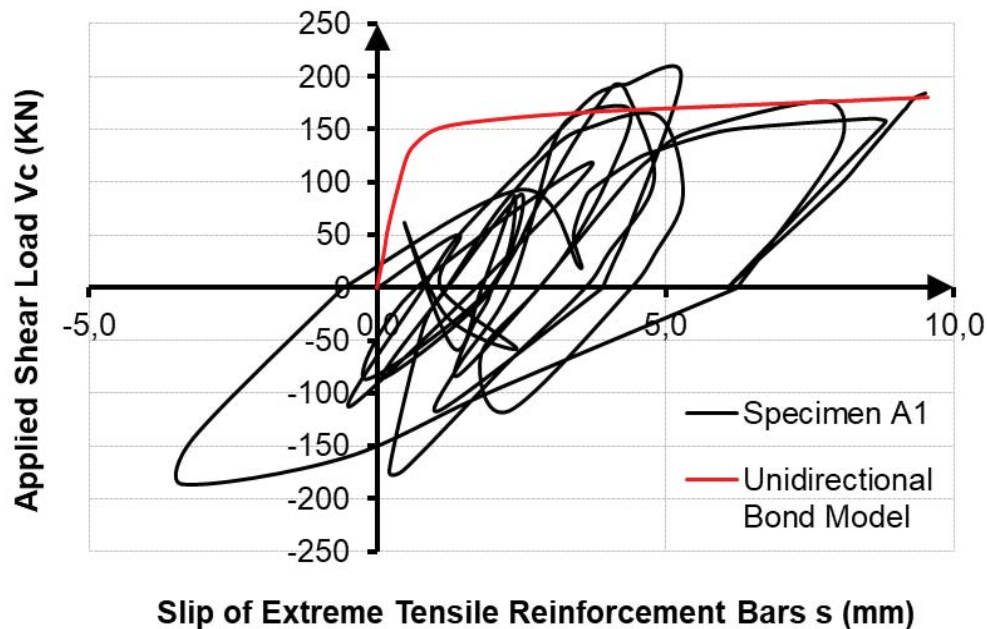


Figure 4: Correlation of the unidirectional bond model with the experimental response of specimen A1.

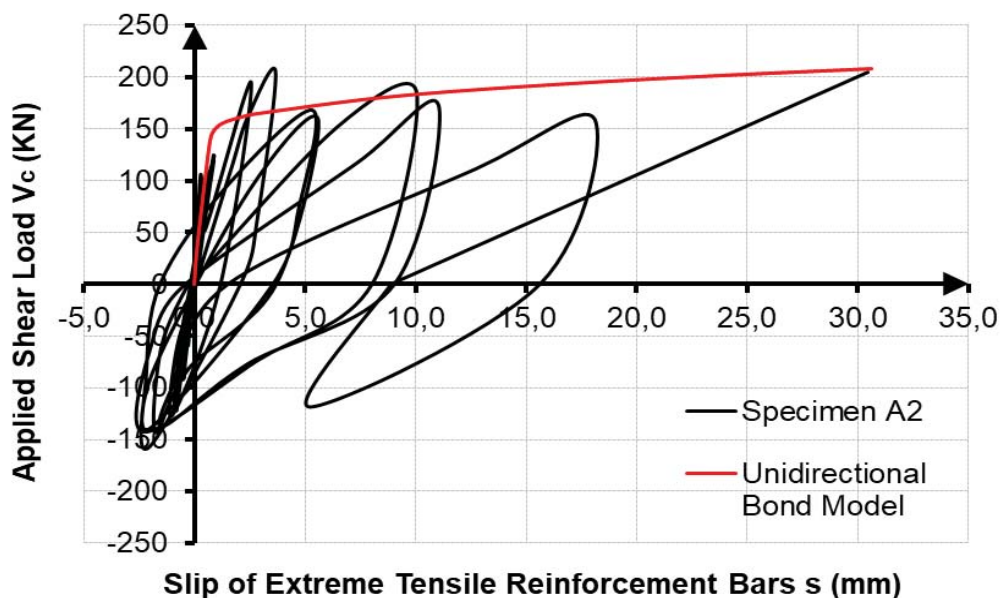


Figure 5: Correlation of the unidirectional bond model with the experimental response of specimen A2.



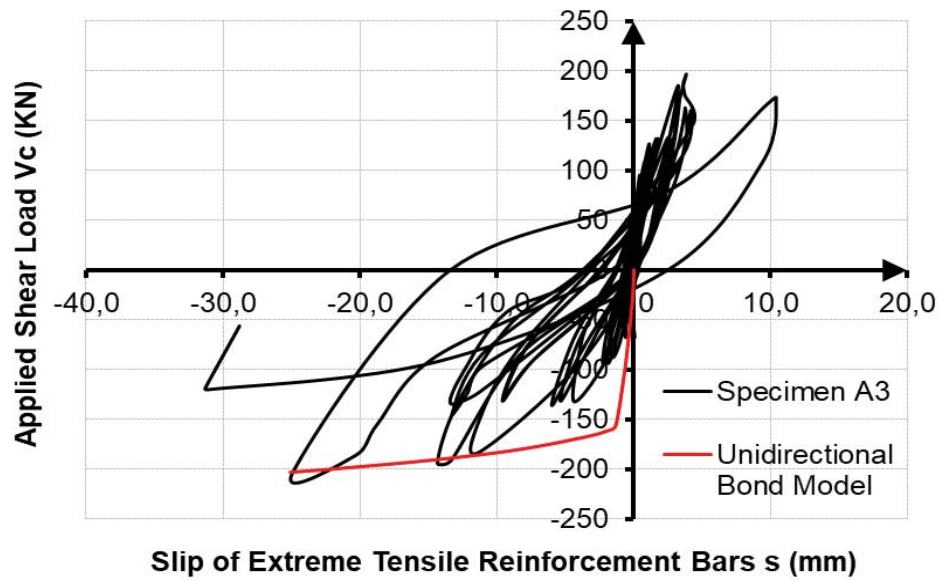


Figure 6: Correlation of the unidirectional bond model with the experimental response of specimen A3.

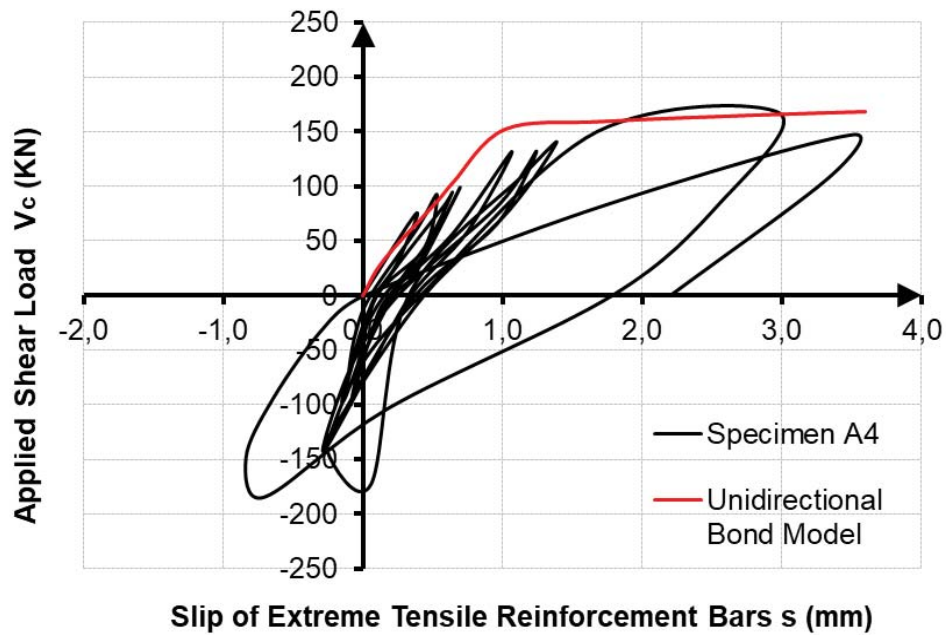


Figure 7: Correlation of the unidirectional bond model with the experimental response of specimen A4.

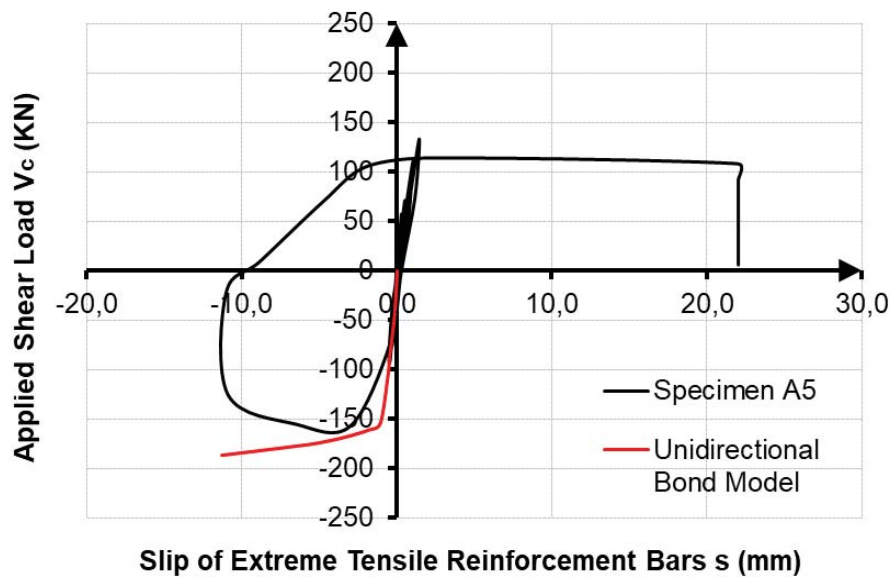


Figure 8: Correlation of the unidirectional bond model with the experimental response of specimen A5.

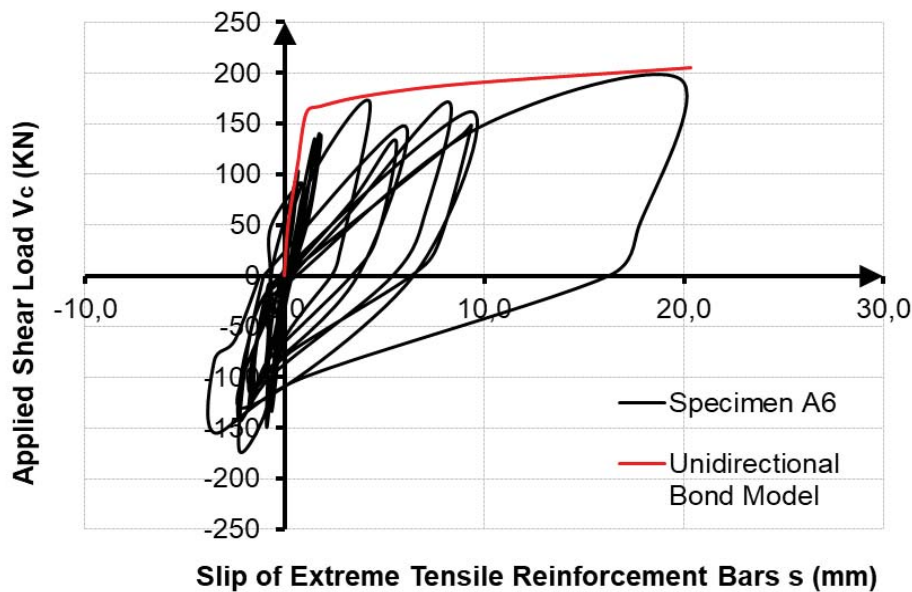


Figure 9: Correlation of the unidirectional bond model with the experimental response of specimen A6.

#### 4 CONCLUSIONS

- The experimental study demonstrated that design and detailing of pier-superstructure monolithic connections according with the EN 1998-2 (2005) [2] leads to a satisfactory performance under earthquake loading. Based on the observed response it was concluded that special care ought to be provided for the design of the anchorages of the pier longitudinal reinforcement according with EN 1992-2 (2005) [4], in order to prevent joint failure due to anchorage pull-out. Placing a fraction of the necessary vertical joint reinforcement in the beams outside the joint, as suggested in EN 1998-2 (2005) [2] for congestion-free alternative detailing did not compromise the strength of the joint, whereas



this practice facilitates placement of the reinforcement during construction. In all cases discontinuities in the joint body such as openings for passage ought to be avoided.

- According to these experimental observations the analytical evidence showed that through the proposed algorithm, the bar strain distributions and the extent of yield penetration from the yielding cross section towards the shear span and towards the support were resolved and calculated analytically by reference to the state of reinforcement strain. The numerical results are well correlated with the experimental evidence and are consistent with the experimental trends described above confirming that the plastic hinge length is controlled by the residual bond that may be mobilized along the yielded reinforcement.

## REFERENCES

- [1] Timosidis D, Megalooikonomou K.G., Pantazopoulou SJ (2015). Monolithic Reinforced Concrete Bridge Joints under Cyclic Excitation, *Engineering Structures*, Vol. 101, p. 477-493.
- [2] EN 1998-2 (2005), Design of Structures for Earthquake Resistance – Part 2 (II): Bridges, CEN, Brussels: European Committee for Standardization.
- [3] California Transportation Agency (2004). Caltrans Seismic Design Criteria Ver.3.1.
- [4] EN 1992-2 (2005). Design of Concrete Structures – Part 2: Concrete Bridges. Design and detailing rules. European Committee for Standardization, (CEN), Brussels.
- [5] Syntzirma D. V., Pantazopoulou S. J. and Aschheim M. (2010). Load history effects on deformation capacity of flexural members limited by bar buckling. *ASCE J. of Structural Eng.*; 136(1): 1–11.
- [6] Inel, M., Aschheim, M. and Pantazopoulou, S. (2004). Deformation Indices for Concrete Columns: Predicted vs. Measured. *13th World Conf. on Earthquake Engineering*, Vancouver, Canada, No. 2397
- [7] EN 1998-3 (2005), Eurocode 8: Design of structures for earthquake resistance -Part 3: Assessment and retrofitting of buildings. European Committee for Standardization (CEN), Brussels.
- [8] Priestley, M.J.N., Seible F., and Calvi M. (1996). Seismic Design and Retrofit of Bridges. J. Wiley & Sons Inc., N. York.
- [9] EN 1998-1 (2004), Eurocode 8: Design of structures for earthquake resistance – Part 1: General rules seismic actions and rules for buildings, European Committee for Standardization (CEN), Brussels.
- [10] Megalooikonomou K.G., Tastani SP, Pantazopoulou SJ. (2018) Effect of Yield Penetration on Column Plastic Hinge Length, *Engineering Structures*, Vol. 156, p. 161-174.
- [11] Fib Model Code (2010), Chapter 6: Interface Characteristics, Ernst & Sohn Publications, Berlin, Germany, pp.434.

## SEISMIC RISK ASSESSMENT OF A PROCESS PLANT UNIT ACCOUNTING FOR DYNAMIC INTERACTION

George Karagiannakis<sup>1,2</sup> and Luigi Di Sarno<sup>1,3</sup>

<sup>1</sup> University of Sannio, Piazza Roma 21, 82100 Benevento, Italy  
[karagiannakis@unisannio.it](mailto:karagiannakis@unisannio.it), [ldisarno@unisannio.it](mailto:ldisarno@unisannio.it)

<sup>2</sup> European Commission Joint Research Centre (JRC), Ispra (VA), Italy  
[georgios.karagiannakis@ec.europa.eu](mailto:georgios.karagiannakis@ec.europa.eu)

<sup>3</sup> University of Liverpool, Liverpool L69 3BX, UK  
[luigi.di-sarno@liv.ac.uk](mailto:luigi.di-sarno@liv.ac.uk)

---

### Abstract

*Analytical fragility curves for structures used in chemical plants are not commonly derived because of the high computational cost. In contrast, empirical curves are utilized within a quantitative risk assessment framework given that they can be found easily and adopted for different structural configurations. Arguably, analytical fragility curves can account for dynamic idiosyncrasies due to the interaction of a supporting structure and equipment that diversify from one process unit to another. Additionally, the use of an efficient and sufficient earthquake intensity measure is essential for deriving robust fragility curves. Peak ground measures that are commonly adopted for risk assessment may not be efficient to describe more complex systems with higher mode effects.*

*Using time-efficient modelling, the present analytical study intends to evaluate the seismic risk to a hydrodesulphurization unit, a process used in modern refineries to remove sulphur from refined petroleum products. The 3D model of the unit consists of an irregular steel supporting structure, several vessels as well as a piping network. To attain a robust modelling, the effects of panel zone configuration is examined. Furthermore, the seismic response of steel structure and piping is seen through the lens of different intensity measures. In the end, the most efficient and sufficient intensity measure is considered to derive fragility functions and estimate the annual frequency of exceedance of two different limit states. The results show that the steel frame is more vulnerable than the piping due to pounding effects of a heavy vessel at high level. In addition, the results highlighted that the spectral acceleration is an efficient and sufficient intensity measure. However, the spectral acceleration should be used at different vibration periods due to higher mode effects of equipment, which cannot always be expressed as a percentage of fundamental period of the structure. Thus, the standard approach based on the average spectral acceleration, as proposed in the literature, may not apply for process units of this type.*

**Keywords:** process unit; steel structure; pipes; seismic hazard; dynamic interaction; fragility; risk assessment

---

## 1 INTRODUCTION

In chemical plants, supporting structures are used to carry piping and equipment for mechanical, safety and maintenance reasons. Supporting structures can vary on purpose and configuration, but two main configurations can be described: 1) pipe racks are used to carry piping that transfers products from one process unit to another and 2) steel towers are constructed to support vessels and piping at different heights. In pipe racks, the supporting structures are quite regular and they are usually considered as cantilevers during design and assessment, because of the lack of diaphragmatic behaviour and because of the point forces of pipes at the top (Figure 1a). In steel towers, structures are more irregular, in terms of mass and stiffness, they present higher mode effects and can be high-rise to accommodate all the required equipment (Figure 1b). In both cases, however, the potential risk due to piping failure can be the reason for catastrophic cascading effects given the hazardous materials involved.

Earthquakes continue to expose European countries, particularly in the Mediterranean sea, to high risk where seismic events have triggered significant destruction over the last decades [1]. Additionally, numerous major accidents events have been triggered by the seismic hazard due to damage to piping and supporting structures, causing human losses, environmental contamination and financial losses ([2]–[4]). The life-saving issue of seismic integrity inside chemical plants was also illustrated by [5], who identified 78 Natech accidents triggered by earthquakes, involving 439 pipework components (directly or indirectly damaged).

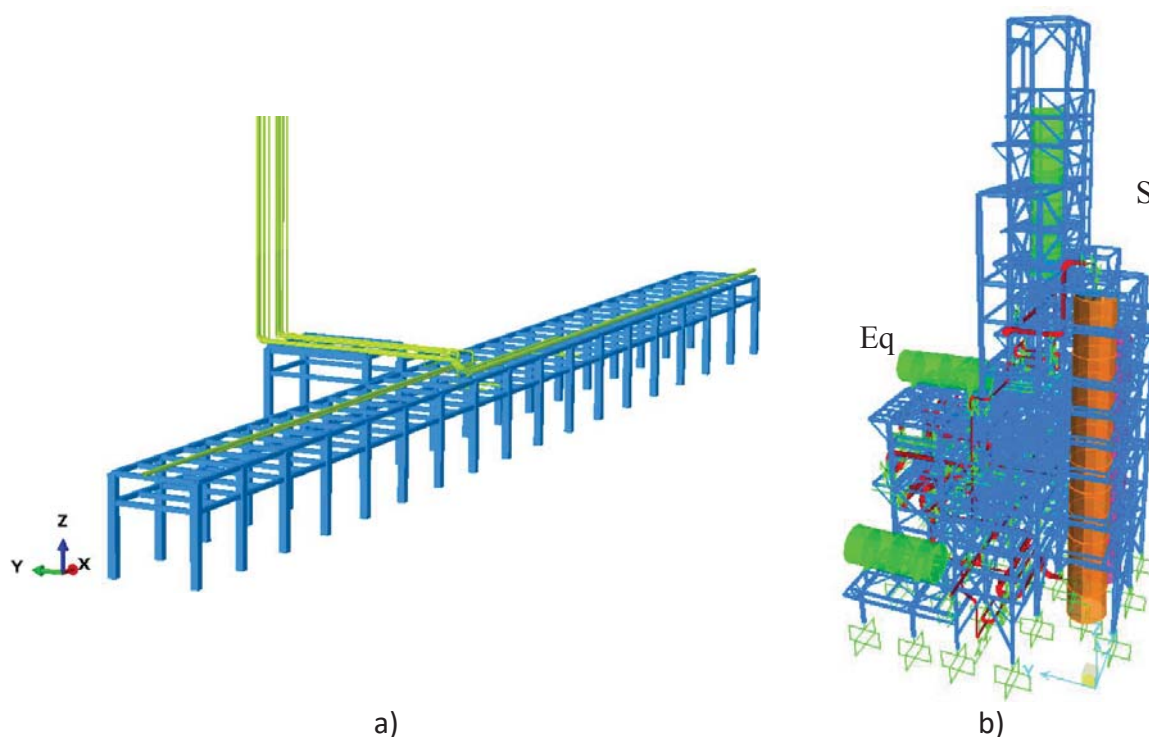


Figure 1: Different types of supporting structures inside chemical plants: a) pipe rack, b) tower with process equipment.

Seismic assessment is essential for risk reduction inside chemical plants. One of the most decisive steps of the risk assessment of major accidents triggered by seismic events is the use of fragility functions [6], which express the conditional probability of reaching or surpassing a specific damage state given an Intensity Measure (IM) of earthquake shaking. Fragility functions can be utilized prior to an earthquake within a consequence-based analysis to design strengthening measures and devise emergency response plans as well as in the aftermath of an

earthquake to prioritize inspection and determine medium- and long-term response and recovery ([7], [8]). Although the robustness of analytical fragility curves for critical process units is crucial for risk reduction inside process plants, many researchers still adopt empirical ones e.g. from HAZUS [9], because they are easily available and have applicability to different process units. Other databases e.g. SYNER-G [10] include both empirical and analytical fragility curves, though they are not exhaustive in terms of the various process units that can be found in petrochemical plants and do not account for the fragility of equipment separately. At least to the Authors' knowledge, the literature on the fragility derivation of supporting structures that account for dynamic interaction with equipment is very scarce. Even though some studies have been conducted in the past, they mainly regarded the fragility assessment at the component level and usually neglected the dynamic coupling between the supporting structures and the equipment ([11]–[14]).

Apart from modelling uncertainties, robust fragility functions should be expressed by selecting seismic IM that are representative of the seismological properties of ground motion related to site and source (sufficiency) and which reduce the record-to-record randomness (efficiency). A sufficient IM is conditionally independent of magnitude,  $M$ , and Joyner-Boore distance,  $R_{jb}$ ; thus, these parameters have little effect on the resulting seismic demand model. Additionally, an efficient measure results in low variability of seismic demand and enables the evaluation of the demand with the least possible number of ground motions. The efficiency and sufficiency of different IMs have already been addressed for common civilian assets, bridges and transport pipelines ([15]–[18]). For example, [18] conducted a literature review on the existing fragility curves for the European building stock, and it was confirmed that typical ground measures, e.g. peak ground acceleration, velocity and displacement as well as spectral measures at the fundamental period of structures were considered efficient. When it comes to buildings with non-structural components, an average spectral acceleration based only on the fundamental period of a building was proposed by [18] and [19], so that it can be easily applied in a risk assessment procedure. However, whether this IM can be applied for high irregular and complex systems, like process units, or not is still an open question that will be discussed in the current work.

The present analytical study intends to: 1) examine the seismic response of a process unit, 2) compare the efficiency and the sufficiency of common and recently-proposed measures for which ground prediction models are easily available and which can be used within a quantitative risk assessment, and 3) estimate the seismic risk in terms of mean annual frequency of collapse for further decision making, e.g. retrofitting or response planning.

## 2 DERIVATION OF ANALYTICAL FRAGILITY

### 2.1 Methodology

Different fragility analysis methods can be adopted to derive the fragility of a structural system. The methods are generally categorized as narrow- and wide-range, depending on the range of IM values. Considering that process units are large in scale and complex, stick modelling should be used, accounting also for the analysis method with the least possible computational cost. In addition, when addressing the fragility of critical plants where high level of damage must be avoided or should occur at large seismic intensity only, it is prudent to localize the investigation of an industrial structure, at least preliminarily, at lower performance level e.g. serviceability or life safety.

To this effect, the so-called cloud analysis that belongs to narrow-range methods will be used for the present study. The probabilistic estimation of an engineering demand parameter

given an IM is attained through the least sum of the squares of the residuals method, as described in [21]. The logarithmic linear regression of seismic demand, EDP, as a function of IM is considered and described by Equation 1:

$$\begin{aligned} EDP &= (a \cdot IM^b) \cdot \varepsilon \\ \eta_\varepsilon &= 1 \text{ and } \sigma_{\ln \varepsilon} = \beta_{EDP|IM} \end{aligned} \quad (1)$$

where  $a$  is an intercept and  $b$  is the slope in log-space. The lognormal random variable  $\varepsilon$  has median,  $\eta_\varepsilon$ , equal to unity and its logarithmic standard deviation,  $\sigma_{\ln \varepsilon}$ , is equal to the standard deviation of the EDP for a given value of IM,  $\beta_{EDP|IM}$ . The latter constitutes a metric of the efficiency of the regression of tested IMs to describe the seismic response of a structure.

Assuming that the EDP follows a logarithmic standard distribution for a given IM, the logarithm of the median,  $\ln(\eta_{EDP|IM})$ , is equal to the mean of the logarithm of EDP,  $\mu_{\ln EDP|IM}$ . The standard deviation of the logarithm of EDP,  $\sigma_{\ln EDP|IM}$ , is equal to the dispersion of EDP,  $\beta_{\ln EDP|IM}$ . Therefore, the parameters of the linear regression,  $a$  and  $b$ , can be obtained by estimating the median using linear regression in the logarithmic space of “cloud” data. The cumulative lognormal distribution of the observed data is expressed by Equation 2:

$$\begin{aligned} P[EDP_D > EDP_C|IM] &= \Phi \left( \frac{\ln(a \cdot IM^b) - \ln \eta_{EDP|IM}}{\beta_{EDP|IM}} \right) \\ &= \Phi \left( \frac{\ln(IM) - \ln \eta_{IM|EDP}}{\beta_{IM|EDP,tot}} \right) \end{aligned} \quad (2)$$

The total dispersion  $\beta_{IM|EDP,tot}$  accounts for three types of uncertainty, namely seismic demand ( $\beta_{EDP|IM}$ ), capacity ( $\beta_C$ ) and limit state ( $\beta_{LS}$ ) definition. The first type of uncertainty will be evaluated via nonlinear dynamic analyses in Section 4. The second and third uncertainty types are set equal to 0.3 and 0.4, respectively, based on common values that can be found in [9]. A more rigorous definition of the last two types of uncertainty would require a further detailed examination, which is beyond the scope of the present study. Finally, the total dispersion is evaluated by Equation 3:

$$\beta_{IM|EDP,tot} = \frac{1}{b} \sqrt{(\beta_{EDP|IM}^2 + \beta_C^2 + \beta_{LS}^2)} \quad (3)$$

### 3 CASE-STUDY

The case-study deals with the seismic assessment of an existing desulphurization process unit that is made of steel (Figure 1b). It was originally designed according to [22] for a high seismicity region. By virtue of a recent update of seismic hazard maps in the region of interest ([23]), the seismic integrity of the process unit should be assessed. The new acceleration values,  $S_1=1.35g$  and  $S_8=0.38g$ , were used for selecting seismic records consistent with the seismic hazard. The system is divided into two parts in order to facilitate the assessment in the following; in particular, the first part regards the high-rise steel structure (S) with the vertical vessel at the top (Figure 2a&b), whilst the second part is composed of a low-rise steel structure with equipment (Eq) that consists of horizontal vessels and pipes (Figure 2b). In this respect, see also Figure 1b. The system was assessed in the nonlinear regime using [24] and [25] as reference codes.

#### 3.1 Modelling characteristics

The structural members are made of steel ASTM A36/A36M with expected yield ( $f_{yes}$ ) and ultimate strength ( $f_{ues}$ ) 372.32 MPa and 439.89 MPa, respectively, modulus of elasticity ( $E$ )



equal to 203 GPa, Poisson ratio ( $\nu$ ) equal to 0.3 and kinematic hysteretic behaviour. The lateral load resisting system is formed by ordinary braced frames in the X direction, and ordinary moment frames in the Y direction. Horizontal bracing is placed in the XY plane and some vertical cross-bracings can also be found in the Y direction.

Several process vessels e.g. heat exchanger, surge drum and steam generator are supported on the steel structure and are considered in the modelling. Also, there is a piping network that connects the vessels at different heights. Pipes have three different nominal diameters (DN), viz DN250 40S, DN500 and DN600 80S. More information about the geometrical properties of pipes can be found in [26]. The pipes are made of steel API 5L X42 with expected yielding ( $f_{yep}$ ) and ultimate strength ( $f_{uep}$ ) equal to 297.00 MPa and 335.50 MPa, respectively. The modulus of elasticity ( $E$ ) and Poisson ratio are equal to 203 GPa and 0.2, respectively. Anew, kinematic hardening is considered with rupture strain at 0.03. The piping is supported on the steel structure mainly with sliding and guided supports, so that pipes are free to move in the longitudinal direction; however, some fixed points are also used particularly at the connection of pipes with equipment at the base floor. The description of supports at different coordinates of the system is omitted for brevity.

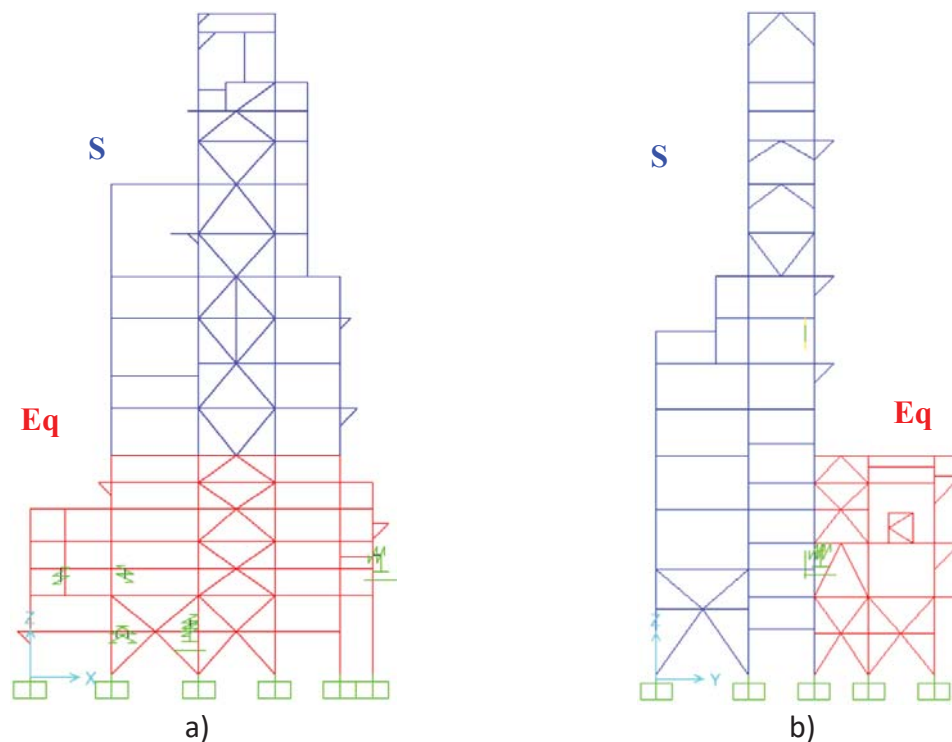


Figure 2: X-Z plane with part S (structure and vertical vessel) and Y-Z plane with part S and Eq (equipment)

Table 1: Impact of panel zone modelling on the first vibration period

Modal Analysis	Panel Zone	T(sec)	$\Delta T(\%)$	Mx/My (%)
X-direction	Centerline	1.084	N.A.	32/7
	Rigid offset	1.115	+2.95	22/18
	Scissor	1.073	-1.01	34/5
Y-direction	Centerline	1.175	N.A.	7/32
	Rigid offset	1.048	-10.71	18/22
	Scissor	1.172	-0.20	7/34

N.A.: Not Available



Before considering the assessment of the system in the nonlinear range using [27], it was necessary to examine a number of modelling aspects. First, three different configurations of panel zone were considered to examine the effects on vibration period of the structure, namely centerline without rigid offset, centerline with offset and scissor model as described in [28]. It can be seen in Table 1 that the maximum reduction of period between the centerline (most flexible) and rigid offset configuration was estimated roughly at 11% in the Y direction, whereas the difference with the scissor model did not exceed 3% in both directions. Furthermore, to examine the influence of flexibility of the beam-to-column connections, mainly in the X direction, two different lateral resisting systems were calibrated. In addition to the original system, a dual system was modelled with both directions being restricted. After comparing the vibration modes for the two different structural types, it was concluded that the maximum difference was 8% and 2% in the X direction and Y direction, respectively. Given that the rigid panel zone and the flexibility of connection did not influence considerably the response, the scissor model with the original configuration of frames was considered in the assessment. Finally, Table 2 quotes the first four vibration periods of the entire system, as inferred from modal analysis.

Table 2: The first four modes of vibration of the system

	Mode #	T(sec)	Mx/My (%)
Structural Part S	Mode 1	1.175	32/7
	Mode 2	1.084	7/32
Structural Part E	Mode 3	0.495	30/0
	Mode 4	0.450	0/17

The plastic deformation of structural members was described by concentrated hinge modeling. Although distributed plasticity formulations may capture the stress-strain behaviour along the structural member or local behaviour such as buckling of flanges, they require high computational effort, which becomes even more prohibitive for large scale models like the process unit under examination. On the other hand, point hinges can be more adequate to capturing the nonlinear degrading response [28]. In the framework of this study, concentrated plasticity was used, allowing for an analysis that is both time efficient and effective, under the condition that the response of the system is not investigated beyond the collapse prevention limit state. Concerning the plastic deformation on pipes, fiber sections with 8 integration points were used. More information about this method can be found in [27] and [28].

### 3.2 Selection of records

The selection of a sufficient number of records for seismic risk assessment is crucial for the accurate prediction of the system response. This comes as a function of the analysis method for deriving fragility functions. For example, the cloud analysis method that the present study employs requires a sufficient number of records with values close to, or larger than, the limit state of interest [29]. Additionally, the method for selecting a set of records consistent with the seismic hazard is equally important for improving the sufficiency and efficiency of the IMs. To this effect, a number of 40 far-field records from NGA West 2 database were selected with the conditional spectrum approach as described by [30]. The spectra of the selected records are shown in Figure 3. The moment magnitude of records,  $M_w$ , varies from 6 to 7.6, the Joyner-Boore distance,  $R_{jb}$ , spans from 22 to 92 km, approximately. Shorter distance was not considered to avoid including pulse-like records, which are being investigated by the Authors. Also, the average shear wave velocity of the upper 30 m of soil profile,  $V_{s30}$ , was found in the range

of 160 km to 360 km which refers to soil type D according to [31]. The records were shortened using the 5-95% significant duration rule and the maximum scale factor was set to 4. Finally, it should be emphasized that the records were conditioned at the first vibration period of the steel structure,  $T_1$ , in the weakest direction Y. This decision was made on the basis of the significant inter-storey drift ratio observed at the point where the vertical vessel is supported at the top of the steel structure. Additionally, [32] showed that risk-based assessments do not vary based on the choice of conditioning period given that hazard consistency is achieved.

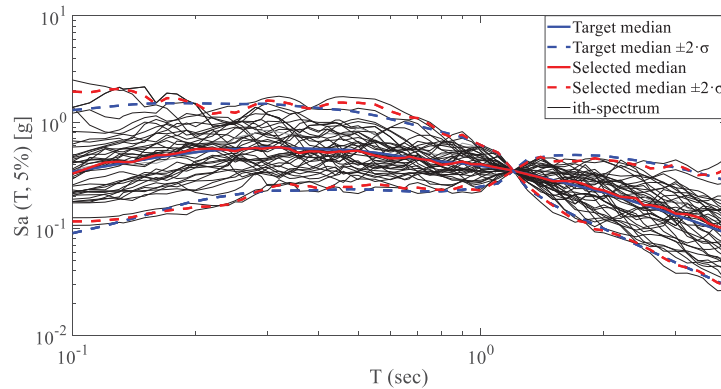


Figure 3: Response spectra of the selected far-field records

## 4 SEISMIC RISK ASSESSMENT

### 4.1 Methodology for nonlinear analysis

Before running nonlinear analyses, the acceptance criteria should be defined. There are three main aspects that need to be accounted for when defining performance levels for irregular systems like the process unit. Firstly, the structural type should be considered. The unit is a concentrically braced frame in the X direction and ordinary moment frame with some bracing in the Y direction as well. Also, it lacks diaphragmatic behaviour, which can result in uneven deformation at the same height. Thus, acceptance criteria should not be the same as for common building structures considering also the higher risk that process plants pose to humans and environment. Secondly, the scale of the model necessitates the use of an engineering parameter that is able to describe the damage at global level and can be monitored easily. The shear or moment force of beams and columns as well as the axial force of braces can be suitable parameters for models with smaller scale. Finally, the selected parameter should be able to describe the damage to pipes. For the aforementioned reasons, the interstorey drift ratio (IDR) was selected as a global and generally recognized demand parameter by seismic codes ([24]) to describe the damage on the steel structure. The acceptance criteria for IDR are shown in Table 3 for two different limit states, namely serviceability (SLS) and safe life (SLLS) limit state. [33] investigated the seismic response of a 4-storey steel moment frame analytically and experimentally, indicating that the beginning of yielding and buckling of members occurs at IDR values equal to 1% and 2%, respectively. Given the higher risk, the presence of bracing and irregularity of the process unit, lower values than those indicated by [33] were set for the SLS and SLLS in Table 3. When it comes to piping, the yielding strain is commonly selected as the lower boundary of SLS both under tension and compression. More information about the limit states of piping can be found in [34] and [35].

Furthermore, preliminary time-history analyses were conducted using 11 unscaled records that examined the seismic response of the structure and defined the scaling factor that is required to equal or to exceed the SLLS, which was set as a performance objective. For the cloud

analysis method, there is a rule of thumb saying that 30% of selected records should exceed the desired limit state ([29]). To attain this goal, the records were initially scaled with a scaling factor that did not exceed 5, and then the factor was scaled down to reduce the bias due to some significant deformation that was observed both on steel structure and pipes.

#### 4.2 Efficiency and sufficiency of tested seismic IMs

The scope of the present study is to find an IM that is sufficient and efficient both for the structure and pipes, and which can be combined with a simple ground prediction model for risk assessment. Considering that the system includes structural and nonstructural components and the deficiency of the literature on the seismic response of petrochemical plants units, it was decided to compare measures of three different categories, namely duration-, amplitude- and period response-based. The first category consisted of Arias Intensity (AI, [36]) cumulative and standardized cumulative average velocity (CAV and SCAV, [28]&[29]) and the second one included the peak ground acceleration and velocity (PGA and PGV). Apart from the spectral acceleration at the first vibration period of both structural parts,  $S_a(T_s)$  and  $S_a(T_{Eq})$ , the effective peak acceleration (EPA, [39]) and the recently introduced equipment average spectral acceleration (E-ASA<sub>R</sub>, [19]) were also considered in the period response-based category.

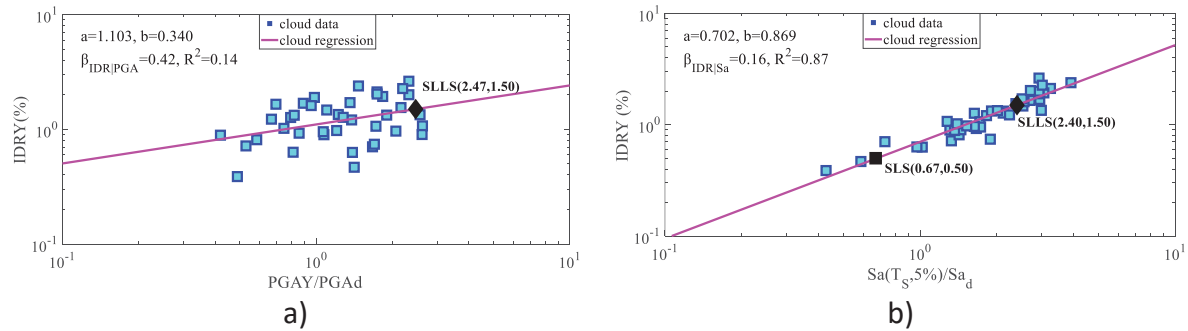


Figure 4: Regression for structural part S using a. PGA in the Y direction, and b. 5%-damped  $S_a$  (design values  $PGA_d$  and  $Sa_d$  are equal to 0.37g and 0.35g, respectively)

Table 3: Median, dispersion and coefficient of determination for structural part S and SLLS

Intensity measure (IM)		$\mu_{\ln EDP IM}$	$\beta_{EDP IM}$	$R^2$
Duration-based	Aly (m/s)	22.77	0.43	0.10
	CAVy(g-s)	3.57	0.40	0.22
Amplitude-based	PGAy/PGA <sub>d</sub>	2.47	0.42	0.14
	PGVy (cm/s)	104.90	0.34	0.44
Period response-based	EPAy (g-s)	0.81	0.29	0.60
	<b>Sa(T<sub>s</sub>)/Sa<sub>d</sub></b>	<b>2.40</b>	<b>0.16</b>	<b>0.87</b>

The results from the linear regression analysis of IDR as a function of PGA and  $S_a$  for the structural part S in the Y direction are shown in Figure 4a&b, respectively. The most remarkable outcome regards the considerably lower dispersion of  $S_a$  compared to the PGA. This outcome stems from the fact that the concentrated mass of the vertical vessel at the top governs the response, resulting in the highest IDR at the same height. The low variability of the response is strengthened further by conditioning the records at the first fundamental mode that pertains mainly to the vibration of the vertical vessel. Obviously, the PGA that is proposed by HAZUS [9] is not efficient and should not be preferred over  $S_a$  for risk assessment of this process unit. Also, the rest of IMs were observed to be less efficient than  $S_a$  (Table 4). It is emphasized that

Table 4 quotes only the dispersion due to record-to-record randomness. The rest two types of uncertainty are not included to avoid blurring the comparison.

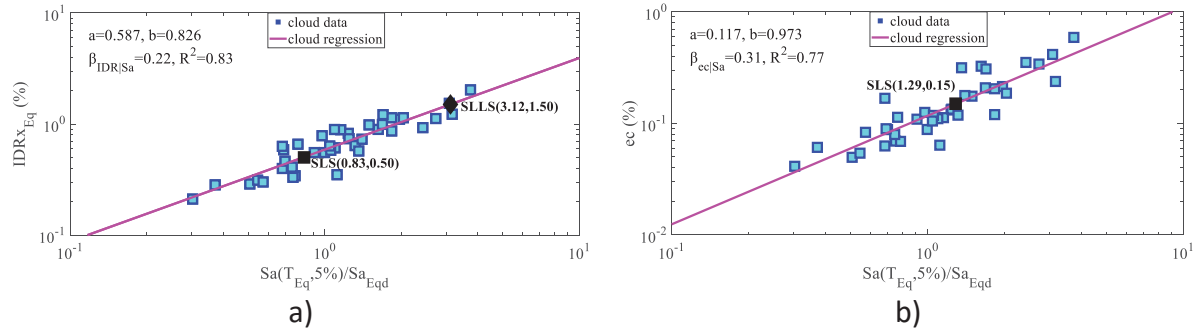


Figure 5: Regression for structural part Eq in terms of a. IDR of steel structure in the X direction and b. compression strain on pipe expressed as a function of 5%-damped  $Sa_{Eq}$  (design value,  $Sa_{Eqd}$ , equal to 0.94g)

Table 4: Median, dispersion and coefficient of determination for structural part Eq

Intensity measure (IM)		$\mu_{lnEDP IM}$	$\beta_{EDP IM}$	$R^2$
Duration-based	$A_{lx}$ (m/s)	6.48	0.54	0.31
	SCAVx (g-s)	1.85	0.59	0.15
Amplitude-based	$PGA_x/PGA_d$	1.48	0.36	0.69
	$PGV_x$ (cm/s)	118.90	0.63	0.05
Period response-based	E-ASA40x (g)	0.94	0.35	0.71
	EPAX (g-s)	0.75	0.44	0.53
	$Sa(T_{Eq})/Sa_{Eqd} _{ec}$	<b>1.29</b>	<b>0.31</b>	<b>0.77</b>
	$Sa(T_{Eq})/Sa_{Eqd} _{IDR}$	<b>3.12</b>	<b>0.22</b>	<b>0.83</b>

Furthermore, the regression for the structural part Eq, which refers to the steel structure out-fitted by the horizontal vessels and pipes, is expressed in terms of interstorey drift,  $IDR_{Eq}$ , and pipe strain due to compression,  $ec$ , as a function of spectral acceleration at the fundamental frequency of the equipment,  $Sa(T_{Eq})$  (mode 3 in Table 2). In this respect, see Figure 5a&b. It can be seen that the SLS for the structure occurred at 36% lower  $Sa$  compared to pipes. Additionally, the dispersion for the seismic response of the structure was lower than the pipe, which can be a clear indication that the vulnerability of the equipment should better be expressed in terms of steel structure deformation. It is reasonable that the response of pipes resulted in higher dispersion, since the dynamic interaction of structure, vessel and pipe can become complex, if the pipe is not rigidly supported on the rack. The rest of IMs that were examined resulted in higher dispersion than the above-mentioned measures (Table 5). It is emphasized herein that in contrast with [19] who formulated  $ESA_R$  ( $R$  means the percentage increase of vibration period) based on the fundamental period of a structure, in this case study, the fundamental period of the structure,  $Sa(T_s)$ , is much greater than the period of equipment,  $Sa(T_{Eq})$ , and thus it was decided to use the latter as a reference period and increase it by 40% in order to account for additional modes of vibration of equipment (not shown in Table 2). Nevertheless, it appeared that higher modes apart from  $T_{Eq}$  did not affect the response of equipment. Other researchers such as [20] have proposed similar IMs, which do not apply to our case due to the high irregularity of the process unit.

Furthermore, the dependency of IMs on magnitude,  $M$ , and Joyner-Boore distance,  $R_{jb}$ , was examined based on the p-value. A p-value greater than 0.05 is commonly accepted as a threshold for accepting the null hypothesis which states that the coefficient of regression is zero. As depicted in Table 6, some measures are sufficient for both parameters and others only for one

of them. It is emphasized that the  $Sa(T_S)$  proved to be sufficient for both seismological parameters, thus it meets the requirements to be used for risk assessment in the following. Even though the  $Sa(T_{Eq})$  was sufficient as a function of IDR, it was not evaluated as sufficient with respect to pipe strain,  $\epsilon_c$  (Table 7). Nevertheless, the dispersion of  $Sa(T_{Eq})|IDR$  is both efficient and sufficient, and thus it can be used as a proper IM for the risk assessment of the equipment. Finally, the PGA was also a sufficient IM, but lower efficiency was estimated compared to  $Sa(T_{Eq})$ .

Table 5: Sufficiency of intensity measures considered for structural part S

Intensity measure (steel structure)		p-value	
		M	Log(Rjb)
Duration-based	$A_{ly}$	0.0094	0.9673
	$CAV_y$	0.2536	0.3713
Amplitude-based	$PGA_y/PGA_d$	0.0029	0.5643
	$PGV_y$	0.1638	0.5775
Period response-based	$EPA_y$	0.0706	0.6480
	<b><math>Sa(T_S)/Sa_d</math></b>	<b>0.7095</b>	<b>0.4879</b>

Table 6: Sufficiency of intensity measures considered for structural part Eq

Intensity measure (equipment)		p-value	
		M	Log(Rjb)
Duration-based	$A_{lx}$	0.0585	0.2069
	$SCAV_x$	0.0514	0.0997
Amplitude-based	$PGA_x/PGA_d$	0.6947	0.5745
	$PGV_x$	0.1601	0.0267
Period response-based	$E-ASA40_x$	0.0884	0.1912
	$EPA_x$	0.1631	0.3594
	<b><math>Sa(T_{Eq})/Sa_{Eqd}  \epsilon_c</math></b>	<b>0.0373</b>	<b>0.2231</b>
	<b><math>Sa(T_{Eq})/Sa_{Eqd}  IDR</math></b>	<b>0.4369</b>	<b>0.5460</b>

### 4.3 Risk estimation

Based on the previous results, the fragility of the system was derived using the  $Sa$  as IM for both structural parts (Figure 6a&b). Also, for the structural part Eq, the fragility for the SLS of the most vulnerable pipe was depicted as well in Figure 6b for the sake of comparison. To derive the mean annual frequency of exceedance for each LS,  $\lambda$ , the fragility curves were integrated with the seismic hazard curves for both parts (Figure 7a&b). The hazard curve provides the mean annual frequency of exceedance, MAF, for each value of  $Sa$ . The values of  $\lambda$  for the SLS and SLLS are quoted in Table 8. For the part S, it can be seen that  $\lambda$  is equal to  $0.0021 \text{ yrs}^{-1}$  or, in other words, the mean return period of exceedance of the SLS is 476 years. Concerning the SLLS and structural part Eq, the mean return period is significantly higher. Based on the fragility analysis results, it can be mentioned that the performance objective of “control damage” on the structure, as stipulated in [24], is met; however, the estimated risk should further be assessed accounting for a greater number of records and soil deformability effects. In such case, the risk can be communicated to a stakeholder for further decision making.

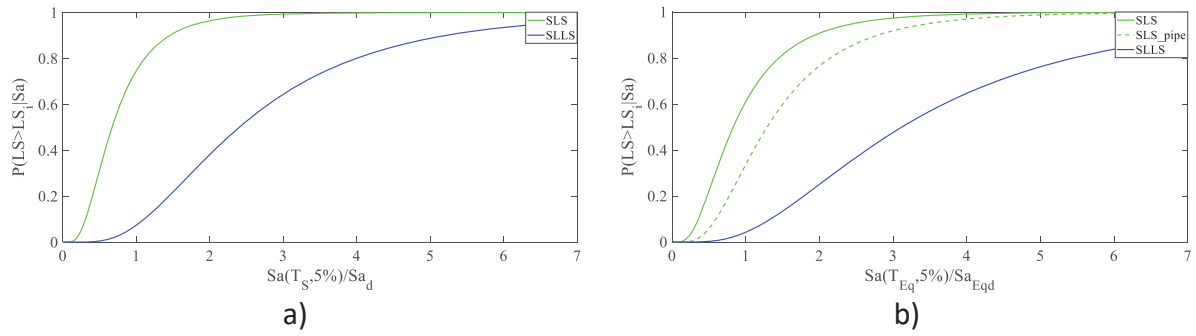


Figure 6: Fragility curves for the a. structural part S and b. structural part Eq

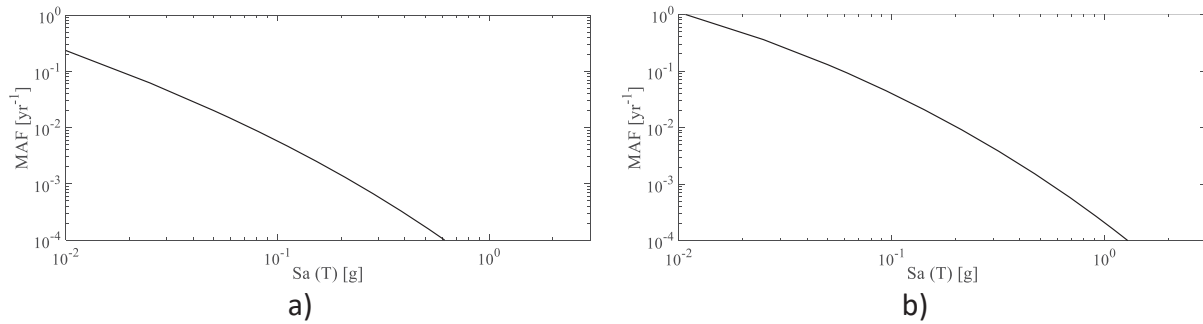


Figure 7: Hazard curves for the a. structural part S and b. structural part Eq

Table 7: Annual frequency of exceedance and return period for the two limit states and structural parts

	PART S		PART Eq	
	$\lambda$ ( $\text{yrs}^{-1}$ )	Return period (yrs)	$\lambda$ ( $\text{yrs}^{-1}$ )	Return period (yrs)
SLS	0.0021	476	0.0014	716
SLLS	$1.32 \cdot 10^{-4}$	7,576	$4.67 \cdot 10^{-5}$	21,426

## CONCLUSIONS

The present analytical study evaluated the seismic risk of a chemical process unit accounting for dynamic interaction with equipment. The main considerations and outcomes can be summarized as follows:

- The system was separated into two different structural parts, part S and Eq. The part S included the high-rise steel structure, affected mainly by a heavy vertical vessel at the top, whilst the part Eq consisted of the low-rise steel structure and horizontal vessels. This separation was necessary, since the two parts exhibited considerably different vibration periods and the second part included the most vulnerable pipe;
- Using a set of far-field records, the steel structure was found to be more vulnerable than the piping network in both parts, S and Eq. This is because of the excessive concentrated mass of vessels that increased the deformation of steel members;
- Different IMs were considered. However, for both structural parts, S and Eq, the spectral acceleration, was evaluated as both the most efficient and sufficient IM to describe the seismic demand both on the steel structure and piping, although considering a different vibration period for each part.. This outcome brings into question the application of average spectral acceleration, as proposed in the literature, for chemical process units with numerous equipment.



- Finally, the seismic risk was derived for each part separately, and the mean period of exceedance was evaluated at 556 and 1011 years for the SLS. However, the soil deformability should also be considered to have a fully realistic estimation of global risk of the petrochemical plant facility.

Apart from far-field seismic motions, a near-field set of records will be used in the future to examine the seismic vulnerability of the system, accounting for soil-structure interaction. In the end, the results from the fragility analysis will be used for determining consequence scenarios.

## ACKNOWLEDGMENTS

The first Author would like to thank Dr. E. Krausmann and Dr. A. Necci for the valuable comments and assistance during the traineeship at Joint Research Center, Ispra. The Authors would like to thank Prof. Carlo G. Lai and Dr. F. Bozzoni from EUCENTRE, Pavia (Italy) for providing the hazard curves for the site under consideration. Finally, the first Author gratefully acknowledges the financial support from the European Commission during the traineeship at the Joint Research Center.

## REFERENCES

- [1] C. Theofili and A. L. V. Arellano, "Lessons learnt from earthquake disasters that occurred in Greece, NEDIES project, EUR 19946 EN," *Jt. Res. Center, Eur. Comm.*, 2001.
- [2] M. Eli, S. Sommer, T. Roche, and K. Merz, "The January 17, 1994 Northridge Earthquake: Effects on Selected Industrial Facilities and Lifelines," 1995.
- [3] E. Krausmann, A. M. Cruz, and B. Affeltranger, "The impact of the 12 May 2008 Wenchuan earthquake on industrial facilities," *J. Loss Prev. Process Ind.*, vol. 23, no. 2, pp. 242–248, 2010.
- [4] E. Krausmann, A. M. Cruz, and E. Salzano, *Natech Risk Assessment and Management: Reducing the Risk of Natural-Hazard Impact on Hazardous Installations*. 2016.
- [5] M. Campedel, "Analysis of Major Industrial Accidents Triggered by Natural Events Reported In the Principal Available Chemical Accident Databases," 2008.
- [6] E. Salzano, I. Iervolino, and G. Fabbrocino, "Seismic risk of atmospheric storage tanks in the framework of quantitative risk analysis," *J. Loss Prev. Process Ind.*, 2003.
- [7] A. S. Elnashai and L. Di Sarno, *Fundamentals of Earthquake Engineering: From Source to Fragility*, Second. Wiley, 2015.
- [8] A. Necci, E. Krausmann, and S. Girgin, "Emergency planning and response for Natech accidents," *Toward an All-Hazards Approach to Emerg. Prep. Response Lessons Learn. from Non-Nuclear Events*, 2018.
- [9] HAZUS-MH MR5, "Multi-hazard Loss Estimation Methodology Earthquake Model," 2010.
- [10] F. T. Kyriazis Pitilakis and K. Kakderi, *Systemic Seismic Vulnerability and Risk Analysis for Buildings, Lifeline Networks and Infrastructures Safety Gain*. 2013.
- [11] R. J. Merino Vela, E. Brunesi, and R. Nascimbene, "Seismic assessment of an industrial frame-tank system: development of fragility functions," *Bull. Earthq. Eng.*, vol. 17, no. 5, pp. 2569–2602, May 2019.

- [12] O. S. Bursi, F. Paolacci, and S. Reza, "Performance-Based Analysis Of Coupled Support Structures And Piping Systems Subject To Seismic Loading," *ASME 2015 Press. Vessel. Pip. Conf.*, vol. 00032, no. July 2015, pp. 1–8.
- [13] O. S. Bursi and M. S. et al Reza, "Component Fragility Evaluation, Seismic Safety Assessment and Design of Petrochemical Plants under Design-basis and Beyond-design-basis Accident Conditions. Mid-Term Report, INDUSE-2-SAFETY Project, Contr. No: RFS-PR-13056, Research Fund for Coal and Ste," 2019.
- [14] Y. S. Salem, P. E. Tiffany Yoo, G. M. Gad, and J. S. Cho, "Analytical Fragility Curves for Pipe Rack Structure," 2019, pp. 292–306.
- [15] N. Luco and C. A. Cornell, "Structure-specific scalar intensity measures for near-source and ordinary earthquake ground motions," *Earthq. Spectra*, 2007.
- [16] G. Tsiniadis, L. Di Sarno, A. Sextos, and P. Furtner, "Optimal intensity measures for the structural assessment of buried steel natural gas pipelines due to seismically-induced axial compression at geotechnical discontinuities," *Soil Dyn. Earthq. Eng.*, 2020.
- [17] J. E. Padgett, B. G. Nielson, and R. DesRoches, "Selection of optimal intensity measures in probabilistic seismic demand models of highway bridge portfolios," *Earthq. Eng. Struct. Dyn.*, 2008.
- [18] R. Maio and G. Tsionis, "Seismic fragility curves for the European building stock: Review and evaluation of analytical fragility curves," 2016.
- [19] M. De Biasio, S. Grange, F. Dufour, F. Allain, and I. Petre-Lazar, "Intensity measures for probabilistic assessment of non-structural components acceleration demand," *Earthq. Eng. Struct. Dyn.*, vol. 44, no. 13, pp. 2261–2280, Oct. 2015.
- [20] M. Kohrangi, P. Bazzurro, D. Vamvatsikos, and A. Spillatura, "Conditional spectrum-based ground motion record selection using average spectral acceleration," *Earthq. Eng. Struct. Dyn.*, 2017.
- [21] C. A. Cornell, F. Jalayer, R. O. Hamburger, and D. A. Foutch, "Probabilistic Basis for 2000 SAC Federal Emergency Management Agency Steel Moment Frame Guidelines," *J. Struct. Eng.*, 2002.
- [22] I. C. Council, *2018 International Building Code*. 2018.
- [23] F. Bozzoni *et al.*, "Probabilistic seismic hazard assessment at the eastern Caribbean Islands," *Bull. Seismol. Soc. Am.*, 2011.
- [24] ASCE/SEI 41-17, *Seismic Evaluation and Retrofit of Existing Buildings*. American Society of Civil Engineers, 2017.
- [25] R. Pekelnicky and C. Poland, "ASCE 41-13: Seismic Evaluation and Retrofit Rehabilitation of Existing Buildings," *SEAOC 2012 Conv. Proc.*, 2012.
- [26] *ASME B36.19M-2004 Stainless steel pipe (Revision of ANSI/ASME B36.19M-1985), American national standard.* .
- [27] CSI, "SAP2000. Analysis Reference Manual v.18.1.1," *CSI: Berkeley (CA, USA): Computers and Structures INC.* p. 496, 2018.
- [28] ATC 114, "Recommended modeling parameters and acceptance criteria for nonlinear analysis in support of seismic evaluation, retrofit, and design," *Nist Gcr 17-917-45*, 2017.

- [29] F. Jalayer, H. Ebrahimian, A. Miano, G. Manfredi, and H. Sezen, “Analytical fragility assessment using unscaled ground motion records,” *Earthq. Eng. Struct. Dyn.*, 2017.
- [30] J. W. Baker and C. Lee, “An Improved Algorithm for Selecting Ground Motions to Match a Conditional Spectrum,” *J. Earthq. Eng.*, 2018.
- [31] ASCE/SEI 7-16, *Minimum Design Loads and Associated Criteria for Buildings and Other Structures*. 2017.
- [32] T. Lin, C. B. Haselton, and J. W. Baker, “Conditional spectrum-based ground motion selection. Part I: Hazard consistency for risk-based assessments,” *Earthq. Eng. Struct. Dyn.*, 2013.
- [33] K. Suita, S. Yamada, M. Tada, K. Kasai, Y. Matsuoka, and Y. Shimada, “Collapse experiment on 4-story steel moment frame: part 2 detail of collapse behavior,” *Proc. 14th world Conf. Earthq. Eng. Beijing, China*, 2008.
- [34] L. Di Sarno and G. Karagiannakis, “On the seismic fragility of pipe rack—piping systems considering soil–structure interaction,” *Bull. Earthq. Eng.*, Feb. 2020.
- [35] M. Vathi, S. A. Karamanos, I. A. Kapogiannis, and K. V. Spiliopoulos, “Performance criteria for liquid storage tanks and piping systems subjected to seismic loading,” *J. Press. Vessel Technol.*, 2017.
- [36] A. Arias, “A measure of earthquake intensity. Seismic Design for Nuclear Power Plants,” in *Seismic Design for Nuclear Power Plants*, 1970.
- [37] J. W. Reed and R. P. Kassawara, “A criterion for determining exceedance of the operating basis earthquake,” *Nucl. Eng. Des.*, 1990.
- [38] EPRI, “Standardization of the cumulative absolute velocity. EPRI TR-100082. Electric Power Research Institute, USA,” 1991.
- [39] ATC, “Tentative provisions for the development of seismic regulations for buildings, ATC-3-06 Report, Applied Technology Council, Redwood City, CA.,” 1978.

## A COMPARATIVE STUDY ON SEISMIC RESPONSE OF A SUPER HIGH-RISE BUILDING USING CONVENTIONAL AND MODAL PUSHOVER ANALYSIS

Xianlong Zhang<sup>1</sup>, Hao Wu<sup>2\*</sup>, Qiao Yu<sup>2</sup>, Yang Liu<sup>1</sup>, Lingzhi Li<sup>2</sup>,  
Wannan Xu<sup>1</sup>, Junyan Zhou<sup>1</sup>

<sup>1</sup>China Construction Seventh Engineering Division (Shanghai) Corp. Ltd.  
235 E. Yunling Rd., Putuo District, Shanghai 200062, China  
1091370813@qq.com, liuyang10@cscec.com, xuwn@cscec.com, 398620137@qq.com

<sup>2</sup>College of Civil Engineering, Tongji University  
1239 Siping Rd., Shanghai 200092, China  
2009wuhao\_tom@tongji.edu.cn, yq\_@tongji.edu.cn, lilingzhi@tongji.edu.cn

---

### Abstract

*For super high-rise buildings, higher order modal shapes may have a significant impact on the structural response under seismic excitations. Since conventional pushover analysis procedure only includes the contribution from the first modal response, it is not able to accurately account for the varying dynamic characteristics of a super high-rise building. Based on mode superposition response spectrum method, modal pushover analysis (MPA) procedure is proposed to consider enough number of modes, which improves the conventional pushover analysis procedure to a certain extent. Based on a case-study super high-rise structure, this paper comparatively investigates the seismic responses of the structure using conventional pushover procedure and MPA procedure, and the accuracy of the results are validated through comparison with nonlinear time history analysis. The results show that the MPA procedure has a great improvement in accuracy as compared to the conventional pushover procedure. It is also demonstrated that the calculated structural response from MPA are in very good agreement with the results from nonlinear time history analysis, such as peak story displacements and story forces, while reducing computing time tremendously which improves the efficiency of seismic analysis of super high-rise buildings.*

**Keywords:** Super High-Rise Buildings, Modal Pushover Analysis, Nonlinear Time-History Analysis, Seismic Response.

---

## 1 INTRODUCTION

The philosophy of seismic design for building structures has been gradually evolved from force-based design to displacement-based and performance-based design during the past decades. Pushover analysis procedure, known as a nonlinear static analysis procedure which could be an alternative to nonlinear time history analysis (NTHA) procedure, has been widely used and adopted within the scope of performance-based design [1]. In spite that the Pushover analysis procedure has the benefits of simplicity and relative accuracy, the fundamental assumptions behind the procedure has limited its use to a certain extent, especially for high-rise structures, which are: 1) the response of the structure is related to a certain equivalent single degree of system (SDOF), and 2) the deformation envelop along the structure height is assumed to maintain constant throughout the entire seismic behavior evolution even for the nonlinear response stage. Obviously, these assumptions have excluded the higher mode responses which should be evident in high-rise and super high-rise structures. For this end, Chopra et al. [2] has proposed a new Pushover analysis procedure, i.e., Modal Pushover Analysis (MPA) procedure, which analyze a structure using Pushover analysis at several selected modes, and combines the modal responses using a certain combination rule to get the final response. Since this procedure is able to include the higher mode responses, it becomes more popular than conventional Pushover analysis for seismic performance assessment of high-rise buildings.

This paper comparatively investigates the seismic response of a case-study super high-rise structure using MPA procedure. Various numbers of modes are selected including only one mode (which becomes traditional Pushover analysis) in order to assess the accuracy of the procedure. The results from MPA are then compared with the results from NTHA to evaluate the accuracy of MPA procedure.

## 2 PROCEDURE OF MODAL PUSHOVER ANALYSIS

A brief introduction to the main process of MPA procedure used in the current study are presented in the following text. More details regarding the theory and any specific attentions that should be paid during analysis could be found in literature [3-6]. The step-by-step illustration of the MPA analysis process are:

- 1) Step 1: Calculate the structural vibration periods  $T_n$  and vibration modes  $\varphi_n$ ;
- 2) Step 2: For the  $n^{\text{th}}$  vibration mode, establish the base shear versus top displacement relationship (i.e., Pushover curve) based on a constant lateral force distribution  $s_n^* = m\varphi_n$ ;
- 3) Step 3: Transfer the analyzed Pushover curve to the idealized double broken Pushover curve for the  $n^{\text{th}}$  vibration mode, then transfer the idealized curve to the capacity curve (i.e., acceleration versus displacement relationship) for the  $n^{\text{th}}$  modal elasto-plastic SDOF system according to the following equations;

$$\frac{F_{sny}}{L_n} = \frac{V_{bny}}{M_n^*} \quad (1)$$

$$D_{ny} = \frac{u_{my}}{\Gamma_n \varphi_m} \quad (2)$$

where,  $M_n^*$  is the equivalent modal mass, and  $\Gamma_n$  is the modal contribution coefficient.

- 4) Step 4: Calculate the structural responses  $r_n$  of the  $n^{\text{th}}$  vibration mode using elasto-plastic response spectrum;

5) Step 5: Repeat the above Steps 3 and 4 for all the vibration modes determined to use in the MPA analysis;

6) Step 6: Obtain the total seismic demands based on a certain combination rule, such as the square root of sum of squares (SRSS) rule;

$$r = \sqrt{\sum r_n^2} \quad (3)$$

where,  $r_n$  is the  $n^{\text{th}}$  modal seismic demand, and  $r$  is total seismic demand.

### 3 THE CASE-STUDY SUPER HIGH-RISE BUILDING

#### 3.1 Description of the building

In this study, a super high-rise building is selected as the case-study structure for MPA analysis. Figure 1 shows the typical floor plan of the structure. As shown, the structural system of the building is frame-core wall system, which is the most commonly used system for super high-rise buildings in China. This system combines reinforced concrete (RC) wall cores (in the plan center) and columns (in the perimeter) to resist later loads, thus obtaining the balance between lateral resistance and stiffness along with architectural functions. The frame columns of the building are concrete filled steel tube (CFT) columns, and the frame beams are RC beams and steel beams. The coupling beams of core walls are steel-concrete coupling beams and RC coupling beams. In order to increase the lateral stiffness, outriggers and mega-braces are used at several stories along the building height. The total height of building is 400 m with 96 stories. Structural concrete strength is C60 based on Chinese design code [7] for columns and core walls, and C35 for floors. The structural steel is Q345, and reinforcing steel is HRB500 for force resisting bars and HRB400 for hoops and stirrups. According to Chinese seismic design code [8], the building is designed for a site of 8 degree representing high seismicity (the peak ground acceleration for design earthquake is 0.2g). The site class is III, and the seismicity group is I, resulting the site characteristic period of 0.45 sec. Dead and live loads for both floor and roof stories are 5 kN/m<sup>2</sup> and 2kN/m<sup>2</sup>, respectively. The design of the building is performed before the analysis of the study using the Chinese structural design software PKPM [9]. A list of the structural member sizes can be referred to as in Table 1 (for horizontal members) and Table 2 (for vertical members).

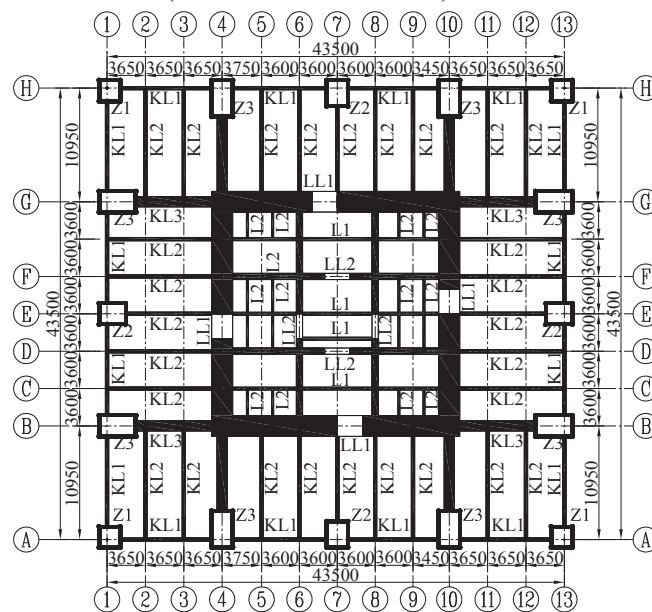


Figure 1: Typical floor plan layout (unit: mm).



Story	KL1	KL2	KL3	LL1	LL2	L1	L2
1~4				2000*2000+1200*1200*50*50			
5~14				1800*2000+1200*1200*50*50			
15~24				1560*1000+800*800*45*45	600*800		
25~27				1320*1000+800*800*45*45			
28~31		900*300	1000*1200	1080*1000+800*400*50*55			
31~37		*25*40					
38~40	1000*300			1320*1000			
41~50	*28*40			1080*1000+800*400*50*55		300*700	200*350
51~53				1080*1000			
54~72			800*1000	800*1000+600*300*40*45	400*800		
73~75		650*300					
		*14*30		600*800			
76~86		900*300					
		*25*40					
87~95	700*300*						
96	16*30	650*300*14*30		300*600		300*700	

Note: 1) The meaning of section size of I-beam is height\*width\*thickness of web\*thickness of flange. 2) The meaning of section size of steel reinforcement concrete beam is section size of full section + section size of I-beam.

Table 1: Horizontal members' section size (Unit: mm).

Story	Z1	Z2	Z3	Inner wall	Exterior wall	Truss	Brace
1~4					2000		
5~11					1800	-	800*800*55*55
12~14					1560	700*700*50*50	-
15~24	2000*2000	2000*3500*	2000*3500*		1320	-	1000*1000*60*60
25~27	*70*70	70*70	70*80	600	1080	700*700*50*50	-
28~37						-	1000*1000*60*60
38~40						700*700*50*50	-
41~50						-	1000*1000*60*60
51~53						700*700*50*50	-
54~66	1500*1500	1500*2000	1500*3000		800	-	1000*1000*60*60
67~72				400	600	700*700*50*50	-
73~75	1200*1200	1200*1600	1200*2000			500*500*30*30	-
76~86	1000*1000	1000*1200	1000*1800	300	600	-	900*1300*100*50
87~89						500*500*30*30	-
90~95	500*500	500*800	650*1000		300	-	-
96						-	-

Note: 1) The meaning of section size of CFT column is height\*width\*thickness of steel plate in height direction\*thickness of steel plate in width direction. 2) The rectangular steel tube is used for truss and brace, and the meaning of section size is height\*width\*thickness of steel plate in height direction\*thickness of steel plate in width direction.

Table 2: Vertical members' section size (Unit: mm).

### 3.2 Numerical modeling

To conduct the MPA nonlinear static analysis, the numerical model of the case-study building is established using PERFORM-3D software [10]. The building core walls are modeled using General Wall element in PERFORM-3D, considering both the axial-flexural interaction as well as nonlinear shear behavior. The axial and flexural behavior of the core walls are modeled using fiber-section-based models, while the shear behavior is modeled by defining shear material in PERFORM-3D. The CFT columns are modeled using fiber section beam-column element, which similarly is capable to simulate the axial-flexural interaction

behavior of the columns. For simplicity, all the beams are modeled using concentrated plasticity beam-column element, and the moment-curvature constitutive relationship for the concentrated plastic hinge in the element could be determined based on the static elasto-plastic method. For coupling beams, it is critical to include shear effect in the element to model shear mechanism of coupling beams. All the material models are determined according to current design codes as well as several reference guidelines [7, 8, 11-14]. Figure 2 shows the elevation view of the considered super high-rise building model. Note that, this building model is analyzed only through only one of the horizontal directions (the X-direction) in the following text for simplicity. Table 3 shows the comparison of the first fifth modal period results (in X-direction) from both PERFORM-3D and PKPM, which indicates good agreement between different analytical software.

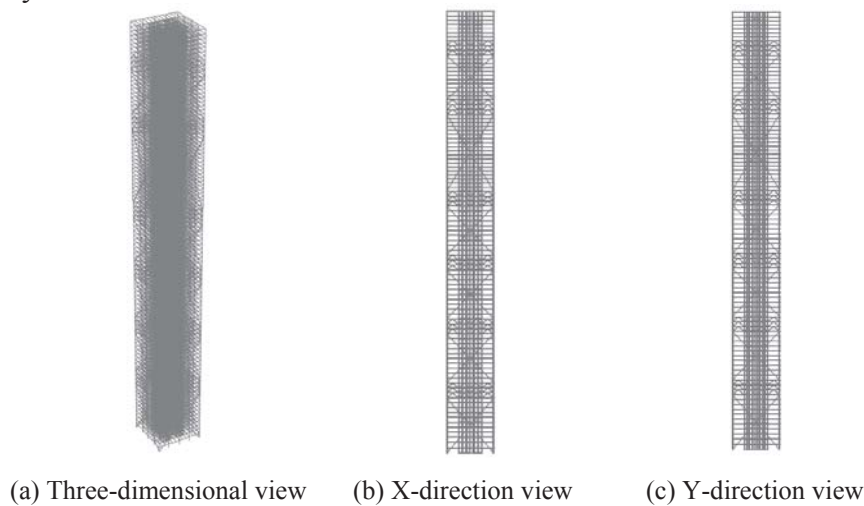


Figure 2: Elevation view of the building model.

Mode (X-direction)	PKPM	Perform-3D	Error
1	6.025	5.999	0.43%
4	1.615	1.569	2.85%
7	0.792	0.762	3.84%
10	0.518	0.493	4.73%
14	0.374	0.352	5.76%

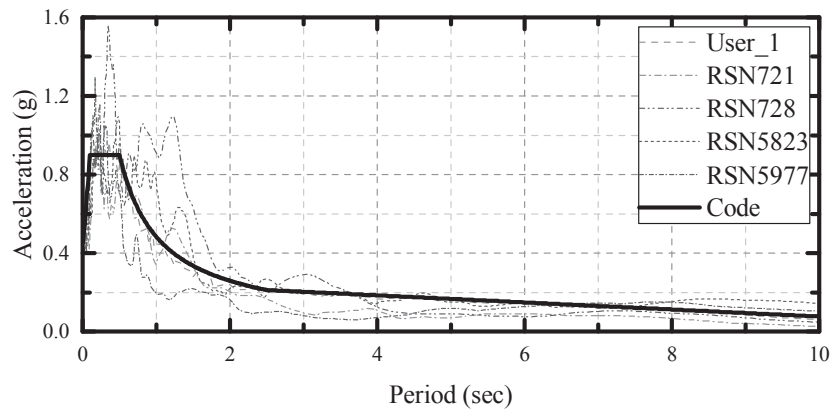
Table 3: Modal analysis results in X-direction.

#### 4 GROUND MOTION DATA

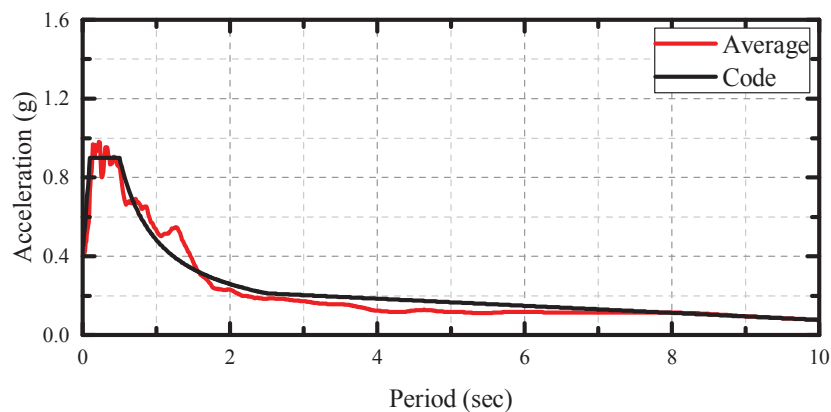
For nonlinear time history analysis, a total of five ground motions are selected in the current study, including four recorded natural seismic excitations from PEER ground motion database, and one artificial ground motion. Table 4 presents the basic information for the five earthquake ground motions, including earthquake records' site station, year and duration time. Figure 3a shows the design spectrum with 5% damping ratio based on Chinese seismic design code [8] along with the individual ground motion spectrum. Figure 3b shows the comparison of the average ground motion spectrum with the design spectrum. It can be referred from the figure that the average spectrum of the ground motions matches well with the design spectrum in an overall sense.

Number	Station	Year	Duration Time (s)
User_1	-	-	43
RSN721	El Centro Imp. Co. Cent	1987	59
RSN728	Westmorland Fire Station	1987	52
RSN5823	Chihuahua Station	2010	83
RSN5977	Chihuahua Station	2010	51

Table 4: Ground motion data.



(a) Acceleration response spectrum of ground motions.



(b) Average acceleration response curve of ground motions.

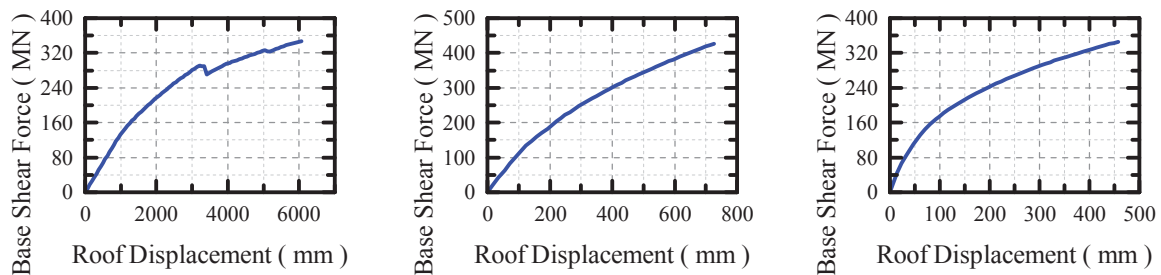
Figure 3: Response spectrum of the ground motions.

## 5 SEISMIC RESPONSE RESULTS

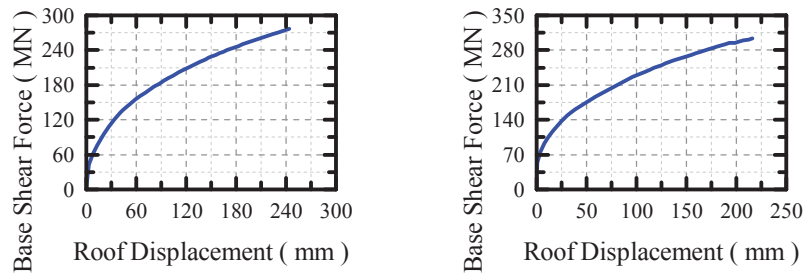
### 5.1 Pushover curves

In this section, seismic analysis results for the case-study building from the MPA analysis and its comparison with traditional Pushover analysis (i.e., use the first mode for MPA only) are presented. As mentioned, the accuracy of the MPA results is assessed through comparison with results from nonlinear time history analysis. As per MPA process illustrated earlier, the building model is subjected to a specific lateral force distribution (i.e., modal force distribution) first, then the static pushover analysis is conducted for each mode, respectively. Since the aim of the current study is to demonstrate the accuracy of the MPA procedure rather than

seismic performance assessment, only the vibration modes in the X-direction are considered. The maximum number of modes in X-direction considered in the current MPA analysis is five. Figure 4 shows the Pushover curves, i.e., base shear versus roof displacement relationships for all the five modal responses. Since the equivalent SDOF system with larger vibration period has less lateral stiffness, the pushover curve tends to be more flexible (larger displacement). Each pushover curve is then transferred to the capacity curves and is used to compare with the demand curve (also transferred from response spectrum as in Section 2) in order to determine the “Performance point”. In this case, the seismic intensity is selected to be the design earthquake level, i.e., 8 degree seismicity ( $PGA = 0.2g$ ). Once the “Performance point” for each mode has been determined, the total response of the structure using MPA could be easily determined through SRSS combination rule.



(a) Mode 1 (mode 1 in X-direction) (b) Mode 4 (mode 2 in X-direction) (c) Mode 7 (mode 3 in X-direction)



(d) Mode 10 (mode 4 in X-direction) (e) Mode 14 (mode 5 in X-direction)

Figure 4: Pushover curves.

## 5.2 Story drifts and peak displacements

Figure 5 and Figure 6 show the story drift response and peak story response along the building height from both the MPA and NTHA analysis results. The relative error for each MPA results (including one mode to five modes) with NTHA results are also given. It can be seen clearly from the figure, with more modes considered in the MPA results, more accuracy results relative to NTHA response could be achieved. Moreover, for the case-study super high-rise building, all the MPA results show quite good results for those stories under 60. However, for those stories above 60, MPA results with more than three modes show evidently much better accuracy as compared with MPA results with only two or one (i.e., traditional Pushover analysis) modes considered. Noted that only the X-direction is considered in the analysis, and for the first three modes in X-direction, the total number of modes should be 11 when all the three directions are included.

### 5.3 Story shear forces and overturning moments

Similarly, Figure 7 and Figure 8 show the story shear force response and story overturning moment response from both the MPA and NTHA analysis results. The relative error for each MPA results (including one mode to five modes) with NTHA results are also given. Similar to the results of story drifts and story displacements presented above, it is referred from the figures that the MPA results with more modes included in the analysis, more accuracy of the results could be achieved relative to NTHA response. For the shear force response, MPA results with 5 modes (blue lines in the figure) shows better accuracy in an overall extent (Figure 7b). However, for overturning moment response, MPA results with 5 modes (blue lines) shows much better results for stories above 25 as compared to results from traditional pushover procedure (i.e., only one mode considered).

## 6 CONCLUSIONS

This study investigates the effects of the Modal Pushover Analysis (MPA) procedure for a case-study super high-rise building, and the accuracy of the MPA results is validated through comparison with NTHA responses. The following conclusions are drawn from the study.

1) Higher mode effects could be included in MPA procedure, which shows the advantage for MPA analysis over traditional Pushover analysis, especially for analyzing high-rise and super high-rise buildings. In this study, the accuracy of MPA is sufficient when more than three modes (in X-direction) are considered in MPA (corresponding to 11 modes when all the three directions are considered).

2) MPA procedure shows a great improvement in accuracy as compared to the conventional pushover procedure (MPA with only one mode considered). It is also demonstrated that the calculated structural response from MPA are in very good agreement with the results from NTHA, in terms of story displacements (and drifts) and story forces (shear force and overturning moment), while reducing computing time tremendously, which in turn improves the efficiency of seismic analysis for super high-rise buildings.

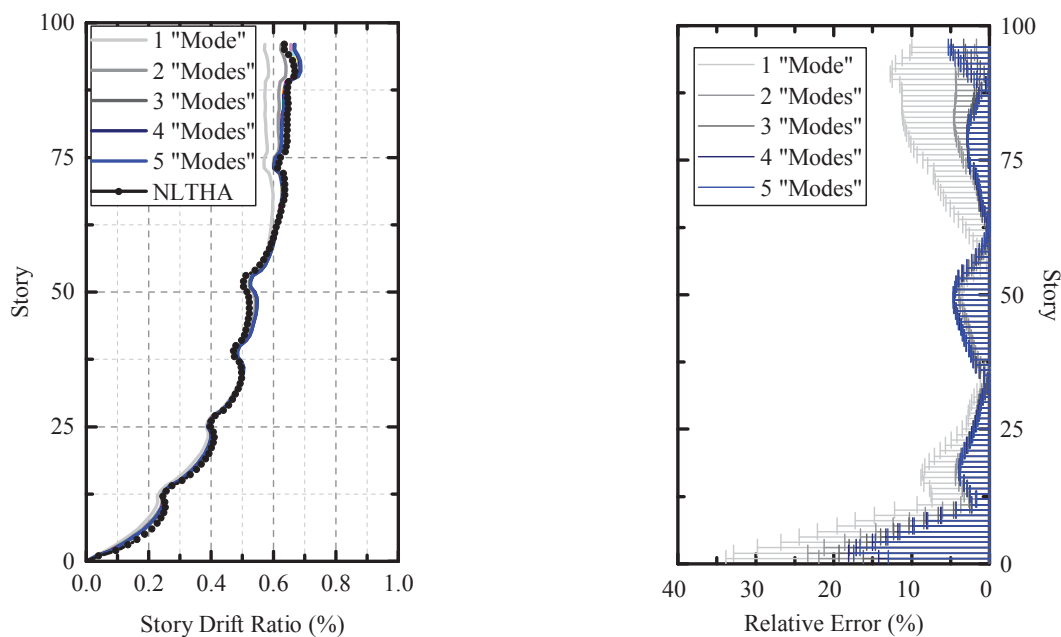


Figure 5: Comparison of the story drift ratios.

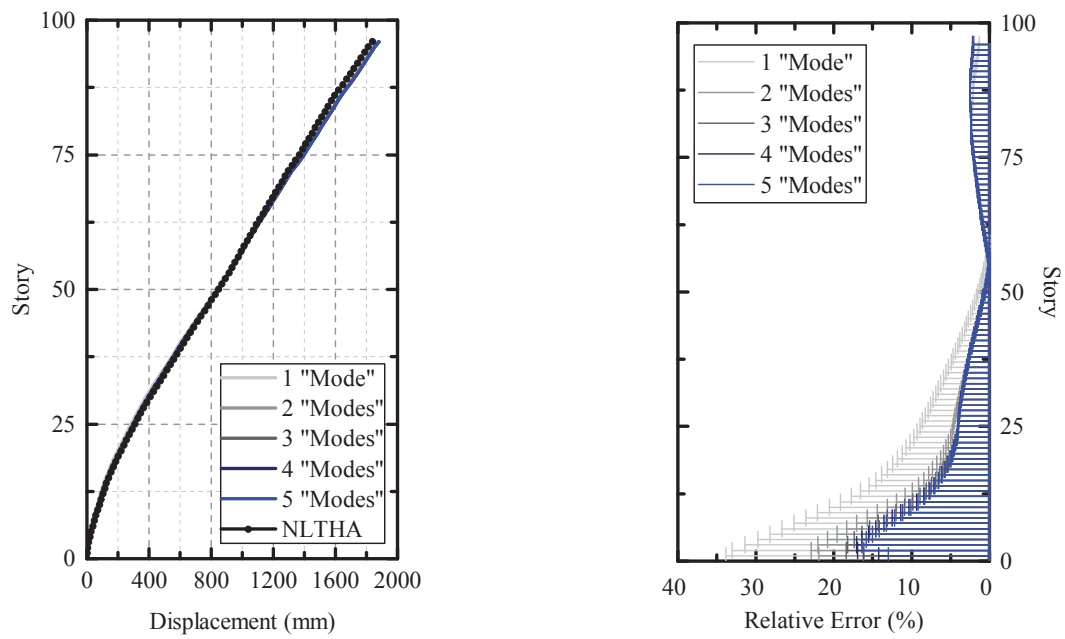


Figure 6: Comparison of the peak story displacements.

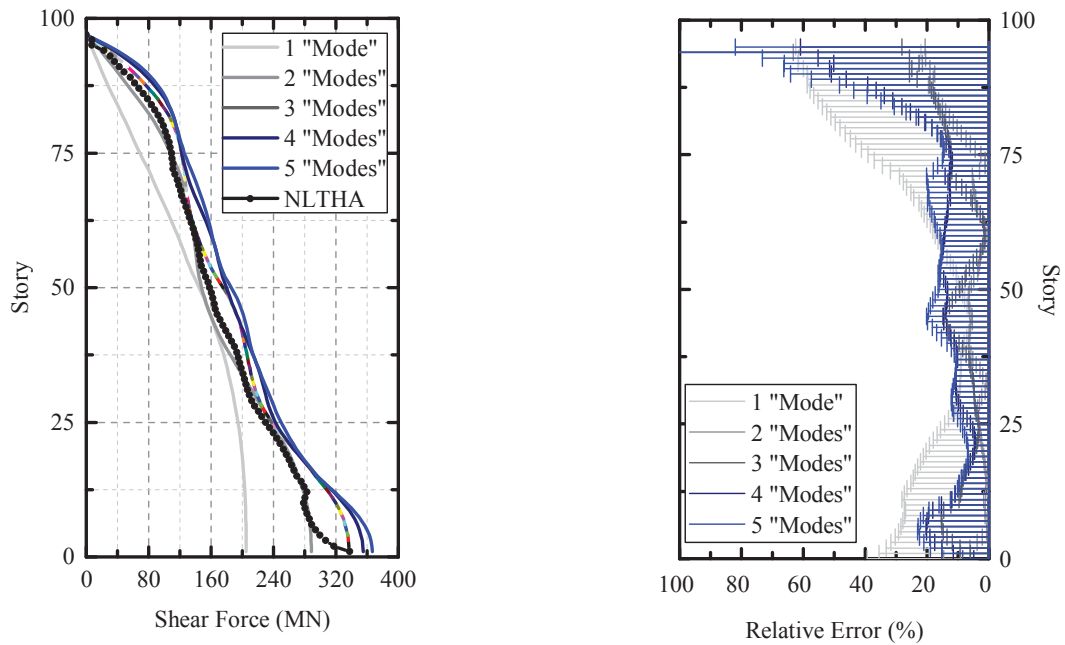


Figure 7: Comparison of the story shear forces.



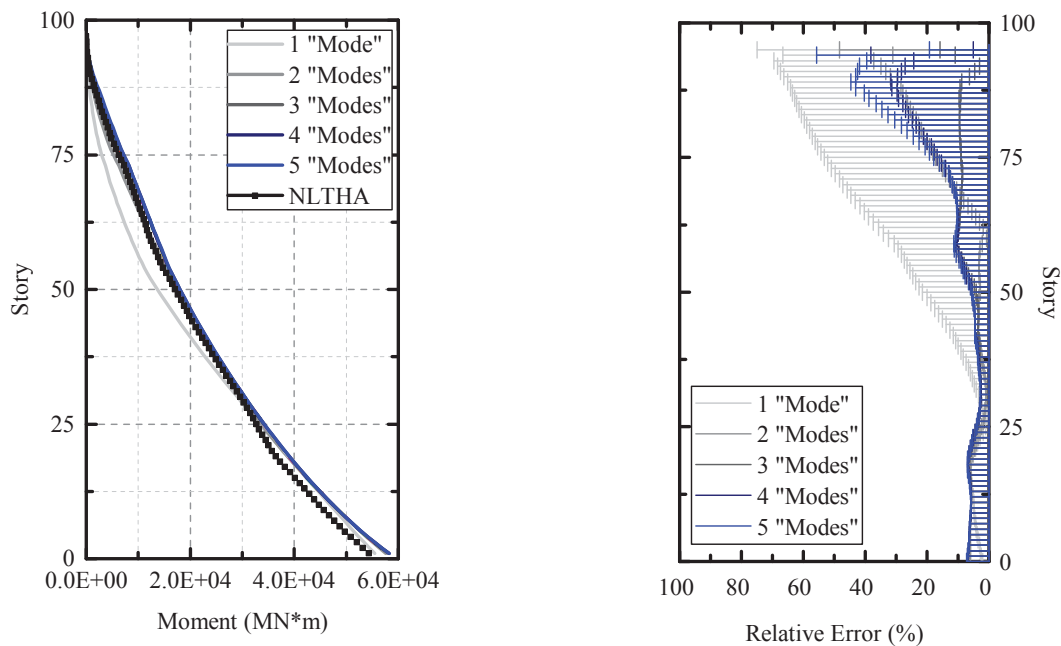


Figure 8: Comparison of the story overturning moments.

## REFERENCES

- [1] Building Seismic Safety Council, NEHRP guidelines for the seismic rehabilitation of buildings. FEMA 273, Federal Emergency Management Agency. Washington, D.C., 1997.
- [2] A.K. Chopra, R.K. Goel. A modal pushover analysis procedure to estimate seismic demands for buildings: theory and preliminary evaluation [R]. Berkeley, CA: Report No. PEER 2001/03, Pacific Earthquake Engineering Research Center, University of California, 2001.
- [3] J. Mao, L. Xie, C. Zhai. Studies on and improvements in modal pushover analysis. *Journal of Earthquake Engineering and Engineering Vibration*, **26(6)**: 50-55, 2006. (in Chinese)
- [4] P. Shen, H. Gong. Multi-mode pushover analysis and seismic evaluation in hybrid structures. *Engineering Mechanics*, **23(8)**, 69-73, 2006. (in Chinese)
- [5] Q. Ma, L. Ye, X. Lu. Comparative evaluation of correctness between MPA and pushover analysis. *Journal of South China University of Technology: Natural Science Edition*, **36(11)**, 121-128, 2008. (in Chinese)
- [6] H. Liu, Q. Guo. Simplified pushover analysis with influence of high-order vibration modes. *Journal of Harbin Institute of Technology*, **41(10)**, 188-192, 2009.
- [7] GB 50010-2010, Code for design of concrete structures. China Architecture & Building Press, Beijing, 2015. (in Chinese)
- [8] GB 50011-2010, Code for seismic design of buildings. China Architecture & Building Press, Beijing, 2016. (in Chinese)

- [9] PKPM. User's manual. Version 4, 2011. (in Chinese)
- [10] PERFORM-3D. User guide PERFORM-3D<sup>TM</sup> nonlinear analysis and performance assessment for 3D structures. Version 7, 2018.
- [11] JGJ 138-2016, Code for design of composite structures. China Architecture & Building Press, Beijing, 2016. (in Chinese)
- [12] JGJ 3-2010, Technical specification for concrete structures of tall building. China Architecture & Building Press, Beijing, 2010. (in Chinese)
- [13] GB 50009-2012, Load code for the design of building structures. China Architecture & Building Press, Beijing, 2012. (in Chinese)
- [14] GB 50017-2017, Standard for design of steel structures. China Architecture & Building Press, Beijing, 2017. (in Chinese)

## NUMERICAL PARAMETRIC STUDY OF GRILLE-TYPE STEEL CONCRETE COMPOSITE SHEAR WALL FOR SEISMIC REGIONS

Tian Wang<sup>1</sup>, Qiao Yu<sup>2\*</sup>, Hao Wu<sup>2</sup>, Yang Liu<sup>1</sup>, Lingzhi Li<sup>2</sup>, Xianlong Zhang<sup>1</sup>

<sup>1</sup>China Construction Seventh Engineering Division (Shanghai) Corp. Ltd.  
235 E. Yunling Rd., Putuo District, Shanghai 200062, China  
1109974324@qq.com, liuyang10@cscec.com, 1091370813@qq.com

<sup>2</sup>College of Civil Engineering, Tongji University  
1239 Siping Rd., Shanghai 200092, China  
yq\_@tongji.edu.cn, 2009wuhao\_tom@tongji.edu.cn, lilingzhi@tongji.edu.cn

---

### Abstract

*Grille-type steel plate concrete composite shear wall (GSPCW) is an innovative shear wall system consisting of steel faceplates, steel tie plates and infilled concrete. Compared with traditional steel plate concrete composite shear wall, GSPCW has the following advantages: 1) high buckling resistance, and 2) simple structural measures and convenient construction. This paper presents a numerical study of the GSPCW using DIANA software and comprehensively investigates the influence of varying design parameters on the seismic performance. First, DIANA models are established for considered GSPCW specimens and validated through comparing numerical results with previous test data. The verified model is further used to perform a parametric study to understand the influence of several design variables on seismic behavior of GSPCW, including steel ratio, axial load ratio, height-width ratio, aspect ratio of grille as well as concrete compressive strength. Results indicate that the former four parameters have remarkable impacts on seismic behavior of GSPCW: 1) The load and deformation capacity of a GSPCW increase significantly as the steel ratio increase; 2) The load capacity and ductility increase to a certain degree with increase of axial load ratio, however excessively high axial load ratio may have a negative impact on ductility behavior; 3) The load capacity and stiffness of a GSPCW decrease with the increase of height-width ratio; 4) The aspect ratio of grille has a hooping effects on the infilled concrete, which should be reasonably considered during design; 5) Compared with other parameters, the influence of concrete compressive strength is negligible. The conclusion from the parametric study might be utilized for engineering practice of GSPCW in future.*

**Keywords:** Steel Plate Concrete Composite Shear Wall, DIANA Software, Finite Element Model Analysis, Seismic Behavior Research.

---

## 1 INTRODUCTION

Steel plate concrete composite shear wall is a shear wall formed by arranging steel plates on one or both sides or inside of the concrete slab, and combining the two materials through shear nails or bolt tie rods on the steel plate. According to the different steel layout of steel plate concrete composite shear wall, it can be roughly classified into three types, single-sided steel plate concrete composite shear wall, double-sided steel plate concrete composite shear wall and embedded steel plate concrete composite shear wall [1]. Domestic and foreign scholars currently have conducted many researches on various steel plate concrete composite shear walls. The previous researches indicate that steel plate concrete composite shear wall has higher load carrying capacity, larger stiffness, better ductility and energy dissipation capacity [3, 4, 5].

To further improve the seismic behavior of steel plate concrete composite shear wall, W. Xu [6] proposes grille-type steel plate concrete composite shear wall, which is consisted of steel faceplates, steel tie plates and infilled concrete. And W. Xu has conducted a series of researches in a certain degree.

The initial study about grille-type steel plate concrete composite shear wall is carried out by X. Guo [7]. He analyzes the influence of different factors on the seismic behavior of grille-type steel plate concrete composite shear wall with embedded corrugated steel plate through experimental research and numerical simulation. The results indicate that the out-of-plane deformation of steel plates on the both sides of the shear wall is restricted due to the existence of concrete slab and ties of corrugated steel plate, thereby improving the out-of-plane buckling resistance of steel plates in the shear wall. Then T. Xu [8] and S. Ye [9] further improve the structure of grille-type steel plate concrete composite shear wall to replace the embedded corrugated steel plate to single independent steel plate. They find the new type of the shear wall has good seismic performance.

The two-dimensional numerical model of the grille-type steel plate concrete composite shear wall (abbreviated as GSPCW) is established in DIANA based on the two shear walls in S. Ye [9]. And 18 GSPCW specimens with various design parameters are designed to systematically investigate the influence of design parameters on GSPCW, including steel ratio, axial load ratio, height-width ratio, aspect ratio of grille as well as concrete compressive strength. The conclusion will provide reference for engineering applications in future construction works.

## 2 BRIEF DISCRIPTION OF PREVIOUS TESTS

This paper selects two GSPCW specimens to verify the accuracy of the simulations. The details of the two walls and material properties are presented in S. Ye [9]. Figure 1 shows views of the shear wall and the material properties are listed in Table 1. The tests were conducted at the Civil Engineering and Transportation Building in Jiulonghu Campus of Southeast University. The two walls had the same height-width ratio of 2.0 and the axial load ratio is the main design variable considered in the experiments. The thickness of steel faceplates and steel tie plates is 4 millimeters. The concrete grade is C40 and the steel grade is Q235B. The loading beam and foundation beam are reinforcement concrete beams. And there is a H steel beam embedded in foundation beam, which is used to improve the stiffness of foundation beam.

As shown in Figure 2, the test setup consists of bottom fixing device, out-of-plane support, vertical and horizontal loading device, and loading method adopts force and displacement-controlled loading history. The vertical load is applied by a hydraulic jack, and a steel beam is placed on the top of loading beam to evenly distribute the vertical load. Before the formal ap-

plication of horizontal load, the pre-load of horizontal load needs to be carried out to determine whether the loading equipment, connected equipment and data acquisition system are normal. Then the single-stage horizontal load is applied until the specimen yields. After specimen yields, displacement controlled multi-stage loading is applied until the horizontal capacity of the specimen decreases to 85% of the peak horizontal load.

No.	Wall dimension W×T (mm×mm)	Steel plate thickness (mm)	Steel channel	Axial load ratio	Concrete strength (MPa)	Steel plate strength (MPa)
GSSW-1	1400×160	4	[16	0.1	26.6	263.2
GSSW-2	1400×160	4	[16	0.4	26.6	263.2

Table 1: Properties of two shear walls of previous test. [9]

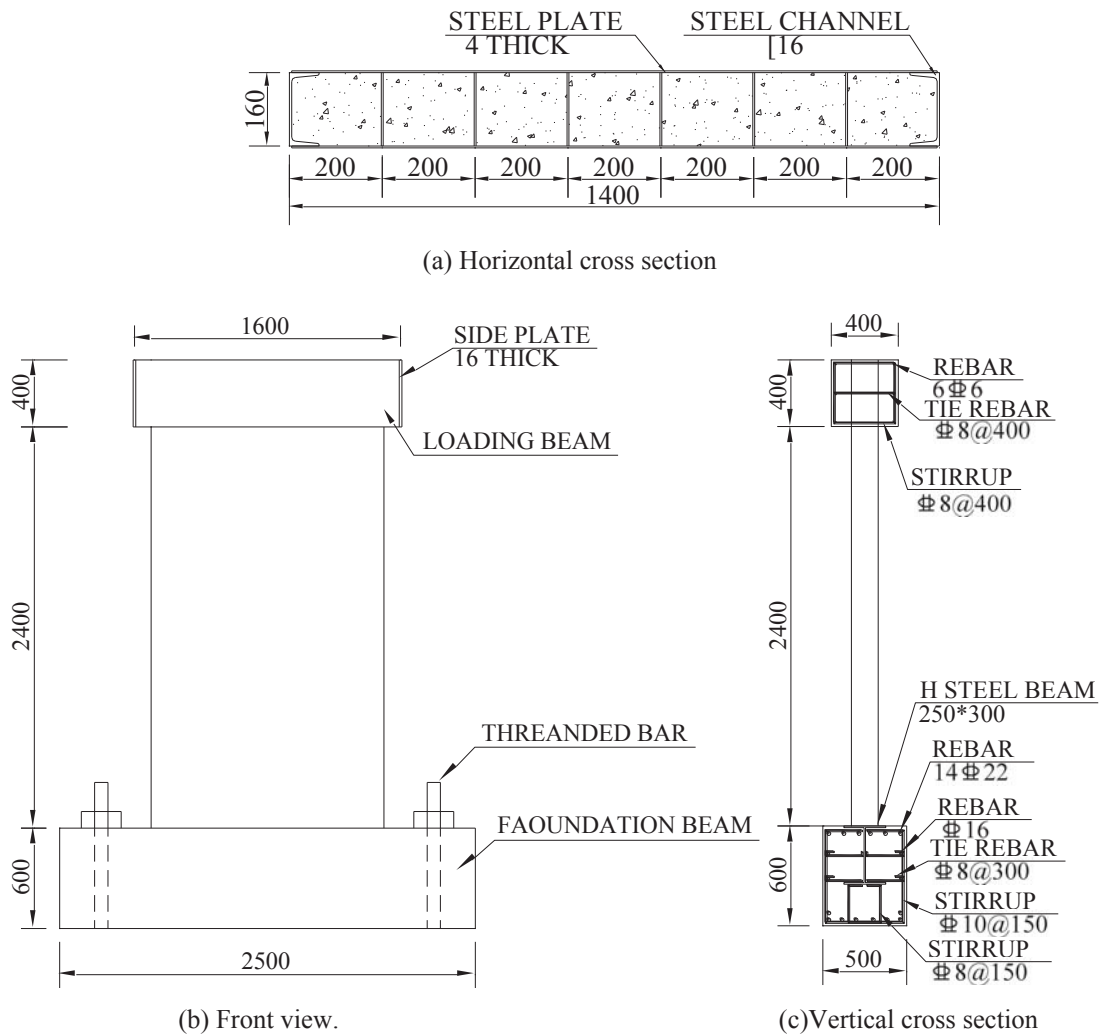


Figure 1: Details of two shear walls of previous test. (Unit: mm, adapted from S. Ye [9])

### 3 METHOD OF NUMERICAL SIMULATION

#### 3.1 Modeling assumption

Two-dimension simulation is adopted in this paper. Figure 3 presents the geometry of the GSPCW developed in DIANA. Eight-node quadrilateral isoparametric plane stress elements are used for the infilled concrete, steel faceplates, loading beam and foundation beam. Bar reinforcement elements are used for the steel tie plates. The size of all elements is 50 mm. The translation of the bottom of the foundation beam is constrained.

The FE models are loaded in two steps as the same as the experiments: 1) the vertical load is applied to the top of the loading beam in a manner of uniform pressure, and 2) cyclic lateral displacement is applied to the centroid of loading beam.

The modified Newton-Raphson method is used for incremental-iterative solution. The convergence criteria combine force norm and displacement norm. Both physical nonlinear analysis and geometrical nonlinear analysis are considered in the analysis procedure.



Figure 2: The loading process of GSSW-1.[9]

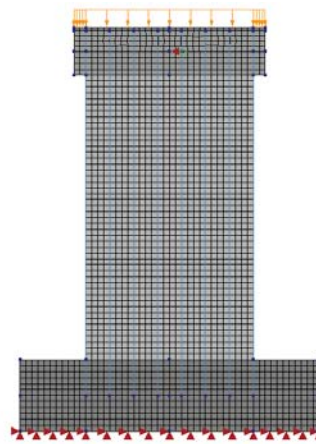


Figure 3: Model of GSPCW in DIANA.

#### 3.2 Material model

The total strain crack model available in DIANA [10] is used for the infilled concrete. The input parameters for this model include linear material properties, crack direction and uniaxial behavior of concrete in compression and tension. The crack direction is rotating direction.

The uniaxial behavior of concrete is represented by a stress-strain curve, see Figure 4. In this paper, the constitute model of concrete in compression adopts the model proposed by J. Mander et al. [11], which is applicable to both circular and rectangular shaped transverse reinforcement. The restraint effect of steel plates on concrete can be regarded as the restraint effect of many transverse reinforcements on concrete. The formula is as follows:

$$f_c = \frac{f'_{cc} x^r}{r - 1 + x^r} \quad (1)$$

$$x = \frac{\varepsilon_c}{\varepsilon_{cc}} \quad (2)$$

$$\varepsilon_{cc} = \varepsilon_{co} \left[ 1 + 5 \left( \frac{f'_{cc}}{f'_{co}} - 1 \right) \right] \quad (3)$$



$$r = \frac{E_c}{E_c - E_{\text{sec}}} \quad (4)$$

$$E_{\text{sec}} = \frac{f'_{cc}}{\varepsilon_{cc}} \quad (5)$$

Where  $f'_{cc}$  is compressive strength of confined concrete,  $\varepsilon_c$  is longitudinal compressive concrete strain,  $f'_{co}$  and  $\varepsilon'_{co}$  is the unconfined concrete strength and corresponding strain,  $\varepsilon'_{co}$  can be assumed as 0.002,  $E_c$  is the tangent modulus of elasticity of the concrete,  $E_c = 5000\sqrt{f'_{co}}$ . The compressive strength of confined concrete  $f'_{cc}$  is determined by the confinement effectiveness for sections confined by steel plates and calculated according to the proposal of J. Cai [12].

The constitute model of concrete in tension is calculated according to CEB-FIP Model 1990 [13], and the formula is given by

$$f_t = \begin{cases} 0.26f_{cu}^{2/3} & (f_{cu} \leq 50\text{MPa}) \\ 0.21f_{cu}^{2/3} & (f_{cu} > 50\text{MPa}) \end{cases} \quad (6)$$

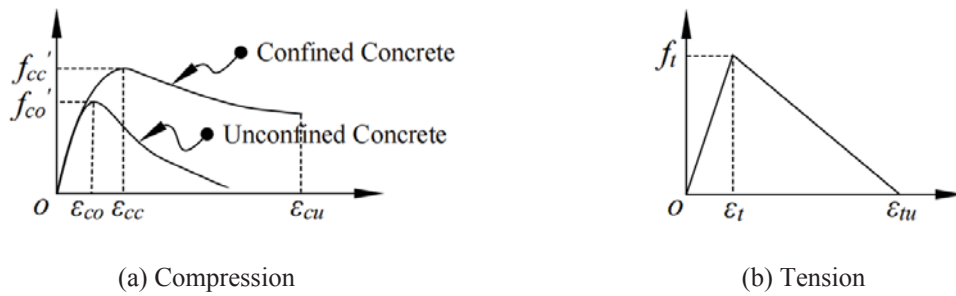


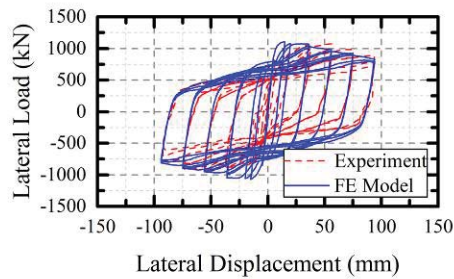
Figure 4: Stress-strain relationship of concrete.

The constitute model of steel uses bilinear elastic hardening model. The elastic modulus, yield strength and ultimate strength are all base on the material properties tests. The Von Mises yield criterion is used to evaluate the yield status of steel.

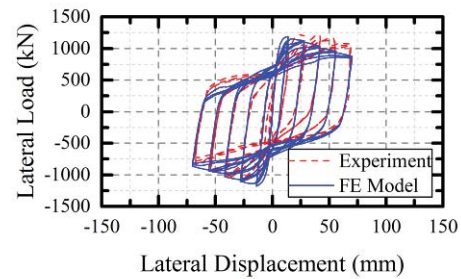
#### 4 NUMERICAL RESULT AND VALIDATION

Figure 5 is the load-displacement hysteric curves of GSSW-1 and GSSW-2. The experiment data of the hysteric curves is available in S. Ye [9]. And according to the hysteric curves, it is easy to calculate the skeleton curves and the rest of the relevant data, see Figure 6~Figure 9 and Table 2. It can be seen from Figure 5 and Figure 6 that the hysteric curves obtained from the numerical simulation are in good agreement with the skeleton curves. The magnitude of the peak load of the numerical simulation is larger than that of the test result, because the test specimens in actual situation have initial defects in a certain degree, and the bottom restraints of the test specimens cannot achieve the perfect effect of complete fixing. From the Figure 7, the stiffness of the FE model at the beginning of loading is greater than that of the experiment result. But as the loading continues, the difference between the two is getting smaller and smaller, because the constraints of the specimens in experiment are not as ideal as the constraints of FE model, so a certain error will occur at the beginning of loading, but as the loading displacement increases, the error caused by the constraint becomes more and more

insignificant. From the perspective of energy consumption and equivalent viscous damping ratio, since the material in the finite element model is uniform and has no initial defects, the energy consumption capacity of the finite element model is stronger than that of the actual specimen.

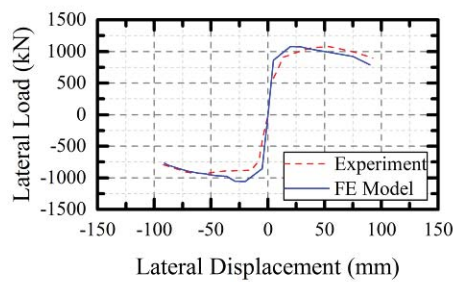


(a) GSSW-1

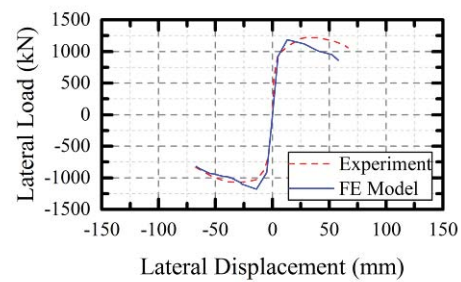


(b) GSSW-2

Figure 5: Comparison of load-displacement hysteric curves.

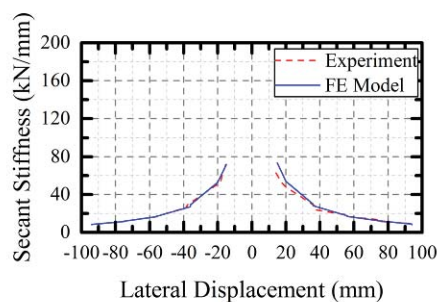


(a) GSSW-1

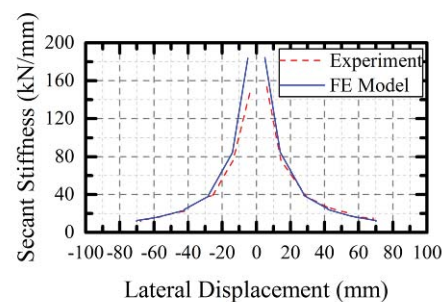


(b) GSSW-2

Figure 6: Comparison of load-displacement skeleton curves.



(a) GSSW-1



(b) GSSW-2

Figure 7: Comparison of secant stiffness degradation curves.

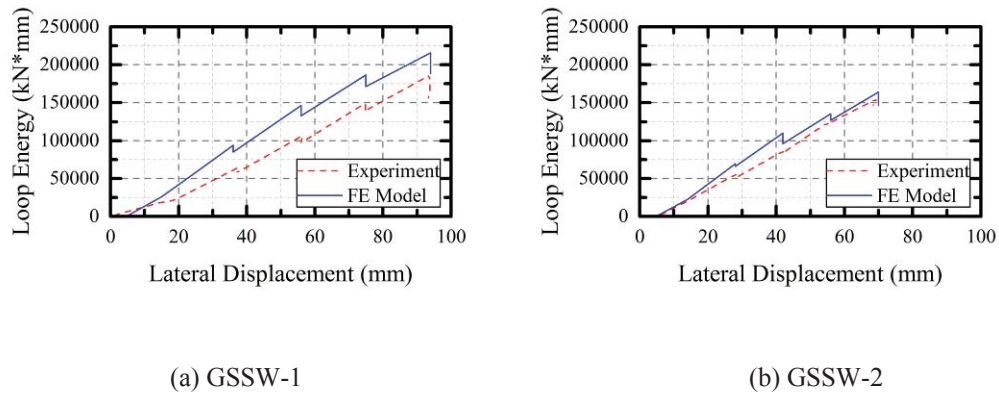


Figure 8: Comparison of energy dissipation curves.

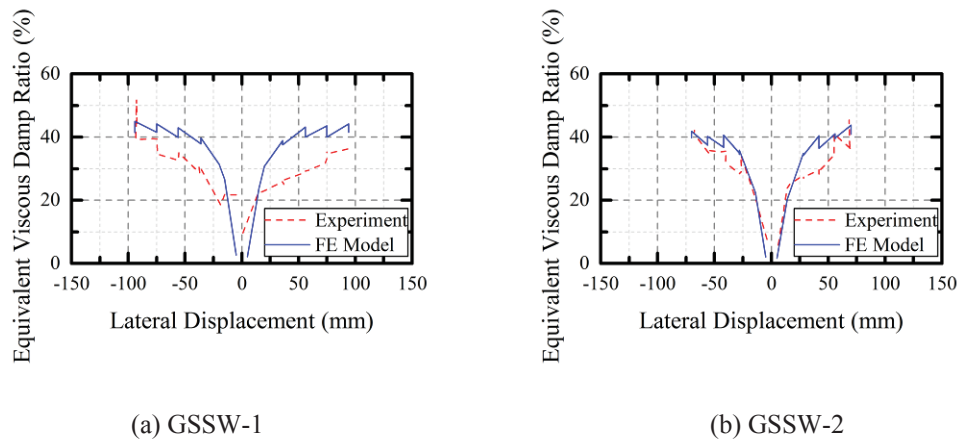


Figure 9: Comparison of equivalent viscous damp curves.

No.		Loading direction	$F_y$ (kN)	$D_y$ (mm)	$F_p$ (kN)	$D_p$ (mm)	$D_u$ (mm)
GSSW-1	Experiment	+	803.47	10.94	1079.54	52.90	92.60
		-	840.59	13.10	930.00	55.40	91.90
	FE model	+	898.69	7.75	1078.70	20.00	75.57
		-	890.34	7.52	1060.00	20.00	91.00
GSSW-2	Experiment	+	931.24	4.81	1223.11	26.64	66.80
		-	885.27	7.55	1070.00	26.40	60.04
	FE model	+	1019.34	7.92	1190.00	13.00	40.07
		-	1002.53	7.90	1180.00	14.00	35.73

Notes:  $F_y$  and  $F_p$  are respectively the horizontal capacity of specimen at yield point and peak point.  $D_y$ ,  $D_p$  and  $D_u$  are respectively the horizontal displacement of loading point of specimen at yield point, peak point and ultimate point. The ultimate point is the point at which the bearing capacity drops to 85% of the peak bearing capacity.

Table 2: Comparison of the features points of skeleton curves.

## 5 PARAMETRIC ANALYSIS

In this study, a total of 18 shear walls were simulated, as shown in Table 3. In the process of parametric analysis of numerical simulation, the values of material strength are taken in accordance with the "Code for Design of Concrete Structures" (GB50010-2010) [14] and "Code for Design of Steel Structures" (GB50017-2017) [15], and the rest of the parameter settings are shown in Section 3. The steel ratio is defined as the ratio of the cross-sectional area of the steel to that of the full cross-section of the specimen, and the steel ratio is reflected by the change of thickness of the steel faceplates and steel tie plates. The height-width ratio is defined as the ratio of the height from the top surface of the loading beam to the top surface of the ground beam to the section width of the member. The axial compression ratio is the ratio of the vertical load to the product of the axial compressive strength and the full cross-sectional area. The aspect ratio of the grille is the ratio of the spacing of the steel tie plates to the thickness of the wall.

No.	Wall dimension W×T (mm×mm)	Height- width ratio	Concrete grade	Aspect ratio of grille	Axial load ratio	Steel plate thickness	Steel ratio
GSPCW1-1	1400×160	2.0	C40	1.25	0.3	3	7.2%
GSPCW1-2	1400×160	2.0	C40	1.25	0.3	4	8.9%
GSPCW1-3	1400×160	2.0	C40	1.25	0.3	5	10.5%
GSPCW1-4	1400×160	2.0	C40	1.25	0.3	6	12.1%
GSPCW2-1	same as GSPCW1-2						
GSPCW2-2	1400×160	2.0	C40	1.25	0.4	4	8.9%
GSPCW2-3	1400×160	2.0	C40	1.25	0.5	4	8.9%
GSPCW2-4	1400×160	2.0	C40	1.25	0.6	4	8.9%
GSPCW2-5	1400×160	2.0	C40	1.25	0.7	4	8.9%
GSPCW3-1	1400×160	1.5	C40	1.25	0.3	4	8.9%
GSPCW3-2	same as GSPCW1-2						
GSPCW3-3	1400×160	2.5	C40	1.25	0.3	4	8.9%
GSPCW3-4	1400×160	3.0	C40	1.25	0.3	4	8.9%
GSPCW3-5	1400×160	3.5	C40	1.25	0.3	4	8.9%
GSPCW4-1	1400×160	2.0	C40	1.75	0.3	4	8.3%
GSPCW4-2	1400×160	2.0	C40	1.46	0.3	4	8.6%
GSPCW4-3	same as GSPCW1-2						
GSPCW4-4	1400×160	2.0	C40	1.09	0.3	4	9.1%
GSPCW5-1	1400×160	2.0	C30	1.25	0.3	4	8.9%
GSPCW5-2	same as GSPCW1-2						
GSPCW5-3	1400×160	2.0	C50	1.25	0.3	4	8.9%
GSPCW5-4	1400×160	2.0	C60	1.25	0.3	4	8.9%

Table 3: The main parameters of numerical models.

### 5.1 Steel ratio

In this study, the change in the steel ratio of the specimens is reflected by the thickness change of the steel plate: the thicker the steel plates, the greater the steel ratio of the specimens. When the thickness of the steel plate is 3 mm to 6 mm, the corresponding steel ratio of the specimen is 7.2% to 12.1%. According to Figure 10 and Table 4, the research results show that the increase of the steel ratio can improve the bearing capacity and lateral stiffness of the shear wall. The lateral stiffness is defined as the ratio of the bearing capacity to the displacement at the yield point. When the thickness of the steel plate is increased from 3 mm to 5 mm, the peak bearing capacity of the specimen is increased by 36.7%, and the lateral stiffness is increased by 14.4%. Because the axial load ratio of the model is relatively small, the lateral stiffness of the specimen is basically the full-section elastic stiffness, and the stiffness of the concrete section accounts for a relatively large amount. Therefore, the increase in the lateral stiffness of the specimen is smaller than the increase in the bearing capacity.

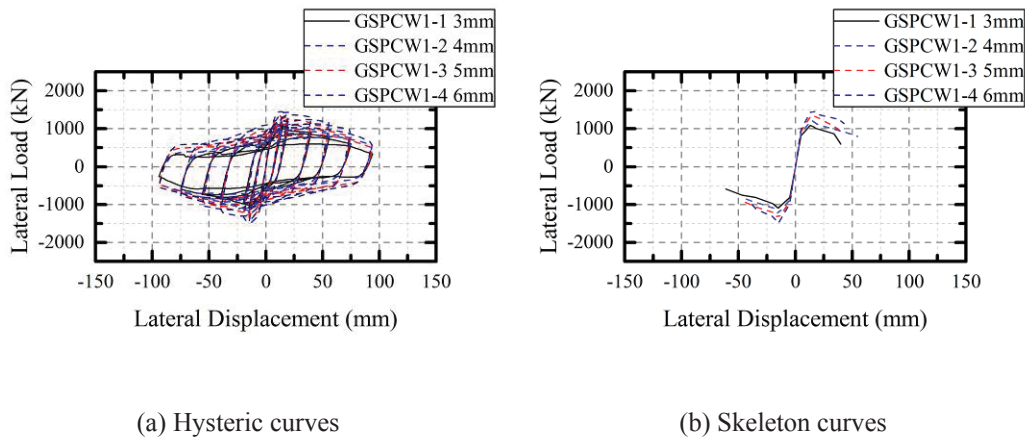


Figure 10: Influence of steel ratio on hysteric curves and skeleton curves.

No.	Loading direction	$F_y$ (kN)	$D_y$ (mm)	$F_y/D_y$ (kN/mm)	$F_p$ (kN)	$D_u$ (mm)
GSPCW1-1	+	927.50	8.31	111.65	1086.68	27.32
	-	914.76	8.56	106.84	1096.87	24.23
GSPCW1-2	+	1027.58	8.96	114.66	1221.49	28.38
	-	1025.83	9.22	111.28	1235.34	23.91
GSPCW1-3	+	1142.42	9.47	120.59	1354.77	28.57
	-	1139.90	9.77	116.67	1370.54	23.92
GSPCW1-4	+	1254.05	9.86	127.16	1480.34	36.01
	-	1257.48	10.25	122.73	1504.66	22.75

Table 4: Influence of steel ratio on feature points of skeleton curves.

### 5.2 Axial load ratio

The variation range of the axial load ratio of the test specimens is 0.3 to 0.7. The hysteric curves, skeleton curves and feature points are shown in Figure 11 and Table 5. It can be seen from the calculation results that when the axial load ratio is in the range of 0.3 to 0.7, the horizontal bearing capacity estimated by finite element varies less, and the difference in the bearing capacity of the specimens is mainly due to the dispersion of material strength. It can also be seen from Table 5 that when the axial compression ratio is less than 0.5, the lateral stiff-

ness of the test specimen increases with the increase of the axial compression ratio. This is because the increase in axial load can delay the development of cracks, thereby improving the lateral stiffness of the specimen. However, when the axial compression ratio is greater than 0.5, due to the large axial load, the specimen enters the plastic development stage in advance, which reduces the lateral stiffness of the specimen. In general, it is recommended that in actual projects, the axial load ratio of the GSPCW should be controlled below 0.5 to ensure its good seismic performance.

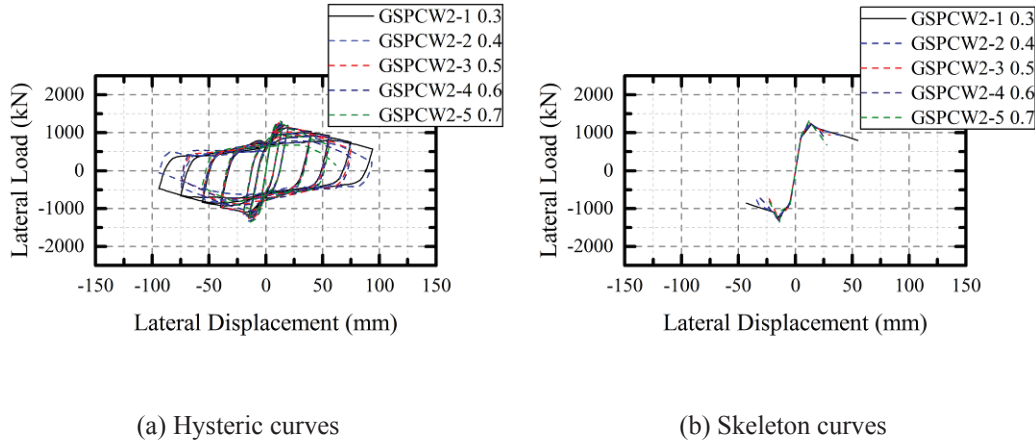


Figure 11: Influence of axial load ratio on hysteric curves and skeleton curves.

No.	Loading direction	$F_y$ (kN)	$D_y$ (mm)	$F_y/D_y$ (kN/mm)	$F_p$ (kN)	$D_u$ (mm)
GSPCW2-1	+	1027.58	8.96	114.66	1221.49	28.38
	-	1025.83	9.22	111.28	1235.34	23.91
GSPCW2-2	+	1054.41	9.04	116.68	1253.29	24.48
	-	1036.89	9.42	110.07	1274.51	20.78
GSPCW2-3	+	1094.41	9.02	121.34	1280.58	21.23
	-	1081.76	9.41	114.93	1308.52	16.93
GSPCW2-4	+	1111.96	9.07	122.62	1300.54	19.15
	-	1055.32	9.76	108.08	1337.08	19.20
GSPCW2-5	+	1141.93	8.94	127.66	1310.83	16.94
	-	997.94	10.17	98.16	1357.47	17.34

Table 5: Influence of axial load ratio on feature points of skeleton curves.

### 5.3 Height-width ratio

The height-width ratio of the shear wall is one of the main factors that determines the failure type of shear wall and affects its seismic performance. The height-width ratio of the model studied in this paper ranges from 1.5 to 3.5. The hysteric curves, skeleton curves and characteristic points are shown in Figure 12 and Table 6. It can be seen from the calculation results that when the height-width ratio is increased from 1.5 to 3.5, its bearing capacity decreases by 58.3%, and its lateral stiffness decreases by 87.6%. The height-width ratio has a distinct effect on the bearing capacity and lateral stiffness of the shear wall. This is because as the height-width ratio increases, the failure mode of the specimen transitions from shear failure to bending failure, so the bearing capacity and lateral stiffness are reduced accordingly. When the height-width ratio is greater than 2.0, the bearing capacity and stiffness of the spec-



imens change slightly with the increase of the aspect ratio, and the descending segment of the skeleton curves of the specimens tends to be flat at the post-stage of loading, and the ultimate displacement gradually increases.

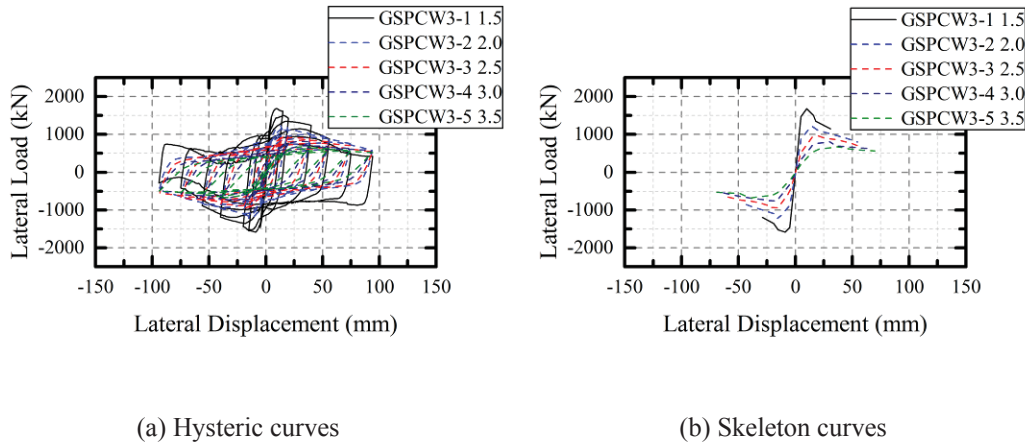


Figure 12: Influence of height-width ratio on hysteric curves and skeleton curves.

No.	Loading direction	$F_y$ (kN)	$D_y$ (mm)	$F_y/D_y$ (kN/mm)	$F_p$ (kN)	$D_u$ (mm)
GSPCW3-1	+	1528.98	6.40	238.75	1680.45	16.93
	-	1488.94	5.78	257.42	1583.03	19.59
GSPCW3-2	+	1027.58	8.96	114.66	1221.49	28.38
	-	1025.83	9.22	111.28	1235.34	23.91
GSPCW3-3	+	852.24	12.97	65.73	969.34	41.54
	-	846.54	12.76	66.34	959.90	31.53
GSPCW3-4	+	729.84	16.47	44.31	814.40	38.01
	-	717.52	15.41	46.55	770.74	45.68
GSPCW3-5	+	602.80	19.70	30.59	682.39	43.83
	-	600.84	19.58	30.69	679.11	47.92

Table 6: Influence of height-width ratio on feature points of skeleton curves.

#### 5.4 Aspect ratio of grille

The aspect ratio of the grille refers to the ratio of the spacing of the steel tie plates to the thickness of the wall. It can be seen from Figure 13 and Table 7 that the aspect ratio of the grille has a certain influence on the seismic performance of the GSPCW. As the aspect ratio of the grille decreases, the horizontal bearing capacity of the specimens increases instead. This is because the steel faceplates and steel tie plates have a certain hoop effect on the filled concrete. When the aspect ratio of the grille increases, the bond between the steel faceplates and the inner concrete is weakened, which cannot effectively limit the out-of-plane deformation of the steel faceplate, so the hoop effect is relatively weakened. The displacements at yield points and ultimate points of the test specimens increase with the decrease of aspect ratio of grille, and the deformation performance of the test specimens have a certain improvement.

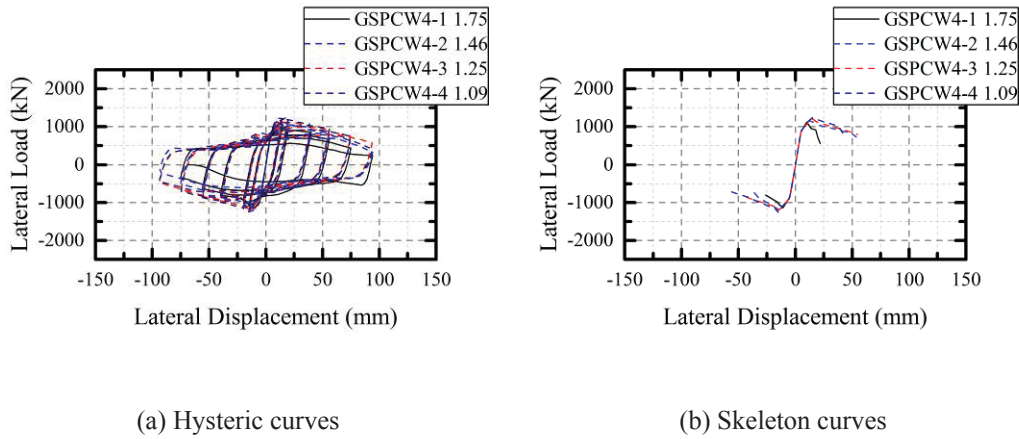


Figure 13: Influence of aspect ratio of grille on hysteric curves and skeleton curves.

No.	Loading direction	$F_y$ (kN)	$D_y$ (mm)	$F_y/D_y$ (kN/mm)	$F_p$ (kN)	$D_u$ (mm)
GSPCW4-1	+	1008.72	7.79	129.54	1124.95	13.98
	-	997.85	8.01	124.55	1134.18	17.28
GSPCW4-2	+	1025.63	8.50	120.65	1183.62	25.44
	-	1010.36	8.88	113.83	1200.99	24.10
GSPCW4-3	+	1027.58	8.96	114.66	1221.49	28.38
	-	1025.83	9.22	111.28	1235.34	23.91
GSPCW4-4	+	1052.53	9.15	115.03	1250.68	31.93
	-	1049.23	9.40	111.58	1263.49	25.39

Table 7: Influence of aspect ratio of grille on feature points of skeleton curves.

### 5.5 Concrete compressive strength

In this study, the compressive strength of concrete was selected to be changed from 30MPa to 60MPa, and the calculation results are shown in Figure 14 and Table 8. The results show that with the increase of concrete strength, the horizontal bearing capacity and lateral stiffness of the specimens have a certain increase, but the growth rate is small. This is because high-strength concrete has a higher elastic modulus. Compared with other research variables, the compressive strength of concrete has less influence on the seismic behaviors of GSPCW.

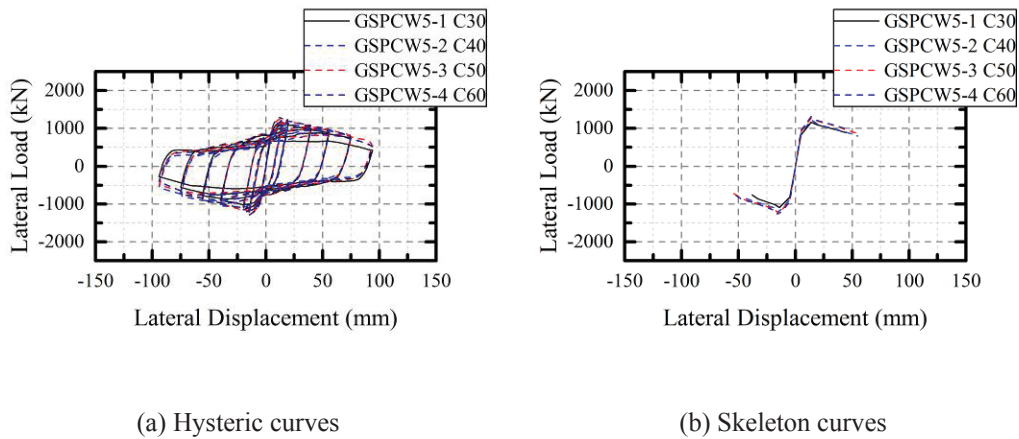


Figure 14: Influence of concrete compressive strength on hysteric curves and skeleton curves.

No.	Loading direction	$F_y$ (kN)	$D_y$ (mm)	$F_y/D_y$ (kN/mm)	$F_p$ (kN)	$D_u$ (mm)
GSPCW5-1	+	976.68	9.06	107.81	1160.86	32.47
	-	927.29	8.36	110.88	1099.01	26.52
GSPCW5-2	+	1027.58	8.96	114.66	1221.49	28.38
	-	1025.83	9.22	111.28	1235.34	23.91
GSPCW5-3	+	1068.95	8.92	119.80	1270.68	33.37
	-	1057.47	9.04	116.98	1272.84	24.41
GSPCW5-4	+	1104.41	8.90	124.15	1312.81	30.16
	-	1080.64	8.90	121.46	1299.76	24.14

Table 8: Influence of concrete compressive strength on feature points of skeleton curves.

## 6 CONCLUSIONS

This paper mainly studies the influence of different design variables on the seismic behavior of GSPCW, including steel ratio, axial load ratio, height-width ratio, aspect ratio of grille as well as concrete compressive strength. The DIANA software was used to establish the finite element models of GSPCW, and the accuracy of the model was verified based on the previous test data. A total of eighteen shear wall models with different design parameters were further established. By comparing their hysteric curves, skeleton curves and feature points, the following conclusions were drawn:

1) To increase the steel ratio of the section can significantly increase the horizontal bearing capacity of the component, and increase the lateral stiffness of the component to a certain extent;

2) When the axial load ratio of the shear wall is less than 0.5, the bearing and deformation capacity will be improved with the increase of the axial load ratio. But when the axial load ratio is greater than 0.5, the increase in the axial compression ratio is more unfavorable to the seismic performance of the specimens. Therefore, the axial load ratio of this type of shear wall below 0.5 is expected in actual projects.

3) As the height-width ratio of the shear wall increases, the failure mode of the shear wall gradually develops from shear failure to bending failure, and the bearing capacity and lateral stiffness of the component decrease rapidly.

4) The aspect ratio of the grille is a meaningful design parameter to determine the hooping effect of the steel plate on the infilled concrete. The smaller the aspect ratio of the grille, the stronger the constraint on the infilled concrete, so the concrete compressive strength is higher, thereby the horizontal bearing capacity of the specimen is developed. In the actual practice, the influence of the aspect ratio of the grille on the seismic performance of the component should be reasonably considered.

5) Compared with other design parameters, concrete compressive strength has little-to-no effect on the seismic performance of GSPCW. The horizontal bearing capacity and lateral stiffness of specimens improve slightly with the increase of concrete strength.

## REFERENCES

- [1] J. Nie, M. Tao, J. Fan, et al. Research advances of composite shear walls with double steel plates and filled concrete. *Building Structures*, **41(12)**, 52-60, 2011. (in Chinese)

- [2] W. Wang, Y. Wang, Z. Lu. Experimental study on seismic behavior of steel plate reinforced concrete composite shear wall. *Engineering Structures*, **160**, 281-292, 2018.
- [3] M. Ozaki, S. Akita, H. Osuga, et al. Study on steel plate reinforced concrete panels subjected to cyclic in-plane shear. *Nuclear Engineering & Design*, **228(1/3)**, 225-244, 2004.
- [4] K. Emori. Compressive and shear strength of concrete filled steel box wall. *Steel Structures*, **2(01)**, 29-40, 2002.
- [5] R. Link, A. Elwi. Composite concrete-steel plate walls: Analysis and behavior. *Journal of Structural Engineering*, **121(02)**, 260-271, 1995.
- [6] W. Xu, T. Xu. Seismic performance test of grille type double steel plate concrete composite shear wall. *Journal of Architecture and Civil Engineering*, **35(02)**, 111-118, 2018. (in Chinese)
- [7] X. Guo. Study on seismic behavior of grid-type steel tube-concrete composite shear walls. *Southeast University*. Nanjing, 2016. (in Chinese)
- [8] T. Xu. Experimental study on grille-type steel plate concrete composite shear wall under low cyclic loading. *Southeast University*. Nanjing, 2017. (in Chinese)
- [9] S. Ye. Study on seismic performance of concrete filled steel tube frame-grille type steel plate shear wall structure. *Southeast University*. Nanjing, 2018. (in Chinese)
- [10] DIANA. User's manual - DIANA Documentation Release 10.3. Version 10.3, 2019.
- [11] J. Mander, M. Prestley, R. Park. Theoretical stress-strain model for confined concrete. *American Society of Civil Engineers*, **114(08)**, 1804-1826, 1988.
- [12] J. Cai, G. Sun. Constitutive relationship of concrete core confined by square steel tube. *Journal of South China University of Technology*, **36(01)**, 105-109, 2008. (in Chinese)
- [13] CEB-FIP Model 1990. Model code for concrete structures (1990): chapter 2: material properties. Lausanne, 1991.
- [14] GB 50010-2010, Code for design of concrete structures. China Architecture & Building Press, Beijing, 2015. (in Chinese)
- [15] GB 50017-2017, Standard for design of steel structures. China Architecture & Building Press, Beijing, 2017. (in Chinese)

## SEISMIC RELIABILITY OF BRIDGES ISOLATED WITH FPS

P. Castaldo<sup>1</sup>, G. Amendola<sup>2</sup>, L. Giordano<sup>2</sup>, D. Gino<sup>2</sup>, and E. Miceli<sup>2</sup>

<sup>1</sup> Department of Structural, Geotechnical and Building Engineering (DISEG), Politecnico di Torino,  
Turin, Italy  
e-mail: paolo.castaldo@polito.it ; pcastaldo@unisa.it

<sup>2</sup> Department of Structural, Geotechnical and Building Engineering (DISEG), Politecnico di Torino,  
Turin, Italy  
{guglielmo.amendola, luca.giordano, diego.gino, elena.miceli}@polito.it

---

### Abstract

*The present analysis deals with the seismic reliability of isolated multi-span continuous deck bridges considering as the main aleatory uncertainties relevant to the problem the sliding friction coefficient of the friction pendulum (FP) isolators together with the seismic records characteristics. A six-degree-of-freedom model is defined to simulate the elastic response of the reinforced concrete pier, the infinitely rigid response of the deck supported by the seismic devices and the non-linear velocity-dependent behavior of the FPS bearings. The reinforced concrete abutment is modelled as a rigid support above which a FPS device is located. A set of natural records with different characteristics is properly selected and scaled to increasing intensity levels. The randomness on the friction coefficient is described by an appropriate probability density function to sample. For different system and isolator properties, fragility curves of both the reinforced concrete pier and FP devices supporting the deck are estimated. In accordance with the hazard curve of the design site, the seismic reliability curves are derived by means of the convolution integral.*

**Keywords:** Seismic isolation, Bridge, Friction pendulum isolators, Performance-based engineering, Seismic reliability.

---

## 1 INTRODUCTION

The aim of seismic isolation for bridges is to uncouple the deck from the horizontal components of the earthquake action, allowing a significant reduction of both acceleration and forces transmitted from the deck to the pier, compared to non-isolated bridges, as demonstrated in [1]-[3]. This topic is very crucial to the issue of the infrastructure safety [4]-[5]. Among the possible seismic retrofitting solutions, single concave friction pendulum system (FPS) devices have been often used because they imply a high dissipation capacity and determine an isolation period independent of the isolated mass as well as for their durability properties [6]-[10].

The use of both elastomeric and FPS bearings is studied in [11], where the efficacy of using simplified models in relation to the flexibility of the deck and of the piers is emphasized. Optimal values for the friction coefficient in seismic isolated bridges are proposed in [12], as function of the structural properties and of the soil condition. Furthermore, a three-dimensional multi-span continuous steel girder bridge, isolated by FPS isolators, is studied in [13], where the effect of modeling parameters and the influence of the design parameters on the response is investigated.

Seismic reliability-based design (SRBD) approach has been proposed in [14]-[18], in the context of investigating new design solutions for these seismic devices in relation to their main uncertainties. In [19] it is presented a probability-based reliability assessment method to consider the variations of the seismic isolation properties under different conditions, referring to a base-isolated two span reinforced concrete (RC) bridge. Seismic reliability analysis of a multi-span bridge pier developed through the response surface method-based metamodeling approach is described in [20]. Different methodologies to deal with seismic fragility assessment of highway bridges is presented in [21]. The research by [22] regards the efficiency of numerous seismic intensity measures to estimate the response of seismic-isolated bridges in relation to ordinary and pulse-like ground motions. Life-cycle reliability analyses of RC bridges are presented in [23]. In [24], the seismic design of RC bridge structures in relation to both ductile and brittle resisting mechanisms is evaluated, by proposing a reliability-based analysis with partial factors.

The present study regards the seismic reliability of multi-span continuous deck bridges isolated with FPS devices through the analysis of fragility curves related to a wide range of bridge properties as well as different seismic intensity levels. Five-degree-of-freedom (dof) models have been adopted, accounting for five vibrational modes representative of the elastic RC pier behaviour and another dof is added to analyze the response of the infinitely rigid RC deck isolated by the FPS devices. The pier-abutment-deck interaction is taken into account by modelling the RC abutment as a rigid support [2],[25],[26]. To model the behaviour of the FPS device the hypothesis of the friction coefficient varying with the velocity is adopted, as proposed by [7]. The friction coefficient has been described by means of an appropriate normal probability density function (PDF) and the Latin hypercube Sampling Method (LHS) [27], is employed as the random sampling technique to define the set of the input data. In addition, seismic uncertainty is accounted by considering 30 natural seismic records with different characteristics, scaled to different increasing intensity levels in line with the seismic hazard of the reference site (i.e., L'Aquila (Italy)). The relation between seismic demand and the capacity of the isolated bridge is analyzed through incremental dynamic analyses (IDAs) [28]. Thus, the response statistics related to both the superstructure (i.e., deck) and the pier have been evaluated. For the former in terms of peak deck displacement (with respect to the pier) and for the latter in terms of peak pier displacement (with respect to the ground). Furthermore, the results regarding the response statistics have been used to evaluate the seismic fragility curves



of both the rigid deck and the RC pier, assuming appropriate values of the corresponding limit state thresholds. The above-mentioned analyses (i.e., fragility curves) have been useful to assess the seismic reliability of bridges isolated with FPS bearings, according to the PEER-like modular approach [29], assuming the hazard curves of the site and a specific design life.

## 2 EQUATIONS OF MOTION

The structural system of an isolated multi-span continuous deck bridge is modelled, according to [2],[25],[26], as the sum of 5dof corresponding to the lumped masses of the RC pier and 1dof related to the rigid RC deck mass. The RC abutment is modeled as rigid and fixed.

The equations of motion of the response of an isolated bridge on FPS devices subjected to the seismic input along the longitudinal direction,  $\ddot{u}_g(t)$ , are:

$$\begin{aligned} m_d \ddot{u}_d(t) + m_d \ddot{u}_{p5}(t) + m_d \ddot{u}_{p4}(t) + m_d \ddot{u}_{p3}(t) + m_d \ddot{u}_{p2}(t) + m_d \ddot{u}_{p1}(t) + c_d \dot{u}_d(t) + f_b(t) + f_a(t) &= -m_d \ddot{u}_g(t) \\ m_{p5} \ddot{u}_{p5}(t) + m_{p5} \ddot{u}_{p4}(t) + m_{p5} \ddot{u}_{p3}(t) + m_{p5} \ddot{u}_{p2}(t) + m_{p5} \ddot{u}_{p1}(t) - c_d \dot{u}_d(t) + c_{p5} \dot{u}_{p5}(t) + k_{p5} u_{p5}(t) - f_b(t) &= -m_{p5} \ddot{u}_g(t) \\ m_{p4} \ddot{u}_{p4}(t) + m_{p4} \ddot{u}_{p3}(t) + m_{p4} \ddot{u}_{p2}(t) + m_{p4} \ddot{u}_{p1}(t) - c_{p5} \dot{u}_{p5}(t) - k_{p5} u_{p5}(t) + c_{p4} \dot{u}_{p4}(t) + k_{p4} u_{p4}(t) &= -m_{p4} \ddot{u}_g(t) \\ m_{p3} \ddot{u}_{p3}(t) + m_{p3} \ddot{u}_{p2}(t) + m_{p3} \ddot{u}_{p1}(t) - c_{p4} \dot{u}_{p4}(t) - k_{p4} u_{p4}(t) + c_{p3} \dot{u}_{p3}(t) + k_{p3} u_{p3}(t) &= -m_{p3} \ddot{u}_g(t) \\ m_{p2} \ddot{u}_{p2}(t) + m_{p2} \ddot{u}_{p1}(t) - c_{p3} \dot{u}_{p3}(t) - k_{p3} u_{p3}(t) + c_{p2} \dot{u}_{p2}(t) + k_{p2} u_{p2}(t) &= -m_{p2} \ddot{u}_g(t) \\ m_{p1} \ddot{u}_{p1}(t) - c_{p2} \dot{u}_{p2}(t) - k_{p2} u_{p2}(t) + c_{p1} \dot{u}_{p1}(t) + k_{p1} u_{p1}(t) &= -m_{p1} \ddot{u}_g(t) \end{aligned} \quad (1)$$

where  $u_d$  represents the horizontal displacement of the deck relative to the pier,  $u_{p,i}$  the displacement of the  $i$ -th ( $i = 1:5$ ) pier mass relative to the  $i$ -th-1 dof,  $m_d$  and  $m_{pi}$  are respectively the mass of the deck and of the  $i$ -th ( $i = 1:5$ ) lumped mass of the pier,  $c_d$  is the viscous damping constant of the isolated deck,  $k_{pi}$  and  $c_{pi}$  respectively the pier stiffness and inherent viscous damping constant of the  $i$ -th ( $i = 1:5$ ) dof of the pier,  $t$  the time instant,  $f_a(t)$  and  $f_p(t)$  are the reactions of the FP bearings, respectively on the abutment and on the pier, equal to:

$$f_a(t) = \frac{m_d g}{2R} \left( u_d(t) + \sum_{i=1}^5 u_{pi}(t) \right) + \frac{1}{2} \left( \mu_a \left( \dot{u}_d(t) + \sum_{i=1}^5 \dot{u}_{pi}(t) \right) \right) m_d g \left( \operatorname{sgn} \left( \dot{u}_d(t) + \sum_{i=1}^5 \dot{u}_{pi}(t) \right) \right) \quad (2)$$

$$f_p(t) = \frac{m_d g u_d(t)}{2R} + \frac{\mu_p(\dot{u}_d) m_d g \operatorname{sgn}(\dot{u}_d)}{2} \quad (3)$$

where  $g$  is the gravity constant,  $R$  is the radius of curvature of the two FPS isolators assumed equal,  $\mu(\dot{u}(t))$  represents the sliding friction coefficient of the isolator on the abutment (subscript  $a$ ) or of the isolator on the pier (subscript  $p$ ), which depends on the bearing slip velocity  $\dot{u}(t)$  (that is a relative velocity with respect to the ground for the isolator on the abutment or to the pier top for the isolator on the pier), and  $\operatorname{sgn}(\cdot)$  denotes the sign function.

Regarding Equations (2)-(3), the first addenda represent the elastic behaviour ( $k_d = m_d g / R$ ), associated to the pendulum motion with fundamental vibration period equal to  $T_d = 2\pi \sqrt{R / g}$  (i.e., only function of the radius of curvature  $R$ ), and the second is the frictional behaviour, related to the sliding friction coefficient of the teflon-steel interface [14]. Experimental results

[7]-[9] suggest adopting the following equation to model the sliding friction coefficient of teflon-steel interfaces:

$$\mu(\dot{u}) = f_{\max} - (f_{\max} - f_{\min}) \cdot \exp(-\alpha |\dot{u}|) \quad (4)$$

where  $f_{\max}$  is the maximum value of friction coefficient at large sliding velocities, and  $f_{\min}$  represents the value at zero velocity. Considering this, the hypothesis of continuous sliding in structures supported by teflon bearings is included by assuming, for simplicity, a ratio  $f_{\max} / f_{\min}$  equal to 3 and an exponent  $\alpha$  equal to 30, based on a regression of the experimental results of [7]-[9].

Note that cracking phenomena [30]-[34] of the RC deck are herein neglected.

### 3 ALEATORY UNCERTAINTIES AND DETERMINISTIC PARAMETERS

The relevant uncertainties assumed in the following parametric study are presented in this section. In particular, the seismic performance of multi-span continuous deck bridges isolated with FP bearings is evaluated for different structural properties, assumed as deterministic parameters.

#### 3.1 Seismic records

The uncertainties regarding the seismic input intensity are separated from the ones related to the characteristics of the record (i.e., record-to-record variability), according to the performance-based earthquake engineering (PBEE) approach [35],[36]. Specifically, a scale factor, i.e., an intensity measure ( $IM$ ), is considered such that the randomness in the seismic intensity is described by a hazard curve while the ground motion randomness for a fixed intensity level can be represented by a set of ground motions with a different duration and frequency content, scaled according to  $IM$ . A set of 30 natural ground motion records are considered in this work, selected from [37]-[39], in line with [40]. Particularly, these records derive from 19 different seismic events. The largest source-to-site distance is 98.2km, the moment magnitude ( $M$ ) varies between 6.0 and 7.6, the PGA between 0.13g and 0.94g. Table 1 illustrates the main properties of these earthquakes.

	Year	Earthquake Name	Recording Station Name	$V_{S30}$ [m/sec]	Source (Fault Type)	$M$ [-]	$R$ [km]	$PGA_{\max}$ [g]
1	1994	Northridge	Beverly Hills - Mulhol	356	Thrust	6.7	13.3	0.52
2	1994	Northridge	Canyon Country-WLC	309	Thrust	6.7	26.5	0.48
3	1994	Northridge	LA - Hollywood Stor	316	Thrust	6.7	22.9	0.36
4	1999	Duzce, Turkey	Bolu	326	Strike-slip	7.1	41.3	0.82
5	1999	Hector Mine	Hector	685	Strike-slip	7.1	26.5	0.34
6	1979	Imperial Valley	Delta	275	Strike-slip	6.5	33.7	0.35
7	1979	Imperial Valley	El Centro Array #11	196	Strike-slip	6.5	29.4	0.38
8	1995	Kobe, Japan	Nishi-Akashi	609	Strike-slip	6.9	8.7	0.51
9	1995	Kobe, Japan	Shin-Osaka	256	Strike-slip	6.9	46	0.24
10	1999	Kocaeli, Turkey	Duzce	276	Strike-slip	7.5	98.2	0.36
11	1999	Kocaeli, Turkey	Arcelik	523	Strike-slip	7.5	53.7	0.22
12	1992	Landers	Yermo Fire Station	354	Strike-slip	7.3	86	0.24
13	1992	Landers	Coolwater	271	Strike-slip	7.3	82.1	0.42
14	1989	Loma Prieta	Capitola	289	Strike-slip	6.9	9.8	0.53
15	1989	Loma Prieta	Gilroy Array #3	350	Strike-slip	6.9	31.4	0.56
16	1990	Manjil, Iran	Abbar	724	Strike-slip	7.4	40.4	0.51
17	1987	Superstition Hills	El Centro Imp. Co.	192	Strike-slip	6.5	35.8	0.36
18	1987	Superstition Hills	Poe Road (temp)	208	Strike-slip	6.5	11.2	0.45

19	1987	Superstition Hills	Westmorland Fire Stat.	194	Strike-slip	6.5	15.1	0.21
20	1992	Cape Mendocino	Rio Dell Overpass	312	Thrust	7.0	22.7	0.55
21	1999	Chi-Chi, Taiwan	CHY101	259	Thrust	7.6	32	0.44
22	1999	Chi-Chi, Taiwan	TCU045	705	Thrust	7.6	77.5	0.51
23	1971	San Fernando	LA - Hollywood Stor	316	Thrust	6.6	39.5	0.21
24	1976	Friuli, Italy	Tolmezzo	425	Thrust	6.5	20.2	0.35
25	1980	Irpinia	Bisaccia	496		6.9	21.3	0.94
26	1979	Montenegro	ST64	1083	Thrust	6.9	21.0	0.18
27	1997	Umbria Marche	ST238	n/a	Normal	6.0	21.5	0.19
28	2000	South Iceland	ST2487	n/a	Strike-slip	6.5	13	0.16
29	2000	South Iceland (a.s.)	ST2557	n/a	Strike-slip	6.5	15.0	0.13
30	2003	Bingol	ST539	806	Strike-slip	6.3	14.0	0.30

Table 1: Selected ground motions for the time history analysis.

### 3.2 Intensity measure in terms of spectral displacement

According to [41]-[44], the selection of the intensity measure should follow the criteria of efficiency, sufficiency and hazard compatibility. For the case of this work, the *IM* is chosen as the spectral-displacement  $S_D(T_d, \xi_d)$  which corresponds to the isolated period of the bridge system,  $T_d = 2\pi / \omega_d$ , and for the damping ratio  $\xi_d$ . As demonstrated in many studies, e.g., [41]-[43],[45], not only the spectral-displacement is more efficient than the peak ground acceleration, but also its use allows to obtain more reliable response estimates for a given number of records and to reduce the response dispersion [22].

In line with other studies [22], the damping ratio  $\xi_d$  is assumed equal to zero [46]. Therefore, in the following, the corresponding *IM* is indicated as  $S_D(T_d)$  and, to compute the IDAs, it is assumed varying from 0.10m to 0.45m (Table 2) in compliance with the seismic hazard of the reference site (L'Aquila (Italy)), from the operational to collapse limit state, as provided by [44].

<i>IM</i>	1	2	3	4	5	6	7	8
$S_D(T_d)$ [m]	0.10	0.15	0.20	0.25	0.30	0.35	0.40	0.45

Table 2: Selected values of the intensity measure  $S_D(T_d)$ .

### 3.3 Random variable of the friction coefficient

According to the experimental data on sheet-type teflon bearings [7]-[9], friction is not constant during sliding, as stated in the friction Coulomb law, but it is a much more complex phenomenon, governed by different mechanisms such as the sliding velocity, apparent pressure and temperature. Moreover, it has also been observed by [47] that the friction coefficient varies in space. That is why the sliding friction coefficient at large velocity  $f_{\max}$  is considered as a random variable described by a truncated normal PDF, with an average equal to 3%, a minimum value of 0.5% and a maximum of 5.5% as also studied in [14],[17],[18]. Furthermore, being valid the relation  $f_{\min} = f_{\max} / 3$ , the values of the friction coefficient at the low velocities,  $f_{\min}$ , have also been assumed as random variables. Finally,  $\alpha$  is considered equal to a deterministic value of 30 [17] (Equation (4)).

To deal with the abovementioned random variables, the LHS method [17] has been used to generate the input data samples starting from their PDFs, with a sample number of 15.

### 3.4 Deterministic structural properties

A parametric analysis has been conducted in this work, which has brought to a set of different isolated bridge models. Specifically, in compliance with [15],[25],[26],[46], the parameters  $\xi_d$  and  $\xi_{pi} = \xi_p$  are assumed respectively equal to 0% and 5%; the isolated deck period  $T_d$  is in the range between 1s and 4s; the RC pier period  $T_p$  equal to 0.2s; the overall mass ratio  $\lambda = \sum_{i=1,5} m_{pi} / m_d$  that is related to the sum of the  $i$ -th mass ratios (assumed equal), is in the range between 0.1, 0.15 and 0.2.

Combining these deterministic values with the above sampled values of the friction coefficient, 90 different types of isolated bridges are defined.

## 4 INCREMENTAL DYNAMIC ANALYSIS RESULTS FOR THE DIFFERENT STRUCTURAL PROPERTIES

The differential equations of motion (Equation (1)) have been solved for each of the 90 bridge models, combining the deterministic ( $T_d$ ,  $\lambda$  and  $T_p$ ) and aleatory parameters and for the 30 different ground motion records (Table 1), scaled to the increasing 8 values of  $S_D(T_d)$  (Table 2). Thus, IDAs [28] are performed in MATLAB-Simulink [48] employing the Runge-Kutta-Fehlberg integration algorithm. For each of the 90 deterministic combinations, a total number of 450 simulations has been carried out by pairing each one of the 30 seismic records with the sampled 15 friction coefficients. The IDAs have been obtained assuming the following engineering demand parameters (EDPs): the deck response with respect to the pier top  $u_d$

and the response of the pier top with respect to the ground  $u_p$ , computed as  $u_p = \sum_{i=1}^5 u_{pi}$ . For all the engineering demand parameters, the peak responses are determined:  $u_{d,max}$  and

$u_{p,max} = \left( \sum_{i=1}^5 u_{pi} \right)_{\max}$ . Following an assumption widely used in PBEE [36], each EDP output has been probabilistically [49]-[56] treated by means of a lognormal PDF: using the maximum likelihood technique [14]-[18], the sample lognormal mean  $\mu_{\ln}(EDP)$  and standard deviation  $\sigma_{\ln}(EDP)$  are computed for each EDP. In the end, the 50<sup>th</sup>, 84<sup>th</sup> and 16<sup>th</sup> percentiles of each lognormal PDF can be easily evaluated [17].

The following figures show the IDA curves for the peak deck displacement at the pier  $u_{d,max}$  (Figure 1) and for the peak pier displacement  $u_{p,max}$  (Figure 2). In particular, the EDPs values are plotted with respect to the  $IM$  and each curve corresponds to different percentiles and  $\lambda$  values.

The deck response (Figure 1) tends to decrease for lower values of  $\lambda$ . For the seismic device, the lognormal mean of the isolation system response increases with lower values of  $T_d$ , because the lower the period the larger the response, due to resonance phenomena occurring between deck and pier.

Regarding the IDA curves related to the pier response (Figure 2), the structural response generally decreases with increasing  $T_d$  due to the effectiveness of the isolation technique. The influence of  $\lambda$  decreases as  $T_d$  increases, while the opposite trend regards the dispersion.

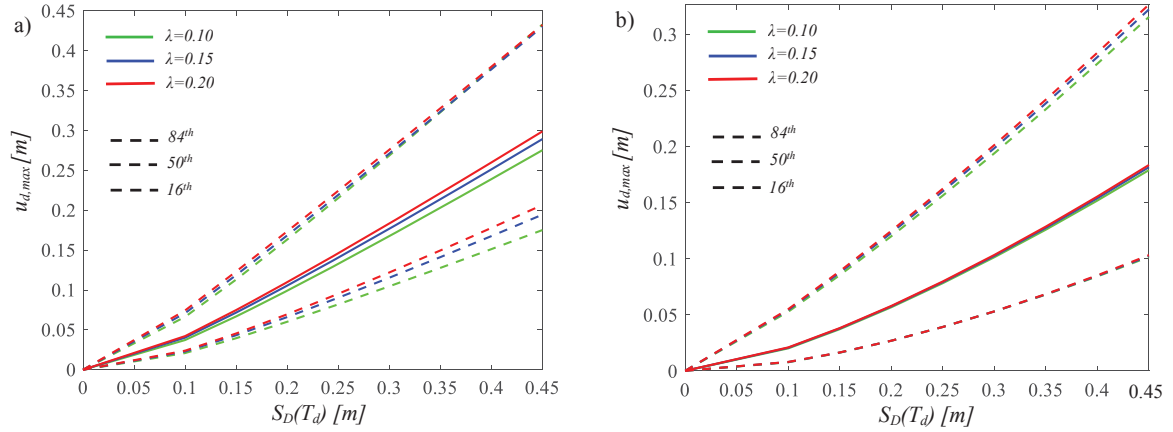


Figure 1: IDA curves of the deck response with respect to the pier, for  $T_p=0.20$ s and  $T_d=1$ s (a),  $T_d=4$ s (b).

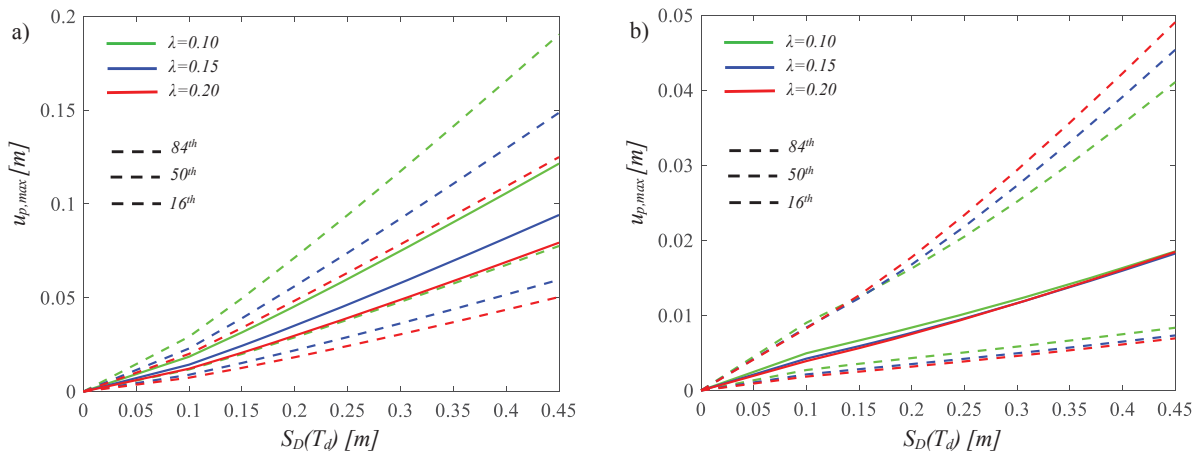


Figure 2: IDA curves of the pier, for  $T_p=0.20$ s and  $T_d=1$ s (a),  $T_d=4$ s (b).

## 5 SEISMIC FRAGILITY ASSESSMENT

The seismic fragility curves represent the probabilities  $P_f$  of exceeding different limit states ( $LS$ s) conditioned to each level of the  $IM$ . This implies the need of defining the  $LS$  threshold related to the isolation system. In particular, nine different values of the in-plan radius for the single concave surface have been assumed [14], herein summed in Table 3.

	1	2	3	4	5	6	7	8	9
$r$ [m]	0.10	0.15	0.20	0.25	0.30	0.35	0.40	0.45	0.50

Table 3: Limit State thresholds for the isolation system.

		PDI	PDI <sub>IB</sub>	$P_f$
$LS1$	Fully Operational	PDI=0.7%	PDI <sub>IB</sub> =0.23%	$5 \cdot 10^{-1}$
$LS2$	Operational	PDI=1.5%	PDI <sub>IB</sub> =0.5%	$1.6 \cdot 10^{-1}$
$LS3$	Life Safety	PDI=2.5%	PDI <sub>IB</sub> =0.83%	$2.2 \cdot 10^{-2}$
$LS4$	Near collapse	PDI=5%	PDI <sub>IB</sub> =1.67%	$1.5 \cdot 10^{-3}$

Table 4: Limit State thresholds for the pier [58].

Regarding the RC pier, four discrete performance levels or  $LS$ s ( $LS1$ ,  $LS2$ ,  $LS3$  and  $LS4$ ), corresponding respectively to “fully operational”, “operational”, “life safety” and “collapse prevention”, are suggested by Vision 2000 [57]. According to the displacement-based seismic

design, the pier drift index ( $PDI$ ), considered as the measurable structural response parameter, is adopted to define the specific  $LS$  threshold related to an acceptable probability of exceeding that  $LS$  [14]-[18], or failure probability, in the design/reference life of a structural system. In particular, the performance  $LS$ s for isolated bridges, in terms of  $PDI_{IB}$ , is defined as 1/3 of the  $PDI$  limit value of a comparable non-isolated bridge, in agreement with FEMA provisions [58]. In the following (Table 4), the  $LS$  thresholds are presented, together with the failure probabilities to respect in 50 years [14]-[18].

From the fundamental period of the RC pier,  $T_p$ , it is finally possible to compute its height [1], needed to assess the seismic fragility of the bridge, as follows:

$$T_p = \frac{2\pi}{(1.875)^2} \cdot \sqrt{\frac{\bar{m}_p h^4}{EI}} \quad (5)$$

where  $\bar{m}_p$  is the mass per unit length of the pier,  $h$  is its height and  $EI$  the flexural rigidity, having assumed a circular cross-section.

### 5.1 Seismic fragility curves

The probabilities  $P_f$  exceeding the  $LS$  thresholds have been numerically computed. Then, lognormal complementary cumulative distribution functions (CCDFs), representing the seismic fragility curves, have been fitted with R-square values higher than 0.8 [14],[17].

The results represented in Figure 3-Figure 4 show the fragility curves for  $T_p=0.2$ s and the different values assumed for  $T_d$ , for each  $LS$  and each value of  $\lambda$ , referring to the deck response with respect to the pier and to the RC pier. As a general behaviour, the seismic fragility decreases for larger values of  $LS$  thresholds. In addition, in compliance with the previous results (i.e., IDA curves), when the isolated vibration  $T_d$  increases, the seismic fragility decreases.

For what concerns the response of the isolation system (Figure 3), the variability of  $\lambda$  causes slight deviations, which are more relevant when  $T_d$  is low. In particular, an increase in  $\lambda$  determines an increase in the isolation response relative to the pier.

Regarding the seismic fragility curves for the pier (Figure 4) a larger influence of the  $\lambda$  variability is present, showing a lower fragility when  $\lambda$  increases.

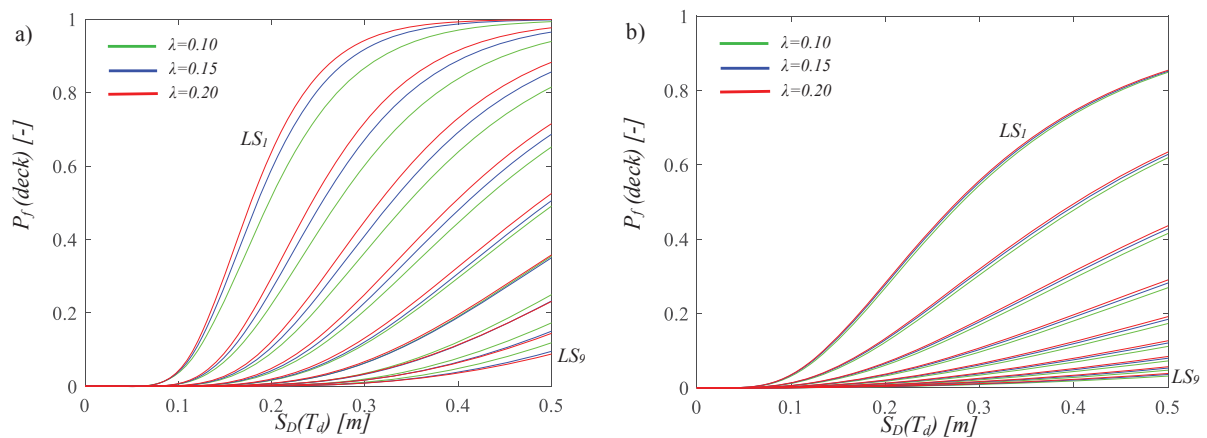


Figure 3: Seismic fragility curves of the deck response with respect to the pier for  $T_p=0.20$ s and  $T_d=1$ s (a),  $T_d=4$ s (b).



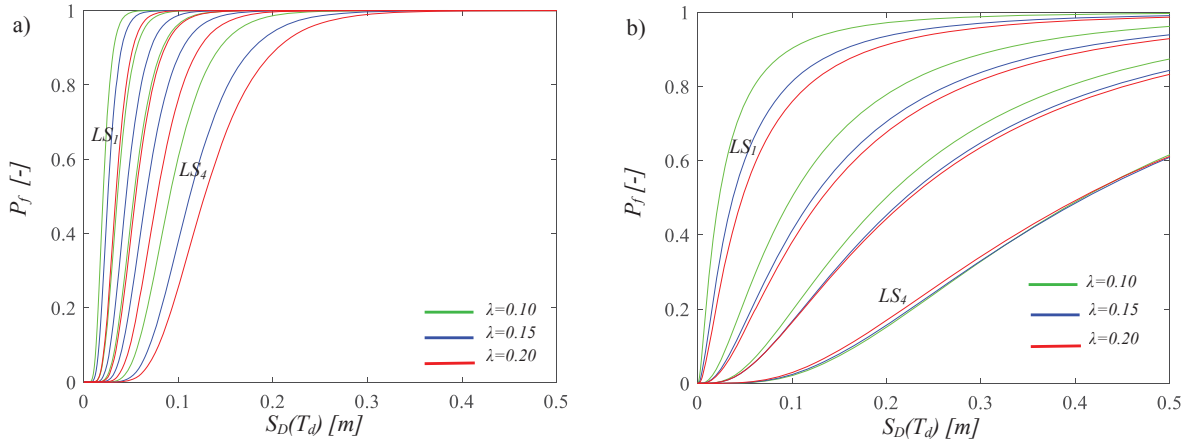


Figure 4: Seismic fragility curves of the pier for  $T_p=0.20s$  and  $T_d=1s$  (a),  $T_d=4s$  (d).

## 6 SEISMIC RELIABILITY OF ISOLATED BRIDGES WITH SINGLE CONCAVE FPS DEVICES

Adopting the Poisson model, the seismic reliability in 50 years can be computed by integrating the seismic fragility curves with the seismic hazard curves, evaluated for the same *IM* and related to the specific site (L'Aquila (Italy)). This allows to obtain the seismic reliability of the isolated multi-span continuous deck bridges, equipped with single concave FPS bearings.

### 6.1 Site seismic hazard

The seismic hazard curves (Figure 5) related to the site under analysis (L'Aquila (Italy)) are herein presented in terms of  $S_D(T_d)$ , as function of the fundamental periods. Each curve refers to the average values ( $50^{th}$  percentile) of the annual rate  $\bar{\lambda}_s$  exceeding the  $IM=S_D(T_d)$ . It is easy to observe that the seismic hazard increases with the increase of the isolated period.

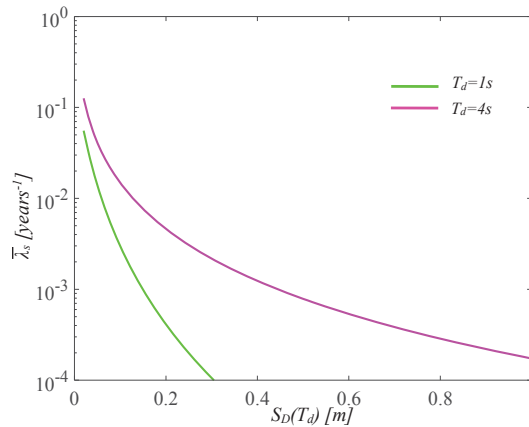


Figure 5: Seismic hazard curves in terms of  $S_D(T_d)$  for the structural periods ( $T_d$ ) related to L'Aquila site.

### 6.2 Seismic reliability curves

In the following, the seismic reliability curves for the pier (Figure 6) are reported for the different thresholds of *LS* as seen in the above Table 4. The limit states *LS1* and *LS2* are always respected demonstrating the effectiveness of the seismic isolation technique.

In addition, the “life safety” *LS3* is not always respected because of the very stringent (equal to 1/3 of the standard ones) limit states for the pier. Moreover, the most flexible RC

piers, with medium-high  $T_p$  values, exceed this  $LS$  also due to the aleatory uncertainty of the sliding friction coefficient. On the other hand, an increase in the vibration period of the FPS devices leads to an increase in seismic demand to the pier also due to the high seismic hazard of the site. Lower is the influence of the mass ratio.

The seismic reliability curves related to for the isolation system with respected to the pier (Figure 7). These reliability curves are almost linear and reveal that the isolation system is seismically less reliable as its fundamental period,  $T_d$ , increases, since higher and higher failure probabilities correspond to the same  $LS$  due to the high seismic hazard of the site. The other structural parameters have a reduced influence.

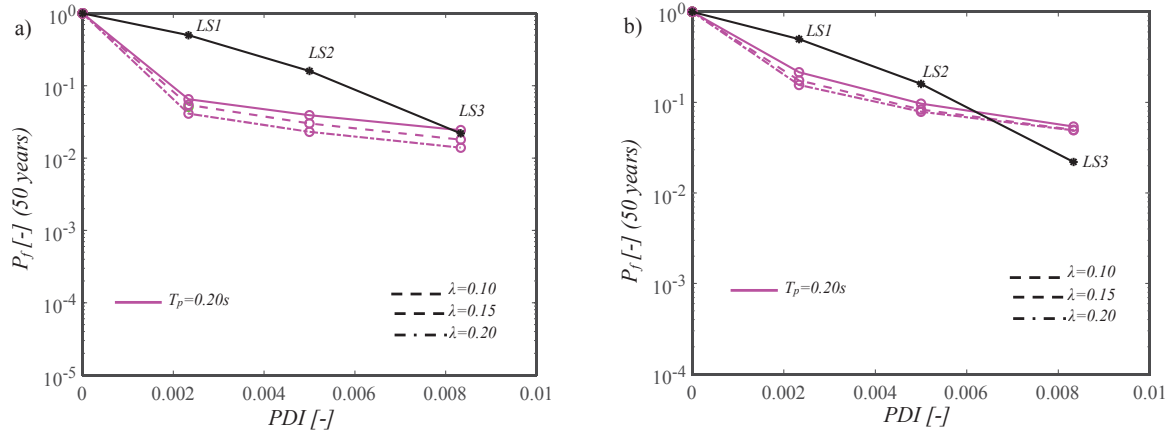


Figure 6: Seismic reliability curves of the pier for  $T_d=1s$  (a),  $T_d=4s$  (b).

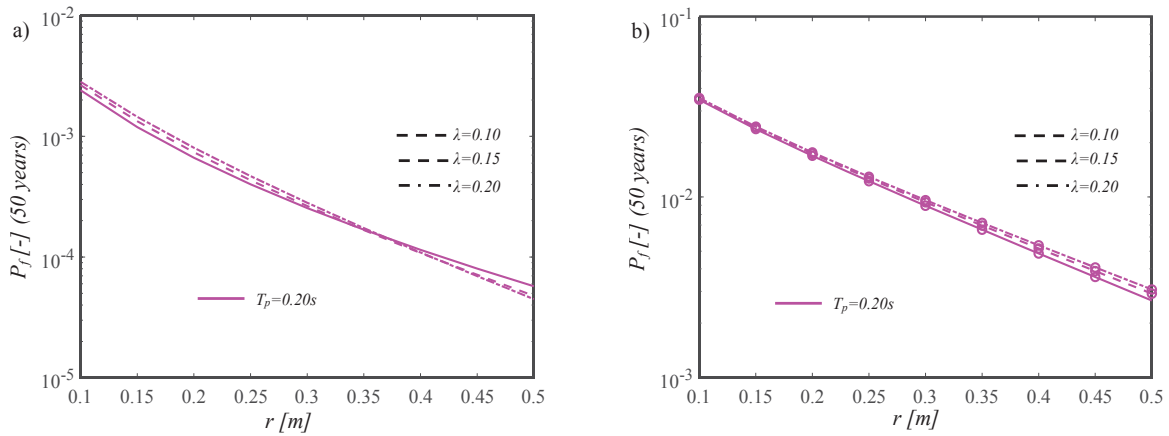


Figure 7: Seismic reliability curves of the deck response with respect to the pier for  $T_d=1s$  (a),  $T_d=4s$  (b).

## 7 CONCLUSIONS

This work regards the evaluation of the seismic reliability of multi-span continuous deck bridges isolated with single concave friction pendulum (FPS), accounting for a large range of isolator and bridge properties (i.e., the isolating system period, the vibration period of the elastic RC pier and the mass ratio, that is the ratio between the masses of the pier and the deck). A 6dof model is adopted, considering the RC pier flexibility, and both the RC abutment and RC deck infinitely rigid on the devices. The FP isolator is described by a wide-spread model, assuming that the friction coefficient varies with the velocity. The record-to-record is considered by defining a set of 30 ground motions, by scaling them to increasing seismic intensity levels. The fragility curves, referred both to the isolation system and the RC substructure/pier, have been computed for each limit state within the parametric analysis.

Then, the failure probabilities are evaluated considering the seismic hazard curves of the site (L'Aquila (Italy)), in a time interval of 50 years. This has resulted in the seismic reliability curves.

The seismic fragility of the seismic device decreases for lower values of the pier period and for increasing values of the isolated period, while the mass ratio has a reduced influence. For the pier, the fragility decreases for low pier periods, for increasing values of the mass ratio and for medium-high isolated periods.

The seismic reliability curves have shown that: it decreases for both higher pier periods and higher isolated periods due to the aleatory uncertainty of the sliding friction coefficient and to the high seismic hazard of the site, for the deck it decreases with the increase of the curvature radius of the isolator. For the pier, the fully operational and operational limit states are always respected demonstrating the effectiveness of the seismic isolation technique.

## REFERENCES

- [1] Jangid, R.S. (2004). Seismic Response of Isolated Bridges. *Journal of Bridge Engineering*, 9(2), 156-166.
- [2] Jangid, R.S. (2008). Stochastic response of bridges seismically isolated by Friction Pendulum System. *Journal of Bridge Engineering*, 13(4), 319-330.
- [3] Chen, L. K., Jiang, L. Z., Qin, H. X., Zhang, N., Ling, L., Zhang, Q. H., Li, Q., & Cao, D. F. (2019). Nonlinear seismic assessment of isolated high-speed railway bridge subjected to near-fault earthquake scenarios. *Structure and Infrastructure Engineering*, 15(11), 1529-1547.
- [4] Troisi R., Alfano G. 2019. Towns as Safety Organizational Fields: An Institutional Framework in Times of Emergency. *Sustainability*, 11: 7025, 2019, doi:10.3390/su11247025.
- [5] Troisi R., Alfano G. 2020. Firms' crimes and land use in Italy. An exploratory data analysis. New Metropolitan Perspectives, International Symposium – 4th edition, 27-30 May 2020, pp 10.
- [6] Zayas, V.A, Low, S.S., & Mahin, S.A. (1990). A simple pendulum technique for achieving seismic isolation. *Earthquake Spectra*, 6(2), 317–33.
- [7] Mokha, A., Constantinou, M.C., & Reinhorn, A.M. (1990). Teflon Bearings in Base Isolation. I: Testing. *Journal of Structural Engineering*, 116(2), 438-454.
- [8] Constantinou, M.C., Mokha, A., & Reinhorn, A.M. (1990) Teflon Bearings in Base Isolation. II: Modeling. *Journal of Structural Engineering*, 116(2), 455-474.
- [9] Constantinou, M.C., Whittaker, A.S., Kalpakidis, Y., Fenz, D.M., & Warn, G.P. (2007). Performance of Seismic Isolation Hardware Under Service and Seismic Loading. *Technical Report MCEER-07-0012*.
- [10] Tsiavos, A., Schlatter, D., Markic, T., & Stojadinovic, B. (2017). Experimental and analytical investigation of the inelastic behavior of structures isolated using friction pendulum bearings, *Procedia Engineering*, 199, 465-470.
- [11] Kunde, M. C., & Jangid, R. S. (2006). Effects of pier and deck flexibility on the seismic response of isolated bridges. *Journal of Bridge Engineering*, 11(1), 109-121.

- [12] Castaldo, P., Ripani, M., & Lo Piere, R. (2018). Influence of soil conditions on the optimal sliding friction coefficient for isolated bridges. *Soil Dynamics and Earthquake Engineering*, 111, 131–148. <https://doi.org/10.1016/j.soildyn.2018.04.056>.
- [13] Eröz, M., & DesRoches, R. (2013). The influence of design parameters on the response of bridges seismically isolated with the friction pendulum system (FPS). *Engineering structures*, 56, 585–599.
- [14] Castaldo, P., Amendola, G., & Palazzo, B. (2017). Seismic fragility and reliability of structures isolated by friction pendulum devices: Seismic reliability-based design (SRBD). *Earthquake Engineering and Structural Dynamics*, 46(3), 425–446, DOI: 10.1002/eqe.2798.
- [15] Castaldo, P., Palazzo, B., Alfano G., & Palumbo, M.F. (2018). Seismic reliability-based ductility demand for hardening and softening structures isolated by friction pendulum bearings. *Structural Control and Health Monitoring*, 25(11), e2256. <https://doi.org/10.1002/stc.2256>
- [16] Palazzo, B., Castaldo, P., & Della Vecchia, P. (2014, September). Seismic reliability analysis of base-isolated structures with friction pendulum system. In 2014 IEEE Workshop on Environmental, Energy, and Structural Monitoring Systems Proceedings (pp. 1–6). IEEE.
- [17] Castaldo, P., Palazzo, B., Ferrentino, T., & Petrone, G. (2017). Influence of the strength reduction factor on the seismic reliability of structures with FPS considering intermediate PGA/PGV ratios. *Composites Part B: Engineering*, 115, 308–315.
- [18] Castaldo, P., & Alfano, G. (2020). Seismic reliability-based design of hardening and softening structures isolated by double concave sliding devices. *Soil Dynamics and Earthquake Engineering*, 129, 105930.
- [19] Nassar, M., Guizani, L., Nollet, M. J., & Tahan, A. (2019). A probability-based reliability assessment approach of seismic base-isolated bridges in cold regions. *Engineering Structures*, 197, 109353.
- [20] Ghosh, S., Ghosh, S., & Chakraborty, S. (2018). Seismic reliability analysis of reinforced concrete bridge pier using efficient response surface method-based simulation. *Advances in Structural Engineering*, 21(15), 2326–2339.
- [21] Muntasir Billah, A. H. M., & Shahria Alam, M. (2015). Seismic fragility assessment of highway bridges: a state-of-the-art review. *Structure and Infrastructure Engineering*, 11(6), 804–832.
- [22] Avşar, Ö., & Özdemir, G. (2013). Response of seismic-isolated bridges in relation to intensity measures of ordinary and pulselike ground motions. *Journal of Bridge Engineering*, 18(3), 250–260.
- [23] Yanweerasak, T., Pansuk, W., Akiyama, M., & Frangopol, D. M. (2018). Life-cycle reliability assessment of reinforced concrete bridges under multiple hazards. *Structure and Infrastructure Engineering*, 14(7), 1011–1024.
- [24] Akiyama, M., Matsuzaki, H., Dang, H. T., & Suzuki, M. (2012). Reliability-based capacity design for reinforced concrete bridge structures. *Structure and Infrastructure Engineering*, 8(12), 1096–1107.

- [25] Wang, Yen-Po., Chung, Lap-Loi., & Liao, Wei-Hsin. (1998). Seismic response analysis of bridges isolated with friction pendulum bearings. *Earth. Eng. & Str. Dyn.*, 27, 1069-1093.
- [26] Kunde, M.C., & Jangid, R.S. (2003). Seismic behavior of isolated bridges: A-state-of-the-art review. *Electronic Journal of Structural Engineering*, 3.
- [27] Celarec, D., & Dolšek, M. (2013). The impact of modelling uncertainties on the seismic performance assessment of reinforced concrete frame buildings. *Engineering Structures*, 52, 340-354.
- [28] Vamvatsikos, D., & Cornell, C.A. (2002). Incremental dynamic analysis. *Earthquake Engineering and Structural Dynamics*, 31(3), 491–514.
- [29] Cornell, C.A., & Krawinkler, H. (2000). Progress and challenges in seismic performance assessment. *PEER Center News*, 4(1), 1-3.
- [30] Bertagnoli, G., Mancini, G., Tondolo, F. Early age cracking of massive concrete piers, *Magazine of Concrete Research*, 2011, 63, 10, 1, 723-736.
- [31] Bertagnoli G., Giordano L., Mancini S. Design and optimization of skew reinforcement in concrete shells, *Structural Concrete*, 2012, 13, 4, 248-258.
- [32] Bertagnoli G., Giordano L., Mancini, S. Optimization of concrete shells using genetic algorithms, *ZAMM Zeitschrift für Angewandte Mathematik und Mechanik*, 2014, 94, 1-2, 43-54.
- [33] Mancini G., Carbone V.I., Bertagnoli G., Gino, D. Reliability-based evaluation of bond strength for tensed lapped joints and anchorages in new and existing reinforced concrete structures, *Structural Concrete*, 2018, 19, 3, 904-917.
- [34] Bertagnoli G., Gino D., Martinelli, E. A simplified method for predicting early-age stresses in slabs of steel-concrete composite beams in partial interaction, *Engineering Structures*, 2017, 140, 286-297.
- [35] Porter, K.A. (2003). An overview of PEER's performance-based earthquake engineering methodology. *Proceedings of the 9th International Conference on Application of Statistics and Probability in Civil Engineering (ICASP9)*, San Francisco, California.
- [36] Aslani, H., & Miranda, E. (2005) Probability-based seismic response analysis. *Engineering Structures*, 27(8), 1151-1163.
- [37] PEER, *Pacific Earthquake Engineering Research Center* <http://peer.berkeley.edu/>
- [38] ITACA, *Italian Accelerometric Archive* [http://itaca.mi.ingv.it/ItacaNet/itaca10\\_links.htm](http://itaca.mi.ingv.it/ItacaNet/itaca10_links.htm)
- [39] ISESD, *Internet-Site for European Strong-Motion Data* [http://www.isesd.hi.is/ESD\\_Local/frameset.htm](http://www.isesd.hi.is/ESD_Local/frameset.htm)
- [40] ATC-63. 2008. Quantification of building seismic performance factors. FEMAP695. Redwood City, CA.
- [41] Shome, N., Cornell, C.A., Bazzurro, P., & Carballo, J.E. (1998). Earthquake, records, and nonlinear responses. *Earthquake Spectra*, 14(3), 469-500.
- [42] Pinto, P.E., Giannini, R., & Franchin, P. (2003). Seismic Reliability Analysis of Structures, *IUSS Press*, Pavia, Italy.



- [43] Luco, N., & Cornell, C.A. (2007). Structure-specific scalar intensity measures for near-source and ordinary earthquake ground motions. *Earthquake Spectra*, 23(2), 357-92.
- [44] NTC18. Norme tecniche per le costruzioni. Gazzetta Ufficiale del 20.02.18, DM 17.01.18, Ministero delle Infrastrutture.
- [45] Iervolino, I., & Cornell, C.A. (2005). Record selection for nonlinear seismic analysis of structures. *Earthquake Spectra*, 21(3), 685-713.
- [46] Ryan, K., Chopra, A. (2004). Estimation of Seismic Demands on Isolators Based on Nonlinear Analysis. *Journal of Structural Engineering*, 130(3), 392-402.
- [47] Wei, B., Fu, Y., Li, S., Jiang, L., & He, W. (2020). Scaling errors of a seismic isolation system with a shear key. *Soil Dynamics and Earthquake Engineering*, 139, 106382.
- [48] Math Works Inc. (1997) MATLAB-High Performance Numeric Computation and Visualization Software: User's Guide. Natick, MA, USA.
- [49] Garzillo C., Troisi R. Le decisioni dell'EMA nel campo delle medicine umane. In EMA e le relazioni con le Big Pharma - I profili organizzativi della filiera del farmaco, G. Giappichelli, 85-133, 2015.
- [50] Golzio L. E., Troisi R. The value of interdisciplinary research: a model of interdisciplinarity between legal re-search and research in organizations. *Journal For Development And Leadership*, 2: 23-38, 2013.
- [51] Nese A., Troisi R. Corruption among mayors: evidence from Italian Court of Cassation judgments, *Trends In Organized Crime*, 1-26, 2018. DOI:10.1007/s12117-018-9349-4.
- [52] Troisi R., Golzio, L. E. Legal studies and organization theory: a possible cooperation. *Manageable cooperation* - European Academy of Management: 16th EURAM Conference, Paris, 1-2, 1-4 June 2016.
- [53] Troisi R., Guida V. Is the Appointee Procedure a Real Selection or a Mere Political Exchange? The Case of the Italian Health-Care Chief Executive Officers. *Journal of Entrepreneurial and Organizational Diversity*, 7 (2): 19-38, 2018, DOI:10.5947/jeod.2018.008.
- [54] De Iuliis, M., & Castaldo, P. (2012). An energy-based approach to the seismic control of one-way asymmetrical structural systems using semi-active devices. *Ingegneria Sismica-International Journal of Earthquake Engineering*, 29(4), 31-42.
- [55] Basone, F., Castaldo, P., Cavaleri, L., & Di Trapani, F. (2019). Response spectrum analysis of frame structures: reliability-based comparison between complete quadratic combination and damping-adjusted combination. *Bulletin of Earthquake Engineering*, 17(5), 2687-2713.
- [56] Troisi R. Le risorse umane nelle BCC: lavoro e motivazioni al lavoro. In Progetto aree bianche. Il sistema del credito cooperativo in Campania, 1: 399-417, 2012.
- [57] SEAOC Vision 2000. 1995. Committee. Performance-based seismic design engineering. Report prepared by Structural Engineers Association of California, Sacramento, CA.
- [58] Building Seismic Safety Council. 1997. NEHRP commentary on the guidelines for the seismic rehabilitation of buildings. Provisions (FEMA 274), Washington, DC.



# INTENSITY MEASURES PROPERTIES AND SELECTION FOR RISK ANALYSIS ON STRUCTURES SUBJECTED TO EARTHQUAKE INDUCED POUNDING WITH A NON-SMOOTH CONTACT DYNAMICS METHOD

T. Langlade<sup>1</sup>, D. Bertrand<sup>1</sup>, S. Grange<sup>1</sup>, G. Candia<sup>2</sup>, and J.C. De La Llera<sup>3</sup>

<sup>1</sup>Laboratory GEOMAS EA7495  
INSA Lyon, Villeurbanne, France  
e-mail: {thomas.langlade,david.bertrand,stephane.grange}@insa-lyon.fr

<sup>2</sup> Research Center for Integrated Disaster Risk 5 Management (CIGIDEN), ANID/FONDAP/15110017  
Facultad de Ingenieria, Universidad Del Desarrollo, Santiago de Chile, Chile  
e-mail: gacandia@gmail.com

<sup>3</sup> Research Center for Integrated Disaster Risk 5 Management (CIGIDEN), ANID/FONDAP/15110017  
Pontificia Universidad Catolica de Chile, Santiago de Chile, Chile  
e-mail: jcllera@ing.puc.cl

**Keywords:** Earthquake induced Building-Pounding, Intensity Measures, Non-Smooth Contact Dynamics, Efficiency-Sufficiency properties

**Abstract.** *This study aims at selecting the best suited Intensity Measures (IMs) in the case of earthquake-induced building pounding to plot fragility functions of civil engineering structures. IMs are indicators representative of the seism "intensity" (e.g. the magnitude, the Peak Ground Acceleration (PGA)) that are intended to be correlated with Engineering Demand Parameters (EDPs) of interest (e.g., interstory drift, shear force). Desirable properties of IMs are efficiency (i.e., the predictability of the EDP for a given IM), and sufficiency (i.e., the independence of the prediction regarding Ground Motions Parameters (GMPs)) on magnitude and source-to-site distance). The study is achieved by means of 1677 Ground Motions (GMs) computed on two Single Degrees Of Freedom (SDOFs) whose modal characteristics are fitted with real-size structures. The numerical treatment of the contact is achieved with the Non-Smooth Contact Dynamics (NSCD) method which showed very good capabilities of reproducing the expected occurrence and number of impacts. Once one or several IMs are considered both efficient and sufficient enough, a future work will compute fragility and risk curves of these adjacent pounding SDOF with various separation distances.*

## 1 INTRODUCTION

Earthquake-induced building pounding occurs typically in denser urban areas where low to mid-height buildings are more likely to be adjacent. Field reports, experimental campaigns, and numerical analysis, have shown and demonstrated the potential negative effects of impact between structures, ranging from minor architectural damages [1, 2], to significant increases in interstory drifts [3, 4] and ductility demand [5, 6], to, in rare occasions, collapse [7]. Figures 1a and 1b illustrate respectively the aftermaths of building pounding in Mexico and Turkey.



(a) Mid-story floor collapse of Hotel de Carlo in Mexico City (Mw 8.1 earthquake) [8]



(b) Pounding damage (Mw 7.4, Izmit earthquake, Turkey, 1999) [9]

Figure 1: Building pounding damage during earthquakes

Building codes such as Eurocode 8 [10] give recommendations on separation distance between adjacent buildings, but they are either too conservative leading to unused land space, or contact occurs due to both large ground motions and buildings uncertainties. Considering the increasing world urban densification, it is acceptable to say that building pounding will continue happening.

Predicting the effects of such phenomenon in engineering design is of importance, especially throughout the lifetime of a given building in a precise geographical and urbanized environment. The purpose of the PBEE (Performance-Based Earthquake Engineering) framework [11] is to assess numerically the IMs correlations with some EDPs of interest. Most often, the IMs chosen are hazard curves of pseudo-acceleration at the structure fundamental period [12]. Probabilities and return periods of critical events are then computed from the statistical data from the studied region. To a further length, damage measures (service state, close to collapse, necessary repairs,...) and decision variables (cost, life,...) can be successively evaluated. Such information is of importance during new phases of life of a project (*e.g.* building design, renovation and expansion) to help decision-makers. To do so, IMs and EDPs are to be correlated for the chief executives to trust the predictions. A trusted IM should then properly reproduce with a reduced variability the EDP value and be conditionally independent on GMPs such as source-to-site distance and magnitude. An efficient and sufficient IM also requires reliable attenuation relationships, or Ground Motion Prediction Equations (GMPEs) to produce trustworthy risk curves. IMs efficiency and sufficiency properties through earthquake and impact are investigated in this paper.

Today, fast (in terms of computational time), robust and ergonomic numerical tools are required in order to run these probabilistic seismic risk analysis. The contact formulation needs

appropriate treatment; classical penalty approaches might give scattered results due to the sensitivity of its parameters [13]. This study uses an alternative way by the use of the Non-Smooth Contact Dynamics (NSCD) method [14, 15]. First, its capabilities are introduced with an idealized test-case. Secondly, a comparison between the experimental and numerical displacements of colliding structures on a shaking table (scale 1:1, EMSI laboratory at CEA Saclay in the frame of national project ANR SINAPS [4, 16]) allows validating the efficiency and robustness of the NSCD method and its use in the efficiency-sufficiency analysis. To the knowledge of the authors, no NSCD-based risk analysis has been carried out in the literature.

## 2 CAPABILITIES OF THE NSCD METHOD

The works by Moreau [17], Jean [14], and Acary [15, 18] have proven the energy conservation, the accuracy, and the application of the NSCD method in finite elements methods. It uses a Moreau-Jean integration scheme associated with a Newton impact law. It allows to apply an instantaneous change in velocities of the nodes in contact. This method has the advantage to depend only on the sole coefficient of restitution  $e$  taken between 0 and 1; it represents the system energy dissipation upon contact.

### 2.1 Test case : two impacting structures with no energy loss

To illustrate NSCD capabilities, a test case involving impact is presented. Two similar SD-OFs named Structure 1 and Structure 2 with fundamental periods  $T_1$  and  $T_2$  both equal to 1s are set adjacent to one another with a null separation distance. They are both subjected to an initial velocity  $V_1$  and  $V_2$  of 1m/s shoving them away in opposite senses before going backwards and impact. Figure 2 presents the set-up. No damping is considered, and the coefficient of restitution equals 1. This way, structures are meant to collide perpetually every 0.5s.

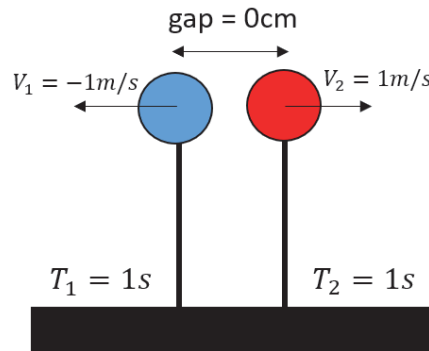


Figure 2: Structures 1 and 2 at initial state for test case

Figure 3 presents the displacements (upper figure) and velocities (lower figure) of the system. The kinematics behaves exactly as expected with a instantaneous change in velocities upon contact, no damping is observed, and collisions are indefinitely perpetuated.

### 2.2 Scale 1:1 reinforced concrete impacting slabs

Ph.D work of Crozet [16] involved the study of scale 1:1 structures colliding both in free motion or subjected to a seismic solicitation. Two instrumented reinforced concrete slabs of 4.6

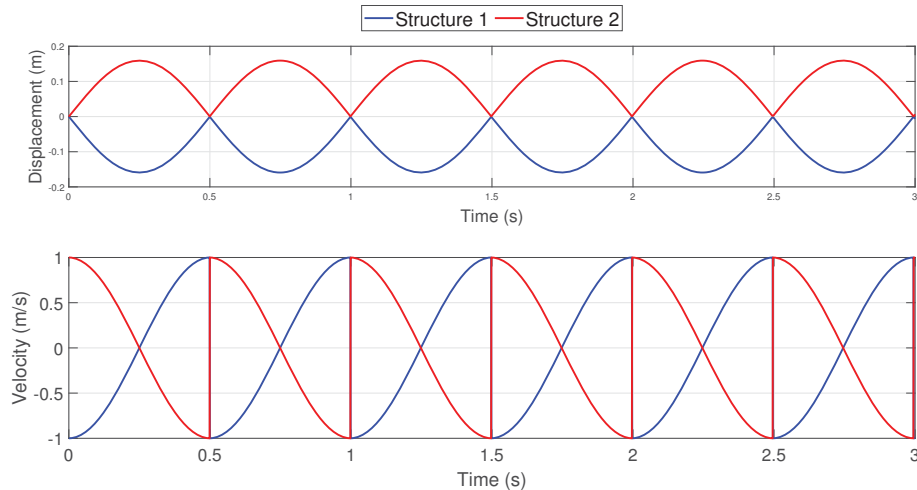
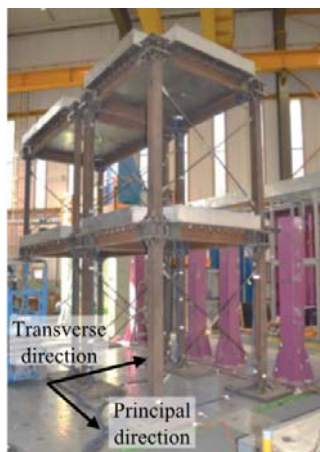
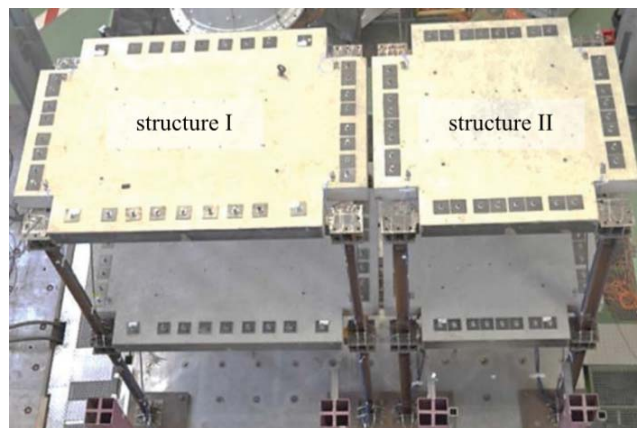


Figure 3: Impacting structures : test case with no damping

tons and 3.5 tons were mounted respectively on four 2.5m high steel HE100AA and HE140AA columns and set a few centimeters next to each other on a shaking table. Additional elements can be added to these single-story structures to make them two-story high, as shown by Figures 4a and 4b. Nevertheless, it is not the case of the present work where only the single-story set-up is considered because behaving like SDOFs. Structures are named 1 and 2, behave in linear elastic fashion, and have respectively their fundamental period equal to 0.28s (heavier, more flexible) and 0.15s (lighter, stiffer).



(a)



(b)

Figure 4: Structure 1 and Structure 2 set on the shaking table [16, 4]

Figure 5 presents the comparison of the experimental outcomes with the numerical model. The coefficient of restitution  $e$  equals 0.6. The comparison shows excellent agreement between the expected and numerical displacements, both in terms of kinematics, and time occurrence of impacts. Only one impact is not reproduced at 9.5s. Even if structures visually seem to collide more, especially between 11s and 14s, the accelerometers set up on the slabs did not detect more contacts.

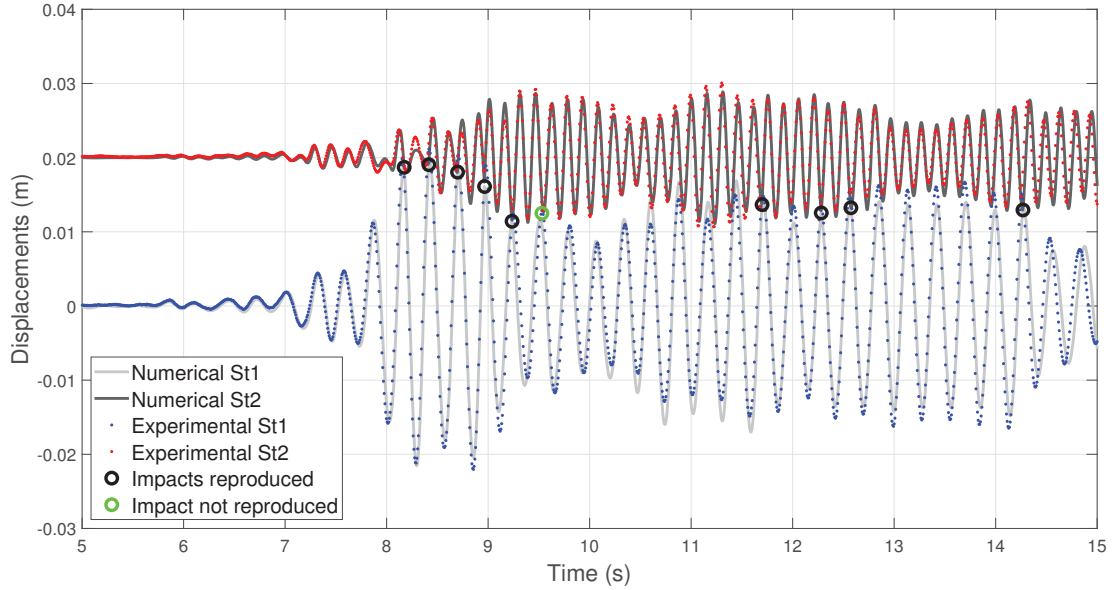


Figure 5: Cadarache 0.25g : Numerical versus Experimental comparison

Additional kinematic and spectral analysis produced very good results that confirmed  $e = 0.6$  is a value of interest in the frame of parallel colliding reinforced concrete slabs, but are not presented in the current work. To reduce the computation cost, the efficiency and sufficiency analysis are run with the structures modelled as SDOFs calibrated on the experimental data.

### 3 IMs EFFICIENCY AND SUFFICIENCY PROPERTIES

This section presents successively the list of IMs that are studied, the GM database, the coefficients used to assess the efficient and sufficient properties, and a discussion on the various gaps studied. Henceforth, the EDP chosen to deduce IM properties is the interstory drift  $\delta$ .

#### 3.1 List of IMs

Six IMs are investigated, the pseudo-acceleration at the fundamental period  $T_f$  of the structure  $S_a(T_f)$ , the *PGA*, the Arias Intensity (*AI*), the Cumulative Absolute Velocity (*CAV*) and Standard CAV (*SCAV*), and the averaged pseudo-acceleration  $S_{avg}(T_f)$ . Considering that earthquake-induced building pounding necessarily involves two buildings,  $S_a(T_f)$  and  $S_{avg}(T_f)$  are studied for  $T_f$  equal both to  $T_1$  and  $T_2$ , the respective fundamental periods of the Structure 1 and 2. Table 1 lists the six IMs studied throughout this work.

#### 3.2 Ground Motion set: Siber-Risk database

The 1677 GM extracted from the Siber-Risk database [19] comply with the properties presented by Table 2. This selection is consistent with the geographic location of the Valparaíso city in Chile. Interface types earthquakes (rupture zone located above 60km under the earth surface) are the most frequent, and the shear velocity in 30 meters below the ground surface  $V_{s30}$  is a class C type soil (very dense). Only ground motions of magnitude greater than five are selected, the authors considering that no significant damages are produced with smaller magnitudes.



$IM$	Formulation	Notes
$S_a(T_f)$	pseudo-spectral acceleration at $T_f$	$T_f$ : fundamental period
$PGA$	$\max( a(t) )$	$a(t)$ : acceleration time history
$AI$	$\frac{\pi}{2g} \int_0^{t_f} a(t)^2 dt$	$g = 9.81 \text{ m/s}^2$ $t_f$ : seism time duration
$CAV$	$\int_0^{t_f}  a(t)  dt$	$t_f$ : seism time duration
$SCAV$	$SCAV = CAV_i + \int_{t_{i-1}}^{t_i}  a(t)  dt$	$a(t)$ : acceleration in one-second interval where at least one value is greater than $0.025g$ $i = 1, \dots, N_r$ with $N_r$ the record length in seconds
$S_{avg}(T_f)$	$(\prod_{i=1}^N S_a(c_i T_f))^{1/N}$	$T_f$ : fundamental period Scalars $c_i$ : $c_1 = 0.5 \leq \dots \leq 1 \leq \dots \leq c_N = 2$ $N$ : length of $[c_1 T_f, \dots, T_f, \dots, c_N T_f]$

Table 1: List of IMs studied

GMP	Min. Value	Max. Value
Magnitude	5	8.8
Vs30	360	800
Type	Interface	

Table 2: GM selection for the Valparaiso region (Chile)

### 3.3 Efficiency

The efficiency of an IM regarding a peculiar EDP is assessed with both the Coefficient Of Variation ( $COV$ ) and the regression coefficient ( $R^2$ ). The first represents the variability around the mean value of the distribution (*i.e.* Eq.(1) where  $\sigma$  is the standard deviation, and  $\mu$  the mean value of the distribution). Unlike  $\sigma$ ,  $COV$  has no dimension which is useful when comparing the efficiency property between EDPs of different natures.

$$COV = \frac{\sigma}{\mu} \quad (1)$$

$R^2$  represents how much the logarithmic EDP-IM correlation is linear, and is calculated directly from a software. A  $R^2 = 1$  value indicates a perfect linear relationship. Henceforth, an IM is arbitrary considered "efficient enough" if  $COV \leq 0.10$  and  $R^2 \geq 0.90$ .

### 3.4 Sufficiency

The sufficiency of IMs is commonly calculated regarding the source-to-site distance (*i.e.*, herein, the distance to the rupture fault) and the magnitude of the GM. The results of the present study are independent of the soil conditions (see Vs30 range in Table 2) and the earthquakes nature (Interface type) accordingly to the selected dataset. Non-exhaustively, the fault rupture mechanism, the directivity of the earthquakes, and the  $\epsilon$  coefficient [12] representing the ran-



domness of the GM are not considered in this study.

Two ways of assessing the sufficiency to magnitude and distance are studied. The p-value "p" (statistical F-test) delivers a binary assessment of the IM, considering it either sufficient if  $p \geq 0.05$  or not sufficient if  $p \leq 0.05$ . This parameter has been notably used by Luco and Cornell [20], and Eads and Miranda [21, 22] in the civil engineering field. This parameter is calculated through a calculation software. The second sufficiency coefficient is the Spearman rank coefficient  $\rho$  presented by Eq.(2).

$$\rho = 1 - \frac{6 \sum_{i=1}^N D^2}{N(N^2 - 1)} \quad (2)$$

With  $D$  the differences between the ranks of the  $N$  dataset values.  $\rho$  measures how much the data fits with a monotonic relationship.  $\rho$  is between -1 and 1, representing respectively a perfect negative linear dependency, and a perfect positive linear dependency. A  $|\rho|$  close to zero denotes the IM is independent from the GMP.

Unlike the p-test, the Spearman coefficient does not produce a binary evaluation of the sufficiency, but it allows a relative comparison of this property, enabling a classification of IMs. To the knowledge of the authors, no risk analysis of building pounding has been carried out with both p-value and Spearman coefficients.  $p(M)$ ,  $p(D)$ ,  $\rho(M)$ , and  $\rho(D)$  are respectively the p-value and Spearman coefficients calculated for magnitude and distance for a given couple of EDP and IM. Henceforth, an IM is considered sufficient if  $p(M)$  and  $p(D)$  are, by definition, greater than 0.05 and if  $|\rho(M)|$  and  $|\rho(D)|$  are arbitrary less than 0.10 (De Biasio [23] considered the IM sufficient if  $|\rho| \leq 0.20$ ).

## 4 RESULTS

One important issue of the building pounding study is the gap separation. Each gap separation chosen consists in itself in a whole single system. For instance, if 11 gaps are studied, then the outcomes to analyse are multiplied by 11 ; *i.e.*, it means first computing 11 times 1677 GM on the structures, retrieving 11 times 1677 EDPs, and inferring 11 times the efficient-sufficient coefficients. The analysis of six coefficients of eight IMs for two structures separated by 11 different gaps is important in terms of computation time. In this work, authors decided to rather obtain a general overlook by averaging the efficient-sufficient coefficients over all the gaps. Thus, the amount of data to analyse is reduced by a factor 11. First, an example is given with the coefficients  $R^2$  and  $COV$  of  $S_a(T_1)$  for Structure 1. Secondly, all efficiency-sufficiency coefficients for both structures are presented.

### 4.1 Example of the average of $R^2$ and $COV$ coefficients $S_a(T_1)$ relationship

Figure 6b presents the interstory drift  $\delta_1$  plots against the  $S_a(T_1)$  of Structure 1, in logarithmic scale, and for both a 5mm and infinite (no-collision case) separation distance. Only the ground motions that actually produced collision in the five millimeters case are plotted.

As expected without contact in a elastic linear structure, a perfect linear fit links the interstory-drift with  $S_a(T_1)$  (*i.e.*, magenta dots and green line are superposed),  $R^2$  and  $COV$  are respectively equal to 1 and 0. On the contrary, the efficiency properties are lesser when impact is

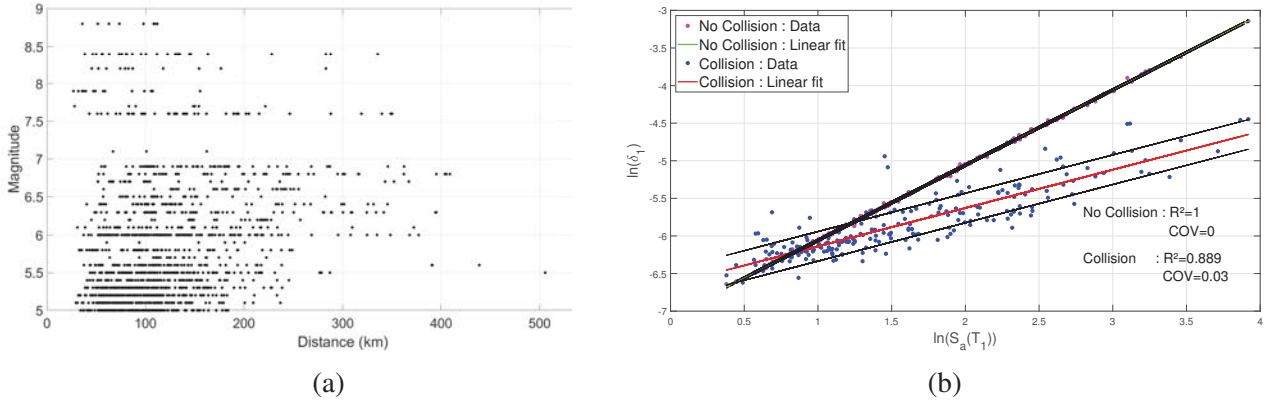


Figure 6: (a) Selected Database : 1677 GM (b) Outcomes of Structure 1 with gap = 5mm

involved with gap=5mm. At this distance, 227 out of the 1677 GM produced impact, resulting in  $R^2$  and  $COV$  respectively equal to 0.89 and 0.03 (*i.e.*, blue dots are scattered around the red linear curve). Thus, for each gap studied,  $R^2$  and  $COV$  will have different values.

As an example, Table 3 presents the  $COV$  results for  $S_a(T_1)$  for  $N=11$  separation distances.  $N_g^{GM}$  corresponds to the number of GM inducing collision for the gap indexed  $g$ .

Gaps (mm)	0	1	2	3	4	5	6	7	8	9	10
Index $g=1,...,N=11$	1	2	3	4	5	6	7	8	9	10	11
$N_g^{GM}$	1677	1020	575	395	297	227	182	148	128	113	106
$S_a(T_1): R_g^2$	0.90	0.91	0.91	0.91	0.91	0.89	0.88	0.85	0.82	0.79	0.82
$S_a(T_1): COV_g$	0.06	0.04	0.04	0.03	0.03	0.03	0.03	0.04	0.04	0.04	0.03

Table 3:  $S_a(T_1)$  :  $R^2$  and  $COV$  values of Structure 1

As expected for a gap null, all 1677 simulations induce impact and the number decreases as the gap increases. At 10mm the number drops to 106 which was decided to be the larger and last gap computed since (i) it is almost the same number (113) as for gap=9mm (ii) it is less than 10% of the totality of the database. In this study case,  $R^2$  decreases from 0.90 to 0.82 (important loss of efficiency) while  $COV$  decreases from 0.06 to [0.03;0.04] (small gain of efficiency) when the gap increases from zero to 10mm.

Let's now note  $R_g^2$  and  $COV_g$  respectively the regression coefficient and coefficient of variation for the  $g$  identified gap (Table 3). All  $R_g^2$  and  $COV_g$  are then averaged and weighted by  $N_g^{GM}$ , the number of ground motions that actually induced collision for the gap number  $g$ ; let's note the results respectively  $R_{avg}^2$  and  $COV_{avg}$ . Eq.(3) presents the formulation used with  $R_{avg}^2$ . Eq.(4) and Eq.(5) respectively present the numerical application for  $R^2$  and  $COV_{avg}$  for  $S_a(T_1)$ . These values can be found in the third column, at the third and fourth lines of Table 4.

$$R_{avg}^2 = \frac{\sum_{g=1}^{N=11} R_g^2 N_g^{GM}}{\sum_{g=1}^{N=11} N_g^{GM}} \quad (3)$$

$$R_{avg}^2 = \frac{0.90 * 1677 + 0.91 * 1020 + \dots + 0.82 * 106}{1677 + 1020 + \dots + 106} = 0.90 \quad (4)$$

$$COV_{avg} = \frac{0.06 * 1677 + 0.04 * 1020 + \dots + 0.03 * 106}{1677 + 1020 + \dots + 106} = 0.043 \quad (5)$$

## 4.2 Identification of the most efficient-sufficient IMs

Tables 4 and 5 present respectively for Structure 1 and Structure 2, the averaged values of the efficiency-sufficiency coefficients. The values are bold if the IM complies with the criterion of validity.

	Validity Criterion	$S_a(T_1)$	$PGA$	$AI$	$CAV$	$SCAV$	$S_{avg}(T_1)$
$R^2$	$\geq 0.90$	<b>0.90</b>	0.87	0.89	0.82	0.82	<b>0.92</b>
$COV$	$\leq 0.05$	<b>0.043</b>	<b>0.046</b>	<b>0.043</b>	0.055	0.054	<b>0.036</b>
$p(M)$	$\geq 0.05$	<b>0.37</b>	6e-6	<b>0.208</b>	<b>0.074</b>	<b>0.211</b>	0.044
$ \rho(M) $	$\leq 0.10$	<b>0.042</b>	<b>0.049</b>	<b>0.046</b>	<b>0.028</b>	<b>0.041</b>	<b>0.024</b>
$p(D)$	$\geq 0.05$	<b>0.66</b>	<b>0.13</b>	<b>0.41</b>	0.002	0.002	<b>0.13</b>
$ \rho(D) $	$\leq 0.10$	<b>0.048</b>	<b>0.037</b>	<b>0.029</b>	<b>0.041</b>	<b>0.039</b>	<b>0.030</b>

Table 4: Structure 1 : Averaged IMs coefficients of Efficiency-Sufficiency

**Efficiency:** For both structures,  $S_{avg}(T_f)$  is the most efficient IM, their respective  $R^2$  and  $COV$  respectively plainly greater and smaller than all the other IMs coefficients.  $S_a(T_f)$ ,  $PGA$ , and  $AI$  show good efficiency properties although closer to the validity criterion than  $S_{avg}(T_f)$ , or even not compliant with the criterion for Structure 2.  $CAV$  and  $SCAV$  are clearly not efficient enough in the regard of that study case.

**Sufficiency:**  $S_a(T_f)$ ,  $AI$ , and  $S_{avg}(T_f)$  are conditionally independent on magnitude and distance parameters for Structure 1, it is validated by both the p-value and Spearman ranking coefficients.  $PGA$  only misses the  $p(M)$  to have also a complete sufficiency validation. The Spearman coefficients of  $S_{avg}(T_f)$  are overall smaller than  $S_a(T_f)$ , implying a better sufficiency.

	Validity Criterion	$S_a(T_2)$	$PGA$	$AI$	$CAV$	$SCAV$	$S_{avg}(T_2)$
$R^2$	$\geq 0.90$	0.88	<b>0.91</b>	<b>0.90</b>	0.82	0.82	<b>0.94</b>
$COV$	$\leq 0.05$	<b>0.048</b>	<b>0.042</b>	<b>0.044</b>	0.06	0.057	<b>0.034</b>
$p(M)$	$\geq 0.05$	<b>0.459</b>	0.011	7e-5	2e-4	2e-4	<b>0.087</b>
$ \rho(M) $	$\leq 0.10$	<b>0.069</b>	<b>0.036</b>	0.054	<b>0.036</b>	<b>0.025</b>	<b>0.028</b>
$p(D)$	$\geq 0.05$	<b>0.77</b>	<b>0.29</b>	0.001	5e-5	4e-5	<b>0.32</b>
$ \rho(D) $	$\leq 0.10$	<b>0.046</b>	<b>0.029</b>	<b>0.040</b>	<b>0.044</b>	<b>0.027</b>	<b>0.051</b>

Table 5: Structure 2 : Averaged IMs coefficients of Efficiency-Sufficiency

## 5 CONCLUSIONS

This article presents the methodology for evaluating the properties of efficiency (predictability of the EDP for a given value of IM) and sufficiency (conditional independence of the IM regarding chosen GMP, herein magnitude and distance) of six IMs in the building pounding framework. It aims to select the best suited IM among  $S_a(T_f)$ ,  $PGA$ ,  $AI$ ,  $CAV$ ,  $SCAV$ , and  $S_{avg}(T_f)$  in the case of risk-assessment studies on elastic buildings colliding at their slab levels. Two different tests, p-value's and Spearman rank's, are used to enforce the conclusions.

The NSCD method used for contact detection and treatment on two SDOFs has produced excellent agreement with both an idealized test case (Figures 2 and 3), and the experimental data extracted from real size colliding structures (Figure 4). These tests validated the NSCD method use in the 1677 GM from the Siber-Risk database are computed on the numerical model for six different gaps as displayed by Table 3. The efficiency-sufficiency coefficients inferred from each gap study are then averaged and weighted (Eq.(3)) to obtain an overview of the IMs properties in this system configuration (two parallel colliding reinforced concrete slabs).

$S_{avg}(T_f)$  is the most efficient IM for the two structures and shows very good sufficiency properties relatively to the other IMs. Although with less interesting grades than  $S_{avg}(T_f)$ , the IMs  $S_a(T_f)$ ,  $PGA$  follow close behind.  $AI$  checks all the cases for Structure 1, but falls short on the p-value test of magnitude and distance for Structure 2. Finally,  $CAV$  and  $SCAV$  are discarded for far behind all the aforementioned IMs.

The continuation of this work is the computation of fragility and risk curves; the first giving the probability of exceeding an EDP value of interest for a given value of IM, the second being the convolution of the first with hazard curves [12].  $S_{avg}(T_f)$  is then the best candidate for fragility curves. For risk curves on the other hand, the more widely known the IM is, the larger the number of existing GMPEs is, and the more accurate and consensual the hazard curves are. In this regard, scientists have more experience using  $S_a(T_f)$  and  $PGA$  rather than  $S_{avg}(T_f)$  whose GMPEs are smaller in number.

## ACKNOWLEDGEMENTS

This work is partly founded by a CDSN Grant (Contrat Doctoral Spécifiques aux Normaliens) and the ECOS-Sud Grant for international collaboration CONICYT-ECOS170044. The authors deeply thanks V. Crozet of the French CEA for the provisioning of the experimental data [13]. Many thanks are also addressed to V. Acary and F. Bourrier respectively of the INRIA (Institut National de la Recherche en sciences et technologies du numérique) and INRAE (Institut National de la Recherche pour l’Agriculture, l’alimentation et l’Environnement) for their guidance into the NSCD method use. In addition, this work has been partially developed within the framework of the federative project I-RISK (L’offre de solutions au traitement des risques naturels) co-funded by the European Union (FEDER) and ”La région Auvergne-Rhône-Alpes” which aims at proposing innovative solutions for natural hazards mitigation. Dr. Candia received support from Facultad de Ingenieria Civil at Universidad del Desarrollo - Chile, FONDECYT Grant 11180937 “Seismic Risk of Mined Tunnels”, the National Research Center for Integrated Natural Disaster Management FONDAP/CIGIDEN 15110017, and FONDECYT Grant Number 1170836, “SIBER-RISK: SIMulation Based Earthquake Risk and Resilience of Interdependent Systems and NetworKs.” The authors are grateful for this support.

## REFERENCES

- [1] Gregory Cole, Rajesh Dhakal, Athol Carr, and Des Bull. Interbuilding pounding damage observed in the 2010 Darfield earthquake. *Bulletin of the New Zealand Society for Earthquake Engineering*, 43(4):382–386, December 2010. Number: 4.
- [2] V Jeng and W. L Tzeng. Assessment of seismic pounding hazard for Taipei City. *Engineering Structures*, 22(5):459–471, May 2000.
- [3] SA Anagnostopoulos. Building pounding re-examined: How serious a problem is it? 11th World Conference on Earthquake Engineering, 1996.
- [4] Vincent Crozet, Ioannis Politopoulos, and Thierry Chaudat. Shake table tests of structures subject to pounding. *Earthquake Engineering & Structural Dynamics*, 48(10):1156–1173, 2019. eprint: <https://onlinelibrary.wiley.com/doi/pdf/10.1002/eqe.3180>.
- [5] Maria J. Favvata. Minimum required separation gap for adjacent RC frames with potential inter-story seismic pounding. *Engineering Structures*, 152:643–659, December 2017.
- [6] Chris G. Karayannis and Maria J. Favvata. Earthquake-induced interaction between adjacent reinforced concrete structures with non-equal heights. *Earthquake engineering & structural dynamics*, 34(1):1–20, 2005. Publisher: Wiley Online Library.
- [7] Roger E. Scholl. Observations of the performance of buildings during the 1985 Mexico earthquake, and structural design implications. *International Journal of Mining and Geological Engineering*, 7(1):69–99, March 1989.
- [8] C Arnold. Pounding damage at hotel de carlo. *The Earthquake Engineering Online Archive NISEE e-Library*, 1985.
- [9] H Sezen. Note effect on pounding. *The Earthquake Engineering Online Archive NISEE e-Library*, 1999.

- [10] Brussels European Committee for Standardization. Design of structures for earthquake resistance. part 1: General rules, seismic actions and rules for buildings. en 1998-1. *Eurocode 8*, 2004.
- [11] Jack Moehle and Gregory Deierlein. A framework methodology for performance-based earthquake engineering. January 2004.
- [12] Jack W Baker. Introduction to Probabilistic Seismic Hazard Analysis. page 79, 2008.
- [13] Sushil Khatiwada and Nawawi Chouw. Limitations in Simulation of Building Pounding in Earthquakes. *International Journal of Protective Structures*, 5(2):123–150, June 2014. Publisher: SAGE Publications.
- [14] Michel Jean. The non-smooth contact dynamics method. *Computer Methods in Applied Mechanics and Engineering*, 177(3-4):235–257, 1999. Publisher: Elsevier.
- [15] Vincent Acary. *Contribution à la modélisation mécanique et numérique des édifices maçonnés*. phdthesis, Université de la Méditerranée - Aix-Marseille II, May 2001.
- [16] Vincent Crozet. *Etude de l'entrechoquement entre bâtiments au cours d'un séisme*. These de doctorat, Institut polytechnique de Paris, November 2019.
- [17] J. J. Moreau. Standard Inelastic Shocks and the Dynamics of Unilateral Constraints. In Gianpiero Del Piero and Franco Maceri, editors, *Unilateral Problems in Structural Analysis*, International Centre for Mechanical Sciences, pages 173–221, Vienna, 1985. Springer.
- [18] Vincent Acary. Energy conservation and dissipation properties of time-integration methods for nonsmooth elastodynamics with contact. *ZAMM - Journal of Applied Mathematics and Mechanics / Zeitschrift für Angewandte Mathematik und Mechanik*, 96(5):585–603, 2016. eprint: <https://onlinelibrary.wiley.com/doi/pdf/10.1002/zamm.201400231>.
- [19] S. Castro, Crempien J. Benavente, R., G. Candia, and J.C. de la Llera. A consistently processed strong motion database for chilean earthquakes. 90, 2021. Submitted.
- [20] Nicolas Luco and C. Allin Cornell. Structure-Specific Scalar Intensity Measures for Near-Source and Ordinary Earthquake Ground Motions. *Earthquake Spectra*, 23(2):357–392, May 2007.
- [21] Laura Eads, Eduardo Miranda, Helmut Krawinkler, and Dimitrios G. Lignos. An efficient method for estimating the collapse risk of structures in seismic regions: an efficient method for estimating the collapse risk of structures. *Earthquake Engineering & Structural Dynamics*, 42(1):25–41, January 2013.
- [22] Laura Eads, Eduardo Miranda, and Dimitrios G. Lignos. Average spectral acceleration as an intensity measure for collapse risk assessment: Average Spectral Acceleration as an IM for Collapse Risk Assessment. *Earthquake Engineering & Structural Dynamics*, 44(12):2057–2073, September 2015.
- [23] Marco de Biasio. Ground motion intensity measures for seismic probabilistic risk analysis. page 169, 2014.



## ESTIMATION OF DUCTILITY IN ASYMMETRIC-PLAN STRUCTURES

Kaan Kaatsız<sup>1</sup> and Halûk Sucuoğlu<sup>2</sup>

<sup>1</sup> Department of Civil Engineering, Ahi Evran University  
40100 Kırşehir, Turkey  
e-mail: kaan.kaatsiz@ahievran.edu.tr

<sup>2</sup> Department of Civil Engineering, Middle East Technical University  
06800 Ankara, Turkey  
e-mail: sucuoglu@metu.edu.tr

---

### Abstract

*Ductility demands observed in asymmetric plan structures due to earthquake excitations are investigated in this study. Torsional Ductility Spectra are utilized to estimate the maximum ductility response of such systems. Dynamic response of these systems are dominated by the lower vibration modes and observed seismic behavior is in conformance with the capacity design principles. In order to utilize the Torsional Ductility Spectra, five parameters of the asymmetric plan systems, namely, first mode period, uncoupled frequency ratio, stiffness eccentricity, stiff-to-flexible edge strength ratio and ductility reduction factor are estimated through a novel procedure. Simple formulations for representing the dynamic properties of shear frame systems in terms of described structural parameters are developed. Parametric equivalents of shear frame structures are obtained. Estimated ductilities from the developed charts are compared with those obtained from dynamic response analyses of shear frame asymmetric-plan systems.*

*The observed results indicate that developed spectra are able to estimate the ductility demands at both stiff and flexible side frames of actual asymmetric-plan systems with reasonable accuracy. Based on the conclusions, Torsional Ductility Spectra charts are considered practical tools for estimating the ductility demands of asymmetric plan structures.*

**Keywords:** Asymmetric-plan Structures, Torsional Coupling, Torsional Ductility, Ductility Distribution, Performance Assessment

---

## 1 INTRODUCTION

Modern seismic design codes employ response reduction factors in design of structural members using linear elastic analysis [1, 2]. The capacity design methodology employing the response reduction factors may result in poor estimation of seismic performance in the case of irregular structures such as asymmetric-plan systems where torsionally coupled behaviour is observed. The resulting poor seismic performance, in turn, yields uneven ductility distribution among plan of asymmetric structures. Hence, varying degrees of inelastic behaviour is observed.

The discussed problem is a well-known issue and in the past it has been addressed in many studies. Comprehensive reviews of these studies has been made by various authors previously [3, 4, 5, 6]. Early research regarding the subject was performed using simple single-story models. Later more advanced studies based in multi-story asymmetric systems have also emerged. In one of the early studies, the reducing effect of torsional coupling with increasing inelastic deformations was observed [7]. An effective eccentricity and associated design torque was introduced to estimate the inelastic deformations of torsionally-coupled systems [8]. Peak ductility demands at the edges of asymmetric systems are determined to be not larger than those of symmetric systems [9, 10]. Moreover, it was proposed that, the inelastic displacements of asymmetric systems can be reduced by modifying the strength distribution along plan by changing the location of center of strength ( $CV$ ). In separate other studies, strength eccentricity has been determined to be more effective than stiffness eccentricity to control inelastic deformations [11, 12, 13]. A displacement-based design approach has also been proposed as an alternative to strength-based approach to limit and make ductility distribution among structural members in asymmetric systems more uniform [14]. A balanced distribution of center of strength and center of stiffness was proposed in order to minimize the edge displacements of torsionally coupled systems [15]. Contribution of load resisting frames that are perpendicular to the direction of earthquake loading to the torsional response was also investigated [16, 17].

The overstrength that is inherent in members of the torsionally coupled systems which are designed with force-based approaches has also been studied. It has been noted that accidental eccentricity formulations in seismic codes does not usually compensate the inelastic deformation demands, rather they increase the overstrength [18, 19]. The explicit inclusion of overstrength in the design of asymmetric systems was suggested in a study regarding the uneven distribution of overstrength in torsionally coupled multistory buildings [20]. Further studying the overstrength in asymmetric systems, uniform ductility spectra which has been proposed by the authors to estimate the optimum strength ratio of stiff and flexible sides of asymmetric systems for achieving balanced ductility demands [21].

The observations and suggestions regarding the torsional response of asymmetric systems vary dramatically among the vast research conducted in the past. Although this is the case for many of the deductions, it has been generally agreed by the researchers that the modification of strength eccentricity is closely related with controlling the inelastic torsional response. The work presented within this study is formulated upon this observation. The inelastic displacements of asymmetric systems are estimated with respect to strength distribution of these simple structures. Seismic response of shear frame systems is represented by simple models using basic dynamic properties.

## 2 TORSIONAL DUCTILITY SPECTRA

A simple tool to assess the ductility demands in simple asymmetric-plan multi degree of freedom systems is proposed. Basic vibration and strength parameters of a simple single story, two degree of freedom asymmetric shear frame are determined as the basic variables for a rigorous parametric study. A shear frame having a stiffness eccentricity ratio of  $e$  is constructed.

It is composed of a stiff side and flexible side structural member, both of which are connected a rigid slab. The system in question is designed under a typical design spectrum by employing the ductility reduction factor  $R\mu$ .

Another parameter that is taken into account is the uncoupled frequency ratio ( $\Omega_r$ ) of the parametric system. A variation for  $\Omega_r$  is introduced so that the variation in seismic response of a torsionally stiff ( $\Omega_r = 1.25$ ), torsionally equally stiff ( $\Omega_r = 1.0$ ) and torsionally flexible ( $\Omega_r = 0.8$ ) systems are investigated. The different parameters considered in this simple, single story shear frames are summarized in Table 1.

$e$	$R\mu$	$\Omega_r$
0.1	3	1.25
0.2	4	1.0
0.3	5	0.8

Table 1: System parameters used in single-story simple structures

The stiffnesses of flexible and stiff side members of the linear elastic system ( $k_F$  and  $k_S$ ) are selected such that the target stiffness eccentricity value is satisfied for each parametric system (Equation 1).

$$e = \frac{k_F - k_S}{2(k_F + k_S)} \quad (1)$$

The uncoupled frequency ratio can also be computed from Equation 2.  $L$  in Equation 2 is the distance between to structural members and  $r$  is the radius of gyration of the system (Equation 3.)

$$\Omega_r = \frac{L}{2r} \quad (2)$$

$$r = \sqrt{\frac{I_{CM}}{m}} \quad (3)$$

The terms  $m$  and  $I_{CM}$  in Equation 3 are the mass and the mass moment inertia of the parametric systems, respectively. Throughout the parametric study,  $L$  and  $m$  are utilized as unity. Solution of Equation 3 for each  $\Omega_r$  value yields the  $L$  parameter which, in turn, used to compute mass moment of inertia and create the mass matrix of the system. In addition, Equation 1 is used to determine  $k_F$  and  $k_S$  for every parametric system having  $e = 0.1, 0.2$ , or  $0.3$ . Upon using the determined stiffness values and  $L$ , the stiffness matrix for each unique system can also be obtained. Consequently, the relationship between modal vibration frequency  $\omega_n$ , stiffnesses  $k_F$  and  $k_S$ , and the inertial properties  $m$  and  $I_{CM}$  of the parametric system can be obtained from the solution of the eigenvalue problem in Equation 4:

$$\det(\underline{k} - \omega_n^2 \underline{m}) = 0 \quad (4)$$

Hence, upon solution of Equation 4, the linear elastic properties of the systems can be obtained for a range of different translational periods ( $T_1$ ). They are designed under the design response spectrum for obtaining the stiff side and flexible side strength demands for selected ductility reduction factors of  $R\mu$ . The schematic representation of the parametric systems and

the distribution of displacements computed under response spectrum analysis is shown in Figure 1. It should be noted here that accidental eccentricity is not included in the design.

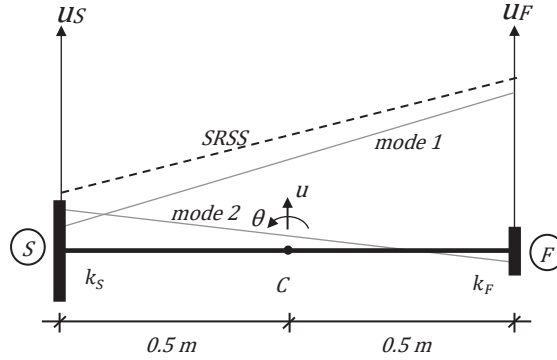


Figure 1: Schematic distribution of displacements for a 2DOF parametric system.

At this stage, another parameter variation is introduced to the parametric systems. The assigned flexible side strength ( $F_F$ ) is kept fixed at its nominal value (i.e. the strength demand); whereas overstrength is introduced to the stiff side members in an incremental manner (Figure 2). Hence, the parameter stiff to flexible edge strength ratio ( $SFSR$ ) is defined (Equation 5).

$$SFSR = \frac{F_S}{F_F} \quad (5)$$

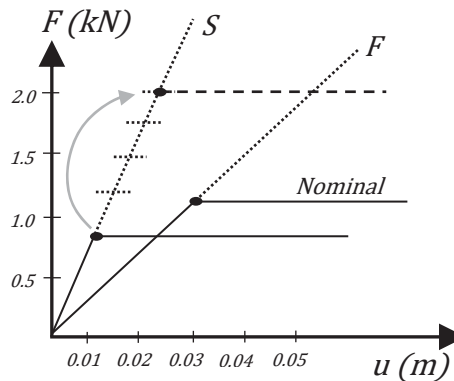


Figure 2: The flexible ( $F_F$ ) and stiff edge ( $F_S$ ) strengths of the parametric systems and variation of  $F_S$ .

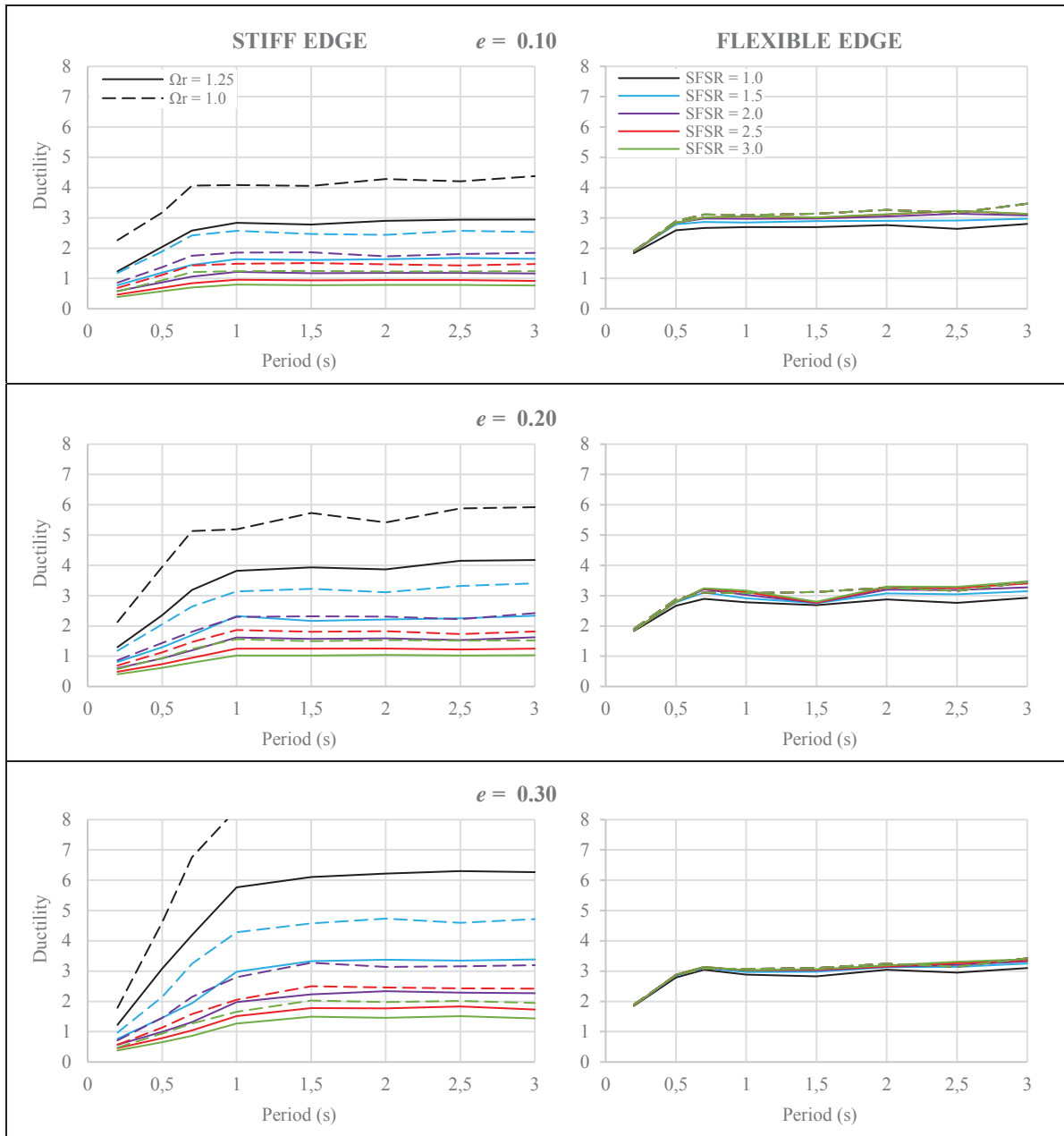
By utilizing this procedure, a family of parametric, two degree of system parametric systems are obtained. Each system is identified by a unique set of parameters ( $T_1$ ,  $\Omega_r$ ,  $e$ ,  $R_\mu$ ,  $SFSR$ ). Nonlinear dynamic response of these systems are then computed under a set of 30 spectrum matched [22] ground motions selected from PEER NGA Database [23]. The unscaled ground motion list and their characteristics are given in Table 2. Generally, they are all recorded in soft soil, at near fault regions. Linear elastic target spectrum is constructed per ASCE 7-16 [1] based on an imaginary location in downtown San Francisco. The site class is assumed as C.

Nonlinear models of the parametric systems have been prepared in OpenSees Platform [24] and elastic-perfectly plastic hysteresis models are employed in numerical representations of load resisting members.

PEER NGA Code	Earthquake	M <sub>w</sub>	Joyner- Boore Dist. (km)	NEHRP Site Class	PGA (g)
TMB205	Parkfield - 1966	6.19	15.96	C	0.29
UC2090	Loma Prieta - 1989	6.93	12.15	C	0.34
WPI046	Northridge-01 - 1994	6.69	2.11	D	0.38
A-TAR000	Whittier Narrows-01 - 1987	5.99	38.24	D	0.60
ABBAR--L	Manjil, Iran - 1990	7.37	12.56	C	0.51
AND250	Morgan Hill - 1984	6.19	3.22	C	0.34
B-PTS225	Superstition Hills-02 - 1987	6.54	0.95	D	0.45
C05085	Parkfield - 1966	6.19	9.58	D	0.38
CPE045	Victoria, Mexico - 1980	6.33	13.80	C	0.57
375-E	Duzce, Turkey - 1999	7.14	3.93	C	0.74
DAY-LN	Tabas, Iran - 1978	7.35	20.63	C	0.35
DZC270	Kocaeli, Turkey - 1999	7.51	13.60	D	0.33
G02090	Loma Prieta - 1989	6.93	10.38	D	0.35
G03090	Loma Prieta - 1989	6.93	12.23	D	0.46
H-E07230	Imperial Valley-06 - 1979	6.53	0.56	D	0.42
H-E08230	Imperial Valley-06 - 1979	6.53	3.86	D	0.54
HEC090	Hector Mine - 1999	7.13	10.35	C	0.31
KAK090	Kobe, Japan - 1995	6.90	22.50	D	0.27
LGP090	Loma Prieta - 1989	6.93	18.46	C	0.78
LOB000	Loma Prieta - 1989	6.93	12.04	C	0.46
MU2035	Northridge-01 - 1994	6.69	12.39	C	0.51
NWH360	Northridge-01 - 1994	6.69	3.16	D	0.70
OBR360	Northridge-01 - 1994	6.69	35.43	D	0.47
ORR360	Northridge-01 - 1994	6.69	20.10	C	0.49
PAR--T	Northridge-01 - 1994	6.69	5.54	D	0.51
A-MAT353	New Zealand-03 - 1987	5.80	26.85	C	0.05
STG000	Loma Prieta - 1989	6.93	7.58	C	0.38
STM360	Northridge-01 - 1994	6.69	17.28	D	0.59
STN110	Whittier Narrows-01 - 1987	5.99	20.35	D	0.12
SYL090	Whittier Narrows-01 - 1987	5.99	38.55	C	0.06

Table 2: Strong ground motions used in the dynamic analyses.

Results obtained from nonlinear dynamic analysis of each parametric system having a distinct  $T_1$  are compiled in a spectrum format to create the Torsional Ductility Spectra. The main response parameter in this spectra set is selected as the mean maximum ductility of the systems. Ductility is a normalized indication of the inelastic response; therefore, it provides an objective response comparison for all parametric systems. Torsional Ductility Spectra produced for  $R_\mu = 3, 4$ , and  $5$  are presented in Figures 3, 4, and 5 respectively. The spectra compiled only for torsionally stiff and torsionally equally flexible systems are displayed in these figures in order to not to make the graphical view too complicated.

Figure 3: Torsional ductility spectra ( $R\mu = 3$ ).

## 2.1 Observations from Torsional Ductility Spectra

As can be seen in Figures 3, 4 and 5 the ductility trends of stiff and flexible side members vary considerably. Flexible side ductilities are invariant of  $SFSR$  and almost equal to  $R\mu$  in each chart. Stiff side ductilities, however, are quite sensitive to  $SFSR$ . It should be noted here that the variation in  $SFSR$  corresponds to the proportional variation of stiff side strength since the flexible side strength is held fixed at its nominal value among designs.

An important observation could be made from Figures 3, 4 and 5. The ductilities observed in flexible edge members are consistent with the ductility reduction factors employed in the design. Therefore, it could be concluded that energy is dissipated mainly through flexible side member. Stiff side member may also experience some inelastic response especially when  $SFSR$



is close to unity (stiff and flexible sides have similar strengths). Although in practice, this observation is not common. Due to relationship between strength and stiffness, the ratio of stiff side to flexible side strength (*SFSR*) is proportional to the ratio of stiff side to flexible side stiffness in most of the cases. This issue, in turn, is the cause of torsional behaviour and the cause of inherent overstrength located in stiff side members. Therefore, it can be deduced that the stiff side members in actual systems behave in a force-controlled manner with fairly small ductility demands. This is visualized in Figures 3, 4 and 5 especially when *SFSR* > 2. It is also well known that ductile seismic detailing supplied to structural members further increase the overstrength for stiff side, hence making the behaviour more unfavorable.

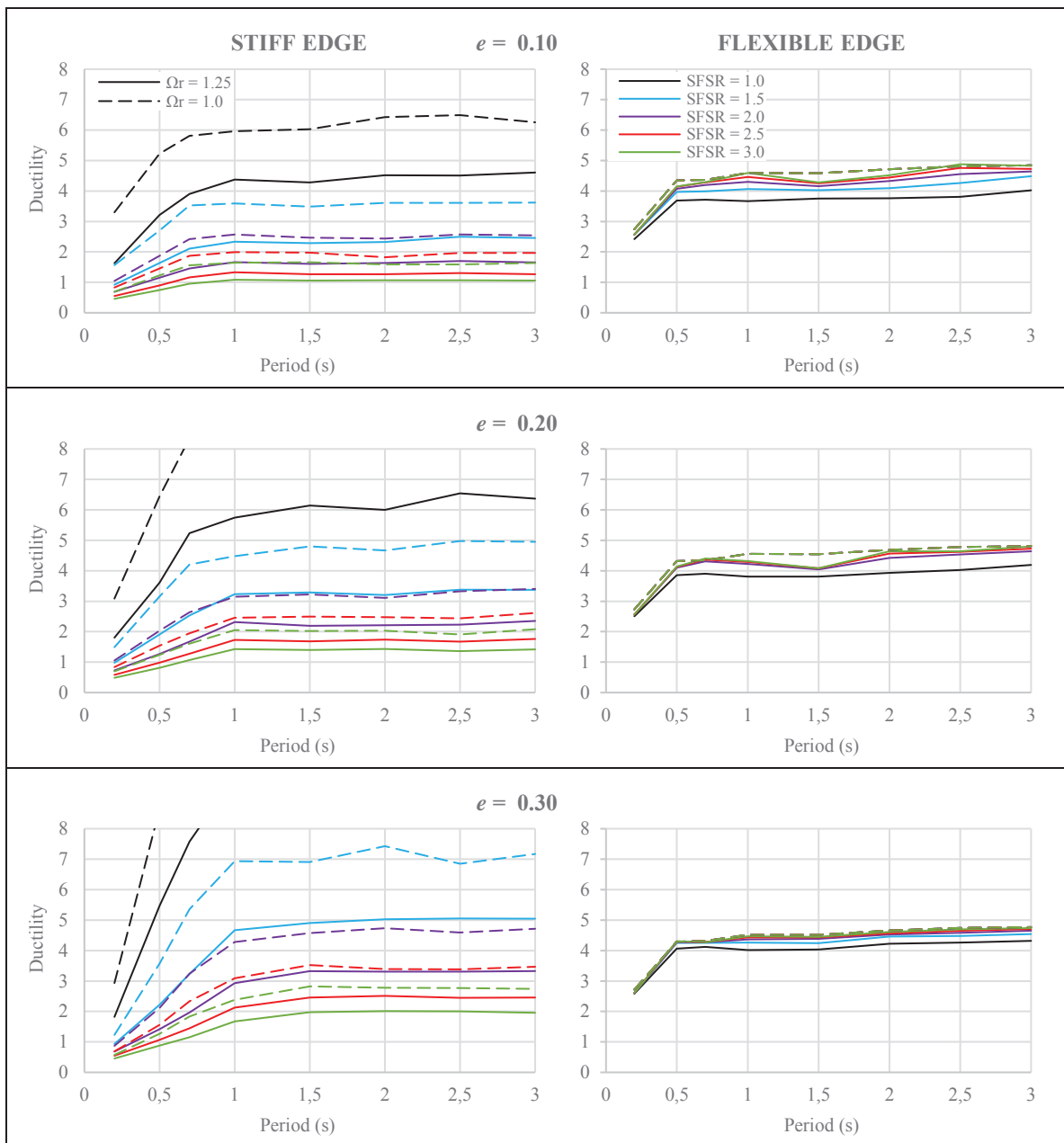
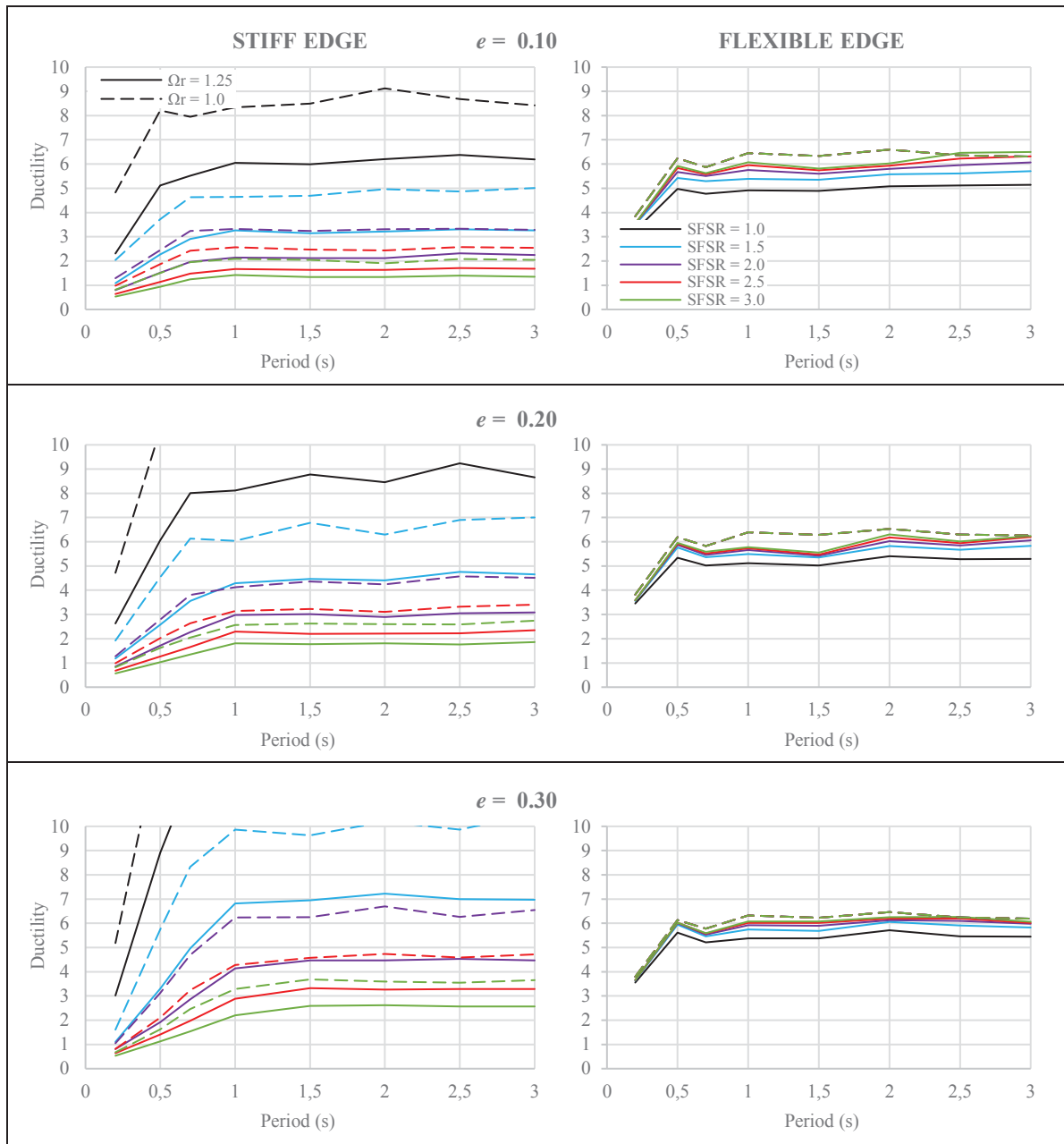
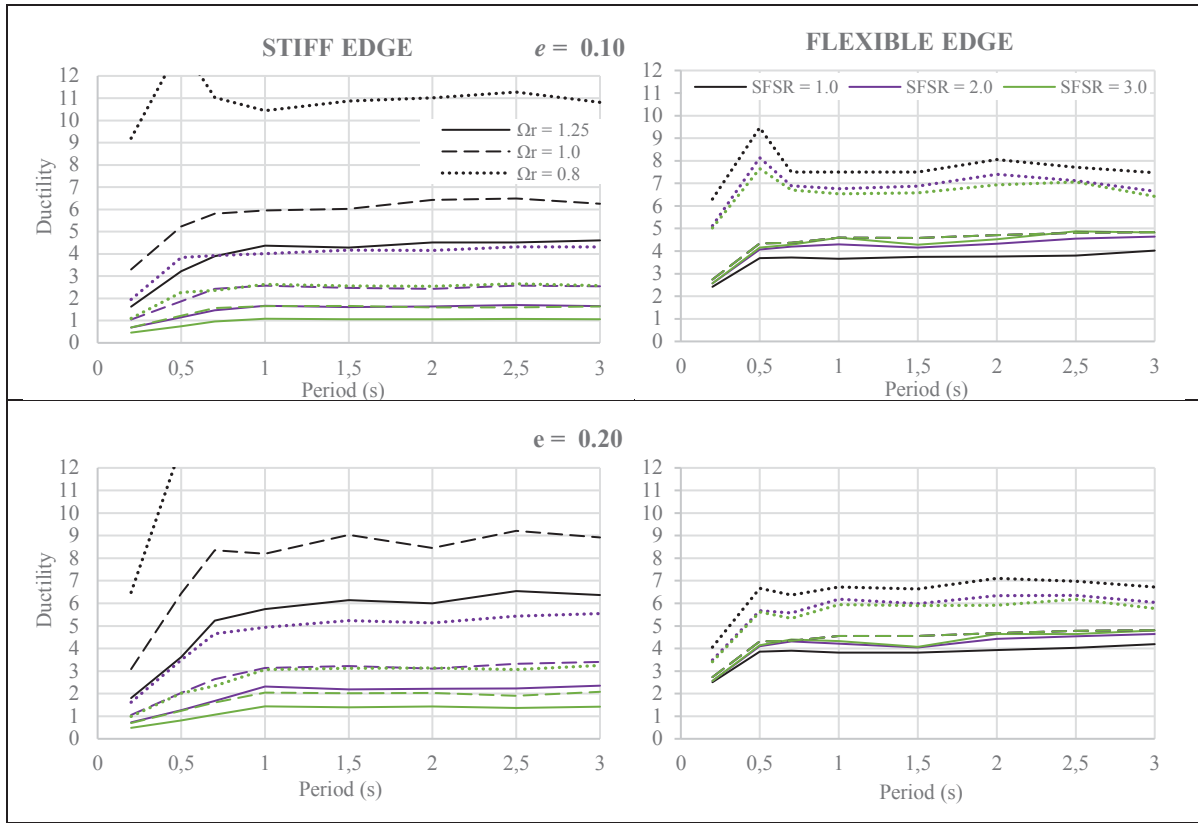


Figure 4: Torsional ductility spectra ( $R\mu = 4$ ).

Figure 5: Torsional ductility spectra ( $R\mu = 5$ ).

The effect of uncoupled frequency ratio is assessed comparatively for uncoupled rotational-to-translational frequency ratios of 1.25, 1.0 and 0.8. The results are presented in a separate figure (Figure 6) for  $R\mu = 4$ ,  $SFSR = 1.0, 2.0, 3.0$  and  $e = 0.1, 0.2$  combinations. It can be seen from Figure 6 that stiff edge ductilities are quite sensitive to increasing values of torsional flexibility whereas flexible edge ductilities are not affected considerably. As a general trend, stiff side ductility demands exhibit an increasing trend with decreasing frequency ratio. Hence, it could be concluded that the torsionally flexible systems display more non-uniform ductility distribution. This observation is consistent with the fact that modern earthquake codes which discourage or penalizes the design of torsionally flexible systems.

Figure 6: Sensitivity of the compiled spectra to uncoupled frequency ratio ( $R\mu = 4$ ).

### 3 ESTIMATION OF DUCTILITIES VIA TORSIONAL DUCTILITY SPECTRA

The torsional ductility spectra presented herein is a tool for estimating the ductility distribution of a 2DOF, 2-member system. In order to utilize the spectra set in performance assessment, more realistic structural systems having varying number of load resisting frames must be “transformed” to the schematic 2DOF system. In this section, a single-story shear frame having four load resisting members is investigated.

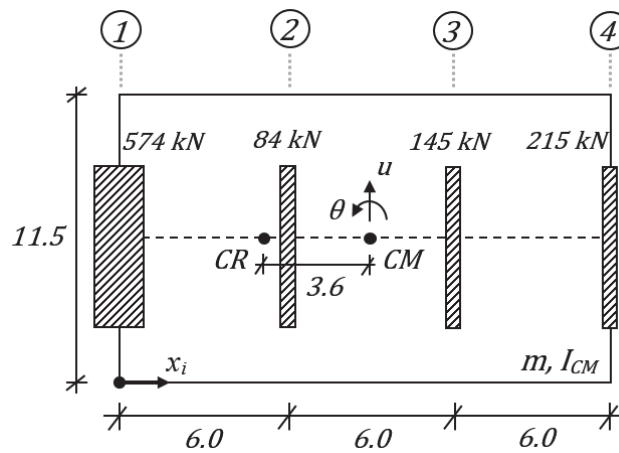


Figure 7: 4-member shear frame system.

The plan view of the 4-member shear frame is shown in Figure 7. The dimensions and related geometric properties of the system are selected such that they represent an actual structure. The rigid slab dimensions are 18 m by 11.5 meters, with a mass of 340 tons. Member 1 is 3.7 times more stiff than members 2, 3, and 4. Consequently, the system has  $e = 0.2$  static eccentricity towards member 1. The lateral stiffness values to the load resisting members are given such that modal vibration periods of  $T_1 = 0.7$  s,  $T_2 = 0.4$  s and uncoupled frequency ratio  $\Omega_r = 1.25$ . The system is designed under the same ASCE 7-16 [1] design spectrum used in parametric study with  $R \equiv R_\mu = 4$ . Since  $R \equiv R_\mu$ , no overstrength is considered for all members. The resulting strengths determined from design and corresponding force-deformation relationships of 4 members are given in Figure 8.

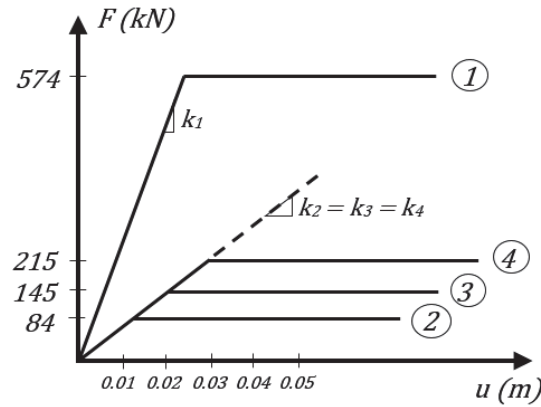


Figure 8: Force-deformation relationships of load resisting members.

All values related with the parametric systems  $[T_1, \Omega_r, e, R_\mu]$  except  $SFSR$  are obtained. Since  $SFSR$  defined within this study depends on single values of  $F_S$  and  $F_F$ , strength capacities of four members should be transformed. This could easily be achieved by satisfying the two equations of force equilibrium in Equation 6.  $x_i$  in Equation 6 is the location of frame  $i$  in the 4-Member system.

$$F_F = \frac{\sum_i (F_i \cdot x_i)}{L}; \quad F_S = (\sum_i F_i) - F_F \quad (6)$$

Using frame strengths and their respective locations in Equation 6,  $F_F = 340$  kN and  $F_S = 678$  kN. Therefore,  $SFSR$  is calculated as 2.0. Since all parameters of the structural system is now known, corresponding Torsional Ductility Spectra given in Figure 4 with associated parameters of  $T_1 = 0.7$  s,  $\Omega_r = 1.25$ ,  $e = 0.2$ ,  $R_\mu = 4$  and  $SFSR = 2.0$  can be used to obtain the estimated ductilities. From the related chart, stiff edge ductility is read as  $\mu_S = 1.7$ , whereas flexible edge ductility is read as  $\mu_F = 4.3$ .

In order to verify the accuracy of this estimation, actual nonlinear performance of the shear frame should be determined. Nonlinear response history analyses (NRHA) are performed on the shear frame system using the ground motion set given in Table 2. Load resisting members are defined with elastic-perfectly plastic hysteretic relationships in OpenSees Platform [24] using the yield force and deformation parameters given in Figure 8. Mean maximum inelastic member displacements are obtained from the dynamic analyses under the ground motion set and corresponding member ductility ratios are computed. Mean member displacements, member yield deformations shown in Figure 8 and corresponding member ductility ratios are given in Equation 7.

$$\begin{array}{l}
\text{Member 1:} \\
\text{Member 2:} \\
\text{Member 3:} \\
\text{Member 4:}
\end{array}
\quad \underline{\mu}_{NRHA} = \begin{Bmatrix} 0.039 \\ 0.055 \\ 0.096 \\ 0.145 \end{Bmatrix} \quad \underline{\mu}_y = \begin{Bmatrix} 0.0241 \\ 0.0129 \\ 0.0224 \\ 0.0331 \end{Bmatrix} \quad \mu_{NRHA} = \begin{Bmatrix} 1.6 \\ 4.3 \\ 4.3 \\ 4.4 \end{Bmatrix} \quad (6)$$

In order to compare the computed ductility ratios with estimations from the Torsional Ductility Spectra, members located at stiff and flexible sides of the shear frame system should be determined. This can be done by inspecting Figure 7 in a fairly straightforward manner. Member 1 is at the stiff side of the shear frame structure with respect to center of rigidity (*CR*); whereas members 2-4 are at the flexible side. Hence, comparison of ductilities estimated from Torsional Ductility Spectra and dynamic analyses can be made accordingly.

Upon comparing the estimation with the dynamic response, a close match can be seen. Mean member ductility ratios obtained from NRHA are seemingly close to the ductility estimations for both sides given by the associated spectrum. It should be noted here that ductility ratios of flexible side members are determined to be close to the imposed value of  $R_\mu = 4$ . On the other hand, mean ductility ratio of the stiff side member is considerably smaller than other members as well as imposed  $R_\mu$ . In practice, significant overstrength is expected to be present in the stiff side member due to factors such as seismic detailing and relationship between strength and stiffness. Therefore, the ductility imbalance shown here is expected to further increase in the case of a more realistic case study structure.

#### 4 SUMMARY AND CONCLUSIONS

Torsional Ductility Spectra as a tool for estimating ductilities and their distribution among asymmetric-plan systems are presented in this study. Basic 2DOF 2-member parametric systems are utilized and through a parametric study considering stiffness eccentricity, frequency ratio, ductility reduction factor, fundamental period and strength ratio, system ductilities are compiled in a spectrum format. Last parameter in question, stiff to flexible strength ratio (*SFSR*) is introduced to the systems such that flexible side members are kept at their nominal strengths whereas overstrength is introduced in stiff side members. By doing so, effect of inherent overstrength present in stiff structural elements to ductility distribution is clearly visualized in charts.

The ductility estimation performance of the spectra set is assessed by utilizing a 4-member shear frame system. Upon designing the system and performing inelastic dynamic analyses, computed mean ductilities are compared with chart estimations. In general, the Torsional Ductility Spectra estimates the expected ductilities of the shear frame members fairly well.

Some observations are also performed on the spectra trends. While flexible side members attain ductilities around imposed ductility reduction factors, this may not be the case for stiff side members especially when overstrength is present. Moreover, it is determined that increasing amount of torsional flexibility have a negative effect in ductility distribution of asymmetric-plan systems.

The proof of concept presented herein and the simple verification with respect to shear frame behaviour are considered as the first phase of the study. As part of the ongoing research, the spectra set defined in this study is to be verified further by computing the ductility distribution of a multi-story, actual asymmetric-plan systems and assessing the estimation performance of Torsional Ductility Spectra.

## REFERENCES

- [1] American Society of Civil Engineers, *Minimum Design Loads for Buildings and Other Structures (ASCE/SEI 7-16)*, 2016.
- [2] European Committee for Standardization, *EN 1998-1 Eurocode 8: Design of structures for earthquake resistance*, 2004.
- [3] A. Rutenberg, Nonlinear response of asymmetric building structures and seismic codes: A state of the art review, in *Nonlinear Seismic Analysis and Design of Reinforced Concrete Buildings*, P. Fajfar, H. Krawinkler eds., Elsevier Publishers, London, 1992.
- [4] A. Rutenberg, Behaviour of irregular and complex structures asymmetric structures – progress since 1998. *Proceedings of the 12th European Conference on Earthquake Engineering*, London, United Kingdom, 2002.
- [5] M. De Stefano, B. Pintucchi, A review of research on seismic behavior of irregular structures since 2002. *Bulletin of Earthquake Engineering*, **6**, 285-308, 2008.
- [6] S.A. Anagnostopoulos, M.T. Krykos, K.G. Stathopoulos, Earthquake induced torsion in buildings: critical review and state of the art. *Earthquakes and Structures*, **121**(2), 305-377, 2015
- [7] C.L. Kan, A.K. Chopra, Torsional coupling and earthquake response of simple elastic and inelastic systems. *Journal of the Structural Division, ASCE*, **107**, 1569-1588, 1981.
- [8] A.M. Chandler, G.L. Hutchinson, Torsional coupling effects in the earthquake response of asymmetric buildings. *Engineering Structures*, **8**, 222-236, 1986.
- [9] A. Rutenberg, M. Eisenberger, G. Shohet, Reducing seismic ductility demand in asymmetric shear buildings. *Proceedings of the 8<sup>th</sup> European Conference on Earthquake Engineering*, Lisbon, Portugal, 1986.
- [10] A. Rutenberg, M. Eisenberger, G. Shohet, Inelastic seismic response of code designed single storey asymmetric structures. *Engineering Structures*, **14**(2), 91–102, 1992.
- [11] R. Goel, A.K. Chopra, Effects of plan asymmetry in inelastic seismic response of one-story systems. *ASCE Journal of Structural Engineering*, **117**, 1492-1513, 1991.
- [12] R. Goel, A.K. Chopra, Dual-level approach for seismic design of asymmetric-plan buildings. *Journal of the Structural Division, ASCE*, **120**(1), 161-179, 1994.
- [13] A.M. Chandler, X.N. Duan, Performance of asymmetric code-designed buildings for serviceability and ultimate limit states. *Earthquake Engineering and Structural Dynamics*, **26**, 717-735, 1997
- [14] T. Paulay, A behaviour based design approach to earthquake induces torsion, in *Seismic Methodologies for the Next Generation of Codes*, P. Fajfar and H. Krawinkler eds., Balkema, Rotterdam, 1997.
- [15] B. Myslimaj, W.K. Tso, A design oriented approach to strength distribution in single-story asymmetric systems with elements having strength-dependent stiffness. *Earthquake Spectra*, **21**(1), 197-212, 2005.
- [16] T. Paulay, Torsional mechanisms in ductile building systems. *Earthquake Engineering and Structural Dynamics*, **27**, 1101–1121, 1998.



- [17] J.L. Humar, P. Kumar, Effect of orthogonal in plane structural elements on inelastic torsional response. *Earthquake Engineering and Structural Dynamics*, **28**, 1071–1097, 1999.
- [18] J.L. Humar, P. Kumar, A new look at the torsion design provisions in seismic building codes. *Proceedings of the 12<sup>th</sup> World Conference on Earthquake Engineering*, Auckland, New Zealand, 2000.
- [19] K.G. Stathopoulos, S.A. Anagnostopoulos, Accidental design eccentricity: Is it important for the inelastic response of buildings to strong earthquakes? *Soil Dynamics and Earthquake Engineering*, **30**(9), 782–797, 2010.
- [20] M. De Stefano, E.M. Marino, P.P. Rossi, Effect of Overstrength on the Seismic Behaviour of Multi-Storey Regularly Asymmetric Buildings. *Bulletin of Earthquake Engineering*, **4**(1), 23–42, 2006.
- [21] K. Kaatsız, H. Sucuoğlu, The role of overstrength on the seismic performance of asymmetric-plan structures. *Earthquake Engineering and Structural Dynamics*, **48**, 412–431, 2019.
- [22] J. Hancock, J. Watson-Lamprey, N.A. Abrahamson, J.J. Bommer, A. Markatis, E. McCoy, R. Mendis, Improved method of matching response spectra of recorded earthquake ground motion using wavelets. *Journal of Earthquake Engineering*, **10**, 67–89, 2006.
- [23] PEER Ground Motion Database available from: <http://ngawest2.berkeley.edu>, 2020.
- [24] Open System for Earthquake Engineering Simulation, available from: <http://open-sees.berkeley.edu>, 2020.

## A MULTI-OBJECTIVE DISPLACEMENT-BASED DESIGN PROCEDURE OF VISCOUS AND HYSTERETIC DAMPED BRACES FOR THE SEISMIC PROTECTION OF RC BUILDINGS

Fabio Mazza<sup>1</sup> and Carlo Pasceri<sup>2</sup>

<sup>1</sup> Dipartimento di Ingegneria Civile, Università della Calabria  
87036, Rende (Cosenza), Italy  
e-mail: fabio.mazza@unical.it

<sup>2</sup> Dipartimento di Ingegneria Civile, Università della Calabria  
87036, Rende (Cosenza), Italy  
e-mail: carlopasceri@libero.it

**Keywords:** RC Framed Buildings, Dual Hysteretic-Viscous Damped Braces, Dual Hysteretic-Hysteretic Damped Braces, Two-Level Displacement-Based Design Procedure.

**Abstract.** *The use of hysteretic damped braces (HYDBs) is an effective and low-cost solution for the seismic retrofitting of reinforced concrete (RC) framed structures. However, notable damage to nonstructural elements can be observed at the serviceability design earthquake (SDE), when too high activation forces of the HYDBs are designed in order to attain structural safety (SS) performance level at the basic (BDE) and/or maximum considered (MCE) earthquakes. On the other hand, HYDBs designed at the immediate occupancy (IO) performance level prevent nonstructural damage of MIs under SDE but may collapse and/or induce structural damage for high intensity seismic loads, due to their early activation which renders them unable to develop large energy dissipation. Aim of this work is the proposal of a multi-objective displacement-based design procedure, where viscous damped braces (VDBs) and HYDBs calculated for IO at the SDE are combined with HYDBs ensuring SS at the MCE. A six-storey RC framed structure, representative of the residential building stock in Italy prior to the 2008-2018 code changes, is to be retrofitted in a high risk-seismic region supposing that is preliminarily designed in L'Aquila (Italy) for moderate seismic loads. The OpenSEES platform is considered for the nonlinear dynamic analysis of the original and retrofitted structures. RC frame members are modelled with lumped plasticity elements while the shear behaviour of the beam-column joints is modelled by means of a scissor model. Masonry infills uniformly distributed in elevation are modelled with a simplified diagonal pin-jointed strut model taking into account the in-plane failure modes. HYDBs are modelled with truss elements characterized by a bilinear force-displacement law, without considering the flexibility of the supports, while nonlinear force-velocity law is considered for VDBs. Nonlinear dynamic analysis is carried out considering three stripes of real records, corresponding to the SDE, BDE and MCE seismic levels assumed in the current Italian code.*

## 1 INTRODUCTION

The use of hysteretic damped braces (HYDBs), based on a plastic deformation mechanism (e.g. axial, bending, shear, torsion) or a combination of some of them, represents an effective and low-cost solution for the seismic retrofitting of reinforced concrete (RC) framed structures [1]. However, notable damage to non-structural elements (e.g. masonry infills, false ceilings and suspended piping) can be observed at the serviceability design earthquake (SDE), when too high activation forces of the HYDBs are considered in order to improve structural performance level at the basic (BDE) and maximum considered (MCE) earthquakes [2, 3]. To overcome this problem, dampers working as fuses can be inserted as sacrificial elements in order to prevent damage of non-structural elements [4], by means of an in-parallel combination of different typologies of dampers [5, 6], or alternatively damping and stiffness properties of dampers arranging in-series minor and major cores can be modulated to different seismic intensity levels [7]. A multi-objective design procedure is proposed in the present work, where viscous (VDBs) and hysteretic (HYDBs) damped braces calculated for immediate occupancy (IO), at SDE, are combined with HYDBs ensuring structural safety (SS), at MCE. To this end, a displacement-based design procedure already proposed in previous works [8-10] is applied, also including the loss of capacity of the existing structure due to previous seismic damage [11-12].

A six-storey RC framed building, representative of the Italian residential housing stock during the 1990s in a medium-risk seismic zone, is assumed as test structure for the numerical investigation [13]. This structure is supposed to be retrofitted by inserting HYDBs and VDBs to attain IO (e.g. no damage to masonry infills, MIs, at SDE) and SS (e.g. limited damage to structural elements at BDE and collapse prevention of HYDBs at MCE) performance levels imposed by current Italian seismic code (NTC18) in a high-risk seismic zone [14]. Specifically, five structural arrangements of damped braces are compared: only HYDBs designed at MCE; in-parallel combination of VDBs and HYDBs designed at SDE and MCE, respectively, possibly with gap-hook elements acting in series with the HYDBs so as to delay their activation at SDE; in-parallel and in-series combinations of small and large HYDBs designed at SDE and MCE, respectively, without and with a gap-hook element positioned in parallel with the small HYDBs, so as to stop their deformation at MCE. Nonlinear dynamic multi-stripe analyses of the original and retrofitted structures are carried out with the OpenSees code [15], considering three different set of records selected and scaled in line with SDE, BDE and MCE intensity levels provided by NTC18 [16]. Brittle and failure mechanisms of the original structure are modelled, considering: a lumped plasticity model for RC frame members, with flexure- or shear-controlled moment-chord rotation at the critical end sections; a scissor model with rigid offsets for shear behaviour of the beam-column joints; a diagonal pin-jointed strut model for MIs, taking into account their in-plane failure modes.

## 2 DISPLACEMENT-BASED DESIGN PROCEDURE OF DAMPED BRACES

A multistep iterative Displacement-Based Design (DBD) procedure of HYDBs, proposed in previous works [8-10], is extended for the seismic retrofitting of RC framed structures with dual hysteretic-viscous and hysteretic-hysteretic damped braces designed at both SDE and MCE, with or without a gap-hook element to avoid activation of small and large dampers at MCE and SDE, respectively.

As first step, the pushover curve of the original structure ( $V-d$ ) is converted to that of an equivalent SDOF system ( $V^*-d^*$ ) and a piecewise linear fit of the initial backbone curve is determined by an ensemble of  $N$  pairs of bilinear elastic-perfectly plastic and elastic-softening damage laws [12]. Then, the damaged backbone curve that envelopes the hysteretic behaviour

of the equivalent SDOF system subjected to seismic loads is evaluated from nonlinear dynamic analysis of the combined plastic-damage hysteretic model. The monotonic and cyclic deterioration of plastic and damage mechanisms is described by a damage loading index  $\Psi$  [11], expressed as function of an ever-increasing curve whose shape depends on a degradation rate parameter (e.g.  $\varepsilon=0.5$ ). A weighting coefficient (e.g.  $C_{wc}=0.25$ ) distinguishes the effect of displacements less or greater than the previous maximum values ( $d_{max}^*$ ) in the same loading direction, while a damage coupling parameter (e.g.  $C_{cd}=0.5$ ) accounts for the influence of the energy dissipation under positive and negative forces on negative and positive values of the loading variable. Finally, the hysteretic energy dissipation of the degraded frame ( $\xi_{h,F}$ ) and the effective stiffness ( $K_{e,F}$ ) related to the performance displacement ( $d_p^*$ ) can be evaluated, while elastic viscous damping of the framed structure (e.g.  $\xi_{v,F}=5\%$ ) can be assigned (Figure 1a).

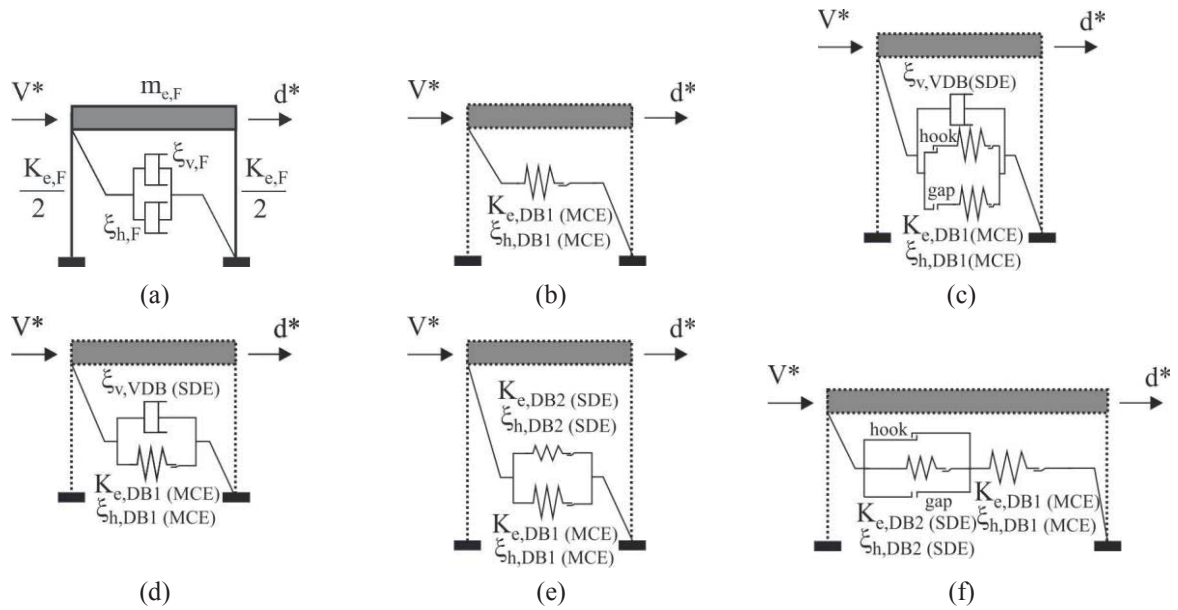


Figure 1. SDOF systems equivalent to the original structure (a), hysteretic (b) and dual hysteretic-viscous (c, d) and hysteretic-hysteretic (e, f) damped braces.

In order to design hysteretic (Figure 1b) and dual hysteretic-viscous (Figures 1c,d) and hysteretic-hysteretic (Figures 1e,f) damped braces at MCE, an iterative procedure is implemented in the acceleration-displacement response spectrum (ADRS) shown in Figure 2, where the bilinear capacity curve of the original structure is represented with a solid blue line. An initial value of the equivalent viscous damping ratio of the damped braced frame (i.e.  $\xi_{e,DBF} > \xi_{v,F} + \xi_{h,F}$ ) is tentatively assumed at the selected performance displacement ( $d_p^*$ ) corresponding to MCE, starting from 5% damped spectrum (solid black line). Then, effective vibration period ( $T_{e,DBF,MCE}$ ) of the retrofitted structure is determined on the reduced ADRS spectrum (dashed black line), starting from the trial performance point corresponding to the target displacement value, so allowing the calculation of effective stiffness  $K_{e,DB}(=K_{e,DBF}-K_{e,F})$  of the equivalent DB at MCE (i.e. DB1). Once ductility demand ( $\mu_{DB1}$ ) and hardening ratio ( $r_{DB1}$ ) of DB1 are assigned, it is possible to calculate the bilinear capacity curve of the damped brace (solid red line in Figure 2) and its viscous damping ( $\xi_{h,DB1}$ ) equivalent to the hysteretic energy dissipation:

$$\xi_{h,DB1}^{(MCE)} (\%) = 63.7 \frac{(\mu_{DB1} - 1) \cdot (1 - r_{DB1})}{\mu_{DB1} [1 + r_{DB1} \cdot (\mu_{DB1} - 1)]} \quad (1)$$

Finally, an updated value of the equivalent viscous damping of the retrofitted structure can be evaluated, being  $V_{p,F}^*$  and  $V_{p,DB1}^*$  strength values of the original frame and damped brace at  $d_p^*$ , respectively:

$$\zeta_{e,DBF}^{(MCE)}(\%) = \zeta_{v,F} + \frac{\zeta_{h,F}^{(MCE)} \cdot V_{p,F}^{*(MCE)} + \zeta_{h,DB1}^{(MCE)} \cdot V_{p,DB1}^{*(MCE)}}{V_{p,F}^{*(MCE)} + V_{p,DB1}^{*(MCE)}} \quad (2)$$

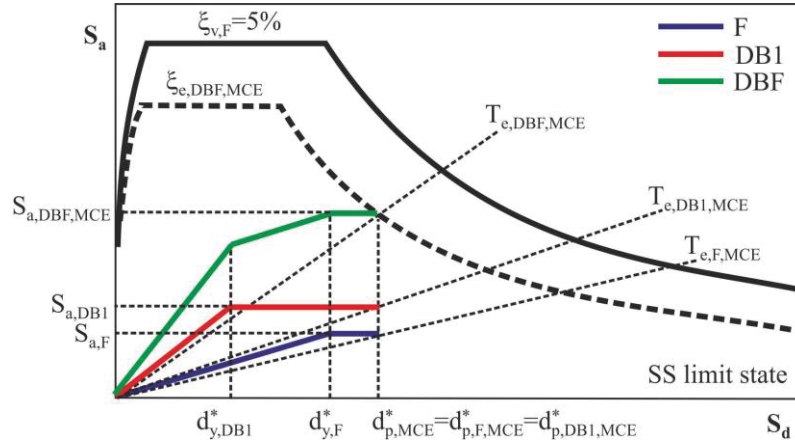


Figure 2. Design procedure of the hysteretic and dual hysteretic-viscous and hysteretic-hysteretic damped braces in the acceleration-displacement response spectrum at MCE.

In a similar way, viscous (Figures 1c,d) and hysteretic (Figure 1e) dampers at SDE, in parallel with the hysteretic damped brace previously designed at MCE (DB1), may be evaluated with an iterative process in the ADRS corresponding to SDE (Figure 3). At this point, the admitted target displacement ( $d_{p,SDE}^*$ ) and first equivalent viscous damping ratio ( $\zeta_{e,DBF,SDE}$ ) of the retrofitted structure will be considered in the evaluation of effective vibration period ( $T_{e,DBF,SDE}$ ) corresponding to dashed black line in Figure 3. Keeping in mind that the effective stiffness of DB1 is already known from the bilinear capacity curve corresponding to  $d_{p,SDE}^*$ , the effective stiffness ( $K_{e,DB1}$ ) of the additional damper (e.g. hysteretic in Figure 1e) for small deformation (DB2) can be determined by a simple subtraction ( $K_{e,DB2} = K_{e,DBF} - K_{e,DB1} - K_{e,F}$ ). It is worth highlighting that contribution of DB1 disappears when it is attached in series to a gap-hook element (Figure 1c), so avoiding its action at SDE.

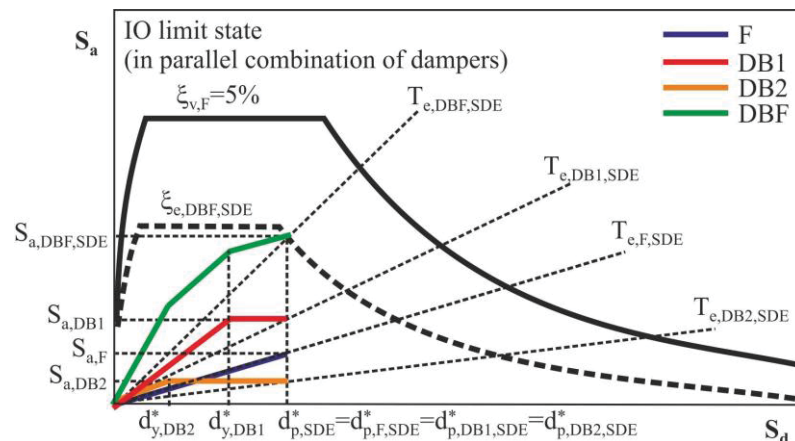


Figure 3. Design procedure of the in-parallel hysteretic-viscous and hysteretic-hysteretic damped braces in the acceleration-displacement response spectrum at SDE.

Once viscous damping equivalent to the hysteretic energy dissipation of DB2 is evaluated ( $\zeta_{h,DB2}$ ) as function of the assigned values of  $\mu_{DB2}$  and  $r_{DB2}$  (see Equation (1)), an updated val-



ue of the equivalent viscous damping can be obtained for the retrofitted structure

$$\zeta_{e,DBF}^{(SDE)}(\%) = \zeta_{v,F} + \frac{\zeta_{h,F}^{(SDE)} \cdot V_{p,F}^{*(SDE)} + \zeta_{h,DB1}^{(SDE)} \cdot V_{p,DB1}^{*(SDE)} + \zeta_{h,DB2}^{(SDE)} \cdot V_{p,DB2}^{*(SDE)}}{V_{p,F}^{*(SDE)} + V_{p,DB1}^{*(SDE)} + V_{p,DB2}^{*(SDE)}} \quad (3)$$

depending on strength values, at the performance displacement  $d_{p,SDE}^*$ , for the original frame ( $V_{p,F}^*$ ) and hysteretic DB1 ( $V_{p,DB1}^*$ ) and DB2 ( $V_{p,DB2}^*$ ). Moreover, the expression

$$\zeta_{e,DBF}^{(SDE)}(\%) = \zeta_{v,F} + \zeta_{VDB}^{(SDE)} + \frac{\zeta_{h,F}^{(SDE)} \cdot V_{p,F}^{*(SDE)} + \zeta_{h,DB1}^{(SDE)} \cdot V_{p,DB1}^{*(SDE)}}{V_{p,F}^{*(SDE)} + V_{p,DB1}^{*(SDE)}} \quad (4)$$

corresponds to viscous damped brace (VDB) at small deformation combined with DB1 at large deformation (Figure 1d), with the further simplification

$$\zeta_{e,DBF}^{(SDE)}(\%) = \zeta_{v,F} + \zeta_{VDB}^{(SDE)} + \zeta_{h,F}^{(SDE)} \quad (5)$$

when DB1 is also combined with a gap-hook mechanism (Figure 1c).

As an alternative, in-series combination of hysteretic-hysteretic dampers (Figure 1f) may be considered adopting the iterative design process described in the ADRS corresponding to SDE (Figure 4), where the gap-hook mechanism acts as a very stiff end-stroke stopper that limits deformations of DB2 at the SDE threshold while ensuring that the energy dissipation at MCE is entrusted to DB1. This time, a starting value of the displacement of DB1 ( $d_{p,DB1}^*$ ) is tentatively assumed at the selected performance displacement ( $d_p^*$ ) at SDE, such to obtain as difference the displacement of DB2 ( $d_{p,DB2}^* = d_p^* - d_{p,DB1}^*$ ). Effective stiffness of both dampers (DB1+DB2) can be evaluated as function of the strength  $V_{p,DB1}^* (= V_{p,DB2}^*)$  corresponding to  $d_{p,DB1}^*$

$$K_{e,DB1}^{(SDE)} = \frac{V_{p,DB1}^{*(SDE)}}{d_{p,DB1}^{*(SDE)}}, K_{e,DB2}^{(SDE)} = \frac{V_{p,DB1}^{*(SDE)}}{d_{p,DB2}^{*(SDE)}} \quad (6a,b)$$

and from these ones the total stiffness

$$K_{e,DBF}^{(SDE)} = K_{e,F}^{(SDE)} + \frac{K_{e,DB1}^{(SDE)} \cdot K_{e,DB2}^{(SDE)}}{K_{e,DB1}^{(SDE)} + K_{e,DB2}^{(SDE)}} \quad (7)$$

and effective period ( $T_{e,DBF,SDE}$ ) of the retrofitted structure are derived. In order to determine the corresponding equivalent viscous damping ratio  $\xi_{e,DBF,SDE}$ , curve passing through the trial performance point is drawn in Figure 4 (solid green line).

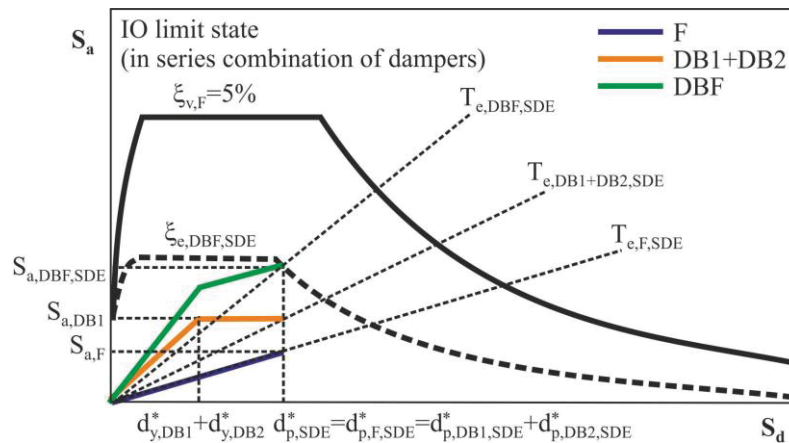


Figure 4. Design procedure of the in-series hysteretic-hysteretic damped braces in the acceleration-displacement response spectrum at SDE.



On the other hand, equivalent viscous damping ratio is analytically evaluated with the expression

$$\zeta_{e,DBF}^{(SDE)}(\%) = \zeta_{v,F} + \frac{\zeta_{h,F}^{(SDE)} \cdot V_{p,F}^{*(SDE)} + \frac{(\zeta_{h,DB1}^{(SDE)} \cdot d_{p,DB1}^{*(SDE)} + \zeta_{h,DB2}^{(SDE)} \cdot d_{p,DB2}^{*(SDE)}) \cdot V_{p,DB1}^{*(SDE)}}{d_{p,DB1}^{*(SDE)} + d_{p,DB2}^{*(SDE)}}}{V_{p,F}^{*(SDE)} + V_{p,DB1}^{*(SDE)}} \quad (8)$$

and an iterative process is triggered until graphical and analytical values are the same.

Finally, vertical distributions of the (elastic) lateral stiffness of the HYDBs and damping coefficients of the nonlinear VDBs are evaluated proportionally to the interstorey drift and design storey shear of the original structure, respectively. Further information is contained in previous papers [8, 17], which complete the necessary detailing of the work.

### 3 ORIGINAL AND RETROFITTED TEST STRUCTURES

A six-storey RC framed structure (Figure 5a), representative of the residential buildings constructed in Italy during the 1990s, is selected from the RINTC project [13]. It is located in L'Aquila and designed as bare frame for a medium-risk zone, in line with provisions of the Italian code DM86 [18], assuming concrete with cylindrical compressive strength of 25 MPa and steel reinforcement with yield strength of 430 MPa. Columns with rectangular cross-section, oriented as shown in Figure 5b, are tapered along the height, considering:  $0,3 \times 0,6 \text{ m}^2$  at the first two levels;  $0,30 \times 0,5 \text{ m}^2$  at the third and fourth levels;  $0,3 \times 0,4 \text{ m}^2$  at the fifth and roof levels. The structure has deep beams along the perimeter and in the knee configuration of the staircase, with cross section  $0,3 \times 0,6 \text{ m}^2$  at the first two levels and  $0,3 \times 0,5 \text{ m}^2$  at the other four levels, while flat beams are considered for all internal frames, with cross-section  $0,6 \times 0,25 \text{ m}^2$  and  $0,8 \times 0,25 \text{ m}^2$  (the latest marked with an asterisk in Figure 5b). Masonry infills with a double leaf (0,08 m, external layer, and 0,12 m, internal layer) of hollow clay bricks are uniformly distributed along the height, with a percentage of openings depending on the in-plan architectural layout: i.e. 0%, MI.B in brown; 22%, MI.Y in yellow; 40%, MI.O in orange; 100%, MI.G in green. Further details can be found in [13].

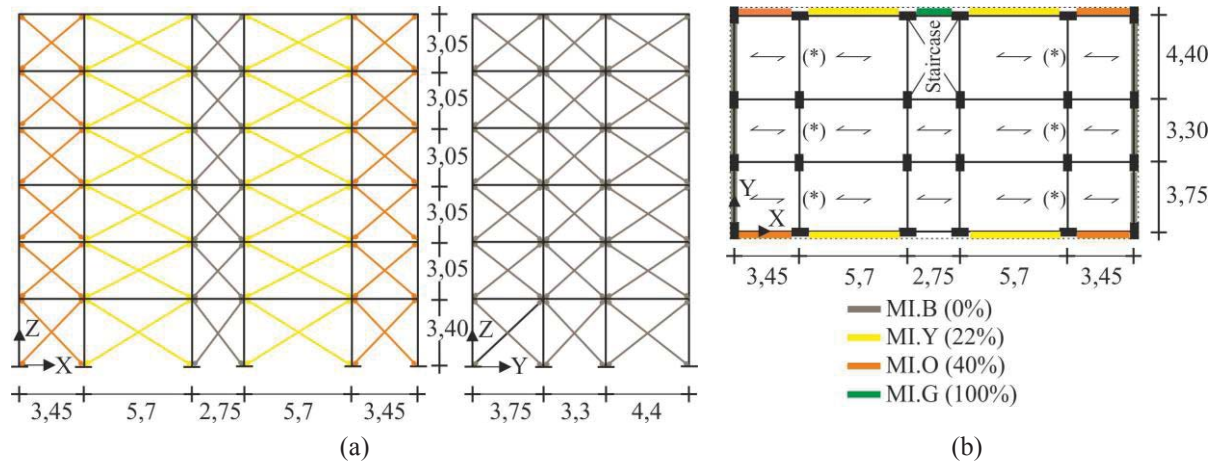


Figure 5. Original test structure (unit in m).

The seismic retrofitting of the original test structure is carried out by the insertion of chevron damped braces, with vertical distribution and in-plan arrangement shown in Figures 6a and 6b, respectively. Five structural configurations of damped braces are compared: i.e. HYDBs designed at MCE (Figure 6b); two in-parallel combinations of VDBs and HYDBs

designed at SDE and MCE, respectively, with (Figure 6c) and without (Figure 6d) gap-hook elements attached in series with HYDBs; in-parallel and in-series combinations of small and large HYDBs designed at SDE and MCE, respectively, without (Figure 6e) and with (Figure 6f) gap-hook elements attached in parallel with the small HYDBs. The deformability of the supporting chevron steel braces is not considered (i.e.  $K_B \rightarrow \infty$ ), so that lateral stiffnesses of the HYDB ( $K_{DB}$ ) and HYD ( $K_D$ ) are assumed equal; this is also for the corresponding stiffness hardening ratios (i.e.  $r_{DB}=r_D$ ). With regard to the VDB, the force developed in the damper is function of a damping exponent  $\beta=0.7$ , which corresponds to nonlinear viscous property.

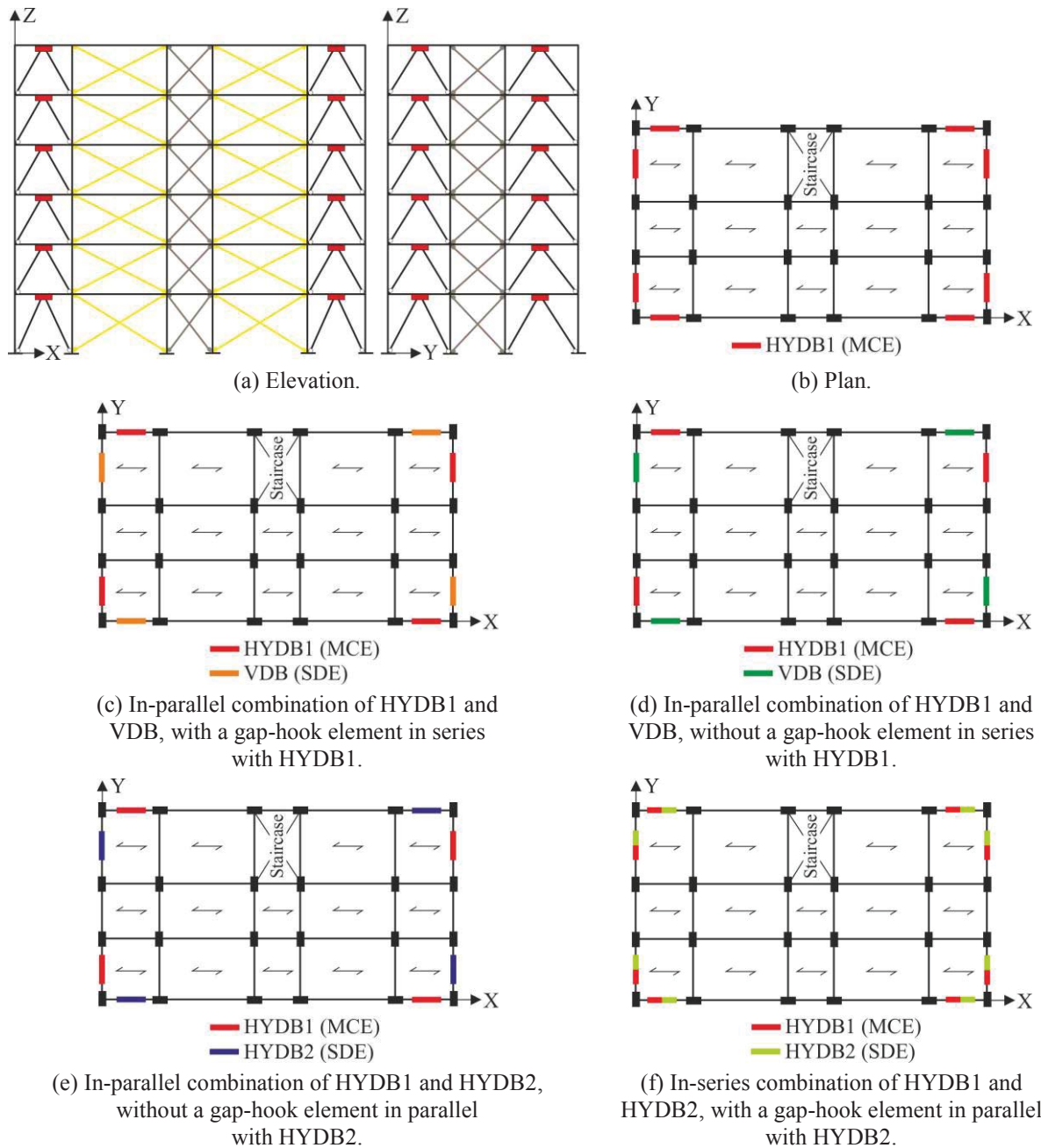


Figure 6. Retrofitted test structures.

Thirteen structural layouts are obtained combining above described five configurations of damped braces with: three ultimate performance levels in terms of top displacement (i.e.

$d_{p,X,MCE}=0,093$  m, 0,14 m and 0.184 m and  $d_{p,Y,MCE}=0,093$  m and 0,14 m), associated with different structural damage scenarios in terms of inter-storey drift ratio (i.e.  $\Delta_X/h=0.5\%$ ,  $0.75\%$  and  $1\%$  and  $\Delta_Y/h=0.5\%$  and  $0.75\%$ ); one serviceability target displacement (i.e.  $d_{p,X,SDE}=0,019$  m and  $d_{p,Y,SDE}=0,042$  m), corresponding to the attainment of the minimum value of peak lateral strength in the masonry infills of each storey, so preventing non-structural damage. Constant design values of damper ductility (i.e.  $\mu_D=5$ ) and hardening ratios (i.e.  $r_F=0\%$  and  $r_D=3\%$ ) are also assumed, except for the in-series arrangement of HYDBs. Main parameters of the equivalent damped braces along the in-plan principal directions are reported in Tables 1-5, with reference to: HYDB1 at MCE (Table 1); in-parallel combination of HYDB1 and VDB at SDE (Table 2); VDB at SDE (Table 3); in-parallel combination of HYDB1 and HYDB2 at SDE (Table 4); in-series combination of HYDB1 and HYDB2 at SDE (Table 5).

Dir.	$d_{p,MCE}^*$	$d_{y,DB1}^*$	$K_{e,F}$	$K_{e,DB1}$	$V_{p,F}^*$	$V_{p,DB1}^*$	$T_{e,F}$	$T_{e,DBF}$	$\xi_{v,F}$	$\xi_{h,F}$	$\xi_{h,DB1}$	$\xi_{e,DBF}$
X	0,072	0,014	23290	14953	1666	1069	1,31	1,03	5	12,00	44,13	29,56
	0,107	0,022	7877	7308	847	785	2,26	1,63	5	14,14	44,13	33,58
	0,143	0,029	2364	4998	338	715	4,13	2,34	5	15,34	44,13	39,84
Y	0,071	0,014	26465	13737	1875	973	1,22	0,99	5	11,73	44,13	27,80
	0,106	0,021	969	10349	103	1101	6,37	1,87	5	14,90	44,13	46,63
	0,106	0,021	969	10349	103	1101	6,37	1,87	5	14,90	44,13	46,63

Table 1. Properties of the SDOF system equivalent to the DBF at MCE: HYDB1 (units in m, kN and s).

Dir.	$d_{p,SDE}^*$	$K_{e,F}$	$V_{p,F}^*$	$T_{e,F}$	$T_{e,DBF}$	$\xi_{v,F}$	$\xi_{v,DB}$	$\xi_{e,DBF}$
X	0,015	57274	851	0,838	0,838	5	42,37	47,37
Y	0,032	62923	1996,69	0,791	0,791	5	0,21	5,21

Table 2. Properties of the SDOF system equivalent to the DBF at SDE: VDB (units in m, kN and s).

Dir.	$d_{p,MCE}^*$	$d_{p,SDE}^*$	$K_{e,F}$	$K_{e,DB1}$	$V_{p,F}^*$	$V_{p,DB1}^*$	$T_{e,F}$	$T_{e,DBF}$	$\xi_{v,DB}$	$\xi_{h,DB1}$	$\xi_{e,DBF}$
X	0,072	0,015	57273	28081	850	953	0,84	0,69	13,51	2,25	19,69
	0,107			16375		483		0,74	23,40	0	28,40
	0,143			14759		331		0,75	27,71	0	32,71
Y	0,071	0,032	62923	28405	1997	901	0,79	0,66	0	32,97	15,25
	0,106			31382		996		0,65	0	20,04	11,67
	0,106			31328		996		0,65	0	20,04	11,67

Table 3. Properties of the SDOF system equivalent to the DBF at SDE: in parallel combination of HYDB1 and VDB (units in m, kN and s).

Dir.	$d_{p,MCE}^*$	$d_{p,SDE}^*$	$d_{y,DB2}^*$	$K_{e,F}$	$K_{e,DB2}$	$K_{e,DB1}$	$V_{p,F}^*$	$V_{p,DB2}^*$	$V_{p,DB1}^*$
X	0,072	0,015	0,003	57273	30367	64398	850	451	956
	0,107		0,003		38933	32499		578	483
	0,143		0,003		40814	22311		606	331
Y	0,071	0,032	0	62923	0	31202	1997	0	990
	0,106		0		0	22329		0	709
	0,106		0		0	22329		0	709
Dir.	$d_{p,MCE}^*$	$d_{p,SDE}^*$	$T_{e,F}$	$T_{e,DBF}$	$\xi_{v,F}$	$\xi_{h,DB2}$	$\xi_{h,DB1}$	$\xi_{e,DBF}$	
X	0,072	0,015	0,84	0,51	5	44,13	2,25	14,76	
	0,107			0,56		44,13	0	18,35	
	0,143			0,58		44,13	0	19,96	
Y	0,071	0,032	0,79	0,65	5	0	32,73	15,85	
	0,106			0,68		0	19,65	10,15	
	0,106			0,68		0	19,65	10,15	

Table 4. Properties of the SDOF system equivalent to the DBF at SDE: in parallel combination of HYDB1 HYDB2 (units in m, kN and s).

Dir.	$d_{p,MCE}^*$	$d_{p,SDE}^*$	$d_{v,DB2}^*$	$d_{p,DB2}^*$	$d_{p,DB1}^*$	$K_{e,F}$	$K_{e,DB2}$	$K_{e,DB1}$	$V_{p,F}^*$	$V_{p,DB2}^*$
X	0,072	0,015	0,003	0,0068	0,0082	57273	81971	68214	850	557
	0,107		0,003	0,0024	0,0127		172000	32511		413
	0,143		0,003	0,0016	0,0130		180333	22272		289
Y	0,071	0,032	-	-	-	62923	-	31202	1997	-
	0,106		-	-	-		-	22329		-
	0,106		-	-	-		-	22329		-
Dir.	$d_{p,MCE}^*$	$d_{p,SDE}^*$	$V_{p,DB1}^*$	$T_{e,F}$	$T_{e,DBF}$	$\xi_{v,F}$	$\xi_{h,DB2}$	$\xi_{h,DB1}$	$\xi_{e,DBF}$	
X	0,072	0,015	557	0,84	0,65	5	35,89	0	11,46	
	0,107		413		0,69		0	0	5	
	0,143		289		0,72		0	0	5	
Y	0,071	0,032	990	0,79	0,65	5	-	32,73	15,85	
	0,106		709		0,68		-	19,65	10,15	
	0,106		709		0,68		-	19,65	10,15	

Table 5. Properties of the SDOF system equivalent to the DBF at SDE: in series combination of HYDB1 and HYDB2 (units in m, kN and s).

#### 4 NUMERICAL RESULTS

In this section, the effectiveness of the proposed multi-objective design procedure and the limitation of use of HYDBs, designed at MCE, in combination with HYDBs and VDBs, designed at SDE, are investigated on the five-storey RC building described in Section 2. Five structural arrangements of damped braces are considered in order to modulate effective damping and stiffness properties to assigned performance targets at the serviceability (e.g. protection of non-structural elements) and ultimate (e.g. upgrading up to full retrofitting of structural parts and collapse prevention of damped braces) limit states. Nonlinear seismic analyses of the original (IF) and retrofitted (DBIF) infilled structures are carried out using the OpenSEES platform [15]. Zero-length flexural- and shear-controlled elements are used to describe the inelastic response at the end-sections of RC frame members, with the internal part modelled with an elastic element, while a zero-length rotational spring is adopted for the beam-columns joints, reproducing shear failure prior to or after the achievement of yielding of the adjacent beams and columns [13]. An equivalent strut acting only in compression represents the in-plane behaviour of masonry infills, where the peak response is evaluated as minimum prediction between diagonal compression, corner crushing, sliding shear and diagonal tension failure mechanisms [19, 20]. Inherent damping equal to  $\xi_{v,F}=5\%$  is assumed for the RC framed structure, using mass and tangent stiffness proportional Rayleigh approach. Nonlinear fluid VDBs are modelled as nonlinear dashpots and linear springs [17], while truss elements with bilinear force-displacement law are considered for the HYDBs, with and without an in-parallel or in-series combination with a gap-link working in parallel to a hook-link. Then, three sets of biaxial accelerograms, each consisting of seven earthquakes, are selected from the PEER database and scaled to three different intensity levels [16]. At the site of L'Aquila (13.40° longitude and 42.35° latitude), design response spectra of acceleration provided by NTC18 are evaluated for moderately-soft subsoil, considering a nominal life  $V_N=50$  years and a functional class II (amplification factor,  $C_U=1.0$ ) resulting in a reference period  $V_R=50$  years. These spectra are matched on average in a suitable range of vibration periods, with reference to SDE (PGA= 0.156 g), BDE (PGA= 0.347 g) and MCE (PGA= 0.407 g).

The beneficial effects offered by the combination of HYDB1, ensuring structural safety (SS) at MCE, and VDB or HYDB2, calculated for immediate occupancy (IO) at SDE, are firstly investigated in Figures 7-9 with reference to the seismic performance of nonstructural elements. Specifically, maximum drift ratio of masonry infills  $\alpha_{\Delta I,max}(=\Delta_{I,max}/\Delta_{I,p}$ , being  $\Delta_{I,max}$  the mean of maximum drift demand at SDE and  $\Delta_{I,p}$  the value corresponding to full cracking)

is evaluated along the building height. As can be observed, the absence of openings in the infill walls along the Y direction (see Figure 5b) results in a significant reduction of  $\alpha_{\Delta I, \max}$ , whose values are less than those corresponding to the attainment of the peak lateral strength (i.e.  $\alpha_{\Delta I}=1$ ) for the IF structure, with a further slight improvement when DBIF structures are considered (Figures 7b, 8b,d and 9b).

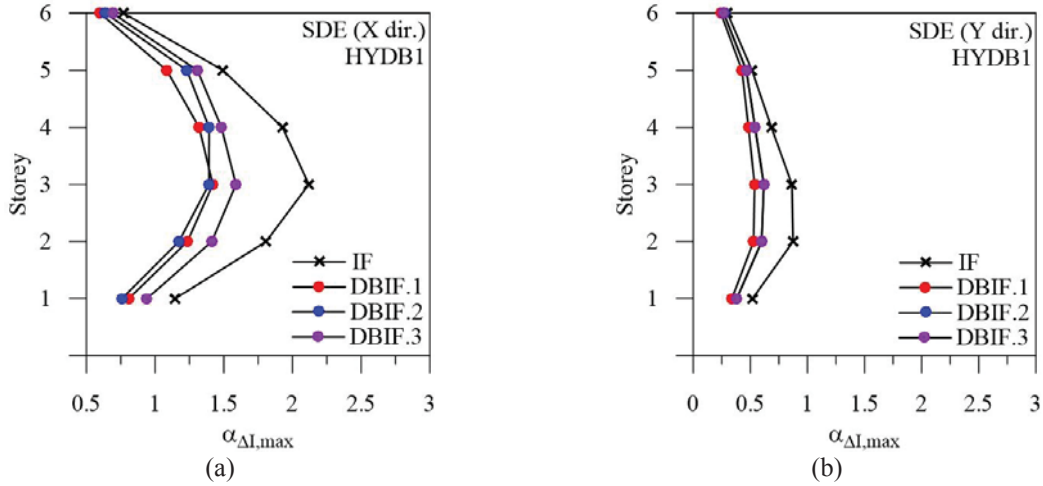


Figure 7. Maximum drift ratio of masonry infills for the original and retrofitted structures, at BDE: HYDB1.

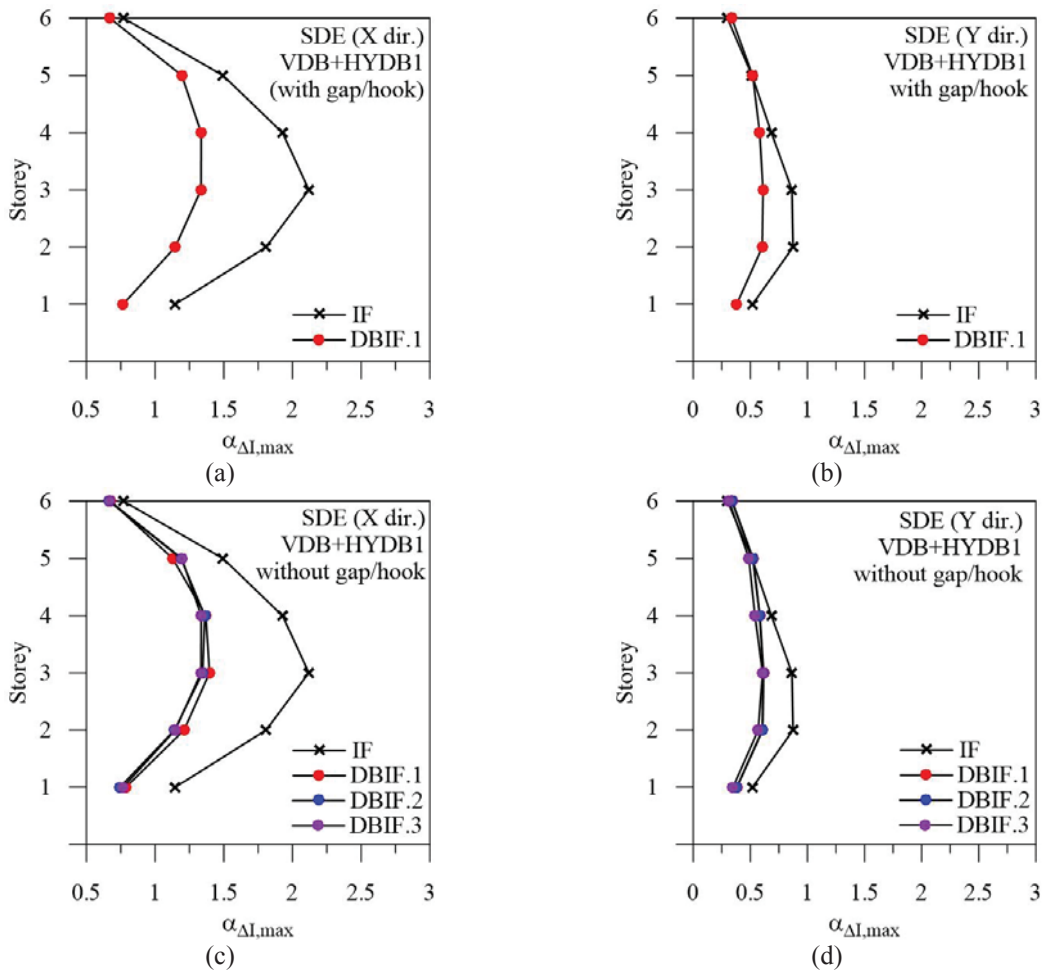


Figure 8. Maximum drift ratio of masonry infills for the original and retrofitted structures, at BDE: in-parallel HYDB1+VDB, with (a, b) and without (c, d) a gap-hook element in series with HYDB1.



On the other hand, extensive damage of masonry infills is resulted for the original structure along the X direction, characterized by infill walls with different percentage of openings, attaining strength reduction at all levels the only exception being the roof (Figure 7a). With regard to the retrofitted structures, the IO condition at SDE is not reached at intermediate storeys for the HYDB1 solution (Figure 7a), where only target performance levels at MCE are checked. The in-parallel combination of HYDB1 and VDB, with (Figure 8a) and without (Figure 8c) a gap-hook element in series with HYDB1, has not produced a marked improvement of the response that has practically unchanged for all examined cases and beyond the damage threshold at the intermediate levels. On the other hand, a significant reduction of  $\alpha_{\Delta I, \max}$  is attained when the in-parallel combination of HYDB1 and HYDB2 is considered, with fulfilment of the IO condition for all values of  $\Delta_x/h$  at MCE (Figure 9a). Finally, results corresponding to the in-series combination of the HYDB1 and HYDB2 are plotted in Figures 9c,d. It should be noted that HYDBs deriving from the in-parallel combination (see Table 4) are adopted when in-series arrangement of HYDBs is considered along X (see Table 5). As can be observed, a different arrangement of the HYDBs impairs their performance, resulting in non-operational condition of the retrofitted structure at SDE (Figure 9c), while the response is essentially the same as that obtained for the in parallel arrangement when Y direction is considered (Figure 9d).

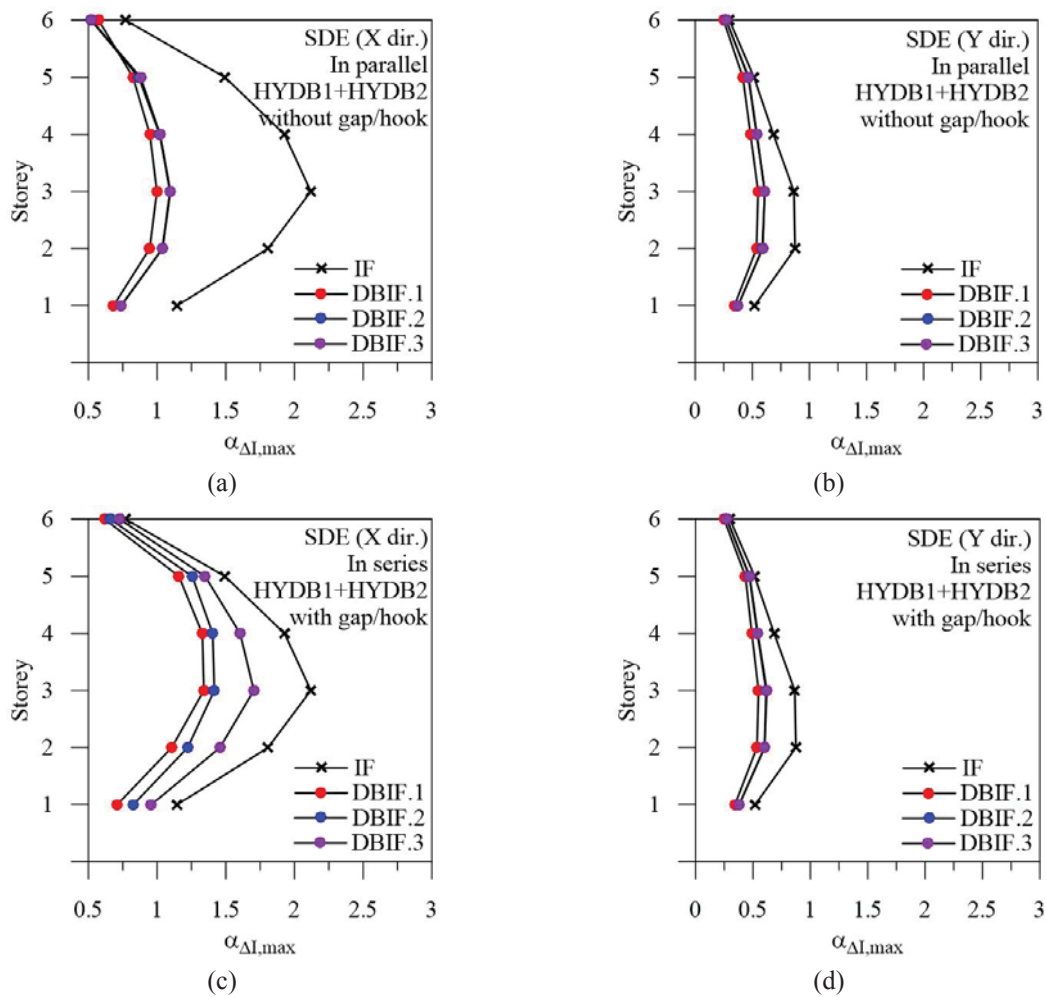


Figure 9. Maximum drift ratio of masonry infills for the original and retrofitted structures, at BDE: in-parallel (a, b) and in-series (c, d) HYDB1+HYDB2.



Afterwards, maximum drift ratio demand  $((\Delta/h)_{\max})$ , with inter-storey displacement  $\Delta_{\max}$  divided by the storey height  $h$  at BDE is shown in Figure 10, only considering HYDB1 since results corresponding to the other four arrangements are practically identical to those obtained for this solution. The effectiveness of the HYDBs is confirmed in both directions, with similar response for all performance levels in the Y direction (Figure 10b). Moreover, target displacements (see dashed lines) are never exceeded in the Y direction, while DBIF.i structures ( $i=1-3$ ) are resulted more flexible compared to the design thresholds in the X direction.

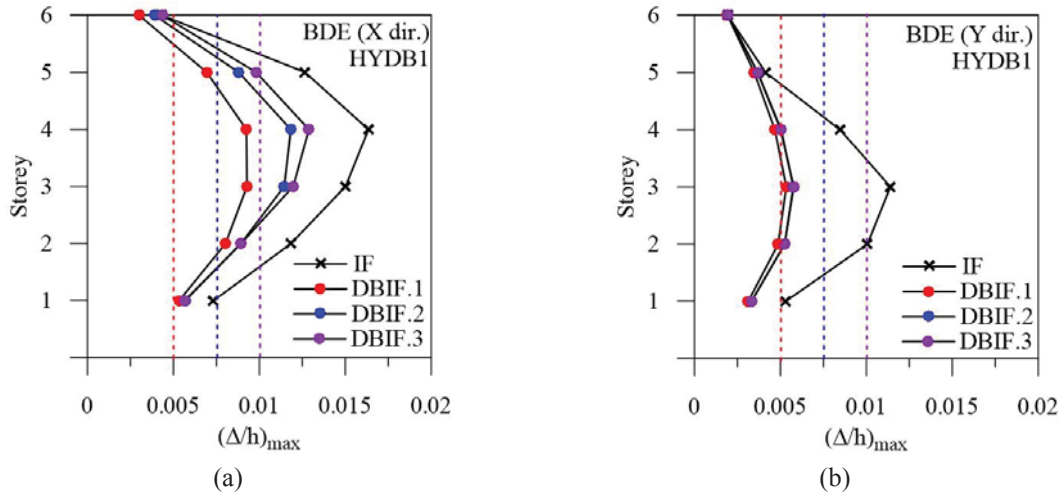


Figure 10. Maximum drift ratio for the original and retrofitted structures, at BDE: HYDB1.

Finally, maximum ductility demand  $(\mu_{D,\max})$  of the HYDBs at MCE are plotted in Figure 11, referring to the in-elevation and in-plan distributions. For all performance levels, the ultimate value ( $\mu_{D,u}=20$ ) is never reached, so avoiding collapse of the dissipative devices, and a rather uniform demand is resulted along Y (Figure 11b). As a confirmation, decreasing values of  $\mu_{D,\max}$  are obtained for increasing values of target displacement.

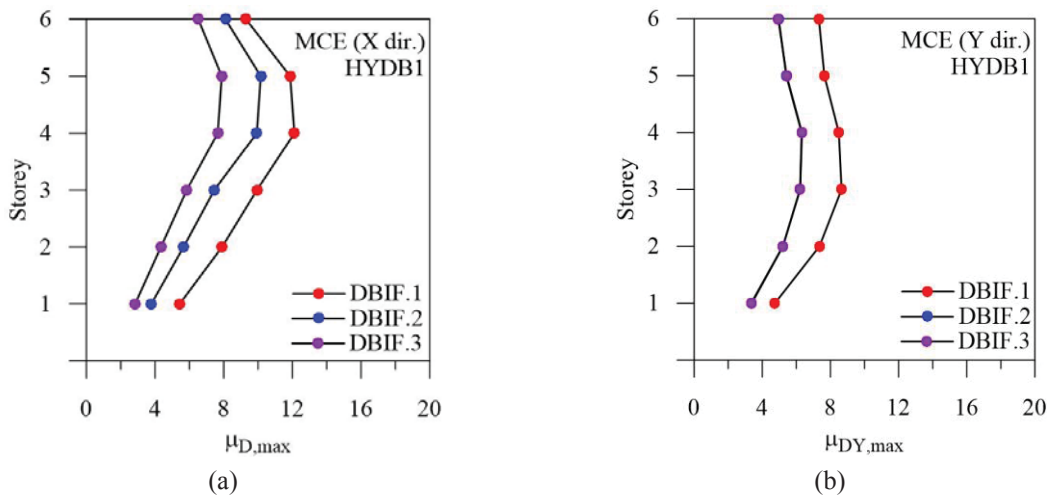


Figure 11. Maximum ductility demand of damped braces for the retrofitted structures, at MCE: HYDB1.

## CONCLUSIONS

A displacement-based design procedure of damped braces is proposed for optimizing the seismic performance of buildings, by minimizing damage of both non-structural and structural

elements at SDE and MCE, respectively. In order to quantify the enhanced seismic protection offered by the combination of HYDBs, designed at MCE, and HYDBs or VDBs, designed at SDE, comparison is made with a traditional solution consisting of HYDBs designed to guarantee the structural safety for severe ultimate limit state seismic events. Four alternative configurations are chosen for retrofitting the original building: in-parallel combination of HYDBs, at MCE, and VDBs, at SDE, with and without a gap-hook element in series with HYDBs; in-parallel and in-series combinations of HYDBs, with and without a gap-hook element in parallel with HYDBs at SDE. The procedure is applied for the seismic retrofitting of an RC framed structure, located in L'Aquila and designed for a medium-risk seismic zone, representative of the residential housing stock built in Italy during the 1990s. By carrying out nonlinear dynamic multi-stripe analysis of the original and retrofitted infilled structures, under three intensity levels provided by Italian seismic code, the following conclusions can be drawn.

The absence of openings along the Y direction results in a significant reduction of damage in the infill walls of the original structure at SDE, differently from strength reduction affecting many infill walls, with different percentage of openings, along the X direction. As expected, HYDBs designed at MCE are not able to ensure the IO condition of the retrofitted structure because too high yielding forces do not allow their activation at SDE. The in-parallel combinations of the HYDBs and VDBs does not produce a marked reduction of damage at SDE for masonry infills at the intermediate storeys, whose drift remains beyond the damage threshold. The in-parallel combination of HYDBs, half designed at SDE and half at MCE, allows the fulfilment of the IO condition; the same HYDBs with an in-series arrangement impairs seismic response of masonry infills at SDE. The effectiveness of the HYDBs is confirmed in both directions at BDE, with target displacements not exceeded in the Y direction, while more flexibility compared to the design thresholds is highlighted in the X direction. Finally, maximum ductility demand of the HYDBs at MCE confirm that their ultimate value is never reached, so avoiding collapse of the dissipative devices.

## ACKNOWLEDGEMENTS

The present work was financed by Re.L.U.I.S. (Italian network of university laboratories of earthquake engineering), in line to the Convenzione D.P.C.-Re.L.U.I.S. 2019-2021, WP15, Code Revisions for Isolation and Dissipation.

## REFERENCES

- [1] C. Christopoulos, A. Filiatrault, *Principles of passive supplemental damping and seismic isolation*. IUSS Press, Pavia, Italy, 2006.
- [2] G. Terenzi, I. Costoli, S. Sorace, Activation control extension of a design method of fluid viscous dissipative bracing systems. *Bulletin of Earthquake Engineering*, **18**, 4017-4038, 2020.
- [3] Gandelli E, Taras A, Distl J, Quaglini V. Seismic retrofit of hospitals by means of hysteretic braces: influence on acceleration-sensitive non-structural components. *Frontiers in Built Environment* 2019; 5:10.3389/fbuil.2019.00100.
- [4] R. Aghlara, M. Md. Tahir, A passive metallic damper with replaceable steel bar components for earthquake protection of structures. *Engineering Structures*, **159**, 85-197, 2018.
- [5] T. Shiomi, K. Fujita, M. Tsuji, I. Takewaki, Dual hysteretic damper system effective for broader class of earthquake ground motions. *International Journal of Earthquake and Impact Engineering*, **2**(3): 175-202, 2018.

- [6] S. Hashizume, I. Takewaki, Hysteretic–viscous hybrid damper system for long-period pulse-type earthquake ground motions of large amplitude. *Frontiers in Built Environment*, **6**, article 62, 2020.
- [7] E. Gandelli, S. Chernyshov, J. Distl, P. Dubini, F. Weber, A. Taras, Novel adaptive hysteretic damper for enhanced seismic protection of braced buildings. *Soil Dynamics and Earthquake Engineering*, doi.org/10.1016/j.soildyn.2020.106522
- [8] F. Mazza, A. Vulcano, Design of hysteretic damped braces to improve the seismic performance of steel and RC framed structures. *Ingegneria Sismica*, **31**(1), 5-16, 2014.
- [9] F. Mazza, Seismic vulnerability and retrofitting by damped braces of fire-damaged RC framed buildings. *Engineering Structures*, **101**, 179-192, 2015.
- [10] F. Mazza, Nonlinear seismic analysis of unsymmetric-plan structures retrofitted by hysteretic damped braces. *Bulletin of Earthquake Engineering*, **14**(4), 1311-1331, 2016.
- [11] F. Mazza, A simplified retrofitting method based on seismic damage of a SDOF system equivalent to a damped braced building. *Engineering Structures*, **200**, 109712, 2019.
- [12] F. Mazza, A plastic-damage hysteretic model to reproduce strength stiffness degradation. *Bulletin of Earthquake Engineering*, **17**(6), 2787-2819, 2019.
- [13] P. Ricci, V. Manfredi, F. Noto, M. Terrenzi, M.T. De Risi, M. Di Domenico, G. Camata, P. Franchin, A. Masi, F. Mollaioli, E. Spacone, G.M. Verderame, RINTC-E: towards seismic risk assessment of existing residential reinforced concrete buildings in Italy. Procs. of the 8<sup>th</sup> ECCOMAS Thematic Conference on Computational Methods in Structural Dynamics and Earthquake Engineering *COMPdyn 2019*, Crete, Greece, 24-26 June 2019.
- [14] NTC18, Norme tecniche per le costruzioni. DM 17-01-2018, Italian Ministry of Infrastructures and Transports, Rome, Italy, 2018.
- [15] F. McKenna, G.L. Fenves, M.H. Scott, Open system for earthquake engineering simulation. University of California, Berkeley, CA, 2000.
- [16] I. Iervolino, A. Spillatura, P. Bazzurro, Seismic structural reliability of code-conforming Italian buildings. *Journal of Earthquake Engineering*, **22**, 5-27, 2018.
- [17] F. Mazza, Dissipative steel exoskeletons for the seismic control of reinforced concrete framed buildings. *Structural Control and Health Monitoring*, **28**(3), e2683. DOI: 10.1002/stc.2683, 2020.
- [18] A. Sepehri, T. Taghikhany, S.M.R. Ahmadi Namin, Seismic design and assessment of structures with viscous dampers at limit state levels: Focus on probability of damage in devices. *The Structural Design of Tall and Special Buildings*, **28**, e1569, 2018.
- [19] DM86, Norme tecniche relative alle costruzioni antisismiche. D.M. 24-01-1986, Italian Ministry of Public Works, Rome, Italy, 1986.
- [20] F. Mazza, In- plane–out- of- plane non- linear model of masonry infills in the seismic analysis of r.c.- framed buildings. *Earthquake Engineering & Structural Dynamics*, **48**(4), 432-453, 2019.
- [21] F. Mazza, A. Donnici, In-plane and out-of-plane seismic damage of masonry infills in existing RC structures: the case study of De Gasperi-Battaglia school in Norcia. *Bulletin of Earthquake Engineering*, **19**, 345-376, 2021.

## EFFECT OF THE DAMPING RATIO OF NON-STRUCTURAL COMPONENTS ON FLOOR ACCELERATION DEMANDS IN TORSIONALLY IRREGULAR BUILDINGS

Ankur Jain and Mitesh Surana

Indian Institute of Technology Ropar  
Rupnagar, Punjab–140001, India  
ankur.19cez0004@iitrpr.ac.in, msurana@iitrpr.ac.in

---

### Abstract

*To investigate the effect of damping ratio of non-structural components on floor acceleration demands in torsionally irregular buildings, reinforced-concrete moment-resisting frame buildings resting on flat ground (regular), and on hill slopes (irregular) are analyzed. Bi-directional linear dynamic analyses are conducted, by applying a suite of far-field ground motions, along two orthogonal axes, to obtain the floor response of the investigated frames. From the obtained floor acceleration response of the investigated buildings, the elastic floor response spectra are derived at two different floor levels: (i) the floor with maximum eccentricity in the irregular building, and the corresponding floor in the reference regular building; and (ii) at the roof levels, for both the regular and irregular buildings, for NSC's damping ratios of 1%, 2%, 5%, and 10%. The effect of damping ratio of the NSCs is studied in terms of damping modification factors, at three different locations on each of the considered floor levels, i.e. (i) at the flexible edge, (ii) at the center of rigidity, and (iii) at the stiff edge. The derived median damping modification factors, as obtained from the time-history analyses are compared with the recommendations of EC 8 and other existing models available in the literature. It is observed that the recommendations of EC 8 underpredict damping modification factors significantly, for non-structural components, tuned to structural modes of vibration, especially, for low damping ratios of the non-structural components, and also for relatively flexible non-structural components, for high damping ratio of the non-structural components.*

**Keywords:** Damping Modification Factors, Floor Response Spectra, Non-structural Component, Seismic Design, Torsional Irregularity.

---

## 1 INTRODUCTION

Components and systems which are neither a part of the gravity load-resisting system nor a part of the lateral load-resisting system, but offer functionality to the buildings are termed as '*non-structural components*' (NSCs) or '*secondary systems*'. The typical examples of these NSCs in a building include electrical and mechanical equipments, architectural elements, bookshelves, suspended ceilings, furniture, and elevators. Typically, NSCs in buildings are either sensitive to the inertia forces, or to the inter-story drifts, or sometimes to both. Thus, based on sensitivity of their response, these NSCs are sub-categorized as: (i) acceleration-sensitive NSCs, (ii) displacement-sensitive NSCs, and (iii) combined acceleration- and displacement-sensitive NSCs. Seismic safety of NSCs is not only crucial due to their higher contributions to the total cost of the buildings (e.g. 70-80% of the total cost of the structure, especially in commercial buildings [1]), but, inoperability of these NSCs due to damage during earthquakes (specifically in lifelines buildings, e.g. hospitals) could lead to increased casualties, and delayed post-earthquake recovery operations. As a result, assessing the adequacy of the existing provisions, and developing new provisions, for ensuring seismic safety of NSCs is considered as an essential step in performance-based earthquake engineering.

It is a well-established fact in the literature [2-8] that dynamic response of the acceleration-sensitive NSCs is affected by the characteristics of both the structure and NSC itself. The typical structural characteristics which affects seismic response of NSCs include e.g. modal periods, height of the structure, stiffness distribution along the height of structure, strength of the structure, and its lateral-load resisting system [2-5]. On the other hand, the NSC's characteristics which affects their seismic response include the location of NSCs in the building, period of the NSCs, and the damping ratio of the NSCs [2-5]. A critical review of the existing literature suggests that most of the NSCs exhibit a low damping ratio, which typically ranges between 1-2% [9-12]. However, the various national building codes [13, 14], as well as most of the past studies [6-8] considered the NSC damping ratio equal to 5%.

Few studies conducted so far [2-5] identified the influence of damping ratio of the NSCs, on their floor acceleration demands. Medina *et al.* [2] conducted a study on the elastic and inelastic regular moment-resisting frame buildings, and observed that a lower damping ratio of the NSCs leads to amplification of the acceleration response, and a reduction in the NSC damping ratio from 5% to 2%, can result approximately 50% amplification in the acceleration demands on NSCs. Anajafi and Medina [4] conducted investigations on code designed structures to study the influence of the damping ratio of the NSC on the floor acceleration demands, and identified that the amplification/de-amplification in the floor accelerations, due to a decrease or increase in the damping ratio of the NSC, is a function of the tuning ratio (defined as the ratio of between the period of the NSC,  $T_s$ , to the fundamental period of the building,  $T_1$ ). Further, the effect of damping ratio of the NSCs was observed to be more pronounced, when NSCs are tuned to any structural modes of vibration, and less pronounced (minimal) for the non-tuned conditions. These findings of the investigations by Anajafi and Medina [4] were further supported by the recorded floor motions in 47 instrumented buildings, located in California [5]. Based on these findings, Anajafi and Medina [4] proposed a simplified tuning ratio dependent model to estimate damping modification factors (DMFs) to scale up or down the ordinates of the 5%-damped elastic floor response spectra, to account for the actual damping ratio of the NSCs.

The studies conducted so far to evaluate the influence of damping ratio of the NSCs on estimated floor acceleration demands are mostly based on NSCs mounted on regular buildings. The dynamic behaviour of the buildings is significantly altered by presence of torsion in the buildings, resulting coupling between translational and torsional motions. Thus, the present



study aims to investigate the influence of the damping ratio of NSCs on the floor acceleration demands, in torsionally irregular buildings. Accordingly, two different buildings, i.e. the reference regular building, and the irregular step-back building are considered for assessments in the present study. Bi-directional linear time-history analyses are conducted using a suite of recorded far-field ground motions. The elastic floor response spectra are obtained at two different floor levels, i.e. (i) at the floor with maximum eccentricity between centre of mass (CM) and centre of rigidity (CR) in the irregular building, and at the corresponding floor in the reference regular building; and (ii) at the roof levels, for both regular and irregular buildings, for NSC's damping ratios of 1%, 2%, 5%, and 10%. From the obtained floor response spectra, DMFs are derived at the CR in the reference regular building, and at CR, flexible edge (FE) and stiff edge (SE) in the irregular step-back building. The derived DMFs from time-history analyses are compared with the recommendations of EC 8 [14] and other models [4] in the existing literature, and the influence of the damping ratio of the NSCs on floor acceleration demands in torsionally irregular buildings is discussed and quantified.

## 2 NUMERICAL STUDY

### 2.1 Details of the investigated buildings

In the present study, two different 4-storied reinforced-concrete (RC) moment-resisting frame buildings, i.e. the reference regular building resting on plain ground, and the step-back irregular building on sloping ground are considered. The plan and elevations of the considered buildings are shown in Fig. 1. The step-back building considered in the assessments rest on a ground, having a slope of 2:1 (H:V), resulting a moderate slope angle of 27.3 degrees. In both, the regular and irregular buildings, the floor-to-floor height is considered as 3.3 m and set constant for all floors. In the irregular building, the ground supported short columns are of two different heights, i.e. 1.1 m and 2.75 m, in the successive storeys. Three-dimensional numerical models of the regular and irregular buildings are developed in OpenSees [15]. The structural elements, i.e. beams and columns are modelled as *ForceBeamColumn* elements, and floor slabs are defined as rigid diaphragms. The effective stiffness of RC beams and columns is modelled as per the recommendations of ASCE 41-17 [13]. Gravity loads (dead and live loads) on the considered buildings are applied as per the relevant Indian Standards [16, 17]. The investigated set of buildings are designed as the Special Moment Resisting Frame (SMRF) buildings, following the provisions of the Indian Standards [18-20], at the rock/stiff site, for the highest seismic zone (Zone V) in India. The member sizes are proportioned to result the longitudinal reinforcement in beams between 0.75-1.5 %, and in columns between 2-4 %, consistent with the typical design practice adopted in North India.

### 2.2 Dynamic characteristics and torsion in the investigated buildings

As highlighted in the past research [2-8], the floor response is significantly affected by the dynamic characteristics of the building, therefore, the dynamic characteristics of the investigated buildings are summarized in Table 1. Past investigations [21] on irregular step-back buildings suggest that in such buildings, the period corresponding to the fundamental mode of vibration is usually controlled by the number of storeys measured on the uphill side (Fig. 1(d)), irrespective of the direction under consideration. The very same effect is evident in the obtained periods of vibration in the present study (Table 1), where the first mode periods for the reference regular and irregular step-back buildings are in close agreements. In addition, the irregular step-back buildings are subjected to torsion, due to non-coincident locations of CM and CR (Fig. 1(b)). In the present study, CR is obtained considering the definition of the



single floor eccentricity. The additional details about estimation of CR in the investigated step-back building is available elsewhere [21]. Based on the obtained estimates of the eccentricity between CM and CR, it is observed that in the investigated irregular step-back building, the maximum torsional effects exist at the base floor (Fig. 1(b)), which further reduces while moving upwards, from base floor to the roof level (Fig. 1(a)). Accordingly, in the present study, the detailed results are reported for these two floor levels only.

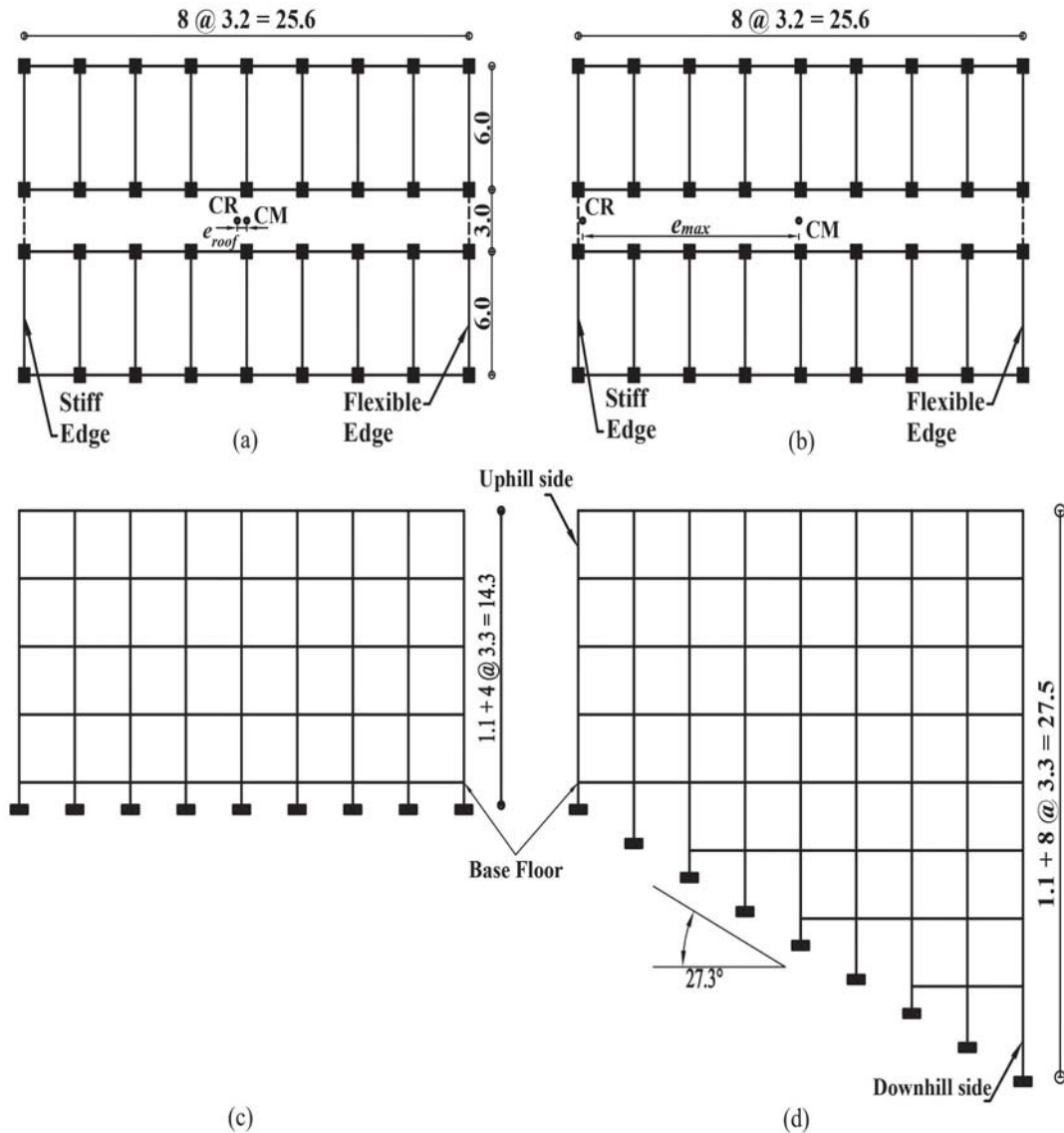


Figure 1: Typical plan and elevation layouts: (a) floor plan of the step-back building, at the roof level, (b) floor plan of the step-back building, at the base foundation level, (c) elevation of the reference regular building, and (d) elevation of the step-back building, in the direction along the slope. The dashed lines define the boundary of the floor slab. CM and CR denotes the locations of the center of mass and center of rigidity in the floor plan. All dimensions are in meters.

### 2.3 Ground motions and linear dynamic time-history analyses

In the present study, the suite of 22 pairs of far-field recorded earthquake ground motions (having moment magnitudes varying between  $M_w$  6.5 to  $M_w$  7.6, with an average value of  $M_w$  7.0, as specified in the FEMA P695 [22]) are considered. For performing the bi-directional time-history analyses, both the horizontal components of seismic ground-motion records are

applied simultaneously, along the two orthogonal axes of the investigated buildings. A total of 44 linear time history analyses have been performed for each of the investigated buildings, by interchanging the two horizontal components of seismic ground-motions, along the two principal axes of the buildings. The viscous damping in the considered buildings is modelled as Rayleigh damping of 2.5% [23], and it is defined corresponding to the periods equal to 1.5 times the fundamental mode period ( $1.5T_1$ ), and the period resulting in a total of 95% cumulative mass participation, in both directions.

Building Type	Mode of Vibration	$T_{ALS}$	$T_{ACS}$	$\alpha_{mx}$ (%)	$\alpha_{my}$ (%)
Regular	First mode	1.23	1.73	72.00	71.00
	Second mode	0.40	0.53	08.07	09.28
	Third mode	0.24	0.28	02.50	03.52
Irregular	First mode	1.21	1.74	52.00	51.00
	Second mode	0.39	0.53	05.78	07.29
	Third mode	0.23	0.29	01.72	14.00

$T_{ALS}$  and  $T_{ACS}$  are the modal periods of vibration in the along and the across-slope directions of excitations, respectively, whereas,  $\alpha_{mx}$  and  $\alpha_{my}$  are the modal mass participation ratios in the along and across-slope directions of excitations, respectively.

Table 1: Dynamic characteristics of the investigated regular and irregular buildings.

### 3 RESULTS AND DISCUSSIONS: DMFS FOR FLOOR RESPONSE SPECTRA

In the present study, a total of 5,104 elastic floor acceleration response spectra are computed at different floor levels, along the height of both the regular and irregular buildings. These floor response spectra are computed at the CR in the regular building, and at the CR, the FE and the SE in the irregular building, for NSC's damping ratios of 1%, 2%, 5% and 10%. The obtained floor acceleration response spectra are used to estimate DMFs, i.e. the ratio between the floor spectral acceleration ordinate at any given period, corresponding to a NSC's viscous damping ratio,  $\xi_s$ , to the floor spectral acceleration ordinate at the same period, corresponding to NSC's viscous damping ratio of 5%, as defined through Eq. 1

$$DMF(T_s, \xi_s) = \frac{S_a(T_s, \xi_s)}{S_a(T_s, 5\%)} \quad (1)$$

where,  $DMF(T_s, \xi_s)$  is the damping modification factor corresponding to NSCs period of vibration,  $T_s$ , and damping ratio,  $\xi_s$ ,  $S_a(T_s, \xi_s)$  is the floor spectral acceleration corresponding to NSCs period of vibration,  $T_s$ , and damping ratio,  $\xi_s$ , and  $S_a(T_s, 5\%)$  is the floor spectral acceleration corresponding to NSCs period of vibration,  $T_s$ , and damping ratio of 5%. These DMFs are derived at all the floors, for both the regular and the irregular building, however, the results at the base floor and at the roof level are reported herein, for the sake of brevity.

Figure 2 presents the variations of DMFs in the across-slope direction (in which the torsional effects are present in case of the irregular step-back building), for the investigated regular and irregular buildings, at the base floor. It is to be noted that at the base floor, the CR and the SE are in close proximity to each other (Fig. 1(b)), and thus, the median floor response spectra at the CR and the SE overlaps with each other, in case of the irregular building. It can be observed that at the base floor level, the median DMFs estimated from the elastic floor re-

sponse spectra (derived from the floor motions) at CR are in close agreement with those recommended in EC 8, for non-tuned response of the NSCs, whereas, non-conservative for the tuned response of the NSCs, especially, when NSCs are tuned to higher modes of vibration. These observations can be attributed to the fact that the NSCs are subjected to limited filtering effects by the structure, due to insignificant contributions of the different modes of vibration at the base floor level.

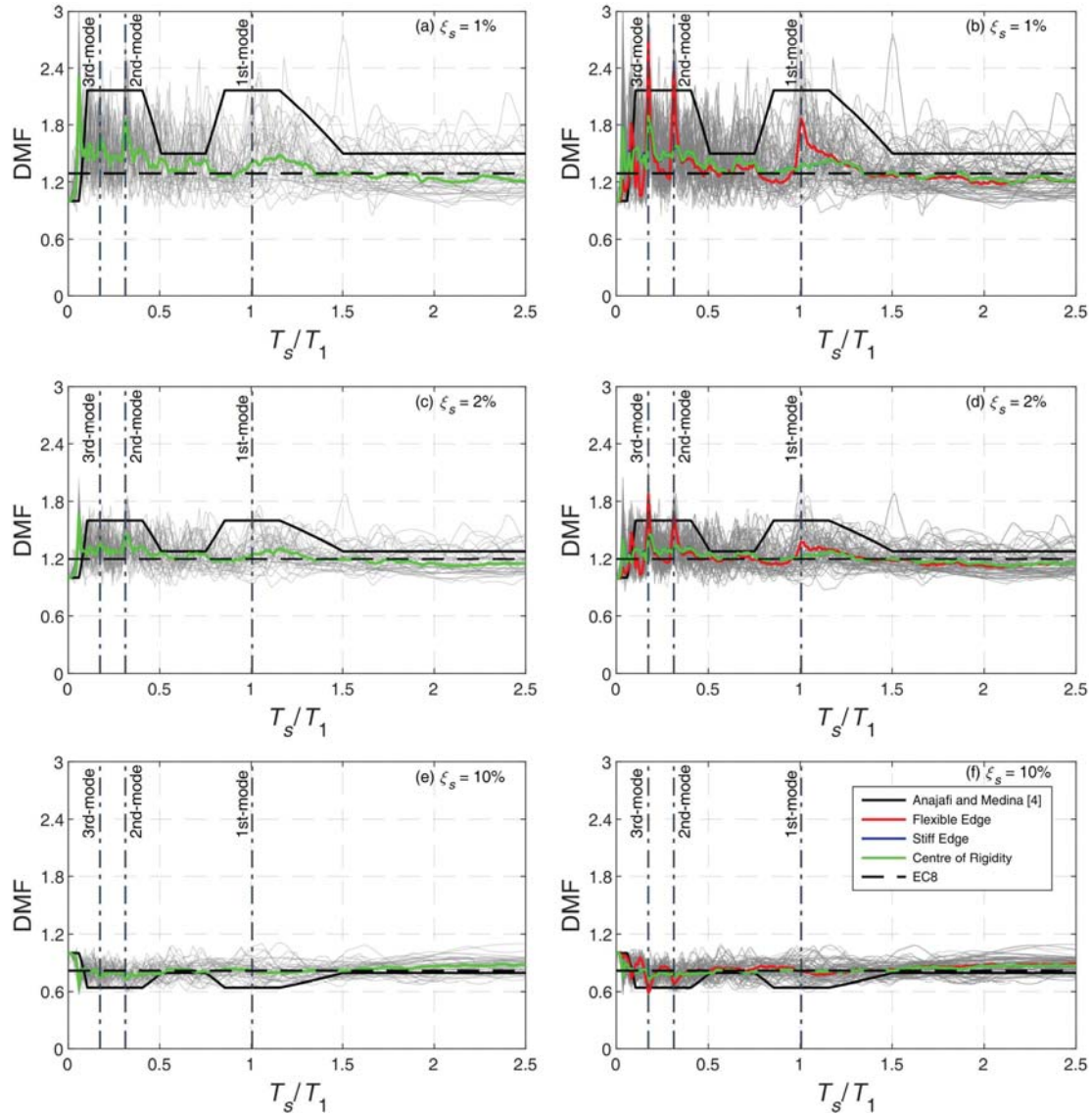


Figure 2: Comparisons of DMFs at the base floor (computed using linear dynamic analyses), with the available model in literature and EC 8. The first column in the plots corresponds to the derived DMFs for the regular building, whereas, the second column corresponds to the derived DMFs for the irregular building.

In case of irregular building, when NSCs are tuned to higher modes of vibration, the estimated DMFs at FE from EC 8 are underestimated by a factor of 2.12 and 1.56 (Fig. 2(b) and 2(d)), for NSC's damping ratios of 1% and 2%, respectively. On the other hand, at the base floor level, the DMF model proposed by Anajafi and Medina [4] provided significantly conservative estimates of the DMFs at the CR (Fig. 2(a)-(d)), for low damping ratios of the NSCs (i.e. 1% and 2%). However, this conservatism vanished at the FE, especially under the tuned response of the NSCs corresponding to higher modes (Fig. 2(b) and 2(d)). Further, the DMFs

obtained from EC 8 (at the CR and the FE), corresponding to NSC's damping ratio of 10% are observed to be reasonable at the base floor, upto tuning ratios of 1.50 (Fig. 2(e)-(f)), for both the regular and irregular buildings. Contrarily, at the base floor, for NSC's damping ratio of 10%, the DMF model proposed by Anajafi and Medina [4] provided non-conservative estimates of the DMFs under tuned response of NSCs (Fig. 2(e)-(f)), at the CR and the FE.

Figure 3 presents similar results at the roof level of regular and irregular buildings investigated in the present study. It is to be noted that at the roof level, only minor eccentricity exist in between CM and CR (Fig. 1(a)), thus, at the roof level, torsional effects are minimal. This effect is manifested in the form of almost overlapping median floor response spectra, for a given damping ratio of interest, at the CR, the FE and the SE (Fig. 3(b), 3(d), and 3(f)).

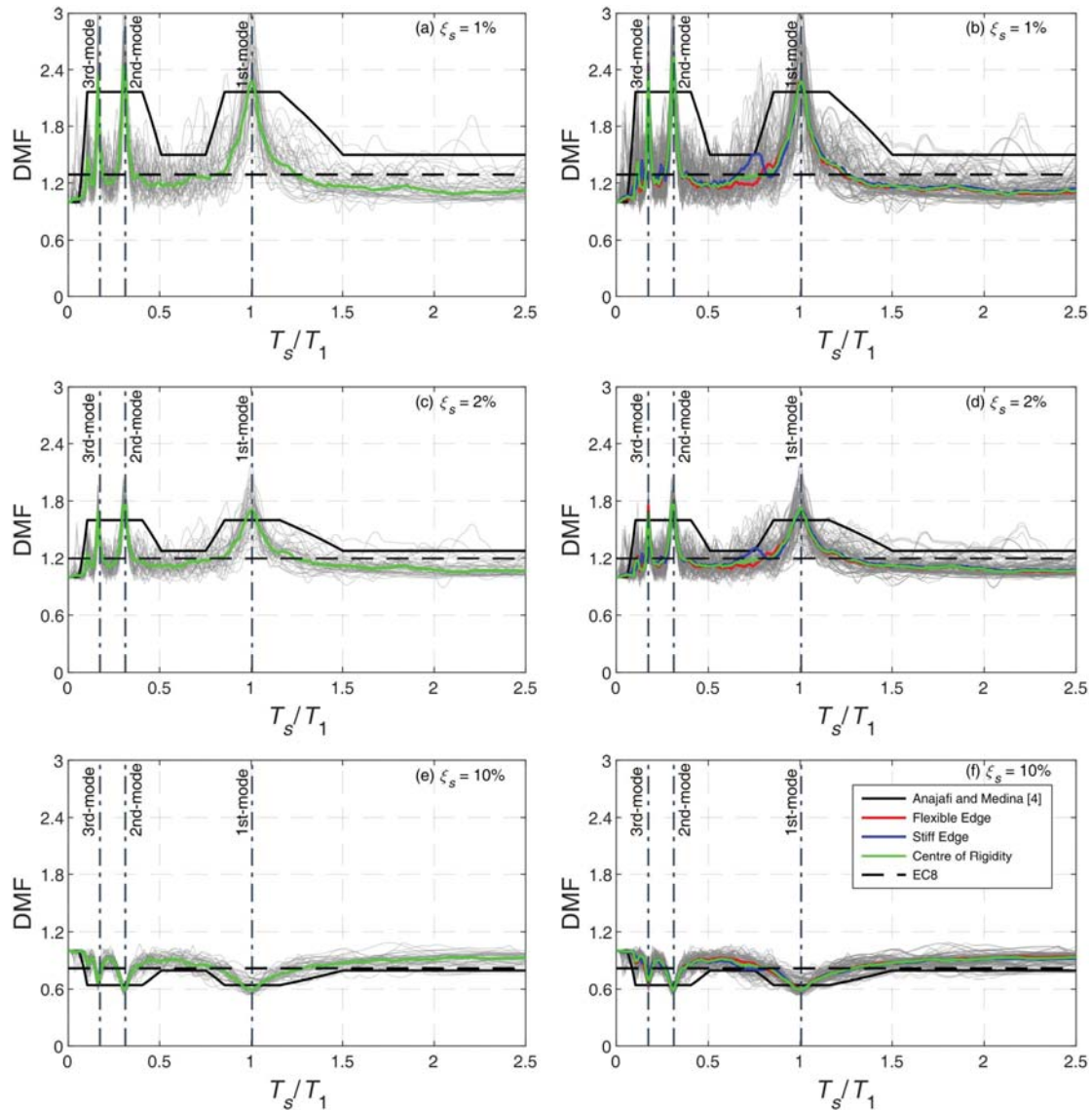


Figure 3: Comparisons of DMFs at the roof level (computed using linear dynamic analyses), with the available model in literature and EC 8. The first column in the plots corresponds to the derived DMFs for the regular building, whereas, the second column corresponds to the derived DMFs for the irregular building.

From Fig. 3, it is further evident that DMFs are tuning ratio dependent, and sharp peaks are observed in DMFs corresponding to the structural modes of vibration. As a result, the DMF model recommended in EC 8 underestimated median DMFs (obtained from floor response

spectra) by a factor of 1.94 and 1.50 (Fig. 3(a)-(d)), for NSC's damping ratios of 1% and 2%, respectively, when NSCs are tuned to the structural modes of vibration. For the non-tuned response of the NSCs having low damping ratios (i.e. 1% and 2%), the DMF model recommended in EC 8 is observed to be reasonable, at the roof level (Fig. 3(a)-(d)). Contrarily, the model proposed by Anajafi and Medina [4] provided slightly non-conservative estimates of DMFs for tuned response of the NSCs to the structural modes of vibration, for both regular and irregular buildings ((Fig. 3(a)-(d))). For high damping ratio of NSCs (i.e. 10%), at the base floor level as well as at the roof level, both the models, i.e. EC 8 and the one proposed by Anajafi and Medina [4] provided slightly non-conservative estimates of DMFs, for tuning ratios more than 1.50 (Fig. 2(e)-(f) and Fig. 3(e)-(f)), at both locations on the floor plan, i.e. at the CR and at the FE.

The observations presented in the study highlighted some of the shortcomings of the existing models in the literature and building codes to account for the actual damping ratio of NSCs in its seismic design and warrants a need for more reliable estimation of DMFs, for seismic design of NSCs.

#### 4 CONCLUSIONS

This study investigated the effects of damping ratio of non-structural components on floor acceleration demands for the reference regular and irregular step-back buildings. A total of 88 bi-directional linear time history analyses were conducted, and 5,104 floor response spectra were evaluated at different floor levels of the investigated buildings. DMFs were computed for the NSC damping ratios of 1%, 2%, 5%, and 10% and compared with the existing DMF prediction model available in the literature as well as in EC 8. The following major conclusions are drawn from this study:

- Consistent with the observations of the earlier studies [4-5], DMFs are observed to be tuning ratio dependent. This observation is found to be valid for both regular and torsionally irregular step-back building, investigated in the present study.
- Due to the presence of severe torsion at the base floor level, the estimated (median) values of DMFs, at the CR and the FE differs significantly, for the irregular step-back building. This effect was observed to be more pronounced for low damping ratio of the NSCs (i.e. 1% and 2%), especially, when NSCs are tuned to structural modes of vibration.
- For the range of damping ratios investigated in the present study, the DMF model recommended in EC 8 under predicted the median DMFs for the floor response spectra upto a factor of 2.12, when NSCs were tuned to structural modes of vibration.
- For higher damping ratio of NSCs (i.e. 10%), due to limited filtering effects at the base floor, the model proposed by Anajafi and Medina [4], provided non-conservative estimates of DMFs, for NSCs tuned to structural modes of vibration. Further, both the investigated models, i.e. the existing DMF prediction model [4] as well as EC 8 were found to be non-conservative, for relatively flexible NSCs ( $T_s/T_1 > 1.50$ ).

The present study was conducted considering mid-rise regular and irregular step-back buildings, exhibiting their elastic response. Further the study used ground motions recorded in far-field. Separate studies are recommended to further examine DMFs for other buildings types, for ground motions having different characteristics, and also considering the inelastic response of the buildings.



## 5 ACKNOWLEDGEMENTS

The first author's fellowship is granted by the Ministry of Education (MoE), Government of India (GoI). The investigations reported in this paper were conducted under the ISIRD project grant (F.No. 9-385/2019/IITRPR/3220) of the second author. The financial support received from both MoE and ISIRD Project Grant of IIT Ropar is gratefully acknowledged. The seismic ground-motion records used in this study were obtained from PEER NGA WEST 2 database.

## REFERENCES

- [1] S. Taghavi, E. Miranda, *Response Assessment of Non-structural Building Elements, PEER 2003/05 Report*, Pacific Earthquake Engineering Research Center, University of California at Berkeley, Berkeley, CA, 2003.
- [2] R. A. Medina, R. Sankaranarayanan, K. M. Kingston, Floor Response Spectra for Light Components Mounted on Regular Moment-Resisting Frame Structures. *Engineering Structures*, **28**, 1927-1940, 2006.
- [3] R. Sankaranarayanan, R. A. Medina, Acceleration Response Modification Factors for Nonstructural Components Attached to Inelastic Moment-Resisting Frame Structures. *Earthquake Engineering and Structural Dynamics*, **36**, 2189-2210, 2007.
- [4] H. Anajafi, R. A. Medina, Damping Modification Factor for Elastic Floor Spectra. *Bulletin of Earthquake Engineering*, **17(11)**, 6079-6108, 2019.
- [5] A. K. Kazantzi, D. Vamvatsikos, E. Miranda, The Effect of Damping on Floor Spectral Accelerations as Inferred from Instrumented Buildings. *Bulletin of Earthquake Engineering*, **18(5)**, 2149-2164, 2020.
- [6] J. Lin, S. A. Mahin, Seismic Response of Light Subsystems on Inelastic Structures, *Journal of Structural Engineering*, **111(2)**, 400-417, 1985.
- [7] S. Taghavi, E. Miranda, Effect of Interaction Between Primary and Secondary Systems on Floor Response Spectra. *The 14th World Conference on Earthquake Engineering*, Beijing, China, October 12-17, 2008.
- [8] A. B. Aldeka, S. Dirar, A. H. C. Chan, P. Martinez-Vazquez, Seismic Response of Non-Structural Components attached to Reinforced Concrete Structures with different Eccentricity Ratios, *Earthquakes and Structures*, **8(5)**, 1069-1089, 2015.
- [9] R. Astroza, E. Pantoli, F. Selva, J. I. Restrepo, T. C. Hutchinson, J. P. Conte, Experimental Evaluation of the Seismic Response of a Rooftop-Mounted Cooling Tower. *Earthquake Spectra*, **31(3)**, 1567-1589, 2015.
- [10] D. A. Watkins, *Seismic Behavior and Modeling of Anchored Nonstructural Components considering the Influence of Cyclic Cracks*. Ph.D. Thesis, University of California, San Diego, 2011.
- [11] D. A. Watkins, L. Chiu, T. Hutchinson, M. Hoehler, *Survey and characterization of floor and wall mounted mechanical and electrical equipment in buildings*. Structural Systems Research Program Report No. SSRP-2009/11, 2009.
- [12] M. Archila, C. Ventura, A. Figueira, Y. Yang, Modal testing of non-structural components for seismic risk assessment, J. Caicedo, F. Catbas, A. Cunha, V. Racic, P. Reyn-



- olds, K. Salyards (eds). *Conference Proceedings of the Society for Experimental Mechanics Series 26*, Topics on the Dynamics of Civil Structures, Vol 1. Springer, Berlin, 239–246, 2012.
- [13] ASCE 41-17, Seismic Evaluation and Retrofit of Existing Buildings, American Society of Civil Engineers, Reston, 2017.
- [14] CEN. EC8: Design of Structures for Earthquake Resistance—Part 1: General rules, Seismic Actions, and Rules for Buildings, EN 1998-1, Brussels, Belgium, 2004.
- [15] Pacific Earthquake Engineering Research Center (PEER), OpenSees (Open System for Earthquake Engineering Simulation), developed by PEER, University of California, Berkeley, California, <http://opensees.berkeley.edu/>, 2009.
- [16] IS 875-Part 1, Indian Standard—Code of Practice for Design loads for Buildings and Structures (Dead Loads), Bureau of Indian Standards, New Delhi, 1987.
- [17] IS 875-Part 2, Indian Standard—Code of Practice for Design loads for Buildings and Structures (Live Loads), Bureau of Indian Standards, New Delhi, 1987.
- [18] IS 456, Indian Standard—Plain and Reinforced Concrete, Code of Practice, Bureau of Indian Standards, New Delhi, 2000.
- [19] IS 1893-Part 1, Indian Standard—Criteria for Earthquake Resistant Design of Structures, Part 1-General Provisions and Buildings, Bureau of Indian Standards, New Delhi, 2016.
- [20] IS 13920, Indian Standard—Ductile Design and Detailing Of Reinforced Concrete Structures subjected to Seismic Forces—Code of Practice, New Delhi, India, 2016.
- [21] M. Surana, Y. Singh, D. H. Lang, Effect of Irregular Structural Configuration on Floor Acceleration Demand in Hillside Buildings, *Earthquake Engineering and Structural Dynamics*, **47(10)**, 2032-2054, 2018.
- [22] Federal Emergency Management Agency (FEMA). Quantification of Seismic Performance Factors, FEMA P695, Washington, D.C., 2009.
- [23] ASCE. Minimum Design Loads and Associated Criteria for Buildings and Other Structures, ASCE 7–16. Reston, Virginia: American Society of Civil Engineers, 2017.

## EXPLORING THE EXPECTED INCREASE OF COSTS AND LOSS REDUCTION BY RAISING THE BAR IN SEISMIC DESIGN: COMPARISON OF ALTERNATIVE DESIGN METHODOLOGIES AND EARTHQUAKE-RESISTANT TECHNOLOGIES

Francesca Gentili<sup>1</sup>, Jonathan Ciurlanti<sup>1</sup>, Simona Bianchi<sup>1</sup>, Stefano Pampanin<sup>1</sup>

<sup>1</sup> Sapienza University of Rome,  
Department of Structural and Geotechnical Engineering, Via Eudossiana 18, 00184, Rome, Italy  
[gentili.1652702@studenti.uniroma1.it](mailto:gentili.1652702@studenti.uniroma1.it), [jonathan.ciurlanti@uniroma1.it](mailto:jonathan.ciurlanti@uniroma1.it),  
[simona.bianchi@uniroma1.it](mailto:simona.bianchi@uniroma1.it), [stefano.pampanin@uniroma1.it](mailto:stefano.pampanin@uniroma1.it)

---

### Abstract

*The severe socio-economic impact of recent earthquakes has further highlighted the existing mismatch between societal expectations and reality of seismic performance of modern buildings. Targeting the traditional Life-Safety level is not enough when dealing with new building design, thus the seismic scientific community is currently aiming to raise the bar in terms of seismic/structural safety. To achieve this goal, different strategies might be adopted, as implementing more advanced design methodologies, increasing the seismic demand (design) level and/or switching from a traditional/monolithic building system to an innovative high performance low-damage structure, capable to withstand high levels of shaking without being (significantly) damaged. Based on this motivation, the paper aims at comparing – through a parametric study – the cost/performance of Reinforced Concrete case-study buildings designed for increasing level of seismic intensity (low-to-high) according to: a) alternative design approaches (force-based vs displacement-based) and b) different earthquake-resisting technologies (monolithic vs low-damage). Thirty-seven parametric configurations are investigated. Analytical/numerical investigations are carried out to determine the building capacity curves and loss assessment investigations are performed to compute the Expected Annual Losses (EAL). Results highlight the convenience of a displacement-based design approach, allowing for a better control of the building performance in the plastic domain, as well as of the adoption of a low-damage technology, leading to a very high performance and significantly reduced economic losses for a small increase of the initial investment costs.*

**Keywords:** Performance-based, Seismic safety, Displacement-based design, Low damage, Post-earthquake losses.

---

# 1 INTRODUCTION

The current performance-based seismic design of new buildings is based on the acceptance of severe level of damage in buildings after major (design level) earthquakes. When subjected to seismic shakings, multi-story structures are expected to concentrate the inelastic demand (therefore damage for traditional technology) in plastic hinges zones located at the end sections of the structural members, according to the hierarchy of strengths or capacity design principles (Figure 1a). Furthermore, according to a Life Safety design approach, attention is typically given to the structural skeleton only, whilst non-structural elements can be very vulnerable and consequently susceptible to high level of damage under low-to-moderate intensity earthquakes. Recent seismic events, in particular the Christchurch earthquake 2011 [1], have further highlighted the limits of this traditional design approach. Although modern buildings behaved as expected, resisting to even higher than code design-level earthquakes, with no collapse and safeguarding humane life, severely damaged buildings were often deemed too expensive to be repaired and were demolished. Targeting the Life-Safety objective is thus not enough when dealing with new building design. As a matter of fact, in recent years research is raising the bar in seismic design aiming at enhanced structural/seismic safety levels for our modern structures in order to fulfil the society demand in terms of seismic resilience, avoiding massive consequences in terms of socio-economic losses.

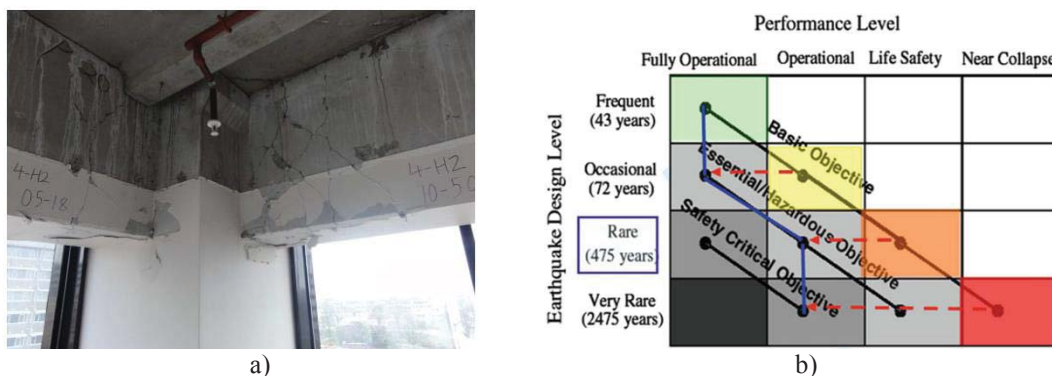


Figure 1. a) Example of beam plastic hinge from a 22 story RC Building [1]; b) Seismic performance design objective matrix [2] modified to emphasise a damage-control objective and design philosophy [3,4].

To reach this aim, different strategies might be adopted to improve the seismic safety and economic resilience of buildings (and communities) as 1) implementing more appropriate and advanced design methodologies and/or 2) increasing the seismic demand design level and/or 3) adopting high-performance earthquake-resistant solutions. In such context, growing attention has been recently dedicated to the development of innovative damage-mitigation technologies, aiming at the control and reduction of the post-earthquake damage. Apart from well-known advanced technologies such as base isolation and supplemental dissipative braces, particular interest is being received by more recently developed “low-damage” systems, based on post-tensioned rocking mechanisms, the so-called PRESSS technology (PREcast Seismic Structural System) for concrete structures [5,6,7,8]. This moment-resisting system combines self-centering capacity, through post-tensioned bars/tendons in the structural elements, and dissipating capabilities, provided either by internally located mild steel bars - as per the first generation of this technology - or using externally replaceable dissipaters, more recently developed [9]. The system behavior results in a dissipative and re-centering Flag-Shape hysteresis cycle [10] allowing for negligible permanent deformations after earthquakes.

Nevertheless, a common obstacle to the wider application of advanced seismic design methodologies and innovative low-damage technologies is often the uninformed perception/prejudice that such approaches would lead to substantially higher and unaffordable costs. Furthermore, rarely the economic benefits associated to a significantly reduced level of damage and thus direct and indirect losses, are computed. This paper intends to shed a light on this important topic, providing robust evidences for informed decision-making on the opportunity (and associated solutions) to raise the bar towards more resilient communities.

## 2 RESEARCH OUTLINE

Based on the above discussion, this work fits into the context of society's growing need for safer and more economically resilient buildings and aims to prove the beneficial effects of designing in a more conscious and controlled way. These objectives are pursued through a parametric study intended to compare the cost/performance of different case-study buildings with different design parameters, design methods, and/or construction technologies. A summary of all the resilient-enhanced strategies and cases investigated within this paper are summarized in the following Figure 2.


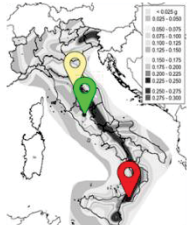
Design methodology		Seismic demand	
Force-Based Design	<div>Drift target</div> <div>1.0%</div> <div>1.5%</div> <div>2.0%</div>	Importance Class → Importance Coeff.	
		II	1.0
Displacement-Based Design		III	1.5
		IV	2.0
Technology		Seismicity area	
Monolithic cast-in situ connections		Low seismicity	
Hybrid low-damage connections		Moderate seismicity	
		High seismicity	

Figure 2: Summary of resilient-enhanced strategies and cases involved in the study.

Alternative design methods are adopted, namely the traditional Force-Based Design (FBD) and the more recently developed and advanced Direct Displacement-Based Design (DDBD), in order to highlight that a design based on (targeting and thus controlling/limiting) displacements rather than forces allows to better control the performance of buildings in the plastic domain. The FBD is implemented following the prescriptions of the Italian code, NTC 2018 [11], thus the method is based on the calculation of the natural period of the structure by alternative formulations and on the choice of the behavior factor,  $q$ , depending on the structural typology, its statically indeterminate level and the design criteria (ductility class). These assumptions do not allow to properly control the building structural behavior. On the other hand, the DDBD method [12] is based on the initial choice of a target drift, thus the seismic behavior/performance of the structure is controlled upfront by the designer and his design choice.

In addition to the two different design methodologies, the increase of seismic safety is studied through the variation of the Importance Level or Class (II, III, IV, i.e. from ordinary/residential buildings to strategic buildings), leading to a consequent increase of the seismic demand (design) level. This means that the buildings are firstly designed as ordinary residential structures, then as strategic structures such as hospitals, firefighter station, police station, etc. According to NTC 2018 [11], the variation of the Importance Class involves a different coefficient, indicated as  $C_u$ , on which the value of the Reference Period ( $V_R$ ) of the building, and consequently of the Return Period ( $T_R$ ) of the seismic demand at different limit states, depends. Thus, in practical terms, this coefficient modifies the design response spectra.

Then, in terms of technology, two different types of structural connections are studied: 1) the traditional/monolithic cast-in-situ system and 2) the hybrid low-damage PRESSS solution. The monolithic connections consist of steel reinforcement (steel B450C) within the structural members (concrete C 45/55) and are designed according to the NTC 2018 [11], while the hybrid connections comprise mild steel bars (dissipation) and unbonded post-tensioning tendons (self-centering).

Furthermore, the case-study buildings are designed referring to three different seismic zones located in Italy: Fabbrica di Roma (low seismicity,  $PGA = 0.15\text{ g}$ ), Subbiano (moderate seismicity,  $PGA = 0.25\text{ g}$ ) and Reggio Calabria (high seismicity,  $PGA = 0.35\text{ g}$ ), selected according to their PGA at the Ultimate Limit State (ULS). Moreover, when the DDBD is adopted, three alternative levels of target drift ratios, namely 1%, 1.5%, 2%, are identified to analyze the structural behavior and the economic losses when targeting different level of drift.

Therefore, a total of 37 parametric building configurations are employed. Analytical/numerical investigations are developed to analyze the building performance of all case-studies. Then, for each configuration, construction costs (material and labour costs) are computed to determine the short-term cost of the alternative technological solutions. Finally, loss assessment analyses are performed to obtain the Expected Annual Losses (EAL) following two alternative procedures [13, 14]. Results are finally compared for all the configurations under consideration in terms of seismic costs at the end of the building service life (50 years). This represents an interesting data for the purpose of the economic comparison, proving that designing for higher levels of safety and resilience is cost-effective, not only beneficial from a seismic performance point of view. In fact, this research will impact with the evidence that the choice of a building system/design strategy should be addressed by its long-term economic convenience. Consequently, highlighting that an improved design approach costs less, would hopefully trigger a step-change in the near future and thus represent a major step forward for the overall society and its well-being.

### 3 COST/PERFORMANCE PARAMETRIC STUDY

#### 3.1 Case-study buildings

The case-study is a 5-story Reinforced Concrete building with geometrical configuration as indicated in Figure 3. This structure has been selected from a previous study developed by *Bianchi et al.* [15]. The first two floors have residential use, while the other two are offices. The structural skeleton consists of seismic resistant four-bay frames in one direction and shear walls in the perpendicular direction.



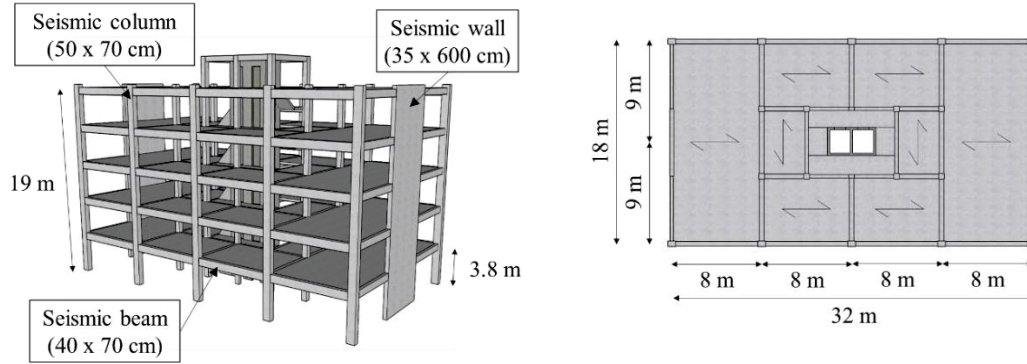


Figure 3: Multi-story case-study RC building (modified after Bianchi et al. 2021).

In this paper, the study is implemented focusing on the frame direction only. As described in the previous section, 37 different combinations of the frame system are considered to develop the proposed investigation. A summary of all the considered frame systems is presented in Table 1. It can be highlighted from this table that the structural cases increase when moving towards a higher seismicity level and importance class. In fact, in these cases the seismic design through the DDBD methodology (the sole to be herein used in case of PRESSS-technology solution) can be developed referring to different (and higher) drift targets.

Seismicity level	Importance Class					
	II		III		IV	
Low	Monolithic	FBD	Monolithic	FBD	Monolithic	FBD
		DDBD (0.8%)		DDBD (0.8%)		DDBD (0.8%)
	PRESSS	DDBD (0.8%)	PRESSS	DDBD (0.8%)	PRESSS	DDBD (0.8%)
Moderate	Monolithic	FBD	Monolithic	FBD	Monolithic	FBD
		DDBD (1.0%)		DDBD (1.0%)		DDBD (1.0%)
	PRESSS	DDBD (1.0%)	PRESSS	DDBD (1.0%)	PRESSS	DDBD (1.0%)
High	Monolithic	FBD	Monolithic	FBD	Monolithic	FBD
		DDBD (1.0%)		DDBD (1.0%)		DDBD (1.0%)
		DDBD (1.5%)		DDBD (1.5%)		DDBD (1.5%)
		DDBD (2.0%)		DDBD (2.0%)		DDBD (2.0%)
	PRESSS	DDBD (1.0%)	PRESSS	DDBD (1.0%)	PRESSS	DDBD (1.0%)
		DDBD (1.5%)		DDBD (1.5%)		DDBD (1.5%)
		DDBD (2.0%)		DDBD (2.0%)		DDBD (2.0%)

Table 1: Selected frame configurations.



### 3.2 Design methodology

The case-study structures are designed at ULS level following two different methodologies: Force-Based Design (FBD) and Displacement-Based Design (DDBD). Taking into account the three different low-to-high seismicity zones (Figure 4a) as well as the three Importance Classes (II, III, IV) described in NTC 2018 [11], accounting for the importance of the building and providing a coefficient (1.0, 1.5, 2.0) which increases/decreases the seismic action, 9 alternative configurations are designed in case of FBD. As an example, Figure 4b presents the response spectra obtained for the case of high seismicity zone and varying the Importance Class.

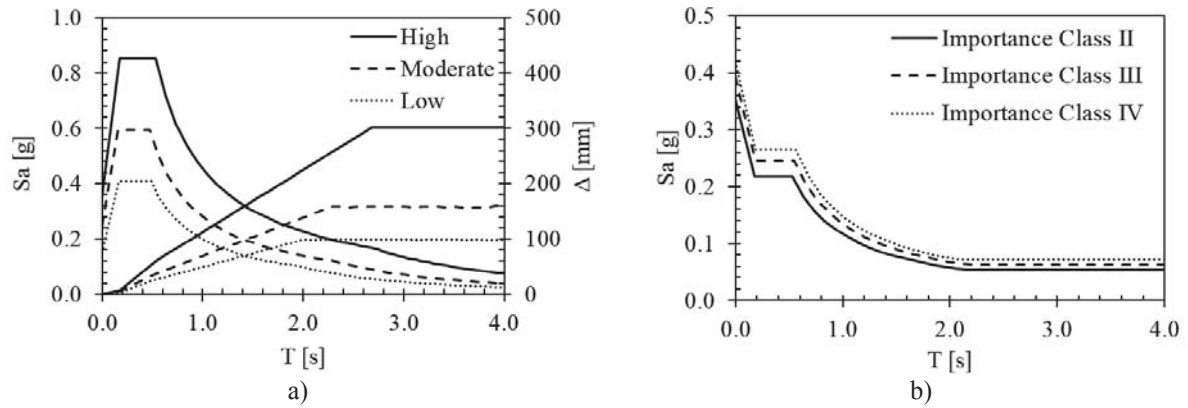


Figure 4: a) Elastic (5% damped) acceleration and displacement response spectra for the three different seismic zones; b) design acceleration response spectra for the case of high seismicity and varying the Importance Class.

Following the NTC 2018 [11] procedure, the design acceleration response spectra at ULS are obtained from the 5% elastic spectra properly scaled by the behaviour factor (i.e.  $q = 3.9$ , for multi-storey frame reinforced concrete structures with regular height and plan, ductility class B). Thus, the base-shear is calculated by multiplying the spectral acceleration at the first natural period of the structure ( $T_1 = 0.68s$ , function of the building height  $H$  and a coefficient  $C$  based on the structural typology) and the building mass (1, 2). Table 2 summaries the seismic response of the case-studies (monolithic) designed following the codified FBD approach.

$$T_1 = C \cdot H^{3/4} \quad (1)$$

$$V_b = S_a(T_1) \cdot m \quad (2)$$

Seismicity level	Importance Class	Base Shear [kN]
Low	II	1206
	III	1391
	IV	1523
Moderate	II	1705
	III	1925
	IV	2122
High	II	2826
	III	3397
	IV	3785

Table 2: Configurations designed by the FBD approach.

Concerning the DDBD, the procedure consists in the evaluation of the equivalent building Single Degree of Freedom (SDoF) system with effective elastic stiffness ( $K_{eff}$ ), effective mass ( $m_{eff}$ ), effective height ( $H_{eff}$ ) and equivalent viscous damping related to the target displacement ( $\Delta_d$ ). Appropriate design inter-story drift limits are selected based on design code, good practice and/or material strain limits. Table 3 summarizes the various configurations designed following the DDBD approach, by reporting the design drift level, the effective period as well as the base shear, calculated as per (3, 4).

$$K_{eff} = (2\pi/T_{eff})^2 \cdot m_{eff} \quad (3)$$

$$V_b = \Delta_d \cdot K_{eff} \quad (4)$$

Seismicity level	Importance Class	Monolithic		PRESSS	
		Design Drift [%]	Base Shear [kN]	Design Drift [%]	Base Shear [kN]
Low	II	0.8	1797	0.8	1865
	III	0.8	1867	0.8	1977
	IV	0.8	1903	0.8	2161
Moderate	II	1.0	2004	1.0	2101
	III	1.0	2006	1.0	2111
	IV	1.0	2269	1.0	2505
High	II	1.0	2415	1.0	3264
	II	1.5	2274	1.5	3008
	III	1.0	3281	1.0	4468
	III	1.5	2874	1.5	3763
	III	1.8	2218	1.8	2989
	IV	1.0	3660	1.0	5822
	IV	1.5	3340	1.5	4614
	IV	2.0	2583	2.0	3041

Table 3: Configurations designed by the DDBD approach.

### 3.3 Numerical investigation

Numerical non-linear static (push-over, push-pull) analyses are carried out in SAP2000 software following a lumped-plasticity approach. The monolithic buildings are modelled by mono-dimensional elastic elements with plastic hinges at the end sections, where the inelasticity is represented by appropriate moment-curvature relationships and stiffness-degrading hysteresis rules (Takeda). The PRESSS connections are modelled using elastic members with two rotational springs working in parallel at the connection interfaces; 1) one simulating the re-centering contribution from the unbonded post-tensioning tendons (non-linear elastic hysteresis), 2) the other one representing the energy dissipation contribution from the mild steel dissipaters (elasto-plastic or bilinear hysteresis).

Non-linear static (pushover) analyses are performed to determine the building capacity curves, then converted into acceleration-displacement functions within an Acceleration Displacement Response Spectra (ADRS) domain. Introducing in the same graphs the code-design spectra and applying the Capacity Spectrum Method (CSM) [16, 17], with the building equivalent viscous damping being derived from push-pull analyses, the maximum expected seismic displacements and accelerations (performance) at each intensity level (namely SLO, SLD, SLV, SLC, or, Immediate Operational, Damage Control, Life Safety and Collapse Prevention, as indicated in the NTC 2018 [11]) can be identified. As an example, Figure 5 shows the acceleration-displacement performance points for the case of SLV, high seismicity and Importance Class IV.

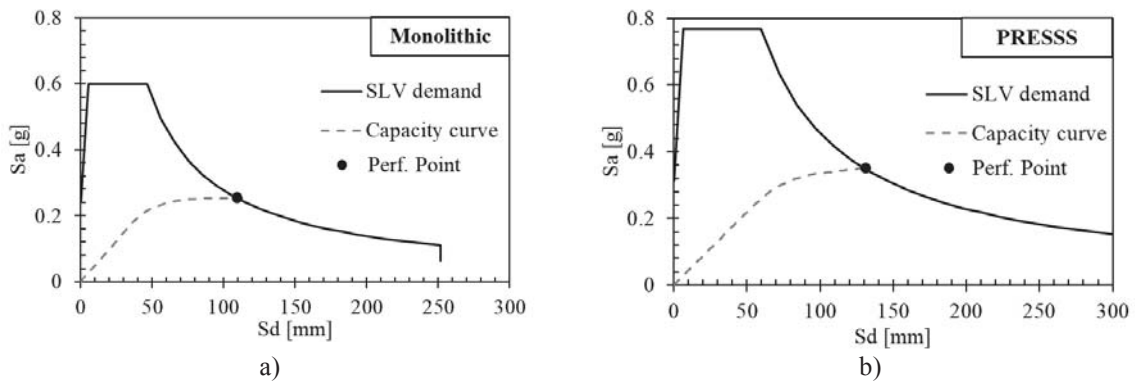


Figure 5: Capacity curves in the Acceleration-Displacement Response Spectrum (ADRS) for both a) Monolithic and b) Low-damage skeletons, high seismicity level (PGA=0.35g), SLV limit state, Importance Class IV.

By comparing the results in terms of base shear for all the case-studies, important considerations supporting the thesis of this paper can be found. Specifically, as presented in Figure 6, ally, the base shear obtained by the FBD has a linear dependence with the Peak Ground Acceleration (PGA) for each seismic zone, however in high seismic zone its value tends to grow faster than the acceleration value. For the cases designed by DDBD, it can be highlighted that the base shear decreases as the design drift increases, due to a greater (accepted) target displacement and thus a lower stiffness, and no direct proportionality between base shear and Peak Ground Acceleration can be found. Furthermore, when considering the hybrid low damage skeleton, a slightly higher base shear – due to the lower hysteretic damping value – is obtained when compared to the traditional solution. This is due to the resisting moment capacity, which is distributed between dissipative and recentring systems, consequently the dissipation is lower when compared to the case of monolithic connections.

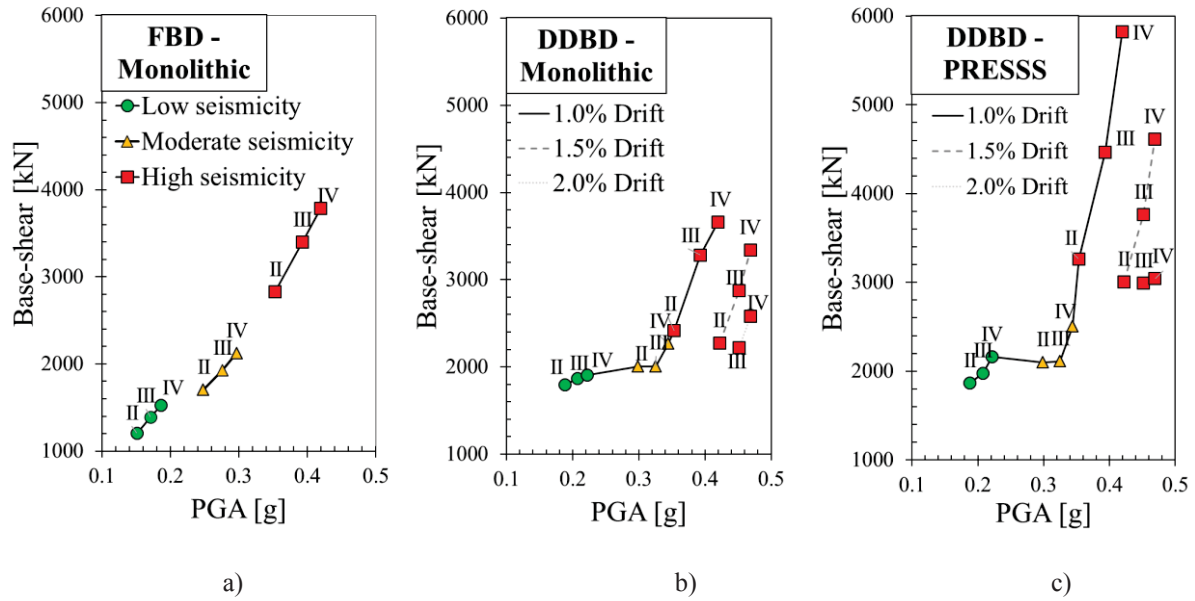


Figure 6: Base shear/PGA curves for: the monolithic structures designed by a) FBD and b) DDBD; c) the low-damage PRESSS structures designed by DDBD (II, III, IV refer to the Importance Class).

Referring to the same seismicity zone, results are also compared by varying the design methodology and type of connection system (Figure 7). Focusing on the monolithic structures, it can be noticed that the FBD underestimates the building base shear in case of low and moderate seismicity zones while overestimate its value in case of high seismicity zone, when compared to the DDBD results, assumed to provide a more reliable (“correct”) structural response. This highlights that the FBD method does not allow to have a proper control on the nonlinear behavior of the structure, due to a design procedure based on the selection of a behavior factor,  $q$ , representing the dissipation capability of the building under consideration.

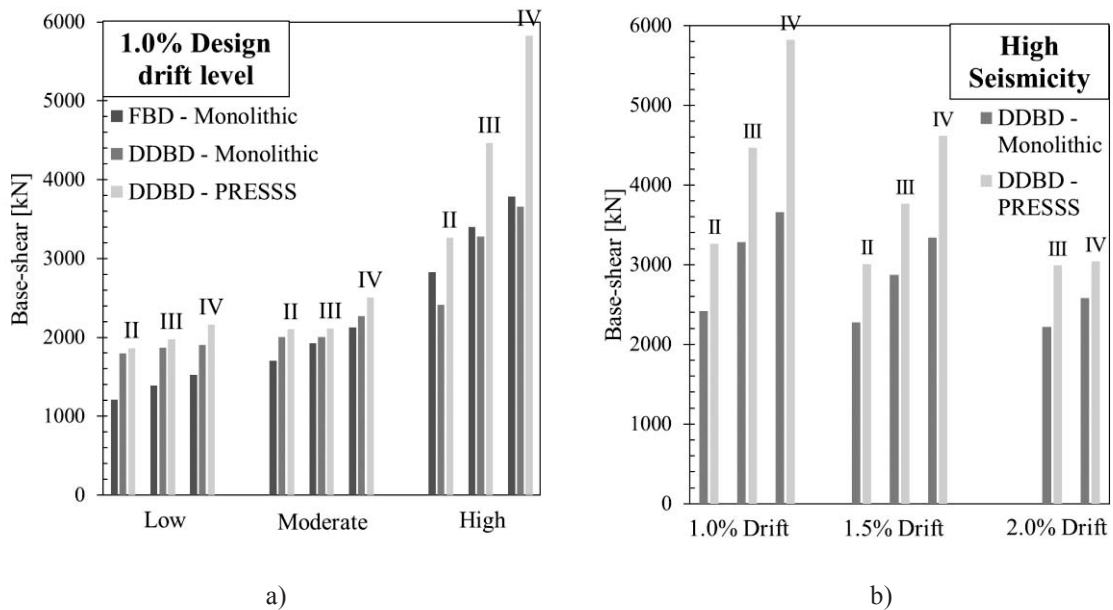


Figure 7: Comparison in terms of Base Shear for: a) alternative design methodologies (at the same design drift level for DDBD) and all the seismicity zones; b) different technological solutions at the same seismicity level, in case of DDBD and various design drift levels.

### 3.4 Construction costs

For each structural configuration involved, construction costs are computed based on the Regional Public Works Price List of the Friuli-Venezia Giulia region (IT), where the cost of each material already account for the specific labour cost. The cost of the monolithic structure is calculated taking into account the quantities of concrete and steel needed for the structural elements, as well as the cost of formworks, safety, excavation, foundations and geotechnical surveys. For the PRESSS structures, the cost of the tendons and their post-tensioning, the corrugated tube and the crane rental are added to the above items (apart from the cost of in-situ formworks, not needed for the precast elements). In order to define an overall cost of the multi-story building, since the seismic-resistant frames have only been designed for the purpose of this study, the other beams, columns and walls have been calculated taking into account code prescriptions and considering standard geometrical dimensions for each element.

A comparison in terms of construction cost for the alternative case-study configurations is reported in the following Figure 8 and Table 4. It can be noticed that the FBD provides costs equal to, or higher than, the DDBD for the same seismicity zone. Moreover, as far as a comparison between technologies is concerned, it can be highlighted that the PRESSS technology leads to an increase of 6.7-8.5% in low and moderate high seismic regions with peaks at 12.5-20.20% in high seismic region, for the construction cost when compared to the monolithic system, due to the presence of tendons/cables and their post-tensioning. In particular, the most expensive cases are those with 1.0 % design drift level in high seismic zone, as confirmed by the results obtained in the previous paragraph in terms of base shear.

Overall for a given seismicity the increase of direct costs associated with a significant raise for the bar, moving from Importance Class II to III and IV, is counter-intuitively rather moderate, ranging between 0.8-2.2%, 0.6-3.8%, 6%-13.3% in low seismic, moderate seismic and high seismic. Thus arguably, a significant level of higher safety of new construction can be achieved with minimal-moderate investment. In the next paragraph the tangible life-span economic benefits of such approach are investigated.

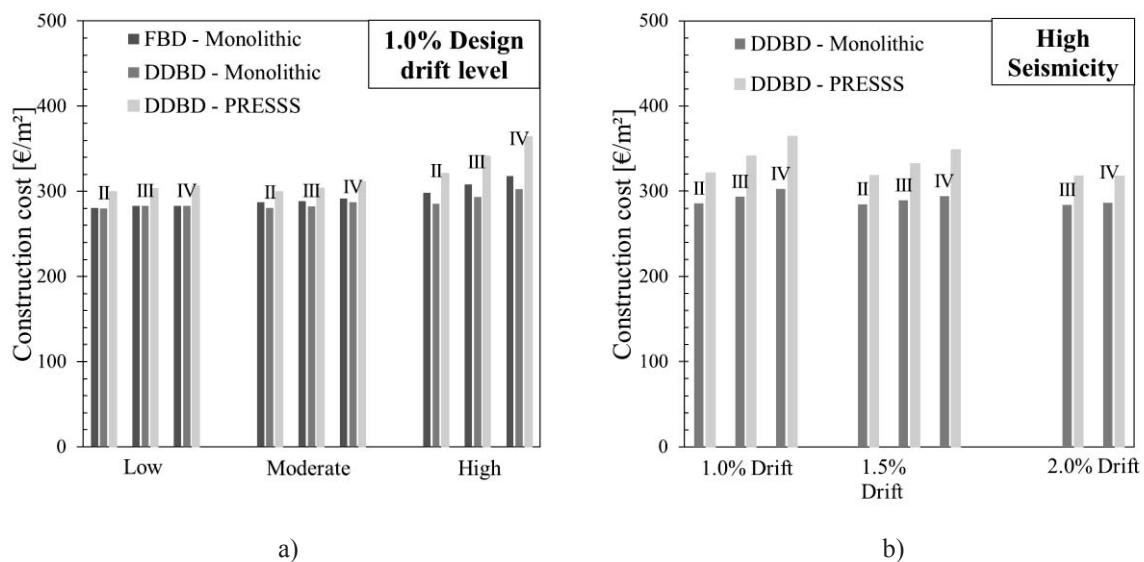


Figure 8: Comparison in terms of Construction Cost for: a) alternative design methodologies (at the same design drift level for DDBD) and all the seismicity zones; b) different technological solutions at the same seismicity level, in case of DDBD and various design drift levels.

Seismicity level	Importance Class	Construction Cost [€/m <sup>2</sup> ]			Cost Difference [%]	
		FBD Monolithic	DDBD Monolithic	DDBD PRESSS	DDBD vs FBD Monolithic	DDBD Monolithic vs PRESSS
Low	II	280.7	280.0	299.8	0.25	7.06
	III	282.9	282.7	303.0	0.07	7.19
	IV	282.9	282.8	306.4	0.04	8.34
Moderate	II	287.0	280.8	299.6	2.21	6.68
	III	288.6	282.6	303.7	2.12	7.45
	IV	291.8	287.3	311.5	1.57	8.44
High (1.0% drift)	II	298.4	285.5	321.2	4.52	12.50
	III	308.3	293.4	341.1	5.08	16.27
	IV	318.2	302.8	364.1	5.09	20.26

Table 4: Comparison in terms of Construction Costs.

#### 4 LOSS ASSESSMENT ANALYSIS

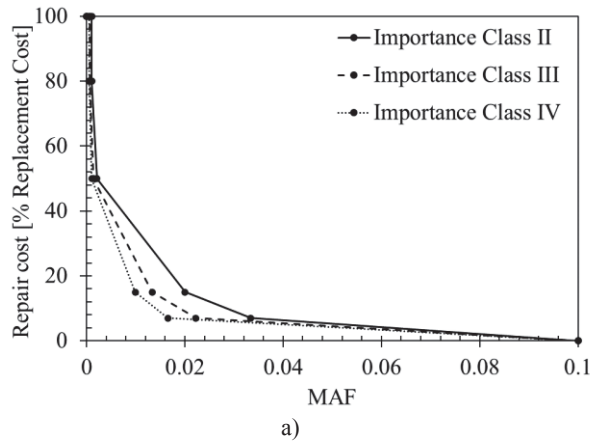
The estimation of seismic economic losses is fundamental to evaluate the actual long-term (structure life-span) convenience of a design strategy when compared to another. As mentioned above, the economic aspect is certainly crucial when a project is carried out, and represents the factor mainly addressing the choice of a technological solution. Proving that a safer solution is also the least expensive (when considering the life-span of the building, not only the initial costs) is therefore essential to spread the idea that current traditional performance-based design approach (limited to Life Safety) is not enough to meet the seismic demands of our modern society.

From a procedural point of view, two assessment approaches are herein involved to evaluate the seismic losses and, specifically, to calculate the Expected Annual Losses (EAL), namely: 1) the simplified procedure by D.M. 65 2017 [13]; 2) the rigorous procedure by FEMA P-58 2012 [14]. The first procedure takes into account the direct losses only and is actually developed for, and calibrated on, existing buildings. On the other hand, the probabilistic FEMA P-58 methodology account for both direct and indirect economic losses, providing an accurate loss estimation if all the building component fragilities (and related fragility curves/consequence functions) are known.

##### 4.1 Simplified methodology

The procedure described in the “Seismic Bonus” guidelines - D.M. 65 2017 [13] - is herein implemented. From the building capacity curves, the capacity Mean Annual Frequencies (MAF) are computed at various seismic intensity levels (SLDI, SLO, SLD, SLV, SLC, SLR, or, respectively Non-structural Damage, Immediate Operational, Damage Control, Life Safety, Collapse Prevention, Demolition and Reconstruction). A Reconstruction Cost is associated with each intensity level and expressed as a percentage of the total building cost. This allows to build the cost/frequency curves and, thus, to determine the EAL value and related class. Since the case-studies are new buildings, the ratio of capacity to demand is equal to (or more than) 1, meaning that the Capacity Return Period is equal to (or more than) the Demand Return Period. The difference between the case-studies is therefore related to the different Importance Class only; as the Importance Class varies, the Return Period associated with each limit state varies. Consequently, only three EAL curves corresponding to the three Importance Classes are obtained for all the 37 cases employed (Figure 9).





Importance Class	EAL [% RC]
II	0.98
III	0.77
IV	0.66

b)

Figure 9: EAL curves and values obtained from the simplified loss assessment analysis.

In all cases, the building systems result in A class ( $0.5 \leq \text{EAL} \leq 1.0$ ) and it can be noted that losses are higher when an Importance Class II is assumed, representing the lower safety-resilience level for the building. Therefore, the implemented procedure highlights that the simplified approach, developed for existing structures, is not applicable for new buildings. In fact, it does not allow to account for between different construction methods as well as technologies.

#### 4.2 Probabilistic-based methodology

The refined loss assessment investigation is implemented using the PACT (Performance Assessment Calculation Tool) provided by the FEMA P-58 [14]. This practical tool allows to calculate the direct and indirect economic losses of a structure. In order to implement the analysis, input data describing the building (geometry, use, components) and hazard are required. Fragility curves and consequence functions need also to be defined for both structural and non-structural elements. Concerning the monolithic cast-in-situ connections, the fragility specifications are selected from the ones available in the FEMA P-58 database considering components with similar geometry to the case-study structure. In the case of PRESSS connections, section-analysis results are elaborated to build up specific fragility functions describing the connection behavior (i.e. fracture of the mild steel bars and yielding of post-tensioned tendons). Then, the seismic demand for each limit state in terms of inter-story drift ratios and floor accelerations, calculated through the pushover-based capacity spectrum method, are considered as additional input data. Moreover, the analysis is carried out including the contribution of residual drift ratios for the monolithic structures (negligible residual displacements characterize the hybrid system due to its self-centering behavior). The loss assessment analysis thus provides a more accurate estimation of the annualized expected repair costs (EAL values). Figure 10 and Table 5 present the results obtained from this probabilistic-based procedure.

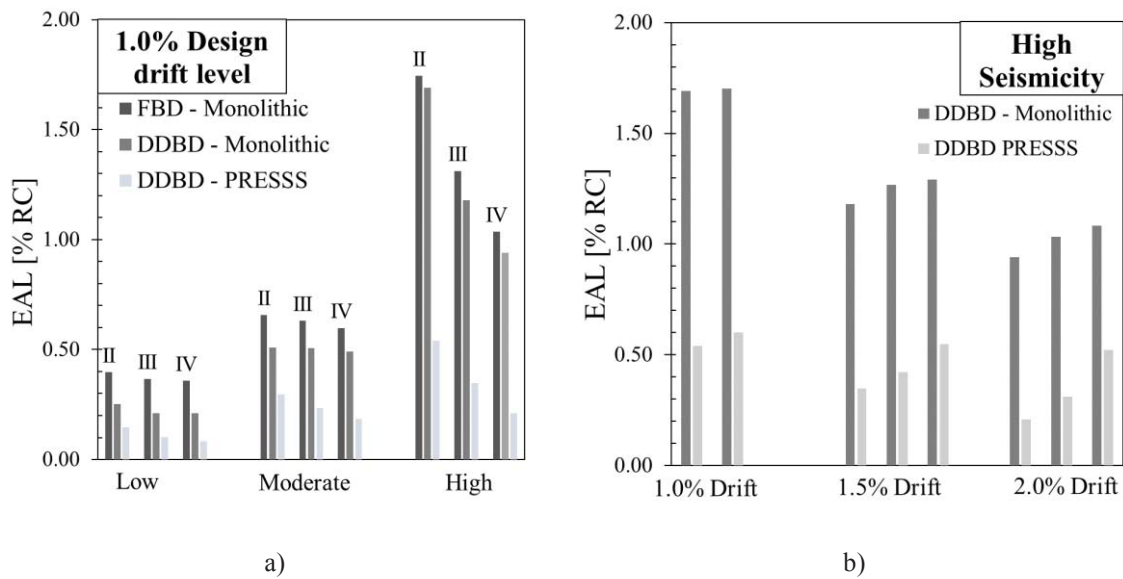


Figure 10: Comparison in terms of Expected Annual Losses for: a) alternative design methodologies (at the same design drift level for DDBD) and all the seismicity zones; b) different technological solutions at the same seismicity level, in case of DDBD and various design drift levels.

Seismicity level	Importance Class	Design Drift [%]	EAL [% Replacement Cost]		
			FBD Monolithic	DDBD Monolithic	DDBD PRESS
Low	II	0.76	0.40	0.25	0.14
	III	0.77	0.37	0.21	0.10
	IV	0.81	0.36	0.21	0.08
Moderate	II	1.0	0.66	0.51	0.30
	III	1.0	0.63	0.51	0.23
	IV	1.0	0.60	0.49	0.18
High	II	1.0	1.74	1.69	0.54
	II	1.5	-	1.70	0.60
	III	1.0	1.31	1.18	0.35
	III	1.5	-	1.27	0.42
	III	1.8	-	1.29	0.55
	IV	1.0	1.04	0.94	0.21
	IV	1.5	-	1.03	0.31
	IV	2.0	-	1.08	0.52

Table 5: Comparison in terms of Expected Annual Loss.

Results in terms of EAL highlight that: 1) as the service class increases, the losses decrease, due to the increased level of safety consequently leading to reduced seismic losses; 2) as the design drift level increases, the value of EAL parameter also increases; this is related to a seismic design for higher levels of displacement which brings to consequent higher damages. When comparing the results obtained for the same construction technology whilst varying the design method, FBD produces greater losses than the DDBD, confirming the disadvantage of applying such traditional design methodology. Moreover, looking at the different types of skeleton systems, PRESS structures lead to significantly lower losses when compared to monolithic structures, due to its inherent low-damage nature.

Referring to the repair costs of each limit state as well as to their Mean Annual Frequency of exceedance, EAL curves are built. These curves provide more reliable loss values when compared to the previous simplified results not accounting for the real repair costs associated with each limit state. The overall repair cost is now properly computed for the various intensity levels and this allows to appreciate the advantages and disadvantages of design methods and technologies. Comparisons in terms of EAL curves are thus carried out for the different seismicity levels as presented in Figure 11 (e.g. different seismicity areas, service class IV, 1.0% design drift level for DDBD). In the same graph a reparability threshold of 65%, i.e. value above which is no longer considered convenient to repair the building, is also included. It is noted that in low seismicity areas this threshold value is never reached.

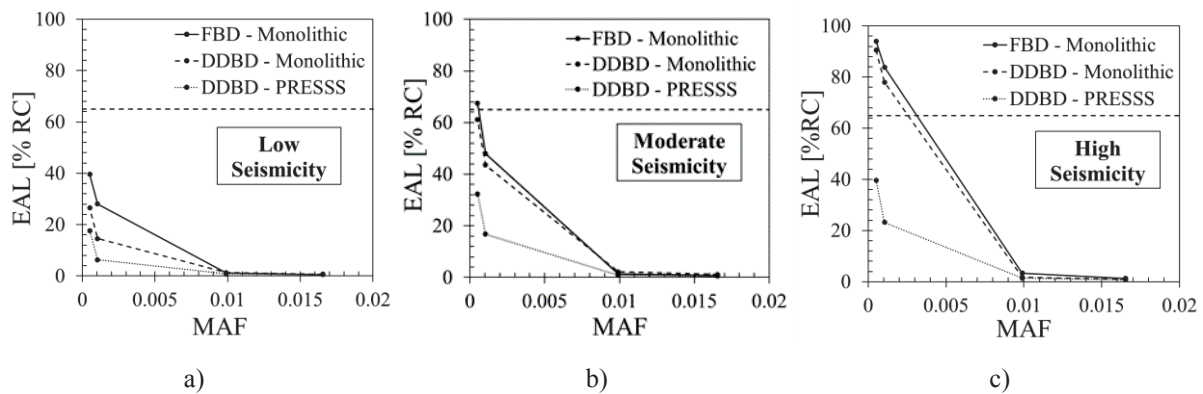


Figure 11: Comparison of design strategies in terms of EAL curves (for different seismic zones: a) low; b) moderate; c) high, an Importance Class IV, 1.0% design drift level for DDBD).

## 5 SEISMIC COSTS IN THE BUILDING LIFE

In order to better appreciate the advantages of a design based on the control of damage and on increased safety levels, the seismic costs of all case-studies are compared at the end of the service life, that is, for example, 50 years after the building construction. This comparison can be carried out by considering the annualized losses (the EAL parameter) distributed along 50 years in order to evaluate the percentage of construction cost which would be lost at the end of the building life. As shown in Figure 13a, the cumulative seismic cost is described by a linear trend going from the initial cost at the time of construction to the cost at the end of the building service life. The intersection between the different lines, representing different design strategies, identify the break-even time at which the initial (if any) difference in the initial construction costs is balanced; therefore, although at the time of initial construction the PRESS technology might be slightly more expensive than the traditional one (notably the implementation of actual buildings have proven to be no more expensive), from the year corresponding to the intersection of their cost lines onward, the trend is completely reversed. For example, it can be noticed that in high seismicity and design drift of 1.0% for DDBD, the difference in the initial cost of 12% (monolithic vs. low damage) at the time of construction can be fully recovered in just ten years. In order to highlight the advantages obtained by switching from FBD to DDBD as well as from monolithic to hybrid connections, the savings after 50 years from the time of construction and for each seismicity area are shown and compared in Figure 12 (b, c) and Table 6.

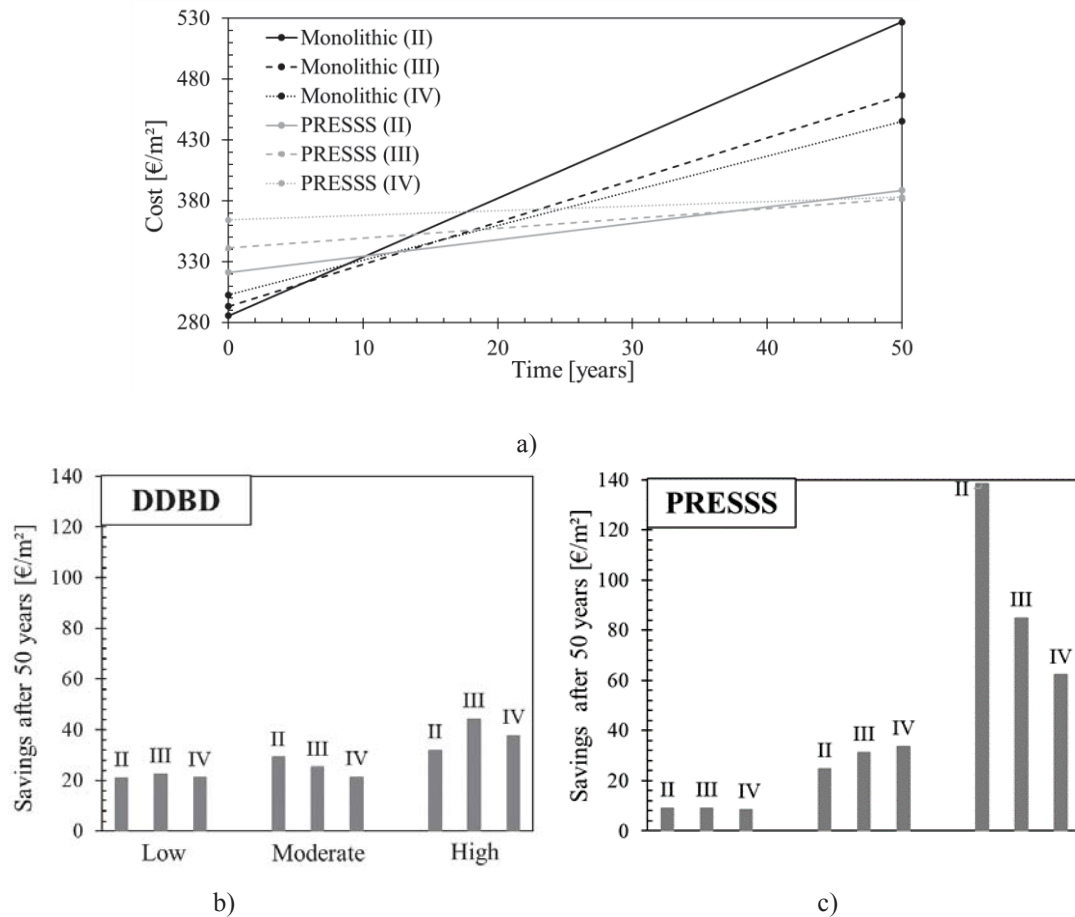


Figure 12: a) Cost/time curves in case of High Seismicity zone; Average savings at the end of the building life for different seismicity zones and due to: b) DDBD method; c) PRESSS technology.

Seismicity level	Importance Class	Savings at 50 years [€/m²]			Savings [€/m²]	
		FBD Monolithic	DDBD Monolithic	DDBD PRESSS	DDBD vs FBD Monolithic	DDBD Monolithic vs PRESSS
Low	II	336.3	315.2	306.1	21.1	9.1
	III	334.8	312.3	303.3	22.5	9.1
	IV	333.5	312.4	304.0	21.1	8.5
Moderate	II	381.3	352.3	327.6	29.0	24.7
	III	379.5	354.2	323.0	25.2	31.2
	IV	379.1	357.7	324.0	21.3	33.7
High (1.0% drift)	II	558.8	527.0	388.5	31.7	138.5
	III	510.6	466.4	381.5	44.1	84.9
	IV	483.0	445.3	383.1	37.7	62.2

Table 6: Comparison in terms of savings at the end of the building life.

The savings are clearly more consistent in high seismicity areas and consequently the advantages of a low-damage technology are more evident. The previous graphs are particularly relevant, as it presents in absolute terms the significant amount of (tax-payers) money that can be saved in 50 years. Cost of construction is correlated with losses over time and money savings are evident. Finally, it is observed that the convenience of implementing low-damage technologies is substantial for the case of high seismicity area and Importance Class II.

## 6 CONCLUSIONS

This paper has focused on the cost/performance-based study and comparison of alternative design strategies which might be adopted to enhance the seismic safety of new buildings. Focusing on Reinforced Concrete structures and considering increasingly levels of seismic intensity (representing either a higher seismic zone or a higher service class or Importance Level), different design methodologies (force-based vs displacement-based) or technologies (monolithic vs low-damage) have been adopted to develop the proposed parametric study.

Results of this research allows for greater awareness of the proper design method/strategy to be used according to the seismic area and the Importance Class of a specific building. In particular, the developed study highlights that the force-based design brings to different (yet not necessarily conservative) results when compared to the displacement-based design. Specifically, the parametric study on alternative structural configurations highlights that the building response in terms of base shear is generally overestimated. However, this does not mean that the force-based design is a more conservative method than the displacement-based approach (as it could in turn underestimate the displacement-ductility demand), while it highlights that this approach does not allow to have a proper control of the real structural behavior, and in general on the obtained seismic results. Furthermore, the parametric study shows that the base-shear, that is a fundamental parameter for the seismic design since it allows to determine the demand moment/shear values on the structural elements, does not necessary nor directly increase with the assumed level of seismic intensity, expressed in terms of Peak Ground Acceleration (PGA). Specifically, looking at the same design displacement, the base shear increases with the acceleration, whilst if the acceleration doubles, the base shear does not. This last consideration proves that designing for higher Importance Classes, and therefore with greater safety and resilience, does not necessarily lead to an equally higher cost. Minor but appropriately focused investments can instead lead to greater safety, resilience and long-term savings.

Taking into account the results in terms of initial construction cost and focusing on high seismicity area, (worst case scenario) it can be noticed that moving from Importance Class II to IV with the same design drift level (e.g. 1%), although the required base shear should be 50% higher, an initial cost increase of only 6% is expected. More importantly, when considering the cumulative seismic cost over time, the slight cost distance is completely recovered in less than 10 years, and at the end of the service life of the structure (50 years) a saving of about 15% is obtained, leading to an increased safety for the building as well as reduced losses over time.

Furthermore, the advantage related to the implementation of a low-damage technology such as the rocking-dissipative PRESSS system is evident, especially for the case-studies where post-earthquake damage causes very high repair costs. In fact, the computed savings at 50 years (service life) after the time of construction show that the greatest savings refer to Importance Class II, design drift of 1% and high seismicity zone. Importance Class II is, in general, the level with the highest losses over time (lower safety), while a design drift of 1% presents the most expensive case in terms of construction cost. However, this consideration does not lead to the conclusion that in areas with a low seismicity, low-damage connections are not convenient; savings are obtained for all seismic-prone areas and Importance Classes, so it is clear that designing better, that means for better performance and greater safety, is always also economically convenient leading to a more resilient community.

Despite this research work represents an initial study aiming to prove the convenience of implementing enhanced-safety design strategies, further investigations are needed to compare alternative design methods and technologies. In particular, more refined numerical studies are required, involving time-history analyses and performing a probabilistic-based approach, looking at the influence of the design approach on the building probability of collapse.

## REFERENCES

- [1] W.Y. Kam, S. Pampanin, K. Elwood, Seismic performance of reinforced concrete buildings in the 22 February Christchurch (Lyttelton) earthquake. *Bulletin of the New Zealand Society for Earthquake Engineering*, **44**, 4, 239-278, 2011.
- [2] Structural Engineers Associate of California, *Performance-based seismic engineering*, SEAOC Vision 2000, Sacramento, California, USA, 2000.
- [3] S. Pampanin, Reality-check and Renewed challenges in Earthquake Engineering: Implementing low-damage structural Systems – from theory to practice. *Bulletin of the New Zealand Society for Earthquake Engineering*, **45**, 4, 137-160, 2012.
- [1] S. Pampanin, Towards the “Ultimate Earthquake-Proof” Building: Development of an Integrated Low-Damage System. *Perspectives on European Earthquake Engineering and Seismology* (A. Ansal, ed.), Geotechnical, Geological and Earthquake Engineering 39, Springer Nature, Switzerland, 2015.
- [2] M.J.N. Priestley, Overview of PRESSS Research Program. *PCI Journal*, **36**, 4, 50–57, 1991.
- [3] M.J.N. Priestley, S. Sritharan, J.R. Conley, S. Pampanin, Preliminary Results and Conclusions From the PRESSS Five-Story Precast Concrete Test Building. *PCI Journal*, **44**, 6, 42–67, 1999.
- [4] S. Pampanin, Emerging solutions for high seismic performance of precast -prestressed concrete buildings. *Journal of Advanced Concrete Technologies*, **3**, 2, 202–222, 2005.
- [5] S. Pampanin, D. Marriott, A. Palermo, New Zealand Concrete Society, *PRESSS Design Handbook*, Auckland, New Zealand, 2010.
- [6] F. Sarti, A. Palermo, S. Pampanin, Fuse-Type External Replaceable Dissipaters: Experimental Program and Numerical Modeling. *Journal of Structural Engineering*, **142**, 12, 2016.
- [7] International Federation for Structural Concrete (fib), *Bulletin No. 27*, Lausanne, Switzerland, 2003.
- [8] Ministero delle Infrastrutture, *Aggiornamento delle Norme Tecniche per le Costruzioni*, Supplemento ordinario n°8 alle G.U. n° 42 del 20/02/2018, serie generale, Rome, Italy, 2018.
- [9] M.J.N. Priestley, G.M. Calvi, M.J. Kowalsky, *Direct Displacement-Based Seismic Design of Structures, 1st edition*, IUSS Press, Pavia, Italy, 2007.
- [10] Ministero delle Infrastrutture, *Linee guida per la classificazione del rischio sismico delle costruzioni*, Decreto Ministeriale 58 del 28/02/2017, Rome, Italy, 2017.
- [11] Federal Emergency Management Agency (FEMA), *Seismic Performance Assessment of Buildings*, Volume 1 – Methodology. Technical Report FEMA-P-58-1, Washington, D.C., USA, 2012.
- [12] S. Bianchi, J. Ciurlanti, S. Pampanin, Comparison of traditional vs low-damage structural and non-structural building systems through a cost/performance-based evaluation. *Earthquake Spectra*, **37**, 1, 366-385, 2021.



- [13] S.A. Freeman, Review of the development of the capacity spectrum method. *ISET J. Earthquake Technology*, **41**, 1, 1–13, 2004
- [14] Applied Technology Council (ATC), *Seismic evaluation and retrofit of concrete buildings*. ATC 40, Redwood City, CA, USA, 1996.

## SEISMIC RESPONSE OF A TRANSPARENT PAVILION MADE OF STRUCTURAL GLASS

Dimitra V. Achillopoulou<sup>1,2</sup>, Nikoleta K. Stamataki<sup>3</sup>

<sup>1</sup> Civil Engineering Department, Democritus University of Thrace  
University Campus, Xanthi  
e-mail: [dimiach@civil.duth.gr](mailto:dimiach@civil.duth.gr)

<sup>2</sup> University of Surrey, Guildford, Surrey GU2 7XH, United Kingdom  
[d.achillopoulou@surrey.ac.uk](mailto:d.achillopoulou@surrey.ac.uk)

<sup>3</sup> Civil Engineering Department, Democritus University of Thrace  
University Campus, Xanthi  
[nikostam3@civil.duth.gr](mailto:nikostam3@civil.duth.gr)

---

### Abstract

*This paper deals with the design of a transparent pavilion (museum) made of structural glass. The fundamental concepts of structural glass are described and its application in public buildings. The work is focused on the seismic analysis of the glass structural members in regions with high seismicity. Particularly in these regions the basic principles of seismic isolation are taken into account and applied in the model building in order to avoid brittle failures. Analytical results show that the elastic behavior of structural glass doesn't affect the overall response of the building in seismic events if it is properly isolated. Especially, glass structural members with pseudo-ductile behavior have favorable effect on the seismic response and contribute towards accomplishing the codes' safety for public buildings.*

**Keywords:** Structural Glass, Public Building, Seismic Design, Base Isolation

---

## 1 INTRODUCTION

Glass has been one of the most well known structural materials since it was discovered back into the 1500 B.C. in Egypt and Mesopotamia and further developed in Rome during the 1<sup>st</sup> century [1]. Lately in 1950, its use in structure become very popular by Alastair Pilkington who developed the process of the float glass production (1,2). Due to its transparency and its high compressive and tensile strength, it was and remains the perfect material for the facades. As the years passed, the material affected the architectural rhythm and lately glass becomes the dominant material of the design [2]. Nowadays, after the progressive development of the material's properties and the new types of structural glass [1,2,3], the modern architecture trend to designing transparent buildings.

Apart from the esthetical value that the structural glass adds to the transparent buildings, it also shifts the negative impact on nature, since it is a full recyclable material [4]. The existing guidelines cover extensively the design of secondary structural elements [5,6] and only lately there is an effort to develop codes for all the structural members. As such, buildings of this kind are rarely met, especially in Northern Europe and US [1], and the vast majority is museums or public buildings. However, there are a few if any examples of transparent buildings in high seismicity regions. For this reason, this paper deals with the investigation of the response of a transparent public building (pavilion) made of structural glass in regions with high probability of severe seismic events.

## 2 STRUCTURAL GLASS

### 2.1 Mechanical properties

The high strength and the glass resistance to acids and salt corrosion, makes glass suitable to be used as a structural material. Especially, due to the lack of porous it is not affected by the climatic conditions and the environmental exposure. This contributes to the durability of the material and hence the structural members.

Glass is an isotropic (density  $\rho=2500\text{Kg/m}^3$ ), elastic material with a modulus of elasticity approximately equal to 70GPa, poisson ratio ranging from 0.2 to 0.3 and a compressive strength more than 500MPa [6]. The tensile strength depends on the chemical process of the production and varies from 45MPa to 120MPa [5,6].

It is worth noticing that, glass is considered a green material since it is fully recyclable and the energy need it for each production is considerably lower than that needed for compatible materials such as concrete and steel [7]. The use of glass needs special attention in order to provide energetically efficient buildings [1,2,3].

### 2.2 Types

The glass when imposed on tensile loads, cracks initiate and propagate. With further chemical process new types of glass are developed with higher tensile strength and more resistant surface on the whole. Consequently, this shift of the tensile strength, leads to different failure modes and patterns. As such there are numerous types of glass e.g. annealed, full tempered, chemically and heat strengthened or composite forms such as laminated and reinforced glass. All these categories have brittle failure mode with large and sharp or round fragments after cracking whereas composite forms present a pseudo-plastic behavior with a combination of the above maintained failure modes.

### 3 DESIGN

#### 3.1 Conceptual design of pavilion

The glass pavilion of this study is orientated to be part of an internal part of an existing museum. The pavilion is considered as a unit which can be an interior or exterior extension and can form various configurations in any natural environment.

The pavilion is a one storey building ( $H_{lev}=3.00\text{m}$ ) and has a total area equal to  $53.00\text{m}^2$  for hosting approximately 20 visitors. It consists of the exhibition room, the meeting room, reception, WC and traffic spaces as they are shown in the function diagram in Figure 1. The use of the spaces can differ according to the pavilion's demands and use. The basic conceptual design idea of the pavilion takes into consideration the proper ventilation and openings of the spaces, as well as the privacy and transparency. In case that there is a requirement for visual isolation, structural glass with controlled transparency can be used [1].

A main issue of the design with structural glass is the energy performance of the building [1,2,3]. Modern technology has lead to the development of various types of glasses e.g. reflective glass, insulating glass units, mirror glass and smart glasses [1,8] that enhance the energy efficiency. It's worth mentioning that in the present work, the energy evaluation and the use of different energy glasses has not been examined and it is a task of future work.

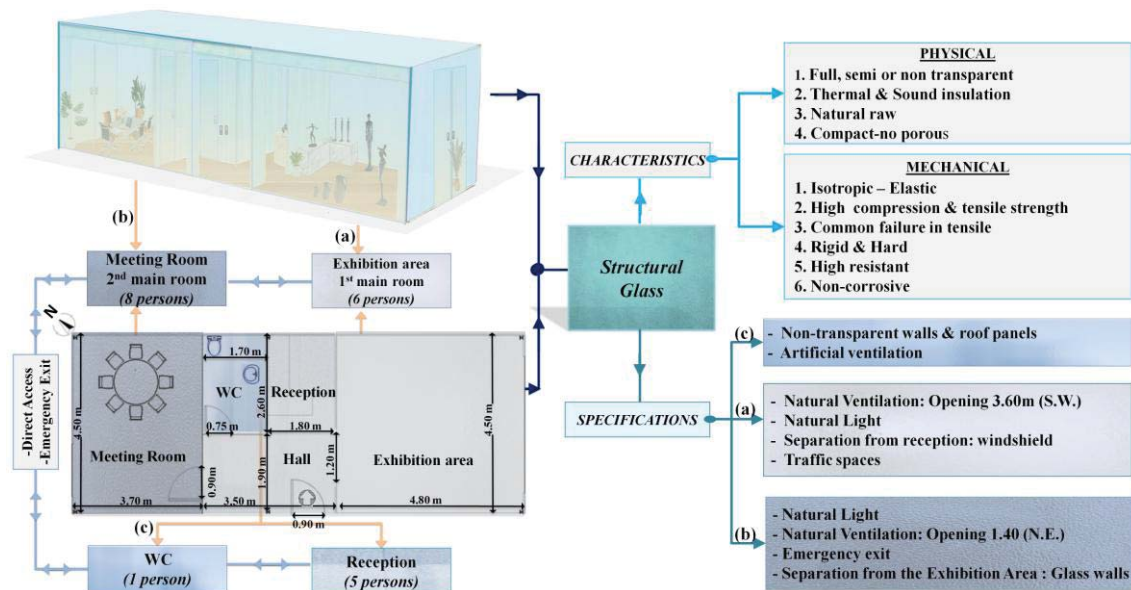


Figure 1: Function diagram of the glass pavilion

#### 3.2 Selection of structural members

Structural glass is mainly a brittle material. Alternative types such as laminated or reinforced glass present a quasi pseudo-plastic behavior [9]. This response is favorable to the overall performance of buildings in high seismicity zones, offering the desirable safety level. As such, safety glass type is preferred to form the structural body of the current study.

The glass moment frame consists of **H** shaped columns ( $250 \times 250 \text{ mm}^2$ ) and rectangular beams ( $66 \times 322 \text{ mm}^2$ ). The cross-section size is chosen so that the frame is resistant to gravity loads. Roof panels are designed to bear wind and snow loads. They are made of four sheets of full tempered laminated glass and they have total thickness equal to 40mm. The exterior glasses have 8.0mm thickness each, in order to protect the middle glasses. The infill panels, which are designed to resist in wind load, are made from triplex laminated glass and each glass panel has 15mm thickness. Columns are made of triplex laminated glass formed by three-layers of tempered glass of 22mm thickness each, assembled with a transparent sentry glass interlayer (SG). This interlayer helps to keep together the fragments in case of failure in tension. Beams contain also a steel rebar ( $22 \times 22 \text{ mm}^2$ ,  $\rho_s = 2.33\%$ ) mounted at the bottom part of the middle glass sheet which is heat-strengthened. The reinforcement is activated after the tensile failure of the cross section's glasses (heat-strengthened and tempered) and bears the tensile stresses developed without affecting significantly the transparency. Beams sheets are also kept together with a glass interlayer. The crack pattern of the fragments and the polymer defines the residual tensile strength of the member as it is shown in Figure 2. The steel reinforcement is also activated once the compressive loads exceed the compressive strength of the glass. Then fragments are created and kept in place by the SG interlayer.

Structural Member	Profile	Dimensions (mm)		Cross Section
Column		Hlev	3000	
		W1	250	
		W2	250	
		W3	250	
		t1	66	
		t2	66	
		t3	66	
Beam		Lz	4600	
		Lx1	6763	
		Lx2	5138	
		H	322	
		B	66	
		bs	22	
		hs	22	
Materials				
	Heat-Strengthened glass	Full tempered glass	Stainless steel type-304	

Table 1: Cross section's geometry

### 3.1 Seismic design of the pavilion

The pavilion's demands for seismic resistance are quantified with response spectra analysis (RSA) according to Eurocode (EC8/EN1998-1) [10] considering the seismic action as an elastic response spectrum. A preliminary modal analysis is performed in order to obtain the modal expansion (shapes).

The dynamic analysis is performed with the elastic response spectrum for the ground accelerations horizontal directions. The seismic action is represented by the elastic response spectrum, Type 1 ( $M_s > 5.5$ ) and the elastic response of the structural glass denotes that the factor  $q$  is equal to 1.00.

According to EC8, the main factors that determine the elastic response spectrum are chosen. That is, soil conditions of type B, brittle type material and importance class of the building III. As such, the reference peak ground acceleration ( $a_{gR}$ ) for soil type B is equal to  $0.36g$  and the values of the characteristics periods ( $T_B$ ,  $T_C$ ,  $T_D$ ) and the soil factor ( $S$ ), are  $0.15\text{sec}$ ,  $0.50\text{sec}$ ,  $2.00\text{sec}$  and  $1.20$  respectively. The building seismic resistance is of importance in view of the consequences associated with a collapse (e.g. schools, museums etc) and thus is classified as importance class III with a corresponding importance factor ( $\gamma_I$ ) equal to  $1.20$ . Therefore the peak ground acceleration is equal to the reference peak ground acceleration ( $a_g = \gamma_I \cdot a_{gR}$ )  $0.43g$  and the damping factor ( $\eta$ ) of the material is equal to  $2\%$ , given the nature of the material [13].

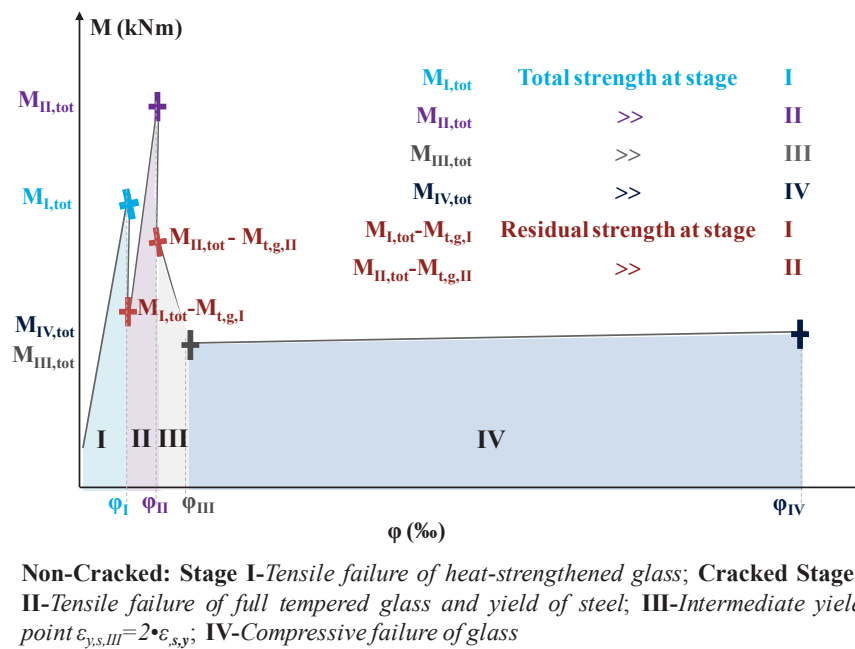


Figure 2: M-φ diagram

### 3.2 Base isolation system

Due to the high importance of the museum demands safety is increased. Especially in high seismicity zones according to EC8 the design should ensure that no collapse occurs. The glass pavilion's response of this study is mainly defined by the elastic nature and brittle failure of glass, which happens in small ranges of deformations. In order to limit them and to prevent failures from extreme earthquake events, the drift of the single degree of freedom (SDOF) pavilion should be reduced.

The glass pavilion is designed to be properly based in separate reinforced concrete foundations. In this paper a solution of base isolation system is chosen in order to decrease the maximum relative displacement of the foundation and the upper level of the structure ( $H_{lev}$ ). Various types of base isolation systems exist e.g. roller and ball bearings, sliding bearings, springs and elastomeric rubber bearings [11], with the most common in use the elastomeric rubber bearings (Low or High Damping Rubber Bearing LDRB/HDRB, Lead Rubber Bearing LRB and Friction Pendulous Systems FPS) [11]. The chosen base isolation system is one LDRB at the base of each column, made of natural rubber (NR) with a rectangular shape ( $250 \times 350 \text{mm}^2$ ) and a total height equal to  $63 \text{mm}$ . The bearing, is also reinforced with steel plates between the elastomer layers which provide high vertical stiffness ( $K_v=418.90 \text{kN/mm}$ ),



considerably higher than the horizontal one ( $K_h=1.50\text{kN/mm}$ ). This type of bearing is chosen since practically vertically it is restricted and incapable to deform. At the same time, it is flexible to withstand horizontal seismic displacements and rotations.

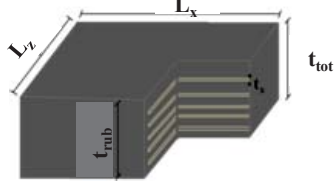


Seismic Isolation	Profile & Cross Section	Dimensions (mm)		Mechanical Characteristics		
<i>Elastomeric Bearing</i>		$L_z$	250	A	$75 \cdot 10^3$	$\text{mm}^2$
		$L_x$	300	$K_z$	$1.5 \cdot 10^3$	$\text{kN/m}$
		$t_{\text{tot}}$	63	$K_x$		
		$t_{\text{rub}}$	45	$K_y$	$4.19 \cdot 10^5$	$\text{kN/m}$
		$t_s$	$t_{\text{tot}} - t_{\text{rub}}$			
		<i>Materials</i>		<div> Natural Rubber</div> <div> Steel Plates</div>		

Table 2: Elastomeric rubber bearings' geometry

#### 4 SIMULATION

The model building was numerically investigated using ANSYS software. The glass structural members (columns and beams) were simulated using a three-dimensional Finite Element Model (FEM). The roof of the building is considered as diaphragm, at the height of 3.0m. Proper finite element types were chosen for the simulation of glass columns (BEAM188), glass beams reinforced with steel rebars (REINF264) and the base isolation system (COMBIN14). Each bearing of the isolation system chosen is simulated with one spring for each direction with suitable stiffness, mechanical properties and stress strain laws, integrating the desired features of a certain base isolation system reducing the acceleration transmitted to the superstructure.

The two scenarios studied in this paper are a) a 3-D model of the glass pavilion without base isolation and b) a 3-D model of the glass pavilion based on elastomeric bearings (Figure 3).

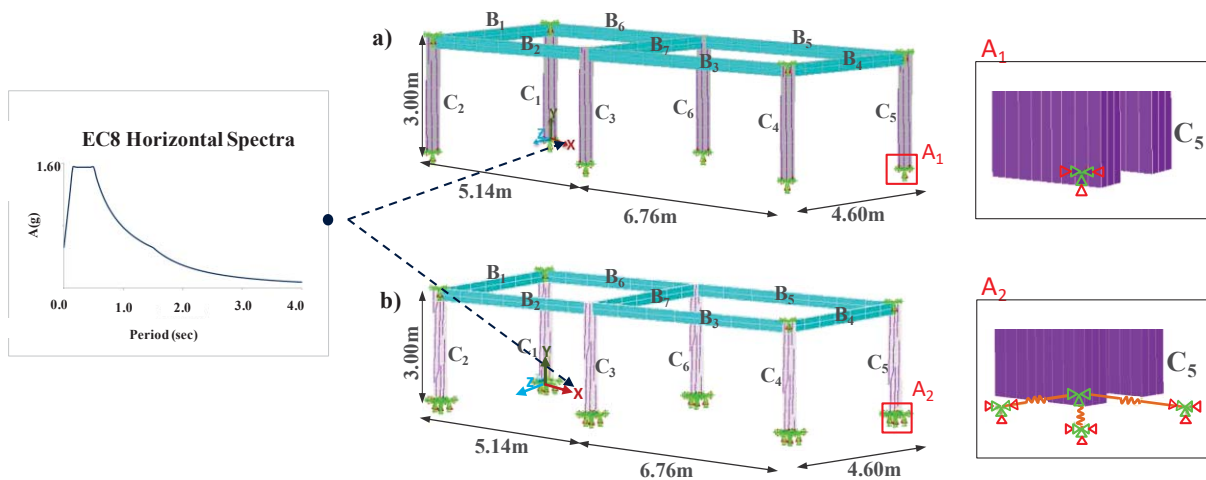


Figure 3: Two scenarios of study a) 3-D model without base isolation and b) 3-D model with base isolation

The seismic design of the pavilion is performed according to the regulations of EC8. An elastic acceleration spectrum is applied representing the seismic load, which is excited in the horizontal plane (directions  $x$  and  $z$ ), neglecting the vertical seismic component (direction  $y$ ). The spectrum's excitation point coincides with the center of the global coordinate system, as shown in Figure 3. For the proper distribution of the pavilion's mass and the calculation of the mode shapes due to gravity, a modal analysis is performed followed by the spectrum analysis. After both the modal and spectrum analysis, the significant modes of the pavilion are combined. The solution in terms of displacement is extracted by using the square route of the sum of squares mode combination method (SRSS). [10,12]

The solution for both models a) without seismic base isolation system or b) isolated with elastomeric bearings, is extracted in terms of the relative displacement of the upper and lower nodes of the columns of each frame.

## 5 RESULTS

The response diagrams of the two different described models are presented. First of the reference model which represents the initial design's performance without base isolation system (circled shaped red dot line) and for the second model which represents the target design performance of the base isolated model (square shaped green dot line). The results are presented in terms of drift ratio of the storey (Figure 4a), maximum displacement vs. the amplitude of the natural frequency of the structure (Figure 4b) and of the maximum acceleration at the base vs. amplitude natural period (Figure 4c).

There is a significant reduction in structure's drift as it is illustrated in Figure 4a corresponding to 83% lower values in respect to the reference model. This reduction of drift expresses the capacity of the bearings to absorb the seismic displacements. Also, the significant decrease of the relative displacement in terms of absolute values is depicted in Figure 4b, where it is shown that the maximum relative displacement of the isolated model happens when the elastomeric bearing reaches its maximum shear capacity (22.5mm), exhibiting also a larger cut off frequency. The cut off frequency of the initial design performance practically coincides with the natural frequency ( $f_n$ ) of the SDOF structure, which is reduced for the isolated model (65%) and exhibiting a sharp increase at the ultimate design state of the elastomeric bearing. The Figure 4c shows the shift of the natural period and response with which the SDOF structure oscillates in the two different models at the ultimate state. Especially, the target design performance has a value of period 2.9 times greater than the initial. This elongation of the period is beneficial as the reference model oscillates with a maximum acceleration of 0.266g, whereas the base isolation decreases the maximum acceleration of the upper structure to 0.014g.

The base isolation system has an overall remarkable effect by favoring glass columns' deformation, eliminating brittle failures. Not only columns, but also beams do not have significant deformation as it shown in Figure 5 in terms of elastic strain. The value range of elastic strains of the isolated structure is between  $\pm 0.10$  (Figure 5b), meaning 85% difference lower than the reference model (Figure 5a). These values of strains in all structural members corresponds to a curvature's value of stage I (Figure 2), which corresponds to non-cracked stage for all type of glasses both in tension and compression.

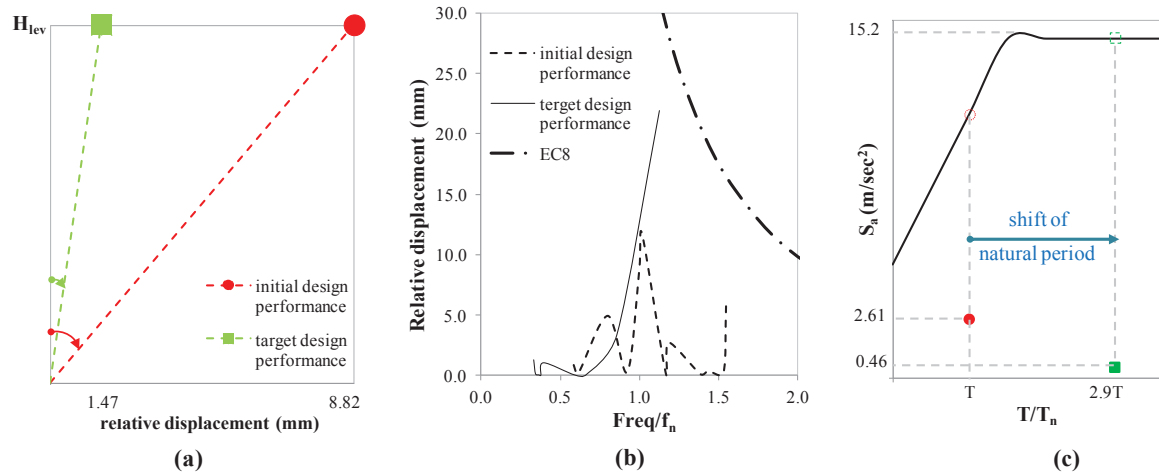


Figure 4: Results of the initial and target design performance in terms of: (a) Drift; (b) Relative displacement-Freq/ $f_n$  and (c)  $S_a(g)$ - $T/T_n$  diagrams

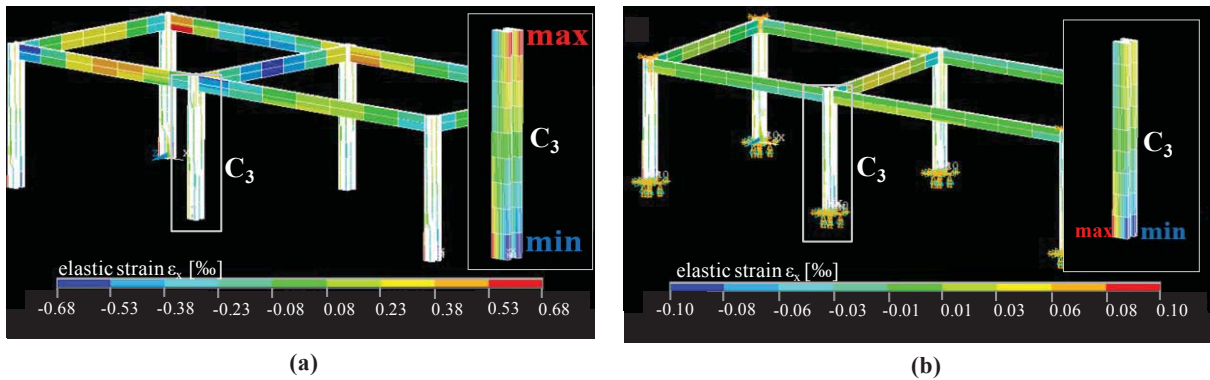


Figure 5: Elastic strain results for (a) non-isolated and (b) base isolated structure

## 6 CONCLUSIONS

- The isolated model exhibits a shift in the SDOF natural period and the significant reduction of the storey drift and the base acceleration, as well as the strains at the critical cross-sections of the structure. As such, glass exhibits no significant fracture or damage, even though is a brittle material. The proper design of the pavilion is proven to exhibit a high ratio of safety.
- A detailed selection of the structural glass type and in addition a proper layering of those types, in combination with structural steel, can lead in avoidance of brittle failures. Even though in the cases of columns the structural glass is proven to have enough resistance to deformations, the base isolation system enhances the overall performance.
- Further research is needed in order to study the connection assemblies between the structural members in order to assure that the abovementioned failure mode is achieved.
- The total displacement provoked from the seismic excitation can be dramatically reduced. Further investigation applying different isolation systems or a combination of them can result to the elimination of the displacement values, especially for different configurations of the unit model either vertically or horizontally.

## REFERENCES

- [1] Garg, N. K. (Ed.). (2007), *Guidelines for use of glass in Buildings*, (P) Limited, Publishers. New Age International.
- [2] Wurm, J. (2007), *Glass structures: design and construction of self-supporting skins*. Walter de Gruyter.
- [3] Institution of Structural Engineers (Great Britain), (1999), *Structural use of glass in buildings*. London: Institution of Structural Engineers.
- [4] DeBrincat, G., & Babic, E. (2018). *Re-Thinking the Life-Cycle of Architectural Glass*, Glasgow: Arup.
- [5] Buildings Department (2018), *Code of Practice for Structural Use of Glass* (the Code).
- [6] Feldmann, M., Kasper, R., & Abeln, B. (2014), *Guidance for European structural design of glass components*. Publications Office of the European Union, 1-196.
- [7] Gutowski, T. G., Sahni, S., Allwood, J. M., Ashby, M. F., & Worrell, E. (2013), *The energy required to produce materials: constraints on energy-intensity improvements, parameters of demand*. Philosophical Transactions of the Royal Society A: Mathematical, Physical and Engineering Sciences, 371(1986), 20120003.
- [8] Gavrilović, D. J., & Stojić, J. (2011). *Usage of "smart" glass panels in commercial and residential buildings*. Facta universitatis-series: Architecture and Civil Engineering, 9(2), 261-268.
- [9] Louter, C., Belis, J., Veer, F., & Lebet, J. P. (2012). *Structural response of SG-laminated reinforced glass beams; experimental investigations on the effects of glass type, reinforcement percentage and beam size*. Engineering Structures, 36, 292-301.
- [10] Code, P. (2005). *Eurocode 8: Design of structures for earthquake resistance-part 1: general rules, seismic actions and rules for buildings*. Brussels: European Committee for Standardization.
- [11] Warn, G. P., & Ryan, K. L. (2012). *A review of seismic isolation for buildings: historical development and research needs*. Buildings, 2(3), 300-325.
- [12] Morante, R., Wang, Y., Chokshi, N., Kenneally, R., & Norris, W. (1999). *Evaluation of modal combination methods for seismic response spectrum analysis*.
- [13] Lenk, P., & Coult, G. (2016, June). *Damping of glass structures and components*. In *Challenging Glass Conference Proceedings* (Vol. 2, pp. 341-350).

## ON THE USE OF INSTANTANEOUS POWER FOR NEAR-FAULT RECORD MODIFICATION

Esra Zengin<sup>1</sup>, Norman A. Abrahamson<sup>2</sup>

<sup>1</sup> Beykent University Department of Civil Engineering, Istanbul, Turkey, 34398  
e-mail: esrazengin@gmail.com

<sup>2</sup> UC Berkeley, Department of Civil and Environmental Engineering, CA, 94720  
e-mail: abrahamson@berkeley.edu

---

### Abstract

*The current seismic design and assessment procedures describe the seismic demand in terms of elastic spectral accelerations, which may not be adequate to capture the destructive effects of near-fault ground motions. The relevant characteristics of near-fault records, such as the presence of a velocity pulse, the pulse amplitude, and the pulse period ( $T_p$ ), make the record selection and modification task more challenging. A newly proposed intensity measure, called Instantaneous Power ( $IP(T_1)$ ), takes into account the effects of velocity pulses on structural response. It has been shown that vector IM including  $IP(T_1)$  and elastic spectral acceleration at the first mode period of structure  $Sa(T_1)$  results in more reliable and accurate structural responses compared to the traditional IM,  $Sa(T_1)$ . A new matching method is developed to incorporate the effects of IP into the record modification process. The procedure combines a widely used time-domain spectral matching algorithm, *RspMatch*, and a velocity adjustment approach to simultaneously match the target response spectrum and IP spectrum. We investigate the extent to which controlling the IP parameter in the modification process affects the nonlinear structural response by comparing the results of single-degree-of-freedom (SDOF) systems and multi-degree-of-freedom (MDOF) system, under the sets of *Sa*-only matched and *Sa*- and *IP*- matched records. Our findings show that the consideration of IP in the record matching can help prevent potential bias in structural response.*

**Keywords:** Near-fault ground motions, Velocity pulses, spectral matching, Record selection and modification

---

## 1 INTRODUCTION

Developing robust approaches for selecting and modifying records that can represent the critical aspects of the design motions is crucial to obtaining reliable and accurate structural response estimates. In current practice, the records having similar implicit causal parameters (e.g., magnitude, distance, site condition) with the scenario earthquake are typically scaled or modified such that their median response spectrum matches the target spectrum within the period range of interest [1]. However, selecting the records on the basis of spectral accelerations may not fully represent the damaging potential of near-fault records containing directivity pulses. For instance, characterization of the near-fault ground motions including velocity pulses requires the determination of the probability of the presence of a pulse, the period of the pulse, as well as the amplitude of the pulse. The recent study showed that the vector IM consisting of  $Sa(T_1)$  and Instantaneous Power ( $IP(T_1)$ ) sufficiently and efficiently captures the destructive impact of the near-fault ground motions on structural response [2]. In order to capture the damaging characteristics of these motions, it is necessary to consider the combined effects of relevant IMs, i.e.  $Sa$  and  $IP$ , in the seismic design and assessment procedures.

One of the most widely used approaches to obtain appropriate input motions for use in response history analysis is the time-domain response spectrum matching procedure, which is also known as RspMatch [3]. This technique adds wavelet function to accelerogram so as to ensure compatibility between record spectrum and target spectrum over a specified period interval. This study presents an  $IP$  matching approach that performs modification on velocity time series to match the target  $IP$  values. The proposed matching algorithm enables near-fault records to match both the target response ( $Sa$ ) spectrum and  $IP$  spectrum. The non-degrading bilinear SDOF systems of varying periods and nonlinearity levels as well as a 2-story steel frame that accounts for stiffness and strength degradation are used as case studies to evaluate the performance of the proposed matching procedure for predicting response of structures to  $Sa$ -only matched records and to  $Sa$ - and  $IP$ -matched records.

## 2 INSTANTANEOUS POWER

The  $IP(T_1)$  is defined as the maximum energy rate of the bandpass-filtered velocity time series over a short time interval given by half of the structural period (i.e.  $0.5T_1$ ) :

$$IP(T_1) = \max\left(\frac{1}{0.5T_1} \int_{t_0}^{t_0+0.5T_1} V_{filtered}^2(t) dt\right) \quad (1)$$

where the  $IP$  is in units of  $\text{cm}^2/\text{s}^2$ ,  $V_{filtered}$  is the bandpass-filtered velocity of the record in  $\text{cm/s}$ . A Butterworth bandpass filter with bandpass period between  $0.2T_1$  and  $3T_1$  is applied to a velocity time series. Figure 1 illustrates the original and filtered velocity time series of the 1979 Imperial Valley-06 earthquake (Agrarias station) record. Figure 1 also shows the variation of  $IP(T_1)$  level over the selected time interval ( $0.5T_1$ ) and the Cumulative Squared Velocity (CSV) of the filtered velocity. It can be seen that the maximum  $IP$  occurs at around 10 seconds, which corresponds to the steepest slope of the CSV. The previous findings showed that the  $IP$  has a significant influence on the structural response after eliminating the effects of spectral shape and amplitude of the ground motions [2-4].



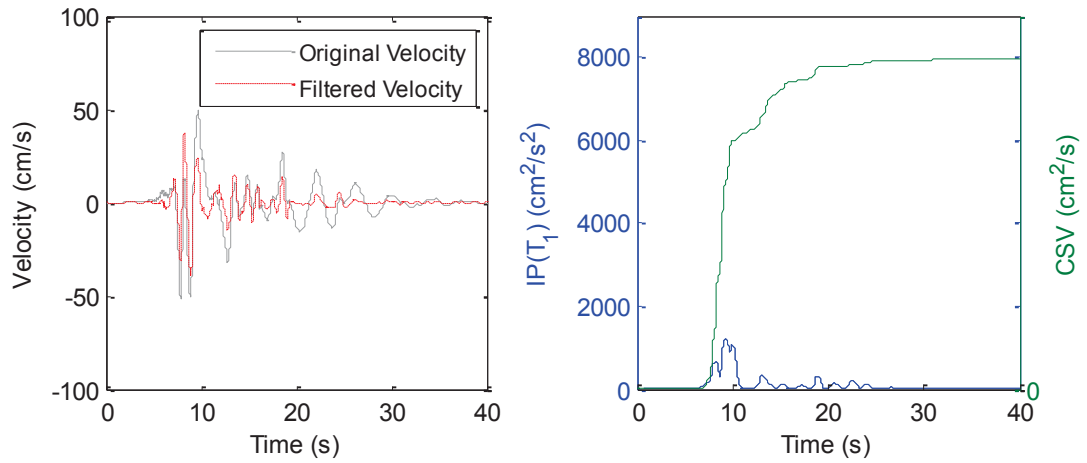


Figure 1. The original and filtered velocity time series of the 1979 Imperial Valley-06 earthquake (Agrarias station) pulse record, and the variation of  $IP(T_1)$  over the selected time interval ( $0.5T_1$ ) and the Cumulative Squared Velocity (CSV) of the filtered velocity.

### 3 CONSTRUCTION OF TARGET SPECTRA FOR MATCHING

Matching of an individual component to a target median can lead to artificial suppression of the spectral variability as the target spectrum generated using geometric-mean or RotD50 (i.e., the median single-component horizontal ground motion across all nonredundant azimuth) of the ground motion does not include the peaks and troughs of the arbitrary component. To maintain the variability of the individual component of the record about the target, we construct a component-specific target spectrum, which is obtained using the Component-Variability Ratio (CVR) given by:

$$CVR_{ij} = \frac{Sa_i^{H_{j,record}}}{Sa_i^{RotD50,record}} \quad (2)$$

where  $Sa^{RotD50,record}$  is the RotD50 spectrum of the record, and  $Sa_i^{H_{j,record}}$  corresponds to the spectral acceleration of the  $j$  component of the record at the  $i$  period. The component-specific target spectrum  $Sa_i^{H_{j,target}}$  is then computed as follows:

$$Sa_i^{H_{j,target}} = CVR_{ij} \times Sa_i^{target} \quad (3)$$

where  $Sa_i^{target}$  is the target spectral accelerations. In computing the CVR for component-specific IP target, we employ geometric-mean IP values of the record instead of the RotD50 because the conditional GMM for the IP is developed based on the geometric-mean horizontal component of ground motion [5]. A conditional ground-motion model (GMM) for  $\sqrt{IP(T)}$  is given by;

$$\ln(\sqrt{IP(T)}) = a_1 + a_2 \ln(Sa(T)) + a_3(M - 6) + a_4 \ln(R_{rup} + 5 \exp(0.4(M - 6))) + \delta B_e + \delta W_{es} \quad (4)$$

in which  $M$  is the moment magnitude,  $R_{rup}$  is the rupture distance in kilometers, and the 5%-damped  $S_a$  in g. The subscripts  $e$  and  $s$  correspond to the indexes of the earthquake and the site, respectively. A more detailed description of the model can be found in [5].

Figure 2 illustrates 50<sup>th</sup> percentile (median) of the target scenario spectrum generated using the Abrahamson et. al. GMM [6], for an earthquake scenario with Magnitude=7,  $R_{rup}$ =3 km, and site condition  $V_{S30}$ = 400m/s, target IP spectrum, as well as component-specific  $S_a$ - and IP- spectra of the selected pulse record that are used as targets in the matching.

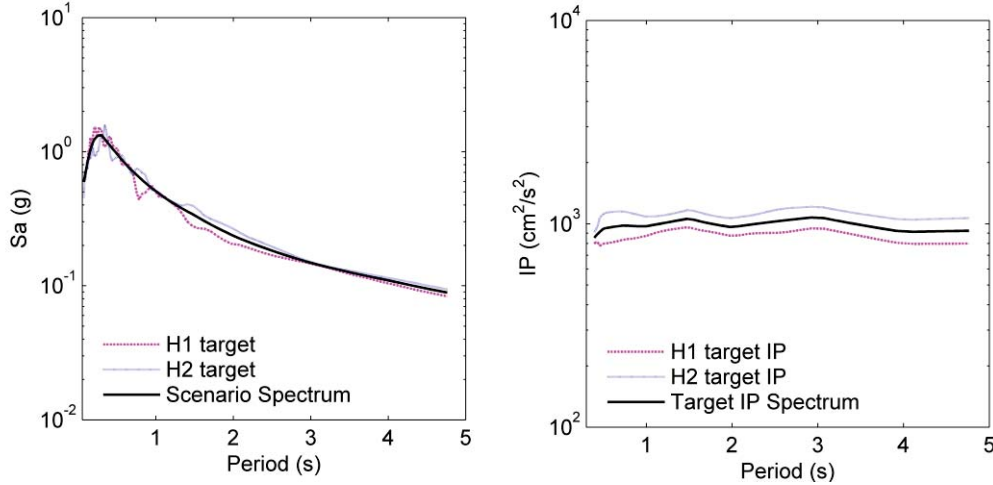


Figure 2. Comparisons of median target spectrum for an earthquake scenario with Magnitude=7,  $R_{rup}$ =3 km, and site condition  $V_{S30}$ = 400m/s, target IP spectrum, and component-specific  $S_a$ - and IP- spectra of the selected pulse record.

#### 4 IP ADJUSTMENT

In this section, we briefly mention about the IP adjustment approach that adds a Ricker wavelet to the velocity time series so as to match the target IP values [7]. The Ricker wavelet has good time localization and a broader frequency spectrum compared to the tapered cosine function, which is added to acceleration time history in response-spectrum matching. This adjustment function is centered at the time of IP occurs ( $tIP_j$ ), for the spectral period  $T_j$ , and is given by

$$h_j(t) = (1 - 2\pi^2 f^2 (t - tIP_j)^2) \exp(-\pi^2 f^2 (t - tIP_j)^2) \quad (5)$$

The adjusted velocity is defined as:

$$V_1(t) = V_o(t) + \gamma_{vel} \delta V_1(t) = V_o(t) + \sum_{j=1}^N b_j h_j(t) \quad (6)$$

where  $\delta V_1(t)$  is the adjustment velocity time history and  $\gamma_{vel}$  is a relaxation factor for the velocity adjustment, where  $b_j$  is a vector of amplitudes of a set of adjustment functions, and  $N$  is the total number of spectral periods. The objective is to equate the change in the IP due to the adjustment to the misfit between target IP and record IP. We refer the reader to the paper by Zengin and Abrahamson [8] for more details.

## 5 MAIN STEPS OF THE SIMULTANEOUS SA- AND IP-MATCHING

The proposed approach sequentially modifies time series to have a close match between records' spectra and target spectra. The flowchart of the proposed algorithm is shown in Figure 3. The required user inputs are target response spectrum, two horizontal components of the ground motion, time step, damping ratio, target peak ground acceleration (PGA). In the first step, the original acceleration time history is initially scaled to the target PGA of the record so as to preserve the shape of the envelope of the time series at high frequencies. The component-specific Sa- and IP- target spectra are then constructed using Equation 3. We subdivide the target periods into smaller subgroups to increase the stability of the matrix inversion as well as to avoid numerical convergence problems. In that regard, we divide Sa- and IP- periods into  $k$  subgroups and select every  $k^{\text{th}}$  element using the equation  $k=(N/n)$ , where  $N$  is the total population size, and  $n$  is the sample size. The maximum sample size is set to 20 because it yields optimum convergence. Moreover, we improve the stability of the matrix inversion by using a Tikhonov regularization method, which is also known as ridge regression [9].

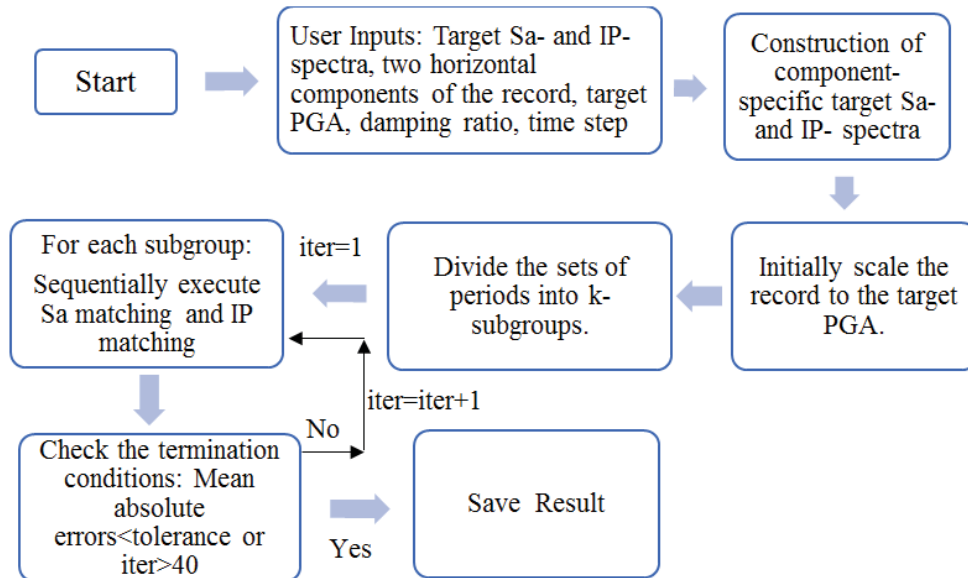


Figure 3. Flowchart of the Sa- and IP-matching algorithm.

Each iteration sequentially performs Sa matching and IP matching stages for each subset. In other words, the accelerogram adjusted using Sa-matching phase is integrated to obtain the velocity time history, which is then used as an input for IP matching. We note that the relaxation factors used to damp the total acceleration and velocity adjustments affect the convergence. Thus, after several trials, we select acceleration relaxation factor of 0.50 and velocity relaxation factor of 0.10. The iterations continue until the desired tolerance levels are achieved, or the maximum number of iterations is reached. Mean Absolute Error (MAE) of the misfit between target spectrum and record spectrum over  $N$  periods is calculated using the following formula:

$$MAE = \frac{1}{N} \sum_{i=0}^N |\ln(y_i) - \ln(x_i)| \quad (7)$$

where  $y$  denotes the target value and  $x$  is the current value of the reference time series. The tolerance levels for the Sa- and the IP- matching are 0.05 and 0.10, respectively. The maximum allowable number of iterations is selected as 40.

## 6 CASE STUDY FOR RECORD MATCHING

Figure 4 shows the acceleration, velocity, and displacement time histories of H2 horizontal component of the pulse record (1979 Imperial Valley-06 earthquake Agrarias station) before and after Sa- and IP- matching. The left panel of the figure illustrates the time histories of the original record, whereas the right panel shows the adjusted time series. It is seen that the addition of wavelets results in some changes in the amplitude and waveforms of the records. However, we assess the suitability of the records for nonlinear response history analysis based on Sa and IP IMs, which are pertinent to the structural response. It should be noted that the consideration of IP in the matching process alleviates the need to preserve the pulse characteristics (i.e., pulse amplitude and pulse period) in the matched record as the IP accounts for the destructive effects of the near-fault ground motion with or without velocity pulses. Thus, we do not check whether the resulting record exhibits velocity pulse.

Figure 5 compares the Sa- and IP spectra of the record and target spectra. Also plotted are the linearly scaled spectra of the record. These results indicate that the proposed matching algorithm performs well in the simultaneous matching of the Sa and IP.

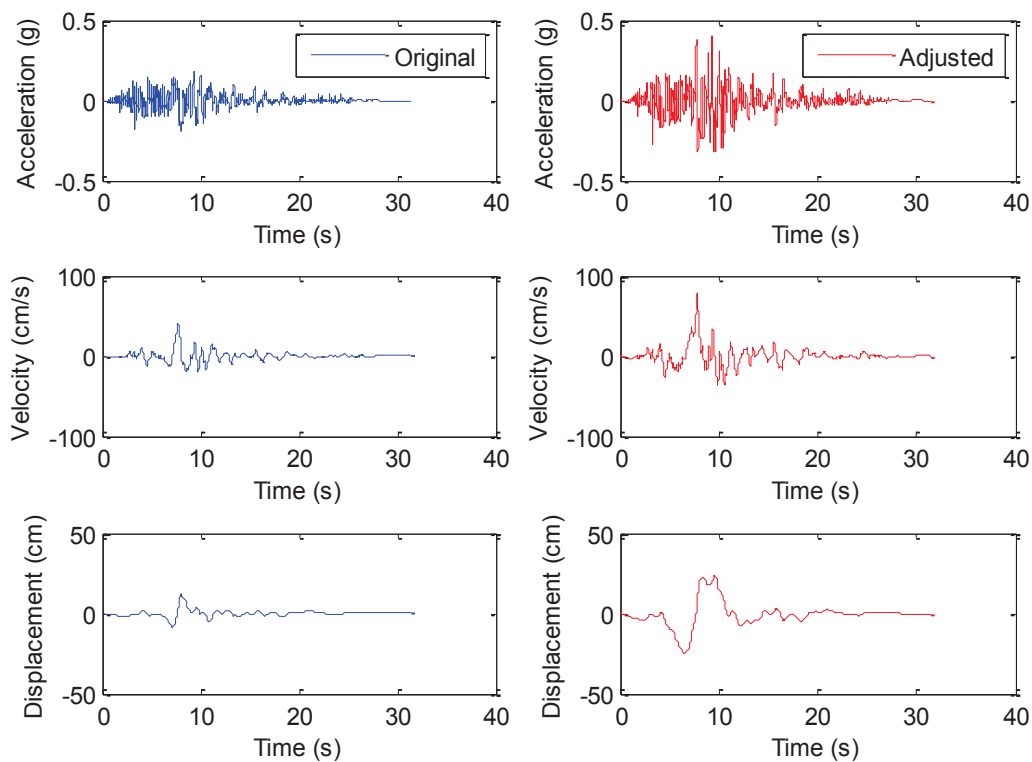


Figure 4. Acceleration, velocity, and displacement time histories of H2 component of the pulse record (1979 Imperial Valley-06 earthquake Agrarias station record) before and after Sa- and IP- matching.

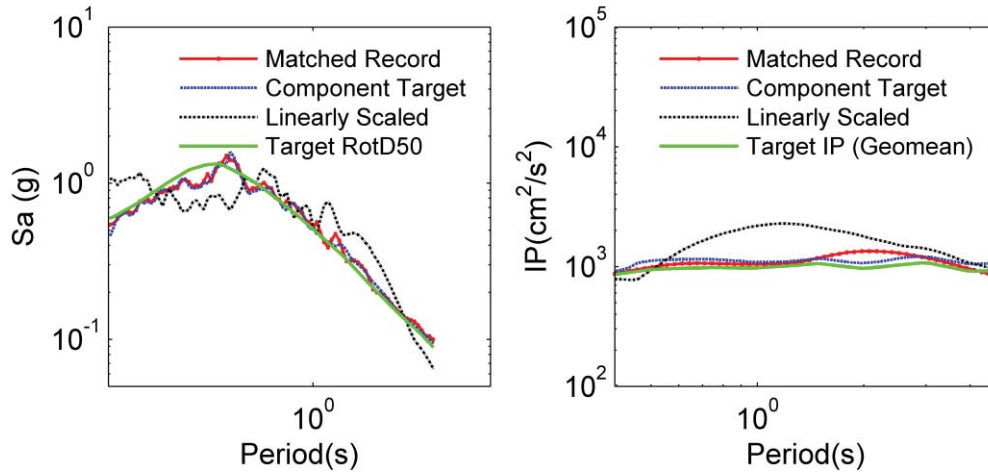


Figure 5. Comparisons of record Sa- and IP- spectra and target spectra

## 7 NONLINEAR STRUCTURAL RESPONSES

Using the proposed matching algorithm, we match 11 near-fault records to the target median scenario spectrum for an earthquake scenario with Magnitude=7,  $R_{rup}=3$  km and site condition  $V_{s,30}=400$  m/s. In our analysis, we utilize both Sa- matched and Sa- and IP-matched records. The records are randomly selected in the magnitude range 6.5-7.5,  $R_{rup}$  range 0-20 km, and  $V_{s,30}$  range 180-760 m/s. We perform nonlinear dynamic analyses of bilinear SDOF systems having five different structural periods between 0.6 and 3.0 seconds and two different inelasticity levels defined by strength reduction factors of  $R=2$  (nearly elastic) and  $R=6$  (highly inelastic). Damping ratio and strain hardening ratio are taken as 5% and  $\alpha=0.10$ , respectively. We also consider a 2-story moment-resisting frame that includes the Modified Ibarra Krawinkler stiffness and strength degradation material model [10][11]. The analytical model also takes into account the P-delta effects. The fundamental period of the frame structure is found to be 0.82 sec. The detail information about this structure can be found in [12]. In this case, the selected records are matched to the 84<sup>th</sup> percentile of the target spectrum to obtain post-elastic maximum interstory drift ratios (MIDRs) of the structure.

Figure 6 plots the mean ratio of the IPs obtained from Sa-matched records to the IPs obtained from Sa- and IP-matched records versus period. It is seen that the mean IP value of the Sa- matched records is lower than that of the Sa- and IP-matched records. Because there is almost no difference between the Sa-values of both record sets, we may attribute the differences observed in structural response to differences in IPs.

Figure 7 shows the results of inelastic displacements of SDOF systems having various periods for  $R=2$  and  $R=6$ . We see that the Sa-only matched records produce a lower mean structural response compared to the Sa- and IP-matched records, suggesting that the effects of IP on structural response are more pronounced for the highly inelastic case. We also observe that, in most cases, the Sa- and IP-matched records produce lower levels of dispersion compared to Sa-only matched records. Figure 8 shows the MIDRs of a 2-story steel frame structure obtained using Sa- matched and Sa- and IP-matched records, where dashed lines show the median results of the record sets. As seen, the MIDRs of Sa-matched records are, on average, lower than that of Sa- and IP -matched records. This indicates that the records having lower IP values than the target IP can produce biased-low responses, relative to the Sa- and IP-matched

record, highlighting the importance of considering the IP parameter in the record modification process.

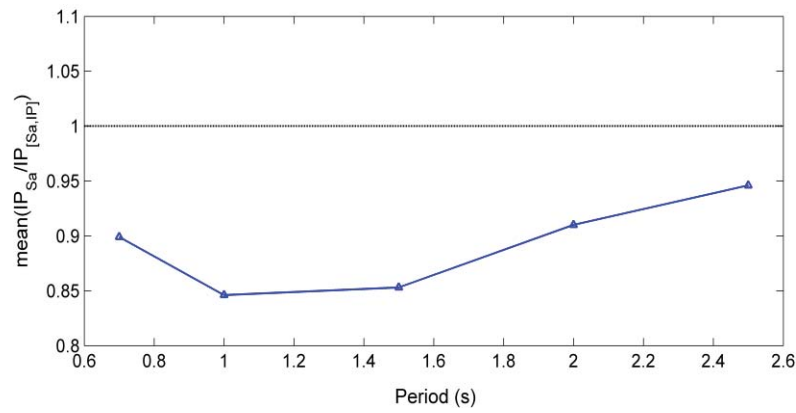


Figure 6. Mean ratio of the IPs obtained from Sa-matched records to the IPs obtained from Sa- and IP-matched records.

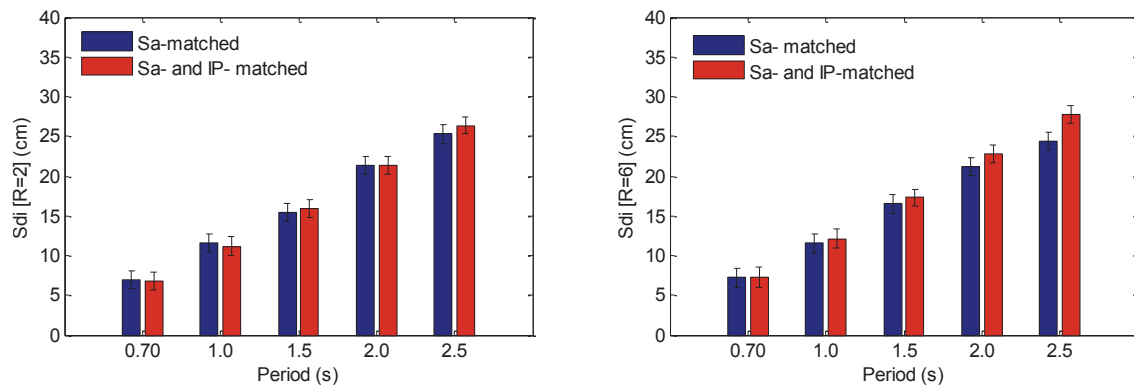


Figure 7. Inelastic displacements of SDOF systems having various periods for R=2 and R=6.

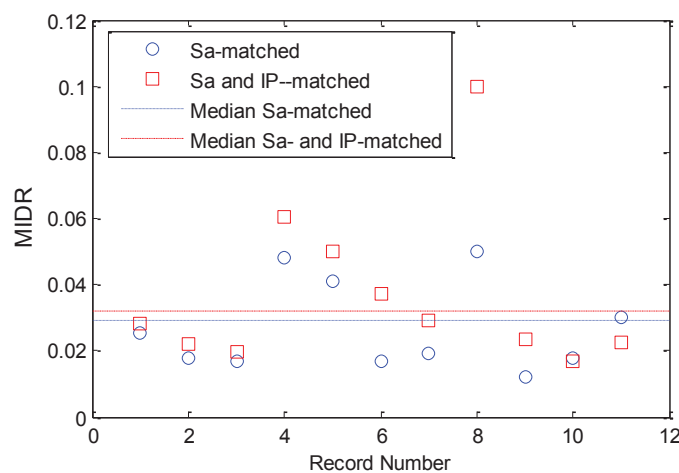


Figure 8. MIDRs of 2-story steel frame ( $T_1=0.82$  s) obtained using Sa- matched and Sa- and IP-matched records.



## 8 CONCLUSIONS

This paper proposes a ground-motion matching procedure that adjusts the near-fault records to simultaneously match target Sa- and IP- spectra. The algorithm builds upon the existing technique, RspMatch, for spectral matching and extends the time-domain modification for IP matching. The case study results show that our algorithm can effectively match the target values over a range of periods. One advantage of considering IP IM is that there is no need to preserve the pulse characteristics in the matching process because IP takes into account the effects of velocity pulses (i.e., pulse amplitude and pulse period). The results of this study indicate that the proposed matching approach can prevent potential bias in nonlinear structural response.

The Matlab source code and the documentation for the Sa- and IP- matching procedure are available at ([https://github.com/zenginesra/Sa\\_IPmatch](https://github.com/zenginesra/Sa_IPmatch)).

## REFERENCES

- [1] ASCE, *Minimum Design Loads for Buildings and Other Structures*, ASCE/SEI 7-16, American Society of Civil Engineers, Washington, D.C., 2016.
- [2] Zengin, E., N. A. Abrahamson, A vector-valued intensity measure for near-fault ground motions, *Earthquake Engineering and Structural Dynamics*, **49.7**, 716-734, 2020.
- [3] Abrahamson, N. A., Non-stationary spectral matching, *Seismological research letters*, **63** (1), 30, 1992.
- [4] Zengin, E., N. A. Abrahamson, S. Kunnath, Isolating the effect of ground-motion duration on structural damage and collapse of steel frame buildings, *Earthquake Spectra*, **36** (2), 718-740, 2020.
- [5] Zengin, E., N. Abrahamson, Conditional ground-motion model for damaging characteristics of near-fault ground motions based on instantaneous power, *Bulletin of the Seismological Society of America*, **110** (6), 2828-2842, 2020.
- [6] Abrahamson, N. A., W. J. Silva, R. Kamai, Summary of the ASK14 ground motion relation for active crustal regions, *Earthquake Spectra*, **30**(3), 1025-1055, 2014.
- [7] Ricker, N., The form and laws of propagation of seismic wavelets, *Geophysics*, **18** (1), 10-40, 1953.
- [8] Zengin, E., N. A. Abrahamson, A Procedure for matching the near-fault ground motions based on spectral accelerations and instantaneous power, *Earthquake Spectra*, in print, 2021.
- [9] Hoerl, A.E., R.W. Kennard, Ridge regression: Biased estimation for nonorthogonal problems, *Technometrics*, 12.1 : 55-67, 1970.
- [10] Ibarra, L.F., R.A. Medina, H. Krawinkler, Hysteretic models that incorporate strength and stiffness deterioration, *Earthquake Engineering and Structural Dynamics*, **34**, 1489-1511, 2005.
- [11] Lignos, D., *Sidesway collapse of deteriorating structural systems under seismic excitations*, Ph.D. Thesis, Stanford University, 2008.
- [12] Eads, L., Dynamic Analysis of 2-Story Moment Frame, [https://opensees.berkeley.edu/wiki/index.php/Dynamic\\_Analysis\\_of\\_2-Story\\_Moment\\_Frame](https://opensees.berkeley.edu/wiki/index.php/Dynamic_Analysis_of_2-Story_Moment_Frame) , last accessed April 2021.

## SEISMIC DESIGN OF STEEL FRAMES WITH INTENTIONALLY ECCENTRIC INDUCTION-HEAT TREATED STEEL BRACES

Thomas Whittall<sup>1</sup> and Konstantinos A. Skalomenos<sup>2</sup>

<sup>1, 2</sup> University of Birmingham  
University of Birmingham, Edgbaston, Birmingham, B15 2TT, United Kingdom  
e-mail: [txw778@student.bham.ac.uk](mailto:txw778@student.bham.ac.uk); [k.skalomenos@bham.ac.uk](mailto:k.skalomenos@bham.ac.uk)

---

### Abstract

*Using induction heat treatment to increase the yield stress of one half of a steel brace section as well as inducing intentional eccentricity along the brace length has been experimentally proven to increase the limited post-yielding stiffness exhibited by concentrically braced steel structures. The high-post yielding stiffness and controllability of the brace response through the two material components and eccentricity provides the brace the capability of satisfying multiple displacement performance objectives offering a reduced section size. Design expressions that describe the mechanical behaviour of the bracing system are developed. The seismic performance of steel braced frames using the two-component composite steel braces with intentional eccentricity is investigated and a direct displacement-based design method (DDBD) is proposed in order to support their implementation to building structures. The design method is validated through a verification study performed on the theoretical design of a 4-storey office building and seismic performance is assessed through dynamic non-linear time history analysis (NTHA). Time-history analysis results demonstrate that a better control is achieved with the proposed bracing system for achieving drift and ductility limitations.*

**Keywords:** Direct Displacement Based Design, Performance Based Design, Concentric Braced Frame, Induction Heating, Eccentricity

---

## 1 INTRODUCTION

A new focus on reducing post-hazard financial losses and recovery time, alongside advances in computational methods, has culminated in the emergence of Performance Based Seismic Design (PBSD). Within PBSD, buildings are designed to respond to seismic loading predictably and reliably to various levels of structural performance, increasing hazard resilience [1]. This provides the ability to optimise structures to reduce total life cycle cost and increase sustainability [2]. The poor inelastic behaviour of certain conventional structures has provided difficulties in the reliable prediction of the non-linear response for these structure types [3]. New systems are under development with better controlled inelastic behaviour, providing satisfaction of PBSD with multi-level performance objectives.

In concentric braced frames (CBFs), the poor inelastic behaviour and early buckling of conventional steel braces (CBBs) leads to rapid loss of storey stiffness, large axial deformations, premature brace fracture and deflection of the brace intercepted beam [4, 5]. The localised inelastic deformations at the plastic hinge leads to a low tangential post-yielding stiffness, resulting in the concentration of residual and maximum drifts. A soft-storey mechanism may be produced, leading to structural instability and collapse in multi-storey buildings [6], observed in the aftermath of large earthquakes, notably the 1989 Loma Prieta [7], Northridge 1994 [8] and Kobe 1995 [9] events. The unfavourable inelastic behaviour of CBBs provides challenges for the application of PBSD with multi-level objectives.

The zero or negative post-yielding stiffness in CBBs leads to the design dominated by the more strenuous objective, leading to an increase in strength demand and larger brace sections [10]. Brace systems that possess and provide control of a large positive post-yielding stiffness will result in improved control of structural performance, a reduction in residual deformations and provide more economical structures through application of PBSD [3]. Several methods have been suggested to increase post-yielding stiffness, such as using reinforcement materials with improved strain hardening behaviour or introducing a secondary parallel inelastic system such as a moment resisting frame in parallel with a CBF [11].

In consideration of the need for alternative brace types, Skalomenos *et al.* [12] propose a brace with intentional eccentricity (BIE). The steel brace is arranged with end plate connections that provide an intentional eccentricity, producing a trilinear curve in tensile loading with a large post-yielding stiffness. Further to this concept, Skalomenos *et al.* [13] investigated applying induction-heating (IH) to the BIEs, increasing post-yielding stiffness and ultimate tensile strength, but decreasing ductility. When cyclic loading is applied, Induction-Heated BIEs (IH-BIEs) exhibit large increases in post-yielding stiffness and ultimate tensile strength. By specifying material properties and eccentricity, combinations of the backbone trilinear curves, with differing strengths and post-yielding stiffness can be specified against multi-level seismic design.

In this paper, a force-deformation model of IH-BIEs and the effect of the material properties and eccentric steel section is discussed. A Direct Displacement Based Design (DDBD) method is then proposed for a steel braced frame with IH-BIEs (FIHB) that satisfies multiple performance objectives, each relating to different level of seismic intensity. For validation, a 4-storey building is designed using the proposed method and non-linear time history analysis is performed. The results are compared against those of the same frame designed using conventional steel braces to Eurocode 8 [14].

## 2 INTENTIONALLY ECCENTRIC INDUCTION HEAT TREATED BRACES

### 2.1 Force-Deformation Behaviour

IH-BIEs comprise a conventional steel hollow member that is induction heated on one half and given a parallel offset from the normal working points of a conventional brace. A rigid brace-to-end gusset plate connection transfers the axial loads from the bracing member to the frame [13]. Figure 1a shows the force-deformation behaviour of a single IH-BIE in tension. A ‘first yield’ and ‘second yield’ point, denoted by  $P_{y1}$  and  $P_{y2}$ , are observed, corresponding to full yielding of the conventional steel and induction-heat treated steel, respectively. In compression, the brace is assumed to act elastic-plastically, and the compressive strength is taken as  $P_{y1}$ . Skalomenos *et al.* [13] found that the induction-heated steel has a fracture ductility 3 times lower than conventional steel and as a result, yielding of the IH-steel may lead to fracture before  $P_{y2}$  is reached. Therefore, in design, it is proposed that a safety factor is applied to give a lower ultimate tensile strength,  $P_u$ , preventing premature fracture of the brace. Figure 1a demonstrates the safety factor,  $\gamma$ , defined by relating the point at which the IH-steel yields to the portion of the section remaining elastic. A value of  $\gamma$  equal to 0.6 was found sufficient to limit the IH-steel from yielding for an IH-ratio, defined as  $F_{y,IH}/F_{y,CS}$ , equal to 4 and a value of 0.5 for all values of an IH-ratio below 4, although this requires verification. The value of this factored ultimate tensile strength is given in terms of  $\gamma$ ,  $P_{y1}$  and  $P_{y2}$  in Equation 1.

$$P_u = (1 - \gamma)P_{y1} + \gamma P_{y2} \quad (1)$$

The design method considers IH-BIEs in a brace pairing, with the maximum storey shear resistance of the brace pair in an inverted- ‘V’ configuration given by the sum of compressive strength,  $P_{y1}$ , and ultimate tensile strength,  $P_u$ .

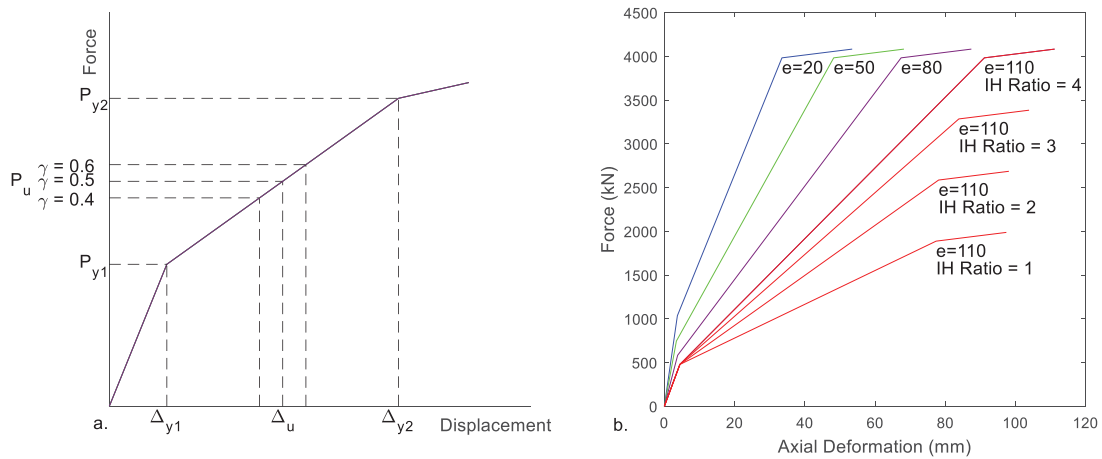


Figure 1: a) Design quantities of a general IH-BIE Member b) Tensile force-deformation behavior of a 244.5 mm x 8 mm CHS IH-BIE member at differing eccentricities and IH-ratios

### 2.2 Effect of eccentricity and induction-heating

Figure 1b shows the effect of the eccentricity and IH-ratio on the idealised behaviour of an 244.5 mm x 8 mm circular hollow section IH-BIE brace member. As eccentricity increases the brace yields earlier, and  $P_{y1}$ , the elastic stiffness,  $K_e$  and post-yielding stiffness,  $K_{in}$  all decrease, increasing deformation for a given force.  $P_{y2}$  is constant as it is not a function of

eccentricity. For a constant eccentricity at increasing IH ratios,  $P_{y1}$  and  $K_e$  are constant, and post-yielding stiffness increases as the induction heat-treated steel remains elastic at greater forces and provides a restoring force to the brace. When combined with the effect of eccentricity, the strain demand on the conventional steel is uniform, preventing a strain concentration that produces local buckling [13]. By varying geometry and material properties a certain controllability of yield points and post-yielding stiffness is afforded, allowing IH-BIEs to be adjustable to satisfy several strength or deformation requirements.

### 3 PROPOSED MULTI-LEVEL DIRECT DISPLACEMENT BASED DESIGN METHOD

The Direct Displacement-Based Design method was selected for the PBSDB of FIHBs, since it has been validated for many cyclic force-deformation behaviours [1] and for application in CBFs [15]. DDBD involves the substitution of the MDOF model for an equivalent SDOF system with a secant stiffness and viscous damping that correspond to that of the real structure at maximum displacement response. In the proposed method, the traditional DDBD method is altered so that the satisfaction of two interstorey drift targets relating to different performance levels are achieved by a singular FIHB design, with no significant iterations.

#### 3.1 Selection of performance objectives

Two performance objectives relating to the interstorey drift, are first selected by the designer for a ‘design’ and a ‘maximum’ performance objective. For the purposes of validating the method, a design interstorey drift limit of 1% associated with life safety and a maximum interstorey drift limit of 2% associated with collapse prevention are later assumed and are comparable with drift limits and performance objectives provided by the SEAOC Blue Book [16] and ASCE 41-13 [17] for steel CBFs. The life safety objective is related to the EC8 design seismic action, 10% probability of exceedance in 50 years (a return period of 475 years), with the collapse prevention objective related to a 2% probability of exceedance in 50 years seismic action (a return period of 2475 years). In addition, the structure will be checked against a 0.5% limit for the damage limitation, ‘frequent’, seismic action, with a 10% probability exceedance in 10 years (a return period of 95 years).

#### 3.2 Design and yield displacement profiles

The selection of a suitable target displacement profile is a key design assumption for translating a MDOF system to a SDOF system and in DDBD methods is generally taken as the first mode inelastic shape of a structure. The high post-yielding stiffness of the FIHB is expected to produce a first mode inelastic displacement profile similar to an MRF due to the prevention of the column-sway inelastic displacement profile that is produced in CBFs. In this method, the equation empirically formulated by Priestley *et al.* [1] for the normalised first mode inelastic shape of moment-resisting frames is used, given in Equation 2. Further research is required to determine the first mode inelastic shape for FIHBs, but this profile provides a good approximation for FIHBs in preliminary analysis. Two design displacement profiles are calculated, one each for the design objective and maximum objective. The first floor is taken as the critical storey, as it is expected to obtain the highest interstorey drift concentration. The design displacement for the  $i^{\text{th}}$  storey,  $\Delta_i$ , can be found by scaling the first-floor design displacement and is given by Equation 3. This step is undertaken twice, using the interstorey drift once for the design event, giving  $\Delta_{i,d}$ , and once for the maximum event, giving  $\Delta_{i,u}$ .

$$n \leq 4 : \delta_i = \frac{H_i}{H_n} \quad (2)$$

$$n > 4 : \delta_i = \frac{4H_i}{3H_n} \left( 1 - \frac{H_i}{4H_n} \right) \quad (3)$$

$$\Delta_i = \delta_i \left( \frac{\Delta_1}{\delta_1} \right)$$

Where  $n$  is the number of storeys,  $\delta_i$  is the normalised lateral displacement of the  $i^{\text{th}}$  storey,  $H_i$  is the elevation of the  $i^{\text{th}}$  storey and  $H_n$  is the elevation of the top storey,  $\Delta_1$  is design displacement of the first storey and  $\delta_1$  is the inelastic mode shape of the first storey.

IH-BIEs exhibits the ‘first yield’ point when the conventional steel is fully yielded and can be considered to occur at the same time in compression and tension. The axial deformation of an IH-BIE brace cannot be determined without knowing section properties or eccentricity. Therefore, to avoid incurring a significant number of iterations in the design procedure, the inter-storey drift at yield is assumed to be 0.2%. In the existing experimental tests, IH-BIEs all yielded at approximately 0.2% interstorey drift [13]. For the purposes of validating the multi-level design method, the braces use the same procedure for the design and maximum displacements, given by Equation 2 and Equation 3, giving  $\Delta_{i,y}$ .

The design, maximum and yield displacement of the SDOF system and equivalent mass can then be determined by Equations 4-7, using mass and displacement of the  $i^{\text{th}}$  storey,  $m_i$  and  $\Delta_i$ . In order to calculate the equivalent viscous damping, the displacement ductility of the equivalent system at both the design event and maximum event is found by Equation 8.

$$\Delta_y = \frac{\sum_{i=1}^n (m_i \cdot \Delta_{i,y}^2)}{\sum_{i=1}^n (m_i \cdot \Delta_{i,y})} \quad (4)$$

$$\Delta_d = \frac{\sum_{i=1}^n (m_i \cdot \Delta_{i,d}^2)}{\sum_{i=1}^n (m_i \cdot \Delta_{i,d})} \quad (5)$$

$$\Delta_u = \frac{\sum_{i=1}^n (m_i \cdot \Delta_{i,u}^2)}{\sum_{i=1}^n (m_i \cdot \Delta_{i,u})} \quad (6)$$

$$M_{eff} = \frac{\sum_{i=1}^n (m_i \cdot \Delta_{i,d})}{\Delta_d} \quad (7)$$

$$\mu_d = \frac{\Delta_d}{\Delta_y}$$

$$\mu_u = \frac{\Delta_u}{\Delta_y} \quad (8)$$

### 3.3 Equivalent viscous damping and calculation of base shear

Priestley *et al.* [1] give an equivalent viscous damping expression for ductile steel frames based on the Ramberg-Osgood hysteretic shape which provides a close fit to that exhibited by FIHBs, given in Equation 9. For the purposes of verifying this method, EVD is not considered critical, and the chosen expression yields satisfactory results. The EVD expression assumes 5% elastic damping, although steel structures feature a lower level, of 2%. Thus, the expression is calibrated with a correction coefficient based on a numerical study by Grant *et al.* [18]. Equation



10 gives equivalent viscous damping using the correction factor  $k$ , provided by Equation 11. A correction coefficient,  $\lambda$ , of -0.617 is taken for tangent stiffness damping [1]. The equivalent viscous damping is found using the displacement ductility between yield and design level,  $\mu_d$ , since  $\xi_{eq}$  is used to reduce the displacement spectrum related to the design seismic action of 10% probability of exceedance in 50 years. Once  $\xi_{eq}$  is obtained, the damping correction factor is found by the expression recommended by Eurocode 8 [14] given in Equation 12.

$$\xi_{steelframe} = 0.05 + 0.577 \left( \frac{\mu - 1}{\mu\pi} \right) \quad (9)$$

$$\xi_{eq} = \xi_{steelframe} - k\Delta\xi_{elastic} \quad (10)$$

$$k = \mu^\lambda \quad (11)$$

$$\eta = \sqrt{\frac{0.1}{0.05 + \xi_{eq}}} \quad (12)$$

The target period,  $T_{eff}$  can be obtained using the reduced damped displacement spectrum by reading the spectral ordinate at  $\Delta_d$ . The secant stiffness is then calculated with Equation 13, and subsequently the base shear for the design objective using  $\Delta_d$  in Equation 14 and storey forces using Equation 15.

$$K_{eff} = 4\pi \frac{M_{eff}}{T_{eff}^2} \quad (13)$$

$$F_b = \Delta_d \cdot K_{eff} \quad (14)$$

$$F_i = \frac{F_b \cdot m_i \cdot \Delta_i}{\sum_{i=1}^n (m_i \cdot \Delta_i)} \quad (15)$$

### 3.4 Brace design

To satisfy both performance objectives, once the design level storey shear is found from the DDBD procedure, the values of displacement ductility at the design and maximum objective, and an assumed value of post-yielding stiffness ratio is used to find a brace section with an eccentricity that satisfies both drift targets. For this procedure, brace sections are considered in terms of brace pairs of an inverted- 'V' configuration. The ratio of storey shear resistance between that at yield and design or maximum level is related in Equation 16 to the corresponding displacement ductility,  $\mu_d$  or  $\mu_u$ , and the post-yielding stiffness ratio,  $\alpha$ . Figure 2 shows the relationships developed by Equation 16, which allows selection of a suitable brace section.

$$\Omega_d = \alpha(\mu_d - 1) + 1 = \frac{P_d + P_{y1}}{2 \cdot P_{y1}} \quad (16)$$

$$\Omega_u = \alpha(\mu_u - 1) + 1 = \frac{P_u + P_{y1}}{2 \cdot P_{y1}}$$

$$\Omega_u = 1 - \frac{\gamma_u}{2} \cdot \left( 1 - \frac{P_{y2}}{P_{y1}} \right) \quad (17)$$

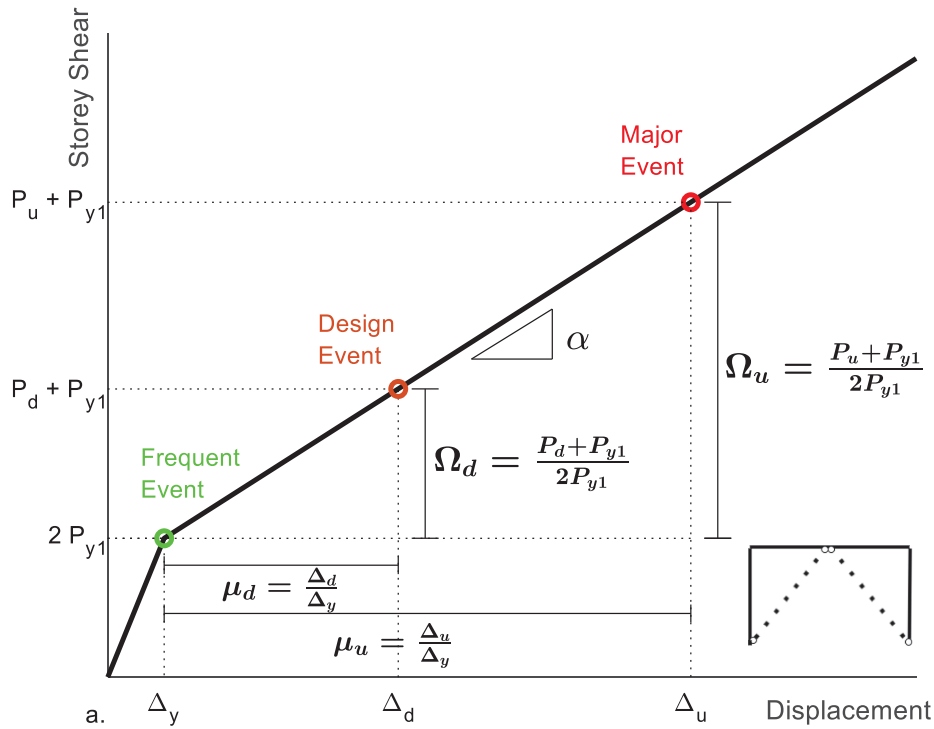


Figure 2: Graph showing the proposed multi-level seismic design and the relationships developed in the proposed design procedure

By using an assumed value for  $\alpha$  and the design displacement ductility,  $\mu_u$ , the ratio  $\Omega_u$  is found using Equation 16. Then, the ratio  $P_{y2}/P_{y1}$ , is calculated using the relationship given in Equation 17, between  $\Omega_u$  and the parameter limiting maximum tensile strength  $\gamma_u$ . After  $P_{y2}/P_{y1}$  is obtained, the dimensionless ratio of eccentricity and radius of gyration is then calculated using Equation 18, considering the level of induction heating on the section. Finally, the brace area is calculated using Equation 19 for a given storey shear,  $V_i$ , the calculated  $e/r$  ratio and the ratio  $\Omega_d$ , given by Equation 18. Eccentricity can be determined from radius of gyration in the ratio  $e/r$ , after brace area has been selected. At this stage, the brace design is checked so that the post-yielding stiffness,  $\alpha$ , is within 5% of the assumed value, assuring the required resistance of the brace pair.

$$\frac{P_{y2}}{P_{y1}} = \frac{1}{2} \cdot \left(1 + \sqrt{2} \frac{e}{r}\right) \cdot \left[ \left( \frac{F_{u,CS}}{F_{y,CS}} \right) + \left( \frac{F_{y,IH}}{F_{y,CS}} \right) \right] \quad (18)$$

$$A_{req} = \left(1 + \sqrt{2} \frac{e}{r}\right) \frac{V_i}{2 \cdot \Omega_d} \cdot \frac{1}{F_{y,CS}} \quad (19)$$

For homogenous dissipative behaviour, the maximum value of storey overstrength at the design level, given by Equation 20, was checked to not differ from the minimum value by more than 25%, to avoid excessive storey shear demand, and the formation of a soft storey mechanism.

$$\Omega_i = \frac{P_d + P_{y1}}{V_i} \quad (20)$$

### 3.5 Capacity design rules

To avoid non-linearity in non-dissipative members, such as beams and columns, capacity design criteria adapted from Eurocode 8 [14] is applied using storey overstrength. The brace-intercepted beams are designed for both the gravity loads not considering the diagonals and the unbalanced force,  $P_{ub}$ , transmitted by the IH-BIE brace pair in an inverted- 'V' configuration at the design event seismic action. This is due to the difference in forces transmitted in tension and compression, given by Equation 21. In conventional braces, the effects of flexural yielding and vertical beam deflection from the unbalanced force leads to the prevention of yielding in tension, an increase in ductility demand, and an impairing of the deformation capacity of braces [5, 19]. To preserve the favourable response of the IH-BIEs in an inverted- 'V' configuration, the beam to vertical brace stiffness ratio is limited to a minimum of 0.2, given by Equation 22.

$$P_{ub} = (P_d - P_{y1})\sin\theta \quad (21)$$

$$K_F = \frac{k_b}{k_{br}} = \frac{48EI_b/L_b^3}{2K_e \sin^2 \theta} \geq 0.2 \quad (22)$$

Where  $P_{ub}$  is the unbalanced force,  $P_{y1}$  is the compressive strength, and  $P_d$  is the design tensile strength,  $k_b$  is the flexural stiffness of the beam, given by  $E$ , the elastic modulus of steel,  $I_b$ , the second moment of area of the beam, and  $L_b$ , the length of the beam span and  $k_{br}$  is the vertical stiffness of the brace pair given by  $K_e$ , elastic stiffness of the IH-BIEs.

### 3.6 Proposed design method flowchart

Figure 3 shows the design flowchart of the proposed method, showing how the direct displacement-based design and brace design produce an FIHB that satisfies two selected performance objectives.

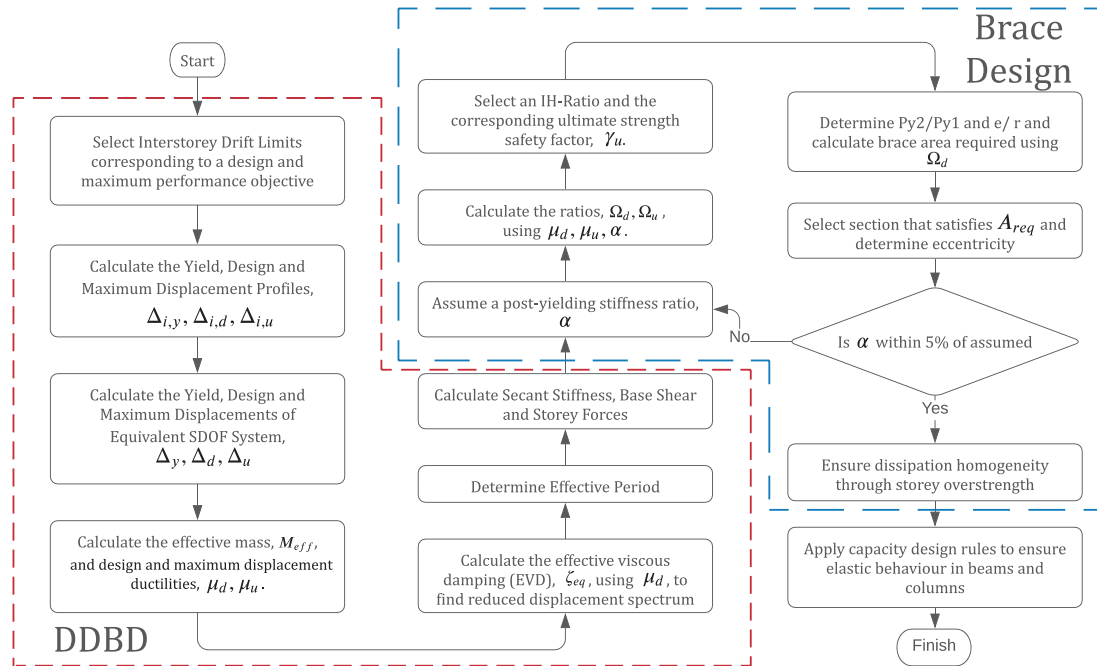


Figure 3: Flowchart of the proposed design method for FIHBs

## 4 VERIFICATION STUDY

### 4.1 Verification case study building

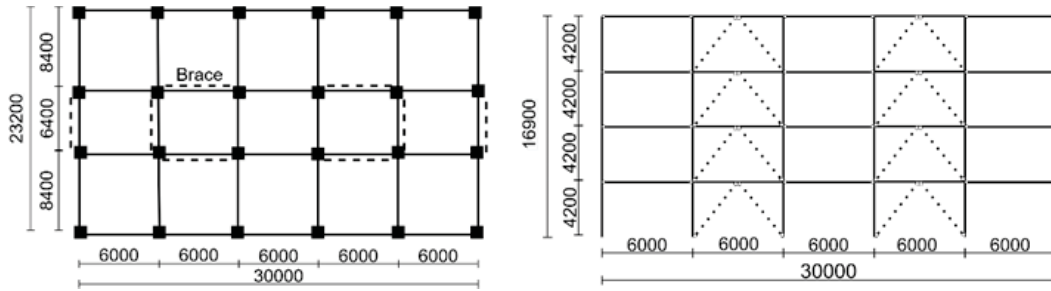


Figure 4: Diagram of a) Floor plan, b) Model elevation plan of the verification study building

A 4-storey mid-rise office building was investigated to verify the proposed design procedure. Figure 4 shows the plans of the 2D frame extracted at the location of the seismic resisting braces in the X-direction, consisting of 2 equally spaced braced bays of 6 metres. An inverted- ‘V’ configuration of the braces was chosen. A constant interstorey height is taken as 4.2 metres and torsional effects are neglected. The frame was designed with conventional braces to EC8 design rules and to the proposed procedure for IH-BIEs, giving two frames in total. The structural design for gravity loads was compliant to EN 1993-1-1 [20]. Permanent and live loads were assumed equal to  $5 \text{ kN/m}^2$  and  $3 \text{ kN/m}^2$  at each storey respectively and the cross sections of all members were selected to satisfy Class 1 requirements. All frames were designed for a ground motion with a probability of exceedance of 10% in 50 years, corresponding to a return period of 475 years, using the 5% damped acceleration spectrum defined by EC8. A peak ground acceleration equal to  $a_{gR} = 0.35g$ , a type B soil, and a Type 1 spectral shape, was assumed. The importance factor,  $\gamma_I$ , was taken as 1, according to EC8 for an ordinary building. The design displacement spectrum was obtained by multiplying the 5% damped acceleration spectral ordinates by the damping correction factor obtained in Equation 12. Non-linear time history analysis

To perform NTHA, the finite element software framework *OpenSees* [21] was used to develop a 2D mixed fibre-distributed frame model of the building. The braces were modelled with the induction heating properties on one half, and with a constant eccentricity. Whilst a 2D frame model, both conventional and IH-BIE braces are modelled in 3D to permit buckling out of plane. To account for second order effects, non-tributary loads were assigned a zero-stiffness leaning column, connected by pinned rigid links. All beam-to-column and columns of the frame are considered pinned, but the braces are fixed, so that only their contribution in resisting the seismic action is considered. The model uses mass-proportional Rayleigh damping, with a damping ratio of 2%, a typical value for steel buildings, and a Newmark acceleration time integration scheme with  $\beta = 0.25$  and  $\gamma = 0.5$ . A suite of 8 semi-artificial ground motions was considered to perform the NTHA, produced by the *Seismic Record Processing program* [22]. Existing ground motion histories were modified to fit the targeted EC8 design elastic response spectrum used in the procedure, so the DDBD method could be validated. For the frequent event and maximum event, the ground motions are scaled by a factor of 0.3 and 1.73, respectively.

## 5 RESULTS

### 5.1 Design summary

Table 1 gives a brief design summary of the FIHB, giving members at each storey of the braced bay. Brace members were selected to meet the slenderness and material properties of the IH-BIEs experimentally validated against the *OpenSees* model, to give confidence in the NTHA. The yield strength of the conventional steel is taken as  $F_{y,cs} = 235 \text{ MPa}$ , and an IH-ratio of 4 was selected, giving  $F_{u,cs} = 940 \text{ MPa}$ . The post-yielding stiffness of the brace pair was assumed to be  $\alpha = 0.16$ , which was later verified, giving the design ratios of  $\Omega_d = 1.64$  and  $\Omega_u = 2.44$ . An  $e/r$  ratio of 0.73 was found and circular hollow sections (CHS) with an area exceeding the calculated value was selected from the Steel Construction Institute Blue Book [23]. Capacity design was then applied to select the frame members.

Storey	IH-BIE Braces						Columns	Beams
	$V_i$ (kN)	D (mm)	t (mm)	e (mm)	$V_r$ (kN)	$\Omega_i$	S355	S355
1	1063.5	244.5	8	60	1303.2	1.23	350 x 10 SHS	HEB 500
2	957.2	244.5	7.1	60	1163.3	1.22	350 x 10 SHS	HEB 500
3	744.5	219.1	6.3	55	919.8	1.24	350 x 10 SHS	HEB 450
4	425.4	168	5.6	40	631.3	1.48	350 x 10 SHS	HEB 400

Table 1: Design summary of the FIHB at the braced bay

### 5.2 Non-linear time history analysis results

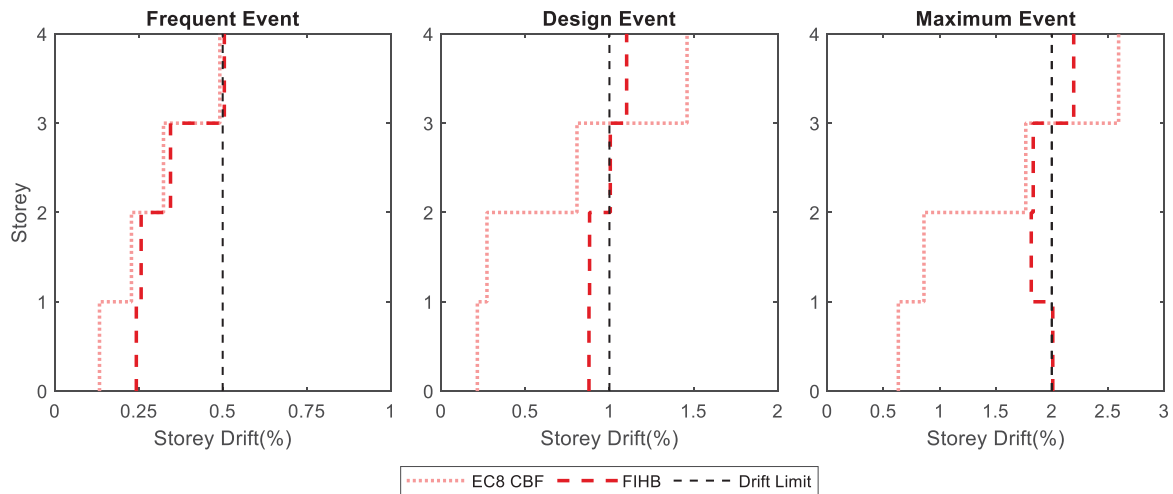


Figure 5: Mean maximum interstorey drift profiles of the FIHB using the proposed method and the CBF designed to EC8

To assess whether the design procedure controlled the response of the FIHB to the chosen interstorey drifts and to compare to a conventionally designed CBF, the mean maximum interstorey drift profiles for both braced frames are given in Figure 5. Both frames compare well against the 0.5% limit for the frequent event, with each experiencing drift concentration at the top storey. At the design and maximum event, the FIHB exhibits a response typical of a shear building, close to the 1% and 2% drift targets, in contrast to the severe cantilever type-response observed for the reference CBF. The response of the CBF designed to EC8 matches existing research [24, 25]. The results show excellent plastic engagement of the IH-BIE braces,

with a uniform drift demand, indicating the favourable characteristic of uniform damage distribution, unlike the conventionally designed CBF. The multi-level design method adequately predicts the storey drift demand at both performance objectives, representing excellent performance and satisfaction of the target drifts.

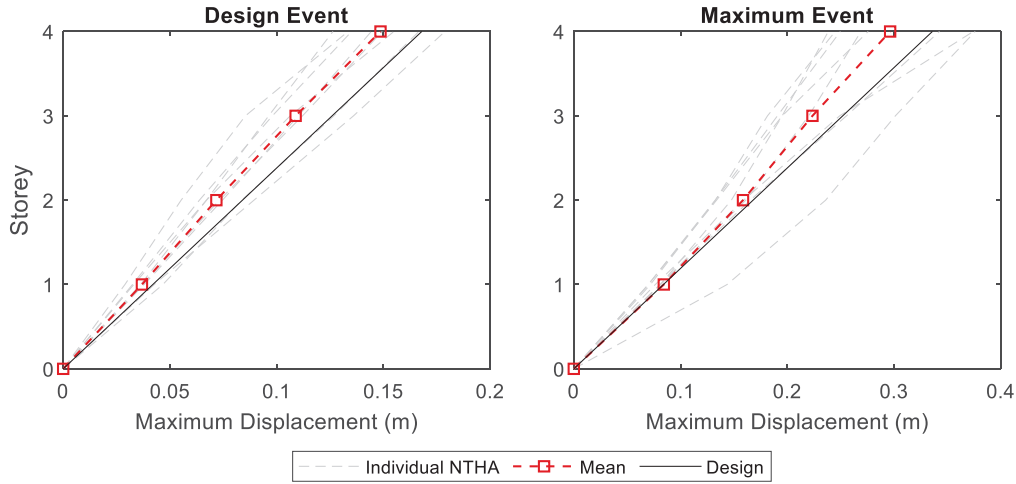


Figure 6: Maximum Displacement Profiles of the FIHBs

The mean and individual NTHA displacement profiles for the FIHB are plotted in Figure 6 against the design displacement profile. The appropriateness of the design displacement profile given in Equation 2 is demonstrated at both the design and maximum event, with only a small difference to the mean displacement profile for both FIHBs. Assumptions made in the DDBD method that the FIHBs provide a similar inelastic first mode shape to steel MRFs are well founded, hence providing an accurate prediction of their behaviour. Further investigation is required to validate Equation 2 for taller FIHBs, with more complex mode effects.

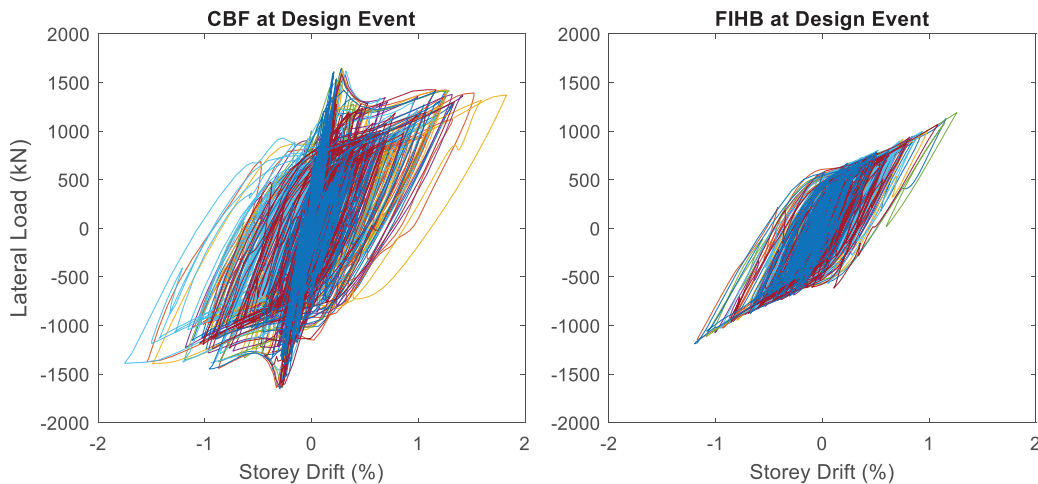


Figure 7: Force-Deformation behaviour of the conventional steel brace pair and the IH-BIE brace pair at the fourth storey at the design seismic action for all ground motions

Figure 7 show the lateral forces in the brace against storey shear drift of the conventional steel braces and the IH-BIEs respectively at the fourth storey, providing the force-deformation behaviour of both conventional steel brace pair and the IH-BIE brace pair system. Compared to a conventional steel brace, which stay elastic at low drifts, the IH-BIE yields earlier at a low



interstorey drift, as predicted, and dissipates energy. This is congruent with the results of Skalomenos *et al.* [13], with a more stable hysteretic behaviour found at low seismic intensities. The brace pairing exhibits a stable, and symmetrical response with a large post-yielding stiffness. The hysteretic shape is similar to that based on the Ramberg-Osgood model used in the assumed expression for equivalent viscous damping. Despite the derivation of Equation 9 relating to ductile steel frames, it provides a suitable translation of the energy dissipation between the IH-BIE system in the MDOF structure to that of the equivalent SDOF system.

## 6 CONCLUSION

In this paper, the performance and a new multi-level direct displacement-based design method has been presented for steel braced frames utilising IH-BIEs (FIHBs). The procedure assumes a displacement profile and equivalent viscous damping ratio developed for steel MRFs. Brace design is achieved by relating displacement ductility and a post-yielding stiffness ratio to the storey shears at a design and maximum performance objective, to find a single brace section with a given induction-heating ratio and eccentricity that can satisfy multiple drift targets corresponding to different levels of seismic intensity. To validate the design method, non-linear time history analysis at three different seismic intensities was performed on a 4-storey FIHB analytical model using *OpenSees*. The results indicate that:

- The design method adequately controls the drift demand of the FIHB
- The FIHB satisfies both the 1% interstorey drift limit at the design performance objective and a 2% interstorey drift limit at the maximum performance objective, without a design change or significant iteration
- FIHBs exhibit a shear building response and produce a hysteretic shape like that of an MRF, indicating the satisfaction of the assumption of a linear displacement profile and the chosen equivalent viscous damping expression
- The FIHB avoids concentration of drifts compared to a reference concentrically braced frame (CBF) designed to Eurocode 8 and promotes reliable and symmetric dissipation of seismic energy

## REFERENCES

- [1] Priestley, M.J.N., G.M. Calvi, and M.J. Kowalsky, *Displacement-based Seismic Design of Structures*. 2007: IUSS Press.
- [2] Welsh-Huggins, S.J. and A.B. Liel, *Evaluating multiobjective outcomes for hazard resilience and sustainability from enhanced building seismic design decisions*. Journal of Structural Engineering, 2018. **144**(8): p. 04018108.
- [3] Ye, L., X. Lu, Q. Ma, G. Cheng, S. Song, Z. Miao, and P. Pan. *Study on the influence of post-yielding stiffness to the seismic response of building structures*. in *Proc., 14th World Conf. on Earthquake Engineering*. 2008.
- [4] Fukuta, T., I. Nishiyama, H. Yamanouchi, and B. Kato, *Seismic performance of steel frames with inverted V braces*. Journal of Structural Engineering, 1989. **115**(8): p. 2016-2028.
- [5] Shen, J., R. Wen, B. Akbas, B. Doran, and E. Uckan, *Seismic demand on brace-intersected beams in two-story X-braced frames*. Engineering Structures, 2014. **76**: p. 295-312.

- [6] Ji, X., M. Kato, T. Wang, T. Hitaka, and M. Nakashima, *Effect of gravity columns on mitigation of drift concentration for braced frames*. Journal of Constructional Steel Research, 2009. **65**(12): p. 2148-2156.
- [7] Kim, H.I., *Seismic evaluation and upgrading of braced frame structures for potential local failures*. 1993, The University of Michigan.
- [8] Tremblay, R., A. Filiatrault, P. Timler, and M. Bruneau, *Performance of steel structures during the 1994 Northridge earthquake*. Canadian Journal of Civil Engineering, 1995. **22**(2): p. 338-360.
- [9] Nakashima, M., *Reconnaissance report on damage to steel buildings structures observed from the 1995 Hyogoken-Nanbu (Hanshin/Awaji) earthquake, Abridged English edition*. Steel Committee of Kinki Branch, the Architectural Institute of Japan (AIJ), 1995.
- [10] Iemura, H., Y. Takahashi, and N. Sogabe, *Two-level seismic design method using post-yield stiffness and its application to unbonded bar reinforced concrete piers*. Structural Engineering / Earthquake Engineering, 2006. **23**.
- [11] Pettinga, D., C. Christopoulos, S. Pampanin, and N. Priestley, *Effectiveness of simple approaches in mitigating residual deformations in buildings*. Earthquake Engineering & Structural Dynamics, 2007. **36**(12): p. 1763-1783.
- [12] Skalomenos, K.A., H. Inamasu, H. Shimada, and M. Nakashima, *Development of a steel brace with intentional eccentricity and experimental validation*. Journal of Structural Engineering, 2017. **143**(8): p. 04017072.
- [13] Skalomenos, K.A., M. Kurata, H. Shimada, and M. Nishiyama, *Use of induction-heating in steel structures: Material properties and novel brace design*. Journal of Constructional Steel Research, 2018. **148**: p. 112-123.
- [14] CEN, *EN 1998-1 in Eurocode 8: Design of structures for earthquake resistance—Part 1: General rules, seismic actions and rules for buildings*. 2004, European Committee for Standardization (CEN): Brussels.
- [15] Wijesundara, K.K. and P. Rajeev, *Direct Displacement-Based Seismic Design of Steel Concentric Braced Frame Structures*. Australian Journal of Structural Engineering, 2012. **13**(3): p. 243-257.
- [16] SEAOC, *SEAOC Blue Book: Seismic Design Recommendations*. Structural Engineers Association of California, Sacramento, CA, 2019.
- [17] ASCE. *ASCE 41-13, Seismic evaluation and retrofit of existing buildings*. 2014. American Society of Civil Engineers.
- [18] Grant, D.N., C. Blandon, and M. Priestley, *Modelling inelastic response in direct displacement-based design*. Journal of Earthquake Engineering, 2005. **9**(sup2): p. pp.257-278.
- [19] D'Aniello, M., S. Costanzo, and R. Landolfo, *The influence of beam stiffness on seismic response of chevron concentric bracings*. Journal of Constructional Steel Research, 2015. **112**: p. 305-324.
- [20] CEN, *EN 1993, in Design of Steel Structures*. 2002, European Committee for Standardization (CEN): Brussels.
- [21] McKenna, F., G.L. Fenves, and M.H. Scott, *Open system for earthquake engineering simulation*. University of California, Berkeley, CA, 2000.
- [22] Karabalis, D.L., G.J. Cokkinides, and D.C. Rizos, *Seismic Record Processing Program (SRP), Version 1.03*, in *International Nuclear Information System*. 1992, International Atomic Energy Agency: United States. p. 74.
- [23] SCI, *Steel building design: design data*. The Steel Construction Institute and The British Constructional Steelwork Association Limited, 2011.

- [24] Costanzo, S., M. D'Aniello, and R. Landolfo, *Seismic design criteria for chevron CBFs: Proposals for the next EC8 (part-2)*. Journal of Constructional Steel Research, 2017. **138**: p. 17-37.
- [25] Bosco, M., G. Brandonisio, E.M. Marino, E. Mele, and A. De Luca,  *$\Omega^*$  method: An alternative to Eurocode 8 procedure for seismic design of X-CBFs*. Journal of Constructional Steel Research, 2017. **134**: p. 135-147.

## AN EFFICIENT RECORD-TRUNCATION SCHEME FOR PULSE-LIKE RECORDS USING A WAVELET-BASED APPROACH

Vicky Dimakopoulou, Michalis Fragiadakis, and Ioannis Taflampas

<sup>1</sup> School of Civil Engineering, National Technical University, Athens, Greece  
e-mail: [vdimak@central.ntua.gr](mailto:vdimak@central.ntua.gr), [mfrag@mail.ntua.gr](mailto:mfrag@mail.ntua.gr), [taflantaflan@gmail.com](mailto:taflantaflan@gmail.com)

---

### Abstract

*The paper shows, that especially for pulse-like ground motions, it is possible to truncate pulse-like signals using a novel wavelet-based definition that identifies the duration of the predominant velocity pulse. The truncated time history can efficiently reproduce the increased seismic demand that near-field records typically produce. Substituting the original ground motion with the truncated signal, significantly accelerates structural analysis and design. The truncated signal is the part of the original accelerogram that coincides with the duration of the predominant pulse, which is identified using a wavelet-based procedure, previously proposed by the authors.*

**Keywords:** Record truncation, effective duration, predominant pulse, pulse-like, pulse index, near-field.

---

## 1 INTRODUCTION

Replacing an acceleration time history with an equivalent, “truncated”, signal has many benefits in terms of accelerating the seismic performance assessment and for understanding structural response. Although this is a very appealing approach, experience has shown that there is no silver bullet to the problem. It is practically impossible to have a record truncation algorithm that is efficient and accurate for all ground motions and all structural systems possible. However, if the problem is narrowed down to the case of pulse-like ground motions, it is possible to achieve an efficient truncation using a novel wavelet-based definition for the record effective duration. The effective duration is calculated first fitting a wavelet on the ground motion and then truncating the record to the time interval that corresponds to the fitted wavelet.

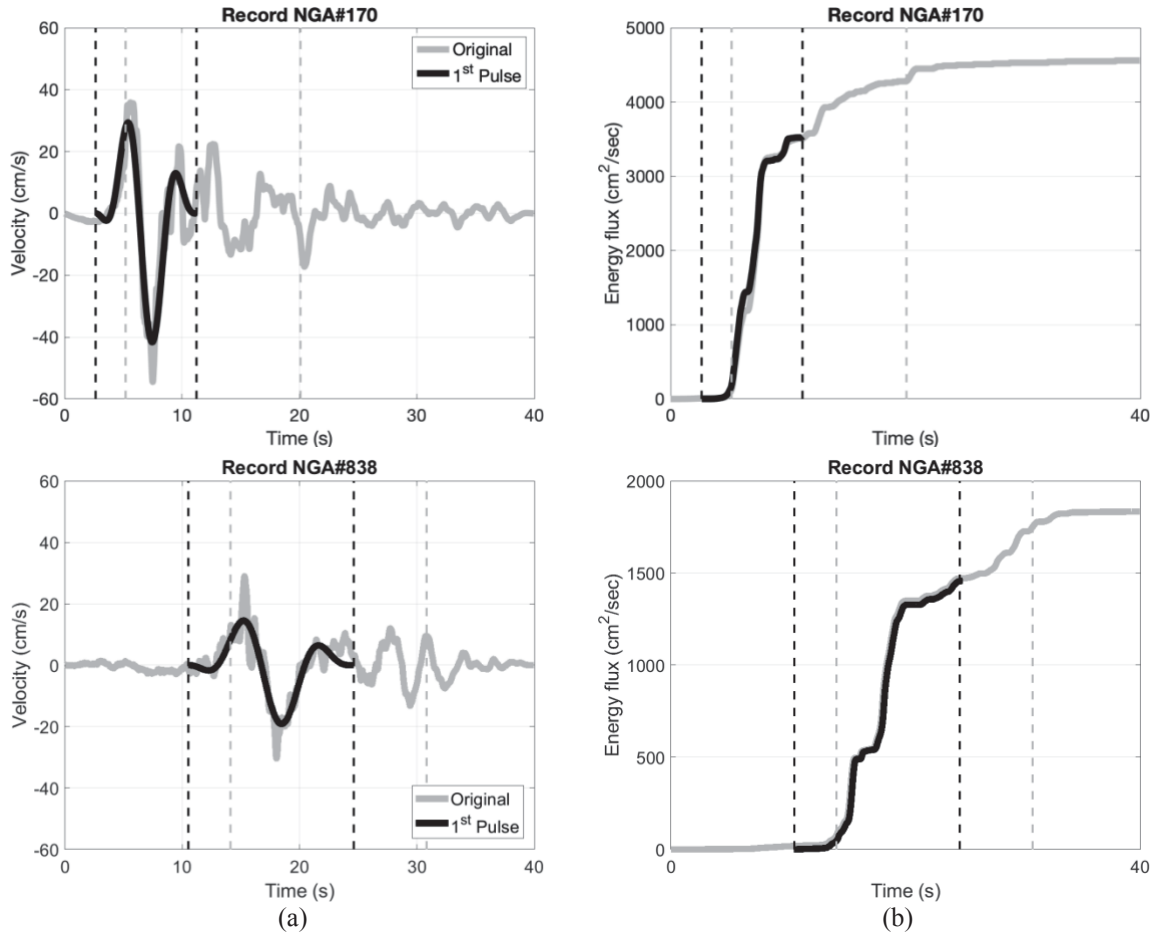
One of the early efforts for record truncation was that of Srivastav and Nau [1] who studied the influence of truncated earthquake records on the response of long-period structures. They recommend truncating the earthquake record at a small value of acceleration in order to reduce the error. However, most efforts are based on Arias intensity [2]. For example, Jin et al. [3] proposed the use of Arias intensity in order to study arch dams, while artificial intelligence approaches have been also proposed [4].

The scope of this study is to adopt the wavelet-based duration definition proposed by Repapis et al. [5] in order to truncate the acceleration time history and obtain a simpler and shorter signal. The paper shows that this practice can efficiently accelerate the simulation time with minor loss of accuracy. The efficiency of the proposed truncation approach depends on the pulse content of the record, which can be quantified with the aid of a pulse index. The approach proposed is quite efficient in the case of pulse-like records, such as those recorded in the case of near-field ground motions with forward directivity. These signals are characterized by strong, coherent, long period pulses that are found mainly in the strike normal direction. The effect of significant velocity pulse on the structural response has been highlighted by several studies, e.g. [6], [7], [8].

## 2 METHODOLOGY

Figure 1 shows two characteristic pulse-like ground motion records and the corresponding significant pulses. The pulses have been identified using the methodology proposed by Mimoglou et al. [9], i.e., appropriately fitting a wavelet on the signal. The plot on the right shows the cumulative energy flux and the time limits that correspond to the proposed “wavelet-based duration” (black dashed lines). The plots also show the 5% and the 95% of the record energy flux (dashed grey lines), which was proposed by Trifunac and Bray [10] as a measure of the record “significant duration”. Clearly, the two definitions of record duration differ considerably (Figure 1a).

In order to calculate the record duration, we first extract the predominant pulse. According to [9] the extraction is based on optimally fitting the Mavroeidis and Papageorgiou wavelet [11] on the signal. This is a versatile wavelet, suitable to represent different duration levels, since it includes a parameter that is explicitly associated with the number of pulse cycles. A further advantage of this wavelet is that it is defined as the product of a sinusoidal periodic function and a bell-shaped envelope.



**Figure 1: (a) Velocity time history showing the total, the proposed wavelet-based and the significant duration definition, (b) Energy flux (records NGA #170 and NGA #838).**

The Mavroeidis and Papageorgiou wavelet [11] depends on four parameters that control the frequency ( $T_p$ ), the amplitude ( $A$ ), the number of cycles ( $\gamma$ ) and the polarity ( $\phi$ ) of the signal. The frequency is obtained as the period value that the product of velocity and displacement spectra becomes maximum. An exhaustive search algorithm is then adopted in order to identify the other three parameters; the search is narrowed to two parameters since the amplitude and the number of cycles are related by the expression proposed by Taflampas *et al.* [12]:

$$CAD = \frac{\gamma A T_p}{\pi} \quad (1)$$

where CAD is the cumulative absolute displacement, obtained as the integral of the absolute value of ground velocity. The wavelet parameters that have the best cross-correlation value with the original signal define the most suitable wavelet model of the record predominant pulse. Once the wavelet is fitted on the ground motion, e.g., see Figure 1a, the wavelet-based effective duration of the signal is defined by the time boundaries of the fitted pulse.

The truncated signal is the part of the original record contained in the time boundaries of the wavelet that represents the predominant pulse (Figure 1a black vertical lines). Therefore, the truncated signal contains all the information, including the high frequency information, of the original ground motion. Moreover, according to Figure 1b, the ends of the proposed duration definition appear at points where the graph of the energy flux shows a horizontal step with zero first gradient. Therefore, there is no significant baseline offset at the beginning and the end of the truncated duration. This is not the case with other duration definitions, e.g. the “significant



duration” definition that use the arbitrary limits of 5 to 95% of the total energy flux in order to truncate the ground motion.

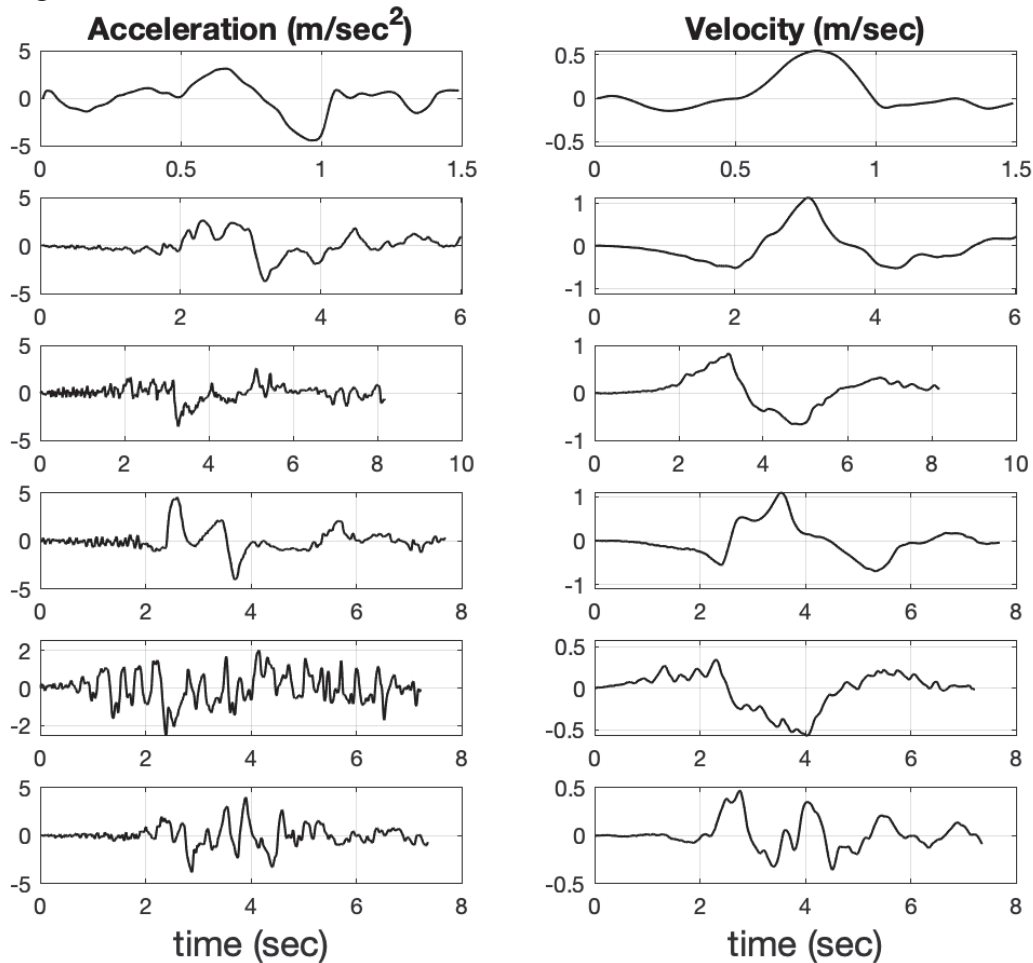


Figure 2: Acceleration and velocity time histories of truncated signals.

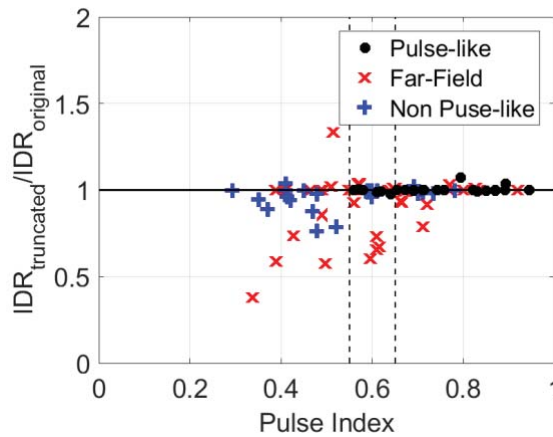
Thanks to the proposed wavelet fitting, the time boundaries identified, ensure that the truncated signal starts and ends at an acceleration value close to zero, similarly to the case of recorded acceleration time histories. Therefore, the limits of the envelope can be considered as boundary tapers that attenuate the harmonic function and smooth the baseline of the cut-off instants. This can be better understood looking at Figure 2, where the acceleration and velocity of six truncated signals are shown. The time histories smoothly converge to zero acceleration and velocity line which allows to use them for structural response history simulations without the need for further processing.

### 3 GROUND MOTION RECORDS

A set of 48 pulse-like ground motion records, included in the PEER-NGA2-West database [13], have been selected for our work. The excitations were recorded on different soil types and distances from the rupture plane and have different values of predominant pulse periods. Moreover, the selected ground motion sample contains records with strong directivity, mainly in the fault-normal direction (e.g., Loma Prieta), or records where both the fault-normal and the fault-parallel components show prominent directivity effects (e.g., Erzincan-Turkey).

#### 4 NUMERICAL INVESTIGATION

The efficiency of the proposed record truncation approach is studied using a nine-storey steel moment-resisting frame. The well-know LA9 frame is used as a testbed multi-degree-of-freedom (MDOF) structure. The building consists of five bays and a hinge-storey basement. The gravity loads and the mass of the internal gravity-resisting frames are placed on a leaning column, which does not contribute to the lateral stiffness. The fundamental period of the frame was found equal to  $T_1=2.35$  sec and the mass modal participation of the first mode amounts to 84% of the total mass. Thus, the frame is essentially dominated by the first mode, while higher modes may also contribute to the response. The cross-sections and more details about the building design can be found in [14]. A centreline model is adopted using the OpenSees platform [15]. The model account explicitly for the geometric nonlinearities in the form of  $P-\Delta$  effects. The columns are assumed linear-elastic, while a quadrilinear model is adopted for the beam-column connections. More specifically, the moment-rotation relationship of all beam-column connections have degrading properties equal to:  $a_h=10\%$ ,  $a_c=-50\%$ ,  $\mu_c=3$  and  $r=50\%$ .



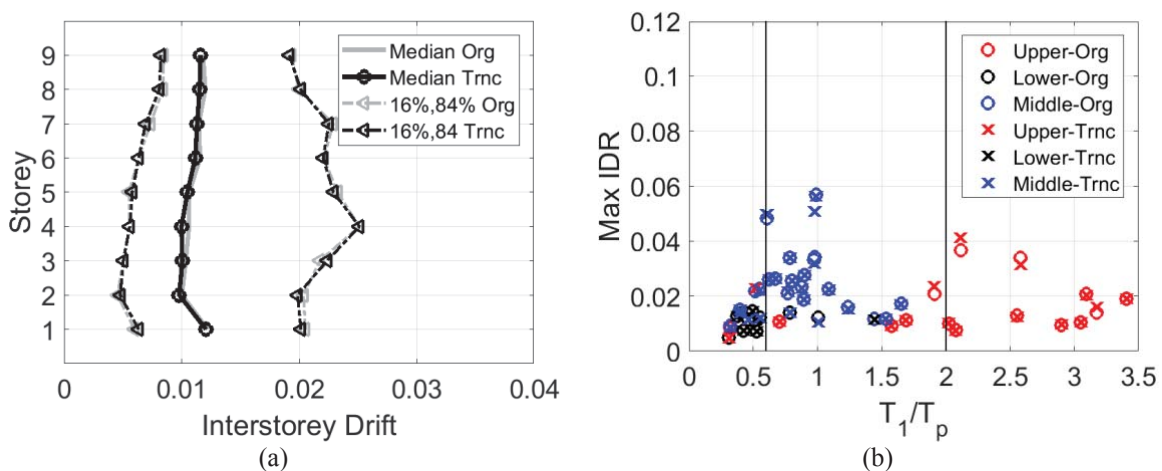
**Figure 3: Ratio of the maximum interstorey drift for the 9-storey steel moment frame versus the calculated cross correlation.**

Primarily, the correlation with a pulse index is studied. Since the proposed wavelet-based truncation, in principle, applies to pulse-like ground motions, the seismic demand obtained with the truncated and the original ground motions is expected to be close. However, often the proposed approach gives sufficiently accurate results also for records that have been a priori classified as non pulse-like. It is, therefore, very useful to have a metric that can be used to determine, prior analysis, if the proposed truncation can be used to substitute the original signal. An obvious metric suitable for this purpose is a “pulse index” such as the one proposed by Kardoutsou *et al.* [16], which is defined as the cross-correlation of the original signal and the extracted wavelet and adopted in our work. This study is also based on fitting the Mavroeidis and Papageorgiou wavelet, as discussed in [9]. The authors recommend that records with  $PI$  less than 0.55 are non-pulse like, while when  $PI > 0.65$  the record is definitely pulse-like. Records with intermediate values, i.e.,  $0.55 < PI < 0.65$ , are characterized as ambiguous.

Figure 3 compares the ratio of peak interstorey drift of the original and the wavelet-based truncated time-history versus the Pulse Index ( $PI$ ). The comparison is based on the record set of FEMA P-695 [17]. A different and well-known record database is adopted in order to use ground motions that are completely different from those used in their previous studies of the authors, [9], [16]. Moreover, the ground motion set of [17] consists of 44 far-field records, 28 near-field records characterized as “pulse-type” and 26 near-field records characterized as “non pulse-type”. The far-field set includes earthquakes of large magnitude ( $M_w > 6.5$ ), recorded on

soil types C and D according to the NEHRP classification. The pulse-type set contains records, with varying pulse periods, corresponding to events of magnitude between 6.5 and 7.6. These records present strong directivity effects in the fault-normal/and or the fault parallel direction.

According to Figure 3, the difference in the maximum peak interstorey drift demand between the original and the truncated records is small for ground motions with a pulse indicator  $PI$  above the 0.65 threshold. This observation holds even for records that belong to the far-field set. The largest differences are again found for the far-field records (red crosses), but even for  $PI < 0.55$  the differences do not seem to exceed on average 18%. Overall, for the building examined, the scatter in the computed drift values is significantly decreased as  $PI$  increases, regardless of the classification of the ground motion record. This indicates the efficiency of the proposed wavelet-based approach for truncating a ground motion record and also the potential on the proposed pulse index  $PI$  metric to quickly assess using the efficiency of the proposed wavelet-based truncation.

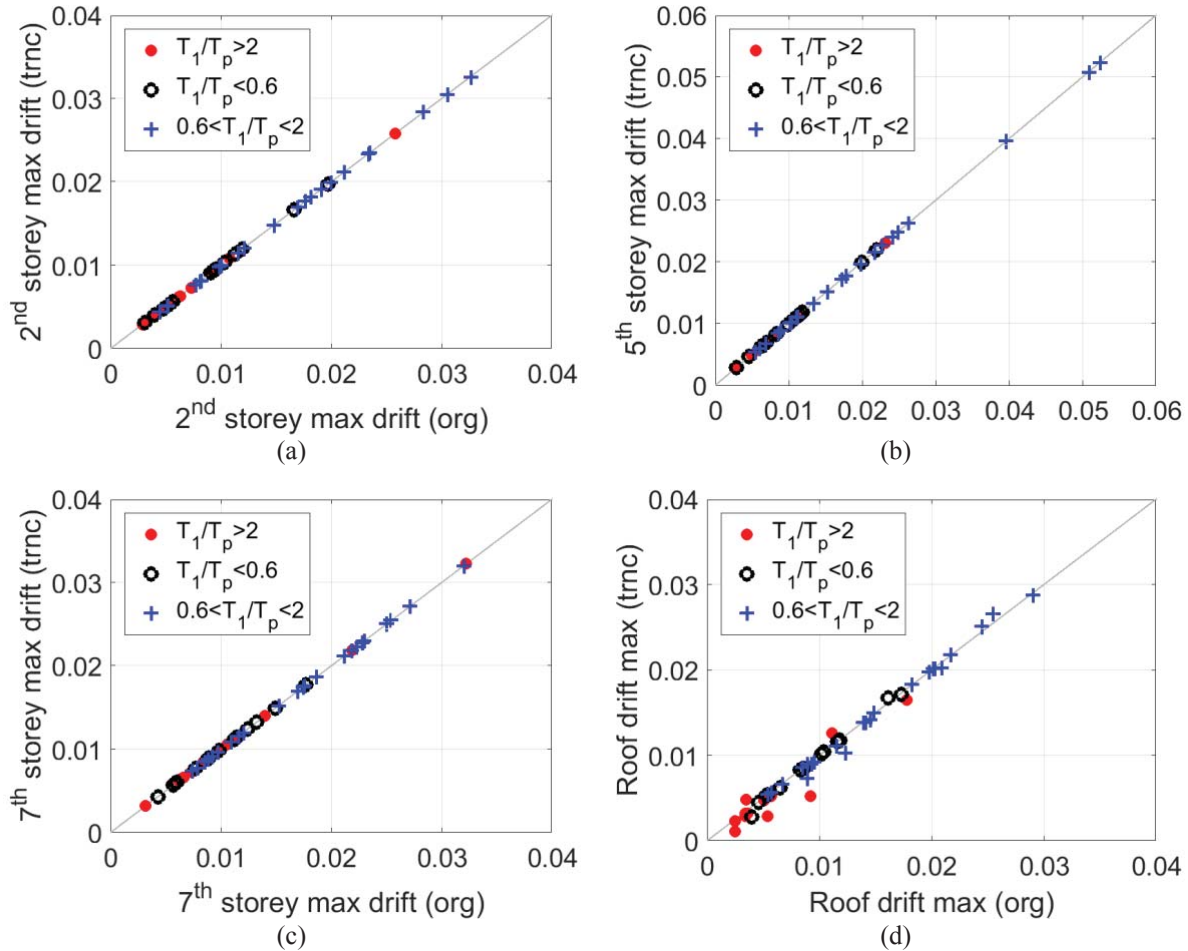


**Figure 4: (a) Profile of the median and the 16 and 84% percentiles drift demand for the 48 pulse-type ground motions; (b) Maximum interstorey drift obtained using the original and the truncated records versus the  $T_1/T_p$  ratio.**

In the following, the LA9 steel frame is subjected to the 48 near-field ground motions with forward directivity. Figure 4a presents the median peak interstorey drift demand and the corresponding 16% and 84% percentile curves of the interstorey drift demand. Excellent agreement for all the stories has been achieved along the height of the frame. Furthermore, the effect of record-to-record variability on the maximum interstorey drift demand is studied in Figure 4b. Although minor differences are seen for individual records, for the majority of ground motions the drift estimates of the original and the truncated signal practically coincide. Figure 4b deserves further attention. A different marker colour has been adopted depending on the storey that the maximum interstorey drift occurred. Overall, the seismic response computed for the truncated signals, follows the same pattern observed for the original records while for most cases the maximum drift demand occurs at the same level. Since the structure studied is sensitive to the first mode, the larger demand is due to records with  $T_1/T_p \leq 1$ . Furthermore, for these records, the peak drift appears at the middle stories (stories 4, 5 and 6).

Our findings are in agreement with Baker and Cornel [18] who discuss the effect of pulse period on the seismic behaviour of MDOF systems. They investigated the effect of the pulse on the higher modes of excitation through MDOF structures sensitive to second mode excitation and suggested that the ratio  $T_1/T_p$  is indicative of the level at which the peak displacement occurs; short period records excite higher modes, while for records with long period pulses the maximum response is expected at the low stories, indicating that first mode response governs

the peak displacements of the building. They proposed the thresholds,  $T_1/T_p < 0.5$  and  $T_1/T_p > 2$  that are also shown as vertical dashed lines in Figure 4b. According to Figure 4, for records with short period pulses,  $T_1/T_p > 2$  the higher modes of vibration are excited and the maximum interstorey drift is located at the upper stories (stories 7, 8 and 9). On the other hand, for records with  $T_1/T_p < 1$ , the maximum drift demand is observed at lower stories, indicating that the response is first mode dominated.



**Figure 5: Maximum interstorey drift at different stories of the building, (a) 2<sup>nd</sup> storey, (b) 5<sup>th</sup> storey, (c) 7<sup>th</sup> storey and (d) 9<sup>th</sup> storey (roof).**

Figure 5 shows the maximum drift demand for the 2<sup>nd</sup>, the 5<sup>th</sup>, the 7<sup>th</sup> and the 9<sup>th</sup> (top) storey. The agreement is practically perfect for all stories with the exception of the top storey where some minor errors appear for ground motions with  $T_1/T_p > 2$ . The maximum interstorey drifts occur mainly for records with  $T_1/T_p$  between 0.6 and 2, and in some cases for  $T_1/T_p > 2$ , while for the structure considered, the peak values appear at the middle stories of the building. Figure 6a shows the profiles of the median shear forces along the height of the building and the corresponding 16% and 84% percentiles. Very good agreement is again obtained, since the damage patterns are very close. Some minor differences are observed with respect to the demand in stories 3, 4 and 5. Furthermore, Figure 6b compares the base shear demand for the original and the truncated signal. It should be pointed out that the maximum values of the base shear are computed in the period range  $0.5 < T_1/T_p < 1$ , while (although not shown) most differences appear at the 1<sup>st</sup> and 5<sup>th</sup> storey, as also applies for the interstorey drifts (Figure 5).

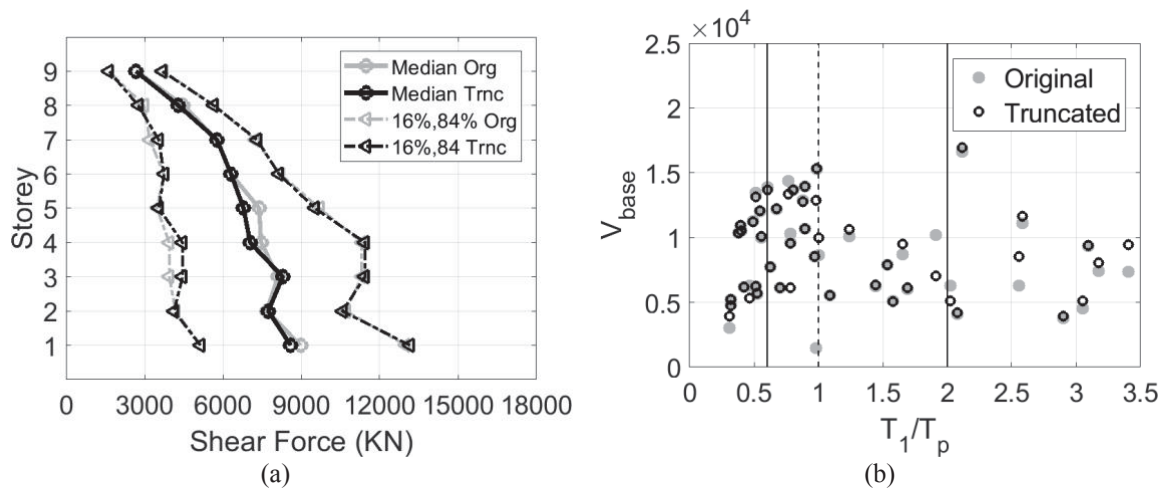


Figure 6: (a) Profiles of the maximum median storey shear force along with the standard deviation of storey shears. (b) Dispersion of the maximum base shear for original and truncated records versus  $T_1/T_p$ .

## 5 CONCLUSIONS

A novel record truncation approach has been presented. The proposed approach simplifies the input signal and accelerates the seismic performance assessment, especially in the case of pulse-like ground motions. The truncation does not require baseline correction and thus it can be integrated to give truncated realistic velocity and displacement time histories. The proposed approach has been validated through the study of a nine-storey steel building. Almost in all cases, the seismic demand, measured in terms of displacement, drift and shear forces, obtained using the truncated signal will produce close estimates. The computational process is performed within a fraction of the CPU time required when the original complete record is used, since the duration reduction lies on average around 80%.

## REFERENCES

- [1] S. Srivastav, J.M. Nau, Structural response to truncated earthquake accelerograms. *J Struct Eng* 114(5), 1189–92, 1988.
- [2] A. Arias, A measure of earthquake intensity. In: Hansen RJ (ed) *Seismic design for nuclear power plants*. MIT Press, pp 438–483, 1970.
- [3] A.-Y. Jin, J.-W. Pan, J.-T. Wang and X.-L. Du, A spectrum-based earthquake record truncation method for nonlinear dynamic analysis of arch dams. *Soil Dynamics & Earthquake Engineering*, 132, 106104, 2020.
- [4] A. Khaloo, S. Nozhati, H. Masoomi, H. Faghihmaleki, Influence of earthquake record truncation on fragility curves of RC frames with different damage indices. *J Build Eng*, 7, 23–30, 2006.
- [5] C.C. Repapis, P.P. Mimoglou, V.V. Dimakopoulou, I.N. Psycharis, I.M. Taflampas, Efficient strong ground motion duration of pulse-like records for nonlinear structural analyses. *Earthquake Engineering & Structural Dynamics*, 49, 479–497, 2020.
- [6] V.V. Bertero, S.A. Mahin, R.A. Herrera, A seismic design implication of near-fault San Fernando earthquake records. *Earthquake Engineering & Structural Dynamics*, 6, 31–42, 1978.



- [7] A.K. Chopra, C. Chintanapakdee, Comparing response of SDF systems to near-fault and far-fault earthquake motions in the context of spectral regions. *Earthquake Engineering & Structural Dynamics*, 30, 1769-1789, 2001.
- [8] C.C. Spyrakos, Ch.A. Maniatakis, J. Taflambas, Evaluation of near source seismic records based on damage potential parameters. Case study: Greece. *Soil Dynamics & Earthquake Engineering*, 28, 738-753, 2008.
- [9] P. Mimoglou, I.N. Psycharis & I.M. Taflampas, Explicit determination of the pulse inherent in pulse-like ground motions. *Earthquake Engineering & Structural Dynamics* 43(15), 2261-2281, 2014.
- [10] M.D. Trifunac & A.G. Brady AG, A study on the duration of strong earthquake ground motion. *Bulletin of the Seismological Society of America*, 65(3), 581-626, 1975.
- [11] G.P. Mavroeidis and A.S. Papageorgiou, A Mathematical Representation of Near-Fault Ground Motions. *Bulletin of the Seismological Society of America*, 93(3), 1099-1131, 2003.
- [12] I.M. Taflambas, Ch.A. Maniatakis, C.C. Spyrakos. Estimation of input seismic energy by means of a new definition of strong ground motion duration. *14th World Conference on Earthquake Engineering*, Beijing, China, October 12-17, 2008.
- [13] Peer-Pacific Earthquake Engineering Research Center. Strong motion database. [http://peer.berkeley.edu/peer\\_ground\\_motion\\_database](http://peer.berkeley.edu/peer_ground_motion_database). Accessed July 2013.
- [14] A. Gupta and H. Krawinkler, Seismic Demands for Performance Evaluation of Steel Moment Resisting Frame Structures. John A. Blume Earthquake Engineering Center Report No. 132, Department of Civil Engineering, Stanford University, 1999.
- [15] F. McKenna F and G.L Fenves, The OpenSees Command Language Manual-Version 1.2. Pacific Earthquake Engineering Research Centre, University of California, 2001.
- [16] V. Kardoutsou, I. Taflampas & I.N. Psycharis, A new pulse indicator for the classification of ground motions. *Bulletin of the Seismological Society of America*, 107(3), 1356-1364, 2017.
- [17] FEMA P-695, Quantification of Building Seismic Performance Factors and commentary for the seismic rehabilitation of buildings, FEMA P-695 Report, prepared by the Applied Technology Council for the Federal Emergency Management Agency Washington DC, 2009.
- [18] J.W. Baker, C.A. Cornell, Vector-valued intensity measures for pulse-like near-fault ground motions. *Eng Str*, 30, 1048–1057, 2008.



## NUMERICAL MODELLING OF SHEAR BOND TESTS ON EXTERNALLY STRENGTHENED MASONRY SPECIMENS

Ottavio Tamborrino<sup>1</sup>, Daniele Perrone<sup>1,2</sup> and Marianovella Leone<sup>1</sup>

<sup>1</sup> University of Salento, Department of Engineering for Innovation, Lecce, Italy  
Via per Monteroni, Campus Ecotekne, 73047, Monteroni di Lecce LE  
{ottavio.tamborrino,daniele.perrone,marianovella.leone}@unisalento.it

<sup>2</sup> University School for Advanced Studies IUSS Pavia, Pavia, Italy  
Palazzo del Broletto n16, Piazza della Vittoria, 27100, Pavia  
daniele.perrone@iusspavia.it

---

### Abstract

*Masonry existing structures are prone to significant structural damages when subjected to seismic actions. Over the last decades, innovative techniques emerged as attractive solutions for repair and retrofit of structures. In particular, composite materials with inorganic matrix (FRCMs-CRMs) have emerged as an alternative to fiber reinforced polymers for their better compatibility with masonry substrates. The effectiveness of the strengthening relies on the FRCM-substrate bond behavior, which needs to be characterized for the design of the reinforcement elements. Shear bond tests are able to determine the stress–slip law and the failure mode that rules the FRCM-substrate stress transfer capacity. In the last years, several experimental investigations on shear bond tests of strengthened masonry prisms were performed even if the knowledge about the influence of each variable parameter is not fully known. In this context, the numerical simulation may be a rapid and economic tool to study the incidence of the most relevant parameters in the bond mechanism.*

*In this paper, a numerical study aimed at simulating the fiber-mortar bond behavior and at calibrating a shear stress ( $\tau$ )–slip ( $s$ ) constitutive bond law, is presented. Advanced 2D numerical models, able to simulate the most probable failure mode occurring in shear bond tests, have been developed. The results of the numerical simulations have been compared with the experimental results of a large database of tests on FRCM/CRM strengthened masonry prisms. An inverse analysis procedure has been used to fit the experimental bond stress versus slip curves and to predict the failure modes.*

**Keywords:** Masonry, FRCM, CRM, Bond, Retrofitting, Finite-element model.

---

## 1 INTRODUCTION

The structural deficiencies of existing masonry structures, in case of horizontal loading, are well-known in the literature. Generally, the strengthening of masonry walls is performed by means of retrofitting techniques which also implies the use of organic-based composite materials. In order to follow the code requirements in terms of lateral load capacity, and to guaranty the chemical compatibility between the substrate and the adopted strengthening solution, the use of the Fabric Reinforced Cementitious Matrix (FRCM) or Composite Reinforced Mortar (CRM) is nowadays considered a suitable solution.

In a large number of structural applications, including the strengthening of masonry walls, the effectiveness of the strengthening is strongly related on the FRCM-substrate bond behavior, which needs to be characterized for the design of the reinforcement and for the assessment of the retrofitted structural members. Experimental investigations have shown that, differently from FRPs, the FRCM-substrate bond failure may take place both within the substrate and within the thickness of the composite. The FRCM-substrate load transfer mechanism may be affected by the textile architecture, the coating or pre-impregnation of the fibers, the mechanical properties and the thickness of the matrix, the mechanical properties of the substrate, as well as by the quality of the application and the curing conditions [1].

In this paper, advanced finite-element 2D models, simulating the failure modes occurred in single-lap shear bond tests, have been developed. The results of the numerical simulations have been compared with the experimental results of a large database of tests on FRCM/CRM strengthened masonry prisms [2-9]. In particular, the database has been divided into two parts: the first one has been used to calibrate a  $\tau$ - $s$  fiber-mortar law, while the second one to validate the proposed  $\tau$ - $s$  fiber-mortar law. An inverse analysis procedure has been used to fit the experimental curve and to obtain the actual failure modes. Both a quantitative and a qualitative method have been used to evaluate the goodness of the fitting. Finally, the influence of some important parameters, such as bond length, grid spacing and grid coating on the shear stress-slip law results has been discussed.

## 2 A DATABASE OF SINGLE-LAP SHEAR BOND TESTS

In the last years, several experimental investigations on shear bond tests of strengthened masonry specimens were performed. A database collecting the results of the main studies available in the literature involving single-lap shear bond tests has been taken into account aiming to collect all the data required for the numerical simulations. In particular, eight different experimental campaigns were analyzed in the database [2-9].

A single-lap shear bond test allows to characterize the FRCM/CRM-substrate bond behavior by providing the following main information: (i) the peak axial stress ( $f_b$ ), referred to the cross-sectional area of the longitudinal fibers of the textile ( $A_f$ ); (ii) the axial stress ( $f$ ) – slip ( $s^*$ ) relationship (Fig. 1a), the slip  $s^*$  being the relative displacement between the substrate and the textile at the loaded end of the bonded area; and (iii) the failure mode that controls the FRCM-substrate load transfer capacity. Analyzing the data available in the literature, six failure modes can be observed (Fig. 1b):

- (a) Debonding with cohesive failure of the substrate;
- (b) Debonding at the matrix-substrate interface;
- (c) Debonding at the textile-matrix interface;
- (d) Textile slippage within the mortar matrix;
- (e) Textile slippage within the matrix with cracking of the outer layer of mortar;
- (f) Tensile rupture of the textile (out of the bonded area) [1].

As reported in Figure 1a, the FRCM-substrate response generally exhibits an initial linear phase, followed by a nonlinear phase up to the attainment of the peak stress value, and a post-peak phase in which the increase of slip is associated to a decrease of the stress.

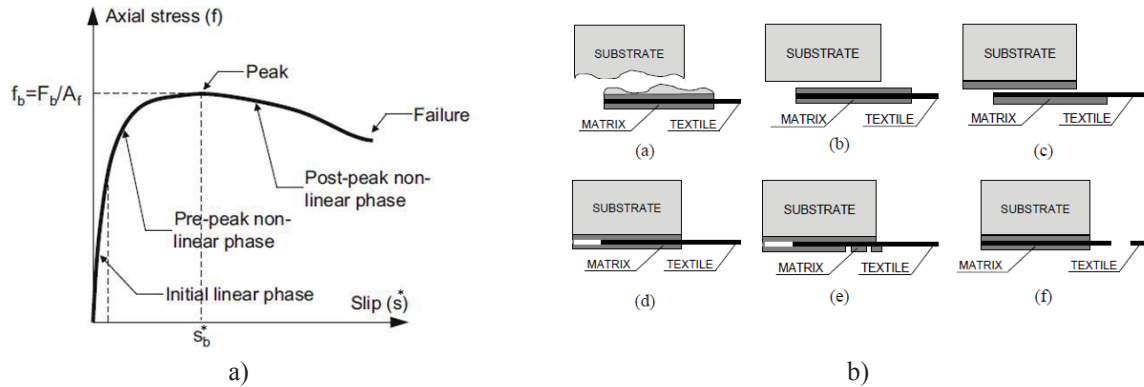


Figure 1: a) axial stress-slip law, b) failure modes [1].

Figure 2 reports both the typical specimen and set-up of a single-lap shear bond test. The grip system is designed “ad hoc” and it is constituted by a steel frame. The tensile force is applied at the specimens through the fabric strengthened at the end. During the tests, the slip between substrate and fiber grid and the slip between substrate and mortar matrix can be recorded [2].

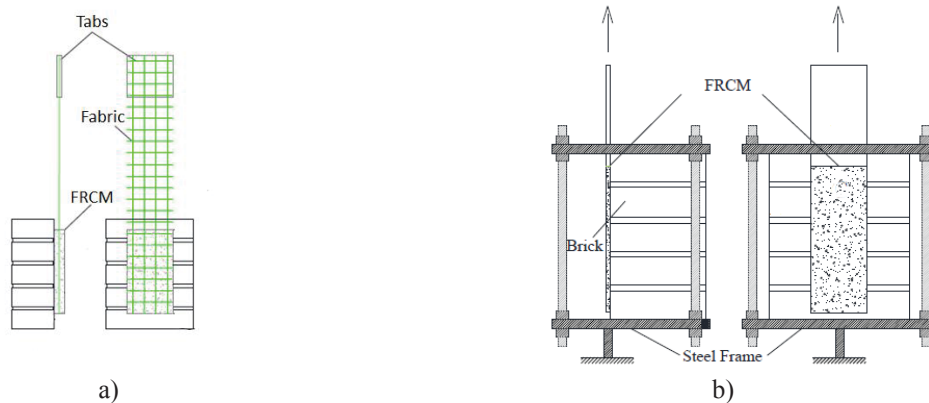


Figure 2: Single lap shear test – a) specimen, b) set-up [2].

Tables 1 and 2 report all the properties of the specimens taken into account to create the database. In particular, Table 1 reports the characteristics of the considered FRCM specimens, while Table 2 reports the properties of the analyzed CRM specimens.

In Lignola et al. [3] the experimental results of bond test between basalt FRCM and masonry, showed that, when the fiber failure is observed, the bond peak stress is similar to the tensile peak stress of the fiber grid; while, when other failure modes occur, the bond peak stress is smaller than the tensile peak stress of the fiber grid. Carozzi et al. [4] observed different failure modes testing carbon FRCM bonded on masonry, the most common being the slippage of the textile within the matrix and the rupture of the textile. Specimens' geometry and curing time of the mortar largely affected the results. The bond tests between glass FRCM and masonry discussed in Bilotta et al. [5] did not underline relevant influence of the mechanical properties of the masonry substrate for the specimens bonded with 1 or 2 grid layers; while this influence is evident for the specimens bonded with 4 grid layers, where the debond-

ing of the reinforcement from the substrate occurred. Leone et al. [6] observed different failure modes performing single face shear test between glass FRCM and masonry: the most common type was the mortar cracking and tensile failure of glass fiber while cohesive failure of the reinforcement from the substrate never occurred. In D'Antino et al. [7] the failure mode of debonding of the PBO fibers at the matrix–fiber interface always occurred except for four specimens where the detachment of the entire composite from the concrete substrate was observed due to the lack of a surface preparation. The experimental results provided by Carloni et al. [8] on concrete specimens reinforced with PBO FRCM indicated that the values of bond peak load are influenced by the adopted test rate of the slip  $s^*$ . In detail, considering  $1V = 0.00084 \text{ mm/s}$ , the peak load increases as the rate increases from 0.5V to 3V; the maximum peak load is achieved for a rate between 3V and 5V; while for rate 5V or greater, it decreases with increasing rate.

Regarding the CRM reinforcement system, Rizzo [2] and Gattesco et al. [9] investigated the bond behavior between glass CRM and clay masonry substrates. In both studies three different bond lengths were considered: 120, 180 and 240 mm. In [2], for each bond length, the failure occurred by tensile rupture of fibers and the mortar layer was undamaged. In [9], caused by the poorer mechanical properties of the mortar, the failure for longitudinal wires rupture was obtained only for 240 mm, while in the other cases, textile slippage within the matrix with cracking of mortar occurred.

For each experimental campaign, the following information are recorded in the database (Tables 1-2) according to the following labels:

- ID = specimen name;
- N = number of specimens;
- $f_{tf}$  = fiber tensile strength, [MPa];
- $E_f$  = fiber elastic modulus, [GPa];
- $f_{cm}$  = mortar compressive strength, [MPa];
- $f_{tm}$  = mortar tensile strength, [MPa];
- $E_m$  = mortar elastic modulus, [GPa];
- $t_f$  = fiber equivalent thickness, [mm];
- $L_{ad}$  = mortar bond length, [mm];
- $b_{ad}$  = mortar width, [mm];
- $t_m$  = mortar thickness, [mm].

ID	N	$f_{tf}$	$E_f$	$f_{cm}$	$f_{tm}$	$E_m$	$t_f$	$L_{ad}$	$b_{ad}$	$t_m$	Failure mode
FRCM4 <sup>3</sup>	5	871	50	15	1.5	8	0.023	260	80	10	F
FRCM4 <sup>3</sup>	5	871	50	15	1.5	8	0.039	260	100	10	F
FRCM3 <sup>3</sup>	5	1201	75	15	1.5	6	0.058	260	75	10	E
FRCM2 <sup>3</sup>	5	2169	112	12	1.2	10	0.033	260	75	10	F
CFRCM4 <sup>4</sup>	5	1944	203	20	2.0	7	0.047	260	100	10	F-D
CFRCM4 <sup>4</sup>	5	1944	197	20	2.0	7	0.047	260	50	10	F-D
CFRCM5 <sup>4</sup>	5	2500	230	38	4.3	16	0.061	260	100	10	F
CFRCM6 <sup>4</sup>	5	1876	187	16	2.8	15	0.047	260	50	10	F
CFRCM6 <sup>4</sup>	5	1876	219	16	2.8	15	0.047	260	60	10	D
G1LMX2 <sup>5</sup>	2	1275	72	12	2.5	8	0.035	300	120	10	F
G2LMX2 <sup>5</sup>	2	1275	72	12	2.5	8	0.070	300	120	10	F
F_unipd <sup>6</sup>	5	1600	80	15	2.7	9	0.031	260	40	10	F
G_polimi <sup>6</sup>	5	1170	72	22	3.3	7	0.144	260	100	10	E

G_zag <sup>6</sup>	5	1170	72	22	3.3	7	0.144	260	100	10	F
H_unina <sup>6</sup>	3	1275	72	15	2.7	8	0.035	260	100	10	F
DS_60U <sup>7</sup>	5	3014	206	28	3.5	6	0.092	450	60	8	C
DS_80U <sup>7</sup>	5	3014	206	28	3.5	6	0.092	450	80	8	C
DS_80V <sup>8</sup>	4	3014	206	23	4.8	6	0.092	450	80	8	C

Table 1: Database bond FRCM [3-8].

ID	N	$f_{t_f}$	$E_f$	$f_{c_m}$	$f_{t_m}$	$E_m$	$t_f$	$L_{ad}$	$b_{ad}$	$t_m$	Failure mode
G66-120 <sup>2</sup>	4	1084	55	25	2.5	20	0.058	120	132	30	F
G66-180 <sup>2</sup>	5	1084	55	25	2.5	20	0.058	180	132	30	F
G66-240 <sup>2</sup>	3	1084	55	25	2.5	20	0.058	240	132	30	F
G33-240 <sup>2</sup>	4	1084	55	25	2.5	20	0.115	240	132	30	E-F
A66-1 <sup>9</sup>	4	1084	55	8	0.8	8	0.058	120	132	30	E
A66-2 <sup>9</sup>	5	1084	55	8	0.8	8	0.058	180	132	30	E
A66-3 <sup>9</sup>	5	1084	55	8	0.8	8	0.058	240	132	30	F

Table 2: Database bond CRM [2, 9].

### 3 NUMERICAL MODELLING

In this study, 2D finite-element models, simulating FRCM/CRM-masonry bond tests, have been developed using Midas FEA [10].

The adopted two-dimensional model, schematized in Figure 3, is able to simulate the main failure modes occurring in a single-lap shear bond test, except for the A and/or B mode that involved the substrate (Fig. 1b). These failure modes were excluded because were not observed in the collected database. This assumption allowed to simplify the numerical model because the masonry substrate was not modelled, and it was replaced by fixed boundaries assigned to the mortar. This assumption is also feasible because the masonry prism is constrained to the steel supporting frame of the test set-up (Fig. 2). In detail, the adopted numerical models are similar to that developed in [11], and composed of:

- Mortar (two layers): it is modelled through four-node plane-stress 2D elements ( $A = 5 \times 5 \text{ mm}^2$ ) with a linear elastic behavior. The behavior was characterized using the elastic modulus and tensile strength provided in the experimental campaigns. The thickness is equal to the mortar width;
- Fiber grid: it is modelled through two-node truss 1D elements ( $l = 5 \text{ mm}$ ), with a linear elastic behavior. The behavior was characterized using the elastic modulus and tensile strength provided in the experimental campaigns. The cross-sectional area ( $A_f$ ) is equal to the sum of transversal areas of each yarn;
- Fiber-mortar interface (two layers): it is modelled through line interface zero-thickness elements, characterized from a nonlinear bond-slip  $\tau$ -s mechanical law. The thickness is equal to the sum of wet perimeters of each yarn;
- Upper-lower mortar interface: it is modelled through point interface zero-thickness elements, characterized from an infinitely rigid behavior.

In this study, a specific cracking modelling of the mortar was not introduced, for this reason is not possible to monitor the cracking development within the mortar. However, it is worth mentioning that this is out of the scope of this work.

The analyses have been conducted in displacement control using the Newton Raphson convergence method. The horizontal maximum displacement is assigned at the loaded end of the equivalent yarn and divided into 50 incremental steps.

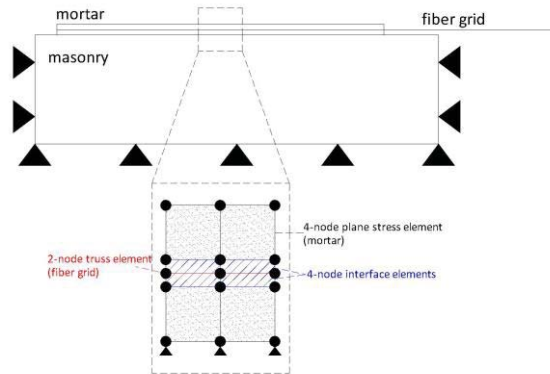


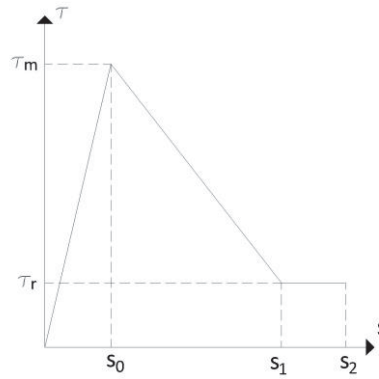
Figure 3: Adopted 2D modelling.

The most critical point in the adopted modelling approach consists in the definition of the nonlinear bond-slip ( $\tau$ - $s$ ) mechanical law. This law will be calibrated for each specimen available in the database in order to find a correlation between the different involved parameters. As a starting point, the shape of the curve has been defined considering some studies available in the literature. In [12], shear bond tests on SRG systems were simulated introducing a steel-mortar nonlinear interface, whose fundamental parameters influence the eventual failure mechanism of the specimen for slippage of the steel cords from the grout.

In particular, with the aim to numerically define this interface, the authors chose a tri-linear constitutive law, taking into account the experimentally observed friction phenomena between textile and matrix (Fig. 4). The same bond stress-slip law form was introduced in [13], where a cohesive interface crack model for the matrix-textile debonding in FRCM composites was developed.

Following a similar approach, in this work, the fundamental values of the adopted bond  $\tau$ - $s$  law are (Fig. 4):  $\tau_m$  (bond strength),  $\tau_r$  (residual bond stress),  $s_0$  (slip corresponding to  $\tau_m$ ),  $s_1$  (slip at the end of softening branch) and  $s_2$  (ultimate slip). All the parameters have been defined through the calibration of the model using the experimental results. The simplified bond stress-slip law of the interface implies a first linear elastic behavior as the pre-peak branch (until the maximum stress  $\tau_m$ ), followed by a linear softening part representing loss of cohesion between the two materials in the interface. The third branch with the constant bond stress of  $\tau_r$  represents the frictional resistance of the interface, this branch is only necessary for convergence reasons.

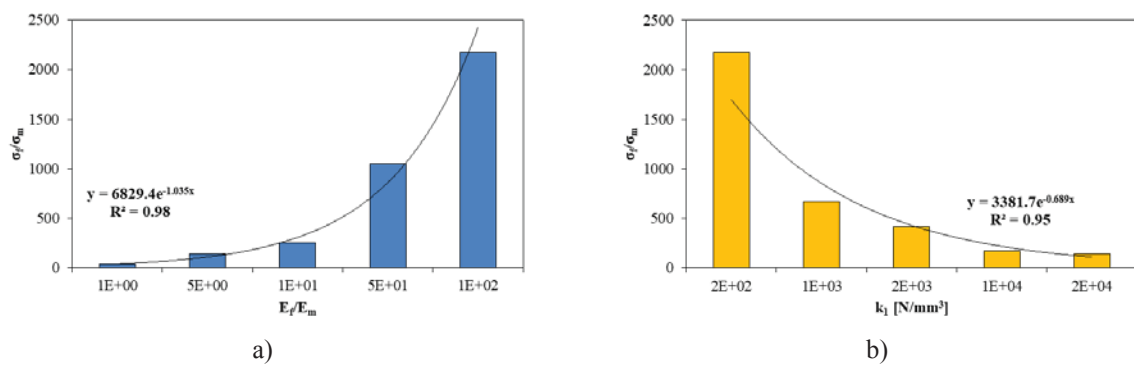



 Figure 4: Adopted bond  $\tau$ - $s$  law.

To demonstrate the effectiveness of the numerical model, a preliminary parametric analysis has been conducted to check the physical robustness of the obtained results. In detail, the ratio between the fiber elastic modulus and the mortar elastic modulus ( $E_f/E_m$ ) and the interface stiffness ( $k_1 = \tau_m/s_0$  – slope of the bond stress versus slip curves) were varied respect to the ratio between the fiber stress and the mortar stress ( $\sigma_f/\sigma_m$ ) at the loaded end.

As expected,  $\sigma_f/\sigma_m$  increases as  $E_f/E_m$  increases (Fig. 5a) while  $\sigma_f/\sigma_m$  decreases as  $k_1$  increases (Fig. 5b). This last is related to the fact that as increasing  $k_1$ , the behavior is closer to the perfect bond behavior and the stresses in the two materials are similar.

Furthermore, with the same purpose to check the robustness of the model, the trend of shear bond stress  $\tau$  in the fiber-mortar interface, along the specimen, respectively for the case of mortar cracking and interface debonding, has been monitored (Fig. 6). The numerical analyses have showed that, if the crisis affects the mortar, the bond stress level in the interface is such that  $\tau$  falls in the first linear elastic phase of the  $\tau$ - $s$  curve (Fig. 4); while when the interface debonding occurs,  $\tau$  falls in the second linear softening phase of the  $\tau$ - $s$  curve. So, it is noticeable that the bond stress trend is opposite between these two cases: in case of mortar cracking,  $\tau$  decreases from loaded end (with higher value of slip) to free end (with lower value of slip); in case of interface debonding  $\tau$  increases from loaded end to free end.


 Figure 5: Validation of the numerical model – a)  $\sigma_f/\sigma_m$  vs  $E_f/E_m$ , b)  $\sigma_f/\sigma_m$  vs  $k_1$ .

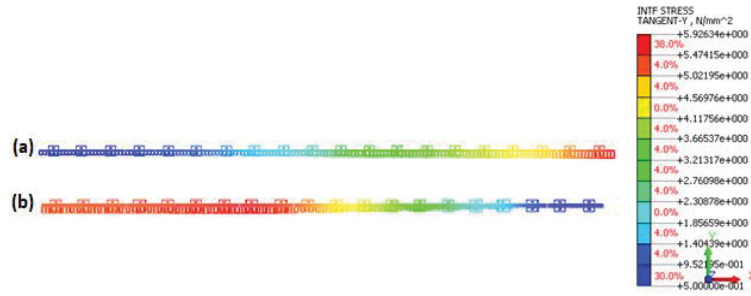


Figure 6: Interface stress mapping – mortar (a) and interface (b) failure.

#### 4 CALIBRATION OF BOND-SLIP INTERFACE LAW

The finite-element model described in Section 3 has been developed to simulate all the results collected in the FRCM/CRM-masonry single-lap shear bond tests database presented in Section 2. The database has been divided into two homogeneous parts: i) the first part has been used to calibrate the fiber-mortar interface laws (76% of the specimens); ii) the second part has been used for validation purpose (24% of the specimens).

The percentage assigned to the calibration and validation part was selected referring to similar studies available in the literature [14].

For each specimen, an inverse analysis has been made, looking for the best fitting between the experimental and numerical axial stress ( $f$ ) - slip ( $s^*$ ) curve to obtain the fiber-mortar  $\tau$ - $s$  interface law. For example, in Figure 7 and Figure 8, the experimental-numerical best fitting with the corresponding  $\tau$ - $s$  output related to the FRCM specimen “FRCM2-01” (Tab. 1) and to the CRM specimen “G66-120-01” (Tab. 2), respectively, are reported.

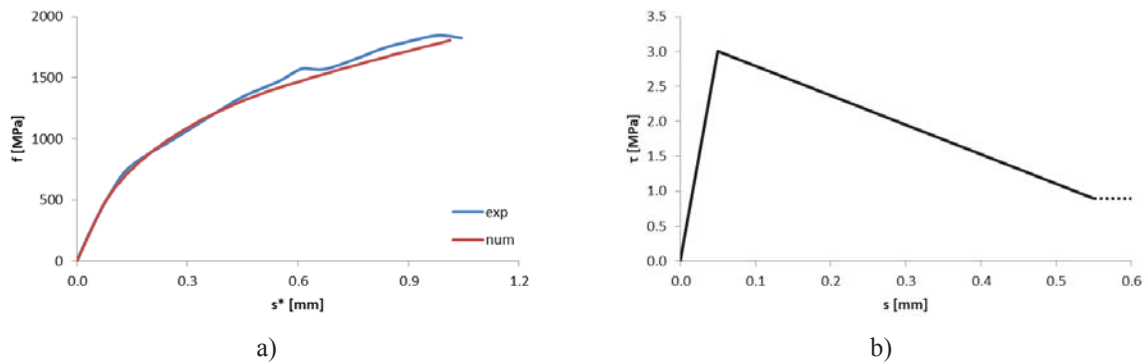


Figure 7: FRCM specimen – a) experimental-numerical best fitting, b) bond interface law.

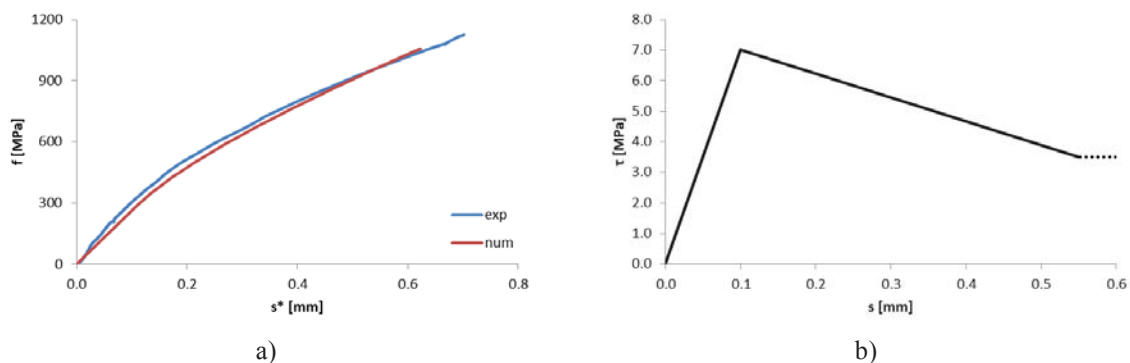


Figure 8: CRM specimen – a) experimental-numerical best fitting, b) bond interface law.

For each inverse analysis, the goodness of the experimental-numerical fitting has been assessed through both qualitative and quantitative methods. The quantitative control has been made comparing the experimental and numerical peak axial stress ( $f_{bexp}$ ,  $f_{bnum}$ ) and corresponding slip ( $s_{bexp}^*$ ,  $s_{bnum}^*$ ).

In Figure 9, each doth represent a different specimen. It can be observed that the correlation in terms of stress is better than slip; in fact, the average value of  $f_{bexp}/f_{bnum}$  is equal to 1.00 (COV=7.4%), while the average value of  $s_{bexp}^*/s_{bnum}^*$  is equal to 1.13 (COV=27.8%).

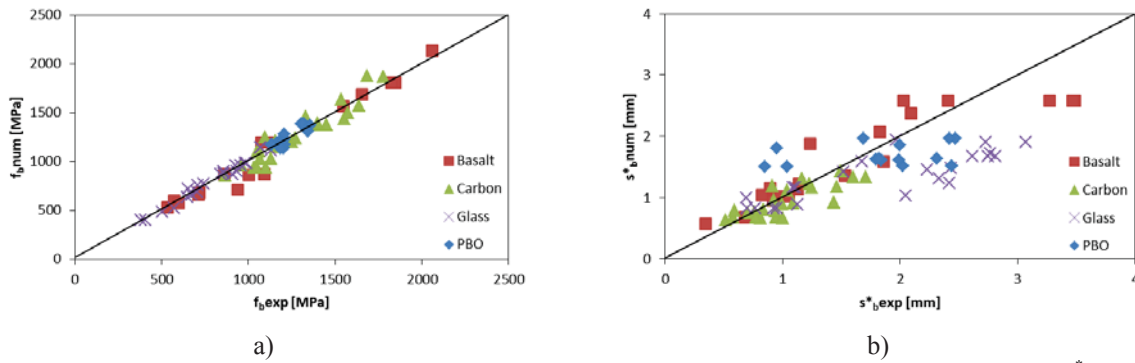


Figure 9: a) experimental-numerical dispersion for  $f_b$ , b) experimental-numerical dispersion for  $s_b^*$ .

In Figure 10 the comparisons between average  $\tau$ - $s$  curves varying  $E_f \cdot t_f$  [kN/mm] and  $f_{tm}$  [MPa], only related to FRCM specimens, are reported. A correlation between the stiffness of the reinforcement and the interface behavior is not completely clear as well as a trend between the tensile strength of the mortar and the peak of the bond-slip curve cannot be defined. Probably other parameters (for example grid coating and spacing), that have been neglected, might affect the obtained results.

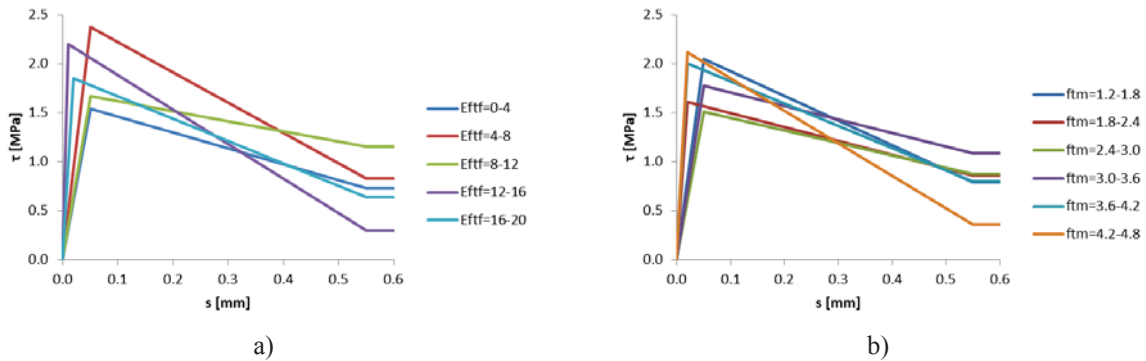


Figure 10:  $\tau$ - $s$  average curves varying a)  $E_f \cdot t_f$  and b)  $f_{tm}$ .

#### 4.1 Discussion

In order to investigate the influence of other parameters that could affect the interface behavior, the superficial grid coating and the grid spacing ( $s_f$ ) have been analyzed. In particular, the incidence of these two parameters on the bond law has been investigated considering two representative specimen groups, extracted from the FRCM database (Tab. 1), composed of specimens characterized by similar properties in terms of mortar and fibers:

- Group 1 ( $E_f = 50$ -80 GPa,  $f_{cm} = 12$ -17 MPa), composed of 13 specimens;
- Group 2 ( $E_f = 80$ -110 GPa,  $f_{cm} = 12$ -17 MPa), composed of 10 specimens.

Each of these two groups is divided into two parts:

- Part a), characterized by a higher spaced grid ( $s_f = 25$  mm);
- Part b), characterized by a lower spaced grid ( $s_f = 10$  mm).

In Figure 11, the blue and the red columns indicates the average value of  $\tau_m$  (Fig. 11a) and  $k_1$  (Fig. 11b), respectively, for the part a) and the part b) of each group. It is expected that the presence of more transversal wires, in case of lower spaced grids, should cause a more significant increment of  $\tau_m$  and  $k_1$  than in higher spaced grids [2]. However, in the analyzed case, as evidenced in Figure 11, this trend is confirmed only for the Group 1 and it's completely opposite for the Group 2.

In fact, while all the specimens belonging to the Group 1 are characterized by the presence of a superficial grid coating; in the Group 2, only the specimens with higher spaced grids are characterized by the coating. So, this opposite trend could be justified by the fact that the presence (or absence) of the coating could have a greater influence than the grid spacing.

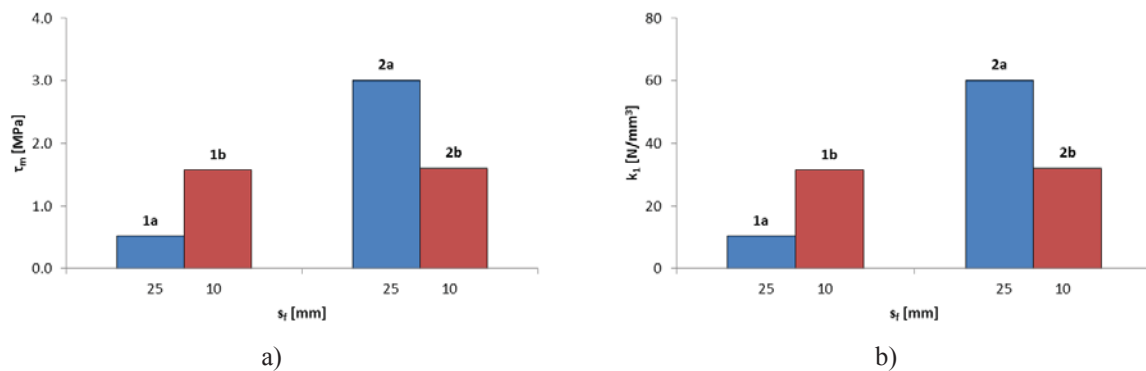


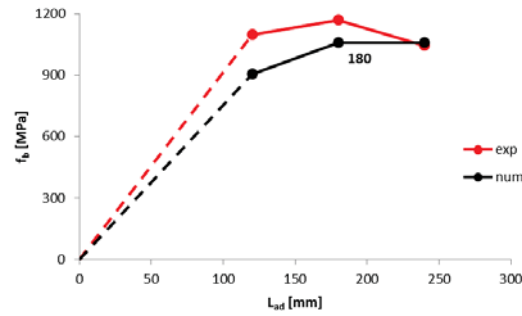
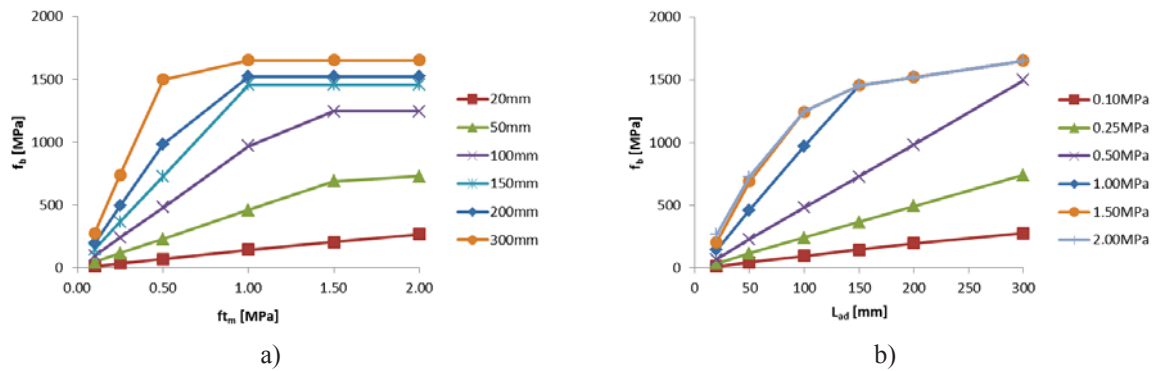
Figure 11: Grid coating and spacing effect in terms of: a)  $\tau_m$  and b)  $k_1$ .

The campaign on shear bond tests between GCRM and masonry, conducted by Rizzo [2] (explained in Section 2), was also used to individuate the effective bond length ( $L_{eff}$ ), beyond which there are no more significant increases in terms of peak axial stress  $f_b$ . The authors observed that  $f_b$  seems to be growing up from 120 mm until 180 mm, after that it remains almost constant at 240 mm. So, the effective bonded length could be estimated equal to 180 mm. From the numerical simulation of these bond tests, the same value of  $L_{eff}$  has been obtained (Fig. 12).

This analysis, with the aim to evaluate an effective bond length, has been extended to FRCM-masonry specimens with different mechanical properties. In detail, the numerical analysis has been made varying the mortar tensile strength  $f_{tm}$  (from 0.10 to 2.00 MPa) and the bond length  $L_{ad}$  (from 20 to 300 mm); while the grid properties have been kept constant:  $E_f = 300$  GPa and  $f_{tf} = 3000$  MPa.

Figure 13 reports the variation of  $f_b$  as a function of  $f_{tm}$  (Fig. 13a) and  $L_{ad}$  (Fig. 13b). In Figure 13a, the constant branch of each curve begins when the failure mode changes from mortar cracking to interface debonding without more increments in terms of  $f_b$ . It is noticeable that increasing the bond length the mode of failure changes for low value of the mortar tensile strength.

From Figure 13b, it is evident that for lower values of  $f_{tm}$ ,  $f_b$  increases as  $L_{ad}$  increases; however, for mortar tensile strength greater than 1.00 MPa and for  $L_{ad}$  values greater than 150 mm, the slope of the curve rapidly decreases and there are no more important increments in terms of  $f_b$ . In conclusion,  $L_{ad}$  equal to 150 mm seems to be the effective bond length ( $L_{eff}$ ) for specimens characterized by  $E_f = 300$  GPa and  $f_{tf} = 3000$  MPa.


Figure 12: Peak axial stress trend in function of  $L_{ad}$ .

Figure 13: Peak axial stress trend – a)  $f_{tm}$  and b)  $L_{ad}$ .

## 5 CONCLUSIONS

The effectiveness of the FRCM/CRM strengthening techniques relies on the composite-substrate bond behavior. In this study, numerical simulations aimed to study the interface behavior have been carried out. The obtained results that represent the first part of a wider study are able to furnish the following conclusions:

- A simplified finite-element 2D model, able to simulate the main failure modes occurring in a single-lap shear bond test between FRCM/CRM and masonry, has been developed.
- An inverse numerical analysis has been used to calibrate the  $\tau$ -s law between fiber and mortar and to simulate the results of single-lap shear bond tests. The comparison between the numerical and experimental results demonstrated the effectiveness of the proposed numerical modelling approach.
- The influence of some important parameters, such as grid spacing and grid coating on the  $\tau$ -s law results has been investigated. For the analyzed cases, it has been observed that for masonry reinforced with coated FRCM, lower spaced grids give higher values of both maximum bond stress ( $\tau_m$ ) and slope of the bond stress versus slip curves ( $k_1$ ).
- The performed numerical analysis seems to be able to estimate the transfer length of the reinforcement.
- At the date, numerical simulations are still in progress with particular reference to shear bond tests between CRM and masonry. In the future, is in the authors' intent to carry out pull-out tests on FRCM and CRM specimens [15] in order to experimentally obtain  $\tau$ -s fiber-mortar relationships for comparison with the numerically obtained laws.

## ACKNOWLEDGEMENTS

This study was supported by the ReLUIS-program 2019-2021, PR 5 – “*Materiali innovativi per applicazioni su costruzioni esistenti*”.

## REFERENCES

- [1] De Felice, G., Aiello, M. A., Caggegi, C., Ceroni, F., De Santis, S., Garbin, E., ... & Viskovic, A. (2018). Recommendation of RILEM Technical Committee 250-CSM: Test method for Textile Reinforced Mortar to substrate bond characterization. *Materials and Structures*, 51(4), 1-9.
- [2] Rizzo, V. (2020). *Bond Behaviour and Durability in Alkaline Environments of Composite Strengthening Systems* (Doctoral dissertation).
- [3] Lignola, G. P., Caggegi, C., Ceroni, F., De Santis, S., Krajewski, P., Lourenço, P. B., ... & Zuccarino, L. (2017). Performance assessment of basalt FRCM for retrofit applications on masonry. *Composites Part B: Engineering*, 128, 1-18.
- [4] Carozzi, F. G., Bellini, A., D'Antino, T., de Felice, G., Focacci, F., Hojdys, Ł., ... & Poggi, C. (2017). Experimental investigation of tensile and bond properties of Carbon-FRCM composites for strengthening masonry elements. *Composites Part B: Engineering*, 128, 100-119.
- [5] Bilotta, A., Ceroni, F., Nigro, E., & Pecce, M. (2017). Experimental tests on FRCM strengthening systems for tuff masonry elements. *Construction and building Materials*, 138, 114-133.
- [6] Leone, M., Aiello, M. A., Balsamo, A., Carozzi, F. G., Ceroni, F., Corradi, M., ... & Saenger, D. (2017). Glass fabric reinforced cementitious matrix: Tensile properties and bond performance on masonry substrate. *Composites Part B: Engineering*, 127, 196-214.
- [7] D'Antino, T., Sneed, L. H., Carloni, C., & Pellegrino, C. (2015). Influence of the substrate characteristics on the bond behavior of PBO FRCM-concrete joints. *Construction and Building Materials*, 101, 838-850.
- [8] Carloni, C., Verre, S., Sneed, L. H., & Ombres, L. (2017). Loading rate effect on the debonding phenomenon in fiber reinforced cementitious matrix-concrete joints. *Composites Part B: Engineering*, 108, 301-314.
- [9] Gattesco, N., & Boem, I. (2017). Characterization tests of GFRM coating as a strengthening technique for masonry buildings. *Composite Structures*, 165, 209-222.
- [10] Midas FEA NX Advanced Nonlinear and Detail Analysis System. Copyright © Since 1989, MIDAS Information Technology Co., Ltd. All Rights Reserved. <http://www.midasuser.com/>.
- [11] Ghiassi, B., Marcari, G., Oliveira, D. V., & Lourenço, P. B. (2012). Numerical analysis of bond behavior between masonry bricks and composite materials. *Engineering Structures*, 43, 210-220.
- [12] Razavizadeh, A., Ghiassi, B., & Oliveira, D. V. (2014). Bond behavior of SRG-strengthened masonry units: Testing and numerical modeling. *Construction and Building Materials*, 64, 387-397.



- [13] Carozzi, F. G., Colombi, P., Fava, G., & Poggi, C. (2016). A cohesive interface crack model for the matrix–textile debonding in FRCM composites. *Composite Structures*, 143, 230-241.
- [14] Haddad, R., & Haddad, M. (2020). Predicting fiber - reinforced polymer – concrete bond strength using artificial neural networks: A comparative analysis study. *Structural Concrete*.
- [15] Barhum, R., & Mechtcherine, V. (2012). Effect of short, dispersed glass and carbon fibres on the behaviour of textile-reinforced concrete under tensile loading. *Engineering Fracture Mechanics*, 92, 56-71.

## A DISPLACEMENT-BASED DESIGN PROCEDURE OF VISCOUS DAMPED STEEL EXOSKELETONS FOR THE SEISMIC RETROFITTING OF RC FRAMED BUILDINGS

Fabio Mazza<sup>1</sup> and Egidio Mollo<sup>2</sup>

<sup>1</sup> Dipartimento di Ingegneria Civile, Università della Calabria  
87036, Rende (Cosenza), Italy  
e-mail: fabio.mazza@unical.it

<sup>2</sup> Dipartimento di Ingegneria Civile, Università della Calabria  
87036, Rende (Cosenza), Italy  
e-mail: egidio.mollo@outlook.it

**Keywords:** RC Framed Buildings, Dissipative Steel Exoskeletons, Nonlinear Fluid Viscous Dampers, Seismic Retrofitting, Design Procedure.

**Abstract.** *The dissipative exoskeleton (DEX), an external framed structure equipped with a damped bracing system and rigidly coupled to the existing building is to be retrofitted, may be more convenient than a dissipative endoskeleton (DEN), constituted of braces connecting adjacent storeys and equipped with dissipative devices. Aim of the present work is the proposal of a displacement-based design procedure of the DEX based on the use of overdamped elastic response spectra, which could prove a valuable tool for practitioners. The DEX includes concentrically braced chevron frames, with pinned joints, and damped bracing systems, incorporating fluid viscous dampers (FVDs). Elastic-linear behaviour of steel frame members and nonlinear pure viscous dashpot for FVDs are hypothesized. A six-storey archetype located in L'Aquila (Italy), representative of many reinforced concrete (RC) framed buildings designed for moderate seismic loads, is to be retrofitted in a high risk-seismic region. The building is regular in plan, with five longitudinal bays (main fronts corresponding to the north- and south-facing façades) and three bays in the transversal one (east- and west-facing façades without apertures). Nonlinear static analysis using the software OpenSEES is preliminarily carried out, to investigate the seismic vulnerability of the existing building. RC frame members are modelled with lumped plasticity elements, with flexure- or shear-controlled moment-chord rotation at critical end sections, while the shear behaviour of the beam-column joints is modelled by means of a scissor model. Interventions with DEXs are designed at the life-safety (LS) limit state, considering parallel (DEX.Pa) and perpendicular (DEX.Pe) dispositions, running around all four façades, and mixed disposition (DEX.Mi), as an enlargement on the eastern and western sides only. In order to demonstrate effectiveness of the retrofitting interventions, nonlinear dynamic analyses of the bare (F) and coupled (DEXF) structures are carried out considering records scaled in line with a high-risk seismic region.*

## 1 INTRODUCTION

The dissipative endoskeleton (DEN) constituted of steel braces supporting devices dissipating energy by means of different mechanisms (metallic yielding, friction sliding, fluid orificing, viscoelastic deformation, phase transformation of metals) offers certain advantages (e.g. ease of inspection and replacement, low maintenance costs) in comparison to traditional retrofitting solutions [1, 2], but it can also induce downsides: e.g. notable increase in the axial load transmitted to columns and foundations; indirect costs associated with the temporary relocation of residents; service interruption during installation. On the other hand, the dissipative exoskeleton (DEX), an external steel framed structure equipped with a damped bracing system, rigidly coupled to the existing building but with an own foundation, exhibits many advantages [3]: the indirect costs associated with downtime during retrofitting are eliminated; the creation of new housing space and the opportunity for an energetic retrofit of the building envelope are possible; the complete reversibility is guaranteed.

Three typological choices are possible depending on the distributive (e.g. available space) and energetic (e.g. thermal loss) features along the perimeter [4-6]: a partial or uniform dissipative exoskeleton, parallel (DEX.Pa) and perpendicular (DEX.Pe) positioned to the façades to which it is connected through standard shear and axial links, respectively; a mixed DEX (DEX.Mi), where DEX.Pa and DEX.Pe are placed on the same façade. It should be noted that DEX.Pa always provides additional torsional stiffness to the original scheme, while the added spatiality in the façades resulting from DEX.Pe allows the creation of new housing space, partially or totally covering the retrofitting costs by means of the increased real estate value, upgrades vertical accessibility (e.g. stairwells and lifts) as well as horizontal private or collective circulation (e.g. balconies and living spaces). However, the increased useful space provided by DEX.Pe corresponds to a non-negligible additional mass of the exoskeleton structure compared to the total mass of the building, thereby inducing seismic loads higher than those corresponding to the DEX.Pa arrangement. As this last solution supports gravity loads due to their self-weight only, large overturning moments induced by the horizontal seismic loads may lead to tensile axial force in its foundation. Both solutions provide the opportunity for an energetic retrofit of the building envelope, but compared to the DEN not only the dissipative bracing system but also the new steel exoskeleton needs to be designed.

A design procedure of DEXs incorporating nonlinear fluid viscous dampers (FVDs) is implemented in this study, which focuses on displacement as the key sizing parameter and employs overdamped elastic response spectra. The procedure is a reformulated version of an approach recently derived for DEN systems [7-11], conceived in such way as to make a clear distinction between the design of a steel exoskeleton (i.e. mass, stiffness and strength) and a dissipative bracing system (i.e. added damping), and an extension including nonlinear FVDs. In the subsequent sections the proposed design procedure is applied for the seismic retrofitting of a six-storey reinforced concrete (RC) archetype in L'Aquila (Italy), representative of many buildings designed for moderate seismic loads prior to the 2008-2018 code changes [12]. Interventions with DEXs are designed at the life-safety (LS) limit state, considering three alternatives: i) parallel disposition running around all four façades (DEX.Pa), with a distance from the existing structure set to suit the new foundation and to allow the opening of windows; ii) perpendicular disposition running around all four façades (DEX.Pe), with a floor slab defining new spaces increasing the wellbeing of the inhabitants along main fronts with north and south exposure; iii) parallel-perpendicular mixed disposition (DEX.Mi), as an enlargement on the eastern and western transversal sides only where energy saving measures could be added. Nonlinear analyses are carried out using the software OpenSEES [13], in order to provide insights into the strength and weaknesses of the examined configurations.

## 2 DISPLACEMENT-BASED-DESIGN PROCEDURE OF THE VISCOUS DAMPED DISSIPATIVE EXOSKELETON

A four-step double-iteration design procedure of the DEX is proposed, whose design parameters are: target performance displacement evaluated through nonlinear static analysis of the existing structure; properties of the nonlinear fluid viscous dampers (FVDs), in terms of maximum equivalent viscous damping ratio ( $\xi_{v,DB0}$ ) and velocity exponent ( $\beta$ ); seismic loads. On the other hand, final unknown parameters are mass, stiffness and strength properties of the steel exoskeleton and damping constant of the FVDs.

By referring to two coupled equivalent single-degree-of-freedom (SDOF) systems shown in Figure 1, representing the original frame (F, black line) with an infinitely rigid but non-dissipative connection to a DEX (blue line), relevant design parameters are mass and stiffness ratios

$$\alpha_m = m_{e,DEX} / m_{e,F}; \quad \alpha_K = K_{e,DEX} / K_{e,F} \quad (1)$$

and uncoupled equivalent damping ratios  $\xi_F$  and  $\xi_{DEX}$ . Equivalent mass of the SDOF system representing the original frame can be evaluated by multiplying the first-mode (horizontal) components ( $\phi_1, \phi_2, \dots, \phi_n$ ) by the corresponding floor masses ( $m_{1,F}, m_{2,F}, \dots, m_{n,F}$ )

$$m_{e,F} = \sum_{i=1}^n (m_{i,F} \cdot \phi_i), \quad (\phi_n = 1) \quad (2)$$

while equivalent (secant) stiffness depends on base shear ( $V_{p,F}^*$ ) at the performance displacement ( $d_p^*$ )

$$K_{e,F} = V_{p,F}^* / d_p^* \quad (3)$$

resulting from the nonlinear static analysis of the original structure. A double iteration process is required because for an assigned value of  $\xi_{DEX}$  and known value of  $\xi_F$ , both corresponding to the assigned displacement demand  $d_p^*$ , the corresponding coupled total damping ( $\xi_{DEXF}$ ) is function of  $\alpha_K$  which in turns depends on the unknown  $\alpha_m$ .

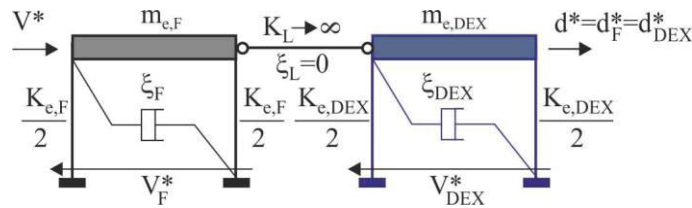


Figure 1. DEXF system as coupling of two equivalent SDOF systems.

The four steps of the proposed design procedure are discussed below. It should be noted that the design procedure requires internal (step 3) and external (steps 3-4) iteration loops related to the stiffness ( $\alpha_K^{(\cdot)}$ ) and mass ( $\alpha_m^{(\cdot)}$ ) ratios, respectively. An initial approximation of these ratios is assigned in step 2 (i.e.  $\alpha_K^{(0)}$  and  $\alpha_m^{(0)}$ ), and then a sequence of iteration loops is performed until convergence to the correct values is attained (i.e.  $\alpha_K^{(i)} \approx \alpha_K^{(i-1)}$  and  $\alpha_m^{(i)} \approx \alpha_m^{(i-1)}$ ).

### 2.1 Properties of the SDOF system equivalent to the original frame (F)

Once base shear ( $V_F$ ) versus roof-storey displacement ( $d$ ) capacity curve of the original framed structure is evaluated from pushover analysis and transformed into the capacity (bilinear) curve ( $V^*-d^*$ ) of an equivalent SDOF system [14], the equivalent viscous damping due to hysteresis  $\xi_{h,F}$  at the performance displacement ( $d_p^*$ ) can be calculated

$$\xi_{h,F}(\%) = \kappa \cdot \left( 63.7 \frac{(\mu_F - 1) \cdot (1 - r_F)}{\mu_F \cdot [1 + r_F \cdot (\mu_F - 1)]} \right) \quad (4)$$

as function of the following parameters (Figure 2b): ductility demand  $\mu_F (=d_p/d_{y,F}$ , being  $d_{y,F}$  the yield displacement); stiffness hardening ratio ( $r_F$ ); reduction factor ( $\kappa$ ), depending on the degrading response of RC frame members [10, 11]. An inherent elastic viscous damping of the framed structure (commonly,  $\xi_{v,F}=5\%$ ) can be also defined (Figure 2a).

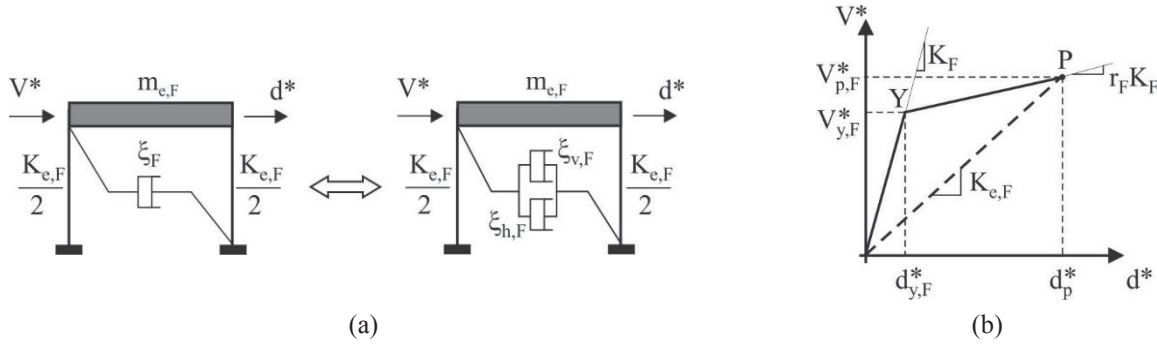


Figure 2. SDOF system equivalent to the original structure (a) and its response (b) idealized as bilinear.

## 2.2 Properties of the SDOF system equivalent to the dissipative exoskeleton (DEX)

Starting from the assumption that the stiffness ( $K_B$ ) of the brace used to install the damper in the exoskeleton (EX) is large enough to eliminate the added stiffness of the FV damped brace (i.e.  $K_{e,DB}=0$ ), the effective (secant) stiffness of the DEX is equal only to the EX part (Figure 3)

$$K_{e,DEX} = K_{e,EX} \quad (5)$$

and its unknown value is assumed as the effective (secant) stiffness of the original frame multiplied by an initial value ( $\alpha_K^{(0)}$ ) of the stiffness ratio

$$K_{e,DEX}^{(0)} = \alpha_K^{(0)} \cdot K_{e,F} \quad (6)$$

Similarly, the effective mass of the equivalent DEX is obtained on the basis of an initial value ( $\alpha_m^{(0)}$ ) of the mass ratio

$$m_{e,DEX}^{(0)} = \alpha_m^{(0)} \cdot m_{e,F} \quad (7)$$

as function of the effective mass of the SDOF equivalent to the original frame (see Equation (2)).

With regard to the nonlinear FVD, the force developed in the damper is function of the damping exponent ( $\beta < 1$ , with  $\beta = 1$  corresponding to linear viscous property)

$$F_{VD} = C_{NL} \cdot \text{sign}(v) \cdot |v|^\beta = F_{VDB} \quad (8)$$

where  $C_{NL}$  is the nonlinear damping coefficient,  $v$  is the relative velocity between the end sections of the device and  $\text{sign}(v)$  is the sign function. Moreover, the equivalent viscous damping ratio for one cycle of harmonic vibration can be expressed as [1, 15]

$$\xi_{v,DB}(\%) = \frac{\lambda \cdot C_{NL} \cdot \omega_{e,DEX}^\beta \cdot d_p^{\beta-1}}{2\pi \cdot K_{DEX}} \quad (9)$$

being

$$\lambda = 2^{2+\beta} \cdot \frac{\Gamma^2 \cdot \left(1 + \frac{\beta}{2}\right)}{\Gamma \cdot (2 + \beta)} \quad (10)$$

and  $\Gamma$  the gamma function. It is easy to verify that the equivalent viscous damping ratio corresponding to  $d_p$  can be computed in terms of an assigned maximum value ( $\xi_{v,DB0}$ ) at the limit of elastic behaviour for the original frame:

$$\xi_{v,DB} (\%) = \xi_{v,DB0} (\%) \cdot (\mu_F)^{\beta-1} \quad (11)$$

For completeness, an inherent elastic damping of the exoskeleton (e.g.  $\xi_{v,EX}=2\%$  is generally used for steel structures) is also defined in Figure 3a.

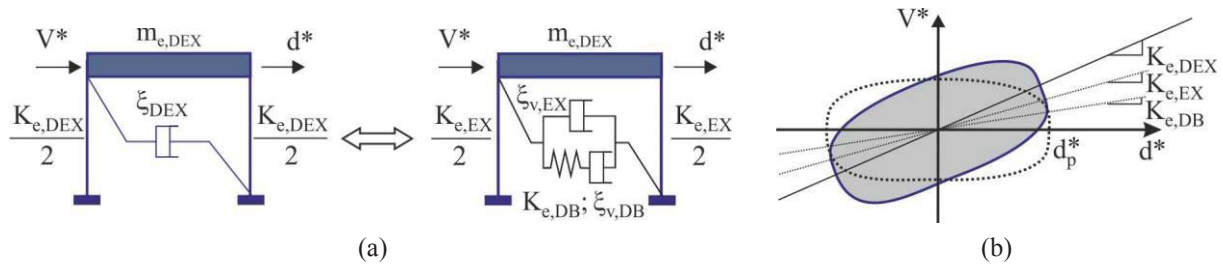


Figure 3. SDOF system equivalent to the DEX (a) and its non-elliptic hysteresis curve (b).

### 2.3 Properties of the SDOF system equivalent to the frame with dissipative exoskeleton (DEXF)

The equivalent viscous damping of the in-parallel system constituted of frame (F) and dissipative exoskeleton (DEX) is function of the stiffness ratio  $\alpha_K^{(\cdot)} (= \alpha_K^{(0)}$  at the first iteration loop)

$$\xi_{DEXF}^{(\cdot)} (\%) = \xi_{v,F} + \xi_{v,E} + \frac{\xi_{h,F} + \xi_{v,DB} \cdot \alpha_K^{(\cdot)}}{1 + \alpha_K^{(\cdot)}} \quad (12)$$

where  $\xi_{h,F}$  and  $\xi_{v,DB}$  are calculated in steps 2.1 and 2.2, respectively. Then, the effective period of DEXF ( $T_{e,DEXF}^{(\cdot)}$ ) is evaluated with reference to the curve of the overdamped displacement-acceleration response spectra corresponding to  $\xi_{DEXF}^{(\cdot)}$  and the performance displacement  $d_p^*$  (Figure 4). Moreover, the acceleration design value ( $a_p^{*(\cdot)}$ ) can be determined as y-coordinate by the same curve.

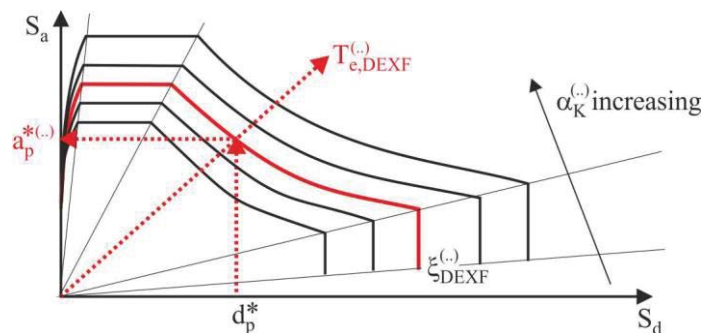


Figure 4. Displacement-acceleration overdamped (elastic) response spectra.



Once the mass of the DEXF is calculated

$$m_{e,DEXF}^{(\cdot)} = m_{e,F} + m_{e,DEX}^{(\cdot)} = (1 + \alpha_m^{(\cdot)}) \cdot m_{e,F} \quad (13)$$

the effective stiffness can be obtained as

$$K_{e,DEXF}^{(\cdot)} = \frac{4 \cdot \pi^2 \cdot m_{e,DEXF}^{(\cdot)}}{(T_{e,DEXF}^{(\cdot)})^2} \quad (14)$$

Finally, an updated value of the stiffness ratio is determined

$$\alpha_K^{(\cdot)} = K_{e,DEX}^{(\cdot)} / K_{e,F} \quad (15)$$

where

$$K_{e,DEX}^{(\cdot)} = K_{e,DEXF}^{(\cdot)} - K_{e,F} \quad (16)$$

As a consequence, an iterative procedure internal to the current step is needed for the solution of Equations (12)-(16) until a final stiffness ratio value is attained.

## 2.4 Properties of the dissipative exoskeleton (DEXF) for the MDOF system

The proportional stiffness criterion [16] allows evaluation of the internal design forces of the steel EX considering the distribution of the lateral loads resulting from the first-mode shape (i.e.  $\phi_i = \phi_{i,F} = \phi_{i,EX}$ ,  $i=1, \dots, n$ ) that remains practically unchanged after the insertion of the EX (Figure 5)

$$F_{EX,i}^{(\cdot)} = \frac{m_{i,F} \cdot \phi_i}{\sum_{i=1}^n (m_{i,F} \cdot \phi_i)} V_{d,EX}^{(\cdot)} \quad (17)$$

where it is proved that the base-shear is equal to

$$V_{d,EX}^{(\cdot)} = \frac{V_{d,DEXF}^{(\cdot)} \cdot \alpha_K^{(\cdot)}}{1 + \alpha_K^{(\cdot)}} = (1 + \alpha_m^{(\cdot)}) \cdot m_{e,F} \cdot a_p^{(\cdot)} \cdot \frac{\alpha_K^{(\cdot)}}{1 + \alpha_K^{(\cdot)}} = V_{d,DEX}^{(\cdot)} \quad (18)$$

It is worth mentioning that base shear expressed by Equation (18) depends on the mass ratio  $\alpha_m^{(\cdot)}$  which is initially unknown. As a consequence, an external iterative procedure needs to be carried out on steps 2.3 and 2.4 for the solution of Equations (12)-(18), until a final mass ratio value is attained.

$$\alpha_m^{(\cdot)} = m_{e,DEX}^{(\cdot)} / m_{e,F} = \sum_{i=1}^n (m_{i,DEX}^{(\cdot)} \cdot \phi_i) / m_{e,F}, (\phi_n = 1) \quad (19)$$

Finally, the distribution of the damping coefficients for the nonlinear FVDs is assumed proportional to the design storey shear of DEX, on the assumption that reduced efficiency of the FVDs generally observed on the upper storeys is related to slower interstorey velocities than those in the lower storeys, through the following expression [17]

$$C_{NL,tot,j} = \frac{(2\pi)^{3-\beta} \cdot (d_p)^{1-\beta} \cdot \zeta_{v,DB}}{(T_{1,DEXF})^{2-\beta}} \cdot \frac{S_j \cdot \sum_{i=1}^n (m_{i,DEXF} \cdot \phi_i^2)}{\lambda \cdot \sum_{i=1}^n [S_i \cdot f_i^{1+\beta} \cdot (\phi_i - \phi_{i-1})^{1+\beta}]}, \quad j = 1, \dots, n \quad (20)$$

where  $f_i$  is the magnification factor of the dampers, depending on their configuration in each storey ( $f_i=1$  for chevron configuration of the FVDB), and  $T_{1,DEXF}$  is the fundamental vibration

period of DEXF. It is clear that, at each storey the shear force is proportional to parameter [18]

$$S_j = \sum_{i=j}^n (m_{i,DEXF} \cdot \phi_i) \quad (21)$$

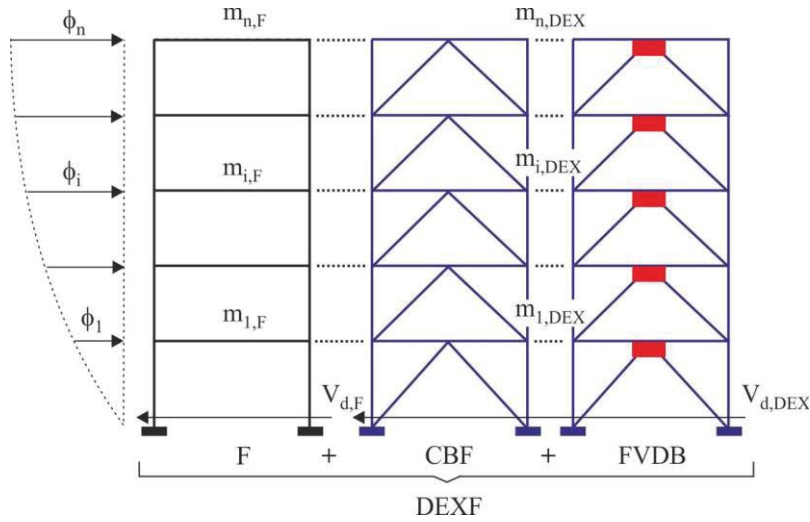


Figure 5. MDOF system representing the original frame (F) combined with DEX.

### 3 LAYOUT AND RETROFITTING OF THE TEST STRUCTURE

An RC framed building located in L'Aquila, representative of the Italian residential housing stock constructed prior to the 2008-2018 code changes [12], is considered as test structure for the numerical investigation. The building is regular in elevation (Figure 6b), while torsion is moderate so the building can be considered also as regular in plan although the staircase is asymmetrically placed along the X direction and bays with different lengths are considered along the Y direction (Figure 6a).

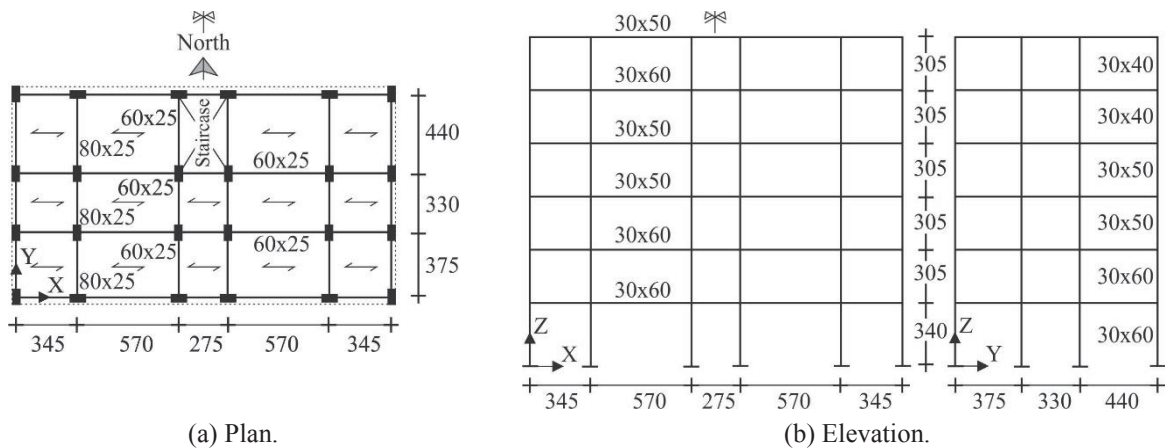


Figure 6. Layout of the archetype (unit in cm).

Cross-section of columns, with the orientation shown in Figure 6a, and deep beams, for perimeter frames and knee configuration of the staircase, are tapered along the building height but constant at each storey (Figure 6b); on the contrary, all internal beams are flat with a constant cross-section at all storeys but this is not the same for different bays (Figure 6a). Masonry infills contribute to the dead load, with a weight of  $3.5 \text{ kN/m}^2$  along the perimeter façades reduced as function of the percentage of apertures. A simulated design of the test structure is

carried out in line with the Italian code DM86 [19], for the seismic loads at the time corresponding to the medium-risk seismic zone and typical subsoil class. Provisions of the Italian code DM92 [20] are also satisfied, assuming the following gravity loads: dead loads of  $4.8 \text{ kN/m}^2$ , on the roof, and  $6.3 \text{ kN/m}^2$ , on the other floors; live loads of  $2.2 \text{ kN/m}^2$ , on the roof (snow),  $2 \text{ kN/m}^2$ , on the other floors, and  $4 \text{ kN/m}^2$  for the staircase. Further details can be found in [12]. Mean compressive cylindrical strength of concrete and steel yield strength equal to  $25 \text{ MPa}$  and  $435 \text{ MPa}$  are assumed, respectively, in the design of the test structure.

Modal and uniform nonlinear static analyses of the original building are preliminarily performed by the OpenSEES platform [13]. A lumped plasticity model is considered for RC frame members, with a trilinear moment-chord rotation backbone curve modified on the basis of the ultimate shear capacity in the event of brittle failure [21, 22]. The shear behaviour of the exterior and interior beam-column joints is modelled by means of a scissor model, with rigid end offsets and double node, considering shear failure prior to or together with yielding of the longitudinal steel reinforcement of beams [23, 24]. Capacity curves reported in Figure 7 represent roof drift ratio (i.e.  $d_{\text{top}}/H_{\text{tot}}$ ,  $d_{\text{top}}$  and  $H_{\text{tot}}$  being the horizontal top displacement and total height) versus normalized base shear (i.e.  $V_{\text{base}}/W_{\text{tot}}$ ,  $W_{\text{tot}}$  being the total seismic weight). Note that pushover curves referring to the positive and negative loading directions are nearly identical, especially in the X direction (Figure 7a), due to the structural symmetry. Maximum strength is always achieved in the Y direction (Figure 7b), depending on the effects of the staircase and in-plan orientation of the cross-sections of all interior columns and most of the exterior ones (Figure 6a), while maximum deformability is attained in the X direction (Figure 7a), where flat interior beams with reduced section are placed. Attention will be focused on the modal capacity curves, that show a maximum  $V_{\text{base}}/W_{\text{tot}}$  ratio roughly between 0.15 (X direction) and 0.2 (Y direction) when one of the aforementioned failure mechanisms is attained for structural elements and joints.

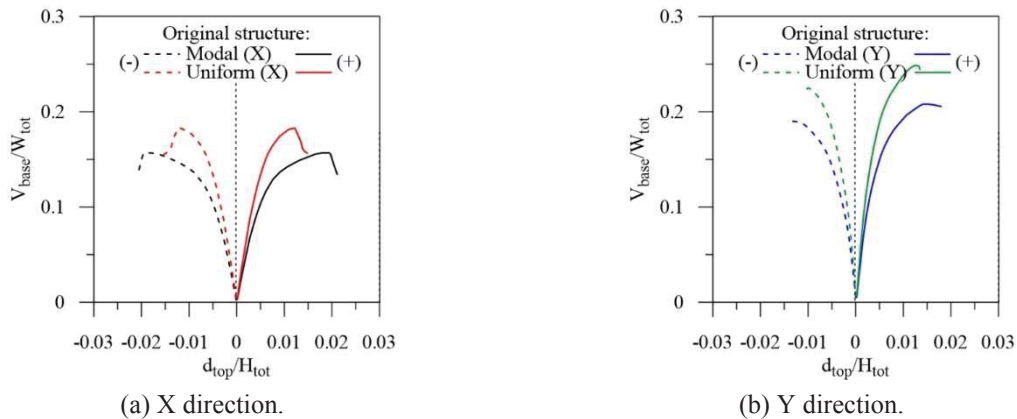


Figure 7. Comparison of pushover curves for modal and uniform lateral load patterns.

Different dissipative exoskeletons are designed at the life-safety (LS) ultimate limit state provided by NTC18 [25] for a residential building (functional class II, coefficient of use  $C_U=1.0$  and expected life of 50 years) located in L'Aquila ( $13.40^\circ$  longitude and  $42.35^\circ$  latitude). Current high-risk seismic zone designation (peak ground acceleration on rock,  $a_g=0.261g$ ) and moderately-soft subsoil (class C, site amplification factor  $S=1.33$ ) are assumed. In particular, concentrically chevron braced frames (CBFs) and chevron braces with fluid viscous dampers (FVDBs) are arranged in three configurations: i) DEX.Pa (Figure 8), configured in adhesion (parallel) to all façades, considerably limiting the external dimensions in the case of urban planning restrictions; ii) DEX.Pe (Figure 9), as an enlargement of the entire building plan, creating additional (perpendicular) living space only along main fronts with

north and south exposure as these are the sides with apertures; iii) DEX.Mi (Figure 10), where DEX.Pa and DEX.Pe are placed as an enlargement on the eastern and western sides without apertures to satisfy both thermal and seismic requirements. The seismic demand for the design of the DEXs assumes as performance objective an elastic behaviour of the original structure (i.e.  $d_p=d_{y,F}$  and  $\xi_{h,F}=0$ ), while the amount of supplemental viscous damping required to limit maximum displacement within this target value is assumed equal to  $\xi_{v,DB0}=20\%$  and elastic viscous damping of the exoskeleton is omitted.

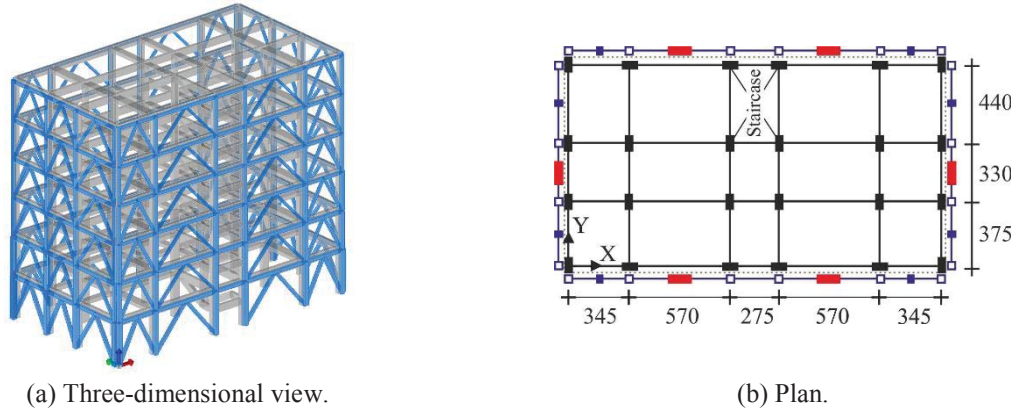


Figure 8. Dissipative exoskeleton parallel (DEX.Pa) to the original building (unit in cm):

■—■—■ chevron brace; ■—■—■ viscous damped chevron brace.

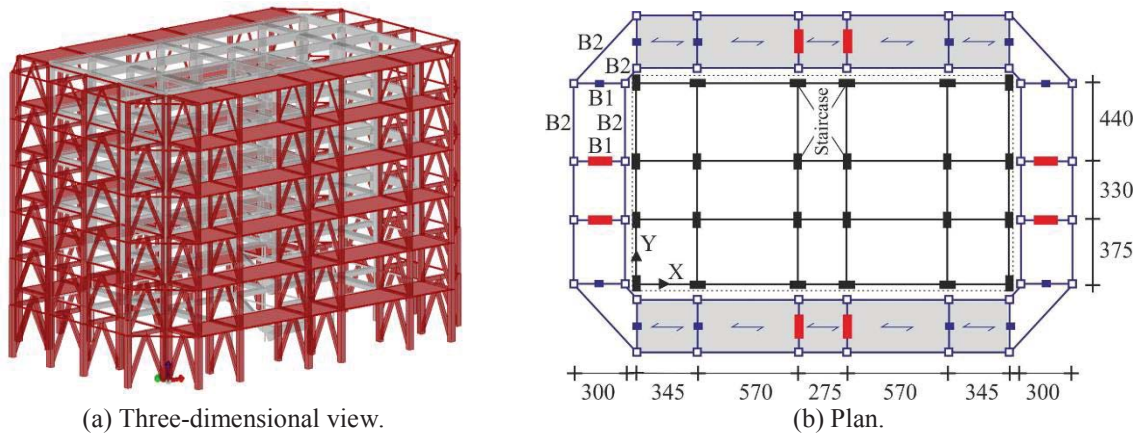


Figure 9. Dissipative exoskeleton perpendicular (DEX.Pe) to the original building (unit in cm):

■—■—■ chevron brace; ■—■—■ viscous damped chevron brace.

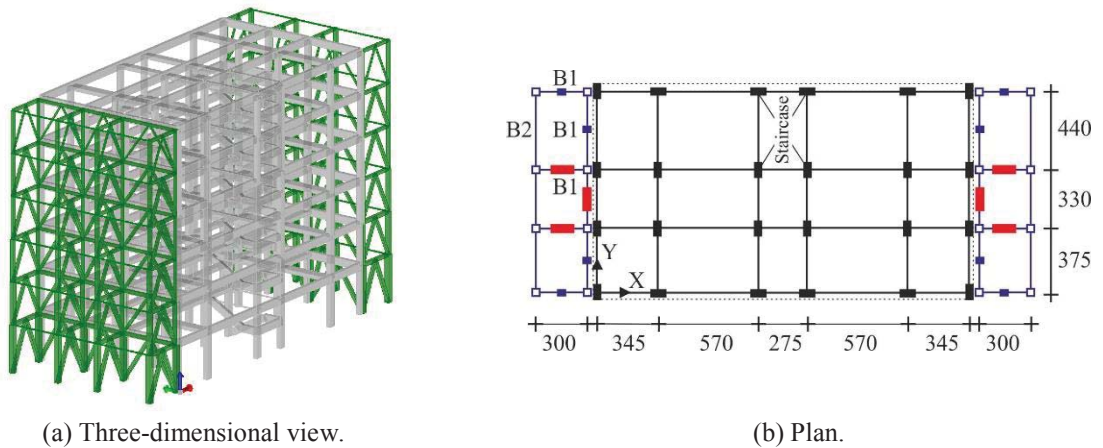


Figure 10. Dissipative exoskeleton with a mixed configuration (DEX.Mi) around the original building (unit in cm): ■—■—■ chevron brace; ■—■—■ viscous damped chevron brace.



The stiffening contribution of the chevron braces arranged in series with the FVDBs is not considered while nonlinear viscous behaviour, with an exponent  $\beta$  equal to 0.7, is assumed for the FVDs. The gravity loads considered for the composite deck with horizontal bracing of DEX.Pe, having a length of 3 metres (see grey areas in Figure 9b), are represented by a dead load of 3.73 kN/m<sup>2</sup> and a live load of 2 kN/m<sup>2</sup>. The design of DEXs is performed in accordance with the four-step procedure presented below, and main parameters of the equivalent SDOF systems are reported in Tables 1a and 1b with reference to the X and Y directions, respectively.

Structure	$K_{e,F}$	$m_{e,F}$	$\xi_{h,F}$	$\alpha_m$	$\alpha_K$	$\xi_{v,DB}$	$\xi_{DEXF}$	$T_{e,DEXF}$	$V_{d,DEXF}$
DEXF.Pa	213	931	0	0.034	6.55	20	22.4	0.487	4678
DEXF.Pe	213	931	0	0.289	8.33	20	22.9	0.489	5778
DEXF.Mi	213	931	0	0.042	6.60	20	22.4	0.487	4709

Table 1a. Properties of the SDOF system equivalent to DEXF along the X direction (units in cm, kN, t and s).

Structure	$K_{e,F}$	$m_{e,F}$	$\xi_{h,F}$	$\alpha_m$	$\alpha_K$	$\xi_{v,DB}$	$\xi_{DEXF}$	$T_{e,DEXF}$	$V_{d,DEXF}$
DEXF.Pa	414	923	0	0.034	6.55	20	22.4	0.347	4638
DEXF.Pe	414	923	0	0.289	8.32	20	22.9	0.349	5728
DEXF.Mi	414	923	0	0.042	6.60	20	22.4	0.347	4668

Table 1b. Properties of the SDOF system equivalent to DEXF along the Y direction (units in cm, kN, t and s).

The tubular square cross-sections selected for primary beams (i.e. typology B1), columns and chevron braces of the CBFs are assumed ductile, in line with class 1 of NTC18. These elements satisfy the ultimate limit states for strength and buckling under the horizontal seismic loads evaluated through Equations (17) and (18). Moreover, secondary (i.e. typology B2) beams with circular (DEX.Pe) and square (DEX.Mi) cross sections are also considered in order to obtain a spatial truss exoskeleton, for which class 3 prevents local buckling until yield strength is reached in a compression fibre. The dimensions obtained for the member cross-sections, assuming yield strength equal to 275 MPa, and damping coefficients of nonlinear FVDs are reported in Table 2 (DEX.Pa), Table 3 (DEX.Pe) and Table 4 (DEX.Mi). It should be noted that FVDs are inserted on chevron braces with the same dimensions as those of the CBFs.

Storey	Beams	Columns	Chevron braces		$C_{NL,tot}$ (FVDs)	
			X direction	Y direction	X direction	Y direction
1	250×8	350×16	220×16	220×16	9999	9118
2	250×8	300×12.5	180×12.5	180×12.5	9657	8818
3	200×8	260×10	180×10	180×10	8839	8092
4	200×8	220×8	180×8	160×10	7438	6830
5	200×8	220×8	180×6.3	150×8	5388	4976
6	200×8	220×8	160×6.3	150×6.3	2702	2513

Table 2. Member cross-sections (mm) and damping coefficient of FVDs (units in kN, s and m) for DEX.Pa.

Storey	Beams		Columns	Chevron braces		$C_{NL,tot}$ (FVDs)	
	B1	B2		X direction	Y direction	X direction	Y direction
1	350×10	88.9×5	400×20	350×16	300×12.5	8467	11545
2	300×10	88.9×5	350×16	260×12.5	260×8	8209	11199
3	300×10	88.9×5	300×10	220×12	250×6.3	7619	10322
4	200×8	88.9×5	300×10	180×12.5	220×6.3	6533	8750
5	200×8	88.9×5	220×8	150×12.5	180×6	4854	6421
6	200×8	88.9×5	220×8	140×12	140×6.3	2496	3299

Table 3. Member cross-sections (mm) and damping coefficient of FVDs (units in kN, s and m) for DEX.Pe.

Storey	Beams		Columns	Chevron braces		$C_{NL,tot}$ (FVDs)	
	B1	B2		X direction	Y direction	X direction	Y direction
1	300×10	50×5	400×16	260×16	250×16	8424	10753
2	250×10	50×5	300×16	220×12	180×12.5	8178	10370
3	250×10	50×5	260×10	200×10	180×10	7560	9442
4	200×8	50×5	220×8	150×12	180×8	6443	7894
5	200×8	50×5	220×8	120×12.5	150×8	4738	5675
6	200×8	50×5	220×8	120×12	150×6.3	2407	2821

Table 4. Member cross-sections (mm) and damping coefficient of FVDs (units in kN, s and m) for DEX.Mi.

#### 4 NUMERICAL RESULTS

Nonlinear seismic analysis of the structure before (i.e. original, F) and after (i.e. retrofitted, DEX.Pa, DEX.Pe and DEX.Mi) the insertion of the dissipative exoskeleton is evaluated by the finite element code OpenSEES [13]. Nonlinear fluid viscous dampers are modelled as twoNodeLink elements, assuming nonlinear dashpot and linear spring acting in series without considering the combined flexibility of the supporting brace and FVD. An elastic linear behaviour, equal for tension and compression, is considered for all truss members of the concentrically steel braced frames. The exoskeleton is connected to the RC framed building at each floor level by means of shear and/or axial rigid steel links. Inherent damping  $\xi_{v,F}=5\%$  for the RC framed structure is modelled using mass and tangent stiffness proportional Rayleigh approach, while the contribution of steel exoskeleton is not considered ( $\xi_{v,EX}=0\%$ ). Seismic input selection for the bi-directional nonlinear dynamic analyses considers earthquakes taken from the Italian accelerometric archive [26] and NGAwest2 database [27], the latter when records reflecting the NTC18 provisions at the site in question were not available, and scaled to match the LS design response spectrum [28].

Mean values of the maximum base shear are reported in Figure 11 for the original (F) and retrofitted (DEX(F) and (DEX)F referring to parallel (Pa), perpendicular (Pe) and mixed (Mi) steel dissipative exoskeleton and RC frame, respectively) structures, which are labelled with letter A when resulting from nonlinear time-history analysis.

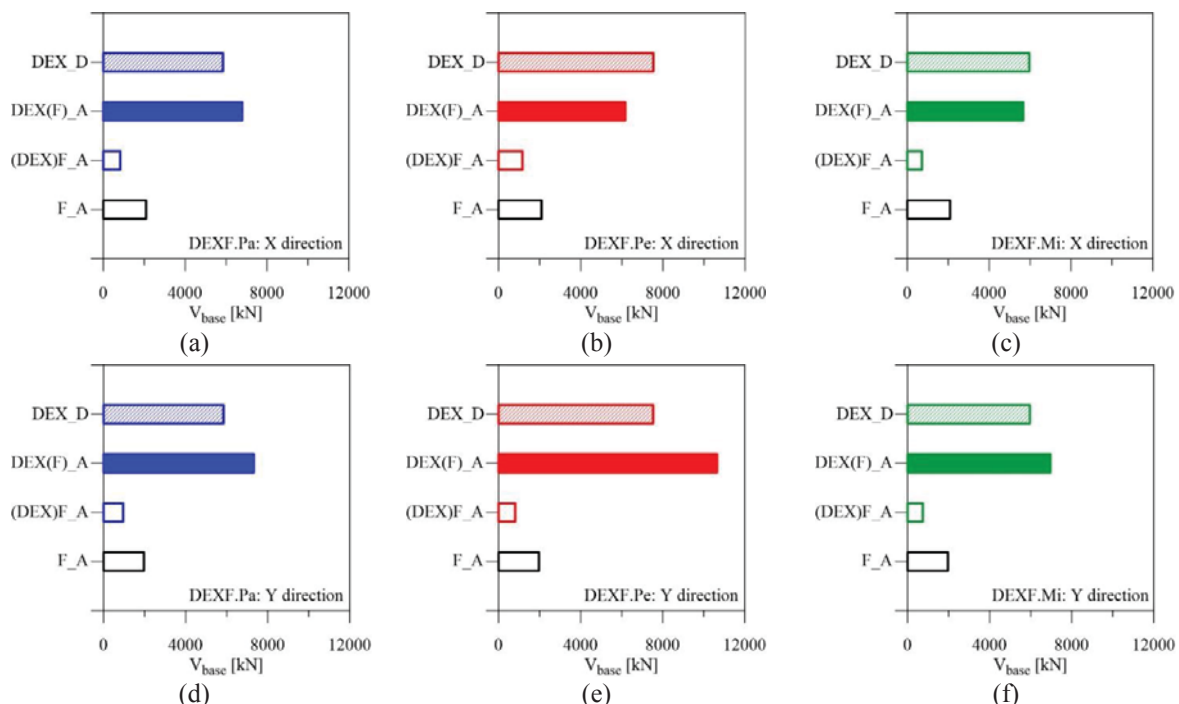


Figure 11. Seismic demand in terms of base shear for the original (F) and retrofitted (DEXF) structures.



As a comparison, design values (letter D) of the base shear obtained for DEXs are also reported with reference to DEXF.Pa (Figures 11a,d), DEXF.Pe (Figure 11b,e) and DEX.Mi (Figures 11c,f). The proportion between the base shear corresponding to DEX(F)\_A and (DEX)F\_A structural parts highlights a good fit with the design value of the stiffness ratio  $\alpha_K$  (see Tables 1a and 1b), thus confirming the reliability of the design procedure of DEXs. This is further demonstrated by the ratio between design (D) and analysis (A) base shear for DEX, whose value falls approximately into the range of -10% to +30%, which represent the lower and upper bound tolerances provided by NTC18 when recorded ground motions are scaled to a certain level of seismic intensity. Evidence of the effectiveness of the proposed retrofitting strategies also results from base shear related to (DEX)F\_A, whose value is between one half (Figure 11e) and one third (Figure 11c) of that given to the corresponding F\_A.

Afterwards, mean values of the storey drift ratio, defined as drift along the in-plan X ( $\Delta_X$ ) and Y ( $\Delta_Y$ ) directions normalized by the storey height (h), are shown in Figure 12. The original structure (F) exhibits an irregular distribution law of the drift ratio, with higher deformability in the X (Figure 12a) rather than in the Y (Figure 12d) direction. The insertion of DEXs generally ensures a reduction of at least half of the drift demand. The only exception is the top floor where an increase in drift demand referring to Y is observed for DEX.Pa and DEX.Pe (Figure 12d), though highlighting values less than 0.5%. Among the three viable retrofitting schemes, DEXF.Pa and DEX.Mi turn out to be the best choice parallel to X (Figure 12a) and Y (Figure 12d), respectively. Graphs of horizontal displacement at the floor levels (Figures 12b,e) confirm the effectiveness of all configurations of the DEX. The acceleration profiles over the elevation of the building, normalised by gravity acceleration g, are displayed in Figures 12c,f. Amplification of acceleration is found in all DEXF systems compared to the original frame, with values increasing towards the upper levels. Moreover, a clear worsening is observed in the Y direction (Figure 12f), where DEX.Pe is the worst solution inducing a threefold increase in top floor acceleration.

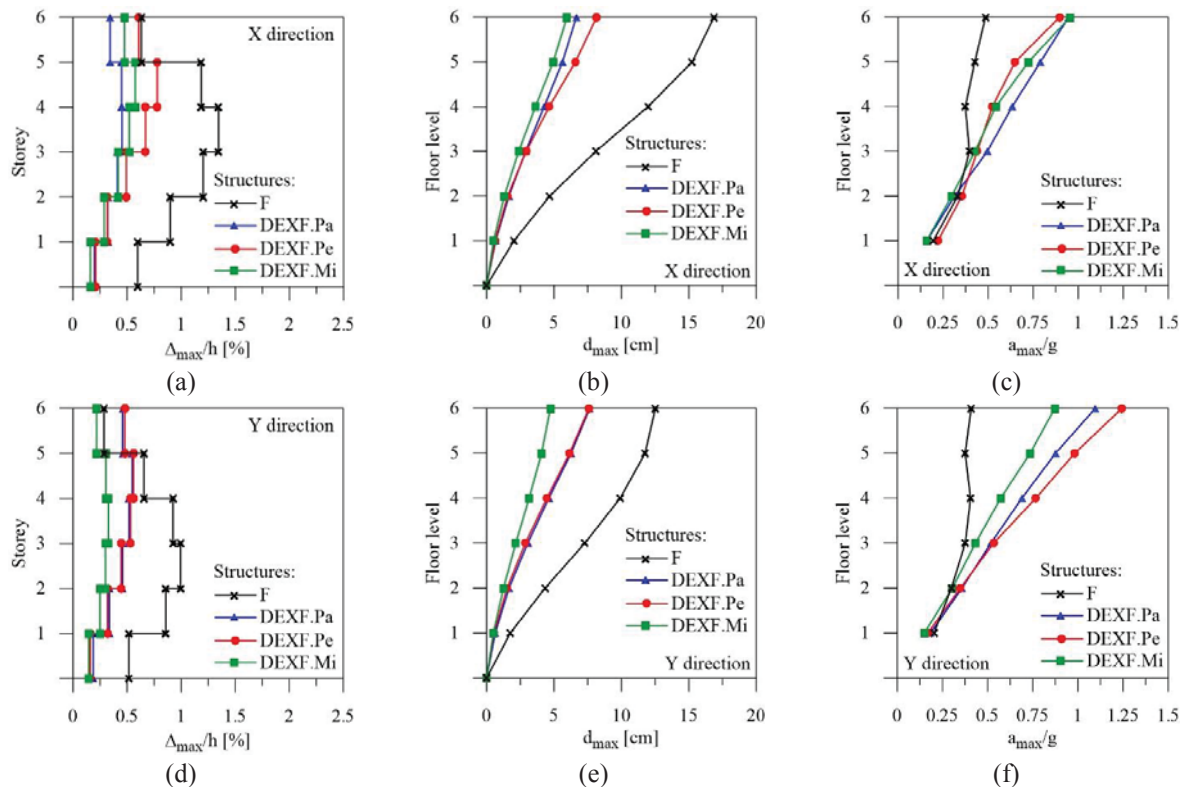


Figure 12. Global response parameters of the original (F) and retrofitted (DEXF) structures over the elevation.

With a view to analysing how different configurations of the exoskeleton (i.e. DEX.Pa, DEX.Pe and DEX.Mi) have an impact on the effectiveness of FVDs, the mean of the maximum values of the total damping force at different storeys are shown in Figure 13. As confirmed experimentally [17], the efficiency of the FVDs in the top storey is reduced by at least half of that at the intermediate levels where maximum values are attained, thereby highlighting that a distribution of damping constants proportional to the storey shear represents an efficient design criterion. The highest energy dissipation corresponds to DEX.Pa and DEX.Pe in the X (Figure 13a) and Y (Figure 13e) directions, respectively, but this does not correspond to significant advantages for the DEX.Pe characterized by the additional mass of balconies. It should be noted that total damping force is only divided between two FVDs for DEX.Pa (Figure 13d) and DEX.Mi (Figure 13f) along the Y direction, thus reducing structural redundancy, contrary to DEX.Pe which instead provides four FVDs at each level (Figure 13e), while all solutions ensure the same number of FVDs in the X direction.

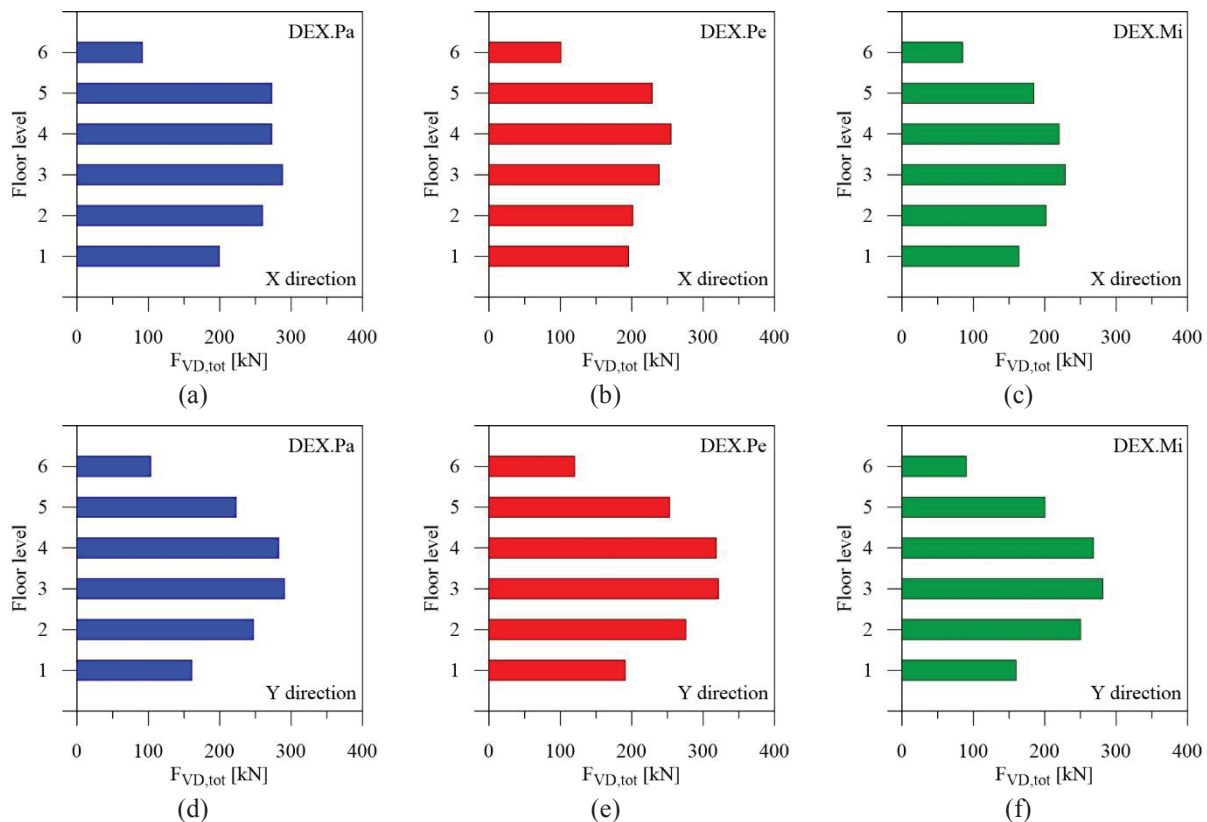


Figure 13. Distribution of the total damping force of FVDs over the elevation of the DEXs.

## 5 CONCLUSIONS

Pros and cons of the seismic retrofitting of RC buildings by means of dissipative exoskeletons is investigated. To this end, a practical procedure for the seismic design is proposed and developed, in such a way as to make a distinction between the steel exoskeleton and the dissipative bracing system. It is based on the rigid coupling of two SDOF systems equivalent to the original frame and dissipative exoskeleton, respectively, assuming elastic behaviour of steel exoskeleton and nonlinear FVDs. A six-storey RC framed structure located in L'Aquila is assumed as an archetype of the residential housing stock built in Italy during the 1990s, designed for medium-risk seismic zone. Three configurations of the DEX along the perimeter are chosen for retrofitting the original building, assuming elastic behaviour as performance

objective in a high risk-seismic zone: i.e. DEX.Pa, representing an envelope parallel to all façades; DEX.Pe, perpendicular to all façades; DEX.Mi, suggested as a compromise solution in which DEX.Pa and DEX.Pe are only placed on the sides without apertures. By carrying out nonlinear seismic analysis the following conclusions can be drawn.

The proportion between base shear demands corresponding to DEX(F) and (DEX)F structural parts matches well with the design value of the stiffness ratio, thus confirming the reliability of the proposed design procedure. Moreover, global and local confirmation of the effectiveness of the seismic retrofitting techniques can be drawn from the base shear and interstorey drift demands to (DEX)F, respectively, whose values are less than half of those corresponding to the original frame. The efficiency of the FVDs is confirmed at the lower and intermediate levels while it is reduced in the top storey, thereby highlighting that a distribution of damping constants proportional to the storey shear represents a good design criterion. DEXF.Pa and DEX.Mi appear the best choice parallel to X and Y, respectively, when drift ratios are considered. As expected, the top displacement target value is frequently exceeded by the building in its original condition, but it is sometimes exceeded when retrofitting with DEX.Pe, while DEXF.Pa and DEXF.Mi are always within the limits of this threshold. However, all DEXs induce amplification of the acceleration towards the upper levels of the original building and this may represent a potential risk in the case of acceleration-sensitive nonstructural components.

## ACKNOWLEDGEMENTS

The present work was financed by Re.L.U.I.S. (Italian network of university laboratories of earthquake engineering), in line to the Convenzione D.P.C.-Re.L.U.I.S. 2019-2021, WP15, Code Revisions for Isolation and Dissipation.

## REFERENCES

- [1] Z. Liang, G.C. Lee, G.F. Dargush, J. Song, *Structural damping: application in seismic response modification*. CRC Press, Boca Raton, 2012.
- [2] C. Christopoulos, A. Filiatrault, *Principles of passive supplemental damping and seismic isolation*. IUSS Press, Pavia, Italy, 2006.
- [3] A. Marini, C. Passoni, A. Belleri, F. Feroldi, M. Preti, G. Metelli, P. Riva, E. Giuriani, G. Plizzari, Combining seismic retrofit with energy refurbishment for the sustainable renovation of RC buildings: a proof of concept. *European Journal of Environmental and Civil Engineering*, 1-21, 2017
- [4] A. Reggio, L. Restuccia, L. Martelli, G.A. Ferro, Seismic performance of exoskeleton structures. *Engineering Structures*, **198**, 109459, 2019.
- [5] G. Di Lorenzo, E. Colacurcio, A. Di Filippo, A. Formisano, A. Massimilla, R. Landolfo, State-of-the-art on steel exoskeletons for seismic retrofit of existing RC buildings. *Ingegneria Sismica*, **37**(1), 33-50, 2020.
- [6] A. Caverzan, M. Lamperti Tornaghi, P. Negro (editors). *Proceedings of SAFESUST Workshop. A roadmap for the improvement of earthquake resistance and eco-efficiency of existing buildings and cities*. Joint Research Centre, Ispra, November 26-27, 2015.
- [7] F. Mazza, A. Vulcano, Design of hysteretic damped braces to improve the seismic performance of steel and RC framed structures. *Ingegneria Sismica*, **31**(1), 5-16, 2014.

- [8] F. Mazza, Seismic vulnerability and retrofitting by damped braces of fire-damaged RC framed buildings. *Engineering Structures*, **101**, 179-192, 2015.
- [9] F. Mazza, Nonlinear seismic analysis of unsymmetric-plan structures retrofitted by hysteretic damped braces. *Bulletin of Earthquake Engineering*, **14**(4), 1311-1331, 2016.
- [10] F. Mazza, A plastic-damage hysteretic model to reproduce strength stiffness degradation. *Bulletin of Earthquake Engineering*, **17**(6), 2787-2819, 2019.
- [11] F. Mazza, A simplified retrofitting method based on seismic damage of a SDOF system equivalent to a damped braced building. *Engineering Structures*, **200**, 109712, 2019.
- [12] P. Ricci, V. Manfredi, F. Noto, M. Terrenzi, M.T. De Risi, M. Di Domenico, G. Camata, P. Franchin, A. Masi, F. Mollaioli, E. Spacone, G.M. Verderame, RINTC-E: towards seismic risk assessment of existing residential reinforced concrete buildings in Italy. Procs. of the 8<sup>th</sup> ECCOMAS Thematic Conference on Computational Methods in Structural Dynamics and Earthquake Engineering *COMPdyn 2019*, Crete, Greece, 24-26 June 2019.
- [13] F. McKenna, G.L. Fenves, M.H. Scott. Open system for earthquake engineering simulation. University of California, Berkeley, CA, 2000.
- [14] H.M. Dwairei, M.J. Kowalsky, J.M. Nau, Equivalent damping in support of direct displacement-based design. *Journal of Earthquake Engineering*, **11**(4), 512-530, 2007.
- [15] Y.-Y. Lin, K.-C. Chang, C.-Y. Chen, Direct displacement-based design for seismic retrofit of existing buildings using nonlinear viscous dampers. *Bulletin of Earthquake Engineering*, **6**(3), 535-552, 2008.
- [16] F. Mazza, M. Mazza, A. Vulcano, Displacement-based seismic design of hysteretic damped braces for retrofitting in-elevation irregular RC framed structures. *Soil Dynamics and Earthquake Engineering*, **69**, 115-124, 2015.
- [17] G. Pekcan, J.B. Mander, S.S. Chen, Design and retrofit methodology for building structures with supplemental energy dissipating systems. *Report No. MCEER-99-0021*. New York at Buffalo, 1999.
- [18] J.-S. Hwang, W.-C. Lin, N.-J. Wu, Comparison of distribution methods for viscous damping coefficients to buildings. *Structure and Infrastructure Engineering: Maintenance, Management, Life-Cycle Design and Performance*, **9**(1), 28-41, 2013.
- [19] DM96, Italian Building Code 86. Norme tecniche relative alle costruzioni antisismiche. DM 24-01-1986, Italian Ministry of Public Works, Rome, Italy.
- [20] DM92, Italian Building Code 92. Norme tecniche per le opere in c.a. normale e pre-compresso e per le strutture metalliche. DM 14-02-1992, Italian Ministry of Public Works, Rome, Italy.
- [21] L.F. Ibarra, R.A. Medina, H. Krawinkler, Hysteretic models that incorporate strength and stiffness deterioration. *Earthquake Engineering and Structural Dynamics*, **34**(12), 1489-1511, 2005.
- [22] F. Mazza, Modelling and nonlinear static analysis of reinforced concrete framed buildings irregular in plan. *Engineering Structures*, **80**, 98-108, 2014.

- [23] S. Alath, S.K. Kunnath, Modeling inelastic shear deformation in RC beam-column joints. *Proceedings of the 10<sup>th</sup> Conference in Engineering Mechanics*, University of Colorado at Boulder, Colorado, 1995.
- [24] F. Mazza, Shear modelling of the beam-column joint in the nonlinear static analysis of RC framed structures retrofitted with damped braces. *Bulletin of Earthquake Engineering*, **108**, 111-129, 2018.
- [25] NTC18, Italian Building Code 18. Norme tecniche per le costruzioni. DM 17-01-2018, Italian Ministry of Infrastructures and Transports, Rome, Italy.
- [26] L. Luzi, S. Hailemichael, D. Bindi, F. Pacor, F. Mele, F. Sabetta, ITACA (ITalian AC-celerometric Archive): a web portal for the dissemination of Italian strong-motion data, *Seismol. Res. Lett.*, **79**, 716-722, 2008.
- [27] T.D. Ancheta, R.B. Darragh, J.P. Stewart, E. Seyhanb, W.J. Silva, B. Chiou, K. Wooddell, R. Graves, A.R. Kottke, D. Boore, T. Kishida, J. Donahue, NGA-West2 database. *Earthquake Spectra*, **30**(3), 989-1005, 2014.
- [28] I. Iervolino, A. Spillatura, P. Bazzurro, Seismic structural reliability of code-conforming Italian buildings. *Journal of Earthquake Engineering*, **22**, 5-27, 2018.

## DEBONDING ANALYSIS OF FRCM COMPOSITES FOR STRUCTURAL UPGRADING OF RC STRUCTURES

Maria Teresa Cristofaro<sup>1</sup>, Angelo D'Ambrisi<sup>1</sup>, Francesco Focacci<sup>2</sup>, Raffaele Nudo<sup>1</sup>,  
Gianfranco Stipo<sup>1</sup>, Marco Tanganelli<sup>1</sup>, Mario De Stefano<sup>1</sup>

<sup>1</sup> Dipartimento di Architettura, Università di Firenze  
piazza Brunelleschi 6, 50121 Firenze, Italy  
mariateresa.cristofaro@unifi.it

<sup>2</sup> Università eCampus  
via Isimbardi 10, 22060 Novedrate (CO), Italy  
francesco.focacci@uniecampus.it

---

### Abstract

*Fiber Reinforced Cementitious Matrix (FRCM) materials are currently widely used for strengthening reinforced concrete (RC) structures and have assumed an important role in the seismic upgrading of these structures. The mechanical parameters for the evaluation of the capacity of strengthened structures, such as the tensile strength and the debonding load of the strengthening material, are determined through standards testing procedures that usually include tensile tests and bond tests. In this work the results of an experimental campaign of beam tests on RC elements strengthened with FRCM composites are presented. Different strengthening configurations and load rates are adopted. The experimental results are discussed and compared with the results available in literature to assess the influence of the testing procedure on the obtained mechanical parameters.*

**Keywords:** FRCM composites, RC structures, Experimental campaign, Beam test.

---



## 1 INTRODUCTION

Fiber reinforced polymers (FRP) [1, 2] and fiber reinforced cementitious matrix (FRCM) materials [3, 4] are widely used for strengthening and repairing masonry and reinforced concrete (RC) structures. The former are made of continuous fibers embedded in a polymeric matrix, while the latter consist of continuous fibers arranged in unidirectional or bidirectional textiles embedded in a cement based matrix. FRCM materials are effective in increasing the flexural [5, 6, 7, 8, 9, 10] and the shear [11, 12, 13] capacity of RC members.

Guidelines have recently been issued for the mechanical characterization and evaluation of the design parameters of FRCM materials [14, 15]. Italian guideline [14] provides for tensile tests both on textiles and on composites and direct shear tests, while US guideline [15] provides for tensile tests on composites and tests on structural elements.

The effectiveness of composite materials in increasing the capacity of concrete and masonry structural elements strongly depend on the bond properties between composite and substrate (FRP) [1, 16, 17] and between fibers and matrix (FRCM) [18, 19].

The shear stress transfer at the reinforcement-substrate interface is experimentally studied through direct shear tests in the single-lap configuration [20, 21, 22, 23, 24, 25, 26] (Figure 1a) or double-lap [27, 22] configuration (Figure 1b). These tests are performed to determine the debonding mechanism, i.e. the interface where debonding occurs, the maximum force transferable at the interface named joint capacity, the maximum force transferable when debonding initiates named debonding load [13, 26], and the minimum length of the interface surface to obtain the bond capacity named effective bond length. The tests performed so far have shown that for many FRCM materials the debonding occurs at the interface between fiber and matrix with significant relative displacements of the fibers with respect to the matrix and without debonding of the matrix from the support [28, 29].

The results of the single-lap or double-lap shear tests can be used to calibrate a cohesive material law (CML) [30, 24, 26], i.e. a relationship between the interfacial shear stress ( $\tau$ ) and the relative displacement or slip ( $s$ ) between the fibers and the substrate. In the case of FRCM materials that show a loss of bond at the interface between fibers and matrix, the CML allows to predict with reasonable accuracy the tensile response obtained through tensile tests [31] performed according to ACI 434 [15].

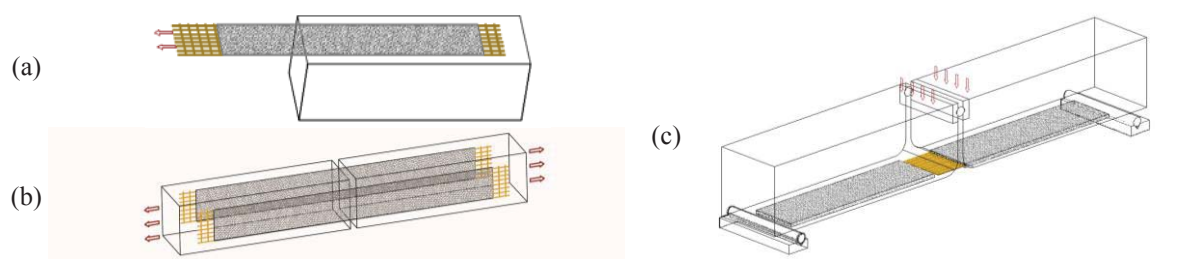


Figure 1. Typical test setup for (a) single-lap shear test, (b) double lap shear test, and (c) beam test.

An alternative to direct shear tests for the evaluation of the interfacial properties is the indirect shear test performed on specimens of the beam test type [32, 33, 34] (Figure 1c). The beams are made up of two concrete blocks connected by a hinge in the compression zone and by the reinforcement in the tensile zone and are subjected to bending test on 3 or 4 load points. The tensile force in the composite material is determined as a function of the applied force  $F$  through the equilibrium conditions.

In this work the results of an experimental campaign of beam tests on a FRCM material with poliparafenilenbenzobisoxazole (PBO) fibers are presented. With regard to the bond

properties of PBO-FRCM materials, many experimental results can be found in literature [13]. In particular the results of single-lap shear tests performed with different bond lengths are reported in [25]. In [26] the results presented in [25] are used to calibrate an interfacial CML based on the relationship between bond length and joint capacity. In [22, 33] the results of single-lap shear tests are compared with the results of double-lap shear tests. In [35] the dependence of the joint capacity evaluated with single-lap shear test on the loading rate is highlighted. Finally in [33] beam test results are compared with single-lap shear test results and it is observed that these two tests provide comparable results in terms of debonding load and joint capacity.

The experimental campaign presented in this paper includes beam tests on PBO-FRCM materials characterized by three different PBO textiles embedded in the same cement matrix. The tests were performed at different loading rates. The obtained experimental results are discussed and compared with the experimental results available in literature with the following aims: i) to compare the dependence of the joint capacity on the loading rate obtained with single-lap shear tests with the dependence of the joint capacity on the loading rate obtained with the beam test; ii) to assess the influence of the fiber arrangement in textiles on the fiber stress associated with the joint capacity; iii) to compare the results of single-lap shear tests with the results of beam tests in terms of joint capacity.

## 2 EXPERIMENTAL PROGRAM

### 2.1 Materials

Three different PBO textiles (Figure 2) embedded in the same cement matrix were used in the experimental campaign: i) bidirectional textile with 70 g/m<sup>2</sup> of fiber in the longitudinal direction (equivalent thickness of 0.046 mm) and 18 g/m<sup>2</sup> of fibers in the transversal direction (equivalent thickness of 0.012 mm); ii) unidirectional textile with 44 g/m<sup>2</sup> of fibers (equivalent thickness of 0.028 mm); iii) unidirectional textile with 105 g/m<sup>2</sup> of fibers (equivalent thickness of 0.067 mm).

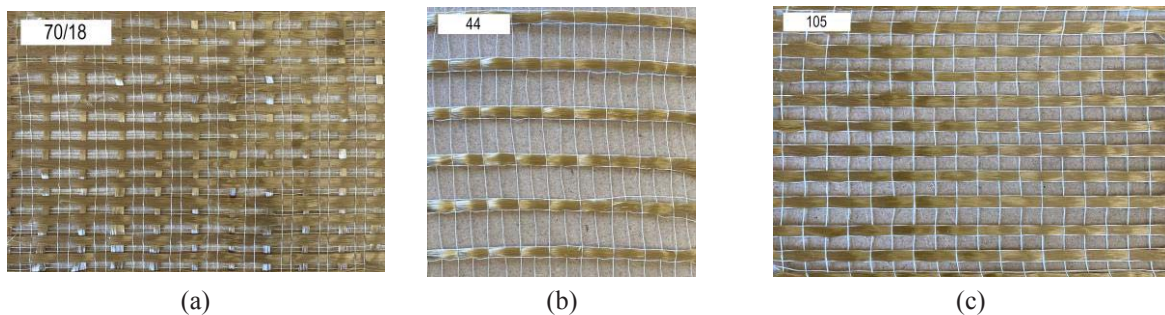


Figure 2. PBO textiles used in the tested FRCM materials: (a) bidirectional textile with 70 g/m<sup>2</sup> of fibers in the longitudinal direction and 18 g/m<sup>2</sup> of fibers in the transversal direction; (b) and (c) unidirectional textiles with 44 g/m<sup>2</sup> and 105 g/m<sup>2</sup> of fibers in the longitudinal direction, respectively.

These PBO textiles are referred to as 70/18, 44, and 105, respectively. The main geometrical and mechanical properties of the PBO textiles are summarized in Table 1, where  $b^*$ ,  $t^*$  and  $i_f$  are the width, thickness and center-to-center distance of the longitudinal yarns, respectively, while  $t_f$  is the equivalent thickness defined as the cross section area per unit width, equal to  $t^*b^*/i_f = p/\gamma_f$ , where  $p=70, 44$ , or  $105$  g/m<sup>2</sup> is the weight of the longitudinal fibers per unit surface of the textile and  $\gamma_f = 1.56$  g/cm<sup>3</sup> is the unit weight of the PBO fibers.  $E_f$  is the elas-

tic modulus of the PBO fiber assumed equal to 206 GPa according to the tensile tests presented in [25], while  $f_t$  is the fiber tensile strength according to the manufacturer.

PBO textile	$p$ [g/m <sup>2</sup> ]	$b^*$ [mm]	$t^*$ [mm]	$i_f$ [mm]	$t_f$ [mm]	$E_f$ [GPa]	$f_t$ [GPa]
70/18	70	4	0.1081	9.5	0.046	206	5.8
44	44	4	0.1645	23.5	0.028		
105	105	4	0.1508	9	0.067		

Table 1. Geometrical and mechanical properties of the three different PBO textiles.

The cement based matrix was characterized through three-point bending tests and compression tests [36]. The performed tests provided an average compressive strength of 29.13 MPa and an average tensile strength of 6.40 MPa. The concrete blocks were casted with a commercial mix design (BIGMAT C25/30 concrete) with the addition of 20% river sand (grain size of 0.3÷1.25 mm) to obtain strength values close to those of existing concretes. Simultaneously to the block casting, 20 cubes with a side of 150 mm were casted. The compression tests of these cubes provided an average compressive strength [37] of 17 MPa (CoV 11%).

## 2.2 Test setup

The bond length  $L$  was the same for the two blocks and was equal to 363 mm while the width of the strip was equal to 94 mm (Figure 3).

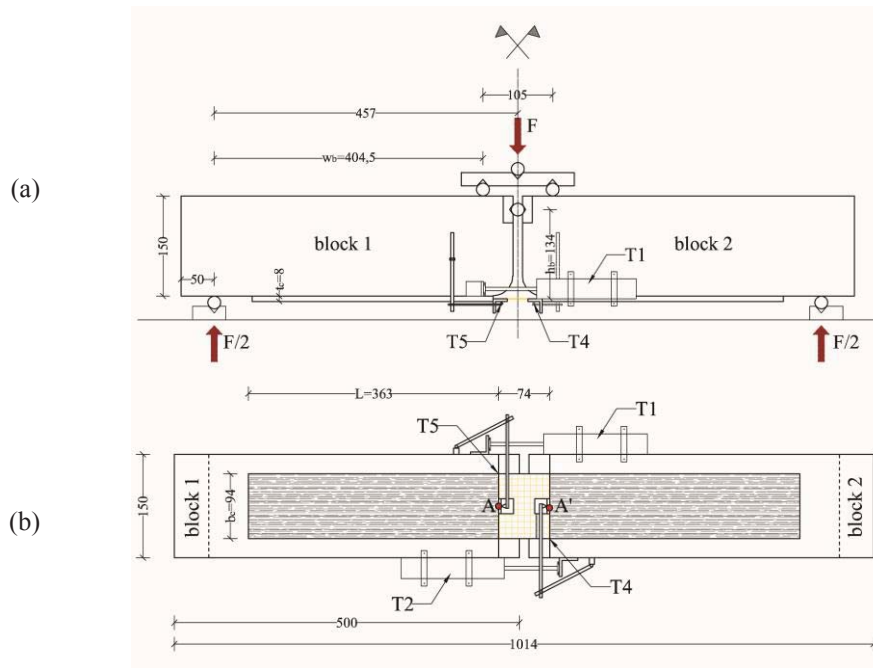


Figure 3. Test setup: (a) front; (b) intrados (dimensions are in millimeters).

The bond length  $L$  was greater than the effective bond length  $L_{eff}$  which is approximately 250-280 mm according to [25, 26, 27, 30]. This allowed to reach the debonding load of the reinforcement and therefore to compare the obtained results with those of single-lap shear tests with  $L \geq L_{eff}$  in terms of debonding load. The edges of the concrete blocks were rounded at the intrados of the hinged cross sections to reduce the transverse compressive stresses at the interface associated with the relative rotation between the blocks during the test [13, 32].

The tests were performed with a servohydraulic universal testing machine (Instron) by controlling the displacement of the load application point at a constant rate. During the test the following response parameters were measured: i) the applied force  $F$  (Figure 3a); ii) the relative displacement between the blocks at the intrados (transducers T1 and T2 in Figure 3a); iii) the slip of the fibers at mid-span with respect to the two blocks (transducers T4 and T5). In particular transducers T4 and T5 measured the maximum relative displacements between the fibers and the concrete blocks (slips at points A and A'), which are referred to as global slips of the interface surfaces. The T1 and T2 transducers were of the CDP (LVDT) type with movable shaft, while the T4 and T5 transducers were of the CE cantilever type. Four displacement rates were used for the force application point: 0.17, 0.34, 0.51 and 0.68 mm/min.

Samples were named  $BT\_x\_yf\_z\_n$ , where  $x$  indicates the type of textile (70/18, 44, or 105),  $y$  the number of yarns,  $z$  the displacement rate, and  $n$  the number of the sample. The samples are listed in Table 2. At least three nominally equal specimens were tested for each textile and for each rate. Pictures of representative test samples are shown in Figure 4.

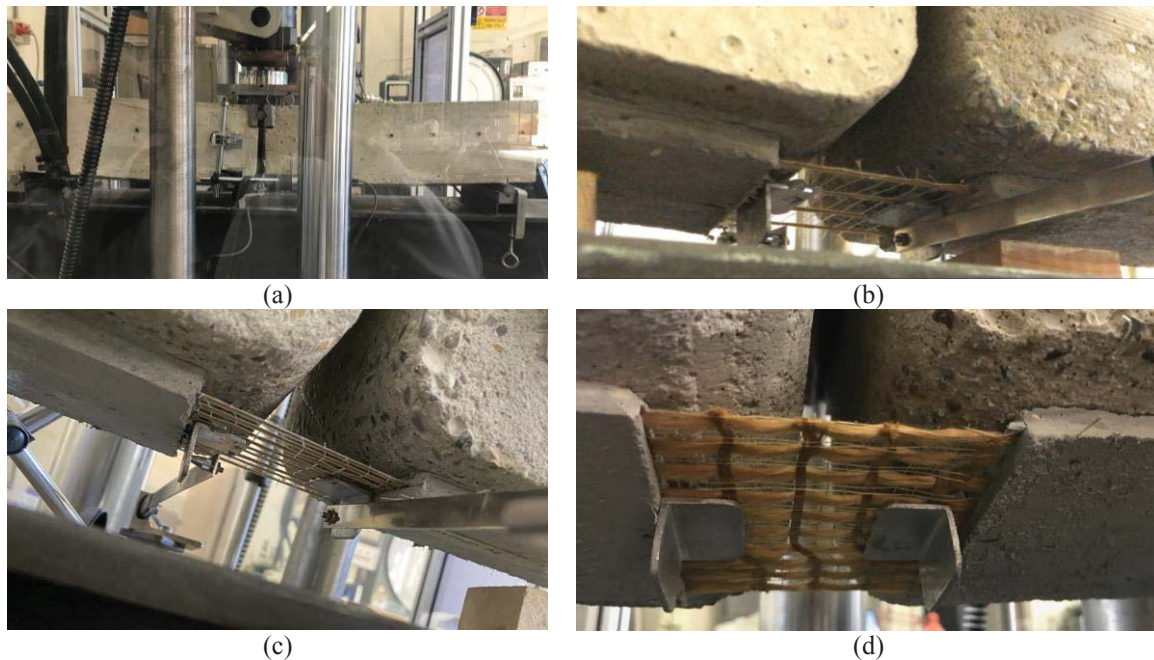


Figure 4. (a) Test set-up; (b) textile 44; (c) textile 105; (d) textile 70/18.

The adopted displacement rates correspond to nominal slip rates of 0.00085, 0.0017, 0.00255 and 0.0034 mm/s, respectively. The nominal slip rate associated with each displacement rate were evaluated neglecting the elastic deformation of the concrete blocks (i.e. rigid rotation of blocks was assumed) and assuming symmetric rotation of the two blocks. The lowest displacement rate was chosen to obtain a nominal slip rate similar to the slip rate adopted for the single-lap shear tests presented in [25]. Figure 5a shows the average of the global slips measured by the transducers T4 and T5 of four specimens with textile 74/18 as a function of time. Figure 5b shows the slip rate (obtained as the derivative of the corresponding curve of Figure 5a) as a function of time for one specimen. Figure 5 shows that after the initial branch the slip rate tends to be constant and proportional to the displacement rate. Nonetheless the slip rate is significantly different from the nominal value evaluated on the base of the rigid blocks assumption. Furthermore the slip rate is almost constant only at the end of the tests when the deboning has already initiated.



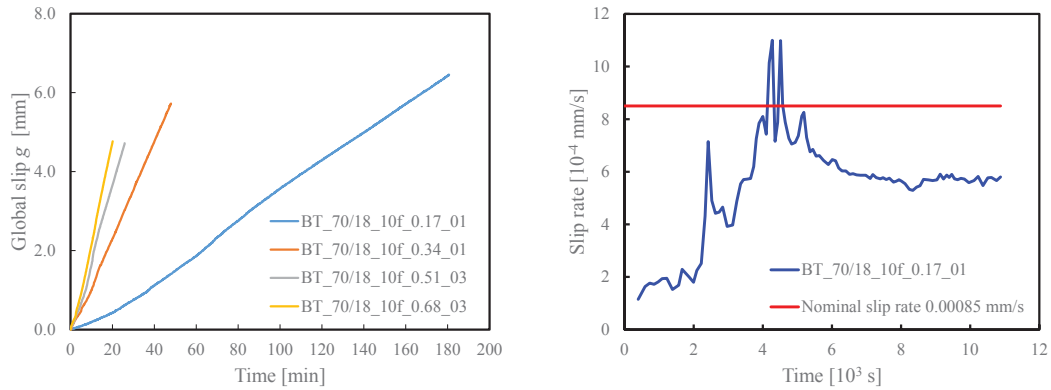


Figure 5. (a) Global slip as a function of time; (b) slip rate as a function of time for specimen BT\_70/18\_10f\_0.17\_1.

### 3 EXPERIMENTAL RESULTS AND DISCUSSION

All the specimens failed due to loss of bond at the fiber-matrix interface with high interfacial slip (Figure 4 (b)-(d)). Longitudinal cracks in a plane parallel to the intrados were observed in the matrix in many of the specimens with 10 yarns of textile 70/18, similar cracks were not observed neither in the specimens with 9 yarns of textile 70/18 nor in the specimens with textiles 44 and 105. With reference to textile 70/18 this is probably related to the ratio between the matrix surface and the textile surface, which is higher in the specimens with 9 yarns compared to the specimens with 10 yarns. With reference to textiles 44 and 105 the lack of longitudinal cracks is probably related to the lack of transverse yarns.

Figure 6 shows a typical experimental response in terms of fiber stress-global slips (transducers T4 and T5) and fiber stress-relative displacement of the blocks at the intrados (average of relative displacements measured by transducers T1 and T2).

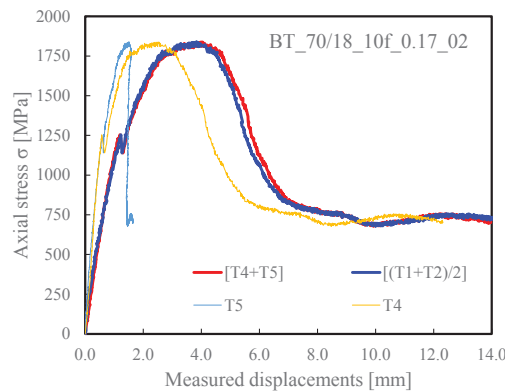


Figure 6. Typical experimental response in terms of fiber stress-measured displacement.

The fiber stress was computed as the ratio between the axial force  $N$  in the fibers and the area  $A_f$  of the fiber cross section.  $N$  was computed as a function of the applied force  $F$  (Figure 3) via equilibrium equations. The global slips measured on the two blocks (points A and A', transducers T4 and T5 in Figure 3b) were similar in the first phase of the loading process, approximately up to a load equal to 50%-60% of the joint capacity. In the second phase of the loading process the global slip increased faster at the loaded end of one of the two interface surfaces (transducer T4 in the case shown in Figure 6) compared to the other interface surface due to the formation and propagation of a crack at the fiber-matrix interface. On this surface

complete debonding occurred at the end of the test. In this phase the global slip of the other interface surface (transducer T5 in the case shown in Figure 6) stopped or decreased. Figure 6 also shows that the global slips measured by the transducers T4 and T5 are consistent with the relative displacement of the blocks at the intrados, since the sum of these slips equals the average relative displacement measured by the transducers T1 and T2.

Table 2 summarizes the specimen characteristics and the experimental results in terms of peak load  $F_{\max}$ , corresponding tensile force in the fibers referred to as peak force  $N_{\max}$ , corresponding stress of the fiber referred to as peak stress  $\sigma_{\max}$ , and global slip of the surface where debonding occurs at the peak load  $g_{\max}$ .

Specimen	$n$ [--]	$b^*$ [mm]	$t^*$ [mm]	$A_f$ [mm <sup>2</sup> ]	$F_{\max}$ [kN]	$N_{\max}$ [kN]	$\sigma_{\max}$ [MPa]	Average $\sigma_{\max}$ [MPa]	$g_{\max}$ [mm]	Average $g_{\max}$ [mm]
BT_70/18_10f_0.17_01	10	4	0.1066	4.26	5.35	8.08	1895	1727 (CoV = 9%)	2.257	2.147 (CoV = 18%)
BT_70/18_10f_0.17_02	10	4	0.1066	4.26	5.19	7.84	1839		2.532	
BT_70/18_10f_0.17_03	10	4	0.1066	4.26	5.08	7.66	1797		2.107	
BT_70/18_10f_0.17_04	10	4	0.1066	4.26	4.78	7.22	1694		1.670	
BT_70/18_10f_0.17_05	10	4	0.1066	4.26	4.12	6.21	1457		1.729	
BT_70/18_10f_0.17_06	10	4	0.1066	4.26	4.75	7.17	1682		2.585	
BT_70/18_10f_0.34_01	10	4	0.1066	4.26	3.53	5.33	1250	1691 (CoV = 23%)	1.526	1.886 (CoV = 26%)
BT_70/18_10f_0.34_02	10	4	0.1066	4.26	5.29	7.98	1872		1.683	
BT_70/18_10f_0.34_03	10	4	0.1066	4.26	5.51	8.32	1952		2.449	
BT_70/18_10f_0.51_01	10	4	0.1066	4.26	4.74	7.16	1680	1529 (CoV = 18%)	1.941	1.579 (CoV = 27%)
BT_70/18_10f_0.51_02	10	4	0.1066	4.26	3.90	5.89	1382		1.615	
BT_70/18_10f_0.51_03	10	4	0.1066	4.26	5.19	7.84	1839		1.763	
BT_70/18_10f_0.51_04	10	4	0.1066	4.26	3.24	4.88	1145		1.700	
BT_70/18_10f_0.51_05	10	4	0.1066	4.26	4.51	6.81	1598		0.859	
BT_70/18_10f_0.68_01	10	4	0.1066	4.26	6.32	9.54	2238	2243 (CoV = 16%)	1.994	2.527 (CoV = 16%)
BT_70/18_10f_0.68_02	10	4	0.1066	4.26	7.49	11.3	2651		2.569	
BT_70/18_10f_0.68_03	10	4	0.1066	4.26	7.23	10.91	2559		2.568	
BT_70/18_10f_0.68_04	10	4	0.1066	4.26	5.44	8.21	1926		2.407	
BT_70/18_10f_0.68_05	10	4	0.1066	4.26	5.20	7.85	1842		3.099	
BT_70/18_9f_0.68_01	9	4	0.1066	3.84	6.11	9.22	2403	2260 (CoV = 6%)	2.232	2.661 (CoV = 14%)
BT_70/18_9f_0.68_02	9	4	0.1066	3.84	5.48	8.27	2156		2.880	
BT_70/18_9f_0.68_03	9	4	0.1066	3.84	5.65	8.52	2221		2.870	
BT_44_4f_0.68_01	4	4	0.16575	2.65	3.83	5.78	2179	2046 (CoV = 7%)	2.821	3.088 (CoV = 12%)
BT_44_4f_0.68_02	4	4	0.16575	2.65	3.60	5.44	2051		2.937	
BT_44_4f_0.68_03	4	4	0.16575	2.65	3.36	5.06	1908		3.505	
BT_105_9f_0.68_01	9	4	0.15145	5.45	9.28	14.01	2570	2516 (CoV = 2%)	3.589	3.610 (CoV = 6%)
BT_105_9f_0.68_02	9	4	0.15145	5.45	9.03	13.63	2500		3.845	
BT_105_9f_0.68_03	9	4	0.15145	5.45	8.95	13.51	2478		3.397	

Table 2. Peak load  $F_{\max}$  and corresponding axial force  $N_{\max}$ , axial stress  $\sigma_{\max}$ , and global slip  $g_{\max}$  of the tested specimens.

The average peak stress of textile 70/18 is between 1529 MPa (displacement rate 0.51 mm/min) and 2260 MPa (displacement rate 0.68 mm/min). The corresponding coefficients of variation (CoV) are equal to 18% and 6%, respectively. The slip at the peak load is between 1.57 mm (displacement rate 0.51 mm/min, CoV=27%) and 2.66 mm (rate 0.68 mm/min, CoV=14%). The average peak stress of textiles 44 and 105 are 2046 MPa (CoV=7%) and 2516 MPa (CoV=2%). The global slip at the peak load exceeds 3 mm for these textiles.

The  $\sigma$ - $g$  responses of the tested specimens are shown in Figure 7 where the fibers tensile stress  $\sigma$  is reported as a function of the global slip  $g$  of the interface surface on which the debonding occurs (maximum of the global slips measured by the transducers T4 and T5). The experimental  $\sigma$ - $g$  responses shown in Figure 7 are consistent with the idealized  $\sigma$ - $g$  response shown in Figure 8a, which is associated with the typical CML shown in Fig 8b [26] and with a bonded length equal to or longer than the effective bond length.



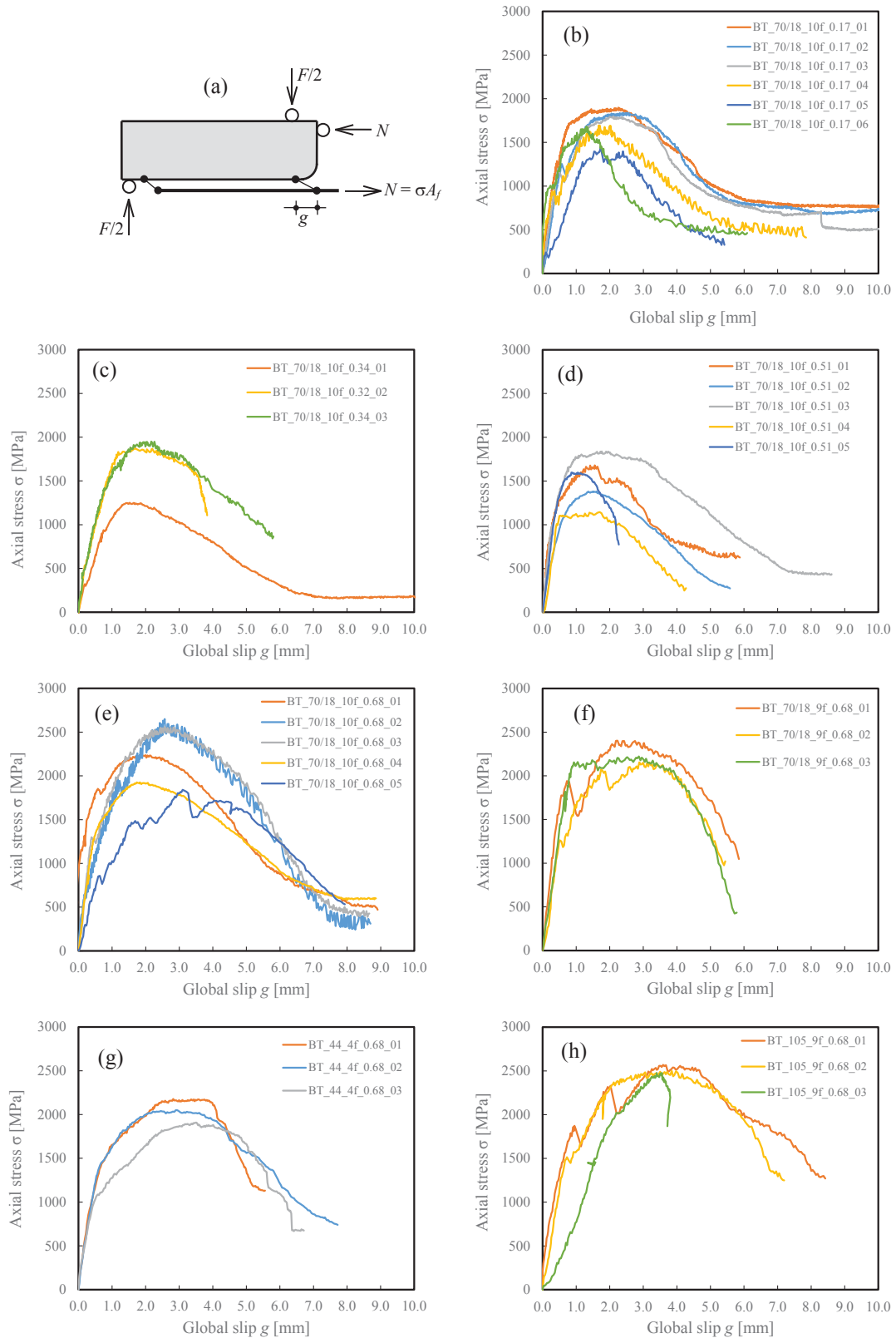
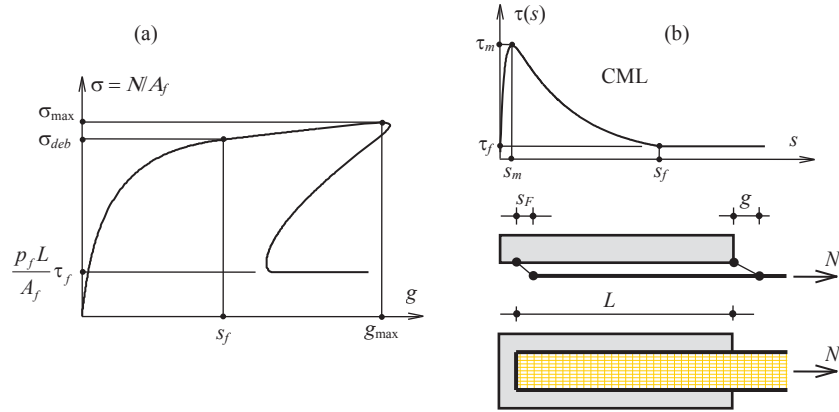


Figure 7. (a) Beam test; (b)-(h)  $\sigma$ - $g$  responses of the tested specimens.

Figure 8. (a) Idealized  $\sigma$ - $g$  response; (b) typical CML.

This response curve exhibits an ascending branch up to the debonding stress  $\sigma_{deb}$ , which correspond to the onset of the interfacial crack propagation that occurs for a global slip equal to  $s_f$  (Figure 8b). A further ascending branch, up to the peak stress  $\sigma_{max}$ , is exhibited if a constant friction branch follows the slip  $s_f$  in the CML and the bonded length is longer than the effective bond length. The slope of this branch is related to the friction shear stress  $\tau_f$  (Figure 8b). Once the peak stress is attained the applied stress decreases until it reaches a constant value due to friction only. The snap back phenomenon shown in Figure 8a, which is due to the elastic energy release associated with the decrease of the force  $N$ , is not experimentally caught by the performed beam tests since they are controlled by the displacement of the load application point.

An initial linear branch is exhibited by all the  $\sigma$ - $g$  responses shown in Figure 7 whose slope is related neither to the type of textile nor to the displacement rate. This branch is followed by an ascending branch with a smaller slope up to the onset of the debonding phenomenon. Once the debonding initiates the increase of the load up to the peak stress  $\sigma_{max}$  is associated with the development of friction shear stress [26] in the debonded region near to the loaded end. The descending branch is associated with the increase of the length of the debonded zone up to the complete debonding and the attainment of a constant stress associated with the interfacial friction shear stress  $\tau_f$  [25]. It should be noted that some beam tests were stopped before reaching the friction branch to save time.

Figure 9 compares the  $\sigma$ - $g$  responses of beam test on textile 70/18, characterized by a nominal slip rate equal to 0.00085 mm/s, with the  $\sigma$ - $g$  responses obtained by D'Antino et al. [25] on the same composite through single-lap shear tests at the slip rate of 0.00084 mm/s with a bonded length equal to 330 mm. Similar responses are obtained with the single-lap and beam tests. In particular the performed beam tests provided a slightly lower peak stress and corresponding global slip and a slightly higher friction stress compared to the values of the corresponding parameters provided by single-lap shear tests. The mentioned differences between the results of these tests are not fully consistent with the experimental results presented by Calabrese et al. [33]. In [33] it is observed that beam tests and single-lap shear tests provide similar peak stress, while beam tests provide friction stress that are roughly the double of those provided by single-lap shear test.

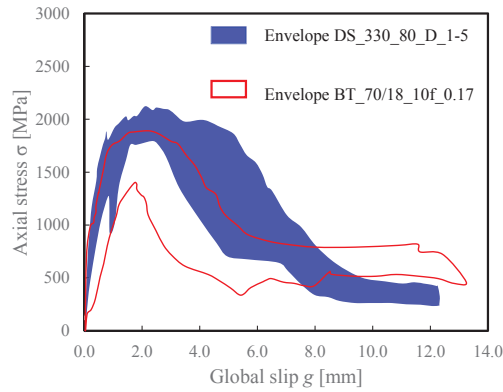


Figure 9. Comparison between the  $\sigma$ - $g$  responses obtained with beam tests and the  $\sigma$ - $g$  responses obtained by D'Antino et al. [25] through single-lap shear tests.

The higher friction stress obtained with beam tests is attributed by the authors of [33] to the transversal compressive stress on the textile at the edge of the blocks (at the mid-span of the specimen) associated with their rotation. The edges of the concrete blocks were rounded at the intrados of the hinged cross sections to reduce the transversal stress on the textile when the blocks rotate. This could explain the difference between the results presented in [33] and the results presented in this paper.

The influence of the displacement rate is shown in Figure 10 in which the peak stress (Figure 10a) and the corresponding global slip (Figure 10b) are reported as a function of the nominal slip rate.

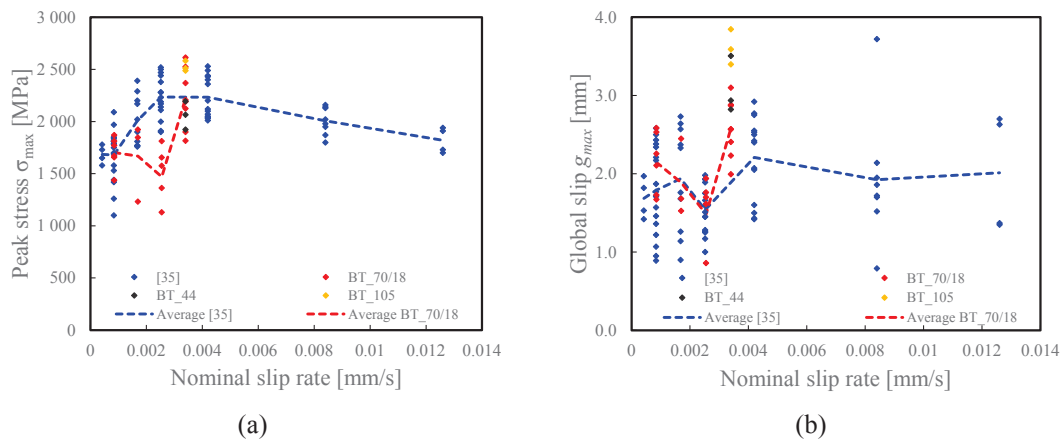


Figure 10. Influence of the slip rate: (a) peak stress vs. slip rate; (b) global slip at peak load vs. slip rate.

In Figure 10 the experimental results are also compared with those obtained by Carloni et al. [35] with single-lap shear tests. Experimental peak stress of single-lap shear tests presented in [35] refer to bonded length equal to 330 mm and 430 mm. It can be observed that the dependencies of the peak stress and corresponding global slip on the slip rate are different from those presented in [35], even if the peak stress corresponding to the slip rate 0.0025 mm/s is similar. The difference between the results of beam tests and the results reported in [35] is probably due to the different test procedure adopted. Indeed the single-lap shear tests presented in [35] are performed imposing a constant rate of the global slip, while the beam tests are performed imposing a constant rate of the load application point. As discussed in section 2.2 the slip rate approaches to a constant value only at an advanced stage of the test (Figure 3). This makes the beam test configuration unsuitable for investigating the influence of the load-

ing rate on the interfacial stress transfer phenomenon, unless the tests are controlled by the global slip measured through the transducers T4 and T5.

Figure 11 shows the comparison among the  $\sigma$ - $g$  responses of the three utilized textiles. It can be observed that the response curves of textiles 44 and 105 are similar to those of textile 70/18. Textile 105 is characterized by slightly higher slip at peak load than those of 70/18.

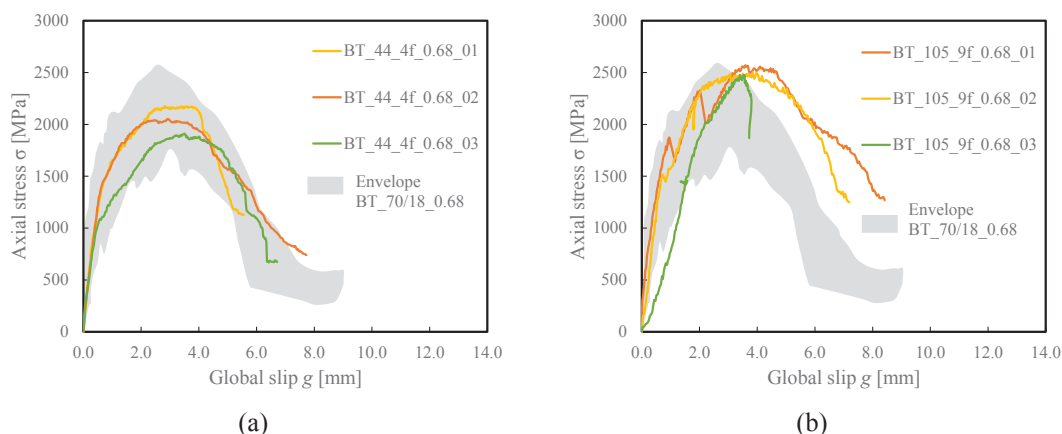


Figure 11. Effect of the fiber arrangement on the  $\sigma$ - $g$  responses: (a) textile 44 vs. textile 70/18; (b) textile 105 vs. textile 70/18.

#### 4 CONCLUSIONS

This paper presents the results of the first step of an experimental campaign for the characterization of the bond between PBO-FRCM materials and concrete by means of beam tests. Three composite materials made of the same matrix and different PBO textiles were tested. The tests were performed with different loading rates. The following conclusions can be drawn.

1. Beam tests provided experimental responses similar to those obtained by several authors through single-lap shear tests.
2. The fiber stress associated with the friction at the fiber-matrix interface was lower than that obtained by other authors with similar tests. This difference can be ascribed to the geometrical characteristics of the employed specimen.
3. It was not possible to observe a clear dependence of the joint capacity and the corresponding global slip on the loading rate. Therefore beam test does not appear suitable for evaluating the effect of the loading rate on the bond properties of PBO-FRCM materials, unless they are performed controlling the relative displacement between the concrete blocks or the interfacial slip at the mid-span of the specimen.
4. Textiles of PBO fibers with different fiber amounts have comparable responses in terms of shear stress transfer mechanism in the investigated range.

The beam test appears to be an alternative to single-lap or double-lap shear tests to characterize the interface between FRCM materials and the substrate. However further investigations are needed to determine the influence of the geometry of the specimen and the test procedure on the measured parameters.

## ACKNOWLEDGMENTS

The authors greatly acknowledge Ruregold s.r.l. (Italy) for providing the composite materials used in this experimental work.

## REFERENCES

- [1] Italian National Research Council (CNR), 'Guide for the Design and Construction of Externally Bonded FRP Systems for Strengthening Existing Structures'. CNR - Rome, Italy, 2004.
- [2] ACI Committee 440.1R-15, 'Guide for the Design and Construction of Structural Concrete Reinforced with Fiber-Reinforced Polymer (FRP) Bars'. ACI 440.1R-15, Farmington Hill, US, 2015.
- [3] Italian National Research Council (CNR), 'Guide for the Design and Construction of Externally Bonded Fibre Reinforced Inorganic Matrix Systems for Strengthening Existing Structures'. CNR - Rome, Italy, 2020.
- [4] ACI Committee 549, 'Guide to Design and construction of externally bonded fabric-reinforced cementitious matrix (FRCM) systems for repair and strengthening concrete and masonry structures'. ACI 549.4R-13, Farmington Hill, US, 2013.
- [5] G. Loreto, L. Leardini, D. Arboleda, and A. Nanni, 'Performance of RC Slab-Type Elements Strengthened with Fabric-Reinforced Cementitious-Matrix Composites', *J. Compos. Constr.*, vol. 18, no. 3, Jun. 2014, doi: 10.1061/(ASCE)CC.1943-5614.0000415.
- [6] S. Babaeidarabad, G. Loreto, and A. Nanni, 'Flexural Strengthening of RC Beams with an Externally Bonded Fabric-Reinforced Cementitious Matrix', *J. Compos. Constr.*, vol. 18, no. 5, p. 04014009, Oct. 2014, doi: 10.1061/(ASCE)CC.1943-5614.0000473.
- [7] C. Escrig, L. Gil, and E. Bernat-Maso, 'Experimental comparison of reinforced concrete beams strengthened against bending with different types of cementitious-matrix composite materials', *Construction and Building Materials*, vol. 137, pp. 317–329, Apr. 2017, doi: 10.1016/j.conbuildmat.2017.01.106.
- [8] F. Bencardino, C. Carloni, A. Cordello, F. Focacci, A. Napoli, and R. Realfonso, 'Flexural behaviour of RC members strengthened with FRCM: State-of-the-art and predictive formulas', *Composites Part B: Engineering*, vol. 148, pp. 132–148, Sep. 01, 2018.
- [9] L. Ombres, 'Structural performances of reinforced concrete beams strengthened in shear with a cement based fiber composite material', *Composite Structures*, vol. 122, pp. 316–329, Apr. 2015, doi: 10.1016/j.compstruct.2014.11.059.
- [10] A. D'Ambrisi and F. Focacci, 'Flexural Strengthening of RC Beams with Cement-Based Composites', *J. Compos. Constr.*, vol. 15, no. 5, pp. 707–720, Oct. 2011, doi: 10.1061/(ASCE)CC.1943-5614.0000218.
- [11] Z. C. Tetta, L. N. Koutas, and D. A. Bournas, 'Textile-reinforced mortar (TRM) versus fiber-reinforced polymers (FRP) in shear strengthening of concrete beams', *Composites Part B: Engineering*, vol. 77, pp. 338–348, Aug. 2015, doi: 10.1016/j.compositesb.2015.03.055.

- [12] Tetta, Zoi C., Triantafillou, Thanasis C., and Bournas, Dionysios A., 'On the design of shear-strengthened RC members through the use of textile reinforced mortar overlays', *Composites Part B: Engineering*, vol. 147, pp. 178–196, Aug. 15, 2018.
- [13] T. D'Antino, F. Focacci, L. H. Sneed, and C. Carloni, 'Relationship between the effective strain of PBO FRCM-strengthened RC beams and the debonding strain of direct shear tests', *Engineering Structures*, vol. 216, p. 110631, Aug. 2020, doi: 10.1016/j.engstruct.2020.110631.
- [14] Consiglio Superiore dei Lavori Pubblici - Servizio Tecnico Centrale, 'Linea Guida per la identificazione, la qualificazione ed il controllo di accettazione di compositi fibrorinforzati a matrice inorganica (FRCM) da utilizzarsi per il consolidamento strutturale di costruzioni esistenti'. Consiglio Superiore dei Lavori Pubblici - Servizio Tecnico Centrale, Dec. 2018.
- [15] AC 434-13, 'Acceptance criteria for masonry and concrete strengthening using fabric-reinforced cementitious matrix (FRCM) composite systems'. 2013.
- [16] C. Carloni and K. V. Subramaniam, 'FRP-Masonry Debonding: Numerical and Experimental Study of the Role of Mortar Joints', *J. Compos. Constr.*, vol. 16, no. 5, pp. 581–589, Oct. 2012, doi: 10.1061/(ASCE)CC.1943-5614.0000282.
- [17] M. Malena, F. Focacci, C. Carloni, and G. de Felice, 'The effect of the shape of the cohesive material law on the stress transfer at the FRP-masonry interface', *Composites Part B: Engineering*, vol. 110, pp. 368–380, Feb. 2017, doi: 10.1016/j.compositesb.2016.11.012.
- [18] M. Bocciarelli and M. A. Pisani, 'Survey on the interface behaviour in reinforced concrete beams strengthened with externally bonded FRP reinforcement', *Composites Part B: Engineering*, vol. 118, pp. 169–176, Jun. 2017, doi: 10.1016/j.compositesb.2017.02.047.
- [19] C. Carloni *et al.*, 'Fiber Reinforced Composites with Cementitious (Inorganic) Matrix', in *Design Procedures for the Use of Composites in Strengthening of Reinforced Concrete Structures*, vol. 19, C. Pellegrino and J. Sena-Cruz, Eds. Dordrecht: Springer Netherlands, 2016, pp. 349–392.
- [20] L. Ombres, 'Analysis of the bond between Fabric Reinforced Cementitious Mortar (FRCM) strengthening systems and concrete', *Composites Part B: Engineering*, vol. 69, pp. 418–426, Feb. 2015, doi: 10.1016/j.compositesb.2014.10.027.
- [21] L. Ascione, G. de Felice, and S. De Santis, 'A qualification method for externally bonded Fibre Reinforced Cementitious Matrix (FRCM) strengthening systems', *Composites Part B: Engineering*, vol. 78, pp. 497–506, Sep. 2015, doi: 10.1016/j.compositesb.2015.03.079.
- [22] L. H. Sneed, T. D'Antino, C. Carloni, and C. Pellegrino, 'A comparison of the bond behavior of PBO-FRCM composites determined by double-lap and single-lap shear tests', *Cement and Concrete Composites*, vol. 64, pp. 37–48, Nov. 2015, doi: 10.1016/j.cemconcomp.2015.07.007.
- [23] F. G. Carozzi *et al.*, 'Experimental investigation of tensile and bond properties of Carbon-FRCM composites for strengthening masonry elements', *Composites Part B: Engineering*, vol. 128, pp. 100–119, Nov. 2017, doi: 10.1016/j.compositesb.2017.06.018.
- [24] C. Caggegi *et al.*, 'Experimental analysis on tensile and bond properties of PBO and aramid fabric reinforced cementitious matrix for strengthening masonry structures', *Composites Part B: Engineering*, vol. 127, pp. 175–195, Oct. 2017, doi: 10.1016/j.compositesb.2017.05.048.



- [25] T. D'Antino, C. Carloni, L. H. Sneed, and C. Pellegrino, 'Matrix-fiber bond behavior in PBO FRCM composites: A fracture mechanics approach', *Engineering Fracture Mechanics*, vol. 117, pp. 94–111, Feb. 2014, doi: 10.1016/j.engfracmech.2014.01.011.
- [26] F. Focacci, T. D'Antino, C. Carloni, L. H. Sneed, and C. Pellegrino, 'An indirect method to calibrate the interfacial cohesive material law for FRCM-concrete joints', *Materials & Design*, vol. 128, pp. 206–217, Aug. 2017, doi: 10.1016/j.matdes.2017.04.038.
- [27] A. D'Ambrisi, L. Feo, and F. Focacci, 'Experimental analysis on bond between PBO-FRCM strengthening materials and concrete', *Composites Part B: Engineering*, vol. 44, no. 1, pp. 524–532, Jan. 2013, doi: 10.1016/j.compositesb.2012.03.011.
- [28] M. R. Valluzzi *et al.*, 'Round Robin Test for composite-to-brick shear bond characterization', *Mater Struct*, vol. 45, no. 12, pp. 1761–1791, Dec. 2012, doi: 10.1617/s11527-012-9883-5.
- [29] S. De Santis *et al.*, 'Round Robin Test on tensile and bond behaviour of Steel Reinforced Grout systems', *Composites Part B: Engineering*, vol. 127, pp. 100–120, Oct. 2017, doi: 10.1016/j.compositesb.2017.03.052.
- [30] A. D'Ambrisi, L. Feo, and F. Focacci, 'Bond-slip relations for PBO-FRCM materials externally bonded to concrete', *Composites Part B: Engineering*, vol. 43, no. 8, pp. 2938–2949, Dec. 2012, doi: 10.1016/j.compositesb.2012.06.002.
- [31] F. Focacci, T. D'Antino, and C. Carloni, 'The role of the fiber-matrix interfacial properties on the tensile behavior of FRCM coupons', *Construction and Building Materials*, vol. 265, p. 120263, Dec. 2020, doi: 10.1016/j.conbuildmat.2020.120263.
- [32] A. S. Calabrese, P. Colombi, and T. D'Antino, 'A Bending Test Set-Up for the Investigation of the Bond Properties of FRCM Strengthenings Applied to Masonry Substrates', *KEM*, vol. 817, pp. 149–157, Aug. 2019, doi: 10.4028/www.scientific.net/KEM.817.149.
- [33] A. S. Calabrese, T. D'Antino, P. Colombi, and C. Poggi, 'Study of the influence of interface normal stresses on the bond behavior of FRCM composites using direct shear and modified beam tests', *Construction and Building Materials*, vol. 262, p. 120029, Nov. 2020, doi: 10.1016/j.conbuildmat.2020.120029.
- [34] A. S. Calabrese, T. D'Antino, and P. Colombi, 'Experimental and analytical investigation of PBO FRCM-concrete bond behavior using direct and indirect shear test set-ups', *Composite Structures*, vol. 267, p. 113672, Jul. 2021, doi: 10.1016/j.compstruct.2021.113672.
- [35] C. Carloni, S. Verre, L. H. Sneed, and L. Ombres, 'Loading rate effect on the debonding phenomenon in fiber reinforced cementitious matrix-concrete joints', *Composites Part B: Engineering*, vol. 108, pp. 301–314, Jan. 2017, doi: 10.1016/j.compositesb.2016.09.087.
- [36] UNI EN 1015-11:2019, 'Metodi di prova per malte per opere murarie - Parte 11: Determinazione della resistenza a flessione e a compressione della malta indurita'. UNI EN, 2019.
- [37] UNI EN 12390-3:2019, 'Prove sul calcestruzzo indurito - Parte 3: Resistenza alla compressione dei provini'. UNI EN, 2019.

## NODAL DISSIPATIVE DEVICES FOR SEISMIC PROTECTION OF PRECAST RC STRUCTURES

Fabrizio Comodini<sup>1</sup>, Angelo D’Ambrisi<sup>2</sup>, and Marco Mezzi<sup>3</sup>

<sup>1</sup> Università eCampus  
via Isimbardi 10, 22060 Novedrate (CO), Italy  
fabrizio.comodini@uniecampus.it

<sup>2</sup> Dipartimento di Architettura, Università di Firenze  
piazza Brunelleschi 6, 50121 Firenze, Italy  
angelo.dambrisi@unifi.it

<sup>3</sup> Dipartimento di Ingegneria Civile e Ambientale, Università di Perugia  
via Duranti 93, 06125 Perugia, Italy  
marco.mezzi@unipg.it

---

### Abstract

*The low seismic performance level of precast reinforced concrete (RC) structures mainly depends on inadequate connections between structural elements. Seismic capacity of precast RC structures can be improved inserting dissipative devices in the nodes between structural elements. With reference to a new conception dissipative device named Joint Torsional Dissipative Device (JTDD) design abaci that represent the main correlations between the geometric and mechanical characteristics of the device are proposed. The design abaci constitute an operative tool that can be used to rapidly determine the optimal dimensions of the individual device as functions of the main characteristics of the structural system, e.g. angular rotation at the elastic limit, torsional stiffness and torsional moment at the elastic limit. The construction of the proposed design abaci is performed for a wide range of possible combinations of geometrical quantities characterizing the shape of the nodal devices.*

**Keywords:** Precast RC Structures, Seismic Capacity, Nodal Dissipative Device, Torsional Behavior, Design Abaci.

---

## 1 INTRODUCTION

In new precast reinforced concrete (RC) structures if typical isostatic schemes are adopted the fulfillment of the capacity requirements provided by current Italian code [1] is obtained only adopting very large column sections. This leads to high construction costs and low market competitiveness [2, 3, 4]. An improvement of the seismic capacity of precast RC structures can be obtained inserting dissipative devices in structural nodes [5, 6]. Many research works are available in technical literature [7], however the scarce application of the results to real precast RC structures suggests a necessary deepening of the constructive and economic aspects in order to ordinarily use these dissipative devices [2]. The research aim is that of defining the characteristics of a specific nodal device able to satisfy the requirements of energy dissipation, of adaptability to the current precast constructive systems and of cost containment. With reference to a device of new conception, described in the following paragraphs, the research activity has been focused on the definition of a design tool that allows to associate the nodal device mechanical characteristics to the geometric and dynamic characteristics of the precast system [8]. Indeed in previously performed studies [9, 10] it has been observed that a nodal dissipative device modifies the degree of constraint among the connected structural elements, producing a stress redistribution and a change of the dynamic characteristics of the precast system. Therefore in order to ensure that the device itself is effective in terms of dissipated energy and does not produce negative effects in terms of stresses, it must be designed appropriately for the specific precast structural system. In particular design abaci that represent the main correlations between the geometric and the mechanical characteristics of the device have been defined. The design abaci constitute an operative tool that can be used to rapidly determine the optimal geometric dimensions of the individual device as a functions of the demand parameters requested by the structural system (e.g.: angular rotation at the elastic limit, torsional stiffness and torsional moment at the elastic limit). The design abaci have been defined for a wide range of possible combinations of geometrical quantities characterizing the shape of the nodal devices.

## 2 DISSIPATIVE DEVICE DESCRIPTION

### 2.1 Operating principles

The JTDD are activated by the relative rotations that occur among the precast structural members (vertical and horizontal) following the system lateral deformation. The device allows horizontal and vertical displacements and restrains the nodal rotations through a hollow cylinder of steel or of a similar material that deforms in torsion in the elasto-plastic range. The amount of dissipated energy is therefore closely related to the extent of rotations and therefore to the floor drifts. This implies that the optimal working conditions of the device are those associated with structures undergoing large horizontal displacements under earthquakes. However the insertion of the JTDD modifies the degree of rotational constraint in the nodes among the structural elements with a consequent stress redistribution on them, that has to be accounted for in the verification of strength. A fundamental condition for a proper functioning of the devices is that the rotation at the elastic limit is larger than the nodal rotation induced by the vertical and horizontal service loads. For rotations lower than the elastic rotation the stress distribution on structural elements is a function of the device elastic stiffness. Therefore as the device constitutive law varies, stress distributions different from those associated to a scheme of isostatic columns and simply supported beams are obtained. In particular a constitutive law characterized by high values of elastic stiffness and plastic threshold leads to a late activation

of the devices in the plastic field, transforming the devices in fixed support constraints and impeding them to dissipate the energy necessary to reduce the seismic action effects. Low values of elastic stiffness and plastic threshold allow an early activation of the device with hysteretic cycles characterized by a small dissipation. In the case of an early device activation a significant part of the seismic action would still affect the columns only. The device calibration is closely related to the geometric and dynamic characteristics of the structure, therefore the present study has the aim of defining design abaci that correlate the geometrical and the mechanical characteristics of the devices. Indeed an incorrect calibration of the devices can compromise the benefits resulting from their insertion in the structural system.

## 2.2 Possible applications

In the last years numerous dissipative or isolation devices able to increase the energy dissipation of a structural system and to reduce the damage have been developed [7]. This approach allows to increase the performance level of precast structures keeping the construction cost at acceptable levels. The possible applications of the JTDD mainly concern new precast RC structures having a static scheme with isostatic columns and simply supported beams. Seismic protection devices can also be installed in existing structures for their seismic retrofitting. As already mentioned in previous paragraphs the proposed dissipative device works as a rotational constraint. Therefore with reference to precast structural system with isostatic columns and simply supported beams the natural positioning of the device is at the beam extrados in correspondence of the beam-column joint and laterally to the columns at the column-foundation joint (Figure 1). In this last case the device can be installed when columns are inserted into sleeve plinths and the internal hollow space between the column and the plinth is constituted by deformable material.

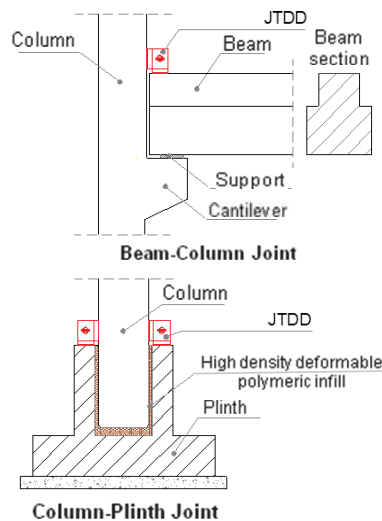


Figure 1: Installation example of the JTDD in the beam-column joint and in the column-plinth joint.

## 2.3 Geometrical and rheological characteristics

All elements constituting the proposed JTDD are made of steel type S275 (Table 1). It has been also studied the possibility of making the hollow cylinder, that is subjected to torsion, with different steel types or different materials characterized by a low elastic modulus and a low plastic threshold as the lead or the aluminum. The use of materials different from the steel type S275 allows to produce devices with lower stiffness and plastic threshold but with a larger dissipative capacity in the plastic field.

Material	E (N/mm <sup>2</sup> )	G (N/mm <sup>2</sup> )	f <sub>yk</sub> (N/mm <sup>2</sup> )	ε <sub>y</sub> (%)
Steel S275	210000	80000	275	0.13
Aluminium	70000	26000	150	0.21
Lead	5000	1785	25	0.50

Table 1: Material mechanical characteristics.

The device is constituted by a hollow section cylinder arranged with the longitudinal axis in the horizontal direction. The cylinder is constrained to a central plate connected to the vertical structural element and to two lateral plates connected to the horizontal structural element. The central plate has a vertical slotted hole, while the lateral plates have horizontal slotted holes. The presence of the slotted holes in the plates allows the structural elements connected by the device of sliding in the horizontal and vertical direction without inducing shear stresses in the hollow cylinder. The steel plates are connected to the structural elements through suitably dimensioned mechanical or chemical anchors (Figure 2). The length, the outer diameter and the internal thickness of the hollow cylinder vary as a function of the geometrical and dynamic characteristics of the precast structure. Indeed the geometrical parameters of the hollow cylinder together with the utilized material type determine the elastic stiffness, the plastic threshold and the ultimate angular strain of the torsional device.

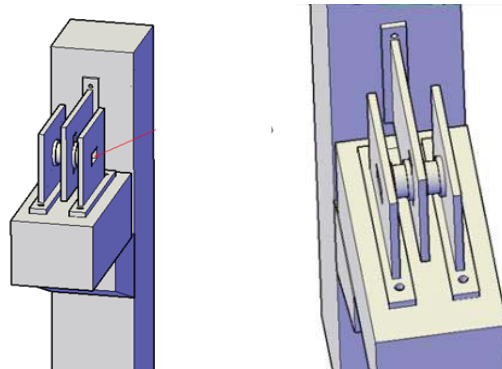


Figure 2: 3D views of the JTDD.

### 3 NONLINEAR BEHAVIOUR

The linear and nonlinear behavior of the device is assimilable to the elastic-plastic behavior of the hollow cylinder subjected to torsional strains. The equations governing the device elastic behavior are those of the torsion classic theory for circular hollow section reported in the following. With reference to Figure 3 the following equations can be defined:

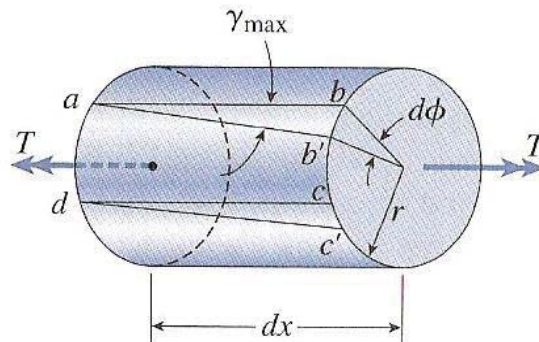


Figure 3: Infinitesimal cylindrical element subjected to torsion.

torsion angle per length unit

$$\vartheta = \frac{d\phi}{dx} \quad (1)$$

outer fiber slip

$$\gamma_{\max} = a \tan\left(\frac{\overline{bb'}}{\overline{aa'}}\right) \approx \frac{Rd\phi}{dx} = R\vartheta \quad (2)$$

linear variation of the distortion  $\gamma$  as a function of  $r$ . In the section the torsion angle is independent of  $r$ , therefore

$$\gamma(r) = r\vartheta = \frac{r}{R}\gamma_{\max} \quad (3)$$

The JTDD has a hollow circular section therefore with reference to Figure 4 the following equations are defined:

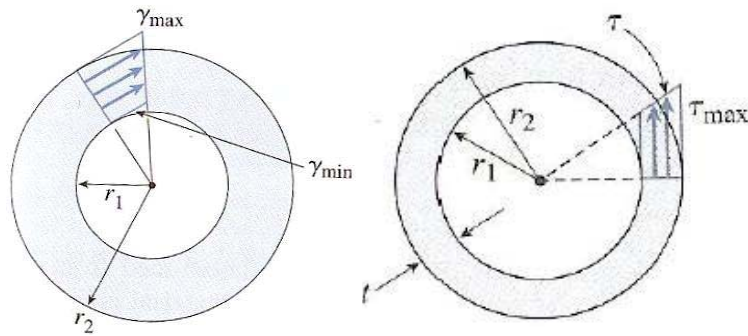


Figure 4: Section of hollow cylindrical element.

polar torsional inertia

$$I_{pol} = \frac{\pi}{2} (r_2^4 - r_1^4) \quad (4)$$

unit torsion angle

$$\vartheta = \frac{\gamma_{\max}}{r_2} \rightarrow \vartheta = \frac{M_t}{GI_{pol}} \quad (5)$$

where  $M_t$  = torsional moment and  $G$  = shear modulus;

total torsion angle between two section placed at a distance  $L$

$$\phi(L) = \frac{M_t L}{GI_{pol}} \quad (6)$$

Assuming the  $\tau_{\max}$  of the outer fiber equal to  $\frac{f_{yk}}{\sqrt{3}}$  the torsional moment at the elastic limit can be evaluated with the following relation:

$$M_{ty} = \frac{\tau_{\max}}{r_2} I_{pol} \quad (7)$$

In order to develop a design procedure for the selection of the device type to install in the precast structural system, the study of the JTDD plastic behavior has been performed in the first instance with a simplified analytical method. The evaluation of the device ultimate angular rotation is based on the maximum axial deformation of the diagonal of the unit element of the hollow cylinder outer fiber (Figure 5).



The element  $abcd$  in Figure 5 is considered deformed in torsion

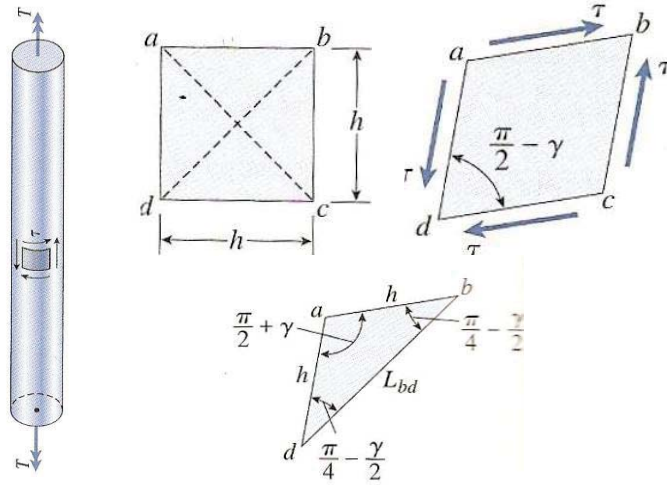


Figure 5: Unit plane element deformed in torsion.

With reference to Figure 5 it is obtained:

$$L_{bd} = \sqrt{2h(1 + \epsilon_{\max})} \quad (8)$$

the same length can be determined with the cosine theorem applied to the  $abd$  triangle:

$$L_{bd}^2 = h^2 + h^2 - 2h^2 \cos\left(\frac{\pi}{2} + \gamma\right) \quad (9)$$

Using both relations it is obtained:

$$(1 + \epsilon_{\max})^2 = 1 - \cos\left(\frac{\pi}{2} + \gamma\right) \rightarrow 1 + 2\epsilon_{\max} + \epsilon_{\max}^2 = 1 + \sin \gamma \quad (10)$$

With this last equation it is possible to relate the ultimate axial deformation of the material  $\epsilon_{\max}$  with the ultimate slip  $\gamma_{\max}$ . Being linear the slip pattern with the radius, in that it derives from the congruence and is independent of the material behavior, it is possible to find the ultimate angular rotation associated to the ultimate slip.

#### 4 DEVICE PROPERTIES

As already introduced in the previous paragraphs the JTDD mechanical characteristics are directly relatable to the elastic stiffness, the plastic threshold and the ultimate rotation of the hollow cylinder subjected to torsional strains. In order to provide an operative tool design abaci for different material types have been defined. They graphically reproduce the analytical relations among the length, the outer radius and the thickness of the hollow cylinder and the mechanical parameters describing the device operation. For this purpose two shape factors, named S1 and S2 respectively, that represent the ratios of the geometric quantities defining the hollow cylinder have been defined. In particular  $S1 = rm/S$  and  $S2 = rm/L$  where  $rm$  is the average radius,  $S$  is the thickness and  $L$  is the length (Figure 6). Relating the shape factors S1 and S2 with the elastic stiffness, the angular rotation at the elastic limit, the plastic threshold and the ultimate angular rotation of the hollow cylinder it has been possible to define the above mentioned abaci. The material constitutive law has been assumed elastic-perfectly plastic. To determine the plastic torsional moment a tangential stress uniform distribution within the thickness of the hollow cylinder has been assumed. This last hypothesis implies that also the moment-angular rotation diagram of the hollow cylinder will show an horizontal plastic branch.

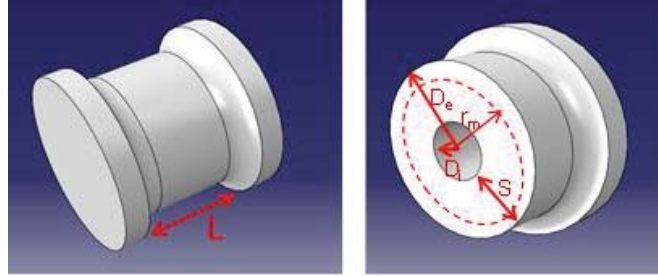


Figure 6: Geometrical quantities of the hollow cylinder.

Different types of JTDD have been designed parametrizing some geometrical quantities of the hollow cylinder to the varying of the utilized materials. The main results obtained with the performed analyses are reported in the following. In particular for different device types Figures 7, 8 and 9 report the torsional moment-total angular rotation diagrams while Figures 10, 11, 12 and 13 report the abaci relating the yielding torsional moment  $M_{ty}$  and the elastic stiffness  $K_t$  with the shape factors  $S_1$  and  $S_2$ .

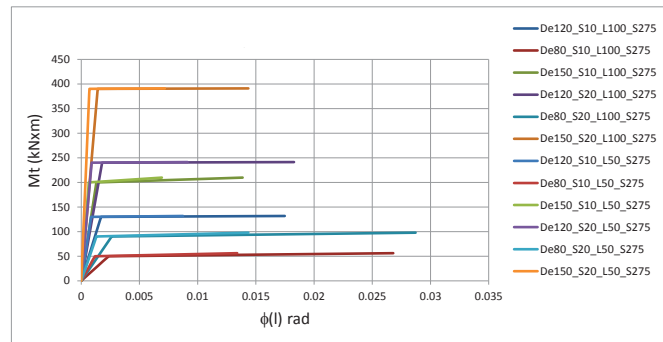


Figure 7: Torsional moment - total angular rotation diagram of steel devices.

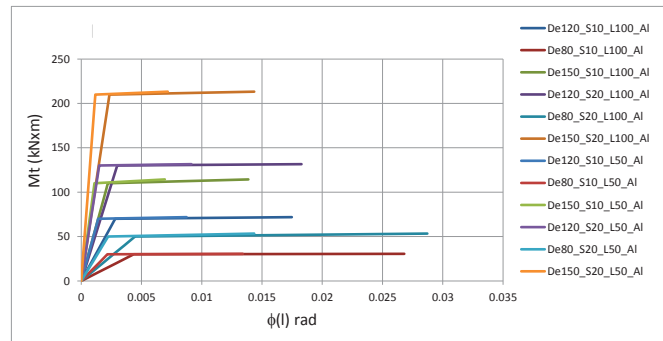


Figure 8: Torsional moment - total angular rotation diagram of aluminum devices.

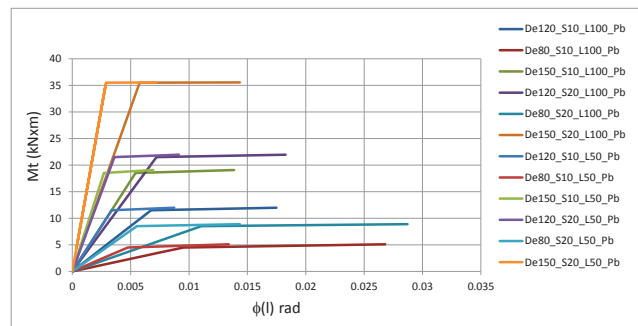


Figure 9: Torsional moment - total angular rotation diagram of lead devices.

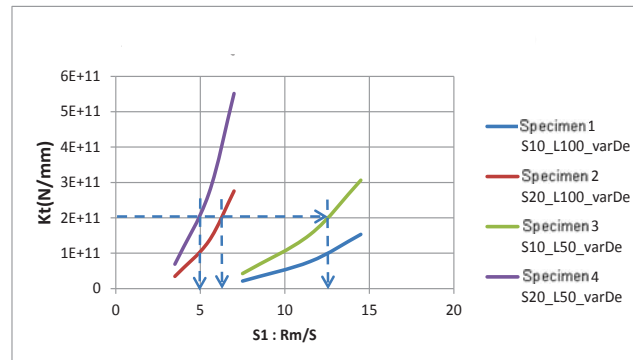


Figure 10: Torsional stiffness  $K_t$  - shape factor  $S_1$  abacus for steel devices.

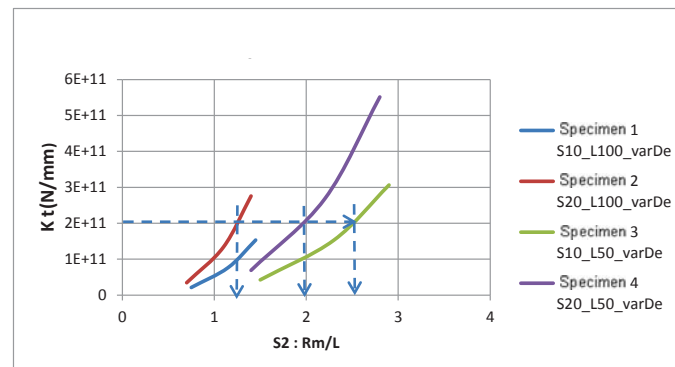


Figure 11: Torsional stiffness  $K_t$  - shape factor  $S_2$  abacus for steel devices.

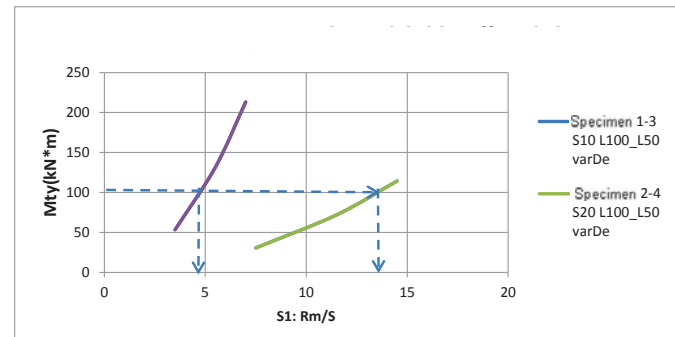


Figure 12: Yielding torsional moment - shape factor  $S_1$  abacus for aluminum devices.

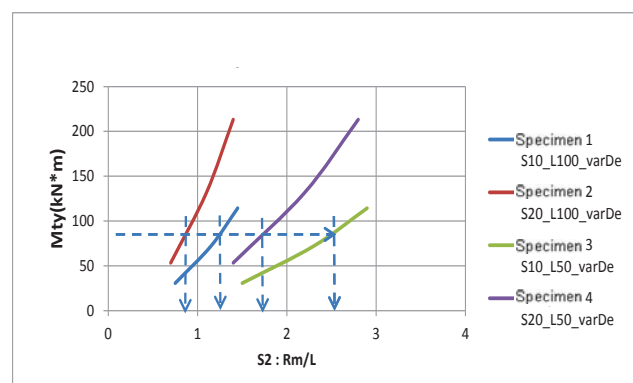


Figure 13: Yielding torsional moment - shape factor  $S_2$  abacus for aluminum devices.

Where the symbols used in the figure legend have the following meaning:  
 $D_e$  = outer diameter,  $S$  = thickness and  $L$  = cylinder length.

In the diagrams reported in Figures 10, 11, 12 and 13 the quantity parametrized to define the devices is  $D_e$ .

Therefore the abaci relating the device mechanical characteristics to the  $S1$  and  $S2$  shape factors and the moment-total angular rotation diagrams constitute an operative tool to design the JTDD. Indeed once defined the device geometry through the  $S1$  and  $S2$  shape factors it is possible to determine the corresponding mechanical characteristics as elastic stiffness and yielding moment. For each device characterized by specific  $S1$  and  $S2$  shape factors it is moreover possible to determine the constitutive law in terms of torsional moment and total angular rotation.

## 5 CONCLUSIONS

- Aim of the present work is the definition of abaci for designing rotational dissipative devices to be placed in the nodes of precast reinforced concrete (RC) structures.
- The insertion in the structure of dissipative devices also at the column base leads to an increase of displacements under seismic action and although the natural consequence is the increase of energy dissipated by the devices, to contain the floor drifts below the thresholds allowed by code it is necessary to calibrate the device cycles also as a function of this last parameter.
- Moreover it has to be noticed that the insertion of these rotational devices produces a benefit in terms of reduction of retrofitting costs and unused costs of the structure subsequent to a seismic event.
- For what concerns the construction costs of a new structure, the proposed device has a low cost, their operation is of mechanical type and their installation and maintenance do not request particular precautions.
- Quick comparison calculations have been performed to evaluate the reduction of the construction costs after the insertion of the dissipative devices. The comparison of the construction costs, relative to the columns only, has shown a savings of about 35%.

## REFERENCES

- [1] NTC2018, Aggiornamento delle "Norme tecniche per le costruzioni", D.M. 17 Gennaio 2018.
- [2] Comodini F., Mezzi M., Rossi L., 2013a. Impiego di dispositivi dissipativi per la riduzione della vulnerabilità di strutture prefabbricate. EDA - Esempi di Architettura, Rivista on-line ISSN 2035-7982.
- [3] Comodini F., Mezzi M., Rossi L., 2013b. Dissipative Devices for Vulnerability Reduction of Precast Buildings. International Conference on seismic design of Industrial Facilities. RWHT Aachen University, Germany.
- [4] Comodini F., Mezzi M., Rossi L., 2013c. Precast Industrial Buildings in Italy - Current Building Code and New Provisions Since the 2012, Earthquake International Conference on seismic design of Industrial Facilities. RWHT Aachen University Germany.

- [5] Pampanin S., 2003. Alternative design philosophies and seismic response of precast concrete buildings, FIB News, University of Canterbury, New Zealand.
- [6] Biondini F., Ferrara L. and Toniolo G., 2008. Capacity design criteria for connections in precast structures The 14th World Conference on Earthquake Engineering October 12-17, 2008, Beijing, China.
- [7] Comodini F., Mezzi M., 2012. Ricerca di sistemi di protezione appropriati per schemi prefabbricati ricorrenti, Eda-esempi di architettura on-line, ISSN 2035-7982.
- [8] Capozzi V., Magliulo G., Manfredi G. e Fabbrocino G., 2009. Caratterizzazione meccanica delle connessioni trave – pilastro spinottate nelle strutture prefabbricate, ANIDIS 2009 Bologna.
- [9] Comodini F., Mezzi M., 2013. Analisi comparative per l'ottimizzazione di dispositivi di protezione sismica a basso costo per strutture prefabbricate. Convegno ANIDIS, Padova, Italy.
- [10] Morgen B.G. and Kurama Y.C, 2004. A friction damper for post-tensioned precast concrete beam-to-column joints, 23th World Conference on Earthquake Engineering Vancouver, B.C., Canada August 1-6, 2004

## INVESTIGATION OF THE RESPONSE OF INTERFACES OF CFRP SHEET STRENGTHENING SCHEMES ENHANCED WITH TOUGHENED EPOXY ADHESIVE LAYERS APPLIED IN CORRODED CONCRETE SUBSTRATES.

Dimitra V Achillopoulou<sup>1,2</sup>

<sup>1</sup> University of Surrey, Guildford, UK  
[d.achillopoulou@surrey.ac.uk](mailto:d.achillopoulou@surrey.ac.uk)

<sup>2</sup> Democritus University of Thrace, Xanthi, Greece  
[dimiach@civil.duth.gr](mailto:dimiach@civil.duth.gr)

---

### Abstract:

*This paper studies the behavior of enhanced strengthening Carbon Fiber Reinforced Polymer (CFRP) strengthening schemes. The CFRP systems are bonded to concrete substrates using toughened adhesive layers to limit the failure propagation in the interface and its brittle nature. Due to the importance of the integrity of the substrate two different scenarios are examined experimentally and analytically: healthy concrete and with corrosion products leached by the corroded reinforcement. The modified shear behavior (stress, slip) of the interfaces between concrete and CFRPs was investigated with a double shear test configuration. The corrosion products leached on the external layers of the substrate affected the interface response of the strengthening scheme, resulting in lower rates of shear stresses corresponding to lower slip ratios. The analysis of the sliding and shear stress distribution along the interface has also been investigated locally by finite elements using a cohesive model (CM) to examine the propagation of failure at the interface length. Toughened adhesives limit the substrate's dislocations and shift the response of the interface from pure elastic to pseudo-ductile in distinct stages. The debonding mode (brittle or pseudo-ductile) depends heavily on the toughness of the adhesive and its tensile modulus, since the higher the modulus is, the more brittle the response becomes.*

**Keywords:** CFRPs, corrosion, strengthening schemes, adhesive layers, toughness, efficiency

---



## 1 INTRODUCTION

In the past few decades, there is a boost in the technological advancement of structural solutions with various strengthening schemes developed for reinforced concrete (RC) members. Bonded composites, that is Fiber Reinforced Polymers (FRPs) made of glass, carbon or other kinds of fibers is a commonly used type. It is commonly accepted that the efficiency of the retrofitting measures is mainly based on the connection of the concrete substrate and the composite [1]. As such, the integrity of the substrate and the connection layer of the strengthening measure are the key elements to a successful intervention.

The use of FRPs orientates towards enhancing the deformability of the strengthened structural members since this type of retrofitting measures are not used to increase the stiffness of a structural member. They are applied on an adhesive layer, which fulfils the requirements of international standards, e.g. EN 1504-4 [2]. Standard epoxy adhesives normally show high tensile modulus and result in brittle fracture of the matrix. The main goal of this research paper is the explanation of the interfacial response of FRP and concrete substrate. FRP measures investigated are enhanced using toughened adhesive layers, which have a lower stiffness matrix and permit higher fracture energy.

This research examines, experimentally and analytically with finite element models (FEM), the use of toughened epoxy adhesive layers as part of strengthening schemes for RC members and has a focus on the examination of the limitation of the substrate's failure propagation due to the use of enhanced retrofitting systems. The toughened adhesives are expected to absorb more energy before debonding, especially under dynamic loads [3], [4]. The interaction with the concrete substrate to the dislocations imposed is examined with double-lap shear tests in carbon FRP (CFRPs) applied to concrete prisms.

Finally, the effectiveness of the bond behavior of these layers is also dependent on the concrete substrate integrity. As structures are exposed to various and at times extreme environmental conditions, the corrosion effect is usually met and has a tremendous impact on the structural integrity of the existing structures. As such, strengthening such members is challenging. A commonly accepted practice in these cases is, first, to define the corrosion rate and then to substitute the concrete substrate with a new one. In cases that the corrosion rate is low, and the bond behavior of concrete is within acceptable limits, strengthening measures can be directly applied. This paper also examines the influence of the corrosion products on the interface response of CFRP measures applied with toughened adhesive layers.

## 2 EXPERIMENTAL INVESTIGATION

For the purposes of the study, an experimental campaign has been designed. The campaign has two phases: a) accelerated corrosion procedure and b) double lap testing. The wider experimental campaign includes three different commercialized FRP systems (fabrics, laminates, Near Surface Mounted bars-NSM) applied in a healthy and corroded concrete substrate using three different adhesive layers, two of which are toughened. In this paper, the specimens including FRP fabrics are presented.

### 2.1 Materials

Nine concrete blocks with dimensions 150x150x250mm were prepared according to [5], [6], [7] with 28-day compressive strength of 37.5MPa corresponding to a tensile strength of 3MPa. All blocks contained steel rebar ( $f_{sy}=500$  MPa) of 18mm diameter in the middle of the cross-section placed longitudinally to the concrete block. CFRP sheets (SikaWrap: density  $\rho=1.8$  kg/L, tensile strength  $\sigma_u=4900$  MPa, modulus of elasticity  $E_{0.05-0.25\%}=230$  GPa, tensile strain  $\varepsilon_{EAB}=1.7\%$ ) were bonded symmetrically on opposite sides of the concrete blocks at a bond

length of 200m. The fibre orientation was  $0^\circ$  along the longitudinal direction of concrete blocks. The systems were applied with a dry lay-up process and according to the technical specification of the manufacturer. The interfaces were treated properly to have a laitance contaminant-free, open-textured surface and were cleaned with air pressure to remove loose material, dust and rust. The two components' epoxy adhesives (Table 1) were mixed according to the manufacturer's recommended ratio and time (4:1 for Sikadur 330 and 100:74 for Sikadur 370). The composites are left to cure at ambient conditions ( $20^\circ\text{C}$ , 50% relative humidity-RH) for at least a week before testing.

type	density $\rho$ [kg/L]	tensile strength $\sigma_u$ [MPa]	E-modulus (0.05-0.25%) [GPa]	tensile strain $\varepsilon$ (EAB) [%]
Sikadur 330	~1.4	29	4000	1
Sikadur 370	~1.7	30	5000	2.5

Table 1: Mechanical properties of epoxy adhesive layers.

## 2.2 Accelerated corrosion

The concrete prisms were exposed to wet conditions in a tank. They were bathed in a 3.5-5% weight NaCl-water solution (Figure 1a), which covered one third of the cross-section size of the concrete blocks [8], [9]. A low ratio of corrosion of the steel rebar cross-section is created almost equal to 6% with a continuous power supply ( $\approx 1\text{mA}$ ) [9] wired in the steel rebars for about three weeks.

## 2.3 Experimental configuration

Various experimental setups of double lap tests exist in the international literature [10]. These configurations permit the direct examination of the shear stresses of the interface. This study adopts a modified double lap shear test (Figure 1b). The concrete block lays on hollow support that permits slip and is hanged from the gripped ends of the FRPs that are fixed to a rigid steel frame. This alteration of the classic setup with two concrete blocks limits the relative slips of the interfaces of the different blocks, eliminates slips at the gripped ends of the FRP and at the same time permits direct shear stress measurement. The tests were performed on a compression machine at a speed of 1mm/min at room temperature ( $20^\circ\text{C}$ ). The measurements of the deformation of the central part of the CFRP were recorded using a high accuracy laser sensor. Also, two Linear Displacement Transducers (LDVT) with a maximum capacity of 100mm, were used to measure the displacement of the upper level of the concrete block and the grips.



(a)



(b)

Figure 1: Experimental campaign: a) accelerated corrosion, b) double lap (DL) setup.

### 3 FINITE ELEMENT SIMULATION

Except for the experimental investigation, a numerical study was conducted in order to study locally the overloading, the response, initiation and propagation of failure of the interface. The debonding of FRP composites applied to the concrete substrate was simulated with a numerical model developed using the commercial software ANSYS. For the realistic representation and simulation of the failure modes of CFRP strengthened concrete substrates a bilinear cohesion zone model (CZM) fracture model was used and calibrated from the experimental results [11]. Concrete and CFRPS were treated as homogeneous isotropic linear-elastic materials and were connected through zero thickness interfaces. Concrete and composites were simulated using a 3d solid element, defined by eight nodes having three degrees of freedom at each node (translations in the nodal x, y, and z directions).

## 4 RESULTS

### 4.1 Experimental results

The results are presented in shear stress- shear deformation diagrams of the average curves for the two categories of specimens, healthy and corroded, with both adhesive layers. Table 2 contains the characteristic values of the experimental results and the average curves.

Specimens wrapped with fabrics (HI330\_1-3, Cr330\_1-3) of unidirectional carbon fibers applied with the epoxy adhesive layer 330 present a response in three distinct stages, shown in Figure 2a. The toughened epoxy layers limit the substrate's failure propagation, allow the fracture to happen in stages and absorb more energy before debonding.

In the first stage the fabric is tensed (Stage I: linear elastic) at a linear rate. The fibers' configuration of the sheets is unidirectional and in parallel to the loading direction. This prevents bridging the crack propagation. In the second stage, there is a progressive crack initiation of the epoxy layer leading to crack opening, followed by a non-linear elastic yielding branch up to the transition point (Stage II: non-linear elastic yielding). The transition point ( $\tau^{\text{trans}}$ ,  $\gamma^{\text{trans}}$ ) practically corresponds to the further propagation of the crack pattern from the resin to the substrate and the overall connection of the two materials. The third stage is characterized by major cracking both at the adhesive layer and the substrate. Plastic regions are created at the concrete, and especially at the initial debonding area at a distance of 5 cm from the loading end. At the ultimate point of this stage (Stage III: major cracking), the specimens exhibit debonding of the FRP ( $\tau^u$ ,  $\gamma^u$ ). The failure mode is mainly caused due to the spalling of concrete at the delamination propagation area after the 5 cm and no FRP rupture is met (Figure 2c).

Figure 2b also shows the effect of corroded steel rebars on the interface response. The green dashed line represents the average curve of specimens with corroded steel rebar with fabrics applied on the concrete substrate with epoxy adhesive layer 330, whereas the red solid line represents the average curve of the healthy specimens containing the same epoxy. There is a clear difference in the response in both cases. The interface of the corroded substrate (330\_corroded\_ave) containing corrosion products presents a 20% decrease in shear strength ( $\tau^u$ ) and 24% lower shear deformation ( $\gamma^u$ ) at the ultimate point (Table 2). Also, the transition point is shifted to lower values of deformations (52%) and strength (18%). The leached corrosion products laying on the sides of the concrete substrate and the minor strains due to the initiation of corrosion are practically mass disturbance creating regions of altered consistency and resistance. Also, even in such low percentages of corrosion, which corresponds to corrosion initiation and to allowable bond values of the substrate, the crack initiation in the concrete mass in

combination with the rust laying on the interface, makes the connection with the FRP strengthening scheme weaker and results in lower values of slip and shear strength.

A higher stiffness matrix corresponding to the specimens with sheets applied with epoxy adhesive layer 370 (Sikadur370) presents a different response (HI370\_1-3, Table 2). Figure 2b shows that the tougher the epoxy resin matrix is, the stages II and III coincide. This means that even though there is a distinct transition point in almost the same levels of shear deformations but in higher values of shear stresses, the crack pattern both in the substrate and in the adhesive layer propagates simultaneously up to the debonding point of the strengthening system. The intrinsic toughened adhesive layer 370 is designed for steel substrates and especially suitable for fatigue cracking applications [4]. The crack width in the cases of concrete substrates is bigger than fatigue cracking in steel substrates. In combination with the stiffness of the matrix, the response alters from pseudo-plastic (case of Sikadur 330) to brittle.

#### 4.2 Finite element results

The finite element simulations' results were calibrated with the corresponding tests. Figure 3a shows the total stresses concentrated at the interface area between the concrete substrate and the FRP sheet. The stresses present a similar value in both cases, that is healthy and corroded substrates. Both cases, have a concentration of stresses near the loading end, presenting similar failure modes. Figure 2c show the differences of the failures and agree with the plastification mechanism of concrete and the sliding distance of the interface, of the FEM simulations' results presented in Figure 3a&b. It is also remarkable that the active length of the interface, meaning the length which concentrates the highest ratios of stresses, is 5% lower in the case of the corroded specimen.

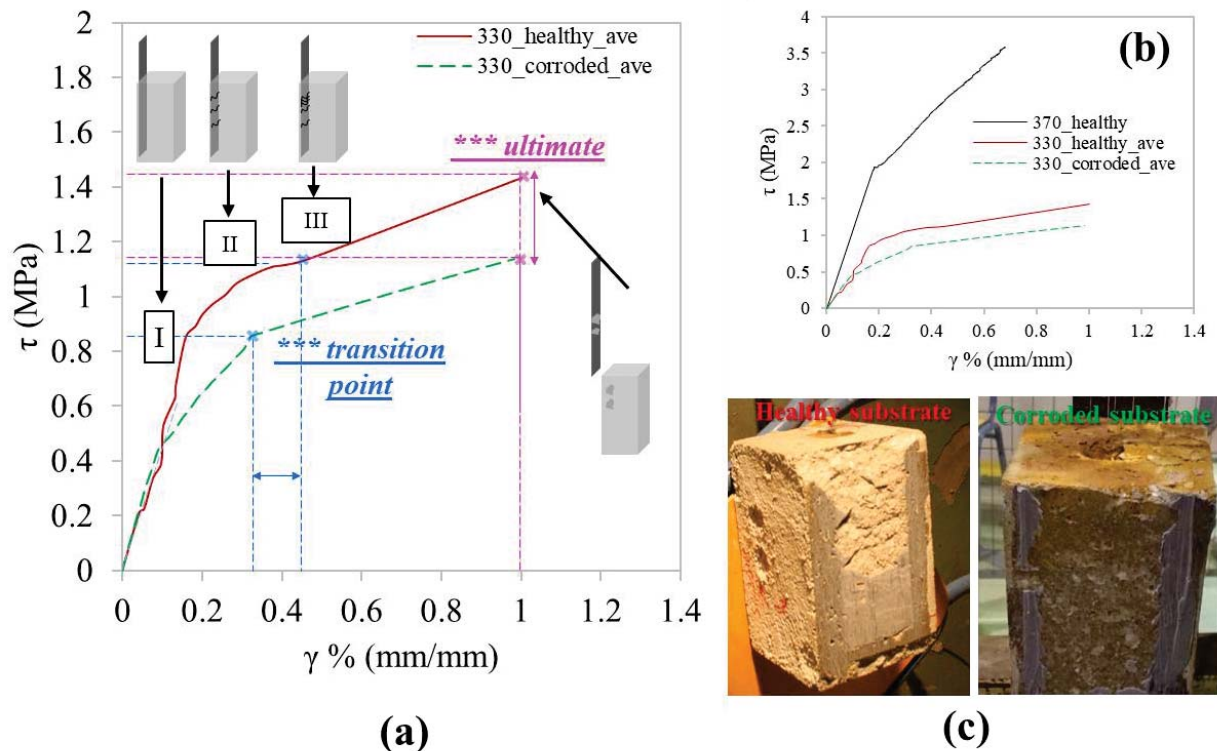


Figure 2: Experimental results of the DL tests: a), b) shear stress vs shear deformation curve, c) failure mode.



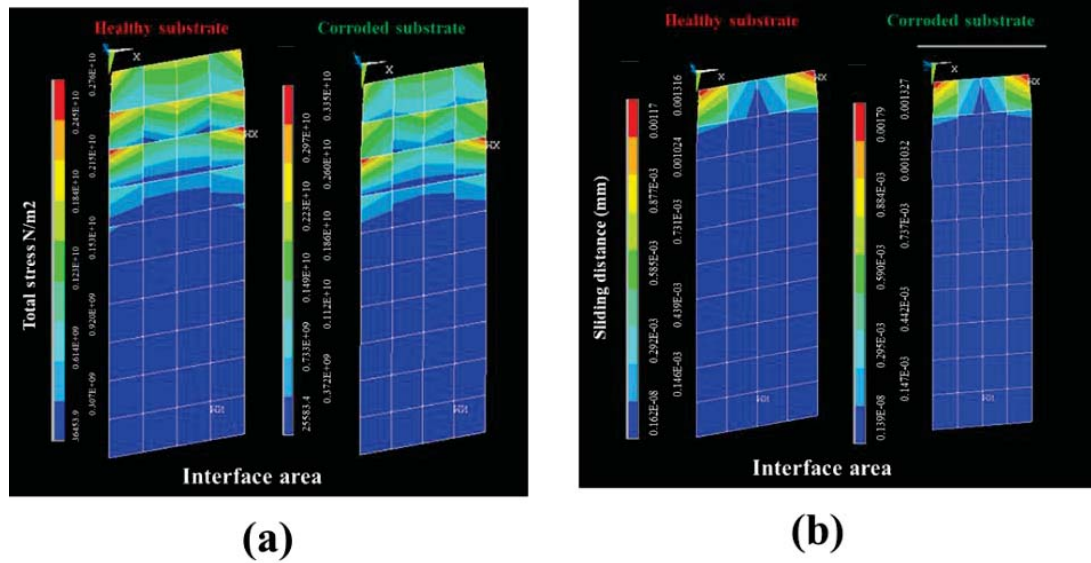


Figure 3: Contour plots of the interface a) total stresses, b) sliding distance.

healthy substrate					corroded products					abs error (healthy-corroded)			
	$\tau^{\text{trans}}$	$\tau^{\text{u}}$	$\gamma^{\text{trans}}$	$\gamma^{\text{u}}$		$\tau^{\text{trans}}$	$\tau^{\text{u}}$	$\gamma^{\text{trans}}$	$\gamma^{\text{u}}$	$\tau^{\text{trans}}$	$\tau^{\text{u}}$	$\gamma^{\text{trans}}$	$\gamma^{\text{u}}$
	(MPa)	(MPa)	(%)	(%)		(MPa)	(MPa)	(%)	(%)	(MPa)	(MPa)	(%)	(%)
HI330_1	1.25	1.48	0.72	1.33	Cr330_1	0.94	1.11	0.47	1.73	25%	25%	35%	30%
HI330_2	1.28	1.38	0.57	1.46	Cr330_2	0.99	1.20	0.32	0.60	23%	13%	44%	59%
HI330_3	0.82	1.37	0.60	0.91	Cr330_3	0.83	1.09	0.12	0.47	1%	20%	80%	48%
average 330	1.12	1.41	0.63	1.23	average 330	0.92	1.13	0.30	0.93	18%	20%	52%	24%
HI370_1	1.97	3.58	0.2	0.67									
HI370_2	1.80	3.57	0.12	0.63									
HI370_3	1.94	3.56	0.20	0.65									
average 370	1.90	3.57	0.18	0.65									
abs error 370-330	41%	61%	263%	90%									

Table 2: Experimental results.

## 5 CONCLUSIONS

- Toughened adhesive layers shift the interface response in comparison with the standard epoxy commonly used, from brittle to pseudo-ductile in distinct stages. The more tough the adhesive layer is, the shorter are the stages before the failure of the wrapped CFRPs.
- The distinct stages of the response of interfaces denote a progressive failure and correspond to the crack propagating stages up to failure.
- The corrosion products affect the interface response. They provoke a decrease of approximately 20% of the ultimate shear strength and corresponding shear deformation, whereas the transition point is met in almost half the shear deformation.
- The length of the CFRP which is overloaded and hence activated, is almost 40% of the total length, whereas, in the case of leached corrosion at the interface, the active length is 5% lower. The majority of stresses are concentrated at a distance of 5 cm of the loading end provoking spalling of the concrete's substrate.

## ACKNOWLEDGEMENTS

This study has received funding from the European Union H2020-Marie Skłodowska-Curie Research Grants Scheme MSCA-IF-2018 (grant agreement no 845549: BRIFACE-Novel assessment of bridge retrofitting measures through Interface Efficiency Indices (InterFeis) using a Guided Wave-based monitoring method).

The authors would like to thank Sika AG, one of the industrial partners of the project, for their contribution to the realization of the experimental program.

Special thanks to the Democritus University of Thrace and the laboratory of Reinforced Concrete and Seismic Design of Structures for collaborating on the experimental campaign.

## REFERENCES

- [1] Jia-Wei Shi, Wen-Hai Cao, Zhi-Shen Wu, Effect of adhesive properties on the bond behaviour of externally bonded FRP-to-concrete joints. *Composites Part B: Engineering*, **177**, 2019.
- [2] EN1504-4:2004, Products and systems for the protection and repair of concrete structures - Definitions, requirements, quality control and evaluation of conformity - Part 4: Structural bonding, European Committee for Standardization.
- [3] T. L. Attard, Toughened carbon-fiber reinforced epoxy via isophorone diisocyanate amine surface modification. *Polymer*, **191**, 122268, 2020.
- [4] Y. Kasper, M. Albiez, T. Ummenhofer, C. Mayer, T. Meier, F. Choffat, Y. Ciupack, H. Pasternak, Application of toughened epoxy-adhesives for strengthening of fatigue-damaged steel structures, *Construction and Building Materials*, Volume **275**, 2021.
- [5] ACI Committee 211, Standard practice for selecting proportions for normal, heavy-weight, and mass concrete, *ACI 211.1-91*, 1991.
- [6] N. Su, K. C. Hsu & H. W. Chai, A simple mix design method for self-compacting concrete, *Cement and concrete research*, **31**(12), 1799-1807, 2001.
- [7] EN 1008, Mixing Water for Concrete – Specification for Sampling, Testing and Assessing the Suitability of Water, Including Water Recovered from Processes in the Concrete Industry, as Mixing Water for Concrete, Brussels: CEN, *European Committee for Standardization*, 1995.
- [8] G. P. van Zijl & S. C. Paul, A novel link of the time scale in accelerated chloride-induced corrosion test in reinforced SHCC, *Construction and Building Materials*, **167**, 15-19, 2018.
- [9] C. Batuwitige, S. Fawzia, D. Thambiratnam, & R. Al-Mahaidi, Durability of CFRP strengthened steel plate double-strap joints in accelerated corrosion environments. *Composite Structures*, **160**, 1287-1298, 2017.
- [10] F. M. Mukhtar & R. M. Faysal, A review of test methods for studying the FRP-concrete interfacial bond behavior, *Construction and Building Materials*, **169**, 877-887, 2018.
- [11] C. Carloni, T. D'Antino, L. H. Sneed & C. Pellegrino, Three-dimensional numerical modeling of single-lap direct shear tests of FRCM-concrete joints using a cohesive damaged contact approach. *Journal of Composites for Construction*, **22**(1), 04017048, 2018.



## SEISMIC RETROFITTING OF SINGLE-STORY RC PRECAST BUILDINGS THROUGH A NOVEL METALLIC HYSTERETIC DEVICE

Chiara Di Salvatore<sup>1</sup>, Gennaro Magliulo<sup>2,3</sup>, Maria G. Castellano<sup>4</sup>, and Nicola Caterino<sup>1</sup>

<sup>1</sup> Department of Engineering, University of Naples Parthenope  
Centro Direzionale, isola C4, 80143 Naples, Italy  
[chiara.disalvatore@uniparthenope.it](mailto:chiara.disalvatore@uniparthenope.it)  
[nicola.caterino@uniparthenope.it](mailto:nicola.caterino@uniparthenope.it)

<sup>2</sup> Department of Structures for Engineering and Architecture, University of Naples Federico II  
via Claudio 21, 80125 Naples, Italy  
[gmagliul@unina.it](mailto:gmagliul@unina.it)

<sup>3</sup> Construction Technologies Institute URT Naples, National Research Council of Italy  
via Claudio 21, 80125 Naples, Italy  
[gmagliul@unina.it](mailto:gmagliul@unina.it)

<sup>4</sup> FIP MEC S.r.l.  
via Scapacchiò 41, 35030 Selvazzano Dentro, Padova, Italy  
[gabriella.castellano@fipmec.it](mailto:gabriella.castellano@fipmec.it)

---

### Abstract

*Structural joints are generally the most critical parts of RC precast structures in terms of seismic assessment, especially in existing buildings, where friction connections can be often found. This issue, widely highlighted in the aftermath of recent earthquakes in Europe, have brought the scientific community to develop retrofitting techniques improving the seismic performance of the connections. The presented work deals with a dissipative hysteretic device, made of two steel rods, arranged as a three-hinged arch, and provided with moon sickle shaped items. It is applied at the beam-to-column connection level and it is intended for both restraining the relative displacements between the joined structural elements and dissipating energy coming from the earthquake. In the presented study, the innovative device is described in detail along with its numerical model, as applied to an existing single-story RC precast structure with beam-to-column friction connections. The results of preliminary numerical analysis showing its efficiency are also reported.*

**Keywords:** Precast RC Structures, Friction Connections, Retrofitting, Nonlinear Analyses, Innovative Device.

---

## 1 INTRODUCTION

Premature failure of structural joints is the main issue detected for the existing RC precast buildings during earthquakes. As demonstrated by recent seismic events in all Europe [1-7], this is caused by either the absence of a mechanical device, i.e., horizontal load transfer relying only on friction, or the inappropriate connection design, both resulting in inadequate seismic performance. Local collapse of structural joints often involves disastrous structural breakdown, due to the loads transfer inability and the loss of support phenomena. For this reason, together with retrofitting techniques at the structure and the element levels, some solutions aiming at improving connection seismic response are developed in last years. The simplest and most obvious intervention consists in the introduction of devices able to reproduce a hinged restrain at the joints level, thus reducing the deformation demand. However, a significant shortcoming for this solution is detected. Indeed, the stresses transmitted to the base of the columns are significantly higher than the ones recorded for the un-retrofitted structure, leading to a greater involvement of plastic hinges and, hence, a higher level of structural damage. Therefore, the state-of-the-art devices are able to both strengthen structural joints, limiting the relative displacement between the connected elements, and dissipate a portion of the seismic energy coming from the ground motion, avoiding high damage. Passive energy dissipation devices represent the easiest and most economical solution in the world of structural control systems, since they do not require any external energy power or electronic hardware and their functioning is simply activated by structural displacements. Martinelli and Mulas [8] investigated the potential application of a connection retrofitting device, already used for cast in situ reinforced concrete and steel buildings, to an RC precast industrial structure. The proposed system is able to both restrain the relative displacement between principal beams and columns and dissipate energy thanks to the friction developed during the rotation of an annular brass plate, inserted between steel components. Two UPN200 channel sections are connected to the beam and the column end respectively, creating the dissipative hinge at their intersection. The provided configuration allows a quick re-centering after the seismic event. Nonlinear dynamic analyses on a structural model are performed, comparing the seismic response of the bare building with the one equipped with rotational friction devices. Outcomes from this assessment show the good behavior of the analyzed retrofitting technique, able to enhance the damping of the structure reducing significantly the hysteretic energy ascribable to plastic hinges at the columns base, despite a moderate increase of the overall stiffness and, thus, of the seismic base shear. Pollini et al. 2018 [9] proposed an innovative connection retrofitting system, combining the deformability of steel with the high strength of composite materials. Carbon-wrapped steel tubes can be connected to the structural elements (beams and columns) thanks to a threaded bar passing through circular holes on the tube basis. Each tube works in compression, dissipating seismic input energy and, thus, limiting the transmission of the stresses to the base; so, for each connection two devices have to be provided. Quasi-static monotonic and cyclic experimental tests were performed on the proposed system in order to assess the energy dissipation capacity, recording very stable hysteretic cycles. A numerical validation was also performed, even if considering a simple structural model, demonstrating the expected beneficial impact of the proposed device on the seismic structural response. Soydan et al. [10] dealt with a new lead extrusion damper (LED), usable in retrofitting interventions for precast structures joints. It is constituted by a cylinder full of lead, a shaft and a cap. Lead is a relatively flexible metallic material, able to dissipate a considerable amount of energy when it is forced to deform. In order to dissipate seismic energy, the cap and the shaft have to be connected to different structural elements (i.e., columns and beams), where relative displacements are expected. A numerical model of an existing RC pre-

cast structure is developed in SeismoStruct [11] and dynamic analyses are performed with ten historical ground motions. The outcomes from the seismic assessment of the bare structure are then compared with the response of the same structure retrofitted with lead extrusion dampers. Even if the recorded acceleration increases for the retrofitted structure, due to the increase in lateral stiffness, shear resistance in the columns is not exceeded and benefits from the application of the LEDs are clear: beam-column relative displacements are strongly reduced, as well as the bending moment at the base. In this way, the plasticization of the structure is limited and the damage level results to be lower.

The present work shows an innovative hysteretic device for the retrofitting of RC precast structural joints. The efficiency of the system is assessed evaluating the seismic response of an existing RC precast structure with beam-to-column friction connections, before and after the application of the hysteretic device. To reach this goal seven nonlinear dynamic analyses are performed, together with an energy balance estimation, demonstrating the ability of the proposed system in both preventing the relative displacements at the connection level and reducing the rotational demand at the base.

## 2 DESCRIPTION OF THE RETROFITTING SYSTEM

The proposed device represents an upgrading of an already patented system for the retrofitting of structural elements connections in precast buildings [12, 13], which consists of two hinged steel profiles, linked through horizontal dowels to the connected elements, i.e., beams and columns. A 2 mm rubber layer surrounds the dowels, since it is demonstrated [13] that this expedient is able to reduce the concrete cracking at the rods connection location, thus improving the device functioning. This arrangement allows turning the horizontal shear forces acting on the connection in axial forces in the rods, thanks to a three hinged-arch behavior. Therefore, it is able to significantly limit, or even prevent, relative displacement between beams and columns. It is possible to take advantage of the device in both existing buildings, often provided with friction connections, and current code-conforming buildings, as a valid alternative to the conventional dowel connection. In the herein presented version (Figure 1), the hysteretic properties are given by some special gadgets, moon sickle shaped, mounted on each profile, which yield under the axial load in the rods and dissipate seismic energy undergoing plastic deformations.



Figure 1: Metallic hysteretic device configuration

The device acts like a structural fuse, in which the seismic damage is concentrated, decreasing the ductility demand at the plastic hinges location. At the end of the ground motion striking the building, these gadgets can be easily replaced, without interrupting the productive activi-

ties. The force-displacement backbone (Figure 2) can be represented as an elastic-hardening curve, characterized by a yielding point ( $d_1, F_1$ ) and a post yielding stiffness, defined thanks to the second point coordinates ( $d_2, F_2$ ). In Table 1, standard mechanical properties for the rods are reported, provided by the manufacturing company. The proposed types underwent qualification tests according to the European code UNI EN 15129 [14], governing the seismic devices design. In the present study, rod type is chosen among the presented ones considering the shear associated to the yielding moment at the columns base, and applying a capacity design safety factor, so as to allow the plasticization of steel gadgets before the yielding of the plastic hinges. However, this is a preliminary study, conducted only to understand how the device works under seismic actions; a proper calibration should be performed, in order to maximize its performance.

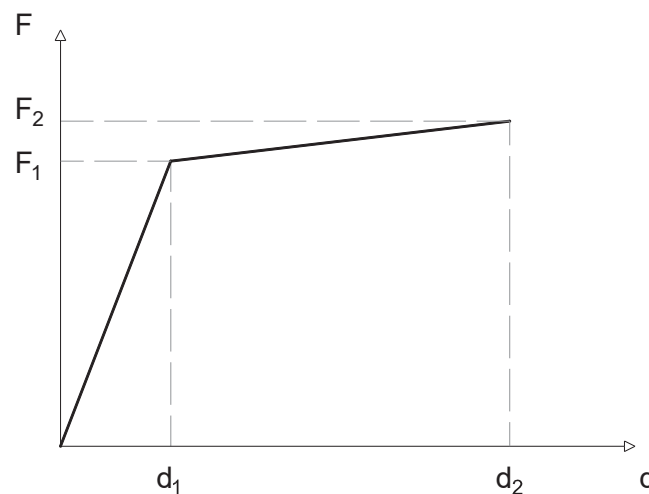


Figure 2: Monotonic force-displacement response

Type	$d_1$ [mm]	$F_1$ [kN]	$d_2$ [mm]	$F_2$ [kN]
1	3.9	34.5	20.0	40.0
2	3.7	43.5	20.0	50.0
3	3.0	52.0	15.0	60.0
4	2.8	75.0	15.0	86.0

Table 1: Rods standard mechanical properties

### 3 CASE STUDY

An existing single-story RC precast structure, dated back to the Seventies, is considered in order to assess the effect of the proposed retrofitting device. The construction is configured with a single bay, 15 m long, in x direction and four bays, each of them 6 m long, in z direction. Columns' total height is equal to 9 m; furthermore, since this kind of buildings are usually intended for industrial activities, design procedure and modeling take into account the presence of a crane and the relative brackets supporting the crane, placed at 7.5 m from the columns' base. Structural layout is presented in Figure 3. A design simulating the elements dimensioning process is performed taking into account codes and regulations of the Seventies, i.e. DM 3/05/1974 [15] and CNR 10012/1967 [16]. The building is located in Catania, an Italian city with a high seismic hazard; nevertheless, at the time of construction, it was not considered as a seismic-prone area, so the design procedure ignored seismic actions. Roof

covering consists of prestressed double T elements, with equivalent section of  $0.40 \times 1.60$  m, placed one near the other on the top of the principal beams and linked together by a 5 cm thick concrete slab. The slope of the covering is assumed to be 10%. The presence of the topping slab involves a rigid diaphragm behavior, i.e. a rigid behavior of the floor in its own plane.

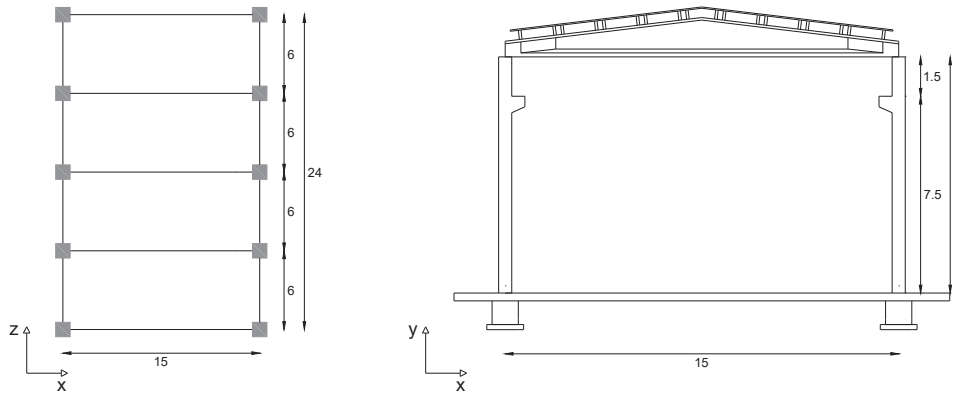


Figure 3: Structural configuration: plan view and transversal view

Roof elements are jointed to the principal beams through steel plates and bolts, ensuring in this way a hinge constrain. Principal beams in transversal direction (x direction) present a variable height and a variable section (T-shaped at the extremities and, after a tapering zone, I-shaped in the middle). However, an equivalent rectangular area ( $0.17 \times 1.14$  m) is assumed, since beams section shape does not affect the results. In z direction, instead, secondary beams are provided in order to both collect rainwater and connect structural frames in longitudinal direction. They usually have a U section, but an equivalent rectangular one is considered, with dimensions  $30 \times 50$  cm. Unlike roof elements and beams, which are dimensioned only for vertical loads (permanent and variable actions), columns are also designed for horizontal (wind) forces acting on the structure. They consist in precast monolithic elements with a square section, whose dimensions and reinforcement are shown in Figure 4a. The presence of socket foundations allows considering the columns fixed at their base. Principal beams are simply supported on columns' head through a neoprene pad, with dimensions  $0.25 \times 0.25 \times 0.01$  meters, generating a friction connection; secondary beams are hinged to the columns' head through steel angles and bolts. Indeed, according to the design practice of the time, the higher value of axial load provided by principal beams on the top of the columns was deemed sufficient to ensure a proper strength to the friction connection. From this assumption follows the most important weakness detected for existing RC precast structures.

#### 4 NONLINEAR MODEL

A nonlinear numerical model is created in OpenSees [17] in order to perform a seismic assessment of the un-retrofitted and the retrofitted structure. Columns and beams are represented as elastic elements through their longitudinal axis; the eccentricities generated at the connection level, typical of precast structures, are modelled thanks to rigid brackets. Roof elements are taken into account only as vertical load and mass, but they are not explicitly modelled since they do not affect the seismic response. Cladding panels are not modelled, only their mass contribution is considered. Even if the cladding affects the seismic behavior of the building, making it stiffer, it should be noted that, in existing structures, panels connections were not provided with earthquake resistance, so panels collapse at very low seismic intensi-

ties, i.e., in the early stages of a ground motion, leaving the structure bare. Therefore, the assumption of neglecting cladding panels in the modelling is reasonable. A lumped plasticity approach is followed, concentrating the nonlinear behaviour at the columns base. Moment-rotation curves are detected performing a fiber analysis of the columns cross section and applying Fardis formulations [18] for the yielding and the ultimate chord rotations. Different backbones are obtained for the two horizontal directions and for corner and lateral columns. These differences are due to the different longitudinal reinforcement provided in the two orthogonal sides of the columns cross-section and to the different value of axial loads on the top of the columns. Figure 4b illustrates the moment-rotation curves. Each column and the corresponding plastic hinge constitute a system working in series, so their stiffness are calibrated in order to return the overall nonlinear stiffness.

Particular attention is paid to the friction connection modelling, since the great impact of its seismic response on the structural global collapse condition. A zero-length element is inserted at the principal beam-to-column intersection, and proper materials are assigned for each degree of freedom. The horizontal translations in x and in z directions (Figure 3) are characterized by a frictional behavior, with an elastic perfectly plastic response; the elastic branch is defined by the lateral stiffness of the neoprene pad, whilst the flat branch is attained in correspondence of the friction force. In the vertical direction an elastic material, identified by the axial stiffness of the pad, is considered as acting only in compression, given that the pad does not react in tension. Rotation around the z axis (in the xy plan) is left free, whereas rotations around x and y axes are constrained.

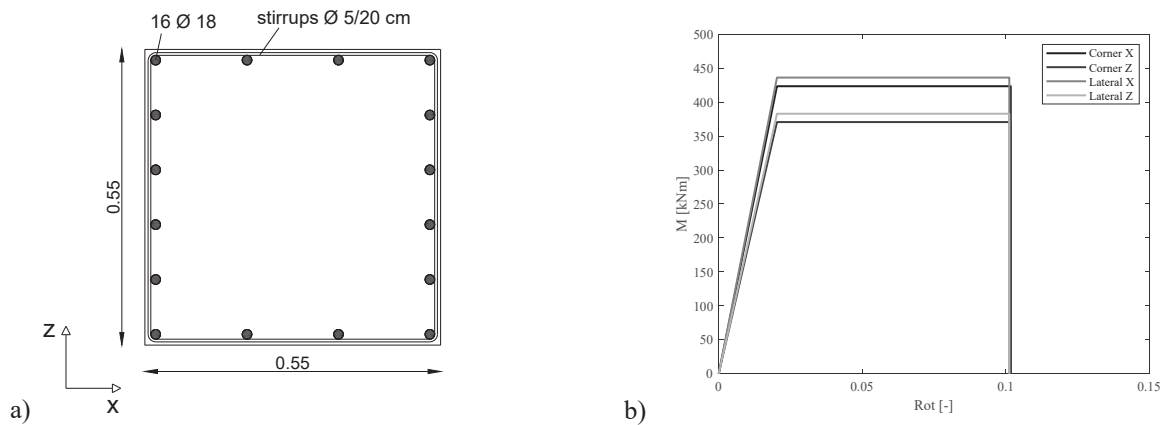


Figure 4: a) Column cross section and b) Moment-rotation backbones at the column plastic hinge

Finally, steel profiles constituting the retrofitting device are modelled thanks to truss elements, i.e., elements absorbing only axial loads. To define the constitutive law, the assigned material is a series of an elastic perfectly plastic gap material, in order to simulate the rubber layer around the dowels, and a hardening material, considering a kinematic hardening response. Parameters to be assigned are calibrated in order to reproduce a Type 1 rod response, according to the design procedure illustrated in Section 2. Following the recommendations provided by the manufacturer company, the device configuration is chosen so as to maintain a difference in the rods length equal to 0.4 m. Rigid brackets are inserted in the model in order to connect the rods to the beam and the column, representing the distance between the longitudinal axis of the structural elements and the connection provided by the device. Retrofitting is performed only in the transverse (x) direction. Figure 5 shows the schematic representation of a typical frame of the retrofitted structure in the x direction.



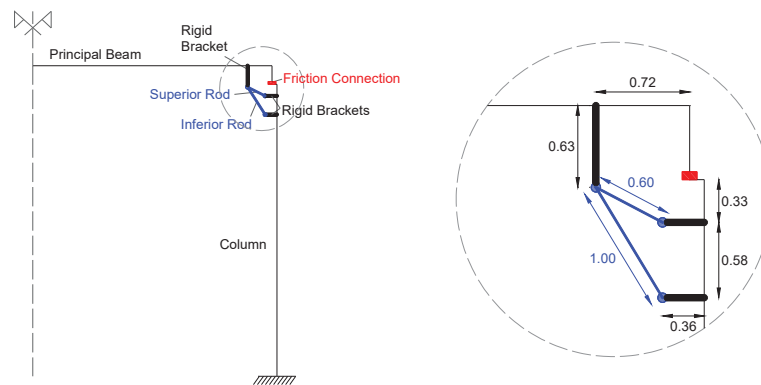


Figure 5: Retrofitted frame layout

## 5 ANALYSES OUTCOMES

In order to demonstrate the functioning of the proposed system, seven ground motions (GM) are selected and applied, first, to the un-retrofitted structure and, then, to the retrofitted one. For the records selection, Conditional Spectrum Method [19, 20] is implemented, according to [21]. All the spectrum coordinates are conditioned to the one corresponding to the fundamental structural period. A soil type C is considered to determine the elastic spectrum. The chosen intensity level refers to a return period,  $T_R$ , equal to 2500 years, i.e., a 2% in 50-years exceedance rate. Seismic records, taken from database of the Italian accelerometric archive (Itaca) [22] and from the database NGwest [23], are properly scaled in order to match the obtained target spectrum. As concern the un-retrofitted structure, outcomes show that the friction connections activate in the very first stages of the ground motions and significant relative displacement between principal beams and columns are recorded. Since, as expected, the sliding begins before the activation of the plastic hinges at the columns base, the structure shows an elastic response until the collapse, due to the loss of support of the beams. Applying the retrofitting device to the structure at each connection location (Figure 5), the first detected benefit is the strong reduction in beam-to-column relative displacements. In Figure 6, the recorded deformations of a friction connection element, corresponding to the relative displacements of the jointed members, is reported in both the case of the un-retrofitted and the retrofitted structure for a single ground motion.

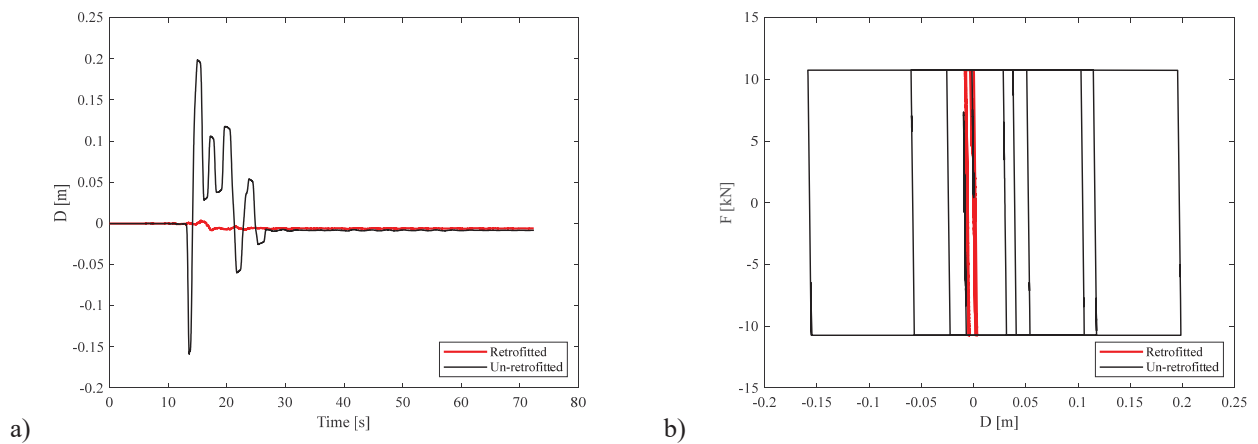


Figure 6: a) Comparison between the relative beam-to-column displacement for the un-retrofitted and the retrofitted structure for GM1, b) comparison between the force-displacement response for the un-retrofitted and the retrofitted structure for GM1

For the same connection and the same seismic input, force-displacement response of the retrofitting device, i.e. of the pair of rods, is reported in Figure 7, confirming the correspondence to the assigned behavior.

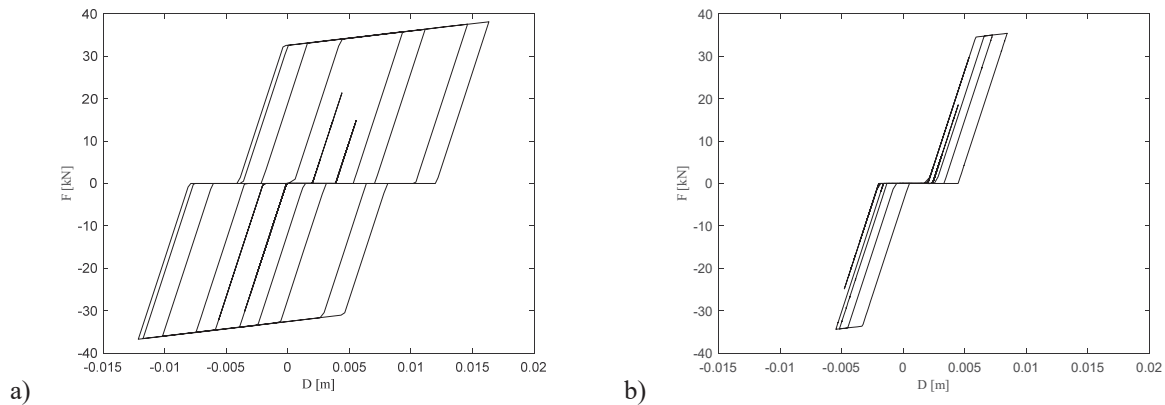


Figure 7: Force-displacement response of a pair of rods, in particular for a) an inferior profile and for b) a superior profile.

The inferior rod shows always a higher engagement, with larger and more numerous hysteretic cycles. It is worth to remember that each rod is provided with a 2 mm gap, simulating the rubber layer around the dowel: it is partially visible only in the superior rod response, represented by the flat branch at force equal to zero. In order to highlight the beneficial effect of the dissipative device on the hysteretic seismic response of the structure, the same set of ground motions is applied to the same structure retrofitted with an identical device but indefinitely elastic. For both the retrofitted systems, the elastic and the hysteretic one, the limitation of the displacements at the connection level is achieved, but in the first case the only source of hysteretic dissipation is provided by the plastic hinges at the columns base. From the comparison between these two solutions, it is possible to understand how much the proposed hysteretic device is able to reduce the plastic rotational demand at the base and, therefore, the structural damage. An energy balance analysis is performed on both the structures, allowing a rapid and synthetic evaluation. The input energy, transferred to the structure by the ground motion, is absorbed and dissipated thanks to energy contributions related to the structural response. In particular: kinetic energy, that is originated by the motion of the building; elastic strain energy, which depends on the level of strain recorded for the structural elements; hysteretic energy, given by the moment-rotation cycles of the plastic hinges at the base, i.e., by the nonlinear response of the structure; frictional energy, provided by the force-displacement cycles generated by the friction connection; viscous damping energy representing the contribution of the damping of the structure (Rayleigh damping is considered). Finally, there is the contribution of the retrofitting devices, which is recoverable for the elastic system and unrecoverable for the hysteretic device, thanks to its dissipative properties. Figure 8 shows the outcomes of the energy balance analysis for both the structures for a single ground motion.

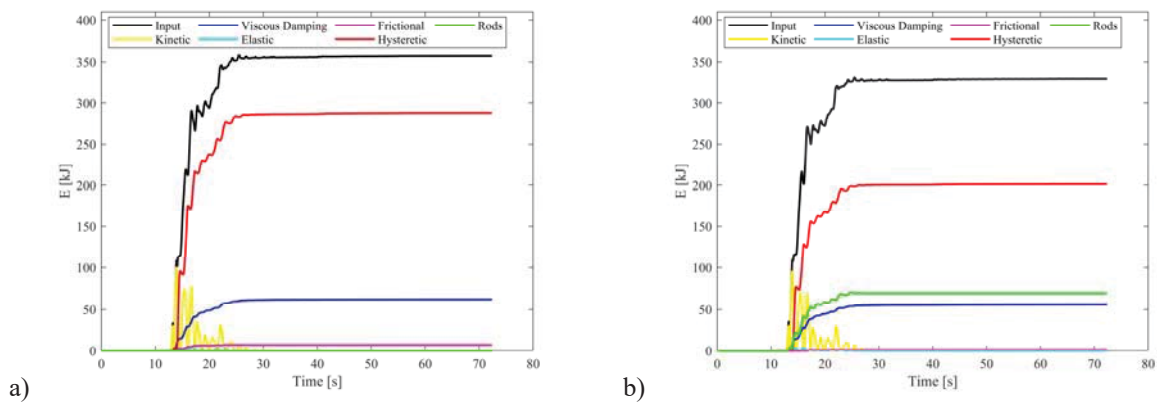


Figure 8: Energy balance for GM1 for a) the structure with an elastic retrofitting device and b) a structure with a hysteretic retrofitting device.

The beneficial effect of the hysteretic device in reducing the dissipated energy of the plastic hinges at the base is evident. The other energetic contributions seem not to be affected by the dissipative behavior of the device. This trend is observed for each of the considered seven ground motions, even if not to the same extent. In Figure 9 the plastic hinges hysteretic energy for both the systems is charted, expressed as a percentage of the total input energy. For some earthquakes, the proposed device slightly reduces the plastic involvement of the structure, and, in any case, it is not able to prevent the yielding of the hinges at the columns base. As already observed, a proper calibration is needed for the hysteretic device and a sensitivity analysis on the parameters conditioning its response should be performed.

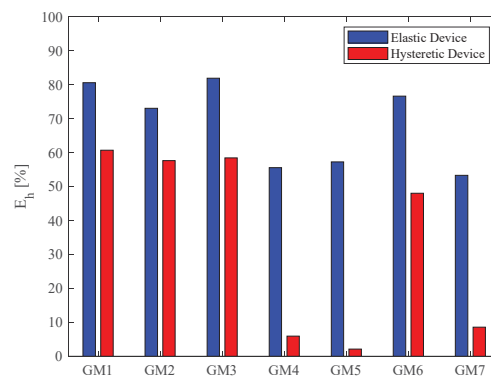


Figure 9: Plastic hinges hysteretic energy in the case of an elastic retrofitting device and a hysteretic retrofitting device for all the ground motions.

## 6 CONCLUSIONS

This paper presents a novel metallic hysteretic device, intended for the seismic retrofitting of beam-to-column connections in RC precast buildings. The proposed system, applied at the joint level, is designed to both restrain the relative displacement between the connected elements, working as a three-hinged arch, and dissipate the ground motion input energy, thanks to special gadgets with hysteretic response. A nonlinear model of a RC precast industrial structure with friction connections is implemented in OpenSees [17], and seven nonlinear dynamic analyses are performed, highlighting the weakness of the structural joints. Indeed, the detected global collapse is due to the beams loss of support, when the structure is still in the

elastic field. Then, hysteretic devices are inserted in the structural model, at the connection levels along the transversal direction, and the same seismic inputs are applied on the retrofitted building. The comparison between the response of the un-retrofitted and the retrofitted structure leads to the following findings.

- i) The proposed device is able to strongly limit the relative displacements between beams and columns, avoiding structural collapse due to loss of support phenomena.
- ii) The seismic demand at the base increases when the device is inserted, resulting in the yielding of the plastic hinges. However, it is demonstrated that the recorded level of damage is lower than the one corresponding to the application of a traditional device, with an elastic behavior.
- iii) The hysteretic properties showed by the metallic device are not sufficient to reduce significantly the plastic deformations at the columns base for all the applied ground motions; indeed, in all the cases, yielding is never prevented. A proper calibration is needed to optimize the retrofitting performance.

## REFERENCES

- [1] Faggiano, B., et al., *Post-event analysis of industrial structures behavior during L'Aquila earthquake*. Progettazione sismica 2009(English Special Edition): p. 203-208.
- [2] Magliulo, G., et al., *The Emilia earthquake: seismic performance of precast reinforced concrete buildings*. Earthquake Spectra, 2014. **30**(2): p. 891-912.
- [3] Deyanova, M., S. Pampanin, and R. Nascimbene. *Assessment of single-storey precast concrete industrial buildings with hinged beam-column connections with and without dowels*. in *Proceedings of the Second European Conference on Earthquake Engineering and Seismology*. 2014.
- [4] Belleri, A., et al., *Seismic performance of precast industrial facilities following major earthquakes in the Italian territory*. Journal of Performance of Constructed Facilities, 2015. **29**(5).
- [5] Liberatore, L., et al., *Failure of industrial structures induced by the Emilia (Italy) 2012 earthquakes*. Engineering Failure Analysis, 2013. **34**: p. 629-647.
- [6] Ozden, S., et al., *Performance of precast concrete structures in October 2011 Van earthquake, Turkey*. Magazine of Concrete Research, 2014. **66**(11): p. 543-552.
- [7] Sezen, H., et al., *Structural Engineering Reconnaissance of the August 17, 1999, Kocaeli (Izmit), Turkey Earthquake*. 2000.
- [8] Martinelli, P. and M.G. Mulas, *An innovative passive control technique for industrial precast frames*. Engineering Structures, 2010. **32**(4): p. 1123-1132.
- [9] Pollini, A.V., N. Buratti, and C. Mazzotti, *Experimental and numerical behaviour of dissipative devices based on carbon - wrapped steel tubes for the retrofitting of existing precast RC structures*. Earthquake Engineering & Structural Dynamics, 2018. **47**(5): p. 1270-1290.
- [10] Soydan, C., E. Yüksel, and E. İrtem, *Seismic performance improvement of single-storey precast reinforced concrete industrial buildings in use*. Soil Dynamics and Earthquake Engineering, 2020. **135**: p. 106167.
- [11] SeismoStruct, *A computer program for static and dynamic nonlinear analysis of framed structures*. (<http://www.seismosoft.com>).
- [12] Cimmino, M., et al., *Seismic retrofit strategies for friction beam-to-column connections of industrial RC precast structures*. Seismic retrofit strategies for friction beam-to-column connections of industrial RC precast structures, 2017: p. 23-34.

- [13] Magliulo, G., et al., *Cyclic shear tests on RC precast beam-to-column connections retrofitted with a three-hinged steel device*. Bulletin of Earthquake Engineering, 2017. **15**(9): p. 3797-3817.
- [14] EN15129, *Anti-seismic device*. Brussels, Belgium. European Committee for Standardization, 2018.
- [15] Legge n. 64, *Provvedimenti per le costruzioni con particolari prescrizioni per le zone sismiche (in Italian)*. 1974, G.U. n. 76 21/3/1974.
- [16] CNR-UNI 10012, *Ipotesi di carico sulle costruzioni (in Italian)*. 1967: Istruzioni del Consiglio Nazionale delle Ricerche e dell'Ente Nazionale Italiano di Unificazioni.
- [17] PEER, C., *OpenSees*. 2007, University of California: Berkeley.
- [18] Fardis, M.N. and D. Biskinis, *Deformation capacity of RC members, as controlled by flexure or shear*, Performance-based engineering for earthquake resistant reinforced concrete structures, Kabeyasawa T, Editor. 2003: University of Tokyo.
- [19] Lin, T., C.B. Haselton, and J.W. Baker, *Conditional spectrum - based ground motion selection. Part I: hazard consistency for risk - based assessments*. Earthquake engineering & structural dynamics, 2013. **42**(12): p. 1847-1865.
- [20] Lin, T., C.B. Haselton, and J.W. Baker, *Conditional spectrum - based ground motion selection. Part II: intensity - based assessments and evaluation of alternative target spectra*. Earthquake Engineering & Structural Dynamics, 2013. **42**(12): p. 1867-1884.
- [21] Iervolino, I., A. Spillatura, and P. Bazzurro, *RINTC Project - Assessing the (implicit) seismic risk of code-conforming structures in Italy* COMPDYN 2017 - 6th ECCOMAS Thematic Conference on Computational Methods in Structural Dynamics and Earthquake Engineering - M. Papadrakakis, M. Fragiadakis (eds.) 15–17 June, 2017.
- [22] Luzi, L., et al., *ITACA (ITalian ACcelerometric Archive): A web portal for the dissemination of Italian strong-motion data*. Seismological Research Letters, 2008. **79**(5): p. 716-722.
- [23] NGwest, *Seismic database*. (<http://peer.berkeley.edu/ngawest2/>).

## COMPRESSIVE STRENGTH EVALUATION OF BLUE MOSQUE MINARET STONES WITH ULTRASONIC TESTING

G. Uncu<sup>1</sup>, Ş.Ö. Dede<sup>2</sup>, and E. Çaktı<sup>3</sup>

<sup>1</sup> Phd Candidate, Earthquake Engineering Department, Kandilli Observatory and Earthquake Research Institute, Boğaziçi University, İstanbul  
e-mail: gulen.uncu@boun.edu.tr

<sup>2</sup> Res. Assistant, Earthquake Engineering Department, Kandilli Observatory and Earthquake Research Institute, Boğaziçi University, İstanbul  
e-mail: sahin.dede@boun.edu.tr

<sup>3</sup> Prof. Dr, Earthquake Engineering Department, Kandilli Observatory and Earthquake Research Institute, Boğaziçi University, İstanbul  
e-mail: eser.cakti@boun.edu.tr

---

### Abstract

*Engineering modeling and analysis of historical structures include various uncertainties and related difficulties. The most important difficulty is to obtain consistent data of structural materials without damaging historical texture as much as possible. The aim of this study is to determine the average compressive strength of the minarets of the Blue Mosque by means of ultrasonic testing. In the scope of the study, cube samples were collected from the unusable stones that were remained from restoration works carried out in the mosque. Compressive strength tests were performed following ultrasonic tests and a highly correlated relation was obtained. This relation was used in a detailed ultrasonic test study carried out in the minarets of the Blue Mosque and afterward, the mean compressive strength distributions for each minaret were estimated. It is thought that the results of the compressive strength test applied for the first time on the Blue Mosque stones as well as the detailed results for each minaret will make a significant contribution to the literature for future restoration studies and analyses.*

**Keywords:** Blue Mosque, compressive strength, non-destructive techniques, cultural heritage, masonry structure

---



## 1 ULTRASOUND TESTING

Ultrasound testing is a nondestructive method that uses high frequency sound wave to determine the material properties. It is based on evaluation of the velocities of P and S waves which are transmitted and reflected back through the material. This study covers the application of ultrasound testing method on Blue Mosque Minarets in İstanbul, Turkey. The equipment utilized for the application is Proceq Pundit Lab Plus. It consists two probes that transmit and receive the sound waves and a device that displays the obtained value. In this study, two probes are used: 250 kHz probe and 54 kHz probe. The 54 kHz probe only generates P waves, whereas the 250 kHz can generate both P and S waves. As can be seen in Figure 1, there are three types of measurement techniques: direct, semi-direct and indirect. The most reliable one is the direct measurement technique, however it is only applicable when the material thickness is appropriate to transfer the waves through the probes which are located reciprocal.

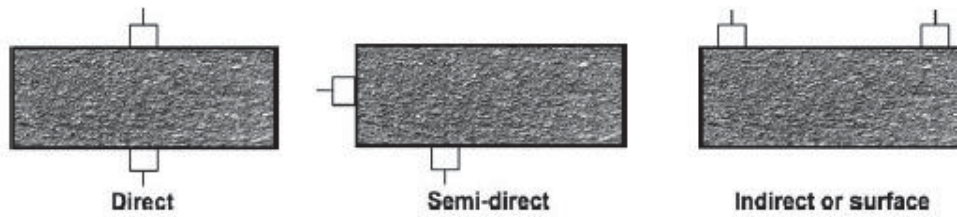


Figure 1. The three types of measurement regarding the arrangement of the probes (Pundit Lab Operating Instructions)

## 2 EXPERIMENTAL STUDIES

Blue Mosque is constructed in between 1609-1616, with its 6 minarets. The laboratory experiments are applied on the stones of the minaret which is under restoration whereas the site investigation is carried on the other 5 minarets of the mosque. The two of those five minarets (M1 and M6) have a height of 57 meters with two balconies; whereas the other three ones (M2, M4, M5) are 66 meter tall with 3 balconies. The minarets are stone masonry constructions. Figure 2 illustrates the settlement of the minarets of the Blue Mosque. While this study is being carried, the honeycomb part of the minaret M3 is removed due to the restoration work. The ultrasound, Schmitt and the compressive strength tests are carried on the stones removed from the honeycomb and will not be reused after the restoration. Besides, ultrasound testing is done on the other five minarets on the site.



Figure 2. Blue Mosque and the settlement of its minaret



Figure 3. The debris removed from the minaret M3 and the cubic specimens obtained by cutting them

Figure 3 shows the debris removed from the minaret M3 and cut to the appropriate shape for the compressive strength test. The 7x7x7 cm and 5x5x5 cm cubic pieces, which are referred as “the large samples” and “the small samples” respectively in this paper, are obtained. First the large ones are worked. Five measurements are done for the each three pair of opposing surfaces to evaluate the P and S wave velocities, not only the numerical value but also with the wave forms. The 54 kHz probes are used for the P waves and the 250 kHz ones for the S waves. When it is completed, P wave velocity values are found to be reliable. However the 250 kHz probes generate the P and S waves together, therefore the velocity value shown on the screen is not respectable and the wave forms are required to be inspected. Nevertheless it should be a detailed observation, since the P and S waves are not clearly detectable due to the limited dimension of the specimens. After the ultrasonic test, the Schmitt Hammer test is carried and then the density of each cubic piece is determined.



Figure 4. The ultrasound and Schmitt Hammer tests application



Figure 5. The samples cracked while the Schmitt Hammer test application

The Schmitt Hammer test is applied on each three non-reciprocal surfaces. After the ultrasonic test, Schmitt Hammer test and the density evaluation, compressive strength test is applied. The small samples are cracked during the Schmitt Hammer test, due to their dimensions, hence it is decided not to apply the test on them. Besides, the test applied on the large samples

is not concluded in reliable correlation with the compressive strength test. Therefore, the Schmitt Hammer test results are not regarded in this study.

It is observed on the cracked specimens that, despite their soft surfaces they have quite stiff cores inside. This fact is considered as one of the reasons for not yielding reliable correlation between Schmitt Hammer test and compressive strength test results.

There are several ultrasound test measurements that resulted in remarkably different outcomes for each surface pairs of the same sample. Besides, it is thought that the compressive strength result is effected by the other two directions that the compression is not applied. Regarding these observations, three different methods are asserted in order to inspect the correlation between the P wave velocity and the compressive strength value.

### 3 THE ANALYSES

The analyses are launched after collecting the data from the previously mentioned tests. The S wave velocities are determined by observing the wave forms, then the regression analysis is carried to evaluate the correlation of the data. First, the correlation between the P wave velocity and the compressive strength is inspected. Concerning the readings on different surfaces of the samples, the correlations between the compressive strength and the following three measurements are regarded respectively: P wave velocity related to the compressed surface; the mean value of the P wave velocity related to each surface; the minimum P wave velocity obtained from each surface.

As can be seen in Figure 6 and 7, the correlations are found to be 66%, 77% and 79% respectively.

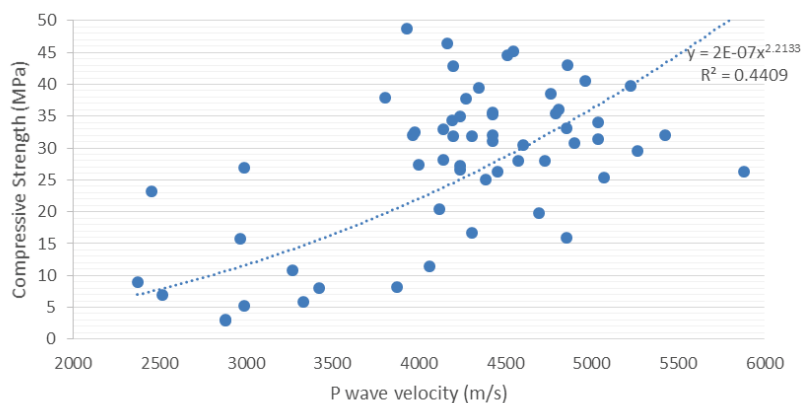


Figure 6. The correlation between the compressive strength and P wave velocity related to the compressed surface

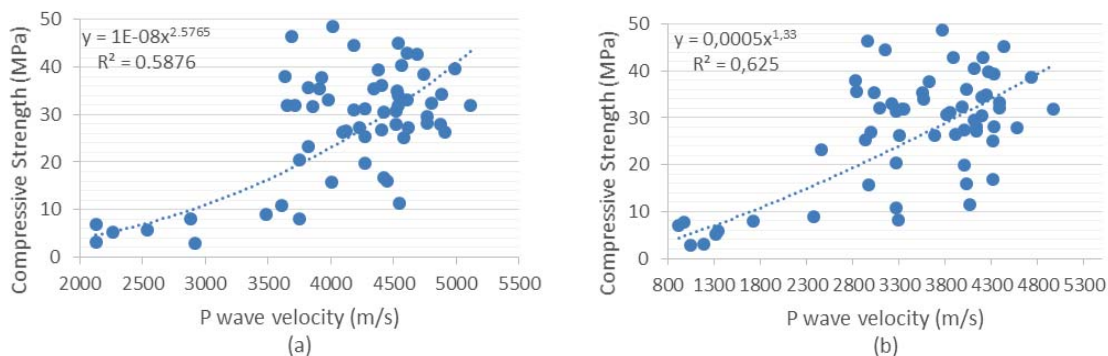


Figure 7. The correlation between the compressive strength and (a) The mean value of the P wave velocity related to each surface (b) the minimum P wave velocity obtained from each surface

Then, the correlation between the minimum P wave velocity obtained from each surface and the compressive strength is observed for the samples having 40MPa and below compressive strength. As Figure 8(a) points, the correlation increases up to 81% in that case. Consequently, the same analysis is carried for the samples with a compressive strength of 35 MPa and below; 30 MPa and below. The correlations are found to be 81% and 85% respectively (Figure 8(b), 8(c)). It is clear that the correlation is the same for the samples with a compressive strength of 40 MPa and below and 35 MPa and below; whereas it increases for the ones with 30 MPa and below. However, there are 55 samples with 40 MPa and below compressive strength out of 61 total samples; whereas only 32 of them have 30 MPa and below compressive strength. It implies that, when only the samples with 30 MPa and below compressive strength are considered, almost the half of the specimens are disregarded.

Figure 8(d) represents that when the samples with a compressive strength of 25 MPa and below are considered, the correlation decreases to 77% and there are only 18 samples tested.

Respecting the previously mentioned results, when the correlation and the number of the tested samples are regarded, the correlation between the compressive strength and the P wave velocity for the specimens with a compressive strength of 40 MPa and below is found to be more reliable among the carried regression analyses.

Furthermore, the correlation between the P and S wave velocities is examined. As explained earlier, the S waves require a detailed eye observation on the waveforms. The observation declines that detecting the S wave velocity on a large cubic is easier and more reliable than that on a small one; since the wave path is longer. Therefore, the correlation between P and S waves is examined regarding the results obtained from the large samples. When the P wave velocity is considered, the mean value of the three surface readings is taken and as can be seen in Figure 9(a), it is found to be 86% correlated to the S wave velocity.

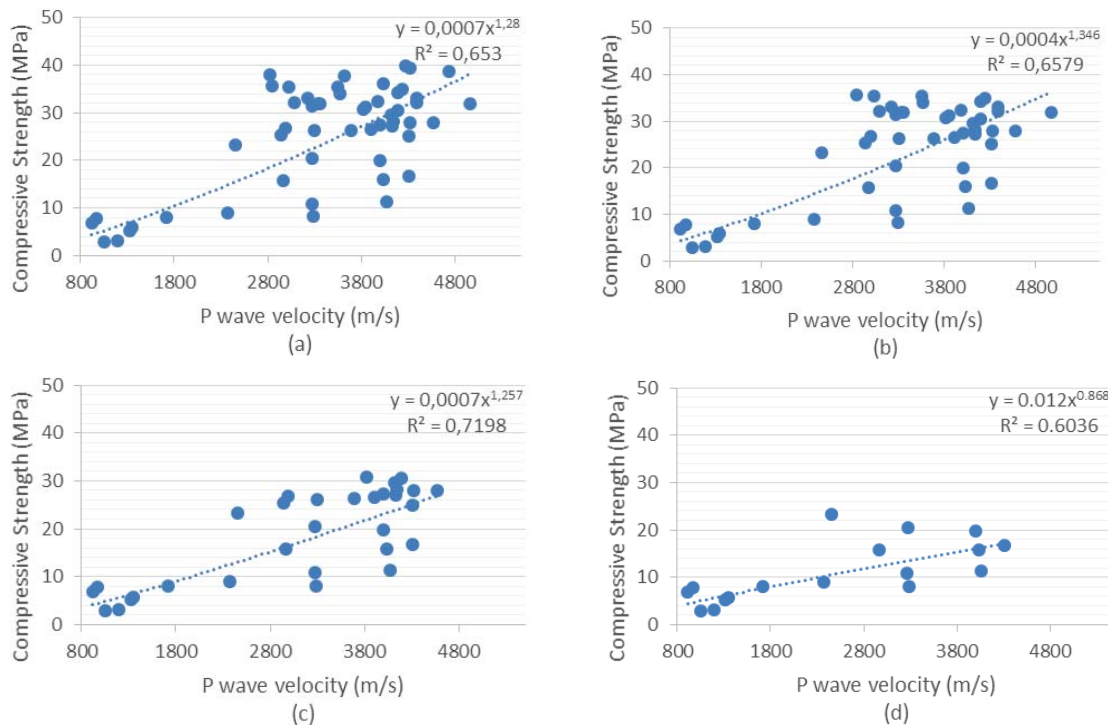


Figure 8. Correlation between the minimum P wave velocity from each surface and the compressive strength for the samples having 40 MPa and below (a), 35 MPa and below (b), 30 MPa and below (c), 25 MPa and below (d)



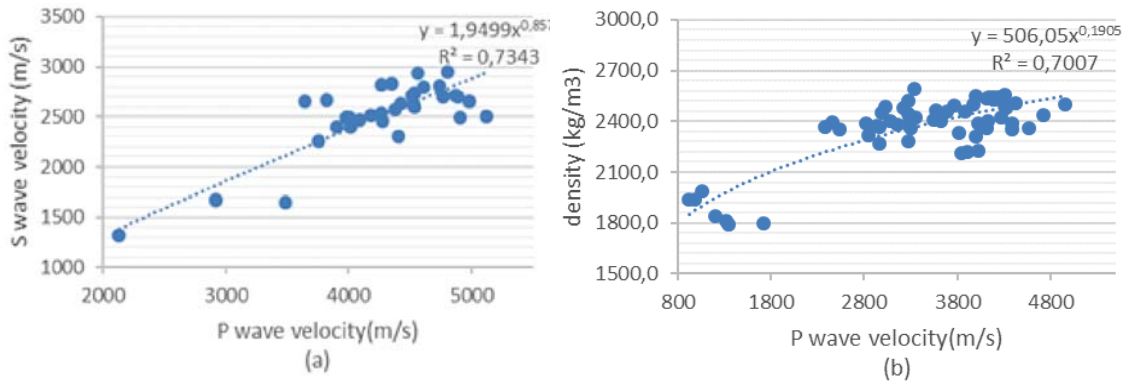


Figure 9. The correlation between (a) Vs and Vp (b) Density and Vp regarding three surfaces of the samples

Furthermore, the correlation between the density and the P wave velocity is examined. The minimum value of the P wave velocity readings from the three surfaces is regarded. First, the analysis is carried concerning the results taken from the samples with a compressive strength of 40 MPa and below; however it is revealed that the correlation and its equation does not change significantly when all the samples are considered. Therefore, the equation found when all samples are analyzed is respected (Figure 9(b)).

The other five minarets M1, M2, M4, M5, M6 are observed by ultrasound testing equipment on site and the results are assessed regarding the laboratory test results mentioned above. The 54 kHz and 250 kHz probes are used for the site survey. Besides, the circular column at the core of the minarets where the stairs are rising, is measured by direct method using 54 kHz probes.

#### 4 RESULTS

First, the equations obtained from the laboratory tests are applied on the site survey results. The regression equation of the P wave velocity and compression strength correlation is adopted on the P wave velocity reading taken from the minarets on site to reveal the compressive strength of the material. The mean compressive strength values of each stone in a minaret is evaluated as following: 28 MPa for M1, 10 MPa for M2, 31 MPa for M4, 10 MPa for M5, 10 MPa for M6. Besides, the samples tested in the laboratory result in 28 MPa of mean compressive strength. The compressive strength of different parts of each minaret is indicated in Figure 11, by a color scale. The color scale is illustrated in Figure 10.

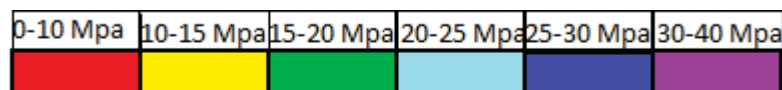


Figure 10. Color scale

#### 5 DISCUSSIONS

This study offers the first application of compressive strength test on Blue Mosque stones, therefore it provides notable contribution to the literature when the future restoration works are considered. The samples tested in the laboratory result in 28 MPa of a mean compressive strength and the compressive strength of the other five minarets on the site is detected part by part for each one.

It is found to have a correlation of 81% between P wave velocity and the compressive strength of the material. Besides, it is assumed that the nonhomogeneous structure has an effect on the compressive strength of the stones.

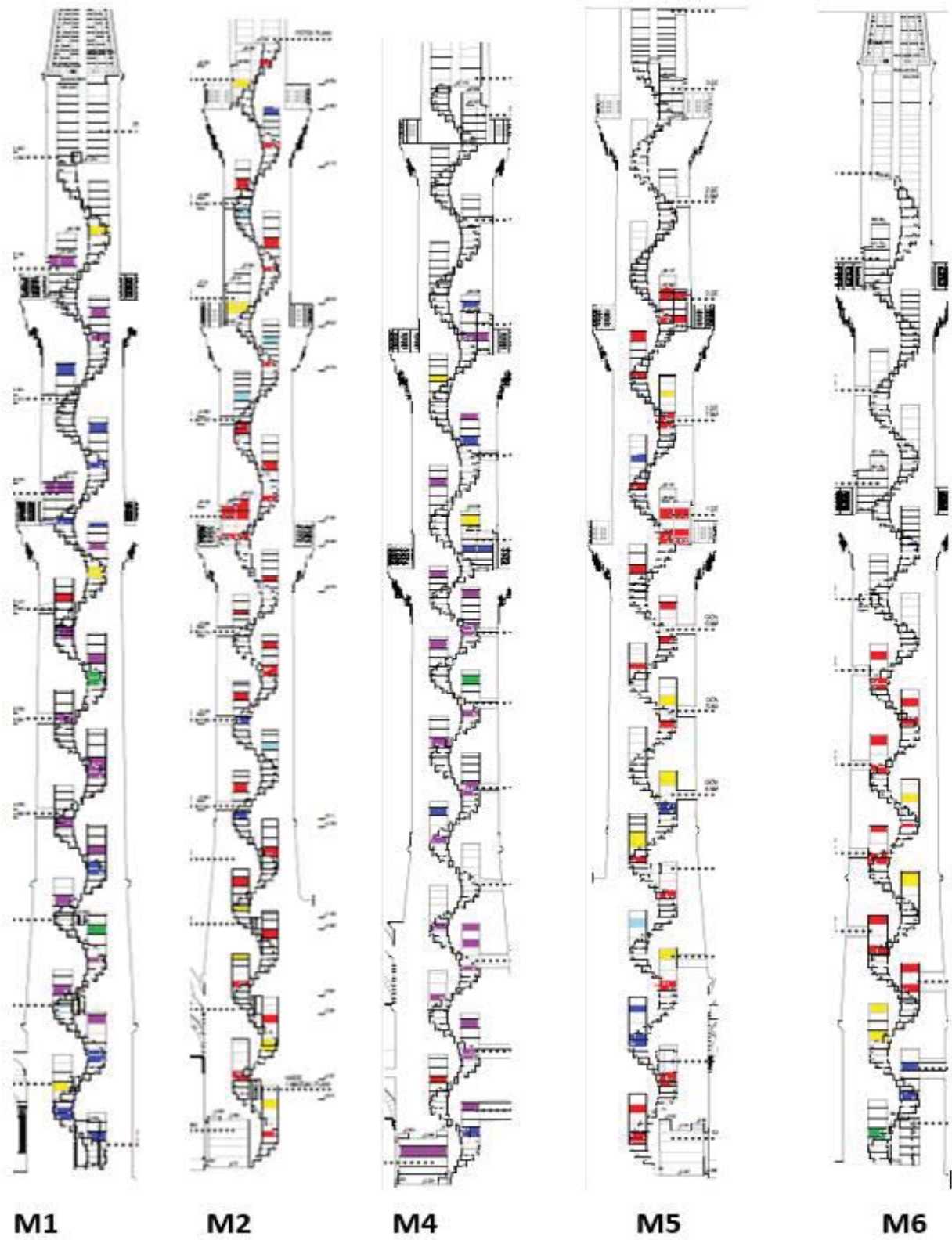


Figure 11. The compressive strength of different parts of each minaret shown by a color scale



Moreover, a number of stones with tough inner cores despite of their soft surfaces are blamed for the unreliable Schmitt Hammer test results. Additionally, the Schmitt Hammer test is observed to damage the samples.

The samples tested in the laboratory reveal that the P wave velocity obtained from different directions of the same cubic is significantly variable and the compressive strength result is highly effected by this diversity. The most reasonable outcome is obtained when the correlation between the minimum of the P wave velocity readings taken from 3 different surfaces of the sample and the compressive strength. However, it must be regarded that, the five minarets on site are not appropriate for taking the readings from all directions of the material.

When the P wave velocity that appears on the screen during the reading and the S wave velocity that obtained by an eye observation on the wave form are compared, the former one is found to be more respectable. Therefore, especially for the site surveys, the limitations of reading the S wave velocity should be concerned. This study offers the idea to determine the material property using the P wave velocity, neglecting the S wave velocity.

When the larger samples are considered higher level of correlation is found between the P and S wave velocities and the correlation between the P wave velocity and the density. This relationship may lead to the evaluation of S wave velocity and the density; therefore the shear and the elasticity modulus, employing the measured P wave velocity. This concept is left for a further study.

## REFERENCES

- [1] Proceq, *Pundit Lab Operating Instructions*, Proceq SA, Schwerzenbach, Switzerland, 2017.

## EXPERIMENTAL INVESTIGATION OF SHEAR STRENGTH OF SOLID BRICK URM WALLS RETROFITTED WITH TRM JACKET

Athanasia K. Thomoglou<sup>1</sup>, Athanasios K. Karabinis<sup>2</sup>

<sup>1</sup> Civil Engineering Department, Democritus University of Thrace (DUTH),

Kimmeria, 67100 Xanthi, Greece  
e-mail: athomogl@civil.duth.gr

<sup>2</sup> Civil Engineering Department, Democritus University of Thrace (DUTH),

Kimmeria, 67100 Xanthi, Greece  
e-mail: karabin@civil.duth.gr

---

### Abstract

*This study is part of an experimental program on full-scale strengthened Un-Reinforced Masonry (URM) walls with Textile reinforced mortars (TRM). Four solid brick walls (one control and three strengthened specimens with central opening), were tested under the diagonal tension (shear) test method in order to investigate the effectiveness of the strengthening system on the in-plane behavior of the walls. All the URM panels consist of solid bricks and a high strength binder mortar. Both of them have increased mechanical properties leading to improved shear behavior of the masonry walls. Several parameters pertaining to the in-plane shear behavior of the retrofitted panels were investigated, including shear capacity, failure modes, the number of layers of the external TRM jacket and the existence of the central opening of the wall. The experimental work allowed an evaluation of the shear behavior in the case of the bidirectional textile (TRM) system applied on URM walls. The experimental results of URM and retrofitted walls with different layers are compared with each other. The purpose is to investigate in depth and to draw conclusions about the in-plane shear behavior.*

**Keywords:** TRM, solid brick URM, in-plane performance, seismic strengthening, diagonal compression test, wall's opening.

---

## 1 INTRODUCTION

The existence of the doors and/or windows openings of the Unreinforced masonry (URM) walls significantly affects the shear behavior of the structure. Hence, there is an urgent need to investigate the influence of the retrofitting technique on URM walls with openings. In the field of rehabilitation and strengthening of the existing masonry buildings, Textile Reinforced Mortar (TRM) has attracted considerable research interest as an alternative to the traditional strengthening methods due to its better compatibility with the URM substrate, fire resistance, excellent mechanical strength and stiffness in the direction of the fibers, while it improves the seismic capacity of URM walls (Thomoglou et al 2020). Nevertheless, there is limited experimental research on full-scale walls.

The existence of openings in masonry walls is often responsible for in-plane collapse mechanism creation, leading to the entire building collapse (Chalioris et al. 2013, Chalioris et al. 2015). Considering this critical parameter, there is a limited experimental study on retrofitting masonry walls with openings. Several works on infill masonry walls with openings were carried out by Kakaletsis and Karayannis (2008), Kakaletsis and Karayannis (2009), Decanini et al. (2014), Mansouri et al. (2014), Sigmund and Penava (2014), Tasnimi and Mohebkah (2011), or without openings by Lee et al. (2010), Rousakis (2017) and Rousakis (2020). From the abovementioned research, it is concluded that openings have a significant effect on the characteristics of masonry infill walls, such as failure mode and lateral strength, and ductility reducing shear strength, stiffness, and energy dissipation capacity.

The work concerns diagonal compression tests on solid brick URM and retrofitted walls with TRM jacket on both sides of the walls. The TRM reinforcement system comprises one, two, or three plies of glass fiber mesh in a cement mortar matrix. This strengthening method has an advantage over other traditional solutions in easy application, excellent adhesion of the mortar to the brick substrate, high tensile strength, and low elasticity increasing compatibility with masonry. The purpose is to investigate and to draw conclusions about the shear behavior of strengthened full-scale brick URM walls with a central opening.

## 2 EXPERIMENTAL PROGRAMM

This experimental study deals with full-scale URM walls comprising solid bricks and a high strength binder mortar (Durostick D-31). The TRM strengthening system consist of one, two or three layers of glass mesh in a cementitious matrix applied to both of the specimen with central opening. The strengthening concept is based on the observation that the strengthening mortar matrix plays a key role to the contribution of the total shear capacity (Thomoglou et al. 2020). All the experiments were conducted at the Laboratory of Reinforced Concrete and Seismic Design of Structures of the Department of Civil Engineering of the Democritus University of Thrace.

## 3 MECHANICAL PROPERTIES OF MATERIALS

### 3.1 Mechanical properties of bricks and mortar and exterior strengthening

The nominal dimensions of the solid bricks were 200 mm (Length) x 100 mm (Width) x 50 mm (Height) (Figure 1a). The compressive behavior of brick units is determined in two load directions: perpendicular and parallel to the bed joints. Six units were tested in total under an axial load after grinding of their loading surfaces according to procedures established in the European standard EN 772-1 (2000). Two displacement transducers (LVDTs) and a laser meter were used to measure the vertical and horizontal deformations,  $\Delta v$  and  $\Delta h$  (Thomoglou et al. 2018). The compressive strength of the bricks equals to 116.17 MPa. A render mortar of

20M class was used to construct all the walls, with a nominal mortar thickness of about 10 mm. The 28-day compressive strength of the Durostick D-31 mortar obtained by testing 40 mm × 40 mm × 160 mm mortar prisms according to EN 1015-11 (1993) with an average value of 38.15 MPa, while the tensile strength is 15.76 MPa (Figure 1b).

Prior to the application of the TRM jacket, the masonry specimen was coated with light-heavy, reinforced cementitious mortar (SikaRep®-200 Multi) in order to smooth the protrusions and to get a flat layer on the external surface. The exterior strengthening system consisted of 1, 2 or 3 plies of glass grid embedded into a cementitious matrix. The glass fibers were arranged along two rectangular directions with axial spacing of 18.1 mm in the longitudinal and 14.2 mm in the lateral direction, respectively, as shown in Figure 1c, while its mass was 360 g/m<sup>2</sup> per unit area. The modulus of elasticity in the longitudinal direction was 80 GPa. Fiber reinforced cementitious mortar with pozzolanic admixtures had a 28-day compressive and flexural strength of 28.85 MPa (based on EN 1015-11) and 6.78 MPa, respectively, while the Modulus of elasticity was 8.03 GPa (according to the manufacturer) (Thomoglou et al. 2019b).

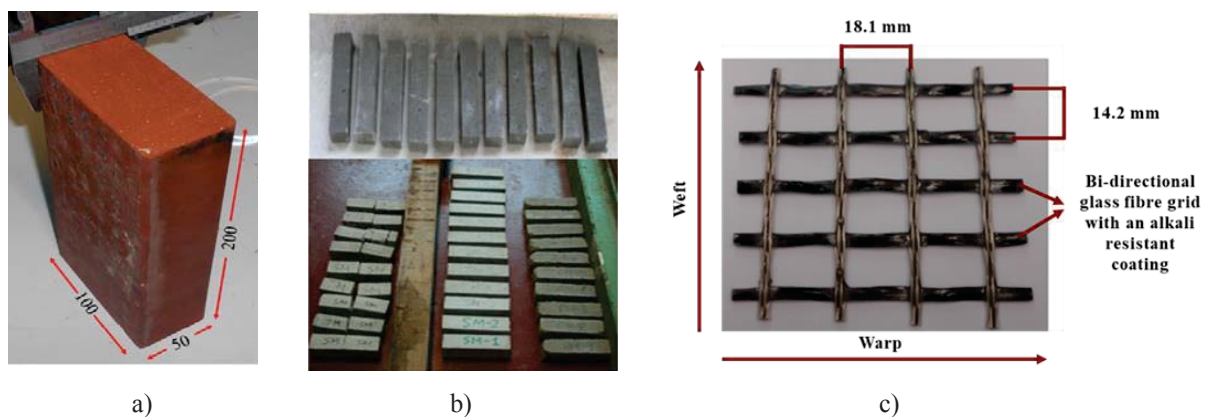


Figure 1 a) Dimensions of solid brick, b) Maturing mortar prisms and test pieces after a three-point bending test, c) Dimensions of fiberglass grid SikaWrap®-350GGrid.

## 4 TEST SET-UP AND LOADING

### 4.1 Main headings

In order to investigate the shear behavior of the strengthened walls under lateral loading, the diagonal compression test, was standardized by ASTM E 519-07 (ASTM 2010) to determine the shear capacity of 1200 mm x 1200 mm masonry panels. The specimens were loaded in compression along one diagonal to cause tension failure, with the specimens splitting apart parallel to the direction of loading. For this study, four specimens were constructed in full scale and the thickness for all panels was 210 mm. All specimens were with central opening (one control and three strengthened walls with 1-ply, 2-ply or, 3-ply glass TRM, respectively). The dimensions of the opening are 450 mm (length) and 300 mm (height) (see Figure 2a). The layers of the glass TRM were applied over each side of the panel.

The in-plane test setup comprises of two steel loading shoes, according to ASTM E519, placed diagonally opposite to the corners of the specimen, while they attached the upper shoe to the MTS servo-hydraulic piston (Figure 2b). Diagonal compression was applied via a 450 kN MTS servo-hydraulic piston. High-performance shrinkage compensated a cementitious,

free-flowing mortar SikaGrout-312 HP which was used to fill the two shoes (capping), maturing for at least 24 hours.

The compressive load applied uniaxially and monotonically to the failure point at a rate of 0.01 mm/s. The diagonal compression test was widely used to broaden the knowledge on masonry subjected to in-plane behavior. Although diagonal compression does not reproduce a field condition behavior of the masonry field, however, it is more conservative because of the limited value of the vertical load and is standardized according to ASTM 2010, (Thomoglou et al. 2019a).

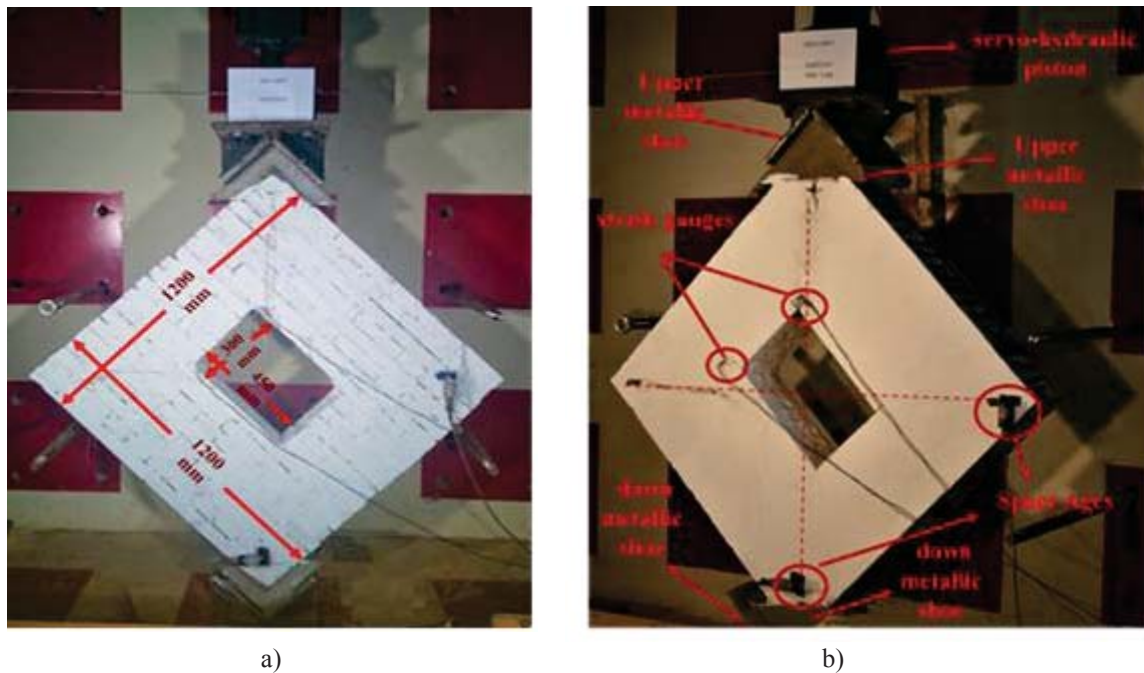


Figure 2 a) Experimental set up of solid brick URM wall with central opening, b) Arrangement of measuring instruments on the URM wall.

## 5 RESULTS-DISCUSSION

### 5.1 Displacement Force Diagram

The mechanical parameters of the tested specimens are presented in Table 1. The results of the experimental tests on the maximum applied load, the ultimate shear stress, the ultimate displacement, the ultimate shear strain, and the failure mode for each specimen are presented in columns (2)-(6) of Table 1, respectively. The production of the reinforcement is defined as the ratio between the maximum load applied to each strengthened panel to the unreinforced control wall. It can be observed that there is an increase in shear capacity and therefore an improvement in the production of external strengthening amounting to 339%, 470%, and 701% for 1, 2, and 3-ply TRM jacket, respectively, compared to the value of 61.49 kN of the control wall. Besides, the displacement of the retrofitted specimen shows 2.31, 2.71 and 3.04 times the value of 4.19 mm of the control one, for 1, 2, and 3-ply TRM jacket, respectively.

The results from those masonry specimens with a central opening retrofitted with 1 to 3-ply TRM jacket are summarized in the response curves of Figure 3 and compared with each other. In the load-displacement diagram, the strengthened masonry specimen with central opening and 3-ply of fiberglass mesh (SS-O-UMG3), presenting more plastic behavior and



showing the best shear response from all the strengthened walls. An important observation is that as the shear capacity so the ultimate displacement of retrofitted masonry walls increases proportionally to the amount of TRM for 1 and 3 plies.

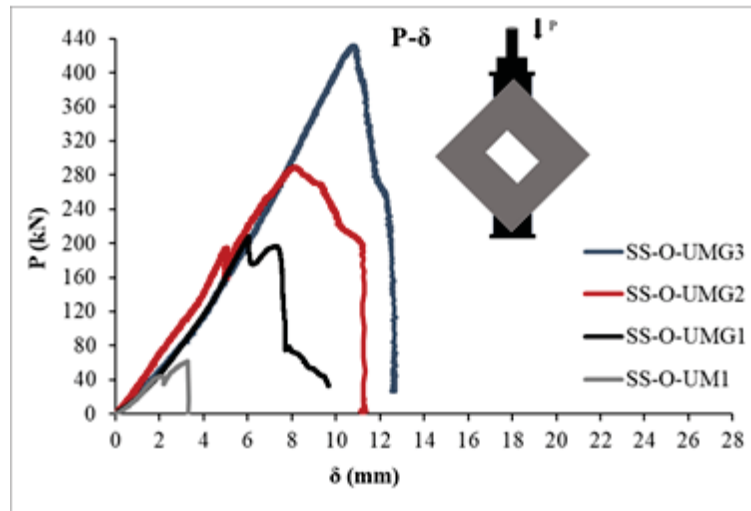


Figure 3 Experimental set up of solid brick URM wall with central opening.

Specimen Codes	Plies of TRM textiles	Maximum applied failure load $P_u$ (kN)	Ultimate Shear stress $\tau_u$ (Mpa)	Displacement $\delta_u$ (mm)	Ultimate Shear strain $\gamma_u$ (mm/mm)	Failure Mode
(1)	(2)	(3)	(4)	(5)	(6)	(7)
SS-O-UM1	Control	61.49	0.17	4.19	0.0028	SF
SS-O-UMG1	1 ply	208.19	0.59	9.67	0.0051	TRM failure-DT
SS-O-UMG2	2 plies	289.23	0.82	11.35	0.0068	TRM failure-DT
SS-O-UMG3	3 plies	431.20	1.22	12.72	0.0091	TRM failure-DT

DT: Diagonal Tension, SF: Shear Friction

Table 1: Experimental results.

## 5.2 URM Failure Modes

The typical crack patterns of the four masonry walls after shear failure are illustrated in Figure 4. The control wall with central opening showed a brittle failure caused by the loss of the bond between the mortar and the bricks, as well as a diagonal tensile stress with a simultaneous fracture of the mortar and bricks, which caused a stair-step cracking and shear friction (Thomoglou et al. 2019a). Hence, the failure mode of the control wall with central opening (SS-O-UM1) is a shear friction. The failure mode of the strengthened wall with 1-ply (SS-O-



UMG1) is diagonal tension, which appears with a thorough crack along the entire length of the diagonal parallel to the direction of the load and across the width of the panel. The evolution of the diagonal crack started from the point where the maximum concentrated tensile stresses appear. This point is the two opposite corners of the hole in the vertical direction, while at the two opposite corners of the other direction maximum compressive stresses develop. Also, two cracks are developed from the external side of the panel and end at the two opposite corners of the opening, which are located almost perpendicular to the load direction (Figure 4a)-b).

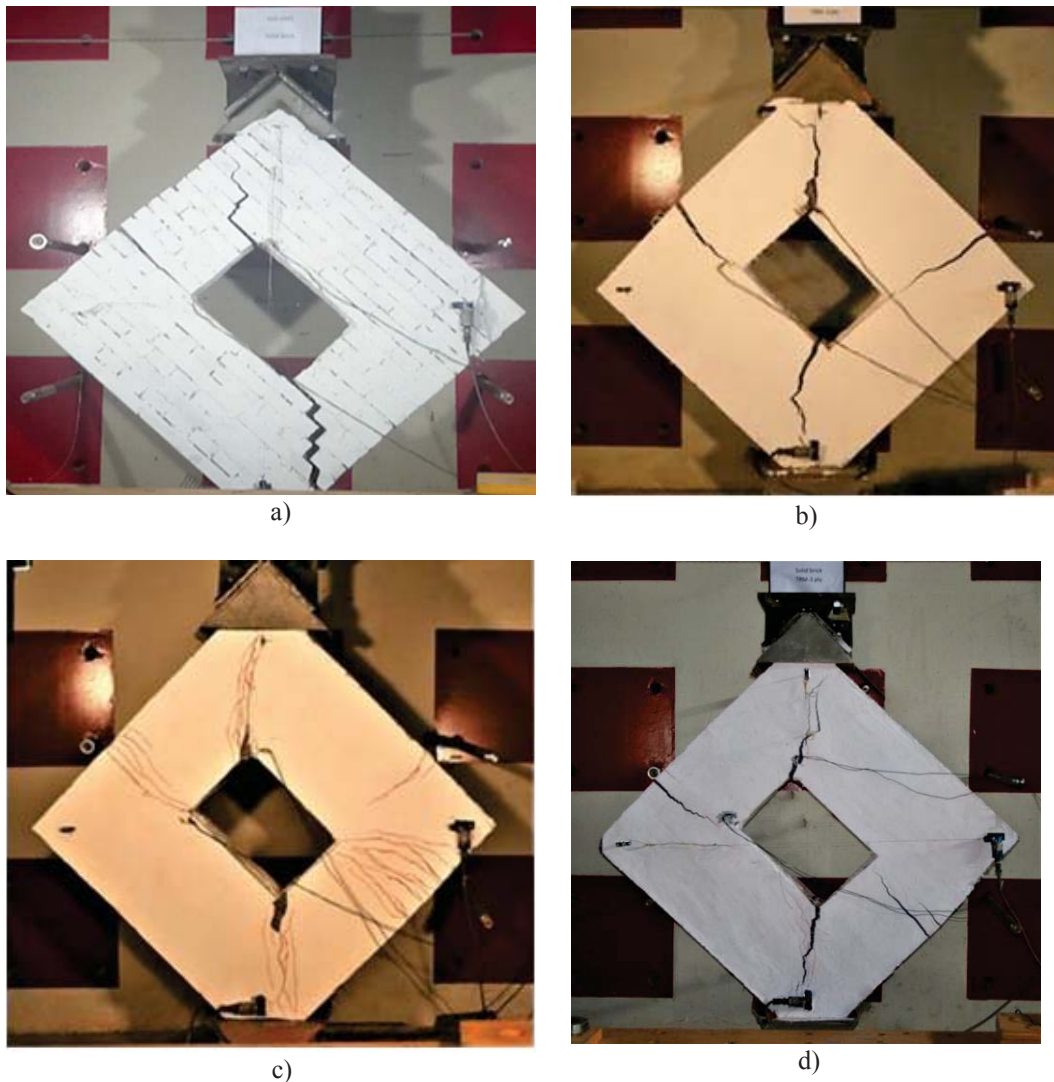


Figure 4 Failure mode of a) control brick URM wall (SS-O-UM1), b), c), d) strengthened wall with 1-ply (SS-O-UMG1), 2-ply (SS-O-UMG2) and 3-ply (SS-O-UMG3) glass textile, respectively.

The failure mode of the retrofitted solid brick URM (SS-O-UMG3) with 3 plies of glass textile and a central opening is similar to the specimens with 1 and 2 plies of TRM jacket (see Table 1 and Figure 4 b)-d)). Nevertheless, a wider vertical crack is observed and parts of the strengthening mortar of the TRM jacket are effectively detached. The glass textile failure is observed here as well as in the case with 1 and 2 plies (SS-O-UMG2, SS-O-UMG3), respectively (Figure 4b)-d)). Finally, the effectiveness of this significant strengthening technical is highlighted, if we include the fact of preventing the final collapse of the masonry, which is very important for the safety of human and material resources.

## 6 ACKNOWLEDGMENTS

We acknowledge KEVE. SA for the supply of Orthoblock K300 bricks and building masonry specimens, as well as Sika Hellas SA for providing all masonry strengthened materials and for our excellent cooperation.

## 7 CONCLUSIONS

A full-scale experimental investigation was aimed to assess the effectiveness of the TRM external jacket in order to improve the in-plane behavior of the four solid brick specimens with a central opening. The masonry panels were retrofitted using three different configurations (with 1, 2, 3 plies of a both-sided TRM application) and were tested under monotonic diagonal tension (shear) test. From the aforementioned results, the following concluding observations arise:

- The TRM jacket has improved the shear capacity and deformation capacity, which caused the failure of the strengthened walls in a more plastic way.
- There is an increase in shear capacity and therefore an improvement in the production of external strengthening amounting to 339%, 470%, and 701% for 1, 2, and 3-ply TRM jacket, respectively, compared to the value of 61.49 kN of the control wall.
- The displacement of the retrofitted specimens shows 2.31, 2.71 and 3.04 times for 1, 2, and 3-ply TRM jacket, respectively, compared to the value of 4.19 mm of the control wall.
- The best shear behavior was demonstrated by the masonry specimen with 3-ply of TRM and a central opening of solid bricks compared to all masonry walls.
- The failure mode of the control wall with central opening is shear friction, while the strengthened masonry specimens exhibited TRM failure and diagonal tension.
- The tests results demonstrated that the glass TRM jacket plays an important role in retaining and protecting the solid brick masonry wall. The strengthening system prevents the abrupt reduction of the resistance and significantly reduces the brittle behavior, avoiding an explosive collapse.

## REFERENCES

- [1] ASTM. "Standard test methods for diagonal tension (shear) in masonry assemblages. ASTM E519 / E519M", West Conshohocken, PA., DOI: 10.1520/E0519\_E0519M-10, 2010.
- [2] Chalioris, C. E., Favvata, M. J., Alexandri, V. G., & Karayannis, C. G., Rehabilitation of a partially collapsed masonry traditional tobacco warehouse of the late 19th century. *In COMPDYN 2013: proceedings of the 4th international conference on computational methods in structural dynamics and earthquake engineering*, Kos Island, Greece, paper (No. 1596, pp. 12-14), 2013.
- [3] Chalioris C.E., Tsioukas V.E., Karayannis C.G., Recording and Rehabilitation Procedures for Historic Masonry Buildings, *Computational Methods in Applied Sciences*, Vol.

- 37**, chapter in the book: “Seismic Assessment, Behavior and Retrofit of Heritage Buildings and Monuments”, Psycharis et al. (eds.), pp. 341-364, 2015.
- [4] Decanini LD, Liberatore L, Mollaioli F., Strength and stiffness reduction factors for infilled frames with openings. *Earthq Eng Vib* 2014; **13**(3): 437-54, 2014.
  - [5] Kakaletsis D. and Karayannis C., Influence of masonry strength and openings on infilled R/C frames under cycling loading. *Journal of Earthquake Engineering* **12**(2): 197–221, 2008.
  - [6] Lee, Y.-H., Kim, M.-S., Byon, E.-H., & Kim, H.-C., Experimental Investigation of The Shear Strengthening of Unreinforced Masonry Infilled RC Frames Using CFRP Sheet. *Journal of the Earthquake Engineering Society of Korea*, **14**(1), 63–70. <https://doi.org/10.5000/eesk.2010.14.1.063>, 2010.
  - [7] Mansouri A, Marefat MS and Khanmohammadi M, Experimental evaluation of seismic performance of low shear strength masonry infills with openings in reinforced concrete frames with deficient seismic details. *Structural Design of Tall and Special Buildings* **23**(15): 1190–1210, 2014.
  - [8] Rousakis, T.C., Rouka, D., Kaloudaki, A., Kwiecien A., Gams, M., Viskovic, A., Zajac, B. Fast Retrofitting of Strong Wall Infill of RC buildings with Fiber Sheets Impregnated with Highly Deformable Polymer. *25th International Conference on Composites/Nano Engineering (ICCE-25)*, Rome, Italy, 16–22 July, 2017.
  - [9] Rousakis T, Ilki A, Kwiecien A, Viskovic A, Gams M, Triller P, Ghiassi B, Benedetti A, Rakicevic Z, Colla C, Halici OF, Zajac B, Hojdys Ł, Krajewski P, Rizzo F, Vanian V, Sapalidis A, Papadouli E, Bogdanovic A., Deformable polyurethane joints and fibre grids for resilient seismic performance of reinforced concrete frames with orthoblock brick infills, *Polymers*, **12**(12), <https://doi.org/10.3390/polym12122869>, 2020.
  - [10] Sigmund V and Penava D, Influence of openings, with and without confinement, on cyclic response of infilled RC frames – an experimental study. *Journal of Earthquake Engineering* **18**(1): 113–146, 2014.
  - [11] Tasnimi AA and Mohebkah A, Investigation on the behavior of brick-infilled steel frames with openings, experimental and analytical approaches, *Engineering Structures* **33**(3): 968–980, 2011.
  - [12] Thomoglou A., Rousakis T. and Karabinis A., Experimental Investigation and 3d Finite Element Analysis of solid and hollow clay bricks, *ICCE-26th Annual International Conference on Composites/Nano Engineering*, Paris, France, 2018.
  - [13] Thomoglou A., Rousakis T. and Karabinis A., Investigation of failure modes of URM walls strengthened with TRM subjected to in plane seismic loads, *2nd International Conference on Natural Hazards & Infrastructure*, Greece, 2019a.
  - [14] Thomoglou A., Rousakis T. and Karabinis A., Experimental Investigation of Shear Behavior of URM strengthened with TRM, *4th Hellenic Conference Mechanical Seismology*, 5-7 September, Athens, Greece, 2019b.
  - [15] Thomoglou A., Rousakis T., Achillopoulou D. and Karabinis A., Ultimate Shear Strength Prediction Model for Unreinforced Masonry Retrofitted Externally with Textile Reinforced Mortar, *Earthquakes and Structures*, **19** (6) 000-000, DOI: <https://doi.org/10.12989/eas.2020.19.6.000>, 2020.

## METAFOUNDATION AS A NEW APPROACH FOR SEISMIC ISOLATION OF BUILDINGS

S.Fiore<sup>1</sup>, D.Magisano<sup>1</sup>, G.Finocchio<sup>2</sup>, M.Chiappini<sup>3</sup>

<sup>1</sup> Department of Computer Engineering, Modeling, Electronics and Systems Engineering  
University of Calabria, Italy  
stefania.fiore@dimes.unical.it, domenico.magisano@unical.it

<sup>2</sup> Department of Mathematical and Computer Sciences, Physical Sciences and Earth Sciences  
University of Messina, Italy  
giovanni.finocchio@unime.it

<sup>3</sup> National Institute of Geophysics and Volcanology  
Italy  
massimo.chiappini@ingv.it

---

### Abstract

*Metamaterials for seismic protection are engineered to filter the low frequency component of seismic waves. In this study, we investigate the performance of a metastructure focusing on the improvement that the concept design of metamaterials can bring in the field of seismic isolation. The metastructure is realized as composite foundation built as a stack of concrete plates having internal resonant elements. The feasibility of the composite foundation is investigated by performing simulations in which at the base of each column of the building a composite metastructure replaces elastomeric isolator. Dynamic linear analyses are set for concrete multi-story frame buildings by using spectrum-compatible accelerograms for the horizontal components of the ground motion. The main result is the achievement of a reduction in the total displacement of the upper structure with respect a classical base isolation system. This work is a step forward in the understanding of the properties and performance of composite foundations as innovative base isolation system.*

**Keywords:** Metamaterials, Seismic isolation.

---

## 1 INTRODUCTION

Research and applications in earthquake engineering are focused on seismic protection methodologies for infrastructures and buildings since a lot of decades. Despite the great developments in geophysics seismic monitoring, the incoming earthquake is a dreadful natural event with a significant impact on the structures and people. The reduction of the buildings seismic vulnerability is an important research field in which two main approaches merge; from one side the design capacity strategies based on exploitation of the ductility resources of the building by preserving global safety condition are widely applied in common design activity; from the other side, seismic protection techniques are explored and improved in order to get the best safety condition for the structures when earthquakes occur. Nowadays, seismic protection system is often designed by combining more than one technology, such as elastomeric and damper elements. Within this context, concepts for seismic protection, related to metamaterials, are introduced by researchers as innovative approaches useful at developing technologies for seismic protection.

## 2 SEISMIC METAMATERIAL

Metamaterials attracted interest from the field of physics, where structures that shown negative refraction and permittivity were realized. From the end of the last century research on metamaterials in optical and electromagnetic field exploded [1]. They can be defined as artificial structures with periodic architecture, not available in nature, designed to produce an optimized response to specific excitation. The most interesting property for the development of seismic metamaterials is the chance to exploit the frequency bandgap in which propagation of seismic wave is attenuated [2]. From this starting point a lot of searches in earthquake engineering started and proposed new approach in seismic protection: seismic cloaks and metabarriers as large-scale protection system of large built areas (and ground volume) and metafoundations, as improvement of seismic protection for the single building by including metamaterial design in the foundation structure [3-9]. The main evidence in all the applications is the low frequency working range (0.1-20 Hz), because both earthquakes frequency content and natural frequencies of most of the building in civil engineering are low. For this reason, seismic metamaterials involve large mass and size.

## 3 STANDARD BASE ISOLATION SYSTEM

Base isolation systems are widely used for seismic protection of concrete multi-story frame buildings. The most popular devices are the elastomeric isolators in which layers of rubber and vulcanized reinforcement steel plates are alternated. Rubber compound guarantees high damping action or other elements with high damping capacity increase this property: the first are called High Damper Rubber Bearings (HDRB), the second Lead Rubber Bearings (LRB). The main features of elastomeric devices are the horizontal low stiffness and vertical load capacity need to transfer the entire dead and live load to the foundation. When this devices are installed at the base of the building, mechanical decoupling between superstructure and ground is achieved and, the vibration period of the structure shifts to higher period and the total acceleration of structural mass is reduced. Their effectiveness is tested by massive experimental tests and, by now, thousands of isolated buildings with this system demonstrate good performance when seismic event occurs.



#### 4 METASTRUCTURE

From analytical point of view, the study of seismic metamaterials is mainly based on the theory of phononic crystals and periodic chains of mass-in-mass system. The bandgap computed with the dispersion relation defines the attenuation regions of metamaterial in the space frequency-wavenumber [10]. Metastructure is proposed in this work, to replace elastomeric devices in standard base isolation system. In this study metamaterial is characterized by external element with inclusions therefore simplified lumped model is a bi-atomic chain or mass-in-mass chain. The parameters of the model are: mass of external element ( $m_1$ ), mass of internal element ( $m_2$ ), stiffness connection between consecutive external elements ( $k_1$ ) and stiffness connection between internal and external elements ( $k_2$ ). The dispersion relation of the periodic chain of the mass-in-mass system is given by:

$$m_1 m_2 \omega^4 - (k_2(m_1 + m_2) + 2m_2 k_1(1 - \cos(kL)))\omega^2 + 2k_2 k_1(1 - \cos(kL)) = 0 \quad (1)$$

Starting point of this study are the results obtained by experimental tests on a demonstrator built of four stacked concrete square plate in each of which five cylindric steel resonators are allocated [11]. Connections was realized by rubber elements excited in tension-compression regime. The demonstrator was tested under dynamic loading with sinusoidal input, from 1 to 8 Hz, applied at the bottom plate. Measurements of displacements confirm a bandgap near 5 Hz. From the bottom to the top, input signal is trapped, and the top plate does not move. Demonstrator was designed with external mass ( $m_1$ ) equal to 317 kg, total internal mass ( $m_2$ ) equal to 245 kg, external stiffness connection ( $k_1$ ) equal to 155e3 N/m and internal stiffness ( $k_2$ ) connection equal to 1080e3 N/m. These values are used in the following, as reference in design of metastructure simulated in this work.

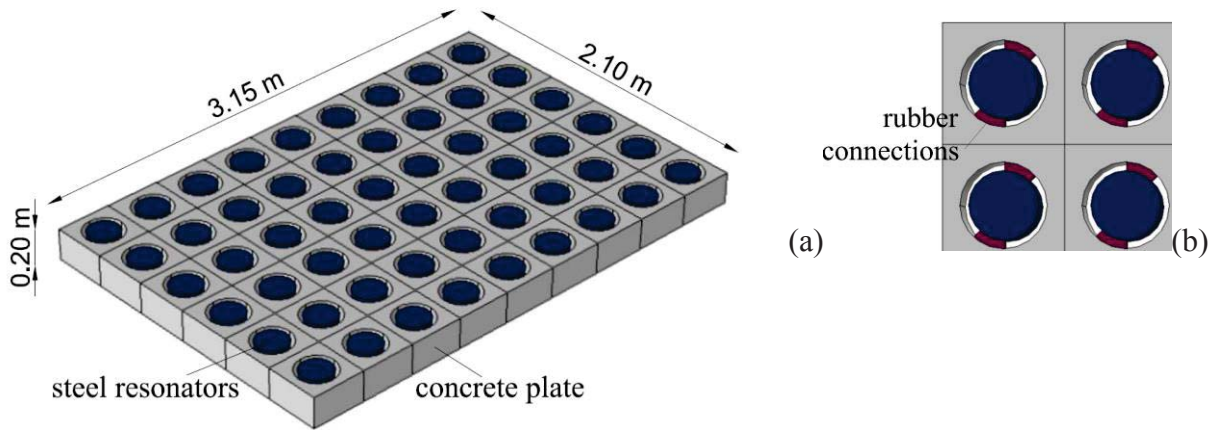


Figure 1: (a) geometry of one plate of the metastructure designed in this work with values shown in Tab 1. (b) details about rubber connection between resonators and concrete plate.

#### 5 NUMERICAL INVESTIGATION

In this part, seismic performance of a square plan concrete four-story frame building is studied. An artificial seismic signal is applied and the results between the performance of the proposed metafoundation and the standard base isolation are compared. The building has a symmetrical geometry, with side equal to 6 m, height of each story equal to 3.5 m, section column of 0.5x0.5m, section beam of 0.4x0.6 m. Concrete floors have thickness equal to 0.2



m and base floor, that ensure rigid motion of the isolated structure, 0.35 m. The dead load is estimated at 7 kN/mq while live load is set at 2 kN/mq.

The design of metastructure is performed in order to define the lower branch of the bandgap by keeping appropriate horizontal stiffness and by limiting structural mass. Reference design is the experimental device [11] whose plate can be used as modular element and in this work by considering six plate in 2x3 array. Fig.1 shows sketch of one plate of the metastructure while Tab. 1 collects geometrical and mechanical data:  $m_1$  is the concrete plate mass,  $m_2$  is the total mass of resonators,  $k_2$  is the liner compression/traction stiffness of rubber elements that connect resonators with concrete plate, while  $k_1$  is the horizontal stiffness between overlapped plates that is realized by appropriate connection elements. Theoretical expected dispersion relation obtained by using this design is shown in Fig.2.

$m_1$	$k_1$	$m_2$	$k_2$
1902 kg	0.31e6 kN/mm	1470 kg	1.08e6 kN/mm

Table 1: Mechanical lumped parameters of metastructure.

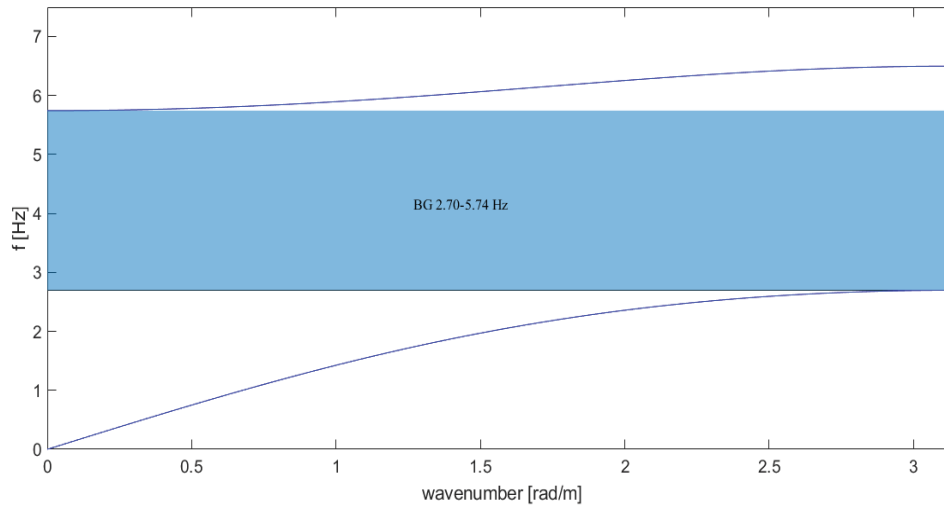


Figure 3: Dispersion curves of mass-in-mass chain with lumped parameters equal to data in Table 1. Theoretical expected bandgap starting at 2.70 Hz.

In order to compare the behavior of metastructure and standard base isolation with elastic devices (named BI in the following for brevity), equivalent linear stiffness for BI is assumed equal to  $k_2$ .

### 5.1 Artificial seismic input

Dynamic loading applied at the building is a set of artificial ground acceleration time-history computed through the software SIMKE\_GR (SIMulation of earthQuaKE ground motions) [12]. Indeed, in compliance with construction standards in design of structures for earthquake resistance (European codes and Italian national codes), seismic analyses can be performed by using a set of spectrum-compatible artificial accelerograms at elastic response spectra with a viscous damping equal to 5%. The source data of artificial earthquakes generation are collected in Table 2 and one of the accelerograms is shown in Figure 3. Accelerograms concern horizontal component of the ground motion while vertical one is neglected.

site	design life	ground type	ag/g	viscous damping
Messina (IT)	50	D	0.337	0.05

Table 2: Spectrum-data for the generation of the artificial horizontal seismic accelerograms.

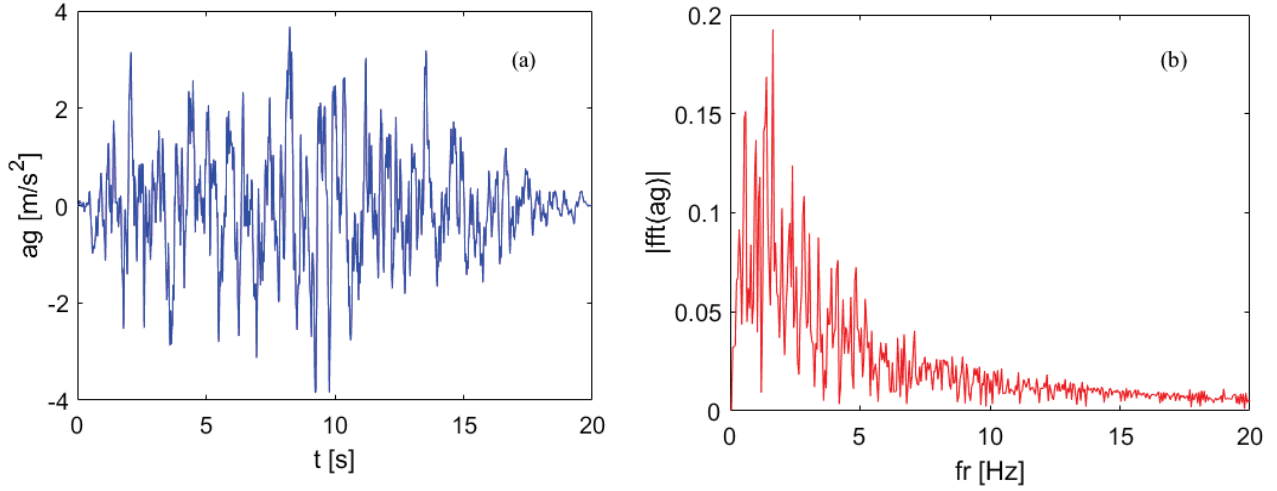


Figure 3: Artificial spectrum-compatible earthquake (a) time-history ground acceleration, (b) ground acceleration in frequency represented by Fourier amplitude spectrum.

## 5.2 Dynamic analysis: model

The building is modeled by using the structural software SAP2000 [13]. A diaphragm constraint is applied at each story to model high stiffness of the concrete floor. Metastructure is modeled by using a simplified configuration of points (one for each plate) connected by mechanical link with linear force-displacement law. Damping in metastructure is neglected in order to observe mechanical response associated with the design configuration of mass and stiffness. Linear dynamic analysis is performed by using direct integration method on Eq. 2 that represents the linear system of equations of motion of the building and metastructure (coupled) in which  $M$  is the stiffness matrix,  $C$  the viscous damping matrix,  $K$  the stiffness matrix,  $\ddot{u}$ ,  $\dot{u}$  and  $u$  are acceleration, velocity and displacement fields and  $\ddot{u}_g$  is the ground acceleration. Vertical motion is neglected in metastructure. Viscous proportional damping is set equal to 5% at 1 and 10 Hz.

$$M (\ddot{u} + \ddot{u}_g) + C \dot{u} + Ku = 0 \quad (2)$$

In addition to artificial earthquake, a sweep signal, modulated between 0.1 and 10 Hz, is applied at the base of the structure to check working frequency range of metastructure and frequency response function is evaluated as ratio between power spectral density of displacement field of the check point and that of input as shown in Eq.3.

$$FRF = 20 \cdot \log_{10} \frac{PSD(u_T)}{PSD(u_g)} \quad (3)$$

Results show comparison between response of structure with fix base, standard elastomeric devices and metastructures.

### 5.3 Results

The total displacement at the top of the building is shown in Fig. 4. Total displacement for isolated structures is almost entirely a rigid motion of the whole structure respect to the plane of the isolation system because bending modes are attenuated. Reduction of displacement when metastructure is set (red line) can be observed in the most time of structural response, in some points is closed at 50% compared to the BI case. This result improves performance in seismic protection because amplitude and number of oscillations of the superstructure is reduced. Fig. 5 shows the frequency response function of metastructures and highlights reduction at lower frequency compared to BI while peaks between 1 and 3 Hz concern local modes of the metastructure (motion in-phase and out-phase between plate and resonators).

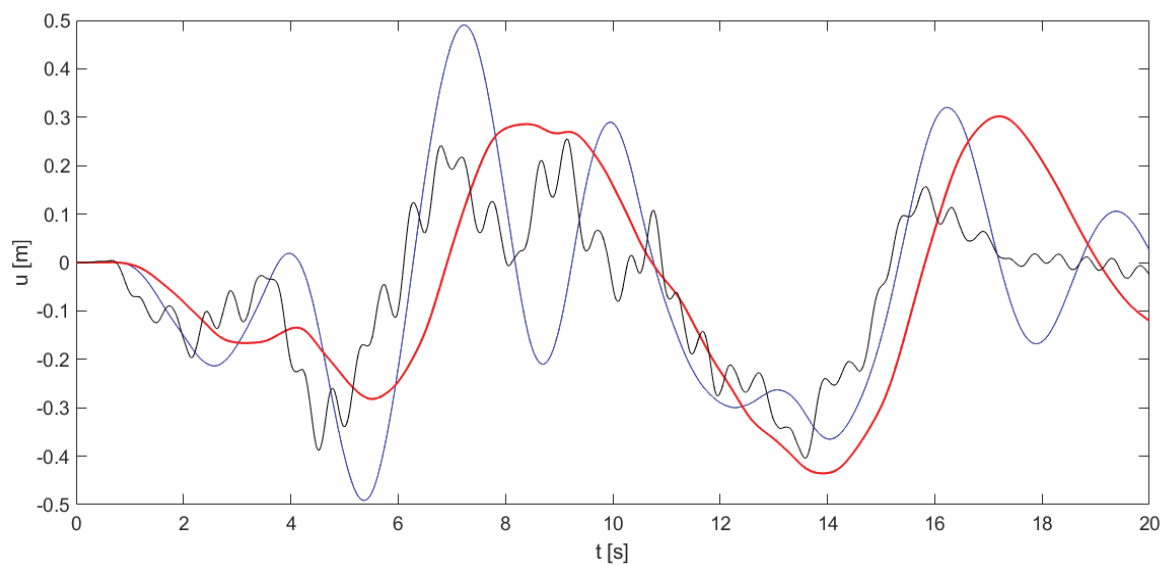


Figure 4: Time-history total displacement at the top of the building ( $u_T$ ) with fix base (black line), BI (blue line), metastructure (red line) by applying artificial earthquake ( $u_g$ ) .

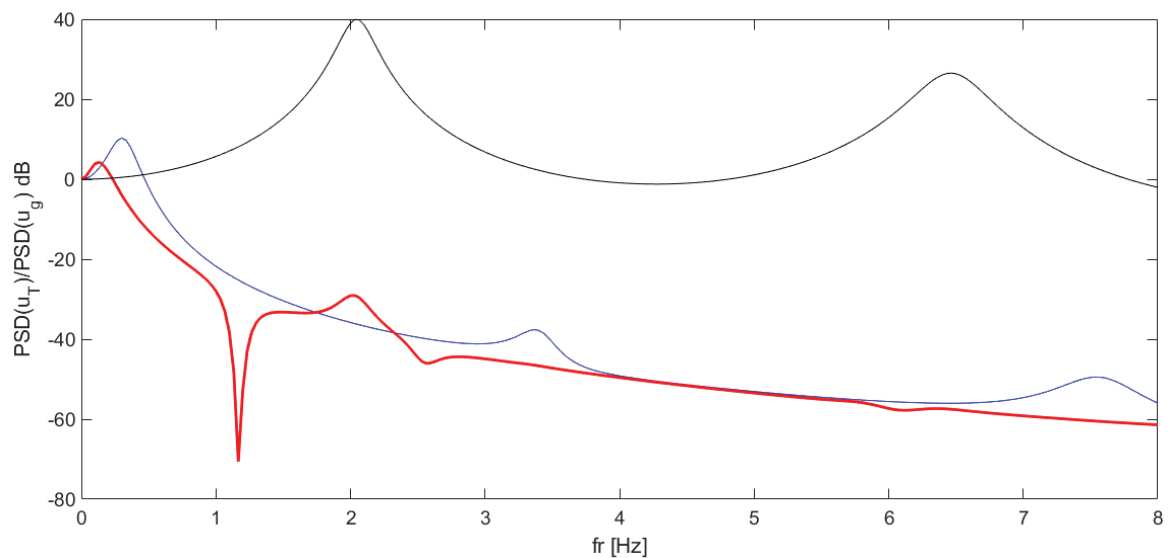


Figure 5: Frequency Response Function evaluated as ratio between power spectral density of total displacement at the top of the building ( $u_T$ ), with fix base (black line), BI (blue line), metastructure (red line), and ground motion ( $u_g$ ) set as modulated sweep signal.

## 6 CONCLUSIONS

- One metastructure characterized by four overlapped plates with inside resonators is proposed as innovative system of base isolation, by starting from good results in experimental investigation;
- The goal of metastructures would be the total isolation of the structure during earthquake but tuning bandgap at very low frequencies is very hard because requires lower stiffness and higher masses;
- By setting appropriate configuration of metastructure bandgap closed to 2 Hz is obtained and filter effect is enforced compared to standard BI system;
- Good reduction in oscillations and amplitude total displacements of four-story frame building under seismic dynamic loading is provided. This can have important benefits for the occupant because perception of earthquake is reduced.

## 7 ACKNOWLEDGEMENT

This work has been supported by MARIS srl (<https://www.maris-ricerca.it/>) and by the Project (Progetto Premiale) “Strategic Initiatives for the Environment and Security -SIES”. The authors acknowledge the discussions and support in learning SAP from the research group in structural mechanical and metamaterials of Professor Eleni Chatzi at ETH Zurich, particularly Dr. Andrea Colombi, Dr. Giulia Aguzzi and Dr. Panagiotis Martakis.

## REFERENCES

- [1] T.J. Cui, D.R. Smith, R. Liu, *Metamaterials, Theory, Design and Applications*, Springer, 2010.
- [2] D. Mu, H. Shu, L. Zhao, S. An; *A Review of Research on Seismic Metamaterials*, Advanced engineering materials (2019).
- [3] A.O. Krushynska, M. Miniaci, F. Bosia, N.M. Pugno, *Coupling local resonance with Bragg band gaps in single-phase mechanical metamaterials*, Extreme Mechanics Letters 12 (2017) 30–36.
- [4] Jing Bao, Zhifei Shi, Hongjun Xiang, *Dynamic Responses of a Structure with Periodic Foundations*, Journal of Engineering Mechanics, Vol.138 Issue 7 (2012).
- [5] Y. Zeng, Y. Xu, K. Deng, P. Peng, H. Yang, M. Muzamil, Q. Du, *A broadband seismic metamaterial plate with simple structure and easy realization*, Journal of Applied Physics, 125, 224901 (2019).
- [6] Z. Chenga, Z. Shia, A. Palermo, H. Xianga, W. Guoc, A. Marzani, *Seismic vibrations attenuation via damped layered periodic foundations*, Engineering Structures 211 (2020) 110427.

- [7] V. Dertimanis, I.A. Antoniadis, E.N. Chatzi, *Feasibility Analysis on the Attenuation of Strong Ground Motions Using Finite Periodic Lattices of Mass-in-Mass Barriers*, J. Eng. Mech., 2016, 142(9): 04016060
- [8] X.H. Shen, C.T. Sun, M.V. Barnhart, G.L. Huang, *Analysis of Dynamic Behavior of the Finite Elastic Metamaterial-Based Structure With Frequency-Dependent Properties*, Journal of Vibration and Acoustics, June 2018, Vol. 140 / 031012-1.
- [9] A. Colombi, R. Zaccherini, G. Aguzzi, A. Palermo, E. Chatzi *Mitigation of seismic waves: metabarriers and metafoundations bench tested*, Journal of Sound and Vibration, Volume 485, 27 October 2020, 115537.
- [10] L. Brillouin, *Wave propagation in periodic structures*, Dover (1953).
- [11] O. Casablanca, G. Ventura, F. Garescì, B. Azzerboni, B. Chiaia, M. Chiappini, and G. Finocchio, *Seismic isolation of buildings using composite foundations based on metamaterials*, Journal of Applied Physics 123, 174903 (2018).
- [12] Gelfi, P. 2009. SIMQKE\_GR, Artificial earthquakes compatible with response spectra, software, Internet site: [http://dicata.ing.unibs.it/gelfi/software/simqke/simqke\\_gr.htm](http://dicata.ing.unibs.it/gelfi/software/simqke/simqke_gr.htm).
- [13] CSI Analysis Reference Manual for SAP2000, ETABS, SAFE and CSiBridge (2017).

## SEISMIC PERFORMANCE OF DOUBLE FRICTION PENDULUM BEARINGS UNDER HORIZONTAL AND VERTICAL EXCITATION

Ioannis E. Kavvadias<sup>1</sup>

<sup>1</sup> Department of Civil Engineering, Democritus University of Thrace  
Campus of Kimmeria, Xanthi 67100, Greece  
e-mail: ikavvadi@civil.duth.gr

---

### Abstract

*In this study the effect of ground motion characteristics on the response of an isolated base using double friction pendulum bearings (DFPBs) is presented. Planar nonlinear time history analyses are performed considering one horizontal and the corresponding vertical component of natural ground motion records. Both far-fault and near-fault ground motion records are considered. In order to focus on the effect of the ground motion intensity measures on the DFPBs response, without taking into account the effect of any other structural characteristics, an analysis model comprised of two DFPBs coupled with a rigid beam is assumed. For this reason, a finite element modeling that can capture the kinematic behavior of the isolation bearing parts is adopted. In order to investigate the effect of the vertical seismic component on the response of the isolated base results in terms of peak developed displacements are presented. Moreover, the performance of ground motion intensity measures for use in probabilistic seismic demand models for isolated base under horizontal and vertical seismic component is assessed.*

**Keywords:** Seismic Isolation, Double Friction Pendulum Bearings, Vertical Ground Motion, Optimal Intensity Measures.

---



## 1 INTRODUCTION

Base isolation consist a seismic protection technique which may applied in both new and existing structures [1]. Two main categories of base isolation devices are in use, the rubber bearings and the friction pendulum ones. The single friction pendulum (SFP) bearings have been studied since 1990 [2-4]. Subsequently, bearings composed by multiple concave spherical surfaces, such as double friction pendulums (DFPs), have been also examined [5].

Isolation devices are principally described by low lateral stiffness. Due to this fact, the superstructure is decoupled from the ground by implementing isolators at a certain level. Thus, the seismic demands of the superstructure are significantly reduced, while large displacements are introduced at the isolators [1]. However, under near-fault ground motions, which are characterized by large amplitude, low frequency, and pulse type of excitation, the performance of the base isolation tends to be reduced [6].

Another feature of near-fault ground motions is the intense vertical component [7, 8]. The detrimental effect of the strong vertical excitation is examined in reinforced concrete buildings, bridges and isolated structures [9-16]. The performance of friction pendulum bearings is strongly affected by the axial load variation during the sliding phase [17, 18]. As such, the effect of vertical ground motions on the response of seismically isolated structures should be studied using more sophisticated models. Given that, in order to assess the seismic response under a probabilistic framework, and set the probabilistic seismic demand model (PSDM), the uncertainties introduced by the ground motions should be examined [19-21]. By this, the efficiency of several intensity measures (IMs) in predicting the seismic response of base isolated structures, under horizontal and vertical ground motions, is investigated.

In the present study the effect of seismic excitation characteristics on the response of an isolated base, formed using DFP bearings, is assessed. Specifically, 21 IMs are examined in order to conclude to the most optimal one upon which the PSDM should be conditioned. Near-fault, as well as far-fault natural ground motion records are considered. Moreover, both horizontal and vertical seismic excitation are assumed, in order to highlight the contribution of the vertical component on the seismic response, examining also the variation of the performance of the IMs in estimating the response of the isolated base.

## 2 OPTIMAL INTENSITY MEASURES

In recent years, probabilistic analysis has become widely used for structural engineering purposes and PSDMs have been developed aiming to predict the response of a structure under earthquakes of certain intensities. The most common tool for this assessment is to develop fragility curves of structures. Specifically, fragility expresses the probability ( $P$ ) that the capacity ( $C$ ) of a specifically measured engineering demand parameter (EDP) of a structure will exceed a certain level of demand ( $D$ ), for a specific ground motion IM, as defined by the following equation [22]:

$$P(D > C | IM) = \Phi \left( \frac{\ln(S_d / S_c)}{\sqrt{\beta_{D|IM}^2}} \right) \quad (1)$$

where  $\Phi$  is the standard normal cumulative distribution function,  $S_c$  is the median value of the capacity which is estimated through the adopted limit states and  $\beta_{D|IM}$  is the dispersion or logarithmic standard deviation for the demand conditioned the IM.

The median seismic demand  $S_d$  is related to an examined IM with the following expression:

$$S_d = a(IM)^b \quad (2)$$

where  $a$  and  $b$  are the linear regression coefficients for the logarithmic expression of the assumed scale law.

The linear regression analysis is performed between the engineering demand parameter calculated via the time history analyses and the corresponding IM values. The dispersion of the median demand is reported by the logarithmic standard deviation of the linear regression analysis (Eq. (3)). This parameter constitutes the demand uncertainty introduced in the probabilistic model.

$$\beta_{D|IM} \cong \sqrt{\frac{\sum (\ln(d_i) - \ln(a(IM)^b))^2}{N - 2}} \quad (3)$$

where  $N$  is the total number of the data.

The appropriate selection of an IM plays an important role in the accuracy of a probabilistic seismic demand analysis (PSDA) for structures. As such, the choice must be made based on criteria, presented in the literature, which help to distinguish the accuracy of the seismic assessment. An optimal IM is defined by primary factors such as efficiency, practicality, proficiency and sufficiency [22-25].

Efficient IMs are the ones that eliminate the dispersion of the results about the median, which means a decrease in the uncertainties introduced to the PSDM, resulting in superior fragility curves during the vulnerability assessment. A distinguished IM according to its efficiency is represented by a lower logarithmic standard deviation  $\beta_{D|IM}$  (Eq. (3)). Moreover, the coefficient of determination of the linear regression analysis ( $R^2$ ) could represent a parameter that denotes the performance of an IM regarding its appropriateness in predicting the structural damage [26]. Practicality refers to whether or not there is any direct correlation between an IM and the demand placed on the structure and is measured by the regression parameter  $b$  in the PSDM. Proficiency is a composite measure that assesses the effect of both efficiency and practicality as follows [25]:

$$\zeta = \frac{\beta_{D|IM}}{b} \quad (4)$$

### 3 EXAMINED GROUND MOTION RECORDS AND IMS

In order to examine the effect of the ground motion characteristics on the response of the isolated base a cloud analysis is performed using the natural ground motions proposed by FEMA P695 [27] are considered. The specific data set is comprised of both far-field and near-field ground motion records. The whole set consists 50 pairs of ground motions. However, due to the fact that vertical excitations records are not provided for 4 seismic events (i.e. RSN725, RSN496, RSN723, RSN1048), 46 pairs of ground motions are used. From those, 21 pairs are far-field records, while 25 are near-fault ones.

In order to designate the earthquake intensity measures (IMs) that affect the seismic response, a large number of seismic parameters is considered in the present study. Specifically, 20 IMs, of the horizontal seismic excitation, are taken into account which can be classified into amplitude, energy, spectral, and frequency parameters [28]. Amplitude parameters include peak ground acceleration (PGA), peak ground velocity (PGV), and peak ground displacement (PGD). The root mean square of acceleration ( $A_{RMS}$ ), of velocity ( $V_{RMS}$ ), and of displacement ( $D_{RMS}$ ), the characteristic intensity [29] ( $I_C$ ), the Arias intensity [30] ( $I_A$ ), the cumulative absolute velocity (CAV), the specific energy density (SED), the strong motion duration [31] ( $t_D$ ), the index proposed by Fajfar-Vidic-Fischinger [32] ( $I_{FVF}$ ) and the characteristic length scale [33, 34] ( $L_m$ ), fall into the class of energy ground motion parameters. Re-

garding the spectrum intensity measures, the acceleration spectrum intensity [35] (ASI), the velocity spectrum intensity [35] (VSI), the Housner spectral intensity [36] ( $SI_H$ ), and the spectral acceleration ( $Sa(T_i)$ ) that correspond to the fundamental vibration period of the superstructure ( $T_i$ ) are considered. The mean period [37] ( $T_m$ ), the ratio PGV/PGA, and the period ( $T_{pred}$ ) corresponding to the peak acceleration of the elastic response spectrum are assumed as frequency parameters.

#### 4 EXAMINED MODEL

Scope of this study is to examine the effect of the ground motion IMs on the response of a seismic isolated base using DFPBs, under horizontal and vertical excitation. As such, the DFPBs are simulated with a full three dimensional continuum modelling using the finite elements method. The analytical presentation of the adopted modelling approach, as well as its validation has been presented by Kavvadias et al. [38]. The detailed model of the bearing's geometry allows a complete description of its kinematic behavior, accounting the restoring forces, the variation of axial forces among the contact surfaces as a consequence of vertical acceleration or overturning moments, and uplift [39]. In order not to count the effect of any structural feature on the dynamic response, a simplified analysis model is examined. The analysis model consists of two identical isolation bearings connected with a rigid and massless beam. The gravity loads  $W$  are considered at the top of the isolators, while the ground motion excitation is applied at the base in terms of seismic acceleration. The schematic of the model, as well as the DFPB properties are presented in Figure 1.

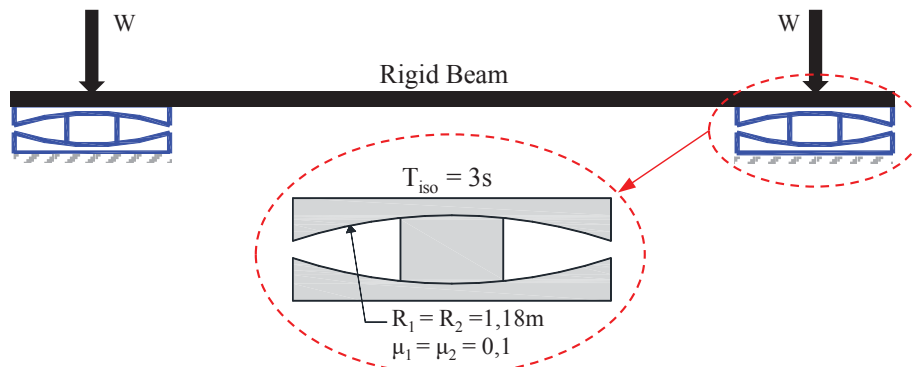


Figure 1: Schematic of the examined numerical model.

#### 5 RESULTS

Planar nonlinear time history analyses are performed using each horizontal component individually. Additionally, in order to examine the effect of the vertical ground motion, time history analyses are conducted assuming also the vertical excitation along with each horizontal one. The data are classified also according to the seismic record type to far-fault and near-fault. In order to evaluate the seismic response of the isolated structural system, the maximum bearing displacement (MBD) is considered as EDP.

In Figure 2 two representative force-displacements loops of the DFPBs are presented. It is obvious that vertical excitation causes an intense variation of the shear forces which can be justified by the variation of the axial forces due to the vertical acceleration. However, in both loops can be observed that the maximum developed displacements do not present a noticeable variation.

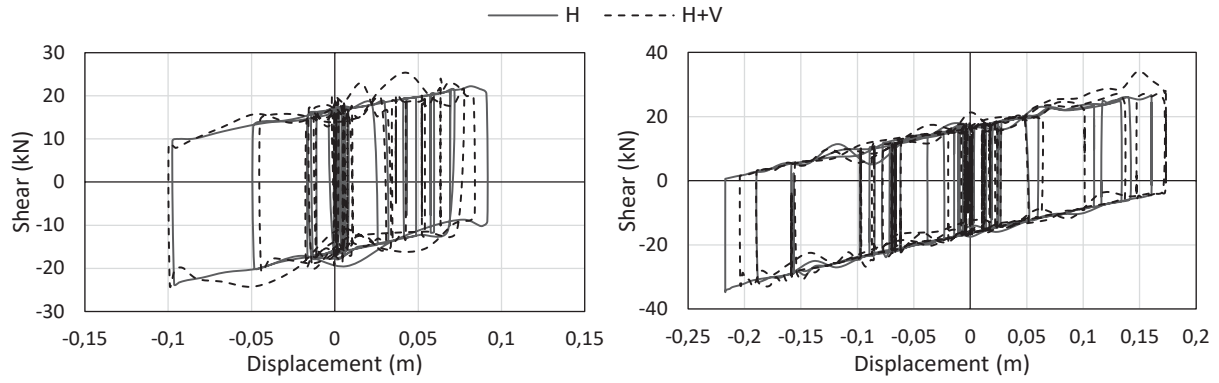


Figure 2: Force-Displacement hysteretic loops of the DFPBs.

In Figure 3 the MBDs for each analysis type is presented. Figure 3(a) depicted the results under far-field seismic records, while in Figure 3(b) the results under the near-fault records are illustrated. It can be observed that the maximum seismic demands are higher under near-fault records. However, regardless the ground motion record type, the maximum response seems not to be affected by the vertical excitation, as the maximum displacements considering only the horizontal component ( $MBD^H$ ) are fairly equal to the displacements assuming also the vertical component of the ground motion ( $MBD^{H+V}$ ). Although the detailed FEA modelling of the DFPBs, the effect of the vertical ground motion component on the MBD is negligible.

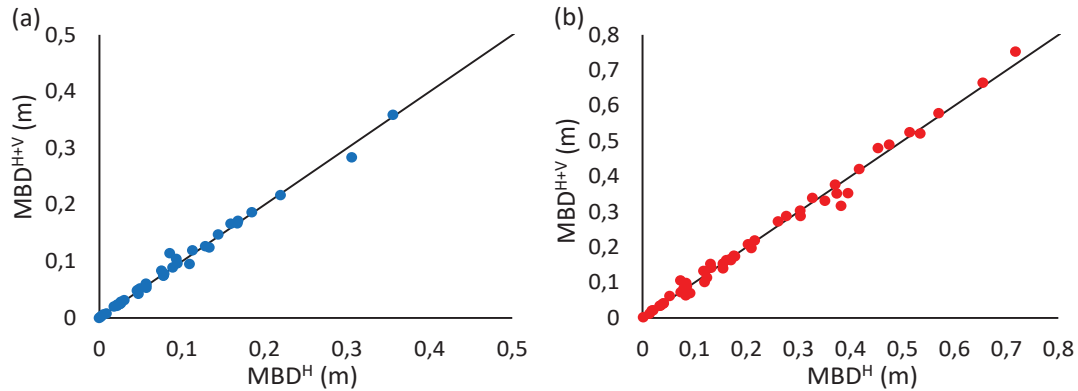


Figure 3: Comparison of the MBDs considering horizontal and horizontal along with vertical seismic excitation under (a) far-fault and (b) near-fault ground motion records.

As indicated above, the identification of an optimal IM in estimating the seismic demands, is based on criteria such as efficiency, practicality and proficiency. In Figure 4 the values of the coefficient of determination ( $R^2$ ), the standard deviation ( $\beta_{D|IM}$ ), the slope of the linear regression ( $b$ ) and the proficiency value ( $\zeta$ ) are presented. The IMs criteria values are presented comparatively regarding the ground motion record type and the consideration of the vertical ground motion on the analysis.

It is obvious that the presence of the vertical component do not affect the performance of the horizontal seismic excitation IMs. Therefore, there is no need to examine the effect of the characteristics of the vertical acceleration signal on the seismic demands, as it should be negligible.

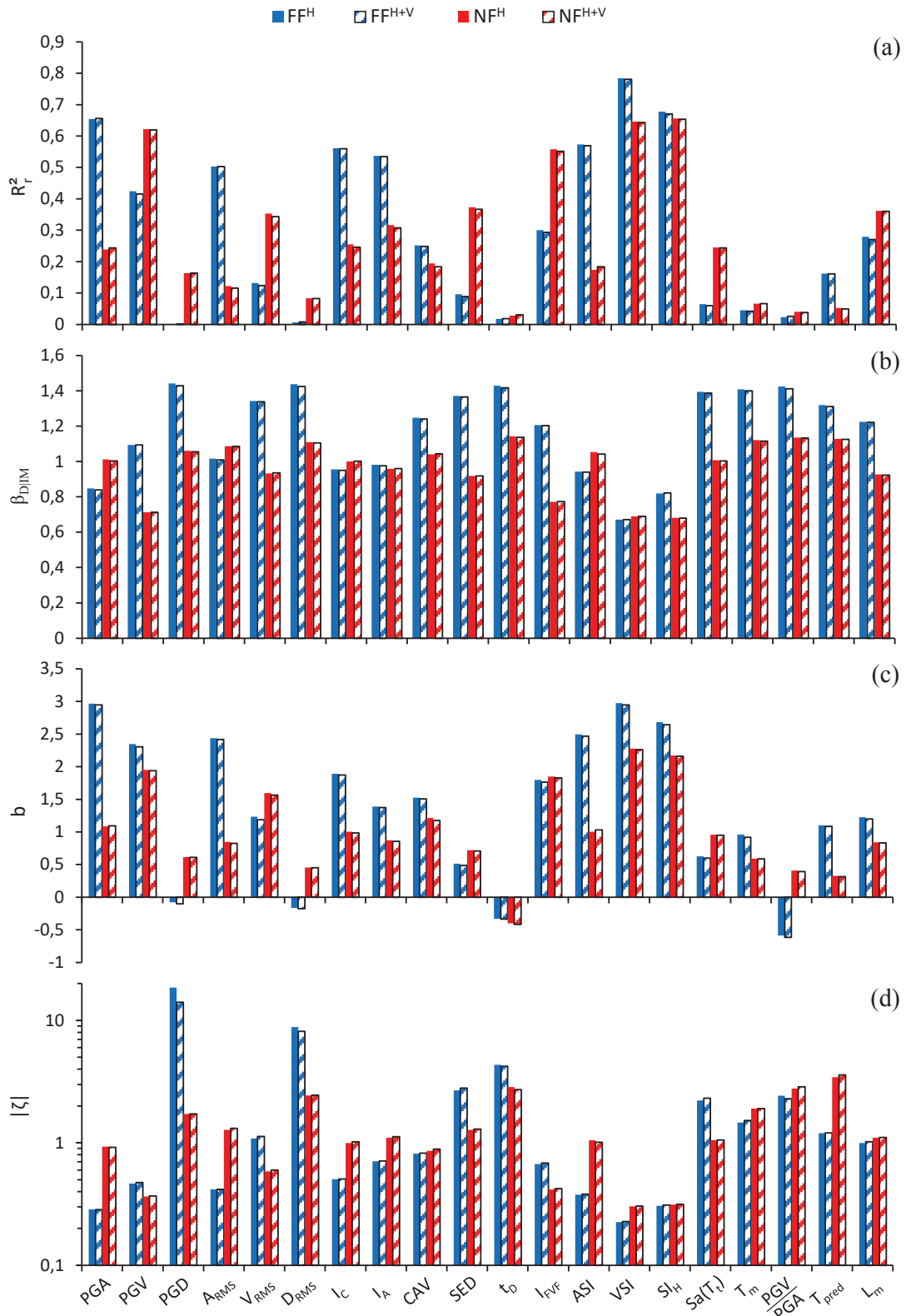


Figure 4: Values of (a) coefficient of determination  $R_r^2$ , (b) standard deviation  $\beta_{D|IM}$ , (c) slope of the linear regression  $b$  and (d) proficiency value  $\zeta$ .

In general the most optimal IMs are the parameters VSI and SI<sub>H</sub>. These two velocity based spectral parameters present at the same time the higher values of  $R_r^2$  and  $b$ , and the lower values of  $\beta_{D|IM}$  and  $\zeta$ . As such these parameters rank as the most optimal ones regardless the as-

assessment criteria. The performance level of the two aforementioned most optimal IMs are almost identical regardless the ground motion record type. Under far-fault excitations, acceleration based parameters such as PGA and ASI demonstrate high enough performance in predicting the seismic response with low uncertainties. Moreover, they present high level of practicality. That can be justified due to the fact that the acceleration level defines the initiation of sliding, given that a vast majority of the far-fault ground motions barely initiates the isolator's sliding. On the other hand, under near-fault excitations these parameters present poor performance. Furthermore, velocity based parameters such as PGV and  $I_{FVF}$  performs quite well in case of near-fault records. Finally, ground motion parameters such as PGD,  $\tau_D$  and frequency based ones are found to be the less optimal IMs to generate PSDMs for seismic isolated structures.

## 6 CONCLUSIONS

In the present study the effect of the ground motion intensity measures on the seismic response of a base isolated with double friction pendulum bearings is investigated. Moreover, the effect of the vertical ground motions is examined. Thus a finite element analysis modeling is adopted that can capture in high accuracy the kinematic response of the bearings. The main concluding remarks can be summarized as follows:

1. Vertical ground motion component may affect the shear forces of the bearings due to the variation of the axial forces, however does not significantly affect the developed maximum displacements.
2. Near-fault seismic records result to higher seismic demands.
3. The characteristics of the vertical excitations does not affect, in a systematic way, the developed maximum displacements of the isolation bearing. Therefore, the performance of the horizontal seismic component IMs presents identical performance regardless the consideration of the vertical seismic component.
4. The velocity spectrum intensity (VSI) and the Housner's spectral intensity ( $SI_H$ ) are identified as the most optimal IMs for use in probabilistic seismic demand models for the examined structural system under both far-fault and near-fault ground motion records.
5. Under far-fault records, peak ground acceleration (PGA) and acceleration spectrum intensity (ASI) follows, while under near-fault records peak ground velocity (PGV) and the intensity proposed by Fajfar-Vidic-Fischinger ( $I_{FVF}$ ) present also a high performance.

## REFERENCES

- [1] F. Naeim, J.M. Kelly, Design of seismic isolated structures. Wiley, New York, USA, 1999.
- [2] V. Zayas, S.S. Low, S.A. Mahin. A simple pendulum technique for achieving seismic isolation. *Earthquake Spectra*, **6**, 317–333, 1990
- [3] M. Constantinou, A. Mokha, A. Reinhorn, Teflon bearings in base isolation I: testing. *Journal of Structural Engineering*, **116**, 438-454, 1990
- [4] M. Constantinou, A. Mokha, A. Reinhorn, Teflon bearings in base isolation II: modeling. *Journal of Structural Engineering*, **116**, 455-474, 1990



- [5] D.M. Fenz, M.C. Constantinou, Behavior of the double concave Friction Pendulum bearing. *Earthquake Engineering and Structural Dynamics*, **35**, 1403–1424, 2006.
- [6] R.S. Jangid, J.M. Kelly, Base isolation for near-fault motions. *Earthquake Engineering and Structural Dynamics*, **30**, 691–707, 2001.
- [7] Y. Bozorgnia, M. Niazi, Distance scaling of vertical and horizontal response spectra of the Loma Prieta earthquake. *Earthquake Engineering and Structural Dynamics*, **22**, 695–707, 1993.
- [8] Y. Bozorgnia, M. Niazi, K.W. Campbell, Characteristics of free-field vertical ground motion during the Northridge earthquake. *Earthquake Spectra*, **11**(4), 515–525, 1995.
- [9] A.J. Papazoglou, A.S. Elnashai, Analytical and field evidence of the damaging effect of vertical earthquake ground motion. *Earthquake Engineering and Structural Dynamics*, **25**, 1109–1137, 1996.
- [10] Y. Bozorgnia, S.A. Mahin, A.G. Brady, Vertical response of twelve structures recorded during the Northridge earthquake. *Earthquake Spectra*, **14**(3), 411–432, 1998.
- [11] L. Di Sarno, A.S. Elnashai, G. Manfredi, Assessment of RC Columns Subjected to Horizontal and Vertical Ground Motions Recorded During the 2009 L'Aquila (Italy). *Engineering Structures*, **33**, 1514–1535, 2011.
- [12] C.C. Harrington, A.B. Liel, Collapse assessment of moment frame buildings, considering vertical ground shaking. *Earthquake Engineering and Structural Dynamics*, **45**(15), 2475–2493, 2016.
- [13] S.K. Kunnath, E. Erduran, Y.H. Chai, M. Yashinsky, Effect of near-fault vertical ground motions on seismic response of highway overcrossings. *Journal of Bridge Engineering*, **13**, 282–290, 2008.
- [14] F. Mazza, A. Vulcano, Effects of Near-Fault Ground Motions on the Nonlinear Dynamic Response of Base-Isolated RC Framed Buildings. *Earthquake Engineering and Structural Dynamics*, **41**, 211–232, 2012.
- [15] L. Landi, G. Grazi, P.P. Diotallevi, Comparison of Different Models for Friction Pendulum Isolators in Structures Subjected to Horizontal and Vertical Ground Motions. *Soil Dynamics and Earthquake Engineering*, **81**, 75–83, 2016.
- [16] F. Mazza, M. Mazza, Nonlinear Seismic Analysis of Irregular RC Framed Buildings Base-Isolated with Friction Pendulum System under Near-Fault Excitations. *Soil Dynamics and Earthquake Engineering*, **90**, 299–312, 2016.
- [17] G.M. Calvi, P. Ceresa, C. Casarotti, D. Bolognini, F. Auricchio, Effects of axial force variation in the seismic response of bridges isolated with friction pendulum systems. *Journal of Earthquake Engineering*, **8**(1), 187–224, 2004.
- [18] P.C. Roussis, M.C. Constantinou, Uplift-restraining friction pendulum seismic isolation system. *Earthquake Engineering and Structural Dynamics*, **35**, 577–593, 2006.
- [19] F. Mazza, R. Labernarda, Structural and non-structural intensity measures for the assessment of base-isolated structures subjected to pulse-like near-fault earthquakes. *Soil Dynamics and Earthquake Engineering*, **96**, 115–127, 2017.

- 
- [20] F. Mollaioli, A. Lucchini, Y. Cheng, G. Monti, Intensity measures for the seismic response prediction of base-isolated buildings. *Bulletin of Earthquake Engineering*, **11**, 1841–1866, 2013.
- [21] H. Ebrahimian, F. Jalayer, A. Lucchini, F. Mollaioli, G. Manfredi, Preliminary ranking of alternative scalar and vector intensity measures of ground shaking. *Bulletin of Earthquake Engineering*, **13**, 2805–2840, 2015.
- [22] P. Giovenale, A.C. Cornell, L. Esteva, Comparing the adequacy of alternative ground motion intensity measures for the estimation of structural responses. *Earthquake Engineering and Structural Dynamics*, **33**, 951–979, 2004.
- [23] N. Luco, C. Cornell, Structure-specific scalar intensity measures for near-source and ordinary earthquake motions. *Earthquake Spectra*, **23**, 357–392, 2007.
- [24] K.R. Mackie, B. Stojadinović, *Fragility basis for California highway overpass bridge seismic decision making*. PEER report, Berkeley, CA, University of California, 2005.
- [25] J.E. Padgett, B.G. Nielson, R. DesRoches, Selection of optimal intensity measures in probabilistic seismic demand models of highway bridge portfolios. *Earthquake Engineering and Structural Dynamics*, **37**, 711–725, 2008.
- [26] A. Elenas, Correlation between seismic acceleration parameters and overall structural damage indices of buildings. *Soil Dynamics and Earthquake Engineering*, 2000, **20**(1), 93–100, 2000.
- [27] FEMA P695, *Quantification of building seismic performance factors*. Federal Emergency Management Agency, Washington, DC, 2009.
- [28] S.L. Kramer, *Geotechnical earthquake engineering*. Prentice-Hall, Upper Saddle River, NJ, 1996.
- [29] A.H.S. Ang, Reliability bases for seismic safety assessment and design. Fourth U.S. National Conference on Earthquake Engineering, Earthquake Engineering Research Institute, Palm Springs, California, USA, 1990.
- [30] A. Arias, *A measure of earthquake intensity*. MIT Press, Cambridge, Massachusetts, 1970.
- [31] M.D. Trifunac, A.G. Brady, A study on the duration of strong earthquake ground motion. *Bulletin of the Seismological Society of America*, **65**, 581–626, 1975.
- [32] P. Fajfar, T. Vidic, M. Fischinger, A measure of earthquake motion capacity to damage medium-period structures. *Soil Dynamics and Earthquake Engineering*, **9**, 236–242, 1990.
- [33] N. Makris, C.J. Black, Dimensional analysis of rigid-plastic and elastoplastic structures under pulse-type excitations. *Journal of Engineering Mechanics*, **130**(9), 1006–1018, 2004.
- [34] E.G. Dimitrakopoulos, A.J. Kappos, N. Makris, Dimensional analysis of yielding and pounding structures for records without distinct pulses. *Soil Dynamics and Earthquake Engineering*, **29**(7), 1170–1180, 2009.
- [35] J. Von Thun, L. Roehm, G. Scott, J. Wilson, Earthquake ground motions for design and analysis of dams. *Earthquake Engineering and Soil Dynamics II—Recent Advances in Ground-Motion Evaluation, Geotechnical Special Publication*, **20**, 463–481, 1988.

- [36] G.W. Housner, Spectrum intensities of strong-motion earthquakes. *Symposium on Earthquakes and Blast Effects on Structures*, Los Angeles, California, USA, 1952.
- [37] E.M. Rathje, N.A. Abrahamson, J.D. Bray, Simplified frequency content estimates of earthquake ground motions. *Journal of Geotechnical and Geoenvironmental Engineering*, **124(2)**, 150–159, 1998.
- [38] I.E. Kavvadias, H.F. Bibo, and L.K. Vasiliadis, Finite element modeling of single and multi-spherical Friction Pendulum Bearings. *6th International Conference on Computational Methods in Structural Dynamics and Earthquake Engineering (COMPDYN 2017)*, Crete, Greece, June, 2017.
- [39] P.C. Tsopelas, P.C. Roussis, M.C. Constantinou, Nonlinear dynamic analysis of multi-base seismically isolated structures with uplift potential I: formulation. *Earthquake Engineering and Engineering Vibration*, **8**, 421-431, 2009.

## SEISMIC DEVICES FOR STEEL STORAGE STRUCTURES

Marco Simoncelli<sup>1\*</sup>, Bonaventura Tagliaferro<sup>2</sup>, Rosario Montuori<sup>2</sup>.

<sup>1</sup>Politecnico di Milano  
Department of Architecture, Built Environment and Construction Engineering Milano, Italy  
claudio.bernuzzi@polimi.it, marco.simoncelli@polimi.it

<sup>2</sup>University of Salerno  
Via Giovanni Paolo II, 132, 84084 Fisciano SA, Italy  
{btagliaferro,r.montuori}@unisa.it

**Keywords:** Steel Structures, Adjustable Pallet Racks, Seismic Standards, Eurocode

**Abstract.** *The importance of the logistics sector has increased even more in the last year, due to the Pandemic event which lead to an increasing of the online purchases. Goods and products are generally located in steel frames known as steel racks or simply racks. Consequently also the safe design of these structures, i.e. preserve their fully functionality and avoid their collapse, is becoming of paramount importance, especially when they are located in strong and moderate seismic zones. Despite pallet rack provisions for seismic loads have been significantly improved in the recent years, only two classic ways to enhance the seismic performance are considered: rack netting and structural strengthening. Both of these suggested solutions are not fully effective to preserve the integrity of the stored products that, when subjected to strong accelerations, can topple and fall down. The only reliable and effective systems seem to be the introduction of seismic devices, such as base-isolation and energy dissipation systems. Since no indications about these techniques are reported in the standards, many researches worldwide are trying to fill this gap. Unfortunately, up to now, just theoretical studies and very limited applications are available in literature. In the present paper a short overview on the base isolation systems available on the market for different steel storage rack typologies is presented highlighting main advantages and defects of each solution.*

## 1 SEISMIC FEATURES OF PALLET RACKING SYSTEMS

Storage racking systems are engineered structures which are designed to withstand high loads during their life. In many countries all over the world, performance requirements and compliant criteria are established either by law or by technical recommendations, which often regard seismic actions as well. Typical rack frames (Figure 1) are made by open cold-formed thin-walled steel members, which lead to significant and non-negligible torsional effects. In fact, designers must be able to account for the calculation of *bimoment distribution* along the members and the associated tangential and normal warping stress during the design of rack frames [1]. In addition, these members are often prone to local and/or distortional buckling phenomena, which largely precede the attainment of the yielding capacity. These profiles do not guarantee the exploitation of the plastic capacities of the cross sections [2]. For this reason, designers cannot rely on the capacity design principles [3] enforced by the mainstream codes worldwide [4, 5]. For the plastic design of such structures, it is important to rely exclusively on the post-yielding capacity of connections. The cyclic response of standard beam-to-column rack joints is remarked by a strong pinched behaviour. The typical relationship between the bending moment and the relative upright-beam rotation shows a considerable loss of stiffness after the first cycle [6, 7, 8]. Also the connections between uprights and building slab are characterised by a very limited degree of flexural stiffness and bending resistance. In most of the cases, when the cross-aisle direction is considered, the seismic action can pose a risk for the overturning, which becomes the most dangerous limit state. Nevertheless, as happened for the beam-to-column connections, the nonlinear cyclic behaviour can provide a non-negligible ductility to the structure. The main peculiarity of these structures is the quite limited self-weight, which is generally not greater than 5% of the payload. This characteristic brings to periods of vibration which are greatly dependent on the considered level of occupancy, affecting hence either the seismic effects and the structural responses. The design is governed by different load conditions: i) the fully loaded rack (100% occupancy); ii) only the top storage level fully occupied and iii) occupancy levels from 50% to 70% of the total load. These conditions are prescribed in both the static (EN15512:2021 [9]) and the seismic (EN16681 [10]) design codes.

For seismic design purposes, racks are often broken down into two planar lateral resisting sub-systems, which can be used to assess the overall performance of the structure. The down-aisle structural scheme can be studied as a moment-resisting frames; they are made up of uprights (vertical elements) that are connected to pallet-beams (horizontal elements) by means of special beam-end connectors. A great body of research focused on studying its performance by exploiting the analogues techniques used for standard buildings [12]. Down-aisle frames have fundamental periods usually longer than 2.00 seconds (see, [11]), which entails a higher demand in terms of displacement.

The cross-aisle structural scheme is often truss-like and tends to have fewer internal degrees of freedom, thus making fragile collapse modes most likely. Hence, as also shown by many works [13, 14, 15]. Hence, its lateral resistance is promoted by the flexural behaviour of the base-plate connections and the stiffness of the braces. Nevertheless, this scheme gives to the upright frames a high degree of stiffness, which may cause excessive accelerations at decks level. This last circumstance sets the stage for the sliding of pallets on the supporting beams, which can lead to shedding of goods, endangering the health of workers/customers or damage some structural parts and thus likely triggering cascading effects. In the cross-aisle direction, the fundamental period is generally short, comprised between 0.5s and 1.0s [16, 17], placing the structure in the most energetic part of the commonly defined design spectra.



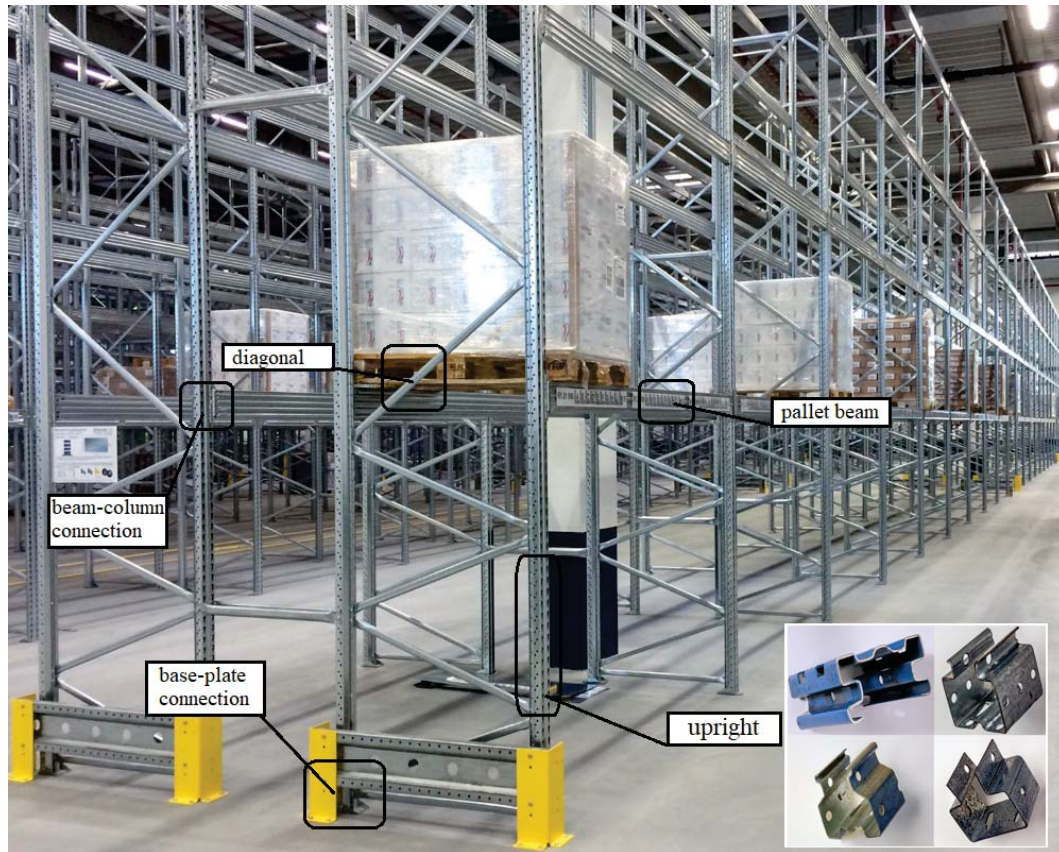


Figure 1: Typical steel storage pallet rack and its main components [11]

Despite the great efforts made to develop more safe and update standards [10], there are issues which still remain not solved. In particular, during a seismic events pallets can overturn and impact against the steel structural skeleton frame causing the well-known *domino effects*, i.e. the progressive collapse of the entire structural system, as showed in 2. An adequate isolation system could be useful to prevent also this phenomena.



Figure 2: Collapse of a warehouse after an earthquake in Italy [18]



## 2 SEISMIC ISOLATION AND ENERGY DISSIPATION DEVICES

Nowadays, a large variety of devices and techniques are available for seismic isolation of structures, often increasing in its use in highly exposed seismic areas [19], where seismic design of structures can be challenging when post-earthquake functionality is considered [20]. Base isolation systems (BIS) are known to be the most cost-effective and efficient devices for earthquake mitigation [21]. In general, BIS introduces a layer between structures and foundations (or bases) consisting of suitable devices with low lateral stiffness, which almost completely retain the previous vertical stiffness. The main effect of inserting the isolation system is a major shift in the fundamental vibration period of the structure that can be selected to be quite distinct from the energy contents of most predicted seismic events.

Similar benefits are demonstrated when the BIS technique is applied to racking systems. The research proposed by [22, 23] shows that if a warehouse is treated as a standard building, several advantages can be obtained when the seismic performance is evaluated. In particular, the proposed solution concerned the application of elastomeric seismic isolators at the base of the huge warehouse, under the concrete slab, as can be done in traditional buildings. Authors demonstrated a non-negligible benefits especially in terms of reduction of relative displacements and torsional effects. However, despite this approach is promising, it is not always applicable, and its convenience may stuck to only one structural direction due to a quite remarkable difference in periods. For this reason some pieces of research focused on proposing purposely developed hardware to be used for rack systems.

### 2.1 Seismic isolators for cross-aisle direction

#### 2.1.1 Pellegrino® isolation system

The trademark Pellegrino® identifies a system that provides seismic isolation along the cross-aisle direction alone to pallet type steel storage racks, by incorporating high damped elastomeric bearings and friction plates (Figure 3). Filiatrault et al. (2008) [24] presents a summary of the experimental results of isolated pallet racking tests performed on the triaxial shake table at the University of Buffalo (USA). The proposed Pellegrino® isolation system works in the cross-aisle direction and can cut down the amount of energy that is transmitted to the superstructure, thus reducing the likelihood of content spillage. Figure 3 shows a detailed view of the system, which consists of a *U-shape* plate (*Horizontal Support*), inserted inside a steel box (*Box Fabrication*) which is welded on the base plate (*Base Plate*). For the sake of brevity more details are not reported here. The base plate must be anchored to a rigid slab by means of anchor bolts. The results obtained from full-scale experimental tests [24] showed: i) the system reduce greatly the top accelerations in the cross-aisle direction but it has also some beneficial effects in reducing the accelerations in the down-aisle direction. The efficiency of the base isolation system in reducing the cross- and down-aisle accelerations increases with the weight of the merchandise. This beneficial effect is directly related to the changing in the fundamental period of vibration which increase in both directions with respect to the natural period of the racks with fixed bases; ii) damage on the uprights and merchandised overturning, which characterised the fixed base tests, have never observed in the base isolated cases; iv) the system brings to a great reduction of the interstorey drifts.

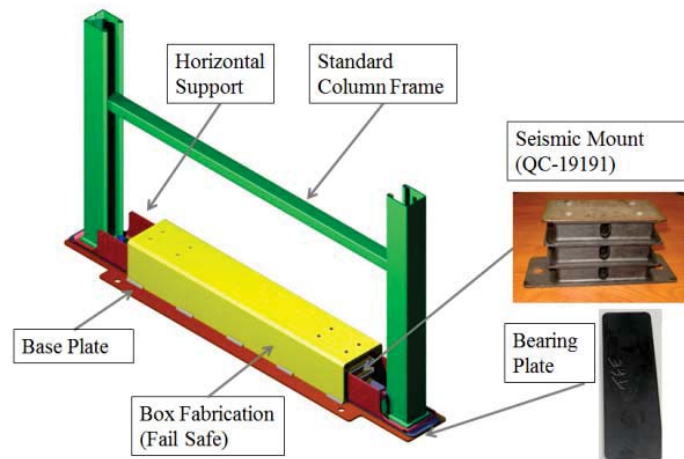


Figure 3: device installed under a single-entry pallet rack, render of Pellegrino® system (font <https://www.ridgurak.com/>)

### 2.1.2 IsolGOODS® isolation system

FIP MEC has developed a quite novel device (Figure 4) that is an unidirectional seismic isolation device that provides seismic isolation to the rack in the cross-aisle direction only. This solution is effective because the fundamental period of racks in the cross-aisle direction is usually short, and thus the isolation system can provide a greater shift in period while keeping a small footprint. This allows to use the pallet slots at ground level, as in a conventional pallet rack, while part of said pallet slots is lost when using multi-directional isolators. Additionally, the system is able to prevent the up-lift of the rack, that could happen in particular load cases under high seismicity actions, in particular in single-entry pallet racks. IsolGOODS® is classified as a pendulum isolator or Curved Surface Slider (CSS), as defined in [25], with a single surface of sliding. Low-lateral flexibility is guaranteed by a low-friction material, and FIP MEC uses a particular material for this device, i.e. FIP friction material (FFM), which ensures very high load-bearing capacity and wear resistance [26]. The performance of the IsolGOODS® device has been assessed by means of shake table test performed at the FIP Laboratory Tests (Italy). A one-bay four-storey pallet rack was equipped with the presented isolation system and its dynamic behaviour was studied under a set of ground motions, as discussed in Tagliaferro et al. (2021) [17].



Figure 4: device installed under a single-entry pallet rack: render view of IsolGOODS® solutions [11]

Together with the two presented solutions, other special devices have been developed by dif-

ferent company during the last years for storage racks, like the LOKI system one (<http://www.lokibase.com>, accessed 2021). However, up to now, there are no scientific results published on international journals for this or other systems.

## 2.2 Energy dissipation

For the points introduced in the previous section, the common procedures enforced by many codes for the seismic design of structures associate a certain structure ductility to a certain degree of energy dissipation. The most common approach foresees the use of a factor used to scale down the seismic demand, by inherently assuming that part of the energy that an earthquake can possibly transmit to a structure is partially dissipated/avoided. In general, a dissipative structure can be designed by either locating ductile zones or adding extra devices to perform that duty. The latter represents the approach that should be followed for inherently fragile structures.

### 2.2.1 Uplifting and sliding friction base-plates

The considered device was proposed as a friction-based devices and can provide energy-dissipation by means of wide and stable loops, with a negligible hardening phenomenon and experiencing no damage. For seismic resistant structures, purposely designed devices are commonly embedded into braces [27], beam-to-column joints, and into column-base joints [28], whereas it is always important to guarantee an even distribution of inter-storey drifts to exploit the displacement-dependent energy dissipation of these devices [29]. A novel dissipation joint was studied by Tang et al. (2017) [30] for adjustable pallet racking systems. It was developed for low and medium-rise racks, and the method consists of inserting a steel sliding friction base-plate connected to all the uprights (Figure 5(a)). The device, presented for the first time in Clifton (2005) [31] (Figure 5(d)), can dissipate energy thanks to a friction-based mechanism rather than forming yielding zones at the base connections. On top of this, this device promotes a rocking behaviour, so that, when the device is activated, the structure benefits from a further shift in period.

## 2.3 Seismic performance of Grana cheese steel racks

As it is well-known, Grana is a type of Italian cheese proposed in the form of large wheels. Generally Parmigiano cheese is stored in structures made by composed steel tubular columns (two tubes of  $50 \times 50$  mm with thickness of 3 or 4 mm and a global height from 7 to 9 m) having 1.5 m of span (Figure 6). Along the cross-aisle direction, each bay is connected by means of wooden panels, on which the cheese wheels rely, and via a continuous tubular steel on the top. Global length can vary from 18 to 40 m. When the steel rack is connected to the concrete wall (case S2 of Figure 6), it is simply supported on the floor, i.e. no anchors are present. On the other hand, when it is anchored to the floor, it is not connected to counter walls (case S1 of 6). Bracings are always present only in the down-aisle direction. A great number of these structures have been designed more than 20 years ago, considering only vertical forces (with no seismic actions) and, therefore, they are generally in an unsafe condition. For this reason, earthquakes occurred in May 2012 in Emilia Romagna (Italy) caused causes severe damages to grana warehouses, that progressively collapsed causing a domino effect leading to the loss/depreciation of several thousands of tons of grana cheese.

After this catastrophic event more attention has been paid to the seismic behaviour of these structures. Franco et al. [32] proposed a complete study on the dynamic behaviour of these racks, focusing the attention on the seismic improvement techniques. A solution proposed

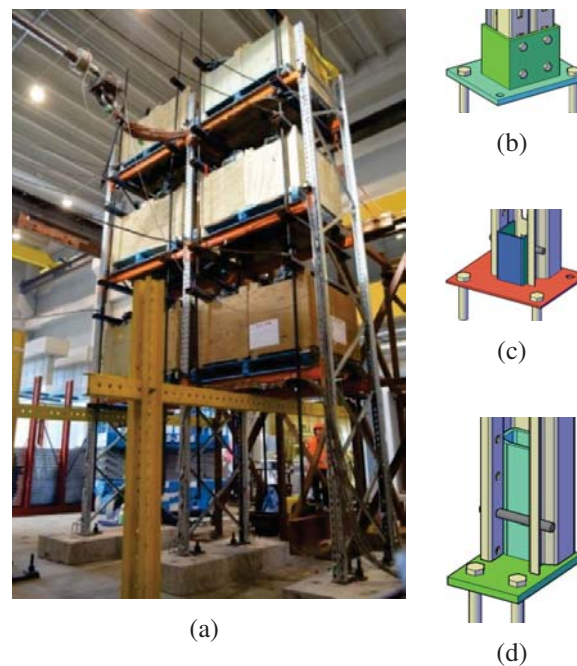


Figure 5: (a) Test setup of the fully loaded frame [30]; sketches of the three connections compared: (b) rigid base-plate, (c) yielding base-plate and (d) friction base-plate

by the Authors is to use a passive-control system: viscous dampers are directly connect to the surrounding concrete structures (see, S3 of Figure 6). The time-history analyses of the proposed configurations have shown that the use of dampers presents noteworthy advantages for all cases in which the constraint degree of the racks is augmented and, consequently, their stiffness is increased. The advantages are in terms of stress reduction in the rack elements, and of reaction forces transmitted to the surrounding support structures.

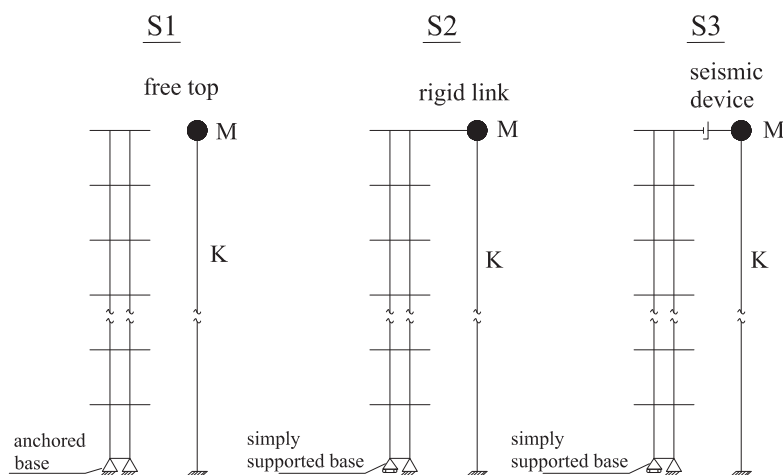


Figure 6: Three structural configurations that can be considered to simulate the *scalere* in the cross-aisle direction (after Franco et al [32]).

Furthermore, as discussed in [33], some producers, instead of performing specific seismic study on their warehouse, decided to renew completely the steel structures by changing com-

pletely the structural system. The brand new structures that store Grana cheese consist of cold-formed columns; the components of the bracing system are made using structural bolts, instead of welding. Boxed composite columns (different from producer to producer) are realised by coupling two open cold-formed mono-symmetric channels or sigma members. Along the columns height (in general about 7-9 m), horizontal L-profiles (angles) are connected, vertically spaced at about 330 mm and protrude beyond the central column as cantilever beams supporting the wooden boards (with 30 mm thickness), on which cheese wheels are directly located. In the longitudinal (down-aisle) direction, the geometry of the oldest and new type cheese rack is the same, differing only for the structural components and for the connection system between columns. This new frames are never connected to the surrounding concrete structure and in seismic areas, rely completely on the hysteric behaviour of the base-plate.

### 3 FINAL REMARKS

The deep understanding of the seismic performance of steel structures used to store good and products, known as steel storage pallet racks, is becoming of a paramount importance. In the specific standards only the classic techniques to improve structural behaviour of racks in seismic zones are provided, with no indications about the seismic isolation or energy dissipation devices. If overturning of stored goods is of concern, there are only two ways reported for the improvement of the safety of racks in seismic zones: rack netting and structural strengthening. The rack netting is a steel netting installed on all sides of the rack, covering the bay openings from top to bottom. It can be noted that if netting is installed, it then needs to be removed and reinstalled every time a storage slot is accessed. As regards the latter provision, it can be noted that it allows the structure to meet the code requirements, but increases the stiffness of the structure at the same time, adding rigidity and introducing higher accelerations throughout the system. The two approaches can be used together, but neither rack netting nor structural strengthening protect the rack and prevent adequately the product shedding.

The product shedding prevention must be always considered in the design process, being the total cost of stored goods generally much higher than the cost of the structural components. Seismic isolation seems to be a very useful and effective solution, and a number of investigations are nowadays in progress in many parts of the world. The paper has shortly discussed the main characteristics of several devices applied to different typologies of steel storage racks, by reporting studies taken from the available literature. The two innovative systems called RIGID-U-RAK system (Pellegrino®) and FIP MEC System (IsolGOODS®) are reported showing main characteristic and advantages of each solution. The results show that the application of a seismic isolation system can reduce accelerations on both cross- and down-aisle directions, and avoid the overturning of the stored goods and damage on the uprights. Finally, the use of dissipative devices is discussed. It can be an effective and low-cost solution as demonstrated by Tang et al. (2017) and Franco et al. (2015). Devices of such kinds can provide rack structures with more resilience, for the design and retrofit of structures, as it is shown in the collected research.

### 4 ACKNOWLEDGEMENTS

The second author's Ph.D. scholarship is granted by the Italian Ministry for Education, University and Research (MIUR) as part of the program "Dottorati Innovativi a caratterizzazione industriale", ID DOT 1328490-3, funded by the European Union (Structural Funding ERDF-ESF for "Research and Innovation" 2014-2020). The authors are grateful for the support.



## REFERENCES

- [1] Claudio Bernuzzi, Alice Pieri, and Veronica Squadrito. Warping influence on the static design of unbraced steel storage pallet racks. *Thin-Walled Structures*, 79:71 – 82, 2014. ISSN 0263-8231. doi: <https://doi.org/10.1016/j.tws.2014.01.024>.
- [2] Rosario Montuori, Giammaria Gabbianelli, Elide Nastri, and Marco Simoncelli. Rigid plastic analysis for the seismic performance evaluation of steel storage racks. *Steel and Composite Structures*, 32(1):1–19, 07 2019.
- [3] Michael N. Fardis. Capacity design: Early history. *Earthquake Engineering & Structural Dynamics*, 47(14):2887–2896, 2018. doi: 10.1002/eqe.3110.
- [4] European Committee for Standardization CEN, EN1998-1. *Eurocode 8 - Design of Structures for Earthquake Resistance-Part 1: General Rules, Seismic Actions and Rules for Buildings*. CEN, 2005.
- [5] ANSI/AISC 360-16. *Specification for structural steel buildings*. American Institute of Steel Construction, US, 2016.
- [6] Claudio Bernuzzi and Marco Simoncelli. An advanced design procedure for the safe use of steel storage pallet racks in seismic zones. *Thin-Walled Structures*, 109:73 – 87, 2016. ISSN 0263-8231. doi: <https://doi.org/10.1016/j.tws.2016.09.010>.
- [7] Federico Gusella, Maurizio Orlando, and Paolo Spinelli. Pinching in steel rack joints: Numerical modelling and effects on structural response. *International Journal of Steel Structures*, 19(1):131–146, Feb 2019. ISSN 2093-6311. doi: 10.1007/s13296-018-0095-x.
- [8] Alper Kanyilmaz, Carlo Andrea Castiglioni, Giovanni Brambilla, and GianPaolo Chiarelli. Assessment of the seismic behaviour of braced steel storage racking systems by means of full scale push over tests. *Thin-Walled Structures*, 107:138–155, 2016.
- [9] EN 15512. *Steel Static Storage Systems – Adjustable Pallet Racking Systems – Principles for Structural Design*. European Committee for Standardization, Brussels, 2021.
- [10] EN 16681. *Steel Static Storage Systems – Adjustable Pallet Racking Systems – Principles for Seismic Design*. European Committee for Standardization, Brussels, 2016.
- [11] Marco Simoncelli, Bonaventura Tagliaferro, and Rosario Montuori. Recent development on the seismic devices for steel storage structures. *Thin-Walled Structures*, 155:106827, 2020. ISSN 0263-8231. doi: <https://doi.org/10.1016/j.tws.2020.106827>.
- [12] Claudio Bernuzzi and Marco Simoncelli. Steel storage pallet racks in seismic zones: Advanced vs. standard design strategies. *Thin-Walled Structures*, 116:291 – 306, 2017. ISSN 0263-8231. doi: <https://doi.org/10.1016/j.tws.2017.03.002>.
- [13] James R. Maguire, Lip H. Teh, G. Charles Clifton, and James B.P. Lim. Residual capacity of cold-formed steel rack uprights following stomping during rocking. *Journal of Constructional Steel Research*, 159:189 – 197, 2019. ISSN 0143-974X. doi: <https://doi.org/10.1016/j.jcsr.2019.04.039>.



- [14] James R. Maguire, Lip H. Teh, G. Charles Clifton, and Timothy J. McCarthy. Equivalent static force method for selective storage racks with uplifting baseplates. *Journal of Constructional Steel Research*, 165:105821, 2020. ISSN 0143-974X. doi: <https://doi.org/10.1016/j.jcsr.2019.105821>.
- [15] Zhaoqi Huang, Yue Wang, Xianzhong Zhao, and Ken S. Sivakumaran. Determination of the flexural behavior of steel storage rack baseplate upright connections with eccentric anchor bolts. *Thin-Walled Structures*, 160:107375, 2021. ISSN 0263-8231. doi: <https://doi.org/10.1016/j.tws.2020.107375>.
- [16] Dimitris Tsarpalis, Dimitrios Vamvatsikos, and Ioannis Vayas. Simplified models for the nonlinear analysis of arsw structures under seismic loading. pages 5756–5771, 01 2019. doi: 10.7712/120119.7343.19687.
- [17] Bonaventura Tagliaferro, Rosario Montuori, and Maria Gabriella Castellano. Shake table testing and numerical modelling of a steel pallet racking structure with a seismic isolation system. *Thin-Walled Structures*, Under review, 2021.
- [18] Alper Kanyilmaz, Carlo Andrea Castiglioni, Giovanni Brambilla, and GianPaolo Chiarelli. Experimental assessment of the seismic behavior of unbraced steel storage pallet racks. *Thin-Walled Structures*, 108:391–405, 2016.
- [19] Antonello De Luca and Laura Giovanna Guidi. State of art in the worldwide evolution of base isolation design. *Soil Dynamics and Earthquake Engineering*, 125:105722, 2019. ISSN 0267-7261. doi: <https://doi.org/10.1016/j.soildyn.2019.105722>.
- [20] Khaled Ghaedi, Zainah Ibrahim, Hojjat Adeli, and Ahad Javanmardi. Invited review: Recent developments in vibration control of building and bridge structures. *Journal of Vibroengineering*, 19:3564–3580, 08 2017. doi: 10.21595/jve.2017.18900.
- [21] Peng Pan, Dan Zamfirescu, Masayoshi Nakashima, Nariaki Nakayasu, and Hisatoshi Kashiwa. Base-isolation design practice in japan: introduction to the post-kobe approach. *Journal of Earthquake Engineering*, 9(1):147–171, 2005. doi: 10.1080/13632460509350537.
- [22] Vojko Kilar, Simon Petrovcic, David Koren, and Simon Silih. Seismic analysis of an asymmetric fixed base and base-isolated high-rack steel structure. *Engineering structures*, 33:3471–3482, 2011.
- [23] Vojko Kilar, Simon Petrovcic, David Koren, and Simon Silih. Cost viability of a base isolation system for the seismic protection of a steel high-rack structure. *International Journal of Steel Structures*, 13(2):253–263, 06 2013.
- [24] Andre Filiatrault, Peter Higgins, Assawin Wanitkorkul, James Courtwright, and Robert Michael. Experimental seismic response of base isolated pallet-type steel storage racks. *Earthquake Spectra - EARTHQ SPECTRA*, 24, 08 2008. doi: 10.1193/1.2942375.
- [25] EN 15129. *Anti-seismic devices*. European Committee for Standardization, Brussels, 2009.

- [26] FIP Industriale. *SCatalogue S04 - Curved Surface Sliders*. Padova, Italy. Available on-line at <http://www.fipindustriale.it>, 2013.
- [27] Vincenzo Piluso, Rosario Montuori, Elide Nastri, and Annabella Paciello. Seismic response of mrf-cbf dual systems equipped with low damage friction connections. *Journal of Constructional Steel Research*, 154:263 – 277, 2019. ISSN 0143-974X. doi: <https://doi.org/10.1016/j.jcsr.2018.12.008>.
- [28] Massimo Latour, Gianvittorio Rizzano, Aldina Santiago, and Luis Simões da Silva. Experimental response of a low-yielding, self-centering, rocking column base joint with friction dampers. *Soil Dynamics and Earthquake Engineering*, 116:580 – 592, 2019. ISSN 0267-7261. doi: <https://doi.org/10.1016/j.soildyn.2018.10.011>.
- [29] R. Montuori, E. Nastri, and B Tagliaferro. An optimal seismic force pattern for uniform drift distribution. *Buildings*, 9(11):231, 2019. doi: <https://doi.org/10.3390/buildings9110231>.
- [30] Z. Tang, G.C. Clifton, J.B.P. Lim, J.R. Maguire, and L.H. Teh. Increasing seismic resilience of pallet racking systems using sliding friction baseplates. New Zealand, 2017. 2017 NZSEE conference.
- [31] George Clifton. Semi-rigid joints for moment resisting steel framed seismic-resisting systems. 01 2005.
- [32] A. Franco and G. Massimiani, S.and Royer-Carfagni. Passive control of steel storage racks for parmigiano reggiano cheese under seismic accelerations. *Journal of earthquake engineering*, 19:1222–1259, 2015.
- [33] Claudio Bernuzzi and Marco Simoncelli. Seismic design of grana cheese cold-formed steel racks. *Buildings*, 10, 246:1–20, 2020.

## ANALYSIS OF THE PARTICLES DISTRIBUTION INFLUENCE ON THE RECYCLED RUBBER PROPERTIES TO BE USED AS A MATRIX OF LOW-COST SEISMIC ISOLATORS

Rojas C. Carolina<sup>1</sup>, Ortega E. Lizeth<sup>2</sup>, Madera S. Ingrid<sup>1</sup>, Losanno Daniele<sup>3</sup>, and Ortiz  
L. Albert<sup>2</sup>

<sup>1</sup> Departamento de Ingeniería Civil e Industrial, Pontificia Universidad Javeriana Cali  
Calle 18 #118-200, Santiago de Cali, Colombia  
e-mail: ingridm@javerianacali.edu.co

<sup>2</sup> Escuela de Ingeniería Civil y Geomática, Universidad del Valle  
Calle 13 #100-00, Santiago de Cali, Colombia  
{lizeth.ortega,albert.ortiz}@correounivalle.edu.co

<sup>3</sup> Department of Structures for Engineering and Architecture, University of Naples Federico II  
Via Claudio 21, 80125, Naples, Italy  
e-mail: danielle.losanno@unina.it

---

### Abstract

*This paper presents the research on recycled rubber material design, made from vehicle tires, to be used as a matrix of low-cost seismic isolators' prototypes for risk mitigation in South America buildings. Four mixes were contrasting to determine the influence of the particle size distribution on the recycled rubber characteristics, three of them with different size particle composition and the last one with a non-control distribution. Mechanical properties such as density, hardness, and tensile stress, were studied, and stereoscopic images were taken. In the controlled size distribution case, the experimental results showed an improvement in the packing capacity of the particles with a better consolidation of the material under the same processing conditions as a consequence. Regarding the tension stress, the controlled mixes achieved a maximum strength higher than the non-controlled mix (up to 70%), and their spectroscopy images show consolidated materials without voids or pores. All the samples presented a similar hardness with values higher than the natural rubber one (60). Therefore, the development of recycled rubber material with a control size distribution allowed to improve the material behavior without changes in the manufactured process.*

**Keywords:** Seismic Isolation, Low-Cost Seismic Isolators, Recycled Rubber, Particle Size Distribution.

---

## 1 INTRODUCTION

Seismic isolators are proposed as technologies for the mitigation of seismic risk to be applied in various structures and are currently accepted by several countries [1]. Current efforts are mainly directed towards reducing manufacturing costs and reducing the weight of devices, exploring variations in the matrix material [2], [3], and the reinforcement material [4]–[6]. Studies focused on the matrix of the devices offer interesting environmental benefits when using recycled rubber for their manufacture. The consolidation of the material from recycled rubber can be with additives such as binders or without using them [7].

The recycled rubber as a raw material of the seismic isolators has been studied by several authors [8 – 12] to gain insight into the possible parameters and their influence on the material performance and presented the viability to use it for commercial production [11]. These studies employed a manufactured molding process to consolidate the material, with additives [12] or without it [8-11]. They also studied the influence of the manufactured process parameter such as molding time and pressure time.

The tensile strength increases with higher pressure and more extensive molding time, which means the cohesion between particles improves to obtain density with values higher than 1.18 g/cm<sup>3</sup>, as shown at the diagram at figure 1 [8]. A relation between the size distribution on the particle rubber and the behavior of the final material was proved.

Higher results in tension were obtained for tertiary distributions with 25% of medium particles and 25% of large particles, in contrast to the distribution composed for 100% of fine material that presented comparable tension values but 62% of maximum elongation [9, 10]. The designed material from the studies mentioned previously were used to produce commercial devices such as anti-vibration tiles and tiles [11].

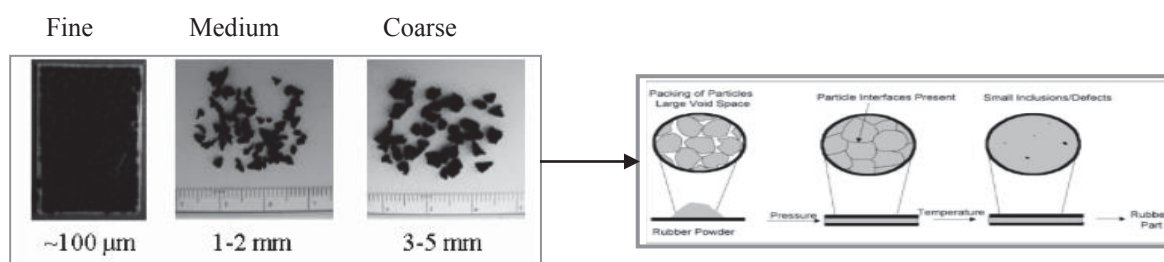


Figure 1: Work diagram of Guglielmotti [8].

According to the studies previously mentioned, the results obtained evidenced the influence of the particle distribution on the material properties for the same processing conditions. The current study proposes the design of a recycled rubber matrix by evaluating different particle size distributions to improve the performance of the recycled rubber material.

## 2 EXPERIMENTAL PROCEDURE

The samples were made with rubber particles recycled from tire used coming from the productive process of a Colombian Company (Occidental de cauchos). This company is dedicated to recycling and reusing tires used to produce simple components, like car mats and others. To obtain the particles of rubber, the tires were classified, separated, adequate, shredder, sieved, and packed; the process uses particles with a primary diameter higher than 2.00mm, which correspond to the material retention of 10 mesh sieves [13]. To consolidate the matrix, the particles were agglomerated with a polyurethane binder manufactured by molding compression.

The design of the rubber matrix was made to obtain insight into the effect of the size distribution in the performance of the rubber matrix, an additional separation after the recycle tyre process mentioned in the raw material section was made with mesh sieves. Table 1 shows the classification of the rubber particles used to design the rubber material.

Size (mesh sieve)	Diameter (mm)	Classification
5-200	0.074-0.297	Fine
10-30	0.595-2.00	Medium
10	>2.00	Coarse

Table 1: Particles classification.

Three size particle distributions were designed using the particle classification presented in Table 1. The denomination letter and composition in weight percentage of each mixer is show at the Table 2. These mixes were evaluated in contrast with a non-control distribution (NC) obtained from the separation process that the company currently uses at their productive process, using sizes of particles of 2.00 mm and less.

Mix	Fine (%)	Medium (%)	Coarse (%)
A	50	25	25
B	50	50	0
C	75	25	0

Table 2: Mixer composition.

The characterization techniques were tensile strength (ASTM D412-06, ASTM D3039), and hardness (ASTM D2240-05) [14]. Due to the dependence of the compression time by the sample size, each test requires different amounts of time to be manufactured. Table 3 shows compression times and molding temperature.

Test	Shear	Tensile	Hardness
Compression time (min)	15, 20	3, 5, 7	10
Compression temperature (°C)	140	140	140

Table 3: Fabrication process of sample rubber matrix.

To evaluate the matrix's conformability regardless of its compatibility and presences of porous, stereoscopic images were taken with a Stereoscopic Stereo Discovery V8 of Carl Zeiss with an AxioCam ERc5s camera in the facilities of the Pontificia Javeriana University.

### 3 RESULTS AND ANALYSIS

#### 3.1 Tensile test

The samples are denominated by letter and compression time, the first one was indicated at Table 2, and the last one was indicated at Table 3. For example, the A3 denomination is for mix A compressed for 3 minutes. Figure 2 shows the experimental results of the tensile test for each Mix and compression time. Results include the samples of non-control distribution made at this study and the results obtained in other studies [15].

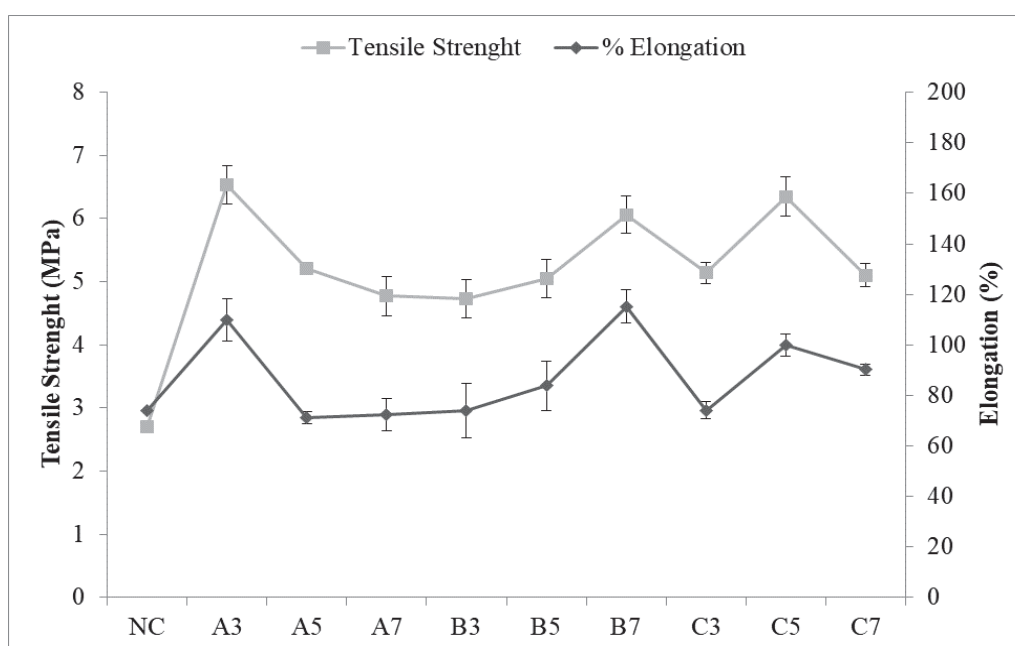


Figure 2: Experimental results for tensile test.

The tension test provides information about the adhesion between the rubber particles; therefore, the material's behavior will depend on its consolidation. Figure 2 shows a proportional relationship between maximum stress and deformation, where the highest values of maximum stress correspond to the largest deformations. The dispersion founded in the results may be due to purely procedural conditions, such as the heat transfer that produced a loss of mold temperature.

In general, all the proposed mixtures (A, B, and C) reached values greater than 6 MPa with deformations greater than 100%. It was found that mixture A showed the highest value of maximum tensile stress, with 6.53 MPa for 109.7 % deformation, with differences of 7.2% and 2.8% compared to the maximum values of maximum stress of mixtures B and C, respectively. The synergy between particle sizes led to improved packing capacity in the material, increasing the contact surface area between them, and the density obtained from these samples was 0.94 g/cm<sup>3</sup>.



### 3.2 Hardness

The hardness samples were denominated similar to the tensile test. The three mixes are indicated by the letter (A, B, C), and the number 1 and 3 indicated 10 and 15 minutes of compression, respectively. Figure 3 shows the results of hardness for the different mixtures.

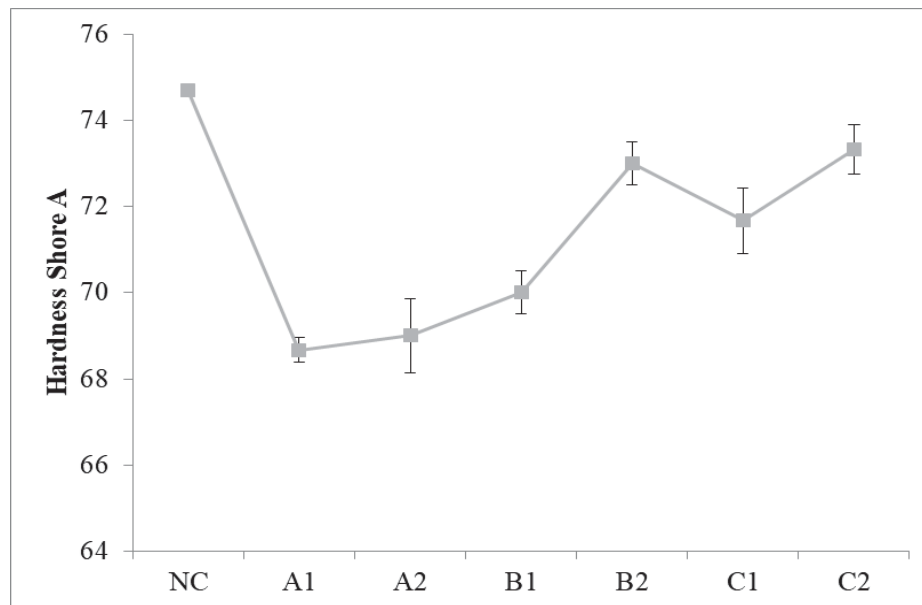


Figure 3: Shore A hardness of the samples.

Hardness is a surface property; it provides an idea of the surface resistance of the samples and the state of consolidation in this area. The hardness results show that mixture C presented the best performance for the shortest molding time evaluated, with 71.67 for 10 minutes, in contrast to 70 and 67.7 for the same molding time of mixtures B and A, respectively.

Similarly, the recycled rubber agglomerate material with the composition of the mixture C presented the highest hardness values, with 73.3 shore A for 15 minutes of molding time. In general, there is an increase in hardness with increasing molding time, although the values are very close to each other. These results are higher than those obtained from materials made from natural rubber, for which 50 Shore A is reported [16], but it is an acceptable difference for use in seismic isolators.

### 3.3 Stereoscopic Images

The stereoscopic images were used to evaluate the sample's failure zone to define the material behavior in the test. Figure 4 shows the 3 mixes (A, B y C) and the non-controlled sizes distribution sample. Each mix exhibits their own and particular surface provided by the compactibility due to different particle sizes where the fine particles fill the voids between the coarser particles.

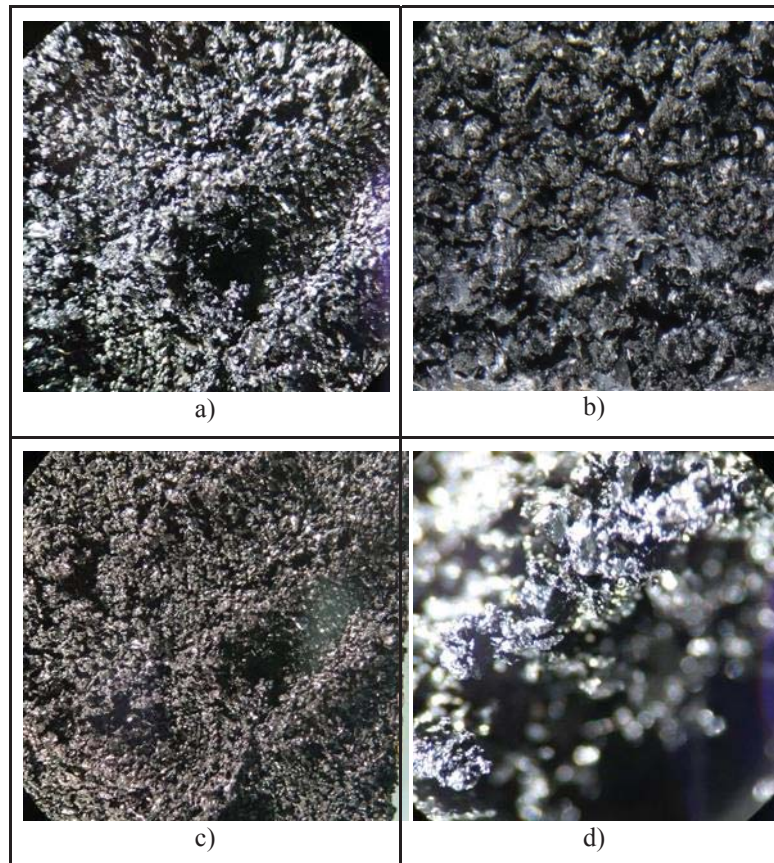


Figure 4: Stereoscopic images of failure zone of the samples.

As shown in figure 4, the material failure occurred in the interface between the rubber particles and through some rubber granules, preserving the integrity of the adhesive and rubber adhesive interfaces. The tensile test proves the relation between compactability and material behavior. The adhesion between rubber particles grows as the compactability increases, producing higher tensile strength and percentage strain due to the bigger superficial area. The hardness does not exhibit a relation with the particle's sizes distribution. That fact could be related to the superficially feature of the property, which shows the adhesion between particle in a superficial way but does not reflect the property across the material.

#### 4 CONCLUSIONS

From the results obtained in this study, it can be concluded that the design of the matrix material made from recycled rubber particles, having the granulometric distribution as a control parameter, allows obtaining materials with good mechanical performance. This happens when 50% of its composition are fine grains, and the remaining percentage is distributed evenly between coarse and medium particles, producing synergy of sizes that increases the compaction capacity.

The stereoscopic images show the effects of different particle size distributions designed to provide synergy between sizes to increase the effective superficial area. These changes in the arrangement of the rubber particles produce a variety of mechanical behavior, affecting properties like tensile strength, as was shown in the experimental results of the present study.

The hardness results for the different mixtures (A, B, and C) presented very similar values, with a small increase with increasing molding time for each mixture. On the other hand, it was found that an improved behavior of the material fabricated with the particle size distribution, where Mix A presented an increase of 71.8% of maximum stress in tension for similar values of deformation concerning the results obtained with granulated rubber matrices without control over the distribution of particle sizes.

## ACKNOWLEDGMENT

This research was funded with resources from the AUTONOMOUS HERITAGE NATIONAL FINANCING FUND FOR SCIENCE, TECHNOLOGY AND INNOVATION FRANCISCO JOSÉ DE CALDAS", by the research project: "ECO-ISOLATORS: LOW-COST ECO-FRIENDLY SEISMIC ISOLATORS FOR RISK LAMITIGATION IN NEW AND EXISTING INFRASTRUCTURE" with code 70694, which is part of the program: EMERGING RISK TECHNOLOGIES FOR MITIGATION CIVIL INFRASTRUCTURE SEISMIC, approved within the framework of THE ANNOUNCEMENT CONNECTING KNOWLEDGE 852-2019, contract RC-463-2020.

## REFERENCES

- [1] S. E. Mason Walters, "Seismic isolation—the gold standard of seismic protection," *STRUCTURE*, vol. 12, 2015.
- [2] M. Spizzuoco, A. Calabrese, and G. Serino, "Innovative low-cost recycled rubber-fiber reinforced isolator: Experimental tests and Finite Element Analyses," *Eng. Struct.*, vol. 76, pp. 99–111, Oct. 2014.
- [3] A. Turer and B. Özden, "Seismic base isolation using low-cost Scrap Tire Pads (STP)," *Mater. Struct. Constr.*, vol. 41, no. 5, pp. 891–908, Jun. 2008.
- [4] J. M. Kelly and I. D. Aiken, "Experimental studies of the seismic response of structures incorporating base-isolation systems," *Nucl. Eng. Des.*, vol. 127, no. 3, pp. 329–338, Jun. 1991.
- [5] G. J. Kang and B. S. Kang, "Dynamic analysis of fiber-reinforced elastomeric isolation structures," *J. Mech. Sci. Technol.*, vol. 23, no. 4, pp. 1132–1141, Apr. 2009.
- [6] I. Gjorgjiev and M. Garevski, "A polynomial analytical model of rubber bearings based on series of tests," *Eng. Struct.*, vol. 56, pp. 600–609, Nov. 2013.
- [7] H. K. Mishra, A. Igarashi, and H. Matsushima, "Finite element analysis and experimental verification of the scrap tire rubber pad isolator," *Bull. Earthq. Eng.*, vol. 11, no. 2, pp. 687–707, Apr. 2013.
- [8] A. Guglielmotti, C. Lucignano, and F. Quadrini, "Production of rubber pads by tyre recycling," *Int. J. Mater. Eng. Innov.*, vol. 1, no. 1, pp. 91–106, 2009.
- [9] A. Gugliemotti, C. Lucignano, and F. Quadrini, "Production of rubber parts by tyre recycling without using virgin materials," *Plast. Rubber Compos.*, vol. 41, no. 1, pp. 40–46, 2012.

- [10] F. Quadrini, D. Bellisario, L. Santo, and I. Hren, "Direct moulding of rubber granules and powders from tyre recycling," *Appl. Mech. Mater.*, vol. 371, pp. 315–319, 2013.
- [11] F. Quadrini, L. Santo, T. Oskorus, W. Wasniowski, and E. Musacchi, "Production of Rubber Goods Made of 100% Ground Tire Rubber," pp. 2016–2019, 2016.
- [12] M. Shen, J. Liu, and Z. Xin, "Mechanical Properties of Rubber Sheets Produced by Direct Molding of Ground Rubber Tire Powder," *J. Macromol. Sci. Part B Phys.*, vol. 58, no. 1, pp. 16–27, 2019.
- [13] L. Ortega et al., "Caracterización mecánica de caucho reciclado de llantas de camión como matriz para la construcción de aisladores sísmicos," *Asoc. Colomb. Ing. Sismica*, no. 1, pp. 631–638, 2019.
- [14] T. A. ATC and T. M. MCEER, *ATC-17-2 Seminar on Response Modification Technologies for Performance-Based Seismic Engineering*. 1986.
- [15] A. Calabrese, "Analytical, Numerical and Experimental Study of a Novel Low-Cost Base Isolation System." p. 249, 2013.
- [16] I. Madera, "Desarrollo tecnologico de un aislador sismico de bajo costo para edificaciones bajas," *Universidad del Valle*, 2018.

## THE EFFECT OF SOIL-STRUCTURE INTERACTION AND LIQUEFACTION ON THE SEISMIC VULNERABILITY OF TYPICAL PORT STEEL LIGHT-FRAME WAREHOUSES

**Stella V. Karafagka<sup>1</sup>, Stavroula D. Fotopoulou<sup>1</sup>, Anna C. Karatzetzou<sup>1</sup>, Georgios E. Malliotakis<sup>2</sup>, and Dimitris Pitilakis<sup>1</sup>**

<sup>1</sup> Aristotle University of Thessaloniki, Greece  
e-mail: {stellak,sfotopou,akaratz,e,pitilakis}@civil.auth.gr

<sup>2</sup> University of Birmingham, UK  
GXM054@student.bham.ac.uk

---

### Abstract

*Ports play a crucial role in the world economy, as they represent critical nodes in regional and national transportation networks. They are usually located in areas prone to geohazards, such as earthquakes and soil liquefaction. Although warehouses constitute a port system's key components, the published literature in the evaluation of their seismic vulnerability considering the effect of soil liquefaction and soil-structure interaction (SSI) is generally inadequate. To bridge this gap, this study's objective is to implement a numerical investigation of the influence of both liquefaction and SSI on the seismic vulnerability of typical port steel light-frame warehouses. The following numerical modelling approaches are applied: i) a 2D fixed-base structure subjected to outcrop bedrock seismic motion neglecting SSI and liquefaction; ii) ) a 2D flexible-base model, considering both SSI and liquefaction; iii) a 3D fixed-base model which is subjected to outcrop bedrock seismic motion and thus neglecting both SSI and liquefaction; iv) a 3D fixed-base model subjected to a free-field motion that considers liquefaction. We conduct nonlinear incremental dynamic analysis for the above numerical approaches to derive seismic fragility and vulnerability curves considering (or not) SSI and/or liquefaction. The earthquake demand is determined based on the selection of actual earthquake records covering a wide range of seismic input motions in terms of amplitude, frequency content, and significant duration. The comparative results show the considerable role of liquefaction and SSI in altering the seismic fragility and port warehouses' vulnerability.*

**Keywords:** Fragility, SSI, liquefaction, steel light-frame warehouse, numerical modelling.

---



## 1 INTRODUCTION

Ports represent critical nodes in regional and national transportation networks, having an important impact on the world economy. Thus, resilience and continuous operation of port structures are interrelated with international, national, and regional growth and development. However, ports are usually located in areas prone to geohazards, such as earthquakes and soil liquefaction. Although warehouses, which are large space steel light-frame buildings (with or without masonry infills), constitute key components of a port system, the published literature in the evaluation of their induced physical damages due to the effect of ground shaking and soil liquefaction is generally inadequate. Also, soil-structure interaction (SSI) may play a significant role in the seismic performance of port structures, modifying their dynamic characteristics, as well as the seismic response at the foundation level. According to PIANC [1], most damage to coastal structures is the result of SSI; thus, design and analysis procedures should include both geotechnical conditions and structural conditions of coastal structures.

Usually, the seismic response of buildings is estimated assuming fixed-base conditions, which is reasonable solely for structures on stiff or rock-type soils. Nevertheless, the seismic response of a structure on soft soil may considerably differ compared to the fixed-base assumption [2]. In general, nonlinear soil behaviour and SSI effects on structures, either beneficial or detrimental, are well-studied [3-5]. Geometrical and material nonlinearities in the soil-foundation-structure system may detrimentally affect the dynamic behaviour of the structure, with respect to the soil characteristics and the intensity of the ground motion [6]. The problem is expected to be even more complicated when soil liquefaction phenomena are present.

Although some progress has already been made on the influence of ground shaking and soil liquefaction on the structural response and vulnerability of steel frame buildings [7-9], studies coupling both phenomena are limited. To estimate the seismic response of buildings, also considering liquefaction, more sophisticated methods can be used [10-11]. Within an effective stress site response concept, a "fully coupled approach" can be adopted that uses a plasticity-based constitutive model to predict both the pore pressure and the stress-strain response of the soil [12]. For estimating seismic performance and damages, the "coupled approach" has already been used for bridge systems [13-15], quay walls [16-17] and other simplified soil-structure systems [18-19]. However, its application to steel frame buildings on soils considering both liquefaction and SSI effects so as to estimate their physical seismic damages, needs further investigation.

To bridge this gap, we implement a numerical investigation of the influence of both SSI and liquefaction on the seismic vulnerability of typical port steel light-frame warehouses. The numerical modelling approaches used for the investigation are a 2D fixed-base structure neglecting SSI and liquefaction, a 2D flexible-base model considering both SSI and liquefaction, a 3D fixed-base model neglecting both SSI and liquefaction as well as a 3D fixed-base model subjected to a free-field motion that considers liquefaction. We conduct nonlinear incremental dynamic analysis for the above numerical approaches to derive seismic fragility and vulnerability curves considering (or not) SSI and/or liquefaction. Comparative results are presented showing the significant role of liquefaction and SSI in altering the seismic fragility and vulnerability of port warehouses.

## 2 CONCEPTUAL MODELLING APPROACHES

We developed four modelling approaches to produce fragility curves considering (or not) SSI and soil liquefaction:

- i. a 2D fixed-base structure subjected to outcrop bedrock seismic motion neglecting SSI and soil liquefaction;



- ii. a 2D flexible-base model, considering both SSI and soil liquefaction. SSI is modelled by applying the direct approach. The soil and the structure are analysed as a single system, while liquefaction is considered by employing a fully coupled (u-P) formulation. Such a formulation is capable of simulating permanent shear-strain accumulation in clean medium-dense cohesionless soils during liquefaction and appropriate constitutive model for the examined soil profiles;
- iii. a 3D fixed-base model which is subjected to outcrop bedrock seismic motion and thus neglecting both SSI and liquefaction and
- iv. a 3D fixed-base model subjected to a free-field motion that considers liquefaction. This two-step uncoupled approach considers the liquefaction effects on the free-field response using the above described u-P formulation and appropriate constitutive model for the examined soil profiles. The free-field response is then applied to the fixed-base structure neglecting, thus, the SSI effects.

### 3 NUMERICAL MODELLING

#### 3.1 Selection of the structural building typology and soil profiles

We study a typical steel light-frame warehouse, representative of Thessaloniki port critical buildings. Figure 1 and Figure 2 illustrate a representative cross-section and the floor plan respectively of the typical warehouse, as provided by Thessaloniki Port authorities and reproduced by the authors. The main characteristics of the building are set equal to total mass  $m=5.1\text{tn}$ , fundamental period  $T_0=0.30\text{s}$ , and yield strength  $f_{ym}=235.0\text{ MPa}$ . Regarding the soil, we consider three representative soil profiles of the port area of Thessaloniki (Greece), simplified with respect to their total depth, denoted as SP1, SP2, and SP3 (Figure 3), based on the available geotechnical information of the port area and the available SPT and laboratory data [20-21]. The fundamental periods  $T_0$  of the three soil profiles are equal to 0.88 s, 0.73 s, and 0.64 s, respectively. Figure 3 presents for all three soil profiles the variation of the shear wave velocities  $V_S$  with depth together with a general geotechnical characterization according to the USCS soil classification scheme. The liquefaction potential of the subsoil layers of the selected soil profiles was quantitatively evaluated following the Eurocode 8 guidelines (EC8)- Part 5 (CEN 2004). For SP1, potentially liquefiable soil formations are found at depths  $z=-9\div-11\text{m}$ ,  $z=-14\div-20\text{m}$ , and  $z=-26.5\div-36\text{m}$ , for SP2 at depths  $z=-3\div-14\text{m}$ , while for SP3 at depths  $z=-4\div-20\text{m}$ , which are basically silty/clayey sands and non-plastic silts with low values of NSPT. Thus, knowing that the liquefaction susceptibility in the port area is rather high, these soil profiles refer to ground type S according to the EC8 soil classification scheme [22].

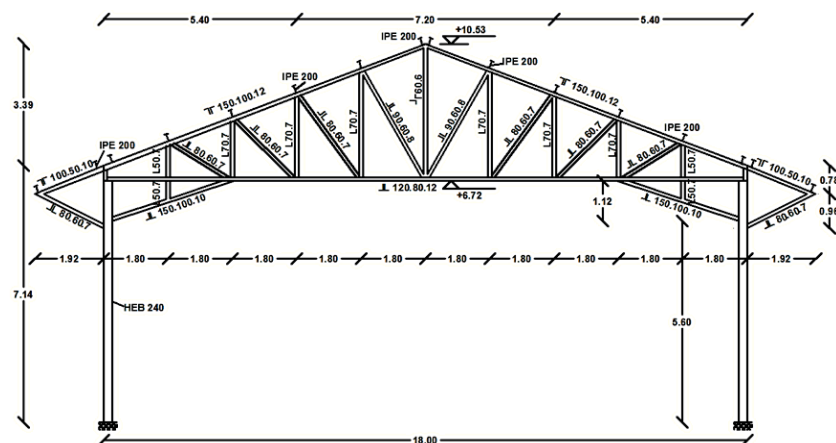


Figure 1: Cross-section of the typical warehouse.

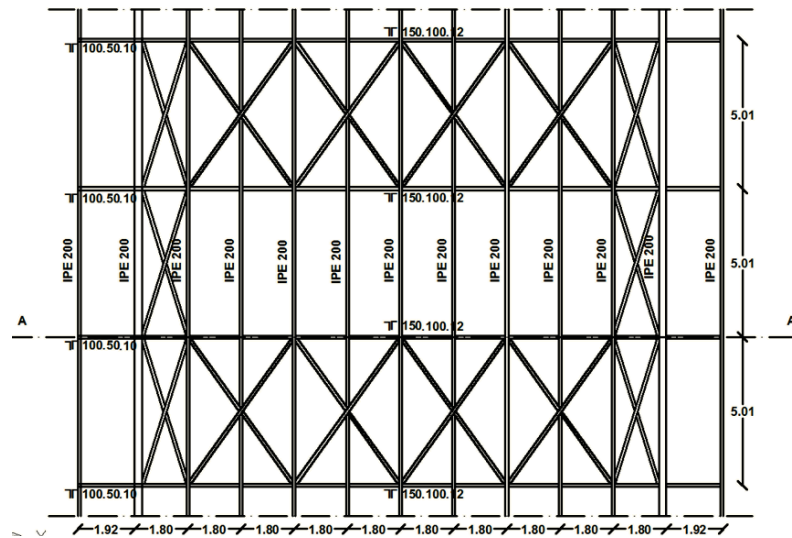


Figure 2: Plan view of the typical warehouse.

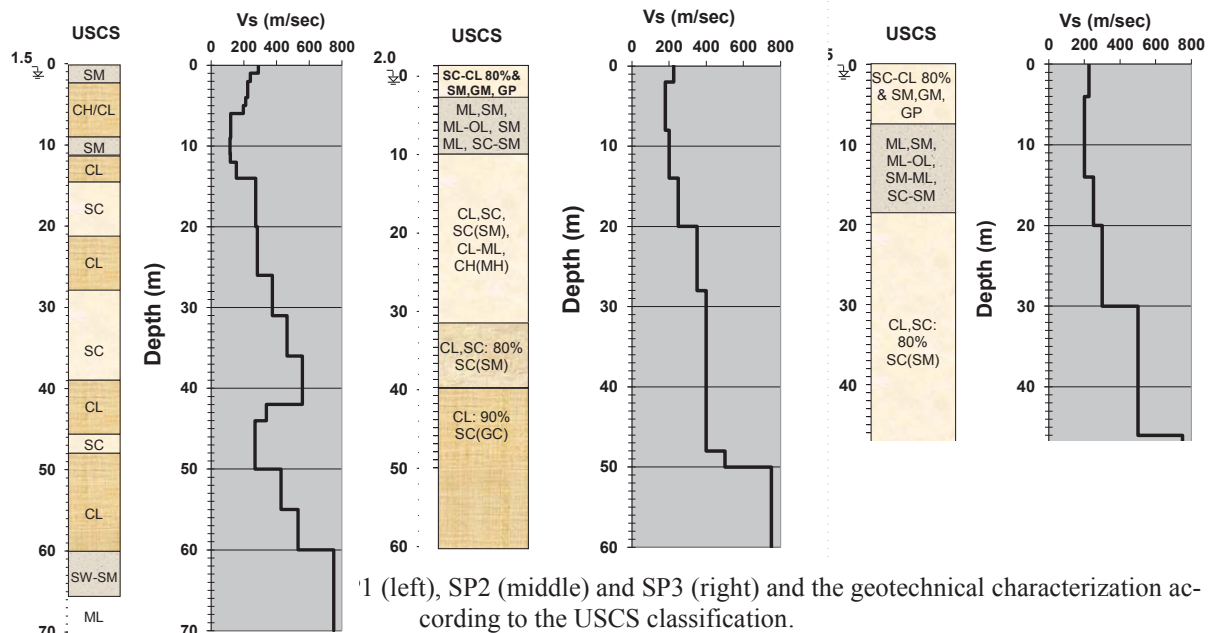


Figure 3: (left), SP2 (middle) and SP3 (right) and the geotechnical characterization according to the USCS classification.

### 3.2 Structural modelling

In the former two conceptual modelling approaches (i.e., i. and ii.), two-dimensional (2D) numerical simulation of the reference building, as shown in Figure 4 left, is conducted using the open-source computational platform OpenSees [23]. Inelastic force-based formulations are implemented for the 2D, three-degree of freedom nonlinear beam-column frame elements modelling, while the roof (trusses) of the building is modelled using "truss" elements (with two degrees of freedom). The uniaxial "Steel01" material is used to construct a uniaxial bilinear steel material object with kinematic hardening. The main parameters required, i.e., the yield strength ( $F_y$ ), the initial elastic tangent ( $E_0$ ), and the strain-hardening ratio ( $b$ ), which is the ratio between post-yield tangent and initial elastic tangent, are taken equal to  $F_y = 235.0$  MPa,  $E_0 = 2.1 \cdot 10^5$  MPa and  $b=0.01$ , respectively. The nonlinear beam-column frame elements are subjected to both axial compression and bending, considering five Gauss-Lobatto [24] integration points along each member's length. The applied formulations allow both geometric

nonlinearities (P-delta and large displacements/rotation effects) and material inelasticity to be captured. Distributed material inelasticity along the element is applied based on the fibre approach to represent the cross-sectional behaviour [25]. Each fibre is associated with a uniaxial stress-strain relationship; the sectional stress-strain state of the beam-column elements is obtained through the integration of the nonlinear uniaxial stress-strain response of the individual fibres in which the section is subdivided. The truss elements are subjected only to axial compression. As they are constructed with a uniaxial material object, they consider strain-rate effects. The masses are applied as distributed along columns and beams (by assigning the specific weight of steel material) plus concentrated vertical loads on joints due to the existence of trusses in the normal direction.

In the latter two conceptual modelling approaches (i.e., iii. and iv.), three-dimensional (3D) numerical simulation of the reference building, as shown in Figure 4 right, is conducted using the SAP2000 finite element program [26]. For all sections, the S235 built-in steel material with isotropic symmetry type is used with the yield stress defined equal to 235 MPa and the maximum tensile stress equal to 360 MPa. A parametric stress-strain curve is utilized to capture the nonlinear behaviour of the steel material comprising an initial linear region, a plastic plateau, a strain hardening region, and finally, a necking region leading to rupture. The main parameters required to construct the backbone stress-strain curve, i.e. the strain at yielding, the strain at the onset of strain hardening, the strain at maximum stress and the strain at rupture, are taken equal to 0.011 for yielding, 0.02 (end of the plateau), 0.14 and 0.20, respectively. The kinematic hardening model is also considered, which is based upon kinematic hardening behaviour that is commonly observed in metals. This model dissipated a significant amount of energy and is appropriate for ductile materials. Under the rules of kinematic hardening, plastic deformation in one direction "pulls" the curve for the other direction along with it. Matching pairs of points are linked. Upon unloading and reverse loading, the curve follows a path made of segments parallel to and of the same length as the previously loaded segments and their opposite-direction counterparts until it re-joins the backbone curve when loading in the opposite direction. We use the fibre approach to represent the cross-sectional behaviour of the beams and columns, while the built-in steel frame sections are utilized to model trusses and braces sections. To consider nonlinear element behaviour, SAP2000 offers various hinges, such as uncoupled moment (M2 or M3), axial force (P), or hinges with axial force and moment interaction. Herein, we consider nonlinear behaviour for beams and columns elements using fibre hinges P-M2-M3, where the hinge force-deformation relationship is input manually, determined from the cross-section fibre model, while for trusses and braces elements, concentrated plastic hinges calculated according to FEMA are used. Once hinges are assigned, material nonlinearity may then characterize the inelastic response of frame elements. For columns and beams, in that way, each point represents a tributary area, having its unique stress-strain law. The axial stresses are integrated over the section to estimate the values of P, M2, M3. Fibre hinges are adapted more effectively to reality, even though they demand a lot of computational workloads. When it comes to strength loss, this is orientated by stress-strain law. In a cross-section, all fibres do not fail at the same time, and, thus, the overall hinges lose their capacity at a steady pace. For trusses and braces, axial hinge type is used. Generally, these sections are not stressed by bending or shear force but only from axial compression load. In addition, the plasticity is distributed at the edges of each element. The hinges behave according to elastoplastic perfectly plastic law, with maximum stress defined by yield point stress. Strength loss is considered to be extrapolated, since sudden loss is often unrealistic and may cause difficulties to analysis, leading to time consuming.

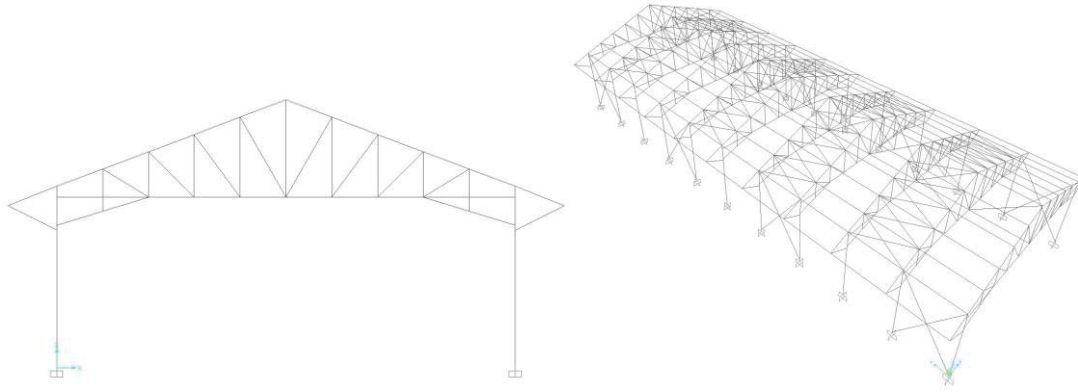


Figure 4: 2D (left) and 3D (right) numerical model of the warehouse.

### 3.3 Soil modelling

Each soil profile comprises several layers of cohesive and cohesionless soil material. The groundwater table is located at a depth of 1.5m, 2.0m and 1.5m for the soil profiles SP1, SP2, and SP3, respectively (Figure 3). Saturated unit weights are used for the soil below this level and effective stress analysis is conducted using nine-node quadrilateral elements with both displacement and pore pressure degrees of freedom. Such elements are able to simulate fluid-solid coupling during the earthquake excitation, based on Biot's theory of porous medium [27]. To account for the finite rigidity of the underlying bedrock, a Lysmer-Kuhlemeyer [28] dashpot is incorporated at the base of the soil profile using a bedrock shear wave velocity of 627.0m/s, 750.0m/s and 750.0m/s for the soil profiles SP1, SP2 and SP3, respectively and a mass density of 2.2Mg/m<sup>3</sup>. The Lysmer-Kuhlemeyer dashpot is assigned based on the viscous uniaxial material model and the 'zeroLength' element formulation at the same location, to connect the two previously defined dashpot nodes. This material model requires a dashpot coefficient that is defined according to Joyner and Chen [29] as the product of the mass density and the shear wave velocity of the underlying bedrock also including the base area of the soil profile. To model the underlying elastic half-space necessitates that the nodes at the base of the soil model are free to displace in the horizontal direction, are all given the same horizontal displacements and finally are fixed against vertical translation only. Mass and stiffness proportional Rayleigh damping is assigned to account for energy dissipation during seismic loading with a damping ratio equal to 2.0%. Periodic boundary conditions are used to ensure that free-field conditions exist at the horizontal boundaries of the model. The displacement degrees of freedom for the nodes on either side of the soil model are tied together, imposing the same translational displacements in x and z directions, and rotation about the y-axis. Each soil profile is excited at the base by a horizontal force time history proportional to the known velocity of the ground motion [29]. Due to the consideration of an elastic half-space it was possible to directly apply the outcropping rock motion at the base of the soil model [30].

We employ a fully coupled (u-P) formulation, capable of simulating permanent shear-strain accumulation in clean medium-dense cohesionless soils during liquefaction and dilation due to increased cyclic shear stiffness and strength. The soil constitutive behaviour is based on the framework of multi-surface plasticity [31], with modifications by Yang [32]. The hardening law, the yield surface and the flow rule constitute the major components of the plasticity model. During the application of the gravity load, at first the material behaviour is linear elastic, while in the second part of the gravity analysis the constitutive behaviour of the soil elements is changed to elastoplastic. In the subsequent dynamic loading phase, the stress-strain response is elastic-plastic. To generate soil hysteretic response under cyclic loading, we adopt a purely deviatoric kinematic hardening rule [31]. This kinematic rule dictates that all



yield surfaces may translate in stress space within the failure envelope [32-33] and be consistent with the Masing unloading/reloading criteria [34]. For the cohesionless soil layers, an elastic-plastic material, namely "PressureDependMultiYield02", is used in Opensees, where the yield function is assumed to follow the Drucker-Prager shape and the yield surface is a function of friction angle and cohesion. Plasticity is formulated based on the multi-surface concept, with a non-associative flow rule [32] that handles the soil contractive/dilative behaviour during shear loading to achieve appropriate interaction between shear and volumetric responses. For the cohesive soil layers, an elastic-plastic material in which plasticity exhibits only in the deviatoric stress-strain response, namely "PressureIndependMultiYield", is used. The volumetric stress-strain response is linear-elastic and is independent of the deviatoric response. This material is implemented to simulate monotonic or cyclic response of materials whose shear behaviour is insensitive to the confinement change. The yield function is assumed to follow the Von Mises shape and the yield surface is a function solely of undrained shear strength. Plasticity is formulated based on the multi-surface concept, with an associative flow rule in which the incremental plastic strain vector is normal to the yield surface.

### 3.4 Soil-structure interaction modelling

For the 2D flexible-base model (modelling approach ii) the direct approach is applied, which accounts simultaneously inertial and kinematic interaction effects. Figure 5 represents the 2D coupled finite element (FE) soil-structure model for the warehouse resting on the liquefiable soil, which is subjected to combined ground shaking and liquefaction. The grids adapted for the different soils SP1, SP2, and SP3 have a total length three times their depth to avoid spurious wave reflections at the vertical boundaries. Their dimensions are defined equal to 60.0m x 180.0m, 50.0m x 150.0m and 46.0m x 138.0m, respectively. Dense discretization is achieved using quadrilateral elements of 0.5m x 2.0m, considering that the maximum frequency of interest is set to 10Hz. This mesh allows an adequate number of elements to fit within the shortest wavelength of the propagating shear wave.

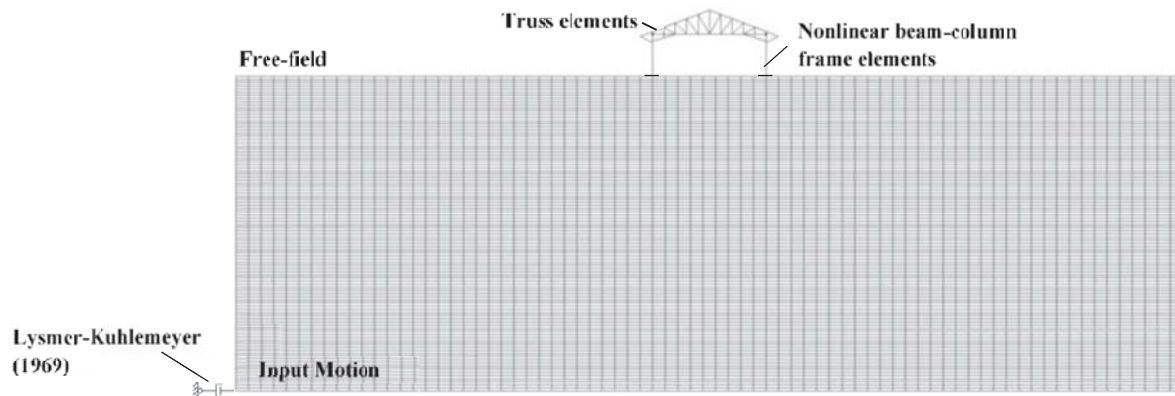


Figure 5: Finite element 2D model for the typical steel light-frame warehouse on liquefiable soil.

A full bond is assumed between the structure's foundation and the soil nodes. The soil and the structure nodes at the level of foundation have appropriate constraints in order to ensure equal displacements. Shallow, relatively flexible foundations are considered, modelled as elastic beam-column elements of infinite rigidity, which allow columns to move differentially. In this case, it is furthermore assumed that no interface has been considered between the structure and the foundation and that failure will take place on the structural elements of the building, while the structural integrity of the foundation itself will not be affected by the liquefaction induced deformation.

## 4 NUMERICAL ANALYSIS

### 4.1 Seismic input motion

A representative set of fifteen real ground motion records (Table 1) is selected from the European Strong-Motion Database to perform nonlinear incremental dynamic analyses. They are all referring to rock type or stiff soils (ground types A and B according to EC8) with moment magnitude ( $M_w$ ) and epicentral distance  $R$  that range between  $5.5 < M_w < 6.5$  and  $0 < R < 45\text{km}$  respectively. The primary selection criterion is the average acceleration spectra of the set to match the corresponding 5% damped median plus 0.5 standard deviations spectrum defined based on the ground motion prediction equation (GMPE) proposed by Akkar and Bommer [35]. The optimization procedure is performed using REXEL software [36] that allows obtaining combinations of accelerograms, which on average are compatible to the reference spectrum. Figure 6 shows the mean elastic response spectrum of the records in comparison with the corresponding median plus 0.5 standard deviations Akkar and Bommer [35] spectrum. As shown in the figure, a good match between the two spectra is achieved.

Earthquake Name	Date	$M_w$	Fault Mechanism	Epicentral Distance [km]	$PGA_{\text{initial}}$ [m/s <sup>2</sup> ]	$PGA_{\text{corrected}}$ [m/s <sup>2</sup> ]	EC8 Site class	Waveform ID
Umbria Marche (aftershock)	6/10/1997	5.5	normal	5	1.838	2.060	A	651
Valnerina SE of Tirana	19/9/1979	5.8	normal	5	1.510	1.472	A	242
Lazio	9/1/1988	5.9	thrust	7	4.037	3.826	A	3802
Abruzzo (aftershock)	11/5/1984	5.5	normal	15	1.411	1.373	A	990
Valnerina	19/9/1979	5.8	normal	5	2.012	2.060	A	242
Kozani	13/5/1995	6.5	normal	17	2.039	2.158	A	6115
Friuli (aftershock)	15/9/1976	6	thrust	12	1.339	1.373	A	149
Umbria Marche 1	26/9/1997	5.7	normal	23	1.645	1.668	A	763
Friuli (aftershock)	15/9/1976	6	thrust	14	2.586	2.649	B	134
Patras	14/7/1993	5.6	strike slip	9	3.337	3.434	B	1932
Kalamata	13/9/1986	5.9	normal	11	2.670	2.747	B	414
Umbria Marche 2	26/9/1997	6	normal	11	5.138	5.592	B	594
Montenegro (aftershock)	24/5/1979	6.2	thrust	17	1.708	1.766	B	229
Kefallinia island	23/1/1992	5.6	thrust	14	2.223	2.060	B	6040
Ano Liosia	7/9/1999	6	normal	14	2.159	2.256	B	1714

Table 1: List of records used for the dynamic analyses.



These records are then filtered between 0.25 and 15.0 Hz, using a fourth-order bandpass Butterworth type filter. Baseline correction linear type is also applied. Table 1 also presents the values of  $PGA_{corrected}$  obtained from the corrected accelerograms used for the analyses.

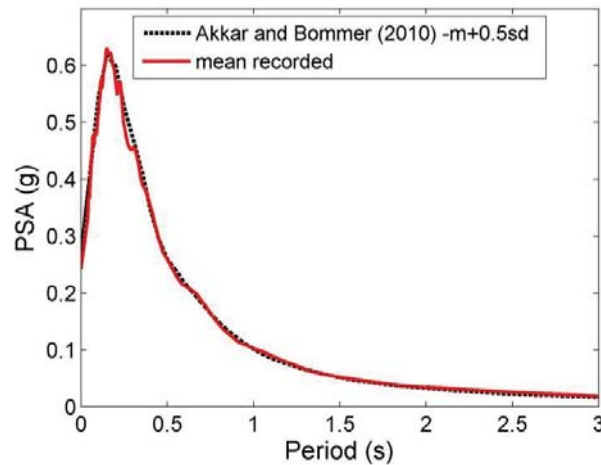


Figure 6: Average elastic response spectrum of the input motions in comparison with the corresponding median plus 0.5 standard deviations Akkar and Bommer [35] spectrum.

## 4.2 Numerical analyses

To examine the effect of liquefaction on the seismic ground response, we initially perform a comparative dynamic analysis of the considered nonlinear soil profiles. In this respect, the utilized earthquake records are scaled at PGA values equal to 0.05g and 0.3g. For PGA equal to 0.05g, it seems that the soil responses are within the linear elastic range, since the effective confinement values with depth do not approach zero. On the contrary, for the dynamic analyses with input motions scaled at 0.30g, liquefaction is taking place. Layers of potential liquefaction may be identified by loss of effective confining stress at certain depths, which is verified by the relative stress-strain loops. Figure 7 shows representative results in terms of effective confinement with depth and stress-strain hysteretic loops at specific depth (i.e., 7 m below surface) indicatively for Soil profile SP2 and Montenegro (aftershock) input motion scaled at 0.05g and 0.3g.

Moreover, an initial elastic modal analysis of both the 2D and 3D fixed-base models is conducted to define the dynamic characteristics of the structure and increase the reliability of the proposed modelling approaches. The fundamental period of the studied structure is computed equal to 0.298 s for the 2D fixed-base model and 0.293 s for the corresponding 3D fixed-base model providing a first verification of their validity.

## 4.3 Incremental dynamic analysis

2D and 3D incremental dynamic analysis (IDA) is then conducted to estimate more thoroughly the seismic performance of the typical steel light-frame warehouse due to ground shaking and liquefaction. To express the scaling level an initial, temporary choice of an intensity measure (IM) is needed. Scaling can be re-expressed in any other scalable IM [37] after the runs are performed. In this study, the IM is initially described by the peak ground acceleration on rock outcropping conditions ( $PGA_{rock}$ ). This IM is considered more appropriate due to its simplicity. Hence, IDA for the fixed-base and the three SSI models is conducted by applying the 15 progressively scaled records, considering a first elastic run at 0.05g, an initial step of 0.1g and a step increment of 0.1 g. A sequence of at least ten runs is performed on

each record. The damage measure (DM) is expressed in terms of maximum inter-story drift (maxISD), which is known to relate well to dynamic instability and structural damage of frame buildings.

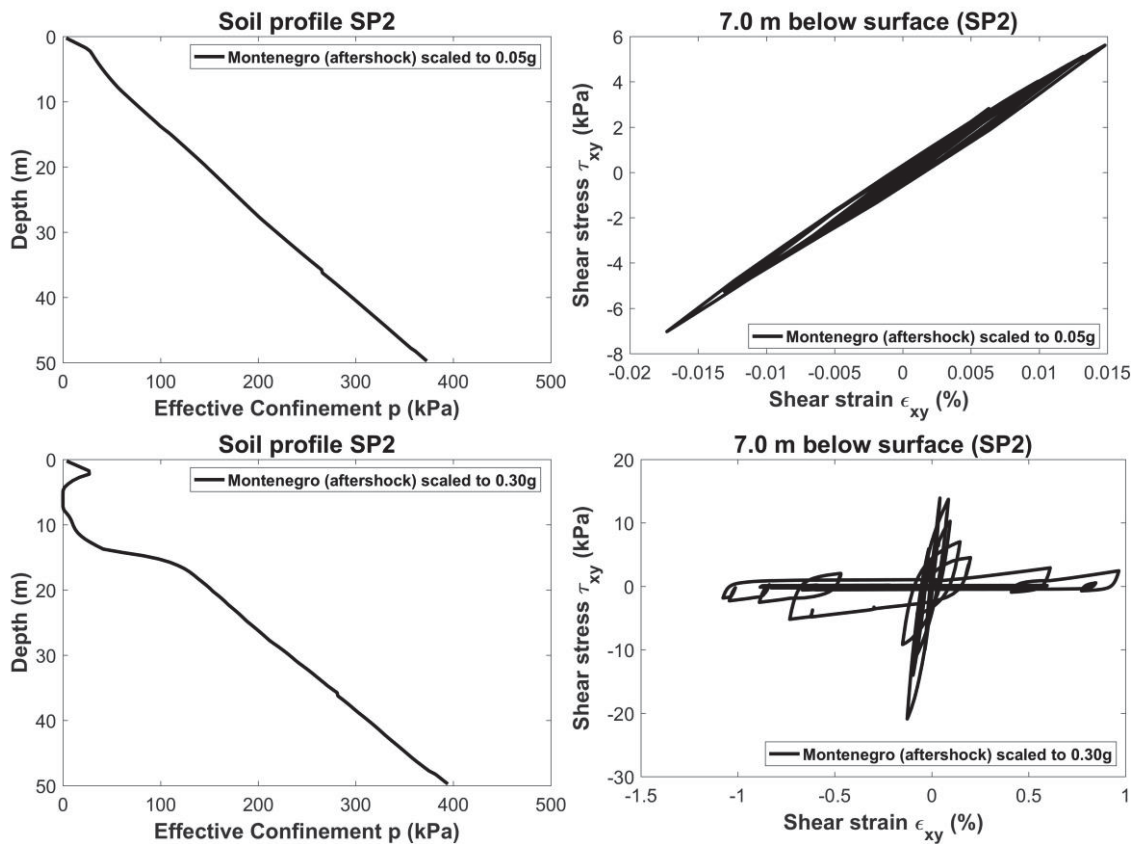


Figure 7: Variation of the effective confinement with depth and stress strain hysteretic loops at specific depth for SP2 and Montenegro (aftershock) input motion scaled at 0.05g (top) and 0.3g (bottom)

## 5 FRAGILITY AND VULNERABILITY CURVES

### 5.1 Definition of limit states

A key factor for the vulnerability assessment is the accurate definition of damage limit states as they directly influence the evaluation of the fragility function parameters. Four damage states are defined in terms of maxISD ratio, describing the exceedance of slight, moderate, extensive, and complete damage of light-weight steel warehouses. According to NIBS [38], "Steel Light Frames" structures are mostly single storey structures combining rod-braced frames in one direction and moment frames in the other. Due to the repetitive nature of the structural systems, the type of damage to structural members is expected to be rather uniform throughout the structure. Consequently, warehouses are considered as "Steel Light Frames" structures. The qualitative description of each damage state for steel light-frame structures adopted in this research work can be found in NIBS [38]. Usually, the damage limit states are defined on the IDA curves derived for the fixed-base building subjected to ground shaking, with the complete/collapse damage limit state placed at a point where the IDA curve is leaning towards the flatline. The damage limit states are selected based on the existing literature [7, 38] combined with the IDA analysis results and objective engineering criteria. The adopted damage limit state values are shown in Table 2.

Limit states	Steel light-frame warehouse
LS 1	0.50%
LS 2	1.00%
LS 3	2.00%
LS 4	3.30%

Table 2: Limit state values in terms of maxISD adopted for steel warehouse.

## 5.2 Development of fragility and vulnerability curves

A fragility curve describes the probability of exceeding a specific damage state under a seismic excitation of a given intensity. They can be produced taking advantage of the results of the nonlinear IDA in terms of PGA and maxISD ratio, as two parameters are required for the lognormal distribution functions given from the following equation:

$$P[LS_i/IM] = \Phi\left(\frac{\ln(IM) - \ln(\overline{IM}_i)}{\beta}\right) \quad (1)$$

where  $\Phi$  is the standard normal cumulative distribution function,  $LS_i$  is the damage limit state,  $IM$  is the intensity measure of the earthquake expressed both in terms of rock outcropping  $PGA_{rock}$  measure in g,  $\overline{IM}$  and  $\beta$  are the corresponding median values at which the building reaches each damage limit state,  $i$ , and log-standard deviations respectively. A linear regression fit of the logarithms of the  $PGA_{rock}$ -maxISD and data pairs which minimize the regression residuals is adopted. Three components of uncertainty are accounted for related to the definition of the limit state value  $\beta_{LS}$  (defined empirically as  $\beta_{LS} = 0.4$ ), the capacity of each structural type  $\beta_c$  (defined empirically as  $\beta_c = 0.30$ ), and the demand  $\beta_D$  [38]. The demand  $\beta_D$  is calculated conducting statistical processing of the numerical results (IM-DM data pairs). In particular, we estimate the dispersion of the logarithms of  $PGA_{rock}$ -maxISD obtained from the numerical analysis using the regression fit. The total parameter  $\beta$ , which represents the total dispersion related to each fragility curve, is finally evaluated as the root of the sum of the squares of the three variability dispersions assuming that they are statistically independent [38]. Figure 8 shows the derived fragility curves along with their fragility parameters (median  $\overline{IM}$  and log-standard deviation  $\beta$ ) in terms of  $PGA_{rock}$  for the steel light-frame warehouse subjected to ground shaking considering the different approaches.

From Figure 8 some interesting conclusions could be derived. First of all, it is noticed, that 2D and 3D configurations for the fixed-base structure, ignoring liquefaction and SSI effects, are generally correlated quite well with the 3D fixed-base model showing lower vulnerability values for all damage states. Secondly, it seems that the vulnerability of a steel light-frame warehouse, when considering liquefaction effects, is very low. More specifically, for  $PGA_{rock}$  values up to 2.0g, the 2D flexible-base and the 3D fixed-base models that consider liquefaction are almost no damaged. For  $PGA_{rock}$  higher than 2.0g, only the "Slight" damage state exists while fragility curves for the other damages are not proposed. A third important conclusion is that the effect of SSI is not significant for the 2D and 3D models which consider liquefaction. Thus, the proposed fragility curve for slight damage state is almost identical for the 2D flexible-base and the 3D fixed-base models implying that the influence of SSI is not of paramount importance for this specific structure.

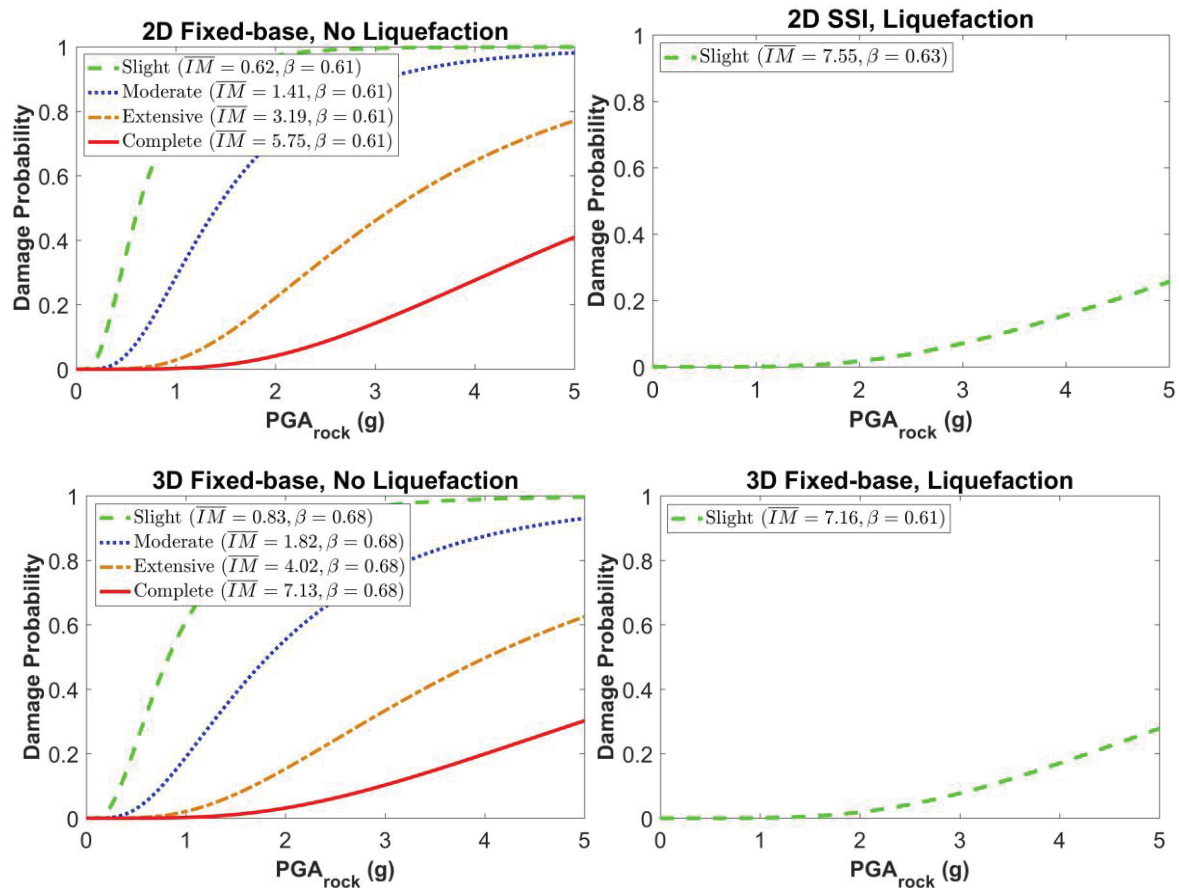


Figure 8: Fragility curves in terms of  $PGA_{rock}$  for the steel light-frame warehouse subjected to ground shaking considering the different approaches.

Next, for the 3D fixed-base approach neglecting liquefaction, we perform a comparison between the herein resulted fragility curves with the ones proposed by Nazri et al. [7] for similar structures (Figure 9). For the "slight" and "moderate" damage states fragility curves are in quite good agreement. For the rest two damage states the correlation between the two approaches is not that good. This is due among other factors to the differences on the structural characteristics and the definition of the complete damage limit state.

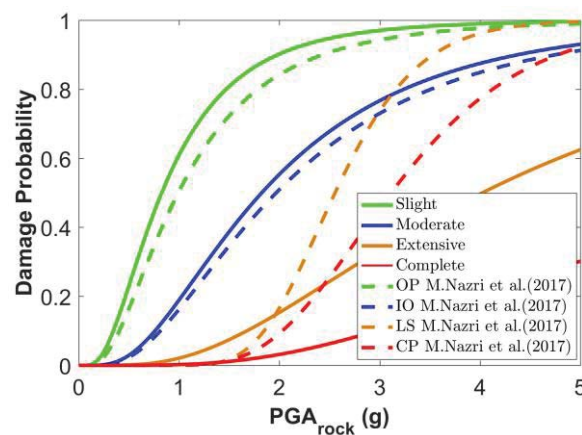


Figure 9: Comparison of the proposed fragility curves for the warehouse using the 3D fixed-base approach neglecting liquefaction with the corresponding analytical ones of Mohamed Nazri et al. [7].

Once the probabilities of exceeding the predefined damage limit states are calculated, the vulnerability (or damage) index  $d_m$  for each level of seismic intensity can be estimated according to the following expression:

$$d_{mj} = \sum_{i=1}^4 P_{ij} \cdot d_i \quad (2)$$

where  $d_{mj}$  is the damage index (taking values from 0: no damage to 1: complete damage) corresponding to each seismic intensity level  $j$ ,  $P_{ij}$  is the discrete damage probability for each damage limit state and  $d_i$  is the damage index at each damage limit state.

Following NIBS [38], we set the central value of the damage index at each damage limit state for the RC buildings equal to 0.10, 0.15, 0.40 and 0.80 for the LS1 (minor), LS2 (moderate), LS3 (extensive) and LS4 (complete), respectively. A vulnerability curve is then generated which provides a unique damage index for each level of seismic intensity.

Figure 10 shows the derived vulnerability curves in terms of  $PGA_{rock}$  for the warehouse subjected to ground shaking considering the different approaches. We observe that the vulnerability of the 2D and 3D fixed-base configurations is in good agreement. When liquefaction is considered, the vulnerability decreases. This is due to the increased nonlinear behaviour of the soil profile introduced by the liquefaction. The 3D fixed-base, and the 2D flexible models that consider soil liquefaction, give almost the same vulnerability curve, which shows that the consideration of SSI has no considerable effect on the vulnerability of the structure.

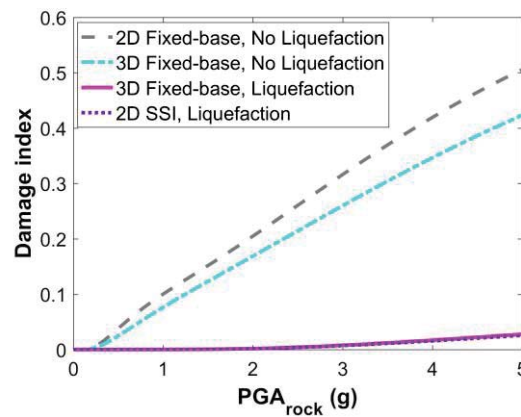


Figure 10: Vulnerability curves in terms of  $PGA_{rock}$  for the steel light-frame warehouse subjected to ground shaking considering the different approaches.

## 6 CONCLUSIONS

Within this study's framework, incremental dynamic analysis was performed for a typical port steel light-frame warehouse using a selected set of earthquake records considering four different modelling approaches. This study aimed to identify soil liquefaction and SSI's role in altering the seismic fragility and vulnerability of port warehouses.

1. We concluded that 2D and 3D configurations for the fixed-base structure, ignoring liquefaction and SSI effects, are generally correlated reasonably well with the 3D fixed-base model showing lower vulnerability values for all damage states.
2. Secondly, it seems that the vulnerability of a steel light-frame warehouse, when considering soil liquefaction effects, is very low, possibly due to the increased nonlinear behaviour of the soil profile introduced by the liquefaction.
3. A third important conclusion is that the impact of SSI is not significant for the 2D and 3D models which consider soil liquefaction. Thus, the proposed fragility curve



for slight damage state is almost identical for the 2D flexible-base and the 3D fixed-base models implying that the influence of SSI is not of paramount importance for this specific structure.

## ACKNOWLEDGMENTS

The research reported in this paper was carried out in the framework of the “Resilient, system-wide seismic risk assessment of port facilities. Application to Thessaloniki Port system” RESPORTS project (<http://resports.gr/>), funded by the Hellenic Foundation for Research and Innovation (HFRI) and General Secretariat for Research and Technology (GSRT) under Grant Agreement Number 754.



## REFERENCES

- [1] PIANC - International Navigation Association, *Seismic design guidelines for port structures*, Chairman: Iai S, Bakelma Publishers, Tokyo, 2001.
- [2] G. Mylonakis, G. Gazetas, Seismic soil-structure interaction: beneficial or detrimental. *J Earthq Eng*, **4**(3), 277-301, 2000.
- [3] M. Ciampoli, P Pinto. Effects of soil-structure interaction on inelastic seismic response of bridge piers. *J Struct Eng ASCE*, **121**(5), 806-814, 1995.
- [4] S. Karapetrou, S. Fotopoulou, K. Pitilakis, Seismic vulnerability assessment of high-rise non-ductile RC buildings considering soil-structure interaction effects. *Soil Dyn Earthq Eng*, **73**, 42-57, 2015.
- [5] C. Petridis, D. Pitilakis, Fragility curve modifiers for RC dual buildings to include non-linear site effects and SSI. *Earthq Spectra*, **36**(4), 1930-1951, 2020.
- [6] D. Pitilakis, A. Modaressi-Farahmand-Razavi, D. Clouteau, Equivalent-Linear Dynamic Impedance Functions of Surface Foundations. *J Geotech Geoenviron Eng*, **139**(7), 1130-1139, 2013.
- [7] F. Mohamed Nazri, S. Tahar, S.N.A. Saruddin, S. Shahidan, Seismic Fragility Curves of Industrial Buildings by Using Nonlinear Analysis. *MATEC Web of Conferences*, **103**, 02017, 2017.
- [8] I. Ntaliakouras, N. Pnevmatikos, Seismic vulnerability curves for industrial steel structures. *Proceedings of the 16<sup>th</sup> European Conference on Earthquake Engineering*, 18-21 June, Thessaloniki, Greece, 2017.
- [9] S. Karafagka, S. Fotopoulou, K. Pitilakis, Vulnerability assessment of RC buildings and warehouses due to liquefaction displacements. *Proceedings of the 16<sup>th</sup> European Conference on Earthquake Engineering*, 18-21 June, Thessaloniki, Greece, 2018.
- [10] S. Karafagka, S. Fotopoulou, D. Pitilakis, Fragility curves of non-ductile RC frame buildings on saturated soils including liquefaction effects and soil-structure interaction. *Bull Earthq Eng*, <https://doi.org/10.1007/s10518-021-01081-5>, 2021.



- [11] S. Karafagka, S. Fotopoulou, D. Pitilakis, Fragility assessment of non-ductile RC frame buildings exposed to combined ground shaking and soil liquefaction considering SSI. *Eng Struct* **229**, 111629, <https://doi.org/10.1016/j.engstruct.2020.111629>, 2021.
- [12] G. Tropeano, A. Chiaradonna, A. D'Onofrio, F. Silvestri, A numerical model for non-linear coupled analysis of the seismic response of liquefiable soils. *Comput Geotech*, **105**, 211-227, 2019.
- [13] M. Bowers, *Seismic fragility curves for a typical highway bridge in Charleston, SC considering soil-structure interaction and liquefaction effects*. MSc Thesis, No 285, Clemson University, 2007.
- [14] B. Aygün, L. Dueñas-Osorio, J.E. Padgett, R. DesRoches, Efficient longitudinal seismic fragility assessment of a multispan continuous steel bridge on liquefiable soils. *J Bridge Eng ASCE*, **16(1)**, 93-107, 2011.
- [15] Z. Wang, L. Dueñas-Osorio, J.E. Padgett, Influence of Soil-Structure Interaction and Liquefaction on the Isolation Efficiency of a Typical Multispan Continuous Steel Girder Bridge. *J Bridge Eng ASCE*, **19(8)**, 2014.
- [16] K. Ichii, *Application of Performance-Based Seismic Design Concept for Caisson-Type Quay Walls*. PhD Dissertation, Kyoto University, 2003.
- [17] K. Ichii, Fragility Curves for Gravity-Type Quay Walls Based on Effective Stress Analyses. *Proceedings of the 13<sup>th</sup> World Conference on Earthquake Engineering*, 2004.
- [18] S. Koutsourelakis, J.H. Prevost, G. Deodatis, Risk assessment of an interacting structure–soil system due to liquefaction. *Earthq Eng Struct Dyn*, **31(4)**, 851-879, 2002.
- [19] F. Lopez-Caballero, A. Modaressi Farahmand-Razavi, Numerical simulation of liquefaction effects on seismic SSI. *Soil Dyn Earthq Eng*, **28(2)**, 85-98, 2008.
- [20] A. Anastasiadis, D. Raptakis, K. Pitilakis, Thessaloniki's detailed microzoning: subsurface structure as basis for site response analysis. *Pure Appl Geophys*, **158(12)**, 2597-2633, 2001.
- [21] K. Pitilakis, S. Argyroudis, S. Fotopoulou, S. Karafagka, K. Kakderi, J. Selva, Application of stress test concepts for port infrastructures against natural hazards. The case of Thessaloniki port in Greece. *Reliab Eng Syst Saf*, **184**, 240-257, 2019.
- [22] CEN, EN 1998-5. *Eurocode 8: Design of structures for earthquake resistance - Part 5: Foundations, retaining structures and geotechnical aspects*. European Committee for Standardization, Brussels, 2004.
- [23] S. Mazzoni, F. McKenna, M.H. Scott, G.L. Fenves, *Open system for earthquake engineering simulation user command-language manual*. Berkeley, California: Pacific Earthquake Engineering Research Centre, 2009.
- [24] A. Neuenhofer, F.C. Filippou, Evaluation of nonlinear frame finite-element models. *J Struct Eng ASCE*, **123(7)**, 958-966, 1997.
- [25] E. Spacone, V. Ciampi, F.C. Filippou, Mixed formulation of nonlinear beam finite element. *Comput Struct*, **58(1)**, 71-83, 1996.
- [26] Computers and Structures Inc., *SAP 2000-Structural Analysis Program: Linear and Nonlinear Static and Design of Three-dimensional structures*. Berkeley, California, USA, 2004.

- [27] M.A. Biot, Mechanics of deformation and acoustic propagation in porous media. *J Appl Phys*, **33(4)**, 1482-1498, 1962.
- [28] J. Lysmer, A.M. Kuhlemeyer, Finite dynamic model for infinite media. *J Eng Mech Div ASCE*, **95**, 859-877, 1969.
- [29] W.B. Joyner, A.T.F. Chen, Calculation of nonlinear ground response in earthquakes. *Bull Seismol Soc of Am*, **65(5)**, 1315-1336, 1975.
- [30] A.O.L. Kwok, J.P. Stewart, Y.M. Hashash, N. Matasovic, R. Pyke, Z. Wang, Z. Yang, Use of exact solutions of wave propagation problems to guide implementation of non-linear seismic ground response analysis procedures. *J Geotech Geoenviron Eng ASCE*, **133(11)**, 1385-1398, 2007.
- [31] J.H. Prevost, A simple plasticity theory for frictional cohesionless soils. *Soil Dyn Earthq Eng*, **4(1)**, 9-17, 1985.
- [32] Z. Yang Z, *Numerical Modeling of Earthquake Site Response Including Dilation and Liquefaction*. PhD Thesis, Department of Civil Engineering and Engineering Mechanics, Columbia University, New York, 2000.
- [33] E. Parra, *Numerical modelling of liquefaction and lateral ground deformation including cyclic mobility and dilation response in soil systems*. PhD thesis, Department of Civil Engineering, Rensselaer Polytechnic Institute, Troy, New York, 1996.
- [34] G. Masing, Eigenspannungen und verfertigung beim messing. *Proceedings of the 2<sup>nd</sup> International Congress for Applied Mechanics*, Zurich, Switzerland, 1926.
- [35] S. Akkar, J.J. Bommer, Empirical equations for the prediction of PGA, PGV and spectral accelerations in Europe, the Mediterranean and the Middle East. *Seismol Res Lett*, **81**, 195-206, 2010.
- [36] I. Iervolino, C. Galasso, E. Cosenza, REXEL: computer aided record selection for code-based seismic structural analysis. *Bull Earthq Eng*, **8(2)**, 339-362, 2010.
- [37] D. Vamvatsikos, C.A. Cornell, Incremental dynamic analysis. *Earthq Eng Struct Dyn*, **31(3)**, 491-514, 2002.
- [38] National Institute of Building Sciences -NIBS, *Direct physical damage-general building stock. HAZUS-MH Technical manual*, Chapter 5. Washington, D.C.: Federal Emergency Management Agency, 2004.

## COMPARATIVE ASSESSMENT OF EMPIRICAL AND MECHANICAL APPROACHES FOR THE ESTIMATION OF THE SEISMIC FRAGILITY OF ORDINARY MASONRY BUILDINGS TYPE OF THE INNER CENTRAL ITALY

Ilaria Capanna<sup>1</sup>, Franco Di Fabio<sup>2</sup>, and Massimo Fragiaco<sup>2</sup>

<sup>1</sup> Department of Civil, Construction-Architectural and Environmental Engineering, University of L'Aquila, Monteluco di Roio, 67100, L'Aquila, Italy  
e-mail: [ilaria.capanna@graduate.univaq.it](mailto:ilaria.capanna@graduate.univaq.it)

<sup>2,3</sup> Department of Civil, Construction-Architectural and Environmental Engineering, University of L'Aquila, Monteluco di Roio, 67100, L'Aquila, Italy  
{[franco.difabio](mailto:franco.difabio@univaq.it), [massimo.fragiacomo](mailto:massimo.fragiacomo@univaq.it)}@univaq.it

---

### ABSTRACT

*The assessment of the built heritage vulnerability is a needful task to mitigate the seismic risk. At this aim, fragility functions estimate the probability of exceedance of a structure at discrete levels of ground motion. The paper focuses on the estimation of seismic fragility of unreinforced masonry buildings typical of the inner Central Italy. Fragility assessments were performed for selected ordinary buildings representative of the urban fabric of the Central Italy, hit by the 2016 earthquake recently. The buildings' stock belongs to a macro-typology defined by structural features, easily available from visual inspections and geometric surveys. The structural performances of the buildings are assessed by means of empirical and numerical approaches, based on a large portfolio of information gathered after the 2016 earthquake swarm. Lastly, the fragility curves for the macro-typology have been derived referred to the attainment of four limit states of interest. A comparison between the obtained results in terms of probabilities of exceedance underlines the main advantages and limitations of each approach in the seismic vulnerability prediction on large scale applications.*

**Keywords:** Masonry un-reinforced buildings, fragility curves estimation, vulnerability assessment, damage scenarios.

---

## 1 INTRODUCTION

Recurring earthquakes in seismic prone areas represent a serious threat for the built environment due to structural vulnerabilities that affect the existing buildings. Particularly, masonry constructions suffer extended damage up to lose their structural stability under an earthquake action. Thus, in recent years, a growing attention has been reserved to the evaluation of the structural vulnerability of existing buildings, also deepened by fragility assessment, to mitigate the seismic risk. A fragility function specifies the probability of a structure of attainment or exceedance a limit states of interest, depending upon a certain ground motion intensity measure [1].

About the estimation of the fragility functions, a significant part of the scientific literature focuses on the derivation of fragility curves based on simplified analysis methods or alternative definition of the limit states [2, 3].

Several approaches are used to derive fragility curves: empirical, analytical and hybrid. Empirical fragility methods aim to predict damage for specific levels of ground motion intensity based on post-earthquake damage data of specific building typologies [4,5,6], through simplified assessment of seismic performance. Analytical methods, also called mechanics-based methods, define the fragility functions based on structural or analytical models that appraisal the seismic behaviour of the structure [7,8]. Limit state are defined in terms of quantitative measure of structural performance, like displacements and deformation indicators [9,10]. Hybrid methods derive fragility curves using features of empirical and mechanics-based methods.

The reliability of each method depends on the availability of data and its accuracy.

Empirical fragility assessment is calibrated on a specific area hit by an earthquake. In general, empirical fragility curves reflect uncertainties on structural data and ground shaking intensity. Analytical fragility assessment requires a numerical or mechanical model of the structure based on an in-depth knowledge of mechanical parameters and structural details, difficultly achievable at territorial scale application.

This paper aims to compare the empirical and numerical approaches to derive fragility curves for ordinary masonry buildings, located in the inner Central Italy, recently hit by a shattering seismic swarm. The investigation of the seismic behavior of these buildings attempts to mirror the entire class, representative of the local built-up.

The mean damage of the buildings' class was, in accordance with the European Macro seismic Scale classification, EMS-98, through an empirical approach proposed by the authors, to derive fragility curves for five damage states. After that, the fragility functions were estimated from the results of non-linear static analysis. A comparison between the typological empirical fragility curves and numerical ones reveals the main advantages and limitations in forecast damage scenarios and supporting resilience-enhancing strategies.

## 2 DESCRIPTION OF THE CASE STUDY

### 2.1 Characterization of the case study

The Italian built environment exhibits typical features for each region, in terms of materials and structural configurations, requiring a classification at local or regional scale [11]. This paper deserves attention to the seismic performance of the masonry ordinary buildings typical of the Central Italy, hit by the last seismic swarm occurred in the 2016. The proposed methodology can be addressed to any buildings' typology by considering structural features of the analyzed facilities, as done by other authors [12,13].

The prevalent typologies of the analyzed built-up consist of low-rise masonry buildings and reinforced-concrete frame buildings. Regarding the masonry facilities, two main typologies could be detected in the selected geographical area: (i) historical constructions and (ii) ordinary buildings. Buildings (i) are located in the historical centers, often built attached to each other up to compose masonry aggregates of structural units with different height, number of stories, structural types and materials heterogeneities [14,15]. In general, historical buildings are conceived to withstand only gravity loads: under an earthquake action, they suffer local mechanisms, like out-of-plane response of masonry walls. Buildings (ii), built in the last century to expand urban centers, follow the empirical rules and the code dispositions in force at the construction period. Most of them are endowed of connections wall-to-wall or anti-seismic devices, like iron ties, that ensure a global response of structures. Often though the poor mechanical properties of the masonry give rise to an unsatisfactory seismic performance.

Fifteen masonry buildings are selected as representative of the ordinary buildings' class of the area hit by the 2016 earthquake. Most of these buildings manifested an in-plane seismic response, with typical shear and bending failure modes. Some of them suffered local mechanisms due to the ineffectiveness of the connections wall to wall. The observed damage was estimated in agreement with the damage classification by Grünthal [16] that ranges from the Level 0 to the Level 5.

Buildings with a suffered damage grade  $D_{k2}$  consist of 13.33% of the sample; with a damage grade  $D_{k3}$  of 80 %, and with a damage grade  $D_{k4}$  of 6.67%.

## 2.2 The Central Italy seismic swarm

In 2016, the Central Italy was hit by a seismic swarm that started on 24 August. The first mainshock, with a magnitude  $M_w = 6.2$ , occurred with an epicenter located in Accumoli (Rieti). The second mainshock, with a magnitude  $M_w = 5.5$ , occurred with an epicenter in Norcia (Perugia). The seismic swarm continued up to 6500 aftershocks with a  $M_w$  until 5.5, affecting four regions: Lazio, Abruzzo, Marche and Umbria. The seismic genetic area concerns a complex structural configuration and different faults, see Fig.1 (INGV) [17]: the soil and topographic configurations drove strong local site effects.

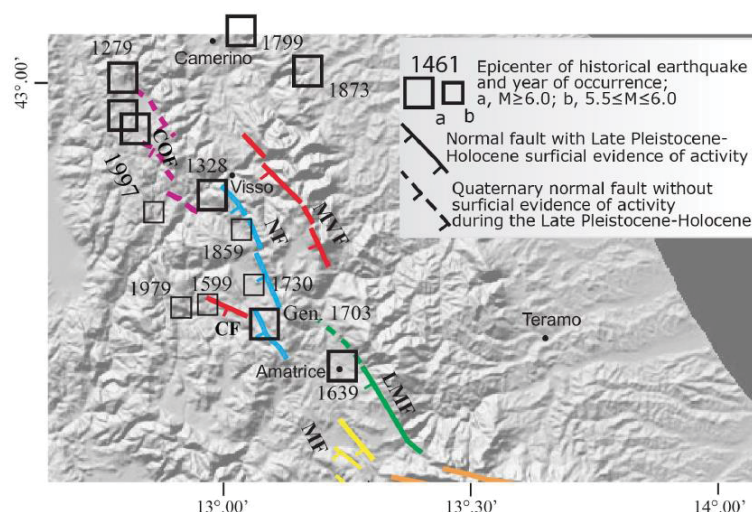


Fig. 1 Scheme of Quaternary and / or active faults in the area between the Monteverde basin (south) and the Colfiorito area (north): COF, Colfiorito fault; MVF, fault of the M. Vettore; NF, Norcia fault; CF, Cascia fault; LMF, Monti della Laga fault; MF, faults in the Monteverde basin (INGV)



Overall, the seismic swarm was shattering giving rise to hundreds of buildings damaged and un-safe.

### 3 SEISMIC VULNERABILITY ASSESSMENT

#### 3.1 Seismic assessment by means an empirical approach.

In the last decades, a significant part of the scientific literature focused on the simplified estimation of the seismic vulnerability of masonry buildings [18,19] to face the estimation of the seismic vulnerability at territorial level.

Empirical approaches attempt to overcome the effort of seismic vulnerability assessment on large-scale application resorting to few structural and mechanical parameters, known from visual inspections or geometric surveys.

The authors proposed a simplified method finalized to provide a vulnerability index (ranging from 0 to 100) for the in-plane seismic behavior, based on ten parameters evaluated through quick formulations, related to three classes of growing vulnerability (from A to C), with different scores associated, see Table 1.

	Parameter of the wall	Weight	
1	Quality of the masonry	1.00	
2	Amount of openings	0.5	
3	Behaviour in plan	0.8	Class A: score 0
4	Behaviour in elevation	0.75	
5	Typology of opening	0.20	Class B: score 50
6	Stiffness of the spandrel beams	0.40	
7	Tensional state in plan	0.8	Class C: score 100
8	Tensional state in elevation	0.8	
9	Position of the wall	1.25	
10	Site effects	1.05	

Table 1: Form of the proposed predictive method.

The method was applied to each building of the case study. The mean value of the vulnerability indices, representative of the entire buildings' sample, was equal to 43.88. The expected mean damage of the typological class  $\mu_D$  was estimated using the macro-seismic method [20], according to Equation 1:

$$\mu_D = 2.5 \left[ 1 + \tanh \left( \frac{(I+6.25V-13.1)}{Q} \right) \right] \quad (1)$$

Where  $I$  is the macro-seismic intensity,  $Q$  is a ductile factor set equal 2.3, and  $V$  is the normalized vulnerability index representative of the entire class. The average vulnerability curves and the confidence bounds associated are derived for different scenarios, expressed in terms of macro-seismic intensity, in Fig.2 (a), and in terms of peak ground acceleration in Fig.2 (b), evaluated according to Murphy O'Brien law correlation [21].



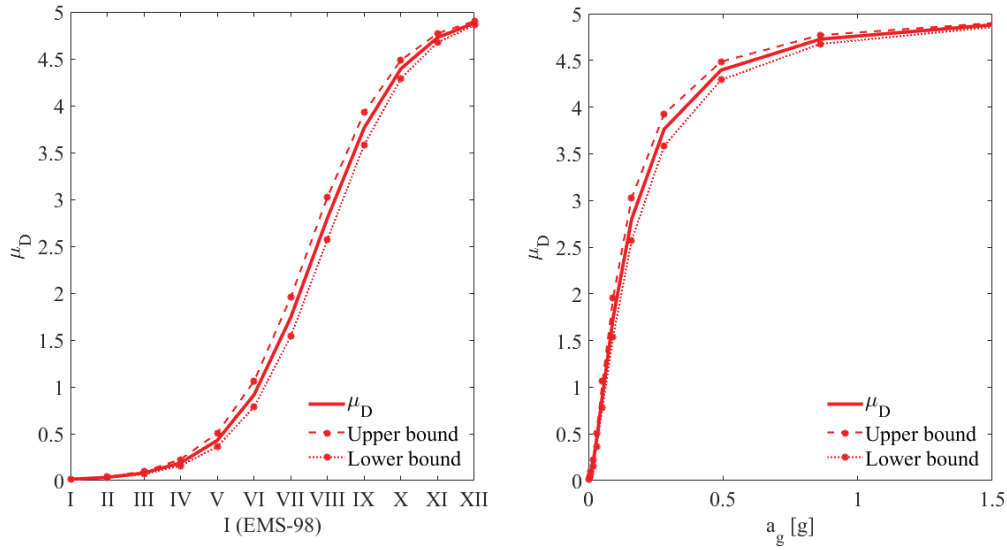


Fig. 2. Mean typological damage curves: in terms of Intensity Measure (a); in terms of  $a_g$  (b).

The probability of occurring the damage grade  $D_k$  is estimated as a function of the  $\mu_D$  according to the Eq. 2, [16]:

$$p_k = \frac{5!}{k!(5-k!)} \left( \frac{\mu_D}{5} \right)^k \left( 1 - \frac{\mu_D}{5} \right)^{5-k} \quad (2)$$

The typological fragility curves, derived by means the empirical method, are plotted in Fig.3: expressed in terms of macro-seismic intensity, in Fig.3 (a), in terms of peak ground acceleration in Fig.3 (b).

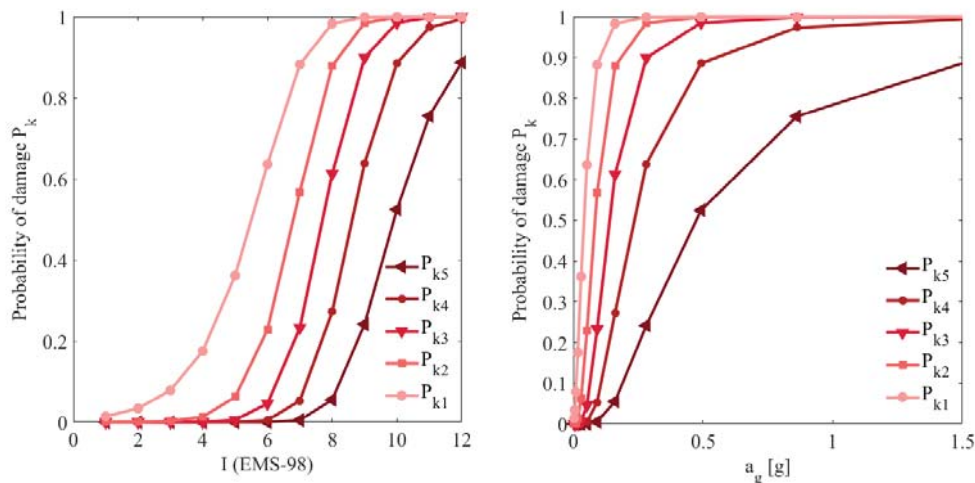


Fig. 3. Typological fragility empirical curves: in terms of Intensity Measure (a); in terms of  $a_g$  (b)

### 3.2 Seismic assessment by means mechanical approaches.

Mechanics-based approaches appraisal the seismic structural performance of buildings accurately based on a numerical or analytical modeling. The achievement of a reliable estimation of the seismic behavior of a structure requires a deep knowledge of the structural system,

detailed data, in-situ diagnostic tests, and a high computational effort. Therefore, the mechanical estimation of the seismic performance at territorial level represents a tricky application.

Nevertheless, the authors derived the fragility curves of the class through numerical analysis to compare the different approaches.

Static no linear analysis was performed using a commercial software package, 3Muri software [22], in which the equivalent frame modelling is implemented. The seismic action corresponds to the design response spectrum, defined to the spectral parameter  $a_g$  (max acceleration value),  $F_0$  (max value of the amplification factor for the horizontal acceleration response spectrum) and  $T_c^*$  (period of the horizontal onset for constant velocity), according to the Italian Seismic Code [23, 24]. The response spectrum is defined for a return period,  $T_r$ , of 30 years, for Operational Limit State, LS1; 50 years, for Damage Limit State, LS2; 475 years, for Significant Damage Limit State, LS3; 975 years, for Collapse Limit State, LS4. Non-linear static analyses were carried out along the longitudinal and transversal direction, by applying two different seismic loads, and an accidental eccentricity between the mass centroid and the stiffness centroid is considered, according to the Italian Design Code. The Acceleration Displacement Response Spectrum, ADRS, was assumed to evaluate the seismic capacity and demand of the structure [25]. Twenty-four pushover analyses were performed from each of the fifteen buildings, yielding 360 analysis.

Still, for each structure, the analysis representative of the lowest safety level.

The probability of collapse,  $P_c$ , descends from the estimation of the standard normal cumulative distribution function  $\Phi$ , as expressed in Equation (3):

$$P[d_s|S_d] = \Phi \left[ \frac{1}{\beta_s} \ln \left( \frac{S_d}{\bar{S}_{ds}} \right) \right] \quad (3)$$

Where  $d_s$  is the displacement of the threshold of damage state,  $S_{ds}$  is the median value of spectral displacement at  $d_s$ ,  $\beta_s$  is the standard deviation of the natural logarithm of spectral displacement of a damage state  $d_s$ . The limit damage thresholds are reported in Table 2:

Damage Limit State		Displacement Limit State
LS1	Operational Limit State	$0.7 \cdot d_y$
LS2	Damage Limit State	$0.8 \cdot d_y + 0.2 \cdot d_u$
LS3	Significant Damage Limit State	$0.5 \cdot (d_y + d_u)$
LS4	Collapse Limit State	$d_u$

Table 2: Damage thresholds definition.

The yielding and ultimate displacement,  $d_y$  and  $d_u$ , correspond to the average of the fifteen values, equal to 0.003 m and 0.011 m, respectively. The standard deviation is equal to 0.15 for the yielding displacement and 0.39 for the ultimate displacement. The typological fragility curves derived by means the numerical method are plotted in Fig. 4.

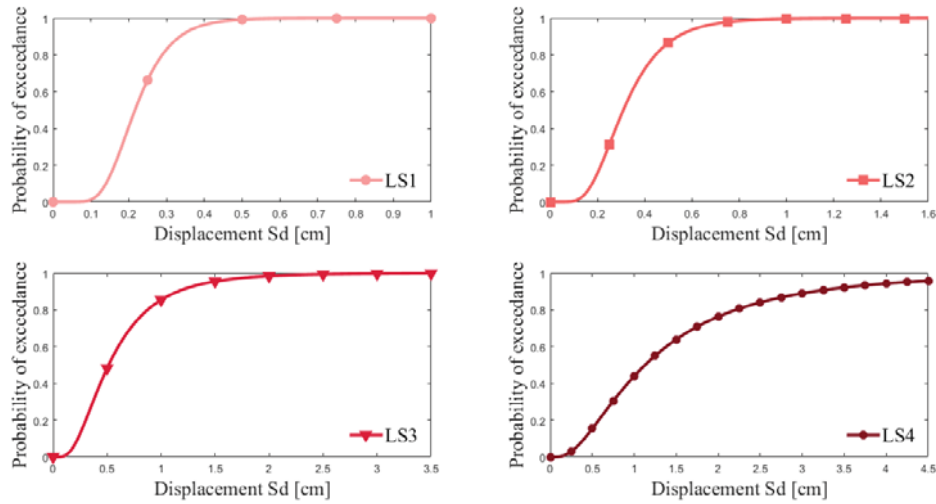


Fig. 4. Typical fragility numerical curves for different limit states.

#### 4 COMPARATIVE ASSESSMENT OF THE FRAGILITY CURVES

Fragility functions estimate the probability of a structure to attain or exceed limit states of interest, depending upon a certain ground motion Intensity Measure. In seismic risk assessment, probabilities of exceedance of limit states of interest are useful to predict the seismic behavior of the built environment before an earthquake occurs.

The authors performed seismic fragility assessment for the class of the ordinary masonry buildings based on the empirical and numerical probabilities of exceedance.

Furthermore, the large portfolio of the gathered information and data allows to estimate the real damage scenario occurred after the 2016 earthquake. The suffered damage of each building of the stock was correlated to the Intensity Measure experienced by the attenuation law proposed by Crespellani [26], see Eq. 4, to prove the reliability of the proposed empirical method in predicting seismic damage scenario:

$$I_{EMS-98} = 6.39 + 1.756M_w - 2.747\ln(R + 7) \quad (4)$$

Where  $M_w$  is the moment magnitude occurred, set equal 6.2, and  $R$  is the distance from the epicenter, equal to 21.5 km. The discrete damage distributions for each buildings of the sample, evaluated for an intensity measure equal to 8.07, is reported in Fig. 5.

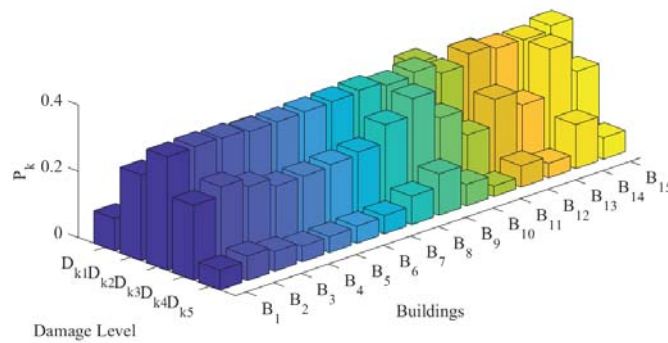


Fig. 5. Discrete damage distributions for  $I=8.07$ .

The percentage of buildings of the sample with a damage grade  $D_{k2}$  was equal to 6.67; with a damage grade  $D_{k3}$  was equal to 86.67, and with a damage grade  $D_{k4}$  equal to 6.67.

The forecast damage shows a good agreement with the real suffered damage: the preponderant level of damage is  $D_{k3}$ , with a discrepancy equal to 6.97 % with the real damage.

Moreover, the correlation law neglects the influence of possible site effects on damage scenario.

The results discussed above prove the capability and reliability of the empirical method to forecast the expected damage of buildings' sample.

Whereupon a comparison in terms of typological fragility curves is performed to compare empirical and mechanics-based methods, see Fig. 6, expressed in terms of  $a_g$ .

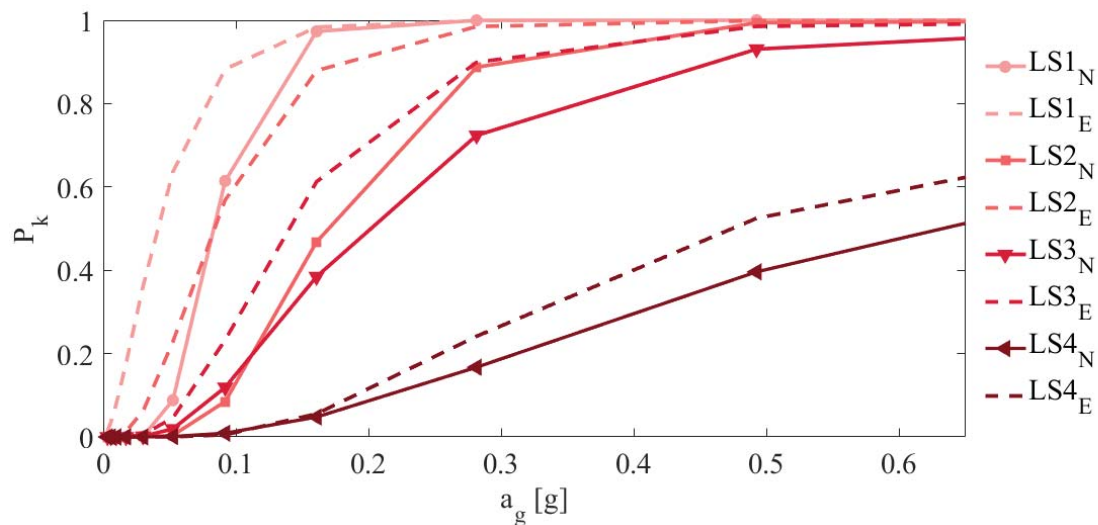


Fig. 6. Fragility curves comparison.

For a seismic demand enclosed in the range 0-0.3 g, the discrepancy in terms of probability of exceedance for the LS1 reaches the value of 29.9 %; for the LS2 reaches the value of 47 %.

The comparison highlights a difference of fragility curves, more remarkable for the LS1 and LS2. Whereas the fragility curves referred to the attainment of the LS3 and LS4 shows a better agreement. For a seismic demand higher than 0.3 g, the discrepancy in terms of probability of exceedance for the LS3 reaches the value of 19 %; for the LS4 reaches the value of 25 %.

The empirical and numerical probability values of exceeding the limit state LS1 and LS2 may be regarded as too scattered to consider equivalently the two approaches.

Overall, the empirical curves overestimate the probabilities of the collapse, on the safe side in predicting the damage scenario.

## 5 CONCLUSIONS

The paper aims to derive fragility curves for masonry buildings' class, composed of fifteen selected buildings typical of the inner Central Italy, by empirical and numerical method. A simplified assessment of the seismic behavior of the buildings is performed, through an empirical method proposed by the authors, to provide a mean vulnerability index representative of the buildings' sample. Based on the empirical results, the mean damage was evaluated, according to the Macro Seismic Methodology to derive empirical fragility curves of the buildings' class. After that, fragility curves are derived from the results of non-linear static analysis. Based on a comparison between the different methodologies, the typological fragility curves show

different values of the expected damage, more scattered for the limit states LS1 and LS2. For a seismic demand enclosed in the range 0-0.3 g, the discrepancy in terms of probability of exceedance for the LS1 reaches the value of 29.9 %; for the LS2 reaches the value of 47 %. Whereas the fragility curves referred to the attainment of the LS3 and LS4 shows a better agreement. For a seismic demand higher than 0.3 g, the discrepancy in terms of probability of exceedance for the LS3 reaches the value of 19 %; for the LS4 reaches the value of 25 %. Thus, the current research results show that a typological approach fails for the LS1 and LS2 states of interest.

To improve the numerical fragility assessment of the buildings' typology, an investigation of the yielding displacements may be useful to propose an appropriate definition of the threshold for the slight and moderate damage states. The identification of suitable limit states for masonry buildings is still an open issue.

Similarly, to improve the empirical fragility assessment, the ductile factor of the masonry structures, set equal to 2.3 in the empirical formulation of the expected mean damage, could be deepened: even within the ordinary masonry class, buildings exhibit different ductile behaviour factors, showing the dispersion of the ductile parameter  $Q$ .

Therefore, the empirical typological fragility assessment ensures accurate and quick seismic vulnerability prediction on large scale, reducing computation time of seismic analysis of buildings' class. For the LS1 and LS2 limit states, the current research points out that a typological approach requires more accurate quantitative parameters to grasp the buildings' seismic behavior, with either approaches. To improve the fragility assessment of the buildings' typological class, an investigation of the onset of the damage may be useful to propose an appropriate definition of the threshold for the slight and moderate damage states. Thus, the limitations of each approach in forecasting damage scenarios and supporting resilience-enhancing strategies could be removed improving observational, experimental and numerical data to better deepen the seismic behavior of buildings under investigation.

## 6 ACKNOWLEDGMENTS

The authors would like to thank S.T.A. DATA company for providing the academic license of the 3Muri software.

## REFERENCES

- [1] A. Aloisio, R. Alaggio, M. Fragiacomò, Fragility functions and behavior factors estimation of multi-story cross-laminated timber structures characterized by an energy-dependent hysteretic model. *Earthquake Spectra*, **37** (1), <https://doi.org/10.1177/8755293020936696>.
- [2] A. Mouyiannou, M. Rota, A. Penna, G. Magenes, Identification of Suitable Limit States from Nonlinear Dynamic Analyses of Masonry Structures. *Journal of Earthquake Engineering*, **18** (2), 231-263, 2014.
- [3] M. Rota, A. Penna, G. Magenes, A methodology for deriving analytical fragility curves for masonry buildings based on stochastic nonlinear analyses. *Engineering Structures*, **32**, 1312-1323, 2010.

- [4] I. Ioannou, T. Rossetto, D. Grant, Use of regression analysis for the construction of empirical fragility curves. *15<sup>th</sup> World Conference on Earthquake Engineering (15 WCEE)*, Lisboa, Portugal, 2012.
- [5] A. Miano, F. Jalayer, G. Forte, A. Santo, Empirical fragility assessment using conditional GMPE-based ground shaking fieldJ.s: application to damage data for 2016 Amatrice Earthquake. *Bulletin of Earthquake Engineering*, **18**, 6629-6659, 2020.
- [6] C. Del Gaudio, G. De Martino, M. Di Ludovico. G. Manfredi, A. Prota, P. Ricci, G. Verderame, Empirical fragility curves for masonry buildings after the 2009 L'Aquila, Italy, earthquake. *Bulletin of Earthquake Engineering*, **17**, 6301-6330, 2019.
- [7] J. Park, P. Towashiraporn, J.I. Craig, B. J. Goodno, Seismic fragility analysis of low-rise unreinforced masonry structures. *Engineering Structures*, **31**, 125-137, 2009.
- [8] S. Saloustros, L. Pelà, F.R. Contrafatto, P. Roca, I. Petromichelakis, Analytical derivation of seismic fragility curves for historical masonry structures based on stochastic analysis of uncertain material parameters. *International Journal of Architectural Heritage*, **13 (7)**, 1142-1164, 2019.
- [9] M. Rota, A. Penna, G. Magenes, A procedure for deriving analytical fragility curves for deriving analytical fragility curves for masonry buildings. *14<sup>th</sup> World Conference on Earthquake Engineering, 14 WCEE*, Beijing, China, 12-17 October 2008.
- [10] A. Mouyiannou, M. Rota, A. Penna, G. Magenes, Identification of Suitable Limit States from Nonlinear Dynamic Analyses of Masonry Structures. *Journal of Earthquake Engineering*, **18 (2)**, 231-263, 2014.
- [11] M. Vettore, M. Donà, P. Carpanese, V. Follador, F. da Porto, M.R. Valluzzi, A multilevel procedure at urban scale to assess the vulnerability and the exposure of residential masonry buildings: the case study of Pordenone, Northeast Italy. *Heritage*, **3**, 1433-1468, 2020.
- [12] N. Chieffo, F. Clementi, A. Formisano, S. Lenci, Comparative fragility methods for seismic assessment of masonry buildings located in Muccia (Italy). *Journal of Building Engineering*, **25**, 2019.
- [13] A. Simoes, J. Milosevic, H. Meireles, R. Bento, S. Cattari, S. Lagomarsino, Fragility curves for old masonry buildings types in Lisbon. *Bulletin of Earthquake Engineering*, **13**, 3083-3105, 2015.
- [14] I. Capanna, A. Aloisio, F. Di Fabio, M. Fragiacomò, Sensitivity Assessment of the Seismic Response of a Masonry Palace via Non-Linear Static Analysis: A case Study in L'Aquila (Italy). *Infrastructures*, **6(1)**, 8, 2021.
- [15] A. Formisano, Theoretical and numerical seismic analysis of masonry buildings aggregates: Case Studies in San Pio Delle Camere (L'Aquila, Italy). *Journal of Earthquake Engineering*, **21**, 227-245, 2017.
- [16] G. Grunthal, European Macroseismic Scale 1998 (EMS-98). *European Seismological Commission on Engineering Seismology*. Sub commission on Engineering Seismology, Working Group Macro Seismic Scales 15:101.
- [17] F. Galadini, E. Falcucci, S. Gori, P. Zimmaro, D. Cheloni, J.P. Stewart, Active faulting in source region of 2016-2017 Central Italy event sequence. *Earthquake Spectra*, **34**, 1557-1583, 2018



- [18] G. Brando, G. De Matteis, E. Spacone, Predictive model for the seismic vulnerability assessment of small historic centres: Application to the inner Abruzzi Region in Italy. *Engineering Structure*, **153**, 81-96, 2017.
- [19] A. Formisano, G. Florio, R. Landolfo, FM. Mazzolani, Numerical calibration of an easy method for seismic behaviour assessment on large scale of masonry building aggregates. *Advances in Engineering Software*, **80**, 116-138, 2015.
- [20] S. Lagomarsino, S. Giovinazzi, Macroseismic and mechanical models for the vulnerability and damage assessment of current buildings. *Bulletin of Earthquake Engineering*, **4**, 415-443, 2006.
- [21] J.R. Murphy, L.J. O'Brien, The correlation of peak ground acceleration amplitude with seismic intensity and other physical parameters. *Bulletin of the Seismological of America*, **67 (3)**, 877-915, 1977.
- [22] S.T.A. DATA 3MURI (2009) Seismic calculation of masonry structures according to M.D. 14/01/2008. New technical codes for constructions.
- [23] Ministerial Decree of Public Works, *Updating of Technical codes for constructions, M.D. 17/01/2018*. Official Gazette of the Italian Republic n.42, 20 February 2018.
- [24] Ministerial Decree of Public Works, *Instructions for the application of the updating "Technical codes for construction, M.D. 17/01/2018*. Official Gazette of the Italian Republic n.42, 20 February 2018.
- [25] A.K. Chopra, R.K. Goel, Capacity-demand-diagram methods based on inelastic design spectrum. *Earthquake Spectra*, **15**, 637-656.
- [26] T. Crespellani, C.A. Garzonio, Seismic risk assessment for the preservation of historical buildings in the city of Gubbio, Geotechnical Engineering for the Preservation of Monuments and Historical Sites. *International Symposium on Geotechnical Engineering for the Preservation of Monuments and Historic Sites*, Napoli, Italy, 3-4 October, 1996.

## EVALUATION OF SEISMIC RESILIENCE OF RC-BUILDING SUBJECTED TO REPEATED EARTHQUAKE USING RESILIENT INDEX AND FRAGILITY SURFACE FUNCTIONS

Moustafa Moufid Kassem<sup>1</sup>, Fadzli Mohamed Nazri<sup>1\*</sup> and Ahmad Mohamad El-Maissi<sup>1</sup>

<sup>1</sup> School of Civil Engineering, Universiti Sains Malaysia, Engineering Campus, 14300 Nibong  
Tebal, Penang, Malaysia.

e-mail: moustafa-kassem@outlook.com

missi\_1993@hotmail.com

\*cefmn7@gmail.com / cefmn@usm.my

---

### Abstract

*Seismic resilience is a modern approach that aims to return the community of damage to its natural condition in a shortest possible time. Seismic resilience could be interpreted as a structure's ability to maintain a degree of functionality over a particular period of time once it is exposed to seismic events. The research study aims to address with an approach of functionality and seismic resilience of a mid-rise Ordinary Moment Resisting Frame (OMRF) structure subjected to repeated earthquakes. Besides, as a vulnerability and functionality study for risk assessments, both the Seismic Resilience Index (SRI) and the fragility surface were used to determine the seismic resilience of the selected building. The fragility surfaces expressed the probability of damages with respect to intensity measure and seismic event period (T). The concept phases of this approach were as follows: (1): Select targeted buildings, (2): Select and scaled a set of repeated Seismic Ground Motion (SGM) records, (3): Generate an Incremental Dynamic Analysis (IDA), (4): Fragility surface and (5): Functionality curve, with seismic resilience index (RI). Eventually, after investigating the structure through the vulnerability assessment, initiating with IDA, and ending with the fragility surface, it is clearly established that the buildings do not have the capacity to withstand a 15 sec repetitive earthquake due to their ordinary structural design related to ductility demand. Meanwhile, with an increase in the possible seismic ground acceleration, the fluctuation in functionality, SRI, robustness, structural losses, and time recovery of distinct performance levels could be estimated.*

**Keywords:** Seismic Resilience Index, Repeated Earthquake, Fragility Surface, Functionality Curve, Damage State, Structural Losses.

---

## 1 INTRODUCTION

In the last decades, the intensity and frequency of earthquakes has increased, causing severe destruction with enormous number of casualties, posing a main disruption and change in the economic, social, and technical conditions for specific communities. Due to this fact, ‘resilience’, ‘vulnerability’, ‘risk reduction’, and ‘recovery’ definitions are trending in research community. However, it is vital to conduct a quantitative procedure to evaluate these intuitive definitions [1].

All these lead to the development of a resilience assessment for earthquakes by using a specific index, which is considered an important factor for managing and planning natural disasters. The main idea of resilience at the beginning was developed by ecologists, however, it expanded to a wider range of fields i.e., social science, psychology, and engineering [2].

The Seismic Resilience Index (SRI) is considered a powerful tool to demonstrate the capability of a structure to sustain a particular standard of performance and usability across a span of time control ( $T_{LC}$ ) [3]. Bruneau et al. [4] introduced a very general definition for resilience, which covered all the precautions that should be taken to reduce the main losses resulting from hazards, and also the study covered the effects of mitigation and recovery. After this broad definition that was introduced by Bruneau and Reinhorn [5], many studies were produced tackling the development and assessment of resilience.

Samadian et al. [6] conducted a study in Iran to determine the seismic resilience of built and rehabilitated RC school buildings, whereby the study was assessed through utilising vulnerability and fragility curves. The main objective of this study is to implement a new approach which focuses on provincial economic conditions, through the use of vulnerability analysis to estimate earthquake-related losses. The results showed that when the magnitude of hazard levels was increased the SRI decreased functionally. The study concluded that retrofitted school buildings had a higher resiliency level. Furthermore, the comparative study between fragility and vulnerability curves showed that the vulnerability curve indicated more efficient results to evaluate the SRI.

Furthermore, Vona et al. [7] introduced a new resilience approach for communities based on numerical assessment and observed post-seismic restoration procedure. The study focused on the housing systems to develop SRI for the communities, by which it was expressed as a combination of SRIs for each building category. The proposed approach could help in assessing different scenarios with more precise results, which could be achieved with more potential choices.

Titi and Biondini [8] tested the reliability of concrete frame structural systems that were affected by corrosion. The results showed that the designed structures designated to have the same level of functionality could display different seismic resilience over a specific time span resulting from the surrounding environmental conditions. Other studies were established to assess resiliency and calculate the SRI for different type of structures. For instance, Alipour and Shafei [9] assessed the seismic resilience transport networks and Banerjee and Chandrasekaran studied the seismic resilience of bridges under the effect of multi-hazards [10].

In addition, Cimellaro et al. [1] introduced a framework for analytical quantification of disaster resilience. This research focused on integrating information from different fields, which were earthquake engineering, social sciences, and economics to develop a disaster resilience framework. The main outcome of this study was to build a decision-making tool that could help both the policy makers and the engineering professionals for better preparedness and restoration plans after disasters.

Various studies tackled the development and assessment of SRI and covered different categories and indicators [11-13], however, the studies that focus on the assessment and development of SRI under repeated earthquakes are limited.

Repeated earthquakes represented two or more incidents, which precisely hit the same fault area and slip, by which it generated the same waveform [14]. The repeated earthquakes could cause a significant deterioration and higher displacement demand for buildings. All these factors could directly impact the resiliency of these buildings [15-17]. Uchida [18] conducted a study to detect the repeated earthquakes and their application in characterising slow fault slip. The author concluded that by measuring the degree of waveform similarity and accurate hypocentre positions could help in recognising the repeated earthquakes and it could assist in evaluating the source-overlap ratio. The fragility curve or surface is considered as an efficient tool to study the effect of repeated earthquakes.

In seismic risk assessment, fragility curves are considered an essential element, which is defined by relating a given level of seismic intensity to the possibility of reaching or exceeding a certain degree of damage. To determine the performance limit states in relation to the Performance Based Seismic Design (PBSD) during earthquakes, structural damage was measured based on the Engineering Demand Parameters (EDP), i.e., vertical displacements, crack patterns or rotations. To establish fragility curves, which are empirical, theoretical, judgmental, and hybrid, different approaches could be used. [19, 20].

The fragility curve is usually defined by one parameter i.e., PGA, Sa, and Arias, but one distinct parameter is insufficient to study the effect of earthquakes on the buildings precisely. From here came the idea of developing fragility surface, by taking into consideration more than one parameter at the same time when studying the effect of the earthquake [21-23]. Many studies developed fragility surface to assess seismic risk on structures. For example, Ardebili and Saouma [24, 25] developed seismic fragility surfaces to study the effect of earthquakes on concrete dams, and Gehl et al. [26] developed fragility surfaces to evaluate the seismic vulnerability assessment for masonry buildings.

This leads to exploring the fact that lends the rise to the significance of seismic resilience and functionality, and the vulnerability risk assessment by using fragility surface. The aim of this paper is to shed the light on studying the seismic vulnerability assessment for an Ordinary Moment Resisting Frame (OMRF) structure that was designed away from any seismic attention under repeated earthquakes. This paper discusses the procedure for combining the vulnerability analysis to know the possibility of damages for four damage states, namely immediate occupancy (IO), damage control (DC), life safety (LS), and collapse prevention (CP), with the functionality of the structure post seismic event in respect to recovery time. Each damage states corresponds to an intensity measure to be determined by using the incremental dynamic analysis (IDA), and fragility surface. From the damaged states the preparedness of recovery procedure was adopted into three retrofitted actions. Firstly, no actions had been taken related to IO; secondly, the action was to apply a retrofitted application related to DC and LS; and thirdly, the action was at the replacement restoration process at CP level. Eventually, the SRI, functionality, loss of resilience and robustness were determined.

## 2 CONCEPTS OF SEISMIC RESILIENCE INDEX (SRI)

The Seismic Resilience Index (SRI) is considered as the main tool for studying the building ability to tolerate a particular standard of performance and reliability across a broad time control ( $T_{LC}$ ). In this paper, the SRI will be developed through applying different steps. Firstly, a model will be developed to the selected building by using finite element platform. Thereafter, ground motions for repeated earthquakes will be selected. Then, the IDA will be performed. This will all lead to the development of fragility surfaces and vulnerability curves. Finally, the functionality curve will be produced, which will help in estimating the SRI, Robustness (R), and Losses of Resilience (LOR). In order to develop the SRI and its functionality curve  $Q(t)$  the following steps should be tracked as shown and illustrated in Figure 1. Each step will be discussed in detail in the following section.

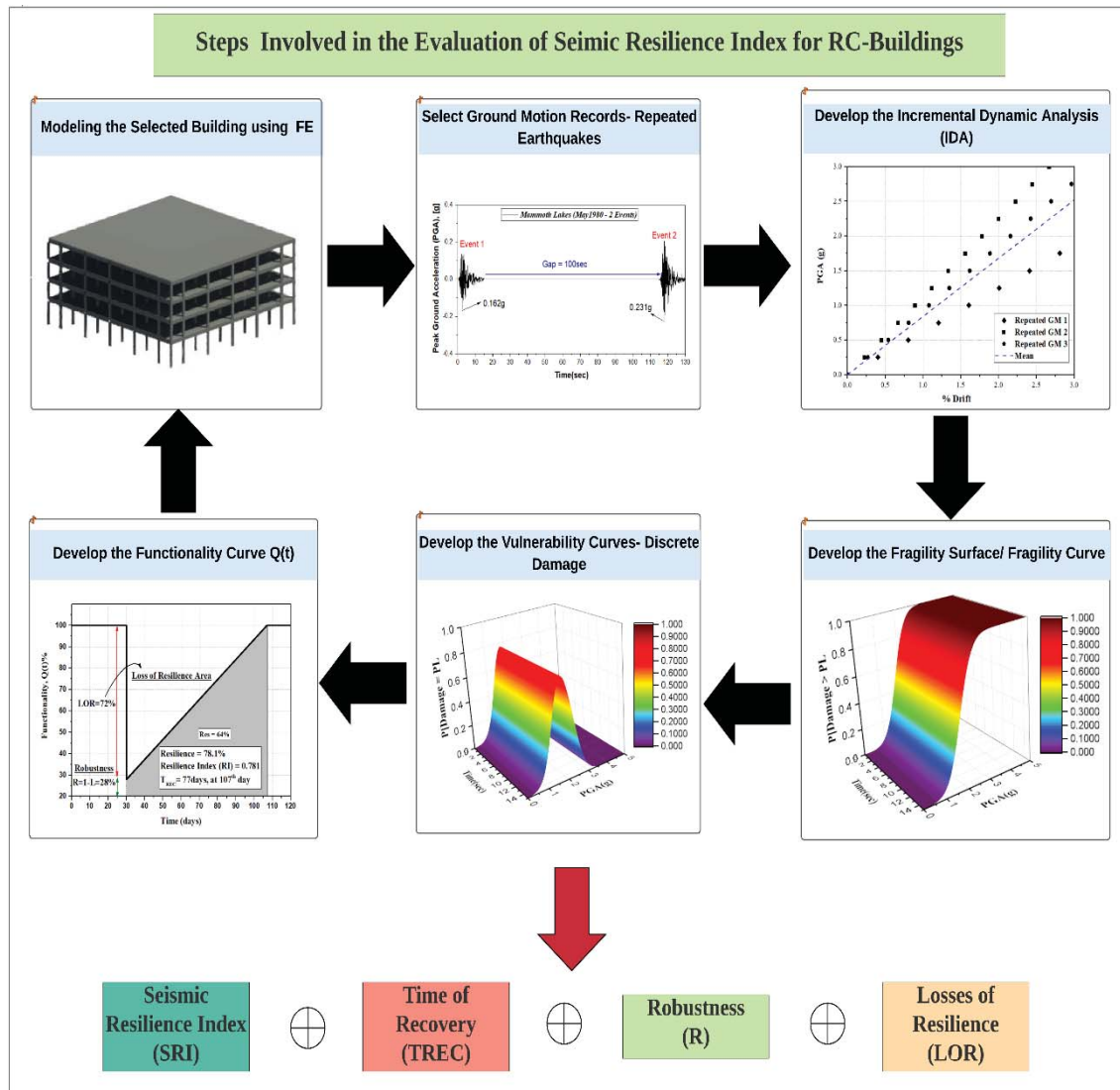


Figure 1: Framework steps for developing SRI.



## 2.1 Modelling structural configuration

A mid-rise model of a 4-storey reinforced concrete building with a total height of 12.0 m and with a common slab thickness of 200 mm was considered in this study. The structural system selected for lateral resistance is considered as Ordinary Moment Resisting Frame (OMRF). The model was designed according to the regulation of ACI318-14 code for gravity loads, and for UBC1997 as OMRF for seismic loads. With reference to the seismic code, the building was assumed to be in seismic zone 4, having soil profile SD, with  $C_a = 0.44$ , and  $C_v = 0.64$  seismic coefficients.

The building materials used were 35 MPa of concrete compressive strength ( $f'_c$ ), and yielding strength ( $f_y$ ) of 420 MPa for the reinforcing steel bars. The gravity loads consisted of dead load and live load which was taken as  $2\text{kN/m}^2$ , and  $4\text{kN/m}^2$ , respectively. The columns cross sections were selected with dimensions of 300 mm x 300 mm, with drop beams of 300 mm x 500 mm. The design calculations supported the use of minimum reinforcement ratio for column longitudinal rebars, which was 1%, whereby 8T12 was used for column reinforcements, with T8 spaced every 300 mm as transversal reinforcement. For the beams, the design expressed the use of 3T12 as bottom longitudinal reinforcement, and 2T12 as top reinforcement. Figure 2 shows the targeted selected building model in three-dimensional (3D) shape, and elevation views.

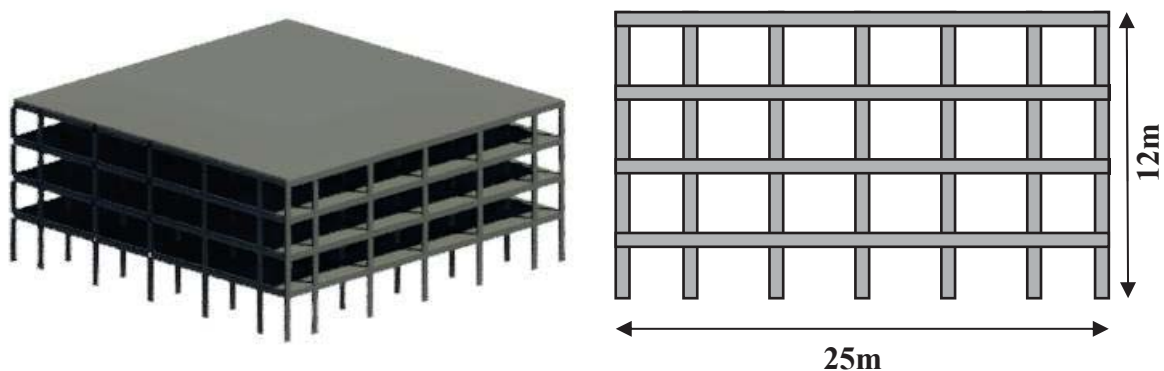


Figure 2: Selected targeted building model in 3D and elevation views.

## 2.2 Repeated ground motion selection

Many studies have considered the impact of repetitive earthquake-induced ground motions on the responsive behaviour of the structures. They found that both the inelastic displacement ratio and its inter-storey drift ratio were significantly influenced by the occurrence of frequent earthquakes. Therefore, in this study, the impact of repeated earthquakes is recognised.

Two real seismic sequences were allocated to each of the ground motion records, namely Chalfant Valley (July 1986 - two events), Imperial Valley (October 1979 - two events) and Mammoth Lakes (May 1980 - two events) from the same station with various record names. For each occurrence, each single ground motion record had a time interval of 15 sec. A gap time interval of 100 sec was added between the two consecutive seismic occurrences. As proposed by Hatzigeorgiou and Liolios [27], this gap had zero spite of potential acceleration values and was completely sufficient to reduce the displacement of any structure due to attenuating and returning to the remaining condition. The three repetitive events were selected from the Pacific Earthquake Engineering Research Center (PEER) database. The selected magnitude ( $M_w$ ) was between 5 and 7 Richter scale, and of intensity measure, PGA ranges between 0.113g, and 0.447g as shown in Figure 3.



Nevertheless, to perform the IDA and establish fragility surfaces or curves, the selection of appropriate ground motion records are very critical as recommended by international standard codes, such as FEMA356, UBC1997, IBC2000, and others [28-30]. These standard provisions also recommended to select a minimum of three ground motion records, or seven to develop a vulnerability assessment analysis. Finally, the selected earthquake events were scaled based on UBC97 target spectrum where the building was located.

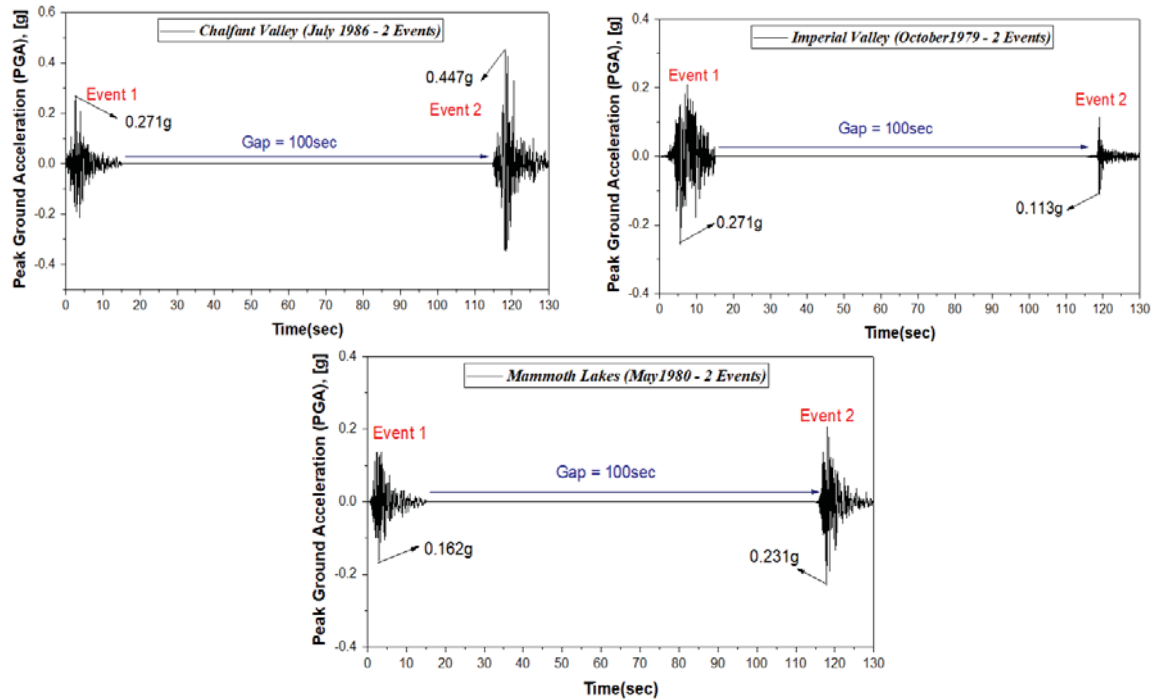


Figure 3: Selection of repeated ground motion seismic events.

### 2.3 Seismic resilience index functionality assessment procedure

Resilience is a specific consideration for evaluating the seismic resistance of the structures and infrastructures, as based on the Multidisciplinary Center for Earthquake Engineering Research (MCEER). Resilience is quantified ranging from 0% to 100% in terms of functionality to be normalised into 0 and 1 to develop its SRI, whereby 0% means spectacular failure and 100% reveals no structure deterioration. It is a wealth of information to develop the SRI as seismic indicator and a recovery application that can help to reduce direct and indirect losses caused by earthquakes.

The SRI is defined as the functionality of a structure after the recovery process or the ability of a structure to withstand earthquakes without any reduction in its functionality [31]. Also, the SRI can be treated as an alternative to deal with the problem of functionality which has been neglected in the seismic codes [32]. Therefore, the SRI is determined by referring to the functionality curves as shown in Figure 4. The area under the curve of functionality demonstrated the structure's resilience, whereby, the functionality of the structure was represented as  $Q(t)$ , as illustrated in Equation (1), and the resilience ( $R$ ) as a function of  $Q(t)$  and time of event ( $t_{OE}$ ) with recovery time ( $T_{REC}$ ) along the total control time ( $T_{LC}$ ), as shown in Equation (2).

Functionality :

$$Q(t) = 1 - \left\{ L(I, T_{REC}) \times [H(t - t_{OE}) - H(t - (t_{OE} + T_{REC}))] \times f_{REC}(t, t_{OE}, T_{REC}) \right\} \quad (1)$$

Resilience (R):

$$R = \int_{T_{OE}}^{T_{REC}} \frac{Q(t)}{T_{LC}} \quad (2)$$

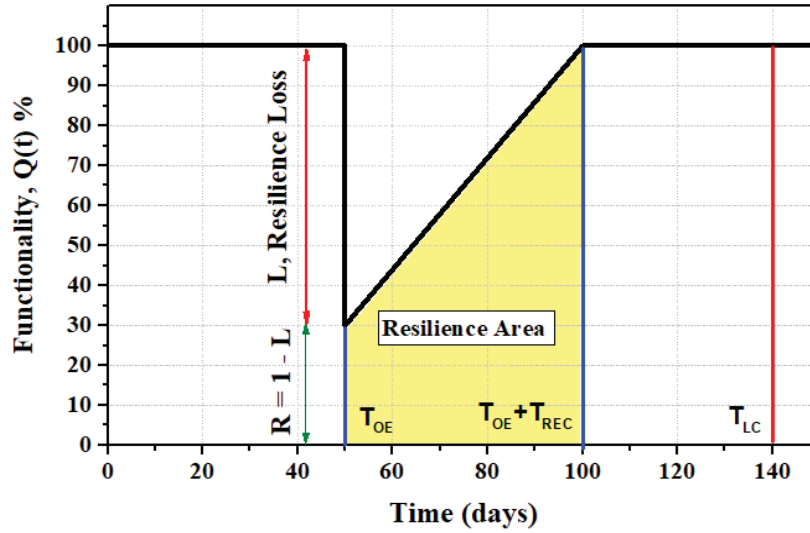


Figure 4: Seismic Resilience with respect to time: Functionality curve.

## 2.4 Loss function evaluation

Losses are very unpredictable in an exceptional case, such as a terrorist attack, blast or other man-made catastrophe, and are different for any scenario discussed. The estimation of losses due to seismic activity is usually questionable and unpredictable. However, it is possible to make some common classifications and identify different types of losses.

Generally, the loss feature usually consists of two types of losses, such as direct losses and indirect losses. The direct loss is referred to structural damages and losses, whereas the indirect losses are referred to casualties, social and economic losses. Since the quantitative analysis of indirect financial damage and human casualties, losses is a complicated procedure, a lot of attention was given to the direct loss in this analysis, as it ultimately depends on the risk of the extensive structural damage.

The direct loss was calculated by using Equation (3) which was required to find the discrete damage probability of four damage states from the fragility surface as a vulnerability analysis. As per FEMA356, by taking into consideration the vertical and horizontal lateral-force resisting components, the state of structural damage during the earthquake determined the performance and output level of a building. These four-performance levels were classified and determined based on % Inter-Storey Drift Ratio (%ISDR) as an Engineering Demand Parameter (EDP). Table 1 describes performance levels of each damage state.

$$L_D = \sum P_E(DS = K) \times r_K \quad (3)$$

Where  $(L_D)$  is the direct loss,  $(K)$  represents the damage state of each performance level,  $P_E(DS = K)$  represents the discrete damage probability,  $(r_k)$  is the corresponding damage ratio for each limit state and damage state that was taken from HAZUS MR4 [33] technical manual, as shown in Table 2. The discrete damage was calculated from the difference between two cumulative distribution functions corresponded to develop fragility surface for each state, as shown from Equation (4) to Equation (8).

$$P[\text{Damage} > DS] = \phi\left(\frac{\ln(IM) - \lambda}{\varsigma}\right) \quad (4)$$

Where  $\phi$  is the cumulative distribution function, IM is an intensity measure,  $\lambda$  is the mean value, and  $\varsigma$  is the standard deviation.

$$P[DS = IO] = P[DS = IO] - P[DS = DC] \quad (5)$$

$$P[DS = DC] = P[DS = DC] - P[DS = LS] \quad (6)$$

$$P[DS = LS] = P[DS = LS] - P[DS = CP] \quad (7)$$

$$P[DS = CP] = P[DS = CP] \quad (8)$$

Damage State (DS)	Damage Description	% Inter-Storey Drift Ratio (%ISDR)
<b>Immediate Occupancy (IO)</b>	There is significant damage to the minor structural elements, but the building stability or lateral ability to resist prior and after the seismic is unaffected.	1.0%
<b>Damage Control (DC)</b>	A certain quantity of repairable damage is appropriate, but the repair cost should be substantially lower than the replacement value.	1.50%
<b>Life Safety (LS)</b>	Due to the higher damage, repair is feasible but economically inefficient and costly. The loss is moderate, but the structure stays stable.	2.0%
<b>Collapse Prevention (CP)</b>	The structure is on the threshold point of local or complete failure being experienced.	2.50%

Table 1: Damage state performance levels description and its damage measures

Damage State (DS)	Damage Ratio ( $r_k$ )
Immediate Occupancy (IO)	0.10
Damage Control (DC)	0.40
Life Safety (LS)	0.80
Collapse Prevention (CP)	1.0

Table 2: HAZUS MR4 technical manual for damage ratios of buildings

## 2.5 Recovery function and time

The progress and the pattern of the structure's post-seismic event rehabilitation will be represented through recovery functions and time. Therefore, for evaluating seismic resilience, recovery time and recovery function are crucial after a seismic event, hence, it should be precisely measured. There are different types of recovery function that could be selected depending on the system and society preparedness response, for example, three possible recovery functions are: linear, exponential, and trigonometric. Where the recovery improvements of the building vary according to the type of recovery functions, it is included to assess the building's functionality, since each function has its own path of restoration. In this study, the linear function is considered to evaluate the building functionality, whereby it is the simplest function commonly used when there is no information available about crisis management and resources. The equations (9, 10 and 11) show the different types of functions that may be used to develop the recovery time and its function path.

Linear function: 
$$f_{rec}(t, t_{OE}, T_{REC}) = \left(1 - \frac{t - t_{OE}}{T_{REC}}\right) \quad (9)$$

Exponential function: 
$$f_{rec}(t, t_{OE}, T_{REC}) = \exp\left(-\frac{(t - t_{OE})(\ln 200)}{T_{REC}}\right) \quad (10)$$

Trigonometric function: 
$$f_{rec}(t, t_{OE}, T_{REC}) = 0.5 \left\{ 1 + \cos \left[ \pi \frac{(t - t_{OE})}{T_{REC}} \right] \right\} \quad (11)$$

## 3 RESULTS AND DISCUSSION

The numerical model of the mid-rise building was developed by using the Finite Element (FE) platform, where the nonlinear time history analysis was generated to develop the incremental dynamic analysis curve. From the IDA curves, the relationship between %ISDR and spectral acceleration of first periodic mode  $S_a(T_1)$  could be determined, and thus, it determined the performance level of the structure based on 4-performance limit state as shown in Figure 5. Where the damage of measured  $S_a(T_1)$  of the repeated earthquakes were increasingly scaled by 0.05 g until it exceeds 2.0 g, the analysis was stopped due to the instability of the structure. The IDA curves are considered an important parametric tool, which evaluates the dynamic behaviour of the structures. This curve clarifies that the building performance is linearly in rapid changes between the damaged states, by which it tends to undergo into three restoration options that will be taken into consideration during post seismic events. The options are; no action at IO stage, restoration action at DC and LS stage, and replacement action at CP stage.

For example, in case of immediate occupancy, no retrofitting action is needed to be applied before exceeding 0.78 g. However, once it reaches the damage control and life safety stages at 1.24 g, and 1.54 g, respectively, it is recommended to apply a retrofitting action before it reaches the collapsed stage, whereby the replacement action is the only choice at 2.15 g and more. Table 3 summarises the structural performance levels, and types of preparedness actions.

Damage State	IM of each Damage State- $S_a(T_1)$ , [g]	Preparedness Action of each Stage
Immediate Occupancy	0.78g	No Action
Damage Control	1.24g	Restoration- repairing action
Life Safety	1.54g	Restoration- repairing action
Collapse Prevention	2.15g	Replacement action

Table 3: IM of each damage state and its preparedness actions.

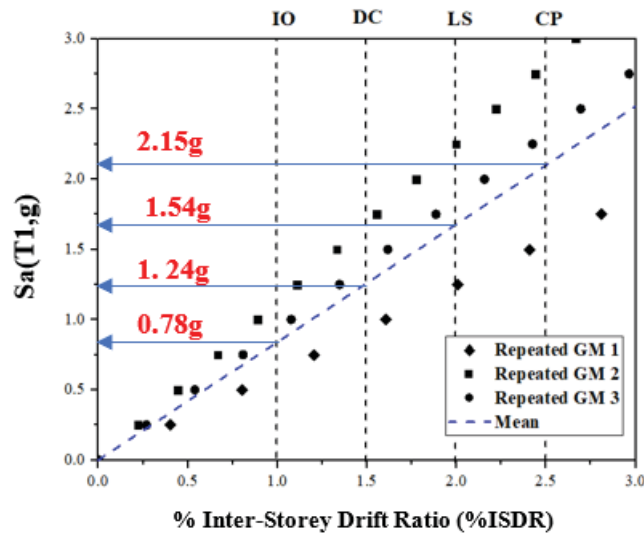


Figure 5: Incremental dynamic analysis curve under repeated earthquakes.

After performing the IDA, the fragility surface and the fragility curve for each damaged state was developed to determine the probability of reaching or exceeding the damaged state at certain Intensity Measure (IM). In this research, the spectral acceleration  $S_a(T_1)$  was chosen as it was used to perform the nonlinear analysis of time history, as well as the seismic events periodic time was selected as another parameter to be used in developing the fragility surface in order to study the effect of 15 sec seismic events with 100 sec gap between two repetitive earthquakes. The mean and standard deviations are needed to establish the fragility surface assessment as shown in Table 4.

Damage State	IO		DC		LS		CP	
	$\lambda$	$\varsigma$	$\lambda$	$\varsigma$	$\lambda$	$\varsigma$	$\lambda$	$\varsigma$
Log-normal parameters for mid-rise building	0.899	0.249	1.333	0.386	1.794	0.517	2.22	0.631

Table 4: Log-normal distribution parameters for developing fragility surfaces for each damage state.

Figure 6 presents all set of fragility surface. The study focused on four intensity measures (1.0 g, 1.5 g, 2.0 g, and 2.5 g) for further applying the preparedness actions of recovery in respect to 15 sec of two repetitive seismic events without considering the 100 sec periodic gap. When 1.0 g ground motion intensity was applied, the building still behaved in the immediate occupancy level with a probability of reaching or exceeding damages of 66%, whereby the rest of the damaged states achieved 19%, 6%, and 2.5% for damage control, life safety, and collapse prevention states, respectively. However, when the structure was exposed to higher intensity measure of 1.50 g, the structure was between two damaged states of damage control and life safety. Whereas, a certain quantity of repairable action was appropriate to be applied with a probability of reaching or exceeding the states of 67%, and 28%, respectively, with slight increases for the collapse stage with 12% possibility of damage. Furthermore, at intensity measure of 2.0 g, the restoration process was mandatory where the loss was moderate, but the structure stays stable that could be classified at life safety stage with probability of reaching the damage of 65%, and 35% for collapse prevention state. Finally, with regard to the IDA curves, when the ground motion intensity surpasses 2.0 g, the structure would suffer from extensive damages and the structure would behave on the threshold point of local or complete experienced damage by achieving 100% probability of damages for the life safety stage. Furthermore, it started to

face a crucial damage by achieving probability of damages of 66% at 2.50 g. Therefore, after analysing the structure through the vulnerability examination, starting with IDA, and finishing with the fragility surface, it was clearly identified that due to its ordinary design moment frame system, the building did not have the ability to resist a 15 sec repetitive earthquake. In addition, the implementation of the resilience assessment was important to plan the recovery process for four different damage states by investigating the structure's functional resilience, degradation, robustness, and recovery time post-seismic events. Table 5 represents the percentage of cumulative damage probability of exceedance for the four damage states.

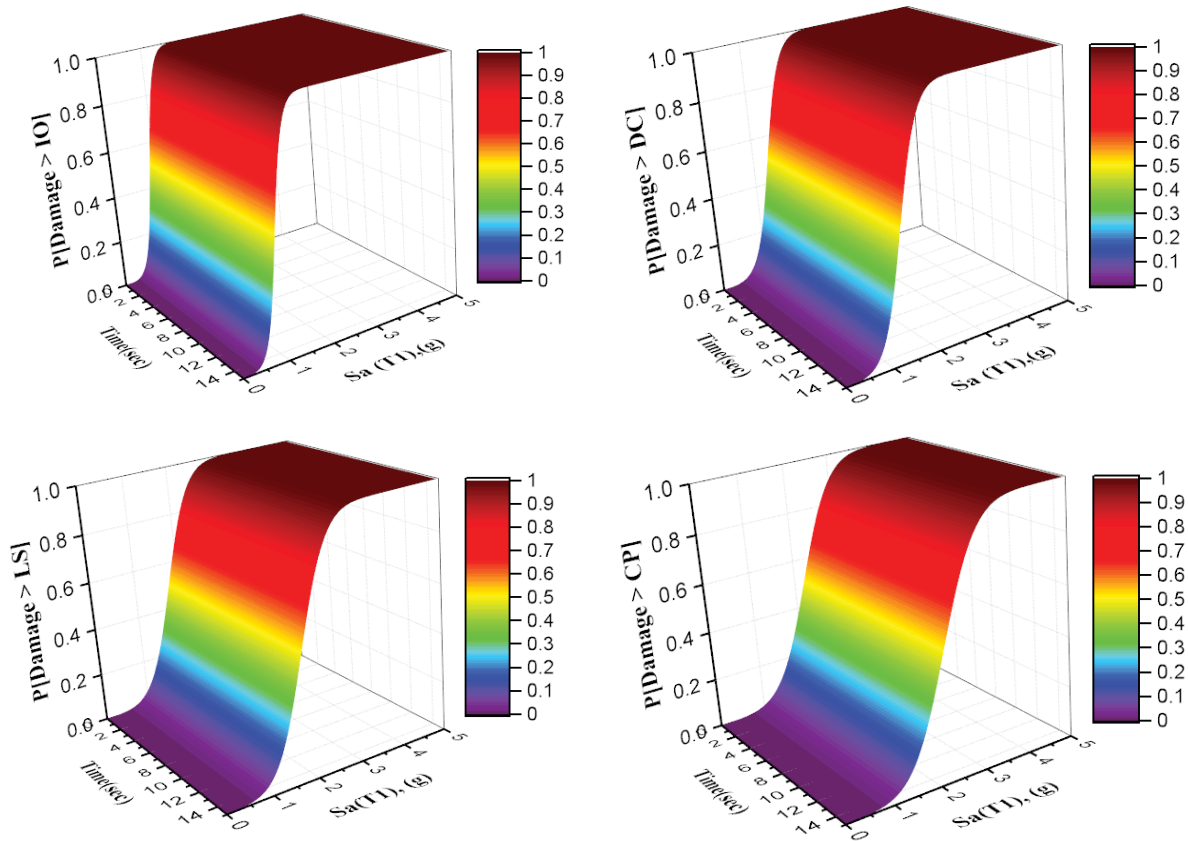


Figure 6: Fragility surfaces for each performance damage state.

Intensity Measure, $S_a(T1)$ , [g]	IO	DC	LS	CP
<b>1.00g</b>	66.00%	19.00%	6.00%	2.50%
<b>1.50g</b>	99.00%	66.00%	28.00%	12.00%
<b>2.00g</b>	100%	95.00%	65.00%	36.00%
<b>2.500g</b>	100%	100%	91.00%	66.00%

Table 5: Probability of damage using CDF for each damage state.



In order to find the SRI and its functionality, the discrete damage probability should be calculated by using Equations (5) to (8). The discrete damage probability was computed from the vulnerability analysis obtained from the fragility surface, known as cumulative distribution function. Table 6 presents the discrete damage probabilities due to post seismic events for each damage state. Subsequently, the direct damage loss ( $L_D$ ) ratio could be computed by the product of  $P_E(DS = K)$  with the damage ratio ( $r_K$ ) as illustrated in Table 7.

Intensity Measure, $S_a(T1)$ , [g]	IO	DC	LS	CP
<b>1.00g</b>	47%	16%	4%	3%
<b>1.50g</b>	32%	38%	16%	12%
<b>2.00g</b>	4%	30%	30%	36%
<b>2.500g</b>	0%	9%	25%	67%

Table 6: Discrete damage probability for different IMs and DS

Intensity Measure, $S_a(T1)$ , [g]	1.0g-IO	1.5g-DC	2.0g-LS	2.50g-CP
<b>Direct Loss (<math>L_D</math>)</b>	0.164	0.438	0.721	0.898

Table 7: Direct damage loss ratio for different IM and DS as a preparedness stages

For instance, the time needed for the recovery approach depends on the damage level of the structure. The time required for full recovery was deemed in this study between the time of occurrence ( $t_{OE}$ ) of seismic event as minimum period, and the control time ( $T_{LC}$ ) as the maximum period. In this study, the time occurrence was assumed to be taken at the 30<sup>th</sup> day of the 120 days of the total control period. This study focused on three types of preparedness actions for different retrofitting stages, which were IO, DC, LS, and CP with different intensity measures of 1.0 g, 1.50 g, 2.0 g, and 2.50 g. These preparedness actions were: No action, retrofitting action, and replacement action based on calculating the SRI and its functionality curve. At 1.0 g represented by IO retrofitting stage, the recovery time was set at 37<sup>th</sup> days which is seven days after earthquake time occurrence to return back to its functionality as before the earthquake. This means that no rehabilitation process needs to be performed. In terms of functionality, the building SRI at this stage was equal to 91.8% (0.918), with robustness of 83.6%. On the other hand, as the ground motion acceleration becomes higher reaching 1.50 g, which was represented by DC retrofitting stage, the recovery time was set to be at 54<sup>th</sup> days which was 24 days after seismic action occurrence, which means a simple retrofitting application is needed for restoration process. Whereas, at this stage the SRI decreased to 78.1% (0.781), with an approximate of 37% drop in its robustness to 56.2%.

Moreover, at the life safety retrofitting stage with 2.0 g, the recovery time was set at 107<sup>th</sup> days from total time control which equals to 77 days after the seismic time occurrence. The building requires a quick retrofitting action to be taken before it reaches the collapse stage, with losses of more than 72% from its robustness, with SRI equals to 64% (0.64) where the robustness equals to 28%.

Furthermore, at the collapse stage the retrofitting actions was not applicable, because the structure resilience loss exceeded 90%, where the structure robustness equals to 11%. Besides, the recovery time was set at 200<sup>th</sup> days which was 170 days after time occurrence, which means it exceeded the total time control, and it was beyond control to apply any of the rehabilitation process. In this stage, at 2.50 g the replacement action was the only option that could be applied, where the building SRI and its functionality equals to 55% (0.55). Although, during the total

time control of 120 days, the functionality of the structure equals to 33% (0.33). Figure 7 shows the variation of functionality curve with respect to time by using the linear function. Furthermore, the shaded area below the functionality curve represented the seismic resilience of the structural system. Table 8 summarises the resilience index, robustness, and losses for each damaged state.

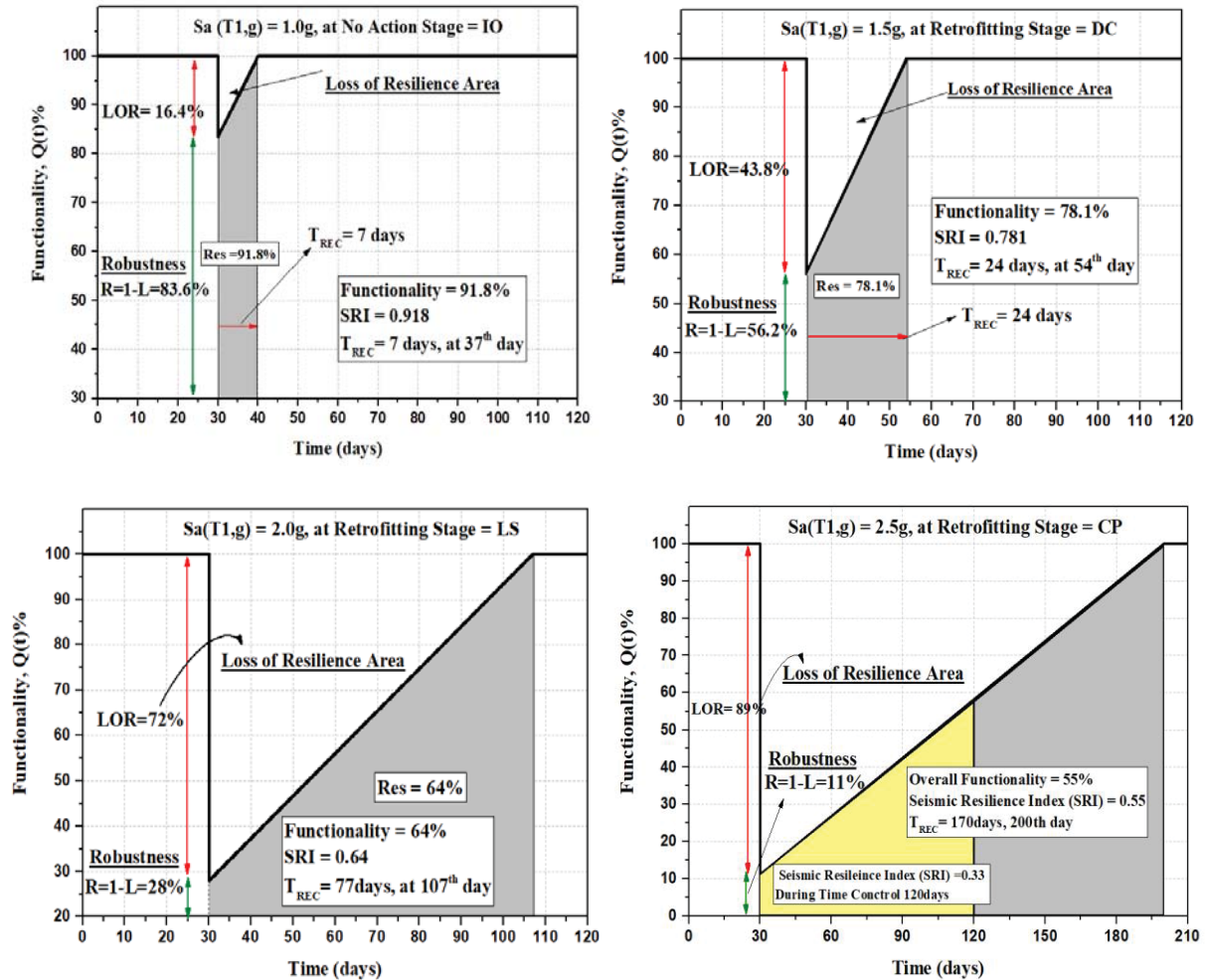


Figure 7: Functionality resilience curves for different preparedness stages.

Seismic Resilience Outcomes	IO	DC	LS	CP
Seismic Resilience Index (SRI)	0.918	0.781	0.64	0.55
Robustness (R)	83.6%	56.2%	28%	11%
Loss of Resilience (LOR)	16.4%	43.8%	72%	89%
Time Recovery ( $T_{REC}$ )	7 days	24 days	77 days	170 days

Table 8: Seismic resilience output results for the targeted building

## 4 CONCLUSION

The aim of the analysis was to determine the impact of the proposed repetitive seismic acceleration on the seismic resilience capability of the Ordinary Moment Resisting Frame (OMRF) building by applying a set of vulnerability assessment.

- From this analysis, the fluctuation in functionality, resilience index, robustness, structural losses, and time recovery of different performance levels could be predicted with an increase in the potential seismic ground acceleration (1.0 g, 1.50 g, 2.0 g, and 2.50 g), which was needed for the post-seismic event strategic recovery planning.
- It could be shown that the increase from 1.0 g to a maximum of 2.50 g as a seismic intensity measure for different damaged states resulted in a substantial increasing trend in the damage loss ratio that further influenced the structure's functionality. As well as it increases the time recovery for the structure to compensate its strength as before the seismic event.
- The disparity in seismic resilience demonstrated the effect of ductility capability and demand ductility of the OMRF structure at the post-seismic event for the various ground accelerations.
- The outcomes showed that despite the performance level, the seismic resilience for different damaged states had to be taken into consideration to assess the seismic vulnerability and functionality of the structural behaviour.

## 5 ACKNOWLEDGMENT

This research was funded under the Research University Individual (RUI) Grant Scheme (8014080).

## REFERENCES

- [1] Cimellaro, G.P., Reinhorn, A.M. and Bruneau, M., 2010. Framework for analytical quantification of disaster resilience. *Engineering structures*, **32**(11), pp.3639-3649.
- [2] Irajifar, L., Alizadeh, T. and Sipe, N., 2013, May. Disaster resiliency measurement frameworks: State of the art. In S. Kajewski, K. Manley, & K. Hampson. Presented at the *World Building Congress*, Brisbane, Australia.
- [3] Cimellaro, G.P., Solari, D. and Bruneau, M., 2014. Physical infrastructure interdependency and regional resilience index after the 2011 Tohoku Earthquake in Japan. *Earthquake Engineering & Structural Dynamics*, **43**(12), pp.1763-1784.
- [4] Bruneau, M., Chang, S.E., Eguchi, R.T., Lee, G.C., O'Rourke, T.D., Reinhorn, A.M., Shinozuka, M., Tierney, K., Wallace, W.A. and Von Winterfeldt, D., 2003. A framework to quantitatively assess and enhance the seismic resilience of communities. *Earthquake spectra*, **19**(4), pp.733-752.
- [5] Bruneau, M. and Reinhorn, A., 2007. Exploring the concept of seismic resilience for acute care facilities. *Earthquake Spectra*, **23**(1), pp.41-62.
- [6] Samadian, D., Ghafory-Ashtiany, M., Naderpour, H. and Eghbali, M., 2019. Seismic resilience evaluation based on vulnerability curves for existing and retrofitted typical RC school buildings. *Soil Dynamics and Earthquake Engineering*, **127**, p.105844.

- [7] Vona, M., Mastroberti, M., Mitidieri, L. and Tataranna, S., 2018. New resilience model of communities based on numerical evaluation and observed post seismic reconstruction process. *International journal of disaster risk reduction*, **28**, pp.602-609.
- [8] Titi, A. and Biondini, F., 2013, June. Resilience of concrete frame structures under corrosion. In *11th International Conference on Structural, Safety & Reliability* (pp. 16-20).
- [9] Alipour, A. and Shafei, B., 2016. Seismic resilience of transportation networks with deteriorating components. *Journal of Structural Engineering*, **142**(8), p.C4015015.
- [10] Banerjee, B. and Chandrasekaran, B., 2013. A framework of voronoi diagram for planning multiple paths in free space. *Journal of Experimental & Theoretical Artificial Intelligence*, **25**(4), pp.457-475.
- [11] Eghbali, M., Samadian, D., Ghafory-Ashtiany, M. and Dehkordi, M.R., 2020. Recovery and reconstruction of schools after M 7.3 Ezgeleh-Sarpole-Zahab earthquake; part II: Recovery process and resiliency calculation. *Soil Dynamics and Earthquake Engineering*, **139**, p.106327.
- [12] Motamed, H., Ghafory-Ashtiany, M., Amini-Hosseini, K., Mansouri, B. and Khazai, B., 2020. Earthquake risk-sensitive model for urban land use planning. *Natural Hazards*, **103**, pp.87-102.
- [13] Mastroberti, M. and Vona, M., 2017. New seismic risk index for existing buildings. In 6th ECCOMAS Thematic Conference on Computational Methods in Structural Dynamics and Earthquake Engineering, COMDYN.
- [14] Uchida, N. and Bürgmann, R., 2019. Repeating earthquakes. *Annual Review of Earth and Planetary Sciences*, **47**, pp.305-332.
- [15] Amadio, C., Fragiaco, M. and Rajgelj, S., 2003. The effects of repeated earthquake ground motions on the non-linear response of SDOF systems. *Earthquake engineering & structural dynamics*, **32**(2), pp.291-308.
- [16] Oyguc, R., Toros, C. and Abdelnaby, A.E., 2018. Seismic behavior of irregular reinforced-concrete structures under multiple earthquake excitations. *Soil Dynamics and Earthquake Engineering*, **104**, pp.15-32.
- [17] Panchireddi, B. and Ghosh, J., 2019. Cumulative vulnerability assessment of highway bridges considering corrosion deterioration and repeated earthquake events. *Bulletin of earthquake engineering*, **17**(3), pp.1603-1638.
- [18] Uchida, N., 2019. Detection of repeating earthquakes and their application in characterizing slow fault slip. *Progress in Earth and Planetary Science*, **6**(1), pp.1-21.
- [19] El-Maissi, A.M., Argyroudis, S.A. and Nazri, F.M., 2021. Seismic Vulnerability Assessment Methodologies for Roadway Assets and Networks: A State-of-the-Art Review. *Sustainability*, **13**(1), p.61.
- [20] Kassem, M. M., Nazri, F. M., & Farsangi, E. N. 2020. The seismic vulnerability assessment methodologies: A state-of-the-art review. *Ain Shams Engineering Journal*, **11**(4), pp. 849-864.
- [21] Gehl, P., Seyedi, D., Douglas, J. and Khiar, M., 2009, June. Introduction of fragility surfaces for a more accurate modeling of the seismic vulnerability of reinforced concrete structures. In *COMPDYN 2009-ECCOMAS Thematic Conference on Computational Methods in Structural Dynamics and Earthquake Engineering*.

- [22] Martin, J., Alipour, A. and Sarkar, P., 2019. Fragility surfaces for multi-hazard analysis of suspension bridges under earthquakes and microbursts. *Engineering Structures*, **197**, p.109169.
- [23] Kassem, M. M., Nazri, F. M., & Farsangi, E. N. 2020. On the quantification of collapse margin of a retrofitted university building in Beirut using a probabilistic approach. *Engineering Science and Technology, an International Journal*, **23**(2), 373-381.
- [24] Hariri-Ardebili, M.A. and Saouma, V.E., 2016. Collapse fragility curves for concrete dams: comprehensive study. *Journal of Structural Engineering*, 142(10), p.04016075.
- [25] Hariri-Ardebili, M.A. and Saouma, V.E., 2016. Seismic fragility analysis of concrete dams: A state-of-the-art review. *Engineering Structures*, **128**, pp.374-399.
- [26] Gehl, P., Sy, S. and Seyedi, D., 2011, May. Developing fragility surfaces for more accurate seismic vulnerability assessment of masonry buildings. In *COMPDYN-3rd Int. Conf. on Computational Methods in Struct. Dynam. & Earthq. Eng.*
- [27] Hatzigeorgiou, G. D., & Liolios, A. A. (2010). Nonlinear behaviour of RC frames under repeated strong ground motions. *Soil dynamics and earthquake engineering*, **30**(10), 1010-1025.
- [28] FEMA-356. 2000. Commentary for the seismic rehabilitation of buildings. Washington, D.C.: Federal Emergency Management Agency, FEMA-356.
- [29] UBC. 1997. Structural design requirement, Division IV. Earthquake Design, **2**(1), 9–37.
- [30] IBC. 2000. International Building Code, International Code Council. Inc. (formerly BOCA, ICBO and SBCCI), 1–796.
- [31] Motlagh, Z. S., Dehkordi, M. R., Eghbali, M., & Samadian, D. 2020. Evaluation of seismic resilience index for typical RC school buildings considering carbonate corrosion effects. *International journal of disaster risk reduction*, **46**, 101511.
- [32] Yu, P., Wen, W., Ji, D., Zhai, C., & Xie, L. 2019. A framework to assess the seismic resilience of urban hospitals. *Advances in Civil Engineering*, 2019.
- [33] HAZUS, MR4 Technical manual. 2003. Multihazard loss estimation methodology. Washington DC, USA: Department of homeland society.



## A SIMPLIFIED APPROACH FOR THE VULNERABILITY ASSESSMENT OF REGULAR AND IRREGULAR REINFORCED CONCRETE BUILDINGS AT THE LARGE SCALE

V. Blasone<sup>1</sup>, A. Basaglia<sup>2</sup>, R. De Risi<sup>3</sup>, F. De Luca<sup>3</sup> and E. Spacone<sup>1,2</sup>

<sup>1</sup> Department of Civil Engineering and Architecture  
University of Pavia  
Via Adolfo Ferrata, 3, 27100 Pavia, Italy  
e-mail: valentina.blasone01@universitadipavia.it

<sup>2</sup> Department of Engineering and Geology  
University “G. d’Annunzio” of Chieti-Pescara  
Viale Pindaro 42, 65127 Pescara, Italy  
e-mail: {alberto.basaglia, enrico.spacone}@unich.it

<sup>3</sup> Department of Civil Engineering  
University of Bristol  
Queen’s Building, University Walk, BS8 1TR, Bristol, UK  
e-mail: {flavia.deluca, raffaele.derisi}@bristol.ac.uk

---

### Abstract

*Several European countries are likely to experience extensive damage following major earthquakes due to high vulnerability and exposure, associated with the age of the built environment and the presence of densely populated areas, respectively. For these reasons, large-scale seismic risk assessment has a pivotal role. Given the large number of buildings to be assessed, indirect methods are usually the preferred option. However, simplified methodologies for reinforced concrete buildings have been recently developed, predominantly using non-linear time history analyses, and have shown to be a suitable alternative to indirect approaches. Simplified methodologies represent buildings as multi-degrees-of-freedom “stick-like” models, with the inter-storey behaviour modelled through an equivalent spring. These methodologies considerably reduce the computational effort yet achieving comparable accuracy with rigorous analyses. A major limitation of these methodologies is that they are applicable only to shear-type buildings, regular both in plan and in elevation. Aimed at overcoming this gap, the present work proposes a simplified method applicable to both regular and irregular reinforced concrete buildings. More specifically, each column is modelled separately with two uncoupled springs, one in each principal direction, to capture the torsional behaviour while retaining high computational efficiency. The proposed method is applied to a case study to demonstrate its capabilities.*

**Keywords:** Vulnerability Assessment, Reinforced Concrete, Shear-Type, Irregular Buildings, Stick-Like Models, Non-Linear History Analyses

---



## 1 INTRODUCTION

Cities are densely populated areas that may experience extensive damage and casualties in the occurrence of major earthquakes. Hence, large-scale seismic risk assessment is of paramount importance to assess expected damage and plan mitigation strategies. Given the high number of buildings to be assessed, indirect methods have been preferred to methods based on detailed structural analyses that use Finite Element (FE) modelling. More specifically, models based on vulnerability indices [1], or on the classification of buildings into typological classes (e.g. [2] and [3]) have been developed. More recently, Polese et al. [4] proposed an innovative method based on buildings inventory (combining Census-based data and interview-based CARTIS approach) and seismic damage assessment. Indirect methods have demonstrated to provide acceptable results in a general framework. However, their reliability is strictly dependent upon the amount and quality of data and they are drastically simplified with respect to a detailed modelling approach. Direct methods include the capacity spectrum method [5], which adopts Single-Degree-Of-Freedom (SDOF) building models and pushover (PO) analysis to predict damage. Lu, Xinzhen et al. [6] showed that the method provides a good estimation of global building behaviour (in terms of strength and ductility), with moderate computational effort but it has important limitations, e.g., it cannot represent concentration of damage at the different storeys.

Recently, as the computational power increases and becomes more easily available, direct Non-Linear History Analysis (NLHA)-based methodologies have become increasingly popular (e.g., [7], [8] and [9]). In this way, it is possible to fully describe the characteristics of the soil on which buildings are based (in time and frequency domain) through suitable ground motion selection, or more sophisticated approaches, along with the non-linear characteristics of the buildings [6]. These methodologies require a direct simplified model for buildings, to compute the Engineering Demand Parameters (EDP) (e.g., inter-storey drift, peak floor acceleration) needed to predict damage. Typically, buildings are directly implemented, usually as Multiple-Degree-Of-Freedom (MDOF) shear systems. More specifically, each storey is represented by a concentrated mass and a non-linear spring, thus considerably reducing the computational effort compared to refined models, yet increasing the accuracy compared to the indirect procedures. Backbone curves of springs are calibrated based on simulated design procedure [7] or adopting a multi-objective Genetic Algorithm (GA) procedure that employs the results of non-linear cyclic pushover analyses done on refined non-linear models (e.g., [9]).

A drawback of the simplified models developed to date is that they are applicable only to shear-type buildings, regular both in plan and in elevation. This drawback is relevant for two main reasons:

- structural irregularities, due to non-symmetric distribution of load resisting elements (stiffness and strength eccentricity) and non-symmetric distribution of masses are particularly common in old buildings;
- torsion can adversely affect the seismic performance of buildings with any type of eccentricity [10], [11] and [12].

For these reasons, a simplified model capable of capturing the torsional behaviour of buildings is needed for NLHA-based methodologies. In this work, a model is proposed which aims to represent the flexural and torsional behaviour of Reinforced Concrete (RC) frame structures in a simplified and light-computational manner. The applicability of the model is general since it is suitable for different structure configurations, not necessary shear-type. It can reproduce the behaviour not only of regular buildings, but also of irregular buildings with torsional behaviour, that have not been considered before. The main software used is OpenSees

along with STKO [13], a Graphical User Interface (GUI) with a pre and post processor for OpenSees.

## 2 METHODOLOGY

In the proposed simplified model, the building is represented by a three-dimensional (3D) MDOF model, fully described by the columns. The non-shear-type behaviour of the building is achieved by adopting calibrated shear-inter storey drift (V-ID) curves for each column. At the local level, each column is represented by two uncoupled translational springs in the two main horizontal directions. If the centre of mass and the centre of stiffness of the building do not coincide, coupling is automatically achieved at the global level, see Figure 1, thus capturing the torsional behaviour.

Each column is modelled in OpenSees as a *zeroLength* element with two nodes. A rigid material is assigned to all the Degrees Of Freedom (DOFs), except for the translations along the local axis (2) and (3) (assuming the local axis (1) always directed along the axis of the column) and for the rotation against the local axis (1) (torsion), which is kept released. Calibrated backbone curves are assigned to the two translational DOFs (see Figure 1).

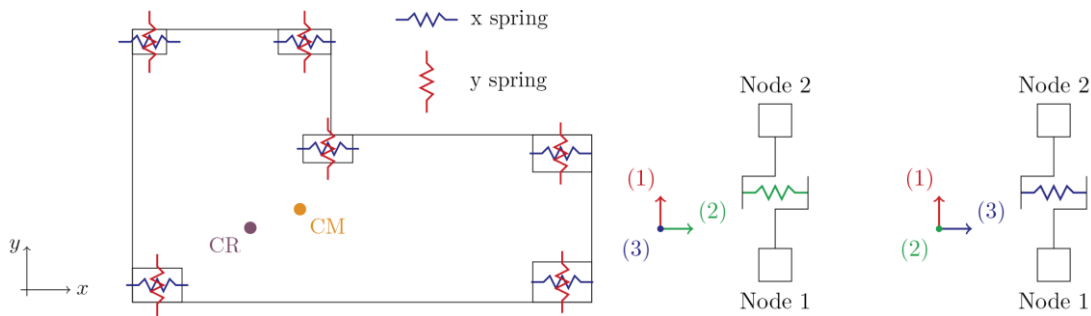


Figure 1. (left) Scheme of the general idea for the storey model (CR: Centre of Stiffness, CM: Centre of Mass); (right) model of the springs, in local axes (2) and (3).

Each spring is defined by an appropriate V-ID backbone curve, that represents the column behaviour in the considered direction. First, an analytical parameter-dependent V-ID curve is defined. A trilinear curve is adopted, and no refined models are needed for this first step. In a second phase, the parameters are calibrated to represent the behaviour of the column in its configuration (e.g., boundary conditions), accounting implicitly for beams flexibility. To derive the analytical parameter-dependent V-ID curve, the method stems from the definition of a trilinear sectional moment-chord rotation ( $M-\theta$ ) curve, which can be simply defined independently from column boundary conditions. The model proposed by Ibarra [14] is used in this work. Using basic structural mechanics relationships and assuming a shear-type configuration for the column, the  $M-\theta$  curve is used to find the corresponding analytical shear-type V-ID curve, which maintains the same shape of the  $M-\theta$  curve, see Figure 2.

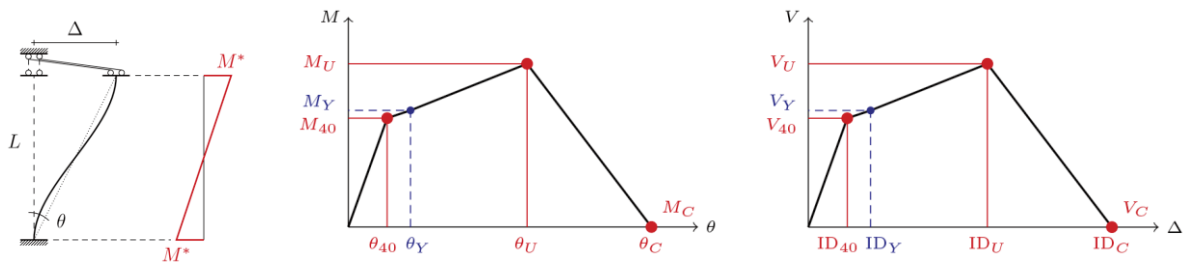


Figure 2. (left) column model with two end rotational springs; (centre) moment-rotation ( $M-\theta$ ) curve by [14]; (right) V-ID curve for the column under the shear-type assumption.

The expressions for the points defining the shear-type V-ID relationship are then modified through a set of five parameters and are presented in Eq. 1 (for details on moment/rotation calculation see [14] and [15]).

$$\begin{aligned}
 V_{40} &= 2 M_{40}/L \cdot \mu & ID_{40} &= \theta_{40} \cdot L/\alpha \\
 V_Y &= 2 M_Y/L \cdot \mu & ID_Y &= \theta_{40} \cdot L/\alpha + (\theta_Y - \theta_{40}) \cdot L/\beta \\
 V_U &= 2 M_U/L \cdot \kappa & ID_U &= \theta_{40} \cdot L/\alpha + (\theta_U - \theta_{40}) \cdot L/\beta \\
 V_C &= 0 & ID_C &= \theta_C \cdot L/\gamma
 \end{aligned} \tag{1}$$

Changes in the values of the parameters (i.e.,  $\alpha$ ,  $\beta$ ,  $\gamma$ ,  $\mu$ ,  $\kappa$ ) modify, in turn, the shape of the V-ID curve. The value of each parameter can be adjusted to represent the realistic behaviour of the column. Indeed, the analytical curves were purposely defined such that the values of the parameters could be directly retrieved making use of some data-driven techniques (e.g., machine learning) that, once developed, would make the definition of the final curve a rapid process. However, the development of this algorithm is beyond the scope of this paper and will be addressed in future works.

Refined reference curves are used in this work. In this perspective, parameters are found by comparison between the analytical and the numerical curves, either by trial-and-error process (i.e., manually changing the values until the approximation is acceptable) or making use of more automatised and accurate procedures. The latter approach is adopted herein, more specifically the parameters values are evaluated using a GA procedure, with the objective of finding the parameters for which the error between the numerical and analytical curves, see Eq. 2, is minimized. More insights about the proposed methodology can be found in [16].

$$\sqrt{\sum_i (V_{numerical,i} - V_{analytical,i})^2} \tag{2}$$

### 3 CASE STUDY

The building considered as case study is adapted from a structure dating back to the 1970s [17], whose characteristics have been slightly modified for the purpose of the current work. The building has three storeys, the first storey is 3.4 m high, the second and third storeys are 3.05 m high. The length of all spans is 3.75 m. Column sections may be divided into three groups, indicated in the following as CA, CB, and CC, see Figure 3. Within each group, columns have also different sections for each floor. Moreover, columns at the first, second and third storey are subject to an axial load of  $0.1 P_{cu}$ ,  $0.2 P_{cu}$  and  $0.3 P_{cu}$ , respectively, where  $P_{cu}$  is the ultimate axial compressive bearing capacity of the column. Beams are all deep with section 30 cm x 50 cm. The concrete and steel reinforcement properties are  $f_c = 23.5$  MPa,  $f_y = 440$  MPa. They are taken from [17] and represent mean values.

A detailed model is considered as benchmark for the simplified model. Both the columns and the beams are modelled as lumped plasticity elements. The model is fixed at the base and a rigid diaphragm is implemented at each storey level. The axial loads are applied as concentrated forces and the masses are added as nodal masses, equal in the three translational DOFs. A Rayleigh damping of 5% is applied, taking as reference the first and second frequencies of vibration of the structure, as derived from the modal analysis.

The simplified model is built as described in Section 2. Figure 4 shows the calibration of the V-ID curves for the frame 2Y of Figure 3. A set of all five coefficients equal to 1 would mean that the shear-type model perfectly captures the behaviour of the specific column.

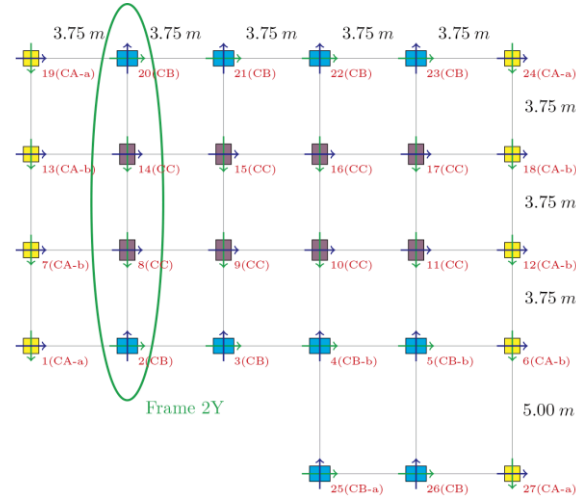


Figure 3. Plan view of the case study building; identification of frame 2Y.

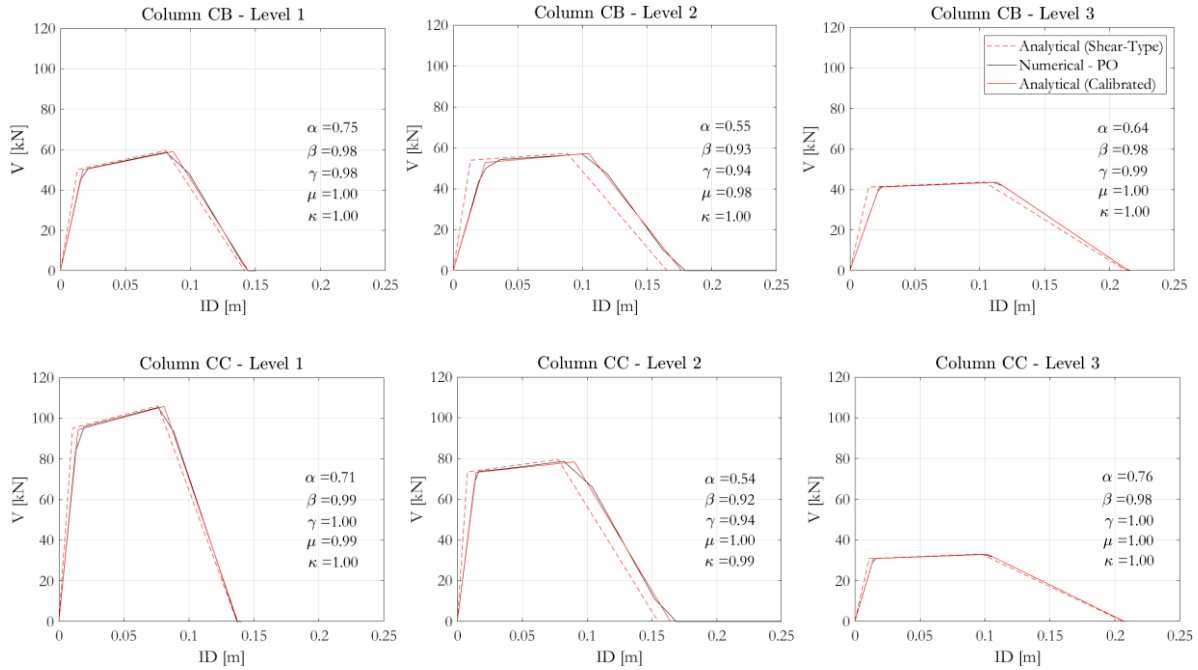


Figure 4. Comparison of analytical (shear-type), numerical and analytical (calibrated) V-ID curves for frame 2Y.

### 3.1 Pushover analysis

A pushover analysis is performed on both detailed and simplified models along both x and y axes of the model (see Figure 1). The pushover load is applied by following a uniform distribution along the height, hence the same load is applied at each storey, at its centre of mass (CM). The load is applied with 2,000 increments through the *DisplacementControl* static integrator in OpenSees, setting the top CM as control node and a target displacement of 0.2 m (corresponding to an average roof drift ratio of  $\sim 2\%$ ). The analysis is repeated in both global horizontal directions, x and y, and results are investigated in the direction of loading.

Results are compared by plotting the total base shear-top displacement curve and the Interstorey Drift Ratio (IDR) values along the height. Figure 5 and Figure 6 show results for the analysis in the x and y directions, respectively. Results show good correspondence between the two models, with the larger differences found in the analysis performed in the global y

direction. Yet, the simplified model underestimates the maximum base shear by only 2.3%. A final comparison is shown in Figure 7, where the deformed shape of the structure at a fixed time instant (step 1,000) is plotted. Both figures refer to the pushover in y, where the torsional behaviour is more evident, and show that the torsional behaviour of the building is perfectly captured by the simplified model.

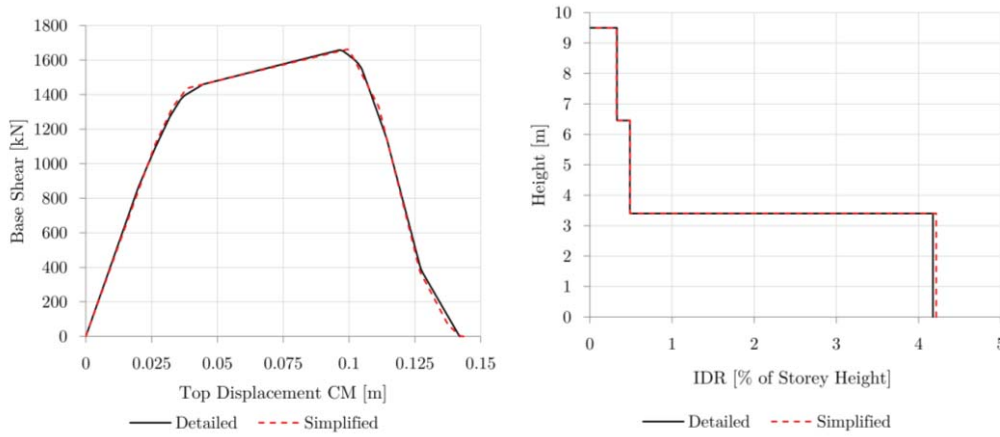


Figure 5. Results from the pushover in x, base shear-top displacement and height-IDR plots.

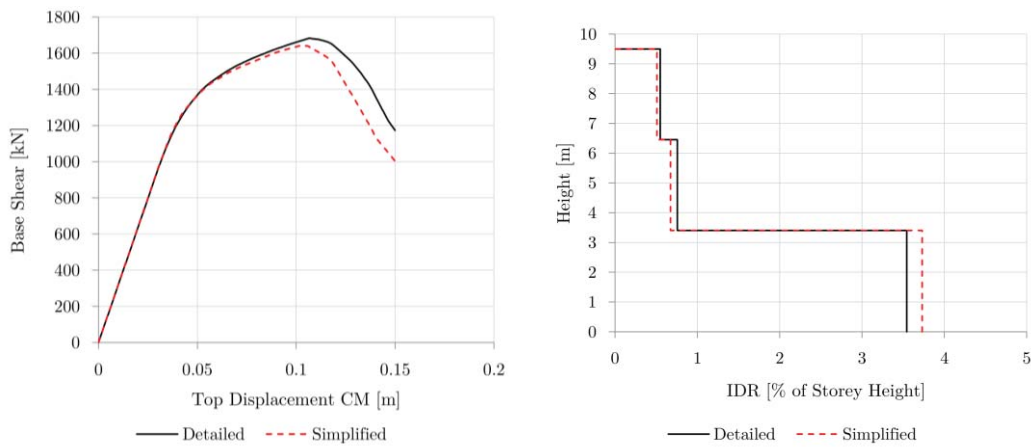


Figure 6. Results from the pushover in y, base shear-top displacement and height-IDR plots.

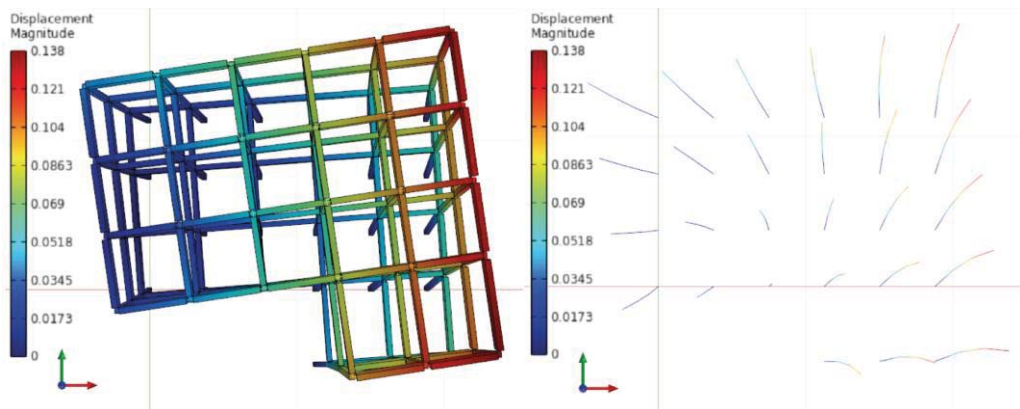


Figure 7. Results from the pushover in y, deformed shape at step 1000 for the (left) benchmark detailed model and (right) simplified model; colours represent the displacement in y (units: m).



### 3.2 Non-Linear History Analysis

A non-linear history analysis is performed on both the detailed and simplified models. The signal is a natural accelerogram selected from the PEER NGA database, related to the Imperial Valley earthquake of 1979, see Figure 8. The PGA is 0.24 g, and the total duration of the signal is 50 s.

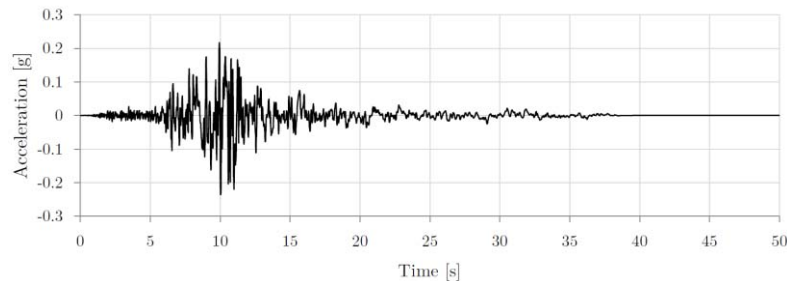


Figure 8. Imperial Valley accelerogram used to perform NLHA.

The acceleration history is defined in STKO as a path time series and is applied through the *UniformExcitation* command. The analysis is performed using the Newmark transient integrator with parameters  $\beta = 0.25$  and  $\gamma = 0.5$ . The time step is 0.01 s and is taken also as time step for the analyses, deriving consequently the initial total number of steps. The adaptive time step is used in the detailed model to achieve convergence. The analysis is first performed separately in the global x and y directions. Then, a last analysis in which the seismic load is applied to both the global directions, x and y, is performed. Due to the non regularity of the building, the results are investigated in both directions. For brevity, only the analysis with the load applied in both directions and the results in the y direction are shown herein. Results from other analyses indicate very similar behaviour, for more details, see [16].

Results in terms of maximum base shear as absolute value show differences lower than 0.5 %, see Table 1 and Figure 9. The negligible difference is further confirmed by the total base shear-top CM displacement plots, see Figure 10. In terms of EDP, the IDR is the parameter that is best represented by the simplified model, with very small differences. The Peak Floor Acceleration (PFA) results show a very good correspondence between the two models too, see Figure 11.

The simplified model presents significant advantages in terms of computational efficiency reaching convergence much faster, with an overall shorter analysis duration. The gain in computational efficiency is more evident when NLHA are performed. More specifically, in the non-linear dynamic case, the simplified model shows a reduced analyses duration to approximately 1/4 of the computational time necessary to bring the detailed model to convergence in a case where no convergence issues arise, and up to approximately 1/100 when convergence problems in the detailed model arise, thus the time step needs to be reduced. The latter case is the one experienced in most of the analyses performed.

Table 1. NLHA - Imperial Valley signal, analysis in x+y, results in terms of maximum base shear.

		Simplified	Benchmark	Relative Difference
Max Base Shear [kN]	x	1513.0	1516.5	0.2 %
	y	1791.7	1786.0	0.3 %



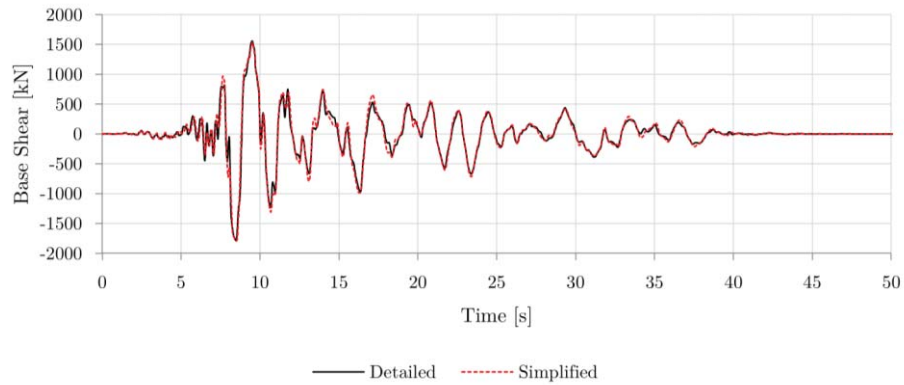


Figure 9. NLHA - Imperial Valley signal, analysis in x+y, results in y, total base shear history.

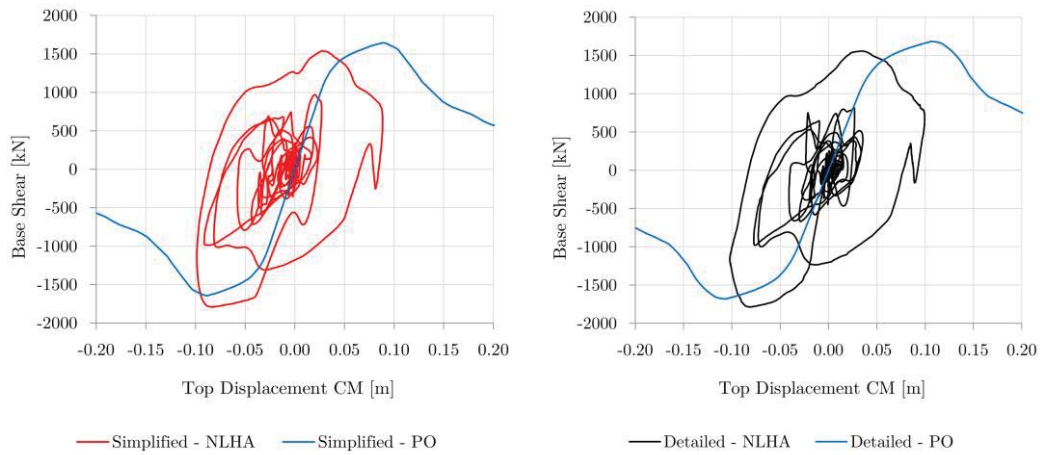


Figure 10. NLHA - Imperial Valley signal, analysis in x+y, results in y, total base shear versus top displacement.

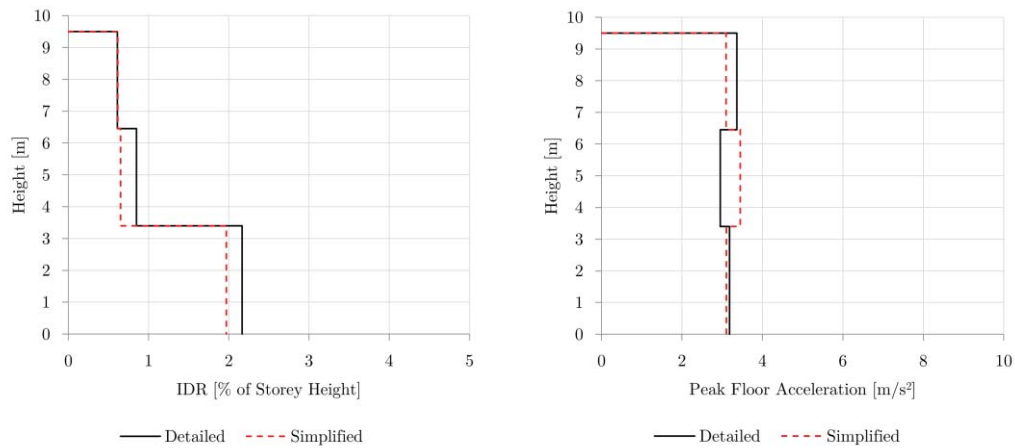


Figure 11. NLHA - Imperial Valley signal, analysis in x+y, results in y, IDR and PFA distribution.

#### 4 SUMMARY AND CONCLUSIONS

In this paper, a simplified model for reinforced concrete buildings that is suitable for large scale non-linear history analysis-based seismic assessment was proposed. The novelty of the proposed model is the applicability also to non-shear-type configurations and the ability to capture the torsional behaviour of irregular buildings. Both aspects are very common when

dealing with an existing building stock. The proposed model is a three-dimensional multiple degree of freedom column-based model, in which each column is represented by two uncoupled translational springs. In this way, coupling at the global level can be automatically obtained, making the model able to represent torsion. The non-shear-type behaviour is instead achieved by specific calibration of the shear-inter-storey drift relationships for the column backbone curves. Refined analyses on two-dimensional sub-frames together with a genetic algorithm are used in this work, however the analytical expressions developed to describe the shear-inter-storey drift curves are suitable for employment in a more efficient data-driven procedure that will be addressed in future research.

The benchmark analyses showed a very good correspondence between the refined and simplified results, both in terms of non-linear static and non-linear dynamic analyses. As for non-linear history analyses, the simplified model is perfectly suitable to represent the base shear history with negligible difference in terms of maximum base shear results. The investigated engineering demand parameters (i.e., inter-storey drift ratio and peak floor acceleration) are correctly captured by the simplified model, too. The model is accurately able to represent the torsional behaviour of the building. In terms of efficiency, the proposed model led to faster convergence and considerable decrease in computational times, making it a competitive option for large-scale assessment applications.

## REFERENCES

- [1] GNDT-SSN, *Scheda di esposizione e vulnerabilità e di rilevamento danni di primo*. 1994.
- [2] G. Grünthal, *European macroseismic scale 1998*. Tech. rep. European Seismological. 1998.
- [3] S. a. S. G. Lagomarsino, *Macroseismic and mechanical models for the vulnerability and damage assessment of current buildings*. Bulletin of Earthquake Engineering, vol. 4.4, pp. 415-443, 2006.
- [4] M. Polese, M. Di Ludovico, M. Gaetani d'Aragona, A. Prota and G. Manfredi, *Regional vulnerability and risk assessment accounting for local building typologies*. International Journal of Disaster Risk Reduction, 2019.
- [5] FEMA, *Multi-hazard Loss Estimation Methodology-Earthquake Model*. 2012.
- [6] X. e. a. Lu, *A coarse-grained parallel approach for seismic damage simulations of urban areas based on refined models and GPU/CPU cooperative computing*. Advances in Engineering Software, vol. 70, pp. 90-103, 2014.
- [7] C. X. a. X. Lu, X. Lin and Z. X. a. L. Ye, *Parameter Determination and Damage Assessment for THA-Based Regional Seismic Damage*. Journal of Earthquake Engineering, 21:3, pp. 461-485, 2017.
- [8] C. Xiong, X. Lu, H. Guan and Z. Xu, *A nonlinear computational model for regional seismic simulation of tall buildings*. Bulletin of Earthquake Engineering, p. 1047–1069, 2016.
- [9] M. G. d'Aragona, M. Polese and A. Prota, *Stick-IT: A simplified model for rapid estimation of IDR and PFA for existing low-rise symmetric infilled RC building typologies*. Engineering Structures, vol. 223, pp. 111-182, 2020.
- [10] S. Anagnostopoulos, M. Kyrkos and K. Stathopoulos, *Earthquake induced torsion in buildings: critical review and state of the art*. Earthquakes and Structures, pp. 305-377, 2015.
- [11] Rajeev, Pathmanathan and Tesfamariam, *Seismic fragilities for reinforced concrete*

- buildings with consideration of irregularities*. Structural Safety, pp. 1-13, 2012.
- [12] Trifunac and Mihailo, *Effects of torsional and rocking excitations on the response of structures*. in Earthquake Source Asymmetry, Structural Media and Rotation Effects, Springer, 2006, pp. 569-582.
- [13] Petracca, M., Candeloro, F. & Camata, G. (2017). *STKO user manual*. ASDEA Software Technology, Pescara.
- [14] Ibarra, Medina and Krawinkler, *Hysteretic models that incorporate strength and stiffness deterioration*. Earthquake Eng. Struct. Dyn., 2005 a.
- [15] Ibarra and Krawinkler, *Global Collapse of Frame Structures Under Seismic Excitations*. Department of Civil and Environmental Engineering Stanford University, 2005 b.
- [16] V. Blasone, *Building and soil modelling for non-linear history analyses at the urban scale: development of a simplified model for reinforced concrete buildings and application to a case study in Benevento*. MS thesis, University of Pavia and IUSS Pavia, 2020.
- [17] I. & D. M. Iervolino, *Foreword to the Special Issue for the RINTC (The Implicit Seismic Risk of Code-Conforming Structures) Project*. Journal of Earthquake Engineering, 2018.

## GENERALIZED MACROELEMENT FOR GEOMETRICALLY AND MATERIALLY NON-LINEAR ANALYSIS OF STEEL MEMBERS

Konstantinos E. Morfidis<sup>1</sup>

<sup>1</sup> Assistant Researcher, Earthquake Planning and Protection Organization (EPPO-ITSAK)  
Terma Dasylliou, 55535, Thessaloniki, Greece  
e-mail: konmorf@gmail.com

---

### Abstract

*The demand for a reliable modelling of steel structures introduces the need for the implementation of advanced techniques. Due to the shape and the properties of steel members, as well as the connections among them, the performance of materially and geometrically non-linear analyses are required in order to approach effectively the actual behavior of the steel structures. To this end, special calculation tools must be available in the software which is used for analysis and design. More specifically, phenomena such as the bending, the torsional and the torsional-flexural buckling as regards the geometric non-linear effects, and the elasto-plastic behavior of steel in critical cross-sections, as regards the materially non-linear effects, require the implementation of appropriate stiffness matrices and load vectors. These calculation tools are available in the literature. However, the inclusion of all required features in a finite element demands a specific formulation. Therefore, the purpose of the present paper is to propose the formulation of a two-noded macroelement with seven degrees of freedom per node, which possesses abilities to model effectively the above-mentioned phenomena in practice. On the basis of a two-stage static condensation technique, the proposed finite element includes features appropriate for the modelling of material non-linearity effects and the semi-rigid connections (through non-linear rotational springs), as well as the modelling of the geometric non-linear effects (using appropriate finite element formulation), and the influence of the rigid joints (through rigid offsets). The proposed macroelement was successfully added to the finite elements' library of an existing professional software for the analysis and design of steel structures. The reliability of the proposed element is tested in the current paper using the solutions of well-known problems selected from the literature.*

**Keywords:** Steel structures, Finite Element Method, Nonlinear Analysis, Buckling, Beam/Column elements.

---

## 1 INTRODUCTION

The analysis and design of members of steel structures require the implementation of specific modelling techniques (see e.g. [1-3]). The requirement of these techniques arises from the fact that the shape and the load conditions of steel beams and columns make them sensitive to the consequences of phenomena which are related with geometric and material nonlinearities. Such phenomena are, for example the bending buckling, the torsional and torsional-flexural buckling as regards the geometric non-linear effects, and the elasto-plastic behavior of steel in critical cross-sections, as regards the materially non-linear effects. The existence of these unfavorable influences on the steel members has been recognized by the former, as well as by the modern, seismic codes, e.g. [4, 5]. Thus, the problem of the effective design of steel structures against static or dynamic (e.g. seismic) loads is treated in the cross-section and member levels. For this reason, specific recommendations are proposed which, however, require the appropriate (and most accurate possible) modelling. A significant number of research studies (e.g. [6-10]) and scientific books (e.g. [11-13]) focused on the effective modelling of steel members have been published. The existing theories regarding the elasto-plastic behavior of steel, as well as the continuous improvement of finite element formulation in combination with the computational abilities of the modern hardware, offer the possibility of a more effective approach to the behavior of steel structural members.

In the current paper, the formulation of a new two-noded macroelement with seven degrees of freedom per node, which can effectively model steel structures members in practice, is presented. Based on a two-stage static condensation technique, the proposed formulation includes features appropriate for the modelling of material non-linearity effects and the semi-rigid connections (through non-linear rotational springs), the modelling of the geometric non-linear effects (using appropriate finite element formulation), and the influence of the rigid joints (through rigid offsets). Using the static condensation method, the proposed element, with 14 degrees of freedom, can be compatible with the classic two-noded elements (with 12 degrees of freedom) and co-exist with them in structures' models. Thus, the problem of the design of steel members in the cross-section and member levels can be handled practically using a compact formulation. The reliability of the proposed element is tested using the solutions of well-known problems selected from the literature.

## 2 FORMULATION OF THE PROPOSED MACROELEMENT

### 2.1 General description of the element

The proposed macroelement consists of three segments, as shown in Figure 1. More specifically:

- the end segment between the external node 1 and the internal (virtual) node 2, and the corresponding end segment between the internal (virtual) node 3 and the external node 4. In each one of these segments, three absolutely rigid rod elements (perpendicular between them) are defined. These elements are the three spatial components of the end rigid offsets (in the local coordinate system of the macroelement) which model the bodies of beam-to-column joints.
- the median segment between the internal nodes 2 and 3. This segment models the flexible part of the macroelement. The type of finite element which is used in this segment can be selected on the basis of the considered problem. For example, Bernoulli or Timoshenko beam elements can be used (see eg. [14]). In the present paper, the formulation which is used for the modelling of the median segment will be described in the following sections.

The connection of the median segment to the rigid offsets is achieved by means of rotational springs. These springs can be considered either as linear for (1<sup>st</sup> or 2<sup>nd</sup> order) elastic analyses, or as nonlinear (in conjunction with  $M-\phi$  diagrams) for materially non-linear analyses in the framework of the concentrated plasticity model.

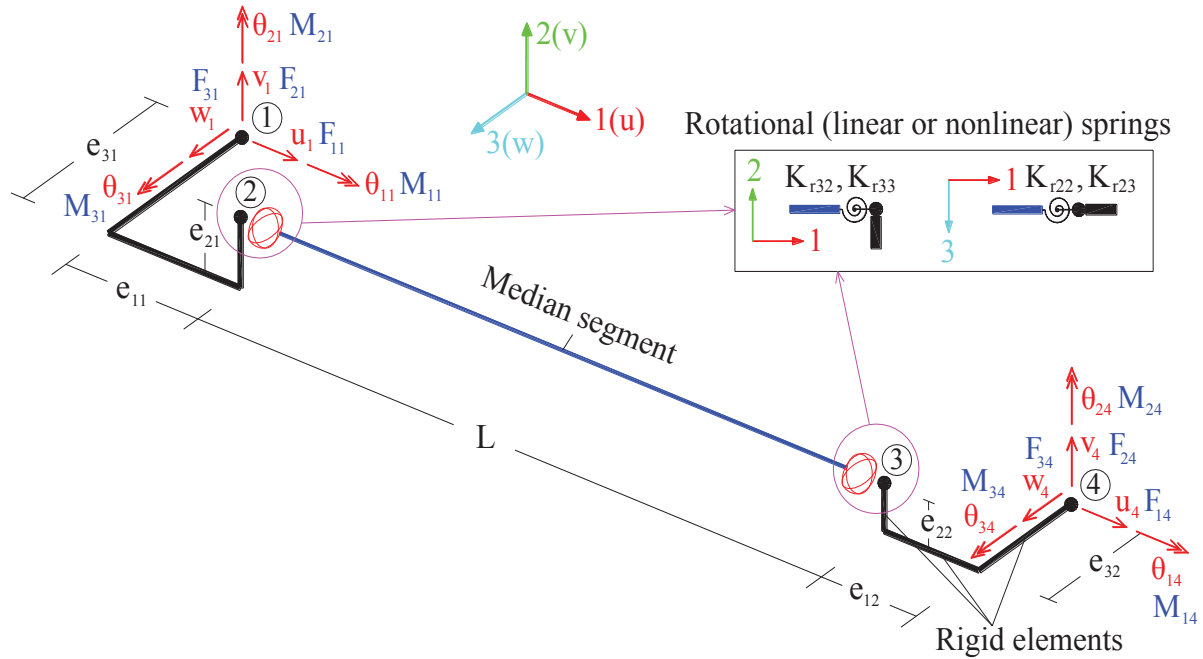


Figure 1: General description of the proposed macroelement

In Figure 1, the degrees of freedom (d.o.f.) of the proposed macroelement are also illustrated. It can be seen that they are 12 in number, as in case of the classic beam/column elements. The 7<sup>th</sup> d.o.f., which is required for the modelling of the effect of warping, is considered only in the median segment. Thus, the median segment can be an element with 14 d.o.f. The procedure of the transformation of the 14 d.o.f. of the median segment to the 12 d.o.f. of the whole macroelement will be described in sections 2.2 and 2.3.

## 2.2 Stiffness matrix derivation

The stiffness matrix of the macroelement is derived in two steps. In the first step, the stiffness matrix of the median segment's element is formed. In the second step, the matrix relation between the stiffness matrix of the median segment and the stiffness matrix of the macroelement is formulated. This relation demonstrates the effect of the rotational springs and the rigid offsets on the stiffness matrix of the macroelement.

### A) Step 1: Derivation of the stiffness matrix for the median segment

The method for the derivation of the stiffness matrix of the median segment's element is based on the static condensation procedure (e.g. [15,16]). In general, static condensation is used in order to reduce the number of the equations which constitute the system of equations of equilibrium. In the present case, static condensation is necessary due to the fact that the stiffness matrix of the median segment is based on the approach of the displacement field through algebraic interpolation functions. These functions are used when the 7<sup>th</sup> d.o.f. must be considered for the modelling of the warping effect, because, in this case, the exact solution of the corresponding differential equations of equilibrium is not available. Thus, the discretization of the median segment is necessary. This discretization causes the increase of the nodes and, consequently, the increase of the d.o.f. of the macroelement. Moreover, when the 7<sup>th</sup> d.o.f.



is considered, the corresponding elements' stiffness matrices are 14x14 matrices, not compatible with the classic 12x12 stiffness matrices which are mainly used in practice.

For this reason, in the present paper, the implementation of the static condensation procedure in two stages is proposed (Figure 2). In the first stage, all the internal d.o.f., which arise from the discretization of the median segment's element, are condensed. Thus, if the number of the sub-elements in which the median segment is discretized is  $n$  (using  $n+1$  nodes:  $n-1$  internal and 2 external), then the corresponding stiffness matrix is a  $[7(n+1)] \times [7(n+1)]$  matrix.

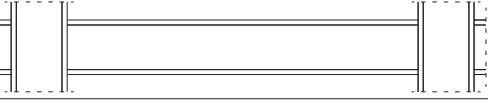
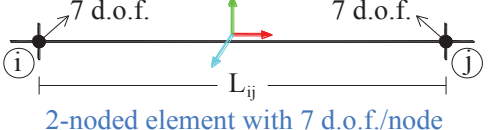
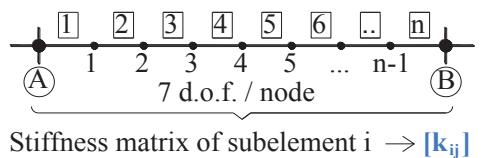
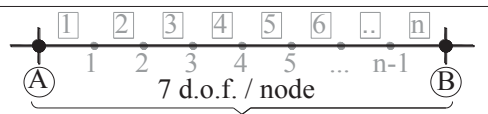
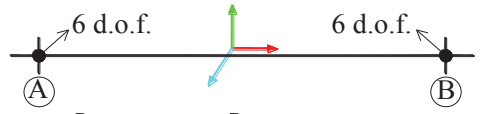
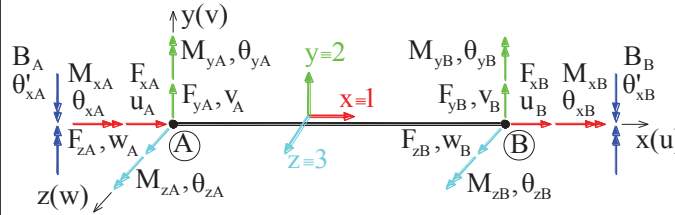
STEP	DESCRIPTION	COMMENTS
Actual member		Beam, member of a steel structure (e.g. steel frame)
<b>First step:</b> Definition of the stiffness matrix for the subelements of the median segment		Stiffness matrix: $[k_{ij}]$ (14x14)
<b>Second step:</b> Discretization of the median segment in $n$ subelements ( $n-1$ internal nodes, 2 external nodes: A,B)	 Stiffness matrix of subelement $i \rightarrow [k_{ij}]$	Formation of a "sub-structure" consisting of $n$ subelements: → Stiffness matrix: $[k_{sub}]$ $[7(n+1) \times 7(n+1)]$ → Load matrix: $[p_{sub}]$ $[7(n+1) \times 1]$
<b>Third step:</b> First stage of static condensation → Condensation of d.o.f. of the internal nodes ↓ Generation of 2-noded macroelement with 7 d.o.f. / node	 $[k_{sub}] = \begin{bmatrix} [k_{sub}^{(AB-AB)}] & [k_{sub}^{(AB-int)}] \\ [k_{sub}^{(int-AB)}] & [k_{sub}^{(int-int)}] \end{bmatrix}$ d.o.f. of the nodes A, B d.o.f. of the internal nodes $[p_{sub}]^T = \begin{bmatrix} [p_{sub}^{(AB-AB)}] & [p_{sub}^{(int-AB)}] \end{bmatrix}$ 14x1      7(n-1)x1	Generation of: Stiffness matrix $[k_{s.c.1}]$ (14x14) Load matrix $[p_{s.c.1}]$ (14x1) → Equation of Equilibrium: $[k_{s.c.1}] \{u_{s.c.1}\} + [p_{s.c.1}] = [F_{s.c.1}]$ $\{u_{s.c.1}\}$ = the (14x1) vector of the displacements of nodes A,B (includes and the warping d.o.f.) $[F_{s.c.1}]$ = the (14x1) vector of the forces of nodes A, B
<b>Fourth step:</b> Second stage of static condensation → Condensation of the warping d.o.f. in nodes A, B ↓ Generation of 2-noded macroelement with the conventional 6 d.o.f. in each of nodes A, B	 $[k_{s.c.1}] = \begin{bmatrix} [k_{s.c.1}^{(cc)}] & [k_{s.c.1}^{(cn)}] \\ [k_{s.c.1}^{(nc)}] & [k_{s.c.1}^{(nn)}] \end{bmatrix}$ conventional d.o.f. of the nodes A, B warping d.o.f. of the nodes A, B $[p_{s.c.1}]^T = \begin{bmatrix} [p_{s.c.1}^{(cc)}] & [p_{s.c.1}^{(nc)}] \end{bmatrix}$ $[F_{s.c.1}]^T = \begin{bmatrix} [F_{s.c.1}^{(cc)}] & [F_{s.c.1}^{(nc)}] \end{bmatrix}$ 12x1      2x1      12x1      2x1	Generation of matrices for the median segment $[k_{ms}]$ (12x12) and $[p_{ms}]$ (12x1) → Equation of Equilibrium of the median segment: $[k_{ms}] \{u_{ms}\} + [p_{ms}] = [F_{ms}]$ $\{u_{ms}\}$ = the (12x1) vector of the displacements of nodes A, B $[F_{ms}]$ = the (12x1) vector of the forces of nodes A, B
		$[u_{s.c.1}]^T = [u_A \ v_A \ w_A \ \theta_{xA} \ \theta_{yA} \ \theta_{zA} \ u_B \ v_B \ w_B \ \theta_{xB} \ \theta_{yB} \ \theta_{zB} \ u'_A \ v'_A \ w'_A \ \theta'_{xA} \ \theta'_{yA} \ \theta'_{zA}]$ $[F_{s.c.1}]^T = [F_{xA} \ F_{yA} \ F_{zA} \ M_{xA} \ M_{yA} \ M_{zA} \ F_{xB} \ F_{yB} \ F_{zB} \ M_{xB} \ M_{yB} \ M_{zB} \ B_A \ B_B]$ $[p_{s.c.1}]^T = [p_{xA} \ p_{yA} \ p_{zA} \ m_{xA} \ m_{yA} \ m_{zA} \ p_{xB} \ p_{yB} \ p_{zB} \ m_{xB} \ m_{yB} \ m_{zB} \ b_A \ b_B]$

Figure 2: The steps of the two-stage static condensation procedure

Eliminating all the internal nodes at the first stage of the procedure, the  $[7(n+1)] \times [7(n+1)]$  stiffness matrix is transformed to a  $14 \times 14$  matrix. Then, at the second stage of the procedure, the 7<sup>th</sup> d.o.f. which corresponds to warping is condensed, transforming the  $14 \times 14$  stiffness matrix  $[k_{s.c.1}]$  to a  $12 \times 12$  stiffness matrix  $[k_{ms}]$  for the median segment (Figure 2).

As regards the matrix transformations which are required for the static condensation in each one of the two stages, it must be noted that, whereas the first one of them is always performed using a specific procedure, the second one depends on the boundary conditions which concern the warping effects in the end nodes of the median segment. Thus, the stiffness matrix  $[k_{s.c.1}]$  and the load matrix  $[p_{s.c.1}]$  of the median segment after the first stage of the static condensation (Figure 2) are given by Eq. (1), (e.g. [17]):

$$\begin{aligned} [k_{s.c.1}] &= [k_{sub}^{(AB-AB)}] - [k_{sub}^{(AB-int)}] \cdot [k_{sub}^{(int-int)}]^{-1} \cdot [k_{sub}^{(int-AB)}] \\ [p_{s.c.1}] &= [p_{sub}^{(AB-AB)}] - [k_{sub}^{(AB-int)}] \cdot [k_{sub}^{(int-int)}]^{-1} \cdot [p_{sub}^{(int-AB)}] \end{aligned} \quad (1)$$

The required matrix transformations for the second stage of the static condensation are summarized in Table 1.

Case	Boundary condition in node A	Boundary condition in node B	Condensed stiffness matrix $[k_{ms}]$	Condensed load matrix $[p_{ms}]$
1	Bimoment $B_A=0$	Bimoment $B_B=0$	$[k_{s.c.1}^{(cc)}] - [k_{s.c.1}^{(cn)}] \cdot [k_{s.c.1}^{(nn)}]^{-1} \cdot [k_{s.c.1}^{(nc)}]$	$[p_{s.c.1}^{(cc)}] - [k_{s.c.1}^{(cn)}] \cdot [k_{s.c.1}^{(nn)}]^{-1} \cdot [p_{s.c.1}^{(nc)}]$
2	$\theta'_{XA}=0$	$\theta'_{XB}=0$	$[k_{s.c.1}^{(cc)}]$	$[p_{s.c.1}^{(cc)}]$
3	Bimoment $B_A=-S_A\theta'_{XA}$	Bimoment $B_B=-S_B\theta'_{XB}$	As in case 1, with: $[\bar{k}_{s.c.1}^{(nn)}] = [k_{s.c.1}^{(nn)}] + \begin{bmatrix} S_A & 0 \\ 0 & S_B \end{bmatrix}$	
4	$B_A=0$	$B_B=-S_B\theta'_{XB}$	As in case 3, with: $[\bar{k}_{s.c.1}^{(nn)}] = [k_{s.c.1}^{(nn)}] + \begin{bmatrix} 0 & 0 \\ 0 & S_B \end{bmatrix}$	
5	Bimoment $B_A=0$	Warping $\theta'_{XB}=0$	$[k_{s.c.1}^{(cc)}] - \frac{1}{k_{s.c.1}^{(nnAA)}} \cdot [k_{s.c.1}^{(cnA)}] \cdot [k_{s.c.1}^{(ncA)}]$	$[p_{s.c.1}^{(cc)}] - \frac{1}{k_{s.c.1}^{(nnAA)}} \cdot [k_{s.c.1}^{(cnA)}] \cdot b_A$
6	$\theta'_{XA}=0$	$B_B=-S_B\theta'_{XB}$	$[k_{s.c.1}^{(cc)}] - \frac{1}{k_{s.c.1}^{(nnBB)} + S_B} \cdot [k_{s.c.1}^{(cnB)}] \cdot [k_{s.c.1}^{(ncB)}]$	$[p_{s.c.1}^{(cc)}] - \frac{b_B}{k_{s.c.1}^{(nnBB)} + S_B} \cdot [k_{s.c.1}^{(cnB)}]$

Table 1: Summary of matrix transformations in the second stage of the static condensation

Where:

$[k_{s.c.1}^{(cc)}], [k_{s.c.1}^{(cn)}], [k_{s.c.1}^{(nn)}], [k_{s.c.1}^{(nc)}]$  are sub-matrices of  $[k_{s.c.1}]$  after the first stage of the static condensation (Figure 2),

$[p_{s.c.1}^{(cc)}], [p_{s.c.1}^{(nc)}]$  are sub-matrices of  $[p_{s.c.1}]$  after the first stage of the static condensation (Figure 2),

$[k_{s.c.1}^{(cnA)}], [k_{s.c.1}^{(ncA)}], [k_{s.c.1}^{(cnB)}], [k_{s.c.1}^{(ncB)}]$  are sub-matrices and  $k_{s.c.1}^{(nnAA)}, k_{s.c.1}^{(nnBB)}$  are elements of  $[k_{s.c.1}]$ , if this matrix is written in the following expanded form:

$$[k_{s.c.1}] = \begin{bmatrix} [k_{s.c.1}^{(cc)}] & [k_{s.c.1}^{(cnA)}] & [k_{s.c.1}^{(cnB)}] \\ [k_{s.c.1}^{(ncA)}] & k_{s.c.1}^{(nnAA)} & k_{s.c.1}^{(nnAB)} \\ [k_{s.c.1}^{(ncB)}] & k_{s.c.1}^{(nnBA)} & k_{s.c.1}^{(nnBB)} \end{bmatrix}$$

It must be noted that cases 3 and 4 in Table 1 correspond to the partial restraint of warping in end nodes A, B (for details see e.g. [18]). Thus,  $s_A$ ,  $s_B$  are the constants of the warping spring elements which partially restrain the warping. Finally, the terms  $b_A$ ,  $b_B$  (see Figure 2) are elements of the median segment's load matrix  $[p_{s.c.1}]$ , which correspond to the warping d.o.f. in the end nodes A, B.

The procedure described in Figure 2 is based on the derivation of the stiffness matrices  $[k_{ij}]$  for the sub-elements (ij) which are the basic components of the macroelement (see the first step of the procedure in Figure 2). The stiffness matrices for these sub-elements are available in the literature (see e.g. [6, 7]). Their formulation is based on the linearized updated Lagrangian formulation of the equation of the incremental virtual work for a beam/column element which possesses 7 d.o.f. in the end nodes (Eq. (2)):

$$\begin{aligned} & \frac{1}{2} \int_0^{L_{ij}} \left[ EA \delta \left( \frac{du}{dx} \right)^2 + EI_{yy} \delta \left( \frac{d^2 w}{dx^2} \right)^2 + EI_{zz} \delta \left( \frac{d^2 v}{dx^2} \right)^2 + EC_\omega \delta \left( \frac{d^2 \theta_x}{dx^2} \right)^2 + GJ \left( \frac{d\theta_x}{dx} \right)^2 \right] dx + \\ & + \frac{1}{2} \int_0^{L_{ij}} F_x \delta \left[ \left( \frac{dv}{dx} \right)^2 + \left( \frac{dw}{dx} \right)^2 \right] dx + \int_0^{L_{ij}} \frac{K_w}{2} \delta \left( \frac{d\theta_x}{dx} \right)^2 dx - \int_0^{L_{ij}} \left[ V_y \delta \left( \frac{du}{dx} \frac{dv}{dx} \right) + V_z \delta \left( \frac{du}{dx} \frac{dw}{dx} \right) \right] dx - \\ & - \int_0^{L_{ij}} M_y \delta \left( \frac{dv}{dx} \frac{d\theta_x}{dx} \right) dx - \int_0^{L_{ij}} M_z \delta \left( \frac{dw}{dx} \frac{d\theta_x}{dx} \right) dx - \frac{1}{2} \int_0^{L_{ij}} M_x \left[ \delta \left( \frac{dv}{dx} \frac{d^2 w}{dx^2} \right) - \delta \left( \frac{d^2 v}{dx^2} \frac{dw}{dx} \right) \right] dx + \\ & + \int_0^{L_{ij}} V_y \delta \left( \frac{dw}{dx} \theta_x \right) dx - \int_0^{L_{ij}} V_z \delta \left( \frac{dv}{dx} \theta_x \right) dx = \{\delta u\}^T (\{^2 f\} - \{^1 f\}) \end{aligned} \quad (2)$$

Where:  $E$  is the modulus of elasticity;  $G$  is the shear modulus;  $A$  is the area of the beam/column's cross-section;  $I_{yy}$ ,  $I_{zz}$  are the moments of inertia of the beam/column's cross-section with respect to local axes  $y$ ,  $z$  (Figure 2);  $J$  is the torsional constant;  $C_\omega$  is the warping constant;  $L_{ij}$  is the length of the element;  $\{du\}$  is the vector of the displacements of nodes  $i$  and  $j$  (Figure 2);  $\{f\}$  is the vector of forces of nodes  $i$  and  $j$  (Figure 2) and  $K_w = [F_x(I_{yy} + I_{zz})]/A$  is the Wagner coefficient. It must also be noted that the right superscripts 1 and 2 of vector  $\{f\}$  refer to the deformed configurations  $C_1$  (the last known state) and  $C_2$  (current deformed state). Both of these configurations are defined in the framework of the updated Lagrangian approach, as the start and the end of each incremental step of external loading (see e.g. [11]).

In order to derive the stiffness matrix  $[k_{ij}]$  starting from Eq. (2), the displacement field of the element (ij) must be defined. For this reason, the following shape functions are used:

$$\begin{aligned} N_1 &= N_1(x) = 1 - (x/L_{ij}) & N_2 &= N_2(x) = (x/L_{ij}) \\ N_3 &= N_3(x) = 1 - 3 \cdot (x/L_{ij})^2 + 2 \cdot (x/L_{ij})^3 & N_4 &= N_4(x) = x - 2 \cdot (x^2/L_{ij}) + (x^3/L_{ij}^2) \\ N_5 &= N_5(x) = 3 \cdot (x/L_{ij})^2 - 2 \cdot (x/L_{ij})^3 & N_6 &= N_6(x) = -(x^2/L_{ij}) + (x^3/L_{ij}^2) \end{aligned} \quad (3)$$

The corresponding matrices of these functions are:

$$\begin{aligned} [N_u] &= [N_1 \quad 0 \quad 0 \quad 0 \quad 0 \quad 0 \quad N_2 \quad 0 \quad 0 \quad 0 \quad 0 \quad 0 \quad \dots \quad 0 \quad 0] \\ [N_v] &= [0 \quad N_3 \quad 0 \quad 0 \quad 0 \quad N_4 \quad 0 \quad N_5 \quad 0 \quad 0 \quad 0 \quad N_6 \quad \dots \quad 0 \quad 0] \\ [N_w] &= [0 \quad 0 \quad N_3 \quad 0 \quad -N_4 \quad 0 \quad 0 \quad 0 \quad N_5 \quad 0 \quad -N_6 \quad 0 \quad \dots \quad 0 \quad 0] \\ [N_\theta] &= [0 \quad 0 \quad 0 \quad N_3 \quad 0 \quad 0 \quad 0 \quad 0 \quad 0 \quad N_5 \quad 0 \quad 0 \quad \dots \quad N_4 \quad N_6] \end{aligned} \quad (4)$$

Thus, the displacement in any point inside the element can be expressed in terms of its end nodes displacements using Eq. (5):

$$\begin{aligned} \mathbf{u} &= [\mathbf{N}_u] \{\mathbf{u}\} \quad \mathbf{v} = [\mathbf{N}_v] \{\mathbf{u}\} \quad \mathbf{w} = [\mathbf{N}_w] \{\mathbf{u}\} \quad \boldsymbol{\theta}_x = [\mathbf{N}_\theta] \{\mathbf{u}\} \\ \{\mathbf{u}\} &= \left[ u_i \quad v_i \quad w_i \quad \theta_{xi} \quad \theta_{yi} \quad \theta_{zi} \quad u_j \quad v_j \quad w_j \quad \theta_{xj} \quad \theta_{yj} \quad \theta_{zj} \quad \theta'_{xj} \quad \theta'_{yj} \right]^T \end{aligned} \quad (5)$$

Eq. (2) also introduces the internal forces of the element (ij):  $F_x$ ,  $V_y$ ,  $V_z$ ,  $M_x$ ,  $M_y$  and  $M_z$ . Assuming that no loads act on the element, these forces can be expressed in terms of the corresponding forces in the element's ends i and j, using the relations of Eq. (6):

$$\begin{aligned} F_x &= F_{xj}, \quad V_y = -\frac{M_{zi} + M_{zj}}{L_{ij}}, \quad V_z = \frac{M_{yi} + M_{yj}}{L_{ij}} \\ M_x &= M_{xj}, \quad M_y = -M_{yi} \left( 1 - \frac{x}{L_{ij}} \right) + M_{yj} \left( \frac{x}{L_{ij}} \right), \quad M_z = -M_{zi} \left( 1 - \frac{x}{L_{ij}} \right) + M_{zj} \left( \frac{x}{L_{ij}} \right) \end{aligned} \quad (6)$$

Inserting Eqs. (5), (6) into Eq. (2), and after a specific transformation (e.g. [6, 8, 19]), the stiffness matrix of the element (ij) can be expressed as follows:

$$\begin{aligned} [k_{ij}] &= EA [k_{uu}^{110}] + EI_{zz} [k_{vv}^{220}] + EI_{yy} [k_{ww}^{220}] + GJ [k_{\theta\theta}^{110}] \\ &\quad + F_{xj} [k_{vv}^{110}] + F_{xj} [k_{ww}^{110}] + V_y [k_{uv}^{110}] + V_y [k_{vu}^{110}] \\ &\quad - V_z [k_{uw}^{110}] - V_z [k_{wu}^{110}] + K_w [k_{\theta\theta}^{110}] - \frac{M_{yi} + M_{yj}}{L_{ij}} ([k_{v\theta}^{100}] + [k_{\theta v}^{010}] + [k_{v\theta}^{111}] + [k_{\theta v}^{111}]) \\ &\quad + M_{yi} [k_{v\theta}^{110}] + M_{yi} [k_{\theta v}^{110}] + M_{zi} [k_{w\theta}^{110}] + M_{zi} [k_{\theta w}^{110}] \\ &\quad - \frac{M_{xj}}{2} [k_{vv}^{120}] - \frac{M_{xj}}{2} [k_{ww}^{120}] + \frac{M_{xj}}{2} [k_{vw}^{210}] + \frac{M_{xj}}{2} [k_{wv}^{120}] \\ &\quad - \frac{M_{zi} + M_{zj}}{L_{ij}} ([k_{w\theta}^{100}] + [k_{\theta w}^{010}] + [k_{w\theta}^{111}] + [k_{\theta w}^{111}]) + EC_\omega [k_{\theta\theta}^{220}] \end{aligned} \quad (7)$$

Where:

$$[k_{gh}^{stv}] = \int_0^{L_{ij}} \frac{d^s [N_g]^T}{dx^s} \cdot \frac{d^t [N_h]}{dx^t} \cdot x^v dx \quad (8)$$

$g = u, v, w \quad h = u, v, w$

$s, t = \text{order of differentiation}$

$v = \text{order of exponent of } x$

From the study of Eq. (7), it can be concluded that the stiffness matrix  $[k_{ij}]$  (which can be used for geometric non-linear analysis, additionally including the influence of the warping effects) consists of 28 matrices. These matrices correspond to contribution of the element's elastic deformations and to the contribution of the element's end forces. On the basis of the above conclusion, the stiffness matrix can be expressed as the summation of two matrices: the linear elastic stiffness matrix  $[k_{ij,e}]$  and the geometric stiffness matrix  $[k_{ij,g}]$ :

$$[k_{ij}] = [k_{ij,e}] + [k_{ij,g}] \quad (9)$$

Where:

$$[k_{ij,e}] = EA[k_{uu}^{110}] + EI_{zz}[k_{vv}^{220}] + EI_{yy}[k_{ww}^{220}] + GJ[k_{\theta\theta}^{110}] + EC_{\omega}[k_{\theta\theta}^{220}] \quad (10a)$$

$$\begin{aligned} [k_{ij,g}] = & F_{xj}[k_{vv}^{110}] + F_{xj}[k_{ww}^{110}] + V_y[k_{uv}^{110}] + V_y[k_{vu}^{110}] \\ & - V_z[k_{uw}^{110}] - V_z[k_{wu}^{110}] + K_w[k_{\theta\theta}^{110}] - \frac{M_{yi} + M_{yj}}{L_{ij}}([k_{v\theta}^{100}] + [k_{\theta v}^{010}] + [k_{v\theta}^{111}] + [k_{\theta v}^{111}]) \\ & + M_{yi}[k_{v\theta}^{110}] + M_{yi}[k_{\theta v}^{110}] + M_{zi}[k_{w\theta}^{110}] + M_{zi}[k_{\theta w}^{110}] \\ & - \frac{M_{xj}}{2}[k_{vv}^{120}] - \frac{M_{xj}}{2}[k_{ww}^{210}] + \frac{M_{xj}}{2}[k_{vw}^{210}] + \frac{M_{xj}}{2}[k_{wv}^{120}] \\ & - \frac{M_{zi} + M_{zj}}{L_{ij}}([k_{w\theta}^{100}] + [k_{\theta w}^{010}] + [k_{w\theta}^{111}] + [k_{\theta w}^{111}]) \end{aligned} \quad (10b)$$

### B) Step 2: Derivation of the stiffness matrix $[k_{me}]$ for the macroelement

After the formulation of the stiffness matrix for the macroelement's median segment according to the procedure which is summarized in Figure 2, the corresponding stiffness matrix for the whole macroelement (Figure 1) can be derived.

At the beginning, the relationships between the displacements of internal nodes 2 and 3, with those of external nodes 1 and 4 (Figure 1) are established. To this end, two factors must be considered: (a) the fact that the rigid offsets are non-deformable elements and behave as absolutely rigid bodies in 3D-space, and (b) the existence of the rotational springs which are located in internal nodes 2, 3, where the median segment is connected to the rigid offsets (Figure 1).

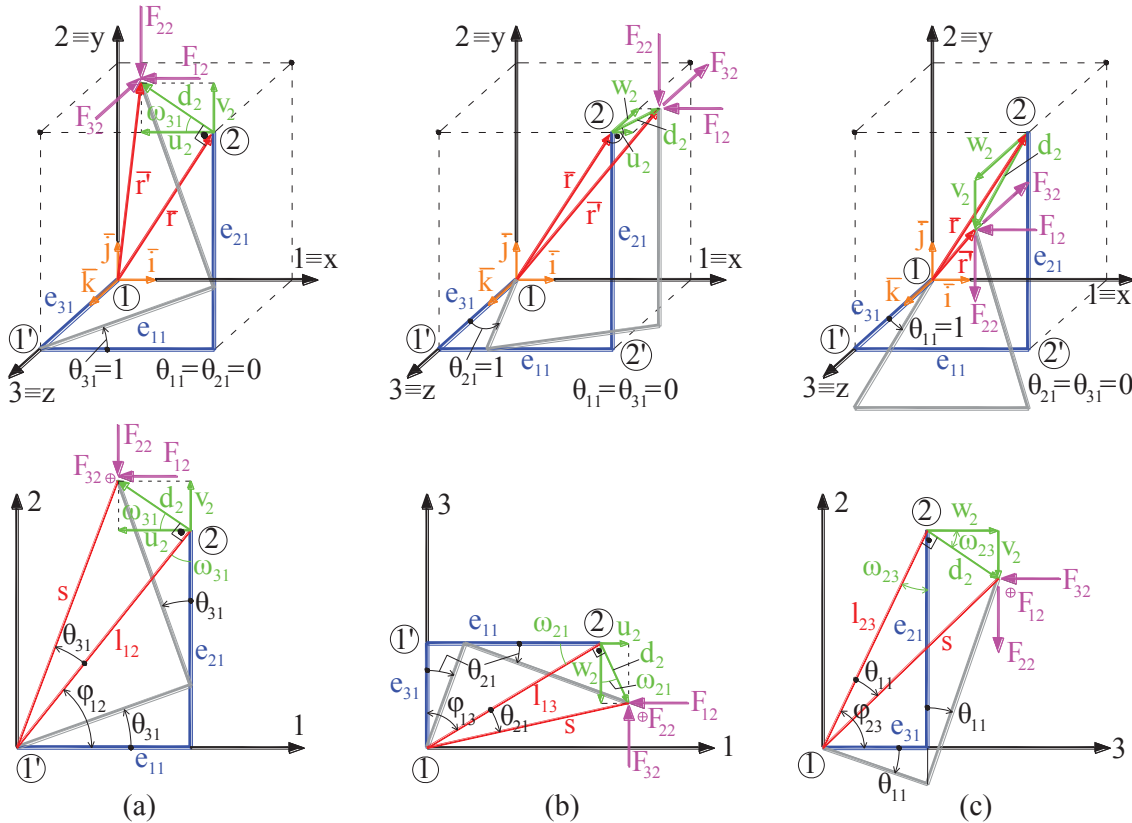


Figure 3: Kinematic conditions of the proposed macroelement's rigid offsets

Due to the fact that the rigid offsets move as rigid bodies in the 3D-space, the displacements of the internal nodes 2 ( $u_2, v_2, w_2$ ), 3 ( $u_3, v_3, w_3$ ) are equal to the displacements of the external nodes 1 ( $u_1, v_1, w_1$ ), 4 ( $u_4, v_4, w_4$ ) respectively, plus the displacements which are caused by the rotations of the rigid offsets about the local axes 1, 2 and 3 (Figure 3). These additional displacements can be calculated on the basis of Figure 3, with the assumption that the displacements are infinitesimal. Moreover, the behavior of the rigid offsets as absolutely rigid bodies leads to the conclusion that the rotations of the internal nodes 2 ( $\theta_{12}, \theta_{22}, \theta_{32}$ ), 3 ( $\theta_{13}, \theta_{23}, \theta_{33}$ ) about the local axes 1, 2 and 3 are equal to the corresponding rotations of the external nodes 1 ( $\theta_{11}, \theta_{21}, \theta_{31}$ ), 4 ( $\theta_{14}, \theta_{24}, \theta_{34}$ ). It can be proved, with the aid of the Figure 3, that (see also [20]):

$$[u_{int}] = [T] \cdot [u] = \begin{bmatrix} [I_3] & [t_{12}] & [0_3] & [0_3] \\ [0_3] & [I_3] & [0_3] & [0_3] \\ [0_3] & [0_3] & [I_3] & [t_{34}] \\ [0_3] & [0_3] & [0_3] & [I_3] \end{bmatrix} \cdot [u] \quad [t_{12}] = \begin{bmatrix} 0 & e_{31} & -e_{21} \\ -e_{31} & 0 & e_{11} \\ e_{21} & -e_{11} & 0 \end{bmatrix} \quad [t_{34}] = \begin{bmatrix} 0 & e_{32} & -e_{22} \\ -e_{32} & 0 & e_{12} \\ e_{22} & -e_{12} & 0 \end{bmatrix} \quad (11a)$$

$$[u_{int}]^T = [u_2 \ v_2 \ w_2 \ \theta_{12} \ \theta_{22} \ \theta_{32} \mid u_3 \ v_3 \ w_3 \ \theta_{13} \ \theta_{23} \ \theta_{33}] \quad (11b)$$

$$[u]^T = [u_1 \ v_1 \ w_1 \ \theta_{11} \ \theta_{21} \ \theta_{31} \mid u_4 \ v_4 \ w_4 \ \theta_{14} \ \theta_{24} \ \theta_{34}]$$

Where  $[I_3]$  is the 3x3 identity matrix and  $[0_3]$  is the 3x3 zero matrix.

The existence of the rotational springs in the internal nodes 2, 3 causes discontinuity of the rotations about the local axes 2 and 3 in these points. This is expressed through the parameter  $\Delta\theta$  and illustrated in Figure 4 for the case of bending of the macroelement in the local plane 1-2, where the rotational springs  $K_{r32}$  and  $K_{r33}$  are activated.

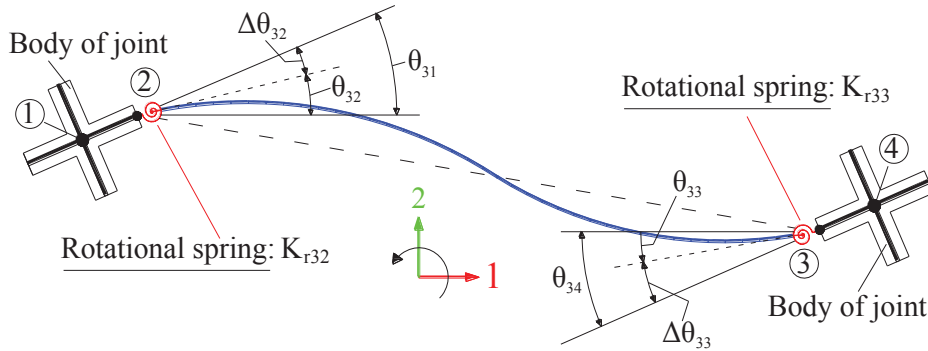


Figure 4: Modelling of semi-rigid connections through the rotational springs in the element's internal nodes

If the rotational springs behave elastically or in the case of inelastic analysis (where, during every incremental step of loading, the tangent stiffness of the rotational springs is used), the equation which gives the value of the discontinuity  $\Delta\theta$  is:

$$\Delta\theta_{2i} = M_{2i}/K_{r2i}, \quad \Delta\theta_{3i} = M_{3i}/K_{r3i} \quad (i = 2, 3) \quad (12)$$

Thus:

$$\begin{aligned} \theta_{22} &= \theta_{21} - (M_{22}/K_{r22}) = \theta_{21} + (-K_{r22}^{-1}) \cdot M_{22} \\ \theta_{23} &= \theta_{24} - (M_{23}/K_{r23}) = \theta_{24} + (-K_{r23}^{-1}) \cdot M_{23} \\ \theta_{32} &= \theta_{31} - (M_{32}/K_{r32}) = \theta_{31} + (-K_{r32}^{-1}) \cdot M_{32} \\ \theta_{33} &= \theta_{34} - (M_{33}/K_{r33}) = \theta_{34} + (-K_{r33}^{-1}) \cdot M_{33} \end{aligned} \quad (13)$$



Taking into consideration Eq. (13), Eq. (11a) is modified as follows:

$$[u_{int}] = [T] \cdot [u] + \underbrace{\begin{bmatrix} [0_3] & [0_3] & [0_3] & [0_3] \\ [0_3] & [K_{R2}] & [0_3] & [0_3] \\ [0_3] & [0_3] & [0_3] & [0_3] \\ [0_3] & [0_3] & [0_3] & [K_{R3}] \end{bmatrix}}_{[T_{KR}]} \cdot [S_{int}] \quad [K_{Ri}] = \begin{bmatrix} 0 & 0 & 0 \\ 0 & -K_{r2i}^{-1} & 0 \\ 0 & 0 & -K_{r3i}^{-1} \end{bmatrix} \quad (i = 2, 3) \quad (14a)$$

$$[S_{int}]^T = [F_{12} \ F_{22} \ F_{32} \ M_{12} \ M_{22} \ M_{32} \ F_{13} \ F_{23} \ F_{33} \ M_{13} \ M_{23} \ M_{33}] \quad (14b)$$

Thus, the matrix equation which relates the displacements of internal nodes 2 and 3 with those of external nodes 1 and 4 is:

$$[u_{int}] = [T] \cdot [u] + [T_{KR}] \cdot [S_{int}] \quad (15)$$

It is also necessary to relate the forces of internal nodes 2 and 3 with those of the external nodes 1 and 4. To this end, the six equations of equilibrium for each one of the two rigid off-sets must be formed. These equations state the equilibrium of the three forces and the three moments which act in each one of the two edges of the rigid off-sets (nodes 1,2 and nodes 3,4). Obviously, the forces which act at the edges of the rigid off-sets are the elements of the vectors  $[S_{int}]$  (Eq. (14b)) and  $[S]$ , which is the vector of the forces of the external nodes 1, 4:

$$[S]^T = [F_{11} \ F_{21} \ F_{31} \ M_{11} \ M_{21} \ M_{31} \ F_{14} \ F_{24} \ F_{34} \ M_{14} \ M_{24} \ M_{34}] \quad (16)$$

It can be proved [20] that the required relation of the forces of the internal nodes 2 and 3 with those of the external nodes 1 and 4 can be expressed in the following matrix form:

$$[S] = [T]^T \cdot [S_{int}] \quad (17)$$

Eq. (17) arises from the rigid off-sets' equilibrium in the undeformed condition of the macroelement. However, in the framework of the geometric non-linear analyses, the equations of equilibrium must be formulated in the element's deformed condition. For this reason, Eq. (17) must be modified. This modification concerns the introduction of the additional moments which are produced when the forces in internal nodes 2, 3 are applied in the deformed state of the element (Figure 3). It can be proved [14] that the modified form of Eq. (17) is:

$$[S] = [T]^T \cdot [S_{int}] + [T_g] \cdot [u] \quad (18)$$

where  $[u]$  is the vector of the displacements of the external nodes 1, 4 (Eq. 11(b)) and the matrix  $[T_g]$  is calculated by means of the following equation:

$$[T_g] = \begin{bmatrix} [0_3] & [0_3] & [0_3] & [0_3] \\ [0_3] & [K_{s12}] & [0_3] & [0_3] \\ [0_3] & [0_3] & [0_3] & [0_3] \\ [0_3] & [0_3] & [0_3] & [K_{s23}] \end{bmatrix} \quad [K_{sij}] = - \begin{bmatrix} F_{3j}e_{3i} + F_{2j}e_{2i} & 0 & 0 \\ 0 & F_{3j}e_{3i} + F_{1j}e_{1i} & 0 \\ 0 & 0 & F_{2j}e_{2i} + F_{1j}e_{1i} \end{bmatrix} \quad (i,j) = \begin{cases} (1,2) \\ (2,3) \end{cases} \quad (19)$$

The relation between the displacements of the internal nodes 2,3 and the external nodes 1,4 (Eq. (15)), as well as the corresponding relation between the forces (Eq. (18)), constitute the basis for the derivation of the stiffness matrix of the macroelement  $[k_{me}]$  as a matrix function of the stiffness matrix of the macroelement's median segment  $[k_{ms}]$  (Table 1). It can be

proved (e.g. [14]) that, after a sequence of matrix transformations using Eqs. (15), (18), the stiffness matrix  $[k_{me}]$  arises from the following equation:

$$[k_{me}] = [T]^T \cdot \{[I_{12}] - [k_{ms}] \cdot [T_{KR}]\}^{-1} \cdot [k_{ms}] \cdot [T] + [T_g] \quad (20)$$

where the  $[I_{12}]$  is the 12x2 identity matrix.

### 2.3 Load matrix derivation

The load matrices for the macroelement are formed using the basic principles of the two-step procedure which is used for the derivation of the stiffness matrix. This procedure was described in Section 2.2. The current section focuses on the points of difference between the procedure for the derivation of the load matrices and the corresponding procedure for the derivation of the stiffness matrix.

#### A) Step 1: Derivation of the load matrix for the median segment

As in case of the derivation of the median segment's stiffness matrix, the corresponding procedure for the formulation of the load matrix is based on the performance of static condensation in two stages (Figure 2). The load matrix of the median segment obviously depends on the shape of the external loading. However, due to the fact that the median segment is discretized in sub-elements, any shape of continuously distributed load can be replaced by concentrated forces which are applied on the generated  $(n-1)$  nodes and the two external nodes A, B (see Second step in Figure 2). As an example, this procedure for the case of a trapezoidal load on a random part of the median segment is illustrated in Figure 5.

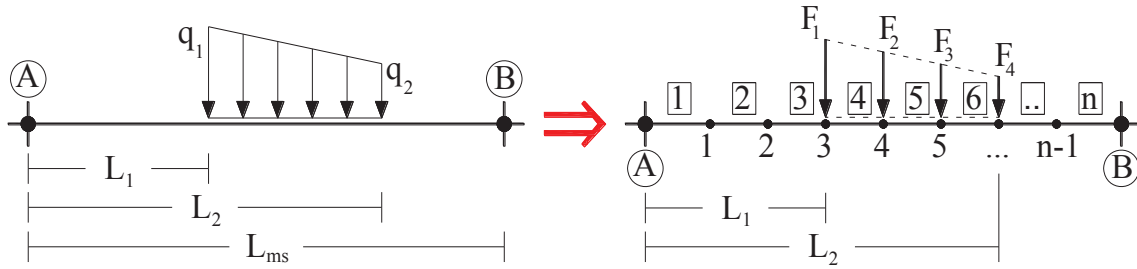


Figure 5: Modelling of distributed load in the median segment through concentrated forces in the generated nodes

Thus, the procedure for the derivation of the load matrix (as is the case with the procedure for the derivation of the stiffness matrix) is based on the consideration of the median segment as a sub-structure which is loaded only by concentrated forces in its nodes. This procedure can generally be programmed, provided that the concentrated forces which replace the actual external load are known. Using this approach, the load matrix  $[p_{sub}]$  (Figure 2) is derived. Then, the next steps of the procedure which is illustrated in Figure 2 (third and fourth step) lead to the generation of the 12x1 load matrix  $[p_{ms}]$  for the macroelement's median segment.

#### B) Step 2: Derivation of the load matrix $[p_{me}]$ for the macroelement

The relation between the displacements and forces of internal nodes 2, 3, considering the external loading of the median segment, is:

$$[S_{int}] = [k_{ms}] \cdot [u_{int}] + [p_{ms}] \quad (21)$$

The corresponding relation for the external nodes 1, 4 is:

$$[S] = [k_{me}] \cdot [u] + [p_{me}] \quad (22)$$

By combining Eqs. (15) and (21), we obtain:

$$[S_{int}] = \{[I_{12}] - [k_{ms}] \cdot [T_{KR}]\}^{-1} \cdot [K_{ms}] \cdot [T] \cdot [u] + \{[I_{12}] - [K_{ms}] \cdot [T_{KR}]\}^{-1} \cdot [p_{ms}] \quad (23)$$

The combination of Eq. (23) and Eq. (18) leads to the following equation:

$$[S] = \{[T]^T \cdot \{[I] - [k_{ms}] \cdot [T_{KR}]\}^{-1} \cdot [k_{ms}] \cdot [T] + [T_g]\} \cdot [u] + \{[T]^T \cdot \{[I] - [k_{ms}] \cdot [T_{KR}]\}^{-1} \cdot [p_{ms}]\} \quad (24)$$

Finally, by comparing Eqs. (22) and (24), the load matrix of the macroelement  $[p_{me}]$  as a function of the stiffness matrix  $[k_{ms}]$  and the load matrix  $[p_{ms}]$  of the median segment is extracted:

$$[p_{me}] = [T]^T \cdot \{[I_{12}] - [k_{ms}] \cdot [T_{KR}]\}^{-1} \cdot [p_{ms}] \quad (25)$$

### 3 NUMERICAL EXAMPLES

In order to check the efficiency of the proposed macroelement in the geometrically non-linear analyses of framed structures, the solution of a set of numerical examples is presented in the current section. A computer program in Fortran was developed for the implementation of the proposed macroelement in these numerical examples.

#### 3.1 Calculation of the critical load of beam/columns

The ability of the proposed macroelement to accurately calculate the critical loads of beam/columns in lateral buckling was tested using a simply supported beam and a cantilever beam. The data and the boundary conditions of these beams are illustrated in Figure 6. It must be clarified that the ends of both beams are free to warp. Thus, the corresponding bimoments are equal to zero.

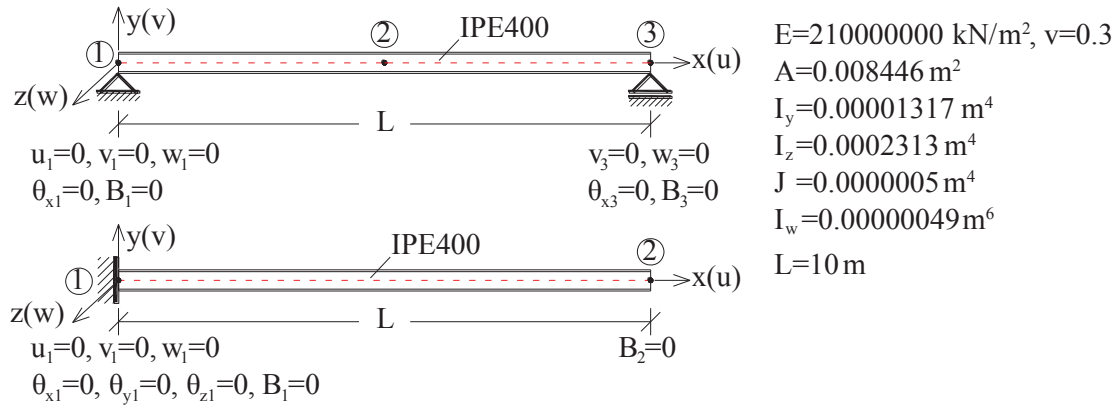


Figure 6: Simple beams for the study of the effectiveness of the new element in the calculation of buckling loads

For the modelling of beams, one macroelement with eight sub-elements was used. Thus, the length of each sub-element is equal to  $L_{se}=10/8=1.25$ m. The calculated critical load values were compared with the corresponding theoretical ones [21]. Three different load cases for the simply supported beam were considered: (a) pure bending i.e. external moments  $M_{ze}$  at its ends, (b) concentrated load  $F_{ye}$  at the middle, and (c) uniform load  $q_{ye}$ . It must be clarified that the force  $F_{ye}$  and the distributed load  $q_{ye}$  are applied at the shear center of the beam's cross section. The above load conditions can cause lateral buckling. In order to estimate the critical load in each load case, two different approaches were adopted. In the first approach, the problem was solved by the addition of a perturbation torsional moment  $M_{xe}$  at the middle of the beam. The value of this torsional moment was taken equal to 1/1000 of the value of each one

of the three considered external loads. In the framework of this approach, the external loads (and the perturbation torsional moment) were applied incrementally (i.e. step by step). In each load step, the solution was achieved through an iterative procedure. The displacements and the internal forces of the beam were stored after the convergence of each load step. The analyses were terminated when the convergence was impossible, after a pre-defined maximum number of iterations. The termination of analyses indicates the values of the critical loads. In the second approach, the calculation of the critical loads was achieved considering and solving the stability problem. Thus, in each load step (without the perturbation torsional moment  $M_x$ ), the value of the determinant  $\det K$  of the stiffness matrix of the restrained beam was calculated and stored. The value of the external load for which the condition  $\det K=0$  is fulfilled corresponds to the value of the critical load.

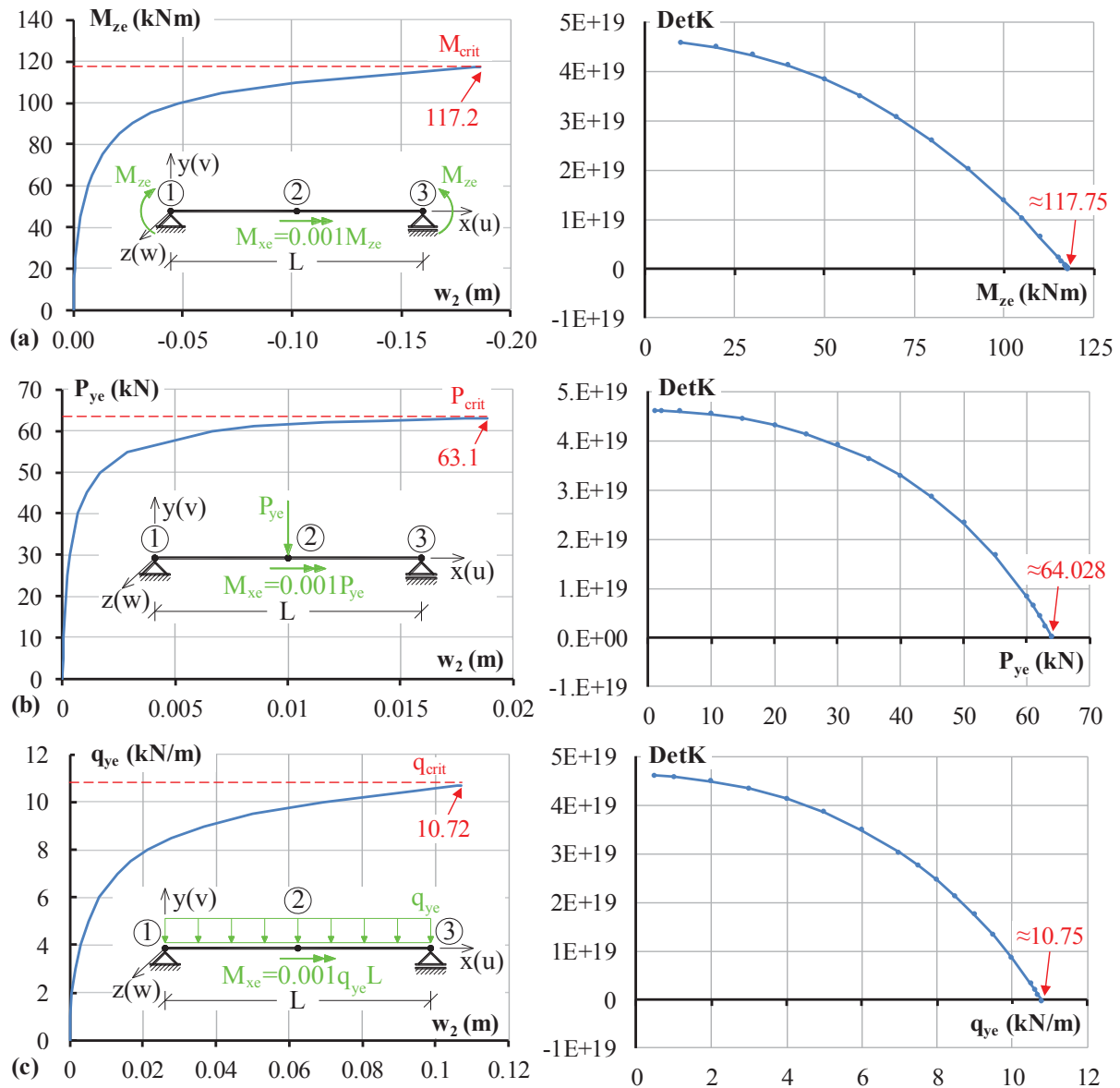


Figure 7: Calculation of critical loads in lateral buckling for a simply supported beam using the new element

Figure 7 illustrates the main results of the analyses described above. The main conclusion to be extracted from this figure is that the implementation of the proposed macroelement can effectively approach the theoretical values of the critical loads for the studied cases (Eqs. (26a)-(26c) [21]). More specifically, the differences of the calculated critical values from the

theoretical ones are 0.47% in the case of the pure bending (Figure 7a), 2.12% in the case of the concentrated load  $F_{ye}$  at the middle of the beam (Figure 7b), and 0.34% in the case of the uniform load  $q_{ye}$  (Figure 7c) when the first approach is adopted. The differences when the second approach is adopted are correspondingly: 0.01%, 0.68% and 0.06%.

$$M_{cr,L}^{s.s.} = \pi \cdot \sqrt{1 + \frac{EI_w}{GJ} \cdot \frac{\pi^2}{L^2}} \cdot \frac{\sqrt{EI_y GJ}}{L} = 117.76 \text{ kNm} \quad (26a)$$

$$P_{cr,L}^{s.s.} = 19.239 \cdot \frac{\sqrt{EI_y GJ}}{L^2} = 64.47 \text{ kN} \quad (26b)$$

$$q_{cr,L}^{s.s.} = 32.1 \cdot \frac{\sqrt{EI_y GJ}}{L^3} = 10.76 \text{ kN/m} \quad (26c)$$

$$P_{cr,L}^c = \frac{4.013}{\left[1 - \sqrt{EI_w / (L^2 GJ)}\right]^2} \cdot \frac{\sqrt{EI_y GJ}}{L^2} = 19.04 \text{ kN} \quad (26d)$$

Similar conclusions are extracted from the results of the solution of the cantilever beam, which are presented in Figure 8. The theoretical value of the critical load (Eq. (26d), [21]) is effectively approached using both types of analysis procedure. More specifically, the differences between the calculated and the theoretical value of the critical load are 0.72% according to the first approach and 0.59% according to the second one.

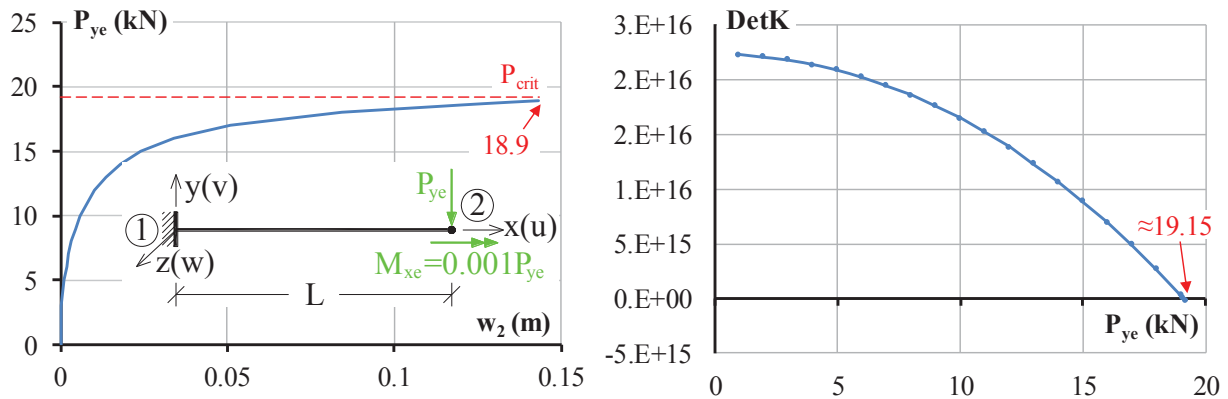


Figure 8: Calculation of the critical load in lateral buckling for cantilever beam using the new macroelement

The efficiency of the proposed macroelement was also studied in the case of an axially loaded column with a cruciform cross-section (Figure 9a). This example was also studied in [22]. The theoretical value of the critical load for pure torsional buckling is available in [21], whereas the corresponding critical value of the axial force for flexural buckling can be calculated by the classic Euler formula. Both of the above critical values of the axial force  $P_{xe}$  are given by Eqs. (27a), (27b).

$$P_{cr,t}^{s.s.} = \frac{A \cdot GJ}{I_y + I_z} = 195 \text{ kN} \quad (27a)$$

$$P_{cr,f}^{s.s.} = \frac{\pi^2 \cdot EI_z}{L^2} = 15791.4 \text{ kN} \quad (27b)$$

For the solution of the two problems, one macroelement with eight sub-elements was used. The procedure which was adopted for the estimation of the critical axial-torsional buckling load was based on the addition of a perturbation torsional moment  $M_{xe}$  equal to 1/1000 of the

applied compressive axial force  $P_{xe}$  at the middle of the column (Figure 9b). Correspondingly, a perturbation concentrated force  $P_{ye}$  was added for the estimation of the critical axial-flexural buckling load (Figure 9c). As in the case of the beam without an axial force, the external forces were applied progressively (step by step). However, in each one of the loading steps, an iteration procedure was adopted for the accomplishment of the equilibrium between the internal and the external forces. As can be seen in Figure 9, as the compressive axial force approaches the theoretical values of the critical load, the displacements and the rotations at the middle of the column are increased rapidly. In addition, the convergence to the solution became slow. Thus, the algorithm fails to converge after the pre-defined maximum number of iterative steps. The solution with the proposed macroelement gives a value for the critical axial-torsional buckling load that is equal to  $P_{cr,t}=194.85\text{kN}$  (0.08% difference from the theoretical value), whereas the corresponding value for the critical axial-flexural buckling load is  $15735\text{kN}$  (0.36% difference from the theoretical value).

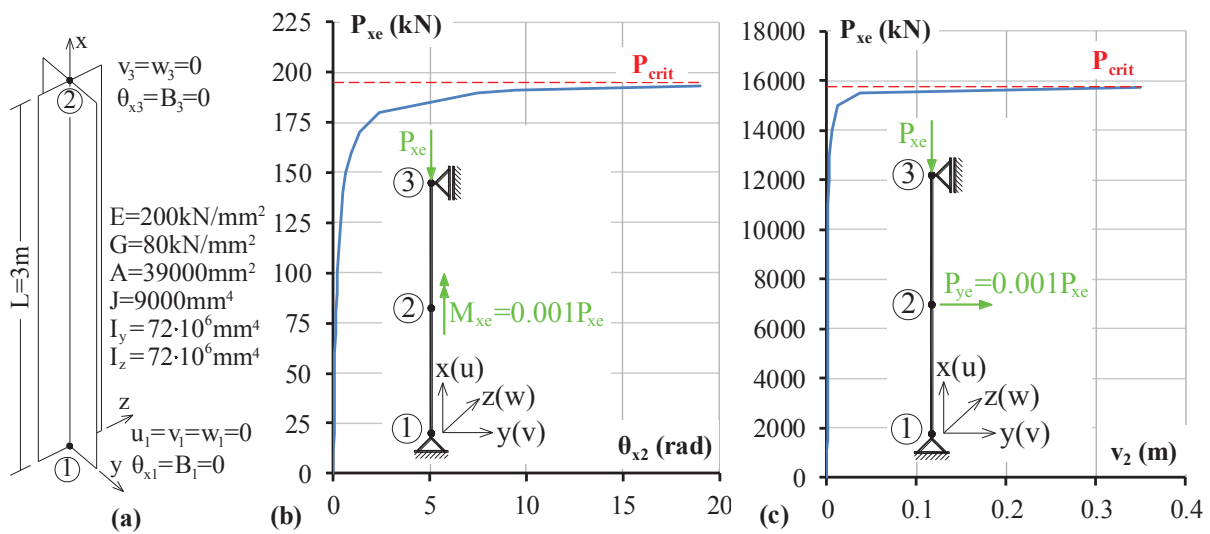


Figure 9: Calculation of critical loads for an axially loaded simply supported column using the new macroelement

### 3.2 Calculation of the critical load of simple framed structures

The scope of the current section is the study of the performance of the proposed macroelement in the geometric nonlinear analysis of simple framed structures. The extracted results are compared with known solutions or with the corresponding results extracted from reliable software.

The first example of this category is a clamped right-angle frame under a load  $P$  at the free end, which was first solved by Argyris et al. [23], as well as by other researchers [22].

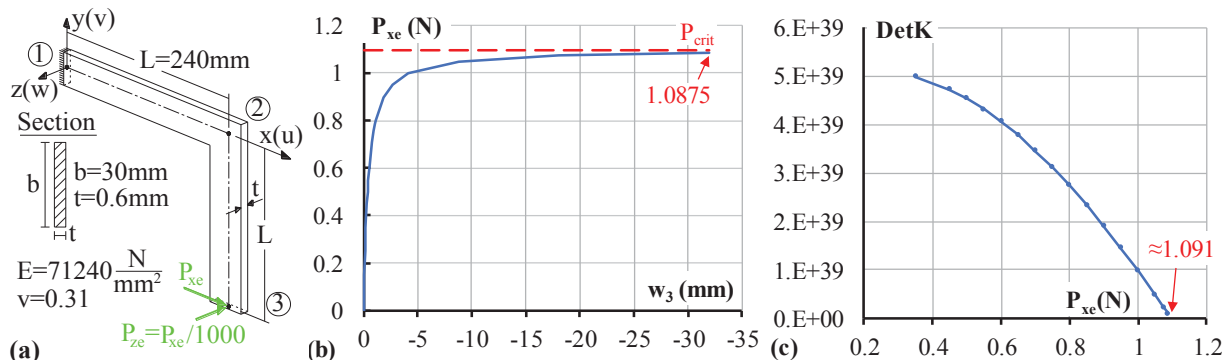


Figure 10: Calculation of the buckling load of a clamped right-angle frame using the new macroelement



The data of this frame are presented in Figure 10. Each one of the two members of the frame was modelled using one macroelement with eight sub-elements.

Following the procedures of the two approaches which were described in the previous section, the values of the frame's critical load were estimated. These values are  $P_{cr}=1.0875N$  (first approach) and  $P_{cr}=1.091N$  (second approach). The corresponding value which was calculated by Argyris et al. [23], using their formulation for the geometric stiffness matrix and 10 beam elements per member, is  $P_{cr}=1.088N$ .

The second example of this category concerns the one-storey steel space frame of Figure 11. This example was selected for the study of the performance of the proposed macroelement when its abilities for the modelling of rigid offsets and semi-rigid connections are activated.

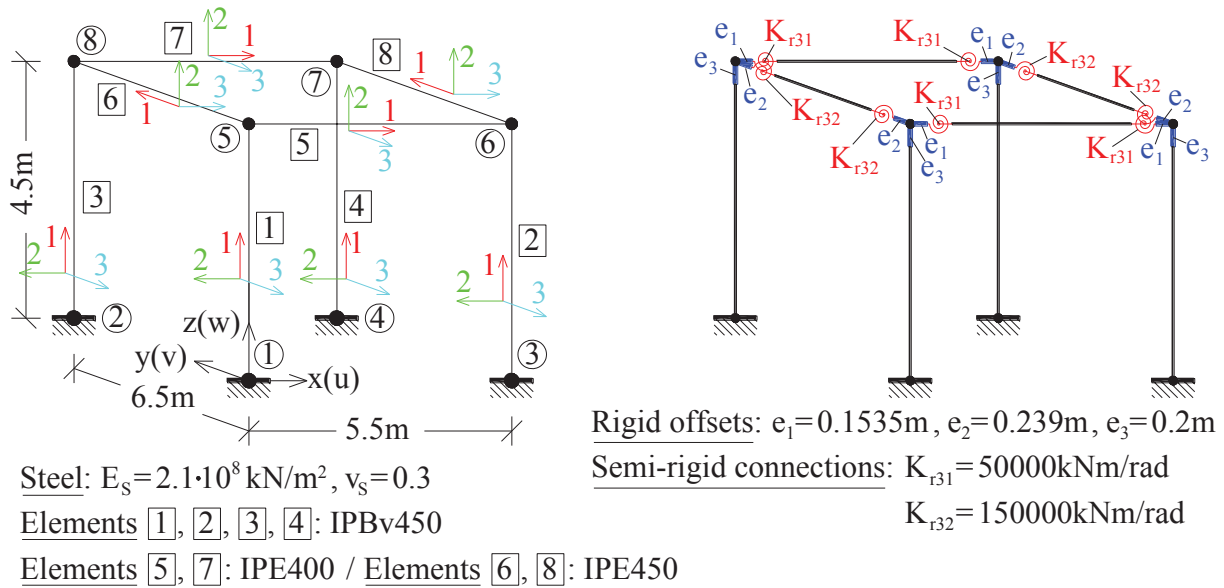


Figure 11: One-storey steel space frame – data and modelling details

Two different types of analyses were performed. The first one concerns the flexural buckling analysis which leads to the calculation of the frame's critical loads. More specifically, the scope of this type of analysis is the calculation of the critical values (eigenvalues) of the load factor  $\lambda$  which correspond to the modes of the overall flexural buckling of the frame for the load pattern of Figure 12. The method which was adopted is based on the estimation of the roots of the equation:

$$\text{Det}[K(P \cdot \lambda)] = 0 \quad (28)$$

where  $K(P \cdot \lambda)$  is the global stiffness matrix of the restrained frame which depends on the external compressive forces  $P$ .

These roots were calculated using the Newton-Raphson algorithm. Details for the shape of the function which relates the  $\lambda$  values with the values of  $\text{det}[K(P \cdot \lambda)]$  for the examined frame are presented in Figure 12. The first five critical values of factor  $\lambda$  were estimated. Definitely, in practical applications only, the first (and smaller) critical value  $\lambda_1$  is useful for the design. However, the calculation of the first five critical values of factor  $\lambda$  was carried out for the further study of the effectiveness of the proposed macroelement.

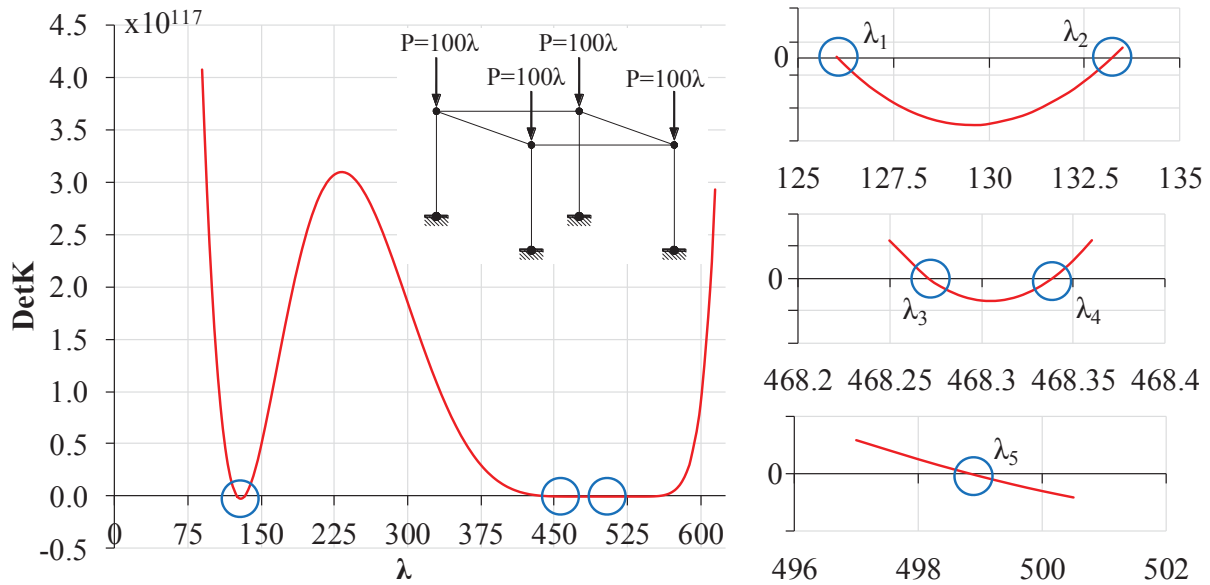


Figure 12: Calculation of the eigenvalues of the overall flexural buckling of the examined space frame using the proposed macroelement

The problem was also solved using the program SAP2000 [24]. Table 2 presents the slight differences of the first five critical  $\lambda$  values between the solution extracted by the SAP2000 program and the corresponding values extracted by the solution using the proposed macroelement.

$\lambda_i$	SAP2000	Proposed Macroelement	Difference (%)
$\lambda_1$	126.06	126.04	0.014%
$\lambda_2$	133.23	133.21	0.019%
$\lambda_3$	468.26	468.27	-0.002%
$\lambda_4$	468.32	468.34	-0.004%
$\lambda_5$	498.86	498.82	0.008%

Table 2: Comparison of the eigenvalues calculated using the new macroelement and the SAP2000 program

The second type of analysis concerns the geometric non-linear analysis of the frame for the vertical (distributed and concentrated) loads and the horizontal concentrated forces which are illustrated in Figure 13.

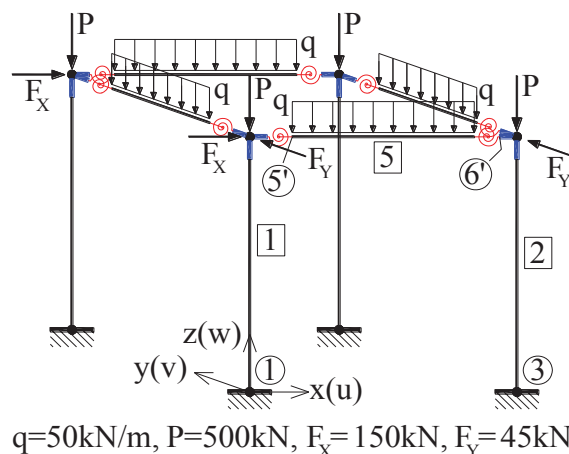


Figure 13: Load case for the geometric non-linear analysis of the space frame

The problem was also solved using the program SAP2000, activating the option for the consideration of the geometric non-linear effects. The comparison between the characteristic results (bending moments and shear forces) which were extracted by SAP2000 and the corresponding results which were extracted by the solution using the proposed macroelement are illustrated in Table 3. This comparison indicates that the proposed macroelement is capable of extracting results very similar to ones extracted by the well-documented SAP2000 program.

Element/Node	Internal Force	Proposed Macroelement	SAP2000	Differences (%)
1/1	$M_{2,1}$	-15.75	-15.72	0.17%
	$M_{3,1}$	178.46	178.37	0.05%
	$V_{2,1}$	-49.40	-49.39	0.02%
	$V_{3,1}$	25.84	25.85	-0.05%
2/3	$M_{2,3}$	-15.82	-15.79	0.22%
	$M_{3,3}$	254.82	254.76	0.02%
	$V_{2,3}$	-100.61	-100.61	0.00%
	$V_{3,3}$	25.85	25.86	-0.03%
5/5'	$M_{3,5'}$	74.33	74.38	-0.07%
	$V_{2,5'}$	78.80	78.75	0.06%
5/6'	$M_{3,6'}$	-190.80	-190.65	0.08%
	$V_{2,6'}$	-180.85	-180.8	0.03%

Table 3: Comparison of values of bending moments and shear forces in characteristic points of the examined space frame using the new macroelement and the SAP2000 program

#### 4 CONCLUSIONS

In the current paper, the formulation and the study of the effectiveness of a proposed beam/column macroelement for non-linear analysis is presented. This macroelement is a two-noded element with seven degrees of freedom per node and possesses abilities to effectively model the members of steel structures. The inclusion of the seventh degree of freedom in each node permits the modelling of the warping effects which are significant in steel members with open thin-walled sections. The proposed formulation is based on a two-stage static condensation technique, which permits the connection of the new element with classic elements with six degrees of freedom per node. The formulation of the new macroelement also includes rotational springs and rigid offsets at ends. It is thus able to model steel members with semi-rigid connections, as well as the influence of the body of rigid joints.

The proposed macroelement was successfully tested using well-known theoretical solutions from the literature and well-documented software (program SAP2000). The macroelement was also inserted to an existing professional software for the analysis and design of steel structures.

#### ACKNOWLEDGMENT

This research has been co-financed by the European Regional Development Fund of the European Union and Greek national funds through the Operational Program ‘Competitiveness, Entrepreneurship and Innovation’, under the call RESEARCH CREATE INNOVATE (project code: T1EDK-01800).

## REFERENCES

- [1] I. Vayas, J. Ermopoulos, G. Ioannidis, *Design of Steel Structures to Eurocodes*, Springer, 2019.
- [2] E. Ellobody, R. Feng, B. Young, *Finite Element Analysis and Design of Metal Structures*, Elsevier, 2014.
- [3] R. Landolfo, F. Mazzolani, D. Dubina, L.S. da Silva, M. D’Aniello, *Design of Steel Structures for Buildings in Seismic Areas, 1<sup>st</sup> Edition*, ECCS, Wiley, 2017.
- [4] EN1993-1-1 (Eurocode 3). Design of steel structures - part 1-1: General rules and rules for buildings, European Committee for Standardization; 2005.
- [5] ANSI, AISC 360-16, Specification for Structural Steel Buildings; American Institute of Steel Construction: Chi-cago, IL, USA, 2016.
- [6] Y.B. Yang, and W. McGuire, Stiffness Matrix for Geometric Nonlinear Analysis, *Journal of Structural Engineering, ASCE*, **Vol. 112**, **No. ST4**, 853-877, 1986.
- [7] Y.B. Yang, and W. McGuire, Joint Rotations and Geometric Nonlinear Analysis, *Journal of Structural Engineering, ASCE*, **Vol. 112**, **No. ST4**, 879-905, 1986.
- [8] S.E. Kim, C.M. Uang, S.H. Choi, and K.Y. An, Practical advanced analysis of steel frames considering lateral torsional buckling, *Thin Wall Struct.*, **44**(7), 709-720, 2006.
- [9] Barsoum RS, Gallagher RH. Finite element analysis of torsional-flexural stability problems, *Int J Numer Methods Eng*, **2**, 335–52, 1970.
- [10] E.J. Sapountzakis, V.G. Mokos, 3-D beam element of composite cross-section including warping and shear deformation effect, *Computers and Structures*, **85**, 102-116, 2007.
- [11] Y-B Yang, S-R Kuo, *Theory and analysis of nonlinear framed structures*, Prentice Hall, NY, 1994.
- [12] *Advanced Analysis of Steel Frames: Theory, Software and Applications*, Ed. W.F. Chen, S. Toma, CRC Press, 1994.
- [13] B. Gorenc, R. Tinyou, A. Syam, *Steel Designer’s Handbook, 7<sup>th</sup> edition*, UNSW press, 2005.
- [14] K. Morfidis, I.E. Avramidis, Generalized beam-column finite element on two-parameter elastic foundation, *Structural Engineering and Mechanics*, **Vol. 21**, **No.5**, 519 – 537, 2005.
- [15] K.J. Bathe, *Finite element procedures*, Englewood Cliffs, NJ: Prentice-Hall, 1996.
- [16] T.J.R. Hughes, *The finite element method: Linear static and dynamic finite element analysis*, Prentice-Hall Inc., New Jersey USA, 1987.
- [17] E.L. Wilson, The static condensation algorithm, *Int. J. Numer. Meth. Engrg.*, **8**, 198–203, 1974.
- [18] Y.B. Yang, and W. McGuire, A Procedure for Analyzing Space Frames with Partial Warping Restraint, *International Journal for Numerical Methods in Engineering*, **Vol. 20**, **No. 8**, 1377-1398, 1984.
- [19] J. Y. R. Liew, H. Chen, N. E. Shanmugam, and W. F. Chen, Improved nonlinear plastic hinge analysis of space frame structures, *Engineering Structures*, **22**, 1324-1338, 2000.

- [20] C. S. Krishnamoorthy, *Finite Element Analysis: Theory and Programming*, McGraw Hill, New Delhi, 1995.
- [21] S.P. Timoshenko, J.M. Gere, *Theory of Elastic Stability*, 2<sup>nd</sup> edition, Dover Publications, Inc., 1961.
- [22] L.H. Teh, M.J. Clarke, Co-rotational and Lagrangian formulations for elastic three-dimensional beam finite elements. *J Constr Steel Res*, **48(2–3)**, 123–44, 1998.
- [23] J.H. Argyris, O. Hilpert, G.A. Malejannakis, D.W. Scharpf, On the geometric stiffness of a beam in space - a consistent V.W. approach, *Comput Methods Appl Mech Eng*, **20(1)**, 105–31, 1979.
- [24] SAP2000 Version 21, Integrated finite element analysis and design of structures. Berkeley, California, USA: Computers and Structures Inc.

## GAUSSIAN AND NON-GAUSSIAN WIND TUNNEL PROCESSES

Di Giovanni M.<sup>1\*</sup>, D'Asdia P.<sup>2</sup>

<sup>1</sup> University G. D'Annunzio, School of Engineering, viale Pindaro 42, 65127, Pescara,  
e-mail: [dgm.studio@outlook.it](mailto:dgm.studio@outlook.it), corresponding author

<sup>2</sup> University G. D'Annunzio, School of Engineering, viale Pindaro 42, 65127, Pescara,  
e-mail: [pierodasdia@gmail.com](mailto:pierodasdia@gmail.com)

---

### Abstract

*The wind-structure interaction for structures sensitive to the wind action is commonly investigated through experimental campaigns in wind tunnel. Aerodynamic tests on rigid body models are carried out to estimate pressure coefficients that in turn are used to estimate the wind action on the prototype surfaces. Pressure taps are located on the model surfaces and pressure scanners acquire pressure time histories. Pressure coefficients are calculated from pressure series, they are dimensionless values and they are nondimensionalized on the wind velocity. In the wind tunnel, the flow is assumed stationary and consequently the mean value of pressure coefficient time history is independent of the experiment time length. However, the acquisition time length affects peak values and in particular the peak factor. In addition, the most of processes acquired near edges and near the flow detachment zones are non-Gaussian, contrary to what codes and standard suggest. It was estimated that several processes on the surfaces of a rigid body are non-Gaussian and, in this case, the mean value is not significant. At contrary, the mean value is mostly assumed as representative value of a measurement and it is used to size the structure. It is true only for some specific zones. In addition, they depend on the wind angle of attack. The purpose of this study is to discuss the Gaussian and non-Gaussian processes localization for two examples of structure families, large span roofs and bridge closed box section using aerodynamic experiments given by literature. The geometries subject of this investigation are typical geometries of roofs and bridge sections sensitive to wind action as for example cable nets roofs and suspended bridges.*

**Keywords:** Wind tunnel, light structure, random processes, Gaussianity, stochastics.

---



## 1 INTRODUCTION

The wind tunnel experimental campaign is largely used to estimate the wind effects on structures sensitive to the wind. Structures very sensitive to the wind action are generally large span roofs [1-5] as for example tensile structures for which the permanent load is smaller than the wind action, suspended bridges [6] that differently than traditional bridges made of reinforced concrete that are sensitive to the seismic action [7] or steel corrosion [8] can be affected by the flutter instability and finally, high-rise buildings [9] that are slender.

The wind tunnel is used to investigate the aerodynamics and the aeroelastic behavior of structures. The aerodynamics is commonly investigated through rigid body models and the test purpose is to estimate pressures using tubes and pressure taps [1] or wind forces using beam balances. The aeroelastic behavior is investigated through dynamic models that reproduces the prototype masses and stiffness based on scaling laws [10-14].

Aerodynamic and aeroelastic wind tunnel tests are both carried out for structures very light and for which instability due to wind effects is expected. However, it is well known that the more common experiments in wind tunnel are intended to estimate the wind action on the structure surface through the pressure distribution. The pressure distributions across the test model have historically been measured by drilling small holes (i.e. pressure taps) along the airflow path and using multi-tube manometers to measure the pressure at each hole. Pressure distributions can more conveniently be measured using pressure-sensitive paint, in which higher local pressure is indicated by lowered fluorescence of the paint at that point. Pressure distributions can also be conveniently measured using pressure-sensitive pressure belts, a recent development in which multiple ultra-miniaturized pressure sensor modules are integrated into a flexible strip. The strip is attached to the aerodynamic surface with tape, and it sends signals depicting the pressure distribution along its surface, [15].

The main results obtained from pressure tests is the pressure coefficients that depend on the building shape and the turbulence flow. The experimental data are time histories and stationary processes. Many codes [16-17] suggest assuming the mean value of the pressure coefficient time history as a representative value for the wind action estimation. It is because codes assuming that the random processes acquired in wind tunnel are gaussian [18] and consequently, the distribution of values is centered around the mean value. However, several studies have shown that in many cases, processes acquired in wind tunnel are not Gaussian, [19-23] and the skewness and kurtosis of the process are not negligible [24]. For these cases the mean value can be not representative of the phenomenon. Another important statistic parameter of a random process is the absolute maximum that depends on the peak factor that in turn depends on the time length of the process. The peak factor can be predicted analytically through models that assume that the process is Gaussian [18] or not-Gaussian [25-31]. This is a hot topic in the scientific literature because codes suggest the common value of the peak factor of 3.5 that is commonly smaller than the experimental value.

This paper discusses the statistics of random processes acquired in wind tunnel during different experimental campaign on roofs and bridge sections. The pressure coefficients time histories peak factors are plotted comparing to the 95% level of confidence given by [18] and the number of Gaussian and non-Gaussian processes were compared.

## 2 RANDOM PROCESSES STATISTICS

In this paper two set of pressure coefficients time histories are discussed. The first one consists of pressure coefficients time histories acquired on hyperbolic paraboloid roofs given by [21] (Fig.1) and the second one consists of pressure coefficients time histories acquired on closed box section of suspended bridges (Fig.2).

The experimental campaign of hyperbolic paraboloid roofs discussed by [21] consists of sixteen different geometries of hyperbolic paraboloid roofs with different plan shape (i.e. square, rectangular, circular, and elliptical), two different curvature (i.e. more curved and flatter) and two different heights (i.e. tall and low). All geometries were tested in wind tunnel to acquire pressure coefficients subsequently published in [16]. Models were equipped with pressure taps (Fig.1) connected to pressure scanners.



Figure 1: Pressure taps tubes on a large span roof test model.

Pressure taps were located on the model external surfaces and more thickly along edges where the flow detachment occurs. In these zones the pressure coefficient is generally bigger than elsewhere for both values, the mean, and the peak value. In these zones the processes are generally non-Gaussian [19].

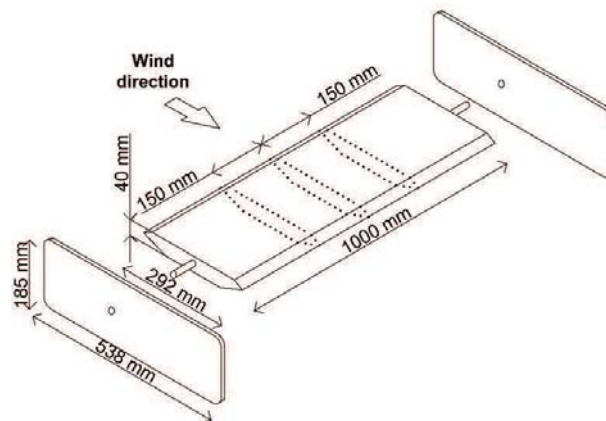


Figure 2: Test model setup for a closed box section model [6, 13].

The pressure coefficients time histories were analysed to estimate the Gaussianity observing the empirical cumulative density function (ECDF), the skewness and the excessive kurtosis of the processes.

If the ECDF of the local peaks of the random process is fitted by a Rayleigh distribution, the processes is Gaussian [18]. Otherwise, if the ECDF of the local peaks is fitted by a Weibull distribution it corresponds to a non-Gaussian condition.

According to [24] the roof regions where the pressure coefficient process is non-Gaussian are identified by the skewness bigger than 0.5 and/or the excessive kurtosis bigger than 0.5.

### 3 GAUSSIAN AND NON-GAUSSIAN PROCESSES

In this study the assumption given by [24] was assumed to select Gaussian and non-Gaussian processes. They were compared with the 95% level of confidence of the Davenport peak factor [18-19], for two set of data, pressure coefficients time history of hyperbolic paraboloid roofs [20] (Figs. 3-5) and of an example of closed box section for suspended pedestrian bridge [6, 13] (Fig.6). In Figs. 3-6, graphs show the peak factor  $g_p$  for each pressure taps #, gray continues line means the 95% Davenport level of confidence [18], green squared dot means non-Gaussian processes and finally red dot means Gaussian processes.

Figures 3 show a comparison between a flutter (Fig.3a) and a more curved (Fig.3b) roofs and it was observed that the curvature promotes the non-Gaussian processes decreasing.

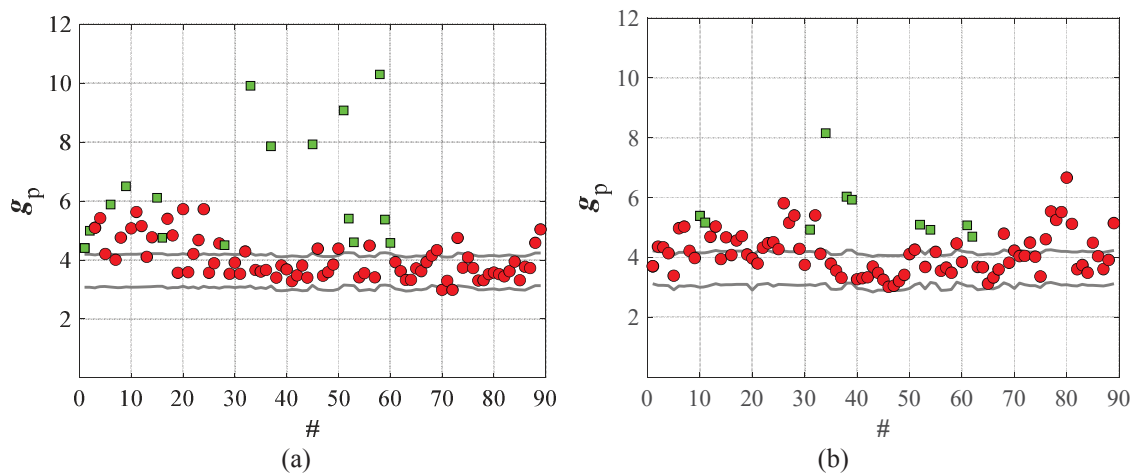


Figure 3: Gaussian and non-Gaussian processes for hyperbolic paraboloid roof: comparison between flatter (a) and more curved (b) roof.

Figure 4 shows a comparison between low (Fig.4a) and tall (Fig.4b) building covered with a hyperbolic paraboloid roof. It was observed that the building height slightly increase the number of non-Gaussian processes.

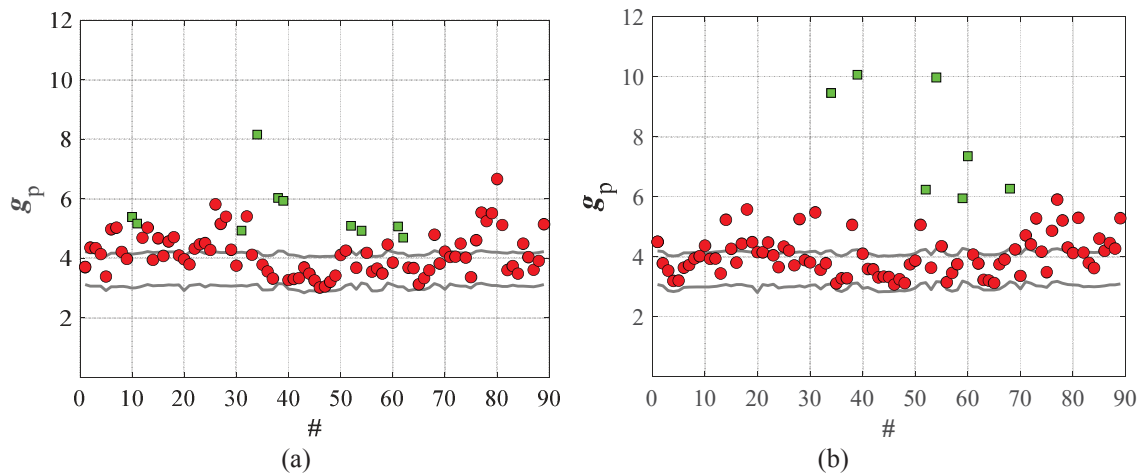


Figure 4: Gaussian and non-Gaussian processes for hyperbolic paraboloid roof: comparison between low (a) and tall (b) building.

Figure 5 shows a comparison between two wind angles,  $0^\circ$  (Fig.5a) and  $90^\circ$  (Fig.5b). For the wind angle equal to  $0^\circ$  the flow is parallel to cables with a downward curvature, for the wind angle equal to  $90^\circ$  the flow is parallel to cables with an upward curvature. It was observed that the wind direction closely affects the Gaussianity. Fig.5b shows that the number of non-Gaussian process for  $90^\circ$  is bigger than  $0^\circ$ .

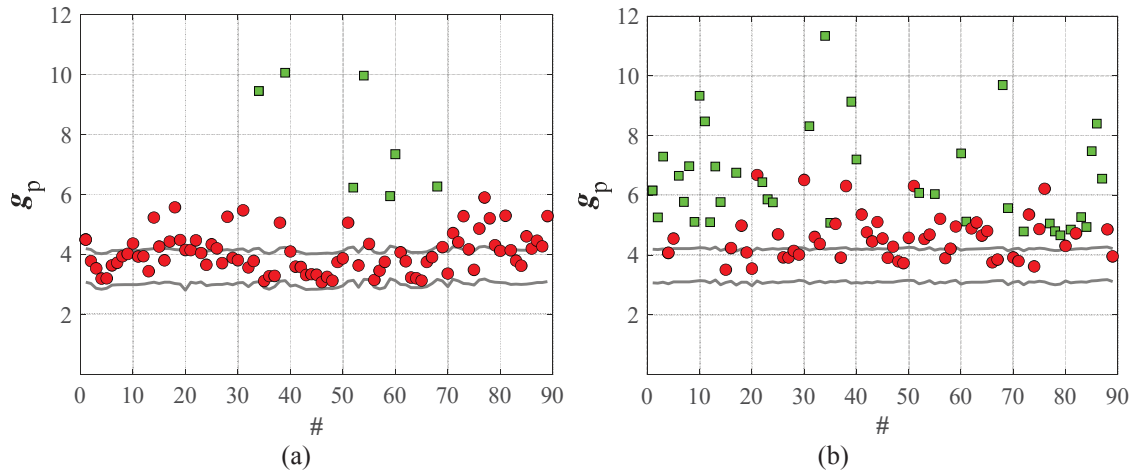


Figure 5: Gaussian and non-Gaussian processes for hyperbolic paraboloid roof: comparison between wind angle equal to  $0^\circ$  and  $90^\circ$ .

Figure 6 shows results for a closed box section (Fig.2) with two angles of attack,  $-10^\circ$  and  $0^\circ$ , respectively. Results show a very relevant difference between the two configurations (Fig.6a and Fig.6b). The number of Gaussian process decreases from  $-10^\circ$  to  $0^\circ$  due to the aerodynamics.

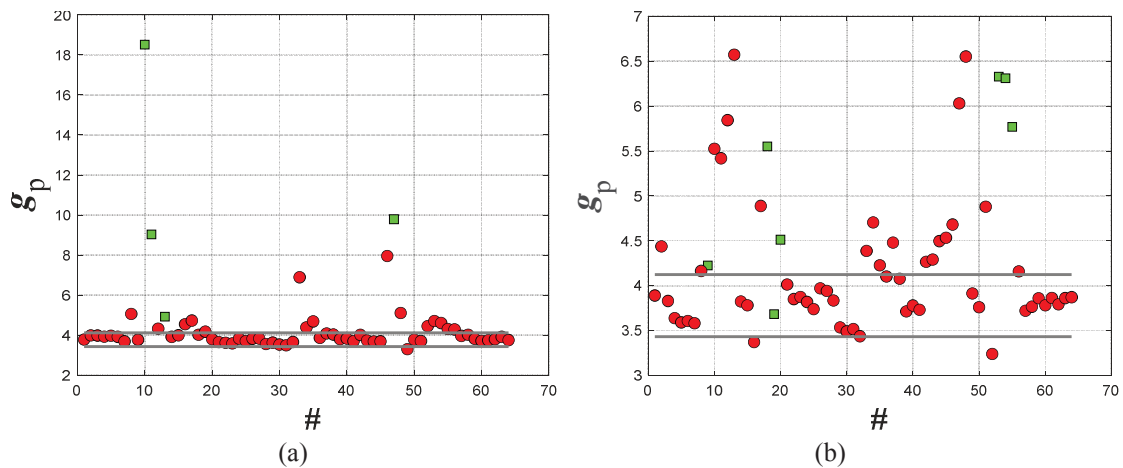


Figure 6: Gaussian and non-Gaussian processes for closed box bridge section: comparison between angle of attack equal to  $-10^\circ$  (a) and  $0^\circ$  (b).

## 4 CONCLUSIONS

The Gaussianity of random processes was investigated on different geometries of roofs and closed box section with different angle of attack. It was observed that:

- For roofs the curvature affects the number of Gaussian processes that increases for flatter roofs.

- The building height is not relevant in term of number of non-Gaussian processes for the geometry investigated.
- The wind direction closely affect the number of non-Gaussian processes for roofs with a double curvature (i.e. Hyperbolic paraboloid roofs) and during the oscillation of a closed box section for a suspended pedestrian bridge.

Data have shown that non-Gaussian processes are mostly located near edges and near the detachment zones. For these zones the davenport peak factor is not reliable because it underestimates the peaks of the random processes.

## REFERENCES

- [1] F. Rizzo, V. Sepe, F. Ricciardelli, A. M. Avossa, Wind pressures on a large span canopy roof'. *Wind and Structures and International Journal*, 30(2): 000-000 DOI: <https://doi.org/10.12989/was.2020.30.2.000>, 2020.
- [2] F. Rizzo, P. Zazzini, Shape dependence of acoustic performances in buildings with a Hyperbolic Paraboloid cable net membrane roof. *Journal of Acoustics Australia*, 45 (2), 2017.
- [3] F. Rizzo, P. Zazzini, Improving the acoustical properties of an elliptical plan space with a cable net membrane roof. *Journal of Acoustics Australia*, 44, 449-456, 2016.
- [4] F. Rizzo, V. Sepe, Static loads to simulate dynamic effects of wind on hyperbolic paraboloid roofs with square plan, *Journal of Wind Engineering & Industrial Aerodynamics*, 137, 46-57, 2015.
- [5] J. Chilton, Tensile Structures-Textiles for Architecture and Design. In: Pöhl G. ed. *Textile Polymers and Composites for Buildings*. Woodhead Publishing Limited, Cambridge, England (UK), 229–257, 2010.
- [6] F. Rizzo, V. D'Alessandro, S. Montelpare, L. Giammichele, Computational study of a bluff body aerodynamics: impact of the laminar-to-turbulent transition modelling. *International Journal of Mechanical Sciences*, 178, 15, 105620, 2020.
- [7] A. Maria Avossa, D. Di Giacinto, P. Malangone and F. Rizzo, Seismic Retrofit Of A Multi-Span Prestressed Concrete Girder Bridge With Friction Pendulum Devices. *Shock and Vibration*, 2018, Article ID 5679480, 2018.
- [8] F. Rizzo, G. Di Lorenzo, A. Formisano, R. Landolfo, A time-dependent corrosion wastage model for Wrought iron Structures. *ASCE's Journal of Materials in Civil Engineering*, 31(8): 04019165, 2018.
- [9] F. Rizzo, F. Ricciardelli, G. Maddaloni, Bonati A., A. Occhiuzzi, Experimental error analysis of dynamic properties for a reduced-scale high-rise building model and implications on full-scale behavior. *Journal of Building Engineering*, 28, 2020.
- [10] F. Rizzo, A. G. Kopp, G. Giaccu, Investigation of wind-induced dynamics of a cable net roof with aeroelastic wind tunnel tests. *Engineering Structures*, 229, 111569, 2021.
- [11] I. Vassilopoulou, C.J. Gantes, Nonlinear dynamic behavior of saddle form cable nets under uniform harmonic load. *Engineering Structures*, 33(10), 2762-2771, 2011.
- [12] I. Vassilopoulou, C.J. Gantes, Vibration modes and natural frequencies of saddle form cable nets. *Computers and Structures*, 88(1-2), 105-119, 2012.



- [13] F. Rizzo, L. Caracoglia, Artificial Neural Network model to predict the flutter velocity of suspension bridges. *Computers and Structures*, 233 (2020) 1062362020.
- [14] Letchford C.W., Denoon R.O., Johnson G., Mallam A., 2002. Dynamic characteristics of cantilever grandstand roofs. *Engineering Structures*, 24(8), 1085-1090.
- [15] Going with the flow, Aerospace Engineering & Manufacturing, March 2009, 27-28 Society of Automotive Engineers.
- [16] National Research Council of Italy (CNR), 2018. Guide for the Assessment of Wind Actions and Effects on Structures. CNR-DT 207/2018, Rome (Italy).
- [17] European Committee for Standardization (CEN), 2005. Eurocode 1: Actions on Structures - Part 1-4: General Actions - Wind Actions. EN-1991-1-4, Brussels (Belgium).
- [18] Davenport A.G., 1964. Note on the distribution of the largest value of a random function with application to gust loading. *Institution of Civil Engineering*, 28(2), 187-196.
- [19] F. Rizzo, M. Barbato, V. Sepe, Peak factor statistics of wind effects for hyperbolic paraboloid roofs. *Engineering Structures*, 173, 313-330, 2018.
- [20] F. Rizzo, C. Demartino, Pressure modes for hyperbolic paraboloid roofs. *Curved and Layer Structure*, 7, 1-21, 2021.
- [21] F. Rizzo, Wind tunnel random processes statistics of pressures on a large span canopy roof. *Iranian Journal of Science and Technology, Transactions of Civil Engineering*, 10.1007/s40996-020-00458-x, 2020.
- [22] J. Colliers, J. Degroote, M. Mollaert, L. De Laet, Mean pressure coefficient distributions over hyperbolic paraboloid roof and canopy structures with different shape parameters in a uniform flow with very small turbulence. *Engineering Structures*, 205, 110043, 2020
- [23] J. Colliers, M. Mollaert, J. Vierendeels, L. De Laet, Collating wind data for doubly-curved shapes of tensioned surface structures (Round Robin Exercise 3). *Procedia Engineering*, 155, 152-162, 2016.
- [24] K. Suresh Kumar, T. Stathopoulos, Wind loads on low building roofs: a stochastic perspective. *Journal of Structural Engineering*, 126(8), 944-956, 2000.
- [25] K.R. Gurley, M.A. Tognarelli, A. Kareem, Analysis and simulation tools for wind engineering. *Probabilistic Engineering Mechanics*, 12(1), 9-31, 1997.
- [26] M.F. Huang, W. Lou, C.M. Chan, N. Lin, X. Pan, Peak distributions and peak factors of wind-induced pressure processes on tall buildings. *Journal of Engineering Mechanics*, 139(12), 1744-1756, 2013.
- [27] C.G. Huntington. The Tensioned Fabric Roof. American Society of Civil Engineers (ASCE), Reston, VA (USA) , 2004.
- [28] C.G. Huntington, Tensile Fabric Structures. Design, Analysis, and Construction. American Society of Civil Engineers (ASCE), Reston, VA (USA) , 2013.
- [29] A. Kareem, J. Zhao, Analysis of non-Gaussian surge response of tension leg platforms under wind loads. *Journal of offshore Mechanics and Arctic Engineering*, 116(3), 137-144, 1994.



- [30] D. Kwon, A. Kareem, Peak factors for non-Gaussian load effects revisited. *Journal of Structural Engineering*, 137(12), 1611-1619, 2011.
- [31] M. Liu, X. Chen, Q. Yang, Characteristics of dynamic pressures on a saddle type roof in various boundary layer flows. *Journal of Wind Engineering and Industrial Aerodynamics*, 150, 1–14, 2016.
- [32] M. Liu, X. Chen, Q. Yang, Estimation of peak factor of non-Gaussian wind pressures by improved moment-based Hermite model. *Journal of Engineering Mechanics*, 143(7):06017006, 2017.

## RANDOM PROCESS PEAKS PREDICTION: A LITERATURE OVERVIEW

Di Giovanni M.<sup>1\*</sup>, D'Asdia P.<sup>2</sup>

<sup>1</sup> University G. D'Annunzio, School of Engineering, viale Pindaro 42, 65127, Pescara,  
e-mail: [dgm.studio@outlook.it](mailto:dgm.studio@outlook.it), corresponding author

<sup>2</sup> University G. D'Annunzio, School of Engineering, viale Pindaro 42, 65127, Pescara,  
e-mail: [pierodasdia@gmail.com](mailto:pierodasdia@gmail.com)

---

### Abstract

*The prediction of the maximum or minimum peaks of a random process in the fields of civil and mechanical engineering is a hot topic for the scientific literature. It is known that the maximum of a random process depends on the process length. For this reason, a probabilistic approach is necessary to estimate a reliable value from the process. Researchers for specific case of studies proposed several analytical models to predict maxima of a random process. Mostly, they are grouped on two families, models for Gaussian processes and models for non-Gaussian processes. Each model was computed and calibrated based on a specific experimental campaign for a specific case of study. This makes difficult to select the best model for every application. In addition, codes and standards neglect this topic and one might happen to make the error to assume the maximum value as the statistical maximum of the random process. Commonly, in the field of the structural engineering, peaks of a wind induced, or wind-induced flow acceleration time histories are estimated following the probabilistic approach of Cook and Mayne. However, from 1950 to today hundreds different probabilistic approach was given by literature. The purpose of this paper is to discuss an overview of models grouped by theoretical underlying assumptions.*

**Keywords:** Random processes, Gaussianity, stochastics, peak factors, wind tunnel.

---

## 1. INTRODUCTION

In the field of wind engineering the experimental tests in wind tunnel are the rule to investigate the building aerodynamics. In wind tunnel random processes of pressure are acquired through pressure taps and tubes located on the building surfaces. Generally, the main result that it is estimated is the pressure coefficient that is dimensionless respect to the wind tunnel velocity. In wind tunnel, processes generally are stationary, and the mean value does not depend on the history time length. However, the mean value of the pressure coefficient time history is not the only one parameter that is important for the building structural analyses. In many cases the most important magnitude is the maxima or minima peak of the random process that are closely important to design structure very sensitive to the wind action differently than structure sensitive to the seismic action [1]. This is a hot topic for the scientific literature in the fields of civil and mechanical engineering. Unfortunately, the absolute maximum (or minimum) of a random process depends on the process time length. Usually, a probabilistic approach is used to estimate a reliable maximum (or minimum) value from the process and several analytical models were proposed by the scientific literature. Mostly, they are grouped on two families, models for Gaussian processes and models for non-Gaussian processes. Each model was computed and calibrated based on a specific experimental campaign for a specific case of study and this makes difficult to select the best model for every application. The purpose of this paper is to discuss an overview of models grouped by theoretical underlying assumptions.

## 2. LITTERATURE OVERVIEW

### *2.1 From Cartwright and Longuet-Higgin, 1956 to Vanmarcke, 1975, through Davenport, 1964.*

One of the first analytical model computed to predict extreme peaks used the field of wind engineering is given by [2] (more recently developed by [3]) and it was computed to predict the peaks of the sea waves. It is based on the assumption that the process is stationery and Gaussian and that the maxima follow a Rayleigh distribution. Starting from this model, Davenport [4], developed the most used model to predict the peak factors of Gaussian processes. It was based on the assumption that largest extreme values of a Gaussian normalized and standardized process, asymptotically follow a Gumbel distribution. This model still today to be the base of all analytical models to predict extreme peaks. About ten year later, [5] accounting for the dependence among the crossing events through a shape factor calculated from the process spectral moments. Unlike Davenport's peak factor, Vanmarcke's [5], peak factor can be applicable to narrow-band response processes while taking consideration of the spectral bandwidth effects [6,7]. Several studies, also recently, have proposed method to extend the [4] and its subsequent updates to non-Gaussian processes, as for example [8] that proposed the extended Davenport peak factor (EDPF). This method relates the descriptors of the resultant, the parameters of the distribution function of the peaks, and the probability of not exceeding a given threshold, however the method seems to have be limited and poorly generalizable.

### *2.2 From Cook and Mayne 1979 to Harris, 2005*

From 1979 to today, the studies published by Cook are a milestone because they proposed a working approach based on a fully probabilistic assessment (i.e. the Gumbel distribution of extremes) to estimate wind loads for the equivalent static design of structures [9, 10]. This approach was born with the precise intent to fill a gap in codes and consequentially it is very

sample. This approach was proposed in [11] and refined in [12] in which the previous approach is extended from the original first-order form, to admit multiple-order corrections through a Monte-Carlo method that replaces the former integral method. This method is still very often used in the field of structural wind engineering [13]. The design fractile of extreme wind load coefficient distribution for a 50-year return period is recommended equal to 79%. According to [14] this value can be increased to 93% to estimate the extremes of the wind velocity, based on the multi-order technique applied by authors.

In Cook, 1982 [15], Cook proposed the peak-factor approach that aims to exceed the limits of the fully probabilistic approach, given by [11], for which fluctuations of load are due to corresponding gusts in the approach flow. These numerical approaches will feed in the designer's guide to wind loading of building structures, Parts 1 and 2 [16, 17]. These methods were based on the assumption that the process is stationary, and this hypothesis is one of the weaknesses on which [18] worked. It has given an extension of the methods given by Cook, to full-scale wind-load measurements where the flow is intrinsically non-stationary. Harris, 1982 [19] provides the [15] theoretical background fully probabilistic approach (i.e. based on the Gumbel distribution of the extremes). It proposed the elimination of the Monte-Carlo corrections, the will be widely used by researchers, as for example [20] that have used this method to estimates peak wind pressures on three-dimensional rectangular buildings with different aspect and side ratios in different atmospheric boundary layers.

Harris will develop the traditional Gumbel extreme value method in [21] through a fitting procedure using weighted least squares that improves set of plotting positions based on the mean values of the order statistics and subsequently, through a direct method given by [22]. This last method does not require Monte-Carlo simulations or the assumption that extreme pressures conform to the ultimate Fisher-Tippett Type I asymptote.

### *2.3 From Holmes and Moriarty, 1999 to Torrielli et al, 2016 through modification of the Cook and Mayne 1979 model*

Several approaches have discussed modification and updates of the [11, 12] approach focused on the probability trend of the extremes in a random process.

The important issue of the extreme peaks of the wind velocity discussed by [23] have inspired [24-26] that have applied the Annual Rate of Independent Events (ARIE) method values, though its modification, to estimate the extremes wind velocity, subsequently discussed for clarification by [27, 28] and [29]. The modification consists on using the Hybrid Weibull model given by [30], to describe the parent distribution of the wind velocity simulations.

Holmes and Moriarty, 1999 [31] proposed the generalized Pareto distribution (GPD) and its application to the statistical analysis of extreme wind speeds. It concluded that generalized extreme value distribution (GEVD) can be used to determine the appropriate value of shape factor,  $k$ , for use in the GEVD. In 2001, [32] and [33] not recommend this approach and discussed the conclusion given by [31], because this method is closely threshold dependent and so not applicable for a process with a Weibull parents. However, [34] confirm the goodness of this method using many and very long acquisitions of pressure series in wind tunnel experiments on a low-rise building as similarly it was done by [35].

Similarly, the Peaks-Over-Threshold (POT) is also affected by limits given by the practical applications of POT method as it was shown by [36]. An and Pandey, 2005 [36] shown that this model fail because the acute threshold sensitivity of wind speed estimates, which can be attributed to erratic variation of model and sampling errors with selected threshold values. In addition, [36], based on results given by [37], proposed a modification based on the assignment of an exponential prior on preconditioned data that is augmented with additional sample information in an optimal sense through the principle of Minimum Cross-Entropy (Cross-

Ent). An update of the POT method was proposed by [38] through a declustering of process to extract independent peaks over a given threshold. for POT method and [39].

#### *2.4 From Grigoriu 1984 to Kwon and Kareem, 2011, though Winterstein models.*

Meanwhile, [40] discussed the mean up-crossing rates for Gaussian and non-Gaussian processes, laying the groundwork for future analytical models that aim to predict extremes of non-Gaussian processes, as for example the analytical models given by [41, 42] and the chaos polynomial theory of which some applications are discussed by [43, 44]. This approach was largely used by researcher through application, as for example by [45, 46] or to develop new models. Winterstein proposed a nonlinear vibration approach using the Moment-based Hermite model to predict extremes of a random vibration, subsequently applied in [47] on a statistical analysis of tension-leg platforms. Kareem and Zhao 1994 [48] developed the model applied by [47]. The given improvement consists of an equivalent statistical quadratization method that permits to derive the response probability density function, crossing rates, and peak value distribution based on the first four cumulants. The method was known as revised Hermite model [49, 50].

This method was developed by [51] using a limited number of statistical moments. Subsequently the model given by [47] and based on the an equivalent statistical quadratization method was developed using a cubicization in [52]. Depending upon the nature of the nonlinearity, the quadratization and the cubicization method may be employed to approximate the process by a quadratic or cubic polynomial. It permits to preserve the nonlinearity using a Volterra functional series approach to attain the response transfer functions. The models is known as modified Hermite model [49]. The distribution of the largest peak values is assumed as a Gumbel distribution, which implies a Weibull distribution for the local peaks of the pressure coefficients.

Yang et al, 2013 [53] proposed a modification of modified Hermite model given by [52] and [54] has given an application. The modification proposed by [53] consists on a numerical inversion of the relationship between skewness, kurtosis and the Hermite model shape parameters and on an approximate solution to improve the accuracy of the Hermite model.

The peak factor for non-Gaussian processes given by [48], was used by [55] to simulate non-Gaussian processes in terms of correlation-distortion methods and application of higher-order spectral analysis. Similarly, the model given by [48] was used to Kareem et al 1998, that developed a technique to model the contribution of the quadratic drag term containing the square of the fluctuating velocity component through the development of a non-Gaussian gust loading factor via moment-based Hermite transformation. This model was based on the concept of a translation process given by [40], moment-based Hermite model given by [42], and the framework of Gaussian peak factor given by [4]. Thirteen years later, after [51] updates, [49] completed the model and it gives the variance of the estimates in standard deviation for the peak factor of non-Gaussian processes on the basis of a moment-based Hermite model [41, 42].

Later, [56] proposed the “L-Hermite” model, an alternative cubic transformation calibrated by the response “L-moments” rather than its ordinary statistical moments. However, this method seems valid only for specific cases of study as for example marine structures in shallow waters [57], because it cannot convey sufficient information to accurately estimate extreme response statistics. The Winterstein, 1988 [42] and 2000 [51] models were developed by [58] to improve their accuracy and simplify their application to measured data in the case of wind pressure data. In particular, [58] proposed a closed form approximate relationship between the skewness and kurtosis and the Hermite models shape

parameters. Based on its results, it suggests that the bandwidth parameter related to the 4th-order spectrum moment should not be introduced.

Several papers proposed new models based on the moment-based Hermite polynomial model as for example the model proposed by [59] that modify the Hermite polynomial method to obtain accurate approximation of extremes of processes with high skewness and Gaussian kurtosis. Many models promoted the Hermite polynomial model to transform non-Gaussian data into a Gaussian process. Huang et al 2016 [60, 61] results suggest that Hermite moment-based should be adopted in the peak value estimation for wind pressures only when the skewness and kurtosis of a process are sufficient to capture its non-Gaussian properties. However, Cook, 2016 [62] refuted these results applying the Bootstrapping methods (EVA ) [63].

Liu et al, 2016 and 2017 [64, 65] proposed a model that aims to solve the problem given by the positive and negative probability distribution tails that affect skewness and kurtosis are statistical moments. To improve the accuracy of the moment-based model approach, it derived a new moment-based translation model by defining a modified probability density function that is symmetric around the median of the original non-Gaussian process. Accordingly, the distributions of maximum and minimum are addressed separately using newly defined two sets of statistical moments with zero skewness. Rizzo et al, 2018 [50] have shown that for strongly non-Gaussian processes this method is not particularly accurate. Rizzo et al, 2018 [50] have given an application of the modified Hermite models on Hyperbolic paraboloid roofs [66-70].

### *2.5 From Sadek and Simiu, 2002 to Huang M. F. et al 2016*

The theory proposed by [71] was innovative because it proposed an automated mapping procedure to estimate the peak distribution of wind-induced non-Gaussian internal forces on low-rise buildings by using a database-assisted design software. This mapping procedure requires identifying an analytical marginal probability distribution for the time series of interest through numerical fitting of the distribution parameters. However, the Sadek and Simiu, 2002 [71] method has been applied only to non-Gaussian processes with an underlying marginal gamma distribution [50]. The result obtained is that a gamma distribution (i.e. three-parameter Gamma distribution) is appropriate for estimating the peaks corresponding to the longer tail of the time series' histograms and a normal distribution corresponding to the shorter tail of the time series' histograms, that are the same conclusions shown by [72]. The distribution of the peaks is then estimated by using the standard translation processes approach given by [40] and developed in [73]. It is found that the peak distribution can be represented by the Gumbel distribution. The estimation obtained through this approach is based on the entire time series and consequently it is more reliable than estimation based only on observed peaks. However, the three-parameter Gamma distribution specific relationship between skewness and kurtosis holds. Once the combinations of skewness and kurtosis of actual samples deviate far away from the relationship, remarkable fitting errors will be incurred [74]. Ma and Xu, 2017 [74], proposed an update of the Gamma method through the Johnson transformation to solve the fitting error. This method depends on the maximum likelihood (MML) [75] to estimate the Johnson transformation parameters.

Using the [71] procedure, [76, 77], estimated the extreme peak pressure distribution based on wind-induced time history pressure data recorded in a wind tunnel and determined the design pressure and load coefficients at any selected probability level of non-exceedance for reliability-based structural design. Recently, Yang et al, 2019 [75] proposed an update using a three-parameter Gamma distribution through formulations for estimating sampling errors of the first four statistical moments.



Based on the [71] results, [6] proposed the Gamma peak factor and it have applied this approach to estimate the wind-induced vibration on tall buildings. This study is one of the few studies that worked on accelerations, discussed in this paper, differently than pressure or wind velocity. For this reason, this contribute will be carefully discussed in the next sections.

From Sadek and Simiu, 2002 [71], Huang et al 2013 [78] and [79], gives an efficient model known as translated-peak-process method (TPP) for the estimation of the peak distribution, peak factor, and variability of extremes, based on the Weibull distribution and point-to-point mapping procedure. The innovation consists on a modification of the [71] from Gamma to Weibull distribution processes [50] and it is particularly efficient for non-Gaussian process. However, it needs to an elaboration of the measured data to fit a Weibull distribution that take only positive bigger than zero values.

### *2.6 Analytical models based on the ACER approach*

The univariate concept of average conditional exceedance rate (ACER) is a method for estimation of extreme wind speed statistics proposed by [80] and by [81] that have given an extension for estimation of extreme wind speed statistics to the case of bivariate wind speed time series based on the previous research on the Monte Carlo methods for estimating the extreme response of dynamic systems [82, 83]. Naess and Karpa, 2015 [81] calibrated and tested the bivariate method for simultaneous wind speed measurements from two separate locations. The univariate approach is based on two separate components: the first component has the capability to accurately capture and display the effect of statistical dependence in the data; the second component is then constructed so as to make it possible to incorporate to a certain extent also the subasymptotic part of the data into the estimation of extreme values [80]. The goodness of this analytical method was confirmed by [84] and it was used by the models developed by [85] and [86]. Finally, Chen, 2014 [87] proposed a model that, based on results given by [88], through the curve-fitting and extrapolation of crossing rate, permits the estimation of extreme values distribution using Poisson distribution of crossings.

## **3. CONCLUSIONS**

This paper discusses the most common analytical models to predict peaks (i.e. local and absolute) from random processes. Models are grouped based to milestones and specifically they are grouped in five families: (I) models for Gaussian process; (II) models from Cook school, (III) models based on Grigoriu studies; (IV) models based on the Sadek and Simiu studies and finally, (V) recent models based on the ACER approach. It is not possible to a priori estimate the best model for a specific case of study investigated and all models are valid until proven otherwise.

## **4. ACKNOWLEDGMENTS**

Professor Mingfeng Huang and Doctor Fabio Rizzo is gratefully acknowledged for sharing data and comments [89].

## **REFERENCES**

- [1] A. Maria Avossa, D. Di Giacinto, P. Malangone and F. Rizzo, Seismic Retrofit Of A Multi-Span Prestressed Concrete Girder Bridge With Friction Pendulum Devices. *Shock and Vibration*, 2018, Article ID 5679480, 2018.

- [2] D.E. Cartwright, M.S. Longuet-Higgins. Statistical distribution of the maxima of a random function. *Proceedings of the Royal Society of London. Series A, Mathematical and Physical Sciences*, 237(1209), 212-232, 1956.
- [3] S.N. Pillai, Y. Tamura, Generalized peak factor and its application to stationary random processes in wind engineering applications. *Journal of Wind and Engineering and Industrial Aerodynamics*, 6(1), 1-9, 2009.
- [4] A.G. Davenport, Note on the distribution of the largest value of a random function with application to gust loading. *Proceedings of the Institution of Civil Engineering*, 28(2), 187-196, 1964.
- [5] E.H. Vanmarcke, Properties of spectral moments with applications to random vibration. *Journal of Engineering Mechanics*, 98(EM2):425-446, 1972.
- [6] M. Huang, C. M. Huang, C. M. Chan, L. ChanWen-juan, K. Chung-Siu, Statistical extremes and peak factors in wind-induced vibration of tall buildings. *Journal of Zhejiang University - Science A: Applied Physics and Engineering* 13(1),18-32, 2012.
- [7] X. Wang, E.M. Rathje, Influence of Peak Factors on Random Vibration Theory Based Site Response Analysis. 6th International Conference on Earthquake Geotechnical Engineering 1-4 November 2015 Christchurch, New Zealand, 2015.
- [8] P. Folgueras, S. Solari, M. Mier-Torrecilla, M. Doblaré, M. Losada, The extended Davenport peak factor as an extreme-value estimation method for linear combinations of correlated non-Gaussian random variables. *Journal of Wind Engineering and Industrial Aerodynamics*, 157, 125-139, 2016.
- [9] F. Rizzo, V. Sepe, F. Ricciardelli, A. M. Avossa, Wind pressures on a large span canopy roof. *Wind and Structures and International Journal*, 30(2): 000-000 DOI: <https://doi.org/10.12989/was.2020.30.2.000>, 2020.
- [10] F. Rizzo, V. Sepe, Static loads to simulate dynamic effects of wind on hyperbolic paraboloid roofs with square plan, *Journal of Wind Engineering and Industrial Aerodynamics*, 137, 46-57, 2015.
- [11] N. J. Cook, J. R. Mayne, A novel working approach to the assessment of wind loads for equivalent static design. *Journal of Wind Engineering and Industrial Aerodynamics*, 4(2), 149-164.17:29 30/03/2020, 1979.
- [12] N.J. Cook, J.R. Mayne, A refined working approach to the assessment of wind loads for equivalent static design, *Journal of Wind Engineering and Industrial Aerodynamics*, 6(1-2), 125-137, 1980.
- [13] M. Xia, C.S. Cai, F. Pan, Y. Yu, Estimation of extreme structural response distributions for mean recurrence intervals based on short-term monitoring, *Engineering Structures*, 126, 121-132, 2016.
- [14] H. Yi, Y. Tamura, Q. Yang. Technical Papers: Estimation of Extreme Wind Load on Structures and Claddings. *Journal of Engineering Mechanics*,143(9), 2017.
- [15] N.J. Cook, Calibration of the quasi-static and peak-factor approaches to the assessment of wind loads against the method of Cook and Mayne. *Journal of Wind Engineering and Industrial Aerodynamics*, 10(3), 315-341, 1982.

- [16] N.J. Cook, The designer's guide to wind loading of building structures. Part 1: Background, damage survey, wind data and structural classification. Building Research Establishment, Butterworths, U.K, 1985.
- [17] N.J. Cook, The designer's guide to wind loading of building structures. Part 2: Static structures. Building Research Establishment, Butterworths, U.K, 1990).
- [18] Hoxey R. P., Richards P. J., Richardson G.M., Robertson A. P., Short J.L., 1996. The folly of using extreme-value methods in full-scale experiments. *Journal of Wind Engineering and Industrial Aerodynamics*, 60, 109-122.
- [19] R. I. Harris, An improved method for the prediction of extreme values of wind effects on simple buildings and structures. *Journal of Wind Engineering and Industrial Aerodynamics*, 9(3), 343-379, 1982.
- [20] J. Wacker, E.J.M. Plate, Local peak wind pressure coefficients for cuboidal buildings and corresponding pressure gust factors. *Journal of Wind Engineering and Industrial Aerodynamics*, 50, 183-192, 1993.
- [21] R.I. Harris, Gumbel re-visited - a new look at extreme value statistics applied to wind speeds. *Journal of Wind Engineering and Industrial Aerodynamics*, 59 (1996) 1-22, 1996.
- [22] R. I. Harris, Extreme value analysis of epoch Maxima-convergence, and choice of asymptote. *Journal of Wind Engineering and Industrial Aerodynamics*, 92, 897-918, 2004.
- [23] R. I. Harris, A new direct version of the Cook-Mayne method for wind pressure probabilities in temperate storms. *Journal of Wind Engineering and Industrial Aerodynamics*, 93, 581-600, 2005.
- [24] A. Torrielli, M. P. Repetto, G. Solari, The annual rate of independent events for the analysis of extreme wind speed. *Journal of Wind Engineering and Industrial Aerodynamics*, 156, 104-114, 2016.
- [25] A. Torrielli, M. P. Repetto, G. Solari, Response to the Discussion on The annual rate of independent events for the analysis of extreme wind speed, by R. Ian Harris. *Journal of Wind Engineering and Industrial Aerodynamics*. 164, 179-181, 2017.
- [26] A. Torrielli, M. P. Repetto, G. Solari, Discussion Response to the further discussion on The annual rate of independent events for the analysis of extreme wind speed, by N. Cook. *Journal of Wind Engineering and Industrial Aerodynamics*, 174, 464-465, 2018.
- [27] R.I. Harris, N.J. Cook, The parent wind speed distribution: Why Weibull? *Journal of Wind and Engineering and Industrial Aerodynamics*, 131, 72-87, 2014.
- [28] R. I. Harris. Discussion of The annual rate of independent events for the analysis of extreme wind speed By Alessio Torrielli, Maria Pia Repetto and Giovanni Solari. *Journal of Wind Engineering and Industrial Aerodynamics*, 164, 174-178, 2017.
- [29] N.J. Cook. Further discussion of The annual rate of independent events for the analysis of extreme wind speed by A. Torrielli, M. P. Repetto and G. Solari. *Journal of Wind Engineering and Industrial Aerodynamics*, 174, 458-463, 2018.
- [30] E.S. Takle, J.M. Brown, Note on the use of Weibull statistics to characterize wind speed data. *Journal of Applied Meteorology*, 17, 556-559, 1978.

- [31] J. D. Holmes, W.W. Moriarty, Application of the generalized Pareto distribution to extreme value analysis in wind engineering. *Journal of Wind Engineering and Industrial Aerodynamics*, 83(1–3), 1–10, 1999.
- [32] N. J. Cook, R. I. Harris, Discussion on Application of the generalized Pareto distribution to extreme value analysis in wind engineering by Holmes J.D., Moriarty W.W. *Journal of Wind Engineering and Industrial Aerodynamics* 89, 215–224, 2001.
- [33] R. I. Harris, Generalized Pareto methods for wind extremes. Useful tool or mathematical mirage? *Journal of Wind Engineering and Industrial Aerodynamics* 93(5), 341–360, 2001.
- [34] J.D. Holmes, L.S. Cochran, Probability distributions of extreme pressure coefficients. *Journal of Wind Engineering and Industrial Aerodynamics* 91, 893–901, 2003.
- [35] C. Sacré, J.M. Moisselin, M. Sabrea, J.P. Floria, B. Dubuisson, A new statistical approach to extreme wind speeds in France. *Journal of Wind Engineering and Industrial Aerodynamics*, 95, 1415–1423, 2007.
- [36] Y. An, M.D. Pandey, Technical note: A comparison of methods of extreme wind speed estimation. *Journal of Wind Engineering and Industrial Aerodynamics*, 93, 535–545, 2005.
- [37] M.D. Pandey, An adaptive exponential model for extreme wind speed estimation. *Journal of Wind Engineering and Industrial Aerodynamics*, 90, 839–866, 2002.
- [38] J. Ding, X. Chen, Assessment of methods for extreme value analysis of non-Gaussian wind effects with short-term time history samples. *Engineering Structures*, 80, 75–88, 2014.
- [39] X. Zhang, X. Chen, Assessing probabilistic wind load effects via a multivariate extreme wind speed model: A unified framework to consider directionality and uncertainty. *Journal of Wind Engineering and Industrial Aerodynamics*, 147, 30–42, 2015.
- [40] M. Grigoriu. Crossings of non-Gaussian translation processes. *Journal of Engineering Mechanics*, 110(4), 610–620, 1984.
- [41] S. R. Winterstein, Moment-based hermite models of random vibration. Report 219, Department of Structural Engineering, Technical University of Denmark, 1987.
- [42] S.R. Winterstein, Nonlinear vibration models for extremes and fatigue. *Journal of Engineering Mechanics*, 114(10), 1772–1790, 1988.
- [43] F. Rizzo, L. Caracoglia, Artificial Neural Network model to predict the flutter velocity of suspension bridges. *Computers and Structures*, 233 (2020) 106236, 2020.
- [44] F. Rizzo, F. Ricciardelli, G. Maddaloni, Bonati A., A. Occhiuzzi, Experimental error analysis of dynamic properties for a reduced-scale high-rise building model and implications on full-scale behavior. *Journal of Building Engineering*, 28, 2020.
- [45] K. Saranyasootorn, L. Manuel, Efficient models for wind turbine extreme loads using inverse reliability. *Journal of Wind Engineering and Industrial Aerodynamics*, 92, 789–804, 2004.
- [46] J. Song, W. Xu, G. Hu, S. Liang, J. Tan, Non-Gaussian properties and their effects on extreme values of wind pressure on the roof of long-span structures. *Journal of Wind Engineering and Industrial Aerodynamics*, 184, 106–115, 2019.

- [47] S.R. Winterstein, T.C. Ude, G. Kleiven, Springing and slow-drift responses: predicted extremes and fatigue vs simulation. Proceedings, Behavior of Offshore Structures at Sea - BOSS-94, MIT, 3, 1-15, 1994.
- [48] A. Kareem, J. Zhao, Analysis of non-Gaussian surge response of tension leg platforms under wind loads. *Journal of Offshore Mechanics and Arctic Engineering*, 116(3), 137-144, 1994.
- [49] D. Kwon, A. Kareem, Peak Factors for Non-Gaussian Load Effects Revisited. *Journal of Structural Engineering*, 137(12), 1611-1619, 2011.
- [50] F. Rizzo, M. Barbato, V. Sepe, Peak factor statistics of wind effects for hyperbolic paraboloid roofs. *Engineering Structures*, 173, 313-330, 2018.
- [51] S.R. Winterstein, T. Kashef, Moment-based load and response models with wind engineering applications. *Journal of Solar Energy Engineering*, 122, 122-128, 2000.
- [52] M.A. Tognarelli, J. Zhao, K. B. Rao, A. Kareem, Equivalent Statistical Quadraticization and Cubicization for Nonlinear Systems. *Journal of Engineering Mechanics*, 123(5), 1772-1790, 1997.
- [53] Q. Yang, Y. Tian, Comparison of non-Gaussian peak factor formulae in wind engineering applications. Proceedings of The Eighth Asia-Pacific Conference on Wind Engineering, December 10–14, 2013, Chennai, India, 2013.
- [54] L.V. Binh, T. Ishihara, P.V. Phuc, Y. Fujino, A Peak Factor for non-Gaussian Response Analysis of Wind Turbine Tower. *Journal of Wind Engineering and Industrial Aerodynamics*, 96, 2217-2227, 2008.
- [55] K.R. Gurley, M.A. Tognarelli, A. Kareem, Analysis and simulation tools for wind engineering. *Probabilistic Engineering Mechanics*, 12(1), 9–31, 1997.
- [56] S.R. Winterstein, C.A. MacKenzie, Extremes of nonlinear vibration: comparing models based on moments, l-moments, and maximum entropy. *Journal of Offshore Mechanics and Arctic Engineering*, 135(2):021602, 2012.
- [57] L. Sant'Anna Nascimento, L. Sagrilo, G. Ellwanger, Extreme Value Analyses of Dynamic Response Parameters of a Wind Tower Structure Under Short-Term Nonlinear Irregular Seastate. Conference: ASME 2017 36<sup>th</sup> International Conference on Ocean, Offshore and Arctic EngineeringAt: Trondheim, Norway, 2017.
- [58] L. Yang, K. R. Gurley, O. D. Prevatt, Probabilistic modeling of wind pressure on low-rise buildings. *Journal of Wind Engineering and Industrial Aerodynamics*, 114, 18–26, 2013.
- [59] M. Choi, B. Sweetman, The Hermite moment model for highly skewed response with application to tension leg platforms. *Journal of Offshore Mechanics and Arctic Engineering*, 132(2), 021602, 2010.
- [60] G. Huang, Y. Luo, K. R. Gurley, J. Ding Ying Luo, Revisiting moment-based characterization for wind pressures. *Journal of Wind Engineering and Industrial Aerodynamics*, 151, 158-168, 2016.
- [61] G. Huang, Y. Luo, K. R. Gurley, J. Ding Ying Luo, Response to Revisiting moment-based characterization for wind pressures. *Journal of Wind Engineering and Industrial Aerodynamics*, 158, 162–163, 2016.



- [62] N. J. Cook, Discussion of Revisiting moment-based characterization for wind pressures. *Journal of Wind Engineering and Industrial Aerodynamics*, 158, 155–161, 2016.
- [63] N.J. Cook, Calibration of EVA methods for peak-over-threshold wind data using Bootstrapping. *Journal of Wind Engineering and Industrial Aerodynamics*, 120, 91–95, 2013.
- [64] M. Liu, X. Chen, Q. Yang, Characteristics of dynamic pressures on a saddle type roof in various boundary layer flows. *Journal of Wind Engineering and Industrial Aerodynamics*, 150, 1–14, 2016.
- [65] M. Liu, X. Chen, Q. Yang, Estimation of peak factor of non-Gaussian wind pressures by improved moment-based Hermite model. *Journal of Engineering Mechanics*, 143(7): 06017006, 2017.
- [66] F. Rizzo, Wind tunnel random processes statistics of pressures on a large span canopy roof. *Iranian Journal of Science and Technology, Transactions of Civil Engineering*, 10.1007/s40996-020-00458-x, 2020.
- [67] F. Rizzo, P. Zazzini, Shape dependence of acoustic performances in buildings with a Hyperbolic Paraboloid cable net membrane roof. *Journal of Acoustics Australia*, 45 (2), 2017.
- [68] F. Rizzo, P. Zazzini, Improving the acoustical properties of an elliptical plan space with a cable net membrane roof. *Journal of Acoustics Australia*, 44, 449-456, 2016.
- [69] F. Rizzo, A. G. Kopp, G. Giaccu, Investigation of wind-induced dynamics of a cable net roof with aeroelastic wind tunnel tests. *Engineering Structures*, 229, 111569, 2021.
- [70] F. Rizzo, C. Demartino, Pressure modes for hyperbolic paraboloid roofs. *Curved and Layer Structure*, 7, 1–21, 2021.
- [71] F. Sadek, E. Simiu, Peak non-Gaussian wind effects for database-assisted low-rise building design. *Journal of Engineering Mechanics*, 128(5), 530-539, 2002.
- [72] M. Gioffrè, M. Grigoriu, M. Kasperski, E. Simiu, Wind induced peak bending moments in low-rise building frames. *Journal of Engineering Mechanics* 126(8), 879–881, 2000.
- [73] M. Grigoriu. *Applied non-Gaussian processes*, Prentice Hall, Englewood Cliffs, N.J. , 1995.
- [74] X. Ma, F. Xu. Peak factor estimation of non-Gaussian wind pressure on high-rise buildings. *The Structural Design of Tall and Special Buildings*, 26(17):e1386, 2017.
- [75] Q. Yang, X. Chen, M. Liu, Bias and sampling errors in estimation of extremes of non-Gaussian wind pressures by moment-based translation process models. *Journal of Wind Engineering and Industrial Aerodynamics*, 186, 214–233, 2019.
- [76] H.W. Tieleman, Z. Ge, M.R. Hajj, Theoretically estimated peak wind loads. *Journal of Wind Engineering and Industrial Aerodynamics*, 95(2), 113–132, 2007.
- [77] H.W. Tieleman, M.A.K. Elsayed, Z. Ge, M.R. Hajj, Extreme value distributions for peak pressure and load coefficients. *Journal of Wind Engineering and Industrial Aerodynamics* 96(6–7), 1111–1123, 2008.
- [78] M.F. Huang, W. Lou, C.M. Chan, N. Lin, X. Pan, Peak distributions and peak factors of wind-induced pressure processes on tall buildings. *Journal of Engineering Mechanics*, 139(12), 1744-1756, 2013.



- [79] M.F. Huang, S. Huang, H. Feng, W.J. Lou, Non-Gaussian time-dependent statistics of wind pressure processes on a roof structure. *Wind and Structures*, 23(4), 275-300, 2016.
- [80] A. Naess, O. Gaidai, O. Karpa, Estimation of Extreme Values by the Average Conditional Exceedance Rate Method. *Journal of Probability and Statistics*, 2013, 797014, 2013.
- [81] A. Naess, O. Karpa, Statistics of bivariate extreme wind speeds by the ACER method. *Journal of Wind Engineering and Industrial Aerodynamics*, 139, 82-88, 2015.
- [82] A. Naess, O. Gaidai, Monte Carlo methods for estimating the extreme response of dynamic systems. *Journal of Engineering Mechanics*, 134(8), 628-36, 2008.
- [83] F. Rizzo, G. Di Lorenzo, A. Formisano, R. Landolfo, A time-dependent corrosion wastage model for Wrought iron Structures. *ASCE's Journal of Materials in Civil Engineering*, 31(8): 04019165, 2018.
- [84] J. Ding, K. Gong, X. Chen, Comparison of statistical extrapolation methods for the evaluation of long-term extreme response of wind turbine. *Engineering Structures*, 57, 100-115, 2013.
- [85] X. Zhang, X. Chen, Assessing probabilistic wind load effects via a multivariate extreme wind speed model: A unified framework to consider directionality and uncertainty. *Journal of Wind Engineering and Industrial Aerodynamics*, 147, 30-42, 2015.
- [86] O. Gaidai, A. Naess, X. Xu, Y. Cheng, Improving extreme wind speed prediction based on a short data sample, using a highly correlated long data sample. *Journal of Wind Engineering and Industrial Aerodynamics* 188 (2019) 102-109, 2019.
- [87] X. Chen, Estimation of extreme value distribution of crosswind response of wind-excited flexible structures based on extrapolation of crossing rate. *Engineering Structures* 60, 177-188, 2014.
- [88] A. Naess, O. Gaidai, Estimation of extreme values from sampled time series, *Structural Safety*, 31(4), 325-334, 2009.
- [89] F. Rizzo, M. F. Huang, Peak value estimation for wind-induced lateral accelerations in a high-rise building, *Structure and Infrastructure Engineering*, in press.

## EFFECT OF SOIL PROFILE CHARACTERISTICS ON THE SEISMIC SLIDING DISPLACEMENT OF SLOPES

Loukas C. Katsenis<sup>1</sup>, Constantine A. Stamatopoulos<sup>2</sup>, Vassilis P. Panoskaltis<sup>1</sup>

<sup>1</sup> Department of Civil Engineering, Demokritos University of Thrace,  
University Campus Xanthi-Kimmeria, 67100 Xanthi, Greece  
e-mails: [katsenisloukas@yahoo.gr](mailto:katsenisloukas@yahoo.gr), [vpanoska@civil.duth.gr](mailto:vpanoska@civil.duth.gr)

<sup>2</sup> Stamatopoulos and Associates Co.; Hellenic Open University; 5 Isavron str, 11471 Athens, Greece  
e-mail: [k.stam@saa-geotech.gr](mailto:k.stam@saa-geotech.gr)

---

### Abstract

*In earthquake analyses, usually the seismic displacement is estimated by the sliding-block model, where a rigid block rests on an inclined plane and every time that the applied horizontal acceleration is larger than the critical horizontal acceleration value for relative motion, the block slides. This model is used for the prediction of permanent seismic movement of slopes along a predefined slip surface, by appropriately selecting the equivalent critical and applied acceleration values of the rigid block. However, the input seismic motion is usually specified at the underlying bedrock and the seismic displacement along a slip surface depends not only on the resistance along the slip surface, but also on the dynamic characteristics of the soil both above and below the slip surface. Based on the above, the present work investigates and proposes expressions relating the ratio of the seismic displacement of slopes along a slip surface and the corresponding displacement of the sliding-block model for similar applied acceleration and critical acceleration of the slip surface in terms of characteristics of the soil profile both above and below the slip surface. The proposed expressions were obtained based state-of-the-art description of the dynamic response and results of previous dynamic seismic sliding displacement analyses. Parametric analyses using a recently developed numerical code were performed to calibrate and validate the proposed expressions. In these analyses, different acceleration histories measured at rock sites are applied below soil layers with a slip surface with varying critical acceleration value and dynamic properties both above and below the slip surface.*

**Keywords:** slopes, sliding-block model, dynamic response, seismic displacement, slip surface, coupled analyses

---

## 1 INTRODUCTION

The seismic displacement of slopes usually occurs along a slip surface [1]. Engineers usually assess the seismic safety of slopes using the dynamic factor of safety calculated from loads. However, evaluations based on the dynamic factor of safety have the serious drawback that they do not consider the seismic displacement, which is directly related to damage. In earthquake analyses, usually the seismic displacement is estimated by the sliding-block model [2], where a rigid block rests on an inclined plane and every time that the applied horizontal acceleration is larger than the critical horizontal acceleration value for relative motion ( $a_c$ ), the block slides. This model is used for the prediction of permanent seismic movement of slopes and retaining structures along a predefined slip surface, by appropriately selecting the equivalent critical and applied acceleration values of the rigid block [1, 3].

Different empirical expressions have been proposed predicting the seismic displacement of the sliding-block model, in terms, primarily, of the ratio of the maximum acceleration of the applied seismic motion by the critical horizontal acceleration for sliding [3]. In addition, some of these expressions use other than the maximum acceleration parameters of the seismic motion, such as the maximum velocity or the Arias Intensity, or parameters of the earthquake that produced the seismic motion, such as its earthquake magnitude or its earthquake fault distance [4,5]. Furthermore, region-specific empirical expressions have been proposed predicting the seismic displacement of the sliding-block model, as different regions have different earthquake faults and geological profiles conditions, and thus potentially different applied seismic motions characteristics [6].

However, the input seismic motion is usually specified at the underlying bedrock and the seismic displacement along a slip surface depends on both the dynamic characteristics of the sliding mass, and the soil profile below [8]. Based on the above, it is of interest for practicing engineers, to relate the seismic displacement along slip surfaces, not only on characteristics of the applied seismic motion and the critical horizontal acceleration for sliding of the slip surface, but also to the dynamic soil properties both above and below the slip surface. Expressions have been proposed predicting the seismic displacement of slopes in terms of not only characteristics of the applied seismic motion and the critical horizontal acceleration for sliding, but also on the dynamic characteristics of the sliding mass [7]. Furthermore, Katsenis et al [9] proposed empirical expressions relating the ratio of the seismic displacement of slopes along a slip surface and the corresponding displacement of the sliding-block model for similar applied acceleration and critical acceleration of the slip surface considering the dynamic soil profile characteristics both above and below the slip surface. Their relationships are in terms of the soil profile type of the slope according to Eurocode 8 [10] and the depth of the slip surface. Yet, the dynamic response of soil layers is related to its dominant period [7, 8], and Eurocode profile types provide only an approximate prediction of the actual dynamic response.

The present work extends the Katsenis et al. [9] work by proposing an empirical expression predicting the seismic displacement of slopes where the soil profile has any shear velocity value and depth both above and below the slip surface. In order to achieve this goal, below, first a critical literature review of the dynamic effect on the seismic displacement of slopes is pre-

sented. Then, based on this critical review, equations simulating the dynamic effect on the seismic displacement of slopes are proposed. Following, a data base of seismic motions measured at rock sites is obtained, mainly recorded in the European-Mediterranean regions and using this data base an evaluation of the model parameters of the proposed equations and an assessment of the accuracy of the model is performed. Finally, the paper discusses further validation and application of the proposed equation.

## 2 CRITICAL LITERATURE REVIEW OF THE DYNAMIC EFFECT ON THE SEISMIC DISPLACEMENT OF SLOPES

### 2.1 Eurocode

According to Eurocode 8 (European Standard, 2003), as illustrated in Fig. 1, the dynamic response of elastic systems ( $S$ ) depends on the critical period of the system ( $T_s$ ) according to the following equations:

$$T_s < T_a \quad S(T_s) = 1 + A T_s / T_a \quad (1)$$

$$T_a \geq T_s \geq T_b \quad S(T_s) = 1 + A$$

$$T_s > T_b \quad S(T_s) = (1 + A) (T_b / T_s)^B$$

Where the parameters  $A$  and  $B$  typically equal 0.25 and 2/3 respectively and the parameters  $T_a$  and  $T_b$  depend on the underlying soil type and for rock sites they equal  $T_a = 0.10s$   $T_b = 0.40s$ .

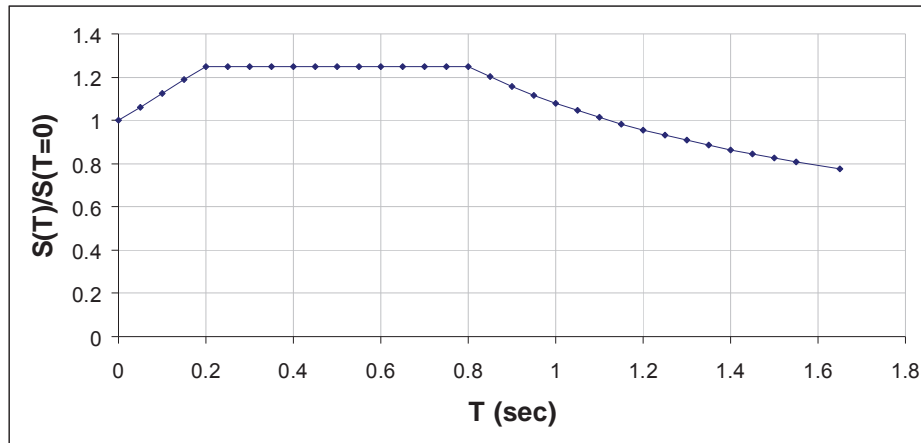


Figure 1: Seismic response in terms of  $T_s$  as predicted by Eurocode 8 (European Standard, 2003) for rock sites.

### 2.2 Work by Rathje and Bray [7] and Bray and Travarasrou [13]

The effect of the dynamic response of the sliding mass on the seismic displacement along slip surfaces has been modelled among others by Rathje and Bray [7]. They consider the 1-dimensional geometry of Fig. 2a where a horizontal shear wave propagates vertically above a

slip surface with critical acceleration  $a_c$  at a body with height  $h$  and shear wave velocity  $V_s$  and identify the critical period of the system, as

$$T_s = 4h / V_s \quad (2)$$

Fig. 2b presents typical predictions of their model: The variation of sliding displacement with  $T_s/T_m$ , where  $T_m$  is the mean period of the applied seismic motion, for the Aegion 1995 seismic motion with  $a_c=0.5\text{m/s}^2$ ,  $h= 15\text{m}$ ,  $\rho= 2 \text{ Mg/m}^3$  and damping  $\lambda=0.15$  is presented. In Fig. 2b it can be observed that, similarly to Fig. 1, the effect of dynamic response (a) does not exist for  $T_s=0$ , (b) as  $T_s$  increases, the dynamic effect increases and it produces maximum response approximately when  $T_s=T_m$  and (c) as  $T_s$  further increases beyond  $T_m$ , it decreases the final seismic displacement along the slip surface ( $u_f$ ) towards zero.

Consistently, Bray and Travasarou [13] proposed empirical expressions relating the seismic displacement, in addition to the critical acceleration  $a_c$  and characteristics of the applied seismic motion such as the earthquake magnitude  $u_f$ , to  $T_s$ .

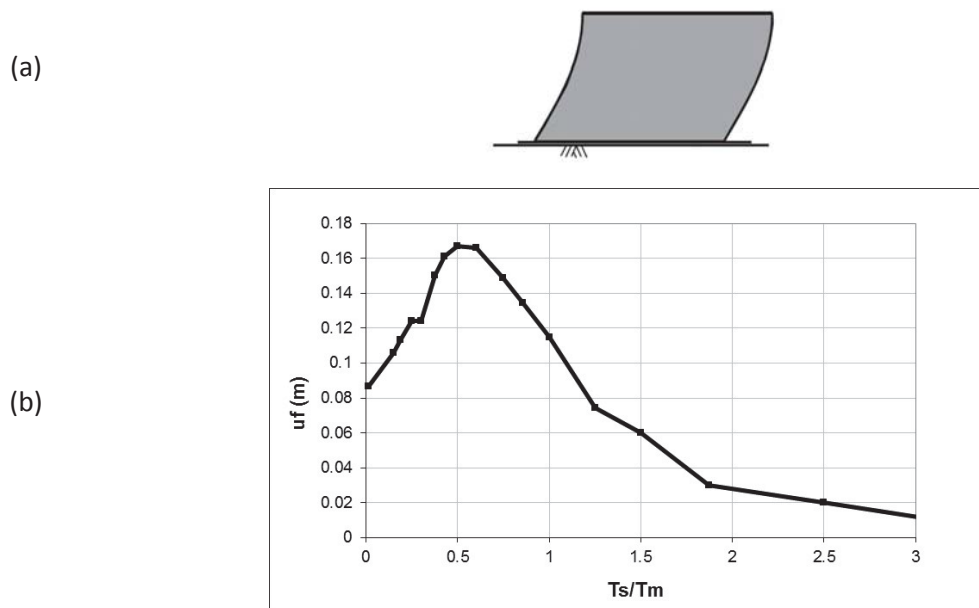


Figure 2: (a) The Rathje and Bray [7] model and (b) typical predictions of the model: Variation of sliding displacement with  $T_s/T_m$  for rigid and dynamic analyses. The Aegion 1995 seismic motion with  $a_c=0.5\text{m/s}^2$ ,  $h= 15\text{m}$ ,  $\rho= 2 \text{ Mg/m}^3$  and  $\lambda=0.15$  is presented.

### 2.3 The Katsenis et al. [9, 11] model

In the analyses described above the effect of the soil profile below the slip surface on the seismic displacement has not been studied. The Katsenis et al [9, 11] model, is a cost-effective

model which can study it: As shown in Fig. 3b, it considers the 1-dimensional dynamic response of a horizontal soil profile of depth  $(h_1+h_2)$  with a slip element at depth  $h_1$ . Different shear wave velocities ( $V_{s-1}$ ,  $V_{s-2}$ ), densities ( $\rho_1$ ,  $\rho_2$ ) and damping ( $\lambda_1$ ,  $\lambda_2$ ) may exist above and below the slip element. The slip element simulates the seismic displacement of the conventional sliding-block model, where its resistance is defined by the critical horizontal value ( $a_c$ ), for which relative movement in only one direction occurs. The two bodies move a horizontal distance  $x_i$ , velocity  $\dot{x}_i$  and acceleration  $\ddot{x}_i$ , where  $i$  takes the values 1 and 2 for bodies 1 and 2 respectively. The corresponding field configuration is that of a slope with a slip surface where seismic displacement may accumulate as a result of a horizontal shear wave, illustrated in Fig. 3a

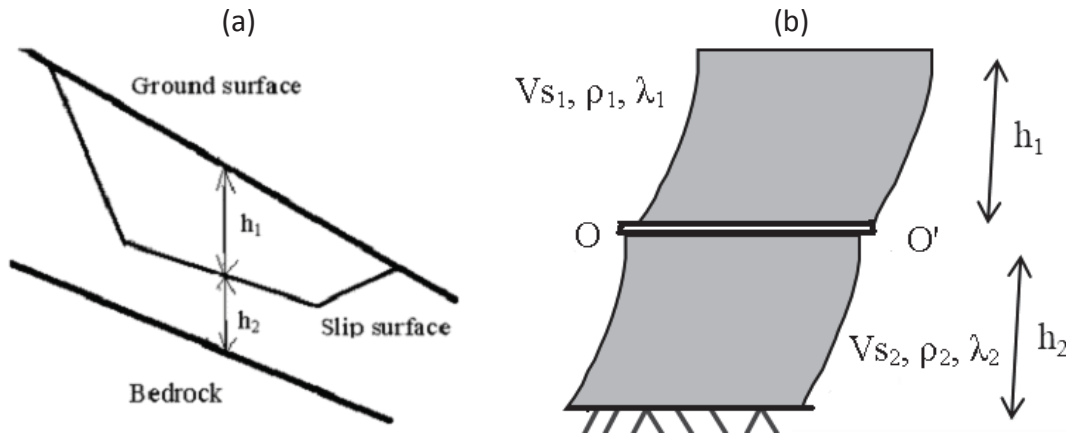


Figure 3: The Katsenis et al, (2020) model: (a) field configuration of a slope with a slip surface where seismic displacement may accumulate as a result of a horizontal shear wave, (b) simulation of (a) with a 1-D dynamic system of 2 continuous bodies separated by a horizontal slip element. In the dynamic system (b) slippage may occur along AA'.

#### 2.4 Results of the Katsenis et al. [11] model

Katsenis et al. [11] define

$$Ts1 = 4 h_1 / V_{s-1} \quad (3a)$$

$$Ts\text{-ave} = 4 (h_1 / V_{s-1} + h_2 / V_{s-2}) \quad (3b)$$

and Fig. 4 presents a typical computed permanent seismic displacement ( $u_f$ ) response of their model. In particular, the computed displacement ( $u_f$ ) for the Aegion 1995 seismic motion with  $a_c = 0.5 \text{ m/s}^2$ ,  $h_1 + h_2 = 30 \text{ m}$ ,  $\rho_1 = \rho_2 = 2 \text{ Mg/m}^3$  and  $\lambda_1 = \lambda_2 = 0.15$  (a) versus  $Ts1/T_m$  for  $V_{s-2} = V_{s-1}$ ,  $h_2 = 1 \text{ m}$ ,  $15 \text{ m}$ ,  $25 \text{ m}$ , (b) versus  $Ts1/T_m$  for  $h_2 = 15 \text{ m}$  and (c) versus  $Ts\text{-ave}/T_m$  for the cases (a) and (b) is presented.

It can be observed that the effect of the soil profile both above and below the slip surface on the seismic displacement is considerable and that if  $u_f$  is plotted in terms of the ratio  $Ts\text{-ave}/T_m$ , the scatter in results for different  $V_{s-2}$  and  $h_2$  values decreases considerably. It is inferred that the dynamic effect on  $u_f$  can partly be interpreted by relating  $u_f$  to  $Ts\text{-ave}$ . In particular, similarly



to the response of Figs. 1 and 2, but replacing  $T_s$  with  $T_{s-ave}$ , it can be observed that the dynamic response (a) does not exist for  $T_{s-ave}=0$ , (b) as  $T_{s-ave}$  increases, the dynamic effect increases and it produces maximum response approximately when  $T_{s-ave}=T_m$  and (c) as  $T_{s-ave}$  further increases beyond  $T_m$ , it decreases the final seismic displacement along the slip surface ( $u_f$ ) towards zero.

Furthermore, Katsenis et al. [11] illustrate that the dynamic response play an important role for small seismic displacement, but a smaller role for large seismic displacement ( $>0.5$  m). Typical results are given in Fig. 5, where the ratio of the rigid and dynamic  $u_f$  value tends to zero as  $a_c$  decreases. Indeed, as identified by previous researchers also [14], large seismic displacement corresponds to low critical acceleration value, which limits the seismic actions transmitted across the slip surface, and thus the dynamic effect.

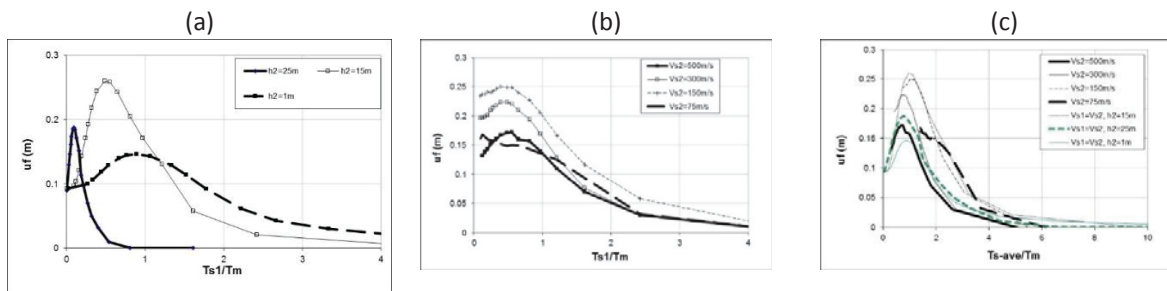


Figure 4: The computed permanent seismic displacement ( $u_f$ ) for the Aegion 1995 seismic motion with  $a_c=0.5\text{m/s}^2$ ,  $h_1+h_2=30\text{m}$ ,  $\rho_1=\rho_2=2\text{ Mg/m}^3$  and  $\lambda_1=\lambda_2=0.15$  (a) versus  $T_{s1}/T_m$  for  $V_{s-2}=V_{s-1}$ ,  $h_2=1\text{m}$ ,  $15\text{m}$ ,  $25\text{m}$ , (b) versus  $T_{s1}/T_m$  for  $h_2=15\text{m}$  and  $V_{s-2}=75, 150, 300, 500\text{m/s}$  and (c) versus  $T_{s-ave}/T_m$  for the cases (a) and (b) [11].

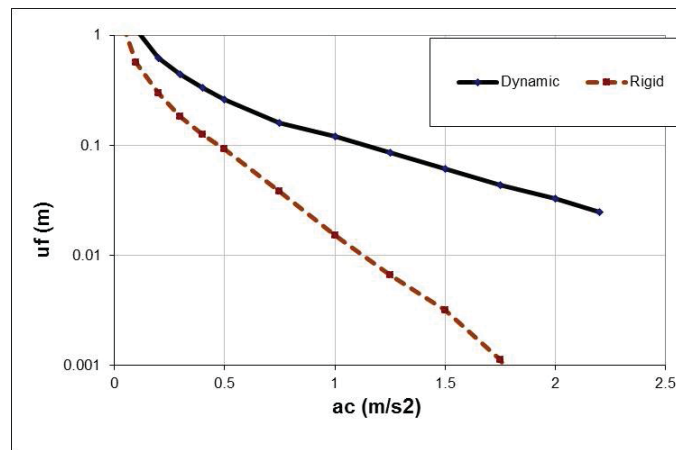


Figure 5: Computed permanent seismic displacement ( $u_f$ ) by [11] for the elastic and rigid analyses in terms of  $a_c$  for the Aegion 1995 seismic motion,  $h_1=h_2=15\text{m}$ ,  $V_{s-1}=V_{s-2}=200\text{m/s}$ ,  $\rho_1=\rho_2=2\text{Mg/m}^3$ ,  $\lambda_1=\lambda_2=0.15$ .

## 2.5 Previous empirical equation

Different empirical expressions have been proposed predicting the seismic displacement of the conventional sliding-block model ( $u_{f-bl}$ ) in terms of  $a_c$  and characteristics of the seismic motion such as  $a_{max}$ , Arias intensity, earthquake magnitude etc. [2-6]. In addition, some of these

expressions are region-specific [7]. Katsenis et al. [9] in order, to separate the dynamic effect from the seismic displacement accumulating along the slip surface for rigid blocks, propose to relate  $u_f$  on the conventional sliding-block model ( $u_{f-bl}$ ) seismic displacement for the same applied seismic motion and critical acceleration value, as

$$u_f = R u_{f-bl} \quad (4)$$

where the factor  $R$  simulates the dynamic effect and depends on various factors such as  $u_{f-bl}$ , the soil profile type and the depth of the slip surface.

### 3 PROPOSED EQUATION PREDICTING THE DYNAMIC EFFECT ON THE SEISMIC DISPLACEMENT OF SLOPES

The problem considered is that of Fig. 3a where a seismic horizontal motion is applied at the bedrock underlying a soil profile where a potential slip surface exists at some depth, which is simulated with the system of Fig. 3b.

In order, to separate the dynamic effect from the seismic displacement accumulating along the slip surface for the same seismic motion, which has been predicted by previously proposed empirical equations, similarly to [9], we relate  $u_f$  on the conventional sliding-block model seismic displacement for the same applied seismic motion and critical acceleration value ( $u_{f-bl}$ ). More specifically, we propose the following equation to predict  $u_f$ :

$$u_f = u_{f-bl} K_{dyn} \quad (5a)$$

At this point it should be noted that  $u_{f-bl}$  equals to  $u_f$  in the case of a very stiff or of a very shallow soil profile, where  $Ts-ave$  tends to 0.

As described above, (i) the dynamic response can be simulated in terms of the critical period by an equation of the form of equation (1), (ii) the dynamic response of the problem considered depends on the value of  $Ts-ave$ , given by equation (3b), (iii) the response of Figs. 4 illustrate that the dynamic response (a) does not exist for  $Ts-ave=0$ , (b) as  $Ts-ave$  increases, the dynamic effect increases and it produces maximum response approximately when  $Ts-ave=T_m$  and (c) as  $Ts-ave$  further increases beyond  $T_m$ , it decreases the final seismic displacement along the slip surface ( $u_f$ ) towards zero and (iv) the dynamic effect is affected by the magnitude of the sliding seismic displacement. Thus, we apply equation (1) by assuming that  $T_a=T_b$  and replacing and  $T_s$  with  $Ts-ave$  and we obtain

$$\begin{aligned} Ts - ave &\leq T_a & K_{dyn}(Ts-ave) &= 1 + A Ts-ave/T_a \\ Ts - ave &> T_a & K_{dyn}(Ts-ave) &= 1 + (1+A) (T_a /Ts-ave)^B \end{aligned} \quad (5b)$$

where  $T_a$  is the  $Ts-ave$  value where  $K_{dyn}$  is maximum and the parameters  $A$ ,  $B$  determine the peak value and the post-peak rate of decrease of the dynamic effect, as illustrated in Fig. 6. Section 2.4 above, described that the dynamic effect diminishes as the seismic displacement increases, or, equivalently, as the critical acceleration value for relative motion increases. Indeed, at the time intervals where seismic displacement accumulates, the body above the slip surface is separated from and moves independently from the body below the slip surface, and thus the relationship between the dynamic effect and the factor  $Ts-ave$  ceases to exist.

We define as ( $R_t$ ) the ratio of the sum of times where the seismic displacement accumulates ( $t_s$ ) by the total duration time of the applied seismic motion:

$$R_t = t_s / t_t \quad (6a)$$

Based on the discussion above, it is inferred that as ( $R_t$ ) increases towards 1, the dynamic effect diminishes. Thus, as  $R_t$  increases, the factors A and B of equation (5b) decrease, and in particular for large values of  $R_t$ , A and B tend to zero.

Yet, the factors  $t_t$ ,  $t_s$  are not usually used or specified on earthquake engineering. On the other hand, the intensity of a seismic motion is best defined by the Arias Intensity measure ( $I_a$ ) [5, 6] and the corresponding magnitude of the relative slip which occurs can be identified by  $u_{f-bl}$ . Thus, we approximate the factor  $R_t$  of equation (6a) with the factor  $R'_t$  defined by commonly used and well defined parameters  $I_a$  and  $u_{f-bl}$  as

$$R'_t = (u_{f-bl} / I_a) \quad (6b)$$

As  $R'_t$  increases, the factors A and B of equation (5b) decrease towards zero and thus we can write

$$A = a_1 (I_a / u_{f-bl})^{a_2} \quad (5c)$$

$$B = b_1 (I_a / u_{f-bl})^{b_2} \quad (5d)$$

where  $a_1$ ,  $a_2$ ,  $b_1$ ,  $b_2$  are model parameters.

It can be noted that equations (5b) and (5d) predict that, similarly to the response described in section 2.4, (a) A and B decrease, and the dynamic response decreases, as  $A_r$  decreases and  $u_f$  increases and (b) A and B tend to zero and the dynamic response diminishes as  $A_r$  tends to zero and as  $u_f$  becomes very large.

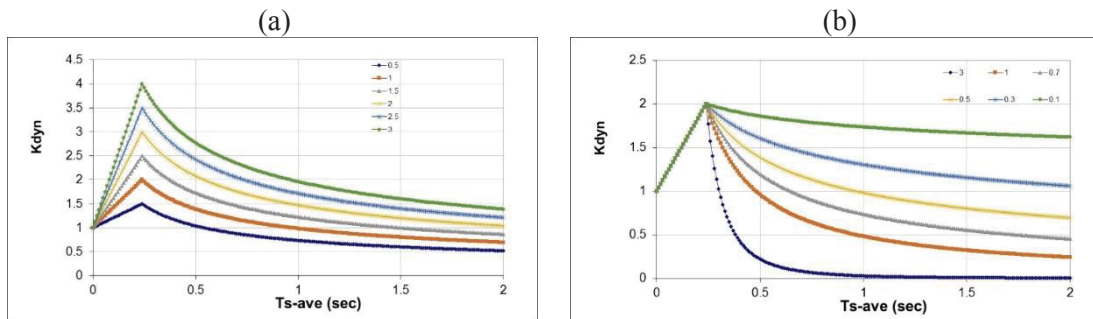


Figure 6: The function  $K_{dyn}$  in terms of (a) A and (b) B. In (a)  $B=0.5$  and in (b)  $A=1$ .

#### 4 DATA BASE AND PARAMETRIC ANALYSES

A data base of seismic motions was obtained using the ESM site (the Engineering Strong-Motion Database), which contains waveforms with magnitude  $\geq 4.0$ , mainly recorded in the European-Mediterranean regions and the Middle-East and provides a set of facilities to search, select, download and analyze ground-motion data. It is obtained by selecting the Northern and Eastern components of seismic motions with the following restrictions: Soil type according to EC8 : A (Rock),  $\max(\text{PGA}) > 100 \text{ cm}^2/\text{s}$ ,  $M > 5$ . The reason of the selection described above is that (a) the Katsenis et al. [9, 11] model input motions must correspond to seismic motions at rock sites without the amplification and modification phenomena that seismic motions exhibit as they pass thru soil layers and (b) seismic motions with  $\max(\text{PGA}) < 100 \text{ cm}^2/\text{s}$  and  $M < 5$  typically do not cause intolerable seismic displacement along slip surfaces.

The data base included 56 cases, sorted in descending PGA order, given in Appendix A. For the present application four seismic motions were selected. In particular, as the seismic displacement greatly depends on PGA, the seismic motions were selected starting from the first and taking the next after passing 12. In this way, the seismic motions No1, 13, 25, 37 were selected, having a variety of PGA values, ranging from large to small PGA. Table 1 gives the main characteristics of these applied seismic motions.

Coupled linear dynamic parametric analyses were performed using the Katsenis et al. [9, 11] model, and more specifically the corresponding numerical code DIAS [11]. All the seismic motions described above were applied at the base of soil column with  $h_1=h_2=15\text{m}$ . The shear wave velocities of the two bodies considered are given in table 2. In each seismic motion, at the slip surface three  $a_c$  values were assumed, selected in such a way that  $u_{f-bl}$  equals 0.01, 0.1, 1m, which cover the range of typical values of typical field problems of instability interest. In addition,  $\lambda_1=\lambda_2=0.05$ ,  $\rho_1=\rho_2=2\text{t/m}^3$  were assumed.

No	Region	Date	ML	Epicentral Distance	PGA ( $\text{cm/s}^2$ )	Ia (cm/s)	Tcr (s)
1	Turkey, Düzce	11/12/1999	6.6	27.4	-1010	1331.53	0.25
2	Montenegro	15/04/1979	6.8	62.9	211	73.32	0.25
3	Turkey, Düzce	12/11/1999	6.6	30.3	-157	44.30	0.25
4	Italy, Umbria	30/10/2016	6.1	46.6	121	19.68	0.13

Table 1: The main characteristics of the applied seismic motions.

$V_{s-1}$ (m/s)	50	100	130	180	270	370	470	580	700	1000	2000
$V_{s-2}$ (m/s)	75	1500	300	500	750	5000					

Table 2: Shear wave velocities applied in the parametric analyses

#### 5 EVALUATION OF MODEL PARAMETERS

Fig. 7 gives the obtained results of the parametric analyses: The ratio  $u_f/u_{f-bl}$  in terms of  $T_{s-ave}$  in terms of applied seismic motion and  $u_{f-bl}$  is given for all seismic motions. Similarly to the theory described above, it can be observed that plotting the results for each case of seismic motion and  $u_{f-bl}$  values in terms of  $T_{ave}$  has small scatter and this is true especially for small

$u_{f-bl}$  values. It is also worth noting that in the results presented in Fig. 7,  $u_f/u_{f-bl}$  was plotted in terms of  $T_{s1}$  instead of  $T_{s-ave}$  also, and it was observed that the scatter was much larger.

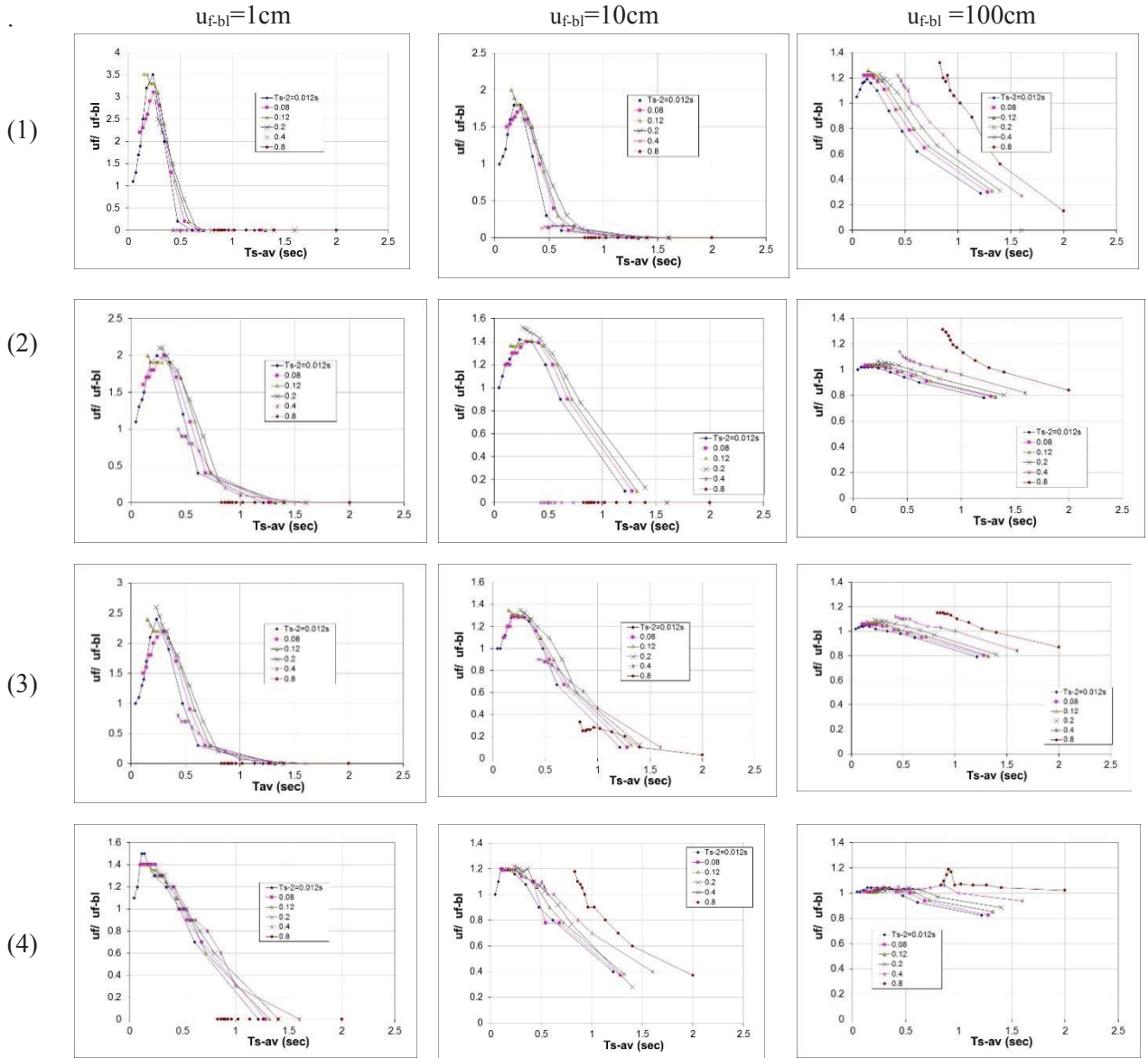


Figure 7: The function  $K_{dyn}$  for the seismic motions (1)-(4) in terms of  $u_{f-bl}$ .

For each case of seismic motion and  $u_{f-bl}$  value, the model parameters simulating the dynamic response according to equation (5) were obtained. In all cases, the seismic response was simulated well when

$$T_a = 0.3s \quad (5.e)$$

It can be noted that this value is consistent with section 2.1 statement that in rock sites  $T_m$  does not exceed 0.4s. With  $T_a = 0.3s$ , table 3 gives the obtained factors A and B. Fig. 8 presents the parameters of table 3: The factors A and B in terms of (a)  $(1/u_{f-bl})$ , (b)  $I_a$ , (c)  $(I_a/u_{f-bl})$  are given.

Strong correlations are observed in all cases and as illustrated in Fig 8c, the best-fit correlations of the relations (5c) and (5d), according to equation (5b), occur when,

$$a1=0.17, a2=0.39 \quad (5.f)$$

$$b1=0.20, b2=0.35 \quad (5.g)$$

As illustrated in Fig. 8c, the coefficient of determination is larger than 0.85 in all cases and as the coefficient of determination is close to unity, it is inferred that the proposed equation describes well the computed response

(a) Factor A

<i>Ia (cm/s):</i>	<i>u<sub>f-bl</sub>(cm): 1331.5</i>	<i>73.3</i>	<i>44.3</i>	<i>19.7</i>
<i>1</i>	2.5	1.2	1.2	0.5
<i>10</i>	1.2	0.4	0.3	0.2
<i>100</i>	0.2	0.2	0.1	0.1

(b) Factor B

<i>Ia (cm/s):</i>	<i>u<sub>f-bl</sub>(cm): 1331.5</i>	<i>73.3</i>	<i>44.3</i>	<i>19.7</i>
<i>1</i>	1.8	0.8	0.8	0.7
<i>10</i>	1	0.55	0.55	0.43
<i>100</i>	0.55	0.1	0.1	0.1

Table 3: The model parameters A and B simulating the dynamic response according to equations (5) , for each case of the  $u_{f-bl}$  (cm) and  $Ia$ (cm/s) of the seismic motion



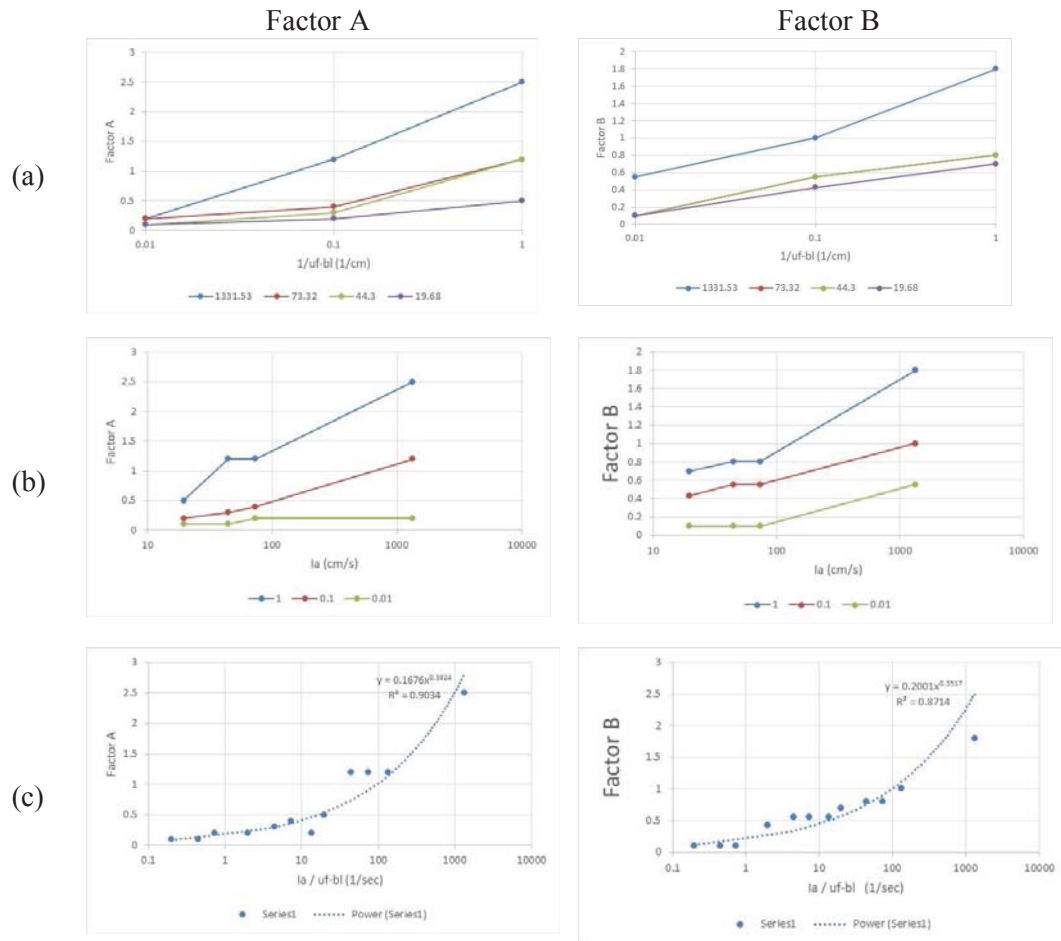


Figure 8: Analysis of the results of the table 3: The factors A and B in terms of (a)  $1/ u_{f-bl}$ , (b)  $I_a$ , (c)  $I_a/ u_{f-bl}$ .

## 6 DISCUSSION

### 6.1 Validation and Application

Partial validation of the proposed equation (5) is the fact that the coefficient of determination ( $R^2$ ) of the fitting parameters  $a_1$ ,  $a_2$  and  $b_1$ ,  $b_2$  of the proposed equation is near unity and certainly larger than 0.8. However, it is desirable to perform additional analyses to validate equation (5), especially as only four seismic motions were used to derive it. For this purpose, more parametric analysis to validate the proposed equation and analyze its error may be performed by applying all the seismic motions of table A1, as well as different soil profiles.

Furthermore, because deterministic methods obtaining empirical expressions predicting the seismic displacement of slopes do not rationally take into account the uncertainty of these expressions, researchers have recently turned to the probabilistic approach: (a) Creating probability curves of an annual exceedance of a specific value [15], or (b) fragility curves which give the possibility of exceeding a certain seismic displacement value in the design time depending on the properties of the seismic excitation and of the slope [16]. Thus, it is desirable

to extend and modify as necessary the proposed equation (5) by applying probabilistic methods.

### 6.2 Effect of non-linearity

Soil behaves linearly only at very small shear strains, well below the typical shear strains exerted in soil profiles near severe earthquakes [11]. It is inferred that for accurate predictions, the linear methods described above must be extended with constitutive equations simulating the non-linear soil response. Under dry conditions the degradation of the shear modulus with shear strain must be simulated. The Katsenis et al [11] model simulates this degradation in terms of the Plasticity Index of the Soil (PI), as proposed by the state-of-the-art model of Vucevic and Dobry [17], shown in Fig. 9a. Typical results of numerical simulations illustrating the profound effect of soil non-linearities on the seismic response are given in Fig. 9b. The case of the Aegion 1995 seismic motion with  $a_c=0.5\text{m/s}^2$ ,  $V_{s-2}=V_{s-1}$ ,  $h_1=h_2=15\text{m}$ ,  $\rho_1=\rho_2=2\text{Mg/m}^3$ ,  $\lambda_1=\lambda_2=0.15$ ,  $PI_1=PI_2=0$  is considered.

Katsenis et al. [11] observed that the effect of soil non-linearities can be simulated in linear analyses by reducing the shear wave velocity to the average value one during the non-linear dynamic simulation. Thus, it is inferred that equation (5) may potentially be extended to predict the non-linear soil response by proposing methods which adequately reduce the  $V_{s-1}$  and  $V_{s-2}$  values in terms of the intensity of the applied seismic motion and the soil stiffness.

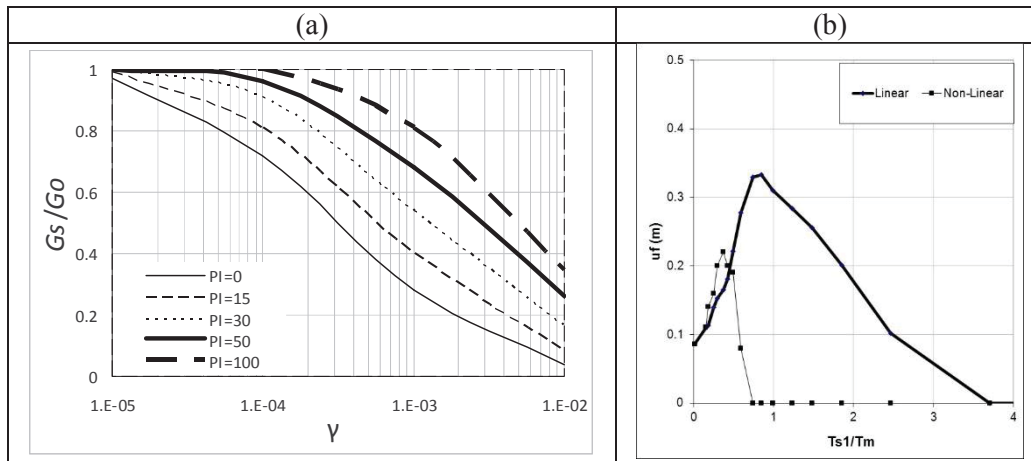


Figure 9: (a) Shear modulus degradation versus shear strain in terms of PI, as proposed by Vucevic and Dobry [17], (b) The computed displacement ( $u_f$ ) by Katsenis et al. [11] for the linear and nonlinear dynamic analyses versus  $Ts1/Tm$  for a specific case, described in the text.

## 7 CONCLUSIONS

- Expressions have been proposed predicting the seismic displacement of slopes in terms of characteristics of the applied seismic motion and the critical horizontal acceleration for sliding and only the dynamic characteristics of the sliding mass [7]. Only Katsenis et al. [9] proposed empirical expressions in terms of the soil profile both above and below the slip surface. Yet, their expressions are in terms of the soil profile type of the slope according to Eurocode 8 and not related to the dominant profile period.
- The present work proposes equation (5) simulating the effect of the dynamic response on the seismic displacement of slopes in terms of the dominant period of the soil profile both above and below the slip surface.
- This equation is based on state-of-the-art descriptions of the dynamic response, results of previous dynamic seismic sliding displacement analyses and numerical predictions of the model of Fig. 3b.
- It is desirable to perform more parametric analysis to validate the proposed equation and analyze its error.
- The proposed equation may be extended to predict the non-linear soil response.

## 8 REFERENCES

- [1] Katsenis L. C. Nonlinear dynamic sliding movement of slopes, Doctoral Dissertation, Democritus University of Thrace, School of Engineering, Department of Civil Engineering, Xanthi, June, 2020.
- [2] Newmark, N. M. Effects of earthquakes on dams and embankments. *Geotechnique*, 55 (2), 139-159, 1965.
- [3] Ambraseys N. and Menu J. Earthquake induced ground displacements, *Earthquake engineering and structural dynamics*, 16, 7, 985-1006, 1998.
- [4] Ambraseys N N, Srbulov M. Attenuation of earthquake-induced displacements. *Journal of Earthquake Engineering and Structural Dynamics* 23: 467–487, 1994.
- [5] Jibson R. W. Regression models for estimating coseismic landslide displacement *Engineering Geology* 91, 209–218, 2007.
- [6] Chousianitis K., Gaudio V., Kalogeras I, Ganas A. Predictive model of Arias intensity and Newmark displacement for regional scale evaluation of earthquake – induced landslide hazard in Greece , *Soil Dynamics and Earthquake Engineering* , 2014.
- [7] Bray J. D. and Travasarou T. (2007). Simplified Procedure for Estimating Earthquake-Induced Deviatoric Slope Displacements, *Journal of Geotechnical and Geoenvironmental Engineering*, 133 (4), 381-392.
- [8] Lin J.-S., and Whitman, R.V. Decoupling Approximation to the evaluation of earthquake-induced plastic slip in earth dams. *Earthquake Engineering and Structural Dynamics*, 11: 667–678, 1983.

- [9] Katsenis L.C, Stamatopoulos C.A., Panoskaltsis V.P., Thomaidou K. Seismic sliding displacement of slopes in terms of soil profile type Non-linear dynamic seismic sliding movement of dry slopes, COMPDYN 2019, 7th International Conference on Computational Methods in Structural Dynamics and Earthquake Engineering, 24-26 June, Crete, Greece, 2019.
  - [10] European Standard. Eurocode 8: Design of structures for earthquake resistance, Final Draft, prEN 1998-5, December, 2003.
  - [11] Katsenis L.C., Stamatopoulos C.A., Panoskaltsis V.P. Non-linear dynamic seismic sliding movement of dry slopes, COMPDYN 2019, 7th International Conference on Computational Methods in Structural Dynamics and Earthquake Engineering, 24-26 June, Crete, Greece, 2019.
  - [12] Katsenis L.C., Stamatopoulos C.A., Panoskaltsis V.P., Di B. Prediction of large seismic sliding movement of slopes using a 2-body non-linear dynamic model with a rotating stick-slip element. Soil Dyn Earthq Eng, 2020.
  - [13] Rathje E. M. and Bray J. D. An examination of simplified earthquake induced displacement procedures for earth structures. Can. Geotech. J. 36: 72–87, 1999.
  - [14] Anastasopoulos I. , Gazetas G., Loli M., Apostolou M., Gerolymos N. Soil failure can be used for seismic protection of structures, Bull Earthquake Eng, 8:309–326, 2010.
  - [15] Rathje E. M., Wang Y., Stafford P. J., Antonakos G. & Saygili G. Probabilistic assessment of the seismic performance of earth slopes. Bulletin of Earthquake Engineering volume 12, 1071–1090, 2014.
  - [16] Jafarian Y., Lashgari A. and Miraei M. Multivariate Fragility Functions for Seismic Landslide Hazard Assessment, Journal of Earthquake Engineering, 2018.
- Vucetic M. And Dobry R. “Effect of soil plasticity on cyclic response, Journal of the Geotechnical Division, ASCE, 117 (1), 1991.

## Appendix

Table A1. Seismic motions collected and their magnitude and distance.

No	Name	Date	M (Mw)	Epic. Distance (km)
1	Turkey, Düzce	12/11/1999	6.6	27.4
2	Turkey, Düzce	12/11/1999	6.6	27.2
3	Italy, Umbria	30/10/2016	6.1	12
4	Italy, Abruzzo	07/04/2009	5.4	3.6
5	Italy, Umbria	30/10/2016	6.1	18.6
6	Turkey, Kocaeli	13/09/1999	5.8	13.8
7	Turkey, Düzce	12/11/1999	6.6	25.9
8	Greece, Ioannina	15/10/2016	5.6	55.9
9	Greece, Ioannina	16/10/2016	4.8	53.3
10	Italy, Umbria	10/30/2016	6.1	10.5
11	Turkey, Düzce	12/11/1999	6.6	32.3
12	Montenegro	15/04/1979	6.8	62.9
13	Italy, Lazio	24/08/2016	6	32.9
14	Italy, Marche	26/10/2016	5.4	11.5
15	Turkey, Kocaeli	17/08/1999	7.25	3.4
16	Italy, Marche	26/10/2016	5.4	16.7
17	Montenegro	15/04/1979	6.8	19.7
18	Italy, Marche	26/10/2016	5.4	15.2
19	Italy, Umbria	06/10/1997	5.4	20.8
20	Italy, Umbria	09/26/1997	5.8	21.6
21	Italy, Calabria	25/10/2012	5	2.4
22	Italy, Umbria	14/10/1997	5.5	8.7
23	Italy, Calabria	09/09/1998	5.5	18
24	Italy, Abruzzo	18/01/2017	5.4	19.2
25	Turkey, Düzce	12/11/1999	6.6	30.3
26	Italy, Umbria	26/09/1997	5.6	24.2
27	Turkey, Düzce	12/11/1999	6.6	27.4
28	Bosnia and Herzegovina	1990-04-03	4.8	22
29	Italy, Abruzzo	18/01/2017	5.1	37.9
30	Italy, Abruzzo	07/04/2009	5.4	15.6
31	Italy, Umbria	30/10/2016	6.1	26
32	Italy, Campania	29/12/2013	5	8.5
33	Turkey, Düzce	12/11/1999	6.6	34.7
34	Greece, Ioannina	16/10/2016	4.5	62.4
35	Italy, Marche	26/10/2016	5.9	31.6
36	Italy, Calabria	25/10/2012	5	10.7
37	Italy, Umbria	30/10/2016	6.1	46.6
38	Croatia, zupanja	27/11/1990	5.6	56.9
39	Greece, Athens	07/09/1999	5.8	19.7
40	Italy, Marche	26/10/2016	5.4	22.8
41	Italy, Marche	26/10/2016	5.9	17.4
42	Greece, Peloponeze	13/10/1997	5.8	51.4
43	Italy, Abruzzo	18/01/2017	5.4	31.4
44	Italy, Calabria	25/10/2012	5	9.4
45	Greece, Rodos	24/01/2019	5.2	86.3
46	Italy, Umbria	07/05/1984	5.9	10.1
47	Italy, Abruzzo	18/01/2017	5.4	20.7
48	Turkey, Düzce	12/11/1999	6.6	15.6
49	Italy, Catania	13/12/1990	5.6	36.9
50	Italy, Abruzzo	18/01/2017	5.3	34.5
51	Italy, Marche	26/10/2016	5.9	60.2
52	Italy, Abruzzo	18/01/2017	5.4	17

Table A2. Characteristics of the seismic motions of table A1.

No	PGA (cm/s <sup>2</sup> )		Ia (cm/s)		Tcr (s)	
	E	N	E	N	E	N
1	-743	-1010	649.35	1331.53	0.26	0.25
2	489	-888	198.95	979.16	0.32	0.4
3	779	-850	555.65	608.67	0.17	0.15
4	652	304	89.77	49.83	0.19	0.2
5	426	385	201.09	192.23	0.25	0.16
6	317	-74	30.49	3.76	0.23	0.22
7	277	298	156.33	185.24	0.37	0.2
8	287	241	64.36	84.47	0.36	0.32
9	284	194	23.12	22.85	0.3	0.34
10	274	273	80.30	70.73	0.65	0.22
11	-254	116	100.62	19.58	0.28	0.32
12	-249	211	45.88	73.32	0.29	0.25
13	242	186	30.33	12.33	0.4	0.12
14	-194	239	23.44	19.74	0.13	0.16
15	229	164	97.78	73.72	0.29	0.28
16	-218	-130	31.84	17.65	0.12	0.12
17	210	173	72.89	61.59	0.7	0.17
18	177	-192	9.88	8.89	0.26	0.13
19	-101	-184	6.57	13.84	0.28	0.22
20	184	164	23.49	27.93	0.32	0.19
21	182	-130	10.69	8.99	0.19	0.28
22	94	-176	5.07	11.43	0.24	0.24
23	-152	-162	10.26	15.68	0.11	0.5
24	82	-161	3.45	9.71	0.13	0.28
25	121	-157	41.07	44.30	0.36	0.25
26	111	152	5.79	11.30	0.25	0.22
27	-133	-148	27.54	37.35	0.19	0.24
28	109	-139	8.00	12.37	0.05	0.08
29	-83	-138	2.47	4.92	0.06	0.1
30	88	131	2.47	4.58	0.1	0.32
31	-131	114	16.15	11.65	0.2	0.22
32	130	-77	9.45	8.56	0.12	0.1
33	-129	98	24.36	22.52	0.32	0.32
34	127	-114	6.37	9.41	0.2	0.3
35	-117	-125	7.22	9.25	0.08	0.13
36	-117	-124	5.38	5.63	0.12	0.19
37	-90	121	9.33	19.68	0.09	0.13
38	-121	121	19.87	18.62	0.35	0.16
39	-119	-108	9.48	6.54	0.1	0.25
40	-119	100	5.88	5.80	0.2	0.2
41	-119	-84	8.59	8.63	0.16	0.2
42	-116	117	28.17	19.12	0.3	0.22
43	109	-116	7.90	10.43	0.1	0.1
44	96	-114	3.20	3.45	0.09	0.1
45	43	112	3.34	11.19	0.35	0.4
46	110	98	5.29	6.23	0.25	0.11
47	95	108	5.97	8.78	0.12	0.29
48	106	74	11.02	6.42	0.1	0.26
49	105	61	5.53	4.71	0.08	0.22
50	-68	103	3.83	6.41	0.1	0.1
51	71	103	4.49	4.29	0.19	0.1
52	-76	-102	3.46	5.78	0.17	0.17



## EFFECT OF 1D VERTICAL VARIABILITY OF SHEAR MODULUS ON THE SEISMIC RESPONSE OF SITES

Mounia Menoun HADJ BRAHIM <sup>1</sup>, Hamid AFRA <sup>2</sup>

<sup>1</sup>National Center of Studies and Integrated Research on Building Engineering (CNERIB) Algiers, Algeria and University of Science and Technology Houari Boumediene (USTHB) Algiers, Algeria.  
[hadj.cnerib@gmail.com](mailto:hadj.cnerib@gmail.com)

<sup>2</sup> National Center of Studies and Integrated Research on Building Engineering (CNERIB) Algiers, Algeria and National Delegation of Major Risks, Algiers, Algeria.  
[hamid.afra@interieur.gov.dz](mailto:hamid.afra@interieur.gov.dz)

---

### Abstract

*Urban development is increased and the construction of building on poor quality soils becomes non avoidable which increases the geotechnical risk. Below these circumstances, the probabilistic approaches to study the behavior of a soil profile in a given environment have been proposed in recent years. The purpose of this research work is to study the effect of vertical variability of soil shear modulus on soil seismic response using the probabilistic approach. Two types of heterogeneity are considered: (1) heterogeneity due to the random distribution of the shear modulus in a soil profile; (2) heterogeneity of soil layer with shear modulus increasing linearly with depth. The first heterogeneous soil models are generated by Monte Carlo simulation. The spatial variation of the shear modulus is controlled by the variation coefficient parameters. The second heterogeneous soil models are assumed to have shear modulus increasing linearly with depth. These heterogeneous soils are generated and then integrated into the computer program based on the one dimensional wave propagation, resulting in seismic responses at the 'free field' soil. To demonstrate and show the importance of considering heterogeneities in the model, the results are compared with examples of deterministic analysis by means of the experimental value of shear modulus obtained from a specific site in Algeria.*

**Keywords:** *Shear Modulus, Heterogeneity, Random Distribution, Increasing Linearly, Soil Seismic Response.*

---

## 1 INTRODUCTION

In geotechnical practice, the determination of soil properties is based on tests carried out on a limited number of samples in the laboratory or on site. Soil state variables in space and time are due to complex geological conditions. Their properties change from a point to another. Due to the uncertainty associated with their inherent spatial variability, and limited available information, soil properties can be considered as random variables. Moreover, poor soil sampling procedures, test procedures, characteristics of the test setup device and operator experience can have a large impact on the measured geotechnical properties. The probabilistic approach is often used in engineering sciences to represent and decrease these uncertainties. It attempts to take into account all the uncertainties affecting the properties of soils, and allow the engineer to make the decision that bringing more objectivity; it assumes that the characteristics are variables defined by a mean, a standard deviation and a distribution law. To consider these uncertainties using the probabilistic approach, soil properties are treated as random variables. These random variables are functions defined on a sample space to represent quantities that can change. In practice, a random variable is where the estimated value is uncertain, but a certain probability can be assigned to any specific value (take values from a finite or countable set) "for discrete random variables" or within any value from an interval on a real line "continuous random variables".

Several studies have been conducted taking into account uncertainty in geotechnical engineering, Tian and Jie [1] conducted a study of the uncertainty of soil parameters, regarding the shear wave velocity (VS), thickness (h), density and damping for the propagating of one-dimensional wave. Specific conclusions were drawn. Nour [2] studied, two-dimensional seismic response, using Monte Carlo simulations combined with the deterministic method of shear modulus, critical damping and Poisson's ratio of soil properties. The results showed a significant attenuation of the tendency of the acceleration at the ground surface compared to the homogeneous case. Dominic et al [3] carried out a study of the importance of the spatial variability of soil properties on the surface response spectrum using Monte Carlo simulation based on the Popescu methodology [4]. They concluded that local conditions are important according to the gradient of the stiffness of the profile and intensity of the movement and that further studies should be performed. Paolo and Cornell [5] presented a probabilistic work to study the effect of soil layers on the estimation of the nonlinear amplification function, AF (f) and the acceleration response spectrum for a frequency range of the oscillator of the structures. The results revealed that AF (f) depends strongly on the intensity of the input soil movement at the same oscillator frequency, for the two soil types studied (sand and clay). Andrade and Borja [6] performed a combined stochastic-deterministic analysis of the local site response. To compare the sensitivities of equivalent linear and non-linear analysis procedures, two computer codes SHAKE and SPECTRA were used. The soil variability as well as the frequency and duration of earthquakes were considered in this study. The results showed that SPECTRA has approximately the same sensitivity as SHAKE.

Other recent typical examples include the work of Li and Assimaki [7], Johari A. [8] and Menzer Pehlivan et al [9] examined the special variability of soil on the prediction of a strong soil motion, where the consequences of spatial variability on the seismic response are not well understood. The basic characteristics of any layer are the shear wave velocity, the thickness and the non-linear properties of soil. The values of these properties in nature through a site vary from one point to another and there is always uncertainty in their measurement, this is a major contributor to uncertainty in geotechnical engineering analyzes.

## 2 PROBABILISTIC METHOD OF INDIRECT SIMULATION OF NON-GAUSSIAN RANDOM FIELDS

The probabilistic method of indirect simulation of non-Gaussian random fields is based on the theory of random fields. This approach is based on the decomposition of random variables as described by Fenton [10].

The algorithm that allows the generation of  $\Delta f_p(z)$  is described as follows:

$$\Delta f_p(z) = \sum_{n=1}^{N_p} \Delta g_{pn}(z) \quad (1)$$

With  $N_p$  is the number of soil properties to be simulated. The Gaussian random field with  $N_p$  variables, one-dimensional, with zero mean and unity variance  $\Delta g_{pn}(z)$  can be simulated as follows [11, 16]:

$$\Delta g_{pn}(z) = \sqrt{2} \sum_{l=0}^N A_{l,pn} \cos(k_l z + \Omega_{l,pn}) \quad (2)$$

With

For multivariate fields

$$A_{l,pn} = H_{pn}(k_l) \sqrt{2\Delta k} \quad (3)$$

For uni-variate fields

$$A_l = \sqrt{2S(k_l)\Delta k} \quad (4)$$

Equation (3) also can ensures the inter-property correlation,  $\Omega_{l,pn}$  are random phases uniformly distributed in the interval  $[0, 2\pi]$ . The coefficients  $H_{pn}$  are obtained from the inter spectral density matrix in the wave number domain  $S(\mathcal{K})$ , the latter is a real, symmetrical matrix, and positive definite. The elements of the matrix  $H$  are obtained from the Cholesky decomposition of the symmetric matrix  $S$  which is defined by:

$$S(k) = \begin{bmatrix} S_{11}(k) & S_{12}(k) & \cdots & S_{1N_p}(k) \\ S_{21}(k) & S_{22}(k) & \cdots & S_{2N_p}(k) \\ \cdots & \cdots & S_{p_i p_i}(k) & \cdots \\ S_{N_p 1}(k) & S_{N_p 2}(k) & \cdots & S_{N_p N_p}(k) \end{bmatrix} \quad (5)$$

The matrix  $H_{pn}$  is assumed to be lower triangular:

$$H(k) = \begin{bmatrix} H_{11}(k) & 0 & \cdots & 0 \\ H_{21}(k) & H_{22}(k) & \cdots & 0 \\ \cdots & \cdots & \cdots & 0 \\ H_{N_p 1}(k) & H_{N_p 2}(k) & \cdots & H_{N_p N_p}(k) \end{bmatrix} \quad (6)$$

with  $\mathcal{K}$  is the number of waves which satisfies:

$$\begin{cases} k_l = l \cdot \Delta k \\ k_u = N \cdot \Delta k \end{cases} \quad (7)$$

The wavenumber step  $\Delta\mathcal{K}$  is evaluated from the representation of  $S\mathcal{K}$  and by evaluating the cut-off wavenumbers values  $\mathcal{K}u$  for  $N$  increments,  $\mathcal{K}u$  is defined by:

$$k_u = \frac{1}{a} \sqrt{\ln\left(\frac{1}{\lambda^4}\right)} ; \lambda = 0.001 \quad (8)$$

$a$  is a parameter statistic, which is obtained from a non-linear regression of experimental data.

In this study, we consider one-dimensional, univariate, homogeneous but non-Gaussian field with mean zero and spectral density function given by [2]:

$$S(k) = \frac{\sigma^2|_{\sigma=1} a}{2\sqrt{\pi}} \exp\left[-\left(\frac{ka}{2}\right)^2\right] \quad (9)$$

In order to considerably reduce the computing time, the digital generation of sample functions of equation (2) is easily calculated using the Fast Fourier Transform (FFT), developed by Yamazaki and Shinozuka [17] and modified by Zerva [18].

The analysis carried out in this paper considers  $\lambda$  (is a small real number close to zero) equal to 0.001.

### 3 SPATIAL VARIABILITY OF UNBOUNDED SOIL PROPERTIES

Soil properties such as elastic modulus  $E$ , shear modulus  $G$ , permeability  $k$ , etc., are assumed to be lognormally distributed. This choice is motivated by the fact that these properties are positive parameters, and that the lognormal distribution makes it possible to analyze their great variability. The expression of the shear modulus for example is given by [2,10]:

$$\lambda_G(z) = \exp[\lambda_{0G}(z) + \xi_G \Delta f_G(z)] \quad (10)$$

With:

$$\begin{cases} \xi_G^2 = Ln(1 + \frac{\sigma_G^2}{\lambda_{0,G}^2}) \\ \lambda_{0G}(z) = \ln(\lambda_{0,G}) - \frac{1}{2} \xi_G^2 \end{cases} \quad (11)$$

Where  $\lambda_{0,G}$  and  $\sigma_G^2$  are respectively stand for shear modulus means and variance.

CV<sub>G</sub>: Coefficient of variation: To provide a dimensionless expression of the uncertainty inherent in a random variable.

### 4 HETEROGENEITY OF SOIL LAYER WITH SHEAR MODULUS INCREASING LINEARLY WITH DEPTH

In this proposed approach the soil profile is assumed to have shear modulus increasing linearly with depth. In the upper layer, of thickness  $h_1$ , the shear modulus is supposed to vary according to [19]:

$$G_1(z) = G_0(z/h_1)^p \quad (12)$$

Where  $z$  is the depth counted positively downwards from ground surface,  $G_0$  is the shear modulus at depth  $h_1$ ,  $p$  is an arbitrary exponent, which takes values in range  $0 \leq p < 2$ . The

parameter  $p$  can be determined by a least square fit through the measured values of the shear wave velocity  $\hat{V}(z)$  and is given by Ref. [20]:

$$p = \ln V_{s1} \frac{1}{h_1} \int_0^{h_1} \ln \left( \frac{z}{h_1} \right) \ln \hat{V}(z) dz \quad (13)$$

Where  $V_{s1}$  is the shear wave velocity at depth  $h_1$

For the underlying layer the shear modulus is assumed to be:

$$G_2(z) = G_0 + G_1(z/h_2) \quad (14)$$

Where  $z$  is counted from the layers interface and  $h_2$  is the thickness of second layer and  $G_0+G_1$  is the shear modulus at depth  $h_2$ .

## 5 RESULTS OF THE DYNAMIC RESPONSE OF A HETEROGENOUS ONE-DIMENSIONAL SOIL PROFILE

### ▪ Site variability Effects (shear modulus): the case of Souidania

This example deals with the vulnerability of a site with an inclined topography, with a slope that varies from 4% to 5%, (figure 10). The site is located at Souidania, located in the southwestern suburbs of Algiers and occupies an area of around 6 ha [21].



**Fig. 1.** Location of the project (Google Earth, October 2016)

It is shown in figures 2 and 3 ten realizations of the shear modulus for different values of  $CVG$ . The effect of site variability is therefore an essential parameter in an urban environment which must be evaluated to better define the lateral variability of the seismic movement of the soil, with immediate consequences on the response of structures and their damage.

### First layer

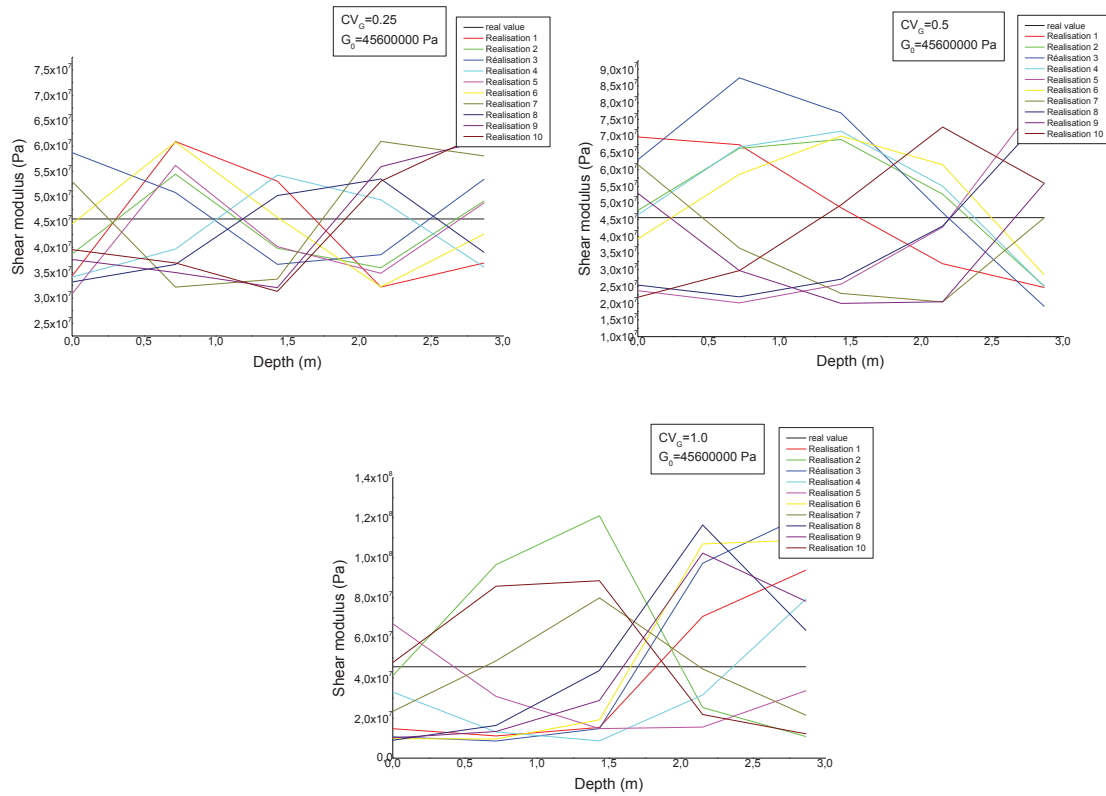
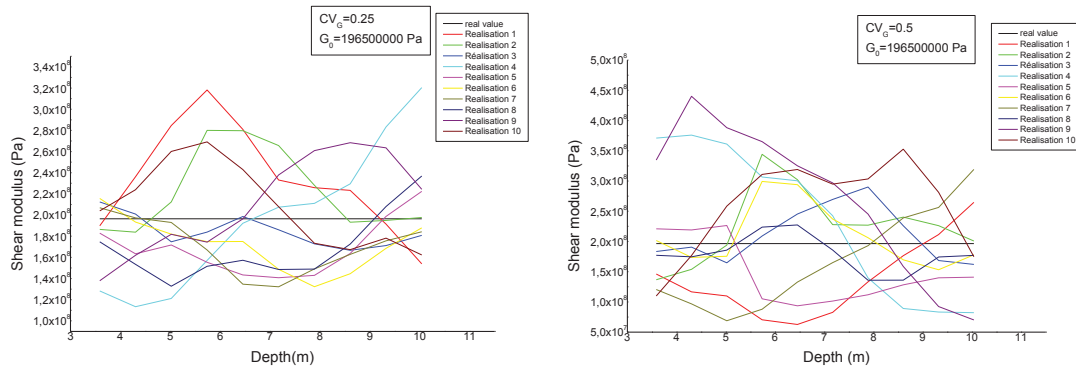
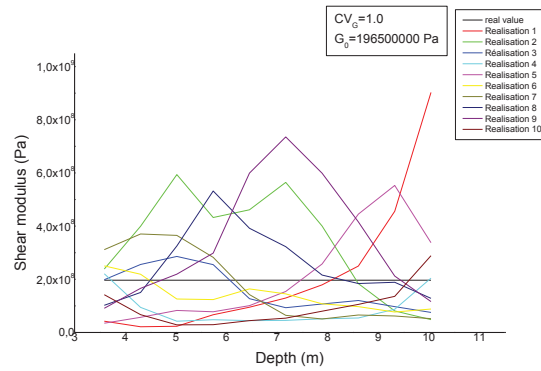


Fig. 2. Ten realizations of variations in shear modulus, first site layer, for different values of  $CV_G$ .

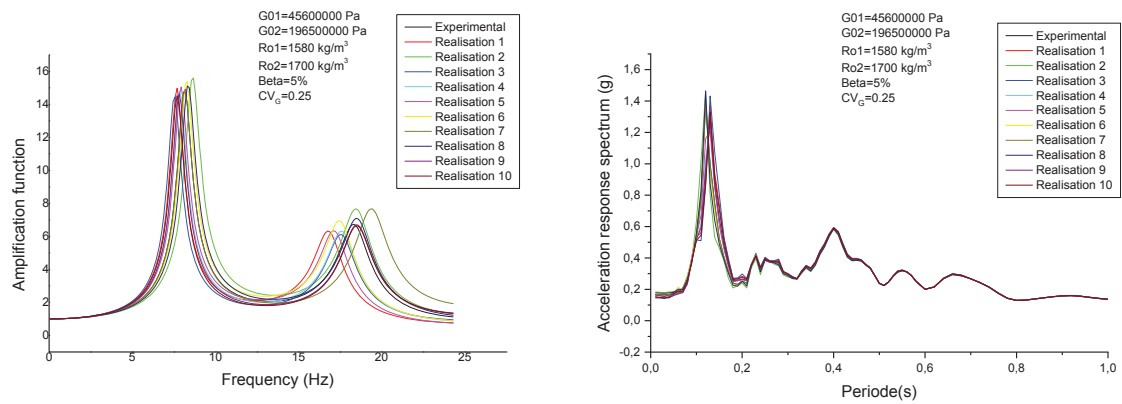
### Second layer



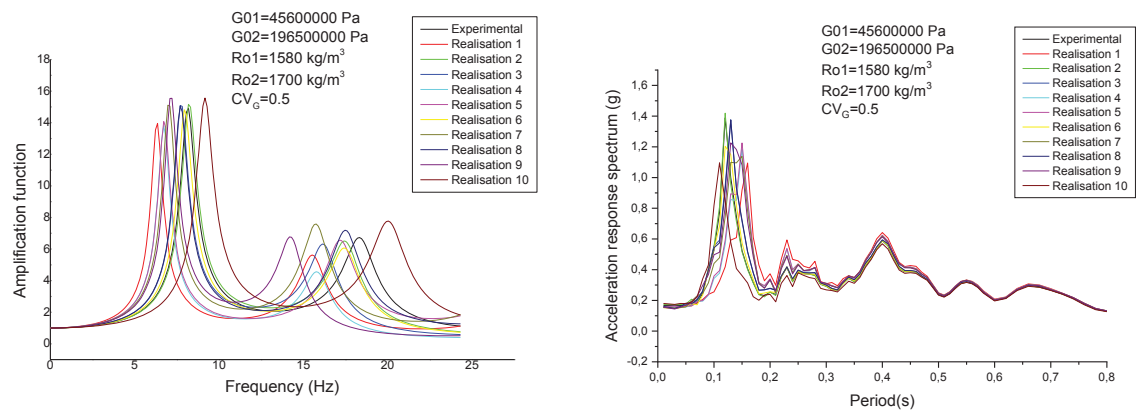




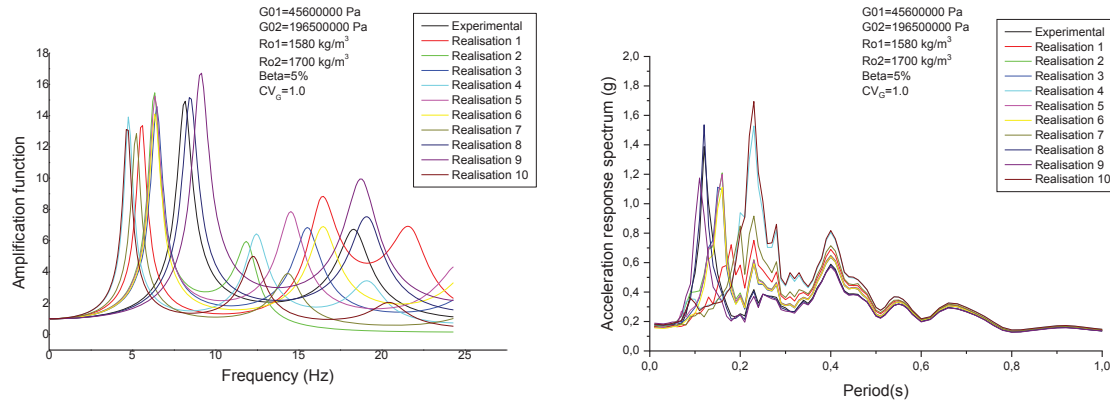
**Fig. 3. Ten realizations of shear modulus variations, second site layer, for different values of  $CV_G$ .**



**Fig. 4. Seismic amplification and the response spectrum in acceleration at the surface of the experimental case and of ten realizations according to the variability of the shear modulus  $G$  for a value of  $CV_G = 0.25$ .**

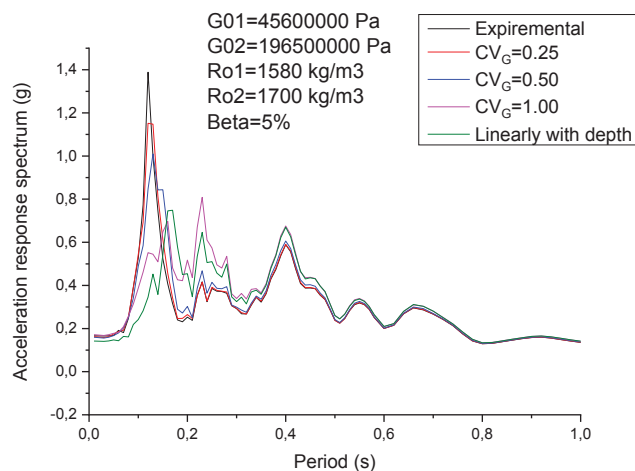


**Fig. 5. Seismic amplification and the response spectrum in surface acceleration of the experimental case and ten realizations according to the variability of the shear modulus  $G$  for a value of  $CV_G = 0.5$ .**



**Fig. 6. Seismic amplification and the response spectrum in acceleration at the surface of the experimental case and of ten realizations according to the variability of the shear modulus  $G$  for a value of  $CV_G = 1$**

From figures 4, 5 and 6, it is clearly seen that the variation of the shear modulus has great importance on the seismic amplification of the soil and this amplification varies according to the coefficient of variation  $CV_G$  where the value of the  $CV_G$  varies from 0.25 slightly heterogeneous to the value 1.00 strongly heterogeneous. Figure 7 shows a comparison between the case of heterogeneous experimental case, the cases of average of the ten realizations for each  $CV$  value and the case of shear modulus increasing linearly with depth.



**Fig.7. Surface acceleration response spectrum difference between the experimental case, the case of Monte Carlo as a function of the variability of the shear modulus  $G$  for different  $CV_G$  values and the case of shear modulus increasing linearly with depth.**

From the curves we can clearly see the differences between the studied cases, and that the probabilistic seismic response of heterogeneous soil profile via Monte Carlo simulations, for the value of  $CV = 0.25$ , is more equivalent to that of the seismic response of experimental case. On the other hand, we have observed an attenuation compared to the other cases of the value of  $CV = 0.5$  and  $CV = 1$ . Furthermore, For the case of the shear modulus increasing linearly with depth, the value of the response spectrum is identical to the probabilistic seismic response of heterogeneous soil profile via Monte Carlo simulations for the case of  $CV = 1$ .

## 6 DISCUSSION AND CONCLUSIONS

In this paper the acceleration response spectrum of the heterogeneous seismic amplification soils is analyzed. The random soil properties considered is the shear modulus, modeled by random spatial fields. The random field for the shear modulus is obtained by adopting the lognormal distribution, which allows its great variability to be analyzed.

As a summary of this article, we can recapitulate the following comments

- The increase in the coefficient of variation of the shear modulus induces a decrease in soil amplification and the peak acceleration response spectrum for the one-dimensional case. On the other hand, it is observed that increasing the coefficient of variation of the shear modulus also causes a filtering effect which slides the fundamental frequency of the system towards low frequencies, and causes attenuation of high frequencies. In this case, the simulated soil becomes softer compared to the homogeneous soil ( $CVG = 0$ ).
- For the case of shear modulus increasing linearly with depth, the value of the response spectrum is identical to the probabilistic seismic response of heterogeneous soil profile via Monte Carlo simulations for case of  $CV = 1$ .

The results obtained indicate that the seismic response is related to the shear modulus variability. In addition, it is observed that the increase in the coefficient of variation of the shear modulus induces a decrease in the peak value of the response spectrum in acceleration for the one-dimensional case. The method described in this paper, by analyzing several realizations, can reduce the geotechnical risk.

## REFERENCES

- [1] Tian, L., and L. Jie. 1992. Influence of random mechanical parameter on earthquake response analysis of site, 10th World Conf. on Earthquake Engineering, Madrid, Spain, 19–24 July.
- [2] Nour, A. 2004. Investigation stochastique sur les milieux hétérogènes par la méthode des éléments finis. Thèse de Doctorat, Université des Sciences et de la Technologie Houari Boumedienne, Algérie.
- [3] Dominic Assimaki, Alain Pecker, Radu Popescu And Jean Prevost. 2003. Effects of spatial variability of soil properties on surface ground motion. Journal of Earthquake Engineering Vol. 07, No. spec01, pp. 1-44.
- [4] Popescu, R., Prevost, J. H. and Vanmarcke, E. H. 1995. Numerical simulations of soil liquefaction using stochastic input parameters, Proc. 3rd International Conference on Recent Advances in Geotechnical Earthquake Engineering and Soil Dynamics, St. Louis, MO.
- [5] Paolo Bazzurro and C. Allin Cornell. 2004. Nonlinear Soil-Site Effects in Probabilistic Seismic-Hazard Analysis Bulletin of the Seismological Society of America, Vol. 94, No. 6, pp. 2110–2123.
- [6] Andrade J.E. et Borja R.I. 2006. Quantifying sensitivity of local site response models to statistical variations in soil properties. Acta Geotechnica 1:3–14.
- [7] Li W. and Assimaki D. 2010. Site- and Motion-Dependent Parametric Uncertainty of Site-Response Analyses in Earthquake Simulations. Bulletin of the Seismological Society of America, Vol. 100, No. 3, pp. 954–968.

- [8] Johari A. Momeni M. 2015. Stochastic analysis of ground response using non-recursive algorithm. *Soil dynamics and earthquake engineering* 69: 57-82.
- [9] Menzer Pehlivan, Ellen M. Rathje and Robert B. Gilbert. 2016. Factors influencing soil surface seismic hazard curves. *Soil dynamics and earthquake engineering* 83, 180-190.
- [10] Fenton G.A. 1990. Simulation and Analysis of Random Fields. Ph.D. thesis, Princeton University.
- [11] Mantoglou A. and Wilson J.L. 1981. Simulation of Random Fields with the Turning Bands Method. Department of Civil Engineering, Report No. 264, Massachusetts Institute of Technology, Cambridge, MA, July.
- [12] Mignolet M.P. and Spanos P.D. 1992. Simulation of homogeneous two-dimensional random fields: Part I – AR and ARMA Models. *ASME J. Appl. Mech.*, 59: 260-269.
- [13] Matheron G. 1973. The Intrinsic Random Functions and Their Applications. *Advances in Applied Probability*; 5: 439-468.
- [14] Fenton G.A. and Vanmarcke E.H. 1991. Spatial Variation in Liquefaction Risk Assessment. *Proc. Of Geotechnical Engrg. Congress, ASCE, Geotech. Div., Boulder, Colorado*, 594 - 607.
- [15] Fenton G.A. 1994. Error evaluation of three random field generators. *Journal of Engineering Mechanics ASCE*, 120(12): 2478–2497.
- [16] Ghanen R.G. and Spanos P.D. 1991. *Stochastic finite elements: a spectral approach*. Springer-Verlag.
- [17] Yamazaki F, Shinozuka M. 1988. Digital generation of non-Gaussian stochastic field. *Journal of Engineering Mechanics ASCE*; 114(7): 1183-1197.
- [18] Zerva A. 1992. Seismic ground motion simulations from a class of spatial variability models. *Earthquake Engineering and Structural Dynamics*; 21: 351-361.
- [19] Afra, H., and Pecker A. 2002. Calculation of free response spectrum of a non-homogeneous soil deposit from bed rock response spectrum. *Soil Dynamics and Earthquake Engineering*, 22: 157-165.
- [20] Pecker A. and Afra H. 1995. Charts for natural frequencies and transfer function on an inhomogeneous soil deposits. *Fifth International Conference on Seismic Zonation, II* : p. 1091-8.
- [21] Rapport géotechnique sur site construction logements AADL/SOUIDANIA wilaya d'Alger 2002. Bureau d'études B.Heba.

## A PARAMETRIC STUDY OF “WEAK LAYER” EFFECTS ON THE SEISMIC RESPONSE OF LIQUEFIABLE SOIL PROFILES

Yannis Z. Tsiapas<sup>1</sup>, Maria S. Spanea<sup>1</sup>, and George D. Bouckovalas<sup>1</sup>

<sup>1</sup> National Technical University of Athens  
Iroon Politexniou 9, 15780 Zografou, Attica, Greece  
e-mail: [ioannis.tsiapas@gmail.com](mailto:ioannis.tsiapas@gmail.com), [marspan53@gmail.com](mailto:marspan53@gmail.com), [gbouck@central.ntua.gr](mailto:gbouck@central.ntua.gr)

---

### Abstract

*The existence of a “weak” layer, of low relative density, within a liquefiable soil profile, may have a beneficial effect on the overall seismic response. The “weak” layer will liquefy earlier and may act as a “Natural Seismic Isolation” system, for the overlying, stronger, liquefiable layers, preventing thus the onset of liquefaction in them. In other words, it is possible that the liquefiable ground above the “weak” layer will not liquefy and may thus form a competent soil crust which will protect the integrity of infrastructure founded on it. The paper presents results of a parametric investigation of the “weak” layer effects on the overall seismic response of liquefiable soil profiles. It is based on nonlinear numerical analyses, performed with the Finite Difference method, and focuses on the effects of (i) soil properties (thickness and relative density) of the “weak” layer and the overlying liquefiable layers as well as (ii) the seismic motion characteristics on the extent of “weak” layer-induced natural seismic isolation.*

**Keywords:** Liquefaction, Numerical Analysis, Seismic Response, Natural Seismic Isolation.

---

## 1 INTRODUCTION

It is widely known that soil formations consisting of saturated, cohesionless soil layers are highly susceptible to earthquake induced excess pore pressure accumulation and liquefaction, with devastating results for infrastructures. However, it is possible that, under certain circumstances, the liquefaction of a soil layer prevents the propagation of seismic waves to the ground surface and leads to the drastic attenuation of seismic actions on infrastructures. Bouckovalas et al. [1] have shown that a uniform liquefiable layer, of adequate thickness and drastically reduced acoustic impedance, may indeed act as a “Natural Seismic Isolation” system for seismic ground motions.

The concept of “Natural Seismic Isolation” can be also generalized for non-uniform liquefiable layers which include an intermediate “weak” layer, with significantly degraded liquefaction resistance. In these soil profiles, the intermediate “weak” layer will liquefy first and will cause the attenuation of seismic motions, an effect which may prove beneficial for the overlying and more stiff sand layers. Hence, it will act as a “Natural Seismic Isolation” system, preventing liquefaction to extent up to the ground surface. In other words, the liquefiable ground above the “weak layer” will not liquefy and consequently it will maintain its strength and may thus act as a foundation bearing soil crust. To date, there are no research studies that systematically examine the above phenomena and suggest methods for their quantitative description. However, the few experimental and numerical studies that are found in the literature (e.g. [2,3]) confirm the abovementioned beneficial “weak” layer effect.

The scope of this paper is to investigate the seismic response and the liquefaction of non-uniform sand deposits, aiming to a qualitative evaluation of the “Natural Seismic Isolation” effect due to a “weak” soil layer embedded within the soil profile. For this purpose, a parametric investigation was performed focusing on the seismic response of non-uniform sand deposits. In total, approximately 100 nonlinear, fully coupled, one-dimensional effective stress numerical analyses aimed to examine the effect of various soil and seismic parameters on the seismic response of liquefiable sites with an intermediate “weak” layer.

## 2 NUMERICAL ANALYSES

All numerical analyses were conducted in the Finite Difference code FLAC [4], for the custom made soil profile depicted in Figure 1, which consists of five distinct soil layers under the groundwater table. The total thickness of the soil profile is 18 m, with the upper and the lower 2 m consisting of non-liquefiable medium plasticity clay with plasticity index  $PI=30$ . The shear wave velocity of the clay crust and the clay bed layers is equal to  $V_s=100$  and  $300$  m/s respectively. The rest 14 m consist of liquefiable sand of variable relative density  $D_{r,o}$ , with a “weak” layer of relative density  $D_r=30\%$  and variable thickness  $H_{weak}$  embedded in it.

The base of the soil column was shaken with a 15-cycle harmonic excitation, of peak acceleration  $a_{max}=0.25$  g and variable period  $T_{exc}$  (Figure 1). The values of: (i) the thickness of the “weak” layer  $H_{weak}$ , (ii) the total thickness of the overlying soil layers  $H_{crust}$  (soil crust), (iii) the period of the seismic excitation  $T_{exc}$  and (iv) the relative density  $D_{r,o}$  of the stiffer sand layers were varied parametrically to cover a wide range site and earthquake conditions encountered in practice. The baseline analysis was conducted for the following reference values of the basic parameters:  $H_{weak}=2$  m,  $H_{crust}=6$  m,  $D_{r,o}=60\%$  και  $T_{exc}=0.3$  sec.

The NTUA-SAND critical state plasticity constitutive model [5,6] was employed to simulate the response of the liquefiable sand, while the simpler Ramberg and Osgood [7] constitutive model was selected to simulate the nonlinear hysteretic response of clay layers. The NTUA-SAND model was calibrated against static and cyclic tests on saturated fine Nevada Sand [8], while the Ramberg and Osgood [7] model was calibrated against the experimental



modulus reduction and damping curves of Vucetic and Dobry [9] for low plasticity ( $PI=30$ ) clays. Free-field lateral boundaries were simulated with the “tied-node” technique, which imposes the same (horizontal and vertical) boundary displacements at grid-points of the same elevation. The “Selective Filtering Method” [10] was used in order to eliminate the numerical noise which is inherent to elastoplastic dynamic analyses with FLAC, while the overall accuracy of the numerical methodology has been successfully evaluated in similar studies in the past [e.g. 11,12].

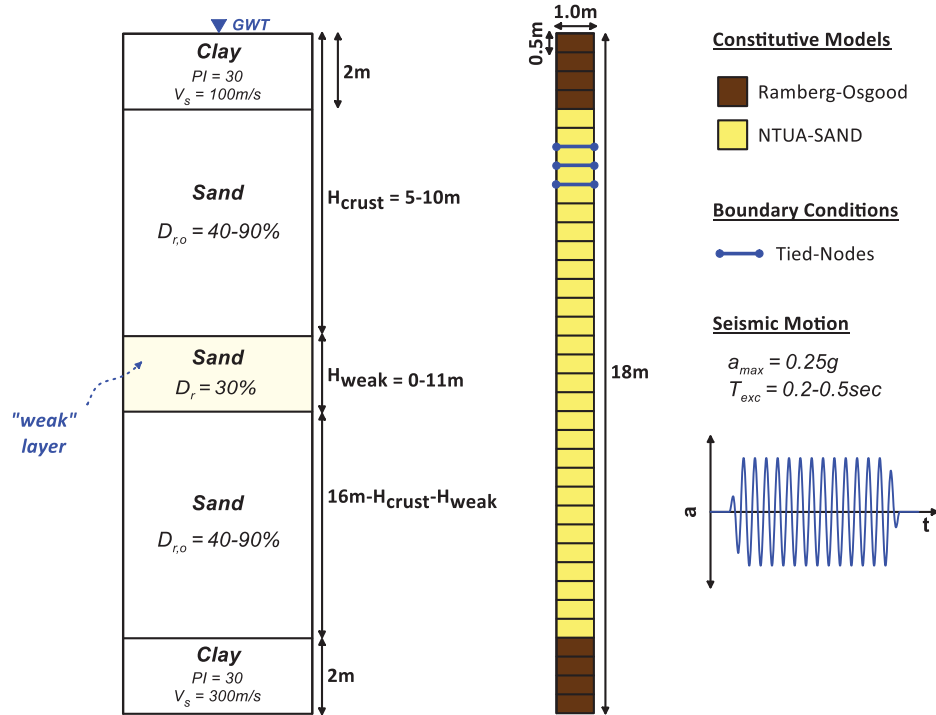


Figure 1: Soil profile, Finite Difference mesh and input motion of the numerical simulations.

### 3 MECHANISMS OF WEAK LAYER EFFECT

To identify the mechanisms which control “weak” layer effects, and demonstrate their consequences on the seismic response of non-uniform sand deposits, the results of a typical analysis with  $H_{weak}=2$  m,  $H_{crust}=8$  m,  $D_{r,o}=60\%$  and  $T_{exc}=0.3$  sec are first presented in more detail. For comparison purposes, the numerical analysis was repeated for the case of uniform sand of relative density  $D_{r,o}=60\%$  over the entire 2 - 16 m depth, namely without intermediate “weak” layer (i.e.  $H_{weak}=0$  m). Figures 2a and 2b compare the time-histories of the excess pore pressure ratio  $r_u$ , defined as the ratio of the excess pore pressures  $\Delta u$  over the initial effective vertical stress  $\sigma'_{v,o}$  (i.e.  $r_u=\Delta u/\sigma'_{v,o}$ ), in the middle of the top sand layer as well as in the middle of the “weak” layer, for the cases of uniform and non-uniform sand respectively. In addition, Figures 2c and 2d present the respective comparisons for the time-histories of the shear stress ratio  $CSR=\tau_d/\sigma'_{v,o}$  (where  $\tau_d$  is the seismic shear stress amplitude).

As depicted by the  $r_u$  time-histories of the non-uniform ground (Figures 2a and 2b), liquefaction occurs first in the “weak” layer at approximately  $t=0.8$  sec, and affects significantly the evolution of the excess pore pressures on the sandy layers above and below the “weak” one. Following the red lines in Figures 2a and 2b, it is observed that after the time instance  $t=0.8$  sec, the excess pore pressure ratio in the “weak” layer becomes almost unity ( $r_u\approx 0.8-1.0$ ) practically diminishing the shearing resistance of that layer. The result of this is to decelerate the excess pore pressure buildup in the overlying layer of relative density  $D_{r,o}=60\%$  and

prevent the onset of liquefaction that would have occurred in the absence of the “weak” layer (black line). The above observations are in total accordance with the respective  $CSR$  time-histories in Figures 2c and 2d, where it is observed that around  $t=1.0$  sec the amplitude of the  $\tau_d/\sigma'_{v,0}$  ratio above the “weak” layer drops to significantly lower levels. This observation, in combination with the small excess pore pressure ratios at these depths, leads to the conclusion that the liquefaction of the “weak” layer actually functions as a “Natural Seismic Isolation” system for the overlying sand layer.

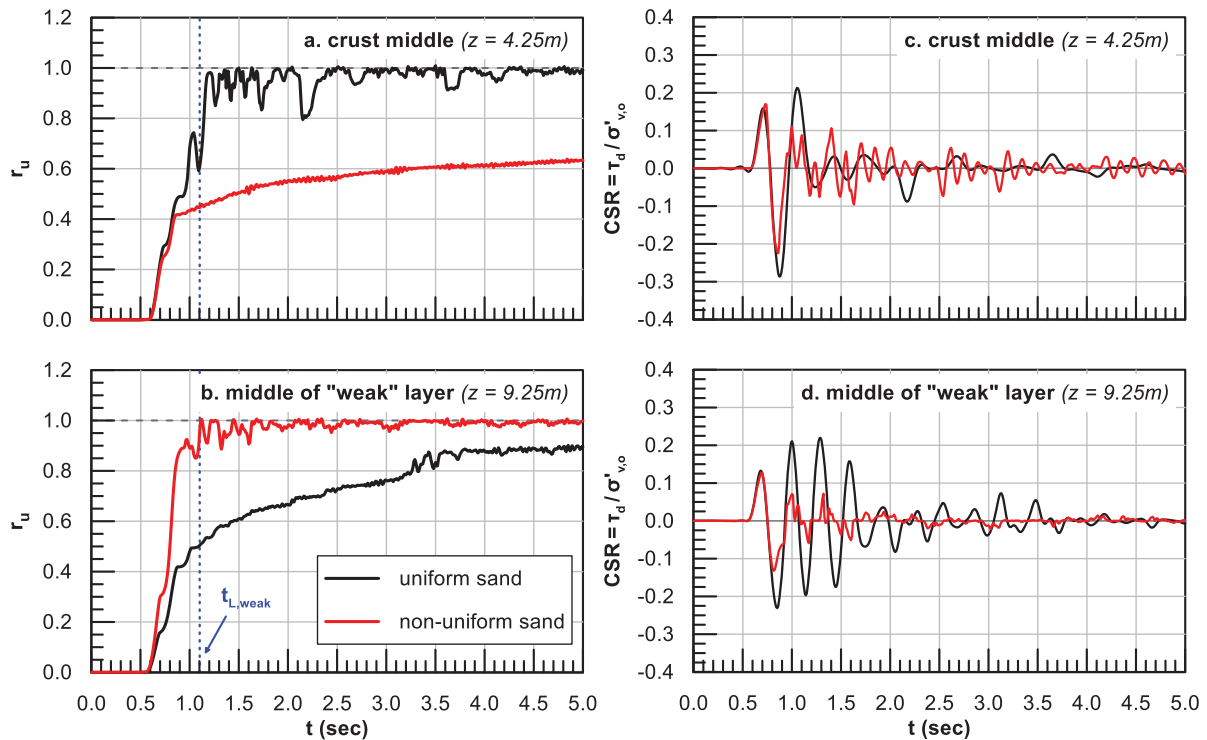


Figure 2: Typical time histories of excess pore pressure ratio  $r_u$  and shear stress ratio  $CSR$  at the middle of the “weak” layer and the overlying layer of sand.

For further insight, Figure 3a compares the variation with depth of the maximum excess pore pressure ratio  $r_{u,max}$  for both the non-uniform and the uniform soil profiles. It is observed that due to the existence of the “weak” layer, liquefaction has not occurred at any depth in the sand layer above it. In particular, the average value of the maximum excess pore pressure ratio above the “weak” layer  $r_u^{cr}$  has been reduced from  $r_u^{cr} \approx 1.0$  for the uniform sand deposit to the value  $r_u^{cr} = 0.65$  in the presence of the “weak” layer. It is also observed that the effect of the “weak” layer is also beneficial on the seismic response of the liquefiable sand layer below it, although less significant and consistent than for the overlying sand layer. For this reason, the following presentation will focus only upon results for the overlying sand layer.

The variation of the factor of safety against liquefaction  $FS_L$  with depth is depicted in Figures 3b and 3c for the case of non-uniform and uniform sand deposit respectively. In both cases, the values of the factor of safety were estimated following two different approaches. Initially,  $FS_L$  was estimated via the empirical methodologies that are commonly utilized in practice (e.g. [13]), based on the results of in-situ SPT or CPT tests. More specifically, it was assumed that the number of SPT blow counts is equal to  $N_{1,60} = 4.1$  and  $16.5$  for  $D_r = 30\%$  and  $D_{r,0} = 60\%$  respectively [14]. For the estimation of the seismic actions, the nonlinear numerical analyses were repeated under drained conditions, i.e. without excess pore pressures

buildup and liquefaction onset. In parallel, the values of  $FS_L$  which correspond to the actual response of each soil element during the numerical simulation were estimated, as follows:

$$FS_L = \left( \frac{N}{N_L} \right)^{-b} \quad (1)$$

where  $N$  is the applied number of cycles by the seismic motion and  $N_L$  the number of loading cycles required to cause liquefaction based on the numerical analysis results. Equation (1) is based on the mathematical expression of the liquefaction resistance curve, namely on the correlation between the cyclic stress ratio  $CSR$  and  $N_L$ :

$$CSR = a \cdot N_L^{-b} \quad (2)$$

where the values of coefficient  $a$  and of exponent  $b$  depend on soil type and loading conditions. For the NTUA-SAND constitutive model and for Nevada Sand, it was assumed that  $b=0.41-0.57$ , based on the previous work of Kalogeraki and Zontanou [15]. More information regarding the estimation of  $FS_L$  from the numerical analysis results can be found in [15-17].

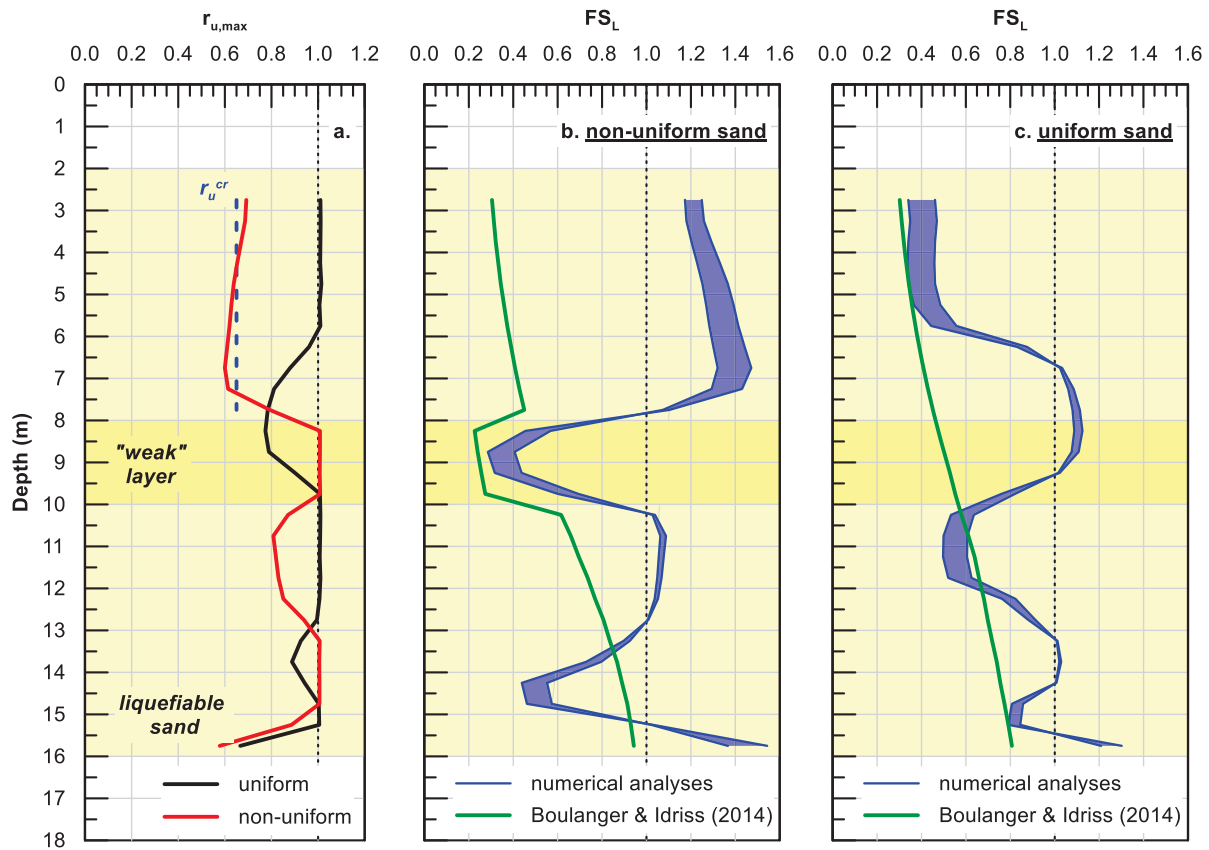


Figure 3: Typical variation with depth of (a) maximum excess pore pressure ratio  $r_{u,max}$  and  $FS_L$  considering (b) non-uniform and (c) uniform sand deposit.

According to Figure 3b, the values of the factor of safety against liquefaction on the top sand layer, based on the numerical analysis results and Eq (1), vary in the range  $FS_L = 1.15 - 1.45$ , compared to the considerably smaller  $FS_L$  values ( $FS_L = 0.30 - 0.45$ ) which were computed for the "weak" layer. It is thus evident that due to the onset of liquefaction in the "weak" layer, the applied shear stress ratio  $CSR$  in more shallow depth is reduced, acting thus benefi-

cially for the overlying sand layers, which have not been already liquefied. As the applied seismic action is reduced, the factor of safety against liquefaction at these depths increases significantly to values larger than unity, implying that the onset of liquefaction has been prevented. On the contrary, it is shown that the empirical methodologies that are used in practice, which cannot take into account the presence of the “weak” layer, are entirely misleading as they predict that the top sand layer will also liquefy and exhibit  $FS_L \approx 0.30-0.40$ . For the “weak” layer, where the onset of liquefaction actually occurs, the two methodologies give compatible results.

Similar conclusions arise even in the case of a uniform sand deposit (Figure 3c). In particular, the empirical methodologies give compatible results with the numerical analyses only for the depths that liquefy first, while they predict considerably smaller  $FS_L$  values in all other depths. This means that the empirical methodologies for the estimation of  $FS_L$ , which are based on in-situ test results, are valid with acceptable accuracy only for the depths which correspond to the minimum factor of safety against liquefaction  $FS_{L,min}$ , as they do not take into account the drastic attenuation of the seismic actions in the soil deposits above the depth where liquefaction is first triggered (or equivalently the minimum  $FS_L$  value).

#### 4 PARAMETRIC INVESTIGATION

In total, about 100 numerical analyses were performed, to explore the effect of the following basic parameters: (i) the thickness of the “weak” layer  $H_{weak}$  ( $=0-11$  m, at 1 m increments), (ii) the thickness of the top sand layer  $H_{crust}$  ( $=5-10$  m, at 1 m increments), (iii) the excitation period  $T_{exc}$  ( $=0.2-0.5$  sec, at 0.1 sec increments) and, finally, (iv) the relative density of the stiffer sand layers  $D_{r,o}$  ( $=40-90\%$  at 10% increments).

Initially, the analysis of Section 3 was repeated for values of the “weak layer” thickness varying in the range  $H_{weak}=0-8$  m, while its top remained constant at  $z=8$  m (namely with constant  $H_{crust}=8$  m). Figure 4a depicts the variation of the average value (with depth) of the maximum excess pore pressure ratio in the top liquefiable sand layer  $r_u^{cr}$  with the thickness of the “weak” layer  $H_{weak}$ . In the same figure, the total range of  $r_{u,max}$  values in the liquefiable zones of the top sand layer is also presented. It is observed that the thickness of the “weak” layer  $H_{weak}$  is a basic parameter as it significantly affects the value of  $r_u^{cr}$ . It is noteworthy that even a very thin liquefiable “weak” layer with  $H_{weak}=1$  m can prevent the onset of liquefaction on the overlying sand layers. In addition, it is observed that for larger  $H_{weak}$  thickness values the  $r_u^{cr}$  diagrams tend to stabilize to a minimum value  $min(r_u^{cr})$ , which denotes the maximum possible reduction of excess pore pressures in the top sand layer, or else the maximum possible “Natural Seismic Isolation” that can be achieved. In the examined case, the increase of the thickness of the “weak” layer  $H_{weak}$  leads to a significant reduction on  $r_u^{cr}$  values until the minimum value  $min(r_u^{cr})=0.49$  is reached, which corresponds to the numerical analyses with thickness equal to  $H_{weak}=8$  m.

The format of Figure 4a was adopted for the presentation of the effect of all examined parameters in the present numerical investigation (i.e.  $H_{crust}$ ,  $T_{exc}$ ,  $D_{r,o}$ ). In particular, the diagrams of the  $r_u^{cr}$  variation with the thickness of the “weak” layer  $H_{weak}$  are depicted in Figure 4b for different top sand layer thicknesses  $H_{crust}$ , in Figure 4c for different excitation periods  $T_{exc}$  and in Figure 4d for different values of the relative density  $D_{r,o}$  of the stiffer sand layers. Figure 4b shows that not only the shape of the  $r_u^{cr}-H_{weak}$  diagrams but also the minimum values  $min(r_u^{cr})$  are similar in all numerical analyses with different thickness of the top sand layer  $H_{crust}$ . In other words, the thickness of the top sand layer, namely the depth where the “weak” layer is met, does not seem to have a significant effect on the values of  $r_u^{cr}$ .

On the other hand, Figure 4c shows that the shape of the diagram alters significantly based on the period  $T_{exc}$  of the seismic excitation. In particular, it is observed that the excitation pe-

riod has no effect on the values of the minimum  $r_u^{cr}$  ratio  $\min(r_u^{cr})$ , which in all cases is approximately equal to  $\min(r_u^{cr}) \approx 0.50$ , but affects the reduction rate of  $r_u^{cr}$  with  $H_{weak}$ , which decreases as the excitation period increases. This effect becomes more prominent for  $T_{exc} = 0.5$  sec. This practically means that for larger  $T_{exc}$  periods the  $H_{weak}$  thickness that is required in order to achieve the maximum possible reduction in the mean pore pressure ratio of the top sand layer increases. In more detail, for  $T_{exc} = 0.2$  sec the minimum ratio  $\min(r_u^{cr})$  is achieved for  $H_{weak} = 3$  m, while for  $T_{exc} = 0.5$  sec it is achieved for  $H_{weak} = 10$  m. It should be noted that this observation is in accordance with the findings of Bouckovalas et al. [1], who showed that the excitation period is one of the basic parameters which affect the minimum thickness of liquefied sand that is required for drastic attenuation of the seismic actions on the ground surface.

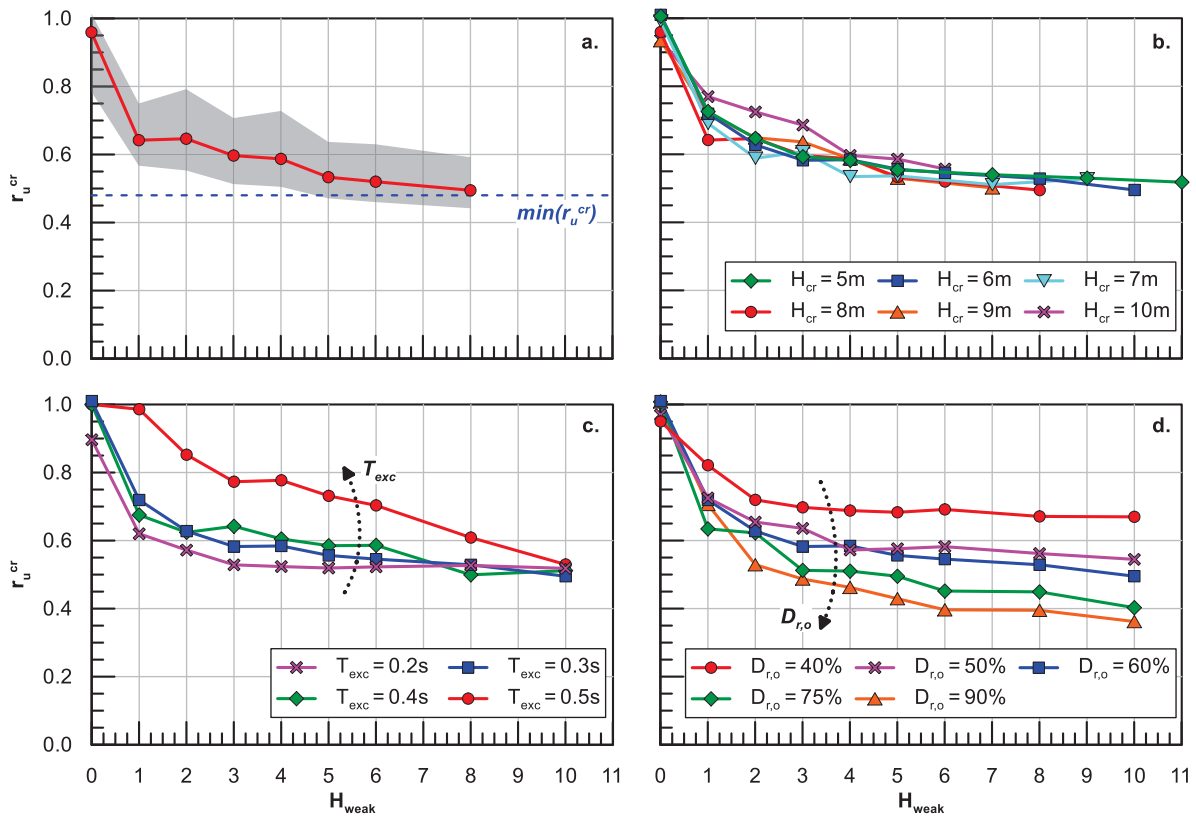


Figure 4: Effect of parameters: (a)  $H_{weak}$ , (b)  $H_{cr}$ , (c)  $T_{exc}$  and (d)  $D_{r,o}$  on the variation of the average pore pressure ratio in the top sand layer  $r_u^{cr}$ .

Finally, Figure 4d shows that the relative density  $D_{r,o}$  of the stiffer sand layers constitutes also a crucial parameter for the definition of the minimum  $r_u^{cr}$  value  $\min(r_u^{cr})$ , which reduces significantly with the increase of  $D_{r,o}$ . Apart from that, the shape of  $r_u^{cr}$ - $H_{weak}$  diagrams is similar for all different relative densities  $D_{r,o}$ . It is worth mentioning that even for relative density  $D_{r,o} = 40\%$ , i.e. slightly larger than that of the “weak” layer ( $D_r = 30\%$ ), a reduction in the values of  $r_u^{cr}$  is observed, which implies that even a small difference in the soil conditions of the “weak” layer, relative to the rest liquefiable ground, is adequate in order to achieve “Natural Seismic Isolation” conditions.

For a more detailed insight in the effect of the relative density of the stiffer layer  $D_{r,o}$  on the values of the minimum ratio  $\min(r_u^{cr})$ , Figure 5 shows the variation of  $\min(r_u^{cr})$  values with the relative density of the top sand layer  $D_{r,o}$ . It is thus observed that the minimum value of

$r_u^{cr}$  reduced from  $\min(r_u^{cr}) \approx 0.67$  for relative density  $D_{r,o} = 40\%$  to  $\min(r_u^{cr}) \approx 0.36$  for  $D_{r,o} = 90\%$ , while the reduction rate of  $\min(r_u^{cr})$  reduces with the increase of  $D_{r,o}$  value.

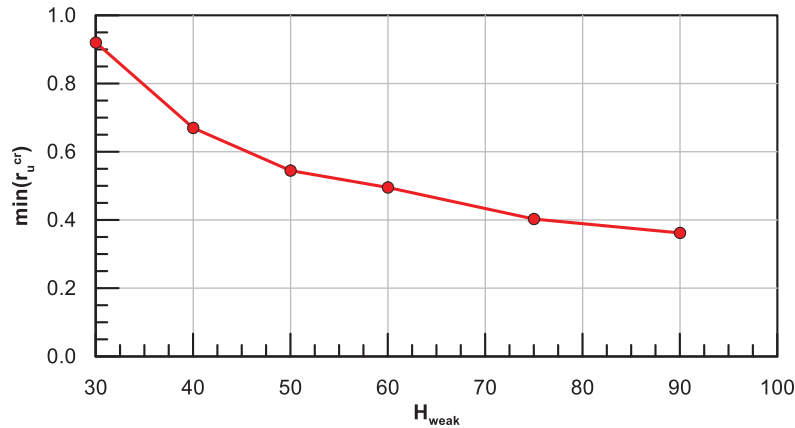


Figure 5: Variation of  $\min(r_u^{cr})$  with the relative density of the top sand layer  $D_{r,o}$ .

## 5 CONCLUSIONS

In the present study, the seismic response of non-uniform liquefiable sand deposits with an embedded “weak” sand layer of low relative density and significantly downgraded liquefaction resistance is examined. In such deposits, the “weak” layer liquefies earlier than the stiffer sand layers above and below it and forms a “Natural Seismic Isolation” system for the stiffer overlying layers, which are now protected and maintain low excess pore pressure ratio values, in the order of  $r_u = 0.40 - 0.70$ . The “weak” layer effect on the seismic response of the underlying liquefiable layer is also beneficial, but not as important and consistent as for the overlying layer.

The parametric analyses of this study revealed that the average values of the maximum excess pore pressure ratio that develop in the overlying sand layer  $r_u^{cr}$  depend on the following site and seismic excitation parameters: (i) the thickness of the “weak” layer  $H_{weak}$ , (ii) the excitation period  $T_{exc}$  and (iii) the relative density  $D_{r,o}$  of the stiffer layers. In particular, the increase of the thickness  $H_{weak}$  leads to reduction of  $r_u^{cr}$  values until a minimum value ( $0 < \min(r_u^{cr}) < 1$ ), the increase of the excitation period  $T_{exc}$  reduces the reduction rate of  $r_u^{cr}$  with the increase of  $H_{weak}$ , without however affecting the aforementioned  $\min(r_u^{cr})$  value, while the increase of  $D_{r,o}$  leads to a reduction of the  $\min(r_u^{cr})$  values. Finally, the depth of the “weak” layer surface ( $H_{crust}$ ) has no substantial effect on the seismic system response.

Furthermore, it has been shown that the empirical methodologies which are widely applied in practice for the estimation of  $FS_L$  based on in-situ test results (e.g. [13]) can be applied with satisfactory accuracy only for the depths corresponding to the minimum factor of safety against liquefaction  $FS_{L,min}$ , while they significantly underestimate the actual value of  $FS_L$  mainly for shallower depths.

It should be finally noted that the present research is currently in progress, aiming to study the effect of additional parameters, such as the relative density of the “weak” layer and the permeability of the liquefiable sand, as well as to propose an analytical methodology for the prediction of the average value (with depth) of the maximum excess pore pressure ratio  $r_u^{cr}$  and of the factor of safety against liquefaction in the top sand layers.

## 6 ACKNOWLEDGEMENTS

This research is co-financed by Greece and the European Union (European Social Fund-ESF) through the Operational Programme “Human Resources Development, Education and



Lifelong Learning” in the context of the project “Reinforcement of Postdoctoral Researchers - 2<sup>nd</sup> Cycle” (MIS-5033021), implemented by the State Scholarships Foundation (IKY).

## REFERENCES

- [1] G.D. Bouckovalas, Y.Z. Tsiapas, A.I. Theocharis, Y.K. Chaloulos, Ground response at liquefied sites: seismic isolation or amplification? *Soil Dynamics and Earthquake Engineering*, 91, 329-339, 2016.
- [2] L. Gonzalez, T. Abdoun, M.K. Sharp, Modeling of seismically induced liquefaction under high confining stress. *International Journal of Physical Modeling in Geotechnics*, 2(3), 1–15, 2002.
- [3] M. Taiebat, B. Jeremić, Y.F. Dafalias, A.M. Kaynia, Z. Cheng, Propagation of seismic waves through liquefied soils. *Soil Dynamics and Earthquake Engineering*, 30(4), 236-257, 2010.
- [4] Itasca, *FLAC version 7.0*. Itasca Consulting Group Inc, 2011.
- [5] A.G. Papadimitriou, G.D. Bouckovalas, Plasticity model for sand under small and large cyclic strains: A multiaxial formulation. *Soil Dynamics and Earthquake Engineering*, 22(3), 191-204, 2002.
- [6] K.I. Andrianopoulos, A.G. Papadimitriou, G.D. Bouckovalas, Bounding surface plasticity model for the seismic liquefaction analysis of geotechnical structures. *Soil Dynamics and Earthquake Engineering*, 30(10), 895-911, 2010.
- [7] W. Ramberg, W.R. Osgood, *Description of stress-strain curve by three parameters*. Technical note 902, National Advisory Committee for Aeronautics, 1943.
- [8] K. Arulmoli, K.K. Muraleetharan, M.M. Hossain, L.S. Fruth, *VELACS: verification of liquefaction analyses by centrifuge studies; Laboratory Testing Program – Soil Data Report*. Research Report, The Earth. Technology Corporation, 1992.
- [9] M. Vucetic, R. Dobry, Effect of soil plasticity on cyclic response. *Journal of Geotechnical Engineering*, 117(1), 89-107, 1991.
- [10] Y.Z. Tsiapas, G.D. Bouckovalas, Selective Filtering of Numerical Noise in Liquefiable Site Response Analyses. *Geotechnical Special Publication, GSP 292*, 248–257, 2018.
- [11] G.D. Bouckovalas, Y.Z. Tsiapas, V.A. Zontanou, C.G. Kalogeraki, Equivalent Linear Computation of Response Spectra for Liquefiable Sites: The spectral envelope method. *Journal of Geotechnical and Geoenvironmental Engineering*, 143(4), 4016115, 2017.
- [12] Y.Z. Tsiapas, G.D. Bouckovalas, Equivalent linear computation of response spectra for liquefiable sites: The spectral interpolation method. *Soil Dynamics and Earthquake Engineering*, 116, 541-551, 2019.
- [13] R.W. Boulanger, I.M. Idriss, *CPT and SPT based liquefaction triggering procedures*. Report No. UCD/CGM-14/01, Center for Geotechnical Modeling, U.C. Davis, 2014.
- [14] I.M. Idriss, R.W. Boulanger, *Soil Liquefaction During Earthquakes*. Earthquake Engineering Research Institute, Oakland, California, USA, 2008.
- [15] C.G. Kalogeraki, V.A. Zontanou, *Re-evaluation of factor of safety against seismic liquefaction*.” Diploma Thesis, NTUA, Athens, 2014.

- [16] Y.Z. Tsiapas, *Seismic Response Analysis of Liquefiable Ground with Computational Methods*. PhD Thesis, Department of Civil Engineering, NTUA, Athens, 2017.
- [17] M.S. Spanea, *Evolution of Earthquake-induced Liquefaction on Sand Deposits with Intermediate “Weak” Layer*. Diploma Thesis, NTUA, Athens, 2019.

## COUPLED ANALYSIS OF SEISMIC PILE-TENDON-PLATFORM INTERACTION IN LIQUEFIABLE SEABED

Yannis K. Chaloulos<sup>1</sup>, Yannis Z. Tsiapas<sup>1</sup>, George D. Bouckovalas<sup>1</sup> and Konstantinos N. Bazeos<sup>1</sup>

<sup>1</sup> National Technical University of Athens  
Iroon Politechniou 9, 15780 Zografou, Attica, Greece  
e-mail: [y.chaloulos@gmail.com](mailto:y.chaloulos@gmail.com), [ioannis.tsiapas@gmail.com](mailto:ioannis.tsiapas@gmail.com), [gbouck@central.ntua.gr](mailto:gbouck@central.ntua.gr),  
[kon\\_bazeos@hotmail.com](mailto:kon_bazeos@hotmail.com)

---

### Abstract

*The paper presents numerical analyses of a pile supported Tension Leg Platform wind turbine, during seismic loading and seabed liquefaction, taking consistently into account the pile-tendon-platform interaction. The emphasis is on the system response when liquefaction in the subsoil is extensive, leading to degradation of the pseudo-static factors of safety against pullout failure of the pile well below unity. It is shown that the pile resistance to pullout failure decreases drastically during shaking, but fully recovers during the following dissipation of earthquake-induced excess pore pressures and even exceeds the initial (pre-shaking) resistance value. Pile head displacements develop steadily during shaking and the following excess pore water pressure dissipation phase, but only during the limited time period when the static pullout factor of safety of the pile remains less than unity. Due to the very high tensional stiffness of the tendons, relative to the buoyancy stiffness of the platform considered in this study, the pile head pullout is mostly transmitted to the platform, with only a very small part corresponding to reduction of tendon elongation. As a result, the potential loss of buoy stability and tendon pretension may prove detrimental, but they are recoverable following a strong seismic event, as is unlikely to threaten the short-term safety of the platform.*

**Keywords:** TLP Platform, Liquefaction, Numerical Analysis, Offshore pile foundation.

---

## 1 INTRODUCTION

Compared to bottom-fixed support platforms (e.g. gravity base, tripod, monopile and “jacket” supporting structures), the cost of Tension Leg Platforms (TLPs) depends on depth only for the station keeping component and becomes competitive for relatively large water depths, beyond about 80 m (e.g. Big Foot TLP, Magnolia TLP, Ursa TLP etc.). In addition to the lower construction cost, the TLP concept is also appealing for high seismicity areas (e.g. Italy, East Mediterranean, California, China, Japan), as it is rather insensitive to seismic actions, especially when the pile foundation response is considered along with the tendon-buoy dynamic model (e.g. [1-4]).

Nevertheless, it should be noted that the previous findings apply to seismically stable soil and foundation conditions, but they are still under consideration for liquefiable sand and silt seafloor soil profiles, where seismic shaking may lead to excess pore pressure buildup and partial or total loss of the pile foundation capacity to sustain the pretension of the tendons [5]. The static design of pile foundations is described with sufficient detail in a number of design guidelines [6-7]. However, available guidance on the seismic design of TLP foundations is limited and practically non-existent for earthquake-induced liquefaction in the foundation soil.

In view of the above objective limitations, the paper presents numerical analyses of a TLP supported wind turbine during seismic loading and seabed liquefaction, taking consistently into account the pile-tendon-platform interaction. The emphasis is on the system response when liquefaction in the subsoil is extensive, leading to degradation of the pseudo static factors of safety against pullout failure of the pile well below unity. For this purpose, it was assumed that the liquefiable soil deposit extends along the entire pile length, instead of forming one or more layers of limited thickness.

## 2 NUMERICAL MODELLING

### 2.1 The POSEIDON Model Floating Platform

The basic data for the numerical analyses are derived from the POSEIDON model TLP (Figure 1a), which was conceptually designed and analyzed for combined wind and wave energy exploitation in Mediterranean Sea conditions [8]. In particular, the system consists of a triangular platform supported by cylindrical floaters with a 5 MW wind turbine mounted at deck's center and three cylindrical oscillating water column (OWC) devices at its corners. The spacing between each OWC is 50 m. In the center of the platform, a cylindrical solid body is arranged to support the wind turbine. When positioned and stabilized, the draught of the platform is 20 m and the tower of the wind turbine is cantilevered at an elevation of 10 m above sea water level (SWL), at the top of the main column of the floating platform.

The floating structure is held in position by a Tension Leg Platform mooring system, which consists of three steel tendons, anchored at the seabed. The tendons are symmetrically placed and mounted at the base of the offset columns, i.e. at a depth of 20 m below the SWL. The diameter of each tendon is 0.130 m, while its length varies in each examined location. In all cases, the pretension load of each tendon is equal to  $F_0 = 10800$  kN. This load is transferred to the foundation system of the platform, which consists of a single driven open-ended steel pile under each tendon. The mass, including ballast, of the floating platform is 2183.6 t. The equivalent, in terms of buoyancy force, cross-section area of the platform is 298.53 m<sup>2</sup>.

The pilot foundation design of the POSEIDON platform was conducted parametrically for two installation locations in the Aegean Sea, assuming typical soil profiles that cover the basic soil types commonly encountered in offshore sites. Of interest for the present study is

the case of the non-cohesive seabed with medium density sand of relative density  $D_r=50\%$ , which is susceptible to earthquake-induced liquefaction.

The foundation piles were properly designed to withstand the combined static and cyclic axial loads applied during the normal and extreme environmental design conditions [9]. In more detail, the static loads come from the pretension of the steel tendons (i.e.  $F_o=10800$  kN), while the cyclic loads are due to sea waves during a storm. The geometry of the pile (length and diameter) was defined in order to ensure a that the factor of safety against static pullout of the pile is greater than 2.0 for normal environmental conditions and greater than 1.50 for extreme environmental conditions [6-7]. This led to the selection of a steel pipe pile of  $L=55$  m length and  $D=2.5$  m outer diameter.

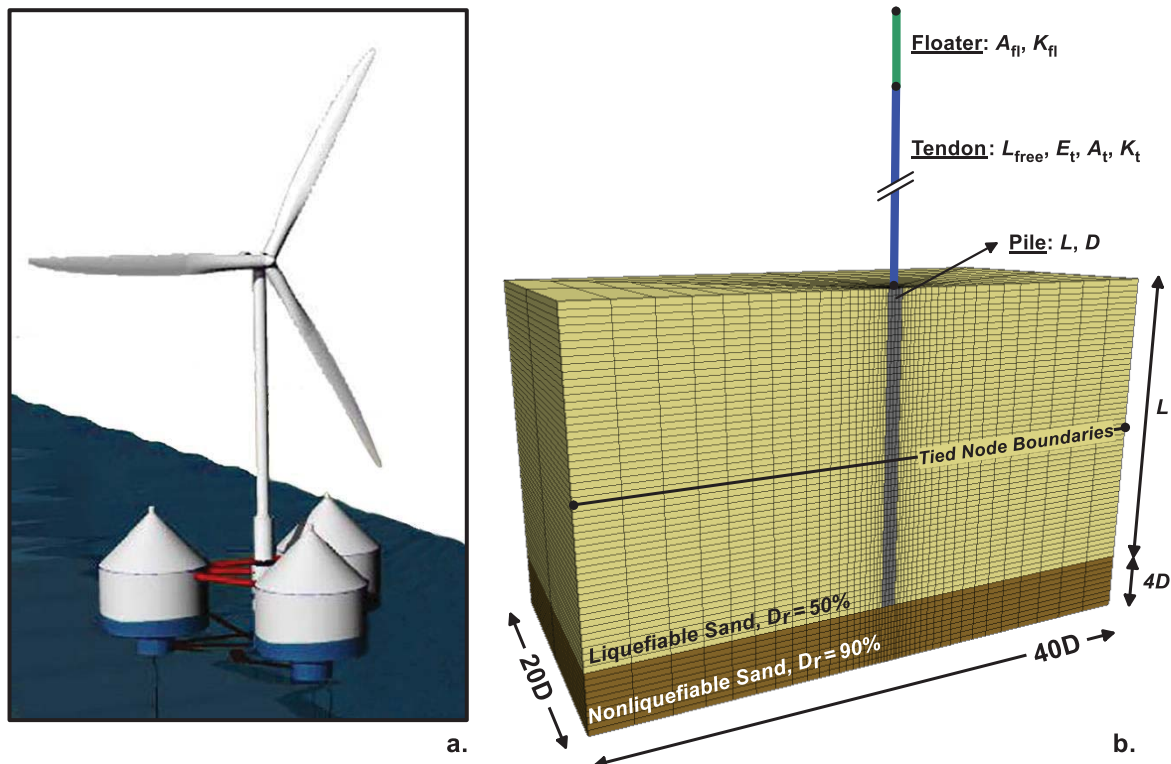


Figure 1: (a) Illustrative presentation of the POSEIDON floating TLP [10], (b) The 3D numerical model of the pile-tendon-floater system.

## 2.2 The 3D Numerical Model

The problem is analyzed numerically by means of 3D coupled dynamic analyses with the finite difference code FLAC3D v6.0 [11]. The specific code employs an explicit scheme for the integration of the equations of motion which is more efficient for highly nonlinear problems like the one analyzed herein, while it allows for coupling between water flow and dynamic loading.

The 3D mesh built to simulate the problem is shown in Figure 1b. A pile of length  $L$  and diameter  $D$  is installed in a liquefiable uniform layer of Nevada Sand of relative density  $D_r$  and permeability  $k$ . As the OWCs are at large distance apart, i.e 50 m, each pile and tendon support is simulated independently. The liquefiable sand layer extends to the depth of the pile tip, followed in depth by a much denser non-liquefiable sand layer of thickness  $4D$ .

The pile supports a floater, defined in terms of its cross-sectional area  $A_f$ , through a pretensioned tendon of free length (before pretension)  $L_{free}$ , cross-sectional area  $A_t$  and Young's modulus  $E_t$ . The floater-tendon system can be adequately represented by two serially connect-

ed springs [12] which are simulated herein by two sets of cable elements. The properties of the cables (length, cross-sectional area and Young's modulus) are properly calibrated to provide the axial stiffness of the tendon  $K_t$  (i.e. the tendon's resistance against unit tensile displacement) and the axial stiffness of the floater  $K_f$  (i.e. the floater's resistance against unit downward displacement), computed as:

$$K_t = \frac{E_t A_t}{L_{\text{free}}} \quad (1)$$

and

$$K_f = A_f \cdot \gamma_w \quad (2)$$

During static uplift loading of the pile, the base of the model is fixed in all three directions and vertical hinges are applied on the vertical boundaries. During seismic shaking the hinges at the lateral boundaries are replaced with "tied-nodes" which impose the same boundary displacements at grid-points of the same elevation, replicating free field conditions, while a harmonic motion of amplitude  $a_{\text{max}}$ , period  $T$  and  $N$  cycles is directly applied at the base assuming rigid bedrock conditions. The in-plane and out-of-plane width of the mesh is 40D and 20D respectively. The thickness of each zone is 1.0m, while the width is approximately equal to 0.2D next to the pile and gradually increases to about 2.7D at the lateral boundaries.

The highly nonlinear response of the liquefiable sand is simulated with NTUA-Sand [13-14] implemented in FLAC3D as a C++ plug-in constitutive model. NTUA-Sand is also used to simulate the response of the dense sand layer below the pile tip, while the pile is simulated through elastic solid elements with the axial stiffness and the unit per length weight of a hollow steel pile with diameter  $D = 2.5$  m and wall thickness  $t = 31.35$  mm.

A key aspect of the numerical methodology is the accurate simulation of the pile-soil interface, as the pile-soil relative slip, as well as the pullout capacity of the pile are both related directly to the strength characteristics and the radial stresses of that interface. Following a trial-and-error approach [15], it was finally decided to install six sets of interface elements, one for each set of zones that encircle the pile. Large values are assigned to the elastic stiffnesses of the interface to ensure that no interface straining occurs before yield. The tensile strength and the shearing cohesion of the interface are set to zero, while an interface friction angle  $\delta$  is adopted and properly calibrated based on relevant guidelines

### 2.3 Numerical Solution Sequence

The seismic response analysis of the pile-tendon-floater system is performed in two stages. Initially, the pretension force  $F_0 = 10800$  kN is applied statically at the structural node corresponding to the top of the floater. In the sequel, the displacement of that node is constrained, and the input seismic motion is applied at the base of the model. The analysis continues beyond the end-of-shaking, until excess pore pressures are fully dissipated. During this second stage, the displacements of the pile head and the floater are continuously monitored, along with the loss of tendon pretension and floater buoyancy. Still, to shed light on the mechanisms that control the system response, it is also necessary to monitor the variation with time, during shaking and following excess pore water pressure dissipation, of the degraded pullout capacity of the pile.

When numerically performed, the latter may extend the computational effort enormously, as it is not part of the main seismic response analysis, but it has to be performed independently at regular time intervals, based on the ever current stress state around the pile. For this reason, the static pullout capacity of the pile was computed analytically, according to the API [7]



and DNV [6] recommendations in connection with the liquefaction-affected radial stresses at the pile-soil interface predicted during the second stage of the seismic response analyses. This semi-analytical methodology has been implemented in the numerical analysis through a user-defined subroutine, written in FLAC3D's inbuilt programming language FISH, to provide the continuous with time variation of the pile capacity to sustain the tendon pretension load.

### 3 LIQUEFACTION EFFECTS ON PILE-TENDON-FLOATER RESPONSE

#### 3.1 Input data and assumptions

The basic analysis presented herein is performed for 120 m water depth, assuming that the relative density of the liquefiable layer is  $D_r=50\%$  and that of the underlying non-liquefiable sand is  $D_r=90\%$ . The permeability is set equal to  $k=6.6 \times 10^{-4}$  m/s for both layers corresponding to a clean sand [16]. The single tendon-pile support considered in the analysis is attached to a floater with equivalent cross-section area  $A_f=99.51 \text{ m}^2$  (i.e. 1/3 of the total), while the free length of the tendon is  $L_{\text{free}}=100$  m, the associated cross section area is  $A_t=0.01327 \text{ m}^2$  and the modulus of elasticity is  $E_t=200 \text{ GPa}$ . According to Eqs. **Error! Reference source not found.** and **Error! Reference source not found.**, the preceding values lead to an axial stiffness  $K_t=62800 \text{ kN/m}$  and  $K_f=995 \text{ kN/m}$  for the tendon and the floater respectively. The input seismic motion consists of  $N=15$  uniform acceleration cycles (corresponding to an  $M_w=7.5$  earthquake) with amplitude  $a_{\text{max}}=0.24 \text{ g}$  and period  $T=0.5 \text{ sec}$ .

#### 3.2 Pile response

Figure 2 summarizes the response of the pile-tendon-floater system. More specifically, Figure 2a presents time-histories of the pile's pullout capacity  $Q_{\text{ult}}$  and the tendon's force  $F$  (black and red line respectively) both during and after the end of shaking until full excess pore pressure dissipation. Similarly, Figure 2b presents the factor of safety against pullout of the pile  $FS=Q_{\text{ult}}/F$  as well as the Stability Safety Factor  $FS_{\text{st}}=U/W_f$  ( $U$  is the total buoyancy force and  $W_f$  is the weight of the floater), while Figure 2c shows the uplift displacement of the pile head and the floater. To further verify the semi-analytical procedure for the estimation of  $Q_{\text{ult}}$ , during and after shaking, a set of undrained numerical analyses is performed at selected time instances in order to compute  $Q_{\text{ult}}$  and is compared with the analytical estimates. The results of these analyses are shown on Figure 2a with the cyan bullets.

Based on the above observations the following critical time instances can be identified:

- Point A ( $t_A=3.5 \text{ sec}$ ): The factor of safety drops below 1.0 for the first time.
- Point B ( $t_B=8.0 \text{ sec}$ ): At the end of shaking  $Q_{\text{ult}}$  reaches a local minimum practically equal to the buoyant weight of the pile.
- Point C ( $t_C=36.5 \text{ sec}$ ): The Factor of Safety becomes again larger than unity.
- Point D ( $t_D=250 \text{ sec}$ ): At the end of consolidation the post-shaking pullout capacity stabilizes to a value that is approximately 38% larger than the initial.

The evolution of the pullout factor of safety is the key factor determining the accumulation of pile displacements. More specifically, as shown on Figure 2c, pile displacements are limited as long as the factor of safety remains greater than 1.0 (up to Point A) and do not exceed 5-6 cm. However, as the  $FS$  becomes and remains lower than unity (between points A and C) the rate of displacement accumulation increases substantially leading to uplift displacements that increase linearly with time. It is noteworthy that at the end of shaking only a fraction of the total pullout displacement has accumulated. Namely, at the end of shaking (Point B) dis-

placements are approximately equal to 30 cm, and at the end of the failure stage (Point C) they are equal to 85 cm. Afterwards (between points C and D), as the factor of safety becomes again larger than unity, displacement accumulation practically ceases and the pile stabilizes. The above observations suggest that the accumulation of pile pullout displacements is primarily influenced by the duration of the failure stage ( $t_A - t_C$  in Figure 2b) and may thus increase considerably when the excess pore water pressure dissipation is delayed (e.g. for silty sand seabed with lower permeability coefficient).

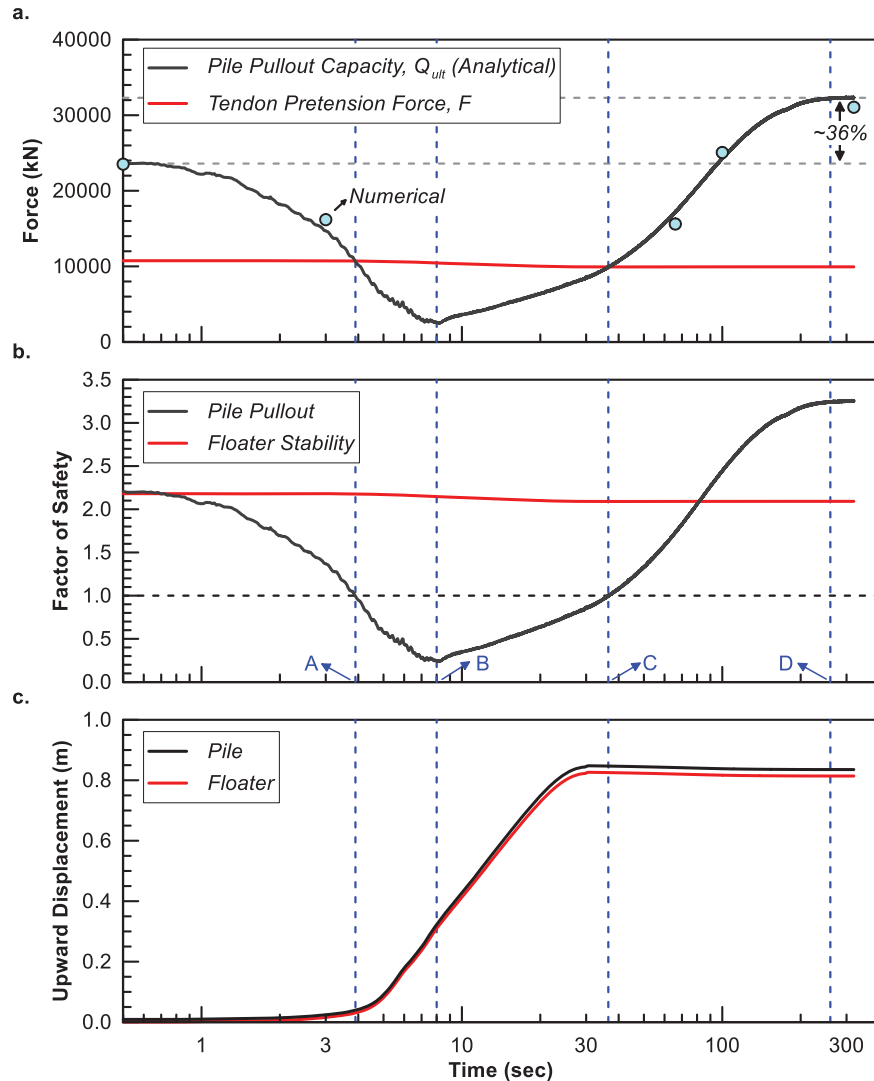


Figure 2: (a) Pile pullout capacity and tendon pretension force, (b) Pullout and Stability Factor of Safety ( $FS$  and  $FS_{st}$ ), (c) Pile head uplift time-histories.

### 3.3 Soil Response

The patterns described in the previous section regarding the pullout capacity of the pile are directly associated with excess pore pressure generation and soil liquefaction. Figure 3 presents time-histories of excess pore pressure ratio  $r_u$ , defined as the ratio of the excess pore pressures  $\Delta u$  over the initial effective vertical stress  $\sigma'_{v,0}$  (i.e.  $r_u = \Delta u / \sigma'_{v,0}$ ), at depths  $z = 1, 10$  and  $40$  m below ground surface both at the free field and next to the pile.

Focusing first on the co-seismic response ( $t = 0 - 8$  sec), the figure shows that complete liquefaction ( $r_u = 0.9 - 1.0$ ) takes place almost in the entire soil mass with the exception of the ar-

ea around the pile head where the excess pore pressure ratio stabilizes at a peak value of  $r_u \approx 0.5-0.6$  (Figure 3). This non-liquefied zone is more clearly illustrated on Figure 4a which shows contours of  $r_u$  at the end of shaking. It has an inverted-cone shape and extends to a depth of about 4-5 m (1.6-2.0 D). Post-seismically ( $t > 8$  sec), excess pore pressures dissipate primarily towards the ground surface as evidenced by the fact that excess pore pressures at large depths dissipate earlier. Furthermore, this upward flow towards areas of lower hydraulic head, causes the pore pressures near the pile head, where the soil hasn't fully liquefied, to notably increase before they also start to dissipate.

It is interesting to observe the correlation between the generation of excess pore pressures and the degradation of the pile's pullout capacity. Namely, as shown in Figure 2b, the factor of safety drops below unity at  $t \approx 3.5$  sec, which, according to Figure 3, coincides with the moment when significant excess pore pressures ( $r_u > 0.6$ ) have started to develop in the soil. Furthermore, the ultimate pullout capacity  $Q_{ult}$  and the factor of safety  $FS$  reach a local minimum at the end of shaking, when the majority of the soil is liquefied (Figure 4a). Finally, as shown on Figure 4b, at  $t \approx 36.5$  sec the dissipation process has progressed significantly, the soil has regained a considerable amount of its shear strength, and thus the factor of safety becomes again larger than unity.

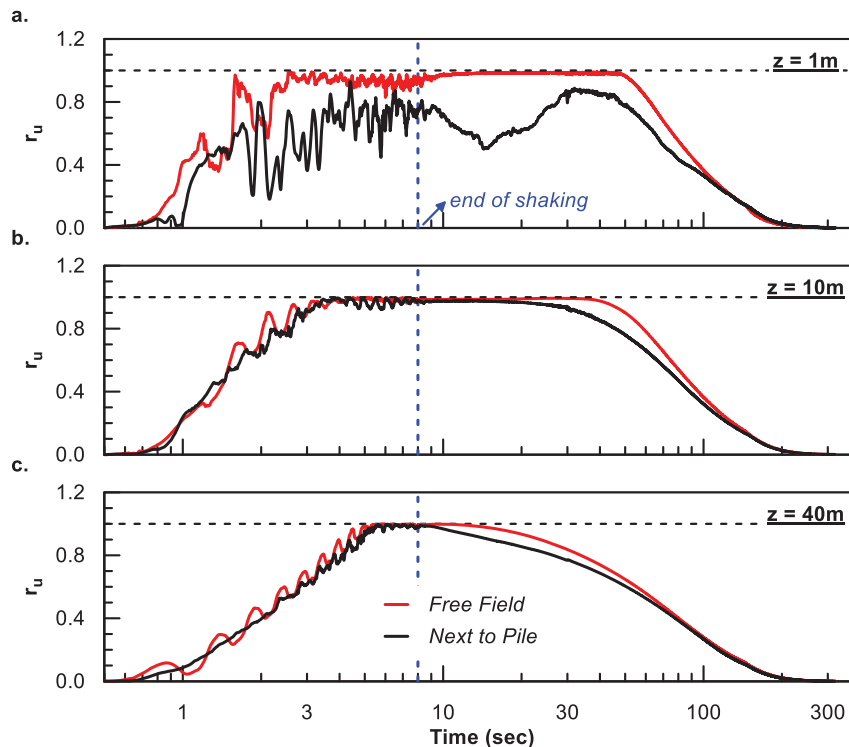


Figure 3: Excess pore pressure ratio ( $r_u$ ) time-histories at the free field and next to the pile at various elevations.

### 3.4 Tendon & floater response

Pullout of the pile causes both the floater to move upwards as well as the tendon's elongation to decrease subsequently decreasing the pretension force. For the platform examined herein, Figure 2c presents the evolution with time of the upward displacement of the floater (red line) compared to that of the pile head (black line). As shown on this figure, the displacement of the floater resembles that of the pile head. Initially the displacement is very limited (up to Point A), while, afterwards, it increases linearly with time until the end of the failure phase (Point C). Finally, the floater stabilizes to an upward displacement of about

82 cm, approximately 3 cm less than that of the pile head. It is thus observed that the pile head displacement is almost entirely (by approximately 96-97%) transmitted to the floater, while only a small portion ( $\sim 3-4\%$ ) causes the length of the tendon to decrease.

As a result, the tension force of the tendon is only marginally reduced by 7.8%, from its initial value  $F_0 = 10800$  kN to approximately  $F = 9950$  kN (Figure 2c). Subsequently the stability safety factor of the floater decreases by 6.2%, from 2.25 to 2.11 (Figure 2b). It should be noted that the system studied herein employs a relatively short tendon (due to the shallow seabed) with high tensional stiffness. For larger water depths and less stiff tendons, the percentage of pile head pullout that is transferred to the floater will substantially decrease, leading to higher loss of pretension platform stability.

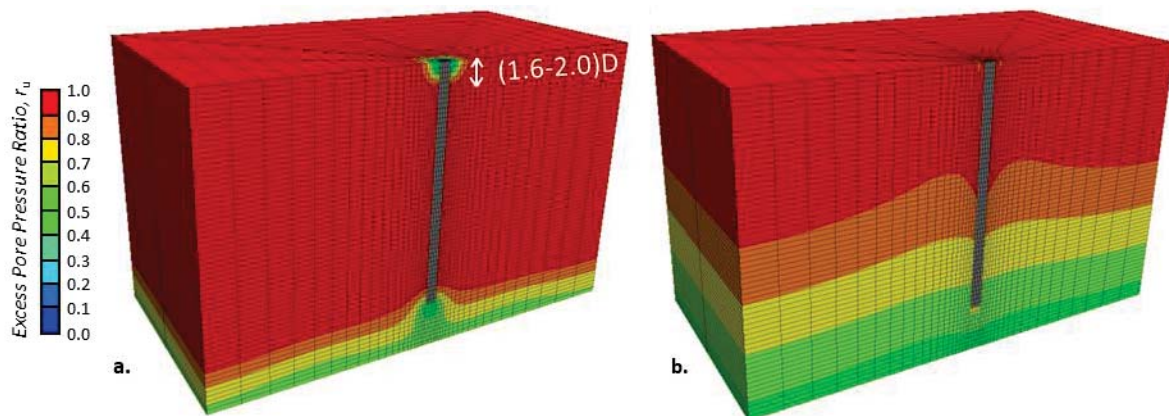


Figure 4: Excess pore pressure ratio  $r_u$  contours (a) at the end of shaking and (b) at  $t = t_c$  when FS becomes greater than 1.0 post-seismically.

#### 4 CONCLUSIONS

In summary, the following findings emerged from the study presented in this paper, with regard to seismic liquefaction effects on TLP foundation-tendon-buoy systems:

- (a) Upon complete free field liquefaction, the excess pore pressure ratio becomes approximately equal to unity ( $r_u = 0.9-1.0$ ) along almost the entire pile length. As a result, the skin friction resistance of the pile is drastically reduced during shaking and it is almost eliminated when free field liquefaction extends over the entire pile length. At that stage, the main force resisting the pretension of the tendons is the buoyant weight of the pile.
- (b) The pile resistance to pullout failure increases with dissipation of the excess pore pressures created during shaking, while the associated factor of safety becomes gradually larger than unity, mainly due to the increase of the total radial soil stresses at the pile-soil interface caused during shaking but also to the loss of tendon pretension. For the analyses of this study, the final value of the ultimate resistance exceeds the initial static design by about 38%, while the corresponding factors of safety increase by approximately 48%.
- (c) Pile head displacements develop essentially in the time period, during and after shaking, when the factor of safety against static pullout of the pile becomes less than unity (i.e. at failure conditions) and may thus increase considerably when the excess pore water pressure dissipation is delayed (e.g. for silty sand seabed with lower permeability coefficient). The displacements are insignificant before and after that time period, when the factor of safety remained larger than unity.

- (d) Due to the very high tensional stiffness of the tendons considered herein, relative to the buoyancy stiffness of the platform, the pile head pullout was almost entirely (96-97%) transmitted to the platform with only a very small percentage (3-4%) corresponding to the reduction of tendon elongation. For larger water depths and less stiff tendons, the percentage of pile head pullout that is transferred to the floater may decrease substantially, leading to higher loss of pretension and platform stability.
- (e) Despite the catastrophic per se effects of liquefaction (loss of pile capacity and large displacements), the overall stability of the floater is not jeopardized and the computed loss of the tendon's elongation and tension force is rather small to induce slackening. In addition, the above effects are potentially recoverable as the pretension force can be restored to its initial or to an even higher value, taking also into account that the post-shaking pullout capacity of the pile has considerably increased.

## 5 ACKNOWLEDGEMENTS

This research is carried out/funded in the context of the project “Seismic design of offshore wind turbines: Effect of pile foundation damping and soil liquefaction” (MIS 5049428) under the call for proposals “Researchers' support with an emphasis on young researchers- 2nd Cycle”. The project is co-financed by Greece and the European Union (European Social Fund-ESF) by the Operational Programme Human Resources Development, Education and Lifelong Learning 2014-2020.

## REFERENCES

- [1] G.-S. Liou, J. Penzien, R.W. Yeung, Response of tension-leg platforms to vertical seismic excitations. *Earthquake Engineering & Structural Dynamics*, 16(2), 157-182, 1988.
- [2] K. Venkataramana, Earthquake response of tension-leg-platforms in steady currents. *Earthquake Engineering & Structural Dynamics*, 23(1), 63-74, 1994.
- [3] S.Chandrasekaran, Gaurav, Offshore triangular tension leg platform earthquake motion analysis under distinctly high sea waves. *Ships & Offshore Structures*, 3(3), 173-184, 2008
- [4] H. Suroor, A. Arablouei, Comparison of Coupled and Decoupled Seismic Analysis of TLP Piles. *Offshore Technology Conference*, Houston, Texas, May 6-9, 2019.
- [5] A.M. Kaynia, Seismic considerations in design of offshore wind turbines. *Soil Dynamics & Earthquake Engineering*, 124, 399–407, 2019.
- [6] DNV, *Design of Offshore Wind Turbine Structures; Offshore Standard*. Det Norske Veritas, 2013.
- [7] API, *Geotechnical and Foundation Design Considerations, ANSI/API RP 2GEO*. American Petroleum Institute, 2014.
- [8] T. Mazarakos, D. Konispoliatis, G. Katsaounis, S. Polyzos, D. Manolas, S. Voutsinas, T. Soukissian, S. Mavrakos, Numerical and experimental studies of a multi-purpose floating TLP structure for combined wind and wave energy exploitation. *Mediterranean Marine Science*, 20(4), 745, 2019.
- [9] G.D. Bouckovalas, S.A. Mavrakos, K.I. Andrianopoulos, T.P. Mazarakos, *Deliverable D5.2: Design of anchor piles in silty-sandy seabed*, 2015.



- [10] T.P. Mazarakos, D.N. Konispoliatis, D.I. Manolas, S.G. Voutsinas, S.A. Mavrakos, Modelling of an Offshore Multi-Purpose Floating Structure Supporting a Wind Turbine Including Second-Order Wave Loads. *11th European Wave and Tidal Energy Conference Series, 11th EWTEC*, Nantes, France, September 6-11, 2015.
- [11] Itasca, *FLAC3D version 6.0*. Itasca Consulting Group Inc, 2017.
- [12] Y.Z. Tsiapas, Y.K. Chaloulos, G.D. Bouckovalas, K.N. Bazaios, Performance Based Design of Tension Leg Platforms under Seismic Loading and Seabed Liquefaction: A Feasibility Study. *Soil Dynamics and Earthquake Engineering*, 2021, (under review).
- [13] A.G. Papadimitriou, G.D. Bouckovalas, Plasticity model for sand under small and large cyclic strains: A multiaxial formulation. *Soil Dynamics and Earthquake Engineering*, 22(3), 191-204, 2002.
- [14] K.I. Andrianopoulos, A.G. Papadimitriou, G.D. Bouckovalas, Bounding surface plasticity model for the seismic liquefaction analysis of geostructures. *Soil Dynamics and Earthquake Engineering*, 30(10), 895-911, 2010.
- [15] Y.K. Chaloulos, Y.Z. Tsiapas, G.D. Bouckovalas, Seismic analysis of a model Tension Leg supported Wind Turbine under Seabed Liquefaction. *Ocean Engineering*, 2021, (under review).
- [16] K. Arulmoli, K.K. Muraleetharan, M.M. Hossain, L.S. Fruth, *VELACS: verification of liquefaction analyses by centrifuge studies; Laboratory Testing Program – Soil Data Report*, Research Report, The Earth. Technology Corporation, 1992.



## STATE-OF-THE-ART INVESTIGATION OF WIND TURBINE STRUCTURES BY CONSIDERING THE SOIL-STRUCTURE INTERACTION PHENOMENON

Dewald Z. Gravett<sup>1</sup>, and George Markou<sup>1</sup>

<sup>1</sup> Department of Civil Engineering, University of Pretoria, South Africa  
e-mail: u16004664@tuks.co.za; george.markou@up.ac.za

---

### Abstract

*Investigating the dynamic response of wind turbine structures is of significant importance when it comes to better understanding how their behaviour is affected by different design considerations and their foundation's interaction with the soil. An extensive numerical investigation is presented herein that foresees the performance of modal and pushover analysis on a wind turbine structure that has an 80 m steel tower and is founded on different clay profiles. The 3D detailed models constructed in this research work consider the effect of soil-structure interaction by discretizing the pile foundation and soil domains through 8-noded hexahedral elements, achieving maximum modelling accuracy. An investigation was also performed on the optimum pile inclination, where based on the numerical findings, the optimum inclination of the battered piles was found to be that of 10 degrees.*

**Keywords:** Wind turbine structures, Battered piles, Push-over analysis, Modal analysis, Soil-structure interaction, Optimum design.

---

## 1 INTRODUCTION

The finite element method has become the most commonly used method to model large-scale reinforced concrete (RC) structures. It is of utmost importance for engineers to model large-scale designs to investigate the dynamic behaviour, understand the mechanical behaviour and to optimize their structural designs. It is evident that to capture the nonlinear dynamic behaviour of RC structures through the use of a 3D detailed modelling approach is very challenging [1-3], however, taking into account the soil-structure interaction (SSI) effect [4-6] is even more challenging due to the computational demand and numerical instabilities during nonlinear monotonic and cyclic analysis.

Due to the large size of wind turbine structures, it is not feasible to perform laboratory tests in the appropriate facilities, as this relates in a large cost for physical experiments. However, through time, to obtain more energy, wind turbines evolved rapidly in size. Therefore, this increase in size forced engineers to design larger towers that are founded on relatively large foundation systems, where the soil would have a larger influence on the overall dynamic response of these structures.

Several numerical methods were developed to investigate the dynamic response of wind turbine structures that account for the SSI effect and help in the better understanding of their mechanical behaviour. Some of these numerical methods are the spring and damper approach [7,8], which were also implemented in a pile foundation by Wang *et al.* [9]. Modelling and analysis of wind turbine structures were performed herein through a 3D detailed modelling approach [1-4], in order to investigate their dynamic response through implementing an accurate soil discretization through hexahedral finite elements (FEs). The soil parameters and wind turbine design were based on data provided by the Wind Africa research project [10].

Research on the SSI phenomenon was presented in [9] where they performed numerical and physical experiments on piled foundations. The spring and damper approach was used in [9] to model the SSI phenomenon. Wang *et al.* [9] based their soil parameters on research work performed by Blanco *et al.* [11]. The piles for the numerical experiment performed by [9] were modelled by using beam-column FEs and a pinned connection were assumed at the bottom of the piles to prevent any displacement or uplift during the numerical analysis. Other research was performed on wind turbine structures supported by monopiles in [12-16].

Prowell *et al.* [17] performed a numerical investigation on the influence of SSI on the dynamic response of wind turbine structure. Prowell *et al.* [17] used beam column FEs to discretize the wind turbine tower and solid FEs for the soil domain. The research work performed by [17] concluded an increase in the natural frequency as the soil became stiffer, however, there was a greater influence on the dynamic behaviour as the soil became softer. Guo *et al.* [18] also presented research work on wind turbine structures by account for the SSI where push over analyses were performed.

As discussed within [19], Reconan FEA [20] was used to reproduce experimental results of a foundation with piles embedded in sand [9] through the use of a push over analysis. The same software was also used [20] to perform modal and push over analyses on 80 m tall wind turbine steel towers founded on soft clay, where the soil domain was discretized through hexahedral FEs. The numerical results that derived from this research work are further discussed in this manuscript.

## 2 MODAL ANALYSIS OF LARGE-SCALE MODELS

Modal analysis was performed in order to get an overview of the expected structures' dynamic response. There are several solution methods for solving the eigenvalue problem that is described by the following equation:

$$\mathbf{K}\boldsymbol{\varphi}_i = \lambda_i \mathbf{M}\boldsymbol{\varphi}_i \quad (1)$$

where,  $\mathbf{K}$  is the stiffness matrix of the model,  $\mathbf{M}$  is the mass matrix of the model,  $\boldsymbol{\varphi}_i$  is a vector that contains the eigenvectors of the system and  $\lambda_i$  is the corresponding eigenvalue  $i$ . The solution method used in this research work is called the subspace iteration algorithm [21]. This solution technique is ideal when dealing with large-scale structures since it calculates few eigenvalues and eigenvectors of a large FE model.

This solution algorithm finds an orthogonal basis of vectors in  $\mathbf{E}_{K+1}$ , calculating in one step the required eigenvectors when  $\mathbf{E}_{K+1}$  converges to  $\mathbf{E}_\infty$ . The developed algorithm foresees the iteration used in the subspace iteration method, i.e., step 2 of the complete solution phase proposed in [21]. For  $k = 1, 2, \dots$ , iterate from  $\mathbf{E}_k$  to  $\mathbf{E}_{k+1}$ :

$$\mathbf{K}\mathbf{X}_{k+1} = \mathbf{M}\mathbf{x}_k \quad (2)$$

then, find the projections of matrices  $\mathbf{K}$  and  $\mathbf{M}$  onto  $\mathbf{E}_{k+1}$ :

$$\mathbf{K}_{k+1} = \mathbf{X}_{k+1}^T \mathbf{K} \mathbf{X}_{k+1} \quad (3)$$

$$\mathbf{M}_{k+1} = \mathbf{X}_{k+1}^T \mathbf{M} \mathbf{X}_{k+1} \quad (4)$$

and solve for the eigensystem of the projected matrices:

$$\mathbf{K}_{k+1} \mathbf{Q}_{k+1} = \mathbf{M}_{k+1} \mathbf{Q}_{k+1} \boldsymbol{\Lambda}_{k+1} \quad (5)$$

Thereafter, find an improved approximation to the eigenvectors:

$$\mathbf{x}_{k+1} = \mathbf{X}_{k+1} \mathbf{Q}_{k+1} \quad (6)$$

and then provided that the vectors  $\mathbf{x}_1$  are not orthogonal to one of the equilibrium eigenvectors,  $\boldsymbol{\Lambda}_{k+1} \rightarrow \boldsymbol{\Lambda}$  and  $\mathbf{X}_{k+1} \rightarrow \boldsymbol{\Phi}$  as  $k \rightarrow \infty$ .

It is important to note that the convergence of this method assumes that within the iteration procedure the vectors in  $\mathbf{X}_{k+1}$  are ordered in such a way that the  $i^{\text{th}}$  diagonal element in  $\boldsymbol{\Lambda}_{k+1}$  is always larger than the previous  $i-1$  element,  $i=2, \dots, p$ . This ensures that the  $i^{\text{th}}$  column in  $\mathbf{X}_{k+1}$  converges linearly to  $\boldsymbol{\Phi}_i$ . Although this is an asymptotic convergence rate, it was found that the smallest eigenvalues converge fastest [21], a finding confirmed by Markou *et al.* [22].

### 3 NUMERICAL MODELS OF WIND TURBINE STRUCTURES WITH SSI CONSIDERATIONS

Initially, two wind turbine geometries were developed, however, it was decided to consider only the first geometry (based on the needs of the project [10]), while it was also decided to remove the blades, nacelle and hub to reduce the computational demand of the model. The wind turbine in Fig. 1 (excluding the nacelle, hub and blades) was used during the parametric investigation that will be presented in this manuscript. It is important to note here that the mass of the nacelle, hub and blades was applied at the top of the tower during the analysis as dead load.

Several soil profiles were investigated that included soil geometries based on the Wind Africa project [10], whereas soil geometries where the piles are embedded in rock or situated on softer soil were analysed. The first soil geometry was the Equal Layer Geometry, which was refined into a model with piles embedded in a rock layer (Fig. 2a) and a model with extra soil underneath the piles Fig. 3a. The second soil geometry will be referred to as the Increasing

Layer Geometry. This geometry was also refined into a model with piles embedded in a rock layer (see Fig. 2b) and a model with extra soil underneath the piles (Fig. 3b). During the soil geometry investigation, the pile inclination was modified to determine the optimal foundation design for the under-study wind turbine structure.

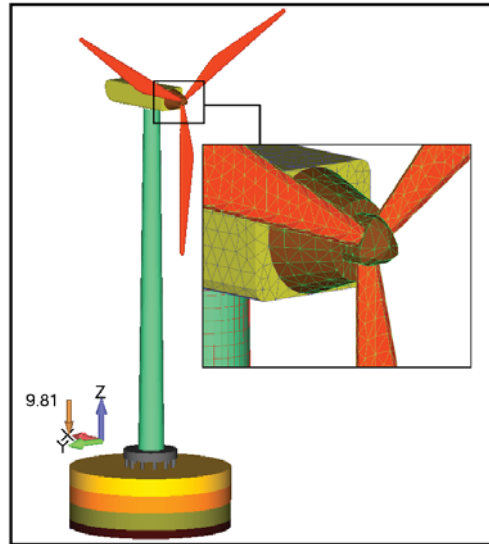


Figure 1. Wind turbine geometry.

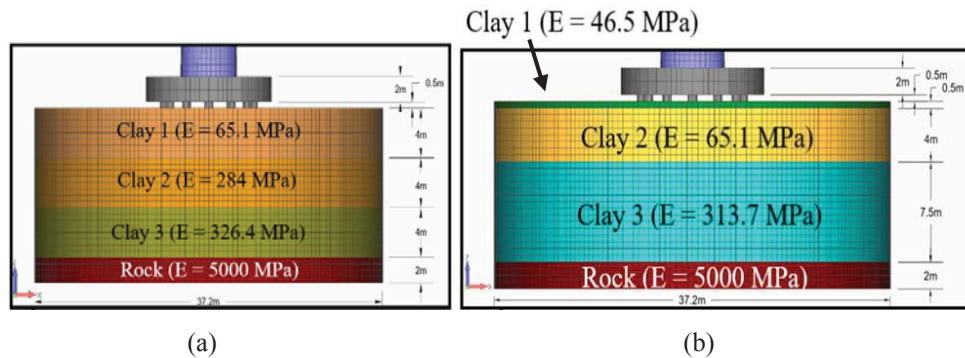


Figure 2. (a) Equal and (b) Increasing Layer Geometry with the piles embedded in a rock layer.

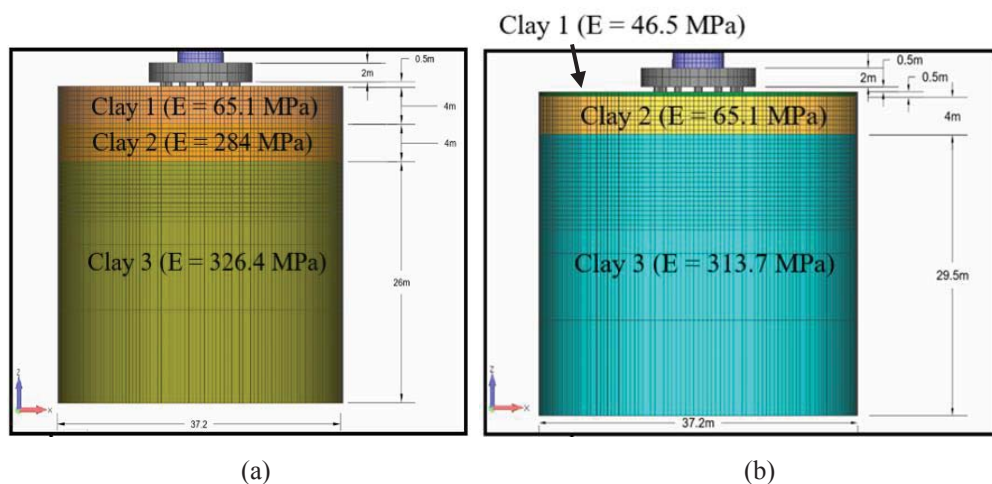


Figure 3. (a) Equal and (b) Increasing Layer Geometry with the piles embedded in extra soil.

The pile inclinations used with each soil geometry was 0-, 5-, 10- and 15-degree battered piles. The battered piles within the Increasing Layer Geometry can be seen in Fig. 4. For additional information on the material properties of soil domains please refer to [17]. It must be

noted at this point that, a mesh sensitivity was also performed by using 25, 50 and 100 cm elements for the discretization of the soil domains. This yielded an optimum mesh geometry when 50 cm hexahedral elements are used. Buckling was also considered during the performance of the pushover analyses.

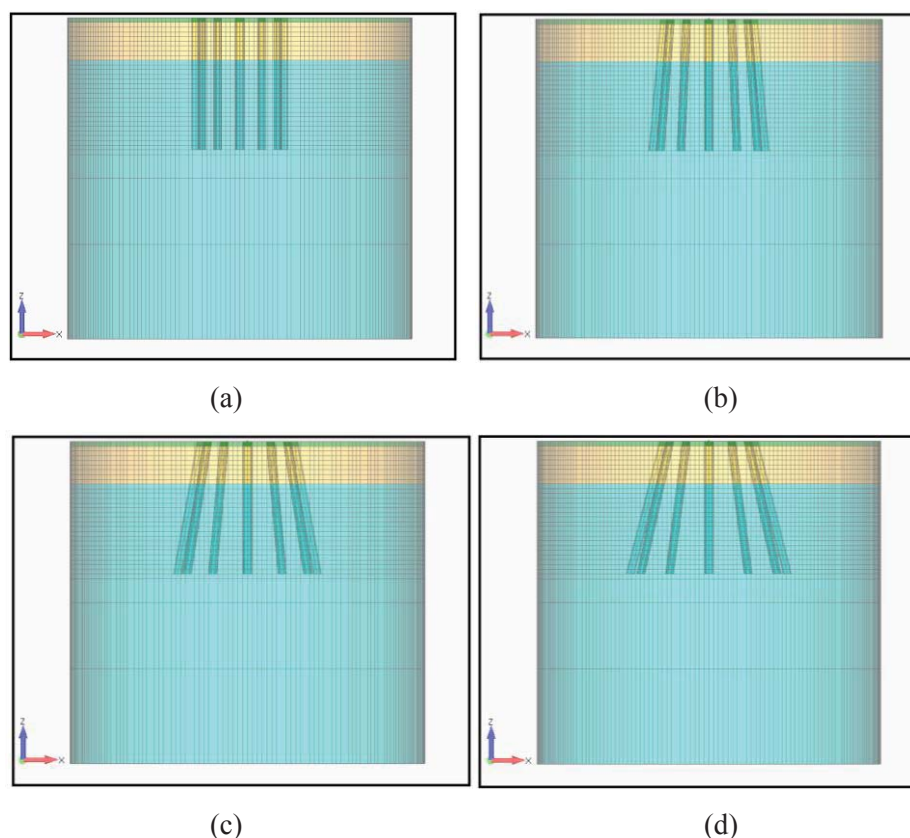


Figure 4. Pile layout of the increasing geometry with extra soil. (a) 0, (b) 5, (c) 10 and (d) 15 degrees of pile inclination.

#### 4 MODAL ANALYSIS RESULTS

Modal analyses were performed for the first 24 modes, where the deformed shapes and the eigenfrequencies will be discussed herein. The eigenmode legend in each figure shows only the critical displacement, therefore, it has no physical meaning in terms of displacement. However, the periods and frequencies have a physical meaning and will be discussed in this section. Fig. 5 shows the fixed model (no SSI considerations), which had the same main eigenmodes as the corresponding eigenmodes of the different geometries with SSI considerations. The deformed shape of a fixed condition can be seen in Fig. 5.

The first three deformed shapes of the Equal Layer Geometry with 5- and 15-degree inclined piles situated on extra soil can be seen in Fig. 6 and 7. The deformed shapes for the other soil geometries can be found in [17].

The Equal Geometry and the Increasing Layer Geometry had the same eigenmodes during this numerical investigation, however, it was evident that the soil geometry has an influence on the stiffness of the Wind Turbine structure. As it can be seen in Fig. 8, the rock layer geometries had the lowest periods due to the hard rock that was practically acting as a fixed base to the piles. The numerical investigation of the 1<sup>st</sup> eigenmode yielded a minimum period value for the 10-degree pile inclination, which was then used to perform further investigations.

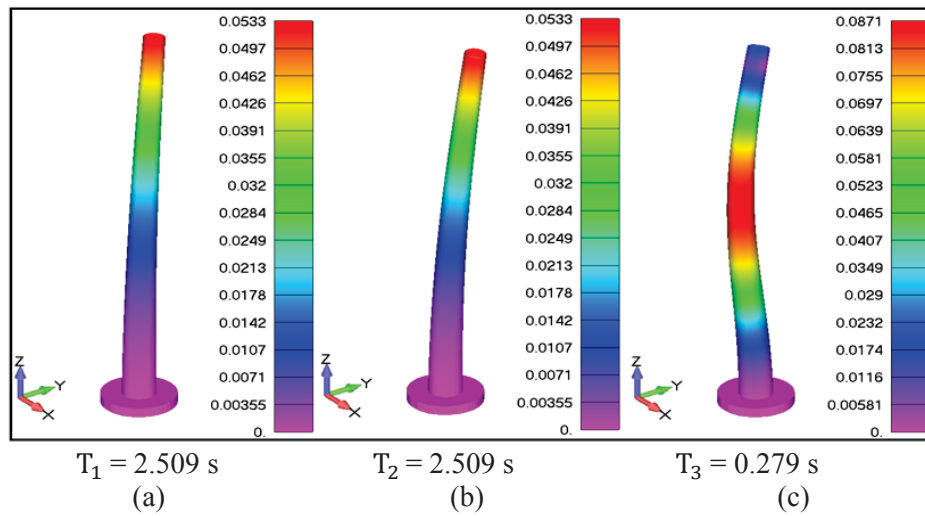


Figure 5: Deformed shapes of the first three eigenmodes with a fixed condition at the bottom of the pile cap. (a) 1st, (b) 2nd and (c) 3rd Mode [17].

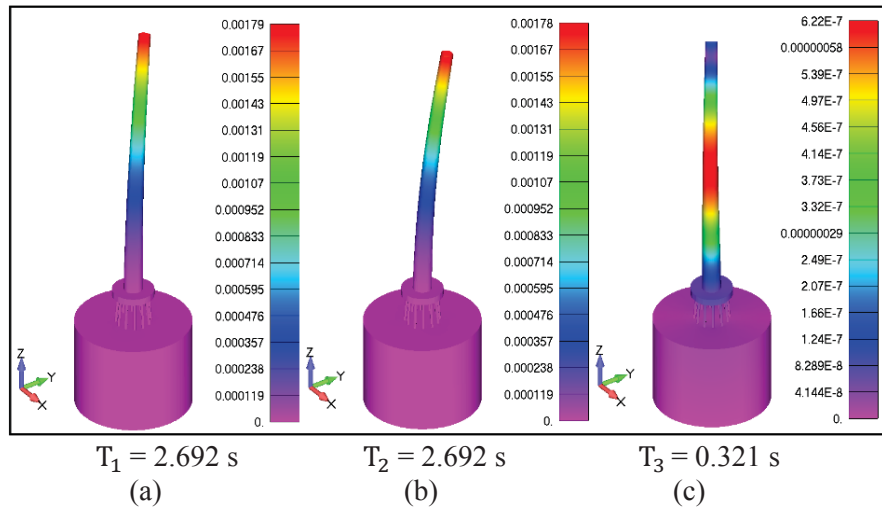


Figure 6: Eigen-shapes of the first three modes with a pile inclination of 5 degrees situated on extra soil. (a) 1<sup>st</sup>, (b) 2<sup>nd</sup> and (c) 3<sup>rd</sup> Mode.

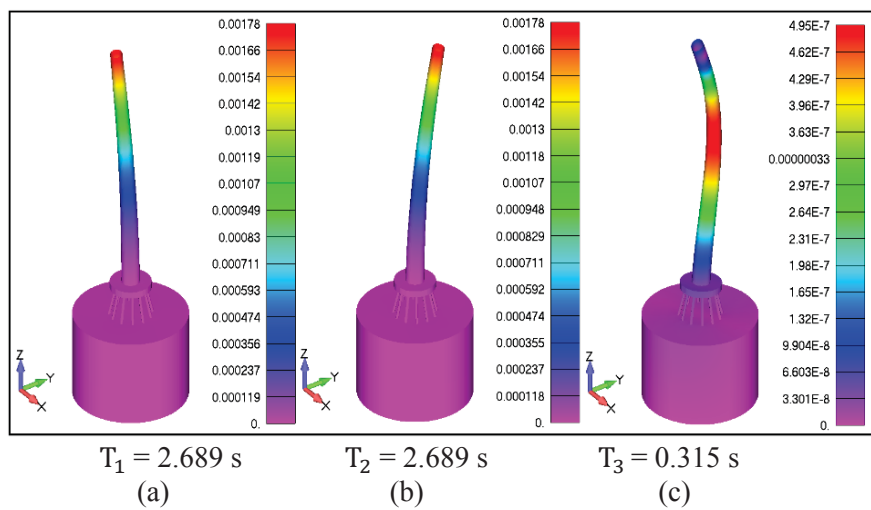
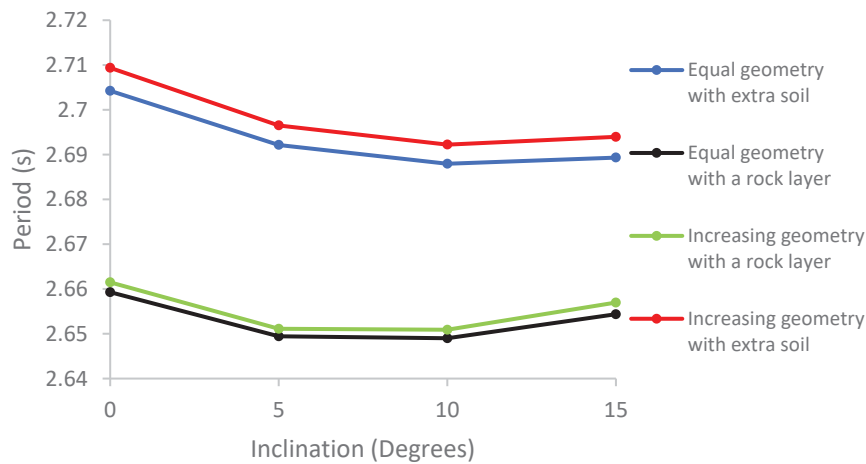


Figure 7: Eigen-shapes of the first three modes with a pile inclination of 15 degrees situated on extra soil. (a) 1<sup>st</sup>, (b) 2<sup>nd</sup> and (c) 3<sup>rd</sup> Mode.

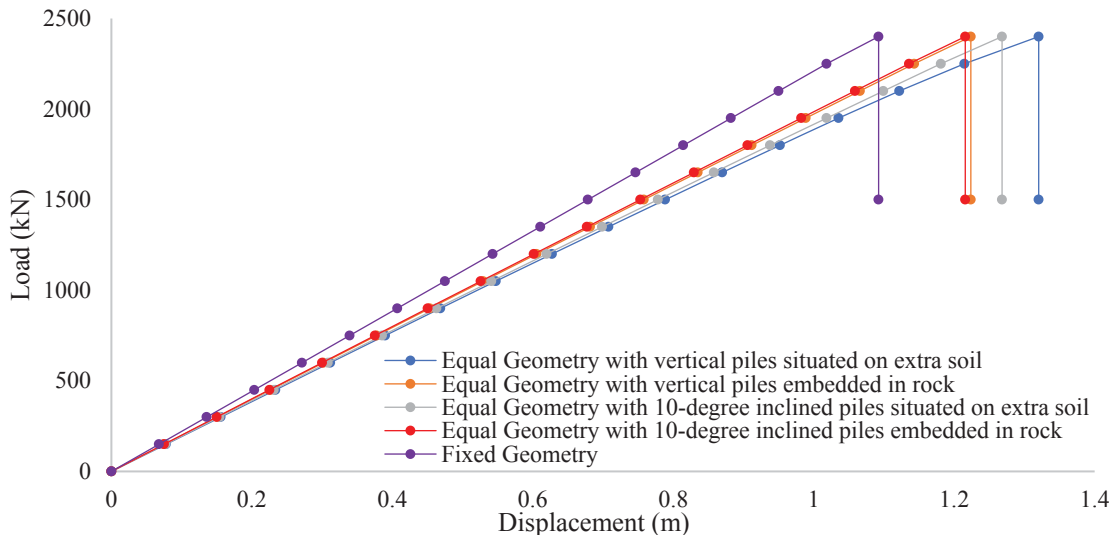


Figure 8: Period comparison of the 1<sup>st</sup> eigenmode.

## 5 PUSHOVER ANALYSES

The pushover analyses were conducted by applying a horizontal force of 3 MN, where all dead loads were accounted for. The vertical and 10-degree inclination piles of the Equal and the Increasing Layer Geometry were analysed. The P- $\delta$  curves for the various models were compared, furthermore, the Load-Rotation relationship for the case of the pile cap was investigated.

The P- $\delta$  curves of the Equal Layer Geometry models can be seen in Fig. 9. It must be noted here that all the models derived a failure due to local buckling at the base of the steel tower. The Equal Layer Geometry with 10-degree inclined piles embedded in rock yielded the smallest displacement at failure. A mechanical behaviour attributed to the stiffness increase due to the rock layer combined with the pile inclination.

Figure 9: P- $\delta$  curves of the Equal Layer Geometry models [17].

The significance of SSI can yet again be observed when comparing the displacement at failure of the SSI models and the Fixed Geometry (Fig. 9). According to the numerical findings, the SSI can derive a total of 26.8 % increase in terms of horizontal displacement prior to failure for the case of the model with vertical piles founded on soft soil.

The rotation of the pile cap for the under-study models can be seen in Fig. 10. As expected, the foundation where the piles are situated on extra soil yielded a larger rotation than that of the

rock layer. The Equal Layer Geometry with 10-degree inclined piles embedded in rock had the lowest rotation of the different investigated foundation and soil profiles.

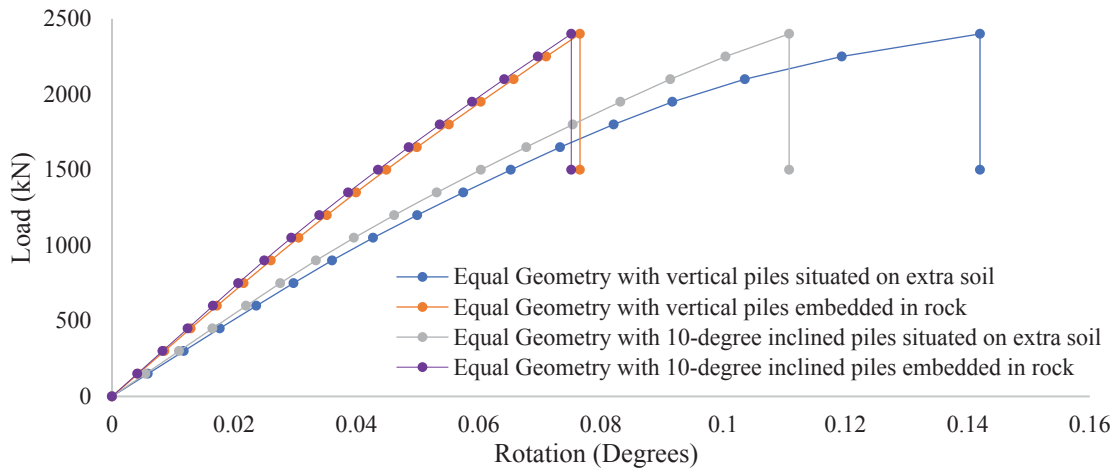


Figure 10: Rotation of the pile cap for the Equal Layer Geometry models [17].

The nonlinear increase in rotation of the pile cap for the Equal Geometry with vertical piles situated on extra soil (Fig. 10) is due to the yielding of the soil that occurred during the nonlinear analysis. The stress exceedance can be observed in Fig. 11, where the soil in the 1<sup>st</sup> layer yielded at 36 kPa (Fig. 11a). The Equal Geometry model with 10-degree inclined piles situated on extra soil had the same behaviour as previously discussed, but the observed level of plastification was less than that of the vertical piles.

The rotation of the pile cap for the optimum foundation design can be seen in Fig. 12. The von Mises stress distribution is also given, where it is easy to observe that the maximum developed stresses were found at the piles' heads.

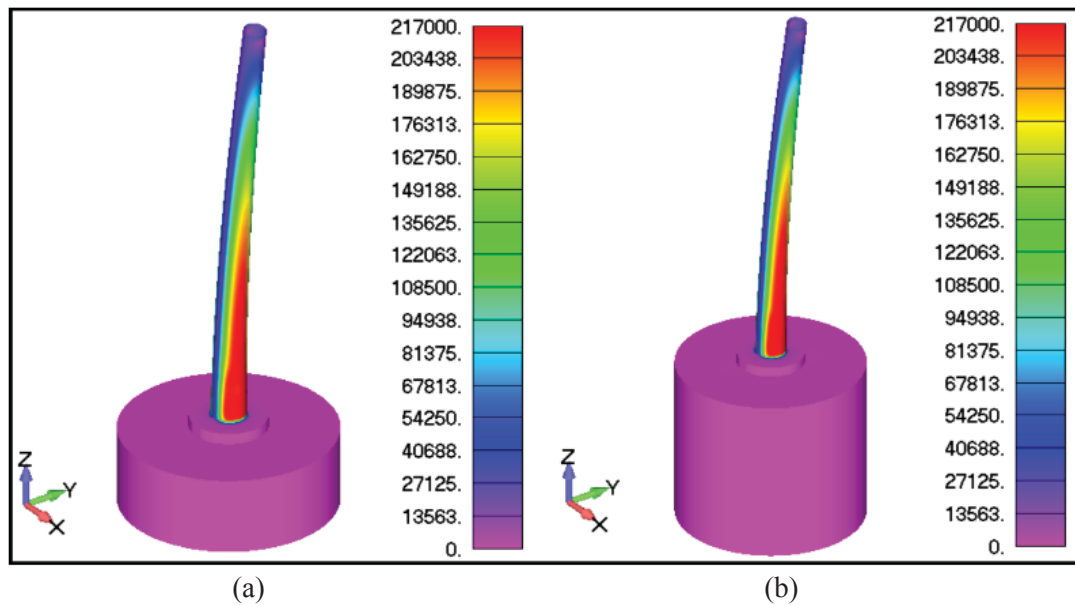


Figure 11: Solid von Mises stress contours. Deformed shape of the tower for (a) Piles embedded in a rock layer and (b) Piles situated on extra soil.

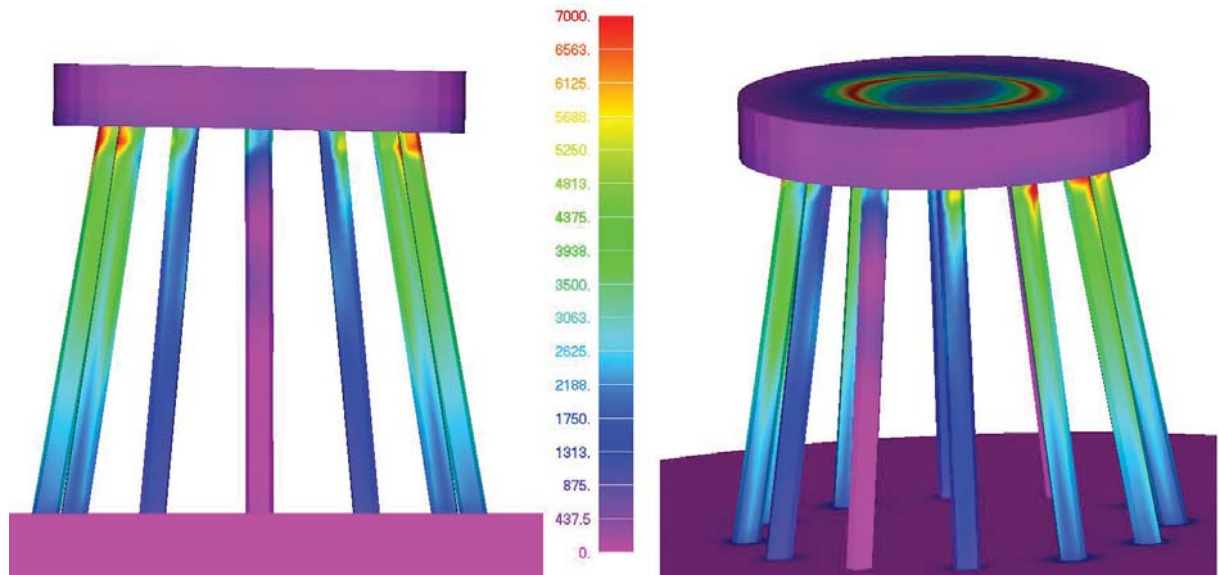


Figure 12: Rotation of the pile cap of 10-degree inclined piles embedded in rock.

The SSI effect for the case of the models that foresee the Increasing Layer Geometry where the model founded on soft soil derived a 13.31% displacement increase prior to failure when compared to the fixed model. This verifies the more flexible behaviour of the SSI models, whereas it is evident that, when the second soil profile is adopted a stiffer behaviour derives when compared to the Equal Layer Geometry soil profile that derived a relevant 16% increase in-terms of horizontal displacements. This is a clear indication that the soil profile plays a significant role in the overall behaviour of the tower.

The 10-degree inclined and vertical piles embedded in rock have a small difference in terms of displacement at failure (see Fig. 13). The 10-degree inclined piles model embedded in rock and situated on extra soil yielded the lowest horizontal displacements.

The rotation of the pile cap for the under-study increasing layer models can be seen in Fig. 14. The Increasing Layer Geometry with 10-degree inclined piles embedded in rock had the lowest rotation out of the investigated increasing layer soil profile models. This verifies the previous finding that the 10-degree pile inclination stiffens the mechanical behaviour of the foundation.

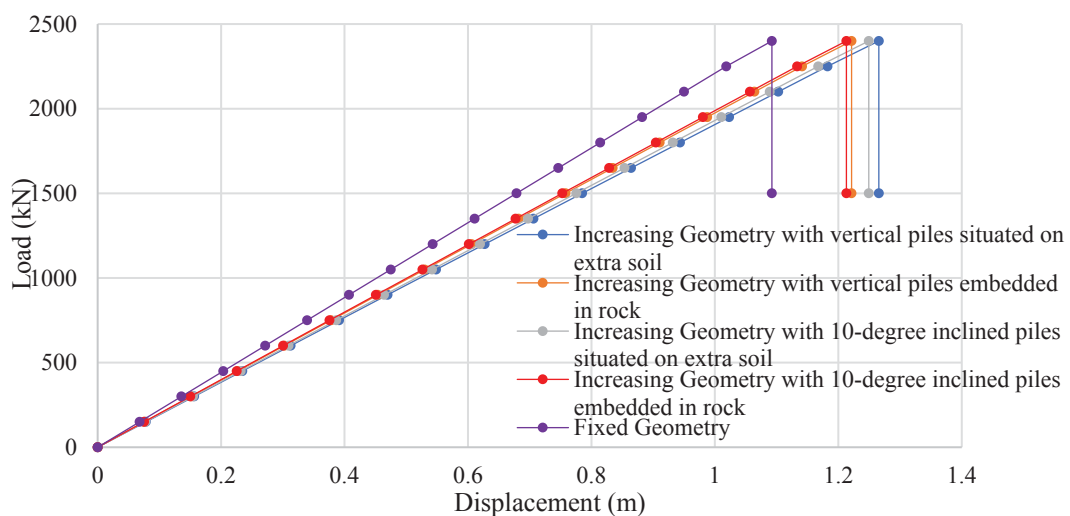


Figure 13: P- $\delta$  curves of the Increasing Layer Geometry models [17].

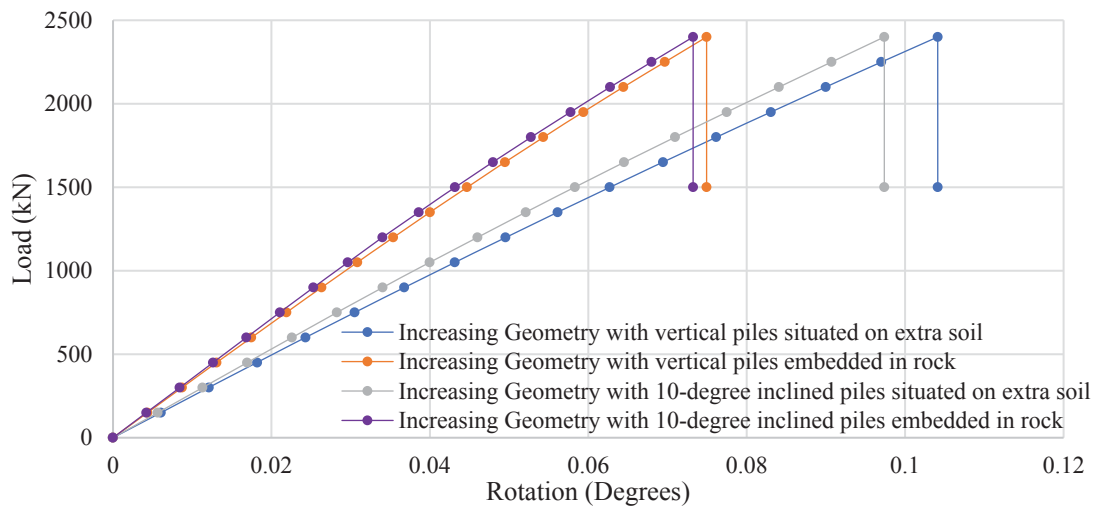


Figure 14: Rotation of the pile cap for the Increasing Layer Geometry models [17].

## 6 CONCLUSIONS

Within this research work a numerical investigation was performed on the effect of the SSI phenomenon on wind turbine structures by using a 3D detailed modelling approach. The modelling approach foresaw the use of hexahedral element to discretize the soil domain as well as the wind turbine structure. Thereafter, modal and pushover analyses were performed.

In regards to the numerical investigation of wind turbine structures and their dynamic response, the numerical investigation of the modal analyses for the Equal Layer Geometry models with extra soil and a rock layer concluded that the optimum inclination of the piles is 10-degrees measured from the vertical. The results obtained within this research work can be used to optimally design the wind turbine foundation according to the relevant site conditions.

The pushover analyses further investigated the optimum foundation that derived from the modal analyses, where the Increasing Layer Geometry with 10-degree pile inclination situated on extra soil and embedded in rock were found to yield the lowest rotations and horizontal displacements prior to failure.

Soil-Structure Interaction has a significant effect on the outcome of an analysis and the mechanical response of the wind turbine structure, thus, the importance of a numerical investigation is crucial. It is essential to thoroughly investigate the effect of SSI on the superstructure prior to finalizing and optimally designing a wind turbine structure.

A future step is to optimize the proposed structural design presented in this research work, where a tower redesign is necessary to be performed so as to adjust the steel thicknesses based on the stress analysis that was performed, minimizing the required material to manufacture the tower. Furthermore, a full-scale nonlinear dynamic analysis will then be performed to further investigate the overall response of the proposed design and parametrically investigate the ability of the proposed design to minimize stress development at the soil, substructure and super-structure domains.

## REFERENCES

- [1] Mourlas, C., Papadrakakis, M. and Markou, G. (2017), "A Computationally Efficient Model for the Cyclic Behavior of Reinforced Concrete Structural Members", *Engineering Structures*, 141, pp. 97–125.

- [2] Mourlas, C., Markou, G. and Papadrakakis, M. (2019), “Accurate and Computationally Efficient Nonlinear Static and Dynamic Analysis of Reinforced Concrete Structures Considering Damage Factors”, *Engineering Structures*, 178 (2019), pp. 258–285.
- [3] Mourlas, C., Markou, G., and Papadrakakis, M., “3D Detailed Modeling of Reinforced Concrete Frames Considering accumulated damage during static cyclic and dynamic analysis – new validation case studies”, *COMPDYN 2019, 7th International Conference on Computational Methods in Structural Dynamics and Earthquake Engineering*, 24-26 June 2019, Crete, Greece.
- [4] Markou, G., Sabouni, R., Suleiman, F. and El-Chouli, R. (2015), “Full-Scale Modeling of the Soil-Structure Interaction Problem Through the use of Hybrid Models (HYMOD)”, *International Journal of Current Engineering and Technology*, 5 (2), pp. 885-892.
- [5] Markou, G., AlHamaydeh, M. and Saadi, D., “Effects of the Soil-Structure-Interaction Phenomenon on RC Structures with Pile Foundations”, *9th GRACM International Congress on Computational Mechanics*, Chania, Greece, 4-6 June 2018, pp. 338-345.
- [6] Mourlas, C., Gravett, D.Z., Markou, G., and Papadrakakis, M., “Investigation of the Soil Structure Interaction Effect on the Dynamic Behavior of Multistorey RC Buildings”, *VIII International Conference on Computational Methods for Coupled Problems in Science and Engineering, COUPLED PROBLEMS 2019*, 3-5 June 2019, Sitges, Catalonia, Spain.
- [7] Austin, S. and Jerath, S. 2017. “Effect of soil-foundation-structure interaction on the seismic response of wind turbines”. *Ain Shams Engineering Journal*, Vol 8, May, pp 323-331.
- [8] De Risi, R., Bhattacharya, S. and Goda, K. 2018. “Seismic performance assessment of monopile-supported offshore wind turbines using unscaled natural earthquake records”. *Soil Dynamics and Earthquake Engineering*, Vol 109, June, pp 154-172.
- [9] Wang, X., Ye, A., He, Z. and Shang, Y. 2015. “Quasi-Static Cyclic Testing of Elevated RC Pile-Cap Foundation for Bridge Structures”. *Journal of Bridge Engineering*, Vol 21, No 2, March, pp 1-16.
- [10] Wind Africa: About the project 2018. Available at: <http://community.dur.ac.uk/wind.africa/about/>. [Accessed 23 Apr 2019].
- [11] Blanco, G., Ye, A., Wang, X. and Goicolea, J. 2018. “Parametric Pushover Analysis on Elevated RC Pile-cap Foundations for Bridges in Cohesionless Soils”. *Journal of Bridge Engineering*, Vol 24, No 1, November, pp 1-16.
- [12] Albiker, J., Achmus, M., Frick, D. and Flindt, F. (2017). 1g model tests on the displacement accumulation of large-diameter piles under cyclic lateral loading. *Geotechnical Testing Journal*, Vol. 40, No. 2, pp. 173-184.
- [13] Frick, D. and Achmus, M. (2019), Model tests on the behaviour of monopiles under general cyclic lateral loading, *2nd International Conference on Natural Hazards & Infrastructure*, 23-26 June, 2019, Chania, Greece.
- [14] Bisoi, S and Halder, S (2019), 3D Modeling of Long-Term Dynamic Behavior of Monopile-Supported Offshore Wind Turbine in Clay, *International Journal of Geomechanics*, Vol 19(7).

- [15] Tziavos, I.N., Hemida, H., Metje, N. and Baniotopoulos, C. (2019), Non-linear finite element analysis of grouted connections for offshore monopile wind turbines, *Ocean Engineering* 171 (2019), pp. 633–645.
- [16] Chun-Bao, Y, Rui, W. and Jian-Min, Z. (2018), Seismic Analysis of Monopile Supported Offshore Wind Turbine, *International Conference on Geotechnical and Earthquake Engineering* 2018, October 20–21, Chongqing, China.
- [17] Prowell, I., Elgamal, A. and Lu, J. 2010. “Modelling the influence of soil structure interaction on the seismic response of a 5MW wind turbine. Scholars’ Mine”. Research 5.09a. San Diego, California.
- [18] Guo, L., Uang, C., Elgamal, A., Prowell, I. and Zhang, S. 2011. “Pushover Analysis of a 53m High Wind Turbine Tower”. *Journal of Computational and Theoretical Nanoscience*, Vol 4, No 3, March, pp 656-662.
- [19] Gravett, Z.D. and Markou, G. (2021), State-of-the-art Investigation of Wind Turbine Structures Founded on Soft Clay by Considering the Soil-Foundation-Structure Interaction Phenomenon – Optimization of Battered RC Piles, *Engineering Structures*, Volume 235, 112013.
- [20] Reconan FEA v2.00, User’s Manual. 2020.
- [21] Bathe, K.J. 1996. “Finite element procedures”. Prentice-Hall, Upper Saddle River, New Jersey.
- [22] Markou, G., Mourlas, C., Bark, H. and Papadrakakis, M. (2018), “Simplified HYMOD non-linear simulations of a full-scale multi-storey retrofitted RC structure that undergoes multiple cyclic excitations - An infill RC wall retrofitted study”, *Engineering structures*, Vol 176, December, pp 829-916.



## MODELLING THE IMPACT OF GAPPING BEHAVIOUR ON MONOPILE MOUNTED OFFSHORE WIND TURBINE DYNAMICS

Stephen A. Williams<sup>1</sup>, Loizos Pelecanos<sup>1</sup>, and Antony P. Darby<sup>1</sup>

<sup>1</sup> Department of Architecture and Civil Engineering  
University of Bath  
Claverton Down, Bath, BA27AY, UK  
e-mail: {sw2007,lp640,absapd}@bath.ac.uk

**Keywords:** SSI, Gapping, Offshore Wind Turbines, Monopile, Winkler

**Abstract.** *Increased demand for renewable energy production has stimulated interest in the offshore wind turbine (OWT) industry as a viable solution, and with OWTs growing larger in scale, further research is required into the dynamics of these newer structures. The majority of installed OWTs to date are built upon monopile foundations, and it is widely acknowledged that the current design methods for offshore piles are not appropriate for the large diameter piles required. This paper uses a novel pile-soil gapping algorithm to simulate the effects of degradation to the soil conditions in the sea bed. Using a 1D Winkler beam-spring approach, a dynamic model is validated for prediction of the natural frequencies of several OWT case studies, and the gapping algorithm is shown to reproduce well the reduction in natural frequency likely attributed to soil degradation measured from an OWT in Kentish Flats wind farm. It is found through the simulation of rotor-stop tests that the presence of gapping decreases the measured natural frequency, and this effect is greater for the monopile foundations with a smaller slenderness ratio.*

## 1 INTRODUCTION

The use of offshore wind power as a means of renewable electricity generation is becoming ever more popular, and is set to continue to grow as an industry. Offshore wind turbines (OWTs) can be mounted on a variety of foundations, including jacket structures, gravity bases, tripods and more recently floating foundation concepts. However, the most common choice is the monopile, due to its relatively simple and economical production. Monopiles are typically long and slender foundations that flex to accommodate the motion of the supported structure. But as energy demands grow, and the construction technology improves, OWTs are rapidly increasing in size, increasing their energy output, and requiring larger diameter and, therefore, more rigid foundations than previously detailed in design recommendations.

OWTs consist of a monopile foundation, a long flexible tower above the water line, and a substructure connecting the two. The nacelle, containing the generators and blade assembly, is affixed atop the tower. Due to the top-heavy nature of this arrangement, OWTs are dynamically sensitive structures, and as such due care must be taken to avoid unwanted resonances once operational. The OWT design paradigm can be described with three categories; stiff-stiff, soft-stiff, and soft-soft [1], referring to the flexibility of the support structure. Displayed in Figure 1, the OWT experiences four main driving frequencies. Wind and wave loading peaks at low frequencies around 0.1 Hz. The rotation of the rotor within the nacelle exerts an additional force on the system, at a frequency of  $1P$ , ranging from around 0.1 to 0.3 Hz. The  $3P$  loading arises from the blade shadowing force exerted on the OWT from the air deficiency created by the blades sweeping in front of the tower as they rotate, with a frequency of  $3 \times 1P$  for a three-bladed turbine, and  $2 \times 1P$  for a two-bladed turbine (i.e  $2P$  rather than  $3P$ ). In response to these driving forces, the soft-soft design regime places the natural frequency of the superstructure less than  $1P$ , the soft-stiff between  $1P$  and  $3P$  and the stiff-stiff above  $3P$ . Since the soft-soft is in danger of becoming excited by environmental loading, and the stiff-stiff requires too much steel to be economically viable, the soft-stiff approach is the most suitable. The bandwidth of non-resonant frequencies is narrow, so it is important to be aware of the the natural frequency of the structure upon installation, and also how it may vary during the operational lifetime.

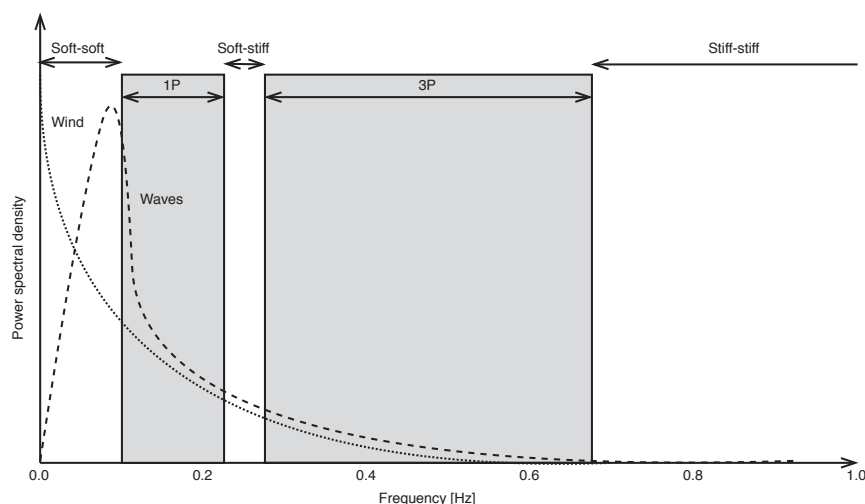


Figure 1: Example power spectrum of an OWT, showing rotor frequency  $1P$ , blade passing frequency  $3P$ , and wind and wave spectra (Figure adapted from [1]).

OWTs experience cyclic loading in the lateral direction from wind and waves, and during its expected operational lifetime of 25-30 years may experience billions of cycles [2]. Currently, the design methods employ beam-on-nonlinear-Winkler-foundation (BNWF) models with prescribed soil reaction  $p$ - $y$  curves given by the DNV [3] and the American Petroleum Institute, or API [4]. They recommend the use of cyclic loading curves based on empirical tests performed on flexible piles under hundreds of loading cycles [5]. It is widely shown that long term cyclic loading has a considerable impact on the soil-structure interaction [6, 7, 8], including the effect of soil degradation and gap formation under cyclic loads. It is therefore important to include these mechanisms in models of OWT dynamics.

Gapping is the formation of a separation between the foundation and soil, causing unresisted lateral motion of the foundation, and a reduction in effective soil stiffness. It is affected by the soil condition, where different soil cohesiveness will affect the subsequent cave-in of a gap under cyclic load, but it has been shown that even cohesionless soils will not cave-in completely under continuous cyclic loading [9]. Changing the properties of the soil will have an impact on the natural frequency of the OWT, which is of specific importance for soft-stiff structures in danger of resonance if they experience drift of this natural frequency. Differences have been reported between the designed natural frequency and the measured value upon operation [10], with Damgaard et al. [11] recording reduction in natural frequency likely attributed to soil erosion in the upper layers around the foundation. It is important then to include in modelling efforts how this frequency may change with soil condition over long term cyclic loading.

In this paper, a simple gapping algorithm is applied to a dynamic BNWF model of several OWT case studies, and the effect of this gapping to the natural frequency is shown for different monopile geometries and levels of loading. The results of this study will have applications in the modelling and design of OWTs, and provide estimations for the condition of the soil after reasonable loading simulations are applied.

## 2 THE MODEL

A BNWF concept model is used with Euler-Bernoulli beams to model the structure, and soil springs with viscous dampers to model soil reaction, as displayed in Figure 2, with  $M_{RNA}$  representing the mass of the rotor-nacelle assembly, and  $F$  the externally applied force.

Soil reaction is modelled using the hyperbolic reaction curve of Duncan & Chang [12], defined as:

$$P = \frac{k_{max}y}{1 + y \frac{k_{max}}{P_{max}}} \quad (1)$$

where  $k_{max}$  is the initial spring stiffness in N/m,  $P_{max}$  is the ultimate capacity of the spring in N,  $y$  the horizontal displacement in m and  $P$  the force in N. Masing rules [13] are used to model the unloading response upon reversal. The value of the initial stiffness  $k_{max}$  used is that of Vesic [14], which is described by:

$$k_{max} = \frac{0.65 L_{EL} E_s}{(1 - \nu^2)} \left( \frac{E_s d_p^4}{E_p I_p} \right)^{\frac{1}{12}} \quad (2)$$

where  $L_{EL}$  is the elemental length in the BNWF model,  $E_s$  the Young's modulus of the soil,  $\nu$  the Poisson's ratio of the soil,  $d_p$  the diameter of the pile and  $I_p$  its second moment of area. The ultimate capacity of the pile is defined by the undrained shear strength of the soil, and given

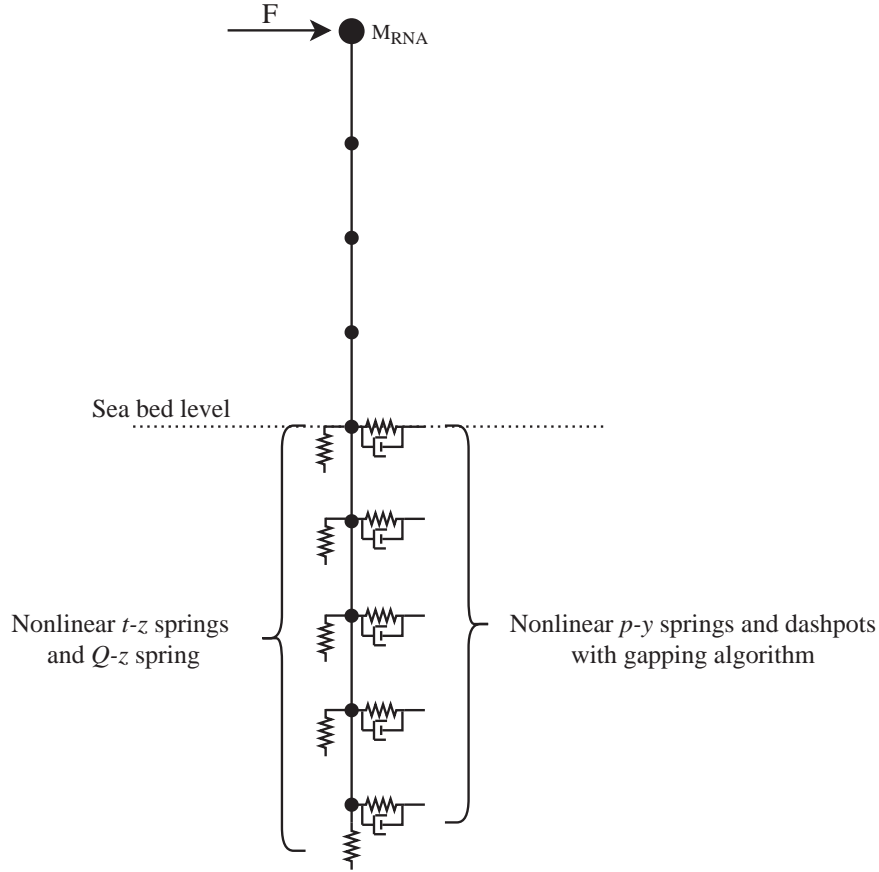


Figure 2: The BNWF model of an OWT where the lateral soil reaction is modelled with  $p$ - $y$  springs and viscous dashpot dampers, and the vertical reaction with  $t$ - $z$  &  $Q$ - $z$  springs. The rotor-nacelle assembly is modelled as a point mass at the top node.

by [15]:

$$P_{max} = L_{EL} N_p S_u d_p \quad (3)$$

where  $N_p$  is a dimensionless coefficient increasing with depth, linearly from a value of 2 to a constant value of 11 from a depth of  $z/d_p = 3$ , and  $S_u$  is the undrained shear strength of the soil. Since the system is exclusively loaded laterally in this study, the axial component of the soil reaction springs can be neglected, as is commonly done for OWT analysis. A Newmark beta method [16] is used to solve the dynamic problem iteratively, with a beta value of 0.3025, and a gamma value of 0.6, in combination with a tangent stiffness method to model nonlinearity in the soil response.

## 2.1 Damping

Damping in the system consists of a superposition of structural, hysteretic and radiation damping. Aerodynamic and hydrodynamic damping sources are neglected for simplicity. Structural damping is modelled using the Rayleigh method, superposing contributions from the mass and stiffness matrices to form the damping matrix, and classical damping formulations for the coefficients. A damping percentage of 1% is used for structural contributions, as it is typically expected to be between 0.5% and 1.5% for OWTs [17]. Radiation damping is modelled with

the damping coefficient of Gazetas & Dobry [18], formulated as:

$$\frac{c_r}{2d_p\rho_s V_s} = \left[ 1 + \left( \frac{3.4}{\pi(1-v)} \right)^{5/4} \right] \left( \frac{\pi}{4} \right)^{3/4} a_0^{-1/4} \quad (4)$$

where  $V_s$  is the shear wave velocity in the soil,  $\rho_s$  is the mass density of the soil, and  $a_0 = 2\pi f d_p / V_s$  is the dimensionless frequency. This damping is tuned to achieve a contribution of 0.5%.

## 2.2 Gapping model

The gapping model is based on an entry condition defined by the soil reaction threshold, and an exit condition based on a displacement threshold. If a node enters a gap, it experiences soil resistance only from the side shear friction, modelled with a reduced stiffness value of 5% of  $k_{max}$ . If a node is no longer in, or has not entered the gap, it continues to move based on the Masing rules and hyperbolic curve.

The entry and exit conditions are modified using parameters  $\alpha_p$  and  $\alpha_y$ . A node enters the gap if its  $p$  value crosses the threshold defined by:

$$p_{pos} = \alpha_p(z) [p] \quad (5)$$

$$p_{neg} = \alpha_p(z) [p] \quad (6)$$

for  $p$  decreasing and increasing respectively, where  $[p]$  is the minimum and  $\lceil p \rceil$  the maximum  $p$  value for that degree-of-freedom over the time history of loading so far. The  $\alpha_p(z)$  value can be calibrated over depth  $z$ , to control the amount of gapping down the pile. Exit threshold values are based on displacement, and are defined by:

$$y_{neg}^N = \begin{cases} \alpha_y [y] & \text{if } y \leq 0 \text{ \& } N = 1 \\ \alpha_y y_{neg,entry}^{N-1} & \text{if } y \leq 0 \text{ \& } N > 1 \end{cases} \quad (7)$$

$$y_{pos}^N = \begin{cases} \alpha_y \lceil y \rceil & \text{if } y \geq 0 \text{ \& } N = 1 \\ \alpha_y y_{pos,entry}^{N-1} & \text{if } y \geq 0 \text{ \& } N > 1 \end{cases} \quad (8)$$

for  $p$  increasing and decreasing respectively, where  $[y]$  is the minimum and  $\lceil y \rceil$  the maximum  $y$  value for that degree-of-freedom over the time history of loading so far. The  $N$  value is the cycle number within the cyclic loading. After cycle 1, the  $y$  threshold values are derived from the displacement upon entry of the gap in the previous cycle. This means that different levels of cave-in can be modelled with the  $\alpha_y$  parameter, with a value of 1 meaning no cave-in occurs, and a value of 0 implying a fully caved-in gap upon exit. The above parameters are shown for reference over two example loading cycles in Figure 3.

## 3 RESULTS

The gapping model has been applied to four case study OWTs located in the UK and Netherlands. They have been selected for their availability of geometry and soil data. The data of these OWTs is summarized in Table 1.

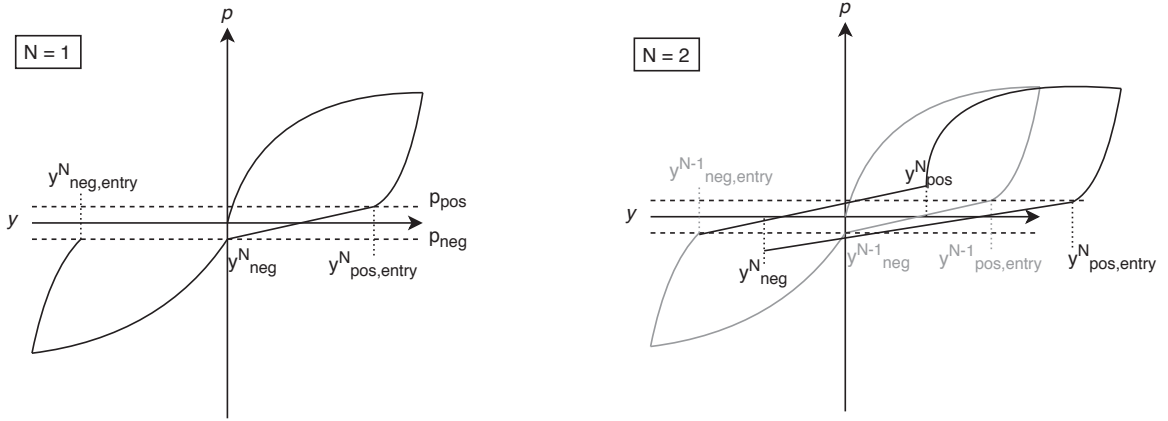


Figure 3: A schematic of a  $p$ - $y$  curve for a node experiencing gapping behaviour. This figure demonstrates how the gapping parameters influence the  $p$ - $y$  curve.

Parameters	Unit	Irene Vorrink	Lely A2	North Hoyle	Walney 1
Tower height	[m]	45.8	37.9	67	67.3
Substructure height	[m]	5.2	12.1	7	37.3
RNA mass	[kg]	35,700	32,000	100,000	234,500
Pile length	[m]	19	13.5	33	23.5
Pile diameter	[m]	3.5	3.2	4	6
Pile wall thickness	[mm]	28	35	30-70	80
Rotor diameter	[m]	43	40.77	80	107
Soil shear modulus $G_s$	[MPa]	55	53	230	70
Eigenfrequency $f$	[Hz]	0.563	0.634	0.35	0.35

Table 1: Parameters defining the OWT case studies. OWT geometry and soil data from [19, 20, 21].

For all case studies, the soil was modelled for simplicity as a linearly increasing stiffness value such that the average over the pile length was equal to the given value in Table 1. Environmental loading is simulated with a sinusoidal load applied to the top node and lateral degree of freedom, with an amplitude given by [19]:

$$F_{ext} = 0.5\rho_a\pi R_T^2 V_w^2 C_T(\lambda_s) \quad (9)$$

where  $\rho_a$  is the density of air, taken to be  $1.25 \text{ kg/m}^3$ ,  $R_T$  is the radius of the turbine rotor blades in m,  $V_w$  the wind speed at the hub, assumed to be  $13.5 \text{ m/s}$ , and  $C_T$  is a dimensionless thrust coefficient due to the fact that the blades are rotating, dependent on the factor  $\lambda_s = \frac{V_{rot} R_T}{V_w}$ , where  $V_{rot}$  is the rotational speed (1P frequency) of the rotor in rad/s. The value of  $C_T$  can then be estimated from the function and graph given in [22].

The natural frequency is found by simulating a rotor-stop test, and then performing a fast Fourier transform (FFT) on the resulting period of free vibration. A rotor-stop test involves spontaneously feathering the OWT blades during operation, causing the turbine to stop spinning and the structure to freely vibrate. In this model, the OWTs are loaded with the force value given by Equation 9 sinusoidally, and then the load removed to simulate the feathering of the blades.

In this study, three rotor-stop tests are simulated; one without the gapping element, to validate



the structure geometries and soil conditions with natural frequency prediction, then two with the gapping enabled. The first is with loading equal to the value predicted in Equation 9, and a loading frequency equal to the 1P value of the OWT. The second normalises the force across all case studies, and they are loaded with a 100 kN force at 0.1 Hz to see the effect of gapping over different foundation geometries. For all tests the effect of gapping on the measured natural frequency is quantified. All the following tests were performed with representative gapping parameters of  $\alpha_y = 0.5$ , and  $\alpha_p = 0.15$  at the sea bed, reducing linearly with depth with a gradient of  $0.05 \text{ m}^{-1}$ .

### 3.1 Validation of the gapping model

In order to validate the use of the gapping model, the results of the natural frequency analysis for an OWT in Kentish Flats are compared to the results found in the study at this wind park by Damgaard et al. [11]. The OWT, with a total superstructure length of 105.56 m, and a 29.5 m monopile was modelled with an average soil shear modulus of 60 MPa. In the experimental results used for comparison, the OWT was monitored over time with accelerometers and a number of rotor-stop tests were performed, and its natural frequency was found to vary, likely attributed to soil erosion in the upper layers of the foundation.

This OWT was modelled, and a rotor-stop test performed with gapping parameters of  $\alpha_y = 0.65$ , and  $\alpha_p = 0.25$  to simulate the soil erosion. The magnitude of the force applied during the sinusoidal loading phase was selected to ensure the acceleration experienced at the top node of the OWT during free vibration aligned with the values measured during the experimental tests, for comparability. As is displayed in Figure 4, the plotted frequency spectrum found from the FFT of the free vibration, the natural frequency was predicted to vary from 0.338 Hz without gapping, to 0.327 Hz with gapping. This agrees well with the recorded data from Damgaard et al., who measured the value to vary between 0.340 Hz and approximately 0.327 Hz.

### 3.2 Calculated loads

Using the expression for expected external wind load in Equation 9, rotor stop tests were performed on the OWT case studies and the effect of gapping on the measured natural frequency tested. The OWTs were loaded for 20 cycles, in order to achieve steady state behaviour before the rotor-stop. Results for these tests are summarised in Table 2.

	Irene Vorrink	Lely A2	North Hoyle	Walney 1
Measured $f$	0.563	0.634	0.35	0.35
Modelled $f$ (no gapping)	0.588	0.647	0.349	0.333
Modelled $f$ (gapping)	0.572	0.596	0.329	0.129
$F_{ext}$ [kN]	99.25	103	343	460
Slenderness ratio $L_p/d_p$	5.43	4.22	8.25	3.92
Change with gapping	2.72%	8.31%	5.71%	61.25%

Table 2: Eigenfrequency results for the modelled rotor-stop tests using external load calculated from Equation 9.

The results in Table 2 show first a satisfactory prediction of the measured OWT eigenfrequency assuming soil condition without gapping, using the listed OWT geometries and soil parameters. Secondly, all four results show a decrease in predicted eigenfrequency value when

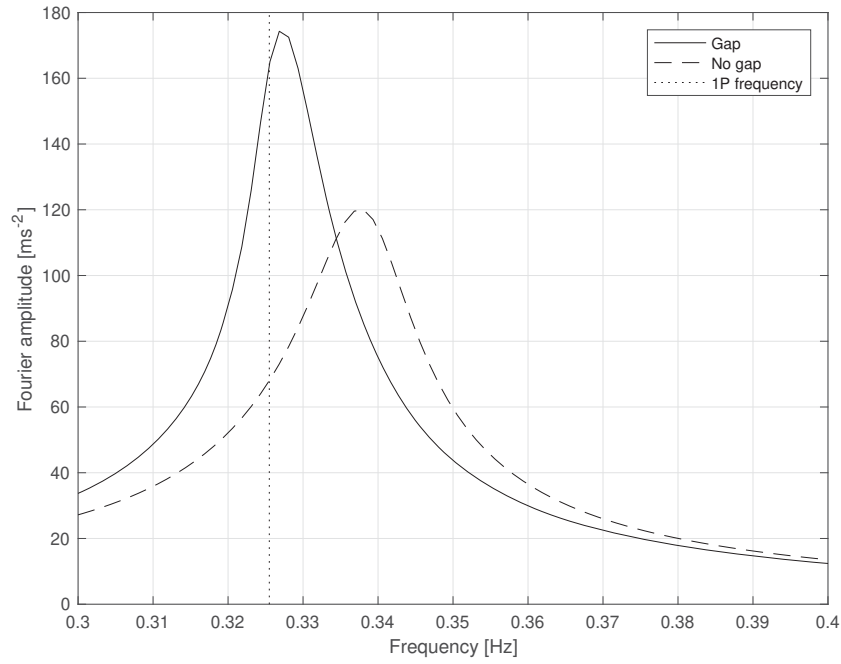


Figure 4: Frequency spectra of the Kentish Flats OWT model during the free vibration after a rotor stop test, with the gap algorithm enabled and disabled, as well as the reference 1P frequency of the OWT. The spectra resonant peaks are located at 0.338 Hz and 0.327 Hz.

the gapping is enabled. This is to be expected, since gapping essentially softens the soil response due to the transition portion of motion while in the gap which is unrestricted from soil reaction. The frequency reduction on the Walney 1 OWT is very large, due to the fact that the applied load was likely an overestimation, causing an exaggerated response.

### 3.3 Equal loads

The same test was then performed with the same load across all case studies, with  $F_{ext} = 100$  kN at a loading frequency of 0.1 Hz. The resulting frequencies identified in the rotor-stop tests are given in Table 3.

	Irene Vorrink	Lely A2	North Hoyle	Walney 1
Measured $f$	0.563	0.634	0.35	0.35
Modelled $f$ (no gapping)	0.588	0.647	0.356	0.338
Modelled $f$ (gapping)	0.575	0.602	0.348	0.302
Slenderness ratio $L_p/d_p$	5.43	4.22	8.25	3.92
Change with gapping	2.41%	6.95%	2.25%	10.65%

Table 3: Eigenfrequency results for the modelled rotor-stop tests using a 100 kN load for all tests.

It is noted that the change in external load and loading frequency has had a small effect on the predicted frequencies without gapping, highlighting the importance of considering a variety of expected loads when predicting the natural frequency, since the value is variable over

a small range once the structure is installed. Similarly to the previous results, the inclusion of gapping has introduced a reduction in the predicted eigenfrequency, but of lower magnitude than prior due to the reduced load magnitude and frequency. However, the results suggest that the size of the reduction may be attributed to the slenderness ratio of the monopile, with the smaller (and therefore more rigid) ratios experiencing a larger change in eigenfrequency. This could be attributed to the more rigid monopiles mobilizing the soil reaction further down the monopile's length, and therefore causing a gap response over a longer pile length. The flexible monopiles can be expected to behave as fixed below a certain critical depth, and therefore will not experience any gapping below that level.

#### 4 CONCLUSION

A simple gapping model was applied to a BNWF model of several offshore wind turbines, and the resulting effect on the natural frequency quantified. The natural frequency was identified with simulations of rotor-stop tests for OWTs of differing geometry and predicted external load. It was found that in all cases the natural frequency was reduced when the gapping effect was introduced, and that the effect appears more severe for the more rigid monopile foundations. The natural frequency is also slightly variable over different magnitudes of loading due to the nonlinear response of the soil, suggesting the importance of considering different weather and loading conditions for foundation design. With OWTs being designed with a natural frequency inside a narrow corridor of stability, it is important then to reliably predict by how much it is likely to drift throughout the operational lifetime. Including soil erosion effects like gapping may, then, assist in the design process and allow for reliable predictions. As well as application to the regular two-way dynamic loading used in this study, the model can be further included for use in stochastic loading simulations, such as more realistic wind and wave loads, and certainly has potential application to the impact of seismic loading on monopile foundations.

#### 5 ACKNOWLEDGEMENTS

The authors gratefully acknowledge the University Research Studentship Award which has supported the work presented in this paper.

#### References

- [1] S. Bhattacharya. Challenges in Design of Foundations for Offshore Wind Turbines. *Engineering & Technology Reference* (2014).
- [2] D. Lombardi, S. Bhattacharya, and D. Muir Wood. Dynamic soil-structure interaction of monopile supported wind turbines in cohesive soil. *Soil Dynamics and Earthquake Engineering* (2013).
- [3] DNV/Risø. *Guidelines for Design of Wind Turbines - 2nd Edition*. 2002.
- [4] API. API RP 2A - Recommended Practice for Planning , Designing and Constructing Fixed Offshore Platforms — Working Stress Design. *Api Recommended Practice* (2007).
- [5] M. Achmus, Y. S. Kuo, and K. Abdel-Rahman. Behavior of monopile foundations under cyclic lateral load. *Computers and Geotechnics* 36.5 (2009), pp. 725–735.
- [6] M. Arshad and B.C. O'Kelly. Analysis and Design of Monopile Foundations for Off-shore Wind-Turbine Structures. *Marine Georesources and Geotechnology* 34.6 (2016), pp. 503–525.

- [7] L. Cui and S. Bhattacharya. Soil–monopile interactions for offshore wind turbines. *Proceedings of the Institution of Civil Engineers: Engineering and Computational Mechanics* 169.4 (2016), pp. 171–182.
- [8] G. Nikitas, Nathan J. Vimalan, and S. Bhattacharya. An innovative cyclic loading device to study long term performance of offshore wind turbines. *Soil Dynamics and Earthquake Engineering* 82 (2016), pp. 154–160.
- [9] R.T. Klinkvort. *Centrifuge modelling of drained lateral pile - soil response: Application for offshore wind turbine support structures*. PhD thesis. Technical University of Denmark, 2012.
- [10] L. Arany, S. Bhattacharya, S. Adhikari, S.J. Hogan, and J.H.G. Macdonald. An analytical model to predict the natural frequency of offshore wind turbines on three-spring flexible foundations using two different beam models. *Soil Dynamics and Earthquake Engineering* 74 (2015), pp. 40–45.
- [11] M. Damgaard, L.B. Ibsen, L.V. Andersen, and J. K.F. Andersen. Cross-wind modal properties of offshore wind turbines identified by full scale testing. *Journal of Wind Engineering and Industrial Aerodynamics* 116 (2013), pp. 94–108.
- [12] J.M. Duncan and C. Chang. Nonlinear analysis of stress and strain in soils. *Journal of Soil Mechanics & Foundations Div* (1970).
- [13] G. Masing. Eigenspannumyen und verfeshungung beim messing. *Proc. Inter. Congress for Applied Mechanics*. 1926, pp. 332–335.
- [14] A.B. Vesic. Bending of beams resting on isotropic elastic solid. *Journal of Engineering Mechanics Division* 87 (1961).
- [15] H. Matlock. Correlation for design of laterally loaded piles in soft clay. *Offshore technology conference*. Offshore Technology Conference. 1970.
- [16] N. M. Newmark. A method of computation for structural dynamics. *Journal of the engineering mechanics division* 85.3 (1959), pp. 67–94.
- [17] R. Shirzadeh, C. Devriendt, M. A. Bidakhvidi, and P. Guillaume. Experimental and computational damping estimation of an offshore wind turbine on a monopile foundation. *Journal of Wind Engineering and Industrial Aerodynamics* 120 (2013), pp. 96–106.
- [18] G. Gazetas and R. Dobry. Simple radiation damping model for piles and footings. *Journal of Engineering Mechanics* 110.6 (1984), pp. 937–956.
- [19] S. Bisoi and S. Halder. Dynamic analysis of offshore wind turbine in clay considering soil-monopile-tower interaction. *Soil Dynamics and Earthquake Engineering* 63 (2014), pp. 19–35.
- [20] S. Adhikari and S. Bhattacharya. Dynamic analysis of wind turbine towers on flexible foundations. *Shock and Vibration* 19.1 (2012), pp. 37–56.
- [21] D. Amar Bouzid, S. Bhattacharya, and L. Otsmane. Assessment of natural frequency of installed offshore wind turbines using nonlinear finite element model considering soil-monopile interaction. *Journal of Rock Mechanics and Geotechnical Engineering* 10.2 (2018), pp. 333–346.
- [22] D. Lombardi. *Dynamics of Offshore Wind Turbines*. PhD thesis. University of Bristol, 2010.

## SOIL-STRUCTURE INTERACTION IN THE SEISMIC VULNERABILITY ANALYSIS OF RC BUILDINGS. APPLICATION TO A CASE STUDY BUILDING LOCATED IN SOUTHWESTERN SPAIN

M.V. Requena-Garcia-Cruz<sup>1</sup>, A. Morales-Esteban<sup>1</sup>, P. Durand-Neyra<sup>1</sup>, E. Romero-Sánchez<sup>1</sup>

<sup>1</sup> Department of Building Structures and Geotechnical Engineering, University of Seville, Spain. Av. Reina Mercedes, 2, 41012, Seville, Spain

{mrequena1, ame, percy, eromero13}@us.es

---

### Abstract

*Most seismic vulnerability analyses do not consider the Soil-Structure Interaction (SSI). However, it has been proved that SSI does not equally affect all types of structures and all types of soils. The analysis of the state of the art reveals that SSI especially affects the performance of mid/high-rise buildings under soft/inelastic soil conditions. This leads to overestimating the capacity of buildings and to obtaining unreliable results. This paper aims to assess the soil influence in the seismic vulnerability analysis of a reinforced concrete (RC) building. Three models of a real case study building have been determined (low-rise (real), mid-rise and high-rise). A pre-code 1970s case study building, located in Huelva, has been selected. This building shares typical constructive and structural characteristics with most RC buildings constructed during that period. The 3D continuum model of the soil has been carried out to simulate its nonlinear behaviour. The most probable soil profile has been defined, observing a clayey soil. Therefore, the analyses have been performed under undrained conditions. Nonlinear static analyses have been carried out to determine the seismic capacity of the models through the finite element method (FEM). The damage has been assessed by means of the local procedure, defined in the European seismic code, and the global fragility procedure. The results have shown that the soil does not significantly influence the behaviour of low-rise buildings. However, in the case of mid- and high-rise buildings, the maximum capacity can be reduced by up to 10% and 30%, respectively.*

**Keywords:** Soil Structure Interaction, Seismic analysis, Reinforced concrete, Buildings, OpenSEEs.

---

## 1 INTRODUCTION

Most seismic vulnerability analyses of buildings are carried out without considering the soil-structure interaction effects (SSI). Despite these notable effects, their consideration in seismic analysis remains unclear. In fact, SSI was assumed to be beneficial in past research [1]. This benefit emerges from the reduction of the internal forces and the drifts due to the soil's increasing flexibility. Hence, the vast majority of seismic vulnerability analyses consider models with a fixed-based configuration to obtain more conservative results. However, recent studies on the influence of SSI in the capacity assessment of buildings has proved that it does not positively affect all types of structures and all types of soils [2]. They have concluded that structures are expected to experience different levels of damage when the soil's influence is taken into account [3]. In fact, the Eurocode-8 Part-1 (EC8-1) [4] establishes that the SSI effects must be born in mind when structures: i) present significant second order ( $p-\Delta$ ) effects; ii) are slender; or, iii) are medium/high-rise buildings. Moreover, it was proved that SSI might affect aspects related to the seismic performance of buildings such as the ductility and the strength [5] or the energy dissipation [6]. Studies have even shown that the SSI can greatly worsen the performance of buildings due to asymmetrical designs [7]. This suggests that further research is needed.

The SSI effects can be taken into account by simulating the flexibility of the soil. To do so, several approaches have been proposed over time. Among others, the most common approaches used in the behaviour assessment of buildings are the Nonlinear Beam on Winkler method (NBWM) and the continuum modelling of soil (in 3D). The first approach is mainly based on simulating the nonlinear behaviour of the soil by adding inelastic springs [8]. These springs present different characteristics which are applied in certain directions. The NBWM can simulate the SSI effects very easily and simply. In this way analyses do not become very tedious [9]. However, this approach presents certain drawbacks: it does not consider the complete behaviour of the soil, the frictional surface between the soil and the foundation and the effects of deeper soil layers. Therefore, this method might not be applicable for all soil and structural characteristics.

The continuum modelling of soils can exhaustively capture the soil constitutive behaviour, obtaining more realistic results [2]. Moreover, this type of analyses has been gaining importance over the past decade due to the availability of new methods and the increase of computational capacity [10]. Some related studies showed that the foundation characteristics and the soil modulus (shear and bulk) are the parameters that most affect the seismic response of buildings [2]. Others proved that the SSI are significant when both the structure and the soil are simulated as inelastic [6]. These parameters cannot be considered in SSI assessment via the NBWM.

Owing to the lack of studies and guidance, this paper aims to analyse the soil's influence in the seismic vulnerability analysis of a reinforced concrete (RC) building. To do so, different models of a real case study building have been simulated (low-rise (real), mid-rise and high-rise). The EC8-1 statement and past research have been proved. The 3D continuum modelling of the soil has been carried out to simulate its nonlinear behaviour. Furthermore, the characterisation of the most probable soil profile at the location has been done by considering different geotechnical studies. As a clayey soil has been observed, the analyses have been carried out under undrained conditions. Nonlinear static analyses have been performed to determine the seismic capacity of models by using the finite element method (FEM). The damage has been assessed by means of the local procedure established in Eurocode-8 Part-3 (EC8-3) [11] and the fragility procedure.



The case study building is a 1970s primary school building located in Huelva (southwestern Spain), which is an earthquake-prone area. This building shares typical constructive and structural characteristics with most RC buildings of the area. What is more, these buildings were constructed prior to the applications of seismic codes.

The key contributions of this paper are: i) the analysis of the soil influence in the seismic vulnerability analysis of RC buildings considering different geometrical characteristics; ii) the characterisation for the 3D continuum modelling of the most probable soil profile in Huelva; iii) 3D FEM models in OpenSees to realistically reproduce the entire system's behaviour (soil+foundation+structure); iv) the analysis of the seismic damage by means of both local and global procedures.

## 2 CASE STUDY

### 2.1 Building configuration

The case study building selected is a primary school building located in Huelva. It has been defined as an index-building of the typology of RC buildings [12]. This typology represents 27% (75 buildings) of the total (279) of the primary school buildings constructed in the province. As they were built during the 1970s, they share constructive and structural characteristics with a major part of the area's RC buildings: insufficient longitudinal and transversal rebar ratio, wide beams, short columns, very slender RC columns sections and low-quality structural materials. Moreover, these buildings have not been designed according to seismic criteria since they were constructed prior to restrictive seismic codes.

The case study building is a two-story RC frame building (Figure 1). Although it is regular in height, it presents short columns on the ground floor. This is a typical constructive configuration that can be commonly found in most RC buildings of the 1970s. Short columns are created due to the elevation of the ground floor from the soil surface to avoid humidity and water problems. This ground-floor construction often leads to isolated footings (superficial or deep). In this case, the building was constructed with isolated footings of a depth of 0.80 m. The structural characteristics of the building are listed in Table 1.

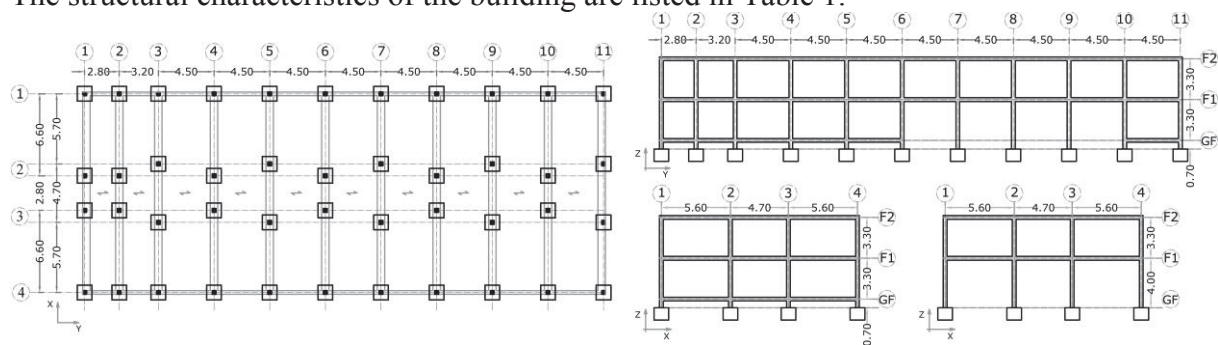


Figure 1: Case study building's configuration.

Characteristic	Columns	Load beams	Tie beams
Dimensions (cm)	30x40	60x30	30x30
Cross-section (cm <sup>2</sup> )	1,200	1,800	900
Longitudinal rebar (cm <sup>2</sup> )	1.572	Top: 0.786 Bottom: 3.495	Top: 0.786 Bottom: 0.786
Transversal rebar (cm <sup>2</sup> )	0.196	0.196	0.196
Spacing of stirrups (cm)	15	20	25

Table 1. Case-study's structural elements geometrical characteristics.

## 2.2 Soil characterisation

A characterisation of the soil under the building has been carried out to properly model its constitutive behaviour. The information has been compiled from 8 nearby geotechnical studies. These studies include information related to laboratory tests done with samples as well as in-situ geotechnical prospections. Based on the available information, an interpretation of the soil layering at the site has been performed. In this study, the most probable soil profile has been considered. To do so, the probability of each stratum according to its depth has been assessed. This determination has considered 17 boreholes. As shown in Figure 2a, four different geotechnical strata have been identified: tilled, grey clay, brown silt and clay loam. The laboratory tests have revealed a predominance of clay. Therefore, only the parameters to perform undrained analyses have been calculated.

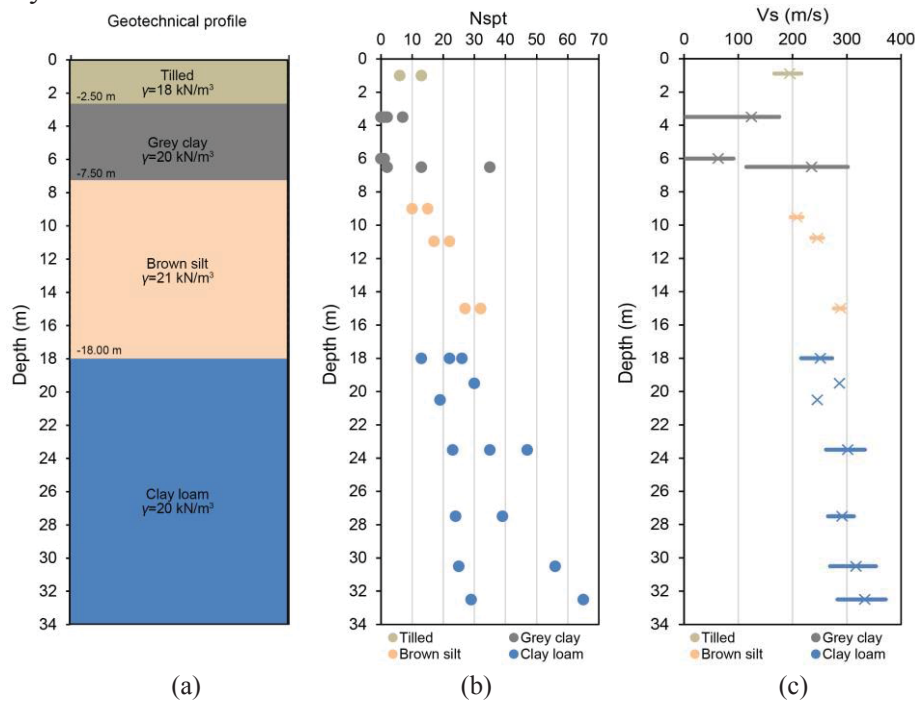


Figure 2: Soil characterization. (a) Soil profile (b)  $N_{spt}$  and  $V_s$  (c) according to depth.

Among other in-situ tests, standard penetration tests (SPT) were executed to determine the  $N_{spt}$ . In Figure 2b, the  $N_{spt}$  for each soil stratum has been plotted. According to [13], the shallow layers can be classified as low-dense soils ( $N_{spt} \approx 11-30$ ) while the deepest layers are dense ( $N_{spt} \approx 31-50$ ).

The shear wave velocity ( $V_s$ ) and the Poisson ratio ( $\nu$ ) are required to numerically model the soil in 3D. In [14], several correlations were defined to obtain  $V_s$ . However, in this work, only the Imai equation (Eq.(1)) has been used since it is widely accepted. In Figure 2c, the  $V_s$  values for each soil layer have been defined according to  $N_{spt}$  and depth. Since there are several values of  $V_s$  for each depth, the most probable value has been used to determine the parameters presented below.

$$V_s = 91 N_{spt}^{0.317} \quad (1)$$

The soil behaviour is defined according to three parameters: shear ( $G$ ), elastic ( $E$ ) and bulk ( $B$ ) modulus and the unit weight ( $\gamma$ ). The moduli have been calculated according to certain widely known geotechnical correlations (Eq.(2)(3)(4)).  $G$ ,  $E$  and  $B$  have been plotted in Figure 3 for each soil stratum. The soil constitutive behaviour has been plotted considering the

medium values of each modulus. As can be observed, the shallow layers are weaker than the deepest ones, which relates to  $N_{spt}$ . The soil stiffness increases at around 5 m depth. The clay loam's modulus rises slightly with depth. In order to take the variability of the modulus into account, four soil layers have been defined following the procedure established in Section 4.2.

$$G = \gamma V_s^2 \quad (2)$$

$$E = 2G(1 + \nu) \quad (3)$$

$$B = E/3(1 - 2\nu) \quad (4)$$

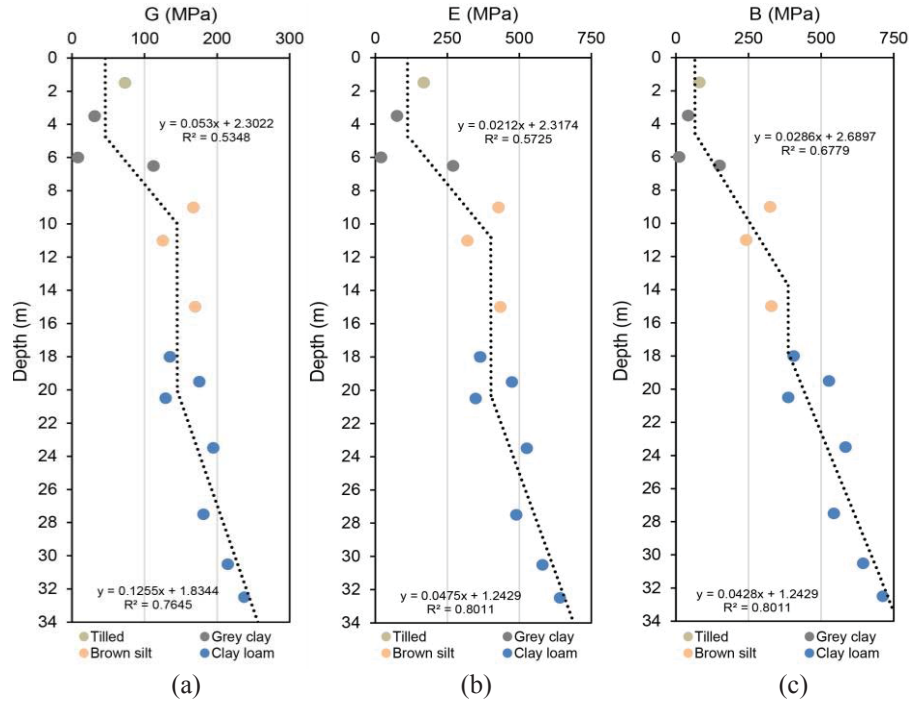


Figure 3:  $G$  (a),  $E$  (b) and  $B$  (c) values obtained from correlations according to geotechnical prospections.

### 3 NONLINEAR STATIC ANALYSES

#### 3.1 Models defined

The state of the art has revealed that SSI must be considered in the seismic analyses of mid- and high-rise buildings. Therefore, in order to better understand their influence, different configurations of the case study building have been determined by varying its height. As shown in Figure 4, three models have been defined: low-rise (real) (M1), mid-rise (M2) and high-rise (M3). The total mass and height of each model have been listed in Table 2. Fixed-base and solid models have been identified with “F” and “S”, respectively. The nodes at the base of the F-models have been fixed in the 6 degrees of freedom (DOF): X, Y, Z,  $R_x$ ,  $R_y$  and  $R_z$ . The modelling of the soil is presented in Section 4.2. It has also been checked that the foundations' dimensions are valid for the soil with each model's configuration.

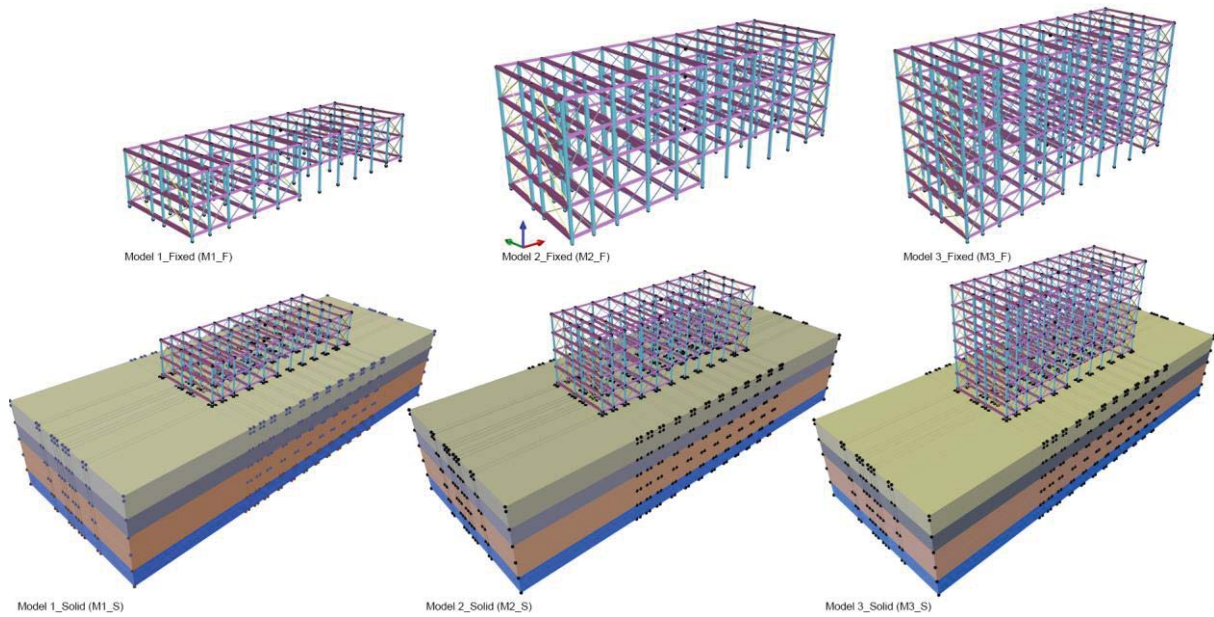


Figure 4: Models' configuration.

Model	Nº of floors	Total mass (ton)	Total height (m)
M1	2	1,058	7.30
M2	4	1,952	13.90
M3	6	2,846	20.50

Table 2. Number of floors, total mass and height of the models analysed.

### 3.2 Analysis procedure

Nonlinear static analyses have been carried out to determine the capacity of the models by using the FEM OpenSees software [15]. Since the models are very large, the analyses have been done using the parallel option available in OpenSees by defying partitions. The outputs have been handled in PYTHON [16]. A load-control and displacement-control integrator have been used to perform the gravity and the pushover analyses, respectively. Only the modal load pattern results have been considered since this has been the most restrictive. Modal analyses have been carried out to define the load pattern. The *-genBandArpack* solver has been used due to the numerous constraints. As models have worked in Mode 1 and 2, torsional effects can be neglected.

### 3.3 Damage determination

The N2-method has been used to determine the single-degree-of-freedom (SDOF) idealised bilinear curves and the target displacement. Its extended version has also been used, which takes the infills' effects into account. A 0.1g PGA for *Huelva* has been used according to the Spanish updated seismic action values [17]. The response spectrum has been constructed using the EC8-1 procedure.

Two approaches have been considered to determine the damage: the local and the global. The first one has borne in mind the demand/capacity ratio (DCR) established in EC8-3 and the local damage of RC structural elements. Three damage states have been determined: damage limitation (DL), significant damage (SD) and near collapse (NC). The NC is calculated considering the ultimate chord rotation ( $\theta_{um}$ ). The SD is determined as  $3/4$  of  $\theta_{um}$ . The DL is worked out by means of the yielding chord rotation ( $\theta_y$ ). The formulae of each parameter are



established in the EC8-3. Each damage state has been calculated when the demand chord of one column reaches the capacity values of  $\theta_{um}$ ,  $\theta_{um}$  and  $\theta_y$ .

The second approach is based on the fragility curves assessment. These curves provide the probability of reaching or exceeding a certain damage state ( $d_s$ ), given a certain spectral displacement ( $S_d$ ). They are determined by the well-known lognormal cumulative distribution (Eq.(5)), where:  $\beta_{ds}$  is the dispersion at  $d_s$  and  $S_{d,ds}$  is the median value of the spectral displacement at which a building reaches the  $d_s$  threshold.

$$P[d_s|S_d]=\Phi[(1/\beta_{ds})\ln(S_d/S_{d,ds})] \quad (5)$$

Both  $\beta_{ds}$  and  $S_{d,ds}$  are statistical parameters that take into account different uncertainties. They should therefore be determined according to the models analysed. However, in this case they have not been studied since further research should be carried out considering many models and including the SSI effects. However, an exhaustive work carried out in [18] has been used to define these parameters. The authors performed the fragility assessment of typical Spanish RC buildings and determined the fragility parameters for low-, mid- and high-rise RC buildings. The values of  $\beta_{ds}$  for each building class are listed in Table 5. The values of  $S_{d,ds}$  have been determined for each of the models analysed and following the provisions established in [18], listed in Table 4. This procedure considers the parameters that characterise the idealised SDOF system curves:  $D_y$  and  $D_u$ , yielding and ultimate displacement.

Damage state/Class	Slight ( $\beta_1$ )	Moderate ( $\beta_2$ )	Severe ( $\beta_3$ )	Complete ( $\beta_4$ )
Low-rise	0.28	0.37	0.82	0.83
Mid-rise	0.28	0.36	0.50	0.61
High-rise	0.28	0.29	0.34	0.45

Table 3.  $\beta_{ds}$  for each RC building class.

Slight ( $S_{d1}$ )	Moderate ( $S_{d2}$ )	Severe ( $S_{d3}$ )	Complete ( $S_{d4}$ )
$0.7D_y$	$D_y$	$D_y+0.25(D_u-D_y)$	$D_u$

Table 4.  $S_{d,ds}$  determination for each damage state threshold.

## 4 NUMERICAL MODELLING

The different models considered in this study have been modelled with the STKO software [19], a Graphical User Interface (GUI) for OpenSees.

### 4.1 Superstructure

The nonlinear behaviour of the RC elements has been simulated through the distributed plasticity approach. This can automatically compute deformations and curvatures, reducing the modelling time. The RC beams and columns have been discretised into different fibres with the fibre section aggregator. In order to take  $p$ -delta ( $p$ - $\Delta$ ) effects into account, force-beams elements have been applied to the RC frames. “Concrete01” has been considered to simulate concrete. The concrete’s core has been defined by increasing its strength and strain according to [20]. “Steel02” has been used to model steel. In this case, the smooth rebars have been considered by decreasing the steel elastic modulus as in [21]. The effects of infills have been taken into account by means of the two-diagonal truss approach defined in [22]. Due to the rigidity of the concrete slabs, rigid diaphragm interactions have been applied to the nodes of each floor. Masses have been applied to each structural member considering the gravitational loads and the self-weights. Gravitational loads have also been applied to each structural element bearing in mind: dead (self- weight and the weight of constructive elements) and live

loads. The characteristics of the structural materials considered in this study are listed in Table 5.

Concrete		Steel		Infills	
$f_c$ (MPa)	28	$f_y$ (MPa)	370	$G_w$ (GPa)	1240
$f_{cu}$ (MPa)	4	$E_s$ (GPa)	310	$\alpha$	0.05
$\varepsilon_c$ (%)	0.002			$\tau_{cr}$ (MPa)	280
$\varepsilon_{cu}$ (%)	0.04			$E_w$ (GPa)	4092

Table 5. Values of the structural materials' parameters.

Where: concrete compressive ( $f_c$ ) and crushing strength ( $f_{cu}$ ); concrete strain at maximum ( $\varepsilon_c$ ) and ultimate strength ( $\varepsilon_{cu}$ ); steel yielding strength ( $f_y$ ); steel modulus of elasticity ( $E_s$ ); infills shear modulus ( $G_w$ ); post-capping degrading branch coefficient ( $\alpha$ ); shear cracking stress ( $\tau_{cr}$ ); masonry elasticity modulus ( $E_w$ ).

## 4.2 Continuum modelling of the soil

The underlying soil of the building has been modelled with a mesh of 125x40x21 m (X, Y and Z directions). The mesh has been defined according to the  $V_s$  and to the frequency ( $\omega$ ) of the models. "SSPbrick" brick elements have been applied to the solid elements to capture the soil small deformation (Figure 5). The mesh is characterised by 51,954 nodes and 120,040 brick elements. The lateral boundaries have been fixed in the corresponding direction and the base in all directions.

According to the different test results (Section 2.2), the soil beneath the building is clayey. Therefore, the analyses have been performed under undrained conditions since this is the most restrictive. Hence, the soil constitutive behaviour has been simulated by means of the "PressureIndependMultiYield" (PIMY) material. This has been implemented in OpenSees to model elasto-plastic undrained clay-type soils, which are independent from pressure. The soil's failure criterion is based on Von Mises' multi-surface plasticity theory (Figure 5) determined in [23]. "EqDOF" has been applied to the interaction between the soil's and the foundation's surfaces. Four soil layers have been defined according to the characterisation performed in Section 2.2, which can be observed in Figure 4.

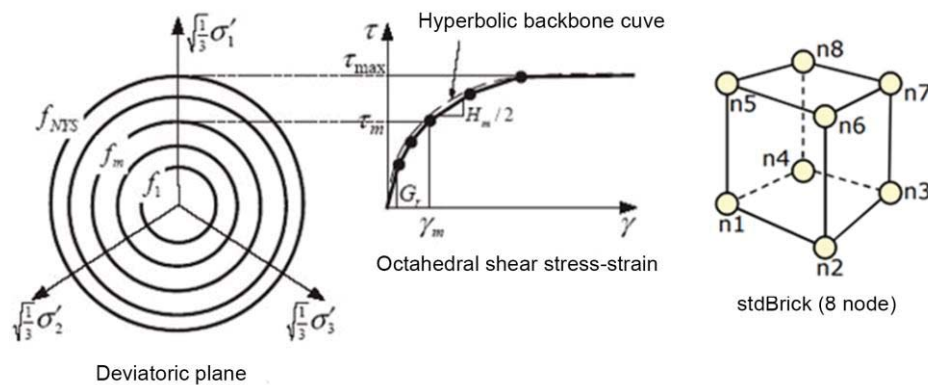


Figure 5: "PressureIndependMultiYield" soil material's failure criterion.

## 5 RESULTS AND ANALYSIS

The results obtained from the analyses appear in this section. In Figure 6, the deformed shape of each model after the application of the gravity loads is shown. As can be observed, the settlement of the structure is higher when the height increases. The displacement in the Z



direction of the control node (in the rooftop) increases 220% and 323% when adding 2 floors (M2) and 4 floors (M3), respectively. Therefore, this increase is not linear.

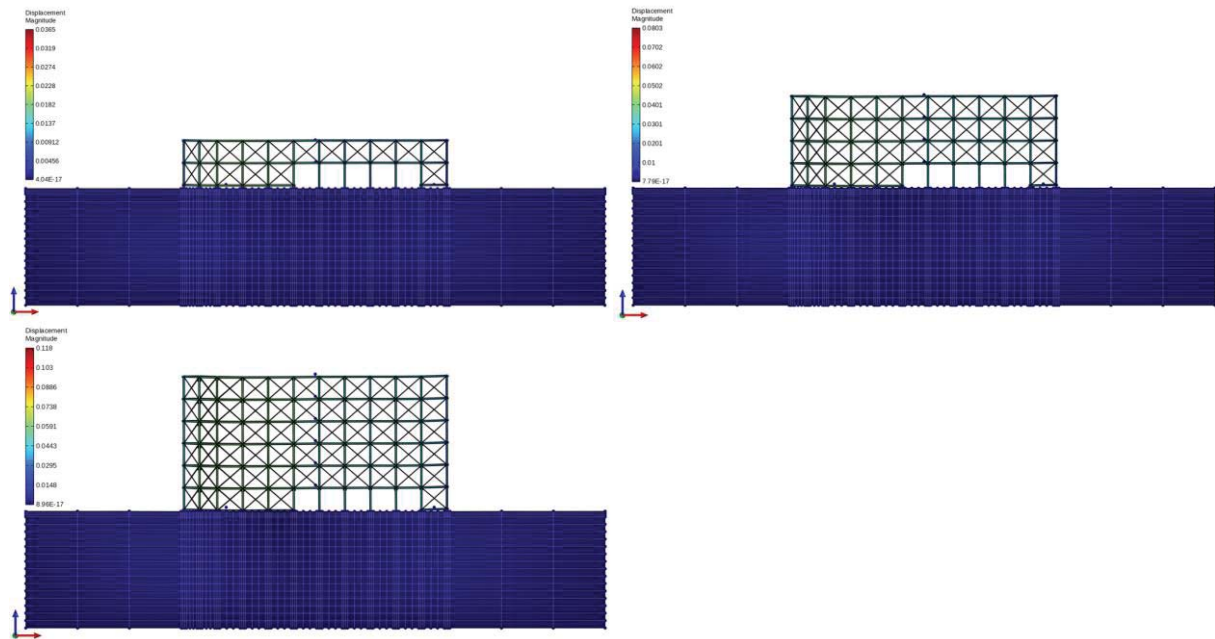
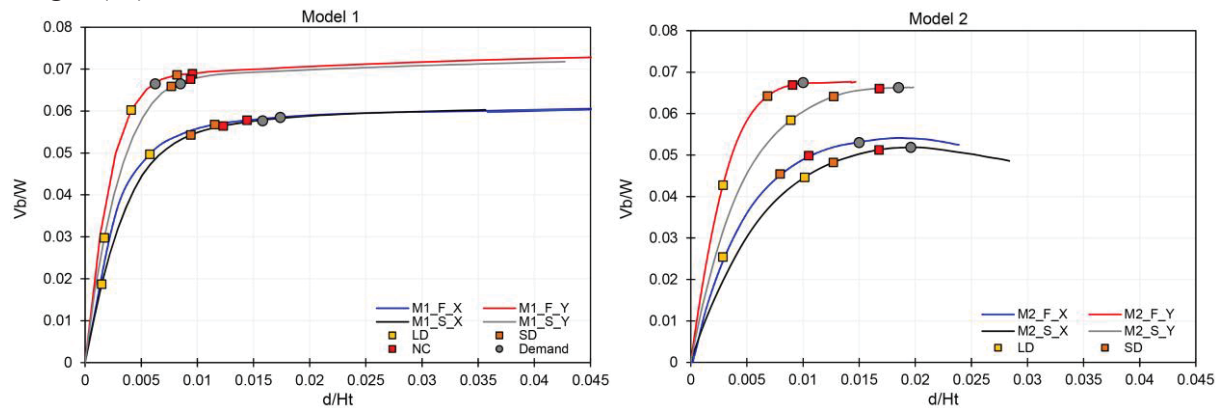


Figure 6: Deformed shape of models analysed after the application of gravity loads.

In Figure 7, the SDOF capacity curves for each of the models have been plotted. Also, the damage states (Section 3.3) and the target displacements (demand) have been determined. In order to compare the results, the multi-degree-of-freedom (MDOF) curves have been normalised by dividing the base shear ( $V_b$ ) by the weight ( $W$ ) and the displacement ( $d$ ) by the total height ( $H_t$ ).



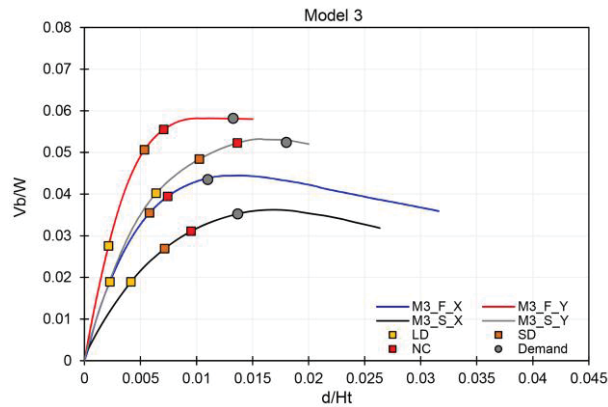
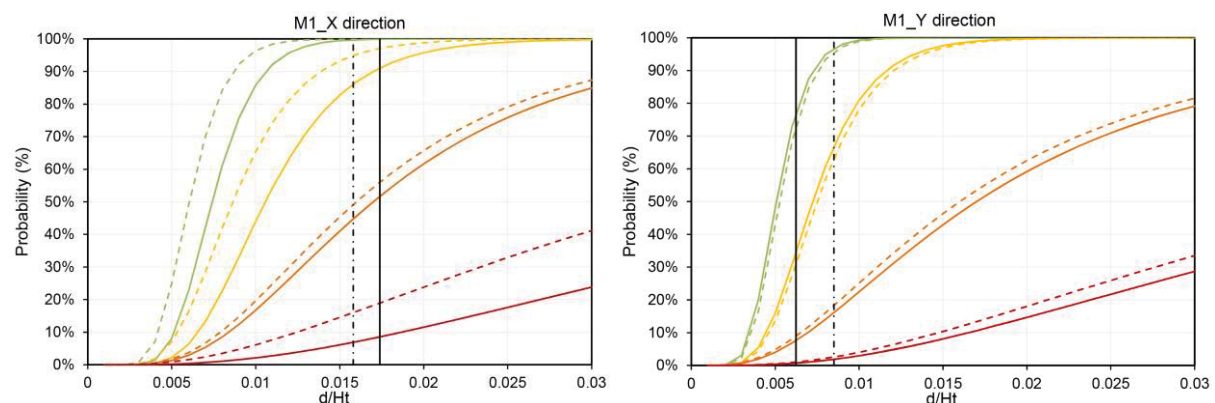


Figure 7: SDOF normalised capacity curves for each of the models assessed.

It can be observed that the higher the structures' height, the higher the soil effects. In the case of the low-rise model (M1), the SSI just decreases the initial stiffness of the systems. In the X direction, the difference between the demand and the NC displacement is higher for the S models. In the Y direction, for the F model, the demand is located between the LD and the SD. However, when considering the SSI, the demand is after the SD; therefore, it will not comply with the EC8 requirements like in the X direction. Mid-rise buildings are more affected by the SSI than low-rise buildings due to the considerable modification of the initial stiffness. The maximum capacity has been reduced by around 10%. In the Y direction, the demand displacement is considerably higher for the S model. High-rise models are the most affected by the SSI, the maximum capacity being reduced by up to 30%. In terms of damage, the models behave worse due to the failure of columns located in the irregularity of the ground floor.

In Figure 8, the fragility curves for each of the models analysed are plotted considering the demand displacement. It can be noted that the fragility curves for the models with SSI are worse than the F-model's curves. Therefore, the probability of reaching higher damage increases in models that bear the soil influence in mind. This probability also increases with the height. As can be seen, the S-model's fragility curves are worse than the F-model's curves when the height increases. This results in the high-rise models being the most affected. Moreover, the fragility curves of high-rise buildings are worse than the rest due to the statistical parameters' values.



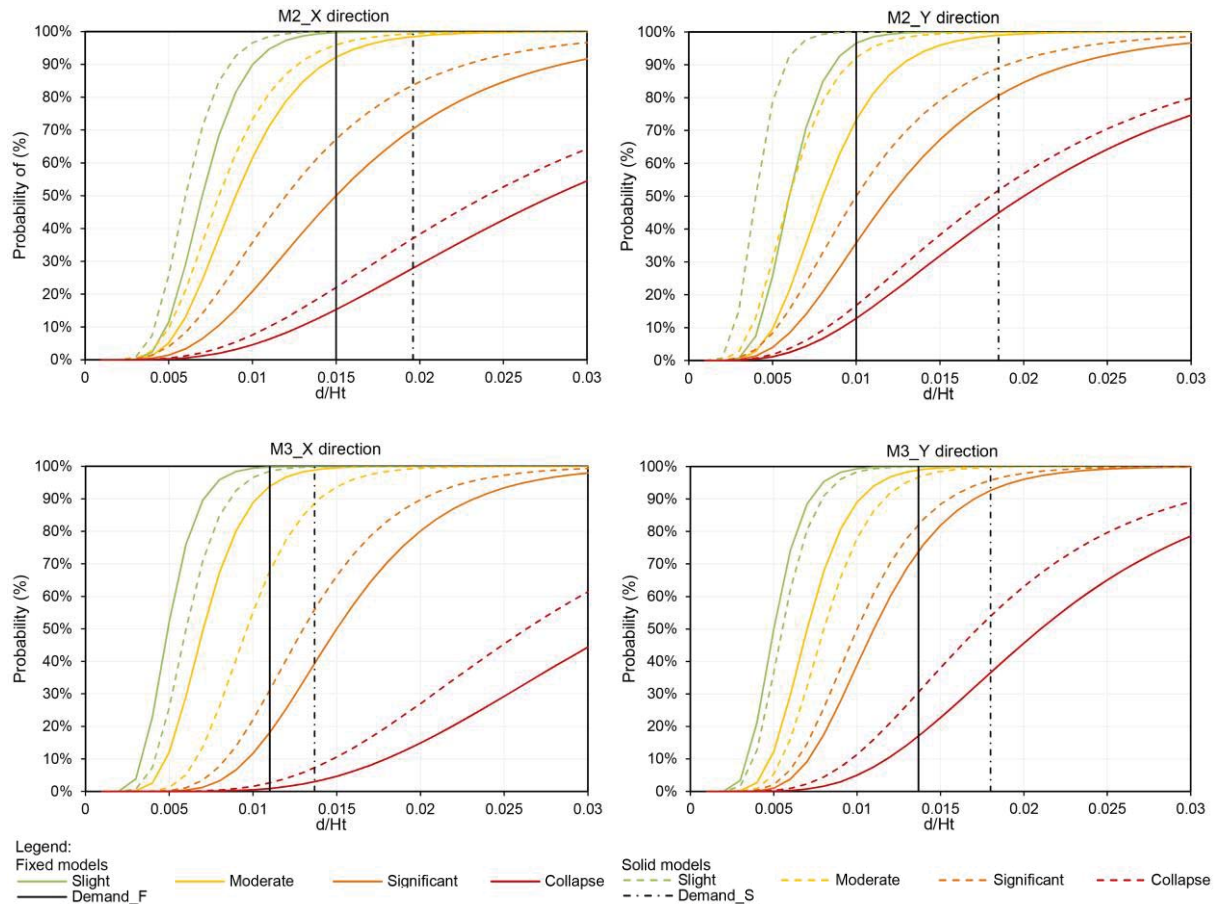


Figure 8: fragility curves considering fixed-based and solid models and low-, mid- and high-rise models.

## 6 CONCLUSIONS

This paper aims to analyse the SSI in the seismic vulnerability analysis of RC buildings. The state of the art has revealed that SSI must be considered in the seismic analyses of mid- and high-rise buildings. Therefore, different configurations of a case study RC building have been defined by varying the height: low- (real), mid- and high-rise. The characterisation of the location's soil profile has been carried out. This characterisation has revealed that the soil is clayey.

Nonlinear static analyses have been performed to assess the models' capacity. The seismic damage has been determined by means of the European seismic code (local damage of elements) and the fragility procedures (global damage). 3D nonlinear models considering the soil as a continuum have been modelled using the FEM to simulate the soil nonlinear behaviour.

The results have shown that the soil does not significantly influence the behaviour of low-rise buildings. However, in the case of mid- and high-rise buildings, the maximum capacity can be reduced by up to 10% and 30%, respectively. Moreover, according to the local damage assessment, structural elements might collapse due to considering the soil, even for low-rise buildings.

In the light of the fragility assessment results, it can be concluded that the probability of reaching higher seismic damage increases when considering the SSI. Moreover, this probability increases with the height.

This work has considered the most probable soil profile that can be found in the area. However, further research should be carried out in order to consider several soil profiles since softer layers could worsen the building's seismic capacity. This research has considered statis-

tical parameters from other works in the fragility assessment. Yet, further research should be assessed to properly determine these values according to the models' characteristics and the type of soil. This research has not considered the element contact between the soil and the foundation's surfaces, which can capture the soil behaviour better, leading to more accurate results.

## REFERENCES

- [1] Kwag, S., Ju, B.S., & Jung, W., Beneficial and Detrimental Effects of Soil-Structure Interaction on Probabilistic Seismic Hazard and Risk of Nuclear Power Plant. *Advances in Civil Engineering*, **2018**, 2018.Epub ahead of print 2018. DOI: 10.1155/2018/2698319.
- [2] Anand, V., & Satish Kumar, S.R., Seismic Soil-structure Interaction: A State-of-the-Art Review. *Structures*, **16**, pp. 317–326, 2018.
- [3] Rajeev, P., & Tesfamariam, S., Seismic fragilities of non-ductile reinforced concrete frames with consideration of soil structure interaction. *Soil Dynamics and Earthquake Engineering*, **40**, pp. 78–86, 2012.
- [4] European Union., Eurocode 8: Design of structures for earthquake resistance. Part 1: General rules, seismic actions and rules for buildings. Belgium, 2004.
- [5] Miranda, E., & Bertero, V. V., Evaluation of strength reduction factors for earthquake-resistant design. *Earthquake Spectra*, **10**(2), pp. 357–379, 1994.
- [6] Karapetrou, S.T., Fotopoulou, S.D., & Pitilakis, K.D., Seismic vulnerability assessment of high-rise non-ductile RC buildings considering soil-structure interaction effects. *Soil Dynamics and Earthquake Engineering*, **73**, pp. 42–57, 2015.
- [7] Badry, P., & Satyam, N., Seismic soil structure interaction analysis for asymmetrical buildings supported on piled raft for the 2015 Nepal earthquake2016.Epub ahead of print 2016. DOI: 10.1016/j.jseaes.2016.03.014.
- [8] Boulanger, R.W., Curras, C.J., Kutter, B.L., Wilson, D.W., & Abghari, A., Seismic Soil-Pile-Structure Interaction Experiments and Analyses. *Journal of Geotechnical and Geoenvironmental Engineering*, **125**(9), pp. 750–759, 1999.
- [9] Harden, C.W., & Hutchinson, T.C., Beam-on-Nonlinear-Winkler-Foundation Modeling of Shallow, Rocking-Dominated Footings. *Earthquake Spectra*, **25**(2), pp. 277–300, 2009.
- [10] Cayci, B.T., Inel, M., & Ozer, E., Effect of Soil-Structure Interaction on Seismic Behavior of Mid-and Low-Rise Buildings. *International Journal of Geomechanics*, **21**(3), pp. 04021009, 2021.
- [11] European Union., Eurocode-8: Design of structures for earthquake resistance. Part 3: Assessment and retrofitting of buildings. Belgium, 2005.
- [12] Morales Esteban, A. et al., *Schools: seismicity and retrofitting (PERSISTAH project)*. Universidad de Sevilla, 2020.
- [13] Spanish Ministry of Public Works [Ministerio de Fomento de España]., Spanish Technical Code of Buildings [Código Técnico de la Edificación (CTE)]. Spain, 2006.

- [14] Naik, S.P., Patra, N.R., & Malik, J.N., Spatial Distribution of Shear Wave Velocity for Late Quaternary Alluvial Soil of Kanpur City, Northern India. *Geotechnical and Geological Engineering*, **32**(1), pp. 131–149, 2014.
- [15] McKenna, F., Fenves, G.L., & Scott, M.H., OpenSees: Open system for earthquake engineering simulation 2000.
- [16] Python Software Foundation., Python 2021.
- [17] Spanish Ministry of Public Works [Ministerio de Fomento de España]., Update of the seismic hazard maps [Actualización de mapas de peligrosidad sísmica de España]. Spain, 2012.
- [18] Barbat, A.H., Pujades, L.G., & Lantada, N., Seismic damage evaluation in urban areas using the capacity spectrum method: Application to Barcelona. *Soil Dynamics and Earthquake Engineering*, **28**(10–11), pp. 851–865, 2008.
- [19] Petracca, M., Candeloro, F., & Camata, G., *"STKO user manual"*. ASDEA Software Technology. Pescara Italy, 2017.
- [20] Mander, J.B., Priestley, M.J.N., & Park, R., Theoretical Stress-Strain Model for Confined Concrete. *Journal of Structural Engineering*, **114**(8), pp. 1804–1826, 1988.
- [21] Couto, R., Requena-García-Cruz, M., Bento, R., & Morales-Esteban, A., Seismic capacity and vulnerability assessment considering ageing effects. Case study: Three local Portuguese RC buildings. *Bulletin of Earthquake Engineering* 2020. Epub ahead of print 2020. DOI: 10.1007/s10518-020-00955-4.
- [22] Celarec, D., Ricci, P., & Dolšek, M., The sensitivity of seismic response parameters to the uncertain modelling variables of masonry-infilled reinforced concrete frames. *Engineering Structures*, **35**, pp. 165–177, 2012.
- [23] Mazzoni, S., McKenna, F., Scott, M.H., & Fenves, G.L., *OpenSees command language manual*. 2006.



## FREE VIBRATION RESPONSE OF LONG MULTI-SPAN BRIDGES ACCOUNTING FOR SOIL-STRUCTURE INTERACTION

Pieter Reumers, Geert Lombaert, and Geert Degrande

KU Leuven, Department of Civil Engineering, Structural Mechanics Section  
Kasteelpark 40, 3001 Leuven, Belgium  
e-mail: {pieter.reumers,geert.lombaert,geert.degrande}@kuleuven.be

**Keywords:** multi-span bridges, soil-structure interaction, modal analysis, piled foundation, periodic structure theory

**Abstract.** *This paper investigates the effect of soil-structure interaction (SSI) on the free vibration response of long multi-span bridges. A numerical case study of a continuous concrete box girder bridge is presented. For several bridge lengths, the influence of SSI on modal characteristics is studied. Furthermore, if the bridge is assumed to be infinitely long, periodic structure theory is used to compute the dispersion curves of the non-decaying waves that propagate through the bridge. The stop- and passbands are related to the natural frequencies of the bridges with finite length.*



## 1 INTRODUCTION

Road and railway bridges are frequently constructed in regions with changing topography or soft sub-soil conditions, and in dense urban areas due to space limitations. Often, these bridges consist of identical spans repeated over a long distance resulting in a convenient and cost-effective design. This paper investigates the effect of soil-structure interaction (SSI) on their free vibration response, which is important as the structure's modal characteristics (mode shapes, natural frequencies, modal damping ratios) are commonly used in structural health monitoring.

The influence of SSI on the modal characteristics of long multi-span bridges is often neglected in finite element model updating procedures [1, 2], as this significantly reduces the model complexity and is typically a valid simplification when the structure is founded on stiff soil. However, for short (single-span) bridges, many studies have highlighted the importance of SSI on modal characteristics. Romero et al. [3] studied the dynamic response of single-span, simply supported railway bridges under moving loads. They conclude that the resonant train speed is lower when dynamic SSI is accounted for, due to the lower natural frequency of the bridge. Furthermore, they report a substantial increase of the modal damping ratio if the soil stiffness is low, resulting in lower bridge deck acceleration at mid-span. Östlund et al. [4] investigate the effect of different foundation types and span lengths on the response and modal characteristics of a single-span railway bridge. They show that the modal damping ratio increases for shorter span lengths and that the bridge deck acceleration is generally higher in the case of fixed supports.

In this paper, a case study of a continuous concrete box girder bridge is presented in order to analyze the influence of SSI on the modal characteristics of long, repetitive bridges. Three cases are considered for the soil stiffness: a soft, medium, and stiff soil. Furthermore, the analysis is performed for a bridge with 5 spans, 15 spans, and an infinitely long bridge.

The paper is organized as follows. Section 2 introduces the numerical case study. Section 3 focuses on the influence of SSI and bridge length on the free vibration response of the bridge; the influence on modal characteristics is studied for the bridges with finite length, which are subsequently linked to dispersion curves of free waves propagating through the infinitely long bridge. Section 4 concludes the paper.

## 2 NUMERICAL CASE STUDY

This section presents a numerical case study of a continuous concrete box girder bridge founded on piled foundations. In the past decades, a large number of such bridges have been built in many European countries [5]. The advantage over simply supported box girder bridges, which remain the standard in China, is their greater slenderness (ranging between 12 and 14) and generally lower dynamic response. The geometry and material properties are based on a literature survey of existing box girder bridges presented by Kang et al. [5], Yan et al. [6], and Cascales Fernández et al. [7].

### 2.1 Bridge geometry

Figure 1a shows a single span of the railway bridge. The span length  $L$  equals 24 m. The bridge cross section is a concrete box girder with uniform height (Figure 1b). The bridge deck is periodically supported by 6 m high piers with a rectangular cross section of 5.5 m by 1 m. At each pier, the bridge deck rests on two bearings. The concrete has a Young's modulus  $E = 30$  GPa, a Poisson's ratio  $\nu = 0.25$ , and a density  $\rho = 2500$  kg/m<sup>3</sup>. Rate-independent hysteretic material damping in the frequency domain is modeled by introducing a complex

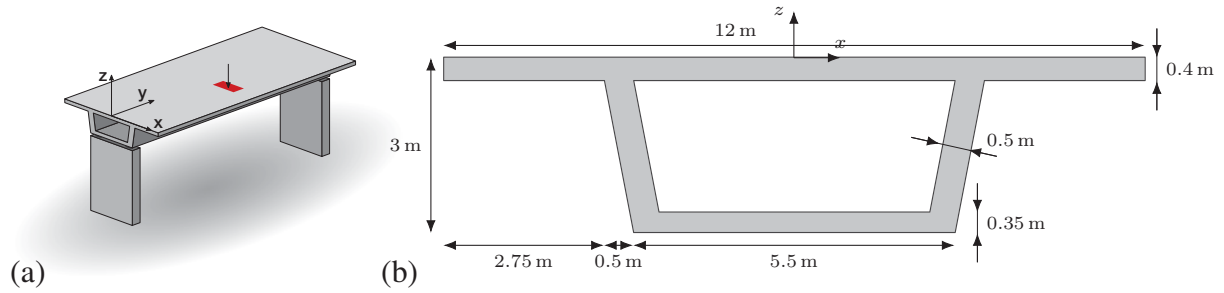


Figure 1: (a) Single bridge span and (b) cross section of the bridge deck. The red area indicates the area to which the load is applied.

Young's modulus  $E^* = E(1 + 2i\beta)$ , where a material damping ratio  $\beta$  of 0.02 is assumed.

The deck and piers are both modeled with 8-node quadratic shell elements based on Reissner-Mindlin plate theory. Figure 2 shows the FE model of the pier and bridge deck. The maximum element size equals 1 m for the deck and 0.5 m for the pier. Each bearing is represented by constraint equations between two nodes on the deck and two corresponding nodes on the pier. For the left bearing (in red), the vertical as well as the lateral displacement of the deck and pier are coupled. For the right bearing (in blue), only the vertical displacement is coupled. In the longitudinal direction, the displacement of the deck and pier is only coupled at one of the bridge piers.

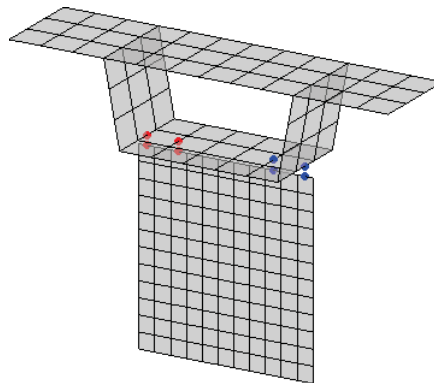


Figure 2: Finite element model of a pier and part of the bridge deck. At the nodes representing the left bearing (in red), vertical and lateral displacements are coupled using constraint equations, while at the right bearing (in blue), only vertical displacements are coupled.

## 2.2 Bridge length

Three bridges are considered in this paper: a bridge with 5 spans, a bridge with 15 spans, and an infinitely long bridge. For the first two cases, the length of the end spans equals half the regular span length. At both bridge ends, constraint equations (as explained in Subsection 2.1) are used to account for the support conditions: the vertical displacements are prohibited by both supports, while lateral displacements are prohibited by the left support.

## 2.3 Piled foundation

Each pier is supported by a piled foundation that consists of eight piles connected to a pile cap with a thickness of 1 m. The pile cap is assumed to be rigid, as is the connection between the pier and the pile cap, and the pile cap and the piles. Figure 3b shows the geometry of the

piled foundation. The piles have a diameter of 0.4 m and a length of 10 m. The piles and pile cap are made of concrete with Young's modulus  $E = 35$  GPa, Poisson's ratio  $\nu = 0.25$ , and density  $\rho = 2500$  kg/m<sup>3</sup>. No material damping is considered for the piled foundation.

Each piled foundation is embedded in a horizontally layered soil (Figure 3a) consisting of a 9 m thick top layer on top of a halfspace. Three cases are considered for the top layer: a soft soil, a medium soil, and a stiff soil. The underlying halfspace consists of stiff soil. Hence, the stiff soil case corresponds to a homogeneous halfspace. The dynamic soil characteristics are specified in Table 1. The piles reach 1 m into the stiff halfspace.

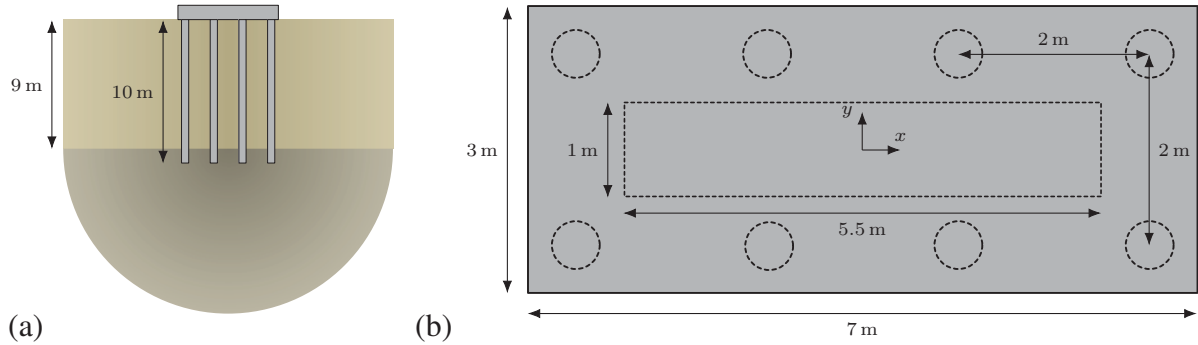


Figure 3: (a) Piled foundation embedded in a horizontally layered halfspace and (b) geometry of the piled foundation.

Soil type	$C_s$ [m/s]	$C_p$ [m/s]	$\rho$ [kg/m <sup>3</sup> ]	$\beta_s$ [-]	$\beta_p$ [-]
Soft soil	100	200	1800	0.02	0.02
Medium soil	200	400	1800	0.02	0.02
Stiff soil	300	600	1800	0.02	0.02

Table 1: Dynamic soil characteristics: shear wave velocity  $C_s$ , dilatational wave velocity  $C_p$ , density  $\rho$ , and material damping ratio's  $\beta_s$  and  $\beta_p$  in shear and dilatational deformation.

The soil and the piles are both modeled with 10-node quadratic tetrahedral elements. A perfectly matched layer (PML) is used to absorb waves at the edges of the FE model [8, 9]. The element size  $l_e$  is chosen such that the distance between two nodes is always less than one-eighth of a shear wavelength for each frequency, both in the physical soil domain and the PML. The width of the physical soil domain between the PML and the foundation is chosen as one half shear wavelength at 50 Hz .

The FE-PML formulation used in this work is described in detail by Papadopoulos et al. [10], and based on the work of Chew and Qiu [8] and Basu and Chopra [9]. As explained in [10], the PML stretch functions consist of third-degree polynomial functions with  $\alpha_0 = \pi C_s / (l_e \omega) - 1$  and  $\alpha_1 = 20 C_s$ , controlling the attenuation of evanescent and propagating waves inside the PML domain, respectively. The FE-PML model of the piled foundation is validated using a finite element-boundary element model (FE-BE) model.

The dynamic stiffness of the piled foundation is defined as the forces or moments required to impose a unit displacement or rotation of the rigid pile cap. The real part determines the stiffness, while the imaginary part depends on the material and radiation damping in the soil.

Figure 4 shows the stiffness and damping coefficients of a single piled foundation modeled with a 3D FE-PML model and a 3D FE-BE model. The pile cap is assumed to be rigid and

massless. Figure 4a shows the vertical stiffness  $\text{Re}(k_{zz})$  of the piled foundation embedded in soft, medium, and stiff soil. The static stiffness increases with increasing soil stiffness. An increase in stiffness is observed for the soft soil around 22 Hz due to interaction between the individual piles. When the shear wavelength in the soil equals twice the pile spacing, the piles vibrate in anti-phase motion leading to a stiffer behavior of the piled foundation [11]. The pile-soil-pile interaction effect is observed around 45 Hz for the medium soil. For the stiff soil, a peak in the stiffness function is expected around 75 Hz. Figure 4b shows the vertical damping  $\text{Im}(k_{zz})$ . In the low frequency range it is observed that, as the soil stiffness of the top layer decreases, the damping decreases as well. This is explained by the fact that, for a soft layer on a stiffer halfspace, wave propagation in the soft top layer only occurs at frequencies above the cut-on frequency, activating radiation damping. This effect is more pronounced as the relative difference in stiffness between the top layer and the halfspace increases. Furthermore, the peaks due to pile-soil-pile interaction are also observed in the damping curves.

Figure 4c shows the rocking stiffness  $\text{Re}(k_{\varphi_x \varphi_x})$  around the  $x$ -axis, which is significantly lower than the rocking stiffness  $\text{Re}(k_{\varphi_y \varphi_y})$  around the  $y$ -axis shown in Figure 4e, due to the smaller eccentricity of the piles with respect to the center. Again, the effect of pile-soil-pile interaction is observed as peaks in the stiffness functions. Figures Figure 4d and Figure 4f show the corresponding damping values  $\text{Im}(k_{\varphi_x \varphi_x})$  and  $\text{Im}(k_{\varphi_y \varphi_y})$  for the rocking motion of the piled foundation around the  $x$ - and  $y$ -axis, respectively. Finally, the results obtained with the 3D FE-PML and 3D FE-BE model are in very good agreement across the entire frequency range. The slight discrepancy in the high frequency range is attributed to the FE discretization.

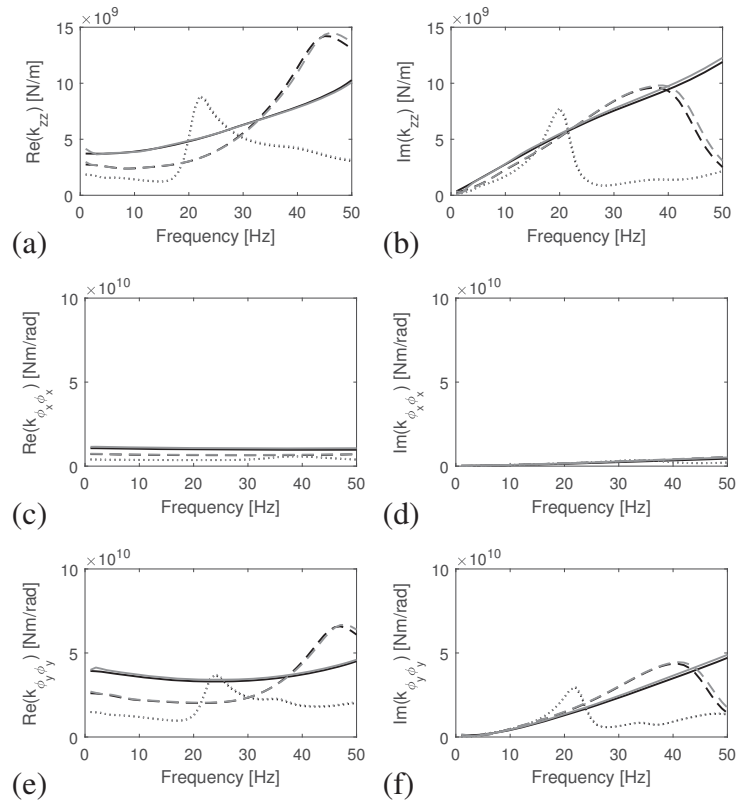


Figure 4: Vertical (a) stiffness  $\text{Re}(k_{zz})$  and (b) damping  $\text{Im}(k_{zz})$ , rocking (c) stiffness  $\text{Re}(k_{\varphi_x \varphi_x})$  and (d) damping  $\text{Im}(k_{\varphi_x \varphi_x})$ , and rocking (e) stiffness  $\text{Re}(k_{\varphi_y \varphi_y})$  and (f) damping  $\text{Im}(k_{\varphi_y \varphi_y})$  for the piled foundation embedded in stiff (solid line), medium (dashed line), and soft soil (dotted line). The black and gray lines correspond to the results obtained with the FE-BE and FE-PML model, respectively.

### 3 FREE VIBRATION RESPONSE

The effect of SSI and bridge length (number of spans) on the natural frequencies and mode shapes is investigated. Furthermore, the dispersion curves of the non-decaying waves propagating through an infinitely long bridge are computed and related to the modal characteristics of the bridges with finite length.

#### 3.1 Modal characteristics

A 3D FE model of the bridge with 5 spans (Figure 5) is constructed in order to compute its modal characteristics. First, SSI is neglected and the piers are assumed fixed at the bottom. Figure 6a shows the first five mode shapes and corresponding natural frequencies of the bridge.



Figure 5: Bridge with 5 spans. The support where longitudinal displacement of the bridge deck and pier are coupled is shown in red.

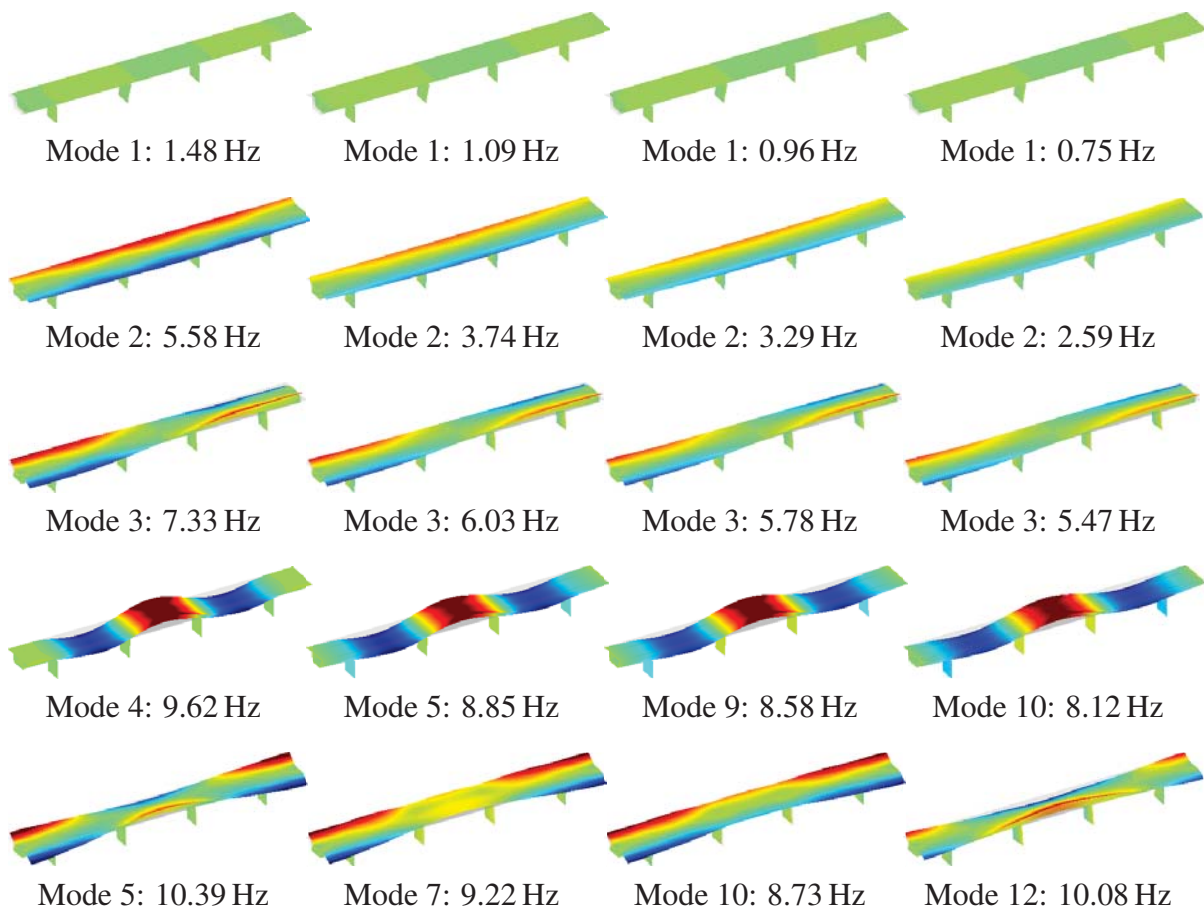


Figure 6: Mode shapes and natural frequencies of the bridge with 5 spans computed for (a) the case without SSI, (b) the stiff soil, (c) the medium soil, and (d) the soft soil. The color scheme indicates the magnitude of the vertical displacement while the undeformed structure is shown in light gray.

The first mode is a longitudinal translation mode of the bridge deck, which is not excited by a vertical load acting on the bridge. The top of the second pier translates with the bridge deck due to the fixed coupling at this support. Modes 2, 3, and 5 are torsional modes for which the dominant vertical displacement is situated in the flanges of the box girder. Mode 4 is a vertical bending modes of the bridge for which neighboring spans oscillate out-of-phase.

### 3.1.1 Influence of SSI

In order to assess the effect of SSI on the modal characteristics, the static foundation stiffness is added to each bridge pier (using springs) and the modal characteristics are recomputed. Alternatively, the dynamic stiffness at a resonance frequency of the bridge without SSI could be used [12]. Note that, in the present case, the dynamic stiffness does almost not depend on the frequency between 0 and 15 Hz (Figure 4), where the first bridge modes are situated, so that the outcome would be very similar.

In order to properly match the mode shapes and corresponding natural frequencies of the bridge with and without SSI, the Modal Assurance Criterion [13] is used. Whenever mode numbers are mentioned in the following, we refer to the modes without SSI. Figure 7a shows the MAC values computed for the first 20 mode shapes without SSI and with the stiff soil. The first 13 modes can be matched reasonably well to the mode shapes of the bridge without SSI. The order of the modes, however, changes when SSI is accounted for. In modes 8 to 10 (with SSI), the piers rotate around the  $x$ -axis and the bridge deck remains still as the piers can rotate freely with respect to the bridge deck. Figure 7b shows the MAC values computed for the medium soil. In this case, only the first five mode shapes can be matched accurately to the modes without SSI. For the soft soil case in Figure 7c, it is observed that only the first three modes are matched relatively well to the modes computed without SSI. Modes 4 to 6 (with SSI) are local rotation modes of the piers, which correspond to lower natural frequencies compared to the case with stiff soil. Mode 4, the first vertical bending mode, now corresponds to mode 7 with SSI.

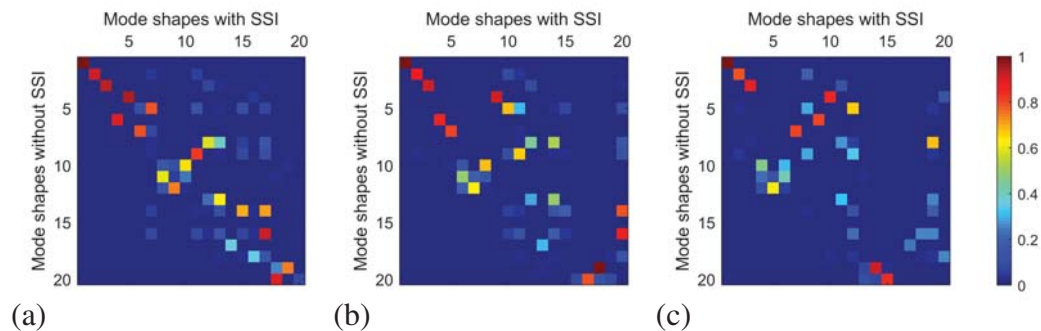


Figure 7: MAC values between the mode shapes computed without and with SSI for the case of (a) stiff soil, (b) medium soil, and (c) soft soil.

Using the MAC values presented in Figure 7, the mode shapes of the bridge with and without SSI are matched. The mode shapes computed with the stiff soil are shown in Figure 6b. Overall, the mode shapes are very similar to those without SSI. For the torsional modes, rocking motion of the piers around the  $y$ -axis is observed due to the flexibility of the soil, resulting in significantly lower natural frequencies. Figure 6c shows the mode shapes computed with the medium soil. The natural frequencies are lower compared to those computed with the stiff soil, but the



mode shapes are very similar. Figure 6d shows the mode shapes computed with the soft soil. Compared to the case without SSI, a reduction of 53 % and 25.4 % on the natural frequency of the first and second torsional mode is predicted. The reduction of the natural frequency for the first vertical bending mode is 15.6 %. For mode 5, almost no decrease in natural frequency is observed, but the MAC value shows a poor agreement with the corresponding mode shape without SSI.

It can be concluded that, as the soil stiffness decreases, the effect of SSI on the modal characteristics of the bridge increases. Torsional modes in particular are significantly affected by SSI. Hence, when predicting the forced vibration response or performing structural health monitoring of multi-span bridges, it is important to account for SSI especially when soft soil conditions prevail.

### 3.1.2 Influence of the bridge length

Next, the influence of the bridge length (number of spans) on the natural frequencies is investigated. For periodic structures, natural frequencies tend to cluster in frequency bands corresponding to the pass-bands of the structure where non-decaying waves propagate. These frequency bands are characterized by a high modal density. This was already illustrated by Zhang et al. [14] for a periodic frame structure, who used free wave propagation constants for model updating purposes; however, the influence of SSI was not yet studied.

Figure 8 shows the natural frequencies of the bridge as a function of the number of spans. The computations are performed for the case without SSI and for the stiff, medium, and soft soil. Figure 8a presents the results for the case without SSI. As the number of spans increases, the natural frequencies tend to a limit value resulting in frequency bands with different modal density. Below 5 Hz, the longitudinal translation modes of the bridge deck are found. The natural frequencies between 5 Hz and 9 Hz correspond to torsional modes, while vertical bending modes as well as torsional modes are found between 9 Hz and 12.5 Hz. Above 12.5 Hz, only torsional modes are found. For the stiff soil, the natural frequencies are shown in Figure 8b. The decrease of the natural frequencies due to the flexibility of the soil is clearly observed. The frequency band of the vertical bending modes is very narrow between 8.5 Hz and 9 Hz, approximately. Furthermore, a narrow band around 10 Hz is observed corresponding to the rotation

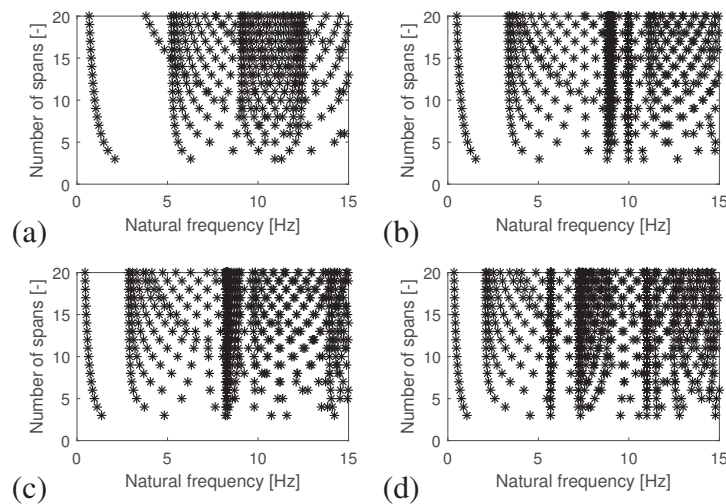


Figure 8: Natural frequencies of the bridge as a function of the number of spans computed for (a) the case without SSI, (b) the stiff soil, (c) the medium soil, and (d) the soft soil.

modes of the piers. This frequency band is also visible for the medium soil in Figure 8c around 8 Hz, nearly coinciding with the band where the vertical bending modes are situated. For the soft soil (Figure 8d), the narrow band around 5.7 Hz corresponds to the rotation modes of the piers, while the vertical bending modes are situated between 7 Hz and 9 Hz, approximately.

### 3.2 Dispersion curves

The dispersion curves of an infinitely long bridge in the wavenumber-frequency domain are presented in this subsection. As the bridge is periodic, the Floquet transform [15] is used to predict the forced vibration response of an infinitely long bridge due to a unit vertical eccentric load at mid-span (Figure 1a).

Figure 9 presents the vertical bridge mobility at mid-span in the wavenumber-frequency domain. Note that, in this model, the frequency dependent dynamic stiffness of the piled foundation is accounted for. The peaks observed in the forced vibration response correspond to the dispersion curves of the free waves propagating through the superstructure. These dispersion curves are obtained as the solution of an eigenvalue problem at each frequency; this originates from the condensation of the interior degrees of freedom of a reference cell and the application of Floquet theory [16, 17]. In order to reduce the computational effort, a methodology was proposed earlier [18] where advantage is taken from the fact that the bridge cross section does not vary between two piers so that the span can be subdivided in a finite number of identical cells. The dispersion curves that are superimposed on Figure 9 are: (1) the longitudinal translation mode, (2) the torsional mode, and (3) the vertical bending mode.

Figure 9a shows the dispersion curves for the case without SSI. The dispersion curves coincide with the peaks in the wavenumber-frequency domain response. The cut-on and cut-off frequencies of the dispersion curves correspond to the frequency bands observed in Figure 8a. The dispersion curve of the longitudinal translation mode does not appear as a peak in the wavenumber-frequency domain response because it is not excited by the applied load. Figure 9b shows the dispersion curves for the stiff soil. The dispersion curve of the vertical bending mode is nearly vertical, corresponding to the narrow frequency band in Figure 8b. For the medium soil, Figure 9c shows that the group velocity  $\partial\omega/\partial\kappa_y$  changes sign for the vertical bending

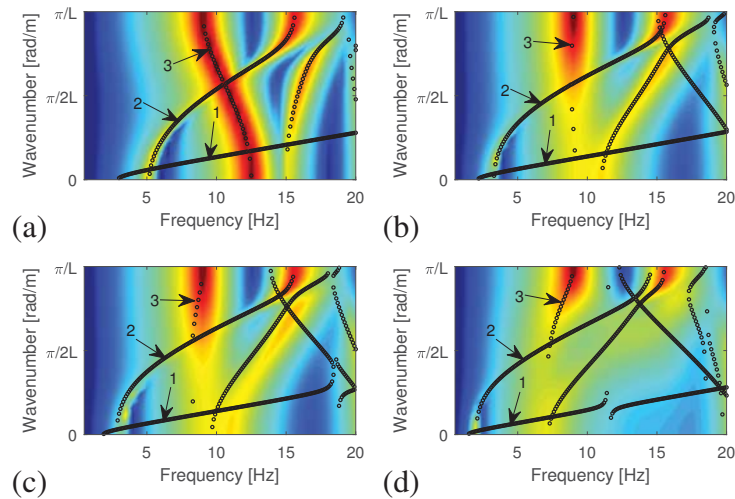


Figure 9: Logarithm of the amplitude of the vertical mobility at mid-span in the wavenumber-frequency domain. Superimposed are the dispersion curves of the non-decaying waves obtained with the WFEM: (1) the longitudinal translation mode, (2) the torsional mode, and (3) the vertical bending mode.

mode compared to the case without SSI. Figure 9d shows the dispersion curves for the soft soil. The cut-on frequency of the torsional mode equals 2 Hz, which is significantly lower than for the case without SSI (around 5 Hz). For the vertical bending mode, the cut-on frequency of the dispersion curve has decreased compared to the medium soil.

#### 4 CONCLUSIONS

A numerical case study of a continuous concrete box girder bridge is presented in this paper. It is shown that the natural frequencies of a bridge are significantly affected by SSI when the soil is soft, particularly for the torsional modes. The influence of SSI on the mode shapes is relatively small for the lower modes, but is important for the higher modes, especially when the soil is soft. Furthermore, it has been shown that as the number of bridge spans increases, the natural frequencies converge to a limit value. These values mark the boundaries of the stop- and passbands that were observed in the dispersion curves of an infinitely long bridge. Inside the passbands, high modal density is observed. As SSI results in shift of the natural frequencies, it also affects the boundaries of the stop- and passbands of the bridge.

#### REFERENCES

- [1] D. Feng and M.Q. Feng. Model updating of railway bridge using in situ dynamic displacement measurement under trainloads. *ASCE Journal of Bridge Engineering*, 20(12):04015019, 2015.
- [2] J. Wiberg, R. Karoumi, and C. Pacoste. Optimized model updating of a railway bridge for increased accuracy in moving load simulations. In X. Perpiñà, editor, *Infrastructure Design, Signalling and Security in Railway*, chapter 8, pages 203–224. InTech, 2012.
- [3] A. Romero, M. Solís, J. Domínguez, and P. Galvín. Soil-structure interaction in resonant railway bridges. *Soil Dynamics and Earthquake Engineering*, 47:108–116, 2013.
- [4] J.L. Östlund, M. Ülker-Kaustell, A. Andersson, and J.-M. Battini. Considering dynamic soil-structure interaction in design of high-speed railway bridges. *Procedia Engineering*, 199:2384–2389, 2017. X International Conference on Structural Dynamics, EUROLYN 2017.
- [5] C. Kang, S. Schneider, M. Wenner, and S. Marx. Development of design and construction of high-speed railway bridges in germany. *Engineering Structures*, 163:184–196, 2018.
- [6] B. Yan, G.-L. Dai, and N. Hu. Recent developments of design and construction of short span high-speed railway bridges in china. *Engineering Structures*, 100:707–717, 2015.
- [7] J. Cascales Fernández, R. Rico Rubio, and S. Couto Wörner. Criterios de diseño sísmico en viaductos de alta velocidad en la zona de levante. *Hormigón y Acero*, 68(281):69–79, 2017.
- [8] W.C. Chew and Q.H. Liu. Perfectly matched layers for elastodynamics: A new absorbing boundary condition. *Journal of Computational Acoustics*, 4(4):341–359, 1996.
- [9] U. Basu and A.K. Chopra. Perfectly matched layers for time-harmonic elastodynamics of unbounded domains: theory and finite-element implementation. *Computer Methods in Applied Mechanics and Engineering*, 192(11–12):1337–1375, 2003.

- [10] M. Papadopoulos, S. François, G. Degrande, and G. Lombaert. The influence of uncertain local subsoil conditions on the response of buildings to ground vibration. *Journal of Sound and Vibration*, 418:200–220, 2018.
- [11] K. Miura, A.M. Kaynia, K. Masuda, E. Kitamura, and Y. Seto. Dynamic behaviour of piled foundations in homogeneous and non-homogeneous media. *Earthquake Engineering and Structural Dynamics*, 23:183–192, 1994.
- [12] J.L. Östlund, A. Andersson, M. Ülker-Kaustell, and J.-M. Battini. Soil-structure interaction for foundations on high-speed railway bridges. TRITA-BKN 166, KTH Royal Institute of Technology, Stockholm, 2017.
- [13] R.J. Allemang and D.L. Brown. A correlation coefficient for modal vector analysis. In *Proceedings of the 1st International Modal Analysis Conference*, pages 110–116, Orlando, Florida, 1982.
- [14] J. Zhang, E. Reynders, G. De Roeck, and G. Lombaert. Model updating of periodic structures based on free wave characteristics. *Journal of Sound and Vibration*, 442:281–307, 2019.
- [15] D. Clouteau, M.L. Elhabre, and D. Aubry. Periodic BEM and FEM-BEM coupling: application to seismic behavior of very long structures. *Computational Mechanics*, 25:567–577, 2000.
- [16] D. Mead. Wave propagation in continuous periodic structures: research contributions from Southampton. *Journal of Sound and Vibration*, 190(3):495–524, 1996.
- [17] B. Mace, D. Duhamel, M. Brennan, and L. Hinke. Finite element prediction of wave motion in structural waveguides. *The Journal of the Acoustical Society of America*, 117(5):2835–2843, 2005.
- [18] P. Reumers, K. Kuo, G. Lombaert, and G. Degrande. Response of periodic elevated structures accounting for soil-structure interaction. In M. Papadrakakis and M. Fragiadakis, editors, *Proceedings of the 7th International Conference on Computational Methods in Structural Dynamics and Earthquake Engineering, COMPDYN 2019*, Crete, Greece, June 2019.

## THREE DIMENSIONAL DYNAMIC INTERACTION OF ADJACENT FOUNDATIONS ON A HALFSPACE WITH LOCAL INHOMOGENEITY APPLYING A COUPLED ITM-FEM APPROACH

Julian Freisinger<sup>1</sup>, Gerhard Müller<sup>1</sup>

<sup>1</sup> Chair of Structural Mechanics, Technical University of Munich  
Arcisstr. 21, 80333 Munich, Germany  
e-mail: julian.freisinger@tum.de, gerhard.mueller@tum.de

**Keywords:** Soil Dynamics, Soil-Structure-Interaction (SSI), Integral-Transform-Method (ITM), Finite-Element-Method (FEM), Foundation-Soil-Foundation Interaction (FSFI), Vibration Mitigation, Wave Impeding Block (WIB)

**Abstract.** *The dynamic subsoil coupling for a finite number of adjacent foundations has a significant effect on the dynamic behaviour of the foundations involved and the structures based on them. As the mutual influence of the foundations on each other is decisively influenced by the properties and the composition of the subsoil, buried structures or inhomogeneities have to be included, in order to model the real soil conditions as exact as possible and to enable an accurate prediction of the interaction phenomena of adjacent foundations. In this contribution an efficient 2.5D coupled Integral Transform Method (ITM) – Finite Element Method (FEM) approach is used in conjunction with a conventional 3D FEM to compute the dynamic stiffness of foundations resting on the surface of a halfspace including a longitudinally invariant structure or inhomogeneity. Herein, the analytical ITM solutions of the dynamic wave equation allow to account for the infinite extension of the soil by satisfying the radiation condition. The 2.5D FEM formulation enables to model complex, spatially limited structures and a part of the surrounding soil within a cylindrical outer boundary, on which both methods are coupled. The finite foundations on the halfspace surface are modelled using 3D finite elements and are coupled to the soil substructure enforcing the compatibility conditions (full coupling or relaxed boundary conditions) at the common interface. The influence of the embedment depth, size and stiffness of the inclusion on the dynamic response of the foundations, taking into account the through soil coupling, is investigated for different configurations of the surface foundations (distance, width). Frequency dependent compliance functions at the soil-foundation interface are calculated for the different parameter settings and compared with existing solutions to verify the method as well as with the results for the homogeneous halfspace to illustrate the influence of an inclusion. Furthermore the displacement distribution over the total surface of a halfspace with a stiff inclusion due to a dynamic excitation of either one or both of the two considered adjacent rigid surface foundations obtained by a post-processing procedure is presented.*



## 1 INTRODUCTION

The dynamic interaction of structures based on a single foundation with the supporting homogeneous or stratified soil has been studied extensively in the past applying a variety of different methods as presented e.g. in [1–8]. However, in the dense urban areas buildings are often not well separated from each other and the dynamic foundation-soil-foundation interaction (FSFI) between the closely spaced structures has a significant effect on the dynamic behaviour of the foundations involved and the structures based on them. This mutual influence is decisively influenced by the properties and the composition of the subsoil.

In the literature, various approaches have been employed to investigate the interaction of foundations located on or embedded in a homogeneous or layered halfspace. Warburton et al. [9] were the first to study the dynamic FSFI of two neighbouring massive foundations resting on a homogeneous halfspace applying an approximate analytical method based on the Bycroft model. The cross interaction of multi-foundation systems located on a viscoelastic stratum due to different excitation types has been investigated by Kobori et al. [10]. Wong and Luco [11] analysed the effect of a layered halfspace on the interaction of two rigid, square surface foundations subjected to external forces by the boundary integral equation technique. Kausel et al. [12] and Lin et al. [13] used the Finite-Element-Method (FEM) together with consistent boundaries to examine the FSFI of rigid foundations resting on or embedded in a stratum over bedrock for harmonic force and moment excitation in all degrees of freedom. An analytical method addressing the dynamic subsoil coupling between a finite number of rigid, rectangular foundations solving the mixed boundary value problem by the Bubnov-Galerkin method has been presented by Triantafyllidis and Prange [14]. The Boundary Element Method (BEM) in the frequency domain has been employed to investigate the 3D FSFI of two adjacent rigid, surface foundations resting on a soil layer over bedrock by Karabalis and Beskos [15] and on a homogeneous halfspace due to seismic resp. harmonic excitation by Qian and Beskos [16] and Qian et al. [17]. Wang et al. [18] also used the BEM to investigate the cross interaction of flexible strip foundations embedded in a homogeneous halfspace. A coupled FEM-BEM approach for the 3D dynamic interaction of two surface foundations in the time domain was presented by Rizos and Wang [19]. More recently Chen et al. [20] employed a time domain Scaled-Boundary-Finite-Element-Method (SBFEM) to investigate the response of two strip foundations embedded in a layered soil. Sbartaï [21] coupled the BEM to the Thin-Layer-Method (TLM) to account for the interaction of two embedded, rigid 3D foundations within a layered soil over bedrock. A precise integration method (PIM) is used by Han et al. [22] to analyse the FSFI of a group of adjacent massless and massive 3D foundations on multilayered ground. Radisic [23] uses the Integral-Transform-Method (ITM) together with a kinematic conditions for the deformation of a rigid foundation to investigate the mutual influence of adjacent foundations.

In reality the ground often contains local inhomogeneities and structures, that have an effect on the wave propagation within the soil. Diffraction and scattering lead to an amplification of the initial vibrations and thus significantly influence both, the distribution and the amplitude of the stresses and displacements near the surface and within the surface foundations. Therefore, in order to model the real soil conditions as exact as possible and to enable an accurate prediction of the interaction phenomena of adjacent foundations, these buried structures or inhomogeneities have to be included in the model. The interaction of foundations on a soil including a spatially limited structure has been investigated in literature mainly in the context of Wave Impeding Blocks (WIB). Chouw et al. [24] used the BEM to analyse the vibration transmission in a soil layer over bedrock caused by a harmonic excitation of a rigid strip foundation and found,



that no wave propagation occurs in the layer, if the excitation frequency is lower than the first eigenfrequency ("cutoff frequency") of the stratum. This effect was used in Chouw and Schmid [25], where a spatially limited WIB was implemented into the soil in order to mitigate the low frequency vibration transmission, induced by the active of two foundations, and thus reduce the dynamic response of the passive foundation. Takemiya and Fujiwara [26] applied a 2D time domain BEM to examine the effect of a single or multiple WIBs located directly beneath or sideways under a rigid strip foundation on a homogeneous halfspace or soil stratum on the response of the system due to an excitation with an impulse load. A 3D BEM frequency domain approach was used by Antes and von Estorff [27] to study the influence of the stiffness of a finite block shaped elastic inclusion within a homogenous halfspace on the dynamic response of a elastic surface foundation. In Peplow and Finnveden [28] a 2D Spectral Finite Element Method (SFEM) is presented analysing the attenuation of surface vibrations by placing a WIB in the near field of the harmonic load applied at the surface of a layered soil stratum. Gao et al. [29] published a 3D BEM, based on Green's functions deduced with the TLM, which allows it to investigate the dynamic interaction of a surface foundation with a WIB located within a saturated, layered ground as well as to predict the vibration screening effectiveness of the WIB for different parameter settings.

In this study a coupled 2.5D ITM-FEM approach in conjunction with a conventional 3D FEM is presented to examine the influence of a local length invariant structure or inhomogeneity buried in the soil on the dynamic response of three dimensional, finite surface foundations. The 2.5D ITM-FEM approach is used to compute the dynamic stiffness at the discretization points within the interaction areas of the foundations with the soil substructure by evaluating its dynamic response due to concentrated harmonic loads. Therefore all interaction phenomena, including the interaction of the induced waves with the buried structure or inhomogeneity, are comprised. The analytical ITM solutions of the dynamic wave equation allow to account for the infinite extension of the soil by satisfying the radiation condition and thus avoid non-physical reflections at artificial boundaries. A 2.5D FEM formulation enables to model complex, spatially limited structures and a part of the surrounding soil within a cylindrical outer boundary, on which both methods are coupled. The foundations at the soil surface are modelled using common 3D finite elements and are coupled to the soil substructure enforcing the compatibility conditions at the common interface, whereby full coupling or relaxed boundary conditions can be applied.

The outline of the paper is as follows. In subsection 2.1 firstly the fundamental ITM solutions are introduced and superposed in order to obtain the stiffness matrix of a halfspace with cylindrical cavity. Subsequently in 2.2 the dynamic stiffness of the 2.5D FEM subsystem is used to model the embedded inclusion is presented, followed by the coupling of the substructures 2.3. In subsection 3.1 the dynamic stiffness of the soil substructure at the contact areas with the foundations is determined and coupled with the dynamic stiffness of the 3D FEM model of the foundations. A post processing procedure which allows to evaluate the displacement field over the total surface of a soil with inclusion due to a harmonic loading of the foundations is presented in subsection 3.3. The accuracy of the proposed method is demonstrated in subsection 4.1 by comparison with literature results for two benchmark examples. In subsection 4.2 the influence of the embedment depth, size and stiffness of the inclusion on the dynamic response of the foundations, also considering the through soil coupling, is investigated for different configurations of the surface foundations (distance, width). Frequency dependent compliance functions at the soil-foundation interface of a soil with inhomogeneity are presented and compared with the results for the homogeneous halfspace to illustrate the influence of the inclusion.

## 2 ITM-FEM FORMULATION FOR ELASTODYNAMICS

### 2.1 ITM Substructure

#### 2.1.1 Fundamental Solutions

The Lamé differential equation describes the dynamic behaviour of a linear elastic, homogeneous and isotropic continuum, which consists of three coupled partial differential equations

$$\mu u^i|_j^j + (\lambda + \mu) u^j|_j^i - \rho \ddot{u}^i = 0 \quad (1)$$

with the displacement field  $u^i$ , the Lamé constants  $\mu$  and  $\lambda$  and the density  $\rho$ . The differential equations are decoupled using a Helmholtz decomposition  $u^i = \Phi|_k^i + \Psi_l|_k \varepsilon^{ikl}$  and thereby expressing the displacement field by the sum of the gradient of a scalar field  $\Phi$  and the rotation of a vector field  $\Psi$ , resulting in an uncoupled system of three wave equations (setting  $\Psi_z = 0$  cp. [30]) only depending on the compressional and the shear wave velocities  $c_p$  and  $c_s$ .

$$\Phi|_j^j - \frac{1}{c_p^2} \ddot{\Phi} = 0 \quad \Psi_i|_j^j - \frac{1}{c_s^2} \ddot{\Psi} = 0 \quad (2)$$

The system halfspace is solved in Cartesian coordinates  $(x, y, z)$  and is derived from Eq. (2) applying a threefold Fourier transform into the wavenumber-frequency domain  $(k_x, k_y, z, \omega)$ . Thus the coupled partial differential equations turn into three decoupled ordinary differential equations that can be solved analytically with an exponential approach [31]:

$$\hat{\Phi} = A_1 e^{\lambda_1 z} + A_2 e^{-\lambda_1 z} \quad \hat{\Psi}_\alpha = B_{\alpha 1} e^{\lambda_2 z} + B_{\alpha 2} e^{-\lambda_2 z} \quad (3)$$

with  $\alpha = x, y$ ,  $\lambda_1 = (k_x^2 + k_y^2 - k_p^2)^{-2}$ ,  $\lambda_2 = (k_x^2 + k_y^2 - k_s^2)^{-2}$  and  $k_p = \frac{\omega}{c_p}$ ,  $k_s = \frac{\omega}{c_s}$ . The wavenumbers are given as  $k_x = o\Delta k_x$  with  $o = -N_x/2, \dots, (N_x/2-1)$  and  $k_y = s\Delta k_y$  with  $s = -N_y/2, \dots, (N_y/2-1)$ , where  $N_x, N_y$  is the number of Fourier series members or sample points in the original domain respectively. Applying the local boundary conditions on the halfspace surface  $\Lambda$  as well as the Sommerfeld radiation condition [32] the unknown coefficients can be determined and the stresses and displacements within the halfspace can be calculated by  $\hat{\sigma}_{hs} = \hat{K}_{hs} \hat{C}_{hs}$  and  $\hat{u}_{hs} = \hat{H}_{hs} \hat{C}_{hs}$  using the matrices given in [33], where  $\hat{K}_{hs}$  and  $\hat{H}_{hs}$  include the fundamental solutions, kinematic and material relations linking the unknowns with the stresses and the displacements. Quantities in the single, twofold resp. threefold Fourier transformed domain are marked with  $\hat{\phantom{x}}$ ,  $\sim$  and  $\wedge$ .

The system fullspace with cylindrical cavity is solved in cylindrical coordinates  $(x, r, \varphi)$  applying a Fourier transform with respect to  $x$  and  $t$  as well as performing a Fourier series expansion along the cylinder circumference  $\varphi \rightarrow n$ . Furthermore the vector field  $\Psi = \Psi g^1 + \chi|_j^j \varepsilon_{ij1} g^i$  is expressed by two independent scalar fields. The respective system of equations in the  $(k_x, r, n, \omega)$  domain is solved with Hankel functions of first and second kind [34]:

$$\hat{\Phi}(k_x, r, n, \omega) = C_{1n} H_n^{(1)}(k_1 r) + C_{4n} H_n^{(2)}(k_1 r) \quad (4)$$

$$\hat{\psi}(k_x, r, n, \omega) = C_{2n} H_n^{(1)}(k_2 r) + C_{5n} H_n^{(2)}(k_2 r) \quad (5)$$

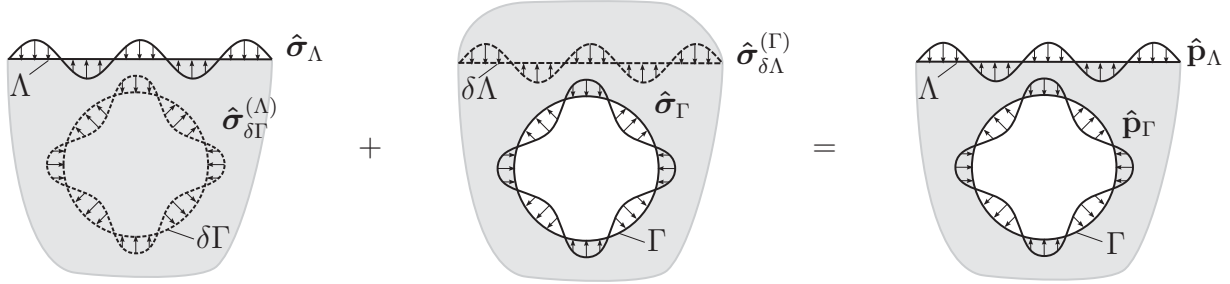
$$\hat{\chi}(k_x, r, n, \omega) = C_{3n} H_n^{(1)}(k_2 r) + C_{6n} H_n^{(2)}(k_2 r) \quad (6)$$

with  $k_1^2 = k_p^2 - k_x^2$  respectively  $k_2^2 = k_s^2 - k_x^2$ . Applying the local boundary conditions at the cylinder surface  $\Gamma$  as well as the radiation condition the stresses and displacements can be determined as  $\hat{\sigma}_c = \hat{K}_c C_c$  and  $\hat{u}_c = \hat{H}_c C_c$  as given in [33].

For a more detailed derivation of the fundamental solutions the reader is referred to [33–36].

### 2.1.2 Superposition of Fundamental Systems

In order to obtain a stiffness matrix for the system halfspace with cylindrical cavity the fundamental solutions presented in 2.1.1 are now superposed in order to satisfy the boundary conditions of the final system on the surface of the halfspace  $\Lambda$  and the cylindrical cavity  $\Gamma$ . For this reason fictitious surfaces  $\delta\Lambda$  resp.  $\delta\Gamma$  are introduced into the fundamental systems allowing a superposition at the common surfaces as depicted in Figure 1. Thus, unit stress states  $\hat{\sigma}_\Lambda$  are



**Figure 1:** Fictitious surfaces and stresses in the fundamental systems halfspace and fullspace with cylindrical cavity for superposition to a halfspace with cylindrical cavity.

applied at  $\Lambda$  for each wavenumber combination  $(k_x, k_y)$  and the stresses  $\hat{\sigma}_{\delta\Gamma}^{(\Lambda)}$  at the fictitious surface  $\delta\Gamma$  are determined. Reciprocally, the stresses  $\hat{\sigma}_{\delta\Lambda}^{(\Gamma)}$  at  $\delta\Lambda$  due to unit stress states  $\hat{\sigma}_\Gamma$  at  $\Gamma$  for each series member  $n$  can be calculated. The sum of the stresses at  $\Lambda$  and  $\Gamma$  has then to coincide with the external loads  $\hat{p}_\Lambda$  and  $\hat{p}_\Gamma$  acting on the total system.

$$C_\Lambda \hat{\sigma}_\Lambda + C_\Gamma \hat{\sigma}_{\delta\Lambda}^{(\Gamma)} = \hat{p}_\Lambda \quad (7)$$

$$C_\Lambda \hat{\sigma}_{\delta\Gamma}^{(\Lambda)} + C_\Gamma \hat{\sigma}_\Gamma = \hat{p}_\Gamma \quad (8)$$

Thereafter it is possible to determine the amplitudes  $C_{ITM} = (C_\Lambda \ C_\Gamma)^T$  of the unit stresses and the stresses at the fictitious boundaries, gathered in  $\hat{S}_{ITM}$ , in dependency of the total external load  $\hat{P}_{ITM} = (\hat{p}_\Lambda \ \hat{p}_\Gamma)^T$  on  $\Lambda$  and  $\Gamma$  as:

$$C_{ITM} = \hat{S}_{ITM}^{-1} \hat{P}_{ITM} \quad (9)$$

Hereinafter, the amplitudes  $C_{ITM}$  are used to scale the displacements due the unit stresses, gathered in  $\hat{U}_{ITM}$ , finally resulting in the displacements  $\hat{u}_{ITM}$  of the halfspace with cylindrical cavity at  $\Lambda$  and  $\Gamma$ :

$$\hat{u}_{ITM} = \hat{U}_{ITM} C_{ITM} \quad (10)$$

Combining equations (9) and (10) the stiffness matrix  $\hat{K}_{ITM} = \hat{S}_{ITM} \hat{U}_{ITM}^{-1}$  of the ITM sub-system for a halfspace with cylindrical cavity is obtained, giving a direct relation between the displacements and the external loads:

$$\underbrace{\begin{bmatrix} \hat{K}_{\Lambda\Lambda ITM} & \hat{K}_{\Lambda\Gamma ITM} \\ \hat{K}_{\Gamma\Lambda ITM} & \hat{K}_{\Gamma\Gamma ITM} \end{bmatrix}}_{\hat{K}_{ITM}} \underbrace{\begin{pmatrix} \hat{u}_{\Lambda ITM} \\ \hat{u}_{\Gamma ITM} \end{pmatrix}}_{\hat{u}_{ITM}} = \underbrace{\begin{pmatrix} \hat{P}_{\Lambda ITM} \\ \hat{P}_{\Gamma ITM} \end{pmatrix}}_{\hat{P}_{ITM}} \quad (11)$$

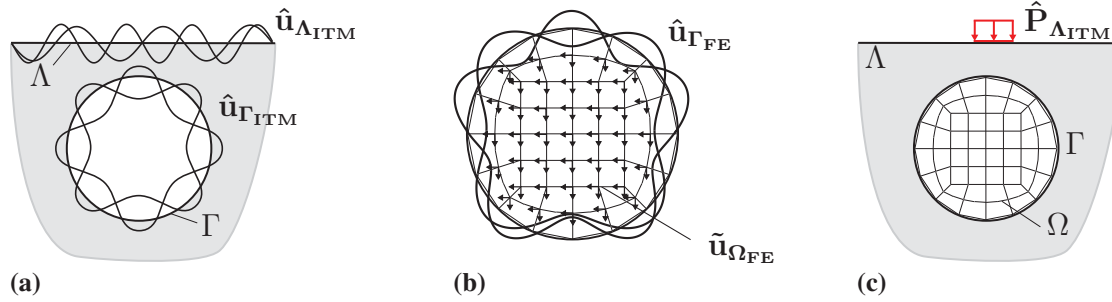
## 2.2 2.5D FEM Substructure

In order to couple a finite element structure to the previously introduced ITM subsystem, both substructures need a matching outer boundary. Therefore the dynamic stiffness matrix of a finite element structure with equally distributed nodes on the cylindrical outer boundary, matching with the discretization points of the ITM on  $\Gamma$ , needs to be computed. The dynamic stiffness matrix of the halfspace with cylindrical cavity was computed in the transformed domain for each combination  $(k_x, \omega)$ . The length invariance of the system allows to reduce the originally 3D computations to a series of 2D calculations for each  $(k_x, \omega)$ , where the information of the third dimension is stored in  $k_x$ . This 2.5D approach allows to represent the cylindrical cavity in the original domain by a circular cavity in the transformed domain. Thus modified 2D quadrilateral finite elements with linear shape functions and an additional degree of freedom (DOF) in the length direction, adopted to the Fourier transformed domain  $(k_x, y, z, \omega)$  as presented in [34], can be used to discretize the cross section. The dynamic stiffness of the 2.5D FEM substructure (with the DOFs separated for the outer boundary  $\Gamma$  and the area inside  $\Omega$ ) can finally be computed as:

$$\begin{bmatrix} \tilde{\mathbf{K}}_{\Gamma\Gamma_{FE}} & \tilde{\mathbf{K}}_{\Gamma\Omega_{FE}} \\ \tilde{\mathbf{K}}_{\Omega\Gamma_{FE}} & \tilde{\mathbf{K}}_{\Omega\Omega_{FE}} \end{bmatrix} \begin{pmatrix} \tilde{\mathbf{u}}_{\Gamma_{FE}} \\ \tilde{\mathbf{u}}_{\Omega_{FE}} \end{pmatrix} = \begin{pmatrix} \tilde{\mathbf{P}}_{\Gamma_{FE}} \\ \tilde{\mathbf{P}}_{\Omega_{FE}} \end{pmatrix} \quad (12)$$

## 2.3 Coupling of Substructures

The coupling of the ITM and the FEM substructure is carried out at the two dimensional circular coupling surface  $\Gamma$  in the reference frame of the ITM. Therefore the dynamic stiffness matrix of the FEM subsystem on  $\Gamma$  needs to be transformed into the  $(k_x, r, n, \omega)$  domain by applying a transformation to a cylindrical reference frame as well as a Fourier series expansion along the circumference. The FEM formulation inside the structure  $\Omega$  is kept in the  $(k_x, y, z, \omega)$  domain (Figure 2).



**Figure 2:** (a) Displacements  $\hat{\mathbf{u}}_{\Lambda_{ITM}}(k_x, k_y, z, \omega)$  on  $\Lambda$  and  $\hat{\mathbf{u}}_{\Gamma_{ITM}}(k_x, r, n, \omega)$  on  $\Gamma$  of the ITM substructure, (b)  $\hat{\mathbf{u}}_{\Gamma_{FE}}(k_x, r, n, \omega)$  on  $\Gamma$  and  $\tilde{\mathbf{u}}_{\Omega_{FE}}(k_x, y, z, \omega)$  within  $\Omega$  of the FEM substructure in the respective reference systems for the coupling on the circular interaction surface  $\Gamma$ . (c) Halfspace with cylindrical inclusion modelled by the coupled 2.5D ITM-FEM approach.

Thereafter, the continuity of displacements as well as the equilibrium of forces are applied at the coupling surface, finally leading to the total dynamic stiffness matrix of the 2.5D ITM-FEM system of a halfspace with cylindrical cavity filled with finite elements.

$$\underbrace{\begin{bmatrix} \hat{\mathbf{K}}_{\Lambda\Lambda_{ITM}} & \hat{\mathbf{K}}_{\Lambda\Gamma_{ITM}} & 0 \\ \hat{\mathbf{K}}_{\Gamma\Lambda_{ITM}} & \hat{\mathbf{K}}_{\Gamma\Gamma_{ITM}} + \hat{\mathbf{K}}_{\Gamma\Gamma_{FE}} & \hat{\mathbf{K}}_{\Gamma\Omega_{FE}} \\ 0 & \hat{\mathbf{K}}_{\Omega\Gamma_{FE}} & \tilde{\mathbf{K}}_{\Omega\Omega_{FE}} \end{bmatrix}}_{\hat{\mathbf{K}}^{hc}} \underbrace{\begin{pmatrix} \hat{\mathbf{u}}_{\Lambda_{ITM}} \\ \hat{\mathbf{u}}_{\Gamma} \\ \tilde{\mathbf{u}}_{\Omega_{FE}} \end{pmatrix}}_{\hat{\mathbf{u}}^{hc}} = \underbrace{\begin{pmatrix} \hat{\mathbf{P}}_{\Lambda_{ITM}} \\ \hat{\mathbf{P}}_{\Gamma} \\ \tilde{\mathbf{P}}_{\Omega_{FE}} \end{pmatrix}}_{\hat{\mathbf{P}}^{hc}} \quad (13)$$

### 3 SOIL-FOUNDATION SYSTEM

#### 3.1 Dynamic Soil Flexibility and Stiffness

With the stiffness matrix  $\hat{\mathbf{K}}^{\text{hc}}$  it is possible to compute the displacements  $\hat{\mathbf{u}}_{\Lambda\text{ITM}}$  on the surface of a halfspace with length invariant FEM inclusion due to an external load  $\hat{\mathbf{P}}_{\Lambda\text{ITM}}$  on the ground surface. As the members  $\hat{F}_{mn}^{ij}$  with  $m, n = x, y, z$  of the complex, dynamic flexibility matrix at the ground surface correspond to the displacements  $\hat{u}_m^i$  at a discretization point  $i$  on  $\Lambda$  due to a concentrated unit load  $\hat{P}_n^j$  in direction  $n$  acting at a discretization point  $j$ , Eq. (13) can be used in the following to set up the flexibility matrix  $\hat{\mathbf{F}}_s^{ij}$  giving the force displacement relationship between a pair of discretization points:

$$\underbrace{\begin{pmatrix} \hat{u}_x^i \\ \hat{u}_y^i \\ \hat{u}_z^i \end{pmatrix}}_{\hat{\mathbf{u}}_s^i} = \underbrace{\begin{pmatrix} \hat{F}_{xx}^{ij} & \hat{F}_{xy}^{ij} & \hat{F}_{xz}^{ij} \\ \hat{F}_{yx}^{ij} & \hat{F}_{yy}^{ij} & \hat{F}_{yz}^{ij} \\ \hat{F}_{zx}^{ij} & \hat{F}_{zy}^{ij} & \hat{F}_{zz}^{ij} \end{pmatrix}}_{\hat{\mathbf{F}}_s^{ij}} \underbrace{\begin{pmatrix} \hat{P}_x^j \\ \hat{P}_y^j \\ \hat{P}_z^j \end{pmatrix}}_{\hat{\mathbf{P}}_s^j} \quad (14)$$

To avoid a singularity under the location of application of the unit load and to keep the numerical errors associated with the discrete calculations small, instead of an unit point force a load uniformly distributed over a small area with a unit resultant is used in the following and referred to as concentrated load [23].

For the later coupling with the finite foundations, modelled by a 3D FEM, the force displacement relationship is needed at the interaction areas of the foundations with the ground surface, as the nodal contact forces and displacements of both substructures must coincide there. Thus, it is necessary, that both substructures exhibit the same discretization at the interaction areas, so that the element nodes of the foundations match with the discretization points of the ITM-FEM soil substructure (Fig. 4), which was discretized on  $\Lambda$  with equidistant points in the original domain  $(x, y, z, \omega)$ . The coordinates of these can be obtained as  $x = o\Delta x$  with  $o = -N_x/2, \dots, (N_x/2 - 1)$  and  $y = s\Delta y$  with  $s = -N_y/2, \dots, (N_y/2 - 1)$ , where  $\Delta x, \Delta y$  are the incremental distances. Outside of the foundations a traction free surface is assumed.

In order to populate the overall flexibility matrix  $\bar{\mathbf{F}}_s$ , which fully represents the coupled 2.5D ITM-FEM system and specifies the force-displacement relationship

$$\bar{\mathbf{u}}_s(x, y, \omega) = \bar{\mathbf{F}}_s(x, y, \omega) \bar{\mathbf{P}}_s(x, y, \omega) \quad (15)$$

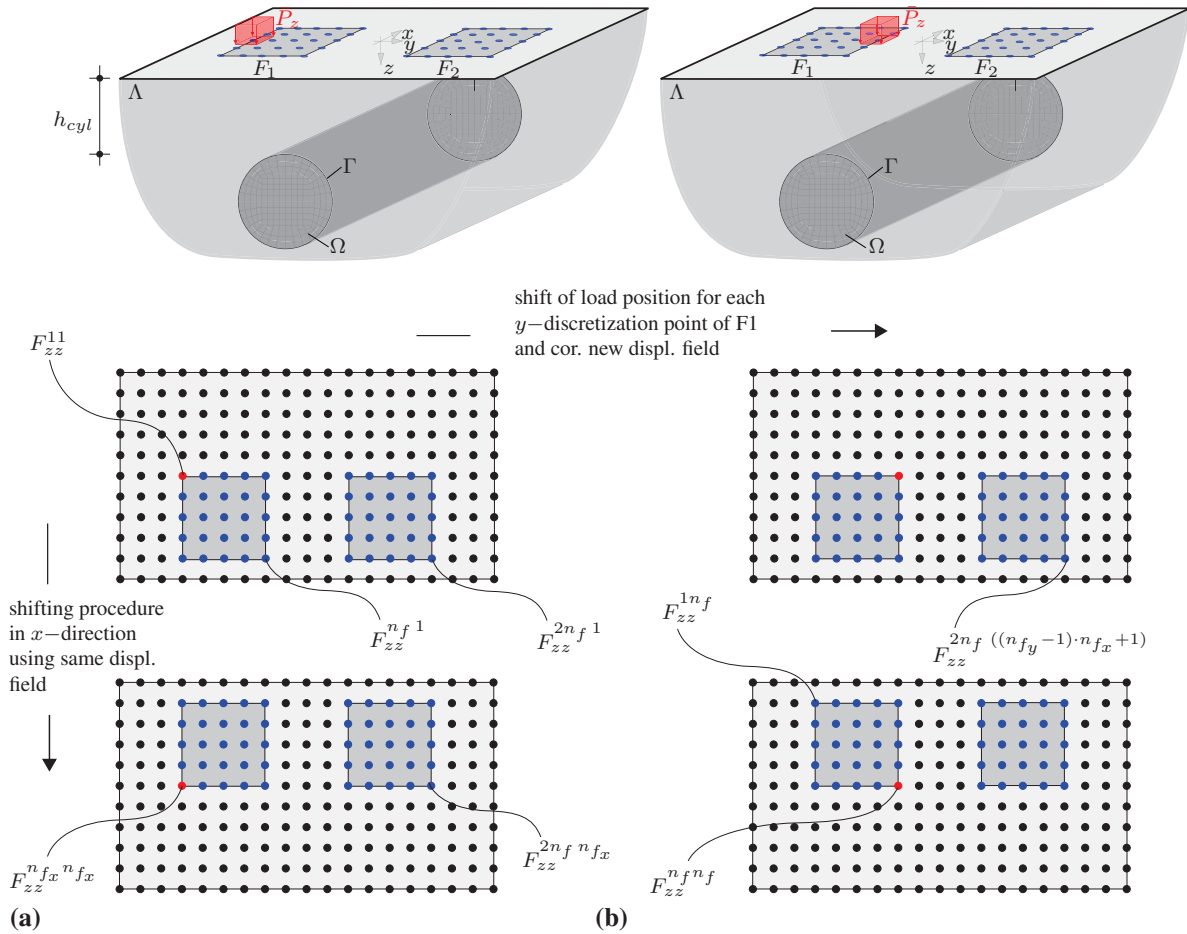
at all  $n_{f,\text{tot}} = N_f \cdot n_f$  discretization points within the soil-foundation coupling regions, the soil response  $\bar{\mathbf{u}}_s^i$  with  $i = 1 \dots n_{f,\text{tot}}$  in all directions at each of these points must be evaluated as a result of a harmonic excitation with concentrated unit loads  $\bar{\mathbf{P}}_s^j$  with  $j = 1 \dots n_{f,\text{tot}}$  in each spatial direction acting on each of these points in turn. Thereby  $N_f$  is the total number of foundations and  $n_f = n_{fx} \cdot n_{fy}$  is the number of discretization points of one foundation at the coupling surface with the soil and results from the product of the amount of discretization points of the foundation in  $x, y$ -direction  $n_{fx}, n_{fy}$ . Since all foundations possess the same size also the number of discretization points is equal. Thus the dimension of  $\bar{\mathbf{F}}_s$  yields to  $[3n_{f,\text{tot}} \times 3n_{f,\text{tot}}]$ .

The displacements and thus also the members of the flexibility matrix, resulting from the application of Eq. (13), are firstly obtained in the  $(k_x, k_y, z, \omega)$  domain. To enable a direct stiffness coupling by enforcing the compatibility conditions at the interaction areas of the soil with the 3D FEM foundations, it is necessary to have the soil stiffness matrix  $\bar{\mathbf{K}}_s = \bar{\mathbf{F}}_s^{-1}$  defined w.r.t. a Cartesian reference frame in the frequency domain  $(x, y, z, \omega)$  as it is the case for the dynamic stiffness of the foundations. Hence, a twofold inverse Fourier transform (IFFT)



is applied to finally attain the dynamic stiffness matrix  $\bar{\mathbf{K}}_s(x, y, z, \omega)$  of the 2.5D ITM-FEM system.

The computational effort to determine the soil flexibility resp. stiffness matrix can be reduced significantly by taking into account the symmetry conditions and in case of the halfspace with inclusion also the length invariance of the system. Instead of placing the concentrated load at each of the  $n_{f,\text{tot}}$  discretization points at the contact areas and evaluating the system response at all of them, the foundation areas can be shifted according to the discretization step size, such that every interaction node is positioned once under the unit concentrated load. In case of a homogeneous halfspace, due to the complete rotational symmetry, the position of the load on  $\Lambda$  is irrelevant and the displacement field only needs to be computed twice (once for the load acting in vertical direction and once for one of the horizontal directions, as the other can be determined via the symmetry conditions). In case of the halfspace with inclusion due to the inhomogeneity in the soil, the position of the concentrated load on  $\Lambda$  is no more irrelevant for the resulting displacement field. However, as the system is length invariant only a different position in  $y$ -direction causes a different system response. Consequently the concentrated load needs to be placed once at each  $y$ -discretization point of the foundations. For two foundations located symmetrically w.r.t. the  $x$ -axis, it is even sufficient to only consider the  $y$ -discretization points of one foundation for the load positions, as the results for the second foundation again can be gained by symmetry considerations. Nevertheless, all load directions have to be considered.



**Figure 3:** Shifting procedure and selection of displacements for (a) concentrated load at first and (b) last load position on discretization points of soil foundation interface in  $y$ -direction of foundation  $F_1$ .



Figure 3 illustrates the shifting procedure for the latter case. The load is positioned one after another on all  $y$ -discretization points of the first foundation  $F_1$  and the response at all interaction points of both foundations with the soil surface  $\Lambda$  is evaluated. A new displacement field is determined using Eq. (13) for each of this load positions. For the discretization points of the foundation  $F_1$  in  $x$ -direction the same system response is used and only the evaluation points are shifted under the point of load application. Thereby the displacements at all nodes of the soil foundation contact area due to a single load position in one direction are sorted into the respective column of  $\bar{\mathbf{F}}_s(x, y, z, \omega)$  after the IFFT. To avoid an ill conditioning of the flexibility matrix, which would result from a shift of the load position by only one discretization point in combination with the distributed uniform load (as then the adjacent columns of  $\bar{\mathbf{F}}_s$  contain very similar values), a coarser mesh is introduced for the shifting procedure as proposed by [23]. The displacements w.r.t. the coarse mesh are computed as the mean value of the displacements w.r.t. the fine mesh within an area  $A = n_\Delta dx n_\Delta dy$ . Thereby  $dx, dy$  are the discretization step sizes of the fine mesh and  $n_\Delta$  is the factor relating the old step size with the new one.

### 3.2 Dynamic Stiffness of Soil-Foundation-System

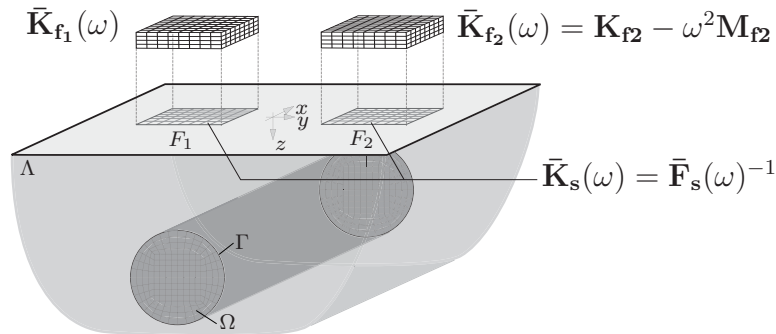
The three dimensional, finite surface foundations, that shall be coupled to the 2.5D ITM-FEM soil substructure, are modelled with conventional finite elements. Either 8-node solid elements or shell elements can be used for this objective. As in this work only foundations satisfying the thin plate assumptions are investigated, a shell element with six DOFs per node presented by Rojas et al. [37] is used due to reasons of computational efficiency. Assembling the element stiffnesses of all elements of one foundation  $n$ , the total dynamic stiffness matrix results as

$$\bar{\mathbf{K}}_{f_n}(\omega) = \mathbf{K}_{f_n} - \omega^2 \mathbf{M}_{f_n} \quad (16)$$

with  $\mathbf{K}_{f_n}$  and  $\mathbf{M}_{f_n}$  being the stiffness and the mass matrix of the respective foundation  $n$  and  $\omega$  as the excitation frequency.

The material properties of the foundations are fully described by the linear elastic parameters, i.e. the Young's Modulus  $E_f$ , the Poisson ratio  $\nu_f$  and the density  $\rho_f$ . For the following investigations only very stiff (subsequently termed as rigid), massless foundations are considered by assigning them a very high modulus of elasticity and close to zero density. However, it is easily possible with the presented approach, to also include elastic, hysteretically damped foundations with mass into the investigations.

For the coupling of the foundations and the soil substructure, the compatibility conditions need to be satisfied at the interaction nodes on the soil surface  $z = 0$  as illustrated in Fig. 4.



**Figure 4:** Coupling of FEM foundations  $F_1$  and  $F_2$  to the 2.5D ITM-FEM system of halfspace with stiff cylindrical inclusion at the common interaction surfaces.

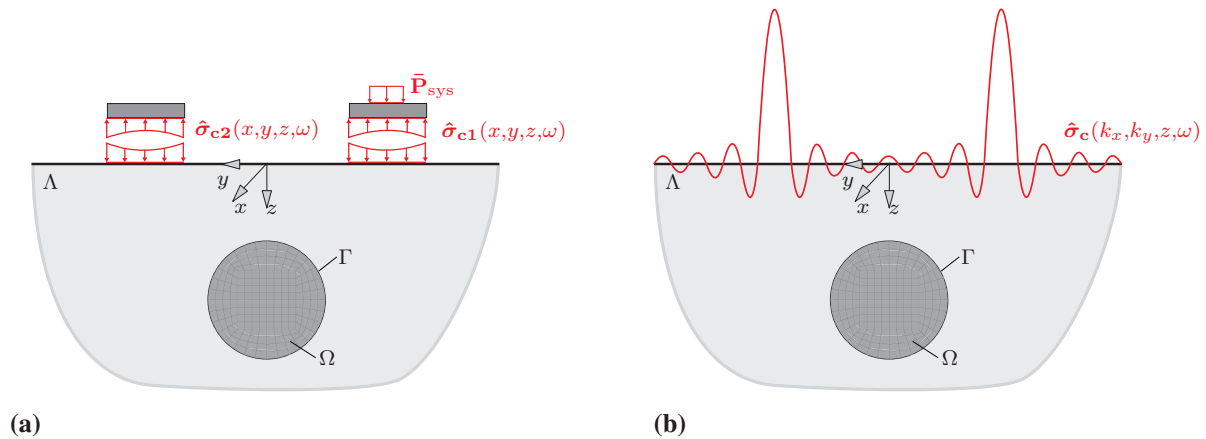
Thereby the soil substructure is fully represented by  $\bar{\mathbf{K}}_s(x, y, \omega)$ , which describes the cross interaction between the foundations under consideration of the interaction via the soil including the inhomogeneity. Since only translational DOFs exist at the discretization points of the soil substructure, the rotational DOFs of the shell elements of the foundations need to be condensed out, before assembling  $\bar{\mathbf{K}}_s(\omega)$  and  $\bar{\mathbf{K}}_{f_n}(\omega)$  into the total dynamic stiffness matrix

$$\bar{\mathbf{K}}_{\text{sys}} \bar{\mathbf{u}}_{\text{sys}} = \bar{\mathbf{P}}_{\text{sys}} \quad (17)$$

where  $\bar{\mathbf{u}}_{\text{sys}}$  is the vector of nodal displacements comprising the DOFs of the foundation nodes and the interface nodes with the soil and  $\bar{\mathbf{P}}_{\text{sys}}$  is the respective system load vector. Either full coupling of all DOFs or relaxed boundary conditions (frictionless contact) can be assumed at the interaction surfaces.

### 3.3 Postprocessing

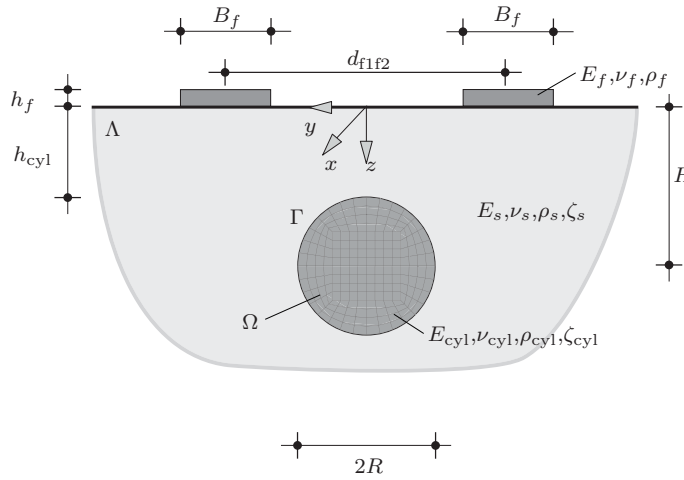
Firstly the total system of equations in Eq. (17) is solved for the nodal displacements at the soil foundation interfaces  $\bar{\mathbf{u}}_c = \bar{\mathbf{u}}_{\text{sys}}(z = 0)$  due to a harmonic load on either one or both foundations. These displacements are used in the following to compute the nodal contact forces  $\bar{\mathbf{P}}_c = \bar{\mathbf{K}}_s \bar{\mathbf{u}}_c$  w.r.t. the  $(x, y, z, \omega)$  domain.  $\bar{\mathbf{P}}_c$  includes the components in all directions for the full coupling, whereas for relaxed boundary conditions only contact forces in the  $z$ -direction remain. Subsequently, these nodal contact forces are applied as external loads on the surface of the halfspace with inclusion, as depicted in Fig. 5a, in order to determine the displacements on the whole ground surface  $\Lambda$  by application of Eq. (13). Thereby the effects of the interaction of the foundations with the soil substructure are completely included. However, the members of the stiffness matrix  $\hat{\mathbf{K}}^{\text{hc}}$  and the load vector  $\hat{\mathbf{P}}^{\text{hc}}$  associated with  $\Lambda$  are given in the Fourier transformed domain. Furthermore, as  $\hat{\mathbf{P}}_{\Lambda\text{ITM}}$  in Eq. (13) consists of the stresses on the halfspace surface, the contact forces  $\bar{\mathbf{P}}_c$  need to be divided by the corresponding load influence area in a first step and have to be transformed into the  $(k_x, k_y, z, \omega)$  domain afterwards to obtain the contact stresses  $\hat{\sigma}_c(k_x, k_y, z, \omega)$ , depicted in Fig. 5b, that can then be sorted into  $\hat{\mathbf{P}}_{\Lambda\text{ITM}}$ . Therewith the displacements  $\hat{\mathbf{u}}_{\Lambda\text{ITM}}(k_x, k_y, z, \omega)$  and finally after a twofold IFFT  $\bar{\mathbf{u}}_{\Lambda}(x, y, z, \omega)$  over the total soil surface  $\Lambda$  can be computed.



**Figure 5:** Postprocessing procedure: Application of the contact stresses at the soil foundation interfaces as external load on the 2.5D ITM-FEM system halfspace with inclusion (a) in the original domain  $(x, y, z, \omega)$  and (b) in the transformed domain  $(k_x, k_y, z, \omega)$  to determine the displacements  $\bar{\mathbf{u}}_{\Lambda}(x, y, z, \omega)$  over the total ground surface.

#### 4 NUMERICAL RESULTS

In this section the above presented coupled ITM-FEM approach is applied to determine the dynamic response of a single or a group of two adjacent 3D square foundations with a side length  $B_f$ , a height  $h_f$  and a midpoint distance of  $d_{f1f2}$  resting on the surface of a halfspace with a length invariant, cylindrical inclusion of radius  $R$ , embedment depth  $H$  and a soil covering height  $h_{cyl}$ , as depicted in Fig. 6. The material properties of the linear elastic foundations, the soil and the inclusion are described by the Young's modulus  $E$ , the Poisson ratio  $\nu$  and the density  $\rho$ . For the soil substructure, whose properties as well as the corresponding wave speeds  $c_p$ ,  $c_s$  and  $c_r$  are listed in Tab. 1, additionally material damping was introduced by means of a complex Young's modulus  $\hat{E} = E(1 + i \text{sign}(\omega)\zeta)$  with the hysteric damping ratio  $\zeta$ .



**Figure 6:** Geometric parameters of the coupled 2.5D ITM-FEM system with two adjacent surface foundations.

For all subsequent calculations, full coupling of all DOFs between soil and foundations is assumed and only rigid, massless square foundations, modelled by choosing a large Young's Modulus  $E_f$ , are considered for reason of comparability with other results from literature. However, the limitation to this rather simple systems in this paper does not imply any confinement on the applicability of the proposed method for more complicated SSI and FSFI problems, including flexible and massive structures with rectangular contact area to the soil as well as more complex inclusion geometries inside the 2.5D FEM substructure with cylindrical outer boundary.

	$E$ (N m <sup>-2</sup> )	$\nu$ ( )	$\rho$ (kg m <sup>-3</sup> )	$\zeta$ (—)	$c_p$ (m s <sup>-1</sup> )	$c_s$ (m s <sup>-1</sup> )	$c_r$ (m s <sup>-1</sup> )
Soil	$26.00 \cdot 10^6$	0.30	2000	0.05	132.5	70.8	65.7
Infill A	$96.00 \cdot 10^6$	0.20	2000	0.04	231.0	141.5	128.9
Infill B	$38.40 \cdot 10^7$	0.20	2000	0.04	461.9	282.9	257.9
Infill C	$15.40 \cdot 10^8$	0.20	2000	0.04	925.2	566.5	516.5
Infill D	$34.00 \cdot 10^9$	0.20	2000	0.04	4347.0	2661.9	2426.8
Foundation	$34.00 \cdot 10^{11}$	0.20	1	0.00	$2.142 \cdot 10^6$	$1.145 \cdot 10^6$	-

**Table 1:** Material parameters of soil, foundation and different inclusion infill materials.

Since only comparably very stiff foundations are considered, all elements of a foundation can be considered as constrained to move like a rigid body and the displacements of each point can be expressed by the displacements and the rotations at the center of the resp. foundation  $\bar{\mathbf{u}}_{c,r}^i = (u_x^i, u_y^i, u_z^i, \varphi_x^i, \varphi_y^i, \varphi_z^i)^T$  at the soil foundation interface  $z = 0$ . In case of two

adjacent foundations, the displacements  $\bar{\mathbf{u}}_{c,r}^i$  of foundation  $i$  due to an external load  $\bar{\mathbf{P}}_{c,r}^j = (P_x^j, P_y^j, P_z^j, M_x^j, M_y^j, M_z^j)^T$  on foundation  $j$  with  $i, j = 1, 2$  can be computed as

$$\begin{pmatrix} \bar{\mathbf{u}}_{c,r}^1 \\ \bar{\mathbf{u}}_{c,r}^2 \end{pmatrix} = \begin{pmatrix} \bar{\mathbf{F}}_{c,r}^{11} & \bar{\mathbf{F}}_{c,r}^{12} \\ \bar{\mathbf{F}}_{c,r}^{21} & \bar{\mathbf{F}}_{c,r}^{22} \end{pmatrix} \begin{pmatrix} \bar{\mathbf{P}}_{c,r}^1 \\ \bar{\mathbf{P}}_{c,r}^2 \end{pmatrix} \quad (18)$$

The main diagonal terms represent the compliance matrices of each rigid foundation itself in case it is loaded with an external load, whereas the off diagonal terms represent the coupling between the foundations. Thereby each member of the total flexibility/compliance matrix of the rigid foundations  $\bar{\mathbf{F}}_{c,r}^{ij}$  consists of

$$\bar{\mathbf{F}}_{c,r}^{ij} = \begin{pmatrix} \bar{F}_{xx}^{ij} & 0 & 0 & 0 & \bar{F}_{x,\varphi_y}^{ij} & 0 \\ 0 & \bar{F}_{yy}^{ij} & 0 & \bar{F}_{y,\varphi_x}^{ij} & 0 & 0 \\ 0 & 0 & \bar{F}_{zz}^{ij} & 0 & 0 & 0 \\ 0 & \bar{F}_{\varphi_x,y}^{ij} & 0 & \bar{F}_{\varphi_x,\varphi_x}^{ij} & 0 & 0 \\ \bar{F}_{\varphi_y,x}^{ij} & 0 & 0 & 0 & \bar{F}_{\varphi_y,\varphi_y}^{ij} & 0 \\ 0 & 0 & 0 & 0 & 0 & \bar{F}_{\varphi_z,\varphi_z}^{ij} \end{pmatrix} \quad (19)$$

In the entries  $\bar{F}_{rs}^{ij}$  the first subscript  $r$  indicates the mode of vibration and the second subscript  $s$  the direction of the force resp. moment.

For the subsequently presented dimensionless compliance functions, defined as

$$C_{rs}^{ij} = \frac{u_r^i G_s B_f / 2}{P_s^j} \quad (20)$$

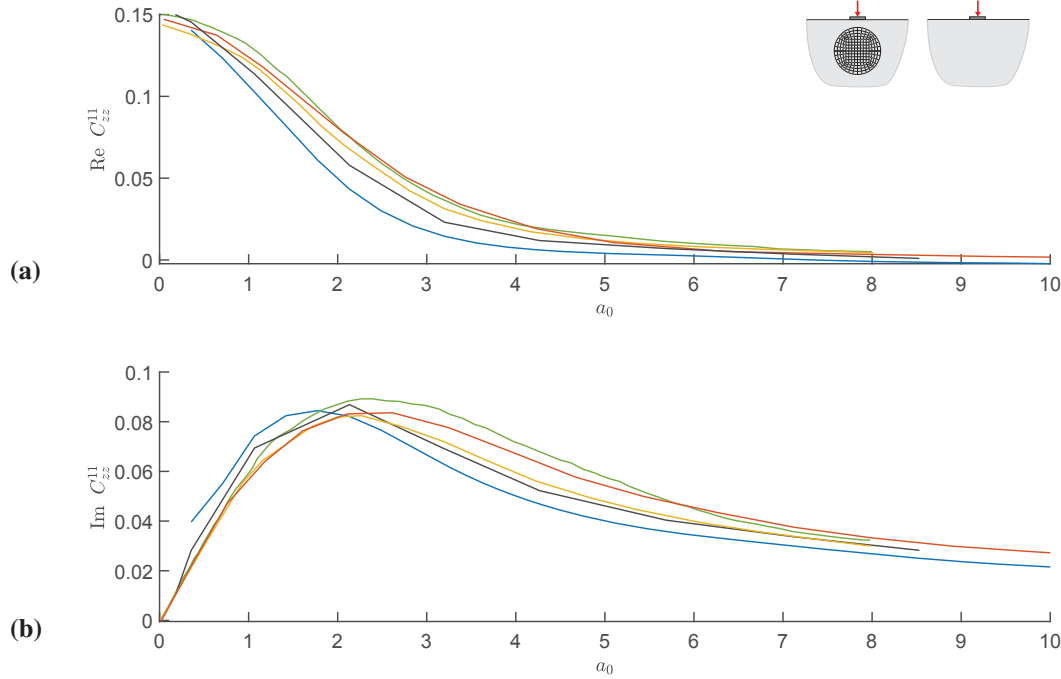
the displacements  $u_r^i$  due to unit force  $|P_s^j| = 1$  with  $r, s = x, y, z, \varphi_x, \varphi_y, \varphi_z$  normalized with the shear modulus of the soil  $G_s$  and the foundation width are evaluated over the dimensionless frequency  $a_0 = \omega B_f / c_s$ , where  $c_s$  is the shear wave velocity of the soil. It is possible to determine the compliance functions for a load either on one or both foundations.

Concerning the dimensions and the discretization of the 2.5D ITM-FEM approach, used to model the soil subsystem, same parameters were chosen for all following computations. A total domain size of  $B_x = B_y = 64$  m with  $N_x = N_y = 2^9$  discretization points resp. Fourier members was chosen, resulting in a original step size of  $dx = dy = 0.125$  m at the halfspace surface. With a factor  $n_\Delta$ , relating the original and the coarse mesh, which is used for the determination of the flexibility, the contact area of each foundation with the soil is meshed with  $n_{\text{elem}} = (B_f / (n_\Delta dx))^2$  quadratic shell elements. The cylindrical 2.5D FEM inclusion was discretized with  $N_\varphi = 32$  equidistant nodes resp. Fourier series members along the circumference, leading to an element size between 0.25 and 0.375 m for the considered inclusion sizes  $R$  and thus ca. four elements per shear wave length  $\lambda_s$  of the soil at the highest regarded frequency.

#### 4.1 Validation

In literature numerous results applying a variety of different methods have been published, dealing with the interaction of surface foundations and a homogeneous halfspace. Therefore, the previously presented approach is used in the following to compute the flexibility resp. compliance functions of a single or two adjacent surface foundations resting on a halfspace with inclusion, whereby the material properties of the latter are chosen to be identical to those of the surrounding soil in order to reproduce a homogeneous halfspace. The obtained results are then compared to the literature results to validate the proposed method.

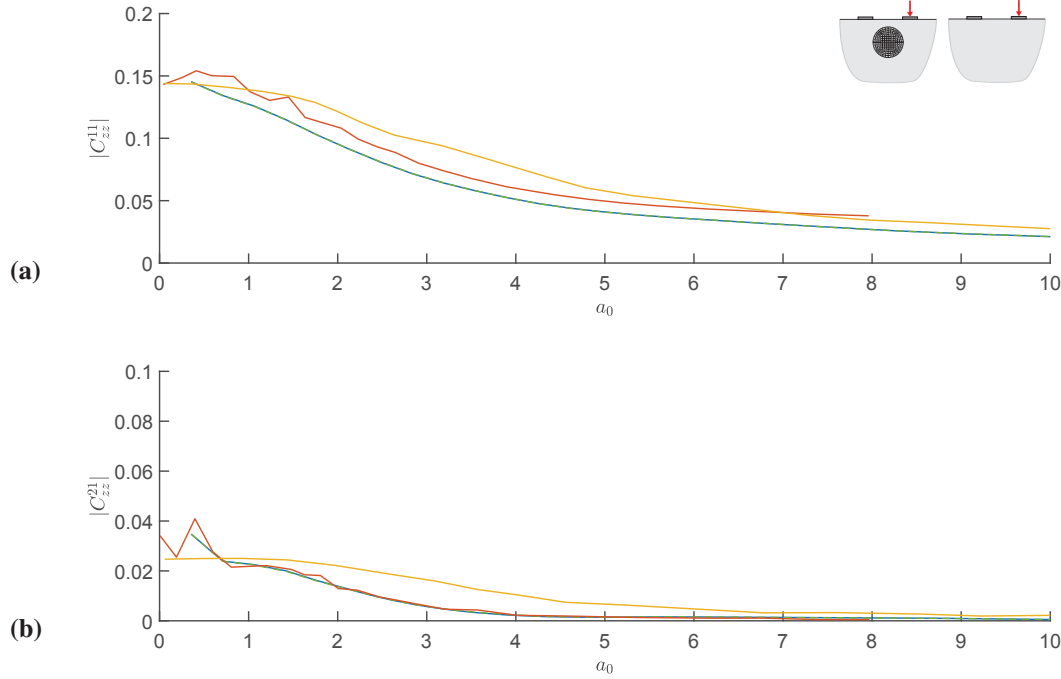
Fig. 7 shows the real and imaginary part of the vertical compliance  $C_{zz}^{11}$  of a single rigid, massless square foundation with  $B_f = 2$  m on a halfspace with cylindrical inclusion (soil material) with  $R = 3$  m and embedment depth  $H = 4$  m obtained with the presented 2.5D ITM-FEM approach. A point load with unit amplitude was applied at the midpoint of the foundation for excitation frequencies from 2 to 60 Hz.



**Figure 7:** Comparison of real and imaginary part of the vertical compliance functions  $C_{zz}^{11}(a_0)$  of a rigid, massless square foundation with  $B_f = 2$  m on a halfspace with cylindrical inclusion (Soil) with  $R = 3$  m and embedment depth  $H = 4$  m obtained with presented ITM-FEM approach with  $N_x = N_y = 2^9$  (—) to the results of the ITM-FEM approach on homogeneous halfspace with  $N_x = N_y = 2^{11}$  (—), Wong and Luco [1] (—), Hirschauer [38] (—) and Shahi and Noorzad [39] (—).

A good agreement of the results with those obtained by Wong and Luco [1], Hirschauer [38] and Shahi and Noorzad [39] can be observed. However, the compliances attained with the presented method show slightly lower values. One reason for that is the hysteretic material damping ( $\zeta = 0.05$ ), whereas the literature results were determined for zero material damping. In addition, the results for a rigid foundation, determined by enforcing the kinematics of a rigid plate as a displacement boundary condition at the soil-foundation interface of a homogeneous halfspace with lower material damping  $\zeta = 0.02$ , larger domain size  $B_x = B_y = 128$ , and larger sample number  $N_x = N_y = 2^{11}$  (possible as there the computational effort is much lower) are shown in Fig. 7, whose courses correspond even better with the literature solutions. However, for the halfspace with inclusion due to the rapidly raising computational effort, as the number of  $y$ -discretization points on the contact surface and thus the load positions, at which a new displacement field for the shifting procedure to populate the flexibility matrix needs to be computed, increases proportional to a decreasing incremental step width, this adaption of the discretization is not reasonable and the agreement of the results gained with the used parameters is considered as sufficient.

In Fig. 8 the absolute value of the vertical compliance of the active (loaded)  $|C_{zz}^{11}|$  and the passive (unloaded)  $|C_{zz}^{21}|$  of two adjacent surface foundations with distance  $d_{f1f2} = 4$  m due to a unit harmonic point load on foundation  $F_1$  are illustrated. The dimensions of the foundations



**Figure 8:** Comparison of absolute vertical compliance functions  $|C_{zz}^{ij}(a_0)|$  for (a) first (loaded) and (b) second of two adjacent rigid, massless square foundations with  $B_f = 2$  m and distance  $d_{f1f2} = 4$  m on a halfspace with cylindrical inclusion (Soil) with  $R = 3$  m and embedment depth  $H = 4$  m obtained with presented 2.5D ITM-FEM approach (—) to the results of the ITM approach on homogeneous halfspace, enforcing the kinematic of a rigid plate as displacement boundary condition (—), Radisic [23] (—) and Karabalis and Mohammadi [40] (—).

as well as the parameters of the halfspace with inclusion are chosen as before. A perfect match of the presented 2.5D ITM-FEM approach with the ITM approach with the kinematic condition can be observed, if same discretization parameters are chosen. Furthermore, the results show good agreement with those obtained by Radisic [23] and Karabalis and Mohammadi [40], who again obtained slightly larger compliances due to zero material damping. At higher frequencies, where mainly the geometrical damping dominates the system response, the deviations diminish.

Overall the comparison with literature results shows, that the proposed method delivers valid results and can further be applied to determine compliance functions of foundations resting on soils with embedded structures or inhomogeneities.

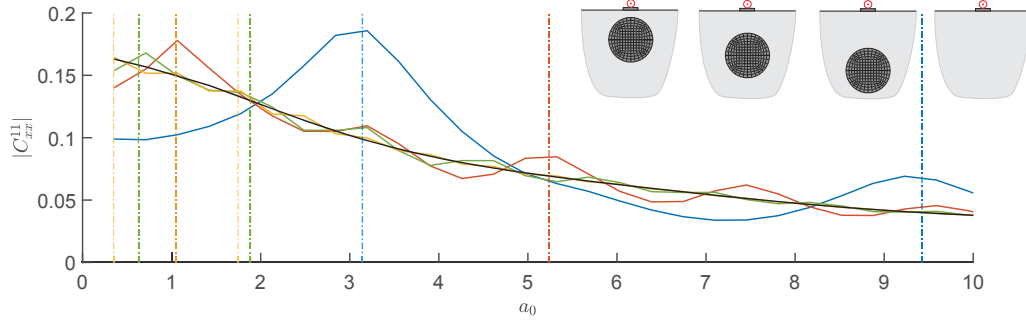
## 4.2 Parameter study

In this subsection the influence of the variation of the inclusion parameters such as embedment depth  $H$ , size  $R$  and stiffness  $E_{\text{cyl}}$  on the dynamic response of a single or two adjacent rigid, massless, square surface foundations, including their cross interaction, is investigated for different configurations of the surface foundations w.r.t. their midpoint distance  $d_{f1f2}$  and width  $B_f$ . The frequency dependent dimensionless compliance functions at the soil-foundation interface are presented for the different system designs and compared with the results for equivalent foundations resting on a homogeneous halfspace to illustrate the influence of the inclusion respectively the change in influence for varying configurations of inclusion and foundations. Furthermore the impact of a stiff, length invariant cylindrical confinement on the displacement distribution over the entire ground surface as a result of a simultaneous harmonic excitation of both foundations, determined by the post-processing method described above, is presented.

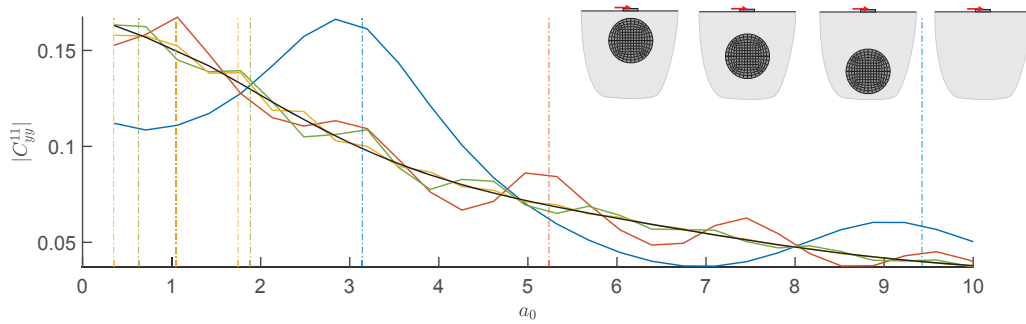


### Variation of embedment depth $H$ - single foundation

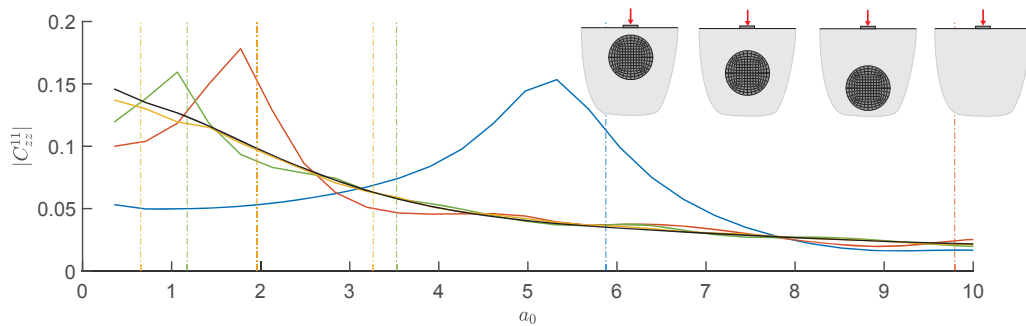
Firstly the influence of a variation of the embedment depth  $H$  of a stiff cylindrical inclusion (Infill D in Tab. 1) directly located beneath a single foundation on the compliance functions is investigated. All other parameters, such as the foundation width  $B_f = 2$  m, the inclusion radius  $R = 3$  m, as well as the soil and inclusion material are kept constant.



**Figure 9:** Absolute horizontal compliance functions  $|C_{xx}^{11}(a_0)|$  of a rigid, massless square foundation with  $B_f = 2$  m on a halfspace with cylindrical inclusion (Infill D) with  $R = 3$  m and varying embedment depth  $H = 4$  m (—),  $H = 6$  m (—),  $H = 8$  m (—),  $H = 12$  m (—) and on a homogeneous halfspace (—).



**Figure 10:** Absolute horizontal compliance functions  $|C_{yy}^{11}(a_0)|$  of a rigid, massless square foundation with  $B_f = 2$  m on a halfspace with cylindrical inclusion (Infill D) with  $R = 3$  m and varying embedment depth  $H = 4$  m (—),  $H = 6$  m (—),  $H = 8$  m (—),  $H = 12$  m (—) and on a homogeneous halfspace (—).



**Figure 11:** Absolute vertical compliance functions  $|C_{zz}^{11}(a_0)|$  of a rigid, massless square foundation with  $B_f = 2$  m on a halfspace with cylindrical inclusion (Infill D) with  $R = 3$  m and varying embedment depth  $H = 4$  m (—),  $H = 6$  m (—),  $H = 8$  m (—),  $H = 12$  m (—) and on a homogeneous halfspace (—).

Figs. 9 and 10 show the horizontal compliance functions due to a harmonic excitation with horizontal unit forces. In case of small embedment depths  $H$ , corresponding to a small thicknesses of the soil layer between the stiff inclusion and the bottom of the foundation  $h_{\text{cyl}}$ , large fluctuations of the flexibilities  $|C_{xx}^{11}|$  and  $|C_{yy}^{11}|$  can be observed. This large influence of the buried structure on the foundation flexibilities decreases with increasing  $H$ , for which the results converge to those obtained for a homogeneous halfspace. However, some waviness in the flexibilities is left, which can be attributed to waves reflected at the soil-inclusion interface and their superposition with the primary waves. The two rather distinct peaks for  $H = 4$  can be linked to the first and second horizontal eigenfrequencies of a soil layer over bedrock (defined equal to the natural frequencies of an equivalent one-dimensional rod featuring the same length as the thickness of the layer like proposed in [24] and also depicted in Figs. 9 and 10)

$$f_{\text{h,res}} = \frac{(2n-1)c_s}{4H_{\text{layer}}} \quad \text{with } n = 1, 2, \dots \quad (21)$$

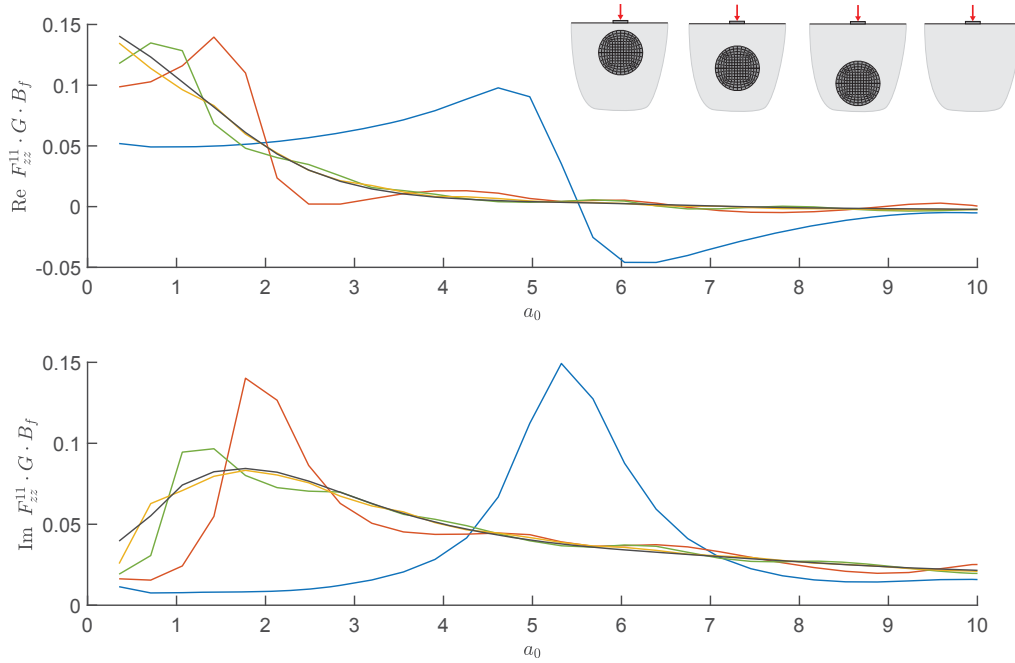
which here result with  $H_{\text{layer}} = h_{\text{cyl}} = 1$  to  $f_{\text{h,res}} = 17.7, 53.1$  Hz resp.  $a_{0,\text{h,res}} = 3.14, 9.42$ . The generally quite resembling qualitative course of  $|C_{xx}^{11}|$  and  $|C_{yy}^{11}|$  can be explained by the rather small foundation width  $B_f = 2$  m compared to the diameter of the inclusion with 6 m, which leads to a similar behaviour in the  $y$ - as in the  $x$ -direction of the fully length invariant inclusion. Nevertheless, the maxima of  $|C_{xx}^{11}|$  are slightly more peaked, show little higher amplitudes and fit better to the horizontal resonance frequencies of a soil layer in Eq. (21).

Also in the vertical compliances  $|C_{zz}^{11}|$  in Fig. 11 the existence of vertical resonances of the soil layer over the inclusion is clearly visible. Depending on the embedment depth  $H$ , distinct peaks occur in the vicinity of the vertical resonance frequencies of an elastic stratum also depicted in Fig. 11 by the vertical lines

$$f_{\text{v,res}} = \frac{(2n-1)c_p}{4H_{\text{layer}}} \quad \text{with } n = 1, 2, \dots \quad (22)$$

However, since the cylindrical inclusion is spatially limited in the  $y-z$ -plane, the behaviour only approximates that of a soil layer over bedrock. This also holds for the corresponding resonance frequencies and explains the shift of the smoother peaks towards lower frequencies. It was shown by Chouw et al. [24] and Kobori et al. [41], that in a perfectly elastic stratum with zero material damping, energy attenuation is only possible by free waves, i.e. Rayleigh and Love waves, travelling in radial direction away from the source and that for an excitation at the surface of the layer with a frequency below the first resonance frequency ("cutoff frequency") no such propagating waves can occur. The imaginary part of the flexibility at the soil foundation interface, associated with the system damping, in this case directly shows the amount of radiation damping due to propagating waves into the laterally infinite medium and is zero below the first natural frequency. In contrast, in a viscoelastic stratum with non zero material damping even in the low frequency range, below the first natural frequency, innumerable modes of the free propagating waves are possible. Consequently both attenuation mechanisms, material and radiation damping, are present in the whole frequency range. However, in the low frequency range each of these modes is highly damped, such that the dissipative attenuation predominates the radiative one greatly and the energy attenuation due to wave radiation is extremely small [41]. At resonance a significant amplification of the flexibility amplitudes can be observed, which decrease again and converge to the solution for the homogeneous halfspace with increasing frequency. This is because for larger layer thicknesses resp. higher excitation frequencies,

implying a larger ratio of  $H/\lambda_p$ , the waves introduced at the source at the ground surface almost attenuate before reaching the layer boundary resp. the stiff inclusion and only scarcely affect the dynamic response of the system. In this case approximately the same amount of energy is dissipated and dispersed as in case of the homogeneous halfspace. Also for the stiff cylindrical inclusion considered before, an imaginary part of the compliance  $C_{zz}^{11}$  in Fig. 12 close to zero can be observed for excitation frequencies below the first vertical resonance frequency. This small values of the imaginary part, which are linked to both, material and geometrical damping, can, according to the above explanations, be associated with an only small dissipative energy attenuation due to material damping in the low frequency range. At resonance, large values of the imaginary part are observed connected to a large amount of dissipated energy, which then is dominated by the energy dispersion of the freely propagating waves occurring from then on. For excitation frequencies, which are large in comparison to the first layer resonance, associated with the respective soil layer thickness  $h_{\text{cyl}}$ , the compliances converge to the halfspace solution.

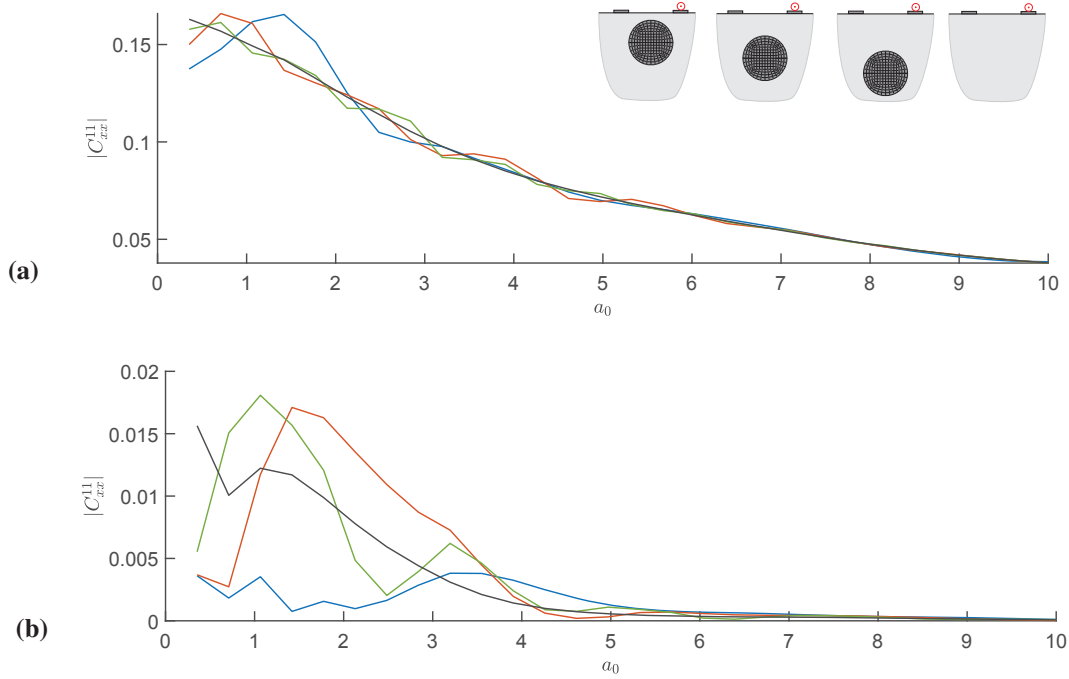


**Figure 12:** Real and imaginary part of vertical compliance functions  $C_{zz}^{11}(a_0)$  of a rigid, massless square foundation with  $B_f = 2$  m on a halfspace with cylindrical inclusion (Infill D) with  $R = 3$  m and varying embedment depth  $H = 4$  m (—),  $H = 6$  m (—),  $H = 8$  m (—),  $H = 12$  m (—) and on a homogeneous halfspace (—).

### Variation of embedment depth $H$ - two adjacent foundations

Now the compliance functions of two adjacent surface foundations with a width of  $B_f = 2$  m and a midpoint distance  $d_{f1f2} = 8$  m, again resting on a halfspace with a stiff cylindrical inclusion (Infill D) of radius  $R = 3$  m and varying embedment depth  $H$  are considered.

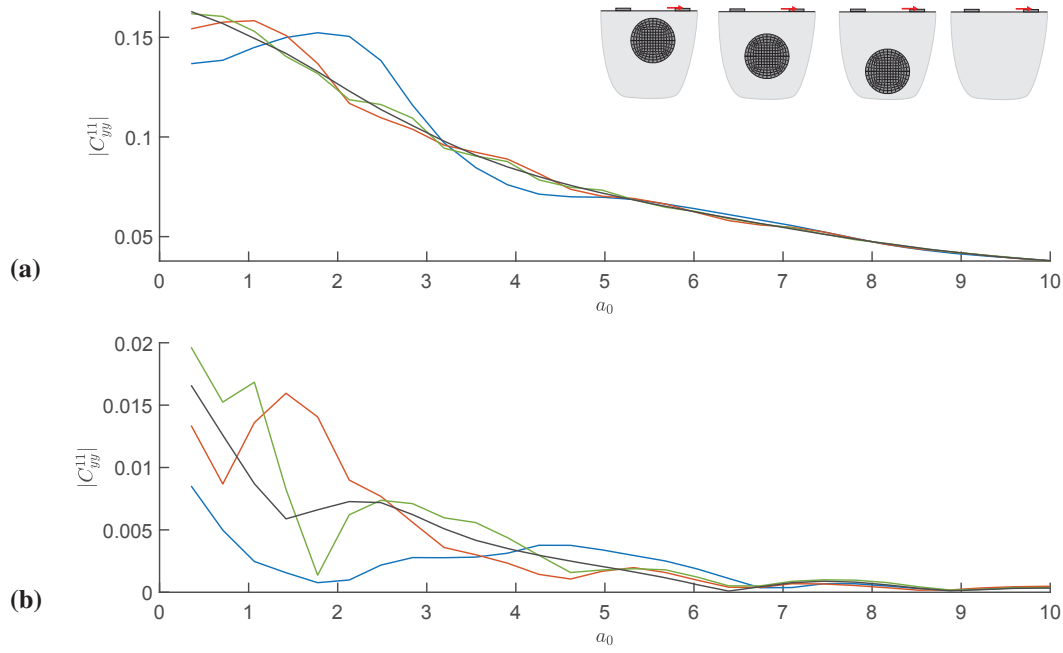
For the horizontal compliance  $|C_{xx}^{11}|$  of the loaded foundation in Fig. 13a, only relatively small deviations from those obtained for the homogeneous halfspace are visible in comparison to the case of the single foundation. This is because here the loaded foundation is located besides the stiff inclusion instead of directly over it. The largest deviations are observed for the smallest embedment depths and in the low frequency range. The then occurring amplification can be traced back to the effect of waves reflected at the inclusion. With increasing  $H$  and



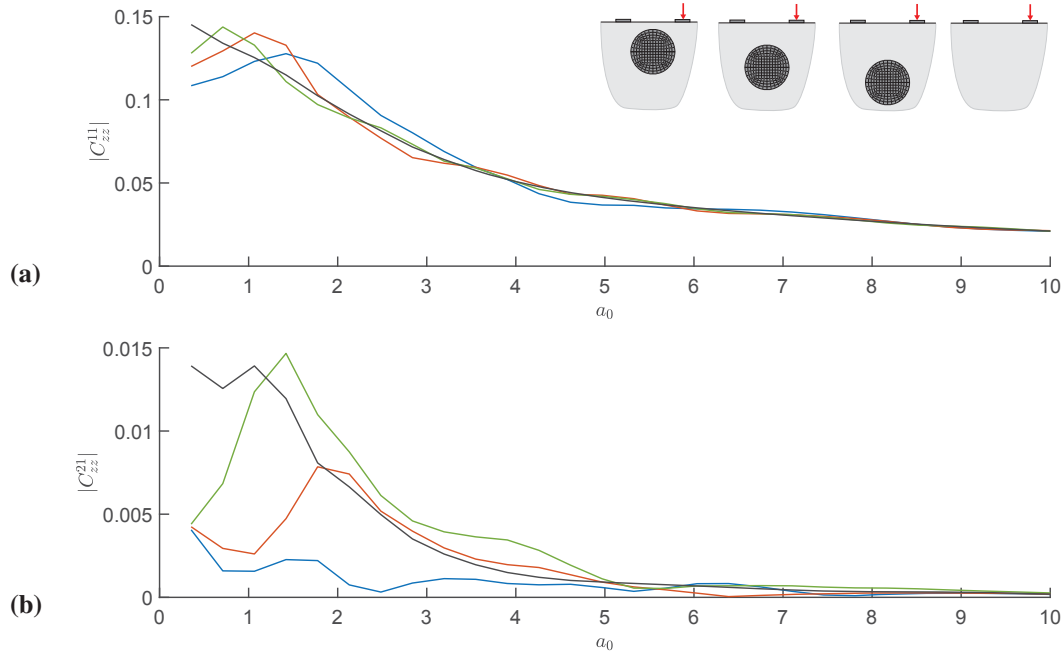
**Figure 13:** Absolute vertical compliance functions  $|C^{ij}_{xx}(a_0)|$  for (a) first (loaded) and (b) second of two adjacent rigid, massless square foundations with  $B_f = 2$  m and distance  $d_{f1f2} = 8$  m on halfspace with cylindrical inclusion (Infill D) with  $R = 3$  m for varying embedment depth  $H = 4$  m (—),  $H = 6$  m (—),  $H = 8$  m (—) and on a homogeneous halfspace (—).

increasing frequency  $|C^{11}_{xx}|$  converges to that for the homogeneous halfspace. The compliance of the passive foundation  $|C^{21}_{xx}|$  is very small for small  $H$ , as the main excitation takes place in the direction of the length invariant inclusion and a propagation of the elastic waves from the excited foundation  $F_1$  to the unloaded foundation  $F_2$  is disturbed by the cylindrical inclusion in the transmission path. Furthermore in the soil layer over the inclusion propagating waves can occur only above the first (here horizontal) layer resonance frequency, which can e.g. be observed by the increase of  $|C^{21}_{xx}|$  for  $H = 4$  at excitation frequencies  $a_0 > 3.14$ . With increasing  $H$  the amplitude of  $|C^{21}_{xx}|$  in the low frequency range increases due to a smaller shielding effect of the cylindrical inclusion. For intermediate values of  $H$ ,  $|C^{21}_{xx}|$  shows to be larger than in case of a homogeneous halfspace, probably due to reflected waves at the top of the inclusion, amplifying the response at  $F_2$ . In case of large  $H$  and with increasing frequencies, the compliance again converges to that obtained for the homogeneous halfspace, as with increasing ratio of the soil layer thickness to the elastic wave lengths the influence of the inclusion diminishes.

Comparing the results of for the compliances in  $x$ - and  $y$ -direction, it can be stated, that  $|C^{11}_{yy}|$  in Fig. 14 converges to the halfspace solution only at higher frequencies as  $|C^{11}_{xx}|$  and the deviations are larger, which is because the direction of excitation in this case directly points towards the inclusion located in the transmission path and thus a bigger portion of elastic waves is reflected as for the excitation in  $x$ -direction, especially as the foundation is located besides the inclusion. For very low frequencies the inclusion size is small compared to the wavelength, wherefore it has no big influence on the direct cross interaction of the adjacent foundations resulting in higher values of  $|C^{21}_{yy}|$ . Again a raise of amplitudes for  $a_0 > 3.14$  can be observed for  $|C^{21}_{yy}|$ .



**Figure 14:** Absolute vertical compliance functions  $|C_{yy}^{ij}(a_0)|$  for (a) first (loaded) and (b) second of two adjacent rigid, massless square foundations with  $B_f = 2$  m and distance  $d_{f1f2} = 8$  m on halfspace with cylindrical inclusion (Infill D) with  $R = 3$  m for varying embedment depth  $H = 4$  m (—),  $H = 6$  m (—),  $H = 8$  m (—) and on a homogeneous halfspace (—).



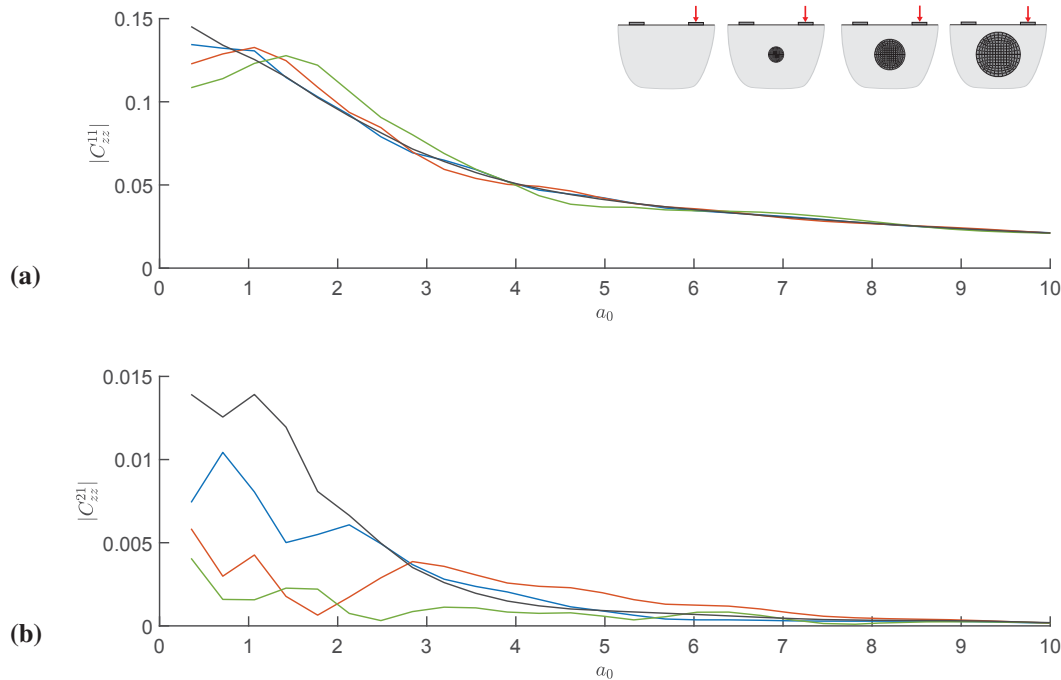
**Figure 15:** Absolute vertical compliance functions  $|C_{zz}^{ij}(a_0)|$  for (a) first (loaded) and (b) second of two adjacent rigid, massless square foundations with  $B_f = 2$  m and distance  $d_{f1f2} = 8$  m on halfspace with cylindrical inclusion (Infill D) with  $R = 3$  m for varying embedment depth  $H = 4$  m (—),  $H = 6$  m (—),  $H = 8$  m (—) and on a homogeneous halfspace (—).

Concerning the vertical compliances  $|C_{zz}^{11}|$  of the active foundation in Fig. 15 only small deviations occur as the foundation is located besides the inclusion and only a little part of the induced elastic waves interacts with it. In general small compliances  $|C_{zz}^{21}|$  are observed over the whole frequency range for small  $H$ . However, above the first vertical resonance frequency of the soil layer over the inclusion at  $a_0 = 5.87$  for  $H = 4$  a slight increase of  $|C_{zz}^{21}|$  can be observed. The overall trend of the compliances tending to those obtained for the homogeneous halfspace for increasing  $H$  and  $a_0$  is also found here.

Due to space limitation for all following cases only the vertical compliances are shown. However the computation of the compliances for any load direction and type is possible.

### Variation of the inclusion radius $R$

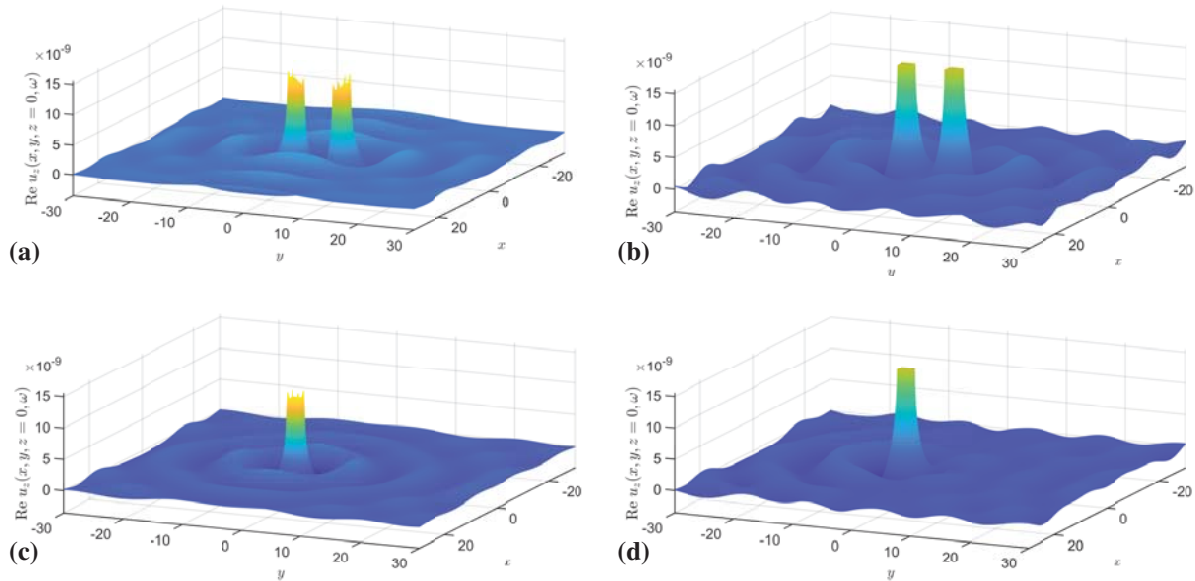
Hereinafter, the embedment depth  $H = 4$  m of the inclusion under two adjacent surface foundations with  $B_f = 2$  m and  $d_{f1f2} = 8$  m is fixed as well as the material properties and only its size  $R$  is varied. Fig. 16 shows, that the vertical compliances  $|C_{zz}^{11}|$  of the loaded foundation on the soil with the inclusion are very close to those for the homogeneous halfspace for small inclusion size  $R$ . Also for the largest considered radius  $R = 3$  m, only small deviations occur, as the foundation is located besides the inclusion and the share of waves travelling downwards or to the inclusion averted side (thus not affected by it) is quite large. The compliances  $|C_{zz}^{21}|$  of the passive foundation show low amplitudes for large  $R$  and converge, due to the effects already pointed out earlier, to those for the homogeneous halfspace with decreasing inclusion size.



**Figure 16:** Absolute vertical compliance functions  $|C_{zz}^{ij}(a_0)|$  for (a) first (loaded) and (b) second of two adjacent rigid, massless square foundations with  $B_f = 2$  m and distance  $d_{f1f2} = 8$  m on halfspace with cylindrical inclusion (Infill D) with embedment depth  $H = 4$  m for varying radius  $R = 1$  m (—),  $R = 2$  m (—),  $R = 3$  m (—) and on a homogeneous halfspace (—).



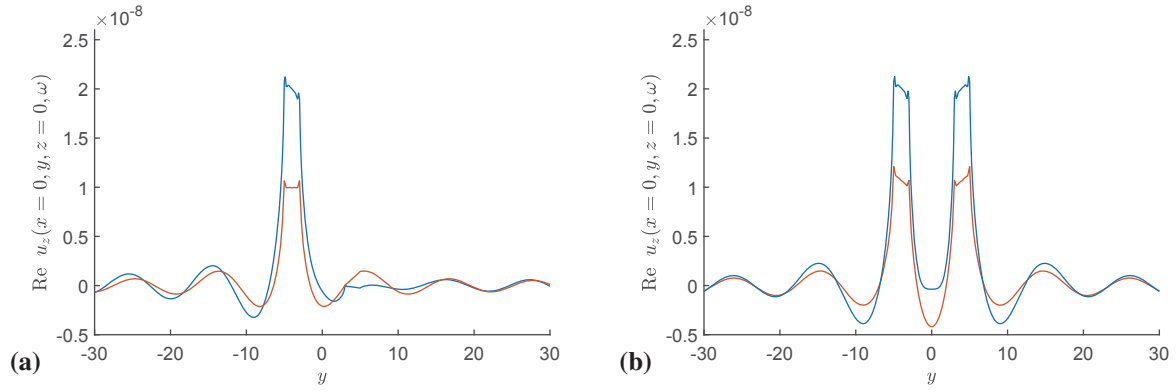
For the system configuration with the maximum inclusion size of  $R = 3$ , the displacements on the whole ground surface have been determined with the post processing procedure outlined in subsection 3.3 applying relaxed boundary conditions, i.e. frictionless contact at the soil foundation interfaces. The left column of Fig. 17 shows the results for the real part of the vertical displacements, obtained for a harmonic excitation with  $f = 6$  Hz of both resp. only one foundation, resting on a homogeneous halfspace. In Fig 17a, a wave propagation concentrated on the direction of the foundation alignment and perpendicular to it can be observed, whereas Fig 17c shows a nearly omnidirectional propagation of the surface waves. The second, unloaded foundation only hardly influences the displacement field on the ground surface, except the area directly under it, where a linear displacement course arises due to the rigidity of the foundation plate. In case of a massive foundation the inertia effects would lead to a much higher influence of the unloaded foundation on the system response. The right column of Fig. 17 shows the results for same foundation and load configuration, but on a halfspace with stiff inclusion. Fig. 17b shows a significant reduction of  $u_z(x, y, z = 0, \omega)$  in a limited area along the entire length of the stiff inclusion compared to the case of the homogeneous halfspace, in turn leading to an increase in amplitudes in the direction perpendicular to the inclusion on both sides. Furthermore, the behaviour of the stiff inclusion as wave barrier can clearly be observed in Fig. 17d, where a considerable reduction of  $u_z(x, y, z = 0, \omega)$  occurs on the load averted side of the inclusion. These effects gets even more obvious, when the displacements along the  $y$ -direction for  $x = 0$  are compared for both cases in Fig. 18.



**Figure 17:** Real part of vertical displacement  $u_z(x, y, z = 0, \omega)$  on whole ground surface due to harmonic loading ( $f = 6$  Hz) on (a),(b) both and (c),(d) only one of the adjacent rigid, massless foundations with  $B_f = 2$  m and  $d_{f1f2} = 8$  m resting on the surface of a (a),(c) homogeneous halfspace and (b),(d) halfspace with a stiff cylindrical inclusion (Infill D) with  $H = 4$  m and  $R = 3$  m, obtained with the post processing procedure.

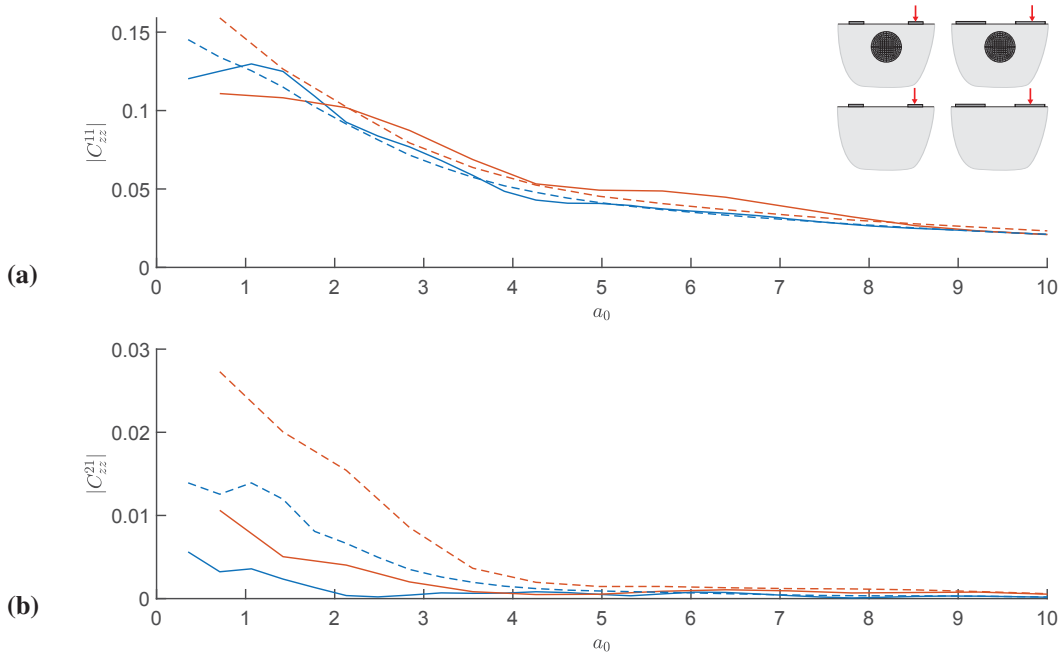
### Variation of foundation size $B_f$

Now the width of the foundations is varied, while keeping the midpoint distance  $d_{f1f2} = 8$  m as well as all other parameters constant. Only relatively minor deviations of  $|C_{zz}^{11}|$  from the homogeneous halfspace response for  $B_f = 2$  and 4 m are observed in Fig. 19. This is



**Figure 18:** Real part of vertical displacement  $u_z(x=0, y, z=0, \omega)$  along  $y$ -direction for  $x=0$  due to harmonic loading with  $f = 6$  Hz on (a) only one and (b) both of the adjacent rigid, massless foundations with  $B_f = 2$  m and  $d_{f1f2} = 8$  m resting on the surface of a homogeneous halfspace (—) and a halfspace with a stiff cylindrical inclusion (Infill D) (—) with  $H = 4$  m and  $R = 3$  m, obtained with the post processing procedure.

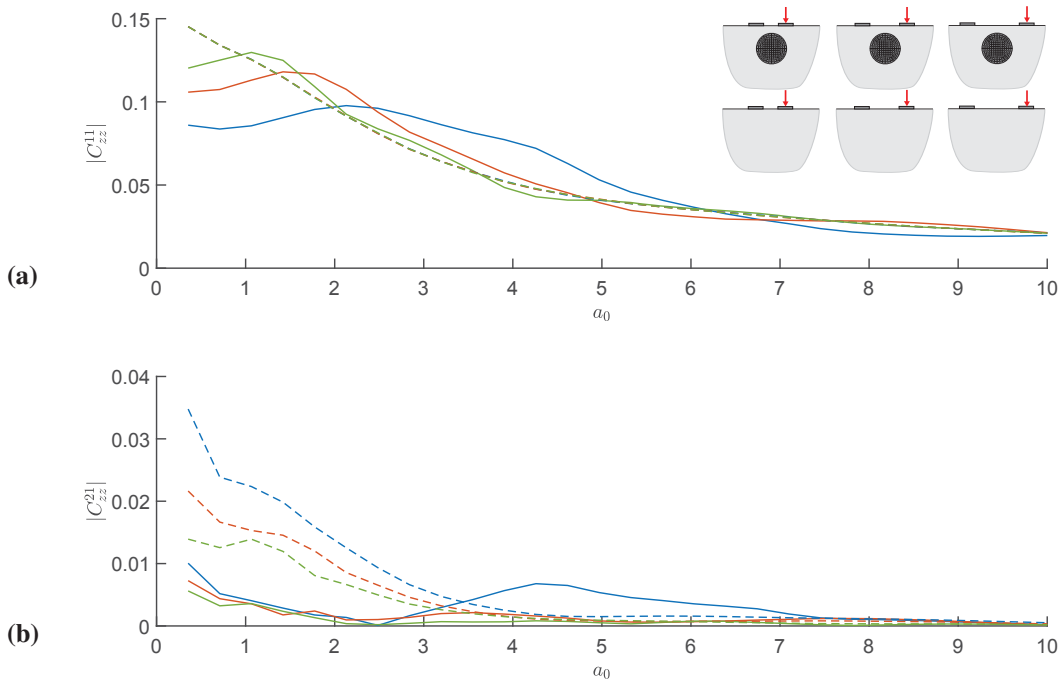
presumably because the center of the foundation is located besides the stiff inclusion. Especially in the high frequency range a comparably small influence of the inclusion turns out, whereas for low excitation frequencies some smaller oscillations of  $|C_{zz}^{11}|$  due to interaction effects with the inclusion are visible. Furthermore a considerably decreased compliance  $|C_{zz}^{21}|$  due to presence of the stiff inclusion, acting as wave barrier, is observed. In general larger  $|C_{zz}^{21}|$  occur in case of  $B_f = 4$ , as then distance of foundation edges is smaller and the mutual interaction effects are therefore stronger.



**Figure 19:** Absolute vertical compliance functions  $|C_{zz}^{ij}(a_0)|$  for (a) first (loaded) and (b) second of two adjacent rigid, massless square foundations with  $B_f = 2$  m (—),  $B_f = 4$  m (—) and distance  $d_{f1f2} = 8$  m on halfspace with cylindrical inclusion (Infill D) with embedment depth  $H = 3$  m and radius  $R = 2$  m (solid lines) and on a homogeneous halfspace (dashed lines).

### Variation of foundation distance $d_{f1f2}$

The variation of the midpoint distance  $d_{f1f2}$  in Fig. 20 for a constant foundation width as well as inclusion size, location and material shows, that the cross interaction between the foundations decreases with increasing distance regardless the underlying soil. For a homogeneous halfspace,  $|C_{zz}^{11}|$  of the loaded foundation is equal for all  $d_{f1f2}$ , whereas the influence of the inclusion is clearly visible for small distances of the foundations and decreases with increasing  $d_{f1f2}$ , thereby converging to the halfspace solution. In general larger  $|C_{zz}^{21}|$  are observed for the homogeneous halfspace, which also decrease with increasing  $d_{f1f2}$  and  $a_0$ . Due to the rather large inclusion located closely to the halfspace surface, only very low compliance values  $|C_{zz}^{21}|$  show up for larger foundations distances. For the likewise nearby foundations with  $d_{f1f2} = 4$  m, an increase of the compliance amplitude above the first horizontal resonance frequency of the soil layer at  $a_0 = 3.14$  can be observed and attributed to the then possible propagation of surface waves, passing through the soil over the inclusion and impinging at the second foundation.



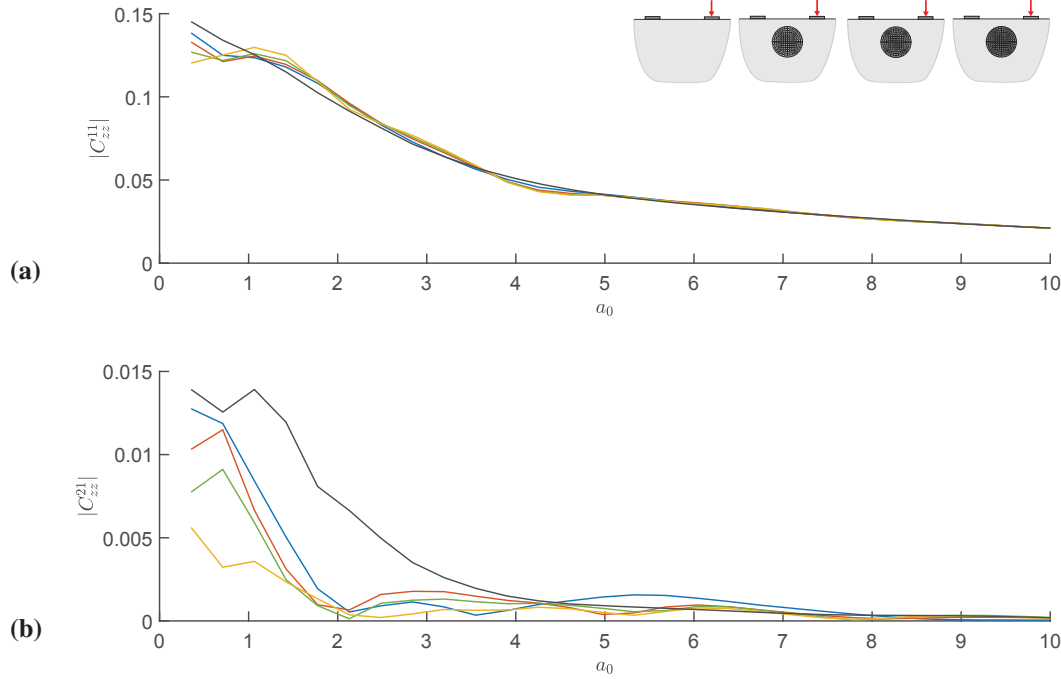
**Figure 20:** Absolute vertical compliance functions  $|C_{zz}^{ij}(a_0)|$  for (a) first (loaded) and (b) second of two adjacent rigid, massless square foundations with  $B_f = 2$  m on halfspace with cylindrical inclusion (Infill D) with embedment depth  $H = 3$  m and radius  $R = 2$  m (solid lines) and on a homogeneous halfspace (dashed lines) for varying distance  $d_{f1f2} = 4$  m (—),  $d_{f1f2} = 6$  m (—) and  $d_{f1f2} = 8$  m (—).

### Variation of inclusion stiffness $E_{cyl}$

Finally, the effect of a varying stiffness of the inclusion is investigated. Therefore the Young's modulus  $E_{cyl}$  is adapted such that the ratio of the shear wave velocity of the infill material and the soil  $c_{s,cyl}/c_s$  takes values between 2 and 8, additionally to the very stiff inclusion with  $c_{s,cyl}/c_s = 37.6$  investigated in the previous cases.

The vertical compliance of the active foundation  $|C_{zz}^{11}|$  in Fig. 21a generally differs only slightly from the results for the homogeneous halfspace. However, an increase of the smooth peak in the low frequency range and an ascending waviness of the course of the compliance is observed for raising stiffness of the inclusion. The compliance of the passive foundation  $|C_{zz}^{21}|$

in Fig. 21b drastically reduces with increasing stiffness  $E_{\text{cyl}}$ . The oscillations in  $|C_{zz}^{21}|$  imply, that, in dependency of the frequency and with that the corresponding wavelengths, the elastic waves interact differently with the inclusion and the wave field resulting from the direct and reflected waves at the inclusion shows amplification and attenuation effects compared to the nearly monolithically decaying of the compliance  $|C_{zz}^{21}|$  in case of the homogeneous halfspace.



**Figure 21:** Absolute vertical compliance functions  $|C_{zz}^{ij}(a_0)|$  for (a) first (loaded) and (b) second of two adjacent rigid, massless square foundations with  $B_f = 2$  m and distance  $d_{f1f2} = 8$  m on halfspace with cylindrical inclusion with embedment depth  $H = 3$  m and radius  $R = 2$  m for varying stiffness of inclusion: Infill A  $c_{s,\text{cyl}} = 141.4 \text{ ms}^{-1}$  (—), Infill B  $c_{s,\text{cyl}} = 282.8 \text{ ms}^{-1}$  (—), Infill C  $c_{s,\text{cyl}} = 565.68 \text{ ms}^{-1}$  (—), Infill D  $c_{s,\text{cyl}} = 2661.45 \text{ ms}^{-1}$  (—) and on a homogeneous halfspace (—).

## 5 CONCLUSIONS

In this paper an efficient approach for the investigation of the dynamic interaction of finite, three dimensional foundations located on the surface of a soil with a buried local, length invariant structure or inhomogeneity is presented. A 2.5D ITM-FEM approach was used for the determination of the complex, dynamic stiffness matrix of the soil substructure, which is coupled to the dynamic stiffness of the foundations (modelled with conventional 3D finite elements), at the common interaction surfaces via the compatibility conditions. Frequency dependent, dimensionless compliance functions of rigid, massless surface foundations resting on a homogeneous halfspace, modelled with the presented approach by choosing the same material properties for the inclusion as for the surrounding soil, were computed and compared to literature results, showing very good agreement and thereby validating the proposed methodology.

The approach was applied to compute the dynamic response of a single or two adjacent surface foundations, taking into account the through soil coupling as well as the interaction with the inclusion inside the soil, for different system configurations. The influence of both, the embedment depth, size and stiffness of the inclusion and the width and distance of the foundations on the compliance functions at the soil foundation interface was investigated.

In general the impact of the inclusion on the response is larger, if it is located closely to the foundations and features a rather large size in comparison to the elastic wavelengths at the corresponding frequency. With increasing distance of the foundations, as well as for raising embedment depths, decreasing inclusion sizes or a reduced stiffness the compliance functions converge to the results for the case, where the foundations are resting on a homogeneous half-space. For the response at the unloaded foundation the resonance frequency of the soil layer over the inclusion showed to play a decisive role, as below this cut-off frequency a propagation of free waves through this soil layer in the transmission path between the two foundations is not possible. This effect, in combination with the behaviour of the inclusion as a wave barrier, leads to a very small reception at the passive foundation, if the excitation frequency is below this first critical frequency.

Furthermore, the displacement field resulting from the interaction of two adjacent surface foundations with a soil including a stiff cylindrical confinement, due to a dynamic excitation of either one or both, was presented. Thereby a significant reduction in displacement amplitudes at the surface was observed in a limited area along the entire length of the stiff inclusion compared to the case of a homogeneous soil, which in turn led to an increase in amplitudes in the direction perpendicular to the inclusion on both sides, in case both foundations are loaded. For a load only on one foundation, the stiff inclusion shows to act as a wave barrier, leading to significantly reduced displacement amplitudes on the opposite site of the confinement.

## REFERENCES

- [1] H. L. Wong, J. E. Luco, Dynamic response of rigid foundations of arbitrary shape, *Earthquake Engineering & Structural Dynamics* 4 (1976) 579–587.
- [2] J. Dominguez, J. M. Roesset, Dynamic stiffness of rectangular foundations, *Nasa Sti/recon Technical Report N 79* (1978).
- [3] S. A. Savidis, T. Richter, Dynamic response of elastic plates on the surface of the half-space, *International Journal for Numerical and Analytical Methods in Geomechanics* 3 (1979) 245–254.
- [4] M. Iguchi, J. E. Luco, Dynamic response of flexible rectangular foundations on an elastic half-space, *Earthquake Engineering & Structural Dynamics* 9 (1981) 239–249.
- [5] H. R. Hamidzadeh-Eraghi, P. Grootenhuis, The dynamics of a rigid foundation on the surface of an elastic half-space, *Earthquake Engineering & Structural Dynamics* 9 (1981) 501–515.
- [6] W. L. Whittaker, P. Christiano, Dynamic response of plate on elastic half-space, *Journal of the Engineering Mechanics Division* 108 (1982) 133–154.
- [7] H. Antes, O. von Estorff, Dynamic response analysis of rigid foundations and of elastic structures by boundary element procedures, *Soil Dynamics and Earthquake Engineering* 8 (1989) 68–74.
- [8] O. von Estorff, E. Kausel, Coupling of boundary and finite elements for soil-structure interaction problems, *Earthquake Engineering & Structural Dynamics* 18 (1989) 1065–1075.
- [9] G. B. Warburton, J. D. Richardson, J. J. Webster, Forced vibrations of two masses on an elastic half space, *Journal of Applied Mechanics* 38 (1971) 148–156.
- [10] T. Kobori, R. Minai, K. Kusakabe, Dynamical characteristics of soil-structure cross-interaction system, *i* (1973).
- [11] H. L. Wong, J. E. Luco, Dynamic interaction between rigid foundations in a layered half-space, *Soil Dynamics and Earthquake Engineering* 5 (1986) 149–158.
- [12] E. Kausel, J. M. Roesset, G. Waas, Dynamic analysis of footings on layered media, *Journal of Engineering Mechanics* 101 (1975).

- [13] H.-T. Lin, J. M. Roesset, J. L. Tassoulas, Dynamic interaction between adjacent foundations, *Earthquake Engineering & Structural Dynamics* 15 (1987) 323–343.
- [14] T. Triantafyllidis, B. Prange, Dynamic subsoil-coupling between rigid rectangular foundations, *Soil Dynamics and Earthquake Engineering* 6 (1987) 164–179.
- [15] D. L. Karabalis, D. E. Beskos, Dynamic response of 3-d rigid surface foundations by time domain boundary element method, *Earthquake Engineering & Structural Dynamics* 12 (1984) 73–93.
- [16] J. Qian, D. E. Beskos, Harmonic wave response of two 3-d rigid surface foundations, *Soil Dynamics and Earthquake Engineering* 15 (1996) 95–110.
- [17] J. Qian, L. G. Tham, Y. K. Cheung, Dynamic analysis of rigid surface footings by boundary element method, *Journal of Sound and Vibration* 214 (1998) 747–759.
- [18] Y. Wang, R. K. N. D. Rajapakse, A. H. Shah, Dynamic interaction between flexible strip foundations, *Earthquake Engineering & Structural Dynamics* 20 (1991) 441–454.
- [19] D. C. Rizos, Z. Wang, Coupled bem–fem solutions for direct time domain soil–structure interaction analysis, *Engineering Analysis with Boundary Elements* 26 (2002) 877–888.
- [20] X. Chen, C. Birk, C. Song, Transient analysis of wave propagation in layered soil by using the scaled boundary finite element method, *Computers and Geotechnics* 63 (2015) 1–12.
- [21] B. Sbartaï, Dynamic interaction of two adjacent foundations embedded in a viscoelastic soil, *International Journal of Structural Stability and Dynamics* 16 (2016) 1450110.
- [22] Z. Han, G. Lin, J. Li, Dynamic 3d foundation–soil–foundation interaction on stratified soil, *International Journal of Structural Stability and Dynamics* 17 (2017) 1750032.
- [23] M. Radisic, Itm-based dynamic analysis of foundations resting on a layered halfspace, Ph.D. thesis, Universität Belgrad, Belgrad, 2018.
- [24] N. Chouw, R. Le, G. Schmid, Propagation of vibration in a soil layer over bedrock, *Engineering Analysis with Boundary Elements* 8 (1991) 125–131.
- [25] N. Chouw, G. Schmid, Building isolation using the transmitting behaviour of a soil layer, in: *Proceedings of the 10th world conference on signal engineering*, Madrid (Spain), volume 4, pp. 2519–2524.
- [26] H. Takemiya, A. Fujiwara, Wave propagation/impediment in a stratum and wave impeding block (wib) measured for ssi response reduction, *Soil Dynamics and Earthquake Engineering* 13 (1994) 49–61.
- [27] H. Antes, O. von Estorff, Dynamic response of 2d and 3d block foundations on a halfspace with inclusions, *Soil Dynamics and Earthquake Engineering* 13 (1994) 305–311.
- [28] A. T. Peplow, S. Finnveden, Calculation of vibration transmission over bedrock using a waveguide finite element model, *International Journal for Numerical and Analytical Methods in Geomechanics* 32 (2008) 701–719.
- [29] G. Gao, J. Chen, X. Gu, J. Song, S. Li, N. Li, Numerical study on the active vibration isolation by wave impeding block in saturated soils under vertical loading, *Soil Dynamics and Earthquake Engineering* 93 (2017) 99–112.
- [30] C. F. Long, On the completeness of the lamè potentials, *Acta Mechanica* 3 (1967) 371–375.
- [31] G. Müller, Ein Verfahren zur Erfassung der Fundament-Boden Wechselwirkung unter Einwirkung periodischer Lasten, Dissertation, Technische Universität München, München, 1989.
- [32] A. Sommerfeld, Partial differential equations in physics, volume 1 of *Pure and applied mathematics*, Acad. Pr, New York, 1964.
- [33] J. Freisinger, M. Hackenberg, G. Müller, A coupled integral transform method - finite element



- method approach to model the soil structure interaction of finite (3d) and length invariant (2.5d) systems, *Journal of Sound and Vibration* 482 (2020) 115443.
- [34] M. Hackenberg, M. Dengler, G. Müller, Implementation of the finite element method in the fourier-transformed domain and coupling with analytical solutions, in: Cunha A., Caetano E., Ribeiro P., Müller G (Ed.), *Eurodyn.*
- [35] G. Frühe, Überlagerung von Grundlösungen in der Elastodynamik zur Behandlung der dynamischen Tunnel-Boden-Bauwerk-Interaktion, Dissertation, Technische Universität München, München, 2010.
- [36] M. Hackenberg, A Coupled Integral Transform Method - Finite Element Method Approach to Model the Soil-Structure-Interaction, Dissertation, Technische Universität München, München, 2016.
- [37] F. Rojas, J. C. Anderson, L. M. Massone, A nonlinear quadrilateral layered membrane element with drilling degrees of freedom for the modeling of reinforced concrete walls, *Engineering Structures* 124 (2016) 521–538.
- [38] R. Hirschauer, Kopplung von finiten Elementen mit Rand-Elementen zur Berechnung der dynamischen Baugrund-Bauwerk-Interaktion: Zugl.: Berlin, Techn. Univ., Diss., 2001, volume 31 of *Veröffentlichungen des Grundbauinstitutes der Technischen Universität Berlin*, Univ.-Bibliothek der Techn. Univ. Abt. Publ. Sekr. FRA-B, Berlin, 2001.
- [39] R. Shahi, A. Noorzad, Dynamic response of rigid foundations of arbitrary shape using half-space green's function, *International Journal of Geomechanics* 11 (2011) 391–398.
- [40] D. L. Karabalis, M. Mohammadi, 3-d dynamic foundation-soil-foundation interaction on layered soil, *Soil Dynamics and Earthquake Engineering* 17 (1998) 139–152.
- [41] T. Kobori, R. Minai, T. Suzuki, The dynamical ground compliance of a rectangular foundation on a viscoelastic stratum (1971).

## NUMERICAL ANALYSIS ON SHALLOW FOUNDATIONS LATERAL DISCONNECTION

Fausto Somma<sup>1</sup>, Alessandro Flora<sup>1</sup>, Emilio Bilotta<sup>1</sup> and Giulia Viggiani<sup>2</sup>

<sup>1</sup> University of Naples Federico II

Via Claudio 26, NA

fausto.somma@unina.it, flora@unina.it, bilotta@unina.it

<sup>2</sup> University of Cambridge

Trumpington Street, Cambridge CB2 1PZ, UK

gv278@cam.ac.uk

---

### Abstract

*The paper presents a numerical study aiming at establish the effects of removing the lateral ground connection between embedded shallow foundations and surrounding soil on dynamic soil-structure interaction. Series of two-dimensional finite element models were developed comparing the behaviour of two identical structures with just one difference: the embedment of their own foundations. In order to find the parameters that most influenced the effect of the lateral disconnection technique, the properties of the two structures (predominant period, aspect ratio, loading bearing, foundation embedment) as well as the ones of the soil were parametrically varied. From the results gathered in here, it was established the effectiveness of the proposed system to reduce the inter-story drifts demand on the structures and increase their predominant periods specially in case of high value of foundation embedment in a medium dense soil.*

**Keywords:** Soil-structure interaction, Seismic actions mitigation, Period Elongation, Geotechnical Seismic Isolation.

---

## 1 INTRODUCTION

The geotechnical seismic isolation techniques transpose the effects of traditional isolation techniques, such as rubber or sliding bearing isolator, into the ground [1]. Several geotechnical seismic isolation strategies have been outlined over time. It has been shown experimentally and numerically that the creation of a surface with a low friction angle, immediately below the foundations, is able to dissipate the energy of earthquakes [2]. Similarly, the creation of an isolated volume of soil, through the use of vertical and horizontal soft barriers, is able to significantly reduce the accelerations in the volume itself [3]. Furthermore, the effectiveness of sand-rubber mixtures, in mitigating seismic accelerations, was demonstrated through numerical models and fields test [4]. All the procedures outlined have, as a common strategy, to increase the natural period or damping of the soil-structure system. An inexpensive and intuitive way to achieve this is to laterally disconnect the shallow foundations of a structure from the adjacent lateral soil as both the rotational and translational stiffness of soil-structure foundation decrease and, consequently, the equivalent natural period, computing the soil structure interaction, will increase [5]. The elongation of the natural period has as a direct consequence a different demand in terms of accelerations and displacement on the structure.

This article refers on a parametric analysis where the period elongation of the structure with the lateral disconnection is compared with the same structure laying on fully embedded foundation in the ground. Different parameters in the structure, such as the aspect ratio, the fixed base period, the embedded of the foundation, have been changed as well as the stiffness properties of the soil. Finally, a series of multiple real earthquakes have been applied to a single scenario with a specific seismic hazard to numerically highlight the potentiality of such G.S.I technique.

## 2 NUMERICAL ANALYSIS

### 2.1 Numerical model

The numerical analysis were carried out by the use of the software Plaxis 2D. The finite element model is presented in Figure 1.

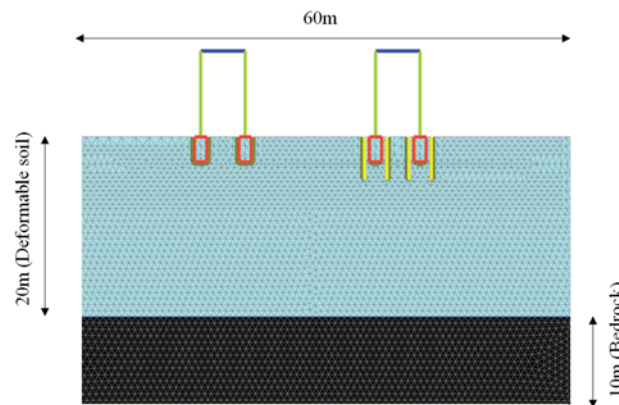


Figure 1. Numerical model with the indication of width and depth of the soil domain and the mesh adopted.

The model has a width dimension of 60m and a total depth of 30meters. The width of the deformable soil is fixed at 20meters while 10 meters of bedrock are included in the model to ensure no significative interference between the bottom base and the soil layer. The ground water is absent. Standard boundary conditions were applied during the initial (static) stage, that

is zero horizontal displacements along the lateral boundaries and fixed nodes at the base of the grid. During the dynamic analysis, the seismic inputs were applied to the bottom nodes of the mesh. In order to take into account the finite stiffness of the underlying bedrock, and to reproduce the upward propagation of shear waves within a semi-infinite domain, the outcrop input accelerations were halved to compute the corresponding upward-propagating wave motion and applied to the bottom nodes together with adsorbing viscous dashpots. Free-field boundary conditions were applied along the lateral sides of the mesh. The element size of the soil has been taken always smaller than one-tenth of the wavelength associated with the highest frequency component of the input wave containing appreciable energy [6]. For this reason, the discretization was carried out using 7872 tetrahedral elements with 15 nodes each. Both the structures, with and without the lateral disconnection, have been studied in the same numerical model. The relative distance between the two structures (13meter) and between the structures and lateral boundaries of the models (16meters) ensures no significant interaction [7].

## 2.2 Static Force and Input Motion Applied

In order to evaluate the elongation of the natural period generated by the lateral disconnection, the Fourier Trasform of crossbeam free oscillation displacement was calculated for both structures. In particular an horizontal static force is applied on the structure crossbeam to impose an initial condition of motion and then the free oscillation was studied in a dynamic phase deactivating the force itself. The procedure was repeated for all the studied scenario.

Consequently, in order to evaluate the effectiveness of the lateral disconnection in terms of acceleration and Arias intensity reduction, a series of multiple earthquakes were selected and applied at the bedrock. The accelerograms were chosen and scaled by using the software Rexel [8] considering the Elastic Design Spectrum of L'Aquila centre (Italy) with a return period of 475 years, corresponding to the life safety limit states as defined by the Italian Code [9]. Since the earthquakes were selected on soil class A (rock) no deconvolution of the earthquakes is needed. Due to the fact that L'Aquila is one of the most affected Italian cities by the seismic events, the frequency content and intensity of L'Aquila hazard was considered a good reference to highlight the applicability of the proposed technique specially in a contest where the seismic hazard is particularly high. All the informations about the selected earthquakes are reported in Table 1 while Figure 1 shows the spectra compatibility of L'Aquila design spectrum with the selected scaled earthquakes.

Record (-)	Location (-)	Year (-)	M (-)	NERHP Site (-)	JB dist (km)	PGA (g)	Arias Intensity (m/s)
1	Campano Lucano	1980	6.9	A	25	0.06	0.06
2	Bingol	2003	6.3	A	14	0.51	1.99
3	South Iceland	2000	6.5	A	13	0.13	0.16
4	Mt. Vatnafjoll	1987	6.0	A	24	0.03	0.006
5	Golbasi	1986	6.0	A	29	0.03	0.01
6	Friuli	1976	6.5	A	23	0.35	0.79
7	South Iceland (after shock)	2000	6.4	A	15	0.12	0.21

Table 1. Main characteristics of the selected accelerograms, before scaled at the Aquila's PGA, for the earthquake analysis

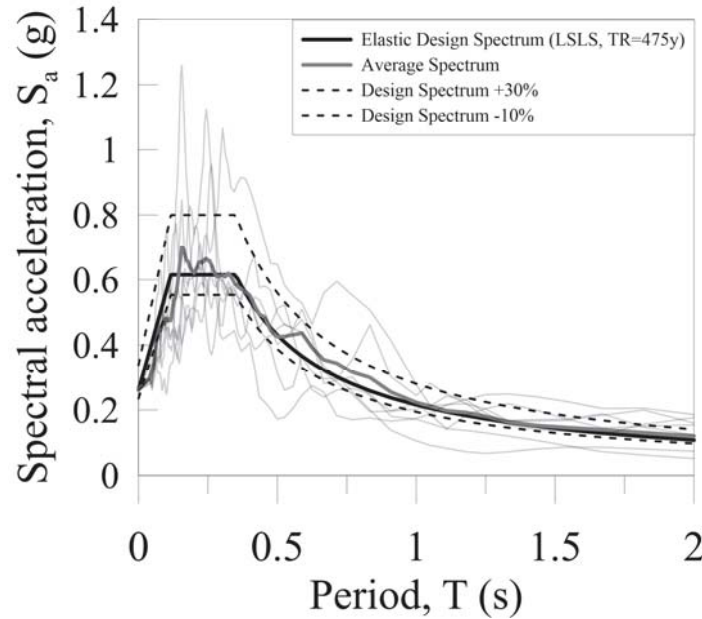


Figure 2. Spectro compatibility of the selected earthquakes with elastic design spectrum of Aquila centre at life safety limit state.

### 2.3 Structural models

The structural model is a linear elastic one bay one frame laying on shallow strip foundations. The foundations of the structures were modelled through the use of a non-porous linear elastic element volume with reinforced concrete properties ( $E=30000\text{Mpa}$ ,  $\nu=0.2$ ,  $\gamma=25\text{kN/m}^3$ ) while beam structural element were used to model the columns and crossbeams. The crossbeam length is equal to 5.00 meters while the distance between the strip shallow foundations ( $W$ ) is equal to 6.36 meters. The SDOF model would represent the main dynamic and static properties of masonry structures. In particular, in order to study the effect of the lateral disconnection on a structure with a different predominant period of vibration, the fixed base period of such structures was set at 0.3, 0.5, 0.8 and 1 sec, calibrating the stiffness of the columns beam and the mass of the crossbeam. Taking advantage of the Eurocode 8[10] formulation:

$$T_{\text{fixed\_base}} = C_t H^{0.75} \quad (1)$$

where  $T_{\text{fixed\_base}}$  is the fundamental period in seconds,  $H$  is the height of the building and  $C_t = 0.05$  is a constant depending on the type of earthquake resistant structural system, it is possible to estimate the total height of the prototype structure and, assuming an interfloors height equal to 3meter, estimate the specific number of floors associated at the fixed base period. Considering an unit load of 10kPa per floor it is possible to calculate the total mass to assign at the crossbeam and thus the stiffness of the column beam to ensure, respectively, the desired average bearing pressure on the soil and fixed base period.

In order to study the impact of the aspect ratio on the lateral disconnection technique, three different heights of the structures ( $H$ ), equal to 4.5, 5.8, 9.8 meters, has been considered. These heights correspond to the structure aspect ratio equal to 0.8-1-1.5.

The width of the strip footing shallow foundation ( $B$ ) was fixed at 1.4 meter while the embedment of the foundation ( $D$ ) was varied from 1.4 to 3.5 meters ( $D/B=1-2.5$ ).

In order to model correctly the contact between the foundation and the soil, interfaces along the foundation has been used assuming a reduction coefficient of 0.7 for the stiffness and strength properties at the interface. The stability of the small trenches, able to generate the lateral disconnection from the soil, is guaranteed by 4 cantilever walls. The viscous damping ratio of the structure is equal to 5% and was assigned to the columns beam with the double frequency approach. Table 2 summarize all the structural variable parameters considered to carry out the parametrical analysis and the fixed ones in the earthquake's analysis.

Type of analysis	Fixed Base period $T_{\text{fixed\_base}}$ (s)	Aspect Ratio $H/W$ (-)	Foundations Aspect Ratio $D/B$ (-)
Parametrical Analysis	0.3-0.5-0.8-1	0.8-1-1.5	1-1.5-2-2.5
Earthquakes Analysis	0.5	1.5	1.5

Table 2. Selected variable and fixed parameters for, respectively, the parametrical and earthquake analysis

## 2.4 Soil Material models

In order to evaluate the elongation of the natural period, the deformable soil was modelled as a homogeneous linear visco-elastic layer with different stiffness and damping properties (Table 3). The different stiffnesses of the soil analysed would represent a large spectrum of possible compliant base conditions for the structure. The bedrock has been modelled as visco-elastic half space with a damping ratio of 0.5%.

Soil type considered	Shear modulus $G$ (MN/m <sup>2</sup> )	Shear waves velocity $V_s$ (m/s)	Viscous Damping ratio (%)
Soil 1	200	350	1.42
Soil 2	141	300	1.60
Soil 3	94	250	2.00
Soil 4	58	200	2.5

Table 3. Different properties of the soil considered to carry out the parametrical analysis.

In order to evaluate the effectiveness of the lateral disconnection in the real earthquake's scenario, an equivalent visco-elastic model was used for the soil. In this case, the properties of Hostun Sand [11], at a relative density of 60%, was used (Table 4).



Maximum void ratio $e_{\max}$ (-)	Minimum void ratio $e_{\max}$ (-)	Specific gravity $G_s$ (-)	Relative Density RD (%)
1.01	0.555	2.65	60

Table 4. Properties of the Hostun Sand considered in the earthquake analysis.

To evaluate the increase of the shear modulus with depth the equation 1, by Hardin and Drenovich [12], was used with the specific parameter for Hostun Sand found by Hoque and Totquoka [13], (Table 5).

$$G_0 = A \cdot f(e) \cdot OCR^k \left( \frac{p'}{p_{ref}} \right)^m \quad (2)$$

Soil (-)	$A$ (-)	$f(e)$ (-)	$k$ (-)	$m$ (-)
Hostun Sand	80	$\frac{(2.17 - e)^2}{1 + e}$	0	0.47

Table 5. Specific parameters of Hostun Sand find by Hoque and Totquoka.

The different shear stiffness of the soil was assigned in the model considering different horizontal layers. In particular, 8 layers of 1 meter have been used for the first 8 meters while 6 layers of 2 meters have been used for the remaining 12 meters (Figure 3a). The mean curves of Seed and Idriss [14] has been selected to model the shear modulus reduction and the increase of damping with the shear strain (Figure 3b).

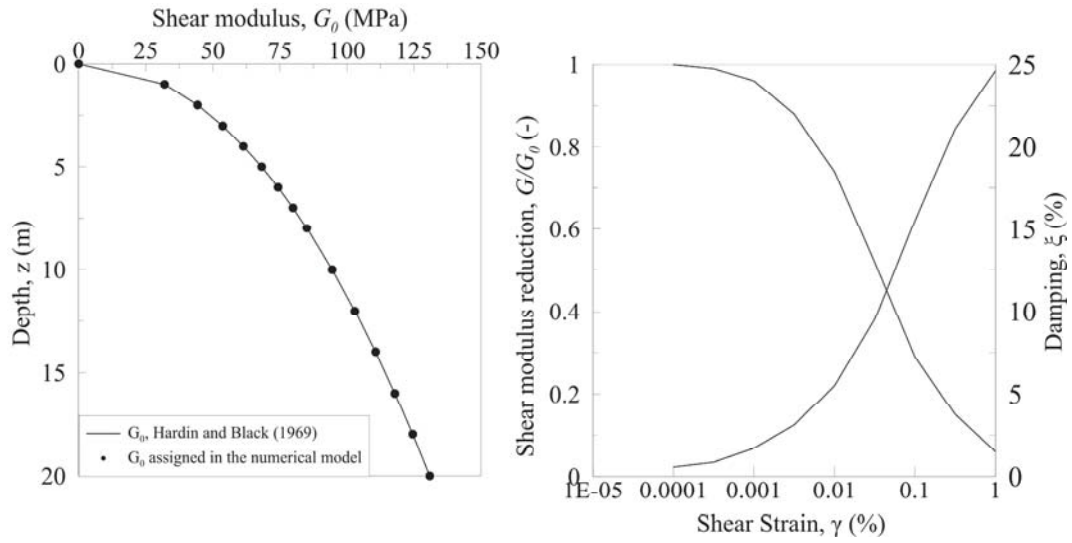


Figure 3. Properties of the sand used for earthquakes analysis: (a) Shear Modulus Profile with depth; (b) Shear modulus reduction and damping increase with shear strain by Seed and Idriss mean curves.

### 3 RESULT AND DISCUSSION

#### 3.1 Parametrical Analysis

Figure 4 summarize all the parametrical analysis carried out combining the different variable parameters.

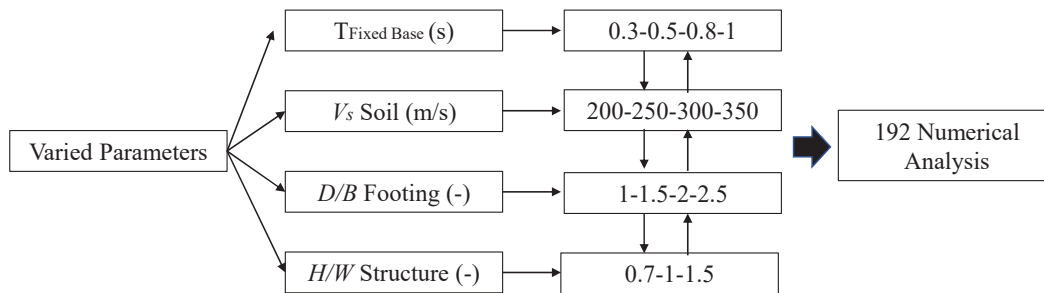


Figure 4. Schematic representation of the parametrical analysis carried out.

From the 192 numerical analysis it was possible to understand the parameters that most influence the period elongation between the two structures. Figure 5 shows the period elongation ( $T_{Var} = (T_{disc} - T_{conn})/T_{conn}$ ) as function of the stiffness of the soil for different value of  $D/B$  with the aspect ratio ( $H/W$ ) equal to 0.7.

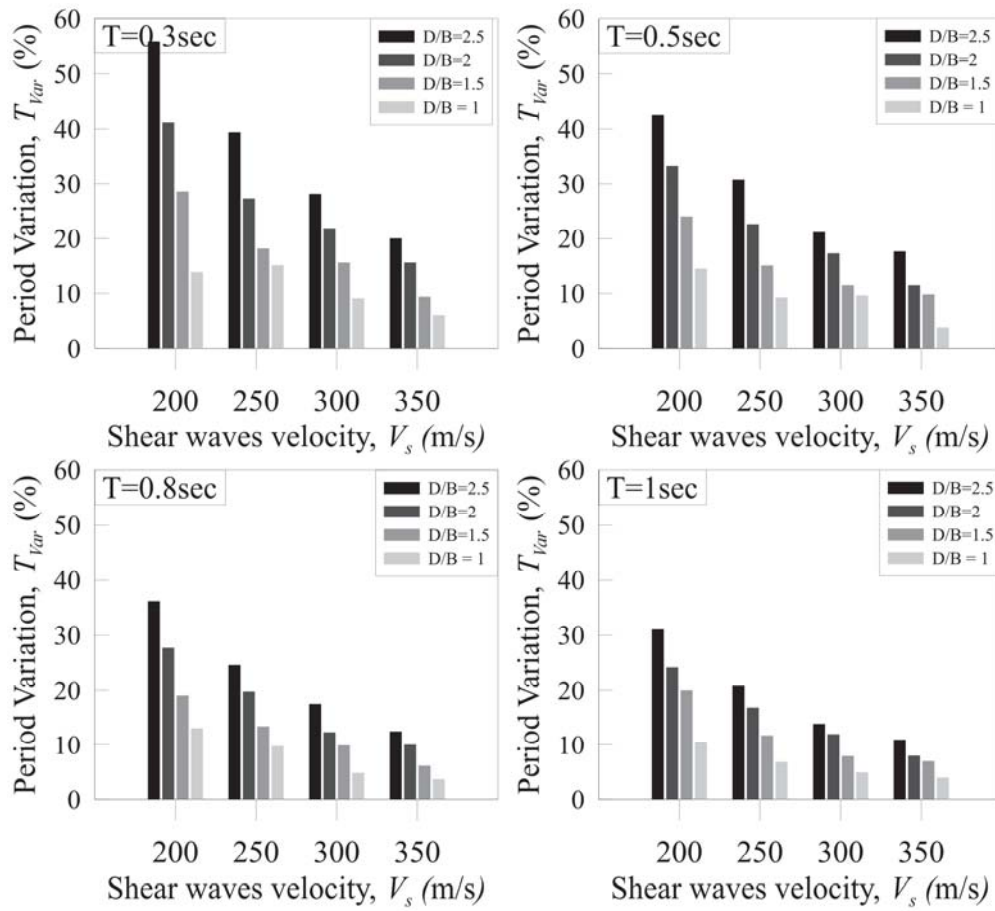


Figure 5. Period variation between the structures with and without lateral disconnection as function of the shear waves velocity and foundation aspect ratio.

It is clear that the period elongation is strictly depended on the value of the ratio  $D/B$ . In relative terms, scaling from  $D/B=1$  to  $D/B=2.5$  the period variation increases to 170% on average all scenarios. However, it is also possible to see, that the period elongation seems to increase as the stiffness of the subsoil decreased. In particular scaling from  $V_s=350$  m/s to  $V_s=200$  m/s the period elongation is increased by 160% on average. A possible explanation is that the high stiffness of the soil beneath the foundation inhibits the rotations more than the lateral soil and for this reason the two structures have almost the same natural period.

The results of the analysis also show that the period elongation seems to slightly reduce as the fixed base period increases. For this reason, the lateral disconnection technique could give more benefits, in terms of period elongation, especially for structures with low fixed base period.

All the results could be summarizing in Figure 7 where the relative soil-structure stiffness parameter,  $H/(V_s \cdot T_{Fixed Base})$ , is plotted against the elongation of period for different  $D/B$  values. Once again, as the stiffness of the structure increases related to the stiffness of the soil the predominant period of the lateral disconnected structure will increase up to 45-50% related to the no disconnected one.

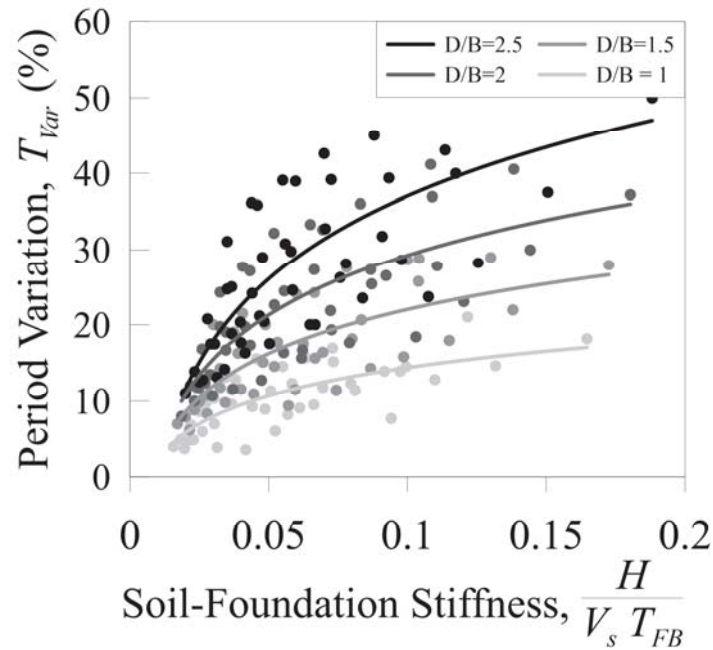


Figure 7. Period variation generated by the lateral disconnection as function of the soil-structure stiffness parameter.

### 3.2 Earthquakes analysis

Two identical structures were modelled with and without the lateral disconnection with the properties reported in Table 2 and the soil properties of section 2.2. The numerical model was then subject to the earthquakes described in Section 2.1. Figure 8 shows the roof total acceleration for Campano Lucano and Friuli earthquakes.

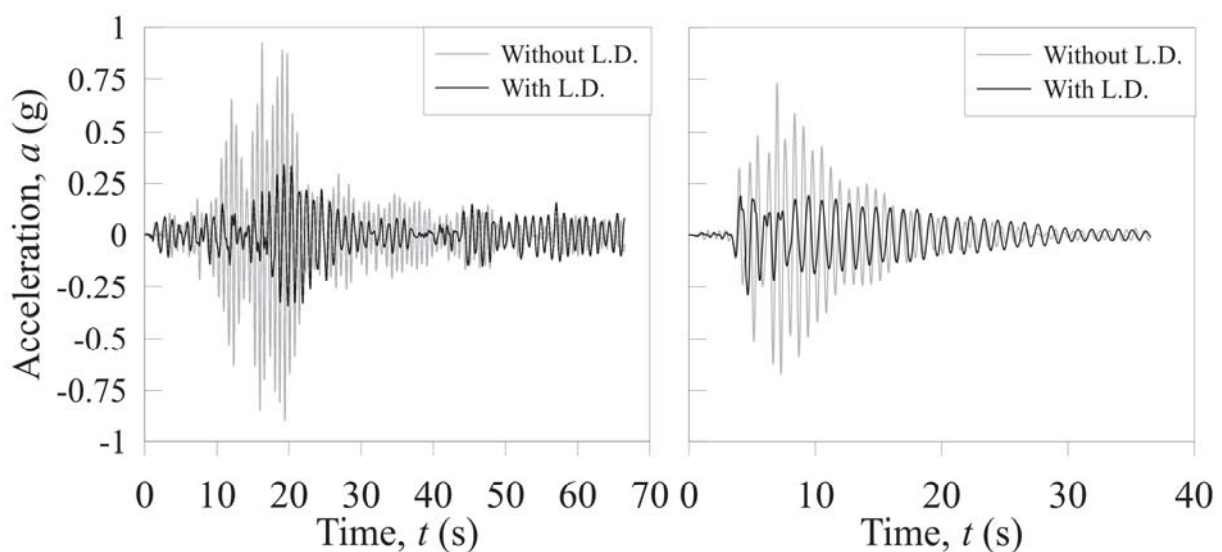


Figure 8 Total crossbeam acceleration on the two-structure considered with and without lateral disconnection: (a) Campano Lucano Earthquake; (b) Friuli Earthquake

Due to the elongation of the predominant period generated by the lateral disconnection, the total roof accelerations are significantly different. Figure 9a shows the acceleration spectrum at the base of the structures with the indication of the elongated predominant periods.

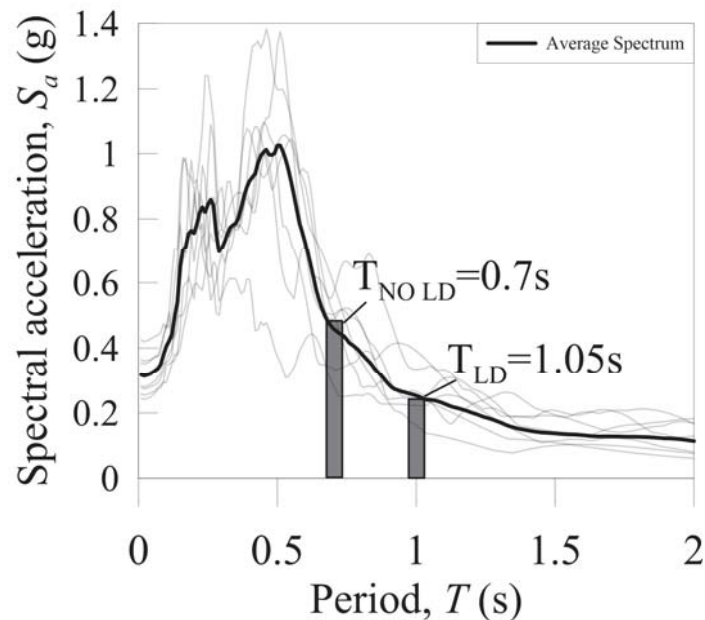


Figure 9. Response spectrum acceleration with the indication of predominant period of the structures computing the S.S.I interaction.

The Arias Intensity variation ( $I.A. Var = I - I.A., LD / I.A., no LD$ ) and maximum total acceleration variation ( $a_{max Var} = I - a_{max, LD} / a_{max, no LD}$ ) provided by the lateral disconnection technique is shown in Table 6 for all earthquakes.

Record (-)	$I.A. Var$ (%)	$a_{max Var}$ (%)
Campano Lucano	80	62
Bingol	50	78
South Iceland	27	27
Mt. Vatnafjoll	64	29
Golbasi	11	0.3
Friuli	69	60
South Iceland(aftershock)	2	5

Table 6. Mitigation of the Arias Intensity and maximum total acceleration provided by the lateral disconnection.

Moreover, the beneficial effects of the lateral disconnection technique could be seen by comparing the structural drift (Figure 10). In fact, subtracting from the total horizontal displacement of the crossbeam the horizontal displacement of the foundations and the horizontal displacement generated by the rocking rigid movement of the structure, it is possible to calculate the structural drift.

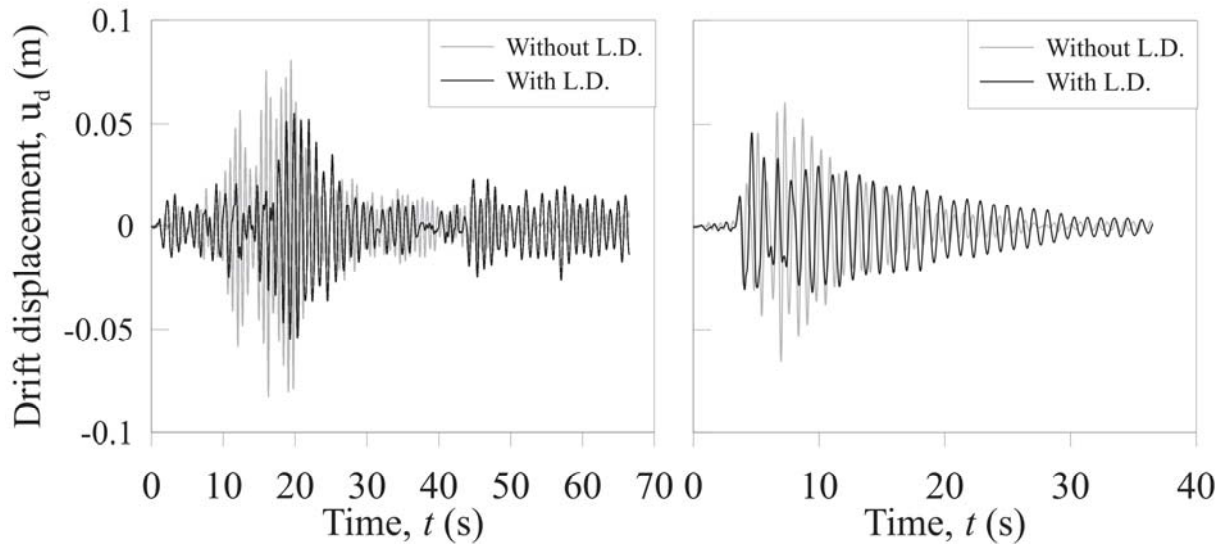


Figure 10. Drift displacement with and without the lateral disconnection: (a) Campano Lucano earthquake; (b) Friuli earthquake.

#### 4 CONCLUSION

This paper has shown the potentiality of a new geo-technical seismic isolation technique called “Lateral Disconnection”. The reduction of the rotational and translational foundation-soil stiffness produced by the lateral disconnection leads to a period increase related to the classical embedment condition. This period lengthening was quantified through parametric analyses where the fixed-base period, the aspect ratio of the structure and foundations and the stiffness of the ground were varied. It was found that the aspect ratio of the foundations, as well as the stiffness of the ground, plays a key role on period lengthening. The more deformable the ground is and the more founded the foundation are, the greater will the period elongation produced by the lateral disconnection be. Under certain conditions the Lateral Disconnection technique can lead to an increase up to 45-50% of the predominant period of vibration related to the classical embedment foundations.

Following the parametric analyses, a series of compatible spectral earthquakes were used to show the effectiveness of such technique in terms of seismic actions (acceleration and drift) reduction. The maximum total acceleration reduction as well as the Arias Intensity reduction could be very high, up to 60%. Similar action reductions can be found if the maximum structural drift expected on the two structures is compared.

It is important to highlight that the lateral disconnection technique is not able to provide a total seismic isolation like rubber or sliding isolators but it can represent a valid seismic improvement strategy especially for its low cost and its low impact on the building. Like any anti-seismic strategy, its effectiveness must be studied in detail, on the basis of the local seismic



hazard and characteristics of the foundation, to predict, with a sufficient margin of reliability, the actions that will affect the modified structure.

## REFERENCES

- [1] H.H. Tsang, Geotechnical seismic isolation. *Earthquake engineering: new research*. Nova Science Publishers. 55–87, 2009.
- [2] M.K. Yegian, M. Catan, Soil isolation for seismic protection using a smooth synthetic liner. *J Geotech Geoenviron Eng*. 130:1131–1139, 2004.
- [3] A. Flora, D. Lombardi, V. Nappa, E. Bilotta, E., Numerical analyses of the effectiveness of soft barriers into the soil for the mitigation of seismic risk. *J. Earthq. Eng.* 22(1):63–93, 2018.
- [4] K. Pitilakis, S. Karapetrou, K. Tsagdi, Numerical investigation of the seismic response of RC buildings on soil replaced with rubber–sand mixtures. *Soil Dynam Earthq Eng.* 79:237–52, 2015.
- [5] R. L. Kuhlemeyer, J. Lysmer, Finite Element Method Accuracy for Wave Propagation Problems. *Journal of Soil Mechanics & Foundations*, Div. ASCE 99(SM5), 421–427, 1973.
- [6] F.Somma, E.Bilotta, A.Florà, G.M. Viggiani. Centrifuge modelling of shallow foundations lateral disconnection to reduce seismic vulnerability. *Manuscript submitted for publication*, 2021.
- [7] X. Jiang, Z. Yan, Earthquake response analysis of building-foundation-building interaction system. *Journal of vibration engineering*. 11(1), 1998.
- [8] I. Iervolino, C. Galasso, E. Cosenza, REXEL: computer aided record selection for code-based seismic structural analysis. *Bulletin of Earthquake Engineering*, 8:339-362, 2009. DOI 10.1007/s10518-009-9146-1
- [9] D.M. 17.01.2018. Nuove Norme Tecniche per le Costruzioni.
- [10] BS EN 1998-1, Design of Structures for Earthquake Resistance. *Eurocode 8*. 3:57, 2004.
- [11] E. Flavigny, J. Desrues, B. Palayer, Le sable d’Hostun. *Revue Française de Géotechnique*. 53:67–70, 1990.
- [12] B. Hardin, V. Drnevich, Shear modulus and damping in soils: measurement and parameter effects. *J. Soil Mech. Found. Div. ASCE*. 98(6):603–624, 1972.
- [13] E. Hoque, F. Tatsuoka, Kinematic elasticity of granular material”. *ISRM International Symposium*, Melbourne, Australia, 2000.
- [14] H.B. Seed, I. M. Idriss, Soil moduli and damping factors for dynamic response analysis. *Report No EERC 70-10*, University of California, Berkeley, California, USA, 1970.

## INFLUENCE OF THE DYNAMIC SOIL-STRUCTURE INTERACTION IN CONCRETE FRAMES WITH INCORPORATED VISCOUS DAMPERS

Andrés M. Cortés<sup>1</sup>, Francisco J. Peña<sup>2</sup>, Orlando Cundumi<sup>1</sup>

<sup>1</sup> Pontificia Universidad Javeriana, Cali, Colombia  
Calle 18#118-250 Avenida Cañasgordas, Cali-Colombia  
e-mail: {andrescortes97, orlando.cundumi}@javerianacali.edu.co

<sup>2</sup> Wiss, Janney, Elstner Associates, Inc. Indianapolis, USA  
8606 Allisonville Road Suite 205 Indianapolis  
email: fpena@wje.com

---

### Abstract

*Essential facilities, such as hospitals, communication systems, highways, bridges, among others, play a significant role in a community. These facilities are vital, especially after being hit by a natural hazard. They must remain functional after a significant event to provide essential services to the community. The implementation of control systems during the structural design and rehabilitation stages enables an attractive manner for this type of structure to dissipate the dynamic response under major disturbance events. Typically, the design stage of structural control systems focuses its attention on the asset's structural configuration. Under seismic events, the structure's response can be altered by the interaction between the structure and the soil underneath. In this paper, the dynamic response's influence is evaluated through numerical simulation by including the effects of soil-structure interaction in a concrete moment resistant frame with viscous fluid-type energy dissipation systems. For this analysis, seven ground motion records were selected for the analysis, considering their frequency and source of content. These records are matched to the corresponding building code design response spectrum for areas prone to high seismicity. Similarly, the soil profiles used for the analysis correlates with the same seismic hazard zone. The analyzed structure corresponds to an essential facility of high importance modeled as a two-dimensional concrete moment resistant frame. The analysis is performed on a seven-story building implementing viscous dampers. Two cases are studied: implementing and neglecting the effects of the soil-structure interaction. The results for the case-study show a significant increase in the dynamic response in terms of displacement, inter-story drift, and base shear when considering soil-structure interaction.*

**Keywords:** Energy Dissipation System, Nonlinear Analysis, Soil-Structure Interaction.

---

## 1 INTRODUCTION

For assets for the built environment, structural damage may occur due to medium to high-intensity seismic events. These effects can damage structural and non-structural elements, and on some unfortunate occasions, they have resulted in casualties. During the last decades, multiple researchers have focused their attention on alternatives for controlling the structure's response due to seismic loads in order to guarantee people's safety and to minimize the amount of inflicted damage into the buildings [1]. The seismic design aims to develop structural configurations to resist earthquake loads, providing reliability, durability, and, most importantly, minimizing casualties. Traditionally, the dissipation of energy has been considered by the deformation and damage of the building components. In the last decades, different methodologies have been developed for the design of structures (e.g., buildings, bridges, dams) with the objective of dissipating the energy while preserving the investment. For instance, displacement-based design and accounting for enough ductility into the structure are used alternatives for energy dissipation. The latter represents the basis of the current building design codes. Alternatively, there are other methods, such as the incorporation of energy dissipation systems, including base isolation, known as control systems. These systems are typically implemented on essential facilities to control the seismic response and remain functional during and after an earthquake [2-7]. Recently, it became evident that the traditional design of structures does not represent a sufficient solution to prevent the collapse of certain structures [8]. Rather, it is necessary to implement solutions that enable immediate occupancy while minimizing required repairs and functionality interruptions after medium to high-intensity earthquakes [8]. This can be achieved by incorporating control systems to reduce structure forces and displacements among seismic events. Incorporating control systems as an alternative for the design of new structures and the rehabilitation of existing structures is becoming more popular among building codes. Some examples of this implementation include the Colombian current code NSR-10 and the new one that is being developed AIS 700 (Asociación Colombiana de Ingeniería Sísmica), ASCE 7-16 (American Society of Civil Engineers), the Eurocode, and the Chilean Standard NCh. Additionally, previous studies have shown that the implementation of control systems may enable a life-time reduction of the structure's cost, in comparison with the cost associated with structures designed in a traditional manner, due to the capability to reach inelastic deformations during earthquakes, suffering minimal damage, providing post-earthquake operability, and reducing the need for repair [8]. Control systems have been implemented in multiple buildings around the world to reduce the dynamic behavior of the structure, for example: St. Francis Towers (Mandaluyong, Philippines), Churchill Hotel (San Diego, California, USA), King County Courthouse (Seattle, Washington, USA), Opera House (San Francisco, California, USA) and 3 Com (Foster City, California, USA) [9, 10].

However, these structures are typically designed neglecting any soil-structure interaction [11]. In structural dynamics, a structure's behavior is analyzed considering a set of discrete elements, modeled following a set of equations of motion to estimate displacements and stresses. For the case of soil dynamic analysis, the study is performed similarly while taking into account the effect of the soil, and therefore the resulting structure's displacements and stresses differ [12]. This effect is known as "Dynamic Soil-Structure Interaction" (DSSI). According to Kausel [13], the DSSI concept is hard to define completely. Still, in general terms, it refers to static and dynamic phenomena that occur between the ground and a much more rigid structure. For example, the seismic wave amplification in the ground and the dynamic interactions between different soil layers are factors to consider during a DSSI analysis. Other studies showed that DSSI consideration could significantly influence the dynamic response of structures [12-18]. This influence is mainly seen in three aspects: i) the change in the dynamic

characteristics of the soil-structure system such as frequencies and modes of vibration; ii) the increasing in damping within the system due to the transference of the structure's energy into the ground; and iii) the soil moving properties influence the analysis [11]. Recent studies have shown that the effects of the DSSI have a greater influence on the structural response in terms of base shear, performance level, and inter-story drifts when is supported on soft soils [17].

To evaluate the influence that the DSSI has on the response of concrete frames with viscous damper devices, we analyzed a seven-story concrete frame with and without implemented control systems. First, seven representative seismic records were selected, considering representative characteristics such as their frequency content. These records were matched to the corresponding response spectrum of a high seismic hazard zone, defined by the design codes. Subsequently, the matched records were filtered through a soil profile to obtain surface records. With the same profile data, the foundation stiffness was calculated at the surface level to perform a more accurate analysis of the structure and the soil at the transition zone between both systems. The soil stiffness and the earthquakes acting at the surface were considered during the analysis. For the seismic response analysis, the analytical model of the structure was done in the finite element software ETABS [21]. The analysis was performed for four cases: fixed and flexible base with and without viscous dampers. The results are presented in terms of the maximum inter-story drift, the base shear, and hysteretic curves for the viscous dampers. Although the complete analysis includes more models of structures with different characteristics (e.g., different number of bays, stories, dimensions) [22], only one structural model with seven stories and five bays are presented within this paper.

## 2 GROUND MOTIONS

### 2.1 Ground motion selection

For the dynamic analysis in the time domain, ground motion records must meet certain criteria [21, 22]: must be a minimum of three different acceleration records or the average value of seven acceleration records, all of them different and representative of the expected ground motions at that zone; they must be events with magnitude, distance to the seismic source and rupture mechanisms similar to the ones for the location of the case-study; and covering the broadest possible range of frequencies.

Following the guidelines outlined above, the seismic acceleration records were selected from the Pacific Earthquake Research Center (PEER), for the NGA-West2 database [25]. Ranges of magnitude and distance to the seismic source were established, according to the analysis of the disaggregation of the seismic threat of the seismic micro zoning project for the city of Cali, Colombia [26]. Two different searches were performed for the analysis: i) magnitude between 5.5 and 6.7 and a distance between 0 and 40 kilometers; ii) magnitude between 7.0 and 8.5 y distance between 110 and 180 kilometers. Also, an average shear wave velocity range of at least 500 m/s was required [27].

Table 1 shows the seven selected ground motion records and a summary of some of their most representative characteristics.

Event	Station	Year	Magnitude Mw	Distance to rupture sur- face (km)	Failure Mechanism	Vs30 (m/s)
ChiChi, Taiwan	TAP046	1999	7.62	118.34	Reverse Oblique	816.9
Kocaeli, Turkey	Eregli	1999	7.51	142.29	Strike Slip	585.09

Niigata	NIG023	2004	6.63	25.82	Reverse	654.76
Northridge-01	LA-Chalon Rd	1994	6.69	20.45	Reverse	740.05
Northridge-01	LA Dam	1994	6.69	5.92	Reverse	628.99
Northridge-01	Santa Susana Ground	1994	6.69	16.74	Reverse	715.12
San Fernando	Lake Hughes #12	1971	6.61	19.3	Reverse	602.1

Table 1: Selected ground motions.

## 2.2 Target response spectrum

The design elastic response spectrum was defined according to the Colombian NSR-10, whose parameters are shown in Table 2, taking into account an importance coefficient ( $I$ ) of 1.25. From this spectrum, the structure is designed without viscous dampers. For the structure with incorporated viscous dampers, a response spectrum of the maximum considered earthquake must be used. According to ASCE 7-16 [24], the response spectrum for the controlled structure must be determined using the code target spectrum amplified by 1.5. Figure 1 shows the two target spectra.

Ground seismicity	Soil Type	Importance Factor	$A_a$	$A_v$	$F_a$	$F_v$
High	D	III	0.25	0.25	1.30	1.90

Table 2: Parameters for the construction of the design spectrum according to Colombian design code NSR-10 [23].

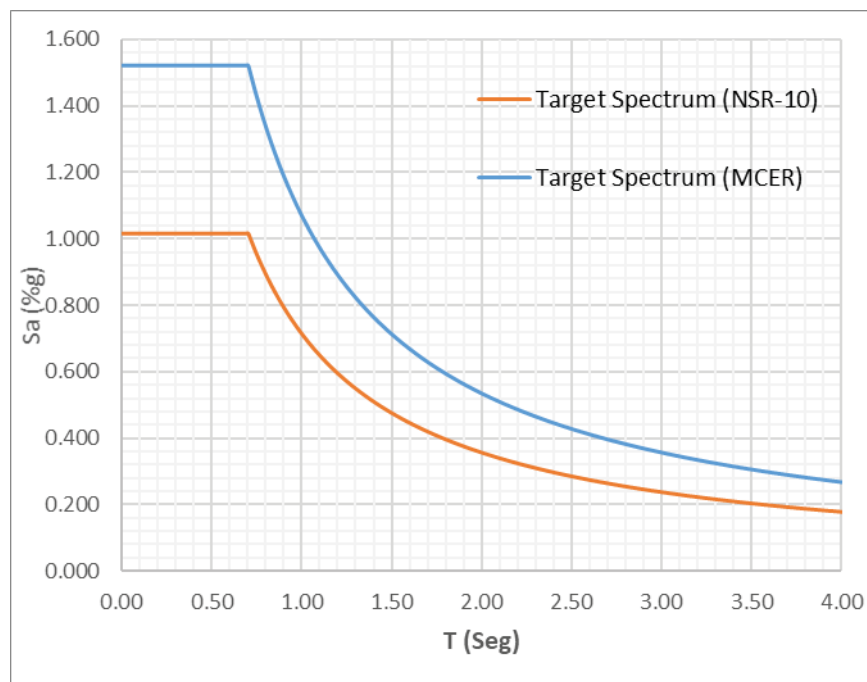


Figure 1: Target response spectra.

## 2.3 Spectral matching

Considering that the acceleration records were selected from a location different than the one from the case-study, it is necessary to match these records according with the target spectrum. This matching process guarantees compatibility in terms of the frequency content and

tectonic regime between the acceleration records and the case-study location. Using the time domain matching methodology described in [28, 29], it is possible to modify the existing acceleration records while preserving the non-stationary character of the reference ground motion records. The methodology implements a tapered cosine wavelet for adjusting the acceleration records, resulting in records without drift in the corresponding displacements and velocities. This adjustment procedure ensures stability, efficiency, and speed in obtaining the numerical solution of the spectral match [29].

The acceleration records are matched to the target response spectrum employing the wavelet algorithm from SeismoMatch, a software by SeismoSoft [30]. Figure 2 shows the comparison between the original acceleration record for the 1971 San Fernando earthquake (recorded at the rock level), and the matched records with respect to the NSR-10 response spectrum and the maximum considered earthquake spectral response ( $MCE_R$ ).

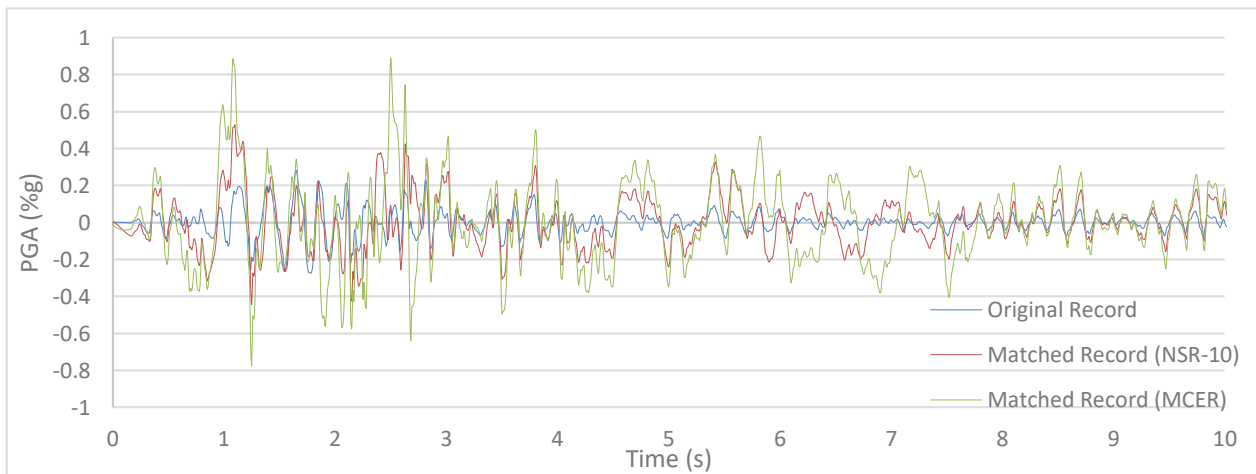


Figure 2: Comparison of original and matched accelerogram records to the Colombian code NSR-10 and MCER target spectrum for 1971 San Fernando Earthquake.

Figure 3 shows the comparison of the mean matched spectrums to its respective target spectrum of the Colombian code NSR-10 (For the model without viscous dampers) and the  $MCE_R$  (For the model with viscous dampers).

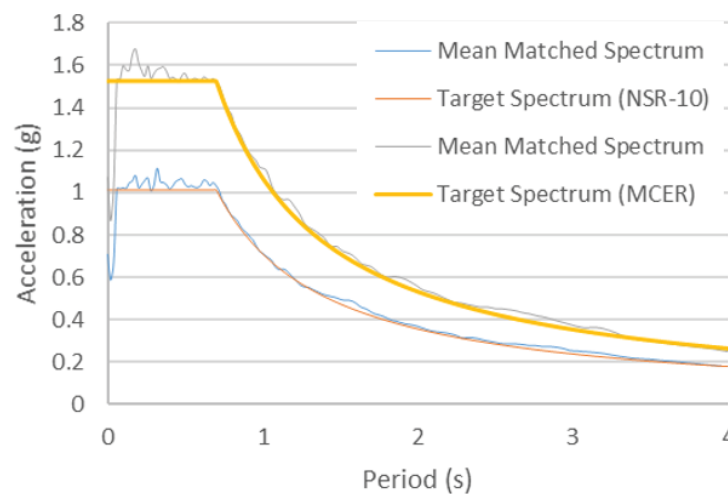


Figure 3: Comparison of the Colombian NSR-10 and MCER target spectrum and their respective mean response spectrum for the original seismic records.



## 2.4 Non-linear properties of the soil

Generally, for stiff structural systems, foundation deformations can represent a significant component of system flexibility and ignoring it can result in bad characterization of properties as fundamental mode frequency and damping ratio [31]. Foundation damping results from the relative movements of the foundation and the supporting soil and these cause displacement and rotations of the structure relative to the free field. The difference between the foundation input motion and free-field motion gives rise to energy dissipation by radiation damping and hysteretic soil damping, and this affects the overall system damping [32].

Site effects are caused by the amplification of the seismic waves as they travel from the rock to the surface. This amplification is the result of the seismic wave traveling through the different layers from the soil profile. The most common physical properties used to characterize these soil layers include their thickness (H), the shear wave velocity ( $V_s$ ), the specific weight ( $\gamma$ ), the friction angle of the material ( $\Phi$ ), the modulus of elasticity (E), and the shear modulus (G) of the soil. Table 3 shows a summary of the soil layers implemented within this study and their representative characteristics.

Soil Layer	H [m]	$V_s$ [m/s]	$\gamma$ [kN/m <sup>3</sup> ]	$\Phi$ [°]	E [MPa]	G [MPa]
Surface Clay	4	157	18.5	25	123.11	46.28
Clay with lens	11	244	18.5	32	297.35	111.79
Hard Clay	7	570	20.0	33	1754.27	659.50
Peat Clay	8	736	21.8	42	3188.07	1198.52

Table 3: Soil profile data.

The implementation of the soil layers effects can be carried out using ProShake 2.0 [33], a software that finds the solution of ground response problem in the frequency domain, whose input acceleration records are represented as a sum of series of sine waves of different amplitudes, frequencies, and phase angles. Filtering the acceleration records using the transfer functions from the different soil layers, the response of the soil profile for each of the waves is obtained. Figure 4 and Figure 5 shows the rock records for the San Fernando earthquake and their comparison with the same record filtered through the soil profile.

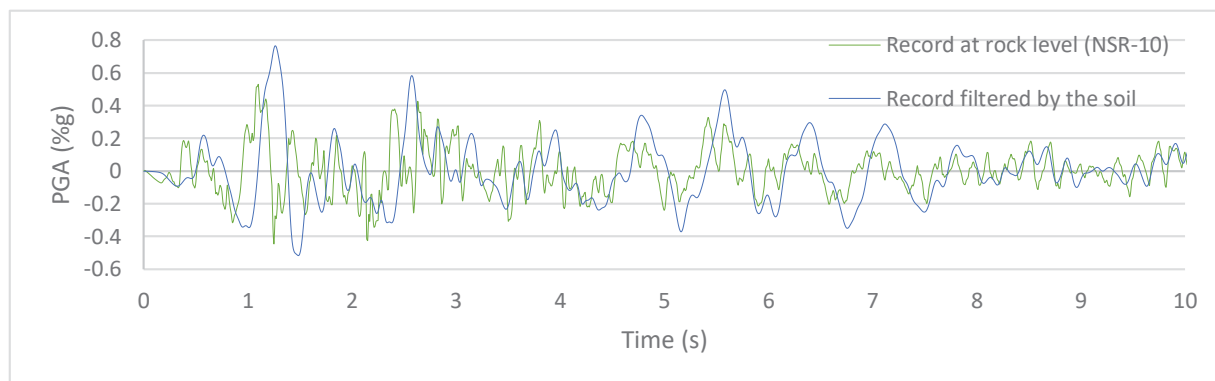


Figure 4: Comparison of matched records to Colombian NSR-10 and the same records filtered through the soil profile for 1971 San Fernando earthquake.

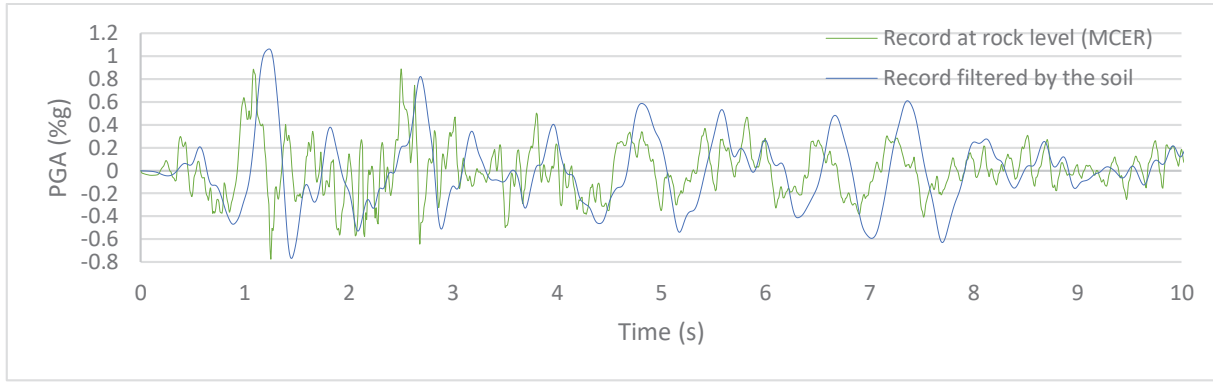


Figure 5: Comparison of matched records to  $MCE_R$  spectrum and the same records filtered through the soil profile for 1971 San Fernando earthquake.

## 2.5 Soil structure interaction

Using the soil profile data shown in Table 3, the stiffnesses of the foundation are calculated at the surface level to posteriorly included in the flexible base model. This calculation is carried out using the following equations from [34]:

$$K_{x,sur} = \frac{GB}{2-\nu} \left[ 3.4 \left( \frac{L}{B} \right)^{0.65} + 1.2 \right] \quad (1)$$

$$K_{z,sur} = \frac{GB}{1-\nu} \left[ 1.55 \left( \frac{L}{B} \right)^{0.75} + 0.8 \right] \quad (2)$$

$$K_{yy,sur} = \frac{GB^3}{2-\nu} \left[ 0.47 \left( \frac{L}{B} \right)^{2.4} + 0.034 \right] \quad (3)$$

where,  $K_{x,sur}$ ,  $K_{z,sur}$ , and  $K_{yy,sur}$  are the stiffnesses for the translation along the X-axis, Z-axis, and the rocking effect about the Y-axis, respectively,  $G$  is the shear modulus,  $\nu$  is the Poisson ratio,  $B$  is the rectangular foundation width, and  $L$  is the rectangular foundation length.

For the flexible base model a foundation beam 0.60 meters wide and discretized in segments of 1.0 meters long, is implemented. Using equations 1 through 3, the following stiffness values are obtained:  $K_{x,sur} = 98752.0$  kN/m,  $K_{z,sur} = 127388.3$  kN/m, and  $K_{yy,sur} = 24402.8$  kN-m.

## 3 NUMERICAL MODEL

The seven-story frame is modeled in ETABS considering the geometry presented in Figure 6 for both cases with and without incorporating viscous dampers.

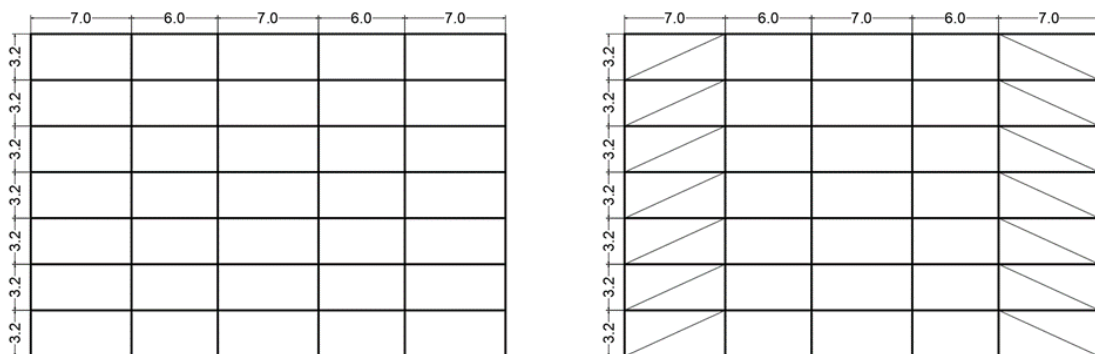


Figure 6: 7-story frame geometry for the case (a) without viscous dampers and (b) with viscous dampers. Dimensions in meters.

Structural elements are modeled using a value of concrete compressive strength of 28 MPa and reinforcing steel with yield strength of 420 MPa. The structural design of the case-study building is performed in accordance with the NSR-10 and performing a dynamic modal spectral analysis to determine that the maximum inter-story drift is less than established limit of one percent. Additionally, an adequate capacity of structural elements needs to be guaranteed with respect to the expected load demands that the structure is expected to withhold.

According to ASCE 7-16, the base shear used for the design of the main system for the structure with viscous dampers must not be less than 75 percent of the originally determined base shear. Consequently, the reduction in the lateral forces for the system results in a reduction on the transversal section of the structural elements from the main system.

Viscous dampers were incorporated into the model using link elements with a non-linear exponential damper. The non-linear properties were introduced considering a moderate damage level in a moderate-height building [35] and following the methodology presented in [36]:

Firstly, the response reduction factor  $B$  was calculated using the following equation:

$$B = \frac{D_{max}}{D_{obj}} \quad (4)$$

where  $D_{max}$  is the maximum drift obtained in the structural analysis and  $D_{obj}$  is the target drift, which in this case is 0.0051 for a moderate damage level according to [35]. A structure's effective damping of 35 percent is set as the target, meaning that viscous dampers must contribute to 30% of total structural damping. Then, the damping coefficient  $C$  was calculated for each floor using the equation below:

$$C = \zeta \frac{k_i}{\eta_i} * \frac{T}{\pi} * \frac{1}{\cos^2 \theta_j} \quad (5)$$

where  $\zeta$  is the damping ratio,  $k_i$  is the stiffness for the  $i$ -th story,  $\eta_i$  is the number of viscous dampers per story,  $T$  is the fundamental period of the structure, and  $\theta_j$  is the inclination angle for the viscous dampers.

The following non-linear properties for the viscous dampers were determined: damping coefficient  $C = 2553.59$  kN-seg/m, velocity exponent  $\alpha = 0.5$ , brace stiffness  $K = 202630.16$  kN/m, obtained by axial stiffness equation of a brace element using physical properties of a steel section HEB200. The maximum damper force can be obtained by using the equations shown on [36]:

$$F = C (V)^\alpha \quad (6)$$

$$V = \frac{2\pi}{T} 0.02xH_{story} \times \cos(\theta) \quad (7)$$

where  $F$  is the damping force,  $V$  is the velocity,  $T$  is the fundamental period,  $H_{story}$  is the height of the analyzed story, and  $\theta$  is the damper inclination angle.

### 3.1 Load considerations

A load assessment was carried out and summarized in Table 4Table 5.

Dead Loads	
Joist slab	3.00 kN/m <sup>2</sup>

Floor finishes	1.50 kN/m <sup>2</sup>
Facade and partition walls	3.00 kN/m <sup>2</sup>
Mechanical, electrical and plumbing systems (MEP)	0.55 kN/m <sup>2</sup>
Ceiling finishes	0.25 kN/m <sup>2</sup>
<b>SUM OF DEAD LOADS</b>	<b>8.30 kN/m<sup>2</sup></b>

Table 4: Dead loads included in the analysis of the seven-story frame building.

Live Loads	
Operating room	4.00 kN/m <sup>2</sup>
<b>SUM OF LIVE LOADS</b>	<b>4.00 kN/m<sup>2</sup></b>

Table 5: Live loads included in the analysis of the seven-story frame building.

## 4 RESULTS

Table 6 shows the Peak Ground Acceleration (PGA) values of the original, matched and filtered acceleration records and it shows that PGA for the matched records to  $MCE_R$  have an increase of approximately 50% comparing them to the matched records to the NSR-10.

Similarly, Table 7 shows the maximum Fourier amplitude for an analysis in the frequency domain. A graphic example of frequency content is shown for the San Fernando Earthquake on Figure 7. It is important to notice that the maximum Fourier amplitude has an average increase of 80% when the soil effects are considered.

Earthquake	Original Record	PGA			
		Matched NSR-10		Matched $MCE_R$	
		Rock	Surface	Rock	Surface
ChiChi	0.083	0.622	0.671	0.953	0.912
Kocaeli	0.087	0.404	0.623	0.596	0.998
Niigata	0.405	0.734	0.774	1.093	1.019
Northridge CHL	0.183	0.562	0.678	0.806	0.926
Northridge LDM	0.324	0.569	0.897	0.864	1.181
Northridge SSU	0.231	0.533	0.717	0.755	0.860
San Fernando	0.282	0.527	0.764	0.887	1.063

Table 6: PGA comparison between the different evaluated cases.

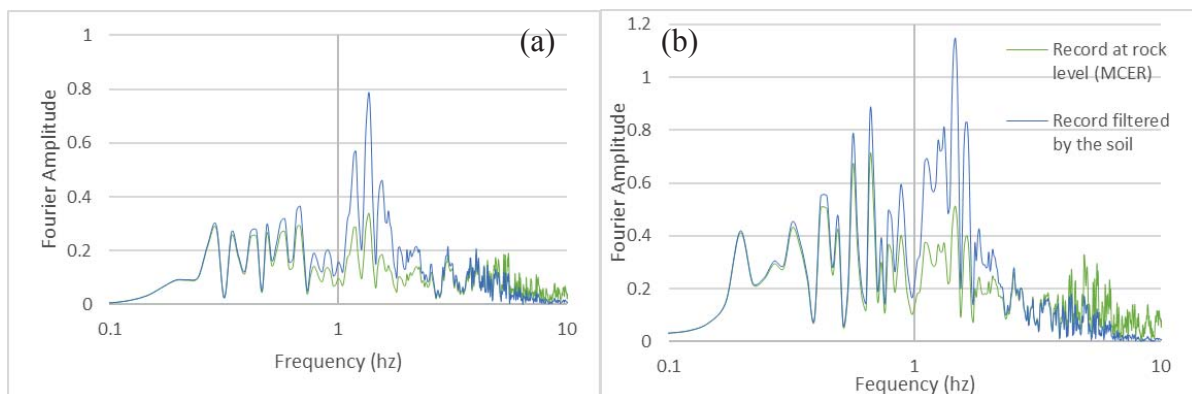


Figure 7: Frequencal content for matched record to the (a) Colombian Code NSR-and the same record filtered through the soil profile for San Fernando earthquake; (b) ASCE 7-16 Spectrum and the same record filtered through the soil profile for San Fernando earthquake.

Event	Original Record	Maximum Fourier Amplitude			
		Matched NSR-10		Matched MCE <sub>R</sub>	
		Rock	Surface	Rock	Surface
ChiChi	0.063	0.445	1.081	0.738	1.508
Kocaeli	0.102	0.613	1.192	0.873	1.390
Niigata	0.140	0.364	0.689	0.518	1.048
Northridge CHL	0.202	0.396	0.785	0.692	1.194
Northridge LDM	0.243	0.379	0.716	0.527	0.875
Northridge SSU	0.142	0.419	1.080	0.537	1.067
San Fernando	0.144	0.338	0.786	0.705	1.148

Table 7: Maximum Fourier amplitude comparison between the different evaluated cases.

For the structural model, the fundamental period for each case is shown in Table 8. The increment in the fundamental period for the structures with the viscous dampers results from the reduced section in structural elements (i.e., reduced stiffness).

Case	Fundamental period (s)
Fixed base without viscous dampers	0.354
Flexible base without viscous dampers	0.382
Fixed base with viscous dampers	0.450
Flexible base with viscous dampers	0.484

Table 8: Fundamental periods for studied cases.

Table 9 show the maximum displacement and acceleration values for response of the structure's top floor, showing values for all seven earthquake records for the 7-story frame building with viscous damper incorporation for the fixed base case and flexible base case, respectively.

Event	Maximum Displacement (mm)		Maximum Acceleration (m/s <sup>2</sup> )	
	Fixed Base	Flexible Base	Fixed Base	Flexible Base
ChiChi	23.7	50.4	10.3	7.7
Kocaeli	26.1	52.9	12.0	13.2
Niigata	38.1	62.2	14.3	11.9
Northridge CHL	23.3	52.7	10.4	8.3
Northridge LDM	24.0	66.1	12.4	13.3
Northridge SSU	24.7	51.6	13.0	10.9
San Fernando	25.0	64.2	11.9	10.8

Table 9: Maximum displacement and acceleration values for the seven records.

The inter-story drift response is also shown in Figure 8 for the fixed base model and the flexible base model incorporating viscous dampers.

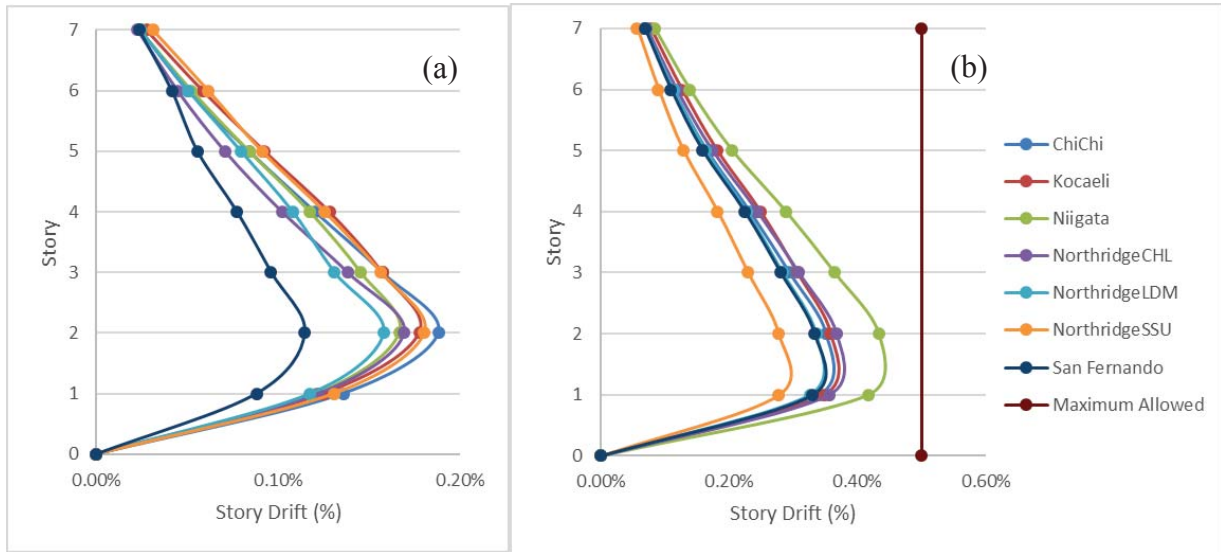


Figure 8: Maximum drift ratio for (a) fixed base model incorporating viscous dampers and (b) flexible base model incorporating viscous dampers.

The inter-story drift has an average increment of 117% for the flexible base than the fixed base case. But for both cases with viscous dampers, the maximum drift is below the limit for a moderate damage level (0.5 percent), according to Hazus [35].

The distribution of the story shear forces for both cases with viscous dampers are shown in Figure 9.

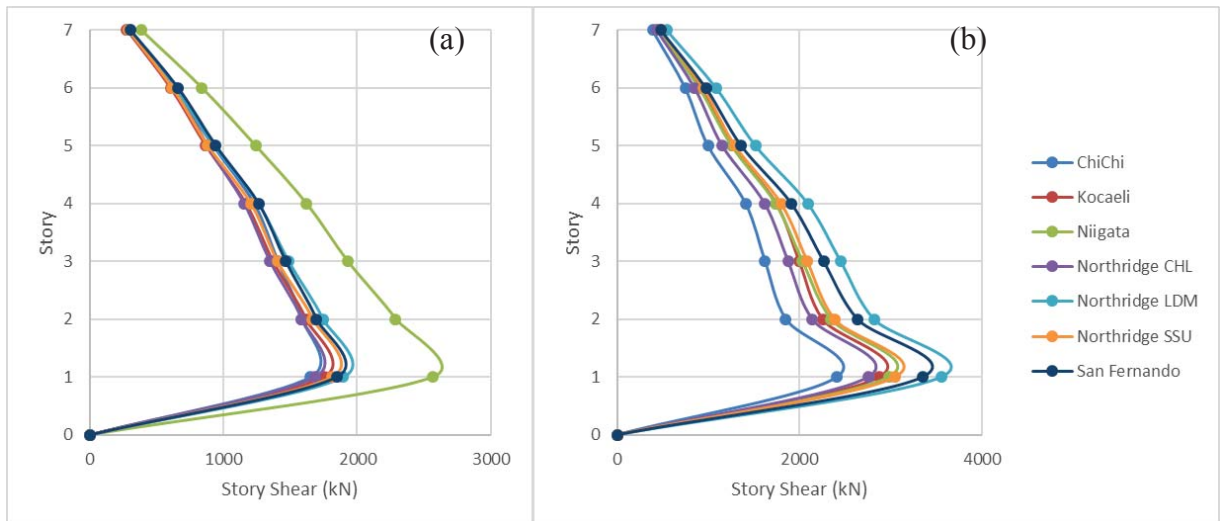


Figure 9: Shear distribution for (a) fixed base model incorporating viscous dampers and (b) flexible base model incorporating viscous dampers.

The maximum shear force increases on average 61% for the flexible base case with respect to the fixed base case.

The obtained results for the viscous dampers show stable hysteretic cycles. For space reasons, two hysteretic curves of the second-story viscous damper were presented for the Kocaeli earthquake for fixed-base and the flexible base cases (Figure 10).



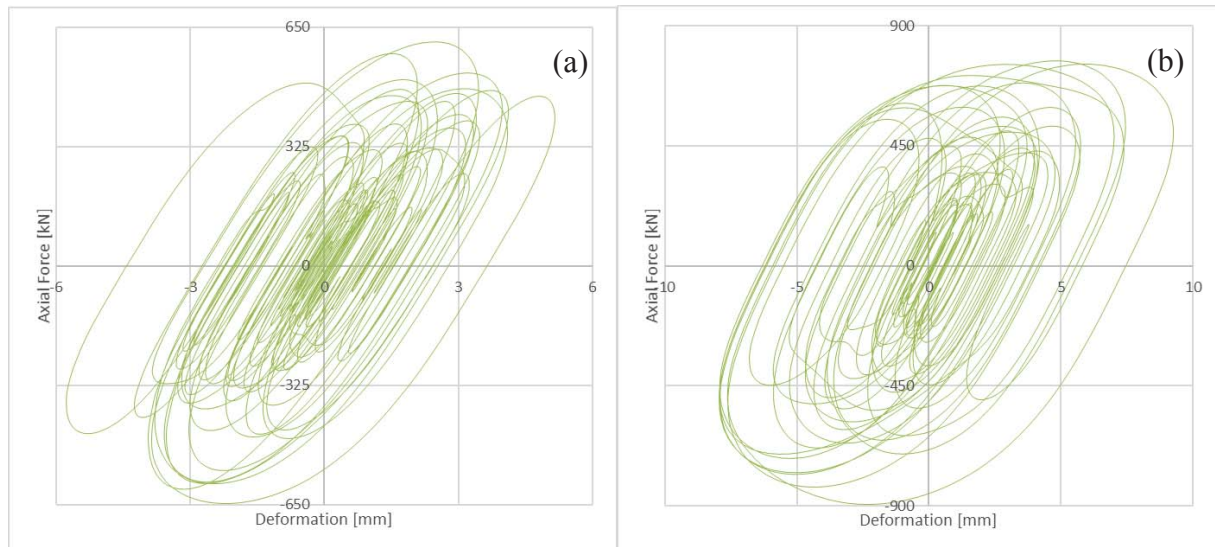


Figure 10: Hysteretic curve for K13 for Kocaeli earthquake of (a) fixed base model and (b) flexible base case.

The figures show that the dampers were successfully dissipating energy and reducing displacements of the structure. The maximum forces and deformations increased for the flexible base model, meaning that the viscous dampers have a wider working range when the soil effects are considered.

## 5 CONCLUSIONS

The SSI effects for concrete frame structures implementing viscous dampers have been investigated. The following conclusions were determined for the 7-story frame building used as case-study:

- In a comparison between the models with fixed and flexible base, the average inter-story drift increased by approximately 115 percent when the SSI is considered. Similarly, the maximum story shear force increased on average by approximately 60 percent for the model with flexible base.
- The results of the study show that the acceleration and displacement responses have inversely proportional effects when SSI is considered. Although the maximum displacement increased on average by approximately 120 percent, the acceleration response shows a slight noticeable reduction of less than 20 percent.
- For both cases implementing viscous dampers, the devices had a stable behavior and a good performance dissipating the energy. The use of viscous dampers enables the dynamic control during a seismic event, which may result in a reduction in the amount and the level of damage that both structural and non-structural elements can sustain. This is the result of the additional capacity to dissipate the energy provided by the control systems.
- There is a noticeable difference of the results when the SSI effects are considered in the analysis. For the case-study, the displacement and distribution of shear forces increases for the selected characteristics of the soil supporting the structure. Therefore, it is of high importance to consider the SSI effects when performing any type of global analysis of structures, and even more significant when the structure is categorized of high importance for a community.

## REFERENCES

- [1] D. Gómez, J. Marulanda, and P. Thomson, "Control systems for dynamic loading protection of civil structures," *DYNA*, vol. 75, no. 155, pp. 77–89, 2008.
- [2] C. Genatios and M. Lafuente, *Introducción al uso de aisladores y disipadores en estructuras*. 2016.
- [3] O. Cundumí Sánchez, "Nonlinear Analysis of Structures Controlled With A New Variable Damping Device," in *14th World Conference on Earthquakes Engineering – 14WCEE 2008*, 2008.
- [4] O. Cundumí Sánchez and L. E. Suárez, "A New Variable Damping Semi-Active Device Seismic Response Reduction of Civil Structure," *J. Mech. Mater. Struct.*, vol. 2, no. 8, 2007.
- [5] O. Cundumí Sánchez and S. Laboy, "Nonlinear Analysis of Structures Controlled with Passive Damper," in *17th Congreso de Ingeniería Sísmica*, 2009.
- [6] O. Cundumí Sánchez and S. Laboy, "Fragility Curves for Concrete Frame Buildings with Passive Controllers," in *9th US National and 10th Canadian Conference on Earthquake Engineering: Reaching Beyond Borders*, 2010.
- [7] F. J. P. Ocampo, "Diseño e implementación de un amortiguador de masa sintonizada (TMD) robusto para disminuir la respuesta dinámica en una tribuna debido a la interacción humano-estructura," Universidad del Valle, 2011.
- [8] S. Mahin, "Lessons from Recent Earthquakes : The Need for More Resilient Cities," pp. 31–42, 2012.
- [9] S. Infanti, J. Robinson, and R. Smith, "Viscous Dampers For High-Rise Buildings," *14th World Conf. Earthq. Eng.*, no. October 2008, 2008.
- [10] ITT ENIDINE, "Viscous Dampers and Tuned Mass Dampers Ensure Buildings Stand Tall," Jun. 2020. <https://www.itt-infrastructure.com/en-US/Applications/Buildings/>.
- [11] L. Menglin and W. Jingning, "Effects of soil-structure interaction on structural vibration control," no. 2, 1998, pp. 189–202.
- [12] I. Chowdhury and S. P. Dasgupta, *Dynamics of Structure and Foundation – A Unified Approach*. 2009.
- [13] E. Kausel, "Early history of soil-structure interaction," *Soil Dyn. Earthq. Eng.*, vol. 30, no. 9, pp. 822–832, 2010, doi: 10.1016/j.soildyn.2009.11.001.
- [14] A. S. Veletsos and J. W. Meek, "Dynamic behaviour of building-foundation systems," *Earthquake Engineering & Structural Dynamics*, vol. 3, no. 2. pp. 121–138, 1974, doi: 10.1002/eqe.4290030203.
- [15] J. Avilés and L. E. Pérez-Rocha, "Evaluation of interaction effects on the system period and the system damping due to foundation embedment and layer depth," *Soil Dyn. Earthq. Eng.*, vol. 15, no. 1, pp. 11–27, Jan. 1996, doi: 10.1016/0267-7261(95)00035-6.
- [16] G. Mylonakis, C. Syngros, G. Gazetas, and T. Tazoh, "The role of soil in the collapse of 18 piers of Hanshin Expressway in the Kobe earthquake," *Earthq. Eng. Struct. Dyn.*, vol. 35, no. 5, pp. 547–575, Apr. 2006, [Online]. Available: <http://doi.wiley.com/10.1002/eqe.543>.

- [17] H. R. Tabatabaiefar, B. Fatahi, and B. Samali, “Seismic behavior of building frames considering dynamic soil-structure interaction,” *Int. J. Geomech.*, vol. 13, no. 4, pp. 409–420, 2013, doi: 10.1061/(ASCE)GM.1943-5622.0000231.
- [18] C. Medina, J. J. Aznárez, L. A. Padrón, and O. Maeso, “Effects of soil–structure interaction on the dynamic properties and seismic response of piled structures,” *Soil Dyn. Earthq. Eng.*, vol. 53, pp. 160–175, Oct. 2013, doi: 10.1016/j.soildyn.2013.07.004.
- [19] I. E. El-arab and S. Sakla, “The effect of seismic soil-structure interaction on the dynamic characteristics of structural systems on shallow foundations,” 2014, no. August 2014.
- [20] F. Behnamfar and M. Banizadeh, “Effects of soil-structure interaction on distribution of seismic vulnerability in RC structures,” *Soil Dyn. Earthq. Eng.*, vol. 80, pp. 73–86, 2016, doi: 10.1016/j.soildyn.2015.10.007.
- [21] I. Computers & Structures, “ETABS User’s Guide.” 2019.
- [22] A. M. Cortés, “Influencia de la Interacción Dinámica Suelo-Estructura en pórticos de concreto con disipadores viscosos incorporados,” Pontificia Universidad Javeriana Cali, 2021.
- [23] Asociación Colombiana de Ingeniería Sísmica, *Requisitos generales de diseño y construcción sismo resistente*, vol. Título A. 2010.
- [24] American Society of Civil Engineers, *Asce 7-16*, vol. 69, no. 1782. 2017.
- [25] U. of California, “NGA West2,” 2018. .
- [26] Departamento Administrativo de Gestión del Medio Ambiente DAGMA and Instituto Colombiano de Geología y Minería INGEOMINAS, “Estudio de Microzonificación Sísmica de Santiago de Cali. Convenio 002 de 2002,” 2002.
- [27] C. F. Grajales, I. F. Otálvaro, and O. Cundumí, “Efectos de horizontes de suelos blandos profundos en la respuesta dinámica del campus de la PUJ Cali,” in *IX Congreso Nacional de Ingeniería Sísmica*, 2020.
- [28] J. Hancock, J. J. Bommer, and P. J. Stafford, “Numbers of scaled and matched accelerograms required for inelastic dynamic analyses,” *Earthq. Eng. Struct. Dyn.*, vol. 37, no. 14, pp. 1585–1607, Nov. 2008, doi: 10.1002/eqe.827.
- [29] L. Alatik and N. Abrahamson, “An improved method for nonstationary spectral matching,” *Earthq. Spectra*, vol. 26, no. 3, pp. 601–617, 2010, doi: 10.1193/1.3459159.
- [30] Seismosoft, “SeismoMatch - A computer program for spectrum matching of earthquake records,” vol. 0. 2020.
- [31] Y.-J. Lee, T.-J. Kim, and F. Maria, “Foundation Modeling Considering the Soil-Structure Interaction,” *J. Earthq. Eng. Soc. Korea*, vol. 16, no. 3, pp. 13–22, 2012, doi: 10.5000/eesk.2012.16.3.013.
- [32] Federal Emergency Management Agency, *Improvement of Nonlinear Static Seismic Analysis Procedures*, vol. 440, no. June. 2005.
- [33] E. P. C. S. Inc, “ProShake 2.0 User’s Manual.” Sammamish, Washington, 2017.
- [34] Federal Emergency Management Agency FEMA 356, *Prestandard and Commentary*

- for the Seismic Rehabilitation of Buildings*, no. November. 2000.
- [35] Federal Emergency Management Agency (FEMA), “HAZUS-MH MR4 Multi-Hazard Loss Estimation Methodology – Earthquake Model: Technical Manual. Department of Homeland Security,” *Fed. Emerg. Manag. Agency, Washington, ...*, 2003, [Online]. Available: [www.fema.gov/plan/prevent/hazus](http://www.fema.gov/plan/prevent/hazus).
- [36] Taylor Devices Inc., *Fluid Viscous Dampers General Guidelines for Engineers Including a Brief History*. 2020.

## COMPUTATIONAL MODELING AND PARAMETRIC STUDY OF PILE GROUPS

**Mariana Lazarini<sup>1</sup>, Miguel Paula<sup>2</sup>, and Manuel Braz-César<sup>3</sup>**

<sup>1</sup> Instituto Politécnico de Bragança

Student

Campus de Santa Apolónia 5300-253 BRAGANÇA - Portugal

mari\_castanheiro@hotmail.com

<sup>2</sup> Instituto Politécnico de Bragança

Assistent Professor

Campus de Santa Apolónia 5300-253 BRAGANÇA - Portugal

mpaula@ipb.pt

<sup>3</sup> Instituto Politécnico de Bragança

Assistent Professor

Campus de Santa Apolónia 5300-253 BRAGANÇA - Portugal

brazcesar@ipb.pt

---

### Abstract

Geotechnics and the study of the behavior of soil with the construction inserted in it is of extrema importance. This study aims at the computational analysis of a group of three reinforced concrete piles with axial and horizontal loads. The piles were inserted in non-cohesive soil (medium and dense sand). The geometric parameters of the piles (diameter, distance between them, and length) and physical parameters of the soil (stratification and angle of friction between them) were varied. The GEO5 "Pile Group" program, the NAVFAC DM 7.2 method was used to determine the bearing capacity. The Poulos & Davis (1980) and FEM methods for settlement, and the p-y method (FEM) to determine the internal forces distribution. The efficiency of the piles is more sensitive the more the distance between them varies. For settlement, Poulos & Davis values are sensitive to distance and diameter, and in FEM they are more sensitive to diameter and length variation.

**Keywords:** Pile group. Computational analysis. Axial load capacity. Horizontal load capacity. Settlement. Group efficiency. Horizontal displacements. Seismic activity.

---

## 1 INTRODUCTION

Knowing the soil and its movements is essential for structural design. Predicting soil behavior is a difficult task due to the heterogeneity of the rock or earth mass, which prevents precise and consistent characteristics. However, it must be ensured that there are no construction failures without over-design.

This study uses deep foundations, which dissipate the loads of the construction into deep soil beds. The objective is to determine the sensitivity of the bearing capacity (with the NAVFAC DM 7.2 method), settlement (Poulos & Davis (1980) and FEM methods), and group efficiency to variations in the piles and soil using the geotechnical analysis software GEO5 version 2020.

Soil has always occupied an important position in human evolution and engineering. The study of soil and its movement is known as geotechnics and dynamics. This knowledge helps to determine the physical and mechanical characteristics of soil, and thus to design its behavior under loads.

Usually, soil studies using empirical methods are found in the academy, which project local results for total volume. Even though they are close to the real ones, the results do not accurately describe soil behavior, which allows design errors. In deep foundations, the error can be even greater because they are inserted in numerous soil layers with different properties. Thus, the construction may encounter unexpected conditions and cause problems in the dispersion of loads.

Finally, studies such as this computer simulation are very important, enabling a range of information from different methods, soils, foundation solutions, and soil stratifications.

## 2 BIBLIOGRAPHIC REVIEW

Deep foundations are necessary when the uppermost soil layers are not strong enough for the building. Therefore, the foundation must reach deep into the soil. The pile group consists of elongated cylindrical or prismatic pieces, which can be precast or cast in the field, joined by a pile cap.

### 2.1 Load capacity

The distribution of structure loads through the piles is carried out in two components. The lateral frictional mobilization along the vertical axis, also called shear, is the  $R_{sk}$  component. The tip or base resistance is the  $R_{bk}$  component. All foundations use both components to transfer their loads. If more than 80% occurs through lateral resistance, the pile is called a floating pile. If 80% of the total occurs through tip resistance, the pile is called a tip pile. The sum of the two components results in the total load capacity of the pile ( $R_k$ ).

For non-cohesive soils, the method of foundation execution must be considered. This is done using the coefficient  $N_q$ , which depends on the angle of internal friction of the soil. For stratified soil, the value corresponding to the greatest angle of friction should be used. The equations determine how the forces are calculated, and the tables show the fixed values.

$$q_{bk} = \gamma D N_q = \sigma'_{vb} N_q \quad (1)$$

$$q_{sk} = \sigma'_n \tan \delta = K \sigma'_v \tan \delta \quad (2)$$



- Where:  $\sigma'_{vb}$ : Effective vertical stress at the base of the pile [kN/m<sup>2</sup>]  
 $\sigma'_v$ : Effective vertical stress in the pile vertical axis [kN/m<sup>2</sup>]  
 $K$ : Lateral thrust coefficient  
 $\delta$ : angle of friction between soil and pile ( $\frac{3}{4}$  of angle of internal friction)

For the bearing capacity it should also be said that the greater the depth in the soil, the greater the limit capacity of the pile. The critical depth is the quota that determines constant capacity values and is determined by the figure below [5].

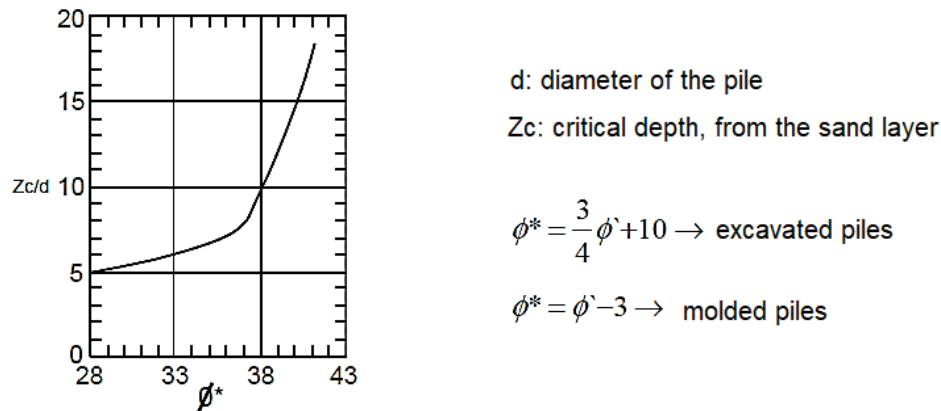


Figure 1: Abacus used for the calculation of the critical depth. [5]

## 2.2 Group load capacity

For a group of piles, Prakash & Sharma (1989) determine that the minimum value of distance between elements should be three times the value of the diameter. If this heat is not placed, the group may behave as a single block.

When piles are placed in a group, there is an influence on the distribution of stresses and soil movement between them, called the group effect. This effect causes the piles not to perform at 100% of their capacity.

The expression that calculates the actual load capacity value is shown below.

$$R_{k;G} = \eta * n * R_k \quad (3)$$

- Where:  $R_{k;G}$ : Pile group load capacity [kN]  
 $\eta$ : Group Efficiency Factor [-]  
 $n$ : Number of piles in the group  
 $R_k$ : Pile load capacity [kN]

To calculate the efficiency factor, there are numerous methods. But none of them is completely reliable, the most widely used being that of Converse-LaBarré (1941), whose equation is shown below.

$$\eta_g = 1 - \psi \left[ \frac{(n_x-1)n_y + (n_y-1)n_x}{90n_xn_y} \right] \quad (4)$$

Where:  $\eta_g$ : Efficiency of the pile group

$\psi$ : Angle with tangent expressed in degrees  $\tan \psi = \frac{d}{s}$ , where s is the axial spacing between piles and d is the diameter of the piles.

$n_x$ : Number of piles in the x direction.

$n_y$ : Number of piles in the y direction.

## 2.3 Horizontal load capacity and displacements

Besides axial loads, structures can suffer horizontal loads, generating displacements, rotations, and bending moments. These loads can occur due to structural requests or, mainly, due to internal soil actions (seismic activities).

For the construction to be safe regarding these loads, it must present materials and strength that avoid rupture and control deformations along the pile [1].

There are many possible methods for structural behavior analysis, but the one that stands out as to its simplicity and coherence with reality is the p-y method, based on the finite element method and Winkler's model (spring method) [2].

### 2.3.1. Winkler Model (Spring Method)

This method was proposed in 1867, it considers the soil as a set of independent springs of elastic and linear behavior. The stiffness of these springs is numerically equal to the unit reaction coefficient of the soil ( $k_h$ ). These values vary with the soil composition and vary according to the following table [2].

Soil	$k$ [MN/m <sup>3</sup> ]
Dense sand	155 – 300
Medium Sand	110 – 280

Table 1: Unit reaction coefficient of soils according to Bowles [2] (adapted).

The final equation of the model follows Hooke's Law, and relates the modulus of elasticity of the pile and the moment of inertia with the soil and its respective displacement.

To determine the resulting values, the pile is considered as floating, in addition to considering the soil characteristics and the type of connection that the pile makes with the heading massif (fixed or with joints).

The GEO5 software determines that you should reduce the stiffness of a unit pile according to the position it is in the group. For horizontal stiffness, the value is reduced by 50% for external positions and 25% for internal ones. As for vertical springs, the reduction is 50% and 10% for exterior and interior positions.

### 2.3.1. P-y method

The p-y curve is a solution of the equation from the previous method. The vertical axis represents the applied load P and the horizontal axis represents the displacement y of the structure. This curve is a non-linear relationship, but it is common to consider it as linear for simplification of the calculations. [2]

The main advantage of this method is that it does not depend on the geometry nor the stiffness of the piles, and it can be used for numerous practical cases [11].

As a disadvantage, Budhu (2013) points out that the method does not consider the soil continuity effect and does not consider the shear strength of the soil, which can generate differences between the calculations and what happens. [10]

## 2.4 Settlement

The settlement of a structure is the displacement of the soil around it, causing vertical displacement. The values can vary for each element of the structure, with the total value being the sum of each. The total value for a group of piles is many times greater than that of an isolated pile, since one element generates the influence over the other as already explained in the group effect. [10]

There are many possible methods to use to estimate settlement, and it is necessary to analyze which one best suit the needs of the project in question. These values are difficult to estimate, they depend directly on the history of stresses over the years in the soil, the way the loads dissipate, the construction method used, among many other factors. [11]

The two types of methods used in this study are that of Poulos & Davis 1980 (theoretical analytical) and that in the finite element method (empirical).

### 2.4.1. Finite element method (FEM)

The finite element method subdivides the pile into small segments, thus determining the displacement for each of them. The total settlement value is the sum of these results. The method also takes into consideration analysis points at the interface between the pile and the soil, promoting values more consistent with reality.

This method also uses the endometric modulus, which determines the compression that occurs in the soil when the foundation is inserted. The equation that determines the settlement of each layer is presented below.

$$s_i = \sum \frac{\sigma_{z,i} h_i}{\frac{E_{def}}{\beta}} \quad (5)$$

Where:  $h_i$ : Layer thickness i.

$\sigma_{z,i}$ : Vertical component of the stress increase at the center of layer i.

$E_{def}$ : Soil deformation modulus.

$\beta$ : Ground scattering angle.

### 2.4.2. Poulos & Davis (1980)

This method is based on the theory of elasticity and considers the soil to have constant and unchanging characteristics, so the soil is homogeneous, isotropic, and elastic. In addition, the authors consider the distribution of stresses along the shaft to also be uniform, and that the resulting settlement values are proportionally linear to the requesting loads.

To determine the maximum settlement of a unit pile, the method uses the equation below.

$$S_{max} = \frac{R_{bk}}{\alpha d E_s} + \left[ R_{bk} - \frac{R_{sk}}{(1-\alpha)} \right] \frac{L}{A_p E_p} \quad (6)$$

Where:  $S_{max}$ : Maximum Pile Settlement.

$R_{bk}$ : Peak load capacity.

$R_{sk}$ : Lateral load capacity.

$E_s$ : Average soil modulus of elasticity.

$d$ : Pile diameter.

$\alpha$ : Proportion of applied load transferred by the base.

$A_p$ : Cross sectional area.

$E_p$ : Modulus of elasticity of the pile.

For group of piles, the study is an extension of the application for a single pile, with the total value multiplied by the group settlement factor. This factor depends on the distance between the elements of the group. The greater the distance, the lower the reduction factor, the inverse occurs for very close piles. The factor ranges from 1 (isolated piles) to values higher than 10 (piles working as a single block). Its use is presented by the equation below.

$$s_g = g_f \cdot s_0 \quad (7)$$

Where:  $s_g$ : Total settlement of the pile group.

$g_f$ : Pile Group Settlement Factor.

$s_0$ : Laying of an isolated pile.

$\beta$ : Ground scattering angle.

## 3 WORK PROGRAM

This paper analyzes a group of three axially and horizontally loaded piles using the geotechnical analysis software GEO5 version 2020. The foundation is inserted in a non-cohesive soil (medium and dense sand). It was verified the behavior of bearing capacity, settlement, and efficiency of the pile group with the variation of geometric parameters of the piles and soil parameters. The diameter, length and distance of the piles, and the internal friction angle of the medium sand were varied. The Spring (Winkler) method was used for determining the

displacements. For the load capacity study, the NAVFAC DM 7.2 method was used. Finally, for the settlement analysis was used the FEM and the method of Poulos & Davis (1980).

The following image represents the three-dimensional model, the stratification and the axes considered in the simulations.

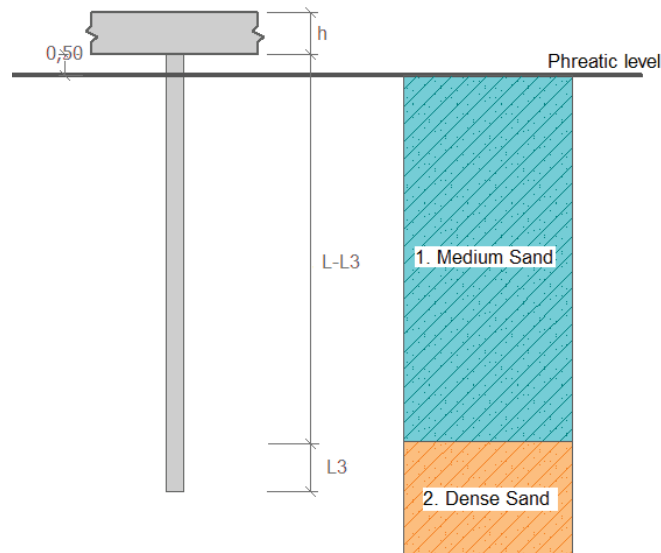


Figure 2: Representation of soil stratification [First author].

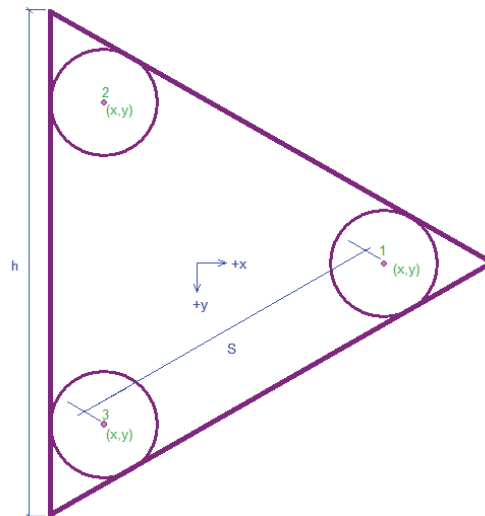


Figure 3: Top view of the pile group and representation of the axes used [first author].

The following tables show the variables and properties of the pile materials and the two soil types.

Piles	
Number of piles	3
Length (L)	10, 15 e 20 m
Diameter (D)	0.4, 0.6 e 0.8 m
Ratio s/d (ratio between the distance and the diameter)	2, 3 e 4
Group efficiency $\eta_g$ (LáBarré)	0.66, 0.76 e 0.82
Axial loads	1980, 2280 e 2460 kN
Horizontal loads	396, 456 e 492 kN
Deformability modulus of concrete	$E_{def} = 29$ GPa
Poisson coefficient of concrete	$\Theta = 0.2$
Characteristic Strengths of concrete	$f_{ck} = 20$ MPa (compression) $f_{ct} = 2.2$ MPa (traction)
Concrete elasticity modulus	$E_{cm} = 29$ GPa
Tensile strength of steel	$f_{yk} = 500$ GPa
Modulus of elasticity of steel	$E = 200$ GPa

Table 2: Variables and properties of the pile materials [first author].

Soil		
Characteristic	Medium Sand	Dense sand
Soil Stratification (m)	L-L3	L3=3xD
Poisson coefficient	$\Theta = 0.35$	
Dry specific weight (kN/m <sup>3</sup> )	19	21
Saturated specific weight (kN/m <sup>3</sup> )	21	23
Soil modulus of deformability (MPa)	50	150
Unit reaction coefficient k (MN/m <sup>3</sup> )	113, 128 e 143	240
Internal friction angle $\Phi$ (°)	26, 28 e 30	40
Soil Cohesion (kPa)	0	
Critical depth	$k_{dc} = 12.5$	

Table 3: Variables and properties of the soils [first author].

## 4 RESULTS AND DISCUSSIONS

To generate the results, the load capacity coefficient  $N_q$  was considered equal to 72, because it corresponds to the value for the 40° internal friction angle of dense sand.

In total 81 simulations were carried out, and problems were observed in some of them. The models with pile lengths of 15 and 20 meters, diameter of 0.4 meters and s/d ratio of 2 and 3, presented excess reinforcement (ratio) with the necessary sizing. However, they will be considered to recognize the sensitivity of the factors.

### 4.1 Load capacity

The analysis is separated in three parameters: the normal end strength ( $q_b$ ), the shear strength ( $q_s$ ) and the pile efficiency  $\eta$ . In the examples of each parameter the intermediate case was sought, which represents the simulations in its great majority.



#### 4.1.1. Normal tip resistance ( $q_b$ )

The tip strength indicates the stress that is transferred to the soil through the cross-sectional area of the pile. It was observed that by increasing the length of the piles, there was an increase in resistance. As for example in the 0.6 meters diameter model with the values are 5,974.43 kPa, 8,710.44 kPa (+45.8%) and 11,446.42 kPa (+91.6%) respectively at 10, 15 and 20 m.

With increasing diameter, the resistance hardly changes. As for example in the model with length 15 m, ratio  $s/d=3$  and friction angle equal to  $28^\circ$  with strength of 8,650.72 kPa, 8,710.44 kPa (+0.7%) and 8,770.12 kPa (+1.4%) respectively at diameters of 0.4, 0.6 and 0.8 m.

As the distance between the piles increases, there is a considerable increase in resistance. This is what is seen in the example of length 15 m, diameter 0.6 m and internal friction angle  $28^\circ$ , with strength of 7,564.33 kPa, 8,710.44 kPa (+15.2%) and 9,398.10 kPa (+24.2%) respectively at  $s/d$  values of 2, 3 and 4.

With increasing the internal friction angle of the medium sand, no change in resistance occurs. As an example, the simulation of 15 m length, 0.6 m diameter and  $s/d=3$  ratio, the resistance value of 8,710.44 kPa is the same for the  $26^\circ$ ,  $28^\circ$  and  $30^\circ$  angles.

It was observed that what generates change in the ultimate strength is the variation in pile properties. The change in the soil friction angle does not affect the results.

#### 4.1.2. Shear or lateral resistance ( $q_s$ )

The lateral resistance indicates the dissipation of loads into the soil through the lateral area along the pile shaft. For the increase of the length of the pile, the lateral resistance hardly changes. As for example in the 0.6 meters diameter pile,  $s/d=3$  ratio and  $28^\circ$  internal friction angle, with values of 22.69 kPa, 22.35 kPa (-1.5%) and 22.18 kPa (-2.3%) respectively for lengths of 10, 15 and 20 m.

For the increase in diameter, there is also an increase in resistance values. This is visible with the model with a length of 15 m, ratio  $s/d=3$  and  $\Phi=28^\circ$ , and the values 15.17 kPa, 22.35 kPa (+47.3%) and 29.27 kPa (+92.9%) respectively for diameters of 0.4, 0.6 and 0.8 m.

When increasing the distance between the piles, an increase in resistance occurs. For example, the simulation of  $L=15$  m, 0.6 m diameter and  $28^\circ$  friction angle, with lateral strength of 19.41 kPa, 22.35 kPa (+15.2%) and 24.12 kPa (+24.2%) corresponding to  $s/d$  ratios of 2, 3 and 4 in order.

Finally, for the increase of the internal friction angle of the medium sand, the resistance also increases a little. This can be verified in the example of length 15 m, diameter 0.6 m and ratio  $s/d=3$ , being the strength 21.80 kPa, 22.35 kPa (+2.5%) and 22.99 kPa (+5.5%) respective to angles  $26^\circ$ ,  $28^\circ$  and  $30^\circ$ .

The following table summarizes the variations generally observed in the analyses and the sensitivity for each parameterization.

Parameter	$Q_b$	% medium	$Q_s$	% medium
increase of L	increases	50%	decreases and increases	2%
increase of D	increases	2%	increases	50%
increase of $s/d$	increases	15%	increases	15%
Increase of $\Phi$	equal	-	increases	2,5%

Table 4: Abstract of sensitivity of the strengths to the increase in the variables studied [first author].

### 4.1.3. Pile efficiency ( $\eta$ )

The pile efficiency is given by the ratio between the total capacity and the theoretical excavated volume ( $R_c/V$ ). As for increasing the length, diameter, and internal friction angle of the medium sand, one can notice derisory changes in efficiency (very low percentages).

The only parameter that generated significant changes in the load transmission efficiency was the increase in the distance between the piles. To exemplify, the simulation with 0.6 m diameter, 10 m length and internal friction angle of  $28^\circ$ , with efficiency of 650.23 kPa, 748.74 kPa (+15.2%) and 807.86 kPa (+24.2%) for s/d ratio of 2, 3 and 4 in order.

The most important thing to analyze in this topic are the values of the most and least efficient piles, which are represented by A and B in the following table.

L	D	s/d	$\Phi$ medium sand	$R_s$	$Q_s$	$R_b$	$Q_b$	$R_c$	$R_c/V$	$R_s/R_c$	$R_b/R_c$
(m)	(m)	-	( $^\circ$ )	(kN)	(kN/m <sup>2</sup> )	(kN)	(kN/m <sup>2</sup> )	(kN)	kPa	(%)	(%)
10	0.6	4	30	470.77	24.98	1822.59	6446.09	2293.36	<b>811.11</b>	20.5	79.5
20	0.4	2	26	316.73	12.60	1242.62	9888.47	1559.36	<b>620.45</b>	20.3	79.7

Table 5: Abstract of sensitivity of the strengths to the increase in the variables studied [first author].

With the previous table it is observed that the least efficient pile was characterized with the largest length, the smallest diameter, the smallest s/d ratio, and the smallest angle of internal friction of the medium sand. The best performing pile, on the other hand, was characterized by the shortest length, largest diameter, largest s/d ratio and largest angle of internal friction. In addition, it is observed that the percentage of load mobilization by lateral friction and by tip resistance in both cases are practically equal.

Finally, one should always remember that each project requires a thorough study of its needs, considering all available resources, material and financial.

## 4.2 Settlement

In this topic some simulations will be discarded. In the models with excess steel, the settlement by the Poulos & Davis method is not generated by the software. These are the simulations characterized by  $L=15$  m,  $d=0.4$  m and  $s/d=3$  and 4, and  $L=20$  m,  $d=0.4$  m and  $s/d=3$  and 4. Another group of simulations will not be used since, for no apparent reason, GEO5 also did not generate results, these are those for  $L=10$  m,  $d=0.4$  m and  $s/d=3$  and 4.

### 4.2.1. FEM

In this method all piles were considered as floating, with the value of the tip resistance equal to zero and the loads distributed only along the shaft.

For the increase in length, a decrease in settlement was observed. As for example the model with 0.6 m diameter, internal friction angle  $28^\circ$  and s/d ratio equal to 3, and maximum settlement values of 7.50 mm, 6.50 mm (-13.3%) and 6.00 mm (-20%) for the lengths 10, 15 and 20 m.

With the increase of the diameter, there was a reduction of the maximum settlement. This is exemplified by the model with length equal to 15 m, angle  $\Phi=28^\circ$  and distance ratio between piles equal to 3, with values of 11.00 mm, 6.50 mm (-40.9%) and 4.60 mm (-58.2%) of settlement, respective to diameters of 0.40 m, 0.60 m and 0.80 m.

The increase of the distance between the piles generated an increase in the final maximum settlement. As for example the model  $L=10$  m, diameter of 0.60 m and  $\Phi=28^\circ$  with values of 7.10 mm, 7.50 mm (+5.6%) and 8.10 mm (+14.1%) of maximum settlement for  $s/d$  ratios of 2, 3 and 4.

Finally, for the increase of the angle of internal friction, a decrease in the maximum settlement value is observed. Which can be verified with the example of  $L=15$  m,  $s/d=3$  and diameter  $d=0.6$  m, with values of 6.60 mm, 6.50 mm (-1.5%) and 6.40 mm (-3%), for  $\Phi$  of  $26^\circ$ ,  $28^\circ$  and  $30^\circ$  in order.

The above data is shown in the graphs below.

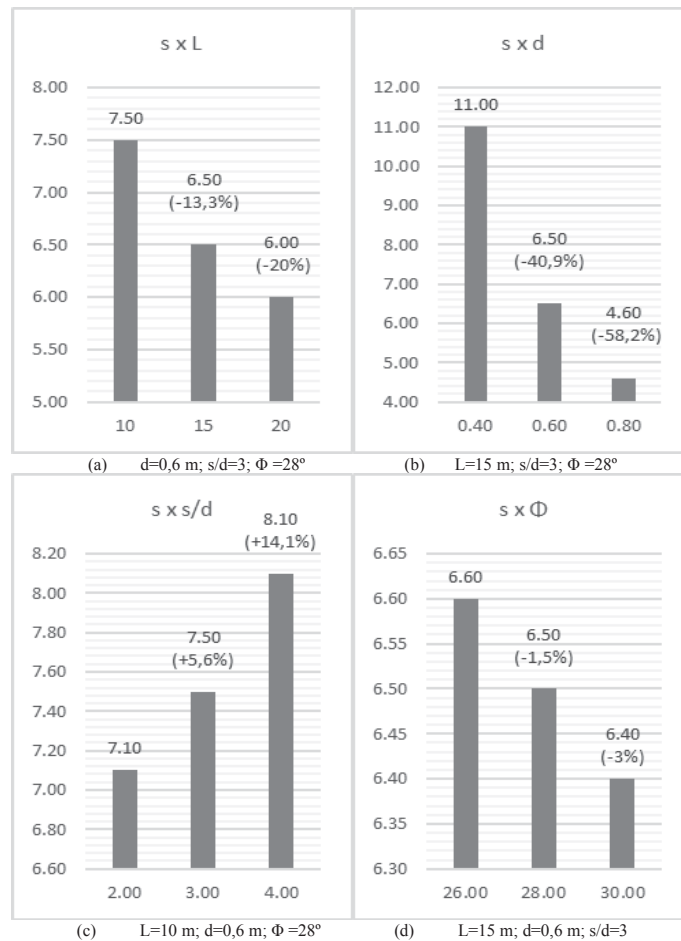


Figure 4: Finite element method settlement plotted A through D [first author].

#### 4.2.2. Poulos & Davis (1980)

In this method a limit settlement of 25 mm was pre-established if the value did not reach the critical settlement of the structure (foundation rupture).

As the length of the piles increased, a reduction in settlement was observed. As for example in the model with diameter 0.6 m, internal friction angle equal to  $28^\circ$  and  $s/d$  ratio equal to 3, the verified values are 8.50 mm, 4.10 mm (-51.8%) and 3.9 mm (-54.1%) for the lengths 10, 15 and 20 m.

For the increase in diameter, the settlement showed a reduction. This is observed with the example  $L=15$  m, angle  $\Phi=28^\circ$  and ratio  $s/d=3$ , the settlements are 22.70 mm, 3.10 mm (-86.3%) and 2.60 mm (-88.5%), respective to diameters of 0.40 m, 0.60 m and 0.80 m.

With the increase of the distance between the piles, the settlement values increased by approximately 35% in most cases. However, the most unfavorable case will be used as an example. In the model with  $d=0.60$  m,  $\Phi=28^\circ$  and  $L=10$  m, the values are 3.80 mm, 8.50 mm (+123.7%) and 13.00 mm (+242.1%) for  $s/d$  equal to 2, 3 and 4, in order.

Finally, for increasing the internal friction angle of the soil, no change was observed in the settlement values.

The above data is shown in the graphs below.

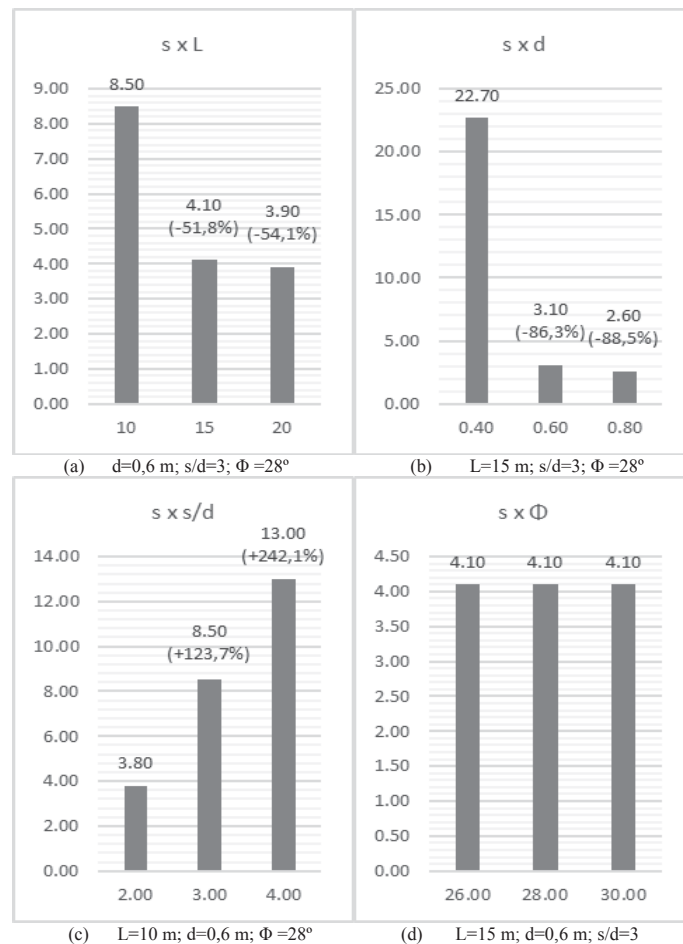


Figure 5: Poulos & Davis (1980) method settlement plotted A through D [first author].

### 4.3 Maximum rotation and displacement of the piles

In this topic it was observed that both increasing the geometric parameters (length, diameter, and distance between the piles) and increasing the angle of internal friction causes the rotation to decrease.

The following graphs show the variation of rotation at the pile head in degrees (y-axis) as a function of the change of parameters cited (x-axis).

The parameter that caused less change in the rotation of the piles was the increase of the internal friction angle of the medium sand, as shown in the images below.

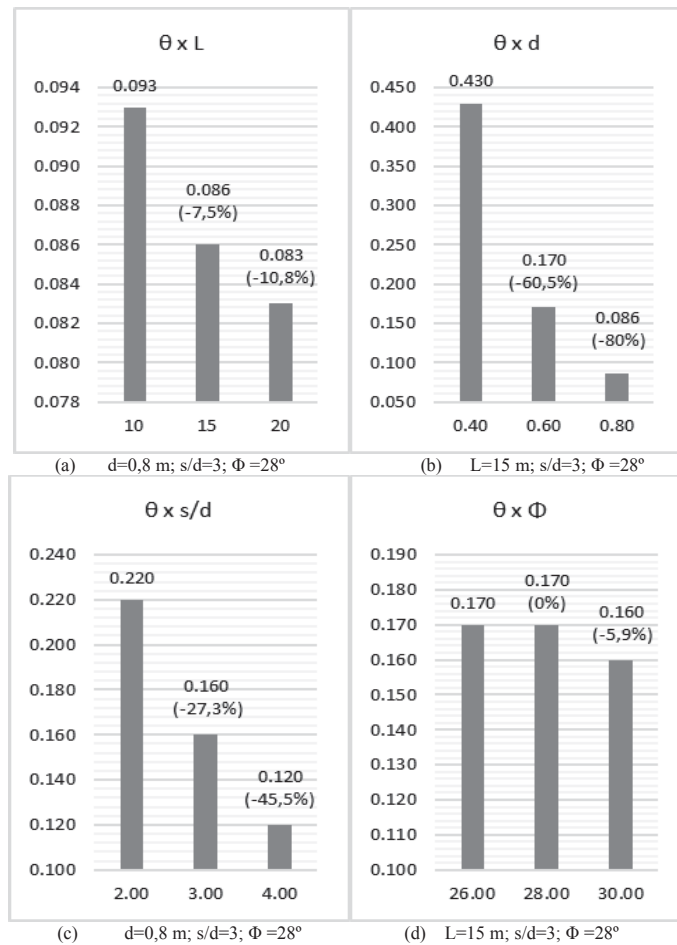


Figure 6: Maximum rotation at the pile head plotted A through D [first author].

For the maximum displacement, an increase only occurs when the length of the pile is changed. For the other parameters there is a decrease in the final values. The following graphs illustrate the percentage of variation of the displacements.

It can be observed that the change that generated the greatest reduction in displacement was the increase in pile diameter.

Finally, it is important to say that all the values presented are negative due to the direction of the axis where the horizontal loads were applied. To facilitate the visualization of the variations, the values are presented as positive, being the y axis the displacement in millimeters and the x axis the variation of the parameters.

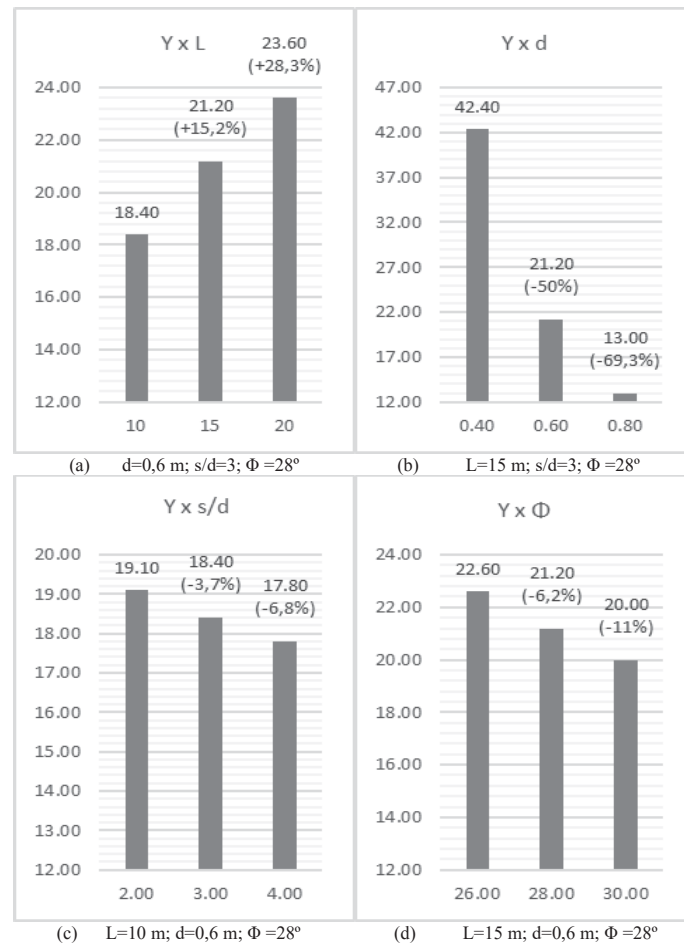


Figure 7: Maximum displacement at the pile head plotted A through D [first author].

## 5 CONCLUSIONS

From the 81 analytical models studied, it can be concluded that the ultimate strength of the piles increases according to the increase of the length and the distance between the group elements. As for increasing the diameter and the angle of internal friction of the medium sand, the change is insignificant. The shear strength shows increase when the values of distance between piles and diameter are increased. With the increase of pile length and angle of internal friction, the change is insignificant.

One of the most important parameters of this study is the efficiency of the cuttings. For this topic, it was observed that the only change that causes efficiency reduction is the increase in length. For alterations in the other parameters there is always an increase, with the distance between the piles being the variable that generates the highest percentage of increase. Furthermore, it can be observed that the most efficient pile has 31% higher results than the least efficient, shown in the item 4.1.3.

In the settlement through the method of Poulos & Davis (1980), the values increased only with the increase of the distance between piles. For the other variables, a decrease in the total values was observed. On the other hand, in the FEM analysis, the increase of all variables studied caused the decrease of the maximum settlement value.

The comparison of the settlement methods allows us to conclude that, in approximately 81% of the cases, the settlement results presented by FEM are higher than those presented by Poulos & Davis (1980) methods. This result was already expected, since the FEM considers analysis points at the soil-pile interfaces and express more faithfully the actual changes that



occurred. Moreover, the values obtained by the Poulos & Davis method presented a high percentage of variation between them, making it difficult to recognize a pattern of variation.

In the strain analysis, both the maximum rotation and the maximum displacement were identified in the pile head. In the rotation, there is a decrease in the results with the increase of all changed parameters. The increase in diameter was the one that generated the highest average percentage influence.

For the  $Y_x$  displacement, the only factor that increased the results was the increase of the length of the piles. Increasing the other variables generated decreases in considerably high percentages.

Finally, if the objective of the structural project is the reduction of the maximum rotation in case of higher horizontal loads, the increase of the pile's diameter would be the main factor for this correction. It is important to remember that any project alteration can imply in problems in the execution of the foundation or in the economics of the enterprise. It is indispensable that a thorough study be carried out, since it may require a larger excavation area or major changes in the reinforcement sizing. Besides, when resuming the previous conclusions, the increase of the pile diameter has almost no influence in the improvement of the pile efficiency.

## REFERENCES

- [1] BOLIN, H.W. (1941). The Pile Efficiency Formula of the Uniform Building Code. Building Standards Monthly, Vol.10, No.1, p 4-5.
- [2] BOWLES, J. E. Foundation Analysis and Design. 5th ed. McGraw-Hill International Editions, Singapore, 1996.
- [3] EN 1997-1. Eurocode 7 - Geotechnical Projects. Portugal, March 2010.
- [4] GEO5, Software 2020 version. Help window and interface of simulations.
- [5] MEYERHOF, G. G. (1976). Bearing Capacity and Settlement of Pile Foundations, 11<sup>a</sup> Presentation Terzaghi, Journal of Geotechnical Engineering Division, ASCE, p. 195 – 228.
- [6] NAVAL FACILITIES ENGINEERING COMAND – NAVFAC. Foundations and Earth Structures: Design Manual 7.02. NAVFAC Publications Transmittal, Alexandria/VA (Estados Unidos), 1986. NEVES, I. C. Principle of Virtual Works. Instituto Superior Técnico, Lisbon (Portugal), 2002.
- [7] POTTS, D. M. & ZDRAVKOVIC, L. Finite element analysis in geotechnical engineering – application. Thomas Telford Ltda. London (United Kingdom), 2002.
- [8] POULOS, H. G. & DAVIS, E. H. Pile Foundation Analysis and Design. Rainbow Bridge Book Co., Sydney (Australia), 1980.
- [9] PRAKASH, S. & SHARMA, H. D. Pile Foundations in Engineering Practice. Wiley-Interscience Publication, New York (United States of America), 1989.
- [10] RUIGROK, J. A. T. Laterally Loaded Piles - Models and Measurements. Faculty of Civil Engineering and Geoscience, Technical University of Delft, Delft (The Netherlands), 2010.
- [11] VENKATRAMAIAH, C.: Geotechnical Engineering. Second edition, New Delhi (India): New Age International Publishers, 19.

## ADVANCES IN COMPUTATIONAL AND ANALYTICAL MODELS FOR COLUMN BASE CONNECTIONS

Pablo Torres-Rodas<sup>1</sup>

<sup>1</sup> Universidad San Francisco de Quito  
Diego de Robles  
e-mail: patorresr@usfq.edu.ec

---

### Abstract

Column Base Connections (CBCs) are one of the most important components of Steel Moment Frames (SMFs) since these connections transfer the loads (e.g., gravity, wind, or earthquake loads) from the superstructure to the foundation. Because of it, CBCs have been extensively studied over the last decade through large-scale experimental programs and computational models that have led to the development of well-developed design guides such as the Design Guide 1 (DG1). Early analytical models were developed to predict the strength of CBCs, while subsequent studies estimated their rotational Stiffness, as well as deformation capacity. Modern studies on the topic have been developed to explore their behavior further with sophisticated finite element simulations. Moreover, their high deformation capacity with desirable hysteretic properties has called the researcher's attention to incorporate CBCs as part of the energy dissipation system.

The broad research conducted on this area points to the importance of CBCs. Motivated by this issue, this paper summarizes the (*state of the art*) analytical and numerical models that characterize the behavior of CBCs. First, the different types of CBCs used in the industry are described. Next, the analytical models to predict their strength, rotational Stiffness, and hysteretic properties are summarized. Strategies for the development of finite element models, as well as results from simulations, are detailed. The influence of column base behavior on the global performance of SMFs (varying in height) is described. Finally, the author's essential results from ongoing research on ductile base plates are discussed, and lines for future investigations are recommended.

**Keywords:** Base Plates, Analytical Models, Numerical Models, Steel Moment Frames

---

## 1 INTRODUCTION

Column Base Connections (CBCs) are, perhaps, the most important component of Steel Moment Frames (SMFs). These connections are designed to transfer the loads from the superstructure (Dead, Live, Wind, Earthquake) into the foundation, being an interface between them (i.e., superstructure and foundation). Depending on the loads that are going to be transferred and the type of building (low rise – high rise), CBCs might be classified into two categories: Exposed Base Plates (EBPs) and Embedded Base Connections (EmBCs). The former consists of a base plate welded to a steel column and anchored to the foundation through steel bolts (a grout pad typically levels the foundation), while the latter detail consists of a steel column with a base plate embedded into a concrete foundation. Typically EBPs are used for low to mid-rise buildings, while EmBCs are the norm for taller buildings. Figure 1 shows a schematic representation of both details.

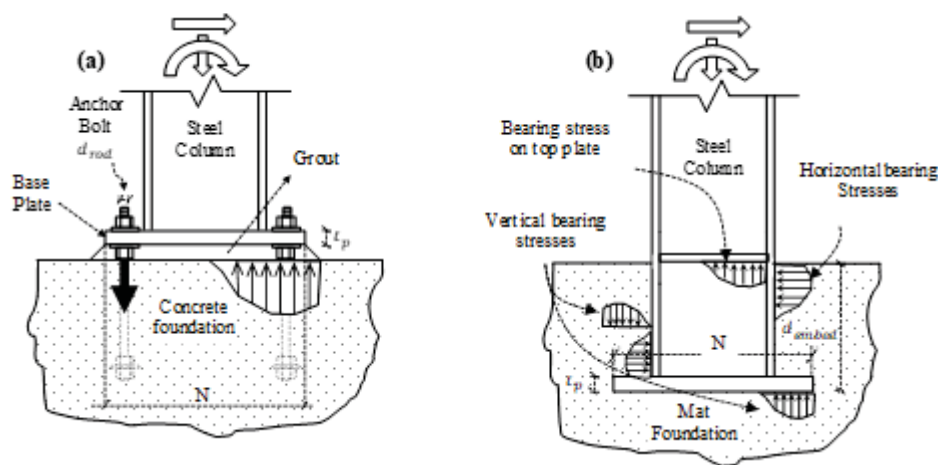


Figure 1: a) EBP detail and the internal force distribution, b) EmBC configuration and the internal force distribution (from Torres-Rodas et al., 2018[12])

The EBPs resist the applied loads by a combination of the bearing stresses developed between the concrete foundation and the base plate and by the tensile forces in the anchor rods. Thus, the axially compressive force is resisted by the bearing stresses in the base plate's compression side, while the Moment is resisted by the couple formed by the resultant compressive force and the tensile force from the bolts (Figure 1a). The shear forces are carried by either friction forces developed between the base plate and the grout/foundation or with a shear key. These connections strongly rely on the level of axial Load applied, and consequently, the relation Moment/Axial Load significantly affects the connection response. Thus, the response of the connection (i.e., Strength, Rotational Stiffness, and Hysteretic characteristics) is defined by complex interactions between its components. Specifically, these interactions refer to the contact and gapping between the base plate and the foundation (or grout pad), and the contact between the top side of the base plate (tension side) and the bottom side of the nut-washers arrangement.

On the other hand, EmBCs resist the applied forces by the horizontal stresses developed between the column flange and the foundation and the vertical stresses in the interface between the embedded base plate and the concrete foundation (Figure 1b). Joint shear forces accompany the horizontal stresses. In contrast with EBPs, EmBCs are no dependent on the ratio of Moment/Axial Load applied. Instead, the experimental evidence [1] indicates that these

connections depend on the Moment/Shear Load's ratio. Thus, the response of EmBCs is dictated by the embedded depth as well as the cross-section of the steel column.

During the last years, CBCs have been extensively studied due to their importance. Early studies on EBPs focus on the development of strength methods based on the modes of failure [2-4]. These models have been validated in experimental programs [2] and further improved [5]. Subsequent studies focused on estimations of their rotational Stiffness [6] and investigation of their hysteretic characteristics [7]. Sophisticated Finite Element Models have been developed to explore the internal stress distribution further [8]. These studies ended up in notably guides for the design of EBPs, such as Design Guide 1 (DG1) [9]. Similarly, large-scale experimental tests have been conducted on EmBCs. These experimental programs lead to the development of methods to compute the strength [1], rotational Stiffness [10] and describe with computational models the hysteretic behavior of EmBCs [11]. Moreover, Torres-Rodas et al., 2018 [12] focus the attention on the seismic demands on these connections with recommendations for their design.

Recent studies on SMFs [13-18] have explored the consequences of weakening the strength of CBCs with the intention to leverage their high deformation capacities and desirable hysteretic properties. These studies show that similar performance (assessed in terms of collapse probability at MCE level) can be achieved in the SMF's behavior if CBCs are sized based on the overstrength seismic load combination rather than with the capacity design criteria. Thus, the idea of protecting the connection with the use of the capacity design criteria may be unnecessary.

Consequently, CBCs play an essential role in the behavior of SMFs. Motivated by this issue, this paper summarizes the main studies (in the author's judgment) about the behavior of both EBPs and EmBCs, describing the state of the art on CBC modeling, and presenting recommendations for new lines of research on the topic. The paper is divided into five sections, beginning with this introductory section, while section two presents models to characterize the Strength, Rotational Stiffness, and Hysteretic behavior of EBPs. Section three details the corresponding models for EmBCs, while section four discusses the findings of the effect of CBC's behavior on the performance of SMFs, finalizing the paper with the Conclusion section.

## **2 MODELS FOR EXPOSED BASE PLATES**

### **2.1 Strength Method**

The analytical methods that quantify the strength of EBPs may be classified into three categories: 1) models that assume a predefined stress distribution on the compression side of the base plate; 2) models that suppose that base plates are rigid and enforce the compatibility of deformation between the components; and 3) sophisticated models that consider the interaction between the modes of deformation of the components. In the context of U.S. construction practice (and in most of the European countries), the first approach is typically adopted for the design of EBPs. The main reason is due to its simplicity in contrast with the other methods. Elkyne and Drake [19] proposed a method that falls in this first category. This method assumes a predefined (either rectangular or triangular) bearing stress form in the connection's compression side. Thus, the Moment is carried by the force-couple developed by the tensile axial forces in the anchor rods and the resultant compressive force from the bearing stresses. The shear forces are taken by either the friction forces in the interface between the base plate and the grout pad/foundation or by a shear key (Figure 1a). On the other hand, the second approach assumes a rigid base plate

neglecting the base flexibility. The model proposed by Wald et al., [20] is an example of this category. However, studies such as Gomez et al., [5] and Kanvinde et al., [21] have indicated that this approach leads to inaccurate results (against test data) on the nonconservative side. Finally, the third method applies the principles of mechanics to propose a procedure to construct Moment – Curvature diagrams [22, 23] given the size of the base plate, anchor rods, their material properties, and the level of Axial Load. Although the results are accurate and based on fundamental principles, the procedure is relatively complex to be implemented in a design office.

In the context of US construction, the design of EBPs is carried out based on the recommendations of DG1 [9]. DG1 assumes a rectangular stress block on the compression side of the base connection. Depending on the level of Axial Compressive Force, the applied Moment is resisted by: 1) bearing stresses in the compressive side of the base plate (low-eccentricity condition), or 2) the force-couple developed between the tensile forces in the anchor bolts and the resultant compressive forces from the bearing stresses (high eccentricity condition). The critical eccentricity, which separates both conditions, may be calculated as:

$$e_{crit} = \frac{N}{2} - \frac{P}{2Bf_{max}} \quad (1)$$

In equation 1,  $N$ , and  $B$  are the length and width of the base plate, respectively.  $P$  is the Axial Load applied, while  $f_{max}$  is the maximum value assumed for the stress block. In the low-eccentricity condition (i.e.,  $e \leq e_{crit}$ ), the only limit state possible is base plate bending in the compressive side, while for the high eccentricity condition (i.e.,  $e \geq e_{crit}$ ), three limit states can occur: 1) fracture of the anchor bolts, 2) bending of the base plate in the tension side, 3) bending of the base plate in the compressive side. The equilibrium equations ( $\sum F_y = 0$ ,  $\sum M_z = 0$ ) are solved to determine the internal forces. For the low-eccentricity case, the unknowns are the magnitude of the bearing stresses ( $f < f_{max}$ ) and the length ( $y$ ) of the rectangular stress block. On the other hand, for the high eccentricity condition, the unknowns are the tensile forces in the anchor rods ( $T$ ) and the length ( $y$ ) of the rectangular stress block. The shear forces in these connections are taken by the friction forces in the interface base plate-grout pad or by a shear key designed for this purpose.

As per DG1, the attainment of one of the before-mentioned limit states represents the capacity of the connection. However, subsequent studies such as Gomez et al., 2010 [5] show that EBPs pose a higher strength capacity. In fact, the maximum capacity is reached once a second component of the connection yields. Thus, the first yield of a component is associated with the called Moment at First Yield of the connection, while the Peak Moment is associated with the formation of a mechanism.

DG1 only deals with the uniaxial bending problem. Hassan et al., 2021 [24] extended the concepts of DG1 to EBPs subjected to biaxial bending with Axial Loads to estimate the internal forces. This procedure implies solving the indeterminacies that take place due to the tensile forces in the anchor rods. The authors suggested a predetermined pattern of the anchor rods' forces based on an assumed Instantaneous Axis of Rotation in conjunction with the rectangular stress block assumption from DG1. An iterative process is required to define the position (inclined) of the Neutral Axis once the equilibrium equations are satisfied. The method was validated against a large set of FE simulations for different base plate configurations.



## 2.2 Rotational Stiffness

Several researchers have studied the flexibility of EBPs (e.g., [22]). Kanvinde et al. 2012 [25] provide a practical method to estimate these connections' rotational Stiffness by aggregating the deformations within its components. The details of this method (which has been validated by [26]) are explained next.

The method leverages the assumptions made by DG1 to characterize the internal force distribution (i.e., a rectangular bearing stress block). The next step is to estimate the Moment at the first yield of the connection, which is defined as the Moment corresponding to the first yield of one of the connection components, i.e., the anchor bolts, base plate at the tension side, or base plate at the compression side. Once this quantity is computed, it is compared with the critical Moment (related to  $e_{crit}$ ) to define if the connection is under high or low eccentricity. For the first case (i.e., high eccentricity), the internal forces are used to compute the deformations of the three sources of base flexibility: anchor rods elongation, base plate bending (in the tension and compression side), and the concrete foundation. For the low eccentricity case, the method considers the concrete foundation as the only source of flexibility since the base plate is not expected to uplift (and consequently, the anchor rods will not elongate). In this manner, the deformations of the components have been estimated. Thus, the rotation of the connection can be computed by dividing the total deformation of the components by the base plate length. Finally, the Rotational Stiffness is defined as the ratio between the Moment at the first yield and the base rotation. Figure 2 illustrates this definition.

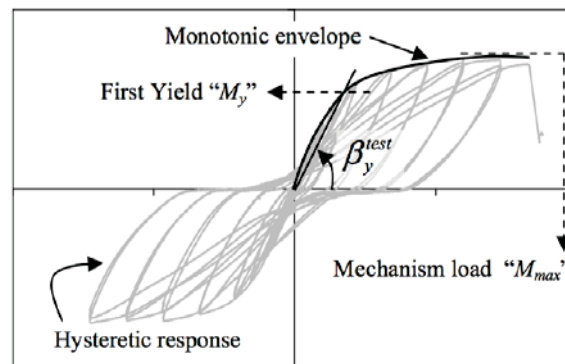


Figure 2: Definition of Rotational Stiffness of EBPs (from [6])

## 2.3 Hysteretic Behavior

The hysteretic characteristics of EBPs have been studied by Torres-Rodas et al., 2016 [7]. These authors proposed a rotational hinge (EBC model) that captures the essential features of the hysteretic behavior of EBPs observed in experimental programs (e.g., [2], [3], [4], [5]). Specifically, this mathematical model consists of a tri-linear backbone curve, a set of hysteretic rules aimed to capture the characteristic shape of the M-Rot curves of EBPs, and rules to capture the modes of deterioration for these connections. Figure 3 illustrates the backbone curve of the model. As per this figure, the backbone curve captures the three initial stages of the connection response. The first stage refers to the linear elastic response. In this phase, the loads are taken by the combination of bearing stresses and tensile forces in the anchor bolts. This phase ends when one of the connection components yields (i.e., base plate or anchor bolts). The element that yielded continues to increase its deformations in the second stage of the response (i.e., strain hardening phase) with an increase in the connection strength. This strength reaches a peak (giving rise to the third phase) when a second component of the connection yields. In this



manner, a yield plateau is formed in the connection response. Thus, the backbone curve is defined by four parameters: 1) the Moment at First Yield ( $M_y$ ), 2) the Peak Moment ( $M_{peak}$ ), 3) the initial Rotational Stiffness ( $K_{init}$ ), and 4) the Rotation associate with the Peak Moment ( $\theta_{peak}$ ). Among these four parameters, the first three of them (i.e.,  $M_y$ ,  $M_{peak}$ ,  $K_{init}$ ) can be estimated by the analytical models described in the sub-sections 2.1 and 2.2, while the latter parameter ( $\theta_{peak}$ ) must be obtained experimentally.

In contrast with the monotonic response, the hysteretic rules from the EBC model capture the characteristic flag shape hysteresis and the related re-centering effect. Figure 3b shows the details of these hysteretic rules defined by four parameters. These parameters are the Initial Moment at the intermediate plateau, the end position of this intermediate plateau, and two parameters that define the pinching behavior. Only the Initial Moment at the intermediate plateau can be estimated from an analytical model, while the rest of the parameters are obtained by empirical calibrations. The Initial Moment at the intermediate plateau corresponds to the connection moment associate with the instant the anchor bolts start to carry axial forces. Finally, the EBC model captures four modes of cyclic deterioration observed in EBPs. These modes reflect the cycle to cycle decrease in 1) the unloading Stiffness, 2) Peak Strength, 3) Intermediate Plateau, and 4) deformation associated with the intermediate plateau. Four empirically calibrated parameters (two for each mode) are necessary to capture these modes of deterioration. EBC model uses the rule proposed by Rahnema and Krawinkler (1993) [27] to simulate the cyclic deterioration. The assumption of this rule is that deterioration depends on the energy dissipated.

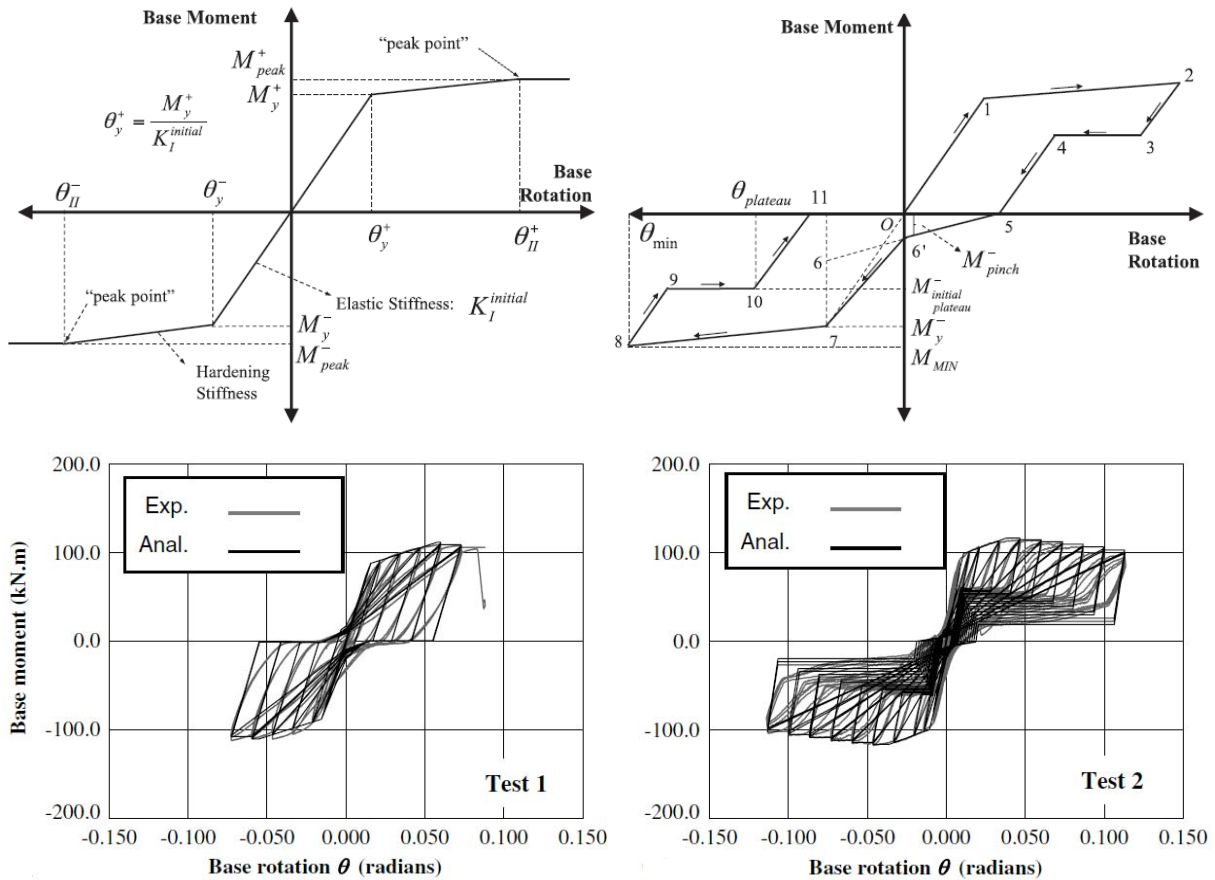


Figure 3: a) Backbone curve of ECB model, b) Hysteretic Rules, c) Calibration Test1, d) Calibration of test 2 (from [7])

Figure 3c,d shows the validation of the EBC model against the experimental test conducted by [5]. A visual inspection of Figure 3c indicates that the EBC captures the hysteretic response's essential features (i.e., the re-centering effect, the hysteretic shape, and the modes of deterioration). Thus, the EBC model is appropriate to capture the overall connection behavior in Non-linear Time History (NTH) frame simulations. However, it is important to detail its limitations. First, the EBC model (as all uniaxial plasticity models) cannot capture the Moment-Axial Load interaction. This problem may be treated in an approximate manner, assuming expected values of Axial Load. Second, the model has been validated against a limited number of tests (5 in total). Thus, it is difficult to generalize the EBC model's functionality for connections with significantly different configurations. Finally, the EBC model has not been validated against connections under tensile Axial Load or Biaxial Bending.

## 2.4 Finite Element Models

Several researchers have developed strategies to conduct Finite Element (FE) simulations on EBPs. Krishnamurty and Thambiratnam (1989) [28] presented one of the earliest FE studies conducted on EBPs to validate design methodologies based on the rigid base plate assumption. Stamapolous and Ermopoulos (2011) [29] conducted an experimental and analytical investigation on EBPs developing of 8 tests. These authors constructed 3D FE models to validate the mathematical formulation suggested in [22], and the results indicate a good agreement between the simulations, the experimental results, and the mathematical model suggested. As mentioned before in the paper, one of the drawbacks of this approach is that it is excessively complicated to be implemented in a design office.

Kanvinde et al., 2013 [8] examined the response of EBPs with sophisticated 3D FE simulations. This paper presents critics to the current assumptions regarding the internal stress distributions and suggests. The FE models include essential features of the connection behavior such as contact and gapping between the components (i.e., base plate and foundation/grout pad, nut-washer arrangement, and base plate) and the nonlinear multiaxial constitutive response of the materials. The models were validated against six large-scale tests conducted by Gomez et al., 2010 [5]. Results of this study indicate that the stress distribution in most of the cases is quite different from the assumed rectangular stress block at DG1. Thicker base plates tend to concentrate the stresses in the base plate's toe, while in thinner base plates, the stresses are concentrated under the compression flange of the column. In contrast to the drawbacks found in the internal stress assumption, the simulations indicate that the anchor bolt forces are well estimated by the equations given at DG1.

More recently, Trautner and Hutchinson 2018 [30] presented a procedure for parametric FE simulations of EBPs (with different details) subjected to combined Axial and Moment loads, validating the models against numerous experimental tests. Hassan et al., 2021 [24] studied with FE simulations the behavior (i.e., internal force distribution) of EBPs under combined Axial Compressive Force and Biaxial Bending. These simulations were validated against experimental test data and constituted the basis of the analytical method detailed in sub-section 2.1 for predicting internal forces in EBPs under Biaxial Bending in the presence of Axial Force. Torres-Rodas et al., 2020 [31] developed FE models to study the behavior of EBPs with extended anchor bolts. This configuration detail intends to concentrate all the inelastic action in the extended region of the anchor bolts, protecting the rest of the connection components.

## 2.5 Reliability Analysis of EBPs

Aviram et al. 2010 [32] carried out a system reliability analysis of the EBPs of a low-rise building located at Berkeley with the intention to evaluate the safety with respect to the different modes of failure reported in the literature. Results of this study indicate that the reliability index for these connections was below the value expected for connections [33]. Torres-Rodas et al., 2020 [34] studied this topic further. These authors evaluated the reliability of EBPs in SMFs designed based on DG1. A statistical approach was suggested to compute strength resistance factors for the modes of failure observed in connections (i.e., concrete bearing, base plate yielding, and anchor bolts failure) [5] to achieve a target reliability index of 4.5. Two buildings were analyzed (2-story and 4-story) using a suite of 120 ground motions from strike-slip and reverse faults. This paper presented a capacity limit state formulation for EBPs considering the M-P interaction, and the focus is on the seismic demands, which are explicitly treated as random variables. Results confirm the reliability index is below the target value. The reliability analysis of EBPs was also studied by Song et al., 2020 [35]. The analysis was conducted using Monte Carlo sampling for the uncertainties from the demands and capacity in this investigation. A total of 59 design scenarios was evaluated. Results confirm the findings from Aviram et al., 2010 and Torres-Rodas et al., 2010 with respect to the reliability index. This study's design recommendation is to eliminate the bearing resistance factor when the flexural demands on the base plate are calculated. Similar to Torres-Rodas et al., 2020, new load resistance factors (with values inferior to the suggested by DG1) are proposed.

## 3 MODELS FOR EMBEDDED BASE CONNECTIONS

### 3.1 Strength Method

Grilli and Kanvinde [1] conducted the first large-scale experimental program on EmBCs for seismic design purposes. The parameters investigated were the embedded length, the column size, and the level of Axial Load. From this experimental program, the modes of failure were identified, and the internal force distribution was postulated. Thus, it is assumed that the Axial Compressive force is resisted by the top stiffener plate as well as the bottom base plate. The applied Moment is resisted through the column flanges at the top of the connection. A fraction of this Moment is resisted by the horizontal stresses against the panel zone, whereas the remainder portion of the Moment is resisted by the vertical bearing stresses at the bottom base plate. The shear forces are resisted by a compression strut formed in the panel zone (Figure 1b).

Once the internal force mechanism is established, the capacities corresponding to each mode of failure can be characterized. Thus, for the horizontal bearing stresses developed in the interface between the column flanges and the concrete foundation, two modes of failure are identified 1) concrete bearing failure and 2) shear failure of the joint panel. On the other hand, the vertical bearing stresses in the bottom base plate entail four modes of failure 1) bearing failure of the concrete surrounding the base plate, 2) concrete breakout under the compression toe of the base plate, 3) concrete breakout above the base plate, and 4) base plate yielding. With these limit states, the Moment capacity associated with the horizontal bearing stresses (i.e.,  $M_{HB}^{capacity}$ ) and the Moment capacity associated with the vertical stresses (i.e.,  $M_{VB}^{capacity}$ ) might be calculated.

The capacity of the connection is determined by combining  $M_{HB}^{capacity}$  and  $M_{VB}^{capacity}$ . These mechanisms are constrained by deformation compatibility, implying that their moment

contributions are additive (i.e., system in parallel). The fraction of the total Moment to each mechanism is solved by the introduction of an empirical equation that relates the embedded length and the relative Stiffness of the column and the surrounding media. Thus, two scenarios can occur 1) failure due to vertical stresses takes place before failure due to horizontal stresses, 2) failure due to horizontal stresses occurs before failure due to vertical stresses. In the first scenario, the capacity of the connection is dictated by the precise mode of failure within the vertical bearing mechanism. In contrast, if the second scenario occurs, the capacity of the connection depends on which of the two modes of failure controls. If the concrete bearing failure controls, then  $M_{HB}^{capacity} = M_{HB}^{bearing}$  and the Moment carried by the horizontal stresses gradually decrease due to an increase in the deformations, and consequently, the vertical stresses will take a larger fraction of the total Moment. If shear failure controls, then no additional moment might be sustained.

### 3.2 Rotational Stiffness

The flexibility of EmBCs has been studied by Tryon 2016 [36] and Torres-Rodas et al., 2017 [10]. Tryon 2016 [36] studied the flexibility of base connections with an overtopping slab, which may be classified as shallowly embedded connections. In this detail, the Moment is carried primarily by the resistance to the uplift of the base plates due to the anchor bolts and by the overlying slab. Usually, the embedded length of these connections is less than 300mm. In contrast, in deeply embedded base connections, the loads are taken by (as described in the previous subsection) the bearing stresses in the column flanges (i.e., horizontal stresses) and the vertical stresses in the bottom base plate.

Torres-Rodas et al., 2017 [10] presented a method to characterize the rotational Stiffness of EmBcs. This method was developed based on the insights gained from the experimental program conducted by Grilli et al., 2018 [1], and consisted of calculating the components' deformations within the connection (i.e., embedded column and concrete foundation). The method was validated against a total of 9 large-scale tests from the programs conducted by [1] and [36]. The details of the method are explained next.

The method assumes from the experimental tests that the Moment at First Yield occurs at 0.7 of the Peak Moment. The latter parameter is obtained from the strength method earlier described. Thus, the connection stiffness is estimated as the ratio between the Moment at First Yield and the base rotation. Based on the internal force distribution postulated by Grilli and Kanvinde [1], the deformations of the embedded steel column and the surrounding foundation are calculated. Figure 4a illustrates the patterns of deformations assumed. Finally, the deformations are aggregated to determine the base flexibility (Figure 4b).

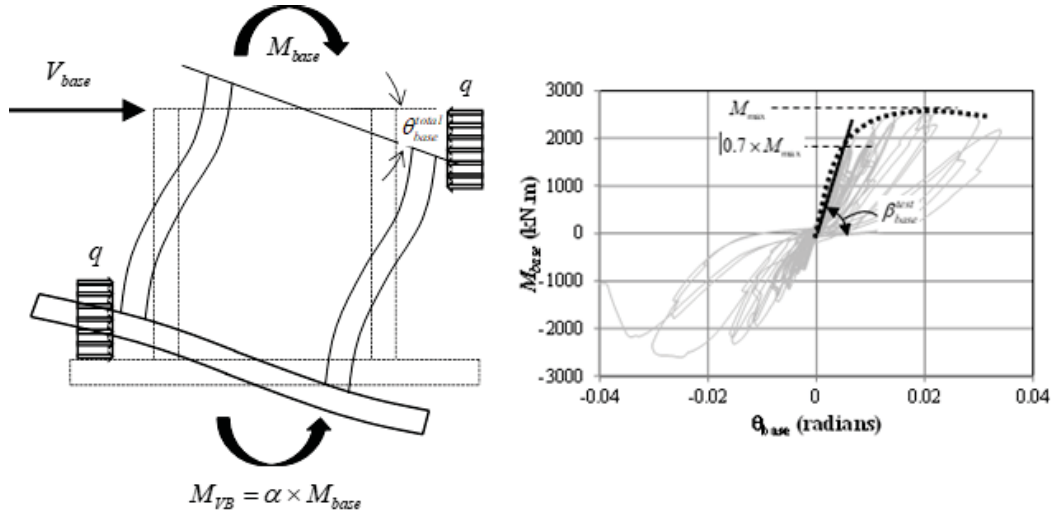


Figure 4: a) Patterns of deformation, b) Definition of Rotational Stiffness (from [10])

### 3.3 Hysteretic Behavior

The experimental studies conducted on EmBCs (e.g., [1],[36]) indicate that these connections are ductile with good hysteretic properties. This issue motivated the study by Torres-Rodas et al., 2018 [11] to formulate a mathematical model (EmBC model) to predict the essential characteristics of the behavior of EmBCs for Nonlinear Time History Simulations. The EmBC model is physically based and validated against Grilli and Kanvinde [1]. The details of this model are briefly explained next.

The EmBC model consists of two rotational springs arranged in parallel, where each spring is associated with the force transfer mechanism, i.e., horizontal bearing stress or vertical bearing stress. In this manner, the degradation of the capacity due to horizontal bearing stresses and the corresponding Moment transfer to the vertical bearing stresses is effectively simulated. Thus, the horizontal bearing mechanism is represented by a trilinear backbone curve defined by the well-known Ibarra-Medina-Krawinkler Pinching Model, while the elastic-perfectly plastic model simulates the vertical mechanism. Four parameters (i.e., Initial Elastic Stiffness, Moment at First Yield, Peak Strength, and Rotation Associate with Peak Strength) are necessary to define the spring that represents the horizontal stresses, while two parameters (i.e., Initial Elastic Stiffness, and Moment at First Yield) are required for the vertical bearing spring.

The cyclic response of these connections is described by the IMK Pinching Model's hysteretic rules detailed in Ibarra et al., 2006 [37]. These hysteretic rules capture two important aspects of the cyclic response: 1) pinching behavior, attributed to the closure of cracks or gaps between the column flange and the concrete foundation, 2) cyclic deterioration of two quantities, i.e., the strength plateau and unloading stiffness. The rules proposed by Rahnama and Krawinkler [27] were used to simulate cyclic deterioration and apply only to the horizontal spring since the experimental tests do not provide evidence of deterioration for the vertical spring. Besides, the vertical mechanism gains strength as the horizontal spring deteriorates.

Figure 5, illustrates the results of the validation of the EmBC model against two tests. Clearly, the essential aspects of the connection response are captured by the model formulation and can be easily implemented in NTH simulations. Although the results are promising, the EmBC model has several limitations that must be considered. The model is validated against a limit



(only five) number of tests. It implies that its results can not be extrapolated to connections with significantly different details. Moreover, it inherits the limitations of a uniaxial plasticity model, i.e., it can not capture the Moment-Axial Load interaction.

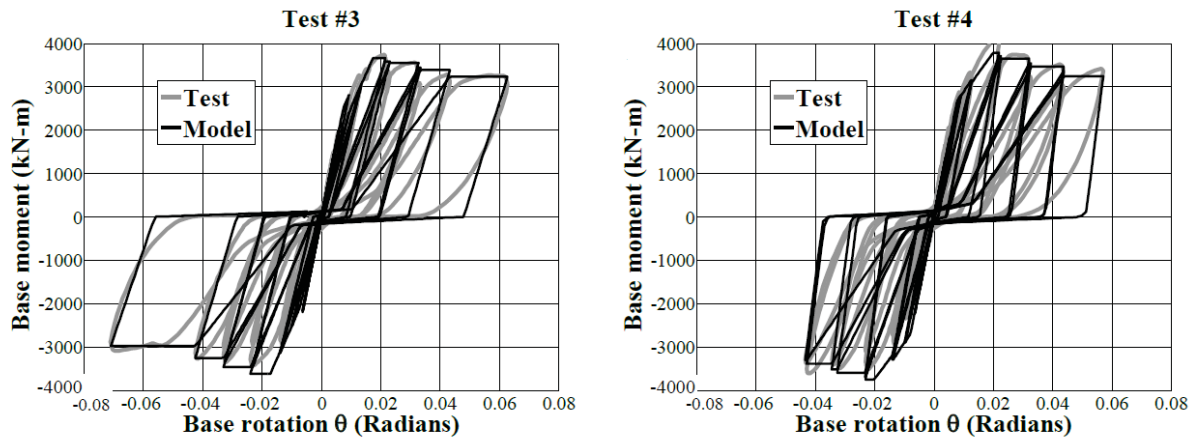


Figure 5: EmBC model validation (from [11])

### 3.4 Finite Element Models

Information about strategies to develop FE models for EmBCs is sparse. Jones 2016 [38] developed 3D FE models for the characterization of the Rotational Stiffness of shallowly embedded base connections. Inamasu et al. [39] studied the seismic design of EmBCs by FE simulations. In this study, the steel column was modeled with shell elements, and the base connection behavior was represented by a rotational spring at the bottom of the column. These models were validated against available tests (e.g., Grilli and Kanvinde [1]). The Finite element models feature the Voce-Chaboche multiaxial plasticity law. The constant parameters were obtained through an optimization process. Local buckling is triggered by considering local imperfections within a certain magnitude. The FE models simulate the response of a design example documented at the AISC Seismic Design Manual. Thus, the connection's response was studied parametrically, being the web local slenderness and the level of Axial Load the parameters investigated. Results indicate that the seismic demands on EmBCs are strongly influenced by the column position (i.e., interior or exterior) and by the cross-section geometry (i.e., local slenderness). Equations empirically calibrated are suggested to promote yielding in the column region above the concrete foundation. More recently, Mora-Bowen and Torres-Rodas [40] further explore the internal force distribution within the components and the patterns of deformation to provide improvements in the design of these connections. This topic is part of the ongoing research projects of the author.

## 4 EFFECT OF CBC'S BEHAVIOR ON THE PERFORMANCE OF SMFs

The effect of CBCs' behavior (i.e., ductility and flexibility) on the seismic response of SMFs has called the attention of researchers during the last years. The main reason is that experimental programs have shown that these connections pose excellent dissipative characteristics with high deformation capacities. Moreover, investigations such as Lignos and Krawinkler 2007 [41] indicate that the ductility of columns in the presence of Axial Compressive Forces might be compromised due to local buckling. Thus, the traditional concept of protecting the connection (remaining elastic) may be unnecessary. This idea may be attributed to the lack of analytical



models capable of predicting base connections' behavior. However, mathematical formulations such as [7, 11, and 16] have permitted to capture the overall connection response and incorporate it in NTH frame simulations.

Falborski et al., 2020 [14] studied the effect of Base Connection Strength, Rotational Stiffness, and Deformation Capacity on the Collapse Probability of four archetype frames parametrically. The authors considered four levels of base strength (and the associate Stiffness) and a range of deformation capacities (from 1% to 5%) to conduct the collapse assessment. Results indicate that if CBCs are detailed to hold rotations of 0.05rad, the seismic demands in the design can be reduced from the Capacity Design Criteria (1.1RyMp) to the Overstrength Seismic Load ( $\Omega=3$ ). This is supported by the similar performances (in terms of probability of collapse) achieved by the SMFs analyzed. The implication is that the strength of the connection is decreased by approximately 40%.

Base connections designed to promote anchor bolt yielding have been investigated by Trautner et al., 2016 [26] and Inamasu et al., 2020 [16]. Trautner et al., [26] conducted a series of large-scale tests to assess the effect of anchor bolt material type, anchor stretch length, column setting method, and base plate hole size on the behavior of the connection. Among these parameters, the setting method and the stretch length appear to be the most influential in the Moment-Rotation response. Moreover, Inamasu et al., 2020 [16] studied the influence of anchor-yield EBPs in the residual deformations of low-rise SMFs. Results from this study indicate that low-rise buildings with anchor-yield EBPs are less likely to experience residual drifts than buildings with EBPs designed based on the strong connection-weak column criteria. Besides, low-rise buildings with ductile EBPs, do not suffer an axial shortening which may significantly complicate the retrofit work.

More recently, Torres-Rodas et al., 2021 [18] studied the interactive effect of column base hysteretic behavior, continuity of gravity columns, and beam-column gravity connections strength on the seismic performance of SMFs. For each archetype frame, different levels of base connection strength, gravity columns rigidity, and beam-column gravity connections were assigned to assess their impact on the Collapse Probability at MCE level of 5 SMFs varying in height. A total of 80 mathematical models were developed, and NTH simulations were conducted as per FEMAp695 methodology. Results indicate that the presence of continuous gravity columns profoundly affects the archetype frames' behavior investigated by reducing their probability of collapse. In this manner, the desirable hysteretic characteristics of ductile CBCs can be incorporated safely as part of the energy dissipative mechanisms. The design implication is that seismic demands can be reduced (similar conclusion as Falborski et al., 2020) safely to the overstrength seismic loads if base connections can rotate up to 0.05rad.

## **5 CONCLUSIONS AND RECOMMENDATIONS FOR FUTURE WORK**

This paper presents a summary (based on the author's judgment) of the numerical and analytical models to characterize the column base connection behavior. Moreover, new findings on the influence of base connection behavior on the seismic performance of SMFs are detailed. The main intention is to synthesize current findings on the topic to highlight the importance of these connections in the overall frame behavior. Thus, the paper is divided into four sections. The first one introduces the topic, while the next two sections describe the main models to simulate

EBPs and EmBCs. A subsequent section is dedicated to examining the influence of the CBCs on building performance metrics (e.g., collapse probability at MCE level).

Traditionally, CBCs have been sized in order to promote plastic strains in the lower region of the column rather than in the connection itself. This approach may be attributed to 1) the intuitive idea that connections are less ductile than members and 2) the lack of available models to predict the behavior of base connections. However, in the last years, several studies have shown that perhaps this criterion is not appropriate for two main reasons 1) ductility in column members in the presence of Axial Load might be compromised due to local buckling, 2) column base connections pose high deformation capacities with desirable hysteretic properties.

Consequently, several researchers have explored the idea of moving from capacity design criteria to a weak base strong column concept. Results from studies such as [15-18] indicate that reducing the seismic design demands in ductile base connections would lead to similar performance to frames designed with stronger base plates. Moreover, column problems such as axial shortening may be eliminated if plastic strains are concentrated in ductile anchor bolts. This topic has called the attention of researchers and deserves further scrutiny. It is recommended to focus on experimental studies on ductile anchor bolt connections, especially with the intention to facilitate the retrofit work after an earthquake event.

## 6 REFERENCES

- [1] Grilli, D.A. and Kanvinde, A.M. (2015). "Embedded Column Based Connections subjected to Flexure and Axial loads," Report 3-11 submitted to the Charles Pankow Foundation.
- [2] DeWolf J.T., and Sarisley, E.F. (1980), "Column Base Plates with Axial Loads and Moments," *Journal of the Structural Division, ASCE*, Vol. 106, No. 11, November 1980, pp. 2167-2184
- [3] Astaneh, A., Bergsma, G., and Shen J.H. (1992). "Behavior and Design of Base Plates for Gravity, Wind and Seismic Loads," *Proceedings of the National Steel Construction Conference*, Las Vegas, Nevada, AISC, Chicago, Illinois.
- [4] Burda, J.J., and Itani, A.M. (1999). "Studies of Seismic Behavior of Steel Base Plates," Report No. CCEER 99-7, Reno (NV): Center of Civil Engineers Earthquake Research, Department of Civil and Environmental Engineering, University of Nevada, NV.
- [5] Gomez I.R., Kanvinde A.M. and Deierlein G.G. (2010). "Exposed Column Base Connections Subjected to Axial Compression and Flexure," Report Submitted to the American Institute of Steel Construction (AISC), Chicago, IL.
- [6] Kanvinde, A.M., Grilli, D.A., and Zareian, F. (2012). "Rotational Stiffness of Exposed Column Base Connections – Experiments and Analytical Models," *Journal of Structural Engineering, ASCE*, 138(5), 549-560.
- [7] Rodas, P. T., Zareian, F., & Kanvinde, A. (2016). Hysteretic model for exposed column–base connections. *Journal of Structural Engineering*, 142(12), 04016137.
- [8] Kanvinde, A. M., Jordan, S. J., & Cooke, R. J. (2013). Exposed column base plate connections in moment frames—Simulations and behavioral insights. *Journal of Constructional Steel Research*, 84, 82-93.

- [9] Fisher, J.M. and Kloiber, L.A. (2006), “Base Plate and Anchor Rod Design,” 2nd Ed., Steel Design Guide Series No. 1, American Institute of Steel Construction, Inc., Chicago, IL.
- [10] Rodas, P. T., Zareian, F., & Kanvinde, A. (2017). Rotational stiffness of deeply embedded column–base connections. *Journal of structural engineering*, 143(8), 04017064.
- [11] Torres-Rodas, P., Zareian, F., & Kanvinde, A. (2018). A hysteretic model for the rotational response of embedded column base connections. *Soil Dynamics and Earthquake Engineering*, 115, 55-65.
- [12] Torres-Rodas, P., Zareian, F., & Kanvinde, A. (2018). Seismic demands in column base connections of steel moment frames. *Earthquake Spectra*, 34(3), 1383-1403.
- [13] Torres-Rodas, P., Flores, F., & Zareian, F. (2018). Seismic response of steel moment frame considering gravity system and column base flexibility. In *Proc. 11th US Natl. Conf. Earthq. Eng.*, June 25–29, Los Angeles, USA.
- [14] Falborski, T., Torres-Rodas, P., Zareian, F., & Kanvinde, A. (2020). Effect of base-connection strength and ductility on the seismic performance of steel moment-resisting frames. *Journal of Structural Engineering*, 146(5), 04020054.
- [15] Torres-Rodas, P., Flores, F., Astudillo, B.X., Pozo, S. (2020). Sensitivity of special steel moment frames to the influence of column-base hysteretic behavior including gravity framing system. *Proceedings of the International Conference on Structural Dynamic , EUROLYN*, 2020, 2, pp. 3629–3642
- [16] Inamasu, H., de Castro e Sousa, A., Güell, G., & Lignos, D. G. (2020). Anchor-yield exposed column bases for minimizing residual deformations in seismic-resistant steel moment frames. *Earthquake Engineering & Structural Dynamics*.
- [17] Y. Cui, F. Wang, S. Yamada, Effect of Column Base Behavior on Seismic Performance of Multi-Story Steel Moment Resisting Frames, *International Journal of Structural Stability and Dynamics*. 19 (2019) 1940007. <https://doi.org/10.1142/S0219455419400078>.
- [18] Torres-Rodas, P., Flores, F., Pozo, S., & Astudillo, B. X. (2021). Seismic performance of steel moment frames considering the effects of column-base hysteretic behavior and gravity framing system. *Soil Dynamics and Earthquake Engineering*, 144, 106654.
- [19] Drake, R. and Elkin, S. (1999). “Beam-Column Base Plate Design LRFD Method”. *Engineering Journal*.
- [20] Wald, F. Column Base Modelling. In *Semi-Rigid Joints in Structural Steelwork*. Vienna:Springer; 2000, p. 227-288.
- [21] Kanvinde A.M., Higgins P., Cooke R.J., Perez J., Higgins J. Column Base Connections for Hollow Steel Sections: Seismic Performance and Strength Models. *Journal of Structural Engineering*, ASCE 2015; 141(7): 04014171.
- [22] Ermopoulos, J. C., & Stamatopoulos, G. N. (1996). Analytical modelling of column-base plates under cyclic loading. *Journal of constructional steel research*, 40(3), 225-238.
- [23] Ermopoulos, J. C., & Stamatopoulos, G. N. (1996). Mathematical modelling of column base plate connections. *Journal of constructional steel research*, 36(2), 79-100.

- [24] Hassan, A; Torres-Rodas, P; Giulietti, L; Kanvinde, A (2021, in press). Strength characterization of exposed column base plates subjected to axial force and biaxial bending. *Engineering Structures*.
- [25] Kanvinde, A. M., Grilli, D. A., & Zareian, F. (2012). Rotational stiffness of exposed column base connections: Experiments and analytical models. *Journal of structural engineering*, 138(5), 549-560.
- [26] Trautner, C. A., Hutchinson, T., Grosser, P. R., & Silva, J. F. (2016). Effects of detailing on the cyclic behavior of steel baseplate connections designed to promote anchor yielding. *Journal of Structural Engineering*, 142(2), 04015117.
- [27] Rahnama, M., and Krawinkler, H. (1993). "Effects of soft soil and hysteresis model on seismic demands" Report No. 108. The John A. Blume Earthquake Engineering Center.
- [28] Thambiratnam, D. P., & Krishnamurthy, N. (1989). Computer analysis of column base plates. *Computers & structures*, 33(3), 839-850.
- [29] Stamatopoulos, G. N., & Ermopoulos, J. C. (2011). Experimental and analytical investigation of steel column bases. *Journal of constructional steel research*, 67(9), 1341-1357.
- [30] Trautner, C. A., & Hutchinson, T. C. (2018). Parametric finite-element modeling for exposed steel moment frame column baseplate connections subjected to lateral loads. *Journal of Structural Engineering*, 144(6), 04018049.
- [31] Torres, P., Medalla, M., Lopez-Garcia, D., Campos, L., & Zareian, F. (2021). Strength method for exposed base plates with extended anchor bolts.
- [32] Aviram, A., Stojadinovic, B., Der Kiureghian, A. (2010). "Performance and Reliability of Exposed Column Base Plate Connections for Steel Moment-Resisting Frames," PEER Report 2010/107, Pacific Earthquake Engineering Research Center, Berkeley, CA.
- [33] Ellingwood, B; Galambos, T; MacGregor, J; Cornell, A. (1980). "Development of a Probabilistic Based Load Criterion for American National Standard A58". National Bureau of Standards.
- [34] Torres-Rodas, P., Fayaz, J., Zareian, F. (2020). Strength resistance factors for seismic design of exposed based plate connections in special steel moment resisting frames. *Earthquake Spectra*, 36(2), 537-553.
- [35] Song, B., Galasso, C., & Kanvinde, A. (2021). Reliability Analysis and Design Considerations for Exposed Column Base Plate Connections Subjected to Flexure and Axial Compression. *Journal of Structural Engineering*, 147(2), 04020328.
- [36] Tryon, J.E., (2016). "Simple models for estimating the rotational stiffness of steel column to footing connections," Masters Thesis, Brigham Young University.
- [37] Ibarra, L. F., Medina, R. A., & Krawinkler, H. (2005). Hysteretic models that incorporate strength and stiffness deterioration. *Earthquake engineering & structural dynamics*, 34(12), 1489-1511.
- [38] Jones, T. A. (2016). Finite Element Modeling of Shallowly Embedded Connections to Characterize Rotational Stiffness.

- [39] Inamasu, H., Kanvinde, A. M., & Lignos, D. G. (2021). Seismic design of non-dissipative embedded column base connections. *Journal of Constructional Steel Research*, 177, 106417.
- [40] Mora-Bowen, N., Torres-Rodas, P. (2021 in press). Nonlinear Finite Element Models for Embedded Base Connections. *COMPADYN* 2021
- [41] Lignos, D. and Krawinkler, H. (2007). "A Database in Support of Modeling of Component Deterioration for Collapse Prediction of Steel Frame Structures". *Structural Engineering Frontiers*.

## **ACKNOWLEDGMENTS**

The author expresses in this paper his profound thanks to his mentors Prof. Farzin Zareian (UC Irvine) and Prof. Amit Kanvinde (UC Davis), for all the lessons learned during and after the doctorate program. The author thanks Universidad San Francisco de Quito for the support given to this publication.

## INFLUENCE OF EARTHQUAKE MECHANISMS TO THE SEISMIC RESPONSE OF STEEL MOMENT FRAMES

Liseth Campos<sup>1</sup>, Pablo Torres-Rodas<sup>2</sup>, Pablo Quinde<sup>2</sup>, and Fabricio Yepez<sup>2</sup>

<sup>1</sup> Universidad San Francisco de Quito  
Diego de Robles  
lcampos@estud.usfq.edu.ec

<sup>2</sup> Universidad San Francisco de Quito  
Diego de Robles  
{patorresr,fyepez}@usfq.edu.ec; pquindem@aisg.com.ec

---

### Abstract

Recent studies conducted on Steel Moment Frames (SMFs) highlight the importance of considering the effect of certain characteristics of earthquake ground motions (GMs) such as duration and spectral shape in their seismic response. Although their acceleration response spectra have mainly characterized ground motions in seismic standards, these studies indicate that the probability of collapse is sensitive to the GMs' duration. This represents a concern in areas with a different tectonic mechanism, such as South-America, and Pacific Northwest U.S., where subduction processes mainly generate GMs. It is well-known that the duration and spectral shape of subductions earthquakes are quite different from crustal earthquakes. Motivated by these issues, this research presents a parametric study to assess building height sensitivity to metrics such as inter-story drift ratios and floor accelerations, considering GMs records from subduction and crustal earthquakes carefully selected and scaled.

The scientific basis of this research is a series of nonlinear dynamic analyses conducted on SMFs (varying in height) at different seismic hazard levels. Two hazard levels are considered in this study: a) Life safety and b) Collapse prevention. The paper intends to understand the sensitivity of engineering demand parameters (i.e., drifts and floor accelerations) of SMFs to different earthquake mechanisms (i.e., crustal earthquakes vs. subduction earthquakes). The GMs records of subduction earthquakes consist of a set of GMs representative of South America and Japan's seismicity. The GMs records set of crustal earthquakes collects large magnitude-long distance events representative of Southern California.

**Keywords:** Steel Moment Frames, EDPs, Floor Accelerations, Megathrust Earthquakes.

---



## 1 INTRODUCTION

Steel Moment Frames (SMFs) are among the most popular systems to resist lateral forces, chiefly due to their architectural versatility. When appropriately designed and detailed, SMFs are among the most ductile available systems for seismic regions [1]. Because of these reasons, these systems have been extensively studied in the past. Early studies on the topic concentrated their attention on the response modes, ending up in the design philosophies [2]. After the 1994 Northridge and 1995 Kobe earthquakes, the focus was on the study of beam-column connections [3]. More recently, with the advances in computational capabilities, SMFs have been studied under the framework of Performance-Based Earthquake Engineering (PBEE). In this manner, extreme limit states such as the collapse probability have been introduced as performance metrics (e.g., [4,5]).

The PBEE approach has enabled researchers to explore profoundly different aspects of SMF response. For instance, the effect of column base behavior on the seismic performance of SMFs has been addressed by several studies (e.g., [6-9]). The influence of the gravity framing system on their collapse probability has been investigated by [10,11]. The soil-structure interaction effects on the response of buildings subjected to earthquakes were assessed by [12,13]. More recently, several researchers have focused on loss estimation after earthquake events [14,15]. Besides, different models have been proposed to predict the behavior of nonstructural elements [16-18]. The technological advances have permitted monitoring buildings entailing the development of new fields such as structural health monitoring [19,20].

The preceding discussion highlights the importance that SMFs have received during the last decades. Besides, it is worldwide accepted that ground motion (GM) parameters such as amplitude, duration, and frequent content, are the most influential on buildings' response. However, practitioner engineers typically carry out their structural designs based on the building codes (e.g., ASCE 7-16), which characterize GMs with the design spectrum. As per this concept, the design spectrum quantifies GMs' amplitude and frequency content, neglecting the influence of duration. Recent studies such as [21-24] have investigated the influence of duration on the collapse probability of buildings by subjecting archetype frames to short and long duration GMs. Results of these studies indicate that duration and spectral shape play a significant influence on the collapse probability of buildings.

Medalla et al. 2020 [25] studied the response of SMFs (i.e., 40 in total) subjected to megathrust earthquakes by performing a hazard-consistent analysis and a comparative collapse evaluation. The authors showed that the collapse probability of SMFs is higher when these systems are subjected to megathrust earthquakes rather than crustal earthquakes. Thus, the seismic demands for the design of buildings located in countries with high seismic activity (e.g., Ecuador) where the GMs are mainly caused by megathrust earthquakes and adopt the US steel design standards may be underestimated, resulting in potentially nonconservative designs.

Motivated by the preceding discussion, this paper presents an evaluation of the earthquake mechanisms' influence, i.e., crustal earthquakes vs. subduction earthquakes on Engineering Demand Parameters (EDPs) such as inter-story drift ratios (IDR) and floor accelerations (FA). For this purpose, a total of 5 archetype frames (varying in height) were subjected to two sets of GMs. The first set represents GMs associated with subductive mechanisms, while the second set contains GMs from crustal earthquakes. Those GMs were carefully selected and scaled to represent two hazard levels a) Life safety and b) Collapse prevention. Thus, the sensitivity of the SMFs to EDPs is assessed through this investigation. In this manner, new insights about SMFs behavior are given. The paper starts by describing the problem in this introductory section. Next, the details of the nonlinear models are described. Then, in a subsequent section of

the paper, the results are presented and discussed, and finally, conclusions, limitations of the current work, and lines for future work are provided.

## 2 METHODOLOGY OF THE PAPER

For the purposes of this paper, i.e., to assess the sensitivity of EDPs to earthquake mechanisms, a total of five archetype frames are developed. The difference among these frames lies in their height (varying from 8.50m to 79.85m). Thus, this investigation's scientific basis consists of a series of Nonlinear Time History (NTH) simulations conducted on the mathematical models developed herein. These archetype frames are part of the study by NIST [26], have been adopted in several studies about SMFs' behavior (e.g., [27-29]), and their salient features are described next.

### 2.1 Mathematical Models

Figure 1a illustrates the typical plan view of all buildings. The SMFs are located at the perimeter of the building, while the rest of the components are part of the gravity framing system. All SMFs are three-bay frames, with a width of 6.10m. The first story's height is 4.50m, while the rest of the stories are 3.90m. The buildings were designed as per ASCE 7-05. On all the floors it was applied a dead load of 4.78 kN/m<sup>2</sup>, and an unreduced live load of 2.38 kN/m<sup>2</sup>, with the exception of the roof, where a live load of 0.95 kN/m<sup>2</sup> was applied. The weight of the cladding was considered with a perimeter load of 1.20 kN/m<sup>2</sup>. For the seismic design of the SMFs it was assumed a Response Coefficient Factor  $R=C_d=8$ , and site class "D" conditions under the seismic design category  $D_{max}$ , which is consistent with the far-field conditions of Los Angeles. The beam-column connections are detailed as RBS connections based on ASIC 341 [30] and AISC 358 [x]. For more details about these SMFs, refer to [31].

Concentrated plasticity models have been adopted for this investigation since this approach has been broadly used for studies on SMFs (e.g., [27, 28, 29, 32, 33]). Thus, beams and columns are idealized as linear-elastic elements with rotational springs (hinges) at their ends. Beam members consist of three linear elastic elements with two hinges located each at the RBS, while column members consist of one linear elastic element with two rotational springs at the ends. These rotational springs are simulated with the well-known Ibarra-Medina-Krawinkler (IMK) bilinear model [34]. This model consists of a trilinear backbone curve with rules that capture cyclic strength and stiffness deterioration. These rules were initially proposed by Ibarra et al. [34] and then modified by Lignos and Krawinkler [35]. The spring properties were calculated by the methodology detailed at NIST [36].

The IMK bilinear models, as all uni-axial plasticity models, are not able to capture the Moment-Axial Load (M&P) interaction. For the springs located at the columns, this phenomenon is captured in an approximate manner. Thus, a reduced bending strength is calculated with the interactive equations from AISC [37] under the presence of an average gravity load (i.e.,  $1.05 P_D + 0.5 P_L$ ). This approach has been adopted in other studies related to the assessment of SMFs behavior (e.g., [27, 28, 29, 32, 33]) mainly because SMFs are drift-controlled rather than force-controlled, and consequently, the columns are lightly loaded. Moreover, studies such as [38] show good agreement between experimental results and this approach. Panel zones are modeled as a parallelogram assembly with rigid elements and with a nonlinear spring placed at one corner to simulate shear distortions in the parallelogram. Column bases were modeled with the rotational springs suggested by Torres-Rodas et al., 2016 [39] for the low-rise buildings (i.e., 2-, 4- story) and with the models by Torres-Rodas et al., 2018 [40] in the case of taller buildings

(i.e., 8-, 12-, 20- story). P-Delta effects were captured using a leaning column connected to the SMFs through rigid elements and loaded with the gravity load equivalent to half of the building at each floor plant.

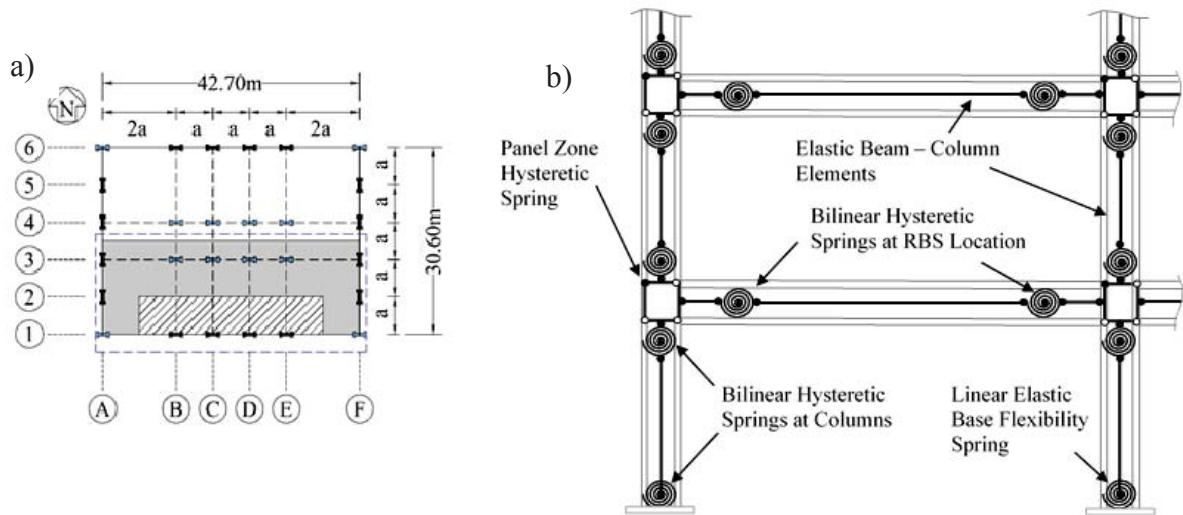


Figure 1: a) Typical plan view of all frames (from [9]), b) Mathematical models of the SMFs (from [32])

## 2.2 Ground Motions Selected

The seismic demands were analyzed using two criteria. On the one hand, several intense ground motions recorded worldwide were analyzed, including both subduction and crustal earthquakes. The earthquakes are shown in Table 1. These earthquakes were scaled linearly so that their intensities cover the accelerations reported in the MCE and DE spectrum of ASCE7-16 [41].

ID	Earthquake	Country	Year	Mw
1	Valparaiso	Chile	1985	7.9
2	Chi-Chi	Taiwan	1999	7.6
3	Sur Peru	Chile	2001	8.4
4	Tokachi-Oki	Japan	2003	8
5	Tocopilla	Chile	2007	7.7
6	Maule	Chile	2010	8.8
7	Tohoku	Japan	2011	9
8	Iquique	Chile	2014	8.1
9	Manabi	Ecuador	2016	7.8
10	Loma Prieta	USA	1989	6.9
11	Landers	USA	1992	7.3
12	Northridge	USA	1994	6.7
13	Kobe	Japan	1995	6.9
14	Duzce	Turkey	1999	7.1
15	Hector	USA	1999	8.1

Table 1: Megathrust earthquakes used for seismic simulation

On the other hand, as mentioned within this research's objectives, the aim is to analyze records of subduction and crustal ground motions representing the tectonic behavior of South America. For this, subduction earthquakes in Chile and Ecuador and crustal earthquakes recorded in Colombia's central region were analyzed. In the seismic accelerometric network of the mentioned countries, there are few records generated during high-intensity ground motions associated with return periods of more than 250 years. Due to this lack of information, seismic simulation was used for analyzes carried out in this study.

The seismic simulations were carried out in two phases. On the one hand, seismological simulation techniques using Green's functions were applied. When it was not possible to reach the design intensities, linear scaling was used to reach the objective thresholds. Linear scaling factors were always lower than 1.8. The simulation technique used is proposed by Kohrs-Sansorny et al. [2005][42]. This methodology uses a two-stages stochastic summation of low-intensity motions (seed motions) that work as empirical Green's functions. Likewise, the simulation employed considers a seismic source point and requires the characterization of two parameters: a) the seismic moment ( $M_0$ ) and b) the stress drop ( $\Delta\sigma$ ). This methodology considers the variation of frequency and energy contents. This technique incorporates wave propagation and site effects in such a way as to eliminate geological uncertainties from the problem when using the same site where the record was obtained [43]. The seed motions for crustal earthquakes used in this paper were recorded during the events under consideration in Table 2 for the Colombian network.

Date	$M_w$	$M_0$ (dyne-cm)	$\Delta\sigma$
25/01/1999	6.3	2.54E+25	40
08/03/2005	5.2	7.94E+23	50
06/02/2017	5.4	1.58E+24	50

Table 2: Seismic parameters for the seeds used in seismic simulations for crustal earthquakes

### 2.3 Nonlinear Time History Simulations

All the mathematical models developed herein were subjected to the two sets (i.e., crustal and megathrust) of GMs detailed in this paper's previous subsection. The software OpenSees is used for all the simulations since it has been extensively verified for NTH analysis [44], and all the modeling features earlier described can be applied. Moreover, several researchers have used this platform to study the behavior of SMFs with the use of NTH analysis [25-29]. Thus, the effect of the earthquake mechanisms (i.e., crustal vs. subductive) in the buildings' seismic performance (i.e., EDPs) is assessed. A total of five mathematical models representing the archetype frames (2-, 4-, 8-, 12- and 20- story) illustrated in Figure 1b have been developed for this investigation. Table 3 summarizes the fundamental periods of each frame. Two seismic hazard levels are considered in this study a) Life safety and b) Collapse prevention. For each simulation, two response metrics are recorded a) Maximum Floor Accelerations (FA) and b) Peak Interstory Drift Ratios (IDR). In this manner, the median values of the EDPs from each set (i.e., crustal vs. subduction) are compared.

Story Frame	First Period (s)
2-	0.69
4-	1.86
8-	2.42
12-	3.18
20-	4.44

Table 3: First Period of the frames

### 3 DISCUSSION OF RESULTS

The results from the NTH simulations of all the mathematical models are discussed in this section of the paper. Table 4 summarizes the results from the median IDR of all the SMFs at the two seismic hazard levels (i.e., DE and MCE level of shaking) analyzed herein, while Table 5 summarizes the results from the peak floor accelerations. As per Table 4, results from the simulations indicate that the IDRs of the low and mid-rise buildings (i.e., 2-, 4-, 8- and 12-stories) are relatively insensitive to the earthquake mechanism (i.e., crustal vs. subduction). The median values of the maximum IDRs associated with each earthquake mechanism are relatively similar, with the only exception in the tall building, i.e., the 20-story building. For this frame, the IDRs tend to be increased by 25% for the subductive earthquakes compared with the GMs' crustal set. This observation might indicate that the earthquake mechanism's influence is associated with the building height (and consequently the first vibration mode).

In contrast to IDRs, Table 5 indicates that the peak floor accelerations (FA) of all the frames are sensitive to the earthquake mechanism. As per Table 5, the subductive GMs entail higher FA than crustal earthquakes. At the Design seismic hazard level, the FA are amplified on average by 35% in the subductive earthquakes, while at MCE level of shaking, the FA are amplified (on average) by 50%. Results from the simulations indicate that the building height does not play an important role in the sensitivity of earthquake mechanisms to FA as apparently it does in IDRs.

Floor accelerations play an essential role in the behavior of nonstructural components. It is worldwide accepted that these components may be divided into two broad groups: the first one, sensitive to IDRs, while the second one, sensitive to floor accelerations [45,46]. Components such as masonry and partition walls fall in the first category, while ducts, parapets, or tanks are examples of the second group [46]. The components from this latter category must carry the forces coming from the building motion. Typically, the acceleration demands acting on these elements are evaluated from the floor response spectrum criteria, where the spectrum is calculated based on the floor accelerations at the desired level. Results from this investigation indicate that the earthquake mechanism (crustal vs. megathrust) profoundly influences the building response in terms of peak floor accelerations, which might affect the anchorage detailing of nonstructural components sensitive to this EDP.

Summary of Results median (I.D.R.) (%)					
Hazard Level	# Stories				
	2	4	8	12	20
M.C.E. with Crustal	3.00	3.12	3.44	3.37	3.46
M.C.E. with Megathrust	3.07	3.82	3.37	3.92	4.79
D.E. with Crustal	2.31	2.44	2.39	2.25	2.79



D.E. with Megathrust	1.97	2.80	2.48	2.48	3.75
----------------------	------	------	------	------	------

Table 4: Summary of Results median (I.D.R.) (%) including collapses.

Summary of Results median Floor Accelerations					
Hazard Level	# Stories				
	2	4	8	12	20
M.C.E. with Crustal	458.68	509.30	572.36	760.84	1018.11
M.C.E. with Megathrust	580.19	763.09	1112.76	1203.07	1746.92
D.E. with Crustal	325.75	379.15	515.21	568.22	640.69
D.E. with Megathrust	440.50	614.40	880.75	880.76	1211.87

Table 5: Summary of Results median floor Accelerations including collapses.

#### 4 SUMMARY, CONCLUSIONS, AND LIMITATIONS

This paper presents the results from NTH simulations conducted on five archetype frames varying in height (i.e., 2-, 4-, 8-, 12- and 20-story) with the intention to evaluate the influence of the earthquake mechanisms (i.e., crustal vs. subduction) on building's metrics such as maximum IDRs and peak floor accelerations. For this purpose, ground motions from both mechanisms were carefully selected and scaled. Two criteria were used for the selecting and scaling process. The first one consists of a linear scaling to the GMs selected with the DE and MCE spectrums from ASCE 7-16 [41], while the second approach uses seismological techniques to simulate GMs.

The results from the NTH simulations conducted in this paper indicate that GMs (scaled at a defined intensity) from megathrust earthquakes cause higher peak floor accelerations than GMs (scaled at the same intensity as the megathrust ones) from crustal earthquakes. On average, the amplification is around 50% when the GMs are scaled to the MCE level of shaking, while it is close to 35% at DE level. This finding might be important in the context of detailing the anchorage of nonstructural components sensitive to accelerations. On the other hand, the IDRs seem to be less sensitive to the earthquake mechanism. Only the 20-story SMF shows an amplification due to the subductive process, which might indicate a potential influence of the building height.

The results of this paper are subjected to limitations that must be addressed appropriately to generalized the findings. First, a limited number of frames is considered (five in total); second, the bias due to ground motion effects, including the GMs' vertical component; third, the modeling assumptions might affect the results (e.g., concentrated plasticity models vs. distributed plasticity models). Finally, this research does not address the soil-structure interaction effects.

#### REFERENCES

- [1] M. Bruneau, C.-M. Uang, R. Sabelli, Ductile design of steel structures, McGraw-Hill, New York; Toronto, 2011. <http://www.myilibrary.com?id=335745> (accessed October 1, 2018).
- [2] Popov, E. P., & Bertero, V. V. (1980). Seismic analysis of some steel building frames. Journal of the Engineering Mechanics Division, 106(1), 75-92.



- [3] Ricles, J. M., Mao, C., Lu, L. W., & Fisher, J. W. (2003). Ductile details for welded unreinforced moment connections subject to inelastic cyclic loading. *Engineering Structures*, 25(5), 667-680.
- [4] Zareian, F., & Krawinkler, H. (2010). Structural system parameter selection based on collapse potential of buildings in earthquakes. *Journal of structural engineering*, 136(8), 933-943.
- [5] Lignos, D. G., & Krawinkler, H. (2011). Deterioration modeling of steel components in support of collapse prediction of steel moment frames under earthquake loading. *Journal of Structural Engineering*, 137(11), 1291-1302.
- [6] Falborski, T., Torres-Rodas, P., Zareian, F., & Kanvinde, A. (2020). Effect of base-connection strength and ductility on the seismic performance of steel moment-resisting frames. *Journal of Structural Engineering*, 146(5), 04020054.
- [7] Inamasu, H., de Castro e Sousa, A., Güell, G., & Lignos, D. G. (2020). Anchor-yield exposed column bases for minimizing residual deformations in seismic-resistant steel moment frames. *Earthquake Engineering & Structural Dynamics*.
- [8] Y. Cui, F. Wang, S. Yamada, Effect of Column Base Behavior on Seismic Performance of Multi-Story Steel Moment Resisting Frames, *International Journal of Structural Stability and Dynamics*. 19 (2019) 1940007. <https://doi.org/10.1142/S0219455419400078>.
- [9] Torres-Rodas, P., Flores, F., Pozo, S., & Astudillo, B. X. (2021). Seismic performance of steel moment frames considering the effects of column-base hysteretic behavior and gravity framing system. *Soil Dynamics and Earthquake Engineering*, 144, 106654.
- [10] F.X. Flores, F.A. Charney, D. Lopez-Garcia, Influence of the gravity framing system on the collapse performance of special steel moment frames, *Journal of Constructional Steel Research*. 101 (2014) 351–362. <https://doi.org/10.1016/j.jcsr.2014.05.020>
- [11] A. Elkady, D.G. Lignos, Effect of gravity framing on the overstrength and collapse capacity of steel frame buildings with perimeter special moment frames: EFFECT OF GRAVITY FRAMING ON STEEL BUILDINGS WITH PERIMETER SMF, *Earthquake Engineering & Structural Dynamics*. 44 (2015) 1289–1307.
- [12] Cruz, C., & Miranda, E. (2017). Evaluation of soil-structure interaction effects on the damping ratios of buildings subjected to earthquakes. *Soil Dynamics and Earthquake Engineering*, 100, 183-195.
- [13] Mylonakis, G., & Gazetas, G. (2000). Seismic soil-structure interaction: beneficial or detrimental?. *Journal of earthquake engineering*, 4(3), 277-301.
- [14] Ramirez, C. M., & Miranda, E. (2012). Significance of residual drifts in building earthquake loss estimation. *Earthquake Engineering & Structural Dynamics*, 41(11), 1477-1493.
- [15] Ordaz, M., Miranda, E., Reinoso, E., & Pérez-Rocha, L. E. (1998). Seismic loss estimation model for Mexico City. Universidad Nacional Autónoma de México, México DF.
- [16] Miranda, E., Kazantzi, A., & Vamvatsikos, D. (2018). New approach to the design of acceleration-sensitive non-structural elements in buildings. In *16th European Conference on Earthquake Engineering* (pp. 18-21).

- [17] Kazantzi, A. K., Miranda, E., & Vamvatsikos, D. (2020). Strength-reduction factors for the design of light nonstructural elements in buildings. *Earthquake Engineering & Structural Dynamics*, 49(13), 1329-1343.
- [18] Fierro, E. A., Miranda, E., & Perry, C. L. (2011). Behavior of nonstructural components in recent earthquakes. In *AEI 2011: Building Integration Solutions* (pp. 369-377).
- [19] Song, G., Wang, C., & Wang, B. (2017). Structural health monitoring (SHM) of civil structures.
- [20] Sergiyenko, O., Rivas-López, M., Miranda-Vega, J. E., Flores-Fuentes, W., Rodríguez-Quinonez, J. C., Lindner, L., ... & Tyrsa, V. (2020). Sensors for structural health monitoring. In *Nanosensors for Smart Cities* (pp. 227-248). Elsevier.
- [21] Chandramohan, R., Baker, J. W., & Deierlein, G. G. (2016). Quantifying the influence of ground motion duration on structural collapse capacity using spectrally equivalent records. *Earthquake Spectra*, 32(2), 927-950.
- [22] Chandramohan, R., Baker, J. W., & Deierlein, G. G. (2016). Impact of hazard-consistent ground motion duration in structural collapse risk assessment. *Earthquake Engineering & Structural Dynamics*, 45(8), 1357-1379.
- [23] Chandramohan, R., Baker, J. W., Deierlein, G. G., & Lin, T. (2013). Influence of ground motion spectral shape and duration on seismic collapse risk.
- [24] Chandramohan, R., Baker, J. W., & Deierlein, G. G. (2018). Accounting for the influence of ground motion response spectral shape and duration in the equivalent lateral force design procedure.
- [25] Medalla, M., Lopez-Garcia, D., & Zareian, F. (2020). Seismic characterization of steel special moment frames subjected to megathrust earthquakes. *Earthquake Spectra*, 36(4), 2033-2057.
- [26] NIST, Evaluation of the FEMA P-695 Methodology for Quantification of Building Seismic Performance Factors, National Institute of Standards and Technology, Gaithersburg, MD, 2010
- [27] Zareian, F., & Kanvinde, A. (2013). Effect of column-base flexibility on the seismic response and safety of steel moment-resisting frames. *Earthquake Spectra*, 29(4), 1537-1559.
- [28] Torres-Rodas, P., Flores, F., & Zareian, F. (2018). Seismic response of steel moment frame considering gravity system and column base flexibility. In *Proc. 11th US Natl. Conf. Earthq. Eng.*, June 25–29, Los Angeles, USA.
- [29] Torres-Rodas, P., Flores, F., Astudillo, B.X., Pozo, S. (2020). Sensitivity of special steel moment frames to the influence of column-base hysteretic behavior including gravity framing system. *Proceedings of the International Conference on Structural Dynamic, EURODDN*, 2020, 2, pp. 3629–3642
- [30] AISC, *Seismic Provisions for Structural Steel Buildings*, (2010).
- [31] AISC, *Prequalified Connections for Special and Intermediate Steel Moment Frames for Seismic Applications*, (2010).
- [32] Torres-Rodas, P., Zareian, F., & Kanvinde, A. (2018). Seismic demands in column base connections of steel moment frames. *Earthquake Spectra*, 34(3), 1383-1403.

- [33] Torres-Rodas, P., Fayaz, J., Zareian, F. (2020). Strength resistance factors for seismic design of exposed based plate connections in special steel moment resisting frames. *Earthquake Spectra*, 36(2), 537-553.
- [34] L.F. Ibarra, R.A. Medina, H. Krawinkler, Hysteretic models that incorporate strength and stiffness deterioration, *Earthquake Engineering & Structural Dynamics*. 34 (2005) 1489–1511. <https://doi.org/10.1002/eqe.495>.
- [35] D.G. Lignos, H. Krawinkler, Deterioration Modeling of Steel Components in Support of Collapse Prediction of Steel Moment Frames under Earthquake Loading, *Journal of Structural Engineering*. 137 (2011) 1291–1302. [https://doi.org/10.1061/\(ASCE\)ST.1943-541X.0000376](https://doi.org/10.1061/(ASCE)ST.1943-541X.0000376).
- [36] NIST, Guidelines for nonlinear structural analysis and design of buildings. part IIa - steel moment frames, National Institute of Standards and Technology, Gaithersburg, MD, 2017. <https://doi.org/10.6028/NIST.GCR.17-917-46v2>.
- [37] AISC, Specification for Structural Steel Buildings, (2016)
- [38] Kanvinde, Micromechanical Simulation of Earthquake Induced Fractures in Steel Structures, Blume Earthquake Engineering Center, Stanford, California, 2004.
- [39] P.T. Rodas, F. Zareian, A. Kanvinde, Hysteretic Model for Exposed Column–Base Connections, *Journal of Structural Engineering*. 142 (2016) 04016137. [https://doi.org/10.1061/\(ASCE\)ST.1943-541X.0001602](https://doi.org/10.1061/(ASCE)ST.1943-541X.0001602).
- [40] P. Torres-Rodas, F. Zareian, A. Kanvinde, A hysteretic model for the rotational response of embedded column base connections, *Soil Dynamics and Earthquake Engineering*. 115 (2018) 55–65. <https://doi.org/10.1016/j.soildyn.2018.08.015>.
- [41] ASCE 7, ed., Minimum design loads and associated criteria for buildings and other structures, American Society of Civil Engineers, Reston, Virginia, 2017.
- [42] Kohrs-Sansorny, C., Courboux, F., Bour, M., & Deschamps, A. (2005). A two-stage method for ground-motion simulation using stochastic summation of small earthquakes. *Bulletin of the Seismological Society of America*, 95(4), 1387-1400.
- [43] Garcia, D., Singh, S. K., Herráiz, M., Ordaz, M., & Pacheco, J. F. (2005). Inslab earthquakes of central Mexico: Peak ground-motion parameters and response spectra. *Bulletin of the Seismological Society of America*, 95(6), 2272-2282.
- [44] S. Mazzoni, F. McKenna, M.H. Scott, G.L. Fenves, *OpenSees Command Language Manual*, (2006).
- [45] Lin J, Mahin SA. Seismic response of light subsystems on inelastic structures. *J Struct Eng* 1985;111:400–17.
- [46] Taghavi S, Miranda E. Response assessment of nonstructural building elements, Report No. PEER 2003/05. Richmond, CA: Dept. of Civil and Environmental Engineering, Stanford University, Stanford, CA. Pacific Earthquake Engineering Research Center; 2003. Singh A, Ang AHS.

## SEISMIC ACTION COMBINATION RULES FOR THE DESIGN OF AZIMUTH-INDEPENDENT STRUCTURES

Nikolaos Karaferis<sup>1</sup>, Dimitrios Vamvatsikos<sup>1</sup>

<sup>1</sup> National Technical University of Athens  
9, Iroon Polytechniou Str., Zografou Campus, GR-15780, Athens, Greece  
e-mail: {nkaraferis, divamva}@mail.ntua.gr

---

### Abstract

*The validity of the typical 100/30 combination rule for horizontal seismic action effects is investigated for the design of structures that are axially symmetric along the vertical direction. The 100/30 rule stipulates that one should combine 100% of the seismic action in one principal direction (as estimated by the design spectrum) with 30% of the action in the other principal direction, and vice-versa. Having been derived for azimuth-dependent structures, having e.g., a rectangular plan, it takes advantage of the fact that the two horizontal components of ground motion are only partially correlated, with peaks that in general do not happen simultaneously, to reduce the overall design loads. On the contrary, vertical liquid-storage tanks, silos and chimneys are examples of azimuth-independent structures, which by virtue of their symmetry will always experience the worst-possible incidence angle of a ground motion. To quantify the effect of axisymmetry we employed a database of 150 records with three components of ground motion. The results show that an 106/106 combination rule, or more accurately a 1.12 amplification factor on the design spectrum in a single direction, rather than the 1.04 implied by the 100/30, is adequate to account for the effects of axisymmetry. Still, this value depends on the definition of the underlying design spectrum, and whether, e.g., the maximum, arbitrary or geometric mean component is employed, which should be accounted for in all calculations.*

**Keywords:** Azimuth Independent Structures, Combination Rules, Horizontal Seismic Components, Structural Dynamics, Earthquake Engineering.

---

## 1 INTRODUCTION

In seismic design, engineers address the structure's seismic capacity by applying an acceleration, and therefore a seismic action to the structure, which corresponds to the site where the structure is going to be located. Those values are provided from hazard maps and are specified in the design code [1-3]. In typical structures, it is also the case that two orthogonal horizontal axes are defined, corresponding to the principal directions of the structure, along which the ground motion and therefore the acceleration is applied. As is often the case in modal response spectra analysis (MRSA) or equivalent lateral force (ELF), the response of the structure is calculated separately by applying the design spectra per each of the principal axes. After the response of the structure has been successfully calculated in each, specific combination rules are applied to combine the results of both directions in a singular peak response for designing the structure [4]. Many combination rules and methods have been described in the literature [5] and have been adopted by different design codes, for example the combination rules described in Eurocode 8 [1], for seismic design, proposes the 100+30% rule [6] that suggests that for a specific response we consider the following cases:

$$\begin{aligned} E_{Edx} "+" 0,30E_{Edy} \\ 0,30E_{Edx} "+" E_{Edy} \end{aligned} \quad (1)$$

where the "+" symbol typically signifies a square-root-sum-of-square (SRSS) combination of the effects of the two horizontal components, rather than an actual addition.

This whole process has been chosen after investigations suggesting that with the assumptions above we can safely combine the responses of a building in its principal axes X and Y, without being overly conservative. It would not be realistic to consider that in each direction the worst case values of acceleration would occur simultaneously [7]. This is of course an effective approach for the usual case of azimuth-dependent structures, but there is an obvious difference in case of structures that are fully symmetric with respect to a vertical axis and therefore have azimuth-independent properties, like cylindrical silos, spherical or vertical cylindrical liquid-storage tanks, circular pillars etc. In those structures the worst case scenario, considering the incidence angle of the ground motion, will always be in effect, as the structure has the same response and is equally vulnerable regardless of the axes defined.

In the following, a symmetrical three-dimensional elastic oscillator will be employed to examine its response after performing dynamic analysis using 150 pairs of strong ground motion records. The goal is to highlight the differences of such vertical axisymmetric structures when it comes to their response, ultimately calculating various amplification factors that allow combining the two horizontal components of motion when performing MRSA or ELF analysis for design purposes.

## 2 GROUND MOTION ACCELERATION DEFINITIONS

To properly clarify the process presented in the following paragraphs, in this segment some definitions [8] of how the ground motion acceleration parameters are usually defined in hazard maps provided by most design codes, are necessary. The following parameters represent the acceleration values calculated for a pair of records of the horizontal components derived for a specific earthquake:

- $Sa_{RotD100}$ : The maximum acceleration value from all possible orientations of the records for a specific response period T.
- $Sa_{RotD50}$ : The median value from all possible orientations for a specific period T.

- $Sa_{GMRotD100}$ : The maximum value of the geometric mean of the horizontal components from all possible orientations of the paired records for period  $T$ .
- $Sa_{GMRotD50}$ : The median value of the geometric mean of the horizontal components from all possible orientations for period  $T$ .
- $Sa_{arb}$ : An "arbitrary" horizontal component of the ground motion for a specific period  $T$ , as estimated by rotating the as-recorded components of the ground motion so that one coincides with a given axis
- $Sa_{GM}$ : Geometric Mean of as-recorded horizontal components for period  $T$ :

$$Sa_{GM}(T) = \sqrt{[Sa_x(T) \times Sa_y(T)]} \quad (2)$$

The above acceleration definitions are generally referring to acceleration values that are taking into account the incidence angle of the ground motion, meaning that for example for a value of  $Sa_{GMRotDXX}$  the response of the structure is calculated by rotating the ground motion records in all angles (for example with a suitable step of  $2^\circ$ ), and calculating the geometric mean value of the horizontal components, with the D50 or D100 value being chosen accordingly, in other words the median or maximum value could be adopted. In most codes the median values are adopted ( $Sa_{RotD50}$ ,  $Sa_{GMRotD50}$ ) taking into account that the principal axes of most structures, would not align to what the critical incidence angle of the ground motion would be, something though that as mentioned, is not true for azimuth independent structures. At this point it should be also clarified that in many cases in design codes the  $Sa_{RotI50}$  (period-independent-rotation-angle measure) is adopted, but according to available literature [9, 10], the differences are insignificant between the RotDXX or RotIXX definitions.

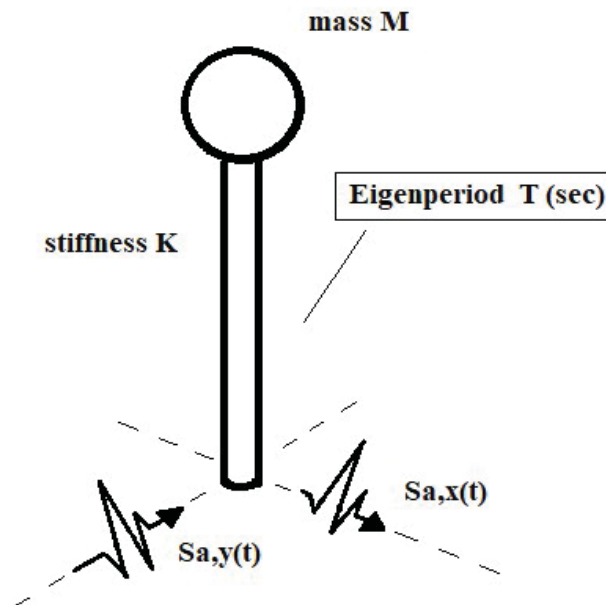


Figure 1: A perspective image of the 3 dimensional elastic and symmetrical oscillator's model, showing the common mass, stiffness and period in both horizontal axes.



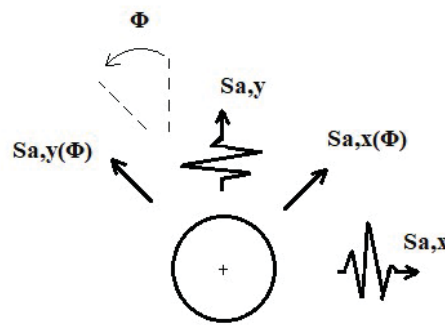


Figure 2: Incident angle rotation of horizontal ground motion components.

### 3 OSCILLATOR MODEL AND DYNAMIC ANALYSIS PARAMETERS

To calculate the acceleration values mentioned above, a three-dimensional elastic and symmetrical oscillator will be used, having the same dynamic parameters in both its major directions X and Y. Using all the aforementioned 150 pairs of ground motion records, from earthquakes of various characteristics, dynamic analysis is performed in each case of record pairs, rotating the ground motion accelerations with an angle step of  $2^\circ$  through a complete circle, essentially altering in each case the incidence angle of the ground motion accelerations.

Through this process and by performing those calculations for all possible incidence angles starting from  $0^\circ$  to  $180^\circ$  (with the previously mentioned  $2^\circ$  step), the accelerations mentioned in the previous paragraph are easily defined, providing a range of responses that can be used to convert the GMRotD50 and RotD50 values in the more suitable D100 cases, that as mentioned before are more reasonable for axisymmetric structures. In Figures 3-4 the results for a specific case of an oscillator with an eigenperiod of  $T=1.0$  sec are presented to put into perspective the process in a more practical way.

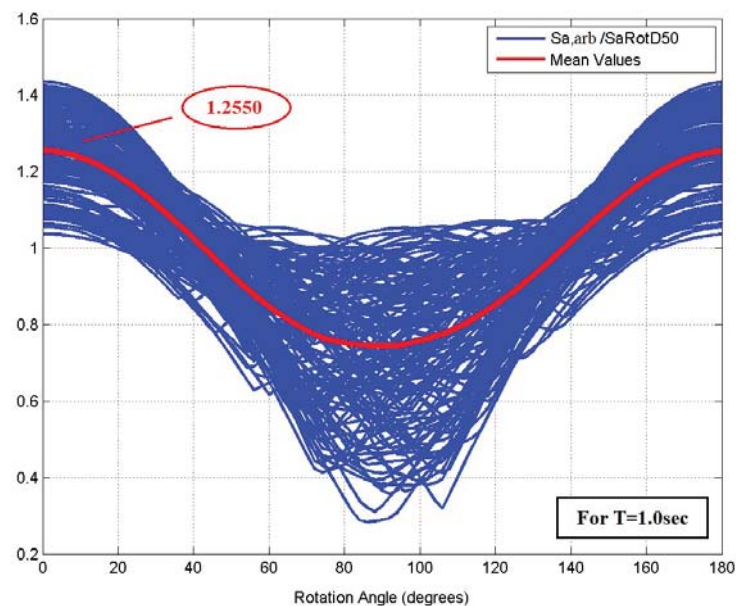


Figure 3 : Results for each record pair, with diagrams for  $Sa_{arb}(\theta)/Sa_{RotD50}$  and the mean value for each rotation angle (arbitrary case).

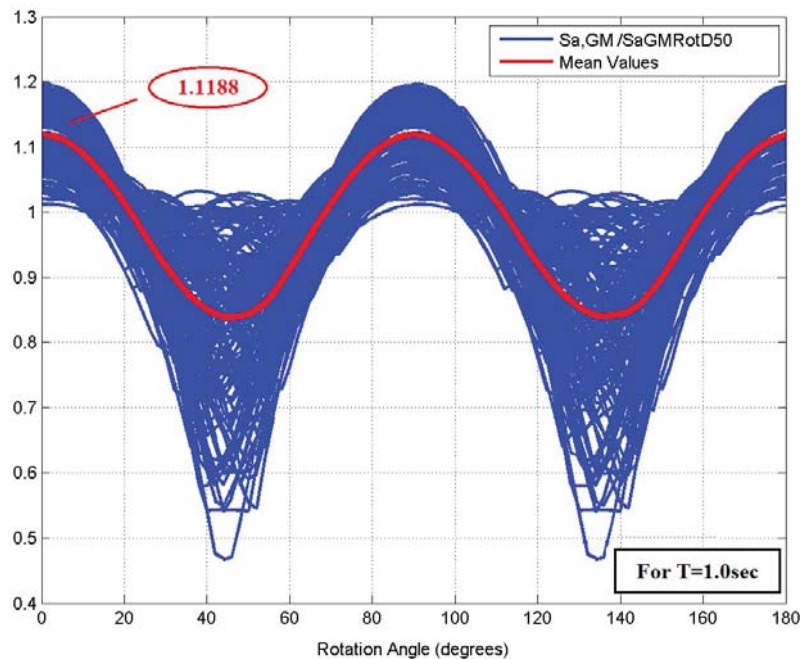


Figure 4 : Results for each record pair, with diagrams for  $Sa_{GM}(\theta)/Sa_{GMRotD50}$  and the mean value for each rotation angle (geomean case).

It is very important to mention that to better identify the output of the results, each diagram for each record was plotted starting from the incidence angle where the maximum acceleration was found. Of course the results were also divided with the equivalent  $Sa_{RotD50}$  and  $Sa_{GMRotD50}$  values accordingly, for the results, concerning each pair of records, to be comparable to each other (in the second case where the geometric mean values are examined, after the  $90^\circ$  angle the diagrams repeat themselves).

#### 4 RESULTS

Using the process mentioned above for a wide spectrum of eigenperiods  $T(\text{sec})$  for the oscillator described, and by identifying the mean value for each of the factors, appearing in Figure 5, for every  $T$ , taking into account all 150 records, the more condensed diagrams were created. They of course provide a wider perspective of how the different definitions of ground motion acceleration relate to one another, examining not only the obvious cases of  $Sa_{RotD100}/Sa_{RotD50}$  and  $Sa_{GMRotD100}/Sa_{GMRotD50}$ , but also cases like  $Sa_{RotD100}/Sa_{GMRotD50}$  and  $Sa_{RotD50}/Sa_{GMRotD50}$ , in case a conversion of that kind could be useful.

According to the results of this investigation, it is obvious that if the peak horizontal acceleration value of a common structure according to the 100+30% rule, and combining the two horizontal components with the SRSS rule would be  $1.044 \cdot a_g$ . In a case where the hazard maps proposed are set up using the  $Sa_{GMRotD50}$  definition, which is expected to be the case of Eurocode, an amplification factor of  $1.117 \cdot a_g$  should be employed. A value between  $1.20 - 1.25 \cdot a_g$  is proper in case of a design spectrum definition based on  $Sa_{RotD50}$ . Those are significant differences that certainly should not be disregarded when axisymmetric structures are examined, as this could lead to non conservative results. At this point a reference of similar works can verify some of the results above especially in cases of the  $Sa_{RotD100}/Sa_{RotD50}$  diagrams for example, as similar results have appeared in the literature [9, 11].

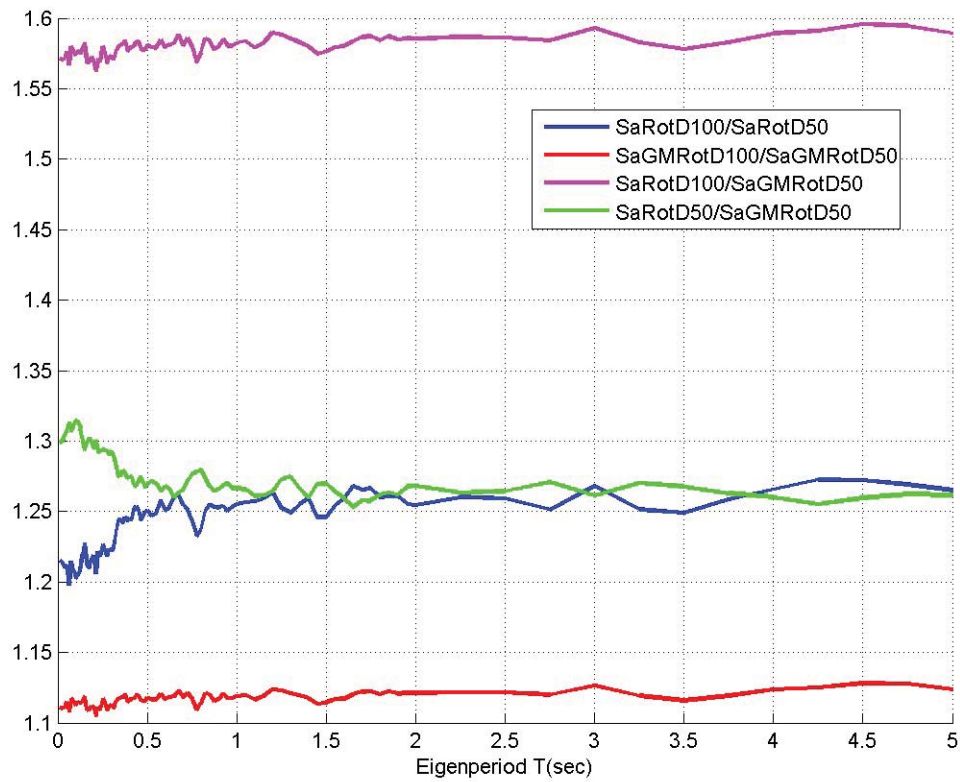


Figure 5 : Aggregated results for various amplification factors for various eigenperiods  $T$ .

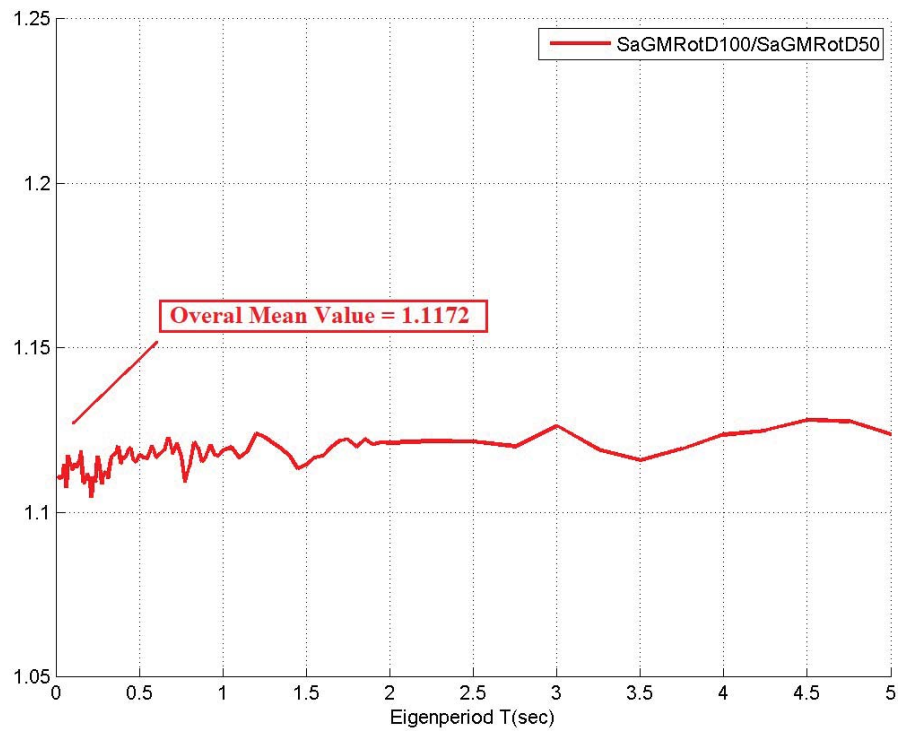


Figure 6 : Aggregated results for the  $Sa_{GMRotD100}/Sa_{GMRotD50}$  conversion factor for various eigenperiods  $T$ .

## 5 CONCLUSIONS

To conclude, the perspective of this article is to propose specific amplification factors in cases of azimuth-independent structures. Their symmetry suggests that the seismic accelerations that would affect them would act upon them in maximum effect, as the incidence angle of the ground motion will affect the structure regardless of the axis X and Y arbitrarily defined in the design process, always subjecting the structure in the peak acceleration produced by the earthquake. That is why we propose amplification factors for the horizontal acceleration component used in design, of 1.12 in a case of an acceleration definition of  $Sa_{GMRotD50}$  in the hazard maps and an amplification factor of 1.25 for the  $Sa_{RotD50}$  case accordingly. Specifically for Eurocode 8 the authors propose the 1.12 case, as an amplification factor for the design spectrum accelerations applied in a single direction to simultaneously account for the combined effect of both horizontal components in axisymmetric structures.

## ACKNOWLEDGEMENT

This research has been co-financed by the European Regional Development Fund of the European Union and Greek national funds through the Operational Program Competitiveness, Entrepreneurship and Innovation, under the call RESEARCH – CREATE – INNOVATE (project code: T1EDK-00956), project: "ARCHYTAS: Archetypal telemetry and decision support system for the protection of monumental structures".

## REFERENCES

- [1] CEN, *Design of structures for earthquake resistance - Part 1: General rules, seismic actions and rules for buildings*, EN1998-1, European Committee for Standardisation, Brussels, 2005.
- [2] T.D. Ancheta, R.B. Darragh, J.P. Stewart, E. Seyhan, W.J. Silva, B.S.J. Chiou, K.E. Wooddell, R.W. Graves, A.R. Kottke, D.M. Boore, T. Kishida, J.L. Donahue, NGA-West2 database, *Earthquake Spectra*, **30**, 989-1005, 2014.
- [3] J.W. Baker, C.A. Cornell, Which spectral acceleration are you using?, *Earthquake Spectra*, **22**, 293-312, 2006.
- [4] O.A. Lopez, A.K. Chopra, J.J. Hernandez, Evaluation of combination rules for maximum response calculation in multi component seismic analysis, *Earthquake Engineering & Structural Dynamics*, **30**, 1379-1398, 2001.
- [5] C. Menun, A. Der Kiureghian, A replacement for the 30%, 40%, and SRSS rules for multicomponent seismic analysis, *Earthquake Spectra*, **14**, 153-163, 1998.
- [6] E. Rosenblueth, H. Contreras, Approximate design for multicomponent earthquakes, *Journal of the Engineering Mechanics Division*, **103**, 881-893, 1977.
- [7] J.P. Stewart, N.A. Abrahamson, G.M. Atkinson, J.W. Baker, D.M. Boore, Y. Bozorgnia, K.W. Campbell, C.D. Comartin, I.M. Idriss, M. Lew, M. Mehrain, J.P. Moehle, F. Naeim, T.A. Sabol, Representation of bidirectional ground motions for design spectra in building codes, *Earthquake Spectra*, **27**, 927-93, 2011.

- [8] D.M. Boore, J. Watson-Lamprey, N.A. Abrahamson, Orientation-independent measures of ground motion, *Bulletin of the seismological Society of America*, **96**, 1502-1511, 2006.
- [9] D.M. Boore, Orientation-independent, nongeometric-mean measures of seismic intensity from two horizontal components of motion, *Bulletin of the Seismological Society of America*, **100**, 1830-1835, 2010.
- [10] K. Beyer, J.J. Bommer, Selection and scaling of real accelerograms for bi-directional loading: a review of current practice and code provisions, *Journal of earthquake engineering*, **11**, 13-45, 2007.
- [11] S.K. Shahi, J.W. Baker, NGA-West2 models for ground motion directionality, *Earthquake Spectra*, **30**, 1285-1300, 2014.

## INVESTIGATING THE OVERTURNING STABILITY OF UNANCHORED CONTAINERS WITH FINITE ELEMENT SIMULATIONS

Stefanos Gkatzogiannis<sup>1</sup>, Peter Knoedel<sup>2</sup>, and Thomas Ummenhofer<sup>1</sup>

<sup>1</sup> KIT Steel and Lightweight Structures  
Research Center for Steel, Timber and Masonry  
Otto-Amman-Platz 1, 76131, Karlsruhe, Germany  
[stefanos.gkatzogiannis@kit.edu](mailto:stefanos.gkatzogiannis@kit.edu)  
[thomas.ummehofer@kit.edu](mailto:thomas.ummehofer@kit.edu)

<sup>2</sup> Dr. Knoedel Engineering Consultants  
Ebersteinburger Str. 9, D-76530 Baden-Baden, Germany  
[info@peterknoedel.de](mailto:info@peterknoedel.de)

---

### Abstract

*Unanchored containers, e.g. for toxic waste, are required to be checked against overturning under seismic actions. Usually this is done by calculating static equilibrium, therewith ensuring stiction and avoiding overturning. When concepting seismic actions as displacement-controlled base excitation with reversals, it becomes obvious that neither the beginning of an overturning motion nor the loss of stiction necessarily causes the structure to fall over. Based on a simplified rigid body assumption for the unanchored container, analytical methods were used to describe the states of no-motion, sliding, overturning and restoring of the overturning motion by reversion of the base displacement in previous work presented by the authors of the current study. Depending on the aspect ratio and a variation of friction coefficients parameter, confidence boundaries were identified, within which the structure is safe against overturning. In the present study this analysis is extended by means of numerical simulation. Dynamic finite element analyses are carried out in order to validate and extend the analytical methods of the previous paper. Successful application of finite element models allows to drop of the rigid body assumption. Thus, deformations of the container, e.g. shell modes, can be considered in a next step. This can lead to more precise and less conservative results, as with the analytical methods dissipation of energy through transformation into deformation energy or damping is neglected.*

**Keywords:** Overturning, Rocking behavior, Toxic waste containers, Slipping, Sticking, Finite Element Method.

---



## 1 NOMENCLATURE

Symbol	Unit	Meaning
$t$	s	time
$F_F^s(t), F_F^d(t)$	N	static and dynamic (Coulomb) friction force
$\mu_s, \mu_d$	-	static and dynamic Coulomb friction coefficient
$G$	N	self-weight
$M_T(t)$	N·m	tilting moment
$m$	kg	mass
$a(t)$	m/s <sup>2</sup>	acceleration
$a, b, c$	m	dimensions of the body
$M_R$	N·m	restoring moment
$A$	m	amplitude of the ground motion
$\mathbf{c}$	N·s/m	damping matrix
$\mathbf{k}$	N/m	stiffness matrix
$p$	N	external load
$C$	-	decay constant with no physical meaning, set equal to 0
$v_{sliding}$	m/s	relative sliding velocity between the surfaces in contact
$\Delta A$	m	relative sliding between ground and base of the prism

## 2 INTRODUCTION

In the present study, the overturning stability of unanchored containers is investigated. A series of numerical investigations is presented, in order to validate and extend an analytical model previously proposed by the authors [1]. Although the nonlinear dynamics of rocking (tilting) and sliding oscillators have been described in the past, see [2], [3], [4] and [2], [5], [6], [7], [8] respectively, to the authors' knowledge no engineering approach existed for describing the behavior of rocking and sliding oscillators, till the recent introduction of the above-mentioned analytical model [1]. Therefore, the Lateral Force Method (LFM) suggested by Eurocode [9] (see also [10]) which leads to overconservative results for this case, had to be applied in practice until now.

Triggering point for the quasi-static analyses of [1] and the present investigations has been an industrial consulting project carried out by the second author regarding the tilting stability of unanchored steel boxes (Figure 1). These boxes are used for fire-proof storage of mercury and they are single-placed on the ground (e.g. on concrete surface) or stacked upon each other, up to three. Proof of the stacks' bearing capacity against earthquake and wind loads is required for receiving a General Type Approval by the German authorities [11]. Since the beginning of this consulting project, the over-conservatism of the LFM for the current case became apparent; loss of stiction or tilting had to be considered as loss of bearing capacity, while in reality these events can respectively lead to sliding, some bumping or even both. Therefore, the authors proposed an enhanced quasi-static solution in [1], based on the mechanical model of Figure 2, which still does not fully describe the physical reality i.e. the full dynamic response of the system, but nevertheless enabled a less conservative investigation of the problem. This was achieved by introducing four different modes for the oscillating system ground – stacked boxes, which are considered to behave as a rigid body<sup>1</sup>:

- The quasi-static or sticking mode with the limit conditions that the base shear does not exceed static friction (Eq. 1) and the tilting moment does not exceed the restoring moment from self-weight (Eq. 2). In this mode the stacked boxes stick to the ground and follow its displacement without any uplift or relative displacement between their base and the ground.

$$F_F^s(t) = m \cdot a(t) \leq F_{F,lim}^s = G \cdot \mu_s, \quad (1)$$

$$M_T(t) = m \cdot a(t) \cdot c/2 \leq M_R = -G \cdot a/2. \quad (2)$$

- The slipping mode, during which the stacked boxes slip on the oscillating ground surface due to loss of stiction. Therefore, there is relative displacement between the stack and the ground. For triggering this mode the base shear must exceed dynamic friction (Eq. 3),

$$F_F^d(t) = m \cdot a(t) \geq G \cdot \mu_d = F_{F,lim}^d, \quad (3)$$

while the tilting moment should not exceed the restoring moment from self-weight so that no uplift takes place (Eq. 2 still stands). When the system is in this mode, the accelerating base shear force is reduced during slipping compared to the stiction mode. Thus, the body is less accelerated, leading to a smaller rotation  $\varphi$  if it simultaneously tilts. Therefore, for same given displacement amplitude  $A$ , the motion of the body becomes less critical.

- The rocking mode, during which uplift of a stack's bottom corner occurs. The limit condition of the base shear not exceeding friction remains unchanged (equation 1 stands) but the tilting moment should exceed the restoring moment from self-weight. As in this mode  $\varphi \neq 0$ , the two moments are estimated as follows,

$$M_T(t) = m \cdot a(t) \cdot \frac{c}{2 \cdot \sin \alpha} \sin(\varphi + \alpha) > M_R = -G \cdot \frac{a}{2 \cdot \cos \alpha} \cos(\varphi + \alpha). \quad (4)$$

It is worth mentioning at this point that slipping, taking place simultaneous to rocking, during this mode cannot be excluded. Due to the uplift, slipping does not any longer refer to two surfaces sliding relative to each other. The Coulomb model theoretically would still stand, as it refers to acting forces and it can therefore, describe both the surface-on-surface and the edge-on-surface friction. Questions arise though, regarding its universal application due to its phenomenological nature. More complex analytical description of the limit conditions for the simultaneous initiation of slipping exceed the scope of the present study. Nonetheless, it is becoming evident from the above-presented argumentation regarding the reduced accelerating base shear during sliding, that neglecting of simultaneous sliding during rocking yields safe results.

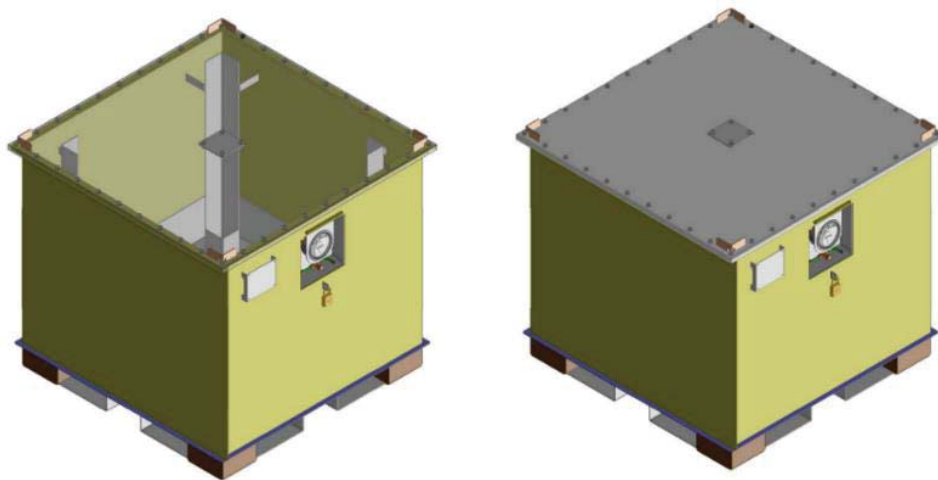


Figure 1: Outer steel box of a double wall mercury container [11]

- Finally, overturning of the system takes place if rocking mode is initiated and the amplitude of the ground motion exceeds the half-length of the stack (we define as length the dimension of the specimen parallel to the ground motion)  $A > a/2$ . In a different case ( $A < a/2$ ), the overturning mode is not initiated and the previous rocking mode continues. In reality, this would lead to bumping due to consecutive ground motion reversals and loss of bearing capacity would be avoided.

It is becoming apparent from the above that the quasi-static model presented by the authors in [1] indeed describes more precisely the physical reality than the LFM, as loss of stiction leading to slipping or rocking without overturning is introduced and is not considered necessarily as loss of bearing capacity. Nonetheless, as the limit conditions of each mode are different from the rest due to changing conditions of friction and moment, the boundaries between the modes are not that discrete. Moreover, it is becoming evident that in reality two of the above-mentioned modes could as well coexist and the dynamic nature of the ground motion could further improve or deteriorate the rocking behavior, an effect that cannot be described by the quasi-static model considering a base shear. In order to enable a better understanding of the involved phenomena, introduce a first step for a future parametric analysis of the problem and extend the currently proposed model a series of full dynamic numerical analyses using the FEM is carried out in the present study.

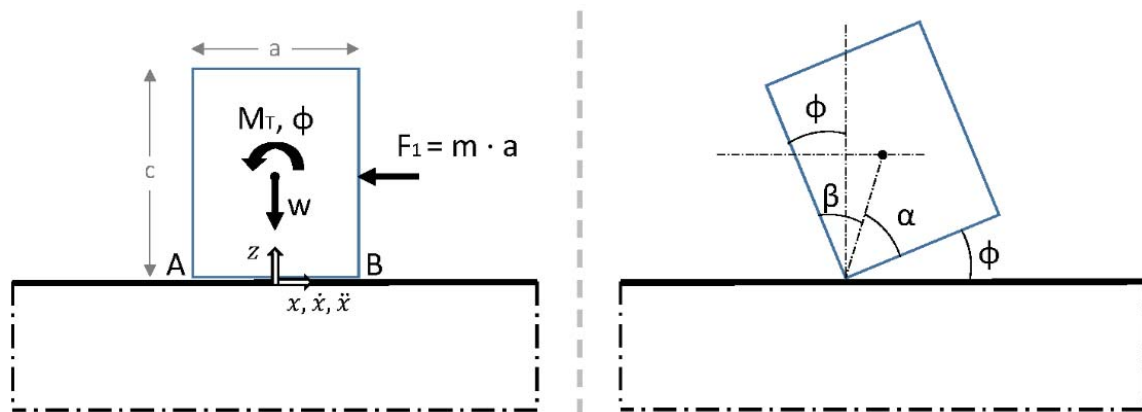


Figure 2: Mechanical model (front view); tilting/sliding body on a rigid surface [1]

### 3 NUMERICAL INVESTIGATIONS

#### 3.1 The finite element model

For the present analyses, a straightforward finite element model was developed with the ground being modelled as a „belt” of solid elements with thickness of 0.01 m and rigid material behavior. When a stack of more than one boxes was modelled, they were considered rigidly connected to each other as in [1] and they were therefore modelled as a single prismatic solid. A virtual density of  $2.066 \text{ kg/m}^3$  was assumed for the boxes considering the steel box structure and the stored material as a homogenous mass based on the suggestion of [1]. Assumption of a rigid body for the prism simulating the single box or the stack of boxes, hereinafter called simply prism, would still stand as for the analytical model. Nonetheless, due to numerical restrictions it was modelled as an elastic body with the mechanical properties of structural steel, which anyway stands closer to physical reality.

The FE Software ANSYS [12] was applied for creating the finite element model, while the explicit dynamic solver LS-Dyna [13] was used for its solution. Based on a convergence study, solid “brick” elements with uniform dimension of 0.05 m were applied (0.01 m in the height

direction for the elements modelling the ground). Linear dynamic analyses were carried out (Eq. 5),

$$m\ddot{u} + c\dot{u} + ku = p(t), \quad (5)$$

while the Coulomb friction model (Eq. 6) was applied for simulating the contact between the bottom surface of the prism and the upper surface of the ground,

$$F_F = \mu \cdot G. \quad (6)$$

LS-Dyna estimates the friction coefficient  $\mu$  by interpolating between the values of the static and dynamic friction coefficient based on the following equation (Eq. 7),

$$\mu = \mu_d + (\mu_s - \mu_d) \cdot e^{-C|v_{sliding}|}. \quad (7)$$

As for the present study  $C$  was set equal to zero,  $\mu = \mu_s$ .

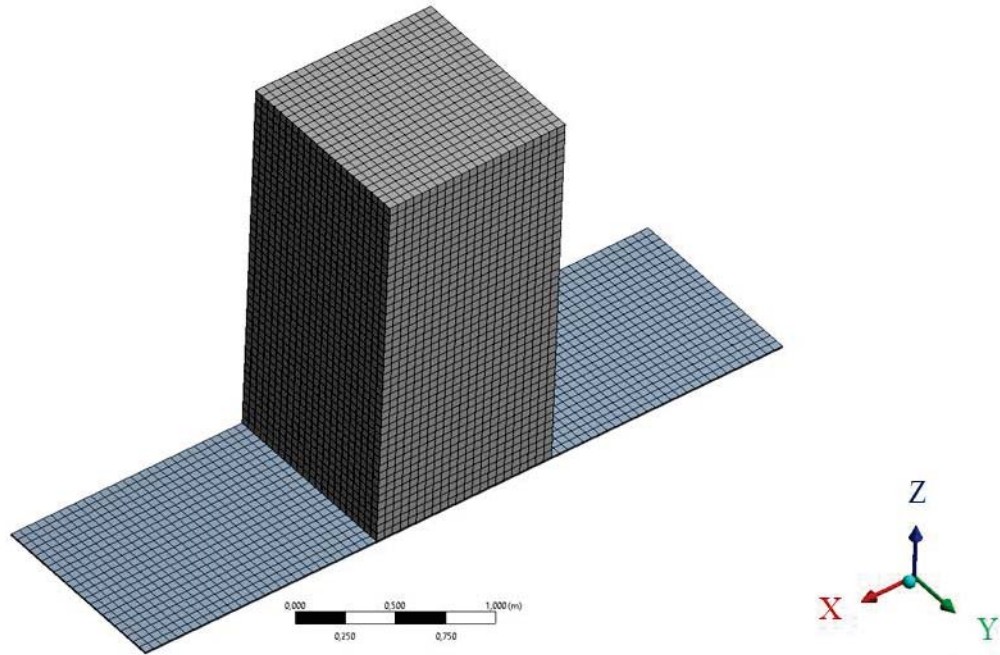


Figure 3: The FE model

### 3.2 Investigated cases

Using the above described FE model, a series of numerical analyses was investigated in order to examine the influence of different input parameters to the rocking behavior of the prism. An overview of the investigated datasets is presented in Table 1, along with the resulting rocking behavior of the prism in each invested case. The geometry of the prism is differentiated, with the height gradually increasing from 1 m to 2 and 3 times respectively the length dimension of a single storage box (1.1 m x 1.1 m x 1 m), for which a fundamental period of 1.98 s is analytically calculated in [1]. For validating this result, prior to the rest of the numerical investigations a simulation was carried out, where the prism was uplifted from the ground around its corner and was left to bounce back to the ground with only gravitational forces acting on it. In all cases, the initial horizontal position of the prism's mass center coincided with the center of the modelled ground "belt" and the gravitational force was pointing the negative direction of the  $z$  axis (Figure 3). Degrees of freedom outside the XZ plane were restrained, as in different case irregular bumping and unexpected displacement out of this plane occurred. This was against initial expectations, as all applied loads were on the XZ plane and although the result is

closer to physical reality (for instance irregularities of real structures and ground can cause out of plane drift) in this case it was attributed to numerical effects and therefore, the additional restraints were imposed.

The seismic action was modelled in all cases as an ideal sinusoidal excitation of 5 periods in the length direction (x direction in Figure 3, the vertical component is neglected). Different values for seismic excitation were tested, with a peak ground acceleration of  $1.6 \text{ m/s}^2$  applied for all analyses, but with various values for the seismic period/frequency: initially, seismic period equal to the fundamental rocking period of the prism was considered and then it was respectively increased and decreased by 10 %. Moreover, as one of the limit conditions, which describe the physical reality, is the relationship between friction and base shear choosing a realistic value for the friction coefficient is crucial for the current problem. Nonetheless, previous experience shows that selection of appropriate values is challenging [14]. Selection of the appropriate friction coefficient  $\mu$  depends on the materials in contact, their roughness, their condition (dry or wet) etc. As a universal value cannot be proposed, two different values for the static friction coefficient 0.4 and 0.57 were tested in the current study, with the former one having been applied in [1] and the second one proposed in [15], for steel surfaces sliding on concrete. The dynamic coefficient in both cases was considered to be 50 % of the static one (see relevant discussion in [1]).

Case	Geometry a/b/c [m]	Seismic period [s]	Friction coefficients [-]	Activated mode of rocking behavior	maxA [mm]	maxΔA [mm]
A1	1.1/1.1/1	1.98	0.40/0.20	sliding - sticking	± 158	31
A2	1.1/1.1/1	2.18	0.40/0.20	sliding - sticking	± 193	37
A3	1.1/1.1/1	1.78	0.40/0.20	sliding - sticking	± 128	25
A4	1.1/1.1/1	1.98	0.57/0.29	sliding - sticking	± 159	14
A5	1.1/1.1/1	2.18	0.57/0.29	tilting & bumping - sticking	± 192	20
A6	1.1/1.1/1	1.78	0.57/0.29	tilting & bumping - sticking	± 128	13
B1	1.1/1.1/2.2	2.50	0.57/0.29	tilting - sticking	± 257	24
C1	1.1/1.1/3.3	3.10	0.57/0.29	tilting - sticking	± 386	22
C2	1.1/1.1/3.3	1.55	0.57/0.29	tilting - overturning	± 399	71*

Table 1: Investigated datasets  
\*at initiation of overturning

## 4 RESULTS AND DISCUSSION

### 4.1 Presented results

For the shake of clarity, only selected results of the above-presented investigations are presented, as some models produced similar results with each other. At first the results of the fundamental period test and the models A2 and A5 regarding the case of a single box are presented. In the former case, the vertical displacement of the prism's upper left corner over time (Figure 5) along with contours of vertical displacement are presented. Tappauf and Taras [16], [17] found quite similar results when they investigated the partial uplift of big tanks. In that case though, a time offset between the bumps was documented due to the sloshing wave along the tanks diameter. For the models A2 and A5, both diagrams of horizontal displacement of the ground and the prism's bottom and top (right corner node for both, Figure 6, 7) and contours of



horizontal displacements at arbitrary but representative times of the simulation (Figure 8, 9) are presented. Later on, C1 and C2 referring to the case, where the height of the prism is three times its length and exhibiting respectively the modes of tilting and overturning are discussed. The results are presented in an analogous way as of those for the models A2 and A5, see Figure 10 – 13.

#### 4.2 Validation of analytically calculated fundamental period

The contours of vertical displacement at three different moments of the simulation, at time 0 s, 0.192 s and 0.360 s, are given in Figure 4. The results of the vertical displacement of the upper left corner over time are provided in Figure 5. During the simulation and after the first contact of the bottom left corner with the ground, the prism entered an irregular bumping sequence, which becomes obvious from the great number of hills and valleys in the diagram of Figure 5, including horizontal displacements as well (x axis). As a result, for the estimation of the fundamental rocking history, only the results up to this moment of first contact are considered. The time, until the initiation of this contact i.e. at 0.384 s constitutes a quarter-period, therefore a fundamental period of 1.536 s is estimated. A significant deviation of 20% with the analytically estimated fundamental period ( $T_{\text{analytical}} = 1.98$  s is given in [1], Eq. 19,  $T_{\text{num}} / T_{\text{analytical}} = 80\%$ ) is met.

#### 4.3 Models A1 – A6

For all the investigations with the prism geometry corresponding to the case of a single box, and despite any change in seismic action no overturning was documented. When the lower values of friction were considered (0.4-0.2 for models A1-A3) slight sliding during initiation of the seismic excitation was observed and the prism stuck to the ground for the rest of the reversals. It has to be highlighted, that after the end of the seismic action the prism slid back to its initial position. The diagram of the horizontal displacements over time presented in Figure 6 and the horizontal displacement contours from the first period of the seismic excitation presented in Figure 8 from the model A2, for which the most severe sliding of approximately 36 mm was observed, validate the above observations.

Nonetheless, when the friction coefficients were increased and for the models A5 and A6 with the lowest and highest seismic periods (A4 exhibited similar behavior with the previous), the prism during the initiation of the seismic action instead of sliding tilted with a slight uplift of the bottom corner on the side of displacement's direction being documented. At the same time the stiction between the left bottom corner and the ground led to a hopping of the prism towards the ground displacement direction, which introduced relative displacement between the ground and the prism. This could be mistakenly attributed to some sort of simultaneous sliding. Observing the diagram of horizontal displacements for the model A5 though, presented in Figure 7, it can be seen that in contrast to the case of A2 the prism exhibits higher horizontal displacement than the ground already from the first quarter of the first loading period. This is physically impossible to be caused by sliding. After the first hopping another uplift of lower magnitude is initiated, after the end of which the prism sticks to the ground for the rest of the excitation. The contours of Figure 9 offer a clearer overview of the above-described phenomenon. Once again after the end of the excitation, reversed uplift and hopping restores the prism to its original position.



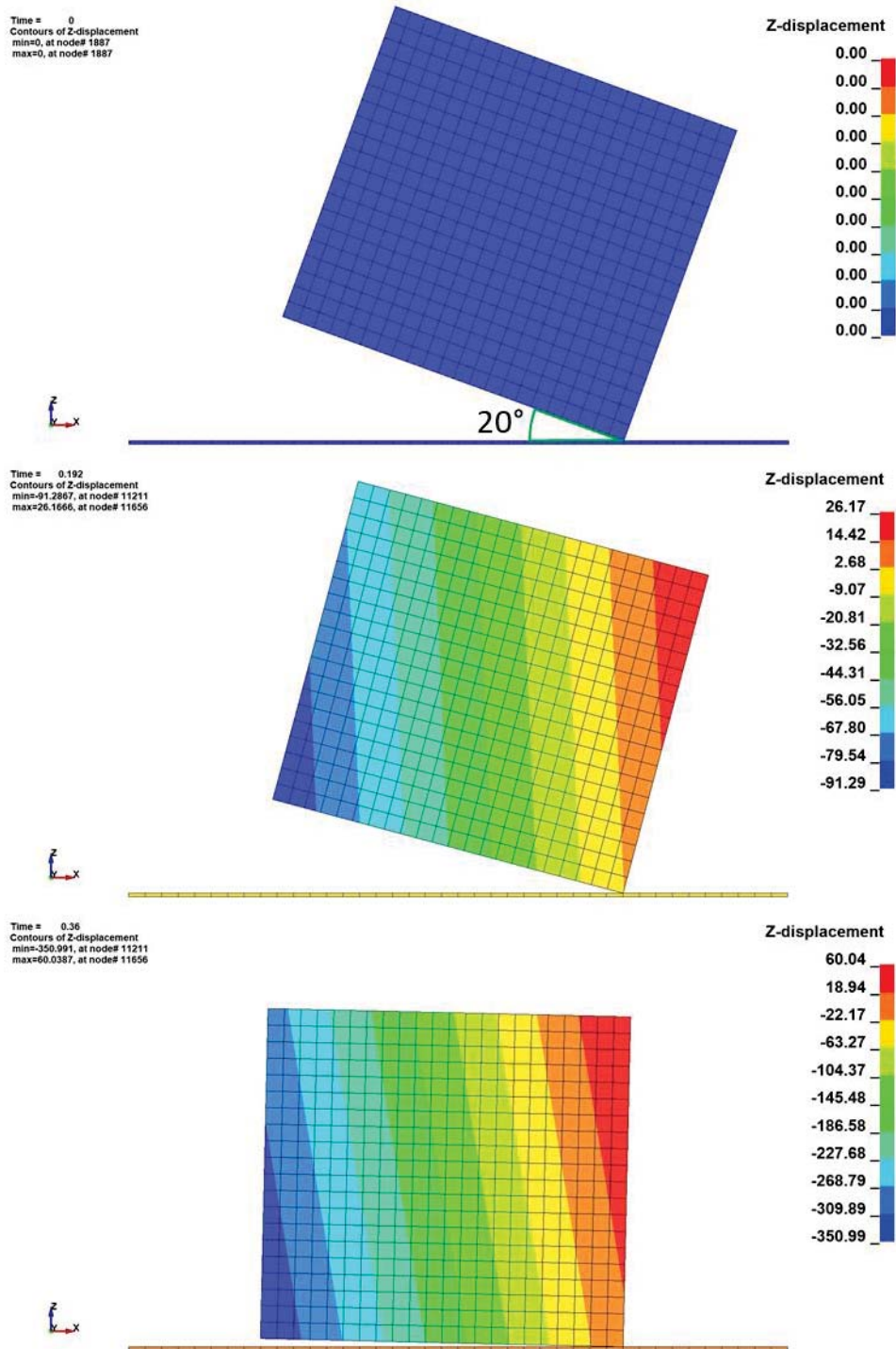


Figure 4: Checking the rocking fundamental period of the prism with dimensions 1.1 m x 1.1 m x 1 m – Contours of vertical displacement, given at mm, at time 0 s, 0.192 s and 0.360 s

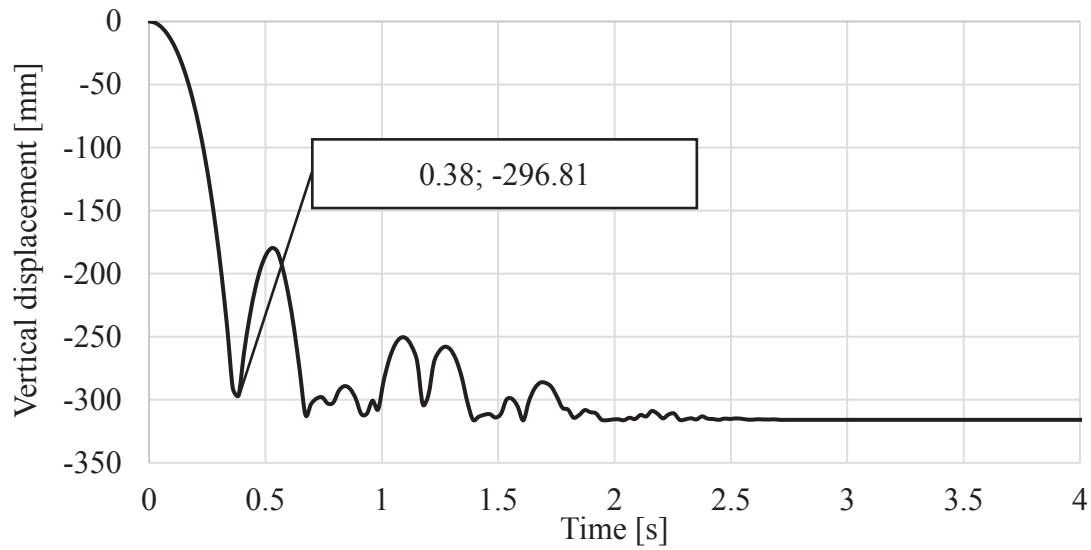


Figure 5: Vertical displacement of the upper left corner over time

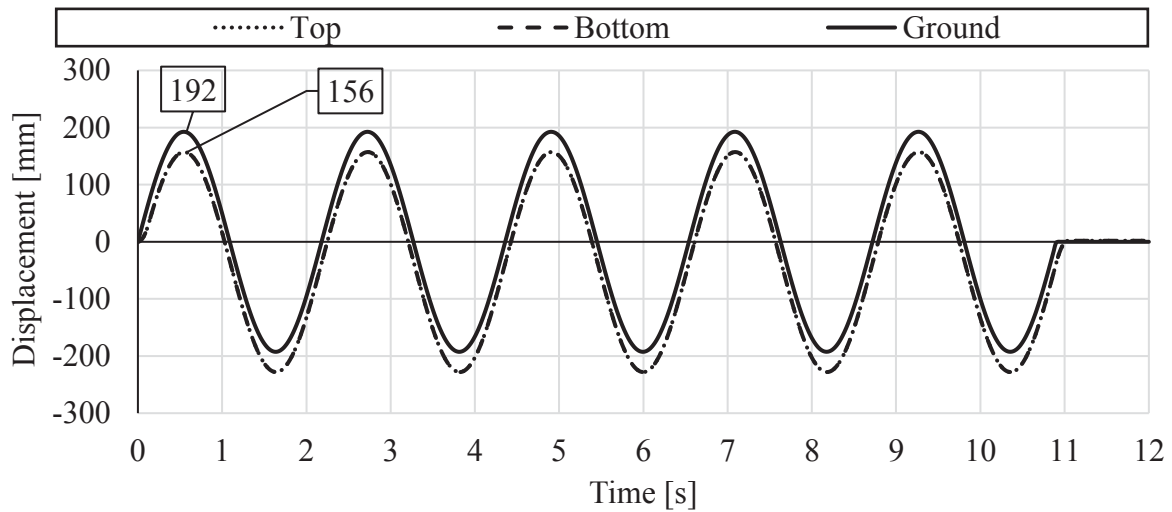


Figure 6: Horizontal displacement of the ground and the top and bottom surfaces of the prism for model A2

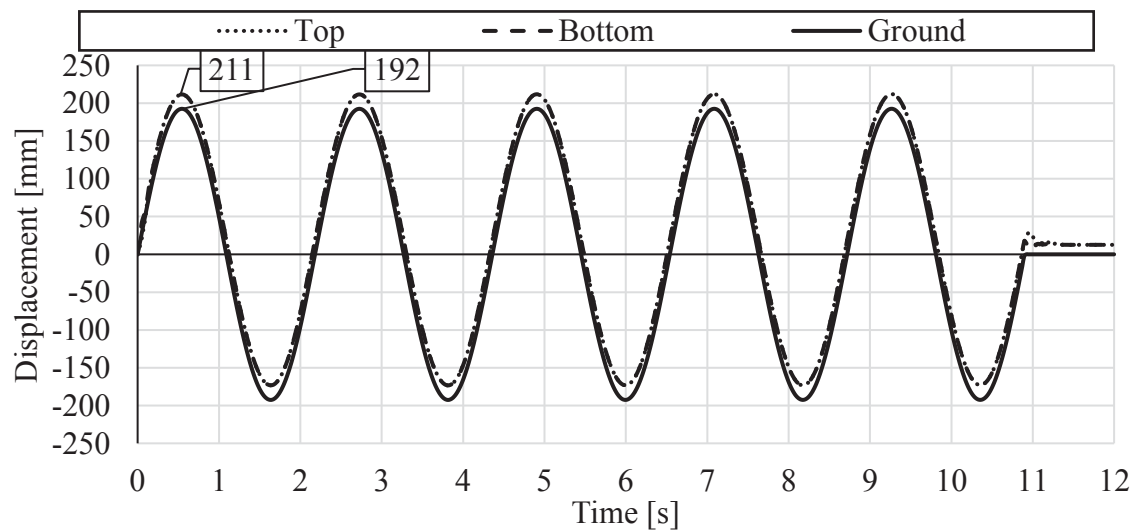


Figure 7: Horizontal displacement of the ground and the top and bottom surfaces of the prism for model A5

This effect of sliding back and forth at the beginning and at the end of the seismic motion is attributed to the simplified modelling of the ground motion. At the beginning and at the end of the loading, sinusoidal displacement is respectively abruptly initiated and changed back to no-motion. With a steady state harmonic oscillation, maximum speed is given at zero-crossing. Thus, in the present way of modelling the displacement, a very high acceleration is imposed onto the prism at these singular points. This in turn activates a very high impulse of inertia forces, which cause a short phase of sliding. This effect is a shortcoming when driving the model by displacements instead of prescribed accelerations. However, in previous work of the authors (e.g. [18], [19]) it was shown, that displacement drives make nonlinear systems with plasticity easier to handle. Note, that the simulations given in [14] are different: there, the displacements of the hammering pin are a priori unknown, and cannot be used to drive the system (see discussion in [14] chap. 5.1). In future simulations, a ramp-up as smooth transition between the states of motion and no-motion could be introduced.

#### **4.4 Models B2, C1, C2**

The increase of height in the model B2 being twice the length and width of the specimen led to qualitatively similar results to the models A5 and A6 with more severe tilting at the initiation of the excitation though, followed once again by a continuous stiction mode till the end of the excitation. Nonetheless, further increase of height in the model C1 led to significant tilting, taking place for more than the first 3 periods of seismic excitation as it is becoming obvious this time by both the horizontal displacement diagrams of Figure 9 and the horizontal displacement contours of Figure 12, but still without leading to overturning. As it can be seen in Figure 11 and Figure 13 though, this was the case for the analysis of model C2, for which the seismic frequency was doubled. Tilting initiated at the beginning of the seismic excitation caused uplift at first to the right side of the prism (direction of the seismic excitation at first quarter of the period), which was reversed after the reversal of the seismic displacement during the second quarter of the seismic period, which initiated at 0.389 s. This almost caused the overturning of the prism, which was nevertheless stalled due to the second reversal of the ground displacement. The prism remained at its uplifted position for the third quarter of the seismic period (0.778 s – 1.167 s) and finally after the third reversal and initiation of the fourth quarter of the 1<sup>st</sup> seismic period overturning was completed leading to loss of the bearing capacity. Once again, the prism carried out several consecutive hops, when in rocking position, during the second and third quarters.

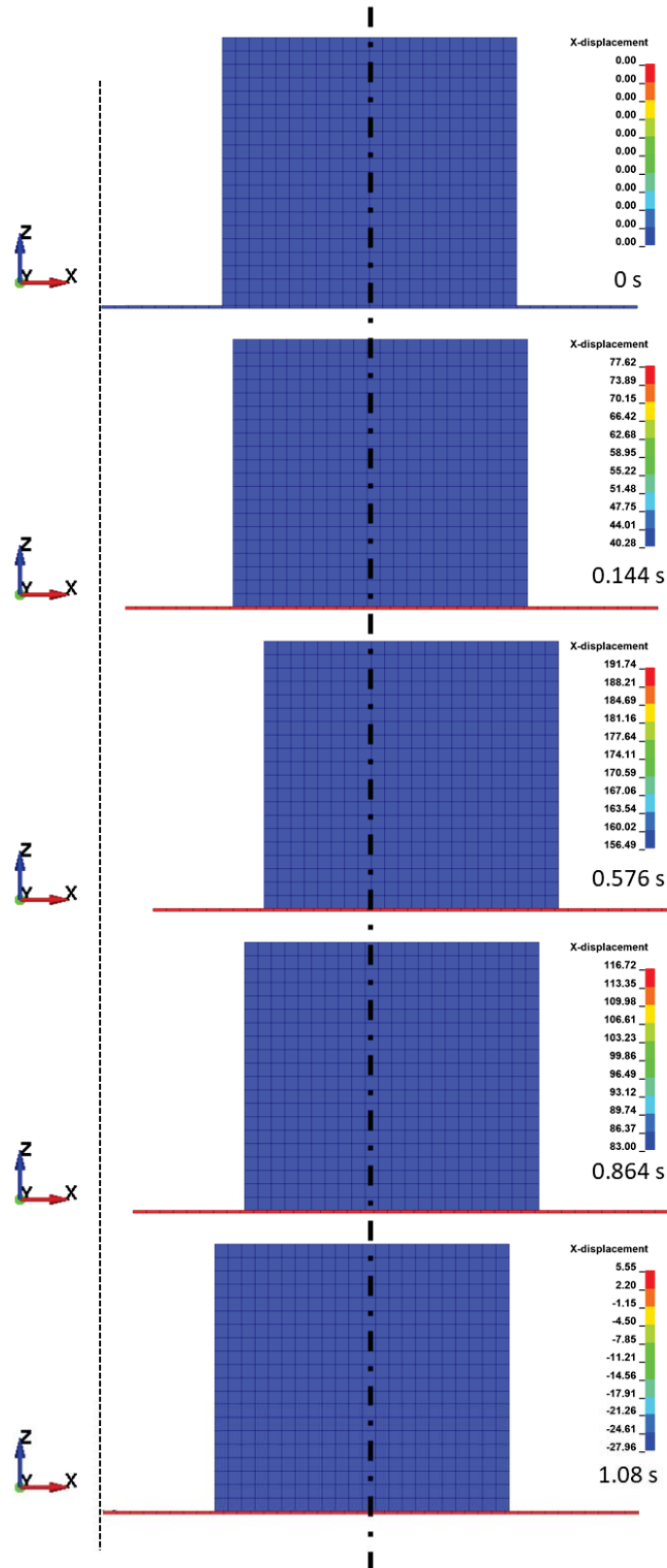


Figure 8: Horizontal displacement contours at arbitrary moments of the 1<sup>st</sup> period of the seismic loading for the model A2 – the broken and the dashed broken line show respectively the initial horizontal position of the ground belt's left edge and the prism's mass center

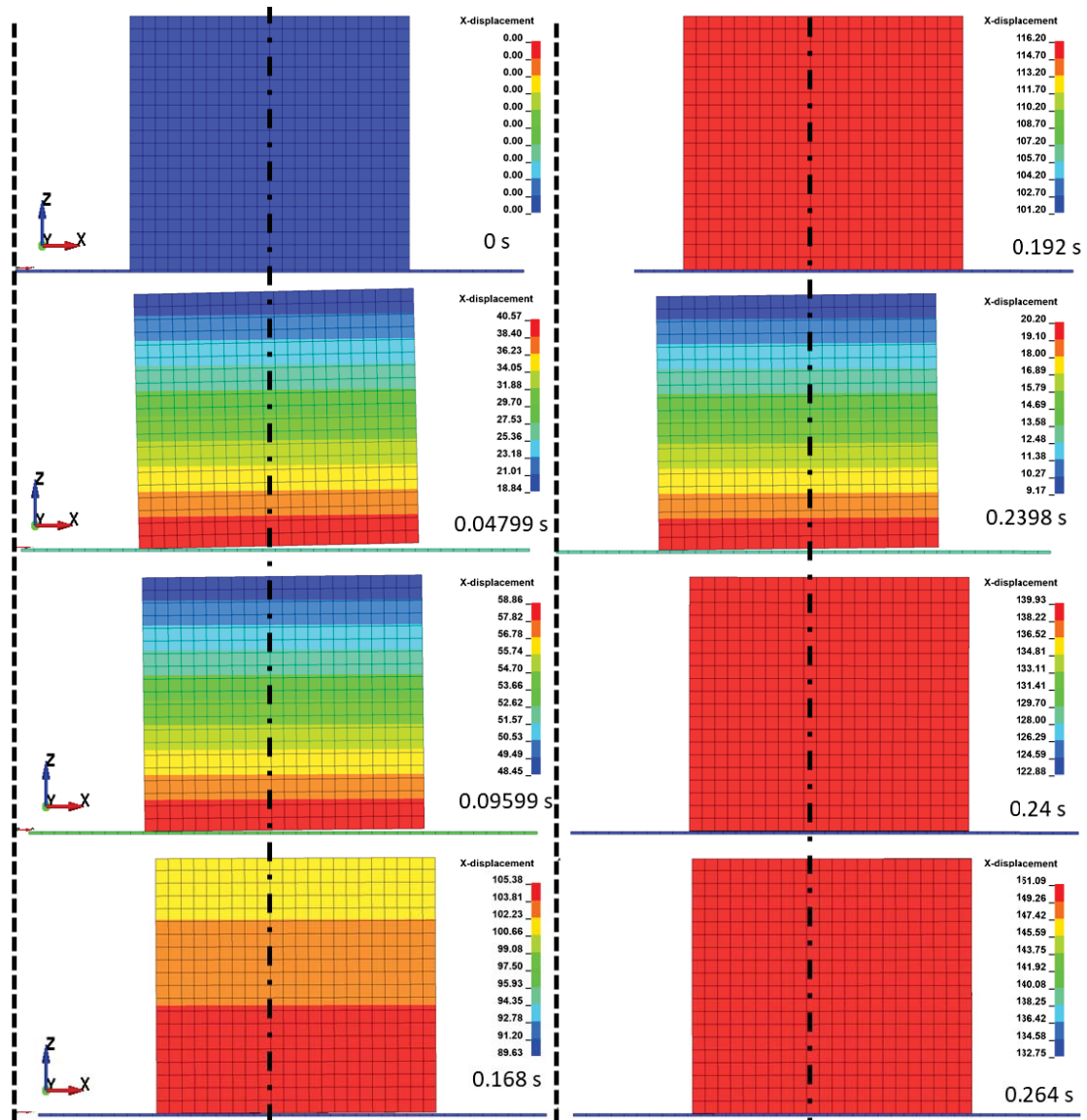


Figure 9: Horizontal displacement contours taken at arbitrary moments of the 1<sup>st</sup> period of the seismic loading for the model A5 - the broken and the dashed broken line show respectively the initial horizontal position of the ground belt's left edge and the prism's mass center

## 5 SUMMARY AND CONCLUSIONS

A series of numerical analyses was carried out in order to investigate the rocking behavior of a single or several steel boxes stacked upon each other, used for safe deposition of chemicals. Goal of the investigations was to test assumptions stated during the introduction of an analytical model in a previous study [1], prove the conservatism of this analytical model and act as a first-step towards the development of a numerical model, which will enable a parametric analysis of the investigated problem. The following conclusions were drawn:

- The numerically estimated rocking fundamental period of the investigated prism deviates significantly from the analytically calculated ( $\sim 20\%$ ). Further investigations are recommended in order to clarify the reasons for this discrepancy.
- The over-conservatism of the approach of the LFM is proven: It is shown that in many cases the loss of stiction does not lead to loss of bearing capacity.

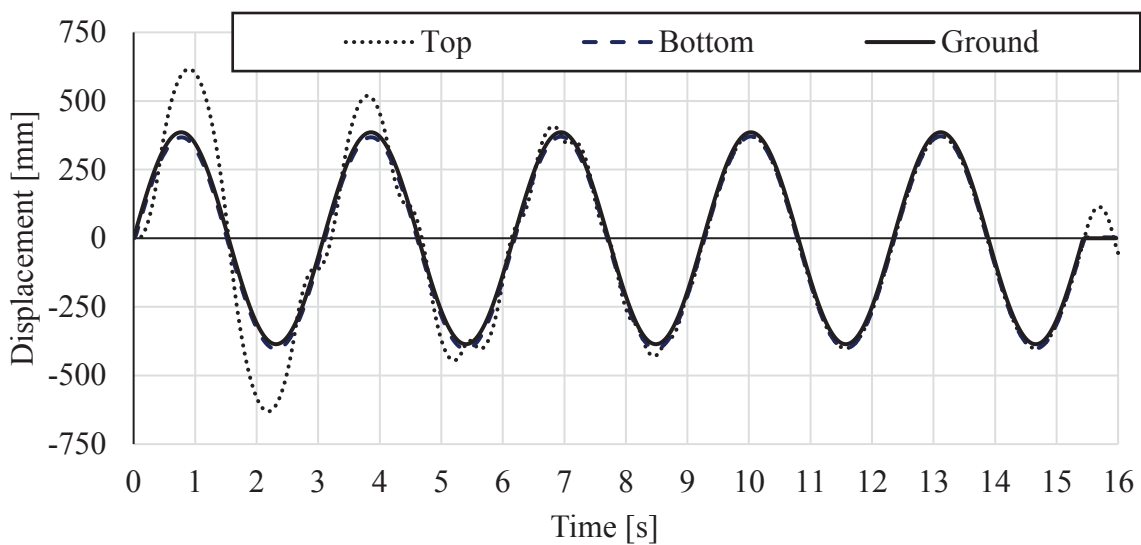


Figure 10: Horizontal displacement of the ground and the top and bottom surfaces of the prism for model C1

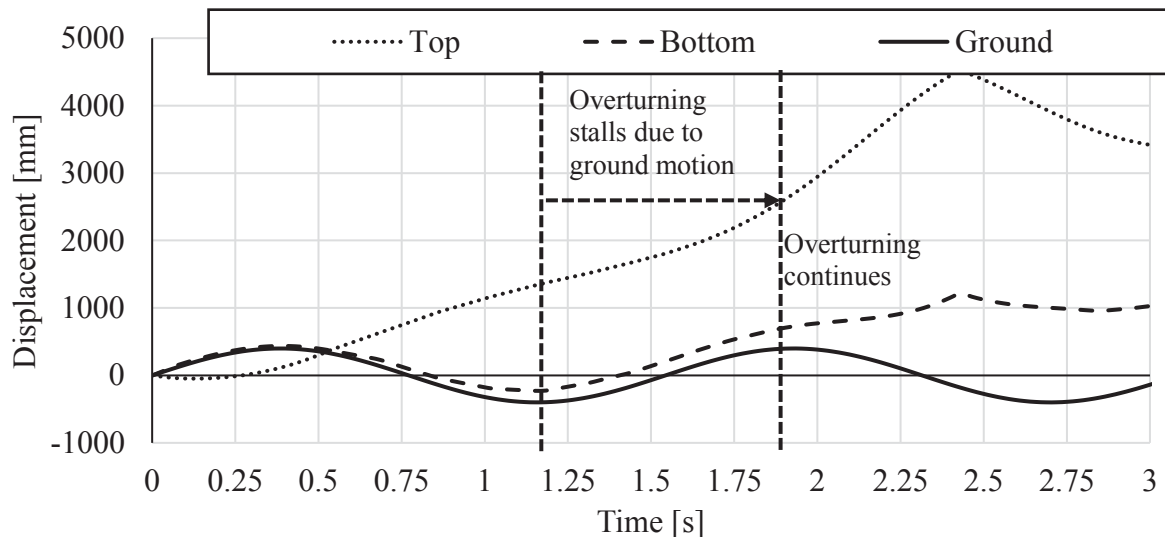


Figure 11: Horizontal displacement of the ground and the top and bottom surfaces of the prism for model C2

- It is shown that the analytical model proposed by the authors is as well conservative, although less than the LMF method. For instance overturning of a structure, although initiated can be stalled due to the ground motion, an effect which cannot be described by the quasi-static model.
- The assumption stated above that different modes (sliding and sticking) can both be met during a seismic excitation is proven. This as well cannot be described by the quasi-static analytical model.
- The above-stated assumption that appropriate selection of friction coefficients is crucial is validated: for identical conditions increase of the static and dynamic friction coefficient from 0.4 to 0.57 and from 0.2 to 0.29 led to change of the rocking behaviour.
- Hopping due to bumping of the prism due to initial tilting of its front corner and action of horizontal stiction forces on its back corner, produces relative displacement between the prism and the ground. This as well cannot be described the quasi-static analytical model introduced by the authors.



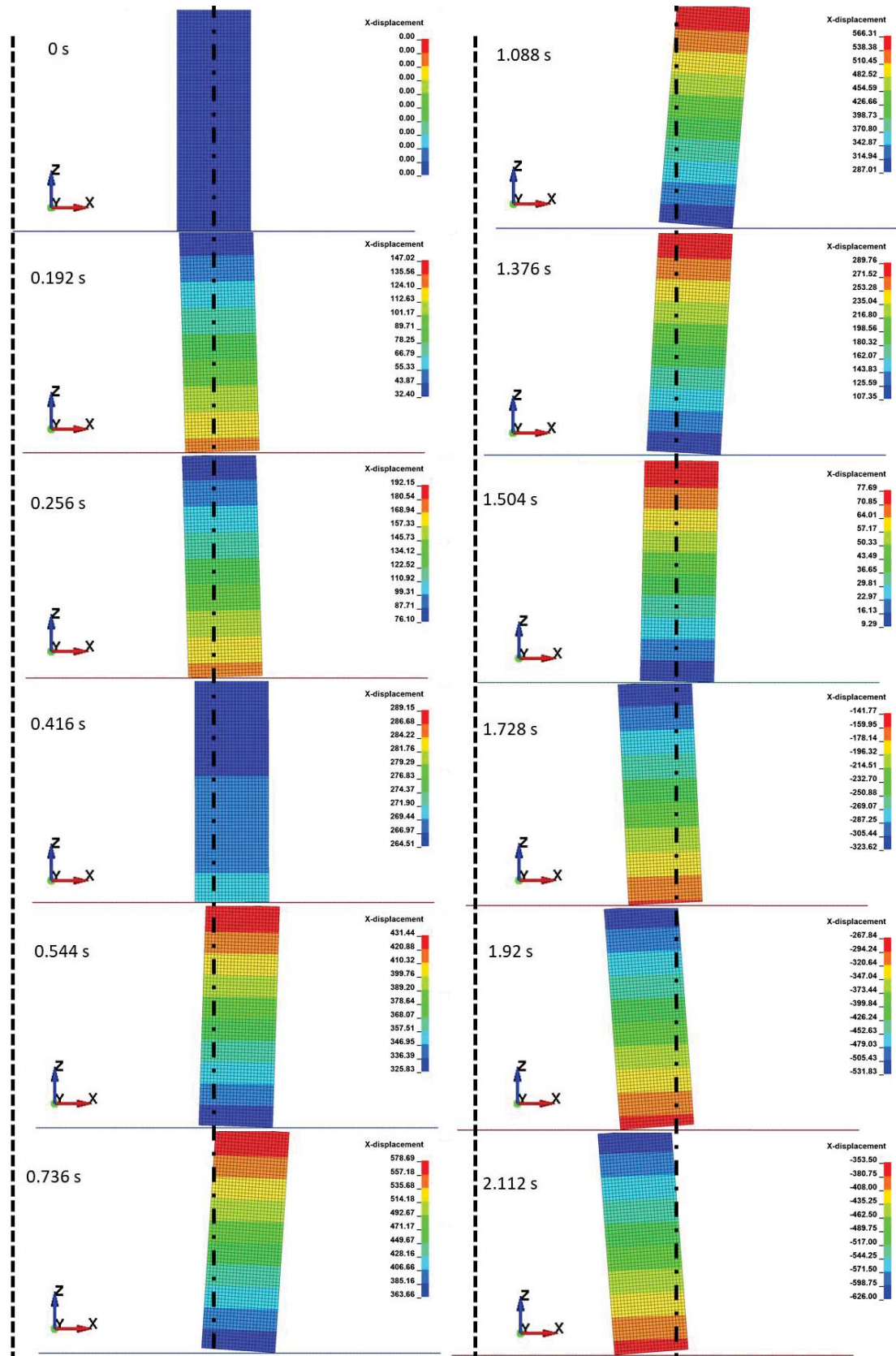


Figure 12: Horizontal displacement contours taken at arbitrary moments of the 1<sup>st</sup> period of the seismic loading for the model C1 – the broken and the dashed broken line show respectively the initial horizontal position of the ground belt's left edge and the prism's mass center

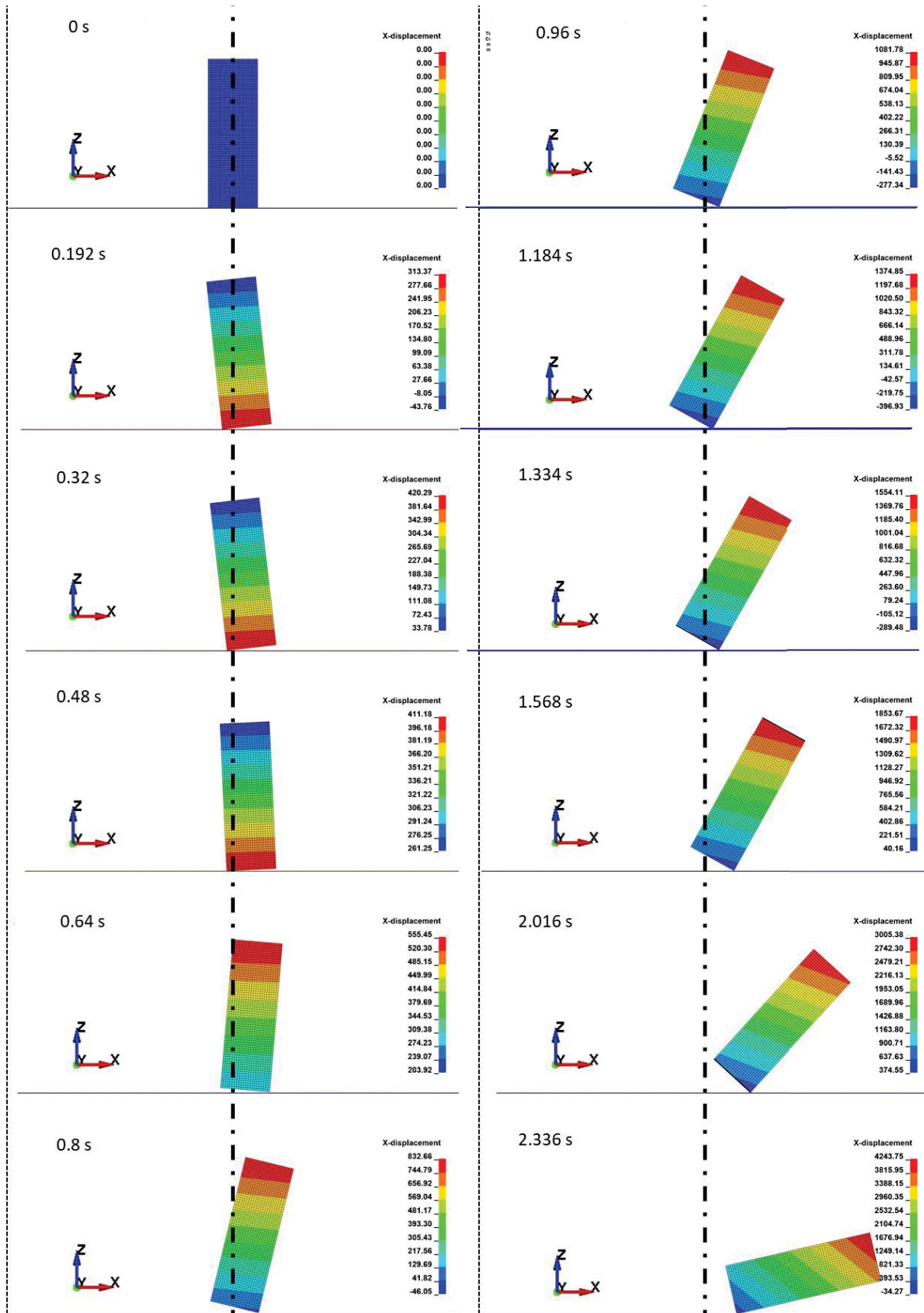


Figure 13: Horizontal displacement contours from the model C2 taken at arbitrary moments – the broken and the dashed broken line show respectively the initial horizontal position of the ground belt's left edge and the prism's mass center

In general, numerical investigations of the current problem show great potential for better understanding of the investigated systems behavior and for achieving less conservative results. A parametrization of the present model in future work in combination with varied and even real seismic excitation, could enable the estimation of the precise limits of transition from one mode of rocking behavior to another. It could be as well interesting to introduce a vertical seismic component, which assumingly could lead more easily to loss of stiction. Finally more detailed modelling of the structures geometry and physical properties could contribute to more accurate solutions.

## ACKNOWLEDGEMENT

The authors would like to thank the company *UTM Umwelt-Technik-Metallrecycling GmbH* for allowing the use of industrial data for the present academic project.

## REFERENCES

- [1] P. Knoedel, S. Gkatzogiannis, T. Ummenhofer, A Simple Stick-Slip Model for the Overturning Stability of unanchored Containers. Published in Butenweg, C., Hoffmeister, B., Holtschoppen, B., Klinkel, S., Rosin, J., Schmitt, T. (eds), *Seismic Design of Industrial Facilities 2020. Proceedings of the 2nd International Conference on Seismic Design of Industrial Facilities*, Apprimus Verlag, Aachen, 201-210, 2020.
- [2] K. Klotter, *Technische Schwingungslehre, Erster Band: Einfache Schwinger. Teil B: Nichtlineare Schwingungen*, 3d Edition. Auflage, Springer-Verlag, Berlin 1980.
- [3] M.J. DeJong, E.G. Dimitrakopoulos, Equivalent Rocking Systems: Fundamental Rocking Parameters. *Proc., 15 WCEE 15th World Congress on Earthquake Engineering*, Lisbon, Portugal, September 24-28, 2012.
- [4] M.F. Vassiliou, N. Makris, Dynamics of the Vertically Restrained Rocking Column. *J. Eng. Mech.* **141** (12), published online May 19, 2015.
- [5] J.P. den Hartog, *Mechanical Vibrations*, Third Edition. McGraw-Hill New York, London, 1947.
- [6] N. Gaus, *Zur Ermittlung eines stochastischen Reibwerts und dessen Einfluss auf reibungserregte Schwingungen*. Diss. Karlsruher Institut für Technologie, Schriftenreihe des Instituts für Technische Mechanik, Band 23, 2014.
- [7] R.I. Leine, D.H. van Campen, A. de Kraker, L. van den Steen, Stick-Slip Vibrations Induced by Alternate Friction Models. *Nonlinear Dynamics* **16**, 41–54, 1998.
- [8] H.-K. Hong, C.-S. Liu, Coulomb Friction Oscillator: Modelling and Responses to Harmonic Loads and Base Excitations. *Journal of Sound and Vibration*, **229** (5), 1171-1192, 2000.
- [9] EN 1998-1: 2004 (English), *Eurocode 8: Design of structures for earthquake resistance – Part 1: General rules, seismic actions and rules for buildings*.

- [10] P. Knoedel, T. Ummenhofer, Mass Variation with dissipative Steel Structures under Seismic Loads. Published in Papadrakakis, M., Fragiadakis, M. (eds), *Proc. COMPDYN 2017, 6<sup>th</sup> ECCOMAS Thematic Conference on Computational Methods in Structural Dynamics and Earthquake Engineering, 15-17 June 2017, Rhodes Island, Greece*, 4928-4942, 2017.
- [11] Allgemeine bauaufsichtliche Zulassung Z-38.12-294, *Kubische doppelwandige Behälter aus Stahl; Hg Storage 150L*. Entwurf, Deutschen Institut für Bautechnik, Berlin, Entwurf 2019. Antragsteller: UTM Umwelt-Technik-Metallrecycling GmbH, Alt-Herrenwyk 12, D-23569 Lübeck.
- [12] ANSYS® Academic Research, Release 21.1, Help System, ANSYS, Inc., 2021.
- [13] LS-DYNA, Theory Manual, Livermore Software Technology Corporation (LSTC), Livermore California, 2016.
- [14] S. Gkatzogiannis, *Finite Element Simulation of Residual Stresses from Welding and High Frequency Hammer Peening*. Doctoral Dissertation, Department of Civil Engineering, Geo and Environmental Sciences, Karlsruhe Institute of Technology, 2020.
- [15] B. G. Rabbat, H. G. Russel, Friction Coefficient of Steel on Concrete or Grout. *J. Struct. Eng.* **111** (3), 505-515, 1985.
- [16] C. Tappauf, A. Taras, Deformation and Strain Histories in Shell-to-Base Joints of Unanchored Steel Storage-Tanks during Seismic Loading. *STESSA 8th Int. Conf. on Behavior of Steel Structures in Seismic Areas, Shanghai, China, July 1-3, 2015*.
- [17] C. Tappauf, *Ermüdungsverhalten von unverankerten Stahltanks bei Erdbeben*. Dissertation, TU Graz, Juni 2018.
- [18] P. Knoedel, J. Hrabowski, Yield Limit vs. Behaviour Factor in Seismic Design. *Proceedings, NSCC 2012 Nordic Steel Construction Conference, 5-7 September 2012, Oslo, Norway*, 147-155, 2012.
- [19] P. Knoedel, T. Ummenhofer, Time History Simulation in Seismic Design. Contribution 379 (USB). *Heinisuo, M., Mäkinen, J. (eds).: Proceedings, NSCC-2015 Nordic Steel Construction Conference 2015, Tampere, Finland, 23-25 September, 2015*.

---

<sup>i</sup> for stacked boxes this implies, that either gapping between the boxes is counterbalanced by the self-weight or the boxes are bolted; the stack remains rigid, “whipping” is excluded.



## GREEN BANK RADIO TELESCOPE: WIND INDUCED EFFECTS ON FEED-ARM

Gian Felice Giaccu<sup>1</sup>, Luca Gallisai<sup>2</sup>, Steven White<sup>3</sup>, Richard Prestage<sup>4</sup>,

Luca Caracoglia<sup>5</sup>

<sup>1</sup>Department of Architecture, Design and Urban Planning, University of Sassari,  
Alghero, Italy  
e-mail: gf.giaccu@uniss.it

<sup>2</sup>Department of Architecture, Design and Urban Planning, University of Cagliari,  
Cagliari, Italy

<sup>3</sup>Green Bank Observatory, National Radio Astronomy Observatory,  
Green Bank, WV, USA

<sup>4</sup>Department of Physics and Astronomy, West Virginia University,  
Morgantown, WV, USA

<sup>5</sup>Department of Civil and Environmental Engineering, Northeastern Univ.,  
Boston, MA, USA

---

### Abstract

*Radio Telescopes have been widely used in deep-space exploration and satellite communications. High pointing accuracy is required to be high in these applications, since the beams involved in these measurements are narrow. However, pointing precision can be influenced by wind load effects, which represent a disturbance source for the support structures of the telescope, especially in the high-frequency range. This paper analyzes the wind load effects on the feed arm of the Green Bank Radio Telescope (GBO) for two different wind directions as a function of the wind speed. A Finite Element (FE) Model of the GBO has been assembled to evaluate the dynamic response of the structure against turbulent wind disturbances. The FE model has been updated according to results derived from previously developed models. The paper focuses the attention on the wind induced displacements of the feed arm, which is, for the examined structure, the main source of wind disturbances. The study shows that wind disturbances can deeply affect the pointing accuracy of GBO even at low wind speeds. Namely, for reference mean wind speed of 4 m/s the total along-wind lateral displacements of the feed arm can reach the maximum threshold associated with an acceptable Pointing Error (PE). Furthermore, displacements are larger for winds acting in the cross-elevation direction and can deeply affect pointing accuracy of the antenna measurements.*

**Keywords:** Radio Telescopes, Large reflector antennas, Wind Turbulence, Wind induced Disturbances.

---

## 1 INTRODUCTION

The Green Bank Radio Telescope is a large reflector antenna located in West Virginia, United States; it is a fully steerable, 100m diameter paraboloidal radio telescope capable of operating with high efficiency in a wide frequency range: from 0.1 to 116 GHz (wavelengths 3.0m – 2.6mm). The telescope is located near the heart of the United States National Radio Quiet Zone, a unique area in North America, close to the city of Green Bank, West Virginia, where authorities restrict all radio broadcasts to avoid emissions interfering with the GBT itself. The position of the telescope inside the zone of radio silence allows the detection of radio frequency signals, avoiding the interference of other weak signals emitted by other sources or human activities. The observatory is bordered by the National Forest and the Allegheny mountains, which shield it from further radio interference. As for the large antennas, which usually operate in open space without any protection from atmospheric loads, variable wind load effects can influence the accuracy of the pointing; in fact, the wind interference becomes one of the causes of PE that can induce structural resonance at low natural frequencies (close to 1Hz).



Figure 1. Picture of Green Bank Radio Telescope (reproduced from [www.skyandtelescope.com](http://www.skyandtelescope.com))

Pointing accuracy of large reflector antennas is influenced by few factors: deformation of the main reflector, lateral movement of the Feed-Arm, lateral displacement of the sub-reflector, rotation of the sub-reflector around the point of focus. Several types of orientation errors may be observed in large telescopes, requiring complex adjustment mechanisms to minimize the undesirable effects. These conditions can be, either integrally or in part, a consequence of the wind loads.

Pointing errors due to wind excitation have been often observed but rarely examined in the literature since the problem is particular to each structure (and telescope). For example, the first documented case of significant wind load effects on PE was documented by Ulich [1]. The current state-of-the-practice and analysis approach considers the combination of wind tunnel tests and computational fluid dynamics to simulate the wind loads [2-4]. Since each



structure is unique and effects are on occasion not fully predicted by simulations (i.e. during design), measurements of the flow field and wind loads around full-scale telescopes have also been considered [5]. In the case of flexible telescopes the issue of large deformation in the antenna may also affect the structural response [6]. Despite all these efforts, several problems are still unresolved and require careful consideration.

In this work the focus has been given to the lateral displacement of the sub-reflector, located at the top of the feed-arm, since it can be considered the largest source of wind induced PE in GBO. This work is part of ongoing research activity, which analyzes the wind-induced PE on large radio telescopes.

## 2 DESCRIPTION OF FINITE ELEMENT MODEL AND WIND LOAD SIMULATION

### 2.1 Finite Element (FE) model of GBO

For the purpose of studying wind effects on GBO, an FE model has been built, using *in Strand7* software package. The model consists of a total of 5702 nodes, 6133 beam elements, 2477 plate elements, 968 brick elements (Figure 2). Despite the geometric complexity of the model, the computational aspects do not require special efforts. Various models aimed to evaluate several load conditions, such as temperature gradient or gravitational effects, were previously built for similar structures [7].

The proposed analysis methodology is based on the application of wind loads on the structure through the FE model, after suitable discretization of the feed-arm in different sectors, each having different pressure distributions [8]. The discretization is schematically illustrated in Figures 2b, 2c. This approach aims to assess the wind load effects on the structure in terms of local displacements of the sub reflector, located at the top of the feed arm and the pointing error (PE), which represents the angle of rotation of the antenna compared to the non-deformed configuration [9-11].

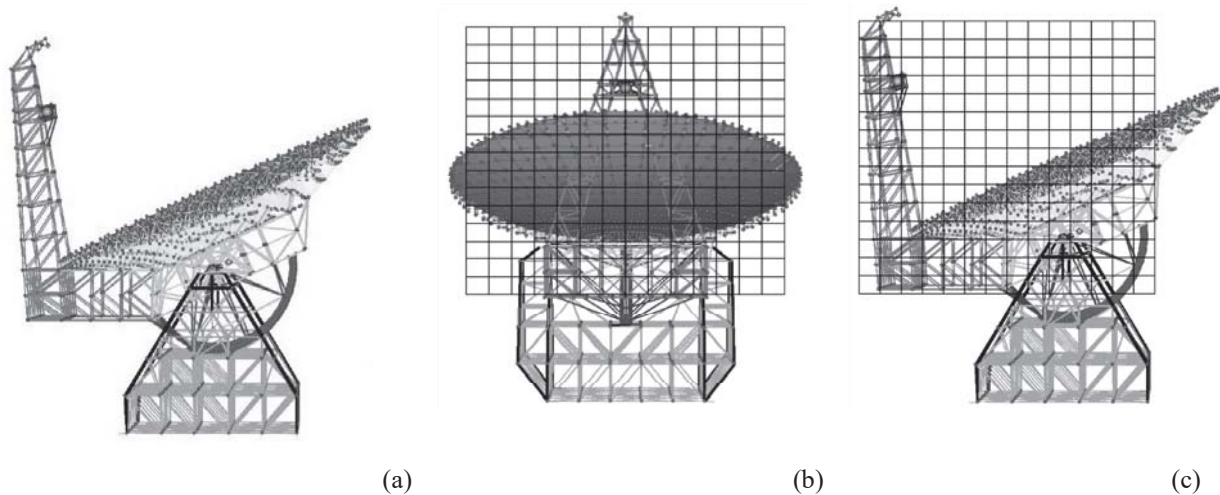


Figure 2. (a) Finite element model of the Green Bank Radio Telescope, Schematic representation of the grid utilized for simulating wind forces on feed-arm, (b) elevation direction, (c) cross-elevation direction.

### 2.2 Application of the wind forces on the model of GBO

Wind load simulation has been studied on the GBO through spatial discretization of the wind field using a  $15 \times 15$  ( $6\text{m} \times 5\text{m}$ ) idealized grid in front of the telescope. At each node of the grid partially-correlated wind turbulence time histories of the along-wind field (primary)

load component are synthetically generated by standard wave superposition method [12]. The turbulent wind load, generated by assuming validity of the quasi-steady aerodynamic theory, which can be used to study a variety of structures (e.g. [13, 14]), has been imposed to simulate pressures and equivalent forces (based on tributary areas). The pressure coefficients of the telescope surface have been extracted and adapted from the results by Liu Yan [8]. The synthetically generated time histories of the loads have a duration equal to 60s, with a time step  $\Delta t = 0.01$ s. The loads have been evaluated for both “elevation” and “cross-elevation” mean wind directions, as shown in Figure 3.

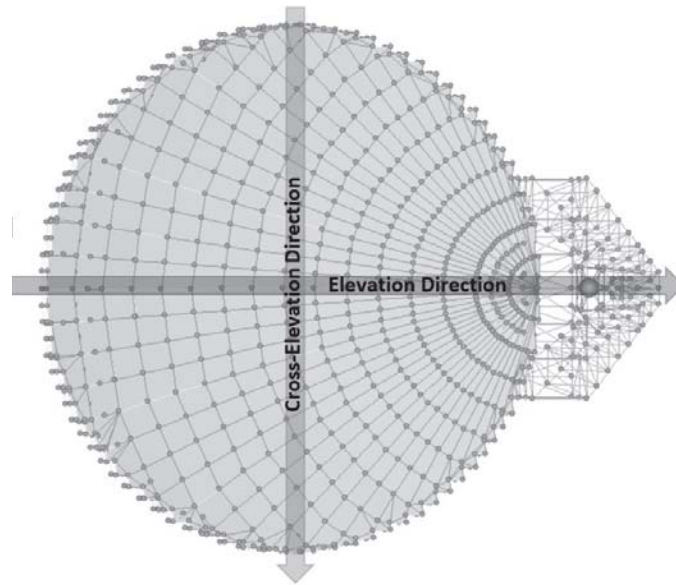


Figure 3. Schematic representation of main, incident wind directions.

### 2.3 Linear dynamic integration approach

A linear, (step-by-step) dynamic integration approach has been applied for examining the wind load effects, described in the previous sections and acting on the feed arm, for the two examined mean wind directions (Figure 3). The Results of the dynamic integration approach of wind load simulation are illustrated in Figure 4 for a reference mean wind speed of 4 m/s at a reference elevation from ground  $z_{ref}=10$  m.

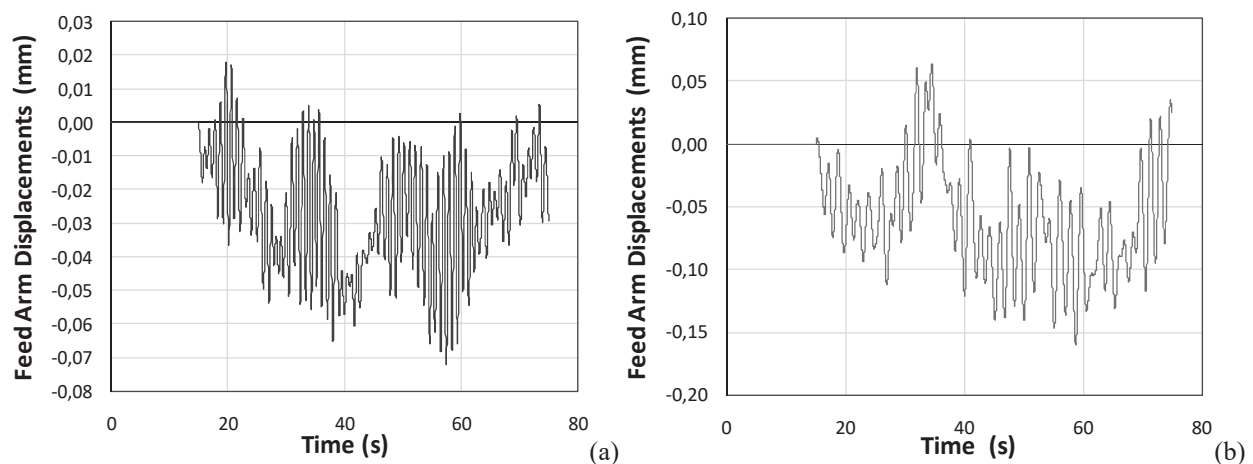


Figure 4. Time history of turbulent along-wind dynamic displacements of the top node of feed-arm, for wind acting in (a) elevation direction and (b) cross- elevation direction, at a reference ground speed of 4m/s.

Figure 4a presents typical along-wind displacements of the feed-arm top node for mean wind acting in the elevation direction; Figure 4b shows an example of along-wind displacements for mean wind acting in the cross-elevation direction.

### 3 CONCLUSIONS

This study discusses the turbulent wind effects on the GBO for two different wind directions: elevation and cross-elevation direction. Along-wind induced displacements of the feed-arm were examined for different ground wind speeds. Results shows that, even for low ground wind speed such as 4m/s, displacements of the-feed arm can approach the maximum threshold for pointing PE. In particular, displacements are greater for the wind acting in cross-elevation direction. Future studies will examine the validity of the quasi-steady aerodynamic theory for the estimation of wind loads, the relevance of transverse loads due to wake excitation along with potential flow-structure interaction.

### 4 ACKNOWLEDGEMENTS

The first author would like to acknowledge the financial support of Regione Autonoma della Sardegna (L.R. n. 3/2008 "Rientro Cervelli" and L.R. n. 7/2007 "Promozione della Ricerca Scientifica e dell'Innovazione Tecnologica in Sardegna").

### REFERENCES

- [1] B.L. Ulich, Pointing errors of large telescopes due to wind, *Very Large Telescopes, their Instrumentation and Programs.*, European Southern Observatory (IAU Colloquium n 79), Garching, Garching, W Ger, 1984, pp. 177-181.
- [2] D.G. MacMynowski, K. Vogiatzis, G.Z. Angeli, J. Fitzsimmons, J.E. Nelson, Wind loads on ground-based telescopes, *Applied Optics* 45(30) (2006) 7912-7923.
- [3] M. Mamou, K.R. Cooper, A. Benmeddour, M. Khalid, J. Fitzsimmons, R. Sengupta, Correlation of CFD predictions and wind tunnel measurements of mean and unsteady wind loads on a large optical telescope, *Journal of Wind Engineering and Industrial Aerodynamics* 96(6-7) (2008) 793-806.
- [4] M. Mamou, A. Tahi, A. Benmeddour, K.R. Cooper, I. Abdallah, M. Khalid, J. Fitzsimmons, Computational fluid dynamics simulations and wind tunnel measurements of unsteady wind loads on a scaled model of a very large optical telescope: A comparative study, *Journal of Wind Engineering and Industrial Aerodynamics* 96(2) (2008) 257-288.
- [5] G.Z. Angeli, M.K. Cho, M. Sheehan, L.M. Stepp, Characterization of wind loading of telescopes, *Workshop On Integrated Modeling of Telescopes*, February 5, 2002 - February 7, 2002, SPIE, Lund, Sweden, 2002, pp. 72-83.
- [6] Z. Cheng, C. Ma, Distributed real-time networked control architecture for suppressing wind load deformation of Fourier telescope, *2014 6th International Conference on Intelligent Human-Machine Systems and Cybernetics, IHMSC 2014*, August 26, 2014 - August 27, 2014, Institute of Electrical and Electronics Engineers Inc., Hangzhou, China, 2014, pp. 364-367.
- [7] F. Buffa, A. Causin, A. Cazzani, S. Poppi, G. Sanna, M. Solci, F. Stochino, E. Turco, The Sardinia Radio Telescope: A comparison between close-range photogrammetry and finite element models, *Mathematics and Mechanics of Solids* (2015) 1–22.
- [8] Q.H. Liu Yan, Fan Feng, Wind load characteristics of large radio telescope, *Infrared and Laser Engineering* 44(1) (2015) 148-156.

- [9] J. Zhang, J. Huang, L. Qiu, R. Song, Analysis of Reflector Vibration-Induced Pointing Errors for Large Antennas Subject to Wind Disturbance: Evaluating the pointing error caused by reflector deformation, *IEEE Antennas & Propagation Magazine* 57(6) (2015) 46-61.
- [10] F. Wang, R. Prestage, R. McCullough, G.-S. M., Green Bank Telescope Sub-reflector Stabilization (Wind), *Metrology and Control of Large Telescopes*, Green Bank, West Virginia, USA, 2016.
- [11] L. Gallisai, Green Bank Telescope: valutazione del pointing error determinato dall'azione turbolenta del vento, University of Cagliari, Italy, 2018.
- [12] M. Di Paola, Digital simulation of wind field velocity, *Journal of Wind Engineering and Industrial Aerodynamics* 74-76 (1998) 91-109.
- [13] C. Borri, C. Costa, Quasi-steady analysis of a two-dimensional bridge deck element, *Computers & Structures* 82(13-14) (2004) 993-1006.
- [14] P.J. Richards, R.P. Hoxey, Quasi-steady theory and point pressures on a cubic building, *Journal of Wind Engineering and Industrial Aerodynamics* 92(14-15) (2004) 1191-1218.

## PARAMETRIC STUDY OF STEEL COLUMN-BASE CONNECTION SUBJECTED TO BIDIRECTIONAL BENDING AND AXIAL COMPRESSION

Md. Asif B. Kabir<sup>1</sup>, and AHM M. Billah<sup>2</sup>

<sup>1</sup> Graduate Research Assistant  
Lakehead University, Thunder Bay, ON, Canada  
e-mail: [mkabir4@lakeheadu.ca](mailto:mkabir4@lakeheadu.ca)

<sup>2</sup> Assistant Professor  
Lakehead University, Thunder Bay, ON, Canada  
e-mail: [muntasir.billah@lakeheadu.ca](mailto:muntasir.billah@lakeheadu.ca)

---

### Abstract

*Column base plate connection is one of the most critical structural components of steel moment-resisting frames which acts as a transfer medium to transmit the reaction forces, shear and moments from the entire building into the foundation. Failure of these base plate connections is critical since it can result in the collapse of the entire structure. Very often these base plates experience bidirectional lateral loadings from natural events such as wind and earthquake. Previous studies considered uniaxial lateral loading combined with axial load but do not provide any guidelines for exposed column base plate connections under axial load and biaxial lateral loading. This study aims to develop an accurate nonlinear finite element (FE) model of exposed column-base connections under combined axial load and bi-axial lateral loading using general purpose finite element software ABAQUS. The developed model is validated against experimental results under monotonic and cyclic loading considering both geometric and material nonlinearities to check the accuracy of the model. After validation, a bidirectional symmetric lateral loading combined with constant axial compressive load is applied in the developed model to analyze the response of the column-base plate connections. Further, the effects of three different parameters of column base plate connection such as base plate thickness, base plate yield strength, and anchor rod diameter are investigated through parametric study. Results show that higher value of base plate thickness and anchor rod diameter significantly affect both the stiffness and strength of column base connections. It also demonstrates that base plate yield strength has no significant influence on column base connections.*

**Keywords:** Column Base Plate Connection, Bidirectional Lateral Loading, Finite Element Modeling, Parametric Study.

---



## 1 INTRODUCTION

In steel moment-resisting frames, column base plate (CBP) connection is one of the most critical structural components that transfer the forces and moments from the superstructure to the substructure. Under dynamic loadings, such as earthquake and wind, the dynamic effects are transferred to the structure through the base plate of this connection. Failure of the CBP connection can result in the collapse of the entire frame as the ductility demand and force distribution in the structure is directly affected [1]. Tremblay et al. [2] and Midorikawa et al. [3] outlined several issues with the exposed type CBP connections experienced during the past major seismic events (e.g. 2011 Tohoku, 1995 Kobe, 1994 Northridge). Exposed column base connections are mostly found in low-rise steel structures around the world. Over the past forty years, researchers have extensively investigated various parameters, both experimentally and numerically, affecting the design, behavior, and strength of CBP connections [4-7]. These research outcomes led to the publication of the AISC Design Guide 1 [8] for column base plate design, which is still widely used in the industry. Fahmy et al. [9] examined the base connection failure mechanisms and categorized them into three main groups as "weak column-strong connection", "balanced mechanism", and "strong column-weak connection". All of these previous studies and design guidelines focused on the base plate design under axial load and uniaxial bending moment although the base plates very often can experience bidirectional bending moment from lateral loads. Though the columns are designed and checked considering axial load and biaxial bending, when it comes to the base plate connection, only the axial load combined with major axis bending is considered.

Lee et al. [10, 11] experimentally and numerically investigated the response of CBP connections under weak axis moments. They concluded that the widely used Drake and Elkin's design method is inadequate for designing CBP connections under minor axis bending. Gomez et al. [12] formulated a new technique for characterizing the strength of the CBP connections by introducing a plastic mechanism through extensive experimental study. This study was further expanded by Kanvinde et al. [13] through finite element (FE) analysis to investigate the stress distribution in different components of CBP connections. Although very effective, both of them concluded that the recommended method is not applicable for designing CBP connections under biaxial bending. Fasaee et al. [14] conducted a numerical investigation to evaluate the capacity of flexible CBP connections under axial load and biaxial bending. They proposed an analytical model to determine the moment capacity along the major and minor axis considering the variation of applied axial load only. Recently, Song et al. [15] performed a reliability analysis of CBP connections under combined axial compression and flexure. They identified AISC Design Guide 1 [8] approach to be inconsistent which underestimated the flexural demand in the base plate and inapplicable for CBP connections under biaxial bending. Although they proposed two alternative design approaches for overcoming these limitations and improving the reliability, however, those are only applicable under uniaxial bending.

Currently, there exists a gap in the literature that comprehensively investigates the behavior of exposed CBP connections subjected to combined axial load and biaxial bending. Hence, this study aims to investigate the behavior of the W-shaped steel CBP connection under combined axial load and biaxial bending through parametric numerical analysis. This is achieved through the pursuit of considering different values for three parameters of CBP connections such as base plate thickness, base plate yield strength, and anchor rod diameter.

## 2 FINITE ELEMENT MODELING – METHODOLOGY AND VALIDATION

A detailed 3D nonlinear finite element (FE) model is developed using ABAQUS [16] simulation platform. FE model constructed for validation in this study considered the geometric



and material properties of CBP connections experimented by Gomez et al. [12]. The FE model is developed and validated in two phases where the model is constructed as a half model first due to the symmetric nature of the specimen under monotonic loading to reduce the simulation time for interpreting a suitable modeling strategy. Later, a full FE model is developed instead of the half-model to simulate the accurate behavior under combined axial load and lateral cyclic loading. A description of the overall methodology to develop the FE model followed by the validation of the developed models is presented in the subsequent sections.

## 2.1 Methodology

All the elements are modelled as 3D deformable solid elements except the column in the full model which is defined as shell elements for validating the complex cyclic simulation with the consideration of global and local buckling behavior [17]. The column is considered as a W200x71 section which reflects the typical members that are used as the first-story interior columns of steel moment resisting frames (SMRF). The length of the column is considered as 2350 mm from the top of the base plate. The cross-sectional dimension of the grout is considered the same as the base plate dimension (356mm x 356mm). A 1220x1220x610 mm concrete footing is considered for the foundation of the CBP connection. Figure 1 shows details of the geometry and dimensions of the specimens used to validate the FE model.

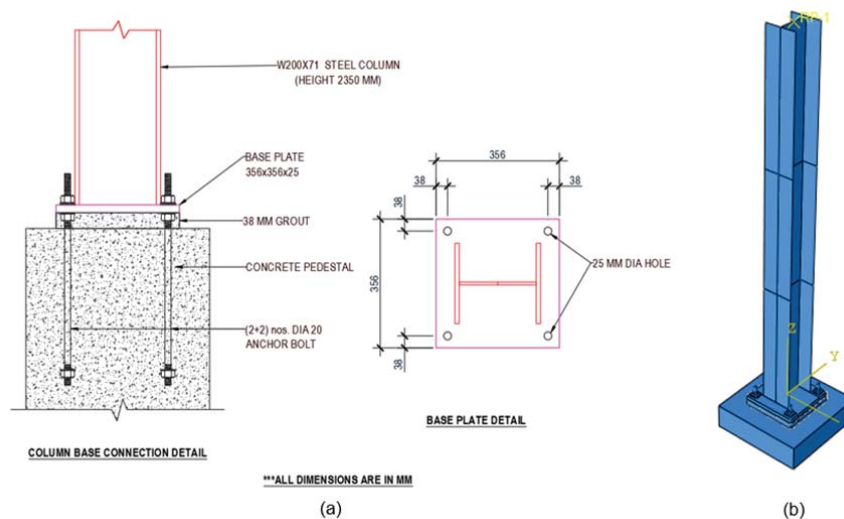


Figure 1: (a) Geometric details (b) Developed FE model

All the 3D solid elements of the developed model are meshed with hexahedral (C3D8R) element whereas the shell element of the column is meshed with quadratic 4-node doubly curved (S4R) shell elements accumulating a total number of 82000 elements. Geometric nonlinearity (NLGEOM) is considered due to the nonlinear effects of large displacement. Column is meshed by dividing its length into three equal parts for computational efficiency. The bottom part is meshed using the same element size as the base plate to neglect the convergence issue while the other parts are meshed using a coarser mesh size. Grout is also meshed by a size similar to the column bottom part and base plate. Anchor rods, nuts and washer are meshed using finer element size to accurately capture the stress behavior of these elements. Since the behavior of footing is not considered in this study, larger mesh size is considered for the footing. A mesh sensitivity study is conducted to accurately predict the results as well as to ensure the computational time efficiency of the developed FE models. For brevity, the details

of the mesh sensitivity study are omitted from this paper. It is very usual for steel structural elements to contain geometric imperfections as well as residual stresses due to the manufacturing and handling process. Geometric imperfection is introduced to capture the global out-of-straightness imperfections of the column. Separate linear perturbation buckling analysis is performed to obtain different buckling modes of the respective column. A global out-of-straightness limit equal to  $L/1500$  [17] is applied with the first buckling mode of the column during the construction of the full model under cyclic loading.

Explicit modeling of component interaction is critical as the contact and gapping of CBP connection components control the overall connection response [13]. Tie constraints are provided between the column and base plate, anchor rods, nuts, and washers, and between the grout and concrete because of their monolithic properties. Surface to surface contact interactions are defined between the interfaces of the base plate and grout, base plate and both the top and bottom washer, and anchor rod-base plate with the finite sliding formulation. Two different interaction properties are defined for these surface to surface interactions. A coefficient of friction of 0.45 is used for the base plate and grout whereas 0.80 is used for the other two interactions [18]. The pressure overclosure for normal behavior is considered as hard contact and separation after contact is allowed whereas the constraint enforcement method is set as default for both the interaction properties. No constraints or interactions are defined between the concrete footing and the anchor rods assuming their interfaces to be free as prescribed by Gomez et al. [12]. Figure 2 illustrates a schematic description of contact and interactions between different components of CBP connection.

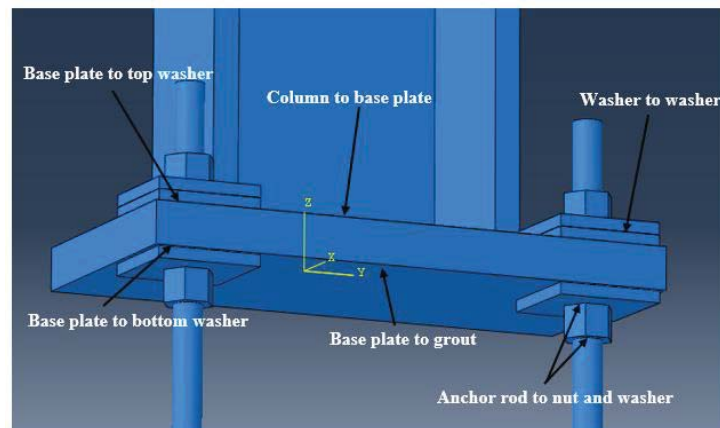


Figure 2: Contact and interactions of different components of CBP connection

The bottom of the concrete footing is restrained in all six degrees of freedom to simulate a fixed-base condition. When the FE model is constructed as a half model under monotonic loading, a symmetric boundary condition is provided parallel to the center plane of the column web to simulate its full-scale behavior. On the other hand, to accurately capture the flexural yielding and geometric instabilities under cyclic loading with full model, a flexible boundary condition is considered at a reference point defined at the cross-section center of the top of the column.

## 2.2 Material modeling

**Steel Elements:** Von-Mises type of material with a nonlinear isotropic/kinematic hardening material model is used to define the column and base plate. In addition to the modulus of elasticity and yield stress, the nonlinear kinematic and isotropic hardening components ( $C$ ,  $\gamma$ ,  $Q^\infty$ ,  $b$ ) are considered for cyclic loading which are derived from the Chaboche [19] model. A

nonlinear monotonic isotropic hardening is modeled for anchor rod whereas nut and washer are modeled as elastic-perfectly plastic material. The hardening parameters used for these parts are from the results of the ancillary experiments conducted by Gomez et al. [12]. Table 1 and 2 provides the values used to define different steel materials for validation of developed FE model for monotonic and cyclic loadings, respectively.

	Yield Stress (MPa)	Modulus of Elasticity (GPa)	Poisson's ratio	Material type
Column	345	200	0.3	nonlinear isotropic hardening
Base Plate	280	200	0.3	nonlinear isotropic hardening
Anchor Rod	786	200	0.3	nonlinear isotropic hardening
Nut & Washer	345	200	0.3	elastic perfectly plastic

Table 1: Steel material for monotonic loading

	Yield Stress (MPa)	Modulus of Elasticity (GPa)	Poisson's ratio	C (MPa)	$\gamma$	$Q_{\infty}$ (MPa)	b
Column	380	200	0.3	3378	20	90	12
Base Plate	255	216	0.3	6895	25	172	2
Anchor Rod	790	200	0.3	nonlinear isotropic hardening			
Nut & Washer	345	200	0.3	elastic perfectly plastic			

Table 2: Steel material for cyclic loading

**Concrete Elements:** Concrete damage plasticity model is developed based on compressive strength for both grout and concrete pedestal. The compressive strengths used for developing concrete damage plasticity model are adopted from the ancillary test results by Gomez et al. [12] for both footing & grout. For monotonic loading phase, the compressive strength of grout and footing is considered as 51 and 27 MPa, respectively. Similarly, the compressive strength of grout and footing is considered as 64 and 30 MPa, respectively for the cyclic loading case. Default values were used for the other parameters to define the concrete damage plasticity model as provided in Table 3.

Parameters	Value
Dilation angle ( $\psi$ )	$36^{\circ}$
Eccentricity (e)	0.1
$f_{b0}/f_{c0}$	1.16
K	0.6667
Viscosity parameter	0.001

Table 3: Concrete damage plasticity parameters

### 2.3 Loading protocol

At first, monotonic loading in the form of lateral displacement (10.58% column drift) is applied along the major axis direction with no axial load. After validating under monotonic load, SAC cyclic loading protocol with a maximum drift of 10.6% is applied in the column major axis direction with a constant 410 KN axial compression at the top of the column to validate the model accuracy under combined axial load and uniaxial cyclic loading.

## 2.4 Validation of developed FE model

The developed FE model is validated against experimental results from Gomez et al. [12] under monotonic and cyclic loading for Test no. 1 and Test no. 5, respectively to check the accuracy of the adopted modeling approach. For monotonic loading, the developed half FE model is validated in terms of anchor rod force and base plate deformation profile as shown in Figure 3 and 4, respectively. From both the Figures, it can be seen that the developed FE model can very well predict the experimental results with reasonable accuracy signifying the suitability of the adopted modeling techniques and material models.

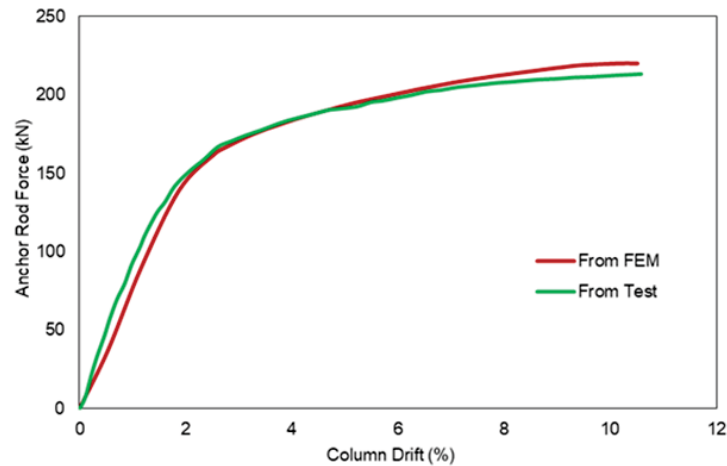


Figure 3: Comparison of experimental (Gomez et al. [12] Test no. 1) and numerical (FE) results

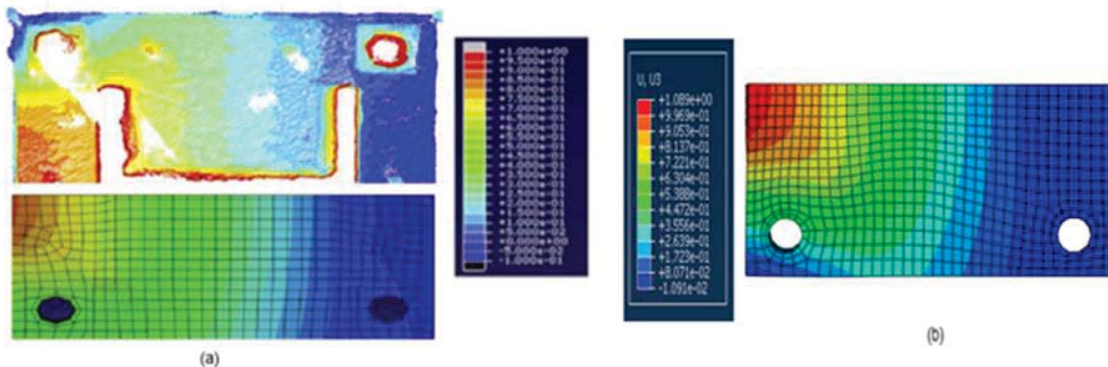


Figure 4: Base plate deformation behavior (a) Gomez et al. [12] Test no.1 (b) developed FE model

Further, the full FE model is validated under cyclic loading protocol in terms of the lateral load-displacement profile as shown in Figure 5. It is found that the variation of maximum lateral load is only 3% between the experimental (Test No. 5 of Gomez et al. [12]) and numerical results. Also, it is evident from Figure 5 that the hysteresis loop for the developed FE model and experimental results are quite similar except for the slipping behavior which is due to the complexity of the interactions among the various CBP connection elements. All these validation results suggest that the adopted modeling techniques can be applied with a high degree of confidence for further investigation.

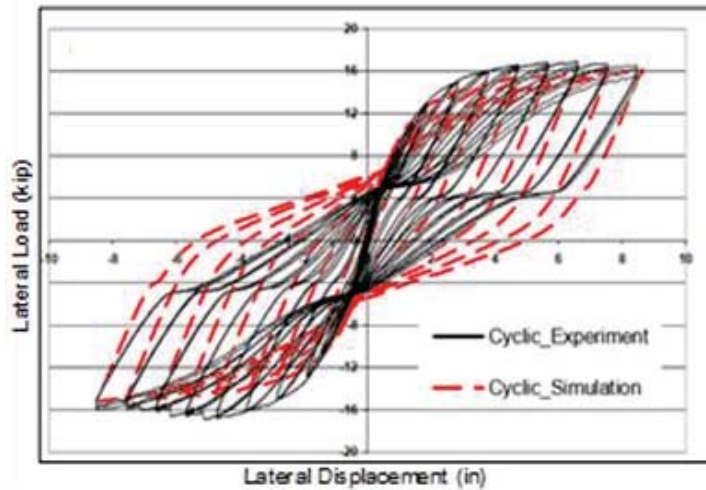


Figure 5: Validation of FE model using cyclic loading

### 3 PARAMETRIC STUDY

Once validated, a total of 12 FE models are developed for the parametric study to understand the behavioral insights of the CBP connections under combined axial load and biaxial bending. These models consider different practical values for three critical column base connection parameters such as base plate thickness, base plate yield strength and anchor rod diameter. Since no symmetric plane is available when the specimen is subjected to biaxial bending, a full model is considered to simulate the behavior of the CBP connection. Details of the test matrix and development of the bidirectional loading protocol are described in the subsequent sections.

#### 3.1 Parametric analysis cases

The three critical parameters of the analytical investigation are selected from the literature review conducted by Grauvilardell et al. [1] as well as the previous parametric study done by Trautner and Hutchinson [20] where they categorized different parameters of CBP connection into low, medium, and high category. Based on these studies, three critical parameters with variable ranges are considered in this study. Table 4 provides the details of the simulation matrix considered in this parametric study where the bold numbers indicate the variable values of different parameters. Each of the cases considered only one variable to understand its effect on the base plate connection considering PR-01 as the base model.

Parameter	Specimen ID	Parameter Values						
		Base Plate Thickness (mm)	Base Plate Yield Strength (Mpa)	Anchor Rod Dia (mm)	No. of Anchor Rod	Embedment Length (mm)	Grout Thickness (mm)	Axial Load Ratio
Base Model	PR-01	<b>25</b>	<b>350</b>	<b>20</b>	<b>4</b>	<b>500</b>	<b>25</b>	<b>0.2</b>
Base Plate Thickness	PR-02	<b>16</b>	350	20	4	500	25	0.2
	PR-03	<b>20</b>	350	20	4	500	25	0.2
	PR-04	<b>30</b>	350	20	4	500	25	0.2
	PR-05	<b>38</b>	350	20	4	500	25	0.2



	PR-06	<b>50</b>	350	20	4	500	25	0.2
Base Plate Yield Strength	PR-07	25	<b>300</b>	20	4	500	25	0.2
	PR-08	25	<b>400</b>	20	4	500	25	0.2
Anchor Rod Dia	PR-09	25	350	<b>16</b>	4	500	25	0.2
	PR-10	25	350	<b>25</b>	4	500	25	0.2
	PR-11	25	350	<b>30</b>	4	500	25	0.2
	PR-12	25	350	<b>38</b>	4	500	25	0.2

Table 4: Simulation matrix of the parametric study

### 3.2 General features of the FE models

All the developed FE models of the parametric analysis cases have similar geometric and material properties. ASTM A992 Grade 50 W250x73 column section (typical interior first story column) having 2000 mm length (2/3rd of typical first story height of SMRFs) is designed according to the requirements of CSA S16-19 [21]. The column is designed considering yield strength ( $F_y$ ) of 345 MPa and modulus of elasticity ( $E$ ) of 200 GPa and the cross-section is selected to prevent local buckling criteria as well as its capacity to ensure its effectiveness before the failure of the base plate connection. A rectangular base plate of 407 mm x 407 mm, welded together with the column, having different thicknesses and yield strength is selected for the study. Anchor rods of different sizes are designed using yield strength and modulus of elasticity of 790 MPa and 200 GPa, respectively following the requirements of CSA S16-19 [21] and CSA A23.3-19 [22] to prevent any type of failure in the concrete by pullout or breakout strength. The nut and washers are selected according to standard geometry for the specific anchor rod. A concrete foundation of 1220 mm x 1220 mm is designed to support all types of loading. Non-shrink grout having 64 MPa compressive strength of various thickness is also considered between the pedestal and the base plate. All the FE models developed for the parametric analysis study have the same configuration of mesh size, geometric imperfection, tie contact, and interaction properties as the validated full FE model. Anchor rods, nuts and washers and concrete material properties of the developed FE models are also the same as the validated model.

### 3.3 Bidirectional lateral loading protocol

A bidirectional symmetric lateral loading protocol is developed for the numerical investigation in pursuance of evaluating the effect of biaxial bending on the exposed CBP connection. This cyclic loading protocol is developed for a four-story steel frame building following the concepts discussed in Krawinkler [23] and Elkady [17]. The loading protocol covers a wide range of story drift ratios starting from 0.375% amplitude up to amplitude of 4% radians in the column's strong axis direction as shown in Figure 6(a). It also covers story drift ratio ranging from 0.25% to 2% amplitude in the column's weak axis direction as shown in Figure 6(b). When combined, it is found that the developed bidirectional loading protocol achieves a maximum drift ratio of 3% in the column's strong axis direction when 2% drift amplitude is reached in the column's weak axis direction as depicted in Figure 6(c). Detail procedure of the developed bidirectional loading protocol is described in Elkady [17].



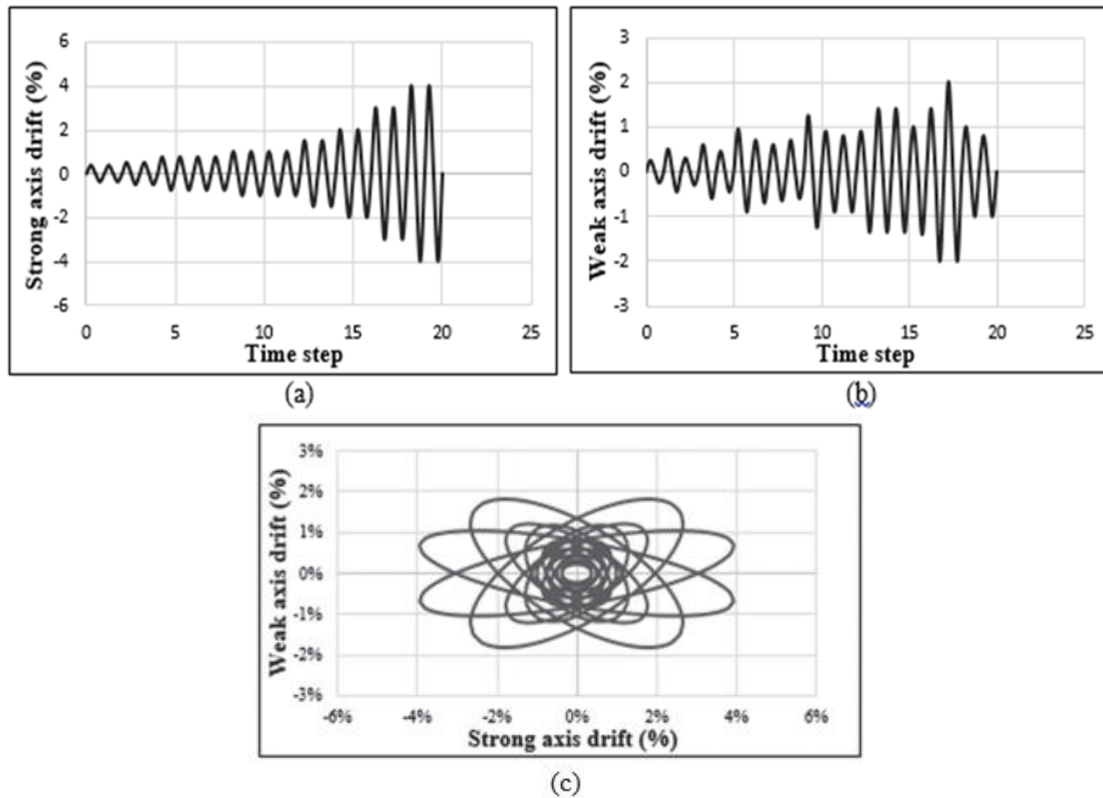


Figure 6: Developed bidirectional symmetric lateral loading protocol: (a) history of strong axis drift ratio; (b) history of weak axis drift ratio; (c) history of strong axis vs weak axis drift ratio

#### 4 RESULTS AND DISCUSSION

The analytical results obtained from the parametric study have been used to further understand the behavior of exposed CBP connections subjected to combined axial load and biaxial bending. Results are scrutinized in terms of moment-rotation curve which is a key output to better understand the connection behavior by defining the rigidity, resistance, and rotational capacity of any connection. Table 5 provides the summary of the results extracted from the FE models.

FE Model ID	Axis	Yield			Ultimate			$K_{\theta(Yield)} / K_{\theta(Ultimate)}$
		M (KN-m)	$\theta \times 10^{-3}$ (rad)	$K_{\theta} \times 10^3$	M (KN-m)	$\theta \times 10^{-3}$ (rad)	$K_{\theta} \times 10^3$	
PR-01	X	120.26	13.89	8.66	184.75	33.87	5.45	1.59
	Y	43.28	6.45	6.71	72.20	15.52	4.65	1.44
PR-02	X	49.58	6.68	7.42	78.10	37.38	2.09	3.55
	Y	24.14	3.64	6.63	40.67	16.89	2.41	2.75
PR-03	X	93.22	10.68	8.72	163.81	34.49	4.75	1.84
	Y	40.5	6.57	6.17	63.54	16.07	3.95	1.56
PR-04	X	150.44	12.69	11.85	220.00	32.43	6.78	1.75
	Y	48.68	6.31	7.71	79.43	15.56	5.10	1.51
PR-05	X	155.60	12.65	12.30	244.29	31.40	7.78	1.58
	Y	51.44	6.34	8.11	85.65	15.42	5.55	1.46

PR-06	X	181.52	11.73	15.47	241.43	31.62	7.64	2.03
	Y	53.36	6.27	8.51	89.00	15.25	5.84	1.46
PR-07	X	149.38	21.59	6.92	182.86	33.63	5.44	1.27
	Y	44.52	6.46	6.89	71.91	15.92	4.52	1.52
PR-08	X	154.74	21.67	7.14	195.71	33.09	5.91	1.21
	Y	46.64	6.72	6.94	74.50	15.72	4.74	1.46
PR-09	X	117.20	13.96	8.39	175.71	33.74	5.21	1.61
	Y	37.96	5.19	7.32	71.77	15.81	4.54	1.61
PR-10	X	133.56	13.53	9.87	197.14	33.17	5.94	1.66
	Y	44.98	6.23	7.22	74.64	15.65	4.77	1.51
PR-11	X	132.88	13.48	9.86	205.71	32.89	6.25	1.58
	Y	47.24	6.38	7.41	75.60	15.68	4.82	1.54
PR-12	X	139.34	13.19	10.57	220.00	32.31	6.81	1.55
	Y	46.98	6.42	7.32	76.56	15.59	4.91	1.49

Table 5: Summary of FE model results

#### 4.1 Moment-rotation behavior

For each FE simulation, the hysteretic response in terms of base moment-rotation is plotted as shown in Figure 7 and compared within the various values of the specific parameter considered in the analytical study. Further bilinear moment-rotation curve, considering yield point and ultimate point, is developed for both the strong (x-axis) and weak axis (y-axis) and analyzed separately for convenient visualization. Column plastic moment capacity ( $M_p$ ) is also shown in the same plot (horizontal line) for both strong and weak axis direction. The column base moment ( $M$ ) and base rotation ( $\theta$ ) are computed from the column lateral force and lateral displacement according to Eq. (1) and Eq. (2), respectively.

$$M = F \times H_{col} \quad (1)$$

$$\theta = \left( \Delta_{top} - \frac{F \times H_{col}^3}{3 \times E_{col} \times I_{col}} \right) \times \frac{1}{H_{col}} \quad (2)$$

Where,  $F$  is the lateral force at the column top,  $H_{col}$  is the column height from the base plate,  $\Delta_{top}$  is the displacement at the top of the column,  $E_{col}$  is the modulus of elasticity of the column,  $I_{col}$  is the column's second moment of inertia in the direction of loading.

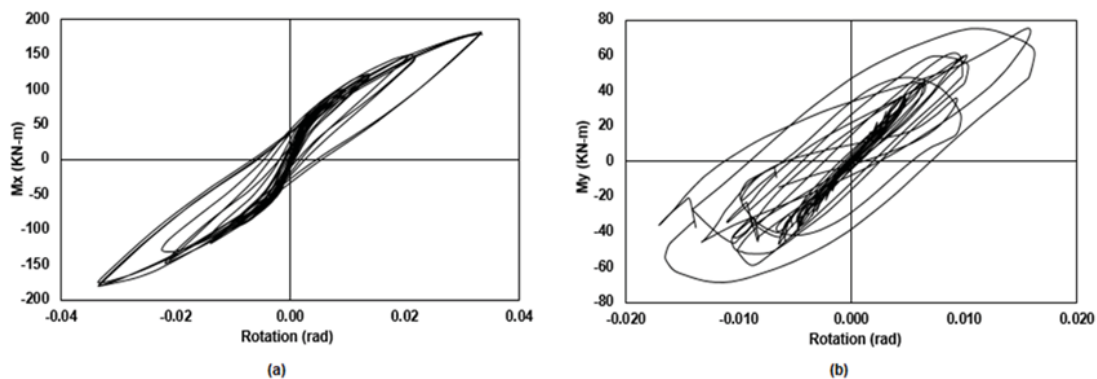


Figure 7: Moment-rotation hysteresis curve for PR-01 model (a) Strong axis (b) Weak axis

#### 4.2 Effect of base plate thickness

Six different base plate thicknesses (PR-01 to PR-06) are considered with values ranging from 16 mm to 50 mm. For the base model (PR-01), the base plate thickness of 25 mm is considered for the study which is widely used in the construction industry. Figure 8 illustrates the comparison of bilinear moment-rotation curves for various base plate thicknesses. It is observed from Figure 8 that a higher value of base plate thickness increases both the stiffness and the strength of the connection for both strong and weak axis direction. This is plausible since an increase in base plate thickness increases the flexural rigidity as well as bending resistance of the plate. However, it should be noted that the effect of base plate thickness is more pronounced in the strong axis direction compared to the weak axis. A significant increase in the strength of the connection is observed after yielding for each of the simulation cases except for the PR-02 where the base plate thickness is considered as 16 mm. Early yielding of the base plate of lower thickness significantly hinders the strength gain of the CBP connection. As reported in Table 5, the average ratio of yield to ultimate rotational stiffness for various base plate thicknesses is 2.06 and 1.7 in the strong and weak axis direction, respectively. It is also found that the strength of all the base connections with different base plate thicknesses is significantly below the column plastic moment capacity in both the strong and weak axis directions. In brief, as the base plate thickness increases, the strength of the base connection is augmented with the reduction in ductility.

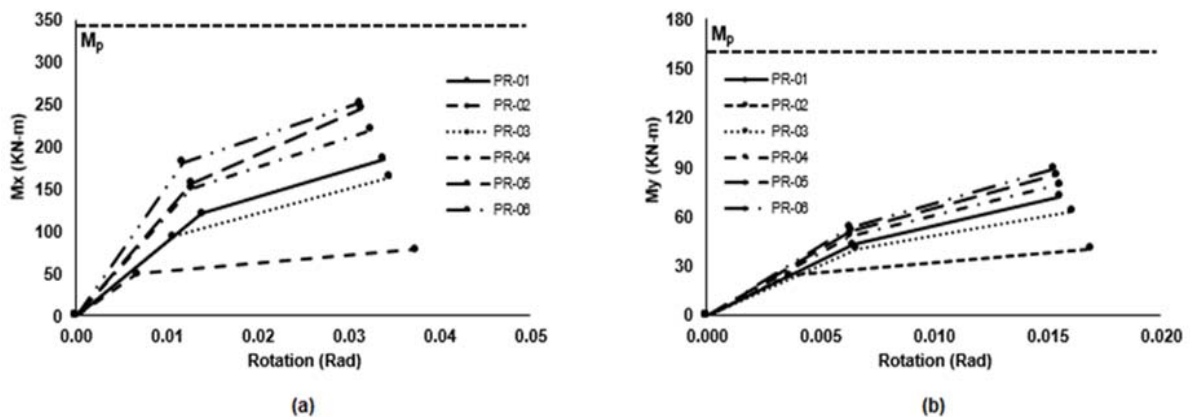


Figure 8: Effect of base plate thickness (a) Strong axis (b) Weak axis

#### 4.3 Effect of base plate yield strength

Different base plate yield strengths of 300, 350 and 400 MPa (PR-01, PR-07 and PR-08) are considered to understand the effect of base plate yield strength on base plate connection behavior. Although base plate yield strength is not considered in the previous experimental study on CBP connections, it is considered in this study due to its contribution on the design of base plate thickness according to AISC Design Guide 1 [8]. The variations in the base plate strengths are considered based on the most commonly used steel grades in industry. It can be seen from Figure 9 and Table 5 that base plate yield strength does not influence the moment-rotation response in the weak axis direction. However, initial stiffness is found to be lower when the base plate yield strength is changed from the base model of 350 MPa in the strong axis direction.

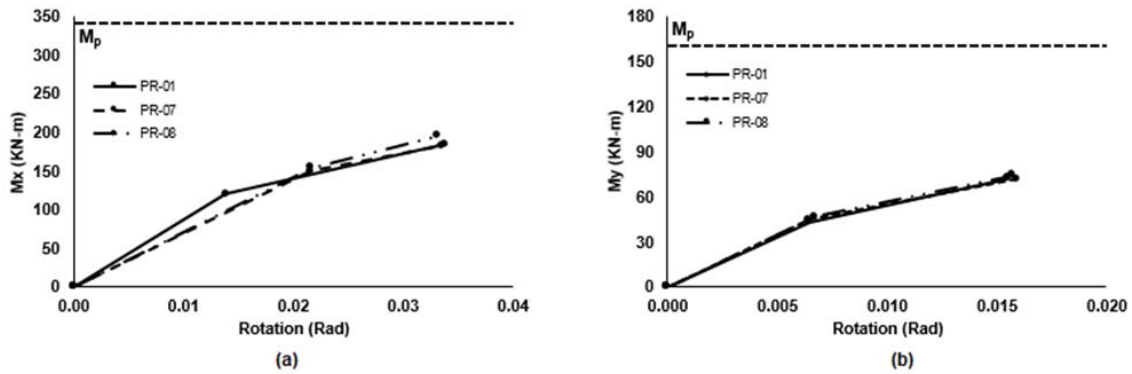


Figure 9: Effect of base plate yield strength (a) Strong axis (b) Weak axis

#### 4.4 Effect of anchor rod diameter

Different anchor bolt diameters ranging from 16 mm to 38 mm (PR-01, PR-09 to PR-12) are selected to scrutinize the moment-rotation behavior of CBP connections. Figure 10 represents the effect of anchor bolt diameter in terms of moment-rotation curves of the base plate connection. It is evident that an increase in anchor bolt diameter increases the initial stiffness as well as the strength in both axes directions. A larger bolt diameter affects the flexibility of the base plate cantilever length by contributing in the base rotation. An increase of 20% is observed for maximum strength in the strong axis direction when the diameter is increased from 20 mm to 38 mm. Conversely, a 6% increment is observed in the weak axis direction for the same configuration. Changes in the initial stiffness are found to be more obvious in the strong axis than the weak axis of the base plate connection. As reported in Table 5, the average ratio of yield to ultimate rotational stiffness is 1.60 and 1.52 in the strong and weak axis direction, respectively.

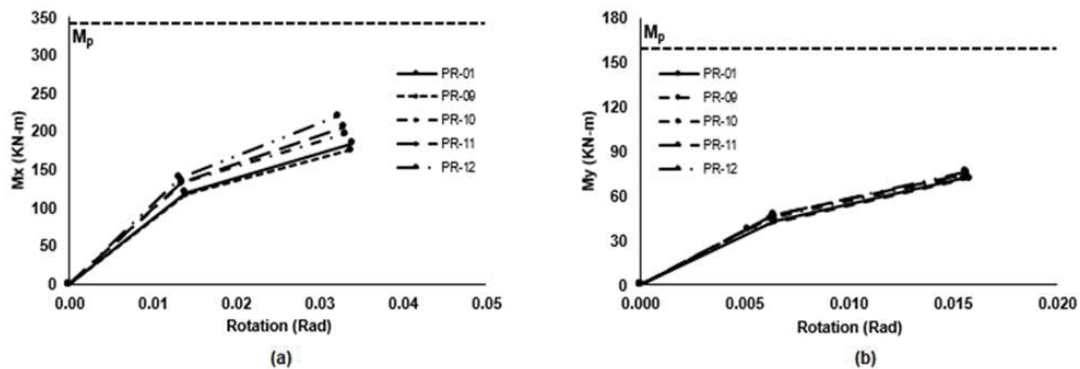


Figure 10: Effect of anchor rod diameter (a) Strong axis (b) Weak axis

## 5 CONCLUSIONS

- Higher value of base plate thickness increases both the stiffness and the strength of the connection for both strong and weak axis directions.
- The effect of base plate thickness is more pronounced in the strong axis direction compared to the weak axis direction.
- Early yielding of the base plate is observed for the thinner (16 mm) base plate of the CBP connection.
- Base plate yield strength has no significant influence on CBP connection within the considered ranges.

- An increase in anchor bolt diameter increases both the initial stiffness and strength in strong and weak axis directions.
- For different anchor rod diameters, changes in the initial stiffness are found to be more obvious in the strong axis than the weak axis of the base plate connection.

## ACKNOWLEDGEMENTS

The financial contributions of the Canadian Institute for Steel Construction (CISC) through CISC Research Grant is gratefully acknowledged.

## REFERENCES

- [1] J.E. Grauvilardell, D. Lee, J.F. Hajjar, R.J. Dexter, Synthesis of design, testing and analysis research on steel column base plate connections in high seismic zones. *Structural Engineering Rep. No. T-04-02, Dept. of Civil Engineering, University of Minnesota, Minneapolis, USA*, 2005.
- [2] R. Tremblay, A. Filiatrault, P. Timler, M. Bruneau, Performance of steel structures during the 1994 Northridge earthquake. *Canadian Journal of Civil Engineering*, **22**(2), 338–360, 1995.
- [3] M. Midorikawa, I. Nishiyama, M. Tada, T. Terada, Earthquake and tsunami damage on steel buildings caused by the 2011 Tohoku japan earthquake. *International Symposium on Engineering Lessons Learned from the 2011 Great East Japan Earthquake*, March. Tokyo, Japan, 2012.
- [4] J. T. DeWolf, E.F. Sarisley, Column base plates with axial loads and moments. *ASCE Journal of Structural Division*, **106**(11), 2167–2184, 1980.
- [5] A. Picard, D. Beaulieu, B. Perusse, Rotational Restraint of a Simple Column Base Connection. *Canadian Journal of Civil Engineering*, **14**, 49-57, 1987.
- [6] A. Astaneh-Asl, G. Bergsma, Cyclic Behavior and Seismic Design of Steel Base Plates. *Proceedings of Structures Congress, ASCE*, 409–414, 1993.
- [7] J.J. Burda, A.M. Itani, Studies of Seismic Behavior of Steel Base Plates. *Report No. CCEER 99-7, Reno (NV): Center of Civil Engineering Earthquake Research, Department of Civil and Environmental Engineering, University of Nevada, NV, USA*, 1999.
- [8] J.M. Fisher, L.A. Kloiber, *Design Guide 1: Base plate and anchor rod design, 2nd Ed.* American Institute of Steel Construction, Chicago, 2006.
- [9] M. Fahmy, B. Stojadinovic, S.C. Goel, Analytical and experimental behavior of steel column bases. *Proceedings of 8th Canadian Conference on Earthquake Engineering, Canadian Association for Earthquake Engineering*, Ottawa, ON, Canada, 1999.
- [10] D.Y. Lee, S.C. Goel, B. Stojadinovic, Exposed Column-Base Plate Connections Bending about Weak Axis: I. Numerical Parametric Study. *International Journal of Steel Structure, KSSC*, **8**(1), 11–27, 2008.

- [11] D.Y. Lee, S.C. Goel, B. Stojadinovic, Exposed column-base plate connections bending about weak axis: II. Experimental Study. *International Journal of Steel Structure*, KSSC, **8**(1), 29–41, 2008.
- [12] I. Gomez, G. Deierlein, A. Kanvinde, Exposed column base connections subjected to axial compression and flexure. *Final Rep. Presented to the American Institute of Steel Construction*, Chicago, USA, 2010.
- [13] A.M. Kanvinde, S.J. Jordan, R.J. Cooke, Exposed column baseplate connections in moment frames—Simulations and behavioral insights. *Journal of Constructional Steel Research*, **84**, 82–93, 2013.
- [14] M.A.K. Fasaee, M.R. Banan, S. Ghazizadeh, Capacity of Exposed Column Base Connections Subjected to Uniaxial and Biaxial Bending Moments. *Journal of Constructional Steel Research*, **148**, 368–370, 2018.
- [15] B. Song, C. Galasso, A. Kanvinde, Reliability Analysis and Design Considerations for Exposed Column Base Plate Connections Subjected to Flexure and Axial Compression. *ASCE Journal of Structural Engineering*, **147**(2), 04020328, 2021.
- [16] SIMULIA Inc. *ABAQUS user's manual, version 6.20*. Providence, RI, USA, 2020.
- [17] A. Elkady, Collapse Risk Assessment of Steel Moment Resisting Frames Designed with Deep Wide Flange Columns in Seismic Regions. *PhD Thesis, Department of Civil Engineering and Applied Mechanics*, McGill University, Montreal, Canada, 2016.
- [18] I.S. Grigoriev, E.Z. Meĭlikhov, A.A. Radzig, *Handbook of Physical Quantities*. CRC Press, Boca Raton, FL, 1997.
- [19] J.L. Chaboche, A review of some plasticity and viscoplasticity constitutive theories. *International Journal of Plasticity*, **24**(10), 1642–1693, 2008.
- [20] C.A. Trautner, T.C. Hutchinson, Parametric Finite-Element Modeling for Exposed Steel Moment Frame Column Baseplate Connections Subjected to Lateral Loads. *ASCE Journal of Structural Engineering*, **144**(6), 04018049, 2018.
- [21] CSA. *Design of Steel Structures. CSA-S16-19*, Canadian Standards Association, Toronto, ON, Canada, 2019.
- [22] CSA. *Design of Concrete Structures. CSA-A23.3*, Canadian Standards Association, Mississauga, ON, Canada, 2019.
- [23] H. Krawinkler, Cyclic loading histories for seismic experimentation on structural components. *Earthquake Spectra*, **12**(1), 1–12, 1996.



## GEOMETRICALLY NON-LINEAR FREE IN-PLANE VIBRATION OF FUNCTIONALLY GRADED CIRCULAR ARCH WITH UNIFORM CROSS-SECTION

O. Outassafte<sup>1</sup>, A. Adri<sup>1</sup>, Y. El khouddar<sup>1</sup>, S. Rifai<sup>1</sup> and R. Benamar<sup>2</sup>

<sup>1</sup> Laboratoire de Mécanique Productique et Génie Industriel, Ecole Supérieure de Technologie  
Hassan II University of Casablanca, B.P.8012, Oasis, Casablanca, Maroc  
e-mail: [omar.outassafte@ensem.ac.ma](mailto:omar.outassafte@ensem.ac.ma), [ahmedadri@gmail.com](mailto:ahmedadri@gmail.com), [yassine.elkhouddar@ensem.ac.ma](mailto:yassine.elkhouddar@ensem.ac.ma)

[Said57.rifai@gmail.com](mailto:Said57.rifai@gmail.com)

<sup>2</sup> Mohammed V University in Rabat, EMI-Rabat, LERSIM  
B.P.765 Agdal, Rabat, Morocco.  
[rhali.benamar@gmail.com](mailto:rhali.benamar@gmail.com)

---

### Abstract

*In this present work the geometrical non-linearity in free in-plane vibration of inextensible functionally graded circular arch with uniform cross-section and pinned-pinned at both ends has been studied. For simplification, the complicating effects such as rotary inertia and shear deformation will be ignored. The sixth order differential partial equation of motion has been obtained after the inextensibility assumption. This study is based on Euler Bernoulli theory and Von Karman's assumptions. The kinetic and total strain energies due to the axial strain and bending have been discretized into a series of a finite spatial functions and derived by applying the Hamilton's principle energy. The non-linear algebraic equations were obtained and solved numerically using an approximate explicit method developed previously the so-called second formulation. A numerical results have been obtained to examine the effects of the volume fraction index on non-linear behavior of the arch. Comparison is made with the available results for the case of isotropic homogeneous circular arches: good agreement is obtained.*

**Keywords:** geometrical non-linearity, free in-plane vibration, functionally graded circular arch, uniform cross-section, second formulation.

---

## 1 INTRODUCTION

Arches have become one of the very important structures elements that are used in many areas such as aeronautics, civil engineering and mechanical engineering due to its ability to transfer loads through the combined action of bending and stretching for in-plane deformations. The equations of free in-plane vibration of an arch are very complex when the complicating effects such as axial extension, shear deformation and rotatory inertia are taken into account. If these effects are neglected, then the equations become much simpler, but the main simplification arises if the arch axis is assumed to be also inextensible.

H. Saffari et al [1] used a finite element technique to obtain the natural frequencies and mode shapes of circular arch in free vibration analysis. The Rayleigh-Ritz method was employed by Laura et al to find the fundamental frequency of arches with various types of cross-section using polynomial functions as a trial function of displacement [2]. G.R. Liu, T.Y. Wu were applied the generalized differential quadrature rule to investigate the free in-plane vibration of inextensible Euler-Bernoulli arches with uniform, continuously varying, and stepped cross-sections. A semi analytical solution for in-plane vibration of circular arch was used by A. Babahammou and R. Benamar [3], [4] to find the linear frequencies and mode shape of arches with various boundary conditions. The results shown a very good agreement with those available in the literature. Recently, the geometrically non-linear in free in-plane vibration of circular arches elastically restrained against rotation at the two ends was investigated by O. Omar et al [5].

Functionally graded material can be defined as a new class of non-homogeneous composite materials made from combination of two different materials. In recent years, a lot of research has been done to study the geometrical non-linearity of the FGM and composite structure based on Benamar's method such as [6]–[10]

The free in-plane vibration of arches made of homogeneous, composite, and FG materials was the interest of numerous researchers such as . Hadi Babaei et al [11] have investigated the large amplitude free vibration of curved beam (shallow arch) resting on elastic foundation. The natural frequencies of a deep circular arch made of FG materials with arbitrary thickness and boundary conditions, have been obtained in [12]. The influence of the temperature, boundary conditions and the material graded index as well as the different geometrical parameters such as the thickness-to-mean radius ratio and the opening angle on the frequency parameters of the FG arches have been investigated by [13]. M. Javan et al [14] have studied a large amplitude thermally induced vibration analysis is investigated for shallow FGM arches under different cases of rapid heating on the top and bottom surfaces. In [15] an analytical solution to study the non-linear thermal bending and buckling of the through-the-thickness FGM shallow arches is presented, taking into account the variation of critical buckling temperature in terms of power law index, geometric parameter and opening angle.

This current work deals with the study of the geometrical non-linearity in free in-plane vibration of a FGM circular arch with uniform cross-section and pinned-pinned at both ends. This theoretical model is based on the Euler-Bernoulli theory and the Von Karman assumptions. The complicating effects such as rotary inertia and shear deformation will be ignored. The kinetic and total strain energies due to the axial strain and bending were discretized into a series of finite spatial functions and derived using Hamilton's principle energy. Then, the non-linear algebraic equations are obtained and solved numerically using an explicit method developed previously, the so-called second formulation. A numerical results have been obtained to

examine the effects of the volume fraction index on the non-linear behavior of the FGM circular arch.

## 2 GENERAL FORMULATION

### 2.1. Non-linear vibration

A functionally graded circular arch made from a mixture of ceramic-metal material with a constant thicknesses is considered in this study. The effective material properties of the FGM circular arch such as Young's modulus  $E(z)$ , and mass density  $\rho(z)$ , with volume fraction index  $p$  are assumed to vary continuously through the thickness of the beam, according to power law form are shown in Fig.1.

The effective of material properties  $P$ , can be expressed as:

$$P = P_m V_m + P_c V_c \quad (1)$$

Where  $P_m$ ,  $V_m$ ,  $P_c$ , and  $V_c$  are the material properties and the volume fraction of the metal and ceramic respectively.

In which  $V_m$  and  $V_c$  are the metal and ceramic volume fractions respectively related by :

$$V_m + V_c = 1 \quad (2)$$

Assuming the power law distribution, the volume fraction can be written with the relation:

$$V_f(z) = \left( \frac{z}{h} + \frac{1}{2} \right)^p \quad (3)$$

Where  $p$  is the volume fraction index,  $0 \leq p \leq \infty$ . When  $p$  is set to zero, the FG arch becomes fully ceramic, when  $p$  is set to infinite, the FG arch becomes fully metal .

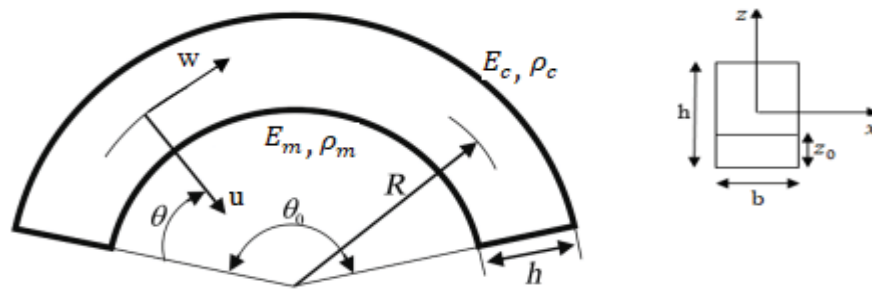


Fig 1: Schematic of a FGM circular arch

According to the power law, the young's modulus  $E(z)$  and mass density are  $\rho(z)$  expressed as:

$$E(z) = E_m + (E_c - E_m)V_f(z) \quad (4)$$

$$\rho(z) = \rho_m + (\rho_c - \rho_m)V_f(z) \quad (5)$$

Where  $(E_m, \rho_m)$  are the material properties for metal and  $(E_c, \rho_c)$  are the material properties for ceramic respectively. The physical parameters of ceramic and metal are presented in Table 1.

Table 1 :The physical parameters of ceramic and metal

Materials	Young's modulus $E / Gpa$	Density $\rho / (kg.m^{-3})$
<b>Ceramic</b>	380	3980
<b>Metal</b>	206	7800

The variation the density and Young's modulus along the height of the cross-section is shown in Fig.2, by taking into account several values of the the volume fraction index.

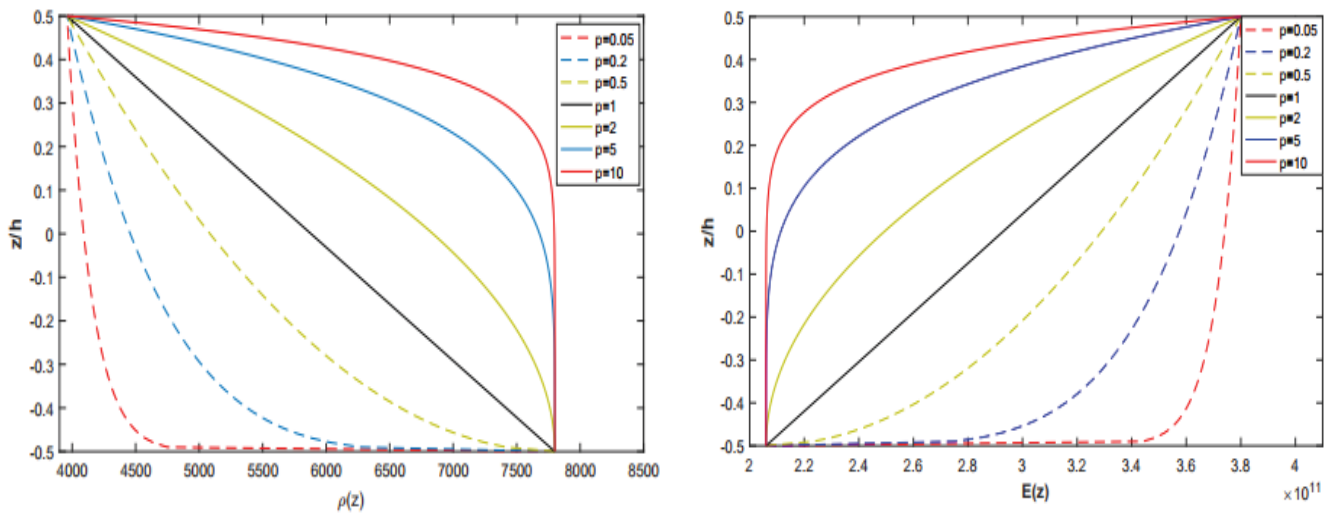


Fig. 2. Variation of the density and Young's modulus through the arch thickness for different values of gradient index p.

In this present study , the complicated effects such as shear deformation and rotary inertia are neglected because the arch is supposed to be thin. The arch axis is supposed to inextensible, the radial displacement  $u$  and tangential displacement  $w$  are related by [16]:

$$\frac{\partial w}{\partial \varphi} = u \quad (6)$$

The sixth order differential equation of motion may be written as:

$$\frac{\partial^6 w}{\partial \varphi^6} + 2 \frac{\partial^4 w}{\partial \varphi^4} + \frac{\partial^2 w}{\partial \varphi^2} + \lambda^2 \frac{\partial^4 w}{\partial t^2 \partial \varphi^4} = 0 \quad (7)$$

$$\lambda_i^2 = \frac{\omega_i^2 R_i^{*4} \int_{-h/2}^{h/2} \rho dy}{\int_{-h/2}^{h/2} E y^{*2} dy} \text{ is the non-dimensional frequency.}$$

$$z_0 = \frac{p(E_m - E_c)}{2(p+2)(pE_c + E_m)} h \quad (8)$$

$$(9)$$

$$z^* = z + z_0$$

$$(10)$$

$$R^* = R + z_0$$

$z_0$  denoted the height of the metal material,  $z$  denoted the neutral axis of isotropic homogenous circular arch,  $z^*$  denoted the neutral axis of the FGM circular arch, of the Where  $R$  denoted the radius of curvature of the geometric median of the arch and  $R^*$  denoted the radius of curvature of the neutral layer.

Considering the arch in a harmonic motion, we put:

$$w(\varphi, t) = W(\varphi) \cos(\omega t) \quad (11)$$

When the form of solution is:

$$W(\varphi) = e^{\Omega \varphi} \quad (12)$$

The characteristic equation may be written as:

$$\Omega^6 + 2\Omega^4 + (1 - \lambda^2)\Omega^2 = 0 \quad (13)$$

The general solution of the differential equation (7) in term of tangential displacement can be written as:

$$W_i(\varphi) = C_1 \sin(\alpha\varphi) + C_2 \cos(\alpha\varphi) + C_3 \sinh(\alpha\varphi) + C_4 \cosh(\alpha\varphi) + C_5(\varphi) + C_6 \quad \text{with} \quad i = 1, \dots, n \quad (14)$$

Where:  $\alpha = \sqrt{\lambda - 1}$ ,  $\beta = \sqrt{\lambda + 1}$  and  $\lambda \geq 1$ .

The pinned-pinned boundary conditions of circular arch in term of tangential displacement may be written as:

$$W_i(\varphi = 0) = W_i(\varphi = \varphi_0) = 0 \quad \left. \frac{dW_i}{d\varphi} \right|_{\varphi=0} = \left. \frac{dW_i}{d\varphi} \right|_{\varphi=\varphi_0} = 0 \quad \left. \frac{d^3W_i}{d\varphi^3} \right|_{\varphi=0} = \left. \frac{d^3W_i}{d\varphi^3} \right|_{\varphi=\varphi_0} = 0 \quad (15)$$

The use of the end conditions and the transfer matrix method leads to a homogeneous system. The determinant of the latest must be set equal to zero to obtain the natural frequencies, determined iteratively by the Newton–Raphson algorithm.

## 2.2. Non-linear vibration

The kinetic energy  $T$  and total strain energy  $V$  of the system presented in Fig. 1 may be written as a sum of the axial energy  $V_a$  and the strain energy due to the bending  $V_b$ . The expression of  $T$ ,  $V_a$  and  $V_b$  are expressed as:

$$T = \frac{R^*}{2} \int_0^{\theta_0} \left[ b \left( \frac{\partial w_i^{(1)}}{\partial t} \right)^2 + \left( \frac{\partial w_i}{\partial t} \right)^2 \int_{-h/2}^{h/2} \rho dy \right] dt \quad (16)$$

$$V_a = \frac{1}{2R^{*3}} \int_0^{\theta_0} \left[ b \left( \frac{\partial w_i}{\partial \theta} + \frac{\partial^3 w_i}{\partial \theta^3} \right)^2 \int_{-h/2}^{h/2} Ey^{*2} dy \right] d\theta \quad (17)$$

$$V_b = \frac{1}{8R^{*3}} \int_0^{\theta_0} \left[ b \left( w_i + \frac{\partial^2 w_i}{\partial \theta^2} \right)^4 \int_{-h/2}^{h/2} E dy \right] d\theta \quad (18)$$

$$V = V_a + V_b$$

Assuming harmonic, the tangential displacement function is expanded in the form of finite basic spatial functions:

$$w_i(\varphi, t) = a_i W_i \sin(\omega t) \quad (19)$$

By replacing  $w_i$  in the expressions for the energies  $T$ ,  $V_a$  and  $V_b$  can be written in the form:

$$T = \frac{1}{2} a_i a_j \omega^2 m_{ij} \cos^2(\omega t) \quad (20)$$

$$V_a = \frac{1}{2} a_i a_j k_{ij} \sin^2(\omega t) \quad (21)$$

$$V_b = \frac{1}{2} a_i a_j a_k a_l b_{ijkl} \sin^4(\omega t) \quad (22)$$

The parameters  $m_{ij}$ ,  $k_{ij}$ ,  $b_{ijkl}$  are the mass tensor, linear and the quadratic non-linear rigidity tensor of the arch in which their expressions are defined as:

$$m_{ij} = R^* \int_0^{\theta_0} b \left( \frac{\partial W_i}{\partial \theta} \frac{\partial W_j}{\partial \theta} + W_i W_j \right) \int_{-h/2}^{h/2} \rho dy d\theta \quad (23)$$

$$k_{ij} = \frac{1}{R^{*3}} \int_0^{\theta_0} b \left[ \left( \frac{\partial W_i}{\partial \theta} + \frac{\partial^3 W_i}{\partial \theta^3} \right) \left( \frac{\partial W_j}{\partial \theta} + \frac{\partial^3 W_j}{\partial \theta^3} \right) \right] \int_{-h/2}^{h/2} Ey^{*2} dy d\theta \quad (24)$$

$$b_{ijkl} = \left\{ \frac{1}{4R^{*3}} b \left[ \int_0^{\theta_0} \left( W_i + \frac{\partial^2 W_i}{\partial \theta^2} \right) \left( W_j + \frac{\partial^2 W_j}{\partial \theta^2} \right) d\theta \int_0^{\theta_0} \left( W_k + \frac{\partial^2 W_k}{\partial \theta^2} \right) \left( W_l + \frac{\partial^2 W_l}{\partial \theta^2} \right) \int_{-h/2}^{h/2} E dy d\theta \right] \right\} \quad (25)$$



The coefficients  $a_i$  are unknowns as well as the frequency  $\omega_i$ . The dynamic behaviour of the conservative system may be obtained by applying Hamilton's principle as defined in equation (27) :

$$\delta \int_0^{2\pi/\omega} (V - T) dt \quad (26)$$

One can obtain the following non-linear algebraic equations:

$$([K] - \omega^2 [M])\{A\} + \frac{3}{2}[B(A)]\{A\} = \{0\} \quad (27)$$

To obtain non-dimensional parameters, ones put:

$$W_i(\varphi) = hW_i^* \left( \frac{\varphi}{\varphi_0} \right) = hW_i^*(\varphi^*) \quad \frac{m_{ij}}{m_{ij}^*} = bR^*h^2, \frac{k_{ij}}{k_{ij}^*} = \frac{b_{ijkl}}{b_{ijkl}^*} = \frac{bh^2}{R^{*3}} \quad (28)$$

Where  $m_{ij}^*$ ,  $k_{ij}^*$  and  $b_{ijkl}^*$  are the non-dimensional generalized parameters given by:

$$m_{ij}^* = \int_0^1 \left( \frac{1}{\theta_0^2} \frac{\partial W_i^*}{\partial \theta^*} \frac{\partial W_j^*}{\partial \theta^*} + W_i^* W_j^* \right) \theta_0 \int_{-h/2}^{h/2} \rho dy d\theta^* \quad (29)$$

$$k_{ij}^* = \left\{ \int_0^1 \left( \frac{1}{\theta_0} \frac{\partial W_i^*}{\partial \theta^*} + \frac{1}{\theta_0^3} \frac{\partial^3 W_i^*}{\partial \theta^{3*}} \right) \left( \frac{1}{\theta_0} \frac{\partial W_j^*}{\partial \theta^*} + \frac{1}{\theta_0^3} \frac{\partial^3 W_j^*}{\partial \theta^{3*}} \right) \theta_0 \int_{-h/2}^{h/2} E y^{*2} dy d\theta^* \right\} \quad (30)$$

$$b_{ijkl}^* = \left\{ \frac{h^2}{4} \int_0^1 \left( W_i^* + \frac{\partial^2 W_i^*}{\theta_0^2 \partial \theta^{2*}} \right) \left( W_j^* + \frac{\partial^2 W_j^*}{\theta_0^2 \partial \theta^{2*}} \right) \theta_0 d\theta^* \int_0^1 \left( W_k^* + \frac{\partial^2 W_k^*}{\theta_0^2 \partial \theta^{2*}} \right) \left( W_l^* + \frac{\partial^2 W_l^*}{\theta_0^2 \partial \theta^{2*}} \right) \theta_0 \int_{-h/2}^{h/2} E dy d\theta^* \right\} \quad (31)$$

By substituting the non-dimensional parameter into equation (28) one obtain the dimensionless non-linear algebraic equations :

$$([K^*] - \omega^{*2} [M^*])\{A\} + \frac{3}{2}[B^*(A)]\{A\} = \{0\} \quad (32)$$

$B_{ijkl}^*$  presents the dimensionless non-linearity tensor,  $K_{ij}^*$  is the dimensionless rigidity matrix,  $M_{ij}^*$  denotes the dimensionless mass matrix and  $\omega^*$  is the dimensionless non-linear frequency. Using the tensorial notation, one put:

$$a_i k_{ir}^* + \frac{3}{2} a_i a_j a_k b_{ijk}^* - a_i \omega^{*2} m_{ir}^* = 0 \quad \text{with} \quad r = 1, \dots, n \quad (33)$$

The called the second formulation [17], it is an approximation which consists to separate the nonlinear term of equation (34) into a terms proportional to  $a_i^3$  and terms proportional to  $a_i^2 \varepsilon_i$  and neglecting terms proportional to  $a_i \varepsilon_i \varepsilon_j$  and terms proportional to  $\varepsilon_i \varepsilon_j \varepsilon_k$  one can write:

$$a_i a_j a_k b_{ijk r} = a_1^3 b_{111 r} + a_1^2 \varepsilon_i b_{11 i r} \quad r = 1, \dots, n \quad (34)$$

After substituting and rearranging, equation (34) may be written in matrix form as:

$$\left( [K_r^*]_R - \omega^2 [M_r^*]_R \right) \{A_r\}_R + \frac{3}{2} [\alpha_r^*]_R \{A_r\}_R = \left\{ -\frac{3}{2} a_r^3 b_{111 r}^* \right\} \quad (35)$$

### 3 RESULTATS AND DISCUSSION

In this present work, the free in-plane vibration of a FGM circular arch made with mixture of ceramic-metal material with uniform section and pinned at the both ends is studied based on multimode approach.

By assuming the material properties in table.1, the material volume fraction p dependence to the variation of the first four in-plane free vibration frequencies of FGM pinned-pinned circular arch are shown in Fig. 2 for radius  $R=60m$ , thicknesses  $h=0.8m$  and an opening angle  $\varphi_0 = 100^\circ$ .

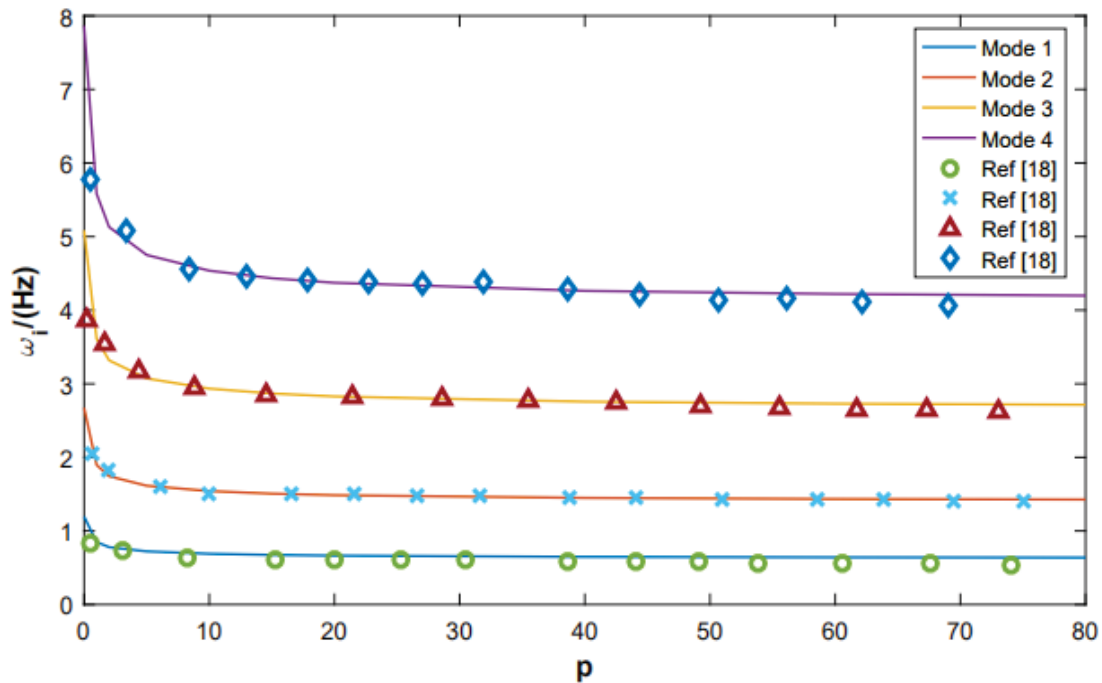


Fig. 2: The material volume fraction p dependence to the variation of the first four in-plane free vibration frequencies of FGM circular arch [18].

The influence of the volume fraction index p on the dimensionless non-linear frequency ratio of pinned-pinned FGM circular arch are presented in Fig.4.

The Fig.2 shows a comparison of the first four linear frequencies of the FGM pinned-pinned circular arch obtained in this present work with the results obtained in [18] as the curvature is constant. Where good agreement is obtained.

The effects of the opening angle of the FGM circular arch with a volume fraction index  $p = 5$  and pinned-pinned ends on the dimensionless non-linear frequency ratios are shown in Fig. 4.

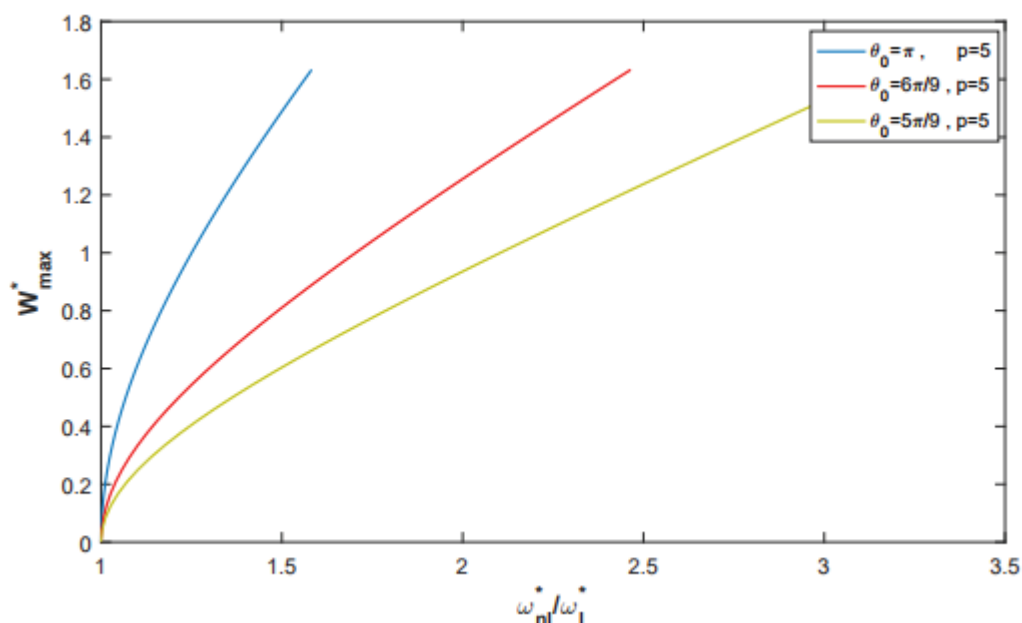


Fig. 3. Influence of the opening angle on the ratio of the dimensionless non-linear frequency ratios to the linear frequency of FGM circular arch beams with volume fraction  $p = 5$ .

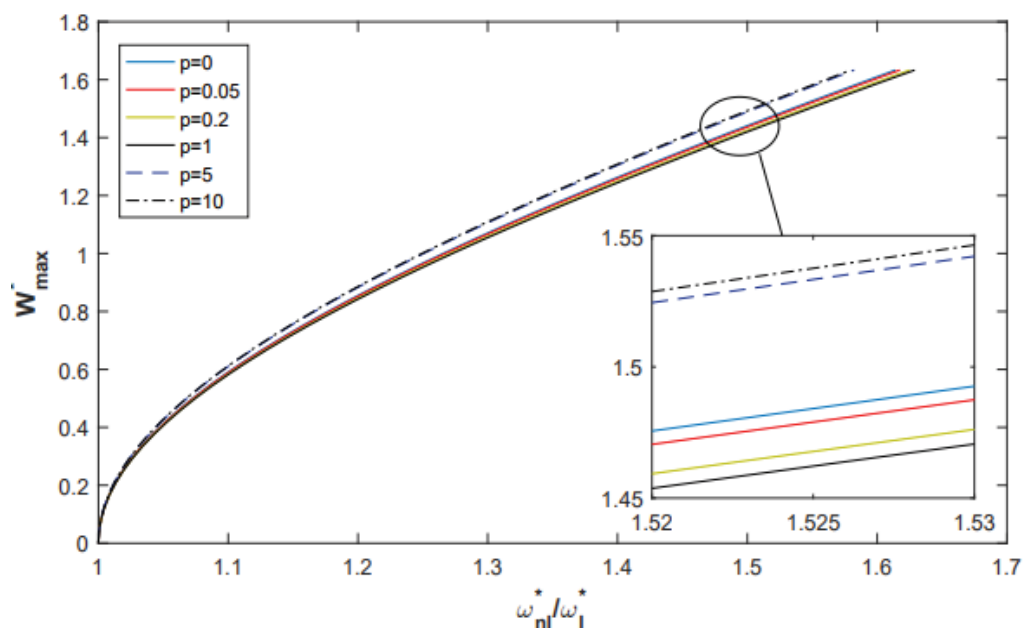


Fig. 4. Effect of The material volume fraction  $p$  on the frequency ratio.

The results in Fig. 4 show that the dimensionless non-linear frequency ratios of arch tend increase with increasing the opening angle increases, due to the increased rigidity.

The influence of the volume fraction index  $p$  on the dimensionless non-linear frequency ratios of the FGM arch by considering the pinned-pinned boundary conditions can be clearly shown in Fig. 3.

A quantitative values of the dimensionless non-linear frequency ratios of the FGM circular arch, for various values of the volume fraction index  $p$  and the non-dimensional amplitude of vibration are presented in Table 2. The results are compared with those obtained in [5].

Table 2: comparison of the dimensionless non-linear frequencies ratios for each value of the volume fraction index  $p$  with isotropic homogenous pinned-pinned circular arch [5].

$W_{\max}^*/h$	$\omega_{nl}^*/\omega_l^*$	Present $\omega_{nl}^*/\omega_l^*$						
		Ref [5]	p=0.0	p=0.05	p=0.2	p=1	p=5	p=10
0.08165	1.002004	1.002004	1.002017	1.002048	1.002064	1.001877	1.001867	1.002004
0.46947	1.064259	1.064259	1.064694	1.065658	1.066144	1.60301	1.059994	1.064259
0.857231	1.200968	1.200968	1.202254	1.205100	1.206531	1.189286	1.188324	1.200968
1.24488	1.390340	1.390340	1.392682	1.397860	1.400463	1.368994	1.367231	1.390340
1.63239	1.613943	1.613943	1.617412	1.625076	1.628927	1.582246	1.579621	1.613943

Table 2 shows the dependence of the frequency ratio of the pinned FG circular arch on the amplitude of vibration for various values of the power law index  $p$ . As may be seen in this figure, by increasing the values of the power law index in the range  $[0, 1]$ , the frequency increases. For values higher than  $p=1.0$ , the frequency decreases when  $p$  increases. This may be expected, since when the power index  $p=0.0$  or  $p=\infty$ , the material becomes pure metallic or pure ceramic, respectively, and the non-dimensional frequency corresponds to the isotropic homogenous material case.

## 4 CONCLUSIONS

The geometrical non-linearity in free in-plane vibration of inextensible FGM circular arches. were analyzed based on the Euler Bernoulli theory and the Von Karman geometrical non-linearity assumptions. For simplification, the complicating effects such as rotary inertia and shear deformation will be ignored. The natural frequencies of arch were obtained iteratively using Newton-Raphson algorithm. The kinetic and total strain energy of the arch were reduced discretized then the problem was reduced into a set non-linear algebraic equations using Hamilton's principle energy and spectral analysis and solved numerically by an approximate explicit method the so-called second formulation. A numerical results were obtained to examine the effects of the volume fraction index on non-linear behavior of the FGM circular arch.

## REFERENCES

- [1] H. Saffari, R. Tabatabaei, and S. H. Mansouri, 'Vibration Analysis of Circular Arch Element Using Curvature', *Shock and Vibration*, vol. 15, no. 5, pp. 481–492, 2008, doi: 10.1155/2008/149393.
- [2] P. A. A. Laura and P. L. V. de Irassar, 'A note on in-plane vibrations of arch-type structures of non-uniform cross-section: The case of linearly varying thickness', *Journal of Sound and Vibration*, vol. 124, no. 1, pp. 1–12, Jul. 1988, doi: 10.1016/S0022-460X(88)81402-0.
- [3] A. Babahammou and R. Benamar, 'Semi-Analytical Solution of In-Plane Vibrations of Circular Arches Carrying Added Point Masses', *Procedia Manufacturing*, vol. 44, pp. 465–472, Jan. 2020, doi: 10.1016/j.promfg.2020.02.269.
- [4] A. Babahammou. B.Rhali, 'The Efficiency of the Rayleigh-Ritz Method Applied to In-Plane Vibrations of Circular Arches Elastically Restrained against Rotation at the Two Ends', *International Journal of Engineering Trends and Technology - IJETT*, Accessed: May 30, 2021.
- [5] O. Outassafte, A.Adri, Y.El khouddar, S.Rifai, B. Rhali, 'Geometrically Non-Linear Free In-Plane Vibration Of Circular Arch Elastically Restrained Against Rotation At The Two Ends', *International Journal of Engineering Trends and Technology - IJETT*, Accessed: Apr. 17, 2021. [Online]. Available: <https://www.ijettjournal.org/archive/ijett-v69i3p215>
- [6] L. Boutahar, el bikri Khalid, and B. Rhali, 'Thermal Behavior Analysis at Large Free Vibration Amplitudes of Thin Annular FGM Plates with Porosities', *Procedia Engineering*, vol. 199, pp. 528–533, Dec. 2017, doi: 10.1016/j.proeng.2017.09.148.
- [7] M. Chajdi, A. Ahmed, K. E. Bikri, and R. Benamar, 'Analysis of the associated stress distributions to the nonlinear forced vibrations of functionally graded multi-cracked beams', *Diagnostyka*, vol. 22, no. 1, pp. 101–112, Feb. 2021, doi: 10.29354/diag/133702.
- [8] Y. E. khouddar, A. Adri, S. Rifai, and R. Benamar, 'Geometrically non-linear forced vibrations of Euler–Bernoulli laminated composite beams', *J. Phys.: Conf. Ser.*, vol. 1896, no. 1, p. 012016, Apr. 2021, doi: 10.1088/1742-6596/1896/1/012016.
- [9] M. Chajdi, E. B. Merrimi, and el bikri Khalid, 'Geometrically Non-Linear Free and Forced Vibration of Clamped-Clamped Functionally Graded Beam with Discontinuities.', *Procedia Engineering*, vol. 199, pp. 1870–1875, Dec. 2017, doi: 10.1016/j.proeng.2017.09.117.
- [10] H. Fakhreddine, A. Adri, M. Chajdi, S. Rifai, and R. Benamar, 'Geometrically nonlinear forced vibrations of fully clamped multi-span beams carrying multiple masses and resting on a finite number of simple supports', *J. Phys.: Conf. Ser.*, vol. 1264, p. 012021, Jul. 2019, doi: 10.1088/1742-6596/1264/1/012021.
- [11] H. Babaei, Y. Kiani, and M. R. Eslami, 'Large amplitude free vibration analysis of shear deformable FGM shallow arches on nonlinear elastic foundation', *Thin-Walled Structures*, vol. 144, p. 106237, Nov. 2019, doi: 10.1016/j.tws.2019.106237.
- [12] M. Javani, Y. Kiani, and M. R. Eslami, 'Free vibration of arbitrary thick FGM deep arches using unconstrained higher-order shear deformation theory', *Thin-Walled Structures*, vol. 136, pp. 258–266, Mar. 2019, doi: 10.1016/j.tws.2018.12.020.
- [13] P. Malekzadeh, M. M. Atashi, and G. Karami, 'In-plane free vibration of functionally graded circular arches with temperature-dependent properties under thermal environment', *Journal of Sound and Vibration*, vol. 326, no. 3–5, pp. 837–851, Oct. 2009, doi: 10.1016/j.jsv.2009.05.016.
- [14] M. Javani, Y. Kiani, and M. R. Eslami, 'Geometrically nonlinear rapid surface heating of temperature-dependent FGM arches', *Aerospace Science and Technology*, vol. 90, pp. 264–274, Jul. 2019, doi: 10.1016/j.ast.2019.04.049.

- [15] H. Asgari and M. Eslami, 'Nonlinear Thermal Buckling Analysis of FGM Shallow Arches Under Linear Temperature Gradient', *ASME 2014 12th Biennial Conference on Engineering Systems Design and Analysis, ESDA 2014*, vol. 1, Jul. 2014, doi: 10.1115/ESDA2014-20402.
- [16] P. Chidamparam and A. W. Leissa, 'Vibrations of Planar Curved Beams, Rings, and Arches', *Appl. Mech. Rev.*, vol. 46, no. 9, pp. 467–483, Sep. 1993, doi: 10.1115/1.3120374.
- [17] M. El kadiri, R. Benamar, and R. G. White, 'IMPROVEMENT OF THE SEMI-ANALYTICAL METHOD, FOR DETERMINING THE GEOMETRICALLY NON-LINEAR RESPONSE OF THIN STRAIGHT STRUCTURES. PART I: APPLICATION TO CLAMPED–CLAMPED AND SIMPLY SUPPORTED–CLAMPED BEAMS', *Journal of Sound and Vibration*, vol. 249, no. 2, pp. 263–305, Jan. 2002, doi: 10.1006/jsvi.2001.3808.
- [18] W. Li and Z. Teng, 'In-plane free vibration analysis of FGM arches with variable curvature', *Zhendong yu Chongji/Journal of Vibration and Shock*, vol. 36, pp. 201–208, May 2017, doi: 10.13465/j.cnki.jvs.2017.09.030.



## ANALYSIS OF GEOMETRICALLY NON-LINEAR FREE VIBRATIONS OF FUNCTIONAL GRADED BEAMS IN A THERMAL ENVIRONMENT

Y. El khouddar <sup>1</sup>, A. Adri <sup>1</sup>, O. Outassafte <sup>1</sup>, S. Rifai <sup>1</sup> and R. Benamer <sup>2</sup>

<sup>1</sup> Laboratoire de Mécanique Productique et Génie Industriel, Ecole Supérieure de Technologie, Hassan II University of Casablanca, B.P.8012, Oasis, Casablanca, Morocco

e-mail: [yassine.elkhouddar@ensem.ac.ma](mailto:yassine.elkhouddar@ensem.ac.ma), [ahmedadri@gmail.com](mailto:ahmedadri@gmail.com), [omar.outassafte@ensem.ac.ma](mailto:omar.outassafte@ensem.ac.ma)

[Said57.rifai@gmail.com](mailto:Said57.rifai@gmail.com)

<sup>2</sup> Mohammed V University in Rabat, EMI-Rabat, LERSIM, B.P.765 Agdal, Rabat, Morocco

e-mail: [rhali.benamer@gmail.com](mailto:rhali.benamer@gmail.com)

---

### Abstract

*The thermal non-linear vibrational behavior of functional graded beams is analyzed using Euler-Bernoulli beam theory and Hamilton's theorem, combined with spectral analysis. A set of non-linear equations is derived based on the von Kármán deformation-displacement relationship and the properties of the functional graded material are assumed to be temperature dependent and to follow a simple power distribution in the thickness direction. Numerical solutions of the non-linear dynamic equations of functional graded beams are obtained by an approximate method called the second formulation. In addition, numerical examples were performed to highlight the accuracy of the method used in this study, and the results are very consistent with those found in the literature. In the numerical examples, the influences played by thermal environmental conditions and volume fraction index are discussed in detail.*

**Keywords:** Functionally graded beams, Non-linear free vibration, Thermal environment, Second formulation.

---

## 1 INTRODUCTION

Functionally graded materials (FGM) are composed of a mixture of ceramic and metal or a combination of different materials. The FGM ceramic provides a barrier against thermal effects and protects the metal from corrosion and oxidation, and the FGM is hardened and strengthened by the metal component. Currently, FGM has been developed as a general structural element in extremely high temperature environments and has been widely used in electronics, chemistry, optics, biology, medical engineering and many other fields.

Due to the above-mentioned advantageous characteristics, many studies have been conducted on the following topics, which are the static and dynamic behavior of the FGM structure. Xiang and Shi [1] proposed an analytical solution to analyze the thermo-elasticity of FGM beams embedded in piezoelectric layers. Assuming a cantilevered beam, he used the Airy stress function method to obtain an accurate solution. Ebrahimi et al. [2] reported an analytical method to control the vibration of an FGM beam containing two piezoelectric layers. A theoretical model is based on the Kirchhoff's-Love hypothesis, which has a non-linear geometric von-Karman-type deformation. Fu and colleagues [3] studied the non-linear analysis of buckling, free vibration, active control and dynamic stability of functionally graded piezoelectric beams in a thermal environment. Based on Hamilton's principle, a non-linear guidance equation is established. Falsone and La Valle [4] solved the differential equations governing the axial equilibrium and bending in the Euler-Bernoulli and Timoshenko theory of an FGM beam. This analysis is obtained in both cases of material variation in the transverse and axial directions. Kiani et al. [5] studied the thermal buckling of piezoelectric FGM beams, in which the piezoelectric layer is bonded to the surface and subjected to a constant thermal load and tension. Bodaghi and Shakeri [6] analytically studied the free vibration and dynamic response of a cylindrical piezoelectric FGM panel, which is simply supported and subjected to time-dependent explosive pulses. In recent years, a lot of research has been done on free and forced non-linear vibrations. Based on the Euler-Bernoulli beam theory and von Kármán's non-linear kinematics, and using Hamilton's principle, Benamar et al. [7] developed a theory and a method to analyze the vibrational response of isotropic beams. El khouddar et al [8] studied the free and forced non-linear vibrations of laminated composite beams under different boundary conditions, using the Euler-Bernoulli beam theory and the Green-Lagrang non-linearity. From the Euler-Bernoulli beam theory, Chajdi et al [9] examined the forced nonlinear vibrations of an FGM beam with multiple cracks. Based on the Euler-Bernoulli beam theory, Outassafte et al [10], [11] contributed to the geometrically non-linear free vibration of a fixed-ended arch. Currently, many results have been obtained when studying the dynamic mechanical properties of FGM beams, but most of them are based on linear theory. Due to the large displacement of the structure in engineering practice, the geometric non-linearity must be taken into account, otherwise it will lead to serious errors. At the same time, the analysis under thermal loading will affect the non-linear vibration of the FGM structure. Therefore, it is necessary to study the non-linear vibration of the FGM beam under thermal loading in more detail.

In the present work, the problem of geometrically non-linear free vibrations of FGM beams in a thermal environment with fixed ends is studied. In this analysis, the material properties change continuously through the thickness of the beam according to the power law, and change with temperature changes. The Hamiltonian principle is used to establish the governing equation of the beam under thermal load, and the second formula is used to obtain the analytical solution of the non-linear free vibration problem. Important conclusions have been drawn.

## 2 BASIC EQUATIONS

Consider an FGM beam of rectangular cross-section with a length of  $L$  and a thickness of  $h$ . This beam is made of a mixture of ceramics and metals. The coordinate system is shown in Figure 1. The material properties, namely Young's modulus  $E$ , Poisson's ratio  $\nu$ , thermal conductivity  $\kappa$ , and coefficient of thermal expansion  $\alpha$ , depend on temperature and vary with thickness.

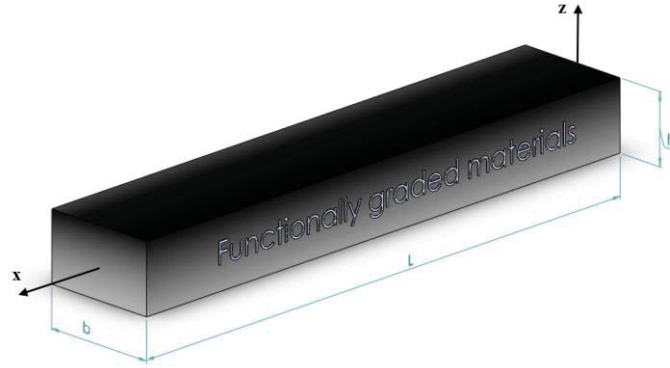


Figure 1: Coordinates and geometry of the FGM beam.

The effective material properties  $P$  of the FGM layer, namely the Young's modulus  $E$ , Poisson's ratio  $\nu$ , thermal conductivity  $\kappa$  and coefficient of thermal expansion  $\alpha$ , can be expressed as follows:

$$P(z, T) = P_m + (P_c - P_m) \left( \frac{1}{2} + \frac{z}{h} \right)^k \quad (1)$$

The characteristic  $P$  of the constituent material depends on the temperature and can be written:

$$P = P_0 (P_{-1} T^{-1} + 1 + P_1 T + P_2 T^2 + P_3 T^3) \quad (2)$$

The temperature distribution on the beam is considered as uniform and can reach  $\Delta T = T - T_0$  to deform the beam. Where  $T_0$  is the reference temperature of the beam in the unstressed state.

### 2.1 linear vibration analysis

Considering the mid-plane stretch and ignoring the axial inertia, the equations of motion to control the axial and lateral vibration of FGM beams are often considered in the literature and have been adopted in reference [12]:

$$\frac{\partial N_x}{\partial x} = 0 \quad (3)$$

$$\frac{\partial^2 M_x}{\partial x^2} + \frac{\partial}{\partial x} \left( N_x \frac{\partial w}{\partial x} \right) = I_0 \frac{\partial^2 w}{\partial t^2} \quad (4)$$

$N_x$  and  $M_x$  are respectively the axial internal force and the bending moment acting at the mid-plane of the beam are defined as follows:

$$N_x = A_{11} \frac{\partial u}{\partial x} - B_{11} \frac{\partial^2 w}{\partial x^2} - N_x^T \quad (5)$$

$$M_x = B_{11} \frac{\partial u}{\partial x} - D_{11} \frac{\partial^2 w}{\partial x^2} - M_x^T \quad (6)$$

Where  $I_0$  is the inertia of the beam:

$$I_0 = \int_{-h/2}^{h/2} \rho_f dz \quad (7)$$

Where  $N_x^T$  and  $M_x^T$  are the resultant and the moment of the thermal force, which are calculated using the following relations:

$$N_x^T = \int_{-h/2}^{h/2} E \alpha \Delta T dz, \quad M_x^T = \int_{-h/2}^{h/2} (z - z_0) E \alpha \Delta T dz \quad (8)$$

In equations (5) and (6),  $A_{11}$ ,  $B_{11}$  and  $D_{11}$  are extension-extension, bending-extension and bending-bending coupling coefficients, respectively, which can be evaluated using the well-known classical theory of FGM beams [13]. Their expressions are defined as follows:

$$A_{11} = \int_{-h/2}^{h/2} E dz, \quad B_{11} = \int_{-h/2}^{h/2} E (z - z_0) dz, \quad D_{11} = \int_{-h/2}^{h/2} E (z - z_0)^2 dz \quad (9)$$

The axial equation (1) of equilibrium is then given by :

$$N_x = A_{11} \frac{\partial u}{\partial x} - B_{11} \frac{\partial^2 w}{\partial x^2} - N_x^T = N_{x0} \quad (10)$$

Considering the fixed ends (i.e.  $u = 0$ , at  $x = 0$  and  $L$ ), the integration of Eq (10) along the x-axis leads to:

$$0 = \int_0^L \frac{\partial u}{\partial x} dx = u(L) - u(0) = \frac{1}{A_{11}} \int_0^L \left[ N_{x0} + N_x^T + B_{11} \frac{\partial^2 w}{\partial x^2} \right] dx \quad (11)$$

Also:

$$N_{x0} = \frac{A_{11}}{L} \int_0^L \left[ -\frac{B_{11}}{A_{11}} \frac{\partial^2 w}{\partial x^2} \right] dx - N_x^T \quad (12)$$

By introducing equation (12) into equation (6), the bending moment can be rewritten as follows:

$$M_x = B_{11} \left[ \frac{N_{x0} + N_x^T}{A_{11}} + \frac{B_{11}}{A_{11}} \frac{\partial^2 w}{\partial x^2} \right] - D_{11} \frac{\partial^2 w}{\partial x^2} - M_x^T \quad (13)$$

Taking  $N_x^T$  and  $M_x^T$  as constants along the x-axis, we can obtain the following linear steering equation for the FGM beam by inserting equations (12) and (13) into equation (4).

$$D_{11} \frac{\partial^4 w}{\partial x^4} + (N_x^T) \frac{\partial^2 w}{\partial x^2} + I_0 \frac{\partial^2 w}{\partial t^2} = 0 \quad (14)$$

Equation (14) can be written in a slightly less complicated way, the result is:

$$w'''' + \lambda w'' - \beta^4 w = 0 \quad (15)$$

In formula (15), the new symbol indicates the following functional relationship:

$$\lambda = \frac{N^T}{D_{11}}, \quad \beta^2 = \frac{\omega}{c}, \quad c^2 = \frac{D_{11}}{I_0} \quad (16)$$

Where  $x^*$  is a dimensionless coordinate, which can be written:  $x^* = \frac{x}{L}$ . Equation (15) is an ordinary differential equation of order 4 with constant coefficients whose general solution is given by:

$$w_i(x^*) = A \sin \left( \sqrt{\frac{1}{2}\lambda + \frac{1}{2}\sqrt{\lambda^2 + 4\beta_i^4}} x^* L \right) + B \cos \left( \sqrt{\frac{1}{2}\lambda + \frac{1}{2}\sqrt{\lambda^2 + 4\beta_i^4}} x^* L \right) + C \sinh \left( \sqrt{-\frac{1}{2}\lambda + \frac{1}{2}\sqrt{\lambda^2 + 4\beta_i^4}} x^* L \right) + D \cosh \left( \sqrt{-\frac{1}{2}\lambda + \frac{1}{2}\sqrt{\lambda^2 + 4\beta_i^4}} x^* L \right) \quad (17)$$

i changes from 1 to n, where n is the number of functions.

## 2.2 Non-linear vibration analysis

Using the displacement fields from the Euler-Bernoulli theory and assuming that the FGM beam has large vibration amplitudes, the Von-Karman relation can be written as follows:

$$\varepsilon_{xx} = \frac{\partial u}{\partial x} - (z - z_0) \frac{\partial^2 w}{\partial x^2} + \frac{1}{2} \left( \frac{\partial w}{\partial x} \right)^2 \quad (18)$$

The kinetic energy  $T_e$  of an FGM beam in vibration is equal to:

$$T_e = \frac{I_0}{2} \int_0^L \left( \frac{\partial w}{\partial t} \right)^2 dx \quad (19)$$

The potential energy  $V$  can be written in terms of transverse displacement  $w$  and longitudinal displacement for our beam as:

$$V = \frac{1}{2} \int_0^L N_x \left( \frac{\partial u}{\partial x} + \frac{1}{2} \left( \frac{\partial w}{\partial x} \right)^2 \right) + M_x \left( -\frac{\partial^2 w}{\partial x^2} \right) dx \quad (20)$$

Using the generalized parameterization that corresponds to the transverse displacement of the beam we have [14], [15]:

$$w = a_i w_i(x) \sin \omega t \quad (21)$$

According to Hamilton's principle, the non-linear algebraic equations of the dynamic behavior of the structure are calculated using the tensor notation:

$$a_i k_{iq} + \frac{3}{2} a_i a_j a_k b_{ijkq} - \omega^2 a_i m_{iq} = 0, i = 1, \dots, n \quad (22)$$

To perform a general parametric study, the following dimensionless formulation is used:

$$x^* = \frac{x}{L}, \quad w_i(x) = r w_i^*(x^*), \quad r^2 = \frac{\int_{-h/2}^{h/2} z^2 dz}{\int_{-h/2}^{h/2} dz} \quad (23)$$

$r$  is the radius of gyration of the piezoelectric FGM beam. The numerical solution of equation (22) can be obtained by using the second formula described in [16]. This approximation consists of ignoring the second-order terms provided by the relevant mode. As mentioned in the reference, in the non-linear expression  $a_i a_j a_k b_{ijkq}$  of equation (22), the second order term of  $\varepsilon_i$  will be ignored.

### 3 NUMERICAL RESULTS AND DISCUSSIONS

In this section, the FGM beam is chosen for the material Si3N4 / SUS304, this beam has a length of  $L = 200$  mm and a thickness of  $h = 10$  mm. Table 1 shows the characteristics of Young's modulus  $E$  (in Pa), thermal expansion coefficient  $\alpha$  (in K) and thermal conductivity  $\kappa$  (in W/mK). For the Poisson's ratio  $\nu$  of the FGM layer is assumed to be constant equal to 0.28. It should also be noted that the upper surface of the substrate ( $z = h / 2$ ) is ceramic rich and the lower surface ( $z = -h / 2$ ) is metal rich. In addition, the temperature  $T_m$  of the lower surface of the FGM beam is assumed to be 300K, and the temperature  $T_c$  of the upper surface is variable.

Table 1. Coefficients material properties as a function of temperature for Si3N4 and SUS304.

Materials	Properties	$P_0$	$P_{-1}$	$P_1$	$P_2$	$P_3$
Si3N4	$E_c$ (Pa)	348.43e+9	0	-3.07e-4	2.160e-7	-8.964e-11
	$\alpha_c$ (1 / K)	5.8723e-6	0	9.095e-4	0	0
	$\kappa_c$ (W / mK)	13.723	0	-1.032e-3	5.466e-7	-7.876e-11
SUS304	$E_m$ (Pa)	201.04e+9	0	3.079e-4	-6.534e-7	0
	$\alpha_m$ (1 / K)	12.33e-6	0	8.086e-4	0	0
	$\kappa_m$ (W / mK)	15.379	0	-1.264e-3	2.092e-6	-7.223e-10

Before further investigation of the non-linear behaviors of the FGM beam, the results between the present method and previous work [17] are compared to prove the accuracy of the proposed method. Table 2 lists the dimensionless linear eigenfrequencies ( $\omega_1 L^2 / h \sqrt{\rho_b / E_b}$ ) of the FGM beam considering the clamped-clamped boundary condition when the length-to-height ratio is  $L/h = 100$ . The results of these comparisons, considering the material properties for the upper ( $E_t$  and  $\rho_t$ : ceramic) and lower ( $E_b$  and  $\rho_b$ : aluminium) surfaces are as follows [17]:  $E_t = 380 \text{ GPa}$ ,  $\rho_t = 3960 \text{ Kg} / \text{m}^3$ ,  $E_b = 70 \text{ GPa}$ ,  $\rho_b = 2702 \text{ Kg} / \text{m}^3$

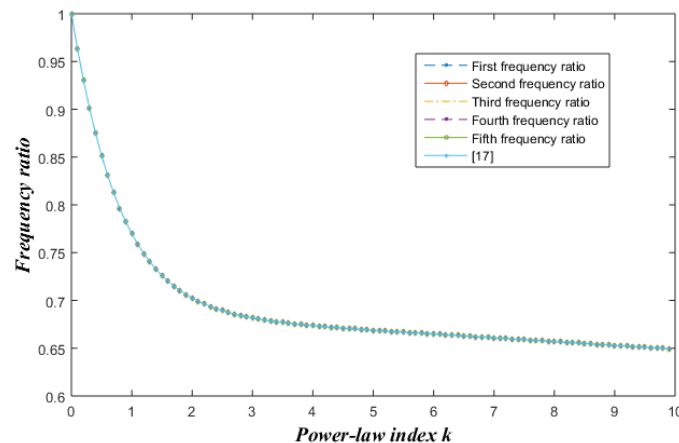


Figure 2: Comparisons of the first five non-dimensional eigenfrequencies of the FGM beam with clamping boundary conditions and for different values of the power index.



It can be seen from Table 2 that the results obtained in this study are in perfect agreement with the results given in the literature, which verifies the effectiveness of the shape function used in this work.

Table 2. Dimensionless linear nature frequency of FGM beam for different volume fraction exponent  $k$ .

k		Modes				
		1	2	3	4	5
0	Present	12.430	34.264	67.171	111.038	165.871
	[17]	12.430	34.258	67.144	110.96	165.69
0.1	Present	11.974	33.009	64.711	106.971	159.796
	[17]	11.974	33.003	64.685	106.90	159.62
0.2	Present	11.565	31.880	62.498	103.313	154.332
	[17]	11.565	31.875	62.473	103.24	154.16
0.5	Present	10.584	29.175	57.195	94.546	141.236
	[17]	10.583	29.170	57.171	94.478	141.08
1	Present	9.5685	26.375	51.707	85.474	127.684
	[17]	9.5680	26.371	51.685	85.410	127.53
2	Present	8.7316	24.069	47.185	77.999	116.517
	[17]	8.7311	24.064	47.162	77.934	116.37
5	Present	8.3137	22.917	44.926	74.266	110.941
	[17]	8.3132	22.912	44.904	74.201	110.79
10	Present	8.0676	22.238	43.597	72.068	107.657
	[17]	8.0672	22.234	43.576	72.008	107.52

Taking into account the material characteristics (see Table 1 [18]), the influence of the thermal load and the volume fraction index on the first three modes of the linear dimensionless eigenfrequency of the FGM beam is studied by considering the boundary condition clamped-clamped. It can be seen from Table 3 that when the temperature of the upper surface of the beam  $T_c$  increases, and when the temperature of the lower surface  $T_m$  remains constant ( $T_m = 300K$ ), the dimensionless eigenfrequency of the beam is stripped, which indicates the temperature-independent material properties have overestimated the stiffness of the structure. As shown in Table 3, in a high-temperature environment, the material properties related to the beam temperature must be considered. In addition, it should be noted that as the volume fraction index  $k$  increases, the frequency decreases due to the fact that the Young's modulus of SUS304 is lower than that of Si3N4.

Table 3. Dimensionless fundamental frequency of the FGM beam under thermal loading with temperature dependent material properties.

Modes	Tc(K)	Volume fraction exponent $k$					
		0	0.2	0.5	2	5	10
1	300	14.930	12.103	10.279	8.094	7.361	7.012
	400	14.162	11.374	9.576	7.433	6.717	6.369
	500	13.353	10.565	8.765	6.632	5.923	5.566
2	300	41.156	33.363	28.335	22.311	20.293	19.331
	400	40.064	32.346	27.369	21.420	19.430	18.473
	500	39.117	31.380	26.388	20.445	18.464	17.497
3	300	80.682	65.405	55.548	43.740	39.783	37.896
	400	79.384	64.224	54.447	42.748	38.829	36.954
	500	78.535	63.306	53.481	41.754	37.836	35.945

Figure 3 shows the influence of the volume fraction  $k$  of the Si3N4 / SUS304 FGM beam on the ratio of non-linear to linear frequency ( $\omega_{NL} / \omega_L$ ), which is a function of the dimensionless vibration amplitude  $W_{max}/r$ . The volume fraction significantly affects the Backbone curve.

On the other hand, when the exponential of the volume fraction diminishes, the frequency ratio increases. All these FGM beams with different volume fractions show typical hardening behavior, i.e., the non-linear frequency increases with increasing vibration amplitude. The effects of uniformly increasing the temperature of the FGM beam with a volume fraction index  $k = 1$  and clamped ends on the relationship between the non-linear to linear frequency are shown in Figure 4. In this example, the temperature of the bottom surface  $T_m$  remains constant ( $T_m = 300$  K), while the temperature of the top surface  $T_c$  varies ( $T_c = 300, 400$  and  $500$  K). The results in Figure 4 show that the curves of the non-linear to linear frequency ratios tend to increase as  $T_c$  increases, and the non-linear effect tends to be higher as  $T_c$  increases. Figure 5 illustrates the effect of simultaneous change in temperature and volume fraction on the non-linear vibration behavior of FGM Si3N4/SUS304 beams. In Figure 5, it is found that increasing the volume fraction ( $k=0, 1$  and  $5$ ) and increasing the temperature of the top surface ( $T_c=300$  and  $500$  K) result in an increase in the ratio of non-linear to linear frequency. It is also interesting to note that as the temperature increases, the effect of the volume fraction exponent  $k$  on the frequency ratio decreases.

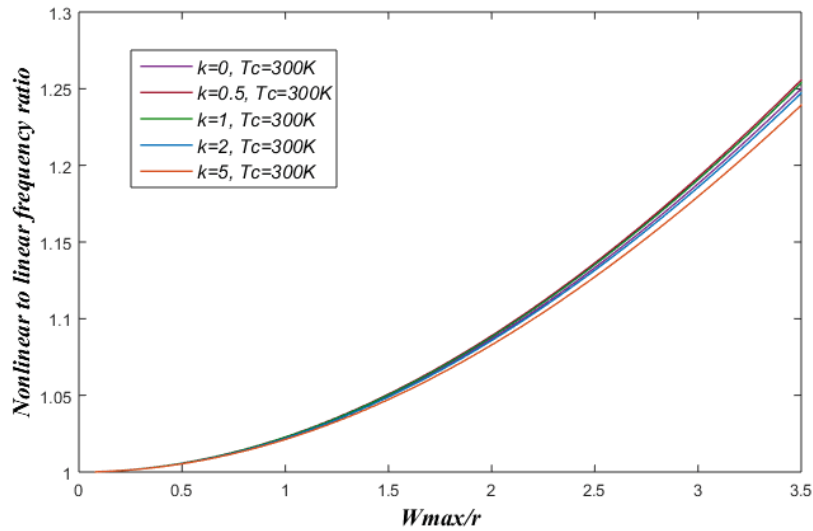


Figure 3: Influence of volume fraction  $k$  on the ratio of non-linear to linear frequency of FGM beams with thermal load  $T_c=300$  K.

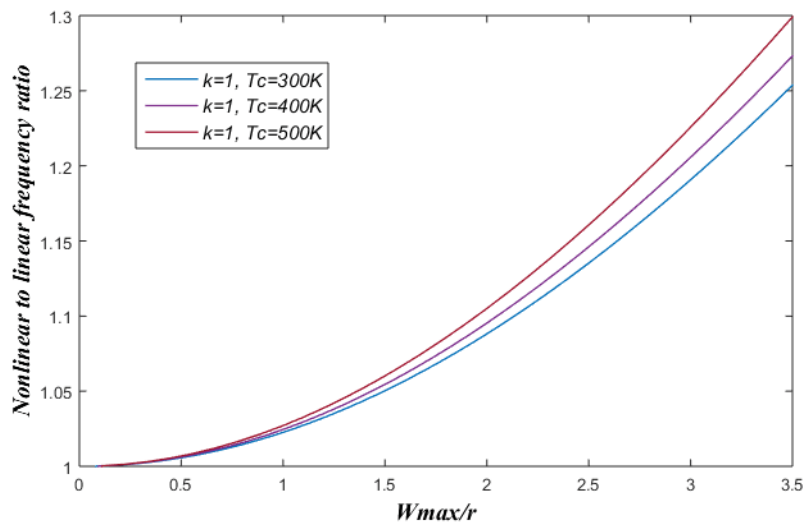


Figure 4: Influence of the thermal load  $T_c$  on the ratio of the non-linear frequency to the linear frequency of FGM beams with volume fraction  $k = 1$ .

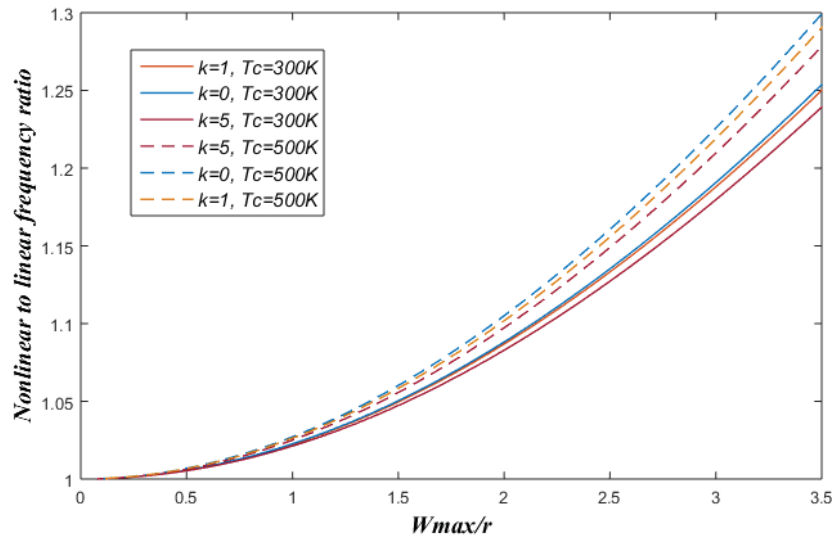


Figure 5: Influence of thermal loading on the ratio of non-linear to linear frequency of FGM beams with different volume fraction indices.

#### 4 CONCLUSIONS

The behavior of clamped FGM beams under free vibration in a thermodynamic environment is studied. The geometrically non-linear vibrational equations are determined in this analysis using an analytical approach based on the Euler-Bernoulli beam model and Hamilton's principle. The effective material properties of FGMs are assumed to be temperature dependent and to follow a simple power distribution in the thickness direction. The effects of volume fraction exposure, thermal loading, and thermal properties of constituent materials on non-linear vibration studies of FGM beams were examined in a parametric study. Numerical results indicate that the volume fraction affects the natural and non-linear frequencies in the ambient temperature fields. The volume fraction has an effect on the non-linear free vibration behavior of an FGM beam, and this effect weakens with increasing temperature. Furthermore, as the temperature increases, the non-linear effect increases, and the relationship between non-linear frequency and non-linear frequency as a function of nondimensional vibration amplitudes increases accordingly.

#### REFERENCES

- [1] H. J. Xiang and Z. F. Shi, 'Static analysis for functionally graded piezoelectric actuators or sensors under a combined electro-thermal load', *European Journal of Mechanics - A/Solids*, vol. 28, no. 2, pp. 338–346, Mar. 2009, doi: 10.1016/j.euromechsol.2008.06.007.
- [2] F. Ebrahimi, M. H. Naei, and A. Rastgoo, 'Geometrically nonlinear vibration analysis of piezoelectrically actuated FGM plate with an initial large deformation', *J Mech Sci Technol*, vol. 23, no. 8, pp. 2107–2124, Aug. 2009, doi: 10.1007/s12206-009-0358-8.
- [3] Y. Fu, J. Wang, and Y. Mao, 'Nonlinear vibration and active control of functionally graded beams with piezoelectric sensors and actuators', *Journal of Intelligent Material Systems and Structures*, vol. 22, no. 18, pp. 2093–2102, Dec. 2011, doi: 10.1177/1045389X11425277.
- [4] G. Falsone and G. La Valle, 'A homogenized theory for functionally graded Euler–Bernoulli and Timoshenko beams', *Acta Mech*, vol. 230, no. 10, pp. 3511–3523, Oct. 2019, doi: 10.1007/s00707-019-02493-w.

- [5] Y. Kiani, S. Taheri, and M. R. Eslami, 'Thermal Buckling of Piezoelectric Functionally Graded Material Beams', *Journal of Thermal Stresses*, vol. 34, no. 8, pp. 835–850, Aug. 2011, doi: 10.1080/01495739.2011.586272.
- [6] M. Bodaghi and M. Shakeri, 'An analytical approach for free vibration and transient response of functionally graded piezoelectric cylindrical panels subjected to impulsive loads', *Composite Structures*, vol. 94, no. 5, pp. 1721–1735, Apr. 2012, doi: 10.1016/j.compstruct.2012.01.009.
- [7] R. Benamar, M. M. K. Bennouna, and R. G. White, 'The effects of large vibration amplitudes on the mode shapes and natural frequencies of thin elastic structures part I: Simply supported and clamped-clamped beams', *Journal of Sound and Vibration*, vol. 149, no. 2, pp. 179–195, Sep. 1991, doi: 10.1016/0022-460X(91)90630-3.
- [8] Y. E. khouddar, A. Adri, S. Rifai, and R. Benamar, 'Geometrically non-linear forced vibrations of Euler–Bernoulli laminated composite beams', *J. Phys.: Conf. Ser.*, vol. 1896, no. 1, p. 012016, Apr. 2021, doi: 10.1088/1742-6596/1896/1/012016.
- [9] M. Chajdi, A. Ahmed, K. E. Bikri, and R. Benamar, 'Analysis of the associated stress distributions to the nonlinear forced vibrations of functionally graded multi-cracked beams', *Diagnostyka*, vol. 22, no. 1, pp. 101–112, Feb. 2021, doi: 10.29354/diag/133702.
- [10] O. Outassafte, A. Adri, Y. el Khouddar, R. Said, and R. Benamar, 'Geometrically Non-Linear Free In-Plane Vibration Of Circular Arch Elastically Restrained Against Rotation At The Two Ends', *International Journal of Engineering Trends and Technology*, vol. 69, pp. 85–95, Mar. 2021, doi: 10.14445/22315381/IJETT-V69I3P215.
- [11] O. Outassafte, A. Adri, R. Said, and R. Benamar, 'Geometrically nonlinear free vibration of Euler-Bernoulli shallow arch', *Journal of Physics: Conference Series*, vol. 1896, p. 012013, Apr. 2021, doi: 10.1088/1742-6596/1896/1/012013.
- [12] L.-L. Ke, J. Yang, and S. Kitipornchai, 'An analytical study on the nonlinear vibration of functionally graded beams', *Meccanica*, vol. 45, no. 6, pp. 743–752, Dec. 2010, doi: 10.1007/s11012-009-9276-1.
- [13] Z. Wu, Y. Zhang, G. Yao, and Z. Yang, 'Nonlinear primary and super-harmonic resonances of functionally graded carbon nanotube reinforced composite beams', *International Journal of Mechanical Sciences*, vol. 153–154, pp. 321–340, Apr. 2019, doi: 10.1016/j.ijmecsci.2019.02.015.
- [14] H. Fakhreddine, A. Adri, M. Chajdi, S. Rifai, and R. Benamar, 'A multimode approach to geometrically non-linear forced vibration of beams carrying point masses', *Diagnostyka*, vol. 21, no. 4, pp. 23–33, Nov. 2020, doi: 10.29354/diag/128603.
- [15] I. el Hantati, A. Adri, H. Fakhreddine, R. Said, and R. Benamar, 'A Multimode Approach to Geometrically Nonlinear Free and Forced Vibrations of Multisteped Beams', *Shock and Vibration*, vol. 2021, pp. 1–18, Apr. 2021, doi: 10.1155/2021/6697344.
- [16] M. El kadiri, R. Benamar, and R. G. White, 'IMPROVEMENT OF THE SEMI-ANALYTICAL METHOD, FOR DETERMINING THE GEOMETRICALLY NON-LINEAR RESPONSE OF THIN STRAIGHT STRUCTURES. PART I: APPLICATION TO CLAMPED–CLAMPED AND SIMPLY SUPPORTED–CLAMPED BEAMS', *Journal of Sound and Vibration*, vol. 249, no. 2, pp. 263–305, Jan. 2002, doi: 10.1006/jsvi.2001.3808.
- [17] J. W. Lee and J. Y. Lee, 'Free vibration analysis of functionally graded Bernoulli-Euler beams using an exact transfer matrix expression', *International Journal of Mechanical Sciences*, vol. 122, pp. 1–17, Mar. 2017, doi: 10.1016/j.ijmecsci.2017.01.011.
- [18] J. N. Reddy and C. D. Chin, 'Thermomechanical Analysis of Functionally Graded Cylinders and Plates', *Journal of Thermal Stresses*, vol. 21, no. 6, pp. 593–626, Sep. 1998, doi: 10.1080/01495739808956165.

## PERSPECTIVES ON THE ACCELERATION OF THE NUMERICAL ASSESSMENT OF FLUTTER AND BUFFETING RESPONSE OF BRIDGE DECKS

**Julien Heremans<sup>1,2</sup>, Anass Mayou<sup>1</sup>, and Vincent Denoël<sup>1</sup>**

<sup>1</sup>Structural & Stochastic Dynamics, University of Lige, Belgium  
Alle de la Dcouverte, 1, B-4000 Lige Belgium  
e-mail: julien.heremans@uliege.be

<sup>2</sup> F. R. S.-FNRS, National Fund for Scientific Research, Belgium  
Rue d'Egmont, 8, B-1000 Bruxelles, Belgium

**Keywords:** Multiple Timescale Spectral Analysis, Background, Resonant.

**Abstract.** *The critical flutter speed of a bridge deck is the result of an eigen value analysis. However, the progressive growth of the response for sub-critical wind velocities, resulting from the buffeting action of the turbulent wind, is also of major concern to the designers. The complete flutter analysis of a bridge structure therefore requires the repeated analysis of the aeroelastic response for various wind velocities, starting from zero (wind off) to the critical flutter speed. In a spectral approach, each of these analyses is typically based on the heavy integration of the power spectral density of the aeroelastic response. It has been recently found that this integration can be facilitated by a background/resonant decomposition as is commonly implemented in a buffeting-only setting. The paper describes a preliminary work showing that this decomposition can be extended to the flutter-and-buffeting configuration. The work is only preliminary since it deals with a single oscillator. However, it shows a massive CPU saving of one to two orders of magnitude, while limiting the error to one percent. This kind of saving is particularly expected to make affordable the analysis of large multi degree-of-freedom structures.*

## 1 INTRODUCTION

The critical flutter speed of a bridge deck corresponds to an aeroelastic instability of the coupled system composed of the bridge and the surrounding air flow [1, 2, 3]. This instability is recognized as potentially very harmful since the famous collapse of the Tacoma-Narrows bridge [4]. Codes and standards [5] take a significant safety margin with respect to this critical wind speed and typically do not allow to overcome 80% of this critical velocity.

Besides, the progressive growth of the response for sub-critical wind velocities, resulting from the buffeting action of the turbulent wind, is also of major concern to the designers [6, 7]. The complete flutter analysis of a bridge structure therefore requires the repeated analysis of the aeroelastic response for various wind velocities, starting from zero (wind off) to the critical flutter speed, or at least to the design wind speed [8]. In a spectral approach, each of these analyses is typically based on the time-consuming integration of the power spectral density (PSD) of the aeroelastic response.

Traditional integration methods struggle to efficiently estimate these integrals because of the significant peakedness of the function in the neighborhood of the natural frequencies. In this paper, we present an extension of the Background/Resonant decomposition (which is commonly applied under the quasi-steady assumption), to aeroelastic analysis, where the stiffness and damping of the coupled system changes with frequency. The study is limited to single degree-of-freedom systems at this stage but constitutes the cornerstone of an extension to multi degree-of-freedom systems, where such an approximation becomes very interesting in terms of computational efficiency.

In the following sections, the mathematical background is presented, then the algorithmic implementation is briefly discussed and the method is illustrated with a few examples. Finally, the perspectives of application to multi degree-of-freedom (MDOF) structures are discussed.

## 2 EXTENSION OF THE BACKGROUND/RESONANT DECOMPOSITION TO THE AEROELASTIC OSCILLATOR

The dynamics of a single degree-of-freedom (SDOF) system subjected to buffeting and aerodynamic loads is governed by

$$m_s \ddot{q}(t) + c_s \dot{q}(t) + k_s q(t) = f_{bu}(t) + f_{ae}(t), \quad (1)$$

where  $m_s$ ,  $c_s$  and  $k_s$  are the mass, viscosity and stiffness of the structural system, and where  $t$  is the time. The loading consists of a buffeting loading  $f_{bu}(t)$  which is here assumed to be characterized as a Gaussian stochastic process and a so-called *unsteady* aerodynamic loading  $f_{ae}(t)$ , which is usually expressed as a convolution of the structural response ( $q(t)$ ,  $\dot{q}(t)$ ) with aeroelastic indicial functions. In the frequency domain,  $F_{ae}(\omega) = [i\omega c_{ae}(\omega) + k_{ae}(\omega)] Q(\omega)$  and the governing equation becomes

$$[-m_s \omega^2 + i\omega c(\omega) + k(\omega)] Q(\omega) = F_{bu}(\omega), \quad (2)$$

where  $c(\omega) = c_s - c_{ae}(\omega)$  and  $k(\omega) = k_s - k_{ae}(\omega)$  gather both the structural and aerodynamic viscosity and stiffness. The later ones can be expressed as a function of Theodorsen's function (flat plate, [9]) or, more generally, as Scanlan's derivatives (e.g. bridge deck [1]).

The power spectral density of the structural response  $q(t)$  is thus obtained by

$$S_q(\omega; U) = \left| [-m_s \omega^2 + i\omega c(\omega) + k(\omega)]^{-1} \right|^2 S_{f,bu}(\omega), \quad (3)$$



and the variance of the response is ultimately obtained by integration of (3),

$$\sigma_q^2(U) = \int_{-\infty}^{+\infty} S_q(\omega; U) d\omega. \quad (4)$$

In a structural design process, this integral has to be computed for several values of the wind velocity  $U$ , which enters in the modeling through  $c_{ae}(\omega)$  and  $k_{ae}(\omega)$  which are expressed as a function of the reduced frequency  $K = \omega B/U$  where  $B$  is a characteristic size of the structural element (deck width). Standard integration schemes based on the trapezoidal rule or Gauss-Lobatto integration schemes [10] do provide an accurate result, they might seem too slow for application in large scale problems or when the bridge stability has to be assessed in a probabilistic manner, which requires many repetitions of the deterministic problem, see Section 5

In the wind engineering community, this type of integral is also encountered in the buffeting-only analysis of structures, i.e. without unsteady forces. The method, implemented in the community by Davenport [11, 12], based on the existing approaches in aeronautics [13], has resulted in the well known Background/Resonant (B/R) decomposition. The use of multiple timescales in the computation of the wind induced response of structures is not new. It has already been used to determine the statistics of non Gaussian responses [14] or of nonlinear aerodynamic loading terms [15]. The general method, based on stretches and rescaling of the frequency bands contributing to the integral has been generalized under the terminology *Multiple Timescales Spectral Analysis* (MTSA) [16].

In the present configuration, under the following assumptions:

- the timescales of the loading and of the system are significantly different. In other words, a distinction is made between the slow dynamics represented by the buffeting loading, and fast dynamics represented by the natural vibrations of the aeroelastic system. The centroid of the power spectral density of the buffeting load shall be substantially lower (5 to 10 times lower) than the natural frequency of the aeroelastic system;
- the structural damping ratio is small, smaller than or of the same order of magnitude as 5%-10%; the quality of the approximation worsens as the damping ratio grows beyond these values;
- the frequency dependent stiffness and damping  $k(\omega)$  and  $c(\omega)$  vary smoothly and moderately in the neighborhood of the resonance peak of the aeroelastic system,

it is actually possible to demonstrate [17], by application of the general concepts of the Multiple Timescale Spectral Analysis [16], that the variance is expressed as a sum of the background and the resonant contributions

$$\sigma_q^2 = \sigma_{q,B}^2 + \sigma_{q,R}^2, \quad (5)$$

where

$$\sigma_{q,B}^2 = \int_{-\infty}^{+\infty} \frac{S_{f, bu}(\omega)}{(k_s - k_{ae}(\omega))^2} d\omega \quad ; \quad \sigma_{q,R}^2 = \frac{S_{f, bu}(\bar{\omega})}{(k_s - k_{ae}(\bar{\omega}))^2} \frac{\pi \bar{\omega}}{2\bar{\xi}} \frac{1}{1 + \frac{1}{2} \frac{\bar{\omega} \partial_{\omega} k_{ae}(\bar{\omega})}{k_s - k_{ae}(\bar{\omega})}}. \quad (6)$$

They are readily interpreted as the aeroelastic extensions of the well known decomposition introduced by Davenport. In this expression  $\bar{\omega}$  represents the resonance frequency of the aeroelastic system; it is defined by

$$\frac{\bar{\omega}^2}{\omega_s^2} = \frac{k_s - k_{ae}(\bar{\omega})}{k_s}. \quad (7)$$

In wind-off conditions,  $k_{ae}(\bar{\omega}; U = 0) = 0$  and  $\bar{\omega} = \omega_s$  is therefore equal to the natural structural frequency. As the wind velocity increases, the natural frequency of the aeroelastic system  $\bar{\omega}$  might drift more or less significantly from  $\omega_s$  depending on the specificities of the aerodynamic stiffness  $k_{ae}(\omega)$ .

### 3 ALGORITHMIC IMPLEMENTATION

This section describes a practical implementation of the algorithm. At this stage, the implemented model is suitable for SDOF models only but its extension to MDOF models is also discussed.

#### 3.1 Algorithm for SDOF structures

The flow-chart of the solution strategy is shown in Figure 1. For a given average wind velocity, the solving process consists of 3 main tasks: the evaluation of the aeroelastic eigen frequency, and that of the background and resonant components. The determination of the eigen frequency of the aerodynamic system relies on an iterative scheme, initiated with the wind-off conditions. Relaxation can be used to improve the convergence of the process. As the wind-off conditions give already an excellent guess of the natural frequency of the aeroelastic system, the convergence is quite straightforward. The resonant component is then evaluated using (6), and Scanlan's formulation for  $k_{ae}(\omega)$ ,  $c_{ae}(\omega)$  and  $\partial_\omega k_{ae}(\omega)$ . The last step is the determination of the background component. Depending on the specificities of  $k_{ae}(\omega)$  and the targeted accuracy, the integration of the buffeting forces according to (6) can be simplified. Indeed, in cases where the background component plays a secondary role,  $\sigma_{q,B} \ll \sigma_{q,R}$ , its accurate determination is no longer a necessity and the denominator in the expression for  $\sigma_{q,B}$  in (6) can be simply replaced by  $k_s^2$ . This leads to a drastic simplification of the computation of the integral since  $\sigma_{q,B}$  then boils down to the usual quasi-static formulation of Davenport. When this assumption can be made —and this is what is done in the rest of this paper—, the background component does not require any integration point, the resonant component just requires one integration point (located at the natural frequency) and the proposed formulation, referred to as MTSA in the sequel, is just based on a single integration point.

All this solving process is embedded in a loop over a range of  $U$ , from wind-off to critical conditions.

#### 3.2 Extension to MDOF structures

Up to now, the use of the background/resonant decomposition for aeroelastic systems was only discussed on SDOF models. For such simple models, the computational load is proportional to the number of wind velocities considered in the analysis. Since the analysis for each wind velocity is rapid, there is no big issue and the process can be repeated for a comfortable number of wind velocities, which allows an accurate evaluation of the transition towards instability on approaching the critical wind velocity. In the case of MDOF models, every single run for a given velocity might turn to be much more expensive. Indeed, if the number of degrees of freedom is large, a very time-consuming operation appears in the algorithm: the projection of the buffeting forces in the modal basis. This is explained by considering that, in a standard linearized model of the buffeting forces, the wind force at each degree-of-freedom is expressed as a linear transformation of the local wind velocity, i.e.

$$\mathbf{F}_{bu}(t) = \mathbf{A}\mathbf{u}(t) + \mathbf{b} \quad (8)$$

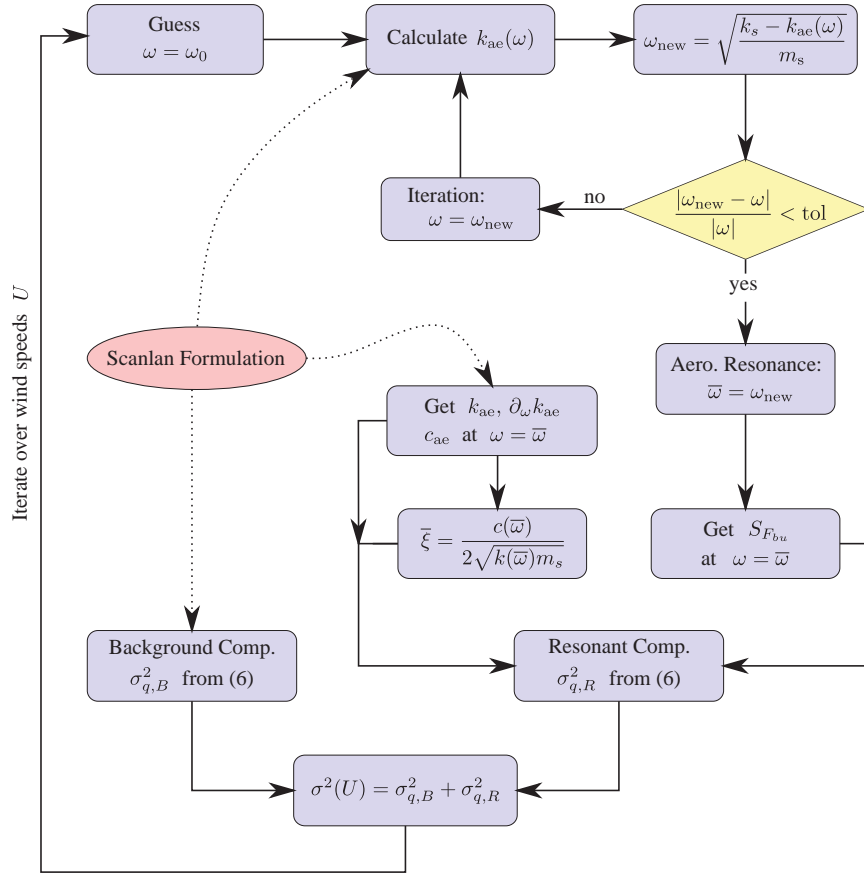


Figure 1: Organigram of the aeroelastic analysis performed with the background/resonant decomposition for evaluating the integral of the response spectra. The solving process is embedded in a loop over the average wind speeds.

where  $\mathbf{u}(t)$  is a column vector containing the fluctuating component of the wind velocities at the nodes of the finite element model, the power spectral density of the buffeting load projected in mode  $i$  reads

$$S_{F_{bu}}^i(\omega) = \phi_i^T \mathbf{A} \mathbf{S}_{\mathbf{u}} \mathbf{A}^T \phi_i. \quad (9)$$

The evaluation of the PSD of the modal forces, including their cross-PSD, is particularly time consuming since it involves the left- and right-multiplication by large matrices.

In short, the computational time for the modal analysis of a large MDOF structure is mostly conditioned by the number of frequencies where the PSD must be sampled, i.e. the number of projections such as (9). As a result, the determination of the variance as the quadrature of the PSD of the structural response (in each mode) is the operation that requires being optimally implemented. Three solutions are studied in the rest of this paper to determine these integrals with various levels of smartness : (i) first, a classical trapezoidal method is implemented; it requires typically a large number of uniformly distributed points to accurately capture the sharp peaks of the spectra, (ii) an adaptative integration scheme is also considered, which is an interesting solution to lighten the computational burden by optimizing the integration mesh, distributing a (smaller) number of points at well chosen locations, (iii) third, a method of integration based on the proposed background/resonant decomposition.

The development of the background/resonant decomposition for spectral aerodynamic analysis is quite straightforward, at least if the modal response is uncoupled. In the latter case, the

analysis is performed mode by mode, and the SDOF model is still applicable provided that the mass, damping and stiffness are replaced by their modal homologue. Cases of structures experiencing modal coupling require however slightly more advanced models [23], but remains in the scope of the approximation that will constitutes the core of the future investigations.

In the next section, these integration methods with uniform and non uniform meshes will be compared with the background/resonant decomposition. A special attention will be paid to the trade-off between number of integration points and accuracy of the results.

#### 4 ILLUSTRATIONS AND EVALUATION OF CPU LOAD SAVING

In this section, the efficiency of the background/resonant decomposition is illustrated on two realistic case studies, namely the Golden Gate bridge and Tacoma Narrows bridge. The aeroelastic behavior of these two structures is characterized by torsional flutter as governing failure mode. The structure behavior is idealized by a SDOF model governed by

$$(-\omega^2 I_s + i\omega(c - c_{ae}(\omega)) + k - k_{ae}(\omega)) \Theta(\omega) = M_b(\omega) \quad (10)$$

where  $I_s$  is the mass moment of inertia per unit length and such that the aeroelastic damping, stiffness, and the buffeting pitching moment are reduced to

$$\begin{aligned} M_{bu}(\omega) &= \frac{qB}{U} \left( \frac{\pi}{2} B A(\omega) \right) W(\omega) \\ k_{ae}(\omega) &= qB^2 \left( \frac{\omega B}{U} \right)^2 A_3^*(\omega) \\ c_{ae}(\omega) &= qB^2 \frac{B}{U} \left( \frac{\omega B}{U} \right) A_2^*(\omega). \end{aligned} \quad (11)$$

The  $A_2^*(\omega)$  and  $A_3^*(\omega)$  coefficients refer to the Scanlan's —or flutter— torsional derivatives (see Figure 2), the admittance  $A(\omega)$  is supposed to be constant and equal to 1 in the following illustrations and  $W(\omega)$  is the spectral representation of the vertical fluctuating component of the wind turbulence. The structural parameters are summarized in Figure 1. For the two test cases, the accuracy and the efficiency of the proposed background/resonant decomposition will be compared to classical integration methods. The trapezoidal scheme is standard, while the adaptative integration scheme is briefly detailed in the Appendix. In each case, the integral in (4) is computed where  $S_q(\omega; U)$  corresponds to  $S_\theta(\omega; U)$ , for these case of torsional flutter. It is also defined by (3) where the aeroelastic stiffness and viscosity are given by (11).

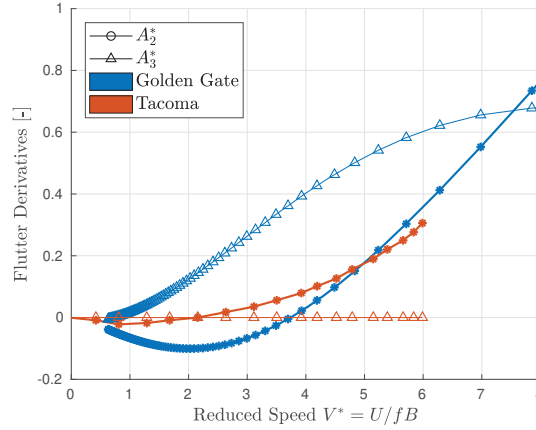
As previously discussed, the number of integration points has a direct impact on the calculation load, and consequently on the computation time: the smaller the number of integration points, the faster the wind flutter analysis. The CPU times are not reported for this simple SDOF structure; they are replaced by the number of integration points which is assumed to give an correct picture of the computational burden for larger problems.

##### 4.1 Golden Gate bridge

Figure 3-a shows the PSD of the torsional degree-of-freedom for a selection of wind velocities. As the wind velocity increases, the resonance peak is shifted to the left and becomes sharper. This is a sign of torsional flutter, i.e. aero-elastic instability by lack of damping. The integral of the PSDs obtained for various wind velocities, i.e. the variance, is used to determine the scaled standard deviation of the angular displacement  $\theta$  shown in Figure 3-b. Each

	Golden Gate	Tacoma
Moment of Inertia $I_s$ [kg.m <sup>2</sup> /m]	$4.4 \cdot 10^6$	$177.73 \cdot 10^3$
Natural frequency $f_s$ [Hz]	0.1916	0.20
Damping Ratio $\xi_s$ [%]	0.5	0.5
Deck width $B$ [m]	27.43	12.0

Table 1: Structural properties of the structures considered in Illustrations 1 and 2.


Figure 2: Flutter derivatives  $A_2^*(\omega)$  and  $A_3^*(\omega)$  of the considered structures .

point of the reference curve was obtained with the trapezoidal integration scheme with a large number (50,000) of integration points. Red dots represents the results obtained with the B/R decomposition while the individual components B and R are also represented to indicate that the instability occurs for this type of cross-section by means of the resonant component. The reference solution and the proposed approximation are in excellent agreement, promising a very low relative error. As shown in Figure 3-c, the damping ratio remains constantly lower than 1% for all wind velocities, indicating that the hypothesis formulated above related to small damping is respected.

In Figure 3-d, the number of integration points required to satisfy a given relative precision is represented for the two usual numerical methods (trapezoidal scheme and adaptative integration) as well as the proposed Multiple Timescale Spectral Analysis approach (background/resonant decomposition). The relative error is calculated with respect to a reference solution obtained from a classical trapezoidal integration method with a mesh of 50,000 points uniformly spaced between 0 and 10 Hz (i.e. 62.8 rad/s). This mesh was kept constant for all considered wind speeds.

The square symbols, associated with the trapezoidal scheme, indicate that this classical integration method requires a minimum of 10,000 integration points to get a relative error of the order of the percent pour all wind speeds. For 1,000 points and below, the error is already way too large and the function is not accurately represented. However, with 1,000 points smartly distributed using an adaptive integration method, the standard deviation is accurately calculated with an error lower than 0.01%. A good compromise can be found around 100 points, where the error is of the order of the percent again. This method reduces the number of integration points required by a factor 100, approximatively. The performance of this adaptive integration method

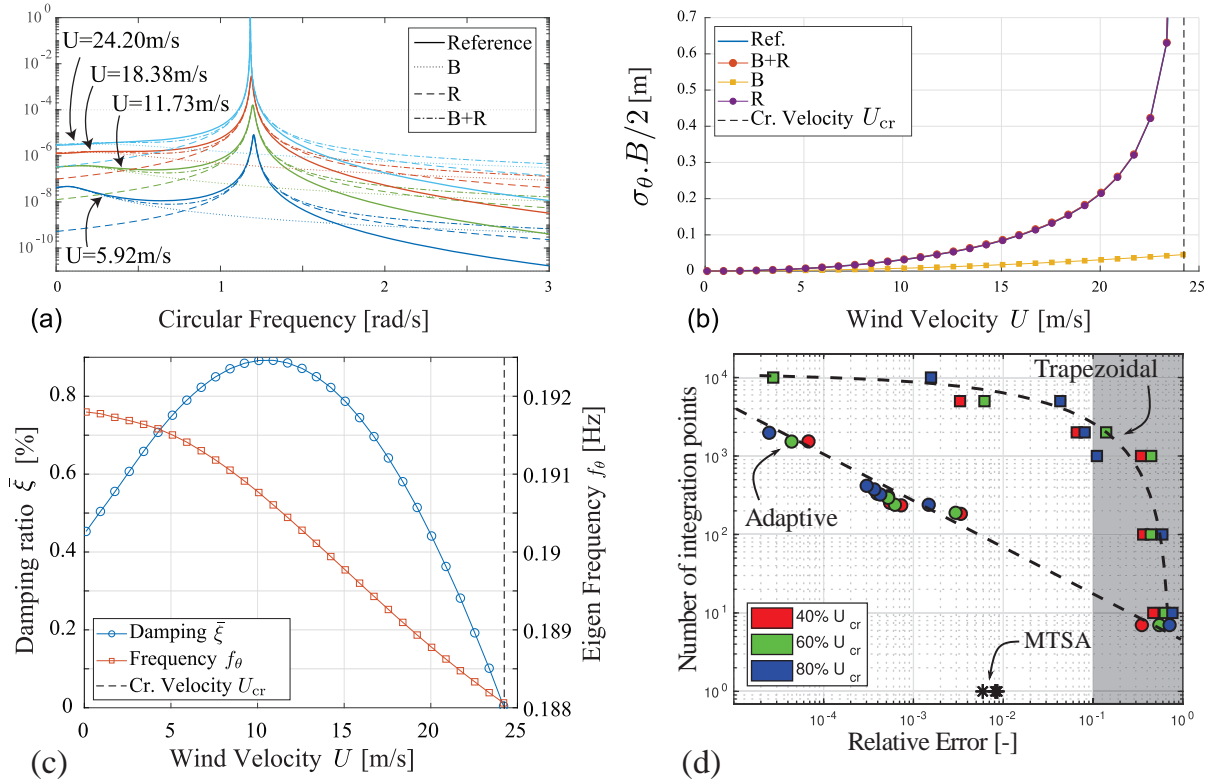


Figure 3: Aerodynamics response under buffeting loads (Golden Gate bridge). (a) PSD and their B and R approximations for different wind velocities. (b) Scaled standard deviations obtained with accurate numerical integration (Reference), background component (B), resonant component (R), and the sum of them (B)+(R). (c) Damping ratio and natural frequency at resonance with respect to avg. wind velocity. (e) Number of integration points required to satisfy a given relative error on  $\sigma_\theta$  for 3 avg. wind velocities and for the three methods discussed (trapezoidal scheme with uniform sampling, adaptive quadrature and the MTSA based B/R decomposition .)

is of course conditioned by the efficiency of the refinement algorithm and also by the parameters passed by the user—for instance the initial mesh. Usage of other adaptive integration scheme than the algorithm presented in the appendix might therefore lead to similar trends but slightly different numbers. The last cluster of points represented in Figure 3-d refers to the B/R decomposition and suggests an error below 1% while being limited a single sampling point, at resonance. This arises from the white noise approximation made in (6). This method appears now to be therefore the best compromise number of points/accuracy.

## 4.2 Tacoma Narrows bridge

The second case study is the Tacoma Narrows bridge. Besides its dangerously low critical velocity of 11 m/s, it behaves very similarly to the Golden Gate bridge such that most of results are globally the same. The output resulting from the aeroelastic analysis are shown in Figure 4.

For this second application the damping related flutter derivative  $A_2^*(\omega)$  is such that the damping ratio at resonance  $\bar{\omega}$  diminishes as  $U$  increases, except at very low wind speeds. The damping ratio remains again below 1% which explains why the quality of the approximation does not drop as the wind velocity increases. The trapezoidal integration scheme, in contrast, fails to capture the sharp resonance peak on approaching the critical flutter speed. More than that, the proposed background/resonant decomposition is even more precise that the damping ratio is small. Because the damping drops as the considered wind velocity approaches the crit-



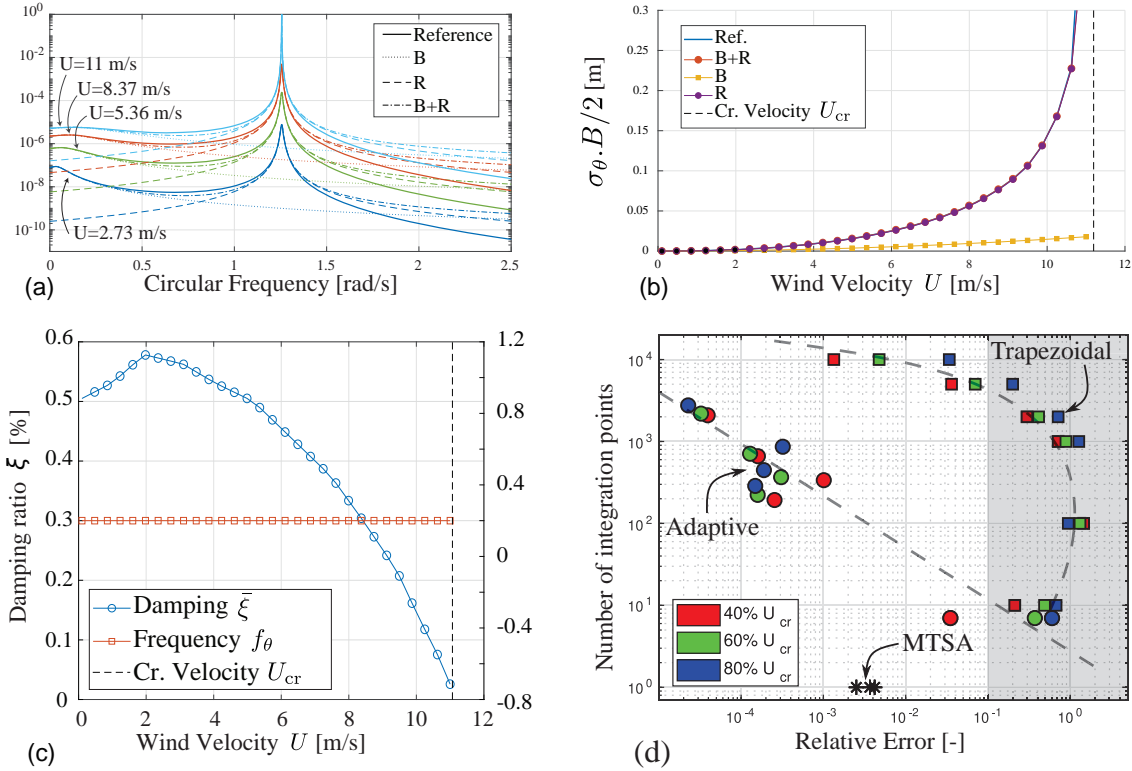


Figure 4: Aerodynamics response under buffeting loads (Tacoma Narrows bridge). (a) PSD and their B and R approximations for different wind velocities. (b) Scaled standard deviations obtained with accurate numerical integration (Reference), background component (B), resonant component (R), and the sum of them (B)+(R). (c) Damping ratio and natural frequency at resonance with respect to avg. wind velocity. (e) Number of integration points required to satisfy a given relative error on  $\sigma_\theta$  for 3 avg. wind velocities and for the three methods discussed (trapezoidal scheme with uniform sampling, adaptive quadrature and the MTSA based B/R decomposition .)

ical velocity, the approximation is even more accurate and appealing as flutter conditions are close. This is unfortunately not applicable to divergence instabilities, where the loss of stiffness is typically accompanied by an increase in damping, see e.g. XXX (bench polimi). Therefore, the approximation should not be recommended for divergence instabilities, particularly close to the flutter conditions.

Regarding the relative error and the integration points, the same 3 tendencies as in the previous applications are observed. A number of 100 integration points are required to accurately integrate the PSD using an adaptive method, and 10.000 points at least should be used if a uniform mesh is used. The MTSA approach provides truly accurate standard deviation with an error lower than 0.5%, slightly lower than in the Golden Gate bridge illustration.

## 5 PERSPECTIVES

The acceleration of the computation of the aeroelastic response of a single degree-of-freedom system could seem ridiculous at the time where the computational power is continuously growing and especially when the multiple mode analysis of large structures has been being available for more than 20 years [18, 19, 20]. We see however two main promising perspectives for this preliminary work.

The first one is immediate and concerns the stochastic stability of the single degree-of-freedom system. Indeed in a probabilistic approach, should it be by means of Monte Carlo simulations [21] or alternatives such as the collocation method or Galerkin approach [22], it is

essential to repeat the solution of the deterministic problem a large amount of times. Any CPU saving is therefore welcome to determine more accurate statistics of the response.

A second perspective of application of the proposed formulation concerns the extension to multi degree-of-freedom systems. They are governed by an equation similar to (I), which reads, in the frequency domain,

$$[-M_s \omega^2 + i\omega C(\omega) + K(\omega)] Q(\omega) = F_{bu}(\omega). \quad (12)$$

The aeroelastic matrices  $M_s$ ,  $C$  and  $K$  combining the structural matrices and aerodynamic unsteady loads might be very large. An analysis in the modal basis is able to drastically decrease the size of the system. The variance of the modal responses in each mode can then be determined with the method proposed in this paper. The main difference with a classical integration of the power spectral densities is that the projection of the buffeting forces in the modal basis is performed for natural frequencies only—or for a very restricted number of points in the most unfavorable case of a large aeroelastic stiffness—and not for the whole set of natural frequencies that a Gauss-Lobatto or trapezoidal integration scheme would require. So the proposed method can be used with very little adaptations as long as modal responses are concerned. Then, the combination of modal responses is necessary to determine structural responses (displacements and internal forces) or, alternatively, equivalent static loads. This requires the estimation of modal correlation coefficients but again, the Multiple Timescale Spectral Analysis has already been used to solve this problem in the buffeting-only case [23] and it is believed that the same extension is possible. Depending on how the eigenmodes of the aeroelastic system are determined, a proper recourse to the smallness of off-diagonal terms might be invoked, similarly to some of the previous results of the authors [24]. All in all, the determination of the response of a single oscillator appears as a major building block for the derivation of a very fast algorithm for the analysis of the aeroelastic response of large bridges. The outlook for future is to make possible the probabilistic analysis of large-scale structures or the rapid parametric analysis of large scale structures (varying the wind incidence, optimization of the aerodynamic deck, etc.).

## 6 CONCLUSIONS

The analysis of an aeroelastic oscillator subjected to low frequency turbulence can be studied by means of background and resonant components, which take a more general form than in the well known case presented by Davenport. They remain simple, however, and offer therefore a straightforward understanding of the response. Beyond this gain in physical insight, the derivation of the two components in an appropriate algorithmic implementation allows to speed up the determination of the stochastic response.

Examples have shown that the number of sampling points is reduced by a factor 10.000 (!) with respect to classical integration method, and by a factor 100 with respect to a smarter adaptive integration technique. This promises massive computational time saving, especially since the projection of the nodal aerodynamic loads vector in modal basis is by far the exhausting operation of the algorithm.

The delicacy of the proposed approximation resides also in the quality of its predictions: in the studied examples, the error committed on the standard deviation is lower than 1% which remains quite accurate when put in perspective to the safety envelope usually taken in civil engineering applications. The approximation method assumes that the damping ratio is small, and this hypothesis is even more respected that the system is close to flutter (except (static) divergence). Therefore the prediction is even more accurate that the resonant peaks are sharp,

as opposed to the trapezoidal integration method with a uniform mesh which struggles to capture accurately the sharpness of the peaks with a reasonable number of points.

These performance are promising for future extensions to probabilistic contexts, or large multiple mode structures, that rely both entirely on the efficiency of the algorithm to be envisaged.

## REFERENCES

- [1] Robert H Scanlan and J Tomo. Air foil and bridge deck flutter derivatives. *Journal of Soil Mechanics & Foundations Div*, 1971.
- [2] Robert H Scanlan and Nicholas P Jones. Aeroelastic analysis of cable-stayed bridges. *Journal of Structural Engineering*, 116(2):279–297, 1990.
- [3] Robert H Scanlan. Problematics in formulation of wind-force models for bridge decks. *Journal of Engineering Mechanics*, 119(7):1353–1375, 1993.
- [4] Peter A Irwin, Stoyan Stoyanoff, Jiming Xie, and Mark Hunter. Tacoma narrows 50 years later? wind engineering investigations for parallel bridges. *Bridge structures*, 1(1):3–17, 2005.
- [5] EN. *EN 1991-1-1 Eurocode 1: Actions on Structures - Part 1-4: Wind actions*, Brussels, 2005. CEN.
- [6] Tajammal Abbas, Igor Kavrakov, and Guido Morgenthal. Methods for flutter stability analysis of long-span bridges: a review. In *Proceedings of the Institution of Civil Engineers-Bridge Engineering*, volume 170, pages 271–310. Thomas Telford Ltd, 2017.
- [7] Giorgio Diana, Stoyan Stoyanoff, Ketil Aas-Jakobsen, Andrew Allsop, Michael Andersen, Tommaso Argentini, Miguel Cid Montoya, Santiago Hernandez, Jose Angel Jurado, Hiroshi Katsuchi, Igor Kavrakov, Ho-Kyung Kim, Guy Larose, Allan Larsen, Guido Morgenthal, Ole Oiseth, Simone Omarini, Daniele Rocchi, Martin Svendsen, and Teng Wu. Iabse task group 3.1 benchmark results. part 1: Numerical analysis of a two-degree-of-freedom bridge deck section based on analytical aerodynamics. *Structural Engineering International*, 0(0):1–10, 2019.
- [8] Ahsan Kareem and Yukio Tamura. *Advanced structural wind engineering*. Springer, 2013.
- [9] Earl Dowell. *A Modern Course in Aeroelasticity*. Springer International Publishing, 01 15.
- [10] William H Press, Saul A Teukolsky, William T Vetterling, and Brian P Flannery. Numerical recipes in c++. *The art of scientific computing*, 2:1002, 1992.
- [11] Alan Garnett Davenport. The application of statistical concepts to the wind loading of structures. *Proceedings of the Institution of Civil Engineers*, 19(4):449–472, 1961.
- [12] Alan G Davenport. The response of slender, line-like structures to a gusty wind. *Proceedings of the Institution of Civil Engineers*, 23(3):389–408, 1962.

- [13] Hans Wolfgang Liepmann. On the application of statistical concepts to the buffeting problem. *Journal of the Aeronautical Sciences*, 19(12):793–800, 1952.
- [14] Vincent Denoël. On the background and biresonant components of the random response of single degree-of-freedom systems under non-gaussian random loading. *Engineering structures*, 33(8):2271–2283, 2011.
- [15] Vincent Denoël and Luigi Carassale. Response of an oscillator to a random quadratic velocity-feedback loading. *Journal of Wind Engineering and Industrial Aerodynamics*, 147:330–344, 2015.
- [16] Vincent Denoël. Multiple timescale spectral analysis. *Probabilistic Engineering Mechanics*, 39:69–86, 2015.
- [17] Julien Heremans, Anass Mayou, and Vincent Denoël. Background/resonant decomposition of the stochastic torsional flutter response of an aeroelastic oscillator under buffeting loads. *Journal of Wind Engineering and Industrial Aerodynamics*, 208:104423, 2021.
- [18] Anurag Jain, Nicholas P Jones, and Robert H Scanlan. Coupled flutter and buffeting analysis of long-span bridges. *Journal of Structural Engineering*, 122(7):716–725, 1996.
- [19] H Katsuchi, NP Jones, RH Scanlan, and H Akiyama. Multi-mode flutter and buffeting analysis of the akashi-kaikyo bridge. *Journal of Wind Engineering and Industrial Aerodynamics*, 77:431–441, 1998.
- [20] YJ Ge and H Tanaka. Aerodynamic flutter analysis of cable-supported bridges by multi-mode and full-mode approaches. *Journal of Wind Engineering and Industrial Aerodynamics*, 86(2-3):123–153, 2000.
- [21] Tommaso Argentini, A Pagani, Daniele Rocchi, and Alberto Zasso. Monte carlo analysis of total damping and flutter speed of a long span bridge: Effects of structural and aerodynamic uncertainties. *Journal of Wind Engineering and Industrial Aerodynamics*, 128:90–104, 2014.
- [22] Thomas Canor, Luca Caracoglia, and Vincent Denoël. Application of random eigenvalue analysis to assess bridge flutter probability. *Journal of Wind Engineering and Industrial Aerodynamics*, 140:79–86, 2015.
- [23] Vincent Denoël. Estimation of modal correlation coefficients from background and resonant responses. *Structural Engineering and Mechanics: an International Journal*, 32(6):725–740, 2009.
- [24] Vincent Denoël and Hervé Degée. Asymptotic expansion of slightly coupled modal dynamic transfer functions. *Journal of Sound and Vibration*, 328(1-2):1–8, 2009.

## 7 APPENDIX: THE ADAPTATIVE INTEGRATION SCHEME

The results obtained and presented in this paper are partly obtained with a simple in-house adaptative integration scheme. The algorithm works as follows. First, the domain of integration is divided into segments separated by the integration points. On each segment, the contribution to the integral is computed by means of the trapezoidal rule. These segments are then iteratively refined, if required, until a desired accuracy is reached.

The refinement procedure consists in adding an integration point in the middle of the interval, creating therefore two sub-segments instead of the initial one. The sum of the contribution on the two sub-segments is compared to the contribution along the domain before subdivision. If the relative difference between both is lower than a user-defined threshold, then this domain is not subdivided anymore. This process is continued until no segments requires being divided anymore.

This algorithm performs better when the original distribution of points includes the inflexion points in the function to integrate. This is due to the fact that the break-down condition originates from a concept built on a curvature with a constant sign along the domain. The termination criteria can indeed be too confident in case of a domain with an inflexion point in the middle.

```
doloop = 1; iter=1;
while doloop
    ir = find(r==1);
    nz = length(ir);
    jr=1;
    while jr<=nz
        iz = ir(jr);
        xn = (x(iz)+x(iz+1))/2;
        fn = fct(xn);
        I1 = trapz( [x(iz) x(iz+1)], [f(iz) f(iz+1)] );
        I2 = trapz( [x(iz) xn], [f(iz) fn] ) + trapz( [xn x(iz+1)], [fn f(iz+1)] );
        err = abs(I2-I1) / (Itot / (x(end)-x(1)) * (x(iz+1)-x(iz)) );
        x = [x(1:iz) xn x(iz+1:end)];
        f = [f(1:iz) fn f(iz+1:end)];
        if err < tol
            r = [r(1:iz-1) 0 0 r(iz+1:end)];
        else
            r = [r(1:iz-1) 1 1 r(iz+1:end)];
        end ir = ir+1; jr = jr+1;
        Itot = trapz( x,f );
    end
    if sum(r) == 0; doloop=0; end
    iter=iter+1;
end
Itot = trapz( x,f );
```

## SIMULATING LOW FREQUENCY SOUND TRANSMISSION LOSS OF MOUNTED PANELS

Moris Kalderon<sup>1</sup>, Andreas Paradeisiotis<sup>1</sup> and Ioannis Antoniadis<sup>1</sup>

<sup>1</sup>National Technical University of Athens Dynamics and Structures Laboratory, School of Mechanical Engineering  
Heroon Polytechniou 9, 15780 Zografou Athens, Greece  
e-mail: moriska@mail.ntua.gr , aparadis@mail.ntua.gr

**Keywords:** low frequency, panel, sound transmission loss, elastic mounts, reverberation room

**Abstract.** *Lightweight panels are very common in the building, aerospace and automotive industry, and their acoustic insulation properties are well studied; nevertheless, low frequency noise is inherently difficult to deal with, mainly due to its high penetration. To encounter this issue, several treatments have been proposed in the form of perforated plates, meta-surfaces and acoustic/elastic meta-materials among others. Despite, the continuous attempts, none of the available solutions has indicated an outstanding performance in the low frequency range. On the other hand, boundary conditions of a vibrating panel are known to have an influence on the sound transmission loss (STL). Driven by the recently extended standards to include frequencies as low as 50 Hz, and the academic community debate about the reliability of low-frequency measurements in reverberant chambers, STL improvement in the region of the first panel resonance is investigated in this paper, considering a panel supported on elastic mounts. Following a general vibration isolation approach, the fundamental eigenfrequency of the panel-mount system is reduced and is explicitly selected below the threshold of human hearing. STL predictions are accomplished utilizing a Finite Element (FE) vibroacoustic model that simulates real test room conditions. Compared to the commonly used models of a baffled plate radiating to infinity, this detailed approach allows not only a more accurate calculation of STL but also reveals the potential issues emerging during laboratory measurements.*



## 1 INTRODUCTION

When considering room-to-room noise transmission inside buildings, sources such as electrical appliances, music and movies in neighboring apartments etc., have notable low frequency content. Another significant component of low frequency noise in residential areas is road noise emitted by vehicles, since their engines operate typically at speeds up to 6000 RPM (100 Hz). Therefore, there is an ever increasing demand for noise mitigation solutions in this range, providing an improvement on the residents quality of life but also for compliance with legal requirements [1].

However, the low frequency range approximately below 200 Hz, has been overwhelmingly overlooked in the past when considering applications and we presently lack understanding to properly model the processes governing the sound transfer in this frequency range. Almost exclusively, the focus is on the region of the coincidence frequency of finite partitions. The lack of complete industrial standardization and guidances for such cases, especially below 100 Hz is also a factor. Yet, a large research program on low frequency sound transmission into buildings was conducted by NGI (the Norwegian Geotechnical Institute) between 2010-2016, comprising of laboratory, full scale and numerical testing [2]. The disseminating research findings of the program have been proven very useful, but there are still uncharted areas in this field.

When it comes to acoustic treatment in rooms there are also a lot of misconceptions among the general public. Full scale tests reveal that when noise transmission occurs inside a building, the peaks of the low frequency sound spectrum are of the same order as the fundamental acoustic room-modes [3], leading to a collection of resonances, which compromise the measurements. International standards describe procedures to extend the measurement range down to the 50 Hz one-third octave band [4, 5, 6]. Prescriptions include use of specific source and receiver positions, however the procedure is complex, with the worst case scenario to propose the use of a sufficiently large number of source-receiver combinations as a means to smooth the large spatial variations in measured levels. Moreover, regarding the laboratory geometry, large rooms with volumes  $V > 200m^3$  and specific room size ratios are suggested when low frequency measurements are conducted. Recently, Ayr et al. [7] presented a detailed low frequency qualification procedure for a typical reverberant test room in order to perform sound power measurements, by taking advantage of a room finite element model. Similarly, Løvholt et al. [8] developed a finite element methodology that incorporates a two-way coupled fluid-structure interaction and they compared their numerical results with experimental measurements including low frequency sound transmission of plain walls, and walls with windows. Vorländer and Aretz also worked on room to room acoustic simulations, focusing on the room boundary conditions [9] and the uncertainties of the computational models [10].

As far as the analytic methods are concerned, the acoustic radiation from plates has long been an important subject in structural dynamics and acoustics, thus numerous mathematical models describing the structural response to noise, acoustic fatigue and sound transmission of partitions have been developed. Beranek and Ver, Cremer et al., Ordubadi and Lyon and London [11, 12, 13, 14] derived equations for the unbounded/infinite partitions ("infinite-panel theory") simplifying the problem and later ad hoc corrections were added to enhance the accuracy of the Sound Transmission Loss (STL) formulas. Although, the infinite panel theory can approximate pretty accurately the panel response when high frequency noise mitigation is concerned, it is known that bounded plates vibrating at frequencies below the critical frequency are very much influenced by the presence of their boundaries [15, 16]. Similarly, Kim [17] approached sound transmission through partitions from the standpoint of impedance mismatch. Despite, the merits

of the aforementioned approaches, in low frequency the modal response of the structure affects the transmission properties.

The aim of this contribution is to investigate the effects of elastic mounting in the STL performance, considering a much relevant specific case of single-leaf plasterboard partitions and show how the uncertainties due to practical factors can be diminished with this approach. Namely, the ways that elastic mounting may be incorporated in already existing panels and set circumstances regarding their spatial configuration, as well as, the effectiveness of the damping of the mounts in the mitigation of the first panel resonance. The analysis is conducted via both simple mathematical models and a coupled finite element vibroacoustic model where the room to room sound transmission is described based on the laboratory set-up in SINTEF Building laboratory in Oslo, Norway [8].

The idea of utilizing "soft mounts" to reduce the fundamental frequency of the system delves into the investigation of what constitutes soft mounting. Therefore, a modeling procedure based on certain approximations [18] is formulated in order to provide a projection of the expected level of stiffness that satisfies this terminology and serves the intended purpose. Intuitively, following the general concepts of vibration isolation for the reduction of the eigenfrequency through the reduction of stiffness, supporting an existing panel on elastic mounts, the 'mass law' behavior may be dragged into lower frequencies and the resonant region of the new system panel-mount will be moved below a critical frequency, for example at 20 Hz considering the threshold of human hearing.

To sum up, in Section 2 the theoretical formulation of the three applied methods, are provided together with the FE model describing the room to room transmission. In Section 3 a parametric investigation is presented to reveal the parameters that affect STL of a rectangular panel and finally in Section 4 the conclusions of this work are briefly discussed.

## 2 MATERIALS & METHODS

By defining the transmission coefficient as

$$\tau = \frac{\Pi_t}{\Pi_i} \quad (1)$$

where  $\Pi_i$  is the incident and  $\Pi_t$  the transmitted (radiated) sound power, the STL is expressed as

$$STL = 10 \log_{10} \left( \frac{1}{\tau} \right) \quad (2)$$

A typical form of the STL curve for sound propagation through a thin panel is described in [19]. In the 'mass law' region, the STL is controlled by the mass per unit area of the panel. Specifically, for a thin panel, neglecting stiffness and damping (limp wall):

$$STL = 10 \log_{10} \left[ \frac{\Omega^2 \bar{m}^2}{4(\rho_0 c_0)^2 / \cos^2 \theta_i} \right] \quad (3)$$

where  $\Omega$  is the cyclical frequency of the propagated incident sound waves,  $\theta_i$  is the angle of incidence,  $c_0$  is the speed of sound in air,  $\rho_0$  is the air density and  $\bar{m} [kg/m^2]$  is the mass per unit area of the panel. Although the mass law is very simple and compact, it is only valid for large simple plates because it is derived from the infinite and rigid plate assumption. Therefore, attention should be given when utilized for STL predictions of general finite panels.

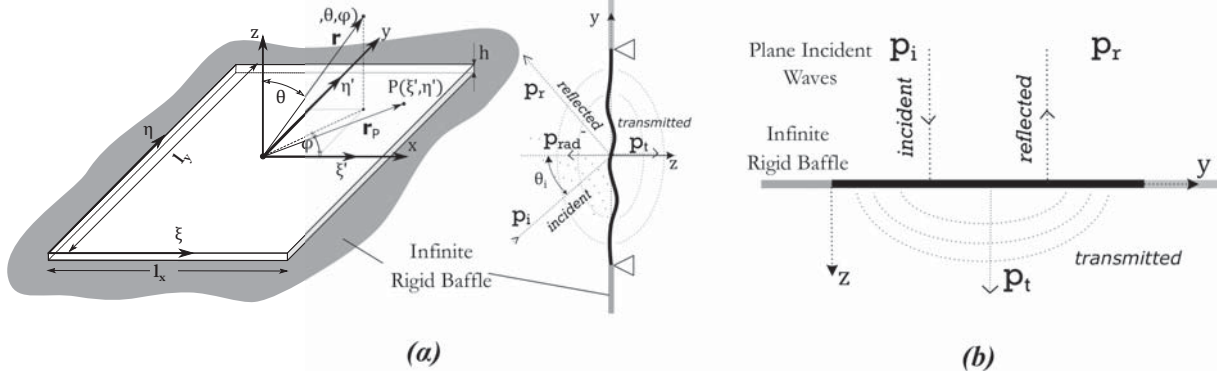


Figure 1: (a) Coordinate systems and transmission geometry of a rectangular plate in a rigid baffle. (b) Transmission geometry of the free finite rigid panel.

## 2.1 Sound radiation from a rectangular panel in an infinite rigid baffle

The fluid domain is assumed homogeneous and compressible. The mass density of air and sound speed are noted as  $\rho_0$  and  $c_0$ , respectively. The infinitely large acoustic rigid baffle divides the space into two domains i.e. the excitation domain  $V^-$  and the receiver domain  $V^+$ . The panel is subjected to the incident pressure  $p_i$ , with incidence angle  $\theta_i$  and azimuth angle  $\phi_i$ . Therefore, the excitation domain consists in the incident pressure  $p_i$ , the reflected pressure  $p_r$ , and the re-radiated pressure  $p_{rad}^-$  due to the motion of the finite panel. The receiver domain consists only in the transmitted pressure  $p_t$ , namely the radiated pressure due to the motion of the panel  $p_{rad}^+$ . Assuming that the incident sound pressure  $p_i$  is a harmonic function, we can express it as

$$p_i(x, y, z, t) = P_i e^{-j(\kappa_x x + \kappa_y y + \kappa_z z)} e^{j\Omega t} = \tilde{p}_i(x, y, z) e^{j\Omega t} \quad (4)$$

where  $\tilde{p}_i(x, y, z)$  the time invariable complex amplitude and  $\kappa = \Omega/c_0$  is the wavenumber with

$$\kappa_x = \kappa \sin \theta \cos \phi, \quad \kappa_y = \kappa \sin \theta \sin \phi, \quad \kappa_z = \kappa \cos \theta \quad (5)$$

The reflected pressure by the surface of the panel is then expressed as

$$p_r(x, y, z, t) = P_r e^{-j(\kappa_x x + \kappa_y y - \kappa_z z)} e^{j\Omega t} = \tilde{p}_r(x, y, z) e^{j\Omega t} \quad (6)$$

denoting the opposite direction from the incident wave. Lord Rayleigh [20] determined a relationship expressing the radiated (transmitted) pressure in terms of the structural velocity based on Green's function,

$$p_{rad}^+(\mathbf{r}, t) = p_t(\mathbf{r}, t) = \frac{j\Omega\rho_0}{2\pi} e^{j\Omega t} \int_{-l_x/2}^{l_x/2} \int_{-l_y/2}^{l_y/2} \frac{e^{-j\kappa R}}{R} \frac{\partial w(\xi', \eta')}{\partial t} d\eta' d\xi' \quad (7)$$

where  $R$  referring to Fig.1, is defined as

$$R = |\mathbf{r} - \mathbf{r}_P| = \sqrt{(x - \xi')^2 + (y - \eta')^2 + z^2} \quad (8)$$

and  $\mathbf{r} = (x, y, z)$  is the position vector of a point in the receiver domain while  $\mathbf{r}_P = (\xi', \eta', 0)$  is the position vector of the center of an elemental radiator with surface  $\delta S$  on the panel, having a normal velocity amplitude  $\dot{w}(\xi', \eta')$ . For the local coordinates holds that  $\xi' = \xi - \frac{l_x}{2}$ ,  $\eta' = \eta - \frac{l_y}{2}$ .

Following the calculation of the expression for the transmitted pressure, there are two different ways used to determine the radiated (transmitted) power. The first is to integrate the

intensity on a hemisphere in the far-field enclosing the plate which is followed in this paper, and the latter is to integrate the acoustic intensity over the surface of the vibrating plate. Both approaches require the knowledge of the distribution of the velocity over the plate and they assume a weak coupling between the vibrating structure and the radiated sound field.

Applying the far-field approximation as described in Section A.1, the transmitted intensity  $I_t$  is calculated as

$$I_t(r, \theta, \phi) = \frac{|p_t(r, \theta, \phi)|^2}{2\rho_0 c_0} \quad (9)$$

Then, the transmitted power  $\Pi_t$  comes by integrating the transmitted intensity on a hemisphere in the far field enclosing the plate as

$$\Pi_t = \int_0^{2\pi} \int_0^{\pi/2} I_t r^2 \sin \theta d\theta d\phi \quad (10)$$

while the incident power on the panel is defined as

$$\Pi_i = \frac{|p_i|^2 l_x l_y \cos \theta}{2\rho_0 c_0} \quad (11)$$

## 2.2 Vibration of a panel subject to external pressure

With reference to Fig.1a, the finite-sized flat panel partition is assumed to be rectangular and baffled, with lengths  $l_x$  and  $l_y$  along the  $x$  and  $y$  axes respectively. The panel of thickness  $h$ , is considered homogeneous and isotropic and is modeled as a classical thin plate, implying that the effects of both the rotary inertia and the transverse shear deformation can be neglected. Hereinafter, the equation of motion governing the bending vibration of the plate is given by

$$\begin{aligned} D \left[ \frac{\partial^4 w(\xi, \eta, t)}{\partial \xi^4} + 2 \frac{\partial^4 w(\xi, \eta, t)}{\partial \xi^2 \partial \eta^2} + \frac{\partial^4 w(\xi, \eta, t)}{\partial \eta^4} \right] + \rho h \frac{\partial^2 w(\xi, \eta, t)}{\partial t^2} = \\ = p_i(\xi, \eta, t) + p_r(\xi, \eta, t) + \bar{p}_{rad} - p_{rad}^+ \end{aligned} \quad (12)$$

where  $D = \tilde{E}h^3/12(1 - \nu^2)$  is the bending stiffness of the plate,  $E$ ,  $h$ ,  $\rho$  and  $\nu$  are the Young's modulus, thickness, mass density and Poisson's ratio of the plate, respectively.  $w(\xi, \eta, t)$  is the instantaneous transverse displacement. In order to account for energy dissipation due to structural damping, a complex modulus of elasticity is introduced  $\tilde{E} = E(1 + jn)$ , where  $n$  is the loss factor.

The right hand side must satisfy the velocity continuity at the surface of the panel ( $z = 0$ ). In that case, it holds that  $p_r = p_i$  and also since  $p_t = p_{rad}^+ = -\bar{p}_{rad}$  the right hand side becomes

$$p_i(\xi, \eta, t) + p_r(\xi, \eta, t) + \bar{p}_{rad} - p_{rad}^+ = 2p_i(\xi, \eta, t) - 2p_t(\xi, \eta, t) \quad (13)$$

The so-called "blocked pressure" [17]  $p_b = 2 p_i$ , is the pressure when the incident wave meets a rigid wall.

## 2.3 Free Finite Rigid (FFR) Panel Approximation

In order to replace the infinite panel approximation (limp wall) with a more appropriate reference for finite panels, the free finite rigid (FFR) panel approximation is formulated. In this case it is assumed that the panel is rigid, consisting only in mass and oscillating freely in an infinite rigid baffle but instead has finite dimensions as demonstrated in Fig.1b.

Since the panel is considered rigid, the spatial derivatives of Eq.(12) are eliminated. Also, considering only the blocked pressure  $p_b = 2p_i$  as the forcing pressure and that  $p_i$  are incident plane waves, the equation of motion becomes:

$$\rho h \ddot{w} = 2P_i e^{j\Omega t} \quad (14)$$

The forcing pressure is a harmonic function, therefore the steady-state transverse displacement of the panel can be expressed as

$$w = W(\xi, \eta) q(t) \quad (15)$$

where

$$q(t) = C e^{j\Omega t} \quad (16)$$

For the rigid assumption, the shape function is independent of the position  $(\xi, \eta)$  on the surface of the panel, namely  $W(\xi, \eta) = 1$ . Substituting the solution into Eq.(14) and solving for  $C$  gives:

$$C_{\text{FFR}} = -\frac{2P_i}{\rho h \Omega^2} \quad (17)$$

The transmission coefficient then comes as

$$\tau_{\text{FFR}} = \frac{1}{l_x l_y} \left( \frac{\rho_0}{\pi} \right)^2 \frac{1}{\overline{m}^2} I_{\theta\phi} \quad (18)$$

where  $\overline{m} = \rho h$  is the mass density (mass per surface area) of the panel, and  $I_{\theta\phi}$  is the double integral over a hemisphere in the receiver domain as given in Eq.(A.10).

## 2.4 Simply Supported Plate First Mode Approximation

Analytic solutions for the problem can be found via modal superposition methods, for example as formulated by Roussos [21]. However, in these analytic approaches, past researchers usually avoided to include in their calculations the re-radiated pressure  $2p_t(\xi, \eta, t)$  (often referred to as "fluid loading") of Eq.(13) in order to reduce complexity. According to Roussos [21] neglecting the effect of the re-radiated pressure allows an accurate solution to be obtained over large frequency range, and gives invalid answers only for frequencies near the panel's fundamental resonant frequency.

Since the low frequency range of interest in the present case is exactly the range near the fundamental resonance of the panel, an attempt for a more accurate and usable approximation is formulated in this section, including the effect of fluid loading.

Considering only the 1<sup>st</sup> vibrational mode of the simply supported plate, the spatially dependent amplitude of the transverse displacement  $w(\xi, \eta) = W_1(\xi, \eta, t) e^{-j\Omega t}$  is assumed by the shape function

$$W_1 = C_1 \sin\left(\frac{\pi\xi}{l_x}\right) \sin\left(\frac{\pi\eta}{l_y}\right) \quad (19)$$

the resulting expression for the transmitted (radiated) power  $\Pi_t$  is given by Eq.(A.25). The detailed analysis is presented in Section A.3.

Assuming normal incident waves ( $\theta_i = 0$ ), the incident power is given by

$$\Pi_i = \frac{P_i^2 l_x l_y}{2\rho_0 c_0} \quad (20)$$

leading to the transmission coefficient  $\tau$  as

$$\tau_1 = \frac{1}{l_x l_y} \frac{(16\Omega^2 \rho_0)^2}{|\pi^3 \rho h (\omega_1^2 - \Omega^2) - 16\Omega^2 \rho_0 \frac{e^{-jkr}}{r}|^2} I_{\theta\phi} \quad (21)$$

where distance  $r$  needs to be large enough to satisfy the far-field approximation and  $\omega_1$  is the natural frequency of the 1<sup>st</sup> mode resulting from the homogeneous form of Eq. (12), as

$$\omega_1^2 = \frac{D\pi^4}{\rho h} \left( \frac{1}{l_x^2} + \frac{1}{l_y^2} \right)^2 \quad (22)$$

Expressing the dynamic behavior of the continuous system of the simply supported panel approximated by the 1<sup>st</sup> mode, as a single degree of freedom (SDoF) lumped parameter model (LPM), the corresponding generalized mass and stiffness [22] come as

$$m_1^* = \frac{\rho h l_x l_y}{4} = \frac{\bar{m} l_x l_y}{4} = \frac{m}{4} \quad (23)$$

$$k_1^* = \frac{D\pi^4 l_x l_y}{4} \left( \frac{1}{l_x^2} + \frac{1}{l_y^2} \right)^2 \quad (24)$$

The transmission coefficient is then calculated as

$$\tau_{\text{LPM}} = l_x l_y \left( \frac{4\Omega^2 \rho_0}{\pi^3} \right)^2 \frac{1}{[m_1^* |\omega_1^2 - \Omega^2|]^2} I_{\theta\phi} \quad (25)$$

## 2.5 Lamped parameter model for elastic mounts

The goal is to formulate a straightforward procedure for the investigation of how the bending stiffness of the panel combines with the mounting stiffness in the case where the panel is supported on elastic mounts and how the acoustic performance is affected. In order to do that, the main assumption is that the bending stiffness of the deformable plate is in a way in series with the stiffness of the mounting. Therefore, the resulting stiffness is

$$k_{\text{tot}} = \frac{k_1^* k_0'}{k_1^* + k_0'} \quad (26)$$

When the mounting is very stiff ( $k_0' \gg k_1^*$ ) leads to  $k_{\text{tot}} = k_1^*$ , namely, the case of the simply supported plate is approached. When  $k_0' \rightarrow 0$ , the plate is essentially free floating. Naturally, when the eigenfrequency of the system is reduced along with the total stiffness, the mass considered in the SDof model increases. In this case this variation is neglected for reasons of simplification. As a result, when the considered mounting stiffness  $k_0'$  is of comparative order of magnitude with  $k_1^*$ , there is some deviation between the resulting eigenfrequency of the model and the actual eigenfrequency. However, in cases when  $k_0' \gg k_1^*$  or  $k_0' \ll k_1^*$  the deviation is nullified. Thus the model is used for an estimation of the required stiffness level and guidance for the design of the mounts.

Fig.2, shows the equivalent dynamic SDOF model of the deformable thin panel when it is supported on elastic mounts according to the 'in-series' assumption. This is achieved by utilizing the generalized values of the structure, namely generalized mass and the corresponding



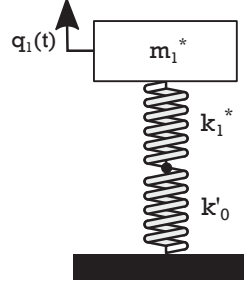


Figure 2: Modelling of a deformable plate on elastic mounts with stiffness  $k'_0$ .

generalized stiffness for the appropriate modes, as calculated from Eqs.(23),(24) for the  $1_{st}$  mode approximation of the simply supported panel.

Since the loss factor ( $n$ ) can represent more accurately the dynamic response of nonlinear systems compared with the damping ratio which is defined on the grounds of the linear single degree of freedom (SDOF) viscous model [23, 24], hysteretic damping is introduced indirectly considering complex stiffness elements as

$$k'_0 = k_0 (1 + jn) \quad (27)$$

$$(28)$$

The STL of the model is then calculated as  $STL = 10 \log_{10} \left( \frac{1}{\tau} \right)$ , where the transmission coefficient  $\tau$  comes as

$$\tau = l_x l_y \left( \frac{4\Omega^2 \rho_0}{\pi^3} \right)^2 \frac{1}{|-\Omega^2 m_1^* + k_{tot}|^2} I_{\theta\phi} \quad (29)$$

## 2.6 3D vibro-acoustic FE model

In addition to the aforementioned analytical methodologies, a 3-D FE coupled vibro-acoustic model was developed on the commercial finite element software package ABAQUS [25]. In the present simulations, the geometry of the SINTEF laboratory [8] is utilized as the computational domain, as shown in Fig.3  $\alpha$  and b. It is noted that the laboratory geometry and the measurement procedure do not follow accurately the proposed from the standards guidance, however, the developed model can be used for room to room sound transmission predictions. The panel is excited by the source located in the left corner of the source room and the incidence and radiated acoustic pressure is extracted from the fluid-structure interface nodes. An arithmetic average is performed by

$$\overline{P}_t = \frac{1}{n} \sum_{i=1}^n |p_{t,i}| \quad (30)$$

$$\overline{P}_i = \frac{1}{n} \sum_{i=1}^n |p_{i,i}| \quad (31)$$

where  $n$  denotes the total number of measuring nodes;  $i$  denotes the node number;  $p_i$  denotes the incidence pressure and  $p_t$  denotes the transmitted pressure. Then the averaged pressures  $\overline{P}_i, \overline{P}_t$  are used to compute the simulated STL by

$$STL = 20 \log_{10} \frac{|\overline{P}_i|}{\overline{P}_t} \quad (32)$$

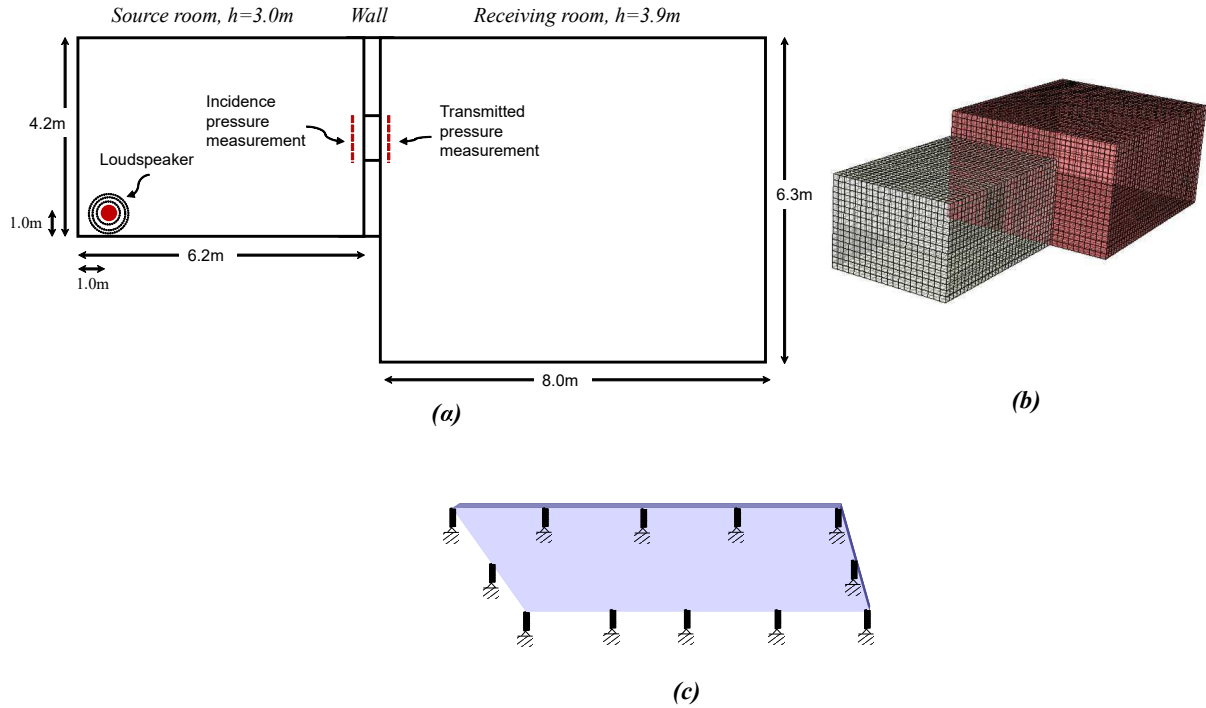


Figure 3: (a) Plan view of the sound laboratory setup used in ABAQUS model. (b) Depiction of the vibro-acoustic model. (c) Positioning of the twelve (12) mounts on the surface of the panel.

The panel is discretized by 20-node quadratic solid hexahedral elements, while the fluid domain is discretized by 20-node quadratic acoustic hexahedral elements. Tie constraints are used to simulate the coupling at the fluid-structure interface, while reflecting boundary conditions were specified to simulate the room conditions. In cases that the plate is supported on elastic mounts, connectors are installed on the required locations with the appropriate properties. Lastly, the discretization of the fluid domain has more than three quadratic elements across the wavelength of interest to increase the accuracy of the computational results [26].

### 3 Numerical Example - Parametric investigation of STL

In this section, the elements that affect STL of a rectangular plate are investigated, especially in case of a single leaf plasterboard partition. Initially, the analytic models proposed in the previous section A  $0.625 \times 1.6m$  rectangular plasterboard is considered, according to real-life masonry applications. The width corresponds to the horizontal distance between the upright supporting beams providing the stable frame of the plasterboard. Typically, the height of such a plasterboard is around 3.2 m, meaning that it can be covered by two pieces with the dimensions consider here. The selected dimensions correspond also to a frontal surface of  $1 m^2$ . The relevant properties of the plasterboard are summarized in Table 1.

Table 1: Plasterboard properties.

$\rho \left[ \frac{kg}{m^3} \right]$	$L_x [m]$	$L_y [m]$	$h [m]$	$E [MPa]$	$\nu [-]$
668	0.625	1.6	$12.5 \cdot 10^{-3}$	2900	0.31

The red dashed line in Fig.4, represents the FFR panel approximation as given by Eq.(18). Intuitively, this approximation should constitute the ideal case regarding the STL of a panel

with finite dimensions and may act as a reference curve for the various comparisons instead of the infinite panel approximation which is invalid in the lower frequency range that is being examined. The yellow line corresponds to the 1<sup>st</sup> mode approximation of the simply supported panel while the blue dotted line is the lumped parameter model as derived from the 1<sup>st</sup> mode approximation. The difference between the two methods is essentially the effect of fluid loading (FL), whereas in the latter model is not included. It is observed that the fluid loading has very little effect on the damping of the first resonance. Thus, the elimination of its participation in the respective models is justified and consists a safe approximation. Lastly, the black dashed line represents the modal superposition method as formulated by Roussos and the grey line with markers shows the STL as calculated from the finite element model. In general a good agreement is observed among all the applied methods.

### 3.1 Mathematical vs Numerical models

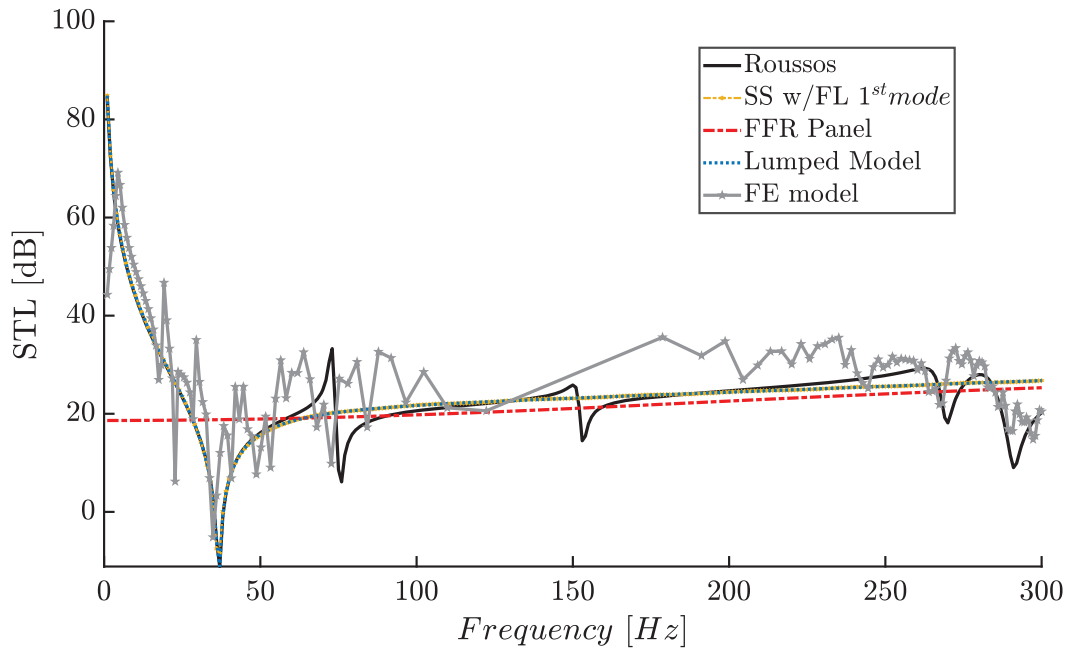


Figure 4: Comparison of 1<sup>st</sup> mode, rigid approximations and numerical model.

The objective of the simplified models is to provide a more straightforward and fast prediction of the acoustic performance of the panel along with the ability to extract intuitive and revealing expressions of the main dynamic parameters that govern its frequency response. Since the higher modes have significantly lower modal participation factors in the frequency response than the fundamental mode, they are relatively easily damped. With that thinking, the approximation using only the 1<sup>st</sup> mode is considered appropriate in order to study this low frequency region, and following, the effect of elastic mounting and damping.

### 3.2 Effect of support conditions in STL

A case for the resulting STL frequency response compared to the simply-supported and clamped configurations are presented in Fig.5 $\alpha$ . The total stiffness of the mounting is considered equal to the generalized stiffness of the simply supported panel ( $k = k_1^* = 1.1 \cdot 10^5 \text{ N/m}$ ),

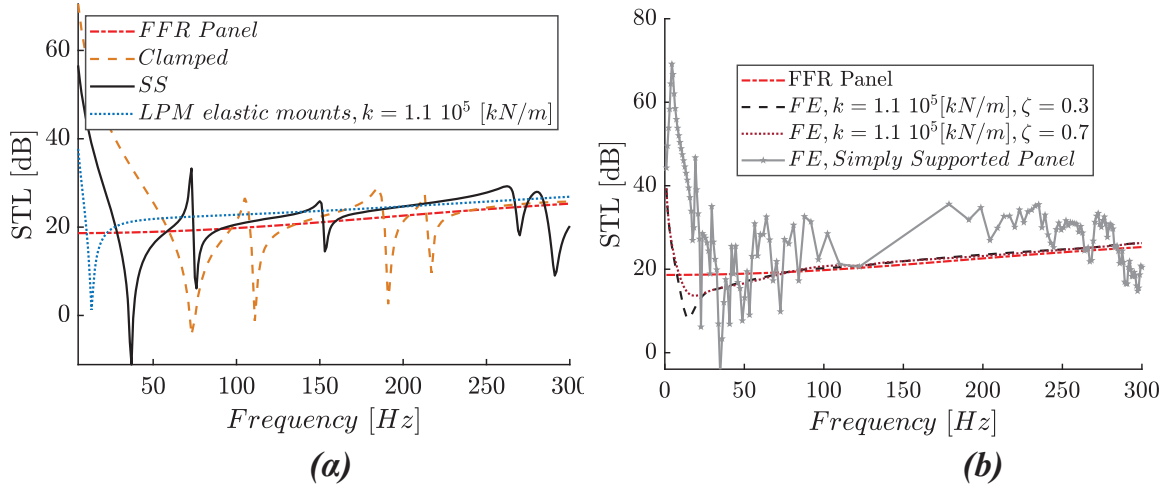


Figure 5: (a) Effect of support conditions in Sound transmission loss (STL). (b) Effect of damping in Sound transmission loss (STL).

while, no damping is considered for the mounts. This choice for the mounting stiffness is based on the Lamped parameter model, described in Section 2.5. Specifically, the total mounting stiffness is selected to drop the  $1_{st}$  resonance below 20 [Hz] and then the estimated stiffness is allocated to the 12 springs of the FE model.

Following the logic of classic vibration isolation, by lowering this frequency enough it can be moved outside the frequency range of interest, e.g. above 20 Hz. However, significantly decreasing this frequency can have certain implications. On one hand, it leads to slightly reduced STL frequency response and on other hand, it may present practical problems including excessive vibration magnitude, possible resonances with other supportive structural elements such as bolts or the frame, or even inadequate rigidity for impact loads. The optimal solution requires a combination that leads to a low enough fundamental eigenfrequency that can be effectively dampend without the need of excessive damping while at the same time is high enough that the overall STL is not significantly reduced and no vibrational implications come into play when the mounting is very soft.

Another purpose of the comparison in Fig.5a is to highlight the deviation of the eigenfrequencies between the simply supported and clamped panels in regards to the uncertainty introduced by this fact in real world installations. Depending on the technique of the installation the exact support conditions may vary between these two cases. However, the inclusion of the soft elastic mounts, eliminates this uncertainty as it produces an explicit, calculated frequency response by design. Additionally, the reduction of the eigenfrequencies alone almost eliminates the participation of the higher modes even without the consideration of any energy diffusive elements besides the structural damping of the panel itself which holds for all three case compared here.

### 3.3 Effect of damping

Further examination considers the effect of damping of the elastic mounts. In order to investigate the effects of damping 12 linear springs were attached to the panel as in Fig.3c. Assuming the same stiffness for the mounts as in the previous case, a comparison is presented in Fig. 5b damping ratios  $\zeta = 0.3$  and  $\zeta = 0.7$ .

The results presented in Fig.5b are meant to demonstrate the expected level of damping in

order to effectively damp the fundamental frequency. As already mentioned, even in cases of low damping the STL response is flattened as the higher eigenfrequencies are very effectively damped while only the first eigenfrequency requires significant damping. How realistic are the actual values of the assumed viscous dampers for high damping ratios is surely a matter of discussion and very much depends on practical factors like the material used for the mounts and spatial considerations of the real world implementation.

Certainly, the positions of the mounts have a significant role on their damping effectiveness. Especially in this case of viscous damping, the velocity amplitude is maximum at the center of the panel and minimum along the edges, therefore a mount positioned at the center would most effectively dampen the fundamental resonance. However, this case would change the dynamic behaviour of the panel and would also require an additional supporting frame along the middle of the panel for example, which is something that is preferably avoided. For this reasons such a modification is not investigated in the current contribution.

## 4 Conclusions

The variation of the support conditions of the panel, between simply supported and clamped, in a real-world implementation affects significantly the eigenfrequencies and therefore the frequency response of the STL.

The term "soft mounts" is approximately defined as the case in which the total stiffness of the mounts is lower than the generalized stiffness of the simply supported panel. When the panel is supported regionally on soft elastic mounts, the values of the eigenfrequencies of the structure are reduced. This has two main consequences:

- The value of the fundamental eigenfrequency can be explicitly defined, depending on the stiffness of the mounts, and be moved outside the frequency range of interest, namely below 20 Hz.
- The contribution of the higher modes is almost nullified without the need of any significant damping in the mounts.

Therefore, the utilization of soft mounts displaces the STL curve towards lower frequencies, providing smooth performance in the entire low frequency range. Additionally, this practice diminishes any uncertainties introduced in the acoustic performance either due to practical support conditions or variations in the rigidity of the panel.

Finally, the analytic models showed good agreement with the developed FE model, indicating that they can be used as a quick tool for the design of soft mounts.

## 5 Acknowledgments

Moris Kalderon has been financed by the European Union's Horizon 2020 research and innovation programme under the Marie Skłodowska-Curie grant (grant agreement No INSPIRE-813424, "INSPIRE - Innovative Ground Interface Concepts for Structure Protection").

## Appendix

### A.1 Far-field approximation

The distance  $R$  can be written as

$$R = \sqrt{r^2 - 2x\xi' - 2y\eta' + \xi'^2 + \eta'^2} \quad (\text{A.1})$$

where  $r = |\mathbf{r}| = \sqrt{x^2 + y^2 + z^2}$ . In spherical coordinates  $R$  becomes

$$R = r \sqrt{1 - 2 \frac{\sin \theta}{r} (\xi' \cos \phi + \eta' \sin \phi) + \frac{\xi'^2 + \eta'^2}{r}} \quad (\text{A.2})$$

The solution of Eq.(7) is not trivial and has been calculated analytically only for a few cases of boundary conditions. A way around this obstacle comes by utilizing the far field approximation. In the far field we can ignore the weak dependence of the amplitude of the integrand on the position but not the dependence of the phase, namely it holds that

$$\frac{1}{R} \approx \frac{1}{r} \quad (\text{A.3})$$

$$e^{-j\kappa R} \approx e^{-j\kappa r \left[ 1 - \frac{\sin \theta}{r} (\xi' \cos \phi + \eta' \sin \phi) \right]} = e^{-j\kappa r} e^{j\kappa \sin \theta (\xi' \cos \phi + \eta' \sin \phi)} \quad (\text{A.4})$$

Since  $r$  is independent of  $\xi'$  and  $\eta'$ , the corresponding terms in Eq.(7) can be moved outside the double integral, leading to

$$p_t(\mathbf{r}, t) = \frac{j\Omega\rho_0}{2\pi r} e^{j(\Omega t - \kappa r)} \int_{-l_x/2}^{l_x/2} \int_{-l_y/2}^{l_y/2} \frac{\partial w(\xi', \eta')}{\partial t} e^{j\kappa (\xi' \sin \theta \cos \phi + \eta' \sin \theta \sin \phi)} d\eta' d\xi' \quad (\text{A.5})$$

which may be analytically calculated.

## A.2 Free Finite Rigid (FFR) Panel Approximation

Then, the transmitted pressure by considering the far-field approximation, is calculated from the expression

$$p_t(\mathbf{r}, t) = \frac{-\Omega^2 \rho_0 W}{2\pi} \frac{e^{-j\kappa r}}{r} e^{j\Omega t} \int_{-\frac{l_x}{2}}^{\frac{l_x}{2}} \int_{-\frac{l_y}{2}}^{\frac{l_y}{2}} e^{j\kappa (\xi' \sin \theta \cos \phi + \eta' \sin \theta \sin \phi)} d\eta' d\xi' \quad (\text{A.6})$$

where the surface integral is calculated

$$I_{\xi'\eta'} = \frac{8 \sin(\sigma_x) \sin(\sigma_y)}{k^2 \sin^2 \theta \sin 2\phi} \quad (\text{A.7})$$

and

$$\sigma_x(\theta, \phi) = k \frac{l_x}{2} \sin \theta \cos \phi \quad (\text{A.8})$$

$$\sigma_y(\theta, \phi) = k \frac{l_y}{2} \sin \theta \sin \phi \quad (\text{A.9})$$

The transmitted intensity  $I_t$  and consequently the transmitted power, are calculated from Eqs.(9),(10) where  $I_{\theta\phi}$  is defined as

$$I_{\theta\phi} = \int_0^{2\pi} \int_0^{\pi/2} |I_{\xi'\eta'}|^2 \sin \theta d\theta d\phi \quad (\text{A.10})$$



### A.3 Simply Supported Plate - First Mode Approximation

Considering only the 1<sup>st</sup> mode for interpolation of the transverse displacement the derivatives to be substituted in the equation of motion are calculated as

$$\begin{aligned}
 \frac{\partial^2 w(\xi, \eta)}{\partial t^2} &= -\Omega^2 W_1(\xi, \eta) e^{-j\Omega t} \\
 \frac{\partial^4 W_1(\xi, \eta)}{\partial \xi^4} &= C_1 \left( \frac{\pi}{l_x} \right)^4 \sin\left(\frac{\pi \xi}{l_x}\right) \sin\left(\frac{\pi \eta}{l_y}\right) = \left( \frac{\pi}{l_x} \right)^4 W_1(\xi, \eta) \\
 \frac{\partial^4 W_1(\xi, \eta)}{\partial \eta^4} &= C_1 \left( \frac{\pi}{l_y} \right)^4 \sin\left(\frac{\pi \xi}{l_x}\right) \sin\left(\frac{\pi \eta}{l_y}\right) = \left( \frac{\pi}{l_y} \right)^4 W_1(\xi, \eta) \\
 \frac{\partial^4 W_1(\xi, \eta)}{\partial \xi^2 \partial \eta^2} &= C_1 \left( \frac{\pi^2}{l_x l_y} \right)^2 \sin\left(\frac{\pi \xi}{l_x}\right) \sin\left(\frac{\pi \eta}{l_y}\right) = \left( \frac{\pi^2}{l_x l_y} \right)^2 W_1(\xi, \eta)
 \end{aligned} \tag{A.11}$$

Considering the far field approximation for the transmitted pressure and normal incident waves ( $\theta_i = 0$ ), the equation of motion becomes

$$\begin{aligned}
 \left[ D\pi^4 \left( \frac{1}{l_x^2} + 2\frac{1}{l_x^2 l_y^2} + \frac{1}{l_y^2} \right) - \Omega^2 \rho h \right] W_1(\xi, \eta) = \\
 2P_i + \frac{\Omega^2 \rho_0}{\pi r} e^{-jkr} I_{\xi' \eta'}
 \end{aligned} \tag{A.12}$$

where  $I_{\xi' \eta'}$  is the double integral on the surface of the plate

$$I_{\xi' \eta'} = \int_{-l_x/2}^{l_x/2} \int_{-l_y/2}^{l_y/2} W_1(\xi', \eta') e^{jk(\xi' \sin \theta \cos \phi + \eta' \sin \theta \sin \phi)} d\eta' d\xi' \tag{A.13}$$

and the local coordinates  $\xi' = \xi - \frac{l_x}{2}$ ,  $\eta' = \eta - \frac{l_y}{2}$ . For  $\xi'$ ,  $\eta'$  the shape function from Eq.(19) becomes

$$W_1(\xi', \eta') = C_1 \cos\left(\frac{\pi \xi'}{l_x}\right) \cos\left(\frac{\pi \eta'}{l_y}\right) \tag{A.14}$$

The surface integral is then calculated as

$$I_{\xi' \eta'} = C_1 I_{\xi \eta} \tag{A.15}$$

where

$$I_{\xi \eta} = 4\pi^2 l_x l_y \frac{\cos(\sigma_x)}{(l_x k \sin \theta \cos \phi)^2 - \pi^2} \frac{\cos(\sigma_y)}{(l_y k \sin \theta \sin \phi)^2 - \pi^2} \tag{A.16}$$

and  $\sigma_x$ ,  $\sigma_y$  are the same as in Eq.(A.8). Solving (19) for  $C_1$ , the surface integral can be written as

$$I_{\xi' \eta'} = \frac{W_1(\xi, \eta)}{\sin\left(\frac{\pi \xi}{l_x}\right) \sin\left(\frac{\pi \eta}{l_y}\right)} I_{\xi \eta} \tag{A.17}$$

Substituting to equation (A.12), multiplying with  $W_1$  and integrating over the panel surface gives

$$\begin{aligned} \int_0^{l_x} \int_0^{l_y} \left[ D\pi^4 \left( \frac{1}{l_x^2} + \frac{1}{l_y^2} \right)^2 - \frac{\Omega^2 \rho_0 e^{-j\kappa r}}{\pi r} \frac{I_{\xi\eta}(\theta, \phi)}{\sin(\frac{\pi\xi}{l_x}) \sin(\frac{\pi\eta}{l_y})} - \Omega^2 \rho h \right] \dots \\ \dots W_1^2(\xi, \eta) d\eta d\xi = \int_0^{l_x} \int_0^{l_y} 2P_i W_1(\xi, \eta) d\eta d\xi \end{aligned} \quad (\text{A.18})$$

and inserting  $\omega_1$  from Eq.(22) leads to

$$\begin{aligned} \rho h(\omega_1^2 - \Omega^2) \int_0^{l_x} \int_0^{l_y} W_1^2(\xi, \eta) d\eta d\xi = \\ = \left[ 2P_i + \frac{\Omega^2 \rho_0}{\pi} \frac{e^{-j\kappa r}}{r} C_1 I_{\xi\eta}(\theta, \phi) \right] \int_0^{l_x} \int_0^{l_y} W_1(\xi, \eta) d\eta d\xi \end{aligned} \quad (\text{A.19})$$

The two integrals are calculated as

$$\int_0^{l_x} \int_0^{l_y} W_1^2(\xi, \eta) d\eta d\xi = \frac{l_x l_y}{4} C_1^2 \quad (\text{A.20})$$

$$\int_0^{l_x} \int_0^{l_y} W_1(\xi, \eta) d\eta d\xi = \frac{4l_x l_y}{\pi^2} C_1 \quad (\text{A.21})$$

Substituting in Eq.(A.19) and solving the quadratic equation for  $C_1$  leads to:

$$C_1 = \frac{8P_i}{\pi^2 [\rho_0 h \frac{(\omega_1^2 - \Omega^2)}{4} - \frac{4\Omega^2 \rho_0}{\pi^3} \frac{e^{-j\kappa r}}{r} I_{\xi\eta}(\theta, \phi)]} = \frac{32P_i + p_t}{\pi^2 \rho h(\omega_1^2 - \Omega^2)} \quad (\text{A.22})$$

Therefore, substituting in Eq.(A.5) for the transmitted pressure, comes:

$$\begin{aligned} p_t(\mathbf{r}, t) &= \frac{\Omega^2 \rho_0 e^{-j\kappa r}}{2\pi r} C_1 I_{\xi\eta}(\theta, \phi) e^{j\Omega t} \\ \Rightarrow p_t(\mathbf{r}, t) &= \frac{16\Omega^2 \rho_0 I_{\xi\eta}(\theta, \phi) P_i}{r [\pi^3 \rho h(\omega_1^2 - \Omega^2) - 16\Omega^2 \rho_0 \frac{e^{-j\kappa r}}{r}]} e^{-j\kappa r} e^{j\Omega t} \end{aligned} \quad (\text{A.23})$$

The transmitted intensity  $I_t$  is calculated from Eq.(9) as

$$I_t(r, \theta, \phi) = \frac{1}{2\rho_0 c_0 r^2} \left( \frac{16\omega^2 |I_{\xi\eta}| P_i}{|\pi^3 \rho h(\omega_1^2 - \Omega^2) - 16\Omega^2 \rho_0 \frac{e^{-j\kappa r}}{r}|} \right)^2 \quad (\text{A.24})$$

and the transmitted power comes from Eq.(10) as

$$\Pi_t = \frac{P_i^2}{2\rho_0 c_0} \frac{(16\Omega^2 \rho_0)^2}{|\pi^3 \rho h(\omega_1^2 - \Omega^2) - 16\Omega^2 \rho_0 \frac{e^{-j\kappa r}}{r}|^2} I_{\theta\phi} \quad (\text{A.25})$$

where  $I_{\theta\phi}$  is the double integral over a hemispheric surface in the receiver domain

$$I_{\theta\phi} = \int_0^{2\pi} \int_0^{\pi/2} |I_{\xi\eta}|^2 \sin \theta d\theta d\phi \quad (\text{A.26})$$

and  $I_{\xi\eta}$  is defined in Eq.(A.16).

### A.3.1 Lumped Parameter Model

Let us rewrite the transverse displacement as

$$w(\xi, \eta, t) = \sin\left(\frac{\pi\xi}{l_x}\right) \sin\left(\frac{\pi\eta}{l_y}\right) q(t) \quad (\text{A.27})$$

where

$$q(t) = C_1 e^{j\Omega t} \quad (\text{A.28})$$

The kinetic energy of the system is defined as

$$\begin{aligned} T &= \frac{1}{2} \rho h \int_0^{l_x} \int_0^{l_y} \left( \frac{\partial w}{\partial t} \right)^2 d\xi d\eta \\ &= \frac{1}{2} \frac{\rho h l_x l_y}{4} \dot{q}^2(t) \\ &= \frac{1}{2} m_1^* \dot{q}^2(t) \end{aligned} \quad (\text{A.29})$$

and the potential energy as

$$\begin{aligned} U &= \frac{1}{2} D \int_0^{l_x} \int_0^{l_y} \left[ \nabla^2 w(\xi, \eta, t) \right]^2 d\xi d\eta \\ &= \frac{1}{2} \frac{D \pi^4 l_x l_y}{4} \left( \frac{1}{l_x^2} + \frac{1}{l_y^2} \right)^2 q^2(t) \\ &= \frac{1}{2} k_1^* q^2(t) \end{aligned} \quad (\text{A.30})$$

where  $m_1^*$  and  $k_1^*$  are the generalized mass and stiffness of the fundamental, 1<sup>st</sup> mode.

The equation of motion of the equivalent SDOF model is

$$m_1^* \ddot{q} + k_1^* q = f^*(t) \quad (\text{A.31})$$

where the generalized excitation, considering only the blocked pressure, comes as

$$f^*(t) = 2p_i \int_0^{l_x} \int_0^{l_y} W_1(\xi, \eta) d\xi d\eta = \frac{8P_i l_x l_y}{\pi^2} e^{j\Omega t} \quad (\text{A.32})$$

Consequently, by substituting in Eq.(A.31), and since  $k_1^* = m_1^* \omega_1^2$ , the factor  $C_1$  is calculated as:

$$C_1 = \frac{8P_i l_x l_y}{\pi^2} \frac{1}{m_1^* (\omega_1^2 - \Omega^2)} \quad (\text{A.33})$$

## REFERENCES

- [1] Vigran E T. *Building Acoustics*. Taylor & Francis Limited, 2019, 2019.
- [2] Norén-Cosgriff K, Løvholt F, Brekke A et al. Countermeasures against noise and vibrations in lightweight wooden buildings caused by outdoor sources with strong low frequency components. *Noise Control Engineering Journal* 2016; 64: 737–752.

- [3] Løvholt F, Madshus C and Norén-Cosgriff K. Analysis of low frequency sound and sound induced vibration in a norwegian wooden building. *Noise Control Engineering Journal* 2011; 59(4): 383–396.
- [4] ISO 717, acoustics — rating of sound insulation in buildings and of building elements. Standard.
- [5] ISO 10140, acoustics — laboratory measurement of sound insulation of building elements. Standard.
- [6] ISO 15186, acoustics — measurement of sound insulation in buildings and of building elements using sound intensity. Standard.
- [7] Ayr U, Martellotta F and Rospi G. A method for the low frequency qualification of reverberation test rooms using a validated finite element model. *Applied Acoustics* 2017; 116: 33–42. DOI:<https://doi.org/10.1016/j.apacoust.2016.09.001>. URL <https://www.sciencedirect.com/science/article/pii/S0003682X16302663>.
- [8] Løvholt F, Norén-Cosgriff K, Madshus C et al. Simulating low frequency sound transmission through walls and windows by a two-way coupled fluid structure interaction model. *Journal of Sound and Vibration* 2017; 396: 203 – 216. DOI:<https://doi.org/10.1016/j.jsv.2017.02.026>.
- [9] Aretz M and Vorländer M. Efficient modelling of absorbing boundaries in room acoustic fe simulations. *Acta Acustica United With Acustica* 2010; 96: 1042–1050.
- [10] Vorländer M. Computer simulations in room acoustics: Concepts and uncertainties. *The Journal of the Acoustical Society of America* 2013; 133(3): 1203–1213. DOI:10.1121/1.4788978.
- [11] Beranek LL and Vér IL. Noise and vibration control engineering: Principles and applications. John Wiley & Sons, New York.
- [12] Cremer L, Heckl M and Petersson BA. *Structure-borne sound: structural vibrations and sound radiation at audio frequencies*. Springer Science & Business Media, 2005.
- [13] Ordubadi A and Lyon RH. Effect of orthotropy on the sound transmission through plywood panels. *The Journal of the Acoustical Society of America* 1979; 65(1): 133–139. DOI:10.1121/1.382255.
- [14] London A. Transmission of reverberant sound through double walls. *The Journal of the Acoustical Society of America* 1950; 22(2): 270–279. DOI:10.1121/1.1906601.
- [15] Callister J, George A and Freeman G. An empirical scheme to predict the sound transmission loss of single-thickness panels. *Journal of Sound and Vibration* 1999; 222(1): 145 – 151. DOI:<https://doi.org/10.1006/jsvi.1998.1624>.
- [16] Pellicier A and Trompette N. A review of analytical methods, based on the wave approach, to compute partitions transmission loss. *Applied Acoustics* 2007; 68(10): 1192 – 1212. DOI:<https://doi.org/10.1016/j.apacoust.2006.06.010>.
- [17] Kim YH. *Sound propagation: an impedance based approach*. John Wiley & Sons, 2010.

- [18] Paradeisiotis A, Kalderon M, Antoniadis I et al. Acoustic Performance Evaluation of a panel utilizing negative stiffness mounting for low frequency noise control. In *Proceedings of EURODYN 2020*. Athens, Greece, 23–26 November: EASD Procedia, pp. 4093–4110.
- [19] Cowan AJ. *Sound Transmission Loss of Composite Sandwich Panels*. PhD Thesis, Department of Mechanical Engineering, University of Canterbury, 2013.
- [20] Rayleigh JWSB. *The Theory of Sound*, volume 1. Macmillan, 1894, 1896. DOI:10.1017/CBO9781139058087.
- [21] Roussos L. Noise transmission loss of a rectangular plate in an infinite baffle. *The Journal of the Acoustical Society of America* 1985; 75. DOI:10.1121/1.2021367.
- [22] Yang Y, Lam NTK and Zhang L. Estimation of response of plate structure subject to low velocity impact by a solid object. *International Journal of Structural Stability and Dynamics* 2012; 12(06): 1250053.
- [23] Koblar D and Boltežar M. Evaluation of the frequency-dependent young's modulus and damping factor of rubber from experiment and their implementation in a finite-element analysis. *Experimental Techniques* 2013; .
- [24] Carfagni M, Lenzi E and Pierini M. The loss factor as a measure of mechanical damping. In *Proc. SPIE, Proceedings of the 16th International Modal Analysis Conference*, volume 3243. p. 580.
- [25] Smith M. *ABAQUS/Standard User's Manual, Version 6.9*. United States: Dassault Systèmes Simulia Corp, 2009.
- [26] Marburg S. Six boundary elements per wavelength: Is that enough? *Journal of Computational Acoustics* 2002; 10(01): 25–51. DOI:10.1142/S0218396X02001401.

## INVESTIGATION OF A METHODOLOGY FOR DESCRIBING FAN BLADE FLUTTER LIMITATIONS INDUCED BY NON-LINEAR FRICTION AT BLADE ROOTS

Nicolas Ombret<sup>1,2,3</sup>, Maxime De Pret<sup>2</sup>, Alain Dugeai<sup>3</sup>, Fabrice Thouverez<sup>1</sup>, Laurent  
Blanc<sup>1</sup> and Thomas Berthelon<sup>3</sup>

<sup>1</sup>École Centrale de Lyon, LTDS UMR 5513  
69130 Ecully France  
e-mail: {nicolas.ombret,fabrice.thouverez,laurent.blanc}@ec-lyon.fr

<sup>2</sup>Safran Aircraft Engines  
77550 Moissy-Cramayel France  
e-mail: {nicolas.ombret,maxime.de-pret}@safrangroup.com

<sup>3</sup>ONERA - The French Aerospace Lab  
92320 Châtillon France  
e-mail: {nicolas.ombret-ext,alain.dugeai,thomas.berthelon}@onera.fr

**Keywords:** Fan flutter, acoustic reflection, Limit Cycle Oscillation, friction damping, nonlinear complex modes.

**Abstract.** *Fan Blade Flutter is an aeroelastic instability which may occur during the operation of a jet engine, depending on the working conditions of the fan stage. It finds its origins in some various mechanisms, including the impact of the environment of the fan stage, which may play an important role in the stability limits due to acoustic effects. If not properly taken into account, flutter can lead to an anticipated ruin of the fan stage as the fluid keeps on giving energy to the structure. However, nonlinear phenomena may appear at some high vibratory amplitude of the blades, resulting in energy dissipation of the aeroelastic system. Blade roots friction is an example of such a case : by dry-friction dissipation at blade roots, a limitation of the vibratory amplitude may be reached, the so-called Limit Cycle Oscillations (LCO), within the unstable regions of the operating domain predicted with a usual linear structural modelling. By taking these nonlinear effects into account, it is then possible to define more precisely the stability limits of the fan stage. In this paper, we describe a methodology to predict LCO induced by blade roots friction, including acoustic effects on stability. First, assuming a linear behaviour of the structure, the stability limits of the fan stage are described using the cyclic symmetry hypothesis and Computational Fluid Dynamics (CFD). Acoustics effects are taken into account by including the fan inlet environment in the numerical model. Then, a nonlinear structural model of the blade is used to compute nonlinear complex modes in order to check for the presence of a LCO. To do so, a reduced model of the fluid response to the blade movement is used. To sum up, this work intends to establish a methodology to be used in an industrial context for the analysis of the nonlinear stability of the fan stage, including LCO phenomena.*



## 1 INTRODUCTION

Aeroelastic stability of fan blades has been studied for decades. It has become more and more important in the recent years to properly predict when this phenomenon does or does not occur, as the reduction of dry mass in jet engines remains one of the toughest objectives for manufacturers to achieve towards less consuming engines to face environmental issues. Moreover, the current trend for manufacturers which consists in developing designs with greater bypass ratio (hence more flexible blades) and shorter inlets allows fluid-structure interactions to have greater effects on blades movement and potentially on its lifecycle. However, physical mechanisms at the origin of fan blade flutter are still not fully understood despite the research done about it and depends on the operating point of the fan stage, as shown in [1].

In this work, we focus on flutter occurring at 75%-80% speed range near stall boundaries. Various experimental and numerical works relate on the mechanisms causing fan blade flutter in this working range, and two major contributions at its origins have been highlighted. The first one refers to a strong interaction between the shock between tip leading edge and mid-chord of the suction side of the blade and the boundary layer around it [2, 3, 4, 5, 6]. It appears that due to blades vibration and depending on the Inter Blade Phase Angle (IBPA), the shock position may oscillate onto the suction side and be responsible of static pressure fluctuations. In addition, the shock interacts with the boundary layer on the blade surface which may detach behind it. For a periodic motion of the blade, it results in positive (unstable) and negative (stable) aerodynamic work areas onto the blade. This may lead to flutter if the overall aerodynamic work on the blade is positive, meaning that the fluid transfers its energy to the structure. The second mechanism contributing to fan blade flutter in the operating range of interest is due to acoustic interactions between the fan stage and the intake of the engine. Considering a slowly varying intake diameter, acoustic waves may propagate through the intake if the frequency of the perturbation is greater than the characteristic frequency of acoustic propagation  $\omega_{cut-on}$  called *cut-on* frequency. Then, if the fan stage blade generates a perturbation at a frequency  $\omega$  greater than  $\omega_{cut-on}$ , an acoustic wave will propagate through the intake [7]. A reflected wave will occur at the opening of the intake and go back to the fan stage. The phase difference between the wave generated by the fan stage and the one reflected on the intake at the axial position of the stage may cause drastic variation of flutter stability for very narrow operating ranges, yielding the term *flutter bite* [8, 9, 10].

Usually, a linear approach of the structure is sufficient to assess the fan stage aeroelastic stability. Two approaches may be used to do so, as well explained in [11] : the first one consists in neglecting the effects of aerodynamics on the fan stage dynamics and then to assess stability by studying aeroelastic stability of the structural modes of the fan with harmonic motion ; the second one consists in using strong coupling (partitionned or monolithic approaches) to take into account the effects of the fluid onto the structure dynamics. However, if it is sufficient to consider a linear structure to assess stability limits, it is possible to find stable solutions of the aeroelastic system beyond the stability limits predicted with a linear structure by taking into account nonlinear effects. In this study, we are interested in nonlinear effects due to blade-disk dry friction at blade roots. First works about flutter limitation by dry friction between the blade and the disk seem to be attributed to Sinha and Griffin [12, 13]. They showed on small degree of freedom systems that in spite of the presence of negative aerodynamic damping, stable and unstable periodic solutions may arise. Since, many works about this subject have been made and new usefull tools have been developped. As we are dealing with nonlinear autonomous systems, there have been many efforts made in order to define the nonlinear dynamics of such systems by

analogy with the linear modes describing the dynamics of autonomous linear systems. Hence, the notion of *nonlinear normal modes* has been established, describing the dynamics of conservative autonomous nonlinear systems [14, 15] and then extended to nonconservative systems [16]. Other definitions have been suggested in more recent years and are particularly suited to dissipative systems like the one we will study in this paper. Some of these methods are based on frequency approach like the Harmonic Balance Method (HBM) [17, 18]. Decoupled approaches have allowed to find Limit Cycle Oscillations (LCO) of the structure by using the HBM procedure, while modelling aerodynamic effects from Computational Fluid Dynamics (CFD) calculations [19, 20]. More recently, a fully coupled method in the frequency domain has been established [21] in order to find LCO by using harmonic formulation in both flow and structure models, and iterating in a fixed point loop between the two physics.

In this study, a methodology for predicting LCO induced by dry friction of a fluttering rotor blade will be investigated by the means of *nonlinear complex modes* [17]. To do so, a decoupled approach will be used. First, the aeroelastic stability of a rotating fan from a typical modern civil engine will be assessed while considering a linear structure. From those results, a simple model of the acoustic effects on flutter stability will be built and used on a phenomenological model representing a blade with nonlinear dry friction effects at its roots. The purpose of this study is to establish a methodology based on nonlinear complex modes that can be applied to the analysis of an industrial fan stage.

## 2 AEROELASTIC STABILITY WITHIN THE SCOPE OF A LINEAR STRUCTURE

### 2.1 Case modeling and flow solver

For this study, a fan model (18 blades) provided by Safran Aircraft Engines has been used with its intake in order to take account of acoustic interactions between these two elements. Figure 1 shows an illustration of this model. Experimental data showed that the fan stage used with this intake became unstable before surge was reached at 75% speed.

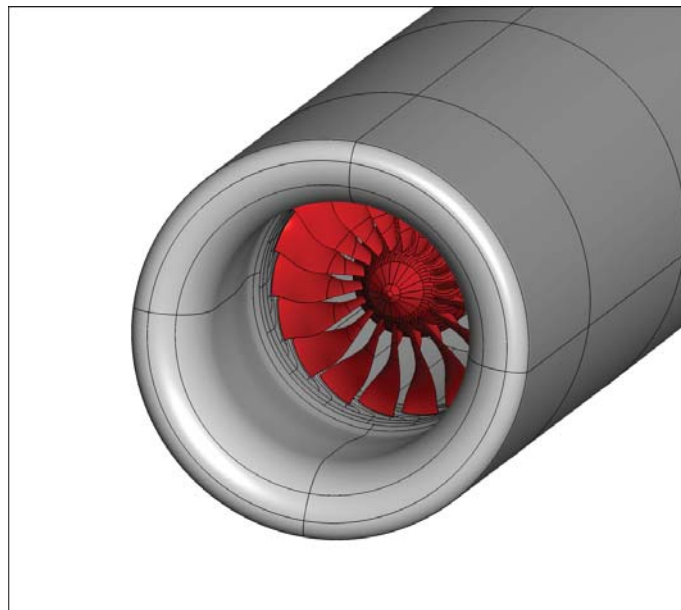


Figure 1: Fan stage model with its intake used for CFD calculations

The mesh used for this model has to be sufficiently dense in the intake to have a good representation of acoustic waves. However, it is of a higher interest to keep the mesh coarse outside of the intake, where a precise representation of the aerodynamic is not required. As a matter of fact, due to the lack of absorbant acoustic boundary conditions, a too high density grid near the external boundaries would lead to unwanted spurious numerical acoustic reflections, which would not have physical meanings. Hence, a coarsening of the mesh has been put in place from the intake to the outside boundaries of the mesh until eventual acoustic waves coming from the intake are sufficiently dissipated by the spatial scheme. Figure 2 shows the boundaries of the mesh and highlights the ratio between the external characteristic dimension  $D$  of the mesh and the intake diameter  $d$  midway between the fan and the intake beginning. This ratio has been set to 30. Since there is no Outlet Guide Vanes (OGV) in the model, same considerations have to be taken for both fan primary and secondary outlets. Mesh coarsening has also been used for these parts of the model.

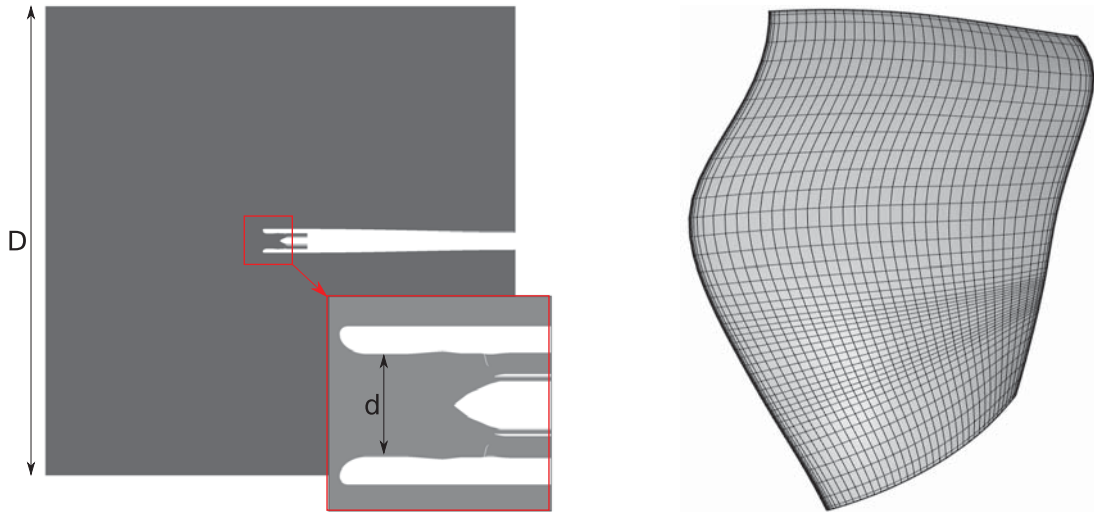


Figure 2: External mesh boundaries on the left, blade mesh on the right

To build the mesh used in this model, the intake and the fan have been meshed separately with two different meshing tools : *ICEM* for the intake and *Autogrid* for the fan. Hence, we are dealing with a structured mesh of the full model containing about 11M cells, with about 3M cells for the intake and 410000 cells per blade passage.

The solver used to perform both steady and unsteady analysis is the finite-volume *elsA* software developed at Onera [22, 23], which solves in our case 3D compressible (U)-RANS equations. Roe flux difference splitting scheme has been used, with the two equations turbulence model  $k - l$  of Smith. Non reflective boundary conditions have been set upon the external boundaries of the domain with atmospheric sea-level conditions. These conditions are efficient to suppress steady reflections, but are not enough when dealing with unsteady acoustic waves, which justifies the external mesh coarsening. The outflow boundary conditions in primary and secondary outlets is based on radial equilibrium equation for static pressure and allows to select the operating point on the constant 75% speed of the fan characteristic.

As mentionned earlier, the global mesh is built from two meshes that have been merged : the fan, which rotates at 75% speed, and the intake which does not move, both in the fixed frame. Therefore, the stator/rotor interface has to be treated to maintain the flow continuity. While performing steady computations, a mixing plane condition is used, transferring azimuthal

averages of the flow quantities from the intake mesh to the fan one. When dealing with unsteady computations, the mixing plane is replaced with an unsteady interface boundary condition so that acoustic waves may propagate from the fan mesh to the intake mesh. This condition take into account the relative positions of the meshes at the interface at each time step to transfert the information from a cell to its corresponding ones on the other side of the interface. Spatial interpolation is performed when there is no perfect match between the facets of the interface.

## 2.2 Aeroelastic model

As mentioned in the introduction, two approaches may be used to assess the aeroelastic stability of the fan stage. The first one consists in neglecting the impact of the flow on the structure dynamics for the evaluation of aerodynamic forces due to vibrations, while the second one consists in a strong aeroelastic coupling. The approach to be used depends on the case, as the flow may have some impact on the structure dynamics [11]. Even if the second approach may be more precise, it may be computationally expensive to apply, as the first one already gives good insights on the flutter stability while lowering the computationnal costs. In this study, the first approach has been chosen. Strong coupling of the fluid and the structure will be adressed in a future study.

It is assumed for now that the structure is linear and that the vibration is small enough so that aerodynamic forces may be linearized regarding structure movement and velocity. Thus, the aeroelastic stability of the fan may be assessed by considering the aeroelastic stability of each structural eigenmodes separately. Let us consider the equation governing the movement of the linear structure (nonlinear effects due to friction at blade root will be adressed later in this study) :

$$\mathbf{M}\ddot{\mathbf{x}} + \mathbf{C}\dot{\mathbf{x}} + \mathbf{K}\mathbf{x} = \mathbf{f}_{aero}(\mathbf{x}, \dot{\mathbf{x}}) \quad (1)$$

Solving the eigenvalue problem while considering cyclic symmetry hypothesis for the structure leads to expressing the structure movement in terms of complex modes  $\Phi$  representing rotating waves. It is then possible to express the structure movement in the modal basis  $\Phi$  :

$$\mathbf{x} = \Phi \mathbf{q} \quad (2)$$

By substituing (2) into (1), one can describe the motion of the structure in  $\Phi$  with the complex generalized coordinates  $\mathbf{q}$  [24]. If considering one eigenmode, this leads to the following scalar differential equation :

$$\mu\ddot{q} + \beta\dot{q} + \gamma q = g_{aero}(q, \dot{q}) \quad (3)$$

where  $\mu$ ,  $\beta$ ,  $\gamma$  and  $g_{aero}$  are respectively the generalized mass, generalized dissipation, generalized stiffness and generalized aerodynamic forces.

As we are dealing with stability issues, we consider that the structure is autonomous (*i.e* there is no external forcing and initial conditions). Moreover, we consider that the movement of the structure is small enough so that the generalized aerodynamic forces may be written as a linear function of the structure movement and velocity (respectively represented by  $q$  and  $\dot{q}$ ). Hence, (3) may be written as :

$$\mu\ddot{q} + \beta\dot{q} + \gamma q = A q + B \dot{q} \quad (4)$$

where :

$$g_{aero}(q, \dot{q}) = A q + B \dot{q} ; A, B \in \mathbb{C}$$

Considering harmonic motion ( $q(t) = q_0 e^{j\omega_0 t}$ ), we have :

$$\begin{aligned}
 g_{aero} &= (A + j\omega_0 B) q \\
 &= \left( \left( \operatorname{Re}(A) - \omega_0 \operatorname{Im}(B) \right) + j\omega_0 \left( \frac{\operatorname{Im}(A)}{\omega_0} + \operatorname{Re}(B) \right) \right) q \\
 &= (\gamma_{aero} + j\omega_0 \beta_{aero}) q
 \end{aligned} \tag{5}$$

In (5),  $\gamma_{aero}$  and  $\beta_{aero}$  may respectively be seen as aerodynamic stiffness and aerodynamic dissipation.

The generalized structural dissipation  $\beta$  may be hard to evaluate. Usually, it is convenient to neglect it in order to assess the flutter stability as the approach remains conservative (*i.e* stability limits will be reached sooner than in a more realistic damped system). Hence,  $\beta$  will be omitted in this section. If  $\bar{q}$  denotes the conjugate of  $q$ , the aerodynamic work on one period of harmonic motion may be written as :

$$\begin{aligned}
 W &= \operatorname{Re} \left( \int_0^{\frac{2\pi}{\omega_0}} g_{aero} \bar{q} dt \right) \\
 &= \operatorname{Re} \left( \int_0^{\frac{2\pi}{\omega_0}} (A + j\omega_0 B) q_0 e^{j\omega_0 t} (-j\omega_0 \bar{q}_0 e^{-j\omega_0 t}) dt \right) \\
 &= 2\pi\omega_0 \beta_{aero} |q_0|^2
 \end{aligned} \tag{6}$$

From (4), we may express  $\beta_{aero}$  as an aerodynamic damping term  $\xi_{aero}$  :

$$\xi_{aero} = -\frac{\beta_{aero}}{2\mu\omega_0} = -\frac{W}{4\pi\mu\omega_0^2 |q_0|^2} \tag{7}$$

Flutter occurs when  $\xi_{aero}$  is below zero, meaning that the fluid gives energy to the blade for a blade movement on the considered mode.

### 2.3 Stability computations

Experimental results showed that at 75% speed, the most unstable mode was the 1F2D for the considered fan stage coupled with its intake. Hence, stability analysis has been performed for this mode. In this conditions, acoustic interactions between the fan and the intake are expected as the eigenfrequency of the mode is greater than the cut-on frequency of some acoustic modes. Figure 3 shows a representation of this mode.

In order to analyse the aeroelastic stability of the selected mode, unsteady aerodynamic simulations with prescribed harmonic motion of the row following its 1F2D vibration mode at its eigenfrequency are performed. The simulation are carried out using the Dual Time Stepping (DTS) approach, with 20 dual iterations between each physical timesteps and 192 timesteps per period of vibration. The forward mode is selected (same rotation direction as the one of the fan) to get the largest frequency of perturbation due to vibration in the fixed frame. In these conditions, intake fan acoustic interactions are expected to occur. As a reminder, the perturbation frequency  $f$  generated by the fan stage is  $f = f_{1F2D} + \Omega \times \text{ND}$  ( $\Omega$  is the rotation frequency of the fan and ND the nodal diameter of the forward mode considered). It has to be greater than the cut-on frequency  $f_{cut-on}$  so that acoustic waves can propagate through the intake represented as a cylindrical duct.





Figure 3: Mode shape for 1F2D

Figure 4 shows the stability analysis results for the 1F2D forward mode, where the evolution of  $\xi_{aero}$  is plotted against the normalized mass flow. The red star represents the stability limits measured during experiments. Stability limit is detected sooner with the numerical model than during experiments, as it was expected since the mechanical damping has been neglected. The approach remains conservative (*i.e* numerical results do not predict a stable behaviour of the fan on an experimental unstable operating point).

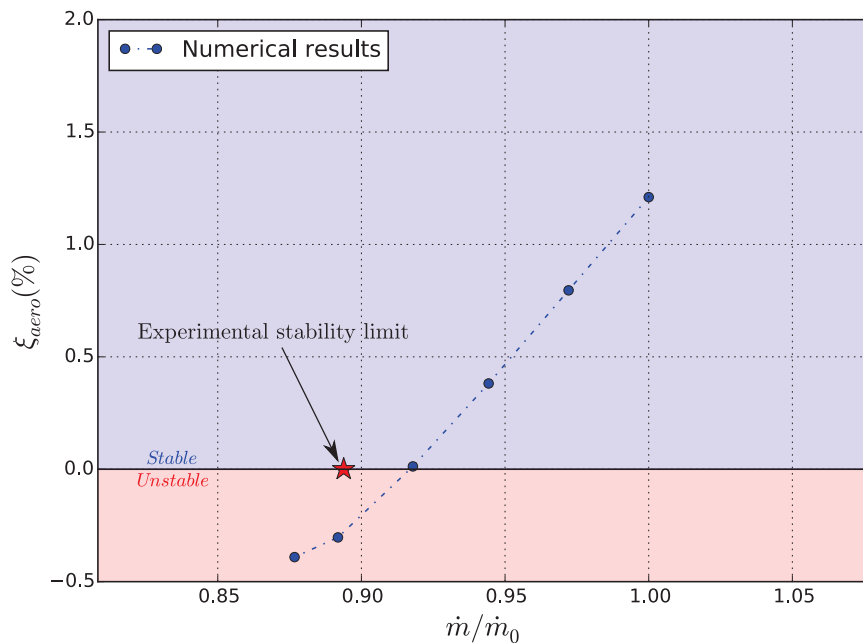


Figure 4: Evolution of  $\xi_{aero}$  on the constant 75% speed characteristic

For the last period of vibration of the fan, a Discrete Fourier Transform (DFT) has been performed on acoustic variables of interest (density, velocities, static pressure) in the whole domain to check for the presence of acoustic waves in the intake. Results of the DFT of unsteady



static pressure are displayed in Figure 5. The amplitude representation of static pressure shows a peak in the middle of the intake, which highlights the presence of acoustic interferences between the acoustic waves generated by the vibrating fan and the ones coming from the reflection at the inlet level. The phase reveals a two diameter perturbation in the intake, which was expected as the studied structural mode is a two diameter as well.

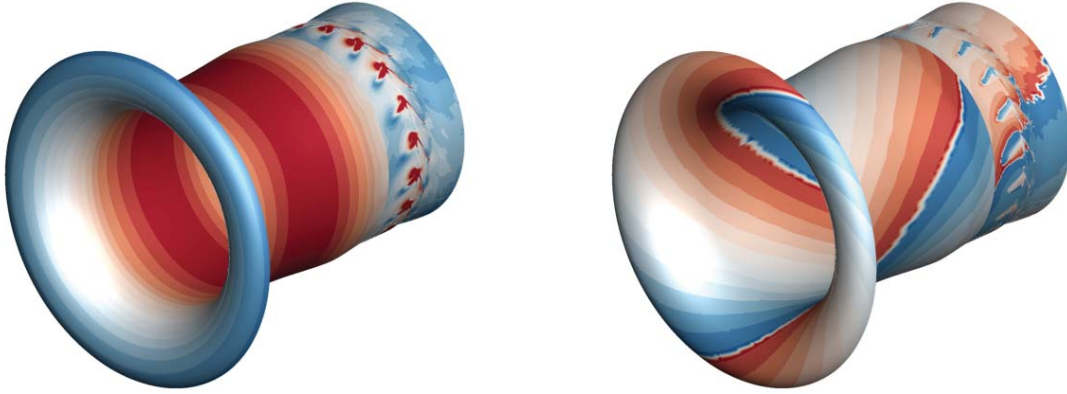


Figure 5: Discrete Fourier Transform of the unsteady static pressure in the intake : amplitude on the left, phase on the right

Hence, for mode 1F2D at 75% speed, acoustic interactions between the fan and the intake may be observed. The impact of this interaction on flutter stability depends on the reflection rate and the phase lag between emitted and reflected acoustic waves, as mentioned in [9, 10]. Both are functions of the excitation frequency as showed in Bontemps et al. [25]. However, in a context of nonlinear dynamics induced by dry friction, free vibration frequencies of the structure may vary depending on its amplitude of vibration. It is then of interest to have a measure of the sensitivity of  $\xi_{aero}$  against the vibration frequency of the blade to build a model of aerodynamic forces that takes into account acoustic effects on stability.

From the operating point at  $\frac{\dot{m}}{\dot{m}_0} = 0.972$  on the constant 75% speed characteristic, a set of computations with different values of excitation frequency has been made, whose results are displayed in Figure 6.

It can be seen from this figure that excitation frequency has a first order impact on stability for the considered operating point. A sharp drop in stability appears around  $0.87 - 0.9f_{1F2D}$ , which corresponds to the excitation frequency  $f$  equaling the cut-on frequency  $f_{cut-on}$  of the activated acoustic mode in the duct. According to Bontemps et al. [25], this leads to a reflection rate near 100% and quick variations of the phase lag between emitted and reflected acoustic waves onto the fan blades : in other terms, this is where one may encounter the greatest variation of flutter stability due to acoustic effects and frequency shifts. Results displayed in Figure 6 will be used in the next section as a simplified model of acoustic effects on blade stability. We are now going to introduce the phenomenological nonlinear model used for computing LCO.

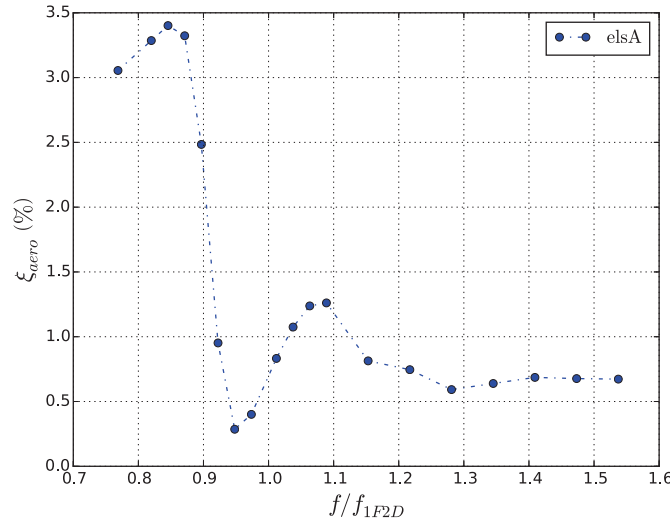


Figure 6: Evolution of  $\xi_{aero}$  against vibration frequency for 1F2D shape mode

### 3 NONLINEAR APPROACH FOR FINDING LIMIT CYCLE OSCILLATIONS

#### 3.1 Phenomenological model

The phenomenological model that has been used to represent a blade with dry friction at its root is represented in Figure 7. It is made of three distinct parts : the blade, its root, and the disk. Dry friction nonlinearities are considered between the blade root and the disk. Relative motions authorized between the different parts are rotations. Let us define  $X, Y$  and  $Z$  the axis of the rotating frame. We assume that there is no rotation of the parts around the  $Y$  axis. Hence, we define :

- $\theta_{1,x}$  as the angle of rotation of the disk around  $X$  ;
- $\theta_{1,z}$  as the angle of rotation of the disk around  $Z$  ;
- $\theta_{2,x}$  as the angle between  $Z_{root}$  (axis of the local frame attached to the root) and  $Z$  ;
- $\theta_{2,z}$  as the angle of rotation of the blade root around  $Z_{root}$  ;
- $\theta_{3,x}$  as the bending angle between  $Z_{root}$  and  $Z_{blade}$  (axis of the local frame attached to the blade) ;
- $\theta_{3,z}$  as the angle of rotation of the blade around  $Z_{blade}$ .

Moreover, we consider that the section of the blade containing its center of gravity is at a height  $H_G$  of its root ( $H_G \gg e$  where  $e$  is the characteristic dimension of the root thickness). Lastly, we consider that the center of gravity of the blade is not aligned with its center of torsion, but is located at a distance  $a$  of it. In that way, when we will consider the modes of the blade with sticking conditions between the blade root and the disk, we will not have pure plunging or twisting modes, but modes with the contributions of those two pure motions.

We are now going to derive the equations of motion of the blade-root-disk system using lagrangian formalism. Some assumptions need to be made first concerning the movement of the

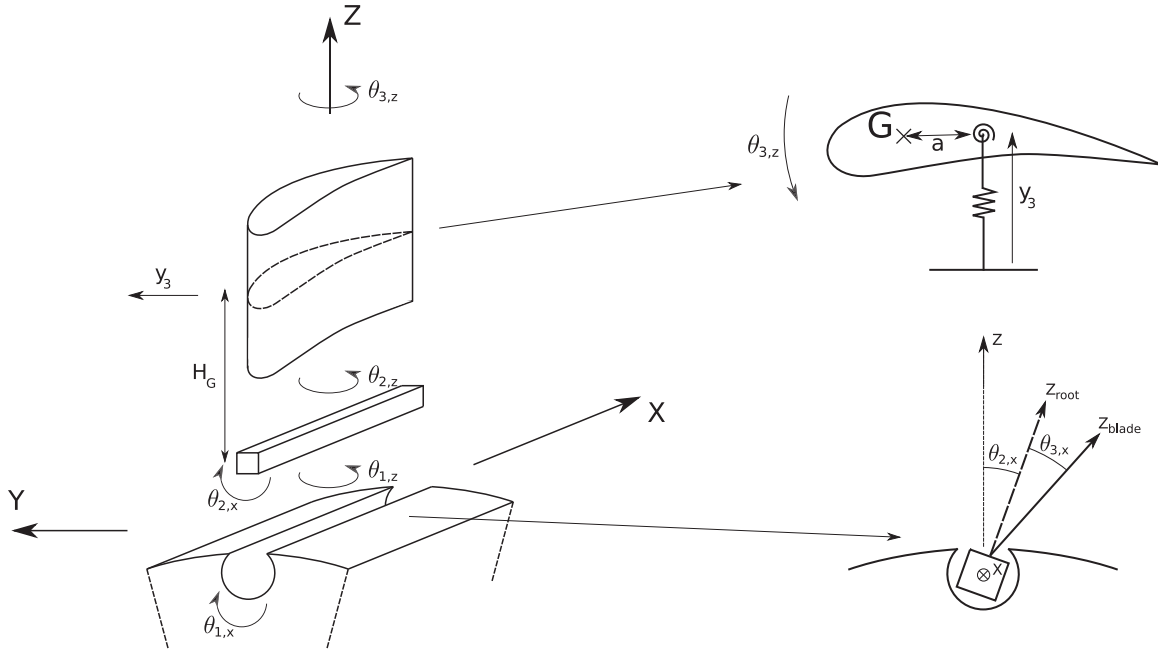


Figure 7: Phenomenological model of a bending-torsion blade with dry friction at blade root

system. We consider that the disk is motionless in the rotating frame due to its high stiffness (in comparison to those of the root and the blade). Moreover, the root is supposed to rotate only along the  $X$  axis due to its high longitudinal dimension in comparison to its thickness. Hence, we have  $\theta_{1,x} = \theta_{1,z} = \theta_{2,z} = 0$ . The system dynamics is then described by the three variables left :  $\theta_{2,x}, \theta_{3,x}, \theta_{3,z}$ . Let us define the variable  $q$  as the vector containing the generalized coordinates of the system  $q = (\theta_{3,x}, \theta_{3,z}, \theta_{2,x})^T$ . We consider at last that we have small perturbations (*i.e*  $\theta \ll 1$ ). For now, the system is assumed to be in vacuum. The Lagrange equations are :

$$\frac{d}{dt} \frac{\partial \mathcal{L}}{\partial \dot{q}} - \frac{\partial \mathcal{L}}{\partial q} = \mathcal{Q} \quad (8)$$

where  $\mathcal{Q}$  is the generalized non conservative torque (here, due to blade root friction), and :

$$\mathcal{L} = \mathcal{T} - \mathcal{V}$$

In these equations,  $\mathcal{T}$  is the kinetic energy, while  $\mathcal{V}$  is the potential energy of the system. Let us denote respectively (1), (2) and (3) the disk, the root and the blade. Then, we have :

$$\mathcal{T} = \mathcal{T}_2 + \mathcal{T}_3$$

with :

$$\mathcal{T}_2 = \frac{1}{2} J_{2x} \dot{\theta}_{2x}^2 \quad (9)$$

$$\mathcal{T}_3 = \frac{1}{2} \left( m_3 v_G^2 + \Omega_3 \cdot \left( \bar{\bar{I}}_{G,3} \cdot \Omega_3 \right) \right) \quad (10)$$

$J_{2x}$ ,  $m_3$ ,  $v_G$ ,  $\Omega_3$  and  $\bar{\bar{I}}_{G,3}$  are respectively the moment of inertia of the blade root around  $X$ , the mass of the blade, the velocity of the center of gravity of the blade in the laboratory frame

of reference, the angular velocity vector and the moment of inertia tensor of the blade expressed at its center of mass  $G$ .

By calculation, we have at first order :

$$v_G^2 = a^2 \dot{\theta}_{3z}^2 - 2 a H_G \dot{\theta}_{3z} (\dot{\theta}_{2x} + \dot{\theta}_{3x}) + H_G^2 (\dot{\theta}_{2x} + \dot{\theta}_{3x})^2 + a^2 (\dot{\theta}_{2x} + \dot{\theta}_{3x})^2 \theta_{3z}^2$$

Since small perturbations are considered ( $\theta \ll 1$ ), it seems reasonable to neglect the last term of this equation, which is of higher order than the other terms :

$$v_G^2 = a^2 \dot{\theta}_{3z}^2 - 2 a H_G \dot{\theta}_{3z} (\dot{\theta}_{2x} + \dot{\theta}_{3x}) + H_G^2 (\dot{\theta}_{2x} + \dot{\theta}_{3x})^2 \quad (11)$$

Under the assumption that the blade has symmetry properties around its center of torsion on the section containing the center of mass, the moment of inertia tensor of the blade is written as follow :

$$\bar{\bar{I}}_{G,3} = \begin{pmatrix} J_{2x} & 0 & 0 \\ 0 & J_{3y} & 0 \\ 0 & 0 & J_{3z} \end{pmatrix} \quad (12)$$

The angular velocity vector of the blade is written :

$$\Omega_3 = \begin{pmatrix} \dot{\theta}_{2x} + \dot{\theta}_{3x} \\ 0 \\ \dot{\theta}_{3z} \end{pmatrix} \quad (13)$$

Hence, we have :

$$\begin{aligned} \mathcal{T} = & \frac{1}{2} J_{2x} \dot{\theta}_{2x}^2 + \frac{1}{2} m_3 a^2 \dot{\theta}_{3z}^2 - m_3 a H_G \dot{\theta}_{3z} (\dot{\theta}_{2x} + \dot{\theta}_{3x})^2 + \frac{1}{2} m_3 H_G^2 (\dot{\theta}_{2x} + \dot{\theta}_{3x})^2 \\ & + \frac{1}{2} J_{3x} (\dot{\theta}_{2x} + \dot{\theta}_{3x})^2 + \frac{1}{2} J_{3z} \dot{\theta}_{3z}^2 \end{aligned} \quad (14)$$

For the potentiel energy of the system, some rotational stiffnesses are considered between each part. Hence, it may be written as follow :

$$\mathcal{V} = \frac{1}{2} C_{23z} \theta_{3z}^2 + \frac{1}{2} C_{23x} \theta_{3x}^2 + \frac{1}{2} C_{12x} \theta_{2x}^2 \quad (15)$$

Using equations (14) and (15) in (8) leads to the following three degree of freedom system :

$$I \begin{pmatrix} \ddot{\theta}_{3x} \\ \ddot{\theta}_{3z} \\ \ddot{\theta}_{2x} \end{pmatrix} + C \begin{pmatrix} \theta_{3x} \\ \theta_{3z} \\ \theta_{2x} \end{pmatrix} = \mathcal{Q} \quad (16)$$

with :

$$I = \begin{pmatrix} m_3 H_G^2 + J_{3x} & -a m_3 H_G & m_3 H_G^2 + J_{3x} \\ -a m_3 H_G & m_3 a^2 + J_{3z} & -a m_3 H_G \\ m_3 H_G^2 + J_{3x} & -a m_3 H_G & m_3 H_G^2 + J_{2x} + J_{3x} \end{pmatrix} \quad (17)$$

and :

$$C = \begin{pmatrix} C_{23x} & 0 & 0 \\ 0 & C_{23z} & 0 \\ 0 & 0 & C_{12x} \end{pmatrix} \quad (18)$$

$\mathcal{Q}$  is a nonlinear torque due to the presence of a friction force between the blade root and the disk. In this approach, the nonlinear friction torque is simply modelled using the following regularized form of the Coulomb law, which will be helpfull to derive the jacobian of the nonlinear algebraic system that will be solved in the next subsection :

$$\mathcal{Q} = \begin{pmatrix} 0 \\ 0 \\ -e \mu N \tanh \left( p \frac{\dot{\theta}_{2x}}{e \mu N} \right) \end{pmatrix} \quad (19)$$

The evolution of the nonlinear torque is plotted in Figure 8. As it can be seen, a  $p$  parameter allows to choose the slope of the nonlinearity : the nonlinear force asymptotically approaches the Coulomb law as one chooses a high value for  $p$ .

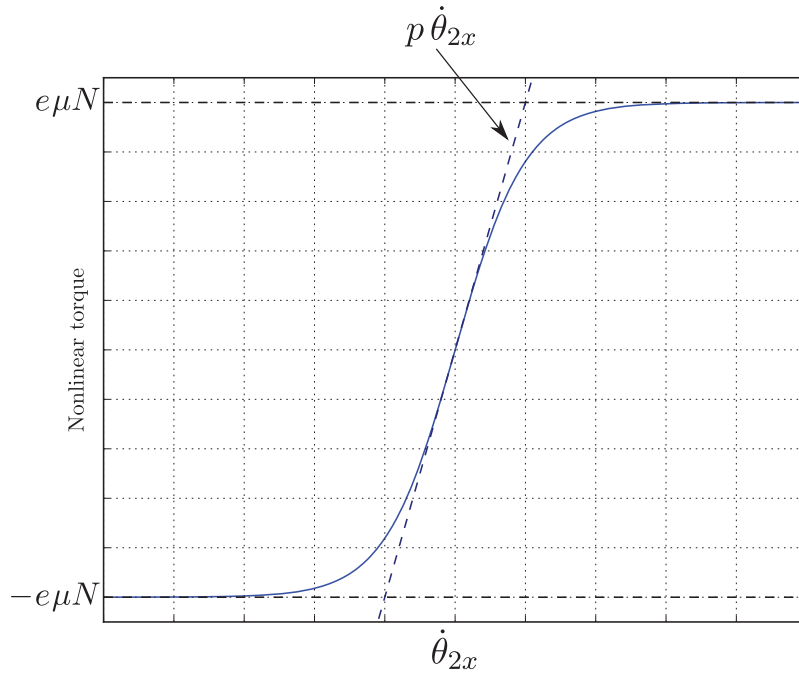


Figure 8: Evolution of the nonlinear torque against the movement of the blade root

Now that the equations of the nonlinear dynamics of the system have been written, we are going to use nonlinear complex modes in order to analyse the occurrence of LCO for the blade-root-disk system.

### 3.2 Nonlinear complex modes

The notion of nonlinear complex mode [17] has been introduced to characterize the nonlinear dynamics of nonconservative autonomous systems. Its formulation is built by analogy with

linear complex modes, as the eigenvalues of such a system may be written in the form :

$$\lambda = \beta + j\omega$$

Let us take the general equation of movement of a structure in presence of some dry friction nonlinear force :

$$\mathbf{M} \ddot{\mathbf{x}} + \mathbf{C} \dot{\mathbf{x}} + \mathbf{K} \mathbf{x} + \mathbf{f}_{nl}(\mathbf{x}, \dot{\mathbf{x}}) = 0 \quad (20)$$

We suppose the solution of this differential equation being in the following nonlinear complex mode form :

$$\mathbf{x}(t) = \mathbf{a}_0 + \sum_{k=1}^{N_h} e^{-k\beta t} (\mathbf{a}_k \cos(k\omega t) + \mathbf{b}_k \sin(k\omega t)) \quad (21)$$

Two time scales may be seen in equation (21) : the first time scale is due to the  $\beta$  term, which may be defined as the dissipation of the nonlinear complex mode by analogy with linear complex mode ; the second time scale is due to the  $\omega$  term. We suppose that the time scale associated to  $\omega$  is much faster than the one associated to  $\beta$  (i.e  $\omega \gg \beta$ ). Moreover,  $\beta$  is supposed to be the same for each harmonic. Defined in that way, the main difference between nonlinear complex modes and linear complex modes is the presence of multi-harmonic content in the nonlinear case.

By the means of a Galerkin procedure, one may rewrite the nonlinear differential equation of the structure into an algebraic one. To do so, a scalar product must be chosen. The scalar product that we consider is the inner product of square integrable functions defined as :

$$\forall f, g \in \mathcal{C} \left( 0; \frac{2\pi}{\omega} \right)^2, \langle f|g \rangle = \frac{\omega}{\pi} \int_0^{\frac{2\pi}{\omega}} f(t) \overline{g(t)} dt \quad (22)$$

Let us consider the Fourier basis functions  $1, \cos(k\omega t), \sin(k\omega t) \forall k \in \{1; N_h\}$ . By reinjecting (21) into the equations of motion and applying the inner product (22) with the Fourier basis functions, the dynamics of the nonlinear system may be described by the following algebraic equation in residual form :

$$\mathcal{R}(\mathbf{X}, \omega, \beta) = \mathbf{Z}(\omega, \beta) \mathbf{X} + \mathbf{F}_{nl}(\mathbf{X}, \omega, \beta) = 0 \quad (23)$$

where the multi-harmonic stiffness matrix  $\mathbf{Z}$  is :

$$\mathbf{Z} = \begin{pmatrix} 2\mathbf{K} & & & & \\ & \mathbf{Z}^1 & & & \\ & & \ddots & & \\ & & & \mathbf{Z}^k & \\ & & & & \ddots \\ & & & & & \mathbf{Z}^{N_h} \end{pmatrix} \quad (24)$$

and :

$$\mathbf{Z}^k = \begin{pmatrix} \mathbf{K} + ((k\beta)^2 - (k\omega)^2) \mathbf{M} - k\beta \mathbf{C} & k\omega \mathbf{C} - 2k^2 \beta \omega \mathbf{M} \\ - (k\omega \mathbf{C} - 2k^2 \beta \omega \mathbf{M}) & \mathbf{K} + ((k\beta)^2 - (k\omega)^2) \mathbf{M} - k\beta \mathbf{C} \end{pmatrix} \quad (25)$$



To perform the scalar product and derive (23), the hypothesis  $\omega \gg \beta$  has been used to neglect the amplitude variation of  $\mathbf{x}$  due to the dissipation  $\beta$  during a period  $\frac{2\pi}{\omega}$ . Hence, orthogonality properties may be used to derive the scalar product of the equation of movement with the Fourier basis functions.

In (23), the unknowns are  $\mathbf{X}$ ,  $\omega$  and  $\beta$ . As the system is autonomous, there are two more unknowns in the system than there are equations, which means that we are dealing with a rectangular system. By adding two more equations, it is possible to make it square. The first equation may be seen as a constraint equation, while the second one as a phase equation. By considering arc-length continuation [26] and a zero phase for an arbitrary harmonic  $k$  and degree of freedom  $q$ , these two equations may be written as :

$$\begin{cases} \mathcal{R}_{arc}(\mathbf{X}, \omega, \beta) = \|\mathbf{X} - \mathbf{X}_0\|^2 + \|\omega - \omega_0\|^2 + \|\beta - \beta_0\|^2 - \Delta s^2 = 0 \\ \mathcal{R}_{phase}(\mathbf{X}, \omega, \beta) = \mathbf{b}_{k,q} = 0 \end{cases} \quad (26)$$

where  $\Delta s$  is the arc-length radius.

A Newton-Raphson procedure is used to solve (23) and (26) simultaneously. Thus, an evaluation of the nonlinear forces in the frequency domain has to be done. Since there is no direct analytical expression of  $\mathbf{F}_{nl}(\mathbf{X}, \omega, \beta)$ , an Alternating Frequency-Time (AFT) method is used, as described in [27]. As previously, under the hypothesis that two different time scales are considered, a periodic movement of the structure is assumed during a pseudo-period  $\frac{2\pi}{\omega}$ , which means that the decrease due to  $\beta$  when performing the AFT method is neglected [17]. It is then assumed that the decrease of the nonlinear forces is the same than the one of the movement.

To get a full branch of nonlinear complex mode, the computation needs to be initialized. To do so, the system is set with small amplitudes of vibration so that the linear sticking case is a good approximation of the solution. Then, the first solution is searched in a subspace of the solutions of (23) at a distance  $\Delta s$  from the linear sticking case with the Newton-Raphson procedure. When converged, the computed solution is stored on one hand and replaces  $(\mathbf{X}_0, \omega_0, \beta_0)$  on the other hand. The next solution is predicted using secant predictor [28]. It is then computed with the Newton-Raphson procedure and so on.

### 3.3 Fluid modeling

We are here interested in taking into account aerodynamic effects on the nonlinear complex mode computation. First, let us consider the asymptotic case when there are sticking conditions between the blade root and the disk (*i.e.*  $\theta_{2,x} = 0$ ). Under the hypothesis that the modal basis of the full blade model used in *elsA* and the phenomenological model are equivalent on the considered bending mode, we assume that we may transfer the aerodynamic damping computed in aeroelastic computations to the equivalent bending mode of the phenomenological model. From (16), we write the movement equation in sticking conditions where  $\theta_{2,x} = 0$  :

$$I_{stick} \begin{pmatrix} \ddot{\theta}_{3x} \\ \ddot{\theta}_{3z} \end{pmatrix} + C_{stick} \begin{pmatrix} \theta_{3x} \\ \theta_{3z} \end{pmatrix} = 0 \quad (27)$$

with :

$$I_{stick} = \begin{pmatrix} m_3 H_G^2 + J_{3x} & -a m_3 H_G \\ -a m_3 H_G & m_3 a^2 + J_{3z} \end{pmatrix} \quad (28)$$

and :

$$C_{stick} = \begin{pmatrix} C_{23x} & 0 \\ 0 & C_{23z} \end{pmatrix} \quad (29)$$

Solving the eigenvalue problem associated to (27) allows to find the modal basis  $\Phi$  of the system in sticking conditions. It is possible to switch from physical base to modal basis using :

$$\begin{pmatrix} \theta_{3x} \\ \theta_{3z} \end{pmatrix} = \Phi \begin{pmatrix} q_{bend} \\ q_{torsion} \end{pmatrix} \quad (30)$$

When switching equation (27) to modal basis in sticking conditions, we have :

$$\mu \begin{pmatrix} \ddot{q}_{bend} \\ \ddot{q}_{torsion} \end{pmatrix} + \gamma \begin{pmatrix} \dot{q}_{bend} \\ \dot{q}_{torsion} \end{pmatrix} = 0 \quad (31)$$

with :

$$\mu = \Phi^T I_{stick} \Phi = \begin{pmatrix} \mu_{bend} & 0 \\ 0 & \mu_{torsion} \end{pmatrix} \quad (32)$$

and :

$$\gamma = \Phi^T C_{stick} \Phi = \begin{pmatrix} \gamma_{bend} & 0 \\ 0 & \gamma_{torsion} \end{pmatrix} \quad (33)$$

Under the assumption that we may use the aerodynamic damping previously computed, a damping modal matrix is added to (31) in the form :

$$\mu \begin{pmatrix} \ddot{q}_{bend} \\ \ddot{q}_{torsion} \end{pmatrix} + \begin{pmatrix} 2\sqrt{\mu_{bend}\gamma_{bend}}\xi_{aero} & 0 \\ 0 & 0 \end{pmatrix} \begin{pmatrix} \dot{q}_{bend} \\ \dot{q}_{torsion} \end{pmatrix} + \gamma \begin{pmatrix} q_{bend} \\ q_{torsion} \end{pmatrix} = 0 \quad (34)$$

Going back in the physical basis gives :

$$I_{stick} \begin{pmatrix} \ddot{\theta}_{3x} \\ \ddot{\theta}_{3z} \end{pmatrix} + D_{stick} \begin{pmatrix} \dot{\theta}_{3x} \\ \dot{\theta}_{3z} \end{pmatrix} + C_{stick} \begin{pmatrix} \theta_{3x} \\ \theta_{3z} \end{pmatrix} = 0 \quad (35)$$

with :

$$D_{stick} = \Phi^{-T} \begin{pmatrix} 2\sqrt{\mu_{bend}\gamma_{bend}}\xi_{aero} & 0 \\ 0 & 0 \end{pmatrix} \Phi^{-1} \quad (36)$$

where  $\Phi$  is the eigenvectors matrix of the system with sticking conditions. Since aerodynamic efforts are applied only on the blade, we make the assumption that  $\theta_{2x}$  will not be affected by aerodynamic damping. Hence, we may use the aerodynamic dissipation matrix  $D_{stick}$  in the full model as :

$$I \begin{pmatrix} \ddot{\theta}_{3x} \\ \ddot{\theta}_{3z} \\ \ddot{\theta}_{2x} \end{pmatrix} + D \begin{pmatrix} \dot{\theta}_{3x} \\ \dot{\theta}_{3z} \\ \dot{\theta}_{2x} \end{pmatrix} + C \begin{pmatrix} \theta_{3x} \\ \theta_{3z} \\ \theta_{2x} \end{pmatrix} = \mathcal{Q} \quad (37)$$

with :

$$D = \begin{pmatrix} D_{stick} & 0 \\ 0 & 0 & 0 \end{pmatrix} \quad (38)$$

Nonlinear complex modes may now be computed as in the previous subsection from (37) by taking into account fluid effects. It is at last assumed that the aerodynamic damping only affects the first harmonic of the nonlinear complex mode : as higher-harmonic content is expected to be much lower than the fundamental content, we may suppose that it does not affect aerodynamic forces. The multi-harmonic stiffness matrix can be expressed as follow :

$$\mathbf{Z} = \begin{pmatrix} 2C & & & \\ & \mathbf{Z}^1 & & \\ & & \ddots & \\ & & & \mathbf{Z}^k & \\ & & & & \ddots & \\ & & & & & \mathbf{Z}^{N_h} \end{pmatrix} \quad (39)$$

with :

$$\mathbf{Z}^1 = \begin{pmatrix} C + (\beta^2 - \omega^2) I - \beta D & \omega D - 2\beta\omega I \\ -(\omega D - 2\beta\omega I) & C + (\beta^2 - \omega^2) I - \beta D \end{pmatrix} \quad (40)$$

and  $\forall k \neq 1$  :

$$\mathbf{Z}^k = \begin{pmatrix} C + ((k\beta)^2 - (k\omega)^2) I & -2k^2\beta\omega I \\ 2k^2\beta\omega I & C + ((k\beta)^2 - (k\omega)^2) I \end{pmatrix} \quad (41)$$

In (40), note that the aerodynamic dissipation matrix  $D$  depends on the free frequency  $\omega$ , meaning that acoustic effects are taken into account.

## 4 NUMERICAL RESULTS

### 4.1 Model identification process

The model derived in the previous section has been used to compute nonlinear complex modes. It should be noticed that in the formulation of  $I$ , all of the terms may be extracted from any FEM model of blade. In this case, the values have been extracted from the blade model used previously in the aeroelastic computations. The remaining terms to choose are those in  $C$ . To do so, let us remind that the nonlinear behaviour of the system is bounded by two asymptotical linear cases respectively defined by sticking or sliding conditions between the blade root and the disk. Hence, rotational stiffnesses have been set so that the eigenfrequencies of the phenomenological blade-root-disk system on asymptotical cases match the eigenfrequencies of the model used for aeroelastic computations on the same asymptotical cases. Table 1 sums up the values that have been used for the phenomenological model. Eigenfrequencies and eigenvectors of the asymptotical linear cases are reported in Table 2.

### 4.2 Nonlinear analysis in vacuum

Results for a branch of nonlinear complex mode are displayed in Figures 9 and 10. The evolutions of free frequency and modal nonlinear damping expressed as  $\frac{\beta}{\omega}$  against the amplitude of the first harmonic of  $\theta_{3x}$  are plotted in the first one. Trajectories in the configuration space of the dynamics of the system during a pseudo-period are plotted in the second one. The trajectories of Figure 10 match the dots of Figure 9.

Parameter	Value
$m_3$	4.3
$H_G$	0.27
$a$	$-\text{chord} \times 0.15$
$J_{3x}(\times 10^{-6})$	159114
$J_{3z}(\times 10^{-6})$	28120
$J_{2x}(\times 10^{-6})$	217
$C_{23x}$	119500
$C_{23z}$	40000
$C_{12x}$	110000
$e$	0.02
$\mu$	0.1
$N$	200000
$p$	123078
$N_h$	15

Table 1: Numerical values of the phenomenological model

Asympt. case	$f$	$\theta_{3x}$	$\theta_{3z}$	$\theta_{2x}$
Sticking	$f_{1F2D}$	-0.919	-0.395	0.
Sliding	$0.7 \times f_{1F2D}$	0.655	0.252	0.712

Table 2: Eigenfrequencies and eigenvectors of the asymptotical linear cases

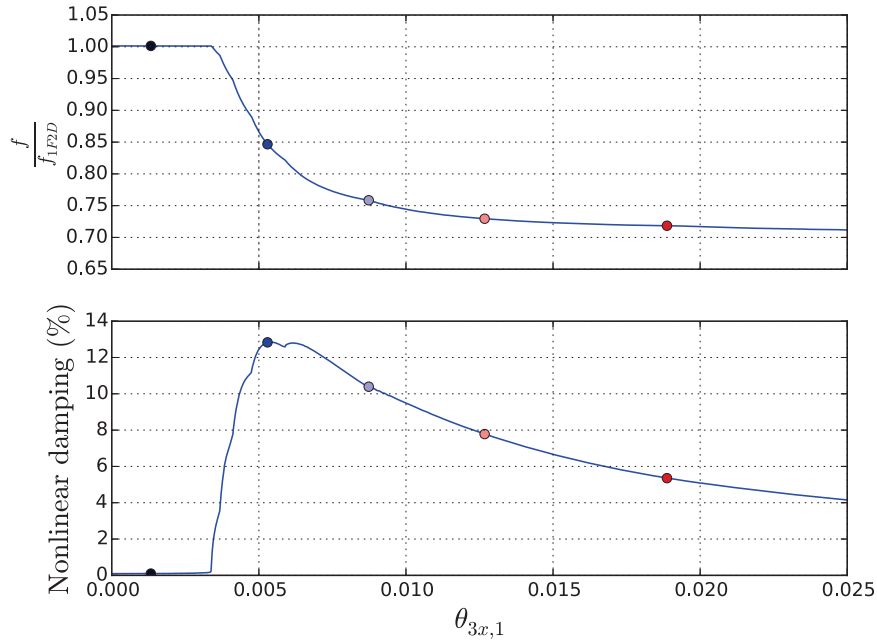


Figure 9: Nonlinear complex mode of the phenomenological model in vacuum

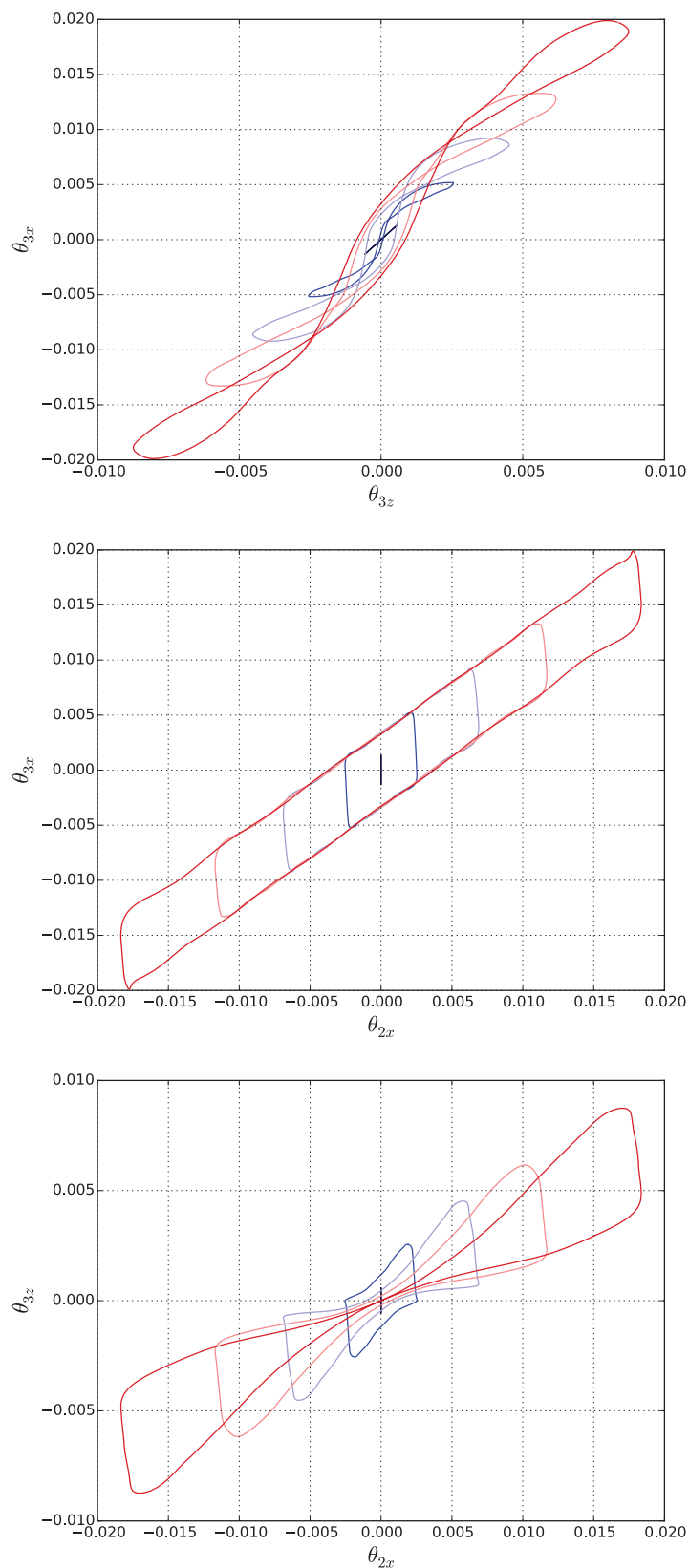


Figure 10: Nonlinear dynamics of the system in the configuration space

The nonlinear behaviour of the system dynamics changes as expected with increasing levels of  $\theta_{3x,1}$  (*i.e* increasing levels of vibration energy). A frequency shift is observed in Figure 9, from the frequency of the linear sticking case to the frequency of the linear sliding one. This frequency shift was expected, as blade root friction may be seen as the liberation of a degree of freedom which reduces the stiffness of the system, thus the free frequency. As  $\theta_{3x,1}$  increases, one may see when nonlinearities start to have a significant impact on the system dynamics, as sharp changes may be observed on the nonlinear damping and free frequency.

It can be seen in Figure 10 the effects of friction nonlinearities onto the system dynamics. Starting in sticking conditions (deep blue curves), the system dynamics evolves along a straight line as the system is nearly linear. With increasing levels of friction nonlinearities (from deep blue to deep red), one may observe an opening and a curvature of the generalized coordinates trajectories. A phase difference between the generalized coordinates appears, leading to hysteresis cycles of the system dynamics. Such cycles are typical of systems with dissipation due to friction nonlinearities.

The system dynamics has been characterized with nonlinear complex modes in vacuum. The previously derived simplified fluid representation is going to be added to the system, using numerical results of the first section.

### 4.3 Nonlinear analysis with simplified fluid representation

In this study, we are interested in predicting LCO with nonlinear complex modes while taking into account flutter instability and changes in acoustic effects due to frequency shifts. To do so, the methodology derived in subsection 3.3 and the results exposed in Figure 6 will be used. A spline has been created to characterize the evolution of  $\xi_{aero}$  with respect to the frequency of vibration. In that way, the evolution of  $\xi_{aero}$  is in regards to  $f$ , and the jacobian may be analytically derived easily. Figure 11 illustrates the spline used for computations.

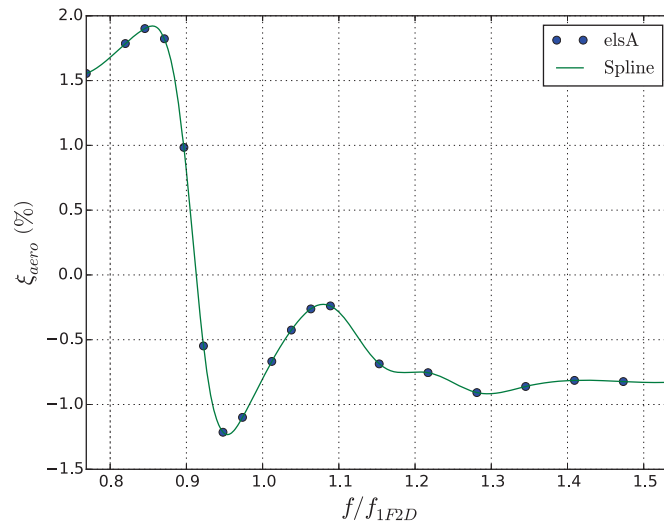


Figure 11:  $\xi_{aero}$  spline implemented in the computation of the nonlinear complex mode

It should be noticed that Figure 11 differs from 6 : the points have been shifted to a lower level in the latter so that we are in presence of negative aerodynamic damping when the system is stuck and vibrates at  $f = f_{1F2D}$ . This shift, which is artificial, has been applied so that the



system may be unstable in absence of friction nonlinearities. The methodology can then be tested to assess the presence of LCO when taking into account aerodynamic effects. Another way to proceed would have been to compute the dependance of  $\xi_{aero}$  against  $\omega$  on a operating point beyond the stability limit computed previously. It is assumed that it would have produced similar results. A nonlinear complex mode has been computed when the system is initialized on the unstable bending mode. Numerical parameters have been kept the same as the case in vacuum. Results are displayed in Figure 12.

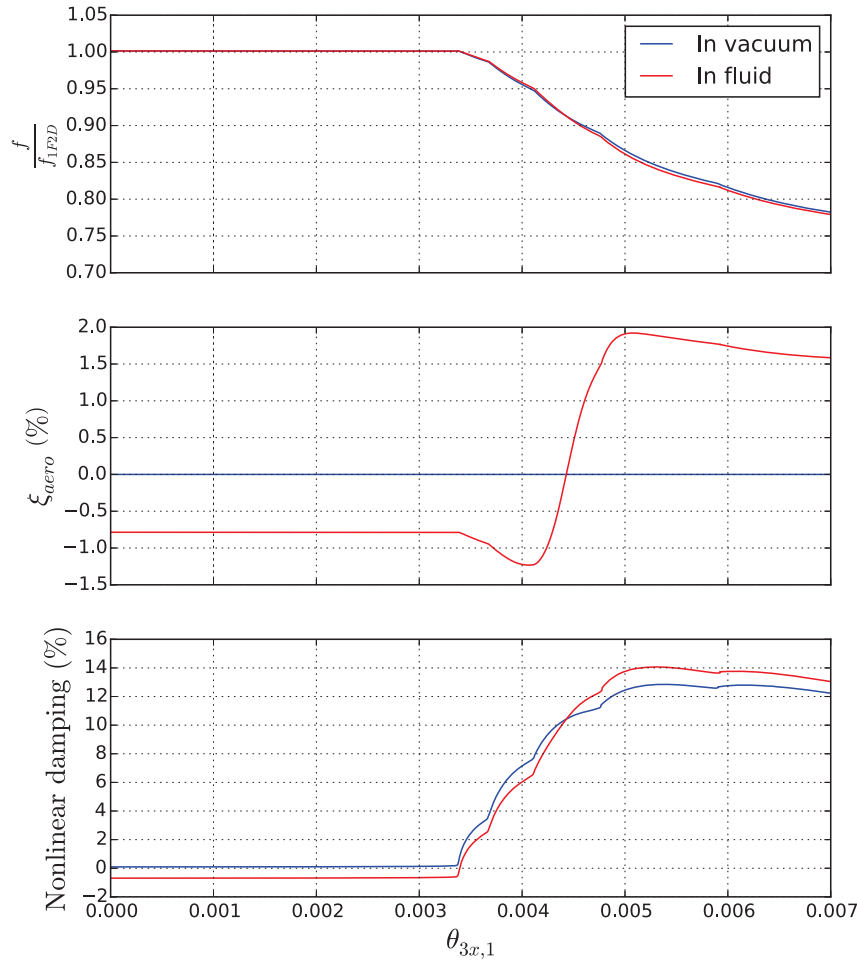


Figure 12: Nonlinear complex mode of the phenomenological model with fluid modeling

Since there is no more information on  $\xi_{aero}$  for values of  $f$  under  $0.77f_{1F2D}$ , the computation has been interrupted for this value of  $f$ . It can be seen that qualitatively we have the same trends for  $f$  and the nonlinear damping as in the case in vacuum, in spite of small discrepancies. What must be noticed is that there is a point on the nonlinear complex mode where the nonlinear damping equals zero, which highlights the presence of a LCO on this point. By using a direct Fourier transform, it is possible to display the dynamics of the system in the state space on the LCO, as shown in figure 13. Finally, it may be seen in Figure 12 that the evolution  $\xi_{aero}$  follows the evolution of the free frequency with increasing values of amplitude, as implemented from Figure 11.

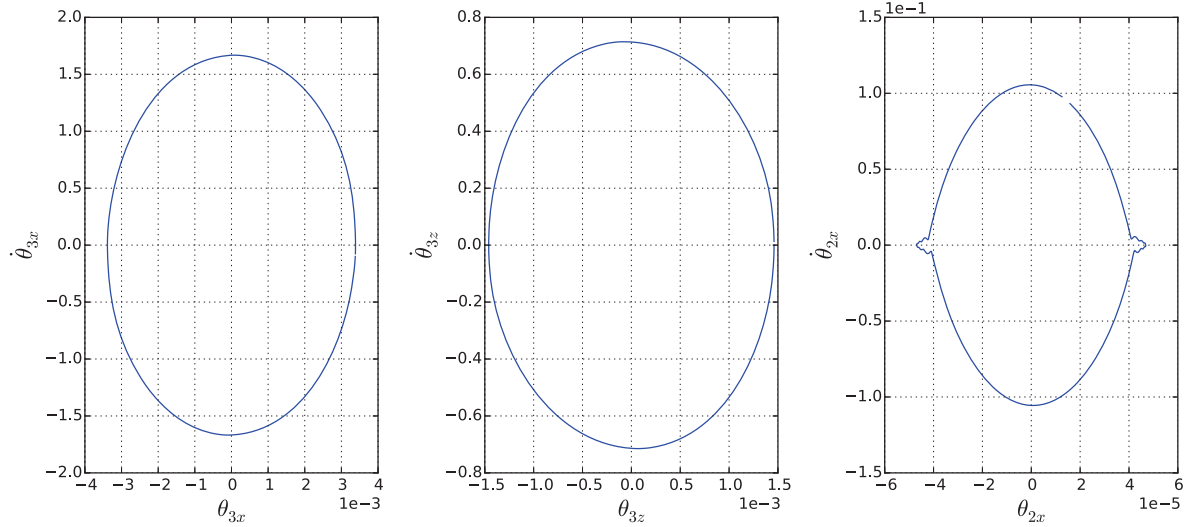


Figure 13: LCO computed by the means of nonlinear complex modes

## 5 CONCLUSIONS

This study has detailed a methodology to assess flutter stability of a fan stage while taking into account friction nonlinearities at blade root. An approach including the use of nonlinear complex modes and stability results from CFD calculations has been developed. It has been tested on a simple three degrees of freedom system that represents a blade-root-disk assembly. It allows to find a dry friction induced LCO while the system is aeroelastically unstable when no friction occurs. Moreover, the sensitivity of the aerodynamic damping to acoustic reflections in the inlet of the engine has been taken into account. The next step would be to apply this methodology in an industrial context, with a typical design of modern civil fan stage. However, some aspects that have been neglected in this study will have to be taken into account. Firstly, assumptions have been made for aeroelastic computations : the effects of the flow on the structure dynamics for the evaluation of aerodynamic forces due to vibration have been neglected. For structures as fan blades, which may be rather large and flexible for modern designs, these assumptions may not be totally realistic. Hence, it will be taken into account in a further study. Concerning the fluid modeling in the nonlinear complex mode computation, it has been chosen to add linear modal fluid effects only on the first harmonic of vibration. However, with increasing levels of energy, the nonlinear shape deformation may change sufficiently so that it has an impact on the flow. Hence, some data exchanges may have to be done between the nonlinear complex mode computation and the CFD based aeroelastic calculations to converge on each physics more accurately.

## 6 ACKNOWLEDGEMENT

The present study has been done thanks to the support of Safran Aircraft Engines.

## REFERENCES

- [1] J.G. Marshall and M. Imregun, A Review of Aeroelasticity Methods with Emphasis on Turbomachinery Applications. *Journal of Fluids and Structures*, Vol. 10, No. 3, 237–267, 1996.
- [2] H. Stargardter, Subsonic/transonic stall flutter study. *NASA CR-165256*, 1979.
- [3] M. Vahdati et al. Mechanisms and prediction methods for fan blade stall flutter. *Journal of Propulsion and Power*, Vol. 17, No. 5, 1100–1108, 2001.
- [4] R. Srivastava, M. A. Bakhle, T. G. Keith Jr. and G. L. Stefko, Flutter Analysis of a Transonic Fan. ASME Paper No. GT-2002-30319.
- [5] M. Aotsuka and T. Murooka, Numerical analysis of fan transonic stall flutter. *ASME Turbo Expo 2014: Turbine Technical Conference and Exposition*, American Society of Mechanical Engineers (2014), Article V07BT35A020.
- [6] X. Dong, Y. Zhang, Y. Zhang, Z. Zhang, X. Lu, Numerical simulations of flutter mechanism for high-speed wide-chord transonic fan. *Aerospace Science and Technology*, Vol. 105, 2020.
- [7] S. W. Rienstra and A. Hirschberg, An introduction to acoustics. *Eindhoven University of Technology*, Vol. 18, 2004.
- [8] M. Vahdati, G. Simpson and M. Imregun, Mechanisms for wide-chord fan blade flutter. *Journal of Turbomachinery*, American Society of Mechanical Engineers Digital Collection, Vol. 133, 2011.
- [9] M. Vahdati, N. Smith and F. Zhao, Influence of intake on fan blade flutter. *Journal of Turbomachinery*, American Society of Mechanical Engineers Digital Collection, Vol. 137, 2015.
- [10] F. Zhao, N. Smith and M. Vahdati, A simple model for identifying the flutter bite of fan blades. *Journal of Turbomachinery*, American Society of Mechanical Engineers Digital Collection, Vol. 139, 2017.
- [11] C. Chahine, T. Verstraete, T and L. He, A comparative study of coupled and decoupled fan flutter prediction methods under variation of mass ratio and blade stiffness. *Journal of Fluids and Structures*, Vol. 85, 110–125, 2019.
- [12] A. Sinha and J. Griffin, Friction Damping of Flutter in Gas Turbine Engine Airfoils. *Journal of Aircrafts*, Vol. 20, No. 4, 372–376, 1983.
- [13] A. Sinha and J. Griffin, Effects of friction dampers on aerodynamically unstable rotor stages. *AIAA journal*, Vol. 23, No. 2, 262–270, 1985.
- [14] R.M. Rosenberg, Normal modes of nonlinear dual-mode systems. 1960.
- [15] R.M. Rosenberg, The normal modes of nonlinear n-degree-of-freedom systems. 1962.
- [16] S.W. Shaw and C. Pierre, Normal modes for non-linear vibratory systems. *Journal of sound and vibration*, Vol. 164, No. 1, 85–124, 1993.

- [17] D. Laxalde and F. Thouverez, Complex non-linear modal analysis for mechanical systems: Application to turbomachinery bladings with friction interfaces. *Journal of sound and vibration*, Vol. 322, No. 4–5, 1009–1025, 2009.
- [18] K. Malte, Nonlinear modal analysis of nonconservative systems: extension of the periodic motion concept. *Computers & Structures*, Vol. 154, 59–71, 2015.
- [19] E.P. Petrov, Analysis of flutter-induced limit cycle oscillations in gas-turbine structures with friction, gap, and other nonlinear contact interfaces. *Journal of Turbomachinery*, American Society of Mechanical Engineers Digital Collection, Vol. 134, No. 6, 2012.
- [20] M. Lassalle and C.M. Firrone, A parametric study of limit cycle oscillation of a bladed disk caused by flutter and friction at the blade root joints. *Journal of Fluids and Structures*, Vol. 76, 349–366, 2018.
- [21] C. Berthold, J. Gross, C. Frey and M. Krack, Analysis of Friction-Saturated Flutter Vibrations With a Fully Coupled Frequency Domain Method. *Journal of Engineering for Gas Turbines and Power*, Vol. 142, No. 11, 2020.
- [22] L. Cambier, M. Gazaix, S. Heib, S. Plot, M. Poinot, J.P. Veuillot, J.F. Boussuge and M. Montagnac, An Overview of the Multi-Purpose *elsA* Flow Solver. AerospaceLab, 2011, p. 1-15. hal-01182452
- [23] L. Cambier, S. Heib and S. Plot, The Onera *elsA* CFD software: input from research and feedback from industry. *Mechanics & Industry*, Vol. 14, No. 3, 159–174, 2013.
- [24] R. Henry, Calcul des fréquences et modes des structures répétitives circulaires. *Journal de Mécanique Appliquée*, Vol. 4, No. 1, 61–82, 1980.
- [25] T. Bontemps, S. Aubert and N. De Cacqueray, Prediction of the acoustic influence of an intake on fan flutter: a comparison of numerical methods. *13th European Conference on Turbomachinery Fluid dynamics & Thermodynamics*, European Turbomachinery Society, 2019.
- [26] A. H. Nayfeh and B. Balachandran, *Applied nonlinear dynamics: analytical, computational, and experimental methods*. John Wiley & Sons, 2008.
- [27] T.M. Cameron and J.H. Griffin, An alternating frequency/time domain method for calculating the steady-state response of nonlinear dynamic systems. *American Society of Mechanical Engineers, Journal of Applied Mechanics*, Vol. 56, No. 1, 149–154, 2019.
- [28] K.B. Blair, C.M. Krousgrill and T.N. Farris, Harmonic balance and continuation techniques in the dynamic analysis of Duffing’s equation. *Journal of Sound and Vibration*, Vol. 202, No. 5, 717–731, 1997.

## GEOMETRICALLY NON-LINEAR FREE IN-PLANE VIBRATION OF STEPPED CIRCULAR ARCH

O. Outassafte<sup>1</sup>, A. Adri<sup>1</sup>, Y. El khouddar<sup>1</sup>, S. Rifai<sup>1</sup> and R. Benamar<sup>2</sup>

<sup>1</sup> Laboratoire de Mécanique Productique et Génie Industriel, Ecole Supérieure de Technologie  
Hassan II University of Casablanca, B.P.8012, Oasis, Casablanca, Maroc  
e-mail: [omar.outassafte@ensem.ac.ma](mailto:omar.outassafte@ensem.ac.ma), [ahmedadri@gmail.com](mailto:ahmedadri@gmail.com), [yassine.elkhouddar@ensem.ac.ma](mailto:yassine.elkhouddar@ensem.ac.ma)

[Said57.rifai@gmail.com](mailto:Said57.rifai@gmail.com)

<sup>2</sup> Mohammed V University in Rabat, EMI-Rabat, LERSIM  
B.P.765 Agdal, Rabat, Morocco.  
e-mail: [rhali.benamar@gmail.com](mailto:rhali.benamar@gmail.com)

---

### Abstract

*The objective of this current work is to study the geometrical non-linearity in free in-plane vibration of stepped circular arch. The first part has been devoted to the study of the linear vibration of stepped arch. The sixth order differential partial equation of motion has been obtained after the inextensibility assumption. For simplification, the complicating effects such as rotary inertia and shear deformation will be ignored. The natural frequencies of arches have been obtained iteratively using Newton-Raphson algorithm, and compared with the available in the literature. The study of the geometrical non-linearity is based on Euler Bernoulli theory and Von Karman's assumptions. The kinetic and total strain energies have been written in each interval of the arch and discretized into a series of a finite spatial functions then derived using Hamilton's principle energy. The problem is reduced into a set of non-linear algebraic equations solved numerically using an approximate explicit method developed previously the so-called second formulation. Consequently, an analysis has been performed in the neighborhood of the first mode, based on the multimode approach, to obtain the stepped circular arches frequency ratio dependence on the maximum vibration amplitude.*

**Keywords:** geometrical non-linearity, free in-plane vibration, stepped circular arch, second formulation, multimode approach.

---

## 1 INTRODUCTION

For a long time, the circular arches are considered one of an important structural element which have large applications in many fields, such as mechanical engineering, civil engineering. Due to the practical importance of the arches, many authors have been studied the static and dynamic behavior of these structures. The challenge today is to find a structure that offers high strength, stability and durability by optimizing the material used in their manufacture. For this reason, the stepped arches are considered. The authors of [1]–[3] used the polynomial co-ordinate functions and Rayleigh-Ritz method to find the fundamental frequency of in-plane vibration of arcs of with thicknesses varying in a discontinuous fashion. In reference [4] an exact solution of the equation of in-plane free vibration of circular arch with uniform cross section has been used to study the free in-plane vibration of a stepped circular arch, the numerical solution have been obtained using ANSYS and performed with the experiments. Using a systematic approach X. TONG et al [5] investigated the free and forced In-plane vibration of circular arch with variable cross-section. The differential quadrature methodology has been presented by the author of [6] to study the free in-plane vibration of circular arches with varying cross-section under a various type of boundary conditions. Recently, the geometrical non-linearity in free and forced vibration of three type of multi- stepped Euler-Bernoulli beams based on single mode approach has been analyzed by El Hantati et al in references [7] and [8].

In this current paper, the geometrically non-linear in free in-plane vibration of a stepped circular arches will be presented. The complicating effects such as rotary inertia and shear deformation will be ignored. Using the inextensibility assumption, the two coupled differential partial equations are reduced to sixth order differential partial equation. The theoretical model is based on the Euler–Bernoulli beam theory and the von Karman geometrical non-linearity assumptions. Harmonic motion is assumed and expended into a series of finites spatial functions. The use of Hamilton’s principle energy, reduces the problem into a set of non-linear algebraic equations solved numerically using an approximate method the so-called second formulation developed in [9] leading to frequency ratio dependence on the maximum vibration amplitude.

## 2 GENERAL FORMULATION

In this study, homogenous stepped circular arches are considered as shown in Fig. 1. Where  $E$  denoted young’s modulus,  $I(\theta)$  is second moment of area,  $A(\theta)$  is the cross section,  $\mu(\theta)$  is the mass per unit length, and  $R$  the radius of the circular. The complicated effects such as shear deformation and rotary inertia are neglected because the arch is supposed to be thin [2].  $u_i$ ,  $w_i$  are respectively radial and tangential displacement of the arches, when the arch axis is supposed to inextensible, radial and tangential displacements are related by [10] :

$$\frac{\partial w}{\partial \varphi} = u \quad (1)$$

Whereas the bending moment  $M(\theta, t)$ , the shear force  $T(\theta, t)$  and the normal force  $N(\theta, t)$  of arch can be expressed as:

$$M(\theta, t) = \frac{-EI(\theta)}{R^2} \left( \frac{\partial^3 w}{\partial \theta^3} + \frac{\partial w}{\partial \theta} \right) \quad (2)$$



$$T(\theta, t) = \frac{-1}{R^3} \frac{\partial}{\partial \theta} \left[ EI(\theta) \left( \frac{\partial^3 w}{\partial \theta^3} + \frac{\partial w}{\partial \theta} \right) \right] \quad (3)$$

$$N(\theta, t) = \frac{1}{R^3} \frac{\partial^2}{\partial \theta^2} \left[ EI(\theta) \left( \frac{\partial^3 w}{\partial \theta^3} + \frac{\partial w}{\partial \theta} \right) \right] + \mu(\theta) R \frac{\partial^3 w(\theta, t)}{\partial \theta \partial t^2} \quad (4)$$

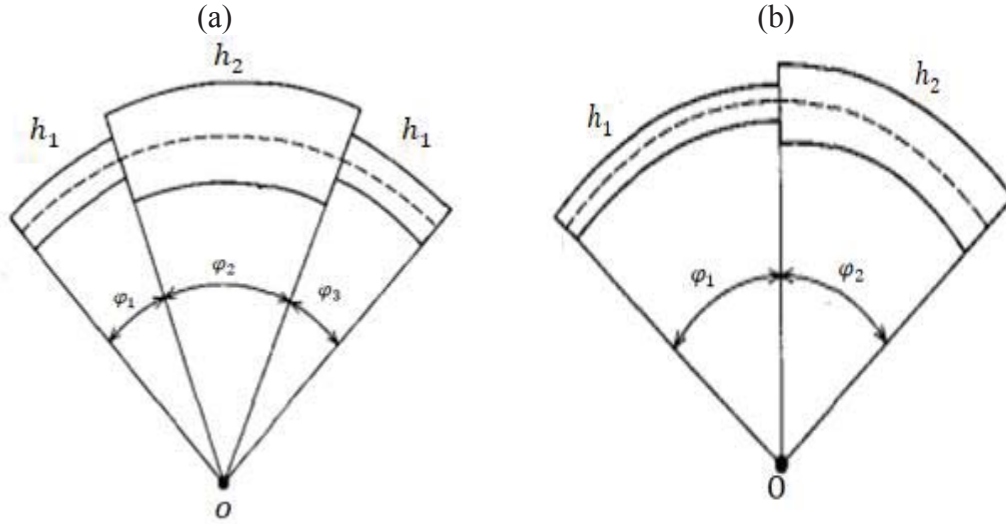


Fig.1: Two stepped arches ( $\eta = h_1/h_2$ ): (a) symmetric stepped arch, (b) unsymmetric stepped arch.

The sixth order differential equation of motion may be written as:

$$\frac{\partial^6 w}{\partial \varphi^6} + 2 \frac{\partial^4 w}{\partial \varphi^4} + \frac{\partial^2 w}{\partial \varphi^2} + \frac{\mu R^4}{EI} \frac{\partial^4 w}{\partial t^2 \partial \varphi^4} = 0 \quad (5)$$

Considering the arch in a harmonic motion, we put:

$$w(\varphi, t) = W(\varphi) \cos(\omega t) \quad (6)$$

If this form of solution is allowed:

$$W(\varphi) = e^{\Omega \varphi} \quad (7)$$

Then it is possible to arrive at this characteristic equation:

$$\Omega^6 + 2\Omega^4 + (1 - \lambda^2)\Omega^2 = 0 \quad (8)$$

Where  $\lambda_j^2 = \frac{\mu R^4 \omega_j^2}{EI_j}$  is the non-dimensional frequency.

The general solution of the differential equation (2) in term of radial displacement in each step of arch can be expressed as:

$$W(\theta) = \begin{cases} W_1(\theta) \rightarrow ]0, \theta_1[ \\ W_j(\theta) \rightarrow ]\theta_{j-1}, \theta_j[ \\ W_{n+1}(\theta) \rightarrow ]\theta_n, 1[ \end{cases} \quad (9)$$

$$W_{ji}(\varphi) = a_j \sin(\alpha_j(\varphi - \varphi_{j-1})) + b_j \cos(\alpha_j(\varphi - \varphi_{j-1})) + c_j \sinh(\alpha_j(\varphi - \varphi_{j-1})) + d_j \cosh(\alpha_j(\varphi - \varphi_{j-1})) + e_j(\varphi - \varphi_{j-1}) + f_j \quad (10)$$

Where:  $\alpha_j = \sqrt{\lambda_j - 1}$ ,  $\beta = \sqrt{\lambda_j + 1}$  and  $\lambda_j \geq 1$

The clamped-clamped boundary conditions of circular arches in term of tangential displacement may be written as:

$$W_{1i}(\varphi = 0) = W_{1i}(\varphi = 1) = 0 \quad \frac{dW_{1i}}{d\varphi} \Big|_{\varphi=0} = \frac{dW_{(n+1)i}}{d\varphi} \Big|_{\varphi=1} = 0 \quad (11)$$

$$W_{1i} \Big|_{\varphi=0} + \frac{d^2 W_{1i}}{d\varphi^3} \Big|_{\varphi=0} = W_{(n+1)i} \Big|_{\varphi=1} + \frac{d^2 W_{(n+1)i}}{d\varphi^2} \Big|_{\varphi=1} \quad (12)$$

The compatibility condition of at the steps of arches may be expressed as:

$$W_{ji}(\varphi = \varphi_i) = W_{(j+1)i}(\varphi = \varphi_i) \quad \frac{dW_{ji}}{d\varphi} \Big|_{\varphi=\varphi_i} = \frac{dW_{(j+1)i}}{d\varphi} \Big|_{\varphi=\varphi_i} \quad (13)$$

$$W_{ji} \Big|_{\varphi=\varphi_j} + \frac{\partial^2 W_{ji}}{d\varphi^3} \Big|_{\varphi=\varphi_j} = W_{(j+1)i} \Big|_{\varphi=\varphi_j} + \frac{\partial^2 W_{(j+1)i}}{d\varphi^2} \Big|_{\varphi=\varphi_j} \quad (14)$$

$$M_{ji}(\theta_i, t) = M_{(j+1)i}(\theta_i, t) \quad T_j(\theta_i, t) = T_{(j+1)i}(\theta_i, t) \quad N_i(\theta_i, t) = N_{(j+1)i}(\theta_i, t) \quad (15)$$

The position of the variation section can be obtained using the Gauss–Lobatto–Chebyshev points:

$$\varphi_i = \frac{1}{2} \left[ 1 - \cos \left[ \frac{(i-1)\pi}{(N-1)} \right] \right] \quad (16)$$

The use of the compatibility conditions corresponding to each step, the end conditions and the transfer matrix method [11] leads to a homogeneous system. The determinant of the latest must be set equal to zero to obtain the natural frequencies, determined iteratively by the Newton–Raphson method [12]

The corresponding dimensionless frequencies  $\lambda_i$  for stepped arches are given respectively in Tables 1 and 2, the results are compared with those of available in the literature.

The corresponding radial  $u_i$  and tangential  $w_i$  displacements of arch are plotted respectively in Fig. 2 and 4. the tangential and radial displacements are projected into a Cartesian coordinate to plot the corresponding first four mode shapes of stepped circular arches in Fig.3.

Table1: First frequency  $\lambda$  of an unsymmetric stepped circular arch.

$\varphi_0$	$\lambda_1$		$\lambda_2$		$\lambda_3$		$\lambda_4$	
	Present	Ref [13]	Present	Ref [13]	Present	Ref [13]	Present	Ref [13]
<b>10</b>	2280	2277.434 2	4029	4027.230	7368	7366.07	10499	10494.09
<b>20</b>	569.2	567.1737	1007	1005.440	1841	1839.008	2624	2622.562
<b>30</b>	252.5	250.4748	446.9	445.7867	817.9	815.4926	1166	1164.457
<b>40</b>	141.7	139.6489	251	249.9069	459.6	457.2812	655.2	654.0919
<b>50</b>	90.37	88.3724	160.3	159.2458	293.8	291.5007	419	417.8631
<b>60</b>	62.5	60.5389	111.1	110.0019	203.7	201.4672	290.7	289.5425
<b>70</b>	45.7	43.7766	81.35	80.3138	149.4	161.9572	213.3	212.1714
<b>80</b>	34.79	32.9173	62.08	61.0496	114.2	127.533	163.1	161.9572

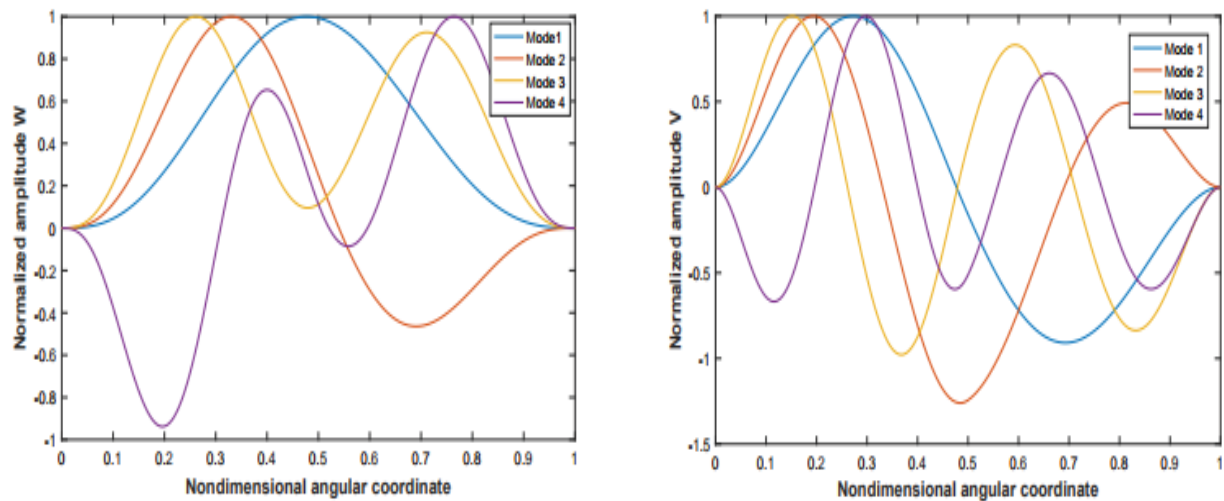
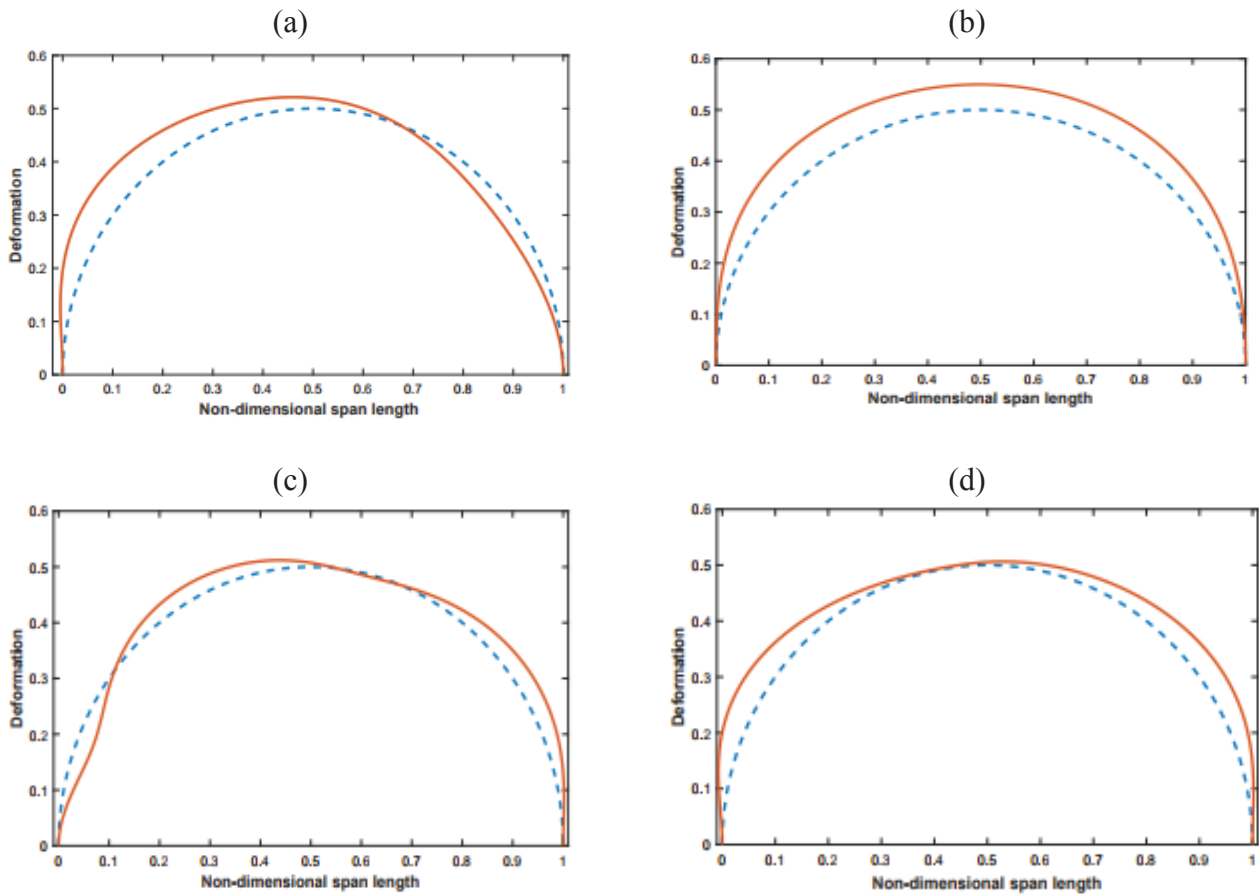


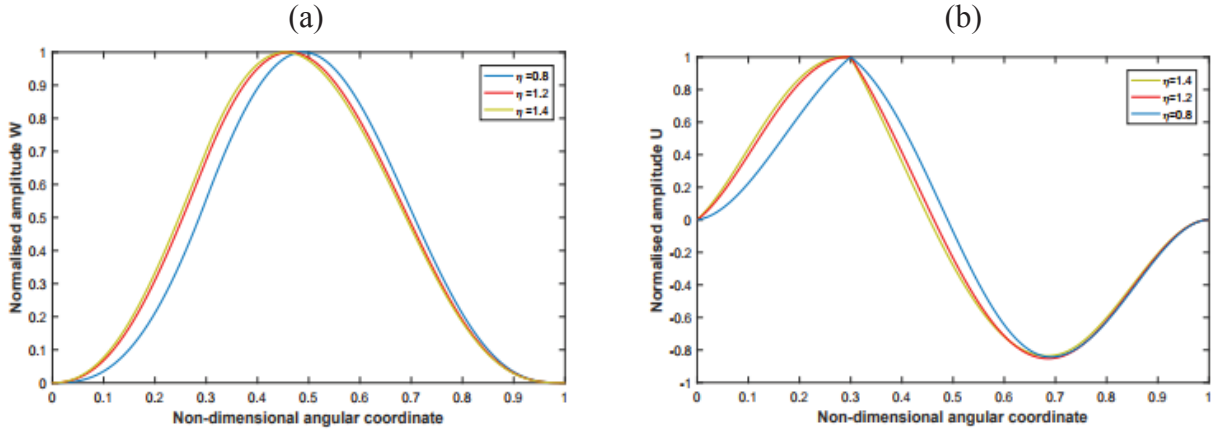
Fig.2: The first fourth tangential and radial displacement  $W$  and  $V$  of an unsymmetrical stepped arch for  $h_1/h_2 = 1.25$ .



**Fig.3:** Representation of the first four mode shapes of unsymmetrical stepped circular arch clamped-clamped at the two ends: (a) the first mode shape, (b) the second mode shape, (c) the third mode shape, (d) the fourth mode shape.

Table2: First frequency  $\lambda$  of symmetric stepped C-C arch with  $\varphi_1/\varphi_0 = 0.3$  and  $\varphi_2/\varphi_0 = 0.7$

$\varphi_0$	$\eta = 0.8$			$\eta = 1.2$			$\eta = 1.4$		
	Present	R-R [2]	C.D.M [2]	Present	R-R [2]	C.D.M [2]	Present	R-R [2]	C.D.M [2]
<b>40</b>	111.9104	121.874	113.15	125.2367	129.42	128.63	128.4396	136.87	130.83
<b>60</b>	49.2784		49.200	54.8975		55.613	56.2268		56.439
<b>80</b>	27.3375		26.86	30.2928		30.134	30.9795		30.494
<b>100</b>	17.1684		16.564	18.9077		18.416	19.3028		18.574
<b>120</b>	11.6317		11.009	12.7214		12.119	12.9611		12.180
<b>140</b>	8.2770		7.6961	8.9859		8.3821	9.1335		8.3940
<b>160</b>	6.0744		5.5784	6.5514		6.0080	6.6401		5.9948
<b>180</b>	4.5085		4.1550	4.8639		4.4230	4.9127		4.3979



**Fig.4:** The first tangential and radial displacement  $W$  and  $V$  of symmetrical stepped arch for various values of  $\eta$ .

In Fig. 4, the corresponding first tangential and radial displacement  $W$  and  $U$  of symmetrical stepped circular arch are plotted for various values of  $\eta$  where  $\varphi_1/\varphi_0 = 0.3$  and  $\varphi_2/\varphi_0 = 0.7$

### 3 NON-LINEAR FORMULATION

The expressions of the kinetic energy  $T$ , the axial strain energy  $V_a$  and the bending strain energy  $V_b$  for the system in Fig. 1 can be written as:

$$T = \frac{R}{2} \left( \mu_1 \int_0^{\varphi_1} \left[ \left( \frac{\partial w_1^{(1)}}{\partial t} \right)^2 + \left( \frac{\partial w_1}{\partial t} \right)^2 \right] dt + \dots + \mu_{N+1} \int_{\varphi_N}^{\varphi_{N+1}} \left[ \left( \frac{\partial w_{N+1}^{(1)}}{\partial t} \right)^2 + \left( \frac{\partial w_{N+1}}{\partial t} \right)^2 \right] dt \right) \quad (17)$$

$$V_a = \frac{E}{2R^3} \left( I_1 \int_0^{\varphi_1} \left( \frac{\partial w_1}{\partial \varphi} + \frac{\partial^3 w_1}{\partial \varphi^3} \right)^2 d\varphi + \dots + I_{N+1} \int_{\varphi_N}^{\varphi_{N+1}} \left( \frac{\partial w_{N+1}}{\partial \varphi} + \frac{\partial^3 w_{N+1}}{\partial \varphi^3} \right)^2 d\varphi \right) \quad (18)$$

$$V_b = \frac{E}{8R^3} \left( A_1 \int_0^{\varphi_1} \left( w_1 + \frac{\partial^2 w_1}{\partial \varphi^2} \right)^4 d\varphi + \dots + A_{N+1} \int_{\varphi_N}^{\varphi_{N+1}} \left( w_{N+1} + \frac{\partial^2 w_{N+1}}{\partial \varphi^2} \right)^4 d\varphi \right) \quad (19)$$

Assuming harmonic, the displacement function is expanded as a series of  $N$  basic spatial functions:

$$w_{ji}(\varphi, t) = a_i W_{ji} \sin(\omega t) \quad (20)$$

Where  $a_i$  are the basic functions contributions coefficients. Using a generalized parameterization  $T$  and the usual summation convention defined in [10] and [9] The kinetic energy  $T$ , the axial strain energy  $V_a$  and the bending strain energy  $V_b$  of the arch can be expressed as:

$$T = \frac{1}{2} a_i a_j \omega^2 m_{ij} \cos^2(\omega t) \quad (21)$$

$$V_a = \frac{1}{2} a_i a_j k_{ij} \sin^2(\omega t) \quad (22)$$

$$V_b = \frac{1}{2} a_i a_j a_k a_l b_{ijkl} \sin^4(\omega t) \quad (23)$$

To obtain non-dimensional parameters, ones put:

$$W_i(\varphi) = h W_i^* \left( \frac{\varphi}{\varphi_0} \right) = h W_i^*(\varphi^*) \quad (24)$$

$$\frac{m_{ij}}{m_{ij}^*} = \mu_1 R^3 h_1^2, \frac{k_{ij}}{k_{ij}^*} = \frac{b_{ijkl}}{b_{ijkl}^*} = \frac{EI_1 h_1^2}{R^3} \quad (25)$$

Using Hamilton's principle as defined in equation (12):

$$\delta \int_0^{2\pi/\omega} (V - T) dt \quad (26)$$

One can obtain the following non-linear algebraic equations:

$$([K^*] - \omega^{*2} [M^*]) \{A\} + \frac{3}{2} [B^*(A)] \{A\} = \{0\} \quad (27)$$

Where  $M_{ij}^*$  denotes the dimensionless mass matrix  $K_{ij}^*$  is the dimensionless rigidity matrix and  $B_{ijkl}^*$  is the dimensionless non-linearity tensor. Using the tonsorial notation, one put:

$$a_i k_{ir}^* + \frac{3}{2} a_i a_j a_k b_{ijk r}^* - a_i \omega^{*2} m_{ir}^* = 0 \quad \text{with} \quad r = 1, \dots, n \quad (29)$$

The called the second formulation, it is an approximation which consists to separate the nonlinear term of equation (29) into a terms proportional to  $a_i^3$  and terms proportional to  $a_i^2 \varepsilon_i$  and neglecting terms proportional to  $a_i \varepsilon_i \varepsilon_j$  and terms proportional to  $\varepsilon_i \varepsilon_j \varepsilon_k$  one can write:

$$a_i a_j a_k b_{ijk r} = a_i^3 b_{111r} + a_i^2 \varepsilon_i b_{i11r} \quad r = 1, \dots, n \quad (31)$$

After substituting and rearranging, equation (29) can be written in matrix form as:

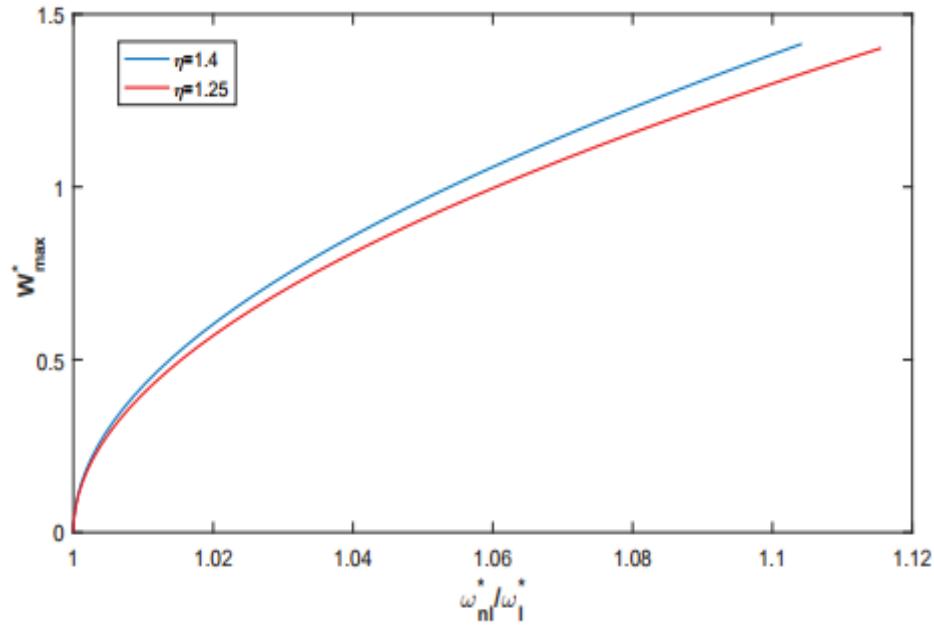
$$([K_r^*] - \omega^2 [M_r^*]) \{A_r\}_R + \frac{3}{2} [\alpha_r^*] \{A_r\}_R = \left\{ -\frac{3}{2} a_r^3 b_{111r}^* \right\} \quad (32)$$

### 3. NUMERICAL RESULTS

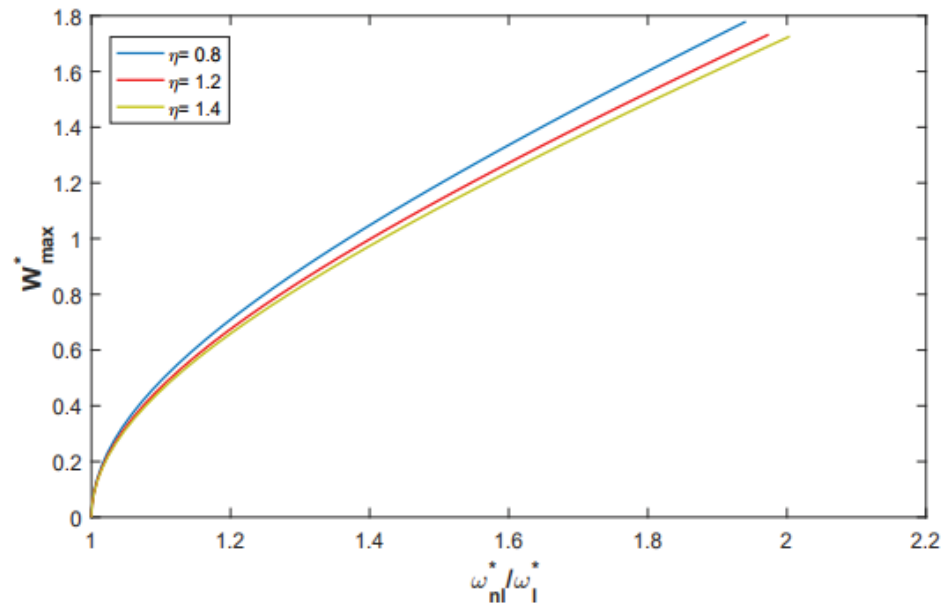
Based on the multimode mode approach, the results obtained here are given for C-C stepped circular arches in the neighborhood of the first mode shape.

The Fig. 4 and 5 show the effect of the variation in the cross-section on the dimensionless frequency ratio dependence on the maximum vibration amplitude.



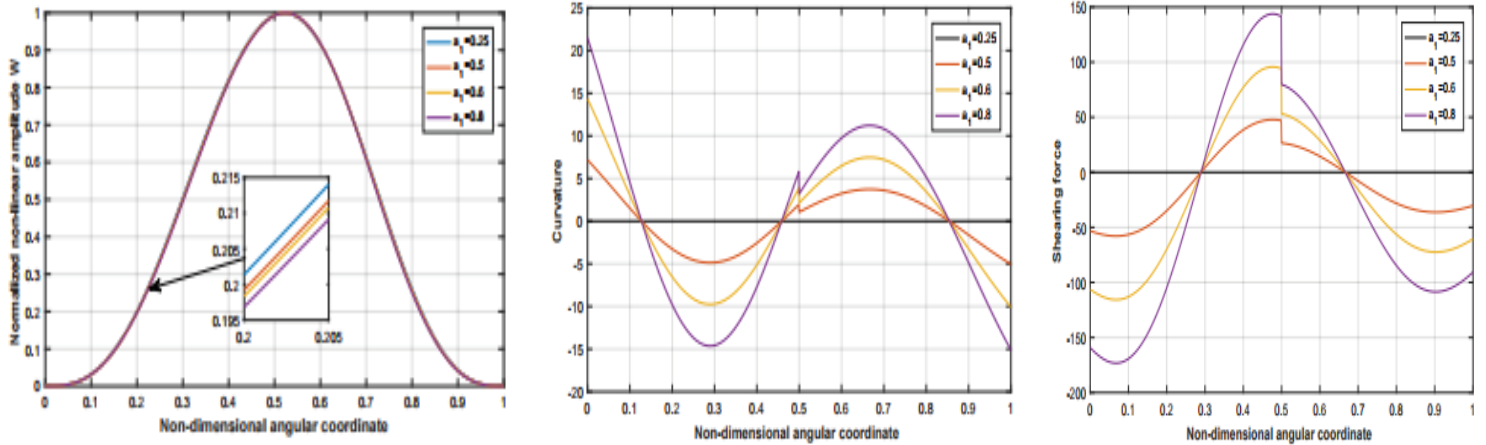


**Fig.4:** Backbone curve of symmetric stepped circular arch for  $\eta = 1.25$  and  $1.4$

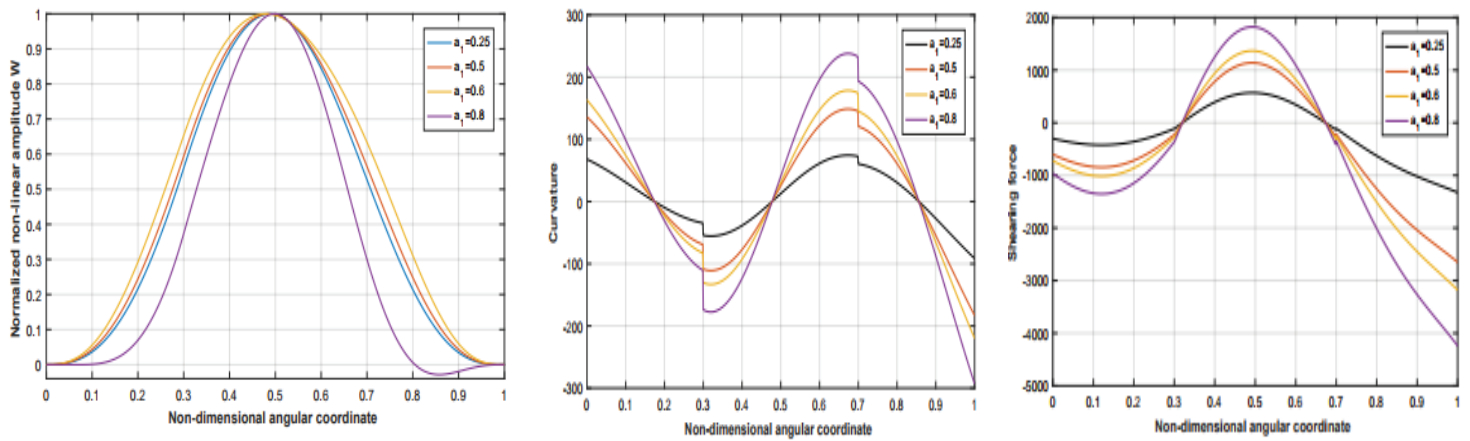


**Fig.5:** Backbone curve of symmetrical C-C stepped arch with  $\varphi_1/\varphi_0 = 0.3$ ,  $\varphi_2/\varphi_0 = 0.7$  and various values of  $\eta$ .

The non-linear frequency ratio versus the non-dimensional vibration amplitude curves of an unsymmetric and symmetric stepped circular arches clamped at both ends are shown respectively in Fig. 4 and 5 for the first non-linear mode shape by taking into account various values of  $\eta$ . The hardening type of geometrical non-linearity can be clearly observed.



**Fig.5:** The associated first normalized non-linear tangential displacement, non-linear curvature and non-linear shearing force of a C-C symmetric stepped circular arch for various vibrations level.



**Fig.5:** The associated first normalized non-linear tangential displacement, non-linear curvature and non-linear shearing force of symmetric stepped circular arch for various vibrations level.

The amplitude dependent normalized first nonlinear mode shape, the corresponding curvature and shearing force of unsymmetric and symmetric stepped circular arches are plotted respectively in Fig. 5 and 6 for various vibration amplitudes.

#### 4 CONCLUSIONS

The geometrical non-linearity in free in-plane vibration of inextensible stepped circular arches were analyzed based on Euler Bernoulli theory and the Von Karman geometrical nonlinearity assumptions. For simplification, the complicating effects such as rotary inertia and shear deformation were ignored. The natural frequencies of arch were obtained iteratively using Newton-Raphson algorithm, and compared with those available in the literature. The linear modes shapes were plotted and used as a basic function on non-linear analysis. The kinetic and total strain energy were written in each interval of the arch and discretized into a set of non-linear algebraic equations. Using the Hamilton's principle energy and spectral analysis, the problem was reduced into a set of non-linear algebraic equations solved numerically by an approximate explicit method the so-called second formulation. Based on the multimode approach, the effects of the variation of the cross section area on non-linear behavior of the arches were studied. The first non-linear deflections, curvatures and shearing forces curves were plotted.

## REFERENCES

- [1] P. A. A. Laura, P. L. Verniere de Irassar, R. Carnicer, and R. Bertero, 'A note on vibrations of a circumferential arch with thickness varying in a discontinuous fashion', *Journal of Sound and Vibration*, vol. 120, no. 1, pp. 95–105, Jan. 1988, doi: 10.1016/0022-460X(88)90336-7.
- [2] N. M. Auciello and M. A. De Rosa, 'Free Vibrations Of Circular Arches: A Review', *Journal of Sound Vibration*, vol. 176, pp. 433–458, Sep. 1994, doi: 10.1006/jsvi.1994.1388.
- [3] R. H. Gutierrez, P. A. A. Laura, R. E. Rossi, R. Bertero, and A. Villaggi, 'In-plane vibrations of non-circular arcs of non-uniform cross-section', *Journal of Sound and Vibration*, vol. 129, no. 2, pp. 181–200, Mar. 1989, doi: 10.1016/0022-460X(89)90577-4.
- [4] E. Tufekci and O. Ozdemirci, 'Exact solution of free in-plane vibration of a stepped circular arch', *Journal of Sound and Vibration*, vol. 295, no. 3, pp. 725–738, Aug. 2006, doi: 10.1016/j.jsv.2006.01.048.
- [5] X. Tong, N. Mrad, and B. Tabarrok, 'IN-PLANE VIBRATION OF CIRCULAR ARCHES WITH VARIABLE CROSS-SECTIONS', *Journal of Sound and Vibration*, vol. 212, no. 1, pp. 121–140, Apr. 1998, doi: 10.1006/jsvi.1997.1441.
- [6] G. Karami and P. Malekzadeh, 'In-plane free vibration analysis of circular arches with varying cross-sections using differential quadrature method', *Journal of Sound and Vibration*, vol. 274, no. 3, pp. 777–799, Jul. 2004, doi: 10.1016/S0022-460X(03)00786-7.
- [7] I. el Hantati, A. Adri, H. Fakhreddine, R. Said, and R. Benamar, *GEOMETRICALLY NONLINEAR FORCED VIBRATIONS OF MULTIPLE-STEPPED EULER-BERNOULLI BEAMS*. 2020. doi: 10.47964/1120.9015.19055.
- [8] I. el Hantati, A. Adri, H. Fakhreddine, R. Said, and R. Benamar, 'A Multimode Approach to Geometrically Nonlinear Free and Forced Vibrations of Multisteped Beams', *Shock and Vibration*, vol. 2021, pp. 1–18, Apr. 2021, doi: 10.1155/2021/6697344.
- [9] M. El kadiri, R. Benamar, and R. G. White, 'IMPROVEMENT OF THE SEMI-ANALYTICAL METHOD, FOR DETERMINING THE GEOMETRICALLY NON-LINEAR RESPONSE OF THIN STRAIGHT STRUCTURES. PART I: APPLICATION TO CLAMPED–CLAMPED AND SIMPLY SUPPORTED–CLAMPED BEAMS', *Journal of Sound and Vibration*, vol. 249, no. 2, pp. 263–305, Jan. 2002, doi: 10.1006/jsvi.2001.3808.
- [10] Y. Zhao and H. Kang, 'In-plane free vibration analysis of cable–arch structure', *Journal of Sound and Vibration*, vol. 312, no. 3, pp. 363–379, May 2008, doi: 10.1016/j.jsv.2007.04.038.
- [11] H. Fakhreddine, A. Adri, S. Rifai, and R. Benamar, 'Nonlinear free and forced vibration of Euler-Bernoulli beams resting on intermediate flexible supports', *MATEC Web Conf.*, vol. 211, p. 02003, 2018, doi: 10.1051/mateconf/201821102003.
- [12] Kiusalaas J 'Numerical Methods in Engineering with MATLAB' Engineering mathematics and programming', *Cambridge University Press*. 2010
- [13] A. Shahba, R. Attarnejad, M. T. Marvi, and V. Shahriari, 'Free Vibration Analysis of Non-uniform Thin Curved Arches and Rings Using Adomian Modified Decomposition Method', *Arab J Sci Eng*, vol. 37, no. 4, pp. 965–976, Jun. 2012, doi: 10.1007/s13369-012-0228-z.

## SIMPLE AND COMPLEX MODELLING OF SEAT-TYPE ABUTMENT-BACKFILL SYSTEMS

Ioannis G. Mikes<sup>1</sup>, Andreas J. Kappos<sup>1</sup>

<sup>1</sup> Department of Civil Infrastructure and Environmental Engineering, Khalifa University  
Abu Dhabi, United Arab Emirates  
e-mails: [ioannis.mikes@ku.ac.ae](mailto:ioannis.mikes@ku.ac.ae), [andreas.kappos@ku.ac.ae](mailto:andreas.kappos@ku.ac.ae)

---

### Abstract

*The response of the seat-type abutment-backfill system under a dynamic excitation and its contribution to the structural system of the entire bridge is usually ignored in practice in Europe, since the designers prefer providing joint gap sizes larger than the required for the design earthquake. In the high seismic hazard areas of the US, various versions of Caltrans Guidelines prescribe a relatively simple way to account for the abutment – backfill interaction. However, the design of Caltrans abutments is based on the ‘fully sacrificial’ approach, wherein the backwall ‘shears off’ at an early stage, while in other countries the detailing of the deck-abutment interface is such that a plastic hinge forms at the base of the backwall which is detailed for ductile behaviour. In all cases, if assessment of the bridge safety beyond the design earthquake is sought (e.g. in fragility analysis), it is essential to properly account for the response of the bridge when the end joint is closed.*

*This paper focuses on seat-type abutments with backwall hinging. In a practical context, a ‘simple’ model in this case consists of a spring-gap element that models the entire abutment-backfill system, while a ‘complex’ model includes explicit modelling of the abutment using beam-column elements, and of the backfill behind it using one or multiple soil springs. For dynamic response-history analysis, dashpots are also needed for modelling radiation damping. The issues of the number and the arrangement of the spring-dashpot systems and their nonlinear constitutive laws are addressed herein and several configurations are studied. SAP 2000 is used for analysing a typical overpass bridge with seat-type abutments and joints in both the longitudinal and transverse directions, for a number of spectrum compatible records. A series of pushover analyses of the ‘complex’ model are also carried out; their output can be used to define the (single) spring properties of the simple model. Interesting conclusions are drawn, both with regard to the spring configuration and to the difficulties in combining the various nonlinear elements in SAP 2000.*

**Keywords:** Bridges, Abutment, Backfill, Seismic design

---

## 1 INTRODUCTION

While in integral abutment bridges it is now customary to model the stiffness of the backfill soil (and indeed the forthcoming new Eurocode 8-2 makes mandatory to model the effect of interaction between soil and abutments in such bridges), in the case of seat-type abutments this interaction is usually ignored in practice. In a number of European countries, designers prefer to provide end joint gaps substantially larger than the expected seismic displacement of the deck under the design earthquake, so that the joint remains open and the contribution of the backfill can be ignored. In various versions of Caltrans' Guidelines [1], which are implemented in the high seismic hazard regions of the US, seat-type abutments backfill systems in straight bridges are taken into account in a simplified way. Specifically, in the longitudinal direction, the simplified recommendations of the current Caltrans are based on the work of Shamsabadi et al. [2], which, in turn, is based on large-scale abutment tests at UCLA. For the transverse direction a nominal spring stiffness is suggested; this stiffness is not directly correlated to the actual stiffness of the shear keys or the abutment-backfill system, but it is simply meant to suppress unrealistic (?) response modes that would emerge in the transverse direction in the case of a completely unrestrained deck end [1]. Modelling of seat-type abutments is reviewed in the reports of Aviram et al. [3] and the more recent one by Omrani et al. [4], where there are also practical guidelines for modelling in SAP 2000 and OpenSees, respectively. However, Caltrans and the aforementioned reports refer to the 'fully sacrificial' backwall approach, i.e. a backwall that 'shears off' almost immediately after gap closure.

In this paper, the behaviour of seat-type abutment-backfill systems with hinging backwall and exterior shear keys is examined using 'simple' models consisting of one spring-gap element at each end that models the entire abutment-backfill system, and 'complex' models including explicit modelling of the abutment using beam-column elements, and of the backfill behind it using one or multiple soil springs. For a real bridge selected as a case study, in the longitudinal direction, nonlinear static analyses of various configurations of this system are conducted and are compared with a similar backwall-backfill system designed following the 'fully sacrificial' approach. In both the longitudinal and transverse directions, nonlinear response history analyses for different levels of seismic action are carried out to investigate the feasibility of the aforementioned configurations and their effect on the response of the entire bridge. The effect of the joint gap size is also investigated herein and several conclusions are drawn, regarding the importance of accounting for the deck-abutment-backfill interaction and the modelling challenges that it poses.

## 2 OVERVIEW OF THE CASE-STUDY BRIDGE

The studied bridge (called T7) is an actual overpass of Egnatia Motorway in northern Greece, designed by a German firm and overall representative of modern bridge design practice in Europe. It is a three-span concrete structure, designed for earthquake according to the 2000 Greek national seismic code (EAK2000), very similar to the then current draft of Eurocode 8-2. The total length of the bridge is 99 m, consisting of a 45 m central span and two 27 m outer spans, while the longitudinal slope of its axis is equal to 7%. The deck consists of a 10 m wide prestressed concrete box girder section with a continuously changing cross section along the length of the bridge. The two piers of the bridge have a circular cross section, with a diameter of 2 m and are monolithically connected to the deck; their clear heights are 5.94 m and 7.93 m (Fig. 1).

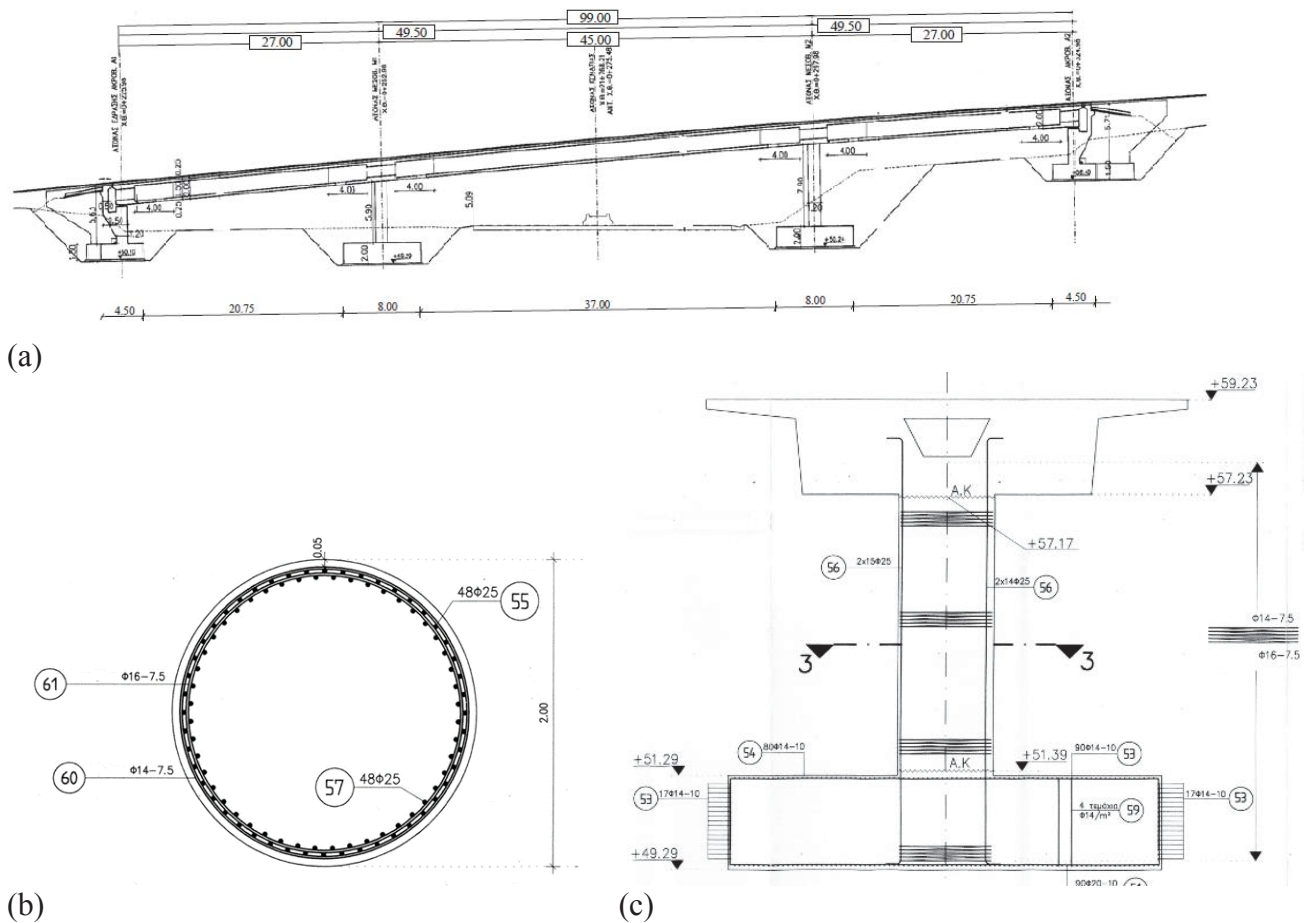


Figure 1: (a) Longitudinal section of the bridge, (b) Pier section, (c) Section close to pier

The deck is supported on seat-type abutments (Fig. 2), which include backwall, wingwalls, and external shear keys, through two elastomeric bearings with dimensions (mm) equal to  $350 \times 450 \times 136$ . The total heights of the abutments are equal to 5.63 m and 5.71 m, while the height of both backwalls is 2.45 m. The deck is separated from the seat-type abutments with joints of 100 mm in the longitudinal direction and 150 mm in the transverse direction.

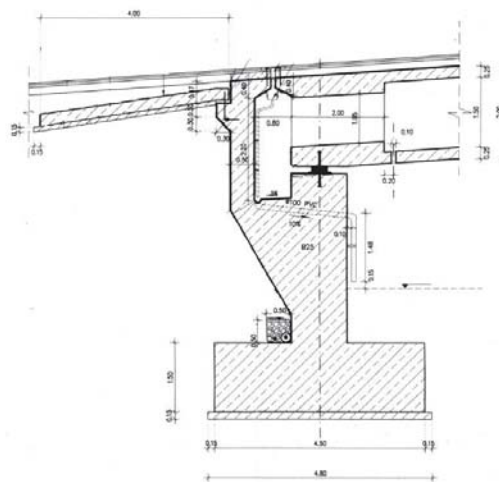


Figure 2: Section at the abutment



The piers, as well as the abutments, rest on surface footings (due to the relatively firm soil). The pier footings are  $9.0 \text{ m} \times 8.0 \text{ m} \times 2.0 \text{ m}$ , while the abutment footings are  $12.0 \text{ m} \times 4.5 \text{ m} \times 1.5 \text{ m}$ . The soil in the bridge area mainly consists of moderately stiff clay formations, corresponding to soil class C according to Eurocode 8 [5]. In the absence of measured data, a shear wave velocity  $V_s = 300 \text{ m/s}$  was assumed for modelling the properties of clay, while its specific weight was taken as  $\gamma = 20 \text{ kN/m}^3$ .

### 3 FINITE ELEMENT MODELLING OF THE BRIDGE

#### 3.1 Modelling of concrete members

The bridge was modelled using the broadly used SAP 2000 software [6] as shown in Fig. 3. The prestressed deck is deemed to remain elastic during the seismic event and it was modelled as a non-prismatic section, varying along its length, to take into account its changing shape along the longitudinal axis. The inelastic behaviour expected to develop at the bridge piers was modelled with plastic hinges at both ends of each pier (monolithic connection to the deck). SAP 2000 uses a moment-rotation curve for its plastic hinge elements, which was defined on the basis of the pertinent moment-curvature diagram. The length of the plastic hinges was calculated as the weighted average of two relationships available for piers [7], [8]:

$$L_{pl} = 0.08L_s + 0.022d_{bl}f_y \quad (1)$$

$$L_{pl} = 0.6D \left[ 1 + \frac{1}{6} \min \left( 9; \frac{L_s}{D} \right) \right] \quad (2)$$

where  $L_{pl}$  is the calculated plastic hinge length,  $L_s$  is the shear span of the pier,  $d_{bl}$  is the diameter of the longitudinal bars,  $f_y$  is the yield strength of concrete and  $D$  is the diameter of the pier. A weighting factor of 0.7, is selected for relationship (2) since it was derived from numerous experimental results and was specifically created for circular columns, whereas relationship (1) is recommended for general use.

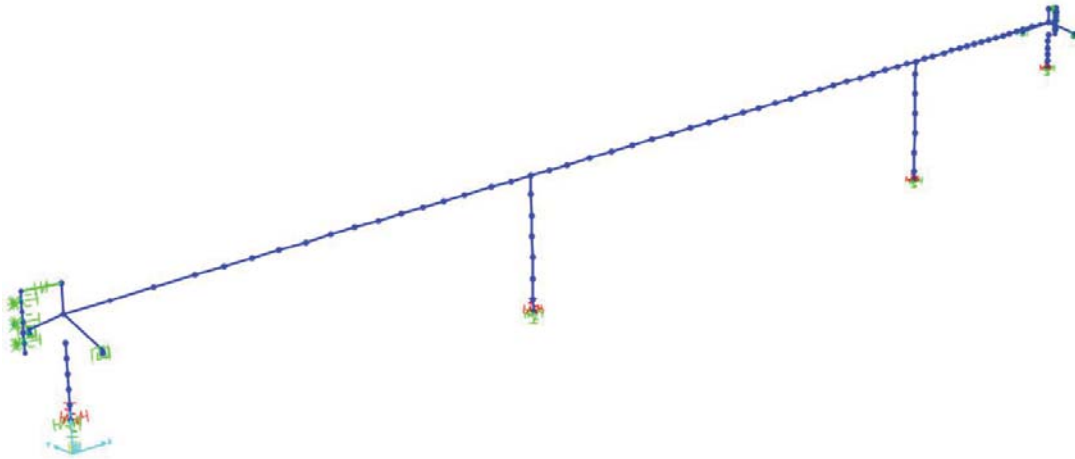


Figure 3: Finite element model of the bridge

Moment-curvature ( $M-\phi$ ) curves are obtained at every pier end, using the section analysis software AnySection [9] for the axial load  $N_{G+0.3}$ . The constitutive models of the materials used in section analysis were the model by Mander et al. as adapted by Paulay & Priestley [7] for confined concrete, the nonlinear model of EN1992-1 [10] for unconfined concrete and the model of Park and Sampson [11] for reinforcing steel. To define the (apparent) yield point,

the  $M-\phi$  curves were bilinearised by adopting the criteria of 15% strength drop and equality of areas under the “exact” and the bilinear curve (equal energy absorption).

The horizontal shear behaviour of the (common) elastomeric bearings was considered bilinear, while in the other directions the bearings are considered to respond linearly. All the relevant stiffnesses, namely initial and post-yield horizontal shear stiffness ( $K_{h,el}$  and  $K_{h,pl}$ ), flexural stiffnesses ( $K_{bx}$  and  $K_{by}$ ) and axial stiffness ( $K_v$ ) were calculated according to [12].

Soil-structure interaction at the foundations of the piers and the abutments of the bridge was taken into account, utilising equivalent linear springs at the bases of the respective beam-column elements of the model. The stiffness values of these springs were calculated according to Mylonakis et al. [13].

The seat-type abutment-backfill system was modelled in detail, as its behaviour is the main focus of this study. This ‘complex’ (in a practical design context) abutment-backfill model is depicted in Fig. 4. It consists of separate beam-column elements which represent the stem wall and the backwall, while the behaviour of the backfill soil was modelled using multiple pairs of springs and dampers (Kelvin-Voigt elements) distributed along the height of the stem wall and the backwall. A moment-curvature ( $M-\phi$ ) curve was derived from AnySection for the expected plastic hinge at the base of the backwall, while the estimated length of this plastic hinge was calculated from the relationship of Biskinis [14], developed for concrete walls:

$$L_{pl} = 0.1L_s + 0.2h \quad (3)$$

A gap element was placed between the top of the backwall and the end of the deck; several initial gap sizes were used, to investigate the effect of the gap size on the response of the bridge. The constitutive models used for the springs and dashpots representing the backfill soil are described in the next section.

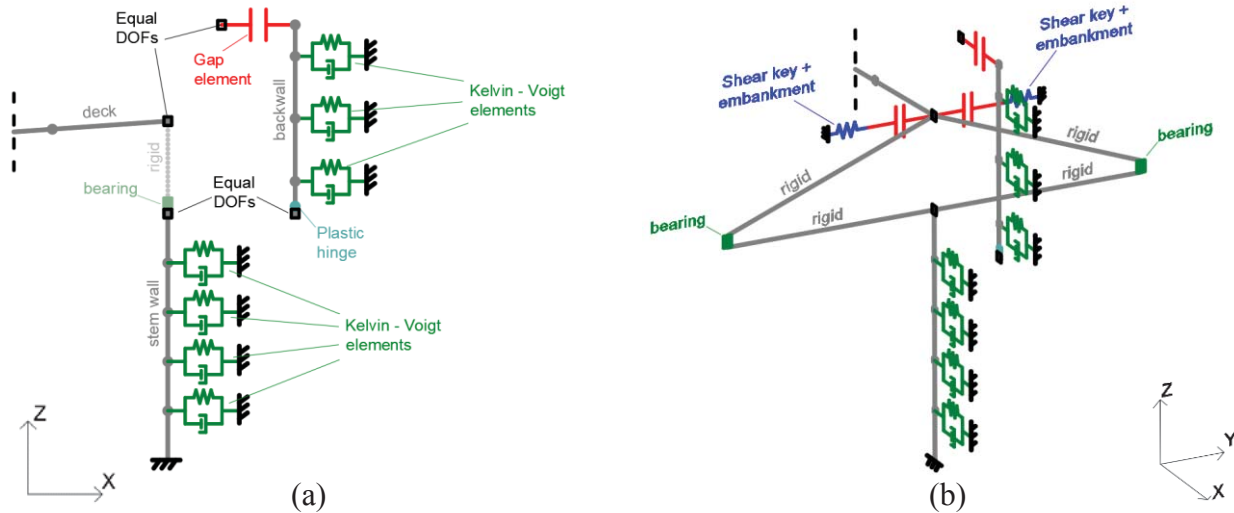


Figure 4: (a) Longitudinal section and (b) 3-d view of the ‘detailed’ abutment-backfill model

### 3.2 Modelling of the backfill soil behaviour

The radiation damping and the hysteretic behaviour of the backfill soil in the longitudinal direction are modelled with the use of multiple spring-dashpots along the abutment, each of which consists of a viscous damper and a nonlinear spring (called “nonlinear link element” in SAP 2000) placed in parallel, as shown in Fig. 4. The effect of the number of these pairs and their position in the abutment-backfill was investigated through a series of non-linear static (pushover) analyses.

The closed-form relationship recently proposed by Khalili-Tehrani et al. [15] was adopted as the backbone curve of the nonlinear backfill springs. This relationship is based on the log-spiral hyperbolic (LSH) model proposed by Shamsabadi et al. [16], which was verified against large-scale experiments on backwall – backfill systems with different types of soil. The relationship is given by:

$$F(y) = f_\delta \frac{a_r y}{\hat{H} + b_r} \hat{H}^n \quad (4)$$

where  $f_\delta$  is a function of the wall – soil interface friction angle,  $a_r$  and  $b_r$  express backfill capacity and wall displacement at capacity, respectively, and  $\hat{H}$  is the normalised value of the wall height.

The above hyperbolic relationship and its parameters were derived from a calibration of multiple experimental results, which were conducted using a 1.7m high backwall specimen, pushed horizontally against backfill of various soil types, considering it a typical sacrificial backwall with almost no shear resistance, i.e. designed to break almost immediately after gap closure, as per the relevant Caltrans provisions [1] (also found in older Caltrans guidelines). As a result, the behaviour of the abutment – backfill was governed by the passive pressures of the backfill soil developing uniformly along the height of the wall. However, in the studied bridge, the backwall is designed to form a plastic hinge at its base. Consequently, after gap closure, it does not shear off but it has a predominantly flexural response, and the backfill soil near the top of the wall deforms more than at its base. Therefore, in the longitudinal direction, the abutment was modelled with separate frame elements representing the stem wall and the backwall, while the backfill soil was modelled with multiple springs to better capture the differing soil deformation along the backwall height.

For the implementation of (4), a dense granular backfill soil, typically suggested by the pertinent codes/guidelines (e.g. [1]) is considered, with  $\phi = 40^\circ$ ,  $c = 0$ ,  $\gamma = 20\text{kN/m}^3$ , soil strain at 50% of the ultimate stress  $\varepsilon_{50} = 0.0035\text{m}$  (according to Shamsabadi et al. [16] for a similar type of soil),  $\nu = 0.35$  and ultimate deformation equal to  $0.05H_{bw} = 0.1225\text{m}$ , where  $H_{bw}$  is the height of the backwall; the value of  $0.05H_{bw}$  is a common estimation of ultimate deformation for granular backfill soil, derived from large-scale experiments [15], [16].

The nonlinear link provided by SAP 2000 is a multilinear one, hence the previously calculated hyperbolic curve was converted to a quadrilinear approximation. Furthermore, to capture the full-range behaviour of the system, a final descending branch was added to this quadrilinear curve, based on a linear approximation of experimental descending branches for granular soils found in Cole & Rollins [17]; both curves are presented in Fig. 5. In the absence of other options, the compression-only “Concrete” hysteresis model, available in SAP 2000, was adopted as the hysteresis rule of the nonlinear backfill springs.

Last, the dashpot coefficient of the viscous dampers was estimated based on the work of Mylonakis et al. [13] which refers to footings rather than backwalls; so an adjustment was made (as also done in [18]) to account for the fact there is no soil above the backwall. The estimated dashpot coefficient was found to be equal to 13.5 MN s/m.

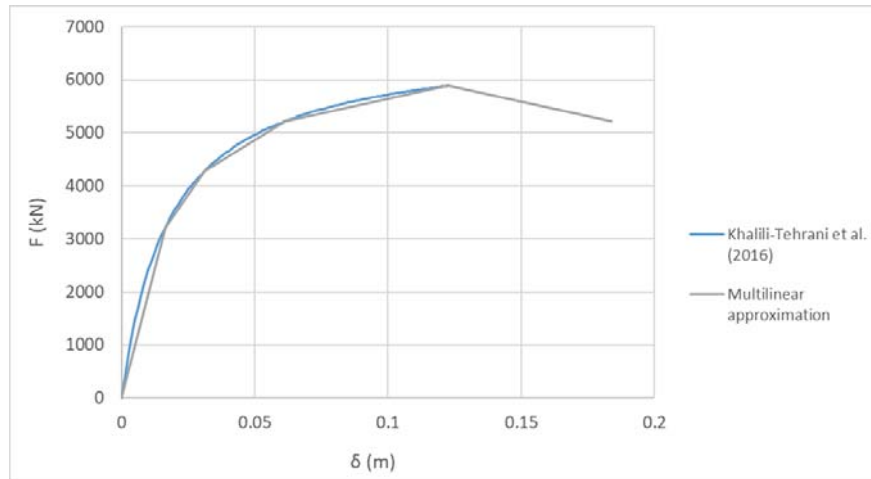


Figure 5: Backfill hyperbolic force-deformation curve according to Khalili-Tehrani et al. [15] and its multilinear approximation made herein

In the transverse direction, it is considered that the external shear keys of the bridge are practically rigid and remain elastic (which was indeed the case here), and the abutment-backfill system was modelled as a pair of p-y springs which represent the bridge-embankment interaction in the transverse direction, according to the model of Xie et al. [19]. This model, which was derived from multiple 3-D continuum finite element analyses of abutment-backfill models verified against the recorded response of Painter Street Bridge during the 1992 Petrolia earthquake, provides closed-form relationships for the calculation of the ultimate embankment capacity at top of the 3D embankment in the transverse direction ( $\Sigma p_{ult,T}$ ), the value of the embankment displacement that corresponds to 50% of  $\Sigma p_{ult,T}$  ( $y_{50,T}$ ) and the value of the transverse secant stiffness at  $y_{50,T}$  ( $K_{s,T}$ ). However, no relationship for the calculation of the embankment displacement at  $\Sigma p_{ult,T}$  or the estimation of the stiffness when the displacements are larger than  $y_{50,T}$  is provided in [19]. In view of this, it was assumed that the full force – deformation curve in the transverse direction is a bilinear one and that the slope of the second branch of this bilinear curve is equal to about 20% of  $K_{s,T}$ . The bilinear curve that was finally derived is shown in Fig. 6, using the same backfill soil properties which have already been described for the longitudinal direction.

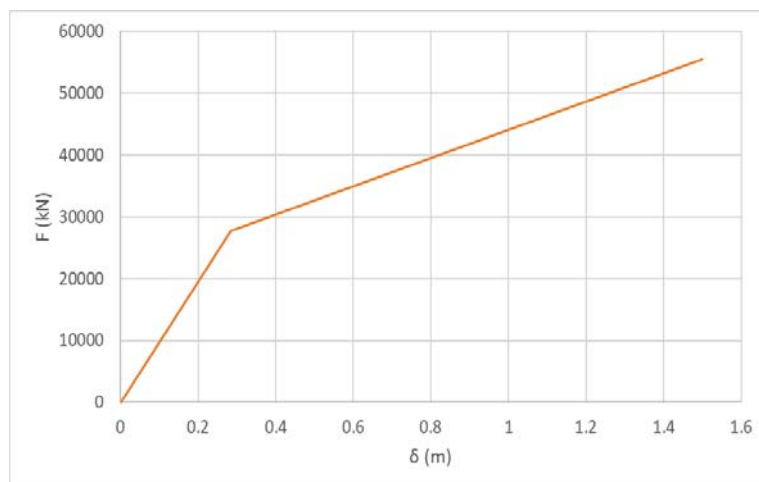


Figure 6: Embankment bilinear force-deformation curve in the transverse direction, based on the model of Xie et al. [19]

## 4 NONLINEAR ANALYSIS OF THE BRIDGE

### 4.1 Nonlinear static (pushover) analysis of the abutment-backfill system

In order to investigate the rather complex inelastic behaviour of the abutment-backfill system in the longitudinal direction, before integrating it into the entire bridge model, multiple pushover analyses of different configurations of the system in the longitudinal direction were conducted. The main goals of these analyses were to define the importance of the contribution of the backfill soil after gap closure, to investigate the effect of the number and the positions of soil springs and dashpots and, finally, to compare the behaviour of backwalls which form a plastic hinge at their base with that of ‘fully sacrificial’ (Caltrans type) backwalls which ‘shear off’ as soon as the joint gap closes.

The first issue to be addressed is whether the contribution of the lower part of the backfill, i.e. the area behind the stem wall, should be taken into account. In order to investigate the influence of this area, two additional analyses were conducted; one of the abutment alone, without any contribution from the backfill, and one with the lower part of the backfill considered. The respective models are shown in Fig. 7b and 7c. and the resistance curve (i.e. base shear vs displacement at the top of the backwall) is depicted in Fig. 8 and compared with the model which has springs along the entire height of the abutment (Fig. 7a). It is clear that the contribution of the examined part of the backfill is negligible and hence, in the following analyses, only the part of the backfill behind the backwall is considered. This result is anticipated, since the very high stiffness of the stem wall results in little deformation of the springs attached to it, consequently leaving them almost inactive.

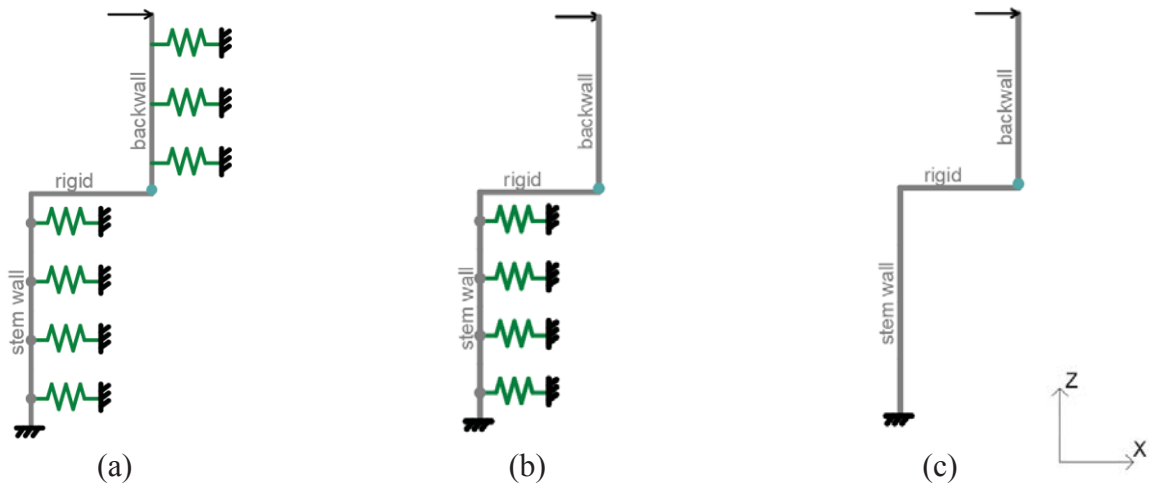


Figure 7: Longitudinal abutment model: (a) with backfill soil springs behind the entire abutment (b) with backfill soil springs behind the stem wall, (c) without backfill soil springs

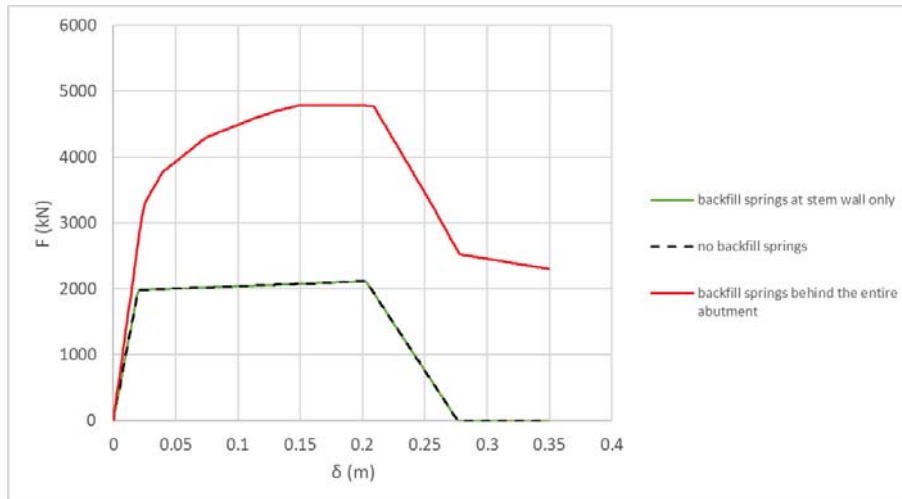


Figure 8: Resistance curve of the abutment with backfill soil springs behind the stem wall, behind the entire abutment and without backfill soil springs

The next issue addressed was the effect of the position and the number of the backfill springs along the height of the backwall. Some of the configurations explored are depicted in Fig. 9; note that in the multiple spring configurations the influence area of each spring is the same. From the resulting resistance (pushover) curves in Fig. 10, it is clear that the number of the springs does not affect the abutment-backfill behaviour significantly, while for 3 springs or more, hardly any difference is observed in the pushover curves, except for the descending branch that follows the failure of the backwall. This difference is caused by the way that the strength drop of the backwall is modelled in the software due to different discretisation of the frame element of the backwall in each case, since the backwall element is divided at each of its connections with the springs; namely, the shorter an element is, the more it is capable of capturing an abrupt strength drop [20]. However, in the case that a single spring is used, placing it at the top of the backwall seriously overestimates the maximum strength of the backfill by almost 60%. It is stressed here that the springs do not contribute to the response of the system in the same way; the closer a spring is to the top of the backwall, the earlier it reaches its maximum strength (Fig. 11), due to the hinging at the base.

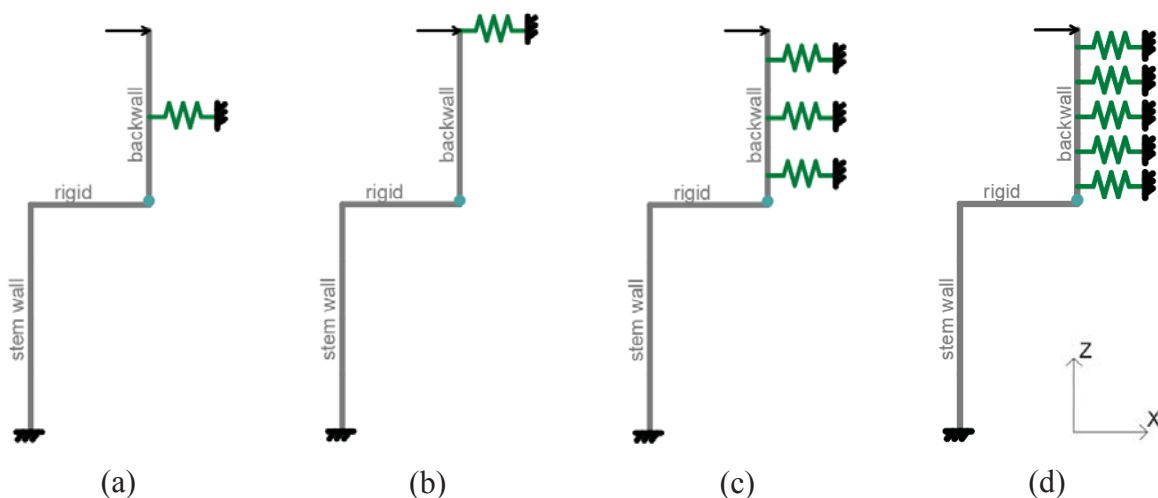


Figure 9: Longitudinal abutment model with: (a) a single backfill soil spring in the middle of the backwall, (b) a single backfill soil spring at the top of the backwall, (c) 3 springs along the height of the backwall, (d) 5 springs along the height of the backwall



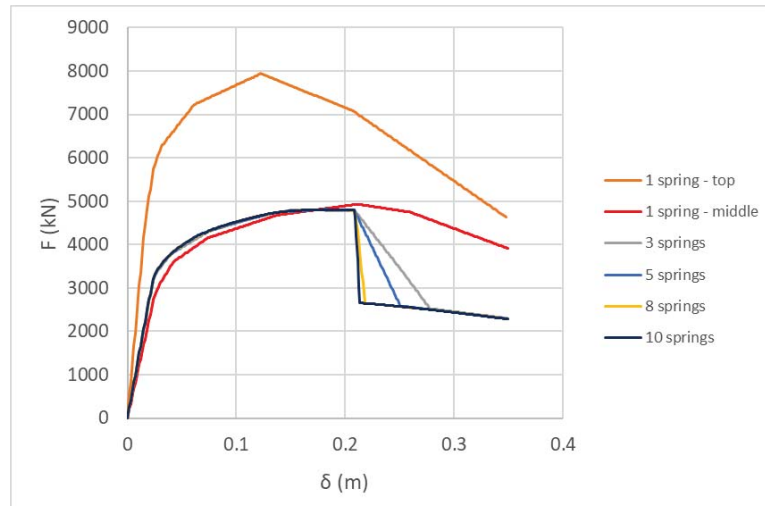


Figure 10: Resistance curves for various numbers of distributed backfill soil springs along the height of the backwall and for a single spring at the top of the backwall

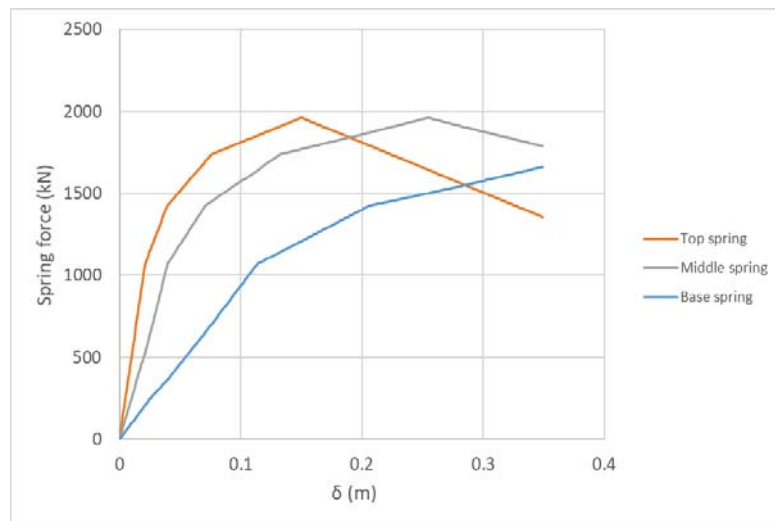


Figure 11: Axial forces developed at the backfill soil springs during the pushover analysis of the abutment-backfill system in the case of 3 used springs along the height of the backwall (Fig. 9c)

The case of the ‘fully sacrificial’ backwall with no shear resistance that shears off right after the gap closure with a lateral force applied at its top, was also examined with the use of a backwall model with a roller support at its base, as shown in Fig. 12a. As seen in Fig. 12b, in this case each of the backfill soil springs contributes equally to the response of the system, meaning that a model which consists of a single spring would be enough for modelling the behaviour of the entire abutment-backfill system adequately. The maximum contribution of the backfill soil springs in the case of the ‘fully sacrificial’ backwall is larger by 15% than in the case that the backwall yields and eventually fails in flexure. The ‘fully sacrificial’ backwall has also higher initial stiffness but it develops its maximum strength at a smaller displacement (Fig. 13). These results can be attributed to the fact that in the case of the ‘fully sacrificial’ backwall every spring along the backwall height is activated simultaneously from the beginning, contrary to the case of the backwall with the plastic hinge at its base.

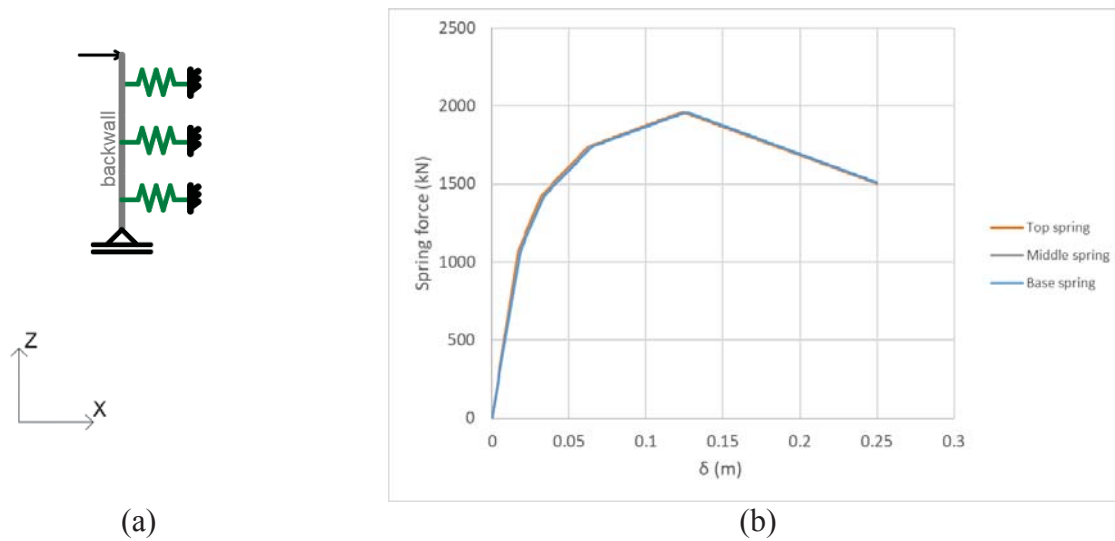


Figure 12: (a) Longitudinal backwall model with no shear resistance ('fully sacrificial') and 3 backfill soil springs along its height, (b) axial forces developed at the backfill soil springs during the pushover analysis of the 'fully sacrificial' backwall-backfill system in the case of 3 used springs along the height of the backwall (Fig. 12a)

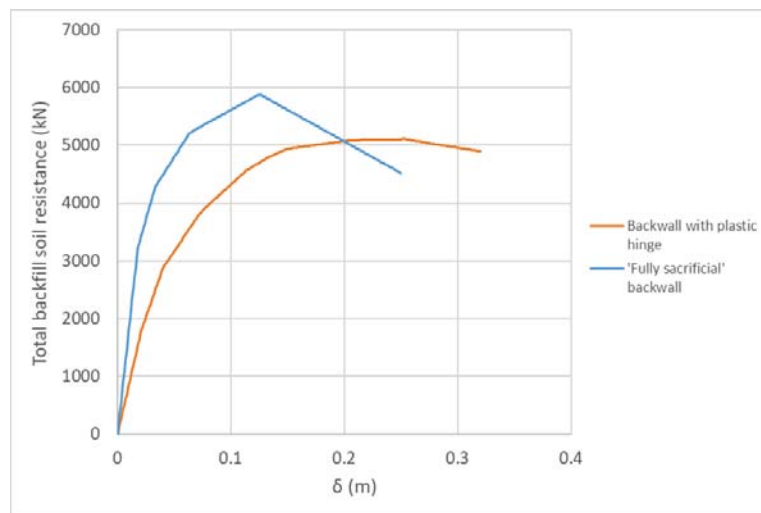


Figure 13: Total contribution of the backfill soil springs in the pushover analyses of backwall with plastic hinge formed at its base and 'fully sacrificial' backwall

#### 4.2 Nonlinear static (pushover) analysis of the bridge model

Having compared the spring configurations that represent the abutment-backfill system, nonlinear static (pushover) analyses of the entire T7 bridge model were conducted, for both the 'fully sacrificial' backwall case and the backwall with a plastic hinge formed at its base. Simple spring configurations (such as a single nonlinear spring for the case of the 'fully sacrificial' case) and more complex models, including detailed modelling with nonlinear beam-column elements representing the abutment and nonlinear springs along the height of the backwall, which represented the backfill soil were used. Five longitudinal joint gap sizes, namely 0 cm, 2.5 cm, 5 cm, 7.5 cm and 10 cm were explored, to study the influence of the gap size. The results are given in Fig. 14 and Fig. 15. The total base shear after gap closure is 23.5% and 30% larger than in the case without gap closure for the 'fully sacrificial' and the backwall with a plastic hinge at its base, respectively.

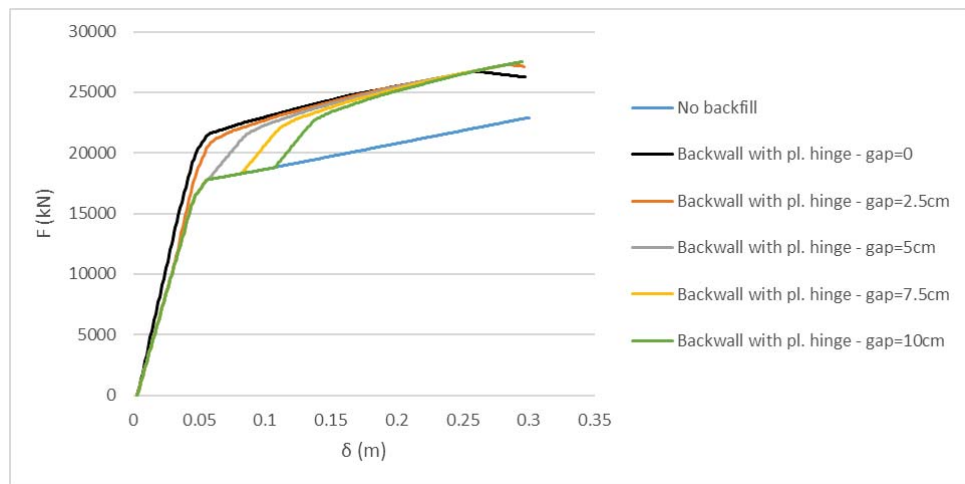


Figure 14: Resistance curves of the entire bridge with 'detailed' abutment-backfill model and backwall with plastic hinge at its base in the longitudinal direction, for various joint gap sizes

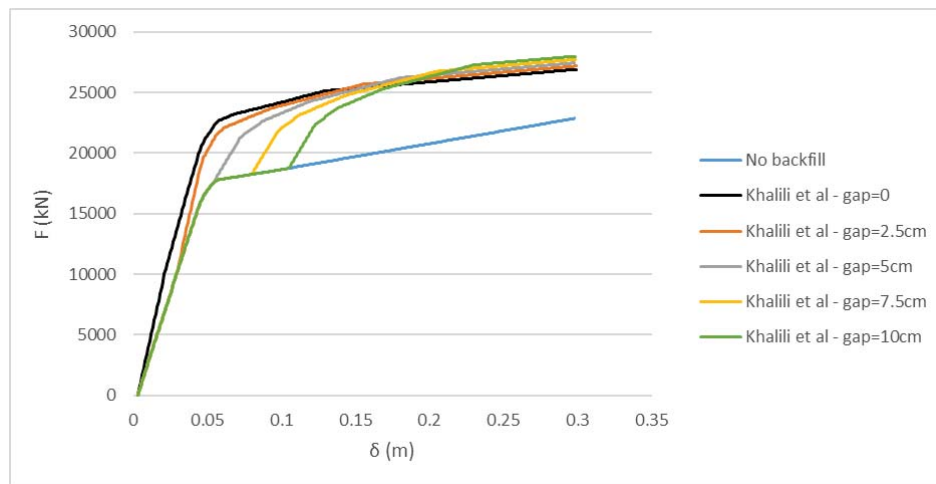


Figure 15: Resistance curves of the entire bridge with single spring according to Khalili-Tehrani et al. [15] representing a 'fully sacrificial' backwall in the longitudinal direction, for various joint gap sizes

The effect of simple or complex modelling of the abutment-backfill system can be seen in Fig. 16, where both the detailed and the single-spring model are used to derive resistance curves for the bridge, and these are compared with the detailed (multi-spring) model and the reference case where the abutment-backfill system is ignored (which is the situation prior to gap closure). It is clear (and expected) that when the single spring is defined from the analysis of the abutment-backfill system, the detailed and the simple model produce practically identical curves; however, when the single spring is based on the Khalili et al. [15] model, which corresponds to the case of a shearing-off backwall, the simple model overestimates the strength of the system for the reasons discussed earlier in the paper. Regarding the effect of gap size, the contribution of a shearing-off backwall and a backwall that forms a plastic hinge at its base were very similar for all examined joint gap sizes.

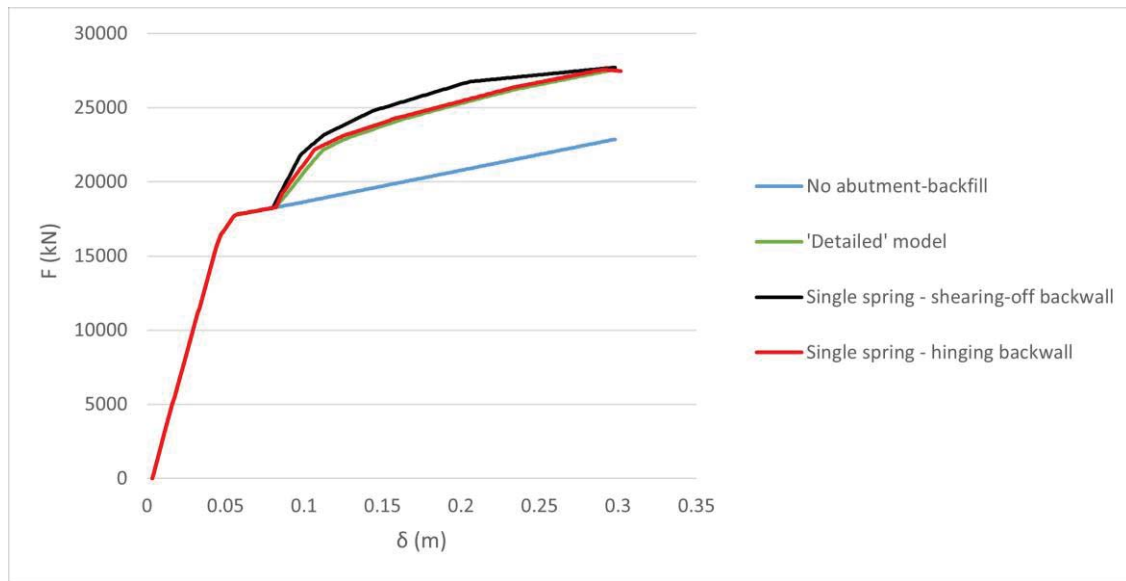


Figure 16: Comparison of the resistance curves of the entire bridge in the longitudinal direction, modelled with 'detailed' and 'simple' (single spring) model representing either a 'fully sacrificial' backwall and a back-wall with plastic hinge at its base, for joint gap size equal to 7.5 cm.

#### 4.3 Nonlinear response history analysis

The nonlinear dynamic response of the bridge was studied to better understand its overall dynamic behaviour and to identify modelling issues that should be further addressed. For the dynamic response history analysis, the bridge is subjected to a set of artificial accelerograms scaled to various levels of intensity, multiples of the design seismic action (0.16g, 0.32g and 0.48g, considering soil class C according to Eurocode 8, but assuming that  $T_D = 4s$  instead of  $T_D = 2s$  suggested by EC8, as a more representative value of high seismicity regions [21], [22]). In the longitudinal direction, 3 pairs of nonlinear spring and dashpots are used to represent the backfill, while in both directions separate gap elements are used.

The issue of modelling the joint gap was one of the focuses of the investigation. In SAP 2000, gaps are modelled with a separate element, which has zero stiffness when it is open and a user-defined stiffness value when it is closed. The latter value is difficult to define in a way such as to avoid numerical instabilities and to appropriately capture the force transfer between the elements which are adjacent to the gap during response history analysis; this is known from the literature [23] and has also been observed in the analyses conducted for the present work. According to Kim & Shinozuka [23], the stiffness of the gap element should not be larger than 1000 times the stiffness of the adjacent elements in order to avoid numerical instabilities. After conducting preliminary response history analyses of the examined bridge model, it was found out that the response quantities are significantly different when the gap element stiffness is equal to 100 times the stiffness of the adjacent elements or lower from those for gap element stiffness 1000 times the stiffness of the adjacent elements or larger. It was decided to set the gap stiffness equal to 1000 times the initial stiffness of the adjacent elements. However, in a nonlinear analysis, the stiffness of the adjacent elements varies with time, and numerical stability is not achieved in every response history analysis. Moreover, the existence of the gap element results in large analysis duration which becomes even larger as the level of the input ground motion increases and, most importantly, the time step at which the base of the backwall yields is very different even for very small differences in the gap element stiffness or the considered initial gap. The use of a nonlinear spring with a backbone curve that starts with a zero slope would be an alternative solution to avoid all the aforementioned prob-

lems. This solution was indeed utilized in the nonlinear *static* analyses with the ‘simple’ single-spring model; however, in the *dynamic* response history analyses with SAP 2000, it could not be implemented, since no compression-only hysteresis model provided by the software is compatible with such a backbone curve.

Some results of the analyses in the longitudinal and the transverse direction are plotted in Figures 17 and 18. In both directions, the deformation of the upper backfill-soil spring, the bearing deformation and the plastic rotations of the pier are depicted for various gap sizes and for the three selected levels of earthquake intensity. In the longitudinal direction, the derived backwall plastic rotations are also shown.

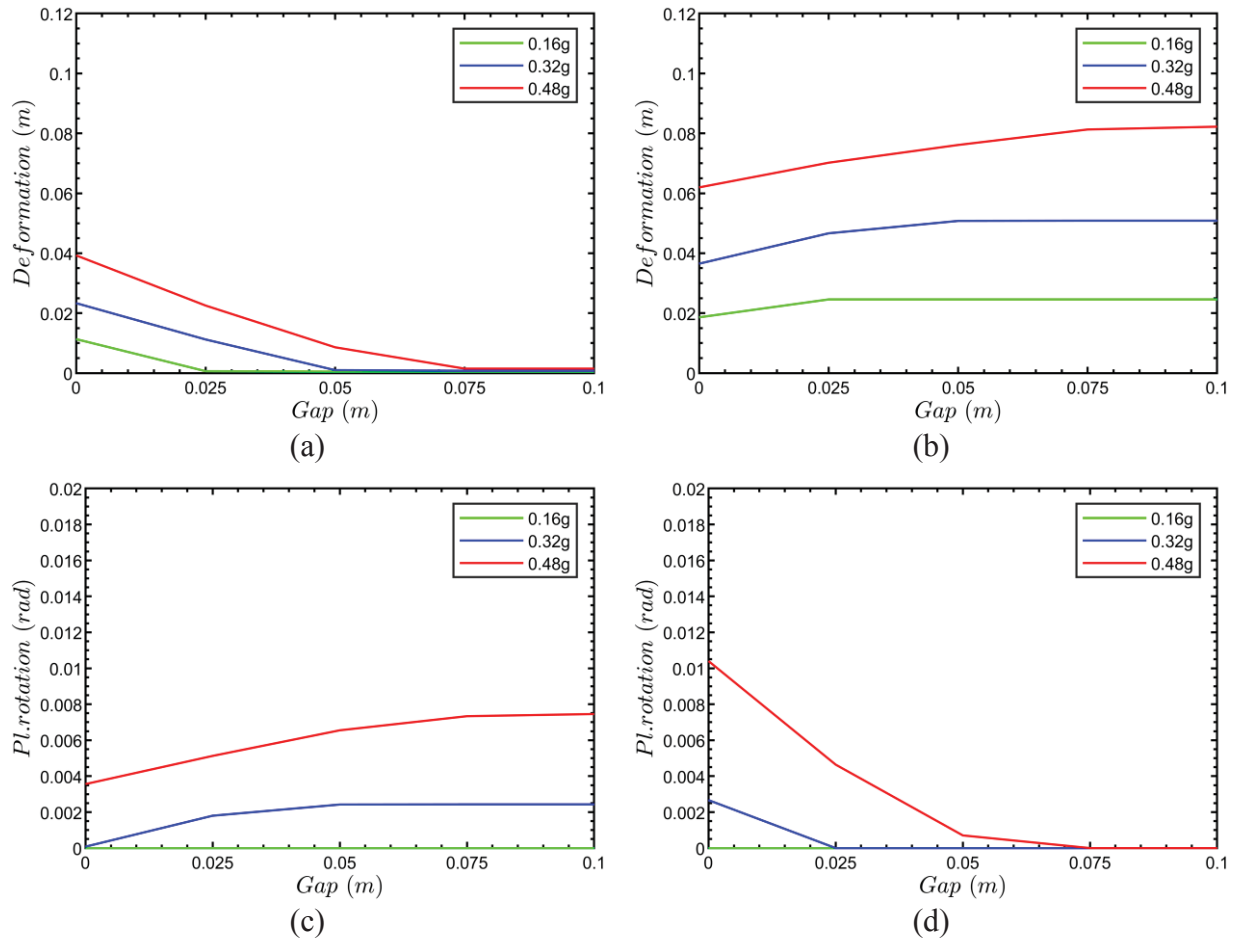


Figure 17: Longitudinal direction: Effect of gap size on: (a) the maximum deformation of the upper backfill spring, (b) the maximum bearing deformation, (c) the maximum pier plastic rotation and (d) the maximum backwall plastic rotation for 3 levels of ground motion

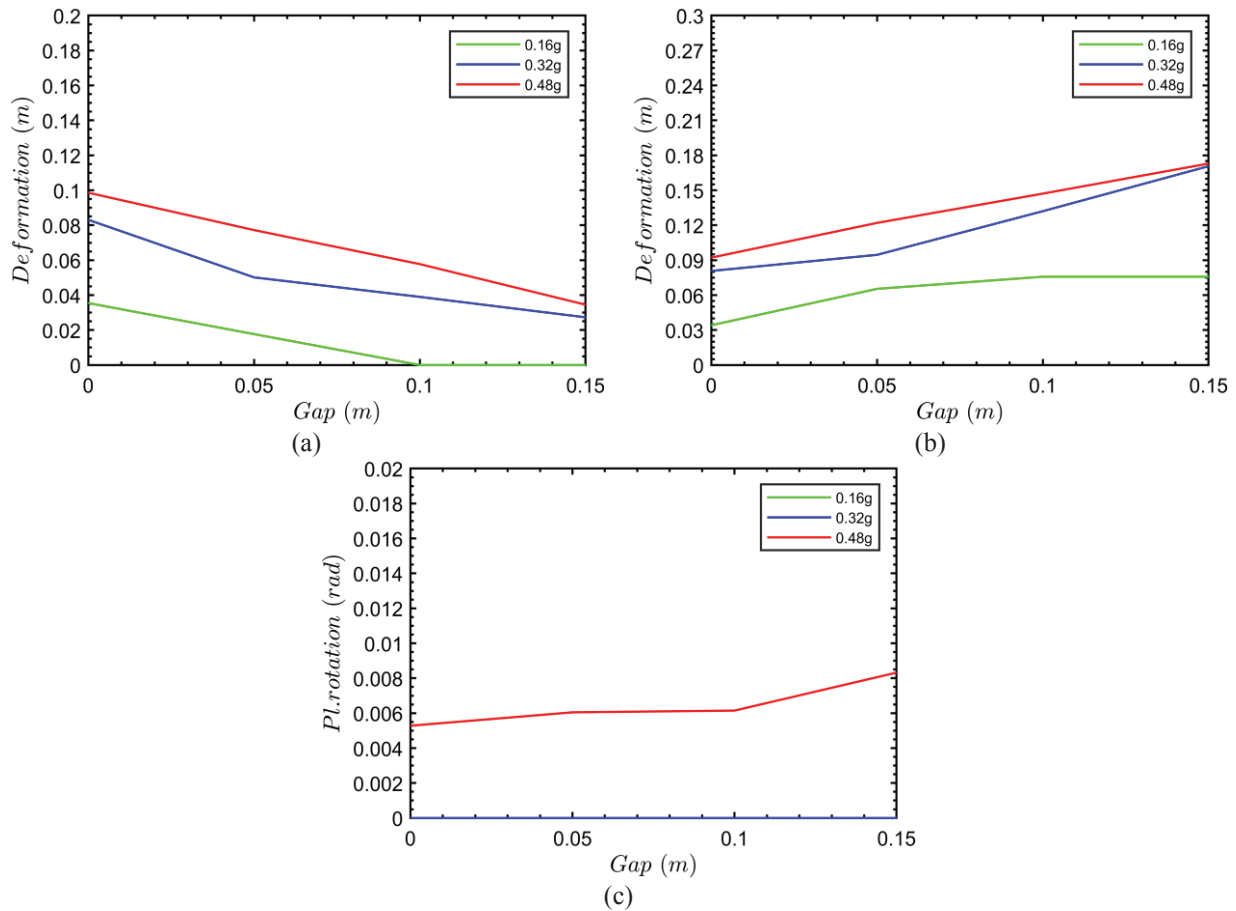


Figure 18: Transverse direction: Effect of gap size on: (a) the maximum deformation of the spring that models the shear key and the embankment resistance, (b) the maximum bearing deformation and (c) the maximum pier plastic rotation for 3 levels of ground motion

The results indicate the importance of accounting for the abutment-backfill system in both directions and the fact that small gap sizes may alter the response of the entire bridge significantly, mainly in cases of high seismic intensities. As expected, the abutment-backfill system is activated more when the gap size is small, and this emerges as beneficial for the piers and the bearings which sustain less damage. Bearings are affected more than piers, particularly in the transverse direction, where an initially closed gap results in approximately 50% decrease of the bearing deformation with respect to 15 cm gap, for ground motion equal to twice the design earthquake. Longitudinal gap sizes larger than 7.5 cm (which is close to the 10 cm gap selected by the designer of the actual bridge), do not make any noticeable difference compared to larger ones, since the displacements in the longitudinal direction are smaller than the largest examined initial gap sizes even for the highest examined level of ground motion.

## 5 CONCLUSIONS

Various configurations of a seat-type abutment-backfill model in the longitudinal and the transverse directions were studied, focusing on an existing overpass designed according to modern code provisions. From both the static and the dynamic (response history) analyses, it emerged that the performance of the bridge improved and that the response of its various components was different when the abutment-backfill system was taken into account, highlighting the importance of modelling this system. Specifically:



- ‘Hinging’ and shearing-off (‘fully sacrificial’) backwalls behave differently when the joint gap closes, hence their modelling should account for this. Abutment-backfill systems with shearing-off backwalls present higher initial stiffness and strength than the ones with ‘hinging’ backwalls; this occurs at the cost of early backwall damage, whereas they reach their strength peak at smaller displacements.
- A single nonlinear spring with a properly defined constitutive law based on passive pressures developing on the backfill is sufficient for modelling the shearing-off system. On the contrary, it is not appropriate for a ‘hinging’ backwall, where the nonlinear behaviour at its base differentiates the response of the entire abutment-backfill system. In this case the single-spring model must be based on the pushover curve derived from the analysis of the abutment-backfill component of the bridge, as described in this paper.
- Modelling the nonlinear behaviour of the backfill soil behind the stem wall of a seat-type abutment is not required, at least in the common case that the stem walls is much stiffer than the backwall, since that part of the soil barely deforms.
- The location of the springs that represent the backfill soil affects the calculated response of the abutment-backfill system, while their number also has some influence. For common backwalls of around 2 m height, use of three springs suffices.
- Modelling the gap element separately, which is necessary for response history analyses with the ‘detailed’ abutment-backfill model, is prone to cause numerical instabilities and/or long computation time. Use of constitutive law with an initial flat slope is clearly preferable, but is not available in all software packages.
- The bearings and the piers are generally relieved as the gap size is made smaller and hence the abutment-backfill system is activated; this occurs at the cost of increased response of the abutment-backfill system that may cause damage to the more critical component of this system.

## REFERENCES

- [1] Caltrans, “Seismic Design Criteria (version 2.0),” CA, USA, 2019.
- [2] A. Shamsabadi, P. Khalili-Tehrani, J. P. Stewart, and E. Taciroglu, “Validated simulation models for lateral response of bridge abutments with typical backfills,” *Journal of Bridge Engineering*, **15**, no. 3, pp. 302–311, 2010.
- [3] A. Aviram, K. R. Mackie, and C. Florida, “PACIFIC EARTHQUAKE ENGINEERING Guidelines for Nonlinear Analysis of Bridge Structures in California,” 2008.
- [4] R. Omrani *et al.*, “Guidelines for Nonlinear Seismic Analysis of Ordinary Bridges: Version 2.0,” *Caltrans Final Report No. 15-65A0454*, no. December, p. 168, 2015.
- [5] CEN (2005), “Eurocode 8: Design of Structures for Earthquake Resistance—Part 2: Bridges,” *European Committee for Standardization, Brussels*, 2005.
- [6] CSI, “SAP2000 v.22: Integrated Software for Structural Analysis and Design.” CA, USA, 2020.
- [7] T. Paulay and M. J. N. Priestley, *Seismic design of reinforced concrete and masonry buildings*. Wiley New York, 1992.
- [8] D. Biskinis and M. N. Fardis, “Stiffness and cyclic deformation capacity of circular RC columns with or without lap-splices and FRP wrapping,” *Bulletin of Earthquake Engineering*, **11**, no. 5, pp. 1447–1466, 2013.
- [9] V. K. Papanikolaou, “Analysis of arbitrary composite sections in biaxial bending and

- axial load,” *Computers & structures*, **98**, pp. 33–54, 2012.
- [10] CEN (2004), “Eurocode 2: Design of concrete structures—Part 1-1: General rules and rules for buildings,” *EN 1992-1-1*, 2004.
  - [11] R. Park and R. A. Sampson, “Ductility of reinforced concrete column sections in seismic design,” in *Journal Proceedings*, 1972, **69**, no. 9, pp. 543–555.
  - [12] F. Naeim and J. M. Kelly, *Design of seismic isolated structures: from theory to practice*. John Wiley & Sons, 1999.
  - [13] G. Mylonakis, S. Nikolaou, and G. Gazetas, “Footings under seismic loading: Analysis and design issues with emphasis on bridge foundations,” *Soil Dynamics and Earthquake Engineering*, **26**, no. 9, pp. 824–853, 2006.
  - [14] D. Biskinis, “Strength and deformation capacity of reinforced concrete members with or without strengthening,” PhD Dissertation, University of Patras, 2007 (in Greek), 2007.
  - [15] P. Khalili-Tehrani, A. Shamsabadi, J. P. Stewart, and E. Taciroglu, “Backbone curves with physical parameters for passive lateral response of homogeneous abutment backfills,” *Bulletin of Earthquake Engineering*, **14**, no. 11, pp. 3003–3023, 2016.
  - [16] A. Shamsabadi, K. M. Rollins, and M. Kapuskar, “Nonlinear soil–abutment–bridge structure interaction for seismic performance-based design,” *Journal of geotechnical and geoenvironmental engineering*, **133**, no. 6, pp. 707–720, 2007.
  - [17] R. T. Cole and K. M. Rollins, “Passive earth pressure mobilization during cyclic loading,” *Journal of Geotechnical and Geoenvironmental Engineering*, **132**, no. 9, pp. 1154–1164, 2006.
  - [18] I. M. Thomaidis, A. J. Kappos, and A. Camara, “Dynamics and seismic performance of rocking bridges accounting for the abutment-backfill contribution,” *Earthquake Engineering & Structural Dynamics*, **49**, no. 12, pp. 1161–1179, Oct. 2020.
  - [19] Y. Xie, Y. Huo, and J. Zhang, “Development and validation of p-y modeling approach for seismic response predictions of highway bridges,” *Earthquake Engineering & Structural Dynamics*, **46**, no. 4, pp. 585–604, 2017.
  - [20] CSI, “Analysis reference manual for SAP2000, ETABS, SAFE and CSIBridge,” *Computers and Structures, Inc., Berkeley, CA, USA*, 2017.
  - [21] K. I. Gkatzogias and A. J. Kappos, “Direct estimation of seismic response in reduced-degree-of-freedom isolation and energy dissipation systems,” *Earthquake Engineering and Structural Dynamics*, **48**, no. 10, pp. 1112–1133, 2019.
  - [22] G. Weatherill, H. Crowley, and L. Danciu, “Preliminary reference Euro-Mediterranean seismic hazard zonation,” 2013.
  - [23] S.-H. Kim and M. Shinozuka, “Effects of Seismically Induced Pounding at Expansion Joints of Concrete Bridges,” *Journal of Engineering Mechanics*, **129**, no. 11, pp. 1225–1234, 2003.

## INFLUENCE OF THE CONTINUITY OF THE BALLASTED TRACK ON THE DYNAMIC RESPONSE OF A SIMPLY SUPPORTED HIGH- SPEED RAILWAY BRIDGES

S. El Hankari, R. Dkiouak, and K. Roky

Laboratory Mechanical and Civil Engineering, UAE/U17FST, Faculty of Sciences and Techniques, University Abdelmalek Essaadi 90000 Tangier, Morocco

[elhankari.said@gmail.com](mailto:elhankari.said@gmail.com)

[rdkiouak@hotmail.com](mailto:rdkiouak@hotmail.com)

[kh.roky@fstt.ac.ma](mailto:kh.roky@fstt.ac.ma)

---

### Abstract

*In a system of soil-structure interaction, in railway lines particularly, the difference in rigidity at the area of interaction ground-pillar or ground-bridge generates a bending moment at the ends of the structure during the passage of high-speed trains. To analyze the phenomenon and its influence on the response of the work, a more realistic schematization of the studied system is necessary. Although the introduction of rotary springs at the ends of the deck enhances the choice of the appropriate analysis model, most of the contributions reported do not consider this effect. In the present work, an analytical approach to analyze the dynamic response of railway bridges especially those with the ballasted track is investigated. The idea of the proposed model is based on analyzing the continuity effect of the ballasted track (rails and ballast) on the dynamic response of railway bridges, with taking into account an axial force that models the effect of prestressing, ballast interface, axial displacement, force braking. The analytic solution is based on Hamilton's principle, two dynamic case studies of a simply supported and simply supported partially clamped Euler-Bernoulli beam are presented. The results revealed that the compression force presents an additional stiffness which affects the critical velocity and the continuity of the track modeled by rotational springs at the beam's end, so as it increases the dynamic response decreases.*

**Keywords:** Resonance; Force axial; Ballasted track; Partially clamped beam.

---

## 1 INTRODUCTION

Nowadays, high-speed train plays an important role in the public transportation strategy of the states. Thus, vertical acceleration in the platform of short or long railway bridges in high-speed lines is still a matter of concern. As dynamic analyzes and experimental tests have shown that vertical acceleration is responsible for this result, these analyzes were carried out by the European Railway Research Institute (EERRI) [1]. So from this, we conclude that the deck vertical acceleration is among the most important specifications required for the design and evaluation of short railway bridges, which have been identified as  $3.5m/s^2$  for ballast tracks [2]. Therefore, the development of precise models working to respect this acceleration factor has become important in applications. So the dynamic performance of railway bridges is playing an increasingly important role in public transportation systems due to the extensive construction of new high-speed lines and the use of old high-speed lines. The regular and repetitive nature of the wheel loads that make up the railway bridges can stimulate resonance situations in these structures. For this latter, it is necessary to continuously modernize the railway infrastructure and especially the bridge structures. Even the axle loads of modern trains are not greater than the forces transmitted in older vehicles, higher design speeds can lead to the occurrence of resonance phenomena. Resonance in a railway bridge occurs when the excitation frequency of the periodic loading of a train approaches a natural frequency of the bridge. In this case, the loads enter the bridge in phase with the natural vibrations of the structure, resulting in a progressive increase in the vibration response of the deck.

In the reported works, Mesuros et al. [3] based on an analytical approach, analyzed and studied the free vibration response of simply and elastically supported beams under moving constant and moving loads, in which the conditions of resonance and cancelation are proved. Resonance vibrations have been observed on railway bridges subjected to high-speed trains. An elementary theoretical model of a bridge has been studied using the integral transformation method, which provides an estimate of the amplitudes of the free vibration. Besides, the analysis gives the critical speeds at which resonant vibration can occur. They are caused by two main reasons: the repeated action of axle loads and the high speed itself [4]. Moreover, it is reported in a work that generally consists of studying the effect of the continuity of the ballasted track on the dynamic response of simply supported railway bridges to assess the influence of the track components and its continuity on the response to the acceleration of the bridge under the passage of railway convoys [5-6].

Additionally, some authors have investigated the effect of axial load on natural frequencies and modal shapes with various types of uniform beam boundary conditions with a concentrated mass at the tip [7]. Some authors investigate the vibration and stability of an infinite Bernoulli-Euler beam on an elastic foundation of the Winkler type when the system is subjected to a static axial force and a moving load with constant or harmonic amplitude variation [8]. The present study takes into account the fact of an axial force that models the effect of prestressing, ballast interface, axial displacement, force braking, and so on. This same idea was discussed by Zhong et al. [9] in which they studied and analyzed the effect of prestressing on the dynamic responses of bridges.

A study that presents a methodology for the comprehensive analysis of railway transition zones (for example, near bridges), which includes: an advanced measurement technique that uses a DIC (Digital Image Correlation) device to measure the dynamic displacements of the rails at multiple locations along the track in transition zones [10]. Also, the authors of this work carried out an experimental study on the problem of the degradation of the railways in the transition zones towards the railway bridges, by numerous measurements on the ground [11].

For this reason, in this study, the interest is to analyze the continuity of the ballasted track in the maximum dynamic response of the bridge (acceleration, displacement) due to rail traffic as a criterion of ballast stability in the case of a ballasted track with taking into account an axial force for the two models, simply supported (SS) beam and simply supported partially clamped (SSPC) beam.

## 2 BASIC ASSUMPTIONS AND PROBLEM FORMULATION

In this section, as cited previously, to understand the track's continuity effects in the dynamic response of a simply supported bridge, the studied bridge is modeled by an E-B simply supported partially clamped beam, as shown in Fig. 1, which connected in its end's by two rotational springs with a constant stiffness  $K_r$ , and an axial Force  $K_s$  is presented which simulate the effect of prestressing, ballast interface, axial displacement, force braking.

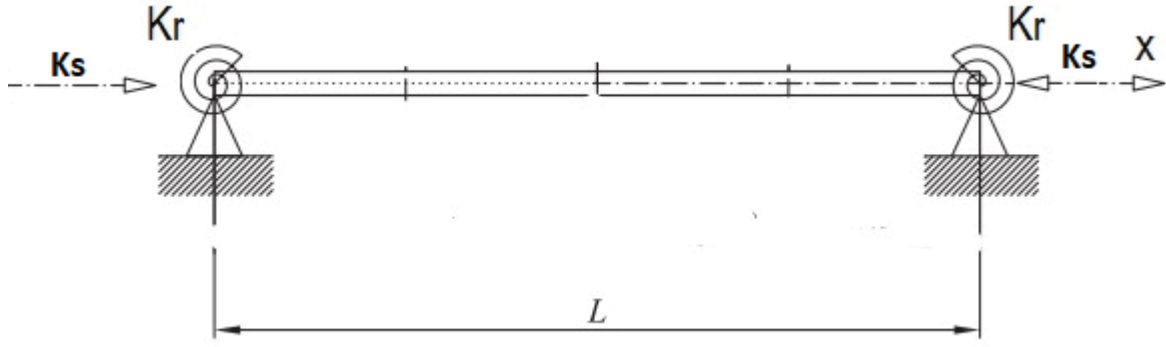


Figure 1: Simply supported partially clamped beam.

By neglecting the damping ratio, the problem of dynamic vibrations of the system can be expressed by Hamilton's principle which is

$$\delta \int_{t_1}^{t_2} (U - T - W) dt = 0 \quad (1)$$

Which  $U$ ,  $T$  and  $W$  are the potential energy, the kinetic energy, and the work of the external forces and defined as

$$U = \frac{1}{2} EI \int_L \left( \frac{\partial^2 v}{\partial x^2} \right)^2 dx + \frac{1}{2} \int_L k_s \left( \frac{\partial v}{\partial x} \right)^2 dx \quad (2a)$$

$$T = \frac{1}{2} \rho A \int_L \left( \frac{\partial v}{\partial t} \right)^2 dx \quad (2b)$$

$$W = \int_L p(x, t) v dx + W_{r,0} \left( \frac{\partial v}{\partial x} \right) + W_{r,L} \left( \frac{\partial v}{\partial x} \right) \quad (2c)$$

With  $v(x, t)$  is the vertical displacement,  $k_s$  is the axial force,  $EI$ ,  $\rho A$  and  $p(x, t)$  are the bending stiffness, the mass per unit length, and the force acting in the structure are assumed to be constant whereas the vehicle-bridge interactions are neglected, then the moving load model HSMA-A is chosen here, which is expressed as follows:

$$p(x, t) = \sum_{k=1}^N P_k \left( H \left( t - \frac{d_k}{c} \right) - H \left( t - \frac{d_k + L}{c} \right) \right) \delta(x - ct + d_k) \quad (2d)$$

The loads presented through Dirac delta function acting along  $(x_v = ct - d_k)$ , where  $c$  is the constant train speed,  $d_k$  is the distance when  $t = 0$  from the  $k$ th to the entrance of the beam,  $N$  is the total number of axle loads,  $P_k$  the value of the  $k$ th load,  $H$  is the Heaviside function and  $L$  stands for the beam length.



$W_{r,i}$   $i = 0, L$  are the general work done by the moments at the boundary sections  $x = 0, L$ , and the moment at these sections are obtained by

$$M_{r,0} = -\frac{\partial W_{r,0} \left( \frac{\partial v}{\partial x} \right)}{\partial \left( \frac{\partial v}{\partial x} \right)}, \quad M_{r,L} = \frac{\partial W_{r,L} \left( \frac{\partial v}{\partial x} \right)}{\partial \left( \frac{\partial v}{\partial x} \right)} \quad (3a)$$

Where  $W_{r,0} \left( \frac{\partial v}{\partial x} \right) = -\frac{1}{2} K_r \left( \frac{\partial v}{\partial x} \right)_{x=0}^2$ ,  $W_{r,L} \left( \frac{\partial v}{\partial x} \right) = -\frac{1}{2} K_r \left( \frac{\partial v}{\partial x} \right)_{x=L}^2$  (3b)

With  $K_r$  is the stiffness of the rotational springs which are identical in this present model, in the same context, the strain energy due to internal axial forces  $N$  and the strain energy produced by the shear force  $V$  is neglected according to the Euler-Bernoulli beam theory. Introducing Eqs. (2) and (3) into Eq. (1) and integrating by parts lead to Eq. (4):

$$\int_{t_1}^{t_2} \left\{ \int_L \left( EI \frac{\partial^4 v}{\partial x^4} - k_s \frac{\partial^2 v}{\partial x^2} + m \frac{\partial^2 v}{\partial t^2} - p \right) \delta v \, dx - \left[ V - k_s h^2 \frac{\partial v}{\partial x} \right]_0^L \delta v - [M - M_r]_0^L \delta \theta \right\} dt = 0 \quad (4)$$

With  $M$ ,  $V$  are the total bending moment and the total shear force defined by

$$M = EI \frac{\partial^2 v}{\partial x^2}; \quad V = EI \frac{\partial^3 v}{\partial x^3} \quad (5)$$

With  $m = \rho A$ .

As the variations  $\delta v$ ,  $\delta \theta$  must vanish at the  $t_1$  and  $t_2$  according to Hamilton's principle, the partial differential governing equation of the system is given by

$$EI \frac{\partial^4 v}{\partial x^4} - k_s \frac{\partial^2 v}{\partial x^2} + m \frac{\partial^2 v}{\partial t^2} = p(x, t) \quad (6a)$$

With the pertaining boundary conditions

$$\left( EI \frac{\partial^3 v(x, t)}{\partial x^3} - k_s \frac{\partial v(x, t)}{\partial x} \right) \delta v_{x=0}^L + \left( EI \frac{\partial^2 v(x, t)}{\partial x^2} - M_r \right) \delta \frac{\partial v^L}{\partial x_{x=0}} = 0 \quad (6b)$$

As mentioned in the Eqs. (6b), it is evident that the beam affected by the presence of the moments ( $M_{r,0}, M_{r,L}$ ) due to the rotational springs and the axial force, were ( $M, V$ ) are the total moment and the total shear force in the considered beam.

As mentioned in the introduction, the interest is to analyze the continuity of the ballasted track in the maximum peak bridge dynamic response (acceleration, displacement) due to the rail traffic as a criterion for the ballast stability in the case of ballasted track. However, as the

frequency band should range from 0 to 30Hz in the dynamical analysis, this is as a reason which allows this limitation of the frequency range, why we use the mode superposition method for solving the equation of motion Eq. (6a), which the general solutions expressed as follows

$$v(x, t) = \sum_{i=1}^{N_m} \Phi_i(x) q_i(t) \quad (7)$$

Where  $\Phi_i$  is  $i$ th the mode shape which depends on the boundary conditions, and  $q_i$  is the time functions response of the beam and  $N_m$  stands for the number of the considered modes.

## 2.1 Simply supported partially clamped beam

As known for a simply supported beam, the mode shape is a sinusoidal function and following the same procedure, attaching the simply supported beam with two rotational springs introduce end moments at the supports. Fig.1 shows the model of a simply supported beam leaning on identical rotational spring with identical rotational stiffness which is constant and equal to  $K_r$ .

From the eq. (7) which is the vertical deflection of the beam, by using the equations 6(a) and 6(b) the mode shapes and the frequency equation of the uniform simply supported partially clamped beam, the frequency equation is given by

$$\frac{4k^2(r_1L)(r_2L)}{\sqrt{\Delta}L^2} (\cosh(r_1L)\cos(r_2L)-1) + k(r_2L)\cos(r_2L)\sinh(r_1L) - k(r_1L)\cosh(r_1L)\sin(r_2L) - \left( \frac{16k^2k_b + (\sqrt{\Delta}L^2)^2}{8\sqrt{\Delta}L^2} \right) \sin(r_2L)\sinh(r_1L) = 0 \quad (8)$$

With

$$\Delta = \left( \frac{k_s}{EI} \right)^2 + \frac{4m\omega_i^2}{EI} ; r_1 = \sqrt{\frac{\sqrt{\Delta} + \frac{k_s}{EI}}{2}} ; r_2 = \sqrt{\frac{\sqrt{\Delta} - \frac{k_s}{EI}}{2}} ; k_b = \frac{k_s L^2}{EI} ; k = \frac{K_r L}{4EI} \quad (9)$$

The parameters  $k$  and  $k_b$  are the ratio of the rotational stiffness of the rotational springs to the flexural rigidity of the beam, and the ratio of the axial force to the flexural rigidity of the beam, respectively.

The stiffness and flexural strength of the abutments should be analyzed in detail for each particular structure. Nevertheless, from the retrofit studies performed by the authors on real

cases, it can be concluded that stiffness and flexural strength of abutments will be usually railway structures [1].

As shown in equation (8), if we neglected the influence of the axial force ( $k_b = 0$ ), the equation becomes

$$2k^2 \cosh(rL) \cos(rL) - 2k^2 + krL \sinh(rL) \cos(rL) - krL \cosh(rL) \sin(rL) - \frac{(rL)^2}{4} \sinh(rL) \sin(rL) = 0 \quad (10).$$

Which is the same frequency equation founded in [14] with the root  $rL = rL(k)$  and  $rL = \pi \sqrt{\frac{\omega_i}{\omega_{ss}}}$ .

The analytical model shape expressed as follows

$$\psi_i(x) = B_i \left( b_1 \left( \cosh \left( r_1 L \frac{x}{L} \right) - \cos \left( r_2 L \frac{x}{L} \right) \right) + \sin \left( r_2 L \frac{x}{L} \right) \right) + \left( b_1 \left( \cosh \left( r_1 L \frac{x}{L} \right) - \cos \left( r_2 L \frac{x}{L} \right) \right) + \sin \left( r_2 L \frac{x}{L} \right) \right) \quad (11a)$$

$$\text{Where } B_i = - \frac{b_1 (\cosh(r_1 L) - \cos(r_2 L)) + \sin(r_2 L)}{a_1 (\cosh(r_1 L) - \cos(r_2 L)) + \sinh(r_1 L)} \quad (11b)$$

$$\Phi_i(x) = \frac{\psi_i(x)}{\max(\psi_i(x))} \quad (11c)$$

$$\text{And } \eta_1 = \frac{4k}{(r_1 L)_i} ; \eta_2 = \frac{4k(r_2 L)_i}{(r_1 L)_i^2} ; x_1 = \left( \frac{(r_2 L)_i}{(r_1 L)_i} \right)^2 ; a_1 = \frac{\eta_1}{1+x_1} ; b_1 = \frac{\eta_2}{1+x_1} \quad (11d)$$

Finally, introducing the Eqs. (7) and (12c) into the Eq. (6a) and multiplying by the  $j$ th mode  $\Phi_j(x)$  with integration over the length of the beam  $L$ , the  $i$ th modal equation of motion is obtained by using the orthogonality conditions, and by introducing a modal damping ratio  $\xi_i$ , the modal damped equation of motion is expressed as:

$$\ddot{q}_i(t) + 2\xi_i \omega_i \dot{q}_i(t) + \omega_i^2 q_i(t) = \frac{1}{M_i} \sum_{k=1}^N \left( H \left( t - \frac{d_k}{c} \right) - H \left( t - \frac{d_k + L}{c} \right) \right) P_k \Phi_i(ct - d_k) \quad (12)$$

Where  $M_i$  is modal mass associated to the  $i$ -th mode

$$M_i = m \int_0^L \Phi_i^2(x) dx = \rho A \int_0^L \Phi_i^2(x) dx \quad (13)$$

$\omega_i$  Represents the  $i$ th circular frequency in  $rad/s$ .

## 2.2 Free vibration of simply supported partially clamped beam

As can be seen, the mode shape (Eq.11) composed by symmetric and axisymmetric modes, we used this expression, if we neglected the damping effect, the solution of the equation of motion of simply supported partially clamped beam for each value of  $r_j L = r_j L(k, k_b)$   $j = 1, 2$  subjected to moving load can be derived as follows

$$\begin{aligned} \frac{q_i(t)}{q_{st}} = B_i & \left[ \frac{\eta_1}{1+x_1} \frac{(\cosh(O_{i1}t) - \cos(\omega_i t))}{1+K_{i1}^2} + \frac{(\sinh(O_{i1}t) - K_{i1} \sin(\omega_i t))}{1+K_{i1}^2} - \frac{\eta_1}{1+x_1} \frac{(\cos(O_{i2}t) - \cos(\omega_i t))}{1-K_{i2}^2} \right] \\ & + \left[ \frac{\eta_2}{1+x_1} \frac{(\cosh(O_{i1}t) - \cos(\omega_i t))}{1+K_{i1}^2} - \frac{\eta_2}{1+x_1} \frac{(\cos(O_{i2}t) - \cos(\omega_i t))}{1-K_{i2}^2} + \frac{(\sin(O_{i2}t) - K_{i2} \sin(\omega_i t))}{1-K_{i2}^2} \right] \quad 0 \leq t \leq L/c \end{aligned} \quad (14)$$

Where  $q_{st}$  is the static solution which is

$$q_{st} = \frac{P}{\omega_i^2 m \int_0^L \Phi_i^2(x) dx} \quad (15)$$

$$\text{And } O_{i1} = \frac{(r_1 L)_i c}{L}; O_{i2} = \frac{(r_2 L)_i c}{L}; K_{i1} = \frac{O_{i1}}{\omega_i}; K_{i2} = \frac{O_{i2}}{\omega_i} \quad (16)$$

The speed parameters  $K_{i1}$  and  $K_{i2}$  are defined by the ratio of the load frequencies,  $O_{i1}$  and  $O_{i2}$  the simply supported partially clamped beam circular frequency  $\omega_i$ ,  $c$  is the speed of the moving load,  $B_i$ ,  $\eta_1$ ,  $\eta_2$  and  $x_1$  are defined in the Eq. (11d),  $(r_1 L)_i$  and  $(r_2 L)_i$  are the roots of the frequency equation correspond to the  $i$ th mode, which is equal in the case of axial force is neglected ( $k_b = 0$ ).

To understand the effect of the axial force in the case of free vibration of a simply supported partially clamped composite beam, as derived in [3] by using the analytical mode shapes of the considered beam, the amplitude of the  $i$ th modal response of the beam after the passage of a unit constant load  $P$  at a constant speed  $c$  in the so-called free vibration phase normalized by the static solution is computed by [3]

$$R_i = \frac{1}{q_{st}} \sqrt{\frac{\dot{q}_i(t=L/c)^2}{\omega_i^2} + q_i(t=L/c)^2} \quad (17)$$

Where  $q_i(t=L/c)$  and  $\dot{q}_i(t=L/c)$  are the initial conditions for the free vibration phase correspond respectively to the  $i$ th modal deflection of the beam and its derivative  $t = L/c$  dur-

ing the forced vibration phase,  $0 \leq t \leq L/c$ . Analytical expressions of these quantities are derived in Eq. (14). Then as can be observed, this equation at  $t = L/c$  is only dependents on the parameters  $k$  which is the ratio of the stiffness of the rotational springs to the flexural stiffness of the beam, the beam length  $L$  and its flexural stiffness  $EI$ , the two no dimensional speed  $K_{i1}$  and  $K_{i2}$  which are defined in the Eq.(16) and the  $k_b$  which is the ratio between of the axial force and the beam bending stiffness.

### 3 NUMERICAL RESULTS

In this section, two cases study is presented, dynamic response of simply supported beam and dynamic response of partially clamped beam, to investigate the effect of the continuity of the ballast track and the axial force in the dynamic response of the aforementioned structure.

#### 3.1 Simply supported beam

the dynamic response of a simply supported and simply supported partially clamped beam is analyzed, the Vinival Bridge [13] is a simply supported, single-track bridge, the main mechanical properties are cited in the Table. 1, in which these properties schematize the total properties of the bridge (include the mass of the track superstructure), the height of the ballast in this bridge is computed by  $h_b = 0.52m$ , then the dynamic response of the bridge under the circulation of High-Speed Load Model-A (HSLM-A) is presented and the maximum dynamic response takes place at mid-span section [14], as noted in the Eurocode and accounting for modes with natural frequencies below  $30Hz$ , Fig .2 shows the maximum vertical acceleration in terms of the circulating velocity in the range  $[140,310]km/h$  every  $1km/h$ . The maximum vertical acceleration reaches  $6.16m/s^2$  and occurs when the train HSLM-A2 crosses the bridge at  $220km/h$  which corresponding to the fourth resonance of the first bending mode. For these reasons, in the following section, the dynamic response of the bridge will be accounted for by the passage of the train A2.

From Table.1, the main properties are calculated considering the mass and the inertia of the track superstructure which is composed of rails, sleepers, and ballast.

Length $L(m)$	9.70
Mass per unit length, $kg/m$	9754
Natural frequency, $f_{0b}(Hz)$	12.8
Modal damping ratio, $\xi(\%)$	2

Table1: mechanical properties of the considered bridge [13]

Besides, the axial force has the following value:  $k_s = 5.37MN$  (18)

The dynamic response of the bridge under the load model HSLM-A2 is evaluated in the time domain with taking into account the first mode of vibration (allow the Eurocode criterion), the figs. 2 (a) and 2(b) show the vertical acceleration and displacement of the bridge at mid-span section, The blue line in the two figures shows the variation of the acceleration and displacement without taking into account the effect of axial force, and the red line shows the variation of the acceleration and displacement with taking into account the axial force with the mentioned value (Eq. 18). From this figure, it can be concluded that critical speed increases as the axial force are introduced, which explain that the axial force such as bracing force, axial displacement introduces a remarkable stiffness (additional stiffness) to the structure which increases the critical velocity, and the displacement amplitude of vibration decreases, especially in the vicinity of resonance at the critical speed  $220 km/h$  which corresponding to a fourth resonance of the first bending mode.



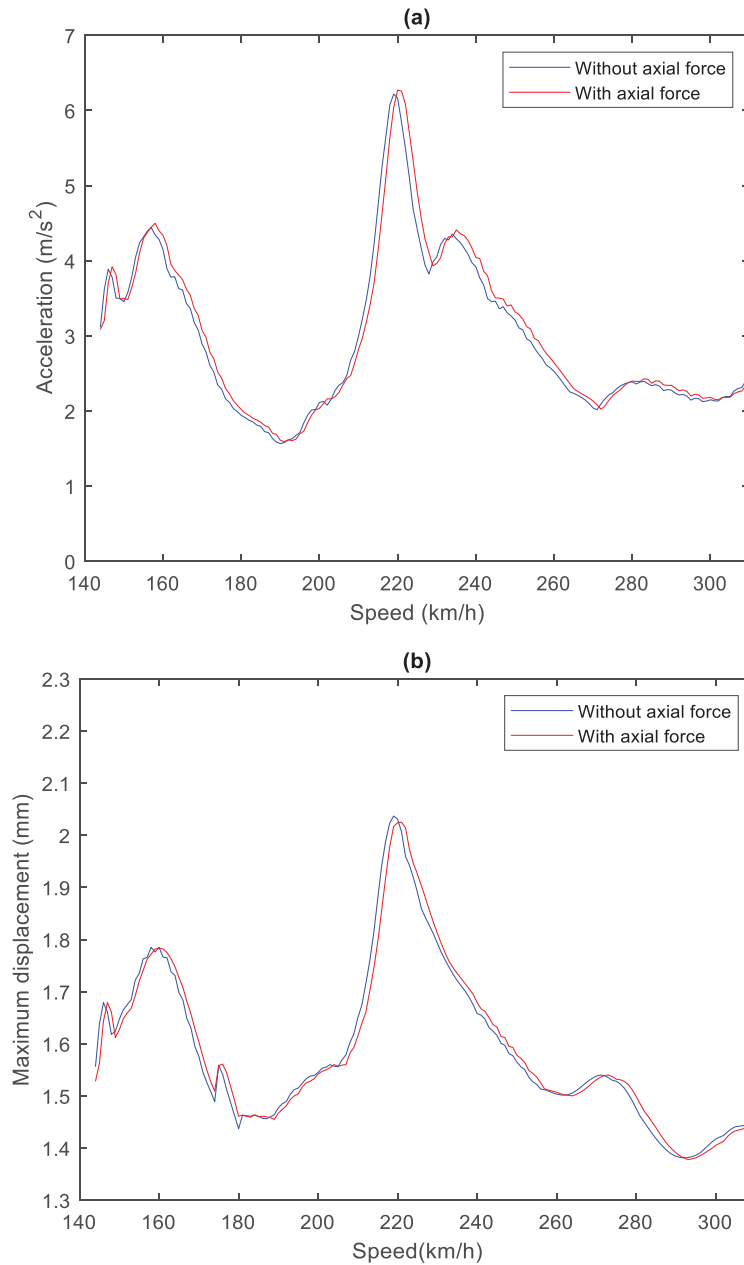


Figure 2: Dynamic response of the beam at mid-span section as a function of the speed of HSLM-A2  
(a) Acceleration, (b) displacement.

### 3.2 Simply supported partially clamped beam

In the following part, as cited in the literature remarkable scientific contributions focused to study the effect of ballast in the response of simply supported bridge, but as the continuity of track introduces a moment of resistance at the beam ends an influence can occur, it is important to study this effect by modeling the bridge as a partially clamped beam schematized by two identical linearly rotational springs attached to the beam ends, to ensure this continuity of the track.

As demonstrated in Eq. (17) the normalized amplitude of the free vibrations of the simply supported partially clamped beam depends on two parameters  $(k, k_b)$ , which represent the effect of the rotational springs and the effect of the axial force. Figure 3 represents the first modal response amplitude of the simply supported partially clamped beam as a function of the speed parameters  $K_{11}$  (Eq. 16)  $k=1.1$ , which represents the ratio between the stiffness of the rotational springs and the beam bending stiffness and which means that the fundamental frequency of the partially clamped beam increases by 50%, with the value of  $k_b$  in the range  $[0, 5k_b]$ . The value  $k_b$  is calculated by using the value of axial force (Eq.18) which corresponds to the value  $k_b = 0.1255$ .

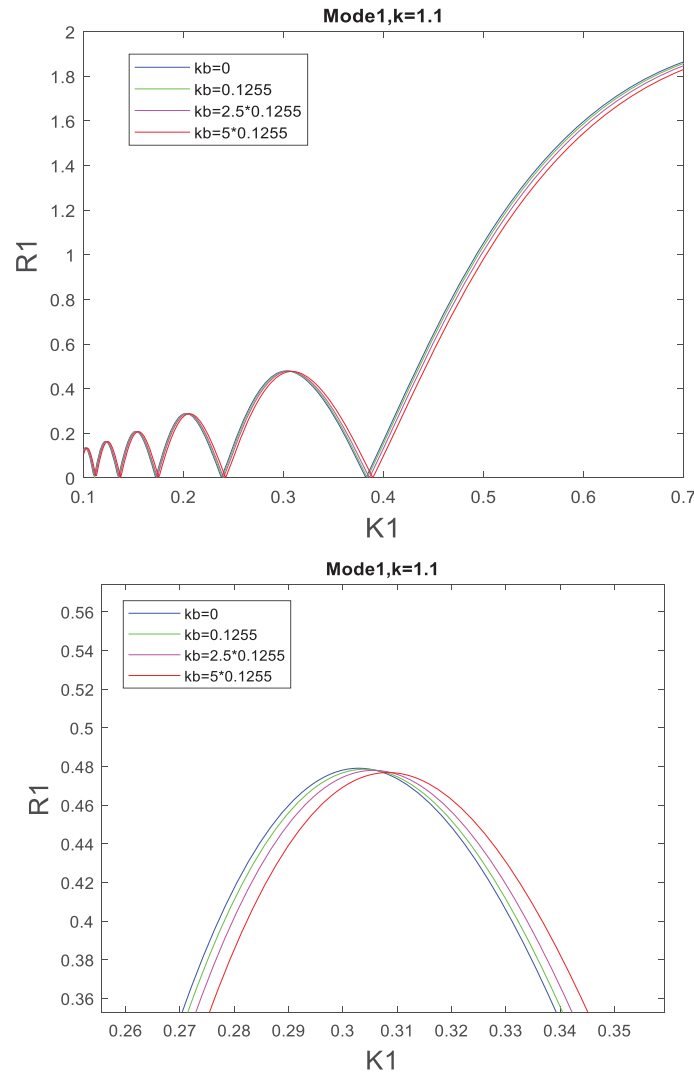


Figure 3: First modal response amplitude vs the speed parameters.

Then as shown in Fig.3, in the case of free vibration of simply supported partially clamped beam, as the ratio  $k_b$  increases, the speed parameters  $K_{11}$  increases which correspond to an increase in the critical speed.

In the case of forced vibration, due to higher modes have frequencies above  $30\text{Hz}$ , the response of the beam is computed from the contribution of its first bending mode, the Figs. 4(a) and 4(b) represent the displacement and acceleration of the simply supported partially clamped beam at the mid-span section of the bridge under the circulation of HSLM-A2 for circulating velocities in the range  $[150, 350]\text{km/h}$  in steps  $1\text{km/h}$ , this wide range of velocities permits the occurrence of a second resonance of the fundamental bridge frequency. Then, from this figure, in comparison with the section (3.1) for a simply supported beam, the critical speed corresponds to  $v_c = 220\text{km/h}$  which theoretical is  $v_{i=1,n=4}^{\text{Res}} = \frac{f_{ss}D}{4} = \frac{12.8.19}{4}.3.6$  [15-16], where  $f_{ss}$  is the fundamental frequency of the SS beam,  $i$  the model number,  $n$  the resonance number and  $D=19\text{m}$  is the characteristic distance of the train HSLM-A2, corresponds to the fourth resonance of the fundamental mode. In the same context, by fixing the value  $k=1.1$ , the fundamental frequency of the beam is changed, due to the rotational spring's stiffness and corresponds to  $\omega_1 = 1.5\omega_{ss}$  which leading to  $f_1 = 19.2\text{Hz}$  the value  $k_b = 0$ . Also, as it can be seen, for  $k_b = 0$  the maximum acceleration reaches the value  $5.21\text{m/s}^2$  which corresponding to a critical velocity  $v_c = 1.5v_{i=1,n=4}^{\text{Res}} = 330\text{km/h}$ , for  $k_b = 5 \times 0.1255$  the acceleration is attained  $5.24\text{m/s}^2$  which corresponding to the critical velocity  $v = 333\text{km/h}$ , the thing explains that for a fixed value  $k=1.1$ , the peak of resonance increases as the ratio  $k_b$  increases. Also, for the displacement, we can conclude that as the ratio  $k_b$  increases the displacement amplitude decreases, and critical velocity increases. Then, this is the same conclusion found in section (3.1) which indicates that the axial force introduces an additional stiffness and independent of the boundary conditions of the beam.

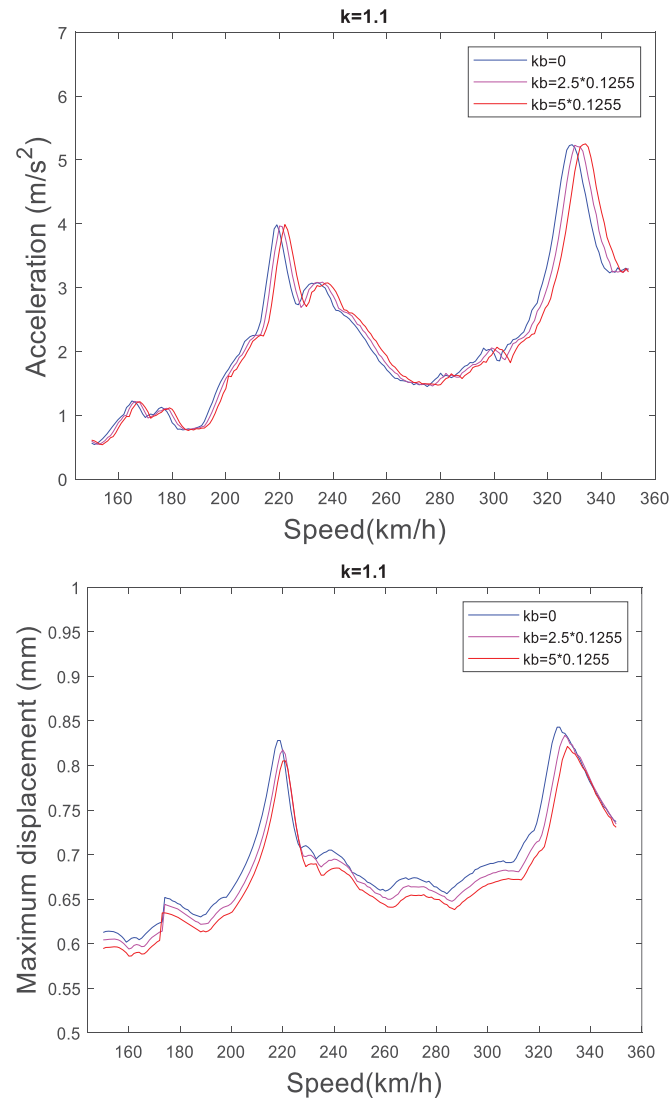


Figure 4: Dynamic response of the beam at mid-span section as a function of the HSLM-A2  
(a) Acceleration, (b) displacement; effect of  $k_b$ .

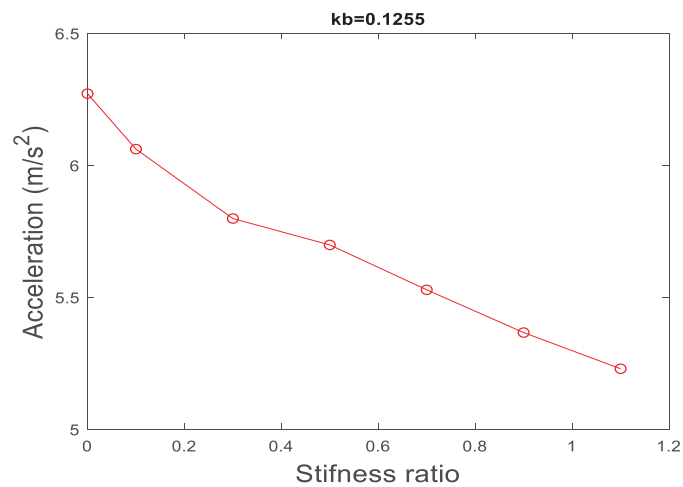


Figure 5: Acceleration as a function of the stiffness ratio  $k$ .

Another parameter that should be also analyzed is the effect of the rotational stiffness due to the rotational springs located at the beam ends, Fig. 5 represents the variation of the acceleration at the mid-point section of the simply supported partially clamped beam under the passage of HSLM-A2 at the critical velocity, as a function of the ratio  $k$  for a fixed value of the ratio  $k_b = 0.1255$ , from this figure we conclude that as the stiffness ratio  $k$  increases, the vertical acceleration decreases, which means that the continuity of track as its rigidity increases the vertical acceleration decreases independent of the influence of the axial forces.

#### 4 CONCLUSION

To summarize, the dynamic response of a simply supported uniform beam and a simply supported partially clamped beam have been studied, with take into account the axial forces and the continuity of the track effects, the results indicate that the axial forces introduce an additional stiffness which modifies the critical velocity and the continuity of the ballast affects largely only the vertical acceleration of the bridge.

#### REFERENCES

- [1] ERRI-D-214/RP9. Ponts Rails pour vitesses > 200 km/h. Rapport final. Brussels: European Committee for Standardization; 2000.
- [2] European Committee for Standardisation (CEN), Eurocode: Basis of Structural Design. Annex A2: Application for bridges, Final PT Draft EN 1990—prAnnex A2 (pre-European Standard), 2002.
- [3] Museros P, Moliner E, Martinez-Rodrigo M.D., (2013). Free vibrations of simply-supported beam bridges under moving loads: Maximum resonance, cancellation and resonant vertical acceleration. *Journal of Sound and Vibration*. 333, 326-345.
- [4] L. Fryba, A rough assessment of railway bridges for high speed trains, *Engineering Structures* 23 (2001) 548–556.
- [5] M.D. Martinez-Rodrigo, A. Romero, E. Moliner, J. Chorda, P. Galvin, Influence of ballast track on vertical response of multispan simply-supported bridges under railway traffic, *ICCES 2020: The 26th International Conference on Computational & Experimental Engineering and Sciences*, 2020.

- [6] E. Moliner, A. Romero, J.C. Sanchez-Quesada, M.D. Martinez-Rodrigo, P. Galvin vertical coupling effect of the ballasted track on the dynamic behavior of multitrack railway bridge composed by adjacent decks. EURODEX 2020. XI International Conference on Structural Dynamics
- [7] Shaker FJ. Effect of axial load on mode shapes and frequencies of beams. NASA Technical Note. Lewis Research Center. 1975.
- [8] Kim, S.-M. (2004). Vibration and stability of axial loaded beams on elastic foundation under moving harmonic loads. *Engineering Structures*, 26(1), 95–105.
- [9] H Zhong, M, Yang, Z; Gao. (2015). Dynamic response of prestressed bridge and vehicle through vehicle-bridge interaction analysis.
- [10] Haoyu Wang, Valeri L. Markine. Methodology for the comprehensive analysis of railway transition zones (2018)
- [11] André Paixão, Eduardo Fortunato, Rui Calçada; Transition zones to railway bridges: Track measurements and numerical modelling (2014)
- [12] Lavado J, Domenech A, Martinez-Rodrigo M.D., (2014). Dynamic performance of existing high-speed railway bridges under resonant conditions following a retrofit with fluid viscous dampers supported on clamped auxiliary beam. *Engineering Structures*, 59, 355-374.
- [13] Moliner E, Museros P, Martinez-Rodrigo M.D., (2012). Retrofit of existing railway bridges of short to medium spans for high speed traffic using viscoelastic dampers. *Engineering Structures*. 40, 519-528.
- [14] European Committee for Standardisation (CEN), Eurocode 1: Actions on structures. Part 2: General actions- Traffic loads on bridges. Final Draft pr EN 1991–1992 (pre-European Standard), 2002.
- [15] P. Mesuros, E. Alarcon, Influence of the second bending mode on the response of high-speed bridges at resonance. *Journal of Structural Engineering* 131(3) (2005) 405-415.
- [16] H. Xia N. Zhang, W. W. Guo, analysis of resonance mechanism and conditions of train-bridge system, *Journal of Sound and Vibration*, 297, (2006) 810-822.



## A FRAMEWORK ON THE DYNAMIC RESPONSE OF TALL STRUCTURES TO NON-STATIONARY WIND USING DESIGN SPECTRUM

Jing Song<sup>1</sup>, Pedro Martinez-Vazquez<sup>2</sup>, Konstantinos A. Skalomenos<sup>3</sup>

Department of Civil Engineering, University of Birmingham, Birmingham, B15 2TT, UK  
<sup>1</sup>[jxs1223@bham.ac.uk](mailto:jxs1223@bham.ac.uk); <sup>2</sup>[p.vazquez@bham.ac.uk](mailto:p.vazquez@bham.ac.uk); <sup>3</sup>[k.skalomenos@bham.ac.uk](mailto:k.skalomenos@bham.ac.uk)

---

### Abstract

*The use of design spectra is common practice in earthquake engineering design as opposed to wind-resisting design. Nonetheless, previous research has identified ways to map such technique to study wind effects on structures. The present investigation introduces a novel framework to deal with the dynamic performance of infrastructure subject to thunderstorm downbursts. It builds on recent developments that demonstrate that spectral analysis is applicable to wind engineering given various equivalences developed to quantify random loading generated through non-synoptic wind environment. The new framework is tested on a benchmark building via a simplified model, which demonstrates its validity. In this framework, the dynamic response of the multi-degree-of-freedom (MDOF) system subjected to non-stationary wind can be obtained assuming that the first mode of vibration is dominant when the mechanical properties of the structure and aerodynamic characteristics of the thunderstorm downburst are identified.*

**Keywords:** Wind design spectrum, Wind-excited response, Thunderstorm downburst, Non-stationary wind, Multi-degree-of-freedom system

---

## 1 INTRODUCTION

The potentially destructive effect of thunderstorm downbursts on structures raises concerns amongst societies for the safety and serviceability of infrastructure. The recorded highest microburst wind reached up to 150 mph, which is in the range of an EF3 tornado [1] with potentially severe damage to the buildings. The peak velocity of such events locates between 30m and 100m above the ground [2, 3], hence covering the height of critical civil engineering infrastructure. The study of the wind actions and damages on structures induced by the downburst outflows becomes crucial for the current wind engineering design.

Various researchers in the past have discussed the downburst wind load and the dynamic response of structures, see for example [4-9]. However, they acknowledge that the transient properties and limited measurements of this complex phenomena make its study uncertain and challenging, starting from the characterisation of the unsteady wind load. Considering the limited experimental measurements of the thunderstorm downburst, the wind field of these typical characteristics has been simulated through hybrid models [5, 6, 10], based on the theoretical velocity profiles. The state of the art is therefore limited to specific yet disperse techniques to estimate wind loading of thunderstorm downbursts.

The short duration and instantaneous properties of the downburst outflow lead to similarities with earthquake loads which are generally evaluated by the response spectra technique [11-13] – widely used in the past to deal with random vibrations, where the structural performance was combined with the inter-storey displacement and roof displacement ductility of the buildings. The proposed framework merges the response spectral technique applied in earthquake engineering with a refined characterisation of wind loads [14, 15]. It revisits the originally developed wind design spectra [16, 17] for the structural vibrations of regular buildings subjected to stationary wind to enhance that basic methodology to study non-stationary wind events.

## 2 MATHEMATICAL FRAMEWORK UNDERPINNING WIND DESIGN SPECTRA

Martinez-Vazquez [17] dealt with the wind design spectra for regular prismatic buildings subjected to stationary wind. The method requires the generalisation of force exerted by wind, structural mass, and stiffness, as well as the characterisation of partially correlated wind fields and its interaction with bluff bodies, to then apply classic spectral techniques for generating design spectra. The design spectra could be used to analyse MDOF systems via modal analysis, which unfolds the response of the oscillators (implicit in the design spectra) to capture the contribution of higher-order modes. The following paragraphs describe how the original formulation by Martinez-Vazquez [17] was tailored to thunderstorm downbursts.

The method departs from establishing the physical relationship between force and acceleration as established by Newton's Second Law on a vertical slender structure – see Eq. (1)-(2). The relationship enables the spectra of the input acceleration induced by the wind on a MDOF system, to be determined. The force spectrum being the scaled wind power spectrum.

$$S_F(z, n) = q^2(z) S_{\tilde{u}'}(z, n) \quad (1)$$

$$S_A(z, n) = \left( \frac{q(z)}{m} \right)^2 S_{\tilde{u}'}(z, n) \quad (2)$$

In these equations,  $S_F$  is the force spectra;  $S_{\tilde{u}'}$  is the power spectra for reduced horizontal fluctuating velocity component  $\tilde{u}'$ , i.e.,  $n S_{\tilde{u}'}(z, n) = \frac{18f}{[1+27f]^{5/3}}$ , where  $f = nz/\bar{U}_{max}(z)$  [18] and  $\bar{U}_{max}$  is the maximum value of the slowly varying mean velocity;  $S_A$  is the input acceleration spectra, i.e., the acceleration imparted by the wind to the structural system;  $m$  is the mass

of the structure excited by the wind force;  $n$  is the frequency of gust wind;  $z$  is the height above the ground;  $q$  is a force factor, expressed as,

$$q(z) = c_D \rho A \bar{U}_{max}^2(z) [1 + 0.5 \bar{I}_u(z)] \bar{I}_u(z) \quad (3)$$

In Eq. (3),  $c_D$  is the drag coefficients,  $\rho$  is the air density,  $A$  is the air exposed to wind,  $\bar{I}_u$  is the slowly varying mean turbulence intensity. It needs to note that the force factor is purely induced by fluctuating turbulence where the fluctuating force  $f' = 0.5 c_D \rho A (2 \bar{U} u' + u'^2)$ . In this case, The second-order term of the fluctuating turbulence,  $u'^2$ , is replaced by  $\sigma_u u'$  to simplify the calculation process, i.e.,  $2 \bar{U} u' + u'^2 = (2 \bar{U} + u') u' \approx (2 \bar{U} + \sigma_u) \sigma_u \tilde{u}' \approx (2 \bar{U} + I_u \bar{U}) I_u \bar{U} \tilde{u}'$ .

Considering the spatial correlation of wind gusts on MDOF system, the normalized cross spectra proposed by Davenport [19] is adopted, given in Eq. (4).

$$\chi(z, n) = \exp \left\{ - \frac{n}{1/2 [\bar{U}_{max}(z_i) + \bar{U}_{max}(z_j)]} \sqrt{(C_y \Delta_y)^2 + (C_z \Delta_z)^2} \right\} \quad (4)$$

In Eq. (4),  $\Delta_y$  and  $\Delta_z$  are the horizontal and vertical distances between two points,  $i, j$ , located at coordinates  $\{y_i, z_i\}$  and  $\{y_j, z_j\}$  respectively.  $C_y$  and  $C_z$  are non-dimensional decay constants along with the horizontal and vertical directions, in this case, assumed equal to 10.  $\bar{U}_{max}(z_i)$  and  $\bar{U}_{max}(z_j)$  represent the maximum value of the slowly varying mean velocity at height  $z_i$  and  $z_j$ , respectively. In this case, we adopted the suggested shape function for the vertical velocity profile of horizontal wind suggested by Wood, et al. [20].

It follows that, by combining the spectra of input acceleration given in Eq. (2) with the cross spectra of the horizontal turbulence component given in Eq. (4), the cross-spectrum of the input acceleration can be obtained, see Eq. (5).

$$S_{A_{ij}}(z_i, z_j, n) = \frac{1}{m^2} q(z_i) q(z_j) \sqrt{S_{\tilde{u}'}(z_i, n) S_{\tilde{u}'}(z_j, n)} \frac{1}{A^2} \chi(z_i, z_j, n) \quad (5)$$

The integration of Eq. (5) across the area exposed to wind flow, contributes to the power spectral density of the generalised input acceleration  $S_{cu}(z_i, z_j, n)$ , given in Eq. (6).

$$S_{cu}(z_i, z_j, n) = \iint_A \phi(z_i) \phi(z_j) S_{A_{ij}}(z, n) dy_i dy_j dz_i dz_j \quad (6)$$

In Eq. (6),  $\phi(z)$  represents the fundamental modal shape at height  $z$  above the ground. This provides the acceleration inputted to a system, therefore the variance of the overall spectral response can be obtained by passing the signal through the transfer function, as shown in Eq. (7). The integration of this equation can be done in two parts, to separate the background and resonant response components. This is expressed in Eq. (8) and Eq. (9) [15]. In this model, we adopt the transfer function with varying frequency ratio for wind excitation given in units of acceleration, i.e.,  $J(n) = \frac{1}{\sqrt{[1 - (n/n_0)^2]^2 + 4\xi^2(n/n_0)^2}}$  ( $n$  is the frequency of the wind,  $n_0$  is the natural frequency of structures,  $\xi$  is the damping ratio) - derived by Martinez-Vazquez [16].

$$\sigma_a^2 = \int_0^\infty |J(n)|^2 S_{cu}(z_i, z_j, n) dn \quad (7)$$

$$\sigma_{a,b}^2 = \int_0^\infty S_{cu}(z_i, z_j, n) dn \quad (8)$$

$$\sigma_{a,r}^2 = S_{cu}(z_i, z_j, n_0) \int_0^\infty |J(n)|^2 dn \cong \frac{\pi n_0 S_{cu}(z_i, z_j, n_0)}{4\xi} \quad (9)$$

Furthermore, the design spectra of the output acceleration can be evaluated by the square root of the sum of the background component (see Eq. (8)) and the resonant component (see Eq. (9)). Therefore, the design spectra for vertical MDOF system are defined as Eq. (10).

$$S_a = \sqrt{\sigma_a^2} = \sqrt{\sigma_{a,b}^2 + \sigma_{a,r}^2} \quad (10)$$

### 3 ESTIMATION OF WIND DESIGN SPECTRA

The input variables of the wind design spectra are investigated based on the building dimensions with the width of 20m, the aspect ratio of 10, and the ratio between chord and width of 1. The damping ratio of this building is 0.025 and the assumed height of peak velocity of downburst wind is 50m. The reference velocity at 10-metre height above the ground is set as 25m/s. Then, the overall design spectra of the output acceleration with varying  $\bar{U}_{max,10}$  is shown in Figure 1 (a) with varying natural period,  $T$ . According to the properties of the structures, it is reasonable to assume that the investigating range of the natural frequency changes from 0.1Hz to 10Hz and the corresponding range of the natural period varies from 10s to 0.1s. When the natural frequency of the structure matches 0.2, the overall design spectra of the output acceleration at 50m/s is about 5 times higher than the counterpart at 25m/s. When the natural frequency reduces to 0.1, the ratio of the overall design spectra at 50m/s and 25m/s is around 5.4.

The dimensions of the structure are also non-negligible, shown in Figure 1(b) for the aspect ratio,  $H/W$  and Figure 1(c) for the ratio of  $L/W$ . The descending dimensions of the structures relative to the structural width can lead to higher design spectra for both ratios of  $H/W$  and  $L/W$ , since lower structures have higher natural frequency with high acceleration. For the natural frequency of 0.2, the ratio of the design spectra when  $H/W = 1$  and  $H/W = 10$  is around 4.2. The ratio of these decreases to 4.0 for the natural frequency of 0.1. Similarly, the ratio of the design spectra when  $L/W = 0.4$  and  $L/W = 2$  is around 5.1 and 5.0 for  $n_1 = 0.2$  and  $n_1 = 0.1$  respectively. This tendency demonstrates that when the natural periods of the structures increase from 5 to 10, the effects of the input parameters mitigate.

A slight influence of the height of peak velocity can be observed in Figure 1 (d), since the height of peak velocity approaching the top of the building can increase the velocity at the top of the building. Therefore, the reference velocities of the downburst outflow and the dimensions of the structures are important parameters for the design spectra of the output acceleration.

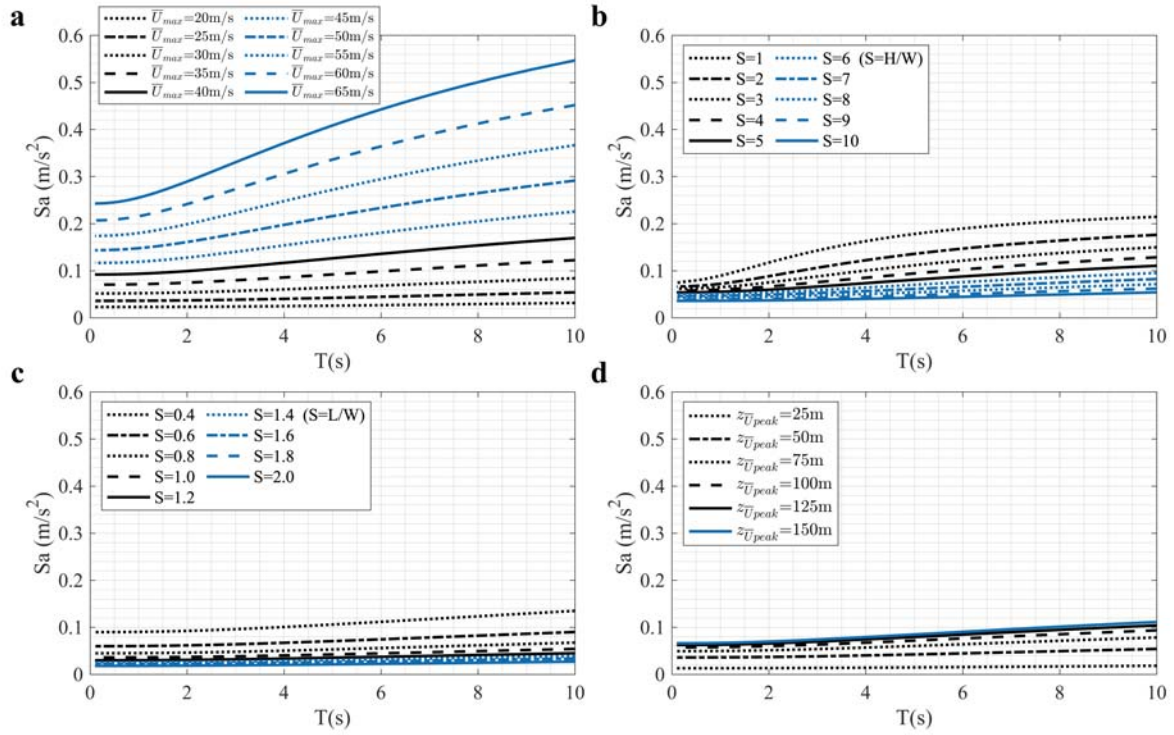


Figure 1: Design spectra of output acceleration with variable parameters, (a)  $\bar{U}_{max}$ ; (b)  $H/W$ ; (c)  $L/W$ ; (d)  $z\bar{U}_{peak}$ .

## 4 DYNAMIC RESPONSE OF CAARC TALL BUILDING

### 4.1 CAARC tall building

The CAARC benchmark building is utilized in this section for the validation of the wind design spectra. The CAARC building was experimentally analysed in five different laboratories and has been regarded as a standard prototype of the tall building to study on the dynamic analysis [21]. The dimensions of the building are shown in Figure 2. The natural frequency of the building is 0.2Hz along the x and y direction. The fraction of the critical damping equals 0.01 and the mass per unit volume of the building is  $160 \text{ kg} \cdot \text{m}^{-3}$ . The turbulence intensity at the top of the building is around 10.57% and a linear relationship of the turbulence intensity with varying height is assumed, where the turbulence intensity at height of 0.5H is around 13.34%.

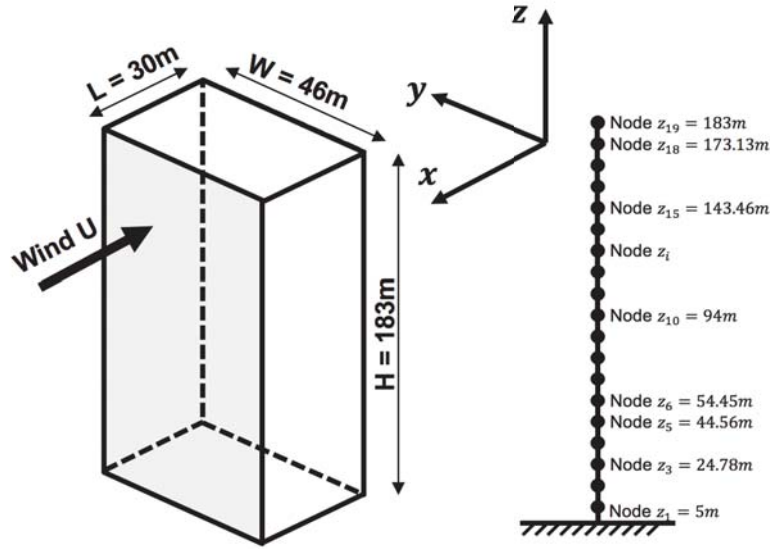


Figure 2: The dimensions of the CAARC benchmark building.

## 4.2 Application of wind design spectra and validation

The CAARC building was assumed as a uniform cantilever structure with a series of single-degree-of-freedom (SDOF) oscillators. This building is equally divided into 18 elements with 19 nodes in the vertical directions of the domain, i.e.,  $z_i = (i - 1) \times 9.89m, i = 1, 2, \dots, 19$  starting from 5m to 183m (see Figure 2). In running a modal spectral analysis (where the proposed design spectra fit), the dynamic displacement response,  $\sigma_d$  (rms of dynamic displacement), can be obtained by using Eq. (11). In addition, the static displacement response of the structure can be obtained with Eq. (12) which is the ratio of the first modal static force (Eq. (13)) and the first modal stiffness  $k_1 = 4\pi^2 n_1^2 m_1$ .

$$\sigma_{1d}(z) = \phi_1(z) \frac{L_1 S_a}{m_1 (2\pi n_1)^2} \quad (11)$$

$$d_{1s}(z) = \frac{\bar{f}_1(z)}{k_1} \quad (12)$$

$$\bar{f}_1(z_i) = c_D \times 0.5 \rho W \bar{U}_{max}^2(z_i) \sum_1^i \left[ \int_{z_i}^{z_{i+1}} \alpha^2(z) \phi_1(z) dz \right] \quad (13)$$

In these equations,  $\phi_1$  is the first modal amplitude at height  $z$  and can approximately take the form  $\phi_1(z) = (z/H)^\psi$  with  $H$  representing the vertical dimension of structures. The constant  $\psi$  is taken as 1 in this case since a frame structure with large columns and shear bracings is considered [22]. Further variables  $n_1$ ,  $m_1$  and  $L_1$  represent the first natural frequencies, first modal mass,  $m_1 = \int_0^H m_l(z) \phi_1^2(z) dz$  (where  $m_l$  is the structural mass per unit height), and first modal excited masses,  $L_1 = \int_0^H m_l(z) \phi_1(z) dz$ , respectively. In Eq. (13),  $i$  represents the  $i$ -th number of recorded velocity time history and  $\alpha(z) = \bar{U}_{max}(z)/\bar{U}_{max}(z_i)$  which is the non-dimensional vertical shape profile of horizontal wind. Finally, the peak displacement response can be obtained by  $d_{1T}(z) = d_{1s}(z) + \sigma_{1d}(z)$ .

The displacements at the top of the building calculated from the wind design spectra are shown in Table 1. In Eq. (4), the correlation function in both vertical and transverse directions of the windward surface of the building is considered. The results from the design spectra combined with the partially correlated function only in vertical direction are also demonstrated in Table 1, where the oscillation amplitude of the displacement at the top of the building in  $x$



direction, i.e., 0.351m, is larger than 0.328m since the correlation in the transverse direction is considered as full correlation, that is the same consequences as the displacement response in y-direction where the counterpart is 0.206m which is higher than 0.196m. Higher correlation can cause higher displacement amplitude of the oscillation. The peak displacements calculated from the simulated wind field using time series analysis methods, i.e., the Newmark method (M1) and interpolation of excitation method (IOE, M2) (detailed in Chopra [23]), are illustrated in Table 1, where the results are slightly higher than those from the wind design spectra.

Direction	Design spectra for thunderstorm downburst					Num. Int. (M1)	Num. Int. (M2)
	Davenport's coherence (vertical and horizontal)			Partial correlated (vertical only)		Partial correlated (vertical only)	
	Static	Dynamic	Total	Dynamic	Total	Total	Total
x	0.200	0.128	0.328	0.151	0.351	0.435	0.434
y	0.112	0.084	0.196	0.094	0.206	0.244	0.243

Table 1: Lateral displacements at the top of the building (Unit: metre).

## 5 CONCLUSIONS

This paper presents a newly developed design spectra technique in the frequency domain subjected to thunderstorm downburst which attempts to extend the successful performance-based design philosophy to wind engineering application. The investigation for the input parameters of the design spectra illustrates that the design spectra of the output accelerations significantly rise with the increasing velocities of the downburst outflow, and obviously mount with the decreasing aspect ratio and cross-sectional ratio of the buildings. The consistent comparison between the results of the wind design spectra in frequency domain and the equivalent numerical simulation in time domain for the benchmark tall building enable design spectra technique to be developed, assuming that the displacement response is mainly reflected on the first mode. This technique identifies the mechanical properties of the structure and aerodynamic characteristics of the outflow winds, which enable to obtain the structural performance for MDOF oscillators. Further validations of the proposed design spectra by using the finite element method will be carried out.

## REFERENCES

- [1] J. R. McDonald and K. C. Mehta, *A recommendation for an Enhanced Fujita scale (EF-Scale)*. Wind Science and Engineering Center, Texas Tech University, 2006.
- [2] T. T. Fujita, "The downburst: microburst and macroburst. University of Chicago," *SMRP Research* vol. 210, p. 112, 1985.
- [3] T. T. Fujita, "Downbursts: meteorological features and wind field characteristics," *Journal of wind engineering and industrial aerodynamics*, vol. 36, pp. 75-86, 1990.
- [4] M. Chay and F. Albermani, "Dynamic response of a SDOF system subjected to simulated downburst wind," 2005.
- [5] L. Chen and C. Letchford, "A deterministic–stochastic hybrid model of downbursts and its impact on a cantilevered structure," *Engineering structures*, vol. 26, no. 5, pp. 619-629, 2004.

- [6] X. Chen, "Analysis of alongwind tall building response to transient nonstationary winds," *Journal of structural engineering*, vol. 134, no. 5, pp. 782-791, 2008.
- [7] E. C. Choi and F. A. Hidayat, "Dynamic response of structures to thunderstorm winds," *Progress in Structural Engineering and Materials*, vol. 4, no. 4, pp. 408-416, 2002.
- [8] J. Holmes, G. Forristall, and J. McConochie, "Dynamic response of structures to thunderstorm winds," in *Proc., 10th Americas Conf. on Wind Eng. (10ACWE)*, 2005, pp. 1-6.
- [9] G. Solari, "Thunderstorm response spectrum technique: theory and applications," *Engineering Structures*, vol. 108, pp. 28-46, 2016.
- [10] G. Solari, D. Rainisio, and P. De Gaetano, "Hybrid simulation of thunderstorm outflows and wind-excited response of structures," *Meccanica*, vol. 52, no. 13, pp. 3197-3220, 2017.
- [11] K. A. Skalomenos, G. D. Hatzigeorgiou, and D. E. Beskos, "Application of the hybrid force/displacement (HFD) seismic design method to composite steel/concrete plane frames," *Journal of Constructional Steel Research*, vol. 115, pp. 179-190, 2015.
- [12] D. N. Serras, K. A. Skalomenos, and G. D. Hatzigeorgiou, "A displacement/damage controlled seismic design method for MRFs with concrete-filled steel tubular columns and composite beams," *Soil Dynamics and Earthquake Engineering*, vol. 143, p. 106608, 2021.
- [13] G. W. Housner, R. Martel, and J. Alford, "Spectrum analysis of strong-motion earthquakes," *Bulletin of the Seismological Society of America*, vol. 43, no. 2, pp. 97-119, 1953.
- [14] G. Solari, "Wind response spectrum," *Journal of Engineering Mechanics*, vol. 115, no. 9, pp. 2057-2073, 1989.
- [15] E. Simiu and R. H. Scanlan, "Wind effects on structures: fundamentals and applications to design," 1996.
- [16] P. Martinez-Vazquez, "Wind-induced vibrations of structures using design spectra," *International Journal of Advanced Structural Engineering*, vol. 8, no. 4, pp. 379-389, 2016.
- [17] P. Martinez-Vazquez, "Wind design spectra for generalisation," *Wind and Structures*, vol. 30, no. 2, p. 155, 2020.
- [18] G. Solari, M. Burlando, P. De Gaetano, and M. Repetto, "Characteristics of thunderstorms relevant to the wind loading of structures," *Wind and Structures*, vol. 20, no. 6, p. 763, 2015.
- [19] A. Davenport, "The prediction of the response of structures to gusty wind," *Safety of structures under dynamic loading*, vol. 1, pp. 257-284, 1977.
- [20] G. S. Wood, K. C. Kwok, N. A. Motteram, and D. F. Fletcher, "Physical and numerical modelling of thunderstorm downbursts," *Journal of Wind Engineering and Industrial Aerodynamics*, vol. 89, no. 6, pp. 535-552, 2001.
- [21] W. Melbourne, "Comparison of measurements on the CAARC standard tall building model in simulated model wind flows," *Journal of Wind Engineering and Industrial Aerodynamics*, vol. 6, no. 1-2, pp. 73-88, 1980.
- [22] C. Eurocode, "1: Actions on structures—Part 1.4: General actions—wind actions," *Brussels: The European Standard EN*, 2010.
- [23] A. K. Chopra, *Dynamics of structures : theory and applications to earthquake engineering*, 4th ed. ed. Upper Saddle River, N.J. : Prentice Hall ; London : Pearson Education [distributor], 2011 (in English), 2011.

## GEOMETRICALLY NONLINEAR FORCED TRANSVERSE VIBRATIONS ANALYSIS OF TAPERED EULER-BERNOULLI BEAMS

I. El Hantati<sup>1,2</sup>, A. Adri<sup>1</sup>, H. Fakhreddine<sup>1,2</sup>, S. Rifai<sup>1</sup>, R. Benamar<sup>3</sup>

<sup>1</sup> Laboratory of Production Mechanics and Industrial Engineering (LMPGI), Higher School of Technology, Hassan II University of Casablanca, Km 7, Route El Jadida, B.P. 8012 Oasis, Casablanca, Morocco  
[hantati.issam@gmail.com](mailto:hantati.issam@gmail.com), [ahmedadri@gmail.com](mailto:ahmedadri@gmail.com), [hatim.fakhreddine@gmail.com](mailto:hatim.fakhreddine@gmail.com), [said57.rifai@gmail.com](mailto:said57.rifai@gmail.com)

<sup>2</sup> Doctoral Studies Centre of National High School of Electricity and Mechanics (ENSEM)

Route d'El Jadida, Km 7, Oasis, Casablanca 8018, Morocco

[hantati.issam@gmail.com](mailto:hantati.issam@gmail.com), [hatim.fakhreddine@gmail.com](mailto:hatim.fakhreddine@gmail.com)

<sup>3</sup> Mohammed V University in Rabat, EMI-Rabat, LERSIM, Agdal,

B.P. 765, Rabat, Morocco

[rhali.benamar@gmail.com](mailto:rhali.benamar@gmail.com)

---

### Abstract

*Tapered beams like structures are widely used in many fields including mechanical and civil engineering, such as high-rise buildings, robot arms, etc. The objective of this paper is to study the geometrically nonlinear free and forced transverse vibrations of tapered beams with a constant width and a linearly varying depth. The theoretical model is based on the Euler-Bernoulli beam theory and the Von Kármán assumptions for geometrical nonlinearity. The motion is assumed to be harmonic and the transverse displacement function of the nonlinear beam is expanded as a series of linear modes, determined by solving the linear problem in terms of Bessel functions satisfying the boundary conditions. The discretized expressions for total beam strain and kinetic energies are derived, and by application of Hamilton's principle, the problem is reduced to a non-linear algebraic system solved using a previously developed approximate method (the so-called second formulation). The effect of the linear variation of depth on the non-linear behaviour of the beam is examined and then illustrated. Using the single-mode approach, the non-linear dynamic behaviour of the tapered beam is studied in the forced case. The effects of the excitation level of the applied harmonic force are investigated and illustrated for various scenarios.*

**Keywords:** tapered beam, transverse vibrations, nonlinear vibrations, forced vibrations

---

## 1. INTRODUCTION

In civil engineering, aeronautics or mechanical engineering, the beams used are commonly non-uniform. This type of beams are often subjected to free or forced vibrations, especially in some applications such as aircraft wings or steel structures. Many works have been devoted to the dynamic behaviour of tapered beams under different boundary conditions and both the Euler-Bernoulli and Timoshenko beam's theory have been used.

The literature review may go back to [1], in which Sanger exposed a general solution in terms of Bessel function of order  $n$  for a range of beams, for different classical boundary conditions as a fixed end, a simply supported end, etc. Goel studied in [2] the transverse vibrations of tapered beams with elastically restrained ends, as well as the effect of a concentrated mass at the free end of a cantilever tapered beam. Craver et al. [3] examined the free vibrations of Euler Bernoulli tapered cantilever beams, elastically restrained at an arbitrary position over its length, using the straight search and bisection method. Abrate [4] gave simple formulas for predicting the fundamental frequencies using one term Rayleigh-Ritz approximations. De Rosa and Auciello [5] investigated a tapered beam of linearly varying width and depth and with rotational and translational springs at both ends using the false position method. In order to solve the natural frequencies of the free vibration of beams with variable flexural rigidity and mass density, Yong Huang and Xian-Fang Li presented in [6] a new approach based on Fredholm's integral equations. S.M. Abdelghany et al. [7] investigated the case of non-uniform circular Euler-Bernoulli beam vibrations using the differential transformation method. Fatemeh Sohani and H. R. Eipakchi [8] studied the flexural vibrations of Euler Bernoulli and Timoshenko beams with an arbitrary varying cross-section using on the perturbation technique.

Despite the large literature devoted to the dynamic behaviour of tapered beams, only few authors have considered the effect of geometrical non-linearity. This effect was studied by L. S. Raju et al. in [9], for a tapered beam of rectangular cross-section with two types of linear taper, one corresponding to the width and the other to the depth. The study was based on Galerkin's method. The analysis of the non-linear behaviour of Timoshenko tapered beams with linear variation in width and depth has been carried out by Minmao Liao and Hongzhi Zhong [10], based on the differential quadrature method. Kumar et al. [11] investigated large amplitudes of free vibrations of axially functionally graded tapered beams under different boundary conditions, taper profiles and material properties. The principle of minimum total potential energy was applied in the static case while Hamilton's principle was used in the dynamic analysis.

The present work is focused on the study of geometrically non-linear free and forced vibrations of tapered beams and constitutes a continuation of the work previously initiated by Benamar et al. [12]–[22] in the perspective of a contribution to a non-linear modal analysis theory of free and forced vibrations of structures. The purpose of this paper is to study the geometrically nonlinear free and forced transverse vibrations of tapered beams with a constant width and a linearly varying depth. The theoretical model is based on Euler-Bernoulli's beam theory and the Von Kármán geometrical nonlinearity assumptions. The motion is assumed to be harmonic and the transverse displacement function of the nonlinear beam is expanded as a series of the linear modes, determined by solving the linear problem in terms of Bessel functions and the boundary conditions. The discretized expressions for total beam strain and kinetic energies are derived, and by applying Hamilton's principle, the problem is reduced to a non-linear algebraic system solved using an approximate method (the so-called second formulation). The effect of the linear variation of depth on the non-linear behaviour of the beam is

examined and then illustrated. Using the single-mode approach, the non-linear dynamic behaviour of the tapered beam is studied in the forced case. The effects of the excitation level of the applied harmonic force are investigated and illustrated for various scenarios.

## 2. GENERAL FORMULATION

### 2.1 Linear formulation

This study concerns a non-uniform fully-clamped tapered Euler-Bernoulli beam subjected to transverse vibrations. A thin rectangular cross-section tapered beam of a constant width and a linearly varying depth, denoted by beam (a) is considered.

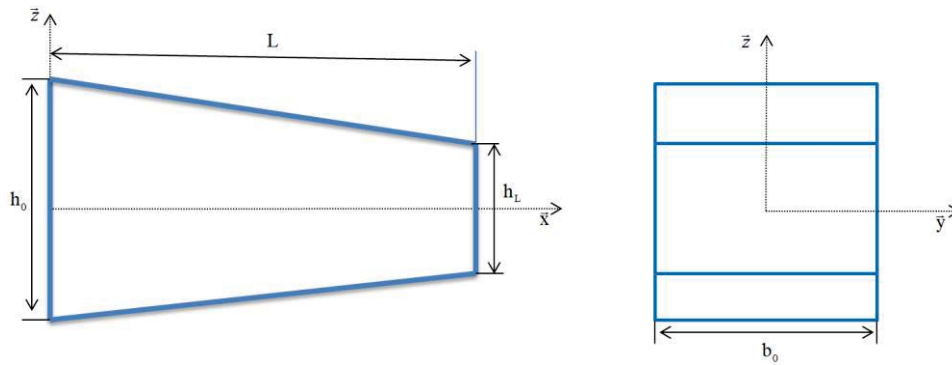


Figure 1: Coordinates system for the tapered beam studied.

Setting that  $h_{(x)} = h_0 \left( 1 - \alpha \left( \frac{x}{L} \right) \right)$ , where  $h_{(x)}$  and  $\alpha$  present the depth of the beam and the taper ratio equal to  $1 - \frac{h_L}{h_0}$ . The area and inertia functions are given as follows:

$$S(x) = h_{(x)} \times b_0 \quad (1)$$

$$I(x) = \frac{h_{(x)}^3 \times b_0}{12} \quad (2)$$

The equation of motion of the tapered beam in the case of free transverse vibrations can be expressed as in [23]:

$$\frac{\partial^2}{\partial x^2} \left\{ EI_{(x)} \frac{\partial^2 w_i}{\partial x^2} \right\} + \rho S_{(x)} \frac{\partial^2 w_i}{\partial t^2} = 0 ; \quad x \in [0, L] \quad (\text{For } i = 1, 2, \dots, 10) \quad (3)$$

Where  $E$ ,  $\rho$  and  $t$  are respectively the Young's modulus, the density of the beam material and time.  $w$  presents the transverse displacement function of  $x$  and  $t$ , supposed to be separated into two functions  $w(x, t) = W(x) \times \varphi(t)$ . By substituting  $\xi = 1 - \alpha \left( \frac{x}{L} \right)$  in the equation of motion (6), leads to the formulation previously stated in [23]:

$$\xi^2 \frac{d^4 W_i}{d\xi^4} + 2(n+2)\xi \frac{d^3 W_i}{d\xi^3} + (n+2)(n+1) \frac{d^2 W_i}{d\xi^2} - \frac{\beta_i^4}{\alpha} W_i = 0 \quad (4)$$

Where:

$$\beta_i = \sqrt[4]{\frac{\rho S_0 \omega_i^2 L^4}{EI_0}} \quad \text{and } n=1 \quad (5)$$

The eigenvalue parameter is denoted by  $\beta_1$ . The solution of Eq. (4) presents the linear modes form given in [23] as follows:

$$W_i(\phi) = \frac{1}{\phi} (A_i J_1(\phi) + B_i Y_1(\phi) + C_i I_1(\phi) + D_i K_1(\phi)) \quad (6)$$

Where  $\phi = (2\beta_1 \sqrt{\xi}) \alpha^{-1}$

In equation (6)  $A_i, B_i, C_i$  and  $D_i$  present constants that can be determined from the boundary conditions,  $J_1$  and  $Y_1$  are Bessel functions of the first and second kinds in order 1,  $I_1$  and  $K_1$  are the modified Bessel functions of first and second kinds in order 1.

After setting  $x^* = x/L$  for  $x^* \in [0, 1]$ , the beam end conditions are given by:

The end conditions at the left side:

$$W_i|_{x^*=0} = \frac{dW_i}{dx^*}|_{x^*=0} = 0 \quad (11)$$

The end conditions at the right side:

$$W_i|_{x^*=1} = \frac{dW_i}{dx^*}|_{x^*=1} = 0 \quad (12)$$

The substitution of equation (6) into equations (11 and 12) leads to four equations, expressed in the following forms:

$$A_i J_1(\phi_0) + B_i Y_1(\phi_0) + C_i I_1(\phi_0) + D_i K_1(\phi_0) = 0 \quad (13)$$

$$A_i J_2(\phi_0) + B_i Y_2(\phi_0) - C_i I_2(\phi_0) + D_i K_2(\phi_0) = 0 \quad (14)$$

$$A_i J_1(\phi_L) + B_i Y_1(\phi_L) + C_i I_1(\phi_L) + D_i K_1(\phi_L) = 0 \quad (15)$$

$$A_i J_2(\phi_L) + B_i Y_2(\phi_L) - C_i I_2(\phi_L) + D_i K_2(\phi_L) = 0 \quad (16)$$

Where  $\phi_0 = \frac{2\beta_1}{\alpha}$  and  $\phi_L = \frac{2\beta_1}{\alpha} \sqrt{1-\alpha}$ .

The satisfaction of equations (13-16) leads to an homogeneous system which can be expressed by the following matrix form:

$$\begin{bmatrix} J_1(\phi_0) & Y_1(\phi_0) & I_1(\phi_0) & K_1(\phi_0) \\ J_2(\phi_0) & Y_2(\phi_0) & -I_2(\phi_0) & K_2(\phi_0) \\ J_1(\phi_L) & Y_1(\phi_L) & I_1(\phi_L) & K_1(\phi_L) \\ J_2(\phi_L) & Y_2(\phi_L) & -I_2(\phi_L) & K_2(\phi_L) \end{bmatrix} \times \begin{Bmatrix} A_i \\ B_i \\ C_i \\ D_i \end{Bmatrix} = \begin{Bmatrix} 0 \\ 0 \\ 0 \\ 0 \end{Bmatrix} \quad (17)$$

The non-trivial solutions corresponding to the natural frequencies are derived from equation (17), solved iteratively by the Newton-Raphson method. Then the constants  $A_i, B_i, C_i$  and  $D_i$  are determined by the usual classical algebra procedure.



## 2.2 Non-linear formulation

### 2.2.1 Free vibration

The kinetic energy  $T$  of the tapered beam can be presented in the following form:

$$T = \frac{\rho}{2} \int_0^L S(x) \left( \frac{\delta w}{\delta t} \right)^2 dx \quad (18)$$

The total strain energy  $V$  is the sum of the strain energy due to bending and the axial strain energy due to the non-linear stretching forces induced by the large deflections, respectively denoted by  $V_f$  and  $V_a$  and written as follows:

$$V = V_f + V_a \quad (19)$$

$$V_f = \frac{1}{2} \int_0^L E I(x) \left( \frac{d^2 w_i}{dx^2} \right) \left( \frac{d^2 w_j}{dx^2} \right) dx \quad (20)$$

$$V_a = \frac{1}{2} \frac{N_x^2}{E} \int_0^L \frac{dx}{S(x)} \quad (21)$$

Where  $N_x$  presents the non-linear axial stretching forces in the beam, which may be written in the form reported in [9]:

$$N_x = \frac{E}{2} \cdot \frac{\int_0^L \left( \frac{dw_i}{dx} \right)^2 dx}{\int_0^L \frac{dx}{S}} \quad (22)$$

The dynamic behaviour of the system is studied by applying Hamilton's principle, stated formally as:

$$\delta \int_0^{\frac{2\pi}{\omega}} (V - T) dt = 0 \quad (23)$$

Assuming a harmonic motion, the transverse displacement can be written as:

$$w(x, t) = a_i W_i(x) \sin(\omega t) \quad (\text{For } i = 1, 2, \dots, n) \quad (24)$$

In which  $W_i(x)$ ,  $a_i$  and  $\omega$  present the linear mode, the basic function contribution coefficients and the associated frequency.

After Substituting equation (24) in the expressions for the kinetic energy, the axial deformation energy due to non-linear stretching forces and the deformation energy due to the bending, one gets:

$$T = \frac{1}{2} \omega^2 a_i a_i (\cos(\omega t))^2 m_{ij} \quad (25)$$

$$V_a = \frac{1}{2} a_i a_j a_k a_l (\sin(\omega t))^4 b_{ijkl} \quad (26)$$

$$V_f = \frac{1}{2} a_i a_i (\sin(\omega t))^2 k_{ij} \quad (27)$$

Where  $k_{ij}$ ,  $b_{ijkl}$  and  $m_{ij}$  denote the matrix of the stiffness due to  $V_f$ , the non-linearity tensor due to  $V_a$  and the mass matrix attributable to  $T$ . Equation (23) is extended by adding equations (25, 26 and 27) into it, which can be expressed in the following form:

$$2a_i k_{ir} + 3a_i a_j a_k b_{ijk r} - 2\omega^2 a_i m_{ir} = 0 \quad ; \quad r = 1, \dots, n \quad (28)$$

Equation (28) can be expressed in a matrix form as follows:

$$2[K]\{A\} + 3[B(\{A\})]\{A\} - 2\omega^2 [M]\{A\} = 0 \quad (29)$$

In which  $(k_{ir}), (m_{ir}), (a_j, a_k, b_{ijkl})$  and  $(a_i)$  are converted into  $[K], [M], [B(\{A\})]$  and  $\{A\}$ . Setting some dimensionless parameters as below:

$$\frac{W_i(x^*)}{W_i^*(x^*)} = h_0; \frac{\omega^2}{\omega^{*2}} = \frac{EI_1}{\rho S_1 L^4}; \frac{M_{ij}}{M_{ij}^*} = \rho S_1 h_0^2 \quad (30, 31, 32)$$

$$k_{ij} = \frac{EI_1 h_0^2}{L^3} k_{ij}^*; b_{ijkl} = \frac{EI_1 h_0^2}{L^3} b_{ijkl}^* \quad (33, 34)$$

After substituting the dimensionless parameters in equation (29), this later becomes:

$$[K^*]\{A\} + \frac{3}{2}[B^*(\{A\})]\{A\} - \omega^{*2} [M^*]\{A\} = 0 \quad (35)$$

In order to determine the frequency ( $\omega$ ) and the column vector of the contribution coefficients  $\{A\}$ , which represent the unknowns of equation (35), the so-called second formulation had been used. This method was previously developed by EL KADIRI et al. in [16].

### 2.2.2 Forced vibrations

To study the non-linear forced vibrations, the tapered beam is supposed to be excited by a concentrated harmonic force. The dynamic behaviour of this beam is then studied using Hamilton's principle including the forcing term, and can be expressed as in ref[18]:

$$\delta \int_0^t (V - T + F) dt = 0 \quad (36)$$

The concentrated harmonic force applied at the point  $x_0$  can be written as in[14]:

$$F_i^c = F^c \cos(\omega t) w_i(x_0) = f_i^c \cos(\omega t) \quad (37)$$

Where the dimensionless force  $f_i^{c*}$  can be written as:

$$f_i^{c*} = \frac{L^3}{EI_1} F^c w_i^*(x_0) \quad (33)$$

The mathematical development of equation (36) obtained after substitution of equations (25, 26, 27 and 37), as well as the dimensionless parameters can be given as follows:

$$[K^*]\{A\} + \frac{3}{2}[B^*(\{A\})]\{A\} - \omega^{*2} [M^*]\{A\} = \{F^{c*}\} \quad (32)$$

Equation (32) was solved using the single mode approach, previously applied by AZRAR et al [14]. This approach consists of using only the predominant mode. The predominant mode and the contribution coefficients are denoted by "i" and "a<sub>i</sub>", leading to the following equation:

$$1 + 3 a_i^2 \frac{B_{iiii}^*}{K_{ii}^*} - \frac{f_i^{c*}}{a_i K_{ii}^*} = \left( \frac{\omega_{nl}^*}{\omega_1^*} \right)^2 \quad (34)$$

Where  $\omega_1^* = \frac{K_{ii}^*}{M_{ii}^*}$ .

### 3. NUMERICAL RESULTS AND DISCUSSION

#### 3.1 Free vibration

The beam investigated in this study is a tapered beam of a constant width, A linearly varying depth and IS characterised by a taper ratio equal to  $\alpha = 0.8$ . The first four eigenvalues of this tapered beam are compared to those of [23] for two end conditions: a tapered beam clamped at the both sides denoted by C-C, and a tapered beam simply-supported at the both sides denoted by S-S. The results of this comparison are summarised in table 1.

Table 1: The first four eigenvalues of tapered beams for different end conditions. The taper ratio

$$\alpha = 0.8 \text{ and } \frac{S(x)}{S_1} = \left(1 - \alpha \left(\frac{x}{L}\right)\right)$$

		Mode index				
		1	2	3	4	5
CC	Present work	11.84165331	32.47545622	63.51175681	104.8670264	156.5532995
	Ref [23]	11.8417	32.4755	63.5118	104.867	156.554
	Rel Diff	3E-04	1E-04	6.7999E-05	2.51307E-05	4E-04
SS	Present work	4.91976	21.34448781	47.48198199	83.82160776	130.436039
	Ref [23]	4.91976	21.3445	47.482	83.8216	130.436
	Rel Diff	5.51534E-05	-5.71158E-05	-3.79301E-05	9.2612E-06	2.98946E-05

$$Rel\ Diff = \left[ \frac{|Present\ work - Ref[23]|}{Present\ work} \right] \times 100$$

The comparisons made in Table (1) show an excellent agreement, with a relative difference not exceeding 0,0004% for the whole range of frequencies considered.

In the nonlinear free vibration case, the tapered beam investigated remains characterised by the same taper ratio and clamped at the both ends. Figure (2) shows the amplitude dependence of the non-linear frequency parameter on the maximum vibration amplitude.

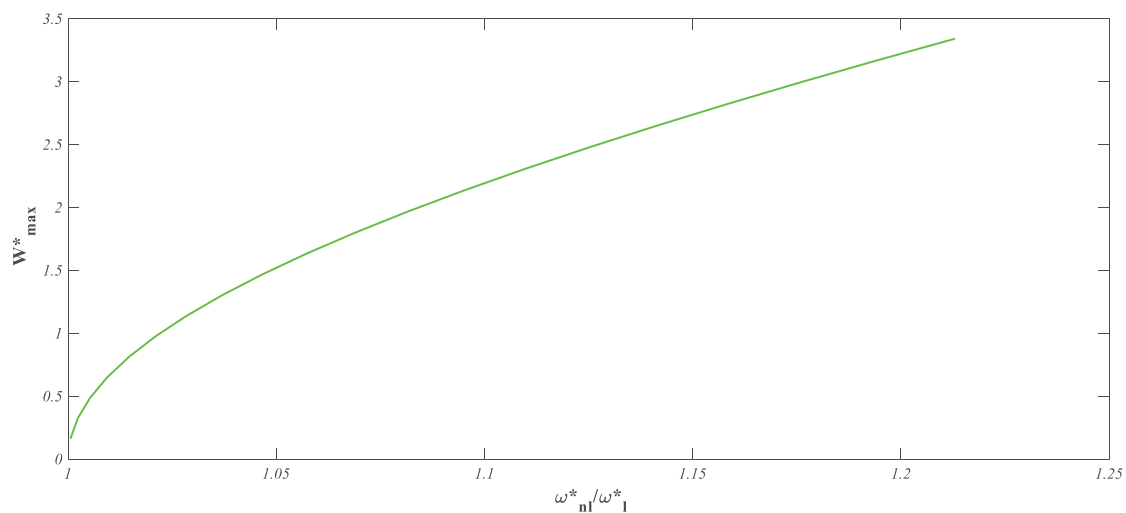


Figure (2) Backbone curve of the tapered beams studied, corresponding to the first nonlinear mode.

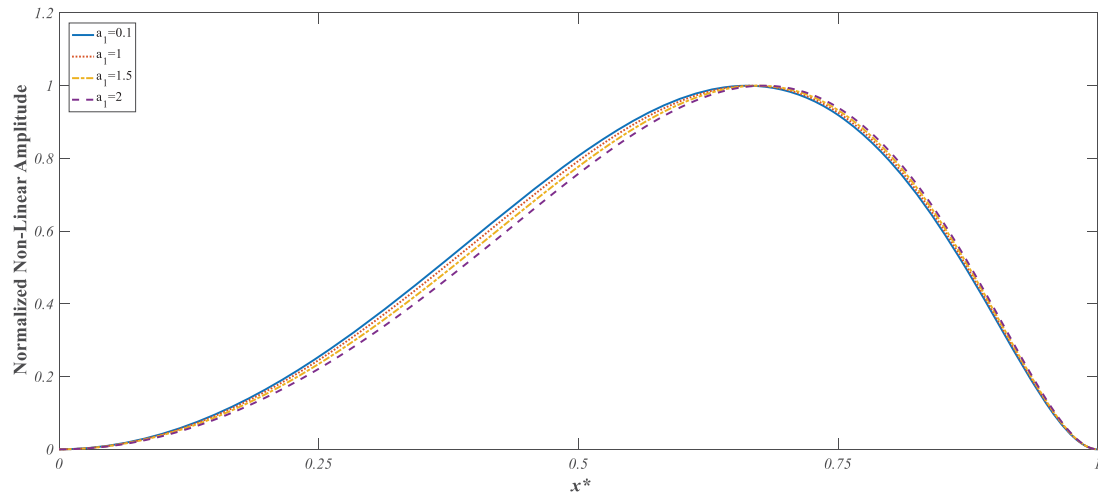


Figure (3): The normalized first non-linear mode of the tapered beam for different amplitude values

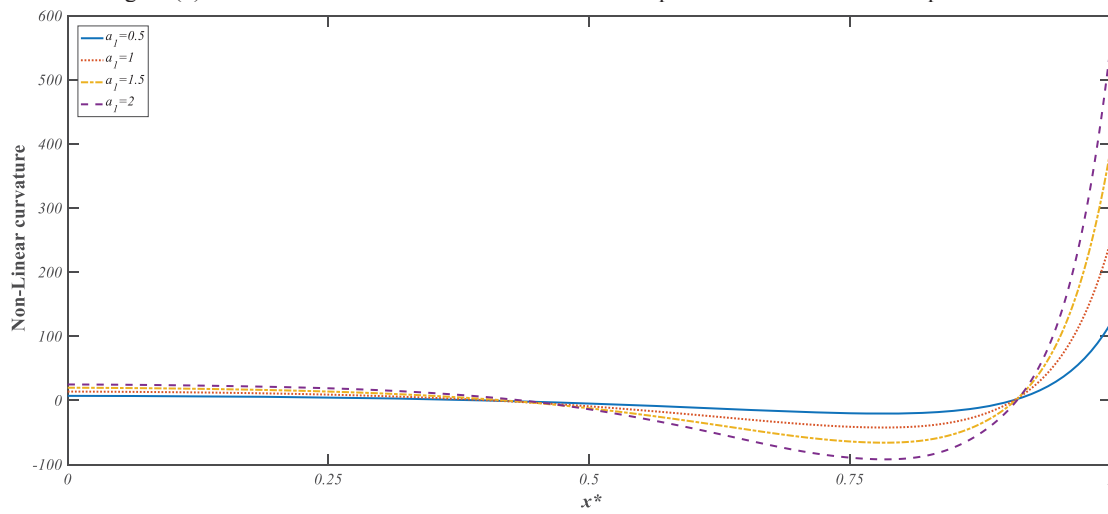


Figure (4): The Non-linear curvature distribution associated to the normalized first non-linear mode for different amplitude values

It may be seen in the backbone curve given in Figure (2) that increasing the maximum non-dimensional amplitude  $W_{\max}^*$  results in an increase the non-linear to linear frequency ratio, which is characteristic of a non-linearity of the hardening type. In addition, the bending moment distribution associated to the non-linear mode shows that the assumption of neglecting the geometrical non-linearity may be misleading. For instance, the non-linear bending moment of the tapered beam at the right end with a contribution coefficient  $a_1 = 1$  is 248.84, while the linear bending moment predicted by linear theory is 237.21, which corresponds to a percentage correction of 4,9%. For  $a_1 = 1.5$ , the non-linear bending moment equals 392.41, while the linear bending moment is 355.81, resulting in a percentage difference of 10,28%. For a contribution coefficient  $a_1 = 2$ , the non-linear and linear bending moments are equal respectively to 553.71 and 474.42, which corresponds to percentage correction of 16,71%.

### 3.2 Forced vibration

The fully-clamped tapered Euler-Bernoulli beam is excited by a concentrated force located at the middle. The generalised forces calculated in Table (2) shows that the first mode remains predominant, which justifies use of the approximate theory developed in [16] for the determination of the non-linear frequency response curve in the neighbourhood of the first mode (NLFRF). The following Table illustrates the type of results obtained.

Table 2: Percentage of generalized forces exciting the first five symmetric modes of tapered beams excited by a concentric force located at the middle of it.

	Modes				
	1	3	5	7	9
$ F^c w_i^*(x_f) $	18,41	9,20	0,35	9,98	16,32

Using the single-mode approach, an investigation of the dynamic behaviour of the tapered beam was carried out in the vicinity of the predominant mode. The response curves were plotted for the tapered beams shown in Figure (1), which was excited by a concentric harmonic force. Five scenarios was investigated in which the excitation level varied in the following way  $[F^c=10^n]$ (for  $n=0,1,2$  and 3).

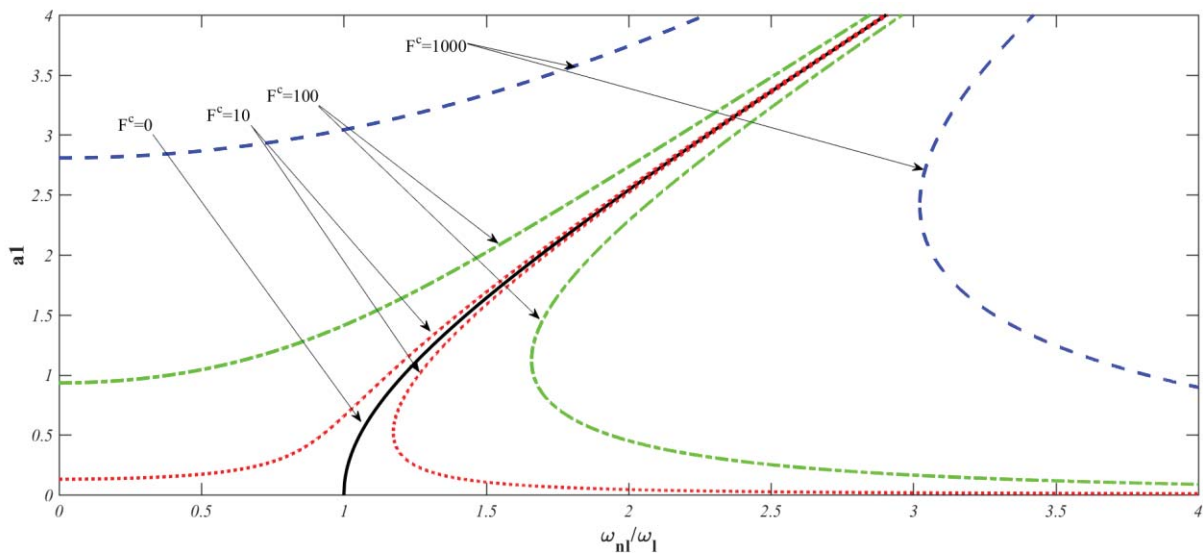


Figure (5): Nonlinear frequency response functions, based on the single mode approach, for the tapered beam subjected to four levels of excitation.

Figure (5) shows the effect of the geometrical non-linearity in the case of forced vibrations, with the jump phenomenon region commonly found in non-linear vibrations. The hardening behaviour is also visible, as well as the non-proportional progression in the frequency response with the excitation intensity.

#### 4. CONCLUSION

Geometrically non-linear transverse vibrations of tapered beams were studied analytically using the Euler-Bernoulli beam theory and Von Karman nonlinearity assumptions. The solution of the linear problem was obtained for a tapered beam of a constant width, a linearly variable depth and a taper ratio equal to 0.8. The linear modes obtained were used as basic functions in the analysis of non-linear vibrations. To solve the non-linear algebraic system derived via application of Hamilton's principle, a previously developed approximate method, called the second formulation, was applied. A comparison was made between the result obtained from the numerical method used here and those obtained using the transfer matrix method. This comparison shows an excellent agreement since the relative difference does not exceed 0.0002 %. Then, the non-linear dynamic behaviour of tapered beams subjected to free vibrations was examined and illustrated by the backbone curve, nonlinear modes and curva-

ture distributions, in which the hardening behaviour can be clearly observed. Using the single-mode approach, a study of the dynamic behaviour of the tapered beams in the forced case was carried out in the vicinity of the predominant mode. The effect of the force level was examined and illustrated for four excitation levels. The results illustrate the effect of geometrical non-linearity with the hardening type behaviour and the instable regions in which the jump phenomena can occur.

## REFERENCES

- [1] D. J. Sanger, "Transverse Vibration of a Class of Non-Uniform Beams," *J. Mech. Eng. Sci.*, vol. 10, no. 2, pp. 111–120, 1968, doi: 10.1243/jmes\_jour\_1968\_010\_018\_02.
- [2] R. P. Goel, "Transverse vibrations of tapered beams," *J. Sound Vib.*, vol. 47, no. 1, pp. 1–7, 1976, doi: 10.1016/0022-460X(76)90403-X.
- [3] W. L. Craver and P. Jampala, "Transverse Vibrations of a Linearly Tapered Cantilever Beam With Constraining Springs," *J. Sound Vib.*, vol. 166, no. 3, pp. 521–529, Sep. 1993, doi: 10.1006/jsvi.1993.1310.
- [4] S. Abrate, "Vibration of non-uniform rods and beams," *J. Sound Vib.*, vol. 185, no. 4, pp. 703–716, Aug. 1995, doi: 10.1006/jsvi.1995.0410.
- [5] M. A. De Rosa and N. M. Auciello, "Free vibrations of tapered beams with flexible ends," *Comput. Struct.*, vol. 60, no. 2, pp. 197–202, 1996, doi: 10.1016/0045-7949(95)00397-5.
- [6] Y. Huang and X.-F. Li, "A new approach for free vibration of axially functionally graded beams with non-uniform cross-section," *J. Sound Vib.*, vol. 329, no. 11, pp. 2291–2303, May 2010, doi: 10.1016/j.jsv.2009.12.029.
- [7] S. M. Abdelghany, K. M. Ewis, A. A. Mahmoud, and M. M. Nassar, "Vibration of a circular beam with variable cross sections using differential transformation method," *Beni-Suef Univ. J. Basic Appl. Sci.*, vol. 4, no. 3, pp. 185–191, Sep. 2015, doi: 10.1016/j.bjbas.2015.05.006.
- [8] F. Sohani and H. R. Eipakchi, "Analytical solution for modal analysis of Euler-Bernoulli and Timoshenko beam with an arbitrary varying cross-section," *Math. Model. Eng.*, vol. 4, no. 3, pp. 164–174, 2018, doi: 10.21595/mme.2018.20116.
- [9] L. S. Raju, G. V. Rao, and K. K. Raju, "Large amplitude free vibrations of tapered beams," *AIAA J.*, vol. 14, no. 2, pp. 280–282, 1976, doi: 10.2514/3.7095.
- [10] M. Liao and H. Zhong, "Nonlinear vibration analysis of tapered Timoshenko beams," *Chaos, Solitons & Fractals*, vol. 36, no. 5, pp. 1267–1272, Jun. 2008, doi: 10.1016/j.chaos.2006.07.055.
- [11] S. Kumar, A. Mitra, and H. Roy, "Geometrically nonlinear free vibration analysis of axially functionally graded taper beams," *Eng. Sci. Technol. an Int. J.*, vol. 18, no. 4, pp. 579–593, 2015, doi: 10.1016/j.jestch.2015.04.003.
- [12] R. Benamar, M. M. K. Bennouna, and R. G. White, "The effects of large vibration amplitudes on the mode shapes and natural frequencies of thin elastic structures part I: Simply supported and clamped-clamped beams," *J. Sound Vib.*, vol. 149, no. 2, pp. 179–195, Sep. 1991, doi: 10.1016/0022-460X(91)90630-3.
- [13] R. Benamar, M. M. K. Bennouna, and R. G. White, "The Effects of Large Vibration Amplitudes on the Mode Shapes and Natural Frequencies of Thin Elastic Structures, Part II: Fully Clamped Rectangular Isotropic Plates," *J. Sound Vib.*, vol. 164, no. 2, pp. 295–316, Jun. 1993, doi: 10.1006/jsvi.1993.1215.
- [14] L. Azrar, R. Benamar, and R. G. White, "SEMI-ANALYTICAL APPROACH TO THE NON-LINEAR DYNAMIC RESPONSE PROBLEM OF S-S AND C-C



- BEAMS AT LARGE VIBRATION AMPLITUDES PART I: GENERAL THEORY AND APPLICATION TO THE SINGLE MODE APPROACH TO FREE AND FORCED VIBRATION ANALYSIS,” *J. Sound Vib.*, vol. 224, no. 2, pp. 183–207, Jul. 1999, doi: 10.1006/jsvi.1998.1893.
- [15] K. El Bikri, R. Benamar, and M. Bennouna, “Geometrically non-linear free vibrations of clamped simply supported rectangular plates. Part I: The effects of large vibration amplitudes on the fundamental mode shape,” *Comput. Struct.*, vol. 81, no. 20, pp. 2029–2043, 2003, doi: 10.1016/S0045-7949(03)00152-4.
- [16] M. EL KADIRI, R. BENAMAR, and R. G. WHITE, “IMPROVEMENT OF THE SEMI-ANALYTICAL METHOD, FOR DETERMINING THE GEOMETRICALLY NON-LINEAR RESPONSE OF THIN STRAIGHT STRUCTURES. PART I: APPLICATION TO CLAMPED–CLAMPED AND SIMPLY SUPPORTED–CLAMPED BEAMS,” *J. Sound Vib.*, vol. 249, no. 2, pp. 263–305, Jan. 2002, doi: 10.1006/jsvi.2001.3808.
- [17] E. bekkaye Merrimi, K. El bikri, and R. Benamar, “Geometrically non-linear steady state periodic forced response of a clamped-clamped beam with an edge open crack,” *Comptes Rendus - Mec.*, vol. 339, no. 11, pp. 727–742, 2011, doi: 10.1016/j.crme.2011.07.008.
- [18] H. Fakhreddine, A. Adri, S. Rifai, and R. Benamar, “A Multimode Approach to Geometrically Non-linear Forced Vibrations of Euler–Bernoulli Multispan Beams,” *J. Vib. Eng. Technol.*, vol. 8, no. 2, pp. 319–326, 2020, doi: 10.1007/s42417-019-00139-8.
- [19] H. Fakhreddine, A. Adri, M. Chajdi, S. Rifai, and R. Benamar, “A multimode approach to geometrically non-linear forced vibration of beams carrying point masses,” *Diagnostyka*, vol. 21, no. 4, pp. 23–33, Nov. 2020, doi: 10.29354/diag/128603.
- [20] I. El Hantati *et al.*, “GEOMETRICALLY NONLINEAR FORCED VIBRATIONS OF MULTIPLE-STEPPED EULER-BERNOULLI BEAMS,” pp. 193–204, 2020, doi: 10.47964/1120.9015.19055.
- [21] I. El Hantati, A. Adri, H. Fakhreddine, S. Rifai, and R. Benamar, “A Multimode Approach to Geometrically Nonlinear Free and Forced Vibrations of Multisteped Beams,” *Shock Vib.*, vol. 2021, no. 4, pp. 1–18, Apr. 2021, doi: 10.1155/2021/6697344.
- [22] O. Outassafte, A. Adri, Y. El Khouddar, S. Rifai, and R. Benamar, “Geometrically Non-Linear Free In-Plane Vibration Of Circular Arch Elastically Restrained Against Rotation At The Two Ends,” *Int. J. Eng. Trends Technol.*, vol. 69, no. 3, pp. 85–95, Mar. 2021, doi: 10.14445/22315381/IJETT-V69I3P215.
- [23] J. R. Banerjee and A. Ananthapuvirajah, “Free flexural vibration of tapered beams,” *Comput. Struct.*, vol. 224, p. 106106, 2019, doi: 10.1016/j.compstruc.2019.106106.

## POWDER SNOW IMPACT OF TALL VIBRATING STRUCTURES

Andrin Caviezel<sup>1</sup>, Stefan Margreth<sup>2</sup>, Kseniya Ivanova<sup>1</sup>, Betty Sovilla<sup>2</sup> and Perry Bartelt<sup>1</sup>

<sup>1</sup>WSL Institute for Climate, Extremes and Alpine Natural Hazards CERC  
Davos Dorf, Switzerland  
e-mail: {caviezel,ivanova,bartelt}@slf.ch

<sup>2</sup>WSL Institute for Snow and Avalanche Research SLF  
Davos Dorf, Switzerland  
e-mail: {margreth,sovilla}@slf.ch

**Keywords:** Powder Snow Avalanche, Impact, Dynamic Magnification, Power Transmission Towers, Pylons, RAMMS

**Abstract.** *Tall structures play an important role in the economic well-being of mountainous regions. They serve to distribute hydroelectric energy (power line transmission towers), generate tourist income (cableway pylons) and protect important infrastructure from natural hazards (trees). It is not uncommon for these structures to be destroyed by the air-blast of a powder avalanche. In this paper we investigate the shock response spectra of an asymmetric steel structure subjected to powder avalanche impact. We perform a spectral analysis of measured accelerations in the in-plane (avalanche flow) and cross-plane (normal to avalanche flow) directions. The structural eigenfrequencies in each direction are likewise calculated using a simple finite element model consisting of three-dimensional beam elements. Mode superposition is then used to reconstruct the measured accelerations, velocities and displacements in order to identify the magnitude and duration of the powder avalanche loading. From the analysis we find that the powder avalanche must contain high-frequency, short-duration blasts ( $f > 2$  Hz) of moderate magnitude ( $p \approx 1$ -10 kPa). High frequency blasts are also present in the cross-plane, transverse flow direction. This result, however, does not exclude the existence of longer duration blasts, which, because of the frequency mismatch, cannot excite the measurement pylon. It appears the high-frequency content of the cloud attenuates to endanger low-frequency structures ( $f \approx 1$  Hz) such as trees at the lateral edges of the flow, or hanging cables located well above the core. The shock response of a specific structure therefore depends on its location relative to the avalanche core, depending on how the blast-structures dissipate in time and space. Because the powder cloud contains a wide range of blast frequencies, tall structures are vulnerable to the action of the powder cloud, even if they are located well outside the avalanche core.*

## 1 INTRODUCTION

A longstanding problem in natural hazards engineering has been to predict the action of snow avalanches on power transmission towers and pylons. These are thin, tall structures, that are exposed to both the impact of the dense avalanche core and powder cloud (Figs. 1 and 2). The avalanche core is composed of clumps and clods of compacted snow with bulk densities reaching  $500 \text{ kg/m}^3$  or even higher (Fig. 3). The avalanche core is primarily a surface flow governed strongly by terrain and slope properties (steepness, roughness, vegetation, gullies, channels, etc) [1]. Although engineers can often position transmission towers and pylons outside the reach of the flow core, exploiting natural terrain features such as elevated ridges and knolls, they are nonetheless subjected to the wind blast of the airborne powder cloud.



Figure 1: Left: The front of a powder snow avalanche. Photograph taken at the Swiss experimental avalanche dynamics site in 2003. The avalanche is moving at a speed between 40-50 m/s. Note the turbulent billow and cleft structures an indication of velocity fluctuations. Right: A powder avalanche overturned this power transmission mast in January 2018. The mast is located in the runout zone of the Val Barcli avalanche track, Zerne, Switzerland. The conductors are still attached to the mast which appears to be severely damaged near the foundation. Note the mangled and twisted truss elements near the foundation suggesting a multi-dimensional loading. The photograph appeared in the newspaper Engadiner Post, January 24th, 2018. The transmission line belongs to the Engadiner Kraftwerke AG (EKW).

The powder cloud consists of suspended ice-dust; it is created when both dense particles and ice-dust are ejected from the avalanche core into the surrounding air, often quickly and to great heights [1]. The suspended dust remains airborne while the larger particles eventually return back to the core. The difference in particle sizes thus leads to a natural separation between the core and cloud. The cloud is created from the core and during the formation phase is continually supplied with mass and momentum from the core. It can reach significant speeds. More importantly, once airborne the flow of suspended ice-dust is free from the terrain and will essentially travel in the initial direction defined by the core/cloud momentum exchange. Thus, while the core is a surface flow, the cloud is an inertial, airborne flow. At formation the flows are combined, but the flows can separate, flow in different directions and velocities and therefore can inundate larger areas.





Figure 2: An avalanche displaced and tilted this cableway mast in East Tirol, Kals, Austria. The mast itself was not damaged and could be brought back into an upright position. The picture appeared in the Dolomitenstadt.at online magazine on November 21, 2019.

Transmission towers and pylons are vulnerable to the action of the powder cloud. For one, because the powder cloud applies wind loadings at significant heights above the ground. The primary purpose of these structures is to carry cables above ground. They are designed for vertical loads and horizontal wind loads. As such, heavy, cable supporting sub-structures are often located well above the ground, Fig. 2. Mass is therefore not equally distributed over the height, but often concentrated near the top of the structure. This makes masts and pylons particularly vulnerable to dynamic loads. If this mass is excited by the avalanche impact, large internal stresses can be generated by the external loading. Another problem is that the cables between towers can also be impacted by the powder cloud. That is, the towers can escape the powder blast, but the cables are often subjected to pressures larger than the wind load. The impact of the cables creates internal stress/deformation waves that propagate back and forth between the towers, with a magnitude and frequency dependent on the elasticity and cross-sectional mass of the cables [2]. This leads to concentrated, dynamic loads on the towers, again at some distance above the ground. Thus, powder avalanches can both directly and indirectly produce dynamic loads on tall tower-type structures (Fig. 4).

The purpose of this paper is the following. We first would like to identify the duration and magnitude of powder avalanche impact loadings on tall, thin structures. This information is the prerequisite for performing a dynamic structural engineering analysis for both man-made structures as well as natural structures such as trees [3]. We do this by back-calculating measured accelerations on a tall, asymmetric structure with known cross-section and material properties. For this purpose we develop a simple three-dimensional finite element beam model. Thus, we are able to approximate both longitudinal and transverse loadings arising from the powder cloud

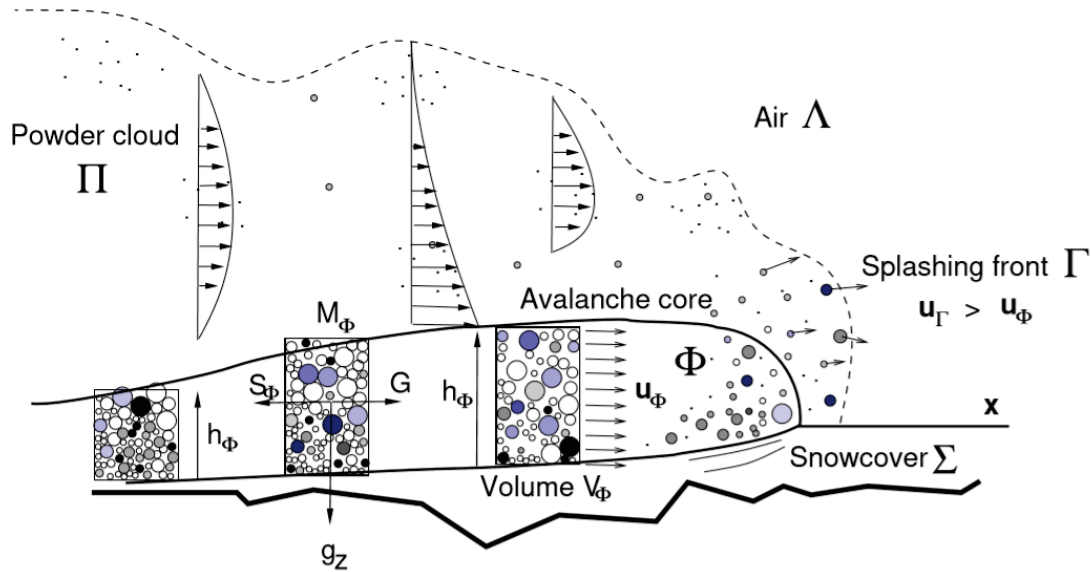


Figure 3: Flowing avalanche core  $\Phi$  and powder cloud  $\Pi$ . Avalanche dynamics models predict the movement of the core and cloud in general terrain. The core contains granular mass in the form of clumps of snow. The cloud contains suspended ice-dust. The layers are not separate, but overlaid and mixed. The height of the core is defined by the location of the highest clump of snow; that is, it includes saltating particles at great heights in the powder cloud. A splashing front exists at the front of the avalanche.

impact. We perform a modal analysis to identify the duration, location and magnitude of the blast [4]. We then apply a mixed flowing/powder avalanche model to calculate the destruction of the mast to demonstrate the important contribution of the dynamic powder blast to overall avalanche loading. Clearly, the primary objective of this paper is to underscore the necessity of including both (internal) inertial forces and (external) impulsive forces when calculating the response of tall structures to powder avalanche impact.

## 2 ACCELERATION MEASUREMENTS and FE-MODAL ANALYSIS

Acceleration measurements on the 20 m high, tubular steel pylon at the Swiss Vallée de la Sionne test site are used to determine the duration and intensity of powder loadings [5, 6]. The width of the pylon is approximately  $w = 0.6\text{ m}$ , with bevelled edges; in the direction of avalanche flow the pylon is 1.6 m long. Accelerometers are fixed on the pylon at four heights (3.8 m, 7.8 m, 12.3 m, 16.3 m) and measure accelerations in both the longitudinal (avalanche direction) and transverse (perpendicular to flow) directions. The pylon is fixed rigidly to the ground via a concrete sub-structure and can be considered a fixed-end cantilever. Because of internal stiffness elements and variable section thickness (1-3 cm), the moments of inertia can vary with height somewhat. Values at the midsection are stated here,  $I_Y = 0.0042\text{ m}^4$  and  $I_Z = 0.0125\text{ m}^4$ . The flexural rigidity of the pylon is subsequently a factor 3 lower in the transverse direction. The modulus of elasticity and density for steel are applied in the analysis,  $E = 200\text{ GPa}$  and  $\rho = 8000\text{ kg/m}^3$ , respectively.

Measured accelerations in the transverse and longitudinal directions are depicted in Fig. 5. The measurements reveal (1) Within six seconds the pylon was struck by a series of short duration blasts lasting less than a fraction of a second, between 0.25 s and 0.50 s. (2) Higher accelerations are measured in the transverse (less stiff) direction, (3) the magnitude of the accelerations at the highest location (16.3 m) reach 10  $g$  in the transverse direction and 4  $g$  in the

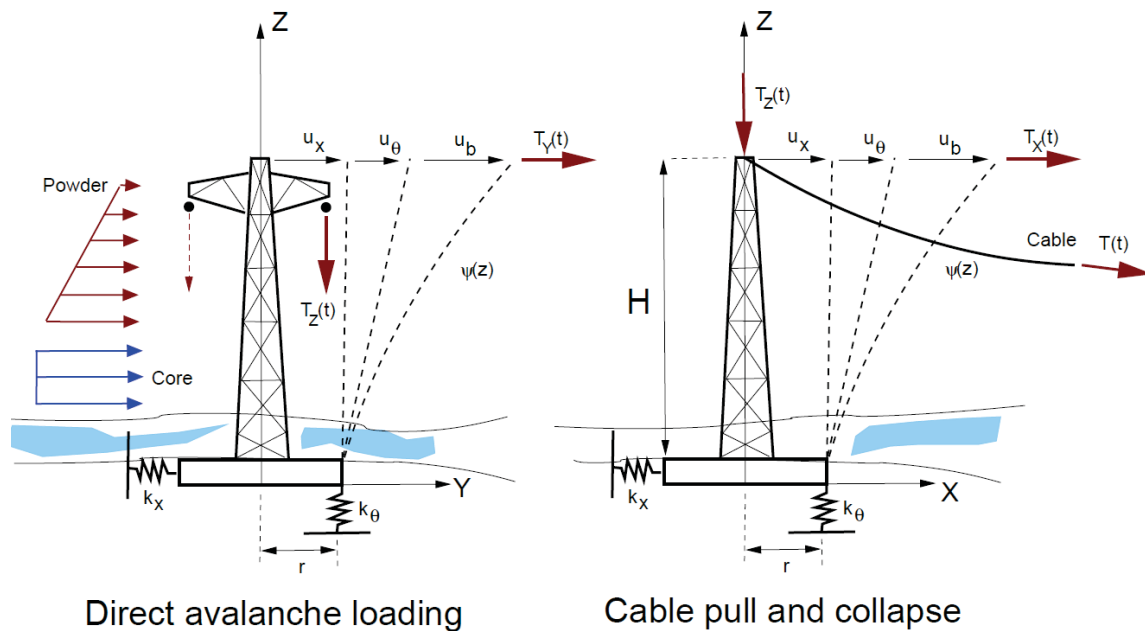


Figure 4: We consider two loading cases: 1) The avalanche core and cloud directly impacts the mast. 2) The mast is outside the reach of the core and cloud and the avalanche impacts only the cables, causing pull and collapse forces on the mast. The avalanche impacts the mast in transverse  $Y$ -direction producing bending moments around the  $X$ -axis. The  $X$ -direction runs parallel to the cable. Cable impact induces pulling forces  $T_X(t)$  in the  $X$ -direction and collapse forces  $T_Z(t)$  in the  $Z$ -direction. These induce bending moments around the  $Y$ -axis. A third loading case is when both the mast and cables are struck by the avalanche.

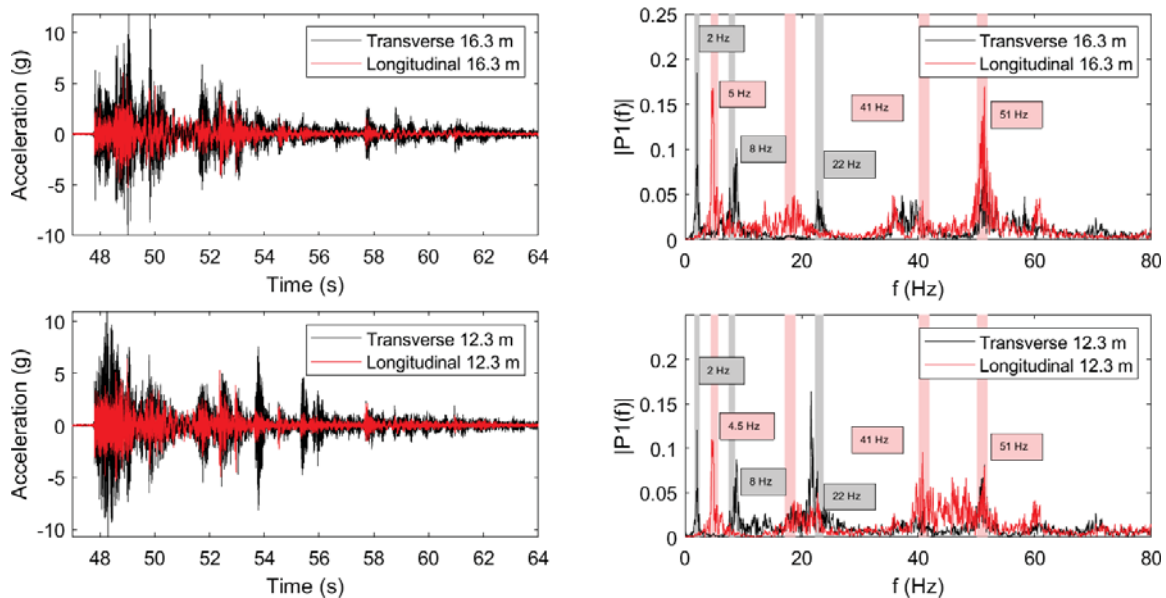


Figure 5: Left: Measured accelerations at heights 16.3 m and 12.3 m in the transverse (black) and longitudinal (red) directions. Right: Frequency analysis of the measured accelerations. The three lowest eigenfrequencies in longitudinal direction are 5 Hz, 18 Hz and around 40 Hz; in the transverse direction 2 Hz, 8 Hz and 18 Hz.



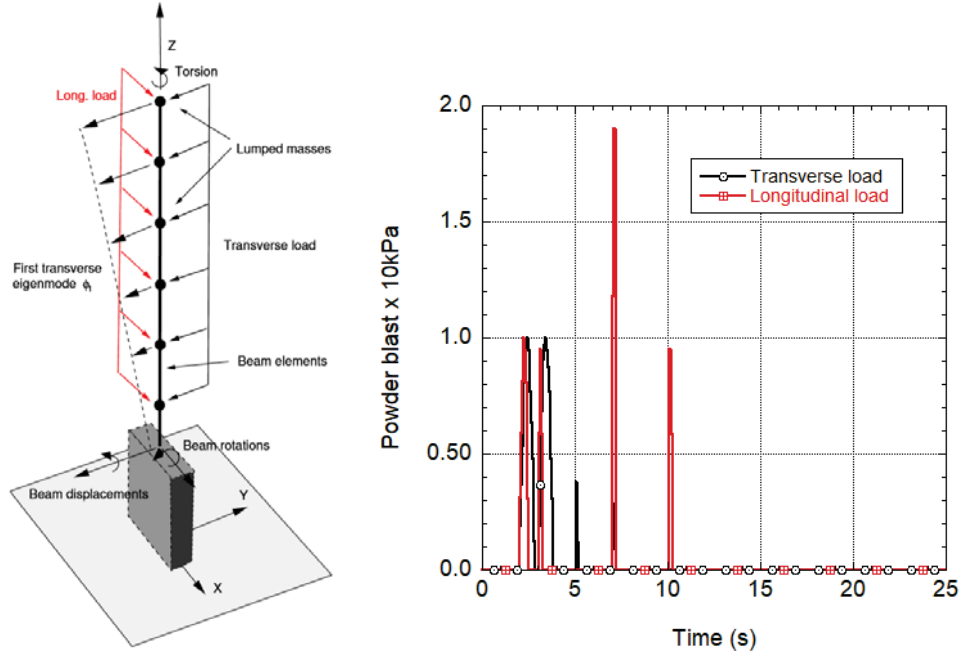


Figure 6: Left: Three-dimensional finite element beam model displaying the transverse and longitudinal directions. The finite element model is used to determine the eigenmodes of the structure. Right: A powder loading is applied to the structure as a series of random pulses.

longitudinal direction and finally (4) the intensity of the blast is clearly highest at or near the avalanche front.

We performed a discrete Fourier transform using the standard fast Fourier transform (FFT) algorithm [7] to identify the eigenfrequencies. Figure 5 shows raw data streams and its according FFTs without applying any data filtering. Likewise, we developed a simple finite element model consisting of three-dimensional beam elements to model the pylon structure (Fig. 6). The finite element model consisted of 7 elements, 8 nodes (48 DOFs). We calculated all  $n = 48$  eigenvalues ( $\omega_n$ ) and eigenvectors ( $\phi_n$ ) using MAPLE [8]. Measured and calculated eigenfrequencies are presented in Table 1.

Mode no.	Longitudinal $X$ -direction	Transverse $Y$ -direction
	Eigenfrequency $\phi_z$ (Hz)	Eigenfrequency $\phi_y$ (Hz)
	Measured/FE	Measured/FE
1	5.0 / 5.1	2.0 / 1.9
2	18.0 / 18.5	8.0 / 8.8
3	41.0 / 41.5	18.0 / 21.3

Table 1: Longitudinal and transverse eigenfrequencies of the impact pylon.

The orthogonality properties of the eigenvectors can be used to uncouple the general equations of motion to arrive at a series of  $n=3$  differential equations in the longitudinal and transverse directions [4],

$$M_n \ddot{Y}_n + C_n \dot{Y}_n + K_n Y_n = P_n(t) \quad (1)$$

where

$$M_n \equiv \phi_n^T m \phi_n \quad K_n \equiv \phi_n^T k \phi_n \quad P_n \equiv \phi_n^T p(t) \quad (2)$$

are the generalized mass (FE mass matrix  $m$ ), stiffness (FE stiffness matrix  $k$ ) and load (FE load vector  $p(t)$ ). The damping  $C_n$  is determined using the usual method of assigning a damping ratio for each mode  $n$ . For the mode-superposition method we took the three lowest eigenfrequencies in the longitudinal and transverse direction and therefore solved a system of six ordinary differential equations to find the dynamic response. Higher frequencies were not included in the analysis.

We matched the experimental results by selecting short duration blasts arranged randomly over the six second interaction time. The load  $p(z, t)$  acted over the entire pylon height. The magnitude of the load did not change between the longitudinal and transverse directions  $p_0 = 5$  kPa. The avalanche core was assumed to act only on the lower region of the pylon ( $h < 5$  m). The measurements appear to be strongly damped and we selected an appropriate damping ratio for each mode.

In order to capture measurements it was necessary to apply several high-frequency blasts of duration  $0.25 \text{ s} \leq \Delta t \leq 0.5 \text{ s}$  (Fig. 6). We applied these loads homogeneously over the entire height. The blasts must be applied in both flow and cross-flow directions. The fact that the pylon structure is asymmetric, and therefore has two dissimilar first bending mode eigenfrequencies, is helpful to quantify the frequency content and blast magnitude in both directions. For the blast loading we found the frequency content and intensity to be similar (Fig. 7).

It would be entirely wrong to conclude the powder cloud contains *only* turbulent structures of duration 0.25s to 0.50s (2Hz - 4Hz). These pulses exist at the eigenfrequency of the pylon, and therefore the pylon reacts to them. Lower frequency (longer duration) pulses could exist in the cloud, but the pylon would not react to them. These pulses would therefore not be seen in the measurements.

Of considerable importance is the fact that we applied significant core loadings to the structure at the same time as the powder blast. The magnitude of the acceleration response, however, was not dominated by the magnitude of the long-duration core load ( $p = 60$  kPa), rather by the short duration of the powder blast, especially in the transverse direction. Using the model it was possible to obtain similar accelerations in both the longitudinal and transverse directions, at different heights. Clearly, the comparison between the measurements and model results could be optimized to obtain the exact magnitude and load timing. We show that with a relatively simple load model a reasonable and good quantitative fit to the experiments can be achieved. Remarkable is the model prediction of the three lowest eigenfrequencies in each direction.

Finally, we note that we applied the powder blasts over the entire pylon. Only in this way could we match the measured accelerations. This result indicates that the pulses have considerable height (20m) in the  $Z$ -direction, larger than the pulse wavelength in the  $X$ - and  $Y$ -directions. Vorticity in the cloud must therefore not be distributed equally in all directions.

### 3 RAYLEIGH ANALYSIS with AVALANCHE DYNAMICS SIMULATIONS

To reinforce the idea that the duration and magnitude of the powder blast contributes a large part to the total structural load, we performed a simple Rayleigh analysis, using a method developed by Wolf [9]. In this section we investigate two of the largest snow avalanches ever recorded at the Swiss Vallée de la Sionne test site. These are the avalanches of the 10th of February and 25th February, 1999. Both avalanches are documented in the SLF internal report No. 732 entitled *Lawinendynamik-Versuchsgelände Vallée de la Sionne-Arbaz, Wallis. Schlussbericht Winter 1998/1999*. These avalanches clearly impacted the pylon structure with a significant core loading.

We construct an equivalent one-dimensional model of the mast (Rayleighs method) given by

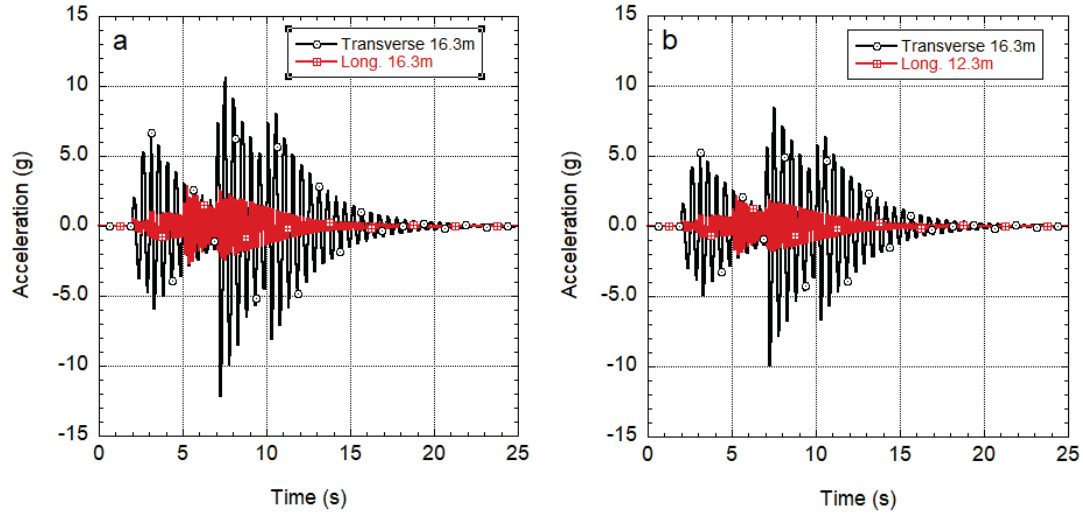


Figure 7: Results of the FE mode-superposition analysis. Transverse (black) and longitudinal (red) accelerations. a)  $z = 16.3$  m. b)  $z = 12.3$  m. The calculations are damped with first mode damping ratios of  $\xi_n = 0.02$ .

the dynamic equation

$$M\ddot{u}(t) + Ku(t) = P(t) \quad (3)$$

where  $M$ ,  $K$  and  $P$  are the effective mass, stiffness and loading values. The deformation at the top of the structure  $z = H$  is  $u(t)$ . For this simple analysis we neglect structural damping. We use the analytical function (see [4])

$$\psi(z) = 1 - \cos \frac{\pi z}{2H}. \quad (4)$$

to model the bending displacement. The effective mass and loading are then found,

$$M = \int_0^H m(z) (\psi(z))^2 dz \quad P(t) = \int_0^H p(z, t) \psi(z) dz. \quad (5)$$

The mass distribution of the steel structure is given  $m(z)$ ; the external avalanche loading  $p(z, t)$ . The effective bending stiffness (flexural rigidity  $EI(z)$ ) is given by

$$k_b = \int_0^H EI(z) \left( \frac{d^2\psi}{dz^2} \right) dz \quad (6)$$

which we modify to include foundation effects according to the procedure of Wolf [9],

$$K = \frac{k_b}{\left[ 1 + \frac{k_b}{k_x} + \frac{k_b H^2}{k_\theta r^2} \right]} \quad (7)$$

where the parameters  $k_x$ ,  $k_b$  and  $r$  characterize the foundation stiffness. The dimensions of the pylon (width 0.6 m, length 1.6 m, avg. plate thickness 25 mm) were used to approximate the flexural rigidity of the tubular steel structure  $EI = 3.5$  GNm<sup>2</sup>. This also provided the approximate mass per running height of the pylon ( $m = 550$  kg/m). We considered a soil strength of  $k_x = k_x = 75$  MN/m. This produced a vibration frequency  $\omega = 12.2$  rad/s ( $f = 1.95$  Hz), in good agreement with the finite element model and the acceleration measurements. The natural vibration frequency of the pylon on an absolutely rigid foundation is  $\omega = 25.0$  rad/s ( $f = 4$  Hz).

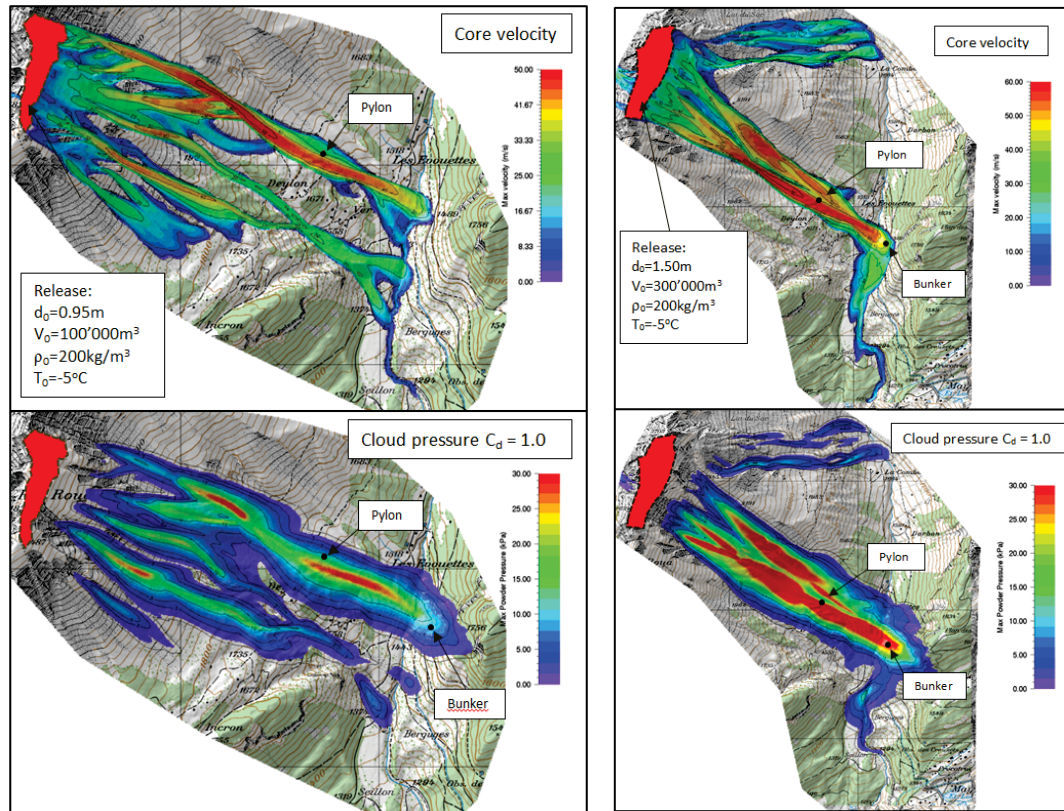


Figure 8: Vallée de la Sionne, 1999. Calculated core velocities and powder cloud impact pressures (**RAMMS**) for two large powder avalanches that occurred on 10.2.1999 and 25.2.1999. The calculated pressures are around 35 kPa ( $C_d = 1$ ).

We first simulated the avalanche events with the **RAMMS** software [10] to determine the core and powder cloud loadings (Fig. 8). An overview of the simulation results is contained in Table 2. Pre- and post event photogrammetric measurements were used to derive the mass balance of both avalanches. The location and extent of the release zones are also defined according to the photogrammetric measurements. The fracture depths  $d_0$  and release volumes  $V_0$  likewise correspond to the experimental observations.

The calculated avalanches reach peak leading-edge velocities of 60 m/s (10.2.1999) and 80 m/s (25.2.1999), close to the observed values (see report). The calculated runout distances correspond to the observations. The avalanche of 25.2.1999 inundated the forested area behind the bunker with pressures large enough to knock down trees (observed and calculated). The powder pressure of the 25.2.1999 avalanche is considerably higher than the avalanche of 10.2.1999. This is in large part due to the fact that the core of 25.2.1999 avalanche impacted the mast directly, whereas the core of the 10.2.1999 avalanche flowed past the pylon on the orographic right side, reducing the magnitude of the calculated powder pressures. This fact suggest large transverse loadings on the structure for the second avalanche. The calculation results were used to construct core and cloud loading that are shown in Fig. 9. Note that the core of the 25.2.1999 avalanche struck the mast at a higher level as it flowed on the deposits of the 10.2.1999 avalanche.

The first surprising result of the Rayleigh analysis is that the powder avalanche load contributes significantly to the effective avalanche loading in both the longitudinal and transverse directions (Fig. 10). The effective loading of the 25.2.1999 avalanche is a factor 5 times larger

Vallée de la Sionne February 1999	10.2.1999	25.2.1999
Release height $d_0$ (m)	0.98/0.95	1.50/1.50
Measured release volume $V_0$ (m <sup>3</sup> )	104'000/105'650	316'000/315'125
Release temperature $T_0$ (°C)	-5	-5
Release density $\rho_0$ (kg/m <sup>3</sup> )	200	200
Snowcover gradient $\Delta h_\Sigma$ (cm/100m)	5	5
Temperature gradient $\Delta T_\Sigma$ (°C/100m)	0.5	0.5
Calculated erosion volume (m <sup>3</sup> )	607'300	1'265'000
Calculated core mass to cloud (t)	33'110	75'100
Cloud deposition volume (m <sup>3</sup> )	74'000	167'000
Measured deposition volume (m <sup>3</sup> )	760'000	1'710'000
Calculated deposition volume (m <sup>3</sup> )	786'950	1'747'125

Table 2: Mass balance of Vallée de la Sionne avalanches February 1999. The size and location of the release zone are taken directly from the experimental report. The total measured deposition volume is compared to the calculated deposition volume which is the sum of the simulated release, erosion and powder cloud deposition volumes.

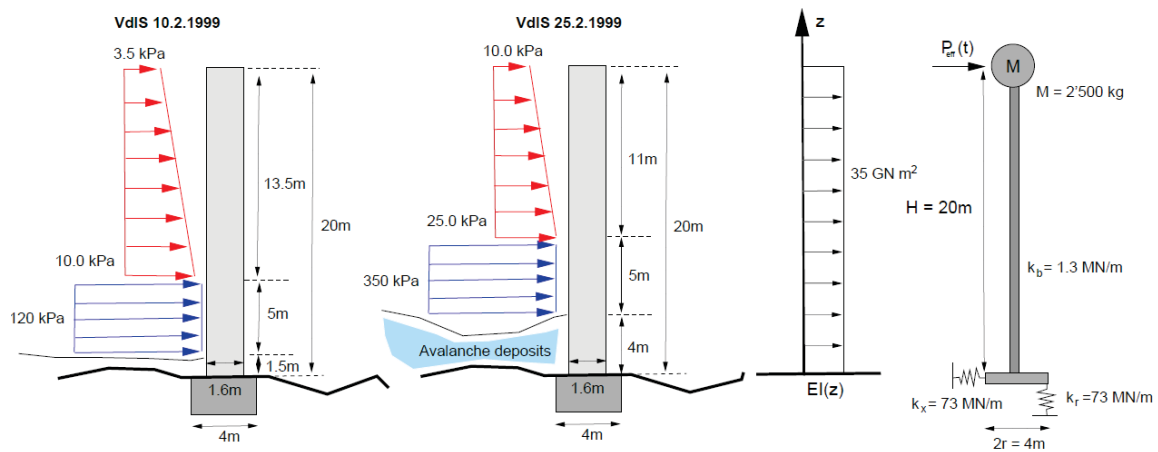


Figure 9: Calculation model of the VDLS pylon for two avalanches (10.2.1999 and 25.2.1999) in 1999. The second avalanche destroyed the pylon. The two loadings produce two different effective loadings  $P_{\text{eff}}(t)$ .

than the avalanche of 10.2.1999 – although the pressure loading from the core and cloud vary only by a factor two. This is due in part to the stronger powder cloud pressure of 25.2.1999, but also due to the fact that the core load is elevated 4 m from the base of the pylon. For the avalanche of 25.2.1999 the effective loading increases from  $P_{\text{max}} = 150$  kN to peak impact pressures of  $P_{\text{max}} = 300$  kN; that is, the effective loading essentially doubles. Note that the duration of the core and powder loadings differ - the core loading is of longer duration (15s) than the powder loading ( $< 1$  s). The Rayleigh analysis effectively quantifies the effect of the loading elevation.

Another interesting result of the Rayleigh analysis is that the elastic limit ( $2000 \mu\epsilon$ ) is reached because of the transverse impact. Strains from the transverse loading are approximately 4 times higher than from longitudinal loading ( $500 \mu\epsilon$ ), see Fig. 10c. The calculated accelerations in the transverse direction have a higher order of magnitude than the experimental measurements ( $15 g > 5 g$ ), but are also longer lasting, suggesting a more intense impact.



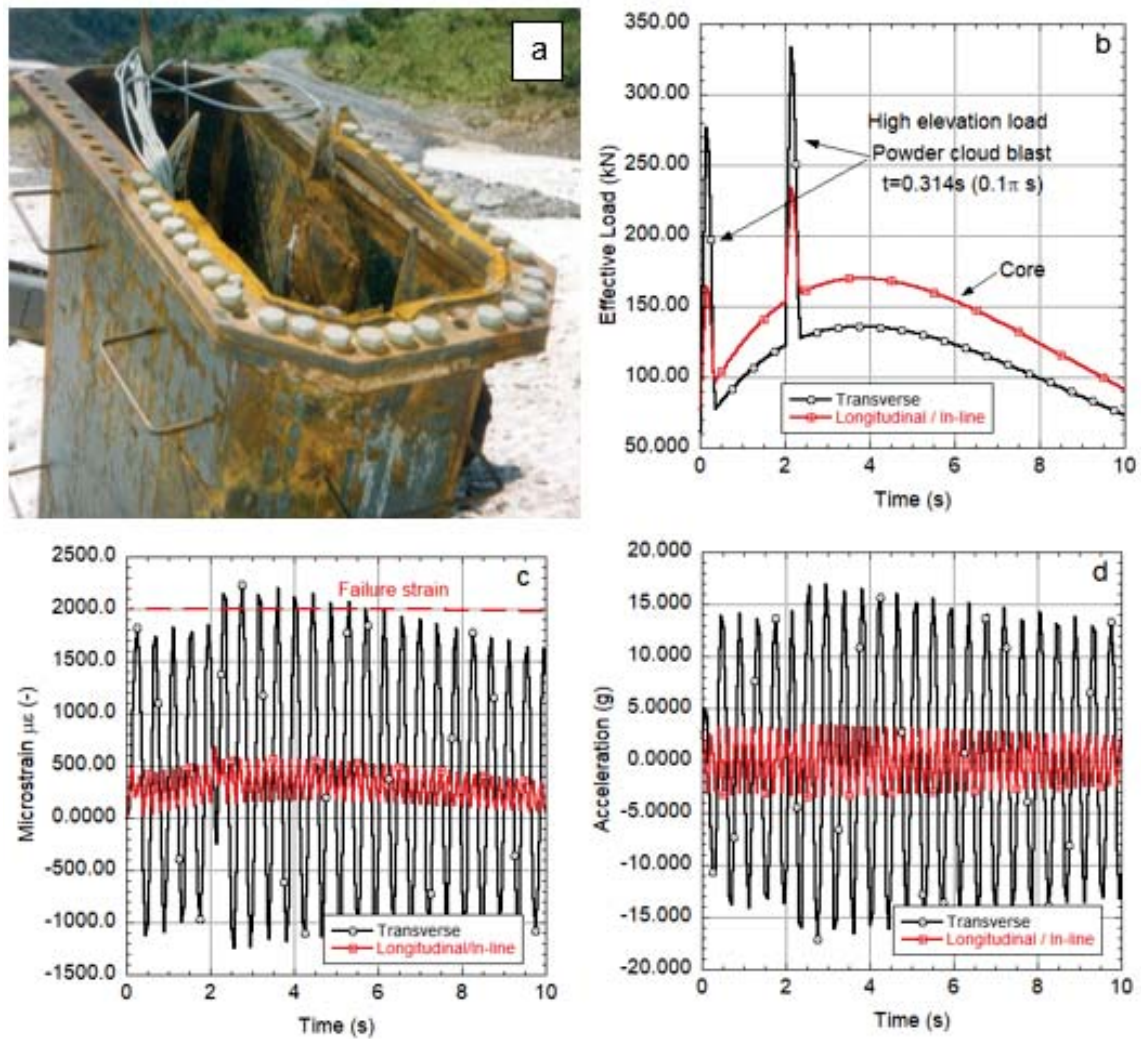


Figure 10: Results of Rayleigh analysis for the two observed avalanches with a loading duration of  $\pi$ s. a) Calculated microstrains for avalanche of 10.02.1999. b) Calculated effective load of 10.02.1999. c) Calculated microstrains for avalanche of 25.02.1999. The powder cloud loading excites the inertial forces such that the failure strains are reached. d) Calculated effective load of avalanche 25.02.1999.



## 4 CONCLUSIONS

We began our work with an analysis of measured structural accelerations induced by powder avalanche impact of a 20 m high cantilever pylon. In the measurements we could clearly identify the first three bending frequencies of the pylon in both the longitudinal and transverse directions. These eigenfrequencies could be reproduced using a simple finite element beam model. Because the pylon cross-section is a rectangular tube (1.6 m x 0.6 m, with some internal stiffening elements), the first mode eigenfrequencies differed in the longitudinal (5 Hz) and transverse (2 Hz) directions. Avalanche impact of the pylon induced accelerations reaching 10 *g* in the transverse direction (pylon top) and smaller accelerations in of 2 *g* in the stiff longitudinal direction. The significance of these results is twofold.

Firstly, a mode superposition analysis reveals that to reproduce the measured accelerations it is necessary to apply short duration blasts with duration times of approximately 0.25 s to 0.50 s. This corresponds to loading frequencies of 2 Hz to 4 Hz. At present it is not possible to model the exact timing of the blasts, but it appears there can be several within the first 10 s of the avalanche passage. It is not possible to conclude that the powder cloud contains structures only of this duration. The pylon reacts to these loading frequencies because they are near the eigenfrequencies of the pylon. It is entirely possible for the cloud to contain many different frequencies. Secondly, the powder blasts appear to be stronger than considered in the transverse direction. These transverse loadings arise as the avalanche head passes to one side of the structure. The lateral blasts are significant, especially for asymmetric structures which reduce the impact area in the longitudinal direction (in this particular case 0.6 m), but increase the length of the structure (in this particular case 1.6 m) in order to increase the flexural rigidity in the line of attack. The primary conclusion of this part of the paper is that inertial effects and dynamic magnification factors must be considered when designing pylon type structures against powder avalanche impact. Presently, this is not performed in avalanche engineering.

In the second part of the paper we performed a Rayleigh analysis of the pylon. That is, we reduced the finite element model to a single degree of system, modelling the response of the structure using only the first bending mode. In this analysis the mass, flexural rigidity and loading distributions are reduced to scalar (effective) quantities by assuming a specific deformation in the *z*-height direction. With this simple modelling approach, it was possible to obtain the eigenfrequencies in the longitudinal and transverse directions, but not with the accuracy of the finite element model. We simulated two large powder avalanches that occurred at the test site during the avalanche winter of 1999, on the 10.02.1999 and 25.02.1999. The second avalanche was so extreme, that it destroyed the pylon. Our analysis reveals that the transverse loading played a significant part in the structural failure, as we could only generate microstrains above the plastic limit (2000  $\mu\epsilon$ ) from this loading case. The first avalanche appeared to stress the pylon up to only 50% of its capacity. Of interest is the fact that the effective loading of the avalanche core contributed only 50% of the total effective loading. Moreover, the short duration powder loading, because it hits the pylon at the right frequency some distance above the ground contributes a significant part of the total effective loading.

Finally, there is considerable empirical evidence that the duration of the powder blast increases with distance from the avalanche core, where the powder cloud is formed. Trees have eigenfrequencies of approximately 1 Hz and would easily survive short duration powder blasts in the 2 Hz to 5 Hz range. This result suggests that the blast frequency of the cloud is continually changing in time and space. The powder cloud contains a wide spectrum of turbulent wavelengths that would excite tall structures. As the cloud turbulence dissipates, we expect

longer duration blasts which would blow-down tree stands. This fact would explain why trees in the runout zone of avalanches (and on the sides of avalanche tracks) are especially vulnerable to the action of the powder cloud. This fact motivates our interest in understanding both the production and decay of vorticity in powder avalanches. For shear flows with varying in space and time vorticity an intermediate model was recently proposed where the governing equations are obtained by depth-averaging the Euler equations without assuming potential flow [12, 13, 14].

## REFERENCES

- [1] Bozhinskiy, A. N., and Losev, K. S., The fundamentals of avalanche science, Mitt. Eidgenöss. Inst. Schnee- Lawinenforsch. 55: 280 p., 1998.
- [2] P. Bartelt, A. Caviezel, M. Christen, O. Buser, Impact of hanging cables and power transmission lines by mixed flowing/powder avalanches, *25th international conference on theoretical and applied mechanics*, Milan, Italy, August 23-28, 2020.
- [3] P. Bartelt, P. Bebi, T. Feistl, O. Buser and A. Caviezel, Dynamic magnification factors for tree blow-down by powder snow avalanche air blasts. *Natural Hazards and Earth System Science*, **18**(3), 759-764, 2018.
- [4] Clough R. and J. Penzien, *Dynamics of Structures*. McGraw-Hill, New York, NY, 1975.
- [5] W. Ammann, A new Swiss test-site for avalanche experiments in Vallée de la Sionne/Valais, *Cold Regions Science and Technology*, **30**(1-3), 3-11, 1999.
- [6] B. Sovilla, J. McElwaine and A. Köhler, The Intermittency Regions of Powder Snow Avalanches, *Journal of Geophysical Research: Earth Surface*, 123. <https://doi.org/10.1029/2018FJ004678>.
- [7] <http://www.fft.w.org>, last accessed 17.03.2021.
- [8] Maple 2019. Maplesoft, a division of Waterloo Maple Inc., Waterloo, Ontario.
- [9] Wolf, J.P., *Dynamic Soil Structure Interaction* Prentice-Hall, Englewood Cliffs, NJ, 1983.
- [10] P. Bartelt, O. Buser, C. Vera Valero and Y. Bühler, Configurational energy and the formation of mixed flowing/powder snow and ice avalanches, **57**(71), *Annals of Glaciology*, 179-188, 2016.
- [11] L. Dreier, Y. Bühler, C. Ginzler and P. Bartelt, Comparison of simulated powder snow avalanches with photogrammetric measurements, **57**(71), *Annals of Glaciology*, 371-381, 2016.
- [12] V. M. Teshukov, Gas dynamic analogy for vortex free-boundary flows, *Journal of Applied Mechanics and Technical Physics*, **48**, 303-309, 2007.
- [13] S. Gavriluk, K. Ivanova, N. Favrie, Multi-dimensional shear shallow water flows: Problems and solutions, *Journal of Computational Physics*, **366**, 252-280, 2018.
- [14] K. Ivanova, S. Gavriluk, Structure of the hydraulic jump in convergent radial flows. *Journal of Fluid Mechanics*, **860**, 441-464, 2019.

## GEOMETRICALLY NONLINEAR FREE VIBRATIONS OF FULLY CLAMPED MULTI-STEPPED BEAMS CARRYING MULTIPLE MASSES

I. El Hantati<sup>1</sup>, A. Adri<sup>1</sup>, H. Fakhreddine<sup>1</sup>, S. Rifai<sup>1</sup>, R. Benamar<sup>2</sup>

<sup>1</sup> Laboratory of Production Mechanics and Industrial Engineering (LMPGI), Higher School of Technology, Hassan II University of Casablanca, Km 7, Route El Jadida, B.P. 8012 Oasis, Casablanca, Morocco

[hantati.issam@gmail.com](mailto:hantati.issam@gmail.com), [ahmedadri@gmail.com](mailto:ahmedadri@gmail.com), [hatim.fakhreddine@gmail.com](mailto:hatim.fakhreddine@gmail.com), [said57.rifai@gmail.com](mailto:said57.rifai@gmail.com)

<sup>2</sup> Doctoral Studies Centre of National High School of Electricity and Mechanics (ENSEM)

Route d'ElJadida, Km 7, Oasis, Casablanca 8018, Morocco

[hantati.issam@gmail.com](mailto:hantati.issam@gmail.com), [hatim.fakhreddine@gmail.com](mailto:hatim.fakhreddine@gmail.com)

<sup>2</sup> Mohammed V University in Rabat, EMI-Rabat, LERSIM, Agdal,

B.P. 765, Rabat, Morocco

[rhali.benamar@gmail.com](mailto:rhali.benamar@gmail.com)

---

### Abstract

*The main objective of this work is to study the geometrically non-linear free vibration of stepped beams carrying multiple masses. These beams are studied on the basis of the Euler-Bernoulli beam theory and the Von Karman geometrical nonlinearity assumptions. The discrete expressions for the beam total strain and kinetic energies are derived. By applying Hamilton's principle, the problem is reduced to a non-linear algebraic system solved by an approximate method (the so-called second formulation). A parametric study is performed to explore the effect of non-linearity on the dynamic behaviour of stepped beams with several added masses. The free vibration case is discussed by considering three types of stepped beams which differ in the cross-section type.*

**Keywords:** Stepped beam, transverse vibrations, nonlinear vibrations, free vibrations

---

## 1 INTRODUCTION

Stepped beams are commonly encountered in practical structures and extensively used in many domains, including mechanical and civil engineering, such as high-rise buildings, robot arms, etc. These structures, often subjected during their lifetime to transverse vibrations, may contain concentric elements that can be assimilated to point masses or to linear or rotational springs. Considerable work has been done to study the dynamic behaviour of these types of beams by means of linear theory, making the analysis relatively easy, but leading to inaccurate results when the beams are subjected to large vibration amplitudes. In such situation, non-linear analysis is needed to obtain with accuracy the deformation of the beam for each amplitude level considered. A review of the literature goes back to Naguleswaran who presents an overview of the existing studies performed to analyse stepped beams using linear approaches[1]. El Hantati[2], [3] presents a literature review of works related to non-uniform beams in the case of linear and non-linear vibrations. A significant number of studies have been conducted on the dynamic response of single and multi-mass beams, using linear and non-linear analyses for both free and forced vibrations. These studies have been mostly reported in an extensive literature review presented by Fakhreddine[4]. Regarding non-uniform beams with concentric masses, many studies have been carried out to analyse their response to free and forced vibrations, considering both the Euler-Bernoulli and the Timoshenko beam theories. Karami[5] investigated free vibrations of arbitrary non-uniform Timoshenko beams with their concentrated mass and rotary inertia and resting on elastic supports based on the differential quadrature element method. Based on the same method, Torabi et al. studied in [6] free vibrations of a non-uniform cantilever Timoshenko beam with multiple concentrated masses. Kohan et al. [7] studied a non-uniform beam carrying a concentrated masses and supported by linear and rotational springs at both sides. The analytical formulation exposed in this work was based on the Ritz method and the orthogonal polynomials within the framework of the first order shear deformation beam theory. Jong-Shyong[8] used the continuous-mass transfer matrix method to investigate free vibrations of a multi-step Timoshenko beam axially loaded and carrying arbitrary concentrated elements. K.Torabi et al [9] investigated multiple-stepped Bernoulli Euler and Timoshenko beams, carrying concentrated masses with rotary inertia at arbitrary points based on the same method. Yusuf Yesilce[10] studied free vibrations of a Timoshenko multiple-step beam under axial load, carrying a number of intermediate lumped masses and rotary inertias based on the Differential transform method and numerical assembly technique. Farghaly and El-Sayed presented in [11] parametric studies for an axially loaded stepped Timoshenko beam carrying several attachments. All of the aforementioned studies were carried out assuming linearity and none of them took into account the effect of geometrical non-linearity. This work, which is a continuation of the work previously carried out by Benamar et al.[12]–[19], is intended to contribute to a non-linear modal analysis of structural vibration by studying the geometrically non-linear free vibration of stepped beams carrying multiple masses using the Euler-Bernoulli beam theory and the Von Karman geometrical nonlinearity assumptions. The beam total strain and kinetic energies are presented as discrete expressions and then derived. By applying Hamilton's principle, the problem is reduced to a non-linear algebraic system solved by an approximate method previously applied to similar problems (the so-called second formulation) [16]. A parametric study is performed to explore the effect of non-linearity on the dynamic behaviour of stepped beams with several added masses. The free vibration case is discussed by considering three types of stepped beams which differ in the cross-section type.

## 1- General formulation

### 1.1 Linear formulation

The current study deals with the three homogeneous Euler-Bernoulli multi-step beams shown in Figure (1), characterised by a thin rectangular cross-section. The first beam rectangular cross-section (a) varied in breadth, the second beam (b) varied in depth, and the third beam (c) varied in both. For the remainder of the work, the beams examined are fully clamped, with a concentrated mass at the middle, and subjected to transverse vibrations.

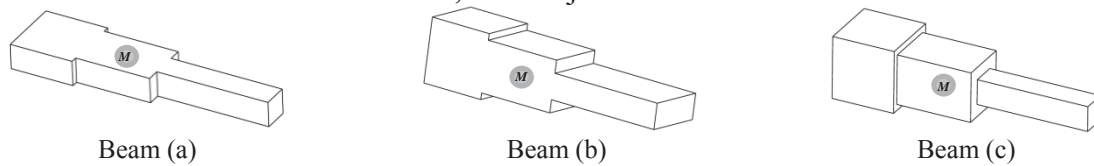


Figure 1: Three representative cases of the stepped beam.

Each of the beams shown in Figure 2 carries a concentric mass in the middle. They are also partitioned into three uniform cross-section parts and are subjected to transverse vibrations.

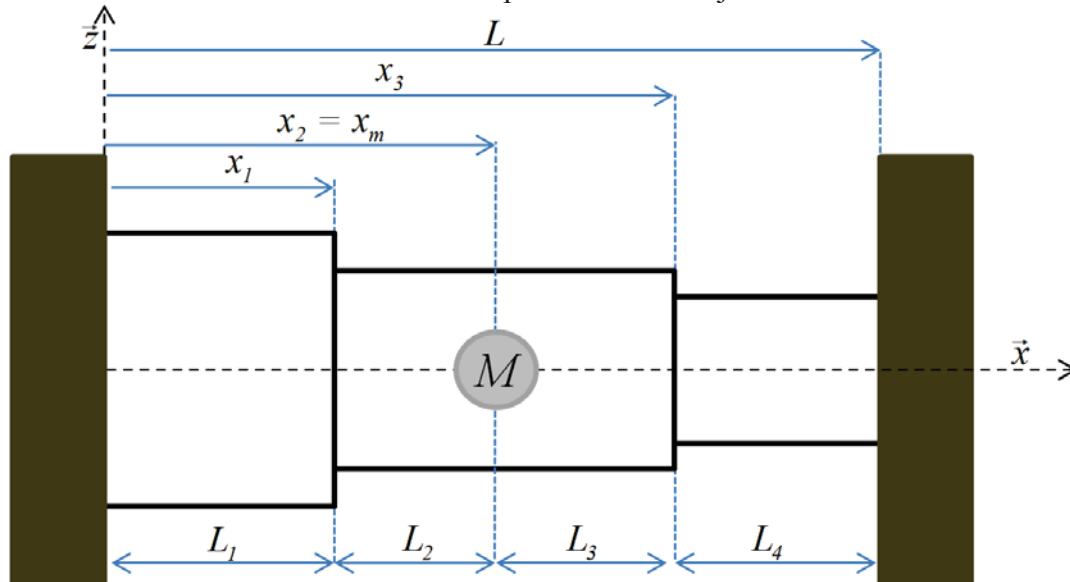


Figure 2: The coordinate system for a multi-stepped beam.

The transverse free vibration in each span is governed by the following equation:

$$\frac{d^4 W_i(x)}{dx^4} - \beta_i^4 W_i(x) = 0 \quad ; x \in [0, L] \text{ (For } i=1, 2, \dots, 12) \quad (1)$$

Where

$$\beta_{ij}^4 = \omega_i^2 \frac{\rho_j S_j}{E_j I_j} \text{ (For } j=1, 2 \text{ and } 4) \quad (2)$$

After putting the parameters of equation (1) into a non-dimensional form, Equation (1) can be written in the following form:

$$\frac{d^4 W_i(x^*)}{dx^4} - \beta_i^4 W_i(x^*) = 0 \quad ; x^* \in [0 \ 1] \quad (3)$$

Where

$$x_j^* = \frac{x_j}{L}; R_j^* = \frac{L_j}{L} \quad ; \quad z_j = \frac{\beta_{ij}}{\beta_{i1}}; u_j = \frac{S_j}{S_1}; v_j = \frac{I_j}{I_1} \quad (4)$$

Each step of the beam is characterized by a ratio of sections, moments of inertia and eigenvalue parameters which are denoted by (  $u_j, v_j$  and  $z_j$  ).

The solution of Eq. (1) presents the linear modes form which can be expressed at each span as:

$$W_i(x^*) = \begin{cases} W_{ij}(x^*) \rightarrow \{x_{j-1}^* \leq x^* \leq x_j^*\} \\ \dots \\ \dots \end{cases}$$

$$W_{ij}(x^*) = A_j \cosh(\beta_{ij} L(x^* - x_{j-1}^*)) + B_j \sinh(\beta_{ij} L(x^* - x_{j-1}^*)) + C_j \cos(\beta_{ij} L(x^* - x_{j-1}^*)) + D_j \sin(\beta_{ij} L(x^* - x_{j-1}^*)) \quad (5)$$

In equation (5), the constants  $A_j, B_j, C_j$  and  $D_j$  can be solved from the compatibility conditions and the boundary conditions.

The boundary conditions at the left side:

$$W_{i1}(x^*) \Big|_{x^*=0} = 0 \quad ; \quad \frac{dW_{i1}(x^*)}{dx^*} \Big|_{x^*=0} = 0 \quad (6,7)$$

The boundary conditions at the right side:

$$W_{i4}(x^*) \Big|_{x^*=1} = 0 \quad ; \quad \frac{dW_{i4}(x^*)}{dx^*} \Big|_{x^*=1} = 0 \quad (8,9)$$

The compatibility conditions at each change in the cross-section are given by:

$$W_{ij}(x^*) \Big|_{x^*=x_j^*} = W_{ij+1}(x^*) \Big|_{x^*=x_j^*} \quad (10)$$

$$\frac{dW_{ij}(x^*)}{dx^*} \Big|_{x^*=x_j^*} = \frac{dW_{ij+1}(x^*)}{dx^*} \Big|_{x^*=x_j^*} \quad (11)$$

$$EI_j \frac{d^2 W_{ij}(x^*)}{dx^{*2}} \Big|_{x^*=x_j^*} = EI_{j+1} \frac{d^2 W_{ij+1}(x^*)}{dx^{*2}} \Big|_{x^*=x_j^*} \quad (12)$$



$$EI_j \frac{d^3 W_{ij}(x^*)}{dx^{*3}} \Big|_{x^*=x_j^*} = EI_{j+1} \frac{d^3 W_{(j+1)i}(x^*)}{dx^{*3}} \Big|_{x^*=x_j^*} \quad (13)$$

The compatibility conditions for an attached mass with a rotary inertia are given by:

$$W_{ji}(x^*) \Big|_{x^*=x_m^*} = W_{(j+1)i}(x^*) \Big|_{x^*=x_m^*} \quad (14)$$

$$\frac{dW_{ji}(x^*)}{dx^*} \Big|_{x^*=x_m^*} = \frac{dW_{(j+1)i}(x^*)}{dx^*} \Big|_{x^*=x_m^*} \quad (15)$$

$$\frac{d^2 W_{ji}(x^*)}{dx^{*2}} \Big|_{x^*=x_m^*} = \frac{d^2 W_{(j+1)i}(x^*)}{dx^{*2}} \Big|_{x^*=x_m^*} + J_j \omega^2 \frac{dW_{ji}(x^*)}{dx^*} \Big|_{x^*=x_m^*} \quad (16)$$

$$\frac{d^3 W_{ji}(x^*)}{dx^{*3}} \Big|_{x^*=x_m^*} = \frac{d^3 W_{(j+1)i}(x^*)}{dx^{*3}} \Big|_{x^*=x_m^*} - \frac{M_j \omega^2 W_{ji}(x^*)}{EI} \Big|_{x^*=x_m^*} \quad (17)$$

Non-trivial solutions corresponding to the natural frequencies are derived by stating that the determinant of the homogeneous system obtained from the boundary and compatibility conditions vanishes. The transcendental equation obtained is solved iteratively by the Newton-Raphson method and the constants  $A_j, B_j, C_j$  and  $D_j$  are determined by classical algebra.

### 2.3. Non-linear formulation

#### 2.2.1 Free vibration

The kinetic energy  $T$  of the beam is given by:

$$T = \frac{\rho}{2} \int_0^L S(x) \left( \frac{\delta w(x^*, t)}{\delta t} \right)^2 dx + \frac{I}{2} M_c \left( \frac{\delta w(x_m^*, t)}{\delta t} \right)^2 \quad (18)$$

The total deformation energy  $V$  is the sum of the deformation energy due to bending and the axial deformation energy due to the non-linear stretching forces induced by the large deflections, respectively denoted by  $V_f$  and  $V_a$  and written as follows:

$$V = V_f + V_a \quad (19)$$

$$V_f = \frac{I}{2} \int_0^L E I(x) \left( \frac{d^2 w_i}{dx^2} \right) \left( \frac{d^2 w_j}{dx^2} \right) dx \quad (20)$$

$$V_a = \frac{I}{2} \frac{N_x^2}{E} \int_0^L S(x) dx \quad (21)$$

Where  $N_x$  present the non-linear stretching forces in the beam. The dynamic behaviour of the system is studied by applying Hamilton's principle, stated formally as follows:

$$\delta \int_0^{2\omega} (V - T) dt = 0 \quad (22)$$

Assuming that the system has a harmonic motion, the transverse displacement can be written as:

$$w(x,t) = a_i W_i(x) \sin(\omega t) \quad (\text{For } i = 1, 2, \dots, n) \quad (23)$$

The linear modes, the basic function contribution coefficients and the associated frequency are denoted by  $W_i(x)$ ,  $a_i$  and  $\omega$ . After Substitution of equation (23) into equations (18, 20 and 21), the expressions for the kinetic energy, the axial deformation energy and the bending strain energy can be written as follows:

$$T = \frac{1}{2} \omega^2 a_i a_i (\cos(\omega t))^2 m_{ij}; \quad (24)$$

$$V_a = \frac{1}{2} a_i a_j a_k a_l (\sin(\omega t))^4 b_{ijkl}; V_f = \frac{1}{2} a_i a_i (\sin(\omega t))^2 k_{ij} \quad (25,26)$$

Where  $k_{ij}$ ,  $b_{ijkl}$  and  $m_{ij}$  denote the stiffness tensor due to  $V_f$ , the non-linearity tensor due to  $V_a$  and the mass tensor attributable to  $T$ . Equation (23) is extended by adding equations (24 and 26) into it, which leads to the following new form:

$$2a_i k_{ir} + 3a_i a_j a_k b_{ijkr} - 2\omega^2 a_i m_{ir} = 0 \quad ; \quad r = 1, \dots, n \quad (28)$$

Equation (28) can be expressed in a matrix form as follows:

$$2[K]\{A\} + 3[B(\{A\})]\{A\} - 2\omega^2 [M]\{A\} = 0 \quad (29)$$

In which  $(k_{ir})$ ,  $(m_{ir})$ ,  $(a_j a_k b_{ijkl})$  and  $(a_i)$  are the general terms of the matrices  $[K]$ ,  $[M]$ ,  $[B(\{A\})]$  and  $\{A\}$ . Setting the dimensionless parameters as follows:

$$\frac{W_i(x^*)}{W_i^*(x^*)} = h_0; \frac{\omega^2}{\omega^{*2}} = \frac{E I_1}{\rho S_1 L^4}; \frac{M_{ij}}{M_{ij}^*} = \rho S_1 h_0^2 \quad (30,31,32)$$

$$k_{ij} = \frac{E I_1 h_0^2}{L^3} k_{ij}^*; b_{ijkl} = \frac{E I_1 h_0^2}{L^3} b_{ijkl}^* \quad (33,34)$$

After substitution of the dimensionless parameters, Equation (29) becomes:

$$[K^*]\{A\} + \frac{3}{2}[B^*(\{A\})]\{A\} - \omega^{*2} [M^*]\{A\} = 0 \quad (35)$$

In order to determine the frequency  $\omega$  and the column vector of the contribution coefficients  $\{A\}$ , which are the unknowns of equation (35), the so-called second formulation, previously developed by EL KADIRI et al. in [16], is used to solve equation (35).

## NUMERICAL RESULTS AND DISCUSSION:

### 1.2 Free vibration:

In order to validate the numerical method mentioned above using the available data, the results corresponding to a uniform beam carrying a point mass at the middle are compared to those obtained in [20], where the section ratios of the 1<sup>st</sup> and 2<sup>nd</sup> steps, designated by  $u_1$  and  $u_2$ , are equal to  $u_1 = u_2 = 1$  and the mass magnitude  $M_c = 1$

$W_{\max}/r$	Present work	Reference [20]	Rel Diff[20]
0.4	1.0035	1.0034	0.01%
0.8	1.0142	1.0137	0.05%
1	1.0221	1.0213	0.08%
2	1.0851	1.0814	0.34%

Table 1:  $\left(\omega_{NL}/\omega\right)$  for clamped beams, in which a concentrated mass is located at its middle with  $r = \sqrt{I/S}$ .

The results show an excellent agreement, with a relative difference not exceeding 0,34%. The cases considered in all figures below are for three stepped beams with two cross-section changes and carrying a concentrated mass at the middle as shown in figure (1). The mass magnitude  $M_c = 1$ , the cross-section ratios at the 1st and 2nd step  $u_1$  and  $u_2$  equal to  $u_1=0.8$  and  $u_2=0.6$ . The three beams keep the same ratios  $u_1$  and  $u_2$ , but each of them is expressed differently. The figures below show the effect of the cross-section variations on the frequency ratio.

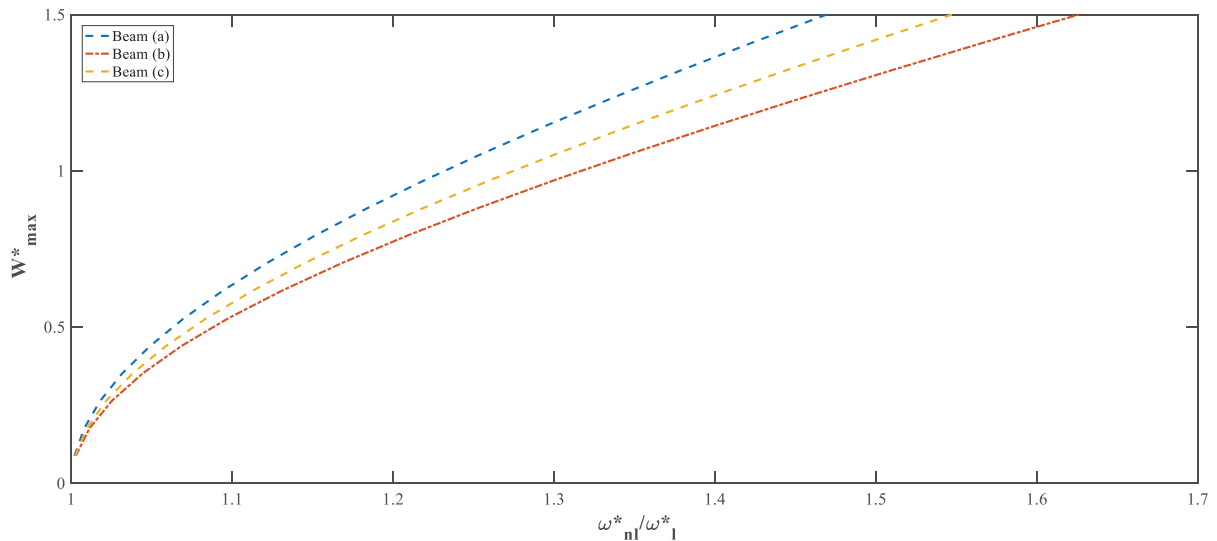


Figure (3): Backbone curves of the three stepped beams studied, corresponding to the first nonlinear mode.

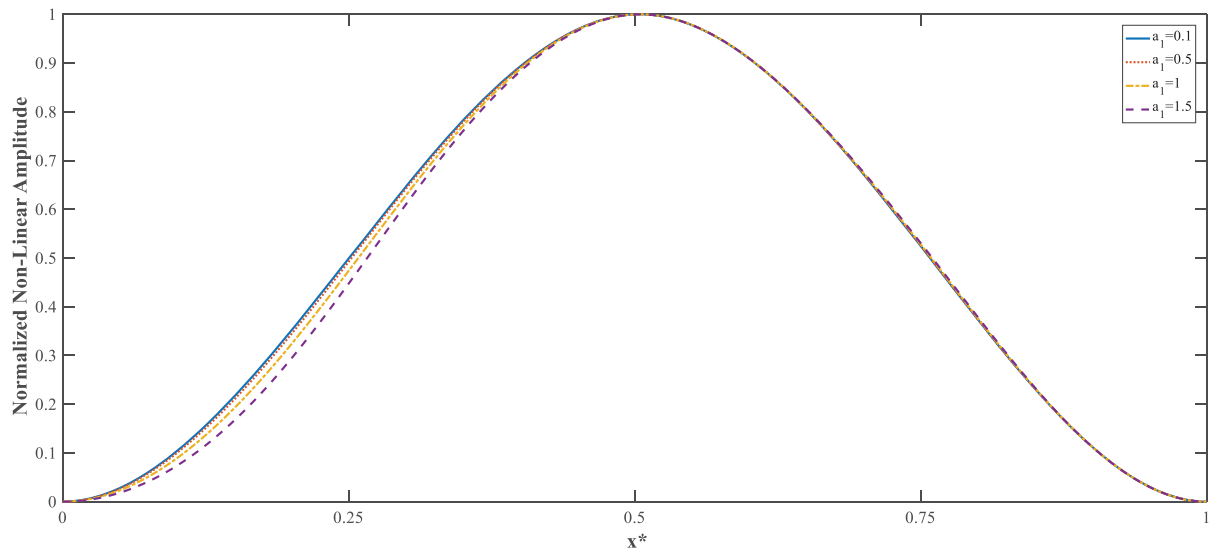


Figure (4): The normalized first non-linear mode of beam (a) for different values of  $a_1$ .

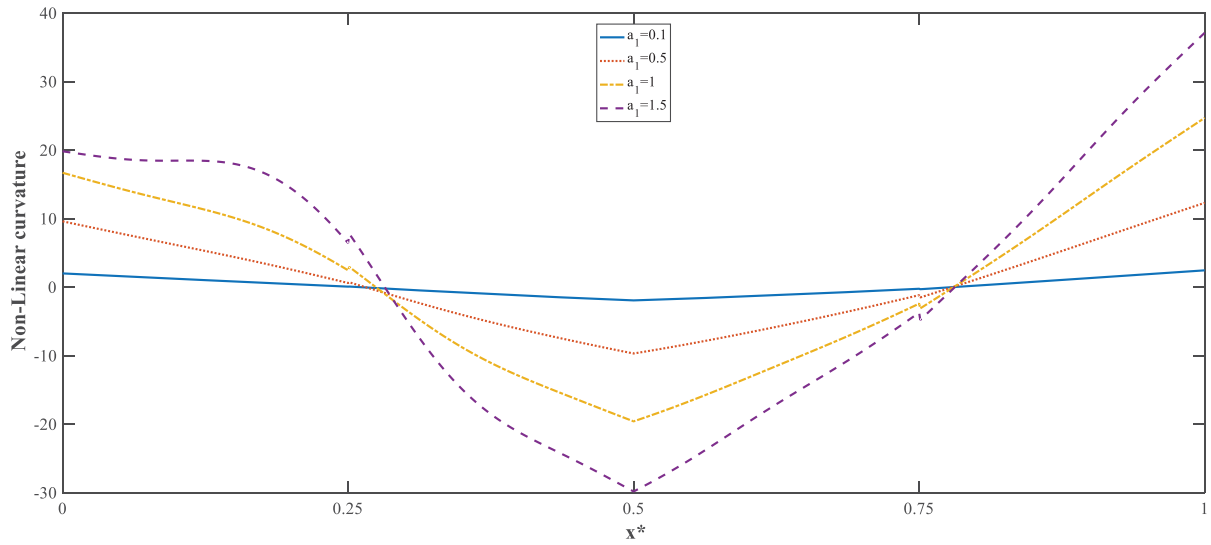


Figure (5): The non-linear curvature distribution of beam (a) associated to the normalized first non-linear mode for different values of  $a_1$ .

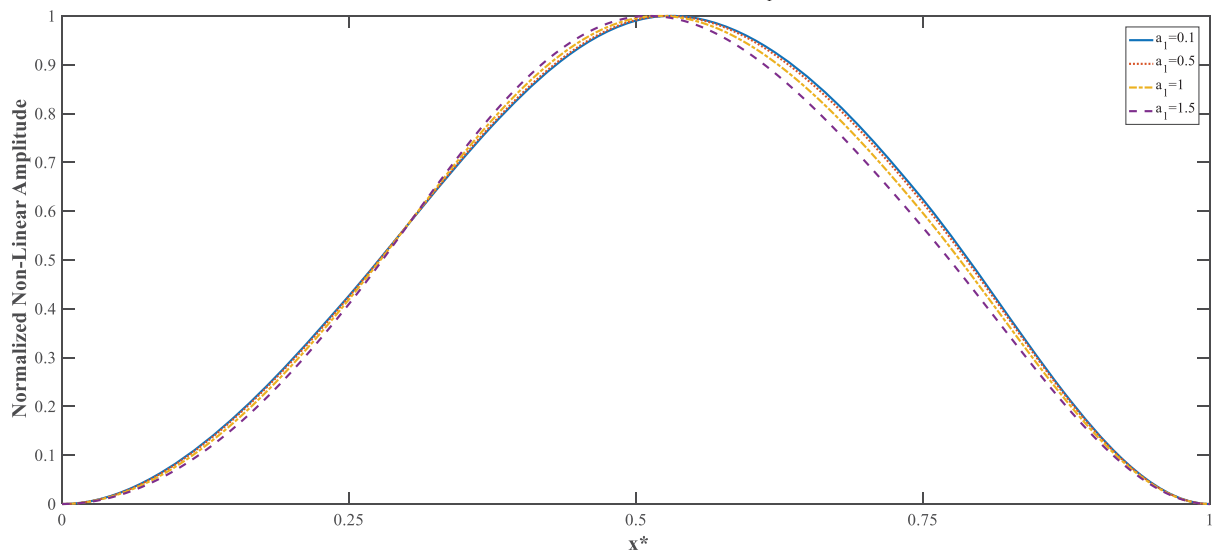


Figure (6): The normalized first non-linear mode of beam (b) for different values of  $a_1$ .

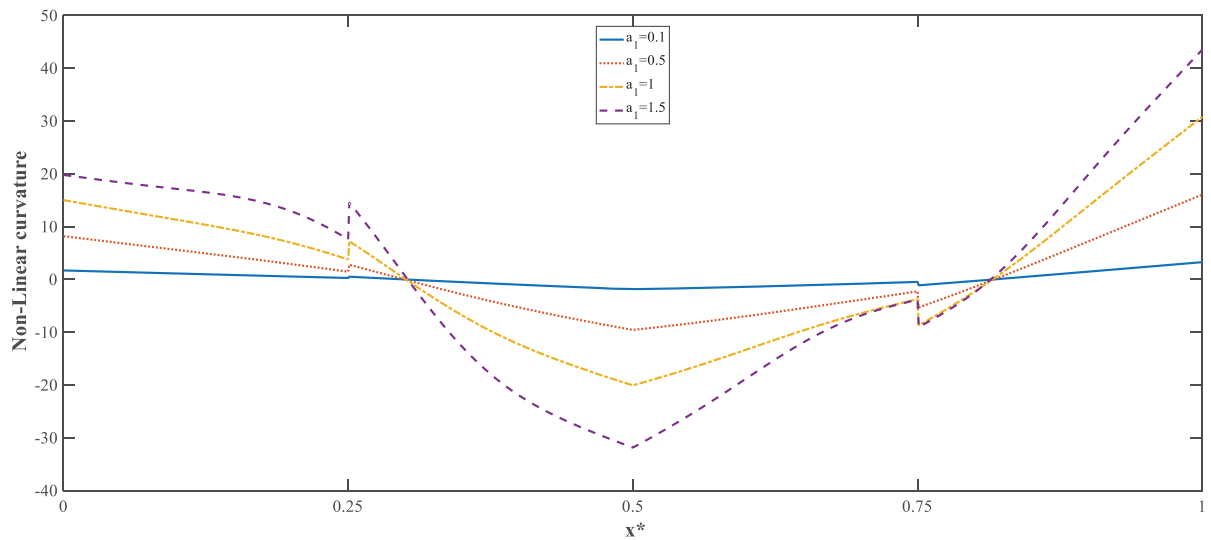
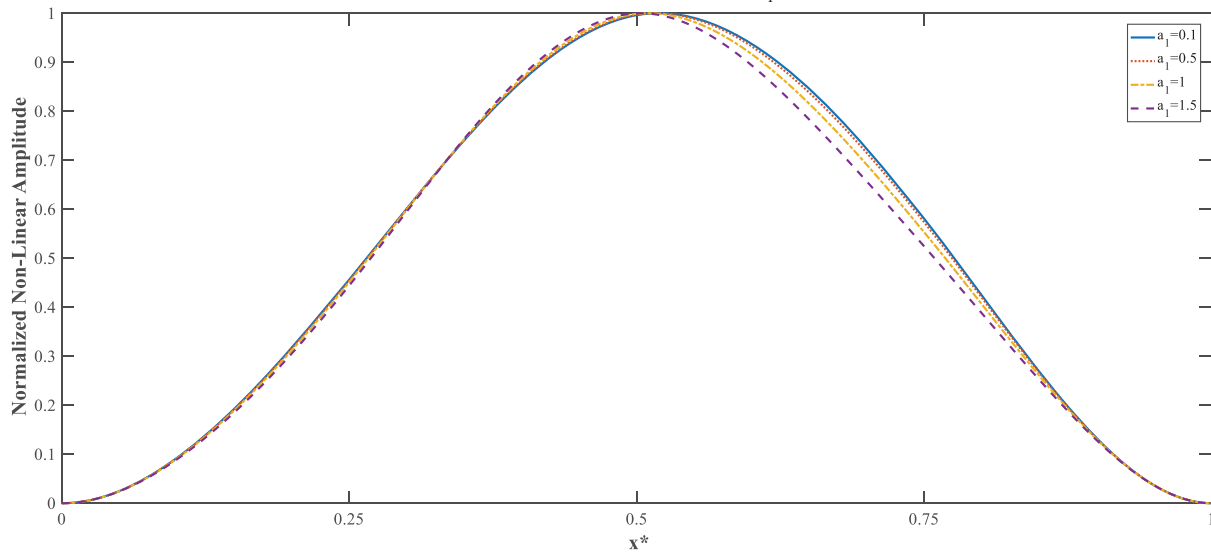
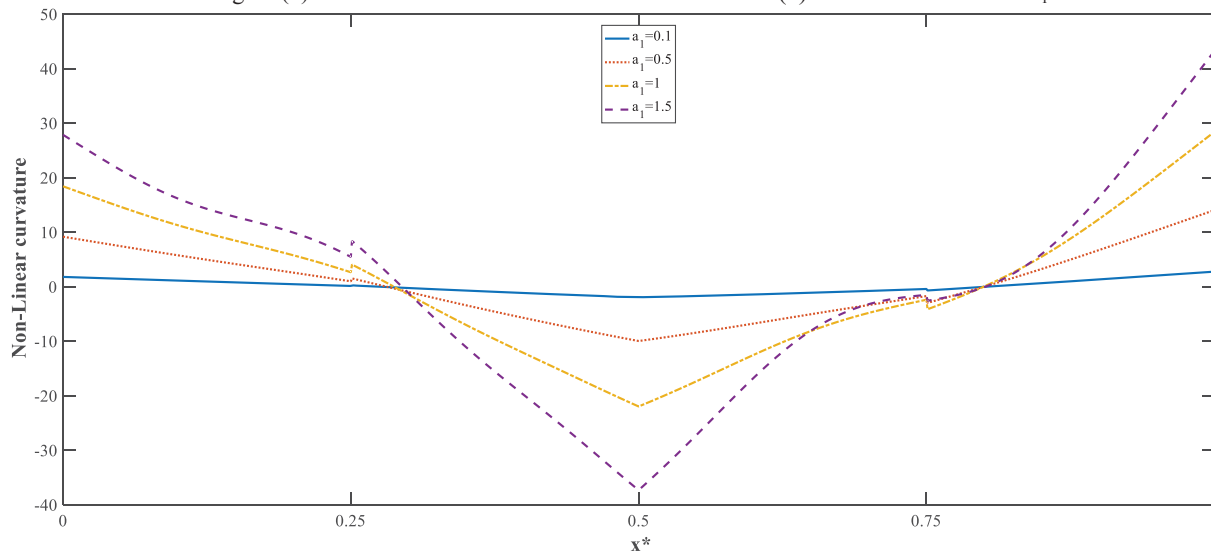


Figure (7): The non-linear curvature distribution of beam (b) associated to the normalized first non-linear mode for different values of  $a_1$ .Figure (8): The normalized first non-linear mode of beam (c) for different values of  $a_1$ .Figure (9): The non-linear curvature distribution of beam (c) associated to the normalized first non-linear mode for different values of  $a_1$ .

beam	Curvature		
	Non-linear theory	Linear theory	percentage correction %
a	49,33	61,43	19,69
b	54,18	81,44	33,47
c	58,56	70,12	19,74

Table 2: The percentage correction between the curvatures estimated at the right end via the linear and nonlinear theories for  $a_1=2$ .

The backbone curves in Figure (3) show that by increasing the maximum non-dimensional amplitude  $W_{\max}^*$ , the frequency ratios also increase. Also, the hardening effect of non-linearity is more accentuated in beam (b) compared to the other. It can be noticed that the geometrical non-linearity is not only related to the section ratio but also to the way it varies. For instance, the results obtained from Table (2) show that the percentage correction of the linear and non-linear bending moment of beam (a) at the right end with a contribution coefficient

$a_1=2$  is 19.69%, and remains higher than the two others, where the percentage correction of beam (c) and beam (a) are respectively 19.74% and 19.69%. Once more, these results reveal that the assumption of neglecting geometrical non-linearity for the same beam can be misleading.

## 2 CONCLUSION

The geometrically non-linear transverse vibrations of multi-stepped fully clamped beams carrying masses at the middle was studied analytically based on the Euler-Bernoulli's beams theory and the Von Karman's nonlinearity assumptions. The solution of the linear problem was obtained for the stepped beams considered. After determining the linear mode shapes, these were employed as basic functions for non-linear vibration analysis. To solve the non-linear algebraic system, the approximate method called the second formulation was applied. A comparison was performed between the result obtained from the numerical method used in the present work and those of Reference [18]. This comparison showed an excellent agreement. Then, the non-linear dynamic behaviour of multi-stepped beams in the free vibration case was examined by considering three types of fully clamped multi-stepped beams carrying masses at the middle. The results were illustrated by backbone curves, amplitude dependent non-linear modes and curvatures, showing a clear hardening non-linear behaviour. The assumption of neglecting the geometrical non-linearity is also illustrated and discussed.

## 3 REFERENCES

- [1] S. Naguleswaran, "Vibration of an Euler-Bernoulli beam on elastic end supports and with up to three step changes in cross-section," *Int. J. Mech. Sci.*, vol. 44, no. 12, pp. 2541–2555, 2002, doi: 10.1016/S0020-7403(02)00190-X.
- [2] I. El Hantati, A. Adri, H. Fakhreddine, S. Rifai, and R. Benamar, "Geometrically nonlinear forced vibrations of multiple-stepped euler-bernoulli beams," *Proc. Int. Conf. Struct. Dyn. , EURODYN*, vol. 1, no. June, pp. 193–204, 2020, doi: DOI: 10.47964/1120.9015.19055.
- [3] I. El Hantati, A. Adri, H. Fakhreddine, S. Rifai, and R. Benamar, "A Multimode Approach to Geometrically Nonlinear Free and Forced Vibrations of Multisteped Beams," *Shock Vib.*, vol. 2021, no. 4, pp. 1–18, Apr. 2021, doi: 10.1155/2021/6697344.
- [4] H. Fakhreddine, A. Adri, M. Chajdi, S. Rifai, and R. Benamar, "A multimode approach to geometrically non-linear forced vibration of beams carrying point masses," *Diagnostyka*, vol. 21, no. 4, pp. 23–33, Nov. 2020, doi: 10.29354/diag/128603.
- [5] G. Karami, P. Malekzadeh, and S. A. Shahpari, "A DQEM for vibration of shear deformable nonuniform beams with general boundary conditions," vol. 25, pp. 1169–1178, 2003, doi: 10.1016/S0141-0296(03)00065-8.
- [6] K. Torabi and H. Afshari, "Free vibration analysis of a non-uniform cantilever Timoshenko beam with multiple concentrated masses using DQEM Free vibration analysis of a non-uniform cantilever Timoshenko beam with multiple concentrated masses using DQEM," no. January, 2013, doi: 10.5267/j.esm.2013.06.002.
- [7] P. H. Kohan, L. G. Nallim, and S. B. Gea, "Dynamic characterization of beam type structures : Analytical , numerical and experimental applications," *Appl. Acoust.*, vol. 72, no. 12, pp. 975–981, 2011, doi: 10.1016/j.apacoust.2011.06.007.
- [8] J. Wu and B. Chang, "European Journal of Mechanics A / Solids Free vibration of axial-loaded multi-step Timoshenko beam carrying arbitrary concentrated elements using continuous-mass transfer matrix method," *Eur. J. Mech. / A Solids*, vol. 38, pp.



- 20–37, 2013, doi: 10.1016/j.euromechsol.2012.08.003.
- [9] K. Torabi, H. Afshari, and H. Najafi, “Vibration analysis of multi-step Bernoulli-Euler and Timoshenko beams carrying concentrated masses,” *J. Solid Mech.*, vol. 5, no. 4, pp. 336–349, 2013.
- [10] S. Engineering, “Differential transform method and numerical assembly technique for free vibration analysis of the axial-loaded Timoshenk ....,” no. February, 2015, doi: 10.12989/sem.2015.53.3.537.
- [11] S. H. Farghaly and T. A. El-sayed, “Exact free vibration of multi-step Timoshenko beam system with several attachments,” *Mech. Syst. Signal Process.*, vol. 72–73, pp. 525–546, 2016, doi: 10.1016/j.ymssp.2015.11.025.
- [12] R. Benamar, M. M. K. Bennouna, and R. G. White, “The effects of large vibration amplitudes on the mode shapes and natural frequencies of thin elastic structures part I: Simply supported and clamped-clamped beams,” *J. Sound Vib.*, vol. 149, no. 2, pp. 179–195, Sep. 1991, doi: 10.1016/0022-460X(91)90630-3.
- [13] R. Benamar, M. M. K. Bennouna, and R. G. White, “The Effects of Large Vibration Amplitudes on the Mode Shapes and Natural Frequencies of Thin Elastic Structures, Part II: Fully Clamped Rectangular Isotropic Plates,” *J. Sound Vib.*, vol. 164, no. 2, pp. 295–316, Jun. 1993, doi: 10.1006/jsvi.1993.1215.
- [14] L. Azrar, R. Benamar, and R. G. White, “Semi-analytical approach to the non-linear dynamic response problem of s–s and c–c beams at large vibration amplitudes part i: general theory and application to the single mode approach to free and forced vibration analysis,” *J. Sound Vib.*, vol. 224, no. 2, pp. 183–207, Jul. 1999, doi: 10.1006/jsvi.1998.1893.
- [15] K. El Bikri, R. Benamar, and M. Bennouna, “Geometrically non-linear free vibrations of clamped simply supported rectangular plates. Part I: The effects of large vibration amplitudes on the fundamental mode shape,” *Comput. Struct.*, vol. 81, no. 20, pp. 2029–2043, 2003, doi: 10.1016/S0045-7949(03)00152-4.
- [16] M. EL KADIRI, R. BENAMAR, and R. G. WHITE, “Improvement of the semi-analytical method, for determining the geometrically non-linear response of thin straight structures. Part i: application to clamped–clamped and simply supported–clamped beams,” *J. Sound Vib.*, vol. 249, no. 2, pp. 263–305, Jan. 2002, doi: 10.1006/jsvi.2001.3808.
- [17] E. bekkaye Merrimi, K. El bikri, and R. Benamar, “Geometrically non-linear steady state periodic forced response of a clamped-clamped beam with an edge open crack,” *Comptes Rendus - Mec.*, vol. 339, no. 11, pp. 727–742, 2011, doi: 10.1016/j.crme.2011.07.008.
- [18] H. Fakhreddine, A. Adri, S. Rifai, and R. Benamar, “A Multimode Approach to Geometrically Non-linear Forced Vibrations of Euler–Bernoulli Multispan Beams,” *J. Vib. Eng. Technol.*, vol. 8, no. 2, pp. 319–326, 2020, doi: 10.1007/s42417-019-00139-8.
- [19] O. Outassafte, A. Adri, Y. El Khouddar, S. Rifai, and R. Benamar, “Geometrically Non-Linear Free In-Plane Vibration Of Circular Arch Elastically Restrained Against Rotation At The Two Ends,” *Int. J. Eng. Trends Technol.*, vol. 69, no. 3, pp. 85–95, Mar. 2021, doi: 10.14445/22315381/IJETT-V69I3P215.
- [20] K. K. Raju and G. Venkateswara Rao, “Non-linear vibrations of beams carrying a concentrated mass,” *J. Sound Vib.*, vol. 48, no. 3, pp. 445–449, Oct. 1976, doi: 10.1016/0022-460X(76)90073-0.

## COMPARISON BETWEEN DYNAMIC NONLINEAR ANALYSIS WITH ASCE 7-10 AND ASCE 7-16 IN CONCRETE FRAMES WITH VISCOUS DAMPERS INCORPORATED

Juan S. Cundumi García<sup>1</sup>, and Orlando Cundumi Sánchez<sup>2</sup>

<sup>1</sup> Pontificia Universidad Javeriana, Cali, Colombia  
Calle18#118-250 Avenida Cañasgordas, Cali-Colombia  
e-mail: cundumi0612@javerianacali.edu.co  
e-mail: sebastian\_cundumi\_ing@hotmail.com

<sup>2</sup> Pontificia Universidad Javeriana, Cali, Colombia  
Calle18#118-250 Avenida Cañasgordas, Cali-Colombia  
e-mail: Orlando.cundumi@javerianacali.edu.co

---

### Abstract

*During the last few years, different methodologies have been developed for the analysis of the structural seismic response, such as the performance-based design, the systems of energy dissipation, seismic isolation. Based on these efforts, a number of devices, known collectively as protection systems have emerged. They are divided into three types of systems: passive, active, and semi-active. Passive systems dissipate energy through friction, viscous fluid dampers, and inelastic behavior of the material, among others. On the other hand, active control systems can be implemented by applying time varying forces to counteract those imposed by the excitation. which can be active, passive, semi-active, active, etc.*

*This paper presents the response of the structure when it enters the nonlinear range and is being controlled by the Viscous Damper. To obtain the nonlinear response of the structure system through numerical simulation are used the Methodologies of ASCE 7-10 and ASCE 7-16. To examine the behavior of the structures and the application of each methodology, simulations using concrete frames of 5, 7 and 11-story buildings were performed. The models were subjected to the horizontal components of different earthquakes, for the ASCE 7-10 were used three earthquakes, for the ASCE 7-16 were used seven earthquakes. These seismic records are subjected to a matching process to obtain records that match the corresponding building code design spectrum for a high seismic risk zone. The history displacement and acceleration results were compared with those obtained with the uncontrolled structure with nonlinear behavior.*

**Keywords:** Energy Dissipation System, Dynamic Nonlinear Analysis, Spectral Matching,

---

## 1 INTRODUCTION

During the last three decades, a number of modern mechanical devices have been proposed to reduce the structural response of buildings to environmental loads. These devices, which are known collectively as protective devices, include viscoelastic dampers, viscous fluid dampers, frictional dampers, tuned-mass dampers, and base isolation systems. The devices themselves and their design methodology are referred to as passive control systems [1]. On the other hand, the highest level of sophistication in seismic protection is provided by the active control systems [2]. There is an intermediate alternative between passive and fully active control systems: they are referred to as “semi-active systems” [3, 4, 5, 11, 12]. The passive systems dissipate the seismic energy through friction in special devices, the inelastic behavior of sacrificial elements, etc. The passive systems have the important advantage that they do not require external energy for their operation.

On the other hand, research on fragility curves in structures with control system incorporated have been developed Taylor and Dike [13], Cundumi and Laboy [6], and among others.

This can be achieved by incorporating control systems to reduce displacements, acceleration and forces among seismic events. Incorporating control systems as an alternative for the design of new structures and the rehabilitation of existing structures is becoming more popular among building codes. Some examples of this Code include the Colombian Code NSR-10 [16], ASCE 7-10 and ASCE 7-16 (American Society of Civil Engineers) [17, 18], the Eurocode [30], and the Chilean Standard NCh [27].

This paper only presents the result abstained for two frames. The frames used were subjected to acceleration at the base by using three earthquakes [16] and seven earthquakes [17]. To obtain the maximum drift, displacement time histories, acceleration time histories, hysteresis, etc. for each one of the frames the program ETABS [19] and programs utilizing Mathlab applications was developed. The amount of damage was quantified by using HAZUS parameter [14, 15], where the damage index was obtained based on the ratio between the maximum displacement and the story height.

Finally, a series of Figures and Table are presented for each frame analyzed in order to represent the difference between using three [17] and seven [18] seismic records.

## 2 EQUATION OF MOTION AND DAMPER FORCE

It is well known that the equations of motion of a structure modeled as a multi-degree of freedom system and subjected to a base acceleration of  $\ddot{x}_g(t)$  at all its supports is:

$$[M]_{n \times n} \{\ddot{x}(t)\} + [C]_{n \times n} \{\dot{x}(t)\} + [K]_{n \times n} \{x(t)\} = -[M]_{n \times n} \{E\} \ddot{x}_g(t) \quad (1)$$

where  $[M]$ ,  $[C]$  y  $[K]$  are the mass, damping and stiffness matrix respectively, the vectors  $\{\ddot{x}(t)\}$ ,  $\{\dot{x}(t)\}$ ,  $\{x(t)\}$  are the acceleration, velocity and displacement of each dynamic degree of freedom of the structure,  $\{E\}$  is the vector of influence coefficients, and  $n$  is the number of degrees of freedom.

When a viscous fluid damper is incorporated in the structure, the damping matrix change. The force-displacement response of a velocity-dependent dashpot-type device is primarily a function of the relative velocity between each end of the device.

$$[M]_{n \times n} \{\ddot{x}(t)\} + [C + C_d]_{n \times n} \{\dot{x}(t)\} + [K]_{n \times n} \{x(t)\} = -[M]_{n \times n} \{E\} \ddot{x}_g(t) \quad (2)$$

The ideal force output of a viscous fluid damper can be expressed as is presented in equation (3).

$$F_d(t) = C_o |\dot{x}(t)|^\alpha \operatorname{sgn}(\dot{x}(t)) \quad (3)$$

where  $F_d$  is the damper force,  $C_o$  is the damping coefficient for the device,  $\dot{x}(t)$  is the relative velocity between each end of the device,  $\operatorname{sgn}$  is the sign um function that in this case defines the sign of the relative velocity term, and  $\alpha$  is the velocity exponent for the device which may take values in the range of about 0.25 to 2 (see reference [10]). The case  $\alpha=1$  correspond to a linear viscous damper in which the damper force is proportional to the relative velocity. When  $\alpha$  smaller than 1 the device is called a nonlinear viscous damper. Values of  $\alpha$  larger than 1 (also a nonlinear damper) have not been used often in practical applications.

The viscous damping ratio in the first mode should be estimated as [7]:

$$\beta_{v1} = \frac{\sum_j (2\pi)^{a_j} T_1^{2-a_j} \lambda_j C_j f_j^{1+a_j} \Delta_{roof}^{a_j-1} \phi_{rj}^{1+a_j}}{8\pi^3 \sum_i \left( \frac{\omega_i}{g} \right) \phi_{i1}^2} \quad (4)$$

where  $\lambda_j$  is a dimensionless parameter given by Equation 14 of Ramirez et al. [10] and all other terms have been defined by Whittaker et Al [7].

### 3 NUMERICAL PROCEDURE AND EXAMPLE

As an initial step, two concrete frames are established for two different buildings, Type I frame is five (5) levels with cover consisting of beams and columns with three lights ranging in length between 4m and 5m with a total height per story of 3m, on the other hand, the type II frame consists of seven (7) levels with cover and four lights ranging in length between 5m and 6m with total height per story of 3m, as shown in the Figure 1.

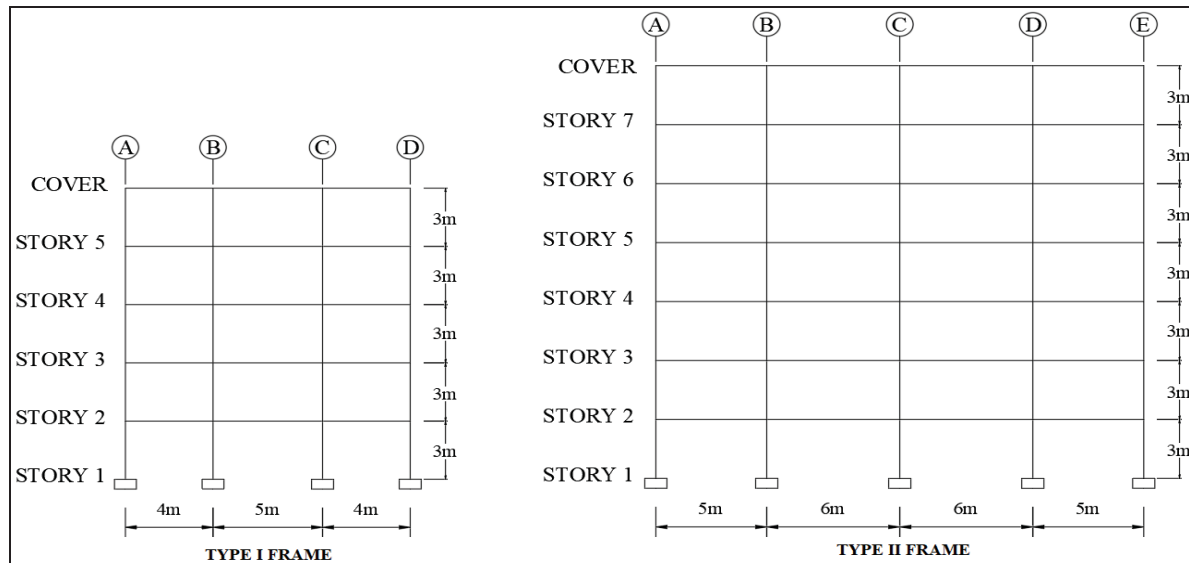


Figure 1: Types frames.

Once the two types of frames are defined to be designed, the next step is to build the design spectrum, where two types of spectrum with different characteristics belonging to a particular area were established, for this, the Colombian earthquake resistant code (NSR-10) was used. establishing the city of "Santiago de Cali" as the area to study because it is an area of high seismic threat, for the spectrum, different couples of results were taken depending on the importance level of the structure and of the type of soil, for the Type I design spectrum, a type "D" soil was used, corresponding to rigid soil profiles with a group III of importance equivalent to "Community care buildings". For the Type II design spectrum, a type "C" soil was used, corresponding to soft soil profiles or formed by soft rock, with a group IV of importance equivalent to "Essential buildings" such as clinics. Based on this data, the rest of the coefficients belonging to the construction of the design spectrum. The Table 1 presents the definitive characteristics for each type of spectrum.

DESIGN SPECTRUM COEFFICIENTS							
ESPECTRUM	SOIL GROUP	Aa	Av	Fa	Fv	IMPORTANCE GROUP	I
Type I espectrum	D	0,25	0,25	1,3	1,9	III	1,25
Type II espectrum	C	0,25	0,25	1,15	1,55	IV	1,5

Table 1: Design spectrum coefficients.

Once the spectrum coefficients are defined, it gives way to calculate and graph the two types of spectrum "Type I" and "Type II", therefore, the maximum expected spectrum "MCEr" is calculated, as indicated by the American regulations, multiplying by 1,5 the accelerations obtained in the previous calculated designs spectrum. Figure 1 shows the design spectrum.

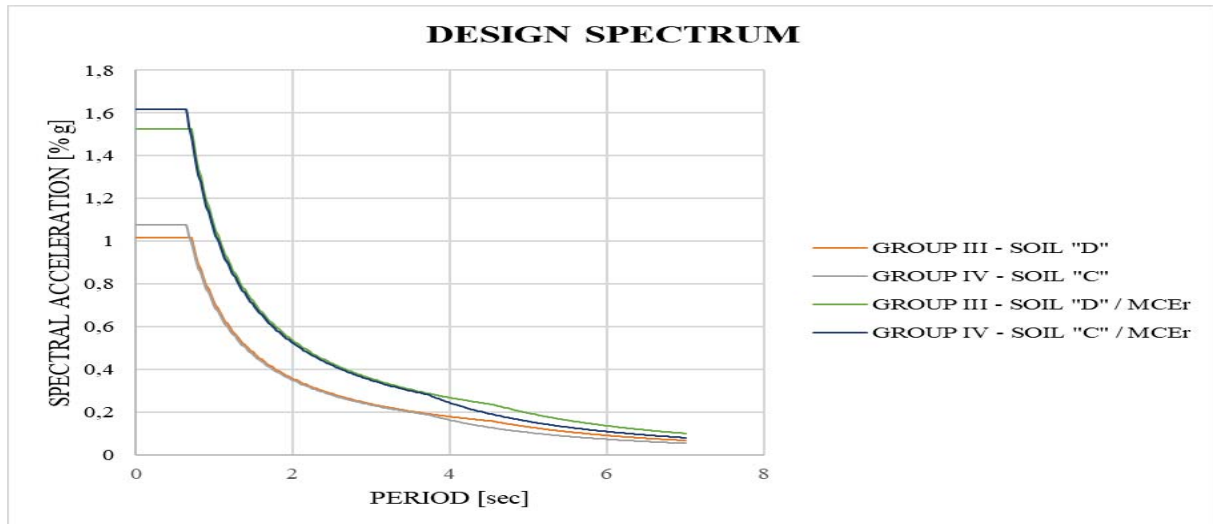


Figure 2: Design spectrum.

For the load assessment of the two frames, an afferent width of 3m was assumed, a 10cm slab and an additional dead load corresponding to walls with an equivalent value to  $2\text{kN/m}^2$ , on the other hand, a live load was assumed for each story equivalent to  $2,5\text{kN/m}^2$  and  $0,5\text{kN/m}^2$  for the cover, therefore, the respective load assessment is obtained. The Table 2 presents the load assessment.

LOAD ASSESSMENT			
FRAME	STOREYS	WD [ $\text{KN/m}^2$ ]	WL [ $\text{KN/m}^2$ ]
Type I	1 - 5	4,4	2,5
Type I	Cover	2,4	0,5
Type II	1 - 7	4,4	2,5
Type II	Cover	2,4	0,5

Table 2: Load Assessment.

After obtaining the load assessment, it gives way to carry out the pre-dimensioning and design of the different structural elements for the two frames, thus obtaining the following dimensions. The Table 3 presents the model dimensions.

MODEL DIMENSIONS					
ESPECTRUM	TYPE FRAME	BASE COLUMN (cm)	HEIGHT COLUMN (cm)	BASE BEAM (cm)	HEIGHT BEAM (cm)
Group III - Soil D	I	40	40	40	40
Group IV - Soil C	II	55	55	55	50

Table 3: Model dimensions.

The code ASCE 7-16 specifies that, for both the design spectrum and the MCER, at least seven (7) seismic records must be selected, each of these records must be escalated to the design spectrum as the MCER, the average of the seven (7) seismic records should not stay below both spectrums mentioned above. For this, the procedure called "Matching" is carried out using the SeismoMatch software [23], where a damping of 5% is determined and the period of



vibration of the structure is specified by the design spectrum and the MCER. next up, the seven (7) seismic records to analyze. The Table 4 presents the seven (7) seismic records.

<b>SEISMIC RECORDS</b>			
<b>NAME</b>	<b>YEAR</b>	<b>MAGNITUDE</b>	<b>PGA [g]</b>
ChiChi	1999	7,3	0,36
Friuli	1976	6,4	0,35
El Centro	1940	6,9	0,32
Kobe	1995	6,9	0,34
Kocaeli	1999	7,4	0,35
Loma Prieta	1989	6,9	0,37
Northridge	1994	6,7	0,57

Table 4: Seven seismic records.

On the other hand, the code ASCE 7-10, specifies that, for both the design spectrum and the MCER, three (3) seismic records must be selected, unlike the standard ASCE 7-16, Each seismic record must be analyzed independently, analyzing the maximum values obtained for each record, without averaging the results of the three records among themselves. Since the objective is to compare the behavior in each frame for both seven (7) and three (3) registers, of the seven (7) mentioned above, three records are chosen to perform the respective calculations and analysis based on the ASCE 7-10. The Table 5 presents the three (3) seismic records to analyze.

<b>SEISMIC RECORDS</b>			
<b>NAME</b>	<b>YEAR</b>	<b>MAGNITUDE</b>	<b>PGA [g]</b>
Friuli	1976	6,4	0,35
Loma Prieta	1989	6,9	0,37
Northridge	1994	6,7	0,57

Table 5: Seven seismic records.

Once the seismic records, design spectrum and dimensions mentioned above are defined, the modeling is carried out using the ETABS Software [19], where four (4) structural models are defined, and each one of the frames are evaluated by the method given by each code. Next up, the four (4) models to analyze. The Table 6 presents the model types.

<b>MODEL TYPES</b>			
<b>MODEL</b>	<b>FRAME TYPE</b>	<b>ESPECTRUM</b>	<b>METHOD</b>
I	I	Group III - Soil D	ASCE-16
II	I	Group III - Soil D	ASCE-10
III	II	Group IV - Soil C	ASCE-16
IV	II	Group IV - Soil C	ASCE-10

Table 6: Model types.

After assigning each model with different properties, it gives way to define the energy dissipaters, in this case, the viscous dampers were modeled as non-linear elements “Link” of the “Damper - Exponential” type, the dampers are located in the external lights of each frame.

Next up, the distribution and selection of the dampers to be analyzed in each frame. The Figure 3 shows the Damper's location and selection.

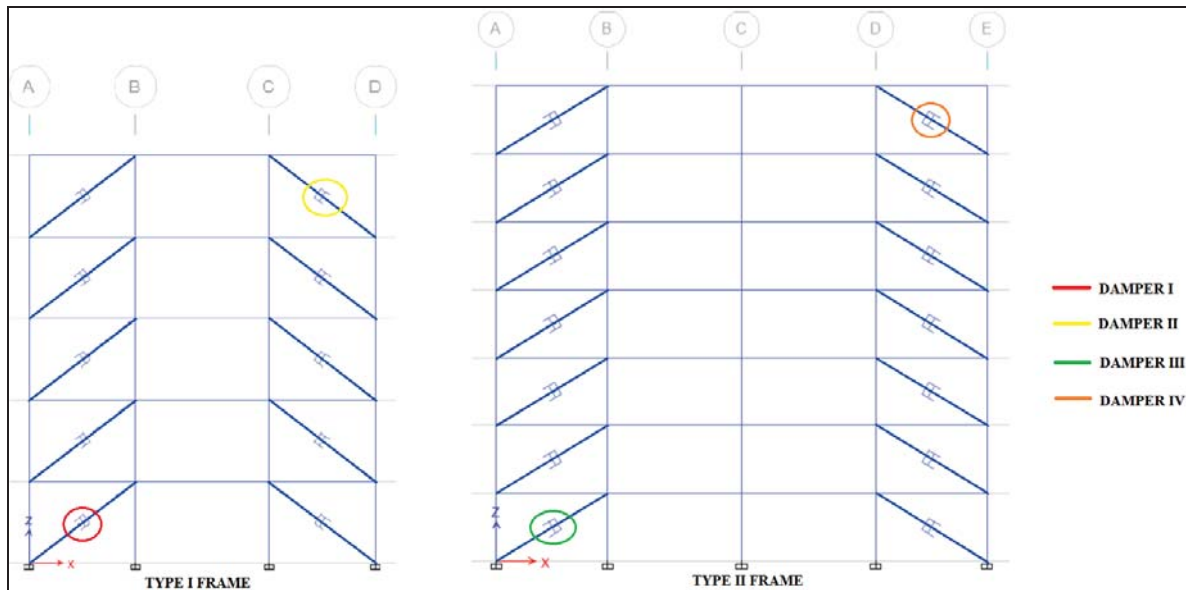


Figure 3: Damper's location and selection.

Each of the dampers are assigned a value of ( $\alpha = 0.3$ ), on the other hand, the damping “C” is included, which is generated by the damper, plus the contribution of the stiffness of the strut connecting the damper, depending on the stiffness value on the diagonal is assigned a metal profile equivalent to that value. Next up, the properties for each damper depending on the model to be analyzed. The Table 7 presents the viscous dampers properties.

VISCOUS DAMPERS PROPERTIES					
FRAME TYPE	ESPECTRUM	METHOD	PROFILE	STIFFNESS [KN/m]	DAMPING [KN*(s/m) <sup>Cexp</sup> ]
I	Group III - Soil D	ASCE-16	W8X24	200000	100
I	Group III - Soil D	ASCE-10	W8X31	250000	100
II	Group IV - Soil C	ASCE-16	W8X35	290000	100
II	Group IV - Soil C	ASCE-10	W8X35	290000	100

Table 7: Viscous dampers properties.

Once each model has been defined with their respective properties for each damper, we proceed to run each of the models in order to analyze the behavior of each of these under the different methods established by the ASCE-10 and ASCE-16 codes. Since the code establishes that when designing a structure with energy dissipaters, said structure must be evaluated against different seismic records. When a structure is exposed to a seismic loading, the structure presents displacement generated by the force, the displacement is in function with the height, that is why the displacement at the maximum point of the structure is analyzed, in this case on the cover, due to this, the maximum displacements generated by each historical record are analyzed in order to analyze said displacements and see if these values are optimal for the structure.

Then the seismic record is shown as in function of the time for the cover displacement in each one (1) of the four (4) models. The Figure 4 shows the cover displacement for Model I and Model II.

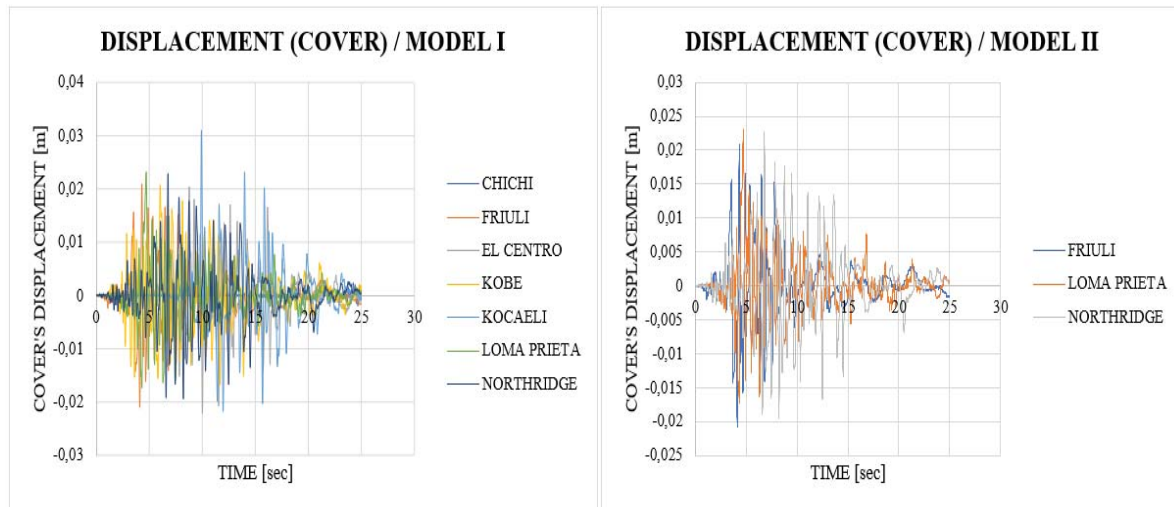


Figure 4: Cover displacement (MI - 7 seismic records vs MII - 3 seismic records).

With regard to “Model I” in Figure 4, it presents a maximum displacement on the cover equivalent to 0,031m corresponding to the seismic record “Kocaeli”, however, the average of the seven (7) seismic records presents a maximum displacement of 0,02m, on the other hand, the “Model II” presents a maximum displacement on the cover of 0,023m corresponding to the “Loma Prieta” seismic record. The Figure 5 shows the cover displacement for Model III and Model IV.

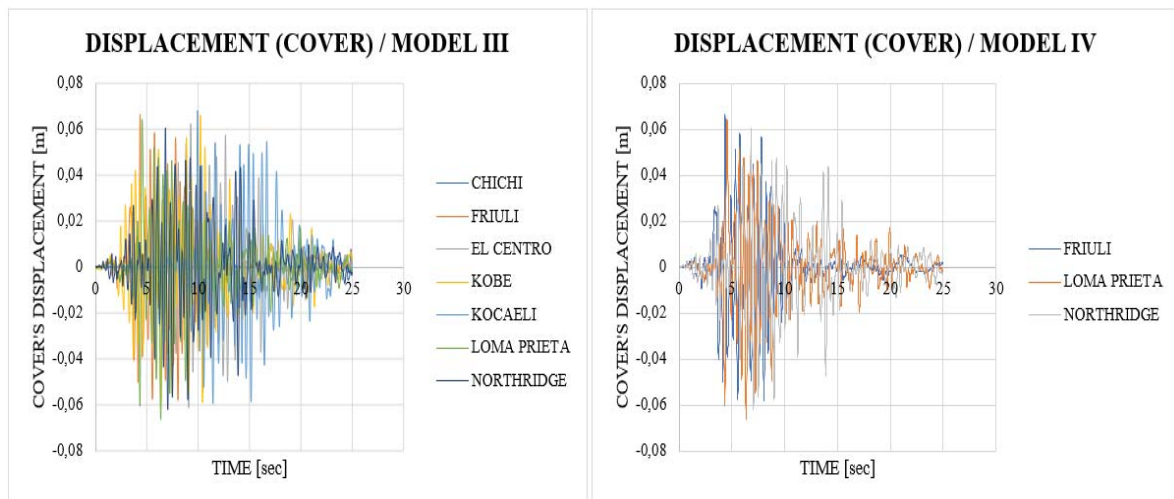


Figure 5: Cover displacement (MIII - 7 seismic records vs MIV - 3 seismic records).

It is observed that in Figure 5, the “Model III” presents a maximum displacement on the cover equivalent to 0,068m corresponding to the seismic record “Kocaeli”, however, the average of the seven (7) seismic records presents a maximum displacement of 0,057m, on the other hand, with regard to the “Model IV” this presents a maximum displacement on the cover of 0,066m corresponding to the “Loma Prieta” seismic record.

The Table 8 presents the maximum cover displacements for each model.

DISPLACEMENT (COVER)		
MODEL	METHOD	MAXIMUM DISPLACEMENT [m]
I	ASCE-16	0,02
II	ASCE-10	0,023
III	ASCE-16	0,057
IV	ASCE-10	0,066

Table 8: Maximum displacement.

Once the maximum displacements on the cover have been found, the corresponding drifts to each model is reviewed in order to analyze if these meet the requirements for design, based on the Methodology "HAZUS" a moderate damage is established for armed concrete frames, for the "Type I" frame with a total height of 15m, a target drift of 0,58% is assigned, on the other hand, for the "Type II" frame with a total height of 21m, a target drift of 0,54% is assigned as presented in the following table. The Table 9 presents the target drifts.

TARGET DRIFTS	
FRAME TYPE	DRIFTS [%]
I	0,58
II	0,54

Table 9: Target drifts.

Based on the aforementioned, the same gantry is compared under the methodologies specified in each code. The Figure 6 shows the maximum story drifts for Model I and Model II.

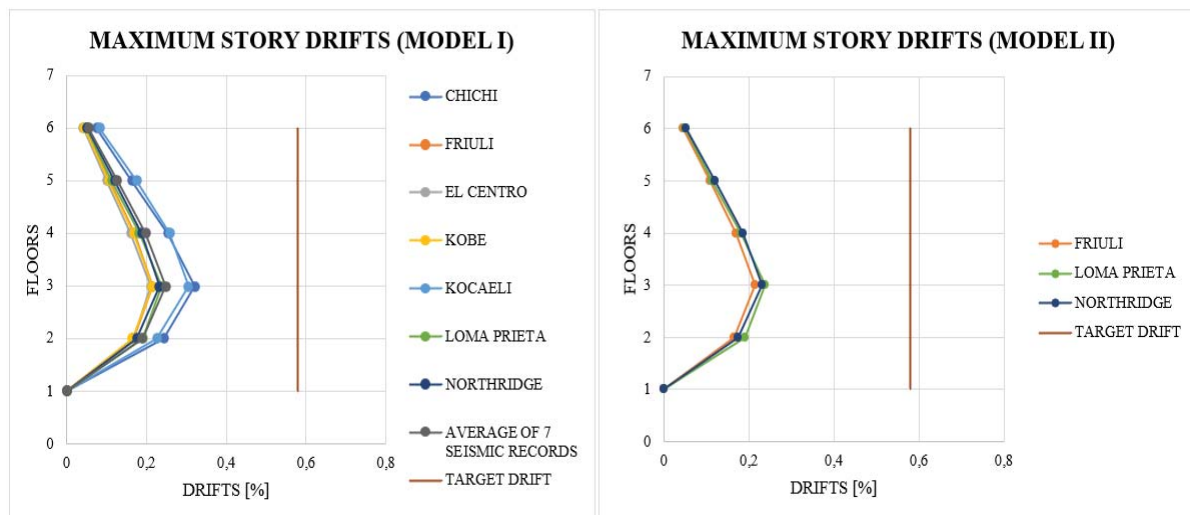


Figure 6: Maximum story drifts (MI - 7 seismic records vs MII - 3 seismic records).

As it can be seen in Figure 6, both models are below the target drift, on one hand, “Model I” presents a maximum equivalent drift to 0,32% corresponding to the “Chichi” seismic record, however, the average of the seven (7) seismic records shows a maximum drift of 0,25%, on the other hand, the “Model II” presents a maximum drift of 0,24% corresponding to the

“Loma Prieta” seismic record. The Figure 7 shows the maximum story drifts for Model III and Model IV.

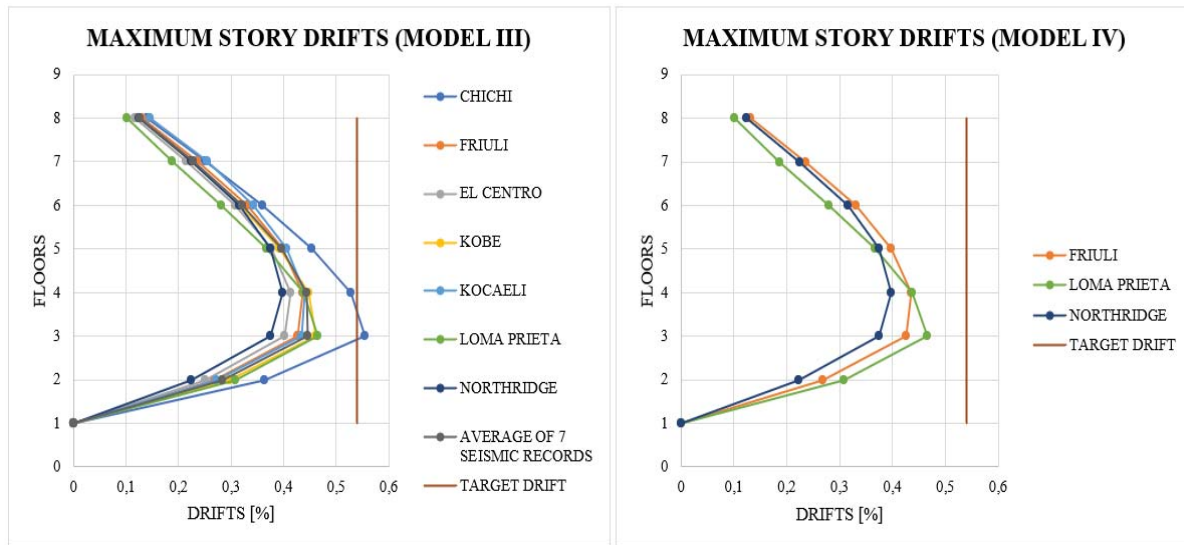


Figure 7: Maximum story drifts (MIII - 7 seismic records vs MIV - 3 seismic records).

In Figure 7, for the “Model III” it is observed that the “Chichi” seismic record exceeds the target drift with an equivalent value to 0,56%, however, the average of the seven (7) seismic records presents a maximum drift of 0,45%, on the other hand, the “Model IV” presents a maximum drift of 0,47% corresponding to the “Loma Prieta” seismic record.

The Table 10 presents the maximum drifts for each model.

MAXIMUM STORY DRIFTS			
MODEL	METHOD	DRIFT [%]	TARGET DRIFT [%]
I	ASCE-16	0,25	0,58
II	ASCE-10	0,24	0,58
III	ASCE-16	0,45	0,54
IV	ASCE-10	0,47	0,54

Table 10: Maximum story drifts.

Therefore, considering the MCEr registers, the force-displacement relationship is analyzed in different dampers located on the first and last story. Next up, the Figure 8, 9, 10 and 11 show the dampers hysteresis cycle with different location in each frame.



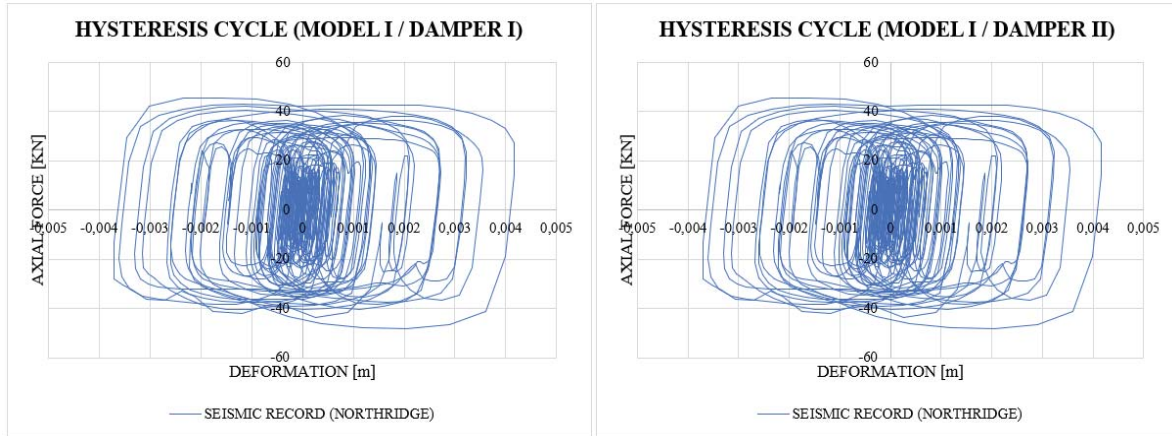


Figure 8: Model I hysteresis cycle.

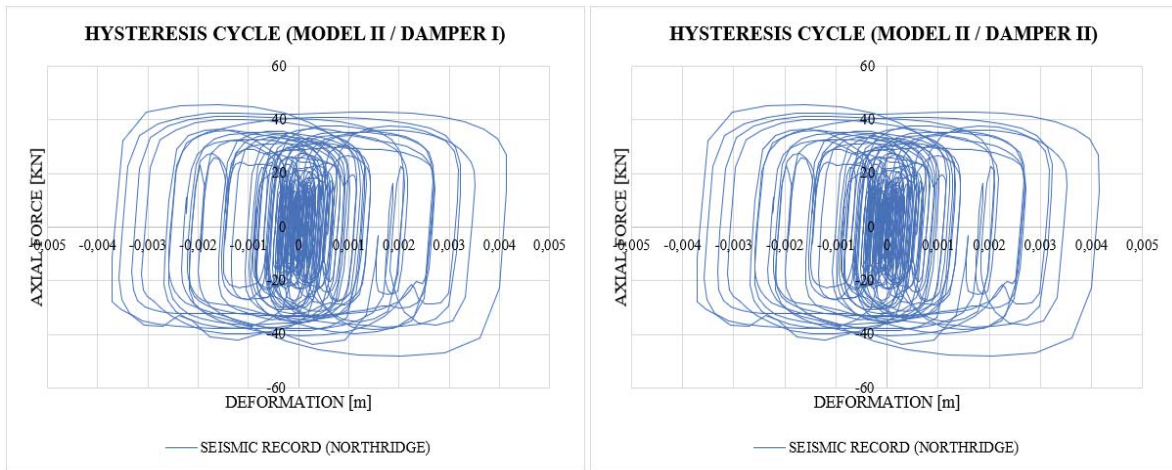


Figure 9: Model II hysteresis cycle.

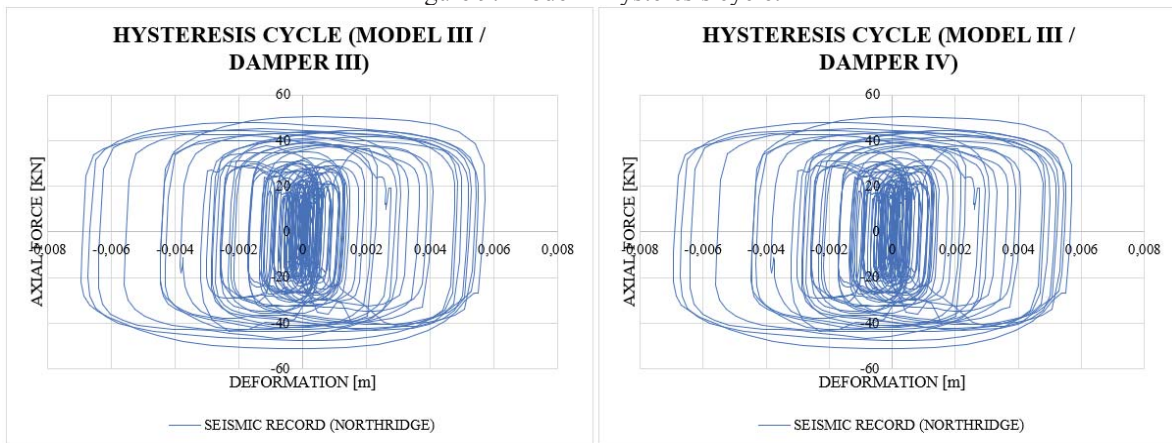


Figure 10: Model III hysteresis cycle.



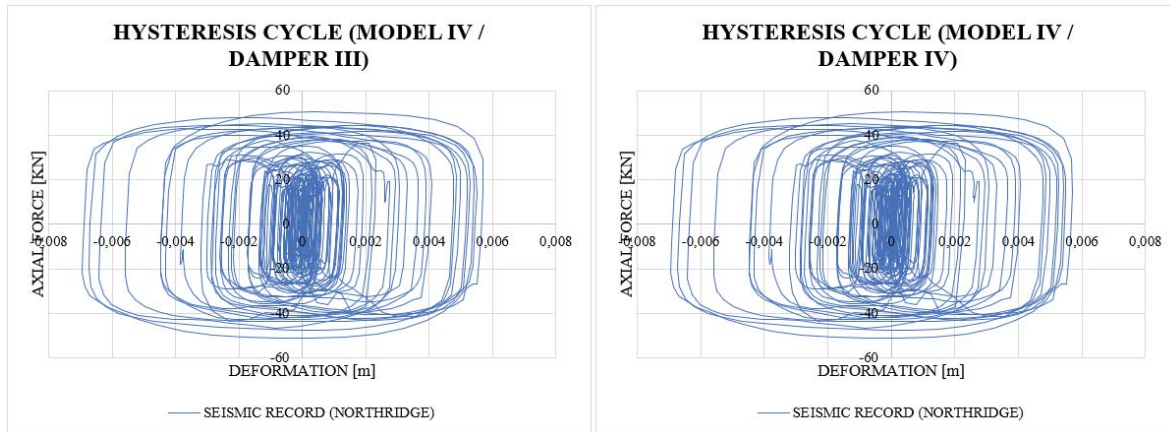


Figure 11: Model IV hysteresis cycle.

Finally, the results of the progressive accumulation of the shear forces in each story are presented, which are reflected in the same base, next up, the seismic record is shown as in function of the time for the base shear in each one (1) of the four (4) models. The Figure 12 shows the base shear results for Model I and Model II.

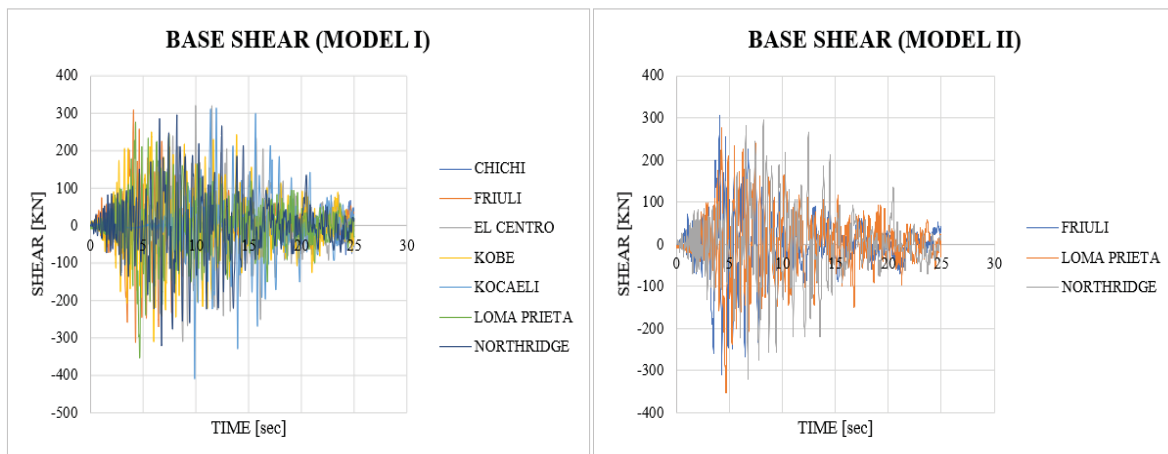


Figure 12: Base shear (MI - 7 seismic records vs MII - 3 seismic records).

With regard to “Model I” in Figure 12, it presents a maximum base shear with a value equivalent to 408,8kN corresponding to the seismic record “Kocaeli”, however, the average of the seven (7) seismic records presents a maximum shear at the base with a value of 300,3kN, on the other hand, the “Model II” presents a maximum base shear with a value of 351,9kN corresponding to the “Loma Prieta” seismic record. The Figure 13 shows the base shear results for Model III and Model IV.

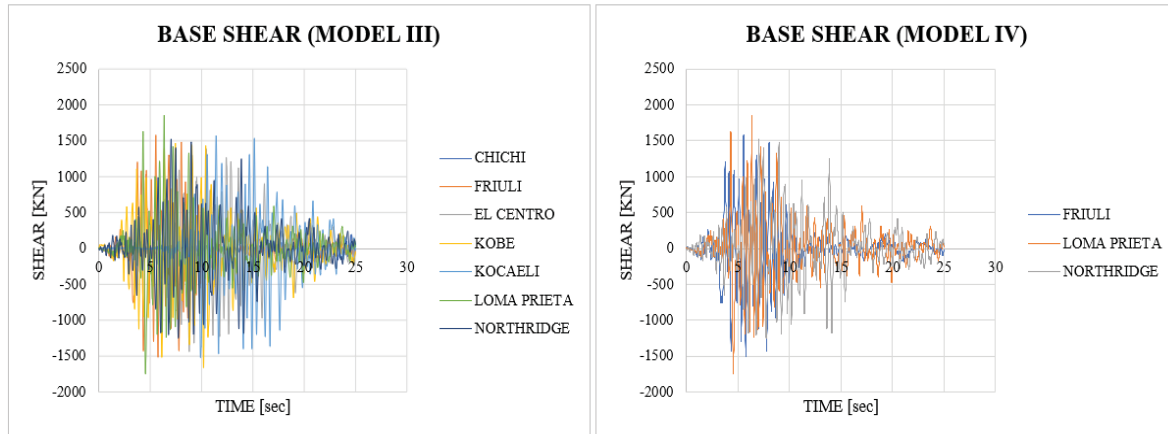


Figure 13: Base shear (MIII - 7 seismic records vs MIV - 3 seismic records).

It is observed that in Figure 13, the “Model III” presents a maximum base shear with a value equivalent to 1851,5kN corresponding to the “Loma Prieta” seismic record, however, the average of the seven (7) seismic records presents a maximum base shear with a value of 1407kN, on the other hand, with regard to "Model IV" this presents a maximum base shear of 1851,7kNm corresponding to the seismic record "Loma Prieta".

The Table 11 present the maximum base shear values for each model.

BASE SHEAR		
MODEL	METHOD	BASE SHEAR [KN]
I	ASCE-16	300,3
II	ASCE-10	351,9
III	ASCE-16	1407
IV	ASCE-10	1851,7

Table 11: Base shear.

## 4 CONCLUSIONS

This paper presented the analysis and result for two concrete frame buildings with passive controllers incorporated using the methodologies ASCE 7-10 (three seismic record) and ASCE 7-16 (seven seismic records). The response of the hysteresis cycle, time histories displacement, acceleration, and base shear were compared for each analysis and corresponding frame. The differences between the two methodologies of the maximum responses obtained were presented in detail in section 3.

The results obtained in the numerical simulations for the frames presented in this article, show in Table 8 differences in the maximum displacement of 15% in the two frames using both methodologies, the displacement results obtained are lower with the methodology of the ASCE 7-16. Similarly, Table 10 presents difference percentages of less than 5% for the maximum drifts, registering the lowest values with the ASCE 7-16 methodology.

## REFERENCES

- [1] Constantinou, M. C., Soong, T. T. & Dargush, G. F. "Passive energy dissipation systems for structural design and retrofit" in *Multidisciplinary Center for Earthquake Engineering Research-MCEER, University at Buffalo, Buffalo, New York*.1998.
- [2] Soong,T.T. "Active Structural Control: Theory and Practice", *John Wiley & Sons, New York City, New York*, 1990.
- [3] O. Cundumí Sánchez, "Nonlinear Analysis of Structures Controlled With A New Variable Damping Device," in *14th World Conference on Earthquakes Engineering – 14WCEE 2008*, 2008.
- [4] O. Cundumí Sánchez and L. E. Suárez, "A New Variable Damping Semi-Active Device Seismic Response Reduction of Civil Structure," *J. Mech. Mater. Struct.*, vol. 2, no. 8, 2007.
- [5] O. Cundumí Sánchez and S. Laboy, "Nonlinear Analysis of Structures Controlled with Passive Damper," in *17th Congreso de Ingeniería Sísmica*, 2009.
- [6] O. Cundumí Sánchez and S. Laboy, "Fragility Curves for Concrete Frame Buildings with Passive Controllers," in *9th US National and 10th Canadian Conference on Earthquake Engineering: Reaching Beyond Borders*, 2010.
- [7] Andrew S. Whittaker et Al, "Equivalent Lateral Force and Modal Analysis Procedures of the 2000 NEHRP Provisions for Buildings with Damping Systems", *Earthquake Spectra*, Vol. 19, no. 4, pages 959–980, November 2003.
- [8] Ramirez, O. M., Constantinou, M. C., Kircher, C. A., Whittaker, A. S., Johnson, M. W., and Gomez, J. D. "Development and Evaluation of Simplified Procedures for Analysis and Design of Buildings with Passive Energy Dissipation Systems", *MCEER Report 00-0010*. Multidisciplinary Center for Earthquake Engineering Research, University at Buffalo, StateUniversity of New York, Buffalo, NY, 2000.
- [9] Ramirez, O. M., Constantinou, M. C., Gomez, J. D., Whittaker, A. S., and Chrysostomou, C. Z.. "Elastic and inelastic seismic response of structures with damping systems", *Earthquake Spectra* **18** (3), 501–530.University at Buffalo, StateUniversity of New York, Buffalo, NY, 2002a.
- [10] Ramirez, O. M., Constantinou, M. C., Whittaker, A. S., Kircher, C. A., and Chrysostomou, C. Z., 2002b. "Evaluation of simplified methods of analysis of yielding structures with damping systems", *Earthquake Spectra* **18** (3), 531–547, 2002b.
- [11] Hrovat, D., Barak, P., and Rabins, M. "Semi-active versus passive or active tuned mass dampers for structural control". *Journal of Engineering Mechanics, ASCE*, Vol. 109, No. 3, pp. 691-705, (1983).
- [12] Symans, M., and Constantinou, M. C. "Seismic testing of a building structure with a semi-active fluid damper control system". *Earthquake Engineering and Structural Dynamics*. Vol. 26, No. 7, pp. 759-777, (1997).
- [13] Taylor, E., and Dyke, S. "The Development of Fragility Relationships for Controlled Structures", *Master Thesis*, Washington University, 2007.
- [14] HAZUS-MH MR1., 2003. *Multi-Hazard Loss Estimation Methodology: EarthquakeModel*, Department of Homeland Security, FEMA, Washington, D.C.

- [15] Federal Emergency Management Agency (FEMA), “HAZUS-MH MR4 Multi-Hazard Loss Estimation Methodology – Earthquake Model: Technical Manual. Department of Homeland Security,” *Fed. Emerg. Manag. Agency, Washington, ...*, 2003, [Online]. Available: [www.fema.gov/plan/prevent/hazus](http://www.fema.gov/plan/prevent/hazus).
- [16] Asociación Colombiana de Ingeniería Sísmica, *Requisitos generales de diseño y construcción sismo resistente*, vol. Título A. 2010.
- [17] American Society of Civil Engineers, *ASCE Standard ASCE/SEI 7-10*, 2010.
- [18] American Society of Civil Engineers, *ASCE 7-16*, vol. 69, no. 1782. 2017.
- [19] I. Computers & Structures, “ETABS User’s Guide.” 2019.
- [20] Departamento Administrativo de Gestión del Medio Ambiente DAGMA and Instituto Colombiano de Geología y Minería INGEOMINAS, “Estudio de Microzonificación Sísmica de Santiago de Cali. Convenio 002 de 2002,” 2002.
- [21] C. F. Grajales, I. F. Otálvaro, and O. Cundumí, “Efectos de horizontes de suelos blandos profundos en la respuesta dinámica del campus de la PUJ Cali,” in *IX Congreso Nacional de Ingeniería Sísmica*, 2020.
- [22] J. Hancock, J. J. Bommer, and P. J. Stafford, “Numbers of scaled and matched accelerograms required for inelastic dynamic analyses,” *Earthq. Eng. Struct. Dyn.*, vol. 37, no. 14, pp. 1585–1607, Nov. 2008, doi: 10.1002/eqe.827.
- [23] Seismosoft, “SeismoMatch - A computer program for spectrum matching of earthquake records,” vol. 0. 2020.
- [24] Federal Emergency Management Agency, *Improvement of Nonlinear Static Seismic Analysis Procedures*, vol. 440, no. June. 2005.
- [25] Federal Emergency Management Agency FEMA 356, *Prestandard and Commentary for the Seismic Rehabilitation of Buildings*, no. November. 2000.
- [26] Taylor Devices Inc., *Fluid Viscous Dampers General Guidelines for Engineers Including a Brief History*. 2020.
- [27] Seismic design of buildings with passive energy dissipation systems - Requirements and test methods. *NCh3411*, 2017.
- [28] ATC/BSSC. *NEHRP Commentary on the Guidelines for the Seismic Rehabilitation of Buildings, FEMA 274 Report*, prepared by the Applied Technology Council for the Building Seismic Safety Council, Federal Emergency Management Agency, Washington, DC, 1997b.
- [29] ATC-13. *Earthquake Damage Evaluation Data for California, Report No. ATC-13*, Applied Technology Council, Redwood City, California, 1985.
- [30] EUROCODES Building the Futures. European Commission.

## FRAGILITY CURVES DEFINITION OF EXISTING REINFORCED CONCRETE BUILDINGS DESIGNED FOR GRAVITY LOADS

A. Basaglia<sup>1</sup>, M. Terrenzi<sup>1</sup> and E. Spacone<sup>1</sup>

<sup>1</sup> University “G. d’Annunzio” of Chieti-Pescara  
Department of Engineering and Geology  
Viale Pindaro 42, 65127 Pescara, Italy  
e-mail: {alberto.basaglia, marco.terrenzi, enrico.spacone}@unich.it

---

### Abstract

*Urban areas with a significant number of buildings designed without earthquake resistant concepts may undergo high losses following major earthquakes. However, an adequate design is the direct result of a comprehensive knowledge of the seismic hazard. In Italy, for example, the seismic zonation was completed in recent years, thus a significant number of buildings lack adequate lateral capacity. For this reason, preventive assessment of their vulnerability and expected damage is crucial.*

*This paper presents the vulnerability assessment of two reinforced concrete buildings designed for gravity loads and representative of the Pescara Province in the Abruzzi Region (Central Italy). Geometrical and structural characteristics of the buildings are initially derived from an existing database based on structured interviews with local technicians. The two buildings are then modeled using a simulated design approach following two different buildings codes. Nonlinear dynamic analyses are carried out in order to derive a suite of fragility curves for different damage states. These curves may be used to predict the expected damage following earthquakes of increasing intensities and plan mitigation strategies.*

**Keywords:** Seismic Risk, Vulnerability Assessment, Reinforced Concrete, Nonlinear Dynamic Analyses, Fragility Curves.

---



## 1 INTRODUCTION

The European Union is actively trying to enhance the understanding of disaster risk by laying out a shared approach for loss assessments [1]. Italy committed to this effort by developing a National Risk Assessment (NRA) [2] which considered all potential disaster risks. Among potential risks, seismic risk induces the second highest loss of lives, especially in the Euro-Mediterranean Region.

A commonly agreed definition of seismic risk is the combination of hazard (H), vulnerability (V) and exposure (E) [3], see Eq. 1:

$$R = H \cdot V \cdot E \quad (1)$$

Hazard relates to the probability of occurrence of an earthquake of a specified intensity in a defined period of time. Vulnerability relates to the potential damage undergone by the asset under assessment (e.g., a building) in the occurrence of the earthquake. Exposure relates to the potential losses (e.g., economic and social) caused by the building's damage.

Among the three aspects of Eq. 1, the vulnerability definition has proven to be the most challenging task, as it requires not only an extensive knowledge of all buildings under assessment, but also a detailed evaluation of their seismic response. The complexity of the task is further increased when dealing with large scale assessments. For these reasons, the concept of “minimal fragility portfolio” has been recently developed [4–6], which focuses on defining a reasonable number of buildings typologies that are representative of the whole built environment. By focusing on the derivation of fragility curves (which relates the probability of exceeding pre-defined damage states for increasing intensities [7]) only for these typologies, the time needed to perform large scale assessments is significantly reduced while keeping a sufficient level of accuracy.

In this paper, an existing database for Italian residential buildings is used to define two reinforced concrete (RC) building typologies that are representative of the Pescara province, Central Italy. These buildings have been modeled using a simulated design approach [8] in order to perform non-linear dynamic analyses (NLDAs). Outputs of these analyses have been used to derive a suite of fragility curves for defined damage states.

## 2 CASE STUDY DEFINITION

The Abruzzo Region, Central Italy, is among the areas with the highest seismic risk in Italy, as showed by the extensive losses in the aftermath of the L'Aquila 2009 [9] and Central Italy 2016-2017 [10] earthquakes.

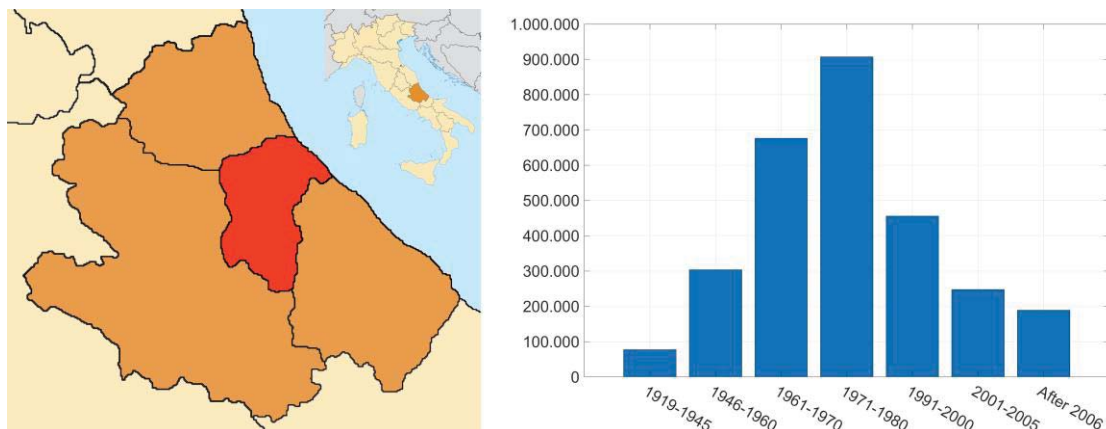


Figure 1. (left) Map of Italy with Abruzzo Region and Province of Pescara highlighted and (right) number of RC buildings in Italy per different construction periods.



In the Abruzzo Region, the Province of Pescara spreads from the coast to the inner mountain areas, see Figure 1a, with the highest population density in the former. The coastal area has been fully included in the seismic zonation in 2003 [11] while the majority of RC buildings in Italy has been built between 1961 and 1980 (source: Census data [12]). For this reason, RC buildings in Pescara were designed considering only gravity loads (GLD) thus making them prone to damage even in the occurrence of earthquakes with moderate intensity.

To collect information on RC buildings in the Pescara Province, the database provided by the CARTIS project [13] has been used. The CARTIS project has been collecting data on the geometrical and structural features of residential buildings in Italy since 2014. The data collection is performed by filling a structured form through interviews with local technicians. The experience and knowledge of the technician ensure that collected data are accurate.

CARTIS data are freely accessible through the pgAdmin platform (<https://www.pgadmin.org/>). For RC buildings, the parameters provided in Table 1 are available.

Parameter
<b>Main resisting system</b>
<b>Number of stories</b>
<b>Construction period</b>
Seismic joints
<b>Unidirectional frames</b>
<b>Ground floor infill walls</b>
Soft story upper floors
Presence of SAP slabs (or similar)
Regularity in plan
Regularity in elevation
Roof material
Roof spread
Structural strengthening

Table 1. Parameters available in the CARTIS database for RC buildings (in bold, those used for the relevant typologies definition).

Parameters of Table 1 in bold have been used to determine the most relevant typologies for the Pescara Province, whose characteristics are listed in Table 2.

ID	Main resisting system	No. of Stories	Construction Period	Design Type	Unidirectional frame	Ground floor infill walls	Regularity in plan
A	Frames with exposed beams and non-sturdy infill walls	4-6	1946-1960	GLD	Yes	Regular configuration	Regular
B	Frames with exposed beams and non-sturdy infill walls	4-6	1971-1980	GLD	Yes	Regular configuration	Regular

Table 2. Characteristics of relevant RC building typologies for the Pescara Province based on CARTIS data.

### 3 MODELING APPROACH

#### 3.1 Design codes, geometry, loads and material properties definition

To model the buildings listed in Table 2, a simulated design approach [8] has been used. Following this approach, the design loads, material properties, and construction details have been determined based on the codes in use at the time of the construction. More specifically, R.D.L. 1939 [14] and D.M. '72 [15] have been used for RC typologies A and B, respectively. In addition, as both typologies were designed for gravity loads and the only load combination used is the sum of dead ( $G$ ) and live ( $Q$ ) loads. This design type does not change for increasing number of stories, the focus has been put on the six-story buildings. The 4 and 5-story buildings have been subsequently derived by taking the upper 4 and 5 stories, respectively.

At first, the buildings' layout is assumed, as no geometrical information was provided by the CARTIS data. The assumed plan layout is derived by existing studies that analyzed buildings of the same period [14,15] and is shown in Figure 2. In the inner frames, beams are present only in the X direction, thus making the Y direction less resistant to lateral forces. Each story is 3 m height, for a total height of 18 m.

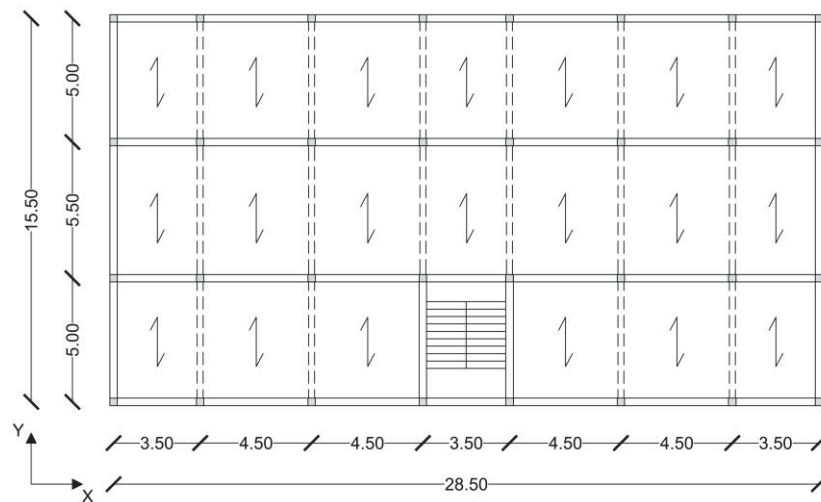


Figure 2. Assumed plan layout (dotted, the bond-beams in the Y direction).

As for the design loads, the R.D.L. 1939 does not provide any value, therefore they had to be assumed based on the experience. On the other hand, the D.M. '72 refers to another code for the definition of  $G$  and  $Q$  [16]. Design loads for Building A and B are assumed equal and are listed in Table 3, divided between story levels 1-5 and 6 (i.e., roof), infills and stairs.

Load type	Story 1-5 [KN/m <sup>2</sup> ]	Story 6 [KN/m <sup>2</sup> ]	Infills [KN/m]	Stairs [KN/m <sup>2</sup> ]
G	6.4	6.1	5.5	5.3
Q	2	1	-	4

Table 3. Assumed design loads.

The material properties for the concrete and the steel reinforcement are assumed based on the codes provision and are listed in Table 4 and Table 5, respectively.

Concrete					
Building A			Building B		
$R'_{bk}$	250	[kg/cm <sup>2</sup> ]	$R'_{bk}$	250	[kg/cm <sup>2</sup> ]
$\sigma_c$	77.8	[kg/cm <sup>2</sup> ]	$\sigma_c$	85	[kg/cm <sup>2</sup> ]
$\tau_{b0}$	4	[kg/cm <sup>2</sup> ]	$\tau_{b0}$	5.3	[kg/cm <sup>2</sup> ]
$\tau_{b1}$	14	[kg/cm <sup>2</sup> ]	$\tau_{b1}$	16.9	[kg/cm <sup>2</sup> ]

Table 4. Assumed material properties for concrete.

Building		Steel Reinforcement			
A		Longitudinal (carbon)		Transversal (mild)	
		$\sigma_y$	[kg/cm <sup>2</sup> ]	2000	$\sigma_y$ [kg/cm <sup>2</sup> ]
B		Longitudinal (FeB44K)		Transversal (FeB32K)	
		$\sigma_y$	[kg/cm <sup>2</sup> ]	2600	$\sigma_y$ [kg/cm <sup>2</sup> ]

Table 5. Assumed material properties for steel reinforcement.

$R'_{bk}$ ,  $\sigma_c$ ,  $\tau_{b0}$ , and  $\tau_{b1}$  are the concrete compressive strength, permissible stress, and shear strength without/with reinforcement, respectively.  $\sigma_y$  is the steel permissible stress at the yielding of longitudinal and transversal reinforcement. Mild and carbon steel are associated to carbon percentages of 0.15-0.25% and 0.4-0.6%, respectively.

### 3.2 Finite element modeling

The vulnerability analysis of Building A and B is performed through a Finite Element Method (FEM) approach. The FEM modeling has been performed in OpenSees [17] using the pre/post processor STKO [18], as shown in Figure 3.

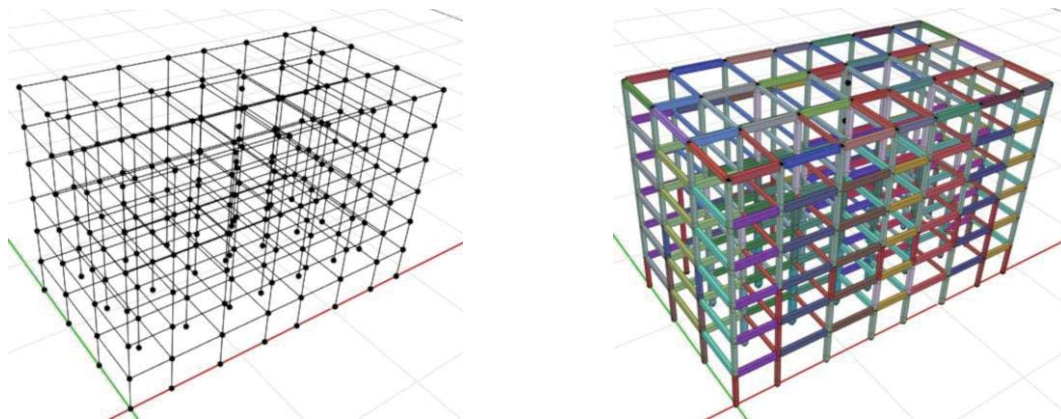


Figure 3. Graphical user interface of STKO.

Beams have been modeled as lumped plasticity elements combining a section based on so-called “phenomenological” laws and two plastic hinges of finite length at both ends with fiber section [19,20]. By combining these sections, it is possible to reduce the model complexity while describing its behavior with high accuracy [21]. Assumed phenomenological laws are different between the two buildings as they are based on the rebars type. Building A adopts smooth rebars, therefore the phenomenological law proposed by Verderame et al. (2018) [22] is assumed. On the other hand, Building B adopts corrugated bars, therefore the phenomenological law based on the Ibarra et al. (2005) [23] model with Haselton et al. (2008) [24] predictive equation is assumed.

Columns have been modeled as fiber sections using the *Concrete01* [25] and *Steel02* [26] model for the RC and steel, respectively. The length of plastic hinges at both ends has been determined based on modern code provisions [27].

To correctly evaluate the seismic behavior of existing buildings, different material properties than those listed in Table 4 and Table 5 are assumed, in order to consider the aging effect. For the RC compressive strength,  $f_c$ , mean values provided by Masi et al. (2014) [28] have been used, which derived from a large scale in situ survey. For the steel yielding strength,  $f_y$ , values provided by the open-access software Stil ([http://www.reluis.it/index.php?option=com\\_content&view=article&id=199&Itemid=136&lang=it](http://www.reluis.it/index.php?option=com_content&view=article&id=199&Itemid=136&lang=it)) have been used [29]. In addition, the elastic modulus,  $E_s$ , of Building A has been modified to consider the bond-slip that may occur with smooth bars. Assumed values for the structural modeling are listed in Table 6.

Building	Concrete				Steel			
A	$f_c$	18	[MPa]	$f_y$	350	[MPa]	$E_s$	175000 [MPa]
B	$f_c$	20	[MPa]	$f_y$	470	[MPa]	$E_s$	206000 [MPa]

Table 6. Assumed values for the concrete and steel in the structural modeling.

Infills and stairs have not been modelled but have been considered only as loads.

## 4 VULNERABILITY ANALYSIS

### 4.1 Seismic input

The ground motions selection is crucial when performing NLDAs as they must be representative of the seismic hazard in the area under assessment [30] and the number must be sufficient to capture all possible damage states. In this paper, the ground motion selection proposed by Paolucci et al. (2020) [31] has been used. This selection includes 125 unscaled input motions have been determined for soil category A (rock) using the L'Aquila hazard spectra (Abruzzo Region, close to the Pescara Province) as target.

### 4.2 Engineering Demand Parameter and Damage states

The maximum interstory drift ratio (IDR) in both horizontal directions is assumed as Engineering Demand Parameter (EDP) to determine the building's damage. Damage is classified according to the European Macroseismic Scale EMS-98 [32] and varies from D0 (no damage) to D5 (destruction or complete collapse). IDR values are associated to EMS-98 damage states by using the ranges proposed by Masi et al. (2015, 2021) [33,34] for medium and high-rise ( $\geq 3$  stories) GLD RC buildings, that are listed in Table 7.

Damage State	IDR (%)
D0 (none)	< 0.1
D1 (slight)	0.1 - 0.25
D2 (moderate)	0.25 - 0.5
D3 (substantial to heavy)	0.5 - 1.0
D4 (very heavy)	1.0 - 2.5
D5 (destruction)	> 2.5

Table 7. Assumed relationships between IDR values and EMS-98 damage states.

### 4.3 Fragility curves definition

Selected ground motions have been applied on both horizontal directions thus obtaining 250 PGA-IDR values, which relate the maximum Peak Ground Acceleration of the considered ground motion to the maximum IDR among all story levels. Then, fragility curves are derived using the formulation proposed by FEMA 2018 [35], see Eq. 2.

$$P(D_k|PGA) = \Phi \left[ \frac{1}{\beta_{D,Dk}} \cdot \ln \left( \frac{PGA}{PGA_{Dk}} \right) \right] \quad k = 1, \dots, 5 \quad (2)$$

where  $P(D_k|PGA)$  is the probability of exceeding the  $k$ -th damage state,  $D_k$ , given a PGA value,  $\Phi$  is the Gaussian cumulative distribution function,  $\beta_{D,Dk}$  and  $PGA_{Dk}$  are the logarithmic standard deviation and median value, respectively.

Obtained fragility curves for Building A and B are shown in Figure 4. As previously mentioned, 4 and 5-story buildings have been derived by the 6-story by taking the four and five upper stories, respectively.

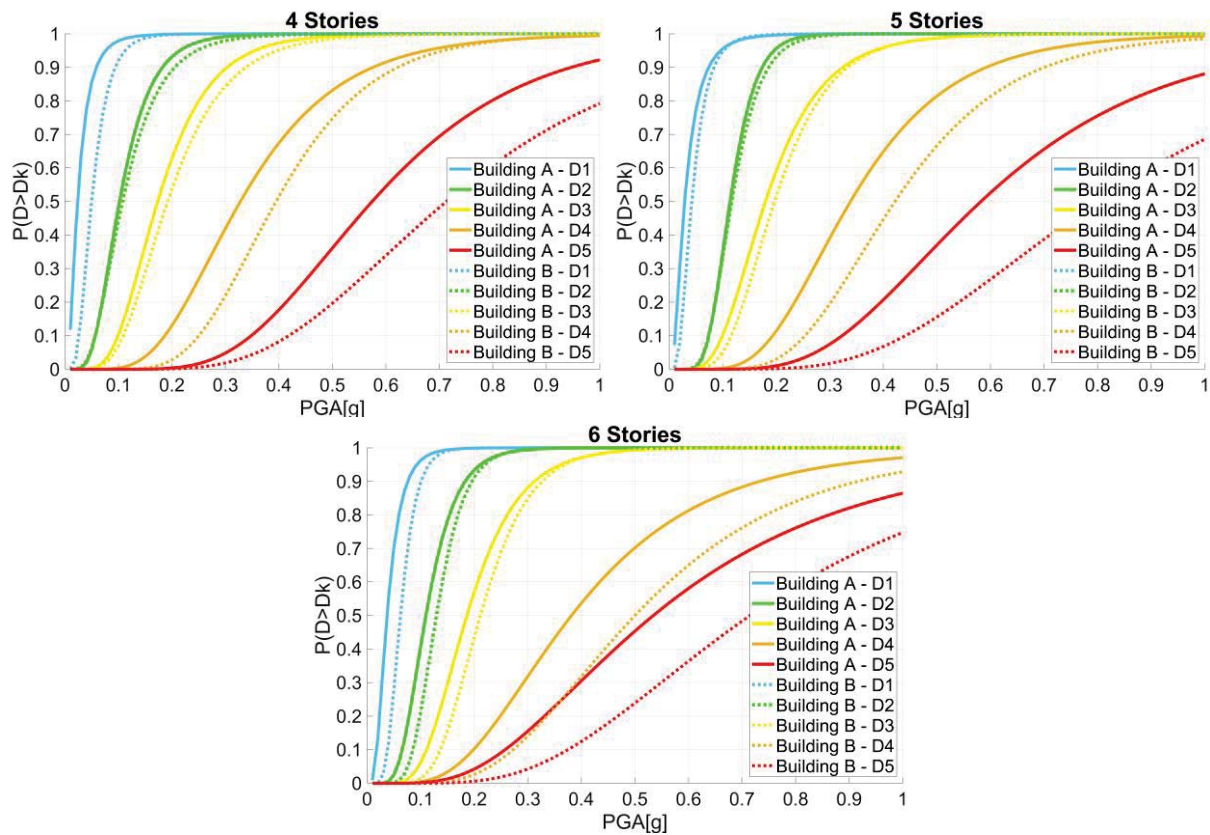


Figure 4. (clockwise) Fragility curves for 4-story, 5-story and 6-story Building A (designed with R.D.L. 1939) and Building B (designed according to D.M. '72).

Observing the graph, it is possible to note that fragility curves of the 4 and 5-story buildings do not significantly differ, while the 6-story buildings is significantly less vulnerable. This is possibly due to the fact that 4-story and 5-story buildings are both considered as “medium-rise”, while the 6-story building is included in the “high-rise” category [36]. Then, Building B is consistently less vulnerable than Building A, thus noting how the evolution of codes is associated to an increase in the seismic performance.



## 5 SUMMARY AND CONCLUSIONS

This paper has presented the vulnerability analysis of two RC building typologies that are representative of the built environment in the Pescara Province, Central Italy. Main characteristics of the typologies have been derived by an existing database of Italian residential buildings. Then, buildings have been modeled through a simulated design approach, also considering the aging effects.

A suite of ground motion records has been used to perform NLDAs whose outputs were used to derive fragility curves for five damage states. Obtained fragility curves show medium-rise buildings have a higher fragility than high rise ones. Finally, the evolution of the building code is associated to an increase in the seismic performance.

## ACKNOWLEDGMENTS

The Authors wish to acknowledge M.Sc. students Michael Palmucci and Matteo Di Simone whose dissertation is part of the project.

## REFERENCES

- [1] C. Corbane, U. Hancilar, D. Ehrlich, T. De Groeve, Pan-European seismic risk assessment: a proof of concept using the Earthquake Loss Estimation Routine (ELER). *Bull Earthq Eng*, **15**:1057–83, 2017.
- [2] ICPD, National risk assessment, Overview of the potential major disasters in Italy: Seismic, volcanic, tsunامي, hydro-geological/hydraulic and extreme weather, droughts and forest fire risks. *Italian Civil Protection Department Technical report*, 2018.
- [3] UNDRO, *Natural Disasters and Vulnerability Analysis*. Geneva, Switzerland, 1980.
- [4] P. Lin, N. Wang, Building portfolio fragility functions to support scalable community resilience assessment. *Sustain Resilient Infrastruct*, **1**:108–22, 2016. <https://doi.org/10.1080/23789689.2016.1254997>.
- [5] M. Mehrdad, A. Navid, M. Hassan, M. Hussam, J.W. van de Lindt, S.F. Pilkington, M.R. Ameri, Minimal Building Fragility Portfolio for Damage Assessment of Communities Subjected to Tornadoes. *J Struct Eng*, **144**:4018072, 2018.
- [6] O.M. Nofal, J.W. van de Lindt, Minimal Building Flood Fragility and Loss Function Portfolio for Resilience Analysis at the Community Level. *Water*, **12**:2277, 2020.
- [7] K. Porter, A Beginner's Guide to Fragility, Vulnerability, and Risk. *Encycl Earth. Eng*, Springer, 2015.
- [8] G.M. Verderame, M. Polese, C. Mariniello, G. Manfredi, A simulated design procedure for the assessment of seismic capacity of existing reinforced concrete buildings. *Adv Eng Softw*, **41**:323–35, 2010.
- [9] T. Rossetto, N. Peiris, J. Alarcon, E. So, S. Sargeant, V. Swords-Daniels, C. Libberton, E. Verrucci, D. Del Re, M. Free, *The L'Aquila, Italy Earthquake of 6 April 2009: a field report by EEFIT*. 2009.
- [10] G. Fiorentino, A. Forte, E. Pagano, F. Sabetta, C. Baggio, D. Lavorato, C. Nuti, S. Santini, Damage patterns in the town of Amatrice after August 24th, 2016 Central Italy earthquakes. *Bull Earthq Eng*, **16**:1399–423, 2018.



- [11] Presidenza del Consiglio dei Ministri, *Primi elementi in materia di criteri generali per la classificazione sismica del territorio nazionale e di normative tecniche per le costruzioni in zona sismica*. Italy: O.P.C.M. 3274 20/3/2003; 2003.
- [12] ISTAT, *Edifici residenziali 2011*. [http://dati-censimentopopolazione.istat.it/Index.aspx?DataSetCode=DICA\\_EDIFICI1](http://dati-censimentopopolazione.istat.it/Index.aspx?DataSetCode=DICA_EDIFICI1) (accessed September 14, 2020).
- [13] G. Zuccaro, M. Dolce, D. De Gregorio, E. Speranza, C. Moroni, La scheda CARTIS per la caratterizzazione tipologico-strutturale dei comparti urbani costituiti da edifici ordinari. Valutazione dell'esposizione in analisi di rischio sismico. *34<sup>th</sup> national conference of GNGTS*, Trieste, 2015.
- [14] M. Bosco, G.A.F. Ferrara, A. Gherzi, E.M. Marino, P.P. Rossi, Predicting displacement demand of multi-storey asymmetric buildings by nonlinear static analysis and corrective eccentricities. *Eng Struct*, **99**:373–87, 2015.
- [15] M. Bosco, A. Gherzi, E.M. Marino, P.P. Rossi, Generalized corrective eccentricities for nonlinear static analysis of buildings with framed or braced structure. *Bull Earthq Eng*, **15**:4887–913, 2017.
- [16] Consiglio Nazionale delle Ricerche and Ente nazionale italiano di unificazione, *Ipotesi di carico sulle costruzioni*. Italy: CNR UNI 10012:67, 1967.
- [17] F. McKenna, G.L. Fenves, M.H. Scott, *Open system for earthquake engineering simulation*. Univ California, Berkeley, CA, 2000.
- [18] M. Petracca, F. Candeloro, G. Camata, STKO user manual. *ASDEA Softw Technol*, Pescara, 2017.
- [19] E. Spacone, F.C. Filippou, F.F. Taucer, Fibre Beam–Column Model for Non-Linear Analysis of R/C Frames: Part I. Formulation. *Earthq Eng Struct Dyn*, **25**:711–25, 1996.
- [20] E. Spacone, F.C. Filippou, F.F. Taucer, Fibre Beam–Column Model for Non-Linear Analysis of R/C Frames: Part II. Applications. *Earthq Eng Struct Dyn*, **25**:727–42, 1996.
- [21] M. Terrenzi, E. Spacone, G. Camata, Comparison Between Phenomenological and Fiber-Section Non-linear Models. *Front Built Environ*, 6:38, 2020.
- [22] G.M. Verderame, P. Ricci, An empirical approach for nonlinear modelling and deformation capacity assessment of RC columns with plain bars. *Eng Struct*, 176:539–54, 2018.
- [23] L.F. Ibarra, R.A. Medina, H. Krawinkler, Hysteretic models that incorporate strength and stiffness deterioration. *Earthq Eng Struct Dyn*, **34**:1489–511, 2005.
- [24] C.B. Haselton, A.B. Liel, S. Taylor Lange, G.G. Deierlein, Beam-column element model calibrated for predicting flexural response leading to global collapse of RC frame buildings. *PEER Report*, 2008.
- [25] K.D. Charles, P. Robert, Flexural Members with Confined Concrete. *J Struct Div*, **97**:1969–90, 1971.
- [26] M. Menegotto, P. Pinto, Method of analysis for cyclically loaded RC plane frames including changes in geometry and non-elastic behavior of elements under combined normal force and bending. *Proceedings of IABSE Symposium on Resistance and Ulti-*

- mate Deform ability of Structures Acted on by Well Defined Repeated Loads*, **11**:15-22, 1973.
- [27] Consiglio Superiore dei Lavori Pubblici, *Istruzioni per l'applicazione dell'aggiornamento delle "Norme tecniche per le costruzioni" di cui al decreto ministeriale 17 gennaio 2018*, 2019.
  - [28] A. Masi, A. Digrisolo, G. Santarsiero, Concrete Strength Variability in Italian RC Buildings: Analysis of a Large DataBase of Core Tests. *Appl Mech Mater*, **597**:283–90, 2014
  - [29] G.M. Verderame, P. Ricci, M. Esposito, F.C. Sansiviero, Le Caratteristiche Meccaniche degli Acciai Impiegati nelle Strutture in ca realizzate dal 1950 al 1980. *XXVI Convegno Nazionale di Geotecnica AICAP*, Padova, 2011.
  - [30] P. Bazzurro, C.A. Cornell, Seismic Hazard Analysis of Nonlinear Structures. I: Methodology. *J Struct Eng*, **120**:3320–44, 1994.
  - [31] R. Paolucci, A.G. Ozcebe, C. Smerzini, A. Masi, V. Manfredi, *Selection and spectral matching of recorded ground motions for earthquake engineering analysis 2020*. <https://143.225.144.186:5001/> (accessed March 19, 2021).
  - [32] G. Grünthal, European macroseismic scale 1998. *Cahiers du Centre Européen de Géodynamique et de Séismologie*, 1998.
  - [33] A. Masi, A. Digrisolo, V. Manfredi, Fragility curves of gravity-load designed RC buildings with regularity in plan. *Earthquakes Struct*, **9**:1–27, 2015.
  - [34] A. Masi, S. Lagomarsino, M. Dolce, V. Manfredi, D. Ottonelli, Towards the updated Italian seismic risk assessment: exposure and vulnerability modelling. *Bull Earthq Eng*, 2021.
  - [35] FEMA P-58-1, *Seismic Performance Assessment of Buildings, Volume 1—Methodology*. Applied Technology Council, Redwood City, California, 2018.
  - [36] FEMA. *Hazus 4.2 SP3 Earthquake Model - Technical Manual*, 2020.

## STOCHASTIC NONLINEAR RESPONSE OF STRUCTURAL SYSTEMS ENDOWED WITH SINGULAR MATRICES SUBJECT TO COMBINED PERIODIC AND STOCHASTIC EXCITATIONS

I.P. Mitseas<sup>1,2</sup>, P. Ni<sup>3</sup>, V.C. Fragkoulis<sup>3</sup>, F. Kong<sup>4</sup>, M. Beer<sup>3,5,6</sup> and M. Fragiadakis<sup>1</sup>

<sup>1</sup>School of Civil Engineering, National Technical University of Athens  
Iroon Polytechniou 9, Zografou 15780, Athens, Greece  
e-mail: Imitseas@mail.ntua.gr, Mfrag@mail.ntua.gr

<sup>2</sup>School of Civil Engineering, University of Leeds  
Leeds LS2 9JT, UK  
e-mail: I.Mitseas@leeds.ac.uk

<sup>3</sup>Institute for Risk and Reliability, Leibniz University Hannover  
Callinstr. 34, Hannover 30167, Germany  
e-mail: peihua.ni@irz.uni-hannover.de, fragkoulis@irz.uni-hannover.de, beer@irz.uni-hannover.de

<sup>4</sup>School of Civil Engineering and Architecture, Wuhan University of Technology  
122 Luoshi Road, Wuhan 430070, China  
e-mail: kongfan@whut.edu.cn

<sup>5</sup>Institute of Risk and Uncertainty, University of Liverpool  
Peach Street, Liverpool L69 7ZF, UK

<sup>6</sup>International Joint Research Center for Engineering Reliability and Stochastic Mechanics, Tongji  
University  
Shanghai 200092, China

**Keywords:** Singular Matrix, Combined Periodic and Stochastic Excitations, Moore-Penrose Inverse Matrix, Nonlinear System, Statistical Linearization.

**Abstract.** *A new technique is proposed for determining the response of multi-degree-of-freedom nonlinear complex multi-body systems with singular parameter matrices subject to combined periodic and stochastic loads. The singular parameter matrices are due to adopting redundant coordinates for modeling the system governing equations of motion. Considering that the system response has a periodic as well as a stochastic component, a harmonic balance method-based scheme is used for treating the deterministic component, followed by the application of the generalized statistical linearization method, in conjunction with an averaging treatment to account for the stochastic component. The validity of the proposed technique is demonstrated by pertinent numerical examples.*

## 1 INTRODUCTION

When the problem of formulating the governing equations of motion of multi-degree-of-freedom (MDOF) dynamical systems is considered, the minimum number of independent coordinates is used. Nevertheless, for several classes of complex multi-body systems and also systems subject to constraints [1, 2], a redundant coordinates modeling is often connected with solution treatments of reduced computational cost [3, 4, 5]. However, this yields singular matrices in the system governing equations of motion. Therefore, several techniques have been developed recently for conducting stochastic response analyses pertaining to systems exhibiting singular parameter matrices; see, indicatively, [6, 7, 8, 9, 10, 11]. This is achieved by resorting to the theory of generalized matrix inverses.

In this paper, a Moore-Penrose (M-P) generalized matrix inverses framework is adopted for determining the response of MDOF nonlinear systems with singular matrices subject to combined periodic and stochastic excitations. To this end, the harmonic balance method is combined with the statistical linearization methodology for systems with singular matrices [12, 13]. Specifically, since the system excitation consists of a periodic and a stochastic component, the corresponding response also has a periodic and a stochastic part. Therefore, a solution treatment based on the harmonic balance method is used for the former, whereas the latter is treated by resorting to the generalized statistical linearization method. Combining the two methods results in the formulation of a coupled system of algebraic equations, which is solved iteratively by invoking the generalized matrix inverse theory [14]. Overall, the proposed technique consists a generalization of the framework developed in [15] to account for systems with singular matrices. Its validity is demonstrated by pertinent numerical examples.

## 2 MATHEMATICAL FORMULATION

The governing equations of motion of an  $l$ -DOF nonlinear system are given by

$$\mathbf{M}_x \ddot{\mathbf{x}} + \mathbf{C}_x \dot{\mathbf{x}} + \mathbf{K}_x \mathbf{x} + \Phi_x(\mathbf{x}, \dot{\mathbf{x}}, \ddot{\mathbf{x}}) = \mathbf{f}_{d,x}(t) + \mathbf{Q}_x(t), \quad (1)$$

where  $\mathbf{x}$  denotes an  $l$  dependent coordinates vector,  $\mathbf{M}_x$ ,  $\mathbf{C}_x$  and  $\mathbf{K}_x$  are, respectively, the  $l \times l$  mass, damping and stiffness matrices, and  $\Phi_x(\mathbf{x}, \dot{\mathbf{x}}, \ddot{\mathbf{x}})$  represents the  $l$  vector of the nonlinearities, which are of the polynomial kind for simplicity. Further,  $\mathbf{f}_{d,x}(t)$  represents the periodic component of the excitation, whereas  $\mathbf{Q}_x(t)$  is a zero-mean Gaussian stochastic excitation. Considering that the system of Eq. (1) is subject to a number of constraint equations of the form  $\mathbf{A}\ddot{\mathbf{x}} + \mathbf{E}\dot{\mathbf{x}} + \mathbf{L}\mathbf{x} = \mathbf{F}$ , where  $\mathbf{A}$ ,  $\mathbf{E}$ ,  $\mathbf{L}$  and  $\mathbf{F}$  denote, respectively,  $m \times l$  matrices and an  $l$  vector, Eq. (1) is recast into

$$\bar{\mathbf{M}}_x \ddot{\mathbf{x}} + \bar{\mathbf{C}}_x \dot{\mathbf{x}} + \bar{\mathbf{K}}_x \mathbf{x} + \bar{\Phi}_x(\mathbf{x}, \dot{\mathbf{x}}, \ddot{\mathbf{x}}) = \bar{\mathbf{f}}_{d,x}(t) + \bar{\mathbf{Q}}_x(t). \quad (2)$$

In Eq. (2),  $\bar{\mathbf{M}}_x$ ,  $\bar{\mathbf{C}}_x$  and  $\bar{\mathbf{K}}_x$  denote the augmented  $(l + m) \times l$  mass, damping and stiffness parameter matrices, which have the form [7]

$$\bar{\mathbf{M}}_x = \begin{bmatrix} (\mathbf{I}_l - \mathbf{A}^+ \mathbf{A}) \mathbf{M}_x \\ \mathbf{A} \end{bmatrix}, \quad \bar{\mathbf{C}}_x = \begin{bmatrix} (\mathbf{I}_l - \mathbf{A}^+ \mathbf{A}) \mathbf{C}_x \\ \mathbf{E} \end{bmatrix}, \quad \bar{\mathbf{K}}_x = \begin{bmatrix} (\mathbf{I}_l - \mathbf{A}^+ \mathbf{A}) \mathbf{K}_x \\ \mathbf{L} \end{bmatrix}, \quad (3)$$

where  $\mathbf{I}_l$  denotes the  $l \times l$  identity matrix, and “+” represents the M-P matrix inverse operation. Further, the augmented  $(l + m)$  vector of the system nonlinearities, and the corresponding periodic and stochastic  $(l + m)$  vectors of the excitation are given by

$$\bar{\Phi}_x = \begin{bmatrix} (\mathbf{I}_l - \mathbf{A}^+ \mathbf{A}) \Phi_x \\ \mathbf{0} \end{bmatrix}, \quad \bar{\mathbf{f}}_{d,x}(t) = \begin{bmatrix} (\mathbf{I}_l - \mathbf{A}^+ \mathbf{A}) \mathbf{f}_{d,x}(t) \\ \mathbf{F} \end{bmatrix}, \quad \bar{\mathbf{Q}}_x(t) = \begin{bmatrix} (\mathbf{I}_l - \mathbf{A}^+ \mathbf{A}) \mathbf{Q}_x(t) \\ \mathbf{F} \end{bmatrix}. \quad (4)$$

A detailed derivation of Eqs. (2)-(4) is found in [7, 12].

Next, considering that the MDOF system in Eq. (2) is subject to combined deterministic and stochastic loads, it is assumed that the corresponding response also consists of a periodic and a stochastic component, namely  $\mathbf{x}(t) = \mathbf{x}_s(t) + \mathbf{x}_d(t)$ . Further, assuming that the stochastic excitation is modeled as a zero-mean Gaussian process, ensemble averaging Eq. (2) yields

$$\bar{\mathbf{M}}_{\mathbf{x}}\ddot{\mathbf{x}}_d + \bar{\mathbf{C}}_{\mathbf{x}}\dot{\mathbf{x}}_d + \bar{\mathbf{K}}_{\mathbf{x}}\mathbf{x}_d + \mathbb{E}[\bar{\Phi}_{\mathbf{x}}(\mathbf{x}_s + \mathbf{x}_d, \dot{\mathbf{x}}_s + \dot{\mathbf{x}}_d, \ddot{\mathbf{x}}_s + \ddot{\mathbf{x}}_d)] = \bar{\mathbf{f}}_{d,\mathbf{x}}(t), \quad (5)$$

which consists of a periodic and a stochastic response component too. In the ensuing analysis, first, the harmonic balance methodology is used in conjunction with the concept of the generalized inverse matrix for treating the deterministic component in Eq. (5). Then, the stochastic component of the system is treated by applying the generalized statistical linearization [12, 13].

## 2.1 Application of the harmonic balance method for treating the periodic component of the response

Assume that  $\bar{\mathbf{f}}_{d,\mathbf{x}}(t)$  in Eq. (4) is modeled as a monofrequency function of period  $T = \frac{2\pi}{\omega_d}$ . Then,  $\bar{\mathbf{f}}_{d,\mathbf{x}}(t) = \bar{\mathbf{f}}_{d1,\mathbf{x}} \cos(\omega_d t) + \bar{\mathbf{f}}_{d2,\mathbf{x}} \sin(\omega_d t)$ , where  $\bar{\mathbf{f}}_{d1,\mathbf{x}}$  and  $\bar{\mathbf{f}}_{d2,\mathbf{x}}$  are the constant coefficient  $(l + m)$  vectors, and thus, the deterministic response of the system in Eq. (5) becomes  $\mathbf{x}_d(t) = \mathbf{x}_{d1} \cos(\omega_d t) + \mathbf{x}_{d2} \sin(\omega_d t)$ , where  $\mathbf{x}_{d1}$ ,  $\mathbf{x}_{d2}$  are constant  $l$  vectors. Next, applying the harmonic balance method yields the overdetermined system of equations

$$\mathbf{P}\mathbf{u} = \mathbf{v}, \quad (6)$$

where the  $2(l + m) \times 2l$  matrix  $\mathbf{P}$ , and the  $2l$ - and  $2(l + m)$  vectors  $\mathbf{u}$ ,  $\mathbf{v}$  are given by

$$\mathbf{P} = \begin{bmatrix} \bar{\mathbf{K}}_{\mathbf{x}} - \omega_d^2 \bar{\mathbf{M}}_{\mathbf{x}} & \omega_d \bar{\mathbf{C}}_{\mathbf{x}} \\ -\omega_d \bar{\mathbf{C}}_{\mathbf{x}} & \bar{\mathbf{K}}_{\mathbf{x}} - \omega_d^2 \bar{\mathbf{M}}_{\mathbf{x}} \end{bmatrix}, \mathbf{u} = \begin{bmatrix} \mathbf{x}_{d1} \\ \mathbf{x}_{d2} \end{bmatrix}, \mathbf{v} = \begin{bmatrix} \bar{\mathbf{f}}_{d1} - \frac{2}{T} \int_0^T \mathbb{E}[\bar{\Phi}_{\mathbf{x}}] \cos(\omega_d t) dt \\ \bar{\mathbf{f}}_{d2} - \frac{2}{T} \int_0^T \mathbb{E}[\bar{\Phi}_{\mathbf{x}}] \sin(\omega_d t) dt \end{bmatrix}. \quad (7)$$

The solution of the system in Eq. (6) leads to the computation of the deterministic component of the response. In this regard, utilizing the generalized matrix inverses theory implies [14]

$$\mathbf{u} = \mathbf{P}^+ \mathbf{v} + (\mathbf{I} - \mathbf{P}^+ \mathbf{P}) \mathbf{y}, \quad (8)$$

which, in essence, corresponds to a family of solutions, since  $\mathbf{y}$  is an arbitrary  $2l$  vector. However, the matrix  $\bar{\mathbf{M}}_{\mathbf{x}}$  in the diagonal entries of matrix  $\mathbf{P}$  in Eq. (7) ensures that the columns of the latter are independent of each other or, equivalently, that matrix  $\mathbf{P}$  has full column rank. Therefore, it holds that  $\mathbf{P}^+ = (\mathbf{P}^* \mathbf{P})^{-1} \mathbf{P}^*$ , and thus, Eq. (8) attains a unique solution corresponding to the deterministic response component of the system in Eq. (2).

## 2.2 Application of the statistical linearization method for treating the stochastic component of the response

The stochastic component  $\mathbf{x}_s(t)$  of the system response is treated by resorting to the generalized statistical linearization methodology for systems with singular parameter matrices [12, 13]; see also [16, 17, 18, 19, 20, 21, 22, 23] for a broader perspective, as well as several examples pertaining to application of the method. First, the difference between the systems in Eqs. (2) and (5) is formed,

$$\bar{\mathbf{M}}_{\mathbf{x}}\ddot{\mathbf{x}}_s + \bar{\mathbf{C}}_{\mathbf{x}}\dot{\mathbf{x}}_s + \bar{\mathbf{K}}_{\mathbf{x}}\mathbf{x}_s + \tilde{\Phi}_{\mathbf{x}}(\mathbf{x}_s, \mathbf{x}_d) = \bar{\mathbf{Q}}_{\mathbf{x}}(t), \quad (9)$$

where  $\tilde{\Phi}_{\mathbf{x}}(\mathbf{x}_s, \mathbf{x}_d) = \bar{\Phi}_{\mathbf{x}}(\mathbf{x}_s + \mathbf{x}_d, \dot{\mathbf{x}}_s + \dot{\mathbf{x}}_d, \ddot{\mathbf{x}}_s + \ddot{\mathbf{x}}_d) - \mathbb{E}[\bar{\Phi}_{\mathbf{x}}(\mathbf{x}_s + \mathbf{x}_d, \dot{\mathbf{x}}_s + \dot{\mathbf{x}}_d, \ddot{\mathbf{x}}_s + \ddot{\mathbf{x}}_d)]$  is the zero-mean vector of the system nonlinearities. Then, the linear equivalent system to Eq. (9) is written as [12, 16]

$$(\bar{\mathbf{M}}_{\mathbf{x}} + \bar{\mathbf{M}}_e)\ddot{\mathbf{x}}_s + (\bar{\mathbf{C}}_{\mathbf{x}} + \bar{\mathbf{C}}_e)\dot{\mathbf{x}}_s + (\bar{\mathbf{K}}_{\mathbf{x}} + \bar{\mathbf{K}}_e)\mathbf{x}_s = \bar{\mathbf{Q}}_{\mathbf{x}}(t). \quad (10)$$

Subsequently, the error function, which is defined as the difference between Eqs. (9) and (10), is formed and minimized by adopting the mean square minimization criterion [12, 13, 16]. In this regard, the elements of the  $(l + m) \times l$  matrices  $\bar{\mathbf{M}}_e$ ,  $\bar{\mathbf{C}}_e$  and  $\bar{\mathbf{K}}_e$  are given by pertinent closed form expressions; more details are found in [13].

Since the nonlinear vector  $\tilde{\Phi}_{\mathbf{x}}(\mathbf{x}_s, \mathbf{x}_d)$  depends on the deterministic and stochastic components of the response, the elements  $m_{ij}^e, c_{ij}^e, k_{ij}^e$  of matrices  $\bar{\mathbf{M}}_e$ ,  $\bar{\mathbf{C}}_e$  and  $\bar{\mathbf{K}}_e$  are also time-dependent. Nevertheless, the slowly varying over a period  $T$  of oscillation components of  $\bar{\mathbf{M}}_e$ ,  $\bar{\mathbf{C}}_e$  and  $\bar{\mathbf{K}}_e$  are approximated by their average over  $T$  [15, 24], i.e.,  $\bar{\mathbf{M}}_e \approx \bar{\mathbf{M}}_e^{av}$ ,  $\bar{\mathbf{C}}_e \approx \bar{\mathbf{C}}_e^{av}$  and  $\bar{\mathbf{K}}_e \approx \bar{\mathbf{K}}_e^{av}$ ; indicatively,  $\bar{\mathbf{M}}_e^{av} = \frac{1}{T} \int_0^T \bar{\mathbf{M}}_e dt$ . This provides with an approximation to the system in Eq. (10), given by the equivalent system

$$(\bar{\mathbf{M}}_{\mathbf{x}} + \bar{\mathbf{M}}_e^{av})\ddot{\mathbf{x}}_s + (\bar{\mathbf{C}}_{\mathbf{x}} + \bar{\mathbf{C}}_e^{av})\dot{\mathbf{x}}_s + (\bar{\mathbf{K}}_{\mathbf{x}} + \bar{\mathbf{K}}_e^{av})\mathbf{x}_s = \bar{\mathbf{Q}}_{\mathbf{x}}(t). \quad (11)$$

Further, the response statistics of the equivalent system in Eq. (11) are determined by employing a frequency domain approach. In this regard, the frequency response function matrix of the system in Eq. (11) is derived and used in conjunction with the generalized input-output relationship for systems with singular parameter matrices, i.e.,  $\mathbf{S}_{\mathbf{x}}(\omega) = \boldsymbol{\alpha}_{\mathbf{x}}(\omega) \mathbf{S}_{\bar{\mathbf{Q}}_{\mathbf{x}}}(\omega) \boldsymbol{\alpha}_{\mathbf{x}}^T(\omega)$ , for determining the response power spectrum  $\mathbf{S}_{\mathbf{x}_s}(\omega)$  [13]. Finally, the second order response statistics of the equivalent system in Eq. (11) are computed by [16]

$$\mathbb{E}[\mathbf{x}_s^2(i)] = \int_{-\infty}^{\infty} \mathbf{S}_{\mathbf{x}_s(i)\mathbf{x}_s(i)}(\omega) d\omega, \quad i = 1, 2, \dots, l. \quad (12)$$

Eq. (12) in conjunction with the generalized input-output relationship for systems with singular parameter matrices, as well as Eq. (8), constitute a coupled nonlinear system of equations to be solved for determining the system response. For its solution, the following iterative procedure is used: *i.* The nonlinear vector  $\tilde{\Phi}_{\mathbf{x}}(\mathbf{x}_s, \mathbf{x}_d)$  in the governing equations of motion is set equal to the null vector and the deterministic response  $\mathbf{x}_d$  is obtained. *ii.* The variance of the stochastic response  $\mathbf{x}_s$  is derived by using the generalized input-output relationship in conjunction with Eq. (12). *iii.* Using step (ii.), Eq. (8) leads to the derivation of the deterministic response, which, in turn, results in calculating the values  $\bar{\mathbf{M}}_e^{av}$ ,  $\bar{\mathbf{C}}_e^{av}$  and  $\bar{\mathbf{K}}_e^{av}$ . *iv.* Steps (ii.) and (iii.) are repeated until reaching satisfactory accuracy for the response variance.

### 3 NUMERICAL EXAMPLE

In this example, the 2-DOF system in Fig. 1 is considered, where mass  $m_1$  is connected to the foundation by a nonlinear damper and a nonlinear spring of forces  $c_1 \dot{q}_1(1 + \varepsilon_1 \dot{q}_1^2)$  and  $k_1 q_1(1 + \varepsilon_2 q_1^2)$ , respectively. Further,  $q_i$  denotes the displacement of the  $i$ -th mass, and  $\varepsilon_1, \varepsilon_2$  the magnitude of the nonlinearities. In addition, mass  $m_2$  is connected to  $m_1$  by a linear spring of stiffness  $k_2$  and a linear damper of damping coefficient  $c_2$ . The system is excited by a combination of a stochastic force  $Q_1(t)$ , which is modeled as a Gaussian white noise stochastic process with spectral density  $S_0$ , and a deterministic force of the form  $f_{d2,1} \sin(\omega_d t)$ . The following set of parameter values is considered:  $m_1 = m_2 = 1$ ,  $c_1 = c_2 = 0.2$ ,  $k_1 = k_2 = 1$ ,  $S_0 = 10^{-2}$  ( $0 < \omega < 2\pi$ ),  $f_{d2,1} = 0.4$ ,  $\omega_d = \pi$  and  $\varepsilon_1 = \varepsilon_2 = 10$ .



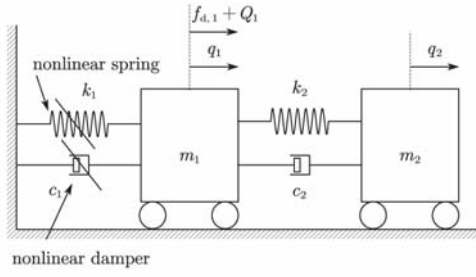


Figure 1: A 2-DOF nonlinear system subject to periodic and stochastic excitations.

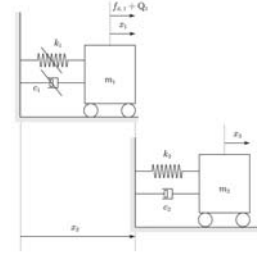


Figure 2: The nonlinear system of Fig. 1 modeled by employing an additional redundant coordinate.

Next, considering the redundant coordinates vector  $\mathbf{x}^T = [x_1 \ x_2 \ x_3]$ , the 2-DOF system of Fig. 1 is decomposed into its partial subsystems, as shown in Fig. 2. The system constraints equation is formed (see section 2), where  $\mathbf{A} = \begin{bmatrix} 1 & -1 & 0 \end{bmatrix}$ ,  $\mathbf{E} = \mathbf{L} = \mathbf{0}_{1 \times 3}$  and  $F = 0$ . Thus, the parameter matrices defined in Eq. (3) are determined, and the  $(l + m)$  vectors in Eq. (4) are computed. For the application of the harmonic balance method, the system response is decomposed into its stochastic  $\mathbf{x}_s$  and deterministic  $\mathbf{x}_d$  components, and ensemble averaging the expression for  $\bar{\Phi}_{\mathbf{x}}$  yields

$$(\mathbb{E}[\bar{\Phi}_{\mathbf{x}}])^T = \left( c_1 \varepsilon_1 (\dot{x}_{d,1}^3 + 3\dot{x}_{d,1} \sigma_{x_{s,1}}^2) + k_1 \varepsilon_2 (x_{d,1}^3 + 3x_{d,1} \sigma_{x_{s,1}}^2) \right) \begin{bmatrix} 0.5 & 0.5 & 0 & 0 \end{bmatrix}. \quad (13)$$

Then, taking into account that the  $8 \times 6$  matrix  $\mathbf{P}$  has full rank (see Eq. (7)), the overdetermined system in Eq. (6) leads to a uniquely defined periodic response component. Next, the iterative scheme in section 2.2 is employed to solve the coupled set of algebraic equations formed by Eqs. (12) and Eq. (8), and thus, to derive the variance of the stochastic response. The scheme is initialized by using  $\bar{\mathbf{C}}_e^{av} = \mathbf{0}$ ,  $\bar{\mathbf{K}}_e^{av} = \mathbf{0}$  and  $x_{d1} = x_{d2} = 0$ . The stochastic and deterministic components are derived based on the criterion  $\left| \frac{\bar{\mathbf{C}}_{e,j+1}^{av} - \bar{\mathbf{C}}_{e,j}^{av}}{\bar{\mathbf{C}}_{e,j}^{av}} \right| < 10^{-5}$  and  $\left| \frac{\bar{\mathbf{K}}_{e,j+1}^{av} - \bar{\mathbf{K}}_{e,j}^{av}}{\bar{\mathbf{K}}_{e,j}^{av}} \right| < 10^{-5}$ , as well as a similar criterion for  $x_{d1}, x_{d2}$ . The iterative scheme is applied until reaching satisfactory accuracy for the response displacement and velocity variances. Finally, considering that  $\mathbf{x}(t) = \mathbf{x}_s(t) + \mathbf{x}_d(t)$  and successively ensemble and temporal averaging the expression  $\mathbf{x}_d(t) = \mathbf{x}_{d1} \cos(\omega_d t) + \mathbf{x}_{d2} \sin(\omega_d t)$  implies

$$\langle \mathbb{E}[x_i^2] \rangle = \sigma_{x_{s,1}}^2 + \frac{x_{d1,i}^2 + x_{d2,i}^2}{2}, \quad \langle \mathbb{E}[\dot{x}_i^2] \rangle = \sigma_{\dot{x}_{s,1}}^2 + \frac{\omega_d^2 (x_{d1,i}^2 + x_{d2,i}^2)}{2}, \quad i = 1, 2, 3, \quad (14)$$

where  $\langle \cdot \rangle$  denotes the temporal averaging operation.

Eq. (14), in conjunction with the results of the iterative scheme above yield  $\sigma_{x_1}^2 = 0.0705$ ,  $\sigma_{\dot{x}_1}^2 = 0.0704$  and  $\sigma_{x_3}^2 = 0.0617$ ,  $\sigma_{\dot{x}_3}^2 = 0.1098$ . Finally, applying the standard solution framework proposed in [15] for deriving the system response variance yields  $\sigma_{q_1}^2 = 0.0705$ ,  $\sigma_{\dot{q}_1}^2 = 0.0704$  and  $\sigma_{q_2}^2 = 0.0617$ ,  $\sigma_{\dot{q}_2}^2 = 0.1098$ . Clearly, comparing the results above, it is seen that the herein proposed framework is in total agreement with the standard approach in [15].

## 4 CONCLUSIONS

In this paper, the response of multi-degree-of-freedom nonlinear systems with singular parameter matrices subject to combined stochastic and deterministic excitations has been determined by resorting to a generalized inverse matrix-based approach. Singular matrices appeared due to a redundant coordinates formulation of the system governing equations of motion. The

latter is associated with solution frameworks of reduced computational cost for certain classes of complex multi-body systems and/or systems with constraints. In this context, considering that the system excitation consists of a periodic and a stochastic component, the corresponding response has been decomposed in two parts, namely a periodic and a stochastic. Then, the system response has been determined by utilizing the generalized matrix inverses theory, in conjunction with the harmonic balance method and the generalized statistical linearization method for systems with singular parameter matrices. The validity of the proposed technique has been demonstrated by pertinent numerical examples.

## 5 ACKNOWLEDGMENTS

The research work herein was supported by the Hellenic Foundation for Research and Innovation under Grant/Project No. 1261. This support is gratefully acknowledged.

## REFERENCES

- [1] A.D. Karageorgos, L. Moysis, V.C. Fragkoulis, I.A. Kougiumtzoglou, A.A. Pantelous, Random vibration of linear systems with singular matrices based on Kronecker canonical forms of matrix pencils. *Mech. Syst. Sig. Process.*, **161**, 107896, 2021.
- [2] A. Pirrotta, I.A. Kougiumtzoglou, A. Di Matteo, V.C. Fragkoulis, A.A. Pantelous, C. Adam, Deterministic and random vibration of linear systems with singular parameter matrices and fractional derivative terms. *J. Eng. Mech.*, **147**(6), 04021031, 2021.
- [3] F.E. Udwadia, R.E. Kalaba, A new perspective on constrained motion. *Proc. R. Soc. London, Ser. A: Math. Phys. Sci.*, **439**(1906), 407–410, 1992.
- [4] A. Schutte, F.E. Udwadia, New approach to the modeling of complex multibody dynamical systems. *J. Appl. Mech.*, **78**(2), 021018-1–021018-11, 2011.
- [5] C.M. Pappalardo, D. Guida, On the Lagrange multipliers of the intrinsic constraint equations of rigid multibody mechanical systems. *Arch. Appl. Mech.*, **88**(3), 419–451, 2018.
- [6] V.C. Fragkoulis, I.A. Kougiumtzoglou, A.A. Pantelous, A. Pirrotta, Higher order matrix differential equations with singular coefficient matrices. *AIP Conf. Proc.*, **1648**(1), 340002, 2015.
- [7] V.C. Fragkoulis, I.A. Kougiumtzoglou, A.A. Pantelous, Linear random vibration of structural systems with singular matrices. *J. Eng. Mech.*, **142**(2), 04015081, 2016a.
- [8] A.A. Pantelous, A. Pirrotta, Modal analysis of multi-degrees-of-freedom systems with singular matrices: Analytical dynamics approach. *J. Eng. Mech.*, **143**(6), 06017005, 2017.
- [9] A. Pirrotta, I.A. Kougiumtzoglou, A.A. Pantelous, Stochastic response determination of structural systems modeled via dependent coordinates: A frequency domain treatment based on generalized modal analysis. *Meccanica*, **54**(9), 1421–1431, 2019.
- [10] G.D. Pasparakis, V.C. Fragkoulis, M. Beer, Harmonic wavelets based response evolutionary power spectrum determination of linear and nonlinear structural systems with singular matrices. *Mech. Syst. Sig. Process.*, **149**, 107203, 2021.

- [11] V.C. Fragkoulis, I.A. Kougiumtzoglou, A.A. Pantelous, M. Beer, Joint statistics of natural frequencies corresponding to structural systems with singular random parameter matrices. *J. Eng. Mech.* (Forthcoming).
- [12] V.C. Fragkoulis, I.A. Kougiumtzoglou, A.A. Pantelous, Statistical linearization of non-linear structural systems with singular matrices. *J. Eng. Mech.*, **142**(9), 04016063, 2016b.
- [13] I.A. Kougiumtzoglou, V.C. Fragkoulis, A.A. Pantelous, A. Pirrotta, Random vibration of linear and nonlinear structural systems with singular matrices: A frequency domain approach. *J. Sound Vib.*, **404**, 84–101, 2017.
- [14] S.L. Campbell, C.D. Meyer, *Generalized inverses of linear transformations*. SIAM, 2009.
- [15] P.D. Spanos, Y. Zhang, F. Kong, Formulation of statistical linearization for M-D-O-F systems subject to combined periodic and stochastic excitations. *J Appl Mech*, **86**(10), 101003, 2019.
- [16] J.B. Roberts, P.D. Spanos, *Random vibration and statistical linearization*. Courier, 2003.
- [17] V.C. Fragkoulis, I.A. Kougiumtzoglou, A.A. Pantelous, M. Beer, Non-stationary response statistics of nonlinear oscillators with fractional derivative elements under evolutionary stochastic excitation. *Nonlinear Dyn.*, **97**(4), 2291—2303, 2019.
- [18] I.P. Mitseas, M. Beer, Modal decomposition method for response spectrum based analysis of nonlinear and non-classically damped systems. *Mech. Syst. Sig. Process.*, **131**, 469–485, 2019.
- [19] M.G.R. Faes, V.C. Fragkoulis, P. Ni, D.J. Jerez, M.A. Valdebenito, M. Beer, Operator Norm-based Statistical Linearization to Bound the First Excursion Probability of Nonlinear Structures Subjected to Imprecise Stochastic Loading. *ASCE-ASME J. Risk Uncertainty Eng. Syst., Part A: Civ. Eng.* (Forthcoming).
- [20] I.P. Mitseas, I.A. Kougiumtzoglou, A. Giaralis, M. Beer, A novel stochastic linearization framework for seismic demand estimation of hysteretic MDOF systems subject to linear response spectra. *Structural Safety*, **72**, 84–98, 2018.
- [21] I.P. Mitseas, I.A. Kougiumtzoglou, P.D. Spanos, M. Beer, Nonlinear MDOF structural system survival probability determination subject to evolutionary stochastic excitation, *J. Mech. Eng.*, **62**(7-8), 440–451, 2016.
- [22] I.P. Mitseas, M. Beer, Fragility analysis of nonproportionally damped inelastic MDOF structural systems exposed to stochastic seismic excitation, *Computers and Structures*, **226**, doi: 10.1016/j.compstruc.2019.106129, 2020.
- [23] I.P. Mitseas, M. Beer M., First-excursion stochastic incremental dynamics methodology for hysteretic structural systems subject to seismic excitation, *Computers and Structures*, **242**, doi: 10.1016/j.compstruc.2020.106359, 2021.
- [24] P. Ni, V.C. Fragkoulis, F. Kong, I.P. Mitseas, M. Beer, Response determination of nonlinear systems with singular matrices subject to combined stochastic and deterministic excitations. *ASCE-ASME J. Risk Uncertainty Eng. Syst., Part A: Civ. Eng.*, **7**(4), 04021049, 2021.



**COMPDYN 2021**

**Proceedings of the  
8<sup>th</sup> International Conference on  
Computational Methods in Structural Dynamics and Earthquake Engineering**

M. Papadrakakis, M. Fragiadakis (Eds.)

First Edition, September 2021

ISBN (set): 978-618-85072-5-8

ISBN (vol II): 978-618-85072-4-1



**Institute of Structural Analysis and Antiseismic Research  
National Technical University of Athens, Greece**